Wolfgang Drexler
James G. Fujimoto
Editors-in-Chief

Optical Coherence Tomography

Technology and Applications

Second Edition

Springer Reference

Optical Coherence Tomography

Wolfgang Drexler • James G. Fujimoto
Editors

Optical Coherence Tomography

Technology and Applications

Second Edition

With 1380 Figures and 33 Tables

Springer Reference

Editors
Wolfgang Drexler
Center for Medical Physics and
Biomedical Engineering
Medical University Vienna
General Hospital Vienna
Vienna, Austria

James G. Fujimoto
Department of Electrical Engineering
and Computer Science and Research
Laboratory of Electronics
Massachusetts Institute of Technology
Cambridge, MA, USA

ISBN 978-3-319-06418-5 ISBN 978-3-319-06419-2 (eBook)
ISBN 978-3-319-06420-8 (print and electronic bundle)
DOI 10.1007/978-3-319-06419-2

Library of Congress Control Number: 2015941449

Springer Cham Heidelberg New York Dordrecht London
1st edition: © Springer-Verlag Berlin Heidelberg 2008
2nd edition: © Springer International Publishing Switzerland 2015
This work is subject to copyright. All rights are reserved by the Publisher, whether the whole or part of the material is concerned, specifically the rights of translation, reprinting, reuse of illustrations, recitation, broadcasting, reproduction on microfilms or in any other physical way, and transmission or information storage and retrieval, electronic adaptation, computer software, or by similar or dissimilar methodology now known or hereafter developed.
The use of general descriptive names, registered names, trademarks, service marks, etc. in this publication does not imply, even in the absence of a specific statement, that such names are exempt from the relevant protective laws and regulations and therefore free for general use.
The publisher, the authors and the editors are safe to assume that the advice and information in this book are believed to be true and accurate at the date of publication. Neither the publisher nor the authors or the editors give a warranty, express or implied, with respect to the material contained herein or for any errors or omissions that may have been made.

Printed on acid-free paper

Springer International Publishing AG Switzerland is part of Springer Science+Business Media (www.springer.com)

Preface

New medical imaging technologies can improve the diagnosis and clinical management of many diseases. Furthermore, advanced imaging also contributes to a better understanding of pathogenesis and therefore to the development of new pharmaceuticals and novel therapies. Thus, imaging plays a critical role in modern medical research and clinical practice. Noninvasive or minimally invasive imaging techniques have revolutionized diagnostic medicine during the last decades, e.g., X-ray computed tomography (CT), magnetic resonance imaging (MRI), functional magnetic resonance imaging (fMRI), radioisotope imaging (position emission tomography (PET)), single-photon emission computed tomography (SPECT), and diffuse optical tomography (DOT). These techniques permit three-dimensional visualization; however, their spatial resolution is typically limited to a few millimeters in standard clinical practice. Optical imaging techniques such as conventional, confocal, fluorescence, as well as two-photon or multiphoton microscopy enable high axial and transverse ($\leq$1 μm) resolution imaging but with limited penetration in biological tissues. Excisional biopsy and histopathology remains the gold standard for many clinical applications including cancer diagnosis. However, biopsy is hazardous or impossible in some tissues, and it can suffer from unacceptable false-negative rates because of sampling errors.

An imaging modality that enables noninvasive or minimally invasive three-dimensional imaging with near cellular resolution or tissue morphology as well as function could significantly improve early diagnosis, contribute to a better understanding of disease pathogenesis, and enable improved monitoring of disease progression and response to therapy. Optical coherence tomography (OCT) is a noninvasive, optical medical diagnostic imaging modality, which enables in vivo cross-sectional and three-dimensional tomographic visualization of internal microstructure in biological systems. Since its invention in the late 1980s and early 1990s, the original concept of OCT was to enable noninvasive optical biopsy, i.e., the in situ imaging of tissue microstructure with a resolution approaching that of histology but without the need for tissue excision and postprocessing. In order to accomplish – or to approach – this challenging goal, recent efforts in OCT research focused on improvements in resolution, data acquisition speed, optimization of tissue penetration, as well as contrast enhancement. The development of state-of-the-art medical devices and patient interfaces facilitated the application of OCT in a variety of medical fields, enabling access to internal body organs using a variety of catheters,

endoscopes, needles, and other imaging probes. Furthermore, extensions of OCT have been developed that enable noninvasive *depth-resolved* functional imaging, providing spectroscopic, polarization-sensitive, blood flow, or physiological tissue information. These functional extensions of OCT not only enhance image contrast but also promise to enable improved differentiation of pathologies via localized metabolic properties or functional (physiological) states.

As a consequence, there have been numerous recent innovations in OCT technology and considerable interest in this topic – especially in the fields of ophthalmology, gastroenterology, and cardiology. OCT is one of the most innovative and rapidly emerging optical imaging modalities in the last decades since unlike histology, it is capable of noninvasively exploiting the wealth of morphological and functional tissue information in living tissues and performing repeated imaging to elucidate dynamics, progression, and treatment response. To date, more than 50 OCT companies have been created; more than 100 international research groups are involved in OCT; over 1,000 OCT patents have been granted; and more than 10,000 research articles have been published – mostly in ophthalmology, followed by technology-related and cardiovascular publications (http://www.octnews.org/; Eric Swanson). In ophthalmic diagnosis, OCT was the fastest adopted imaging technology in the history of ophthalmology. In 2010, there were 108 million X-ray, 30 million SPECT, PET, and CT, and 26 million MRI examinations compared with approximately 30 million ophthalmic OCT scans. In more than 110 years of X-ray imaging development, ionizing radiation dose was reduced by 1,500 times; imaging speed became 257,000 times faster; contrast increased significantly; and the images became of much finer resolution. It is interesting to note that in less than 20 years of OCT development, its axial resolution has improved by more than 10 times; imaging speed has increased by more than half a million times; image contrast is greatly enhanced; and many functional extensions of OCT have been developed.

In 2008, the first edition of this book was successfully published and has contributed to the extremely rapid development and dissemination of OCT. Since then, significant advances in photonics, detection and OCT technology, as well as a broad and continuously growing spectrum of successful OCT applications in a variety of medical fields have occurred. The second edition of this book seeks to comprehensively summarize and critically highlight the state of the art of OCT technology and its applications. The book includes contributions from the leading international experts in OCT technology and its clinical applications. The number of chapters more than doubled from 42 in the first edition to more than 80 in this second edition. The chapters have been grouped into five themes:

- Two chapters present an overview, history, and basic theory of OCT. Modeling of light tissue interactions in OCT systems is described in the third chapter.
- In Part II, 21 chapters summarize the state-of-the-art *OCT Technology* including Spectral/Fourier, Frequency Domain OCT, Swept Source OCT, Inverse Scattering OCT, Ultrahigh-Resolution OCT, Ultrahigh-speed OCT, superluminescent diodes, rapid swept sources, ultrashort pulse and tuneable light sources for OCT as well as optical designs, linear OCT systems, and OCT signal and image processing, including digital signal processing enhancements.

- In Part III, seven chapters focus on *Optical Coherence Microscopy* including flying spot-based en face OCT, scanning OCM, time domain, spectral domain and swept source full field OCT, OCM with engineered wavefront, interferometric synthetic aperture microscopy, and holographic OCT.
- In Part IV, 23 chapters introduce *extensions of OCT* describing Doppler flow, microangiography, polarization-sensitive, spectroscopic, molecular contrast, phase-resolved OCT, OCT combined with fluorescence, multiphoton microscopy, ultrasound, photoacoustic imaging, fluorescence laminar tomography, elastic scattering spectroscopy combined with OCT, optical tissue clearing for OCT, nonlinear interferometric vibrational imaging, optical coherence elastography, as well as multimodal OCT endoscopy.
- In Part V, the final 31 chapters summarize the broad spectrum of medical OCT applications including tissue engineering, developmental biology, ophthalmology (including 2 chapters on cellular resolution (adaptive optics) OCT, small animal retinal OCT, as well as choroidal OCT), gastrointestinal and intracoronary endoscopy, dermatology, laryngology, neuroscience, dentistry, kidney transplantation, as well as applications in the oral cavity, pulmonary area, gynecology, urology and large hollow organs, but also nondestructive material testing and examination of artwork by OCT. A final chapter describes the OCT technology transfer and the OCT market.

Three-dimensional ultrahigh-resolution OCT in combination with ultrafast scanning/data acquisition enabled a quantum leap in OCT performance. OCT can now be considered as an optical analogue to CT or MRI but with microscopic resolution. OCT is in a unique position because it enables not only three-dimensional structural imaging of tissue architecture and pathology but also depth-resolved, three-dimensional imaging of functional tissue information. Integrated structural and functional imaging might ultimately be performed with a single acquisition combined with innovative data post processing. With the continuing development of functional OCT, this technique has the potential to revolutionize medical diagnosis in multiple specialties in the near future. It is unlikely, however, that OCT will replace excisional biopsy and histology or other existing diagnostic modalities. Rather, it would be used as an adjunct to increase coverage, reduce sampling error, and improve sensitivity. In addition, OCT promises to have impact on the screening and diagnosis of diseases and to enable new insight into the pathogenesis and therapy of many diseases. The unique features of this technology enable a broad range of research and clinical applications, which not only complement the existing imaging technologies available today but can also reveal previously unseen morphological, dynamic, and functional changes in applications spanning different biological tissues and medical fields.

Due to recent dramatic technological advances, there may be a concern that key OCT performance parameters, e.g., resolution, scanning/data acquisition speed, sensitivity, and penetration may have reached a plateau. At the same time, it is difficult to predict the future of a technology. Ten years ago, it was difficult to predict the development of Fourier domain detection methods that enabled multiple-order-of-magnitude increases in imaging speed. The full impact of these

extremely high data rates remains yet to be realized, especially in the context of new functional imaging methods. In addition, many challenges in medical device development for OCT remain to be solved.

However, it is clear that the future of OCT clinical applications requires major research efforts by multidisciplinary teams of investigators spanning academics, industry, and clinical medicine. Fundamental studies, engineering, clinical feasibility studies, product development, and multicenter clinical trials must be performed to demonstrate efficacy and outcome. Regulatory and reimbursement hurdles must be addressed and development and educational efforts undertaken to disseminate OCT into the international clinical community. This represents an enormous effort because it must be performed on a specialty-by-specialty and indication-by-indication basis. This translational process requires partnerships between engineers and clinicians, academics and industry, as well as government funding and regulatory agency involvement. These challenges are great, but the potential impact on health care and society is also great.

The editors are especially grateful to the numerous coeditors and their teams for their significant efforts and indispensable contributions that resulted in an extremely comprehensive, state-of-the-art description of OCT. The editors and coeditors have all agreed not to accept any royalty income for this book in order to maintain a low sales price, making it accessible to the widest possible audience. We wish to offer special thanks to the numerous companies and organizations who are advertisers of this book. Their contributions enabled the book to be printed with full color (rather than black and white) figures at an economical price. Finally, we are also especially grateful to Springer Publishing for their efforts to make this book possible.

On behalf of all the coeditors, we hope you find this book and the field of OCT as interesting, enlightening, and stimulating as we do.

Wolfgang Drexler
Vienna, Austria

James G. Fujimoto
Cambridge, MA, USA
Editors

Contents

Volume 1

Part I Introduction to OCT 1

1 Introduction to OCT 3
James G. Fujimoto and Wolfgang Drexler

2 Theory of Optical Coherence Tomography 65
Joseph A. Izatt, Michael A. Choma, and Al-Hafeez Dhalla

3 Modeling Light–Tissue Interaction in Optical Coherence Tomography Systems 95
Peter E. Andersen, Thomas M. Jørgensen, Lars Thrane, Andreas Tycho, and Harold T. Yura

Part II OCT Technology 141

4 Inverse Scattering and Aperture Synthesis in OCT 143
Adolf F. Fercher

5 Spectral/Fourier Domain Optical Coherence Tomography 165
Johannes F. de Boer

6 Complex and Coherence-Noise Free Fourier Domain Optical Coherence Tomography 195
Rainer A. Leitgeb and Maciej Wojtkowski

7 Optical Frequency Domain Imaging 225
Brett E. Bouma, Guillermo J. Tearney, Benjamin Vakoc, and Seok Hyun Yun

8 Complex Conjugate Removal in SS Optical Coherence Tomography 255
Oscar Carrasco-Zevallos and Joseph A. Izatt

9 Ultrahigh Resolution Optical Coherence Tomography 277
Wolfgang Drexler, Yu Chen, Aaron D. Aguirre, Boris Považay, Angelika Unterhuber, and James G. Fujimoto

10 Ultrahigh Speed OCT 319
Ireneusz Grulkowski, Jonathan J. Liu, Benjamin Potsaid, Vijaysekhar Jayaraman, Alex E. Cable, and James G. Fujimoto

11 Optical Design for OCT 357
Zhilin Hu and Andrew M. Rollins

12 Linear OCT Systems 385
Gereon Hüttmann, Peter Koch, and Reginald Birngruber

13 Data Analysis and Signal Postprocessing for Optical Coherence Tomography 407
Tyler S. Ralston, Daniel L. Marks, Adeel Ahmad, and Stephen A. Boppart

14 DSP Technology and Methods for OCT 437
Murtaza Ali, Adeel Ahmad, and Stephen A. Boppart

15 OCT Motion Correction 459
Martin F. Kraus and Joachim Hornegger

16 Image Processing in Intravascular OCT 477
Zhao Wang, David L. Wilson, Hiram G. Bezerra, and Andrew M. Rollins

17 Superluminescent Diode Light Sources for OCT 505
Vladimir R. Shidlovski

18 SLEDs and Swept Source Laser Technology for OCT 527
Marcus Duelk and Kevin Hsu

19 Broad Bandwidth Laser and Nonlinear Optical Sources for OCT 563
Angelika Unterhuber, Boris Považay, Aaron D. Aguirre, Yu Chen, Franz X. Kärtner, James G. Fujimoto, and Wolfgang Drexler

20 Wavelength Swept Lasers 619
Seok Hyun Yun and Brett E. Bouma

21 Swept Light Sources 639
Bart Johnson, Walid Atia, Mark Kuznetsov, Christopher Cook, Brian Goldberg, Bill Wells, Noble Larson, Eric McKenzie, Carlos Melendez, Ed Mallon, Seungbum Woo, Randal Murdza, Peter Whitney, and Dale Flanders

22 VCSEL Swept Light Sources 659
Vijaysekhar Jayaraman, James Jiang, Benjamin Potsaid, Martin Robertson, Peter J. S. Heim, Christopher Burgner, Demis John, Garrett D. Cole, Ireneusz Grulkowski, James G. Fujimoto, Anjul M. Davis, and Alex E. Cable

23 Akinetik Swept Sources 687
Michael Minneman, Jason Ensher, Michael Crawford, Marco Bonesi, Behrooz Zabihian, Paul Boschert, Erich Hoover, Dennis Derickson, Brian E. Applegate, Thomas Milner, and Wolfgang Drexler

24 FDML (incl. Parallelization) 741
Robert Huber

Volume 2

Part III Optical Coherence Microscopy 789

25 Time Domain Full Field Optical Coherence Tomography Microscopy 791
Fabrice Harms, Anne Latrive, and A. Claude Boccara

26 Assessment of Breast, Brain and Skin Pathological Tissue Using Full Field OCM 813
Eugénie Dalimier, Osnath Assayag, Fabrice Harms, and A. Claude Boccara

27 Digital Holoscopy 839
Dierck Hillmann, Gesa Franke, Christian Lührs, Peter Koch, and Gereon Hüttmann

28 Optical Coherence Microscopy 865
Aaron D. Aguirre, Chao Zhou, Hsiang-Chieh Lee, Osman O. Ahsen, and James G. Fujimoto

29 OCM with Engineered Wavefront 913
Rainer A. Leitgeb, Theo Lasser, and Martin Villiger

30 Holographic Optical Coherence Imaging 941
David D. Nolte, Kwan Jeong, John Turek, and Paul M. W. French

31 Interferometric Synthetic Aperture Microscopy (ISAM) 965
Steven G. Adie, Nathan D. Shemonski, Tyler S. Ralston, P. Scott Carney, and Stephen A. Boppart

Part IV Contrast Enhanced, Functional and Multimodal OCT 1005

32 Optical Coherence Elastography 1007
Brendan F. Kennedy, Kelsey M. Kennedy, Amy L. Oldenburg, Steven G. Adie, Stephen A. Boppart, and David D. Sampson

33 Polarization Sensitive Optical Coherence Tomography 1055
B. Hyle Park and Johannes F. de Boer

34 MUW Approach of PS OCT 1103
Christoph K. Hitzenberger and Michael Pircher

35 Jones Matrix Based Polarization Sensitive Optical Coherence Tomography 1137
Yoshiaki Yasuno, Myeong-Jin Ju, Young Joo Hong, Shuichi Makita, Yiheng Lim, and Masahiro Yamanari

36 Spectroscopic Low Coherence Interferometry 1163
Nienke Bosschaart, T. G. van Leeuwen, Maurice C. Aalders, Boris Hermann, Wolfgang Drexler, and Dirk J. Faber

37 Motility Contrast Imaging and Tissue Dynamics Spectroscopy 1189
David D. Nolte, Ran An, and John Turek

38 Elastic Scattering Spectroscopy and Optical Coherence Tomography 1207
Adam Wax, Michael Giacomelli, and Francisco Robles

39 Nonlinear Interferometric Vibrational Imaging (NIVI) with Novel Optical Sources 1237
Stephen A. Boppart, Matthew D. King, Yuan Liu, Haohua Tu, and Martin Gruebele

40 Ultrasensitive Phase-Resolved Imaging of Cellular Morphology and Dynamics 1257
Michael A. Choma, Audrey Ellerbee, and Joseph A. Izatt

41 Doppler Optical Coherence Tomography 1289
Zhongping Chen and Jun Zhang

42 Doppler Fourier Domain Optical Coherence Tomography for Label-Free Tissue Angiography 1321
Rainer A. Leitgeb, Maciej Szkulmowski, Cedric Blatter, and Maciej Wojtkowski

43 Dual Beam Doppler Optical Coherence Angiography 1353
Yoshiaki Yasuno, Shuichi Makita, and Franck Jaillon

44 Optical Microangiography Based on Optical Coherence Tomography 1373
Roberto Reif and Ruikang K. Wang

45 Optical Coherence Tomography in Cancer Imaging 1399
Ahhyun Stephanie Nam, Benjamin Vakoc, David Blauvelt, and Isabel Chico-Calero

46 Clinical Applications of Doppler OCT and OCT Angiography 1413
Ou Tan, Yali Jia, Eric Wei, and David Huang

47 Molecular Optical Coherence Tomography Contrast Enhancement and Imaging 1429
Amy L. Oldenburg, Brian E. Applegate, Jason M. Tucker-Schwartz, Melissa C. Skala, Jongsik Kim, and Stephen A. Boppart

48 Optical Tissue Clearing to Enhance Imaging Performance for OCT 1455
Ruikang K. Wang and Valery V. Tuchin

49 Second Harmonic OCT and Combined MPM/OCT 1489
Zhongping Chen and Shuo Tang

50 Combined Endoscopic Optical Coherence Tomography and Laser Induced Fluorescence 1515
Jennifer K. Barton, Alexandre R. Tumlinson, and Urs Utzinger

51 Integrated Optical Coherence Tomography (OCT) with Fluorescence Laminar Optical Tomography (FLOT) 1557
Chao-Wei Chen and Yu Chen

52 Photoacoustic / Optical Coherence Tomography 1579
Michelle Gabriele Sandrian, Edward Zhang, Boris Považay, Jan Laufer, Aneesh Alex, Paul Beard, and Wolfgang Drexler

53 Multi-modal Endoscopy: OCT and Fluorescence 1599
Jessica Mavadia-Shukla, Jiefeng F. Xi, and Xingde D. Li

Volume 3

Part V OCT Applications 1615

54 Application of Fourier Domain OCT Imaging Technology to the Anterior Segment of the Human Eye 1617
Maciej Wojtkowski, Susana Marcos, Sergio Ortiz, and Ireneusz Grulkowski

55 Anterior Eye Imaging with Optical Coherence Tomography 1649
David Huang, Yan Li, and Maolong Tang

56 Retinal Optical Coherence Tomography Imaging 1685
Wolfgang Drexler and James G. Fujimoto

57 OCT Imaging in Glaucoma 1737
Jessica E. Nevins, Gadi Wollstein, and Joel S. Schuman

58 Intraoperative Retinal Optical Coherence Tomography 1771
Justin Migacz, Oscar Carrasco-Zevallos, Paul Hahn, Anthony Kuo, Cynthia Toth, and Joseph A. Izatt

59 En-face Flying Spot OCT/Ophthalmoscope 1797
Richard B. Rosen, Patricia Garcia, Adrian Gh. Podoleanu, Radu Cucu, George Dobre, Irina Trifanov, Mirjam E. J. van Velthoven, Marc D. de Smet, John A. Rogers, Mark Hathaway, Justin Pedro, and Rishard Weitz

60 Choroidal OCT 1833
Marieh Esmaeelpour and Wolfgang Drexler

61 Retinal AO OCT 1849
Robert J. Zawadzki and Donald T. Miller

62 Acousto Optic Modulation Based En face AO SLO OCT 1921
Michael Pircher and Christoph K. Hitzenberger

63 Small Animal Retinal Imaging 1941
WooJhon Choi, Wolfgang Drexler, and James G. Fujimoto

64 Optical Coherence Tomography in Tissue Engineering 1965
Youbo Zhao, Ying Yang, Ruikang K. Wang, and Stephen A. Boppart

65 4-D OCT in Developmental Cardiology 2003
Michael W. Jenkins and Andrew M. Rollins

66 OCT and Coherence Imaging for the Neurosciences 2025
Jonghwan Lee and David A. Boas

67 Optical Coherence Tomography for Gastrointestinal Endoscopy 2051
Wei Kang, Xin Qi, Hui Wang, and Andrew M. Rollins

68 Endoscopic Optical Coherence Tomography 2077
Chao Zhou, James G. Fujimoto, Tsung-Han Tsai, and Hiroshi Mashimo

69 Imaging Coronary Atherosclerosis and Vulnerable Plaques with Optical Coherence Tomography 2109
Guillermo J. Tearney, Ik-Kyung Jang, Manubu Kashiwagi, and Brett E. Bouma

70 Cardiovascular Optical Coherence Tomography 2131
Taishi Yonetsu, Martin Villiger, Brett E. Bouma, and Ik-Kyung Jang

71 Intravascular OCT 2153
Joseph M. Schmitt, Desmond Adler, and Chenyang Xu

72 Development of Integrated Multimodality Intravascular Imaging System for Assessing and Characterizing Atherosclerosis 2173
Zhongping Chen

73 OCT in Dermatology 2189
John Holmes and Julia Welzel

74 Dental OCT 2209
Petra Wilder-Smith, Linda Otis, Jun Zhang, and Zhongping Chen

75 Anatomic Optical Coherence Tomography of Upper Airways . . . 2245
Anthony Chin Loy, Joseph Jing, Jun Zhang, Yong Wang, Said Elghobashi, Zhongping Chen, and Brian J. F. Wong

76 Optical Coherence Tomography in Pulmonary Medicine 2263
Septimiu Dan Murgu, Matthew Brenner, Zhongping Chen, and Melissa J. Suter

77 OCT in Gynecology 2305
Irina A. Kuznetsova, Natalia D. Gladkova, Valentin M. Gelikonov, Jerome L. Belinson, Natalia M. Shakhova, and Felix I. Feldchtein

78 Endoscopic Optical Coherence Tomography in Urology 2335
Yingtian Pan, Wayne Waltzer, and Zhangqun Ye

79 Optical Coherence Tomography in Kidney Transplantation 2363
Peter M. Andrews, Jeremiah Wierwille, and Yu Chen

80 Intraoperative OCT in Surgical Oncology 2393
Fredrick A. South, Marina Marjanovic, and Stephen A. Boppart

81 Optical Coherence Tomography in a Needle Format 2413
Dirk Lorenser, Robert A. McLaughlin, and David D. Sampson

82 OCT for Examination of Artwork 2473
Piotr Targowski, Magdalena Iwanicka, Bogumiła J. Rouba, and Cecilia Frosinini

83 Nondestructive Material Testing Using OCT 2497
D. Stifter

84 OCT Technology Transfer and the OCT Market 2529
Eric A. Swanson

Contributors

Maurice C. Aalders Department of Biomedical Engineering and Physics, Academic Medical Center, University of Amsterdam, The Netherlands

Steven G. Adie Department of Biomedical Engineering, Cornell University, Ithaca, NY, USA

Desmond Adler St. Jude Medical, Westford, MA, USA

Aaron D. Aguirre Massachusetts General Hospital, Boston, MA, USA

Department of Electrical Engineering and Computer Science and Research Laboratory of Electronics, Massachusetts Institute of Technology, Cambridge, MA, USA

Adeel Ahmad Biophotonics Imaging Laboratory, Beckman Institute for Advanced Science and Technology, University of Illinois at Urbana-Champaign, Urbana, IL, USA

Osman O. Ahsen Department of Electrical Engineering and Computer Science and Research Laboratory of Electronics, Massachusetts Institute of Technology, Cambridge, MA, USA

Aneesh Alex Department of Electrical and Computer Engineering, Lehigh University, Bethlehem, PA, USA

Murtaza Ali Embedded Processing Systems Lab, Texas Instruments Inc, Dallas, TX, USA

Ran An Department of Basic Medical Sciences, Purdue University, West Lafayette, IN, USA

Peter E. Andersen Department of Photonics Engineering, Technical University of Denmark, Roskilde, Denmark

Peter M. Andrews Department of Biochemistry, Molecular and Cellular Biology, Georgetown University Medical Center, Washington, DC, USA

Brian E. Applegate Department of Biomedical Engineering, Texas A&M University, College Station, TX, USA

Osnath Assayag Institut Langevin, ESPCI-ParisTech, Paris, France

Walid Atia Axsun Technologies, Billerica, MA, USA

Jennifer K. Barton Biomedical Engineering, The University of Arizona, Tucson, AZ, USA

Optical Sciences, The University of Arizona, Tucson, AZ, USA

Paul Beard Department of Medical Physics and Bioengineering, Malet Place Engineering Building, London, UK

Jerome L. Belinson Cleveland Clinic Foundation, Cleveland, OH, USA

Hiram G. Bezerra Cardiovascular Imaging Core Laboratory, University Hospitals Case Medical Center, Cleveland, OH, USA

Reginald Birngruber Institute of Biomedical Optics, University of Lübeck, Lübeck, Germany

Medical Laser Center Lübeck GmbH, Lübeck, Germany

Cedric Blatter Center for Medical Physics and Biomedical Engineering, Medical University of Vienna, Vienna, Austria

David Blauvelt Wellman Center for Photomedicine, Massachusetts General Hospital and Harvard Medical School, Boston, MA, USA

David A. Boas Martinos Center for Biomedical Imaging, Massachusetts General Hospital, Harvard Medical School, Charlestown, MA, USA

A. Claude Boccara LLTech SAS Pépinière Paris Santé Cochin, Paris, France

LLTech, Princeton, NJ, USA

Institut Langevin, ESPCI–ParisTech, Paris, France

Marco Bonesi Medical University of Vienna, Vienna, Austria

Stephen A. Boppart Biophotonics Imaging Laboratory, Beckman Institute for Advanced Science and Technology, University of Illinois at Urbana-Champaign, Urbana, IL, USA

Departments of Bioengineering, Electrical and Computer Engineering, and Medicine, University of Illinois at Urbana-Champaign, Urbana, IL, USA

Paul Boschert Insight Photonic Solutions, Lafayette, CO, USA

Nienke Bosschaart Department of Biomedical Engineering and Physics, Academic Medical Center, University of Amsterdam, The Netherlands

Brett E. Bouma Wellman Center for Photomedicine, Massachusetts General Hospital, Harvard Medical School, Boston, MA, USA

Matthew Brenner Pulmonary and Critical Care Medicine, UC Irvine Medical Center, Orange, CA, USA

Christopher Burgner Praevium Research, Inc., Santa Barbara, CA, USA

Alex E. Cable Advanced Imaging Group, Thorlabs Inc., Newton, NJ, USA

P. Scott Carney Beckman Institute for Advanced Science and Technology, University of Illinois at Urbana-Champaign, Urbana, IL, USA

Oscar Carrasco-Zevallos Fitzpatrick Institute for Photonics and Department of Biomedical Engineering, Duke University, Durham, NC, USA

Chao-Wei Chen Fischell Department of Bioengineering and Department of Electrical and Computer Engineering, University of Maryland, College Park, MD, USA

Yu Chen Department of Electrical Engineering and Computer Science and Research Laboratory of Electronics, Massachusetts Institute of Technology, Cambridge, MA, USA

Biomedical Optics and Imaging Laboratory, Fischell Department of Bioengineering, University of Maryland, College Park, MD, USA

Zhongping Chen The Edwards Life Sciences Center for Advanced Cardiovascular Technology, Beckman Laser Institute, Irvine, CA, USA

Department of Biomedical Engineering, Beckman Laser Institute, University of California Irvine, Irvine, CA, USA

Isabel Chico-Calero Wellman Center for Photomedicine, Massachusetts General Hospital and Harvard Medical School, Boston, MA, USA

Anthony Chin Loy Department of Otolaryngology Head and Neck Surgery, The Beckman Laser Institute, University of California Irvine, Irvine, CA, USA

WooJhon Choi Department of Electrical Engineering and Computer Science and Research Laboratory of Electronics, Massachusetts Institute of Technology, Cambridge, MA, USA

Michael A. Choma Departments of Diagnostic Radiology, Pediatrics, Biomedical Engineering, and Applied Physics, Yale University, New Haven, CT, USA

Garrett D. Cole Advanced Optical Microsystems, Mountain View, CA, USA

Christopher Cook Axsun Technologies, Billerica, MA, USA

Michael Crawford Insight Photonic Solutions, Lafayette, CO, USA

Radu Cucu Applied Optics Group, School of Physical Sciences, University of Kent, Canterbury, UK

Eugénie Dalimier LLTech SAS Pépinière Paris Santé Cochin, Paris, France

LLTech, Princeton, NJ, USA

Anjul M. Davis Thorlabs, Newton, NJ, USA

Johannes F. de Boer Department of Physics and Astronomy, LaserLaB Amsterdam, Vrije Univ Amsterdam, Amsterdam, The Netherlands

Marc D. de Smet Academic Medical Center, Amsterdam, The Netherlands

Dennis Derickson California Polytechnic State University, San Luis Obispo, CA, USA

Al-Hafeez Dhalla Bioptigen, Inc, Durham, NC, USA

George Dobre Applied Optics Group, School of Physical Sciences, University of Kent, Canterbury, UK

Wolfgang Drexler Center for Medical Physics and Biomedical Engineering, Medical University of Vienna, General Hospital Vienna, Vienna, Austria

Marcus Duelk EXALOS, Schlieren, Switzerland

Said Elghobashi Department of Mechanical and Aerospace Engineering, University of California Irvine, Irvine, CA, USA

Audrey Ellerbee Ginzton Laboratory and Department of Electrical Engineering, Stanford University, Palo Alto, CA, USA

Jason Ensher Insight Photonic Solutions, Lafayette, CO, USA

Marieh Esmaeelpour Center for Medical Physics and Biomedical Engineering, Medical University of Vienna, Vienna, Austria

Dirk J. Faber Department of Biomedical Engineering and Physics, Academic Medical Center, University of Amsterdam, The Netherlands

Felix I. Feldchtein Imalux Corporation, Cleveland, OH, USA

Institute of Applied Physics Russian Academy of Sciences, Nizhny Novgorod, Russia

Adolf F. Fercher Medical University Vienna, Vienna, Austria

Dale Flanders Axsun Technologies, Billerica, MA, USA

Gesa Franke Institute of Biomedical Optics, University of Lübeck, Lübeck, Germany

Medical Laser Center GmbH, Lübeck, Germany

Paul M. W. French Imperial College, London, UK

Cecilia Frosinini Opificio delle Pietre Dure e Laboratori di Restauro, Firenze, Italy

James G. Fujimoto Department of Electrical Engineering and Computer Science and Research Laboratory of Electronics, Massachusetts Institute of Technology, Cambridge, MA, USA

Patricia Garcia New York Eye and Ear Infirmary Advanced Retinal Imaging Center, New York, NY, USA

Valentin M. Gelikonov Institute of Applied Physics Russian Academy of Sciences, Nizhny Novgorod, Russia

Michael Giacomelli Department of Electrical Engineering and Computer Science and Research Laboratory of Electronics, Massachusetts Institute of Technology, Cambridge, MA, USA

Natalia D. Gladkova Medical Academy, Nizhny Novgorod, Russia

Brian Goldberg Axsun Technologies, Billerica, MA, USA

Martin Gruebele Beckman Institute for Advanced Science and Technology, University of Illinois at Urbana-Champaign, Urbana-Champaign, USA

Ireneusz Grulkowski Department of Electrical Engineering and Computer Science and Research Laboratory of Electronics, Massachusetts Institute of Technology, Cambridge, MA, USA

Paul Hahn Duke Eye Center and Department of Ophthalmology, Duke University Medical Center, Durham, NC, USA

Fabrice Harms LLTech SAS Pépinière Paris Santé Cochin, Paris, France

LLTech, Princeton, NJ, USA

Mark Hathaway Ophthalmic Technology Inc., Toronto, Canada

Peter J. S. Heim Thorlabs Quantum Electronics (TQE), Jessup, MD, USA

Boris Hermann Center for Medical Physics and Biomedical Engineering, Medical University of Vienna, Vienna, Austria

Dierck Hillmann Thorlabs GmbH, Lübeck, Germany

Christoph K. Hitzenberger Center for Medical Physics and Biomedical Engineering, Medical University of Vienna, Vienna, Austria

John Holmes Michelson Diagnostics Ltd, Orpington, UK

Young Joo Hong Computational Optics Group, University of Tsukuba, Tsukuba, Ibaraki, Japan

Erich Hoover Insight Photonic Solutions, Lafayette, CO, USA

Joachim Hornegger Pattern Recognition Lab, University Erlangen–Nürnberg, Erlangen, Germany

School of Advanced Optical Technologies (SAOT), University Erlangen–Nürnberg, Erlangen, Germany

Kevin Hsu EXALOS, Schlieren, Switzerland

Zhilin Hu Case Western Reserve Department of Biomedical Engineering, Cleveland, OH, USA

David Huang Center for Ophthalmic Optics and Lasers, Casey Eye Institute and Department of Ophthalmology, Oregon Health and Science University, Portland, OR, USA

Robert Huber Institut für Biomedizinische Optik, Universität zu Lübeck, Lübeck

Gereon Hüttmann Institute of Biomedical Optics, University of Lübeck, Lübeck, Germany

Medical Laser Center GmbH, Lübeck, Germany

Magdalena Iwanicka Institute for the Study, Restoration and Conservation of Cultural Heritage, Nicolaus Copernicus University, Toruń, Poland

Joseph A. Izatt Fitzpatrick Institute for Photonics and Departments of Biomedical Engineering and Ophthalmology, Duke University Medical Center, Durham, NC, USA

Franck Jaillon Computational Optics Group, University of Tsukuba, Tsukuba, Ibaraki, Japan

Ik-Kyung Jang Division of Cardiology, Massachusetts General Hospital and Harvard Medical School, Massachusetts, Boston, MA, USA

Vijaysekhar Jayaraman Praevium Research, Inc., Santa Barbara, CA, USA

Michael W. Jenkins Department of Pediatrics, Case Western Reserve University, Cleveland, OH, USA

Kwan Jeong Physics Department, Korean Military Academy, Soeul, South Korea

Yali Jia Casey Eye Institute, Oregon Health and Science University, Portland, OR, USA

James Jiang Thorlabs, Newton, NJ, USA

Joseph Jing Department of Biomedical Engineering, The Beckman Laser Institute, University of California Irvine, Irvine, CA, USA

Demis John Praevium Research, Inc., Santa Barbara, CA, USA

Bart Johnson Axsun Technologies, Billerica, MA, USA

Thomas M. Jørgensen Department of Photonics Engineering, Technical University of Denmark, Roskilde, Denmark

Myeong-Jin Ju Computational Optics Group, University of Tsukuba, Tsukuba, Ibaraki, Japan

Wei Kang St. Jude Medical, Westford, MA, USA

Franz X. Kärtner Center for Free-Electron Laser Science, DESY (Deutsches Elektronen-Synchrotron), Hamburg, Germany

Manubu Kashiwagi Wellman Center for Photomedicine, Massachusetts General Hospital, Boston, MA, USA

Brendan F. Kennedy Optical+Biomedical Engineering Laboratory, School of Electrical, Electronic and Computer Engineering, The University of Western Australia, Crawley, WA, Australia

Kelsey M. Kennedy Optical+Biomedical Engineering Laboratory, School of Electrical, Electronic and Computer Engineering, The University of Western Australia, Crawley, WA, Australia

Jongsik Kim Department of Electrical and Computer Engineering, Bioengineering, Medicine, and the Beckman Institute for Advanced Science and Technology, University of Illinois at Urbana-Champaign, Champaign, IL, USA

Matthew D. King Beckman Institute for Advanced Science and Technology, University of Illinois at Urbana-Champaign, Urbana-Champaign, USA

Peter Koch Institute of Biomedical Optics, University of Lübeck, Lübeck, Germany

Medical Laser Center Lübeck GmbH, Lübeck, Germany

Martin F. Kraus Pattern Recognition Lab, University Erlangen–Nürnberg, Erlangen, Germany

School of Advanced Optical Technologies (SAOT), University Erlangen–Nürnberg, Erlangen, Germany

Anthony Kuo Duke Eye Center and Department of Ophthalmology, Duke University Medical Center, Durham, NC, USA

Mark Kuznetsov Axsun Technologies, Billerica, MA, USA

Irina A. Kuznetsova Nizhny Novgorod Regional Hospital, Nizhny Novgorod, Russia

Noble Larson Axsun Technologies, Billerica, MA, USA

Theo Lasser Laboratoire d'Optique Biomedicale, Ecole Polytechnique Federal de Lausanne, Lausanne, Switzerland

Anne Latrive Institut Langevin, ESPCI ParisTech, Paris, France

LLTech SAS Pépinière Paris Santé Cochin, Paris, France

Jan Laufer Institut für Optik und Atomare Physik, Sekretariat ER 1–1, Technische Universität Berlin, Berlin, Germany

Institut für Radiologie, Charité – Universitätsmedizin Berlin, Berlin, Germany

Hsiang-Chieh Lee Department of Electrical Engineering and Computer Science and Research Laboratory of Electronics, Massachusetts Institute of Technology, Cambridge, MA, USA

Jonghwan Lee Martinos Center for Biomedical Imaging, Massachusetts General Hospital, Harvard Medical School, Charlestown, MA, USA

Rainer A. Leitgeb Center for Medical Physics and Biomedical Engineering, Medical University of Vienna, Vienna, Austria

Xingde D. Li Department of Biomedical Engineering, Johns Hopkins University, Baltimore, MD, USA

Yan Li Center for Ophthalmic Optics and Lasers, Casey Eye Institute and Department of Ophthalmology, Oregon Health and Science University, Portland, OR, USA

Yiheng Lim Computational Optics Group, University of Tsukuba, Tsukuba, Ibaraki, Japan

Jonathan J. Liu Department of Electrical Engineering and Computer Science and Research Laboratory of Electronics, Massachusetts Institute of Technology, Cambridge, MA, USA

Yuan Liu Beckman Institute for Advanced Science and Technology, University of Illinois at Urbana-Champaign, Urbana-Champaign, USA

Dirk Lorenser Optical+Biomedical Engineering Laboratory, School of Electrical, Electronic and Computer Engineering, The University of Western Australia, Crawley, WA, Australia

Christian Lührs Thorlabs GmbH, Lübeck, Germany

Shuichi Makita Computational Optics Group, University of Tsukuba, Tsukuba, Ibaraki, Japan

Ed Mallon Axsun Technologies, Billerica, MA, USA

Susana Marcos Instituto de Óptica "Daza de Valdés", Consejo Superior de Investigaciones Científicas, Madrid, Spain

Marina Marjanovic Beckman Institute for Advanced Science and Technology, University of Illinois at Urbana-Champaign, Urbana, IL, USA

Daniel L. Marks Biophotonics Imaging Laboratory, Beckman Institute for Advanced Science and Technology, University of Illinois at Urbana-Champaign, Urbana, IL, USA

Hiroshi Mashimo Veteran Affairs Boston Healthcare System, Harvard Medical School, Boston, MA, USA

Jessica Mavadia-Shukla Department of Biomedical Engineering, Johns Hopkins University, Baltimore, MD, USA

Eric McKenzie Axsun Technologies, Billerica, MA, USA

Robert A. McLaughlin Optical+Biomedical Engineering Laboratory, School of Electrical, Electronic and Computer Engineering, The University of Western Australia, Crawley, WA, Australia

Carlos Melendez Axsun Technologies, Billerica, MA, USA

Justin Migacz Department of Ophthalmology and Vision Science, University of California at Davis, Davis, CA, USA

Donald T. Miller School of Optometry, Indiana University, Bloomington, IN, USA

Thomas Milner University of Texas, Austin, TX, USA

Michael Minneman Insight Photonic Solutions, Lafayette, CO, USA

Randal Murdza Axsun Technologies, Billerica, MA, USA

Septimiu Dan Murgu The University of Chicago, Chicago, IL, USA

Ahhyun Stephanie Nam Wellman Center for Photomedicine, Massachusetts General Hospital and Harvard Medical School, Boston, MA, USA

Jessica E. Nevins UPMC Eye Center, Eye and Ear Institute, Ophthalmology and Visual Science Research Center, Department of Ophthalmology, University of Pittsburgh School of Medicine, Pittsburgh, PA, USA

David D. Nolte Department of Physics, Purdue University, West Lafayette, IN, USA

Department of Basic Medical Sciences, Purdue University, West Lafayette, IN, USA

Amy L. Oldenburg Department of Physics and Astronomy and the Biomedical Research Imaging Center, University of North Carolina at Chapel Hill, Chapel Hill, NC, USA

Sergio Ortiz Instituto de Óptica "Daza de Valdés", Consejo Superior de Investigaciones Científicas, Madrid, Spain

Linda Otis Oncology and Diagnostic Sciences, University of Maryland School of Dentistry, Baltimore, MD, USA

Yingtian Pan Stony Brook University, Stony Brook, USA

B. Hyle Park Department of Bioengineering, UC Riverside, Riverside, CA, USA

Justin Pedro Ophthalmic Technology Inc., Toronto, Canada

Michael Pircher Center for Medical Physics and Biomedical Engineering, Medical University of Vienna, Vienna, Austria

Adrian Gh. Podoleanu Applied Optics Group, School of Physical Sciences, University of Kent, Canterbury, UK

Benjamin Potsaid Department of Electrical Engineering and Computer Science and Research Laboratory of Electronics, Massachusetts Institute of Technology, Cambridge, MA, USA

Advanced Imaging Group, Thorlabs Inc., Newton, NJ, USA

Boris Považay Center for Medical Physics and Biomedical Engineering, Medical University of Vienna, Vienna, Austria

OptoLab, HuCe - Bern University of Applied Sciences (BUAS), Postfach, Biel/Bienne, Switzerland

Xin Qi Rutgers University, Piscataway, NJ, USA

Tyler S. Ralston Biophotonics Imaging Laboratory, Beckman Institute for Advanced Science and Technology, University of Illinois at Urbana-Champaign, Urbana, IL, USA

Roberto Reif Department of Bioengineering, University of Washington, Seattle, WA, USA

Martin Robertson Praevium Research, Inc., Santa Barbara, CA, USA

Francisco Robles Department of Chemistry, Duke University, Durham, NC, USA

John A. Rogers Ophthalmic Technology Inc., Toronto, Canada

Andrew M. Rollins Department of Biomedical Engineering, Case Western Reserve University, Cleveland, OH, USA

Richard B. Rosen New York Eye and Ear Infirmary Advanced Retinal Imaging Center, New York, NY, USA

Bogumiła J. Rouba Institute for the Study, Restoration and Conservation of Cultural Heritage, Nicolaus Copernicus University, Toruń, Poland

David D. Sampson Optical+Biomedical Engineering Laboratory, School of Electrical, Electronic and Computer Engineering, The University of Western Australia, Crawley, WA, Australia

Centre for Microscopy, Characterisation and Analysis, The University of Western Australia, Crawley, WA, Australia

Michelle Gabriele Sandrian Department of Ophthalmology, Department of Bioengineering Eye and Ear Institute, University of Pittsburgh, Pittsburgh, PA, USA

Joseph M. Schmitt St. Jude Medical, Westford, MA, USA

Joel S. Schuman UPMC Eye Center, Eye and Ear Institute, Ophthalmology and Visual Science Research Center, Department of Ophthalmology, University of Pittsburgh School of Medicine, Pittsburgh, PA, USA

Natalia M. Shakhova Institute of Applied Physics Russian Academy of Sciences, Nizhny Novgorod, Russia

Nathan D. Shemonski Beckman Institute for Advanced Science and Technology, University of Illinois at Urbana-Champaign, Urbana, IL, USA

Vladimir R. Shidlovski Superlum Diodes Ltd., Moscow, Russia

Melissa C. Skala Department of Biomedical Engineering, Vanderbilt University, Nashville, TN, USA

Fredrick A. South Beckman Institute for Advanced Science and Technology, University of Illinois at Urbana–Champaign, Urbana, IL, USA

Department of Electrical and Computer Engineering, University of Illinois at Urbana–Champaign, Urbana, IL, USA

D. Stifter Center for Surface and Nanoanalytics (ZONA), Johannes Kepler University (JKU) Linz, Linz, Austria

Melissa J. Suter Pulmonary and Critical Care Unit, Harvard Medical School and Massachusetts General Hospital, Boston, MA, USA

Eric A. Swanson Gloucester, MA, USA

Maciej Szkulmowski Faculty of Physics, Astronomy and Informatics, Institute of Physics, Nicolaus Copernicus University, Toruń, Poland

Ou Tan Casey Eye Institute, Oregon Health and Science University, Portland, OR, USA

Maolong Tang Center for Ophthalmic Optics and Lasers, Casey Eye Institute and Department of Ophthalmology, Oregon Health and Science University, Portland, OR, USA

Shuo Tang Department of Electrical and Computer Engineering, University of British Columbia, Vancouver, BC, Canada

Piotr Targowski Institute of Physics, Department of Physics, Astronomy and Informatics, Nicolaus Copernicus University, Toruń, Poland

Guillermo J. Tearney Wellman Center for Photomedicine, Massachusetts General Hospital, Harvard Medical School, Boston, MA, USA

Department of Pathology, Massachusetts General Hospital, Boston, MA, USA

Lars Thrane Department of Photonics Engineering, Technical University of Denmark, Roskilde, Denmark

Cynthia Toth Duke Eye Center and Departments of Ophthalmology and Biomedical Engineering, Duke University Medical Center, Durham, NC, USA

Irina Trifanov Applied Optics Group, School of Physical Sciences, University of Kent, Canterbury, UK

Tsung-Han Tsai Department of Electrical Engineering and Computer Science and Research Laboratory of Electronics, Massachusetts Institute of Technology, Cambridge, MA, USA

Haohua Tu Beckman Institute for Advanced Science and Technology, University of Illinois at Urbana-Champaign, Urbana-Champaign, USA

Valery V. Tuchin Research–Educational Institute of Optics and Biophotonics, Saratov State University, Saratov, Russia

Laboratory of Laser Diagnostics of Technical and Living Systems, Institute of Precise Mechanics and Control RAS, Saratov, Russia

Optoelectronics and Measurement Techniques Laboratory, University of Oulu, Oulu, Finland

Jason M. Tucker-Schwartz Department of Biomedical Engineering, Vanderbilt University, Nashville, TN, USA

Alexandre R. Tumlinson Carl Zeiss Meditec, Inc., Dublin, CA, USA

John Turek Department of Basic Medical Sciences, Purdue University, West Lafayette, IN, USA

Andreas Tycho Department of Photonics Engineering, Technical University of Denmark, Roskilde, Denmark

Angelika Unterhuber Center for Medical Physics and Biomedical Engineering, Medical University of Vienna, Vienna, Austria

Urs Utzinger Biomedical Engineering, The University of Arizona, Tucson, AZ, USA

Optical Sciences, The University of Arizona, Tucson, AZ, USA

Benjamin Vakoc Wellman Center for Photomedicine, Massachusetts General Hospital and Harvard Medical School, Boston, MA, USA

T. G. van Leeuwen Department of Biomedical Engineering and Physics, Academic Medical Center, University of Amsterdam, The Netherlands

Mirjam E. J. van Velthoven Academic Medical Center, Amsterdam, The Netherlands

Martin Villiger Wellman Center for Photomedicine, Massachusetts General Hospital, Harvard Medical School, Boston, MA, USA

Wayne Waltzer Stony Brook University, Stony Brook, USA

Hui Wang American Medical Systems, San Jose, CA, USA

Ruikang K. Wang Department of Automation Engineering, Northeastern University at Qinhuangdao, Hebei, Peoples' Republic of China

Department of Bioengineering, University of Washington, Seattle, WA, USA

Yong Wang Department of Mechanical and Aerospace Engineering, University of California Irvine, CA, USA

Zhao Wang Department of Biomedical Engineering, Case Western Reserve University, Cleveland, OH, USA

Adam Wax Department of Biomedical Engineering and Medical Physics, Duke University, Durham, NC, USA

Eric Wei Casey Eye Institute, Oregon Health and Science University, Portland, OR, USA

Rishard Weitz Ophthalmic Technology Inc., Toronto, Canada

Bill Wells Axsun Technologies, Billerica, MA, USA

Julia Welzel Klinikum Augsburg, Augsburg, Germany

Peter Whitney Axsun Technologies, Billerica, MA, USA

Jeremiah Wierwille Fischell Department of Bioengineering, University of Maryland, College Park, MD, USA

Petra Wilder-Smith Beckman Laser Institute, University of California Irvine, Irvine, CA, USA

David L. Wilson Department of Biomedical Engineering, Case Western Reserve University, Cleveland, OH, USA

Maciej Wojtkowski Faculty of Physics, Astronomy and Informatics, Institute of Physics, Nicolaus Copernicus University, Toruń, Poland

Gadi Wollstein UPMC Eye Center, Eye and Ear Institute, Ophthalmology and Visual Science Research Center, Department of Ophthalmology, University of Pittsburgh School of Medicine, Pittsburgh, PA, USA

Brian J. F. Wong Department of Otolaryngology Head and Neck Surgery, Department of Biomedical Engineering, Department of Surgery, The Beckman Laser Institute, University of California Irvine, Irvine, CA, USA

Seungbum Woo Axsun Technologies, Billerica, MA, USA

Jiefeng F. Xi Department of Biomedical Engineering, Johns Hopkins University, Baltimore, MD, USA

Chenyang Xu St. Jude Medical, Westford, MA, USA

Masahiro Yamanari Computational Optics Group, University of Tsukuba, Tsukuba, Ibaraki, Japan

Ying Yang Institute for Science and Technology in Medicine, School of Medicine, Keele University, Stoke-on-Trent, UK

Yoshiaki Yasuno Computational Optics Group, University of Tsukuba, Tsukuba, Ibaraki, Japan

Zhangqun Ye Tonji Medical College and Affiliated Hospital, Wuhan, Peoples' Republic of China

Taishi Yonetsu Department of Cardiology, Tsuchiura Kyodo Hospital, Tsuchiura, Ibaraki, Japan

Seok Hyun Yun Partners Research Building, Wellman Center for Photomedicine, Cambridge, MA, USA

Wellman Center for Photomedicine, Massachusetts General Hospital, Harvard Medical School, Boston, MA, USA

Harold T. Yura The Aerospace Corporation, Electronics and Photonics Laboratory, Los Angeles, CA, USA

Behrooz Zabihian Medical University of Vienna, Vienna, Austria

Robert J. Zawadzki Vision Science and Advanced Retinal Imaging Laboratory (VSRI) Department of Ophthalmology and Vision Science, University of California Davis, Sacramento, CA, USA

UC Davis RISE Eye–Pod Laboratory, Department of Cell Biology and Human Anatomy, University of California Davis, Davis, CA, USA

Edward Zhang Department Medical Physics and Bioengineering, Malet Place Engineering Building, University College London, London, UK

Jun Zhang Department of Biomedical Engineering, The Beckman Laser Institute, University of California Irvine, Irvine, CA, USA

Youbo Zhao Biophotonics Imaging Laboratory, Beckman Institute for Advanced Science and Technology, University of Illinois at Urbana-Champaign, Urbana, IL, USA

Chao Zhou Department of Electrical Engineering and Computer Science and Research Laboratory of Electronics, Massachusetts Institute of Technology, Cambridge, MA, USA

Department of Electrical and Computer Engineering, Lehigh University, Bethlehem, PA, USA

Part I

Introduction to OCT

Introduction to OCT

1

James G. Fujimoto and Wolfgang Drexler

Keywords

Optical coherence tomography • OCT • Optical biopsy • Fourier domain OCT • Spectral domain OCT • Swept source OCT • Optical frequency domain imaging • Ophthalmic imaging • Intravascular imaging • Endoscopic imaging • Catheter/endoscope • Technology translation

1.1 Introduction

Optical coherence tomography (OCT) has evolved to become a major optical imaging modality in biomedical optics and medicine. OCT performs high-resolution, cross-sectional, and three-dimensional volumetric imaging of the internal microstructure in biological tissues by measuring echoes of backscattered light [1]. Tissue pathology can be imaged in situ and in real time with resolutions of 1–15 μm, one to two orders of magnitude finer than conventional ultrasound. The unique features of OCT make it a powerful imaging modality with applications spanning many multiple clinical specialties as well as fundamental scientific and biological research.

OCT performs cross-sectional and volumetric imaging by measuring the magnitude and echo time delay of backscattered light. Cross-sectional images are generated by transversely scanning the incident optical beam and performing sequential axial measurements of echo time delay (axial scans or A-scans), as shown in Fig. 1.1.

J.G. Fujimoto (✉)
Department of Electrical Engineering and Computer Science and Research Laboratory of Electronics, Massachusetts Institute of Technology, Cambridge, MA, USA
e-mail: jgfuji@mit.edu

W. Drexler
Center for Medical Physics and Biomedical Engineering, Medical University of Vienna, General Hospital Vienna, Vienna, Austria
e-mail: wolfgang.drexler@meduniwien.ac.at

© Springer International Publishing Switzerland 2015

W. Drexler, J.G. Fujimoto (eds.), *Optical Coherence Tomography*,
DOI 10.1007/978-3-319-06419-2_1

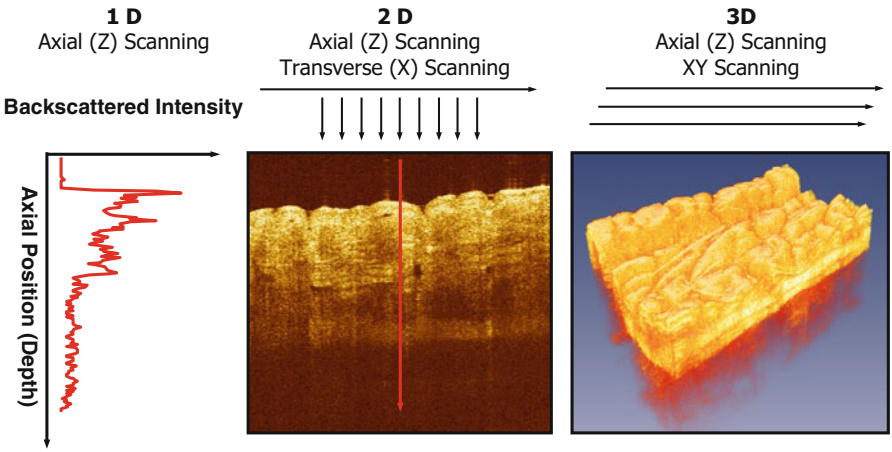

Fig. 1.1 Optical coherence tomography (OCT) generates cross-sectional or three-dimensional images by measuring the magnitude and echo time delay of light. Measurements of backreflection or backscattering versus depth known as axial scans (A-scans). Cross-sectional images are generated by scanning the OCT beam in a transverse direction to acquire a series of axial scans. This generates a two-dimensional data set (B-scan) which can be displayed as a gray scale or false color image. Three-dimensional volumetric data sets (3D-OCT) can be acquired by raster scanning to generate a series of two-dimensional data sets (B-scans)

This produces a two-dimensional data set which represents the optical backscattering in a cross-sectional plane through the tissue. Images, or B-scans, can be displayed in false color or gray scale in order to visualize internal tissue structure of pathology. Three-dimensional, volumetric data sets are generated by acquiring sequential cross-sectional images, scanning the incident optical beam in a raster or other two-dimensional pattern. Three-dimensional OCT (3D-OCT) data contains comprehensive volumetric structural information and can be displayed similar to MR or CT images.

OCT is a powerful medical imaging technology because it performs "optical biopsy," the real time, in situ visualization of tissue microstructure and pathology, without the need to remove and process specimens [2, 3]. Although histopathology is the gold standard for assessing pathology, it requires excision, fixation, embedding, microtoming, and staining of tissue specimens. OCT has applications in several general clinical situations: (1) Where standard excisional biopsy is hazardous or impossible. Applications include tissues such as the eye, arteries, or nervous tissues. (2) Where standard excisional biopsy has sampling error. Excisional biopsy and histopathology is used for diagnosis of many diseases including cancer; however, if the biopsy misses the lesion, this causes a false negative. OCT can guide excisional biopsy to reduce the number of biopsies required and to improve sensitivity by reducing sampling errors. If sufficient sensitivities and specificities can be achieved, OCT may be used to diagnose pathology in real time. Since imaging is performed in situ, OCT has the advantage that much larger regions of tissue can be assessed than by excisional biopsy. (3) For guidance of interventional procedures. In ophthalmology, OCT can visualize changes in retinal structure and markers of disease such

as neovascularization or edema to assess pharmaceutical treatment response. In cardiology and intravascular imaging, the ability to see cross-sectional and three-dimensional structure enables the guidance of procedures such as stent placement. The ability to see beneath the tissue surface enables guidance of ablative therapies such as laser or radio-frequency ablation, as well as surgical and microsurgical procedures. (4) For performing functional measurement and imaging. Doppler OCT enables quantitative measurement of blood flow. Complementary methods such as OCT angiography enable three-dimensional imaging of vascular structure using motion contrast from moving blood cells. Polarization-sensitive OCT enables measurement of birefringence, a marker for cellular and subcellular organization. Spectroscopic, displacement, vibrometry, and many other measurements are possible. Although the imaging depth of OCT is limited by attenuation from light scattering, OCT can be integrated with many medical devices such as catheters, endoscopes, laparoscopes, or needles, to access luminal organ systems such as the GI tract and airway as well as solid organs and masses.

OCT has become a standard of care in clinical ophthalmology and promises to have a powerful impact on many medical applications ranging from intravascular imaging to the assessment of neoplasia and guidance of minimally invasive surgical procedures. This chapter reviews the background and development of OCT.

1.2 OCT and Ultrasound

OCT has features which are common to both ultrasound and microscopy. In order to understand OCT imaging, it is helpful to compare it with these related medical imaging techniques. Figure 1.2 shows the resolution and imaging depth for several imaging modalities. The resolution of clinical ultrasound imaging is typically 0.1–1 mm and depends on the frequency of the sound wave (3–40 MHz) used for imaging [4–6]. Sound waves at standard ultrasound frequencies are transmitted with minimal absorption in biological tissue and it is possible to image structures deep in the body. High frequency ultrasound has been used for research and clinical applications such as intravascular imaging. Resolutions of 15–20 μm and finer have been achieved with frequencies of ~100 MHz. However, these high frequencies are strongly attenuated in biological tissues and imaging depths are limited to only a few millimeters.

Microscopy and confocal microscopy are examples of imaging techniques which have extremely high transverse image resolutions of 1 μm or finer. Imaging is typically performed in an en face plane and resolutions are determined by optical diffraction. The imaging depth in biological tissue is limited because image signal and contrast are significantly degraded by unwanted scattered light. In most biological tissues, imaging can be performed to depths of only a few hundred microns.

OCT fills a gap between ultrasound and microscopy. The axial image resolution in OCT is determined by the bandwidth of the light source. OCT technologies have axial resolutions ranging from 1 to 10 μm, approximately 10–100 times finer than standard ultrasound imaging. The high resolution of OCT imaging enables the visualization of tissue architectural morphology. OCT has become a clinical

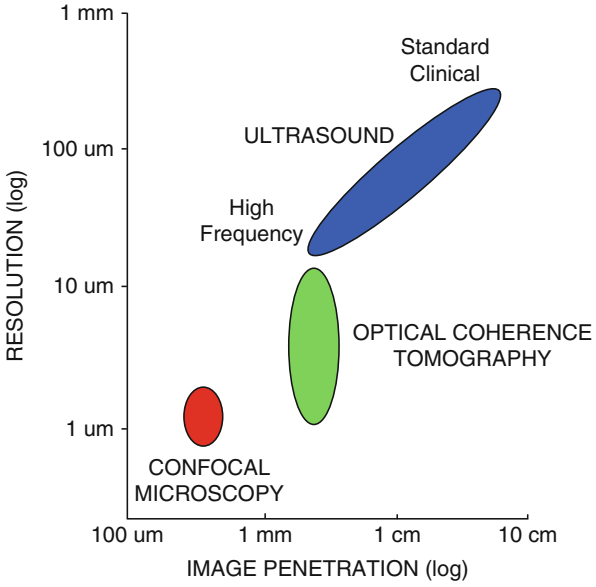

Fig. 1.2 Comparison of ultrasound, OCT, and confocal microscopy resolution and imaging depth. Standard clinical ultrasound achieves deep imaging depths, but has limited resolution. Higher sound frequencies yield finer resolution, but ultrasonic attenuation increases, reducing image penetration. OCT axial image resolution ranges from 1 to 15 μm, determined by the coherence length of the light source. In most biological tissues attenuation from optical scattering limits OCT imaging depth to 2–3 mm. Confocal microscopy has submicron resolution, but imaging depth is only a few hundred microns in most tissues

standard in ophthalmology, because the transparency of the eye provides easy optical access to the retina and noncontact high-resolution imaging is possible [7]. The major limitation of OCT is that light is highly scattered by most tissues and attenuation from scattering limits the imaging depths to ~2 mm in most tissues. However, because OCT uses fiber optics, it can be integrated with a wide range of medical instruments such as catheters, endoscopes, laparoscopes, or needles which enable imaging in luminal organ systems or even solid tissues inside the body.

OCT imaging is analogous to ultrasound imaging except that it uses light instead of sound. There are several different detection methods for performing OCT, but essentially imaging is performed by measuring the magnitude and echo time delay of backreflected or backscattered light from internal microstructures in materials or tissues. OCT images are two-dimensional or three-dimensional data sets which represent optical backreflection or backscattering in a cross-sectional plane or 3D volume. Ultrasound and OCT are analogous in that when a beam of sound or light is incident into tissue, it is backreflected or backscattered differently from structures which have varying acoustic or optical properties, as well as from boundaries between structures. The dimensions of these internal structures can be determined by measuring the "echo" time it takes for sound or light to travel different axial distances.

In ultrasound, the axial measurement of distance or depth is called A-mode scanning, while cross-sectional imaging is called B-mode scanning. Volumetric or 3D imaging can be performed by acquiring multiple B-mode images. The principal difference between ultrasound and optical imaging is that the speed of light is extremely high. The speed of sound is ~1,500 m/s, while the speed of light is approximately 3×10^8 m/s. In order to measure distances with a 100 μm resolution, a typical resolution for ultrasound imaging, a time resolution of ~100 ns is required. This resolution is well within the limits of electronic detection. Ultrasound technology has advanced significantly in recent years with the availability of high-performance, low-cost analog to digital converters and digital signal processing technology. Unlike sound, the detection of light echoes requires much higher time resolution. Light travels from the moon to the earth in only ~2 s. The measurement of distances with a 10 μm resolution, a typical resolution for OCT imaging, requires a time resolution of ~30 fs (30×10^{-15} s). A femtosecond is extremely fast; the ratio of 1 fs–1 s is equal to the ratio of 1 s to the time since the age of dinosaurs. Direct electronic detection is impossible with this time resolution and measurement methods such as high-speed optical gating, optical correlation, or interferometry must be used.

1.3 Measuring Optical Echoes

1.3.1 Photographing Light in Flight

Using optical echoes to see through biological tissue was proposed by Michel Duguay, more than 30 years ago, in 1971 [8, 9]. These pioneering studies demonstrated an ultrafast optical shutter based on the laser-induced Kerr effect which could "photograph light in flight." Figure 1.3 shows a schematic of the ultrahigh-speed Kerr shutter and an ultrashort light pulse propagating though a scattering solution of diluted milk [9]. The Kerr shutter operates by using an intense laser pulse to induce birefringence (the Kerr effect) in an optical medium placed between two crossed polarizers. If the induced birefringence is electronically mediated, it has an extremely rapid response time and the Kerr shutter can achieve picosecond or femtosecond time resolution.

Optical scattering limits the ability to image biological tissues, and Duguay proposed that an ultrahigh-speed shutter could remove unwanted scattered light and detect light echoes from inside tissue [9]. Ultrahigh-speed optical shutters might be used to "see through" tissues and noninvasively image internal pathology. The major limitation of the high-speed optical Kerr shutter is that it requires high intensity, short laser pulses to induce the Kerr effect and operate the shutter.

1.3.2 Femtosecond Time Domain Measurement

An alternate method for detected optical echoes is to use nonlinear optical processes such as harmonic generation, sum frequency generation, or parametric

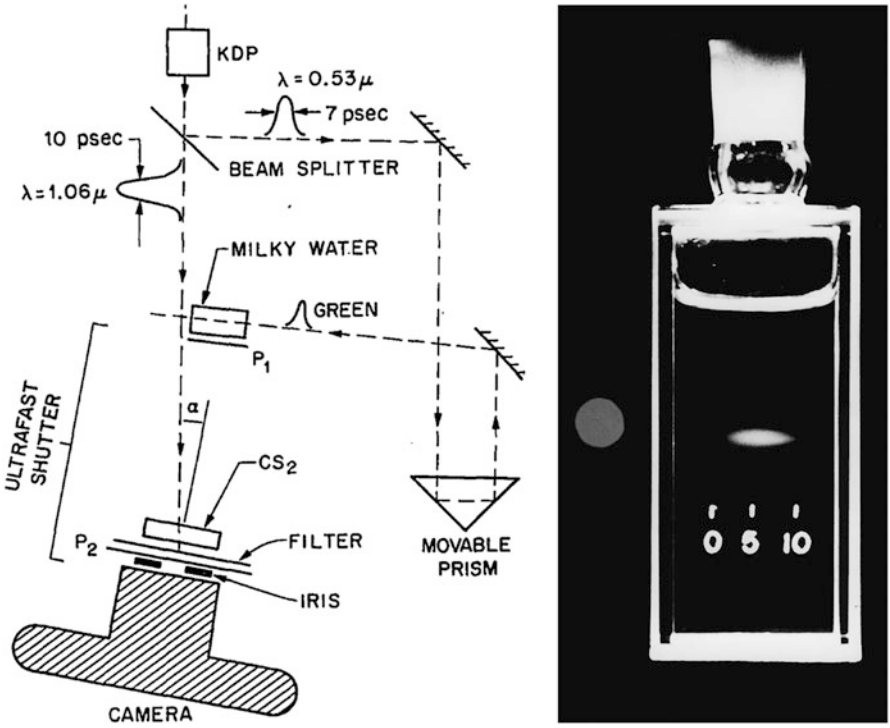

Fig. 1.3 Photographing light in flight. (*left*) A high-speed optical shutter is created using a CS2 cell placed between crossed polarizers. An intense laser pulse induces transient birefringence (the Kerr effect) and opens the shutter (*right*). Photograph of an ultrashort laser pulse propagating through a cell of milk and water. The shutter speed was 10 ps. These early studies suggested that high-speed optical gating could be used to see inside biological tissues by rejecting unwanted scattered light (Duguay and Mattick [9])

conversion [10–12]. Short pulses illuminate the tissue and the backscattered light is nonlinearly mixed with a reference pulse in a nonlinear optical material. The nonlinear process can measure the intensity and time delay of the optical signal with a time resolution determined by the pulse duration. Figure 1.4 shows a schematic of how transient light echoes are detected using nonlinear second harmonic generation cross correlation. The reference pulse is generated by the same laser source and is delayed by a variable time delay ΔT using a mechanical optical delay line. The nonlinear mixing process creates an ultrahigh-speed optical gate. If $I_S(t)$ is the signal that is being detected and $I_r(t)$ is the reference pulse used as the gate, the response function $S(\Delta T)$ is

$$S(\Delta T) \sim \int_{-\infty}^{\infty} I_s(t) I_r(t - \Delta T)\, dt$$

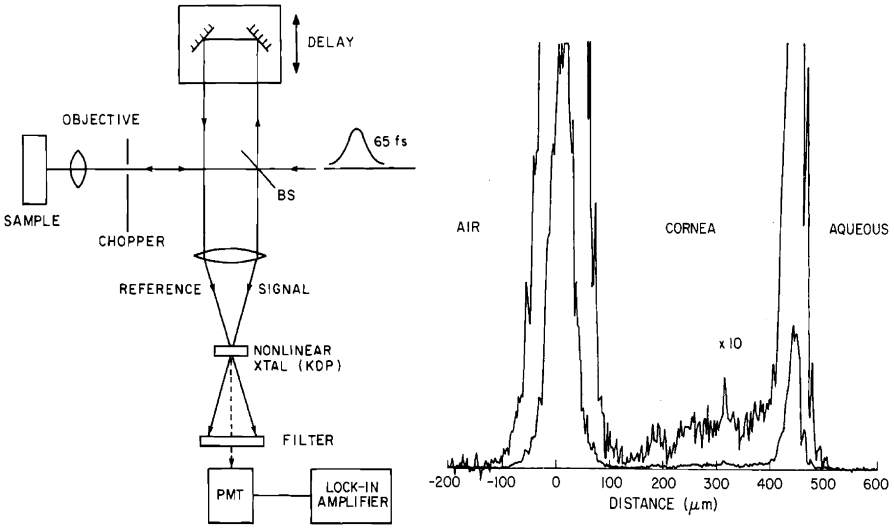

Fig. 1.4 Early demonstration of femtosecond optical ranging in biological systems. (*left*) Femtosecond echoes of backscattered light (signal) are detected using nonlinear second harmonic generation, mixing the signal with a delayed reference pulse. (*right*) Measurement of corneal thickness in an in vivo rabbit eye using femtosecond pulses, showing an axial scan of backscattering versus depth. An axial resolution of 15 μm (in air) was achieved using a femtosecond dye laser generating 65 fs pulses at 625 nm wavelength. The detection sensitivity was −70 dB or 10^{-7} (From Fujimoto et al. [12])

Figure 1.4 shows a measurement of corneal thickness in a rabbit eye in vivo. Very low scattering from the corneal stroma can be detected. The measurement had a 15 μm axial resolution and was performed using 65 femtosecond duration pulses from a femtosecond dye laser at 625 nm wavelength. Sensitivities of −70 dB or 10^{-7} of the incident intensity were achieved. However, these sensitivities were still not high enough to image most biological tissues. Current OCT systems achieve sensitivities 1,000× higher, approaching −100 dB or 10^{-10} of the incident intensity.

1.3.3 Low-Coherence Interferometry

Interferometry is a powerful technique for measuring the magnitude and echo time delay of backscattered light with very high sensitivity. OCT is based on a classic optical measurement technique known as low-coherence interferometry, or white light interferometry, first described by Sir Isaac Newton. Low-coherence interferometry was used in photonics to measure optical echoes and backscattering in optical fibers and waveguide devices in the 1980s [13–15]. The first biological application of low-coherence interferometry for the measurement of axial eye length was reported by Fercher et al. in 1988 [16]. Different versions of low-coherence interferometry were developed for noninvasive measurement in biological tissues [17–20].

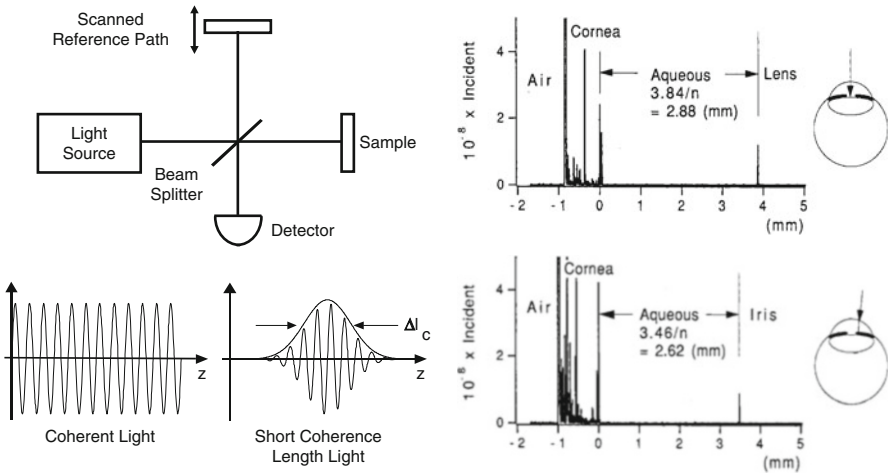

Fig. 1.5 Low-coherence interferometry. (*left*) Backreflected or backscattered light is interfered with light from a scanning reference path delay. Using low-coherence length light, interference only occurs when the path lengths are matched to within the coherence length. The interferometer output is detected as the reference path delay is scanned (time domain detection). The echo magnitude versus delay or axial scan is obtained by demodulating the interference signal. (*right*) Measurement of the anterior chamber in an ex vivo bovine eye. A 10 μm axial resolution was achieved using a low-coherence diode light source at ~800 nm. Interferometry enables high sensitivity detection of optical echoes and is the basis for optical coherence tomography (From Huang et al. [21])

Interferometry techniques perform correlation measurements by interfering light that is backscattered from the tissue with light that has traveled through a reference path with a known time delay. Also, interferometry measures the electric field of the light wave rather than its intensity. Figure 1.5 shows a schematic diagram of a classic Michelson interferometer. The incident light source is divided into a reference beam $E_r(t)$ and a measurement or signal beam $E_s(t)$ which travel different distances in the two interferometer arms. The electric field of the interferometer output is the sum of the signal and reference fields, $E_r(t) + E_s(t)$, and a detector measures the output intensity, which is proportional to the square of the total field:

$$I_o \sim |E_r|^2 + |E_s|^2 + 2 \cdot E_r \cdot E_s \cos(2 \cdot k \cdot \Delta L)$$

ΔL is the path length difference between the signal and reference arms of the interferometer. If the reference path length is scanned, interference fringes will be generated as a function of time. This process can also be understood by noting that the scanning reference arm produces a Doppler shift of the reference field. If a coherent (narrow linewidth) light source is used, interference will be observed over a wide range of path length differences. However, in order to detect optical echoes, a low-coherence (broad bandwidth) light source is required.

Low-coherence light can be characterized as having statistical phase discontinuities over a distance known as the coherence length, which is inversely proportional to the frequency bandwidth of the light. When low-coherence light is used, interference is only observed when the measurement and reference path lengths are matched to within the coherence length. The interferometer essentially measures the field autocorrelation of the light wave. The magnitude and echo time delay of light echoes can be measured by scanning the reference arm and demodulating, detecting the envelope of the interference signal. The coherence length of the light source determines the axial image resolution. Shorter coherence lengths from broadband light sources provide finer resolution.

Figure 1.5 shows an early ex vivo measurement of the anterior chamber of the bovine eye with a 10 μm axial resolution using an 800 nm wavelength, low-coherence diode light source with a bandwidth of 29 nm [21]. Sensitivities of −100 dB or 10^{-10} of the incident intensity were achieved. Scanning the beam in the transverse direction yielded information on different structures, such as the lens and iris. The axial measurements of backscatter versus depth using low-coherence interferometry provided the foundation for optical coherence tomography. Low-coherence interferometry has the advantage that can be performed with continuous wave light sources, without requiring short pulse lasers. Since interferometry measures the field rather than the intensity, it is equivalent to heterodyne detection in optical communication. Weak signals $E_s(t)$ are multiplied by a strong reference field $E_r(t)$ to produce heterodyne gain and very high, shot noise-limited sensitivities can be achieved. In addition, since the intensity is the square of the field, very high dynamic ranges are possible.

1.4 The Development of OCT

1.4.1 Early OCT Technology and Systems

Optical coherence tomography imaging was demonstrated in 1991 by Huang et al. [1]. Figures 1.6 and 1.7 show the first OCT images of the retina and human coronary artery ex vivo with corresponding histology [1]. These examples demonstrate OCT imaging in transparent as well as optically scattering tissues. Imaging was performed with 15 μm axial resolution in tissue at 830 nm wavelength. The image is displayed using a log false color scale with a signal level ranging between ∼ −60 and −90 dB of the incident intensity. The OCT image of the retina in Fig. 1.6 shows the contour of the optic nerve head as well as retinal vasculature near the nerve head. The retinal nerve fiber layer can also be visualized emanating from the optic nerve head. This image was ex vivo and postmortem retinal detachment is evident. The OCT image of the coronary artery in Fig. 1.7 shows fibrocalcific plaque on the right of the specimen and fibroatheromatous plaque on the left. The plaque scatters light and therefore attenuates the OCT beam, limiting the image penetration depth. Ophthalmic and intravascular imaging have emerged as two of the major applications of OCT which are now in clinical practice.

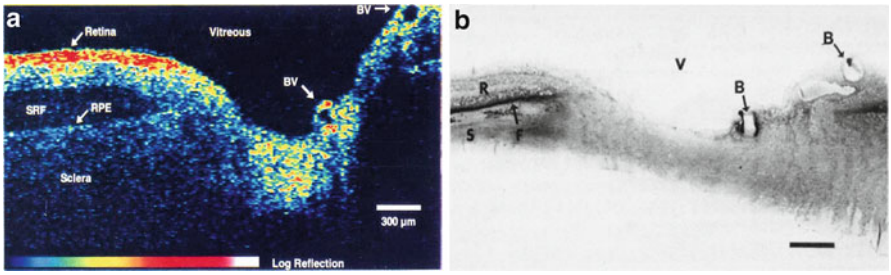

Fig. 1.6 OCT image of the human retina ex vivo and corresponding histology. Imaging was performed with 15 µm axial resolution in tissue at 830 nm wavelength. The OCT image is displayed using a log false color scale spanning –60 to –90 dB of the incident light intensity. The image shows the optic nerve head contour and vasculature. The retinal nerve fiber layer can be visualized and there is postmortem retinal detachment with subretinal fluid accumulation (From Huang et al. [1])

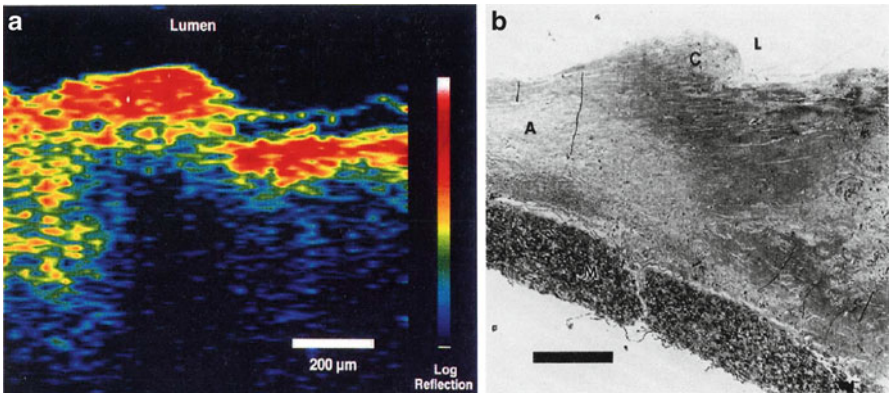

Fig. 1.7 OCT image of human artery ex vivo and corresponding histology. The OCT image shows fibrocalcific plaque (*right* three-quarters of specimen) and fibroatheromatous plaque (*left*). The fatty-calcified plaque scatters light and attenuates the OCT beam, limiting the image penetration depth (From Huang et al. [1])

Optical coherence tomography has the advantage that it can be implemented using fiber-optic components and integrated with a wide range of medical instruments. OCT systems can be divided into an imaging engine (consisting of an interferometer, light source, and detector) and imaging devices or probes. Early OCT imaging engines employed time domain detection with an interferometer using a low-coherence light source and scanning reference arm delay. Figure 1.8 shows an example of an OCT system using a fiber-optic Michelson-type interferometer with time domain detection. A low-coherence light source is coupled into the interferometer. One arm of the interferometer emits a beam which is directed and scanned on the sample being imaged, while the other arm is a reference with

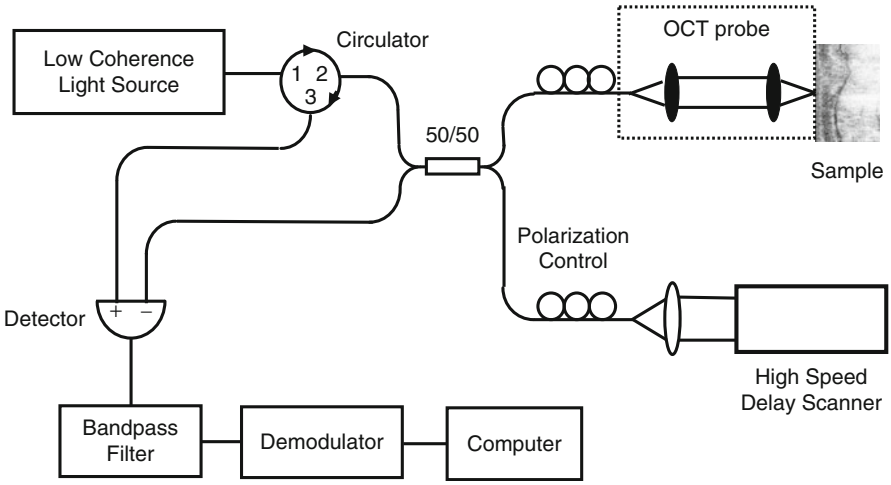

Fig. 1.8 OCT imaging system based on a fiber-optic Michelson interferometer. OCT has the advantage that it uses photonics and fiber optics technology. This schematic shows a Michelson interferometer with a circulator for dual balanced detection. Dual balanced detection adds the signal from the interference of the sample and reference arms and subtracts excess noise from the light source. The sample/probe arm may be interfaced to a variety of imaging devices. OCT interferometers can be built in many different configurations depending on design requirements

a scanning delay. The interferometer shown in Fig. 1.8 uses a circulator to collect the interference signal which returns to the light source to improve efficiency. This interference signal is out of phase with the other interferometer output. When these two signals are subtracted, the desired interference signal adds and excess noise from the light source is cancelled. This configuration is known as dual balanced detection and is used in coherent optical communications systems [22]. There are many different embodiments of the interferometer and imaging engine which have different power delivery and detection efficiency advantages [23]. ▶ Chapter 11, "Optical Design for OCT," discusses aspects of OCT system design in more detail.

Because the eye is optically accessible and optical imaging methods are widely used in ophthalmology, many of the earliest OCT studies were in the eye. The first in vivo retinal images were obtained independently in 1993 by Fercher et al. [24] and Swanson et al. [25]. Figure 1.9 shows an early in vivo OCT image of the normal human retina from Hee et al. in 1995 [26]. Imaging was performed at 800 nm wavelength with ~10 μm axial resolution in tissue. The nerve fiber layer as well as other architectural features can be visualized with higher resolution than was previously possible. Several thousand patients were imaged at the New England Eye Center in the mid-1990s. These early clinical studies investigated OCT for the diagnosis and monitoring of a variety of macular diseases [27], including macular edema [28, 29], macular holes [30], central serous chorioretinopathy [31], and age-related macular degeneration and choroidal

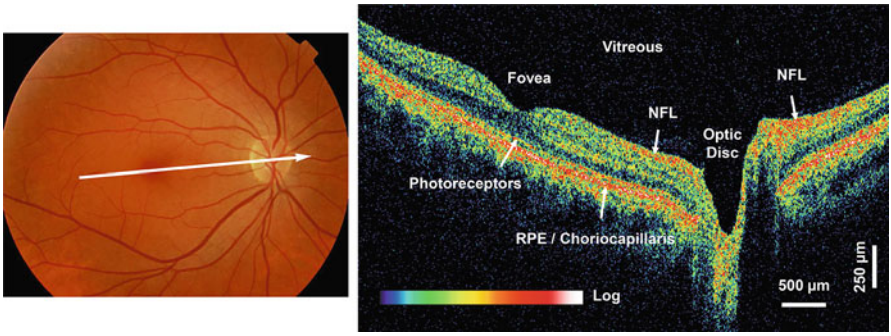

Fig. 1.9 Early in vivo OCT image of the normal retina in a human subject. Imaging was 10 µm axial resolution at 800 nm wavelength. The retinal pigment epithelium, choroid, and retinal nerve fiber layers are visible as highly backscattering layers. OCT can noninvasively visualize and quantitatively measure retinal pathology and is now a standard of care in clinical ophthalmology (From Hee et al. [26])

neovascularization [32]. The retinal nerve fiber layer thickness, an indicator of glaucoma, can be quantified in normal and glaucomatous eyes and correlated with conventional measurements of the optic nerve structure and function [33,34]. Many of the measurement protocols that were developed in these early studies were adopted in current OCT ophthalmic instruments [7].

The high detection sensitivity of OCT enables imaging structures such as the retina which have very low optical scattering. Typical retinal images have signal levels of −50 to −90 dB of the incident intensity. For retinal imaging, safety standards govern the maximum permissible light exposure and set limits for OCT imaging speeds [25, 26]. However, the majority of OCT applications require imaging in tissues which are not transparent, but instead are highly scattering. In this case, detection sensitivity is also important because light is highly attenuated by scattering and the sensitivity determines the imaging depth.

OCT imaging in tissues other than the eye became feasible with the recognition that using longer optical wavelengths can reduce scattering and increase image penetration depths [3, 35, 36]. Figure 1.10 shows an early example from Brezinski et al. 1996 showing OCT imaging in a human epiglottis ex vivo, comparing imaging at 850 nm and 1,300 nm wavelengths [3]. The dominant absorbers in most tissues are melanin and hemoglobin, which have absorption at visible and near-infrared wavelengths [37]. Water absorption becomes dominant for longer wavelengths, approaching 1,900–2,000 nm. In most tissues, scattering at near-infrared wavelengths is one to two orders of magnitude higher than absorption, and scattering decreases for longer wavelengths. Therefore, imaging at 1,300 nm improved image penetration and has become a standard wavelength for most non-ophthalmic OCT applications.

Early studies investigated the mechanisms of OCT image contrast as they are related to tissue optical properties [35, 38]. ▶ Chapter 3, “Modeling Light–Tissue Interaction in Optical Coherence Tomography Systems” considers these

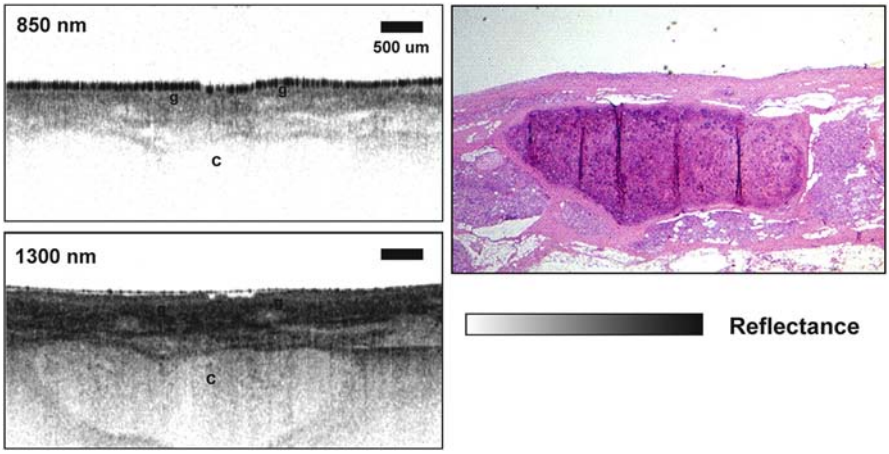

Fig. 1.10 OCT imaging penetration depth. OCT in scattering tissues was made possible using longer wavelengths which are less attenuated by scattering. OCT images of human epiglottis ex vivo performed with 850 nm and 1,300 nm wavelengths. Superficial glandular structures (*g*) can be seen in images with 850 nm and 1,300 nm wavelengths, but the underlying cartilage (*c*) is better visualized with longer 1,300 nm wavelength. With a detection sensitivity of ~90–100 dB, image penetration depths of up to 2–3 mm are possible in most scattering tissues (From Brezinski et al. [3])

mechanisms in detail. In OCT images, tissue structures are visible because they have different optical scattering properties. OCT images show true tissue dimensions (correcting for index of refraction and beam refraction effects); however, if OCT is displayed using a false color image, the colors represent different optical properties and not necessarily different tissue morphologies. In histology, histological sections are stained in order to produce selective contrast between different tissue structures. There are multiple stains available for histology which are highly specific. OCT relies on intrinsic differences in optical properties of different tissues in order to produce image contrast. On one hand this is a limitation because tissue structures, for example, nuclei of cells, may not have contrast in OCT imaging. However, histology is a time-consuming process which requires tissue excision, processing, embedding, sectioning, and staining, while OCT imaging can be performed on tissue in situ and in real time, without the need for excision and processing.

Several early OCT imaging studies were performed using ex vivo surgical specimens [3, 39–50]. These studies helped to define which structural features were visible using OCT and to establish a baseline for comparison to histology. Figure 1.11 shows an example of one of the first OCT images of arterial plaque ex vivo and corresponding histology from Brezinski et al. 1996 [3]. The OCT image has an axial resolution of ~15 μm in tissue and imaging was performed at 1,300 nm wavelength. The figure shows an unstable plaque characterized by a thin intimal cap layer, adjacent to a heavily calcified plaque with low lipid content.

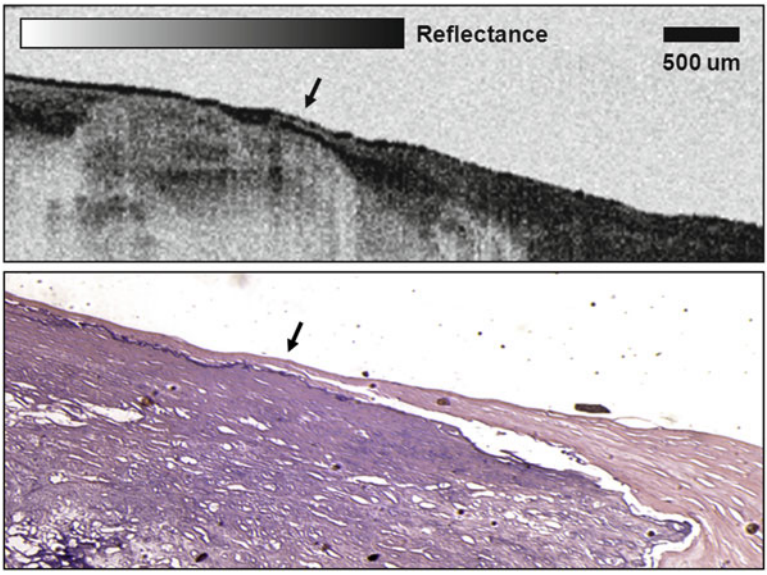

Fig. 1.11 Early OCT image of atherosclerotic plaque ex vivo and corresponding histology. The plaque is highly calcified with relatively low lipid content and a thin intimal cap. This result demonstrated that OCT can resolve morphological features associated with unstable plaques (From Brezinski et al. [3])

The demonstration that OCT could resolve unstable plaque in ex vivo specimens was an important milestone which helped lead to the later clinical development of intravascular OCT imaging.

Another active area of OCT research is the detection of neoplastic changes. Early studies were performed ex vivo to correlate OCT images with histology for gastrointestinal [40, 41, 44, 50], biliary [45], female reproductive [47, 49], pulmonary [46], and urinary [42, 48] pathologies. Figure 1.12 shows an example from an early OCT imaging study of gastrointestinal neoplasia. The figure shows OCT images and corresponding histology of normal colon and adenocarcinoma ex vivo. Imaging was performed with an axial resolution of ~15 μm in tissue at 1,300 nm wavelength. The OCT image of normal colon shows normal glandular organization associated with columnar epithelial structure. The mucosa and muscularis mucosa can be differentiated by the different backscattering characteristics within each layer. Architectural morphology, such as crypts or glands within the mucosa, can be visualized. The OCT image of adenocarcinoma shows disruption of architectural morphology or glandular organization. However, assessing cancer pathology is an extremely challenging application. OCT has significant limitations in both tissue contrast and resolution compared with the gold standard of excisional biopsy and histopathology. These challenges have been a factor in the slower development of OCT for cancer applications.

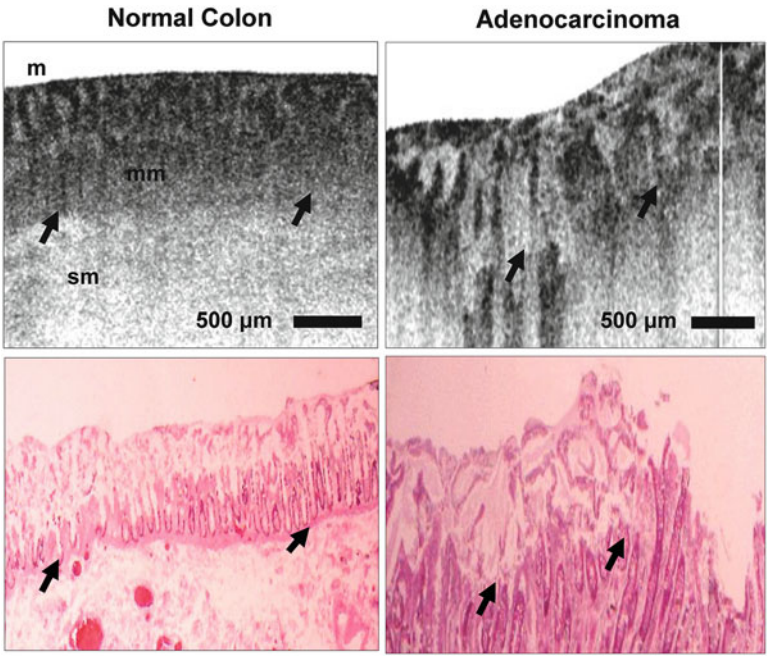

Fig. 1.12 OCT imaging of neoplastic changes. Early ex vivo OCT image of normal colon (*left*) and adenocarcinoma (*right*) with corresponding histology. The mucosal (*m*), muscularis mucosa (*mm*), and submucosal (*sm*) layers of the normal colon are visible. Dilated and disorganized crypts (*c*) are visible in the specimen with adenocarcinoma. OCT can visualize changes in architectural morphology (Pitris et al. [50])

1.4.2 Ophthalmic OCT Imaging

The earliest clinical studies with OCT were performed in ophthalmology, and to date OCT has had the largest clinical impact in this specialty. OCT is a powerful technique in ophthalmology because it can identify markers of early disease at treatable time points before visual symptoms and irreversible vision loss occurs. Furthermore, repeated imaging can be performed to track disease progression or monitor the response to therapy. The development of a prototype clinical instrument was a key step to enabling early studies in ophthalmology. Figure 1.13 shows a photograph of an early prototype instrument for OCT retinal imaging that was designed and built by Eric Swanson at MIT Lincoln Laboratories in the mid-1990s. The instrument was based on a slit lamp biomicroscope and provided a simultaneous view of the retinal fundus for aiming and registering the OCT imaging beam. This instrument was used in the New England Eye Center to perform the first clinical studies of OCT in ophthalmology [25–27, 51]. Several thousand patients were imaged in cross-sectional as well as longitudinal studies during the mid-1990s.

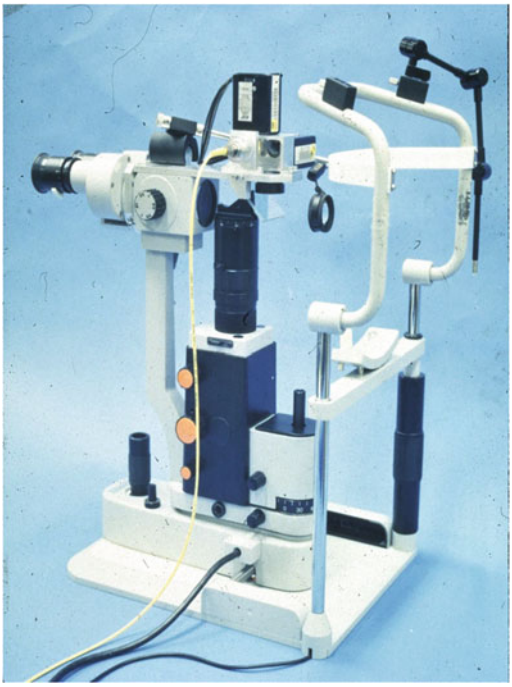

Fig. 1.13 Photograph of an early retinal imaging prototype instrument. The OCT system is interfaced with a slit lamp biomicroscope. The OCT beam is scanned using a pair of galvanometer-actuated mirrors. This system was used at the New England Eye Center and imaged several thousand patients during the mid-1990s (Courtesy of Eric Swanson)

Figure 1.14 shows a schematic diagram of the optical design for retinal imaging. Similar design principles were used for OCT using low numerical aperture microscopes imaging developmental biology specimens in vivo as well as for surgical imaging applications [39, 52, 53]. An objective lens relays an image of the retina onto an intermediate image plane where it can be viewed by the operator or a video camera. The OCT beam is coupled into the instrument using a beam splitter and focused onto the intermediate image plane using a relay lens and then imaged onto the retina by the objective lens and the subject's eye. The transverse spot size of the OCT beam on the retina is typically ~20 μm and is limited by ocular aberrations. The transverse position of the OCT beam is scanned by two perpendicular x-y galvanometer scanning mirrors. The optical system is designed so that the beam pivots about the pupil of the eye when it is scanned. This prevents the OCT beam from being vignetted by the pupil and enables a wide field of view on the retina. OCT imaging can be performed at different locations on the retina by controlling the scanning of the OCT beam. When the OCT beam is scanned, it is visible on the retina that is visible to the operator, enabling aiming. The OCT beam is also visible to the patient as a small spot or scanned line, whose position in the patient's visual field corresponds to the points on the retina that are being scanned. Since the scanning trajectory of the OCT beam on the retina can be controlled, different scan patterns can be designed and adopted as part of the diagnostic protocol for specific retinal diseases.

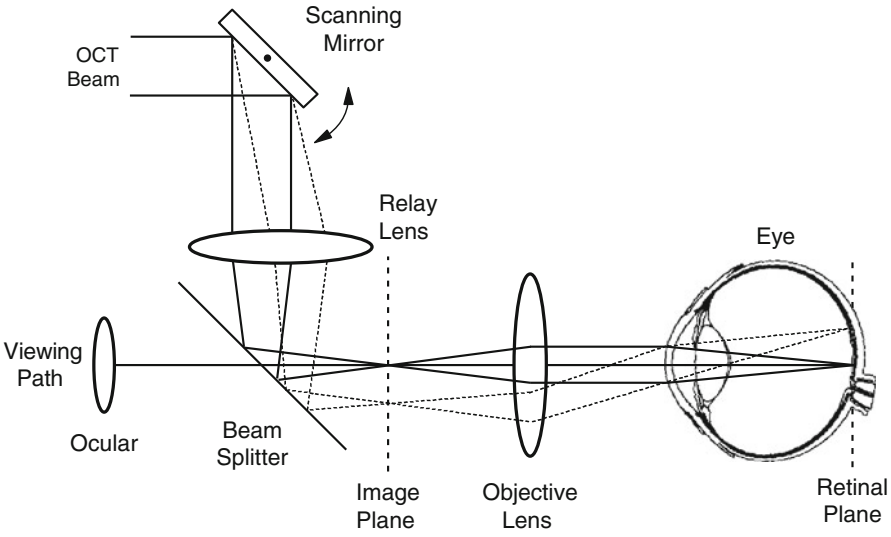

Fig. 1.14 Schematic of OCT instrument design for retinal imaging. An objective lens relay images the retina to a plane in the OCT instrument. Operator viewing of the fundus is performed by imaging with a video camera. Computer-controlled galvanometer scanning mirrors positions and scan the OCT beam. A relay lens focuses the OCT beam onto the image plane, and the objective lens directs the OCT beam through the pupil onto the retina. The OCT beam is focused on the retina by adjusting the objective lens. The OCT beam pivots about the pupil of the eye in order to minimize vignetting

OCT is important for the diagnosis and monitoring of diseases such as glaucoma, age-related macular degeneration, and diabetic retinopathy because it provides quantitative information on retinal pathology which is a measure of disease progression or response to therapy [29, 33, 54]. Images can be analyzed quantitatively and processed using intelligent algorithms to extract features such as retinal or retinal nerve fiber layer thickness. Mapping and display techniques have been developed to display OCT data in alternate forms, such as thickness maps, in order to aid interpretation. Figure 1.15 shows an early example of an OCT topographic map of retinal thickness [29]. The thickness map was constructed by performing six standard OCT scans at varying angular orientations through the fovea. The OCT images are segmented to detect the retinal thickness which is then linearly interpolated over the macular region and represented as a false color topographic map. For quantitative interpretation, the macula is divided into different regions and averaged values of retinal thickness are displayed. The ability to reduce image information to numerical information is important because it enables the development of normative databases and the use of statistical criteria for disease diagnosis.

OCT technology was transferred to industry by our group at MIT and introduced commercially for ophthalmic diagnostics in 1996 (Carl Zeiss Meditec). Early instruments had an axial resolution of 10 um and an imaging speed of 100 A-scans/s.

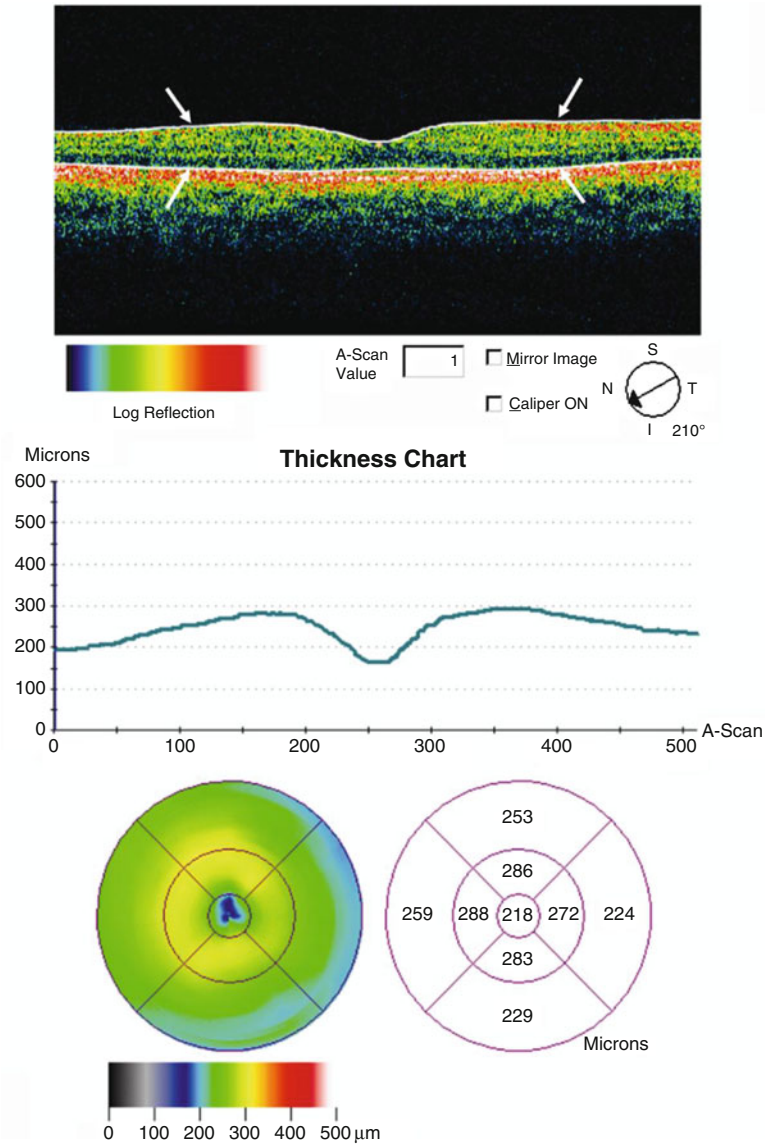

Fig. 1.15 OCT topographic map of retinal thickness. (*Top*) OCT image of the macula which has been segmented in order to measure retinal thickness. The anterior and posterior retinal surfaces are automatically identified. (*Middle*) Quantitative measurement of retinal thickness based on the segmented OCT image. (*Bottom*) Topographic map of macular retinal thickness. The topographic map is constructed by segmenting multiple OCT scans which are radially oriented in the macula, measuring the retinal thickness, and interpolating the retinal thickness in the regions between the scans. Retinal thickness is represented by a color table and has the advantage that it can be directly compared with the retinal fundus image

A third generation ophthalmic instrument, the Stratus OCT, was introduced in 2002 which had similar resolution, but faster speed of 400 A-scans/s. The increased speed enabled an increase in image pixel density. The large amount of published clinical data from previous generation instruments, coupled with technological improvements and reimbursement, helped the clinical adoption of OCT. By the mid-2000s, OCT became a standard of care in ophthalmology and is considered essential for the diagnosis and monitoring of many retinal diseases [7]. With increases in imaging speed provided by spectral/Fourier domain detection, many companies entered the ophthalmic marketplace in the mid-2000s.

1.4.3 Catheter and Endoscopic OCT Imaging Technology

Flexible imaging probes such as catheters and endoscopes were key to enabling internal body OCT imaging [55, 56]. Figure 1.16 shows one of the first OCT catheter/endoscopes devices. This device was a prototype for modern OCT intravascular imaging catheters and endoscopic probes. The catheter/endoscope has a single-mode optical fiber in a hollow rotating torque cable, coupled to a distal lens and microprism that reflects the OCT beam radially. The torque cable and distal optics are contained in a transparent housing. The OCT beam is scanned by rotating the torque cable to generate a transverse image in luminal structures or hollow organs. Imaging may also be performed in a longitudinal plane by push-pull movement or a spiral rotation and pullback of the torque cable assembly [57]. The early catheter/endoscope shown in Fig. 1.16 had a diameter of 2.9 French or 1 mm, similar to a standard IVUS catheter. The development of catheter imaging devices is challenging because of the simultaneous mechanical, optical, and biocompatibility requirements. Early commercial devices (such as the LightLab

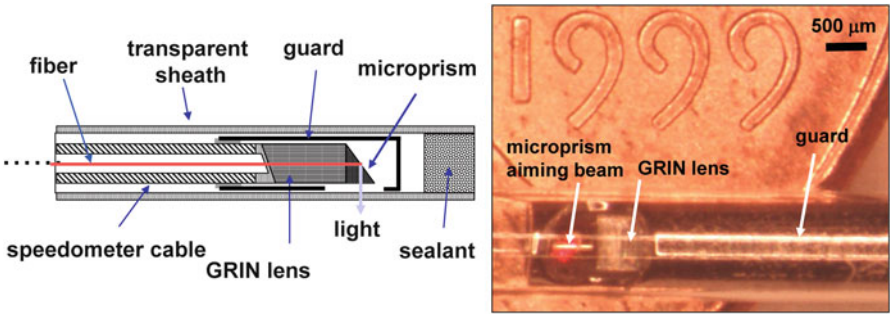

Fig. 1.16 Catheter/endoscopic OCT imaging. Schematic and photograph of an early OCT catheter/endoscope for intraluminal imaging. A single-mode fiber is contained in a rotating flexible speedometer cable which is enclosed in a protective plastic sheath. The distal end has a lens and prism/mirror which focuses the beam at 90° from the catheter axis. The diameter of the catheter is 2.9 French or ~1 mm. The catheter is shown on a United States coin for scale. OCT can be integrated with a wide range of diagnostic and interventional devices

Imaging ImageWire™ and Helios™ occlusion balloon catheters) used micro-optic fabrication methods to create lenses and beam-directing elements which have diameters of optical fibers (80–250 μm), significantly smaller than can be achieved with IVUS catheters.

1.4.4 Intravascular OCT Imaging

Intravascular imaging is the second most developed clinical OCT application. Figure 1.17 shows the first catheter-based image of a human coronary artery ex vivo using an early prototype 2.9 F OCT catheter, from Tearney et al. in 1996 [58]. The figure shows a comparison of OCT with 30 MHz intravascular ultrasound (IVUS). The OCT image shows excellent differentiation of the intima, media, and adventitia and suggested the utility of intravascular OCT. In vivo intravascular OCT imaging was challenging because of the need to develop suitable catheter imaging devices which could be used in animals and human subjects. In addition, since blood is highly optically scattering, it was necessary to develop saline/contrast flushing or balloon occlusion protocols to remove blood or to significantly dilute the hematocrit in the imaging field. Intravascular OCT animal imaging studies were performed in a rabbit model by Fujimoto et al. in 1999 [59]. Imaging was performed using a 2.9 F optical catheter using a time domain OCT system with a broadband femtosecond laser at 1,280 nm wavelength to achieve 10 um axial resolution. Imaging speeds were 4 frames/s with a 512 axial pixel images. Because blood is highly optically scattering at normal hematocrit, saline flushing was required to dilute the hematocrit during imaging. Intravascular animal imaging studies were performed in a porcine model using saline flushing by Tearney et al. in 2000 [60].

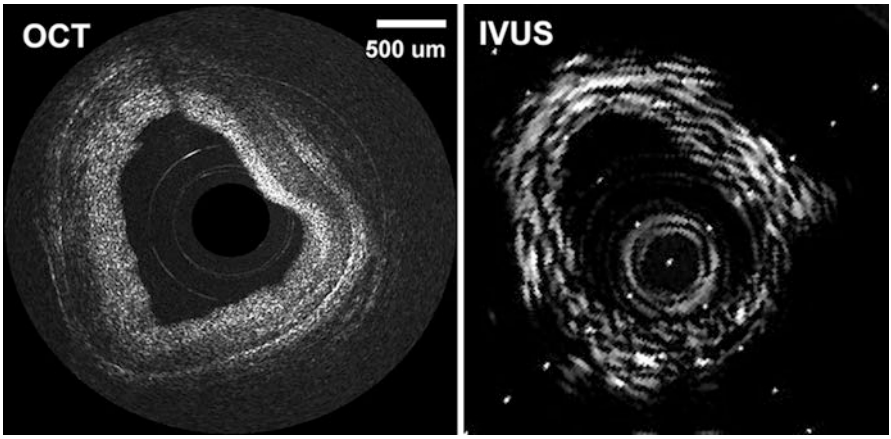

Fig. 1.17 Early OCT image of a human artery ex vivo and comparison with intravascular ultrasound (*IVUS*). The OCT image has 15 μm axial resolution and enables the differentiation of the intima, media, and adventitia. Intimal hyperplasia is evident. IVUS has deeper image penetration, but lower resolution (From Tearney et al. [58])

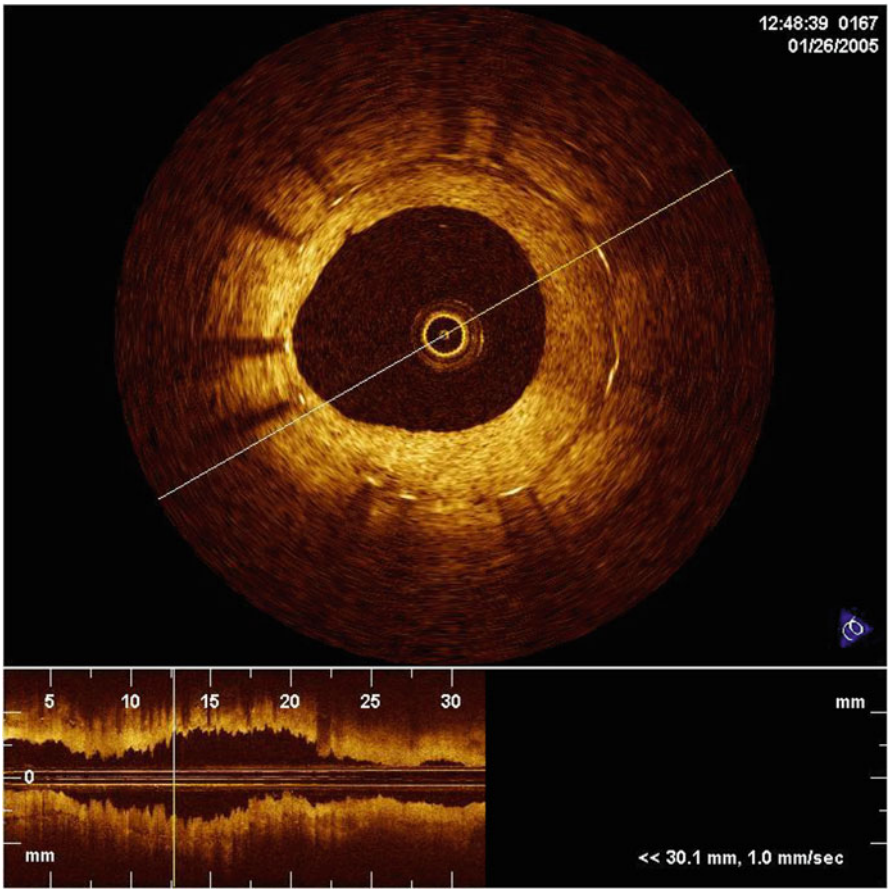

Fig. 1.18 Intravascular OCT. Early OCT image and pullback of a stent with neointimal growth in a human artery in vivo. Saline flushing was used to remove blood from the imaging field. Imaging was performed with the LightLab M2 and an occlusion balloon catheter. Modern intravascular OCT instruments use contrast flushing without occlusion (Courtesy of LightLab Imaging)

This study reported OCT imaging of normal coronary arteries, intimal dissections, and stents with 10 μm resolution.

OCT imaging in human patients was first reported by Jang et al. in 2001 [61]. This pioneering study used a 3.2 F OCT imaging catheter and demonstrated imaging of tissue prolapse in a stent, comparing OCT with IVUS. The study was a significant landmark because it addressed multiple technological, clinical, and administrative challenges. Independent clinical demonstrations by Grube et al. at the Siegburg Heart Center were reported in 2002 using a prototype instrument developed by LightLab Imaging [62]. Other early studies compared OCT with IVUS for visualization of stent placement and apposition [63, 64]. Figure 1.18 shows an early example of intravascular OCT imaging of a partially restenosed

stent with a corresponding L-mode pullback image (courtesy of Osaka City University Hospital and LightLab Imaging). This image was acquired using an occlusion balloon catheter and shows neointimal growth over a stent. Modern intravascular OCT instruments use flushing with contrast agents to dilute hematocrit combined with high-speed imaging.

Intravascular OCT imaging is currently an active area of both research and commercialization. The commercial development of intravascular OCT was performed by an MIT startup in 1998. The first commercial intravascular OCT instrument generated images with 200 A-scans at 15 frames/s and was introduced in Europe in 2004. A higher performance system with 240 A-scan per frame at 20 frames/s was introduced in 2007. A system based on swept source/Fourier domain detection achieved 500 A-scans per frame at 100 frames per second, and FDA approval was obtained in 2010. ▶ Chapters 69, "Imaging Coronary Atherosclerosis and Vulnerable Plaques with Optical Coherence Tomography" and ▶ 70, "Cardiovascular Optical Coherence Tomography" describe intravascular OCT in more detail. ▶ Chapter 71, "Intravascular OCT" discusses the process of commercialization of OCT from the perspective of intravascular imaging.

1.4.5 Endoscopic OCT and Cancer Detection

The first demonstrations of in vivo endoscopic OCT imaging were performed in 1997 [56, 65]. Figure 1.19 shows an example of OCT imaging of the rabbit esophagus in vivo and corresponding histology, from Tearney et al. [56]. This image demonstrates visualization of the esophageal layers including the mucosa (m), the submucosa (sm), the inner muscularis (im), outer muscularis (om), and serosa (s). The first clinical studies of endoscopic OCT imaging in human subjects were reported by Sergeev et al. in 1997 [65] and Feldchtein et al. in 1998 [66].

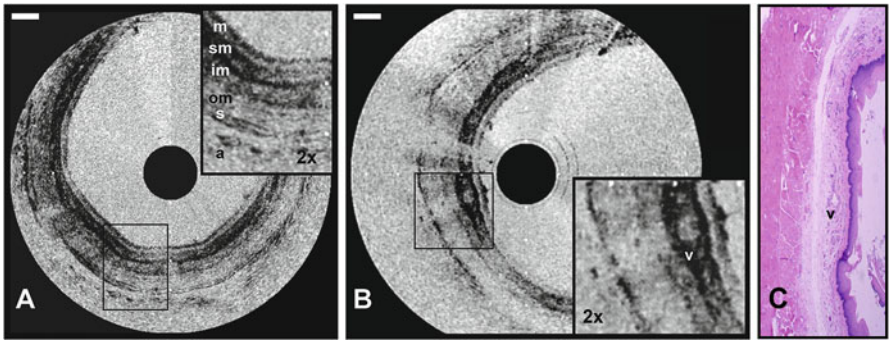

Fig. 1.19 Endoscopic OCT image of the rabbit esophagus in vivo demonstrating internal body imaging. (**a**) Esophageal layers including the mucosa (*m*), submucosa (*sm*), inner muscular layer (*im*), outer muscular layer (*om*), serosa (*s*), and adipose and vascular supporting tissues (*a*) can be visualized. (**b**) A blood vessel (*v*) can be seen within the submucosa. (**c**) Corresponding histology. Scale 500 um (Tearney et al. [56])

OCT imaging was performed with a flexible forward scanning probe in the working channel of a standard endoscope, bronchoscope, or trocar. The imaging device was a 1.5–2 mm diameter probe which used a miniature magnetic scanner to image in the forward direction. These early studies demonstrated the feasibility of performing clinical OCT imaging of organ systems such as the esophagus, larynx, stomach, urinary bladder, and uterine cervix.

Gastrointestinal (GI) endoscopy received considerable attention due to the prevalence of esophageal, stomach, and colon cancers. In contrast to conventional endoscopy that visualizes surface features, OCT can image subsurface tissue morphology. Early studies of endoscopic OCT imaging suggested the ability of OCT to differentiate GI pathologies such as the Barrett's esophagus, adenomatous polyps, and adenocarcinoma [57, 65, 67–73]. However, the development of OCT imaging for cancer detection remains extremely challenging. Conventional histopathology is an extremely powerful diagnostic technique because it enables the use of selective stains to enhance contrast between different cellular or tissue structures. Histology also provides extremely fine image resolutions, enabling the visualization of not only larger scale tissue architectural morphology but also subcellular structure. OCT imaging relies on intrinsic contrast produced by variations in scattering properties of different tissue structures. On the positive side, OCT enables real time imaging of tissue pathology in situ, without the need for excision and processing as in conventional biopsy and histopathology. When used to guide biopsy, it is not necessary for OCT to perform at the level required for diagnosis, but it must have sufficient sensitivity to detect pathology and improve the sensitivity of excisional biopsy by reducing sampling errors.

The development of OCT for cancer detection will require detailed clinical studies which investigate its ability to identify relevant pathologies. These types of studies are challenging because the sensitivity and specificity of OCT imaging must be evaluated relative to biopsy and histopathology which is the gold standard for diagnosis. Since pathology varies depending upon location, precise registration of OCT imaging and excisional biopsy is required. This is an especially challenging problem in endoscopic applications. Sufficient numbers of patients having a given pathology must be investigated in order to ensure that the sample size is large enough to generate statistically significant results. Because many types of dysplasia or cancer have a low incidence, patient enrollments may be large. For these reasons, the investigation and development of OCT for cancer diagnosis remains a challenging and ongoing area of research. Part 2 of this book, Optical Coherence Tomography Applications, includes several chapters which survey a broad range of OCT applications, including the detection of early neoplastic changes in different organ systems.

In addition to catheters and endoscopes, many other early OCT imaging instruments were developed including forward imaging devices that perform one- or two-dimensional beam scanning. Rigid laparoscopes use relay imaging with Hopkins-type relay lenses or graded index rod lenses. OCT can be integrated with laparoscopes to permit internal body OCT imaging with a simultaneous en face view of the region being imaged [65, 74, 75]. Handheld imaging probes have

also been demonstrated [75, 76]. These devices resemble pens and use piezoelectric or galvanometric beam scanning. Handheld probes can be used in open field surgical situations to enable the clinician to view subsurface tissue structure by aiming the probe at the desired location. These devices can also be integrated with conventional scalpels or laser surgical devices to permit simultaneous, real time viewing as tissue is being resected. There has been considerable interest in the use of MEMS scanning devices for OCT imaging probes. MEMS devices enable one- or two-dimensional beam scanning and are a promising technology for developing miniature OCT imaging devices [77–80].

1.5 Advances in Image Resolution

1.5.1 Axial Resolution and Depth of Field

Image resolution is one of the most important parameters governing OCT image quality and developing methods to achieve ultrahigh resolution was a major focus of early research. In contrast to standard microscopy, OCT can achieve fine axial resolution independent of the beam focusing and spot size. The axial image resolution in OCT is determined by the measurement resolution for echo time delays of light. In low-coherence interferometry, the axial resolution is given by the width of the field autocorrelation function, which is inversely proportional to the bandwidth of the light source. For a Gaussian-shaped spectrum, the axial resolution is

$$\Delta z = \frac{2\ln 2}{\pi} \cdot \frac{\lambda^2}{\Delta\lambda}$$

where Δz is the full-width-at-half-maximum of the autocorrelation function, $\Delta\lambda$ is the full-width-at-half-maximum of the power spectrum, and λ is the center wavelength of the light source [81]. Figure 1.20 shows a plot of axial resolution versus bandwidth for light sources with different wavelengths. Since axial resolution is inversely proportional to the bandwidth of the light source, broad bandwidth light sources are required to achieve high axial resolution.

The transverse resolution in OCT imaging is the same as in optical microscopy and is determined by the diffraction limited spot size of the focused optical beam. The diffraction limited minimum spot size is proportional to wavelength and inversely proportional to the numerical aperture or the focusing angle of the beam. The transverse resolution is

$$\Delta x = \frac{4\lambda}{\pi} \cdot \frac{f}{d}$$

where λ is the wavelength, d is the size of the incident beam on the objective lens, and f is the focal length. Fine transverse resolution can be obtained by using a large numerical aperture that focuses the beam to a small spot size. At the same time,

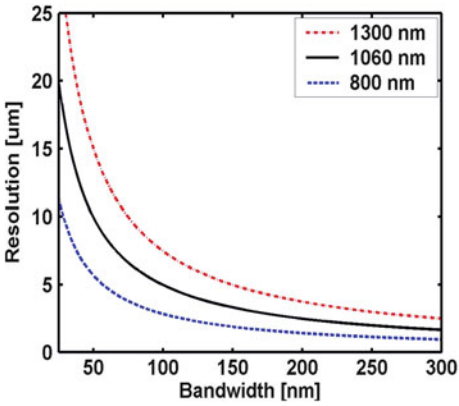

Fig. 1.20 Axial image resolution in OCT. Axial resolution versus light source bandwidths for center wavelengths of 800 nm, 1,000 nm, and 1,300 nm. Micron scale axial resolution requires extremely broad optical bandwidths and bandwidth requirements increase dramatically for longer wavelengths

because of diffraction, the transverse resolution also governs the depth of field or confocal parameter b, which is $2z_R$ or two times the Rayleigh range:

$$b = 2z_R = \frac{\pi \Delta x^2}{\lambda}$$

Thus, there is a trade-off between transverse resolution and depth of field; increasing the transverse resolution decreases the depth of field.

Figure 1.21 shows the relationship between focused spot size and depth of field for low and high numerical aperture focusing. Typically, OCT imaging is performed with low numerical aperture focusing in order to have a large depth of field. The confocal parameter is larger than the coherence length, $b > \Delta z$, and the axial resolution is governed by the measurement resolution for echo time delays of light. In contrast to microscopy, OCT can achieve fine axial resolution independent of the numerical aperture of the focusing. This feature is especially powerful for applications such as ophthalmic imaging or catheter/endoscope imaging, where numerical apertures are limited. However, low numerical aperture focusing also limits the transverse resolution because the focused spot sizes are large.

1.5.2 Optical Coherence Microscopy and En Face OCT

In order to improve the transverse image resolution, it is necessary to perform OCT imaging with high numerical aperture focusing to decrease the focused spot size (see Fig. 1.21). However, this results in a decreased depth of field. High numerical aperture imaging with fine transverse resolution is the typical operating regime for microscopy or confocal microscopy. Because of the limited depth of field, if very fine transverse resolution imaging is required, then it is more efficient to perform en face imaging, rather than cross-sectional imaging. In the limiting case of very high numerical aperture focusing, the depth of field can be comparable to or shorter than the coherence length, $b < \Delta z$, and a combination of confocal as well as coherence

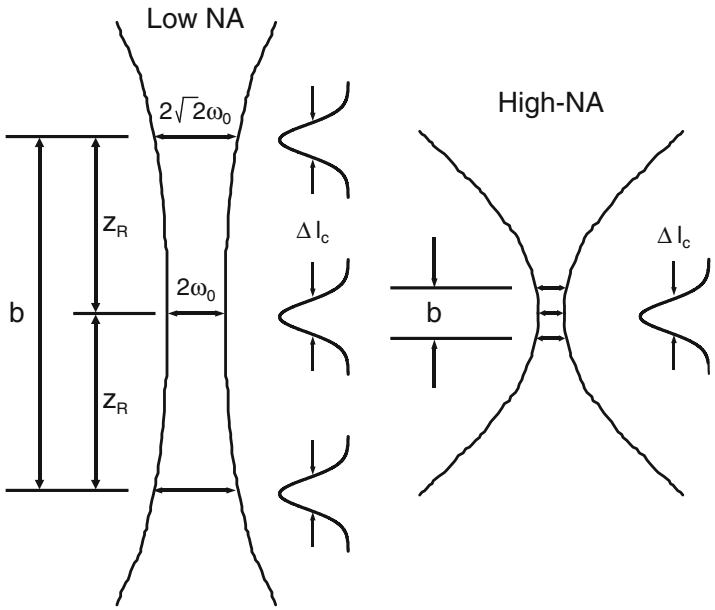

Fig. 1.21 Transverse image resolution in OCT. Transverse image resolution is determined by the focused spot size of the OCT beam and diffraction forces a trade-off between resolution and depth of field. OCT imaging is usually performed with low numerical aperture (*NA*) focusing, with the confocal parameter much longer than the coherence length, in order to generate cross-sectional images. A high NA focusing limit achieves fine transverse resolution, but has reduced depth of field. High NA focusing is used in optical coherence microscopy (*OCM*) for en face imaging

gating can be used to detect backscattered or backreflected signals from different depths and reject unwanted scattered light. This mode of operation is known as optical coherence microscopy (OCM) [40, 82, 83]. OCM achieves extremely fine transverse image resolution, on the order of 1–2 μm, and is useful for imaging tissues because the coherence gating rejects unwanted scattered light more effectively than confocal gating alone. OCM can achieve improved imaging depth and contrast compared with confocal microscopy.

Figure 1.22 shows an early example of OCT and OCM imaging of ex vivo lower GI pathology specimens [84]. Imaging was performed using a Nd:glass femtosecond laser at 1,060 nm that was spectrally broadened in a high numerical aperture optical fiber to a bandwidth of ~200 nm, yielding a 4 um axial image resolution. A combined OCT/OCM system was developed where OCM was performed by modulating the reference beam in the interferometer, raster scanning the sample beam, and demodulating the interference. The sample interface resembled a scanning confocal microscope and used 40× water immersion microscope objective which achieved <2 um transverse image resolution. The system imaged at 2 frames/s with 500 × 750 en face pixels over a 400 × 400 um field of view. Figure 1.22a, b shows ultrahigh-resolution cross-sectional OCT images of

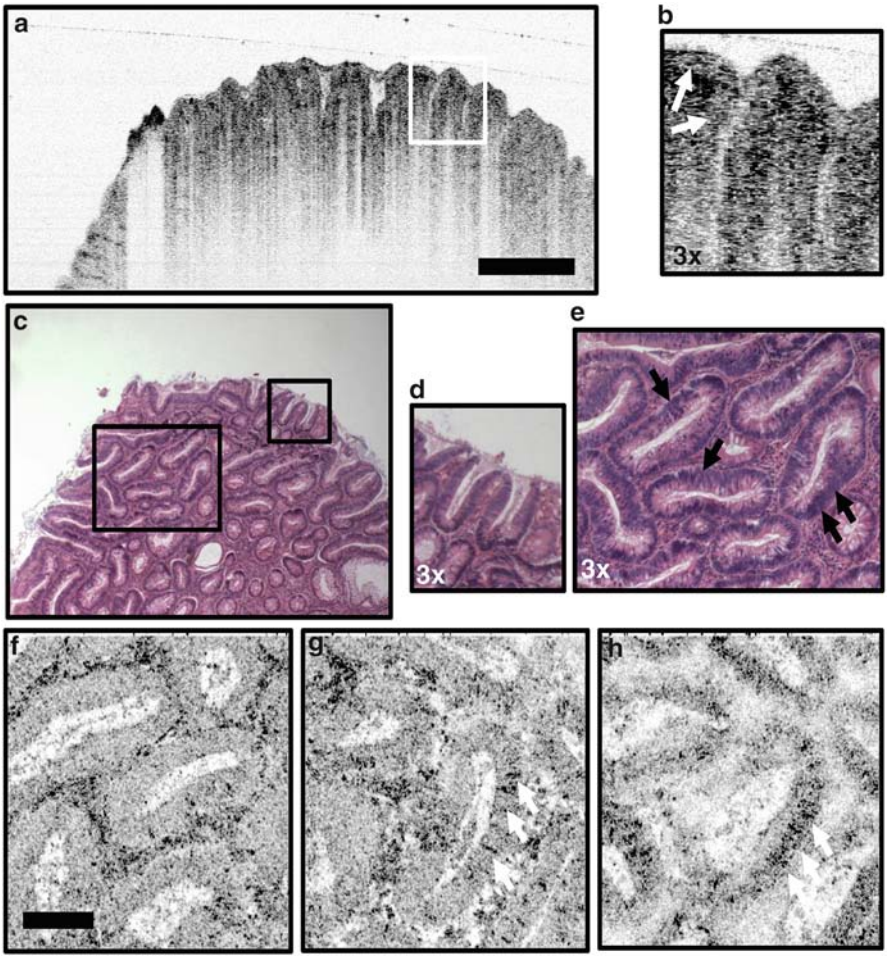

Fig. 1.22 OCT and OCM images of lower GI pathology ex vivo. (**a**, **b**) OCT of tubular adenoma shows parallel arrangement of long, slender crypt units, with the crypt epithelium identifiable from the lamina propria (**b**, *arrows*). (**c**–**e**) Corresponding histology. (**f**–**h**) OCM visualizes architecture en face, showing eccentric crypt lumens with varying shape and arrangement as well as oval-shaped nuclei. (**e**) Histology in the transverse plane shows corresponding features. OCM image depths for (**f**–**h**) were 80, 90, and 190 um, respectively. Scale bars: (**a**, **c**) 500 um; (**f**–**h**) 100 um (Aguirre et al. [84])

a tubular adenoma. The cross-sectional structure of the crypts is visible, but the OCT signal decreases with depth because of scattering as well as depth of field limitations, producing a signal gradient in the cross-sectional image. In contrast, the OCM images of Fig. 1.22f–h have uniform intensity and resolution because they are in en face planes. OCM images can be obtained at different depths by adjusting the focus depth while matching the reference arm path delay to the focus depth.

The en face OCM images have excellent image resolution, enabling visualization of the columnar epithelial structure as well as cell nuclei.

Although OCM has advantages in resolution, early OCM methods were difficult to implement because it was necessary to match the interferometer reference arm delay to the scanned beam path delay in the microscope sample arm interface. Standard confocal or multiphoton microscopes do not require constant path delay beam scanning and therefore it was difficult to make early OCM technology compatible with existing microscope designs. In addition, OCM requires acquiring one axial scan for each pixel in the image, because the image is in the en face plane. Therefore, high imaging speeds were needed in order to generate high pixel resolution images using standard OCT detection methods. Advances in OCT image speeds using spectral/Fourier domain and swept source/Fourier domain OCT (described in the next section) provided a solution to the problem of path delay matching because the dramatic increase in imaging speed enabled multiple en face depths, spanning the focal depth, to be acquired during a fast raster scan [85]. Related techniques, known as en face OCT, were developed in fields such as ophthalmology [86–88]. With the advent of high-speed imaging techniques, the low numerical aperture focusing meant that en face images at multiple depths could be generated from a single volumetric data set [89–91]. This was especially powerful in ophthalmology because it enables direct comparison with standard clinical imaging methods such as fundus photography or fluorescein angiography which image the retina in an en face plane.

The development of a technique known as full-field optical coherence tomography enabled optimized en face plane imaging and achieved extremely high pixel density images over wide fields of view [92–94]. Full-field OCT performs high-resolution en face imaging with coherence-gated detection using a Linnik interferometer and CCD cameras. Full-field OCT achieves cellular resolution imaging, and because a single spatial mode light is not required, it has the advantage that high axial resolution is possible using low-cost thermal or gas discharge light sources. Part II of this book, Optical Coherence Microscopy, includes several chapters which describe different approaches for en face imaging.

Since improving transverse resolution requires a trade-off in depth of field, to date, the majority of early studies have focused on improving axial resolution. Early OCT systems had axial resolutions of 10–15 μm. However, OCT systems can now achieve ultrahigh axial image resolution of <5 μm for endoscopic and catheter imaging and 2–3 μm for ophthalmic imaging [95–97]. These improvements in axial image resolution have been primarily driven by advances in superluminescent and laser light sources. ▶ Chapter 9, "Ultrahigh Resolution Optical Coherence Tomography" describes ultrahigh-resolution OCT in more detail.

1.5.3 Light Sources for Ultrahigh-Resolution OCT

Superluminescent diodes (SLDs) are the most commonly used light sources in OCT because they are compact and relatively inexpensive. Early ophthalmic OCT

instruments employed commercially available, GaAs superluminescent diodes which operated near 800 nm with bandwidths of ~30 nm to achieve axial resolutions of ~10 μm in tissue. Imaging in scattering tissues requires the use of longer wavelengths. Commercially available superluminescent diodes operating at 1,300 nm achieved axial resolutions of ~10 μm in tissue with output powers of several tens of mW. Since their early development, the performance of superluminescent diode light sources has improved dramatically and it is possible to multiplex diodes to achieve bandwidths of >150 nm, corresponding to axial resolutions as fine as 3–5 μm. ▶ Chapters 17, "Superluminescent Diode Light Sources for OCT" and ▶ 18, "SLEDs and Swept Source Laser Technology for OCT" describe advances in superluminescent diode technologies.

For research applications, femtosecond lasers are powerful light sources for ultrahigh-resolution OCT imaging because they can generate extremely broad bandwidths across a range of wavelengths in the near IR. Figure 1.20 shows the axial resolution in air as a function of bandwidth at center wavelengths of 800 nm, 1,000 nm, and 1,300 nm. These wavelengths can be generated using solid-state Ti:Al_2O_3, Nd:glass or Yb fiber, and Cr:forsterite lasers.

The Kerr lens mode-locked (KLM) Ti:Al_2O_3 laser is the most commonly used laser in femtosecond optics and ultrafast phenomena. Early OCT imaging studies by Bouma et al. in 1995 used Ti:Al_2O_3 lasers to demonstrate an axial image resolution of ~4 μm [98]. More recently, high-performance Ti:Al_2O_3 lasers have been made possible through the development of double-chirped mirror (DCM) technology [99]. Double-chirped mirrors can compensate high-order dispersion and have extremely broadband reflectivity, enabling the generation of few cycle optical pulses. Ti:Al_2O_3 lasers can achieve pulse durations of ~5 fs, corresponding to only two optical cycles and octave bandwidths at 800 nm [100–102]. Using state-of-the-art Ti:Al_2O_3 lasers, record OCT axial image resolutions of ~1 μm have been demonstrated [103]. Figure 1.23 shows a comparison of the optical bandwidth and interferometer traces showing the axial resolution of a superluminescent diode (SLD) and a Ti:Al_2O_3 laser. Optical bandwidths of ~260 nm were transmitted through the OCT instrument, corresponding to axial image resolution of ~1 μm. The first studies of ultrahigh-resolution imaging in the retina were reported by Drexler et al. in 2001 [95]. Figure 1.24 shows an example of the first ultrahigh-resolution OCT image of the human retina. The figure shows a ~3 μm axial resolution OCT obtained using a femtosecond laser light source. The middle and bottom images show enlargements of the macular region showing individual retinal layers. For ophthalmic applications, ultrahigh-resolution OCT enables visualization of internal retinal layers, including detailed features of the photoreceptors and photoreceptor outer segments which could be early markers of disease [104, 105].

Femtosecond Ti:Al_2O_3 lasers, in combination with high nonlinearity, air-silica microstructure fibers, or tapered fibers, can generate a broadband continuum. These fibers have enhanced nonlinearity because of their dispersion characteristics, which shift the zero dispersion to shorter wavelengths, and the small core diameters, which provide tight mode confinement. Microstructure and tapered fibers have been used with femtosecond Ti:Al_2O_3 lasers to achieve bandwidths spanning the

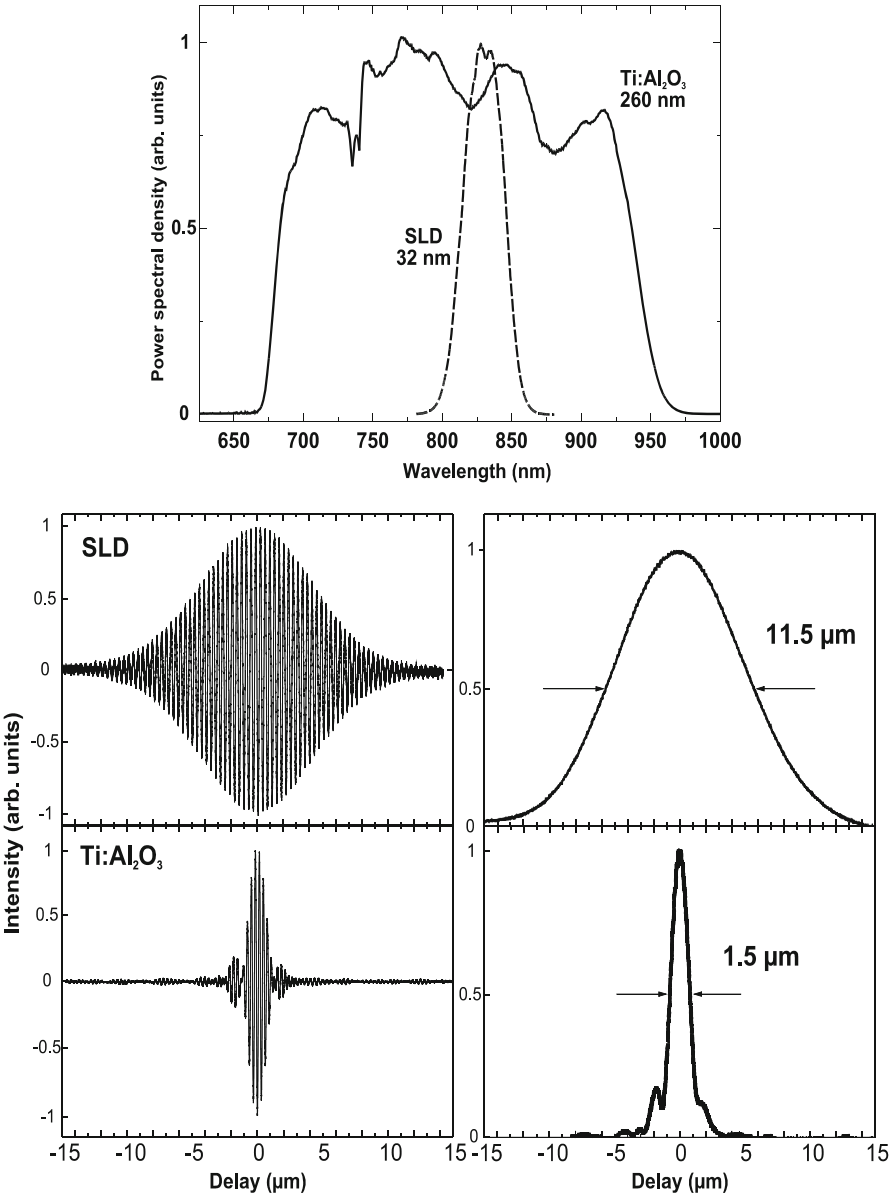

Fig. 1.23 Ultrahigh-resolution OCT. Optical spectrum, OCT interference signals and point spread functions using femtosecond Ti:Al_2O_3 laser versus a standard resolution superluminescent diode light source. The femtosecond laser has a bandwidth of 260 nm and achieves an axial resolution of 1.5 μm in air, corresponding to ~1 μm in tissue. In contrast, the superluminescent diode has a bandwidth of 32 nm and achieves a resolution of 11.5 μm (Drexler et al. [103])

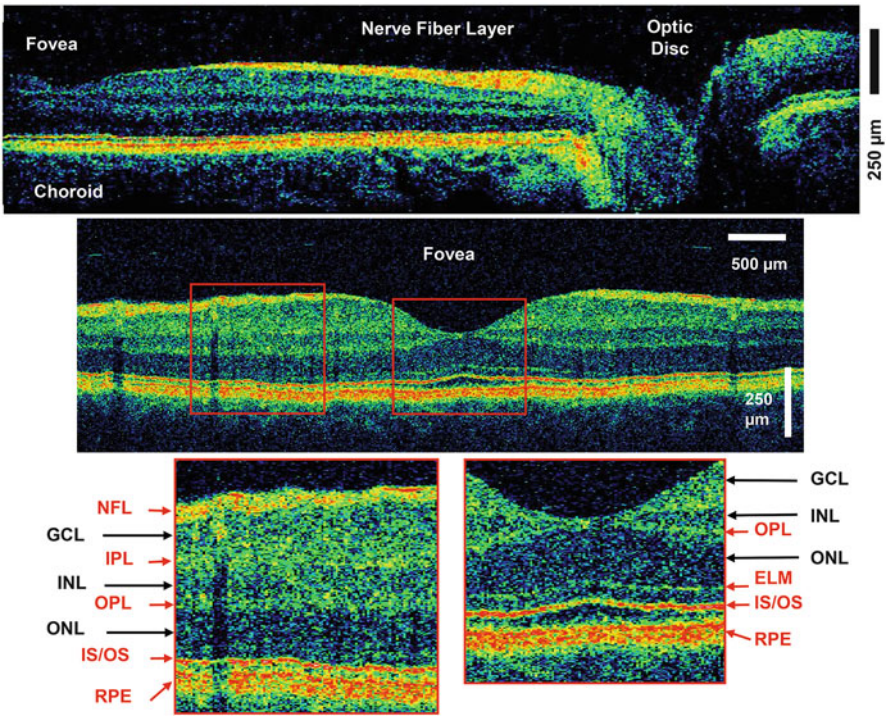

Fig. 1.24 Ultrahigh-resolution OCT image of the normal human retina in vivo. Ultrahigh-resolution OCT with 3 µm axial resolution at 800 nm wavelength enables visualization of the individual retinal layers including the nerve fiber layer (*NFL*), ganglion cell layer (*GCL*), inner and outer plexiform layers (*IPL* and *OPL*), inner and outer nuclear layers (*INL* and *ONL*), external limiting membrane (*ELM*), boundary between the inner and outer segments of the photoreceptors (*IS/OS*), and the retinal pigment epithelium (*RPE*) (Drexler et al. [95])

visible and near-infrared [106, 107]. Continuum generation from a femtosecond Ti:Al_2O_3 laser with air-silica microstructured photonic crystal fibers was demonstrated to achieve OCT axial image resolutions of 2.5 µm in the spectral region 1.2–1.5 µm [108], resolutions of 1.3 µm in the spectral region 800–1,400 nm [109], and record resolutions of <1 µm in the spectral region of 550–950 nm [110]. Although they have outstanding performance, femtosecond laser light sources are relatively costly and complex. Recently new Ti:Al_2O_3 lasers have been developed that can operate with much lower pump powers than previously thought possible, thereby greatly reducing cost [111, 112]. At the same time, there have been advances in multiplexed superluminescent diode SLD technology, and bandwidths >150 nm can be achieved, but with limited output power [113].

Longer wavelengths of 1,300 nm are required for most OCT imaging applications because they enable deeper imaging than shorter wavelengths.

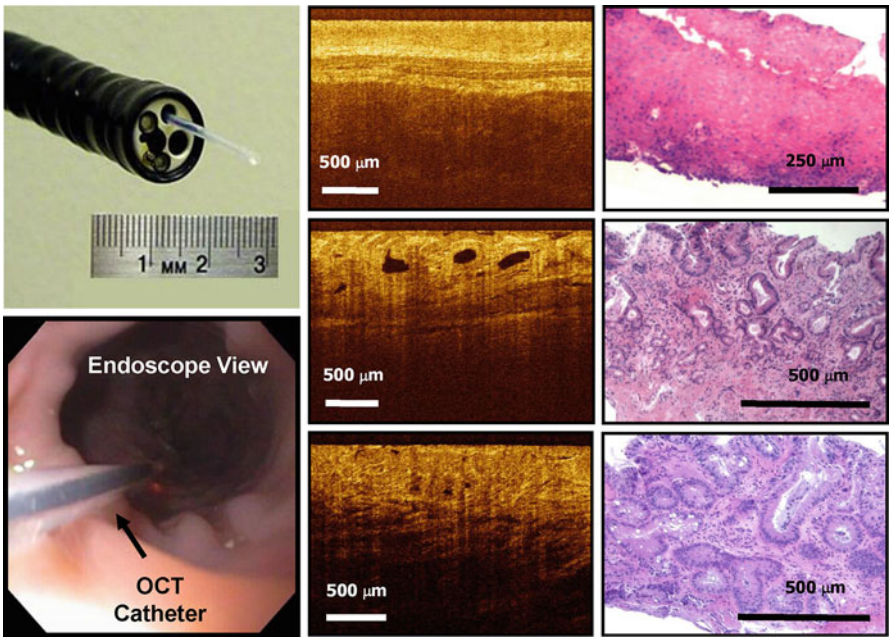

Fig. 1.25 Ultrahigh-resolution endoscopic OCT. (*left*) OCT imaging can be performed using an imaging probe introduced in the biopsy port of a standard endoscope. (*right*) Ultrahigh-resolution endoscopic OCT images of the esophagus in a human subject, acquired with 5 μm axial resolution at 1,300 nm wavelength and pinch biopsy histology. (*right*, *top* to *bottom*) Normal squamous epithelium, Barrett's esophagus, and high-grade dysplasia (From Chen et al. [97])

KLM femtosecond Cr^{4+}:forsterite lasers operate at wavelengths near 1,300 nm and have the advantage that they can be directly pumped at 1 μm wavelengths using compact Yb fiber lasers. OCT imaging studies using femtosecond Cr^{4+}:forsterite lasers were performed as early as 1996 and demonstrated axial image resolutions of 5–10 μm by coupling the femtosecond laser output into a nonlinear fiber and broadening the spectrum by self-phase modulation [114]. Early Cr^{4+}:forsterite laser technology was challenging to use because the lasers required intracavity prisms for dispersion compensation. However, with the development of double-chirped mirror technology, femtosecond Cr^{4+}:forsterite laser performance improved significantly and it became possible to generate pulse durations as short as 14 fs and bandwidths of up to 250 nm directly from the laser [115]. The Cr^{4+}:forsterite laser can also be operated with longer duration pulses and broad bandwidths obtained using nonlinear self-phase modulation in optical fibers. Bandwidths of ∼180 nm, corresponding to OCT axial image resolutions as fine as ∼3.7 μm in tissue have been achieved [96]. Figure 1.25 shows an early example of an ultrahigh-resolution in vivo endoscopic OCT image of the human gastrointestinal tract [97]. Imaging was performed with <5 μm axial resolution in tissue with an imaging speed of 3,000 axial scans/s. The images show normal squamous

mucosa, glandular architecture associated with Barrett's metaplasia, and high-grade dysplasia. Improved axial image resolution reduces speckle noise as well as improves the visibility of clinically significant features. Advances in resolution promise to be important for improving the identification of early neoplastic changes and guiding excisional biopsy.

Imaging at 1,000 nm wavelengths is an attractive compromise between the fine axial resolution, but limited image penetration available at 800 nm wavelengths, versus the reduced resolution, but increased image penetration at 1,300 nm wavelengths [116]. A wide range of commercially available femtosecond laser sources, including mode-locked Nd:glass lasers and Yb fiber lasers, are available at 1,000 nm. Commercial femtosecond lasers in combination with high nonlinearity optical fibers are an attractive and robust approach for achieving the broad bandwidths necessary for ultrahigh-resolution OCT imaging. Femtosecond Nd:glass lasers and nonlinear fibers can generate bandwidths of 200 nm centered around 1,050 nm, corresponding to axial image resolutions of ~3.5 μm in tissue [117]. Commercial laser systems such as femtosecond Nd:glass or Yb fiber lasers are well suited for in vivo ultrahigh-resolution OCT imaging studies that would be performed outside the research laboratory. ▶ Chapter 19, "Broad Bandwidth Laser and Nonlinear Optical Sources for OCT" describes ultrahigh-resolution OCT light sources in more detail.

1.6 Advances in Imaging Speed

There have been powerful advances in OCT detection technology which enable dramatic increases in imaging speeds. These techniques are known as spectral/Fourier domain OCT (SD-OCT) and swept source/Fourier domain OCT (SS-OCT), also termed optical frequency domain imaging (OFDI) [118–125]. Early OCT instruments used a low-coherence light source and interferometer with a scanning reference delay arm. This method is known as time domain detection. However, it is also possible to perform detection in the Fourier domain using a low-coherence interferometer with a broadband light source, measuring the interference spectrum with a spectrometer and a high-speed line scan camera [118, 126–129]. This method is known as spectral/Fourier domain OCT and was first proposed by Fercher et al. almost two decades ago in 1995 [118]. In 2003, three different research groups, working independently, demonstrated that spectral/Fourier domain detection (SD-OCT) has a powerful sensitivity advantage over time domain detection, since spectral/Fourier domain detection essentially measures all of the echoes of light simultaneously [123, 130, 131]. This discovery drove a boom in OCT research and development. The sensitivity is enhanced by the ratio of the axial resolution to the axial imaging depth. For most OCT systems, this corresponds to a sensitivity increase of 50–100 times, enabling a corresponding increase in imaging speeds. ▶ Chapter 2, "Theory of Optical Coherence Tomography" presents a comprehensive theoretical description of sensitivity and imaging speed for different Fourier domain techniques. ▶ Chapters 5, "Spectral/Fourier Domain

Optical Coherence Tomography" and ▶ 6, "Complex and Coherence-Noise Free Fourier Domain Optical Coherence Tomography" describe this technique in detail.

The second type of Fourier domain detection, known as swept source/Fourier domain OCT (SS-OCT), or optical frequency domain imaging (OFDI), uses an interferometer with a narrow-bandwidth, frequency swept light source and detectors which measure the interference output as a function of time [119, 121, 123]. Swept source/Fourier domain OCT has the advantage that it does not require a spectrometer and line scan camera. Therefore, it can operate at longer wavelengths where camera technology is less developed and it can achieve imaging speeds which are much faster than spectral/Fourier domain OCT which is limited by the camera speed. The primary challenge in swept source/Fourier domain OCT is that it requires a high-speed, swept narrow linewidth light source. ▶ Chapters 7, "Optical Frequency Domain Imaging" and ▶ 8, "Complex Conjugate Removal in SS Optical Coherence Tomography" describe swept source/Fourier domain OCT.

1.6.1 Spectral/Fourier Domain OCT

Spectral/Fourier domain OCT (SD-OCT) detection uses a broad bandwidth light source and detects the interference spectrum from the interferometer using a spectrometer and a line scan camera [118, 126–129]. Spectral/Fourier domain OCT has had a major impact in the field of ophthalmology. The first demonstration of retinal imaging was performed by Wojtkowski et al. in 2002 [126]. This result demonstrated that high enough sensitivities to image the retina could be achieved using spectral/Fourier domain OCT and motivated a renewed interest in this technology. Pioneering studies by Nassif et al. demonstrated video rate retinal imaging using spectral/Fourier OCT with line scan cameras to achieve 29,000 axial scans per second with 6 μm axial image resolution [132]. Cense et al. demonstrated ultrahigh-resolution spectral/Fourier domain OCT retinal imaging with 3.5 μm resolution in tissue at 14,600 axial scans per second using a multiplexed superluminescent diode light source [128]. Wojtkowski et al. demonstrated ultrahigh-resolution retinal imaging with 2.1 μm resolution in tissue at 19,000 axial scans per second using a femtosecond laser light source [129].

Figure 1.26 shows a schematic of how spectral/Fourier domain OCT detection works. Spectral/Fourier domain can be understood by recalling that a Michelson interferometer acts like a periodic frequency filter, where the periodicity depends on the path difference between the sample and reference arms. The output from a broad bandwidth light source is split into two beams. One beam is directed onto the tissue to be imaged and is backreflected or backscattered from internal structures at different depths. The second beam is reflected from a reference mirror whose position is fixed. The signal beam and the reference beam have a relative time delay determined by the path length difference, which is related to the depth of the structure in the tissue. The interference of the two beams will have a spectral modulation as a function of frequency which can be measured using a spectrometer. The periodicity of this modulation will be inversely related to the echo time delay.

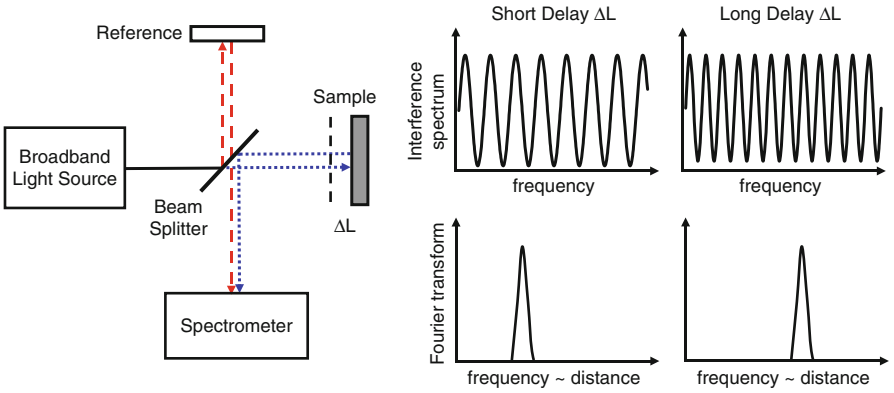

Fig. 1.26 Spectral/Fourier OCT detection. Spectral/Fourier domain OCT uses an interferometer with a broadband light source. The spectrum of the interferometer output is measured with a spectrometer. The Michelson interferometer acts like a spectral filter which has a periodic output spectrum depending on path length mismatch ΔL. Fourier transforming the interference spectrum yields axial scan information (echo magnitude vs. time delay). The technique is somewhat analogous to MR imaging in that spatial information is encoded as frequency

Therefore, different echo delays will produce different frequency modulations. The echo delays can be measured by rescaling the spectrometer output from wavelength to frequency and then Fourier transforming the interference signal. This results in an axial scan measurement of the magnitude and echo delay of the light signal from the tissue.

Figure 1.27 shows a schematic of a typical spectral domain OCT instrument. The light source is a broad bandwidth superluminescent diode or femtosecond laser and the interferometer is implemented using fiber optics. The example shows an ophthalmic imaging instrument where the interferometer sample arm is a patient interface which directs the OCT beam through the pupil and scans the retina. The interferometer reference path has an attenuator to set the reference power as well as materials which approximately match the dispersion in the patient interface and eye. The interference signal is measured by a spectrometer and a high-speed line scan camera. The line scan rate of the camera determines the axial scan rate of the OCT instrument. The spectrometer is typically a refractive spectrometer, using lenses for collimating the optical fiber output onto a diffraction grating and for focusing the angularly dispersed spectrum on the line scan camera. Lenses are superior to mirrors for obtaining diffraction limited focusing of the spectrum over the wide field of view required by most line scan cameras. Transmission diffraction gratings are typically used because the diffraction efficiencies are less polarization dependent than reflective gratings. The spectrometer generates an interference spectrum which is a function of wavelength; therefore, the spectrum must be numerically resampled from wavelength to frequency or wavenumber k before Fourier transforming. The Fourier transform of the spectrum generates the axial scan.

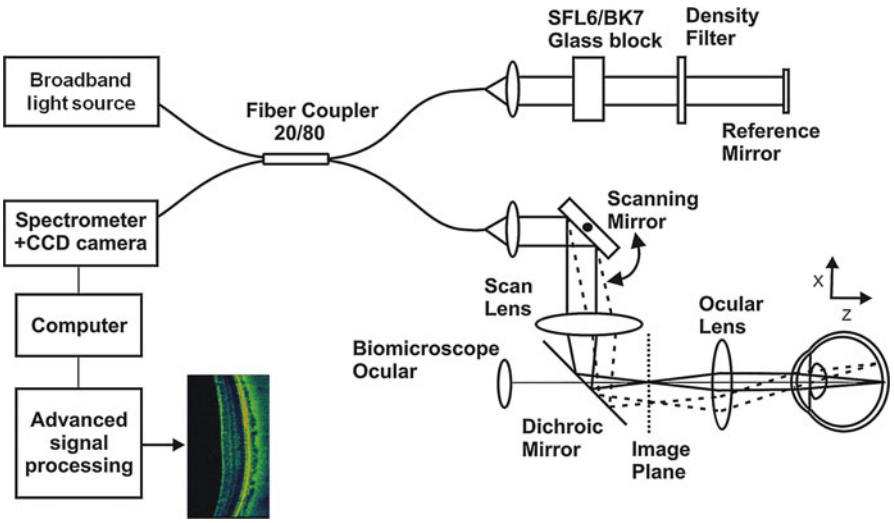

Fig. 1.27 Schematic of a typical spectral domain OCT instrument. This system consists of a fiber-optic interferometer with a low-coherence light source. The reference arm has a fixed delay and is not scanned. The example shows a sample arm with an ophthalmic user interface. Interference is detected with a spectrometer and a high-speed, line scan camera. A computer reads the spectrum, rescales it from wavelength to frequency or k, and Fourier transforms to generate axial scans. Spectral domain OCT has a dramatic sensitivity and speed advantage because it simultaneously detects light from all delays. It also allows direct access to the spectrum which enables numerical dispersion compensation and spectral shaping

Although OCT using spectral/Fourier domain detection has powerful imaging speed advantages, it also has artifacts which are not present in OCT time domain detection. Spectral/Fourier domain OCT is subject to "mirror" artifacts in the images, when the sample is positioned incorrectly or when features span a large depth range. As shown in Fig. 1.27, spectral/Fourier domain detection measures axial scans from the Fourier transform of the interference spectrum of backreflected or backscattered light from the sample with light from a reference path delay which determines a "zero delay." Standard spectral/Fourier domain detection cannot distinguish between positive versus negative time delays compared to this zero delay. Therefore, if the sample is exactly at the reference zero delay position, or if features cross this zero delay, then the OCT image appears folded about this zero delay producing a "mirror" artifact. Stated another way, the magnitude of the Fourier transform is symmetric for positive or negative values and therefore cannot distinguish positive or negative time delays. In addition, measuring a spectrum with N samples results in an axial scan with $N/2$ samples and therefore line scan cameras with large numbers of pixels are required to generate axial scans with high pixel resolution.

In addition to the "mirror" artifact, the detection sensitivity varies as a function of the measurement range in spectral/Fourier domain detection. This is often referred to as "sensitivity roll-off." Spectral/Fourier domain detection is most sensitive to echoes which are close to the zero delay position and sensitivity

decreases further from zero delay. This occurs because the spectrometer has a limited spectral resolution. Echoes which are further from the zero delay position produce progressively high frequency spectral oscillations which can no longer be resolved. The spectral resolution is governed by multiple factors including the optical aberrations in the spectrometer lenses, the resolution of the diffraction grating, camera pixel size, and electronic pixel cross talk.

Figure 1.28 shows a series of OCT retinal images which illustrate the mirror artifact. The different images, from the top to the bottom, are acquired by moving the OCT instrument toward the eye, so that the distance to the eye is decreasing. The echoes of light from the retina are measured with respect to a specific delay, the "zero delay" position from the instrument, which is determined by the interferometer reference path. The retina appears in a normal position when it is farther than the zero delay. However, when the instrument is moved toward the eye so that the retina is exactly at the zero delay reference position, the portions of the retina which cross the zero delay appear folded or mirrored around the zero delay because positive versus negative delays are not distinguishable. Finally, when the instrument is moved even closer to the eye, the retina is closer than the zero delay reference position and the retina appears inverted. The sensitivity roll-off can also be seen in the images of Fig. 1.28, where the retina appears brighter when it is near zero delay. Conversely, features which are further from zero delay appear dimmer. Depending upon the application, it may be desirable to set the zero delay position in order to have increased sensitivity to signals from deeper in the sample versus avoiding mirror artifacts.

Spectral/Fourier domain detection enables OCT imaging with a ~50–100 times increase in imaging speed compared with first generation OCT systems. At the same time it is important to note that spectral/Fourier domain detection must be operated at high speeds because specimen motion produces averaging of the interference fringes if the acquisition speed is too slow. High-speed imaging is a major advance because it is possible to increase the number of axial scans or transverse pixels per B-scan image to yield high-definition images as well as to increase the number of cross-sectional or B-scan images acquired in a sequence to yield denser three-dimensional data (3D-OCT). Figure 1.29 shows a comparison of standard OCT and high-speed, ultrahigh-resolution OCT images of the optic nerve head of the human retina. Figure 1.29a shows a standard 10 μm axial resolution OCT image with 512 axial scans, acquired in ~1.3 s. Figure 1.29b shows a high-speed, ultrahigh-resolution OCT image with ~2 μm axial resolution and 2,048 axial scans, acquired in 0.13 s. The higher resolution and greater number of transverse pixels in the high-speed, ultrahigh-resolution OCT image improve the visualization of internal retinal structure. The ability to visualize internal retinal features promises to enable the identification of early markers of disease and disease progression.

In addition, high-speed OCT imaging enables the acquisition of complete 3D-OCT data sets in a time comparable to that of first generation OCT protocols that acquired several individual images [133]. Figure 1.30 shows 3D-OCT imaging of the optic disc using a raster scan pattern [134]. The 3D-OCT volumetric data set contains comprehensive structural information. An en face OCT image, identical to a standard retinal fundus view, can be generated by summing the data in

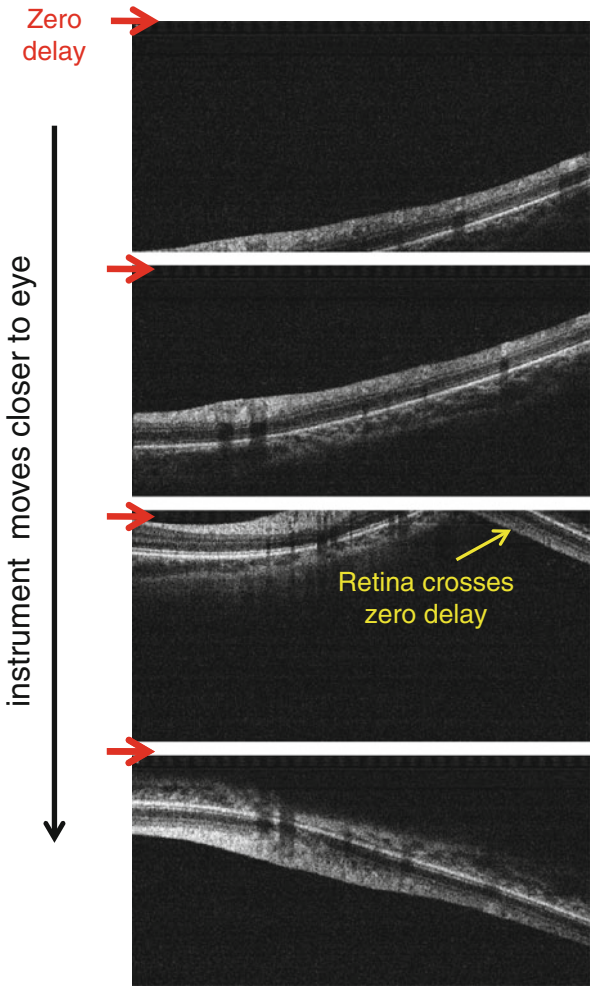

Fig. 1.28 Artifacts in spectral/Fourier domain OCT detection. Spectral/Fourier domain detection cannot distinguish between positive or negative echo time delays and has a "mirror image" artifact. The series of OCT retinal images (*top* to *bottom*) was acquired as the instrument was moved closer to the eye. When the retina crosses the interferometer zero delay position, it produces a folded or mirror image appearance in the OCT image. When the instrument is even moved closer, with the retina in back of the zero delay, the image appears inverted. Care must be taken to avoid misinterpreting mirror artifacts in OCT images

the axial direction. Individual cross-sectional OCT images can be precisely and reproducibly registered to en face features of the retina. Figure 1.31 shows an example of retinal nerve fiber layer (RNFL) thickness measurement from a 3D-OCT data set. Figure 1.31a shows an RNFL thickness map, Fig. 1.31b shows a measurement of RFNL thickness in a virtual circumpapillary scan, and Fig. 1.31c shows a virtual circumpapillary scan extracted from the 3D-OCT data set. Because 3D-OCT contains comprehensive structural information, the position of the circumpapillary scan can be adjusted in post processing to achieve precise registration with fundus features and improve measurement reproducibility.

With the development of improved camera technology, it became possible to increase spectral/Fourier domain imaging speeds. In 2008, Potsaid et al. demonstrated record imaging speeds of up to 312,500 axial scans per second using

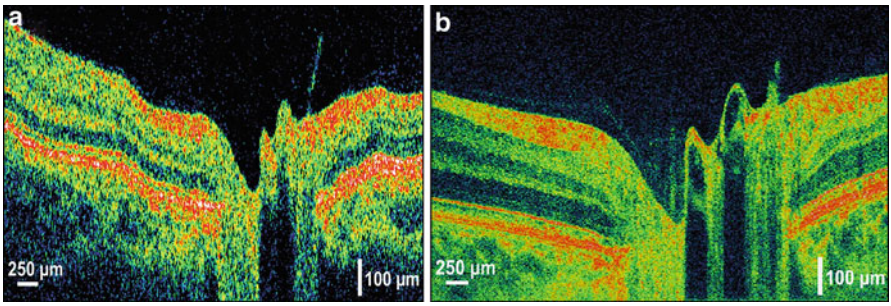

Fig. 1.29 Spectral/Fourier OCT imaging of the retina. Comparison of standard time domain OCT and high-speed, ultrahigh-resolution OCT using spectral/Fourier domain detection. (**a**) Standard OCT of the optic nerve head with ~10 µm axial image resolution and 512 axial scans, acquired in ~1.3 s. (**b**) High-speed, ultrahigh-resolution image with ~2 µm axial resolution and 2048 axial scans, acquired in 0.13 s

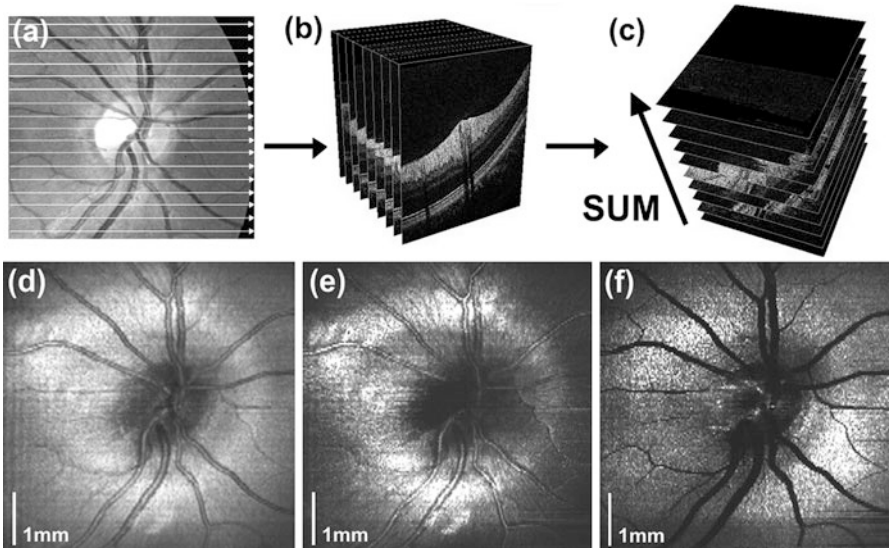

Fig. 1.30 En face imaging using 3D-OCT data. (**a**, **b**) High-speed OCT enables the acquisition of 3D-OCT data which contains comprehensive volumetric information. (**c**, **d**) An en face OCT retinal fundus image can be generated directly from 3D-OCT data by summing the signal along the axial direction. Individual images in the data set are precisely registered with fundus features. (**e**, **f**) En face OCT images can also be generated by displaying individual retinal layers such as (**e**) the nerve fiber layer or (**f**) retinal pigment epithelium, enabling visualization of specific features (Wojtkowski et al. [134])

a CMOS line scan camera [135]. The camera (Sprint spL4096-140 k from Basler Vision Technologies) had 4 k pixels that were read at 70 kHz line rate, but progressively higher rates could be achieved by reducing the number of pixels used. Line rates of 312.5 kHz could be achieved by reading 576 pixels. The ability

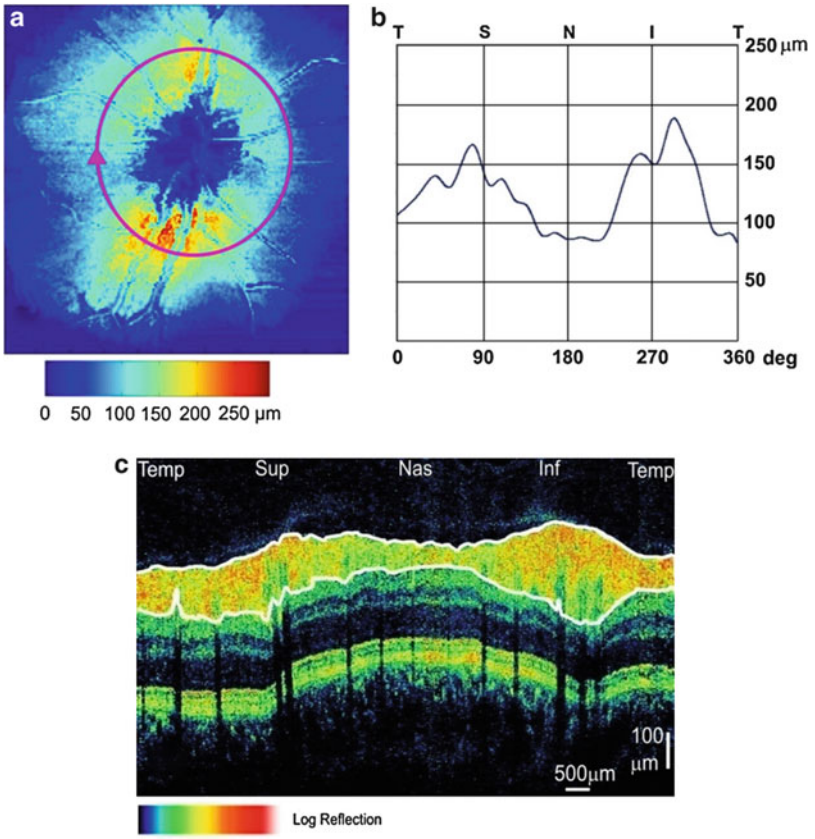

Fig. 1.31 3D-OCT. (**a**) RNFL thickness map from 3D-OCT data. (**b**) Plot of RNFL thickness on a 3.4-mm diameter circumpapillary circle from 3D-OCT. (**c**) Virtual circumpapillary image extracted from 3D-OCT. (INF) inferior, (NAS) nasal, (SUP) superior, and (TEMP) temporal portions of NFL (Wojtkowski et al. [134])

to adjust the number of pixels enables optimization of performance. Ultrahigh axial image resolutions of 2.5–3 um can be achieved with 100 kHz read speeds, while ultrahigh speeds of 312.5 kHz require a trade-off in axial resolution to ~9 um. Reducing parasitic sensitivity roll-off requires a spectrometer design that uses more pixels for a given wavelength span, resulting in slower imaging speeds.

Spectral/Fourier domain OCT has had a dramatic impact in ophthalmology. The improved imaging capabilities promise to provide earlier diagnosis of retinal disease as well as more sensitive assessment of progression and response to therapy. Numerous commercial organizations have developed spectral/Fourier domain OCT instruments for the ophthalmic marketplace and the technology is now widely available to the clinical community.

1.6.2 Swept Source/Fourier Domain OCT

Swept source/Fourier domain detection (SS-OCT), also known as optical frequency domain interferometry (OFDI), uses an interferometer with a frequency swept, narrow-bandwidth light source [119, 121, 123]. The sweep in frequency with time essentially labels different time delays in the light beam, which can then be detected by interference and Fourier transforming. The basic concept of SS-OCT was described in patents as early as 1991 and experimental studies in 1997 [119, 120, 136]. These detection techniques were used in the 1990s to perform measurements in fiber optic and photonics components [137–139]. The basic concept of frequency chirped coherent ranging and imaging, as well as the associated signal-to-noise and performance advantages, actually date back to the 1980s and where they were used in coherent laser radar [140]. OCT using swept source/Fourier domain detection was demonstrated as early as 1997 by Chinn et al. [119] and Golubovic et al. [120], but the sensitivity and speed advantages were not recognized in these studies and performance was limited by the available laser technology. Pioneering studies by Yun et al. in 2003 demonstrated OCT imaging with 19,000 axial scans per second and 13–14 μm axial resolution in free space [121]. Record imaging speeds of 115,000 axial scans per second were achieved in 2005 using a novel swept laser technology based on a grating and rotating polygon mirror filter [141].

Figure 1.32 shows a schematic of how swept source/Fourier domain detection works. The output from a narrow-bandwidth, frequency swept light source is divided into a signal and a reference beam. The signal beam is directed onto the tissue to be imaged and is backreflected or backscattered from internal structures at different depths. The reference beam is reflected from a reference mirror at a fixed delay. The signal and reference beams have a time offset determined by the path length difference, which is related to the depth of the structure in the tissue. Because the frequency of the light is swept as a function of time, the light echoes in the signal beam will have a frequency offset from the reference beam. When the signal and reference beams interfere, a modulation or beat in intensity is produced at a frequency which is given by this frequency offset. Therefore, different echo delays will produce different frequency modulations. The axial scan can be measured by digitizing the photodetector signal over a single frequency sweep of the light source, correcting any nonlinearity in the frequency sweep as a function of time and then Fourier transforming this beat frequency signal. This results in an axial scan measurement of the magnitude and echo delay of light from the tissue.

Figure 1.33 shows a schematic of a typical swept source OCT instrument. The light source is a swept laser with a narrow instantaneous linewidth. The example shows a catheter/endoscopic imaging instrument where the interferometer sample arm is a fiber-optic imaging probe. The interferometer uses circulators in both the sample and reference paths to extract the return light from the sample and references arms which are then interfered in a 3 dB coupler. This configuration provides access to two interference signals and enables dual balanced detection where the reference arm power and excess noise in the light source are subtracted, while the interference signal is added. This interferometer configuration is more

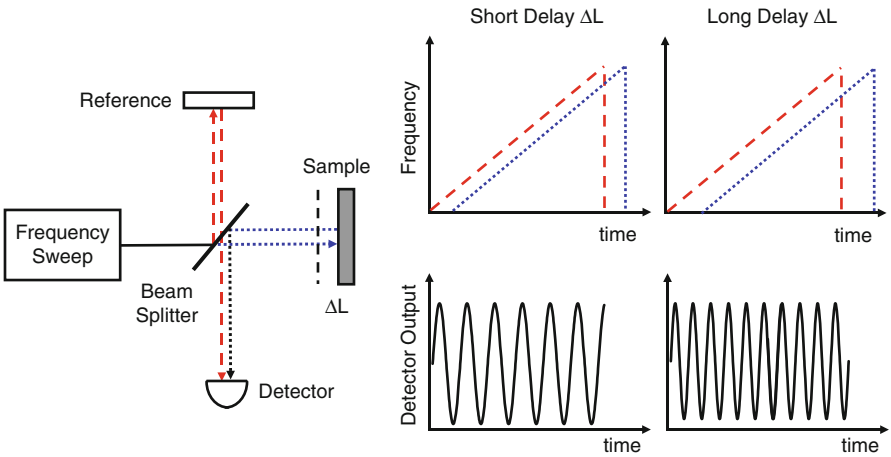

Fig. 1.32 Swept source/Fourier domain OCT detection. Swept source/Fourier domain OCT uses an interferometer with a narrow-band, frequency swept laser and photodetectors. The Michelson interferometer interferes two frequency sweeps which are time delayed with respect to each other and generates a beat frequency which is proportional to the path length mismatch ΔL. Fourier transforming the beat signal from the detector yields axial scan information (echo magnitude vs. time delay)

efficient than the classic Michelson interferometer because all of the light is detected. The output of the dual balanced detector is digitized by a high-speed A/D.

Frequency swept light sources usually generate frequency sweeps that are not linear in time. Therefore, it is necessary to either rescale the digitized interference signal so that it is sampled with equal frequency or k intervals rather than equal time intervals. If a calibration of frequency versus time is available, this resampling can be performed by numerically processing the interference signal. However, modern swept source/Fourier domain detection systems avoid this computational cost by clocking the A/D at equal frequency or k intervals. This optical clocking or k-clocking is typically performed using a Mach-Zehnder interferometer to detect the frequency sweep and clock the A/D at a variable rate corresponding to the frequency sweep rate. The technique of optical clocking has the advantage that it increases data processing speed by removing the computationally expensive step of resampling the interference signal and also reduces the amount of data that is acquired, but it requires special A/D instrumentation which can clock accurately with a variable clock rate. Furthermore, the optical and electronic propagation delays in swept source/Fourier domain instruments must be carefully managed because a timing mismatch between the clock and interference signal results in sampling at incorrect times which distorts the interference signal. The requirement of high-speed A/D as well as precise synchronization makes swept source/Fourier domain detection more challenging than spectral/Fourier domain detection.

Like spectral/Fourier domain detection, swept source/Fourier domain detection measures all of the optical echoes at the same time, rather than sequentially as in

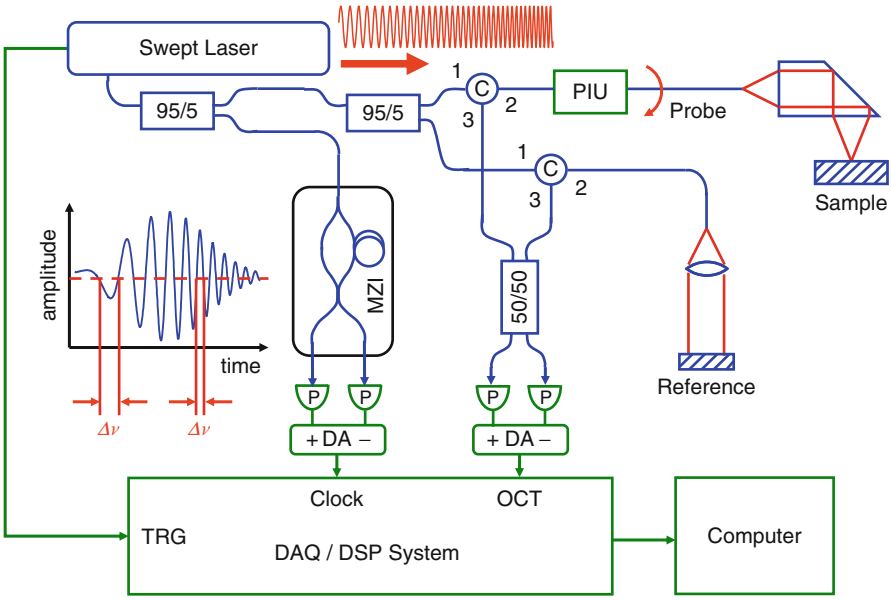

Fig. 1.33 Schematic of a typical swept source OCT instrument. This system consists of a fiber-optic interferometer with a frequency swept light source. The reference arm has a fixed delay and is not scanned. The example shows a sample arm with catheter/endoscope interface and the system is assumed to operate at 1.3 um wavelengths. Two circulators are used to collect light from the sample and reference arms and generate interference in a 50/50 coupler. This geometry enables dual balanced detection, cancelling excess noise in the laser for better utilization of the D/A dynamic range. A portion of the frequency swept light is directed into a Mach-Zehnder interferometer (*MZI*) which acts as a periodic frequency filter to generate a clock signal for the D/A. This optical clock triggers that D/A at varying time intervals to remove frequency sweep nonlinearity, yielding spectral data sampled with constant frequency or k interval. Swept source OCT is extremely versatile and avoids the spectral resolution and pixel limitations which are inherent in spectrometers and line scan cameras

time domain detection. This enables a dramatic improvement in detection sensitivity. Swept source/Fourier domain methods have the advantage that they can be used in the 1,300 and 1,000 nm wavelength ranges where silicon-based cameras lack sensitivity and more expensive InGaAs cameras are required. The axial image resolution and axial scan rate in swept source OCT are determined by the sweep range and sweep repetition rate of the laser, respectively. If the laser can achieve high sweep repetition rates, imaging can be performed much faster than spectral domain OCT which is limited by camera read rates.

1.6.3 Light Sources for Swept Source OCT

Because swept source OCT can achieve high imaging speeds at wavelengths of 1,300 nm, it has had a powerful impact on intravascular and endoscopic

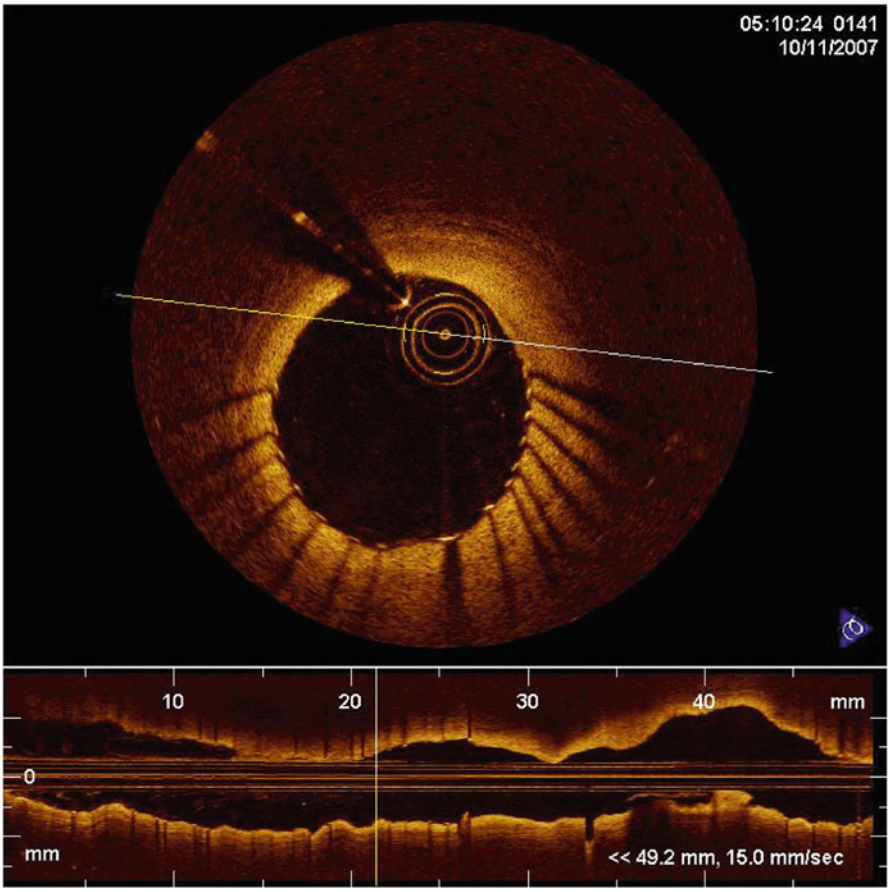

Fig. 1.34 High-speed intravascular OCT imaging. High-speed OCT imaging using swept source/Fourier domain OCT with a Fourier domain mode-locked (FDML) laser. The image shows a stented human LAD coronary artery in vivo using a LightLab M4 prototype instrument operating at 45,000 axial scans per second and 100 frames/s with a 15 mm/s pullback speed. Imaging speeds are ~100 times faster than previous generation OCT systems enabling rapid imaging with minimal ischemia (Courtesy of LightLab Imaging)

imaging applications. Swept source 3D-OCT imaging was demonstrated in the porcine esophagus and coronary artery at speeds of 10,000 and 54,000 axial scans/s, respectively [142, 143]. Figure 1.34 shows an example of high-speed OCT intravascular imaging in the porcine artery in vivo using a LightLab prototype instrument which operates at 45,000 axial scans/s, acquiring 100 frames per second with a 15 mm/s pullback speed using a 10 mL contrast injection to remove blood from the imaging field. These high imaging speeds enable rapid pullbacks, mapping long segments of artery while minimizing ischemia.

Figure 1.35 shows an example of in vivo endoscopic 3D-OCT imaging in the rabbit, using high-speed, swept source/Fourier domain OCT [144]. In vivo 3D-OCT

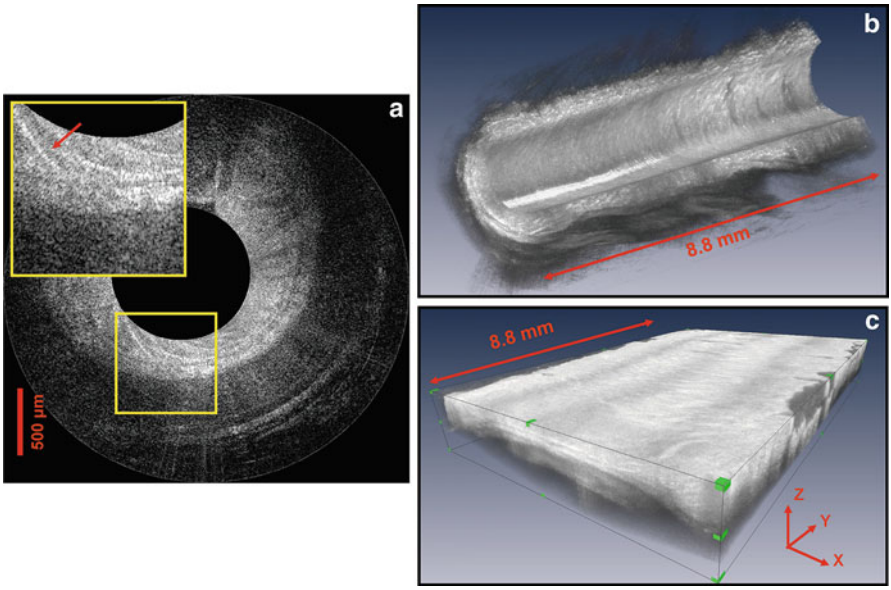

Fig. 1.35 High-speed endoscopic OCT. Volumetric data is acquired at 100,000 axial scans per second and 50 frames/s using a rotary fiber-optic endoscope probe with swept source/Fourier domain OCT and a Fourier domain mode-locked (FDML) laser. Volumetric renderings of the rabbit colon in vivo. (**a**) Single radial frame acquired in 20 ms. Inset shows enlarged view of epithelium, with crypt indicated by *red arrow*. (**b**) Cutaway view of the rendered volume. (**c**) Unfolded data set showing the cylindrical volume as a rectangular tissue slab. The entire volume was acquired in 17.7 s (Adler et al. [144])

was demonstrated with axial image resolutions of 5–7 µm, at speeds of 100,000 axial lines/s, equivalent to 50 frames/s and rates of 61 Megavoxels/s. 3D-OCT enables virtual manipulation of tissue geometry, speckle reduction, synthesis of en face views similar to endoscopic images, generation of virtual cross-sectional images with arbitrary orientation, and quantitative measurements of morphology. These technological advances promise to enable a wide range of applications.

Because the performance of swept source OCT systems depends directly on the swept light source, advances in laser technology have become an active area of research in OCT. Frequency swept lasers consist of a laser gain and a tunable filter. There is a fundamental limit on the tuning rate of a frequency swept laser because the lasing of a given frequency must build up from spontaneous emission and be amplified up to saturation as the filter is tuned in order to achieve a narrow linewidth [145]. Therefore, short laser cavities which have a rapid round trip time can tune faster than long cavity lasers. However, the development of Fourier domain mode locking (FDML) in 2006 by Huber et al. provided a novel approach for breaking the tuning speed limit [125]. FDML lasers use a long optical fiber delay inside the laser which stores the entire frequency sweep in the cavity and synchronously tune the filter such that a given frequency arrives at the filter when it is tuned

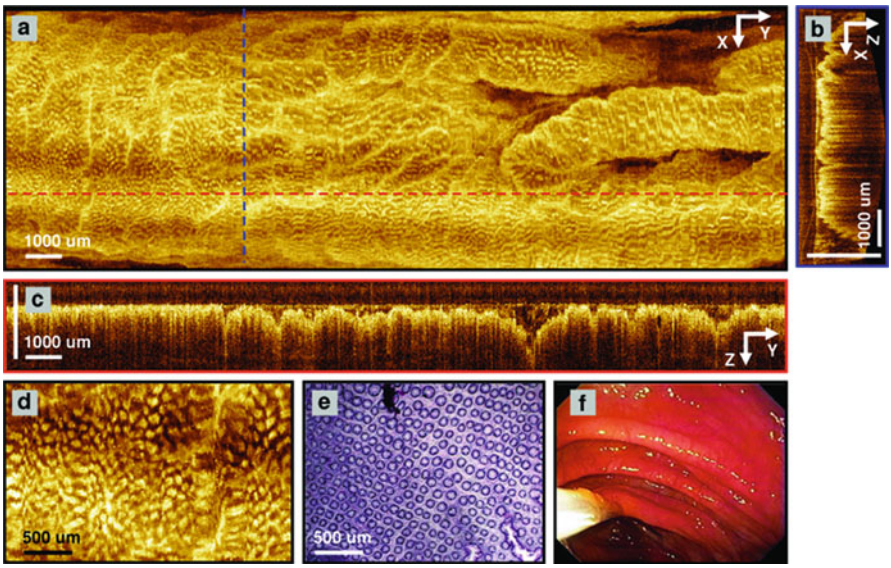

Fig. 1.36 Endoscopic OCT imaging of the normal human colon. 3D-OCT images of columnar epithelial tissue in the human colon. (**a**) En face OCT image constructed by axial summation of the data set. *Dashed lines* show locations of cross sections. (**b**) XZ cross section showing typical columnar epithelial structure. (**c**) YZ cross section. (**d**) Enlarged view of (**a**), showing en face crypt pattern. (**e**) Representative en face histology of human colon. (**f**) White light video endoscopy of region imaged with 3D-OCT (Adler et al. [148])

to pass it. This avoids the need to build up lasing at each frequency and enables record sweep speeds. Fourier domain mode locking is described in detail in ▶ Chap. 24, "FDML (incl. Parallelization)". Early FDML lasers achieved record imaging speeds of 370,000 axial scans per second [146]. This technology was enabling for both endoscopic/catheter as well as ophthalmic applications. Record catheter/endoscope imaging speeds of 100,000 axial scans per second with 5–7 μm axial resolutions were demonstrated in an animal model in 2007 [147]. FDML lasers were also demonstrated in human endoscopic imaging studies and achieved a 62 kHz axial scan rate with 180 nm tuning range at 1,310 nm, corresponding to an axial image resolution of 5 um in tissue [148]. Figure 1.36 shows an example of endoscopic imaging in the normal human colon. A volume of $7 \times 20 \times 1.6$ mm in dimension was acquired in 20 s using rotary fiber-optic probe with pullback. The volumetric data enables the generation of arbitrary cross sections as well as en face images which display the uniform crypt pattern in the normal epithelium of the colon. The ability to assess the 3D structure of crypts is therefore of potential value for future applications in cancer detection and treatment. Ophthalmic imaging with speeds of greater than one million axial scans/s has recently been achieved [149]. These extremely rapid imaging speeds enable wide-field retinal coverage.

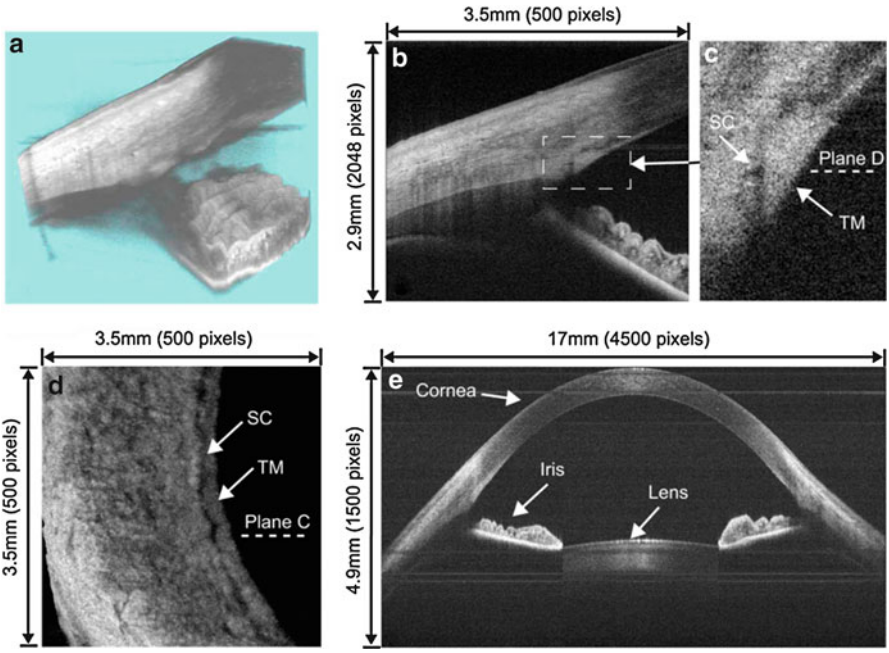

Fig. 1.37 Anterior eye OCT. Example showing a 10 mm imaging range in air (7.5 mm in tissue) acquired at 100 kHz axial scan rates. (**a**) 3D-OCT of the angle consisting of 500 × 500 axial scans over 3.5 × 3.5 mm acquired in 2.6 s. (**b**) Cross-sectional image of the angle from (**a**) averaging two adjacent cross-sectional images. (**c**) Enlarged region from (**b**) showing Schlemm's canal (*SC*) and the trabecular meshwork (*TM*). (**d**) En face OCT image extracted from (**a**) averaging over two en face planes showing a coronal section through structures related to outflow. (**e**) OCT cross-sectional image of the cornea, iris, and anterior lens acquired using 1 GSPS sampling with an oscilloscope to achieve high axial resolution over a long imaging range. The image is cropped in depth to span 4.9 mm (Potsaid et al. [150])

In addition to research systems, commercial swept laser technologies also made critical advances. The development of a commercial short cavity swept laser (Axsun Technologies) enabled intravascular as well as ophthalmic applications. The short cavity swept laser uses a high finesse tunable filter and a gain medium with a few centimeter cavity length. Retinal imaging with a 5.3 um axial resolution at 1,050 nm wavelength was demonstrated at 100 kHz axial scan rates using direct swept laser output, and 200 kHz scan rates were achieved by multiplexing the laser sweeps [150]. The short cavity laser also enabled narrower instantaneous linewidths and therefore supported longer imaging ranges than previous swept lasers. Figure 1.37 shows an example imaging the anterior eye with a 10 mm imaging range in air (7.5 mm in tissue) acquired at 100 kHz axial scan rates. The long image range required an A/D acquisition at a 1 GSPS rate. Short cavity swept laser technology is described in more detail in ▶ Chap. 21, "Swept Light Sources" entitled 1,060 nm Swept Source OCT Engine.

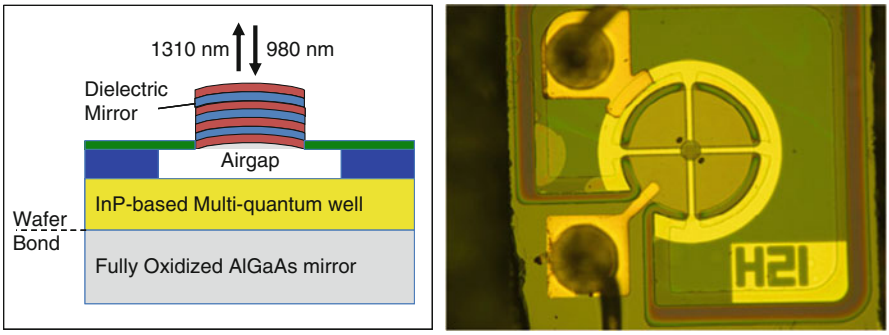

Fig. 1.38 Schematic and photograph of a VCSEL laser. The laser consists of a semiconductor mirror, quantum well gain material, and dielectric mirror fabricated on a MEMS. The gain is optically pumped by a laser diode (not shown). The VCSEL cavity is short and can operate in a single longitudinal mode providing very narrow linewidth. The MEMS mirror is electrostatically actuated and can vary the cavity length to sweep the laser frequency/wavelength. The MEMS mirror can achieve rapid sweep rates as well as adjustable sweep ranges

The development of the vertical cavity surface-emitting laser (VCSEL) enabled advances in both imaging speed and imaging range. Figure 1.38 shows a schematic and photograph of a VCSEL laser. The laser is optically pumped and consists of a quantum well gain medium in a micro-cavity formed by a semiconductor mirror and a dielectric mirror on a MEMS structure [151]. The MEMS is electrostatically actuated in order to change the cavity length and tune the laser. Because the MEMS can be actuated at high speed and the cavity is extremely short, the laser can be frequency swept at high repetition rates. ▶ Chapter 22, "VCSEL Swept Light Sources" describes VCSEL light sources in more detail.

Figure 1.39 shows an example of wide-field retinal and choroidal imaging using SS-OCT with the VCSEL at 580 kHz axial scan rate [152]. A wide-field 12 × 12 mm region of the retina can be imaged with 1,000 × 1,000 axial scans acquired in ~2 s. The high axial scan density enables high-resolution en face OCT images where each pixel in the en face image requires an axial scan in the volumetric data. The longer 1,050 nm wavelength compared with 840 nm in standard OCT instruments enables increased penetration into the choroid and reduced attenuation from ocular opacities.

Depending on the swept laser linewidth as well as the A/D sampling rate, swept source OCT can achieve much longer imaging ranges than spectral domain OCT, with reduced sensitivity roll-off. Swept source OCT also has the advantage that the resolution, axial scan rate, and imaging range can be dynamically adjusted by adjusting the laser sweep range, repetition rate, and A/D sampling rates. Since VCSEL lasers operate with a single longitudinal mode, instantaneous linewidths are much narrower than other swept lasers and they can achieve extremely long imaging ranges. Figure 1.40 shows an example of full eye length imaging at 45 kHz axial scan rate [152]. The VCSEL sweep range was reduced to 45 nm centered around 1,050 nm, corresponding to an axial resolution of 12.4 um in tissue. An A/D rate of 1 GSPS was used to achieve an imaging range of 37.7 mm in tissue. The extremely narrow

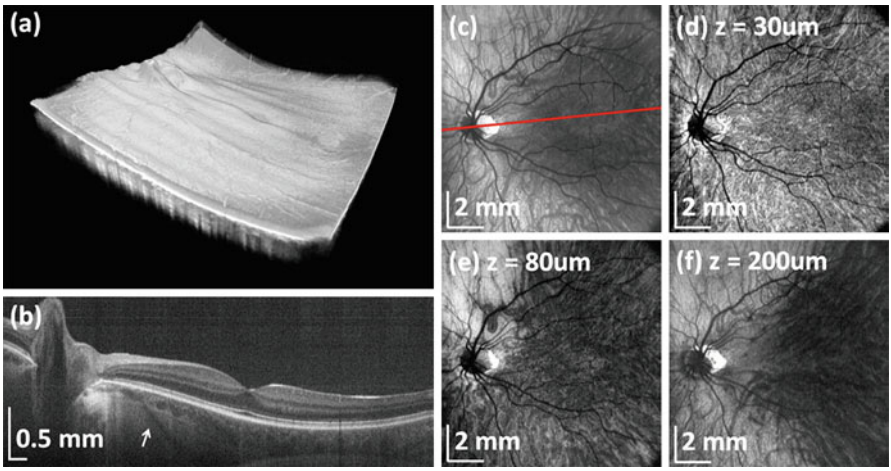

Fig. 1.39 Wide-field retinal and choroidal OCT imaging. Swept source OCT using VCSEL light source at 580 kHz axial scan rate. (**a**) Rendering of volumetric wide-field 3D-OCT data. (**b**) Virtual (arbitrary) cross-sectional image showing deep image penetration and ability to visualize choroid and sclera. *Arrow* indicates scleral vessel. (c) En face OCT image of the choroid obtained by integrating signal below the RPE. *Red line* indicates orientation of cross section in (**b**). En face OCT images at depths (**d**) 30 μm, (**e**) 80 μm, and (**f**) 200 μm below the RPE showing choroidal layers and sclera. Signal was integrated from 40 μm thick slices (Grulkowski et al. [152])

instantaneous linewidth of the VCSEL means that there is virtually no sensitivity roll-off across the imaging range, enabling a wide range of new applications [153].

1.7 Functional OCT

There are many methods for functional OCT which enhance tissue contrast or assess physiological state, as well as multimodal techniques which integrate other imaging modalities with OCT. Here we only briefly mention early methods for functional OCT which involve Doppler flow, polarization-sensitive, and spectroscopic techniques. Early Doppler OCT was performed using techniques that directly detected the interferometric output in the time domain, rather than demodulating the interference fringes [154–157]. Movement or flow produces a Doppler shift in the backscattered or backreflected light which can be measured by Fourier transforming the interference fringe signal. The development of spectral as well as swept source/Fourier domain detection enabled direct access to the phase of the interference signal and enabled a wide range of Doppler techniques [158, 159]. Related techniques, broadly known as OCT angiography, use customized OCT scanning protocols to detect changes in successive B-scan images to assess either phase or speckle variation [160–163]. These techniques can generate motion contrast from moving blood and enable visualization of microvasculature in three dimensions. Polarization-sensitive OCT (PS-OCT) techniques were

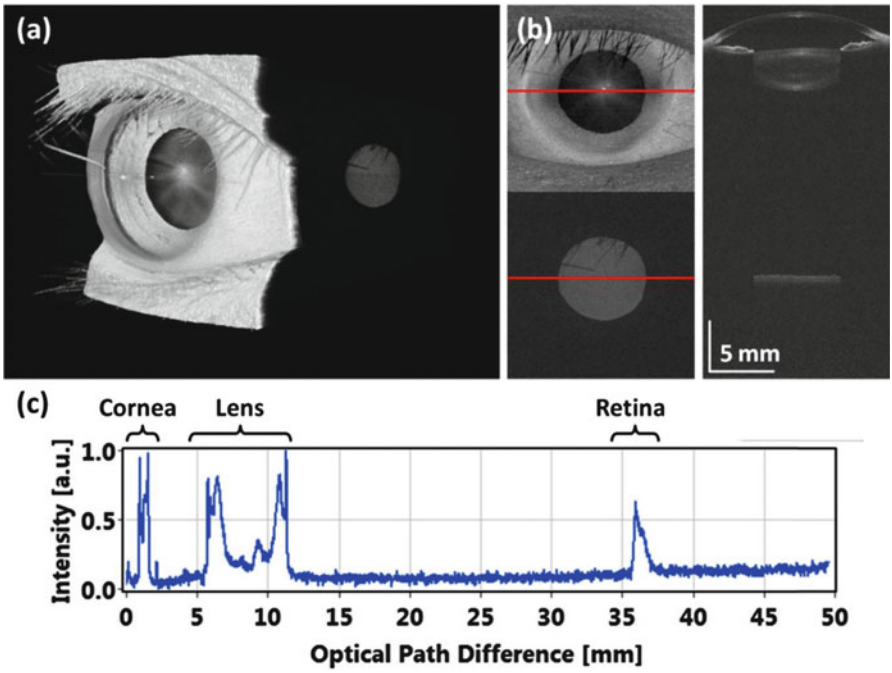

Fig. 1.40 Full eye length imaging. Swept source OCT using a VCSEL light source with ultralong depth range at 45 kHz axial scan rate. (**a**) Rendering of 3D-OCT data showing anterior eye and retina. (**b**) En face OCT images and central B-scan extracted from 3D-OCT data set uncorrected for light refraction. (**c**) Axial scan with echoes from the cornea, crystalline lens, and the retina enables measurement of intraocular distances (Grulkowski et al. [152])

developed using multichannel interferometers that simultaneously detect different interference polarization states [164, 165]. These techniques permit quantitative imaging of the birefringence properties of materials and tissues. Early studies also demonstrated the feasibility of obtaining spectroscopic information by detecting and Fourier transforming the interferometric output [166, 167]. The development of Fourier domain detection has been an enabling advance for many of the functional techniques because there is now direct access to the phase and spectral components of the interference. In addition, many functional methods require high data rates which are supported by Fourier domain detection. These methods are described in more than 20 chapters in Part IV of this book.

1.8 Conclusion

OCT is a powerful imaging technology in biomedical research and medicine because it enables in situ visualization of tissue structure and pathology without the need to excise and process specimens, as in conventional excisional biopsy and

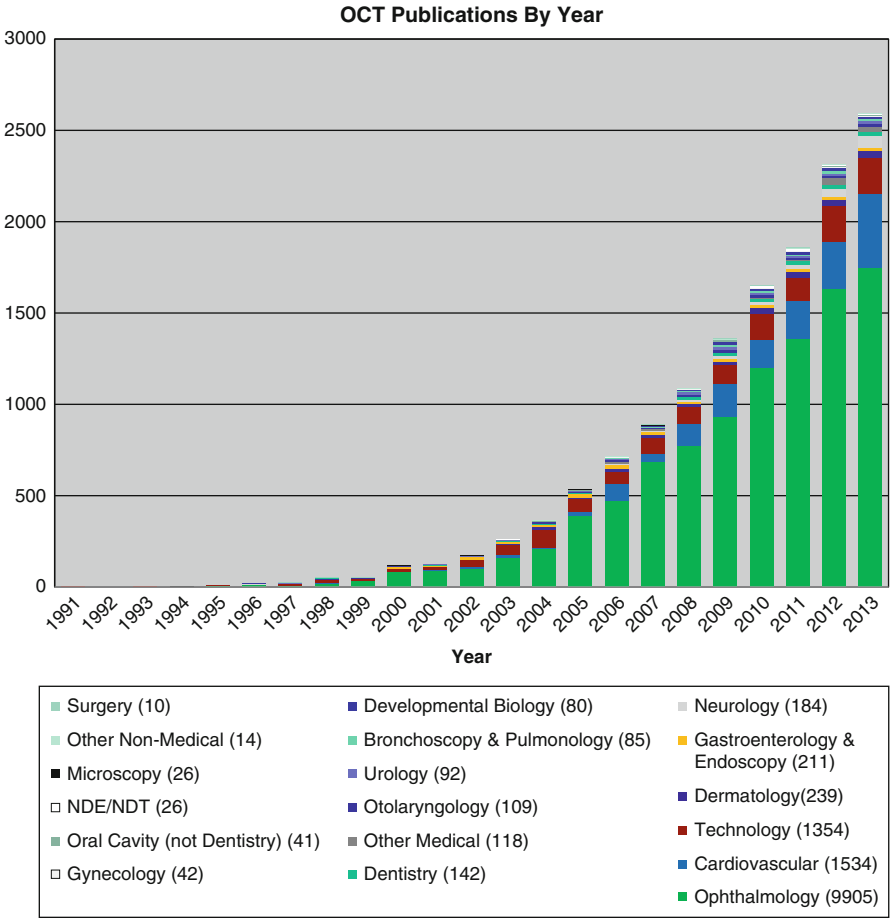

Fig. 1.41 Growth of journal publications involving OCT. Publications are an indicator of scientific and clinical progress. Ophthalmology and cardiovascular imaging are currently the largest applications of OCT. OCT technology remains an active area and was in second place until 2010 when cardiology applications increased. The growth in clinical publications is closely linked to commercial development of technology and is one indicator for clinical impact (Courtesy of E. Swanson)

histopathology. Non-excisional "optical biopsy," the ability to visualize tissue morphology in real time under operator guidance, can be used for a wide variety of applications. Figure 1.41 shows a plot of journal publications which involved OCT as a function of year. Journal articles are one marker for scientific development as well as clinical adoption. The factors which govern the adoption of OCT in different clinical specialties as well as the technology translation process are discussed in detail in ▶ Chap. 84, "OCT Technology Transfer and the OCT Market".

The largest number of publications is in ophthalmology. OCT has had the most clinical impact in ophthalmology, where it provides structural, quantitative, and functional information that cannot be obtained by any other modality. OCT improves the diagnosis of retinal disease as well as the monitoring of disease progression and response to therapy. In ophthalmology OCT played a significant role in the development of new therapies for age-related macular degeneration. It is now a standard clinical imaging modality in this clinical specialty.

The second largest number of publications at the time this book is written is in cardiology. Intravascular OCT has contributed to the understanding of plaque morphology and its role in myocardial infarction as well as percutaneous coronary interventions such as the implantation of stents. OCT is a powerful imaging modality for cardiovascular research; however, it is not yet widely used in interventional cardiology. Extensive clinical studies are still required to determine if OCT will become a standard imaging modality in this specialty. If successful in cardiology, OCT could have a major impact on morbidity and mortality from heart disease and the market could far surpass that in ophthalmology.

The third largest volume of publications is in technology research. Technology development has been an active area of research for more than a decade and although there may be the perception that technology development is saturating, it is difficult to predict future enabling advances. The development of Fourier domain detection not only enabled dramatic improvements in imaging speed, but will also enable countless new functional imaging methods. However, these advances would have been difficult to predict before 2003. Additional powerful new technologies and methods for OCT may be discovered in the near future.

Irrespective of innovations in OCT technology, there are many clinical specialties where OCT can be applied. OCT can be interfaced to a wide range of instruments and devices such as endoscopes, catheters, laparoscopes, and imaging needles, which enable the imaging of luminal or solid organs. The application of OCT in oncology is an active area of investigation and, although this is challenging area, OCT could have a significant impact on improving cancer diagnosis by guiding excisional biopsy to reduce sampling errors. OCT could also be integrated with therapies to guide methods such as ablative therapy or surgical resection. A wide range of smart surgical devices using image guidance remain to be developed and validated.

From the viewpoint of fundamental research, OCT has a broad spectrum of applications spanning such diverse topics as materials research, tissue engineering, developmental biology, and small animal imaging. Preclinical applications of OCT are especially interesting because imaging technologies which enable longitudinal follow-up can improve the speed of pharmaceutical discovery and development. The development of clinical applications across multiple specialties and subspecialties is an enormous task requiring extensive clinical studies to assess efficacy on an indication-by-indication basis. These studies will be performed by multidisciplinary collaborative teams of scientists, engineers, and clinicians. The infrastructure to perform these studies will require government, industry, and foundations support as well as academic and industrial innovation. However, despite these

challenges, there is an enormous potential to advance scientific and clinical knowledge, improve patient care, and reduce morbidity and mortality.

Acknowledgments The authors would like to thank Aaron Aguirre, Osman Ahsen, WooJhon Choi, Erich Ippen, Franz Kartner, Hsiang-Chieh Lee, Jonathan Liu, Chen Lu, and Tsung-Han Tsai from the Department of Electrical Engineering and Computer Science and Research Laboratory of Electronics at the Massachusetts Institute of Technology; Eric Swanson, Entrepreneur; Jay S. Duker, Caroline Baumal, Elias Reichel, Adam Rogers, Nadia Waheed, and Andre J. Witkin from the New England Eye Center, Tufts New England Medical Center, Tufts University; Joel S. Schuman, Hiroshi Ishikawa, Larry Kagemann, and Gadi Wollstein from the University of Pittsburgh Medical Center Eye Center, Department of Ophthalmology, Eye and Ear Institute, University of Pittsburgh School of Medicine; David Huang and Yali Jia from the Oregon Health Sciences University; James Connolly from the Beth Israel Deaconess Medical Center; Allen Clermont and Edward Feener from the Beetham Eye Institute, Joslin Diabetes Center, Harvard Medical School; Robert Huber from the University of Lubeck; Hiroshi Mashimo and Qing Huang from the Boston VA Healthcare System and Harvard Medical School; David Boas and Vivek Srinivasan from the Martinos Imaging Center, Massachusetts General Hospital; Joachim Hornegger and Martin Kraus from the Friedrich-Alexander-Universität Erlangen-Nürnberg; Maciej Wojtkowski, Iwona Gorczynska, and Irek Grulkowski from the Institute of Physics, Nicolaus Copernicus University, Torun, Poland; Vijaysekhar Jayaraman from Praevium Research; Ben Potsaid, Alex Cable, and James Jiang from Thorlabs; Desmond Adler and Joseph Schmitt from LightLab; and Tony Ko from Optovue.

This work was sponsored at MIT by the National Institutes of Health R01-CA75289, R01-CA178636, and R01-EY11289 and the Air Force Office of Scientific Research FA9550-10-1-0551 and FA9550-12-1-0499. This work is supported by the Medical University of Vienna, the European projects FAMOS (FP7 ICT 317744) and FUN OCT (FP7 HEALTH 201880), Macular Vision Research Foundation (MVRF, USA), Austrian Science Fund (FWF) project number S10510-N20, and the Christian Doppler Society (Christian Doppler Laboratory "Laser development and their application in medicine").

References

1. D. Huang, E.A. Swanson, C.P. Lin, J.S. Schuman, W.G. Stinson, W. Chang, M.R. Hee, T. Flotte, K. Gregory, C.A. Puliafito, J.G. Fujimoto, Optical coherence tomography. Science **254**, 1178–1181 (1991)
2. J.G. Fujimoto, M.E. Brezinski, G.J. Tearney, S.A. Boppart, B.E. Bouma, M.R. Hee, J.F. Southern, E.A. Swanson, Biomedical imaging and optical biopsy using optical coherence tomography. Nat. Med. **1**, 970–972 (1995)
3. M.E. Brezinski, G.J. Tearney, B.E. Bouma, J.A. Izatt, M.R. Hee, E.A. Swanson, J.F. Southern, J.G. Fujimoto, Optical coherence tomography for optical biopsy. Properties and demonstration of vascular pathology. Circulation **93**, 1206–1213 (1996)
4. R. Erbel, J.R.T.C. Roelandt, J. Ge, G. Gorge, *Intravascular Ultrasound* (Martin Dunitz, London, 1998)
5. T.L. Szabo, *Diagnostic Ultrasound Imaging: Inside Out* (Elsevier/Academic, Burlington, 2004)
6. W.R. Hedrick, D.L. Hykes, D.E. Starchman, *Ultrasound Physics and Instrumentation*, 4th edn. (Elsevier/Mosby, St. Louis, 2005)
7. J.S. Schuman, C.A. Puliafito, J.G. Fujimoto, *Optical Coherence Tomography of Ocular Diseases*, 2nd edn. (Slack, Thorofare, 2004)
8. M.A. Duguay, Light photographed in flight. Am. Sci. **59**, 551–556 (1971)

9. M.A. Duguay, A.T. Mattick, Ultrahigh speed photography of picosecond light pulses and echoes. Appl. Optics **10**, 2162–2170 (1971)
10. A.P. Bruckner, Picosecond light scattering measurements of cataract microstructure. Appl. Optics **17**, 3177–3183 (1978)
11. H. Park, M. Chodorow, R. Kompfner, High resolution optical ranging system. Appl. Optics **20**, 2389–2394 (1981)
12. J.G. Fujimoto, S. De Silvestri, E.P. Ippen, C.A. Puliafito, R. Margolis, A. Oseroff, Femtosecond optical ranging in biological systems. Opt. Lett. **11**, 150–153 (1986)
13. K. Takada, I. Yokohama, K. Chida, J. Noda, New measurement system for fault location in optical waveguide devices based on an interferometric technique. Appl. Optics **26**, 1603–1608 (1987)
14. R. Youngquist, S. Carr, D. Davies, Optical coherence-domain reflectometry: a new optical evaluation technique. Opt. Lett. **12**, 158–160 (1987)
15. H.H. Gilgen, R.P. Novak, R.P. Salathe, W. Hodel, P. Beaud, Submillimeter optical reflectometry. IEEE J. Lightwave Technol. **7**, 1225–1233 (1989)
16. A.F. Fercher, K. Mengedoht, W. Werner, Eye-length measurement by interferometry with partially coherent light. Opt. Lett. **13**, 1867–1869 (1988)
17. X. Clivaz, F. Marquis-Weible, R.P. Salathe, Optical low coherence reflectometry with 1.9 μm spatial resolution. Electron. Lett. **28**, 1553–1554 (1992)
18. J.M. Schmitt, A. Knuttel, R.F. Bonner, Measurement of optical-properties of biological tissues by low- coherence reflectometry. Appl. Optics **32**, 6032–6042 (1993)
19. N. Tanno, T. Ichimura, Reproduction of optical reflection-intensity-distribution using multimode laser coherence. Trans. Inst. Electron. Inf. Commun. Eng. C-I **J77C-I**, 415–422 (1994)
20. Y. Wang, T. Funaba, T. Ichimura, N. Tanno, Optical multimode time-domain reflectometry. Rev. Laser Eng. **23**, 273–279 (1995)
21. D. Huang, J. Wang, C.P. Lin, C.A. Puliafito, J.G. Fujimoto, Micron-resolution ranging of cornea and anterior chamber by optical reflectometry. Lasers Surg. Med. **11**, 419–425 (1991)
22. G.L. Abbas, V.W.S. Chan, T.K. Yee, Local-oscillator excess-noise suppression for homodyne and heterodyne detection. Opt. Lett. **8**, 419–421 (1983)
23. A.M. Rollins, J.A. Izatt, Optimal interferometer designs for optical coherence tomography. Opt. Lett. **24**, 1484–1486 (1999)
24. A.F. Fercher, C.K. Hitzenberger, W. Drexler, G. Kamp, H. Sattmann, In vivo optical coherence tomography. Am. J. Ophthalmol. **116**, 113–114 (1993)
25. E.A. Swanson, J.A. Izatt, M.R. Hee, D. Huang, C.P. Lin, J.S. Schuman, C.A. Puliafito, J.G. Fujimoto, In vivo retinal imaging by optical coherence tomography. Opt. Lett. **18**, 1864–1866 (1993)
26. M.R. Hee, J.A. Izatt, E.A. Swanson, D. Huang, J.S. Schuman, C.P. Lin, C.A. Puliafito, J.G. Fujimoto, Optical coherence tomography of the human retina. Arch. Ophthalmol. **113**, 325–332 (1995)
27. C.A. Puliafito, M.R. Hee, C.P. Lin, E. Reichel, J.S. Schuman, J.S. Duker, J.A. Izatt, E.A. Swanson, J.G. Fujimoto, Imaging of macular diseases with optical coherence tomography. Ophthalmology **102**, 217–229 (1995)
28. M.R. Hee, C.A. Puliafito, C. Wong, J.S. Duker, E. Reichel, B. Rutledge, J.S. Schuman, E.A. Swanson, J.G. Fujimoto, Quantitative assessment of macular edema with optical coherence tomography. Arch. Ophthalmol. **113**, 1019–1029 (1995)
29. M.R. Hee, C.A. Puliafito, J.S. Duker, E. Reichel, J.G. Coker, J.R. Wilkins, J.S. Schuman, E.A. Swanson, J.G. Fujimoto, Topography of diabetic macular edema with optical coherence tomography. Ophthalmology **105**, 360–370 (1998)
30. M.R. Hee, C.A. Puliafito, C. Wong, J.S. Duker, E. Reichel, J.S. Schuman, E.A. Swanson, J.G. Fujimoto, Optical coherence tomography of macular holes. Ophthalmology **102**, 748–756 (1995)

31. M.R. Hee, C.A. Puliafito, C. Wong, E. Reichel, J.S. Duker, J.S. Schuman, E.A. Swanson, J.G. Fujimoto, Optical coherence tomography of central serous chorioretinopathy. Am. J. Ophthalmol. **120**, 65–74 (1995)
32. M.R. Hee, C.R. Baumal, C.A. Puliafito, J.S. Duker, E. Reichel, J.R. Wilkins, J.G. Coker, J.S. Schuman, E.A. Swanson, J.G. Fujimoto, Optical coherence tomography of age-related macular degeneration and choroidal neovascularization. Ophthalmology **103**, 1260–1270 (1996)
33. J.S. Schuman, M.R. Hee, A.V. Arya, T. Pedut-Kloizman, C.A. Puliafito, J.G. Fujimoto, E.A. Swanson, Optical coherence tomography: a new tool for glaucoma diagnosis. Curr. Opin. Ophthalmol. **6**, 89–95 (1995)
34. J.S. Schuman, M.R. Hee, C.A. Puliafito, C. Wong, T. Pedut-Kloizman, C.P. Lin, E. Hertzmark, J.A. Izatt, E.A. Swanson, J.G. Fujimoto, Quantification of nerve fiber layer thickness in normal and glaucomatous eyes using optical coherence tomography. Arch. Ophthalmol. **113**, 586–596 (1995)
35. J.M. Schmitt, A. Knuttel, M. Yadlowsky, M.A. Eckhaus, Optical-coherence tomography of a dense tissue: statistics of attenuation and backscattering. Phys. Med. Biol. **39**, 1705–1720 (1994)
36. J.G. Fujimoto, M.E. Brezinski, G.J. Tearney, S.A. Boppart, B. Bouma, M.R. Hee, J.F. Southern, E.A. Swanson, Optical biopsy and imaging using optical coherence tomography. Nat. Med. **1**, 970–972 (1995)
37. P. Parsa, S.L. Jacques, N.S. Nishioka, Optical properties of rat liver between 350 and 2200 nm. Appl. Opt. **28**, 2325–2330 (1989)
38. J.M. Schmitt, A. Knuttel, Model of optical coherence tomography of heterogeneous tissue. J. Opt. Soc. Am. A Opt. Image Sci. Vis. **14**, 1231–1242 (1997)
39. M.E. Brezinski, G.J. Tearney, S.A. Boppart, E.A. Swanson, J.F. Southern, J.G. Fujimoto, Optical biopsy with optical coherence tomography: feasibility for surgical diagnostics. J. Surg. Res. **71**, 32–40 (1997)
40. J.A. Izatt, M.D. Kulkarni, H.-W. Wang, K. Kobayashi, M.V. Sivak Jr., Optical coherence tomography and microscopy in gastrointestinal tissues. IEEE J. Sel. Top. Quantum Electron. **2**, 1017–1028 (1996)
41. G.J. Tearney, M.E. Brezinski, J.F. Southern, B.E. Bouma, S.A. Boppart, J.G. Fujimoto, Optical biopsy in human gastrointestinal tissue using optical coherence tomography. Am. J. Gastroenterol. **92**, 1800–1804 (1997)
42. G.J. Tearney, M.E. Brezinski, J.F. Southern, B.E. Bouma, S.A. Boppart, J.G. Fujimoto, Optical biopsy in human urologic tissue using optical coherence tomography. J. Urol. **157**, 1915–1919 (1997)
43. S.A. Boppart, M.E. Brezinski, C. Pitris, J.G. Fujimoto, Optical coherence tomography for neurosurgical imaging of human intracortical melanoma. Neurosurgery **43**, 834–841 (1998)
44. K. Kobayashi, J.A. Izatt, M.D. Kulkarni, J. Willis, M.V. Sivak Jr., High-resolution cross-sectional imaging of the gastrointestinal tract using optical coherence tomography: preliminary results. Gastrointest. Endosc. **47**, 515–523 (1998)
45. G.J. Tearney, M.E. Brezinski, J.F. Southern, B.E. Bouma, S.A. Boppart, J.G. Fujimoto, Optical biopsy in human pancreatobiliary tissue using optical coherence tomography. Dig. Dis. Sci. **43**, 1193–1199 (1998)
46. C. Pitris, M.E. Brezinski, B.E. Bouma, G.J. Tearney, J.F. Southern, J.G. Fujimoto, High resolution imaging of the upper respiratory tract with optical coherence tomography: a feasibility study. Am. J. Respir. Crit. Care Med. **157**(5 Pt 1), 1640–1644 (1998)
47. C. Pitris, A. Goodman, S.A. Boppart, J.J. Libus, J.G. Fujimoto, M.E. Brezinski, High-resolution imaging of gynecologic neoplasms using optical coherence tomography. Obstet. Gynecol. **93**, 135–139 (1999)
48. C.A. Jesser, S.A. Boppart, C. Pitris, D.L. Stamper, G.P. Nielsen, M.E. Brezinski, J.G. Fujimoto, High resolution imaging of transitional cell carcinoma with optical coherence

tomography: feasibility for the evaluation of bladder pathology. Br. J. Radiol. **72**, 1170–1176 (1999)
49. S.A. Boppart, A. Goodman, J. Libus, C. Pitris, C.A. Jesser, M.E. Brezinski, J.G. Fujimoto, High resolution imaging of endometriosis and ovarian carcinoma with optical coherence tomography: feasibility for laparoscopic-based imaging. Br. J. Obstet. Gynaecol. **106**, 1071–1077 (1999)
50. C. Pitris, C. Jesser, S.A. Boppart, D. Stamper, M.E. Brezinski, J.G. Fujimoto, Feasibility of optical coherence tomography for high-resolution imaging of human gastrointestinal tract malignancies. J. Gastroenterol. **35**, 87–92 (2000)
51. C.A. Puliafito, M.R. Hee, J.S. Schuman, J.G. Fujimoto, *Optical Coherence Tomography of Ocular Diseases* (Slack, Thorofare, 1996)
52. S.A. Boppart, M.E. Brezinski, B.E. Bouma, G.J. Tearney, J.G. Fujimoto, Investigation of developing embryonic morphology using optical coherence tomography. Dev. Biol. **177**, 54–63 (1996)
53. S.A. Boppart, B.E. Bouma, C. Pitris, G.J. Tearney, J.F. Southern, M.E. Brezinski, J.G. Fujlmoto, Intraoperative assessment of microsurgery with three-dimensional optical coherence tomography. Radiology **208**, 81–86 (1998)
54. J.S. Schuman, T. Pedut-Kloizman, E. Hertzmark, M.R. Hee, J.R. Wilkins, J.G. Coker, C.A. Puliafito, J.G. Fujimoto, E.A. Swanson, Reproducibility of nerve fiber layer thickness measurements using optical coherence tomography. Ophthalmology **103**, 1889–1898 (1996)
55. G.J. Tearney, S.A. Boppart, B.E. Bouma, M.E. Brezinski, N.J. Weissman, J.F. Southern, J.G. Fujimoto, Scanning single-mode fiber optic catheter-endoscope for optical coherence tomography. Opt. Lett. **21**, 543–545 (1996)
56. G.J. Tearney, M.E. Brezinski, B.E. Bouma, S.A. Boppart, C. Pitvis, J.F. Southern, J.G. Fujimoto, In vivo endoscopic optical biopsy with optical coherence tomography. Science **276**, 2037–2039 (1997)
57. B.E. Bouma, G.J. Tearney, Power-efficient nonreciprocal interferometer and linear-scanning fiber-optic catheter for optical coherence tomography. Opt. Lett. **24**, 531–533 (1999)
58. G.J. Tearney, M.E. Brezinski, S.A. Boppart, B.E. Bouma, N. Weissman, J.F. Southern, E.A. Swanson, J.G. Fujimoto, Catheter-based optical imaging of a human coronary artery. Circulation **94**, 3013 (1996)
59. J.G. Fujimoto, S.A. Boppart, G.J. Tearney, B.E. Bouma, C. Pitris, M.E. Brezinski, High resolution in vivo intra-arterial imaging with optical coherence tomography. Heart **82**, 128–133 (1999)
60. G.J. Tearney, I.K. Jang, D.H. Kang, H.T. Aretz, S.L. Houser, T.J. Brady, K. Schlendorf, M. Shishkov, B.E. Bouma, Porcine coronary imaging in vivo by optical coherence tomography. Acta Cardiol. **55**, 233–237 (2000)
61. I.K. Jang, G. Tearney, B. Bouma, Visualization of tissue prolapse between coronary stent struts by optical coherence tomography: comparison with intravascular ultrasound. Circulation **104**, 2754 (2001)
62. E. Grube, U. Gerckens, L. Buellesfeld, P.J. Fitzgerald, Images in cardiovascular medicine. Intracoronary imaging with optical coherence tomography: a new high-resolution technology providing striking visualization in the coronary artery. Circulation **106**, 2409–2410 (2002)
63. I.K. Jang, B.E. Bouma, D.H. Kang, S.J. Park, S.W. Park, K.B. Seung, K.B. Choi, M. Shishkov, K. Schlendorf, E. Pomerantsev, S.L. Houser, H.T. Aretz, G.J. Tearney, Visualization of coronary atherosclerotic plaques in patients using optical coherence tomography: comparison with intravascular ultrasound. J. Am. Coll. Cardiol. **39**, 604–609 (2002)
64. B.E. Bouma, G.J. Tearney, H. Yabushita, M. Shishkov, C.R. Kauffman, D. DeJoseph Gauthier, B.D. MacNeill, S.L. Houser, H.T. Aretz, E.F. Halpern, I.K. Jang, Evaluation of intracoronary stenting by intravascular optical coherence tomography. Heart **89**, 317–320 (2003)

65. A.M. Sergeev, V.M. Gelikonov, G.V. Gelikonov, F.I. Feldchtein, R.V. Kuranov, N.D. Gladkova, N.M. Shakhova, L.B. Suopova, A.V. Shakhov, I.A. Kuznetzova, A.N. Denisenko, V.V. Pochinko, Y.P. Chumakov, O.S. Streltzova, In vivo endoscopic OCT imaging of precancer and cancer states of human mucosa. Opt. Express **1**, 432–440 (1997)
66. F.I. Feldchtein, G.V. Gelikonov, V.M. Gelikonov, R.V. Kuranov, A. Sergeev, N.D. Gladkova, A.V. Shakhov, N.M. Shakova, L.B. Snopova, A.B.. Terent'eva, E.V. Zagainova, Y.P. Chumakov, I.A. Kuznetzova, Endoscopic applications of optical coherence tomography. Opt. Express **3**, 257 (1998)
67. A.M. Rollins, A. Chak, C.K. Wong, K. Kobayashi, M.V. Sivak, R. Ung-arunyawee, J.A. Izatt, Real-time in vivo imaging of gastrointestinal ultrastructure using endoscopic optical coherence tomography with a novel efficient interferometer design. Opt. Lett. **24**, 1358–1360 (1999)
68. S. Jäckle, N. Gladkova, F. Feldchtein, A. Terentieva, B. Brand, G. Gelikonov, V. Gelikonov, A. Sergeev, A. Fritscher-Ravens, J. Freund, U. Seitz, S. Soehendra, N. Schrödern, In vivo endoscopic optical coherence tomography of the human gastrointestinal tract–toward optical biopsy. Endoscopy **32**, 743–749 (2000)
69. S. Jäckle, N. Gladkova, F. Feldchtein, A. Terentieva, B. Brand, G. Gelikonov, V. Gelikonov, A. Sergeev, A. Fritscher-Ravens, J. Freund, U. Seitz, S. Schröder, N. Soehendra, In vivo endoscopic optical coherence tomography of esophagitis, Barrett's esophagus, and adeno-carcinoma of the esophagus. Endoscopy **32**, 750–755 (2000)
70. M.V. Sivak Jr., K. Kobayashi, J.A. Izatt, A.M. Rollins, R. Ung-Runyawee, A. Chak, R.C. Wong, G.A. Isenberg, J. Willis, High-resolution endoscopic imaging of the GI tract using optical coherence tomography. Gastrointest. Endosc. **51**(4 Pt 1), 474–479 (2000)
71. B.E. Bouma, G.J. Tearney, C.C. Compton, N.S. Nishioka, High-resolution imaging of the human esophagus and stomach in vivo using optical coherence tomography. Gastrointest. Endosc. **51**(4 Pt 1), 467–474 (2000)
72. X.D. Li, S.A. Boppart, J. Van Dam, H. Mashimo, M. Mutinga, W. Drexler, M. Klein, C. Pitris, M.L. Krinsky, M.E. Brezinski, J.G. Fujimoto, Optical coherence tomography: advanced technology for the endoscopic imaging of Barrett's esophagus. Endoscopy **32**, 921–930 (2000)
73. J.M. Poneros, S. Brand, B.E. Bouma, G.J. Tearney, C.C. Compton, N.S. Nishioka, Diagnosis of specialized intestinal metaplasia by optical coherence tomography. Gastroenterology **120**, 7–12 (2001)
74. F.I. Feldchtein, G.V. Gelikonov, V.M. Gelikonov, R.V. Kuranov, A.M. Sergeev, N.D. Gladkova, A.V. Shakhov, N.M. Shakhova, L.B. Snopova, A.B.. Terent'eva, E.V. Zagainova, Y.P. Chumakov, I.A. Kuznetzova, Endoscopic applications of optical coherence tomography. Opt. Express. **3**(6), 239–250 (1998)
75. S.A. Boppart, B.E. Bouma, C. Pitris, G.J. Tearney, J.G. Fujimoto, M.E. Brezinski, Forward-imaging instruments for optical coherence tomography. Opt. Lett. **22**, 1618–1620 (1997)
76. F.I. Feldchtein, G.V. Gelikonov, V.M. Gelikonov, R.R. Iksanov, R.V. Kuranov, A.M. Sergeev, N.D. Gladkova, M.N. Ourutina, J.A. Warren, Jr, D.H. Reitze, In vivo OCT imaging of hard and soft tissue of the oral cavity. Opt. Express. **3** (1998b)
77. J.M. Zara, S.W. Smith, Optical scanner using a MEMS actuator. Sens. Actuators A Phys. **A102**, 176–184 (2002)
78. T. Xie, H. Xie, G.K. Fedder, Y. Pan, Endoscopic optical coherence tomography with new MEMS mirror. Electron. Lett. **39**, 1535–1536 (2003)
79. P.H. Tran, D.S. Mukai, M. Brenner, Z.P. Chen, In vivo endoscopic optical coherence tomography by use of a rotational microelectromechanical system probe. Opt. Lett. **29**, 1236–1238 (2004)
80. A. Jain, A. Kopa, Y.T. Pan, G.K. Fedder, H.K. Xie, A two-axis electrothermal micromirror for endoscopic optical coherence tomography. IEEE J. Sel. Top. Quantum Electron. **10**, 636–642 (2004)

81. E.A. Swanson, D. Huang, M.R. Hee, J.G. Fujimoto, C.P. Lin, C.A. Puliafito, High-speed optical coherence domain reflectometry. Opt. Lett. **17**, 151–153 (1992)
82. J.A. Izatt, M.R. Hee, G.M. Owen, E.A. Swanson, J.G. Fujimoto, Optical coherence microscopy in scattering media. Opt. Lett. **19**, 590–592 (1994)
83. A.D. Aguirre, P. Hsiung, T.H. Ko, I. Hartl, J.G. Fujimoto, High-resolution optical coherence microscopy for high-speed, in vivo cellular imaging. Opt. Lett. **28**, 2064–2066 (2003)
84. A.D. Aguirre, Y. Chen, B. Bryan, H. Mashimo, Q. Huang, J.L. Connolly, J.G. Fujimoto, Cellular resolution ex vivo imaging of gastrointestinal tissues with optical coherence microscopy. J. Biomed. Opt. **15**, 016025 (2010)
85. B.W. Graf, S.G. Adie, S.A. Boppart, Correction of coherence gate curvature in high numerical aperture optical coherence imaging. Opt. Lett. **35**, 3120–3122 (2010)
86. A.G. Podoleanu, G.M. Dobre, D.A. Jackson, *En-face* coherence imaging using galvanometer scanner modulation. Opt. Lett. **23**, 147–149 (1998)
87. A.G. Podoleanu, J.A. Rogers, D.A. Jackson, OCT en-face images from the retina with adjustable depth resolution in real time. IEEE J. Sel. Top. Quantum Electron. **5**, 1176–1184 (1999)
88. M.E.J. Van Velthoven, F.D. Verbraak, L.A. Yannuzzi, R.B. Rosen, A.G.H. Podoleanu, M.D. De Smet, Imaging the retina by en face optical coherence tomography. Retin. J. Retin. Vitreous Dis. **26**, 129–136 (2006)
89. I. Gorczynska, V.J. Srinivasan, L.N. Vuong, R.W. Chen, J.J. Liu, E. Reichel, M. Wojtkowski, J.S. Schuman, J.S. Duker, J.G. Fujimoto, A. Manassakorn, H. Ishikawa, J.S. Kim, G. Wollstein, R.A. Bilonick, L. Kagemann, M.L. Gabriele, K.R. Sung, T. Mumcuoglu, J.S. Duker, J.G. Fujimoto, J.S. Schuman, Projection OCT fundus imaging for visualizing outer retinal pathology in non-exudative age related macular degeneration Comparison of optic disc margin identified by color disc photography and high-speed ultrahigh-resolution optical coherence tomography. Br. J. Ophthalmol. **28**, 28 (2008)
90. B. Lumbroso, M.C. Savastano, M. Rispoli, A. Balestrazzi, A. Savastano, E. Balestrazzi, Morphologic differences, according to etiology, in pigment epithelial detachments by means of en face optical coherence tomography. Retin. J. Retin. Vitreous Dis. **31**, 553–558 (2011)
91. B. Lumbroso, D. Huang, A. Romano, *Clinical En Face OCT Atlas* (Jaypee Brothers Medical, Romano, 2013)
92. A. Dubois, L. Vabre, A.-C. Boccara, E. Beaurepaire, High-resolution full-field optical coherence tomography with a Linnik microscope. Appl. Optics **41**, 805–812 (2002)
93. L. Vabre, A. Dubois, A.C. Boccara, Thermal-light full-field optical coherence tomography. Opt. Lett. **27**, 530–532 (2002)
94. A. Dubois, K. Grieve, G. Moneron, R. Lecaque, L. Vabre, C. Boccara, Ultrahigh-resolution full-field optical coherence tomography. Appl. Opt. **43**, 2874–2883 (2004)
95. W. Drexler, U. Morgner, R.K. Ghanta, F.X. Kärtner, J.S. Schuman, J.G. Fujimoto, Ultrahigh-resolution ophthalmic optical coherence tomography. Nat. Med. **7**, 502–507 (2001)
96. P.R. Herz, Y. Chen, A.D. Aguirre, J.G. Fujimoto, H. Mashimo, J. Schmitt, A. Koski, J. Goodnow, C. Petersen, Ultrahigh resolution optical biopsy with endoscopic optical coherence tomography. Opt. Express **12**, 3532–3542 (2004)
97. Y. Chen, A.D. Aguirre, P.L. Hsiung, S. Desai, P.R. Herz, M. Pedrosa, Q. Huang, M. Figueiredo, S.W. Huang, A. Koski, J.M. Schmitt, J.G. Fujimoto, H. Mashimo, Ultrahigh resolution optical coherence tomography of Barrett's esophagus: preliminary descriptive clinical study correlating images with histology. Endoscopy **39**, 599–605 (2007)
98. B. Bouma, G.J. Tearney, S.A. Boppart, M.R. Hee, M.E. Brezinski, J.G. Fujimoto, High-resolution optical coherence tomographic imaging using a mode-locked Ti:Al2O3 laser source. Opt. Lett. **20**, 1486–1488 (1995)
99. F.X. Kärtner, N. Matuschek, T. Schibli, U. Keller, H.A. Haus, C. Heine, R. Morf, V. Scheuer, M. Tilsch, T. Tschudi, Design and fabrication of double-chirped mirrors. Opt. Lett. **22**, 831–833 (1997)

100. U. Morgner, F.X. Kartner, S.H. Cho, Y. Chen, H.A. Haus, J.G. Fujimoto, E.P. Ippen, V. Scheuer, G. Angelow, T. Tschudi, Sub-two-cycle pulses from a Kerr-lens mode-locked Ti:sapphire laser. Opt. Lett. **24**, 411–413 (1999)
101. D.H. Sutter, L. Gallmann, N. Matuschek, F. Morier-Genoud, V. Scheuer, G. Angelow, T. Tschudi, G. Steinmeyer, U. Keller, Sub-6-fs pulses from a SESAM-assisted Kerr-lens mode-locked Ti:sapphire laser: at the frontiers of ultrashort pulse generation. Appl. Phys. B. 631–633 (1999/2000)
102. R. Ell, U. Morgner, F.X. Kärtner, J.G. Fujimoto, E.P. Ippen, V. Scheuer, G. Angelow, T. Tschudi, M.J. Lederer, A. Boiko, B. Luther-Davies, Generation of 5-fs pulses and octave-spanning spectra directly from a Ti:sapphire laser. Opt. Lett. **26**, 373–375 (2001)
103. W. Drexler, U. Morgner, F.X. Kartner, C. Pitris, S.A. Boppart, X.D. Li, E.P. Ippen, J.G. Fujimoto, In vivo ultrahigh-resolution optical coherence tomography. Opt. Lett. **24**, 1221–1223 (1999)
104. W. Drexler, H. Sattmann, B. Hermann, T.H. Ko, M. Stur, A. Unterhuber, C. Scholda, O. Findl, M. Wirtitsch, J.G. Fujimoto, A.F. Fercher, Enhanced visualization of macular pathology with the use of ultrahigh-resolution optical coherence tomography. Arch. Ophthalmol. **121**, 695–706 (2003)
105. T.H. Ko, J.G. Fujimoto, J.S. Duker, L.A. Paunescu, W. Drexler, C.R. Baumal, C.A. Puliafito, E. Reichel, A.H. Rogers, J.S. Schuman, Comparison of ultrahigh- and standard-resolution optical coherence tomography for imaging macular hole pathology and repair. Ophthalmology **111**, 2033–2043 (2004)
106. T.A. Birks, W.J. Wadsworth, P.S. Russell, Supercontinuum generation in tapered fibers. Opt. Lett. **25**, 1415–1417 (2000)
107. J.K. Ranka, R.S. Windeler, A.J. Stentz, Visible continuum generation in air-silica microstructure optical fibers with anomalous dispersion at 800 nm. Opt. Lett. **25**, 25–27 (2000)
108. I. Hartl, X.D. Li, C. Chudoba, R.K. Hganta, T.H. Ko, J.G. Fujimoto, J.K. Ranka, R.S. Windeler, Ultrahigh-resolution optical coherence tomography using continuum generation in an air-silica microstructure optical fiber. Opt. Lett. **26**, 608–610 (2001)
109. Y. Wang, Y. Zhao, J.S. Nelson, Z. Chen, R.S. Windeler, Ultrahigh-resolution optical coherence tomography by broadband continuum generation from a photonic crystal fiber. Opt. Lett. **28**, 182–184 (2003)
110. B. Povazay, K. Bizheva, A. Unterhuber, B. Hermann, H. Sattmann, A.F. Fercher, W. Drexler, A. Apolonski, W.J. Wadsworth, J.C. Knight, P.S.J. Russell, M. Vetterlein, E. Scherzer, Submicrometer axial resolution optical coherence tomography. Opt. Lett. **27**, 1800–1802 (2002)
111. A.M. Kowalevicz, T.R. Schibli, F.X. Kartner, J.G. Fujimoto, Ultralow-threshold Kerr-lens mode-locked Ti:Al2O3 laser. Opt. Lett. **27**, 2037–2039 (2002)
112. A. Unterhuber, B. Povazay, B. Hermann, H. Sattmann, W. Drexler, V. Yakovlev, G. Tempea, C. Schubert, E.M. Anger, P.K. Ahnelt, M. Stur, J.E. Morgan, A. Cowey, G. Jung, T. Le, A. Stingl, Compact, low-cost Ti:Al_2O_3 laser for in vivo ultrahigh-resolution optical coherence tomography. Opt. Lett. **28**, 905–907 (2003)
113. A.M. Kowalevicz, T. Ko, I. Hartl, J.G. Fujimoto, M. Pollnau, R.P. Salathe, Ultrahigh resolution optical coherence tomography using a superluminescent light source. Opt. Express. **10**(7), 349–353 (2002) http://dx.doi.org/10.1364/OE.10.000349
114. B.E. Bouma, G.J. Tearney, I.P. Bilinsky, B. Golubovic, J.G. Fujimoto, Self-phase-modulated Kerr-lens mode-locked Cr:forsterite laser source for optical coherence tomography. Opt. Lett. **21**, 1839–1841 (1996)
115. C. Chudoba, J.G. Fujimoto, E.P. Ippen, H.A. Haus, U. Morgner, F.X. Kärtner, V. Scheuer, G. Angelow, T. Tschudi, All-solid-state Cr:forsterite laser generating 14 f. pulses at 1.3 μm. Opt. Lett. **26**, 292–294 (2001)
116. Y. Wang, J.S. Nelson, Z. Chen, B.J. Reiser, R.S. Chuck, R.S. Windeler, Optimal wavelength for ultrahigh-resolution optical coherence tomography. Opt. Express. **11**(12), 1411–1417 (2003) http://dx.doi.org/10.1364/OE.11.001411

117. S. Bourquin, A.D. Aguirre, I. Hartl, P. Hsiung, T.H. Ko, J.G. Fujimoto, T.A. Birks, W.J. Wadsworth, U. Bunting, D. Kopf, Ultrahigh resolution real time OCT imaging using a compact femtosecond Nd: glass laser and nonlinear fiber. Opt. Express **11**, 3290–3297 (2003)
118. A.F. Fercher, C.K. Hitzenberger, G. Kamp, S.Y. Elzaiat, Measurement of intraocular distances by backscattering spectral interferometry. Opt. Commun. **117**, 43–48 (1995)
119. S.R. Chinn, E.A. Swanson, J.G. Fujimoto, Optical coherence tomography using a frequency-tunable optical source. Opt. Lett. **22**, 340–342 (1997)
120. B. Golubovic, B.E. Bouma, G.J. Tearney, J.G. Fujimoto, Optical frequency-domain reflectometry using rapid wavelength tuning of a Cr^{4+}:forsterite laser. Opt. Lett. **22**, 1704–1706 (1997)
121. S.H. Yun, G.J. Tearney, B.E. Bouma, B.H. Park, J.F. de Boer, High-speed spectral-domain optical coherence tomography at 1.3 mu m wavelength. Opt. Express **11**, 3598–3604 (2003)
122. S.H. Yun, G.J. Tearney, J.F. de Boer, N. Iftimia, B.E. Bouma, High-speed optical frequency-domain imaging. Opt. Express **11**, 2953–2963 (2003)
123. M.A. Choma, M.V. Sarunic, C.H. Yang, J.A. Izatt, Sensitivity advantage of swept source and fourier domain optical coherence tomography. Opt. Express **11**, 2183–2189 (2003)
124. R. Huber, K. Taira, T.H. Ko, M. Wojtkowski, V. Srinivasan, J.G. Fujimoto, High-speed, amplified, frequency swept laser at 20 kHz sweep rates for OCT imaging, in *Conference on Lasers and Electro-Optics/Quantum Electronics and Laser Science and Photonic Applications, Systems and Technologies 2005*, Baltimore, 2005, p. JThE33
125. R. Huber, M. Wojtkowski, J.G. Fujimoto, Fourier domain mode locking (FDML): a new laser operating regime and applications for optical coherence tomography. Opt. Express **14**, 3225–3237 (2006)
126. M. Wojtkowski, R. Leitgeb, A. Kowalczyk, T. Bajraszewski, A.F. Fercher, In vivo human retinal imaging by Fourier domain optical coherence tomography. J. Biomed. Opt. **7**, 457–463 (2002)
127. N. Nassif, B. Cense, B.H. Park, S.H. Yun, T.C. Chen, B.E. Bouma, G.J. Tearney, J.F. de Boer, In vivo human retinal imaging by ultrahigh-speed spectral domain optical coherence tomography. Opt. Lett. **29**, 480–482 (2004)
128. B. Cense, N. Nassif, T.C. Chen, M.C. Pierce, S. Yun, B.H. Park, B. Bouma, G. Tearney, J.F. de Boer, Ultrahigh-resolution high-speed retinal imaging using spectral-domain optical coherence tomography. Opt. Express **12**, 2435–2447 (2004)
129. M. Wojtkowski, V.J. Srinivasan, T.H. Ko, J.G. Fujimoto, A. Kowalczyk, J.S. Duker, Ultrahigh-resolution, high-speed, fourier domain optical coherence tomography and methods for dispersion compensation. Opt. Express **12**, 2404–2422 (2004)
130. R. Leitgeb, C.K. Hitzenberger, A.F. Fercher, Performance of fourier domain vs. time domain optical coherence tomography. Opt. Express **11**, 889–894 (2003)
131. J.F. de Boer, B. Cense, B.H. Park, M.C. Pierce, G.J. Tearney, B.E. Bouma, Improved signal-to-noise ratio in spectral-domain compared with time-domain optical coherence tomography. Opt. Lett. **28**, 2067–2069 (2003)
132. N.A. Nassif, B. Cense, B.H. Park, M.C. Pierce, S.H. Yun, B.E. Bouma, G.J. Tearney, T.C. Chen, J.F. de Boer, In vivo high-resolution video-rate spectral-domain optical coherence tomography of the human retina and optic nerve. Opt. Express. **12**(3), 367–376 (2004) http://dx.doi.org/10.1364/OPEX.12.000367
133. V.J. Srinivasan, M. Wojtkowski, A.J. Witkin, J.S. Duker, T.H. Ko, M. Carvalho, J.S. Schuman, A. Kowalczyk, J.G. Fujimoto, High-definition and 3-dimensional imaging of macular pathologies with high-speed ultrahigh-resolution optical coherence tomography. Ophthalmology **113**, 2054–2065 (2006)
134. M. Wojtkowski, V. Srinivasan, J.G. Fujimoto, T. Ko, J.S. Schuman, A. Kowalczyk, J.S. Duker, Three-dimensional retinal imaging with high-speed ultrahigh-resolution optical coherence tomography. Ophthalmology **112**, 1734–1746 (2005)

135. B. Potsaid, I. Gorczynska, V.J. Srinivasan, Y.L. Chen, J. Jiang, A. Cable, J.G. Fujimoto, Ultrahigh speed spectral/fourier domain OCT ophthalmic imaging at 70,000 to 312,500 axial scans per second. Opt. Express **16**, 15149–15169 (2008)
136. E.A. Swanson, D. Huang, J.G. Fujimoto, C.A. Puliafito, C.P. Lin, J.S. Schuman, Method and apparatus for optical imaging with means for controlling the longitudinal range of the sample, United States Patent 5,321,501, 1994
137. W. Eickhoff, R. Ulrich, Optical frequency-domain reflectometry in single-mode fiber. Appl. Phys. Lett. **39**, 693–695 (1981)
138. H. Barfuss, E. Brinkmeyer, Modified optical frequency-domain reflectometry with high spatial-resolution for components of integrated optic systems. J. Lightwave Technol. **7**, 3–10 (1989)
139. U. Glombitza, E. Brinkmeyer, Coherent frequency-domain reflectometry for characterization of single-mode integrated-optical wave-guides. J. Lightwave Technol. **11**, 1377–1384 (1993)
140. A.L. Kachelmyer, Range-Doppler imaging: waveforms and receiver design, in *Laser Radar III* (1998), pp. 138–161
141. W.Y. Oh, S.H. Yun, G.J. Tearney, B.E. Bouma, 115 kHz tuning repetition rate ultrahigh-speed wavelength-swept semiconductor laser. Opt. Lett. **30**, 3159–3161 (2005)
142. S.H. Yun, G.J. Tearney, B.J. Vakoc, M. Shishkov, W.Y. Oh, A.E. Desjardins, M.J. Suter, R.C. Chan, J.A. Evans, I.K. Jang, N.S. Nishioka, J.F. de Boer, B.E. Bouma, Comprehensive volumetric optical microscopy in vivo. Nat. Med. **12**, 1429–1433 (2006)
143. B.J. Vakoc, M. Shishko, S.H. Yun, W.Y. Oh, M.J. Suter, A.E. Desjardins, J.A. Evans, N.S. Nishioka, G.J. Tearney, B.E. Bouma, Comprehensive esophageal microscopy by using optical frequency-domain imaging (with video). Gastrointest. Endosc. **65**, 898–905 (2007)
144. D.C. Adler, Y. Chen, R. Huber, J. Schmitt, J. Connolly, J.G. Fujimoto, Three-dimensional endomicroscopy using optical coherence tomography. Nat. Photonics **1**, 709–716 (2007)
145. R. Huber, M. Wojtkowski, K. Taira, J.G. Fujimoto, K. Hsu, Amplified, frequency swept lasers for frequency domain reflectometry and OCT imaging: design and scaling principles. Opt. Express **13**, 3513–3528 (2005)
146. R. Huber, D.C. Adler, J.G. Fujimoto, Buffered Fourier domain mode locking: unidirectional swept laser sources for optical coherence tomography imaging at 370,000 lines/s. Opt. Lett. **31**, 2975–2977 (2006)
147. D.C. Adler, Y. Chen, R. Huber, J. Schmitt, J. Connolly, J.G. Fujimoto, Three dimensional endomicroscopy using optical coherence tomography. Nat. Photonics. 709–716 (2007)
148. D.C. Adler, C. Zhou, T.H. Tsai, J. Schmitt, Q. Huang, H. Mashimo, J.G. Fujimoto, Three-dimensional endomicroscopy of the human colon using optical coherence tomography. Opt. Express **17**, 784–796 (2009)
149. T. Klein, W. Wieser, C.M. Eigenwillig, B.R. Biedermann, R. Huber, Megahertz OCT for ultrawide-field retinal imaging with a 1,050 nm Fourier domain mode-locked laser. Opt. Express **19**, 3044–3062 (2011)
150. B. Potsaid, B. Baumann, D. Huang, S. Barry, A.E. Cable, J.S. Schuman, J.S. Duker, J.G. Fujimoto, Ultrahigh speed 1,050 nm swept source/fourier domain OCT retinal and anterior segment imaging at 100,000 to 400,000 axial scans per second. Opt. Express **18**, 20029–20048 (2010)
151. V. Jayaraman, G.D. Cole, M. Robertson, A. Uddin, A. Cable, High-sweep-rate 1,310 nm MEMS-VCSEL with 150 nm continuous tuning range. Electron. Lett. **48**, 867–868 (2012)
152. I. Grulkowski, J.J. Liu, B. Potsaid, V. Jayaraman, C.D. Lu, J. Jiang, A.E. Cable, J.S. Duker, J.G. Fujimoto, Retinal, anterior segment and full eye imaging using ultrahigh speed swept source OCT with vertical-cavity surface emitting lasers. Biomed. Opt. Express **3**, 2733–2751 (2012)

153. I. Grulkowski, J.J. Liu, B. Potsaid, V. Jayaraman, J. Jiang, J.G. Fujimoto, A.E. Cable, High-precision, high-accuracy ultralong-range swept-source optical coherence tomography using vertical cavity surface emitting laser light source. Opt. Lett. **38**, 673–675 (2013)
154. Z. Chen, T.E. Milner, D. Dave, J.S. Nelson, Optical Doppler tomographic imaging of fluid flow velocity in highly scattering media. Opt. Lett. **22**, 64–66 (1997)
155. Z. Chen, T.E. Milner, S. Srinivas, X. Wang, A. Malekafzali, M.J.C. van Gemert, J.S. Nelson, Noninvasive imaging of in vivo blood flow velocity using optical Doppler tomography. Opt. Lett. **22**, 1119–1121 (1997)
156. J.A. Izatt, M.D. Kulkami, S. Yazdanfar, J.K. Barton, A.J. Welch, In vivo bidirectional color Doppler flow imaging of picoliter blood volumes using optical coherence tomography. Opt. Lett. **22**, 1439–1441 (1997)
157. S. Yazdanfar, M.D. Kulkarni, J.A. Izatt, High resolution imaging of in vivo cardiac dynamics using color Doppler optical coherence tomography. Opt. Express. **1**(13), 424–431 (1997) http://dx.doi.org/10.1364/OE.1.000424
158. R.A. Leitgeb, L. Schmetterer, W. Drexler, A.F. Fercher, R.J. Zawadzki, T. Bajraszewski, Real-time assessment of retinal blood flow with ultrafast acquisition by color Doppler fourier domain optical coherence tomography. Opt. Express **11**, 3116–3121 (2003)
159. B.R. White, M.C. Pierce, N. Nassif, B. Cense, B.H. Park, G.J. Tearney, B.E. Bouma, T.C. Chen, J.F. de Boer, In vivo dynamic human retinal blood flow imaging using ultra-high-speed spectral domain optical Doppler tomography. Opt. Express **11**, 3490–3497 (2003)
160. S. Makita, Y. Hong, M. Yamanari, T. Yatagai, Y. Yasuno, Optical coherence angiography. Opt. Express **14**, 7821–7840 (2006)
161. R.K. Wang, S.L. Jacques, Z. Ma, S. Hurst, S.R. Hanson, A. Gruber, Three dimensional optical angiography. Opt. Express **15**, 4083–4097 (2007)
162. J. Fingler, D. Schwartz, C.H. Yang, S.E. Fraser, Mobility and transverse flow visualization using phase variance contrast with spectral domain optical coherence tomography. Opt. Express **15**, 12636–12653 (2007)
163. B.J. Vakoc, R.M. Lanning, J.A. Tyrrell, T.P. Padera, L.A. Bartlett, T. Stylianopoulos, L.L. Munn, G.J. Tearney, D. Fukumura, R.K. Jain, B.E. Bouma, Three-dimensional microscopy of the tumor microenvironment in vivo using optical frequency domain imaging. Nat. Med. **15**, 1219–1223 (2009)
164. J.F. De Boer, T.E. Milner, M.J.C. van Gemert, J.S. Nelson, Two-dimensional birefringence imaging in biological tissue by polarization-sensitive optical coherence tomography. Opt. Lett. **22**, 934–936 (1997)
165. M.J. Everett, K. Schoenenberger, B.W. Colston Jr., L.B. Da Silva, Birefringence characterization of biological tissue by use of optical coherence tomography. Opt. Lett. **23**, 228–230 (1998)
166. U. Morgner, W. Drexler, F.X. Kartner, X.D. Li, C. Pitris, E.P. Ippen, J.G. Fujimoto, Spectroscopic optical coherence tomography. Opt. Lett. **25**, 111–113 (2000)
167. D.J. Faber, E.G. Mik, M.C. Aalders, T.G. van Leeuwen, Light absorption of (oxy-) hemoglobin assessed by spectroscopic optical coherence tomography. Opt. Lett. **28**, 1436–1438 (2003)

Theory of Optical Coherence Tomography

2

Joseph A. Izatt, Michael A. Choma, and Al-Hafeez Dhalla

Keywords
Biomedical optics • Biophotonics • Coherent Imaging • Fourier analysis • Imaging • Interferometry • Noise analysis • Optical coherence tomography • Optics • Photonics • SNR

2.1 Introduction

Several previous publications have addressed the theory of optical coherence tomography (OCT) imaging. These have included original articles [1–12], reviews [13, 14], and books/book chapters [15, 16]. Many of these publications were authored before the major revolution that Fourier-domain techniques (here termed FDOCT) brought to OCT since their sensitivity advantage was confirmed in 2003 [10–12]. Thus, many of these prior works were written primarily from the perspective of time-domain OCT (TDOCT). Also, relatively few prior publications have addressed lateral resolution in OCT systems, which, from an end user perspective, is of equal importance to the axial resolving power derived from low-coherence interferometry. The goal of this chapter is to present a unified theory of OCT, which includes a discussion of imaging performance in all three dimensions and which treats both Fourier- and time-domain OCT on equal footing as specializations of the same underlying principles.

J.A. Izatt (✉)
Fitzpatrick Institute for Photonics and Departments of Biomedical Engineering and Ophthalmology, Duke University Medical Center, Durham, NC, USA
e-mail: jizatt@duke.edu

M.A. Choma
Departments of Diagnostic Radiology, Pediatrics, Biomedical Engineering, and Applied Physics, Yale University, New Haven, CT, USA

A.-H. Dhalla
Bioptigen, Inc, Durham, NC, USA

© Springer International Publishing Switzerland 2015

W. Drexler, J.G. Fujimoto (eds.), *Optical Coherence Tomography*,
DOI 10.1007/978-3-319-06419-2_3

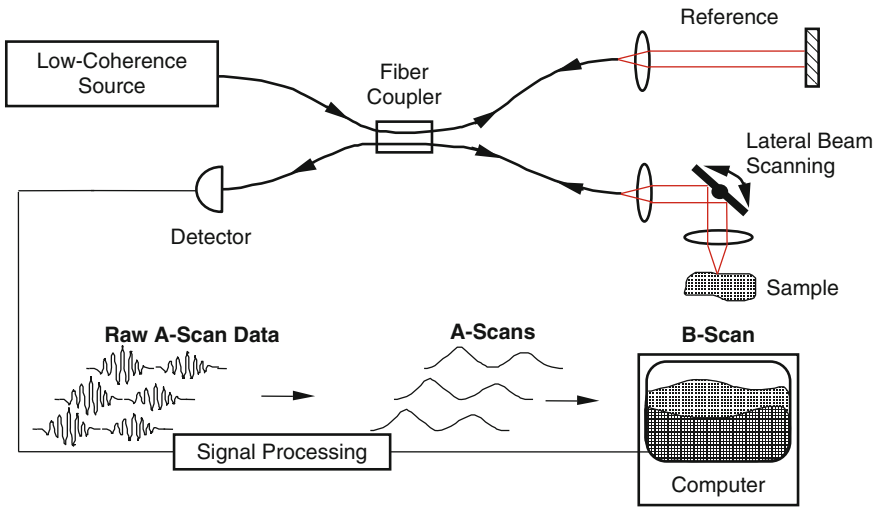

Fig. 2.1 Schematic of a generic fiber-optic OCT system. *Bold lines* represent fiber-optic paths, *red lines* represent free-space optical paths, and *thin lines* represent electronic signal paths

A generic OCT system schematic is illustrated in Fig. 2.1. Light from a low-coherence source is directed into a 2 × 2 fiberoptic coupler implementing a simple Michelson interferometer. The coupler is assumed to split the incident optical power evenly into sample and reference arms, although many practical OCT system designs take advantage of unbalanced power splitting, as has been described both theoretically and experimentally [8, 9]. Light exiting the reference fiber is incident upon a reference delay path and redirected back into the same fiber. Light exiting the sample fiber is incident upon an optical subsystem designed to focus the beam on the sample and to scan the focused spot in one or two lateral directions, typically under computer control. Many specialized scanning systems have been developed for OCT imaging applications in microscopy, ophthalmoscopy, endoscopy, catheterization, and others. The light backscattered or reflected from the sample is redirected through the same optical scanning system back into the sample arm fiber, where it is mixed with the returning reference arm light in the fiber coupler, and the combined light is made to interfere on the surface of a photoreceiver or detector. The electronic signals detected at the photoreceiver are processed into an A-scan, representing the depth-resolved reflectivity profile of the sample at the focal spot of the sample beam at a fixed lateral position of the scanning mechanism. As the scanning mechanism sweeps or steps the focused beam position across the sample, multiple A-scans are acquired and assembled in the computer into a two-dimensional cross-sectional image of the sample in the vicinity of the focal spot, termed a B-scan. Optionally, various alternative combinations of multidimensional lateral scanning and A-scan acquisition under computer control may be combined to create repeated A-scans at the same location as a function of time (termed M-scans), B-scans with lateral rather than depth priority, en face images at a fixed axial depth position (termed C-scans),

three-dimensional OCT volume data sets, and/or image improvement from OCT signal averaging in various combinations of dimensions.

In the case of TDOCT, the low-coherence source in Fig. 2.1 is broadband and continuous wave (cw), the reference arm delay is repetitively scanned in length, a single-channel (spectrally integrating) photoreceiver is employed, and the required signal processing consists of detecting the envelope of the detected fringe burst pattern corresponding to constructive interference between the reference arm light and each successive scattering site in the sample. FDOCT systems are subdivided into spectral-domain (or spectrometer-based) systems referred to as SDOCT and swept-source systems termed SSOCT (alternatively called OFDI by some authors). In the case of SDOCT, the source is broadband and cw, the reference arm length is fixed at a position approximately corresponding to the position of the sample, and the spectral interference pattern between the light returning from the reference arm and all depths in the sample is dispersed by a spectrometer and collected simultaneously on an array detector such as a charge-coupled device (CCD) or complementary metal-oxide-semiconductor (CMOS) camera. In the case of SSOCT, the source has narrow instantaneous linewidth but is rapidly swept in wavelength, and the spectral interference pattern is detected on a single photoreceiver as a function of time. The reference arm length is also fixed in SSOCT. In both SDOCT and SSOCT forms of FDOCT, the spectral interference pattern encodes in its spectral frequency content the entire depth-resolved structure of the sample at the position of the focal spot, and the A-scan may be recovered as described below using inverse Fourier transformation. Additional signal processing steps may also be required in FDOCT to prepare the spectral interferogram for the inverse Fourier transform, such as interpolation, so that the data is linearly sampled in wave number, addition of phase terms to correct for dispersion mismatches between the sample and reference arms, and others.

2.2 Confocal Gating and Lateral Resolution in OCT Systems

Some previous analyses have described the lateral resolution and axial field of view of OCT systems, as illustrated in Fig. 2.1 as the spot size and depth of focus of an assumed Gaussian profile sample arm beam in the region of the beam focus. This approach is a reasonable approximation and provides useful insight into the trade-off between these quantities specifically that spot size is proportional to the numerical aperture (NA) of the sample arm focusing optics, while the depth of focus is proportional to NA^2. However, it is more correct to treat the sample arm of an OCT system as a reflection-mode scanning confocal microscope, in which the single-mode optical fiber serves as a pinhole aperture for both illumination and collection of light from the sample. Even for OCT systems that do not employ fiber optics, the antenna response function of the homodyne wave mixing inherent to OCT can be shown to be equivalent to confocality [17]. Confocal microscopes using fiberoptic delivery and detection have been well described in the literature, including their lateral and axial point spread function behavior for single- and multimode fiber operation [18–20]. For single-mode optical fibers such as those used in OCT, the expressions for both lateral

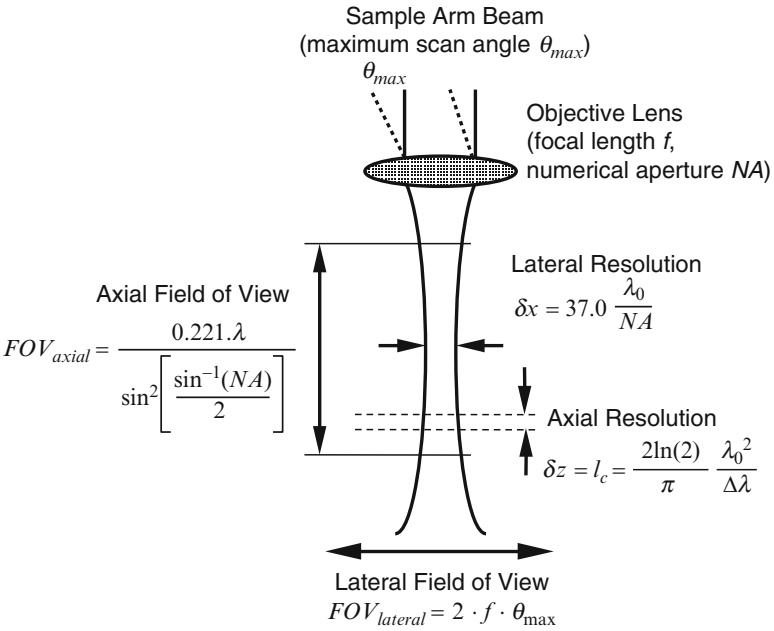

Fig. 2.2 Schematic of generic OCT sample arm optics. Formulas are provided for axial field of view FOV_{axial} and lateral resolution δx (assuming these quantities are dominated by the confocal geometrical optics), axial resolution δz (assuming it is limited by the low-coherence interferometer), and for lateral field of view FOV_{lateral} (assuming a simple f-theta scanning system)

and axial detected intensities reduce to those for an ideal confocal microscope with a diminishingly small pinhole aperture. Confocal microscopes have the advantage of slightly improved lateral resolution over conventional bright-field microscopes and the ability to perform "optical sectioning" due to their peaked axial response (unlike conventional bright-field microscopes, for which out-of-focus light is blurred, but not attenuated). A summary of results characterizing these quantities in lateral and axial directions is presented in Fig. 2.2. The optical system is assumed to be cylindrically symmetric, so only one lateral dimension is depicted.

An expression for the detected intensity from a point reflector placed in the focal plane of an ideal reflection confocal microscope as a function of lateral position is given by

$$I(v) = \left(\frac{2 \cdot J_1(v)}{v}\right)^4, \tag{2.1}$$

where $J_1(v)$ is a first-order Bessel function of the first kind and v is the normalized lateral range parameter defined by $v = 2\pi \cdot x \cdot \sin(\alpha)/\lambda_0$. Here, x is the lateral distance from the optical axis, α is half the angular optical aperture subtended by the objective, and λ_0 is the center wavelength of the light source. Note that the numerical aperture of the objective is given by $NA = \sin(\alpha)$, assuming that it is properly filled. We interpret Eq. 2.1 as the lateral point spread function of an OCT system at the

position of its focal plane and characterize it by defining the lateral resolution δx as its full width at half-maximum (FWHM) power, which calculates to

$$\delta x = 0.37 \cdot \frac{\lambda_0}{\sin(\alpha)} = 0.37 \frac{\lambda_0}{NA}. \tag{2.2}$$

The lateral field of view for an OCT system depends greatly upon the details of the lateral scanning system employed. A particularly simple scanning system employs some means to rotate the sample arm beam through the input aperture of the objective lens to a maximum one-sided scan angle $\theta_{\max}$ in one or two lateral dimensions. In this case, the lateral field of view of the OCT system is simply given by

$$FOV_{lateral} = 2 \cdot f \cdot \theta_{\max}.$$

We follow the convention in confocal microscopy [18, 19] and describe the axial response of the OCT sample arm optics as the confocal response to a planar rather than point reflector. The detected intensity of an ideal confocal microscope from a planar reflector as a function of the reflector position along the optic axis is given by

$$I(u) = \left(\frac{\sin(u/2)}{(u/2)} \right)^2, \tag{2.3}$$

where u is the normalized axial range parameter defined by $u = 8\pi \cdot z \cdot \sin^2(\alpha/2)/\lambda_0$. The axially peaked response of a confocal microscope gives it its well-known depth-sectioning capability. This is also the response we would expect by translating a mirror axially through the focus of an OCT sample arm. If the length of this function is comparable to the axial response of the OCT system arising from low-coherence interferometry (as described below), then the overall axial response of the OCT system should properly be described as the convolution of these two functions. OCT systems operating in this regime have been referred to as optical coherence microscopy or OCM systems [2, 21, 22]. In OCM, however, considerable effort must be expended to align the "confocal" and "coherence" gates and to keep them aligned as depth scanning is performed. In most OCT applications designed for practical clinical and research applications, a relatively low numerical aperture objective is used so that the lateral resolution δx is approximately matched to the axial resolution δz defined by the low-coherence interferometer (see Eq. 2.8), and thus approximately isotropic resolution imaging is performed. Under this condition, the confocal gate length is much larger than the lateral resolution since it scales as the square of the numerical aperture. However, the confocal gate length still limits the axial range over which the low-coherence interferometric depth scanning may usefully operate. We define the FWHM power of the confocal axial response function as the axial field of view FOV_{axial} of the OCT system, which calculates to

$$FOV_{axial} = \frac{0.221 \cdot \lambda}{\sin^2[\alpha/2]} = \frac{0.221 \cdot \lambda}{\sin^2\left[\frac{\sin^{-1}(NA)}{2}\right]}. \tag{2.4}$$

2.3 Spatial Coherence Gating in Full-Field OCT Systems

While the preceding discussion has assumed a point-scanning implementation of OCT, the expressions derived for lateral resolution and axial field of view are equally applicable for full-field OCT (FFOCT). FFOCT refers to a class of techniques wherein the entire en face slice of an OCT volume is acquired simultaneously by using a two-dimensional array camera as the detector in a wide-field interferometer. FFOCT has been demonstrated in both time-domain [23, 24] and Fourier-domain [25, 26] implementations. Fourier-domain FFOCT has only been demonstrated using swept sources since a three-dimensional camera would be necessary to obtain the two spatial and one spectral dimensions that would be required for spectrometer-based spectral-domain FFOCT.

An important consideration in the design of FFOCT systems is the management of multiple scattering and crosstalk artifacts [27, 28]. Cross talk originates in scattering samples when multiply scattered light reaches the detector and interferes with singly scattered light originating from the coherence-gated imaging depth in the reference. In point-scanning OCT, the confocal aperture of the single-mode fiber largely rejects multiply scattered light. However, FFOCT systems are implemented in free space and thus lack this confocal aperture. Therefore, multiply scattered photons are detected by the camera, and a subset of these multiply scattered photons will have traveled the correct optical path length to interfere with the reference field.

Cross talk artifacts can be avoided by employing a light source with low spatial coherence [29]. This prevents multiply scattered light in the sample arm from interfering with the reference field, effectively creating a spatial coherence gate that serves the same function as the confocal pinhole in point-scanning OCT. Because of this, thermal sources are often used in FFOCT systems [30, 31]. However, the average number of photons within a coherence volume of blackbody radiation is always on the order of unity [32], which limits the speed and sensitivity of OCT systems employing thermal sources [29, 33, 34]. A strategy to overcome this limit, while still achieving cross talk rejection, is to reduce the spatial coherence of a coherent source, such as a superluminescent diode or femtosecond laser. This can be achieved by piping light of high spatial but low temporal coherence through a multimode fiber that is either dynamically mode mixed [34] or whose length is appropriately selected [35]. In addition, "random" lasers can also produce light with moderate temporal coherence and low spatial coherence and have been used to demonstrate speckle-free laser imaging [36] and cross talk reduction in FFOCT [37].

2.4 Axial Ranging with Low-Coherence Interferometry

The fundamental quality that differentiates optical coherence tomography (OCT) from other forms of optical microscopy is that the predominant axial component of image formation derives from a ranging measurement performed using low-coherence interferometry. Consider the Michelson interferometer illustrated in Fig. 2.3. The interferometer is illuminated by a polychromatic plane wave whose

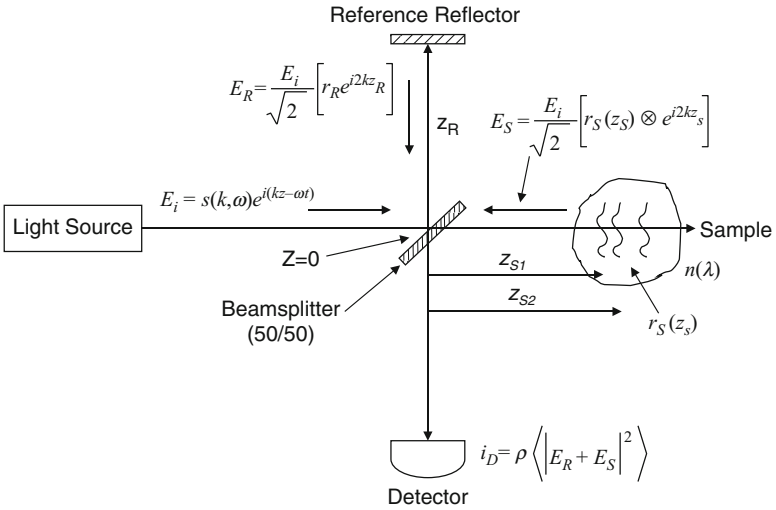

Fig. 2.3 Schematic of a Michelson interferometer used in OCT

electric field expressed in complex form is $E_i = s(k, \omega)e^{i(kz-\omega t)}$. Here, $s(k, \omega)$ is the electric field amplitude as a function of the wave number $k = 2\pi/\lambda$ and angular frequency $\omega = 2\pi v$, which are respectively the spatial and temporal frequencies of each spectral component of the field having wavelength λ. The wavelength λ and frequency v are coupled by the index of refraction $n(\lambda)$ (which is wavelength dependent in dispersive media) and vacuum speed of light c according to $c/n(\lambda) = \lambda v$. For simplicity of exposition in this section, all distances are assumed to be in free space and thus must be scaled by the appropriate index of refraction to obtain real-space measurements; the detailed effects of sample index and dispersion in OCT are discussed in Sect. 2.7. The beam splitter is assumed to have an achromatic (wavelength-independent) power splitting ratio of 0.5, although a generalization of OCT systems to unequal power splitting [8, 9] or other interferometer topologies (e.g., [8, 38]) is straightforward. The reference reflector is assumed to have electric field reflectivity r_R and power reflectivity $R_R = |r_R|^2$. The reference path is assumed to be in air, and the distance from the beam splitter to the reference reflector is z_R.

The sample under interrogation is characterized by its depth-dependent electric field reflectivity profile along the sample beam axis $r_s(z_s)$, where z_s is the path length variable in the sample arm measured from the beam splitter. In general, $r_s(z_s)$ is continuous, resulting from the continuously varying refractive index of biological tissues and other samples. It may also be complex, encoding the phase as well as the amplitude of each reflection. However, for an illustrative example, we assume a series of N discrete, real delta-function reflections of the form $r_S(z_s) = \sum_{n=1}^{N} r_{Sn}\delta[(z_S - z_{Sn})]$, with each reflection characterized by its electric field reflectivity r_{S1}, r_{S2} ... and path length from the beam splitter of z_{S1}, z_{S2} ... (see Fig. 2.4).

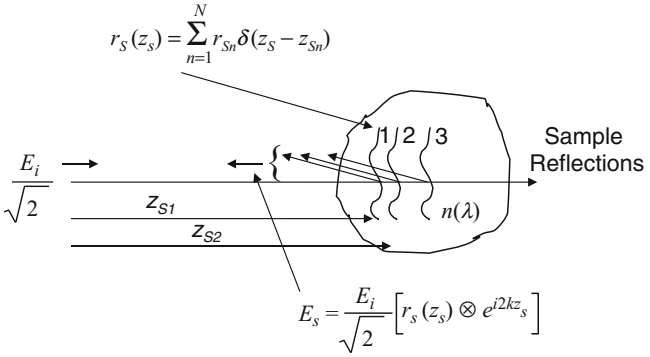

Fig. 2.4 Exemplary model for a sample comprising a series of discrete reflectors

The power reflectivity of each reflector is given by the magnitude squared of the electric field reflectivity, for example, $R_{S1} = |r_{S1}|^2$. **The reconstruction of the function $\sqrt{R_S(z_s)}$ from noninvasive interferometric measurements is the goal of low-coherence interferometry in OCT**. The electric field passing through the beam splitter after returning from the sample arm is $E_s = \frac{E_i}{\sqrt{2}}\left[r_s(z_s) \otimes e^{i2kz_s}\right]$, where $\otimes$ represents convolution and the factor of 2 in the exponential kernel accounts for the round-trip path length to each sample reflection. Note that for most samples such as biological tissues imaged with OCT, sample reflectivities R_{S1}, R_{S2} ... are typically very small (on the order of $\sim 10^{-4}$ to 10^{-5}); thus, the returned reference field typically dominates the reflected sample field. Indeed, selection of the appropriate reference reflectivity is an important criterion in OCT system design [7, 8].

For the example of discrete reflectors, the fields incident on the beam splitter after returning from the reference and sample arms are given by $E_R = \frac{E_i}{\sqrt{2}} r_R e^{i2kz_R}$ and $E_s = \frac{E_i}{\sqrt{2}} \sum_{n=1}^{N} r_{Sn} e^{i2kz_{Sn}}$, respectively. The returning fields are halved in power upon passing through the beam splitter again and interfere at the square-law detector, which generates a photocurrent proportional to the square of the sum of the fields incident upon it, given by $I_D(k,\omega) = \frac{\rho}{2}\left\langle |E_R + E_S|^2 \right\rangle = \frac{\rho}{2}\langle (E_R + E_S)(E_R + E_S)^* \rangle$. Here, ρ is the responsivity of the detector (units amperes/watt), the factor of 2 reflects the second pass of each field through the beam splitter, and the angular brackets denote integration over the response time of the detector. Arbitrarily setting $z = 0$ at the surface of the beam splitter and expanding for the detector current give

$$I_D(k,\omega) = \frac{\rho}{2}\left\langle \left| \frac{s(k,\omega)}{\sqrt{2}} r_R e^{i(2kz_R - \omega t)} + \frac{s(k,\omega)}{\sqrt{2}} \sum_{n=1}^{N} r_{Sn} e^{i(2kz_{Sn} - \omega t)} \right|^2 \right\rangle. \tag{2.5}$$

Expanding the magnitude squared functions in Eq. 2.5 eliminates the terms dependent upon the temporal angular frequency $\omega = 2\pi v$, which is reasonable

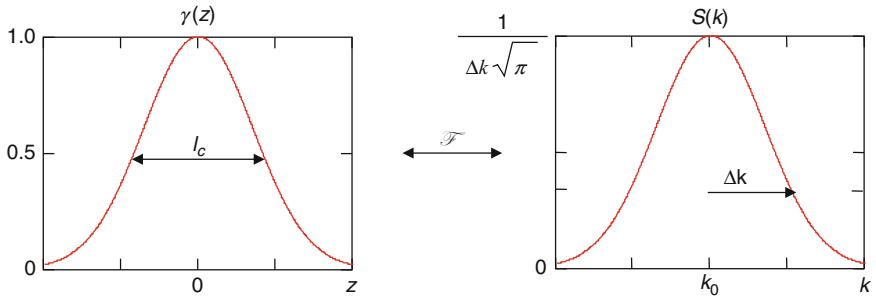

Fig. 2.5 Illustration of Fourier transform relationship between the Gaussian-shaped coherence function $\gamma(z)$ (characterized by the coherence length l_c) and the light source spectrum $S(k)$ (characterized by the central wave number k_0 and wave number bandwidth Δk)

since v oscillates much faster than the response time of any detector. This leaves the temporally invariant terms:

$$\begin{aligned} I_D(k) = &\frac{\rho}{4}\left[S(k)\cdot(R_R + R_{S1} + R_{S2} + \ldots)\right] \\ &+ \frac{\rho}{4}\left[S(k)\sum_{n=1}^{N}\sqrt{R_R R_{Sn}}\left(e^{i2k(z_R - z_{Sn})} + e^{-i2k(z_R - z_{Sn})}\right)\right] \\ &+ \frac{\rho}{4}\left[S(k)\sum_{n\neq m=1}^{N}\sqrt{R_{Sn}R_{Sm}}\left(e^{i2k(z_{Sn} - z_{Sm})} + e^{-i2k(z_{Sn} - z_{Sm})}\right)\right]. \end{aligned} \tag{2.6}$$

Here, $S(k) = \langle |s(k,\omega|^2 \rangle$ is substituted, which encodes the power spectral dependence of the light source. As an illustrative example, a Gaussian-shaped light source spectrum is convenient to use in modeling OCT because it approximates the shape of actual light sources and also has useful Fourier transform properties. The normalized Gaussian function $S(k)$ and its inverse Fourier transform $\gamma(z)$ are given by

$$\gamma(z) = e^{-(z)^2\Delta k^2} \xleftrightarrow{F} S(k) = \frac{1}{\Delta k\sqrt{\pi}} e^{-\left[\frac{(k-k_0)}{\Delta k}\right]^2} \tag{2.7}$$

and are illustrated in Fig. 2.5. Here, k_0 represents the central wave number of the light source spectrum, and Δk represents its spectral bandwidth, corresponding to the half-width of the spectrum at $1/e$ of its maximum. As will be seen below, the inverse Fourier transform $\gamma(z)$, hereafter called the "coherence function," dominates the axial point spread function (PSF) in OCT imaging systems (in OCT systems employing a low numerical aperture focusing objective, as pointed out in Sect. 2.2). The PSF is commonly characterized by its full width at half the maximum (FWHM) value and is the definition of the round-trip "coherence length" of the light source l_c. The free-space coherence length is an explicit function of the light source bandwidth, stated in both wave number and wavelength terms as

$$l_c = \frac{2\sqrt{\ln(2)}}{\Delta k} = \frac{2\ln(2)}{\pi}\frac{{\lambda_0}^2}{\Delta\lambda}. \tag{2.8}$$

Here, $\lambda_0 = \frac{2\pi}{k_0}$ is the center wavelength of the light source, and $\Delta\lambda$ is its wavelength bandwidth, defined as the FWHM of its wavelength spectrum $\left(\text{so that } \Delta k = \frac{\pi}{\sqrt{\ln(2)}}\frac{\Delta\lambda}{\lambda_0^2}\right)$. Note the inverse relationship between the coherence length and the light source bandwidth.

Using Euler's rule to simplify Eq. 2.6 generates a real result for the detector current as a function of wave number, commonly known as the "spectral interferogram":

$$\begin{aligned} I_D(k) = {} & \frac{\rho}{4}[S(k)[R_R + R_{S1} + R_{S2} + \ldots]] \quad \text{“DC Terms”} \\ & + \frac{\rho}{2}\left[S(k)\sum_{n=1}^{N}\sqrt{R_R R_{Sn}}(\cos[2k(z_R - z_{Sn})])\right] \quad \text{“Cross-correlation Terms”} \\ & + \frac{\rho}{4}\left[S(k)\sum_{n\neq m=1}^{N}\sqrt{R_{Sn}R_{Sm}}\cos[2k(z_{Sn} - z_{Sm}]\right] \quad \text{“Auto-correlation Terms”} \end{aligned} \tag{2.9}$$

The result in Eq. 2.6 includes three distinct components:

1. A path length-independent offset to the detector current, scaled by the light source wave number spectrum and with amplitude proportional to the power reflectivity of the reference mirror plus the sum of the sample reflectivities. This term is often referred to as "constant" or "DC" component. This is the largest component of the detector current if the reference reflectivity dominates the sample reflectivity.
2. A "cross-correlation" component for each sample reflector, which depends upon both the light source wave number and the path length difference between the reference arm and sample reflectors. This is the desired component for OCT imaging. Since these components are proportional to the square root of the sample reflectivities, they are typically smaller than the DC component. However, the square root dependence represents an important logarithmic gain factor over the direct detection of sample reflections.
3. "Autocorrelation" terms representing interference occurring between the different sample reflectors appear as artifacts in typical OCT system designs (exceptions occur in common-path system designs, in which the autocorrelation component represents the desired signal). Since the autocorrelation terms depend linearly upon the power reflectivity of the sample reflections, a primary tool for decreasing autocorrelation artifacts is the selection of the proper reference reflectivity so that the autocorrelation terms are small compared to the DC and interferometric terms.

It is useful to gain an intuitive understanding of the form of Eq. 2.9, as well as the effect that different source spectra and different numbers of sample reflectors and

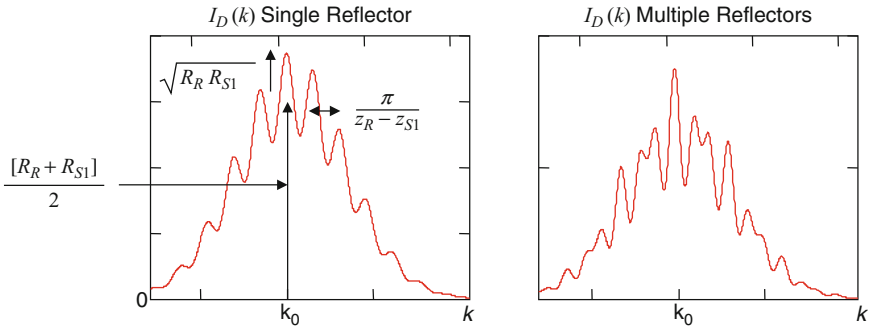

Fig. 2.6 Important features of the spectral interferogram. For a single sample reflector of field reflectivity $r_{S1} = 0.1$ (*left*), the cross-correlation component with amplitude $\sqrt{R_R R_{S1}}$ and wave number period $\frac{\pi}{z_R - z_{S1}}$ rides on top of the DC term of amplitude $\frac{[R_R + R_{S1}]}{2}$ (factors of $\rho S(k)$ are left out for clarity). For multiple reflectors, the cross-correlation component is a superposition of cosinusoids

their distributions have upon it. For a single reflector, only DC and a single interferometric term are present, and the source spectrum is modulated by a simple cosinusoid whose period is proportional to the distance between the sample and reference reflectors, as illustrated in Fig. 2.6. In addition, the amplitude of spectral modulation or "visibility" of the spectral fringes is proportional to the amplitude reflectivity of the sample reflector $\sqrt{R_{S1}}$. For the case of multiple reflectors, the spectrum is modulated by multiple cosinusoids, each having a frequency and amplitude characteristic of the sample reflection that gives rise to it. In addition, if more than one reflector is present in the sample, autocorrelation components modulated according to the path length difference between the sample reflectors and proportional to the product of their amplitude reflectivities also appear. Since the sample amplitude reflectivities are usually small compared to the reference reflection, the autocorrelation terms are usually small compared to the cross-correlation terms. Also, since reflections in the sample tend to be clumped closely together compared to the distance between the sample and the reference reflector, the autocorrelation term modulation frequencies also tend to be small.

2.5 Fourier-Domain Low-Coherence Interferometry

In Fourier-domain OCT (FDOCT), the wave number-dependent detector current $I_D(k)$ in Eq. 2.9 is captured and processed using Fourier analysis to reconstruct an approximation of the internal sample reflectivity profile $\sqrt{R_S(z_s)}$. The process for capturing $I_D(k)$ depends upon the experimental details of the detection apparatus. In spectral-domain OCT (SDOCT, also called spectrometer-based OCT), a broadband light source is used, and all spectral components of $I_D(k)$ are captured simultaneously on a detector array placed at the output of a spectrometer [39–41]. In swept-source OCT (SSOCT, also called optical frequency-domain imaging or OFDI), the spectral

components of $I_D(k)$ are captured sequentially by recording the signal in a single detector while synchronously sweeping the wave number of a narrowband swept-laser source [42–45].

The sample reflectivity profile $r_s(z_s)$ is estimated from the inverse Fourier transform of $I_D(k)$. Making use of the Fourier transform pair $\frac{1}{2}(\delta[(z+z_0)]+\delta[(z-z_0)]) \overset{F}{\longleftrightarrow} \cos kz_0$ and the convolution property of Fourier transforms $x(z)\otimes y(z) \overset{F}{\longleftrightarrow} X(k)Y(k)$, the inverse Fourier transform of Eq. 2.9 may be calculated as

$$\begin{aligned} i_D(z) = {} & \frac{\rho}{8}[\gamma(z)[R_R + R_{S1} + R_{S2} + \ldots]] \text{“DC terms”} \\ & + \frac{\rho}{4}\left[\gamma(z)\otimes\sum_{n=1}^{N}\sqrt{R_R R_{Sn}}(\delta[(z\pm 2(z_R - z_{Sn}))])\right] \text{“Cross-correlation terms”} \\ & + \frac{\rho}{8}\left[\gamma(z)\otimes\sum_{n\neq m=1}^{N}\sqrt{R_{Sn}R_{Sm}}(\delta[(z\pm 2(z_{Sn} - z_{Sm}))])\right] \text{“Auto-correlation terms.”} \end{aligned} \tag{2.10}$$

Note that the desired sample field reflectivity profile $\sqrt{R_S(z_s)} = \sum_{n=1}^{N}\sqrt{R_{Sn}}\delta[(z_S - z_{Sn})]$ is indeed embedded within the cross-correlation terms of Eq. 2.10, although it is surrounded by several confounding factors. Carrying out the convolutions by taking advantage of the sifting property of the delta function, we obtain the result of the interferometric measurement, referred to as the “A-scan”:

$$\begin{aligned} i_D(z) \quad = {} & \frac{\rho}{8}[\gamma(z)[R_R + R_{S1} + R_{S2} + \ldots]] \\ & + \frac{\rho}{4}\sum_{n=1}^{N}\sqrt{R_R R_{Sn}}[\gamma[2(z_R - z_{Sn})] + \gamma[-2(z_R - z_{Sn})]] \\ & + \frac{\rho}{8}\sum_{n\neq m=1}^{N}\sqrt{R_{Sn}R_{Sm}}[\gamma[2(z_{Sn} - z_{Sm})] + \gamma[-2(z_{Sn} - z_{Sm})]]. \end{aligned} \tag{2.11}$$

The results in Eqs. 2.10 and 2.11 for the example of discrete sample reflectors and a Gaussian-shaped source spectrum are plotted in Fig. 2.7. As can be seen in the figure, the sample field reflectivity profile $\sqrt{R_S(z_s)} = \sum_{n=1}^{N}\sqrt{R_{Sn}}\delta[(z_S - z_{Sn})]$ is reproduced in the cross-correlation terms, with the following modifications: First, the sample reflectivity profile appears as a function of the reference coordinate z_R, rather than the sample coordinate z_S. Second, the apparent displacement of each sample reflector from the reference position is doubled (which can be understood from the fact that the interferometer measures the round-trip distance to each reflector). We accommodate this by defining a new single-pass depth variable $\widehat{z} = 2z$.

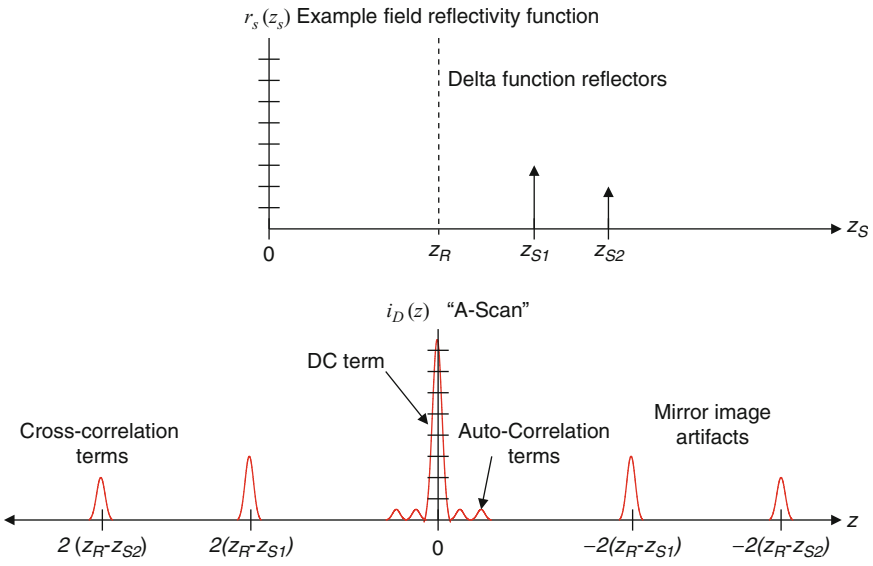

Fig. 2.7 Illustration of the example discrete-reflector sample field reflectivity function $r_S(z_s) = \sum_{n=1}^{N} r_{Sn}\delta(z_S - z_{Sn})$ (*top*) and the A-scan resulting from Fourier-domain low-coherence interferometry

Third, each reflector appears broadened or blurred out to a width of about a coherence length by convolution with the function $\gamma(z)$. This is precisely the definition of an imaging system PSF. Given the inverse relationship of the coherence length to the light source bandwidth, the clearest path to increasing the fidelity of the estimate of $\sqrt{R_S(z_s)}$ is to use as broad-bandwidth sources as possible. Fourth, the magnitude of the detected sample reflectivity, which can be very small, is amplified by the large homodyne gain factor represented by the strong reference reflectivity $\sqrt{R_R}$. All of the modifications listed so far can be dealt with through proper interpretation of the data, that is, the realization that the zero position corresponds to the position of the reference reflector, relabeling axial distances to account for the factor of 2, and accounting for the homodyne gain factor.

A number of additional modifications to the field reflectivity profile are termed artifacts and are more serious. First, as seen in the cross-correlation terms in Eqs. 2.10 and 2.11, a mirror image of the blurred version of $\sqrt{R_S(z_s)}$ appears on the opposite side of zero path length, that is, the reference reflector position. This is termed the complex conjugate artifact in FDOCT and is simply understood from the fact that since the detected interferometric spectrum is necessarily real, its inverse Fourier transform must be Hermitian symmetric, that is, its values at positive and negative distances are complex conjugates of each other, and therefore if they are real, they must be identical. This artifact is not disabling so long as the sample can be kept entirely to one side of zero path length, in which case it can be dealt with by

simply only displaying the positive or negative distances. However, if the sample strays over the zero path length border, it begins to overlap its mirror image, an effect that cannot be removed by image processing alone. A number of approaches have been described for removing this complex conjugate artifact ([46–53]; also see Sect. 2.8.2).

Additional image artifacts also arise from the DC and autocorrelation terms in Eqs. 2.10 and 2.11. The DC terms give rise to a large artifactual signal centered at zero path length difference. The FWHM value of the DC artifact is only one coherence length wide; however, the signal amplitude is so much larger than the desired cross-correlation terms that the wings of the Gaussian-shaped PSF from Eq. 2.7 can overwhelm the desired signal components much farther away. Since the largest component of the DC artifact comes from the reference reflector (with reflectivity near 1), a simple method to eliminate that component is to record the amplitude of the spectral interferometric signal Eq. 2.9 with the reference reflector but no sample present and then to subtract this signal component from each subsequent spectral interferometric signal acquired. The autocorrelation terms in Eqs. 2.10 and 2.11 also give rise to artificial signals at and near the zero path length position, since the distance between reflectors in a sample is typically much smaller than the distance between the sample reflectors and the reference arm path length. The best method to eliminate the autocorrelation signals is to ensure that the reference reflectivity is sufficient so that the amplitude of the autocorrelation terms is very small compared to the cross-correlation terms.

2.6 Time-Domain Low-Coherence Interferometry

In traditional or time-domain OCT (TDOCT), the wave number-dependent detector current $I_D(k)$ in Eq. 2.9 is captured on a single receiver, while the reference delay z_r is scanned to reconstruct an approximation of the internal sample reflectivity profile $\sqrt{R_S(z_s)}$. The result is obtained by the integration of Eq. 2.9 over all k:

$$I_D(z_R) = \frac{\rho}{4}[S_0[R_R + R_{S1} + R_{S2} + \ldots]] \quad \text{“DC offset”}$$
$$+ \frac{\rho}{2}\left[S_0 \sum_{n=1}^{N} \sqrt{R_R R_{Sn}}\, e^{-[(z_R - z_{Sn})]^2 \Delta k^2} \cos\left[2k_0(z_R - z_{Sn})\right]\right] \quad \text{“Fringe bursts.”} \tag{2.12}$$

Here, $S_0 = \int_0^\infty S(k)dk$ is the spectrally integrated power emitted by the light source. The time-domain “A-scan” resulting from such a measurement is illustrated in Fig. 2.8. Note that the sample reflectivity profile convolved with the source coherence function is again recapitulated in the result, resident on a DC offset proportional to the sum of the reference and sample power reflectivities. In addition,

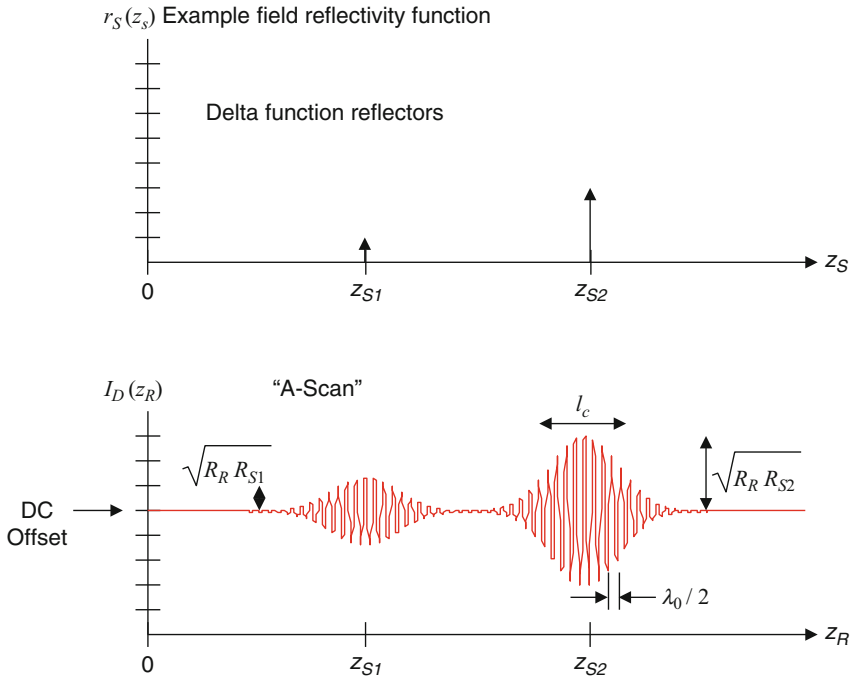

Fig. 2.8 Illustration of the example discrete-reflector sample field reflectivity function $r_S(z_s) = \sum_{n=1}^{N} r_{Sn}\delta(z_S - z_{Sn})$ (*top*) and the A-scan resulting from time-domain low-coherence interferometry

the convolved sample reflectivity profile is modulated by a cosinusoidal carrier wave modulation at a frequency proportional to the source center wave number k_0 and the free-space difference between reference and sample arm lengths $(z_R - z_{Sn})$. Since the reference arm length z_R is typically scanned as a function of time in TDOCT systems, this carrier provides a convenient modulation frequency for lock-in detection, which provides for high-sensitivity detection of the reflectivity envelope and rejection of the DC offset.

2.7 Effects of Index of Refraction and Dispersion

In the preceding sections, all distances were assumed to be in free space, and the effects of varying media in the interferometer arms were not considered. In reality, both reference and sample arms may contain a variety of materials with various indices of refraction, such as optical fiber, glass, air, and biological tissue. In this case, the fields returning from the reference and each reflection from the sample are more correctly written as

$$E_R = \frac{E_i}{\sqrt{2}} r_R \exp\left[i2\int \beta_R(\omega) dz_r\right]; \qquad E_S = \frac{E_i}{\sqrt{2}} r_S \exp\left[i2\int \beta_S(\omega) dz_s\right], \tag{2.13}$$

where $\beta_R(\omega)$ and $\beta_S(\omega)$ are the frequency-dependent propagation constants of the respective media. As is clear from Eq. 2.6, in OCT only the difference in net propagation between reference and sample arms is preserved; thus, so long as all fiber and air path lengths in each arm are closely matched, we denote the residual difference in propagation between the arms as occurring in a single medium (corresponding perhaps to the residual unmatched fiber length between the arms or to tissue in the sample, which is not present in the reference) with propagation constant $\beta(\omega)$. Similar to the analysis performed for optical pulse propagation in dispersive media, for low-coherence light, the dispersion constant $\beta(\omega)$ may be expanded as a Taylor series expansion around the central frequency ω_0, as

$$\begin{aligned} \beta(\omega) &= \beta(\omega_0) + \beta'(\omega_0)(\omega - \omega_0) + \frac{1}{2}\beta''(\omega_0)(\omega - \omega_0)^2 + \ldots \\ &= \frac{\omega_0}{v_p} + \frac{\omega - \omega_0}{v_g} + \ldots . \end{aligned} \tag{2.14}$$

Here, the first three terms of the approximation correspond to zero-order (nondispersive), first-order, and second-order dispersion, respectively, and the zeroth and first-order terms are expressed in terms of the phase velocity (v_p) and group velocity (v_g) of light in the medium at the central frequency. Hee [15] and Dhalla [54] have performed analyses of the cross-correlation component of the OCT signal up to second order for time-domain and Fourier-domain OCT, respectively.

The effects on the OCT signal of unmatched dispersion up to first order result in simple modifications to the A-scan expressions derived above. Directly analogous to pulse propagation in dispersive media, the "fringe bursts" in TDOCT are modulated according to the phase velocity, while the coherence function in both TDOCT and FDOCT is both scaled by and delayed by the group velocity. Particularly, simple expressions result from expressing the phase and group velocities in terms of phase (n_p) and group (n_g) indices of refraction, expressed as

$$n_p = c/v_p = n(\lambda_0); \;\; n_g = c/v_g = n_p - \lambda_0 n'(\lambda_0). \tag{2.15}$$

Here, $n(\lambda)$ is the index of refraction, λ_0 is the central wavelength as above, and c is the vacuum speed of light. Expressions correct to first order in dispersion for the coherence length in the medium and the A-scan signal in FDOCT and TDOCT appear in Table 2.1.

In practical terms, the effect of dispersion up to first order in media of practical interest is quite small if limited to small unmatched path lengths. For example, the difference between phase and group index averages less than 0.015 index units over the wavelength range 0.6–1.3 μm in fused silica optical fibers. For many purposes, the phase index (i.e., the index of refraction at the central wavelength

Table 2.1 Real-space expressions for the coherence length, Fourier-domain OCT A-scan signal, and time-domain OCT A-scan signal in a sample, correct to first-order dispersion. Expressions are in terms of the phase (n_p) and group (n_g) indices of refraction of the sample

Coherence length	$l_c = \frac{2\sqrt{\ln(2)}}{\Delta k \cdot n_g} = \frac{2\ln(2)}{\pi \cdot n_g}\frac{{\lambda_0}^2}{\Delta\lambda}$
Fourier-domain OCT detector current (A-scan)	$i_D(z) = \frac{\rho}{8}\left[\gamma(z/n_g)\left[R_R + R_{S1} + R_{S2} + \ldots\right]\right]$ $+ \frac{\rho}{4}\sum_{n=1}^{N}\sqrt{R_R R_{Sn}}\left[\gamma\left[2(z_R - z_{Sn})/n_g\right] + \gamma\left[-2(z_R - z_{Sn})/n_g\right]\right]$ $+ \frac{\rho}{8}\sum_{n\neq m=1}^{N}\sqrt{R_{Sn}R_{Sm}}\left[\gamma\left[2(z_{Sn} - z_{Sm})/n_g\right] + \gamma\left[-2(z_{Sn} - z_{Sm})/n_g\right]\right]$
Time-domain OCT detector current (A-scan)	$I_D(z_R) = \frac{\rho}{4}\left[S_0\left[R_R + R_{S1} + R_{S2} + \ldots\right]\right]$ $+ \frac{\rho}{2}\left[S_0\sum_{n=1}^{N}\sqrt{R_R R_{Sn}}e^{-\left[\left(z_R - z_{Sn}/n_g\right)\right]^2\Delta k^2}\cos\left[2k_0(z_R - z_{Sn})/n_p\right]\right]$

of the light source) is sufficiently accurate. However, it is important to realize that all free-space distances in other sections of this chapter must be divided by the appropriate index of refraction to obtain real-space measurements.

On the other hand, second-order (group velocity) and higher-order dispersion can distort OCT signals substantially, particularly for unmatched path lengths exceeding several mm in highly dispersive glasses or away from the minimum dispersion wavelength in optical fibers.

2.8 Practical Aspects of FDOCT Signal Processing

2.8.1 Sensitivity Falloff and Sampling Effects in FDOCT

While the FDOCT spectral interferogram of Eq. 2.9 and its continuous-time inverse Fourier transform (Eq. 2.11) illustrate the fundamental principle underlying spectrometer-based (SD) and swept-source (SS) OCT, in practical implementations of these devices, several additional factors must be taken into account. The spectral interferogram data is generated by instrumentation having real-world limitations and is typically acquired by a sampling operation for rapid digital signal computation of its inverse Fourier transform. Figure 2.9 illustrates conceptually the effects of finite spectral resolution and sampling upon the spectral interferogram and its inverse Fourier transform.

First, the instrumentation for acquiring the spectral interferogram always has limited spectral resolution, here denoted by $\delta_r k$. In SSOCT, $\delta_r k$ is limited by the instantaneous line shape of the swept-laser source, while in SDOCT, $\delta_r k$ is the spectral resolution of the spectrometer (including the finite spacing of the CCD or CMOS pixels, whose effect on resolution in SDOCT has also been modeled explicitly [55]). We model the effect of finite spectral resolution by convolving the ideal spectral interferogram from Eq. 2.9 with a Gaussian function having

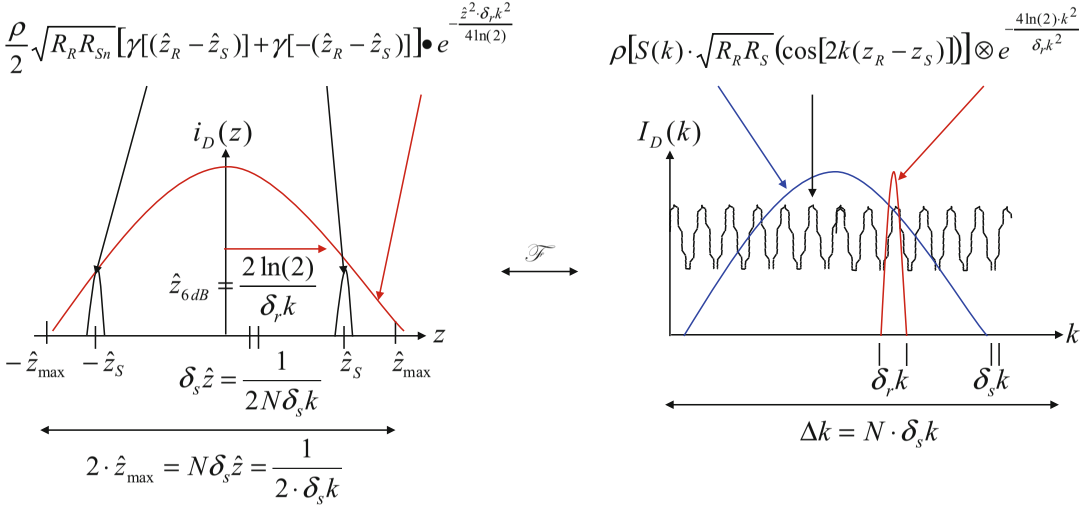

Fig. 2.9 Conceptual basis for sensitivity falloff and maximum imaging depth in FDOCT. Note that the depth-dependent falloff in sensitivity is directly related to the resolution of the interference spectrum, which is dominated by the source linewidth in SSOCT and the spectrometer resolution in FDOCT

half-maximum width $\delta_r k$, which we interpret as the FWHM spectral resolution. Via the convolution property, the A-scan data is thus multiplied by a sensitivity "falloff" factor whose shape is given by the inverse Fourier transform of the Gaussian-shaped resolution factor, which is also a Gaussian:

$$i_D(\hat{z}) \bullet \exp\left[-\frac{(\hat{z})^2 \cdot \delta_r k^2}{4\ln(2)}\right] \overset{F}{\longleftrightarrow} I_D(k) \otimes \exp\left[-\frac{4\ln(2) \cdot k^2}{\delta_r k^2}\right]. \tag{2.16}$$

The use here of the rescaled depth variable $\hat{z} = 2z$ removes the apparent depth-doubling factor in FDOCT and allows processed A-scan data to be compared directly to the sample structure. The exponential falloff of sensitivity with depth can be understood as the decreasing visibility of higher fringe frequencies corresponding to large sample depths. It may be characterized by defining the one-sided depth at which the sensitivity falls off by a factor of ½ or 6 dB in optical SNR units:

$$\hat{z}_{6dB} = \frac{2\ln(2)}{\delta_r k} = \frac{\ln(2)}{\pi} \frac{{\lambda_0}^2}{\delta_r \lambda}. \tag{2.17}$$

Here, $\hat{z}_{6dB}$ is given in terms of the FWHM spectral resolution in both wave number ($\delta_r k$) and wavelength ($\delta_r \lambda$) terms, the latter of which is recognizable as one-half of the coherence length corresponding to the spectral resolution.

The second major consideration in real-world processing of FDOCT data is that computer-based detection involves sampling the spectral interferogram. We assume that the interferogram is sampled with spectral sampling interval $\delta_s k$ into M spectral channels linearly spaced in k. The total wave number range collected is thus $\Delta k = M \cdot \delta_s k$, and this in turn sets the sampling interval in the z-domain $\delta_s \hat{z} = 2\pi/(2\Delta k)$, where the extra factor of 2 in the denominator arises from the use of the rescaled depth parameter $\hat{z}$. The maximum and minimum depth samples are thus given by the Nyquist criterion as

$$\pm z_{\max} = \pm \frac{\pi}{2 \cdot \delta_s k} = \pm \frac{n_0 {\lambda_0}^2}{4 \cdot \delta_s \lambda}. \tag{2.18}$$

A summary of the results of this section is provided in Table 2.2. In addition to these limitations imposed by spectral resolution and sampling, which are difficult to overcome, additional real-world complications arise that can be handled with appropriate digital signal processing. First, the spectral interferogram data may not be acquired as a linear function of optical wave number, which is the required conjugate variable for imaging depth in the inverse Fourier transform operation underlying FDOCT. For example, grating-based spectrometers typically disperse spectra approximately linearly in wavelength rather than wave number, and swept-wavelength laser sources may be subject to any number of nonlinearities. For each of these cases, solutions involving clever spectrometer designs, clever k-triggering schemes, or, as a last resort, digital spectral resampling after acquisition have all been described. In addition, dispersion effects due to mismatched glass or tissue

Table 2.2 Effects of sampling and finite spectral resolution in Fourier-domain OCT (FDOCT) systems. δ_s and δ_r represent the spectral sampling interval and FWHM spectral resolution, respectively. The maximum imaging depth $z_{\max}$ may be doubled by the use of methods for removing the complex conjugate ambiguity artifact. Depths listed are in free space and should be divided by the group index of refraction in media

	Maximum one-sided imaging depth $\widehat{z}_{\max}$	6 dB SNR falloff point $\widehat{z}_{6dB}$
Wave number units ($k = 2\pi/\lambda$)	$\frac{\pi}{2 \cdot \delta_s k}$	$\frac{2\ln(2)}{\delta_r k}$
Wavelength units	$\frac{{\lambda_0}^2}{4 \cdot \delta_s \lambda}$	$\frac{\ln(2)}{\pi} \frac{{\lambda_0}^2}{\delta_r \lambda}$

lengths in the sample and reference arms may also be corrected by the addition of appropriate phase factors to the spectral interferometric data prior to inverse Fourier transformation.

2.8.2 Artifact Removal in FDOCT by Phase Shifting

The DC, autocorrelation, and complex conjugate artifacts in FDOCT may in principle be removed by utilizing principles and techniques borrowed from phase-shift interferometry [47, 48, 56, 57]. If the interferometer is modified to provide for the introduction of a variable single-pass phase delay ϕ (round-trip phase delay 2ϕ) between the reference and sample arms, then a set of spectral interferograms may be acquired with different phase delays that can be combined in signal processing to eliminate the undesired artifacts. For example, Fig. 2.10 illustrates an FDOCT interferometer with a variable phase modulator placed in the reference arm, such that the reference field returning from the reference arm is modified to $E_R = \frac{E_i}{\sqrt{2}} r_R e^{i(2kz_R + 2\phi)}$. There are a number of approaches for introducing such phase delays. Phase modulators based on electro-optic, acousto-optic, and photoelastic modulators may be utilized, or the reference mirror itself may be dithered by mounting it on a piezoelectric transducer. Such transducers have the advantage of relative simplicity; however, their use requires that phase-shifted spectral interferograms be acquired sequentially; thus, the resulting artifact reduction occurs at the cost of increased acquisition time. Phase-shifted spectral interferograms may also be acquired simultaneously on separate detectors by employing interferometer topologies that intrinsically separate phase-shifted signals into different detector channels. Such simultaneous phase-shifted interferometers have been constructed that use orthogonal polarization states to carry phase-shifted signals or that employ 3×3 or higher-order fiber couplers to separate phase channels. While the analysis to follow assumes that the phase delay is inserted in the reference arm, it is the phase difference between reference and sample arms that matters; thus, phase-shifting elements may be placed in either arm.

Rewriting the spectral interferogram from Eq. 2.5 with this additional phase delay explicitly included yields

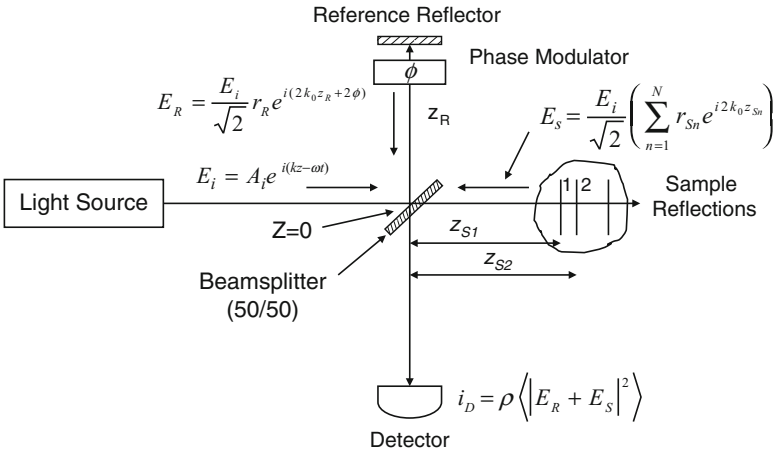

Fig. 2.10 FDOCT interferometer with addition of variable round-trip phase delay ϕ in the reference arm

$$
\begin{aligned}
I_D(k,2\phi) \;=\; & \frac{\rho}{4}[S(k)[R_R + R_{S1} + R_{S2} + \ldots]] \text{ “DC Terms”} \\
& + \frac{\rho}{2}\left[S(k) \sum_{n=1}^{N} \sqrt{R_R R_{Sn}} (\cos[2k(z_R - z_{Sn}) + 2\phi]) \right] \text{ “Cross-correlation Terms”} \\
& + \frac{\rho}{4}\left[S(k) \sum_{n \neq m = 1}^{N} \sqrt{R_{Sn} R_{Sm}} \cos[2k(z_{Sn} - z_{Sm}] \right] \text{ “Auto-correlation Terms”}
\end{aligned}
\tag{2.19}
$$

2.8.2.1 Stepped Phase-Shifting Interferometry Approach

If a spectral interferogram with round-trip phase delay $2\phi = \pi$ is acquired and subtracted from a spectral interferogram acquired with no phase delay, then it follows from Eq. 2.9 that the DC and autocorrelation terms will be eliminated and the cross-correlation terms doubled:

$$
I_D(k, 2\phi = 0) - I_D(k, 2\phi = \pi) = \rho \left[S(k) \sum_{n=1}^{N} r_{Sn} (\cos[2k(z_R - z_{Sn})]) \right]. \tag{2.20}
$$

The reversal of the sign of the cosine, which gives rise to this result, clearly depends only upon the $2\phi = \pi$ phase difference between the spectral interferograms and not upon any arbitrary phase offset to both of them; thus, it is important for this and all of the following results in this section that the phase-shifted interferograms be acquired either simultaneously or else quickly compared to any substantial phase drifting time in the interferometer. The A-scan that results from the inverse Fourier transform of Eq. 2.10 also contains only cross-correlation terms; thus, the DC and autocorrelation artifacts (but not the complex conjugate artifact) may be eliminated using this 2-step algorithm:

$$\begin{aligned} & i_D(z, 2\phi = 0) - i_D(z, 2\phi = \pi) \\ & = \frac{\rho}{2} \sum_{n=1}^{N} \sqrt{R_R R_{Sn}} [\gamma[2(z_R - z_{Sn})] + \gamma[-2(z_R - z_{Sn})]]. \end{aligned} \tag{2.21}$$

To remove the complex conjugate artifact, at least two spectral interferograms with noncomplementary phase delays (i.e., with 2ϕ different than π radians) must be acquired. For example, if a spectral interferogram with round-trip phase delay $2\phi = 3\pi/2$ is subtracted from a spectral interferogram acquired with round-trip phase delay $2\phi = \pi/2$, the result is a spectral interferogram containing only cross-correlation terms, which is in phase quadrature with the previous result:

$$\begin{aligned} & I_D(k, 2\phi = 3\pi/2) - I_D(k, 2\phi = \pi/2) \\ & = \rho \left[S(k) \sum_{n=1}^{N} \sqrt{R_R R_{Sn}} (-\sin [2k(z_R - z_{Sn})]) \right]. \end{aligned} \tag{2.22}$$

Combining all four phase-shifted interferograms yields the result:

$$\begin{aligned} & I_D(k, 2\phi = 0) - I_D(k, 2\phi = \pi) + j[I_D(k, 2\phi = \pi/2) - I_D(k, 2\phi = 3\pi/2)] \\ & = \rho \left[S(k) \sum_{n=1}^{N} r_{Sn} (\cos [2k(z_R - z_{Sn})] - j \sin [2k(z_R - z_{Sn})]) \right]. \end{aligned} \tag{2.23}$$

This 4-step combination of phase-shifted spectral interferograms inverse transforms to an A-scan free of DC, autocorrelation, and complex conjugate artifacts:

$$\begin{aligned} & i_D(z, 2\phi = 0) - i_D(z, 2\phi = \pi) + j[i_D(z, 2\phi = \pi/2) - i_D(z, 2\phi = 3\pi/2)] \\ & = \rho \sum_{n=1}^{N} \sqrt{R_R R_{Sn}} [\gamma[2(z_R - z_{Sn})] + \gamma[-2(z_R - z_{Sn})] + \gamma[2(z_R - z_{Sn})] - \gamma[-2(z_R - z_{Sn})]] \\ & = \rho \sum_{n=1}^{N} \sqrt{R_R R_{Sn}}\ \gamma[2(z_R - z_{Sn})]. \end{aligned} \tag{2.24}$$

It should be noted that if the DC and autocorrelation artifacts are removed through some independent means, that is, by subtracting averaged spectral interferogram data as described above, then only two-phase steps separated by $2\phi = \pi/2$ are required, that is,

$$i_D(z, 2\phi = 0) + j[i_D(z, 2\phi = \pi/2)] = \rho \sum_{n=1}^{N} \sqrt{R_R R_{Sn}} \gamma[2(z_R - z_{Sn})] \tag{2.25}$$

is also true if the component A-scans contain only cross-correlation terms.

2.8.2.2 Quadrature Projection Phase Correction

In many practical implementations, the phase shifts imposed through external means may not be achievable exactly or may be achromatic. For example, the phase shift imposed on reference arm light by physical modulation of the reference arm delay by, for example, a piezoelectric modulator depends upon wave number. In this case, an additional signal processing step may be introduced to ensure that the supposedly orthogonal signal components are in fact exactly orthogonal, independent of wave number. Sarunic has introduced a technique termed quadrature projection phase correction for complex conjugate resolution in FDOCT, which achieves this goal by simply taking the projection of phase-separated signal components upon orthogonal basis vectors [58]. For the example of the simplest two-phase techniques such as in the last section, this procedure proceeds as follows:

First, the inverse Fourier transforms of the ostensibly real and imaginary phase-separated signal vectors are separately computed, creating intermediary complex functions A and B:

$$\begin{aligned} A &= I.F.T[-E_1 + E_2 + E_3 - E_4] \\ B &= I.F.T[-E_1 + E_2 - E_3 + E_4]. \end{aligned} \tag{2.26}$$

Second, the vectors A and B are rotated to lie exactly on the real and imaginary axes. This is done by zeroing out the phase of vector A and subtracting the phase of vector A from that of vector B:

$$\begin{aligned} A' &= |A| \\ B' &= |B| e^{\angle B - \angle A}. \end{aligned} \tag{2.27}$$

Finally, the completely complex conjugate resolved output is computed from the following combination of A' and B':

$$\text{Output} = \text{Im}[\text{Re}(A') + j\,\text{Im}(B')]. \tag{2.28}$$

2.9 Sensitivity and Dynamic Range in OCT Systems

One of the advantages of OCT among biophotonic sensing techniques is that since it borrows so heavily from optical communication technologies, well-developed and inexpensive methodologies for signal optimization are available to approach the quantum detection limit of a single reflected photon. Sensitivity, signal-to-noise ratio (SNR), and dynamic range are often used interchangeably in the OCT literature to denote the minimum detectable reflected optical power compared to a perfect reflector, usually expressed in decibel units. Here, we concur with the first two definitions but reserve dynamic range to refer to the dynamic range of optical reflectivities observable within a single acquisition or image.

2.9.1 SNR Analysis for Time-Domain OCT

The signal-to-noise ratio for any system is defined as the signal power divided by the noise process variance. We follow the historical development of SNR analysis in OCT by first deriving expressions for TDOCT and then extending the analysis to FDOCT. SNR analysis in TDOCT followed directly from its predecessor technique of optical low-coherence domain reflectometry [59]. To simplify the analysis, we consider only a single sample reflector at position z_S and neglect autocorrelation terms. In this case, we can write the total detected photocurrent in a TDOCT system from Eq. 2.12 as

$$I_D(z_R) = \frac{\rho S_{TDOCT}}{2}\left[R_R + R_S + 2\sqrt{R_R R_S}e^{-(z_R - z_S)^2\Delta k^2}\cos\left[2k_0(z_R - z_S)\right]\right]. \quad (2.29)$$

Here, $S_{TDOCT} = \frac{S_0}{2}$ is the instantaneous source power incident in the sample and reference arms and is thus the quantity limited by ocular or skin maximum permissible exposure [] and other safety considerations. The desired OCT signal resides in the third term, whose mean-square peak signal power occurs at $z_R = z_S$ and is given by $\langle I_D\rangle^2_{TDOCT} = \frac{\rho^2 S_{TDOCT}{}^2}{2}[R_R R_S]$. Complete SNR analysis for OCT systems requires consideration of many possible noise sources in addition to shot noise (i.e., bandlimited quantum noise), which is the fundamental limiting noise process for optical detection. The contributions of these noise sources to OCT system performance including design approaches for obtaining shot noise-limited operation have been described in detail for both TDOCT and FDOCT systems. Here, we derive expressions for shot noise-limited performance. Shot noise variance in an optical receiver is given by $\sigma^2_{sh} = 2e\bar{I}B$, where e is the electronic charge, $\bar{I}$ is the mean detector photocurrent, and B is the electronic detection bandwidth. In a TDOCT system whose reference arm scans over a depth range $z_{\max}$ during an A-scan acquisition time Δt with velocity $v_{ref} = z_{\max}/\Delta t$, the reference light frequency is Doppler shifted by $f_D = 2v_{ref}/\lambda_0 = k_0 z_{\max}/(\pi\Delta t)$, and the resulting FWHM signal power bandwidth is $\Delta f_D = \Delta k_{FWHM} z_{\max}/(\pi\Delta t)$ (in Hz). The optimal detection bandwidth is approximately twice this value or $B_{TDOCT} \approx 2\Delta k_{FWHM} z_{\max}/(\pi\Delta t)$ [59]. Assuming the light intensity backscattered from the sample is much smaller than that reflected from the reference, the mean detector photocurrent is dominated by the reference arm power and thus, $\sigma^2_{TDOCT} = \rho e S_{TDOCT} R_R B_{TDOCT}$. The well-known expression for the SNR of a TDOCT system is thus given by

$$SNR_{TDOCT} = \frac{\langle I_D\rangle^2_{TDOCT}}{\sigma^2_{TDOCT}} = \frac{\rho S_{TDOCT} R_S}{2eB_{TDOCT}}. \quad (2.30)$$

This result, that the SNR is proportional to the detector responsivity ρ and to the power returning from the sample ($= S_{TDOCT}R_S$) but is independent of the reference arm power level, is reasonable. Note that the detection bandwidth must be increased to accommodate either increased image depth for a given resolution or increased resolution for a given scan depth for a given A-scan acquisition time; thus, these modifications are penalized in TDOCT.

2.9.2 SNR Analysis for Fourier-Domain OCT

The first indication that the techniques of Fourier-domain OCT may provide a significant SNR advantage over TDOCT was published by Hausler et al. in 1997 [60]. The analysis was not experimentally confirmed and as a conference proceedings paper was not widely available. It was not until late 2003 that the publication of three papers in quick succession by independent groups confirmed the advantage both theoretically and experimentally for the case of spectrometer-based FDOCT or SDOCT [10–12]. One of these papers was also the first to recognize the inherent connection between swept-source and spectrometer-based systems and to demonstrate the identical advantage both theoretically and experimentally for both implementations [11].

To obtain comparable expressions to that of Eq. 2.20 for SSOCT and SDOCT systems, we must understand how both signal and noise propagate through the spectral sampling and inverse Fourier transform processes. Under the same assumptions of a single sample reflector and no autocorrelation terms, the sampled version of the spectral interferogram in FDOCT systems (from Eq. 2.9) is

$$I_D[k_m] = \frac{\rho}{2} S_{FDOCT}[k_m]\left[R_R + R_S + 2\sqrt{R_R R_S}\cos\left[2k_m(z_R - z_S)\right]\right]. \tag{2.31}$$

Here, $S_{FDOCT}[k_m] = \frac{S(k)|_{k=k_m}}{2}$ is that portion of the instantaneous power incident on the sample that corresponds to spectral channel m of the detection system, whether time multiplexed in SSOCT or on separate detectors in SDOCT. In the discrete case, the inverse Fourier transform operation is implemented as an inverse discrete Fourier transform:

$$i_D[z_m] = \sum_{m=1}^{M} I_D[k_m] e^{+ik_m z_m/M}. \tag{2.32}$$

Again, for the special case of a single sample reflector located at depth $z_R = z_S$, the peak value of the interferometric term in Eq. 2.21 inserted into Eq. 2.22 is

$$\begin{aligned} i_D[z_m = (z_R - z_S) = 0] &= \frac{\rho}{2}\sqrt{R_R R_S}\sum_{m=1}^{M} S_{FDOCT}[k_m] \\ &= \frac{\rho}{2}\sqrt{R_R R_S} S_{FDOCT}[k_m] \cdot M, \end{aligned} \tag{2.33}$$

the latter expression being under the assumption that each spectral channel has equal power in it (i.e., for a rectangular-shaped source spectrum). For a more realistic Gaussian-shaped source spectrum centered at pixel $M/2$ and clipped at its $1/e^2$ points, that is, $S_{FDOCT}[k_m] = S_{FDOCT}[k_{M/2}]\exp[-2 \cdot (k_m - k_{M/2})^2/(k_{M/2})^2]$, then the last factor is $\sum_{m=1}^{M} S_{FDOCT}\left[k_{M/2}\right] = S_{FDOCT}\left[k_{M/2}\right] \cdot M \cdot 0.598$. The interpretation of Eq. 2.23 is that the cosinusoidal spectral interference pattern in each separate detection channel from a single reflector adds coherently to give a peak signal

Table 2.3 Shot noise-limited SNR expressions for time-domain (TDOCT), spectral-domain (SDOCT), and swept-source OCT (SSOCT), normalized to the sample arm instantaneous power S_{TDOCT} and detection bandwidth D_{TDOCT} used in TDOCT

	Time-domain OCT (TDOCT)	Swept-source OCT (SSOCT)	Spectral-domain OCT (SDOCT)
Mean-square peak signal power $\langle I_D \rangle^2$	$\frac{\rho^2 S_{TDOCT}{}^2}{2}[R_R R_S]$	$\frac{\rho^2 S_{TDOCT}^2}{4}[R_R R_S] \cdot M^2$	$\frac{\rho^2 S_{TDOCT}^2}{4}[R_R R_S]$
Noise variance σ^2	$\rho e S_{TDOCT} R_R B_{TDOCT}$	$e\rho S_{TDOCT} R_R B_{TDOCT} \cdot M$	$\frac{e\rho S_{FDOCT}[k_m] R_R B_{FDOCT}}{M}$
Signal-to-noise ratio $SNR = \frac{\langle I_D \rangle^2}{\sigma^2}$	$\frac{\rho S_{TDOCT} R_S}{2eB_{TDOCT}}$	$\frac{\rho S_{TDOCT} R_S}{2eB_{TDOCT}} \cdot \frac{M}{2}$	$\frac{\rho S_{TDOCT} R_S}{2eB_{TDOCT}} \cdot \frac{M}{2}$

power much greater than the signal power in each channel alone. Each detection channel in FDOCT senses interference over a much longer coherence length than the single detection channel in TDOCT due to its restricted spectral extent. This coherent addition of signal power in FDOCT is not isolated to the trivial choice of $z_m = (z_R - z_S) = 0$ in Eq. 2.23; any other choice of $z_m = (z_R - z_S)$ would give rise to phase factors in the Fourier kernel, which would still coherently sum to an equivalent combined signal peak. The mean-square peak signal power in FDOCT is thus $\langle i_D \rangle^2_{FDOCT} = \frac{\rho^2 S^2_{FDOCT}[k_m]}{4}[R_R R_S] \cdot M^2$.

To complete the calculation of the SNR of FDOCT, we must address the issue of how noise transforms from the k-domain to the z-domain. $I_D[k_m]$ can be generalized to include an additive, uncorrelated Gaussian white noise term $\alpha[k_m]$. $\alpha[k_m]$ has a mean of zero, a standard deviation $\sigma[k_m]$, and a lower limit set by shot noise. Again, assuming $R_R >> R_S$, in the shot noise limit, $\sigma^2_{TDOCT}[k_m] = e\rho S_{FDOCT}[k_m] R_R B_{FDOCT}$. In this case, however, the noise in each spectral channel is uncorrelated; thus, the noise variances add incoherently in the inverse discrete Fourier summation to give $\sigma^2_{FDOCT}[z_m] = \sum_{m=1}^{M} \sigma^2_{FDOCT}[k_m] = e\rho S_{FDOCT}[k_m] R_R B_{FDOCT} \cdot M$. Thus, the SNR of FDOCT in general is given by

$$SNR_{FDOCT} = \frac{\langle i_D \rangle^2_{FDOCT}}{\sigma^2_{FDOCT}} = \frac{\rho S_{FDOCT}[k_m] R_S}{4eB_{FDOCT}} \cdot M. \tag{2.34}$$

To specialize this general expression for SDOCT and SSOCT specifically and to compare the resulting sensitivities to that of TDOCT, we assume an identical A-scan length $z_{\max}$ and acquisition time Δt for all three systems and that the instantaneous sample arm power (which is limited by safety or source availability considerations in practice) is the same. We also assume a source with rectangular-shaped spectrum, at least initially. A summary of the results of this section is provided in Table 2.3. For an SSOCT system, the allowable sample illumination power for each spectral channel is the same as the total illumination power in TDOCT since only one channel is illuminated at a time. Thus, $S_{SSOCT}[k_m] = S_{TDOCT}$. The detection bandwidth in

SSOCT is limited by the analog-to-digital sampling frequency $f_s = M/\Delta t = 1/(2\pi) \cdot 4z_{\max}\Delta k/\Delta t = 2\Delta k z_{\max}/(\pi\Delta t)$, where Eq. 2.15 relates $z_{\max}$ to $\delta_s k$ and $\Delta k = M \cdot \delta_s k$ is the entire range of wave numbers scanned. Assuming a scanning range of $\Delta k = 2 \cdot k_{FWHM}$ is chosen and that an antialiasing filter is used to limit the detection bandwidth to $B_{SSOCT} = f_s/2$, then $B_{SSOCT} = B_{TDOCT}$. For an SDOCT system, where all spectral channels are illuminated and detected simultaneously, the allowable power per spectral channel is decreased by the factor M, that is, $S_{SDOCT}[k_m] = S_{TDOCT}/M$. Also, the SDOCT detection bandwidth $B_{SDOCT} = B_{TDOCT}/M$ since the signals from each channel are integrated over the entire A-scan time. Thus, we can write expressions for the SNR of both SSOCT and SDOCT systems compared to TDOCT:

$$SNR_{SDOCT} = SNR_{SSOCT} = \frac{\rho S_{TDOCT} R_S}{4eB_{TDOCT}} \cdot M = SNR_{TDOCT} \cdot \frac{M}{2}. \tag{2.35}$$

The factor of $M/2$ improvement in both SSOCT and SDOCT over TDOCT can be simply understood from the fact that both FDOCT methods sample all depths all of the time, giving rise to a potential SNR improvement by a factor M; however, both FDOCT methods generate redundant data for positive and negative sample displacements relative to the reference position, decreasing the SNR improvement by a factor of 2. The factor M in Eq. 2.35 also depends upon the assumption of the source having equal power in all spectral channels, which is unrealistic and would lead to undesirable ringing in the inverse transformed data in any case. More realistic spectral shapes, such as the Gaussian shape discussed above, would decrease the SNR by an additional factor of about 2. It is clear, however, that filling the spectral channels with as much power as possible translates directly into increased SNR. Taking these factors into account and assuming that $M \approx 10^3$ for a realistic swept-source laser or detector array, we conclude that FDOCT systems are theoretically capable of up to 20 dB greater sensitivity than TDOCT systems.

It is also important to note that the theoretical SNR gain of SDOCT and SSOCT compared to TDOCT derived above rests upon the assumption of shot noise-limited detection in each detection channel. As has been addressed in previous publications for the case of TDOCT, achievement of this limit requires sufficient reference arm power to assure shot noise dominance but usually requires significant reference arm attenuation to minimize excess noise. In the case of SSOCT, the SNR of the spectral-domain interferometric signal output by the photodetector is equal to the SNR of a time-domain OCT system photodetector output operating at the same line rate and reference arm power; thus, the optimal reference arm power level for SSOCT is expected to be similar to that for TDOCT. In SDOCT, where the reference arm power is dispersed onto M photodetectors, the total reference power required to achieve shot noise-limited detection on all receivers simultaneously is more than that required for SSOCT and TDOCT by a factor of M. However, whether or not this requires a redesign of the interferometer coupling ratio depends upon the desired A-scan rate and the noise performance of the detectors used.

Acknowledgments We gratefully acknowledge the contributions of past and present graduate student and postdoctoral members of the Izatt Biophotonics Laboratory at Duke University.

References

1. J.M. Schmitt, A. Knuttel, M. Yadlowsky, M.A. Eckhaus, Optical-coherence tomography of a dense tissue – statistics of attenuation and backscattering. Phys. Med. Biol. **39**(10), 1705–1720 (1994)
2. J.A. Izatt, M.R. Hee, G.M. Owen, E.A. Swanson, J.G. Fujimoto, Optical coherence microscopy in scattering media. Opt. Lett. **19**(8), 590–592 (1994)
3. Y. Pan, R. Birngruber, J. Rosperich, R. Engelhardt, Low-coherence optical tomography in turbid tissue: theoretical analysis. Appl. Opt. **34**, 6564–6574 (1995)
4. J.A. Izatt, M.D. Kulkarni, H.W. Wang, K. Kobayashi, M.V. Sivak, Optical coherence tomography and microscopy in gastrointestinal tissues. IEEE J. Sel. Top. Quantum. Electron. **2**(4), 1017–1028 (1996)
5. J.M. Schmitt, A. Knuttel, Model of optical coherence tomography of heterogeneous tissue. J. Opt. Soc. Am. A Opt. Image. Sci. Vis. **14**(6), 1231–1242 (1997)
6. L.S. Dolin, A theory of optical coherence tomography. Radiophys. Quantum Electron. **41**(10), 850–873 (1998)
7. A.G. Podoleanu, D.A. Jackson, Noise analysis of a combined optical coherence tomograph and a confocal scanning ophthalmoscope. Appl. Opt. **38**(10), 2116–2127 (1999)
8. A.M. Rollins, J.A. Izatt, Optimal interferometer designs for optical coherence tomography. Opt. Lett. **24**(21), 1484–1486 (1999)
9. A.G. Podoleanu, Unbalanced versus balanced operation in an optical coherence tomography system. Appl. Opt. **39**(1), 173–182 (2000)
10. R. Leitgeb, C.K. Hitzenberger, A.F. Fercher, Performance of Fourier domain vs. time domain optical coherence tomography. Opt. Express **11**(8), 889–894 (2003)
11. M.A. Choma, M.V. Sarunic, C. Yang, J.A. Izatt, Sensitivity advantage of swept-source and Fourier-domain optical coherence tomography. Opt. Express **11**(18), 2183–2189 (2003)
12. J.F. de Boer, B. Cense, B.H. Park, M.C. Pierce, G.J. Tearney, B.E. Bouma, Improved signal-to-noise ratio in spectral-domain compared with time-domain optical coherence tomography. Opt. Lett. **28**(21), 2067–2069 (2003)
13. A.F. Fercher, Optical coherence tomography. J. Biomed. Opt. **1**(2), 157–173 (1996)
14. J.M. Schmitt, Optical Coherence Tomography (OCT): a review. IEEE J. Sel. Top. Quantum Electron. **5**(4), 1205–1215 (1999)
15. M.R. Hee, Optical coherence tomography: theory, in *Handbook of Optical Coherence Tomography*, ed. by B.E. Bouma, G.J. Tearney (Marcel Dekker, New York, 2002), pp. 41–66
16. M.E. Brezinski, Optical coherence tomography theory, in *Optical Coherence Tomography Principles and Applications* (Academic Press, Burlington, MA, 2006), pp. 97–146
17. T. Sawatari, Optical heterodyne scanning microscope. Appl. Optics **12**(11), 2768–2772 (1973)
18. T. Wilson, *Confocal Microscopy* (Academic, London, 1990)
19. M. Gu, C. Sheppard, X. Gan, Image formation in a fiber-optical confocal scanning microscope. J. Opt. Soc. Am. B **8**, 1755–1761 (1991)
20. M. Gu, *Principles of Three-Dimensional Imaging in Confocal Microscopes* (World Scientific, Singapore, 1996)
21. J.M. Schmitt, S.L. Lee, K.M. Yung, An optical coherence microscope with enhanced resolving power in thick tissue. Opt. Commun. **142**, 203–207 (1997)
22. S.-W. Huang, A.D. Aguirre, R.A. Huber, D.C. Adler, J.G. Fujimoto, Swept source optical coherence microscopy using a Fourier domain mode-locked laser. Opt. Express **15**(10), 6210–6217 (2007)

23. E. Beaurepaire, A.C. Boccara, M. Lebec, L. Blanchot, H. Saint-Jalmes, Full-field optical coherence microscopy. Opt. Lett. **23**(4), 244–246 (1998)
24. A. Dubois, L. Vabre, A.-C. Boccara, E. Beaurepaire, High-resolution full-field optical coherence tomography with a Linnik microscope. Appl. Opt. **41**(4), 805–812 (2002)
25. M.V. Sarunic, S. Weinberg, J.A. Izatt, Full-field swept-source phase microscopy. Opt. Lett. **31**(10), 1462–1464 (2006)
26. B. Povazay, A. Unterhuber, B. Hermann, H. Sattmann, H. Arthaber, W. Drexler, Full-field time-encoded frequency-domain optical coherence tomography. Opt. Express **14**(17), 7661–7669 (2006)
27. B. Karamata, M. Laubscher, M. Leutenegger, S. Bourquin, T. Lasser, P. Lambelet, Multiple scattering in optical coherence tomography. I. Investigation and modeling. J. Opt. Soc. Am. A **22**(7), 1369–1379 (2005)
28. B. Karamata, M. Leutenegger, M. Laubscher, S. Bourquin, T. Lasser, P. Lambelet, Multiple scattering in optical coherence tomography. II. Experimental and theoretical investigation of cross talk in wide-field optical coherence tomography. J. Opt. Soc. Am. A Opt. Image Sci. Vis. **22**(7), 1380–1388 (2005)
29. B. Karamata, P. Lambelet, M. Laubscher, R.P. Salathe, T. Lasser, Spatially incoherent illumination as a mechanism for cross-talk suppression in wide-field optical coherence tomography. Opt. Lett. **29**(7), 736–738 (2004)
30. L. Vabre, A. Dubois, A.C. Boccara, Thermal-light full-field optical coherence tomography. Opt. Lett. **27**(7), 530–532 (2002)
31. B. Laude, A. De Martino, B. Drévillon, L. Benattar, L. Schwartz, Full-field optical coherence tomography with thermal light. Appl. Optics **41**(31), 6637–6637 (2002)
32. L. Mandel, E. Wolf, *Optical Coherence and Quantum Optics* (Cambridge University Press, Cambridge, UK, 1995)
33. A.F. Fercher, C.K. Hitzenberger, M. Sticker, E. Moreno-Barriuso, R. Leitgeb, W. Drexler, H. Sattmann, A thermal light source technique for optical coherence tomography. Opt. Commun. **185**(1–3), 57–64 (2000)
34. J. Kim, D.T. Miller, E. Kim, S. Oh, J. Oh, T.E. Milner, Optical coherence tomography speckle reduction by a partially spatially coherent source. J. Biomed. Opt. **10**(6), 064034 (2005)
35. A.H. Dhalla, J.V. Migacz, J.A. Izatt, Crosstalk rejection in parallel optical coherence tomography using spatially incoherent illumination with partially coherent sources. Opt. Lett. **35**(13), 2305–2307 (2010)
36. B. Redding, M.A. Choma, H. Cao, Speckle-free laser imaging using random laser illumination. Nat Photon **6**(6), 355–359 (2012)
37. B. Redding, M. Choma, and H. Cao, "Spatially Incoherent Random Lasers for Full Field Optical Coherence Tomography," in CLEO:2011 - Laser Applications to Photonic Applications, OSA Technical Digest (CD) (Optical Society of America, 2011), paper PDPC7
38. T. Klein, W. Wieser, C.M. Eigenwillig, B.R. Biedermann, R. Huber, Megahertz OCT for ultrawide-field retinal imaging with a 1050 nm Fourier domain mode-locked laser. Opt. Express **19**(4), 3044–3062 (2011)
39. A.F. Fercher, C.K. Hitzenberger, G. Kamp, S.Y. Elzaiat, Measurement of intraocular distances by backscattering spectral interferometry. Opt. Commun. **117**(1–2), 43–48 (1995)
40. G. Hausler, M.W. Lindner, "Coherence radar" and "spectral radar" – new tools for dermatological diagnosis. J. Biomed. Opt. **3**(1), 21–31 (1998)
41. M. Wojtkowski, R. Leitgeb, A. Kowalczyk, T. Bajraszewski, A.F. Fercher, In vivo human retinal imaging by Fourier domain optical coherence tomography. J. Biomed. Opt. **7**(3), 457–463 (2002)
42. S.R. Chinn, E.A. Swanson, J.G. Fujimoto, Optical coherence tomography using a frequency-tunable optical source. Opt. Lett. **22**(5), 340–342 (1997)
43. B. Golubovic, B.E. Bouma, G.J. Tearney, J.G. Fujimoto, Optical frequency-domain reflectometry using rapid wavelength tuning of a Cr4+:forsterite laser. Opt. Lett. **22**(22), 1704–1706 (1997)

44. F. Lexer, C.K. Hitzenberger, A.F. Fercher, M. Kulhavy, Wavelength-tuning interferometry of intraocular distances. Appl. Opt. OT **36**(25), 6548–6553 (1997)
45. U.H.P. Haberland, V. Blazek, H.J. Schmitt, Chirp Optical coherence tomography of layered scattering media. J. Biomed. Opt. **3**(3), 259–266 (1998)
46. M. Wojtkowski, A. Kowalczyk, R. Leitgeb, A.F. Fercher, Full range complex spectral optical coherence tomography technique in eye imaging. Opt. Lett. **27**(16), 1415–1417 (2002)
47. R.A. Leitgeb, C.K. Hitzenberger, A.F. Fercher, T. Bajraszewski, Phase-shifting algorithm to achieve high-speed long-depth-range probing by frequency-domain optical coherence tomography. Opt. Lett. **28**(22), 2201–2203 (2003)
48. M.A. Choma, C. Yang, J.A. Izatt, Instantaneous quadrature low-coherence interferometry with 3×3 fiber-optic couplers. Opt. Lett. **28**(22), 2162–2164 (2003)
49. S.H. Yun, G.J. Tearney, J.F. De Boer, B.E. Bouma, Removing the depth-degeneracy in optical frequency domain imaging with frequency shifting. Opt. Express **12**, 4822–4828 (2004)
50. E. Gotzinger, M. Pircher, R.A. Leitgeb, C.K. Hitzenberger, High speed full range complex spectral domain optical coherence tomography. Opt. Express **13**(2), 583–594 (2005)
51. M.V. Sarunic, M.A. Choma, C. Yang, J.A. Izatt, Instantaneous complex conjugate resolved Fourier domain and swept-source OCT using 3×3 couplers. Opt. Express **13**, 957–967 (2005)
52. A.M. Davis, M.A. Choma, J.A. Izatt, Heterodyne swept-source optical coherence tomography for complete complex conjugate ambiguity removal. J. Biomed. Opt. **10**(6), 064005 (2005)
53. J. Zhang, J.S. Nelson, Z.P. Chen, Removal of a mirror image and enhancement of the signal-to-noise ratio in Fourier-domain optical coherence tomography using an electro-optic phase modulator. Opt. Lett. **30**(2), 147–149 (2005)
54. A.-H. Dhalla, Development of Extended-Depth Swept Source Optical Coherence Tomography for Applications in Ophthalmic Imaging of the Anterior and Posterior Eye, Ph.D. Thesis, *Biomedical Engineering Department*, Duke University, Durham, North Carolina, 2013
55. S.H. Yun, G.J. Tearney, B.E. Bouma, B.H. Park, J.F. de Boer, High-speed spectral-domain optical coherence tomography at 1.3 mu m wavelength. Opt. Express **11**(26), 3598–3604 (2003)
56. B. Bhushan, J.C. Wyant, C.L. Koliopoulos, Measurement of surface topography of magnetic tapes by Mirau interferometry. Appl. Opt. **24**, 1489–1497 (1985)
57. A. Dubois, Phase-map measurements by interferometry with sinusoidal phase modulation and four integrating buckets. J. Opt. Soc. Am. A **18**, 1972–1979 (2001)
58. M.V. Sarunic, B.E. Applegate, J.A. Izatt, Real-time quadrature projection complex conjugate resolved Fourier domain optical coherence tomography. Opt. Lett. **31**(16), 2426–2428 (2006)
59. E.A. Swanson, D. Huang, M.R. Hee, J.G. Fujimoto, C.P. Lin, C.A. Puliafito, High-speed optical coherence domain reflectometry. Opt. Lett. **17**(2), 151–153 (1992)
60. M. Bail, G. Hausler, J.M. Hermann, F. Kiesewetter, M.W. Lindner, A. Schutz. *Optical Coherence Tomography by Spectral Radar for the Analysis of Human Skin*, (SPIE, 1997)

Modeling Light–Tissue Interaction in Optical Coherence Tomography Systems

3

Peter E. Andersen, Thomas M. Jørgensen, Lars Thrane, Andreas Tycho, and Harold T. Yura

Keywords

Absorption • Light propagation • Light tissue interaction • Optical coherence tomography • Scattering • Theoretical model

3.1 Introduction

Optical coherence tomography (OCT) has developed rapidly since its potential for applications in clinical medicine was first demonstrated in 1991 [1]. OCT performs high-resolution, cross-sectional tomographic imaging of the internal microstructure in materials and biologic systems by measuring backscattered or backreflected light.

Mathematical models [2–11] have been developed to promote understanding of the OCT imaging process and thereby enable the development of better imaging instrumentation and data processing algorithms. One of the most important issues in the modeling of OCT systems is the role of the multiple-scattered photons, an issue which has become fully understood through the works of Thrane et al. [12] and Turchin et al. [13] representing the most comprehensive modeling.

Experimental validation of models on realistic sample structures, e.g., layered sample structures, would require manufacturing of complex tissue phantoms with well-controlled optical properties. However, a useful alternative to validate the analytical predictions on such geometries is to apply a Monte Carlo (MC)-based simulation model [14], because there are few limitations on which geometries may be modeled using MC simulations. MC models for analyzing light propagation are based on

P.E. Andersen (✉) • T.M. Jørgensen • L. Thrane • A. Tycho
Department of Photonics Engineering, Technical University of Denmark, Roskilde, Denmark
e-mail: peta@fotonik.dtu.dk.

H.T. Yura
The Aerospace Corporation, Electronics and Photonics Laboratory, Los Angeles, CA, USA

© Springer International Publishing Switzerland 2015

W. Drexler, J.G. Fujimoto (eds.), *Optical Coherence Tomography*,
DOI 10.1007/978-3-319-06419-2_4

simulating the radiative equation of transfer by tracing a large number of energy packets each considered to represent a given component of the incident light energy [15, 16]. Hence, as a numerical experiment, one has full control of all parameters.

The scope of this chapter is to present analytical and numerical models that are able to describe the performance of OCT systems including multiple-scattering effects in heterogeneous media. Such models, where the contribution to the OCT signal from multiple-scattering effects is taken into account, are essential for the understanding and in turn optimization of OCT systems. An analytical model based on the extended Huygens–Fresnel (EHF) principle meeting these requirements is presented here. An MC analysis is presented in order to handle the modeling of heterodyne/coherent detection OCT systems with a radiative transfer-type photon packet MC approach. Using this MC model results are obtained, which validate the EHF model. In general, these models, analytical as well as numerical, may serve as important tools for improving the interpretation of OCT images.

3.1.1 Modeling Light–Tissue Interactions Relevant to OCT

Since the first paper describing the use of the OCT technique for noninvasive cross-sectional imaging in biological systems [1], various theoretical models of the OCT system have been developed. The primary motivation for deriving an appropriate model has been the potential optimization of the OCT technique leading to an improvement in imaging capabilities and to the possibility of extracting physical parameters.

The first theoretical models were based on single-scattering theory [2, 3]. These models are restricted to superficial layers of highly scattering tissue in which only single scattering occurs. Single scattering or single backscattering refers to photons which do not undergo scattering either to or from the backscattering plane of interest, i.e., ballistic photons.

At larger probing depths, however, the light is also subject to multiple scattering. The effects of multiple scattering have been investigated on an experimental basis [5], by using a hybrid Monte Carlo/analytical model [6] and analysis methods of linear systems theory [7], on the basis of solving the radiative transfer equation in the small-angle approximation [8, 13], by using models based on the extended Huygens–Fresnel (EHF) principle [9, 12, 17], and MC simulations [10, 14]. Note that modeling using MC simulations is treated in greater detail in Sect. 3.4.2.

In the present context, the main objective is the analysis of multiple-scattering effects. As shown by several investigations, the primary effects of multiple scattering are a reduction of the imaging contrast and resolution of the OCT system. In Ref. [4], the authors suggested solving the multiple-scattering problem by using the EHF principle [9] known from atmospheric propagation of laser beams [18]. Their analysis contains one important inaccuracy because in their end result, the ballistic component is included twice leading to erroneous calculations. As a result, their analysis should be applied with care. In addition, the effects of the so-called shower-curtain effect [18] are not accounted for in their analysis. Thrane et al. [12] succeeded in applying the EHF principle for the OCT geometry; see Sect. 4.2. Following their analysis,

Feng et al. [17] aimed at expanding on the use of EHF in modeling the OCT geometry. In particular, their aim is to simplify the analysis, but several mistakes are introduced in the attempt: firstly, an imaginary lens is introduced with the purpose of obviating the shower-curtain effect leading to errors in the final calculation of the OCT signal. Secondly, an erroneous lateral coherence length is introduced, i.e., the lateral coherence length should be calculated as resulting from reflecting off a rough surface and not, as done in Ref. [17], a specular surface. Hence, their model should be approached with caution.

A statistical optics approach to adequately model the effects of multiple scattering was proposed by Karamata et al. [19]. However, their analysis, based on a heuristic argument, is misleading and incorrect. The main error is due to their assumption regarding spatial coherence, where it is alleged that transverse spatial coherence is not degraded due to multiple scattering. The argument used by Karamata et al. [19] is valid only for the case of a focused beam reflecting off a rough surface with no scattering medium in between the reflection site and the collection aperture; see, for example, pages 210–211 of Ref. [20]. This is definitely not the case for OCT in turbid media (i.e., tissue). The degradation of spatial coherence of a beam propagating through a multiple-scattering media is well known and documented in the literature; see Ref. [21] and references therein. Therefore, the analysis given in Ref. [19] is not considered further, and the results and conclusions should not be used in modeling light propagation in turbid media.

Turchin et al. [13] expanded the analysis of Dolin [8] to an OCT geometry. Their analysis is based on the radiative transfer equation (RTE) in the small-angle approximation, of which Arnush [22] first obtained the closed-form solution. It should be noted that in this approximation, the solution of the RTE and the EHF is identical [23, 24]. In general, the analysis of Ref. [13] is consistent with that of the EHF model, which is presented below. However, technically there are two important differences that need to be pointed out. Firstly, the choice of scattering phase function in Ref. [13]: as in Ref. [12], the forward scattered part is modeled by a Gaussian distribution, but additionally a small backscattered fraction is included. This way of taking into account tissue backscattering was previously suggested by Raymer et al. [25–27] and discussed by Yura et al. [24]. However, it was not included in the EHF analysis of the OCT geometry [12], but it is incorporated below. Hence the RTE [13] and EHF [12] descriptions are equivalent. Secondly, Thrane et al. [12] present an analytical engineering expression for the OCT signal current based on an accurate analytical approximation for the irradiance distribution in the backscatter plane (see Appendix for details). Turchin et al. [13] do not use this approximation, and consequently their end results require numerical computations, which yield highly accurate values for the OCT signal current. They also obtain accurate results in the extraction of optical scattering properties of the sample, which is further addressed in Sect. 3.5.1. Furthermore, it is noted that the analysis of Turchin et al. [13] is restricted to the special case where the focusing lens in the sample arm is in direct contact with the tissue being investigated. This is in contrast to the analysis of Ref. [12] where the ABCD ray-matrix formalism was used to readily include an arbitrary configuration of the sample arm. Finally, in

contrast to the totally numerical results of Ref. [13], the multiple-scattering EHF analysis presented below yields accurate analytical expressions for the OCT signal for a wide range of optical configurations that both are amenable to physical interpretation (see, e.g., [28]) and are desirable for use in parametric studies for OCT system optimization.

Strictly speaking, the OCT model developed in Ref. [12] and further extended here is based on the assumption that the detected signal return arises only from photons that have been backscattered from a target layer selected by the coherence gate of the light source. Backscattered photons from the bulk tissue between the light source and the target layer have been assumed to be negligible in comparison with photons arising from the tissue discontinuity. Realistically, photons backscattered from the intervening bulk tissue whose optical path-length difference between the reference light is within the coherence length will also be detected. Bulk backscattered detected light contributes to the noise in the OCT signal because it does not furnish any local information about the target layer. Yao and Wang [29] used a Monte Carlo-based technique to simulate the OCT signal from homogeneous turbid medium. They considered a single mode fiber emitting a pencil beam that is in direct contact with the turbid medium and divided the OCT signal return into two categories: one from a target imaging layer in the medium (Class I photons) and the other from the intervening bulk tissue (Class II photons). The simulation results of Ref. [29] reveal that these two classes of photons have very different spatial and angular distributions which make OCT possible. The Class II signal has a much broader spatial distribution than the Class I signal. Although the spatial distributions of both signals broaden with probing depth, the Class II signal is broadened much faster than the Class I signal, and thus, limiting the detection area will reject most of the Class II signal. Additionally, Class II photons have a wider angular distribution than the corresponding Class I photons, and a correspondingly larger fraction of Class II photons that impinge on the detector area will not be effectively heterodyne coupled with the reference light. For large probing depths, however, the simulation results for the homogeneous turbid medium indicated that Class II signal photons will eventually become dominant. The actual crossover point is ultimately related to the efficiency of Class II signal rejection, whether or not the medium contains refractive index discontinuities, and the effects of Class II photon rejection due to imaging configurations such as dynamic focusing. With these considerations in mind, the extended Huygens–Fresnel-based OCT model developed in Ref. [12], updated to incorporate the attenuating effects of tissue backscatter, is presented below.

3.1.2 Organization of this Chapter

The chapter is divided into three sections covering specific topics in modeling OCT systems. In Sect. 3.2, an analytical model for the detected OCT signal is derived based on the EHF principle. In Sect. 3.3, the effects of multiple scattering on the detected Doppler OCT signal are investigated. In the field of biomedical optics, Monte Carlo simulations have already proved their value. In Sect. 3.4, an advanced

Monte Carlo model for calculating the OCT signal is presented, and comparisons to the analytical model are made. In general, good agreement is obtained, thus validating the EHF model. Section 3.5 overviews the impact of extracting optical scattering properties from OCT images on the diagnostic potential of OCT.

3.2 Analytical OCT Model Based on the Extended Huygens–Fresnel Principle

In the present section, a general theoretical description [12, 30, 31] of the OCT technique when used for imaging in highly scattering tissue is presented, which is valid for an arbitrary ABCD optical configuration. The description is based on the EHF principle. In a standard OCT system [1] with diffuse backscattering from the tissue discontinuity being probed, and a distance between the focusing lens and the tissue, the so-called shower-curtain effect [18, 32] is present, which is uniquely included in Ref. [12]. This effect is not described by previous ad hoc theoretical models [9]. Furthermore, because the sample arm focusing lens in Turchin et al. [13] is assumed to be in direct contact with the tissue being probed, shower-curtain effects are not present in the geometry and hence not in their analysis.

3.2.1 The Extended Huygens–Fresnel Principle

When an optical wave propagates through a so-called random medium, e.g., tissue, both the amplitude and phase of the electric field experience fluctuations caused by small random changes in the index of refraction across the sample. For tissue [33] it can in general be assumed that the depolarization term of the associated vectorial wave equation can be neglected, if the wavelength of the radiation, λ, is much smaller than l_0, where l_0 is a measure of the smallest random inhomogeneities in the medium [34, 35] (the structures that dominate light propagation in tissue, e.g., cells, have a size of 2 μm or more). With this assumption, the wave equation can be simplified to three scalar equations, one for each component of the field. Letting $U(\mathbf{R})$ denote one of the scalar components transverse to the direction of propagation along the positive z-axis, the following scalar stochastic equation is obtained:

$$\nabla^2 U + k^2 n^2(\mathbf{R}) U = 0, \tag{3.1}$$

where k is the wave number, $\mathbf{R}$ is a point in space, and $n(\mathbf{R})$ is the index of refraction. Considering a random medium, $n(\mathbf{R})$ acts as a stochastic variable for different realizations of tissue with given macroscopic optical parameters. Equation 3.1 cannot be solved exactly in closed form. Some early attempts to solve Eq. 3.1 were based on the geometric optics approximation [36], which ignores diffraction effects, and on perturbation theories widely known as the Born

approximation and Rytov approximation [37]. An alternative method was developed, independent of each other, by Lutomirski and Yura [38] and by Feizulin and Kravtsov [39]. This technique is called the extended Huygens–Fresnel (EHF) principle. It extends the Huygens–Fresnel principle to deal with media that exhibit a random spatial variation in the index of refraction. This principle follows directly from Green's theorem [40] and the Kirchhoff approximation [40] applied to the scalar wave equation together with the use of a field reciprocity theorem. Yura and Hanson [41, 42] have applied the EHF principle to paraxial wave propagation through an arbitrary ABCD system in the presence of random inhomogeneities. An arbitrary ABCD system refers to an optical system that can be described by the so-called ABCD ray-transfer matrix [43]. For the present cases of interest, the ABCD ray-transfer matrix is real, and the field in the output plane is then given by [41]

$$U(\mathbf{r}) = \int U_0(\mathbf{p}) G(\mathbf{p},\mathbf{r}) d\mathbf{p} \tag{3.2}$$

where $\mathbf{r}$ and $\mathbf{p}$ are two-dimensional vectors transverse to the optical axis in the output plane and input plane, respectively. The spatial integrals are to be carried out over the entire plane in question. The quantity $U_0(\mathbf{p})$ is the field in the input plane, and $G(\mathbf{p},\mathbf{r})$ is the EHF Green's function describing the response at $\mathbf{r}$ due to a point source at $\mathbf{p}$ given by [38, 41]

$$G(\mathbf{p},\mathbf{r}) = G_0(\mathbf{p},\mathbf{r}) \exp[i\varphi(\mathbf{p},\mathbf{r})], \tag{3.3}$$

where $G_0(\mathbf{p},\mathbf{r})$ is Huygens–Fresnel Green's function for propagation through an ABCD system in the absence of random inhomogeneities and $\varphi(\mathbf{p},\mathbf{r})$ is the random phase of a spherical wave propagating in the random medium from the input plane to the output plane. Huygens–Fresnel Green's function $G_0(\mathbf{p},\mathbf{r})$ is given by [41]

$$G_0(\mathbf{p},\mathbf{r}) = -\frac{ik}{2\pi B} \exp\left[-\frac{ik}{2B}\left(Ap^2 - 2\mathbf{p}\cdot\mathbf{r} + Dr^2\right)\right], \tag{3.4}$$

where A, B, and D are the ray-matrix elements for propagation from the input plane to the output plane.

3.2.2 Calculating the OCT Signal: Time Domain

A time-domain OCT system [1] is based on a broad bandwidth light source (SLD), a Michelson interferometer with a movable reference mirror, and a photodetector. The rotationally symmetric sample arm geometry of such an OCT system is depicted in Fig. 3.1, where a lens with focal length f is placed at a distance d from the tissue surface. The optical path length of the reference arm in the

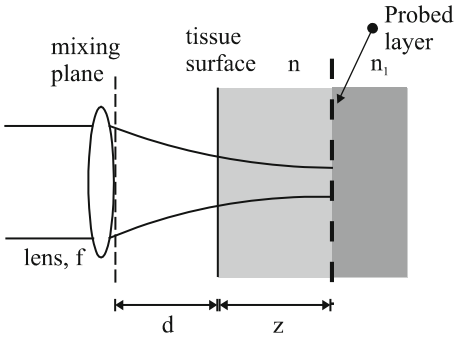

Fig. 3.1 Sample arm geometry of the OCT system

Michelson interferometer is matched to the optical depth of the focal plane, whereby the configuration – due to backscattering – is probing the layer of the tissue coinciding with the focal region.

For the wavelengths of interest in the NIR region and, e.g., in the case of human skin, light scattering in the bulk tissue is predominantly taking place in the forward direction [44]. Hence, the scattering phase function $\sigma(\theta,z)$ can be modeled as a sum of a small-angle scattering phase function $\sigma_1(\theta,z)$ that tends to zero for $\theta > \pi/2$ and a constant but relative small isotropic term included to incorporate a backscattered contribution [8, 13]:

$$\sigma(\theta, z) = [1 - 2p_b(z)]\sigma_1(\theta, z) + 2p_b(z), \tag{3.5}$$

where $p_b(z)$ denotes the backscattering coefficient as a function of the depth. For tissues, the quantity p_b will normally be much smaller than unity, i.e., $p_b << 1$; see, for example, Ref. [13].

It was noted above that the EHF principle is based on the paraxial approximation and therefore valid for small-angle forward scattering. In particular, it can be shown that the paraxial approximation is valid up to 30°, i.e., 0.5 rad [43]. Because most tissues are characterized by *rms* scattering angles below this limit, the EHF principle may be used to describe light propagation in tissue retaining both amplitude and phase information. Also, the bulk tissue absorption is neglected in the present calculation, because in the case of most tissues, the scattering essentially accounts for the signal attenuation [44]. Basically including the absorption would result in an overall exponential decay. Thus, bulk homogeneous tissue is characterized by a scattering coefficient μ_s, a root-mean-square scattering angle θ_{rms} or asymmetry parameter g [45], and a mean index of refraction n. Furthermore, the bulk tissue is modeled as a material with scatterers randomly distributed over the volume of interest.

Consider an optical field that is narrowband and non-monochromatic, i.e., the spectral width of the light source $\Delta\nu$ is much smaller than the center frequency ν. Light sources characterized as "broad band" in relation to OCT also fulfills this condition. At a spatial coordinate $\mathbf{p}$ and time t, such an optical field may be expressed in terms of a (temporally) slowly varying complex amplitude $A(t)$

where the characteristic temporal scale of the complex envelope amplitude A is much less than $1/\nu_0$. In addition it is assumed that the reference field, U_R, and the incident sample field, U_{Si}, are of Gaussian shapes:

$$U_R(\mathbf{p},t) = \sqrt{\frac{P_R}{\pi w_0^2}\exp\left[-\frac{|\mathbf{p}|^2}{2}\left(\frac{1}{w_0^2}+\frac{ik}{f}\right)\right]}A(t)\exp[i\omega_R t+\varphi_R(t)], \tag{3.6}$$

$$U_{Si}(\mathbf{p},t) = \sqrt{\frac{P_s}{\pi w_0^2}\exp\left[-\frac{|\mathbf{p}|^2}{2}\left(\frac{1}{w_0^2}+\frac{ik}{f}\right)\right]}A(t)\exp[i\omega_s t+\varphi_s(t)], \tag{3.7}$$

where P_R and P_S are the powers of the reference and input sample beams, respectively; w_0 is the $1/e$ intensity radius of these beams in the lens plane, $k = 2\pi/\lambda$; λ is the center wavelength of the source in vacuum; ω_R and ω_S are the angular frequencies of the reference and input sample beams, respectively; and φ_R and φ_S are the phases of the reference field and input sample field, respectively.

The mixing of the backscattered or reflected sample field U_S from the probed layer with the reference field U_R on the photodetector of the OCT system gives rise to a heterodyne signal current $i(z)$ [9]:

$$i(z) \propto |\gamma(\tau)|\mathrm{Re}\left[\int U_R(\mathbf{p})\,U_S^*(\mathbf{p})d\mathbf{p}\right], \tag{3.8}$$

where the integration is taken over the area of the photodetector. Re[·] denotes the real part, and τ denotes the time difference between the propagation times of the reference and sample beams. $|\gamma(\tau)|$ is the modulus of the normalized temporal coherence function of the source.

Because a random medium is considered, the mean square heterodyne signal current $\langle i^2(z)\rangle$ should be calculated, which is proportional to the heterodyne signal power. It can be shown to be given by [9, 18]:

$$\langle i^2(z)\rangle = 2\alpha^2|\gamma(\tau)|^2\mathrm{Re}\left[\iint \Gamma_S(\mathbf{p}_1,\mathbf{p}_2;z)\Gamma_R(\mathbf{p}_1,\mathbf{p}_2)d\mathbf{p}_1 d\mathbf{p}_2\right], \tag{3.9}$$

where

$$\Gamma_R(\mathbf{p}_1,\mathbf{p}_2) = \langle U_R(\mathbf{p}_1)U_R^*(\mathbf{p}_2)\rangle = U_R(\mathbf{p}_1)U_R^*(\mathbf{p}_2) \tag{3.10}$$

$$\Gamma_s(\mathbf{p}_1,\mathbf{p}_2;z) = \langle U_s(\mathbf{p}_1;z)U_s^*(\mathbf{p}_2;z)\rangle \tag{3.11}$$

are the mutual coherence functions of the reference and the reflected sample optical fields in the mixing plane. The angular brackets denote an ensemble

average over the statistical properties of the tissue. Physically, the heterodyne mixing process takes place on the photosensitive surface of the detector in the focal plane of the "mixing" lens. However, Fried [46] has shown mathematically that one can identically compute the mean square heterodyne photocurrent in a plane directly in front of the mixing lens at the side facing the sample, and, accordingly, $\mathbf{p}_1$, $\mathbf{p}_2$ are two-dimensional vectors in this plane transverse to the optical axis. The quantity α is a conversion factor for power to current and equals $(q_e\eta/h\nu)$, where q_e is the electronic charge, η the detector quantum efficiency, ν the optical center frequency, and h Planck's constant. In the present analysis, without loss of generality, the temporal coherence function is approximated with a rectangular function of width τ_c, the coherence time of the source.

Details of the derivation of the mutual coherence function Γ_S are given in Appendix under the assumption that the forward propagated light can be considered statistically independent from the backscattered light. To obtain a closed-form expression including the intermediate ranges of propagation, the single-scattering solution and the solution for large optical depths are interpolated, as outlined in Appendix, yielding the following squared signal contribution from within the coherence gate around the depth z:

$$\left\langle i^2(z)\right\rangle_{coh_gate} \approx \frac{2\alpha^2 P_R P_S \sigma_b}{\pi^2} \int \left[\frac{e^{-\mu_s z}\exp\left\{-r^2/w_H^2\right\}}{w_H^2} + \frac{(1-e^{-\mu_s z})e^{-2p_b\mu_s z}\exp\left\{-r^2/w_S^2\right\}}{w_S^2}\right]^2 d\mathbf{r}, \tag{3.12}$$

where the effective backscattering cross section of the layer being probed is defined as $\sigma_b = 4\pi p_b \mu_s l_c/k^2$. Here l_c denotes the coherence length of the source given by $c\tau_c$. In Eq. 3.12 it is assumed that $\mu_s l_c << 1$.

The quantities w_H and w_S are the $1/e$ irradiance radii in the target plane in the absence and presence of scattering, respectively, given by [12]

$$w_H^2 = w_0^2\left(A - \frac{B}{f}\right)^2 + \left(\frac{B}{kw_0}\right)^2, \tag{3.13}$$

$$w_S^2 = w_0^2\left(A - \frac{B}{f}\right)^2 + \left(\frac{B}{kw_0}\right)^2 + \left(\frac{2B}{k\rho_0}\right)^2, \tag{3.14}$$

where ρ_0 denotes the lateral coherence length of the reflected sample field in the plane in which the mixing calculated [12]

$$\rho_0(z) = \sqrt{\frac{3}{\mu_s z}}\frac{\lambda}{\pi\theta_{\text{rms}}}\left(\frac{nB}{z(1-2p_b)}\right). \tag{3.15}$$

Here the root-mean scattering angle, θ_{rms}, is related to the anisotropy parameter g:

$$\theta_{\mathrm{rms}} \approx \sqrt{2(1-g)}. \tag{3.16}$$

Performing the integration over the probed layer (see Fig. 3.1) in Eq. 3.12 and simplifying, the following expression for the mean square heterodyne signal current is obtained:

$$\begin{aligned}\left\langle i^2(z)\right\rangle_{coh_gate} &\approx \frac{\alpha^2 P_R P_s \sigma_b}{\pi w_H^2} \\ &\times \left[e^{-2\mu_s z} + \frac{4e^{-\mu_s z}e^{-2p_b\mu_s z}(1-e^{-\mu_s z})}{1+\frac{w_S^2}{w_H^2}} + (1-e^{-\mu_s z})^2 e^{-4p_b\mu_s z}\frac{w_H^2}{w_S^2} \right] \\ &= \left\langle i^2\right\rangle_0 \Psi(z).\end{aligned} \tag{3.17}$$

Assuming $p_b << 1$, Eq. 3.17 reduces to

$$\begin{aligned}\left\langle i^2(z)\right\rangle_{coh_gate} &\approx \frac{\alpha^2 P_R P_s \sigma_b}{\pi w_H^2} \\ &\times \left[e^{-2\mu_s z} + \frac{4e^{-\mu_s z}(1-e^{-\mu_s z})}{1+\frac{w_S^2}{w_H^2}} + (1-e^{-\mu_s z})^2 \frac{w_H^2}{w_S^2} \right] \\ &= \left\langle i^2\right\rangle_0 \Psi(z).\end{aligned} \tag{3.18}$$

The quantity $\langle i^2\rangle_0 = \alpha^2 P_R P_S \sigma_b/\pi(w_H)^2$ is the mean square heterodyne signal current in the absence of scattering, and the terms contained in the brackets are the heterodyne efficiency factor $\Psi(z)$. The quantity $\Psi(z)$ is the reduction in the heterodyne signal-to-noise ratio due to the scattering of the tissue. The first term in the brackets of Eq. 3.17 represents the contribution due to single scattering. The third term is the multiple-scattering term, and the second term is the cross term. Physically, the cross term is the coherent mixing of the unscattered and the multiple-scattered light. A comparison between the analytical approximation of $\Psi(z)$, given in Eq. 3.17, and the exact numerical calculation is given in Ref. [47] showing reasonable agreement. The validity of the above expression has been explored by comparing the model with advanced Monte Carlo studies and confirms that the analytical result provides a feasible model for investigating the qualitative behavior of the OCT configuration; see Sect. 3.4.

3.2.2.1 Dynamic Focusing: Diffuse Reflectance

If one applies dynamic focusing, the focal plane will ideally be arranged to move in accordance with the position of the coherence gate. This situation can be analyzed by setting $fA = B$ and $A = 1$ in Eqs. 3.13 and 3.14:

$$w_H = \frac{f}{kw_0}, w_S = \sqrt{w_H^2 + \left(\frac{2f}{k\rho_0}\right)^2}, \tag{3.19}$$

$$\frac{w_H^2}{w_S^2} = \frac{1}{1 + \left(\frac{2w_0}{\rho_0(z)}\right)^2}. \tag{3.20}$$

For lateral separations much less (greater) than the coherence length, $\rho_0(z)$, the field can be considered to be mutually coherent (incoherent). Because of the diffuse backscattering from the layer being probed, $\rho_0(z)$ is determined only by the propagation back through the tissue from this layer to the mixing plane. As a consequence, $\rho_0(z)$ is the lateral coherence length in the mixing plane of a point source located in the tissue plane being probed. For the geometry of interest, it can be shown [47] that

$$\rho_0(z) = \sqrt{\frac{3}{\mu_s z}} \frac{\lambda}{\pi\theta_{\text{rms}}} \left(\frac{z + nd(z)}{z\sqrt{1 - 2p_b}}\right) \tag{3.21}$$

where $d(z) = f - z/n$, and $\theta_{\text{rms}} \approx [2(1 - g)]^{1/2}$. The second term in the brackets of Eq. 3.21 indicates that the lateral coherence length increases with increasing distance between the tissue surface and the mixing plane.

The dependence of the lateral coherence length on the position of the scattering medium relative to the observation plane is the so-called shower-curtain effect [18, 32]. In general, the shower-curtain effect implies that the lateral coherence length obtained for the case when the scattering medium is close to the radiation source is larger than for the case when the scattering medium is close to the observation plane. Physically, this is due to the fact that a distorted spherical wave approaches a plane wave as it further propagates through a non-scattering medium. As a consequence, e.g., from a distance, one can see a person immediately behind a shower curtain, but the person cannot see you. The effect is well known for light propagation through the atmosphere as discussed by Dror et al. [32], but has been omitted in previous theoretical OCT models [9]. However, due to the finite distance between the focusing lens and the tissue, the effect is inevitably present in practical OCT systems. Finally, the reflection characteristics of the tissue play a vital role for the shower-curtain effect.

It is only in the very superficial layers of highly scattering tissue that it is possible to achieve diffraction-limited focusing. In this region, the spot size is given by $2w_H$. At deeper probing depths, the spot size is dependent on the scattering properties and

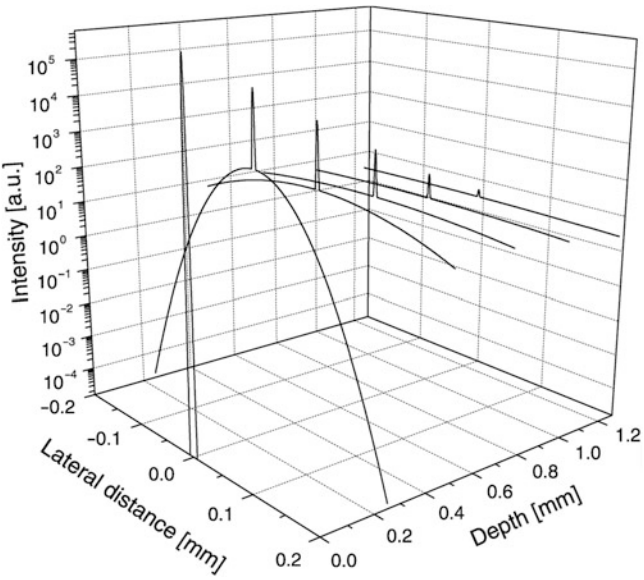

Fig. 3.2 The intensity pattern as a function of the probing depth z in the tissue ($\lambda = 814$ nm, $\mu_s = 10\ \text{mm}^{-1}$, $g = 0.955$ ($\theta_{\text{rms}} = 0.3$ rad), $n = 1.4, f = 5$ mm, $w_0 = 0.5$ mm)

given by $2w_S$. It is seen from Eqs. 3.20 and 3.21 that the spot size is degraded due to multiple scattering when the probing depth is increased. This is illustrated in Fig. 3.2, where the intensity pattern is shown as a function of the probing depth z in the tissue using Eq. 3.72, thus illustrating spot size degradation in, e.g., microscopy.

From Eq. 3.18 an expression for the OCT signal for large optical depths can be obtained as

$$\left\langle i^2(z)\right\rangle \propto \frac{\exp(-4p_b\mu_s z)}{\mu_s(1-g)z^3}, \mu_s z >> 1. \tag{3.22}$$

From this expression it is observed that the denominator is proportional to the reduced scattering coefficient $\mu_s(1\text{-}g)$, while the numerator will be close to 1 for small values of p_b. Consequently, if the signal for large optical depths is observed, it cannot be expected to derive both μ_s and g from the measured depth profiles.

3.2.2.2 Dynamic Focusing: Specular Reflectance

If, instead of diffuse backscattering, one had a specular reflection at the layer being probed, the corresponding mutual coherence function for plane waves would apply. Using this mutual coherence function and $p_b << 1$, the following expression is obtained for the heterodyne efficiency factor:

$$\Psi(z) = \left[e^{-2\mu_s z} + \left(1 - e^{-2\mu_s z}\right) \frac{w_H^2}{w_s^2} \right] \tag{3.23}$$

and

$$\rho_0(z) = \sqrt{\frac{1}{2\mu_s z}} \frac{\lambda}{\pi \theta_{rms}}. \tag{3.24}$$

It is obvious from Eq. 3.24 that the shower-curtain effect would not be present in the case of specular reflection at the tissue discontinuity, in contrast to the case of diffuse backscattering. However, it is important to note that it is diffuse backscattering which actually occurs in the case of tissue.

3.2.2.3 Collimated Sample Beam

In the case of a collimated sample beam, the expressions for w_H and w_S in Eqs. 3.13 and 3.14 need to be rewritten:

$$w_H^2 = \lim_{f \to \infty} \left[w_0^2 \left(1 - \frac{d + z/n}{f} \right)^2 + \left(\frac{d + z/n}{k w_0} \right)^2 \right] = w_0^2 + \left(\frac{d + z/n}{k w_0} \right)^2 \tag{3.25}$$

$$\begin{aligned} w_S^2 &= \lim_{f \to \infty} \left[w_H^2 + \left(\frac{2(d + z/n)}{k \rho_0} \right)^2 \right] \\ &= w_0^2 + \left(\frac{d + z/n}{k w_0} \right)^2 + \left(\frac{2(d + z/n)}{k \rho_0} \right)^2, \end{aligned} \tag{3.26}$$

where it has been used that $A = 1$ and $B = d + z/n$. In order to find the heterodyne efficiency factor, these expressions must be inserted in Eq. 3.17, and moreover, the expression for ρ_0 should be chosen in accordance with the reflection characteristics of the probed layer.

3.2.2.4 Numerical Results

In Fig. 3.3, the calculated heterodyne efficiency factor $\Psi(z)$ from Eq. 3.18 is shown as a function of depth z of the tissue sample for typical parameters of human skin tissue. The curves are shown for the cases of diffuse backscattering with (dashed) and without (dash-dot) the shower-curtain effect included and for the specular reflection (solid), respectively. In addition, the case of pure single scattering (dotted) is included for comparison. At shallow depths single backscattering dominates. Due to multiple scattering, the slope is changed and $\Psi(z)$ becomes almost constant for three cases (curves 1–3). The important difference is, however, that the change of slope occurs at different depths. This is due to the shower-curtain effect leading to an appreciable

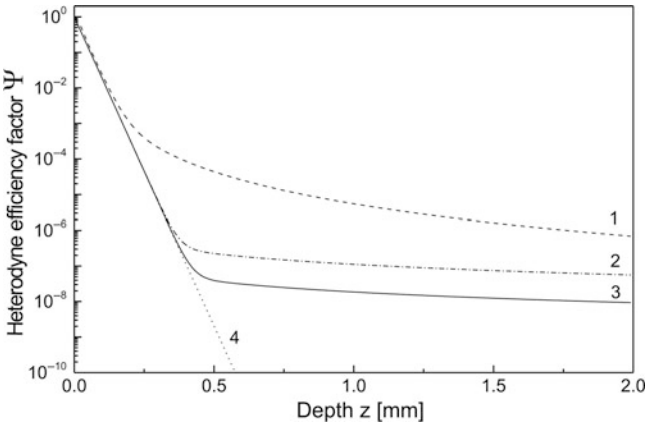

Fig. 3.3 $\Psi(z)$ as a function of z for diffuse backscattering with the shower-curtain effect included (curve 1) and for specular reflection (curve 3). Curve 2 is calculated for diffuse backscattering without the shower-curtain effect, and curve 4 is the case of pure single backscattering; $\lambda = 814$ nm, $\mu_s = 20\ \text{mm}^{-1}$, $g = 0.955$ ($\theta_{\text{rms}} = 0.3$ rad), $n = 1.4$, $f = 5$ mm, $w_0 = 0.5$ mm (From Ref. [12])

enhancement of $\Psi(z)$ and with it the heterodyne signal, which is obtained by comparing curves 1 and 2 in Fig. 3.3. Physically, this increase in the heterodyne signal is due to an enhanced spatial coherence of the multiple-scattered light.

In Fig. 3.4, $\Psi(z)$ from Eq. 3.18 is shown as a function of depth z for $\mu_s = 10\ \text{mm}^{-1}$ and three values of g within the range of validity of the EHF principle. The curves are computed for the case of diffuse backscattering. This figure demonstrates the degree of sensitivity of the heterodyne efficiency factor with respect to changes in the asymmetry parameter. Moreover, in Fig. 3.5, $\Psi(z)$ from Eq. 3.18 is shown as a function of depth z for $g = 0.95$ and three values of μ_s within the range of interest with respect to tissue [44]. The curves are again computed for the case of diffuse backscattering. This figure demonstrates the degree of sensitivity of the heterodyne efficiency factor with respect to changes in the scattering coefficient.

3.2.2.5 Choice of Scattering Function

In the present modeling of the OCT geometry, a Gaussian volume scattering function [20] for the forward scattered part is used; see Eqs. 3.5 and 3.64. The motivation for this choice of scattering function is the ability to obtain an accurate analytical engineering approximation, valid for all values of the optical depth. Using the Henyey–Greenstein scattering function [48], which is widely used in approximating the angular scattering dependence of single-scattering events in some biological media [44, 49], the corresponding analytical approximation is not as accurate as for the case of a Gaussian scattering function. However, a numerical computation using the exact expressions may be carried out instead. Hence, both scattering functions may be used in the modeling of the OCT geometry presented in this chapter.

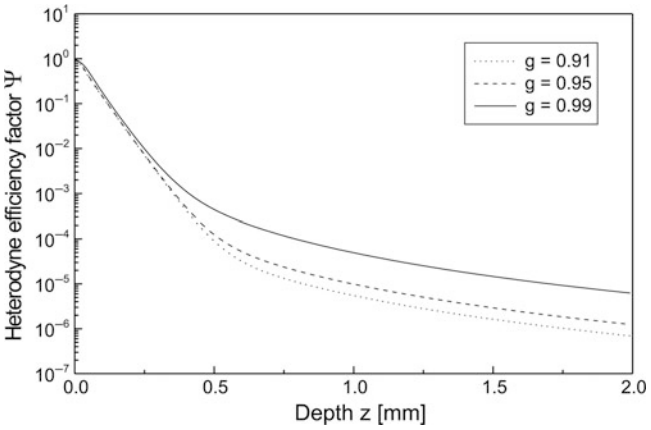

Fig. 3.4 $\Psi(z)$ as a function of z for $\mu_s = 10\ \text{mm}^{-1}$ and three values of g. The curves are for the case of a diffuse backscattering at the discontinuity and inclusion of the shower-curtain effect ($\lambda = 814$ nm, $n = 1.4, f = 5$ mm, $w_0 = 0.5$ mm)

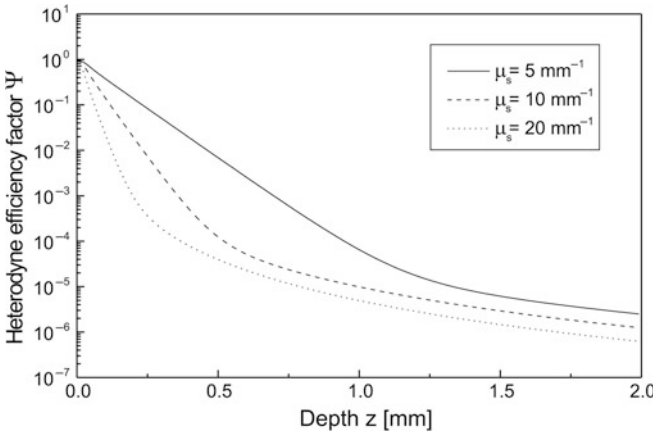

Fig. 3.5 $\Psi(z)$ as a function of z for $g = 0.95$ and three values of μ_s within a range of interest with respect to tissue. The curves are for the case of a diffuse backscattering at the discontinuity and inclusion of the shower-curtain effect ($\lambda = 814$ nm, $n = 1.4, f = 5$ mm, $w_0 = 0.5$ mm)

3.2.2.6 Signal-to-Noise Ratio (SNR) and Estimation of the Maximum Probing Depth

Without loss of generality, an OCT system with shot-noise-limited operation is considered here for calculating the signal-to-noise ratio (SNR) with the purpose of estimating the maximum probing depth. The only significant source of noise is the shot noise caused by the reference beam. For a photoconductive detector, the mean square noise power N_p can then be expressed as [50]

$$N_p = 2\alpha q_e G_{ca}^2 R_l B_w P_R, \tag{3.27}$$

where R_l is the resistance of the load, G_{ca} the gain associated with the current amplifier, and B_w the system bandwidth. The corresponding mean heterodyne signal power $S(z)$ is given by [46]

$$S(z)\langle i^2(z)\rangle G_{ca}^2 R_l \tag{3.28}$$

where $\langle i^2(z)\rangle$ is given by Eq. 3.17. Hence, the mean signal-to-noise ratio $SNR(z)$ is given by

$$SNR(z) = \frac{S(z)}{N_p} = (SNR)_0 \Psi(z), \tag{3.29}$$

where the signal-to-noise ratio in the absence of scattering $(SNR)_0$ is given by

$$(SNR)_0 = \frac{\eta P_S}{2h\nu B_w}\left(\frac{\sigma_b}{\pi w_H^2}\right). \tag{3.30}$$

In the case of interest where the focal plane coincides with the probed layer, the following expression for $(SNR)_0$ is obtained:

$$(SNR)_0 = \frac{4p_b \eta P_S}{h\nu B_w}\left(\frac{w_0}{f}\right)^2, \tag{3.31}$$

where it has been used that $\sigma_b = 4\pi p_b \mu_s l_c / k^2$.

The maximum probing depth is of considerable interest in the characterization and optimization of an OCT system when used for imaging in highly scattering tissue. The maximum probing depth may be calculated by using the model presented above. Details of the calculation are found in Ref. [31], where the calculation of the maximum probing depth z_{max} is based on the minimum acceptable SNR in the case of shot-noise-limited detection. In the calculations, a value of 3 is used as the minimum acceptable signal-to-noise ratio, i.e., $SNR(z_{max}) = 3$.

An important conclusion of Ref. [31] is that, in general, z_{max} depends on the focal length at small values of the scattering coefficient, but is independent of the focal length at larger values of the scattering coefficient. A similar behavior is observed for z_{max} as a function of μ_s and the $1/e$ intensity radius of the sample beam being focused. This behavior is due to multiple scattering of the light in the tissue. At scattering coefficients found in human skin tissue [44, 51], for example, it is concluded that the maximum probing depth is independent of the focal length f. This is an important conclusion because the depth of focus and the lateral resolution of the OCT system may then be chosen independently of z_{max}. For example, if no scanning of the focal plane in the tissue is desirable and, therefore, a large depth of

focus has been chosen, the same maximum probing depth is obtained as for a system with a short depth of focus where the focal plane is scanned to keep it matched to the reference arm. This conclusion is not surprising or contrary to assumptions already held in the field. However, the theoretical analysis in this section provides a theoretical foundation for such statements. Moreover, this agreement may also be taken as a further validation of the OCT model presented here.

3.3 Doppler OCT Analysis

Noninvasive localization and measurement of blood flow is of great interest in many medical applications, e.g., ophthalmology, dermatology, and gastroenterology. Optical Doppler tomography (ODT) [52, 53] combines Doppler velocimetry and optical coherence tomography. Thus, ODT is feasible for noninvasive localized diagnostics of particle flow velocity in highly scattering media, and it is important for functional imaging. In contrast to conventional OCT, where the reflectivity profile of the sample is obtained by envelope detection of the interferometric signal, ODT employs coherent phase-sensitive demodulation of the heterodyne detector current to obtain depth profiles of blood flow velocity. Basically, depth-resolved velocity estimates are obtained directly from the corresponding mean [52, 53] or standard deviation [54, 55] of the observed Doppler-frequency spectrum.

In this section, the results of a theoretical analysis of ODT based on EHF with multiple-scattering effects included are presented. Experiments by Yazdanfar et al. [56] suggest the presence of multiple-scattering effects in ODT. Another study also confirmed the impact of multiple-scattering effects estimating the impact on the determination of flow parameters [57]. The purpose of the analysis below is to determine how multiple scattering affects the estimation of the depth-resolved localized flow velocity, i.e., to obtain the dependence of the mean and standard deviation of the Doppler-frequency spectrum on the scattering properties of the medium.

3.3.1 Multiple-Scattering Effects in ODT

The ODT probe geometry being analyzed is shown in Fig. 3.6. In the absence of multiple scattering, and if the scattering geometry is precisely known, an estimate of the blood flow velocity at a given probing depth can be obtained as [52, 53]

$$V = \frac{f_S \lambda_0}{2n \cos \varepsilon}, \tag{3.32}$$

where λ_0 is the center wavelength of the light source, n is the index of refraction of blood, ε is the angle between the incident light and the direction of blood flow, and f_S is the centroid frequency of each depth-resolved spectrum, which is used as a measure of the corresponding backscattered Doppler frequency.

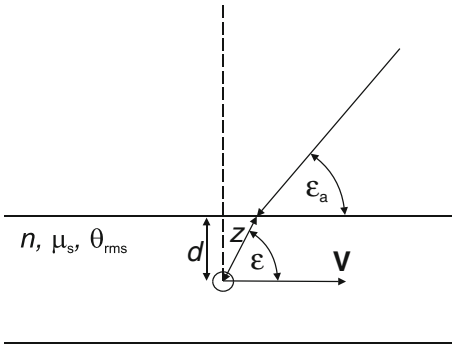

Fig. 3.6 The ODT probe geometry

In a multiple-scattering analysis of ODT, two effects must be taken into account: (a) the incident light on a moving particle contains a stochastic distribution of wave vectors at each optical frequency, and (b) in the round-trip propagation path to the backscattering event, the light will accumulate a random series of Doppler shifts due to the light being scattered by moving constituents along the path. Taking these multiple-scattering effects into account, the following equation for the mean Doppler shift may be derived [58]:

$$\overline{f}_D(d) = \frac{2n\cos\varepsilon}{\lambda_0}\left\{V(d)\exp\left(-\left\langle\theta^2\right\rangle/2\right) + \overline{V}(d)\left[1-\exp\left(-\left\langle\theta^2\right\rangle/2\right)\right]\right\}, \tag{3.33}$$

where $\langle\theta^2\rangle = \mu_s z\theta^2{}_{\mathrm{rms}}$. The quantities μ_s and θ_{rms} are the scattering coefficient and root-mean-square scattering angle of blood, respectively, and the probing depth $z = d/\sin\varepsilon$, where d is the transversal position in the vessel as indicated in Fig. 3.6. Furthermore, $V(d)$ is the flow velocity as a function of the transversal position in the vessel, and $\overline{V}$ is the mean velocity of the flow along the propagation path to the probing depth z. If multiple-scattering effects are neglected, Eq. 3.33 reduces to Eq. 3.32 as expected. In addition, for a constant velocity profile where $\overline{V} = V_0$, Eq. 3.33 yields $\overline{f}_D = 2V_0 n\cos\varepsilon/\lambda_0$ in agreement with Eq. 3.32, i.e., no multiple-scattering effects are present in this case as expected [59]. In the case of laminar flow in the vessel, the velocity and mean velocity profiles are given by [58]

$$V(d) = V_0\left[1-(1-d/a)^2\right] \quad \text{for} \quad 0 \le d \le 2a \tag{3.34}$$

$$\overline{V}(d) = V_0\frac{d}{a}\left(1-\frac{d}{3a}\right), \tag{3.35}$$

where a and V_0 are the radius of the vessel and the flow speed at the center of the vessel, respectively. In Fig. 3.7, the mean Doppler shift for laminar flow is shown with and without multiple-scattering effects included using Eqs. 3.33 and 3.32, respectively. The multiple scattering gives rise to a bias at the proximal end of the

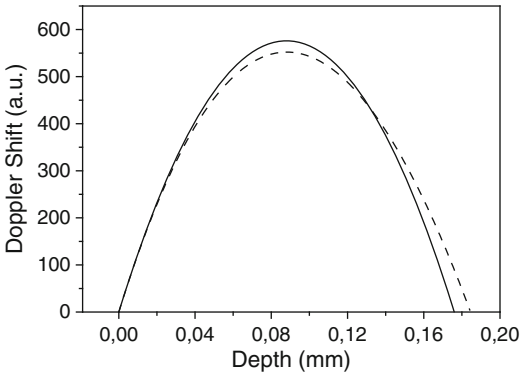

Fig. 3.7 The mean Doppler shift for laminar flow is shown with (*dashed*) and without (*solid*) multiple-scattering effects included using Eqs. 4.33 and 4.32, respectively ($\lambda_0 = 832$ nm, $\varepsilon = 80°$, $a = 88$ μm [56]; $\mu_s = 150\ \text{mm}^{-1}$, $\theta_{\text{rms}} = 0.141$ rad. [59]; $n = 1.38$ [91])

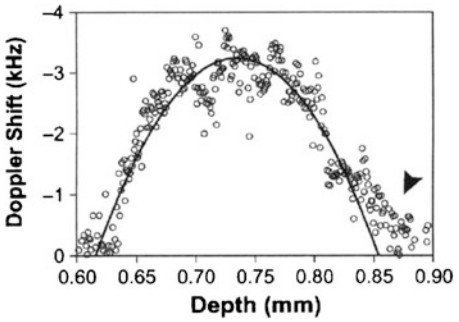

Fig. 3.8 Measurement of depth-resolved retinal flow profile taken (From Ref. [56]). The *arrow* indicates the effect of multiple scattering

profile, which is in qualitative agreement with ODT measurements of a depth-resolved retinal flow profile obtained by Yazdanfar et al. [56] and shown in Fig. 3.8. Typical scattering parameters for blood [59] are used in Fig. 3.7 together with ODT system parameters and vessel diameter from Ref. [56]. The bias increases with larger μ_s and θ_{rms} (or smaller anisotropy factor). No such bias was predicted by Lindmo et al. [59] because of their neglect of the stochastic distribution of wave vectors incident on the backscattering particle.

Furthermore, the dependence of the standard deviation of the Doppler-frequency spectrum on the scattering properties of the flowing medium is also obtained. Thus, the following approximate expression of the standard deviation of the Doppler-frequency spectrum valid for all values of $\mu_s z$ is obtained [58]:

$$\begin{aligned}\Delta f_T(d) &= \sqrt{\Delta f_D^2 + \Delta f_{D0}^2} \\ &= \sqrt{\frac{V^2(d) n^2 \sin^2 \varepsilon}{\lambda_0^2} \mu_s z \theta_{\text{rms}}^2 [2 + p(d)] + \Delta f_{D0}^2}\end{aligned} \tag{3.36}$$

where Δf_{D0} is the standard deviation of the Doppler-frequency spectrum in the absence of multiple scattering as reported previously in Ref. [55] and Δf_D is

the multiple-scattering contribution to the standard deviation of the ODT signal. The quantity $p(d)$ is given by [58]

$$p(d) = \frac{V_{\mathrm{rms}}^2(d) + \overline{V}(d)^2 - 4V(d)\overline{V}(d)}{V^2(d)}, \tag{3.37}$$

where $V_{\mathrm{rms}}(d)$ is the root-mean-square velocity of the flow along the propagation path to the probing depth z and is given by [58]

$$V_{\mathrm{rms}}(d) = \sqrt{\frac{1}{d}\int_0^d V^2(t)dt}. \tag{3.38}$$

The standard deviation increases with larger μ_s and θ_{rms} (or smaller anisotropy factor). As expected, a multiple-scattering contribution to the standard deviation of the ODT signal is obtained, which is identically zero for a constant velocity profile. This is in contrast to the work by Lindmo et al. [59], who arrived at a nonzero contribution from multiple scattering for this case.

3.4 Advanced Monte Carlo Simulation of OCT Systems

In the present section, the derivation of a Monte Carlo (MC) model capable of dealing with the heterodyne detection scheme. Adequate MC modeling may serve as a numerical phantom for further theoretical studies in cases where analytical modeling may be cumbersome.

It is important to note that the MC method only describes the transport of energy packets along straight lines and therefore the approach is incapable of describing coherent interactions of light. These energy packets are often referred to as photon packets or simply photons, and this terminology is adopted here. However, it should be emphasized that no underlying wave equation is guiding or governing these photons. Accordingly, any attempt to relate these to real quantum mechanical photons should be done with great care as argued in Ref. [60] commenting on a suggested approach of including diffraction effects into MC simulations [61, 62]. An MC photon packet represents a fraction of the total light energy, and for some applications, especially continuous wave, it may be useful to think of the path traveled by a photon as one possible path in which a fraction of the power flows. A collection of photon packets may then be perceived as constituting an intensity distribution due to an underlying field, and it can, accordingly, seem tempting to infer behavior known to apply to fields upon photon packets. Consider, as an example, that one wishes to determine whether the photon packets are able to enter an optical fiber. It can then seem intuitively correct to restrict the access of photons impinging on the fiber end to those which fall within the numerical aperture of the fiber. However, such an angular restriction may not be correct, because the individual photon packet does not carry information of the

entire field and its phase distribution. It is therefore impossible to determine whether a portion of the energy carried by a photon packet will enter the fiber due to a mode match between the fiber mode and the field underlying the collective intensity distribution of the photon packets. This discussion is treated in greater detail in Ref. [14].

With the above discussion of MC photons in mind, it may seem futile to investigate if MC simulation is applicable to estimate an OCT signal, which is the result of heterodyne mixing, and thus depends upon the coherence properties of the light. However, the problem may be reformulated to investigate whether or not the effect of the lack of coherence information in an MC simulation may be circumvented, or at least minimized. Others [63–66] have attempted to model similar optical geometries by interpreting the heterodyne process as a rejection process in which the detected photons must conform to a set of criteria on position and angle. Such a set of criteria is referred to as a detection scheme. However, these criteria were found by ad hoc considerations of the optical system, which may easily lead to incorrect results as exemplified above. Instead a mathematical derivation of the true criteria of the detection scheme will be given in the present section.

3.4.1 Theoretical Considerations

In the following, the EHF principle is used to derive an important result: an expression for the OCT signal depending on the intensity of the light only. This is obtained by calculating the mixing of the reference and sample beams in the plane conjugate to the plane in the sample probed by the system. The result is surprising, because the expression for the OCT signal depends on the coherence properties of the light [12]. However, it is shown that the formula used for calculating the OCT signal in this particular plane is mathematically identical to the result obtained in Ref. [12]. These results are valid for the, from a biomedical point of view, important case of a signal arising from a diffusely reflecting discontinuity embedded in a scattering sample. Note that this proves the viability of MC simulation to model the OCT technique, because it is shown that only intensity, and not field and phase, is necessary for this case.

The optical geometry of the sample arm is shown in Fig. 3.9, and it should be noted that the enclosed section corresponds to the geometry used for the EHF calculation in Sect. 3.2.2. An optical fiber end is positioned in the p-plane. The fiber emits a beam, which hits the collimating lens L1. The focusing lens L2 is positioned in the r-plane, and in this plane, the beam is a Gaussian beam with $1/e$ width, w_0, of the intensity. The beam is focused by L2 upon a diffusely reflecting discontinuity positioned at the depth z_f inside a scattering sample a distance d from L2. The sample is taken to be a slab infinite in the transverse direction. The part of the light that is reflected from the discontinuity propagates out through the sample, through lenses L2 and L1 to the optical fiber, where it is collected. The lenses L1 and L2 have the focal length f and are taken to be identical, perfect, and infinite in

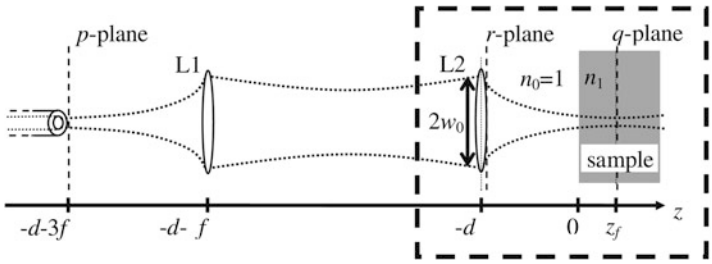

Fig. 3.9 Sample arm setup of the OCT system. The lenses L1 and L2 are considered to be identical, perfect, and have infinite radius. The setup is essentially a 4 F system (From Ref. [14])

radius. This means that the q- and p-planes are conjugate planes with magnification unity. The purpose of using the 4 F geometry is to have a physical representation of the conjugate plane to the probe plane. However, in Ref. [14] it is shown that the OCT signal term calculated from the conjugate plane is mathematically equivalent to the OCT signal calculated in the plane where the mixing physically takes place. Accordingly, the important result of Eq. 3.40 below is not restricted to the 4 F geometry. Hence, this proves the feasibility of using MC modeling in the analysis of OCT systems.

The OCT signal is produced by the mixing of the light from the reference and sample arms on the photodetector of the OCT system. Due to the symmetry of the system, in Sect. 3.2.2 the EHF prediction of the mixing between signal and reference beam was conveniently calculated at the r-plane. The mean square of the signal current $\langle i^2 \rangle$ is given by Eq. 3.9 and rewritten according to the notation in Fig. 3.9 to yield

$$\langle i^2(z) \rangle = 2\alpha^2 |\gamma(\tau)|^2 \mathrm{Re}\left[\iint \Gamma_S(\mathbf{p}_1, \mathbf{p}_2; z) \Gamma_R(\mathbf{p}_1, \mathbf{p}_2; z) d\mathbf{p}_1 d\mathbf{p}_2 \right] \equiv \Psi_r \langle i_0^2 \rangle, \quad (3.39)$$

where $\Gamma_R(\mathbf{r}_1, \mathbf{r}_2) = \langle U_R(\mathbf{r}_1) U_R{}^*(\mathbf{r}_2) \rangle = U_R(\mathbf{r}_1) U_R{}^*(\mathbf{r}_2)$ is the cross correlation of the scalar reference field, $\Gamma_S(\mathbf{r}_1, \mathbf{r}_2) = \langle U_S(\mathbf{r}_1) U_S{}^*(\mathbf{r}_2) \rangle$ is the cross correlation of the sample field, and $\mathbf{r}_1$ and $\mathbf{r}_2$ are vectors in the r-plane; see Fig. 3.9. Ψ_r is the heterodyne efficiency factor (defined in Eq. 3.17; subscript r refers to it being calculated in the r-plane), which quantifies the reduction in signal due to scattering, and $\langle i_0{}^2 \rangle$ is the OCT signal current in the absence of scattering.

It is important to note that by using the EHF principle, the investigation is limited to the paraxial regime as discussed in Sect. 3.2.1. In addition, most tissues are highly forward scattering in the near-infrared regime in which most OCT systems operate. It is assumed that the coherence length of the light source is short enough that signal powers from other reflections than the probed discontinuity are negligible. On the other hand, the coherence length is assumed long enough so that the temporal distortion of the sample field, or the path-length distribution of the reflected photons, is assumed negligible compared to the coherence length of the

light source. Assuming that the optical path length of the reference beam and sample beam reflected from the discontinuity are perfectly matched, then $\gamma(\tau) \approx 1$. To obtain the best comparison with the EHF model, the MC model presented in this section adopts this approximation.

The approximation of $\gamma(\tau) \approx 1$ is a justified approximation for highly forward scattering tissues [9]. However, it does render the EHF model unsuitable to investigate the effect of scattering on the axial resolution of an OCT system in general, because the coherence gate due to the limited coherence length of the light source is not incorporated. Others have suggested using MC simulation and the total optical path length traveled by a photon packet to determine the influence of the coherence gate [10, 29, 66]. While this may very well be a valid approach, it is clear from the above discussion of photon packets and coherence that, how intuitively correct it may seem, this may not be the case. However, no efforts have been published to establish the meaning of a photon packet in such a temporal mixing of fields, so future work is required to establish such a relation. It is the intention that the MC model of the OCT signal presented in this chapter may be instrumental in such studies.

The OCT signal depends upon the lateral cross correlation of the light from the scattering sample, as indicated by Eq. 3.17, and the lateral coherence length ρ_0 of the sample field in the r-plane for a single layer in front of the discontinuity is given by Eq. 3.21. With a nonzero lateral coherence length, ρ_0, it is seen that the OCT signal depends heavily upon the coherence properties of the field from the sample. As discussed above, an MC simulation does not describe the spatial coherence properties of light, and thus a direct simulation of Eq. 3.39 is not possible. As in Sect. 3.2.2, it is assumed that the discontinuity is diffusely reflecting, and this infers that the lateral coherence will be zero immediately after reflection. The motivation for envisioning the system geometry considered in Sect. 3.2.2 as part of a 4 F setup is to obtain a conjugate plane to the q-plane, here the p-plane; see Fig. 3.9. Through the conjugate relation, it is given that, in the absence of scattering, the lateral coherence length in the p-plane will also be zero. Hence, the sample field will be delta-correlated [20] and the OCT signal will only depend upon the intensities of the reference and sample field. In Appendix B of Ref. [14], it is shown that within the paraxial regime, the sample field is delta-correlated even in the presence of scattering. It is also shown that the heterodyne efficiency factor calculated in the p-plane Ψ_p is mathematically identical to the heterodyne efficiency factor calculated in the r-plane, so that

$$\Psi_p = \frac{\langle i^2 \rangle}{\langle i_0^2 \rangle} = \frac{\int I_R(\mathbf{p}) \langle I_S(\mathbf{p}) \rangle d^2\mathbf{p}}{\int I_R(\mathbf{p}) \langle I_{S0}(\mathbf{p}) \rangle d^2\mathbf{p}} = \Psi_r, \tag{3.40}$$

where I_R is the intensity at the reference beam and I_S, I_{S0} are the received intensities of the sample beam with and without scattering, respectively. The quantity $\mathbf{p}$ is

a vector in the p-plane; see Fig. 3.9. Equation 3.40 shows the viability of applying an MC simulation to an OCT system provided a good estimate of the intensity distribution of the sample field is achieved. This requires a method to simulate a focused Gaussian beam, and a method for modeling such a beam using MC simulation is discussed in Ref. [14]. Note that the identity proven in Eq. 3.40 is only strictly valid within the approximations of the EHF principle and thus also within the paraxial regime. However, for geometries with scattering that is not highly forward, directed coherence effects are expected to be of even less importance, and thus Eq. 3.40 should at least be a good first approximation even when the paraxial approximation is not strictly valid.

3.4.2 Monte Carlo Simulation of the OCT Signal

In Sect. 3.4.1, it is shown that the heterodyne efficiency factor of the OCT signal may be found using the knowledge of the intensity distributions of the sample and reference fields in the p-plane (see Fig. 3.9), where the fiber end is situated:

$$\Psi_p = \frac{\int I_R(\mathbf{p})\langle I_S(\mathbf{p})\rangle d^2\mathbf{p}}{\int I_R(\mathbf{p})\langle I_{S0}(\mathbf{p})\rangle d^2\mathbf{p}}. \tag{3.41}$$

In the EHF principle, the effect of a scattering medium is treated as a random phase distortion added to the deterministic phase of the light as it propagates through the medium. In the derivation of Eq. 3.41 (see also Appendix B of Ref. [14]), it is necessary to assume that the phase distortion added to the light propagating towards the discontinuity is statistically independent from the phase distortion added to the light propagating away from the discontinuity. It is important to note that this assumption is inherently fulfilled by MC methods such as that used by the MCML computer code [67]: a photon is traced through a dynamic medium in the sense that the distance to the next scattering event and scattering angle is a random variable independent upon the past of the photon. Hence, after each stochastic event, the photon experiences a different realization of the sample. Therefore, an ensemble averaging over the stochastic sample in Eq. 3.41 is carried out through a single simulation. Moreover, to also obtain an averaging in the modeling of the diffusely reflecting discontinuity, each reflected photon must experience a new realization of the discontinuity. Thus, the macroscopic intensity distribution of a Lambertian emitter [20] to sample the reflected angle is used

$$I_r(\theta_r) = I_T \cos\theta_r. \tag{3.42}$$

Here I_T is reflected intensity at $\theta_r = 0$ and θ_r is the reflected angle. By following the method outlined by Prahl et al. [68] of sampling a physical quantity using a computer-generated pseudorandom numbers, the following relations are obtained:

$$\theta_r = \arcsin(\xi), \tag{3.43}$$

$$\varphi_r = 2\pi\xi, \tag{3.44}$$

where φ_r is the azimuthal angle of the reflected photon and ξ and ζ are both random numbers uniformly distributed between 0 and 1.

Accordingly, the method of simulating the OCT signal is carried out as follows. The MC photon packet is launched from the focusing lens in the r-plane (see Fig. 3.9), using the focusing method (new hyperboloid method, Ref. [14]). The interfacing with specular surfaces, such as the sample surface and the propagation through the scattering medium, is carried out using the MCML computer code. When a photon packet is reflected off the diffusely reflecting discontinuity,[1] Eqs. 3.43 and 3.44 are used to determine the direction of the photon after reflection. As a photon exits the sample after interaction with the discontinuity, its position and angle are used to calculate its position in the p-plane after propagation through the 4 F system. To evaluate Eq. 3.41 numerically, consider that the mth photon packet exiting the medium contributes to the intensity at the point p_m in the p-plane by the amount

$$I_{S,m} \propto \frac{w_m}{\Delta p^2}, \tag{3.45}$$

where w_m is the energy, or weight, carried by the photon packet and Δp^2 is a differential area around p_m. Using this and Eq. 3.41, the MC estimated heterodyne efficiency factor Ψ_{MC} is then given by

$$\Psi_{\mathrm{MC}} = \frac{\sum_m^M I_R(p_m) I_{S,m} \Delta p^2}{\langle i_0^2 \rangle} = \frac{\sum_m^M I_R(p_m) W_m}{\langle i_0^2 \rangle}, \tag{3.46}$$

where $I_R(p)$ is the intensity distribution of the reference beam in the p-plane, and it is noted that the reference beam has a Gaussian intensity distribution of width w_f in the p-plane. The signal in the absence of scattering $\langle {i_0}^2 \rangle$ may be either simulated or calculated. The latter is straightforward, because with the conjugate relationship between the p- and q-plane, the intensity distribution of the sample beam will be identical to that of the reference beam in the absence of scattering.

[1] The reflection can also be treated as bulk backscattering; see, e.g., Ref. [28].

Equation 3.46 reveals the important detection criterion of the MC simulation of the OCT signal: a photon must hit the p-plane within the extent of the reference beam. While detection schemes of previously published MC models of OCT also incorporate that photons must hit the detector, the key element of this detection scheme is the analytically derived size and necessary position in the p-plane. Furthermore, contrary to these schemes, the model does not incorporate an angular criterion that a photon packet must fulfill in order to contribute to the signal. It may seem counterintuitive that photon packets contribute to the desired signal without penalty regardless of the angle of incidence upon the fiber in the p-plane. However, as demonstrated in Ref. [14], the inclusion of an angular criterion related to the angular extent of the incident beam, or equivalently the numerical aperture of the fiber, yields incorrect results.

3.4.3 Validation

3.4.3.1 Comparison to Experimental Data

The MC model has been verified by comparison to experimental data. In Ref. [12], an experimental setup is described and from this experimental data are obtained. The sample is an aqueous (refractive index 1.33) solution of microspheres (refractive index 1.59; diameter 2.04 μm). The experiment is carried out with the following parameters: source center wavelength $\lambda = 814$ nm, anisotropy $g = 0.929$ (calculated from Mie theory [45] using the particle diameter and refractive index), cuvette thickness $z = 0.5$ mm, focal length $f = 16$ mm, and beam radius $w_0 = 0.125$ mm. Hence, the probe depth remains fixed at $z = 0.5$ mm, and then the scattering coefficient is varied by changing the particle concentration.

From the experimental data, the heterodyne efficiency Ψ factor is derived. The result is plotted in Fig. 3.10 showing Ψ as a function of the scattering coefficient for the above parameters. The measurements are shown as open circles (○) connected with a straight dashed line. The MC data is shown as stars (*) connected with a solid line. For reference, the single-scatter case is plotted as the dotted line. As indicated in Fig. 3.10, good agreement between experiments and the MC model is obtained.

3.4.3.2 Beam Geometries for Numerical Comparison

A set of beam geometries has been selected for numerical comparison between the EHF model and the MC model. These geometries are selected so that the two approaches are compared for different degrees of focusing and distances between the lens L2 and the sample. The selected cases are listed in Table 3.1 and are referred to as cases 1 through 4, respectively.

For all cases the mean refractive index of the sample before the discontinuity and the surroundings are assumed to be matched so that $n_0 = n_1 = 1$. The subject of the investigation is the effect of scattering on the OCT signal. A difference in the refractive index between the sample and the surroundings will impose a Snell's law refraction at the interface, which in turn imposes a focus distortion not treated in the paraxial approximation ($\sin\theta \approx \theta$) and thus not described by the EHF model.

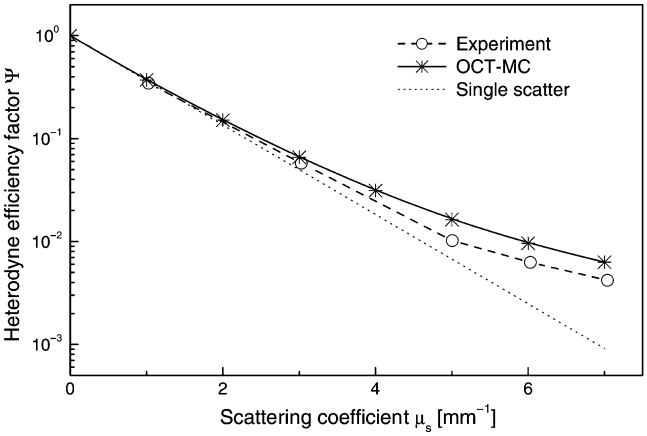

Fig. 3.10 Heterodyne efficiency factor as a function of the scattering coefficient for an aqueous solution of microspheres. Experimental data: *open circles* (○) connected with *dashed line*. MC simulations: stars (*) connected with *solid line*. *Dotted line* shows single-scatter regime for reference. Parameters used: source center wavelength $\lambda = 814$ nm, anisotropy $g = 0.929$ (calculated from the particle diameter and refractive index), cuvette thickness $z = 0.5$ mm, focal length $f = 16$ mm, and beam radius $w_0 = 0.125$ mm

Table 3.1 Beam geometries for the four cases

Case number	f [mm]	d [mm]	z [mm]	w_0 [mm]	w_0/f
1	16.0	15.5	0.5	0.125	0.008
2	8	7.5	0.5	0.4	0.05
3	0.5	0.0	0.5	0.125	0.25
4	16.0	15.0	1.0	4	0.25

Such a distortion will be difficult to separate from the effects of scattering and is thus omitted here. As discussed in Ref. [14], there is only a severe distortion for very tightly focused beams.

In all cases discussed in the following, the wavelength of the light is chosen to be 814 nm, which is one relevant wavelength for biomedical applications of OCT. The sample is assumed to exhibit scattering described by a Gaussian scattering function (see, e.g., Chap. 13 in Ref. [37]). The motivation for this choice is to enable comparison to analytical models of the propagation of Gaussian beams in random media [41] and the OCT signal (see Sect. 3.2.2), which both applies the Gaussian scattering function. The comparisons presented here are carried out for different degrees of scattering and for two relevant values of the asymmetry parameter in tissue [44]: very highly forward scattering ($g = 0.99$) and highly forward scattering ($g = 0.92$). The value $g = 0.92$ was the value of the asymmetry factor in the experiments performed to validate the EHF model by Thrane et al. [12]. With these two cases, the two approaches are compared for a sample geometry where the paraxial approximation is well satisfied

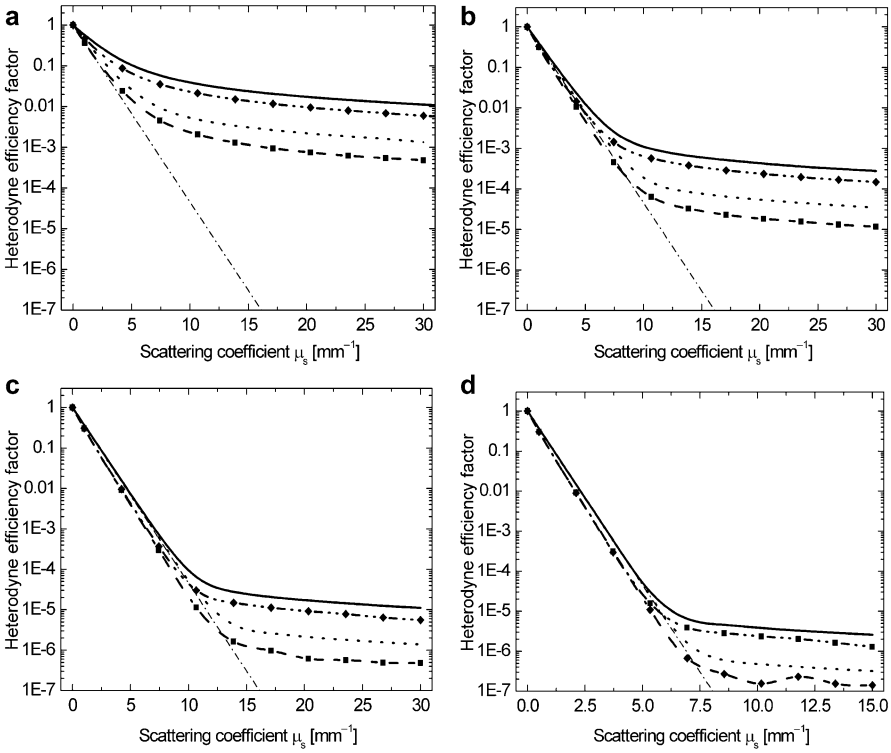

Fig. 3.11 Heterodyne efficiency factors estimated using, respectively, the EHF model and the MC method for two cases of g. (**a–d**) Show the estimated values for geometries 1, 2, 3, and 4 in Table 4.1, respectively. The *solid line* and *dotted line* curves are the results of the EHF model for $g = 0.99$ and $g = 0.92$, respectively. *Dash-dot-dot* and *dashed curves* are the results of the MC simulations for $g = 0.99$ and $g = 0.92$, respectively. *Diamonds* (◆) and *squares* (■) mark the actual data points obtained by the MC simulation method. For comparison, the exponential reduction in signal due to scattering obtained by a single-scatter model is shown as a *dash-dot curve*

and for a sample geometry, which is close to the limit of the paraxial approximation. Accordingly, it is expected that the best agreement will be found for $g = 0.99$.

3.4.3.3 Comparison to Analytical Model

In Fig. 3.11, Ψ is plotted for cases 1 through 4 as a function of the scattering coefficient μ_s, and for reference the case of single backscattering, i.e., $\Psi_{\text{single}} = \exp(-2\mu_s z)$, has been included. Three important observations may be made from Fig. 3.11. Firstly, fine agreement between the MC method and the EHF model for the four cases tested is observed. Thus, these plots are considered the validation of the MC model. Alternatively, the MC results can be considered as the confirmation of the EHF results. Secondly, it is inferred that the OCT signal for high optical depths is a result of multiple-scattering effects in agreement with Sect. 3.2.2. This is seen by

comparing the single-scattering curve to the plots of the MC and EHF. Finally, an important result of Sect. 3.2.2 was the inclusion of the so-called shower-curtain effect [18]. It is an effect caused by multiple scattering and thus plays an important role in calculating the OCT signal as the optical depth increases. Omitting this effect leads to an underestimation of the OCT signal of several orders of magnitude. Due to the good agreement between the EHF model (with the shower-curtain effect included) and the MC model, the important result that the MC model inherently takes the effect into account is obtained.

For cases where the approximation of the EHF model is well satisfied, the observed deviation between the EHF and MC models is likely to be caused by coherence effects in the intensity distribution of the sample field. Apparently, from Fig. 3.11, the lack of coherence information leads to an underestimation of Ψ, but the specific cause for this has yet to be determined. Ψ is by definition unity in the absence of scattering, and for large optical depths, coherence effects are expected to be negligible. Accordingly, the two models are expected to agree for small and large values of the optical depth of the discontinuity, whereas some deviation is to be expected in the intermediate region. As a highly forward scattering event perturbs the field only to a small degree, it is expected to distort coherence effects less than a more isotropic scattering case. In order to plot the relative deviation as a function of the effective distortion of the coherence, the ratio $\Psi_{\mathrm{EHF}}/\ \Psi_{\mathrm{MC}}$ is considered as a function of the transport reduced optical depth of the discontinuity given by

$$S_{tr} = \mu_s z_f (1 - g). \tag{3.47}$$

The relative difference between the EHF model and the MC method behaves, qualitatively, identical as a function of s_{tr} independent of beam geometry and g. This is illustrated in Fig. 3.12 for cases 2 ($g = 0.92$ and 0.99), 3 ($g = 0.92$), and 4 ($g = 0.92$), respectively. The difference between the two approaches increases as a function of s_{tr} until $s_{tr} \approx 0.5$ after which it levels off. This is mainly attributed to the coherence effects in the intensity distribution discussed above. The more abrupt behavior of the curve for geometry 4 is attributed to a higher numerical uncertainty in the case, caused by a more tightly focused beam. According to the detection scheme applied in these simulations, this implies that fewer photons will contribute to the signal resulting in an increased variance. Therefore, due to the good agreement between the results of the EHF model and MC simulations borne out in Figs. 3.11 and 3.12, it is concluded that the MC simulation presented in this section is a viable method of simulating the heterodyne efficiency factor of an OCT signal.

3.5 Applications of Modeling in OCT

The interpretation of OCT images displaying structural information only may be a difficult task, i.e., making adequate assessment of the imaged sample or tissue.

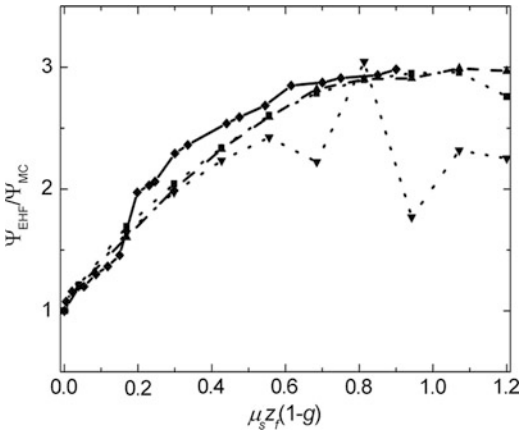

Fig. 3.12 The relative numerical difference between the results of the EHF model and the MC model from Fig. 4.11 for a representative selection of the considered geometries. The ratio Ψ_{EHF}/Ψ_{MC} is plotted for case 2 and $g = 0.99$ with symbols (♦) and *solid curve*, for case 2 and $g = 0.92$ with symbols (■) and *dash-dot-dot curve*, for case 3 and $g = 0.92$ with symbols (▼) and *dashed curve*, and for case 4 and $g = 0.92$ with symbols (•) and *dotted curve* (From Ref. [14])

An OCT signal, i.e., the detected envelope function of the A-scan, measured at a given position in a nonabsorbing scattering medium is the result of the amount of light reflected at the given position and the attenuation due to scattering when the light propagates through the scattering medium. Therefore, in order to make images, which give a direct measure of the amount of light reflected at a given position, it is necessary to be able to separate reflection and scattering effects; see, e.g., Refs. [47, 69] for details on the so-called true-reflection OCT imaging algorithm. Such kind of post processing is similar to the correction for attenuation well known in ultrasonic imaging. In that field, a mathematical model describing the relationship between the received signal and the two main acoustic parameters, backscatter and attenuation, has been considered [70]. The model has then been used to guide the derivation of a processing technique with the aim of obtaining ultrasonic images that faithfully represents one acoustic parameter, such as backscatter [70].

Extraction of optical scattering parameters from OCT images is a method to obtain more quantitative information from these images in order to improve the diagnostics (see, e.g., Ref. [71]), i.e., an alternative method of functional imaging. Accordingly, one may envisage a novel functional imaging method where, in addition to tissue morphology, parameters such as the scattering parameters, g and/or μ_s, or mean refractive index is obtained.

In the following, the viability of the suggested approach in OCT is briefly overviewed. First, a method based on the modeling in Sect. 3.2 is discussed showing that the method may be expanded to more than one layer and that optical scattering properties may be successfully extracted. Finally, some examples highlighting the extraction of optical scattering properties in tissues in vitro and in vivo are given.

3.5.1 Extracting Optical Scattering Properties from an MC-Simulated Heterogeneous Multilayered Sample

It was shown in Sect. 3.2.2 that the mean square heterodyne signal current for light reflected at depth z in the tissue may be expressed as $\langle i^2(z)\rangle = \langle i^2(z)\rangle_0 \Psi(z)$, where $\langle i^2(z)\rangle_0$ is the mean square heterodyne signal current in the absence of scattering and $\Psi(z)$ is the heterodyne efficiency factor, which includes all of the scattering effects. The maximum of the envelope of the measured interference signal corresponds to $[\langle i^2(z)\rangle]^{1/2}$. In practice, μ_s and θ_{rms} may be obtained by fitting the expression for $[\langle i^2(z)\rangle]^{1/2}$ to a measured (or simulated) depth scan of the homogeneous backscattering tissue. It is important to note that in addition to the system parameters λ, f, and w_0, knowledge about the mean index of refraction n of the scattering medium is necessary in order to perform the fitting. Otherwise, the refractive index should be fitted as well as in Ref. [72].

For OCT images of tissue, a multilayered analytical OCT model with multiple-scattering effects included is essential in order to extract optical scattering parameters. In this section, details are given of a method for multilayered extraction of optical scattering parameters [69] by expanding the OCT model developed in Sect. 3.2. Thus, the model makes it straightforward to model OCT imaging in heterogeneous multilayered tissue together with different focusing conditions, i.e., dynamic focusing or fixed focus position.

3.5.1.1 Expressions for Two-Layered Medium

The analytical expressions for the OCT signal of the two layers are obtained from the general expression given by Eq. 3.18. Note that the OCT signal is the root-mean-square (rms) heterodyne signal current $\langle i^2(z)\rangle^{1/2}$. In the case of dynamic focusing, $\langle i^2\rangle_0$ is a constant proportional to the effective backscattering cross section of the sample. For the first layer, characterized by the optical parameters μ_{s1}, θ_{rms1}, and n_1, μ_s and z in Eq. 3.18 are replaced by μ_{s1} and z_1, respectively, where z_1 is the probing depth in the first layer. The lateral coherence length $\rho_{01}(z)$ is then given by [69]

$$\rho_{01}(z_1) = \sqrt{\frac{3}{\mu_{s1} z_1}} \frac{\lambda}{\pi \theta_{\text{rms1}}} \left[\frac{n_1 f}{z_1}\right]. \tag{3.48}$$

For the second layer, characterized by μ_{s2}, θ_{rms2}, and n_2, z and $\mu_s z$ in Eq. 3.18 are replaced by z_2 and $\mu_{s1}\Delta_1 + \mu_{s2} z_2$, respectively, where Δ_1 is the thickness of the first layer and z_2 is the probing depth in the second layer. Furthermore, for the second layer, $\rho_{02}(z)$ is given by [69]

$$\rho_{02}(z_2) = \frac{\sqrt{3}}{\pi} \sqrt{\frac{\left\{\lambda n_2 \Delta_1 + \lambda n_1 \left[z_2 + n_2\left(f - \frac{\Delta_1}{n_1} - \frac{z_2}{n_2}\right)\right]\right\}^2}{n_2^2 \Delta_1 \left(\Delta_1^2 + 3\Delta_1 z_2 + 3z_2^2\right)\theta_{\text{rms1}}^2 \mu_{s1} + n_1^2 z_2^3 \theta_{\text{rms2}}^2 \mu_{s2}}}. \tag{3.49}$$

Table 3.2 The input parameters of the MC simulation together with the extracted parameters obtained by using the EHF model and the relative difference (%). Leave-one-out cross-validation [92] with respect to the MC data points has been used to estimate the standard deviations

Layer	MC input μ_s [mm^{-1}]	Extracted μ_s [mm^{-1}]	Rel. diff. [%]	MC input g-	Extracted g-	Rel. diff. [%]
1	5.000	4.98 ± 0.05	−0.4	0.9900	0.974 ± 0.007	−1.6
2	4.000	4.4 ± 0.1	10	0.9200	0.940 ± 0.003	2.2
2	6.000	6.3 ± 0.1	5.0	0.9200	0.893 ± 0.003	−2.9
2	8.000	8.2 ± 0.1	2.5	0.9200	0.874 ± 0.005	−5.0
2	10.00	9.9 ± 0.2	−1.0	0.9200	0.864 ± 0.006	−6.1

3.5.1.2 Extracting the Optical Scattering Parameters from Layered MC Model

The MC model presented in Sect. 3.3 is used as a numerical phantom. Hence, the versatility of the MC model is demonstrated; for example, it may be used to investigate the performance of the EHF model for sample geometries difficult to produce in the laboratory. By using this model, depth scans of layered scattering structures (tissue) may be obtained. In the present context, a layer is here defined as a plane-parallel homogeneous region characterized by a scattering coefficient μ_s, an anisotropy factor g, and an index of refraction n.

Next the two-layer EHF expression for the OCT signal is fitted to the MC-simulated signal, the optical scattering properties μ_s and g of each of the two layers are extracted, and the MC input values are compared with them. Strictly speaking, the extracted g is the effective anisotropy factor given by the cosine of θ_{rms}, where θ_{rms} is the rms scattering angle defined as the half-width at $1/e$ maximum of a Gaussian curve fit to the main frontal lobe of the scattering phase function of the sample [12]. Because the scattering phase function used in the MC OCT model is also Gaussian, the extracted g values can be directly compared with the MC input g values. The system parameters in this case are $\lambda = 800$ nm, $w_o = 0.4$ mm, and $f = 8.0$ mm. The first layer is 0.3 mm thick (Δ_1) with $\mu_{s1} = 5.0\ mm^{-1}$ and $g_1 = 0.99$. The second layer is 0.9 mm thick with $\mu_{s2} = 10.0\ mm^{-1}$ and $g_2 = 0.92$. Without the loss of generality, the refractive indices of the sample and the surroundings are matched and equal unity.

Table 3.2 shows the main result by comparing the input optical scattering parameters used in the MC simulation to the extracted values including the relative difference. The absolute relative differences between the extracted mean values and the values used in the MC simulation follow a kind of structured pattern with increasing values of μ_{s2}, and the "true" values are not contained within the estimated standard deviations. This observation is an indication of a bias between the EHF model and the MC simulations. On the other hand, the small relative differences demonstrate the capability of the EHF OCT model to extract optical scattering parameters from multilayered tissue. In general, the index of refraction of each layer may also be extracted, but that is outside the scope of the present analysis.

Notice that μ_s and g_{eff} can only be separated if the optical depth of each layer is sufficiently large that multiple scattering occurs. In case the optical depth is too small, only single scattering occurs and therefore only μ_s can be extracted. For large optical depths, i.e., totally diffused light, the EHF model predicts the OCT signal to be determined by the reduced scattering coefficient, and hence, μ_s and g_{eff} cannot be separated for this case (cf. Eq. 3.22, Sect. 3.2.2.1).

3.5.2 Extraction of Optical Scattering Properties from Tissues

As mentioned at the beginning of the present section, attenuation compensation is widely accepted within ultrasonic imaging. Therefore, it has also been among the first attempts to improve on OCT imagery. In fact, attenuation compensation is a method to remove the attenuation caused by scattering in OCT images. This should improve the diagnostic capabilities due to a better differentiation of different tissue types. There have been few attempts to do attenuation compensation in OCT images of tissue by using the single-scattering OCT model [73]. However, due to the fact that multiple-scattered photons contribute to the OCT signal, the single-scattering OCT model is insufficient for this purpose. Attenuation compensation was verified on a single-layer phantom by using an OCT model taking multiple-scattering effects into account [74].

The optical scattering properties themselves, however, also contain information about the tissue. For example, cell mitochondria are affected or changed in several malignant conditions, and through these changes the scattering changes. Conversely, provided that information about the scattering properties can be obtained with good accuracy and good (high) spatial resolution, new diagnostics can be performed [71]. This fact is one important motivation for attempting to extract optical scattering properties in order to improve the diagnostic potential of OCT.

By using the single-scattering OCT model [2], studies have been carried out with the aim to extract only the scattering coefficient μ_s from OCT images of tissue. This approach was applied in various important applications. For example, glucose monitoring was investigated by using the single-scatter approach [75] and expanded to include phase-sensitive OCT [76]. The anisotropy factor g may also be extracted as demonstrated by Kodach et al. [77]. In their study, they showed that monitoring this parameter might offer a contrast mechanism for changes in back-scattering and, hence, indicate morphological changes. Determining optical scattering properties of blood is also of high importance. Faber et al. [78, 79] demonstrated that the optical absorption spectra of oxygenated and deoxygenated hemoglobin, corrected for optical scattering, may be obtained by using spectral OCT. The underlying OCT modeling was based on a single-scattering approach.

Important contributions have been made in in vitro characterization of atherosclerotic plaque by several groups. Studying in vitro samples with various stages of atherosclerotic plaque, van der Meer et al. extracted the optical scattering coefficient [80]. Although the model applied was based on a single-scattering model, their findings provide important data on the optical scattering coefficient of these plaques. A larger study also demonstrated that the scattering coefficient may provide valuable,

additional information, thus improving diagnosis [81]. Some data for the scattering coefficients reported in [81] correlate well with other findings, but some data showed significant deviations: these deviations can, however, be explained by different sample handling and fit to different models, respectively; see also below. In their review paper, Kubo et al. [82] provided an excellent overview on sample handling, extraction of optical parameters, and its diagnostic potential in the clinic. Because OCT is established in cardiology, e.g., stent deployment, such added diagnostic potential seems highly feasible.

Extraction of optical properties has also been investigated targeting other diseases. Quantitative analysis of rectal cancer by spectral domain OCT was demonstrated [83]. Their study involved 16 samples in vitro comprising 1,000 measurement: one half benign and one half malignant. In particular, their results showed that the quantitative analysis of rectal tissue can be used as a promising diagnostic criterion of early rectal cancer. This is noteworthy because early diagnosis has great value for clinical application and earlier onset of treatment. Oral mucosal tissue has also been investigated [84] by using swept source OCT showing promise for early diagnosis. Both studies were carried out under the assumption that single scattering was sufficient to describe the light–tissue interaction. Woolliams and Tomlins [85] claimed that multiple scattering is not affecting the OCT signal at longer wavelengths, but this seems to have been dismissed by several other reports showing clear evidence of the opposite fact. Their statement [85] might, however, be correct with respect to their specific system (data fitting) or application (also mentioned by the authors [85]). Note that for superficial lesions, multiple scattering might be negligible; hence for such applications simplified modeling may suffice.

In general, multiple scattering is impacting the formation of the OCT signal (A-scan). Provided an OCT model is used that takes into account multiple scattering, both μ_s and the anisotropy factor g may be extracted. Extraction for a two-layer geometry has been carried out [69, 86], where both μ_s and g were obtained for each (tissue) layer. In Ref. [69] MC simulations were used as numerical phantom as discussed in detail in the previous subsection.

Lee et al. [28] compared single-scattering and multiple-scattering models for extracting optical scattering properties, and using calibrated scattering phantoms, the validity of the single-scattering and multiple-scattering models for both highly scattering and weakly scattering media was investigated. They showed, with a proper correction for the confocal properties of the sample arm, both models are appropriate to extract the scattering coefficients of weakly scattering media. For highly scattering media, the multiple scattering must be taken into account, and the multiple-scattering model provides much higher accuracy. In their study, they applied the EHF model described in this chapter and in Ref. [12] modeling the multiple scattering. They also investigated the scattering properties of in vitro rat liver and in vivo human skin and concluded that the EHF model is useful for quantitatively characterizing tissue scattering.

A number of in vitro studies have been reported. The characterization of atherosclerotic plaque using a single, multiple-scattering layer model has been reported [87]. The method of extracting the optical scattering properties was

verified using well-controlled and calibrated, single-layer tissue-like phantoms. The study provided the optical scattering properties in 1,300 nm range for lesions in different stages including the anisotropy parameter. Based on the extracted parameters, normal tissue could be separated from malignant tissue. It should be noted that some discrepancies occur between the reported values for the scattering coefficients in Refs. [87, 80]. Possible explanations for the differences may be due to different sample handling and fit to different models. The results reported in both Refs. [87, 80] are encouraging although further studies are required to fully establish these criteria and thereby demonstrate the feasibility of the method in this particular area.

The EHF model, as described in the present chapter and Ref. [12], has been validated and expanded by other groups. Most notably, the work of Kuo et al. [88] concluded that multiple scattering had to be taken into account in the assessment of arterial characteristics in human atherosclerosis. Moreover, they expanded the extraction to also include polarization parameters, thus establishing a refined criterion as compared to previous work; see, e.g., [87].

In Ref. [13], an excellent study comprising rigorous application of the RTE modeling (small-angle approximation) in the extraction of optical parameters is presented. First, the authors verified their modeling on a well-controlled tissue-like phantom. By estimating covariance and confidence regions for the extracted optical properties, they point to specific regimes of the OCT signal decay where extraction is likely to fail. These regimes depend on both the optical properties and sample beam geometry. Hence, their findings provide important insight of how to optimize the OCT system for a specific application. The authors applied their method to cervical tissue (cervical dysplasia 2–3 and leukoplakia). In their in vitro investigation, they demonstrated that cervical dysplasia 2–3 and leukoplakia could be distinguished on the basis of the extracted optical scattering properties. Hence, their excellent contribution should be an encouragement for expanding to other clinical applications and finally in vivo applications.

In vivo studies are sparse; however, Knüttel et al. [72] took the approach of extracting optical scattering properties using the EHF model [12] and refractive index aiming at relating the effects of skin hydration to the optical properties extracted from OCT images. Their investigation showed the applicability of the approach and the potential in dermatology to provide new diagnostic information.

3.6 Summary

Advanced models for describing the light–tissue interactions in optical coherence tomography (OCT) systems have been reviewed. Firstly, an analytical model based on the extended Huygens–Fresnel (EHF) principle is presented valid for the single- and multiple-scattering regimes simultaneously. Because the model is based on the general *ABCD*-matrix formalism, it is applicable to any sample arm geometry, and it leads to closed-form solutions for the OCT heterodyne signal. Expressions for

static and dynamic focusing were presented. Furthermore, expressions for the effects of multiple scattering on the detected OCT signal in Doppler OCT were presented and reasonable agreement with experimental data shown. Notice that the multiple-scattering EHF analysis presented here yields accurate analytical expressions for the OCT signal for a wide range of optical configurations that both are amenable to physical interpretation and are desirable for use in parametric studies for OCT system optimization.

From the EHF model a mathematical proof may be established showing that Monte Carlo (MC) simulations indeed may be used to model OCT system despite the fact that the MC model is restricted to the calculation of intensities and calculation of the OCT heterodyne signal involves the optical fields. Both the analytical and the numerical model compared favorably to experimental data. Moreover, good agreement between the analytical model and the MC simulations was found over a large range of optical scattering parameters and sample arm geometries.

Extraction of optical scattering parameters from OCT images is a method to obtain more quantitative information from these images in order to improve the diagnostics, i.e., an alternative method of functional imaging. Accordingly, one may envisage a novel functional imaging method where, in addition to tissue morphology, parameters such as the optical scattering parameters or mean refractive index are obtained. In addition, other functional parameters, such as polarization properties, can also be combined with the aforementioned scattering properties. The optical scattering properties themselves contain information about the tissue. For example, cell mitochondria are affected or changed in several malignant conditions, and through these changes the scattering changes. Conversely, provided that information about the scattering properties can be obtained with good accuracy and good (high) spatial resolution, new diagnostics can be performed. A survey highlighting important investigations aiming at bringing the modeling of the light–tissue interaction into OCT diagnostics was presented. The examples spanned theoretical/numerical in vitro and in vivo investigations. Although further work is needed, it seems that, in addition to or in combination with other functional imaging modalities, the extraction of optical scattering properties seems feasible and may ultimately improve OCT imagery and its diagnostic potential.

Appendix: Calculation of Γ_S

In the determination of the mutual coherence function Γ_S in Eq. 3.9, the EHF principle is applied in order to obtain a viable expression for $U_S(\mathbf{p};z)$, i.e., the reflected sample optical field. Using Eq. 3.2, $U_S(\mathbf{p};z)$ is related to the reflected sample field $U_B(\mathbf{r};z)$ in the probing plane, where $\mathbf{r}$ defines a two-dimensional vector in this plane:

$$U_S(\mathbf{p};z) = \int U_B(\mathbf{r};z)G(\mathbf{r},\mathbf{p};z)d\mathbf{r}. \tag{3.50}$$

Here $G(\mathbf{r},\mathbf{p};z)$ is Green's function response at $\mathbf{p}$ due to a point source at $\mathbf{r}$, which includes the effects of scattering in the intervening medium. Combining Eqs. 3.11 and 3.50 yields

$$\Gamma_S(\mathbf{p}_1,\mathbf{p}_2;z) = \iint \langle U_B(\mathbf{r}_1;z)U_B(\mathbf{r}_2;z)G(\mathbf{r}_1,\mathbf{p}_1;z)G^*(\mathbf{r}_2,\mathbf{p}_2;z)\rangle d\mathbf{r}_1 d\mathbf{r}_2, \quad (3.51)$$

where $\mathbf{r}_1$, $\mathbf{r}_2$ are associated two-dimensional vectors in the transverse plane. For simplicity in notation, the explicit dependence of the various quantities on z is omitted in the following.

If the forward propagated light is assumed to be statistically independent from the backscattered light, thereby neglecting coherent backscattering, the following relation holds:

$$\left\langle U_B(\mathbf{r}_1)U_B^*(\mathbf{r}_2)G(\mathbf{r}_1,\mathbf{p}_1)G^*(\mathbf{r}_2,\mathbf{p}_2)\right\rangle = \left\langle U_B(\mathbf{r}_1)U_B^*(\mathbf{r}_2)\right\rangle \langle G(\mathbf{r}_1,\mathbf{p}_1)G^*(\mathbf{r}_2,\mathbf{p}_2)\rangle. \quad (3.52)$$

If, furthermore, diffuse backscattering is assumed from the layer being probed, one gets [18, 89]

$$\left\langle U_B(\mathbf{r}_1)U_B^*(\mathbf{r}_2)\right\rangle = \frac{4\pi}{k^2}\delta(\mathbf{r}_1-\mathbf{r}_2)\langle I_B(\mathbf{r}_1)\rangle, \quad (3.53)$$

where $\delta(\mathbf{r})$ is the two-dimensional Dirac delta function and $I_B(\mathbf{r}_1)$ is the mean backscattered irradiance distribution in the plane of the discontinuity. Combining Eqs. 3.51, 3.52, and 3.53 and simplifying yields

$$\Gamma_S(\mathbf{p}_1,\mathbf{p}_2) = \frac{4\pi}{k^2}\int \langle I_B(\mathbf{r})\rangle \langle G(\mathbf{r},\mathbf{p}_1)G*(\mathbf{r},\mathbf{p}_2)\rangle d\mathbf{r}. \quad (3.54)$$

Using Eq. 3.3, the second term in the integral on the right-hand side of Eq. 3.54 may be written as

$$\langle G(\mathbf{r},\mathbf{p}_1)G^*(\mathbf{r},\mathbf{p}_2)\rangle = G_0(\mathbf{r},\mathbf{p}_1)G_0^*(\mathbf{r},\mathbf{p}_2)\Gamma_{pt}(\rho), \quad (3.55)$$

where $G_0(\mathbf{r},\mathbf{p})$ is Huygens–Fresnel Green's function when propagating from the probing plane to the lens plane and Γ_{pt} is the mutual coherence function of a point source located in the probing plane and observed in the lens plane given by

$$\Gamma_{pt} = \langle \exp[i\{\phi(\mathbf{p}_1)-\phi(\mathbf{p}_2)\}]\rangle. \quad (3.56)$$

The mutual coherence function Γ_{pt} contains the effects of the scattering inhomogeneities. Using Eq. 3.4, Green's function $G_0(\mathbf{r},\mathbf{p})$ is given by

$$G_0(\mathbf{r},\mathbf{p}) = -\frac{ik}{2\pi B_b}\exp\left[-\frac{ik}{2B_b}\left(A_b r^2 - 2\mathbf{r}\cdot\mathbf{p} + D_b p^2\right)\right], \tag{3.57}$$

where A_b, B_b, and D_b are the ray-matrix elements for back propagation to the lens plane. These quantities are given by $A_b = D = 1$, $B_b = B = d + z/n$ and $D_b = A = 1$ [39].

$\langle I_B(\mathbf{r})\rangle$ in (3.54) is simply related to the incident mean irradiance distribution $\langle I(\mathbf{r})\rangle$ in the probing layer dz around z by the following relation:

$$\langle I_B(\mathbf{r})\rangle = p_b \mu_s dz \langle I(\mathbf{r})\rangle \tag{3.58}$$

The EHF principle yields that the mean irradiance distribution is given by [39]

$$\langle I(\mathbf{r})\rangle = \left(\frac{k}{2\pi B}\right)^2 \int K(\rho)\exp\left\{\frac{ik}{B}\rho\cdot\mathbf{r}\right\}\Gamma_{pt}(\rho)d^2\rho, \tag{3.59}$$

where

$$K(\rho) = \int \exp\left\{-\frac{ikA}{B}\boldsymbol{\rho}\cdot\mathbf{P}\right\} U_{Si}(\mathbf{P} + \boldsymbol{\rho}/2)U_{Si}^*(\mathbf{P} - \boldsymbol{\rho}/2)d^2P, \tag{3.60}$$

and $\boldsymbol{\rho} = \mathbf{p}_1 - \mathbf{p}_2$. With the considered OCT setup focusing at depth z, $A = 1$ and $B = f$. The mutual coherence function Γ_{pt} can then be found to be [89]:

$$\Gamma_{pt} = \langle \exp\{i[\phi(\mathbf{p}_1) - \phi(\mathbf{p}_2)]\}\rangle = \exp\{-s[1 - b_\phi(\rho)]\}, \tag{3.61}$$

where it has been assumed that the phase ϕ is a normally distributed zero-mean random process. The quantity s is the phase variance, and $b_\phi(\rho)$ is the normalized phase autocorrelation function for a point source whose origin is at the probing depth z. It can be shown [90] that the phase variance is equal to the optical depth, $s = \mu_s z$. The normalized phase autocorrelation function $b_\phi(\rho)$ is given by [89]

$$b_\phi(\rho) = \frac{\int_0^L dz' \int_0^\infty \sigma(\theta; z')J_0(kp_s\theta)\theta d\theta}{\int_0^L dz' \int_0^\infty \sigma(\theta; z')\theta d\theta}, \tag{3.62}$$

where J_0 is the Bessel function of the first kind and of order zero, and

$$P_s = \frac{B_b(z')}{B_b}\rho, \tag{3.63}$$

where $B_b(z')$ is the B-matrix element for back propagation from the probing depth z to a distance z' and $\sigma(\theta; z')$ is the volume scattering or phase function with θ being the scattering angle. For the OCT geometry treated here $B_b(z') = z'/n$ for $0 \le z' \le z$, $L = d + z$, and $\sigma(\theta; z') = \sigma(\theta)$ for $0 \le z' \le z$, and zero otherwise. As described in Eq. 3.5, the phase function is modeled as a combination of a forward scattering term and a small isotropic term. The forward part is modeled here as a Gaussian volume scattering function, which in the small-angle approximation gives a phase function of the following form:

$$\sigma_1(\theta, z) = \exp\left[-\theta^2/\theta_0^2\right], \tag{3.64}$$

where $g = \langle \cos\theta \rangle \approx 1 - \langle\theta^2\rangle/2$, and $\theta_0 = \sqrt{\langle\theta^2\rangle} \approx \sqrt{2(1-g)}$. Substituting Eqs. 3.63 and 3.64 into Eq. 3.62 and performing the indicated integrations yield the following equation for the normalized phase autocorrelation function:

$$b_\phi(\rho) = \frac{\sqrt{\pi}}{2}\frac{\rho_\phi}{\rho}\mathrm{erf}\left(\rho/\rho_\phi\right)[1 - 2p_b], \tag{3.65}$$

where erf(·) denotes the error function and ρ_ϕ is the phase correlation length given by

$$\rho_\phi = \frac{\lambda}{\pi\sqrt{2(1-g)}}\left(1 + \frac{nd}{z}\right). \tag{3.66}$$

Hence, the mutual coherence function Γ_{pt} is given by Eq. 3.61 with $b_\phi(\rho)$ defined by Eq. 3.65. Thus, for specific values of both s and g, the mutual coherence-function is completely determined, and for a given value of the initial optical wave function U_{Si}, numerical results for the mean irradiance can be obtained directly from Eq. 3.59. Here U_{Si} is given by Eq. 3.7, and the following expression for the mean irradiance distribution is obtained at the probing depth z in the tissue:

$$\langle I(\mathbf{r})\rangle = \frac{P_S}{2\pi(f/kw_0)^2}\int_0^\infty \exp\left\{-x^2/4\right\} x J_0(ux)\Gamma_{pt}(xw_0)dx, \tag{3.67}$$

where J_0 is the Bessel function of the first kind of order zero and

$$u = \frac{r}{f/kw_0} \tag{3.68}$$

is a normalized transverse coordinate.

As indicated above, numerical results can readily be obtained. However, it is useful to have an analytical approximation so that OCT system parameter studies can be performed. Examination of Eq. 3.61 reveals for large values of the optical depth that Γ_{pt} is nonzero for $s\{1 - b_\phi(\rho)\}$ less than the order unity, i.e., for $b_\phi(\rho)$

near unity. Expanding $b_\phi(\rho)$ in powers of ρ and retaining the first two nonzero terms yield from Eq. 3.65 that $b_\phi(\rho) \approx (1 - \rho^2/3(\rho_\phi)^2)(1 - 2p_b)$ from which it follows that

$$\Gamma_{pt} \approx \exp\left[-2p_b s - \rho^2/\rho_0^2\right], s >> 1, \tag{3.69}$$

where the lateral coherence length, ρ_0, is defined as $\rho_0 = \rho_\phi[(3/s)/(1 - 2p_b)]^{1/2}$. It is expected that the ballistic, i.e., unscattered, component of the irradiance pattern is proportional to $e^{-\mu s z}$. Thus, by interpolation [12]

$$\Gamma_{pt} \approx \exp(-\mu_s z) + [1 - \exp(-\mu_s z)]e^{-2p_b\mu_s z}\exp\left(-\rho^2/\rho_0^2\right). \tag{3.70}$$

Substituting Eqs. 3.7 and 3.70 into Eq. 3.59 and performing the integration yield the following approximate expression for the mean irradiance distribution at the probing depth z in the tissue:

$$\langle I(\mathbf{r})\rangle \approx \frac{P_S}{\pi}\left[\frac{e^{-\mu_s z}\exp\left\{-r^2/w_H^2\right\}}{w_H^2} + \frac{(1 - e^{-\mu_s z})e^{-p_b\mu_s z}\exp\left\{-r^2/w_S^2\right\}}{w_S^2}\right]. \tag{3.71}$$

For p_b<<1 the expression can be further simplified:

$$\langle I(\mathbf{r})\rangle \approx \frac{P_S}{\pi}\left[\frac{e^{-\mu_s z}\exp\left\{-r^2/w_H^2\right\}}{w_H^2} + \frac{(1 - e^{-\mu_s z})\exp\left\{-r^2/w_S^2\right\}}{w_S^2}\right]. \tag{3.72}$$

The first term in the brackets on the right-hand side of Eq. 3.72 can be interpreted to represent the attenuated distribution obtained in the absence of the inhomogeneities, and the corresponding second term represents a broader halo resulting from scattering by the inhomogeneities. The quantities w_H and w_S are the $1/e$ irradiance radii in the absence and presence of scattering, respectively, given by

$$w_H^2 = w_0^2\left(A - \frac{B}{f}\right)^2 + \left(\frac{B}{kw_0}\right)^2, \tag{3.73}$$

$$w_S^2 = w_0^2\left(A - \frac{B}{f}\right)^2 + \left(\frac{B}{kw_0}\right)^2 + \left(\frac{2B}{k\rho_0}\right)^2. \tag{3.74}$$

For the OCT system in question,

$$w_H = \frac{f}{kw_0}, \tag{3.75}$$

$$w_S = \sqrt{w_H^2 + \left(\frac{2f}{k\rho_0}\right)^2}. \tag{3.76}$$

From Eqs. 3.58 and 3.72, an expression for the intensity is obtained:

$$\langle I_B(r)\rangle \approx \frac{p_b \mu_s dz P_s}{\pi}\left[\frac{e^{-\mu_s z}\exp\{-r^2/w_H^2\}}{w_H^2} + \frac{(1-e^{-\mu_s z})\exp\{-r^2/w_S^2\}}{w_S^2}\right]. \tag{3.77}$$

Substituting Eqs. 3.10, 3.6, 3.77, 3.54, 3.55, 3.57, and 3.70 into Eq. 3.9 and performing the indicated Gaussian integrations over $\mathbf{p}_1$,$\mathbf{p}_2$ and simplifying finally yield for p_b<<1

$$\begin{aligned}\left\langle i^2(z)\right\rangle \approx{}& \frac{8\alpha^2 P_R P_S \pi p_b \mu_s |\gamma(\tau)|^2 dz}{\pi^2 k^2} \\ &\int\left[\frac{e^{-\mu_s z}\exp\{-r^2/w_H^2\}}{w_H^2} + \frac{(1-e^{-\mu_s z})\exp\{-r^2/w_S^2\}}{w_S^2}\right]^2 d\mathbf{r}.\end{aligned} \tag{3.78}$$

Performing the integration over the probed plane in Eq. 3.12 and simplifying, the following expression for the mean square heterodyne signal current is obtained:

$$\begin{aligned}\left\langle i^2(z)\right\rangle \approx{}& \frac{4\alpha^2 P_R P_s p_b \mu_s |\gamma(2(z-l_r)/c)|^2 dz}{w_H^2 k^2} \\ &\times\left[e^{-2\mu_s z} + \frac{4e^{-\mu_s z}(1-e^{-\mu_s z})}{1+\frac{w_S^2}{w_H^2}} + (1-e^{-\mu_s z})^2\frac{w_H^2}{w_S^2}\right], \\ ={}& \left\langle i^2\right\rangle_0 \Psi(z)\end{aligned} \tag{3.79}$$

where l_r is the traversed optical path length of the reference beam and c is the speed of light in vacuum. In order to incorporate the total signal contribution obtained from within the coherence gate of the sample volume, we finally integrate (3.79) along the z-axis. This corresponds to a convolution with respect to the square modulus of the temporal coherence function $|\gamma(z/c)|^2$. Assuming a rectangular coherence function of width l_c/c, where l_c is the coherence length of the source, and $\mu_s l_c$ <<1,

$$\begin{aligned}\left\langle i^2(z)\right\rangle_{coh_gate} &\approx \frac{\alpha^2 P_R P_s \sigma_b}{\pi w_H^2} \\ &\times \left[e^{-2\mu_s z} + \frac{4e^{-\mu_s z}(1-e^{-\mu_s z})}{1+\frac{w_S^2}{w_H^2}} + (1-e^{-\mu_s z})^2 \frac{w_H^2}{w_S^2} \right] \\ &= \left\langle i^2 \right\rangle_0 \Psi(z)\end{aligned} \tag{3.80}$$

where $\sigma_b = 4\pi p_b \mu_s l_c / k^2$ denotes the effective backscattering cross section of the backscattering volume selected by the coherence gate. The quantity $\langle i^2 \rangle_0 = \alpha^2 P_R P_S \sigma_b / \pi (w_H)^2$ is the mean square heterodyne signal current in the absence of scattering, and the term contained in the brackets is the heterodyne efficiency factor $\Psi(z)$.

References

1. D. Huang, E.A. Swanson, C.P. Lin, J.S. Schuman, W.G. Stinson, W. Chang, M.R. Hee, T. Flotte, K. Gregory, C.A. Puliafito, J.G. Fujimoto, Optical coherence tomography. Science **254**, 1178–l181 (1991)
2. J.M. Schmitt, A. Knüttel, R.F. Bonner, Measurement of optical properties of biological tissues by low-coherence reflectometry. Appl. Opt. **32**, 6032–6042 (1993)
3. J.M. Schmitt, A. Knüttel, A.S. Gandjbakhche, R.F. Bonner, Optical characterization of dense tissues using low-coherence interferometry. Proc. SPIE **1889**, 197–211 (1993)
4. J.M. Schmitt, A. Knüttel, M. Yadlowsky, M.A. Eckhaus, Optical-coherence tomography of a dense tissue: statistics of attenuation and backscattering. Phys. Med. Biol. **39**, 1705–1720 (1994)
5. M.J. Yadlowsky, J.M. Schmitt, R.F. Bonner, Multiple scattering in optical coherence microscopy. Appl. Opt. **34**, 5699–5707 (1995)
6. M.J. Yadlowsky, J.M. Schmitt, R.F. Bonner, Contrast and resolution in the optical coherence microscopy of dense biological tissue. Proc. SPIE **2387**, 193–203 (1995)
7. Y. Pan, R. Birngruber, R. Engelhardt, Contrast limits of coherence-gated imaging in scattering media. Appl. Opt. **36**, 2979–2983 (1997)
8. L.S. Dolin, A theory of optical coherence tomography. Radiophys. Quantum Electron. **41**, 850–873 (1998)
9. J.M. Schmitt, A. Knüttel, Model of optical coherence tomography of heterogeneous tissue. J. Opt. Soc. Am. A **14**, 1231–1242 (1997)
10. D.J. Smithies, T. Lindmo, Z. Chen, J.S. Nelson, T.E. Milner, Signal attenuation and localization in optical coherence tomography studied by Monte Carlo simulation. Phys. Med. Biol. **43**, 3025–3044 (1998)
11. A.F. Fercher, W. Drexler, C.K. Hitzenberger, T. Lasser, Rep. Prog. Phys. **66**, 239 (2003)
12. L. Thrane, H.T. Yura, P.E. Andersen, Analysis of optical coherence tomography systems based on the extended Huygens-Fresnel principle. J. Opt. Soc. Am. A **17**, 484–490 (2000)
13. I.V. Turchin, E.A. Sergeeva, L.S. Dolin, V.A. Kamensky, N.M. Shakhova, R. Richards-Kortum, Novel algorithm of processing optical coherence tomography images for differentiation of biological tissue pathologies. J. Biomed. Opt. **10**, 064024 (2005)
14. A. Tycho, T.M. Jørgensen, H.T. Yura, P.E. Andersen, Derivation of a Monte Carlo method for modeling heterodyne detection in optical coherence tomography systems. Appl. Opt. **41**, 6676–6691 (2002)

15. H. Kahn, T.E. Harris, Estimation of particle transmission by random sampling", in *Monte Carlo Methods*. National Bureau of Standards Applied Mathematics Series (U. S. Government Printing Office, Washington, DC, 1951)
16. B.C. Wilson, G. Adam, A Monte Carlo model for the absorption and flux distributions of light in tissue. Med. Phys. **10**, 824–830 (1983)
17. Y. Feng, R. Wang, J. Elder, Theoretical model of optical coherence tomography for system optimization and characterization. J. Opt. Soc. Am. A **20**, 1792–1803 (2003)
18. H.T. Yura, Signal-to-noise ratio of heterodyne lidar systems in the presence of atmospheric turbulence. Opt. Acta **26**, 627–644 (1979)
19. B. Karamata, M. Laubscher, M. Leutenegger, S. Bourquin, T. Lasser, P. Lambelet, Multiple scattering in optical coherence tomography. I. Investigation and modeling. J. Opt. Soc. Am. A **22**, 1369–1379 (2005)
20. J.W. Goodman, *Statistical Optics* (Wiley, New York, 1985)
21. R.G. Frehlich, M.J. Kavaya, Coherent laser radar performance for general atmospheric refractive turbulence. Appl. Opt. **30**, 5325–5352 (1991)
22. D. Arnush, Underwater light-beam propagation in the small-angle-scattering approximation. J. Opt. Soc. Am. **62**, 1109–1111 (1972)
23. H.T. Yura, A multiple scattering analysis of the propagation of radiance through the atmosphere, in *Proceedings of the Union Radio-Scientifique International Open Symposium*, (La Baule, France, 1977), pp. 65−69; see also Ref. [44], pp. 54–55
24. H.T. Yura, L. Thrane, P.E. Andersen, Closed-form solution for the Wigner phase-space distribution function for diffuse reflection and small-angle scattering in a random medium. J. Opt. Soc. Am. A **17**, 2464–2474 (2000)
25. M.G. Raymer, C. Cheng, D.M. Toloudis, M. Anderson, M. Beck, Propagation of Wigner coherence functions in multiple scattering media, in *Advances in Optical Imaging and Photon Migration*, ed. by R.R. Alfano, J.G. Fujimoto. OSA Trends in Optics and Photonics Series, vol. 2 (Optical Society of America, Washington, DC, 1996), pp. 236–238
26. C.-C. Cheng, M.G. Raymer, Long-range saturation of spatial decoherence in wave-field transport in random multiple-scattering media. Phys. Rev. Lett. **82**, 4807–4810 (1999)
27. M.G. Raymer, C.-C. Cheng, Propagation of the optical Wigner function in random multiple-scattering media, in *Laser-Tissue Interaction XI: Photochemical, Photothermal, and Photomechanical*, ed by D.D. Duncan, J.O. Hollinger, S.L. Jacques, Proc. SPIE **3914**, 376−380 (2000)
28. P. Lee, W. Gao, X. Zhang, Performance of single-scattering model versus multiple-scattering model in the determination of optical properties of biological tissue with optical coherence tomography. Appl. Opt. **49**, 3538–3544 (2010)
29. G. Yao, L.V. Wang, Monte Carlo simulation of an optical coherence tomography signal in homogeneous turbid media. Phys. Med. Biol. **44**, 2307–2320 (1999)
30. P.E. Andersen, L. Thrane, H.T. Yura, A. Tycho, T.M. Jørgensen, M.H. Frosz, Advanced modeling of optical coherence tomography systems. Phys. Med. Biol. **49**, 1307–1327 (2004)
31. L. Thrane, H.T. Yura, P.E. Andersen, Calculation of the maximum obtainable probing depth of optical coherence tomography in tissue. Proc. SPIE **3915**, 2–11 (2000)
32. I. Dror, A. Sandrov, N.S. Kopeika, Experimental investigation of the influence of the relative position of the scattering layer on image quality: the shower curtain effect. Appl. Opt. **37**, 6495–6499 (1998)
33. J.M. Schmitt, G. Kumar, Turbulent nature of refractive-index variations in biological tissue. Opt. Lett. **21**, 1310–1312 (1996)
34. J. Strohbehn (ed.), *Laser Beam Propagation in the Atmosphere* (Springer, New York, 1978)
35. R.L. Fante, Wave propagation in random media: a systems approach, in *Progress in Optics XXII*, ed. by E. Wolf (Elsevier, New York, 1985)
36. S.M. Rytov, Y.A. Kravtsov, V.I. Tatarskii, Principles of statistical radiophysics, in *Wave Propagation Through Random Media*, vol. 4 (Springer, Berlin, 1989)

37. A. Ishimaru, *Wave Propagation and Scattering in Random Media* (IEEE Press, Piscataway, 1997)
38. R.F. Lutomirski, H.T. Yura, Propagation of a finite optical beam in an inhomogeneous medium. Appl. Opt. **10**, 1652–1658 (1971)
39. Z.I. Feizulin, Y.A. Kravtsov, Expansion of a laser beam in a turbulent medium. Izv. Vyssh. Uchebn. Zaved. Radiofiz. **24**, 1351–1355 (1967)
40. J.W. Goodman, *Introduction to Fourier Optics*, 2nd edn. (McGraw-Hill, Singapore, 1996)
41. H.T. Yura, S.G. Hanson, Optical beam wave propagation through complex optical systems. J. Opt. Soc. Am. A **4**, 1931–1948 (1987)
42. H.T. Yura, S.G. Hanson, Second-order statistics for wave propagation through complex optical systems. J. Opt. Soc. Am. A **6**, 564–575 (1989)
43. A.E. Siegman, *Lasers* (University Science, Mill Valley, 1986), pp. 626–630
44. M.J.C. Van Gemert, S.L. Jacques, H.J.C.M. Sterenborg, W.M. Star, Skin optics. IEEE Trans. Biomed. Eng. **36**, 1146–1154 (1989)
45. C.F. Bohren, D.R. Huffman, *Absorption and Scattering of Light by Small Particles* (Wiley, New York, 1983)
46. D.L. Fried, Optical heterodyne detection of an atmospherically distorted signal wave front. Proc. IEEE **55**, 57–67 (1967)
47. L. Thrane, *Optical Coherence Tomography: Modeling and Applications*. PhD dissertation, Risø National Laboratory, Denmark, 2000, ISBN 87-550-2771-7)
48. L.G. Henyey, J.L. Greenstein, Diffuse radiation in the galaxy. Astrophys. J. **93**, 70–83 (1941)
49. S.L. Jacques, C.A. Alter, S.A. Prahl, Angular dependence of He-Ne laser light scattering by human dermis. Lasers Life Sci. **1**, 309–333 (1987)
50. C.M. Sonnenschein, F.A. Horrigan, Signal-to-noise relationships for coaxial systems that heterodyne backscatter from the atmosphere. Appl. Opt. **10**, 1600–1604 (1971)
51. V.V. Tuchin, S.R. Utz, I.V. Yaroslavsky, Skin optics: modeling of light transport and measuring of optical parameters, in *Medical Optical Tomography: Functional Imaging and Monitoring, IS11*, ed. by G. Mueller, B. Chance, R. Alfano et al. (SPIE Press, Bellingham, 1993), pp. 234–258
52. J.A. Izatt, M.D. Kulkarni, S. Yazdanfar, J.K. Barton, A.J. Welch, In vivo bidirectional color Doppler flow imaging of picoliter blood volumes using optical coherence tomography. Opt. Lett. **22**, 1439–1441 (1997)
53. Z. Chen, T.E. Milner, D. Dave, J.S. Nelson, Optical Doppler tomographic imaging of fluid flow velocity in highly scattering media. Opt. Lett. **22**, 64–66 (1997)
54. Y. Zhao, Z. Chen, C. Saxer, Q. Shen, S. Xiang, J.F. de Boer, J.S. Nelson, Doppler standard deviation imaging for clinical monitoring of in vivo human skin blood flow. Opt. Lett. **25**, 1358–1360 (2000)
55. H. Ren, K.M. Brecke, Z. Ding, Y. Zhao, J.S. Nelson, Z. Chen, Imaging and quantifying transverse flow velocity with the Doppler bandwidth in a phase-resolved functional optical coherence tomography. Opt. Lett. **27**, 409–411 (2002)
56. S. Yazdanfar, A.M. Rollins, J.A. Izatt, Imaging and velocimetry of the human retinal circulation with color Doppler optical coherence tomography. Opt. Lett. **25**, 1448–1450 (2000)
57. J. Kalkman, A.V. Bykov, D.J. Faber, T.G. van Leeuwen, Multiple and dependent scattering effects in Doppler optical coherence tomography. Opt. Express **18**, 3883–3892 (2010)
58. H.T. Yura, L. Thrane, P.E. Andersen, Analysis of multiple scattering effects in optical Doppler tomography. SPIE Proc. **5690**, 475–479 (2005)
59. T. Lindmo, D.J. Smithies, Z. Chen, J.S. Nelson, T.E. Milner, Accuracy and noise in optical Doppler tomography studied by Monte Carlo simulation. Phys. Med. Biol. **43**, 3045–3064 (1998)
60. A. Tycho, T.M. Jørgensen, Comment on 'excitation with a focused, pulsed optical beam in scattering media: diffraction effects. Appl. Opt. **41**, 4709–4711 (2002)
61. V.R. Daria, C. Saloma, S. Kawata, Excitation with a focused, pulsed optical beam in scattering media: diffraction effects. Appl. Opt. **39**, 5244–5255 (2000)

62. Q. Lu, X. Gan, M. Gu, Q. Luo, Monte Carlo modeling of optical coherence tomography imaging through turbid media. Appl. Opt. **43**, 1628–1637 (2004)
63. J. Schmitt, A. Knüttel, M. Yadlowski, Confocal microscopy in turbid media. J. Opt. Soc. A **11**, 2226–2235 (1994)
64. J.M. Schmitt, K. Ben-Letaief, Efficient Monte carlo simulation of confocal microscopy in biological tissue. J. Opt. Soc. Am. A **13**, 952–961 (1996)
65. C.M. Blanca, C. Saloma, Monte Carlo analysis of two-photon fluorescence imaging through a scattering medium. Appl. Opt. **37**, 8092–8102 (1998)
66. Y. Pan, R. Birngruber, J. Rosperich, R. Engelhardt, Low-coherence optical tomography in turbid tissue—theoretical analysis. Appl. Opt. **34**, 6564–6574 (1995)
67. L.-H. Wang, S.L. Jacques, L.-Q. Zheng, MCML—Monte Carlo modeling of photon transport in multi-layered tissues. Comput. Methods Prog. Biomed. **47**, 131–146 (1995)
68. S.A. Prahl, M. Keijzer, S.L. Jacques, A.J. Welch, A Monte Carlo model for light propagation in tissue", in *Dosimetry of Laser Radiation in Medicine and Biology*. SPIE Institute Series IS, vol. 5 (SPIE Press, Bellingham, 1998)
69. L. Thrane, M.H. Frosz, A. Tycho, T.M. Jørgensen, H.T. Yura, P.E. Andersen, Extraction of optical scattering parameters and attenuation compensation in optical coherence tomography images of multi-layered tissue structures. Opt. Lett. **29**, 1641–1643 (2004)
70. D.I. Hughes, F.A. Duck, Automatic attenuation compensation for ultrasonic imaging. Ultrasound Med. Biol. **23**, 651–664 (1997)
71. C. Xu, J.M. Schmitt, S.G. Carlier, R. Virmani, Characterization of atherosclerosis plaques by measuring both backscattering and attenuation coefficients in optical coherence tomography. J. Biomed. Opt. **13**, 034003 (2008)
72. A. Knüttel, S. Bonev, W. Knaak, New method for evaluation of in vivo scattering and refractive index properties obtained with optical coherence tomography. J. Biomed. Opt. **9**, 265–273 (2004)
73. G.J. Tearney, S.A. Boppart, B.E. Bouma, M.E. Brezinski, N.J. Weissman, J.F. Southern, J.G. Fujimoto, Scanning single-mode fiber optic catheter-endoscope for optical coherence tomography. Opt. Lett. **21**, 543–545 (1996)
74. L. Thrane, T.M. Jørgensen, P.E. Andersen, H.T. Yura, True-reflection OCT imaging. Proc. SPIE **4619**, 36–42 (2002)
75. R.O. Esenaliev, K.V. Larin, I.V. Larina, M. Motamedi, Noninvasive monitoring of glucose concentration with optical coherence tomography. Opt. Lett. **26**, 992–994 (2001)
76. K.V. Larin, T. Akkin, R.O. Esenaliev, M. Motamedi, T.E. Milner, Phase-sensitive optical low-coherence reflectometry for the detection of analyte concentrations. Appl. Opt. **43**, 3408–3414 (2004)
77. V.M. Kodach, D.J. Faber, J. van Marle, T.G. van Leeuwen, J. Kalkman, Determination of the scattering anisotropy with optical coherence tomography. Opt. Express **19**, 6131–6140 (2011)
78. D.J. Faber, M.C.G. Aalders, E.G. Mik, B.A. Hooper, M.J.C. van Gemert, T.G. van Leeuwen, Oxygen saturation-dependent absorption and scattering of blood. Phys. Rev. Lett. **93**(028102), 1–4 (2004)
79. D.J. Faber, E.G. Mik, M.C.G. Aalders, T.G. van Leeuwen, Toward assessment of blood oxygen saturation by spectroscopic optical coherence tomography. Opt. Lett. **30**, 1015–1017 (2005)
80. F.J. van der Meer, D.J. Faber, D.M.B. Sassoon, M.C. Aalders, G. Pasterkamp, T.G. van Leeuwen, Localized measurement of optical attenuation coefficients of atherosclerotic plaque constituents by quantitative optical coherence tomography. IEEE Trans. Med. Imaging **24**, 1369–1376 (2005)
81. G. van Soest, T. Goderie, E. Regar, S. Koljenovic, G.L.J.H. van Leenders, N. Gonzalo, S. van Noorden, T. Okamura, B.E. Bouma, G.J. Tearney, J.W. Oosterhuis, P.W. Serruys, A.F.W. van der Steen, Atherosclerotic tissue characterization in vivo by optical coherence tomography attenuation imaging. J. Biomed. Opt. **15**, 011105 (2010)

82. T. Kubo, C. Xu, Z. Wang, N.S. van Ditzhuijzen, H.G. Bezerra, Plaque and thrombus evaluation by optical coherence tomography. Int. J. Cardiovasc. Imaging **27**, 289–298 (2011). doi:10.1007/s10554-010-9790-1
83. Q.Q. Zhang, X.J. Wu, T. Tang, S.W. Zhu, Q. Yao, B.Z. Gao, X.C. Yuan, Quantitative analysis of rectal cancer by spectral domain optical coherence tomography. Phys. Med. Biol. **57**, 5235–5244 (2012). doi:10.1088/0031-9155/57/16/5235
84. O.K. Adegun, P.H. Tomlins, E. Hagi-Pavli, G. Mckenzie, K. Piper, D.L. Bader, F. Fortune, Quantitative analysis of optical coherence tomography and histopathology images of normal and dysplastic oral mucosal tissues. Lasers Med. Sci. **27**, 795–804 (2012). doi:10.1007/s10103-011-0975-1
85. P.D. Woolliams, P.H. Tomlins, The modulation transfer function of an optical coherence tomography imaging system in turbid media. Phys. Med. Biol. **56**, 2855–2871 (2011). doi:10.1088/0031-9155/56/9/014
86. N.M. Shakhova, V.M. Gelikonov, V.A. Kamensky, R.V. Kuranov, I.V. Turchin, Clinical aspects of the endoscopic optical coherence tomography: a method for improving the diagnostic efficiency. Laser Phys. **12**, 617–626 (2002)
87. D. Levitz, L. Thrane, M.H. Frosz, P.E. Andersen, C.B. Andersen, J. Valanciunaite, J. Swartling, S. Andersson-Engels, P.R. Hansen, Determination of optical scattering properties of highly-scattering media in optical coherence tomography images. Opt. Express **12**, 249–259 (2004)
88. W.-C. Kuo, M.-W. Hsiung, J.-J. Shyu, N.-K. Chou, P.-N. Yang, Assessment of arterial characteristics in human atherosclerosis by extracting optical properties from polarization-sensitive optical coherence tomography. Opt. Express **16**, 8117–8125 (2008)
89. H.T. Yura, S.G. Hanson, Effects of receiver optics contamination on the performance of laser velocimeter systems. J. Opt. Soc. Am. A **13**, 1891–1902 (1996)
90. V.I. Tatarskii, *The Effects of the Turbulent Atmosphere on Wave Propagation* (National Technical Information Service, Springfield, 1971)
91. A.N. Yaroslavsky, I.V. Yaroslavsky, T. Goldbach, H.-J. Schwarzmaier, Influence of the scattering phase function approximation on the optical properties of blood determined from the integrating sphere measurements. J. Biomed. Opt. **4**, 47–53 (1999)
92. M. Stone, Cross-validatory choice and assessment of statistical predictions. J. R. Stat. Soc. B **36**, 111–147 (1974)

Part II

OCT Technology

Inverse Scattering and Aperture Synthesis in OCT

4

Adolf F. Fercher

Keywords
OCT • Inverse scattering • Aperture synthesis (AS) • Optical diffraction tomography • 3D imaging • Interferometric synthetic aperture microscopy (ISAM)

Scattering and diffraction are basically the same basic physical phenomena, though their treatments tend to be separated, depending on the dimensions of the light propagation obstacle compared to the wavelength. Scattering (diffraction) theory determines the relation between the input and output waves, given the details of the target met by light (or other waves). Inverse scattering (IS) determines properties of the target, given sufficiently details of input and scattered waves [1–3].

Many important tomographic techniques, like X-ray and emission photon tomography in the medical field, can rely on straight rays. With ultrasound, microwaves, and optical waves, diffraction plays an important role [4]. Here, IS is dominated by the problem of diffraction inversion; E. Wolf has presented a general solution for a wave field $U^{(s)}(\mathbf{r})$ diffracted by a sample, now known as "basic theorem of optical diffraction tomography (ODT)" [5]. Carney and Wolf [6] also discuss the use of the power extinguished on scattering from weakly scattering objects to obtain three-dimensional reconstructions of the object structure. This so-called power-extinction diffraction tomography relies on interference within the domain of the scatterer; it does not require the phase of the scattered field to be measured. Another IS approach, based on spectral changes, yields the correlation function of the scattering potential of the medium [7].

A.F. Fercher
Medical University Vienna, Vienna, Austria
e-mail: adolf.fercher@meduniwien.ac.at

© Springer International Publishing Switzerland 2015

W. Drexler, J.G. Fujimoto (eds.), *Optical Coherence Tomography*,
DOI 10.1007/978-3-319-06419-2_5

Diffraction-limited resolution is a concern in many imaging systems. Using two-photon entangled states can lead to a twofold increase in resolution due to its doubled photon energy [8]. Another approach to break the diffraction limit and substantially increase optical resolution is near-field optics. Bao et al. [9] have developed a regularized recursive linearization method for two-dimensional inverse medium scattering arising in photon scanning tunneling microscopy and numerically demonstrate its capability to provide subwavelength resolution.

Explicit inversion formulas for inverse scattering with diffusing optical waves have been presented by Konecky et al. [10]. Quantitative images of complex phantoms with millimeter-sized features located centimeters deep within a highly scattering medium were reconstructed using a fast image reconstruction algorithm based on an analytic solution.

This chapter concentrates on optical backscattering-based IS techniques; we shall, however, not be concerned with related problems like enhanced intensity in coherent backscattering [11] and the T-matrix method [12].

Inversion of optical backscattered fields has led to extremely successful distance measurement (partial coherence interferometry, PCI) and imaging techniques (optical coherence tomography, OCT), in particular in the medical field [13]. Since imaging based on inverse scattering replaces the imaging lens by photoelectric detection of the complex amplitude of light scattered by the sample, its detection area can be adapted to various requirements. Besides aiming an optimal reconstruction of the sample structure, an objective is to extract the structure of anomalous areas that differ from a predefined set of features [14].

The techniques described below are based on linearized inverse scattering. In a mathematical linear imaging system, there is an object function and an image function; both are elements of the same or of different ($\mathbf{r}$ versus $\mathbf{K}$) Euclidian spaces. Here, the object function is the sample source strength $S(\mathbf{r})$; the image function is the scattered wave spectrum $\hat{U}^{(S)}(\mathbf{K})$. A linear mapping is assumed which associates the two functions:

$$\hat{U}^{(S)}(\mathbf{K}) = \mathrm{O} \cdot S(\mathbf{r}) + N. \tag{4.1}$$

(Usually, there will be some noise N too.) O is a linear operator describing the scattering process. Here, the experimental procedure involves sampling and in particular severe bandwidth limitations (Fig. 4.2); hence, an inversion of Eq. 4.1 is not a well-posed problem. A similar problem occurs in optical imaging by lenses; here aperture limits of the spatial frequency components in image are countersteered by deconvolution techniques. Such ill-posed problems are usually treated by regularization. The regularization method is based on approximate solutions depending on a regularization parameter that tends to zero, when the approximate solution converges to the exact solution [15].

4.1 Optical Diffraction Tomography-Based Inverse Scattering

4.1.1 Basic Theorem of Diffraction Tomography

Optical diffraction tomography (ODT) is based on IS. The scattering operator O essentially is a three-dimensional (3D) Fourier transform (FT). Tikhonov regularization [16] can be used to improve both, signal-to-noise ratio and image qualities. In formulating the basic theorem of diffraction tomography [5], E. Wolf considers direct scattering on a nonmagnetic sample with an isotropic dielectric constant varying weakly over distances of the order of a wavelength. That sample is assumed illuminated by a plane wave or positioned at the beam waist of a monochromatic Gaussian beam with amplitude

$$U^{(i)}(\mathbf{r}) = A^{(i)}(\mathbf{r})\exp[-i\omega t]. \tag{4.2}$$

Wolf's solution is based on the first-order Born approximation as an approximate solution for weak scatterers. Weyl's expansion of the 3D free-space Green function of the wave equation lets him represent the scattered field as an angular spectrum of plane waves. In a first step Wolf thus obtains an expression for the angular spectrum of homogeneous waves of the scattered field $\hat{U}^{(S)}(\mathbf{K})$ in terms of the 3D Fourier inverse of the sample scattering potential $F(\mathbf{r})$. As a second step Wolf determines the homogeneous part of the angular spectrum of scattered waves by a two-dimensional (2D) FT $\hat{U}_h^{(S)}(\mathbf{K})$ of the scattered field $U^{(s)}(\mathbf{r})$ in detection planes in front and behind the scattering object and adds a phase factor corresponding to the distance between sample and detection plane [1].

Alternative approaches to determine the spatial distribution of magnitude and phase of wave fields under far-field and near-field conditions have been given by Schmidt-Weinmar [17, 18]. The first applications of the ODT theorem were demonstrated by Carter [2], who considered the special case of a rectangular scatterer and compared the computed projection of the scattering potential along a planar section through the object with experimental measurements and furthermore, by Carter and Ho [19], who considered a semitransparent bar with nonuniform index of refraction and stated agreement between the computed 1D (one-dimensional) scattering potential along a line through the object with known object parameters within errors of a few percent.

Another frequently used solution of the inverse scattering problem is the Rytov expansion; it models the phase of the scattered field as exponentially dependent on the scattering potential [5]. Whereas the first-order Born approximation is accurate when the product of the index contrast and object size is less than one-quarter wavelength, the Rytov approximation is accurate when the square of the phase gradient is much less than the index contrast divided by the wavelength squared [20]. If continuities of the sample parameters are located on smooth surfaces, the Kirchhoff approximation is a preferred solution [21].

In 2002 Lauer [22] has presented a new approach to optical diffraction tomography. In this technique the sample is successively illuminated by a series of plane waves having different directions; the sample structure is then reconstructed from these recorded waves.

At present, the basic theorem of diffraction tomography forms the physical basis of many PCI and OCT techniques as well as of the recently put forward synthetic-aperture technique [23].

4.1.2 Far-Field Approximation

Far-field diffraction or Fraunhofer conditions are defined with respect to sample size and detection plane to sample distance. In this case the scattered field is observed at a distance $d \gg a^2/\lambda$ or at a Fresnel number $FN = \frac{a^2}{d\cdot\lambda} \ll 1$; a is a length of the order of the size of the sample. Under these conditions the first-order Born approximation for an incident wave $U^{(i)}(\mathbf{r}') = A^{(i)} \cdot \exp[i \cdot \mathbf{k^{(i)}} \cdot \mathbf{r}']$ yields a spherical wave for the scattered field at the detection plane with a complex amplitude determined by the FT of the sample scattering potential $F(\mathbf{r})$ [3]:

$$U^{(S)}(\mathbf{r},k) = -\frac{1}{4\pi}\int\limits_{Vol} U^{(i)} \cdot (\mathbf{r}') \cdot F(\mathbf{r}') \cdot \frac{\exp[i\cdot k\cdot|\mathbf{r}-\mathbf{r}'|]}{|\mathbf{r}-\mathbf{r}'|} \cdot d^3\mathbf{r}'; \tag{4.3}$$

the fraction in this equation is the Green function of the wave equation. With direct space origin in or close to the sample, we can use the approximation $k \cdot |\mathbf{r} - \mathbf{r}'| \approx \mathbf{k^{(S)}} \cdot (\mathbf{r} - \mathbf{r}')$, $k = |k^{(i)}| = |k^{(S)}| = 2\pi/\lambda$. $\mathbf{r}$ is the far-field position vector. (We have omitted the self-evident time-dependence $\exp[-i \cdot \omega \cdot t]$.)

Equation 4.3 can now be written as

$$\begin{aligned}\hat{U}^{(S)}(\mathbf{K}) &= -\frac{1}{4\cdot\pi}\int\limits_{Vol} F(\mathbf{r}')\cdot A^{(i)}(\mathbf{r}')\cdot\frac{\exp\left[i\cdot\mathbf{k^{(S)}}(\mathbf{r})\right]}{|\mathbf{r}-\mathbf{r}'|}\cdot\exp[-i\cdot(\mathbf{r}'\cdot\mathbf{K})]\cdot d^3\mathbf{r}' \\ &= -\frac{\exp(i\cdot k\cdot d)}{4\cdot\pi\cdot d}\int\limits_{Vol} A^{(i)}(\mathbf{r}')\cdot F(\mathbf{r}')\cdot\exp(-i\cdot\mathbf{K}\cdot\mathbf{r}')\cdot d^3\mathbf{r}',\end{aligned} \tag{4.4}$$

since, in the far-field, both the scattering vector $\mathbf{K} = \mathbf{k}^{(S)} - \mathbf{k}^{(i)}$ and the vector of the scattered wave $\mathbf{k^{(S)}}$ can be used to define the position $\mathbf{r}$ of field detection. $\mathbf{k^{(i)}}$ is the wave vector of the incident wave ($|\mathbf{k^{(i)}}| = |\mathbf{k^{(S)}}| = k = 2\pi/\lambda$). d is the distance between direct space origin at or near the sample and the field position. $F(\mathbf{r})$ is the sample scattering potential – see Eq. 4.7 below. Hence, the scattered wave comprises a spectrum of spherical waves with radius of curvature d and a complex amplitude equal to the inverse Fourier transform of the sample source strength

$$S(\mathbf{r}) = A^{(i)}(\mathbf{r}) \cdot F(\mathbf{r}); \tag{4.5}$$

This corresponds to the first step of Wolf's solution. In the far-field approximation Wolf's second step occurs by light propagation to the detector matrix. Using that facilitation Fercher et al. [3] were the first to demonstrate a full 3D reconstruction of a 3D object based on ODT. Computer simulations based on Mie scattering by coated spheres and reconstructions based on experimentally obtained scattered field data were presented. However, these early (1979) investigations suffered from limitations of light source and computer technology at that time.

For simplification of the subsequent discussion of the properties of diffraction tomography, we shall use the far-field approximation of the basic ODT theorem. This approximation in particular describes digital microscopic imaging but is easily extended to large samples as well; see Sect. 4.2.1.6 below. In this approximation the complex amplitude of the scattered wave $\hat{U}^{(S)}(\mathbf{K})$ represents the Fourier components of the sample source strength accessible by scattered field measurements:

$$S(\mathbf{r}) = FT\left\{\hat{U}^{(s)}(\mathbf{K})\right\} \tag{4.6}$$

As depicted in Fig. 4.1 forward and backward scattering provide access to quite different Fourier components of the sample structure.

4.1.3 Basic Properties of Optical Diffraction Tomography-Based Inverse Scattering

1. Sample structure, represented as source strength $S(\mathbf{r}) = A^{(i)}(\mathbf{r}) \cdot F(\mathbf{r})$, is obtained from a Fourier transform of the complex amplitude of the far-field scattered sample wave.
2. Source strength structure is mainly determined by the scattering potential $F(\mathbf{r})$ (also called "scattering contrast," or "sample susceptibility") of the sample:

$$F(\mathbf{r}) = k^2 \cdot \left[m^2(\mathbf{r}) - 1\right], \tag{4.7}$$

   $m(\mathbf{r}) = n(\mathbf{r}) \cdot [1 + i \cdot \kappa \cdot (\mathbf{r})]$ is the complex refractive index distribution of the sample structure, with $n(\mathbf{r}) =$ phase refractive index and $K(\mathbf{r}) =$ attenuation index. (A more general expression of the scattering potential is achieved if the changes in refractive index are measured relative to the background refractive index [24].)
3. Far-field scattered field data $\hat{U}^{(S)}(\mathbf{K})$ are located on a sphere in $\mathbf{K}$-space (Ewald sphere) [5].
4. The lateral extent of the transfer function for both, forward and backscattering, is the same. In both cases lateral resolution is the same (depending on aperture angle ß).

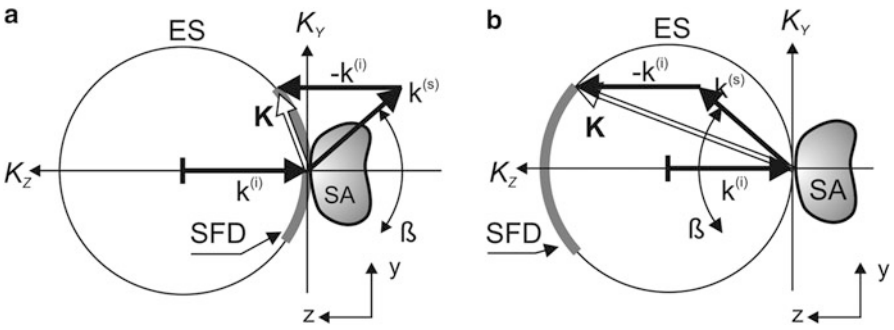

Fig. 4.1 Forward and backward far-field scattering: (**a**) scattered field data (*SFD*) in forward scattering are located around $K_Z \sim 0$; (**b**) scattered field data in backscattering are located around $K_Z \sim -2k$. *ES* Ewald sphere, *SA* sample, *SFD* accessible scattered field data. ß is the aperture angle

4. Forward scattering, even at moderately large aperture angles, provides access only to Fourier data near the K_x–K_y plane ($K_z \sim 0$). Hence, with respect to depth structure, forward scattering techniques act as low-pass filter. The image obtained in standard optical imaging, for example, by lenses, is a projection of the sample structure in z-direction [25]. High depth resolution in standard imaging demands for rather large aperture angles, as used, e.g., in high-resolution microscopy.
6. Standard OCT techniques use low numerical apertures (NAs) of the probing sample beam optics. Hence, the major contribution to the detected light comes from backscattering. For further details see Sheppard et al. [24].
7. Backscattering techniques act as high depth frequency band-pass filter and, therefore, show corresponding structures. However, single Fourier components sample different parts of the whole object's spatial frequency spectrum [26, 27] but do not yield depth resolution.
8. Resolution is determined by the Fourier uncertainty relation:

$$\Delta j \cdot \Delta K_j \sim \frac{1}{2}; j = x, y, z. \tag{4.8}$$

Even at moderate aperture angles ß (Fig. 4.1), relatively large ranges of transversal Fourier components are accessible in forward and backward scattering, and thus relatively high transversal resolution Δx and Δy can be obtained. In contrast to standard optical imaging, high depth resolution in PCI and OCT A-scan signals is provided by a broad wavelength spectrum $\Delta\lambda$. Here depth resolution is usually defined by the coherence length $l_C = \frac{2\ln 2}{\pi} \frac{\overline{\lambda}^2}{\Delta\lambda}$ (Gaussian spectrum assumed, $\overline{\lambda}$ is the mean wavelength).

9. Backscattering detector signal strength is, besides its dependence on the detector aperture, proportional to K^2 and, therefore, proportional to the second-order derivative $F^{(2)}(z)$ of the scattering potential [26]:

$$F^{(2)}(z) = -2 \cdot k_0^2 \cdot \left[n^{(1)}(z)^2 + n(z) \cdot n^{(2)}(z) \right]. \tag{4.9}$$

LCI and OCT signals, therefore, increase with increasing steepness and variability of the sample refractive index. (The same prediction has recently been obtained from another scattering model, based on the Kirchhoff approximation [24].)

10. Finally, the photoelectric OCT signal is proportional to the interferogram intensity at the photodetector and its quantum efficiency.

In this chapter, inversion of backscattered light in the far-field approximation provides the key to Fourier domain PCI and OCT. However, inversion problems also occur in forward scattering, for example, in near-field optics; in diverse areas of biological and industrial applications, such as the imaging of biological samples; in the inspection and manipulation of nano-electronic components in semiconductor technology; and in the inspection and activation of nano-optical devices.

4.2 Inverse Scattering-Based OCT Techniques

4.2.1 Far-Field Diffraction Techniques

In near-field Fresnel diffraction tomography, the operator O comprises two consecutive FTs [1]. Far-field diffraction tomography, on the other hand, is based on one FT only. Hence, we shall concentrate on far-field diffraction tomography and may expect most results to be applicable in near-field Fresnel diffraction tomography as well.

Based on optical diffraction tomography, a hierarchy of tomographic techniques can be formulated [28, 29], each based on a wavelength spectrum from λ_1 to λ_2 – starting from 3D imaging as indicated in Fig. 4.2 down to the point detector that measures scattering strength of the complete illuminated volume of a sample.

Note: In the subsequent figures standard illumination and reference beam optics as indicated in Fig. 4.2a are omitted.

4.2.1.1 Inverse Scattering 3D Imaging

The optical scheme depicted in Fig. 4.2a is a basic arrangement for 3D ODT giving access to the full 3D sample structure. Basically, in each detector pixel amplitude and phase of the interferogram, formed by the scattered sample wave and the reference wave, have to be measured for the wavelength range $\lambda_1 \rightarrow \lambda_2$. In the first approach monochromatic light had been used [3]. However, a 3D sample requires the recording of a 3D scattering data set. This can be achieved by illuminating the sample in more than one direction and/or by more than one wavelength [30]. Figure 4.2 depicts the situation when light of a wavelength range $\lambda_1 \leq \lambda \leq \lambda_2$, for example, from a swept source (LS), is used. Here, scattered field data between Ewald sphere windows ES1 and ES2 can be recorded.

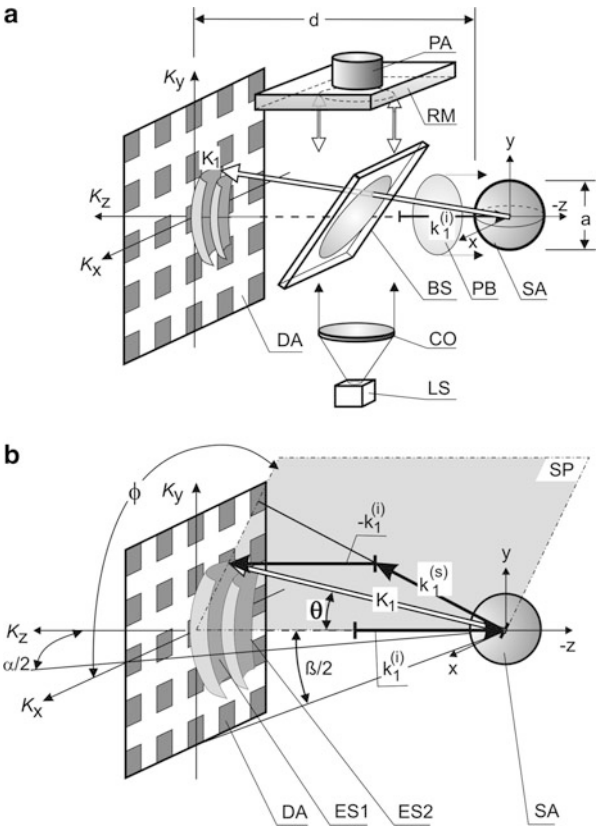

Fig. 4.2 3D far-field DOT. (**a**) basic optical scheme for inverse scattering-based OCT (and PCI). The illuminating beam vector is assumed antiparallel to the K_z-axis of the 2D detector-matrix DA. *BS* beam splitter, *CO* collimator, *LS* tunable or frequency-swept light source, *PA* piezo actuator for phase-shifting technique, *PB* probe beam cross section (sample illumination), *RM* reference mirror, *SA* sample (homogeneous sphere assumed); (**b**) **K**-space geometry of backscattering. Note: here, and in the subsequent figures, the $K_z = 0$ position is at the origin of the x,y,z-system. *ESi* scattered field data Ewald spheres of wavelength λ_i, *SP* scattering plane. K_1 = scattering vector of wavelength λ_1; $\mathbf{k}_1^{(i)}$ = wave vector of illuminating wave of wavelength λ_1; $\mathbf{k}_1^{(s)}$ = wave vector of scattered wave of wavelength λ_i. Fourier data points of wavelength λ_n are in a rectangular window ESn on the surface of the corresponding Ewald spheres. a is the sample size, d is the distance sample/image sensor, ß is the aperture angle, ϕ is the scattering azimuth, θ is the scattering angle

Basically, spectral amplitude and spectral phase have to be determined at each detector pixel. Spectral amplitude can easily be obtained from the pixel signal magnitude. There are several approaches to retrieve spectral phase data. For example, the phase-shifting technique enables registering the phase of the scattered

field at each detector pixel. In phase-shifting interferometry [31–33], the relative phase of the reference beam is shifted by discrete steps. From the interferometic intensity variation generated by these phase shifts, the phase of the scattered object wave is obtained. Hlubina et al. record two spectral interferograms to obtain the spectral interference signal and retrieve from it the spectral phase [34]. Also, a fast Gabor wavelet transform for high-precision phase retrieval in spectral interferometry that is significantly insensitive toward experimental noise has been described [35]. Using a swept source requires sampling the 2D interferogram intensity formed by the scattered sample wave and the reference wave at each pixel while the frequency of the source is scanned.

These methods are somewhat hindered by the fact that interference spectrum data recorded by single photodetector elements have to be rescaled from wavelength to frequency; furthermore, wavelength-dependent scattering vector space coordinates have to be scaled for wavelength, scattering azimuth, and scattering angle. Such a data set, however, enables a 3D reconstruction of the sample structure, also providing the basis for 2D tomograms.

In contrast, today, standard 3D OCT-based instruments typically use two-axis galvano mirrors for transverse 2D sample scanning by an A-scan probing beam. A-scan information is acquired by spectral interferometry (SI) by either using a broad-bandwidth light source and a spectrometer, spectral domain (SD)-PCI, or sweeping a narrow-bandwidth source through a broad range of frequencies, swept source (SS)-PCI. In both cases A-scan depth information is obtained by a Fourier transform of the detected spectra [36]. A comparison of a recently available commercial 3D OCT system operating at 800 nm with three laboratory systems operating with higher A-scans/s and one different wavelength can be found by Povazay et al. [37].

4.2.1.2 Inverse Scattering Sample Slice Generation

Direct access to tomographic sample sections is provided by projected scattering data. This follows from the Fourier projection/slice theorem [38]. Section position and orientation can be chosen within wide limits. For example, a slice $S(x_0, y, z)$ of the sample source strength in the y–z plane at x-coordinate x_0 is obtained from a projection of the scattering data including a phase factor:

$$S(x_0, y, z) = \iint \left\{ \left[\int \hat{U}^{(s)}(\mathbf{K}) \cdot \exp(i \cdot x_0 \cdot K_x) \cdot dK_x \right] \cdot \exp\left[i \cdot \left(y \cdot K_y + z \cdot K_z \right) \right] \right\} \cdot dKy \cdot dKz. \tag{4.10}$$

(In case of $K_x - K_y - K_z -$ factorizable spectra, a sequence of 1D FTs could be used.)

A slice at $x = 0$ is simply obtained as a 2D FT of the complex scattering data $\hat{U}^{(s)}(\mathbf{K})$ projected in K_x-direction in the detection plane

$$S(0,y,z) = \iint \left\{ \left[\int \hat{U}^{(s)}(\mathbf{K}) \cdot dK_x \right] \cdot \exp\left[i \cdot \left(y \cdot K_y + z \cdot K_z \right) \right] \right\} \cdot dKy \cdot dKz. \tag{4.11}$$

Such a projection performance in the detection plane can be achieved by binning sensor pixels of the detector matrix to form corresponding super-pixels in various azimuthal directions. Using programmable detector arrays very flexible OCT sample data acquisition systems can thus be implemented: Besides full 3D imaging, sample slices and sample projections in various orientations could be quickly achieved with such a system.

Projection performance in the detection plane can also be achieved by a linear detector array with reasonable large detector height:

Sample slice generation is analogous to parallel 2D FD-OCT: Grajciar et al. [39], for example, used a cylindrical lens to produce a sheet-of-light illumination on the sample in a study on a fully parallel FD-OCT system that allowed real time imaging of human eye structures. An alternative has been proposed by Zuluaga et al. [40]. These authors used a spatially resolved spectral interferometer. Here the depth in the sample is encoded as wavelength-dependent spatial frequency in the spectrogram whereas transverse information is imaged directly.

4.2.1.3 Inverse Scattering Sample Projection

Consider a 2D slice through the scattered field in the K_y–K_z plane at $K_x = 0$:

$$\begin{aligned} \hat{U}^{(S)}\left(0,K_y,K_z\right) &= \iiint S(x,y,z) \cdot \exp\left[-i \cdot \left(x \cdot K_x + y \cdot K_y + z \cdot K_z \right) \right] \cdot dx \cdot dy \cdot dz|_{K_x=0} \\ &= \iint \left\{ \left[\int S(x,y,z) \cdot dx \right] \cdot \exp\left[-i \cdot \left(y \cdot K_y + z \cdot K_z \right) \right] \right\} \cdot dy \cdot dz \end{aligned} \tag{4.12}$$

Hence, an FT of that 2D slice through the scattered field yields a parallel projection of the sample source strength onto the y–z plane:

$$P_x(y,z) = \int S(x,y,z) \cdot dx = \iint \hat{U}\left(0,K_y,K_z\right) \cdot \exp\left[i \cdot \left(y \cdot K_y + z \cdot K_z \right] \right] \cdot dK_y \cdot dK_z, \tag{4.13}$$

See Figs. 4.3 and 4.4.

4.2.1.4 Inverse Scattering Line Projection

Next we consider a linear stitch $\hat{U}^{(s)}\left(0,K_y,0\right)$ through the scattered field along the K_y-axis at $K_x = K_z = 0$. A Fourier transform yields a condensation of the sample source strength $S(x,y,z)$ along the y-coordinate. Slightly modifying Eq. 4.12 for $\hat{U}^{(s)}\left(0,K_y,0\right)$ readily yields the sample source strength condensed onto the y-axis:

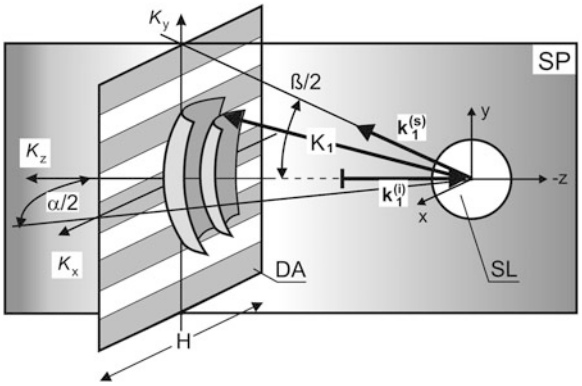

Fig. 4.3 IS sample slice generation by scattered field data projection. Here a line-array detector integrates the complex scattering amplitudes $\hat{U}^{(s)}(\mathbf{K})$ along the height H of the detector elements normal to the symmetry axis (K_y). Inversion reconstructs an OCT slice SL through the sample (a sphere) along the illuminating beam axis ($\mathbf{k}_\mathbf{n}^{(\mathbf{i})}$) and contains the detector symmetry axis (K_y). *DA* detector array, *SP* slice plane. Note: here, and in the subsequent figures, the $K_z = 0$ position is at the origin of the x,y,z-system

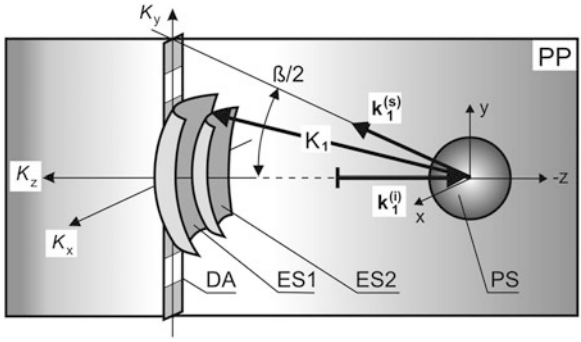

Fig. 4.4 IS sample projection. Projection plane PP is parallel to the illuminating beam axis ($\mathbf{k}_\mathbf{n}^{(\mathbf{i})}$) and contains the array axis (K_y). PS, projected sample structure. *DA* detector array, *ESi* scattered field data Ewald spheres of wavelength λ_i

$$P_{x,z}(y) = \iint S(x,y,z)\cdot dx.dz = \int \hat{U}^{(S)}(0,K_y,0)\cdot\exp\left[i\cdot y\cdot K_y\right]\cdot dK_y,$$

See Figs. 4.5 and 4.6.

Such a projection might not be useful. However, a linear field slice $\hat{U}^{(s)}(0,0,K_z)$ yields a central projection of the sample source strength along the z-direction:

$$P_{x,y}(z) = \int U^{(s)}(0,0,K_z)\cdot\exp(i\cdot z\cdot K_z)\cdot dK_z \tag{4.14}$$

Using a slim focused probing beam, that equation is the A-scan signal in FD-PCI and FD-OCT [41]. Transversal resolution is provided by the transverse diameter of the probing beam – leading to the resolution/depth-of-field contradiction (!). Depth

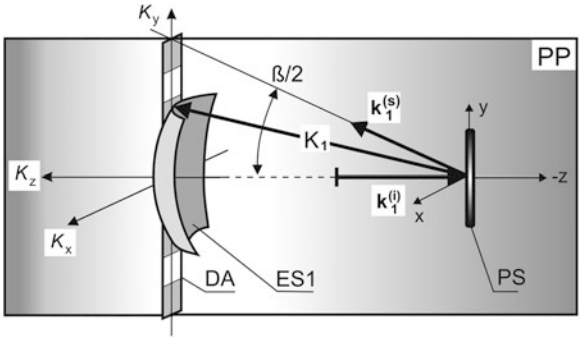

Fig. 4.5 Twofold IS sample projection. Sample = homogeneous sphere. Projection plane # 1 = PP ($K_y - K_z -$ plane). Projection plane # 2 = $K_x - K_y -$ plane. PS, projected sample structure (homogeneous sphere assumed as sample). *DA* detector array, *ES1* scattered field data Ewald spheres of wavelength λ_1

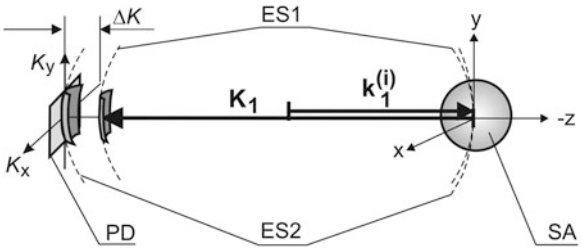

Fig. 4.6 Line projection. A single photodetector PD records a point in the scatter field spectrum. Depth distribution of the scattering potential along the z-axis is obtained from the $\hat{U}^{(s)}(0,0,K_z)$ spectrum. ES_n Ewald sphere of wavelength λ_n, *SA* sample. ΔK determines depth resolution

resolution is determined by the coherence length. This technique (together with an interferometric reference beam) has been implemented as spectral interferometry (SI), using a spectrometer, or as wavelength tuning interferometry (WTI) based on wavelength tuning or swept lasers. Taking the Fourier transform of $\hat{U}^{(s)}(0,0,K_z)$ yields the z-dependent "time-domain" A-scan signal. The logarithm of that signal is used as standard OCT image function. FD techniques provide superior sensitivity [42–44] compared to the original time-domain PCI [45–48] used in early OCT and related techniques [49–51].

Early wavelength tuning techniques have used a grating-tuned external cavity superluminescent LED or injection current modulation [52–54]. However, these techniques suffered either from low wavelength precision or from low tuning speed. Recently, high-speed frequency-swept laser sources have been used by Huber et al. [55], for wavelength tuning interferometry and OCT imaging. These laser sources use a fiber-coupled semiconductor amplifier and a tunable fiber Fabry-Perot filter yielding, for example, 20 kHz sweep rates with a tuning range of ~120 nm full width (mean wavelength 1,300 nm, ~ 45 mW instantaneous peak power). 108 dB sensitivity and ~10 μm axial resolution in tissue have been achieved.

Modern ultrafast wavelength-swept lasers achieve scan speeds >9,000 nm/ms, repetition rates >100 kHz, and tuning ranges >50 nm [56]. Tsai et al. [57] have demonstrated a frequency comb (FC)-swept laser and a frequency comb Fourier domain mode locked (FC-FDML) laser for applications in optical coherence tomography (OCT). A 135 nm tuning range centered at 1,310 nm with average output powers of 50 mW at a sweep rate of 1 kHz and 120 kHz has been achieved. The narrow bandwidth (0.015 nm) of the frequency comb filter enabled an ~ -1.2 dB sensitivity roll off over ~3 mm range, compared to conventional swept source and FDML lasers which have −10 dB and −5 dB roll offs, respectively.

4.2.1.5 Definite Integral Theorem

Finally, for scattered field data recorded by a single detector, the definite integral theorem says that

$$\iiint S(x,y,z)\cdot dx\cdot dy\cdot dz = \hat{U}^{(s)}(0,0,0); \tag{4.15}$$

i.e., scattering strength, cumulated over the complete illuminated volume of a sample, determines the power of the beam backscattered against the direction of the illuminating beam. This retraces time-domain PCI and OCT: Transverse resolution is defined by the illumination beam diameter, whereas depth resolution is provided by the interferometric coherence gate.

Other projections and slices are easily obtained by modification of the above examples.

Resolution vs depth-of-field. It should be noted that the techniques 4.2.1.1 to 4.2.1.5 do not need a focusing lens, hence do not suffer from the usual transverse-resolution vs depth-of-field contradiction of standard OCT. Nevertheless, smart focusing the illuminating wave into the region of interest can be desirable in many situations, since, besides resolution, it will also improve the signal-to-noise ratio.

4.2.1.6 Large Samples

Far-field techniques typically require small samples and/or scattered field detection at large distances from the sample plane. That limits their applicability. However, in case of plane samples or plane areas of interest in large samples, and as an approximation, the spatial Fourier transforming property of lenses can be used. Corresponding smart optics allow Fourier transforming of thin samples with large transversal extension. This approach requires an aberration free lens with the sample at the one focal plane of the lens and the detector array at the other focus of the lens [58].

4.2.2 Inverse Scattering in Near-Field Fresnel Diffraction Techniques

Near-field Fresnel *diffraction* is specified by Fresnel numbers $FN \sim 1$, whereas far-field diffraction optics on the other hand is specified by Fresnel numbers $FN \ll 1$.

Near-field *optics* is concerned with evanescent waves that appear in the passage of light through subwavelength structures within a few wavelengths from the diffracting feature. IS plays a role here too [59]; however, we only consider near-field diffraction PCI and OCT.

The operator O in near-field diffraction comprises two steps: (1) to determine a 2D FT of the homogeneously scattered field $U_h^{(S)}(\mathbf{r})$ in planes in front and/or behind the scattering object and (2) to determine a 3D FT of the angular spectrum $\hat{U}_h^{(S)}(\mathbf{K})$ of the scattered field with a phase factor to obtain the scattering potential $F(\mathbf{r})$ [1]. Hence, Fourier projection/slice theorem-based techniques, as described above for far-field techniques, could be used in both steps. Keeping in mind that a projection yields a slice in the Fourier transformed data and a slice yields a projection in the Fourier transformed data suggests the following: A slice- or a projection-procedure performed on the scattered field data $U_h^{(S)}(\mathbf{r})$ at step 1 yields a slice respectively a projection of the final sample data as well, whereas performing a slice- or a projection-procedure on the angular spectrum of the scattered field $\hat{U}_h^{(S)}(\mathbf{K})$ yields a projection respectively a slice of the final sample data.

Note: Since aperture data in DOT are registered mutually coherent, ODT is conformed to aperture synthesis, even if, from practical reasons, the aperture form is rather restricted.

4.3 Aperture Synthesis-Based Inverse Scattering

Aperture synthesis (AS) in imaging means to synthesize a large aperture by a series of smaller and more easily accessible apertures. AS needs both amplitude and phase of the fields to be measured. For radio frequencies, this is possible by electronics. Hence, AS synthesis imaging has been introduced at radio wavelengths by M. Ryle [60]. Optically, to record these data, the electromagnetic field cannot be measured directly and correlated in software, but must be propagated by sensitive optics and interfered [61]. The earliest synthetic-aperture experiments in the optical domain were performed by T. S. Lewis and H. S. Hutchins [62] using moving targets. The first image of a fixed, diffusely scattering target generated by synthetic-aperture imaging laser radar (SAIL) has been reported in 2005 [63].

Recently, former incoherent compiling of A-scan signals to form the OCT B-scan has obtained an alternative by coherently assembling A-scan signals forming a synthetic aperture, also called "interferometric synthetic-aperture imaging" [64]. The initial promise of AS in PCI and OCT has been to provide space-invariant resolution, in particular to suspend the resolution/depth-of-field contradiction. Since aperture synthesis requires phase stability between signals to be assembled, its demands on mechanical stability in optics are considerable. A closely related synthetic-aperture tomography technique in the terahertz field has been reported by Heimbeck et al. [65]. Sheppard et al. [24] state that these synthetic-aperture techniques use the same hardware like standard OCT; however, those image reconstruction techniques resemble known holographic image reconstruction.

4.3.1 B-Scan-Based Aperture Synthesis

Ralston et al. [64] have developed a solution to the inverse problem for OCT with a linearly scanned Gaussian beam. The mathematical model connects the acquired OCT A-scan signal with the three-dimensional object structure, taking into account scattering, diffraction, and probe beam parameters like transverse position, its finite width and focusing under paraxial approximation. A linear relationship between sample susceptibility η and the measured signal V is assumed:

$$V = O \cdot \eta. \tag{4.16}$$

O is an operator characterizing the OCT system. Light propagation is described by a scalar model based on the reduced wave. The sample is assumed to be illuminated by a Gaussian beam emerging from the sample fiber of a Michelson interferometer, projected by a thin lens onto the sample and laterally displaced for consecutive A-scans with its transverse position registered. Backscattered light is collected and projected back into the fiber. The light at the detector is determined assuming the first-order Born approximation and Green function formulation. A 2D photoelectric signal is assembled from the series of 1D A-scan photoelectric signals coherently detected at adjacent lateral positions. For such a multiplexed signal, mutual phase stability of the single A-scan signal is essential. Since, due to noise and bandwidth limitations, the inverse problem is ill-conditioned, a minimum norm solution of the least-squared error problem has been used. Analogous to Wolf's result [1], the Fourier transform of the observed signal is related to the Fourier transform of the sample susceptibility.

The potential of that solution has been explored by numerical simulation. A synthetic object was created as a collection of sub-resolution-sized point scatterers randomly distributed throughout a simulated imaging area of 1,024 μm by 1,024 μm. The simulated lens had a focal length of 10 mm, a spot size of 4 μm, and a confocal parameter of 30 μm, corresponding to an NA of 0.2. Gaussian white noise was added to simulate SNRs of 35 dB and -5 dB. In both cases the Tikhonov regularized solution [16, 66] resolved objects outside of the confocal region with minimal loss.

In a further step Ralston et al. [67] optimized the IS algorithm to improve the speed. An optimized algorithm has been presented that can generate cross-sectional reconstructed images at frame rates of 2.25 frames per second for 512 × 1,024 pixel images on a personal computer with two 3.0 GHz processors.

4.3.2 AS in Microscopy

Microscopy usually requires high NA optics. Hence, Ralston et al. [68] have resolved the inverse scattering problem analytically relying on a scalar wave model without resorting to the paraxial approximation. The results are demonstrated by numerical simulation. Spatial invariant resolution has been confirmed.

Any computational model for image formation in a high numerical aperture microscope must account for polarization effects on scattering and propagation. Hence, the vectorial diffraction theory is needed to predict imaging correctly. Davis et al. [69] have extended interferometric synthetic-aperture microscopy (ISAM) to non-paraxial full vectorial treatment of the light waves and to describe the effects of polarization on scattering and propagation. Numerical simulations confirm that the depth of focus is limited only by measurement noise and/or detector dynamic range. Furthermore, their model is suitable for the quantitative study of polarimetric coherent microscopy systems. Extensive numerical and noise simulations confirm inter alia diffraction-limited resolution even outside the focal plane.

Ralston et al. have presented the first ISAM photomicrographs of human tissue [23]. A fiber-optic Michelson interferometer illuminated by femtosecond pulses has been used. A spectral interferometer at one of the interferometer exits measures the interferometric cross-correlation between a fixed-delay reference pulse and the pulses reflected back from the sample. Transverse resolution is determined by the NA of the probing beam objective. A planar scanning geometry has been used: The probing beam is laterally translated in two dimensions through the sample by moving a stage or by steering the beam with a pair of galvanometer-driven mirrors before entering the objective.

Human breast tumor tissue was resected and imaged ex vivo. Sections were marked with India ink after imaging and before embedding to register locations. Whereas the histological images were obtained by destroying the sample, ISAM could readily be applied for in vivo applications because signal collection is in the backscattered epi-direction. Figure 4.7 presents images for depths of $z = 591$ μm (Sect. 4.3.1) and $z = 643$ μm (Sect. 4.3.2), where $z = 0$ μm is the focal plane. The ISAM reconstructions resolve features in the tissue that are not decipherable from the unprocessed data (Fig. 4.8).

4.3.3 ISAM with Computational Adaptive Optics

In retinal and catheter-based OCT imaging, astigmatism is a common aberration that becomes more prominent at higher resolution. Adie et al. [70] have demonstrated that ISAM, of course, does not correct aberrations of the sample probing beam. However, with computational adaptive optics correction of aberrations, high-resolution reconstruction of the tissue is obtained. Astigmatism correction in ISAM provides high-resolution reconstruction of the tissue structures and, additionally, a significant increase in signal-to-noise ratio of point-like scatterers.

Furthermore, Davis et al. [71] have shown that ISAM does not suffer from autocorrelation and conjugate image artifacts. ISAM algorithm defocuses the autocorrelation and conjugate image artifacts, mitigating their effects in most cases without requiring supplementary instrumentation or signal processing.

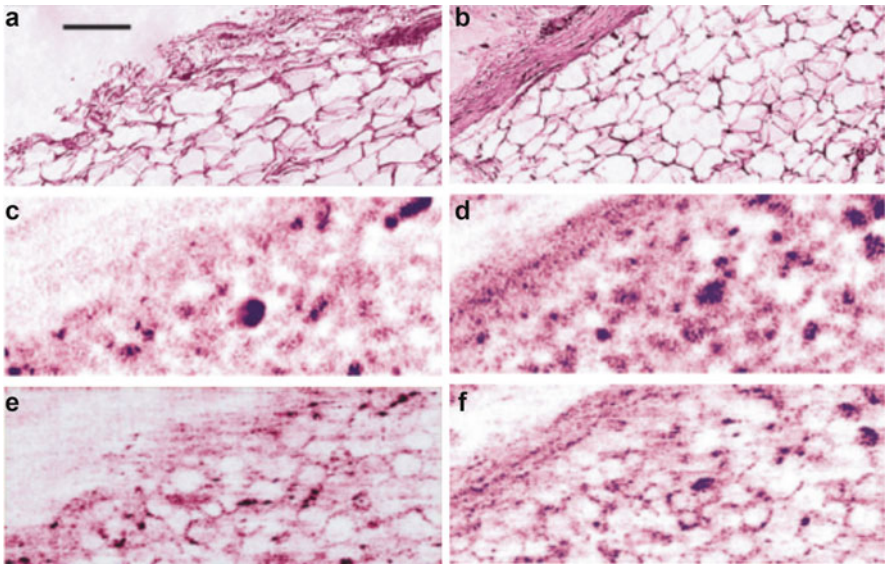

Fig. 4.7 Histological sections (**a**, **b**) show comparable features with respect to the unprocessed interferometric data (**c**, **d**) and the ISAM reconstructions (**e**, **f**). The scale bar represents 100 μm (From [23], by permission from the author)

4.3.4 Rotationally Scanned Synthetic Aperture in OCT

Another adaptation of IS is presented by Marks et al. [72] to angularly scanned OCT. Angularly scanned OCT is used in endoscopic OCT to explore tubular lumens within the human gastrointestinal tract or, for example, in cardiovascular imaging. Here the sample probing beam is typically focused at a fixed distance from the catheter. Hence, in standard endoscopic OCT instruments, the depth of focus of the resulting images is confined to a narrow annulus making clear interpretations of clinical findings difficult. An algorithm based on earlier-developed IS scheme [64] has been developed to compensate for that resolution localization. The simulation performed with a synthetic object comprising of point-like scatterers in fact demonstrated a clear improvement; however, a range-dependent resolution remained: Resolution is high between OCT catheter and focus radius of the Gaussian probing beam but decreases farther from the catheter.

4.3.5 Aperture Synthesis in Full-Field OCT

Full-field OCT images an entire plane of scatterers simultaneously, for example, in OCT microscopy: The objective is focused at the depth of features of interest. The reference beam path length is matched to that plane forming an interferogram that is

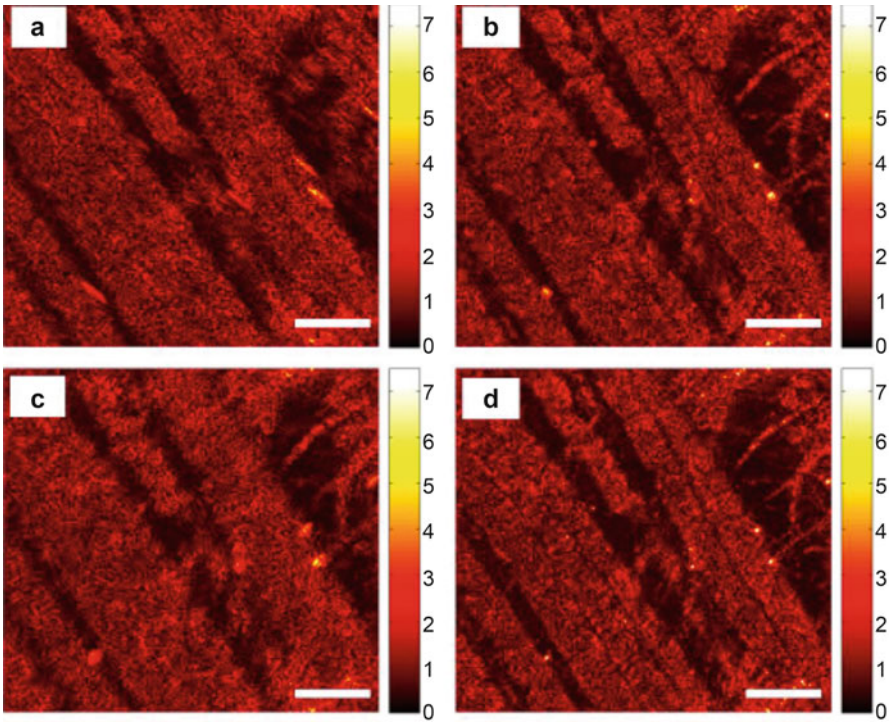

Fig. 4.8 ISAM and aberration correction in highly scattering rabbit muscle tissue. En face planes from 3D data acquired with a highly astigmatic illumination beam. (**a**) Uncorrected OCT, (**b**) aberration-corrected OCT, (**c**) uncorrected ISAM, and (**d**) aberration-corrected ISAM. The scale bar denotes 200 μm. (Note the structure at the top right of the images) (By permission from the author [70])

imaged onto a matrix array. By recording the interferogram, an image of a slice of the sample around the focal plane is obtained, and the out-of-focus contributions are removed by coherence gating. The usual technique is then to translate the sample through the focal plane so that the scatterers at many different depths may be imaged and a 3D structure obtained. This, however, requires a delicate movement of sample and microscope objective relative to each other.

Marks et al. [73] analyzed a full-field OCT system that uses a Köhler-type illumination system. By adjusting the size of the aperture iris, the spatial coherence of the beam illuminating the sample can be varied from very low (when the iris is opened) to very high (when the iris is closed). Both, sample plane and reference beam, are imaged by relay telescopes afocally and telecentrically to the focal plane detector array. The intensity of the interference pattern produced by the superimposed reference and sample signals is recorded there.

In the case of scanned-beam OCT, a focused beam is scanned through the sample, and data measured at each transverse position of the beam are taken at different times. Hence, no interference can occur between the fields produced for

different scan positions. Using incoherent full-field illumination of the sample is equivalent to a superposition of discrete mutually incoherent beams in the transverse direction, since here too, no interference can occur between the fields produced at different scan positions. Such an instrument may produce data similar to those that can be acquired with the scanned-beam implementations, but in a highly parallel fashion. Varying the source spatial coherence by adjusting the iris size allows a transition from full-field to confocal operation. In the one limit inverse scattering is identical to the inverse scattering for the full-field system, and in the other limit it reduces to the confocal ISAM inverse processing. The intermediate regime has also been examined, with the result that the ISAM Fourier domain resampling varies as a function of the source coherence.

The performance of partially coherent full-field AS with regard to image reconstruction and rejection of multiple scattering has been investigated using numerical simulations. These demonstrate the main points of full-field ISAM: High spatial coherence (multiple scattering tolerant) can produce artifacts corrupting the desired single-scatter signal; for the low spatial coherence case (single-scatter signal), ISAM processing corrects the blurring observed in OCT outside the depth of focus. Decreased spatial coherence of the source can thus be used to reduce the multiple-scatter artifact. The depth over which the signal strength is constant can be made many times larger than the Rayleigh range given a prudent choice of coherence properties.

Note: Since aperture data in DOT are registered mutually coherent, ODT is conformed to aperture synthesis, even if, from practical reasons, the aperture form is rather restricted.

Note: Full-field OCT can also be implemented as IS sample slice generation in Fourier domain based on projected scattering data (Sect. 4.2.1.2) obtained from DOT, either based on scattered field detection at large distances from the sample or based on the spatial Fourier transforming property of lenses (Sect. 4.2.1.6).

Acknowledgment The author thanks primarily his colleagues at the former Institute of Medical Physics at the Medical University of Vienna, in particular W. Drexler, C. K. Hitzenberger, M. Pircher, and B. Grajciar as well as M. Wojtkowski and R. Zawadzki (then) from the University of Torun/Poland.

The author is furthermore indebted to Tyler Ralston, Steven G. Adie, and Stephen A. Boppart from the University of Illinois at Urbana-Champaign, USA, for permission to reproduce Figs. 4.7 and 4.8.

References

1. E. Wolf, Three-dimensional structure determination of semi-transparent objects from holographic data. Opt. Commun. **1**, 153–156 (1969)
2. W. Carter, Computational reconstruction of scattering objects from holograms. J. Opt. Soc. Am. **60**, 306–314 (1970)
3. A.F. Fercher, H. Bartelt, H. Becker, E. Wiltschko, Image formation by inversion of scattered field data: experiments and computational simulation. Appl. Opt. **18**, 2427–2439 (1979)
4. A.C. Kak, M. Slaney, *Principles of Computerized Tomographic Imaging* (IEEE Press, New York, 1988)

5. M. Born, E. Wolf, *Principles of Optics* (Cambridge University Press, Cambridge, 2006)
6. P.S. Carney, E. Wolf, Power-excitation diffraction tomography with partially coherent light. Opt. Lett. **26**, 1770–1772 (2001)
7. E. Wolf, D.F.V. James, Correlation-induced spectral changes. Rep. Prog. Phys. **59**(1996), 771–818 (1996)
8. J.C. Schotland, Quantum imaging and inverse scattering. Opt. Lett. **35**, 3309–3311 (2010)
9. G. Bao, P. Li, Numerical solution of inverse scattering for near-field optics. Opt. Lett. **32**, 1465–1467 (2007)
10. S.D. Konecky, G.Y. Panasyuk, K. Lee, V. Markel, A.G. Yodh, J.C. Schotland, Imaging complex structures with diffuse light. Opt. Express **16**, 5048–5060 (2008)
11. Y.L. Kim, V.M. Turzhitsky, Y. Liu, H.K. Roy, R.K. Wali, H. Subramanian, P. Pradhan, V. Backman, Low-coherence enhanced backscattering: review of principles and applications for colon cancer screening. J. Biomed. Opt. **11**(4), 041125–1–041125–10 (2006)
12. D. Petrov, Y. Shkuratov, G. Videen, Optimized matrix inversion technique for the T-matrix method. Opt. Lett. **32**, 1168–1170 (2007)
13. A.F. Fercher, Optical coherence tomography – development, principles, applications. Z. Med. Phys. **20**, 251–276 (2010)
14. E.L. Miller, A.S. Willsky, Multiscale, statistical anomaly detection analysis and algorithms for linearized inverse scattering problems. Multidim. Syst. Sign. Process. **8**, 151–184 (1997)
15. M. Bertero, P. Boccacci, *Introduction to Inverse Problems in Imaging* (IOP Publishing, Bristol, 1998)
16. G.-V.Y. Tikhonov-AN, *Solutions of Ill-Posed Problems* (Winston, Washington, DC, 1977)
17. H.G. Schmidt-Weinmar, Spatial distribution of magnitude and phase of optical-wave fields. J. Opt. Soc. Am. **63**, 547–555 (1973)
18. H.G. Schmidt-Weinmar, Optical-wave near field specified from far-field data. J. Opt. Soc. Am. **65**, 1059–1066 (1975)
19. W.H. Carter, P.C. Ho, Reconstruction of inhomogeneous scattering objects from holograms. Appl. Opt. **13**, 162–172 (1974)
20. D.L. Marks, A family of approximations spanning the Born and Rytov scattering series. Opt. Express **14**, 8837–8848 (2006)
21. G. Beylkin, R. Burridger, Linearized inverse scattering problems in acoustics and elasticity. Wave Motion **12**, 15–52 (1990)
22. V. Lauer, A new approach to optical diffraction tomography yielding a vector equation of diffraction tomography and a novel tomographic microscope. J. Microsc. **205**, 165–176 (2002)
23. T.S. Ralston, D.L. Marks, P.S. Carney, S.A. Boppart, Interferometric synthetic aperture microscopy. Nat. Phys. **3**, 129–134 (2007)
24. C.J.R. Sheppard, S.S. Kou, C. Depeursinge, Reconstruction in interferometric synthetic aperture microscopy: comparison with optical coherence tomography and digital holographic microscopy. J. Opt. Soc. Am. **A29**, 244–250 (2012)
25. E. Evans, Comparison of the diffraction theory of image formation with the three-dimensional, first Born scattering approximation in lens systems. Opt. Commun. **2**, 317–320 (1970)
26. A.F. Fercher, C.K. Hitzenberger, Optical coherence tomography, in *Progress in Optics*, vol. 44 (Elsevier, Amsterdam, 2002), pp. 215–302
27. M. Villiger, T. Lasser, Image formation and tomogram reconstruction in optical coherence tomography. J. Opt. Soc. Am. **A27**, 2216–2228 (2010)
28. A.F. Fercher, OCT techniques. Proc. SPIE **2930**, 164–175 (1996)
29. A.F. Fercher, Inverse scattering, dispersion, and speckle in optical coherence tomography, in *Optical Coherence Tomography*, ed. by W. Drexler, J.G. Fujimoto (Springer, Berlin, 2008)
30. R. Dändliker, K. Weiss, Reconstruction of the three-dimensional refractive index from scattered waves. Opt. Commun. **1**, 323–328 (1970)
31. J. Schwider, Phase shifting interferometry: reference phase error reduction. Appl. Opt. **28**, 3889–3892 (1989)

32. R. Leitgeb, C.K. Hitzenberger, A.F. Fercher, T. Bajraszewski, Phase-shifting algorithm to achieve high-speed long-depth-range probing by frequency-domain optical coherence tomography. Opt. Lett. **28**, 2201–2203 (2003)
33. P. Hariharan, *Optical Interferometry* (Academic, Salt Lake City, 2003)
34. P. Hlubina, D. Ciprian, J. Lunacek, M. Lesnak, Dispersive white-light spectral interferometry with absolute phase retrieval to measure thin film. Opt. Express **14**, 7678–7685 (2006)
35. J. Bethge, C. Grebing, G. Steinmeyer, A fast Gabor wavelet transform for high-precision phase retrieval in spectral interferometry. Opt. Express **15**, 14313–14321 (2007)
36. M.L. Gabriele, G. Wollstein, H. Ishikawa, L. Kagemann, J. Xe, J.S. Schuman, Optical coherence tomography: history, current status, and laboratory work. Invest. Ophthalmol. Vis. Sci. **52**, 2425–2436 (2011)
37. B. Považay, A. Unterhuber, B. Hermann, H. Sattmann, H. Arthaber, W. Drexler, Full-field time-encoded frequency-domain optical coherence tomography. Opt. Express **14**, 7661–7669 (2006)
38. R. Bracewell, *The Fourier Integral and its Applications* (Mc Graw Hill, New York, 2000)
39. B. Grajciar, M. Pircher, A.F. Fercher, R.L. Leitgeb, Parallel Fourier domain optical coherence tomography for in vivo measurement of the human eye. Opt. Express **13**, 1131–1137 (2005)
40. A.F. Zuluaga, R. Richards-Kortum, Spatially resolved spectral interferometry for determination of subsurface structure. Opt. Lett. **24**, 519–521 (1999)
41. A.F. Fercher, C.K. Hitzenberger, G. Kamp, S.Y. El-Zaiat, Measurement of intraocular distances by backscattering spectral interferometry. Opt. Commun. **117**, 43–48 (1995)
42. R. Leitgeb, C.K. Hitzenberger, A.F. Fercher, Performance of Fourier domain vs. time domain optical coherence tomography. Opt. Express **11**, 889–894 (2003)
43. J. deBoer, B. Cense, B.H. Park, M.C. Pierce, G.J. Tearney, B.E. Bouma, Improved signal-to-noise ratio in spectral-domain compared with time-domain optical coherence tomography. Opt. Lett. **28**, 2067–2069 (2003)
44. M.A. Choma, M.V. Sarunic, C. Yang, J.A. Izatt, Sensitivity advantage of swept source and Fourier domain optical coherence tomography. Opt. Express **11**, 2183–2189 (2003)
45. A.F. Fercher, Ophthalmic laser interferometry. Proc. SPIE **658**, 48–51 (1986)
46. A.F. Fercher, K. Mengedoht, W. Werner, Eye-length measurement by interferometry with partially coherent light. Opt. Lett. **13**, 186–188 (1988)
47. A.F. Fercher, Measurement of intraocular optical distances using partially coherent laser light. J. Microw. Optoelectron. **38**, 1327–1333 (1991)
48. D. Huang, J. Wang, C.P. Lin, C.A. Puliafito, J.G. Fujimoto, Micron-resolution ranging of cornea anterior chamber by optical reflectometry. Lasers Surg. Med. **11**, 419–425 (1991)
49. A.F. Fercher, Ophthalmic interferometry, in *Optics in Medicine, Biology and Environmental Research. Selected Contributions to the First International Conference on Optics Within Life Sciences (OWLS I), Garmisch-Partenkirchen, Germany, 12-16 August 1990 (ICO-15 SAT)*, ed. by G. von Bally, S. Khanna (Elsevier, Amsterdam/London/New York/Tokyo, 1993), pp. 221–228
50. A.F. Fercher, C.K. Hitzenberger, W. Drexler, G. Kamp, H. Sattmann, In vivo optical coherence tomography. Am. J. Ophthalmol. **116**, 113–114 (1993)
51. E.A. Swanson, J.A. Izatt, M.R. Hee, D. Huang, C.P. Lin, J.S. Schuman, C.A. Pulliafito, J.G. Fujimoto, In vivo retinal imaging by optical coherence tomography. Opt. Lett. **18**, 1864–1866 (1993)
52. S.R. Chinn, E.A. Swanson, J.G. Fujimoto, Optical coherence tomography using a frequency-tunable optical source. Opt. Lett. **22**, 340–342 (1997)
53. F. Lexer, C.K. Hitzenberger, A.F. Fercher, M. Kulhavy, Wavelength-tuning interferometry of intraocular distances. Appl. Opt. **36**, 6548–6553 (1997)
54. B. Golubovic, B.E. Bouma, G.J. Tearney, J.G. Fujimoto, Optical frequency-domain reflectometry using rapid wavelength tuning of a Cr/sup 4+/:forsterite laser, 1997. Opt. Lett. **22**, 1704–1706 (1997)

55. R. Huber, M.W. Wojtkowski, K. Taira, J.G. Fujimoto, Amplified, frequency swept lasers for frequency domain reflectometry and OCT imaging: design and scaling principles. Opt. Express **13**, 3513–3528 (2005)
56. W.Y. Oh, S.H. Yun, G.J. Tearney, B.E. Bouma, 115 kHz tuning repetition rate ultrahigh-speed wavelength-swept semiconductor laser. Opt. Lett. **30**, 3159–3161 (2005)
57. T.H. Tsai, C. Zhou, D.C. Adler, J.G. Fujimoto, Frequency comb swept lasers. Opt. Express **17**, 21257–21270 (2009)
58. J. Goodman, *Introduction to Fourier Optics* (Robert & Company, Colorado, 2005)
59. P.S. Carney, R.A. Frazin, S.I. Bozhevolnyi, V.S. Volkov, V. Boltasseva, J.C. Schotland, A computational lens for the near-field. Phys. Rev. Lett. **92**, 163903–1–163903–4 (2004)
60. M. Ryle, The mullard radio astronomy observatory, Cambridge. Nature **180**, 110–112 (1957)
61. C. van der Avoort, S.F. Pereira, J.J.M. Braat, J.-W. den Herder, Optimum synthetic-aperture imaging of extended astronomical objects. J. Opt. Soc. Am. **A24**, 1042–1052 (1970)
62. T.S. Lewis, H.S. Hutchins, A synthetic aperture at 10.6 microns. Proc. IEEE **58**, 1781–1782 (1970)
63. S.M. Beck, J.R. Buck, W.F. Buell, R.P. Dickinson, D.A. Kozlowski, N.J. Marechal, T.J. Wright, Synthetic-aperture imaging laser radar: laboratory demonstration and signal processing. Appl. Opt. **44**, 7621–7629 (2005)
64. T.S. Ralston, D.L. Marks, P.S. Carney, S.A. Boppart, Inverse scattering for optical coherence tomography. J. Opt. Soc. Am. A **23**, 1027–1037 (2006)
65. M.S. Heimbeck, D.L. Marks, D. Brady, H.O. Everitt, Terahertz interferometric synthetic aperture tomography for confocal imaging systems. Opt. Lett. **37**, 1316–1318 (2012)
66. A.N. Tikhonov, On the stability of inverse problems. Dokl. Akad. Nauk SSSR **39**, 195–198 (1943)
67. T.S. Ralston, D.L. Marks, P.S. Carney, S.A. Boppart, Real-time interferometric synthetic aperture microscopy. Opt. Express **16**, 2555–2569 (2008)
68. T.S. Ralston, D.L. Marks, S.A. Boppart, P.S. Carney, Inverse scattering for high-resolution interferometric microscopy. Opt. Lett. **31**, 3585–3587 (2006)
69. B.J. Davis, S.C. Schlachter, D.L. Marks, T.S. Ralston, S.A. Boppart, P.S. Carney, Nonparaxial vector-field modeling of optical coherence tomography and interferometric synthetic aperture microscopy. J. Opt. Soc. Am. **A24**, 2527–2542 (2007)
70. S.G. Adie, A. Ahmad, N. Shemonski, B.W. Graf, H. Kim, W.-M.W. Hwu, P.S. Carney, S.A. Boppart, (2012) *Interferometric Synthetic Aperture Microscopy with Computational Adaptive Optics for High-Resolution Tomography of Scattering Tissue*. Paper BW2A.1. OSA Conference on Biomedical Optics and 3D Imaging OSA 2012, Miami, 28 April 2012.
71. B.J. Davis, T.S. Ralston, D.L. Marks, S.A. Boppart, P.S. Carney, Autocorrelation artifacts in optical coherence tomography and interferometric synthetic aperture microscopy. Opt. Lett. **32**, 1441–1443 (2007)
72. D.L. Marks, T.S. Ralston, P.S. Carney, S.A. Boppart, Inverse scattering for rotationally scanned optical coherence tomography. J. Opt. Soc. Am. **A23**, 2433–2439 (2006)
73. D.L. Marks, B.J. Davis, S.A. Boppart, P.S. Carney, Partially coherent illumination in full-field interferometric synthetic aperture microscopy. J. Opt. Soc. Am. **A26**, 376–386 (2009)

Spectral/Fourier Domain Optical Coherence Tomography

5

Johannes F. de Boer

Keywords
Depth dependent sensitivity • Frequency domain OCT • Fringe washout • Shot noise limited detection • SNR advantage • Spectral domain OCT

5.1 Introduction

Optical coherence tomography is a low-coherence interferometric method for imaging of biological tissue [1, 2]. For more than a decade after its inception between 1988 and 1991, the dominant implementation has been time domain OCT (TD-OCT), in which the length of a reference arm is rapidly scanned. The first spectral or Fourier domain OCT (SD/FD-OCT) implementation was reported in 1995 [3]. In SD-OCT the reference arm is kept stationary, and the depth information is obtained by a Fourier transform of the spectrally resolved interference fringes in the detection arm of a Michelson interferometer. This approach has provided a significant advantage in signal-to-noise ratio (SNR), which despite reports as early as 1997 [4, 5] has taken about half a decade to be recognized fully by the OCT community in 2003 [6–8]. The first demonstration of SD-OCT for in vivo retinal imaging in 2002 [9] was followed by a full realization of the sensitivity advantage by video rate in vivo retinal imaging [10], including high-speed 3-D volumetric imaging [11], ultrahigh-resolution video rate imaging [12, 13], and Doppler blood flow determination in the human retina [14, 15]. The superior sensitivity of SD-OCT, combined with the lack of need for a fast mechanical scanning mechanism, has opened up the possibility of much faster scanning without loss of image quality and provided a paradigm shift from point sampling to

J.F. de Boer
Department of Physics and Astronomy, LaserLaB Amsterdam, Vrije Univ Amsterdam, Amsterdam, The Netherlands
e-mail: jfdeboer@few.vu.nl

© Springer International Publishing Switzerland 2015

W. Drexler, J.G. Fujimoto (eds.), *Optical Coherence Tomography*,
DOI 10.1007/978-3-319-06419-2_6

volumetric mapping of biological tissue in vivo. The technology has been particularly promising for ophthalmology [16, 17]. In this chapter, the principles and system design considerations of SD-OCT will be discussed in more detail.

5.1.1 Introduction to Signal to Noise

In the standard time domain (TD) implementation of OCT, the position of the reference mirror in the interferometer is rapidly scanned by mechanical means in order to obtain a depth profile (A-line) within a sample. An alternative method of retrieving depth information examines the cross-spectral density by detecting the interference signal in the detection arm of a Michelson interferometer as a function of wavelength [3, 4, 18]. In spectral domain OCT (SD-OCT), also known as Fourier domain OCT (FD-OCT), no mechanical scanning of the reference arm is required. Instead, the cross-spectral density at the detection arm of the interferometer is measured by means of a spectrometer [3]. In SD-OCT, the depth range z is inversely proportional to the spectral resolution $\delta\lambda$ and given by [4] $z = \lambda_0^2/4n\delta\lambda$. Although this technique has been demonstrated for in vivo dermal and retinal imaging [4, 9], it has only recently been demonstrated both theoretically and experimentally that a sensitivity improvement of several orders of magnitude could potentially be realized in SD-OCT compared to TD-OCT [6, 7]. SD-OCT does not require modulation of the reference arm length and therefore has potential for faster image acquisition rates.

TD-OCT has been applied extensively in ophthalmology, where cross-sectional OCT images of the retina have provided useful information regarding the presence or progression of specific ocular diseases [19]. The acquisition rate of current clinical and preclinical TD-OCT systems is limited by sensitivity and the maximum permissible incident power on the eye [20], preventing comprehensive screening of large retinal areas. The sensitivity improvement of SD-OCT allows for dramatically increased acquisition speeds without compromising image quality. Three-dimensional data sets can therefore be rapidly acquired, opening the possibility of comprehensive screening.

Although this method has long been proposed and demonstrated, only recently have there been efforts to explicitly show that SD-OCT can produce a better detection sensitivity than the time domain method [6–8]. Recent work has experimentally demonstrated a 148-fold (21.7 dB) sensitivity improvement with SD-OCT [10] and a near shot noise limited performance. Reaching shot noise limited performance in SD-OCT requires a careful analysis of noise contributions, which will be presented first.

In essence the SNR advantage of SD-OCT over TD-OCT is based on the significant reduction of shot noise obtained by replacing the single-element detector with a multielement array detector. In a TD-OCT system, each wavelength is uniquely encoded as a frequency by scanning the length of the reference arm, and shot noise has a white noise characteristic. In a single detector TD-OCT system, the shot noise generated by the power density at one particular wavelength is present at all frequencies and therefore adversely affects the SNR at all other wavelengths.

By spectrally dispersing each wavelength to a separate detector, the cross shot noise term is eliminated in both hybrid and fully parallel SD-OCT systems [7].

5.1.2 Noise Analysis of SD-OCT Using Charge-Coupled Devices (CCDs)

The core of an SD-OCT system is the spectrometer in the detection arm. In general, light detection in the spectrometer is achieved by a charge-coupled device (CCD) like a line array. Alternative implementations have been suggested that require individual processing of pixel charges [21]. To facilitate the noise analysis in the case of detection by CCDs, the signal and noise terms will be expressed in charge squared (e^2). Only the real part of the complex cross-spectral density is detected in SD-OCT, resulting in a signal S_{SD} given by [6, 7]

$$S_{SD} = \frac{\eta^2 e^2 P_{ref} P_{sample} \tau_i^2}{E_v^2} \left[e^2\right] \tag{5.1}$$

with e the electron charge; P_{ref} and P_{sample}, respectively, the reference arm and sample arm power per detector element at the detection arm fiber tip; τ_i the integration time; and E_v the photon energy.

The readout and dark noise, shot noise, and relative intensity noise (RIN) contributions to the overall noise in electrons squared per read out cycle and per detector element are given by, respectively [6, 7],

$$\sigma_{noise}^2 = \sigma_{r+d}^2 + \frac{\eta e^2 P_{ref} \tau_i}{E_v} + \left(\frac{\eta e P_{ref}}{E_v}\right)^2 \tau_i \tau_{coh} \quad \left[e^2\right], \tag{5.2}$$

where the sample arm power was assumed to be much smaller than the reference arm power [22], with σ_{r+d}^2 the sum of readout noise and dark noise and $\tau_{coh} = \sqrt{2 \ln 2/\pi}\ \lambda_0^2/c\delta\lambda$ the coherence time, with c the speed of light [23]. The optimal signal-to-noise performance is achieved when shot noise dominates both readout noise and relative intensity noise (RIN) [22]. Shot noise dominates readout noise and dark noise when $\eta e^2 P_{ref} \tau_i / \sigma_{r+d}^2 E_v > 1$, and shot noise dominates RIN when their ratio is larger than one, i.e., $E_v/\eta P_{ref}\ \tau_{coh} > 1$. The optimal reference arm power is found when readout noise and dark noise are equal to the RIN [24]:

$$\sigma_{r+d}^2 = \left(\frac{\eta e P_{ref}}{E_v}\right)^2 \tau_i \tau_{coh}. \tag{5.3}$$

Thus, for a system to operate close to shot noise limited performance, shot noise should dominate thermal and RIN at the optimal reference arm power:

$$P_{ref} = \frac{\sigma_{r+d} E_v}{\eta e \sqrt{\tau_i \tau_{coh}}}. \tag{5.4}$$

At this optimal reference arm power, the inequalities describing shot noise dominance over readout noise and RIN, respectively, reduce to the same equation:

$$\frac{e\sqrt{\tau_i}}{\sigma_{rd}\sqrt{\tau_{coh}}} > 1. \tag{5.5}$$

In general, one would like to choose the integration time τ_i as short as possible and the coherence time τ_{coh} as long as possible. The coherence time is inversely related to the spectral resolution of the spectrometer which in turn relates linearly to the maximum depth range of the system. In conclusion, the parameter that most determines the system performance is the readout and dark noise of the detector σ_{rd}.

5.1.3 Autocorrelation Noise: Dynamic Range and Digitization Depth

SD-OCT is based on spectral interferometry, where recombined light from reference and sample arms is spectrally separated, detected, and converted into a depth profile. The detected interference signal at the spectrometer may be expressed as [4]

$$I(k) = I_r(k) + 2\sqrt{I_s(k) I_r(k)} \sum_n \alpha_n \cos(k z_n) + I_s(k) \tag{5.6}$$

where $I_r(k)$ and $I_s(k)$ are the wavelength-dependent intensities reflected from reference and sample arms, respectively, and k is the wave number. The second term on the right-hand side of Eq. 5.6 represents the interference between light returning from reference and sample arms. α_n is the square root of the sample reflectivity at depth z_n. Depth information is retrieved by performing an inverse Fourier transform of Eq. 5.6, yielding the following convolution [4]:

$$\left|FT^{-1}[I(k)]\right|^2 = \Gamma^2(z) \otimes \left\{ \delta(0) + \sum_n \alpha_n^2 \delta(z - z_n) + \sum_n \alpha_n^2 \delta(z + z_n) + \; O\left[I_s^2/I_r^2\right] \right\}, \tag{5.7}$$

with $\Gamma(z)$ representing the envelope of the coherence function. The first term in the braces on the right-hand side describes the autocorrelation signal from the reference arm and has magnitude unity. The second and third terms are due to interference between light returning from reference and sample arms and form two images, where each has magnitude on the order of I_s/I_r. These two terms provide mirror images, where one is retained. The final term, with magnitude on the order of I_s^2/I_r^2,

describes autocorrelation noise due to interference within the sample arm [4, 9]. I_s and I_r represent the total intensity reflected from sample and reference arms, respectively. Equation 5.7 indicates that the relative contribution of sample autocorrelation noise can be reduced by increasing the reference arm power with respect to the signal. Decreasing the detector integration time permits an increase in the reference arm power without saturating the detector, decreasing the ratio I_s^2/I_r^2 and consequently reducing the contribution of autocorrelation noise in ultrahigh-speed SD-OCT.

In the shot noise limit, the signal-to-noise ratio (*SNR*) in the spectral domain system has been shown to be [7]

$$SNR_{SD} = \frac{\eta P_{sample} \tau_i}{E_v}, \tag{5.8}$$

where η is the spectrometer efficiency, P_{sample} is the sample arm power returning to the detection arm, τ_i is the detector integration time, and E_v is the photon energy. Unlike the SNR in the time domain, Eq. 5.8 demonstrates that in the shot noise limit, SNR_{SD} is independent of the spectral width of the source. This implies that the axial resolution can be increased at no penalty to the SNR, provided that the full spectral width of the source can be imaged onto an array detector. However, this result should be interpreted with some care. The sample arm power returning to the detection arm is assumed to come from a single reflecting surface. In tissue, however, the reflected power comes from multiple structures along a depth profile. The SNR for a particular position along the depth profile is given on average by the total power reflected by all structures within the coherence length of the source. As the resolution increases (the coherence length decreases), the total reflected power within the coherence length decreases. As a consequence, the SNR at a particular position along the depth profile will reduce as the resolution increases by increasing the source optical bandwidth.

5.1.4 Bit Resolution and Well Depth of the CCD, Dynamic Range, and Sensitivity

Earlier SD-OCT system designs emphasized the necessity of large well depth (number of electrons that could be stored in a single element of the CCD) and large bit depth as an important consideration to realize the high sensitivity and dynamic range that can be achieved by OCT. Sensitivity is the ratio of maximum signal over noise floor, where the maximum signal is defined by placing a perfect reflector in the sample arm. The dynamic range of a system is the maximum signal over the noise floor that a particular system can measure without, e.g., saturating a detector, overloading an amplifier, or exceeding a digitization range. In practice, no TD- or SD-OCT system realizes a dynamic range equal to the sensitivity, which can easily be over 100 dB. In general, this is not necessary, since tissue reflectivity

is at least four orders of magnitude smaller than a perfect reflector. A system dynamic range of 40–60 dB suffices in most cases.

A 60-dB dynamic range in a TD-OCT system would require at least a 10-bit A/D range (6 dB per bit) digitizing the interference modulation on the DC background. An advantage of TD-OCT systems is that the signal can be high-pass filtered to remove the DC component and only pass the interference modulation to the digitization circuitry. In SD-OCT, the CCD detectors do not easily permit removal of a DC component, and considerations similar to that for a TD-OCT system suggest that for an SD-OCT system the A/D range needed to capture the interference modulation on top of the DC background with sufficient resolution to provide 40–60-dB dynamic range would require an A/D resolution significantly exceeding that of a TD-OCT system. Fortunately, the required bit resolution capturing the interference modulation to achieve 40–60-dB dynamic range turns out to be much smaller.

In SD-OCT the reflectivity in z-space is given by the square of the Fourier component in k-space (Eq. 5.7). The resolution of the Fourier component is proportional to the resolution of the modulation depth of the spectrum, multiplied with the number of illuminated pixels of the camera (on the order of ~1,000). Thus, a relative small resolution of the modulation depth of the spectrum (on the order of a few bits) gets amplified by the number of illuminated pixels, easily providing a dynamic range in z-space exceeding 40–60 dB. The presence of multiple reflecting structures complicates matters. For example, two strong reflectors in the sample arm each create a periodic modulation of the spectrum. These modulations are summed and create a larger modulation depth of the spectrum on the DC background that should be captured without saturation of the CCD or clipping of the digitization circuitry. Therefore, the calculation of the dynamic range of an SD-OCT system is not a straightforward calculation of the strongest single reflector that can be measured, but depends on the total power reflected by the sample. As the total reflected power increases, the dynamic range with which the reflectivity of a particular location can be measured decreases.

5.1.5 Experimental Demonstration of SNR Advantage

A number of groups have presented empirical evidence demonstrating the SNR advantage of SD-OCT over time domain OCT. The following section describes a direct comparison between a TD-OCT and an SD-OCT system [10]. To compare directly the SNR performance of TD- and SD-OCT, a weak reflector was placed in the sample arm of our system (Fig. 5.1).

The power reflected by the weak reflector measured at the fiber tip in the detection arm was 1.3 nW. The polarization states of sample and reference arm light were carefully aligned to maximize interference. First, 256 depth profiles at a speed of 4 ms per depth profile were acquired with our TD-OCT system, scanning over a depth of 1.4 mm in air. The signal pass bandwidth (BW) was 100 kHz. Then the detection arm was connected to the spectrometer, and 256 spectra were acquired

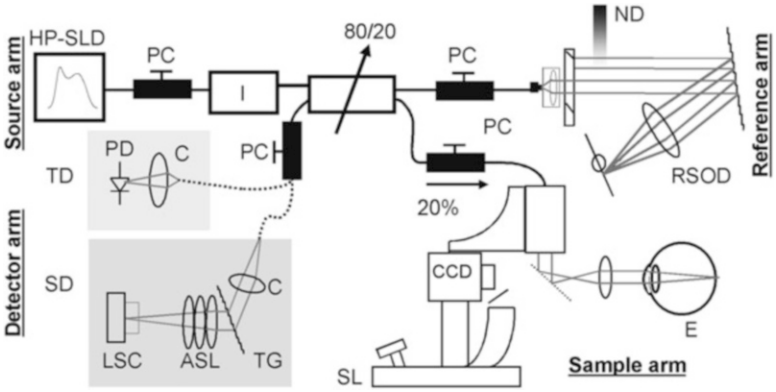

Fig. 5.1 Time and spectral domain system integrated into a single instrument for a direct comparison of the SNR (Reproduced from Ref. [10] with permission from the Optical Society of America)

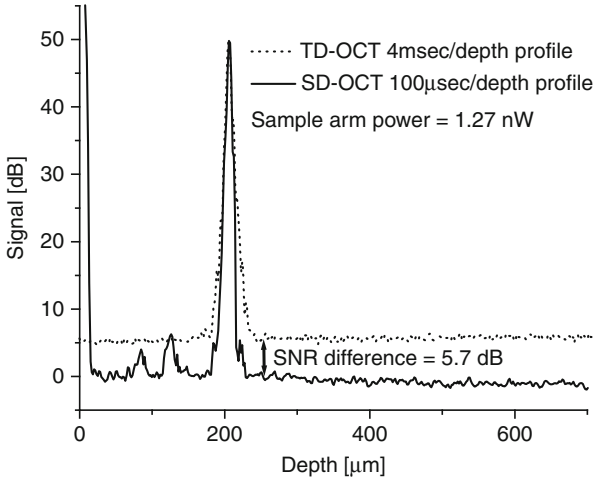

Fig. 5.2 Direct comparison of the SNR between SD- and TD-OCT (Reproduced from Ref. [10] with permission from the Optical Society of America)

at a speed of 100 µs per spectrum. To reduce fixed pattern noise in the SD-OCT measurement [6], each individual spectrum was divided by the average spectrum of 1,000 reference arm spectra. The resulting spectrum was multiplied by a Gaussian to reshape the spectrum [25]. A Fourier transform links z- and k-space. Because of the nonlinear relation between k and λ, the spectra were interpolated to create evenly spaced samples in the k domain [9] before Fourier transformation of the spectra to generate depth profiles.

Figure 5.2 shows the averaged depth profiles acquired with the respective configurations, demonstrating an SNR of 44.3 and 50 dB for TD- and SD-OCT, respectively. Both depth profiles were normalized on the reflectivity peak. The TD measurement was shifted such that the peaks coincide. Some fixed pattern noise

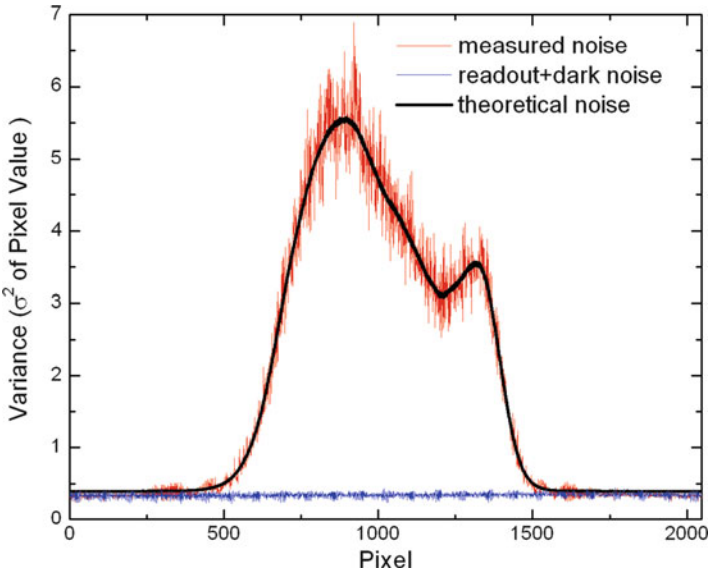

Fig. 5.3 Noise components in the detector. The shot noise level was determined with illumination of the reference arm only and was used to determine the A/D resolution of the detector. The theoretical shot noise curve was fit using Eq. 5.10 to the measured noise, giving a Δe of 173 electrons and a corresponding well depth of 177,000 electrons (Reproduced from Ref. [11] with permission from the Optical Society of America)

was still present in the SD-OCT measurement, resulting in peaks at 84 and 126 μm. Since the SD-OCT system was 5.7 dB more sensitive, operated at a speed 40 times faster (corresponding to 16 dB) than the TD-OCT system, the combined sensitivity improvement was 21.7 dB or a factor of 148. The theoretical shot noise limited SNR in TD and SD is given by, respectively [6, 7],

$$SNR_{TD} = \frac{\eta P_{sample}}{E_v BW}, \quad SNR_{SD} = \frac{\eta P_{sample} \tau_i}{E_v} \tag{5.9}$$

resulting in 46.7 dB (TD) and 51.9 dB (SD), where $\eta = 0.85$ was used for a PIN diode in TD. The measured TD and SD SNRs were, respectively, 2.4 and 1.9 dB less than the theoretical optimal performance, where 1 dB in TD was determined to be due to thermal noise contributing to the total noise. The measured coherence function FWHM in air was 6.3 μm in both TD and SD.

5.1.6 Shot Noise Limited Detection

The different noise components present in the system were measured and analyzed to demonstrate that performance was shot noise limited. The readout and shot noise at a 29.3 kHz readout rate are shown in Fig. 5.3.

The noise was determined by calculating the variance at each camera pixel for 1,000 consecutive spectra. Dark noise measurements were taken with the source light off. Only light returning from the reference arm was used to measure the shot noise in the system. The shot noise expressed in number of electrons is $(I_{PV}(\lambda)\Delta e)^{1/2}$, where $I_{PV}(\lambda)$ is the pixel value corresponding to the intensity at each CCD element, with values ranging from 0 to 1,024 (10 bits), and Δe is the analog-to-digital conversion resolution, which corresponds to the number of electrons required for an incremental increase of 1 pixel value. Thus, the variance as measured in pixel values is defined as

$$\sigma^2(\lambda) = I_{PV}(\lambda)/\Delta e \ + \sigma^2_{r+d}. \tag{5.10}$$

The first term on the right-hand side of Eq. 5.10 is the shot noise contribution and the second term is the readout contribution to the total noise. The CCD well depth was determined by fitting the theoretical expression for shot noise to the measured shot noise, using Δe as the fitting parameter, and limiting the fit to the central 700 pixels. From this measurement, Δe was calculated to be 173 electrons. Assuming that the maximum pixel value corresponds to the full well depth, a well depth of 177,000 electrons was calculated, in agreement with our previously published result [10]. Shot noise dominated readout and dark noise when the intensity reached 6 % of the saturation value. Relative intensity noise (RIN) is never dominant in this setup, since the maximum power per pixel (4.6 nW) at a 34.1 μs integration time does not meet the criteria for RIN-dominated noise [10].

5.1.7 Remapping to k-Space, Sensitivity Drop-Off as a Function of Depth, Spectrometer Resolution, Fixed Pattern Noise Removal

In SD-OCT, the structural information, i.e., the depth profile (A-line), is obtained by Fourier transforming the optical spectrum of the interference as measured by a spectrometer at the output of a Michelson interferometer [3, 9]. Fourier transformation relates the physical distance (z) with the wave number ($k = 2\pi/\lambda$). The spectra obtained with SD-OCT are not necessarily evenly spaced in k-space. A proper depth profile can be obtained only after preprocessing to obtain data that is evenly spaced in k-space [9], and this requires accurate assessment of the wavelength corresponding to each spectral element.

Determination of this wavelength mapping is typically performed using separate measurements of a reflective surface at different positions in the sample arm [9, 26]. The importance of proper wavelength assignment for SD-OCT was first noted by Wojtkowski et al. [9]. Incorrect wavelength mapping generates a depth-dependent broadening of the coherence peak similar in appearance to dispersion in structural OCT images. The disadvantage of such calibration methods is that they typically require separate measurements of a reflective surface. Using the example of a clinical ophthalmic system, calibration data from a model eye are acquired

before or after imaging of the patient in order to later determine the appropriate wavelength mapping. The calibration procedure may be necessary for each measurement session due to thermal and mechanical instabilities of the spectrometer, which is not practical in a clinical setting. Recently we proposed an autocalibration technique wherein the calibration data does not have to be acquired separately, but is contained within the data of interest [27].

Proper wavelength assignment can be achieved by imposing onto the spectrum a known modulation that can be used for calibration. In the system presented here, we introduce a perfect sinusoidal modulation as a function of k by passing the light through a microscope cover slip in the interferometer's source arm. This slide creates spectral modulation by combining the light that passes directly through the glass with the light that is internally reflected twice before transmission. The interference can be characterized by an optical path mismatch of $2dn$, where n is the refractive index and d is the thickness of the glass cover slip, and is of the form $\cos(2dnk)$. This spectral modulation is a perfect cosine as a function of k, assuming that n is independent of the wavelength for the bandwidth of the light source.

The presence of this spectral modulation is key in assigning the correct wavelength to each pixel of the CCD in the spectrometer case. In general, the pixels do not correspond to evenly distributed k, and therefore, the detected intensity modulation is not a perfect sinusoid. The autocalibration technique alters the wavelength assignments until the resulting spectral modulation matches a perfect sinusoid as a function of k. This sinusoidal intensity modulation produces in all A-lines an identical strong peak along z corresponding to the optical thickness of the slide. This peak can be easily removed as fixed pattern noise from the structural intensity images in a patient scan.

Figure 5.4a shows a typical intensity modulation generated by the slide for the spectrum of a Ti:sapphire laser (INTEGRAL OCT, FEMTOLASERS, Austria) with a spectral bandwidth of 150 nm centered at 800 nm. This spectrum has been obtained from a patient scan by taking the mean of 1,000 spectra corresponding to one OCT image. The interference fringes resulting from the retinal structure are washed out in this mean, while the fringes from the slide in the source arm are unaffected since they are the same in each spectrum. The spectral interference fringes from the slide are isolated with a band-pass filter in Fourier space, and the result is shown in Fig. 5.4b in the CCD pixel space. By keeping only the peak from the slide, we also remove the DC component of the spectral interference, illustrated in Fig. 5.4b as a zero-mean interferogram. When represented as a function of k, the fringes in Fig. 5.4b should be perfectly periodic. For a perfect sinusoid, the phase, or the argument of the sinusoidal oscillation, is linearly related to k. This condition is used to determine the accuracy of the wavelength assignment; an improper wavelength assignment results in phase nonlinearity as a function of k. The wavelength mapping is determined by minimizing the nonlinearity of this phase. An initial estimate of the wavelength array W is generated using the grating equation based on the geometrical design of the spectrometer [26] or, alternatively, with a third-order polynomial bringing the generated wavelengths in the spectral range of the light source. W is used to interpolate the spectral interference fringes to equally spaced

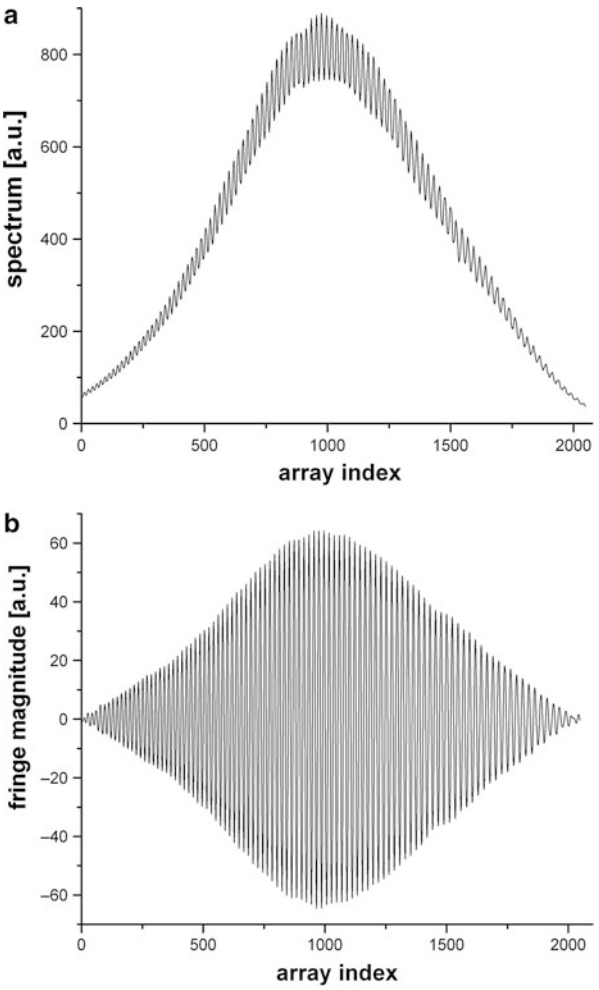

Fig. 5.4 (**a**) Spectrum (in arbitrary units) of interference generated by the slide as a function of the index of the CCD pixels. The spectrum was obtained by averaging 1,000 spectra from a retinal scan of a patient. Since the retinal structural information changes in each consecutive spectrum, but the spectral modulation by the glass cover slip is constant, only the spectral modulation by the cover slip is retained after averaging 1,000 spectra. (**b**) Spectral interference fringes (in arbitrary units) corresponding to the slide, shown in CCD pixel space (Reproduced from Ref. [27] with permission from SPIE)

k values. The quality of this interpolation process is improved by zero padding the spectrum. The next step is to iteratively determine and apply corrections to the wavelength assignment by reducing the phase nonlinearity. The phase of the zero-padded and k-space interpolated spectrum is determined and fit with a third-order polynomial. The nonlinear part $\sigma(k)$ of the polynomial fit (which only has the quadratic and cubic dependence on k and represents the deviation from a perfect linear phase) is used for correcting the wavelengths W based on the assumption that this nonlinearity is generated by wrong wavelength assignment.

Therefore, we calculate a new k-array k', starting from the previous $k = 2\pi/W$ array and $\sigma(k)$, using the equation $k' = k + \sigma(k)/z_{peak}$, where z_{peak} is given by $z_{peak} = 2\pi\text{Peak_Index}/(k_{\max} - k_{\min})$. Peak_Index is the location of the coherence

peak corresponding to the slide in index space, and k_{max} and k_{min} are the extremes of k. This correction is applied iteratively to the original spectral interference, and the final result is the wavelength array $W' = 2\pi/k'$ that corresponds to basically linear phase as a function of k'. The condition to be met in order to exit the loop could be either a maximum number of iterations or a tolerance in the change of the wavelength array after each iteration. The wavelength array W' can now be used to map the spectrometer data to the correct k values for processing the data into depth profiles.

5.1.8 Dispersion Compensation

One difficulty that arises from using ultra-broadband sources in a fiber-based OCT setup is chromatic dispersion in optically dense materials like glass, tissue, and water. The speed of light depends on the refractive index *n(k)* of the material, slowing down certain spectral components to a greater extent than others, hence dispersing the light. The total amount of dispersion increases linearly with length of the dispersive medium as well. Chromatic dispersion in air is negligible. Considerable amounts of dispersion can be tolerated if the dispersion in the two arms of the interferometer is equal, thus creating a coherence function that will be free of dispersion artifacts. However, when sample and reference arms contain different lengths of optical fiber or other dispersive media, a dispersion mismatch occurs. In the sample arm, the introduction of an eye with unknown axial length creates a similar effect. The coherence function will not only be broadened by unbalanced dispersion, but its peak intensity will decrease as well [28]. Second-order or group-velocity dispersion can be compensated for by changing the lens to grating distance in a rapid-scanning optical delay line [29]. However, this method does not compensate for higher orders of dispersion. Alternatively, one can balance dispersion in an OCT system by inserting variable-thickness BK7 and fused silica prisms in the reference arm [30]. The previously mentioned unknown factor introduced by an eye with unknown axial length requires a flexible method for dispersion compensation. An alternative to compensation in hardware is dispersion compensation in software. De Boer et al. induced dispersion in the delay line of a TD-OCT system equipped with an optical amplifier-based source (AFC technologies, $\lambda_0 = 1{,}310$ nm, $\Delta\lambda = 75$ nm) and compensated for dispersion artifacts in structural intensity images obtained in an onion [31]. Fercher et al. compensated for dispersion induced by a glass sample [32, 33]. Other dispersion compensation algorithms are described by Marks et al. [34, 35]. Below we will give an example of compensation in software for dispersion induced by an ultra-broadband source and remove artifacts from retina data [12]. A nearly identical approach was virtually simultaneously published [13].

A dispersion mismatch introduces a phase shift $e^{i\theta(k)}$ in the complex cross-spectral density *I(k)* as a function of wave vector. Since spectrometer data is acquired as a function of wavelength, data has to be transformed to *k*-space first

as detailed above. The relation between the phase $\theta(k)$ and the multiple orders of dispersion can best be described by a Taylor series expansion:

$$\theta(k) = \theta(k_0) + \left.\frac{\partial\theta(k)}{\partial k}\right|_{k_0}(k_0 - k) + \frac{1}{2}\cdot\left.\frac{\partial^2\theta(k)}{\partial k^2}\right|_{k_0}(k_0 - k)^2 + \ldots + \frac{1}{n!}\cdot\left.\frac{\partial^n\theta(k)}{\partial k^n}\right|_{k_0}(k_0 - k)^n \tag{5.11}$$

with λ_0 the center wavelength and k_0 equal to $2\pi/\lambda_0$. The first two terms describe a constant offset and group velocity, respectively, and are not related to dispersive broadening. The third term represents second-order or group-velocity dispersion. Dispersion mismatch in sample and reference arms is largely compensated by this term, although adjustment of higher-order dispersion can be necessary as well, especially when an ultra-broadband source is used. Dispersion can be removed by multiplying the dispersed cross-spectral density function $I(k)$ with a phase term $e^{-i\theta(k)}$.

We will illustrate a method to obtain the phase term $e^{-i\theta(k)}$. To determine this phase term for dispersion compensation of data obtained in the human eye in vivo requires a coherence function obtained from a well-reflecting reference point in the eye. We found that it is possible to use the center of the fovea (foveal umbo) for this purpose because this part of the eye acts as a good reflector [12]. To determine the phase term, after linear interpolation to k-space, the spectrum is Fourier transformed to z-space, where it is shifted such that the coherence function is centered on the origin. A complex spectrum in k-space is obtained after an inverse Fourier transformation. The phase term $\theta(k)$ is equal to the arctangent of the imaginary component divided by the real component and indicates how much subsequent wave numbers k are out of phase with each other. This function was fit to a polynomial expression of the 9th order, yielding a set of coefficients α_{1-9}. Individual spectra obtained from a volunteer were first multiplied with a phase $e^{-i\theta(k)}$ as determined from the last seven polynomial coefficients and then inversely Fourier transformed into A-lines, thus removing dispersion.

The source was a BroadLighter (Superlum, Russia), in which two super luminescent diodes at center wavelengths of approximately 840 nm and 920 nm were combined in one system with a center wavelength of 890 nm, an FWHM bandwidth of over 150 nm, and an optical output power of approximately 4.5 mW. Figure 5.5 shows the source spectrum and a reference arm spectrum that were recorded with a commercial optical spectrum analyzer (OSA). The reference spectrum was also recorded with our high-speed spectrometer (HS-OSA). By comparing the blue and red curves of Fig. 5.5, one can see a significant drop in sensitivity of the line scan camera above 850 nm. The plot amplitudes are adjusted so that all three curves fit within the same graph.

A detailed description and drawing of our setup can be found in our earlier work [10, 11]. In order to compensate for dispersion, coherence functions were obtained from a reflecting spot in the foveal umbo of a human eye, from a mirror in a

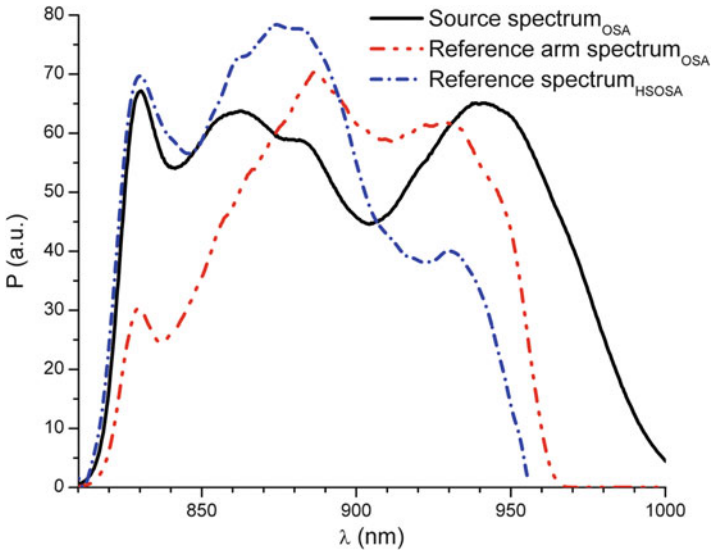

Fig. 5.5 Source spectrum of the BroadLighter (*black*); spectrum returning from the reference arm (*red*). Both spectra were measured with a commercial optical spectrum analyzer. The reference spectrum in blue was recorded with our high-speed spectrometer, and by comparing the blue and red line, it demonstrates the decrease in sensitivity of the line scan camera above 850 nm. Spectrum amplitudes were adjusted so that all three curves fit within the same graph (Reproduced from Ref. [12] with permission from the Optical Society of America)

water-filled model eye (Eyetech Ltd.) and a mirror in air. In vivo measurements were performed on the undilated right eye of a healthy volunteer. The right eye was stabilized using an external fixation spot for the volunteer's collateral eye. Multiple sets of B-scans were taken in the macular area. B-scans that contain specular reflections from the foveal surface were analyzed in detail to compensate for dispersion.

In the graph of Fig. 5.6, the phase term $\theta(k)$, obtained from a mirror in a model eye (black line, averaged over 100 A-lines) and from a specular reflective spot in the fovea (red line, averaged over 5 A-lines), is shown. The quadratic phase term (group-velocity dispersion) was minimized in hardware by a rapid-scanning optical delay line (RSOD) [29]. Figure 5.6 shows that the dispersion is dominated by a cubic phase term. The differences between the measured phase terms and polynomial fits (9th order) to the data are shown as well (light and dark blue lines), with the corresponding axis on the right. Both phases show the same pattern, which indicates that both the model eye and the real eye experience similar amounts of dispersion. The in vivo image shown in Fig. 5.7 was compensated using the phase that was obtained from the specular reflection of the fovea itself (red curve of Fig. 5.6).

In the graph of Fig. 5.8, the coherence function obtained from a mirror in air is plotted. The data shows the amplitude as a function of depth, where the amplitude is given by the absolute value of the Fourier components after transform of the measured spectrum. In the same graph, a coherence function compensated for dispersion is plotted. For this plot, the same technique as applied in Fig. 5.6 was

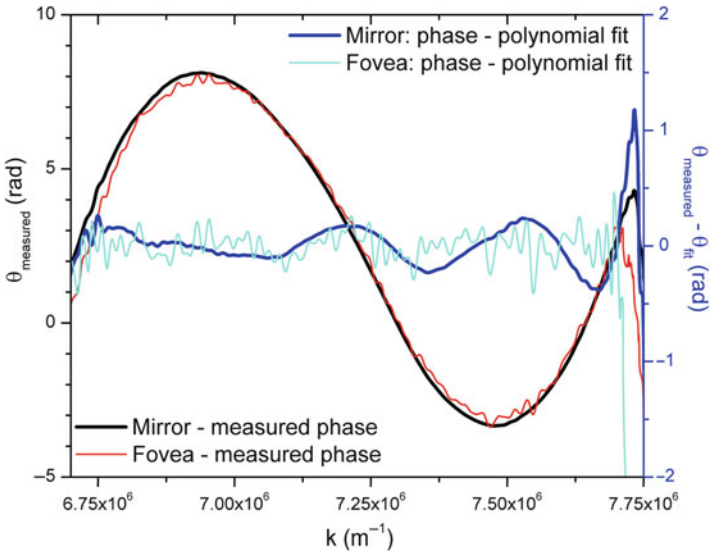

Fig. 5.6 The phase $\theta(k)$ obtained from a mirror in a model eye and from a specular reflection in the fovea (*left axis*). The residual dispersion not compensated for by the polynomial fit is given as a function of k (*right axis*) (Reproduced from Ref. [12] with permission from the Optical Society of America)

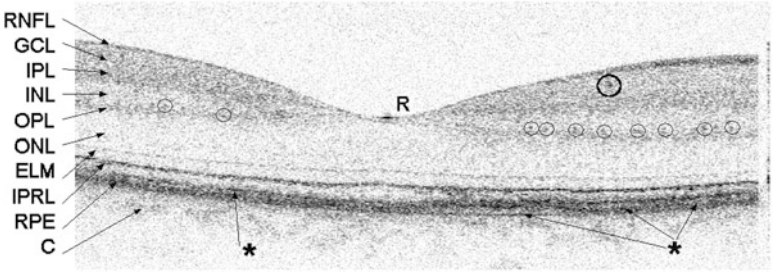

Fig. 5.7 Structural image of the fovea. The dimension of the image is 3.1 × 0.61 mm. The image is expanded in vertical direction by a factor of 2.5 for clarity. Layers are labeled as follows: *RNFL* retinal nerve fiber layer, *GCL* ganglion cell layer, *IPL* inner plexiform layer, *INL* inner nuclear layer, *OPL* outer plexiform layer, *ONL* outer nuclear layer, *ELM* external limiting membrane, *IPRL* interface between the inner and outer segments of the photoreceptor layer, *RPE* retinal pigmented epithelium, *C* choriocapillaris and choroid. A highly reflective spot in the center of the fovea is marked with an *R*. A blood vessel is marked with a large circle (*BV*). Small highly reflecting black dots can be seen in the outer plexiform layer (marked with smaller *circles*). We conclude that they are not caused by speckle because they consistently appear at the same location over consecutive images. The dots seem to be almost regularly spaced in the outer plexiform layer. We believe that these black dots are very small blood vessels. Snodderly et al. measured the distribution of blood vessels in an enucleated macaque eye by means of microscopy in frozen samples [36]. They report a very similar spacing of small blood vessels in the plexiform layers near the fovea. Two layers at the location of the RPE at the left and right are marked with *arrows* and an *asterisk* (*) (Reproduced from Ref. [12] with permission from the Optical Society of America)

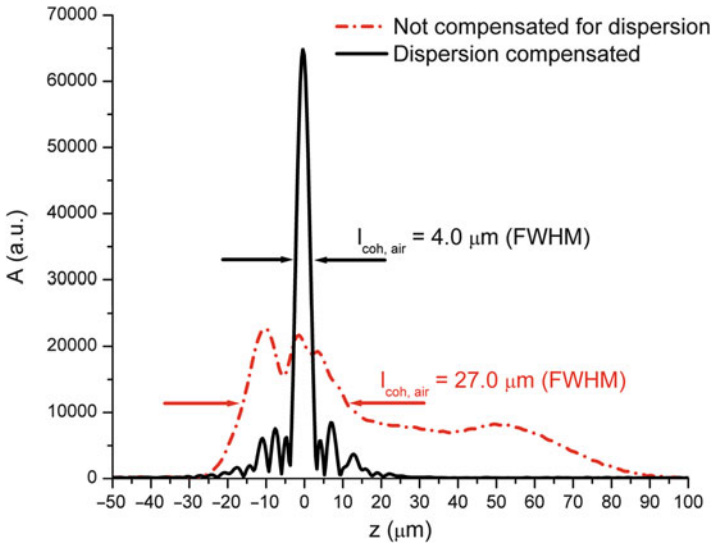

Fig. 5.8 Coherence function obtained from a mirror in air. Uncompensated data (*red*) is compared with a coherence function after dispersion compensation (*black*). The density of points was increased by a factor of 8 using a zero-padding technique (Reproduced from Ref. [12] with permission from the Optical Society of America)

used, yielding a different set of coefficients, since the mirror was not located in the water-filled model eye.

The dispersion compensation technique gives a significant reduction in coherence length as well as a threefold increase in peak height. Without dispersion compensation, the coherence length was 27.0 μm. After dispersion compensation it was estimated to be 4.0 μm ($n = 1$), equivalent to 2.9 μm in tissue with a refractive index of $n = 1.38$. After dispersion compensation, side lobes are present at both sides of the coherence function. These side lobes are a result of the non-Gaussian-shaped reference arm spectrum (Fig. 5.5).

An alternative method to compensate for dispersion exploits the observation that the maximum peak height is achieved when the dispersion compensation is optimized [13, 37]. In this method, the variance of an OCT image is calculated, and the variance is used as a figure of merit for optimal dispersion compensation. In an iterative procedure, quadratic dispersion is introduced to maximize the variance. Next, cubic and higher-order dispersion terms can be optimized for. The advantage of this method is that it does not require a priori knowledge of the dispersion in the system.

5.1.9 Fixed Pattern Noise Removal

The interference of sample with reference arm light generates a modulation of the spectrum that is associated with structural properties of the sample

(second term in Eq. 5.6). There are other effects that cause modulation of the spectrum, which can lead to structural artifacts in SD-OCT images. Many of these modulations are constant or fixed over many spectra. Examples are variations in the response of pixels in the CCD camera or spurious etalons in the interferometer, such as the deliberately introduced cover slip in the section **remapping to k-space** to calibrate the mapping to wave vector (see Fig. 5.4). The artifacts or fixed pattern noise associated with constant modulations of the spectra can be removed by generating a reference spectrum, either by a recording of the reference arm spectrum or by averaging many spectra of an actual measurement. The latter method assumes that spectral modulation caused by structural information changes from spectrum to spectrum by translating the sample arm beam over the sample to generate a 2-D image. The reference spectrum can be subtracted from each spectrum. In a slightly improved version of the fixed pattern removal algorithm, for each image, two background spectra are generated: one by averaging all spectra from that image and the second by subsequently low-pass filtering this averaged spectrum to represent a smooth source spectrum. Each individual spectrum is then divided by the averaged background spectrum and then multiplied by the smoothed spectrum [11]. The latter method has the advantage of removing sidebands generated by particularly strong fixed spectral modulations.

5.1.10 Post Processing

After acquisition data is first processed to remove fixed pattern noise as described above. Next, spectrometer data is mapped as a linear function of k prior to Fourier transformation to recover the depth information. Mapping errors due to linear interpolation can appear at greater depths as an increased background signal or shoulders around the peaks [8, 38]. This error can be corrected by using a zero-filling technique [38] to quadruple the number of points in the spectrum. This correction included Fourier transformation, zero padding to increase the data array length fourfold, and inverse Fourier transformation back to the spectral domain but with 4 times as many points in the data array compared to the original. This spectrum was then linearly interpolated in k-space [9] and Fourier transformed into z-space to recover the depth profile, free of shoulders at longer depths. Results of this procedure are shown in Fig. 5.9.

5.1.11 Depth-Dependent Sensitivity

In SD-OCT, signal sensitivity is strongly dependent on depth within an image. To characterize system sensitivity as a function of ranging depth, 1,000 A-lines were acquired at an acquisition speed of 34.1 μs/A-line for nine different positions of a weak reflector in the sample arm. The reflected sample arm power was 1.18 nW for all reflector positions. The noise floor without zero padding decayed by 5 dB between a depth of 500 μm and 2 mm, and the peak signal dropped by 21.7 dB over the first 2 mm. Due to fixed pattern noise, the true noise floor could not be

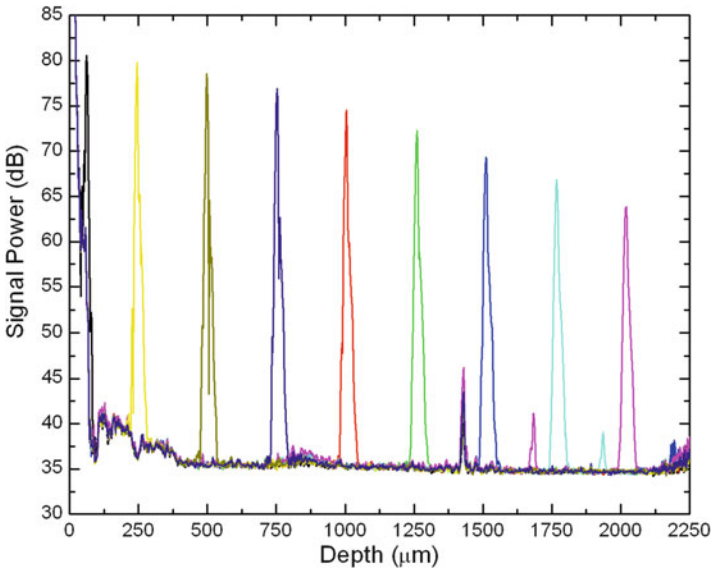

Fig. 5.9 The depth-dependent loss in signal sensitivity from a weak reflector. The signal decayed 16.7 dB between 0 and 2 mm. The peaks at 1.4 mm, 1.6 mm, and 1.85 mm are fixed pattern noise (Reproduced from Ref. [11] with permission from the Optical Society of America)

determined between 0 and 500 μm. The removal of fixed pattern noise as described above was not applied to this sensitivity measurement. After zero-filling to correct mapping errors as described above, a 16.7-dB loss in peak signal was noted across the first 2 mm, whereas the noise level dropped by only 0.4 dB between 500 μm (35.1 dB) and 2 mm (34.7 dB) (Fig. 5.9). The zero-filling method produced a nearly constant noise level and improved the signal by more than 5 dB at the greatest depths in the scan. Although zero-filling did not change the local SNR, this method eliminated the shoulders that are present at larger scan depths [8]. The decay in both the signal and the noise level across the entire scan length of 2.4 mm has been theorized to amount to 4 dB as a result of the finite pixel width [6]. As demonstrated by the experimental data, the noise level decayed by less than 4 dB over the entire scan length, which we attribute to the statistical independence of the shot noise between neighboring pixels of the array. Thus, the finite pixel width does not introduce a decay of the noise level.

The finite spectrometer resolution introduces a sensitivity decay [24] similar to that introduced by the finite pixel size [6]. Convolution of the finite pixel size with the Gaussian spectral resolution yields the following expression for the sensitivity reduction, R, as a function of imaging depth, z [24]:

$$R(z) = \frac{sin^2(\pi z/2d)}{(\pi z/2d)^2} \exp\left[-\frac{\pi^2\omega^2}{8\ln 2}\left(\frac{z}{d}\right)^2\right] \tag{5.12}$$

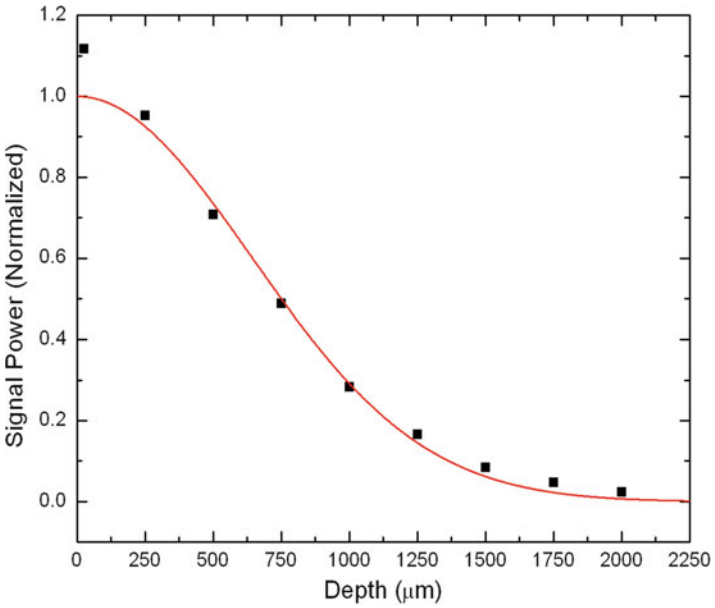

Fig. 5.10 Decay of sensitivity across the measurement range. Symbols: peak intensities of data presented in Fig. 5.9. Solid line: fit of Eq. 5.12 to the data points (Reproduced from Ref. [11] with permission from the Optical Society of America)

where d is the maximum scan depth and ω is the ratio of the spectral resolution to the sampling interval. Equation 5.12 was fit to the signal decay data presented in Fig. 5.9 with ω as a free parameter and the result shown in Fig. 5.10. Due to its proximity to the autocorrelation peak, the first data point was not included in the fit. The value for ω obtained from the fit was 1.85, demonstrating that the working spectral resolution was 0.139 nm.

The SNR was determined by the ratio of the peak at 250 μm (79.8 dB) and the noise level. Due to the fixed pattern noise at 250 μm, the noise level was determined to be 35.2 dB by extrapolation of the linear region between 0.5 and 2 mm. The resulting SNR of 44.6 dB for 1.18 nW returning to the detection arm was 2.2 dB below the theoretical value given by Eq. 5.8 of 46.8 dB, for an integration time of 34.1 μs, a central wavelength of 840 nm, and a spectrometer efficiency of 28 %. With 600 μW of power incident on an ideal reflector in the sample arm, the measured power returning to the detection arm was 284 μW. The sum of the SNR at 1.18 nW (44.6 dB) and the 10 Log ratio of maximum (284 μW) over measured (1.18 nW) power (53.8 dB) gives a sensitivity of 98.4 dB.

5.1.12 Motion Artifacts and Fringe Washout

As OCT utilizes lateral point scanning, motion of the sample or scanning beam during the measurement causes SNR reduction and image degradation in SD-OCT

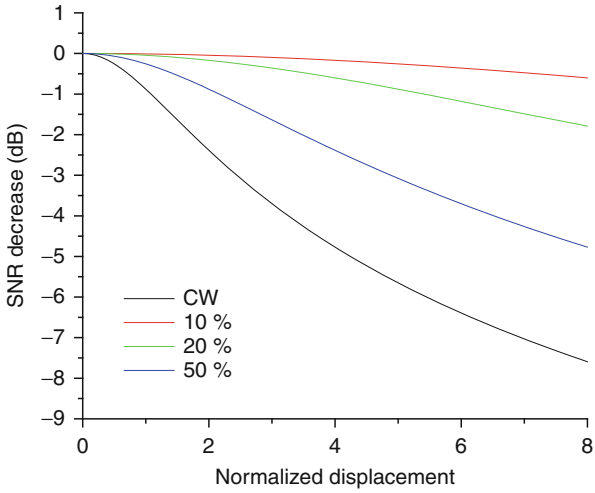

Fig. 5.11 Theoretical SNR decrease due to lateral motion for a CW source and for pulsed illumination with different duty cycles (Reproduced from Ref. [42] with permission from the Optical Society of America)

and OFDI [39]. Yun et al. theoretically investigated axial and lateral motion artifacts in continuous wave (CW) SD-OCT and swept-source OFDI and experimentally demonstrated reduced axial and lateral motion artifacts using a pulsed source and a swept source in endoscopic imaging of biological tissue [39, 40]. Stroboscopic illumination in full-field OCT was demonstrated, resulting in reduced motion artifacts for in vivo measurement [41]. In ophthalmic applications of SD-OCT, SNR reduction caused by high-speed lateral scanning of the beam over the retina may be dominant over axial patient motion. Using pulsed illumination can reduce lateral motion artifacts. We analyzed the SNR benefit of pulsed illumination over CW SD-OCT, demonstrating that pulsed illumination provides a better SNR for in vivo high-speed human retinal imaging.

For a CW source, the SNR decrease is given by [39]

$$\text{SNR decrease} \cong -5\log_{10}\left(1 + 0.5\frac{\Delta x^2}{{w_o}^2}\right), \tag{5.13}$$

where Δx is the scanning distance during the camera integration time and w_o denotes full width at half maximum (FWHM) of the beam profile. The normalized displacement is defined as $\Delta x/w_o$. For pulsed illumination, Δx is replaced by $(\tau_{pulse}/\tau_{camera})\cdot\ \Delta x$, where τ_{pulse} is the pulse width in time and τ_{camera} is the integration time of the camera for a single A-line. As can be seen in Fig. 5.11, pulsed-illumination SD-OCT has a significant SNR benefit over CW SD-OCT when the displacement Δx is larger than the FWHM w_o of the beam profile with the same average power. For example, at a normalized displacement of 4, a 20 % duty cycle pulsed illumination has a 4.2 dB better SNR than CW illumination.

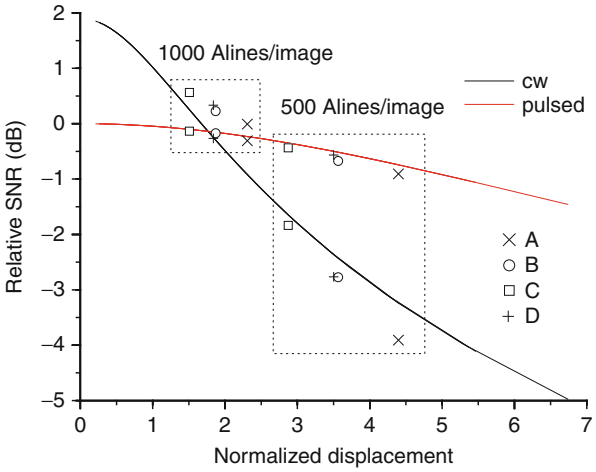

Fig. 5.12 Relative SNR for CW and pulsed illumination, fitted with w_o and offset as parameters for the four different zones *A–D* as a function of normalized displacement. The theoretical fit for CW illumination (*continuous line*) starts 1.9 dB above the theoretical fit for pulsed illumination (*dotted line*) because of the higher average CW power. Despite the lower average power for pulsed illumination, the SNR is better for normalized displacements larger than 2 (Reproduced from Ref. [42] with permission from the Optical Society of America)

Figure 5.11 also shows that for CW illumination, a normalized displacement of 1 gives 1 dB decrease in SNR. At a source center wavelength of 841 nm, an axial motion of 50 nm per A-line would also result in a 1-dB SNR reduction [39]. At an A-line rate of 29.3 kHz, this corresponds to an axial velocity of about 1.5 mm/s, which for retinal imaging is, in general, much higher than encountered in practice.

According to the ANSI standard for safe use of lasers, the maximum permissible exposure expressed as the average power of a pulse train depends on the repetition rate and increases with the pulse repetition rate up to a frequency of 55 kHz, where the limit to continuous wave exposure is reached. Due to this safety restriction, the average power for pulsed illumination was lower than the average power for CW illumination in these experiments [42]. The sample arm power after the slit lamp of CW and pulsed illumination was set to 600 μW and 385 μW, respectively. The 385 μW average power for pulsed illumination will cause a 1.9 dB smaller SNR compared to the 600 μW for CW. This has been accounted for in the SNR analysis comparing pulsed and CW illumination.

Pulsed illumination was applied to human retinal imaging, and the SNR was analyzed by direct comparison with CW illumination. The pulse width was 8 μs and the pulse repetition rate was 29.3 KHz, synchronized with the integration time of the high-speed line scan camera. Four different zones (A–D) on the retina were analyzed. The actual scan range was 8.6 mm on the retina and the normalized displacement was calculated based on a fit of a constant spot size within each zone

to the data for two different lateral scan speeds (500 and 1,000 A-lines over the 8.6-mm scan range), giving two different normalized displacements in each of the four zones (A–D). The normalized displacement is slightly different in each zone due to the variation of w_o. The SNR values in each zone and the theory are shown in Fig. 5.12.

The 1.9 dB better relative SNR for CW illumination over pulsed illumination at zero normalized displacement in Fig. 5.12 reflects the higher average power permitted under the ANSI standards. We can see that the SNR was almost the same at 1,000 A-lines per image with CW and pulsed illumination, but it was 1.4–3.0 dB higher with pulsed illumination for larger normalized displacement. The variation in beam diameter is attributed to a difference in curvature between the retina and the focal plane of the imaging system, where the best overlap between retina and focal plane was realized in zone A, good overlap was realized in zones B and D, and the worst overlap was realized in zone C.

5.1.13 The Effect of Pulsed Illumination on RIN

One consideration that should be taken into account is that shortening the pulse length while maintaining average power and pulse repetition rate will decrease the lateral motion artifact but also increases the ratio of RIN over shot noise. For a shot noise limited system, this ratio needs to be smaller than 1. Using Eq. 5.2 in ref [10] and replacing P_{ref} with J_p/τ_i, with J_p the energy of the pulse and τ_i the pulse duration, gives

$$\sigma^2_{\text{noise}} = \sigma^2_{r+d} + \frac{\eta e^2 J_p}{E_v} + \left(\frac{\eta e J_p}{E_v \tau_i}\right)^2 \tau_i \tau_{coh} \quad \left[e^2\right] \tag{5.14}$$

The reference arm pulse energy J_p to saturate the spectrometer to 90 % of the full well capacity is independent of pulse length. The pulse energy for which the shot noise still dominates over RIN is given by $J_p < \frac{E_v \tau_i}{\eta \tau_{coh}}$, which shows that reducing the pulse length also reduces this pulse energy. In our case of an 8 μs pulse length, the pulse energy is still more than a factor of two below the value where RIN is equal to shot noise [10].

5.1.14 Phase Stability and Doppler

In the past, phase-resolved optical Doppler tomography (ODT) based on time domain OCT (TD-OCT) has proven able to make high-resolution, high-velocity-sensitivity cross-sectional images of in vivo blood flow [43–48]. ODT measurements of blood flow in the human retina have been demonstrated [49, 50],

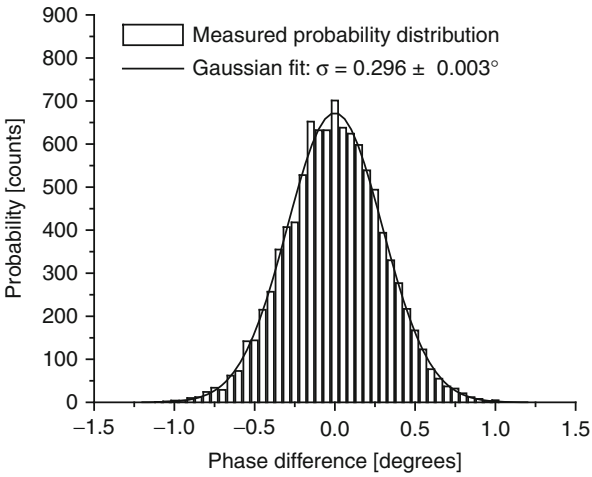

Fig. 5.13 Probability distribution of the measured phase difference between adjacent A-lines, with a stationary reflector in the sample arm. *Bars*: counted phase difference for 9990 A-lines. Bin size = 0.05°. *Solid line*: Gaussian fit to the distribution, with a measured standard deviation of 0.296 ± 0.003° (Reproduced from Ref. [15] with permission from the Optical Society of America)

yet the accuracy and sensitivity were compromised by A-line rate and patient motion artifacts, which can introduce phase inaccuracy and obscure true retinal topography. Combining optical Doppler tomography with the superior sensitivity and speed of SD-OCT has allowed a significant improvement in detecting Doppler signals in vivo. In the first combination of these technologies, velocity of a moving mirror and capillary tube flow was demonstrated [51], followed by in vivo demonstration of retinal blood flow [14, 15].

In SD-OCT, a phase-sensitive image is generated by simply determining the phase difference between points at the same depth in adjacent A-lines. This parallels the time domain method pioneered by Zhao et al. [43, 44]. The superior phase stability of SD-OCT, due to the absence of moving parts, is demonstrated in Fig. 5.13. The data was acquired with a stationary mirror in the sample arm, without scanning the incident beam. Ideally, interference between sample and reference arm light should have identical phase at the mirror position for all A-lines. This condition underlies the assumption that any phase difference between adjacent A-lines is solely due to motion within the sample. The actual phase varies in a Gaussian manner about this ideal, as demonstrated in Fig. 5.13, where we present the measured probability distribution of phase differences with a standard deviation of 0.296 ± 0.003°. This value is over 25 times lower than previously quantified figures for time domain optical Doppler tomography systems [31, 48] and at an acquisition speed of 29 kHz corresponds to a minimum detectable Doppler shift of ±25 Hz. With a time difference of 34.1 μs between acquired A-lines, phase wrapping occurs at Doppler shifts greater than 15 kHz. Thus, the system dynamic range described by the ratio of maximum to minimum detectable Doppler shifts before phase wrapping occurs is a factor of 600.

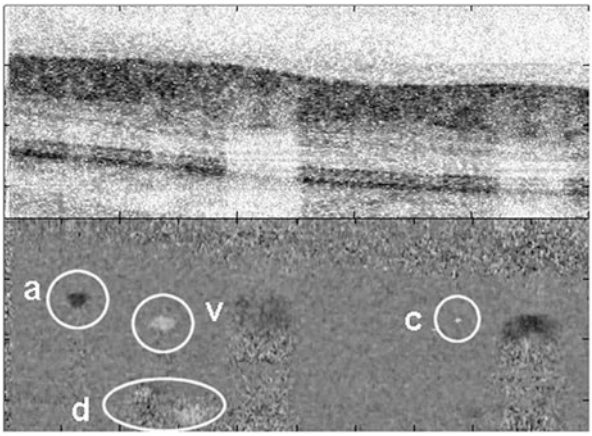

Fig. 5.14 Movie of structure (*top panel*) and bidirectional flow (*bottom panel*) acquired in vivo in the human eye at a rate of 29 frames per second. The sequence contained 95 frames, totaling 3.28 s (See Ref. [15]). Image size is 1.6 mm wide by 580 μm deep. *a* artery, *v* vein, *c* capillary, *d* choroidal vessel (Reproduced from Ref. [15] with permission from the Optical Society of America)

In vivo images of structure and Doppler flow were acquired at 29 frames per second (1,000 A-lines per frame) and subsequently processed. The images presented in Fig. 5.14 are 1.6 mm wide and have been cropped in depth to 580 μm, from their original size of 1.7 mm. The layers of the retina visible in the intensity image have been identified and described previously [19], with the thick, uppermost layer being the nerve fiber layer and the thinner, strongly scattering deep layer being the retinal pigmented epithelium. One can see the pulsatility of blood flow in the artery (a), while the flow in the vein (v) is less variable (See Ref. [15]). At the lower left center of the image, it is possible to distinguish blood flow deep within the retina (d). With reference to the intensity image, one can see that this blood flow is being detected *below* the retinal pigmented epithelium, and we believe this is the first time that optical Doppler tomography imaging techniques have been able to observe and localize blood flow within the choroid. To the left of the large vessel on the right-hand side of the image, note the appearance of a very small vessel (c). The diameter of this vessel is slightly under 10 μm.

5.1.15 Retinal Imaging with SD-OCT

Many examples of retinal imaging with SD-OCT are available in the literature. Commercial systems are being introduced into the market at this point. Below, two typical examples of high-quality SD-OCT images are presented, acquired with a system providing a depth resolution of 3 μm in tissue. Both figures consist of approximately 1,000 A-lines or depth profiles. Figure 5.15 shows a cross section centered on the optic nerve head and the corresponding en face image (Fig. 5.16) generated from the 3-D data set. Figure 5.17 shows an image centered on the fovea and the corresponding en face image (Fig. 5.18) generated from the 3-D data set.

Fig. 5.15 High-resolution SD-OCT image of a human retina in vivo, centered on the optic nerve head. The image is magnified in depth by a factor of 2. Image size, 4.662 × 1.541 mm

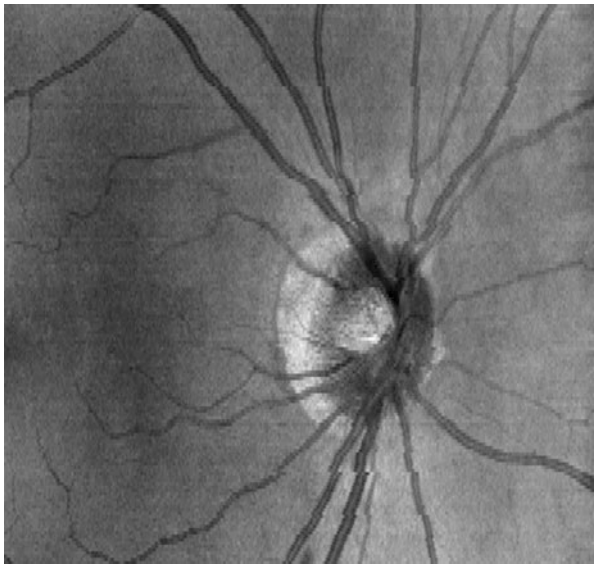

Fig. 5.16 En face reconstruction of the optic nerve head region of the retina from a 3-D volumetric SD-OCT data set of 170 images. Image size, 4.66 × 4.41 mm

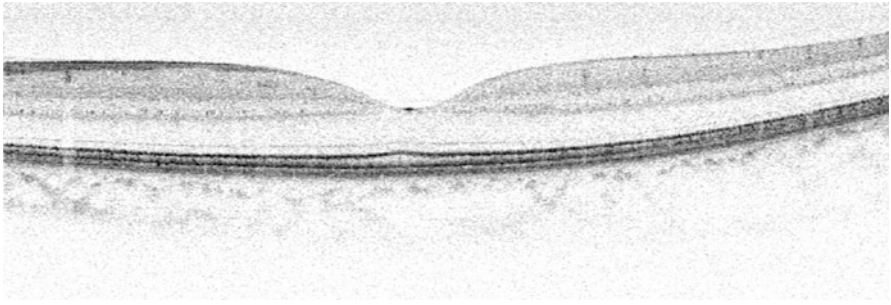

Fig. 5.17 High-resolution SD-OCT image of a human retina in vivo, centered on the fovea. The image is magnified in depth by a factor of 2. Image size, 4.973 × 0.837 mm.

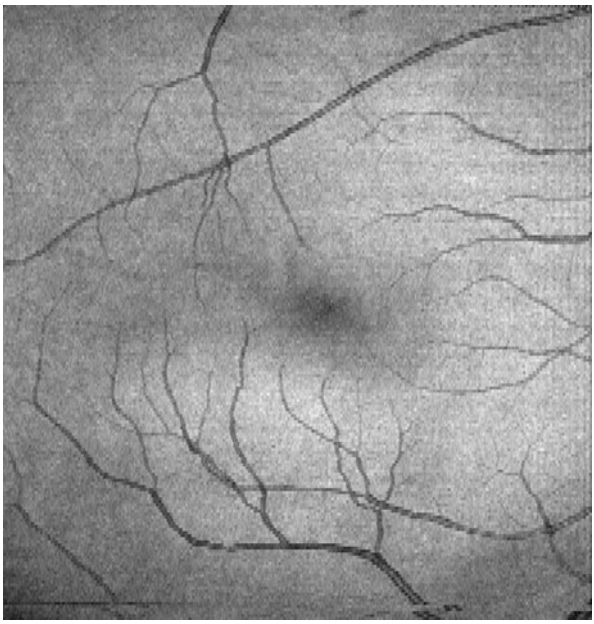

Fig. 5.18 En face reconstruction of the fovea region of the retina from a 3-D volumetric SD-OCT data set of 200 images. Image size, 4.97 × 5.18 mm

5.2 Conclusion

Spectral domain or frequency domain OCT (SD/FD-OCT) has become the preferred method for retinal imaging owing to its high imaging speed [10, 11], enhanced signal-to-noise ratio (SNR) [5–8], and the availability of broadband sources permitting ultrahigh-resolution retinal imaging [12, 13]. However, the state-of-the-art spectrometers are hindering further improvements (1) with limited detection efficiency (∼25 %) [11], and (2) the obtainable spectral resolution causes approximately a 6-dB sensitivity drop over a 1-mm depth range [11]. Furthermore, rapid scanning of the probe beam in SD-OCT has the adverse effect of fringe washout, which causes SNR to decrease [40]. The limited depth range can be addressed by acquiring the complex cross-spectral density as described in the next chapter. Fringe washout can be addressed by pulsed illumination [42]. A competing technique such as optical frequency domain imaging (OFDI), the dominant implementation of Fourier domain OCT technologies at 1.3 μm [52], has the advantage of larger depth range and better immunity to motion artifacts. OFDI has recently been demonstrated in the 800- and 1,050-nm range [53–55], but has not reached the superior resolution of SD-OCT [12, 13].

Acknowledgment This research was supported in part by research grants from the National Institutes of Health (1R24 EY12877, R01 EY014975, and RR19768), Department of Defense (F4 9620-01-1-0014), CIMIT, and a gift from Dr. and Mrs. J.S. Chen to the optical diagnostics program of the Wellman Center of Photomedicine. The author would like to thank a number of

graduate students and postdoctoral fellows that have contributed to the results presented in this chapter, Barry Cense, Nader Nassif, Brian White, Hyle Park, Jang Woo You, and Mircea Mujat. Special thanks to Teresa Chen, MD, my invaluable collaborator at the Massachusetts Eye and Ear Infirmary, without whom all this work would not have been possible.

References

1. A.F. Fercher, K. Mengedoht, W. Werner, Eye-length measurement by interferometry with partially coherent-light. Opt. Lett. **13**(3), 186–188 (1988)
2. D. Huang, E.A. Swanson, C.P. Lin, J.S. Schuman, W.G. Stinson, W. Chang, M.R. Hee, T. Flotte, K. Gregory, C.A. Puliafito, J.G. Fujimoto, Optical coherence tomography. Science **254**(5035), 1178–1181 (1991)
3. A.F. Fercher, C.K. Hitzenberger, G. Kamp, S.Y. Elzaiat, Measurement of intraocular distances by backscattering spectral interferometry. Opt. Commun. **117**(1–2), 43–48 (1995)
4. G. Hausler, M.W. Lindner, Coherence radar and spectral radar – new tools for dermatological diagnosis. J. Biomed. Opt. **3**(1), 21–31 (1998)
5. T. Mitsui, Dynamic range of optical reflectometry with spectral interferometry. Jpn. J. Appl. Phys. **38**(10), 6133–6137 (1999)
6. R. Leitgeb, C.K. Hitzenberger, A.F. Fercher, Performance of fourier domain vs. time domain optical coherence tomography. Opt. Express **11**(8), 889–894 (2003)
7. J.F. de Boer, B. Cense, B.H. Park, M.C. Pierce, G.J. Tearney, B.E. Bouma, Improved signal-to-noise ratio in spectral-domain compared with time-domain optical coherence tomography. Opt. Lett. **28**(21), 2067–2069 (2003)
8. M.A. Choma, M.V. Sarunic, C.H. Yang, J.A. Izatt, Sensitivity advantage of swept source and Fourier domain optical coherence tomography. Opt. Express **11**(18), 2183–2189 (2003)
9. M. Wojtkowski, R. Leitgeb, A. Kowalczyk, T. Bajraszewski, A.F. Fercher, In vivo human retinal imaging by Fourier domain optical coherence tomography. J. Biomed. Opt. **7**(3), 457–463 (2002)
10. N. Nassif, B. Cense, B.H. Park, S.H. Yun, T.C. Chen, B.E. Bouma, G.J. Tearney, J.F. de Boer, In vivo human retinal imaging by ultrahigh-speed spectral domain optical coherence tomography. Opt. Lett. **29**(5), 480–482 (2004)
11. N.A. Nassif, B. Cense, B.H. Park, M.C. Pierce, S.H. Yun, B.E. Bouma, G.J. Tearney, T.C. Chen, J.F. de Boer, In vivo high-resolution video-rate spectral-domain optical coherence tomography of the human retina and optic nerve. Opt. Express **12**(3), 367–376 (2004)
12. B. Cense, N. Nassif, T.C. Chen, M.C. Pierce, S.H. Yun, B.H. Park, B.E. Bouma, G.J. Tearney, J.F. de Boer, Ultrahigh-resolution high-speed retinal imaging using spectral-domain optical coherence tomography. Opt. Express **12**(11), 2435–2447 (2004)
13. M. Wojtkowski, V.J. Srinivasan, T.H. Ko, J.G. Fujimoto, A. Kowalczyk, J.S. Duker, Ultrahigh-resolution, high-speed, Fourier domain optical coherence tomography and methods for dispersion compensation. Opt. Express **12**(11), 2404–2422 (2004)
14. R.A. Leitgeb, L. Schmetterer, W. Drexler, A.F. Fercher, R.J. Zawadzki, T. Bajraszewski, Real-time assessment of retinal blood flow with ultrafast acquisition by color Doppler Fourier domain optical coherence tomography. Opt. Express **11**(23), 3116–3121 (2003)
15. B.R. White, M.C. Pierce, N. Nassif, B. Cense, B.H. Park, G.J. Tearney, B.E. Bouma, T.C. Chen, J.F. de Boer, In vivo dynamic human retinal blood flow imaging using ultra-high-speed spectral domain optical Doppler tomography. Opt. Express **11**(25), 3490–3497 (2003)
16. M. Wojtkowski, T. Bajraszewski, I. Gorczynska, P. Targowski, A. Kowalczyk, W. Wasilewski, C. Radzewicz, Ophthalmic imaging by spectral optical coherence tomography. Am. J. Ophthalmol. **138**(3), 412–419 (2004)
17. T.C. Chen, B. Cense, M.C. Pierce, N. Nassif, B.H. Park, S.H. Yun, B.R. White, B.E. Bouma, G.J. Tearney, J.F. de Boer, Spectral domain optical coherence tomography – ultra-high speed, ultra-high resolution ophthalmic imaging. Arch. Ophthalmol. **123**(12), 1715–1720 (2005)

18. A.F. Fercher, W. Drexler, C.K. Hitzenberger, T. Lasser, Optical coherence tomography – principles and applications. Rep. Prog. Phys. **66**(2), 239–303 (2003)
19. W. Drexler, H. Sattmann, B. Hermann, T.H. Ko, M. Stur, A. Unterhuber, C. Scholda, O. Findl, M. Wirtitsch, J.G. Fujimoto, A.F. Fercher, Enhanced visualization of macular pathology with the use of ultrahigh-resolution optical coherence tomography. Arch. Ophthalmol. **121**(5), 695–706 (2003)
20. American National Standards Institute, *American National Standard for Safe Use of Lasers Z136.1* (Orlando, 2000)
21. A.B.. Vakhtin, K.A. Peterson, W.R. Wood, D.J. Kane, Differential spectral interferometry: an imaging technique for biomedical applications. Opt. Lett. **28**(15), 1332–1334 (2003)
22. W.V. Sorin, D.M. Baney, A simple intensity noise-reduction technique for optical low-coherence reflectometry. IEEE Photon. Technol. Lett. **4**(12), 1404–1406 (1992)
23. L. Mandel, E. Wolf, Measures of bandwidth and coherence time in optics. Proc. Phys. Soc. Lond. **80**(516), 894–897 (1962)
24. S.H. Yun, G.J. Tearney, B.E. Bouma, B.H. Park, J.F. de Boer, High-speed spectral-domain optical coherence tomography at 1.3 mu m wavelength. Opt. Express **11**(26), 3598–3604 (2003)
25. R. Tripathi, N. Nassif, J.S. Nelson, B.H. Park, J.F. de Boer, Spectral shaping for non-Gaussian source spectra in optical coherence tomography. Opt. Lett. **27**(6), 406–408 (2002)
26. B.H. Park, M.C. Pierce, B. Cense, S.H. Yun, M. Mujat, G.J. Tearney, B.E. Bouma, J.F. de Boer, Real-time fiber-based multi-functional spectral-domain optical coherence tomography at 1.3 mu m. Opt. Express **13**(11), 3931–3944 (2005)
27. M. Mujat, B.H. Park, B. Cense, T.C. Chen, J.F. de Boer, Autocalibration of spectral-domain optical coherence tomography spectrometers for in vivo quantitative retinal nerve fiber layer birefringence determination. J. Biomed. Opt. **12**(4), 041205 (2007)
28. C.K. Hitzenberger, A. Baumgartner, W. Drexler, A.F. Fercher, Dispersion effects in partial coherence interferometry: implications for intraocular ranging. J. Biomed. Opt. **4**(1), 144–151 (1999)
29. G.J. Tearney, B.E. Bouma, J.G. Fujimoto, High-speed phase- and group-delay scanning with a grating-based phase control delay line. Opt. Lett. **22**(23), 1811–1813 (1997)
30. W. Drexler, U. Morgner, F.X. Kartner, C. Pitris, S.A. Boppart, X.D. Li, E.P. Ippen, J.G. Fujimoto, In vivo ultrahigh-resolution optical coherence tomography. Opt. Lett. **24**(17), 1221–1223 (1999)
31. J.F. de Boer, C.E. Saxer, J.S. Nelson, Stable carrier generation and phase-resolved digital data processing in optical coherence tomography. Appl. Optics **40**(31), 5787–5790 (2001)
32. A.F. Fercher, C.K. Hitzenberger, M. Sticker, R. Zawadzki, B. Karamata, T. Lasser, Dispersion compensation for optical coherence tomography depth- scan signals by a numerical technique. Opt. Commun. **204**(1–6), 67–74 (2002)
33. A.F. Fercher, C.K. Hitzenberger, M. Sticker, R. Zawadzki, B. Karamata, T. Lasser, Numerical dispersion compensation for partial coherence interferometry and optical coherence tomography. Opt. Express **9**(12), 610–615 (2001)
34. D.L. Marks, A.L. Oldenburg, J.J. Reynolds, S.A. Boppart, Digital algorithm for dispersion correction in optical coherence tomography for homogeneous and stratified media. Appl. Optics **42**(2), 204–217 (2003)
35. D.L. Marks, A.L. Oldenburg, J.J. Reynolds, S.A. Boppart, Autofocus algorithm for dispersion correction in optical coherence tomography. Appl. Optics **42**(16), 3038–3046 (2003)
36. D.M. Snodderly, R.S. Weinhaus, J.C. Choi, Neural vascular relationships in central retina of Macaque Monkeys (Macaca-Fascicularis). J. Neurosci. **12**(4), 1169–1193 (1992)
37. J.F. de Boer, *Systems and methods for imaging a sample*. U.S. Patent 6,980,299, 2005
38. C. Dorrer, N. Belabas, J.P. Likforman, M. Joffre, Spectral resolution and sampling issues in Fourier-transform spectral interferometry. J. Opt. Soc. Am. B-Opt. Phys. **17**(10), 1795–1802 (2000)
39. S.H. Yun, G.J. Tearney, J.F. de Boer, B.E. Bouma, Motion artifacts in optical coherence tomography with frequency-domain ranging. Opt. Express **12**(13), 2977–2998 (2004)

40. S.H. Yun, G.J. Tearney, J.F. de Boer, B.E. Bouma, Pulsed-source and swept-source spectral-domain optical coherence tomography with reduced motion artifacts. Opt. Express **12**(23), 5614–5624 (2004)
41. G. Moneron, A.C. Boccara, A. Dubois, Stroboscopic ultrahigh-resolution full-field optical coherence tomography. Opt. Lett. **30**(11), 1351–1353 (2005)
42. J.W. You, T.C. Chen, M. Mujat, B.H. Park, J.F. de Boer, Pulsed illumination spectral-domain optical coherence tomography for human retinal imaging. Opt. Express **14**(15), 6739–6748 (2006)
43. Y.H. Zhao, Z.P. Chen, C. Saxer, S.H. Xiang, J.F. de Boer, J.S. Nelson, Phase-resolved optical coherence tomography and optical Doppler tomography for imaging blood flow in human skin with fast scanning speed and high velocity sensitivity. Opt. Lett. **25**(2), 114–116 (2000)
44. Y.H. Zhao, Z.P. Chen, C. Saxer, Q.M. Shen, S.H. Xiang, J.F. de Boer, J.S. Nelson, Doppler standard deviation imaging for clinical monitoring of in vivo human skin blood flow. Opt. Lett. **25**(18), 1358–1360 (2000)
45. A.M. Rollins, S. Yazdanfar, J.K. Barton, J.A. Izatt, Real-time in vivo color Doppler optical coherence tomography. J. Biomed. Opt. **7**(1), 123–129 (2002)
46. V. Westphal, S. Yazdanfar, A.M. Rollins, J.A. Izatt, Real-time, high velocity-resolution color Doppler optical coherence tomography. Opt. Lett. **27**(1), 34–36 (2002)
47. Z.H. Ding, Y.H. Zhao, H.W. Ren, J.S. Nelson, Z.P. Chen, Real-time phase-resolved optical coherence tomography and optical Doppler tomography. Opt. Express **10**(5), 236–245 (2002)
48. V.X.D. Yang, M.L. Gordon, B. Qi, J. Pekar, S. Lo, E. Seng-Yue, A. Mok, B.C. Wilson, I.A. Vitkin, High speed, wide velocity dynamic range Doppler optical coherence tomography (Part I): system design, signal processing, and performance. Opt. Express **11**(7), 794–809 (2003)
49. S. Yazdanfar, A.M. Rollins, J.A. Izatt, Imaging and velocimetry of the human retinal circulation with color Doppler optical coherence tomography. Opt. Lett. **25**(19), 1448–1450 (2000)
50. S. Yazdanfar, A.M. Rollins, J.A. Izatt, In vivo imaging of human retinal flow dynamics by color Doppler optical coherence tomography. Arch. Ophthalmol. **121**(2), 235–239 (2003)
51. R. Leitgeb, L.F. Schmetterer, M. Wojtkowski, C.K. Hitzenberger, M. Sticker, A.F. Fercher, *Flow velocity measurements by frequency domain short coherence interferometry*. Proc. SPIE **4619** (2002)
52. S.H. Yun, G.J. Tearney, B.J. Vakoc, M. Shishkov, W.Y. Oh, A.E. Desjardins, M.J. Suter, R.C. Chan, J.A. Evans, I.K. Jang, N.S. Nishioka, J.F. de Boer, B.E. Bouma, Comprehensive volumetric optical microscopy in vivo. Nat. Med. **12**(12), 1429–1433 (2006)
53. E.C.W. Lee, J.F. de Boer, M. Mujat, H. Lim, S.H. Yun, In vivo optical frequency domain imaging of human retina and choroid. Opt. Express **14**(10), 4403–4411 (2006)
54. H. Lim, J.F. de Boer, B.H. Park, E.C.W. Lee, R. Yelin, S.H. Yun, Optical frequency domain imaging with a rapidly swept laser in the 815–870 nm range. Opt. Express **14**(13), 5937–5944 (2006)
55. H. Lim, M. Mujat, C. Kerbage, E.C.W. Lee, Y. Chen, T.C. Chen, J.F. de Boer, High-speed imaging of human retina in vivo with swept-source optical coherence tomography. Opt. Express **14**(26), 12902–12908 (2006)

Complex and Coherence-Noise Free Fourier Domain Optical Coherence Tomography

6

Rainer A. Leitgeb and Maciej Wojtkowski

Keywords.
Coherence noise • Complex signal reconstruction • Dispersion • Doppler OCT • Dispersion • Full range imaging • Phase noise • Phase sensitive OCT • Phase shifting

6.1 Introduction

Fourier domain optical coherence tomography (FdOCT) [1, 2] provides significant improvement of detection sensitivity and imaging speed as compared to time domain OCT [3–5]. The delay and magnitude of backscattered or back-reflected light detected by any OCT system carry information about axial structure of semitransparent objects. FdOCT devices reconstruct the sample structure by spectral analysis of the spectral interference fringe signal. FdOCT detection can be performed in two ways: spectral OCT using a spectrometer with an array or matrix of photodetectors (CCD, CMOS, or photodiode arrays) [1, 6–9] and swept source OCT using a tunable laser source [1, 10–17]. Spectral OCT has demonstrated superior imaging speed as compared to time domain OCT when applied to ophthalmic imaging in the anterior eye segment and the retina [7–9, 18–22]. Spectral OCT and swept source OCT are also promising for ultrahigh-resolution imaging because they overcome imaging speed limitations of time domain OCT. Therefore, it is possible to use these techniques for three-dimensional ultrahigh-resolution imaging [8, 18–20, 23].

R.A. Leitgeb (✉)
Center for Medical Physics and Biomedical Engineering, Medical University of Vienna, Vienna, Austria
e-mail: rainer.leitgeb@meduniwien.ac.at

M. Wojtkowski
Faculty of Physics, Astronomy and Informatics, Institute of Physics, Nicolaus Copernicus University, Toruń, Poland

© Springer International Publishing Switzerland 2015

W. Drexler, J.G. Fujimoto (eds.), *Optical Coherence Tomography*,
DOI 10.1007/978-3-319-06419-2_7

An advantage of Fourier domain OCT is the possibility of having direct access to the spectral fringe pattern, enabling a wide range of novel applications such as tissue absorption measurement [24] and tissue contrast enhancement [25]. Additionally the high speed combined with simultaneous registration of all spectral components (spectral OCT) provides stable phase information. The availability of signal phase information due to the coherent signal detection is one of the most important advantages of OCT. It allows pushing the resolution limits down to the nanometer range and extending the capabilities of FdOCT from purely structural towards a potential functional imaging modality with high temporal resolution [26–28].

It is beyond the scope of the chapter to give an entire overview of all the various facets of phase-sensitive detection. The main motivation is to clarify the notions of signal phase and to introduce the reader to the problem of phase-sensitive FdOCT detection and complex FdOCT signal formation. We discuss the meaning of complex signal content and the implications of complex FdOCT signal reconstruction for cross-sectional image formation. We will also demonstrate the potential of phase-sensitive FdOCT techniques for improving the quality of obtained FdOCT reconstructions [29–39].

6.2 The Complex OCT Signal

Optical coherence tomography (OCT) is an interferometric imaging modality. This simple fact has several far-reaching implications on the achievable system performance and on the amount of information that is contained in an OCT signal. This is best seen by first analyzing the properties of a complex OCT signal and in particular of a Fourier domain OCT (FdOCT) signal.

6.2.1 The Signal Registered by FdOCT Instrument

Assume ρ_R to be the in general complex valued amplitude reflection coefficient of the reference and accordingly ρ_i the coefficients of the backscattering sample sites along the optical axis located at z_i. Clearly the amplitude of the field that is backscattered at a certain sample interface will be apart from the actual interface reflectivity also affected by all previous interfaces. The situation is schematically shown with the layer model of Fig. 6.1 where $E_i(z,t)$ are the individual optical fields back-reflected from interfaces z_i. The interfaces are artificial boundaries separating two regions at which the refractive index difference causes a reflected wave that can be detected by the OCT system. The optical fields $E_i(z,t)$ are not independent but related via

$$E_i(z,t) = \sigma_{i-1}{}^2 \rho_i E_{i-1}(z,t), \tag{6.1}$$

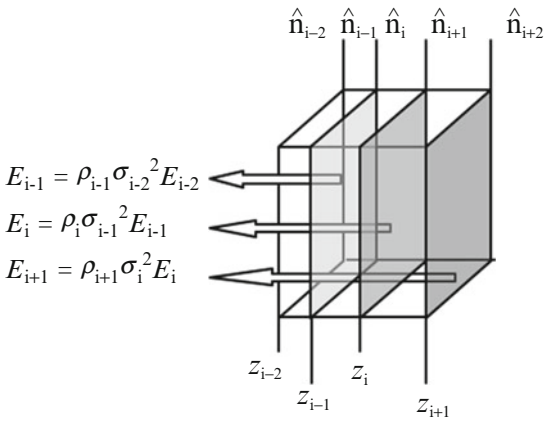

Fig. 6.1 Layer model to describe the field contributions to the OCT signal. The layers are described by their complex refractive index $\hat{n}$

where σ_{i-1} is the amplitude transmission of the $(i-1)$th interface. It is related to the reflectivity coefficient of the corresponding interface via $|\sigma_{i-1}|^2 = 1 - |\rho_{i-1}|^2$. One can account for the effective amplitude attenuation as the beam propagates through the different interfaces in a non-absorbing sample by introducing a reduced amplitude reflectivity:

$$\rho_i' = \prod_{j=0}^{i-1} \sigma_j^2 \rho_i, \tag{6.2}$$

with $\sigma_0 = 1$. Standard OCT systems actually display logarithmic plots of the reduced rather than actual sample structure reflectivities. The structure function including the reference interface is therefore approximated by a sum of delta functions as

$$g(z) = \sum_i \rho_i' \delta(z - (z_0 - z_i)) + \rho_R \delta(z - (z_0 - z_R)), \tag{6.3}$$

where z_R, z_i relate to optical distances with respect to a common reference point z_0. For a certain layer with refractive index n, the optical distances are related to the corresponding geometric values by $z_{opt} = n \cdot z_{geom}$.

Again standard OCT displays optical distances rather than geometric ones. The true geometric sample structure can be retrieved by using elaborate ray tracing algorithms [40, 41].

Having now set the model for the sample structure, we come back to the actual OCT signal. There we measure the coherent superposition of all waves scattered back from the sample together with the reference wave. Assume the power spectral density of the employed broad-bandwidth light source to be $P(\nu)$, where ν is the optical frequency. Then the total optical power at the interferometer entrance is

$$P_0(\nu_C, \Delta\nu) = \int_{-\infty}^{\infty} P(\nu, \Delta\nu) d\nu, \tag{6.4}$$

where Δv is the optical line width, usually the full width at half maximum value, and v_C the center frequency of the employed light source. The total backscattered wave at the common reference point, which is without loss of generalization assumed to be the detector position, can be written as

$$E_D(z_0, t, K) = \int g(z - z_0) E_0(k) \exp(-i2\pi \nu t - iKz) dz. \tag{6.5}$$

The integral ranges over the axial sample structure including the reference site, E_0 is the incident field amplitude, $g(z)$ represents the in general complex valued sample structure, and K is the absolute value of the scattering wave vector, $K = -2\,k$. The expression for the scattering field can be rewritten as

$$E_D(z_0, t, K) = E_0(k) \exp(-i2\pi \nu t) FT_K\{g(z - z_0)\}, \tag{6.6}$$

with $FT\ g(z)\}$ being the Fourier transform of $g(z)$. The intensity of this field becomes:

$$I_D(K) = E_0(k) {E_0}^*(k) |FT_K\{g(z)\}|^2. \tag{6.7}$$

The simple layer model that is used for describing the backscattering structure may be extended to include absorption and scattering losses by introducing a complex refractive index $\hat{n} = n + i\alpha$. A monochromatic wave of wave number k and optical frequency v that travels along z within an homogeneous and isotropic medium of complex refractive index $\hat{n}_i$ is then written as

$$E_i(z, t) = E_{i,0} \exp\{-i[2\pi \nu t - k n_i z]\} \exp(-k \alpha_i z). \tag{6.8}$$

Comparing the expression for the intensity of this wave with Lambert-Beer's law allows immediately finding the relation of α with the extinction coefficient μ_e as

$$\alpha = \mu_e \lambda / 4\pi. \tag{6.9}$$

As indicated by the layer model in Fig. 6.1 and the explanations in the text, the sample function basically represents abrupt changes in refractive index along the axis that give rise to reflection and scattering. Within the layers the complex refractive index $\hat{n}(v)$ can assumed to be an analytic function. Hence its components the dispersion $n(v)$ and the absorption $\alpha(v)$ are linked via Kramers-Kronig (KK) relations. We give the definitions of Ahrenkiel [42] for singly subtractive KK relations that include a known reference point and converge more rapidly than the original integrals:

$$\alpha(v) = \alpha(v_0) - \frac{2}{\pi}\left(v^2 - v_0^2\right)P\int_0^\infty \frac{v' n(v')}{\left(v^2 - v'^2\right)\left(v_0^2 - v'^2\right)}dv',$$
$$n(v) = n(v_0) + \frac{2}{\pi}\left(v^2 - v_0^2\right)P\int_0^\infty \frac{v' \alpha(v')}{\left(v^2 - v'^2\right)\left(v_0^2 - v'^2\right)}dv', \tag{6.10}$$

where P indicates the Cauchy principal value of the integrals. Later Palmer et al. [43] introduced multiply subtractive algorithms to optics that allow including more than one reference point. The KK equations state that with known dispersion over a certain optical frequency range, it is possible to reconstruct the absorption and vice versa. Faber et al. [44] used the simply subtractive KK relations of Eq. 6.10 to calculate the complex index of refraction of oxygenated and deoxygenated hemoglobin by using the accurately known absorption spectra together with a reference measurement at a single wavelength.

The phase as argument of the Fourier transform in FdOCT has no direct meaning; only the phase difference over time or spatially allows to access in a quantitative way changes of the optical path length down to small fractions of the central wavelength. The optical path length is defined by the transit time of light as $OD = \Delta z\, n$, where Δz is the geometric distance and n is the refractive index of the medium. In OCT broadbandwidth light sources are applied and therefore the displacement Δz is multiplied to the group refractive index $n_g = d\omega/dk$, where ω is defined as $w = 2\pi v$. However, the phase of the spectral interference pattern recorded in FdOCT contains in fact the full dispersion properties of the medium. The slope of this phase at the central wavelength is related to the group refractive index, whereas higher-order phase terms relate to higher-order dispersion contributions. In order to extract this spectral phase curve, we need a Hilbert transform or Fourier filtering of the recorded signal. This is easily done by filtering the FdOCT signal of clear sample interfaces, e.g., cuvette interfaces, or glass slides of microscopy samples. Analyzing the spectral phase offers the possibility to extract additional chemical sample information, due to dispersion properties of the sample. It has been demonstrated how to measure analyte concentrations in mixture based on the spectral phase information [45]. Recent work demonstrated the possibility to use the spectral phase information for highly sensitive label-free investigation of cell dynamics [46–48]. Finally, the access to the spectral phase allows in combination with high-speed swept source FdOCT to access fast vibrations with subnanometer resolution on time scales of down to 10^{-9} s. This has been used for all optical detection of photoacoustic signals and parallel acquisition with FdOCT [49].

6.2.2 Reconstruction of Structural Information from FdOCT Signal

The inverse Fourier transform of the field intensity at the detector Eq. 6.7 retrieves the structure function $g(z)$. In fact it yields the autocorrelation function of the structure convoluted with the inverse Fourier transform of the spectral field intensity, i.e.,

$$FT^{-1}{}_z\{I_D(k)\} = FT^{-1}{}_z\{I_0\} \otimes ACF\{g(z)\} \\ = \tau_{\exp} P_0 \gamma(\tau = z/c) \otimes ACF\{g(z)\}. \tag{6.11}$$

For the last step we used the Wiener-Khintchin theorem according to which the complex degree of coherence $\gamma(\tau)$ is connected to the power spectral density via a Fourier transform:

$$\gamma(\tau) = 1/P_0 \int_{-\infty}^{\infty} P(v) \exp(-i2\pi v\tau) dv. \tag{6.12}$$

The importance of this Fourier relation cannot be overemphasized. It is the basic theorem that links time domain with frequency domain interferometry. The superposition of the individual backscattered fields together with the reference wave will form interference fringes only if the temporal delays between the different light fields are smaller than the range of temporal coherence. According to the bandwidth product, the width of the coherence function must be inversely proportional to the spectral bandwidth of the light source. For Gaussian-shaped power spectral density, the expression for the coherence length becomes

$$l_c = \frac{4 \ln 2}{\pi} \frac{{\lambda_c}^2}{\Delta\lambda}. \tag{6.13}$$

The axial resolution of any OCT system is given by half the coherence length since the wave travels twice the sample arm. The temporal coherence function is equal to the normalized field autocorrelation function $\Gamma(\tau) = \langle E(t), E(t-\tau) \rangle$, with brackets indicating an ensemble average. In the case of statistically stationary fields, the ensemble average equals time average. The complex degree of coherence is then defined as the normalized temporal coherence function $\gamma(\tau) = \Gamma(\tau)/\Gamma(0)$. If we use now our definition of the structure function $g(z)$, we finally obtain from Eq. 6.11 the expression for the absolute value of the measured Fourier domain signal:

$$|I_D(\tau)| \propto I_0|\gamma(\tau)| \left[\sum_i |\rho_i|^2 + |\rho_R|^2\right] + I_0|\gamma(\tau)| \\ \otimes \left[\sum_{i,j;i>j} \rho_i {\rho_j}^* \delta\left[\tau - \left(\tau_i - \tau_j\right)\right] + \sum_i \rho_i {\rho_R}^* \delta[\tau - (\tau_i - \tau_R)]\right] + c.c. \tag{6.14}$$

where $\tau = z/c$ and $\delta(\tau)$ is the Dirac delta function. The first term of the rhs corresponds to the total intensity of the signal that appears as DC term at $\tau = 0$. The following two terms are self-cross correlations between fields back-reflected at individual sample structure layers. These terms are commonly referred to as autocorrelation terms or coherence noise terms. Only the last two terms actually display the actual axial sample structure. Still there is an ambiguity with

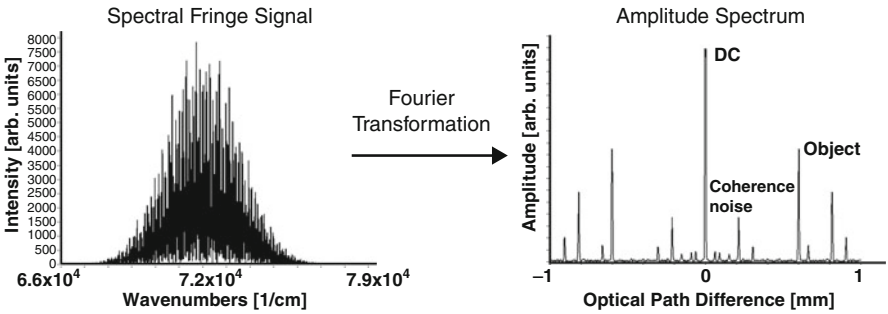

Fig. 6.2 Reconstruction of the axial structure of an object in FdOCT: structural information, DC signal, and coherence noise terms are residual in the amplitude spectrum of the spectral fringe signal

respect to the zero delay associated with the Hermitian nature of the inverse Fourier transform as it is applied to the real-valued signal I_D. Each structure term has its mirror term in the adjoint Fourier space. Figure 6.2 shows the signal measured by FdOCT instrument and how this signal is processed to obtain the reconstruction corresponding to amplitudes of back-reflected intensity versus one-dimensional distribution of scattering points (optical A-scan).

All three extra signal components described by Eq. 6.14 (DC signals, coherence noise, and symmetrical redundant image) limit the useful measurement range and can lead to misinterpretation of reconstructed structure. There are two main types of the coherence noise in FdOCT. The first type represented by term is associated with mutual interferences of light waves back-reflected or scattered from different points within a measured object, located along the penetration beam. In this case each light wave can interfere with others and gives contribution to OCT signal. This signal is present in OCT images even if the reference arm of the interferometer is blocked. Another source of coherence noise affecting Fourier domain imaging is caused by interference of light waves scattered from optical components of the OCT system. Due to the high sensitivity of FdOCT imaging and relatively long axial coherence range (some millimeters), the contribution of light scattered on optical components of the OCT device can be significant. In order to avoid an overlap between various signal components, one needs to take care that all structure terms are confined to one half space.

In practice one adjusts the reference arm delay accordingly. Figure 6.3 shows results of image reconstruction for a sample consisting of four reflecting interfaces. Three measurements have been simulated with different positions of the reference mirror. In the first case (Fig. 6.3a), the optical distance (optical path delay) between reference mirror and the sample is longer than the thickness of the entire set of four interfaces. This enables distinguishing between sample and coherence noise artifacts. Shortening the distance between the reference mirror and the sample can lead to overlapping of terms representing the sample and the coherence noise. In result the structure cannot be distinguished (Fig. 6.3b). The situation can be even more

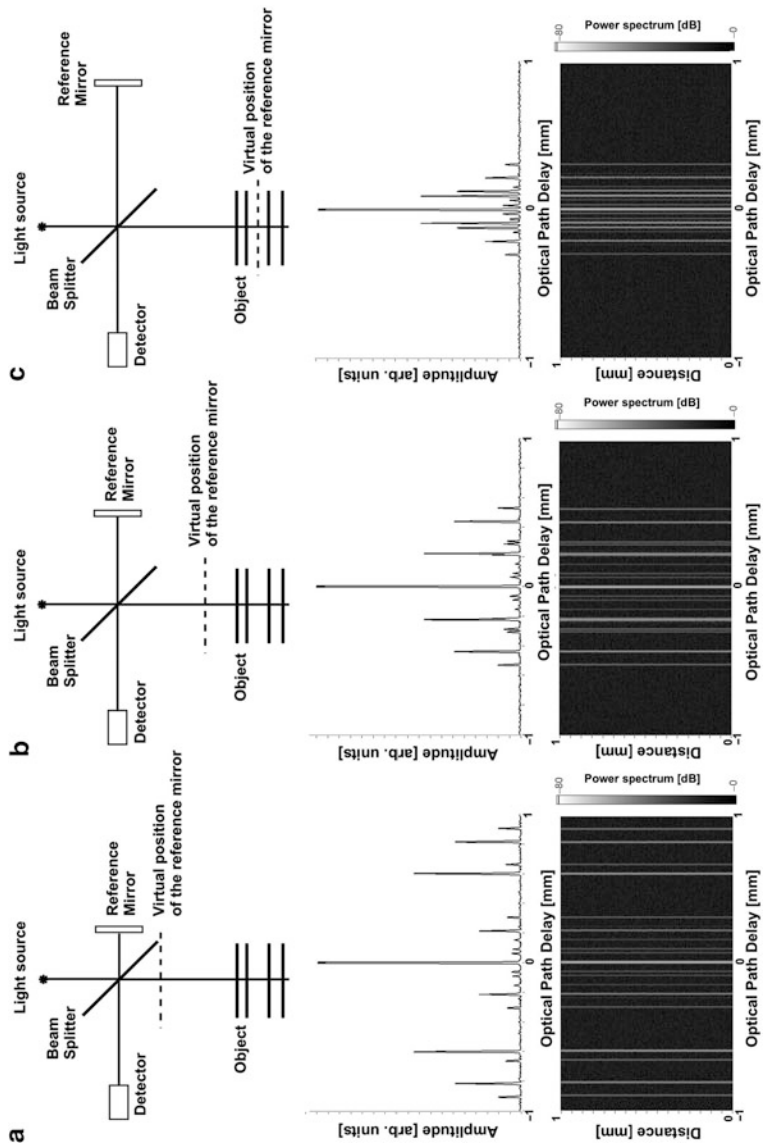

Fig. 6.3 Simulation of Fourier domain OCT reconstruction for a sample comprising four smooth reflecting interfaces registered for three different positions of the reference mirror. *Upper row* shows the scheme of the interferometer configuration chosen for each measurement. *Middle* and *bottom rows* demonstrate axial scans and cross-sectional images, respectively

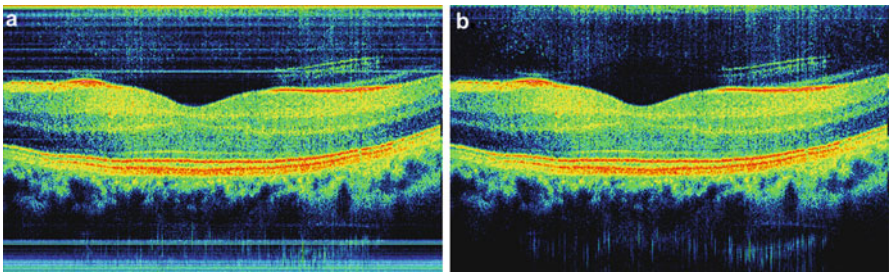

Fig. 6.4 Cross-sectional images of the human retina in vivo (macular region) obtained by FdOCT: (**a**) including all coherence noise terms, (**b**) after background subtraction

complex when the virtual position of the reference mirror is placed "inside" the object. In this case both the coherence noise terms and symmetrical images mix altogether with the signal representing the actual axial sample structure. In both cases (Fig. 6.3b, c), direct reconstruction of true architecture of the measured sample is impossible.

Usually the coherence noise components introduced by the object structure are irregular and distributed close to the zero optical path delay. In contrary coherence noise terms associated with light reflections from optical components of the device usually create characteristic regular stripe patterns, which are randomly distributed along the axial direction (Fig. 6.4). To eliminate such coherence noise terms, it is sufficient to register the spectral fringe pattern in the absence of the sample (background) and subtract it from the spectral fringes registered with the sample in place. Assuming that mutual interferences between light waves scattered from optical components of the OCT system and sample interfaces are negligible, the simple subtraction procedure can effectively reduce the regular stripe pattern that otherwise disturbs the reconstructed cross-sectional image. Practically it is possible to measure the background signal by deflecting the sample beam in an OCT interferometer during the background measurement. Random instabilities of the optical system, which are usually present in OCT devices, such as mechanical vibrations of optical components or thermal expansion of optical fibers can be taken into account and compensated by using an average over several spectral fringe patterns of the background signal. Figure 6.4b shows an example of the background subtraction algorithm applied to a FdOCT tomogram of the human retina measured in vivo.

Nevertheless the autocorrelation terms will still be present (Fig. 6.4) and give rise to coherent noise background that may lead to misinterpretation of the actual sample structure. The question arises whether it is possible to remove all coherence noise terms together with the inherent ambiguity of the FdOCT signal. An answer can be found by taking advantage of the fact that FdOCT being an interferometric method is sensitive to the relative phase between the individual fields that coherently add up at the detector. Note that in particular any reference delay τ_R will only affect the phase of the structure terms in Eq. 6.14

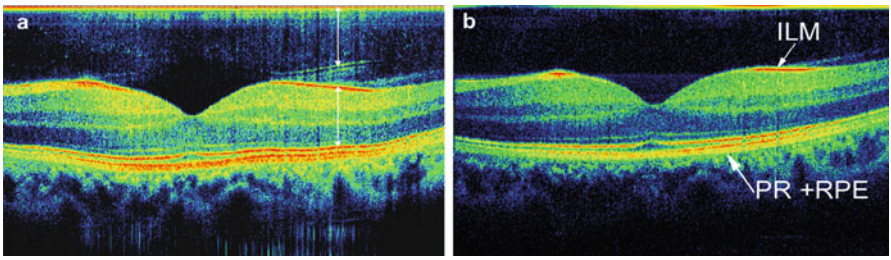

Fig. 6.5 Spectral OCT cross-sectional images of the retina in vivo (macular region). The images were taken with (**a**) 256 μs/A-scan (103 dB sensitivity) and (**b**) 32 μs/A-scan (94 dB sensitivity). Coherence noise components are clearly visible in the top of the panel (**a**), while for (**b**) the dominant noise is the shot noise; *ILM* inner limiting membrane, *PR* photo receptors, *RPE* retinal pigment epithelium. *Arrows* in (**a**) indicate the equal optical distances

but has no effect on the autocorrelation and the DC terms. This observation is the basis for phase-shifting techniques that eventually allow for the elimination of all signals apart from the true structure terms. The important fact is that these methods allow a direct reconstruction of the true depth resolved phase function of the sample field and thus of the complex valued structure function $g(z)$ Eq. 6.3.

In practice it is often impossible to predict the thickness of measured sample. Artifacts created by coherence noise terms may be misinterpreted as details of a real structure. This problem arises, paradoxically, as a result of the high sensitivity of FdOCT. The FdOCT imaging is performed at an optical energy (optical power multiplied by exposure time) that is about hundredfold lower than for traditional time domain OCT. It is therefore tempting to increase optical power to the same energy level in order to enhance sensitivity. Unfortunately, beneficial results of higher power on the sensitivity level are counterbalanced by the fact that simultaneously artifacts caused by coherence noise will emerge and will be visible above shot noise. However, it is possible to choose optimal optical power levels used for FdOCT imaging to keep the coherence noise components under the shot noise level [50]. Illustration of this phenomena is presented in Fig. 6.5. Coherence noise artifacts can be observed, for example, in retinal imaging as a result of cross-interference of waves originating from two strongly reflecting layers in the retina: internal limiting membrane (ILM) and retinal pigment epithelium (RPE). Figure 6.5 demonstrates an influence of the total exposure time (sensitivity) on the visibility of the coherence noise artifacts in retinal FdOCT imaging. Using 740 μW of optical power of light entering the eye and 256 μs of exposure time, several parasitic cross correlations produce artificial features, which are especially visible above the right part of the retinal surface in Fig. 6.5a. It is easy to verify that distances between ILM and structures around RPE match distances between position $\tau = 0$ and corresponding artifacts. The eightfold reduction of the exposure time (−9 dB in sensitivity) results in strong suppression of those artifacts (Fig. 6.5b). Under these circumstances the quality of the image is sufficient to delineate all retinal layers.

Considering the measurement configuration with significant contribution of the coherence noise terms, their amplitudes may be expressed as

$$|\Xi(\tau_{nm})| = \rho \frac{P_0 \kappa}{N} \sum_{n,m} \sqrt{R_m R_n} \tag{6.15}$$

where $\rho = e^{-}\eta/hv$ is the efficiency of photoelectric conversion of photodetector, e^{-} is an electron charge, η is the total efficiency of the spectrometer, h is Planck's constant, P_0 is the integrated optical power of the beam entering the interferometer assumed to be Gaussian across optical frequencies $\omega\left(P_0 = \sqrt{\pi/4\ln 2} P(\omega_0) FWHM\{P(\omega)\}\right)$, $\kappa - a$ double path coupling ratio of the beam splitter, N is the number of samples taken in optical frequency domain, and $R_{m,n}$ are reflectivities of consecutive back-reflecting or scattering points in the object distributed along the probing beam.

The most optimal performance of OCT instruments is usually achieved with shot noise as the dominant source of noise. In FdOCT the signal registered by the detector is Fourier transformed. Therefore, the power spectrum of the resultant shot noise may be expressed as [50]

$$N_{shot} = \frac{e^{-}\rho}{T} \frac{P_0}{N^2} \kappa \left(R_{ref} + \sum_n R_n \right), \tag{6.16}$$

where T is the exposure time needed to register one A-scan (N samples in Fourier domain), R_{ref} is the effective reflectivity of the reference mirror, and R_n is the reflectivity of consecutive back-reflecting or scattering point in the sample distributed along the probing beam. The ratio of coherence noise to shot noise in terms of electrical power of obtained signals is expressed by

$$\frac{N_{coherence}}{N_{shot}} = \frac{|\Xi(\tau_{nm})|^2}{N_{shot}} = \frac{\rho T P_0 \kappa}{e^{-}} \frac{\left(\sum_{n,m} \sqrt{R_m R_n} \right)^2}{\left(R_{ref} + \sum_n R_n \right)}. \tag{6.17}$$

In order to simplify Eq. 6.17, let us assume that there are only two strongly reflecting interfaces with identical reflectivity R contributing to the coherence noise. In this case the ratio of the coherence noise terms to the shot noise may be expressed as

$$\left(\frac{N_{coherence}}{N_{shot}} \right)' = \frac{\rho T P_0}{e^{-}} \frac{R^2 \kappa}{(R_{ref} + 2R)} = Sensitivity(T) \cdot \frac{R^2}{(R_{ref} + 2R)}. \tag{6.18}$$

Plots of the ratio of coherence noise to shot noise level as a function of sample reflectivity calculated according to Eq. 6.18 are shown in Fig. 6.6. These theoretical

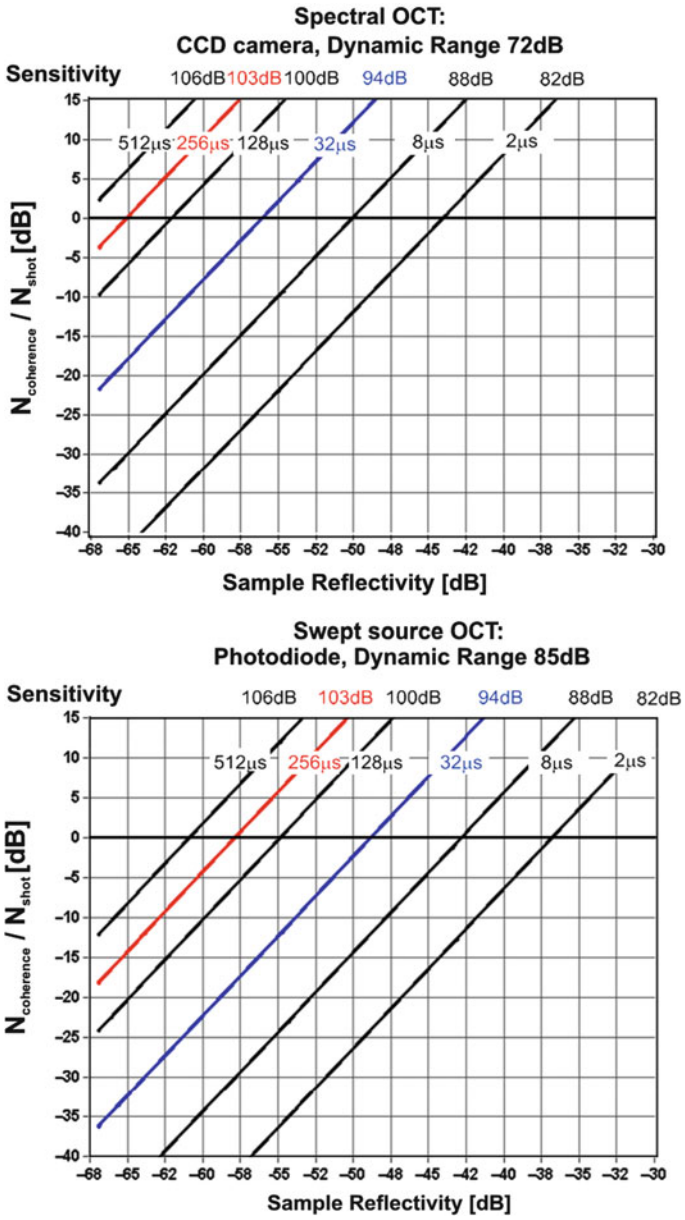

Fig. 6.6 Ratio of coherent noise to shot noise versus reflectivity of the sample calculated from (Eq. 6.17) for different values of exposure time, corresponding sensitivity, and dynamic range. The optimal exposure time to perform an experiment avoiding coherence noise terms from two surfaces of reflectivity R can be chosen by taking exposure time values, for which the oblique lines presented in the graphs are localized below 0 dB horizontal line. *Red* and *blue* lines were calculated for exposure times used in the retinal experiment, which results are shown in Fig. 6.5

plots are calculated for two values of dynamic range corresponding to detection using spectrometer ($DR = 72$ dB) and swept source system with photodiode in dual balanced configuration ($DR = 85$ dB). For these calculations the value of input optical power was assumed to be $P_0 = 2$ mW (740 uW reaching the object), the double path coupling ratio $\kappa = 0.20$, and the spectrometer efficiency $\eta = 0.14$ and the double path losses associated with collimating, back coupling to the fiber, passing through X–Y scanner to be 0.4. These parameters give sensitivities from 82 to 106 dB for exposure times varying from 2 to 512 μs per A-scan measured close to the zero path delay.

The analyzed range of reflectivity values (i.e., −30 dB to −70 dB) and sensitivities (82–106 dB) covers the typical values of reflectivity and sensitivity used in biomedical imaging. For example, in retinal OCT imaging the most reflective layers in the posterior eye are inner limiting membrane (ILM) and retinal pigment epithelium (RPE). Coming back to results presented in Fig. 6.5, the imaging parameters of FdOCT system are given above and were also used to plot relations presented in Fig. 6.6. Cross-sectional retinal images were obtained twice in the same subject using two values of exposure time: 32 us and 256 us. Taking into account the exact value of the instrument sensitivity, it was possible to find the effective average reflectivities of ILM in the presented OCT scans to be approximately −60 dB. Using the graph shown in Fig. 6.6 along with measured values of effective reflectivity of retinal layers, it is possible to estimate the maximum sensitivity corresponding to coherence noise-free imaging of the posterior segment of the human eye to be approximately 97 dB in spectral OCT systems (72 dB of dynamic range) and 102 dB (85 dB of dynamic range) in swept source OCT. The abovementioned optimization causes a limitation of the sensitivity and dynamic range. For example, in the system characterized by the dynamic range of originally 85 dB, it is possible only to image without coherence noise artifacts within a dynamic range of 45 dB.

The limitation of dynamic range due to power optimization can be overcome by using a dual balanced detection (called also differential Fourier domain detection method (dFdOCT)) [6, 51]. This method takes advantage of the fact that terms carrying direct information on the location of reflecting layers depend on the reference mirror position, while the remaining coherence noise terms do not (see Eq. 6.14). In order to completely remove the parasitic terms, it is sufficient to measure one additional spectral fringe pattern $I_D(k)$, with a phase shift of π introduced into the reference arm. Subtraction of these two spectral fringe patterns will yield terms associated exclusively with the sample structure. The π phase shift of the reference beam in differential measurements can be achieved either mechanically by attaching the reference mirror to a moving element such as a piezo actuator or electro-optically, e.g., by a phase modulator placed in the reference arm of the interferometer. The effective measurement time is doubled as compared to standard FdOCT. In swept source OCT it can be also realized by using differential measurement with additional fiber coupler introducing adequate phase shift for two detection channels (the so-called dual balanced detection). Figure 6.9a, b show examples of cross-sectional images of porcine anterior segment obtained with standard and the differential FdOCT technique. The coherence noise and strong DC signal in the central part of the image representing zero path delay are totally removed after two-frame procedure.

Nevertheless, the overlap between conjugate images is still present and can only be removed by application of complex FdOCT techniques.

6.3 Complex Fourier Domain Optical Coherence Tomography

The Fourier transform of the real-valued spectrum yields redundant information for positive and negative fringe frequencies corresponding to positive and negative path length differences between the sample and the reference. Even using the coherence noise-free imaging, one needs to adjust the reference arm delay so that it is slightly shorter than the relative distance of the first sample interface. In this case the axial structure does not mix with its mirrored representation in the conjugate Fourier half space. Hence only half of the Fourier space can be used for the sample structure.

The reconstruction of the complex representation of spectral fringe signal resolves this ambiguity and the image space is doubled (Fig. 6.9c). This needs at least two phase-shifted copies (the so-called frames) of the cross correlation between sample and reference signal. The most straightforward realization of the phase shift is done by changing the path length of the reference arm using, for example, a mirror mounted on a moving mechanical element (Fig. 6.7). A faster and more precise way of shifting the optical delay in the reference arm using electro-optic modulator has been reported by Gotzinger et al. [37]. An alternative approach has been used by Yasuno et al. where phase-shifted spectra are recorded

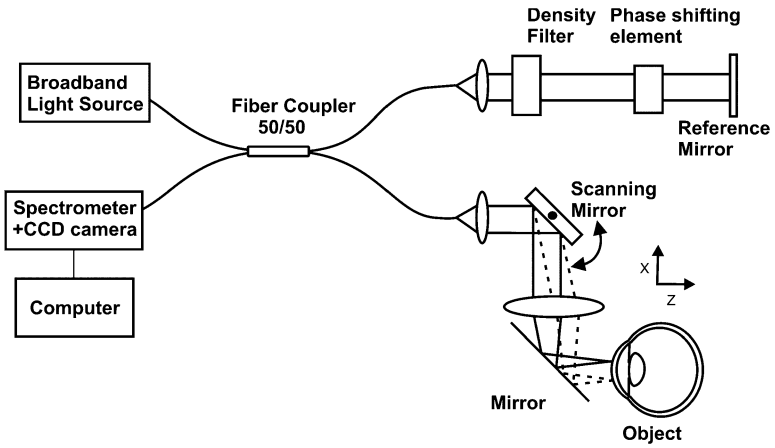

Fig. 6.7 Drawing of spectral OCT system with phase-shifting element used for complex OCT measurements. Similar to other SOCT devices, the system is based on the Michelson interferometer setup with custom-designed highly efficient spectrometer with high-speed linear photodetector. The sample arm enables lateral scanning of probing light beam. The difference between complex SOCT instrument and standard spectral OCT system is in additional phase-shifting device placed in the reference arm and more complex electronic synchronization of the lateral scanners, the phase shifter, and the spectrometer

simultaneously on different lines of an area detector [38]. However, the need for an area detector reduces the speed performance of the technique and the light efficiency is critical.

6.3.1 Complex Two-Frame Technique

In principle the complex reconstruction can be based only on two frames with a relative phase shift of $\pi/2$ [29]:

$$\hat{I}_D(k) = I'_D{}^{(0^\circ)}(k) - jI'_D{}^{(90^\circ)}(k), \tag{6.19}$$

where the role of the dashes will be explained in due course. A simple combination of two shifted spectra will still suffer from a strong DC component as well as coherence noise terms. The necessary approximation is that the reference intensity is much larger than the sample intensity which is the case in most biomedical applications. Then it is sufficient to subtract a reference spectrum from each spectral interference pattern and one is effectively left with a small sample intensity DC term together with the cross-correlation terms.

In this case the dashes in Eq. 6.19 indicate that a reference subtraction has been applied. Since only two phase-shifted copies of the recorded interference pattern are needed, it is possible to realize fast complex in vivo spectral FdOCT systems [37]. However, as pointed out such method works only well for a limited range of optical bandwidths.

For wavelength tuning FdOCT on the other hand, it is possible to perform true heterodyne detection by locking the detector to a sinusoidal reference arm delay modulation. In this case the dashes indicate that only the modulated cross-correlation terms between reference and sample are considered.

One way to achieve a wavelength-independent modulation of the actual structure terms in Eq. 6.14 is to employ frequency-shifting devices such as acousto-optic frequency shifters (AOFS). They are easy to implement into FdOCT systems based on wavelength tuning and allow for high-speed quadrature detection with fast PIN diodes [33, 34]. Nevertheless for spectral FDOCT systems, the array detectors cannot follow the fast signal modulations in the MHz range. Bachmann et al. demonstrated a solution using two slightly detuned AOFS in the sample and reference arm respectively [52]. A quadrature detection scheme is realized by locking the array detector to the resulting lower beating frequency and recording the shifted spectral interference patterns via an integrated bucket method as shown in Fig. 6.8b. Figure 6.8a shows a tomogram of the fingernail region evaluated with standard FdOCT. The strong overlapping between sample structure and its mirror adjoint renders it impossible to determine the actual structure. Figure 6.8d demonstrates the capability of complex signal reconstruction based on Eq. 6.19. A reference subtraction has been performed; nevertheless a spurious DC term might still be visible. Figure 6.8c shows the result if a complex differential technique is applied. Such reconstruction is

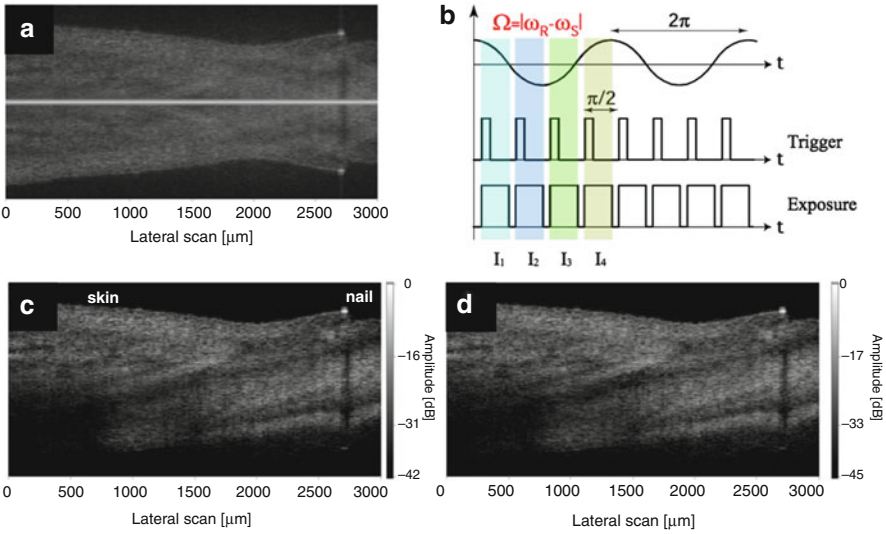

Fig. 6.8 (**a**) Tomogram of a fingernail fold region with standard FDOCT [52]. The zero delay is clearly visible as bright line due to the strong DC signal. (**b**) Integrated bucket method: the detector integrates over sections within the beating signal period. Four successive spectra I_{1-4} have an incremental delay of $\pi/2$. (**c**) Result of complex signal reconstruction according to Eq. 6.19 with reference subtraction. (**d**) As (**c**) but reconstruction of complex signal according to differential complex method. All tomograms are based on the same dataset. The depth range is 1.75 mm (in air)

achieved by the substitution $I'_D{}^{(0°)} = I_1 - I_3$ and $I'_D{}^{(90°)} = I_2 - I_4$ (Fig. 6.8b) into Eq. 6.2 [52]. It should however be mentioned that integrated bucked methods used in spectral OCT suffer in general from fringe washout, an effect discussed in Sect. 6.3.6. Still, this method has the potential together with array detectors based on CMOS technology to perform true heterodyne detection with spectral OCT. CMOS technology allows on-chip demodulation of the heterodyne signal such that only the AC part will subsequently be amplified and digitized.

Choma et al. followed a completely different approach by using the phase relation between the arms of a 3 × 3 fiber coupler and recording two phase-shifted copies of the interference pattern on separate detectors [53, 54].

6.3.2 Complex FdOCT with Phase-Shifting Techniques: *N* Frames

The first complex FdOCT systems [30, 55] needed five phase-shifted signals for five-frame phase retrieval algorithms adapted from white light interferometry [56]. In the simplified case of an interferometric setup with two virtual light sources, the light intensity measured by the detector is expressed as

$$I_D(\tau,\omega) = I_1 + I_2 + 2\sqrt{I_1 I_2}\cos\left(\phi(\tau,\omega)\right) \tag{6.20}$$

where I_1 and I_2 are DC light intensities and ϕ is the phase of the interferometric fringe signal, which can be analyzed as a function of optical delay (time domain) or optical frequencies (Fourier domain). I_1, I_2, and $\phi(\omega,\tau)$ are in general unknowns. In order to calculate these three unknowns, it is necessary to create set a minimum three linearly independent equations. This can be done by measuring three times the intensity signal with the additional phase shift introduced to each interference fringe pattern. The phase shift between adjacent measurements can be anything between 0 and π. Taking into account the phase shift errors, it is also possible to create overdetermined system of equations measuring $N > 3$ fringe patterns:

$$I_D^{[n]}(\tau,\omega) = I_1 + I_2 + 2\sqrt{I_1 I_2}\cos\left(\phi(\tau,\omega) + \Delta\phi_n\right) \qquad n = 1\ldots N, \tag{6.21}$$

with $\Delta\phi$, for example, given by $\Delta\phi = (n-1)\pi/2$. There are many possible algorithms retrieving the phase information based on extended set of measurements with linear phase shifts including three-, four-, five-, and six-frame techniques; Carre method; and others [56]. The five-frame method has been chosen for OCT applications because of its optimal performance in phase reconstruction [57] already known from white light interferometry. In this technique five consecutive measurements of the spectral fringes $I(\omega)$ are needed with a phase increment of π/2. The phase $\phi(\omega,\tau)$ and the amplitude of the fringe signal are calculated according to the following formulas:

$$\phi = \arctan\frac{2\left(I^{[2]} - I^{[4]}\right)}{2I^{[3]} - I^{[5]} - I^{[1]}} \tag{6.22}$$

$$2\sqrt{I_1 I_2} = \frac{1}{4}\sqrt{\left[2\left(I^{[2]} - I^{[4]}\right)\right]^2 + \left[2I^{[3]} - I^{[5]} - I^{[1]}\right]^2}, \tag{6.23}$$

where $\Delta\varphi = (n-1)\frac{\pi}{2}, \qquad n = 1, 2, \ldots, 5$, according to Eq. 6.21.

Figure 6.9 shows results of complex FdOCT imaging of porcine anterior segment in vitro obtained by the five-frame technique. The reconstruction is free from any ambiguities caused by the overlapping mirror images as well as presence of the coherence noise and DC terms. As a result the maximum achievable depth range is doubled.

6.3.3 Heterodyne Fourier Domain OCT Techniques

Fourier domain detection can be applied to optical coherence tomography either by simultaneous measurement of all spectral components of applied light by a spectrometer (Spectral OCT) or by detecting each single spectral component in

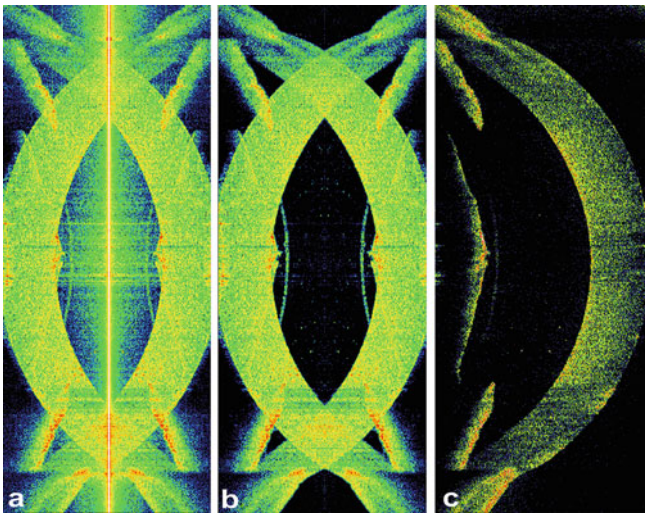

Fig. 6.9 Cross-sectional images of porcine anterior segment in vitro obtained with: (**a**) standard FdOCT technique, (**b**) differential FdOCT, (**c**) five-frame complex FdOCT

time by current generating photodiode synchronized with optical frequency sweeping light source (swept source OCT). The latter technique enables overlapping time-dependent effect of heterodyne beating with also time-dependent sweeping of optical frequencies. In result it is possible to introduce the carrier frequency to the spectral fringe signal and remove the complex conjugate artifacts by quadrature detection without doubling the measurement range. This idea has been introduced simultaneously by three groups [33, 34, 36] In the case of frequency shift of the spectral fringe signal, the carrier frequency introduced by the phase modulator placed in the reference arm of the OCT interferometer establishes the reference point for the zero optical path delay. The frequency shift is possible because the time domain and frequency domain detection both are mixed in the single OCT measurement:

$$I^{(\omega)}(\tau) = I_1^{(\omega)}(\tau) + I_2^{(\omega)}(\tau) + 2\sqrt{I_1^{(\omega)}(\tau) I_2^{(\omega)}(\tau)} \cos\left(\omega \cdot \tau_{Av} + \omega \cdot \tau(t)\right), \qquad (6.24)$$

where the measured light intensity fluctuation $I^{(\omega)}(\tau)$ is a function of optical delay τ varying in time with the parameter ω, which is also continuously swept in time, and τ_{Av} denotes the optical delay between the reference mirror and an object interface at the moment when the phase modulation is switched off. Even for very small amplitudes of $\tau(t)$ (order of magnitude of one optical wavelength), there is a full modulation of the detected light intensity signal – time domain interference fringe pattern. The optical delay $\tau(t)$ can vary periodically (phase modulator introduced to the reference arm of the OCT interferometer) giving the carrier frequency for the

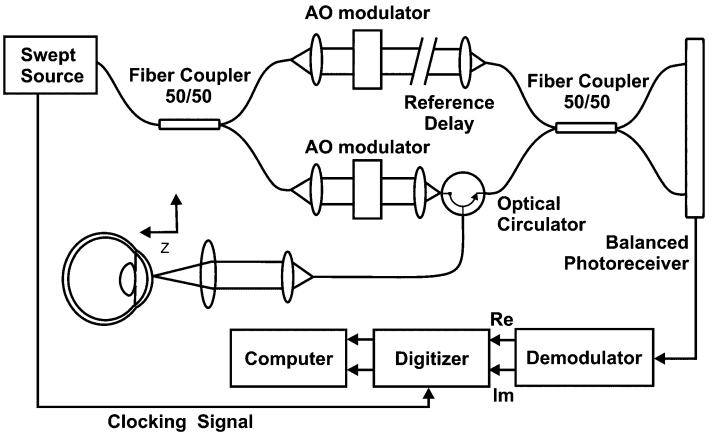

Fig. 6.10 Drawing of the heterodyne complex swept source FdOCT system with courtesy from Davis et al.

light intensity fluctuation signal. Additional sweep of the optical frequencies ω in time will provide light intensity fluctuations with the signal frequency proportional to the average optical delay between the reference mirror and an object – frequency domain interference fringe pattern. The carrier frequency from the time domain heterodyne modulation is then added to the Fourier domain frequency corresponding to the position of measured object, and in turn the zero path delay is shifted to arbitrary chosen position. Coherence noise terms and DC terms are automatically separated from the signal representing the axial structure of measured object. Appropriate frequency shift enables reconstructing OCT images without any image cross talk between positive and negative optical delays [36]. Also the real and imaginary terms of the interferometric signals can be found either numerically [34, 35] or by quadrature demodulation [33], and in turn the complex representation of the spectral interference fringe signal can be calculated. Figure 6.10 shows simplified schematic of the swept source OCT system with heterodyne complex detection proposed by Davis et al. Slightly different systems were also used by Zhang et al. and Yun et al. Davis et al. proposed design of the heterodyne complex FdOCT system using swept source with 1,310 nm central wavelength with 250 Hz sweeping rate, pair of acousto-optic modulators enabling the differential frequency shift of 1 MHz, and dual balanced receiver as a detector. Additional quadrature analog demodulation was applied. Part of the optical energy was also split to generate frequency clock enabling wavelength number triggering.

6.3.4 B-Mode Complex FdOCT Signal

Another interesting concept of complex OCT system combining heterodyne time domain beating with Fourier domain detection was proposed by Yasuno et al. [39].

This technique works analogically to the heterodyne complex method of the previous chapter. Instead of the carrier frequency in the single A-scan introduced by the phase modulator, the entire set of cross-sectional OCT data (B-scan direction) is analyzed. The phase modulation is introduced by periodical and continuous axial movement of the reference mirror synchronized with the lateral scanning. The time-dependent lateral scanning and time-dependent phase modulation mix together. Assuming low speed of the transverse scanning and analyzing each optical frequency separately, the low-frequency light intensity modulation caused by the lateral structure of an object and speckle pattern is now shifted by the frequency introduced by the beating of the time domain signal. In turn the low-frequency cross-correlation and DC terms are separated from the signals corresponding to the lateral structure of measured object. Similarly like in [34], a numerical Hilbert transformation is used, which together with high-pass filtering enables reconstructing the complex and coherence noise-free Fourier domain OCT signal. This technique has later on been reformulated for continuous reference arm shifting using the Hilbert transform [58].

Analysis of the influence of phase-shifting errors on the performance of this B-mode complex reconstruction shows much higher stability with respect to phase fluctuations. The same holds true for chromatic phase-shifting errors. This is manifested in terms of high mirror term suppression. Still, optimal B-mode reconstruction depends on the width of the lateral spatial frequency spectrum. It should be avoided that the width of the spatial frequency spectrum extends to the conjugate frequency plane. In case of under-sampling, in the presence of large motion artifacts, or for signals of flowing blood, conjugate mirror terms might be visible again, or structures might appear flipped in the conjugate Fourier plane.

The B-mode technique is the basis for an elegant, robust, and low-cost complex OCT system realization: instead of using a phase-shifting device such as piezo, electro-optic modulator, or AOFS, the natural path length change in case of off-pivot scanning is used for modulating the phase. Transverse scanning of the sample will then automatically produce a dynamic phase shift that serves as carrier frequency across the B-scan [59, 60]. The only drawback of this system is the rigid coupling between beam offset on the scanner from the pivot, scanning distance, and A-scan rate.

The essence of B-mode reconstruction is to analyze the signal in the spatial frequency domain. This opened in fact new perspectives not only for complex signal retrieval but also for advanced Doppler OCT methods [61–67]. Furthermore, the spatial carrier frequency across the B-scan can be used to encode signals for parallel registration, with a simple spatial Fourier filtering as decoding step. The latter principle of spatial frequency signal multiplexing has been applied for high-speed PSOCT with a single CMOS sensor [68]. A further extension is to use a time sequence of B-scans and analyze after careful registration the spatial frequency content in the temporal direction for each pixel. Such technique has been used for extracting stimulus responses from retinal photoreceptors using optical testing by FdOCT [69].

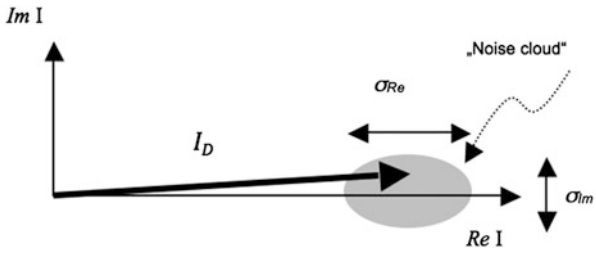

Fig. 6.11 Fluctuations of OCT signal phasor describe a "noise cloud" in the complex plane

6.3.5 Phase-Shifting Errors

The accuracy of reconstruction of the full complex sample field depends on the accuracy of the phase shift and on the phase stability of the interferometer in general. Phase-shifting errors will reduce the ability of the complex signal reconstruction to suppress the mirrored sample structure associated with the complex ambiguity. The most efficient way to reduce such errors is to increase the imaging speed. This has however the drawback of decreasing the system sensitivity. Another more time-consuming way are image processing techniques applied in a post-processing step. One can distinguish between system intrinsic statistical phase noise and systematic phase errors that are due to the phase-shifting process.

6.3.5.1 Statistical Phase Noise

Mechanical instabilities of the phase-shifting unit will contribute to stochastic errors. Such stochastic sample motion during in vivo measurements is in general problematic for phase-shifting methods. It might cause insufficient suppression of mirror terms and eventually deteriorate the actual sample structure reconstruction. Assuming that the FdOCT signal after Fourier transform is $\tilde{I}_D = \mathrm{Re}\,\tilde{I}_D + j\,\mathrm{Im}\,\tilde{I}_D$, both real and imaginary parts are subject to statistical noise. Hence the tip of the actual signal phasor lies within a noise cloud which boundaries are defined by the standard deviation of the complex signal fluctuations (Fig. 6.11). Without loss of generality we can assume the average signal phasor to point along the real axis. The fluctuations may be due to photon shot and excess noise, 1/f noise, detector dark and readout noise, or Johnson noise of the electronic amplification circuit. Let us assume that the system is shot noise limited, i.e., that photon shot noise is the dominating noise source.

Following Goodman [70], the noise variances of the real and imaginary part of the Fourier transformed spectral interference pattern $\tilde{I}_D$ are un-correlated and can be individually analyzed. In the shot noise limit, both variances are shown to be identical, i.e., $\sigma_{\mathrm{Im}}{}^2 = \sigma_{\mathrm{Re}}{}^2$. Now in view of Fig. 6.11, we can assume that the amplitude error is related to the fluctuations of the real part, whereas the phase error is related to the variance of the imaginary part which is responsible for the angular deviation from the original orientation along the real axis. The signal-to-noise ratio (SNR) can then be defined as $SNR = \left|\tilde{I}_D\right|^2 / \sigma_{\mathrm{Re}}{}^2$. In general the length of the phasor will

be much larger than the extensions of the noise cloud. Thus one can finally write for the statistical phase error in the shot noise limit

$$\sigma_{\varphi} \cong \sigma_{\mathrm{Im}} / \mathrm{Re}\, \tilde{I}_D \cong 1/\sqrt{\mathrm{SNR}}. \tag{6.25}$$

This phase error corresponds to a path length jitter amplitude of $\delta z = \lambda / \left(4\pi n \sqrt{SNR}\right)$, where λ_C is the center wavelength of the source and n is the refractive index of the medium. The same result was obtained by Choma et al. [71] with an alternative approach.

6.3.5.2 Systematic Phase-Shifting Noise

The main source of systematic errors is related to the fact that OCT employs broad optical bandwidth sources to achieve high axial resolution. A change in optical path length of the reference arm causes a corresponding phase shift of the cross-correlation terms according to

$$\Delta\Phi = \frac{4\pi\Delta z}{\lambda_c}, \tag{6.26}$$

where we took already into account the round trip path length in a Michelson interferometer setup. The associated change in reference arm delay is $\Delta\tau_R = \Delta\Phi\lambda_C/4\pi c$. Note the dependency on wavelength of the phase shift. A phase shift of $\pi/2$ corresponds therefore to different changes in path length Δz for each wavelength. Hence a phase shifting that is realized via reference path length variation gives rise to chromatic phase errors. As result one needs to look for achromatic phase-shifting techniques that allow combining high-axial-resolution OCT with complex detection. Section 6.3.5 gives an overview to different phase-shifting techniques including multiframe techniques to reduce systematic phase errors such as chromaticity. Creath and Schmid give a thorough phase error analysis for different multiframe phase reconstruction methods [57].

Nevertheless they are only of limited use for in vivo applications since sample motion introduces stochastic phase errors that can only be handled by elaborate post-processing algorithms. We saw earlier that under certain conditions, it is possible to reconstruct the complex sample structure by simply combining two frames with a $\pi/2$ phase shift. Equation 6.20 describes the chromatic phase errors that have to be considered, if the phase shifting is realized via reference path length modulation. If the chromatic phase error increases, the mirror terms in the adjoint Fourier space will no longer be suppressed and the complex reconstruction fails. Figure 6.12 shows a simulated FdOCT signal based on a simple two-frame complex signal reconstruction. The right Fourier half space contains the actual signals that correspond to a single interface in the sample arm. A central wavelength of 800 nm is assumed keeping always the same ratio between spectral width of the spectrum and that of the spectrometer. The adjoint mirror peak P* is visible in the gray-shaded left half space. The signal peaks are

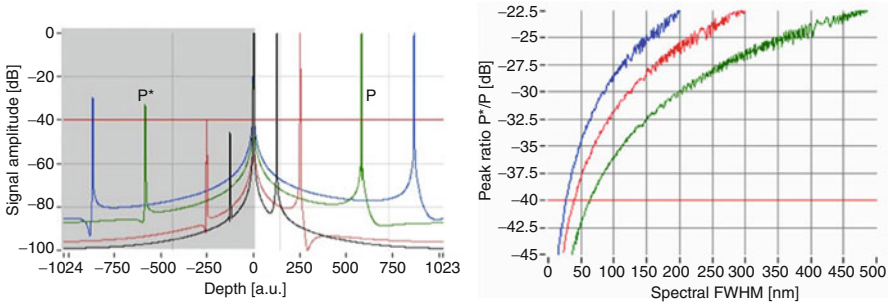

Fig. 6.12 Above −40 dB mirror terms become visible and the reconstruction algorithm fails. Leakage after discrete FFT causes the "noisy" characteristics of the curves on the (rhs) at larger bandwidths. The simulations assume Gaussian-shaped spectra

normalized to the true signal peak maximum P. The resulting signals for four different optical bandwidths are shown (20 nm (black), 40 nm (red), 100 nm (green), and 150 nm (blue)). Figure 6.12 (rhs) displays the suppression ratio of the mirror term peak P* with respect to the actual signal peak P for three different central wavelengths as a function of optical bandwidth ($\lambda_0 = 550$ nm (blue), $\lambda_0 = 800$ nm (red), $\lambda_0 = 1{,}300$ nm (green)). Assuming a typical dynamic range in an OCT tomogram of 30–40 dB, we observe that the mirror terms are suppressed only for standard resolution complex FdOCT corresponding to a bandwidth at 800 nm of ∼20 nm. However, for high-resolution systems with bandwidths above 40 nm, mirror terms become visible. The two-frame algorithm is better suited for in vivo complex FdOCT due to higher registration speed than multiframe algorithms. The simulation presented in Fig. 6.12 however stresses the need for a true achromatic complex reconstruction scheme in particular for high-resolution FdOCT.

6.3.6 Fringe Washout

Spectral OCT has the advantage of being highly phase stable since the full interference pattern is recorded at once. This advantage is shared neither by conventional time domain OCT nor by wavelength tuning FdOCT. Nevertheless this advantage turns to a disadvantage in the presence of relative axial movements between sample and reference. In this case the fringe pattern across the array detector will shift during the signal integration. As a result the effective modulation depth and thus the system sensitivity decrease. This effect has been first pointed out in 2003 [3, 29] and has been analytically analyzed by Yun et al. [72] and later on by Bachmann et al. [73]. Let us assume for the sake of simplicity a single interface in the sample arm of a Michelson interferometer that is moving a distance $\delta z = v\tau$ at constant speed v during integration time τ. Neglecting the intensity DC offset, the spectral interference pattern $I_{AC}(k)$ becomes

$$I_{AC}(k) = 2\sqrt{I_r I_s} \int_{-\tau/2}^{+\tau/2} \cos\left[2k(\Delta z + vt)\right]dt = 2\sqrt{I_r I_s}\,\mathrm{sinc}(k\delta z)\cos\left(2k\Delta z\right). \quad (6.27)$$

The axial motion gives then approximately rise to decay in SNR proportional to $\mathrm{sinc}^2(k_0\delta z)$, with k_0 the center wavenumber of the source spectrum. The approximation holds for small displacements during integration $|\delta z| << \Delta z$. In 2002 first in vivo images of retinal structures obtained with spectral OCT were presented by employing a chopper to limit the exposure time to reduce fringe washout [6]. Yun et al. [74] suggested to use pulsed sources for in vivo imaging. In both cases the actual illumination time is much shorter than the overall integration time, and motion artifacts are less prominent.

The effect of fringe washout is even more critical in case of Doppler OCT when structures with axial motion components need to be resolved. Large blood vessels appear therefore often with empty central areas in spectral OCT, since the high velocities cause interference fringe blurring at thus complete SNR loss. The associated effect for swept source FdOCT in the presence of axial motion is a spectral chirp. As a consequence the swept source FdOCT signal will be broadened. This causes as well-reduced signal peak height, since the OCT signal energy needs to be conserved. Nevertheless, the experienced loss due to axial motion as much less pronounced than for spectral OCT.

As a final remark, fringe washout can also be turned to an advantage, especially when used as filtering technique. Using a heterodyne signal modulation, for example, by oscillating the reference path length causes static structures to be reduced in SNR, whereas commonly fluctuating sample signals will be enhanced. This principle is used in resonant Doppler OCT [73] as well as in a recent realization of thermal contrast OCM [75].

6.3.7 Software Methods (Ghosts Cleaning Algorithms, Dispersion)

Discrete frame methods have the advantage of being quasi achromatic and correct for the intrinsic phase error. Nevertheless their use for in vivo imaging [32] is limited since motion artifacts introduce stochastic phase errors that can only be handled by elaborate post-processing algorithms [31, 76]. Phase errors cause the appearance of residual conjugate images. In order to cancel such "ghost" images Targowski et al. [31] proposed a post-processing iterative phase optimization technique. In this technique the first approximation of phase shifts $\Delta\phi_n$ may be determined from known N mirror displacements. These phases are introduced into the system of Eq. 6.26, and an "unwrapped" image can be reconstructed using a general least square algorithm [56]. In order to remove "ghost" images caused by sample motion (stochastic phase error), N values of $\Delta\phi_n$ have to be adjusted to minimize the function:

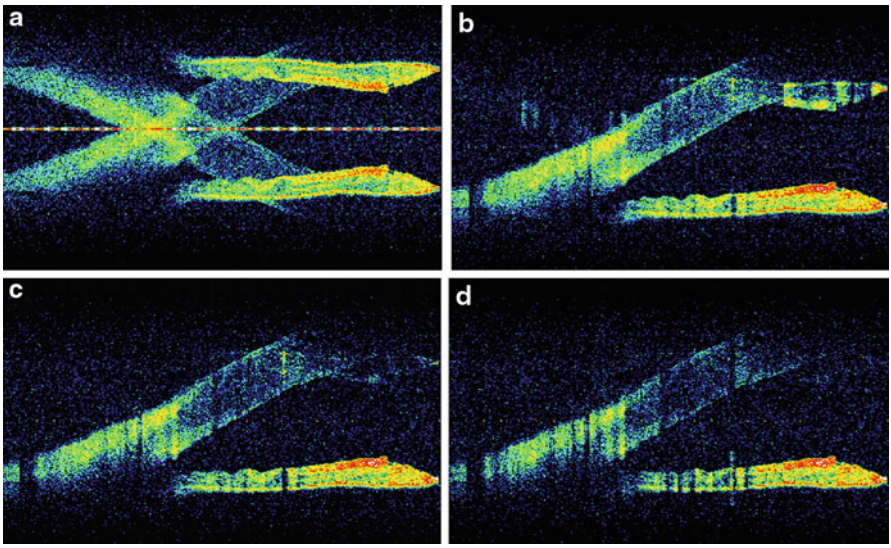

Fig. 6.13 Cross-sectional images of the corneoscleral angle of the human eye in vivo obtained with: (**a**) regular spectral OCT system, (**b**) complex FdOCT measurement with random value of the phase shift increment, (**c**) complex FdOCT measurement with calibrated value of the phase shift increment and (**d**) complex FdOCT measurement with optimized phase shift increment

$$R(\Delta\phi_1, \Delta\phi_2, .., \Delta\phi_N) = \frac{1}{K}\sum_k [\mathbf{V}_k \cdot \mathbf{V}_{k-k}] \tag{6.28}$$

where $\mathbf{V}_k$ is the intensity in kth point of A-scan obtained with complex method, $\mathbf{V}_{K-\,k}$ is the intensity at its mirror image, and the function R represents the level of correlation between the A-scan ($\mathbf{V}_k$) and its mirror image ($\mathbf{V}_{K-k}$).

Directly measured SOCT image and three complex SOCT images of human corneoscleral angle in vivo reconstructed by different algorithms are compared in Fig. 6.13. Application of the complex technique with random value for the phase shift increment causes appearance of a strong residual conjugate image that overlaps with the actual structure of the measured sample (Fig. 6.13b). Exact calibration of the phase shift increment based on complex measurements of a single reflector reduces the intensity of the "ghost" image. Still, involuntary movements of the subject's head prevent its complete cancellation (Fig. 6.13c). Additional iterative phase optimization Eq. 6.28 enables a total removal of the parasitic images from the cross-sectional complex reconstruction.

For completeness we should mention two additional techniques that allow for suppression of coherent FdOCT imaging artifacts in post-processing without the need for phase-shifting devices. The first technique offers the possibility to reduce autocorrelation noise artifacts. This is achieved by adapting a technique known from ultrasound imaging that operates on the logarithmically scaled recorded

spectrum, the so-called cepstrum [77]. The logarithm basically allows separation of autocorrelation from cross-correlation terms Eq. 6.14, in case, the cross-correlation terms do not overlap with their complex conjugate. Hence it does not yield the full complex sample signal by suppressing also the complex conjugate mirror terms. This is possible with the second mentioned technique that uses the fact that dispersion acts differently on the signal and its complex conjugate. This is easily seen from expanding the dispersion into a Taylor series and from the fact that the complex conjugate term exhibits negative path length differences. Hence impair terms flip the sign of path length differences of the complex conjugate term causing an asymmetry with respect to dispersion. Dispersion encoded complex reconstruction (DEFR) iteratively broadens and as such reduces then the complex conjugate signals by adapting a numerically introduced dispersion term [78].

6.4 Summary

This chapter gives a detailed analysis of phase-sensitive FdOCT detection starting from modeling of a complex sample structure to explaining the meaning of FdOCT signal phase and demonstrating different phase reconstruction schemes. For a better understanding of limitations of signal phase reconstruction, a full section is devoted to phase errors. The chapter outlines the problems of FdOCT detection and gives solutions of how to avoid, reduce, and remove FdOCT signal reconstruction artifacts. Some examples of phase-sensitive FdOCT applications are added to underline the potential of coherent detection having phase information at hand.

Acknowledgments We would like to acknowledge Andrzej Kowalczyk and Maciej Szkulmowski from NCU Torun for their assistance in the theoretical and experimental work on phase-sensitive SOCT. We also gratefully acknowledge helpful advices from Robert Zawadzki from UC Davis; Christoph Hitzenberger, Wolfgang Drexler, Leopold Schmetterer, and Michael Pircher from Medical University of Vienna; and Theo Lasser and Adrian Bachmann from EPFL Lausanne. We also would like to place special acknowledgments to Prof. Adolf Fercher for his scientific contribution and support.

References

1. A.F. Fercher, C.K. Hitzenberger, G. Kamp, S.Y. Elzaiat, Measurement of intraocular distances by backscattering spectral interferometry. Opt. Commun. **117**, 43–48 (1995)
2. G. Hausler, M.W. Linduer, Coherence radar and spectral radar-new tools for dermatological diagnosis. J. Biomed. Opt. **3**, 21–31 (1998)
3. R. Leitgeb, C.K. Hitzenberger, A.F. Fercher, Performance of Fourier domain vs. time domain optical coherence tomography. Opt. Express **11**, 889–894 (2003)

4. J.F. de Boer, B. Cense, B.H. Park, M.C. Pierce, G.J. Tearney, B.E. Bouma, Improved signal-to-noise ratio in spectral-domain compared with time-domain optical coherence tomography. Opt. Lett. **28**, 2067–2069 (2003)
5. M.A. Choma, M.V. Sarunic, C. Yang, J. Izatt, Sensitivity advantage of swept source and Fourier domain optical coherence tomography. Opt. Express **11**, 2183–2189 (2003)
6. M. Wojtkowski, R. Leitgeb, A. Kowalczyk, T. Bajraszewski, A.F. Fercher, In vivo human retinal imaging by Fourier domain optical coherence tomography. J. Biomed. Opt. **7**, 457–463 (2002)
7. M. Wojtkowski, T. Bajraszewski, P. Targowski, A. Kowalczyk, Real-time in vivo imaging by high-speed spectral optical coherence tomography. Opt. Lett. **28**, 1745–1747 (2003)
8. N.A. Nassif, B. Cense, B.H. Park, M.C. Pierce, S.H. Yun, B.E. Bouma, G.J. Tearney, T.C. Chen, J.F. de Boer, In vivo high-resolution video-rate spectral-domain optical coherence tomography of the human retina and optic nerve. Opt. Express **12**, 367–376 (2004)
9. M. Wojtkowski, V.J. Srinivasan, T.H. Ko, J.G. Fujimoto, A. Kowalczyk, J.S. Duker, Ultrahigh-resolution, high-speed, Fourier domain optical coherence tomography and methods for dispersion compensation. Opt. Express **12**, 2404–2422 (2004)
10. F. Lexer, C.K. Hitzenberger, A.F. Fercher, M. Kulhavy, Wavelength-tuning interferometry of intraocular distances. Appl. Opt. **36**, 6548–6553 (1997)
11. S.H. Yun, G.J. Tearney, B.E. Bouma, B.H. Park, J.F. de Boer, High-speed spectral-domain optical coherence tomography at 1.3 mu m wavelength. Opt. Express **11**, 3598–3604 (2003)
12. S.H. Yun, C. Boudoux, G.J. Tearney, B.E. Bouma, High-speed wavelength-swept semiconductor laser with a polygon-scanner-based wavelength filter. Opt. Lett. **28**, 1981–1983 (2003)
13. S.H. Yun, C. Boudoux, M.C. Pierce, J.F. de Boer, G.J. Tearney, B.E. Bouma, Extended-cavity semiconductor wavelength-swept laser for biomedical imaging. IEEE Photon Technol. Lett. **16**, 293–295 (2004)
14. R. Huber, M. Wojtkowski, K. Taira, J.G. Fujimoto, K. Hsu, Amplified, frequency swept lasers for frequency domain reflectometry and OCT imaging: design and scaling principles. Opt. Express **13**, 3513–3528 (2005)
15. R. Huber, M. Wojtkowski, J.G. Fujimoto, J.Y. Jiang, A. Cable, Three-dimensional and C-mode OCT imaging with a compact, frequency swept laser source at 1300 nm. Opt. Express **13**, 10523–10538 (2006)
16. S.R. Chinn, E.A. Swanson, J.G. Fujimoto, Optical coherence tomography using a frequency-tunable optical source. Opt. Lett. **22**, 340–342 (1997)
17. M.A. Choma, K. Hsu, J.A. Izatt, Swept source optical coherence tomography using an all-fiber 1300-nm ring laser source. J. Biomed. Opt. **10**, 44009 (2005)
18. M. Wojtkowski, T. Bajraszewski, I. Gorczynska, P. Targowski, A. Kowalczyk, W. Wasilewski, C. Radzewicz, Ophthalmic imaging by spectral optical coherence tomography. Am J. Ophthalmol. **138**, 412–419 (2004)
19. M. Wojtkowski, V. Srinivasan, J.G. Fujimoto, T. Ko, J.S. Schuman, A. Kowalczyk, J.S. Duker, Three-dimensional retinal imaging with high-speed ultrahigh-resolution optical coherence tomography. Ophthalmology **112**, 1734–1746 (2005)
20. U. Schmidt-Erfurth, R.A. Leitgeb, S. Michels, B. Povazay, S. Sacu, B. Hermann, C. Ahlers, H. Sattmann, C. Scholda, A.F. Fercher, W. Drexler, Three-dimensional ultrahigh-resolution optical coherence tomography of macular diseases. Invest. Ophthalmol. Vis. Sci. **46**, 3393–3402 (2005)
21. B.J. Kaluzny, J.J. Kaluzny, A. Szkulmowska, I. Gorczynska, M. Szkulmowski, T. Bajraszewski, P. Targowski, A. Kowalczyk, Spectral optical coherence tomography: a new imaging technique in contact lens practice. Ophthalmic Physiol. Opt. **26**, 127–132 (2006)
22. R.J. Zawadzki, S.M. Jones, S.S. Olivier, M.T. Zhao, B.A. Bower, J.A. Izatt, S. Choi, S. Laut, J.S. Werner, Adaptive-optics optical coherence tomography for high-resolution and high-speed 3D retinal in vivo imaging. Opt. Express **13**, 8532–8546 (2005)

23. Y. Yasuno, V.D. Madjarova, S. Makita, M. Akiba, A. Morosawa, C. Chong, T. Sakai, K.P. Chan, M. Itoh, T. Yatagai, Three-dimensional and high-speed swept-source optical coherence tomography for in vivo investigation of human anterior eye segments. Opt. Express **13**, 10652–10664 (2005)
24. R. Leitgeb, M. Wojtkowski, A. Kowalczyk, C.K. Hitzenberger, M. Sticker, A.F. Fercher, Spectral measurement of absorption by spectroscopic frequency-domain optical coherence tomography. Opt. Lett. **25**, 820–822 (2000)
25. R.A. Leitgeb, B. Hermann, B. Povazay, H. Sattmann, S. Michels, U. Schmidt-Erfurt, W. Drexler, Spectroscopic analysis of the human retina using three-dimensional spectroscopic ultrahigh resolution optical coherence tomography. Invest. Ophthalmol. Vis. Sci. **46**, 4273 (2005)
26. R.A. Leitgeb, L. Schmetterer, W. Drexler, A.F. Fercher, R.J. Zawadzki, T. Bajraszewski, Real-time assessment of retinal blood flow with ultrafast acquisition by color Doppler Fourier domain optical coherence tomography. Opt. Express **11**, 3116–3121 (2003)
27. R.A. Leitgeb, L. Schmetterer, C.K. Hitzenberger, A.F. Fercher, F. Berisha, M. Wojtkowski, T. Bajraszewski, Real-time measurement of in vitro flow by Fourier-domain color Doppler optical coherence tomography. Opt. Lett. **29**, 171–173 (2004)
28. B.R. White, M.C. Pierce, N. Nassif, B. Cense, B.H. Park, G.J. Tearney, B.E. Bouma, T.C. Chen, J.F. de Boer, In vivo dynamic human retinal blood flow imaging using ultra-high-speed spectral domain optical Doppler tomography. Opt. Express **11**, 3490–3497 (2003)
29. R.A. Leitgeb, C.K. Hitzenberger, A.F. Fercher, T. Bajraszewski, Phase-shifting algorithm to achieve high-speed long-depth-range probing by frequency-domain optical coherence tomography. Opt. Lett. **28**, 2201–2203 (2003)
30. M. Wojtkowski, A. Kowalczyk, R. Leitgeb, A.F. Fercher, Full range complex spectral optical coherence tomography technique in eye imaging. Opt. Lett. **27**, 1415–1417 (2002)
31. P. Targowski, W. Gorczynska, M. Szkulmowski, M. Wojtkowski, A. Kowalczyk, Improved complex spectral domain OCT for in vivo eye imaging. Opt. Commun. **249**, 357–362 (2005)
32. P. Targowski, M. Wojtkowski, A. Kowalczyk, T. Bajraszewski, M. Szkulmowski, W. Gorczynska, Complex spectral OCT in human eye imaging in vivo. Opt. Commun. **229**, 79–84 (2004)
33. A.M. Davis, M.A. Choma, J.A. Izatt, Heterodyne swept-source optical coherence tomography for complete complex conjugate ambiguity removal. J. Biomed. Opt. **10**, 64005 (2005)
34. J. Zhang, J.S. Nelson, Z.P. Chen, Removal of a mirror image and enhancement of the signal-to-noise ratio in Fourier-domain optical coherence tomography using an electro-optic phase modulator. Opt. Lett. **30**, 147–149 (2005)
35. J. Zhang, W.G. Jung, J.S. Nelson, Z.P. Chen, Full range polarization-sensitive Fourier domain optical coherence tomography. Opt. Express **12**, 6033–6039 (2004)
36. S.H. Yun, G.J. Tearney, J.F. de Boer, B.E. Bouma, Removing the depth-degeneracy in optical frequency domain imaging with frequency shifting. Opt. Express **12**, 4822–4828 (2004)
37. E. Gotzinger, M. Pircher, R.A. Leitgeb, C.K. Hitzenberger, High speed full range complex spectral domain optical coherence tomography. Opt. Express **13**, 583–594 (2005)
38. Y. Yasuno, S. Makita, T. Endo, G. Aoki, H. Sumimura, M. Itoh, T. Yatagai, One-shot-phase-shifting Fourier domain optical coherence tomography by reference wavefront tilting. Opt. Express **12**, 6184–6191 (2004)
39. Y. Yasuno, S. Makita, T. Endo, G. Aoki, M. Itoh, T. Yatagai, High-speed full-range Fourier domain optical coherence tomography by simultaneous B-M-mode scanning, in *Coherence Domain Optical Methods and Optical Coherence Tomography in Biomedicine IX*, ed. by V.V. Tuchin, J.A. Izatt, J.G. Fujimoto (SPIE, San Jose, 2005), pp. 137–142
40. V. Westphal, A.M. Rollins, S. Radhakrishnan, Correction of geometric and refractive image distortions in optical coherence tomography applying Fermat's principle. Opt. Express **10**, 397–404 (2002)

41. R.J. Zawadzki, C. Leisser, R. Leitgeb, A.F. Fercher, 3D refraction corrected optical coherence tomography measurements of the anterior chamber in vitro. Invest. Ophthalmol. Vis. Sci. **44**, U141–U141 (2003)
42. R. Ahrenkie, Modified Kramers-Kronig analysis of optical spectra. J. Opt. Soc. Am. **61**, 1651 (1971)
43. K.F. Palmer, M.Z. Williams, B.A. Budde, Multiply subtractive Kramers-Kronig analysis of optical data. Appl. Opt. **37**, 2660–2673 (1998)
44. D.J. Faber, M.C.G. Aalders, E.G. Mik, B.A. Hooper, M.J.C. van Gemert, T.G. van Leeuwen, Oxygen saturation-dependent absorption and scattering of blood. Phys. Rev. Lett. **93**, 028102 (2004)
45. S.M. Bagherzadeh, B. Grajciar, C.K. Hitzenberger, M. Pircher, A.F. Fercher, Dispersion-based optical coherence tomography OCT measurement of mixture concentrations. Opt. Lett. **32**, 2924–2926 (2007)
46. F.E. Robles, L.L. Satterwhite, A. Wax, Nonlinear phase dispersion spectroscopy. Opt. Lett. **36**, 4665–4667 (2011)
47. B. Grajciar, Y. Lehareinger, A.F. Fercher, R.A. Leitgeb, High sensitivity phase mapping with parallel Fourier domain optical coherence tomography at 512,000 A-scan/s. Opt. Express **18**, 21841–21850 (2010)
48. B. Grajciar, M. Herdin, C. Blatter, M. Groeschl, R.A. Leitgeb, High-resolution phase mapping with parallel Fourier domain optical coherence microscopy for dispersion contrast imaging. Photonics Letters of Poland **3**, 135–137 (2011)
49. C. Blatter, B. Grajciar, P. Zou, W. Wieser, A.J. Verhoef, R. Huber, R.A. Leitgeb, Intrasweep phase-sensitive optical coherence tomography for noncontact optical photoacoustic imaging. Opt. Lett. **37**, 4368–4370 (2012)
50. A. Szkulmowska, M. Wojtkowski, I. Gorczynska, T. Bajraszewski, M. Szkulmowski, P. Targowski, A. Kowalczyk, J.J. Kaluzny, Coherent noise-free ophthalmic imaging by spectral optical coherence tomography. J. Phys. D-Appl. Phys. **38**, 2606–2611 (2005)
51. R. Leitgeb, L. Schmetterer, M. Wojtkowski, C.K. Hitzenberger, M. Sticker, A.F. Fercher, Flow velocity measurements by frequency domain short coherence interferometry, in *Coherence Domain Optical Methods in Biomedical Science and Clinical Applications VI*, ed. by V.V. Tuchin, J. Izatt, J.G. Fujimoto (SPIE, San Jose, 2002), pp. 16–21
52. A.H. Bachmann, R.A. Leitgeb, T. Lasser, Heterodyne Fourier domain optical coherence tomography for full range probing with high axial resolution. Opt. Express **14**, 1487–1496 (2006)
53. M.V. Sarunic, M.A. Choma, C.H. Yang, J.A. Izatt, Instantaneous complex conjugate resolved spectral domain and swept-source OCT using 3x3 fiber couplers. Opt. Express **13**, 957–967 (2005)
54. M.A. Choma, C. Yang, J.A. Izatt, Instantaneous quadrature low-coherence interferometry with 3 x 3 fiber-optic couplers. Opt. Lett. **28**, 2162–2164 (2003)
55. A.F. Fercher, R. Leitgeb, C.K. Hitzenberger, H. Sattmann, M. Wojtkowski, Complex spectral interferometry OCT, in *Medical Applications of Lasers in Dermatology, Cardiology, Ophthalmology, and Dentistry II,* ed. by G.B. Altshuler, S. Andersson-Engels, R. Birngruber, P. Bjerring, A.F. Fercher, H.J. Geschwind, R. Hibst, H. Hoenigsmann, F. Laffitte, H. Sterenborg (SPIE, 1999), pp. 173–178
56. K. Creath, Phase-measurement interferometry techniques. Prog. Opt. **26**, 349–393 (1988)
57. J. Schmit, K. Creath, Extended averaging technique for derivation of error-compensating algorithms in phase-shifting interferometry. Appl. Opt. **34**, 3610–3619 (1995)
58. R.K. Wang, In vivo full range complex Fourier domain optical coherence tomography. Appl. Phys. Lett. **90**, 054103 (2007)
59. R. A. Leitgeb, R. Michaely, T. Lasser, S.C. Sekhar, Complex ambiguity-free Fourier domain optical coherence tomography through transverse scanning. Opt. Lett. **32**, 3453–3455 (2007)

60. B. Baumann, M. Pircher, E. Götzinger, C.K. Hitzenberger, Full range complex spectral domain optical coherence tomography without additional phase shifters. Opt. Express **15**, 13375–13387 (2007)
61. Y.K. Tao, A.M. Davis, J.A. Izatt, Single-pass volumetric bidirectional blood flow imaging spectral domain optical coherence tomography using a modified Hilbert transform. Opt. Express **16**, 12350–12361 (2008)
62. L. An, J. Qin, R.K. Wang, Ultrahigh sensitive optical microangiography for in vivo imaging of microcirculations within human skin tissue beds. Opt. Express **18**, 8220–8228 (2010)
63. I. Grulkowski, I. Gorczynska, M. Szkulmowski, D. Szlag, A. Szkulmowska, R.A. Leitgeb, A. Kowalczyk, M. Wojtkowski, Scanning protocols dedicated to smart velocity ranging in spectral OCT. Opt. Express **17**, 23736–23754 (2009)
64. A. Szkulmowska, M. Szkulmowski, D. Szlag, A. Kowalczyk, M. Wojtkowski, Three-dimensional quantitative imaging of retinal and choroidal blood flow velocity using joint spectral and time domain optical coherence tomography. Opt. Express **17**, 10584–10598 (2009)
65. D.Y. Kim, J. Fingler, J.S. Werner, D.M. Schwartz, S.E. Fraser, R.J. Zawadzki, In vivo volumetric imaging of human retinal circulation with phase-variance optical coherence tomography. Biomed. Opt. Express **2**, 1504–1513 (2011)
66. C. Blatter, J. Weingast, A. Alex, B. Grajciar, W. Wieser, W. Drexler, R. Huber, R.A. Leitgeb, In situ structural and microangiographic assessment of human skin lesions with high-speed OCT. Biomed. Opt. Express **3**, 2636–2646 (2012)
67. T. Schmoll, A.S.G. Singh, C. Blatter, S. Schriefl, C. Ahlers, U. Schmidt-Erfurth, R.A. Leitgeb, Imaging of the parafoveal capillary network and its integrity analysis using fractal dimension. Biomed. Opt. Express **2**, 1159–1168 (2011)
68. T. Schmoll, E. Götzinger, M. Pircher, C.K. Hitzenberger, R.A. Leitgeb, Single-camera polarization-sensitive spectral-domain OCT by spatial frequency encoding. Opt. Lett. **35**, 241–243 (2010)
69. T. Schmoll, C. Kolbitsch, R.A. Leitgeb, In vivo functional retinal optical coherence tomography. J. Biomed. Opt. **15**, 041513–041518 (2010)
70. J.W. Goodman, *Statistical Optics* (Wiley, New York, 1995)
71. M.A. Choma, A.K. Ellerbee, C. Yang, T.L. Creazzo, J.A. Izatt, Spectral-domain phase microscopy. Opt. Lett. **30**, 1162–1164 (2005)
72. S.H. Yun, G.J. Tearney, J.F. de Boer, B.E. Bouma, Motion artifacts in optical coherence tomography with frequency-domain ranging. Opt. Express **12**, 2977–2998 (2004)
73. A.H. Bachmann, M.L. Villiger, C. Blatter, T. Lasser, R.A. Leitgeb, Resonant Doppler flow imaging and optical vivisection of retinal blood vessels. Opt. Express **15**, 408–422 (2007)
74. S.H. Yun, G.J. Tearney, J.F. de Boer, B.E. Bouma, Pulsed-source and swept-source spectral-domain optical coherence tomography with reduced motion artifacts. Opt. Express **12**, 5614–5624 (2004)
75. C. Pache, N.L. Bocchio, A. Bouwens, M. Villiger, C. Berclaz, J. Goulley, M.I. Gibson, C. Santschi, T. Lasser, Fast three-dimensional imaging of gold nanoparticles in living cells with photothermal optical lock-in optical coherence microscopy. Opt. Express **20**, 21385–21399 (2012)
76. J. Oh, B. Kim, Artifacts removal in complex frequency domain optical coherence tomography with numerical least-square phase-shifting algorithm, in *Coherence Domain Optical Methods and Optical Coherence Tomography in Biomedicine IX*, ed. by V.V. Tuchin, J.A. Izatt, J.G. Fujimoto (SPIE, San Jose, 2005), pp. 132–136
77. C.S. Seelamantula, M.L. Villiger, R.A. Leitgeb, M. Unser, Exact and efficient signal reconstruction in frequency-domain optical-coherence tomography. J. Opt. Soc. Am. A Opt. Image Sci. Vis. **25**, 1762–1771 (2008)
78. B. Hofer, B. Povazay, B. Hermann, A. Unterhuber, G. Matz, W. Drexler, Dispersion encoded full range frequency domain optical coherence tomography. Opt. Express **17**, 7–24 (2009)

Optical Frequency Domain Imaging

7

Brett E. Bouma, Guillermo J. Tearney, Benjamin Vakoc, and Seok Hyun Yun

Keywords

Detection sensitivity • Motion artifacts • Nonlinear tuning • OFDI • Optical frequency domain imaging • Phase sensitive imaging • Swept laser • Swept source OCT

7.1 Introduction

In most OCT systems, one-dimensional (depth) ranging is provided by low-coherence interferometry [1, 2] in which the optical path length difference between the interferometer reference and sample arms is scanned linearly in time. This embodiment of OCT, referred to as "time-domain OCT," has demonstrated promising results for minimally invasive, early detection of disease. The relatively slow imaging speed (approximately 2 kHz A-line rate) of time-domain OCT systems, however, has precluded its use for the screening of large tissue volumes, which is required for a wide variety of medical applications. Imaging speed has a fundamental significance because of its relationship to detection sensitivity (minimum detectable reflectivity). As the A-line rate increases, the detection bandwidth should be increased proportionally, and therefore, the sensitivity drops. The sensitivity of state-of-the-art time-domain OCT systems that operate at 2 kHz ranges between −105 and −110 dB. Most biomedical applications require this level of

B.E. Bouma (✉) • G.J. Tearney • B. Vakoc
Wellman Center for Photomedicine, Massachusetts General Hospital and Harvard Medical School, Boston, MA, USA
e-mail: bouma@mgh.harvard.edu

S.H. Yun
Partners Research Building, Wellman Center for Photomedicine, Cambridge, MA, USA

Wellman Center for Photomedicine, Massachusetts General Hospital, Harvard Medical School, Boston, MA, USA

© Springer International Publishing Switzerland 2015

W. Drexler, J.G. Fujimoto (eds.), *Optical Coherence Tomography*,
DOI 10.1007/978-3-319-06419-2_8

sensitivity for sufficient depth of penetration and cannot tolerate a reduction in sensitivity to achieve a higher frame rate. Although increasing the optical power would, in principle, improve the sensitivity, available sources and maximum permissible exposure levels of tissue represent significant practical limitations.

One potential solution to high-speed imaging is offered by spectral-domain OCT ("spectral radar") where individual spectral components of low-coherence light are detected separately by the use of a spectrometer and a charge-coupled device (CCD) array [3, 4]. The fast readout speed of CCD arrays and the signal-to-noise ratio (SNR) advantage of the spectral-domain OCT [5–7] make it promising for some high-speed and low-power applications. However, the use of CCD arrays may cause problems associated with phase washout by changes in the sample-arm length during the pixel integration time [7]. Furthermore, for this scheme, the implementation of balanced detection and polarization diversity which may be needed for in vivo endoscopic imaging is challenging.

In this chapter, we discuss another frequency-domain approach, optical frequency-domain imaging (OFDI), which is based on optical frequency-domain reflectometry [8–10] and uses a wavelength-swept laser and standard single-element photodetectors. The chapter begins with an overview of the fundamental aspects of the technology, including the detected signal, sensitivity, depth range, and resolution, and then goes on to discuss specific component technologies including the light source, interferometer and acquisition electronics, and image processing. The final section of the chapter provides a brief glimpse at some of the biomedical applications that most directly take advantage of the improved speed and sensitivity of OFDI.

7.2 Principles of Operation

7.2.1 Frequency-Domain Signal

Figure 7.1 shows the basic configuration of OFDR using a tunable light source and a fiber-optic interferometer. The output of the source is split into a reference arm and a sample arm which illuminates and receives the light reflected from within the sample. The interference between the reference- and sample-arm light is detected with a square-law photodetector, while the wavelength of the monochromatic source is swept and the path lengths of the reference and sample arm are held

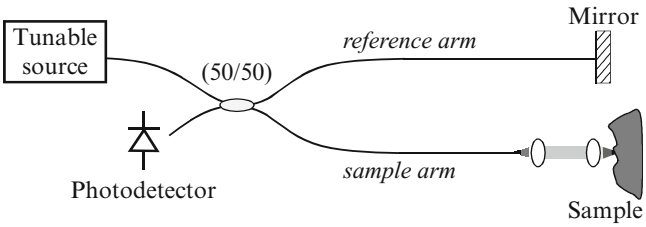

Fig. 7.1 Basic configuration of OFDR optical system

constant. The axial reflectivity profile (A-line) is obtained by discrete Fourier transform (DFT) of the sampled detector signals [8].

The detector current can be expressed as

$$i_{\mathrm{det}}(t) = \frac{\eta q}{hv}\left(P_r + P_o\int r^2(z)dz + 2\sqrt{P_r P_o}\int r(z)\Gamma(z)\cos\left(2k(t)z + \phi(z)\right)dz\right), \tag{7.1}$$

where η is the detector sensitivity, q the quantum of electric charge (1.6×10^{-19} C), hv the single photon energy, P_r the optical power reflected from the reference arm at the photodetector, and P_o the optical power illuminating the sample. The third term represents the interferometric signal, and the first and second terms contribute to the noninterference background. Here, z is the axial coordinate where $z = 0$ corresponds to zero optical path length difference between the two interferometric arms, $r(z)$ and $\phi(z)$ are the amplitude and phase of the reflectance profile of the sample, respectively; $\Gamma(z)$ is the coherence function of the instantaneous laser output; and $k(t) = 2\pi/\lambda(t)$ is the wavenumber which is varied in time monotonically by tuning of the laser. It can be readily seen that the interferometric signal current is related to the reflection profile via the Fourier transform relation. In practice, the detector output is digitized and sampled into a finite number of data points, and a discrete Fourier transform (DFT) is performed to construct an axial scan or A-line.

For a wavelength-swept laser with a Gaussian-profile spectral envelope, the axial resolution is given by [11]

$$\delta z = \frac{2\ln 2}{\pi}\frac{{\lambda_o}^2}{n\Delta\lambda}, \tag{7.2}$$

where λ_o is the center wavelength, $\Delta\lambda$ is the full width at half maximum (FWHM) of the spectral envelope (tuning range), and n is the group refractive index of the sample. The depth range Δz in the Fourier domain is given by [4]

$$\Delta z = \frac{{\lambda_o}^2}{4n\delta\lambda}, \tag{7.3}$$

where $\delta\lambda = \Delta\lambda/N_s$ is the sampling wavelength interval and N_s is the number of samples within FWHM range of the spectrum $\Delta\lambda$. The sampling interval should be smaller than the instantaneous linewidth of the source; otherwise, the amplitude of the coherence function will decay with z, limiting the usable ranging depth.

7.2.2 Detection Sensitivity

For simplicity, let us consider the case of a single reflector located at $z = z_0$ with reflectivity r^2. We assume that the linewidth is sufficiently narrow so that $\Gamma(z) = 1$ within the depth range. The signal current, $i_s(t)$, can be expressed as

$$i_s(t) = \frac{\eta q}{h\nu} \cdot 2\sqrt{P_r P_s} \cos\left(2k(t)z_0\right), \tag{7.4}$$

where $P_s = r^2 P_0$ denotes the optical power reflected from the sample at the photodetector. In reality, the detector current consists of both signal and noise components such that $i(t) = i_s(t) + i_n(t)$. The well-known expression for the noise power $\langle {i_n}^2 \rangle$ is given by [12]

$$\left\langle i_n^2(t) \right\rangle = \left(i_{th}^2 + 2\frac{\eta q^2}{h\nu}(P_r + P_s) + \left(\frac{\eta q}{h\nu}\right)^2 RIN(P_r + P_s)^2 \right) BW, \tag{7.5}$$

where the three terms on the right-hand side represent thermal noise, shot noise, and the relative intensity noise (RIN) of the source (polarized), respectively. Brackets $< >$ denote a time average, *i*th the detector noise current, *RIN* the relative intensity noise given in unit of Hz^{-1}, and *BW* the detection bandwidth. The detection bandwidth can be chosen equal to half the sampling rate as specified by the Nyquist.

For simplicity, let us assume a square-profile spectral envelope and 100 % tuning duty cycle, i.e., the output power of the source is constant in time. Let F_s and F_n denote the Fourier transform samples of signal and noise currents, i_s and i_n, respectively, following DFT via

$$F(z_l) = \sum_{\mathrm{m}=0}^{\mathrm{N_s}-1} i(k_m) \cdot \exp^{-j2\pi lm/N_s} \tag{7.6}$$

Note that the wavenumber and axial coordinate are conjugates to each other through DFT. In the Fourier domain, the absolute square of the peak value of F_s at $z_l = z_0$ is proportional to the reflectivity. Parseval's theorem, $\sum F^2 = N_s \sum i^2$, holds for both signal and noise. In the case of Nyquist sampling (i.e., the sampling rate is equal to twice the detection bandwidth), the sampled data of noise current are mutually uncorrelated [6, 7]. Therefore, the noise power level in the Fourier domain is given by $\langle F_n^2 \rangle = N_s \langle i_n^2 \rangle$. On the other hand, the signal power ${F_s}^2$ is zero except at $z_l = z_0$. Since there are two peaks corresponding to positive and negative frequency components, using $|F_s(z_0)|^2 = (N_s^2/2)\langle i_s^2 \rangle$ leads to

$$(SNR)_{FD} = \frac{|F_s(z_0)|^2}{\left\langle F_n^2 \right\rangle} = \frac{N_s}{2}(SNR)_{TD}, \tag{7.7}$$

where

$$(SNR)_{TD} = \frac{\left\langle i_s^2(t) \right\rangle}{\left\langle i_n^2(t) \right\rangle} \tag{7.8}$$

Here, the latter is defined as the ratio of the signal and noise power in the time domain. These equations indicate that frequency-domain ranging provides an SNR

improvement by a factor of $N_s/2$ compared with time-domain ranging [13]. A similar expression to Eq. 7.7 has been identified by Leigeb et al. [7] and de Boer et al. [6] for spectral-domain OCT and also by Choma et al. [5] for OFDR using a wavelength-swept laser.

It can be shown that Eq. 7.7 is valid for a more general case where the tuning duty cycle is less than 100 %, the source's spectral envelope has a Gaussian profile, and the sampling range spans beyond the FWHM of the source spectrum. In this case, N_s is the number of sampling points within the FWHM of the source and the optical powers, P_r and P_s, would be the time-average value over one tuning cycle. For a shot-noise-limited system, Eqs. 7.5 and 7.7 with $P_s \ll P_r$ lead to

$$(SNR)_{FD} \approx \frac{\eta P_s}{h\nu f_A}, \tag{7.9}$$

where f_A is the A-line rate which is the same as the tuning rate of the source. Therefore, the effective detection bandwidth in OFDR is equal to the A-line scan rate instead of the detector bandwidth.

Equation 7.7 can also be expressed in terms of the number of spatially resolvable points in a ranging depth, $N_R = \Delta z/\delta z$, as

$$(SNR)_{FD} = N_R (SNR)_{TD} \tag{7.10}$$

This expression compares the SNR of two ranging methods, time domain and frequency domain, at the same imaging speed (A-line rate), axial resolution, and ranging depth. Note that a time-domain OCT system requires a detection bandwidth of $N_R f_A$, whereas the effective noise bandwidth of OFDI is f_A.

The sensitivity is defined as the reflectivity that produces signal power equal to the noise power. Therefore, it follows from Eq. 7.9 and $P_s = r^2 P_0$ that

$$Sensitivity[dB] = -10 \log\left(\frac{\eta P_0}{h\nu f_A}\right) \tag{7.11}$$

The relative intensity noise (RIN) of polarized thermal light is proportional to the reciprocal of the linewidth [12] and would have a value of −97 dB/Hz for a linewidth of 0.06 nm (10 GHz). In general, RIN of laser light is different from that of thermal light. However, laser light consisting of many longitudinal modes with random phases would exhibit a peak RIN level similar to that of thermal light of the same linewidth. The mode hopping associated with wavelength tuning and mode competition contributes to the frequency dependence of RIN. The RIN level of our laser had a peak value of approximately −100 dB/Hz near DC frequency, decreasing to −120 dB/Hz at 5 MHz. To reduce the source's RIN, dual-balanced detection was employed [14]. The differential current of two InGaAs detectors D1 and D2 was amplified using transimpedance amplifiers (TIA, total gain of 56 dB) and passed through a low-pass filter (LPF) with a 3-dB cutoff frequency at 5 MHz and excess voltage loss of 3 dB. The common-noise rejection efficiency of the

receiver was approximately 25 dB in the range between DC and 5 MHz. In addition to RIN reduction, the balanced detection provides multiple benefits; it suppresses self-interference noise [7] originating from multiple reflections within the sample and optical components; it also improves the dynamic range and reduces fixed-pattern noise by greatly reducing the strong background signal from the reference light.

In the case of dual-balanced detection, the signal power in Eq. 7.4 can be expressed as

$$\left\langle i_s^2(t)\right\rangle = \left(\frac{\eta q}{h\nu}\right)^2 \left\langle \sum^2 2p_r p_s \cos\left(kz\right)\right\rangle^2 = 8\left(\frac{\eta q}{h\nu}\right)^2 p_r p_s, \tag{7.12}$$

where $p_r = P_r/2$ and $p_s = P_s/2$ denote the reference and signal power per photodiode. The noise power expression in Eq. 7.5 can be modified to

$$\begin{aligned}\left\langle i_n^2(t)\right\rangle = &\left(\frac{i_{qn}^2}{G^2} + \frac{i_{ex}^2}{G^2} + i_{th}^2 + 2\frac{\eta q^2}{h\nu}\sum^2 \left(p_r + p_s\right)\right.\\ &\left. + \left(\frac{\eta q}{h\nu}\right)^2 RIN\left\{\sum^2 \zeta\left(p_r^2 + p_s^2\right) + \sum^2 2p_r p_s\right\}\right) BW\end{aligned} \tag{7.13}$$

Here, the first and second terms are introduced to take into account the quantization noise and excess electrical noise generated in the DAQ board. G denotes the total gain of the receiver. The third term is the thermal noise of the dual-balanced receiver. The fourth term represents the total shot noise which is a sum of the shot noise from the individual photodiodes. The fifth term expresses the RIN noise with ζ denoting the common-mode rejection efficiency of the balanced receiver. It should be noted that the dual-balanced receiver provides RIN suppression only to the RIN component associated with intraband self-beating. The cross-beating noise, as a result of the incoherent interference between p_r and p_s, is not canceled. When $\zeta \ll 1$, the cross-beating RIN component may not be negligible compared to the self-beating RIN component although p_s is weaker than p_r. In practice, the first two terms, quantization and excess noise, can be made negligible by choosing a sufficiently high gain (e.g., $G = 2 \times 10^5$) [13].

7.3 Instrumentation

7.3.1 Light Source and Interferometer

Light sources appropriate for OFDI are discussed in detail in ▶ Chap. 12, "Linear OCT Systems". In the context of this chapter, it will be sufficient to briefly consider the relevant laser characteristics and their implications for high-speed imaging.

The laser specifications having the greatest significance for OFDI include wavelength sweep range, sweep repetition rate, linearity of sweep, power, and instantaneous linewidth. The primary relevance of the source wavelength-scanning range for OFDI is axial resolution. For imaging at a center wavelength of 1.3 μm where attenuation in biological tissues is low, a scanning range of more than 100 nm is required to achieve a resolution comparable with previous-generation time-domain OCT systems. Consideration of laser repetition rate is similarly straightforward; the image A-line acquisition rate is directly determined by the laser repetition rate. For imaging at speeds of 100 frames per second, a repetition rate of >50 kHz is required. The linearity of the wavelength-scan, however, is somewhat more subtle. Although nonlinear scanning can, in principle, be accommodated by sophisticated acquisition electronics, the ideal laser for OFDI would provide a highly linear k-space scan. Fortunately, achieving all of these specifications is now possible while simultaneously producing sufficient power in order to preserve clinically relevant sensitivity. Typical performance specifications have been on the order of 10s of mW of polarized laser power.

As described in the previous sections of this chapter, the instantaneous linewidth of the laser determines the ranging depth and the falloff of sensitivity with ranging depth. For many OFDI applications, an instantaneous linewidth of 0.1 nm-0.2 nm (roughly 20–40 GHz) is sufficient. It is interesting to note that this linewidth is significantly greater than that provided by most wavelength-swept lasers that preceded the development of OFDI. Prior swept lasers were primarily developed for high-resolution spectroscopy where single-longitudinal-mode oscillation is essential and linewidths below 1 MHz are routinely achieved. Relaxing the linewidth specification allows for more rapid tuning without concerns for longitudinal mode hopping.

In order to achieve the greatest possible ranging depth, it would be preferred to use the full instantaneous coherence length of the laser source. Equation 7.4, however, indicates that positive and negative depths, relative to the reference delay, are encoded by the same magnitude of frequency. Since it is not possible to distinguish between a positive and negative electrical frequency in conventional interferometry, OFDI requires alternative interferometer designs to break the depth degeneracy and achieve full ranging depth. Solutions to this challenge can be achieved through the use of quadrature interference signals. Approaches have included active- or passive-phase biasing using piezoelectric actuators [15], birefringent plates [16], and fused fiber 3 × 3 couplers [17]. These techniques can unfold otherwise overlapping images associated with positive and negative depths, but tend to leave residual artifacts due to the difficulty of producing stable quadrature signals. An alternative approach uses an optical frequency shifter in the interferometer to provide a constant frequency shift of the detector signal. This method allows both sides of the coherence range to be used without crosstalk and doubles the ranging depth. The same concept has been described previously in the context of 1-dimensional optical frequency-domain reflectometry using rotating birefringent plates [19] at 58 Hz or a recirculating frequency-shifting loop [16].

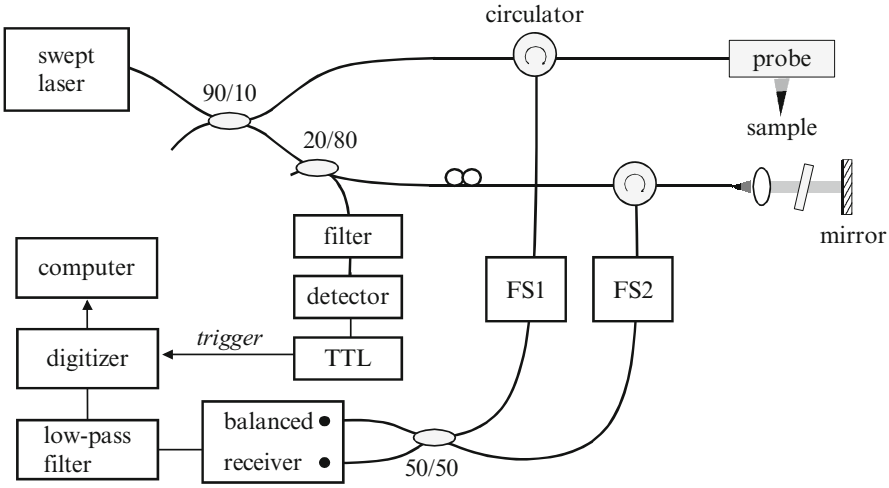

Fig. 7.2 OFDI system schematic

Figure 7.2 depicts a simplified OFDI system comprising a wavelength-swept source, a single-mode-fiber interferometer employing an optical frequency shifter in the reference arm, a photodetector, and a signal processor [18]. Since the optical glass used in acousto-optic frequency shifters can exhibit high dispersion, it is preferable to insert a matching glass within the interferometer sample arm. With a round-trip frequency shift of Δf in the reference arm and an interferometer path length difference (or depth) of z, the detector signal can be expressed as

$$i_s(t) = 2\eta\sqrt{P_r(t)P_s(t)}\int \sqrt{R(z)}\;\; G(|z|)\cos\left[\frac{4\pi}{c}v(t)z + \phi(z) + 2\pi\Delta f t\right]dz, \quad (7.14)$$

where η denotes the quantum efficiency of the detector; $P_r(t)$ and $P_s(t)$ the optical powers of the reference and sample-arm light, respectively; $R(z)$ the reflectivity profile of the sample; $G(|z|)$ the coherence function corresponding to the fringe visibility; c the speed of light; $v(t)$ the optical frequency; and $\phi(z)$ the phase of backscattering. For linear tuning, i.e., $v(t) = v_0 - v_1 t$, the frequency of the detector signal is given by

$$f_s = \left|v_1\frac{2z}{c} - \Delta f\right|. \quad (7.15)$$

A signal frequency of zero (DC) corresponds to a depth $z = c\Delta f/(2v_1)$. Therefore, by choosing Δf and v_1 to have opposite signs, the zero signal frequency can be made to point to a negative depth.

7.3.2 Sampling and Data Processing

Nonlinearity in the frequency sweep of the laser results in a chirping of the signal at a constant depth and causes a degradation of axial resolution [16, 19]. As a solution to this problem, the detector signal may be sampled with nonlinear time intervals compensating for the frequency chirp. Alternatively, the detector signal can be sampled with a constant time interval if the sampled data is remapped to a uniform v-space by interpolation prior to discrete Fourier transform (DFT) [20]. Both methods have been demonstrated to yield a transform-limited axial resolution given by the tuning spectral range of the source.

These methods, however, are not directly applicable in the frequency-shifting technique. Both nonlinear sampling and the interpolation method result in artificial chirping of the frequency shift, leading to suboptimal axial resolution. Alternatively, a modified interpolation method based on frequency shifting and zero padding can be used to achieve nearly transform-limited axial resolution over the entire ranging depth. An exemplary algorithm includes the following:

Step 1. Obtain N samples of the signal with uniform time interval during each wavelength sweep of the source.
Step 2. Calculate DFT of N data points in the electrical frequency domain.
Step 3. Separate two frequency bands below and above Δf corresponding to negative and positive depths, respectively.
Step 4. Shift each frequency band such that the zero depth is aligned to the zero electrical frequency.
Step 5. Apply zero-padding to each frequency band and calculate inverse DFT resulting in an array of increased number of samples in the time domain with smaller time interval for each frequency band.
Step 6. Interpolate each array in the time domain into a uniform v space using a mapping function calibrated to the nonlinearity of the source with linear interpolation. The mapping function can be obtained using an unbalanced interferometer.
Step 7. Calculate DFT of each interpolated array.
Step 8. Combine the two arrays (images) by shifting the array index.

Yun et al. [18] have demonstrated that the above algorithm, coupled with the interferometer design of Fig. 7.2, can be used to achieve a twofold increase of the effective ranging depth of OFDI. Measurements of the system axial resolution indicated that the interpolation algorithm compensated for laser tuning nonlinearity and yielded transform-limited resolution throughout the extended ranging depth.

7.4 Motion Artifacts

Image artifacts resulting from motion have been important topics of research in nearly all medical imaging modalities because they may degrade the image quality and cause inaccurate clinical interpretation of images [21–23]. Artifacts can arise when an object being imaged (sample) is moved during data acquisition but is assumed stationary in the image reconstruction process. In each imaging modality, motion artifacts can present in different forms and with different magnitudes. Understanding basic motion effects in a particular imaging method is an essential step toward the development of techniques to avoid or compensate resulting artifacts.

In the following analysis, it is assumed that the source emits light according to $k(t) = k_0 + k_1 t$, where $k = 2\pi/\lambda$ is the wavenumber, λ is the optical wavelength, t is the time spanning from $-T/2$ to $T/2$, and T is the wavelength-sweep period or equivalently A-line period. Further, we assume a Gaussian tuning envelope given by

$$P_{out}(t) = P_0 \ \exp\left[-4\ln 2 t^2/(\sigma T)^2\right], \tag{7.16}$$

where $P_{out}(t)$ denotes the output power of the source and σT the full width at half maximum (FWHM) of the tuning envelope. Equation 7.16 also describes the Gaussian spectral envelope of the source, where $\sigma k_1 T$ corresponds to the FWHM tuning range in wavenumber. Let (x, y, z) denote the coordinate of a reference frame fixed to the sample, $r(x, y, z)$ represents the complex-valued backscattering coefficient of the sample which is characterized by both local variations of the refractive index and the round-trip attenuation of light in the sample, $g(x, y, z)$ denotes the intensity profile of the probe beam normalized to $\int\int g\, dx\, dy = 1$, and (x_b, y_b, z_b) denotes the coordinates of the probe beam at zero path length difference of the interferometer. For a Gaussian beam with a large confocal parameter, the intensity profile is given by

$$g(x, y, z) \approx \frac{4\ln 2}{\pi {w_0}^2} \exp\left[-4\ln 2\left(x^2 + y^2\right)/{w_0}^2\right], \tag{7.17}$$

where w_0 denotes the full width at half maximum (FWHM) of the beam profile. The explicit dependence of the OFDI signal on the intensity profile, g, rather than an electric field profile of the probe beam can be understood by considering the mode field profile of the sample-arm fiber, which is by definition given by Eq. 7.17 at the sample location. The amplitude of the backscattered light received by the sample-arm fiber is determined by an overlap integral between the scattered field and the mode field.

It has been shown [24] that the complex-valued depth profile can be represented using the above notation as

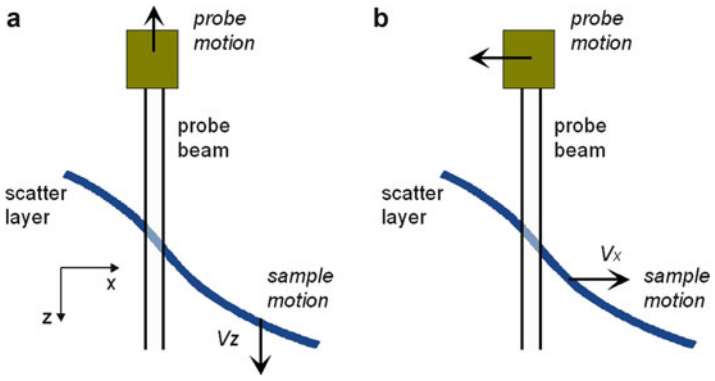

Fig. 7.3 Geometry for considering the effects of axial and transverse motion

$$F(Z) \propto \frac{\gamma P_0}{{w_0}^2 \delta z_0} \iiint dxdydz \;\; r(x,y,z) e^{-i2k_0(z-z_b)} \\ e^{-4\ln 2 \frac{(x-x_b)^2}{{w_0}^2}} e^{-4\ln 2 \frac{(y-y_b)^2}{{w_0}^2}} e^{-4\ln 2 \frac{\{Z+z_b-z(x,y)\}^2}{{\delta z_0}^2}}, \tag{7.18}$$

where $\delta z_0 = 41\mathrm{n}2/(k_1 T\sigma)$ denotes the FWHM axial resolution neglecting the effect of truncation of a Gaussian spectrum. Equation 7.18 states that the amplitude of $F(Z)$ is proportional to a coherent sum of all backscattered light from a coherence volume that has a size $w_0 \times w_0 \times \delta z_0$ and is located at a depth Z in the sample.

7.4.1 Axial Motion

Figure 7.3a depicts a situation with an axially moving sample and probe. The interference signal is solely dependent on the relative motion between the scatterer and the probe beam; sample motion is identical to probe motion with the opposite velocity. Therefore, we will assume a stationary probe and consider a sample moving at a uniform velocity without loss of generality.

The signal in the presence of axial motion can be obtained by substituting $z_b(t) = z - z_0 - v_z t$ into Eq. 7.18 where $z_0 = z\text{–}z_b(0)$ denotes the mean path length difference and v_z the axial velocity of the sample. The depth profile is obtained via the Fourier transform:

$$F(Z) \approx \gamma P_0 \iiint dxdydz \;\; r(x,y,z) g(x-x_b, y-y_b) \\ \int_{-\infty}^{\infty} e^{-4\ln 2 \frac{\kappa^2}{(2k_1 T\sigma)^2}} e^{i(2k_0+\kappa)\left(Z - z_0 - \frac{v_z}{2k_1}\kappa\right)} d\kappa \tag{7.19}$$

$$\propto \frac{\gamma P_0}{{w_0}^2 \delta z} \iiint dxdydz \;\; r(x,y,z) e^{-i2k_0 z_0} e^{-4\ln 2 \frac{(x-x_b)^2}{{w_0}^2}} e^{-4\ln 2 \frac{(y-y_b)^2}{{w_0}^2}} e^{-4\ln 2 \frac{\{Z-[z_0+(k_0/k_1 T)\Delta z]\}^2}{{\delta z_0}^2 (1+4\sigma^2 \Delta z^2/{\delta z_0}^2)}} \tag{7.20}$$

where $\Delta z = v_z T$ denotes the axial displacement of the sample during a single A-line acquisition time. Equation 7.20 illustrates two effects of axial motion. First, depth in the image is given by $Z = z_0 + z_D$, where

$$z_D \equiv \frac{k_0}{k_1 T} \Delta z = \frac{\pi \sigma}{2\ln 2} \frac{\delta z_0}{\lambda} \Delta z. \tag{7.21}$$

The axial shift, z_D, originates from the Doppler frequency shift generated by the moving sample. That is, a moving sample would create a signal modulation even in the absence of tuning. The Doppler frequency is given by $(2v_z/c)v$, where c is the light speed and v is the optical frequency. For frequency-swept light, the Doppler frequency is added to the original modulation frequency of the OFDI signal, resulting in an erroneous depth offset. Typical values for σ and $\delta z_0/\lambda$ may be 0.5–0.8 and 4–12, respectively. Therefore, the Doppler error could be 5–22 times the actual displacement Δz.

The second effect is broadening in axial resolution, given by

$$\frac{\delta z}{\delta z_0} = \sqrt{1 + 4\sigma^2 \frac{\Delta z^2}{{\delta z_0}^2}} \tag{7.22}$$

The broadening arises due to signal chirping represented by the κ^2 term in the phase in Eq. 7.19. Even a modest displacement equal to the unperturbed axial resolution, i.e., $\Delta z = \delta z_0$, could result in a 70 % broadening ($\sigma = 0.71$).

7.4.2 Transverse Motion

Figure 7.3b illustrates a situation where the probe and sample are moved relative to each other along a transverse coordinate, x. Without loss of generality, we will assume a stationary probe again and consider a scattering layer (sample) moving at constant velocity v_x. Substituting $x_b(t) = x_b - v_x t$ in Eq. 7.18, we get

$$F(Z) \approx \frac{\gamma P_0}{{w_0}^2} \iiint dxdydz \;\; r(x,y,z) e^{-i2k_0 z_0} e^{-4\ln 2 \frac{(y-y_b)^2}{{w_0}^2}} \int_{-k_1 T}^{k_1 T} e^{-4\ln 2 \frac{\kappa^2}{(2k_1 T\sigma)^2}} e^{-4\ln 2 \frac{\left(x - x_b + \frac{\Delta x}{2k_1 T}\kappa\right)^2}{{w_x}^2}} e^{i\kappa(Z-z_0)} d\kappa, \tag{7.23}$$

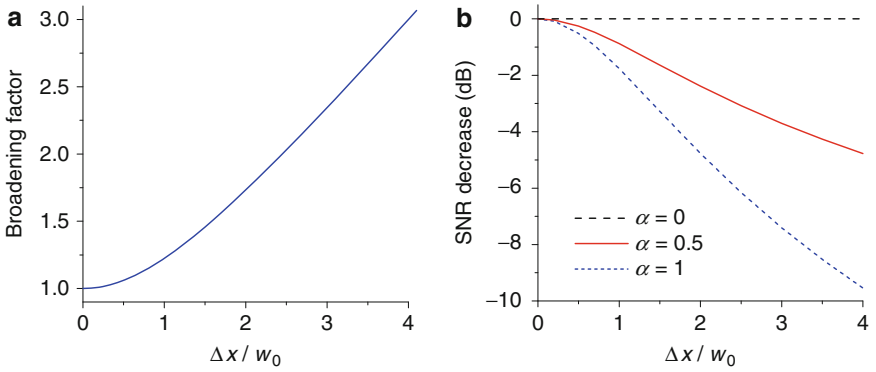

Fig. 7.4 (**a**) The magnitude of broadening in axial and transverse resolution and (**b**) SNR decrease arising from transverse motion as a function of normalized displacement Dx/ w_0 for $s^2 = 0.5$

where $\Delta x = v_x T$ denotes the transverse displacement of the sample during the acquisition of a single A-line.

For a scattering sample, the integral over κ can find an approximate solution which yields

$$F(Z) \propto \frac{\gamma P_0}{w_0 w_x \delta z_0} \iiint dxdydz \; r(x,y,z) e^{-i2k_0 z_0} e^{-4\ln 2 \frac{(y-y_b)^2}{w_0^2}} e^{-4\ln 2 \frac{(x-x_b)^2}{w_x^2}} e^{-4\ln 2 \frac{(Z-z_0)^2}{\delta_{z^2}}}, \tag{7.24}$$

where

$$\frac{w_x}{w_0} = \frac{\delta z}{\delta z_0} = \sqrt{1 + \sigma^2 \frac{\Delta x^2}{w_0{}^2}}. \tag{7.25}$$

This equation describes a broadening of the axial and transverse resolution due to transverse motion. Figure 7.4a shows a plot of the broadening factor as a function of normalized displacement $\Delta x/w_0$ *for* $\sigma = 0.71$. The broadening in transverse resolution is obvious because the effective size of the probe beam is increased by the transverse motion. The broadening in axial resolution occurs because the spectral width that one scattering point on the sample experiences during a single A-line acquisition is reduced as a result of the transverse motion. For a mirrorlike sample, represented by $r(x, y, z) = r_0\delta(z)$, Eq. 7.23 can be readily solved by performing the space integration first to show that both transverse and axial resolutions are invariant as anticipated since the beam scanning over a mirror does not alter the signal. Equations 7.24 and 7.25 are valid for a random scattering sample.

Equation 7.24 also describes the effect of the transverse motion in signal-to-noise ratio (SNR). The SNR is influenced by the transverse motion because a larger number of scatterers are illuminated with motion, but the signal from each scatterer

is collected by only a fraction of the duration of each A-line acquisition. Here, we define the SNR as a ratio $|F_s(z)|^2/|F_n(z)|^2$ where $F_s(z)$ and $F_n(z)$ denote the signal and noise components, respectively, obtained from a DFT of signal and noise photocurrents. The change in SNR by motion depends on the specific type of a sample. For a mirrorlike sample, SNR is invariant since the transverse motion does not alter the signal and noise, as can be derived from Eq. 7.23. For a single-point scatterer sample expressed as $r(x, y, z) = r_0\delta(x)\delta(y)\delta(z)$, it can be shown from Eq. 7.24 that the SNR decrease is given by $(1 + \sigma^2\Delta x^2/{w_0}^2)^{-1}$. For a bulk random scattering medium which leads to a fully developed speckle [25], the speckle-averaged signal power is given as an incoherent sum of signal powers from individual scatters. Assuming a homogenous scattering coefficient, it can be shown from Eq. 7.24 that the mean signal power is proportional to $1/({w_0}^2\delta z)^2$ $\iiint e^{-8\ln 2\frac{(x-x_b)^2}{{w_x}^2}} e^{-8\ln 2\frac{(y-y_b)^2}{{w_0}^2}} e^{-8\ln 2\frac{(Z-z_0)^2}{\delta z^2}} dxdydz$ which is invariant against the transverse motion. On the other hand, for a 2-dimensional scattering layer oriented in the x-y or y-z plane, the SNR is given by $(1 + \sigma^2\Delta x^2/{w_0}^2)^{-0.5}$. The scattering property of the actual biological sample may vary between a point scatterer and bulk homogenous random scattering medium. Therefore, we may expect that the SNR decrease for a biological sample may be given by

$$SNR\ \ decrease \approx \left(1 + \sigma^2 \frac{\Delta x^2}{{w_0}^2}\right)^{-\alpha}, \tag{7.26}$$

where α ranges from 0 to 1 depending on the sample. Figure 7.4b depicts the SNR decrease for three different α values.

As defined in Eq. 7.16, σT is equal to a FWHM width of optical intensity profile and, therefore, can be interpreted as an effective integration time of the signal. This accounts for the dependence on σ in Eqs. 7.21, 7.25, and 7.26 since Δz and Δx were defined as total displacements integrated over the entire A-line acquisition time of T rather than σT.

7.4.3 Nonlinear Tuning Slope

In general, the tuning of a swept source is not always linear in k-space and it is well known that nonlinear sampling in k-space gives rise to a poor spatial resolution [8]. To avoid this problem, the detector output may be sampled with nonuniform time intervals so as to produce uniform sampling in k-space. Alternatively, the detector output may be sampled with a uniform time interval, and subsequently, the acquired data is resampled by interpolation to a uniform spacing in k-space. This method is commonly implemented in practice. Mathematically, both methods are equivalent to a coordinate transform from t to a normalized time variable τ, defined as

$$t = T\tau - (k_2/k_1)T^2\tau^2 + \left[2(k_2/k_1)^2 - (k_3/k_1)\right]T^3\tau^3 + ..., \tag{7.27}$$

where τ spans from -0.5 to 0.5 for a single A-line acquisition. The wavenumber function then becomes linear in τ, i.e., $k(\tau) = k_0 + k_1 T\tau$. The depth profile is readily obtained with transform-limited spatial resolution by a Fourier transform with respect to $\kappa = k_1 T\tau$.

Let us consider an axially moving sample described as $z_b(t) = z - \sum z_m t^m$ where $z_0 = z - z_b$ (0) denotes the mean path length difference, $z_1 = v_z$ the velocity, and z_2 the acceleration. Using Eq. 7.27, we get

$$i(\xi) = \gamma\sqrt{P_r(\tau)P_s(\tau)}\iiint dxdydz \;\; r(x,y,z)g(x-x_b, y-y_b)\exp\left[-i\sum \omega_m \tau^m\right], \tag{7.28}$$

where

$$\begin{aligned} \omega_0 &= 2k_0 z_0, \omega_1 = 2(k_1 z_0 + k_0 z_1)T, \\ \omega_2 &= 2\left\{k_1 z_1 - \frac{k_0 k_2}{k_1}\right)z_1 + k_0 z_2\Big\}T^2. \end{aligned} \tag{7.29}$$

Here, ω_0 is a constant-phase term. ω_1 corresponds to the signal frequency in τ and is responsible for the Doppler shift in Eq. 7.21. ω_2 represents quadratic signal chirping and therefore results in broadening of the axial resolution. The coefficient of the cubic term, ω_3, plays a similar role to third-order chromatic dispersion, leading to asymmetry of the point spread function.

It can be shown [24] that the axial resolution is given by

$$\frac{\delta z}{\delta z_0} = \sqrt{1 + \frac{\sigma^4 \omega_2^2}{(4\ln 2)^2}}. \tag{7.30}$$

This leads to Eq. 7.22 for the special case of linear-k tuning and linear motion. For linear-λ tuning (linearly varying output wavelength in time), the axial resolution is found to be independent of z_1; a pure linear motion does not affect the axial resolution in this special case.

7.5 Phase-Sensitive (Doppler) OFDI

The foregoing sections of this chapter described the core OFDI system element and explored fundamental aspects of the technology. The system architecture that was considered reflects what has become the standard implementation for OFDI. This section will focus on a measurement technique that extends the core capabilities of OFDI to include Doppler-flow characterization through phase-sensitive detection.

Phase-resolved OCT systems measure both the amplitude and phase of the light reflected from the sample as a function of depth. The amplitudes are used to

generate intensity-based structural images. Although the phases are generally random for biological samples, additional functional information can be obtained by measuring changes in phase. For example, spatially resolved flow imaging can be accomplished by comparing the phases between successive A-lines at the same depth. A translation of the sample by distance δ during the time interval between two A-lines will induce a change in the measured phase of the reflected light given by $\Delta\phi = 2n\langle k\rangle\delta$, where n is the refractive index of the sample and $<k>$ is the average wavenumber of the OCT source ($k = 2\pi/\lambda$). Calculating this phase difference at each depth yields spatially resolved measurements of both the magnitude and direction of the axial (parallel to the imaging beam) flow velocity. Assuming that the imaging beam intersects the flow velocity vector at an angle β, the flow velocity is given by $v = \Delta\phi(2n\langle k\rangle\tau\cos(\beta))^{-1}$ where τ is the time between A-lines. This method was originally demonstrated in TD-OCT [26] and later in SD-OCT [27] and is the method applied in the current work. To ensure correlation between the phase measurements of successive A-lines, the transverse displacement of the imaging beam between A-lines must be small relative to the beam size. This constraint can be met by effectively oversampling in the transverse direction.

The sensitivity of the flow measurement is fundamentally limited by the phase sensitivity of the OCT system, which, in turn, is limited by the OCT system noise floor. It has been shown that the noise in the measured phase difference of a given signal, $\sigma^2_{\Delta\phi}$ (rad^2), with an SNR given by X can be written as [28, 29]

$$\sigma^2_{\Delta\phi} = \left(\frac{1}{X}\right). \tag{7.31}$$

Note that because calculation X of the phase difference requires two measurements of phase, the noise level of phase difference measurements as given by Eq. 7.31 is twice that of single-phase measurements. Most signals reflected from biological samples have SNRs below 50 dB, suggesting an ultimate phase difference measurement accuracy of ~3 mrad, corresponding to a flow velocity of 0.02 mm/s at $\beta = 80°$, $n = 1.3$, and $\tau^{-1} = 15.6$ kHz. Signals returning from depths greater than several hundred microns, where blood vessels are likely to be located, typically have SNRs below 30 dB and would yield ultimate phase accuracies of ~30 mrad. To achieve high-sensitivity flow imaging, other (less fundamental) noise sources, including interferometric instabilities, should be minimized such that phase sensitivity is SNR-limited up to an SNR of approximately 50 dB.

Because flow is calculated from the phase difference between successive A-lines, it is essential that phase measurements be repeatable from one A-line to the next. Changes in the measured phase resulting from systematic or interferometric instabilities increase the phase noise floor of the system, reducing the ability of the system to image low flow rates. In SD-OCT, the inherent stability of the source, interferometer, and spectrometer enables highly repeatable phase measurements and, correspondingly, high-sensitivity flow imaging. In OFDI, variations in the synchronization/timing of the wavelength-swept source relative to the

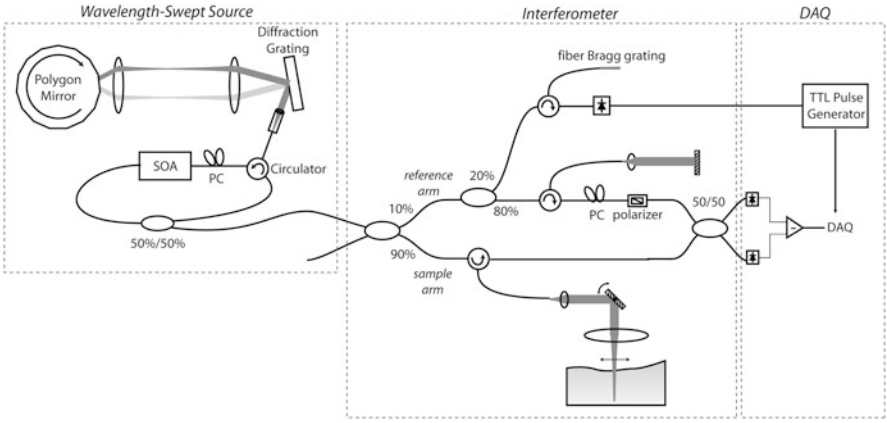

Fig. 7.5 Basic configuration of a phase-sensitive OFDI system

acquisition electronics can induce variations in the measurement of phase that degrade sensitivity. This effect is examined in the following section.

Figure 7.5 depicts the OFDI system configuration that will be discussed in this section [13]. The system comprises three modules: the wavelength-swept source, the interferometer, and the digital acquisition (DAQ) electronics. The source is constructed from a fiber ring laser using a semiconductor optical amplifier (SOA) as the gain element and a narrowband sweeping filter based on a polygon scanner [30]. The polarized source output is coupled to the interferometer where it is split into a reference arm and a sample arm. The sample-arm light is delivered to and collected from the sample through a single fiber. An optical circulator directs the reflected light to the interferometer output coupler. The reference-arm light reflects from the reference mirror, passes through a polarizer to remove any acquired variation in polarization state as a function of wavelength, and is directed to the other port of the output coupler. Resulting interference fringes are detected on both output ports. These signals are subtracted in a balanced-receiver configuration that reduces source intensity noise as well as autocorrelation noise from the sample. A portion of the reference-arm light is directed to a narrowband fiber Bragg grating (FBG) to generate a synchronization pulse for the acquisition electronics. This pulse is detected and converted into a TTL signal with a low-to-high transition that is coincident with the optical pulse and a high-to-low transition that is electrically tunable.

The DAQ board digitizes the balanced-receiver output using the high-to-low transition of the FBG-generated TTL pulse as a trigger signal. In response to the trigger signal, the DAQ board performs N analog-to-digital (A2D) conversions at its internal sample clock rate where the conversion occurs on the sample clock transitions. Although the polygon filter is driven by a signal derived from the sample clock, the phasing of the swept source output and the sample clock drifts slowly over time, causing the trigger signal to fall arbitrarily within the sample clock cycle. As a result, the delay between the trigger signal and the subsequent A2D conversion can vary by one period of the sample clock.

To understand how this variation in delay affects phase-resolved measurements, consider the interference fringe resulting from a stationary mirror at depth z with reflectivity R. The resulting interference signal, $S(t)$, is given by

$$S(t) \propto \sqrt{R}\cos\left(2k_o z + 2\alpha z[t+\varepsilon]\right) \tag{7.32}$$

where the laser is assumed to sweep linearly in wavenumber, i.e., $k(t) = k_o + \alpha t (\alpha = -6.1 \times 10^9 \mathrm{m}^{-1}\mathrm{s}^{-1}$ for our source. Because in practice the source sweep contains higher-order terms, the detected signal is resampled in time to recover the signal given by Eq. 7.32 [13]. The parameter ε describes the delay between the trigger signal and the subsequent A2D conversion. This delay ranges from 0 to the sample clock period T_{cl} (= 0.1 μs) and is different for each A-line. The phase of the interference fringe associated with the mirror is given by $\phi = 2k_o z + 2\alpha z\varepsilon$, and the range of phase differences between successive A-lines, $\Delta\phi$, is given by

$$|\Delta\phi| = 2\alpha z|\Delta\varepsilon| \leq 2\alpha z T_{cl} \equiv \pi Z. \tag{7.33}$$

where $\Delta\varepsilon$ is the change in the delay, ε, from one A-line to the next and is maximally equal to T_{cl}. A normalized depth parameter $Z = 2z\alpha T_{cl}/\pi$ has been defined where $Z = 0$ at the path-matched depth and $Z = 1$ at the Nyquist-limited imaging depth. Equation 7.33 indicates that timing variations produce phase jumps that increase linearly with depth up to a maximum value of π at the Nyquist-limited imaging depth ($Z = 1$). As shown previously, SNR-limited noise levels can be as low as a several mrads, and therefore, phase differences of the magnitude predicted by Eq. 7.33, if uncorrected, would severely degrade the sensitivity of the system.

There are several potential methods to correct the timing-induced phase jumps. Optical generation of the sample clock would improve the synchronization between the source and the DAQ board and reduced timing-induced phase jumps. To achieve this, a small portion of the source output could be directed to a periodic optical filter, generating an optical clock signal that is converted to a suitable TTL sample clock signal [31]. When the laser sweeps nonlinearly in k, the resulting sample clock is frequency chirped and abruptly changes frequency between the end of one sweep and the beginning of the next. As such, there are potential compatibility issues between optically generated clocks and higher-speed (∼100 MS/s) DAQ boards which incorporate phase-locked loop circuits on the external sample clock input. A second solution is to subtract from the measured phase difference of each A-line pair that portion which varies linearly with depth in a manner similar to a correction technique applied in phase-resolved TD-OCT systems [32]. Although straightforward and likely valid for cases in which flow is localized in a small region, this approach can distort the measured flow by subtracting linear portions of actual flow distributions.

To allow for the accurate measurement of arbitrary flow distributions, we have implemented a solution in which a separate calibration signal is used to measure timing-induced phase variations. These variations are then subtracted from the

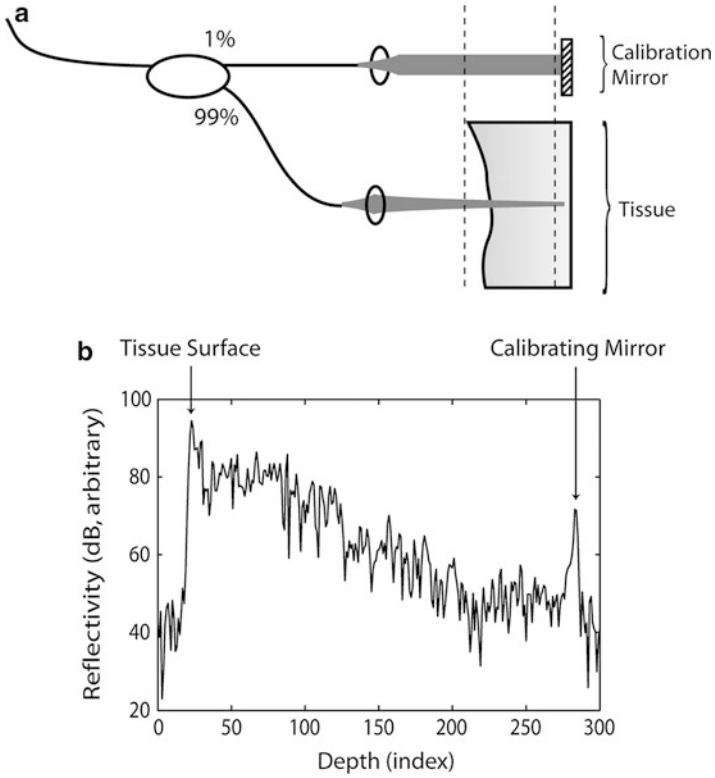

Fig. 7.6 (**a**) The implementation of a calibration mirror used to generate a calibration signal which allows measurement of the timing-induced phase variations for each A-line pair. (**b**) A representative A-line showing the signal from the sample (tissue) and the calibration signal

measured phase differences at all remaining depths. Figure 7.6a shows a sample arm modified to provide this calibration signal. A 1 % tap coupler is used to direct light to both a stationary calibration mirror (1 % port) and the sample to be imaged (99 % port). The calibration mirror is positioned such that its resultant signal appears near the maximum imaging depth, which is optimal for two reasons. Firstly, the calibration mirror creates a line artifact in the image. By locating the calibration mirror near the maximum imaging depth, this artifact appears near the image edge, minimizing the degree to which it can obscure the sample image. Secondly, the magnitude of the timing-induced phase differences is maximized at large depths and can therefore be most accurately measured at these depths. Hereafter, the signal from the calibration mirror is referred to as the calibration signal and the signal from the sample is referred to as the sample signal. The amplitude of the calibration signal is adjusted to ensure that it is large enough to dominate the sample signal at large depths but not so large that it induces significant autocorrelation noise [4]. Figure 7.6b shows a representative A-line

from a tissue image. Notice that the calibration signal obscures only a small portion of the image near the edge of the imaging depth.

Corrected phase differences are calculated by subtracting a fraction of the measured phase difference of the calibration signal from the measured phase difference of the sample signal. The magnitude of the applied correction is scaled linearly with the sample signal depth as dictated by Eq. 7.33. In the following, the parameters $\Delta\phi_{i,j}$ and $\Delta\hat{\phi}_{i,j}$ are used to describe the directly measured phase difference and calculated corrected phase difference, respectively, at depth index i between A-lines j and (j-1). If the calibration signal is located at depth index m, the corrected phase difference at depth index i is calculated as

$$\Delta\hat{\phi}_{i,j} = \Delta\phi_{i,j} - \left(\frac{i}{m}\right)\Delta\phi_{m,j}. \tag{7.34}$$

The first term is the measured phase difference at depth index i and the second term is the applied correction, scaled according to the sample signal depth by the multiplicative factor (i/m). Appropriate phase unwrapping is performed on all measurements. Finally, bulk motion artifacts can be removed by subtracting the median phase difference from each A-line pair [32].

The phase sensitivity of the system is given by the noise level of the corrected phase differences. Ideally, the correction procedure described by Eq. 7.34 reduces the impact of timing-induced phase jumps to negligible levels, leaving only the fundamental SNR-limited noise. To test this, a stationary mirror was used to generate a sample signal and corrected phase differences were calculated according to Eq. 7.34. The measured phase (ϕ), phase difference ($\Delta\phi$), and corrected phase difference ($\Delta\hat{\phi}$) of a sample signal at depth $Z = 0.54$ are plotted in Fig. 7.7a–c, respectively. A depth of $Z = 1$ corresponds to 2.6 mm in these measurements. The imperfect synchronization between the source and sample clock can be seen in the slow drift of the measured phase (Fig. 7.7a). The large jumps in phase occur when the acquisition delay switches by one clock cycle. The magnitude of these phase jumps (see scale bar on right of Fig. 7.7b) is in agreement with the prediction of Eq. 7.33 for a signal at this depth. Figure 7.7c shows that the large phase jumps have been eliminated in the corrected phase difference. Additionally, the baseline noise level has been reduced by 7 dB due to the correction of smaller phase jumps resulting from variations in acquisition delay that are less than one clock cycle.

To confirm the effectiveness of the correction method, the noise on the corrected phase differences was measured and compared to the SNR-limited noise predicted by Eqs. 7.31 and 7.34 as

$$\sigma^2_{\Delta\hat{\phi}} = \left(\frac{1}{X_s}\right) + \left(\frac{Z_s}{Z_c}\right)^2\left(\frac{1}{X_c}\right) \tag{7.35}$$

where X_s is the SNR of the sample signal located at depth Z_s and X_c is the SNR of the calibration signal located at depth Z_c. Phase difference measurements were performed at sample signal depths of $Z_s = 0.07$ (0.2 mm), 0.54 (1.4 mm),

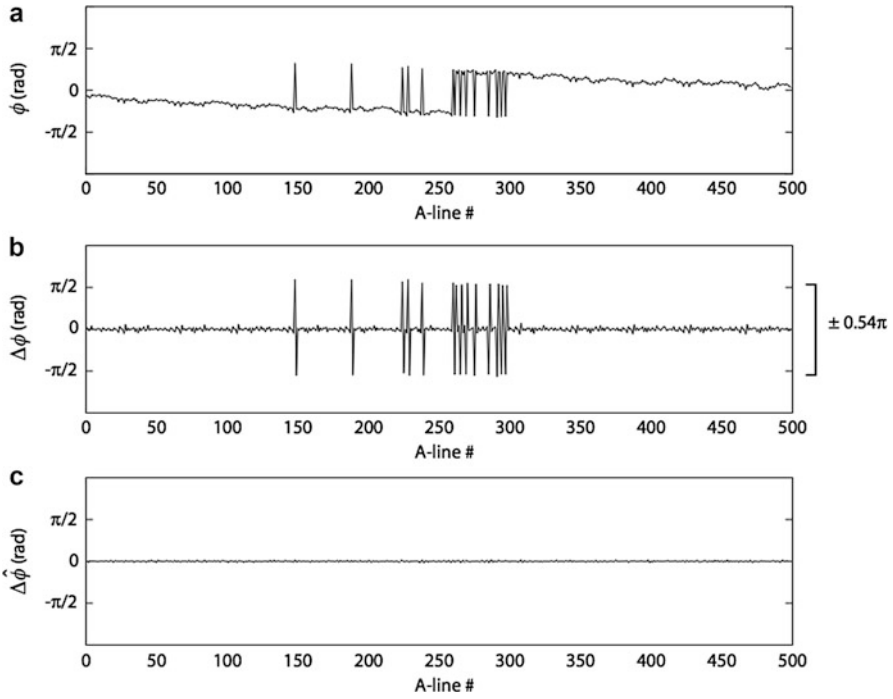

Fig. 7.7 A typical measured phase (**a**), phase difference (**b**), and corrected phase difference (**c**) for a sample signal at depth Z = 0.54

and 0.84 (2.2 mm). In all measurements, the calibration signal was located at depth $Z_c = 0.96$ (2.50 mm) and had an SNR $X_c \sim 31$ dB. The sample signal SNR, X_s, at each depth was adjusted from 10 dB to 50 dB through the use of a variable neutral-density filter located in the sample arm. Figure 7.8 plots the measured noise (calculated from 500 measurements) as a function of the sample signal SNR for two of the measured depths. The measurements show excellent agreement with the predicted noise level given by Eq. 7.35. Measurements at the intermediate depth of $Z_s = 0.54$ (not shown) also show excellent agreement with predictions. This agreement indicates that the proposed correction method is able to reduce timing-induced phase noise to negligible levels for this range of SNRs.

As indicated by Eq. 7.35, both the noise in the sample signal (first term) and the noise in the calibration signal (second term) contribute to the noise in the corrected signal, with the calibration signal contribution scaling with the sample signal depth, Z_s. At the large depth shown in Fig. 7.8b, the calibration signal noise dominates when the sample signal SNR exceeds ~35 dB. Assuming that, in practice, the SNR of sample signals from large depths is limited below 30 dB, and that from shallow depths is limited below 50 dB, one can see from Fig. 7.8 that the resulting noise over this range is sample signal SNR-limited. In the event of higher sample signal SNRs, the calibration signal SNR can be increased to reduce its noise contribution.

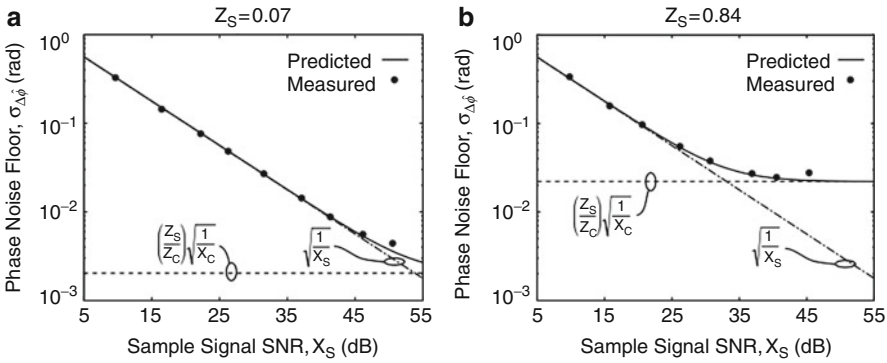

Fig. 7.8 The measured (*circle*) and predicted (*solid curve*) phase noise as a function of the sample signal SNR (X_s) at depths (**a**) $Z_s = 0.07$ and (**b**) $Z_s = 0.84$. The individual contribution to the overall noise resulting from only the sample signal noise (*dash-dot curve*) and calibration signal noise (*dashed curve*) are also shown. In both cases, the calibration signal was located at a depth $Z_c = 0.96$ with $X_c \sim 31$ dB

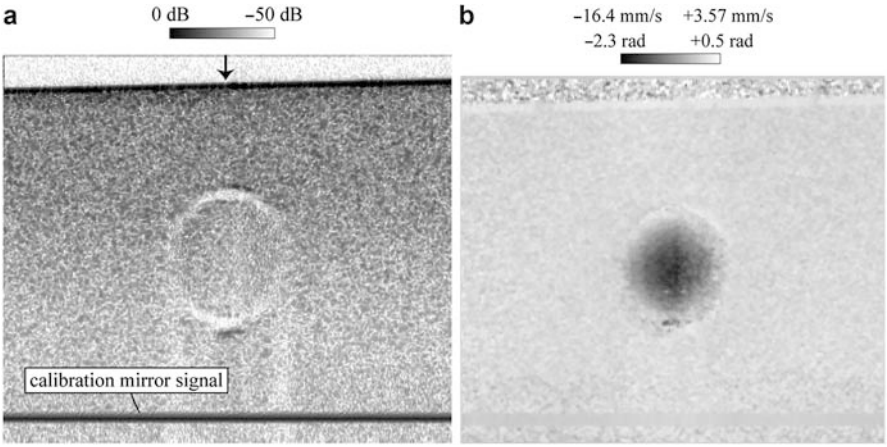

Fig. 7.9 Images of Intralipid flow through an 800-μm tube immersed in stationary Intralipid. (**a**) Structural image. (**b**) Flow image. The transverse distance is 3 mm and the imaging depth is 2.6 mm in air. Each image comprises 2,000 A-lines

As a test of the phase-resolved OFDI system and correction method described above, pulsatile flow of 0.25 % Intralipid in an 800-μm tube surrounded by stationary Intralipid of the same concentration was imaged. The angle between the tube and imaging beam was set at 80°. Figure 7.9 shows the resulting structural and flow images. The images were acquired at an A-line rate of 15.6 kHz and are 3 mm in width and 2.6 mm in depth (in air). Each frame contains 2,000 A-lines (displacement of 1.5 μm per A-line) yielding a frame rate of 7.8 frames per second. A moving median filter of size 20 × 3 pixels (30 × 25 μm) was applied to the corrected

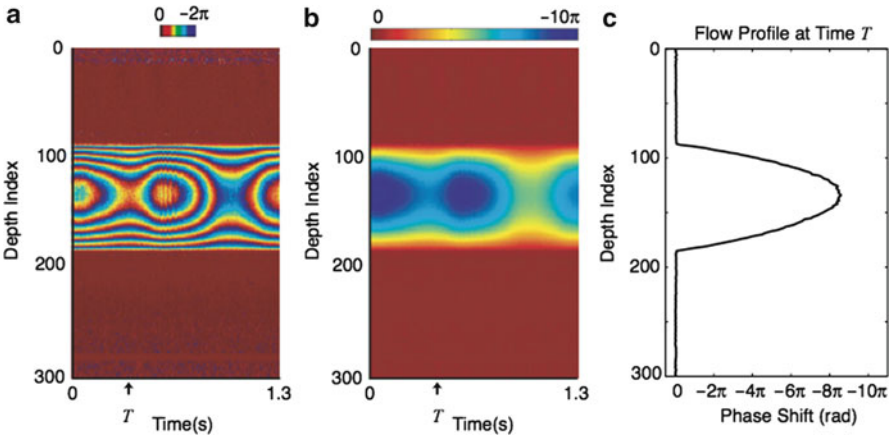

Fig. 7.10 M-mode image showing depth-resolved Intralipid flow as a function of time for high-rate, pulsatile flow. The beam was positioned at the center of the tube (see *arrow* in Fig. 7.5). In (**a**), the measured phase difference is shown without unwrapping phase discontinuities. In (**b**), a phase unwrapping algorithm is used to reconstruct the flow. Note the difference in scale between the images. In (**c**) the flow profile at time T (indicated on the time axis) is plotted. The maximum flow in (**c**) induced a phase difference of -8.5π corresponding to a flow rate of 61 mm/s

phase (flow) image. The flow image clearly differentiates the region of flow inside the tube from the surrounding stationary Intralipid. The phase difference and corresponding flow velocity (assuming an index of refraction of $n = 1.32$) are given in the colorbar. As mentioned previously, OFDI does not suffer from fringe washout due to sample motion. As such, phase-resolved OFDI is well suited to measure high flow rates that induce phase shifts greater than 2π. To demonstrate this, the imaging beam was positioned at the center of the tube shown in Fig. 7.9 and A-lines were recorded without scanning the beam while an increased pulsatile flow rate was induced. Figure 7.10a shows the resulting M-mode image. Phase is mapped to a color scale and the image coordinates are depth index (vertical axis) and time (horizontal axis). The increased flow rate results in measured phase differences that exceed 2π and produce phase wrapping artifacts. Because OFDI does not suffer from fringe washout effects, no SNR penalty is incurred as a result of these large phase shifts. The apparent depth, however, is displaced from the actual depth due to the large Doppler shift [33], an artifact that does not directly impact the ability of OFDI to measure large flow rates. Figure 7.10b shows the phase image unwrapped to remove discontinuities of 2π, yielding the depth-resolved time-varying flow distribution in the tube. Note the change of color scale between Fig. 7.10a, b. Figure 7.10c shows an unwrapped flow profile acquired at the time T as marked in the phase images. The images shown in Fig. 7.10 are constructed by averaging over 100 consecutive A-lines. Figure 7.11 shows cross-sectional structural and flow images obtained from a human nail bed in vivo. The image size is the same as in Fig. 7.10. Two blood vessels (circled), not observed in the structural image, can be clearly seen in Fig. 7.11b.

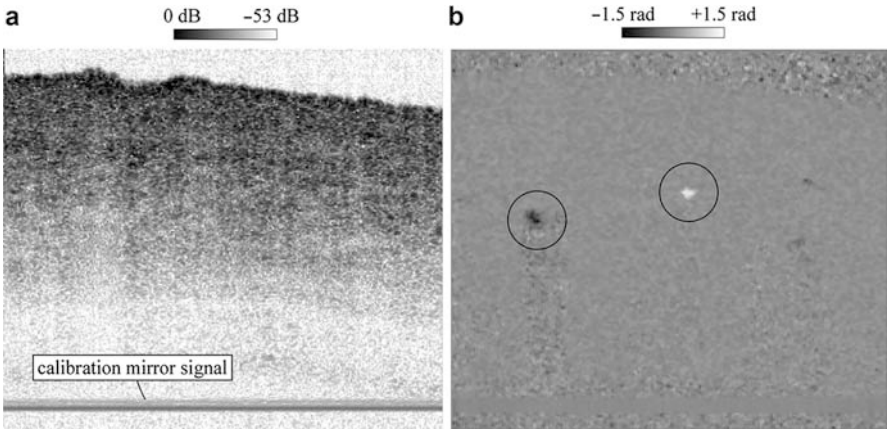

Fig. 7.11 Images of the human finger near the nail bed. Figure 7.6a shows the structural image and Fig. 7.6b shows the flow image. Two blood vessels (*circled*) are clearly visible in the flow image. The transverse dimension is 3 mm and the depth is 2.6 mm. Each image contains 2,000 A-lines

7.6 Applications

Comprehensive volumetric microscopy with OFDI is performed using a minimally invasive procedure such as catheterization or endoscopy is used to deliver the OFDI probe to the target organ or system (Fig. 7.1) [34]. Through rotation and longitudinal pullback of the internal portion of the probe, the OFDI system records the full three-dimensional microstructure of the tissue. Subsequent image processing can then be used to produce a form of virtual histology, where arbitrary cross-sectional views of the tissue can be viewed to screen for disease. The OFDI systems developed for these studies provide an approximately 30-fold increase in imaging speed over prior time-domain OCT systems. Given the individual voxel dimensions of 15 μm × 15 μm × 10 μm, the systems obtain data at a rate of 60 mm^3/s, permitting visualization of large tissue volumes with microscopic resolution.

7.6.1 Gastrointestinal Tract Imaging In Vivo

The management of patients with specialized intestinal metaplasia (SIM) of the esophagus (Barrett's esophagus) exemplifies the need for comprehensive volumetric microscopy. The standard protocol comprising undirected (random) four-quadrant biopsy provides only sparse sampling and is prone to sampling artifacts in the search for focal dysplasia and cancer. The inadequacy of biopsy surveillance is highlighted by the common recommendation for esophagectomy following diagnosis of high-grade dysplasia, a rare scenario in which a costly and highly

morbid procedure is indicated without histopathologic evidence of cancer. The high speed of OFDI imaging may provide a solution for this problem by enabling comprehensive imaging of the esophagus. Figure 7.12 depicts data acquired in the esophagus of a living swine. A 4-cm segment of the esophagus was imaged using a balloon catheter to stabilize and center the optics of the OFDI catheter within the esophageal lumen [34]. The entire volume of data was acquired in 5.8 min using an OFDI system operating at an A-line repetition rate of 10 kHz. This rate was reduced from the maximum operating speed of 64 kHz in order to facilitate continuous data archival to a computer hard drive. One volumetric dataset comprises 14 GB. Volumetric renderings (Fig. 7.12a) depict the tubular anatomy and allow visualization of the vascular network supplying the esophagus. Two-dimensional cross sections can be rendered from this volume in arbitrary orientations (Fig. 7.12b, c) and permit identification of each layer of the esophageal wall including the squamous epithelium, lamina propria, submucosa, and inner and outer muscularis propria (Fig. 7.12d and corresponding histology Fig. 7.12e). The dimension and optical properties of these anatomical features are similar in swine and humans.

7.6.2 Intracoronary Imaging In Vivo

One of the most significant current topics in interventional cardiology is the hypothesis of a vulnerable plaque. Autopsy studies have found that most acute myocardial infarctions (AMIs) are secondary to thrombotic occlusion at the site of a disrupted lipid-rich plaque. It is hypothesized that prior to disruption, these plaques are characterized by large necrotic, lipid-rich cores, thin fibrous caps, and abundant macrophages and represent a significant risk for AMI. In order to test this hypothesis, develop appropriate therapeutic measures, and potentially guide intervention, there is a clear need for a screening technology capable of identifying these lesions in living patients prior to disruption. OCT criteria for the focal characterization of coronary atherosclerotic plaques have previously been identified and validated [35, 36]; the missing capability, however, has been for comprehensive coronary screening. Images acquired in the right coronary artery of a living swine following balloon angioplasty and stenting are shown in Fig. 7.13 [34]. Image data was acquired at an A-line rate of 54 kHz and an imaging speed of 108 images per second using a coronary OFDI catheter that operated at a rotational speed of 6,480 RPM. The volumetric OFDI image (Fig. 7.13a) delineates the metallic wire mesh of the stent (color-coded blue), the intima and media (red), and the remainder of the vessel and surrounding tissues including denuded adventitia (gray). The luminal diameter in the region of balloon inflation (Fig. 7.13c–e) is considerably expanded relative to the reference vessel diameters (Fig. 7.13b, f). The wire struts of the stent are opaque to infrared light and appear as bright local reflections at the lumen with occluded sectors radially behind them. Cross-sectional images revealed portions of the dissected intima and media inside the stent (Fig. 7.13c, d) and exposed adventitia and flaps of intima and media (Fig. 7.13d, e).

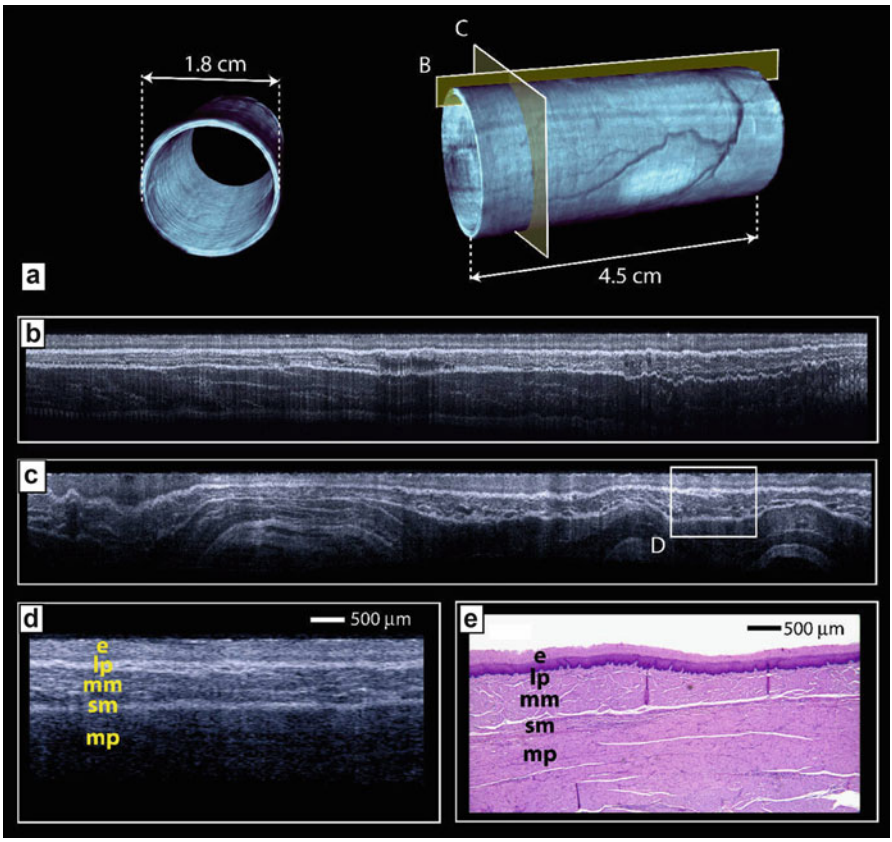

Fig. 7.12 Comprehensive microscopy of a porcine esophagus in vivo [34]. (**a**) The 14 GB volumetric dataset can be rendered and downsampled for presentation in arbitrary orientations and perspectives. The vascular network within the submucosa is readily apparent without image enhancement or exogenous contrast agents. Cross-sectional images can be located on the volume image for higher-resolution viewing. (**b**) Longitudinal cross section through the esophageal wall at location denoted in A (inverted with epithelium at the *top*; dimensions: 45 mm horizontal, 2.6 mm vertical). In the raw data, we observed a periodic vertical offset corresponding to the motion of the beating heart. A simple surface-aligning algorithm was used to reduce this artifact, but a residual vertical banding can still be observed with a period of 300 µm corresponding to a heart rate of 90 beats/min. The longitudinal pitch between adjacent A-lines was 32 µm. (**c**) Unwrapped transverse section (cylindrical coordinates r & θ are mapped to vertical and horizontal) at location denoted in A (dimensions: 57 mm horizontal, 2.6 mm vertical). Both sections (**b**) and (**c**) demonstrate imaging through the entire esophageal wall and permit identification of the squamous epithelium (*e*), lamina propria (*lp*), muscularis mucosa (*mm*), submucosa (*s*), and muscularis propria (*mp*), as labeled in expanded panel (**d**). (**e**) Representative histology section (H&E stain) obtained from the anatomical region corresponding to (**d**)

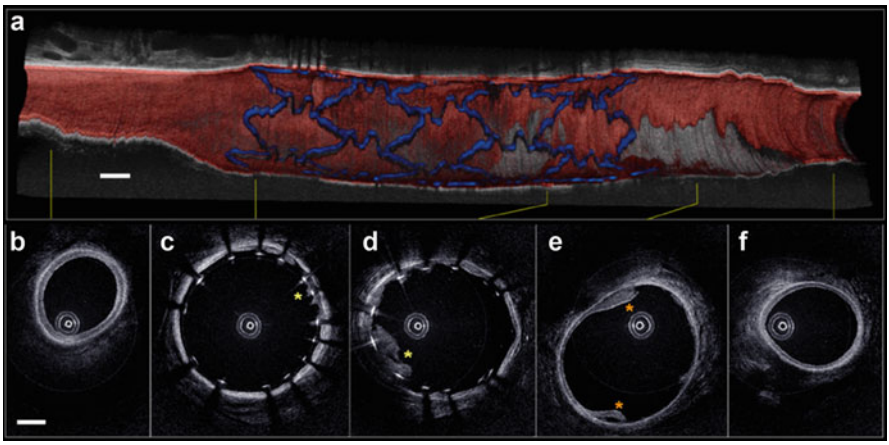

Fig. 7.13 Volumetric imaging of a stented porcine coronary artery in vivo [34]. (**a**) Three-dimensional cutaway rendering of the volumetric dataset acquired with an intravascular catheter in the circumflex coronary artery of a living swine after balloon angioplasty and stent implantation. The stent is represented as *blue*, the intima and media as *red*, and the adventitia and surrounding tissue as a *gray* scale. The volume comprises 500 circular (r-θ) sections at a pitch of 50 μm acquired in 6 s during the injection of saline at a rate of 3 cm^3/s. (**b–f**) Individual OFDI cross-sectional images at corresponding locations marked in (**a**). The metal-based stent produces strongly reflected signals and leaves radial shadow patterns in (**c**) and (**d**). The dissected intima and media layers are shown (**e** *orange asterisk*). Tissue prolapse between the stent struts is visualized in (**c**, **d** *yellow asterisk*). Scale bars, 1 mm

7.6.3 4-Dimensional Imaging of an Embryo Heart

In addition to screening and surveillance, high-speed OFDI also enables dynamic processes to be captured. This capability may be particularly useful in 4-dimensional phenotyping of the heart in models for developmental biology. Using a two-dimensional galvanometric scanner, the entire volume of the heart can be imaged in a xenopus embryo with a three-dimensional image acquisition rate of 20 Hz (Fig. 7.14) [34]. The real-time dynamics of the ventricle, atrium, and truncus arteriosus were recorded without the need for time-gating techniques. The displacements associated with cardiac dynamics were calculated directly from the volumetric images by computing the distance between homologous locations on the cardiac surface at end diastole and end systole on a frame-by-frame basis. Displacement was displayed using a color lookup table. At end systole, OFDI demonstrated that the ventricle was at its smallest volume; the volumes of the atrium and truncus were conversely at their maxima. At end diastole, the ventricle was dilated to its greatest volume, whereas the volumes of the atrium and truncus were at their minima.

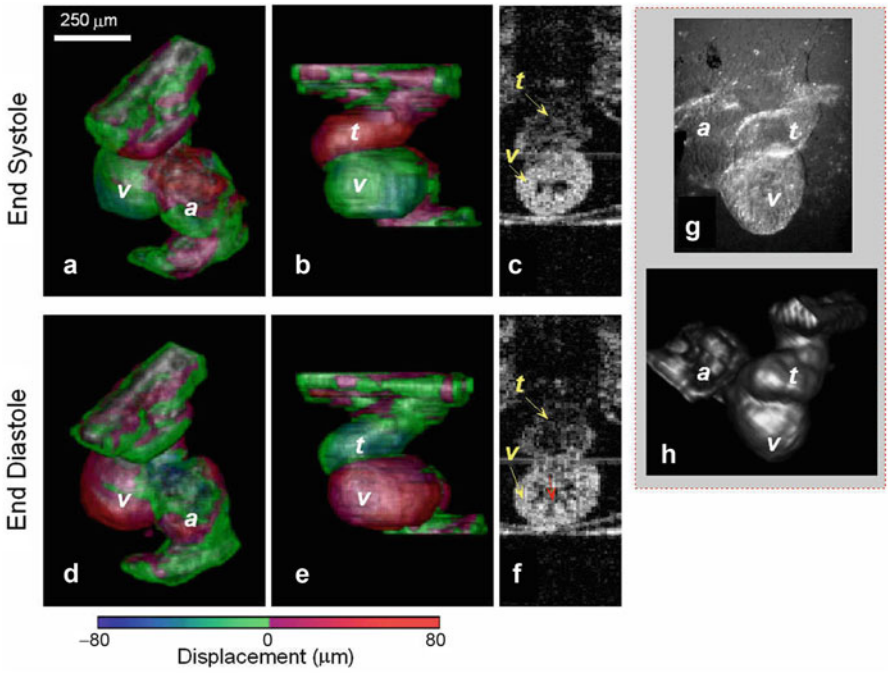

Fig. 7.14 Three-dimensional rendered images of xenopus embryo heart in vivo. The dynamics of the heart motion are visualized by the color-coded displacement maps, which have been overlaid on rendered three-dimensional datasets. Volumetric images including the entire heart were acquired in 50 ms, considerably shorter than the period of the heart beat (approximately 0.5 s). In end systole (**a**, **b**, **c**), the atrium (*a*) is expanded and the ventricle (*v*) is compressed. During diastole, the atrium gets compressed and the ventricle expands. At end diastole (**d**, **e**, **f**), the ventricle is at its largest size. In systole, it compresses and the truncus arteriosus (*t*), expands, and rotates. (**c**, **f**) represent cross-sectional images showing trabeculae (*red arrow*, **f**) in compressed and expanded ventricles, respectively. Each cross-sectional image was acquired in 1 ms. A bright-field picture of the dissected heart and corresponding image are shown (**g**, **h**). Scale bar, 250 μm

References

1. K. Takada, I. Yokohama, K. Chida, J. Noda, New measurement system for fault location in optical wave-guide devices based on an interferometric-technique. Appl. Opt. **26**, 1603–1606 (1987)
2. R.C. Youngquist, S. Carr, D.E.N. Davies, Optical coherence-domain reflectometry – a new optical evaluation technique. Opt. Lett. **12**, 158–160 (1987)
3. A.F. Fercher, C.K. Hitzenberger, G. Kamp, S.Y. El-Zaiat, Measurement of intraocular distances by backscattering spectral interferometry. Opt. Commun. **117**, 43–48 (1995)
4. G. Hausler, M.W. Linduer, "Coherence radar" and "spectral radar"-new tools for dermatological diagnosis. J. Biomed. Opt. **3**, 21 (1998)
5. M.A. Choma, M.V. Sarunic, Y. Changhuei, J.A. Izatt, Sensitivity advantage of swept source and Fourier domain optical coherence tomography. Opt. Express **11**(18), 2183–2189 (2003)

6. J.F. de Boer, B. Cense, B.H. Park, M.C. Pierce, G.J. Tearney, B.E. Bouma, Improved signal-to-noise ratio in spectral-domain compared with time-domain optical coherence tomography. Opt. Lett. **28**, 2067–2069 (2003)
7. R. Leitgeb, C.K. Hitzenberger, A.F. Fercher, Performance of Fourier domain vs. time domain optical coherence tomography. Opt. Express **11**, 889 (2003)
8. E. Brinkmeyer, R. Ulrich, High-resolution OCDR in dispersive wave-guides. Electron. Lett. **26**, 413–414 (1990)
9. S.R. Chinn, E.A. Swanson, J.G. Fujimoto, Optical coherence tomography using a frequency-tunable optical source. Opt. Lett. **22**, 340–342 (1997)
10. B. Golubovic, B.E. Bouma, G.J. Tearney, J.G. Fujimoto, Optical frequency-domain reflectometry using rapid wavelength tuning of a Cr4+:forsterite laser. Opt. Lett. **22**, 1704–1706 (1997)
11. F. Lexer, C.K. Hitzenberger, A.F. Fercher, M. Kulhavy, Wavelength-tuning interferometry of intraocular distances. Appl. Opt. **36**, 6548–6553 (1997)
12. W.V. Sorin, D.M. Baney, A simple intensity noise-reduction technique for optical low-coherence reflectometry. IEEE Photon. Technol. Lett. **4**, 1404–1406 (1992)
13. S.H. Yun, G.J. Tearney, J.F. de Boer, N. Iftimia, B.E. Bouma, High-speed optical frequency-domain imaging. Opt. Express **11**, 2953–2963 (2003)
14. K. Takada, Y. Ken-ichi, M. Kobayashi, J. Noda, Rayleigh backscattering measurement of single-mode fibers by low coherence optical time-domain reflectometer with 14 mum spatial resolution. Appl. Phys. Lett. **59**, 143–145 (1991)
15. M. Wojtkowski, A. Kowalczyk, R. Leitgeb, A.F. Fercher, Full range complex spectral optical coherence tomography technique in eye imaging. Opt. Lett. **27**, 1415–1417 (2002)
16. X.Q. Zhou, K. Iiyama, K. Hayashi, Extended-range FMCW reflectometry using an optical loop with a frequency shifter. IEEE Photon. Technol. Lett. **8**, 248–250 (1996)
17. M.A. Choma, C. Yang, J.A. Izatt, Instantaneous quadrature low-coherence interferometry with 3×3 fiber-optic couplers. Opt. Lett. **28**, 2162–2164 (2003)
18. S.H. Yun, G.J. Tearney, J.F. de Boer, B.E. Bouma, Removing the depth-degeneracy in optical frequency domain imaging with frequency shifting. Opt. Express **12**, 4822–4828 (2004)
19. H. Barfuss, E. Brinkmeyer, Modified optical frequency domain reflectometry with high spatial resolution for components of integrated optics systems. J. Lightwave Technol. **7**, 3–10 (1989)
20. C. Dorrer, N. Belabas, J.P. Likforman, M. Joffre, Spectral resolution and sampling issues in Fourier-transform spectral interferometry. J. Opt. Soc. Am. B **17**, 1795–1802 (2000)
21. R.J. Alfidi, W.J. MacIntyre, R. Haaga, The effects of biological motion in CT resolution. Am. J. Radiol. **127**, 11–15 (1976)
22. S.K. Nadkarni, D.R. Boughner, M. Drangova, A. Fenster, In vitro simulation and quantification of temporal jitter artifacts in ECG-gated dynamic three-dimensional echocardiography. Ultrasound Med. Biol. **27**, 211–222 (2001)
23. M.L. Wood, R.M. Henkelman, NMR image artifact from periodic motion. Med. Phys. **12**, 143–151 (1985)
24. S.H. Yun, G.J. Tearney, J.F. de Boer, B.E. Bouma, Motion artifacts in optical coherence tomography with frequency-domain ranging. Opt. Express **12**, 2979–2998 (2004)
25. J.M. Schmitt, S.H. Xiang, K.M. Yung, Speckle in optical coherence tomography. J. Biomed. Opt. **4**, 95–105 (1999)
26. Y.H. Zhao, Z.P. Chen, C. Saxer, S.H. Xiang, J.F. de Boer, J.S. Nelson, Phase-resolved optical coherence tomography and optical Doppler tomography for imaging blood flow in human skin with fast scanning speed and high velocity sensitivity. Opt. Lett. **25**, 114–116 (2000)
27. B.R. White, M.C. Pierce, N. Nassif, B. Cense, B.H. Park, G.J. Tearney, B.E. Bouma, T.C. Chen, J.F. de Boer, In vivo dynamic human retinal blood flow imaging using ultra-high-speed spectral domain optical Doppler tomography. Opt. Express **11**, 3490–3497 (2003)
28. B.H. Park, M.C. Pierce, B. Cense, S.H. Yun, M. Mujat, G.J. Tearney, B.E. Bouma, J.F. de Boer, Real-time fiber-based multi-functional spectral-domain optical coherence tomography at 1.3 μm. Opt. Express **13**, 3931–3944 (2005)

29. S. Yazdanfar, C. Yang, M.V. Sarunic, J.A. Izatt, Frequency estimation precision in Doppler optical coherence tomography using the Cramer-Rao lower bound. Opt. Express **13**, 410–416 (2005)
30. S. Yun, C. Boudoux, G. Tearney, B. Bouma, High-speed wavelength-swept semiconductor laser with polygon-scanner-based wavelength filter. Opt. Lett. **28**, 1981–1983 (2003)
31. M.V. Sarunic, M.A. Choma, C.H. Yang, J.A. Izatt, Instantaneous complex conjugate resolved spectral domain and swept-source OCT using 3x3 couplers. Opt. Express **13**, 957–967 (2005)
32. M.C. Pierce, B.H. Park, B. Cense, J.F. de Boer, Simultaneous intensity, birefringence, and flow measurements with high-speed fiber-based optical coherence tomography. Opt. Lett. **27**, 1534–1536 (2002)
33. S.H. Yun, G.J. Tearney, J.F. de Boer, B.E. Bouma, Pulsed-source and swept-source spectral-domain optical coherence tomography with reduced motion artifacts. Opt. Express **12**, 5614–5624 (2004)
34. S.H. Yun, G.J. Tearney, B.J. Vakoc, M. Shishkov, R. Yelin, W.Y. Oh, A. Desjardins, R.C. Chan, D. Yelin, J.A. Evans, I.K. Jang, N.S. Nishioka, J.F. de Boer, B.E. Bouma, Comprehensive volumetric optical microscopy in vivo. Nat. Med. **12**, 1429–1433 (2006)
35. G.J. Tearney, I.K. Jang, B.E. Bouma, Optical coherence tomography for imaging the vulnerable plaque. J. Biomed. Opt. **11**, 021002 (2006)
36. H. Yabushita, B.E. Bouma, S.L. Houser, H.T. Aretz, I.-K. Jang, K.H. Schlendorf, C.R. Kauffman, M. Shishkov, D.-H. Kang, E.F. Halpern, G.J. Tearney, Characterization of human atherosclerosis by optical coherence tomography. Circulation **106**, 1640–1645 (2002)

Complex Conjugate Removal in SS Optical Coherence Tomography

8

Oscar Carrasco-Zevallos and Joseph A. Izatt

Keywords

Complex conjugate removal • Increased axial range • Fourier domain Optical Coherence Tomography • Complex conjugate ambiguity

8.1 Introduction

Optical coherence tomography (OCT) enables tomographic imaging with micron-scale axial and lateral resolution. Since its inception in 1991 [1], OCT revolutionized ophthalmic imaging by visualizing retinal layers with exquisite detail for the first time. OCT was also extended for imaging of the anterior segment of the eye [2].The development of Fourier domain OCT (FDOCT) systems significantly improved sensitivity and imaging speed, catalyzing the commercialization of OCT technology. FDOCT is now the clinical gold standard for retinal imaging. However, the transition from time-domain OCT to Fourier domain detection was not without cost; imaging artifacts inherent to FDOCT acquisition and processing were introduced. The most prominent, the complex conjugate artifact, results in reducing the OCT depth imaging range by a factor of 2. In this chapter, techniques for complex conjugate removal in swept-source OCT (SSOCT) are discussed. Complex conjugate removal in spectral domain OCT (SDOCT) will be only briefly reviewed; a thorough analysis of such techniques can be found in ► Chap. 7, "Optical Frequency Domain Imaging".

O. Carrasco-Zevallos (✉)
Fitzpatrick Institute for Photonics and Department of Biomedical Engineering, Duke University, Durham, NC, USA
e-mail: omc3@duke.edu

J.A. Izatt
Fitzpatrick Institute for Photonics and Departments of Biomedical Engineering and Ophthalmology, Duke University Medical Center, Durham, NC, USA

© Springer International Publishing Switzerland 2015

W. Drexler, J.G. Fujimoto (eds.), *Optical Coherence Tomography*,
DOI 10.1007/978-3-319-06419-2_9

8.1.1 Fourier Domain Optical Coherence Tomography

Direct detection of the interferometric OCT signal in the Fourier domain revolutionized OCT and increased imaging speeds dramatically. FDOCT can be separated into two categories, SDOCT and SSOCT. In SDOCT, a broadband source, such as a super-luminescent diode, is utilized similar to time-domain OCT. However, instead of detecting with a photodiode, the backscattered spectrum is now collected with a spectrometer, comprised of an array or matrix of photodetectors [3, 4]. As discussed in ▶ Chap. 3, "Modeling Light–Tissue Interaction in Optical Coherence Tomography Systems," collection in the Fourier domain introduces a "signal fall-off" effect, in which the imaging depth range is governed by the spectral resolution of the detected interferogram. Spectral resolution of SDOCT is given by the spectral resolution of the spectrometer. To mitigate this effect, swept-source technology was introduced in OCT. In SSOCT, a tunable source that is swept as a function of time is used and the interferogram is collected with a photodiode [5, 6]. The spectral resolution in SSOCT is determined by the instantaneous linewidth of the swept source, which has much finer spectral resolution than any spectrometer.

As alluded to above, FDOCT enabled faster imaging than time-domain OCT due to increased sensitivity [7–9]. This paradigm shift in OCT had significant impact in ophthalmology. Faster line-rates enabled volumetric imaging, noise reduction via averaging, and real-time imaging, with both SDOCT [10–14] and SSOCT [15–20]. Additionally, simultaneous detection of the backscattered spectra in SDOCT facilitated functional extensions of OCT that measure wavelength-dependent scattering and absorption [21, 22]. Furthermore, the phase stability of FDOCT enables detection of nanometer-scale motions [23–25].

Despite these numerous advantages, the shift from time domain to Fourier introduces several nontrivial artifacts. Included are autocorrelation artifacts, which result from interference from separate reflectors in the sample located within a coherence length from each other. In addition, the so-called DC artifact is introduced after Fourier transforming the backreflected spectra to the spatial domain. Finally, the complex conjugate artifact, which is the focus of this chapter, originates from performing a Fourier transform on real data resulting in a Hermitian symmetric A-scan. The origins of these artifacts are evident from the theoretical treatment of FDOCT, which will be briefly reviewed here. For more in-depth analysis, see ▶ Chap. 3, "Modeling Light–Tissue Interaction in Optical Coherence Tomography Systems".

Assuming a standard Michelson interferometer, photocurrent at the detector is given by

$$D_i[k_m] \propto \rho \cdot S[k_m] \cdot \left(R_R + R_S + 2\sqrt{R_R R_S}\cos\left(2\Delta x k_m + \varphi_i\right)\right) \tag{8.1}$$

where D_i is the photocurrent at one detector; k_m is the wavenumber; ρ is the detector responsivity; S is the source spectral density in watts per wavenumber; R_R and R_S are the reflectivity from the reference and sample arm, respectively; and φ_i is

a trivial phase offset of the interferometric signal. The detector elements are $i = 1$: M where, in SDOCT, M is the number of pixels of the camera in the spectrometer or, in SSOCT, M is the number of spectral samples over the entire bandwidth of the wavelength-swept laser. The difference in optical path length between the reflectors in the sample and the reference arm is encoded by the frequency of the cosine term, and sample reflectivity is encoded in the fringe visibility of the interferometric signal. The detected signal in FDOCT essentially represents the real part of a Fourier transform of an OCT A-line given by

$$D_i[x_m] = \sum_{m=1}^{M} D_i[k_m] e^{-(j2\pi(2k_m x_n))}, n \in \{1, M\} \tag{8.2}$$

In the space domain, the channel spaces are given by $1/\Delta k$ where Δk is the bandwidth of the source in wavenumber units. As previously mentioned, the scan depth is given by the spectral resolution of system $1/\delta k$ where δk is the spectral resolution. Performing the Fourier transform shown in (8.2), the OCT A-line in the space domain is then represented by the following:

$$D_i[x_n] \propto S[x_n] \bigotimes \left((R_R + R_S)\delta(x_n) + 2\sqrt{R_R R_S}(\delta(x_n + \Delta x) + \delta(x_n - \Delta x)) \right) \tag{8.3}$$

Because the detected signal is necessarily real, the resulting Fourier transform will result in a Hermitian symmetric A-line, evidenced by the presence of two delta functions offset by $+\Delta x$ and $-\Delta x$ from DC. Therefore, a reflector at $+\Delta x$ cannot be distinguished from a reflector located $-\Delta x$. This ambiguity is termed the complex conjugate artifact [26], which effectively reduces the scan depth by a factor 2. Lastly, the DC artifact is given by the first delta function in the brackets.

The typical manner of resolving the complex conjugate artifact is to ensure that the region of interest in the sample is located solely on one side of the zero path length position, given by the position of the reference mirror. Duplicate data from the other side of the zero path length position is simply cropped out. While the majority of FDOCT systems utilize this technique, it is inefficient since half of the collected data is redundant and thus discarded. Complex conjugate removal (CCR) techniques in FDOCT aim to suppress or altogether eliminate this artifact to double imaging range, thereby enabling the entire collected data to be utilized efficiently. Some CCR techniques, such as phase-shifting OCT, are applicable in either SD or SSOCT, while others such as Heterodyne OCT are more suitable for SSOCT, as discussed below. This chapter will focus on CCR in SSOCT, while CCR in SDOCT, which is the focus of ▶ Chap. 7, "Optical Frequency Domain Imaging," will be briefly reviewed.

8.1.2 Complex Conjugate Removal in Spectral Domain OCT

As previously stated, the main drawback of adopting FDOCT is the complex conjugate artifact. Therefore, a major focus of OCT research was on techniques

that suppress or eliminate the complex conjugate artifact. The majority of these techniques were developed for SDOCT and will be reviewed here. CCR in SSOCT will be discussed in the following sections.

The complex conjugate artifact originates from the collection of only the real part of the complex OCT signal in FDOCT. However, if the entire complex OCT signal can be collected, then the Fourier transform of the complex signal back to the spatial domain would yield a complex conjugate free A-line. Because optical detectors necessarily acquire real data, reconstructing the complex OCT signal is not trivial. A method of acquiring both the real and imaginary components of the complex OCT signal involves acquiring multiple (at least two) interferograms at the same location but with a relative phase shift – a technique termed phase-shifting OCT. Phase shifting can be done in a variety of ways, including dithering the reference mirror with a piezoelectric transducer (PZT) [26, 27] or incurring a phase shift with an electro-optic modulator [28]. Using a PZT for phase stepping tends to severely hinder imaging speed since the OCT frame rate is now limited by the response time of the PZT. As a consequence, phase stepping with a PZT is more sensitive to patient motion than when using electro-optic modulator.

Once the phase-shifted interferograms are acquired, the complex OCT signal must be reconstructed. The first phase-shifting OCT systems employed a five shifted frame algorithm, first developed for white-light interferometry [29]. Five frames were necessary to correct for chromatic phase error induced by phase shifting using the reference mirror. Once again, collecting five frames sequentially is time consuming, and therefore the algorithm is vulnerable to patient motion that may introduce phase error. Other algorithms have been developed that only necessitate two phase-shifted to reduce imaging time; however, such algorithms are only applicable for limited optical bandwidths [28, 30]. Another group developed a system in which the phase-shifted spectra can be collected on different line arrays of a 2D detector to increase speed of imaging [31]. However, five phase-shifted frames were still necessary for every complex conjugate-resolved B-scan.

In addition to phase shifting, other phase modulation techniques for CCR in SDOCT have been developed. Sinusoidal phase modulation of the reference mirror and a high-speed integrating buckets acquisition scheme has also been utilized for reconstruction of the complex OCT signal [32]. Another algorithm was explored to retrieve the in-phase and quadrature components of the complex OCT signal from the first and second harmonics of the phase-modulated interferogram [33]. Instead of moving the reference arm, phase modulation of the interferogram can also be induced by offsetting the beam away from the pivot of the fast scanning mirrors. This incurs a phase shift that is proportional to the rate of the scanning mirrors and is therefore a simple way in which the complex OCT signal can be reconstructed after phase modulation [34, 35]. Another technique, termed B-M-mode OCT, uses phase modulation of a reference beam while transverse scanning to retrieve the complex OCT signal [36].

A completely different approach utilizes multiple reference arms to circumvent the complex conjugate artifact rather than suppress it. This technique simply uses two

reference arms, with the zero path length of each located at different positions in the sample. Therefore, two images, collected from different regions of the sample, can be captured and later registered to produce an image with greater depth range and free of the complex conjugate ambiguity. A fiber-based optical switch can be used to minimize the time it takes to switch between reference arms [37].

Another method to obtain for CCR is applying an electronic carrier frequency to the interferogram using frequency-shifting devices. This method does not induce any chromatic phase shift error, unlike most phase-shifting techniques, and allows for quadrature detection of the OCT signal. Frequency shifting in OCT is termed Heterodyne OCT and is more suitable for SSOCT since spectral domain detectors cannot follow MHz signal modulations. However, frequency shifting has also been applied to SDOCT using acousto-optic frequency shifters [38]. After applying a constant carrier frequency to the spatial OCT interferogram, a Hilbert transform can be used to capture the quadrature components of the OCT signal [39].

There are some disadvantages with the previously discussed methods, which include reduced imaging time since most CCR techniques in SDOCT necessitate the acquisition of multiple, phase-shifted frames or the use of multiple reference arms. Furthermore, phase-stepping or modulation techniques are subject to phase noise incurred by either patient movement or mechanical instability of the system. The accuracy of the complex OCT signal is dependent on the phase stability of the system. That is, for phase-shifting OCT, "phase calibration" is usually required, in which the phase shift between frames is predetermined and chosen carefully for the algorithm to work. Any phase noise will cause deviations from these predetermined phase shifts and therefore cause errors in the reconstruction of the complex FDOCT signal, resulting in "ghost images" because the complex conjugate artifact is not fully suppressed. Furthermore, chromatic phase error is incurred when phase shifting by dithering the reference mirror and can again contribute to ghost images. These phase-shifting techniques described above are more suitable for SDOCT because of greater source phase stability than in SSOCT. A true achromatic method for CCR is heterodyne OCT, in which a frequency carrier is imparted on the interferometric signal. This technique is more suitable for SSOCT since spectral domain detectors cannot follow fast signal modulations in the MHz range.

8.2 Heterodyne SSOCT

A method for true achromatic complex FDOCT signal reconstruction uses frequency shifting devices to create a beating signal with the detected interferometric signal. Termed heterodyne OCT, this technique is especially suitable for SSOCT in which large bandwidth detectors that can capture fast signal modulations in the MHz to 1 GHz range are used. A carrier signal can be imparted to enable quadrature detection of the complex OCT signal and subsequent suppression of the complex conjugate ambiguity. Furthermore, frequency shifting can also be used to establish a new zero optical path delay and eliminate the complex conjugate ambiguity altogether.

8.2.1 Heterodyne SSOCT Theory

As stated previously, the photocurrent collected by the detectors can be expressed as (8.1). In the case for SSOCT, the wavenumber k is swept as a function of time and can be represented as $k = k_0 + t(\mathrm{d}k/\mathrm{d}t)$ where k_0 is the starting wavenumber in the sweep and $\mathrm{d}k/\mathrm{d}t$ is the instantaneous sweep velocity. Optical sweeping in the time domain leads to the conversion of the cross-correlation and autocorrelation to electronic frequency in the time-varying photocurrent $D[t]$. Note that in Eq. 8.1, photocurrent is expressed as a function of k. However, since wavenumber is swept as function of time in SSOCT, photocurrent can be recast in terms of t.

The cross-correlation frequencies can be represented by the multiplication of OPL mismatch between the sample and reference arm and the sweep velocity $\omega_n = (\mathrm{d}k/\mathrm{d}t)\ (z_R - z_n)$, while the autocorrelation frequencies are given by $\omega_{nm} = (\mathrm{d}k/\mathrm{d}t)\ (z_n - z_m)$. If a beat frequency ω_d is induced in the reference arm, then the time-varying photocurrent can be represented by

$$D_i[t] \propto \rho \cdot S[t] \cdot \left\{ R_R + \sum\nolimits_n R_n + 2\sqrt{R_R}\sum\nolimits_n \sqrt{R_n}\cos\left[(\omega_n + \omega_D)t + \varphi_n\right] \right.$$
$$\left. +2\sum\nolimits_n \sum\nolimits_{m\neq n} \sqrt{(R_n R_m)}\cos\left(\omega_{nm}t + \varphi_{nm}\right) \right\} \tag{8.4}$$

where φ_n and φ_{nm} are trivial initial phase offsets. As evident in the equation, the autocorrelation artifacts, given by the last term inside the brackets, are still centered around the baseband, while the cross-correlation terms, given by the third term inside the brackets, are now shifted away from DC and centered around the carrier frequency ω_D. Although the Fourier transform of the frequency-shifted signal is still Hermitian symmetric, the frequency-shifted fringes are far away enough from baseband such that negative and positive displacements can be differentiated. Positive displacements are located above ω_D, while negative displacements are below ω_D but above the baseband, as long as ω_D is higher than the highest frequency signal, i.e., the maximum ω_n.

A frequency shift of ω_D corresponds to a path length shift of z_D, where $z_D = \omega_D \Delta t/(2\Delta k)$ where Δt is the time it takes for the source to sweep over the entire bandwidth and Δk is the bandwidth of the source in wavenumber units. This shift in frequency is not subject to conventional FDOCT signal falloff, governed by the spectral source instantaneous linewidth in SSOCT. Instead, the frequency shift merely creates a time-varying beat frequency that is not dependent on source linewidth or source sweep rate.

8.2.2 Heterodyne OCT with Frequency-Shifting Devices

There are several algorithms in heterodyne OCT to recover a complex conjugate-free image. The first to be discussed, implemented by Davis et al. [40], utilized

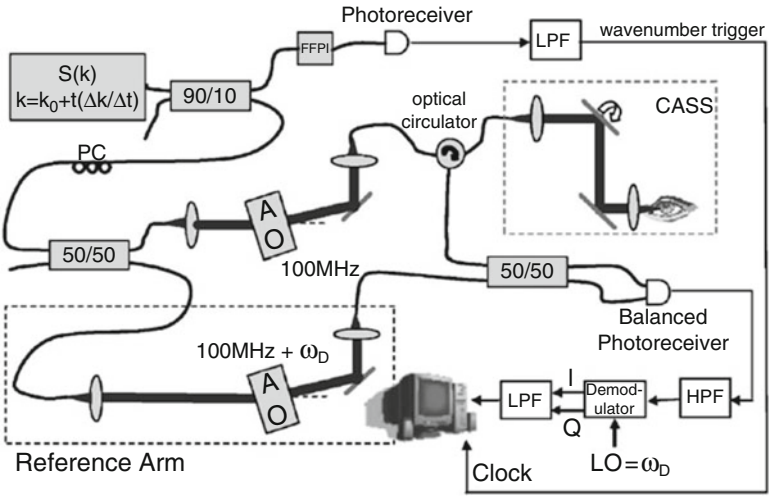

Fig. 8.1 Heterodyne SSOCT system using AOMs to frequency upshift interferogram. The swept laser was centered at 1,300 nm with a bandwidth of 100 nm. Balanced detection is used for common noise rejection. *AO* acousto-optic modulator, *PC* polarization controller, *FFPI* Fabry-Perot interferometer, *CASS* corneal anterior segment scanner

a band-pass filter around the carrier frequency and subsequent demodulation to recover the inphase and quadrature components of the complex OCT signal. The optical setup, depicted in Fig. 8.1, employed two acousto-optic modulators centered at 100 MHz, with a user tunable offset frequency in one modulator to provide the carrier frequency. Circulators were used to minimize the amount of optical power loss through the AOMs. Wavenumber triggering was used to remap the sweep linearly in wavenumber.

After the heterodyned interferometric signal was collected, a high-pass filter was used to remove the DC and autocorrelation artifacts. The filtered signal is then demodulated by mixing with a local oscillator of the same frequency as the carrier frequency. The in-phase and quadrature components can then be recovered to reconstruct the complex OCT signal. Furthermore, after demodulation, the resulting signal is only dependent on ω_n; therefore, conventional wavenumber triggering can be used to remap the sweep linearly in time. Figure 8.2 depicts captured interferometric fringes with and without the frequency shift. Two different interferograms are analyzed, with frequencies corresponding to reflectors at +/−50 μm displacements. As evident, with no frequency shift, the interferograms cannot be differentiated due to the complex conjugate ambiguity. However, collection of the same exact reflectors but with a carrier frequency of 20 kHz depicts how the two interferograms are now at different frequencies and can be easily differentiated. The fringe frequency for the positive displacement is greater than the fringe frequency for the negative displacement.

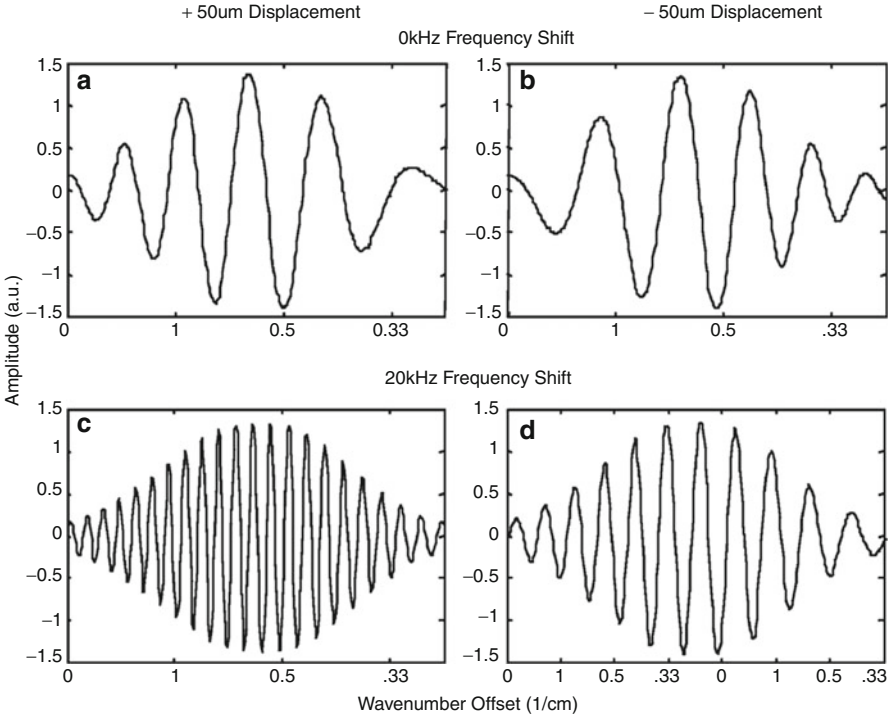

Fig. 8.2 Interferograms captured from reflectors at +/−50 μm displacements using homodyne and heterodyne SSOCT. The top row illustrates the homodyne case, while the bottom row illustrates the effect of frequency shifting by 20 kHz. As evident, the two reflectors in the homodyne case are indistinguishable, while the reflector at the positive displacement has much higher frequency fringes than the reflector at the negative displacement. Notice that the frequency-shifted signals are chirped, indicating that the signal must first be demodulated before wavenumber triggering

As previously mentioned, frequency shifting not only resolves the complex conjugate ambiguity but also eliminates the DC and autocorrelation artifacts. The anterior segment of the eye was imaged using heterodyne SSOCT to illustrate the utility of frequency shifting. The power on the eye was 60 μm and the images were constructed using 500 lines/image acquired at 250 Hz. With homodyne SSOCT, the entire anterior segment cannot be visualized simultaneously; however, frequency shifting doubles the imaging depth range and enables simultaneous imaging of the cornea, sclera, and iris, as shown in Fig. 8.3.

Zhang et al. utilized an electro-optic phase modulator (EOM) to induce a carrier frequency, similar to the frequency-shifting process described above [41, 42]. To compensate for group-velocity dispersion mismatch induced by the EOM, a rapid scanning optical delay line was used. The upshifted signal was band-pass filtered and demodulated to retrieve the complex OCT signal and resolve the complex conjugate ambiguity. As mentioned before, the demodulation of the

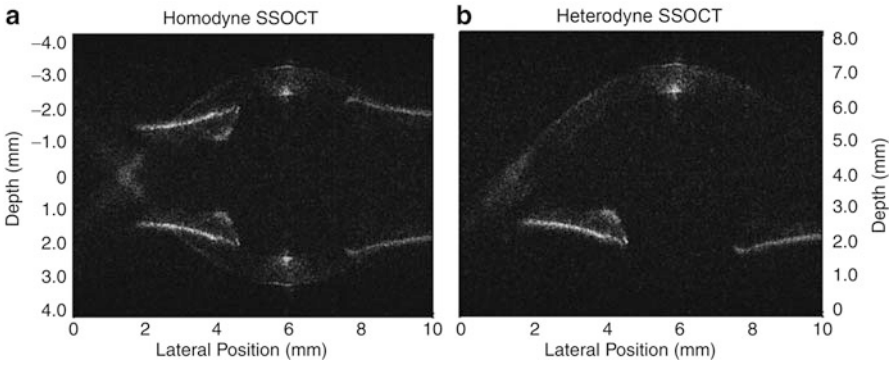

Fig. 8.3 In vivo images of the anterior segment of a human eye with homodyne (**a**) and heterodyne (**b**) SSOCT. The complex conjugate artifacts are resolved in the heterodyne case, doubling depth imaging range to about 8 mm and enabling visualization of the entire anterior segment

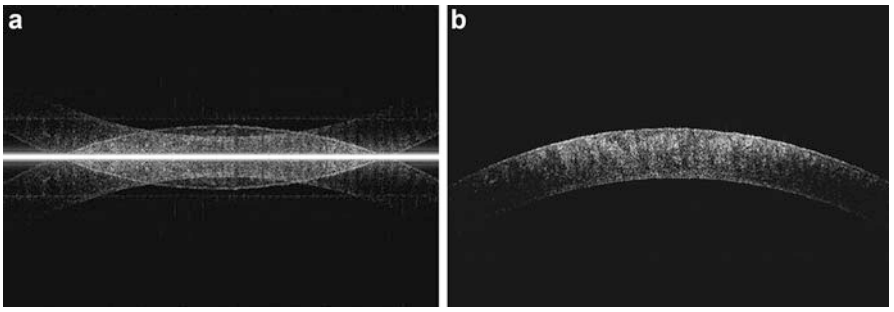

Fig. 8.4 Images of rabbit cornea obtained without (**a**) and with (**b**) the EOM. As evident, frequency upshifting results in a doubling of imaging depth range. The entire corneal curvature can be imaged only after removal of the complex conjugate ambiguity

frequency-shifted signal before remapping the source sweep linearly in wavenumber is necessary to avoid chirping. Furthermore, removal of low-frequency noise as well as autocorrelation artifacts improved system sensitivity by 20 dB. As with the previous technique, removal of the complex conjugate artifact resulted in an increased imaging range by a factor of 2 and was demonstrated by imaging rabbit cornea. Figure 8.4 illustrates the ability to image the entire corneal depth after removal of the complex conjugate artifact.

Another group demonstrated CCR with AOMs, similar to Davis et al. As before, a carrier frequency was applied to electronically shift interferometric signal away from baseband. However, unlike the previously discussed techniques, IQ demodulation was not performed, and the interferometric signal at the carrier frequency was digitized and processed. Instead of performing IQ demodulation to reconstruct the complex OCT signal, the authors relied on the frequency shift induced by the AOMs to be far away enough from baseband such that the negative

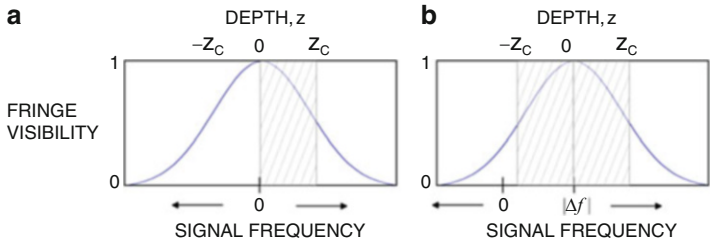

Fig. 8.5 Plot of fringe visibility versus fringe signal frequency without (**a**) and with (**b**) frequency shifting. Frequency shifting enables both sides of the coherence range to be utilized, therefore doubling the imaging range. Negative and positive path lengths are readily differentiated after frequency shifting

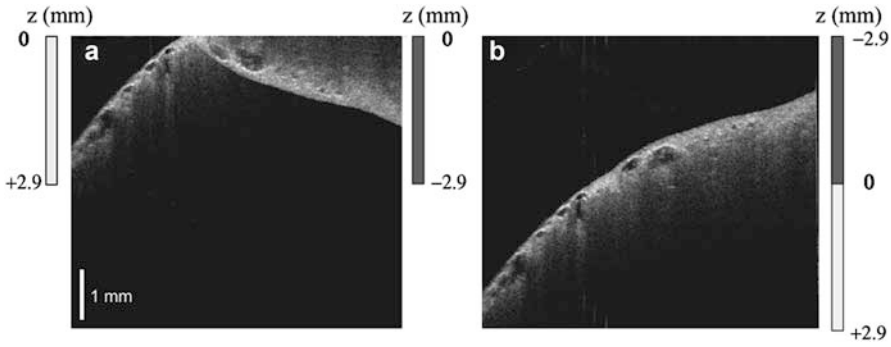

Fig. 8.6 Heterodyne (*right*) and homodyne (*left*) OCT ex vivo images of human lung tissue. The frequency shift of −2.5 MHz corresponds to a path length shift of 2.9 mm. The frequency-shifted image results in doubling of the depth range

path length differences are still above DC. A Fourier transform of this signal is still Hermitian symmetric; however, the complex conjugate ambiguity is still resolved since the entire imaging range is located above baseband. Therefore, as long as a digitizer and photoreceiver with large enough bandwidths are utilized, the upshifted interferometric signal can be collected directly, resulting in a complex conjugate free A-line. Figure 8.5 illustrates this concept. As shown, the zero path delay is now upshifted to some carrier frequency, resulting in locating the entire coherence range on the positive frequency side of DC, doubling the effective ranging depth [43].

CCR was demonstrated on ex vivo images of human lung tissue. A −2.5 MHz frequency shift, corresponding to a 2.9 mm path length shift, was induced using AOMs. The upshifted interferogram was captured and digitized without any demodulation. Therefore, the zero path length position in the heterodyne OCT image is now located 2.9 mm deeper relative to the homodyne OCT image, effectively doubling the imaging range, as shown in Fig. 8.6.

8.2.3 Heterodyne OCT with Coherence Revival

Coherence revival refers to observing interference fringes in an interferometer not only when the sample and reference arms OPLs are matched but also when the OPL mismatch is an integer multiple of the cavity length of the source [44]. This phenomenon can occur if the laser oscillates at multiple longitudinal modes simultaneously; if so, then the multimode field emitted exhibits periodicity. The period at which the interference fringes are seen is equal to the reciprocal of the mode space or alternatively equal to the round-trip optical delay of the cavity length. Therefore, by inserting a "virtual" cavity in either the sample or reference arm by mismatching the OPL difference by an integer multiple of the cavity length, interference fringes are still observed. This phenomenon is present in some external cavity lasers used in SSOCT.

Of particular importance is frequency shifting in coherence revival. For the two swept-source lasers investigated in [45], inserting a virtual cavity also results in phase modulation of the interferometric fringes seen in coherence revival. This phase modulation results in a frequency upshift, equivalent to imparting a carrier frequency with AOMs, as described above. Therefore, phase modulation in coherence revival enables CCR by the same principles as frequency upshifting with AOMs. Although the exact origin of the phase modulation in coherence revival is unknown, it is suggested that a change in the physical length of the cavity or a modulation of the refractive index of the gain media may be responsible [46]. Nevertheless, coherence revival heterodyne OCT behaves exactly the same as the previous heterodyne OCT methods, except that it does not require a frequency-shifting device such as an AOM.

CCR using coherence revival is illustrated in Fig. 8.7, shown below. Falloff plots, which are compiled plots of A-lines for a single, perfect reflector located at different depths, are illustrated for −1, 0, and +1 cavity length offsets. Notice that at −1 and +1 cavity length offsets, the peak sensitivity of the fall of plots is upshifted to around 6 mm, indicating that the interferogram has been upshifted with a carrier frequency corresponding to a path length shift of 6 mm. Coherence revival results in almost doubling the imaging, as defined by the −6 dB cutoff in the falloff plots.

The increased imaging range was illustrated in volumetric in vivo imaging of the anterior segment of the human eye, depicted in Fig. 8.8. Two swept sources (centered at 840 and 1,050 nm) exhibiting coherence revival were used.

Coherence revival OCT was further extended for whole eye imaging [47]. Using polarization encoding, a hybrid anterior segment and retinal imaging system was constructed, as seen in Fig. 8.9. A cavity length offset was added to the sample OPL of the beam focused at the anterior segment to enable CCR. The OPL of the beam focused at the retina and the reference arm were matched. Therefore, the interferogram signal collected from the retina was centered at the baseband, while the upshifted interferogram signal from the anterior segment was centered at a carrier frequency far enough away from baseband to prevent crosstalk between the two interferograms.

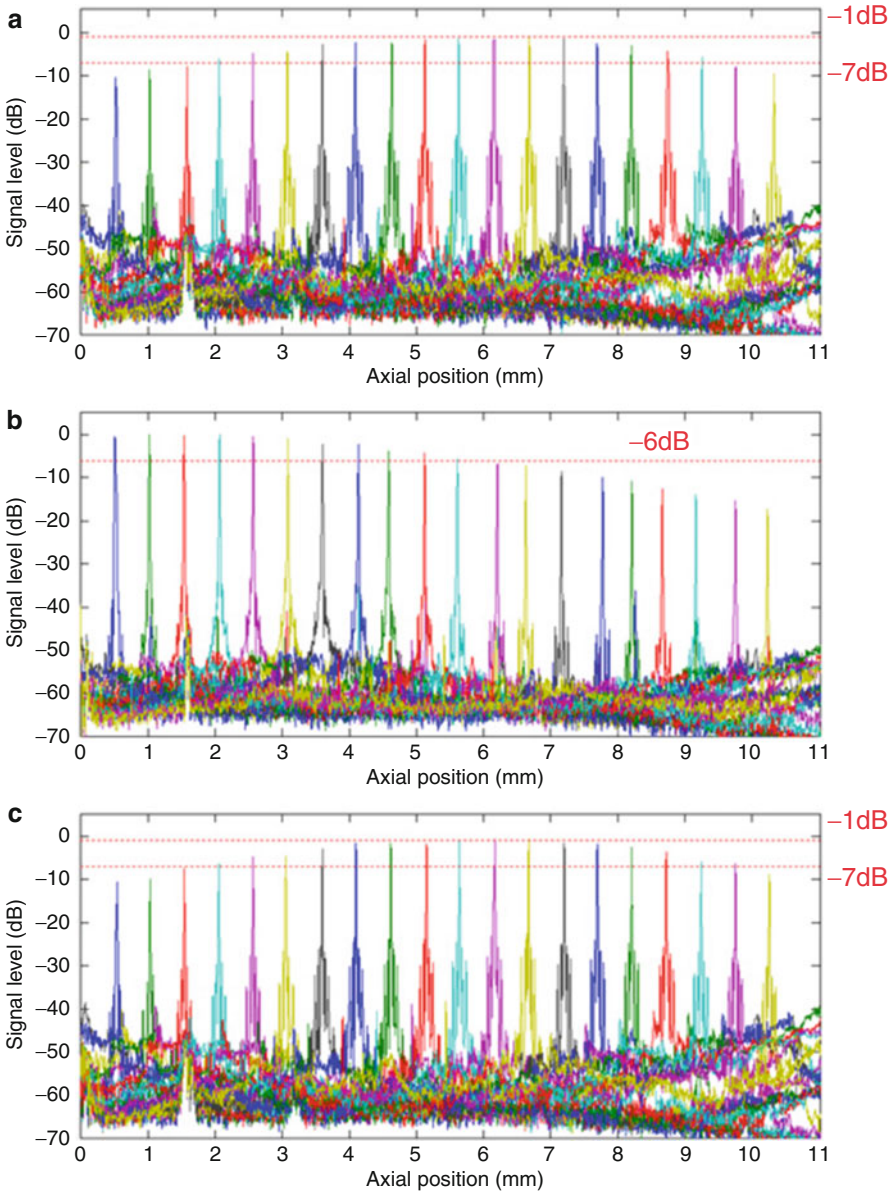

Fig. 8.7 Falloff plots, generated by recorded the reflection of a mirror at different depth locations, are shown for −1 (**a**), 0 (**b**), and +1 (**c**) cavity length offsets. Offsetting the OPL mismatch between the reference and sample arm by +/−1 cavity length results frequency-shifted interferograms, as evidenced by a shift in the peak sensitivity to about 6 mm

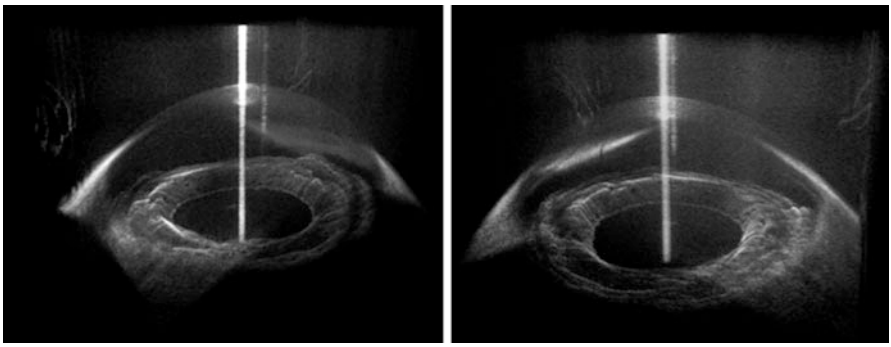

Fig. 8.8 Volumetric imaging of the anterior segment of the human eye with an 840 nm (*left*) and 1,040 nm (*right*) systems. CCR via coherence revival enables imaging of the full anterior segment, including the cornea, iris, and sclera

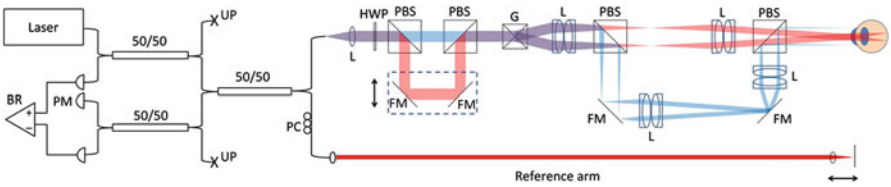

Fig. 8.9 A coherence revival heterodyne OCT system that enables whole eye imaging. Polarization encoding is used to simultaneously image the anterior eye segment and the retina. A cavity length offset in the sample arm enables CCR imaging of the anterior segment of the eye. Simultaneous detection of the baseband and frequency-shifted interferogram, from the retina and anterior segment, respectively, is achieved with a balanced receiver

Whole eye imaging with polarization-encoded coherence revival OCT is shown in Fig. 8.10. The zero path length position and the one cavity length offset position are labeled. The frame acquired before cropping the image is shown in (A) and illustrates how both the retina and anterior segment can be imaged simultaneously.

It is important to note the nonlinear sweep of the source as a function of time in relation to frequency shifting. That is, in standard homodyne SSOCT, the nonlinear sweep causes chirping of the interferometric signal resulting in a loss of axial resolution. Several techniques can be implemented to compensate for the nonlinear sweep. The detector can be sampled at nonlinear time intervals, utilizing an interferometric clock (or "optical clock"), which essentially provides an interferometric signal at a constant frequency. The zero crossings of the fringes of the interferometric clock are used to trigger the detector to enable nonlinear sampling of the OCT interferometric signal. This technique is usually referred to as wavenumber triggering. Another technique simply employs linear time sampling of the OCT signal and subsequent interpolation to remap the sweep linearly in

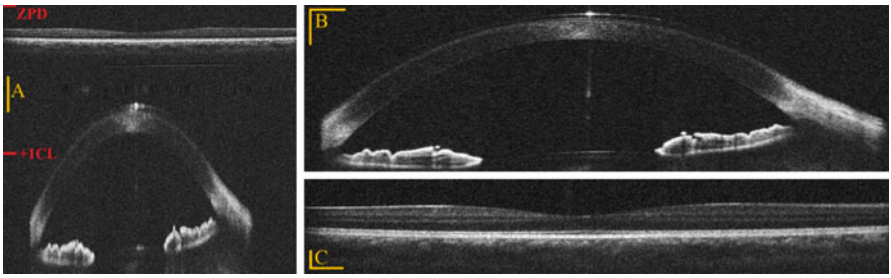

Fig. 8.10 Whole eye imaging with coherence revival OCT. (**a**) shows the simultaneously acquired images of the anterior segment and retina. (**b**) and (**c**) show cropped and average B-scans of the CCR anterior segment and retina, respectively

wavenumber before Fourier transforming to the space domain. When frequency shifting, these standard sampling techniques can result in chirping of the upshifted interferometric signal if it is not demodulated back to baseband. This problem is particularly relevant to frequency-shifting CCR by Yun et al. [43] and coherence revival CCR by Dhalla et al. [48].

To mitigate chirping of the upshifted interferogram, Yun et al. proposed the following algorithm. First, the OCT upshifted interferometric is sampled at uniform time intervals. The DFT is calculated to obtain the electronic frequency of the signal. The frequency bands above and below the carrier frequency are separated and downshifted such that the zero position for each frequency band is aligned with the zero electrical frequency. Zero padding is then applied on each frequency band to increase time resolution in the electrical time domain. With higher time resolution, each band can now be linearly interpolated using a mapping function calibrated for the nonlinear sweep of the source, as is done with conventional SSOCT.

Dhalla et al. proposed a much simpler algorithm. The optical clock from the swept source is designed for calibrating a mapping function such that the interferometric signal can be resampled linearly in wavenumber. However, some of these interferometric clocks are typically designed for maximum imaging depths of 3.7 mm (Axsun Technologies). For imaging depths greater than 3.7 mm, achieved by heterodyne SSOCT, using the conventional optical clock to sample the signal will result in chirping of frequencies corresponding to depths greater than 3.7 mm. The optical clock can then simply be interpolated to increase the fringe frequency to correspond to a depth at least twice that of the carrier frequency. Then, this interpolated calibration vector can be used to interpolate and resample the upshifted SSOCT signal linearly in wavenumber.

Heterodyne OCT is a useful technique that allows complete elimination of the complex conjugate artifact. The complex OCT signal can be retrieved by IQ demodulation or the upshifted interferogram can be directly captured to achieve CCR SSOCT. Heterodyne OCT necessitated the use of frequency-shifting devices such as AOMs, but the recent discovery of coherence revival and phase modulation in popular swept-frequency lasers allow for frequency shifting by simply offsetting

the OPL difference between the sample and reference arms by an integer multiple of the roundtrip delay of the laser cavity length. Heterodyning is an attractive choice for CCR SSOCT due to its simplicity and complete elimination of the complex conjugate artifact.

8.3 Phase-Shifting SSOCT with 3 × 3 Fiber Coupler

Another method for CCR, which is applicable to both SD and SSOCT, utilizes the inherent phase shift in 3 × 3 fiber couplers to enable simultaneously acquisition of phase-shifted interferograms to reconstruct the complex OCT signal [49–51].

8.3.1 3 × 3 Fiber Coupler Phase-Shifting Theory

Phase shifting with 3 × 3 couplers enables instantaneous acquisition of the in-phase and quadrature components of the complex OCT waveform, unlike typical phase-shifting OCT techniques which necessitate the sequential acquisition of phase-shifted frames, resulting in increased imaging time. As discussed above, reconstruction of the complex OCT signal yields a complex conjugate-resolved A-line. Note that unlike the heterodyne CCR SSOCT techniques above, using 3 × 3 fiber couplers suppresses the complex conjugate artifact rather than completely eliminating it, where the suppression ratio is dependent on the reconstruction accuracy of the complex OCT signal.

Recall that the detectors utilized in SSOCT necessarily acquire the real part of the complex OCT signal given by (8.2). As discussed above, the Fourier transform of the real part of (8.2) yields a Hermitian symmetric signal resulting in the complex conjugate ambiguity. To further discuss phase-shifting theory in CCR SSOCT, it proves helpful to rewrite the complex OCT signal in terms of its in-phase and quadrature components. These can be obtained by collecting two interferograms with a relative $\pi/2$ phase shift:

$$D_i[k_m] = D_i^0[k_m] + jD_i^{90}[k_m] \tag{8.5}$$

Recasting Eq. 8.5 and in terms of trigonometric functions and taking the Fourier transform of the complex signal yields an A-scan in which the negative and positive displacements can be unambiguously determined, as shown below:

$$D_i[k_m] \propto S[k_m] \cdot \left(2(R_R + R_S) + 2\sqrt{R_R R_S}\cos\left(2\Delta x k_m + \varphi_i\right) + j2\sqrt{R_R R_S}\sin\left(2\Delta x k_m + \varphi_i\right)\right) \tag{8.6}$$

$$D_i[x_n] \propto S[x_n] \bigotimes \left(2(R_R + R_S)\delta(x_n) + 4\sqrt{R_R R_S}(\delta(x_n + \Delta x))\right) \tag{8.7}$$

As previously mentioned, to acquire the complex OCT signal, other phase-shifting techniques necessitate dithering or stepping of the reference arm to acquire sequential, phase-shifted interferograms. A Michelson interferometer constructed with a 3 × 3 fiber coupler, as shown in Fig. 8.10, introduces an inherent phase delay between the detector ports. If the 3 × 3 fiber coupler has even power splitting rations, then the phase shift between the detector ports is ideally 120° [50]. The true advantage of phase shifting with higher-order couplers is that the phase-shifted interferograms can be acquired simultaneously on the two different ports, which allows for instantaneous CCR SSOCT.

Once the phase-shifted interferograms are collected and assuming that the splitting ratios of the 3 × 3 coupler are know, the in-phase and quadrature components of the complex OCT signal can then be retrieved. Defining the first and second interferograms collected as i_n and i_m, respectively, one of the collected interferograms can be treated as the real part of the complex signal ($i_n = i_{Re}$ shown in (8.5). The imaginary component i_{Im} can be obtained through trigonometric manipulation, as follows:

$$i_{Im} = \frac{i_n \cos\left(\Delta\phi_{mn}\right) - \beta_{mn} i_m}{\sin\left(\Delta\phi_{mn}\right)} \tag{8.8}$$

where ϕ_{mn} is the relative phase shift between the detector ports and β_{mn} is the wavelength-dependent power splitting ratio, which is further discussed in [50].

8.3.2 CCR SSOCT imaging with 3 × 3 Fiber Couplers

Using a 3 × 3 fiber coupler and the system shown in Fig. 8.11, suppression of the complex conjugate-resolved ambiguity was demonstrated [51]. Figure 8.12 shows falloff plots depicting the complex conjugate-resolved A-scans for various path lengths. The peak SNR of the SSOCT system was 112 dB, while the maximum suppression of the complex conjugate artifact was about 25 dB.

An anterior eye segment SSOCT imaging system with a conventional imaging depth of 4 mm, as defined by the finite linewidth of the swept source, was utilized.

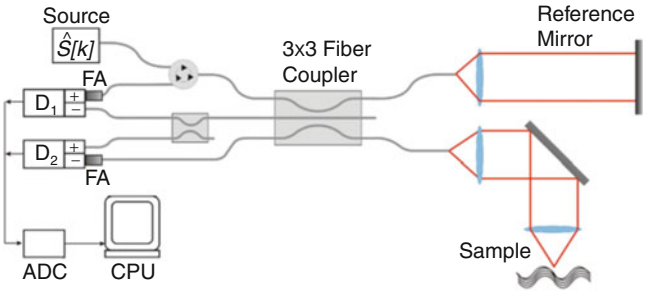

Fig. 8.11 Phase-shifting OCT using a 3 × 3 fiber coupler. The phase-shifted interferograms are simultaneously acquired at the two separate detectors to reconstruct the complex OCT signal

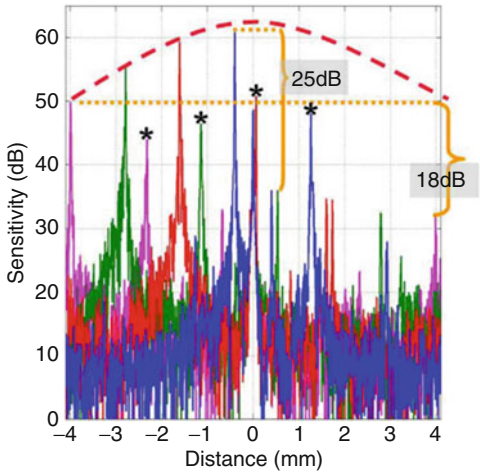

Fig. 8.12 Complex conjugate-resolved A-scans. Maximum suppression of about 25 dB of the complex conjugate artifact is shown. The asterisks indicate peaks corresponding to reflections from an attenuation filter

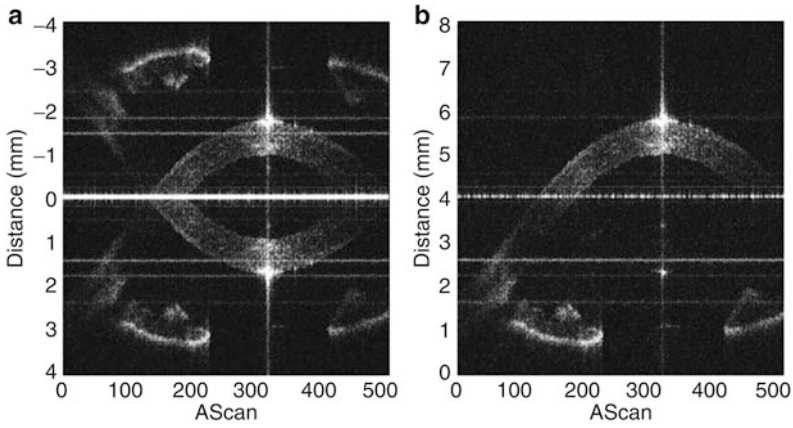

Fig. 8.13 Conventional SSOCT (**a**) and CCR SSOCT (**b**) imaging of the anterior segment of the eye. The origin of the spurious reflections between 1.5 and 2.6 mm is unknown

Resolving the complex conjugate ambiguity with the 3 × 3 fiber coupler doubled the imaging depth to 8 mm, enabling visualization of the entire anterior eye segment, shown in Fig. 8.13.

It should be noted that the wavelength-dependent power splitting is a limiting factor in the reconstruction of the complex OCT single and contributes to the imperfect suppression of the complex conjugate artifact. Furthermore, similar to the phase-stepping techniques used in CCR SDOCT, introducing additional phase steps by using higher-order coupler (e.g., 4 × 4) may improve reconstruction accuracy of the complex signal. As noted above, a suppression of 25 dB was achieved with this previously discussed implementation.

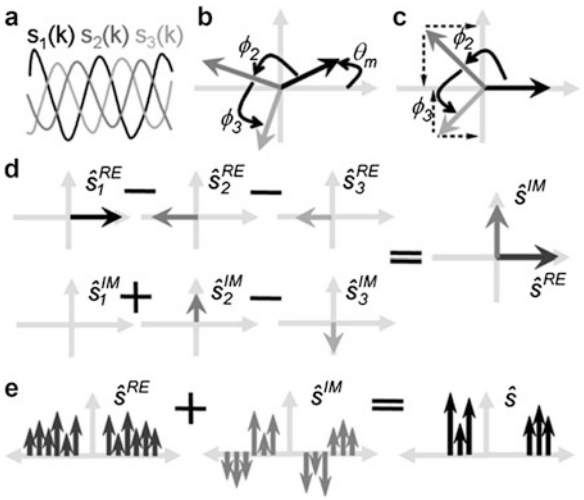

Fig. 8.14 Quadrature projection processing for complex conjugate-resolved FDOCT. The processing steps are described in detail in the text. 3 × 3 fiber coupler phase-shifting OCT does not necessitate any mechanically induced phase shifting. Instead, the phase shift between collected interferograms is inherent to the fiber coupler. Furthermore, multiple detector ports enable simultaneous acquisition of the shifted interferograms and reduce imaging time compared to other phase-shifting OCT techniques

Phase-shifting OCT techniques in general usually have imperfect suppression of the complex conjugate ambiguity because of miscalibration of the phase shift and chromatic phase shift error when dithering the reference mirror. When using 3 × 3 couplers, chromatic phase shift error is not induced; however, the technique may still be sensitive to phase shift miscalibration. A different complex OCT reconstruction algorithm – intended for use in 3 × 3 coupler phase shifting but applicable to any phase-shifting OCT techniques – is insensitive to miscalibrated phase shifts in 90° interferometry and only requires knowledge of the Re/Im quadrant location for each phase in non-90° interferometry [49]. In this algorithm, illustrated in Fig. 8.14, the phase-shifted interferograms can be represented in the Fourier domain (a) and the complex plane (b). Phase subtraction enables the phase shift of the first signal to align onto the real positive axis. The shifted interferograms are now offset from the real positive axis by some angle ϕ given by the relative phase shift (c). The real and complex projections of each vector can then be summed to obtain a single complex signal (d). The complex conjugate ambiguity can then be resolved by summing the real and imaginary components of the reconstructed complex signals (e). A more detailed description and analysis of the algorithm can be found in [49]. This algorithm is advantageous since it can be utilized with an arbitrary number of phase shifts and enabled complex conjugate artifact suppression of >30 dB with 3 × 3 fiber coupler phase-shifting OCT.

8.4 Polarization-Based Optical Demodulation in SSOCT

Another method for retrieving the IQ components of the complex OCT signal in SSOCT is through polarization-based optical demodulation [52]. In essence, the detected interferogram is polarization encoded such that one polarization state (first interferogram) is 90° out of phase with the second polarization state (second interferogram), thereby allowing reconstruction of the complex signal. The system utilized is depicted in Fig. 8.15, where the dashed box delineates the optical demodulation circuit [53, 54] for retrieval of the IQ components.

Light from the sample and reference arm paths are orthogonally polarized using a polarized beam combiner. The light is then coupled to a 50/50 coupler where each arm of the coupler directs light to a polarization controller and then a polarized beam splitter. The output from the polarized beam splitter converts polarization modulation to intensity modulation detected by a balanced receiver. It is important to note that the phase shift between light in each arm of the 50/50 splitter can be arbitrarily set by the polarization controllers. Therefore, to retrieve the IQ components of the complex OCT signal, the polarization-encoded interferograms can be phase-shifted by 90°. CCR SSOCT using polarization-encoded optical demodulation was demonstrated with images of a finger, shown in Fig. 8.16.

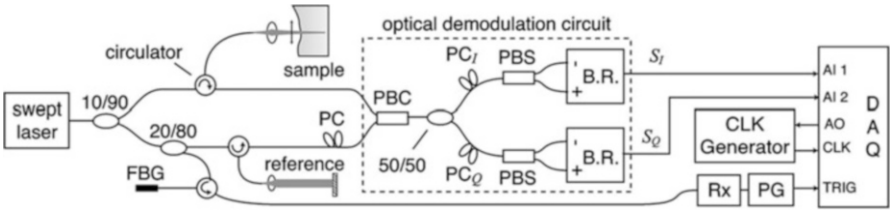

Fig. 8.15 Retrieval of IQ components using polarization-encoded optical demodulation. *PC* polarization controller, *PBC* polarization beam combiner, *PBS* polarized beam splitter, *BR* balanced receiver

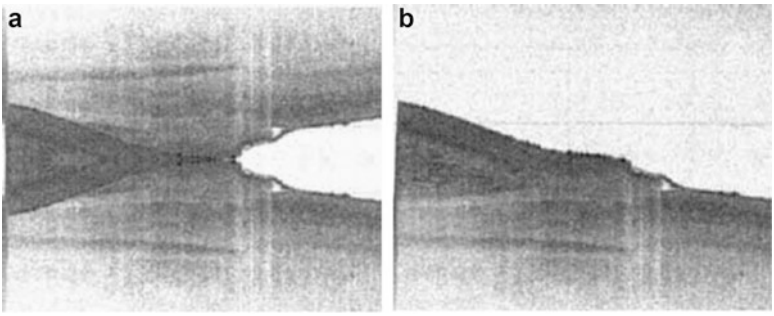

Fig. 8.16 Images of a human finger without (**a**) and with (**b**) optical demodulation

Polarization-based optical demodulation is unique since it does not require RF demodulation or phase shifting. As long as the relative phase delay between the orthogonally polarized interferograms is carefully controlled, the complex OCT signal can be readily reconstructed.

8.5 Conclusion

The complex conjugate ambiguity is a nontrivial artifact resulting from direct Fourier detection in FDOCT. While most FDOCT systems avoid this artifact by limiting their imaging range, CCR FDOCT seeks to suppress or eliminate the complex conjugate ambiguity. CCR for SSOCT, by either phase shifting, heterodyning, or optical demodulation, increases the imaging range by a factor of 2 compared to conventional FDOCT. This technological development is important in many OCT applications, including ophthalmology in which the increased imaging range in necessary to visualize the entire anterior segment of the human eye.

References

1. D. Huang, E.A. Swanson, C.P. Lin, J.S. Schuman, W.G. Stinson, W. Chang, M.R. Hee, T. Flotte, K. Gregory, C.A. Puliafito, J.G. Fujimoto, Optical coherence tomography. Science **254**(5035), 1178–1181 (1991)
2. J.A. Izatt, M.R. Hee, E.A. Swanson, C.P. Lin, C.A. Puliafito, J.G. Fujimoto, Micrometer-scale resolution imaging of the anterior eye in vivo with optical coherence tomography. Arch. Ophthalmol. **112**, 1584–1589 (1994)
3. F. Fercher, K. Hitzenberger, G. Kamp, Measurement of intraocular distances by backscattering spectral interferometry. Opt. Commun. **117**, 43–48 (1995)
4. G. Huasler, M.W. Lindner, Coherence radar and spectral radar – new tools for dermatological diagnosis. J. Biomed. Opt. **3**(1), 21–31 (1998)
5. S.R. Chinn, E.A. Swanson, J.G. Fujimoto, Optical coherence tomography using a frequency-tunable optical source. Opt. Lett. **22**(5), 340–342 (1997)
6. F. Lexer, C.K. Hitzenberger, A.F. Fercher, M. Kulhavy, Wavelength-tuning of interferometry of intraocular distances. Appl. Optics **36**(25), 6548–6553 (1997)
7. M. Choma, M. Sarunic, C. Yang, J. Izatt, Sensitivity advantage of swept source and Fourier domain optical coherence tomography. Opt. Express **11**(18), 2183–2189 (2003)
8. R. Leitgeb, C. Hitzenberger, A. Fercher, Performance of fourier domain vs. time domain optical coherence tomography. Opt. Express **11**(8), 889–894 (2003)
9. J.F. de Boer, B. Cense, B.H. Park, M.C. Pierce, G.J. Tearney, B.E. Bouma, Improved signal-to-noise ratio in spectral-domain compared with time-domain optical coherence tomography. Opt. Lett. **28**(21), 2067–2069 (2003)
10. N.A. Nassif, B. Cense, B.H. Park, M.C. Pierce, S.H. Yun, B.E. Bouma, G.J. Tearney, T.C. Chen, In vivo high-resolution video-rate spectral-domain optical coherence tomography of the human retina and optic nerve. Opt. Express **12**(3), 367–376 (2004)
11. M. Wojtkowski, R. Leitgeb, A. Kowalczyk, T. Bajraszewski, A.F. Fercher, In vivo human retinal imaging by Fourier domain optical coherence tomography. J. Biomed. Opt. **7**(3), 457–463 (2002)
12. R. Leitgeb, W. Drexler, A. Unterhuber, B. Hermann, T. Bajraszewski, T. Le, A. Stingl, A. Fercher, Ultrahigh resolution Fourier domain optical coherence tomography. Opt. Express **12**(10), 2156–2165 (2004)

13. J.A. Goldsmith, Y. Li, M.R. Chalita, V. Westphal, C.A. Patil, A.M. Rollins, J.A. Izatt, D. Huang, Anterior chamber width measurement by high-speed optical coherence tomography. Ophthalmology **112**(2), 238–244 (2005)
14. M. Wojtkowski, V. Srinivasan, J.G. Fujimoto, T. Ko, J.S. Schuman, A. Kowalczyk, J.S. Duker, Three-dimensional retinal imaging with high-speed ultrahigh-resolution optical coherence tomography. Ophthalmology **112**(10), 1734–1746 (2005)
15. S.H. Yun, C. Boudoux, G.J. Tearney, B.E. Bouma, High-speed wavelength-swept semiconductor laser with a polygon-scanner-based wavelength filter. Opt. Lett. **28**(20), 1981–1983 (2003)
16. R. Huber, M. Wojtkowski, K. Taira, J. Fujimoto, K. Hsu, Amplified, frequency swept lasers for frequency domain reflectometry and OCT imaging: design and scaling principles. Opt. Express **13**(9), 3513–3528 (2005)
17. R. Huber, M. Wojtkowski, J.G. Fujimoto, J.Y. Jiang, A.E. Cable, Three-dimensional and C-mode OCT imaging with a compact, frequency swept laser source at 1300 nm. Opt. Express **13**(26), 10523–10538 (2005)
18. Y. Yasuno, V.D. Madjarova, S. Makita, K. Chan, Three-dimensional and high-speed swept-source optical coherence tomography for in vivo investigation of human anterior eye segments. Opt. Express **13**(26), 10652–10664 (2005)
19. M.A. Choma, K. Hsu, J.A. Izatt, Swept source optical coherence tomography using an all-fiber 1300-nm ring laser source. J. Biomed. Opt. **10**(4), 44009 (2005)
20. Y. Yasuno, Y. Hong, S. Makita, M. Yamanari, M. Akiba, M. Miura, T. Yatagai, In vivo high-contrast imaging of deep posterior eye by 1-microm swept source optical coherence tomography and scattering optical coherence angiography. Opt. Express **15**(10), 6121–6139 (2007)
21. F.E. Robles, C. Wilson, G. Grant, A. Wax, Molecular imaging true-colour spectroscopic optical coherence tomography. Nat. Photonics **5**(12), 744–747 (2011)
22. A. Wax, C. Yang, J.A. Izatt, Fourier-domain low-coherence interferometry for light-scattering spectroscopy. Opt. Lett. **28**(14), 1230–1232 (2003)
23. M.A. Choma, A.K. Ellerbee, C. Yang, T.L. Creazzo, J.A. Izatt, Spectral-domain phase microscopy. Opt. Lett. **30**(10), 1162–1164 (2005)
24. A.K. Ellerbee, T.L. Creazzo, J.A. Izatt, Investigating nanoscale cellular dynamics with cross-sectional spectral domain phase microscopy. Opt. Express **15**(13), 8115–8124 (2007)
25. E.J. McDowell, A.K. Ellerbee, M.A. Choma, B.E. Applegate, J.A. Izatt, Spectral domain phase microscopy for local measurements of cytoskeletal rheology in single cells. J. Biomed. Opt. **12**(4), 044008 (2007)
26. M. Wojtkowski, A. Kowalczyk, R. Leitgeb, A.F. Fercher, Full range complex spectral optical coherence tomography technique in eye imaging. Opt. Lett. **27**(16), 1415–1417 (2002)
27. P. Targowski, M. Wojtkowski, A. Kowalczyk, T. Bajraszewski, M. Szkulmowski, I. Gorczyńska, Complex spectral OCT in human eye imaging in vivo. Opt. Commun. **229**(1–6), 79–84 (2004)
28. E. Götzinger, M. Pircher, R. Leitgeb, C. Hitzenberger, High speed full range complex spectral domain optical coherence tomography. Opt. Express **13**(2), 583–594 (2005)
29. J. Schmit, K. Creath, Extended averaging technique for derivation of error-compensating algorithms in phase-shifting interferometry. Appl. Optics **34**(19), 3610–3619 (1995)
30. R.A. Leitgeb, C.K. Hitzenberger, A.F. Fercher, T. Bajraszewski, Phase-shifting algorithm to achieve high-speed long-depth-range probing by frequency-domain optical coherence tomography. Opt. Lett. **28**(22), 2201–2203 (2003)
31. Y. Yasuno, S. Makita, T. Endo, G. Aoki, H. Sumimura, M. Itoh, T. Yatagai, One-shot-phase-shifting Fourier domain optical coherence tomography by reference wavefront tilting. Opt. Express **12**(25), 6184–6191 (2004)
32. Y.K. Tao, M. Zhao, J.A. Izatt, High-speed complex conjugate resolved retinal spectral domain optical coherence tomography using sinusoidal phase modulation. Opt. Lett. **32**(20), 2918–2920 (2007)
33. A.B.. Vakhtin, K.A. Peterson, D.J. Kane, Resolving the complex conjugate ambiguity in Fourier-domain OCT by harmonic lock-in detection of the spectral interferogram. Opt. Lett. **31**(9), 1271–1273 (2006)

34. R.A. Leitgeb, R. Michaely, T. Lasser, S.C. Sekhar, Complex ambiguity-free Fourier domain optical coherence tomography through transverse scanning. Opt. Lett. **32**(23), 3453–3455 (2007)
35. L. An, R.K. Wang, Use of a scanner to modulate spatial interferograms for in vivo full-range Fourier-domain optical coherence tomography. Opt. Lett. **32**(23), 3423–3425 (2007)
36. Y. Yasuno, S. Makita, T. Endo, G. Aoki, M. Itoh, T. Yatagai, Simultaneous B-M-mode scanning method for real-time full-range Fourier domain optical coherence tomography. Appl. Optics **45**(8), 1861–1865 (2006)
37. H. Wang, Y. Pan, A.M. Rollins, Extending the effective imaging range of Fourier-domain optical coherence tomography using a fiber optic switch. Opt. Lett. **33**(22), 2632–2634 (2008)
38. A. Bachmann, R. Leitgeb, T. Lasser, Heterodyne Fourier domain optical coherence tomography for full range probing with high axial resolution. Opt. Express **14**(4), 1487–1496 (2006)
39. R.K. Wang, In vivo full range complex Fourier domain optical coherence tomography. Appl. Phys. Lett. **90**(5), 054103 (2007)
40. A.M. Davis, M.A. Choma, J.A. Izatt, Heterodyne swept-source optical coherence tomography for complete complex conjugate ambiguity removal. J. Biomed. Opt. **10**(6), 064005 (2005)
41. J. Zhang, J.S. Nelson, Z. Chen, Removal of a mirror image and enhancement of the signal-to-noise ratio in Fourier-domain optical coherence tomography using an electro-optic phase modulator. Opt. Lett. **30**(2), 147–149 (2005)
42. J. Zhang, W. Jung, J. Nelson, Z. Chen, Full range polarization-sensitive Fourier domain optical coherence tomography. Opt. Express **12**(24), 6033–6039 (2004)
43. S. Yun, G. Tearney, J. de Boer, B. Bouma, Removing the depth-degeneracy in optical frequency domain imaging with frequency shifting. Opt. Express **12**(20), 4822–4828 (2004)
44. S.-Y. Baek, O. Kwon, Y.-H. Kim, High-resolution mode-spacing measurement of the blue-violet diode laser using interference of fields created with time delays greater than the coherence time. Jpn. J. Appl. Phys. **46**(12), 7720–7723 (2007)
45. A.-H. Dhalla, D. Nankivil, J.A. Izatt, Complex conjugate resolved heterodyne swept source optical coherence tomography using coherence revival. Biomed. Opt. Express **3**(3), 633–649 (2012)
46. H.X. Jiang, J.Y. Lin, Mode spacing 'anomaly' in InGaN blue lasers. Appl. Phys. Lett. **74**(8), 1066 (1999)
47. A.-H. Dhalla, D. Nankivil, T. Bustamante, A. Kuo, J.A. Izatt, Simultaneous swept source optical coherence tomography of the anterior segment and retina using coherence revival. Opt. Lett. **37**(11), 1883–1885 (2012)
48. A.-H. Dhalla, J.A. Izatt, Complete complex conjugate resolved heterodyne swept source optical coherence tomography using a dispersive optical delay line: erratum. Biomed. Opt. Express **3**(3), 630–632 (2012)
49. M.V. Sarunic, B.E. Applegate, J.A. Izatt, Real-time quadrature projection complex conjugate resolved Fourier domain optical coherence tomography. Opt. Lett. **31**(16), 2426–2428 (2006)
50. M.A. Choma, C. Yang, J.A. Izatt, Instantaneous quadrature low-coherence interferometry with 3×3 fiber-optic couplers. Opt. Lett. **28**(22), 2162–2164 (2003)
51. M. Sarunic, M.A. Choma, C. Yang, J.A. Izatt, Instantaneous complex conjugate resolved spectral domain and swept-source OCT using 3×3 fiber couplers. Opt. Express **13**(3), 957–967 (2005)
52. B.J. Vakoc, S.H. Yun, G.J. Tearney, B.E. Bouma, Elimination of depth degeneracy in optical frequency-domain imaging through polarization-based optical demodulation. Opt. Lett. **31**(3), 362–364 (2006)
53. F.D.E. Fornel, M.P. Varnham, D.N. Payne, Fibre gyroscope with passive quadrature detection. Electron. Lett. **20**(10), 399–401 (1984)
54. Y. Zhao, Z. Chen, C. Saxer, S. Xiang, J.F. de Boer, J.S. Nelson, Phase-resolved optical coherence tomography and optical Doppler tomography for imaging blood flow in human skin with fast scanning speed and high velocity sensitivity. Opt. Lett. **25**(2), 114–116 (2000)

Ultrahigh Resolution Optical Coherence Tomography

9

Wolfgang Drexler, Yu Chen, Aaron D. Aguirre, Boris Považay, Angelika Unterhuber, and James G. Fujimoto

Keywords

Ultrahigh axial resolution • Broad bandwidth light sources • Ti:sapphire • Super continuum • Resolution limitations

The performance of an OCT system is mainly determined by its longitudinal (axial) resolution, transverse resolution, dynamic range (i.e., sensitivity), and data acquisition specifications, including digitization resolution and speed [11]. For application in medical diagnosis, additional factors, e.g., noncontact vs. contact applicability,

W. Drexler (✉)
Center for Medical Physics and Biomedical Engineering, Medical University of Vienna, General Hospital Vienna, Vienna, Austria
e-mail: Wolfgang.Drexler@meduniwien.ac.at

Y. Chen
Department of Electrical Engineering and Computer Science and Research Laboratory of Electronics, Massachusetts Institute of Technology, Cambridge, MA, USA

Biomedical Optics and Imaging Laboratory, Fischell Department of Bioengineering, University of Maryland, College Park, MD, USA

A.D. Aguirre
Massachusetts General Hospital, Boston, MA, USA

Department of Electrical Engineering and Computer Science and Research Laboratory of Electronics, Massachusetts Institute of Technology, Cambridge, MA, USA

B. Považay • A. Unterhuber
Center for Medical Physics and Biomedical Engineering, Medical University of Vienna, Vienna, Austria

J.G. Fujimoto
Department of Electrical Engineering and Computer Science and Research Laboratory of Electronics, Massachusetts Institute of Technology, Cambridge, MA, USA

© Springer International Publishing Switzerland 2015

W. Drexler, J.G. Fujimoto (eds.), *Optical Coherence Tomography*,
DOI 10.1007/978-3-319-06419-2_10

possible penetration into the investigated tissue, image contrast, as well as extraction of functional or biochemical information in addition to the visualization of micro-structural morphology, have to be considered. In addition, for clinical applications, compactness, user-friendliness, robustness, flexibility, overall costs of the OCT system, as well as the possibility to interface it to existing diagnostic technology are decisive factors.

9.1 Longitudinal and Transverse Resolution in OCT

In contrast to conventional and confocal microscopy, OCT achieves very high-axial image resolutions independent of focusing conditions (cf. Fig. 9.1). The axial and transverse resolutions of OCT are decoupled:

- Axial (depth) resolution – defined by the coherence length of the light source (rather than the depth of field as in microscopy)
- Transverse resolution – defined by the focal spot size

As in conventional microscopy the transverse resolution and the depth of focus are determined by the focused transversal spot size, defined as the $1/e^2$ beam waist of a Gaussian beam (cf. Fig. 9.1). Assuming Gaussian rays and only taking into account Gaussian optics, the transverse resolution can be defined by

$$\Delta x = \frac{4\lambda}{\pi}\frac{f}{d}, \tag{9.1}$$

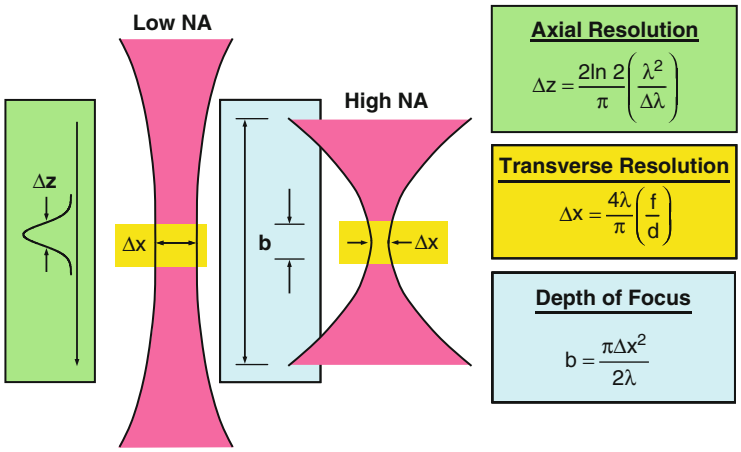

Fig. 9.1 *Resolution limits of OCT*. OCT can achieve high-axial resolutions independent of numerical aperture. Using low-coherence interferometry, the axial resolution is inversely proportional to the bandwidth of the light source. The transverse resolution is given by the focus spot size. The depth of field is determined by the confocal parameter of the focused beam

where f is the focal length of the lens and d is the spot size on the objective lens. Increasing the numerical aperture of the objective increases the transverse resolution by reducing the focal spot size, but it decreases the depth of field, quantified by the confocal parameter b, which is $2z_R$ or twice the Rayleigh length $2z_R = b = \pi\Delta x^2/2\lambda$. Thus, improving the transverse resolution can be accomplished by increasing the numerical aperture (NA) of the objective, but at the same time decreasing b. A solution to this limitation is the use of a dynamic focus tracking system. Especially for ophthalmic retinal OCT imaging, low numerical aperture focusing is employed, because it is desirable to have a large depth of field and to use OCT to achieve high-axial resolution.

The interference signal detected at the output of the interferometer is the electric field autocorrelation of the light source. As mentioned before, the full width at half maximum (FWHM) of this autocorrelation is the coherence length l_c, which gives the axial resolution Δz and is inversely proportional to the width of the power spectrum. The envelope of this field autocorrelation is equivalent to the Fourier transform of the power spectrum. For a source with a Gaussian spectral distribution, the axial resolution Δz is primarily determined by the coherence length of the optical light source given by

$$\Delta z = \frac{2\ln 2}{\pi} \frac{\lambda^2}{\Delta\lambda}, \tag{9.2}$$

where λ is the center wavelength of the source and $\Delta\lambda$ the spectral bandwidth (cf. Fig. 9.1) [12]. Hence, high-axial resolution may be achieved even with low numerical aperture (NA) beam delivery optics. Since the coherence length of a light source is inversely proportional to its spectral bandwidth, broad-bandwidth optical sources are required to improve the axial resolution in OCT, which are important to detect early changes of various diseases occurring at cellular level. To improve axial OCT resolution, the spectral bandwidth must be either increased or the center wavelength decreased. Therefore, novel light sources are necessary – ultrabroad bandwidth solid state lasers have the advantage of providing broad bandwidths necessary for high resolution as well as high power [13]. Since the wavelength in material with a higher refractive index becomes shorter, the actual axial resolution within the imaged tissue can be estimated by dividing the free space resolution by the group refractive index, i.e., 1.35–1.4 for most of the biological tissue. Nevertheless, the axial resolution is also limited not only by the dispersion of the sample but also by absorption and scattering within the sample, where photons with the same path, but backreflected from various imaging depths, are detected.

Improving the axial resolution in OCT is challenging and requires the use of highly sophisticated ultrabroad bandwidth light sources. Figure 9.2 depicts "iso-resolution lines," i.e., the optical bandwidth (at full-width-at-half-maximum (FWHM)) for a given central wavelength necessary to achieve a desired axial OCT resolution. The iso-resolution lines range from 16 to 0.125 μm, measured in free space. For the standard wavelength region used for OCT retinal imaging (800 nm), assuming a Gaussian spectrum of the light source as well as nondispersive imaging medium, this

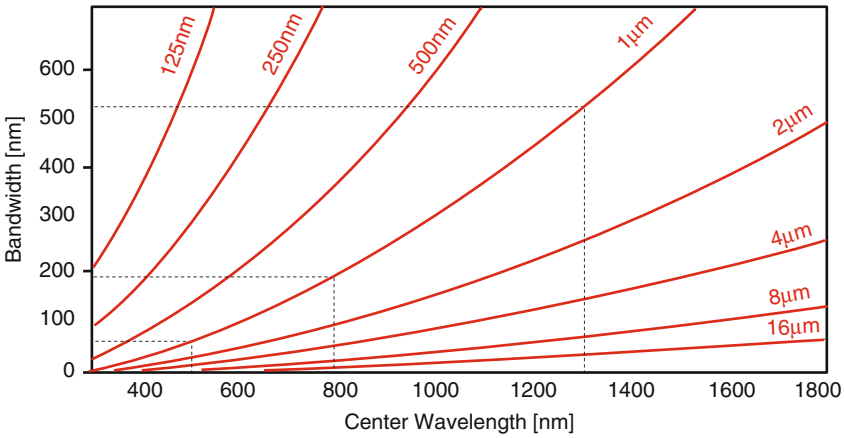

Fig. 9.2 *Axial OCT resolution*. "Iso-resolution lines" for certain axial OCT resolutions (ranging from 16 to 0.125 µm) indicating necessary optical bandwidth as a function of central wavelength. Significantly broader optical bandwidth is needed for the same axial OCT resolution with increasing central wavelength (cf. *dashed lines* for 500 nm, 800 nm, and 1,300 nm, respectively)

figure shows that for 1 µm axial resolution, an optical bandwidth of ~200 nm is needed. It also illustrates that in order to achieve the same axial resolution at 1,300 nm, more than 500 nm of optical bandwidth (FWHM) is needed, i.e., more than two times more, compared to what is needed at 800 nm. Finally, in the visible wavelength region (500 nm), only 75 nm is need to achieve 1 µm axial OCT resolution. This demonstrates the significant wavelength dependence and the challenge to balance resolution versus penetration/contrast depending on the particular OCT application.

9.2 Axial Resolution Limits for OCT

9.2.1 Group Velocity Dispersion Limitations to Resolution

Group velocity dispersion (GVD) causes different frequencies to propagate with nonlinearly related phase velocities. A short pulse in dispersive media will broaden if significant dispersion is present. In analogy to the case for short pulses, the interferometric autocorrelation (i.e., the axial PSF) will also broaden if there is GVD mismatch between reference and sample arms. Both the fiber optics and the sample may introduce a significant amount of GVD. To include GVD in the analysis, the propagation constants β_R and β_S used in the propagation equation are Taylor expanded to second order around the central frequency ω_0.

$$\beta(\omega) = \beta(\omega_0) + \beta^{(1)}(\omega_0)(\omega - \omega_0) + \frac{1}{2}\beta^{(2)}(\omega_0)(\omega - \omega_0)^2 + \ldots \qquad (9.3)$$

where a GVD mismatch is assumed in a length L of the sample and reference paths. The frequency-dependent phase mismatch

$$\Delta\phi(\omega) = 2\beta_S(\omega)l_S - 2\beta_R(\omega)l_R \tag{9.4}$$

is

$$\begin{aligned}\Delta\varphi\ \ (\omega) &= \beta\,(\omega_0)(2\Delta l) + \beta^{(1)}(\omega_0)(\omega-\omega_0)(2\Delta l)\\ &\quad + \frac{1}{2}\Delta\beta^{(2)}(\omega_0)(\omega-\omega_0)^2(2L) + \ldots,\end{aligned} \tag{9.5}$$

where Δl is defined as the additional geometric path difference and $\Delta\beta'' = \beta''_S(\omega_0) - \beta''_R(\omega_0)$ is the GVD mismatch between the reference and sample paths. Note that only the difference in GVD between the two interferometer arms enters Eq. 9.5. Thus, the deleterious effects of dispersion may be decreased by equalizing the GVD in the two interferometer arms. Inserting $\Delta\phi(\omega)$ into the propagation equation gives the photocurrent

$$\begin{aligned}I \propto \Bigg\{ &\exp[-j\omega_0\Delta\tau_P]\int_{-\infty}^{\infty} S(\omega-\omega_0)\exp\left[-j\frac{1}{2}\Delta\beta''(\omega_0)(\omega-\omega_0)(2L)\right]\\ &\times\exp\left[-j(\omega-\omega_0)\Delta\tau_g\right]\frac{d(\omega-\omega_0)}{2\pi}\Bigg\},\end{aligned} \tag{9.6}$$

where $\Delta\tau_P$ is the phase delay mismatch and $\Delta\tau_g$ is the group delay mismatch. The GVD mismatch multiplies the source power spectral density $S(\omega - \omega_0)$ in a frequency dependent, quadratic phase term. The interferometric signal looks like a short pulse, with its Fourier transform being $S(\omega - \omega_0)$, which propagates through a length L of dispersive medium with second-order dispersion equal to the difference in GVD between the interferometer arms. Thus, just as a short pulse broadens and chirps after propagation through a dispersive medium, the interferometric signal should also broaden and chirp due to GVD mismatch in the two interferometer arms.

To establish the analogy further, we assume that the source has a Gaussian power spectral density distribution and after substitution into Eq. 9.6 a modulated interferometric signal with a complex Gaussian envelope is obtained

$$I \propto \frac{\sigma_\tau}{\Gamma(2L)}\exp\left[-\frac{\Delta\tau_g}{2\Gamma(2L)^2}\right]\exp\left[-j\omega_0\Delta\tau_p\right], \tag{9.7}$$

where σ_τ is the single-sided standard deviation. The characteristic width of the axial point spread function in the presence of dispersion $\Gamma(2L)$ is a complex parameter that depends on both the round trip length of GVD mismatch $2L$ and σ_τ via

$$\Gamma(2L)^2 = \sigma_\tau^2 + j\Delta\beta''(\omega_0)(2L). \tag{9.8}$$

The real and imaginary components of $1/\Gamma(2L)^2$ describe the broadening and chirping, respectively, of the interferometric signal and are

$$\frac{1}{\Gamma(2L)^2} = \frac{\sigma_\tau^2}{\sigma_\tau^4 + \tau_{\text{critical}}^4} - j\frac{\tau_{\text{critical}}^2}{\sigma_\tau^4 + \tau_{\text{critical}}^4}, \tag{9.9}$$

where we have defined the dispersion parameter

$$\tau_{\text{critical}} = [\Delta\beta''(\omega_0)(2L)]^{\frac{1}{2}}. \tag{9.10}$$

Substituting the expression for $1/\Gamma(2L)^2$ into Eq. 9.7, we discover that the Gaussian envelope is broadened to the new standard deviation width

$$2\widetilde{\sigma}_\tau = 2\sigma_\tau\left[1 + \left(\frac{\tau_{\text{critical}}}{\sigma_\tau}\right)^4\right]^{\frac{1}{2}}. \tag{9.11}$$

The broadening factor becomes appreciable when the magnitude of the dispersion parameter τ_{critical} becomes greater than the non-broadened temporal standard deviation σ_τ. For a typical fused silica fiber at 800 nm, $\beta'' = 350\ \text{fs}^2/\text{cm}$. For a standard resolution achieved by OCT, $\Delta l = 10\ \mu\text{m}$, implying $\sigma_\tau = 28$ fs. Thus, dispersive broadening becomes a factor if the fiber arm lengths are mismatched by at least 1 mm.

The chirping of the interferometric signal with increasing path length mismatch Δl can be described by differentiating the phase in the exponent of Eq. 9.7, leading to

$$k = \frac{d\phi}{d\Delta l} = 2\beta(\omega_0) - \frac{\tau_{\text{critical}}^2}{\sigma_\tau^4 + \tau_{\text{critical}}^4}\left[4\Delta\beta''(\omega_0)^2\right]\Delta l, \tag{9.12}$$

where k describes the spatial frequency of the interference fringes versus the distance measured Δl. For example, in the positive dispersion mismatch regime $\Delta\beta''(\omega_0) > 0$, when the reference arm path length is increased, Δl decreases, the wavenumber k increases, and the interference fringes occur at the detector more often. It is important to note that GVD changes the phase but not the bandwidth of the interference signal.

Dispersion mismatch also degrades the peak height of the interferometric envelope, which reduces the system dynamic range. The degradation in the photocurrent amplitude is described by the multiplicative factor of Eq. 9.7.

$$\frac{\sigma_\tau}{|\Gamma(2L)|} = \frac{1}{\left[1 + (\tau_{\text{critical}}/\sigma_\tau)^4\right]^{\frac{1}{4}}}. \tag{9.13}$$

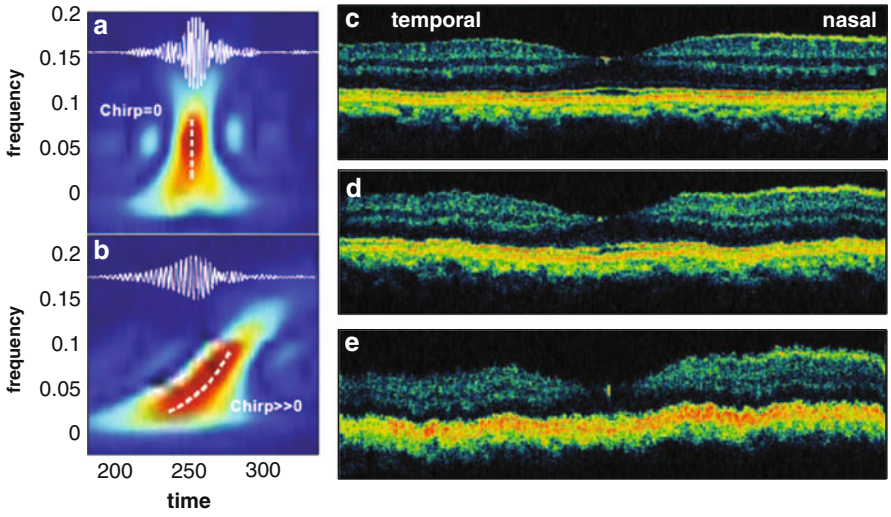

Fig. 9.3 *Group velocity dispersion effect on axial resolution in ultrahigh-resolution OCT*. Dispersion effect on an actual pulse (**a**, **b**); inlet: measured cross-correlation interference pattern and time-frequency diagram of a pulse pair without (**a**) and with (**b**) high-order dispersion difference. Frequencies are shifted in time (*chirp*) and the amplitude is reduced, while the envelope is broadened. Effect of dispersion mismatch in in vivo ultrahigh-resolution retinal imaging (**c**–**e**). Dispersion matched (**c**); artificially introduced dispersion mismatch by 3 mm (**d**) as well as 9 mm (**e**) fused silica in the reference arm. Clear axial resolution as well as sensitivity (–5 dB) degradation is observed

The reduction of the signal amplitude peak scales as the square root of the broadening. Assuming that the dynamic range is measured in terms of reflected optical power, which is proportional to photocurrent power, the loss in dynamic range scales linearly with the broadening.

While first-order dispersion only affects the electromagnetic phase inside the envelope of the signal, leaving the envelope itself unaffected, the second-order frequency dependent refractive index of material introduces a time-dependent change of the instantaneous frequency and an increase of the envelope's width, which are associated with a loss of signal intensity. Commonly this effect is also called "chirp," since the acoustic analogue for dispersion is found in the sound that songbird makes. The different frequencies are also shifted in respect to each other, resulting in a high pitched tone that falls for each chirp. The zero-order term of dispersion only introduces a temporal shift of the whole pulse and is equivalent to the refractive index; the higher indices distribute the phase of different frequencies in time and alter the shape of the pulse envelope (cf. Fig. 9.3). Dispersion distributes signal power away from the central peak where all spectral components are in phase to the wings, thereby distorting the envelope of the signal. In case of an originally unchirped pulse with Gaussian envelope second-order dispersion, also called group dispersion delay (GDD) generates symmetric side lobes where parts of the different continuous wave components interfere constructively. Higher-order dispersion,

such as third-order dispersion (TOD) or fourth-order dispersion (FOD), introduces satellite pulses, in the form of a pulse train. In contrast to the generation of ultrashort pulses, the dispersion effects in OCT do not involve complete reversion, but can be cancelled (in the case of static dispersion) by balancing the dispersion in both arms of the interferometer. Therefore, the cross-correlation becomes a linear autocorrelation again, which is indistinguishable if the spectral content is constant. Compensation of a lens systems consisting of multiple exotic glass types involves a comparable, complex mixture of dispersion compensation materials.

In summary, the two arms of an OCT interferometer must have almost the same delay as well as similar second- and higher-order dispersion (GDD, TOD). The first-order dispersion, however, does not play a role for the interference envelope and therefore is irrelevant for measuring the position. However, FOD does affect the phase and changes the readings for complex analysis of material properties (see in the following chapters). For ultrahigh-resolution retinal OCT imaging, the dispersion of approximately 25 mm ocular media can be compensated by using 25 mm of water in the reference arm, since previous in vivo studies of dispersion measurements have shown that the dispersion of ocular media averaged over 25 mm is similar to the that of 25 mm of water [14]. Balancing the higher-order contributions to dispersion of the 25 mm ocular media in front of the retina is more critical for obtaining high resolution than balancing the dispersion of the system itself. Figure 9.3 depicts the effect of dispersion mismatch in the case of in vivo ultrahigh-resolution retinal imaging of a normal human fovea (cf. Fig. 9.3c). By artificially introducing dispersion mismatch by inserting 3 mm (cf. Fig. 9.3d) and 9 mm (cf. Fig. 9.3e) fused silica in the reference arm of the OCT interferometer, it is obvious that both OCT resolution and sensitivity (up to –5 dB) decrease. Clinical studies with ultrahigh-resolution ophthalmic OCT utilizing ~100 nm broad spectra revealed that by using a dispersion compensation of 25 mm of water in the reference arm of the interferometer, patients with axial eye lengths between 23 mm and about 27 mm can be imaged with tolerable dispersion mismatch-induced axial resolution loss. Furthermore, numeric compensation can be used for further enhancement and fine tuning of the physical compensation, but not as a replacement. This is the result of the inevitable detection and amplification noise in the original signal. In case the signal is so strongly dispersed, that it is below the noise level, the signal is completely corrupted by noise and cannot be recovered numerically. Therefore, it is favorable to physically compensate static dispersion mismatch.

9.2.2 Dispersion and Resolution in FD OCT

The interference signal in spectrometer-based frequency-domain OCT can be recorded as a function of wavelength rather than time. In case of a single reflecting surface in the sample arm, it is of the general form

$$I(\lambda) = I_r(\lambda) + I_s(\lambda) + 2\sqrt{I_r(\lambda)I_s(\lambda)}\cos\left(2f(\lambda)\Delta z + g(\lambda)\right), \tag{9.14}$$

where I_r and I_s are the intensity of the reference and sample arm light, respectively, and Δz is the relative optical path length between both arms. The functions $f(\lambda)$ and $g(\lambda)$ are crucial, since they determine the resolution of the OCT system. In general one needs to Fourier transform the backscattered intensity as a function of wavenumber k or frequency v in order to reconstruct the associate time-domain depth profile. Ideally $g(\lambda)$ is only an arbitrary phase constant that can be neglected without loss of generality, and $f(\lambda) = K = 2\pi/\lambda$. Assuming, however, a dispersion mismatch between both arms associated with a material thickness d, $g(\lambda)$ will no longer be constant but of the form $g(\lambda) = 2d/f(\lambda)(n(\lambda) - 1)$, where $n(\lambda)$ is the wavelength-dependent refractive index of the dispersive material. It is well known that the dispersion $dn(\lambda)/d\lambda$ and higher-order terms cause a broadening of the envelope of the time-domain signal; therefore, the dispersion mismatch between reference and sample arm needs to be minimized to achieve optimal depth resolution. Especially in the case of retinal imaging, one also needs to compensate for the dispersive ocular media that the light double passes on its way to the retina and back to the detector [15].

In order to minimize $g(\lambda)$ one needs to balance the dispersion mismatch between both interferometer arms. Once $g(\lambda)$ has been optimized, we are still left with $f(\lambda)$ which describes a nonlinear phase as a function of wavelength λ in the cosine term of Eq. 9.14. This nonlinearity causes an additional broadening of the coherence envelope after discrete Fourier transform (DFT) of Eq. 9.14. Apart from the relation $\lambda \leftrightarrow K$, it is due to dispersion of the diffraction grating, imaging errors of the optical system in front of the CCD, misalignment, finite CCD pixel sizes, or surface imperfections of the optics. The actual nonlinear phase function needs to be resampled to provide equally spaced interference fringes. There is a residual nonlinearity due to the factors that have been mentioned previously which causes a broader coherence envelope as compared to that obtained with the resampling technique. It is obvious that a small nonlinearity already causes a significant decrease of depth resolution. Further resolution and sensitivity loss occurs as a result of the finite pixel width of the spectrometer together with the limited dynamics of the individual pixel. Due to the recorded chirped interference pattern, there will be always higher frequencies at one end of the modulated spectrum which appear with a reduced modulation depth, as will be explained in the next section. Hence, the effective spectral width of the FD OCT signal is reduced, which results in a resolution loss for structures which are closer to the maximal depth position.

9.2.3 Spectral Shape of Ultrabroad Bandwidth Light Sources

Light sources for UHR OCT not only require high spatial coherence and ultrabroad bandwidth emission with enough output power and low noise but should also have an optimal spectral shape. Since the coherence length is defined as the full width at half maximum of the field autocorrelation measured by the OCT interferometer, the width and also the shape of the coherence function of an OCT system depend on the spectral shape of the light source as well as on the transfer function of the OCT

system. The transfer function is mainly determined by the optical properties of the interferometer, as described in detail later. The ideal spectrum for OCT would have Gaussian spectral shape, resulting in a Gaussian coherence function with no side lobes. Large spectral modulations would reduce sensitivity and resolution, due to the presence of side lobes in the fringe pattern that appear symmetrically to the coherence-function maximum. There are several approaches to change the shape of the emission spectrum of the light source. The easiest way is to introduce optical dichroic or interference filters that suppress certain wavelength regions. Another possibility, especially for very wide spectra, is to spatially disperse the optical beam with prisms and to induce local and therefore wavelength-dependent losses by filtering the dispersed light beam. Especially for nonlinear laser sources, the temporal stability of the spectral properties, i.e., at the time frame of the single depth measurement is essential to maintaining high resolution. Spectral noise, which cannot be optically filtered, can be reduced numerically during post-processing, but always results in a loss of dynamic range and reduction in the full spectral potential.

9.2.4 Chromatic Aberration Limitations to Resolution

Another limitation for achieving ultrahigh resolution is the chromatic aberration of the optics used in the system. Conventional lenses have a focal length which varies with wavelength and thus focus ultrabroad bandwidth light to different planes. This variation in focal position for different wavelengths alters the local effective bandwidth and therefore degrades resolution. For specially corrected achromatic optics, different imaging distances introduce a wavelength-independent attenuation of the whole spectrum, thereby maintaining the spectral shape, optical bandwidth, and therefore axial resolution. Hence, appropriate achromatic objectives have to be used to maintain the ultrabroad bandwidth of the light in order to achieve ultrahigh resolution. Alternatives are reflective objectives like catadioptrics, consisting of parabolic mirrors that have no chromatic aberration and do not introduce dispersion as found in transmittive elements. For ophthalmic OCT chromatic aberration of the eye itself ultimately limits the axial resolution of ultrahigh-resolution retinal OCT imaging if not properly compensated [16–18].

9.2.5 Other Limitations to Resolution

9.2.5.1 Polarization

Another effect that limits axial OCT resolution in UHR OCT systems is polarization mismatch between the interferometer arms and polarization dispersion (loss of polarization) that introduce a phase difference and therefore a change in the shape of the coherence function and axial resolution, respectively. Polarization changes of the static system can be compensated; however, the loss of a single polarization state and sample birefringence leads to an improper overlapping of the reference

and sample light, with severe modulations of the interference spectrum. UHR OCT therefore requires careful polarization control and the polarization dependence of light sources is also an important parameter.

9.2.5.2 Optical Components

The optical transmittance, coating, and wavelength-dependent losses of the bulk or fiber optics, delivery system optics, and also the human eye itself – in case of ultrahigh-resolution ophthalmic OCT – strongly influence the axial resolution as well as the sensitivity of the OCT system. Single-mode and sometimes polarization-maintaining fibers with appropriate cutoff wavelengths should be used to provide light propagation without intra- and inter-fiber interference. Conventional fiber couplers are designed to maintain 3 dB splitting over a narrow wavelength range of typically $\pm$ 10 nm. By using these fiber couplers for delivery of broad bandwidth laser light, unequal beam-splitting with respect to wavelength and power can occur and reduce resolution. Hence, special broad bandwidth and wavelength flattened fiber or bulk optic beam splitter have to be used to maintain broad bandwidths and consequently high-axial resolution. Optical circulators are often used in OCT systems in order to design more power efficient and sensitive interferometers, since nonreciprocal elements reduce power delivery losses from the source to the sample and signal losses from the sample to the detector. However, the large optical bandwidths of more than a fourth of an optical octave (e.g., 200 nm bandwidth at 800 nm) require extremely broad band components to avoid impose wavelength-dependent losses.

9.2.5.3 Detection System

Depending on the method of acquiring the interference signal, the detection system, including electronics as well as digitization and acquisition of the interference signal, must avoid degradation of axial OCT resolution. Hence, the transimpedance amplifier used in time-domain and tunable laser-driven FD-OCT systems, and in particular the electronic band pass filtering, must be designed properly and adapted to the ultrabroad optical bandwidth. The electronic bandwidth of the band pass filter must not be too narrow to reduce the axial resolution, but must also not be too broad to reduce sensitivity by introducing noise. Real-time adaptive filtering can help to optimize sensitivity and maintain axial resolution. In time-domain OCT hardware demodulation must be adapted to the scanning speed and optical bandwidth to avoid broadening caused by the time response of the electronics, resulting in a larger coherence length of the envelope as compared to the full interference fringe signal. Finally, the signal must be correctly temporally digitized with at least five to ten times over sampling in respect to the central wavelength, Doppler shift, as well as scanning speed in order to not degrade the achieved axial resolution. With tunable lasers, the linearity of the scan has to be adjusted or alternatively the k-trigger can be used to generate a scan discretely sampled in k-space. Most tunable laser technology, however, usually is limited to standard bandwidths and cannot achieve ultrahigh resolution. To utilize broadband light sources in the frequency domain, the camera technology and the already-mentioned nonlinearities and sampling problems are the factor that can be compensated with sophisticated post-processing techniques.

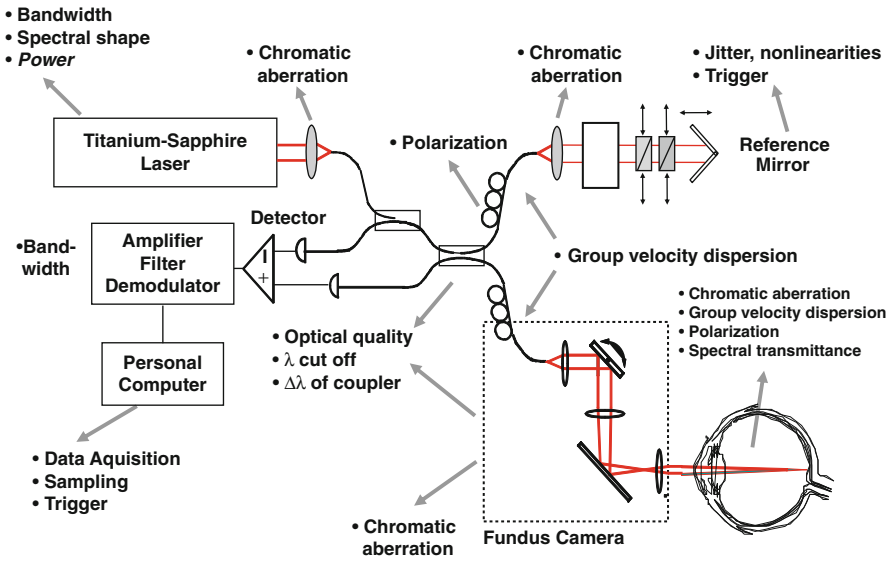

Fig. 9.4 *Axial resolution limits in ultrahigh-resolution OCT*. Summary of all limitations for a time-domain OCT based system for ophthalmic imaging: light source, spectral transmittance of OCT system, delivery system, spectral properties of sample (in this case the human eye), as well as detection and data acquisition specifications

9.2.5.4 Mechanical Components

Finally the mechanical performance of the scanners used for transverse and/or depth scanning should be accurately selected and correctly controlled. Mechanical jitter or displacement of adjacent depth scans as well as noisy control signals of the scanner might result in distorted and therefore degraded resolution UHR OCT tomograms.

Figure 9.4 summarizes the different factors that limit axial resolution performance in OCT for a time-domain-based ophthalmic UHR OCT system. In this case, the delivery systems as well as the eye itself impose challenges for accomplishing ultrahigh-axial OCT resolution. The limitations indicated are also valid for swept source OCT and Fourier-domain OCT systems. In addition to the limitations mentioned in Figure 9.4, specifications of the tunable light source (e.g., linearity, speed, and linewidth of the sweep across a certain optical bandwidth) for swept source/Fourier-domain OCT as well as specifications of the spectrometer for spectral/Fourier-domain OCT have to be taken into account.

9.3 Ultrahigh-Resolution OCT at 800 nm

As mentioned above, a significant difference between OCT and conventional microscopy is that OCT achieves very high-axial image resolutions independent of focusing conditions, because the axial and transverse resolution are determined

independently by different physical mechanisms. The axial OCT resolution can be enhanced using broad bandwidth, low-coherence length light sources. It is important to note that the light source not only determines axial OCT resolution via its bandwidth and central emission wavelength but also influences both the penetration in the sample (biological tissue) and the OCT transverse resolution. A tissue-specific output power and low noise is necessary to enable high sensitivity and high-speed, real-time, OCT imaging. Hence, it is obvious the light source is *the* key technology for an OCT system and proper choice is imperative [13].

Historically the longitudinal resolution of OCT systems was limited by the optical bandwidth of the light source. Typically superluminescent diodes with 20–30 nm bandwidth yielded ~10–15 μm axial resolution. In ophthalmic applications, this provided more detailed structural information than any other standard retinal imaging technique. However, the resolution is significantly below what can be achieved technically and is insufficient to identify individual cells or to assess subcellular structures such as nuclei or mitotic figures. Due to the lack of broad bandwidth, spatially coherent light sources, OCT imaging has been mainly limited to the 800 nm and 1,300 nm wavelength region. Incandescent light sources, although broad bandwidth, produce very little intensity in a single spatial mode. Nevertheless, some research groups have demonstrated these broadband light sources for improving axial imaging resolution by employing a technique that uses a multitude of mutually incoherent low-coherence interferometry channels in order to increase the probe beam power [19] or by using a Linnik-type interference microscope in combination with a CCD camera-based parallel detection scheme [20, 21]. 1 μm isotropic free space axial resolution could be accomplished for in vitro UHR OCT. The first demonstration of sub-10-μm-axial-resolution was achieved by using broadband fluorescence from organic dye [22] and fluorescence from titanium:sapphire [23]. However, biological imaging could not be performed with these light sources due to their low brightness. By multiplexing spectrally displaced superluminescent diodes to increase optical bandwidth [24–26], OCT tomograms with improved ~7 μm axial resolution in the retina were demonstrated several years ago [27]. More recently, cost-effective, broad bandwidth advanced SLD light sources have become available which approach the image resolutions achieved by femtosecond lasers [28, 29]. These light sources are multiplexed SLDs consisting of two or three spectrally displaced SLDs which are combined to synthesize a broad bandwidth spectrum. Multiplexed SLD light sources have the disadvantage of having spectrally modulated emission spectra that can produce sidelobes in the coherence function or axial point spread function, resulting in image artifacts. In addition, the emission wavelength of multiplexed SLDs is typically centered at the longer 900 nm wavelength range, overlapping the water absorption at 980 nm, which can limit the resolution for retinal imaging. On the positive side, multiplexed SLD light sources are much lower cost and more robust than femtosecond lasers and promise to enable wider availability of ultrahigh-resolution OCT. However, at the present time, the price vs. performance trade-off remains such that UHR OCT instruments with 2–3 μm axial resolution are still

limited to research applications. The newest commercial ophthalmic instruments have broad bandwidth, single SLDs and provide 5–8 μm axial image resolution.

Nowadays, ultrashort light pulses can be generated by a range of laser technologies and have widespread applications for ultrafast measurement. Femtosecond laser development has concentrated mainly on the temporal features of the pulses, which were sometimes optimized to the detriment of the spectral shape. In OCT, the pulse shape and duration are irrelevant, while the spectral shape and width play a crucial role. However, unlike ultrafast femtosecond time-resolved measurements where special care must be exercised to maintain the short pulse duration, OCT measurements depend on field correlation, rather than intensity correlation, and every wavelength component interferes independently. Field correlation is preserved even if the pulse duration is long. Femtosecond mode-locked solid state lasers can generate ultrabroad bandwidth, low-coherence light with a single spatial mode and high power, providing both high resolution and high power necessary for high-speed OCT imaging. These lasers can operate over a broad range of wavelengths extending beyond their gain bandwidth by employing nonlinear broadening effects. These spectra are useful for ultrahigh-resolution as well as spectroscopic OCT imaging in tissue. In an early demonstration, a titanium:sapphire laser was used for in vitro OCT imaging in nontransparent tissues with 4 μm axial resolution [30]. In preliminary studies, an OCT system was developed and optimized to support 260 nm of optical bandwidth from a state-of-the-art titanium:sapphire laser [8]. This laser was developed in collaboration with other investigators (Franz Kaertner and Erich Ippen) at M.I.T. and generated pulses of <5.5 fs duration, corresponding to bandwidths of more than 350 nm at 800 nm center wavelength [31]. This high performance was achieved using specially designed double chirped mirrors with high reflectivity bandwidth and controlled dispersion response. Figure 9.5 shows a comparison of the spectra and resolution of an OCT

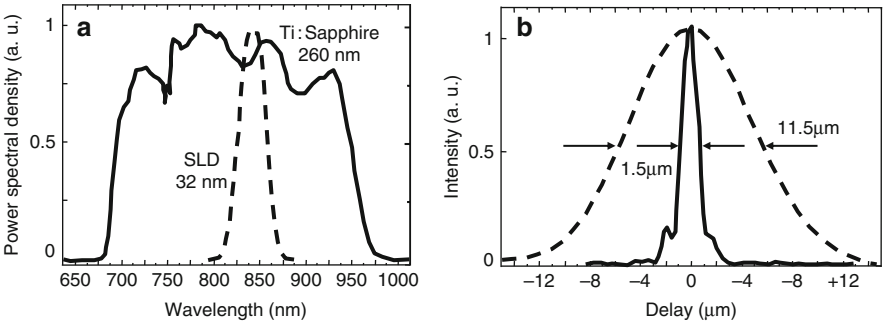

Fig. 9.5 *Light source technology for ultrahigh-resolution OCT*. Solid state laser light sources enable ultrahigh-resolution imaging. The spectrum of the titanium:sapphire laser versus a standard superluminescent diode (*SLD*) is shown depicting their respective wavelength bandwidths (**a**). Demodulated OCT axial scan showing the axial resolution of OCT using titanium:sapphire (*solid*) versus a superluminescent diode SLD (*dashed*) light sources (**b**). Solid state lasers enable almost a 10× improvement in resolution [8]

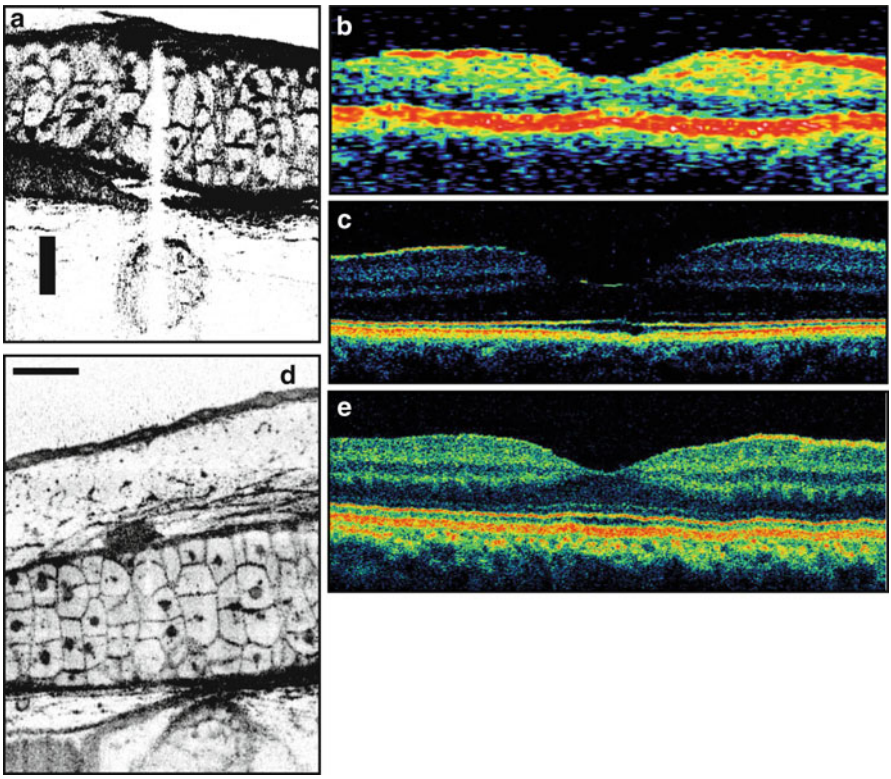

Fig. 9.6 *First in vivo ultrahigh-resolution OCT*. In vivo subcellular resolution OCT (**a**, **d**) in a developmental biology animal model (African tadpole). Standard resolution OCT (performed with the second generation commercial OCT system – OCT II; **b**) versus ultrahigh-resolution ophthalmic OCT (**c**–**e**) of the living human retina. Preliminary results presented in 1999 at SPIE Photonics West (**a**–**c**); improved results published in [8, 9] (**d**, **e**)

A-scan using a conventional superluminescent diode light source versus the femtosecond titanium:sapphire laser source. The ultrabroad bandwidths which are generated by the femtosecond laser enable the axial resolution of OCT to be improved by a factor of nearly 10× compared to standard OCT technology. This femtosecond laser source was used for imaging studies using an OCT microscope as well as an ophthalmic system interfaced to a biomicroscope system.

Figure 9.6a, d show the first in vivo UHR OCT results (presented at SPIE – Photonics West in San Jose, CA in January 1999). The images demonstrate the feasibility of this novel OCT system for in vivo subcellular imaging of a *Xenopus laevis* (African tadpole, left) mesenchymal cells at 1 × 3 μm (longitudinal × transverse) resolution, consisting of 1,600 × 1,200 pixels and 0.4 × 0.5 μm pixel spacing. Figure 9.7b, c, d show preliminary results demonstrating in vivo ultrahigh-resolution retinal OCT imaging in human subjects [9, 32]. These results were achieved with an ultrahigh OCT system based on

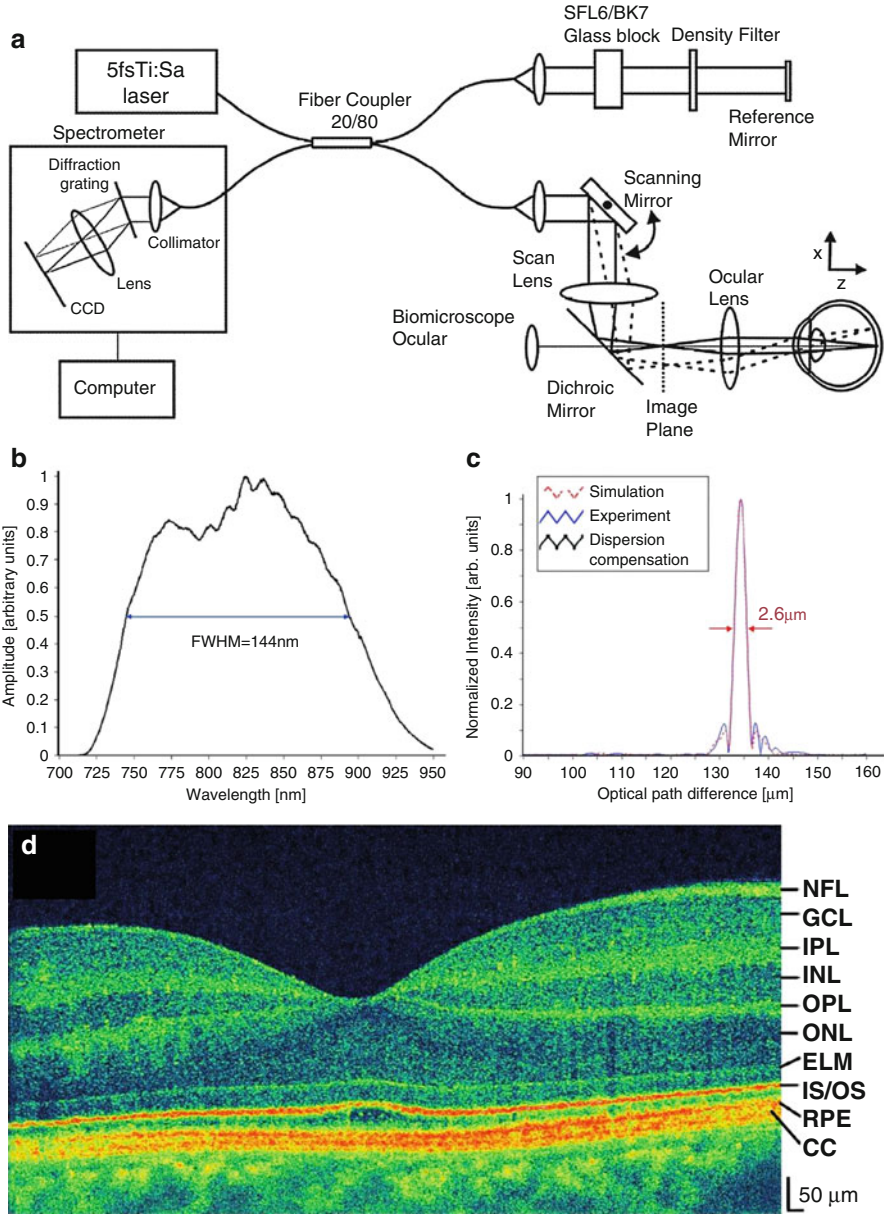

Fig. 9.7 *High-speed, ultrahigh-resolution OCT imaging of the human retina*. A spectral/Fourier-domain OCT system (**a**) using a 5 fs laser was used to demonstrate high-speed, ultrahigh-resolution imaging with an axial line rate of 16,000 lines/s. Source bandwidth (**b**) measured ~144 nm, which provided resolution of ~2.1 um in tissue (**c**). The system enabled high-definition, motion-free imaging of the human retina (**d**)

a laboratory laser system that was not suited for clinical studies. Therefore, a new generation of compact ultrahigh-resolution OCT system was developed. Femtosecond lasers with record low pump requirements enabled a significant reduction in cost [33]. With advanced mirror technology, dispersion control, and adapted cavity design, optical bandwidth of up to 300 nm at full width of half maximum (FWHM) centered at 790 nm could be achieved resulting in sub-μm axial resolution OCT in tissue. Light sources were optimized with respect to compactness, cost-effectiveness, and applicability in the clinical environment with the aim of realization of a commercially available product for UHR OCT. An integrated and sealed system including a low-cost pump laser on a small footprint of about 500 mm × 180 mm was developed. Due to its compactness, the system shows a high stability and reproducibility and facilitated the technology transfer to a commercial product. With the release of compact, cost-effective, user-friendly state-of-the-art titanium:sapphire laser (*Integral* OCT), Femtolasers Produktions GmbH has established this novel OCT light source in industry. A compact design as well as active feedback loops guarantees output parameters of unprecedented quality, stability, and reproducibility. In addition, recently reported, cost-effective approaches for broad bandwidth light sources also took advantage of the lower power demand with ultrahigh-resolution OCT imaging [33–37].

Ophthalmic UHR OCT using these state-of-the-art light sources achieves superior axial image resolutions of 2–3 μm as compared to ∼10 μm resolution in standard OCT, enabling the visualization of intraretinal structure. UHR OCT is a key step toward achieving noninvasive optical biopsy of the human retina, i.e., visualization of intraretinal morphology in retinal pathologies approaching the level achieved with histopathology. UHR OCT technology has been investigated in clinical settings to assess its clinical utility. Cross-sectional studies in ∼1,000 eyes with different pathologies demonstrated unprecedented visualization of all major intraretinal layers and provided especially significant information about the photoreceptor layer [10, 38–46]. These studies demonstrated visualization of photoreceptor layer impairment in macular pathologies such as macular holes, central serous chorioretinopathy, age-related macular degeneration, foveomacular dystrophies, Stargardt's dystrophy, and retinitis pigmentosa (cf. also ▶ Chap. 34, "MUW Approach of PS OCT").

More recently, high-speed and three-dimensional techniques have been developed for ultrahigh-resolution ophthalmic OCT. Spectral/Fourier-domain OCT methods make use of a spectrometer and a line scan camera to acquire all depths of the OCT axial scan simultaneously in the frequency domain [47, 48]. Fourier-domain OCT can also be performed using the swept source method, whereby a narrowband laser source is scanned in wavelength over a broad bandwidth and the frequency encoded OCT axial scan is acquired as a function of time with a balanced photoreceiver [49]. In either case, the signal is reconstructed using a Fourier transform. The Fourier-domain approaches are performed without the need for moving part scanners in the reference arm and are therefore scalable to

much higher speeds than traditional time-domain OCT scanners. High-speed imaging is further facilitated by the fact that spectral and swept source OCT leads to a sensitivity advantage compared to time-domain OCT that scales with the number of points in the acquired data set and is typically in the range of 20–30 dB improvement [50–52]. High-speed ophthalmic OCT was first demonstrated with standard resolution using the spectral domain approach at 800 nm [47, 48]. Subsequent work then demonstrated high-speed, ultrahigh-resolution OCT [53–55]. Figure 9.7 presents results from a high-speed, ultrahigh-resolution OCT system using a 5 fs Ti: Sapphire laser source [53]. The system schematic in Fig. 9.7a illustrates the spectrometer detection system and the static reference arm. The broadband spectrum measuring ~144 nm FWHM is shown in Fig. 9.7b. This resulted in an axial resolution of 2.1 um in tissue, shown in Fig. 9.7c. The high-phase stability of Fourier OCT systems facilitates numerical processing techniques there were previously difficult with time-domain OCT, such as numerical dispersion compensation. A representative image of the human macula is shown in Fig. 9.7d. High-speed acquisition of ultrahigh-resolution scans enables motion-free, high-definition images.

High-speed, ultrahigh-resolution OCT imaging has also been investigated as a research tool for assessment of retinal disease in rodent model systems [56]. Rat and mouse models of ocular disease provide powerful tools for analysis and characterization of disease pathogenesis and response to treatment, but retinal imaging in these models is challenging because of the small size and thin retina of the animal eye compared to the human eye. The advent of ultrahigh-resolution OCT promises to overcome these limitations, however. Similarly, the development of high-speed, ultrahigh-resolution OCT provides for high-quality two- and three-dimensional OCT imaging of the retina with minimal motion artifact. Figure 9.8 presents high-speed ultrahigh-resolution OCT imaging results from the rodent retina [56]. The optical spectrum from a multiplexed superluminescent diode laser source was spectrally shaped to provide axial resolution of 2.8 um in tissue with low sidelobe levels. High-speed acquisition enabled three-dimensional volumetric imaging of the rodent retina. Figure 9.8c demonstrates a 3D OCT volume rendering of the rat retina. Individual cross-sectional OCT images with ultrahigh resolution demonstrate excellent visualization of fine retinal layers and compare well to histology.

To test the performance of the novel, compact, and cost-effective ultrabroad bandwidth titanium:sapphire laser, as well as the ability of sub-μm axial resolution OCT to image subcellular morphological features, tomograms were acquired from sympathetic ganglion cell cultures obtained from rat superior cervical ganglia. The cultures were prepared on protein-coated glass cover slips and were placed in a custom-designed perfusion chamber filled with nutritious solution to preserve the normal condition and electrical activity of the cells. Tomograms were acquired with 0.9 μm axial and 2 μm transversal resolution and SNR of 100 dB, for 2 mW average incident power. Figure 9.9c–e shows tomograms of single and groups of cells as compared to representative images of the cells obtained with a regular microscope (Fig. 9.9a) and scanning electron tunneling microscope (Fig. 9.9b). The

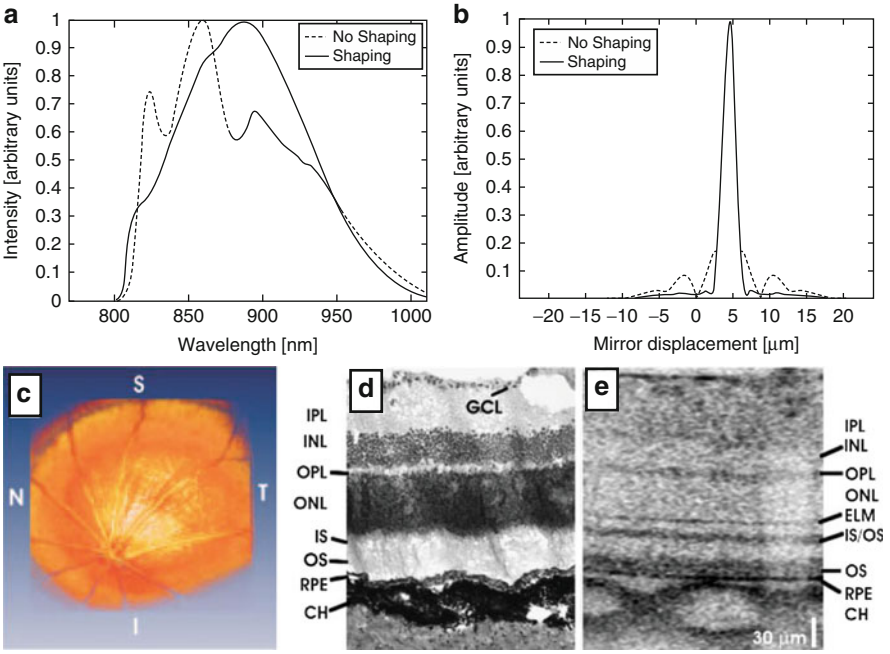

Fig. 9.8 *High-speed, ultrahigh-resolution OCT retinal imaging in rodent models*. A small animal imaging system was constructed using a multiplexed superluminescent diode light source with 145 nm optical source bandwidth at 800 nm center wavelength (**a**) capable of producing ~2.8 um axial resolution in tissue (**b**). The high-speed system acquired 24,000 axial scans per second and was capable of generating in vivo 3D volumetric renderings of the retina (**c**). Individual cross-sectional images (**e**) with ultrahigh resolution compared well with histology (**d**) in visualizing the many fine layers of the retina

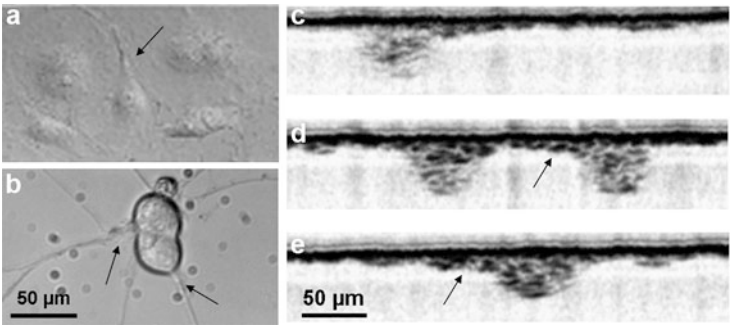

Fig. 9.9 *In vivo ultrahigh-resolution OCT of ganglion cells*. Images of living ganglion cells acquired with scanning electron microscope (**a**), regular optical microscope (**b**) and UHR OCT (C-E). The OCT tomograms (0.34 mm × 0.07 mm) were obtained at $\lambda_c = 785$ nm with spatial resolution 0.9 μm × 2 μm (axial x lateral) and sensitivity of 100 dB for 2 mW optical power at the sample. *Black arrows* indicate axono-dendritic extensions of the ganglion cells

thick black line in the upper part of all OCT images corresponds to a reflection from the glass cover slip, to which the cells tend to attach themselves. The highly reflective (black) spots most likely correspond to various cell organelles, judging from the high optical density and the size of the objects. Although the cell membrane is not clearly visualized, the boundaries of the cell cytoplasm (pale gray color) are distinctly visible. Furthermore, the high spatial OCT resolution permits imaging of the thin axonal extensions of the ganglion cells (marked with black arrows on Fig. 9.9). Therefore, UHR OCT might be capable of acquiring information on the dynamic interaction of neuronal cells via the synaptic connection between the cell dendrites and the axon.

To investigate the feasibility of UHR OCT for imaging brain tissue morphology and to evaluate the potential of this technique as an intraoperative optical biopsy tool in neurosurgery, OCT images were acquired from both healthy and pathological human brain tissues including transitional, fibrous, and atypical meningioma and ganglioglioma [57, 58]. The objective of this research project was to investigate the ability of UHR OCT to discriminate between healthy and pathological human brain tissues by visualization of fine morphological features characteristic for neuropathologies and normally absent in healthy brain tissue. In addition, this study aimed to establish a correlation between structural details present both in the OCT tomograms and in the corresponding histological cross sections. Because postmortem brain tissue quickly looses optical quality due to cell death, all brain tissue samples were fixed in 4 % paraformaldehyde solution. The brain slices were placed in a custom-designed chamber with an optical window (~150 μm thick glass cover slip), through which the tissue was imaged. The OCT system was evaluated to provide 1.3 × 3 μm (axial × lateral) resolution in air, ideally corresponding to 0.9 × 2 μm in biological tissue, and sensitivity of 112 dB for 5 mW at the sample surface. During the imaging procedure care was taken to properly compensate the dispersion mismatch introduced by the glass cover slip and the excess fixation solution between the glass and the tissue surface in order to preserve the high OCT axial resolution in all imaged tissue samples. Standard histological cross sections of the imaged brain tissue samples were prepared after completion of the imaging procedure and compared with the acquired UHR OCT images.

In addition to healthy brain tissue, three different types of meningiomas and one type of ganglioglioma were imaged. Figure 9.10a shows a representative OCT tomogram acquired from a fibrous meningioma biopsy, while the corresponding H&E-stained histological section is presented in Fig. 9.10b. Under the current imaging conditions, the image penetration depth in the fibrous meningioma tissue appears limited to about 400 μm and no structural details can be distinguished deeper in the sample. The dark horizontal line in the tomogram is an imaging artifact. At shallow depths up to ~250 μm, clusters of highly reflective (black) spots are distinctly visible even after application of a speckle reduction [59, 60] image processing algorithm (oversampling of the acquired data – 20 nm separation between adjacent points in a single A-scan, 0.5 μm separation between adjacent A-scans, and subsequent application of directional spatial averaging). An enlarged view (Fig. 9.10c) of a selected region in the biopsy sample, marked with red dotted

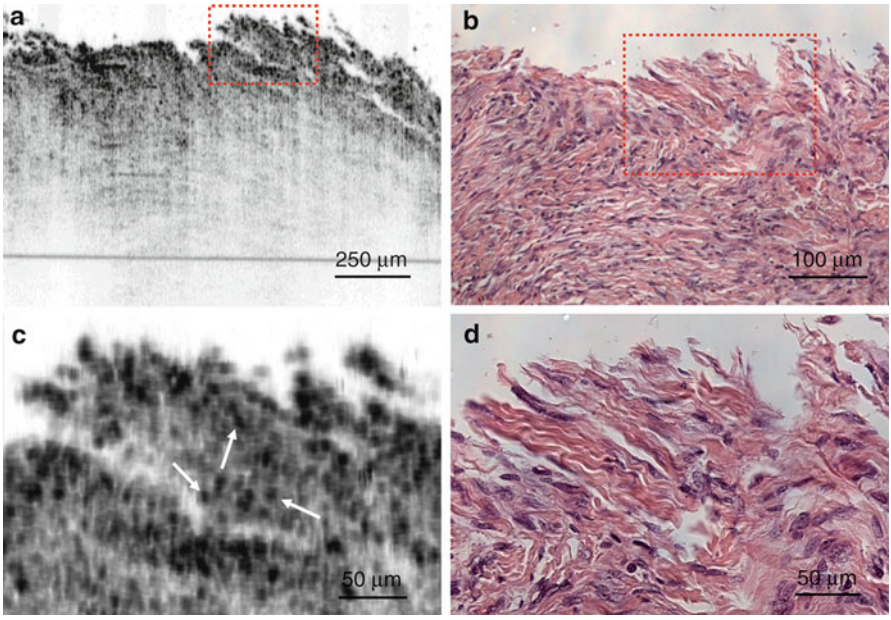

Fig. 9.10 *In vitro ultrahigh-resolution OCT of neuropathologic biopsies*. UHR OCT tomogram (1 mm × 0.69 mm) of fibrous meningioma (**a**) and corresponding H&E-stained histological section (**b**). (**c**) shows an enlarged view of the region in the tomogram (**a**) marked with the *red dotted line*, while (**d**) shows a proportional enlargement of the histological image. *White arrows* in (**c** and **d**) indicate enlarged nuclei of tumor cells [58]

line in Fig. 9.10a, shows that the black spots (marked with white arrows) vary in shape and range in size between 5 and 15 µm. A magnified view of the histological section (Fig. 9.10d) reveals that the nuclei of tumor cells are ∼2–5 times larger than the nuclei of normal neuron/glial cells and that they fill up to ∼80 % of the cell volume. Since cell nuclei are optically much denser than the cell cytoplasm, they scatter light more strongly. Therefore, it is very likely that the highly reflective black spots observed in the UHR OCT tomogram correspond to enlarged nuclei of tumor cells (marked with white arrows). The fact that no highly reflective small spots are visible on the OCT tomogram beyond a depth of ∼300 µm most probably results from loss of contrast and resolution with imaging depth.

The dimension, architecture, and accessibility of human skin make dermatology a compelling field of application for OCT imaging. Current clinical diagnosis by human- or camera-assisted visual inspection is advantageous for fast screening of large surfaces. However, almost no depth information is included and pathologies are mainly distinguished by overall appearance and symptoms. This is not easily possible for diseases like melanoma (cancer) in their early stages, which are often developing at the dermal-epidermal (D-E) junction. OCT with radiation in the near-infrared enables visualization of the full epidermis and can give access to the D-E junction and

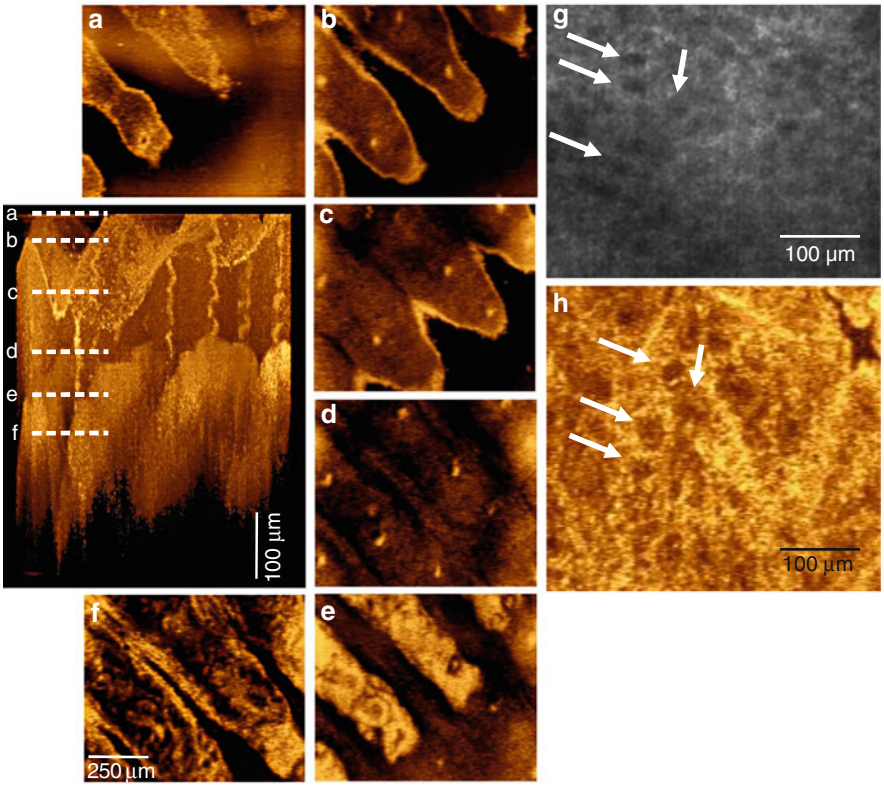

Fig. 9.11 *In vivo ultrahigh-resolution OCT of human skin*. Three-dimensional rendering and C-mode sections (**a**–**e**) of a human finger tip. Consecutive sections extracted from the data stack (**a**–**e**). Comparison to scanning laser microscopy (**g**) with ultrahigh-resolution OCT (**h**) at stratum basale (thin skin). *Arrows* depict cellular structures that might resemble stronger absorbing melanocytes next to the less scattering keratinocytes, though further investigation has to prove the origin of the enhanced contrast

structures below already in vitro. For in vivo imaging, contrast usually improves due to stronger differences between cells and intracellular material in living tissue.

A common problem with time-domain OCT is the slow speed (about 5 s per 1,000 sampling points). Frequency-domain OCT enables scanning of volumetric data sets of 512^3 sample points, equaling ~130 million voxels, within a time frame of about 10–30 s. High-speed frequency-domain OCT is compatible with ultrahigh resolution as well, with systems demonstrating to date about 3 µm axial resolution and less than 6 µm transversal resolution. Results in dermatology using high-speed, frequency-domain OCT are shown in Fig. 9.11. A cube of 512^3 voxels with lateral excursion of 1.5 mm and 1 mm sampling depth was acquired. A volume rendering of the glabrous skin including the typical ripple of dermatoglyphics (responsible for the fingerprints) is shown, with individual en face renderings at varying depths displayed in Fig. 9.11a–f.

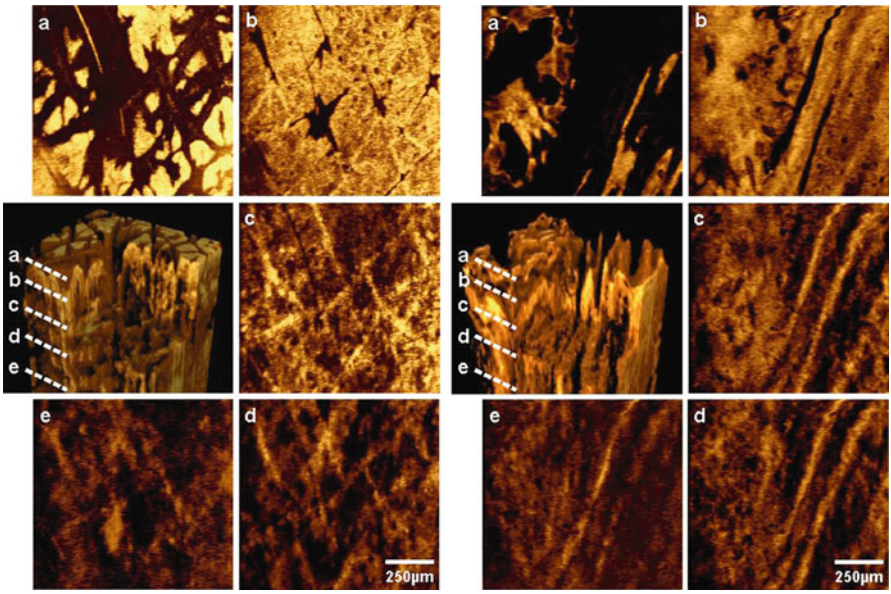

Fig. 9.12 *In vivo ultrahigh-resolution OCT of human skin*. Rendering and virtual C-mode scans (**a**–**e**) of a pigmented mole (*left*). The epidermis is much thinner than at the fingertip. Penetration is lower, but highly absorbing structures of about 10–30 µm at the basal layer (**b**, **c**) and a wide vascular meshwork can be appreciated in the deeper dermal layers (**d**, **e**). Vascular nevus (*right*); strongly folded surface with an unordered network of capillaries, missing mesoscopic structure visualized in virtual C-mode scans (**a**–**e**)

As an example of highly absorbing tissue, a nevus was investigated in vivo. This structure either appears as a mole, as a benign pigmented cluster of melanocytes with tan brown appearance, or as a vascular nevus being a benign blood vessel tumor consisting of a high concentration of capillaries. In Fig. 9.12 the rendering of the pigmented nevus (mole) is demonstrated, located in an area of thin skin. In contrast to the fingertip, the epidermis is much thinner and the dermal layers show a loose vascular reticulum (cross sections C, D). Just beneath the epidermis already, a high concentration of strongly absorbing spheroids, 10–30 µm in diameter, can be visualized, which seem to be interconnected by fine, almost vertical capillaries that are part of the larger vascular meshwork. At an alternate location OCT in vivo imaging at 800 nm of a vascular nevus is demonstrated in Fig. 9.12. Already the overall appearance at the surface is completely different. Deep puckers with a single main orientation separate the tissue. The reflectivity change with depth is not as prominent as with the mole and the internal structuring is much less ordered. Although tiny vessels appear already close to the surface, their squamous fabric seems to lack any alignment. En face sections taken at different depth already loose connections within 20 µm and lack of mesoscopic structure, although their overall texture seems to stay constant.

For investigation of internal organs with ultrahigh resolution, OCT miniaturized probes that can be positioned in the vicinity of the respective surfaces are needed. Several catheter imaging probes for UHR OCT at 800 nm have been demonstrated [61, 62]. Widespread clinical application of OCT endoscopy requires that probes be quickly replaceable by hospital staff, however. Since uncompensated inter-endoscope path length differences of less than 1 mm adversely affect performance of conventional Michelson interferometer-based OCT devices, designs insensitive to minor variations in the endoscopes geometry are desirable. UHR OCT presents a special challenge because chromatic aberrations must be minimized over a large optical bandwidth and dispersion and polarization matching between arms of the interferometer must be performed over a wide bandwidth that may be centered far away from the zero dispersion point of the materials used. Numerical methods for compensating dispersion are computationally expensive, are sensitive to noise, and perform best when the real dispersion mismatch is already well compensated in the system. Endoscopic ultrahigh-resolution optical coherence tomography OCT enabled collection of minimally invasive cross-sectional images in vivo, which may be used to facilitate rapid development of reliable mouse models of colon disease as well as assess chemopreventive and therapeutic agents [63, 64]. The small physical scale of mouse colon made light penetration less problematic than in other tissues and high resolution acutely necessary. In a 2 mm diameter endoscopic time-domain OCT system, isotropic ultrahigh resolution is supported by a center wavelength of 800 nm and full-width-at-half-maximum bandwidth of 150 nm mode-locked titanium:sapphire laser combined with 1:1 conjugate imaging of a small core fiber. A pair of KZFSN5/SFPL53 doublets provides excellent color correction to support wide bandwidth throughout the imaging depth (Fig. 9.13). A slight deviation from normal beam exit angle suppresses collection of the strong back reflection at the exit window surface. UHR endoscopy with axial resolution of 3.2 μm in air and 4.4 μm lateral spot diameter with 101 dB sensitivity could be accomplished. Microscopic features too small to see in mouse tissue with conventional resolution systems, including colonic crypts, are clearly resolved (Fig. 9.13). Resolution near the cellular level is potentially capable of identifying abnormal crypt formation and dysplastic cellular organization.

9.4 Ultrahigh-Resolution OCT at 1,300 nm

For OCT to be successfully used as an in vivo optical biopsy tool in nontransparent tissue, micrometer-scale resolution and millimeter range penetration depth is required. In the range between 800 and 1.8 μm, scattering is the predominant mechanism limiting image penetration depth. Since scattering depends strongly on wavelength and decreases for longer wavelengths, a much higher image penetration depth in nontransparent tissue can be achieved with light at 1.3 μm than at 800 nm. It has been shown that optimum wavelengths for imaging in nontransparent biological tissues are in the 1.3–1.5 μm range [65]. In this wavelength range imaging depths of 2 mm are possible before multiple scattering blurs the OCT

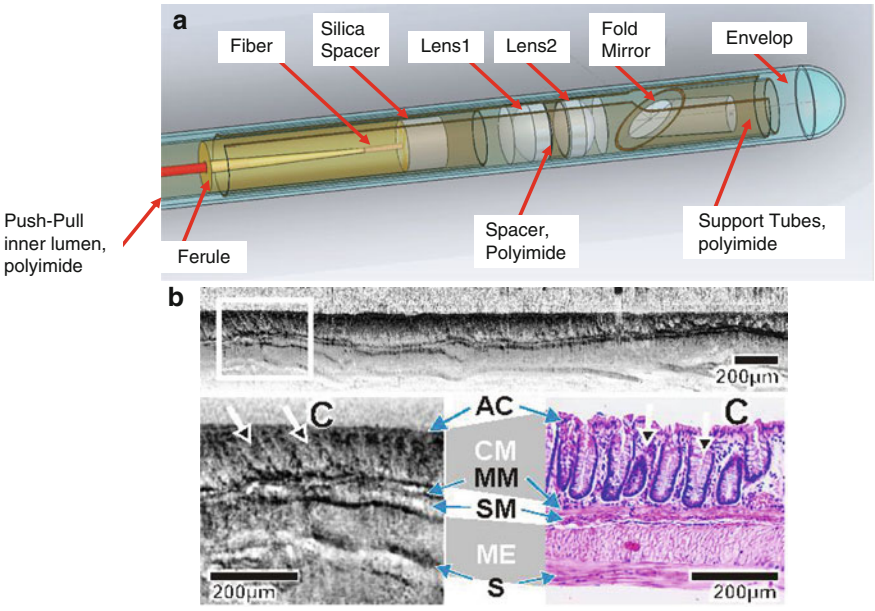

Fig. 9.13 *In vivo ultrahigh-resolution endoscopy of mouse colon*. Solid model shows the mechanical construction of the endoscope tip. The outer dimension of the tubing is 2 mm. The scanning range is 35 mm. All parts are designed to be aligned by location in tight tolerance polyimide tubing (**a**). Endoscopic UHR OCT tomogram (**b** *top* and *left*) versus stained histologic cross section (**c** *right*) of in vivo mouse colon with distally integrated beam splitter enables visualization of colonic mucosa (*CM*), muscular mucosa (*MM*), submucosa (*SM*), muscularis externa (*ME*), and serosa (*S*) layers. Contrast-enhanced portion, using local histogram equalization, shows a surface layer of apical crypt cells (*AC*) as well as vertical structures in the mucosa that may correspond to crypt boundaries (**c**). Corresponding structures are marked in the age and strain matched histology image. Inset graph shows axial point spread function detail [63, 64]

signal. In the 1,300 nm wavelength region, ultrashort pulse solid state lasers are also promising light sources for ultrahigh-resolution OCT. In an early demonstration, a self-phase-modulated KLM Cr:forsterite laser was used for in vivo OCT imaging in nontransparent tissues with 6 µm axial resolution [66]. Recent efforts focused on developing even broader bandwidth light sources in the 1,300 nm wavelength range that would permit OCT micrometer-scale resolution along with millimeter range penetration depth. As an example, broad bandwidth light covering the 1,230–1,580 nm wavelength region with an optical bandwidth of 250 nm (FWHM) was generated directly from an all-solid state Cr:forsterite laser [67].

Figures 9.14 and 9.15 show examples of ultrahigh-resolution OCT imaging of normal and pathologic human tissues ex vivo [68–70]. OCT imaging was performed on surgical specimens in the hospital pathology laboratory. Imaging in the pathology laboratory enables the access to tissues with various pathologies immediately after surgical excision and allows for the precise registration of OCT images and histology. In addition, imaging in a pathology laboratory is also an

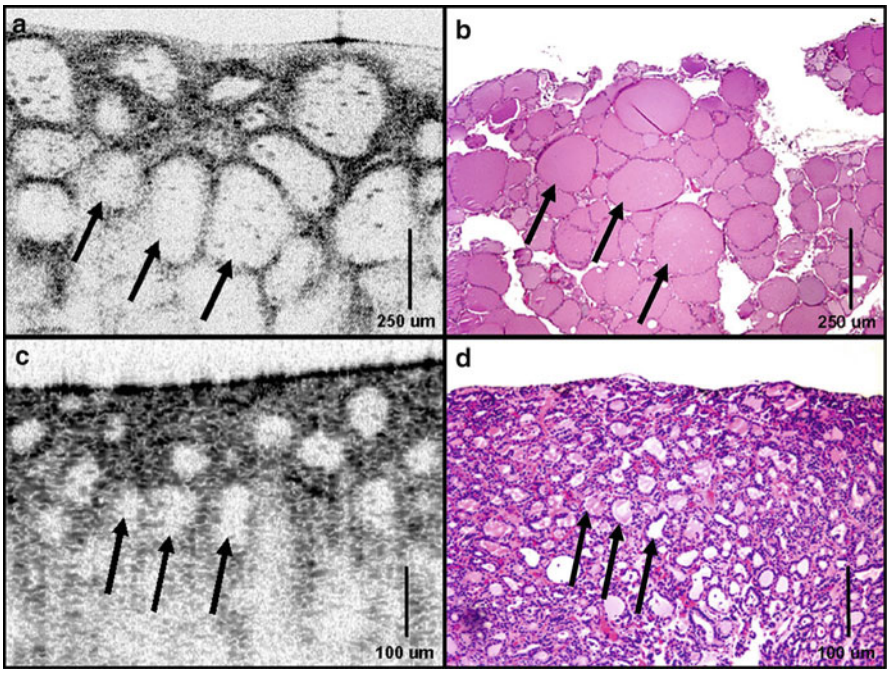

Fig. 9.14 *Ultrahigh-resolution OCT of human thyroid* ex vivo. (**a**) Normal thyroid tissue imaged ex vivo showing multiple colloid-filled follicles (*arrows*), and the corresponding histology is shown in (**b**). (**c**) Thyroid adenoma comprised of a predominantly microfollicular growth pattern, and the corresponding histology is shown in (**d**). *Arrows* indicate microfollicles. OCT images were obtained at central wavelength of 1.26 μm with resolutions of 4.5 μm axial × 11 μm transverse [70]

important step toward developing and validating new technology for future endoscopic studies. OCT imaging was performed with a 4.5 μm axial resolution and 11 μm transverse resolution using a Cr:forsterite laser light source. Since the OCT imaging light was in the near-infrared range and invisible to the naked eye, tissue registration was performed with a visible green light guiding beam. When necessary, irrigation of specimens (isotonic saline or RPMI 1640) was used to prevent dehydration during imaging. Specimens were marked with India ink to designate the plane of OCT imaging. The samples then underwent routine histologic processing. Figure 9.14a shows an OCT image of normal thyroid. Individual follicles with lumens containing colloid could be identified. The smallest follicle visible measured 15 μm in greatest dimension. In normal thyroid glands the follicles were found to be round to oval in shape, with only occasional focal irregularities noted. Colloid appeared low scattering, and occasional follicles contained colloid with focal regions of high scattering. Normal follicular epithelium appeared as a thin, highly scattering, dark layer lining larger follicles and as a slightly thicker, dark rim around smaller follicles. In contrast, adenomas consist predominantly of microfollicles averaging 90 μm in greatest diameter (Fig. 9.14c).

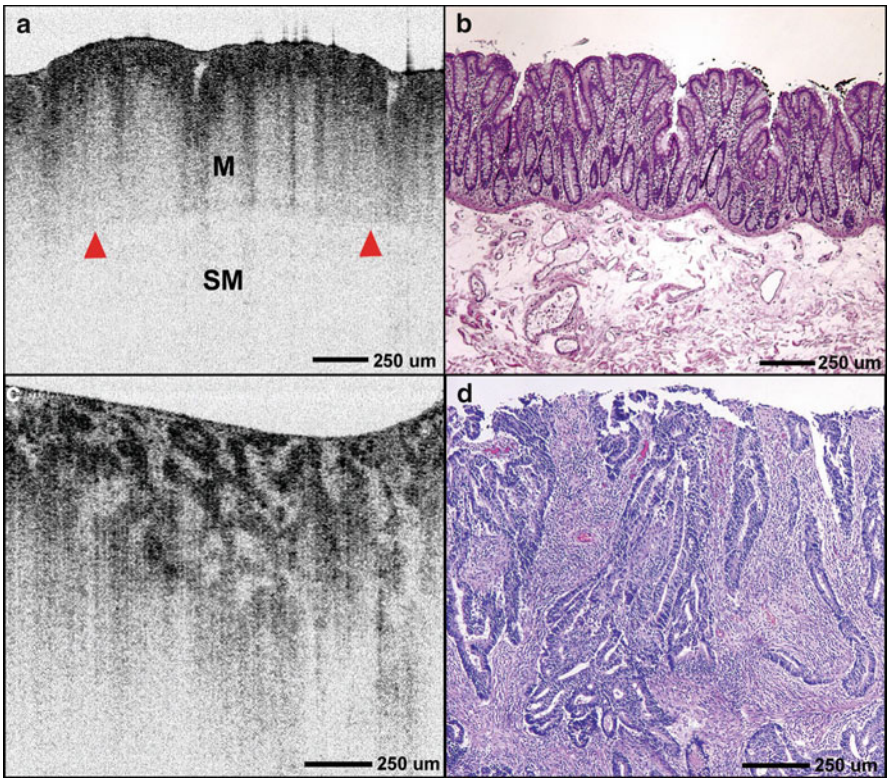

Fig. 9.15 *Ultrahigh-resolution OCT of human colon ex vivo*. (**a**) Ultrahigh-resolution OCT image of normal colon. Mucosa (*M*) is clearly delineated from underlying submucosa (*SM*) by a scattering band corresponding to the thin muscularis mucosa (*arrows*). The submucosa is visible as less optically scattering layer. (**b**) Corresponding histology. (**c**) Ultrahigh-resolution OCT image of well-differentiated adenocarcinoma. Highly irregular invasive glands are visible in a desmoplastic stroma. No clear boundary between mucosa and submucosa is evident in this case. (**d**) Corresponding histology. OCT images were obtained at central wavelength of 1.26 μm with resolutions of 4.5 μm axial × 11 μm transverse [70]

Even small abortive follicles could be recognized. Many of the follicles present within adenomas were oval in shape. Figure 9.15a, b shows a representative ultrahigh-resolution OCT image of the normal colon and corresponding histology. OCT clearly visualized the full thickness of the colonic mucosa. The submucosa appeared as a lighter and less optically scattering layer. The muscularis mucosa appeared as a scattering band in the OCT image separating the mucosa and submusoca. Figure 9.15c, d show an OCT image and corresponding histology of adenocarcinoma. OCT image of adenocarcinoma revealed complete loss of normal mucosal architecture and invasion of the submuscosa. Highly scattering and irregular invasive glands were visible in OCT images of adenocarcinoma.

In vivo ultrahigh-resolution endoscopy imaging of the rabbit gastrointestinal tract was demonstrated at a threefold higher resolution (3.7 μm in tissue), using

such a broadband Cr:forsterite laser as the optical light source [71]. Images acquired from the esophagus, trachea, and colon reveal high-resolution details of tissue architecture. Definitive correlation of architectural features in OCT images and histological sections could be shown. The ability of ultrahigh-resolution endoscopic OCT to image tissue morphology at an unprecedented resolution in vivo advances the development of OCT as a potential imaging tool for the early detection of neoplastic changes in biological tissues. A rapid scanning delay line in the reference arm provided real-time imaging at up to 3,125 axial scans per second. Imaging was performed at a frame rate of 4 Hz, which corresponded to a transverse pixel image density of up to 780 axial scans per image. The OCT beam was scanned in both longitudinal and rotational directions to generate cross-sectional images of tissue structures in orthogonal imaging planes. To match optical dispersion within the system, SFL6 and LaKN22 dispersion-compensating glasses were inserted in the reference arm to compensate for the catheter focusing optics in the sample arm, and an air gap coupling was used in the sample arm to compensate for the air path in the reference arm from the collimator to the scanning delay mirror. The use of the dispersion-compensating glass and air gap coupling allowed precise dispersion compensation for ultrahigh-resolution imaging performance. The backcoupled OCT signal was divided into two orthogonal polarization channels by a polarizing beam splitter, and the two detector outputs were digitally demodulated using a DSP board. A polarization diversity signal was obtained from the square root of the sum of the squared signal intensities from the two polarization channels.

Figure 9.16a shows an in vivo OCT image of the esophagus in the rabbit taken with the linear scanning catheter. The corresponding histology is also shown in Fig. 9.16b. The layered structure of the esophagus is clearly delineated, with good definition to the squamous epithelium (e), lamina propria (lp), muscularis mucosa (mm) submucosa (sm), and the inner (im) and outer muscular (om) layers. The OCT image correlated well with the histology in both the order of the layers and the layer thickness. Figure 9.16c shows a composite image of five OCT linear scans acquired sequentially as the catheter was withdrawn during imaging. Images were acquired over a 12 mm scanning range from the epiglottis to the inner esophagus. This image illustrates the capability to visualize continuous morphology over a large field of view at ultrahigh resolution, a method that permits suspect regions to be rapidly surveyed. Figure 9.17a shows an in vivo OCT image of the esophagus and trachea in the rabbit. The tracheal hyaline cartilage (hc) is visible through the esophageal wall, thus demonstrating the ability of the endoscopic OCT system to image deeply within the tissue. In addition, the structural details of the tracheal mucosa and trachealis muscle are visible. The vacuous region below the tracheal wall located at the bottom of the image is the tracheal airway. The corresponding histology in Fig. 9.17b shows good correlation with the architecture seen in the OCT image. Trichrome staining was used in the histological section to enhance delineation of cartilage rings in the trachea. With the high speed of the OCT system used for this study, it was possible to image large regions within the gastrointestinal tract while maintaining high-axial and transverse image resolutions.

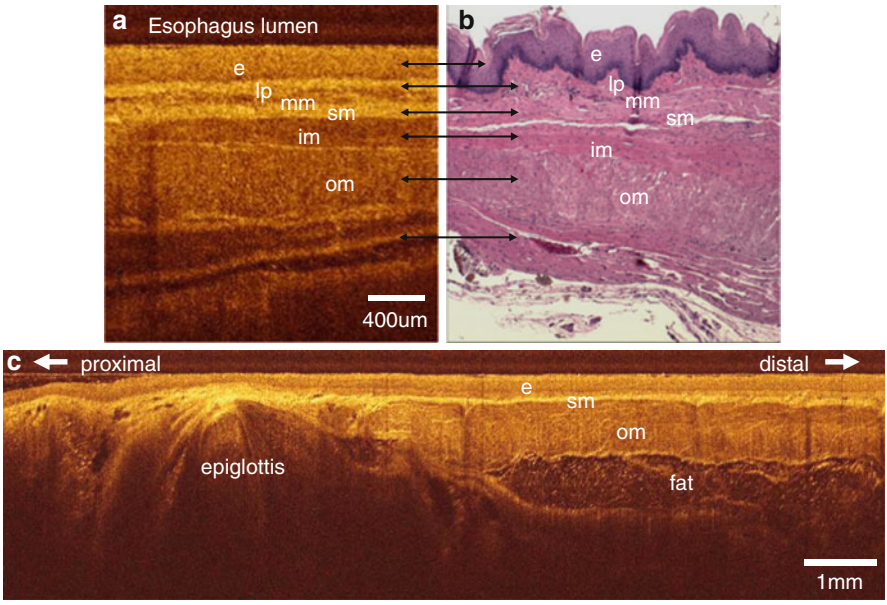

Fig. 9.16 *In vivo ultrahigh-resolution endoscopy of the rabbit gastrointestinal tract.* In vivo endoscopic OCT image of rabbit esophagus (**a**) with corresponding histology (**b**). Good correlation is seen between OCT and histology. The epithelium (*e*), lamina propria (*lp*), muscularis mucosa (*mm*), submucosa (*sm*), inner (*im*), and outer muscular (*om*) layers are visible on both the OCT image and histology. In vivo UHR OCT image (**c**) showing sequential OCT scans spanning the rabbit epiglottis to the inner esophagus. Ultrahigh-resolution imaging capability is maintained over a large field allowing detailed discrimination of tissue structure. Architectural morphology of the proximal esophagus is well defined, as is the transition from the mouth to the esophagus at the epiglottis [71]

Clinical endoscopic OCT studies have been performed using UHR OCT in patients previously diagnosed with Barrett's esophagus [72]. UHR OCT images were compared with endoscopic diagnosis and pinch biopsy histology. UHR OCT images of normal esophagus, Barrett's esophagus, high-grade dysplasia, and esophageal adenocarcinoma were evaluated. UHR OCT images of the normal esophagus exhibited characteristic layered architecture with uniform epithelium, while images of Barrett's esophagus corresponded to crypt-like glandular structures (cf. Fig. 9.18). High-grade dysplasia and esophageal adenocarcinoma images exhibited more heterogeneous structures corresponding to irregular, heterogeneous tissue morphology from distorted and cribriform or villiform glandular architecture. Fine features can be discerned more clearly with endoscopic UHR OCT. Additional studies are required to evaluate the impact of improved resolution on the sensitivity and specificity for detecting high-grade dysplasia.

Spectra much broader than one optical octave can be produced via nonlinear propagation of laser pulses in microstructured fibers. Owing to the geometry of these fibers, the cross section of the fundamental mode is unusually small, which enhances the peak power and thus the nonlinearity. At the same time, the fiber

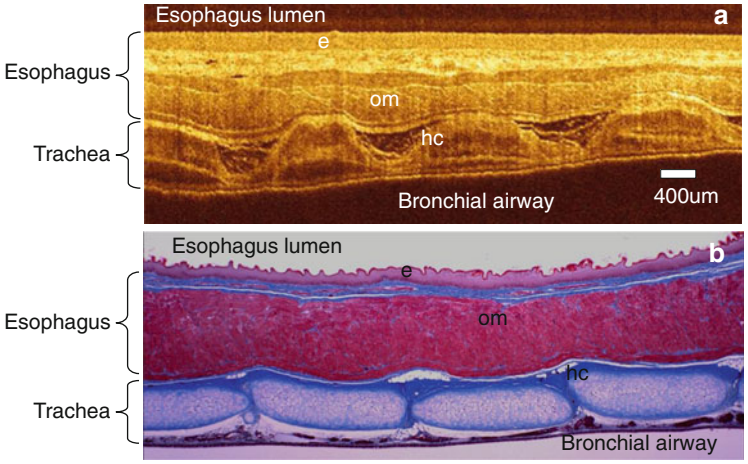

Fig. 9.17 *In vivo ultrahigh-resolution endoscopy of the rabbit gastrointestinal tract*. In vivo UHR OCT image (**a**) and histology (**b**) of rabbit esophagus and trachea viewed intraluminally from the esophagus. Tracheal hyaline cartilage (*hc*) between the tracheal mucosa and trachealis muscle is well defined. The image demonstrates the ability of the endoscopic OCT system to image deeply within the tissue. Trichrome stain was used to highlight cartilage and muscle layers [71]

dispersion can be engineered to avoid rapid temporal broadening. Due to these effects, spectra covering more than one optical octave can be produced even with pulses having moderated energies of a few nJ. This spectral width could never be generated directly from the linear laser oscillator, because it exceeds the fluorescence bandwidth of the crystal. In order to avoid an excessively strong spectral modulation (inherent to the spectral broadening processes – self phase modulation and four wave mixing), only moderate spectral broadening should appear during the nonlinear fiber propagation, i.e., the initial bandwidth of the pulses emerging from the oscillator should already be as broad as possible. High nonlinearity, air-silica microstructure fibers [73] or tapered fibers [74] have been used to generate an extremely broadband continuum using low-energy femtosecond pulses. So far, the highest reported OCT axial resolution in biological tissue in the 1,300 nm wavelength region was realized by use of a complex laboratory prototype PCF-based light source [75]. With a bandwidth of 450 nm at a 1.3 μm center wavelength, 2.5 μm axial resolution in free space, corresponding to 2 μm in tissue, was achieved by employing an OCT system that could support 370 nm bandwidth. In vivo ultrahigh-resolution image of a Syrian hamster's cheek pouch could be demonstrated. Unprecedented sub-2 μm axial resolution OCT in the 1,300 nm wavelength range in nontransparent biological tissue was achieved with a broad bandwidth light source, based on a several meter long dispersion matched optical fiber (Menlo Systems) [68]. This light source is based on a pulsed erbium fiber laser, the amplified output of which is coupled into a highly nonlinear fiber to generate a supercontinuum ranging from 1,100 to 1,800 nm at its pedestal, with a power output of ∼50 mW at 50 MHz repetition rate. Because of a 12 dB modulation

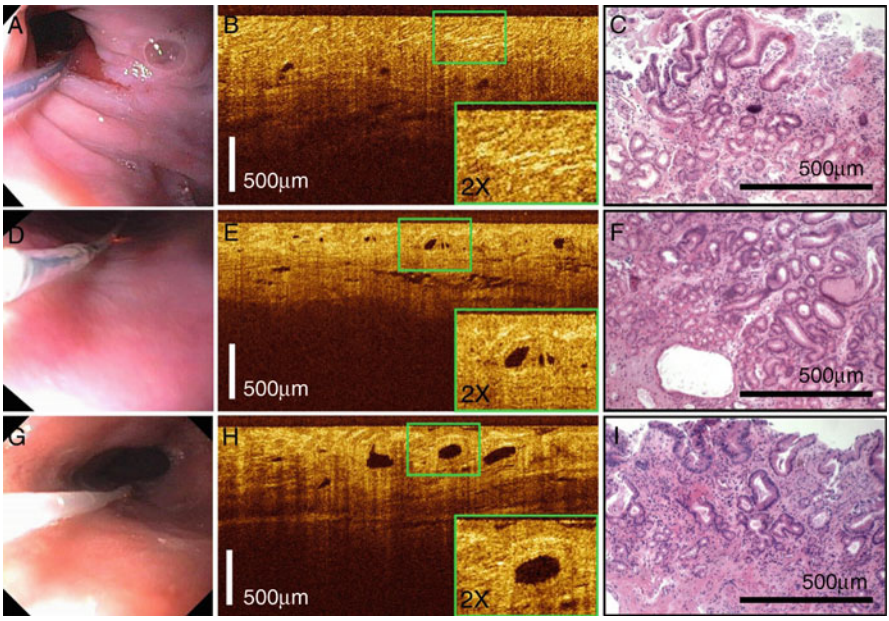

Fig. 9.18 *In vivo ultrahigh-resolution endoscopy of the human gastrointestinal tract*. Endoscopic view (**a**, **d**, **g**), in vivo UHR OCT images (**b**, **e**, **h**), and corresponding histology (**c**, **f**, **i**) of Barrett's esophagus. OCT images were obtained at central wavelength of 1.26 µm with resolutions of 5 µm axial × 15 µm transverse. As compared to normal esophagus that exhibited characteristic layered architecture with uniform epithelium, images of Barrett's esophagus reveal crypt-like glandular structures [72]

at ∼1,550 nm, only the shorter wavelength portion of the emission spectrum was utilized for OCT imaging by blocking the wavelength range beyond 1,550 nm with an edge filter. The filtered fiber laser spectrum was moderately modulated, centered at 1,375 nm with a full width at half maximum (FWHM) of 470 nm and a power output of 4 mW. By interfacing the light source to a free space OCT system, resolution of 2 µm in axial and 4 µm in lateral direction (measured with a resolution target), corresponding to ∼1.4 µm and ∼3 µm in biological tissue, respectively, and 95 dB sensitivity for 500 µW incident power were achieved. The feasibility for ex vivo sub-2 µm axial resolution OCT was demonstrated, but due to insufficient power and noise problems, this source was not used for in vivo OCT studies.

9.5 Ultrahigh-Resolution OCT at 1,000 nm

Imaging at 1,000 nm wavelength range represents an attractive compromise between the ultrahigh-axial resolution, but limited image penetration at 800 nm wavelength range, and the reduced resolution, but enhanced image penetration at 1,300 nm wavelength range. In addition, it has been shown that at 1,000 nm the water dispersion is near zero; therefore, it is possible to eliminate the influence of

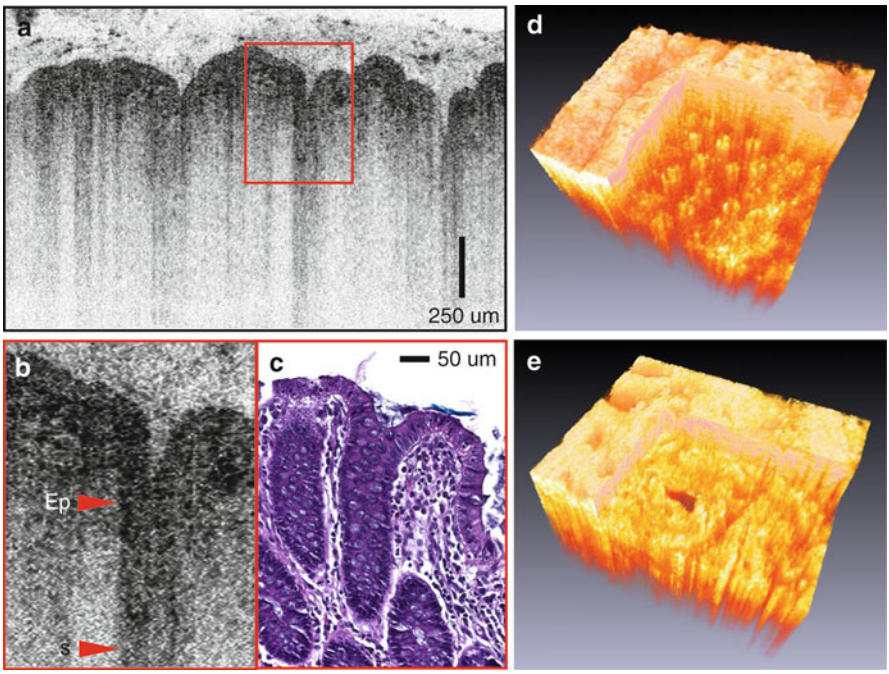

Fig. 9.19 *Ultrahigh-resolution and three-dimensional OCT imaging of human colon ex vivo.* (**a**) Ultrahigh-resolution OCT image of normal colon mucosa with enlarged view (**b**). (**c**) Corresponding histology. (**d**) Volume rendering of normal colon mucosa showing organized crypt pattern. (**e**) Volume rendering of a polypoid adenoma of the colon showing irregular glandular structures. OCT images were acquired at 1,000 nm wavelength range with the resolution of 3.5 μm axial × 6 μm transverse. 3D volume size: 1 mm × 1.2 mm × 1.3 mm [70]

depth-dependent dispersion in tissue by choosing OCT light sources at 1,000 nm [76]. Furthermore, a wide range of commercially available femtosecond laser sources including mode-locked Nd:glass lasers and Yb fiber lasers are available at this wavelength range. The use of these commercial femtosecond lasers in combination with high nonlinearity optical fibers represents an attractive and robust approach for achieving bandwidths necessary for ultrahigh-resolution OCT imaging. For example, the compact diode-pumped femtosecond Nd:glass laser (High Q Laser Productions) can generate pulse durations of $<$100 fs at repetition rates of $\sim$50 MHz with average powers of $\sim$100 mW. Nonlinear self phase modulation in a high numerical aperture fiber can be used to generate bandwidths of $>$200 nm centered around 1,050 nm [77]. The measured FWHM of the point spread function is 4.2 μm in air, corresponding to 3.5 μm in tissue. The Nd:glass laser is robust and provides turn-key operation. This system is well suited for in vivo ultrahigh-resolution OCT imaging studies which would be performed outside the research laboratory, especially in the clinic settings.

Figure 9.19 shows an example of an ultrahigh-resolution OCT image of the human colon ex vivo [70]. Imaging was performed with a 3.5 μm axial resolution

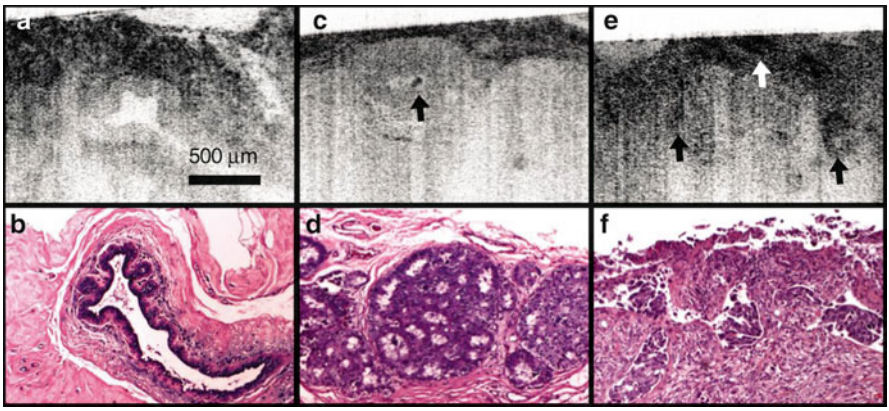

Fig. 9.20 *OCT imaging of normal and neoplastic breast tissue*. (**a**, **b**): normal lactiferous duct. (**c**, **d**): ductal carcinoma in situ with microcalcifications (*arrow*). (**e**, **f**): infiltrating ductal carcinoma (*arrows*)

and 6 µm spot size using a Nd:glass laser light source. Figure 9.19a–c shows a representative OCT image and corresponding histology of normal colon at 1 µm wavelength. The finer transverse resolution more clearly delineates the individual crypt structures and the epithelial layer than images at 1.3 µm wavelength. The epithelium is visible as a distinct layer, approximately 40–50 µm in thickness, delineated by a thin, highly scattering band from the supporting lamina propria. Individual crypts as well as the epithelial layer lining the crypts are visible. Figure 9.19d, e shows representative 3D OCT volume renderings of normal colon and a polypoid adenoma of the colon, respectively. Rendered 3D OCT data can be viewed from a virtual surface perspective, yielding a view similar to that of magnification endoscopy. Normal colon exhibits a well-organized distribution of crypts which are uniform in size and spacing in the en face plane. In contrast, polypoid adenoma exhibits irregular glandular structure.

Ultrahigh-resolution OCT imaging of human breast specimens was also performed using a Nd:glass laser system at 1 um wavelength [78]. Imaging was performed in 119 freshly excised specimens from 35 women with 3.5 µm axial × 6 µm transverse resolution at 1,060 nm wavelength. Both cross-sectional and 3D OCT images were acquired. Microstructure of normal breast parenchyma, including glands, lobules, and ducts, as well as stromal changes associated with infiltrating cancer, was visible from OCT images. Furthermore, fibrocystic changes and benign fibroadenomas were identified. Imaging of ductal carcinoma in situ revealed microcalcifications. Figure 9.20 shows example of OCT images of the breast. A normal lactiferous duct is shown in (a, b) with low scattering epithelium compared to surrounding fibrous stroma. Ductal carcinoma in situ (DCIS) is shown in (c, d) with dilation and distortion of lobules and the presence of a microcalcification. Infiltrating ductal carcinoma (e, f) shows heterogeneous, patchy scattering consistent with disorganized glandular elements within tumor

stroma. The results of this study suggest the potential of OCT to visualize breast disease and motivate further investigation.

9.6 Ultrahigh-Resolution OCT in the Visible Wavelength Region

Using PCF fibers in combination with femtosecond light sources, extremely broad spectra can be generated in the visible wavelength range. A stable, slightly modulated spectrum ranging from 550 to 950 nm (at its pedestal) supercontinuum (SC) spanning more than 325 nm (FWHM) with spectral modulations less than 1.5 dB, centered at 725 nm and providing 27 mW of average output power, was generated starting with a titanium:sapphire laser generating sub-10 fs pulses with 120 nm bandwidth (FWHM) an average output power of 400 mW at 100 MHz repetition rate. The fiber was a PCF with a 2.3 μm core diameter and 6 mm length and matching polarization to the main polarization axis of the fiber and precompression of the pulses to compensate for the positive chirp introduced by the air and the coupling elements was required [79]. This study achieved 0.5 μm axial image resolutions in the visible. The broad bandwidth of this light source also provides access to a spectral region covering the absorption bands of a number of biological chromophores; thus, it has great potential for spectroscopic OCT. This new spectral region is interesting because of the ultrahigh resolution of the OCT images (sub-μm resolution, rather than several microns in the near-infrared) and also the fact that changes in refractive index and therefore image contrast are stronger in this wavelength region and absorption of biological chromophores is stronger. These three properties are extremely interesting for medical applications, since human cells with common sizes of several micrometers can only be visualized with sub-μm resolution. In addition, intra- and extracellular processes involve changes in optical properties in this range of the optical spectrum and can be observed in real time, without additional staining.

Imaging of in vitro human cancer cells could be performed using OCT in combination with this light source. Intracellular structures obtained by visible light OCT were compared with histologically stained samples of the same cells. Nucleoli and the Golgi apparatus might be visualized. Further investigations will help to interpret the results with more accuracy. Considering that the emission bandwidth of the light source overlaps with the so-called therapeutic window, covering absorption features of several biological chromophores, such as melanin, oxyhemoglobin, and desoxyhemoglobin, visible OCT also offers the potential for enhanced noninvasive spatially resolved spectroscopy. To test the ability of UHR OCT to image cellular morphology, tomograms of human colorectal adenocarcinoma cells HT-29 as well as animal ganglion cells were acquired in vitro. In the case of HT-29 cells, monolayers of cultured cells were grown on glass plates at 37 °C in a humidified atmosphere of 95 % air and 5 % CO_2. OCT tomograms of these specimens were obtained 48 h after seeding. Subsequently the cells were fixated and stained and histological cross sections of 1 μm thickness in

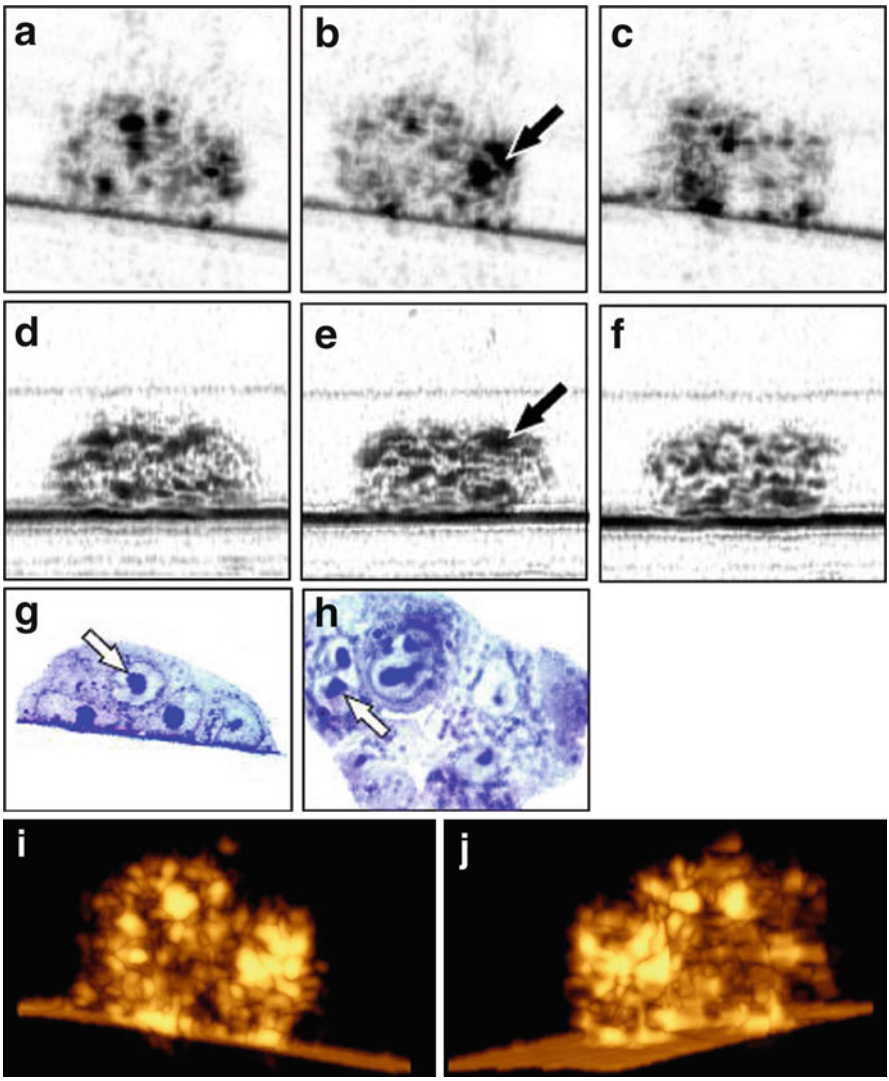

Fig. 9.21 *In vitro sub-micrometer resolution OCT of human colorectal adenocarcinoma cells HT-29*. UHR OCT with 0.5 μm axial and ~2 μm transverse resolution, covering an area of 50 × 50 μm, equally spaced by 2 μm. (**a**–**f**). *Arrows* indicate features that may correspond to nucleoli with ~3–5 μm diameter. Histological sections parallel (**g**, **h**) to the OCT imaging direction. Three-dimensional rendering (**i**, **j**); the different size of three-dimensional scatters, possibly associated with the dense nucleoli of these highly active cells is clearly visible [79]

direction parallel and perpendicular to the OCT imaging direction were prepared and analyzed using standard light microscopy with comparable but isotropic resolution and obvious reduced contrast-at-depth and penetration (Fig. 9.21). Multiple OCT cross-sectional images of a group of HT-29 cells, equally spaced by

2 μm, were acquired in vitro with 0.5 μm axial and ~2 μm transverse resolution (PCF-based light source with visible spectrum) and SNR of 87 dB for 1 mW average power at the sample surface and covering an area of 50 × 50 μm (500 × 500 pixels, Fig. 9.21). In addition, tomograms of the same cells were acquired with the picosecond laser pumped fiber based light source centered at 1,130 nm, with 1.1 axial and 2.5 μm transverse resolution in tissue, and SNR of 93 dB for 11 mW average incident power. The UHR OCT images were compared with histological cross sections of the cells (Fig. 9.21g, h). The observed cell size was ~20 μm, while the nucleoli, parts of the active nucleus, were about 2–3 μm. Comparison with histology revealed that the intercellular-structures visualized in the OCT tomograms might correspond to some cell components as nuclei or mitochondria as well as other intracellular components. Due to the better contrast in the 700 nm region (Fig. 9.21a–c), small features can easily be resolved with the visible light source, while the tomograms acquired at 1,130 nm (Fig. 9.21d–f) look less distinct regardless of the higher intensity.

Since the OCT axial resolution scales with the center wavelength of the optical source, smaller bandwidths are required to achieve micrometer scale resolution in the visible wavelength range. Here the image contrast is enhanced due to stronger modulation of the backscattering profile of biological tissue. Major limitations for UHR OCT in the visible wavelength range are the relatively low image penetration depth as well as stability and inherent noise of current light sources. Dispersion mismatch which deteriorates the imaging quality is more critical in the visible than in the near-infrared wavelength regime especially at 1,060 nm where the zero dispersion point of water is located. The diversity in nonlinear fiber-based light sources with respect to center wavelength, bandwidth, and output power makes them extremely attractive for UHR OCT applications. However, their excess noise is higher compared to Kerr lens mode-locked lasers, and currently their setup is more complex and therefore not easy to handle.

9.7 Conclusion

Novel ultrabroad bandwidth light source technology has been developed to enable UHR OCT imaging in the visible and near-infrared wavelength region with unprecedented axial resolution. Subcellular structures were resolved with sub-micrometer axial resolution in human cancer and animal ganglion cells, while the different contrast and improved penetration depth with increasing wavelength were demonstrated. Different medical fields such as ophthalmology, gastroenterology, dermatology, neurology, gynecology, urology, laryngology, etc. impose various demands to the performance, size, and user-friendliness of UHR OCT systems.

Since its first biological application in the early 1990s, OCT has successively matured from a simple cross-sectional imaging method to a complex, ultrahigh-

resolution, volumetric imaging technique. Broadband light sources and frequency-domain detection were major milestones at the laboratory stage and promise to achieve widespread application. The majority of time-domain instruments with narrow bandwidth and much lower speeds will ultimately be replaced by this newer technology. These developments promise to make OCT as well known as computer-assisted tomography or magnetic resonance imaging. Meanwhile, extremely fast tunable and broader bandwidth light sources at new wavelengths as well as sensitive, fast, high-resolution detectors are emerging. All these technologies can be explored, tested, and evaluated for OCT applications in medicine and other fields, and promising results are rapidly emerging.

Ultrahigh-resolution OCT has the potential to provide real-time, in situ visualization of tissue microstructure without the time intensive need to excisionally remove and process a specimen as in conventional biopsy and histopathology. Non-excisional optical biopsy and the ability to visualize tissue morphology in vivo at the cellular level resolution can be used both for diagnostic imaging and for guiding therapeutic and surgical intervention. By improving axial resolution by two orders of magnitude as compared to conventional ultrasound, ultrahigh-resolution OCT represents a quantum leap in imaging performance. By providing unprecedented noninvasive in vivo optical sectioning to visualize microscopic morphometric features with subcellular level resolution in tissue at depths approaching that of in vitro conventional bright-field and confocal microscopes, OCT promises to enhance early cancer diagnosis as well as the early detection of ocular pathologies that are worldwide leading causes of blindness.

In tissues other than the eye, optical scattering limits image penetration depths to 2 mm. However, because OCT is an optical technology, it can be interfaced to a wide range of instruments such as endoscopes, catheters, or laparoscopes, which enables the imaging of internal organ systems. UHR OCT promises to have a powerful impact on many medical applications ranging from the screening and diagnosis of neoplasia to enabling new microsurgical and minimally invasive surgical procedures.

The broad bandwidths available from short pulse light sources also enable spectroscopic OCT imaging which may be used analogously to stain in histopathology, to enhance image contrast, and to provide better differentiation of tissue pathologies. With further development, spectroscopic techniques hold the promise of enabling functional imaging, for example, cross-sectional mapping of tissue oxygenation at micron level resolution. This extension should not only improve image contrast, but should also enable the differentiation of tissue pathologies via localized spectroscopic properties and functional state.

Acknowledgments The authors would like to thank B. Herrmann, B. Hofer, and J.E. Morgan, from the School of Optometry and Vision Science, Cardiff University; A.F. Fercher, R. Leitgeb, L. Schachinger, und H. Sattmann from the Centre of Biomedical Engineering and Physics, Medical University, Vienna, Austria; K. Bizheva, University of Waterloo, Canada; and A. Stingl and T. Le from Femtolasers Produktions GmbH, Vienna, Austria.

The authors would also like to thank Desmond Adler, Iwona Gorczynska, Robert Huber, Tony H. Ko, Jonathan Liu, Vivek J. Srinivasan, Maciej Wojtkowski, Pei-Lin Hsiung, and Paul Herz, from the Department of Electrical Engineering and Computer Science at the Massachusetts Institute of Technology; Jay S. Duker, Royce Chen, Caroline Baumal, Janice Lem, Brian Monson, Elias Reichel, Adam Rogers, and Andre J. Witkin, from the New England Eye Center, Tufts-New England Medical Center, Tufts University; Joel S. Schuman, Michelle Gabriele Larry Kagemann, Gadi Wollstein, and Hiroshi Ishikawa from the UPMC Eye Center, Department of Ophthalmology, Eye and Ear Institute, University of Pittsburgh School of Medicine; Allen Clermont and Sven-Erik Bursell, from the Beetham Eye Institute, Joslin Diabetes Center, Harvard Medical School, Boston; Andrzej Kowalczyk, from the Institute of Physics, Nicolaus Copernicus University, Torun, Poland; Vladimir Shidlovski and Sergei Yakubovich from Superlum Diodes, Ltd.

Financial support is acknowledged to Cardiff University, FP6-IST-NMP-2 STREPT (017128), the Christian Doppler Society, NP Photonics (Arizona, US), FEMTOLASERS GmbH (Vienna, Austria), Carl Zeiss Meditec Inc. (Dublin, CA, USA), Maxon Computer GmbH (Friedrichsdorf, Germany). FWF P14218-PSY, FWF Y 159, CRAF-1999-70549, Christian Doppler Gesellschaft, FEMTOLASERS Produktions GmbH, Carl Zeiss Meditec Inc. This research was also supported at M.I.T. by the Air Force Office of Scientific Research and Medical Free Electron Laser Program FA9550-040-1-0046 and FA9550-040-1-0011, National Institutes of Health R01-EY011289-21 and R01-CA75289-10, and National Science Foundation ECS-0501478 and BES-0522845.

References

1. A.F. Fercher, E. Roth, Ophthalmic laser interferometer. Proc. SPIE **658**, 48–51 (1986)
2. J.G. Fujimoto, S. De Silvestri, E.P. Ippen, C.A. Puliafito, R. Marglois, A. Oseroff, Femtosecond optical ranging in biological systems. Opt. Lett. **11**, 150–152 (1986)
3. R.C. Youngquist, S. Carr, D.E.N. Davies, Optical coherence domain reflectometry: a new optical evaluation technique. Opt. Lett. **12**, 158 (1987)
4. A.F. Fercher, K. Mengedoht, W. Werner, Eye length measurement by interferometer with partially coherent light. Opt. Lett. **13**, 186–188 (1988)
5. D. Huang, E.A. Swanson, C.P. Lin, J.S. Schuman, W.G. Stinson, W. Chang, M.R. Hee, T. Flotte, K. Gregory, C.A. Puliafito, J.G. Fujimoto, Optical coherence tomography. Science **254**, 1178–1181 (1991)
6. J.G. Fujimoto, M.E. Brezinski, G.J. Tearney, S.A. Boppart, B. Bouma, M.R. Hee, J.F. Southern, E.A. Swanson, Optical biopsy and imaging using optical coherence tomography. Nat. Med. **1**, 970–972 (1995)
7. A.F. Fercher, Optical coherence tomography. J. Biomed. Opt. **1**, 157–173 (1996)
8. W. Drexler, U. Morgner, F.X. Kartner, C. Pitris, S.A. Boppart, X.D. Li, E.P. Ippen, J.G. Fujimoto, In vivo ultrahigh-resolution optical coherence tomography. Opt. Lett. **24**, 1221–1223 (1999)
9. W. Drexler, U. Morgner, R.K. Ghanta, F.X. Kartner, J.S. Schuman, J.G. Fujimoto, Ultrahigh-resolution ophthalmic optical coherence tomography. Nat. Med. **7**, 502–507 (2001)
10. W. Drexler, H. Sattmarin, B. Hermann, T.H. Ko, M. Stur, A. Unterhuber, C. Scholda, O. Findl, M. Wirtitsch, J.G. Fujimoto, A.F. Fercher, Enhanced visualization of macular pathology with the use of ultrahigh-resolution optical coherence tomography. Arch. Ophthalmol. **121**, 695–706 (2003)
11. W. Drexler, Ultrahigh-resolution optical coherence tomography. J. Biomed. Opt. **9**, 47–74 (2004)
12. E.A. Swanson, J.A. Izatt, M.R. Hee, D. Huang, C.P. Lin, J.S. Schuman, C.A. Puliafito, J.G. Fujimoto, In-vivo retinal imaging by optical coherence tomography. Opt. Lett. **18**, 1864–1866 (1993)
13. A. Unterhuber, B. Považay, K. Bizheva, B. Hermann, H. Sattmann, A. Stingl, T. Le, M. Seefeld, R. Menzel, M. Preusser, H. Budka, C. Schubert, H. Reitsamer, P.K. Ahnelt,

J.E. Morgan, A. Cowey, W. Drexler, Advances in broad bandwidth light sources for ultrahigh resolution optical coherence tomography. Phys. Med. Biol. **49**, 1235–1246 (2004)
14. W. Drexler, C.K. Hitzenberger, A. Baumgartner, O. Findl, H. Sattmann, A.F. Fercher, Investigation of dispersion effects in ocular media by multiple wavelength partial coherence interferometry. Exp. Eye Res. **66**, 25–33 (1998)
15. C.K. Hitzenberger, A. Baumgartner, W. Drexler, A.F. Fercher, Dispersion effects in partial coherence interferometry: implications for intraocular ranging. J. Biomed. Opt. **4**, 144–151 (1999)
16. E.J. Fernandez, W. Drexler, Influence of ocular chromatic aberration and pupil size on transverse resolution in ophthalmic adaptive optics optical coherence tomography. Opt. Exp. **13**, 8184–8197 (2005)
17. E.J. Fernandez, A. Unterhuber, B. Povazay, B. Hermann, P. Artal, W. Drexler, Chromatic aberration correction of the human eye for retinal imaging in the near infrared. Opt. Exp. **14**, 6213–6225 (2006)
18. E.J. Fernandez, A. Unterhuber, P.M. Prieto, B. Hermann, W. Drexler, P. Artal, Ocular aberrations as a function of wavelength in the near infrared measured with a femtosecond laser. Opt. Exp. **13**, 400–409 (2005)
19. A.F. Fercher, C.K. Hitzenberger, M. Sticker, E. Moreno-Barriuso, R. Leitgeb, W. Drexler, H. Sattmann, A thermal light source technique for optical coherence tomography. Opt. Commun. **185**, 57–64 (2000)
20. A. Dubois, K. Grieve, G. Moneron, R. Lecaque, L. Vabre, C. Boccara, Ultrahigh-resolution full-field optical coherence tomography. Appl. Opt. **43**, 2874–2883 (2004)
21. L. Vabre, A. Dubois, A.C. Boccara, Thermal-light full-field optical coherence tomography. Opt. Lett. **27**, 530–532 (2002)
22. H.H. Liu, P.H. Cheng, J. Wang, Spatially coherent white light interferometer based on a point fluorescent source. Opt. Lett. **18**, 678–680 (1993)
23. X. Clivaz, F. Marquis-Weible, R.P. Salathe, Optical low coherence tomography with 1.9 9 μm mu;m spatial resolution. Electron. Lett. **28**, 1553–1554 (1992)
24. Y.J. Rao, Y.N. Ning, D.A. Jackson, Synthesized sources for white-light sensing systems. Opt. Lett. **18**, 462–464 (1993)
25. D.N. Wang, Y.N. Ning, K.T.V. Grattan, A.W. Palmer, K. Weir, Optimized multi wavelength combination sources for interferometric use. Appl. Opt. **33**, 7326–7333 (1994)
26. W. Drexler, C.K. Hitzenberger, A. Baumgartner, O. Findl, H. Sattmann, A.F. Fercher, Multiple wavelength partial coherence interferometry. Proc. SPIE. **2930**, 194–201 (1996)
27. A. Baumgartner, C.K. Hitzenberger, H. Sattmann, W. Dresler, A.F. Fercher, Signal and resolution enhancements in dual beam optical coherence tomography of the human eye. J. Biomed. Opt. **3**, 45–54 (1998)
28. T.H. Ko, D.C. Adler, J.G. Fujimoto, D. Mamedov, V. Prokhorov, V. Shidlovski, S. Yakubovich, Ultrahigh resolution optical coherence tomography imaging with a broadband superluminescent diode light source. Opt. Exp. **12**, 2112–2119 (2004)
29. D.S. Adler, T.H. Ko, A.K. Konorev, D.S. Mamedov, V.V. Prokhorov, J.J. Fujimoto, S.D. Yakubovich, Broadband light source based on quantum-well superluminescent diodes for high-resolution optical coherence tomography. Quantum Electron. **34**, 915–918 (2004)
30. B. Bouma, G.J. Tearney, S.A. Boppart, M.R. Hee, M.E. Brezinski, J.G. Fujimoto, High-resolution optical coherence tomographic imaging using a mode-locked Ti-Al2O3 laser source. Opt. Lett. **20**, 1486–1488 (1995)
31. U. Morgner, F.X. Kärtner, S.H. Cho, Y. Chen, H.A. Haus, J.G. Fujimoto, E.P. Ippen, Scheuer, G. Angelow, T. Tschudi, Sub-two-cycle pulses from a Kerr-lens mode-locked Ti:sapphire laser. Opt. Lett. **24**, 411–413 (1999)
32. W. Drexler, U. Morgner, R.K. Ghanta, J.S. Schuman, F.X. Kärtner, M.R. Hee, E.P. Ippen, J.G. Fujimoto, New technology for ultrahigh resolution optical coherence tomography of the retina, in *The Shape of Glaucoma,* eds. by H. Lemij, J.S. Schuman (2000), Kugler, The Hague, Netherlands, pp. 75–104

33. A.M. Kowalevicz, T.R. Schibli, F.X. Kärtner, J.G. Fujimoto, Ultralow-threshold Kerr-lens mode-locked Ti: Al_2O_3 laser. Opt. Lett. **27**, 2037–2039 (2002)
34. S. Uemura, K. Torizuka, Generation of 10 f. pulses from a diode-pumped Kerr-lens mode-locked Cr:LiSAF laser. Jpn. J. Appl. Phys. **39**, 3472 (2000)
35. I. Sorokina, E. Sorokin, E. Wintner, A. Cassanho, H.P. Jensen, R. Szipöcz, 14-fs pulse generation in Kerr-lens mode-locked prismless Cr:LiSGaf and Cr:LiSAF lasers: observation of pulse self-frequency shift. Opt. Lett. **22**, 1716–1718 (1997)
36. P.C. Wagenblast, U. Morgner, F. Grawert, T.R. Schibli, F.X. Kärtner, V. Scheuer, G. Angelow, M.J. Lederer, Generation of sub-10-fs pulses from a Kerr-lens mode-locked Cr 3+: LiCAF laser oscillator by use of third-order dispersion-compensating double-chirped mirrors. Opt. Lett. **27**, 1726–1728 (2002)
37. P.C. Wagenblast, T.H. Ko, J.G. Fujimoto, F.X. Kaertner, U. Morgner, Ultrahigh-resolution optical coherence tomography with a diode-pumped broadband Cr3+: LiCAF laser. Opt. Exp. **12**, 3257–3263 (2004)
38. T.H. Ko, J.G. Fujimoto, J.S. Duker, L.A. Paunescu, W. Drexler, C.R. Baumal, C.A. Puliafito, E. Reichel, A.H. Rogers, J.S. Schuman, Comparison of ultrahigh- and standard-resolution optical coherence tomography for imaging macular hole pathology and repair. Ophthalmology **111**, 2033–2043 (2004)
39. E. Ergun, B. Hermann, M. Wirtitsch, A. Unterhuber, T.H. Ko, H. Sattmann, C. Scholda, J.G. Fujimoto, M. Stur, W. Drexler, Assessment of central visual function in Stargardt's disease/fundus flavimaculatus with ultrahigh-resolution optical coherence tomography. Invest. Ophthalmol. Vis. Sci. **46**, 310–316 (2005)
40. G. Wollstein, L.A. Paunescu, T.H. Ko, J.G. Fujimoto, A. Kowalevicz, I. Hartl, S. Beaton, H. Ishikawa, C. Mattox, O. Singh, J. Duker, W. Drexler, J.S. Schuman, Ultrahigh-resolution optical coherence tomography in glaucoma. Ophthalmology **112**, 229–237 (2005)
41. T.H. Ko, J.G. Fujimoto, J.S. Schuman, L.A. Paunescu, A.M. Kowalevicz, I. Hartl, W. Drexler, G. Wollstein, H. Ishikawa, J.S. Duker, Comparison of ultrahigh- and standard-resolution optical coherence tomography for imaging macular pathology. Ophthalmology **112**, 1922 (2005)
42. M.G. Wirtitsch, E. Ergun, B. Hermann, A. Unterhuber, M. Stur, C. Scholda, H. Sattmann, T.H. Ko, J.G. Fujimoto, W. Drexler, Ultrahigh resolution optical coherence tomography in macular dystrophy. Am. J. Ophthalmol. **140**, 976–983 (2005)
43. L.A. Paunescu, T.H. Ko, J.S. Duker, A. Chan, W. Drexler, J.S. Schuman, J.G. Fujimoto, Idiopathic juxtafoveal retinal telangiectasis: new findings by ultrahigh-resolution optical coherence tomography. Ophthalmology **113**, 48–57 (2006)
44. T.H. Ko, A.J. Witkin, J.G. Fujimoto, A. Chan, A.H. Rogers, C.R. Baumal, J.S. Schuman, W. Drexler, E. Reichel, J.S. Duker, Ultrahigh-resolution optical coherence tomography of surgically closed macular holes. Arch. Ophthalmol. **124**, 827–836 (2006)
45. C. Scholda, M. Wirtitsch, B. Hermann, A. Unterhuber, E. Ergun, H. Sattmann, T.H. Ko, J.G. Fujimoto, A.F. Fercher, M. Stur, U. Schmidt-Erfurth, W. Drexler, Ultrahigh resolution optical coherence tomography of macular holes. Retina **26**, 1034–1041 (2006)
46. A.J. Witkin, T.H. Ko, J.G. Fujimoto, A. Chan, W. Drexler, J.S. Schuman, E. Reichel, J.S. Duker, Ultra-high resolution optical coherence tomography assessment of photoreceptors in retinitis pigmentosa and related diseases. Am. J. Ophthalmol. **142**, 945–952 (2006)
47. M. Wojtkowski, T. Bajraszewski, P. Targowski, A. Kowalczyk, Real-time in vivo imaging by high-speed spectral optical coherence tomography. Opt. Lett. **28**, 1745–1747 (2003)
48. N. Nassif, B. Cense, B.H. Park, S.H. Yun, T.C. Chen, B.E. Bouma, G.J. Tearney, J.F. de Boer, In vivo human retinal imaging by ultrahigh-speed spectral domain optical coherence tomography. Opt. Lett. **29**, 480–482 (2004)
49. E.A. Swanson, D. Huang, M.R. Hee, J.G. Fujimoto, C.P. Lin, C.A. Puliafito, High-speed optical coherence domain reflectometry. Opt. Lett. **17**, 151–153 (1992)
50. R. Leitgeb, C.K. Hitzenberger, A.F. Fercher, Performance of fourier domain vs. time domain optical coherence tomography. Opt. Exp. **11**, 889–894 (2003)

51. J.F. de Boer, B. Cense, B.H. Park, M.C. Pierce, G.J. Tearney, B.E. Bouma, Improved signal-to-noise ratio in spectral-domain compared with time-domain optical coherence tomography. Opt. Lett. **28**, 2067–2069 (2003)
52. M.A. Choma, M.V. Sarunic, C.H. Yang, J.A. Izatt, Sensitivity advantage of swept source and Fourier domain optical coherence tomography. Opt. Exp. **11**, 2183–2189 (2003)
53. M. Wojtkowski, V.J. Srinivasan, T.H. Ko, J.G. Fujimoto, A. Kowalczyk, J.S. Duker, Ultrahigh-resolution, high-speed, Fourier domain optical coherence tomography and methods for dispersion compensation. Opt. Exp. **12**, 2404–2422 (2004)
54. R.A. Leitgeb, W. Drexler, A. Unterhuber, B. Hermann, T. Bajraszewski, T. Le, A. Stingl, A.F. Fercher, Ultrahigh resolution Fourier domain optical coherence tomography. Opt. Exp. **12**, 2156–2165 (2004)
55. B. Cense, N.A. Nassif, Ultrahigh-resolution high-speed retinal imaging using spectral-domain optical coherence tomography. Opt. Exp. **12**, 2435–2447 (2004)
56. V.J. Srinivasan, T.H. Ko, M. Wojtkowski, M. Carvalho, A. Clermont, S.E. Bursell, Q.H. Song, J. Lem, J.S. Duker, J.S. Schuman, J.G. Fujimoto, Noninvasive volumetric imaging and morphometry of the rodent retina with high-speed, ultrahigh-resolution optical coherence tomography. Invest. Ophthalmol. Vis. Sci. **47**, 5522–5528 (2006)
57. K. Bizheva, A. Unterhuber, B. Hermann, B. Povazay, H. Sattmann, W. Drexler, A. Stingl, T. Le, M. Mei, R. Holzwarth, H.A. Reitsamer, J.E. Morgan, A. Cowey, Imaging ex vivo and in vitro brain morphology in animal models with ultrahigh resolution optical coherence tomography. J. Biomed. Opt. **9**, 719–724 (2004)
58. K. Bizheva, A. Unterhuber, B. Hermann, B. Povazay, H. Sattmann, A.F. Fercher, W. Drexler, M. Preusser, H. Budka, A. Stingl, T. Le, Imaging ex vivo healthy and pathological human brain tissue with ultra-high-resolution optical coherence tomography. J. Biomed. Opt. **10**, 11006-1-7 (2005)
59. J.M. Schmitt, S.H. Xiang, K.M. Yung, Speckle in optical coherence tomography. J. Biomed. Opt. **4**, 95–105 (1999)
60. F.A. Sadjadi, Perspective on techniques for enhancing speckle imagery. Opt. Eng. **29**, 25 (1990)
61. A.R. Tumlinson, L.P. Hariri, U. Utzinger, J.K. Barton, Miniature endoscope for simultaneous optical coherence tomography and laser-induced fluorescence measurement. Appl. Opt. **43**, 113–121 (2004)
62. X.M. Liu, M.J. Cobb, Y.C. Chen, M.B. Kimmey, X.D. Li, Rapid-scanning forward-imaging miniature endoscope for real-time optical coherence tomography. Opt. Lett. **29**, 1763–1765 (2004)
63. A.R. Tumlinson, J.K. Barton, B. Povazay, H. Sattman, A. Unterhuber, R.A. Leitgeb, W. Drexler, Endoscope-tip interferometer for ultrahigh resolution frequency domain optical coherence tomography in mouse colon. Opt. Exp. **14**, 1878–1887 (2006)
64. A.R. Tumlinson, B. Povazay, L.P. Hariri, J. McNally, A. Unterhuber, B. Hermann, H. Sattmann, W. Drexler, J.K. Barton, In vivo ultrahigh-resolution optical coherence tomography of mouse colon with an achromatized endoscope. J. Biomed. Opt. **11**, 064003 (2006)
65. J.M. Schmitt, A. Knuttel, M. Yadlowsky, M.A. Eckhaus, Optical-coherence tomography of a dense tissue – statistics of attenuation and backscattering. Phys. Med. Biol. **39**, 1705–1720 (1994)
66. B.E. Bouma, G.J. Tearney, I.P. Bilinsky, B. Golubovic, J.G. Fujimoto, Self-phase-modulated Kerr-lens mode-locked Cr: forsterite laser source for optical coherence tomography. Opt. Lett. **21**, 1839–1841 (1996)
67. C. Chudoba, J.G. Fujimoto, E.P. Ippen, H.A. Haus, U. Morgner, F.X. Kärtner, V. Scheuer, G. Angelow, T. Tschudi, All-solid-state Cr: forsterite laser generating 14-fs pulses at 1.3 μm. Opt. Lett. **26**, 292–294 (2001)
68. K. Bizheva, B. Považay, B. Hermann, H. Sattmann, W. Drexler, M. Mei, R. Holzwarth, T. Hoelzenbein, V. Wacheck, H. Pehamberger, Compact, broad-bandwidth fiber laser for sub-2-mu m axial resolution optical coherence tomography in the 1300-nm wavelength region. Opt. Lett. **28**, 707–709 (2003)

69. L. Pantanowitz, P.L. Hsiung, T.H. Ko, K. Schneider, P.R. Herz, J.G. Fujimoto, S. Raza, J.L. Connolly, High-resolution imaging of the thyroid gland using optical coherence tomography. Head Neck **26**, 425–434 (2004)
70. P.L. Hsiung, L. Pantanowitz, A.D. Aguirre, Y. Chen, D. Phatak, T.H. Ko, S. Bourquin, S.J. Schnitt, S. Raza, J.L. Connolly, H. Mashimo, J.G. Fujimoto, Ultrahigh-resolution and 3-dimensional optical coherence tomography ex vivo imaging of the large and small intestines. Gastrointest. Endosc. **62**, 561–574 (2005)
71. P.R. Herz, Y. Chen, A.D. Aguirre, J.G. Fujimoto, H. Mashimo, J. Schmitt, A. Koski, J. Goodnow, C. Petersen, Ultrahigh resolution optical biopsy with endoscopic optical coherence tomography. Opt. Exp. **12**, 3532–3542 (2004)
72. Y. Chen, A.D. Aguirre, P.L. Hsiung, S. Desai, P.R. Herz, M. Pedrosa, Q. Huang, M. Figueiredo, S.W. Huang, A. Koski, J.M. Schmitt, J.G. Fujimoto, H. Mashimo, Ultrahigh resolution optical coherence tomography of Barrett's esophagus: preliminary descriptive clinical study correlating images with histology. Endoscopy **39**, 599–605 (2007)
73. J.K. Ranka, R.S. Windeler, A.J. Stentz, Visible continuum generation in air-silica microstructure optical fibers with anomalous dispersion at 800 nm. Opt. Lett. **25**, 25–27 (2000)
74. T.A. Birks, W.J. Wadsworth, P.S.J. Russel, Generation of an ultra-broad supercontinuum in tapered fibers. Opt. Lett. **25**, 1415–1417 (2000)
75. I. Hartl, X.D. Li, C. Chudoba, R.K. Ghanta, T.H. Ko, J.G. Fujimoto, J.K. Ranka, R.S. Windeler, Ultrahigh-resolution optical coherence tomography using continuum generation in an air-silica microstructure optical fiber. Opt. Lett. **26**, 608–610 (2001)
76. Y.M. Wang, J.S. Nelson, Z.P. Chen, B.J. Reiser, R.S. Chuck, R.S. Windeler, Optimal wavelength for ultrahigh-resolution optical coherence tomography. Opt. Exp. **11**, 1411–1417 (2003)
77. S. Bourquin, A.D. Aguirre, I. Hartl, P. Hsiung, T.H. Ko, J.G. Fujimoto, T.A. Birks, W.J. Wadsworth, U. Bunting, D. Kopf, Ultrahigh resolution real time OCT imaging using a compact femtosecond Nd: glass laser and nonlinear fiber. Opt. Exp. **11**, 3290–3297 (2003)
78. P.L. Hsiung, D.R. Phatak, Y. Chen, A.D. Aguirre, J.G. Fujimoto, J.L. Connolly, Benign and malignant lesions in the human breast depicted with ultrahigh resolution and three-dimensional optical coherence tomography. Radiology **244**, 865–874 (2007)
79. B. Považay, K. Bizheva, A. Unterhuber, B. Hermann, H. Sattmann, A.F. Fercher, W. Drexler, A. Apolonski, W.J. Wadsworth, J.C. Knight, P.S.J. Russell, M. Vetterlein, E. Scherzer, Submicrometer axial resolution optical coherence tomography. Opt. Lett. **27**, 1800–1802 (2002)

Ultrahigh Speed OCT

10

Ireneusz Grulkowski, Jonathan J. Liu, Benjamin Potsaid, Vijaysekhar Jayaraman, Alex E. Cable, and James G. Fujimoto

Keywords

Optical coherence tomography • Vertical cavity surface-emitting laser • Ophthalmic imaging • Optical coherence microscopy • Ocular biometry • Profilometry

10.1 Introduction

Optical coherence tomography (OCT) is an imaging modality that can generate micrometer resolution, two-dimensional cross-sectional images, and three-dimensional volumetric data on the internal structure of optically scattering and reflective tissues and materials. OCT has been integrated with a wide range of imaging devices and has numerous applications. First-generation OCT systems detected the time delay of optical echoes by mechanically scanning the path length of an interferometer reference arm (time-domain OCT; TD-OCT) [1]. The development of Fourier-domain detection enabled a breakthrough in OCT imaging

I. Grulkowski (✉) • J.J. Liu • J.G. Fujimoto
Department of Electrical Engineering and Computer Science and Research Laboratory of Electronics, Massachusetts Institute of Technology, Cambridge, MA, USA
e-mail: igrulkowski@fizyka.umk.pl

B. Potsaid
Department of Electrical Engineering and Computer Science and Research Laboratory of Electronics, Massachusetts Institute of Technology, Cambridge, MA, USA

Advanced Imaging Group, Thorlabs Inc., Newton, NJ, USA

V. Jayaraman
Praevium Research Inc., Santa Barbara, CA, USA

A.E. Cable
Advanced Imaging Group, Thorlabs Inc., Newton, NJ, USA

© Springer International Publishing Switzerland 2015

W. Drexler, J.G. Fujimoto (eds.), *Optical Coherence Tomography*,
DOI 10.1007/978-3-319-06419-2_11

sensitivity and speed. The performance advantages of Fourier-domain OCT were recognized independently by several research groups in 2003 [2–5]. Although most current commercial OCT instruments are built with spectrometers and line-scan cameras (spectral/Fourier-domain OCT; SD-OCT), the newest generation of OCT is based on wavelength swept light sources (swept source/Fourier-domain OCT; SS-OCT) [4, 6–8]. The advantages offered by SS-OCT are especially important for in vivo biomedical imaging applications, yet SS-OCT can also be applied to many other scientific disciplines and industrial applications.

SS-OCT uses high-speed, balanced photodetectors instead of a spectrometer and line-scan camera that is used in SD-OCT. SS-OCT detection losses are reduced compared with SD-OCT because of the higher detection efficiency of photodetectors. In addition, the parasitic signal roll-off with imaging depth which is present in SD-OCT can be significantly reduced in SS-OCT due to the coherence properties of tunable lasers and the ability to detect high-frequency signals with broad bandwidth detection and data acquisition systems. Moreover, SS-OCT systems imaging at 1,000 nm and 1,300 nm wavelengths, longer than typical wavelengths of 840 nm which are used in SD-OCT, enable better penetration of light and improved imaging depths in scattering tissues. These features allow greater optimization of OCT performance parameters, i.e., to achieve high imaging speeds, image deep tissue structures, and achieve long imaging range, which increases the functionality of OCT instruments and enables a broader range of applications.

Advances in swept laser technology have helped achieve high sweep rates, which have a number of important implications. High speeds enable decreasing the acquisition time for in vivo imaging to reduce motion artifacts. High speeds also enable the acquisition of more data to achieve denser sampling within a given acquisition time or a wider field of view for a given sampling density. Moreover, advances in imaging speed are critical for en face OCT imaging, providing a high-transverse resolution visualization perspective perpendicular to standard cross-sectional OCT images in volumetric (3-D) data sets. High-speed imaging is also enabling for functional imaging methods which extract additional contrast parameters from the OCT data. High speed facilitates techniques such as Doppler OCT which measures blood flow and OCT angiography which visualizes vasculature without requiring exogenous contrast agents. Finally, the measurement of dynamic structural and functional processes using 4-D (3-D + time) imaging, which require repeated acquisition of volumetric data sets as a function of time, is also possible with high-speed OCT technology.

SS-OCT imaging has recently benefited from advances in high bandwidth A/D systems and developments in laser technology. Using high bandwidth detection, it is possible to achieve imaging ranges that are not accessible with SD-OCT. The improvement in the instantaneous coherence length of swept light sources using microelectromechanical systems (MEMS technology) reduces parasitic sensitivity roll-off and enables more efficient use of the available imaging range and detection bandwidth. Extended imaging ranges make OCT a viable tool for imaging and measuring larger objects and enable new classes of applications, including large-scale 3-D profiling for nondestructive evaluation and metrology.

Finally, SS-OCT using new vertical cavity surface-emitting laser (VCSEL) light sources has the advantage that the wavelength sweep range and repetition rate can be adjusted in order to tailor the image resolution, imaging range, and imaging speed to match specific applications. Different operating modes of the system enable versatile functionalities and multimodal applications. This adjustability is not possible with SD-OCT because these operating parameters are set by the spectrometer optical design.

Wavelength swept lasers are a key technology for SS-OCT. One of the first wavelength swept lasers in 1997 used in OCT employed a cavity design with either a galvanometer-tuned grating or prism sequence, where 10 Hz and 2 kHz sweep repetition rates were achieved, respectively [6, 7]. Dramatic increases in speed were achieved when improved tuning elements such as dispersion prisms, rotating polygons, resonant scanning mirrors, diffraction gratings, and scanning Fabry-Perot filters were used [9–15]. Conventional tunable lasers use bulk optics or fiber components, which make resonators relatively long and therefore limit the sweep rate because of the long round trip time. This limitation was overcome using a new laser technique known as Fourier-domain mode locking (FDML) [16]. FDML lasers have long optical fiber cavities which store the entire sweep in the laser cavity, overcoming the laser buildup times which limit conventional swept lasers. Current swept laser designs can achieve MHz range sweep rates [17, 18]. Recent advances include the development of fully integrated lasers as well as miniaturization using microelectromechanical systems (MEMS) technology [19–24]. New swept light sources using vertical cavity surface-emitting laser (VCSEL) technology offer many advantages for OCT imaging [25–28]. The micron-scale cavity length of the VCSEL and the rapid MEMS response enable high imaging speeds as well as real-time adjustability of both the sweep rate and wavelength sweep range [29]. Moreover, the VCSEL operates with a single longitudinal mode instead of multiple modes and therefore has an extremely narrow instantaneous linewidth. This yields a very long coherence length and enables long imaging ranges. Therefore, MEMS-tunable VCSELs can serve as platform for the exploration and demonstration of both high-speed and long-range OCT imaging.

In this chapter, we will describe high-imaging speed and long-depth range SS-OCT with an emphasis on SS-OCT technology using VCSELs operating at 1,050 nm and 1,310 nm wavelengths. We will also review representative applications using high-speed and long-range SS-OCT including ophthalmic imaging (retinal, anterior segment, and full eye length imaging), optical coherence microscopy, endoscopy, ocular biometry, metrology, profilometry, and nondestructive material evaluation.

10.2 Swept Source OCT Technology

A schematic diagram of a typical SS-OCT imaging system and photograph of an ophthalmic prototype OCT instrument (designed and built at the Massachusetts Institute of Technology) are shown in Fig. 10.1. The VCSEL was designed and

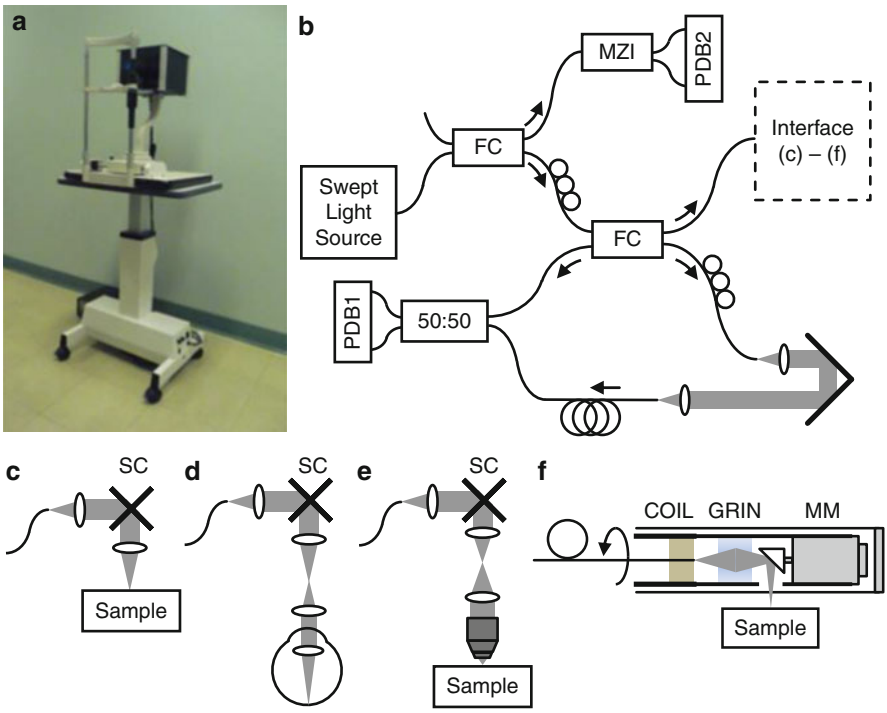

Fig. 10.1 SS-OCT system and examples of imaging interfaces. (**a**) Photograph of the SS-OCT ophthalmic interface. (**b**) Schematics of the SS-OCT system along with the different interface designs for (**c**) anterior segment, full eye length imaging and long-range OCT imaging, (**d**) retinal imaging, (**e**) SS-OCM, and (**f**) endoscopic imaging (micromotor probe). *FC* fiber coupler, *PDB1*/*PDB2* balanced photodetector, *MZI* Mach-Zehnder interferometer, *SC* galvanometric scanners, *COIL* torque coil, *GRIN* gradient index lens, *MM* micromotor

manufactured by Praevium Inc. and Thorlabs Inc. The output of the swept source laser was divided between the OCT interferometer and a sweep calibration Mach-Zehnder interferometer (MZI). The light entering the OCT interferometer was split into the sample and reference arms by a second fiber coupler. The sample arm of the OCT interferometer was attached to an imaging interface.

Figure 10.1 shows a schematic for a representative swept source imaging system at 1,050 nm wavelengths. The system uses a transmission geometry for the reference arm because high-quality optical circulators are not available at this wavelength. Several different OCT imaging systems were used to generate the data shown in this chapter. SS-OCT systems can be interfaced to microscopes, handheld imaging probes, as well as catheters and endoscopes. Different interface designs can be developed depending on the application (Fig. 10.1c–f). In the simplest microscope configuration, the interface has galvanometric scanners at the back focal length of a lens to provide telecentric scanning (Fig. 10.1c). This design is used to image the anterior segment and the full eye length as well as to image non-biomedical objects with long-range OCT. Retinal imaging requires an interface with an adapter lens to collimate the

incident beam on the eye and relay the beam scanning to pivot at the pupil of the eye (Fig. 10.1d) [30]. For swept source optical coherence microscopy (SS-OCM), the sample arm is interfaced to a scanning confocal microscope (Fig. 10.1e) [31]. The fiber output is collimated and relayed to the objective by a pair of compound lenses. Objectives with 10×, 20×, and 40× magnifications can be used, thereby enabling imaging with different fields of view and transverse resolutions. Another example configuration shown in Fig. 10.1f is a micromotor-based miniature catheter for ultrahigh-speed endoscopic OCT imaging [32]. The OCT beam was focused by a fiber-GRIN lens assembly, reflected by the rotating microprism, and focused outside the catheter sheath. The motor and GRIN lens are mounted inside a metal hypotube, and the entire assembly is covered by a transparent plastic sheath. The rotating optics could be pulled back within the sheath to produce a spiral volumetric scan pattern. The endoscopic configuration operated at 1,310 nm wavelength, and circulators were used in the interferometer for improved light collection efficiency.

In the SS-OCT configuration shown in Fig. 10.1b, light from the sample and reference arms was interfered with a fiber coupler and the signal was detected by a high-speed, dual-balanced InGaAs photodetector receiver PDB1. The photodetector signal was digitized by a high-speed A/D converter. A trigger for starting sweep acquisition was synchronized with the MEMS VCSEL. A second dual-balanced photodiode PDB2 detected interference fringes from an MZI to generate an optical clock signal. When fixed frequency A/D clocking is used, the MZI signal is used to recalibrate the OCT interference fringes, i.e., to resample the OCT signal from constant time interval to evenly sampled frequency or wave number before Fourier transforming to obtain the axial scan. If optical clocking is used, the MZI generates the optical clock signal with a constant frequency or wavenumber interval determined by the MZI delay. Several A/D acquisition boards (digitizers) were used including a 12-bit 500MSPS A/D converter (ATS9350; Alazar Technologies Inc.) and 8-bit card 1GSPS A/D converter (ATS9870; Alazar Technologies Inc.).

Frequency swept lasers are a core technology for SS-OCT. The studies presented in this chapter were performed with two types of swept light sources utilizing MEMS technology: a short cavity laser (Axsun Technologies Inc.) and a vertical cavity surface-emitting laser (VCSEL, Praevium Inc./Thorlabs Inc.). The short cavity laser had few centimeter cavity lengths and was tuned with an MEMS-tunable Fabry-Perot filter. The VCSEL had a micrometer length cavity and was tuned with a movable MEMS cavity mirror. The micrometer cavity length means that only one longitudinal mode is within the laser gain bandwidth. Single mode operation and absence of mode hopping makes the VCSEL coherence length extremely long and significantly reduces parasitic sensitivity roll-off with imaging range. The coherence length of the VCSEL was compared with an MEMS Fabry-Perot tunable short cavity laser by acquiring interference signals from a Mach-Zehnder interferometer with high bandwidth oscilloscope. Figure 10.2 shows sensitivity versus depth, where the total optical path delay is two times the depth. The VCSEL light source coherence length exceeds 1 m (measurement limited by the oscilloscope bandwidth), whereas the commercial MEMS Fabry-Perot tunable short cavity laser has a coherence length of ~12 mm.

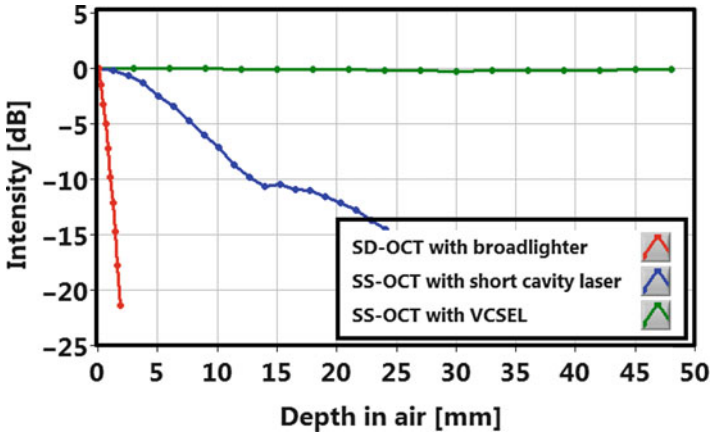

Fig. 10.2 Comparison of the parasitic sensitivity roll-off with depth: MEMS-tunable short cavity laser (sweep rate 100 kHz, tuning range 100 nm), MEMS VCSEL (sweep rate 50 kHz, tuning range 45 nm), and typical high-resolution SD-OCT (810 nm broadband light source)

10.3 High-Speed Imaging with SS-OCT

10.3.1 Imaging Speed in OCT

The imaging speed in OCT is typically specified as the axial scan rate or number of axial scans acquired per unit time. Imaging speed also governs the system sensitivity, i.e., the ability to detect weak signals trades off with increased imaging speed. The imaging speed and the resulting acquisition time is one of the key parameters for ophthalmic imaging as well as many other in vivo imaging applications. With the maturation in OCT technology, systems with higher and higher speeds have become available. The imaging speed in TD-OCT is determined by the periodic mechanical scanning of the reference arm. In practice, TD-OCT instruments are unable to reach speeds higher than ~2 kHz due to mechanical limitations in the reference arm as well as limitations in detection sensitivity [33]. In SD-OCT, imaging speed is determined by the reading speed of the line-scan camera in the spectrometer. Early SD-OCT instruments operated at 19 kHz axial scan rates, but the development of new line-scan camera technology allowed significant increases in speed so that current SD-OCT systems can operate at more than 100 kHz rates [34]. On the other hand, the imaging speed in SS-OCT is determined by the sweep repetition rate of the swept light source, and modern systems can achieve MHz axial scan rates [18, 26, 32, 35].

Different techniques have been developed to increase OCT imaging speed. The use of multiple beams in the sample arm enabled multiplication of the effective speed, although this approach is complex and requires more sophisticated hardware [18, 22, 36–38]. A parallel solution in SD-OCT is to use a dual-camera system which doubles the acquisition speed [39]. Multiboard acquisition and optical

demultiplexing has been used to achieve speeds of 60,000,000 axial scans per second [40]. Using certain swept light sources, it is possible to obtain higher SS-OCT imaging speeds by more efficient usage of the sweep duty cycle. In this approach, imaging speeds can be increased by using both forward and backward sweeps or buffering to combine time-delayed copies of the sweep [16, 22, 41].

10.3.2 High-Speed Retinal SD-OCT and SS-OCT Imaging

The most common application of OCT is retinal imaging. OCT enables imaging the morphology of retinal layers in the fovea and optic disc regions for diagnosis and monitoring therapeutic response in diseases such as age-related macular degeneration, glaucoma, and diabetic retinopathy. Initial retinal TD-OCT instruments had imaging speeds of a few hundred axial scans per second [1, 42, 43]. The introduction of Fourier-domain detection resulted in a sensitivity increase of 50–100 times over previous time-domain technology. These increases in speed enabled dramatic improvements in image quality and retinal coverage, as well as three-dimensional OCT (3-D OCT) imaging. SD-OCT retinal imaging was first demonstrated by Wojtkowski et al. in 2002 [44]. With high-speed line-scan cameras, studies demonstrating SD-OCT at 26,000–29,000 axial scans per second were reported by several groups [45–47]. Ultrahigh SD-OCT imaging speeds of >300,000 axial scans per second were demonstrated by Potsaid et al. in 2008 using advanced CMOS camera technology [34]. Meanwhile, SS-OCT has also undergone similar development. The first SS-OCT retinal instruments operated at imaging speeds of 19,000 axial scans per second [6]. With the advent of new laser technologies, ultrahigh-speed OCT imaging of the retina became possible. Although fundamental laser sweep rates reach 400 kHz, different methods to increase the effective sweep rate were developed including buffering or simultaneous multi-spot imaging. These advances enabled imaging at the rates of several MHz [18, 48]. With these technological improvements, the term “high-speed imaging” was extended to hundreds of thousands of axial scans per second and the term “ultrahigh-speed imaging” referred to speeds which approach ∼1,000,000 axial scans per second [18]. By contrast, current commercial retinal SD-OCT and SS-OCT instruments at 840 nm and 1,050 nm wavelengths have imaging speeds of up to ∼100 kHz.

High acquisition speeds enable 3-D OCT volumetric imaging by raster scanning multiple cross-sectional images. Unlike standard ophthalmic examination techniques such as fundus photography, OCT provides depth-resolved information and enables visualization of 3-D retinal structure. Volumetric data sets provide detailed structural information on the retina that is unavailable with other imaging modalities. The volumetric data sets can be displayed in multiple ways. Figure 10.3 shows SS-OCT retinal imaging with a short cavity laser at 1,050 nm wavelength. Methods of OCT data presentation include 3-D rendering, cross-sectional images, and en face views (OCT projection and C-scan images). Another advantage of 3-D OCT imaging is the ability to extract arbitrary (virtual) cross-sectional images which are precisely registered to retinal fundus features. OCT retinal fundus images

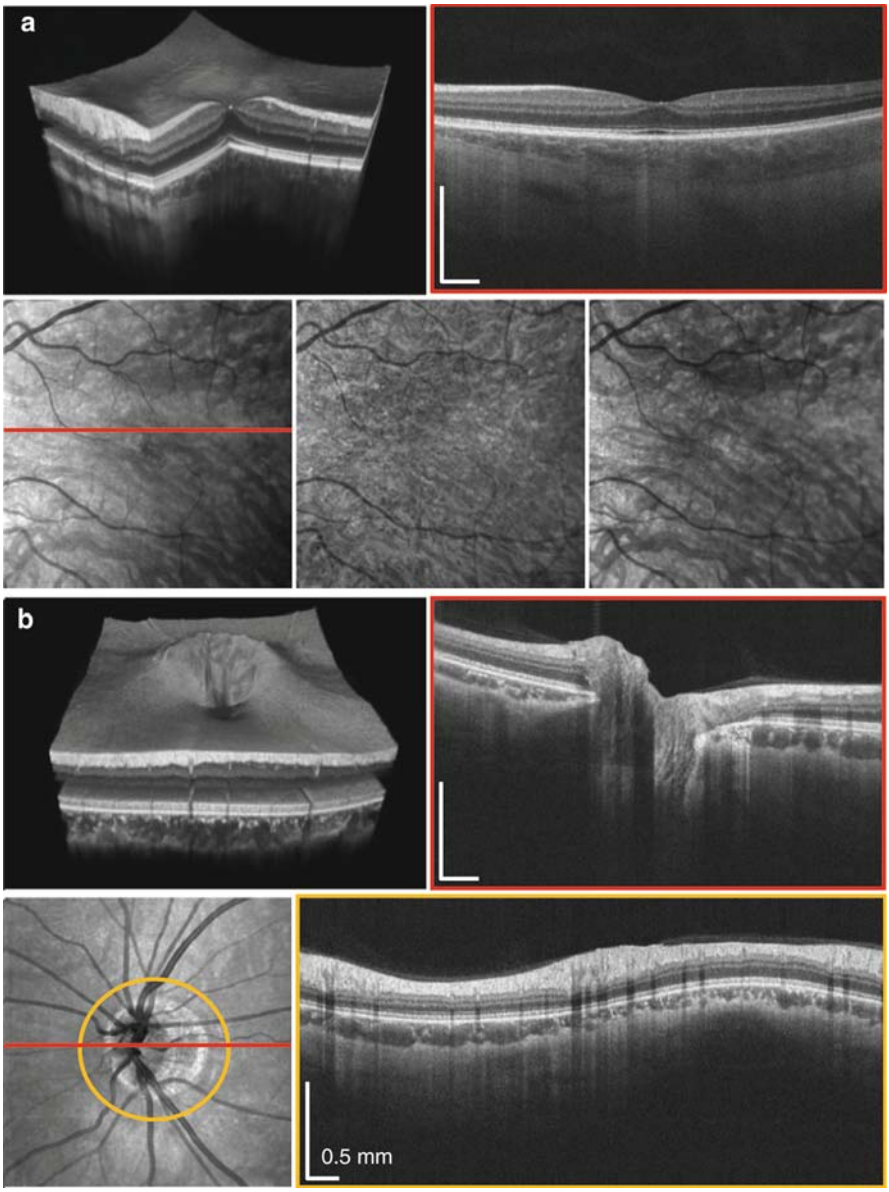

Fig. 10.3 Volumetric SS-OCT retinal imaging at 1,050 nm of the macula (**a**) and optic nerve head (**b**) at 1,050 nm wavelength. 3-D data sets enables generation of generating volumetric renderings, OCT fundus images, different cross-sectional images, and C-scans or en face images. Two perpendicularly scanned data sets, each with 700 × 700 axial scans, were acquired at 100 kHz, and an OCT motion correction algorithm was applied to remove motion artifacts

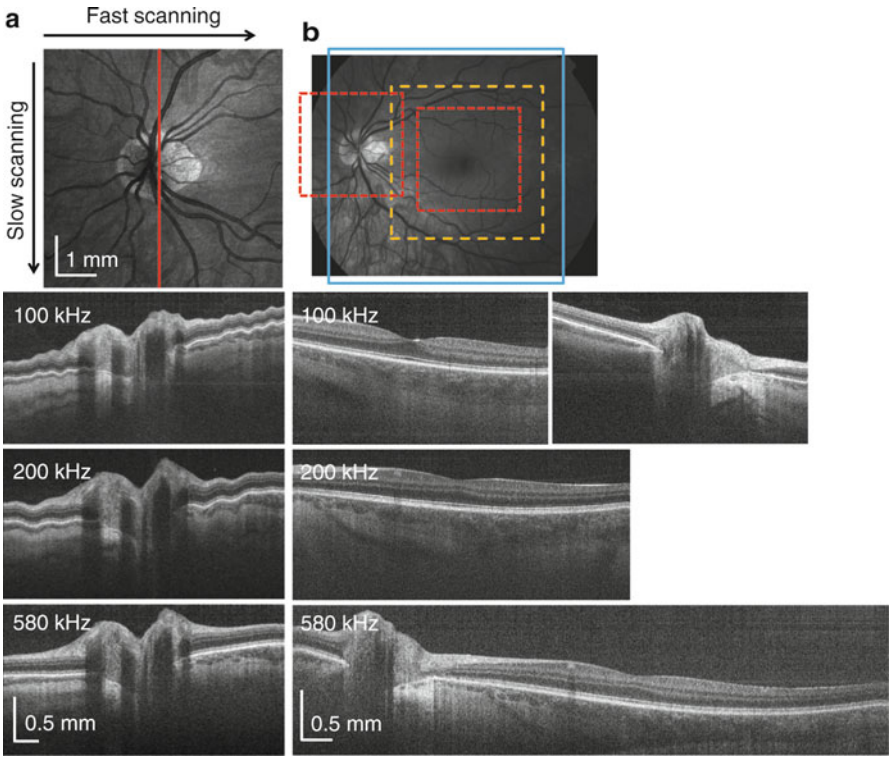

Fig. 10.4 Retinal OCT imaging using SS-OCT with a VCSEL light source. (**a**) Imaging of the optic nerve head region at different speeds. Extracted central cross sections in the slow scan direction, perpendicular to the raster scan directions, show reduced motion artifacts with increased speed. In each case, the data consisted of 500 × 500 axial scans from a 6 × 6 mm^2 area. (**b**) Impact of the imaging speed on retinal coverage. Red-free fundus photograph indicates scanned areas at different speeds. Selected cross sections from volumetric data sets acquired at 100 kHz, 200 kHz, and 580 kHz. Transverse sampling density and acquisition time are kept constant. Aspect ratios of all cross sections are the same (From Ref. [30])

can be obtained by summing the entire signal in axial direction. Other types of en face images include projection views that can be generated either by choosing specific depth level or by integrating the signal from selected depth range [49]. The wide variety of data presentation options enhances the diagnostic utility of 3-D OCT imaging in clinical practice and forms a basis for quantitative data analysis.

Eye and head motion during acquisition generates artifacts in OCT images. Different approaches have been developed to minimize or compensate motion artifacts, including reducing acquisition times, software-based methods (e.g., OCT registration and motion correction) [50], and hardware techniques (e.g., eye tracking) [51]. Ultrahigh imaging speeds enable rapid acquisition of dense volumetric data to reduce motion artifacts. Figure 10.4a shows 3-D OCT data sets of the

optic nerve head of the same subject acquired at three different speeds. Since the lateral scanning density (500 axial scans and 500 B-scans over a 6 × 6 mm^2 retina area) was kept constant, different axial scan rates resulted in reduced acquisition times ranging from 2.6 to 0.5 s. Fundus features were used to confirm that corresponding cross-sectional OCT images are extracted from the same position for comparison. These data demonstrate that motion artifacts in the slow scan direction, perpendicular to the raster, are significantly reduced as the imaging speed increases.

High-speed OCT imaging of the retina also enables better retinal coverage for a given sampling density. This feature of high-speed imaging is shown in Fig. 10.4b. Volumetric OCT data sets were acquired by raster scanning at axial scan rates of 100 kHz, 200 kHz, and 580 kHz. Fundus views and corresponding cross-sectional images are presented. A measurement time of ∼2 s was used for each volume, consistent with a typical clinically acceptable acquisition time. The data sets comprise of 400 × 400, 600 × 600, and 1,000 × 1,000 axial scans and cover areas of 5 × 5 mm^2, 7 × 7 mm^2, and 12 × 12 mm^2 at the sweep rates of 100 kHz, 200 kHz, and 580 kHz, respectively. Whereas at 100 kHz the scanned area requires separate acquisitions for the central macular region versus the optical nerve head, imaging at 580 kHz enables an almost sixfold increase in scanned area covering both the macular region and optical nerve head in a single scanned area. In this case, a wide-field OCT coverage comparable to standard fundus photography is achieved (Fig. 10.5b compared to Figs. 10.4a and 10.5h), and the sampling density in the transverse direction is high enough to image focal retinal pathologies. Whereas fundus photographs reveal two-dimensional information, OCT volumetric data can be used to display cross-sectional and en face projections of different retinal and choroidal layers. Cross-sectional images in Fig. 10.4 demonstrate the ability to visualize deep choroidal layers, the choroid-scleral interface, and even scleral vasculature due to the high sensitivity and deep image penetration at 1,000 nm wavelengths. Axial summation of the OCT signal intensity from 40 μm thick slices at different depths below the retinal pigment epithelium (RPE) was used to generate projection OCT en face images of the choroid. OCT projection images corresponding to the chriocapillaris, Sattler's layer, and Haller's layer can be identified and characterized by choroidal structure and vasculature appearance, as shown in Fig. 10.5 d–g.

Standard clinical angiographic modalities require intravenous administration of dyes such as fluorescein or indocyanine green (ICG). However, OCT can be used to visualize vascular networks and generate images analogous to angiography without the need for exogenous contrast agents. This complementary information can be obtained from the same OCT data sets. Figure 10.5 c, h–k show comparisons of ICG angiography and OCT intensity-based retinal and choroidal images. Since retinal vessels generate shadows in OCT cross-sectional images, it is possible to increase contrast in a projection image by summing the intensity from a 50 μm thick layer around the RPE. On the other hand, choroidal vasculature can be visualized by using an inverted gray scale in the projection image of the signal below the RPE. Due to shadowing effects, retinal vessels also appear in the choroidal vasculature

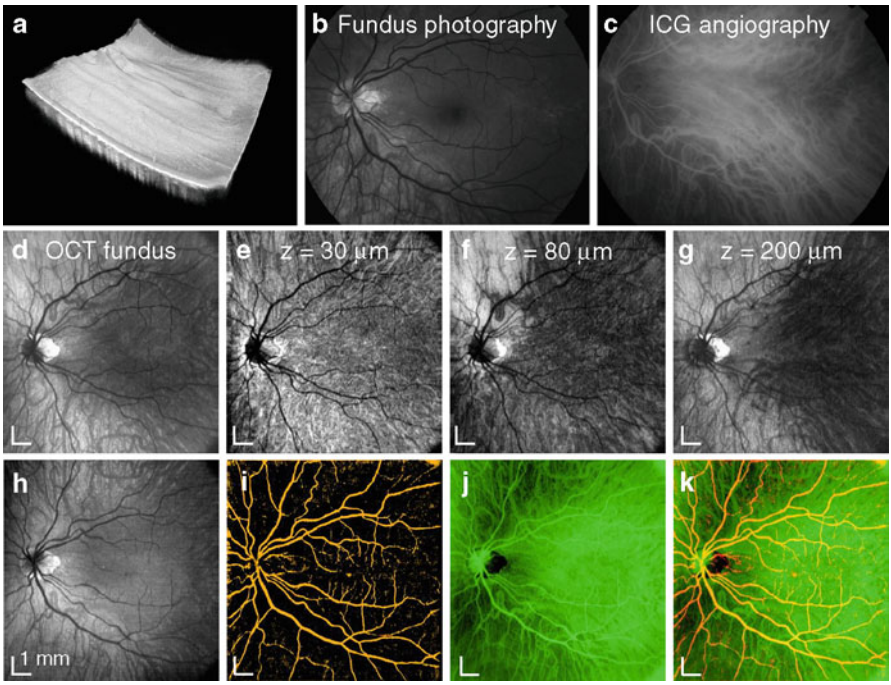

Fig. 10.5 Wide-field choroidal OCT imaging using SS-OCT with a VCSEL light source. (**a**) Rendering of a volumetric wide-field data set. (**b**) Red-free fundus photography and (**c**) indocyanine green (ICG) angiography of the same subject. (**d**) OCT fundus image. (**e**) – (**g**) OCT projection images at different depths below RPE showing choroidal layers and sclera. The OCT signal was integrated from 40 µm thick slices. (**h**) OCT wide-field fundus image. OCT angiographic images showing: (**i**) segmented retinal, (**j**) choroidal vasculature and (**k**) combined angiographic image. (From Ref. [30])

en face image. Volumetric OCT data can be used to visualize vascular networks in the eye by a combination of retinal and choroidal projection OCT images. In addition, a variety of Doppler and angiographic OCT methods have been developed that can measure flow using the Doppler phase shift or enhance the contrast of vasculature using phase variance or intensity speckle decorrelation [52–62].

10.3.3 High-Speed Anterior Segment Imaging with SS-OCT

Imaging the anterior segment of the eye requires a combination of long depth range and high imaging speed to obtain clinically useful information. Generally speaking, the challenge of anterior segment OCT imaging comes from the fact that the anterior segment has multiple structures: some of which are anatomically thick, others are heavily pigmented, and one, the cornea, has steep curvature. Additionally, as in other ophthalmic applications, high acquisition speeds are important to minimize motion artifacts.

The first demonstration of anterior segment OCT imaging was performed in 1994 by Izatt et al. [63]. Multiple studies demonstrated time-domain OCT and Fourier-domain OCT for anterior segment imaging at different wavelengths and speeds [11, 22, 64–68]. Challenges encountered in SD-OCT could be addressed by reducing parasitic sensitivity roll-off and improving light penetration into tissue [69, 70]. These requirements can also be fulfilled by SS-OCT technology which offers better performance over SD-OCT at wavelengths longer than the traditional 840 nm used for retinal imaging [4]. Light at wavelengths longer than 840 nm exhibits less scattering and therefore enables deeper imaging [71, 72]. The first SS-OCT systems for anterior segment imaging utilized light sources at 1,300 nm wavelength, and the imaging speed increased from 20 to 200 kHz [11, 66]. Recent demonstrations of anterior segment imaging achieved imaging speeds of 1,600 kHz at 1,310 nm wavelength and 100 kHz at 1,050 nm wavelength [22, 73]. Finally, SD-OCT and SS-OCT systems for simultaneous anterior segment and retinal imaging have also been demonstrated [74, 75].

High-speed and reduced parasitic sensitivity roll-off is important for 3-D imaging of the anterior eye. Figure 10.6a shows a rendering of a volumetric data set covering a 13 × 13 mm^2 area of the anterior eye. The volume consists of 500 × 500 axial scans acquired in 2.6 s. The en face image of the anterior segment reveals a rhombus-like polarization artifact from the cornea. Due to the long coherence length of the VCSEL light source, there is virtually no parasitic sensitivity roll-off. This enables direct visualization of the entire anterior segment. The cross-sectional image in Fig. 10.6a shows the cornea, iris, and entire crystalline lens and spans the entire transverse width of the anterior chamber, from limbus to limbus. The crystalline lens is not an optically homogenous structure; the nucleus and cortex can be distinguished. It should be noted that anterior segment OCT images do not display the true shape of the eye unless refraction correction algorithms are used. The refraction-corrected cross-sectional image where the OCT beam propagation direction has been corrected using the interfaces and refractive indices of ocular structures is also shown. The uncorrected image has an artificial posterior displacement of the iris and anterior lens which is produced by refraction of the OCT beam at the air-corneal interface, while the refraction-corrected image displays the iris and anterior lens in their true anatomical positions.

The same scanning protocol was applied to scan the eye of a subject after cataract surgery. As shown in the en face image in Fig. 10.6b, the intraocular lens (IOL) causes strong reflections in OCT images. Visualization of 3-D data enables identification of regions with floaters behind the posterior IOL surface.

In addition to wide-field OCT, scanning can be performed over specific structures such as the limbus and anterior chamber angle [76]. Figure 10.6c shows corneoscleral imaging of the anterior eye. This does not require long imaging range, and therefore the system was operated at 100 kHz in high-resolution mode, similar to that used for retinal imaging. The volumetric data set consisted of 500 × 500 axial scans and covered a 7 × 7 mm^2 area. This dense scan over the anterior chamber angle enabled visualization of the limbal region along with

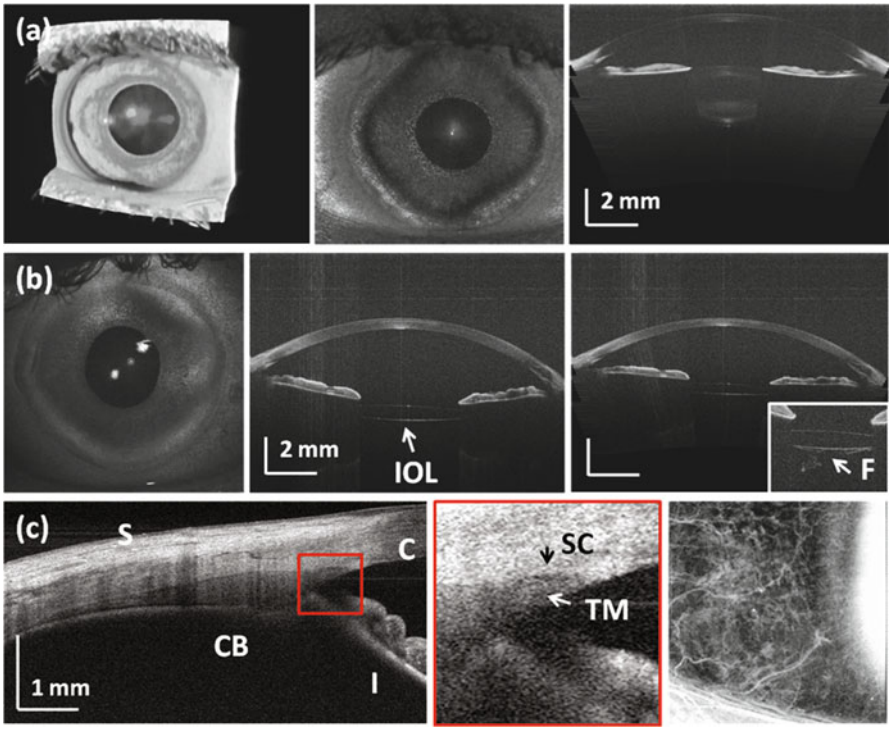

Fig. 10.6 Anterior segment imaging with SS-OCT. (**a**) Volumetric rendering, en face OCT, and cross section taken from the volumetric OCT data of a healthy subject. (**b**) En face OCT and cross-sectional images of an eye after cataract surgery and intraocular lens (*IOL*) implantation (*F* floaters). (**c**) Cross section and en face image of the corneoscleral junction with enlargements showing Schlemm's canal and scleral vasculature (*S* sclera, *CB* ciliary body, *C* cornea, *I* iris, *SC* Schlemm's canal, *TM* trabecular meshwork)

landmarks such as the corneoscleral junction and rich scleral vasculature. Elements of the outflow system such as Schlemm's canal can also be identified.

After refraction correction of anterior segment OCT data sets, qualitative 3-D structure can be accurately visualized and quantitative information about the shape of ocular structures can be extracted. Figure 10.7 shows example maps of clinically relevant parameters which can be measured from 3-D OCT data. Mapping biometric parameters is important for the diagnosis of ocular diseases as well as in pre-and postoperative assessment of the eye for keratorefractive surgery or IOL implant.

10.3.4 Dynamics of the Anterior Segment of the Eye and 4-D OCT Imaging

Apart from its structural complexity, the eye is also a highly dynamic organ that can adapt to changing conditions and provide the best optical imaging of objects

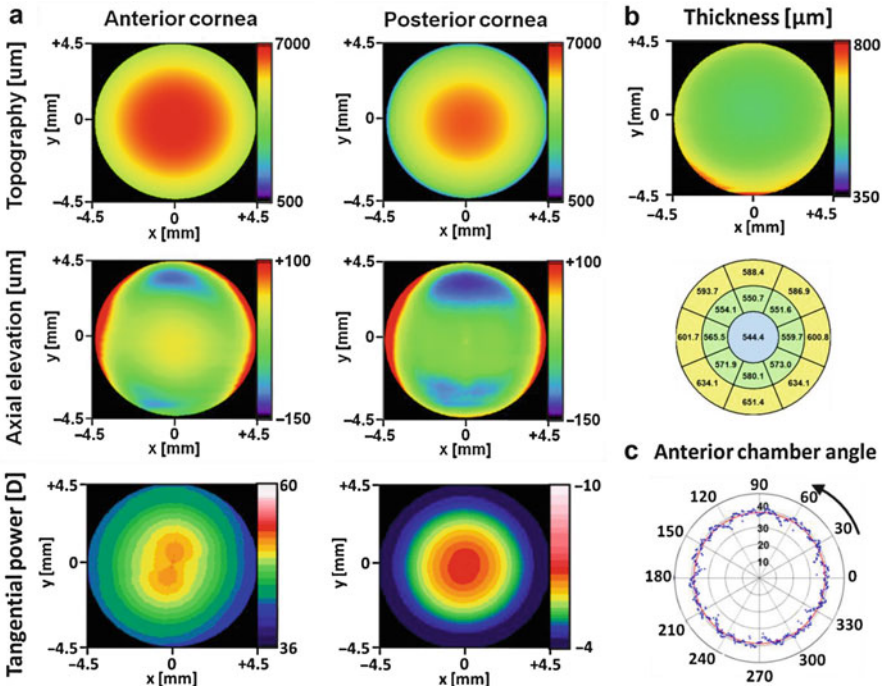

Fig. 10.7 OCT ocular biometry. (**a**) Topography, elevation, and tangential power (keratometry) maps of both corneal surfaces obtained from 3-D OCT data. (**b**) Corneal thickness map and corresponding sector map showing average thickness in central (0–3 mm diameter), paracentral (3–6 mm diameter annulus), and pericentral (6–9 mm diameter annulus) region. (**c**) Polar plot of anterior chamber angle for different meridionals. Mean anterior chamber angle is shown in *red*

onto the retina. Ultrahigh-speed OCT enables visualization of dynamic processes within the eye [77]. Studies of dynamic processes are an important indicator of ocular functionality and can be performed using rapid, repeated volumetric scanning in time. This demanding scanning mode combines 3-D scanning with time as the fourth dimension and therefore is often described as 4-D imaging. In this subsection, we will discuss applications of high-speed anterior segment imaging for visualizing processes such as tear film breakup and pupillary reflex.

The first example demonstrates measurement of tear film dynamics for tear evaluation and diagnosis of dry eye. The tear film is the first refractive surface for light incident on the eye and plays an important role in the optical quality of the eye. Tear film breakup time is usually measured with fluorescein dye [78]. OCT can enable indirect but noninvasive imaging of tear film dynamics by integrating the detected OCT signal over the lens region where optical shadowing from tear film breakup appears. Figure 10.8a shows the shadows caused by tear film breakup which appear over the lens region in repeated volumetric OCT data sets. A 4-D scan protocol was used with 300 × 300 axial scan volumes over a central 8.5 × 8.5 mm^2 area at a rate of ~0.5 volumes per second for 20 s with an axial scan rate of 50 kHz. The shadowing

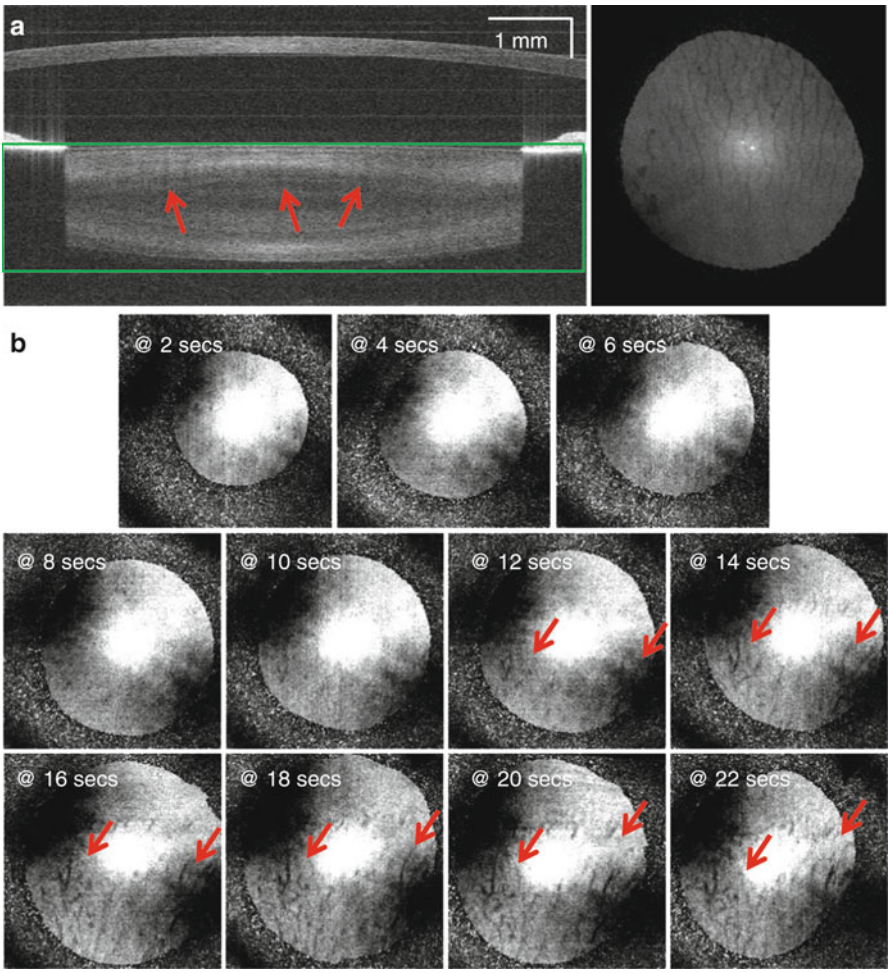

Fig. 10.8 SS-OCT visualization of tear film breakup. (**a**) Shadowing effect in a cross-sectional image of the anterior segment. The signal from the crystalline lens region can be integrated to generate projection OCT image with a characteristic pattern which shows tear film breakup. (**b**) Tear film breakup observed in en face images from 4-D OCT data. Tear film breakup is observed to begin at ~12 s (From Ref. [77])

effect can be observed, and the signal between the anterior and posterior surface of the crystalline lens was used to generate projection OCT images (Fig. 10.8b). Tear film breakup appears as randomly distributed spots in the OCT projection image within the pupil area. Tear film breakup can be determined by the frame-by-frame analysis of the projections and is approximately 12 s in the example shown.

The iris is a dynamic structure whose configuration changes in response to light and during accommodation. Studying the dynamic response of the pupil to dark-light stimulus may provide a more comprehensive assessment of risks from

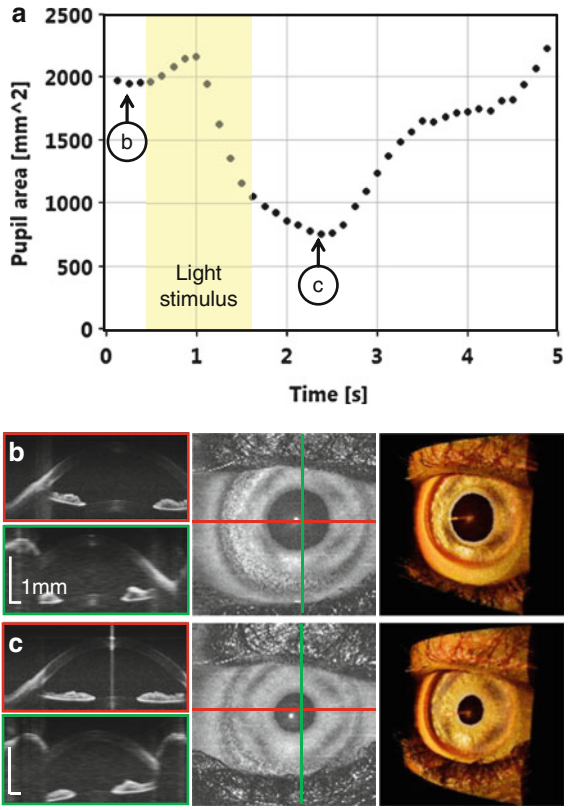

Fig. 10.9 4-D OCT imaging of pupillary reflex. (**a**) Plot of pupil area versus time measured from 3-D OCT data. Application of light stimulus is indicated in yellow. (**b**) 3-D rendering, en face OCT, and cross-sectional images extracted from the volumetric OCT data of the eye before light stimulus. (**c**) 3-D rendering, en face OCT, and cross-sectional images extracted from the volumetric OCT data of the eye at the time of maximum pupil constriction (From Ref. [77])

primary-angle closure development and may help understand the pathophysiology of angle closure glaucoma [79, 80]. Figure 10.9 shows the pupil response to light stimulus from an LED positioned adjacent to the eye. Sequential 150 × 150 axial scan volumes over a 17 × 17 mm^2 area were acquired with an ~8 volumes per second volume rate at an axial scan rate of 200 kHz. The acquisition required ~5 s and enabled visualization of 3-D changes in the iris as a function of time. The pupillary response to light stimulus can be quantitatively analyzed by measuring the pupil size/area changes. As shown in Fig. 10.9, the pupil area decreased rapidly when light stimulus was applied. In contrast, the time constant of the pupil recovery was longer than the constriction reflex.

10.3.5 High-Speed Microscopy and Endoscopy

High imaging speeds which can be achieved with SS-OCT are also important for applications such as microscopy and endoscopy. In conventional microscopy, transverse resolution is determined by the numerical aperture of the objective, which in turn limits the depth of field. OCT has the advantage that it decouples

the diffraction-limited axial and transverse parameters of the focused beam. In most OCT applications, high axial resolutions can be achieved with broadband light sources, but the transverse resolution is not sufficient to reveal cellular or subcellular features. Optical coherence microscopy (OCM) combines low coherence detection with confocal microscopy to improve the transverse resolution of OCT images [81, 82]. The utility of OCM to identify pathologies has been demonstrated in ex vivo studies on human breast, thyroid, and renal tissue [81–83]. OCM also has a broad range of applications in research and biological microscopy, ranging from cellular level imaging of the cortex in small animals to in vivo imaging of developmental biology specimens.

OCM has several advantages over traditional confocal microscopy. OCM uses coherence gating to remove out-of-focus light, and compared with confocal microscopy, OCM can image scattering tissues with improved contrast [84, 85]. The imaging depth in confocal microscopy is limited by loss of contrast due to unwanted scattered light and aberrations. The optical sectioning provided by coherence gating significantly improves image quality by removing unwanted scattered light, and OCM enables deeper imaging of biological specimens. OCM was originally developed using time-domain detection, which allows video-rate en face imaging [81]. However, since time-domain OCM (TD-OCM) enables acquisition of only a single coherence-gated depth, both confocal and coherence-gate depths must be carefully matched. This increases the complexity of the system. In addition, variations in path length delay arising from the non-coincident pivot locations of the galvanometer mirrors in scanning microscope systems produce a curved en face image surface which does not match the objective focal plane [86]. Fourier-domain detection enables simultaneous imaging of multiple depths, which reduces the complexity of acquiring en face images and enables the reconstruction of en face images at multiple depths [87, 88]. Post-processing algorithms may be applied to volumetric Fourier-domain OCM data in order to compensate for path length variations across the scan field as well as dispersion mismatch between sample and reference arms [89, 90]. However, since each en face OCM pixel requires the acquisition of an axial scan, ultrahigh imaging speeds are important in order to achieve acceptable en face frame rates. Swept source OCM (SS-OCM) offers ultrahigh speed that is critical for real-time imaging and display to provide diagnostic feedback in clinical settings such as the pathology laboratory or endoscopy suite. SS-OCM systems also require wide wavelength sweep bandwidths to achieve high axial resolution at 1,000 nm and 1,300 nm wavelengths.

High-speed OCT/OCM can be performed using swept source/Fourier-domain detection with a VCSEL light source. VCSEL light sources are well suited for SS-OCM because they can operate at MHz sweep rates and are broadly tunable at 1,000 nm and 1,300 nm wavelengths. The example shows a VCSEL operating at 1,310 nm with a 280 kHz sinusoidal sweep frequency and bidirectional axial scan rate of 560 kHz [31]. A tuning range of 117 nm was achieved, which provided an axial resolution of 13.1 μm in air, corresponding to 8.1 μm in tissue. Fourier-domain detection has the advantage that the dispersion mismatch between the sample and reference arms can be numerically compensated enabling sample arm

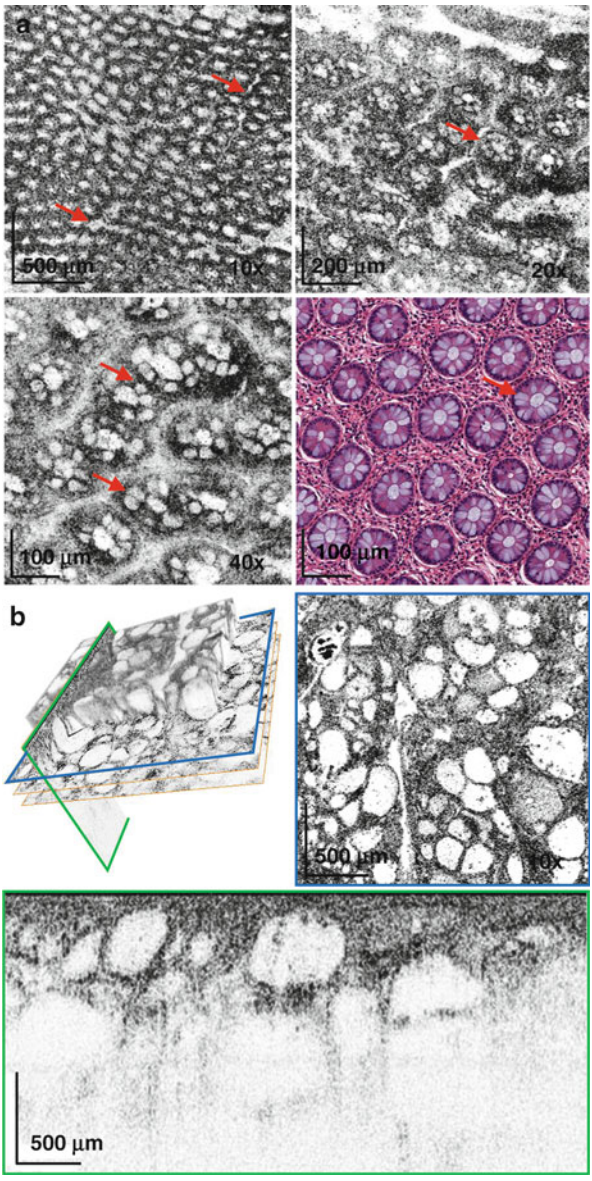

Fig. 10.10 High-speed ex vivo optical coherence microscopy (OCM) using swept source/Fourier-domain detection with a VCSEL light source at 1,310 nm wavelength and 560,000 axial scans per second imaging speed. (**a**) SS-OCM images of a fresh ex vivo human colon specimen with different magnification objectives. Goblet cells are indicated with arrows. Lower right image shows corresponding histology image of colon tissue for comparison. (**b**) Volumetric SS-OCM of a fresh ex vivo thyroid specimen. En face OCM images provide high transverse image resolution and uniform signal compared with cross-sectional images (Figure from Ref. [31])

optics and magnification to be easily changed. As mentioned in Sect.10.2, SS-OCT can be interfaced to a confocal microscope. The microscope had interchangeable objectives (40×, 20× and 10×) for different transverse resolutions (0.86–3.42 µm) and different fields of view (600 × 600 µm^2, 1 × 1 mm^2 and 2 × 2 mm^2). Figure 10.10a shows example ex vivo OCM images of a normal human colon

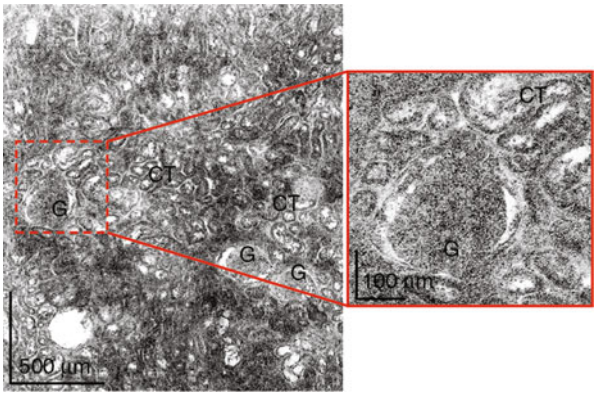

Fig. 10.11 Example mosaic large-field SS-OCM image of a normal human kidney specimen ex vivo. Stitching of 30 individual en face images was performed. *CT* convoluted tubules, *G* glomerulus (Figure from Ref. [31])

specimen taken with three different magnification objectives demonstrating multi-scale imaging. The specimen can be surveyed with a low magnification 10× objective with large field of view (FOV; 2 × 2 mm^2) to show the general architecture of the specimen. With the aid of higher magnification 20× and 40× objectives, details of the colon crypt structures can be visualized. SS-OCM images delineate the mucin secreting goblet cells residing in the crypts and correspond well with features visualized in histology.

SS-OCM also enables volumetric imaging by simultaneously acquiring signals from multiple en face depths. Figure 10.10b shows a 3-D rendering of a fresh ex vivo human thyroid specimen where different en face images and cross sections can be extracted from the volumetric data, similar to the 3-D ophthalmic images presented previously. As an example, an en face plane from the same volumetric data set was selected 50 μm below the specimen surface. Depth-dependent features of follicular architecture can also be clearly observed in the OCM images. The en face images enable high transverse image resolution, but the ability to extract multiple depths is limited by the depth of field and confocal parameter which trades off against high transverse resolution.

Another approach is to perform image mosaicking to preserve high resolution but also obtain wide field of view. A large specimen area can be imaged at high resolution using a high magnification objective and acquiring multiple partially overlapping volumes with a small field of view which are stitched to generate a large field of view image. Figure 10.11 shows an example of a wide-field SS-OCM image from a fresh ex vivo normal human kidney specimen. The image was generated by combining 30 frames taken with a 40× objective to obtain a 1.8 × 2.1 mm^2 total field of view. Glomeruli and convoluted tubules can be observed throughout the imaging field, consistent with the characteristics of normal renal cortex. Detailed examination can be performed by zooming into regions of interest.

OCT imaging has also been applied in fiber-optic-based endoscopes [91, 92]. OCT can visualize microstructural features of internal luminal organs to detect pathology associated with disease such as cancer or atherosclerosis. However, in vivo endoscopic OCT imaging is challenging because high-speed optical

scanning must be implemented inside a miniaturized imaging probe [93]. Many scanning mechanisms have been realized in catheter-based endoscopic OCT systems, such as proximal rotation of a torque cable and fiber with a distal microprism [91, 94–96], actuating a distal fiber tip using a galvanometer [97], actuating a fiber on a cantilever by piezoelectric transducer [98–100], beam scanning using microelectromechanical systems (MEMS) [101–104], and rotary beam scanning in a tethered capsule [105].

High-speed SS-OCT endoscopy requires high-speed endoscopic scanning devices. This example shows ultrahigh-speed endoscopic SS-OCT imaging using a VCSEL light source at 1,310 nm wavelength with a micromotor imaging catheter [32]. The system imaged at 400 frames per second with 1 MHz axial scan rate, 11 μm axial resolution, 7 μm transverse resolution, and 1.65 mm imaging range in air (corresponding to 8 μm axial resolution, 8 μm transverse resolution, and 1.2 mm imaging range in tissue). The micromotor could operate at 1,200–72,000 rpm (corresponding to 20–1,200 fps). Volumetric data sets were obtained by proximally pulling back the micromotor and optics inside the endoscopic probe sheath in order to obtain a spiral scan pattern. The high frame rate can reduce the total data acquisition time, while distal actuation reduces nonuniform rotation artifacts, improving volumetric data acquisition. Image quality can also be enhanced by averaging consecutive frames to reduce speckle.

High imaging speed enables rapid acquisition of a densely sampled 3-D volumetric data set covering a wide field with minimum motion artifacts in vivo. In the following example, volumetric data in the rabbit colon consisting of 3,000 frames of 2,500 axial scans each was acquired in 7.5 s, covering an area of 7.5×7.5 mm^2. Figure 10.12a shows volumetric data and representative cross sections. The image quality was improved by averaging three consecutive images perpendicular to the viewing direction. The en face image in Fig. 10.12a shows crypt structures in the colon as well as vessels below the surface (indicated with arrows). The megahertz speed imaging also makes 3-D-OCT acquisition less sensitive to motion, which can be seen in cross sections. Two cross-sectional images are also included in Fig. 10.12a: a cross-sectional image along the longitudinal pullback direction and a cross-sectional image along the rotary direction. The architectural morphology of the colon, such as the epithelium, mucosa, submucosa, and muscular layers can be identified and correspond to representative histology of the rabbit colon.

Figure 10.12b shows example 3-D SS-OCT data from the rabbit esophagus. The scanning protocol was similar to the previous example. The cross-sectional OCT images allow visualization of normal esophageal layers including the epithelium, lamina propria/muscularis, submucosa, circular muscle, and longitudinal muscle. The layered structure in the OCT images correlates well with representative histology. The projection view in Fig. 10.12b shows features such as vessels over a large field of view. Although vessels have similar structures to dilated glands in cross-sectional images, they are distinguishable in en face images. Periodic motion due to the cardiac cycle is also visible in the en face view.

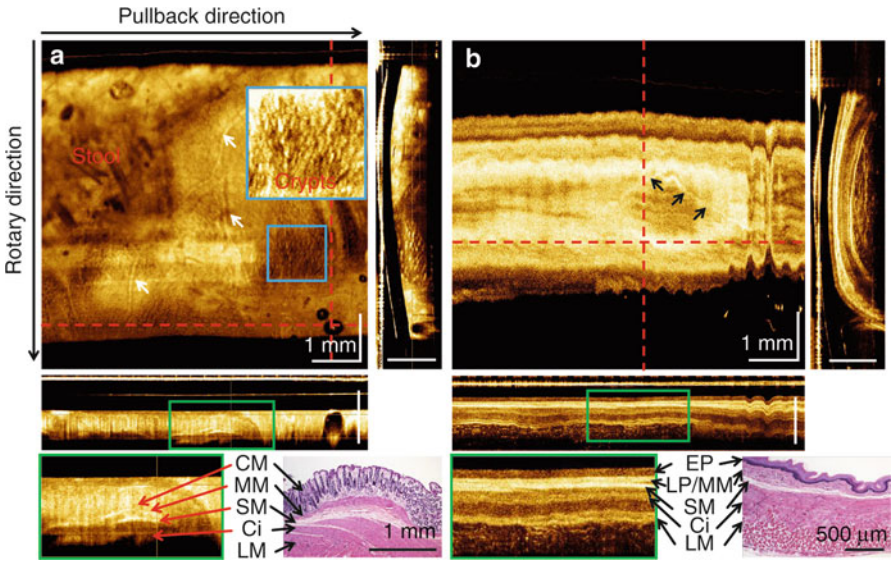

Fig. 10.12 Ultrahigh-speed volumetric SS-OCT endoscopy in the rabbit. The VCSEL light source operated at 1,310 nm wavelength and 1 MHz axial scan rate. (**a**) SS-OCT images of the rabbit colon. Projection OCT image at 300 um depth. *Arrows* indicate blood vessels. Cross-sectional images along the rotary and pullback directions. Representative H&E histology of the rabbit colon. (**b**) SS-OCT image of the rabbit esophagus. Projection OCT image averaged over 15 µm at 190 µm depth. *Arrows* indicate blood vessels. Cross-sectional image averaged over 12 µm. Longitudinal image averaged over 7.5 µm. Representative histology of the rabbit esophagus. *EP* epithelium, *LP* lamina propria, *MM* muscularis mucosa, *SM* submucosa, *Ci* circular muscle, *LM* longitudinal muscle, *CM* columnar mucosa (Figure from Ref. [32])

10.4 Long-Range Imaging and Optical Metrology

10.4.1 Depth Range in OCT

The performance of Fourier-domain OCT systems is also governed by the axial imaging range (depth range), which is limited by the coherence length of the light source and the highest detectable OCT fringe frequency. The imaging range of the OCT system and light source is often characterized by the −6 dB intensity roll-off depth, i.e., the range at which the interference amplitude signal decreases to one half of its maximum [106].

The imaging range in TD-OCT depends on the mechanical scanning range of the reference arm. However, the imaging range (maximum detectable optical path difference) in SD-OCT systems is limited by the spectral resolution of the spectrometer. Therefore, the spectrometer design (optics, dispersive element, and camera specifications) plays a key role in determining the imaging range in SD-OCT. On the other hand, SS-OCT systems detect interferometric signals in time, and therefore different factors determine the imaging range. The light source coherence

length, related to its instantaneous linewidth, is a key parameter which determines the imaging range in SS-OCT. The maximum range which can be measured by an SS-OCT system also depends on other laser and hardware specifications such as sweep rate of the swept light source, the wavelength sweep range, the detector bandwidth, and the sampling rate (bandwidth) of the acquisition (A/D card).

Currently, standard clinical ophthalmic SD-OCT instruments have imaging ranges of 2–3 mm which are sufficient to image the retina assuming moderate patient eye motion. Additionally, current clinical ophthalmic or intravascular SS-OCT devices can image up to ~6 mm range, sufficient for imaging the anterior chamber of the eye for ophthalmic applications or imaging a typical coronary artery diameter for intravascular applications.

10.4.2 Hardware Requirements for Long-Range OCT

OCT systems require special design in order to image long ranges. First, the OCT sample arm depth of focus of the beam incident on the sample should match the imaging range of the system. This provides optimized light collection efficiency from all depths imaged. In practice, if high transverse resolution is desired, it is difficult to meet this requirement even for standard imaging range systems. When the imaging range increases, the numerical aperture of the lens decreases, and long focal lenses should be used resulting in a loss of transverse resolution (Fig. 10.13). Methods using non-diffracting beams (e.g., Bessel beams) or a combination of multiple focal depths have been investigated to address these depth of focus limitations [107–110].

In SS-OCT, given the availability of high bandwidth detection and acquisition electronics, the primary factor determining the ability to image large depths is the coherence length of the swept laser. MEMS VCSEL laser technology enables mode-hop-free tuning which in turn allows coherence lengths of much more than 10 cm. Furthermore, state-of-the-art signal detection and acquisition systems for SS-OCT can acquire signals at GHz sampling rates. Both of these features improve the performance of new SS-OCT instruments, enabling imaging far beyond previous depth ranges [73, 111, 112].

10.4.3 Methods for Depth Range Extension

Early optical methods for measuring depth profiles of samples were based mainly on interferometric reflectometry [113, 114]. Early long image range OCT systems used time-domain detection and were driven by anatomical OCT applications which required reconstructing the internal anatomy of large hollow organs [115, 116]. With the development of Fourier-domain OCT technology, multiple approaches for extending imaging range were investigated. A twofold increase of available imaging range can be obtained using complex conjugate removal techniques. However, these full-range techniques require varying the reference arm

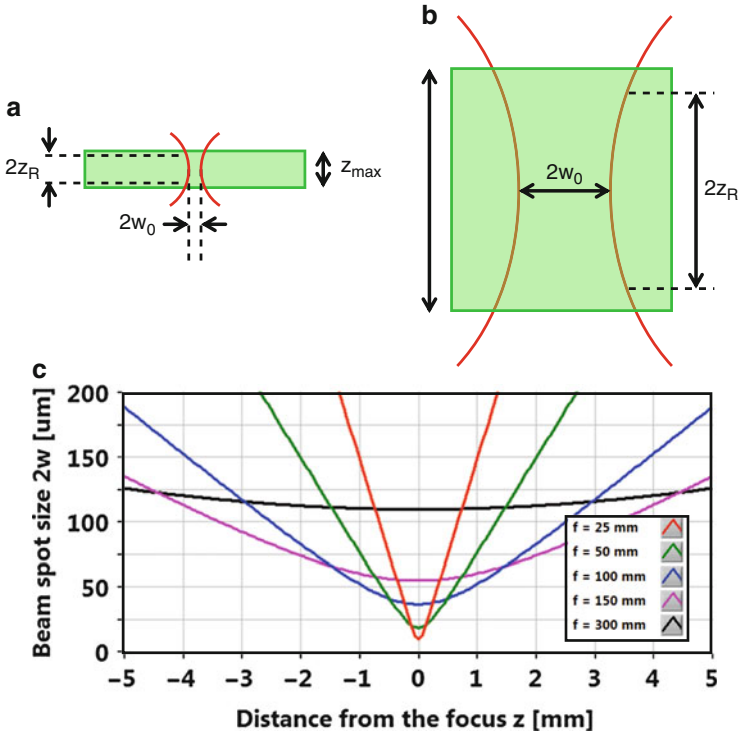

Fig. 10.13 Relationship between the imaging lens numerical aperture and depth range: (**a**) standard OCT system, (**b**) long-range OCT requires longer depth of focus, (**c**) lateral resolution is sacrificed if longer depth of focus is required

length by phase modulation, frequency shifting (acousto-optic modulation), numerical approaches, interpixel shifting, Talbot band effects, or recirculation loops [117–119]. Other approaches use two or more reference arms with a well-defined offset, or optical switches, which enable simultaneous measurement of different imaging ranges within an object when a single imaging range is insufficient to accommodate the entire depth [120–122]. Similar concepts have been demonstrated with polarization-encoded, dual depth range SS-OCT [75].

10.4.4 Full Eye Length OCT Imaging and OCT-Based Ocular Biometry

Measurements of intraocular distances, known as ocular biometry, are essential for accurate outcomes in cataract and keratorefractive surgeries. Precisely measured axial intraocular distances are important for proper intraocular lens (IOL) power calculation [123]. Early studies in the late 1950s and early 1960s used ultrasound for measuring intraocular distances [124]. Currently, ocular biometry with

ultrasound is a gold standard in ophthalmology. Ultrasound devices can perform axial length measurements with a resolution of ~200 μm. However, ultrasound techniques require contact of the eye by a transducer in order to measure axial distance. Early optical methods based on interferometry utilized short pulse light sources [113]. Full eye length measurement using partial coherence interferometry and related methods was demonstrated by multiple groups [2, 125–129]. The most important advantages of optical biometry are that it is noncontact and has higher resolution (10–20 μm) compared with ultrasound. Investigation and validation studies resulted in the introduction of commercial optical devices based on low coherence time-domain interferometry including the IOL Master (Zeiss) and LensStar (Haag-Streit) [130–132]. Other modalities used clinically for postoperative axial eye length measurements include MRI and x-ray tomography, although these have limited resolution and are not clinical standards [133, 134].

The initial reports showing the ability to generate cross-sectional images of the entire eye were confined to small animal studies. Whole mouse eye imaging by TD-OCT at 1,300 nm wavelength and pig and rodent eye imaging with SS-OCT at 1,050 nm wavelength were reported [112, 135, 136]. Fourier-domain reflectometry with two reference arms (well-defined offset) for eye length measurement was also reported [117, 137]. Recently, multiple imaging range OCT systems for simultaneous anterior segment and retinal imaging as well as for full eye length imaging have been demonstrated [74, 121, 138].

OCT full human eye length imaging requires an axial measurement range of at least ~40 mm in air, accounting for refractive indexes of ocular components and patient eye length variations. Full eye length imaging can be achieved using SS-OCT with VCSEL light source technology. The VCSEL light source can be adjusted to optimize the imaging range, while trading off the sweep range and imaging speed. Figure 10.14 shows a 3-D rendering of a volumetric OCT data set obtained at an acquisition rate of 50 kHz with an axial resolution of 23 μm in tissue. Ocular structures such as the cornea, crystalline lens, iris, and retina are displayed with different colors. Telecentric scanning of the cornea was used; therefore, with the refraction of the eye, it means that the spot position on the retina is not scanned. The retinal image converges to a single point after correction for OCT beam refraction (Fig. 10.14b, c).

Apart from imaging from the anterior eye to posterior pole, full eye length imaging is extremely useful in ocular biometry, i.e., in quantitative measurements of intraocular distances. This can be performed by constructing an averaged depth profile of the eye from the central area of the pupil which enables reflections from ocular interfaces to be identified and intraocular distances measured [139, 140]. OCT-based biometry was validated and compared with a clinical ocular optical biometer (IOL Master, Carl Zeiss Meditec) and an immersion A-scan ultrasound biometer (Axis II PR, Quantel Medical) with excellent reproducibility and repeatability. Table 10.1 shows the precision of intraocular distance measurements, and Fig. 10.15 shows the correlation of axial eye length measurements with SS-OCT,

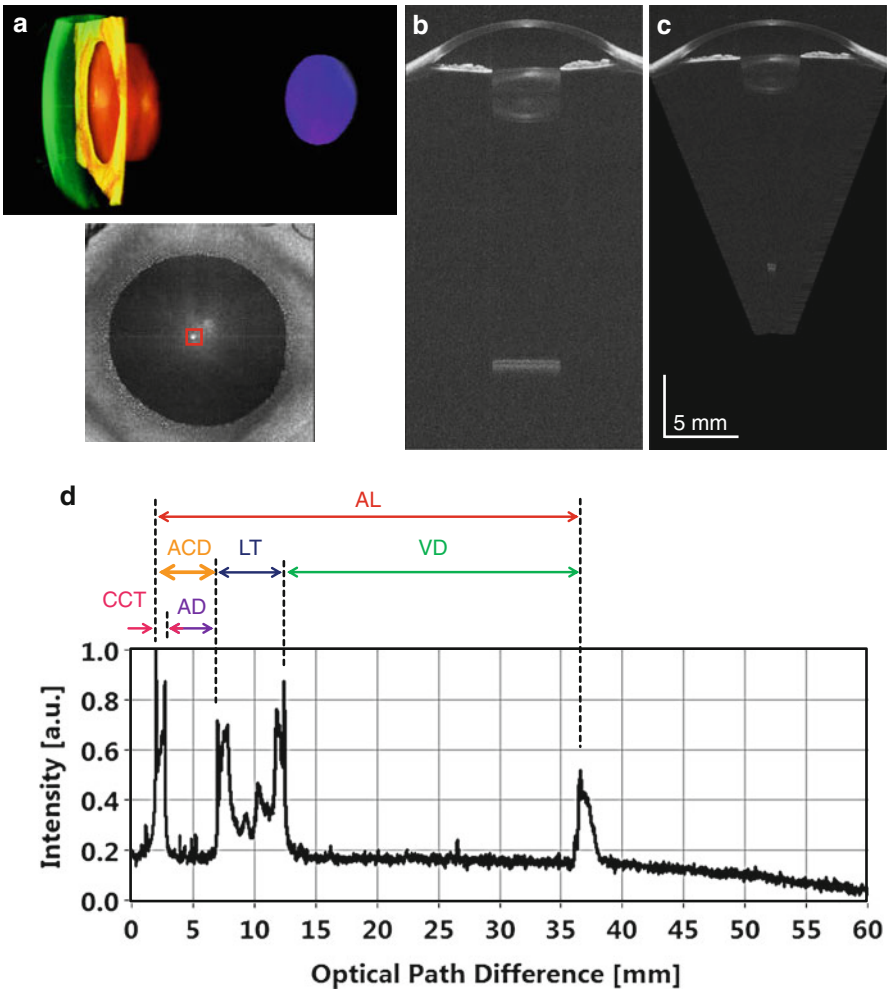

Fig. 10.14 Full eye length SS-OCT imaging using a VCSEL light source. (**a**) 3-D rendering of volumetric OCT data and the en face OCT image. (**b**) Central cross section before refraction correction. (**c**) Central cross section after refraction correction. (**d**) Averaged axial scan (depth profile) generated from the center region of the pupil enables the identification of light reflections from intraocular surfaces and measurement of intraocular distances: *CCT* central corneal thickness, *ACD* anterior chamber depth, *AD* aqueous depth, *LT* lens thickness, *VD* vitreous depth, *AL* axial eye length (From Ref. [139])

the IOL Master, and immersion ultrasound. SS-OCT can provide comprehensive biometric information needed for intraocular lens (IOL) power calculation, is noninvasive and noncontact, and promises to be useful in patients with lens opacities.

Table 10.1 Precision of the measurement of intraocular distances with long-range SS-OCT (From Ref. [139])

Parameter	Mean (mm)	Standard deviation (mm)	Coefficient of variation (%)
Central corneal thickness (CCT)	0.519	0.006	1.08
Anterior chamber depth (ACD)	3.743	0.016	0.43
Aqueous depth (AD)	3.225	0.014	0.42
Lens thickness (LT)	3.810	0.013	0.34
Vitreous depth (VD)	18.304	0.014	0.08
Axial length (AL)	25.857	0.016	0.06

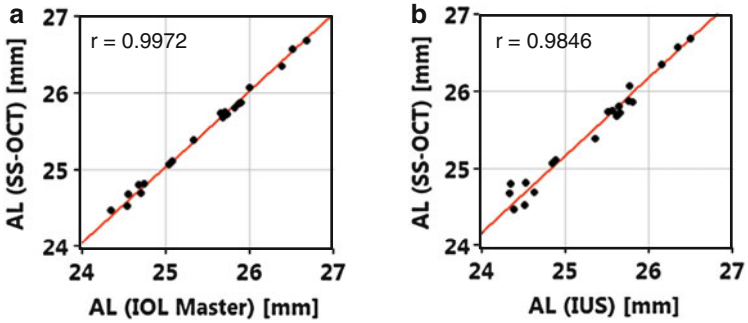

Fig. 10.15 Comparison of methods for axial eye length measurement. (**a**) Correlation between SS-OCT and IOL Master. (**b**) Correlation between SS-OCT and immersion ultrasound A-scan biometry (IUS) (From Ref. [139])

10.4.5 Non-biomedical Applications of Long-Depth Range and Ultralong-Depth Range OCT

10.4.5.1 Optical Profilometry, Metrology, and Testing

SS-OCT can be used to image surface topography as well as the internal structure of turbid objects such as plastic polymers, material coatings, and circuit components to verify manufacturing processes and to assess possible flaws [141–143]. Figure 10.16a shows 3-D OCT data obtained from a printed circuit board that shows both the layout and cross sections of circuit components. Information on internal structures in multilayer boards can be obtained nondestructively. Figure 10.16b shows a commercial MEMS mirror device imaged with SS-OCT at 1,050 nm wavelength which is transmitted through silicon. The support structure on the bottom of the scanning mirror can be seen by displaying signals from behind the

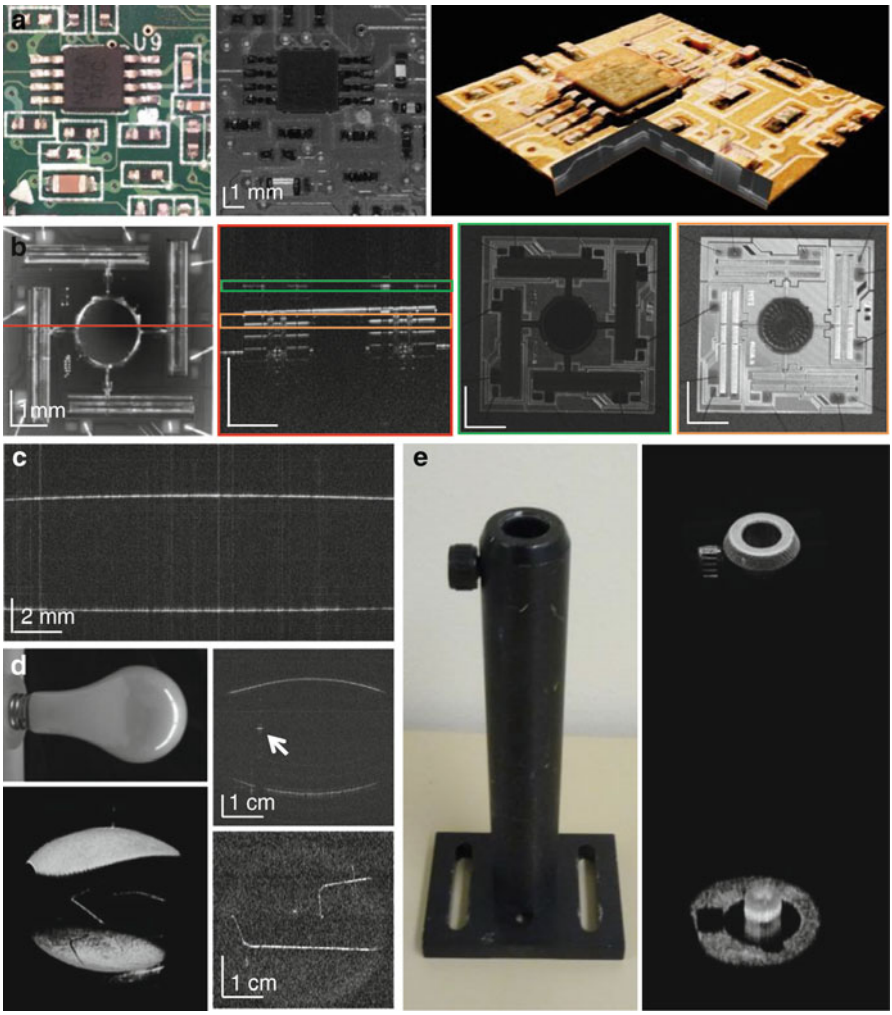

Fig. 10.16 Material applications of long-range SS-OCT imaging. (**a**) OCT profilometry of a circuit board. (**b**) Imaging of an MEMS mirror. (**c**) Imaging of a singlet lens for extracting data on the radii of curvature and thickness. (**d**) Long-range imaging in a light bulb as an example of an opaque material. Both surfaces of the bulb can be visualized along with the filament. (**e**) Ultralong range imaging of the 6 in. tall optomechanical component (Figures (**a**, (**b**) courtesy of Chen D. Lu, Massachusetts Institute of Technology. Figures (**c**, **d**, **e**) from Ref. [140])

mirror surface. In these two examples, SS-OCT was performed using an MEMS Fabry-Perot tunable short cavity laser. The high imaging speeds enable multiple scanned volumes to be obtained versus time to perform four-dimensional (4-D) imaging for MEMS mirror vibration analysis.

Optical component evaluation plays an essential role in optical fabrication since the measurement accuracy of the optics directly limits the fabrication accuracy. Optical testing entails the measurement of geometry, such as surface curvature, surface homogeneity, and surface roughness [144, 145]. The advantage of long-range OCT is that it can distinguish and measure multiple surface layers simultaneously with micrometer resolution, without requiring a reference test plate. Therefore, OCT has the unique capability to provide information on not only surface profiles but also multiple surface curvatures and refractive indices. As an example, the optical properties of a lens were characterized using long-range OCT measurement of the front and back surfaces. Figure 10.16c demonstrates visualization of a thick singlet lens where the top and bottom surfaces of the lens are clearly visualized with an imaging range of 26 mm. The axial resolution was 25 μm in air and imaging was performed at 1,050 nm wavelength. The radius of curvature and central thickness were measured based on OCT images and compared with manufacturer specifications.

Long-range OCT enables nondestructive evaluation and inspection of nontransparent objects. Figure 10.16d shows an example of imaging inside a frosted white light bulb. SS-OCT was performed at 25 kHz axial scan rate with an axial resolution of 30 μm and a record depth range of 15.5 cm in air. 3-D volumetric images showing wires leading to the filament in the light bulb were obtained through the optically scattering light bulb glass. Long depth range can be also used for 3-D visualization of large objects. A 300 mm focal length objective lens was used to provide a long depth of focus and SS-OCT was performed at 25 kHz axial scan rate. Figure 10.16e shows renderings of volumetric OCT data sets (250×250 axial scans). Ultralong imaging depth range enabled visualization of a 6-in. tall optomechanical element from its top to base. This example geometry was chosen because it is difficult to perform precise measurements of high-aspect ratio objects, such as bore holes, using other measurement methods.

10.4.5.2 Reflectometry

Optical reflectometry enables measurement of optical reflections versus delay or distance, equivalent to an axial scan, and can be regarded as the precursor of OCT. There are multiple approaches to optical reflectometry [146]. In the classic optical reflectometer, distance information is obtained using time delay measurement, but these methods were typically applied to long distances of the order of several kilometers and with meter resolution. In optical coherence domain reflectometry (OCDR), a low coherence interferometer with a scanning reference arm path length is used, and in optical Fourier-domain reflectometry (OFDR), wavelength swept light sources are used [147]. An attractive feature of OFDR is that the measurement can be performed without scanning the reference arm path delay. Other reflectometry techniques use light intensity modulation with vector signal analysis or mixing the detected signal with RF frequency-swept waveform modulating the laser output [148, 149]. Very long-range depth measurements are possible with limited resolution. The applications of optical reflectometry include metrology, optical component evaluation, nondestructive fiber inspection

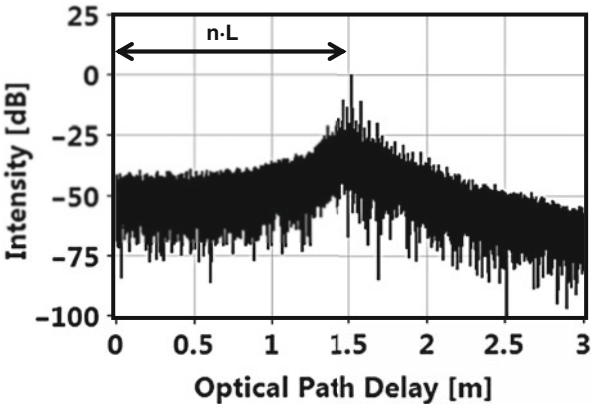

Fig. 10.17 Optical reflectometry using SS-OCT with the VCSEL light source. The example demonstrates the measurement of a length of optical fiber length and represents a record range for SS-OCT (From Ref. [140])

(e.g., differential group delay, distributed birefringence, strain, distributed gain in optical fiber amplifiers), and remote spectroscopic sensing of environmental conditions and industrial processes [114, 148–153].

VCSEL-based SS-OCT can also be used for optical reflectometry. This example shows precision measurement of a length of optical fiber. The VCSEL operated at the sweep rate of 20 kHz with an axial resolution of 70 μm, and the interference signal was recorded using a 1 GHz bandwidth oscilloscope. Figure 10.17 shows the light reflection profile versus depth. In order to obtain the geometric length of the fiber, the optical path measurement must be corrected for the refractive index of fiber ($n = 1.4696$). There was excellent correlation between the measurements using the reflectometer and physical fiber length [140].

10.5 Summary and Perspectives

Modern SS-OCT systems using state-of-the-art swept laser technologies provide powerful platforms for both high-speed and long-range OCT imaging. MEMS VCSEL light sources have the advantage that laser operating parameters can be adjusted to enable imaging with different imaging speeds, resolutions, and ranges, optimizing performance within detector and A/D bandwidth limits. High imaging speeds enable rapid acquisition times as well as wider field of view and are especially important for applications which involve en face OCT imaging. High speeds are also important for functional imaging techniques such as Doppler flow or OCT angiography which use repeated scan protocols. High speed also enables 4-D imaging of dynamical processes where 3-D volumetric data is acquired as a function of time. Long imaging range trades off against high speed or high resolution. The MEMS VCSEL provides unprecedented imaging ranges due to its long coherence length. These extended imaging ranges promise to enable a wide range of new applications in nondestructive evaluation, industrial imaging, and process control. In biomedical applications, long imaging ranges have immediate applications in ophthalmology for biometry of the anterior eye and full eye length

imaging as well as diverse applications ranging from anatomic OCT and surgical guidance. These exciting developments suggest that SS-OCT may become the dominant implementation of OCT in the future.

Acknowledgements The authors thank Osman Ahsen, WooJhon Choi, Dr. Al-Hafeez Dhalla, ByungKun Lee, Hsiang-Chieh Lee, Chen D. Lu, Kathrin Mohler, Dr. Yuankai Tao, and Dr. Tsung-Han Tsai from the Department of Electrical Engineering and Computer Science and Research Laboratory of Electronics at the Massachusetts Institute of Technology; Dr. David Huang from Oregon Health and Science University; Dr. Jay S. Duker, Mehreen Ahdi, and Jason Y. Zhang from the New England Eye Center at the Tufts University; Dr. Bernhard Baumann from Medical University of Vienna; Dr. Joachim Hornegger and Martin F. Kraus from University of Erlangen; and Dr. James Jiang from Thorlabs Inc. The studies were supported by the National Institutes of Health (R01-EY011289-27, R01-EY013178-12, R01-EY018184-05, R01-CA075289-16, R01-EY019029-03, R01-NS057476-05, R44-CA101067-05, R44-EY022864-01) and the Air Force Office for Scientific Research (FA9550-10-1-0551, FA9550-10-1-0063, FA9550-12-1-0499).

References

1. D. Huang, E.A. Swanson, C.P. Lin, J.S. Schuman, W.G. Stinson, W. Chang, M.R. Hee, T. Flotte, K. Gregory, C.A. Puliafito, J.G. Fujimoto, Optical coherence tomography. Science **254**, 1178–1181 (1991)
2. A.F. Fercher, C. Hitzenberger, M. Juchem, Measurement of intraocular optical distances using partially coherent laser light. J. Mod. Opt. **38**, 1327–1333 (1991)
3. R. Leitgeb, C.K. Hitzenberger, A.F. Fercher, Performance of fourier domain vs. time domain optical coherence tomography. Opt. Express **11**, 889–894 (2003)
4. M.A. Choma, M.V. Sarunic, C.H. Yang, J.A. Izatt, Sensitivity advantage of swept source and Fourier domain optical coherence tomography. Opt. Express **11**, 2183–2189 (2003)
5. J.F. de Boer, B. Cense, B.H. Park, M.C. Pierce, G.J. Tearney, B.E. Bouma, Improved signal-to-noise ratio in spectral-domain compared with time-domain optical coherence tomography. Opt. Lett. **28**, 2067–2069 (2003)
6. S.R. Chinn, E.A. Swanson, J.G. Fujimoto, Optical coherence tomography using a frequency-tunable optical source. Opt. Lett. **22**, 340–342 (1997)
7. B. Golubovic, B.E. Bouma, G.J. Tearney, J.G. Fujimoto, Optical frequency-domain reflectometry using rapid wavelength tuning of a Cr4+: forsterite laser. Opt. Lett. **22**, 1704–1706 (1997)
8. E.A. Swanson, S.R. Chinn, *Method and apparatus for performing optical measurements using a rapidly frequency-tuned laser*, Patent 5,956,355 1999
9. S.H. Yun, C. Boudoux, G.J. Tearney, B.E. Bouma, High-speed wavelength-swept semiconductor laser with a polygon-scanner-based wavelength filter. Opt. Lett. **28**, 1981–1983 (2003)
10. S.H. Yun, C. Boudoux, M.C. Pierce, J.F. de Boer, G.J. Tearney, B.E. Bouma, Extended-cavity semiconductor wavelength-swept laser for biomedical imaging. IEEE Phot. Technol. Lett. **16**, 293–295 (2004)
11. Y. Yasuno, V.D. Madjarova, S. Makita, M. Akiba, A. Morosawa, C. Chong, T. Sakai, K.P. Chan, M. Itoh, T. Yatagai, Three-dimensional and high-speed swept-source optical coherence tomography for in vivo investigation of human anterior eye segments. Opt. Express **13**, 10652–10664 (2005)
12. M.A. Choma, K. Hsu, J.A. Izatt, Swept source optical coherence tomography using an all-fiber 1300-nm ring laser source. J. Biomed. Opt. **10**, 044009 (2005)
13. R. Huber, M. Wojtkowski, K. Taira, J.G. Fujimoto, K. Hsu, Amplified, frequency swept lasers for frequency domain reflectometry and OCT imaging: design and scaling principles. Opt. Express **13**, 3513–3528 (2005)

14. B.D. Goldberg, S. Nezam, P. Jillella, B.E. Bouma, G.J. Tearney, Miniature swept source for point of care optical frequency domain imaging. Opt. Express **17**, 3619–3629 (2009)
15. Y. Okabe, Y. Sasaki, M. Ueno, T. Sakamoto, S. Toyoda, S. Yagi, K. Naganuma, K. Fujiura, Y. Sakai, J. Kobayashi, K. Omiya, M. Ohmi, M. Haruna, 200 kHz swept light source equipped with KTN deflector for optical coherence tomography. Electron. Lett. **48**, 201–202 (2012)
16. R. Huber, M. Wojtkowski, J.G. Fujimoto, Fourier Domain Mode Locking (FDML): a new laser operating regime and applications for optical coherence tomography. Opt. Express **14**, 3225–3237 (2006)
17. W.Y. Oh, B.J. Vakoc, M. Shishkov, G.J. Tearney, B.E. Bouma, $>$ 400 kHz repetition rate wavelength-swept laser and application to high-speed optical frequency domain imaging. Opt. Lett. **35**, 2919–2921 (2010)
18. W. Wieser, B.R. Biedermann, T. Klein, C.M. Eigenwillig, R. Huber, Multi-megahertz OCT: high quality 3D imaging at 20 million A-scans and 4.5 GVoxels per second. Opt. Express **18**, 14685–14704 (2010)
19. T. Amano, H. Hiro-Oka, D. Choi, H. Furukawa, F. Kano, M. Takeda, M. Nakanishi, K. Shimizu, K. Ohbayashi, Optical frequency-domain reflectometry with a rapid wavelength-scanning superstructure-grating distributed Bragg reflector laser. Appl. Optics **44**, 808–816 (2005)
20. A.Q. Liu, X.M. Zhang, A review of MEMS external-cavity tunable lasers. J. Micromech. Microeng. **17**, R1–R13 (2007)
21. N. Fujiwara, R. Yoshimura, K. Kato, H. Ishii, F. Kano, Y. Kawaguchi, Y. Kondo, K. Ohbayashi, H. Oohashi, 140-nm quasi-continuous fast sweep using SSG-DBR lasers. IEEE Photon. Technol. Lett. **20**, 1015–1017 (2008)
22. B. Potsaid, B. Baumann, D. Huang, S. Barry, A.E. Cable, J.S. Schuman, J.S. Duker, J.G. Fujimoto, Ultrahigh speed 1050 nm swept source/Fourier domain OCT retinal and anterior segment imaging at 100,000 to 400,000 axial scans per second. Opt. Express **18**, 20029–20048 (2010)
23. K. Totsuka, K. Isamoto, T. Sakai, A. Morosawa, C.H. Chong, MEMS scanner based swept source laser for optical coherence tomography. Proc. SPIE **7554**, 75542Q (2010)
24. M.P. Minneman, J. Ensher, M. Crawford, D. Derickson, All-semiconductor high-speed akinetic swept-source for OCT. Proc. SPIE **8311**, 831116 (2011)
25. V. Jayaraman, J. Jiang, H. Li, P.J.S. Heim, G.D. Cole, B. Potsaid, J.G. Fujimoto, A. Cable, OCT Imaging up to 760 kHz axial scan rate using single-mode 1310 nm MEMS-Tunable VCSELs with $>$ 100 nm Tuning Range, in *2011 Conference on Lasers and Electro-Optics* (IEEE, 2011), pp. 1–2
26. B. Potsaid, V. Jayaraman, J.G. Fujimoto, J. Jiang, P.J.S. Heim, A.E. Cable, MEMS tunable VCSEL light source for ultrahigh speed 60 kHz–1 MHz axial scan rate and long range centimeter class OCT imaging. Proc. SPIE **8213**, 82130M (2012)
27. V. Jayaraman, J. Jiang, B. Potsaid, G. Cole, J. Fujimoto, A. Cable, Design and performance of broadly tunable, narrow line-width, high repetition rate 1310 nm VCSELs for swept source optical coherence tomography. Proc. SPIE **8276**, 82760D (2012)
28. V. Jayaraman, G.D. Cole, M. Robertson, C. Burgner, D. John, A. Uddin, A. Cable, Rapidly swept, ultra-widely-tunable 1060 nm MEMS-VCSELs. Electron. Lett. **48**, 1331–1333 (2012)
29. V. Jayaraman, B. Potsaid, J. Jiang, G.D. Cole, M.E. Robertson, C.B. Burgner, D.D. John, I. Grulkowski, W. Choi, T.H. Tsai, J. Liu, B.A. Stein, S.T. Sanders, J.G. Fujimoto, A.E. Cable, High-speed ultra-broad tuning MEMS-VCSELs for imaging and spectroscopy. Proc. SPIE **8763**, 87630H (2013)
30. I. Grulkowski, J.J. Liu, B. Potsaid, V. Jayaraman, C.D. Lu, J. Jiang, A.E. Cable, J.S. Duker, J.G. Fujimoto, Retinal, anterior segment and full eye imaging using ultrahigh speed swept source OCT with vertical-cavity surface emitting lasers. Biomed. Opt. Express **3**, 2733–2751 (2012)

31. O.O. Ahsen, Y.K. Tao, B.M. Potsaid, Y. Sheikine, J. Jiang, I. Grulkowski, T.-H. Tsai, V. Jayaraman, M.F. Kraus, J.L. Connolly, J. Hornegger, A.E. Cable, J.G. Fujimoto, Swept source optical coherence microscopy using a 1310 nm VCSEL light source. Opt. Express **21**, 18021–18033 (2013)
32. T.-H. Tsai, B. Potsaid, Y.K. Tao, V. Jayaraman, J. Jiang, P.J.S. Heim, M.F. Kraus, C. Zhou, J. Hornegger, H. Mashimo, A.E. Cable, J.G. Fujimoto, Ultrahigh speed endoscopic optical coherence tomography using micromotor imaging catheter and VCSEL technology. Biomed. Opt. Express **4**, 1119–1132 (2013)
33. G.J. Tearney, B.E. Bouma, J.G. Fujimoto, High-speed phase- and group-delay scanning with a grating-based phase control delay line. Opt. Lett. **22**, 1811–1813 (1997)
34. B. Potsaid, I. Gorczynska, V.J. Srinivasan, Y. Chen, J. Jiang, A. Cable, J.G. Fujimoto, Ultrahigh speed Spectral/Fourier domain OCT ophthalmic imaging at 70,000 to 312,500 axial scans per second. Opt. Express **16**, 15149–15169 (2008)
35. S. Moon, D.Y. Kim, Ultra-high-speed optical coherence tomography with a stretched pulse supercontinuum source. Opt. Express **14**, 11575–11584 (2006)
36. M.K.K. Leung, A. Mariampillai, B.A. Standish, K.K.C. Lee, N.R. Munce, I.A. Vitkin, V.X.D. Yang, High-power wavelength-swept laser in Littman telescope-less polygon filter and dual-amplifier configuration for multichannel optical coherence tomography. Opt. Lett. **34**, 2814–2816 (2009)
37. S. Makita, F. Jaillon, M. Yamanari, M. Miura, Y. Yasuno, Comprehensive in vivo micro-vascular imaging of the human eye by dual-beam-scan Doppler optical coherence angiography. Opt. Express **19**, 1271–1283 (2011)
38. N. Suehira, S. Ooto, M. Hangai, K. Matsumoto, N. Tomatsu, T. Yuasa, K. Yamada, N. Yoshimura, Three-beam spectral-domain optical coherence tomography for retinal imaging. J. Biomed. Opt. **17**, 106001–106001 (2012)
39. L. An, P. Li, T.T. Shen, R. Wang, High speed spectral domain optical coherence tomography for retinal imaging at 500,000 A-lines per second. Biomed. Opt. Express **2**, 2770–2783 (2011)
40. D. Choi, H. Hiro-Oka, H. Furukawa, R. Yoshimura, M. Nakanishi, K. Shimizu, K. Ohbayashi, Fourier domain optical coherence tomography using optical demultiplexers imaging at 60,000,000 lines/s. Opt. Lett. **33**, 1318–1320 (2008)
41. R. Huber, D.C. Adler, J.G. Fujimoto, Buffered Fourier domain mode locking: unidirectional swept laser sources for optical coherence tomography imaging at 370,000 lines/s. Opt. Lett. **31**, 2975–2977 (2006)
42. A.F. Fercher, C.K. Hitzenberger, W. Drexler, G. Kamp, H. Sattmann, In vivo optical coherence tomography. Am J. Ophthalmol. **116**, 113–114 (1993)
43. E.A. Swanson, J.A. Izatt, M.R. Hee, D. Huang, C.P. Lin, J.S. Schuman, C.A. Puliafito, J.G. Fujimoto, In vivo retinal imaging by optical coherence tomography. Opt. Lett. **18**, 1864–1866 (1993)
44. M. Wojtkowski, R. Leitgeb, A. Kowalczyk, A.F. Fercher, T. Bajraszewski, In vivo human retinal imaging by Fourier domain optical coherence tomography. J. Biomed. Opt. **7**, 457–463 (2002)
45. B. Cense, N. Nassif, T. Chen, M. Pierce, S.-H. Yun, B. Park, B. Bouma, G. Tearney, J. de Boer, Ultrahigh-resolution high-speed retinal imaging using spectral-domain optical coherence tomography. Opt. Express **12**, 2435–2447 (2004)
46. R. Leitgeb, W. Drexler, A. Unterhuber, B. Hermann, T. Bajraszewski, T. Le, A. Stingl, A. Fercher, Ultrahigh resolution Fourier domain optical coherence tomography. Opt. Express **12**, 2156–2165 (2004)
47. M. Wojtkowski, V. Srinivasan, T. Ko, J. Fujimoto, A. Kowalczyk, J. Duker, Ultrahigh-resolution, high-speed, Fourier domain optical coherence tomography and methods for dispersion compensation. Opt. Express **12**, 2404–2422 (2004)
48. T. Klein, W. Wieser, C.M. Eigenwillig, B.R. Biedermann, R. Huber, Megahertz OCT for ultrawide-field retinal imaging with a 1050 nm Fourier domain mode-locked laser. Opt. Express **19**, 3044–3062 (2011)

49. I. Gorczynska, V.J. Srinivasan, L.N. Vuong, R.W.S. Chen, J.J. Liu, E. Reichel, M. Wojtkowski, J.S. Schuman, J.S. Duker, J.G. Fujimoto, Projection OCT fundus imaging for visualising outer retinal pathology in non-exudative age-related macular degeneration. Br. J. Ophthalmol. **93**, 603–609 (2009)
50. M.F. Kraus, B. Potsaid, M.A. Mayer, R. Bock, B. Baumann, J.J. Liu, J. Hornegger, J.G. Fujimoto, Motion correction in optical coherence tomography volumes on a per A-scan basis using orthogonal scan patterns. Biomed. Opt. Express **3**, 1182–1199 (2012)
51. R.D. Ferguson, D. Hammer, L.A. Paunescu, S. Beaton, J.S. Schuman, Tracking optical coherence tomography. Opt. Lett. **29**, 2139–2141 (2004)
52. Y.H. Zhao, Z.P. Chen, C. Saxer, S.H. Xiang, J.F. de Boer, J.S. Nelson, Phase-resolved optical coherence tomography and optical Doppler tomography for imaging blood flow in human skin with fast scanning speed and high velocity sensitivity. Opt. Lett. **25**, 114–116 (2000)
53. B.R. White, M.C. Pierce, N. Nassif, B. Cense, B.H. Park, G.J. Tearney, B.E. Bouma, T.C. Chen, J.F. de Boer, In vivo dynamic human retinal blood flow imaging using ultra-high-speed spectral domain optical Doppler tomography. Opt. Express **11**, 3490–3497 (2003)
54. S. Makita, Y. Hong, M. Yamanari, T. Yatagai, Y. Yasuno, Optical coherence angiography. Opt. Express **14**, 7821–7840 (2006)
55. Y. Yasuno, S. Makita, T. Endo, G. Aoki, M. Itoh, T. Yatagai, Simultaneous B-M-mode scanning method for real-time full-range Fourier domain optical coherence tomography. Appl. Optics **45**, 1861–1865 (2006)
56. J. Fingler, D. Schwartz, C. Yang, S.E. Fraser, Mobility and transverse flow visualization using phase variance contrast with spectral domain optical coherence tomography. Opt. Express **15**, 12636–12653 (2007)
57. A.H. Bachmann, M.L. Villiger, C. Blatter, T. Lasser, R.A. Leitgeb, Resonant Doppler flow imaging and optical vivisection of retinal blood vessels. Opt. Express **15**, 408–422 (2007)
58. L. An, R.K.K. Wang, In vivo volumetric imaging of vascular perfusion within human retina and choroids with optical micro-angiography. Opt. Express **16**, 11438–11452 (2008)
59. M. Szkulmowski, A. Szkulmowska, T. Bajraszewski, A. Kowalczyk, M. Wojtkowski, Flow velocity estimation using joint spectral and time domain optical coherence tomography. Opt. Express **16**, 6008–6025 (2008)
60. Z.C. Luo, Z.G. Wang, Z.J. Yuan, C.W. Dua, Y.T. Pan, Optical coherence Doppler tomography quantifies laser speckle contrast imaging for blood flow imaging in the rat cerebral cortex. Opt. Lett. **33**, 1156–1158 (2008)
61. A. Mariampillai, B.A. Standish, E.H. Moriyama, M. Khurana, N.R. Munce, M.K.K. Leung, J. Jiang, A. Cable, B.C. Wilson, I.A. Vitkin, V.X.D. Yang, Speckle variance detection of microvasculature using swept-source optical coherence tomography. Opt. Lett. **33**, 1530–1532 (2008)
62. Y.K. Tao, A.M. Davis, J.A. Izatt, Single-pass volumetric bidirectional blood flow imaging spectral domain optical coherence tomography using a modified Hilbert transform. Opt. Express **16**, 12350–12361 (2008)
63. J.A. Izatt, M.R. Hee, E.A. Swanson, C.P. Lin, D. Huang, J.S. Schuman, C.A. Puliafito, J.G. Fujimoto, Micrometer-scale resolution imaging of the anterior eye in-vivo with optical coherence tomography. Arch. Ophthalmol. **112**, 1584–1589 (1994)
64. K. Grieve, M. Paques, A. Dubois, J. Sahel, C. Boccara, J.F. Le Gargasson, Ocular tissue imaging using ultrahigh-resolution, full-field optical coherence tomography. Invest. Ophthalmol. Vis. Sci. **45**, 4126–4131 (2004)
65. C. Kerbage, H. Lim, W. Sun, M. Mujat, J.F. de Boer, Large depth-high resolution full 3D imaging of the anterior segments of the eye using high speed optical frequency domain imaging. Opt. Express **15**, 7117–7125 (2007)
66. M. Gora, K. Karnowski, M. Szkulmowski, B.J. Kaluzny, R. Huber, A. Kowalczyk, M. Wojtkowski, Ultra high-speed swept source OCT imaging of the anterior segment of human eye at 200 kHz with adjustable imaging range. Opt. Express **17**, 14880–14894 (2009)

67. I. Grulkowski, M. Gora, M. Szkulmowski, I. Gorczynska, D. Szlag, S. Marcos, A. Kowalczyk, M. Wojtkowski, Anterior segment imaging with Spectral OCT system using a high-speed CMOS camera. Opt. Express **17**, 4842–4858 (2009)
68. M.X. Shen, L.L. Cui, M. Li, D.X. Zhu, M.R. Wang, J.H. Wang, Extended scan depth optical coherence tomography for evaluating ocular surface shape. J. Biomed. Opt. **16**, 056007 (2011)
69. C.K.S. Leung, R.N. Weinreb, Anterior chamber angle imaging with optical coherence tomography. Eye **25**, 261–267 (2011)
70. W.J. Dupps, Anterior segment imaging: new milestones, new challenges. J. Cataract Refract. Surg. **32**, 1779–1783 (2006)
71. A. Unterhuber, B. Povazay, B. Hermann, H. Sattmann, A. Chavez-Pirson, W. Drexler, In vivo retinal optical coherence tomography at 1040 nm-enhanced penetration into the choroid. Opt. Express **13**, 3252–3258 (2005)
72. B. Povazay, B. Hofer, C. Torti, B. Hermann, A.R. Tumlinson, M. Esmaeelpour, C.A. Egan, A.C. Bird, W. Drexler, Impact of enhanced resolution, speed and penetration on three-dimensional retinal optical coherence tomography. Opt. Express **17**, 4134–4150 (2009)
73. W. Wieser, T. Klein, D.C. Adler, F. Trépanier, C.M. Eigenwillig, S. Karpf, J.M. Schmitt, R. Huber, Extended coherence length megahertz FDML and its application for anterior segment imaging. Biomed. Opt. Express **3**, 2647–2657 (2012)
74. C. Dai, C. Zhou, S. Fan, Z. Chen, X. Chai, Q. Ren, S. Jiao, Optical coherence tomography for whole eye segment imaging. Opt. Express **20**, 6109–6115 (2012)
75. A.-H. Dhalla, D. Nankivil, T. Bustamante, A. Kuo, J.A. Izatt, Simultaneous swept source optical coherence tomography of the anterior segment and retina using coherence revival. Opt. Lett. **37**, 1883–1885 (2012)
76. I. Grulkowski, J.J. Liu, B. Baumann, B. Potsaid, C. Lu, J.G. Fujimoto, Imaging limbal and scleral vasculature using swept source optical coherence tomography. Photon. Lett. Poland **3**, 132 (2011)
77. J.J. Liu, I. Grulkowski, B. Potsaid, V. Jayaraman, A.E. Cable, M.F. Kraus, J. Hornegger, J.S. Duker, J.G. Fujimoto, 4D dynamic imaging of the eye using ultrahigh speed SS-OCT. Proc. SPIE **8567**, 85670X (2013)
78. M.A. Lemp, J.R. Hamill Jr., Factors affecting tear film breakup in normal eyes. Arch. Ophthalmol. **89**, 103 (1973)
79. C.K.-s. Leung, C.Y.L. Cheung, H. Li, S. Dorairaj, C.K.F. Yiu, A.L. Wong, J. Liebmann, R. Ritch, R. Weinreb, D.S.C. Lam, Dynamic analysis of dark–light changes of the anterior chamber angle with anterior segment OCT. Invest. Ophthalmol. Vis. Sci. **48**, 4116–4122 (2007)
80. C.Y.-l. Cheung, S. Liu, R.N. Weinreb, J. Liu, H. Li, D.Y.-l. Leung, S. Dorairaj, J. Liebmann, R. Ritch, D.S.C. Lam, Dynamic analysis of iris configuration with anterior segment optical coherence tomography. Invest. Ophthalmol. Vis. Sci. **51**, 4040–4046 (2010)
81. A.D. Aguirre, Y. Chen, B. Bryan, H. Mashimo, J.L. Connolly, J.G. Fujimoto, Q. Huang, Cellular resolution ex vivo imaging of gastrointestinal tissues with optical coherence microscopy. J. Biomed. Opt. **15**, 016025–016025 (2010)
82. C. Zhou, D.W. Cohen, Y. Wang, H.-C. Lee, A.E. Mondelblatt, T.-H. Tsai, A.D. Aguirre, J.G. Fujimoto, J.L. Connolly, Integrated optical coherence tomography and microscopy for ex vivo multiscale evaluation of human breast tissues. Cancer Res. **70**, 10071–10079 (2010)
83. H.-C. Lee, C. Zhou, D.W. Cohen, A.E. Mondelblatt, Y. Wang, A.D. Aguirre, D. Shen, Y. Sheikine, J.G. Fujimoto, J.L. Connolly, Integrated optical coherence tomography and optical coherence microscopy imaging of ex vivo human renal tissues. J. Urol. **187**, 691–699 (2012)
84. J.A. Izatt, M.R. Hee, G.M. Owen, E.A. Swanson, J.G. Fujimoto, Optical coherence microscopy in scattering media. Opt. Lett. **19**, 590–592 (1994)
85. A.D. Aguirre, P. Hsiung, T.H. Ko, I. Hartl, J.G. Fujimoto, High-resolution optical coherence microscopy for high-speed, in vivo cellular imaging. Opt. Lett. **28**, 2064–2066 (2003)

86. S. Tang, Z. Chen, B.J. Tromberg, T.B. Krasieva, Combined multiphoton microscopy and optical coherence tomography using a 12-fs broadband source. J. Biomed. Opt. **11**, 020502–020502 (2006)
87. S.-W. Huang, A.D. Aguirre, R.A. Huber, D.C. Adler, J.G. Fujimoto, Swept source optical coherence microscopy using a Fourier domain mode-locked laser. Opt. Express **15**, 6210–6217 (2007)
88. H.-C. Lee, J.J. Liu, Y. Sheikine, A.D. Aguirre, J.L. Connolly, J.G. Fujimoto, Ultrahigh speed spectral-domain optical coherence microscopy. Biomed. Opt. Express **4**, 1236–1254 (2013)
89. B.W. Graf, S.G. Adie, S.A. Boppart, Correction of coherence gate curvature in high numerical aperture optical coherence imaging. Opt. Lett. **35**, 3120–3122 (2010)
90. B.W. Graf, S.A. Boppart, Multimodal in vivo skin imaging with integrated optical coherence and multiphoton microscopy. IEEE J. Sel. Top. Quant. Electron. **18**, 1280–1286 (2012)
91. G.J. Tearney, S.A. Boppart, B.E. Bouma, M.E. Brezinski, N.J. Weissman, J.F. Southern, J.G. Fujimoto, Scanning single-mode fiber optic catheter-endoscope for optical coherence tomography. Opt. Lett. **21**, 543–545 (1996)
92. G.J. Tearney, M.E. Brezinski, B.E. Bouma, S.A. Boppart, C. Pitris, J.F. Southern, J.G. Fujimoto, In vivo endoscopic optical biopsy with optical coherence tomography. Science **276**, 2037–2039 (1997)
93. Z. Yaqoob, J. Wu, E.J. McDowell, X. Heng, C. Yang, Methods and application areas of endoscopic optical coherence tomography. J. Biomed. Opt. **11**, 063001–063001 (2006)
94. S.H. Yun, G.J. Tearney, B.J. Vakoc, M. Shishkov, W.Y. Oh, A.E. Desjardins, M.J. Suter, R.C. Chan, J.A. Evans, I.-K. Jang, N.S. Nishioka, J.F. de Boer, B.E. Bouma, Comprehensive volumetric optical microscopy in vivo. Nat. Med. **12**, 1429–1433 (2006)
95. D.C. Adler, Y. Chen, R. Huber, J. Schmitt, J. Connolly, J.G. Fujimoto, Three-dimensional endomicroscopy using optical coherence tomography. Nat. Photon. **1**, 709–716 (2007)
96. M.J. Suter, B.J. Vakoc, P.S. Yachimski, M. Shishkov, G.Y. Lauwers, M. Mino-Kenudson, B.E. Bouma, N.S. Nishioka, G.J. Tearney, Comprehensive microscopy of the esophagus in human patients with optical frequency domain imaging. Gastrointest. Endosc. **68**, 745–753 (2008)
97. A. Sergeev, V. Gelikonov, G. Gelikonov, F. Feldchtein, R. Kuranov, N. Gladkova, N. Shakhova, L. Snopova, A. Shakhov, I. Kuznetzova, A. Denisenko, V. Pochinko, Y. Chumakov, O. Streltzova, In vivo endoscopic OCT imaging of precancer and cancer states of human mucosa. Opt. Express **1**, 432–440 (1997)
98. A.D. Aguirre, J. Sawinski, S.-W. Huang, C. Zhou, W. Denk, J.G. Fujimoto, High speed optical coherence microscopy with autofocus adjustment and a miniaturized endoscopic imaging probe. Opt. Express **18**, 4222–4239 (2010)
99. X. Liu, M.J. Cobb, Y. Chen, M.B. Kimmey, X. Li, Rapid-scanning forward-imaging miniature endoscope for real-time optical coherence tomography. Opt. Lett. **29**, 1763–1765 (2004)
100. T.-H. Tsai, B. Potsaid, M.F. Kraus, C. Zhou, Y.K. Tao, J. Hornegger, J.G. Fujimoto, Piezoelectric-transducer-based miniature catheter for ultrahigh-speed endoscopic optical coherence tomography. Biomed. Opt. Express **2**, 2438–2448 (2011)
101. Y. Pan, H. Xie, G.K. Fedder, Endoscopic optical coherence tomography based on a microelectromechanical mirror. Opt. Lett. **26**, 1966–1968 (2001)
102. J. Woonggyu, D.T. McCormick, Z. Jun, L. Wang, N.C. Tien, C. Zhongping, Three-dimensional endoscopic optical coherence tomography by use of a two-axis microelectromechanical scanning mirror. Appl. Phys. Lett. **88**, 163901–163903 (2006)
103. K.H. Kim, B.H. Park, G.N. Maguluri, T.W. Lee, F.J. Rogomentich, M.G. Bancu, B.E. Bouma, J.F. de Boer, J.J. Bernstein, Two-axis magnetically-driven MEMS scanning catheter for endoscopic high-speed optical coherence tomography. Opt. Express **15**, 18130–18140 (2007)
104. J. Sun, S. Guo, L. Wu, L. Liu, S.-W. Choe, B.S. Sorg, H. Xie, 3D In Vivo optical coherence tomography based on a low-voltage, large-scan-range 2D MEMS mirror. Opt. Express **18**, 12065–12075 (2010)

105. M.J. Gora, J.S. Sauk, R.W. Carruth, K.A. Gallagher, M.J. Suter, N.S. Nishioka, L.E. Kava, M. Rosenberg, B.E. Bouma, G.J. Tearney, Tethered capsule endomicroscopy enables less invasive imaging of gastrointestinal tract microstructure. Nat. Med. **19**, 238–240 (2013)
106. B.R. Biedermann, W. Wieser, C.M. Eigenwillig, T. Klein, R. Huber, Dispersion, coherence and noise of Fourier domain mode locked lasers. Opt. Express **17**, 9947–9961 (2009)
107. K.-S. Lee, J.P. Rolland, Bessel beam spectral-domain high-resolution optical coherence tomography with micro-optic axicon providing extended focusing range. Opt. Lett. **33**, 1696–1698 (2008)
108. B.A. Standish, K.K. Lee, A. Mariampillai, N.R. Munce, M.K. Leung, V.X. Yang, I.A. Vitkin, In vivo endoscopic multi-beam optical coherence tomography. Phys. Med. Biol. **55**, 615 (2010)
109. N. Weber, D. Spether, A. Seifert, H. Zappe, Highly compact imaging using Bessel beams generated by ultraminiaturized multi-micro-axicon systems. J. Opt. Soc. Am. A **29**, 808–816 (2012)
110. J. Mo, M. de Groot, J.F. de Boer, Focus-extension by depth-encoded synthetic aperture in optical coherence tomography. Opt. Express **21**, 10048–10061 (2013)
111. C. Chong, T. Suzuki, A. Morosawa, T. Sakai, Spectral narrowing effect by quasi-phase continuous tuning in high-speed wavelength-swept light source. Opt. Express **16**, 21105–21118 (2008)
112. C.H. Chong, T. Suzuki, K. Totsuka, A. Morosawa, T. Sakai, Large coherence length swept source for axial length measurement of the eye. Appl. Optics **48**, D144–D150 (2009)
113. J.G. Fujimoto, S. Desilvestri, E.P. Ippen, C.A. Puliafito, R. Margolis, A. Oseroff, Femtosecond optical ranging in biological systems. Opt. Lett. **11**, 150–152 (1986)
114. E.A. Swanson, D. Huang, M.R. Hee, J.G. Fujimoto, C.P. Lin, C.A. Puliafito, High-speed optical coherence domain reflectometry. Opt. Lett. **17**, 151–153 (1992)
115. J. Armstrong, M. Leigh, I. Walton, A. Zvyagin, S. Alexandrov, S. Schwer, D. Sampson, D. Hillman, P. Eastwood, In vivo size and shape measurement of the human upper airway using endoscopic long-range optical coherence tomography. Opt. Express **11**, 1817–1826 (2003)
116. R.A. McLaughlin, J.P. Williamson, M.J. Phillips, J.J. Armstrong, S. Becker, D.R. Hillman, P.R. Eastwood, D.D. Sampson, Applying anatomical optical coherence tomography to quantitative 3D imaging of the lower airway. Opt. Express **16**, 17521–17529 (2008)
117. S. Nezam, B.J. Vakoc, A.E. Desjardins, G.J. Tearney, B.E. Bouma, Increased ranging depth in optical frequency domain imaging by frequency encoding. Opt. Lett. **32**, 2768–2770 (2007)
118. Y. Wang, A. Lu, J. Gil-Flamer, O. Tan, J.A. Izatt, D. Huang, Measurement of total blood flow in the normal human retina using Doppler Fourier-domain optical coherence tomography. Br. J. Ophthalmol. **93**, 634–637 (2009)
119. A. Bradu, A.G. Podoleanu, Attenuation of mirror image and enhancement of the signal-to-noise ratio in a Talbot bands optical coherence tomography system. J. Biomed. Opt. **16**, 076010 (2011)
120. E. Jonathan, Dual reference arm low-coherence interferometer-based reflectometer for optical coherence tomography (OCT) application. Opt. Commun. **252**, 202–211 (2005)
121. M. Ruggeri, S.R. Uhlhorn, C. De Freitas, A. Ho, F. Manns, J.M. Parel, Imaging and full-length biometry of the eye during accommodation using spectral domain OCT with an optical switch. Biomed. Opt. Express **3**, 1506–1520 (2012)
122. P. Li, L. An, G. Lan, M. Johnstone, D. Malchow, R.K. Wang, Extended imaging depth to 12 mm for 1050-nm spectral domain optical coherence tomography for imaging the whole anterior segment of the human eye at 120-kHz A-scan rate. J. Biomed. Opt. **18**, 016012–016012 (2013)
123. T. Olsen, Calculation of intraocular lens power: a review. Acta Ophthalmol. Scand. **85**, 472–485 (2007)

124. F. Jansson, Measurements of intraocular distances by ultrasound. Acta. Ophthalmol. **41**, 9–48 (1963)
125. A.F. Fercher, K. Mengedoht, W. Werner, Eye-length measurement by interferometry with partially coherent light. Opt. Lett. **13**, 186–188 (1988)
126. C.K. Hitzenberger, Optical measurement of the axial eye length by laser Doppler interferometry. Invest. Ophthalmol. Vis. Sci. **32**, 616–624 (1991)
127. C.K. Hitzenberger, W. Drexler, C. Dolezal, F. Skorpik, M. Juchem, A.F. Fercher, H.D. Gnad, Measurement of the axial length of cataract eyes by Laser-Doppler Interferometry. Invest. Ophthalmol. Vis. Sci. **34**, 1886–1893 (1993)
128. A.F. Fercher, C.K. Hitzenberger, G. Kamp, S.Y. Elzaiat, Measurement of intraocular distances by backscattering spectral interferometry. Opt. Commun. **117**, 43–48 (1995)
129. W. Drexler, O. Findl, R. Menapace, G. Rainer, C. Vass, C.K. Hitzenberger, A.F. Fercher, Partial coherence interferometry: a novel approach to biometry in cataract surgery. Am J. Ophthalmol. **126**, 524–534 (1998)
130. J. Santodomingo-Rubido, E.A.H. Mallen, B. Gilmartin, J.S. Wolffsohn, A new non-contact optical device for ocular biometry. Br. J. Ophthalmol. **86**, 458–462 (2002)
131. H. Eleftheriadis, IOLMaster biometry: refractive results of 100 consecutive cases. Br. J. Ophthalmol. **87**, 960–963 (2003)
132. P.J. Buckhurst, J.S. Wolffsohn, S. Shah, S.A. Naroo, L.N. Davies, E.J. Berrow, A new optical low coherence reflectometry device for ocular biometry in cataract patients. Br. J. Ophthalmol. **93**, 949–953 (2009)
133. K. Takei, Y. Sekine, F. Okamoto, S. Hommura, Measurement of axial length of eyes with incomplete filling of silicone oil in the vitreous cavity using X ray computed tomography. Br. J. Ophthalmol. **86**, 47–50 (2002)
134. G. Bencic, Z. Vatavuk, M. Marotti, V.L. Loncar, I. Petric, B. Andrijevic-Derk, J. Skunca, Z. Mandic, Comparison of A-scan and MRI for the measurement of axial length in silicone oil-filled eyes. Br. J. Ophthalmol. **93**, 502–505 (2009)
135. C.Q. Zhou, J.H. Wang, S.L. Jiao, Dual channel dual focus optical coherence tomography for imaging accommodation of the eye. Opt. Express **17**, 8947–8955 (2009)
136. J.J. Liu, I. Grulkowski, M.F. Kraus, B. Potsaid, C.D. Lu, B. Baumann, J.S. Duker, J. Hornegger, J.G. Fujimoto, In vivo imaging of the rodent eye with swept source/Fourier domain OCT. Biomed. Opt. Express **4**, 351–363 (2013)
137. B. Grajciar, M. Pircher, C.K. Hitzenberger, O. Findl, A.F. Fercher, High sensitive measurement of the human axial eye length in vivo with Fourier domain low coherence interferometry. Opt. Express **16**, 2405–2414 (2008)
138. A. Tao, Y. Shao, J. Zhong, H. Jiang, M. Shen, J. Wang, Versatile optical coherence tomography for imaging the human eye. Biomed. Opt. Express **4**, 1031–1044 (2013)
139. I. Grulkowski, J.J. Liu, J.Y. Zhang, B. Potsaid, V. Jayaraman, A.E. Cable, J.S. Duker, J.G. Fujimoto, Reproducibility of a long-range swept-source optical coherence tomography ocular biometry system and comparison with clinical biometers. Ophthalmology **120**, 2184–2190 (2013)
140. I. Grulkowski, J.J. Liu, B. Potsaid, V. Jayaraman, J. Jiang, J.G. Fujimoto, A.E. Cable, High-precision, high-accuracy ultralong-range swept-source optical coherence tomography using vertical cavity surface emitting laser light source. Opt. Lett. **38**, 673–675 (2013)
141. S. Kuwamura, I. Yamaguchi, Wavelength scanning profilometry for real-time surface shape measurement. Appl. Opt. **36**, 4473–4482 (1997)
142. M. Kinoshita, M. Takeda, H. Yago, Y. Watanabe, T. Kurokawa, Optical frequency-domain imaging microprofilometry with a frequency-tunable liquid-crystal Fabry-Perot etalon device. Appl. Opt. **38**, 7063–7068 (1999)
143. S.H. Wang, C.J. Tay, Application of an optical interferometer for measuring the surface contour of micro-components. Meas. Sci. Technol. **17**, 617 (2006)
144. V. Srinivasan, H.C. Liu, M. Halioua, Automated phase-measuring profilometry: a phase mapping approach. Appl. Opt. **24**, 185–188 (1985)

145. D.C. Adler, R. Huber, J.G. Fujimoto, Phase-sensitive optical coherence tomography at up to 370,000 lines per second using buffered Fourier domain mode-locked lasers. Opt. Lett. **32**, 626–628 (2007)
146. K. Yuksel, M. Wuilpart, V. Moeyaert, P. Megret, *Optical frequency domain reflectometry: a review*, in 11th International Conference on Transparent Optical Networks, 2009. ICTON '09, (2009), p. 1–5
147. R.C. Youngquist, S. Carr, D.E.N. Davies, Optical coherence-domain reflectometry: a new optical evaluation technique. Opt. Lett. **12**, 158–160 (1987)
148. U. Glombitza, E. Brinkmeyer, Coherent frequency-domain reflectometry for characterization of single-mode integrated-optical waveguides. J. Lightwave Technol. **11**, 1377–1384 (1993)
149. K. Yüksel, M. Wuilpart, and P. Mégret, *Optical-Frequency Domain Reflectometry: Roadmap for High-Resolution Distributed Measurements*, in Proceedings of the IEEE Laser and Electro-Optics Society Symposium-Benelux Chapter, (2007), pp. 231–234
150. W.V. Sorin, D.F. Gray, Simultaneous thickness and group index measurement using optical low-coherence reflectometry. IEEE Photon. Technol. Lett. **4**, 105–107 (1992)
151. H. Kao-Yang, G.M. Carter, Coherent optical frequency domain reflectometry (OFDR) using a fiber grating external cavity laser. IEEE Photon. Technol. Lett. **6**, 1466–1468 (1994)
152. P. Oberson, B. Huttner, O. Guinnard, L. Guinnard, G. Ribordy, N. Gisin, Optical frequency domain reflectometry with a narrow linewidth fiber laser. IEEE Photon. Technol. Lett. **12**, 867–869 (2000)
153. W. Wieser, B.R. Biedermann, T. Klein, C.M. Eigenwillig, R. Huber, Ultra-rapid dispersion measurement in optical fibers. Opt. Express **17**, 22871–22878 (2009)

Optical Design for OCT

11

Zhilin Hu and Andrew M. Rollins

This chapter aims to provide insights and tools to design high-quality optical subsystems for OCT. First, we discuss the various optical subsystems common to OCT and relevant optical design criteria. Second, we review several fundamental optical design principles important for OCT designs. Finally, we discuss a number of examples of designed optical systems for OCT.

To simplify the discussion, the following schematics of OCT in the time domain and spectral domain (or frequency or Fourier domain) are shown below in Fig. 11.1. The major subsystems are labeled by Roman numerals. Illumination sources and sample scanners are labeled by I and II, respectively, in both schematics in Fig. 11.1. Numeral III refers to a scanning optical delay line (ODL), while numeral IV refers to a fixed-path length ODL. Numeral V refers to a single-point detector, and numeral VI refers to an array-based spectrometer (for spectrometer-based frequency-domain OCT). This notation will refer to these subsystems throughout the chapter.

11.1 Optical Design Considerations for OCT

11.1.1 Unique Optical Design Needs for OCT

OCT presents unique design needs different than, for example, microscopy or photography or laser scanning. Therefore, custom optical subsystems are typically designed especially for OCT and often for a specific application. For example, OCT sample scanning optics (II) are typically confocal systems that scan 0.05–0.1 NA beams over a range of several millimeters. Time-domain OCT (TD-OCT) systems typically use fast-scanning, reflective ODLs (III). In spectrometer-based frequency

Z. Hu
Case Western Reserve Department of Biomedical Engineering, Cleveland, OH, USA

A.M. Rollins (✉)
Department of Biomedical Engineering, Case Western Reserve University, Cleveland, OH, USA
e-mail: rollins@case.edu

© Springer International Publishing Switzerland 2015

W. Drexler, J.G. Fujimoto (eds.), *Optical Coherence Tomography*,
DOI 10.1007/978-3-319-06419-2_12

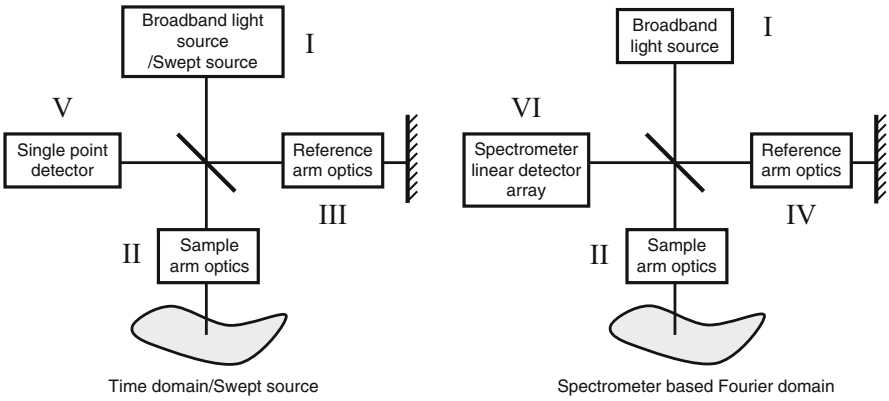

Fig. 11.1 Sketches of OCT configuration

domain OCT (FD-OCT) (or spectral domain OCT, SDOCT) systems, the interfering spectra are collected by a linear array spectrometer (VI). The following six design considerations will be discussed:

1. Clear sample spot profile
2. Uniform chromatic coupling and high coupling efficiency
3. Spectral response
4. Depth of focus versus lateral resolution (numerical aperture)
5. Frequency resolution
6. Spectrometer spot size and falloff

Where items 1–3 are critical for the optical delay line design (III or IV), 1–4 are important for scanner optics (II), and 1–3 and 5–6 are key for the spectrometer designs (VI). The next three subsections *b*, *c*, and *d* will discuss these items in more detail. As a general principle, telecentric and achromatic optics will be used in the system designs to help achieve the design goals.

11.1.2 Sample Scanners

11.1.2.1 Clear Spot Profile

To achieve a high-resolution, high-contrast OCT image, a clean probe beam spot profile is necessary. Ideally, the clean spot profile will be maintained over the entire range of the scan, not merely on the optical axis. OCT makes two-dimensional or three-dimensional images by using spot scanning optics. The spot profile of the paraxial beam is usually closer to Gaussian than the skew beams or the beam significantly off the optical axis because of spherical and chromatic aberrations of the optical components. Sometimes, commercially available lenses with a small aperture are used to build scanners with a large lateral scanning range that degrades the spot profile toward the edge the lenses due to significant spherical and chromatic aberrations.

The use of certain lens types and design principles can be used to reduce design time, construction difficulties, and alignment issues. To minimize difficult design considerations, achromatic and aspheric lenses and a telecentric configuration are suggested in the sample arm scanner (II) design. Design software such as Zemax is usually a suitable tool for optimizing the spot profiles over the entire scanning range, while a beam analyzer is useful for measuring the real spot profile to optimize the assembled design [1]. The use of these tools will help to ensure a minimum amount of work and maximum results when designing OCT optical systems.

11.1.2.2 Uniform and High Coupling Efficiency

Coupling efficiency refers to any point where the light enters and or exits the OCT system. The efficiency refers to both the amount of power lost during transitions from, for example, air to fiber or fiber to air and the chromatic efficiency of the transitions. Proper consideration of these parameters will ensure that optimal use of the light source occurs, and maximum axial resolution is maintained throughout the length of the scan.

The sample scanner of an OCT system typically delivers the light to the sample and collects the scattered light back from the sample through the same optics, as shown in Fig. 11.1. The higher the coupling efficiency, the lower the source power that is needed to achieve the same image quality. Besides the neutral attenuation due to optical surfaces, both the spherical and the chromatic aberrations of the lenses affect the coupling efficiency. In most scanner designs, the light is delivered by an optical fiber to the scanner (II). The wavefront of the back-reflected (scattered) beam is changed because of spherical and chromatic aberrations. These changes result in both misalignment and mode mismatch between the fiber and the back-reflected beam, which lead to some loss of the coupling efficiency. Coupling efficiency may also vary as a function of the lateral scan position.

A telecentric optical configuration can minimize misalignment, while achromatic and aspheric lenses can minimize spherical and chromatic aberrations. Optical design software can help the designer create an optimum arrangement of the components to build a scanner with a uniform and high coupling efficiency.

11.1.2.3 Spectral Response

The spectral response of an OCT subsystem affects the axial resolution of the images, the system's sensitivity to dispersion, and the degree to which optical corrections have to be made. Appropriate design, taking into account the spectral response, can ensure that image quality remains high even in conditions such as imaging through large volumes of water. Designing for an appropriate spectral response profile will result in optimal use of the bandwidth of the light source and the highest quality images.

The variation of the coupling efficiency as a function of wavelengths filters the spectrum of the light. The center wavelength, bandwidth, and amplitude are all altered by the optics and the sample between the light source and the detector. These variations may not be identical in the sample arm scanner (II) and the optical

delay line (III or IV). In general, this filter function generated by the nonconstant spectral response of the optics affects the signal amplitude and the axial resolution of the OCT image [2]. Since the coupling efficiency may be different at different transversal positions, the spectral response will be different as well.

11.1.2.4 Depth of Focus Versus Resolution

To obtain high lateral resolution and large depth of focus are always the goals in an OCT scanner design. Unfortunately, the depth of focus and the lateral resolution vary inversely so that increasing the depth of focus typically worsens the lateral resolution. An optical designer must consider the tradeoff between the two parameters. The intended application must be carefully considered when designing these parameters.

Assuming the OCT beam is Gaussian, the depth of focus is defined as twice the Rayleigh range [3]:

$$2z_0 = \frac{2\pi W_0^2}{\lambda}, \tag{11.1}$$

where W_0 and λ are the radius of the beam waist at focus and the wavelength, respectively. The Rayleigh range z_0 is measured from the waist to the spot size $\sqrt{2}$ times of the waist. For instance, if the wavelength is $\lambda = 1.3$ μm and the radius of waist is $W_0 = 5$ μm, the depth of focus will be 121 μm. The dependence of the beam radius on z is expressed as

$$\begin{aligned} W(z) &= \left[W_0^2 + \left(\frac{\lambda}{\pi W_0} z \right)^2 \right]^{1/2} \\ &= \left[\left(\frac{\lambda}{\pi \theta_0} \right)^2 + (z\theta_0)^2 \right]^{1/2}, \end{aligned} \tag{11.2}$$

where the beam divergence $\theta_0 = W_0/z_0$ and the distance variable z is measured from the point of the waist. The value of $\sin(\theta_0)$ is defined as the numerical aperture (NA). Equation 11.2 indicates that the spot size is smaller for a higher numerical aperture and that the higher the lateral resolution, the shorter the depth of focus.

11.1.3 Scanning Optical Delay Lines

11.1.3.1 Uniform Coupling Efficiency

In OCT, the function of the optical delay line (ODL) (III or IV) is to produce the optical path or the phase match with the sample arm (II). Numerous scanning ODL designs have been demonstrated [4]. Although only a small amount of reference light is needed, the coupling efficiency can affect system sensitivity. More importantly, the reference ODL should have a uniform coupling efficiency. The coupling pattern of the rapid scanning optical delay line (RSOD) is described in Sect. 11.3.

11.1.3.2 Spectral Response

The spectral response requirement in the reference arm or the optical delay line is of the same importance as discussed previously for the sample arm scanner design. Although the optics of the optical delay line are usually simpler than that of the sample scanner, they still normally create a nonuniform coupling efficiency over the spectrum. This creates a curved spectral response filter that operates on the spectrum of the light source. This spectral response is normally different from the spectral filter of the scanner, which results in a degradation of the amplitude and the axial resolution of OCT signal [2].

11.1.4 Spectrometers

11.1.4.1 Resolution

In spectrometer-based frequency domain OCT, three parameters primarily influence the quality of the spectrometer and hence the OCT image quality: the frequency resolution, spectral response, and spot size of the beam. These determine the falloff characteristic and the axial resolution of the image.

A spectrometer based on a linear detector array samples the spectrum illuminating the array, resulting in a discrete signal. The frequency interval of the pixels in the dispersive direction of the spectrum (i.e., the distance between each pixel) determines the un-aliased imaging range of FD-OCT according to the sampling theorem. The higher the frequency resolution, the longer the image range of the FD-OCT. Because the pixel number of the detector array is finite, the tradeoff between the imaging range and the axial resolution (spectrum bandwidth) should be considered in the spectrometer design.

11.1.4.2 Spectral Response

The spectral response of the spectrometer is important in the same way as discussed previously for both scanner and delay line designs. Besides going through the reference and sample arms, the light travels through the optics of the spectrometer before it is collected by the detector array. A nonuniform spectral response filters the interfering spectra, which changes the axial resolution and the contrast of the OCT image.

One of the design goals is to minimize the difference between the coherence spectra and the spectrum of the light source in order to achieve an optimum image quality. The design example of a spectrometer in Sect. 11.5.1 presents an example of a case where there is a trade-off between the flatness of the spectral response and the throughput of the spectrometer.

11.1.4.3 Spot Size and Falloff

The penetration depth of spectrometer-based FD-OCT is also limited by the signal falloff due to the interference fringe washout due to the window in frequency space. In other words, the falloff is mostly determined by the spot size of a single wavelength component of the beam illuminating the array and the pixel width of

the detector in the spectral dispersion direction [5] such that the smaller the spot size or the pixel size, the better the falloff.

11.2 Some Key Optical Design Principles for OCT

11.2.1 Telecentric Optics

Telecentric optical systems are characterized by a flat imaging plane and are important to the design of OCT systems because they increase coupling efficiency. The flat imaging plane decreases the amount of post-image processing needed to display geometrically correct images and increases the coupling efficiency because the back-reflected light returns close to the same incident path.

The definition of a telecentric optical system is a system in which all of the chief rays on the image side are parallel to the local optical axis and perpendicular to the planar image plane. Telecentric optics generally reduce image artifacts caused by off-axis optical aberrations. This leads to several advantages for an OCT scanner, including constant magnification, constant spot size both on- and off-axis, and a flat imaging plane. Figure 11.2 shows the ray trace of three examples of approximately telecentric lens systems (modeled by Zemax) in which the stop is located at the front focus. Three collimated incident beams at different angles pass through the optical system and are focused on the almost-flat image plane at the back focus. All of the chief rays on the image side are parallel to the optical axis. This feature results in a maximum reflection or scattering from the sample at and around the focus and back through the same optics.

In Fig. 11.2(a1–a3), the foci of off-axis beams were closer to the lens than the paraxial focus by 0.36 mm, 3.15 mm, and 0.012 mm, respectively, for the three simulated configurations. Figure 11.2(a1) is sometimes the most economical configuration since a singlet is much cheaper than a second achromatic doublet (a3), yet the performance is much superior to a doublet alone (a2). For a telecentric design, the scanning mirrors of an OCT scanner (or their image) should be placed at the front focus of the optics, which results in a more consistent image quality over a wide lateral scanning range. It should be noted that telecentric optics do not necessarily require an achromatic doublet, but the achromatic doublet generally provides good performance.

11.2.2 Aspheric Optics

The use of aspheric optics in an OCT system provides several distinct advantages. First, it reduces the effects of spherical aberrations in the system. Second, because of this reduction, imaging spot profiles are more clean. Third, a clean spot profile results in an increased coupling efficiency.

The curvature of an aspheric surface varies with the height of the incident ray [6]. Aspheric surfaces are usually used to collimate a beam with a large

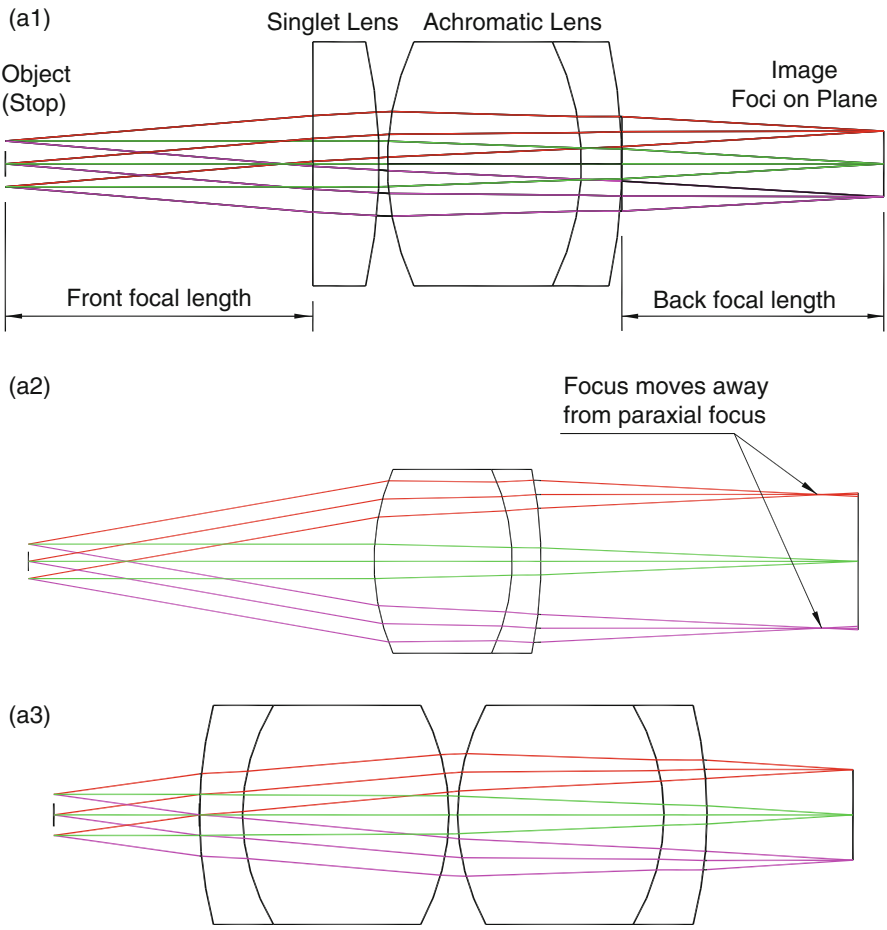

Fig. 11.2 Telecentric setup by Zemax

numerical aperture. Spherical aberration is defined as the variation of the focus with the aperture, which is because a spherical surface is only an approximation of an ideal focusing surface. Figure 11.3(b1) is a somewhat exaggerated sketch of a simple lens forming an "image" of an axial object point a great distance away. The ray close to the optical axis comes to a focus (intersects the axis) very near the paraxial focus position. The higher the ray height at the lens, the farther the position of the ray intersection with the optical axis moves from the paraxial focus. The distance between the paraxial focus and the axial intersection of the ray is also called the longitudinal spherical aberration.

The spherical aberration can be improved by correctly orienting the lens. For instance, the aberration of the optics in Fig. 11.3(b1) was improved by just flipping this lens to Fig. 11.3(b2). It is always a preferred setup that the more curved surface

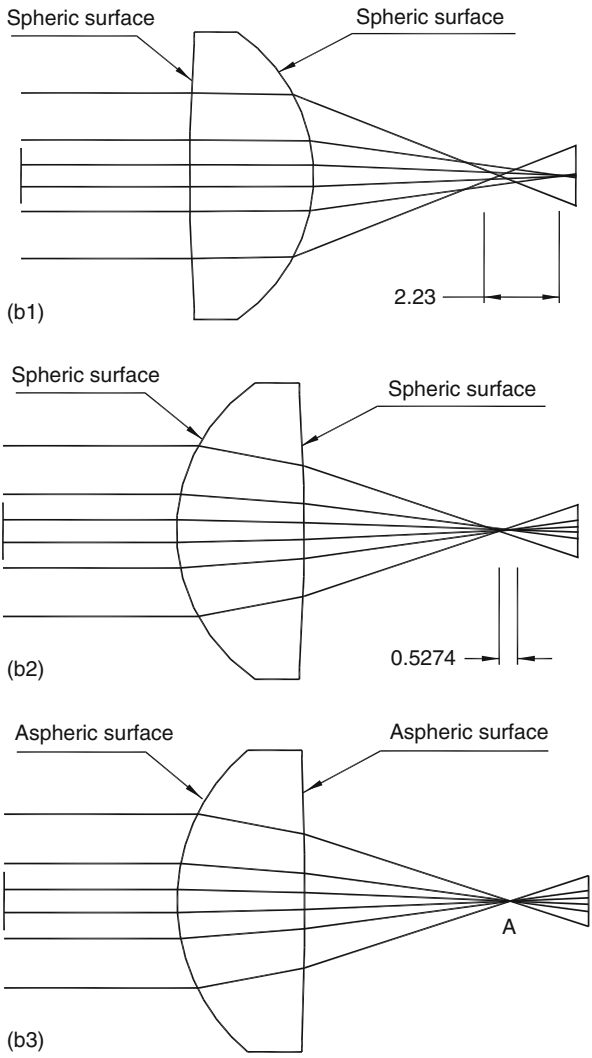

Fig. 11.3 A simple converging lens with under-corrected spherical aberration. (**b1**) The rays farther from the axis are brought to a focus nearer the lens; (**b2**) a correctly oriented spherical lens; (**b3**) an aspheric collimator

faces the collimated beam and the less curved surface faces the focused beam. In order to achieve high-order removal of the spherical aberration, an aspheric lens should be used as shown in Fig. 11.3(b3).

11.2.3 Achromatic Optics

The use of achromatic optics in an OCT system has several advantages. They preserve axial resolution, reduce the dispersion effects of the optical system, improve coupling efficiency, and produce a clean spot profile. For these reasons,

it is advantageous to use achromatic optics when designing an OCT system. Again, achromatic optics are more expensive, but the result is typically worthwhile.

Chromatic aberration is the longitudinal variation of focus (or image position) with wavelength. The refractive index of the glass varies as a function of the wavelength of light, which results in the focal length of the lens varying as a function of the wavelength. For most optical materials, the longer the wavelength, the lower the refractive index. This index feature of the material causes the short wavelengths to be more strongly refracted than the long wavelengths at the surface. For example, the blue light rays (shorter wavelengths) going through a simple positive lens are brought to a focus closer to the lens than the red rays (longer wavelengths) as shown in Fig. 11.4(c1) (detailed later). The distance along the axis between the two focus points is the longitudinal axial chromatic aberration [7].

To clearly demonstrate chromatic aberration, we virtually "dissected" an achromatic doublet lens (Edmund Optics 45805), shown in Fig. 11.4. The lens materials are, respectively, LAKN22 (index: 1.6536@550 nm; 1.6333@1,350 nm) for the AB layer and SFL6 (index: 1.8118@550 nm; 1.7665@1,350 nm) for the BC layer. The radii of curvature of surfaces A, B, and C are, respectively, 43.96 mm, −43.96 mm, and −321.46 mm. The center thicknesses are 6 mm for AB and 4 mm for BC. After the removal of the BC layer, Fig. 11.2c1 shows the significant chromatic aberration of a simple positive element. In Fig. 11.4(c1), the short (550 nm) and long (1,350 nm) wavelength rays incident at point A on the first surface of the lens were separated by the dispersion of the glass shown in the zoom-in window at point B of the second surface. The zoom-in window at focus F indicates an aberration of 1.12 mm for a beam with height of 12 mm and that the focal length of the long wavelength is longer than that of the short wavelength.

Compared to the first piece AB, the second piece BC is made of a glass with different dispersion and polished to lower power (curvature). Figure 11.4(c2) shows that an achromatic doublet lens is made by bonding pieces AB and BC together using an index matching epoxy. Observe that the positions of long and short wavelengths are swapped during propagation from surface B to C, and the longitudinal aberration at the focus is reduced to 0.005 mm from 1.12 mm for the wavelengths of 550 nm and 1,350 nm.

OCT optics must support broad optical bandwidths in order to achieve high-quality, high-resolution imaging.

11.3 Scanning ODL Design Example

All OCT systems require an optical delay line (ODL) to provide a reference field to interfere with the sample field. A FD-OCT system uses a fixed-path ODL, but a TD-OCT system requires a high-speed scanning ODL for real-time imaging. The most commonly used ODL for real-time TD-OCT in the Fourier-domain rapid-scanning ODL (RSOD) [8–11].

In this section, we will review the optical design and the performance analysis of the RSOD and demonstrate how to address the design requirements 2–3 in Sect. 11.1.1

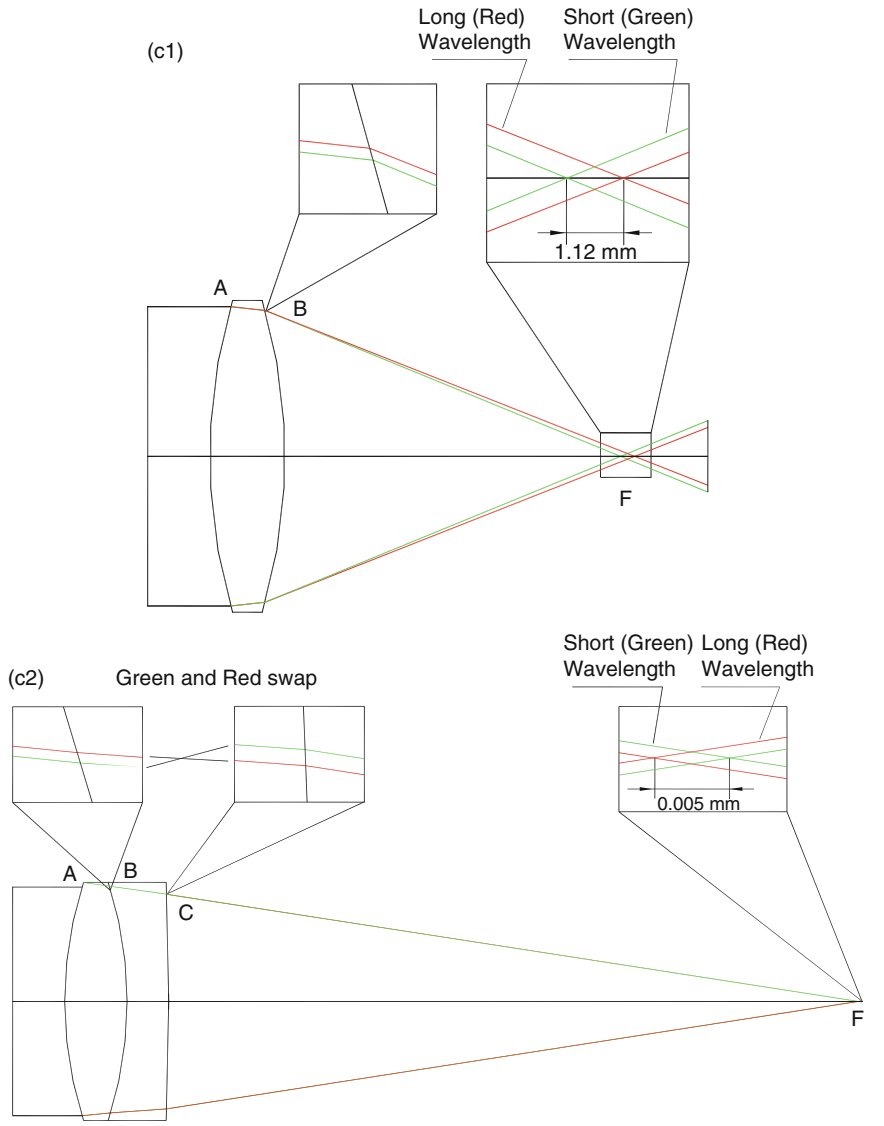

Fig. 11.4 Schematic diagram of chromatic aberration and correction by use of an achromatic doublet. The lens is simulated by Zemax. (**c1**) is a simple double convex positive lens and part of the doublet of (**c2**). (**c2**) is the achromatic doublet lens. *Green* and *red* represent the short and long wavelengths, respectively

and the use of telecentric and achromatic optics in Sects. 11.2.1 and 11.2.3. The coupling efficiency and the spectral response will be addressed by simulations using a Zemax model of a previously reported RSOD design [11]. Figure 11.5b1 shows a schematic drawing of the RSOD [11], while the Figs. 11.5b2, b3 are

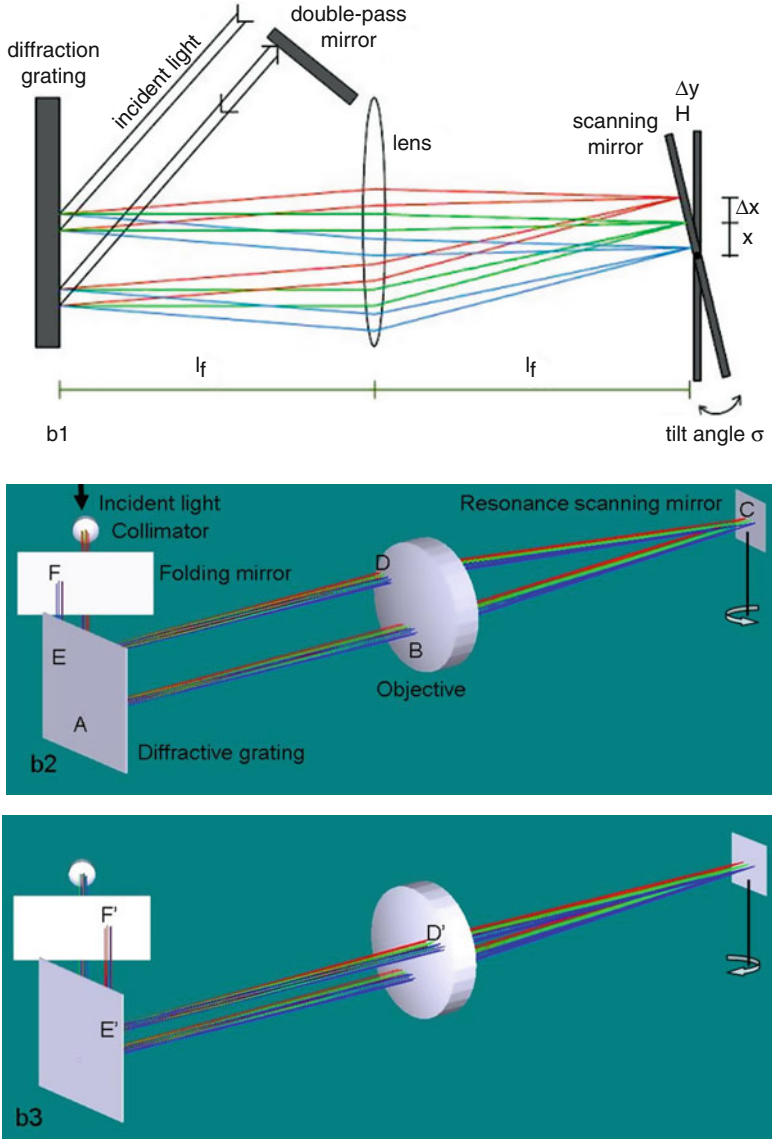

Fig. 11.5 Schematic of the Fourier domain optical delay line. (**b1**) The top view from ref. [11]. (**b2**, **b3**) Zemax modeling at two different scanning angles. Round trip by going through the fiber – collimator – A – B – C – D (D′) – E (E′) – F (F′) – E (E′) – D (D′) – C – B – A – collimator – fiber. The incident and output rays at the lower parts of the grating and the objective in b2 and b3. The folded part of the travel are scanning in horizontal lines from D to D′, E to E′, and F to F′ on the upper part of the objective, grating, and folding mirror, respectively

the Zemax models at two different scanning angles showing the ray propagation step by step on which we will discuss the design procedure.

Figures 11.5b2 and b3 show that the collimated broadband light is dispersed by a diffraction grating at point A. The dispersed beam passes through the lower part of the objective at point B before it is focused onto a resonant scanning mirror at point C (an alternative design is a galvanometric scanning mirror). The objective collimates the spectrum and images or focuses every wavelength onto the scanning mirror. The resonant scanning mirror vibrates on a vertical axis reflecting the dispersed beam back to the upper part of the objective from D to D′. Then, the objective collimates each single wavelength and reconverges the spectrum to point E (through E′ when the resonant mirror scans) on the diffraction grating which recombines the dispersed spectrum into a single collimated beam and directs the collimated beam toward the folding mirror at point F (through F′ when the resonant mirror scans). To the folding mirror, one-half of the round trip is completed. The next propagation is identical to the first series but opposite in order. In summary, the ray finishes a round trip by going through the following steps: the fiber – collimator – A – B – C – D (D′) – E (E′) – F (F′) – E (E′) – D (D′) – C – B – A – collimator – fiber.

The group delay (in the units of distance) resulting from the tilting of the resonant scanning mirror can be expressed as

$$\Delta l_g = 4\sigma\left(x - \frac{l_f \lambda}{p}\right), \tag{11.3}$$

where x is the offset distance between the mirror pivot and the center wavelength, σ is the tilting angle in radians of the resonance mirror, l_f is the effective focal length (not the back focal length) of the objective, λ is the center wavelength of the light source, and p is the pitch of the diffractive grating [11]. The design goal is to achieve a large scanning range and fast scanning speed without significantly distorting the spectrum. The first step is to determine the required axial scanning range. For this design example, we select the axial scanning range to be about 4 mm, which is reasonable considering that the penetration depth of 1310 nm OCT is no more than 3 mm for most biological tissue. The second step is to begin selecting components based on design equations and commercial availability. For example, for this design, we choose a commercially available 2 kHz resonant scanner, a 600 lines/mm (pitch = 1.667 μm) diffraction grating optimized for 1,310 nm light, and a 77 mm focal-length achromatic doublet for the objective lens. The design also assumes a usable duty cycle of $\eta = 0.86$ because the resonant scanner motion is a sinusoidal function of time, so the ends of the scan will not be used.

With the assumed duty cycle, the group delay $\Delta l_g = 4$ mm can be calculated by substituting the above parameters and the titling angle $\sigma = \pm 0.5°$ into Eq. 11.3. A telecentric configuration shown in Fig. 11.5b1 is advantageous because this objective lens is used to collimate the spectrum and focus the beam on the scanning mirror (although for purposes of dispersion compensation, the grating-lens distance

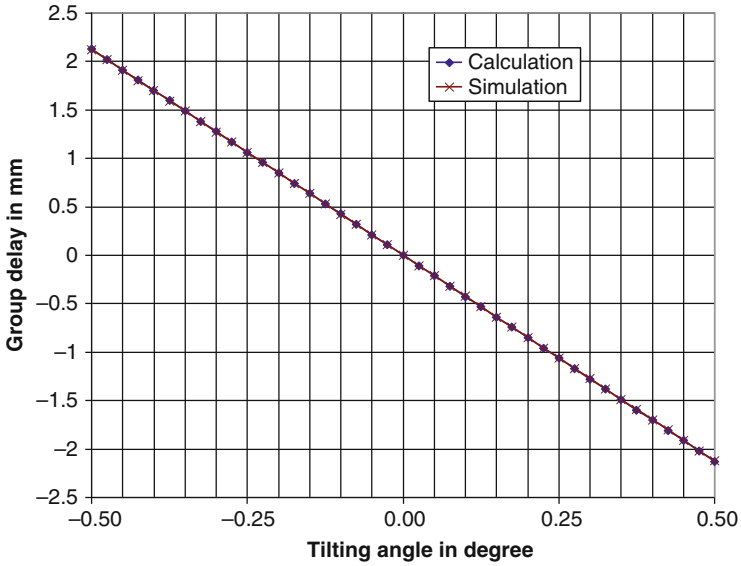

Fig. 11.6 Group delay as a function of the angle of the tilting mirror. Cross is simulated by Zemax simulation and diamond is calculated by Eq. 11.3

is often adjusted after the delay line is aligned). Therefore, the grating should be at the front focus, while the scanning mirror should be at the back focus of the lens. The grating is modeled as normal to the diffracted forward ray. The exact alignment of the components is optimized using optical design software (Zemax).

Three characteristics of the delay line will be evaluated at two opposite tilting angles using the Zemax model: the group delay, the coupling efficiency, and the transmission spectrum as a function of the tilting angle.

First, the group delay is evaluated by comparing the calculation using Eq. 11.3 and the simulation using Zemax, as shown in Fig. 11.6. The delay versus the tilting angle is very linear. The delay produced by this Zemax RSOD model agrees closely with the calculation of Eq. 11.3 in which the effective focal length is used.

Second, a uniform coupling efficiency is important for preserving image quality across an image. The coupling efficiency varies with the tilting angle of the resonance mirror and this variance changes significantly with slight changes in the alignment of the optical components. The goal is to minimize this variance. The achromatic lens combination as shown in Fig. 11.2a1 was used in this design in order to minimize the chromatic dispersion, improving uniformity of coupling efficiency. The coupling efficiencies for three wavelengths versus the tilting angle are shown in Fig. 11.7. The upper three curves are the coupling efficiencies at three different wavelengths, while the lower three are the relative variations versus the scanning angle corresponding to each wavelength. It indicates that the maximum relative tolerance is less than 5/10,000 in the scanning range −0.5, 0.0, and +0.5° and that the coupling efficiency is quite stable in the scanning range.

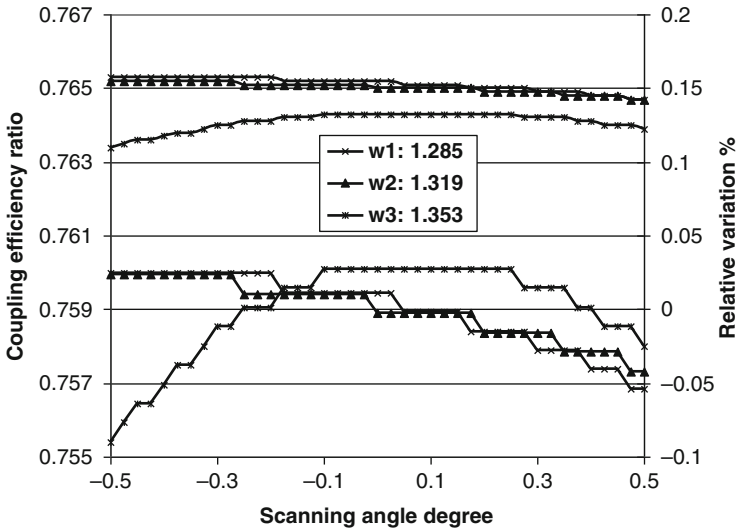

Fig. 11.7 Coupling efficiency as a function of wavelength and tilt angle. Upper three curves: the coupling efficiencies at three wavelengths (*left*). Lower three curves: the relative tolerances at each wavelength (*right*)

Third, the spectral response versus tilting angle is another critical parameter of the RSOD because a filtered spectrum will affect the axial resolution and the amplitude of the interference signal [2]. In order to obtain the spectral response of the optical system using optical design software, we calculate the coupling efficiency as a function of wavelength. The spectral responses are obtained at the angles −0.5, 0, and +0.5° and shown in Fig. 11.8. The upper three curves represent the coupling efficiencies at the three different tilting angles, −0.5, 0, and +0.5°, respectively, while the lower one represents averaged relative variation of the scanning at each wavelength. The results indicate that the spectrum of the light source is just very slightly filtered by the optics, about one percent at shorter wavelengths, and that the relative variation of the spectra is less than 6/10,000.

In summary of this section, we designed and analyzed an RSOD using optical design software and making use of telecentric and achromatic optics. The simulated group delay agrees with the theoretical predication; the coupling efficiency varies only slightly with the tilting angle of the scanning mirror and with wavelength. An achromatic lens is necessary for the objective because the incident light has a broad bandwidth spectrum. A telecentric design is also required because the lens should collimate the spectrum and focus the beam for every single wavelength. Notable lessons from this design example are that the recoupling as a function of tilt angle and wavelength is much worse without the use of achromatic and telecentric optics and that the distance between the lens and the scanning mirror is much more critical than the distance between the lens and the grating.

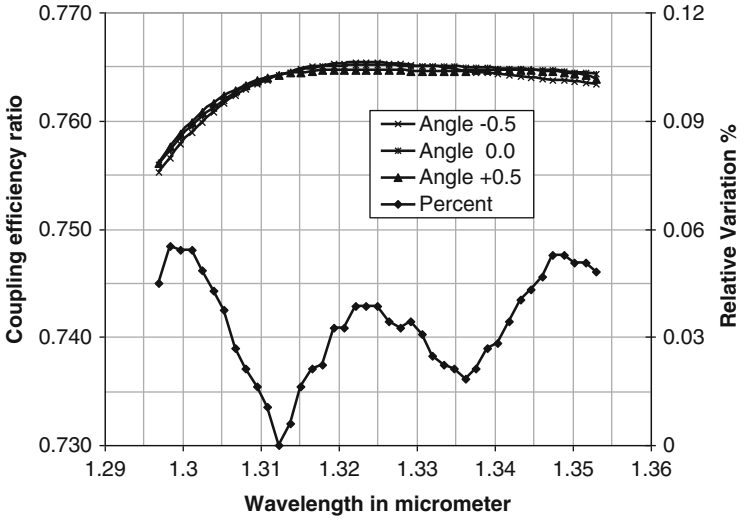

Fig. 11.8 Transmission spectrum at various tilt angles. Upper three spectra at three different tilting angles: −0.5, 0, and +0.5° (*left*). Lower: percentage of relative variations averaged over three angles (*right*)

11.4 OCT Scanner Design Examples

11.4.1 Overview of OCT scanners

The OCT sample scanner (II) is one arm of the two-beam OCT interferometer and is used to deliver and focus the probe light into the tissue and to collect the scattered light back to the interferometer to generate the image signal by interference of the sample light with the reference light returned from the ODL.

Many types of scanners have been demonstrated for a variety of applications [4]. Recent developments include high-resolution devices involving adaptive optics [12, 13, 20] and high numerical aperture systems [14, 15], high scanning speed using micro-motors [16, 17], and three-dimensional imaging [18, 19, 21].

In the rest of this section, we will discuss two examples of OCT sample arm (II) designs. For sample arm design, as with reference arm design, coupling efficiency and spectral response are important. In addition, the spot profile and the scanning range are critical parameters.

11.4.2 Design Example: Bench-Top Scanner

The purpose of this design example is to demonstrate how to address the design requirements 1–4 in Sect. 11.1.1 by making use of telecentric and achromatic optics (Sects. 11.2.1, 11.2.2, and 11.2.3). The example that will be used in the design

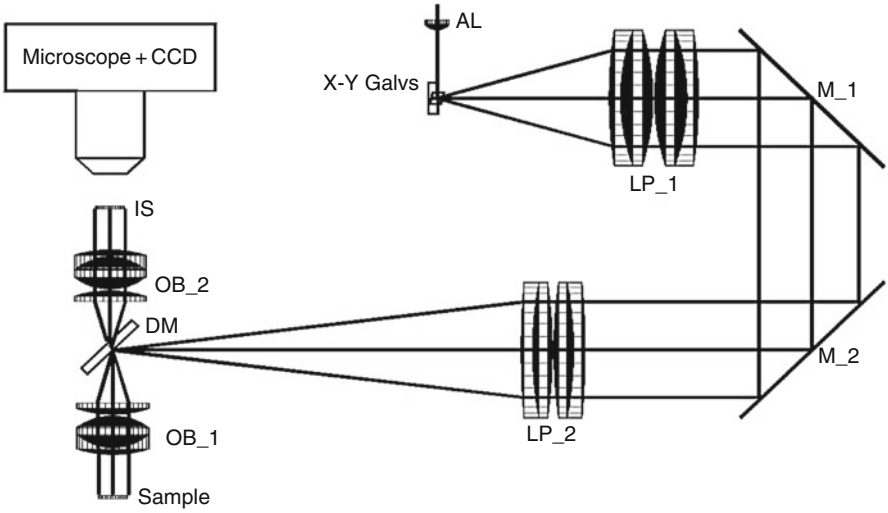

Fig. 11.9 Layout of quasi-telecentric OCT scanner optical design with view port and microscope, modeled by Zemax. *AL*, aspheric lens; *X-Y Galvs*, x-y galvanometric scan head; *LP-1* and *LP-2*, achromatic lens pairs; *M_1* and *M_2*, folding mirrors; *OB-1* and *OB-2*, identical objectives; *DM*, dichroic mirror; *IS*, 1:1 image of sample (view port)

discussion is a bench-top OCT scanner described previously [1]. The goal of this design was to develop an OCT scanner with high lateral resolution, long working distance (the distance between the final optical component and the sample), and large lateral scanning range. In addition, we attempted to achieve a uniform spot size and image quality over the entire lateral scan range. Another design goal was to provide a view port for a microscope to visualize the sample simultaneously while OCT imaging. The primary purpose of this scanner is for use with an OCT system intended for bench-top studies of biomedical samples under the guidance of a microscope [1].

Figure 11.9 shows the optical design of the scanner [1]. The illuminating light delivered via optical fiber is collimated by an aspheric lens AL (see Sect. 11.2.2) into a diameter of 2.2 mm and then deflected by a commercially available, small, and compact x-y galvanometric scan head. The x-y scan head (Cambridge Technology, Cambridge, MA) used in our design provides high scanning speed and has a distance (d) of 5.4 mm between the x and y mirrors which leads to a small deviation from telecentric optics. The relay optics consist of two pairs of achromatic lenses, LP-1 and LP-2, which magnify the OCT beam by a factor of two. In order to minimize spherical aberration in a large angle scan, LP-1 and LP-2 are pairs of identical achromatic lenses face-to-face (see Fig. 11.2(a3)). The focal lengths of LP-1 and LP-2 are $f_1 = 62$ mm and $f_2 = 124$ mm, respectively, and they are separated by $f_1 + f_2$. Folding mirrors M1 and M2 are used to make the scanner compact. A dichroic mirror DM at 45° incident angle is employed to deflect infrared light and transmit visible light and is located at the back focus f_2 of LP-2

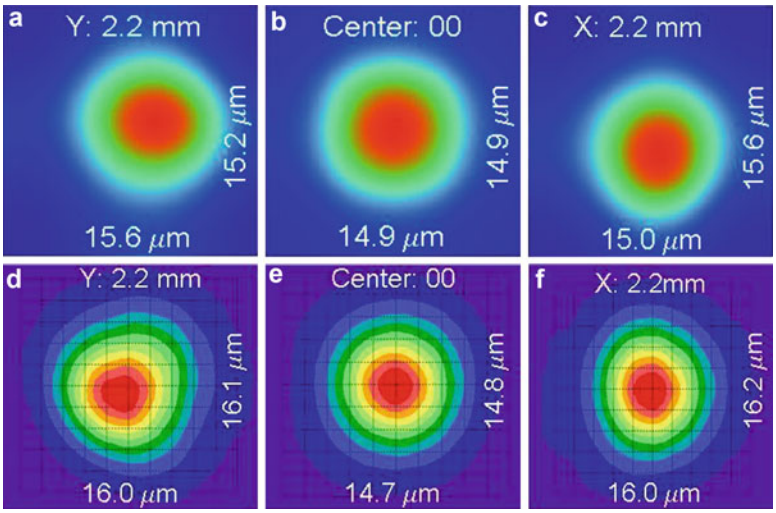

Fig. 11.10 (**a–c**) Cross-section profiles of the spots simulated by Zemax; (**d–f**), spot profiles corresponding to (**a–c**) measured by beam analyzer. Mesh grid and Zemax windows are 20×20 μm. Center means the beam goes through the center of the optics (on axis), while x and y mean tilting the x and y mirrors, respectively, to translate the beam in either x or y direction by 2.2 mm

and the front focus $f_3 = 20$ mm of the objective OB-1. DM deflects the OCT beam through the objective lens OB-1 which then focuses the beam onto the sample. OB-1 is a combination of singlet and achromatic lenses, which is a simplified method of minimizing spherical aberration similar to LP-1 or LP-2. The OCT signal reflected or scattered from the sample placed at the back focus f_4 of OB-1 is collected back through the same path to the OCT detector, while visible light passes through OB-1, DM and OB-2 to the microscope and CCD camera. OB-2 is identical to OB-1, so that they constitute a finite conjugate system to provide a 1:1 image of the sample at conjugate plane IS and allows the microscope to indirectly image the sample at IS. All optical components used in the design are commercially available and the alignment was optimized using optical design software (Zemax).

Spot analysis and characterization: Fig. 11.10(a)–(c) shows the spot profiles on the flat image plane simulated by Zemax in physical optics propagation (POP) mode, while Fig. 11.10(d)–(f) shows the same spot profiles measured by a beam analyzer placed at the image plane 16.5 mm away from last surface of the objective lens. The $1/e^2$ diameter of the simulated central spot was 14.9 μm, while the diameter of the simulated 2.2 mm y-offset spot was 15.4 μm, and the diameter of the simulated 2.2 mm x-offset spot was 15.3 μm. This achieves our design goal of not exceeding 17 μm $1/e^2$ spot diameter. The maximum fractional spot size deviation is 2.3 % over the full lateral scan range of 4.4 mm, which is better than our tolerance criterion of 5 %. The average ellipticity of x- and y-scans is 3.2 %, which also meets our tolerance criterion of 5 %. The measured $1/e^2$ diameter of the central beam was 14.8 μm, while the measured diameters of the 2.2 mm y-offset

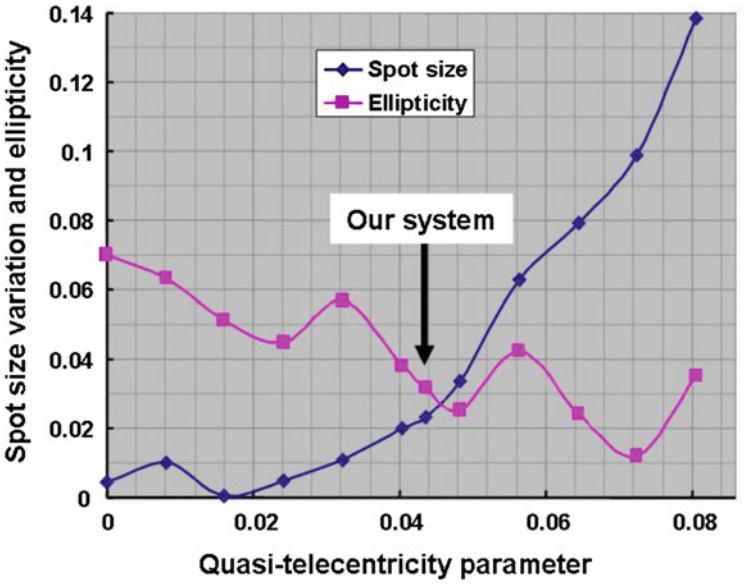

Fig. 11.11 Simulations showing variation of the relative off-axis spot profile with QTP. Diamond and square represent spot size variation and ellipticity respectively

beam and 2.2 mm x-offset beam were 16.1 μm. This corresponds well to above-simulated spot profiles. The spot size remained below our design goal of 17 μm over the full scan range, and the maximum fractional spot size deviation of 4.4 % meets our tolerance criterion. The average measured ellipticity of x- and y-scans in Fig. 11.10 is 1 %, which is better than our tolerance criterion of 5 %.

Comparing Fig. 11.10(a)–(c) with (d)–(f), we note that except for the central beam, the spot size measured by the beam analyzer is slightly larger than the one simulated by Zemax. One possible explanation is that we assumed the core diameter of the SMF-28 optical fiber to be 9 μm, but the diameter of the actual fiber may vary by ±0.4 μm. Another possible explanation is that the beam analyzer might not be precisely aligned with the image plane. The off-axis spot profiles are slightly elliptical, which is a typical problem for a system with slight uncorrected spherical aberration. The further the spots are from the optical axis, the more elliptical they become. Another important property shown in Fig. 11.10 is the purity of the spot profile. There are no side lobes, which would decrease the image contrast.

In order to investigate the effects of varying the degree of quasi-telecentricity, we varied the distance between the two scanning mirrors in our Zemax model while keeping both the front focal length of LP-1 constant and the focus of LP-1at the middle distance between the two mirrors (see Fig. 11.9). The quasi-telecentricity parameter (QTP, the ratio of the half separation between the two scanning mirrors to the front focal length of the optics that follow) value of zero in Fig. 11.11 represents a telecentric system. We varied the distance between the mirrors up to 10 mm, which varies the quasi-telecentricity parameter up to approximately 8 %.

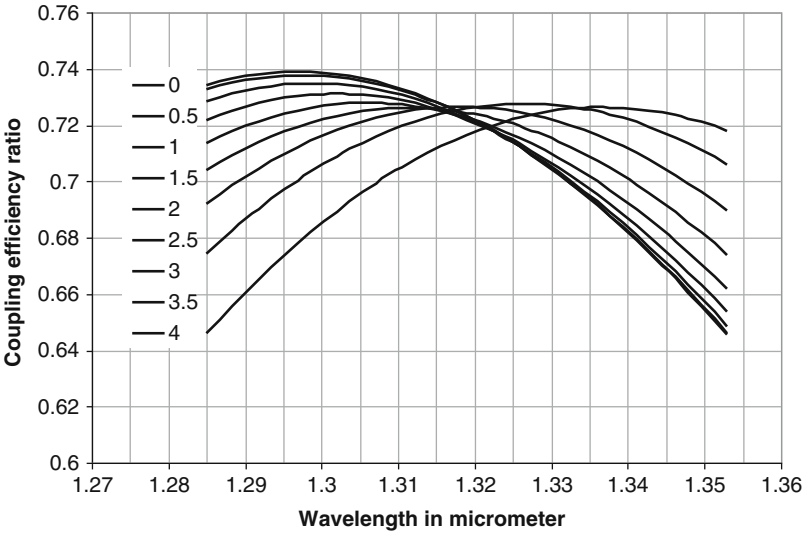

Fig. 11.12 Coupling efficiencies versus wavelength at different tilting angles in degree

In Fig. 11.11, we plotted the variation of the two spot parameters at the maximum of the lateral scan range as a function of the quasi-telecentricity parameter: the spot size variation and spot ellipticity. The average values for the x- and y-spots are plotted.

The results shown in Fig. 11.11 indicate that the relative spot size increases slowly until the QTP reaches approximately 5 % then increases more rapidly. The ellipticity generally decreases slowly with QTP. We observe an oscillation in ellipticity with QTP, but have no explanation for this observation at this time. The arrow in Fig. 11.11 represents the QTP of our implemented system, 4.4 %. At this value, as discussed above, both spot size variation and ellipticity are well below our tolerance criteria.

Coupling efficiency: As discussed in Sect. 11.4.2, the coupling efficiency directly relates the signal amplitude and affects the axial resolution since it filters the spectrum of the light source. Evaluating the coupling efficiency of this scanner via the Zemax model requires ray-tracing the light propagating through the optical components from the optical fiber to the sample (the end mirror in Zemax model) and reflected through the same optical path back to the optical fiber. The model should be built as a round trip, and both the emission and receiving fibers should have the same numerical aperture at the given wavelength before evaluating the coupling efficiency. For instance, the numerical aperture of SMF-28 fiber is 0.14 at 1,550 nm wavelength but is 0.118 at 1,310 nm wavelength. Steering the optical beam by tilting the scanning mirror from the center to the edge of the field of view, we obtained the coupling efficiencies as a function of wavelength at different transversal positions, as shown in Fig. 11.12. The incident spectrum in the simulation was normalized to unity in the calculation range. Figure 11.12 shows that the

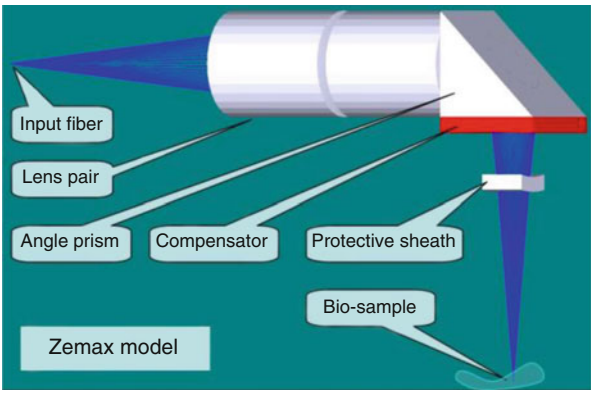

Fig. 11.13 Zemax model of a high NA, long working distance catheter probe design using refractive lenses, and a cylindrical lens for the compensation of the astigmatism due to the protective sheath

spectral bandwidth will be slightly narrowed by the filtering effect of the wavelength-dependent coupling efficiency and that the peak of the function shifts toward the longer wavelengths as the tilting angle increases from 0 to 4° or the beam is moved toward the edge of the scanning range. For a typical OCT light source, this filter function will not significantly affect the spectrum. In the case of a light source with ultra-broad bandwidth, for instance, 200 nm, this effect could be significant and require more careful design. To achieve a flat spectral dependence of the coupling efficiency, telecentric optics for the last objective and careful compensation of chromatic dispersion are essential.

11.4.3 Design Example: Catheter Probe

In this section, we examine the design of a relatively high numerical aperture (NA) and long working distance catheter probe (II). Catheter probes with high NA require a beam with a large diameter to produce a sufficiently small spot size that leads to a high-resolution image. A probe with a long working distance requires an even larger beam in order to maintain a small spot size. This requirement of a large beam makes careful optical design important in order to meet design specifications. A GRIN lens is typically used in catheter probe designs in order to achieve a small probe diameter. Here, we choose conventional refractive lenses with around 2 mm diameter to achieve a high NA and a long working distance probe because of improved off-axis performance. The astigmatism due the probe sheath also needs to be compensated in the design of high NA probe.

Figure 11.13 shows the Zemax model of a catheter probe using conventional lenses. The light out of the fiber is focused by a spherical lens pair, reflected by an angle prism and adjusted by two orthogonal cylindrical lenses as well as the compensator and the protective sheath. The working distance between the outside surface of the sheath and the focus is about 2.6 mm. The outer diameter of the sheath is 3 mm. Figures 11.14, 11.15, and 11.16 compare the spot profiles of the probe design with and without astigmatism compensation. The spot achieved with

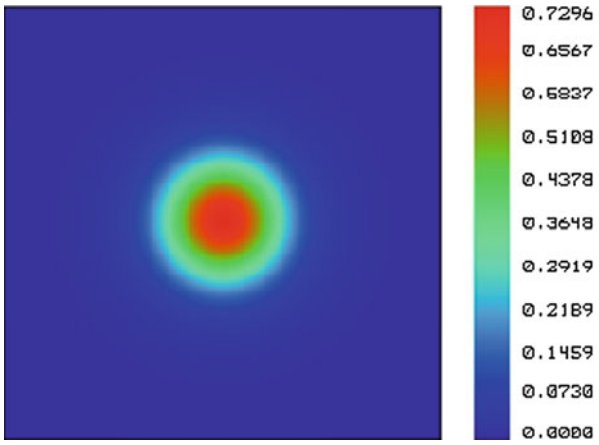

Fig. 11.14 Spot profile of the high NA catheter probe design with astigmatism compensation. Image window is 32 × 32 μm

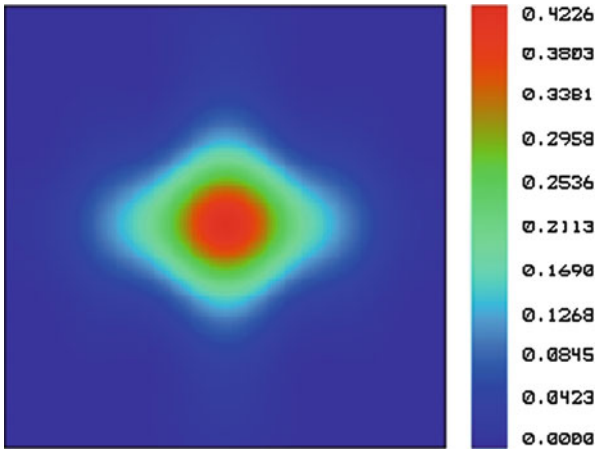

Fig. 11.15 Spot profile of the high NA catheter probe design without astigmatism compensation. Image window is 32 × 32 μm

the compensation lens, shown in Fig. 11.14, shows a clear profile with a high relative irradiance and a Strehl ratio of 0.73. The spot achieved without the compensation, shown in Fig. 11.15, shows some fuzzy or star pattern with a lower relative irradiance of 0.423. The "star pattern" spreads the energy from the peak of the spot, which reduces the contrast and the resolution of the image. Figure 11.16 shows the cross section of the spot profiles achieved with and without astigmatism compensation, which are normalized to the spot with compensation. The curves represent the cross sections through the center of the spot images orthogonally in two directions. The $1/e^2$ diameters of the spots are 13 μm and 20 μm, respectively, for the designs with and without the compensator. The profile of spot with the compensation lens is symmetric around the center, while the profile without the compensation lens is not symmetric.

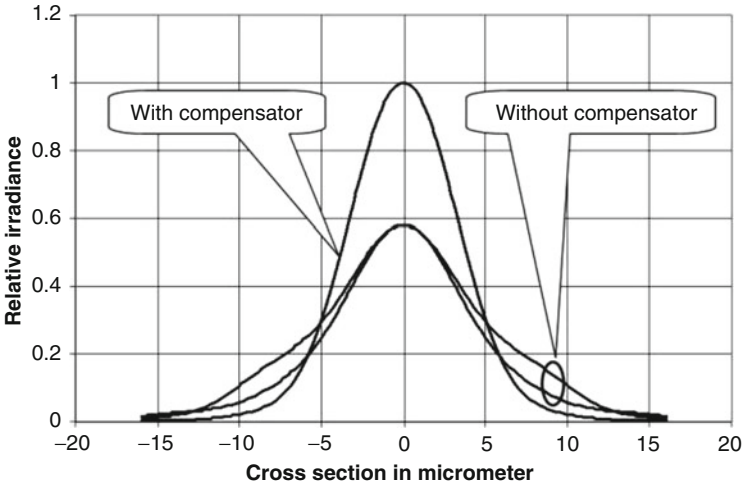

Fig. 11.16 Cross sections of the spot profiles for the high NA catheter probe design with and without compensation. The orthogonal cross sections with compensation are identical, whereas the orthogonal cross sections without compensation are not

As a summary of this subsection, in order to accommodate the relatively large beam necessary for a higher NA and longer working distance catheter probe, refractive optics may be advantageous, and correction for the astigmatism caused by the curved catheter probe sheath is important.

11.5 SD-OCT Spectrometer Design Example

The spectrometer (VI) is a critical component of array-based frequency-domain OCT (SD-OCT). The typical components of a fiber-coupled spectrometer include the collimator, diffractive grating, objective lens, and linear detector array as shown in Fig. 11.17. The spectral coverage of the spectrometer determines the axial resolution of the FD-OCT system together with the bandwidth of the light source. The spectral range integrated by each pixel, together with the optical resolution of the spectrometer, determines the axial signal falloff, which is a result of fringe visibility washout. The spectral spacing between pixels determines the unambiguous imaging range (limited by aliasing). To design a high-quality spectrometer, the chromatic aberration, optical resolution, and detector array resolution should be taken into account. Chromatic aberration could be avoided by using all reflective optics, i.e., curved mirrors, but the optical resolution (the spot profile) would be more difficult to control than if refractive lenses were used. The following two subsections will describe a refractive lens-based spectrometer design and the performance analysis.

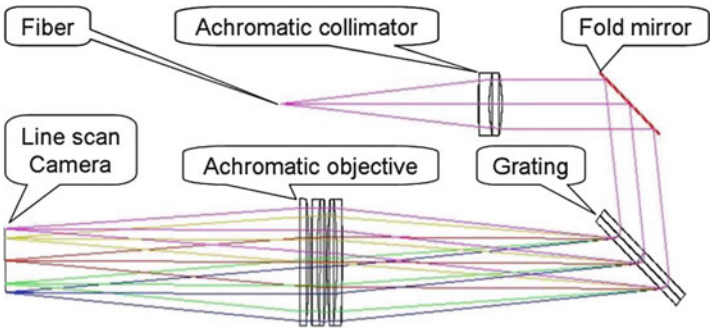

Fig. 11.17 Zemax model of spectrometer for FDOCT at 1,310 nm. Pixel number of detector array: 512; Pixel size: 50 μm; average wavelength spacing: 0.2 nm

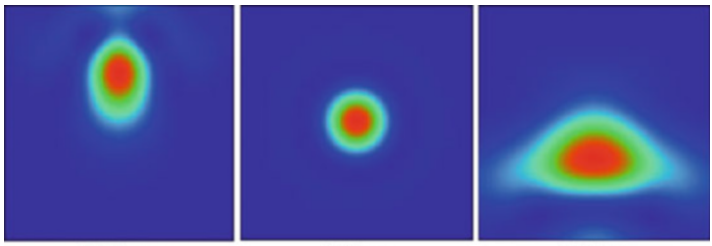

Fig. 11.18 Spot images at wavelengths 1,257 nm, 1,310 nm, and 1,359 nm, window size: 50 × 50 μm. Vertical is the dispersion direction

11.5.1 Achromatic Spectral Response

In this subsection, we discuss the correction of chromatic aberration due to the dispersion of the glass of the lenses and analyze the spectral response in this design. Figure 11.17 is the Zemax model of a refractive lens-based spectrometer. The specifications of this spectrometer are the following: The wavelength coverage is 102 nm and the center wavelength of the spectrum, located at the center of the detector array, is 1,310.6 nm. The detector array contains 512 pixels; this is 50 μm wide. The orientation of the grating is fixed at the optimum incident angle at the center wavelength for the expected light source spectrum, which makes the design relatively simple. The broad bandwidth coverage requires good achromatic optics. According to the principles discussed in Sect. 11.2, we used one achromatic lens to collimate the beam before the grating and three lenses for the objective. This consideration provided acceptable spot profiles through the entire spectrum of the light source as shown in Fig. 11.18. Figure 11.18 shows in that the spot sizes at wavelengths 1,257 nm and 1,359 nm are slightly broader in the dispersive direction than the spot at the center wavelength, 1,310 nm, which is optimized in this design. They are all significantly smaller than the pixel width of 50 μm. The optimized

optical design gives a flat throughput covering the entire spectrum of this spectrometer (data not shown).

11.5.2 Spectral Resolution and Optical Resolution

Both spectral resolution and detector array resolution affect the axial image range of the spectrometer-based FD-OCT. According to the Nyquist theorem, the maximum axial imaging range ΔD is limited by the following equation:

$$\Delta D = \frac{1}{4}\frac{{\lambda_c}^2}{\Delta\lambda}N. \tag{11.4}$$

where λ_c, $\Delta\lambda$, and N are the center wavelength, spectral range covered by the spectrometer, and the pixel number of the detector array. The spectral resolution $\delta\lambda$ is defined as $\delta\lambda = \Delta\lambda/N$ and represents the spectral range integrated by a single pixel. According to Eq. 11.4, the better the spectral resolution $\delta\lambda$, the larger the imaging range ΔD. For instance, at $\lambda_c = 1{,}307.8$ nm, $\Delta\lambda = 102$ nm, and $N = 512$, the maximum imaging range ΔD is 2.142 mm. This distance can be thought of as the "folding range," or the maximum range from which an image signal can be collected without aliasing. The imaging range will be doubled to 4.284 mm if the pixel number N is increased by a factor of 2 or the spectral coverage is alternatively decreased by the same factor. In other words, the smaller the wavelength or frequency spacing, the longer the folding range will be. Therefore, for a given number of pixels available, there is a design tradeoff between axial resolution and axial range.

In addition, the resolution of the spectrometer determines the falloff of the FD-OCT. The signal amplitude $I(x_j)$ at pixel number j can be expressed as [5],

$$\begin{aligned} I(x_j) = {} & \frac{1}{4}Erf\left(\frac{\Delta y\sqrt{\ln 2}}{a}\right) \\ & \cdot \int_0^\infty \left[Erf\left(\frac{(\Delta x - 2x(k) + 2x_j)\sqrt{\ln 2}}{a}\right) + Erf\left(\frac{(\Delta x + 2x(k) - 2x_j)\sqrt{\ln 2}}{a}\right)\right] \\ & \cdot \left[S_{ref}(k) + S_{sam}(k) + 2\sqrt{S_{ref}(k)S_{sam}(k)}\cos(2k\,\Delta D)\right]dk. \end{aligned} \tag{11.5}$$

where coordinate function $x(k)$ varies with wave number k and is defined by the optical design of the spectrometer. Where Erf, Δy, Δx, and x_j are, respectively, the error function, the pixel height, the pixel width of the detector array, and the position of the center of pixel j. The spot diameter a is defined as the FWHM of the beam focused on the detector and is assumed to be constant. The variable in the error function $k = 2\pi/\lambda$ is the wave number of the illuminating light. The spectral densities of reference and sample fields S_{ref} and S_{sam} are not necessarily the same. In Eq. 11.5, the quantum efficiency is assumed to be constant and the system

attenuation factor was normalized. The pixel height Δy in Eq. 11.5 comes out of the integral and does not affect the spectral interference or the falloff of the FD-OCT signal, but it affects the amplitude when it is not large enough compared to the spot size a. The pixel width Δx of the detector and the spot diameter a determine the fall-off of FD-OCT.

In the extreme condition when the spot diameter a goes to infinitely small, the sum of the two error functions under integral in Eq. 11.5 degrades into three special expressions: a step function either 2 in the pixel area or 0 outside the pixel if Δx has a finite and nonzero size ($\Delta x > a$), a Delta function with a maximum value of 1.68 if Δx goes to infinitely small ($\Delta x = a$), and zero if $\Delta x = 0$. Therefore, Eq. 11.5 degrades correspondingly into the following expressions:

$$I(x_j) = \frac{1}{2}\left[S_{ref}(k_j) + S_{sam}(k_j) + \sqrt{S_{ref}(k_j)S_{sam}(k_j)} \bullet \cos\left(2\Delta D k_j\right) \frac{\sin\left(\Delta D \Delta k_j\right)}{\Delta D \Delta k_j}\right] \quad (\Delta x > a), \tag{11.6}$$

$$I(x_j) = \frac{1}{2}\left[S_{ref}(k_j) + S_{sam}(k_j) + \sqrt{S_{ref}(k_j)S_{sam}(k_j)} \bullet \cos\left(2\Delta D k_j\right)\right] \quad (\Delta x = a). \tag{11.7}$$

where k_j is the wave number at position x_j and Δk_j is the segment of wave number around k_j covered by the j^{th} pixel. Equation 11.6 shows a clear sinc falloff when Δk_j is a constant over the spectrum, representing the case where the spectral resolution is dominated by the pixel size. Equation 11.7 is the familiar formula describing OCT interference, representing the case of infinitesimal spectral resolution and negligible falloff.

As an example, we evaluate the falloff versus different spot sizes for a spectrometer at center wavelength 1307.8 nm with bandwidth coverage of 102 nm. The design layout of this spectrometer is similar to the one in Fig. 11.17 except the grating is aligned for the center of the spectrum to be 1,307.8 nm. After integrating Eq. 11.5 over k space and Fourier transforming, the falloff curves at different ratios of the spot size to pixel size (pixel width: 50 μm), 0, 0.002, 0.25, 0.5, 0.75, 1.0, and 1.5 from top to bottom, are shown in Fig. 11.19. As expected, the calculations show that the smaller spot size leads to a better falloff. In the cases of the ratio < 0.25, the falloff is close to a sinc function, dominated by the pixel width. In order to easily compare the image attenuation versus the spot size ratio, we evaluated the image attenuation at -3 dB and -10 dB as a function of the spot size ratio (Fig. 11.20). This plot indicates that as long as the spot size ratio is less than 0.25, the falloff is near optimum.

11.5.3 Linear-k Spectrometer in OCT

A linear wavenumber (k) spectrometer design significantly improves the reliability and performance of SD-OCT [22], providing several advantages. First, there is no

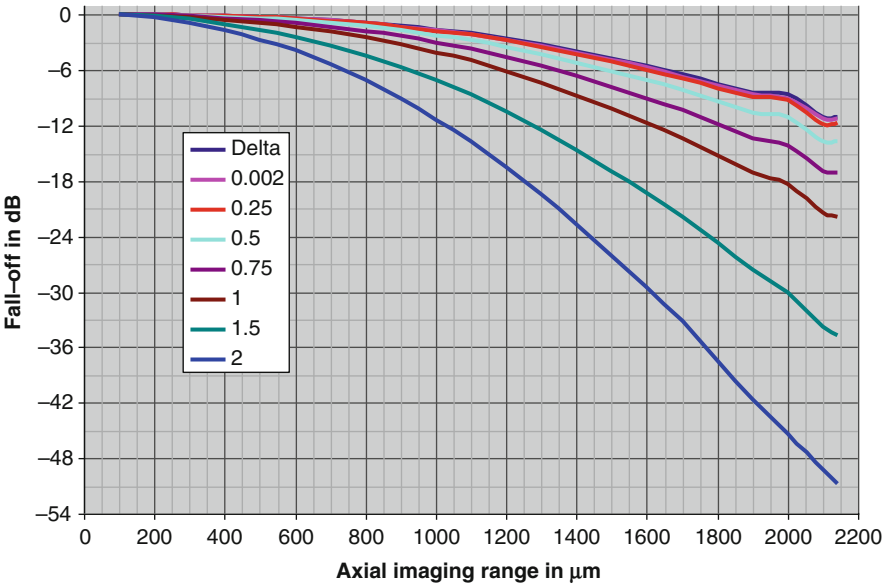

Fig. 11.19 Falloff curves at 8 different spot sizes ratios, falloffs for 0, 0.002, and 0.25 are very close. The higher the curve, the smaller the spot size. Pixel size = 50 μm; center wavelength = 1307.8 nm; wavelength coverage = 102 nm

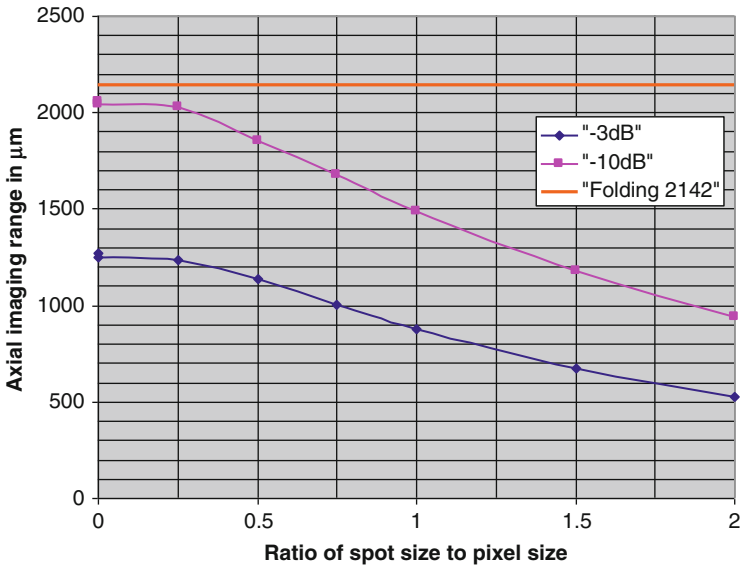

Fig. 11.20 Falloff distances at −3 dB ad −10 dB as a function of the ratio of spot size to pixel size. The falloff is near optimum when the ratio is less than 0.25

need to numerically transform the spectral interferogram into a function of k, which saves imaging reconstruction time. Furthermore, there is no need for a lookup table and wavelength calibration that requires the alignment of the camera to specific wavelengths of the spectrum. Also, the axial imaging falloff and SNR are significantly improved because of the uniformity of spectral sampling.

11.6 Conclusion

In summary, the quality of the design of critical components, including sample scanners, spectrometers, and delay lines, will significantly impact the performance of OCT imaging systems. The conscientious use of appropriate optics (e.g., achromatic and aspheric optics), design strategies (e.g., telecentric systems), and design tools (e.g., optical modeling software for computer-aided design) are important ways to design high-quality OCT subsystems.

Acknowledgements The authors thank Yinsheng Pan. Research presented here was supported in part by the National Institutes of Health (R01CA114276, R01HL083048, R01HL095717).

References

1. Z. Hu, A.M. Rollins, Quasi-telecentric optical design of a microscope-compatible OCT scanner. Opt. Express **13**(17), 6407–6415 (2005)
2. Z. Hu, A.M. Rollins, Theory of two beam interference with arbitrary spectra. Opt. Express **14**(26), 12751 (2006)
3. B.E.A. Saleh, M.C. Teich, Fundamentals of photonics, in *Wiley Series in Pure and Applied Optics*, ed. by J.W. Goodman (Wiley, New York, 1991)
4. B.E. Bouma, G.J. Tearney, *Handbook of Optical Coherence Tomography* (Marcel Dekker, New York, 2002), p. 741
5. Z. Hu et al., Analytical model of spectrometer-based two-beam spectral interferometry. Appl. Opt. **46**(35), 8499 (2007)
6. M. Laikin, *Lens Design*, 3rd edn. (Marcel Dekker, New York, 2001), p. 474
7. W.J. Smith, *Modern Optical Engineering*, 3rd edn. (McGraw-Hill, New York, 2000), p. 617
8. K.F. Kwong et al., 400-Hz mechanical scanning optical delay line. Opt. Lett. **18**(7), 558 (1993)
9. G.J. Tearney et al., In vivo endoscopic optical biopsy with optical coherence tomography. Science **276**(5321), 2037 (1997)
10. G.J. Tearney, B.E. Bouma, J.G. Fujimoto, High-speed phase- and group-delay scanning with a grating-based phase control delay line. Opt. Lett. **22**(23), 1811 (1997)
11. A.M. Rollins et al., In vivo video rate optical coherence tomography. Opt. Express **3**(6), 219 (1998)
12. A. Roorda et al., Adaptive optics scanning laser ophthalmoscopy. Opt. Express **10**(9), 405 (2002)
13. R.J. Zawadzki et al., Adaptive-optics optical coherence tomography for high-resolution and high-speed 3D retinal in vivo imaging. Opt. Express **13**(21), 8532 (2005)
14. W. Drexler et al., In vivo ultrahigh resolution optical coherence tomography. Opt. Lett. **24**, 1221 (1999)
15. B. Povazay et al., Submicrometer axial resolution optical coherence tomography. Opt. Lett. **27**(20), 1800 (2002)

16. P.R. Herz et al., Micromotor endoscope catheter for in vivo, ultrahigh-resolution optical coherence tomography. Opt. Lett. **29**(19), 2261 (2004)
17. P.H. Tran et al., In vivo endoscopic optical coherence tomography by use of a rotational microelectromechanical system probe. Opt. Lett. **29**(11), 1236 (2004)
18. A.G. Podoleanu, J.A. Rogers, D.A. Jackson, Three dimensional OCT images from retina and skin. Opt. Epress **7**(9), 292 (2000)
19. C.K. Hitzenberger et al., Three-dimensional imaging of the human retina by high-speed optical coherence tomography. Opt. Epress **11**(21), 2753 (2003)
20. D.T. Miller, O.P. Kocaoglu, Q. Wang, S. Lee, Adaptive optics and the eye (super resolution OCT). Eye **25**, 321 (2011)
21. W. Kang et al., Endoscopically guided spectral-domain OCT with double-balloon catheters. Opt. Express **18**(16), 17364 (2010)
22. Z. Hu, M.A. Rollins, Fourier domain optical coherence tomography with a linear-in-wavenumber spectrometer. Opt. Lett. **32**(24), 3525 (2007)

Linear OCT Systems

12

Gereon Hüttmann, Peter Koch, and Reginald Birngruber

Keywords
Linear OCT • L-OCT • Parallel OCT • Parallel detection

12.1 Introduction

Optical coherence tomography (OCT) determines the distances of scattering structures by interferometry in order to reconstruct A-scans and B-scan images of three-dimensional objects. In time-domain OCT (TD-OCT) the intensity at the output of the interferometer is measured with a point detector, while the optical path length in one interferometer arm is changed [1]. As an approach to avoid moving parts, linear OCT (L-OCT) employs a parallel detection scheme to measure the interference by introducing spatially varying path length differences on an array of individual detectors. According to Fig. 12.1, L-OCT is one of the four basic groups of OCT systems, which can be distinguished by the measured parameter (interference pattern or spectrum) and the type of acquisition (time-dependent point measurement or spatially multiplexed parallel measurement). TD-OCT and L-OCT measure an interference pattern, whereas spectral or Fourier domain OCT (FD-OCT) [2, 3] and swept source OCT (SS-OCT) [2, 4], which is also named optical frequency domain imaging (OFDI), measure the cross-correlation spectrum, which is converted to the A-scan by a Fourier transform.

G. Hüttmann (✉) • P. Koch • R. Birngruber
Institute of Biomedical Optics, University of Lübeck, Lübeck, Germany

Medical Laser Center GmbH, Lübeck, Germany
e-mail: huettmann@bmo.uni-luebeck.de

© Springer International Publishing Switzerland 2015

W. Drexler, J.G. Fujimoto (eds.), *Optical Coherence Tomography*,
DOI 10.1007/978-3-319-06419-2_13

		Sampling of the A-Scan	
		Sequentially by Point Measurement	Spatially Multiplexed by Parallel Detection
Measured Parameter	Spectrum (Frequency Domain)	Swept Source OCT (Optical Frequency Domain Imaging)	Spectral Domain OCT (Spectral Radar)
	Coherence Function (Time Domain)	Time Domain OCT	Linear OCT

Fig. 12.1 The four fundamental implementations of OCT

FD- and SS-OCT offer superior sensitivity and signal-to-noise ratio (SNR) over time-domain and linear OCT. But they also have some disadvantages. FD-OCT needs high performance optics for the spectrometer, SS-OCT is based on sophisticated rapidly tunable light sources, and the necessary Fourier transform requires some processing power. Additionally, the correlation of the reflectivity distribution in the sample, which is incorporated in the FD- and SS-OCT signals, may obscure the image. This is especially the case when strong reflecting surfaces are present in the image. By their working principle, TD-OCT and L-OCT avoid the autocorrelation problem and give unique information about the structure of the sample.

One of the main technological challenges for TD-OCT was to build an optical delay line that worked at high frequencies with a constant velocity [5], and still the delay line is an important factor that limits the acquisition speed and makes TD-OCT systems complex and sensitive to unwanted changes of the alignment. Obviously, TD-OCT without moving parts would be of great advantage, especially for commercial systems.

Linear OCT, which combines the principle of TD-OCT with a parallel detection scheme, is a way to overcome these limitations by projecting the interference pattern on a line detector. A problem of L-OCT was the high number of pixels which were needed to sample the interference pattern without aliasing. At a wavelength of 800 nm a ranging depth of 2 mm required at least 10,000 pixels. This problem was overcome by optically reducing the fringe frequency of the interference pattern without influencing the information-carrying parts. The advances in CCD and CMOS detector technology in the recent years made linear OCT devices possible.

This chapter describes theory, implementation, and performance of linear OCT systems and discusses possible applications. Line-field versions of linear OCT are briefly introduced.

12.2 Theory

12.2.1 The Principle of Linear OCT

The depth z_s of reflecting or scattering tissue structures can be measured by interferometry because the propagation time of radiation with a frequency ω travelling through tissue with a phase velocity c introduces a phase shift of $\Phi_S = (\omega/c)\, z_S$. In OCT this phase shift is recovered by superposing the radiation from the sample with a reference beam. With the electric fields for sample and reference radiation given by $\sqrt{j_S(\omega)}\exp(i\,\Phi_S(\omega))$ and $\sqrt{j_R(\omega)}\exp(i\,\Phi_R(\omega))$, respectively, the intensity of the interference signal on a detector at the output of the interferometer results in

$$I = j_S + j_R + 2\sqrt{j_S j_R}\cos(\Delta\Phi) \tag{12.1}$$

$\Delta\Phi = \Phi_S - \Phi_R = \omega/c\,(2z_S - 2z_R)$ is the phase difference between sample and reference irradiation. For monochromatic light the interference signal I changes periodically with the difference $\Delta z = z_S - z_R$ of the path lengths in sample and reference arm and gives no unique information for a Δz larger than the half of the wavelength λ. Therefore, OCT uses polychromatic light to recover Δz. The phase difference and subsequently the interference pattern are dependent on the frequency of the radiation. Hence the change of $\Delta\Phi$ with the frequency contains in a unique way the depth information. In TD- and L-OCT a nearly zero phase difference is detected by superposing all frequency components on the detector. This is described mathematically by integrating Eq. 12.1 over the whole frequency range of the radiation.

$$I = I_S + I_R + 2\int \sqrt{j_S(\omega) j_R(\omega)}\cos(\Delta\Phi(\omega))d\omega \tag{12.2}$$

I_s and I_R are the integrals over spectral densities j_s and j_R which yield the intensities for reference and sample radiation. When the dispersions in both arms of the interferometer are balanced, the interference signal consists of a harmonic function with the central frequency ω_0, which is modulated by the Fourier transform $\sqrt{2\pi}F\{S(\omega-\omega_0)\} = \sqrt{j_S j_R}\,\gamma(2\Delta z/c)$ of the radiation spectrum $s(\omega)$ [6]:

$$I = I_S + I_R + 2\sqrt{I_S I_R}\gamma(2\Delta z/c)\cos(\omega_0/c\,2\Delta z) \tag{12.3}$$

The modulation of the cosine actually contains the normalized coherence function γ of the radiation source. The interference pattern is only observed if the difference of the optical path lengths $2\Delta z/c$ is within the width of the coherence function γ. This coherence gate allows to separate the signals from different depths in the sample by evaluating I, while the optical delay in one arm of the interferometer is changed over a certain range.

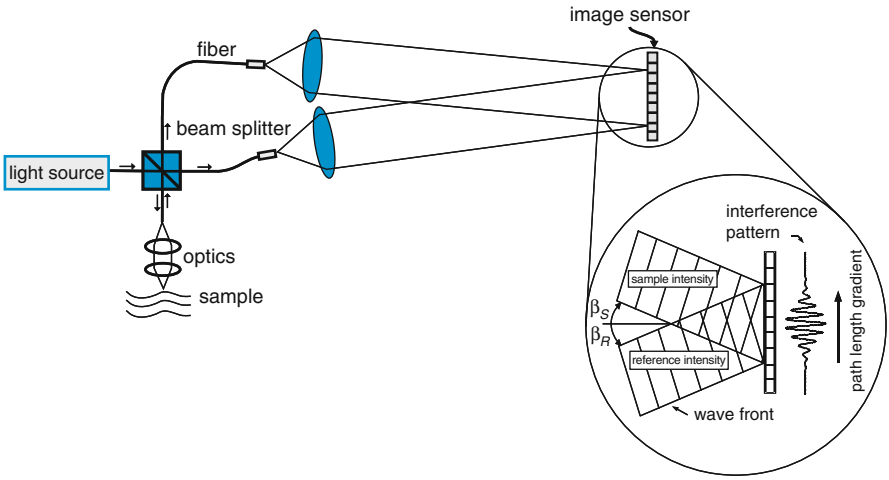

Fig. 12.2 The basic principle of linear OCT (L-OCT). An interference pattern is formed on the image sensor by the tilted sample and reference beams

In linear OCT the interference pattern is measured in parallel by spatially extending the interference pattern on a line or array detector (Fig. 12.2). A simple way for this is to expand sample and reference beam and superpose them under the angles β_s and β_R on the detector (see inset in Fig. 12.2).

In that case, the phases of both beams depend linearly on the lateral position on the detector and the resulting phase difference is given by

$$\Delta\Phi = \omega/c\,(2\Delta z + x(\sin\beta_S - \sin\beta_R)) \tag{12.4}$$

With this expression for the phase difference, Eq. 12.3 changes to:

$$I = I_S + I_R + 2\sqrt{I_S I_R}\gamma((x\xi\lambda_0 + 2\Delta z)/c)\cos(2\pi x\xi + \omega_0/c\;2\Delta z) \tag{12.5}$$

The interference pattern now contains the carrier frequency $\xi = (\sin\beta_S - \sin\beta_R)/\lambda_0$, which can be controlled by the incidence angles of both beams. Without moving parts a whole A-scan can be measured.

The time-dependent modulation of a signal from a single point detector at the output of the interferometer is exchanged by the measurement of a spatial intensity distribution with an extended detector. Differences in the performance and layout between TD-OCT and L-OCT arise, therefore, only from the parallel acquisition of data for the complete A-scan, the discrete sampling of the interference pattern, and the performance characteristics of the different classes of detectors used.

One important restriction for L-OCT is that the pixel frequency ξ_P of the detector has to be at least two times the modulation frequency ξ to fulfill the Nyquist criterion. Since a full cycle of the interference signal corresponds to a path length difference of $\lambda/2$, at least $4\Delta d/\lambda$ pixels are needed for a certain

measurement depth Δd. Hence, the depth range is limited by the number of available pixels. The information that is detected by OCT has a bandwidth that is the reciprocal of the coherence length l_c (typically 5–20 μm), which is significantly smaller than ξ. To reduce the number of necessary pixels, it would be desirable to reduce the bandwidth of the interference pattern by reducing or removing the carrier frequency ξ. In fact there is the possibility of an optical control of the carrier frequency without loss of information.

12.2.2 Optical Control of the Carrier Frequency

12.2.2.1 Transmission Grating in Near Field

In radio technology, a reduction of the carrier is often done by mixing, i.e., the multiplication with a second fixed frequency. Optically, this can be facilitated by the transmission of the interference pattern through a mask with a periodically changing absorption, i.e., by a transmission grating (Fig. 12.3). The intensity directly behind the grating is the product of the interference pattern with the transmission of the mask. With a grating of a frequency ξ_g and a harmonic transmission $\tau = (1 + \cos(2\pi\xi_g x))/2$, the following intensity pattern results to [7].

$$I(x) = \frac{1}{2}(I_S + I_R)\left(1 + \cos\left(2\pi\xi_g x\right)\right) + \frac{1}{2}\sqrt{I_S I_R}\gamma((x\xi\lambda_0 + 2\Delta z)/c)$$
$$\left(\cos\left(2\pi\left(\xi - \xi_g\right)x + \omega_0/c\,2\Delta z\right) + \cos\left(2\pi\xi x + \omega_0/c\,2\Delta z\right) + \cos\left(2\pi\left(\xi + \xi_g\right)x + \omega_0/c\,2\Delta z\right)\right) \tag{12.6}$$

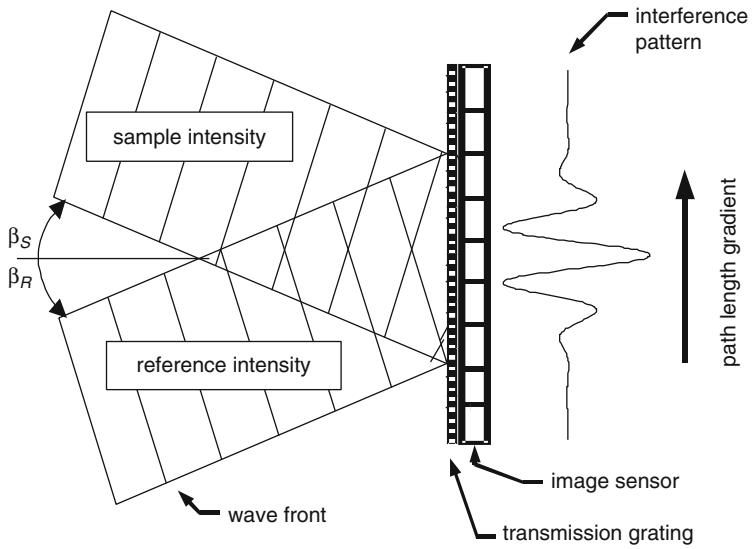

Fig. 12.3 Reduction of the fringe frequency of the interference pattern by a periodic transmission grating

$I(x)$ now consists of four bands with the center frequencies at $\xi - \xi_g$, ξ_g, ξ, and $\xi + \xi_g$. All frequency components but ξ_g are modulated by the information from the sample. With choosing ξ_g and ξ in a way that $\xi - \xi_g$ is below the half sampling frequency and that ξ and $\xi + \xi_g$ are above the pixel frequency ξ_P, the Nyquist criterion can be fulfilled and the high-frequency components of the interference pattern will be averaged out on the light-sensitive area of the pixels [7]. Only the signal component $1/2\sqrt{I_S I_R}\gamma((x\xi\lambda + 2\Delta z)/c)\cos\left(2\pi\left(\xi - \xi_g\right)x + \omega_0/c\,2\Delta z\right)$ and a constant background will be measured. The spectral components of the coherence function γ and, therefore, the structure information of the sample are not affected by the transmission mask.

By this principle, the carrier frequency can be reduced to any value. If ξ_g is exactly ξ, the carrier is completely removed, and only the modulation multiplied by a phase term will appear on the sensor. In this case the intensity on the detector becomes sensitive to the relative phase between reference and sample irradiation which modulates the signal between zero and the maximal level. The simplest way to avoid the resulting ambiguity is to use a low-frequency carrier. For a reconstruction of γ, two cycles of the carrier per coherence length l_c are sufficient. Without transmission mask l_c/λ cycles, which appear under γ, have to be sampled. Therefore, at a fixed number of pixels the grating increases the image depth by a factor of $l_c/2\lambda$. At 800 nm wavelength and 15 µm coherence length, this is about an order of magnitude. Unfortunately the mask reduces the signal due to transmission losses of the grating and the fact that 50 % of the signal power is mixed into the sum frequency where it cannot be detected. The modulation amplitude of the signal is thereby reduced to 25 % compared to L-OCT without transmission mask.

12.2.2.2 Diffraction by a Phase Grating

A control of the fringe frequency of the interference pattern with minimal signal loss is possible by the use of a phase grating. In a beam diffracted by a grating, parallel light rays, which emerge from each groove, have different propagation times. The direction of the newly formed phase front, which determines the carrier frequency in the interference pattern, is decoupled from the group front (the time delay of wave packages), which determines the width of the coherence function (Fig. 12.4). An individual control of the group and phase delay across the beam diameter is therefore possible by a phase grating. This principle, which was used for femtosecond pulse measurements [8, 9], in delay lines for TD-OCT [10, 11], and for coherent microscopy [12], can also be applied to L-OCT [13].

A reduction of the fringe frequency occurs when different diffraction orders of the reference and sample beam are superposed on the detector (Fig. 12.4). The m^{th} diffraction order introduces an achromatic phase shift of $2\pi m$ between parallel rays from neighbored grating lines. Therefore, a phase which varies by $2\pi\ m\ \xi_g\ x$ is introduced across the beam. This phase term changes Eq. 12.3 to

$$I(x) = I_S + I_R + 2\sqrt{I_S I_R}\gamma((x\ \xi\ \lambda_0 + 2\Delta z)/c)\cos\left(2\pi\left(\xi - \Delta m\xi_g\right)x + \omega_0/c\ 2\Delta z\right), \quad (12.7)$$

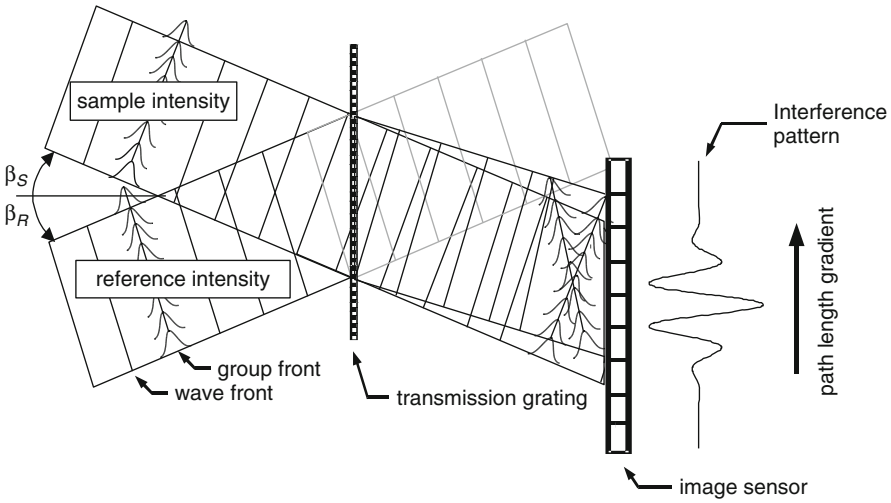

Fig. 12.4 Reduction of the fringe frequency by a diffraction grating. A grating forms new phase fronts in the diffracted beam, in which the propagation time varies across the diameter. Phase and group fronts are tilted against each other

where Δm is the difference of the diffraction orders of the sample and reference beam which interfere on the detector. Compared to Eq. 12.5, an expression appears, in which the fringe frequency is reduced by Δm times the grating frequency ξ_g. In contrast to the transmission mask, only the term with the difference frequency appears, and the losses in the sample beam can be kept small by adequate design. In the configuration of Fig. 12.4, a low diffraction efficiency of the grating causes only negligible losses to the sample beam. The high losses to the reference beam can be tolerated, because only the intensity from the sample is affecting the sensitivity of the system. Therefore, with a phase grating a control of the fringe frequency is possible without compromising the sensitivity of the OCT signal. With an additional beam splitter, a reflection grating can be used as well (Fig. 12.5). An open Michelson interferometer, in which the reference mirror is replaced by a grating in Littrow configuration, offers here an elegant way [14, 15]. The carrier frequency is adjusted by the angle between reference and sample beam. The path length difference over the detector is determined by the tilt angle of the grating.

12.2.3 Sensitivity and Signal-to-Noise Ratio (SNR)

In principle L-OCT can reach the same sensitivity and signal-to-noise ratio (SNR) as T-OCT [16]. According to Eq. 12.3 the OCT signal S, which shall reflect the intensity of the radiation scattered by tissue structures, is calculated as the square of the detected modulation integrated over the coherence function γ.

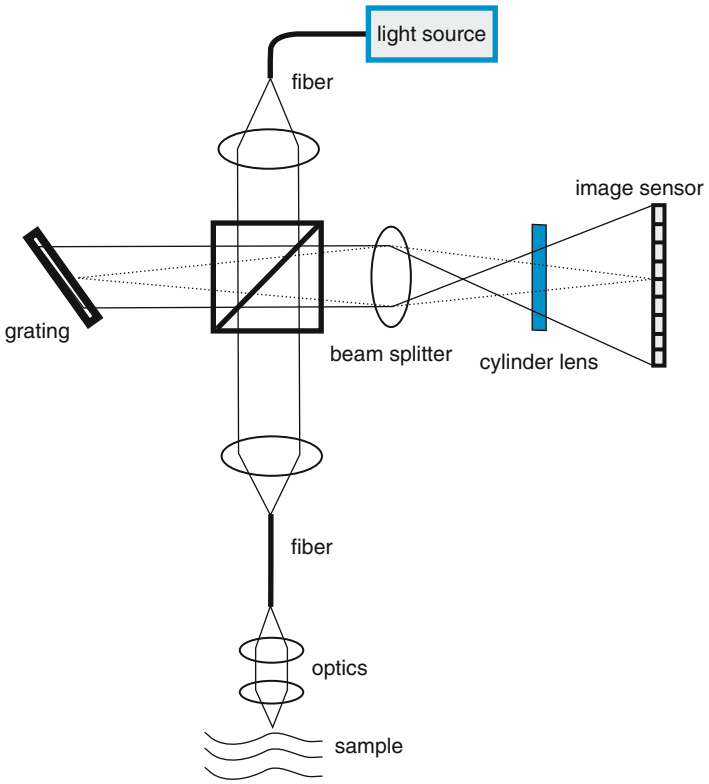

Fig. 12.5 Reduction of the fringe frequency by a reflection grating

$$S = 4n_R n_S \int \gamma^2(2\Delta z/c)\cos^2(\omega_0/c2\Delta z)d\Delta z \approx l_c n_R n_S, \tag{12.8}$$

where n_R and n_S are the numbers of photoelectrons generated by the reference and the sample radiation, respectively. Noise arises from the shot noise mainly generated by the constant background signal n_B in the interference pattern and the noise n_D of the detector and electronics.

$$N = n_B \int \gamma^2(2\Delta z/c)d\Delta z + n_D \approx l_c n_B + n_D, \tag{12.9}$$

For small signal intensities (the reference intensity is much larger than the sample intensity) and quantum noise limited performance (detector noise is smaller than shot noise), n_B is given by n_R and the SNR is just the number n_S of detected photons from the sample. n_S can be expressed by the intensity I_s received from the sample, the exposure time τ, and the quantum efficiency η of the detector:

$$SNR = \frac{S}{N} = n_S = I_s \tau \frac{\eta}{\hbar\omega} \frac{l_c}{\Delta d} \tag{12.10}$$

Besides the power I_S from the sample, also the ratio between coherence length l_c and measuring range Δd determines the SNR, because I_S, which is spread over the whole detector length, only contribute to the signal n_s within the window of the coherence function γ. This fraction can be approximated by $l_c/\Delta d$. A similar equation is obtained for TD-OCT systems. In FD- and SS-OCT the SNR is higher by the factor $\Delta d/l_c$, because the sample intensities from all depth contribute to the signal in every pixel of the detector [3]. Hence, the number of signal photons n_s is only given by $I_s\tau\eta/\hbar\omega$.

In contrast to standard TD-OCT systems, in L-OCT as well as FD-OCT incident power on their primary sensors is limited. The photodiodes used in TD-OCT show a linear response up to a few mW well exceeding the output power of standard OCT light sources like SLDs. Here the analog demodulation electronics is the bottleneck. It is especially difficult to build a rectifier with a dynamic range larger than 80 dB. In L-OCT devices the full well capacity (FWC) of the image sensors is the limiting factor. The number of detectable sample electrons n_s in one readout cycle cannot be larger than the half of FWC times the average number of pixels under the coherence function, which is given by the total pixel number N_P times $l_c/\Delta d$. Therefore, the maximum SNR_{max} can be expressed in terms of the FWC by

$$SNR_{max} = \frac{FWC}{2} \frac{N_P l_c}{\Delta d} \tag{12.11}$$

For a measurement range of 1 mm, a coherence length of 20 μm, a line detector with 1,024 pixel, and 6 million electrons FWC, SNR_{max} is 78 dB. Equation 12.11 also gives the dynamic range of an L-OCT system, defined by the highest detectable signal divided by the signal which can be detected with an SNR of one.

The sensitivity σ of an OCT device is defined by the reciprocal of the smallest reflectivity in the sample that can be detected with an SNR larger than one. It is calculated by replacing I_S by $1/\sigma$ times the irradiation I_{OS} falling on the sample

$$\sigma = \frac{\eta\tau I_{OS} l_c}{\hbar\,\omega\Delta z} \tag{12.12}$$

In principle σ can be increased arbitrarily by increasing the light level that falls on the sample. However, in practical applications the sensitivity is limited by the dynamic range of the OCT system, because usually high and low reflection should be measured at the same time. If, for example, a specular reflection at the surface of the tissue should not saturate the detector, the sensitivity is approximately given by the dynamic range divided by the surface reflectivity (about 4 %).

12.3 Detectors for Linear OCT

The detector arrays for L-OCT should be selected with great care because their performance is crucial for the quality of the L-OCT images. In biomedical applications a high sensitivity is necessary to visualize internal tissue structures. This means that small modulations on a large background signal have to be detected with low noise. Relevant properties of the detectors are noise, linearity, maximum signal (FWC), pixel size and number. Similar criteria, as will be discussed in the following section, are also valid for FD-OCT detectors, but a high dynamic range of the line detector is even more important for L-OCT, because a strong signal from one image point is not distributed over all the pixels, but sampled locally.

12.3.1 Systematical Errors and Detector Noise

For an optimal performance the systematic measurement errors, which are always present in image sensors, have to be removed. Every pixel of the sensor has a specific offset error, which is usually called dark signal nonuniformity (DSNU), and a certain gain error, the pixel response nonuniformity (PRNU). DSNU is in the order of a few percent of the full well capacity. PRNU is usually also about a few percent. To gain an optimal performance, DSNU has to be removed by subtracting the dark response of the sensor from every scan. Gain errors are corrected by dividing the measured data by a reference scan which is obtained under uniform illumination of the sensor.

If all systematic errors are removed properly, a noise floor N of the sensor is left which depends on the photon shot noise N_{PSN} of the photoelectrons n_{Ph}, the dark noise N_{Dark}, which is the shot noise of dark signal electrons n_{Dark}, and the additional signal-dependent noise components from the sensor and the electronics N_{Elec}.

$$N^2 = N_{PSN}^2 + N_{Dark}^2 + N_{Elec}^2 = n_{Ph} + n_{Dark} + N_{Elec}^2 \tag{12.13}$$

For a quantum noise limited performance of an L-OCT system, the photon shot noise must be larger than the two other noise contributions. This is achieved by increasing the number of photoelectrons n_{Ph} in the pixel until the sensor nearly saturates. The maximal exposure (FWC) and the dark noise actually define the optimal working range of the sensor and determine the achievable SNR of the L-OCT system.

For a quantitative comparison of different detectors, the photon transfer function (PFT) can be used [17], which relates the noise N of the output to the average number n_{Ph} of measured photoelectrons. The PTF allows to identify the exposure region in which the performance of the sensor is closest to the quantum noise limit. The closer the PTF of a detector is to the straight line $N = \sqrt{n_{Ph}}$ of an ideal detector, the better the performance. A real sensor (e.g., the LIS 1024 CMOS sensor from Photon Vision Systems) has usually three distinct areas (Fig. 12.6). At very low intensities a constant dark noise is dominant. In the case of CMOS sensors, the dark noise is generated by switching the different pixels on a common video signal bus. At medium intensities the quantum noise is the dominant noise source, and at very

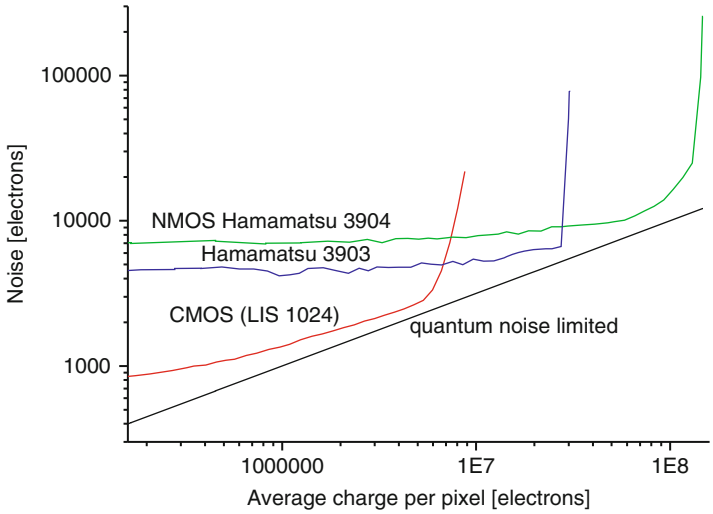

Fig. 12.6 Photon transfer functions (PTF) of different image sensors. The Hamamatsu 3903 and 3904 are passive NMOS diode array detector and the LIS 1024 (Photo Vision Systems) is a CMOS image sensor with an active pixel technology

high intensities close to the FWC, the performance is degraded by nonlinearities of the image sensors.

For useful L-OCT devices the design has to allow for some fluctuations of the reference intensity. Therefore, it is important for an image sensor to have a certain range of intensities in which quantum noise limited performance is possible.

Compared to PIN photodiodes, which are used in TD-OCT, line detectors have a considerably smaller intensity range (an order of magnitude or less) in which they work with optimal performance.

12.3.2 Spatial Resolution and MTF

The spatial resolution of the image sensor has to be high enough to measure the interference pattern with good contrast. The sensitivity of an array detector to a harmonic wave of a given frequency is described by the modulation transfer function (MTF). The MTF can be calculated by the Fourier transformation of the point spread function (PSF), which is the spatial sensitivity distribution of a pixel to a point illumination. For an ideal pixel the PSF would be a rectangular function with the width of the pixel pitch. Correspondingly, the MTF of an ideal sensor would be a sinc function (Fig. 12.7). The modulation would decrease with increasing spatial frequencies of the fringe pattern and reach zero, when the period of the modulation equals the pixel pitch. At higher frequencies the side lobes of the sinc function cause a certain modulation response, which gives an ideal sensor a sensitivity to frequency components higher than the pixel frequency. This would cause additional

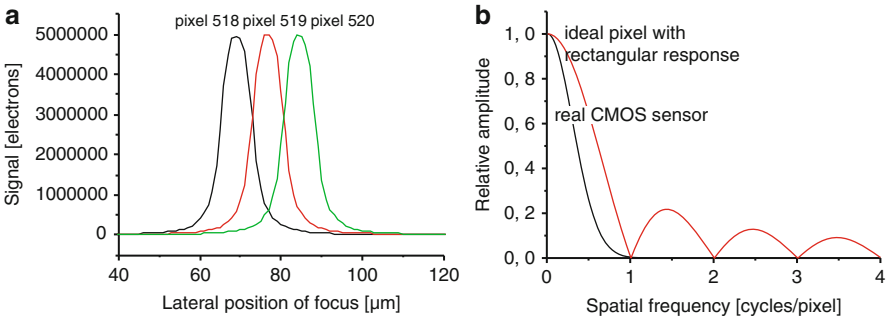

Fig. 12.7 (**a**) Sensitivity distribution of three neighboring pixels measured with a CMOS image sensor (LIS 1024, Photo Vision Systems). The sensor was illuminated with monochromatic light ($\lambda = 830$ nm) focused on the detector by a microscope objective. (**b**) Modulations transfer function (MTF) from calculated the measured data in comparison to the MTF of an image sensor with a rectangular pixel response

interfering signals when a transmission grating attached to the sensor is used for a reduction of the fringe frequency. In reality cross talk between the pixels (see Fig. 12.7a) results in a more or less bell curve-shaped spatial sensitivity of a pixel and therefore also in a bell curve-shaped MTF, which does not extend beyond the pixel frequency. The MTF of real sensors can already drop by almost an order of magnitude toward half of the pixel frequency (Nyquist frequency). Measurements with a contrast close to one are therefore limited to spatial frequencies significantly below that frequency.

12.3.3 Practical Considerations and Choice of the Detector

Price and performance of the detectors favor today linear OCT in the spectral range from the visible down to 1,000 nm, because inexpensive, high performance silicon-based detectors are available for that spectral range. However, IR line detectors were used for FD-OCT [18] and should also be applicable for L-OCT. A small pitch is advantageous for building compact systems. A high aspect ratio of the pixels makes the devices robust against misalignment and a large number of pixels enable a high imaging depth or according to Eq. 12.11 a high maximum SNR. Additionally, large pixel numbers allow to work in a range of high MTF values. However, since usually the pixel readout frequency is limited to a certain value, increasing the number of pixels decreases the A-scan rate.

Three different kinds of detectors (CCD, CMOS, and NMOS) were used for L-OCT [7, 13, 16, 19]. They work on different power levels due to different readout noise and different maximal signal levels. Nearly quantum noise limited performance was only demonstrated with CMOS and CCD detectors. NMOS diode array with a photodiode and a storing capacitor at each pixel have a relatively high readout (switching) noise of 5,000–10,000 electrons and large pixel to pixel

variation, which prevent shot noise limited performance despite of the high full well capacity of 10^7–10^8 electrons (Fig. 12.6).

CMOS sensors have active pixels with an integrated readout amplifier, which reduces the readout noise to less than 1,000 electrons. The saturation level lies between that of CCD and NMOS diode array. Nearly shot noise limited performance over one order of magnitude is possible with these characteristics (Fig. 12.6).

CCD detectors which shift the trapped photogenerated charges from the pixels to an optimized readout amplifier can reach readout noise and pixel response nonuniformity (PRNU) down to a few tens of electrons. With values between 10^5 and 10^6 electrons, the full well capacity of CCD detectors is quite small compared to CMOS and NMOS diode arrays. Two-dimensional CCD detectors provide increased FWC by binning or the simultaneous acquisition of complete B-scan images [12, 14].

Usually, OCT uses superluminescent diodes with a power of a few mW of which due to losses at the beam splitter and other optical components, typically only 100 μW fall onto the detector. This corresponds at 800 nm to 4×10^{14} photons per second. With a quantum efficiency of 25 % and a line detector with 1,000 pixel, 10^{11} electrons per second and pixel are generated. Depending on the FWC of the detector, scan times between 1 μs and 1 ms provide an optimal exposure. CCD detectors are therefore suited for limited sample exposure and high-speed applications, whereas CMOS sensors are very attractive at lower and high readout frequencies offering shot noise performance over one order of magnitude and high SNR.

A uniform illumination of an array detector without intensity losses is difficult, because the spatially coherent radiation, which has to be used in OCT, has usually a Gaussian intensity profile. Either the illumination at the rim of the detector is smaller than at the central part or photons from the sample have to be discarded. In both cases the sensitivity is reduced.

12.3.4 Signal Processing

In TD-OCT, the output of the photodetector is either demodulated by analog electronics or sampled by a fast A/D converter. In principle, both analog and digital processing of the output of the array detector are also possible for L-OCT. However, up to now only a direct digitalization with a software-based demodulation was demonstrated.

The standard procedure for signal processing in L-OCT, which consists of band-pass filtering, rectification, and low-pass filtering, is shown in Fig. 12.8. As an example, the digitized signal of a single glass-air interface is depicted in the leftmost graph. The Gaussian beam profile causes the intensity distribution to drop toward the left most and rightmost pixel to about a third of the maximum value. The fringe pattern caused by the object is visible around pixel number 500.

In a first processing step, the offset error is subtracted for every pixel. Following the A-scan is divided by a calibration dataset to compensate for the different gains and exposure of the pixels. The graph in the middle of Fig. 12.8 shows the normalized signal. In the next step, excess noise is removed by digital band-pass

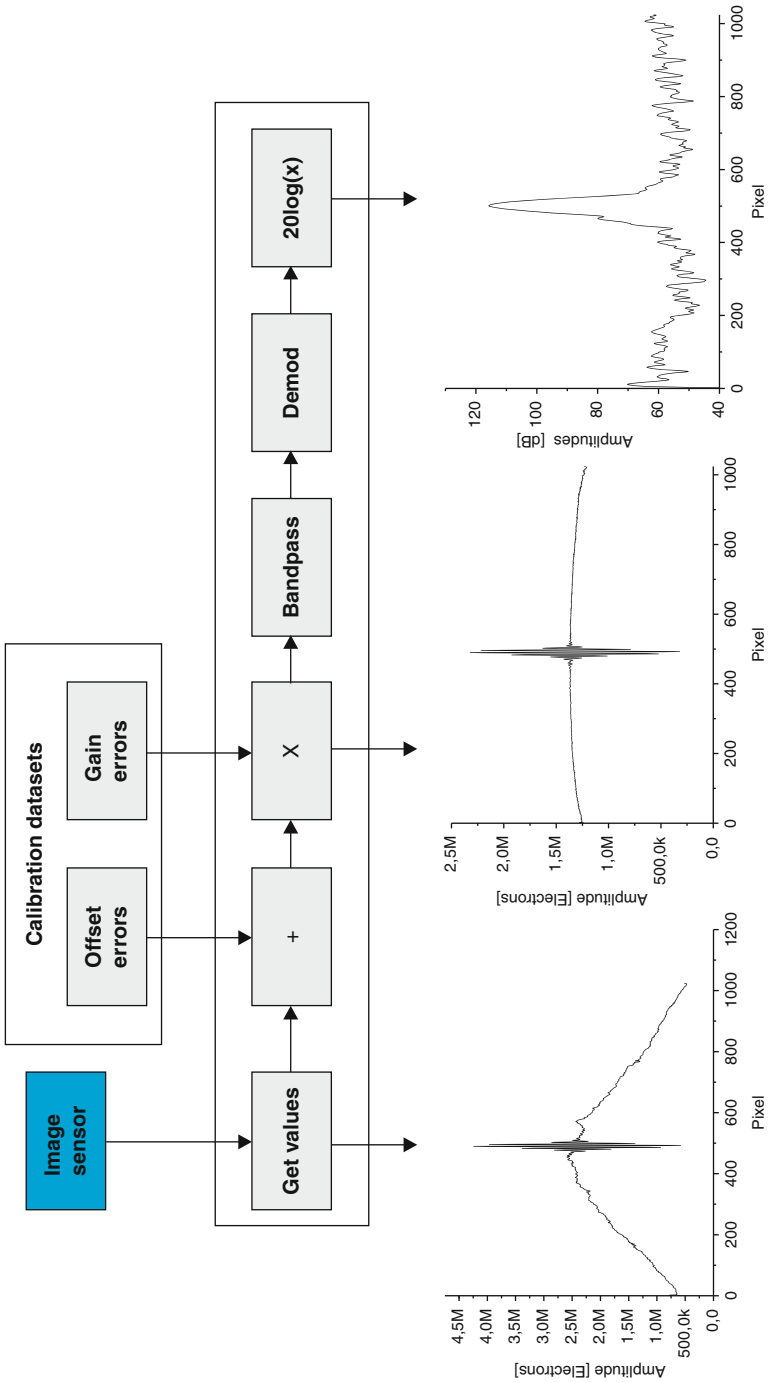

Fig. 12.8 Signal processing in L-OCT

filtering. The center frequency f_c of the filter is adjusted to the fringe frequency of the interference pattern. The demodulation is either done by taking the absolute value (rectification) and averaging (low-pass filtering) or by directly sampling of the signal at fixed intervals (e.g., after each $\lambda/3$). The demodulated amplitude is depicted on a logarithmic scale in the rightmost graph in Fig. 12.8. The noise floor which is in the order of 50 dB in the center of the image sensor increases toward the right most and leftmost pixel by about 10 dB, because at the edges the SNR is reduced by the significant smaller light intensity from the sample. Correction to a constant amplitude over the sensor area causes the increased noise level.

With a reflection grating in Littrow configuration, which replaces the reference mirror of a Michelson interferometer, OCT imaging at zero carrier frequency was demonstrated [15]. The phase changes, which are needed for the demodulation of the interference signal, were generated either by moving the grating by a piezo transducer or by lateral gradients in the phase when the sample was scanned.

12.4 Examples of L-OCT Systems

Only a few L-OCT systems were described up to now. As far as we know, the first system built was based on an NMOS diode array with 512 pixels and provided a ranging depth of only 70 μm [19]. The interferometer was built with a fiber coupler, and the two output fibers were positioned side by side in a certain distance from the detector (Fig. 12.9). One fiber carried the radiation from the reference arm, the other the radiation from the sample. Similar to Young's double slit experiment, a spatially varying interference pattern with a nearly constant frequency was formed on the detector. This setup demonstrated that L-OCT systems can be built of a few simple optical components: superluminescence diode, fiber coupler, cylindrical lens, and detector array. The performance of the system was demonstrated by scanning the surface of an MEMS acceleration sensor (Fig. 12.10). Here the required imaging depth was less than 70 μm, and the advantage of stable phase measurements due to the lack of moving parts was exploited for high-resolution profiling. The reflection signal from a surface consisted only of the coherence peak. By either calculating the centroid or fitting a Gaussian curve to the measured data, the position of the surface was determined with submicrometer resolution though the coherence length was 13 μm. Additionally, the phase of the OCT signal which is sampled together with the amplitudes could be used in order to increase the resolution.

With a similar interferometer design and a 7,926 element CCD image sensor, Hauger et al. demonstrated for the first time L-OCT images of biological tissue. They verified theoretical predictions of the fringe frequency and the depth resolution and showed with 0.6 mW illumination on the sample and 200 Hz A-scan rate images of porcine brain and heart in vitro, as well as human skin in vivo. Quantitative numbers on SNR and sensitivity were not given.

L-OCT with 1.1 mm measuring range was demonstrated with a transmission mask attached in front of a 1,024 pixel CMOS sensor [7]. Due to losses caused by the mask and the common path interferometer design, which introduced an additional

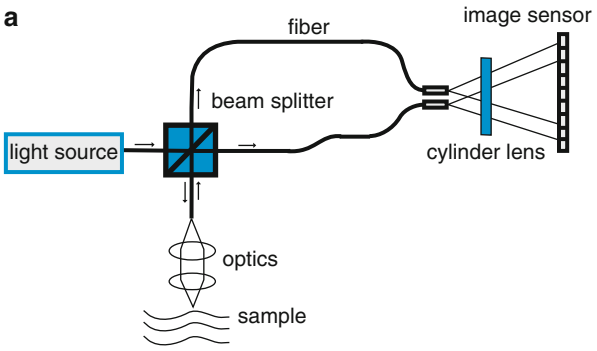

Fig. 12.9 (**a**) Simple setup for an L-OCT system, based on Young's double slit experiment. (**b**) Image of the main optical components

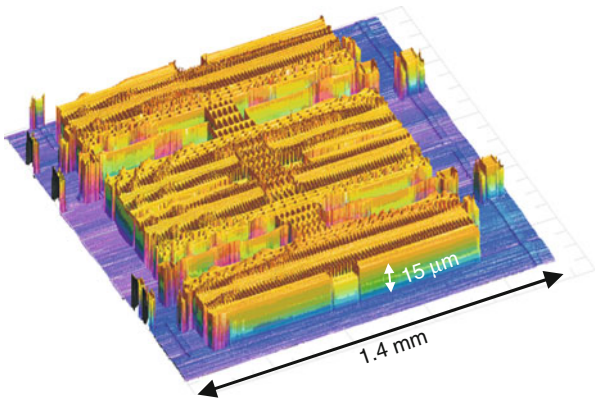

Fig. 12.10 Surface structure of an MEMS technology acceleration sensor measured by linear OCT (*L-OCT*)

incoherent background, a sensitivity below 61 dB was attained and only images of surface structures were possible with good quality. The common path interferometer enabled a flexible system with a high phase stability which is well suited for profilometry. However, the sensitivity was too low for imaging tissues with satisfactory quality.

Using the same CMOS sensor with a phase grating for the reduction of the fringe frequency and a modified Mach-Zehnder interferometer, a sensitivity of 80 dB was

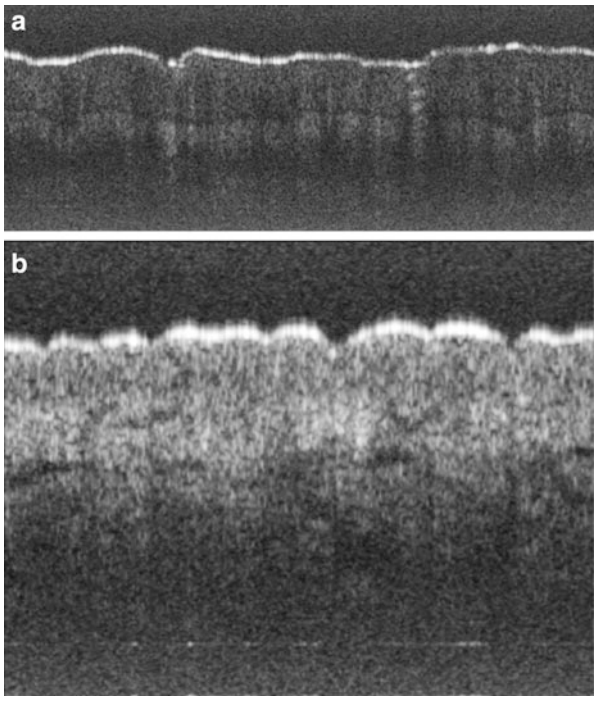

Fig. 12.11 In vivo images of human skin acquired by linear OCT (*L-OCT*) with a 1,024 pixel CMOS sensor and a phase grating at 1,200 A-scans per second were acquired. (**a**) Skin of the thumb with visible boundary between horny layer and dermis. Ducts of sweat glands are visible in the right half of the B-scan. The image dimensions were 940 µm × 4 mm. (**b**) B-scan image of the skin of the forearm. The boundary between dermis and epidermis and single vessels were observed. Measured range was 940 µm × 2 mm

possible [13]. This allowed imaging of skin at 1.2 kHz A-scan rate with good quality (Fig. 12.11). With increased output from the SLD, even scan rates of more than 5 kHz should be possible with this detector. The image quality was comparable to standard TD-OCTs which usually work at lower scan rates of 20–200 Hz [20, 21]. However, with an FD-OCT system based on the same detector, a significantly better image quality was possible [22] due to the fundamentally higher SNR of OCT systems working in the spectral domain.

With high-speed line cameras and 3 mW exposure to the tissue at a wavelength of 1,300 nm, imaging faster than video rate is possible [15]. With the variant of L-OCT, which used a Michelson interferometer with a reflection grating and a fast InGaAs-camera, images of human skin were demonstrated at 94 frame/s corresponding to 47,000 kHz A-scans rate. A sensitivity of 93 dB was reached. Structures of the skin near the nail fold were visible 1 mm deep.

12.5 Extensions of Linear OCT

12.5.1 Discontinuous Depth Range

Some applications require a long measurement range, which is essentially discontinuous. For example, for the measurement of the positions of the refractive surfaces of the anterior part of the eye and the retina, an imaging depth is needed, which is

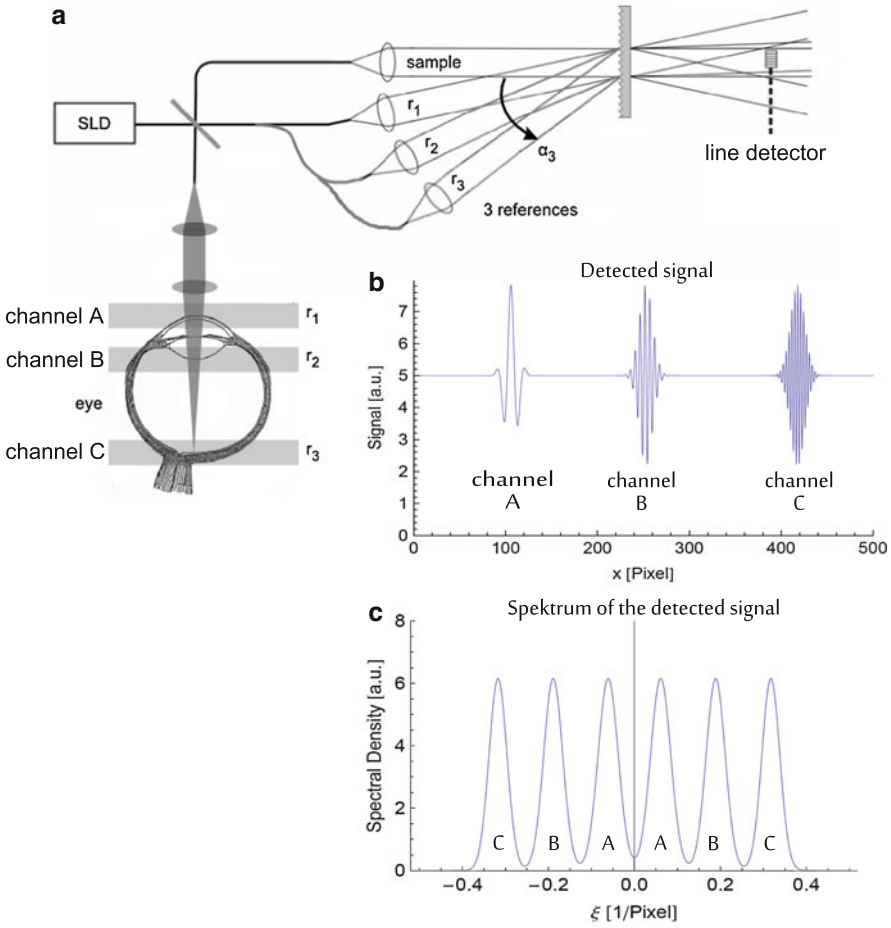

Fig. 12.12 Principle of multiple-reference linear OCT (*MRL-OCT*). Several reference waves interfere with the sample radiation at different angles α_i (**a**). The interference signals of the channels (here **a**, **b**, and **c**) are separated by different carrier frequency (**b**). The *angles* of the reference beams define the carrier frequencies (**c**)

difficult to achieve with Fourier domain OCT in one continuous A-scan, because either a spectrometer with a very high resolution or a tunable laser with a very high coherence is needed. With TD-OCT a large depth range is possible, but the signal-to-noise ratio (SNR) scales directly with the ratio between depth resolution and depth range [23]. A long imaging depth will significantly decrease the SNR.

L-OCT with a discontinuous measurement range is possible by using multiple-reference waves with different path lengths (Fig. 12.12a). An unambiguous discrimination of the information from the depth ranges is possible by introducing different carrier frequencies in the interference patterns, which result from different angles between the sample beam and the reference beams (Fig. 12.12b, c).

In multiple-reference linear OCT (MRL-OCT), the sample wave E_S interferes with n reference waves E_i. The intensity distribution I, which is measured by the line detector, then consists of the reference and sample intensity ($R_i = |E_i|^2$ and $S = |E_i|^2$), the interference of the complex sample wave with the n reference waves ($I_{si} = E_s E_i^* + E_s^* E_i$), and the $n(n-1)/2$ mutual interferences between the different reference waves ($I_{ij} = E_i E_j^* + E_i^* E_j$).

$$\begin{aligned} I &= \left(E_s + \sum E_i\right)\left(E_s^* + \sum E_i^*\right) \\ &= S + \sum_{i=1}^{n} R_i + \sum_{i=1}^{n} I_{si} + \sum_{i<j}^{n} \sum I_{ij} \end{aligned} \tag{12.14}$$

Different angles α_i of the reference beams result in different carrier frequencies which can be used to record the sample radiation in n different channels. The zero position of each channel can be adjusted individually by the length of the delays z_i of the respective reference beams. It can be shown that the width of the channels is approximately given by reciprocal depth resolution of L-OCT, which itself is given by spectral width δk of the OCT light source. By choosing an appropriate grating frequency and suitable angles, the usable bandwidth of the line detector, which is limited according to the Nyquist criterion to 0.5 per pixel distance, can be filled with several channels (Fig. 12.12c). The frequency distance of the channels depends on the acceptable cross talk (i.e., frequency overlap) and a proper sampling of the envelope of the coherence function γ. The reference waves will also interfere with each other on the detector. Combinations of angles and path length differences between the reference beams exist so that all signals are separated, either by the carrier frequency or by placing the interference outside the measurement range.

With multiple-reference beams each channel will experience an additional noise contribution of the noninterfering reference arm intensities, which will increase the quantum noise without increasing modulation by the signal. For equal reference intensity R_i, the SNR is reduced by the number n of reference arms:

$$SNR_{MRL-OCT} = \frac{SNR_{TD-OCT}}{n} \propto \frac{n_s}{n} \frac{\delta z}{\Delta z}, \tag{12.15}$$

where n_s is the number of photons detected from a reflecting structure during one A-scan. Though in each channel the SNR is reduced by the number of channels, MRL-OCT can cover a depth range of approximately $n\ \Delta z$. Measuring this depth range with only one reference arm would result in a similar SNR. The use of several reference arms in MRL-OCT does not systematically decrease nor increase the SNR compared to L-OCT. For a proof of concept, an L-OCT with a phase grating for fringe frequency reduction [13] was amended by a second reference arm (Fig. 12.13a). The sample light was collimated to a parallel beam and then focused by a further achromat. A glass plate, which was placed in the parallel sample beam, and a mirror in the focus of the second achromat served as two objects which were separated by 69 mm. By the two reference arms two carrier frequencies (0.063 per

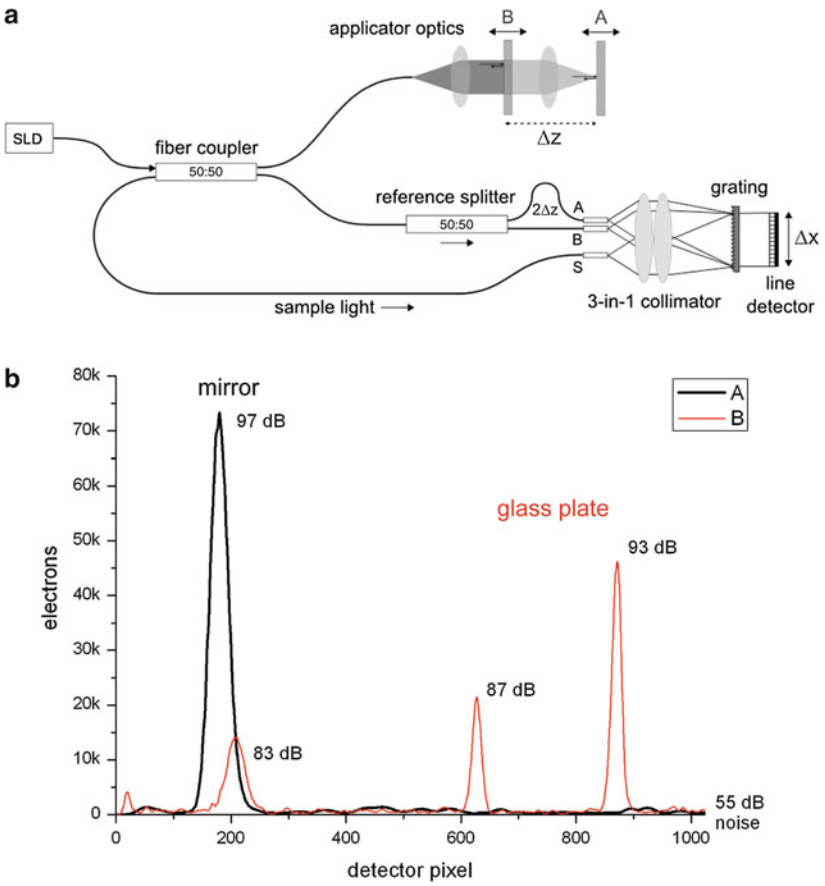

Fig. 12.13 (**a**) Setup of an MRL-OCT with two reference arms. (**b**) Demodulated signals when imaging a mirror in channel A and glass plate with two surface in channel B

pixel and 0.19 per pixel) are introduced, which defined the channels A and B. The mirror signal in channel A was recorded with an SNR of 42 dB. In channel B both surface reflections of the glass plate were measured with an SNR of 32 dB and 38 dB, respectively. The cross-channel rejection was about 35 dB in channel A but only 15 dB in channel B. MRL-OCT with multiple reference beams offers a simple and robust approach for parallel OCT measurements in different depths. However, a certain cross talk has to be expected.

12.5.2 Line-Field Linear OCT

The main advantage of L-OCT is the simplicity of the setup. No moving parts are needed for the depth scan. A line-field L-OCT, i.e., an L-OCT which measures

a B-scan without scanning does further simplify the device. On a two-dimensional camera, one axis can be used for L-OCT and the other axis for imaging one coordinate of the sample. A first device was demonstrated by Zeylikovich and Alfano [12]. Here a reflection grating was used in a Mach-Zehnder type interferometer to completely remove the fringe frequency. The thickness of the fiber cladding was measured. Later a simplified version using a Michelson interferometer was demonstrated [14] and applied to biological tissues [24]. In-vivo measurements were not demonstrated possibly because of fringe washout caused by the long exposure time of the camera. With the introduction an ultrahigh-speed CMOS camera, in-vivo images of human skin became possible [25]. With a zoom lens and by varying the diffraction order of the grating, lateral and axial field of view were adjustable [26].

12.6 Conclusion

Linear OCT which works without moving parts is in principle able to give a similar image quality than TD-OCT. Disadvantages are a higher sensitivity to movements and some signal losses at the edges of the detector due to the Gaussian beam profiles, with which the detector is illuminated. The progress in sensor technology and the control of the fringe frequency by a phase grating allowed to build a compact L-OCT system which can be used for imaging scattering tissues with a quality comparable to that of TD-OCT, avoiding the problems of a scanning optical delay line. Simple and rugged design, fast acquisition speed, and stable phase detection are advantages over TD-OCT. These properties are also shared by FD-OCT which offers a significantly higher sensitivity. However, the lack of interfering autocorrelation signals, a simpler signal evaluation without Fourier transform, and a less complex optical layout, which does not need high-quality optics to achieve diffraction limited resolution of the spectrometer, are advantages over FD-OCT.

L-OCT systems might be the better choice in cases where the superior SNR of FD-OCT is not needed and complexity and price are important design parameters. This may be in applications with low to moderate resolution where a stable and simple system without the ultimate dynamic range is needed. L-OCT may find its place in profilometry and measurements of distances in low scattering technical and biological objects.

References

1. D. Huang, E. Swanson, C. Lin, J.S. Schuman, W.G. Stinson, W. Chang, M.R. Hee, T. Flotte, K. Gregory, C.A. Puliafito, J.G. Fujimoto, Optical coherence tomography, Science **254**, 1178–1181 (1991)
2. A.F. Fercher, C.K. Hitzenberger, G. Kamp, S.Y. El-Zaiat, Measurement of intraocular distances by backscattering spectral interferometry, Opt. Commun. **117**, 43–48 (1995)
3. G. Häusler, M.W. Lindner, "Coherence radar" and "Spectral radar"- new tools for dermatological diagnosis, J. Biomed, Opt. **3**, 21–31 (1998)

4. S.H. Yun, G.J. Tearney, J.F.D. Boer, N. Iftimia, B.E. Bouma, High-speed optical frequencydomain imaging, Opt. Express **11**, 2953–2963 (2003)
5. B.E. Bouma, G.J. Tearney, *Handbook of Optical Coherence Tomography* (Marcel Dekker, New York, 2002)
6. A.F. Fercher, W. Drexler, C.K. Hitzenberger, T. Lasser, Optical coherence tomography–principles and applications, Rep. Prog. Phys. **66**, 239–303 (2003)
7. P. Koch, G. Hüttmann, H. Schleiermacher, J. Eichholz, E. Koch, Linear optical coherence tomography system with a downconverted fringe pattern, Opt. Lett. **29**, 1644–1646 (2004)
8. A.M. Weiner, D.E. Leaird, J.S. Patel, J.R. Wullert, Programmable femtosecond pulse shaping by use of a multielement liquid-crystal phase modulator, Opt. Lett. **16**, 326 (1990)
9. K.F. Kwong, D. Yankelevich, K.C. Chu, J.P. Heritage, A. Dienes, 400-Hz mechanical scanning optical delay line, Opt. Lett. **18**, 558 (1993)
10. A. Rollins, S. Yazdanfar, M. Kulkarni, R. Ung-Arunyawee, J. Izatt, In vivo video rate optical coherence tomography, Opt. Express **3**, 219–229 (1998)
11. G.J. Tearney, B.E. Bouma, J.G. Fujimoto, High-speed phase- and group-delay scanning with a grating-based phase control delay line, Opt. Lett. **22**, 1811–1813 (1997)
12. I. Zeylikovich, R.R. Alfano, Ultrafast dark-field interferometric microscopic reflectometry, Opt. Lett. **21**, 1682–1684 (1996)
13. P. Koch, V. Hellemanns, G. Hüttmann, Linear OCT System with extended measurement range, Opt. Lett. **31**, 2882–2884 (2006)
14. I. Zeylikovich, A. Gilerson, R.R. Alfano, Nonmechanical grating-generated scanning coherence microscopy, Opt. Lett. **23**, 1797–1799 (1998)
15. Y. Watanabe, F. Sajima, T. Itagaki, K. Watanabe, Y. Shuto, High-speed linear detection time domain optical coherence tomography with reflective grating-generated spatial reference delay, Appl. Opt. **48**, 3401–3406 (2009)
16. C. Hauger, M. Worz, T. Hellmuth, Interferometer for optical coherence tomography, Appl. Opt. **42**, 3896–3902 (2003)
17. J. R. Janesick, *Scientific Charge-Coupled Devices* (SPIE, Bellingham, Washington, USA, 2001)
18. S. Yun, G. Tearney, B. Bouma, B. Park, B. J. d, High-speed spectral-domain optical coherence tomography at 1.3 μm wavelength, Opt. Express **11**, 3598–3604 (2003)
19. M. Wosnitza, *Optische Kohärenztomographie mit MOS-Zeilensensoren*, (University of Applied Science Lübeck, Lübeck 2000)
20. J. Welzel, C. Reinhardt, E. Lankenau, C. Winter, H.H. Wolff, Changes in function and morphology of normal human skin: evaluation using optical coherence tomography, Br. J. Dermatol. **150**, 220–225 (2004)
21. J. Welzel, M. Bruhns, H.H. Wolff, Optical coherence tomography in contact dermatitis and psoriasis, Arch. Dermatol. Res. **295**, 50–55 (2003)
22. P. Koch, D. Boller, E. Koch, J. Welzel, G. Hüttmann, Ultrahigh-resolution FDOCT system for dermatology, in *Coherence Domain Optical Methods and Optical Coherence Tomography in Biomedicine IX*, ed. by V.V. Tuchin, J.A. Izatt, J.G. Fujimoto (SPIE, San Jose, 2005), pp. 24–30
23. J.A. Izatt, M.A. Choma, Theorie of Optical Coherence Tomography, in *Optical Coherence Tomography*, ed. by W. Drexler, J. Fujimoto (Springer, Berlin/Heidelberg/New York, 2008), pp. 47–72
24. A. Gilerson, I. Zeylikovich, R.R. Alfano, High-speed grating-generated electronic coherence microscopy of biological tissue without moving parts, V.V.T.J.A. Izatt (ed.), (SPIE, 1999), pp. 213–215
25. Y. Watanabe, K. Yamada, M. Sato, Three-dimensional imaging by ultrahigh-speed axial-lateral parallel time domain optical coherence tomography, Opt. Express **14**, 5201–5209 (2006)
26. Y. Watanabe, Y. Takasugi, K. Yamada, M. Sato, Axial-lateral parallel time domain OCT with optical zoom lens and high order diffracted lights for variable imaging range, Opt. Express **15**, 5208–5217 (2007)

Data Analysis and Signal Postprocessing for Optical Coherence Tomography

13

Tyler S. Ralston, Daniel L. Marks, Adeel Ahmad, and Stephen A. Boppart

Keywords
Deconvolution • Image processing • Noise reduction • Signal processing • Speckle

13.1 Introduction

The quality of images obtained with optical coherence tomography (OCT), like many other imaging modalities, can be enhanced by using signal processing to numerically infer properties of the object being studied. While a great deal of insight can be gained by understanding OCT intuitively as a range-finding mechanism, more sophisticated analysis can reveal additional detail and features to the extent data quality allows. To maximize the utility of the data, signal processing is used to reject noise and to ensure the resulting image conforms to known properties of the object. We briefly summarize concepts of inference in signal processing. These ideas are applied when reviewing and examining methods of reducing noise, improving resolution through deconvolution, reducing speckle, correcting for material dispersion and OCT system imperfections, and deblurring the defocusing effects outside of the depth-of-field of the OCT instrument.

T.S. Ralston • D.L. Marks • A. Ahmad
Biophotonics Imaging Laboratory, Beckman Institute for Advanced Science and Technology, University of Illinois at Urbana-Champaign, Urbana, IL, USA

S.A. Boppart (✉)
Biophotonics Imaging Laboratory, Beckman Institute for Advanced Science and Technology, University of Illinois at Urbana-Champaign, Urbana, IL, USA

Departments of Bioengineering, Electrical and Computer Engineering, and Medicine, University of Illinois at Urbana-Champaign, Urbana, IL, USA
e-mail: boppart@illinois.edu

© Springer International Publishing Switzerland 2015

W. Drexler, J.G. Fujimoto (eds.), *Optical Coherence Tomography*,
DOI 10.1007/978-3-319-06419-2_14

To understand the rationale for signal processing, we consider the process of imaging with OCT. The goal of OCT imaging is to determine which one of many possible objects are being imaged. In this context, an "object" does not refer simply to an entire class of objects, such as tadpoles or retinas. Rather, an object refers to all possible variations on a type of object that could be plausibly expected to be imaged. For example, for tadpoles, this would include all tadpoles, of all sizes, shapes, relative body dimensions, etc., that one would expect to find. All possible objects are those mutually distinguishable by the operator and would not be rejected as impossible or overly unlikely to be observed by the operator.

When an object is measured by an OCT instrument, the OCT instrument produces data. The data is all of the information learned about the object using the instrument. All measurements, including those of OCT, are subject to noise and uncertainty. Therefore, the observation of a given object may produce one of many possible data sets because of randomness introduced by the measurement process. In particular, two different objects may randomly produce the same data; so based on the data alone, it is not possible to specify incontrovertibly that the data was observed from any of the objects that could have produced that data.

To represent the object in a way that the operator can perceive visually, the data is transformed using signal processing into an image. An image ideally relays enough information about the object to the operator to distinguish which objects are consistent with the data. Images are typically employed because the human visual system can more readily assimilate and process the large amount of data as an image rather than as raw samples or other descriptions of the data. A human operator can also be trained to interpret the data in a more flexible and versatile manner than most automated data processing methods.

In general, there will be a multitude of similar images that correspond to physical objects that could be explained by the data. The image produced by signal processing should at the very least be plausible given what is known about the object and ideally would be a unique estimate given the data. Often, signal processing is neglected or grossly simplified because the resultant images are similar enough to a plausible image to satisfy the operator. However, when there is a large amount of uncertainty or noise or there is specific information about the object that one wishes to incorporate into the image, the methods of signal processing must be carefully considered.

As a simple example of inference for a particular set of objects, the measured data, and their corresponding images, consider Fig. 13.1. In this case, we know that we have only one of two possible objects, either the smiling tadpole or the frowning tadpole. Because of noise, the data measured for each of the tadpoles will not map onto a unique data set. Rather, some data sets may be observed for only smiling or frowning tadpoles, and some may be observed for either object. Each of the data sets will be processed into an image, which is shown on the right side of Fig. 13.1. While being noisy, two of the images will correspond to one of the objects. However, one of the images is ambiguous and could be observed for either tadpole.

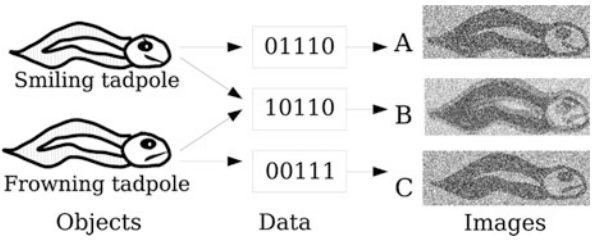

Fig. 13.1 A simple object, data, and image combination to illustrate the process of inference

Signal processing ideally presents the data, often in the form of an image, to the operator so that there will be the minimal ambiguity inferring which object is present. The process of inference can be seen as a mapping from data outcomes to the most likely object that the data could have been observed for.

Unfortunately, in practice, we usually do not have the possible objects narrowed down to two possibilities, and there are a nearly unlimited number of data observations one could make for these objects. While a rigorous enumeration of all possibilities is almost always not practical or even possible, we can still specify the general properties of what is known about the object and tailor the signal processing to produce images of these objects consistent with the data and the prior knowledge of the object. Within the limits of the available computational devices and methods, signal processing can help relieve the operator of some of the burden of recognizing and classifying the image by removing artifacts and noise in the image that is not consistent with what the object is believed to be.

There are two properties that a useful signal processing method must have. First, a method must be stable. This means that very small changes in the data should not produce large changes in the reconstructed image or ultimately in the object that is believed to correspond to the data. This is necessary so that the image is robust to the variations in the data produced by noise and measurement error. Also, there should be a unique image estimate corresponding to a particular data set. This is so that the operator is not confronted with one of many possibly very different images given the same data. Both of these problems can be addressed partially by the use of regularization. Regularization is a constraint on the image that specifies aspects of the image that cannot be determined by the data. For example, a common regularization method penalizes the energy of an image. If an OCT system is designed to measure an object using wavelengths between 1,250 and 1,350 nm, the instrument does not provide information about the scattering of the object outside of this bandwidth. By minimizing the energy of the image, the estimate of the scattering of the object outside the bandwidth of the OCT system, say between 500 and 600 nm, is estimated to be zero. This is a reasonable assumption and one that is commonly made (implicitly or explicitly) when analyzing OCT data. By examining the stability, uniqueness, and the properties of an image that a given signal processing algorithm assumes, one can better understand whether a given signal processing algorithm will be useful in a specific situation.

13.2 Speckle Reduction and Signal Improvement

Speckle is one of the most distracting artifacts of OCT images (and other coherent ranging techniques such as ultrasound). It is often difficult to separate the features that are caused by speckle, and those of other features of interest. However, the phenomenon of speckle is what enables methods such as OCT to be useful. Because scatterers tend to be randomly placed in most objects, every frequency band in which the object can be probed contains some useful details of the object. This is why most coherent ranging techniques are useful in practice. If scatterers were not randomly placed so that speckle did not occur, it is possible that the object may not yield any detail whatsoever in the frequency band in which it is being probed (an example is when one images a Bragg grating with a resonant frequency outside the probed bandwidth). Unfortunately, if one is distinguishing detail at the resolution limit of the instrument, it is likely that it will be modulated by speckle and therefore appear very noisy.

Speckle occurs when the scatterers are randomly placed, and their backscattered reflections each superimposes with a random phase and amplitude in the OCT interferogram. This can be visualized as a "random walk" of two-dimensional vectors [1], each vector representing the complex-valued reflectance of each unresolved scatterer. The sum of these vectors is approximated by a complex-Gaussian random variable [1], which has a length given by a Rayleigh probability distribution. Note that this implies that the magnitude squared of the vector has an exponential or Boltzmann probability distribution. When multiple polarizations of return signal are accounted for, the magnitude squared of the reflectance conforms more to a gamma distribution [2, 3].

This persistent problem has been addressed by several different approaches. One method [4], the sticks method adapted from ultrasound, was used to despeckle coronary artery images. This method fits short line segments of various orientations to features in the image to approximate the boundaries of the vessel. Another method [5] applies the rotating kernel transformation to coronary images, which matches edges in the image to a set of binary-valued two-dimensional square kernels to enhance the edges and suppress speckle noise. A promising technique [6] uses an undecimated wavelet filter transformation on the logarithm of the magnitude of the OCT image to remove the uncorrelated speckle features but retain the scale-invariant features that produce the largest wavelet coefficients. This method enhances the discrimination of noise by exploiting the correlations between wavelet coefficients at multiple scales due to object features. The logarithm of the magnitude is processed because speckle can be modeled as multiplicative noise to the image, which becomes additive noise once the logarithm is taken. Additionally, a multidimensional wavelet method utilizes correlations in time-series data to suppress noise via decorrelation [7]. An example of denoising using this technique is shown in Fig. 13.2. A similar method, except based on the curvelets transform, has also been demonstrated as shown in Fig. 13.3 [8, 9]. Another speckle suppression method [10] simultaneously constrains the magnitude to match a blurred version of the image, while retaining the detail by constraining the image to fit

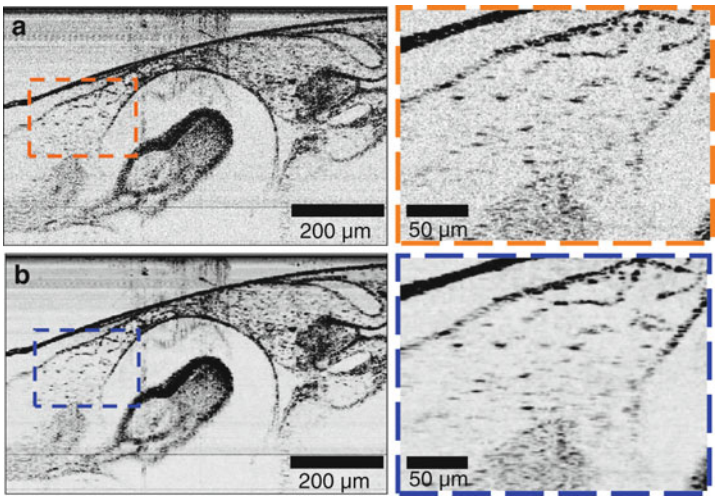

Fig. 13.2 Representative frame of multidimensional denoising of a sequence of OCT images acquired in real time. (**a**) Originally acquired data of *Xenopus laevis* tadpole. (**b**) Image after denoising. The zoomed-in figures at the *left panel* correspond to the *boxed* regions (Images used with permission from [7])

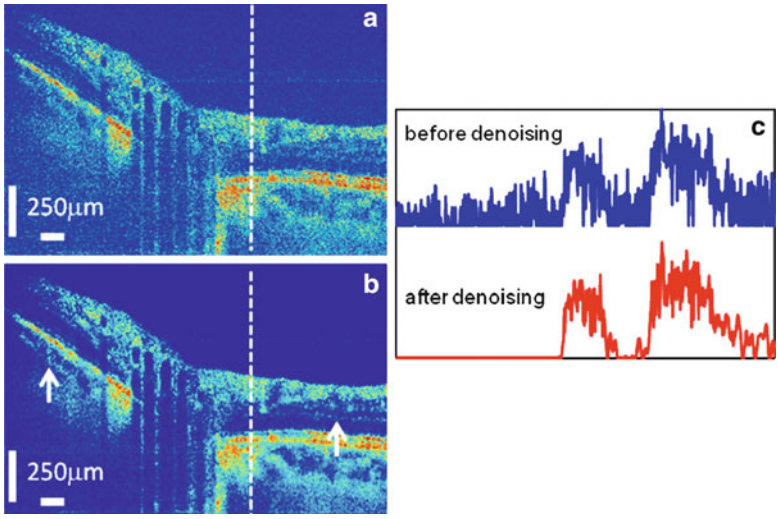

Fig. 13.3 Image of an optical nerve head (**a**) before and (**b**) after speckle reduction by shrinkage in the curvelet domain. Depth-resolved line-plots (**c**) along the vertical dashed lines in (**a** and **b**) illustrate speckle reduction, making features more distinguishable (*white arrows*) (Images used with permission from [8])

the data in a least-squares sense. The blurred OCT image acts as a "default" image that is used to assign the magnitude of the data where the data leaves the magnitude of the reconstructed image unspecified. The actual constraint used is a relative entropy constraint called the I-divergence [11] between the default image and the reconstructed image.

One straightforward way to remove the effects of speckle is to incorporate several images into a single image [2, 3]. The speckle effect occurs because most objects have features at length scales smaller than the smallest resolvable area of an OCT instrument. Speckle is caused by the interference between randomly placed scatterers that are individually unresolvable due to the finite bandwidth and focused spot size of the OCT instrument. In OCT images, speckle appears as a random modulation to the demodulated amplitude image due to the interference between the scattered waves from these unresolved scatterers. Unfortunately, in practice, the features caused by the random interference of speckle and those of other features of interest are frequently indistinguishable.

Two or more images of the same object that does not itself change between the image acquisition sequences will exhibit identical speckle patterns even if the noise is independent between the images. Therefore, if these images are averaged together, the speckle pattern will remain even if the signal-to-noise ratio is improved. To reduce speckle, the averaged images must each be slightly different by probing different coherent superpositions of the sub-resolution scatterers that produce the speckle. To achieve this, one may employ a diversity mechanism intended to vary the phase of the interference between the sub-resolution scatterers. The diversity mechanism ideally produces an independent amplitude modulation due to speckle at each resolvable point in each image. By measuring different combinations of interference between the sub-resolution scatterers, the density of scatterers in the image can be better estimated by averaging together the randomized amplitudes of the constituent images.

There are four main diversity methods used to reduce speckle. Frequency compounding [12] merges the images of the same object taken in two different optical frequency bands. Most particles will scatter at wavelengths in the near infrared (NIR). By choosing two different frequency bands in the NIR, the phase shift of the interference between scatterers is altered to produce two different speckle patterns in each band. Because the speckle patterns in both frequency bands are largely uncorrelated, compounding them significantly decreased the speckle in the image. Polarization diversity [13] measures the same object with orthogonal polarizations with the goal of producing different speckle patterns for each polarization that can be averaged. Angular compounding [14–16] measures the sample with various tilts of the axial scan relative to the transverse scan direction, rather than always having the axially focused beam normal to the transverse scanning direction. By illuminating the scatterers in the object at different angles, different combinations of the scatterers are measured to change the speckle pattern. Finally, spatial compounding [17] reduces speckle noise by averaging together various parts of an image, which is helpful when the object properties are uniform such as a sample of human skin. In some recent methods, an

increasing strain is applied to the sample, which effectively decorrelates the speckle between successive B-scans. Incoherent averaging of these decorrelated images reduces the speckle noise [18, 19]. In another method, image registration followed by averaging of multiple B-scans is used to reduce speckle [20].

Similar signal processing methods have been developed to remove and suppress image artifacts commonly seen in spectral-domain OCT systems. Fixed pattern noise artifacts which show up in OCT images as horizontal lines are the most prominent. These artifacts can come from the non-flatness of the reference spectrum, spectral structure in the source spectrum, and optical interferences from spurious back-reflections [21]. These artifacts can be removed by measuring the reference spectrum in the absence of the sample and subtracting it from the measured spectrum. The reference spectrum can be estimated from the acquired data itself. A common method is to average several A-scans, and due to the sample inhomogeneity, the random phase distribution would wash out the fringe pattern leaving behind the reference spectrum. Subsequently, each interferometric spectrum is subtracted by the reference spectrum to remove the fixed-pattern noise. However, a small number of high-amplitude back-reflections mainly due to the air–tissue interface can cause errors in estimating the mean reference spectrum [21, 22]. A number of alternative approaches to overcome this limitation of the mean-spectrum subtraction method have been proposed. In one technique called the minimum-variance mean-line subtraction, each horizontal line is divided into segments and the mean value corresponding to the segment having the minimum variance is assigned to a given axial position. As the segment containing high-amplitude reflection points would exhibit higher variances, this method can potentially give more robust estimates [21, 23]. Another method is based on the median estimator which is known to be less sensitive to high-amplitude data points. In this method, a complex median value is calculated for each axial position and this complex median A-line is then subtracted from each of the A-lines to remove the fixed-pattern noise artifacts [21–23].

One of the simplest and most intuitive ways in which images can be enhanced is to take several images of the same object and incorporate these into a single image with superior resolution and/or signal-to-noise ratio to any of the individual images. The resultant denoised image is often the average of the samples of the individual images. There are two reasons that signal averaging is done to OCT images. This first is to improve the signal-to-noise ratio of the resultant image. If one can assume that the noise component of each of the constituent images is independent of each other, then averaging together several images of the same object (which are ideally identical except for different realizations of added noise), the average of the images will converge to an image with a lower variance than the constituent images. This averaging can be done on the interferograms of the OCT axial scans or more often is performed on the demodulated gray-scale image. While this method works, the penalty is a slower data acquisition which is often not acceptable in practice.

Recent attention has been given to compressive sampling (CS) strategies for image recovery in medical sensors [24, 25]. The idea behind CS is to exploit an

aspect of sparsity in a transform domain where fewer measurements can be used to recover missing data with higher accuracy. Of course, this is reliant on the accuracy of your choice of transform domain. This means that the choice of sparse representation is a key to recovering good image quality. Some authors have described a method that exploits the sparsity in point-like scattering within an A-mode OCT scan [26, 27]. By using the fact that the frequency domain representation of a sparse numbers of point-scatterers is overdetermined, fewer measurements of the Fourier signal space can be used to form a reconstruction. Other methods rely on the spatial sampling as the sparsity constraint [28, 29]. For instance, if one intends to reconstruct an object with three to five times oversampling, then the redundancy in the measurements can be exploited by using CS. That is, fewer measurements can be used to reconstruct the object to full oversampled resolution. This method has been demonstrated with both B-mode and 3-D imaging in real-time systems [28]. One study evaluated the performance of different transform domains for recovery of OCT volumes from sparse data sets [30]. The Fourier basis, wavelet basis, Dirac basis, discrete-cosine basis (DCT), and surfacelet basis are examples of common bases examined. Another study showed an approach for using a modified-CS algorithm to increase the local contrast, the signal-to-noise ratio (SNR), and the contrast-to-noise ratio (CNR) [31]. Further quality improvements are gained from averaging the reconstructions.

13.3 Deconvolution and Spectral Shaping

Another common goal of post-processing is to achieve the best resolution and highest signal-to-noise ratio that the data will allow. In OCT, the primary limiting factor for axial resolution is the bandwidth of the source, and the limiting factor for transverse resolution is the focused spot size. The process of deconvolution attempts to extrapolate somewhat more detail from the data limited by the signal-to-noise ratio of the data. In addition, deconvolution can reject noise and remove sidelobes from the image.

To understand what deconvolution does, we consider Fig. 13.4 which contains the interferogram of an axial scan of a reflection off of a glass–air interface in an OCT system. This interface between glass and air is extremely abrupt and so is much sharper than the features that can be resolved with a typical OCT system. The length of the interferogram in this case is limited by the bandwidth of the source and not by the detail of the object.

Because we know this interferogram corresponds to a single reflection, we may decide to infer the location and the position of the surface as the peak of the interferogram. The error in the estimate of the position of the surface is potentially much less than that suggested by the width of the interferogram, because we already have knowledge that there is only one reflector. By using a priori knowledge about the object and the optical source spectrum, scatterers can be better resolved than would be suggested by the interferogram width alone.

If there are multiple reflections, each of the reflections produces an interference pattern that is superimposed on the interferogram. The mathematical operation that

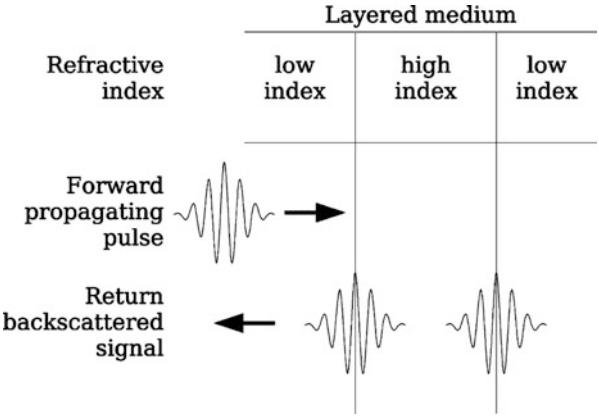

Fig. 13.4 A diagram showing how an optical pulse reflects off of interfaces between regions of varying indices of refraction. Even though the interfaces are sharp, the reflections are all copies of the original pulse and therefore the length of the pulse

finds the interferogram caused by a set of reflectors by superimposing the interference patterns for each reflector is called convolution. Therefore, the operation of finding the reflectors based on the interferogram is called deconvolution. Because of the relatively wide width of the interferograms and noise, deconvolution is necessarily an imperfect process where the reflectors corresponding to a particular interferogram cannot be recovered with certainty.

A simple way of locating reflectors in an OCT image is based on the CLEAN algorithm [32, 33]. In this algorithm, one attempts to locate the highest reflectivity scatterer in the data by scanning for the largest magnitude interference pattern. The position and magnitude of this interference pattern is used to infer the location of the scatterer in the final image, and then the interference pattern due to the scatterer is subtracted from the data. This process is repeated on the data to successively infer the positions and magnitudes of weaker scatterers as they are subtracted from the data. Because this method identifies individual point scatterers, it tends to work best on objects with discrete particles. However, many biological specimens are not similar to a collection of point-like reflectors. In one method, it is assumed that the signal at each point is superimposed by the sidelobes of other points in the same A-scan. A method to suppress the sidelobes called gradual iterative subtraction is implemented by iteratively subtracting the influence of the sidelobes from other points in an A-scan [34].

Rather than determining the position and magnitude of every point scatterer in the sample, most deconvolution methods produce an image where the features appear more point-like. This is done by applying a post-processing filter to concentrate the signal of a scatterer around its center position on the interferogram. Highly nonuniform spectra will cause the image of a point scatterer to have many and large-amplitude sidelobes. Sources such as ultrahigh numerical aperture fibers [35, 36] and microstructured fibers [37, 38] produce a large bandwidth, but the sidelobes caused by these sources can severely degrade the practically achievable resolution. Deconvolution methods help improve resolution, reject noise outside of the laser spectrum, and make the resolution more robust to variations in the source spectrum.

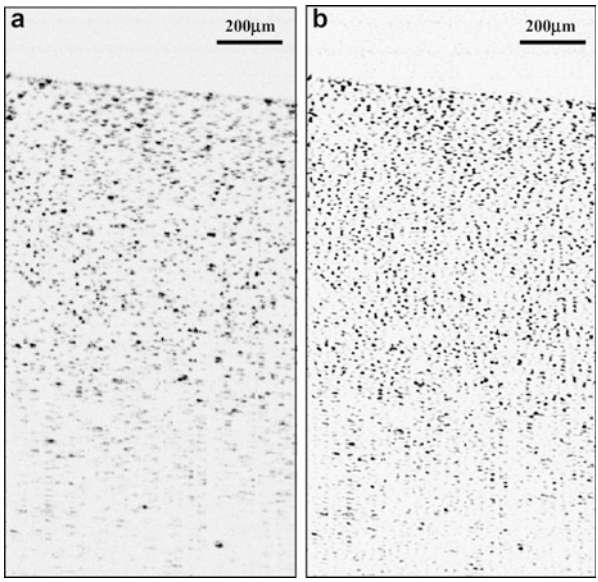

Fig. 13.5 Deconvolution using the Richardson–Lucy algorithm on a tissue phantom. (**a**) Original and (**b**) Richardson–Lucy corrected image (Images used with permission from [46])

To apply these methods, the interferograms themselves [39] need to be sampled rather than just the demodulated envelope. A method of deconvolution of the demodulated magnitude data [40] has been achieved, but may have problems accounting for interference effects between scatterers. Many OCT systems provide only demodulated interference fringes. This method uses a positivity constraint to somewhat overcome the lack of phase information. The benefit of directly processing the interferograms is that they are typically linear in the scattering amplitude of the sample (in the weak scattering approximation). One of the simplest methods [41] infers what the image would have looked like if it was taken with a low-sidelobe Gaussian source rather than the actual source used. This method effectively numerically "reshapes" the spectral envelope of the laser to become Gaussian-like which helps reduce sidelobes, perhaps at the expense of increasing noise. Other methods [42] apply a linear filter that inverts the source spectrum shape, to attempt to make the numerically reshaped source spectrum uniform. Another method applies a filter that provides the linear least-squares estimate of the sample scattering [43], taking into account the quantum efficiency and photon noise of photodetection. A further method [44] modifies this result to reduce sidelobes. Additional methods use deconvolution in conjunction with dispersion management to minimize the point-scatterer image size [45]. Another paper describes regularized inversion methods for deconvolution that mitigate the depth-dependent blurring of the transverse point spread function caused by the focusing optics [46]. An example is shown in Fig. 13.5 where after the deconvolution operation, the point scatterers in the image are sharper and better defined. In a similar method described, a set of Gaussian PSFs of different spot sizes were used to deconvolve defocused images using the Richardson–Lucy algorithm. The Richardson–Lucy algorithm is based on

the maximum-likelihood solution in regard to Poisson statistical data. One study introduced a method to improve the resolution on OCT system by step-frequency encoding [47]. In this method, two A-scans of slightly different frequencies are added together resulting in a beating pattern which reduces the FWHM of the central lobe in the interferograms. However, the beating also introduces sidelobes in the interferograms which can lead to artifacts in the reconstructed images [47].

While many of these methods successfully mitigate the blurring of OCT, a full formalized quantitative deconvolution of the focusing optics is solved in interferometric synthetic aperture microscopy (ISAM) [48]; the details of which can be found in ▶ Chap. 31, "Interferometric Synthetic Aperture Microscopy (ISAM)".

13.4 Dispersion Correction

Apart from speckle, the chromatic dispersion of the OCT signal is one of the most image-degrading distortions. Dispersion appears in OCT images as the blurring and interference of adjacent reflectors. A signal pulse propagating through a dispersive medium tends to develop a "chirp," so that the signal increases or decreases in frequency as it passes a particular point in the medium. This changes a formerly sharp point in an image into a blurred region within an axial scan. Dispersion degrades the axial resolution because of this blurring. However, dispersion can be corrected. A simple way to do this is to insert a dispersive medium into the reference arm to balance the dispersion of the sample signal. However, it is desirable to correct dispersion using digital post-processing rather than a physical adjustment. Signal processing is more flexible and can adapt to the dispersion of the medium of the object. In addition, it is possible to automatically adjust digital post-processing without necessarily knowing the medium dispersion beforehand.

The dispersion of a medium is usually characterized by a dispersion relation. This relation can be specified in a number of ways: commonly by the index of refraction as a function of wavelength or the spatial frequency wavenumber in the medium as a function of temporal frequency. This dispersion determines the total propagation phase a particular temporal frequency component of the signal acquires when traveling a certain physical distance in the medium. By applying the opposite phase to each frequency component of the detected interference signal in post-processing, the effect of dispersion can be cancelled out. This method has been successfully demonstrated on OCT interferograms [49, 50] to produce the digital equivalent of optical dispersion balancing. The method is implemented as a cross-correlation and therefore can be implemented together with other convolution signal processing techniques as used for resolution enhancement, sidelobe reduction, and noise reduction.

One disadvantage of optical or digital dispersion balancing is that the dispersion is only compensated at one depth in the axial scan. To overcome this, consider that the interferogram in OCT is typically measured in the time domain using a delay line. The interferogram may be Fourier analyzed to find the temporal frequencies in the measured interferogram. Each temporal frequency has a corresponding spatial frequency in the sample medium. Because of medium dispersion, the spatial and

temporal frequencies in media are not necessarily proportional to each other, as they are in free space. The relationship between temporal and spatial frequency is given by the medium dispersion relation. Compensating for material dispersion involves changing the coordinates of the Fourier representation of the interferogram from temporal frequency to spatial frequency. In practice, this is achieved numerically by a resampling or "warping" of the Fourier space. This process has been demonstrated [43, 51] to correct the dispersion for all of the points in the axial scan simultaneously. This resampling method can be performed more easily in spectral domain OCT [51] where the interferogram data is already measured in the Fourier domain and needs to be resampled anyways to compensate for nonlinearities in the spectrometer. Parameterizing a Taylor series expansion of the frequency-dependent dispersion often allows estimation of the dispersion correction [52].

In addition, it is possible in some cases to determine the amount of dispersion directly from the data without previous knowledge of the composition of the sample. A method of automatically finding the dispersion parameters minimizes the entropy of the image given a set of dispersion parameters [51]. Minimizing entropy tends to produce point-like and sharp features in the reconstructed image. Because uncorrected dispersion is expected to blur out the image, minimizing entropy tends to favor the images with the least dispersion. The method adjusts trial dispersion parameters and recomputes an image corrected by the trial parameters, searching for the parameters that produce an image with minimum entropy. Others find the best parameters by using a metric that minimizes the total number of points in the axial scan above some threshold [53].

Several others have described approaches to achieve dispersion compensation with similar results using noteworthy estimation techniques or advanced interpolation schemes. One paper describes a method in analogy to the Shack–Hartmann wavefront sensor, which provides an equivalent solution [54]. Here a short-time Fourier transform provides a means to calculate the nonlinear phase. A fractional Fourier transform has been used to achieve an optimal rotation of the time-frequency plane for correcting second-order dispersion [55]. Nonuniform discrete Fourier transforms or nonuniform fast Fourier transforms are methods of correcting the nonlinear frequency-dependent dispersion effect [56, 57]. These transforms perform as highly accurate band-limited interpolators. Additional dispersion compensation methods have been developed for nonconventional scanning methods, such as an electro-optical modulator [58]. This method involves making two measurements with a mirror at two different depths and subtracting the phases of the spectral fringes to get the resampling parameters.

To see the effect of dispersion correction on OCT axial scan data, Fig. 13.6 shows the measured interferogram before and after correction. This data is measured from the air–glass and polymer–glass interfaces of a polydimethylsiloxane microfludic channel. By applying a resampling to the interferogram in the Fourier domain, the effect of material dispersion can be compensated for, to restore the bandwidth-limited resolution. An example of dispersion compensation applied to data in a tadpole image is shown in Fig. 13.7. In this case, the dispersion parameters were inferred from the image itself and then were used to correct the image.

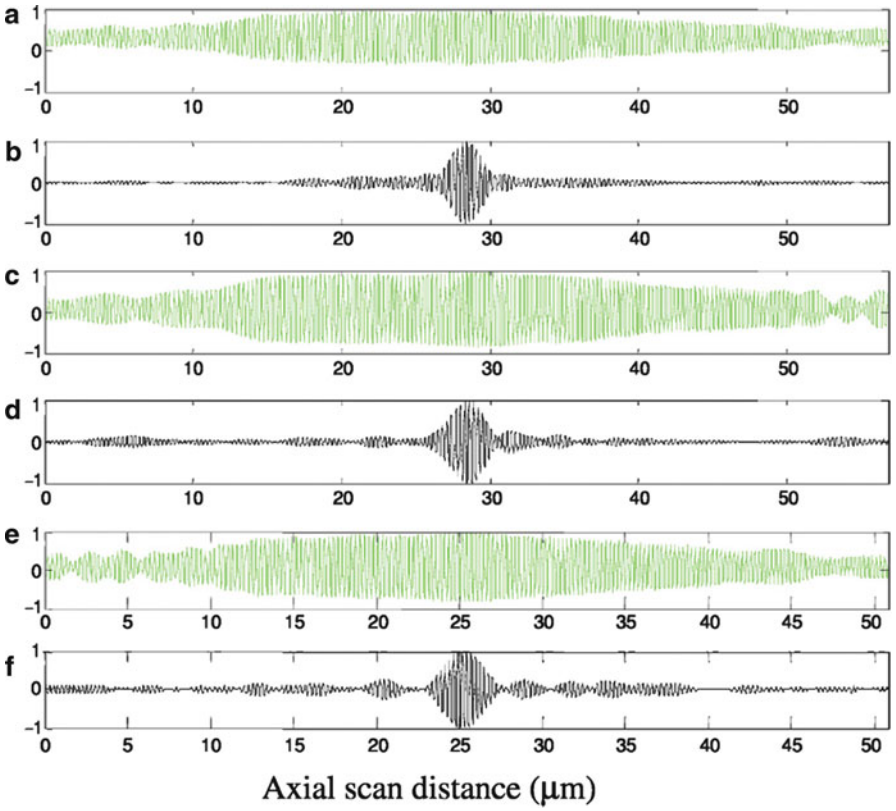

Fig. 13.6 Interferograms of reflections of air-glass and polymer-glass interfaces measured by OCT from a polydimethylsiloxane microfluidic channel. Parts (**a**), (**c**), and (**e**) are the interferograms before digital dispersion correction and (**b**), (**d**), and (**f**) are after correction (Image used with permission from [43])

In swept source (SS-) OCT, the sweep of the wavelength happens over a time frame, whereby phase coherency can be lost with motion. The motion induces a Doppler effect on the chirp sweep, which has a similar appearance to that of dispersion. A method of cross-correlation of sub-bandwidth reconstructions has been used to compensate for this motion-induced dispersion [59]. Other OCT modalities, where the compressed pulse is used for imaging, do not have this effect within the A-scans. In the next section, these motions that affect the consecutive A-scans, and motion compensation algorithms, are discussed.

A sample having a nonuniform medium can also suffer other distortions due to the refraction of the focused OCT beam as it scans through the sample. The refraction of the beam can change the apparent dimensions of the sample and the apparent locations of scatterers in the sample. It is then desirable to find the true spatial locations of scatterers inside the medium with knowledge of the refractive indices of the layers that comprise the medium. A method has been proposed [60] to

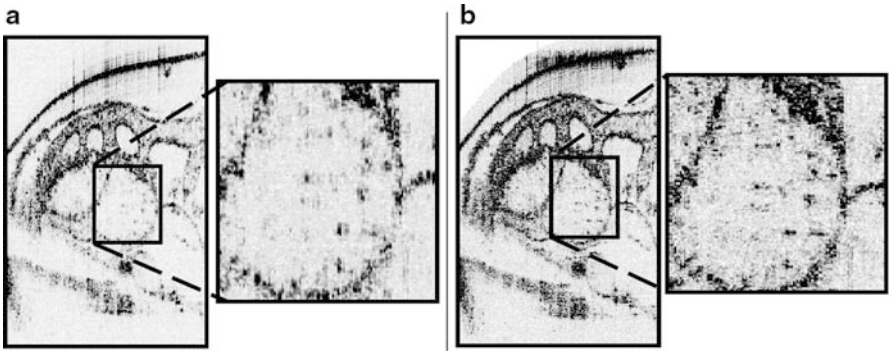

Fig. 13.7 Example of automatic removal of dispersion artifacts from an image of *Xenopus laevis* tadpole. The image (**a**) is the original OCT image, and (**b**) is the image with the dispersion parameters inferred from the image, and then used to remove the speckle from the image. This method uses an entropy minimization criterion to determine the dispersion parameters (Image used with permission from [51])

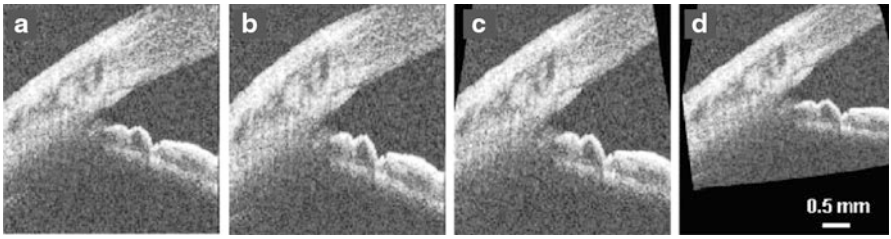

Fig. 13.8 Example of refraction correction of an image of the anterior chamber angle of a human eye. Image (**a**) is the raw acquired OCT image. Image (**b**) includes the correction for the nonlinear delay of the axial scanner. Image (**c**) further includes the correction of the divergent scan geometry due to telecentric scanning. Image (**d**) corrects for the refraction at the air–cornea and endothelium–aqueous boundaries (Images used with permission from [60])

correct for the refraction of the object and was demonstrated on a phantom and on the anterior chamber angle of a human eye. This method can correct the nonlinear scanning profile of a resonant scanning delay line and also non-telecentric imaging distortions. An example of an image corrected this way is given in Fig. 13.8. It accounts for the refraction of the OCT beam at the surfaces of the object by using ray tracing. Another method [61] uses the distortions caused by the refractive index variations to find the refractive index of the medium itself. Another method [62, 63] measures the refractive index by using coherence gating to measure the delay between light scattered from two foci in the medium along the axial scan. In another approach, the refractive index and thicknesses of multilayered phantoms were calculated by utilizing a matrix formulation of Fresnels's equations [64]. One study used the Delaunay triangulation method to represent the surfaces in ocular images followed by 3-D ray tracing to correct for optic distortions caused by

refractive index variations [65]. With knowledge of the refractive index, it seems likely that the refraction of a non-layered medium can be corrected as well.

13.5 Motion and Phase

Motion estimation and compensation methods have widespread applicability in imaging modalities including OCT. Numerous OCT modalities such as Doppler OCT [66], speckle variance imaging [67], optical micro angiography (OMAG) [68], optical coherence elastography (OCE) [69], and magnetomotive OCT (MM-OCT) [70] explicitly rely on motion for estimating the flow and viscoelastic properties of the specimen. Motion artifacts arising from physiological fluctuations such as heart beat and respiration and involuntary movement of a living subject, in addition to fluctuations caused by a noisy environment and galvanometer jitter, can be detrimental to these imaging modalities. Motion artifacts can not only degrade image quality but also limit the accuracy and reproducibility of quantitative measurements in OCT [71]. Motion artifacts arise when the sample moves during data acquisition and the OCT image reconstruction process assumes the sample to be stationary. High-speed data acquisition can mitigate the impact of motion artifacts to some extent; however, acquiring OCT volumes for a large field-of-view still takes a few seconds, and motion compensation algorithms need to be applied in post-processing to minimize the impact of motion artifacts.

Techniques based on the cross-correlation have been widely used for motion compensation and estimation. These methods are primarily based on finding the shifts corresponding to the maximum cross-correlation values. It is usually helpful to upsample the data prior to finding the cross-correlation values to detect sub-pixel shifts. Cross-correlations between successive A-scans have been used to correct for axial motion [72], while others used cross-correlations between orthogonal B-scans to correct for both axial and transverse motion [73]. Similar techniques were used to correct phase fluctuations due to cardiac and respiratory motions [74]. Some of the more recent methods include optimizing a set of objective functions for image registration [75]. Histogram-based bulk motion estimation methods have been applied to phase-resolved techniques such as Doppler OCT and optical angiography. In these methods, the phase differences between two adjacent A-scans are calculated and the bulk motion is estimated based on the phase difference corresponding to the mode of histogram distribution of these phase differences. This phase difference is then subtracted from the second A-scan to compensate for motion artifacts [76]. Motion compensation techniques have also been used for OCT image formation while manually scanning a probe over a sample. By measuring the de-correlation of the adjacent A-scans, the velocity of the movement of the probe can be measured and used to correct for motion artifacts due to nonuniform scanning [77, 78].

Sub-wavelength motion can induce a phase change in the measured OCT signal. With the advancement of phase-stable Fourier-based systems, techniques have been

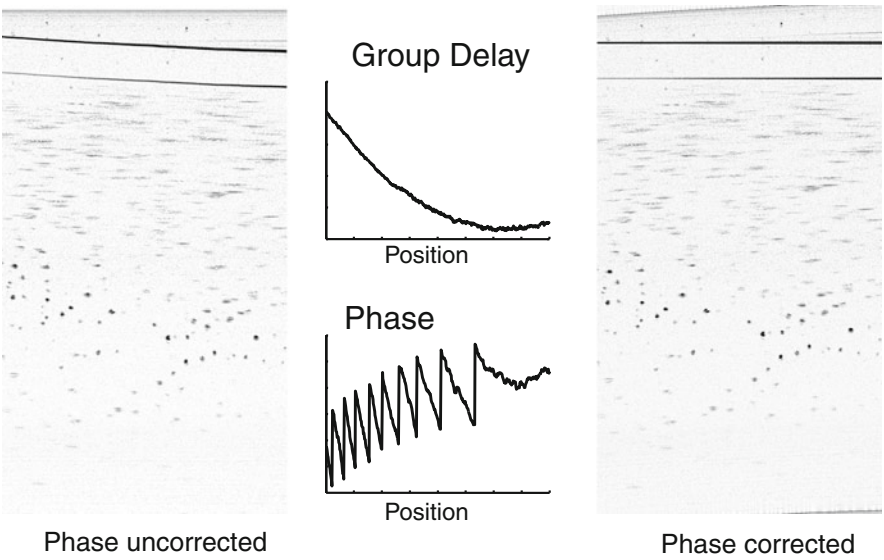

Fig. 13.9 Example of phase correction by using a coverslip placed on the top of the tissue phantom as a phase reference. Phase uncorrected image (*left*). Image after phase correction (*right*). Images used with permission from [80]. The plots show the group delay and phase as a function of transverse position on the coverslip interface

developed to estimate the phase values and infer a displacement. Furthermore, based on these phase measurements, some authors use a finite difference (numerical derivative) approach to solve the velocity or acceleration. Some authors use this approach combined with cross-correlation to improve sensitivity of the OCT system [79]. One study used the group velocity and phase of a common scatterer to stabilize the system before solving the inverse problem of interferometric synthetic aperture microscopy (ISAM) [80]. Figure 13.9 shows an example where phase correction was applied using a coverslip as a phase reference. Another study performed Doppler flow imaging of cytoplasmic streaming using a common path interferometer [81]. One study developed a magnetomotive optical coherence elastography approach to detect the elastic moduli of a medium by detecting the position and displacement of nanoparticles, which have displacements induced by an external magnetic field that switches on and off [82]. Measuring phase to within a wavelength can be difficult, so some authors use phase unwrapping techniques. One technique in particular involves calculating a synthetic wavelength, longer than the center wavelength, by dividing the spectra into subbands for processing [83].

A range of techniques based on taking the Fourier transform along the lateral direction (time or the coupled transverse-time (x-t) axis) have been proposed for detecting moving scatterers within a sample. Spatial oversampling is necessary to separate out the static sample structure from the moving scatterers within the sample. In OMAG, for instance, the separation is obtained by applying a constant

carrier frequency during B-scan acquisition, and a subsequent Hilbert transform is used to separate out the moving scatterers from the static tissue structure [68]. In some techniques such as OCE [84] and MM-OCT [70], the displacements induced by an external modulating force are detected by bandpass filtering the Fourier transform of the phase differences around the modulation frequency. In one study, the peak of the Fourier transform at the modulation frequency was used to calculate the sub-nanometer displacements [85].

13.6 Analysis and Classification

The purpose of OCT, as with any other biomedical imaging technique, is to extract diagnostically important information from acquired images. Many times, this information may not be apparent from the displayed data and further data analysis might be required. Computational techniques, being quantitative in nature, can give an objective assessment of the images, reduce inter-observer and intra-observer variability, extract diagnostically significant image features not easily observable by the human eye, and greatly increase the speed and accuracy of diagnosis. Moreover, with the rapid increase in OCT data acquisition speeds, analyzing these volumetric data sets can be challenging. Automated image analysis can reduce the burden of analyzing all these images and alert the user to significant landmarks and important information in these data sets.

The methods developed for automated image classification in OCT can be divided into two broad categories, i.e., algorithms that evaluate A-scans by exploiting differences in the attenuation coefficients, intensity histograms, spatial frequencies, etc. [86, 87], and techniques that take into account the 2-D and 3-D spatial information of OCT images such as differences in the texture patterns [88, 89].

Scattering properties of tissues can change due to morphological changes induced by disease progression. For instance, tumor tissues are in general known to be highly scattering due to changes in the regular cellular structure and the increase in the nuclear-to-cytoplasmic ratio. These changes can be quantitatively evaluated by measuring the attenuation coefficients from the OCT data and can be used for classifying different tissue types. The two main models used for the description of the OCT signal are the single-backscattering and the multiple-backscattering model. In the single-backscattering model, it is assumed that only light that has been scattered once contributes to the OCT signal. Beer's law can be used to express the attenuation of the OCT signal in single backscattering where the intensity of the OCT signal is represented by an exponential relation, related to the depth and the attenuation coefficient. A more accurate description of the OCT signal can be obtained by taking into account the confocal properties of the OCT beam in the sample arm. The attenuation coefficients are usually calculated by performing an exponential fit onto the intensity of the A-scan or a linear fit after taking the logarithm of the A-scan data [90]. This method has been used to differentiate between normal and tumor tissues in rectal [91] and renal tissues [92], characterization of atherosclerotic plaques [93], and classification of human

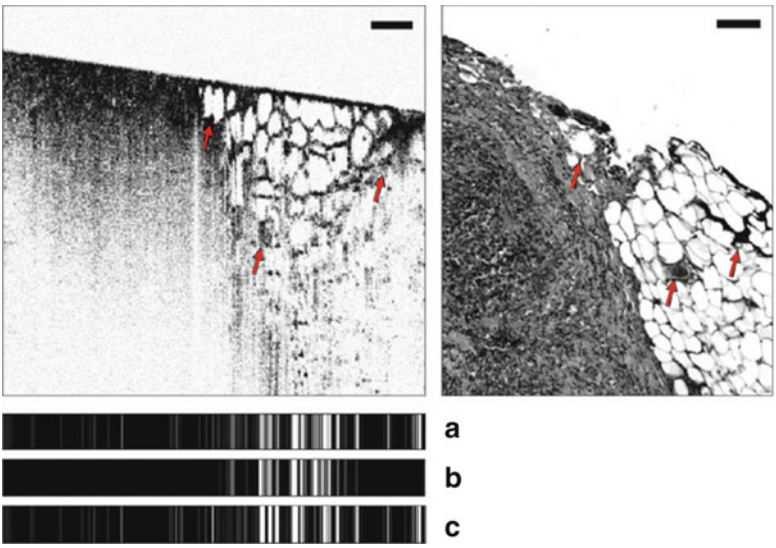

Fig. 13.10 OCT image of a vertical tumor margin (*left*) and the corresponding H&E stained histology (*right*) from human breast tissue. Highly correlated image features are indicated with *arrows*. An A-scan-based analysis was performed for each A-scan within the image using (**a**) both Fourier domain and periodicity analysis, (**b**) Fourier domain classification, and (**c**) periodicity analysis, for each scan line. *Black*, *white*, and *gray* regions represent tumor, adipose, and stroma classifications, respectively. Scale bars represent 200 μm (Images used with permission from [87])

breast tissue types [86, 87, 93]. In Fig. 13.10, information content in the A-scan data such as the spatial frequencies and the mean distances between the high-intensity back-reflections were used for classification of stroma, tumor, and adipose tissues in the human breast [87].

The spatial variation in image intensities forming certain repeated patterns constitutes texture. Texture in OCT images may arise due to the tissue structure or the speckle pattern. Speckle is an important contributor to the texture patterns in OCT images, especially when morphological features are not apparent in the image. Since speckle depends upon the size and distribution of the scatterers within the sample, different tissue types would form distinct speckle patterns. Texture analysis of these speckle patterns can potentially be used for tissue classification [88]. Three main approaches have traditionally been used to quantify texture: statistical methods, structural methods, and model-based methods. In structural methods, it is assumed that a set of texture units and primitives define the texture of the image and the geometric properties of these textural units are used to classify texture. In the model-based approach, an image-based model is used to describe and synthesize the image texture, and the model parameters are used for the purpose of classification. Statistical methods are based on the spatial distributions of the gray-level values between each pixel and its neighboring pixels. Gray-level co-occurrence matrices calculate the second-order joint conditional probability

distribution of intensity values between two pixels for various distances and specified directions. Texture features such as contrast, correlation, homogeneity, entropy, and energy can be calculated from these matrices. Usually, a number of texture features are calculated from an image or a subset of the image and it is not very apparent as to which image features would give the best discriminating power. Moreover, for optimum classification and to overcome the so called curse of dimensionality, dimensionality reduction techniques such as principal component analysis are applied prior to classification [94, 95]. With an optimum combination of the features, it is hoped that the feature vector would cluster into distinct groups corresponding to each tissue type in the multidimensional feature space. The extracted features are compared with the features calculated from the training set and classified into a tissue type. Texture analysis due to its intuitive simplicity has been widely applied to OCT images. Texture analysis has been used for diagnosis of dysplasia in Barrett's esophagus [96], for automated classification of gastrointenstinal tissues [97], and for differentiating between different human breast tissue types [98]. Texture analysis has also been combined with wavelets to improve classification performance by reducing the impact of system-dependent variations in the speckle pattern [99]. More recently, the fractal dimension, which is a measure of the self-similarity and complexity of the object, has been used to characterize texture. One-dimensional fractal analysis has been applied for distinguishing between stroma and tumor tissues in the breast [100] and arterial tissue [101].

13.7 Visualization and Representation

An issue perhaps equally as important as the computational post-processing of data is how this data is to be presented as an image. The same data can be presented in many ways that can help, hinder, aid, or mislead the instrument operator. OCT data is 3-D in nature and can potentially include many properties such as Doppler shift, polarization, birefringence, and spectral shift, among others. Careful consideration to the representation of data is essential to maximize the utility of the data and ensure that the relevant features can be rapidly ascertained.

The conventional way standard 2-D OCT images are represented is using a density plot. The horizontal axis typically corresponds to the direction of transverse scanning, and the vertical axis corresponds to sample depth, with the downward direction in the image corresponding to increasing depth. A gray level is usually plotted at a particular pixel on an image corresponding to the magnitude of the interferogram at a particular depth and transverse scanning position. Usually, the pixel intensity is mapped to the logarithm of the interferogram magnitude because of the high dynamic range and speckle noise present in OCT images, but visual improvements can be made by using an adaptive method [102] of selecting the lookup tables between pixel intensity and interferogram magnitude. In addition to gray levels, lookup tables utilizing color can aid the human visual system by varying hue as well as pixel intensity. Lower and upper thresholding of the pixel values is

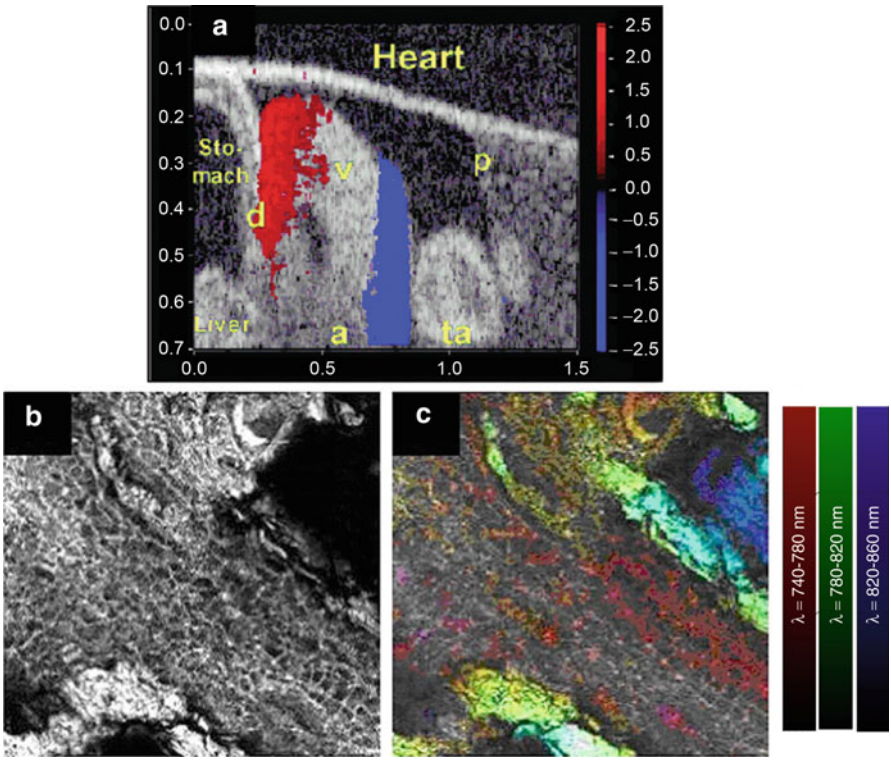

Fig. 13.11 Image (**a**) is an example of color Doppler and structure superimposed on the image of a *Xenopus laevis* heart. Image used with permission from [104]. Images (**b**, **c**) show a representation of spectroscopic OCT data. (**b**) Structural optical coherence microscopic image of a rat tissue showing regions of adipose cells and muscle and the corresponding spectroscopic representation (**c**) generated by assigning the intensity in three equally spaced subbands to the *red*, *green*, and *blue* channels (Images used with permission from [107])

commonly done to conserve the dynamic range of the display device, especially when the dynamic range is dominated by large magnitude specular reflections.

False color images where the colormaps represent different optical properties of the tissues rather than the tissue structure are also widely used. This method has been commonly used in ophthalmological imaging to overlay the thickness of different segmented layers over the structural image. The use of color for Doppler imaging in OCT is a practice adopted from Doppler ultrasound imaging. Typically, a reddish hue is used to denote movement away from the source of the illumination beam (for a "red-shifted" or lower-frequency Doppler signal) and blue is used to denote movement towards the beam (likewise for a "blue-shifted" higher-frequency signal). Note that in standard Doppler imaging, only the component of velocity parallel to the illumination beam can be measured. The red-blue coloring method

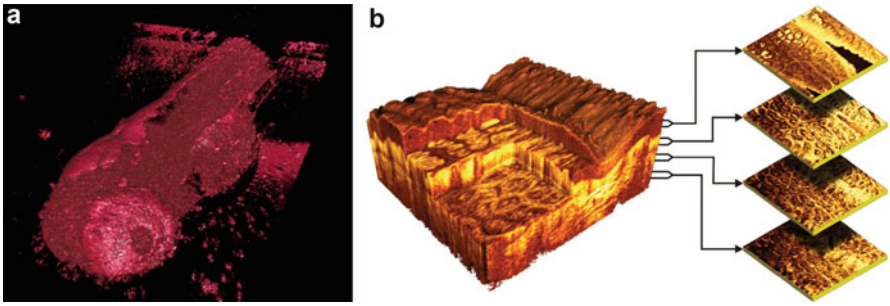

Fig. 13.12 Examples of 3-D volumetric renderings of (**a**) a zebra fish (at the fry stage of development) using a transfer function for isosurface generation and (**b**) human skin showing different sublayers of epidermis and dermis. The en face sections are separated in depth by 360 μm (Image used with permission from [130])

typically superimposes a red-blue hue on an otherwise gray-level image of structure [103, 104], but it can also be plotted separately [105] so the intensity better indicates the magnitude of the Doppler shift. Figure 13.11a shows an example of color Doppler OCT, with the color Doppler information superimposed on the structural information. The color Doppler representation has been commonly used, but others have been proposed, such as using colors to denote the frequency band of the Doppler-shifted OCT signal [106], which indicates the magnitude of the velocity shift. Spectroscopic OCT data can be represented in the form of images in a variety of ways. One commonly used approach is metameric imaging shown in Fig. 13.11c where the source spectrum is divided into three equally spaced subbands, and the intensity from these frequency bands are assigned to the red, green, and blue channels [107, 108]. Another method maps the center of mass of the spectrum onto a red–green hue in the image where a green hue shows a spectral shift to shorter wavelengths and a red hue indicates a shift to longer wavelengths [109]. A nontraditional way to represent data is in the form of nonspeech audio signals. This process known as sonification has been used for OCT data where different parameters extracted from the data were mapped into an audio signal for the purpose of tissue classification [110].

One innovation that has made a major impact on medical imaging and OCT in particular is computer-based volume-rendered 3-D OCT images. A 2-D image can be insufficient to recognize a feature of interest, e.g., a blood vessel or tissue boundary, because the planes in which the individual images are taken each contains only one cross section of the larger feature. By using 3-D rendering, the operator is not required to mentally assemble a complete picture of a feature, so the operator can concentrate on recognizing and classifying features. With the advent of Fourier/spectral domain OCT, data acquisition has become very rapid [111], and complete 3-D data sets can be acquired within seconds. This rapid acquisition and the large quantities of data produced need ingenious ways to convey their

significance to the operator, and 3-D rendering is a good candidate for this. When mapping a 3-D voxelized data set to a scene, there are several options for rendering and thresholding. For rendering, the volume surfaces may be rendered by slices or ray casting. In an isosurface, some voxels as indicated by a boundary intensity value may be interconnected into a polygonal mesh and rendered. Regardless of the rendering type, the thresholds for every channel (red, blue, green, alpha) may be selected. These channel thresholds are often set based on a histogram of voxel intensity values. The alpha channel allows for transparency through the object. In more sophisticated thresholding schemes, a 2-D transfer function is used to map the voxels based on intensity and gradient values. Examples of 3-D rendered volumetric data sets are shown in Fig. 13.12. With ongoing developments in 3-D computation hardware, the widespread availability of hardware acceleration devices such as graphics processing units (GPUs), display technology, and user interfaces, volume rendering will almost certainly be standard technology for OCT data visualization.

To see what has been done, we consider examples taken from the electronic and free Optical Society of America Optics Express journal (World Wide Web address: http://www.opticsexpress.org/) which has readily downloadable animations of 3-D renderings. One of the simplest ways to represent a 3-D volume is by an animation of B-mode slices. For example, animations of a human finger and tadpole [36] and a retina [53] show adjacent two-dimensional slices in successive frames. B-scan images can be synthesized from C-scan (en face) images and then animated, showing a projection image of a human retina in a manner similar to a confocal scanning laser ophthalmoscope [112]. Animations of B-scan images [113, 114] include color-coding of the fast-axis of the birefringence and the retardation. However, full 3-D rendering can help one visualize the complete object and not just individual sections. Volume rendering allows the visualization of a discretely sampled 3-D data set in the form of 2-D projections. A simple example [115] is a 3-D volume rendering of a "cloud of points" representing the scattering of an object, in this case a frog, where the spinal cord and notochord can be identified. Several examples exist where authors both plotted slices and created an animation of 3-D surface rendering, which provides a good comparison between the utility of the two methods. Two examples include renderings of a Syrian hamster cheek pouch [116] and a human finger pad [113]. The maximum intensity projection method, which is based on projecting the voxels in the projection path that correspond to the maximum intensities, has been used to visualize vascular perfusion [117, 118]. More recently, the processing capabilities of GPUs have been utilized for real-time volume rendering of OCT data. A ray-casting method was used to demonstrate real-time rendering of the human finger at the rate of 10 volumes/s. In addition, multiple 2-D frames were rendered in real-time using different model view matrices [119, 120]. A further example shows a hair being burned by a laser both as three orthogonal sections and an animated 3-D rendering [121]. In another example, volumetric rendering at 41 volumes/s is

shown as the human eye undergoes constriction and dilation on the shining of a laser beam [122]. These are examples of rendering a four-dimensional data set, including both three dimensions of space and one of time.

13.8 Conclusions

Great strides have been made to increase the utility of OCT images by using image post-processing. It seems likely that future OCT instruments will feature combinations of post-processing that include deconvolution, despeckling, dispersion correction, and 3-D visualization. Such advances will almost certainly provide the clinician with a portable, noninvasive, cellular level, in vivo diagnostic tool perhaps capable of obviating the need for many biopsies. Perhaps one day, OCT may even provide the physician with a 3-D visualization of cellular-level structure and processes inside the living human. While this may perhaps not be as complete as the intravascular submersible imagined in the science fiction film Fantastic Voyage, these capabilities may still be well beyond the mostly static 3-D images of tissue and organ structures that physicians use today.

Further improvements are needed to make many of these methods cost-effective and practical. To be useful clinically, processing methods must work in real time, presenting processed and analyzed results to the operator with little delay or lag time. Furthermore, processing methods must operate automatically, requiring little or no adjustment by the operator. Advances in digital signal processing and computational hardware continue to close the gap between the possible and the practical. The 3-D rendering hardware commonly used for computer gaming will also benefit portable medical imaging. Clinicians will need to be trained to interpret the images with the additional processing and hopefully with feedback on which methods enhance their diagnostic accuracy. Eventually, methods of image enhancement will be standardized among OCT instruments.

It is important to note that other coherent ranging modalities have already developed a body of knowledge on signal processing, much of which is likely useful to the OCT community. The similarities between ultrasound imaging and OCT are great, though they use different types of radiation at vastly different frequencies. How signal processing has been incorporated into ultrasound instruments [123] can provide guidance on how to succeed in integrating signal processing into OCT. In addition, tomographic algorithms [124, 125] developed for ultrasound may also find use for OCT. Synthetic aperture radar (SAR) extensively utilizes image processing because of the inherently tomographic nature of the backscattered signal in this method. For example, methods of deconvolution and despeckling [126–128], which are developed within the formalism of statistical signal processing, may serve as a starting point for similar algorithms developed for OCT. In fact, there is a resemblance between the method of stripmap SAR and axial priority scanning OCT [129]. Additionally, methods in magnetic resonance

imaging and X-ray computed tomography also have algorithms that may translate well to OCT, particularly in the sampling strategies. It seems likely that such cross-fertilization of disciplines and modalities will continue the convergence and use of medical imaging techniques.

References

1. J. Goodman, *Statistical Optics* (Wiley, New York, 1985)
2. J.M. Schmitt, S.H. Xiang, K.M. Yung, Speckle in optical coherence tomography. J. Biomed. Opt. **4**, 95–105 (1999)
3. M. Bashkansky, J. Reintjes, Statistics and reduction of speckle in optical coherence tomography. Opt. Lett. **25**, 545–547 (2000)
4. J. Rogowska, M.E. Brezinski, Optical coherence tomography image enhancement using Sticks technique, in *Conference on Lasers and Electro-Optics (CLEO)* (Optical Society of America, Washington, DC, 2000), pp. 418–419
5. J. Rogowska, M.E. Brezinski, Evaluation of the adaptive speckle suppression filter for coronary optical coherence tomography imaging. IEEE Trans. Med. Imag. **19**, 1261–1266 (2000)
6. D.C. Adler, T.H. Ko, J.G. Fujimoto, Speckle reduction in optical coherence tomography images by use of a spatially adaptive wavelet filter. Opt. Lett. **29**, 2878–2880 (2004)
7. T.S. Ralston, I. Atkinson, F. Kamalabadi, S.A. Boppart, Multi-dimensional denoising of real-time OCT imaging data, in *Proceedings of the IEEE, ICASSSP International Conference on Acoustic, Speech and Signal Processing* EEE, Piscataway, 2006), pp. II-1148–II-1151
8. Z. Jian, Z. Yu, L. Yu, B. Rao, Z. Chen, B.J. Tromberg, Speckle attenuation in optical coherence tomography by curvelet shrinkage. Opt. Lett. **34**, 1516–1518 (2009)
9. Z. Jian, L. Yu, B. Rao, B.J. Tromberg, Z. Chen, Three-dimensional speckle suppression in optical coherence tomography based on the curvelet transform. Opt. Express **18**, 1024–1032 (2010)
10. D.L. Marks, T.S. Ralston, S.A. Boppart, Speckle reduction by I-divergence regularization in optical coherence tomography. J. Opt. Soc. Am. A **22**, 2366–2371 (2005)
11. I. Csiszar, Why least squares and maximum entropy? An axiomatic approach to inference for linear inverse problems. Ann. Stat. **19**, 2032–2066 (1991)
12. M. Pircher, E. Götzinger, R. Leitgeb, A.F. Fercher, C.K. Hitzenberger, Speckle reduction in optical coherence tomography by frequency compounding. J. Biomed. Opt. **8**, 565–569 (2003)
13. T. Storen, A. Royset, N.-H. Giskeodegard, H. M. Pedersen, and T. Lindmo, Comparison of speckle reduction using polarization diversity and frequency compounding in optical coherence tomography, in *Proceedings of the SPIE, Coherence Domain Optical Methods and Optical Coherence Tomography in Biomedicine VIII* (Bellingham, 2004), pp. 196–204
14. N. Iftimia, B.E. Bouma, G.J. Tearney, Speckle reduction in optical coherence tomography by "path length encoded" angular compounding. J. Biomed. Opt. **8**, 260–263 (2003)
15. J.M. Schmitt, Array detection for speckle reduction in optical coherence microscopy. Phys. Med. Biol. **42**, 1427 (1997)
16. A.E. Desjardins, B.J. Vakoc, W.Y. Oh, S.M. Motaghiannezam, G.J. Tearney, B.E. Bouma, Angle-resolved optical coherence tomography with sequential angular selectivity for speckle reduction. Opt. Express **15**, 6200–6209 (2007)
17. D.P. Popescu, M.D. Hewko, M.G. Sowa, Speckle noise attenuation in optical coherence tomography by compounding images acquired at different positions of the sample. Opt. Commun. **269**, 247–251 (2007)
18. B.F. Kennedy, T.R. Hillman, A. Curatolo, D.D. Sampson, Speckle reduction in optical coherence tomography by strain compounding. Opt. Lett. **35**, 2445–2447 (2010)

19. B.F. Kennedy, A. Curatolo, T.R. Hillman, C.M. Saunders, D.D. Sampson, Speckle reduction in optical coherence tomography images using tissue viscoelasticity. J. Biomed. Opt. **16**, 020506 (2011)
20. D. Alonso-Caneiro, S.A. Read, M.J. Collins, Speckle reduction in optical coherence tomography imaging by affine-motion image registration. J. Biomed. Opt. **16**, 116027 (2011)
21. S. Moon, S.-W. Lee, Z. Chen, Reference spectrum extraction and fixed-pattern noise removal in optical coherence tomography. Opt. Express **18**, 24395–24404 (2010)
22. B. Hofer, B. Považay, B. Hermann, S.M. Rey, V. Kajić, A. Tumlinson, K. Powell, G. Matz, W. Drexler, Artefact reduction for cell migration visualization using spectral domain optical coherence tomography. J. Biophotonics **4**, 355–367 (2011)
23. Y. Huang, J.U. Kang, Real-time reference A-line subtraction and saturation artifact removal using graphics processing unit for high-frame-rate Fourier-domain optical coherence tomography video imaging. Opt. Eng. **51**, 073203-1 (2012)
24. D.L. Donoho, Compressed sensing. IEEE Trans. Inf. Theory **52**, 1289–1306 (2006)
25. E.J. Candes, J. Romberg, T. Tao, Robust uncertainty principles: exact signal reconstruction from highly incomplete frequency information. IEEE Trans. Inf. Theory **52**, 489–509 (2006)
26. N. Mohan, I. Stojanovic, W.C. Karl, B.E.A. Saleh, M.C. Teich, Compressed sensing in optical coherence tomography, in *Proceedings of the SPIE: Three-Dimensional and Multidimensional Microscopy: Image Acquisition and Processing XVII* (SPIE, Bellingham, 2010), pp. 75700L1–75700L5
27. X. Liu, J.U. Kang, Compressive SD-OCT: the application of compressed sensing in spectral domain optical coherence tomography. Opt. Express **18**, 22010–22019 (2010)
28. M. Young, E. Lebed, Y. Jian, P.J. Mackenzie, M.F. Beg, M.V. Sarunic, Real-time high-speed volumetric imaging using compressive sampling optical coherence tomography. Biomed. Opt. Express **2**, 2690–2697 (2011)
29. E. Lebed, P.J. Mackenzie, M.V. Sarunic, F.M. Beg, Rapid volumetric OCT image acquisition using compressive sampling. Opt. Express **18**, 21003–21012 (2010)
30. B. Wu, E. Lebed, M. Sarunic, M. Beg, Quantitative evaluation of transform domains for compressive sampling-based recovery of sparsely sampled volumetric OCT images. IEEE Trans. Biomed. Eng. **60**, 470–478 (2013)
31. D. Xu, N. Vaswani, Y. Huang, J.U. Kang, Modified compressive sensing optical coherence tomography with noise reduction. Opt. Lett. **37**, 4209–4211 (2012)
32. J.M. Schmitt, Restoration of optical coherence images of living tissue using the CLEAN algorithm. J. Biomed. Opt. **3**, 66–75 (1998)
33. D. Piao, Q. Zhu, N.K. Dutta, S. Yan, L.L. Otis, Cancellation of coherent artifacts in optical coherence tomography imaging. Appl. Opt. **40**, 5124–5131 (2001)
34. Y. Wang, Y. Liang, K. Xu, Signal processing for sidelobe suppression in optical coherence tomography images. J. Opt. Soc. Am. A **27**, 415–421 (2010)
35. D.L. Marks, A.L. Oldenburg, J.J. Reynolds, S.A. Boppart, Study of an ultrahigh-numerical-aperture fiber continuum generation source for optical coherence tomography. Opt. Lett. **27**, 2010–2012 (2002)
36. S. Bourquin, A. Aguirre, I. Hartl, P. Hsiung, T. Ko, J. Fujimoto, T. Birks, W. Wadsworth, U. Bünting, D. Kopf, Ultrahigh resolution real time OCT imaging using a compact femtosecond Nd:Glass laser and nonlinear fiber. Opt. Express **11**, 3290–3297 (2003)
37. I. Hartl, X.D. Li, C. Chudoba, R.K. Ghanta, T.H. Ko, J.G. Fujimoto, J.K. Ranka, R.S. Windeler, Ultrahigh-resolution optical coherence tomography using continuum generation in an air-silica microstructure optical fiber. Opt. Lett. **26**, 608–610 (2001)
38. B. Považay, K. Bizheva, A. Unterhuber, B. Hermann, H. Sattmann, A.F. Fercher, W. Drexler, A. Apolonski, W.J. Wadsworth, J.C. Knight, P.S.J. Russell, M. Vetterlein, E. Scherzer, Submicrometer axial resolution optical coherence tomography. Opt. Lett. **27**, 1800–1802 (2002)
39. K.M. Yung, S.L. Lee, J.M. Schmitt, Phase-domain processing of optical coherence tomography images. J. Biomed. Opt. **4**, 125–136 (1999)

40. M.D. Kulkarni, C.W. Thomas, J.A. Izatt, Image enhancement in optical coherence tomography using deconvolution. Electron. Lett. **33**, 1365–1367 (1997)
41. R. Tripathi, N. Nassif, J.S. Nelson, B.H. Park, J.F. de Boer, Spectral shaping for non-Gaussian source spectra in optical coherence tomography. Opt. Lett. **27**, 406–408 (2002)
42. R.K. Wang, Resolution improved optical coherence-gated tomography for imaging through biological tissues. J. Mod. Opt. **46**, 1905–1912 (1999)
43. D.L. Marks, A.L. Oldenburg, J.J. Reynolds, S.A. Boppart, Digital algorithm for dispersion correction in optical coherence tomography for homogeneous and stratified media. Appl. Opt. **42**, 204–217 (2003)
44. D.L. Marks, P.S. Carney, S.A. Boppart, Adaptive spectral apodization for sidelobe reduction in optical coherence tomography images. J. Biomed. Opt. **9**, 1281–1287 (2004)
45. I.J. Hsu, C.-W. Sun, C.-W. Lu, C.C. Yang, C.-P. Chiang, C.-W. Lin, Resolution improvement with dispersion manipulation and a retrieval algorithm in optical coherence tomography. Appl. Opt. **42**, 227–234 (2003)
46. T.S. Ralston, D.L. Marks, F. Kamalabadi, S.A. Boppart, Deconvolution methods for mitigation of transverse blurring in optical coherence tomography. IEEE Trans. Image Process. **14**, 1254–1264 (2005)
47. E. Bousi, I. Charalambous, C. Pitris, Optical coherence tomography axial resolution improvement by step-frequency encoding. Opt. Express **18**, 11877–11890 (2010)
48. T.S. Ralston, D.L. Marks, P. Scott Carney, S.A. Boppart, Interferometric synthetic aperture microscopy. Nat. Phys. **3**, 129–134 (2007)
49. A. Fercher, C. Hitzenberger, M. Sticker, R. Zawadzki, B. Karamata, T. Lasser, Numerical dispersion compensation for partial coherence interferometry and optical coherence tomography. Opt. Express **9**, 610–615 (2001)
50. A.F. Fercher, C.K. Hitzenberger, M. Sticker, R. Zawadzki, B. Karamata, T. Lasser, Dispersion compensation for optical coherence tomography depth-scan signals by a numerical technique. Opt. Commun. **204**, 67–74 (2002)
51. D.L. Marks, A.L. Oldenburg, J.J. Reynolds, S.A. Boppart, Autofocus algorithm for dispersion correction in optical coherence tomography. Appl. Opt **42**, 3038–3046 (2003)
52. B. Cense, N. Nassif, T. Chen, M. Pierce, S.-H. Yun, B. Park, B. Bouma, G. Tearney, J. de Boer, Ultrahigh-resolution high-speed retinal imaging using spectral-domain optical coherence tomography. Opt. Express **12**, 2435–2447 (2004)
53. M. Wojtkowski, V. Srinivasan, T. Ko, J. Fujimoto, A. Kowalczyk, J. Duker, Ultrahigh-resolution, high-speed, Fourier domain optical coherence tomography and methods for dispersion compensation. Opt. Express **12**, 2404–2422 (2004)
54. W. Choi, B. Baumann, E.A. Swanson, J.G. Fujimoto, Extracting and compensating dispersion mismatch in ultrahigh-resolution Fourier domain OCT imaging of the retina. Opt. Express **20**, 25357–25368 (2012)
55. N. Lippok, S. Coen, P. Nielsen, F. Vanholsbeeck, Dispersion compensation in Fourier domain optical coherence tomography using the fractional Fourier transform. Opt. Express **20**, 23398–23413 (2012)
56. K. Wang, Z. Ding, T. Wu, C. Wang, J. Meng, M. Chen, L. Xu, Development of a non-uniform discrete Fourier transform based high speed spectral domain optical coherence tomography system. Opt. Express **17**, 12121–12131 (2009)
57. K.K.H. Chan, S. Tang, High-speed spectral domain optical coherence tomography using non-uniform fast Fourier transform. Biomed. Opt. Express **1**, 1309–1319 (2010)
58. S. Makita, T. Fabritius, Y. Yasuno, Full-range, high-speed, high-resolution 1-μm spectral-domain optical coherence tomography using BM-scan for volumetric imaging of the human posterior eye. Opt. Express **16**, 8406–8420 (2008)
59. D. Hillmann, T. Bonin, C. Lührs, G. Franke, M. Hagen-Eggert, P. Koch, G. Hüttmann, Common approach for compensation of axial motion artifacts in swept-source OCT and dispersion in Fourier-domain OCT. Opt. Express **20**, 6761–6776 (2012)

60. V. Westphal, A. Rollins, S. Radhakrishnan, J. Izatt, Correction of geometric and refractive image distortions in optical coherence tomography applying Fermat's principle. Opt. Express **10**, 397–404 (2002)
61. A.M. Zysk, J.J. Reynolds, D.L. Marks, P.S. Carney, S.A. Boppart, Projected index computed tomography. Opt. Lett. **28**, 701–703 (2003)
62. S.A. Alexandrov, A.V. Zvyagin, K.K.M.B. Dilusha Silva, D.D. Sampson, Bifocal optical coherenc refractometry of turbid media. Opt. Lett. **28**, 117–119 (2003)
63. A. Zvyagin, K.K.M.B. Silva, S. Alexandrov, T. Hillman, J. Armstrong, T. Tsuzuki, D. Sampson, Refractive index tomography of turbid media by bifocal optical coherence refractometry. Opt. Express **11**, 3503–3517 (2003)
64. P.H. Tomlins, R.K. Wang, Matrix approach to quantitative refractive index analysis by Fourier domain optical coherence tomography. J. Opt. Soc. Am. A **23**, 1897–1907 (2006)
65. S. Ortiz, D. Siedlecki, I. Grulkowski, L. Remon, D. Pascual, M. Wojtkowski, S. Marcos, Optical distortion correction in optical coherence tomography for quantitative ocular anterior segment by three-dimensional imaging. Opt. Express **18**, 2782–2796 (2010)
66. Z. Chen, Z. Yonghua, S.M. Srinivas, J.S. Nelson, N. Prakash, R.D. Frostig, Optical Doppler tomography. IEEE J. Sel. Top. Quantum Electron. **5**, 1134–1142 (1999)
67. A. Mariampillai, M.K. Leung, M. Jarvi, B.A. Standish, K. Lee, B.C. Wilson, A. Vitkin, V.X.D. Yang, Optimized speckle variance OCT imaging of microvasculature. Opt. Lett. **35**, 1257–1259 (2010)
68. R.K. Wang, Optical microangiography: a label-free 3-D imaging technology to visualize and quantify blood circulations within tissue beds in vivo. IEEE J. Sel. Top. Quantum Electron. **16**, 545–554 (2010)
69. D.D. Duncan, S.J. Kirkpatrick, Processing algorithms for tracking speckle shifts in optical elastography of biological tissues. J. Biomed. Opt. **6**, 418–426 (2001)
70. A.L. Oldenburg, V. Crecea, S.A. Rinne, S.A. Boppart, Phase-resolved magnetomotive OCT for imaging nanomolar concentrations of magnetic nanoparticles in tissues. Opt. Express **16**, 11525–11539 (2008)
71. S.H. Yun, G.J. Tearney, J.F. de Boer, B.E. Bouma, Motion artifacts in optical coherence tomography with frequency-domain ranging. Opt. Express **12**, 2977–2998 (2004)
72. E.A. Swanson, J.A. Izatt, M.R. Hee, D. Huang, C.P. Lin, J.S. Schuman, C.A. Puliafito, J.G. Fujimoto, In vivo retinal imaging by optical coherence tomography. Opt. Lett. **18**, 1864–1866 (1993)
73. R.J. Zawadzki, A.R. Fuller, S.S. Choi, D.F. Wiley, B. Hamann, J.S. Werner, Correction of Motion Artifacts and Scanning Beam Distortions in 3D Ophthalmic Optical Coherence Tomography Imaging, in *Proceedings of the SPIE: Ophthalmic Technologies XVII* (2007), pp. 642607 1–11
74. J. Lee, V. Srinivasan, H. Radhakrishnan, D.A. Boas, Motion correction for phase-resolved dynamic optical coherence tomography imaging of rodent cerebral cortex. Opt. Express **19**, 21258–21270 (2011)
75. S. Ricco, M. Chen, H. Ishikawa, G. Wollstein, J. Schuman, Correcting motion artifacts in retinal spectral domain optical coherence tomography via image registration, in *Proceedings of Medical Image Computing and Computer-Assisted Intervention (MICCAI)*, vol. 12 (2009), pp. 100–107
76. S. Makita, Y. Hong, M. Yamanari, T. Yatagai, Y. Yasuno, Optical coherence angiography. Opt. Express **14**, 7821–7840 (2006)
77. A. Ahmad, S.G. Adie, E.J. Chaney, U. Sharma, S.A. Boppart, Cross-correlation-based image acquisition technique for manually-scanned optical coherence tomography. Opt. Express **17**, 8125–8136 (2009)
78. X. Liu, Y. Huang, J.U. Kang, Distortion-free freehand-scanning OCT implemented with real-time scanning speed variance correction. Opt. Express **20**, 16567–16583 (2012)
79. P.H. Tomlins, R.K. Wang, Digital phase stabilization to improve detection sensitivity for optical coherence tomography. Meas. Sci. Technol. **18**, 3365–3372 (2007)

80. T.S. Ralston, D.L. Marks, P.S. Carney, S.A. Boppart, Phase stability technique for inverse scattering in optical coherence tomography, in *Proceedings of the 3rd IEEE Int. Symp. on Biomedical Imaging: Nano to Macro* (IEEE, Piscataway, 2006), pp. 578–581
81. M.A. Choma, A.K. Ellerbee, S. Yazdanfar, J.A. Izatt, Doppler flow imaging of cytoplasmic streaming using spectral domain phase microscopy. J. Biomed. Opt. **11**, 024014–024018 (2006)
82. V. Crecea, A.L. Oldenburg, X. Liang, T.S. Ralston, S.A. Boppart, Magnetomotive nanoparticle transducers for optical rheology of viscoelastic materials. Opt. Express **17**, 23114–23122 (2009)
83. H.C. Hendargo, M. Zhao, N. Shepherd, J.A. Izatt, Synthetic wavelength based phase unwrapping in spectral domain optical coherence tomography. Opt. Express **17**, 5039–5051 (2009)
84. X. Liang, S.G. Adie, R. John, S.A. Boppart, Dynamic spectral-domain optical coherence elastography for tissue characterization. Opt. Express **18**, 14183–14190 (2010)
85. R.K. Wang, A.L. Nuttall, Phase-sensitive optical coherence tomography imaging of the tissue motion within the organ of Corti at a subnanometer scale: a preliminary study. J. Biomed. Opt. **15**, 056005–056009 (2009)
86. M. Mujat, R.D. Ferguson, D.X. Hammer, C. Gittins, N. Iftimia, Automated algorithm for breast tissue differentiation in optical coherence tomography. J. Biomed. Opt. **14**, 034040 (2009)
87. A.M. Zysk, S.A. Boppart, Computational methods for analysis of human breast tumor tissue in optical coherence tomography images. J. Biomed. Opt. **11**, 054015 (2006)
88. K.W. Gossage, T.S. Tkaczyk, J.J. Rodriguez, J.K. Barton, Texture analysis of optical coherence tomography images: feasibility for tissue classification. J. Biomed. Opt. **8**, 570–575 (2003)
89. F. Bazant-Hegemark, N. Stone, Towards automated classification of clinical optical coherence tomography data of dense tissues. Lasers Med. Sci. **24**, 627–638 (2009)
90. D. Faber, F. van der Meer, M. Aalders, T. van Leeuwen, Quantitative measurement of attenuation coefficients of weakly scattering media using optical coherence tomography. Opt. Express **12**, 4353–4365 (2004)
91. Q.Q. Zhang, X.J. Wu, T. Tang, S.W. Zhu, Q. Yao, B.Z. Gao, X.C. Yuan, Quantitative analysis of rectal cancer by spectral domain optical coherence tomography. Phys. Med. Biol. **57**, 5235–5244 (2012)
92. K. Barwari, D.M. de Bruin, D.J. Faber, T.G. van Leeuwen, J.J. de la Rosette, M.P. Laguna, Differentiation between normal renal tissue and renal tumours using functional optical coherence tomography: a phase I in vivo human study. BJU Int. **110**, E415–E420 (2012)
93. B.D. Goldberg, N.V. Iftimia, J.E. Bressner, M.B. Pitman, E. Halpern, B.E. Bouma, G.J. Tearney, Automated algorithm for differentiation of human breast tissue using low coherence interferometry for fine needle aspiration biopsy guidance. J. Biomed. Opt. **13**, 014014–014018 (2008)
94. K.W. Gossage, C.M. Smith, E.M. Kanter, L.P. Hariri, A.L. Stone, J.J. Rodriguez, S.K. Williams, J.K. Barton, Texture analysis of speckle in optical coherence tomography images of tissue phantoms. Phys. Med. Biol. **51**, 1563–1575 (2006)
95. F. Bazant-Hegemark, N. Stone, Near real-time classification of optical coherence tomography data using principal components fed linear discriminant analysis. J. Biomed. Opt. **13**, 034002–034008 (2008)
96. X. Qi, J.M.V. Sivak, G. Isenberg, J.E. Willis, A.M. Rollins, Computer-aided diagnosis of dysplasia in Barrett's esophagus using endoscopic optical coherence tomography. J. Biomed. Opt. **11**, 044010 (2006)
97. P.B. Garcia-Allende, I. Amygdalos, H. Dhanapala, R.D. Goldin, G.B. Hanna, D.S. Elson, Morphological analysis of optical coherence tomography images for automated classification of gastrointestinal tissues. Biomed. Opt. Express **2**, 2821–2836 (2011)
98. M. Bhattacharjee, P.C. Ashok, K.D. Rao, S.K. Majumder, Y. Verma, P.K. Gupta, Binary tissue classification studies on resected human breast tissues using optical coherence tomography images. J. Innov. Opt. Health Sci. **4**, 59–66 (2011)

99. C.A. Lingley-Papadopoulos, M.H. Loew, J.M. Zara, Wavelet analysis enables system-independent texture analysis of optical coherence tomography images. J. Biomed. Opt. **14**, 044010 (2009)
100. A.C. Sullivan, J.P. Hunt, A.L. Oldenburg, Fractal analysis for classification of breast carcinoma in optical coherence tomography. J. Biomed. Opt. **16**, 066010 (2011)
101. C. Flueraru, D.P. Popescu, Y. Mao, S. Chang, M.G. Sowa, Added soft tissue contrast using signal attenuation and the fractal dimension for optical coherence tomography images of porcine arterial tissue. Phys. Med. Biol. **55**, 2317–2331 (2010)
102. K. Yu, L. Ji, L. Wang, P. Xue, How to optimize OCT image. Opt. Express **9**, 24–35 (2001)
103. S. Yazdanfar, A.M. Rollins, J.A. Izatt, Imaging and velocimetry of the human retinal circulation with color Doppler optical coherence tomography. Opt. Lett. **25**, 1448–1450 (2000)
104. S. Yazdanfar, M. Kulkarni, J. Izatt, High resolution imaging of in vivo cardiac dynamics using color Doppler optical coherence tomography. Opt. Express **1**, 424–431 (1997)
105. J.A. Izatt, M.D. Kulkarni, S. Yazdanfar, J.K. Barton, A.J. Welch, In vivo bidirectional color Doppler flow imaging of picoliter blood volumes using optical coherence tomography. Opt. Lett. **22**, 1439–1441 (1997)
106. T.G. van Leeuwen, M.D. Kulkarni, S. Yazdanfar, A.M. Rollins, J.A. Izatt, High-flow-velocity and shear-rate imaging by use of color Doppler optical coherence tomography. Opt. Lett. **24**, 1584–1586 (1999)
107. C. Xu, C. Vinegoni, T.S. Ralston, W. Luo, W. Tan, S.A. Boppart, Spectroscopic spectral-domain optical coherence microscopy. Opt. Lett. **31**, 1079–1081 (2006)
108. F.E. Robles, C. Wilson, G. Grant, A. Wax, Molecular imaging true-colour spectroscopic optical coherence tomography. Nat. Photon. **5**, 744–747 (2011)
109. U. Morgner, W. Drexler, F.X. Kärtner, X.D. Li, C. Pitris, E.P. Ippen, J.G. Fujimoto, Spectroscopic optical coherence tomography. Opt. Lett. **25**, 111–113 (2000)
110. A. Ahmad, S.G. Adie, M. Wang, S.A. Boppart, Sonification of optical coherence tomography data and images. Opt. Express **18**, 9934–9944 (2010)
111. M. Wojtkowski, High-speed optical coherence tomography: basics and applications. Appl. Opt. **49**, D30–D61 (2010)
112. C. Hitzenberger, P. Trost, P.-W. Lo, Q. Zhou, Three-dimensional imaging of the human retina by high-speed optical coherence tomography. Opt. Express **11**, 2753–2761 (2003)
113. M. Pircher, E. Goetzinger, R. Leitgeb, C. Hitzenberger, Three dimensional polarization sensitive OCT of human skin in vivo. Opt. Express **12**, 3236–3244 (2004)
114. M. Pircher, E. Götzinger, R. Leitgeb, H. Sattmann, O. Findl, C. Hitzenberger, Imaging of polarization properties of human retina in vivo with phase resolved transversal PS-OCT. Opt. Express **12**, 5940–5951 (2004)
115. B. Hoeling, A. Fernandez, R. Haskell, E. Huang, W. Myers, D. Petersen, S. Ungersma, R. Wang, M. Williams, S. Fraser, An optical coherence microscope for 3-dimensional imaging in developmental biology. Opt. Express **6**, 136–146 (2000)
116. P.-L. Hsiung, Y. Chen, T. Ko, J. Fujimoto, C. de Matos, S. Popov, J. Taylor, V. Gapontsev, Optical coherence tomography using a continuous-wave, high-power, Raman continuum light source. Opt. Express **12**, 5287–5295 (2004)
117. R.K. Wang, L. An, Doppler optical micro-angiography for volumetric imaging of vascular perfusion in vivo. Opt. Express **17**, 8926–8940 (2009)
118. R.K. Wang, S. Hurst, Mapping of cerebro-vascular blood perfusion in mice with skin and skull intact by Optical Micro-AngioGraphy at 1.3 μm wavelength. Opt. Express **15**, 11402–11412 (2007)
119. K. Zhang, J.U. Kang, Real-time 4D signal processing and visualization using graphics processing unit on a regular nonlinear-k Fourier-domain OCT system. Opt. Express **18**, 11772–11784 (2010)
120. K. Zhang, J.U. Kang, Real-time intraoperative 4D full-range FD-OCT based on the dual graphics processing units architecture for microsurgery guidance. Biomed. Opt. Express **2**, 764–770 (2011)

121. M. Laubscher, M. Ducros, B. Karamata, T. Lasser, R. Salathe, Video-rate three-dimensional optical coherence tomography. Opt. Express **10**, 429–435 (2002)
122. D.-h. Choi, H. Hiro-Oka, K. Shimizu, K. Ohbayashi, Spectral domain optical coherence tomography of multi-MHz A-scan rates at 1310 nm range and real-time 4D-display up to 41 volumes/second. Biomed. Opt. Express **3**, 3067–3086 (2012)
123. H. Xiaohui, G. Shangkai, G. Xiaorong, A novel multiscale nonlinear thresholding method for ultrasonic speckle suppressing. IEEE Trans. Med. Imag. **18**, 787–794 (1999)
124. C.H. Frazier, W.D. O'Brien Jr., Synthetic aperture techniques with a virtual source element. IEEE Trans. Ultrason. Ferroelectr. Freq. Control **45**, 196–207 (1998)
125. S.J. Norton, M. Linzer, Ultrasonic reflectivity imaging in three dimensions: Exact inverse scattering solutions for plane, cylindrical, and spherical apertures. IEEE Trans. Biomed. Eng **28**, 202–220 (1981)
126. S.R. DeGraaf, SAR imaging via modern 2-D spectral estimation methods. IEEE Trans. Image Process. **7**, 729–761 (1998)
127. D.L. Snyder, J.A. O'Sullivan, M.I. Miller, The use of maximum likelihood estimation for forming images of diffuse radar targets from delay-Doppler data. IEEE Trans. Inf. Theory **35**, 536–548 (1989)
128. M. Cetin, W.C. Karl, Feature-enhanced synthetic aperture radar image formation based on nonquadratic regularization. IEEE Trans. Image Process. **10**, 623–631 (2001)
129. T.S. Ralston, G.L. Charvat, S.G. Adie, B.J. Davis, P.S. Carney, S.A. Boppart, Interferometric synthetic aperture microscopy: Microscopic laser radar. Opt. Photon. News **21**, 32–38 (2010)
130. A. Alex, B. Považay, B. Hofer, S. Popov, C. Glittenberg, S. Binder, W. Drexler, Multispectral in vivo three-dimensional optical coherence tomography of human skin. J. Biomed. Opt. **15**, 026025 (2010)

DSP Technology and Methods for OCT

14

Murtaza Ali, Adeel Ahmad, and Stephen A. Boppart

14.1 Introduction

Medical imaging devices are continually changing and evolving. In recent years, these devices have been evolving towards portable and handheld point-of-care systems. This is reminiscent of many other industries where semiconductors play a key role. A PC with a 1 GB hard drive and a 100 MHz processor was considered state of the art about 15 years ago. Cell phones were brick-sized voice-only devices. Today, processors ten times faster are available in handheld smartphones that run for days without recharging. These phones now are smaller than a deck of cards, are capable of streaming TV-quality video, and have become an integral part of personal entertainment. This has been possible with the advancement of both analog and embedded processing technology available from the semiconductor industry. This technology today powers consumer and industrial electronics, including medical imaging devices.

Ultrasound imaging devices used for medical evaluations and diagnostics are prime examples of how the advanced analog and embedded processing technology

M. Ali (✉)
Embedded Processing Systems Lab, Texas Instruments Inc, Dallas, TX, USA
e-mail: mali@ti.com

A. Ahmad
Biophotonics Imaging Laboratory, Beckman Institute for Advanced Science and Technology, University of Illinois at Urbana-Champaign, Urbana, IL, USA

S.A. Boppart
Biophotonics Imaging Laboratory, Beckman Institute for Advanced Science and Technology, University of Illinois at Urbana-Champaign, Urbana, IL, USA

Departments of Bioengineering, Electrical and Computer Engineering, and Medicine, University of Illinois at Urbana-Champaign, Urbana, IL, USA

© Springer International Publishing Switzerland 2015

W. Drexler, J.G. Fujimoto (eds.), *Optical Coherence Tomography*,
DOI 10.1007/978-3-319-06419-2_15

is changing the use of these devices. Cart-based systems were the only devices available a few years ago. Now these systems are being complemented by portable and handheld devices. Portability of medical devices creates a paradigm shift by bringing advanced health care to the patient instead of forcing the patient to travel to a facility. This allows development of new devices for use by medical professionals, in patient rooms in hospitals, in disaster and remote areas, in assisted living facilities, and even in ambulances. Portable devices complimented with wireless communication systems have been increasingly used for telemedicine in rural areas, which lack both medical experts and diagnostic facilities.

Today, optical coherence tomography (OCT) systems are mostly cart-based or desktop systems. Like ultrasound imaging devices, we expect portable and handheld OCT systems to open up new opportunities for their use. Recent advances in optics and scanning techniques have led to miniaturization of the optics used to acquire the raw data. This has certainly opened up the potential for creating smaller OCT systems. However, we have also seen the development of very high data acquisition rate systems that can operate at a rate on the order of several hundred thousand A-lines per second, or more [1]. This high rate of acquisition allows 3D volume imaging in real time, as well as imaging fast moving structures at high temporal resolution. The signal processing chain to convert the raw acquired data into a useful structural image is computationally intensive. In addition to the formation of the structural image, many advanced computational techniques like interferometric synthetic aperture microscopy (ISAM) have been proposed to improve the image quality [2]. Additional processing is also necessary to extract further information like Doppler-shifted signals for velocity information [3, 4], elasticity [5], birefringence, and optical axis rotation [6] of the tissues. Today, researchers have responded to this computational need through the use of high-performance personal computers (PC) that include high-end general purpose multi-core central processing units (CPU) coupled with graphics processing units (GPU) [7–9]. While these systems serve well the need for cart-based and desktop systems available today, creating a true embedded system for portability and low-power operation requires coupling the available miniaturized optics with high-performance embedded processing elements.

Digital signal processor (DSP) technology has served the signal processing community over the last three decades by providing low-power, computationally efficient, programmable embedded solutions [10]. DSPs are especially designed for real-time, deadline critical, compute-intensive operations as well as for harsh operating conditions. DSPs have been processing signals in many forms, e.g., to transmit and receive signals through wired and wireless media; to encode and decode speech, audio, and video signals; to identify objects for surveillance; to extract structural and Doppler information in medical ultrasound imaging machines; to enhance images in consumer cameras and camcorders; and in medical devices like X-ray machines. DSP technology is, therefore, an excellent choice of an embedded processor for developing low-power, low-cost, handheld, and portable OCT systems.

14.2 DSP Technology and Medical Imaging

DSPs are among a class of embedded processors that are often used for low-power, low-latency signal processing functions. Modern DSPs can be broadly grouped into three categories:

- Single-core DSP: These DSPs are mostly used in very low-power, low-frequency signal processing. Though there are many medical applications that benefit from these devices, these devices are not suitable for the OCT signal chain.
- Multi-core DSP: These devices bring a large amount of computational power at a comparatively low power through the use of parallel instantiations of DSP cores. These devices are widely used in the wireless infrastructure market. They are also used in various compute-intensive medical imaging modalities. These devices seem to be the most appropriate to handle the compute-intensive signal processing challenges encountered in OCT.
- Systems-on-chip (SoC): These devices are typically based on heterogeneous compute elements that include graphics, display, user input, as well as control. Some versions of these devices also have decent compute capabilities. These devices are ideal for performing the back-end tasks typical in medical imaging applications.

Embedded processors like DSPs are playing a key role in developing both new medical imaging devices and new imaging modalities [11, 12]. Some of the key advantages of DSPs in medical imaging systems are noted below:

- Reduced research to development time: DSPs are programmable devices just like a CPU or GPU in a PC. They are programmed in standard "C" with some specialized extensions called "intrinsics." The programming paradigm is very similar to PC-based programming methods where researchers originally develop their new algorithms. Thus, DSPs provide a much faster path to implementation compared to field-programmable gate arrays (FPGAs) or application-specific integrated circuits (ASICs). FPGA development time is shorter than ASIC and is often used for prototyping complex systems. FPGAs are useful to bring in and process a large number of parallel data and perform fixed tasks which are not expected to change during the lifetime of the product.
- Field upgradability: Due to the programmable nature of DSPs, they provide a path to future proofing the system. New algorithms and new tasks can be easily brought in within the limits of the available computational power. DSP-based systems are often designed with enough headroom to account for future extensions. ASICs functionality cannot be changed without changing the chip. FPGA is, in theory, configurable, but the design and verification time for FPGA implementation is much longer than software-based implementation in DSPs.
- Real-time processing: DSPs are designed to be deterministic in compute time. They have very low-latency interrupt reaction time. In addition, they run low-overhead, real-time operating systems. As a result, they can respond to time critical events quickly. This allows the system to perform low-latency implementations which can be very important in surgical imaging systems.

DSPs also have very low boot-up or start-up time since they do not need to run a full operating system. This is an advantage where it is critical to reduce the time from device start-up to medical image acquisition, such as in ambulances and field medical stations. The operating systems in PCs are inherently non-real time and the response time to a particular event cannot be guaranteed. Though there are embedded operating systems running on PCs which alleviates this problem somewhat, they do not come close to the response time of DSP-based solutions.

- Reliability: The components that are used to build a medical imaging system must be highly reliable. The components must not fail even after years of rough handling in the field. Reliability also includes the ability to recover quickly from failures due to software bugs and immunity to electromagnetic interference. Reliability affects a system's total cost of ownership for the end user, such as hospitals and physician groups. It also affects brand reputation and the competitive positions of system vendors. DSPs have a history of operating under extreme conditions in industrial electronics as well as under rough handling in consumer electronics.
- Scalability: The multi-core DSP platforms provide the system vendor a choice of scaling the end system based on specific needs. Many medical imaging technologies have the same underlying technology but need to scale the functionalities based on capabilities and usage. For example, some ultrasound systems measuring blood flow will require high rates of acquisition, some will require larger depths in imaging, and some will require additional functionalities like elasticity imaging. Similarly, OCT systems, providing various functionalities like B-mode imaging versus 3D volume imaging, and structural versus flow or polarization-sensitive imaging, will benefit from the scalable nature of this class of embedded processors. The functionalities can be implemented for a given architecture of DSP core once, and then various instantiations of the multi-core DSP can be used based on the scale of computation needed for a particular implementation.
- Low power: DSPs are designed for power-sensitive battery-operated systems. The specific architectural features of a DSP core, coupled with the already discussed low-overhead real-time operating systems and the ability to use the compute elements with very high efficiency, all contribute to a low-power system when designed with these embedded processors. Multi-core DSPs usually run from a few watts to a few tens of watts, thereby giving the system vendor the capability to trade off computational need with power need. DSPs are considered to be the lowest power for programmable or configurable embedded processing elements commercially available. A properly designed ASIC will definitely be lower power, but that low power comes with inflexibility of future extension and long development time.

As with many other established and new medical imaging modalities, DSP-based embedded systems will provide the necessary platforms for portable and handheld OCT devices. Multi-core DSPs are suited to take the signal processing tasks from the raw data processing to the manipulation of displayed images. In addition to multi-core DSPs to handle the OCT signal chain, a complete system will potentially be composed of other embedded processing elements. This may include FPGAs to collect and manage the raw data, to transfer the data to the DSP as well as an SoC at

the back-end to control the system, to drive a user interface, and to display the processed images along with any other relevant information.

14.3 Architectural Overview of a Multi-core Digital Signal Processor (DSP)

In this section, we provide an overview of the architectural aspects of the TMS320C6678 multi-core DSP from Texas Instruments (TI) [13]. This is currently the highest performance DSP commercially available. This device is capable of a peak performance of 128 billion floating-point operations per second (GFLOPS) running at 1 GHz clock frequency with a power dissipation of only 10 W. The OCT implementations described in this chapter are based on this particular DSP. Some results on DSP-based embedded implementation of OCT signal processing have been reported in the literature [14, 15]. The results in [14] are based on an earlier generation of DSP architecture and the analysis in [15] is on the architecture described here.

This device incorporates eight DSP cores code-named C66x [16]. The block diagram of each core is shown in Fig. 14.1. Each core is based on very long instruction word (VLIW) architecture. The core has eight units arranged in two sides. The four units on each side are termed as L, M, S, and D units. Each unit is

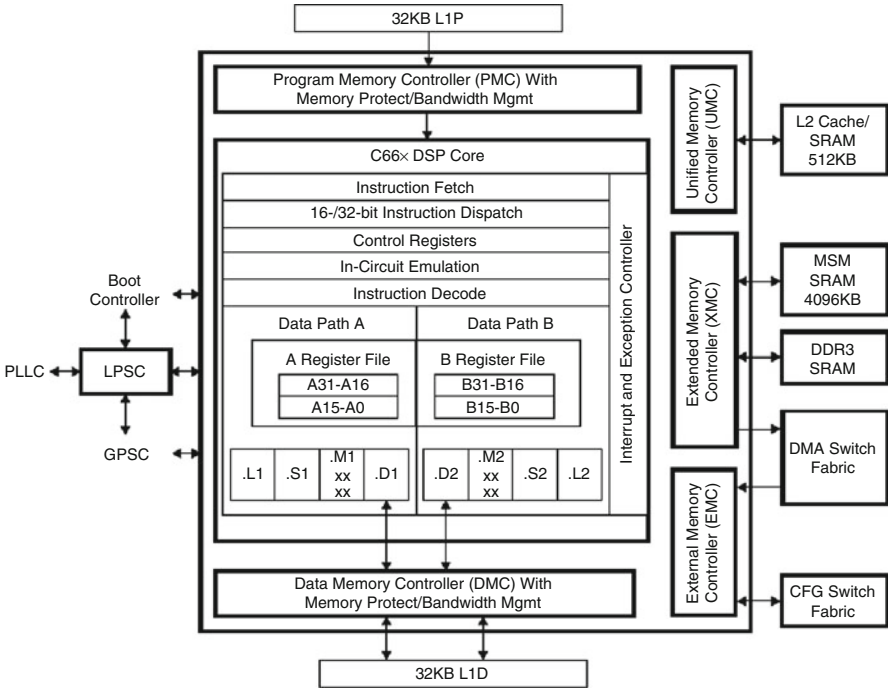

Fig. 14.1 Block diagram of an individual C66x DSP core

designed to perform different sets of operations. For example, the M unit primarily performs multiply operations. The D unit is used for load/store operations from memory. The additions and logical operations are distributed across the L and S units. This is thus an 8-way VLIW machine where eight instructions can be issued across these eight parallel units in one cycle.

The instruction set also includes single instruction, multiple data (SIMD) format. SIMD is often used for vector data processing where the same processing (multiplication, addition, etc.) can be done in parallel on multiple input datasets producing multiple output datasets. This architecture allows up to 128-bit vector processing. The 128-bit vector can hold up to four single precision numbers in IEEE754 format. The M unit can do four single precision multiply operations per cycle. Each of L and S can do two single precision additions per cycles. The two sets of L, S, and M can then do eight single precision multiply-add operations per cycle (i.e., 16 floating-point operations or FLOP per cycle). There is also the ability to do double precision operations as well as integer operations of various widths (8 bit or byte, 16 bit or half word, and 32 bit or full word). Various mixed mode operations are also allowed.

There are two general purpose register files, one on each side, which feeds data to the units of that side. There is also a cross connect so that units on one side can use the data from the units on the other side. The art of efficient programming a VLIW engine like the C66x DSP core lies in the ability to feed as many instructions as possible to the parallel units without overwhelming the registers. Fortunately, a large amount of the standard signal and image processing functions is available as standard libraries, and the user would not need to write optimized functions for these.

The overall block diagram of the TMS320C6678 DSP with eight cores is shown in Fig. 14.2. In addition to the eight cores, the device comes with a rich set of standard interfaces like PCI express, Serial Rapid I/O (SRIO), and gigabit Ethernet.

14.3.1 Memory Hierarchy

The memory hierarchy available in a particular processor is an important design consideration for embedded processors. The TMS320C6678 DSP has 32 KB of L1 program (L1P) and 32 KB of L1 data (L1D) cache memory, as well as 512 KB of L2 cache memory per core, integrated in the chip. Unlike a conventional CPU, both L1 and L2 memory in the TMS320C6678 can be configured as RAM or cache or part cache/part RAM. This flexibility is exploited in this implementation of the OCT signal chain. In addition to this per-core memory, the device also integrates 4,096 KB of multi-core shared memory (referred to as MSMC). This part of the memory is accessible by all the cores.

All L2 memory incorporates error detection and error correction which acts as auto fault detection and correction for device and memory errors. This may be an important aspect in safety critical applications like medical imaging devices. The device includes 64-bit DDR3 external memory which runs at 1,333 MHz, giving a maximum DDR3 (with error correction DRAM support) bandwidth of about

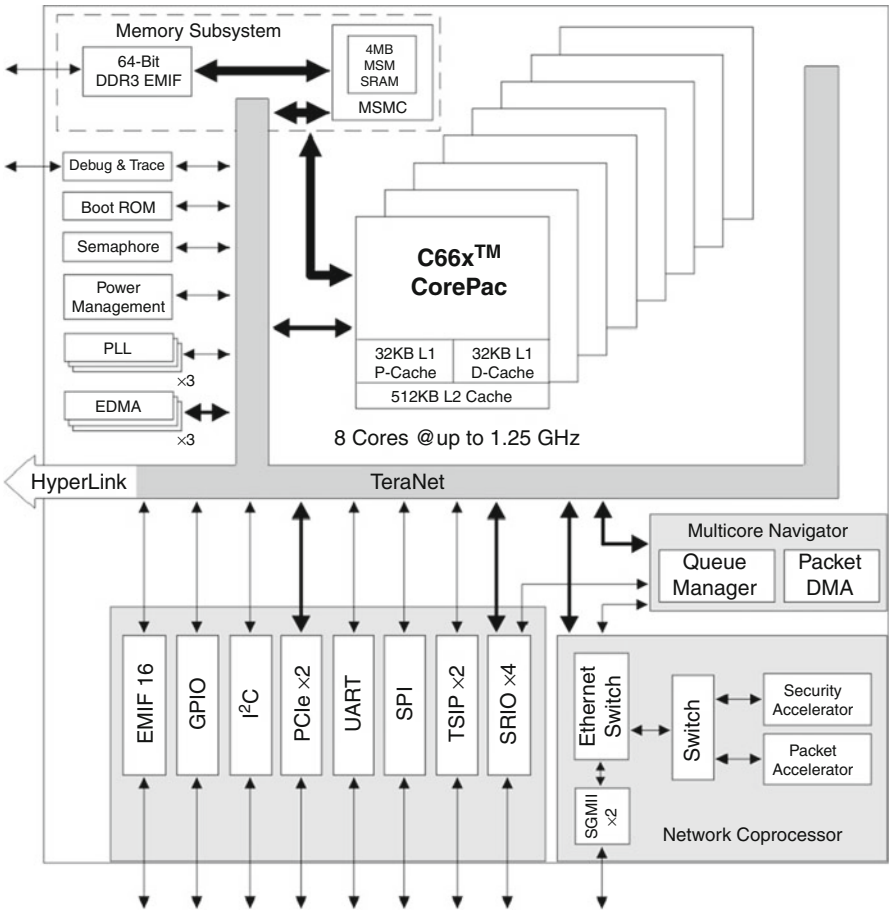

Fig. 14.2 Block diagram of the eight-core TMS320C6678 DSP

10.6 GB/s. The total addressable memory of this device is 8 GB. This gives enough space to hold a 3D volume of OCT images. For example, a $512 \times 512 \times 512$ volume of single precision data requires 0.5 GB of memory space.

14.3.2 Programming Model

The TMS320C6678 is mainly programmed through standard C. Texas Instruments provides a C/C++ compiler as part of its code generation tools. Virtually all C89 compliant C programs can be directly ported to this device. To achieve efficient implementation tuned to the architecture, the compiler provides a rich set of optimization and tuning flags. It supports optimizations through the use of pragma

```
omp_set_num_threads(NUM_THREADS);  // set thread count
#pragma omp parallel for private(i) shared(a, b, c, n)
// The following for loop will be parallelized across multiple threads
// variables a, b, c and n are shared across all threads
// variable i is unique/private to each core
For(i=0;i<n;i++)
{
    c[i] = a[i] + b[i]
}
```

Fig. 14.3 Simple OpenMP-based parallelization of vector addition

and intrinsic. The pragmas can be used to provide useful information to the compiler (e.g., certain variables are multiples of a number; certain addresses are double word aligned) which allows the compiler to perform important optimizations to extract as much efficiency as possible from the underlying core architecture. The intrinsics allow the programmer to guide the compiler to use specific instructions available in the architecture. The compiler also provides important feedback to the programmer, such as how much the units are loaded in a particular loop. This lets the programmer understand bottlenecks and rewrite the code to remove these bottlenecks as he/she iterates through the compiler searching for an optimum implementation. This allows quick port and optimizations of existing code into DSP-based embedded systems.

TI's DSPs run a lightweight real-time native operating system known as SYSBIOS available through the multi-core software development kit (MC-SDK) [17]. SYSBIOS is highly configurable. The user can choose specific parts of the operating system that are needed. This is also an important difference compared to general purpose CPUs available in PCs. Such configurability allows low memory footprint implementation of a system, thereby reducing overall cost, size, and power.

TI's multi-core DSPs support multi-threading through the use of an OpenMP 3.0 model [18]. A simple example of OpenMP-based parallelization is shown in Fig. 14.3. The pragma allows defining shared variables that are accessible by all threads as well as private variables which will be local to each thread. The "#pragma omp parallel" statement shows the boundaries of the parallel regions. The "#pragma omp for" statement tells the device that the "for loop" will need to be distributed across parallel threads. In the multi-core DSP, one thread corresponds to one core.

TI's compiler translates OpenMP into a multi-threaded code with calls to a custom runtime library. The runtime library provides support for thread management, scheduling, and synchronization. The current implementation of the runtime library sits on top of the SYSBIOS operating system and uses the interprocess communication (IPC) protocols running on each core of the DSP. Since these multi-core DSPs have both local private and shared memory, they map well into the OpenMP framework. Shared variables are stored in shared on-chip or DDR3 memory, while private variables are stored in local on-chip L1 or L2 memory.

However, there is no hardware support for cache coherency of data between cores. Hence, special care may need to be taken to keep the data in shared memory coherent. TI's OpenMP implementation does allow support for software cache coherency of DDR3 memory. This can be enabled with a slight loss of computational efficiency, if desired.

14.4 OCT Signal Chain on Multi-core DSP

In this section, we analyze the implementation details of a typical OCT signal chain in the TMS320C6678 multi-core DSP. In spectral-domain OCT systems, a single A-scan is normally acquired simultaneously, and as the beam scans over the sample, the sequence of A-scans collected can be assembled to form 2D or 3D datasets. The typical OCT image reconstruction steps are shown in Fig. 14.4. These steps, which include background subtraction, linearization in wave number (k), dispersion compensation, Fourier transforms, and dynamic range compression, can be performed independently on each A-scan. This parallel nature of OCT image reconstruction can be exploited by parallel processing techniques and multi-core platforms to significantly increase the speed for processing. DSPs have several cores that can process the data independently and in parallel to each other. Efficient utilization of the multi-core capabilities of the DSP would require partitioning the data and algorithms into independent subunits and assigning these to the DSP cores. In addition, memory hierarchy needs to be taken into consideration for efficient implementation. The data-intensive operations should be performed by placing the data in the limited but fast internal memory.

14.4.1 Dataflow

Typically, an acquired OCT frame would be copied from the frame grabber or data acquisition device onto the external memory on the DSP board. The OCT processing can be partitioned in a number of ways using the DSPs. An example

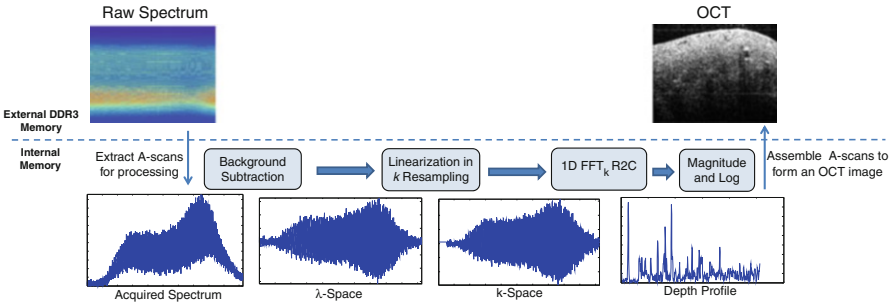

Fig. 14.4 Steps in the OCT signal chain. R2C is real-to-complex

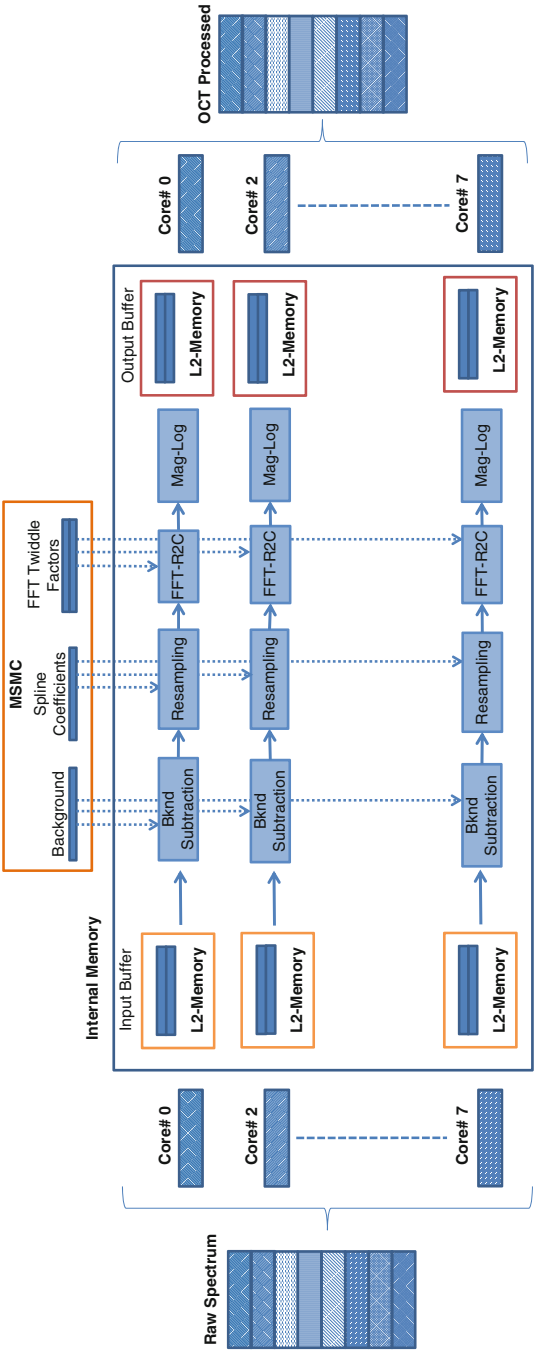

Fig. 14.5 OCT implementation on the multi-core DSP

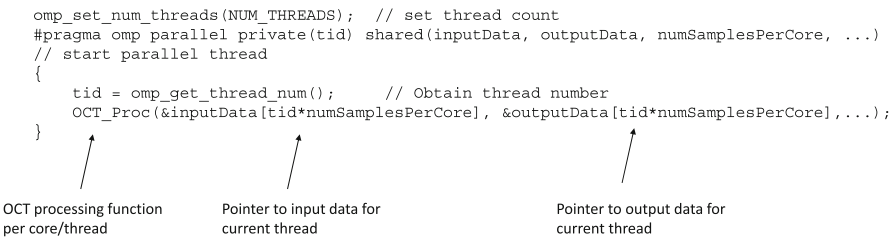

Fig. 14.6 Partitioning of OCT frames through OpenMP pragma

is shown in Fig. 14.5 where a single OCT frame is partitioned into several subsets of A-scans and each of these subsets would be operated independently and in parallel by a different DSP core. Within each core, all the processing on the A-scans are done serially, and finally the processed subsets from all the cores are assembled back to form the final processed frame. The partitioning of the frames into subsets can easily be done using OpenMP pragmas as shown in Fig. 14.6.

In principle, all processing on the data can be performed with the data residing in external memory. However, it is preferable to do the data-intensive operations by moving the data into the fast internal memory available on the DSP chip itself. Often it would be necessary to further divide the data subsets (that have been assigned to each core) into small enough patches that can fit within the limited amount of available internal memory. Each of these patches would contain several A-scans depending on the initial frame size, the number of available cores, and the amount of available internal memory. Each patch once moved inside the internal memory can be accessed at high speeds and, after completion of the processing, is copied back to the external memory. This additional overhead due to memory transfers between the external and internal memory can be minimized using direct memory access (DMA) controllers which can overlap the data transfer with data processing. Typically, memory buffers are configured in the internal memory and are operated as ping-pong buffers (double buffering) to overlap data transfer with the processing. An example of this dataflow within a single core is shown in Fig. 14.7, where the data subset assigned to the core is divided into patches and moved into the internal memory using the DMA controller. Four buffers each of which has a size equivalent to a single patch are configured in internal memory and are used for input, output, and processing purposes. As the Nth patch is being processed by utilizing the processing buffer (and temporary buffer for holding intermediate values), the (N – 1)th patch is copied back to the external memory from the output buffer after undergoing processing in the previous iteration. At the same time, the (N + 1)th patch is being copied into the input buffer, which would be processed in the next iteration. These buffers are then interchanged at the end of each iteration and hence are used alternatively for input, data processing, and output tasks. This procedure continues until all the N patches within the core have been processed.

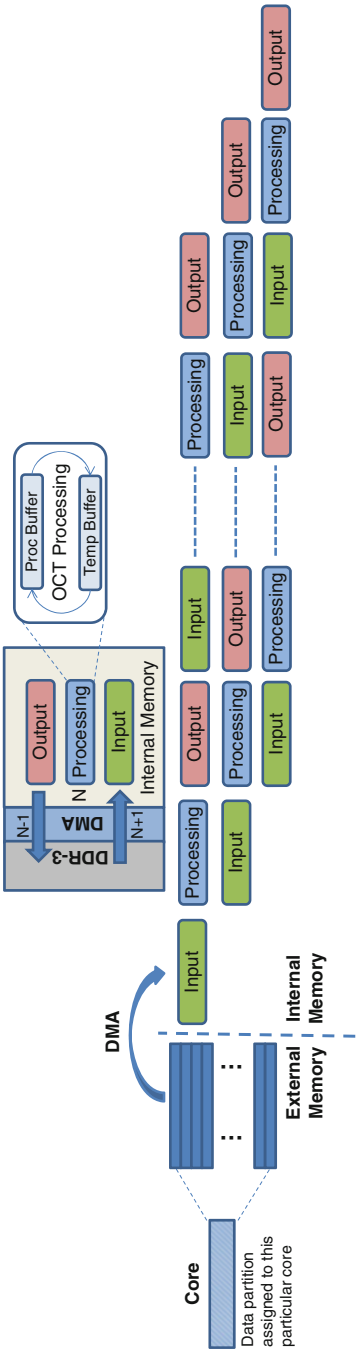

Fig. 14.7 Dataflow through buffers for OCT/ISAM implementation

14.4.2 OCT Data Processing on the DSP

Several chapters in this book present OCT processing methods in detail. Therefore, in this chapter, we will only focus on DSP implementation of standard OCT processing tasks which primarily include resampling and Fourier transform operations. In OCT, several inputs such as background spectrum, resampling indices, and the twiddle factors for the fast Fourier transform (FFT) can be precomputed. These precomputed values will need to be accessed by all the A-scans in each of the cores; hence, it is generally preferable that they be stored in a global memory with fast access times. One such option is utilizing the MSMC.

14.4.2.1 Resampling

The acquired spectrum measured by the spectrometer or obtained from swept-source OCT systems is a function of wavelength, hence, making the λ-k resampling a necessary step in OCT processing. A variety of interpolators (e.g., linear, cubic B-spline) have been employed by different OCT groups to perform the resampling. There is always an inherent compromise between the computational complexity and image quality of the different interpolators employed. Cubic spline interpolation, however, remains a relatively popular interpolator and its implementation on the DSP will be discussed here.

The resampling indices can be computed using a third-order polynomial function: $i_n = n + \beta_2\left(\frac{n}{N} - \omega_{ctr}\right)^2 + \beta_3\left(\frac{n}{N} - \omega_{ctr}\right)^3$, where ω_{ctr} is the center wavelength and N is the number of points in a single A-scan. The nonlinear mapping between the k-domain and the wavelength is adjusted using the parameters β_2 and β_3. These parameters are used to compute the integer and fractional parts that can be subsequently used to determine the spline table coefficients. The resampling indices/spline table coefficients, however, only need to be calculated once in the initialization phase, and the same indices can be reused for resampling every A-scan.

In our implementation, we have followed the technique described in [19]. Prior to using the interpolator, first-order causal and noncausal infinite impulse response (IIR) filters were employed to prefilter the data. This prefiltering is necessary to obtain an exact interpolated value at the original sampling indices. A first-order causal IIR filter, i.e., $b_k = x_k + \alpha b_{k-1}$, would require that the previous output value be available before the current output value can be computed. This operation is inherently serial in nature. Implementation of straightforward IIR filtering cannot take advantage of the parallelism available inside a core through the availability of multiple compute units and SIMD instructions. In order to improve the parallelization of computations, the equation $b_k = x_k + \alpha b_{k-1}$ was unrolled to up to three levels, as shown below.

$$
\begin{aligned}
b_{k-3} &= x_{k-3} + \alpha b_{k-4} \\
b_{k-2} &= x_{k-2} + \alpha x_{k-3} + \alpha^2 b_{k-4} \\
b_{k-1} &= x_{k-1} + \alpha x_{k-2} + \alpha^2 x_{k-3} + \alpha^3 b_{k-4} \\
b_k &= x_k + \alpha x_{k-1} + \alpha^2 x_{k-2} + \alpha^3 x_{k-3} + \alpha^4 b_{k-4}
\end{aligned}
$$

Four output values can now be calculated at each iteration. Though this unrolling increases the total number of computations per output value, the number of cycles used to produce the output, on average, is reduced due to better use of available compute units and SIMD instructions.

Similarly, first-order noncausal IIR filtering, i.e., $c_k = \alpha(c_{k+1} - b_k)$, was also executed by unrolling the equation to up to three levels to generate four outputs per cycle, as shown below.

$$
\begin{aligned}
c_{k+3} &= \alpha(c_{k+1} - b_{k+3}) \\
c_{k+2} &= \alpha^2 c_{k+4} - \alpha^2 b_{k+3} - \alpha b_{k+2} \\
c_{k+1} &= \alpha^3 c_{k+4} - \alpha^3 b_{k+3} - \alpha^2 b_{k+2} - \alpha b_{k+1} \\
c_k &= \alpha^4 c_{k+4} - \alpha^4 b_{k+3} - \alpha^3 b_{k+2} - \alpha^2 b_{k+1} - \alpha b_k
\end{aligned}
$$

After pre-filtering the data, the cubic spline interpolator based on the Farrow structure was employed. Mathematically, the output from the structure can be expressed as

$$
y_k = \begin{bmatrix} 1 & d & d^2 & d^3 \end{bmatrix}
\begin{bmatrix} 1 & 4 & 1 & 0 \\ 3 & 0 & -3 & 0 \\ 3 & -6 & 3 & 0 \\ 1 & -3 & 3 & -1 \end{bmatrix}
\begin{bmatrix} c_{k+1} \\ c_k \\ c_{k-1} \\ c_{k-2} \end{bmatrix}
$$

where each row in the second matrix corresponds to one of the four filters, d is the fractional part of the resampling indices, and c_k is the prefiltered data. The amount of run-time computations can be significantly reduced (up to four times) if the first two matrices are combined together and the resulting coefficients are precomputed during the initialization phase and stored in memory.

$$
y_k = \begin{bmatrix} bm0 & bm1 & bm2 & bm3 \end{bmatrix}
\begin{bmatrix} c_{k+1} \\ c_k \\ c_{k-1} \\ c_{k-2} \end{bmatrix}, \text{ where }
\begin{aligned}
bm0 &= 1 + 3d + 3d^2 + d^3 \\
bm1 &= 4 - 6d^2 - 3d^3 \\
bm2 &= 1 - 3d + 3d^2 + 3d^3 \\
bm3 &= -d^3
\end{aligned}
$$

Although this significantly reduces the processing time, the storage requirements for these coefficients (5 coefficients per output value) can be prohibitively large.

14.4.2.2 Fast Fourier Transform

TI provides optimized 1D FFT functions as part of its offering in MC-SDK. However, only a complex-to-complex FFT is currently available in this library. Our implementation uses the following steps to obtain a 2 N point 1D real-to-complex FFT from the available N point 1D complex-to-complex FFT:

1. The even and odd indices of a 2 N sequence of real numbers are combined to form an N-point sequence of complex numbers.
2. An N-point complex-to-complex FFT $X(k)$; $0 \leq k \leq N - 1$ is computed of the N-point complex sequence.

3. 1D FFT real-complex $G(k)$ is then computed by using the expression

$$G(k) = X(k)\left\{\frac{1}{2}\left(1 - jW_{2N}^{k}\right)\right\} + X^{*}(N-k)\left\{\frac{1}{2}\left(1 + jW_{2N}^{k}\right)\right\}, \quad 0 \le k \le N-1$$

where $W_N = e^{-j(2\pi/N)}$ and the factors $A(k) = \frac{1}{2}\left(1 - jW_{2N}^{k}\right)$ and $B(k) = \frac{1}{2}\left(1 + jW_{2N}^{k}\right)$ are precomputed and stored in memory.

14.5 2D ISAM Signal Chain on Multi-core DSP

In addition to the standard OCT processing, more computationally demanding operations can be performed using the DSP. As an example, we discuss the implementation of a computationally intensive technique called interferometric synthetic aperture microscopy (ISAM) on the DSP. The basic motivation behind ISAM is to overcome one of the inherent limitations that exists in traditional OCT, i.e., the trade-off between higher (better) transverse resolution and depth-of-field where tighter focusing degrades the transverse resolution outside the confocal region. ISAM is a computational technique that solves the depth-of-focus problem in OCT, hence yielding a spatially invariant transverse resolution throughout the imaging depth.

Briefly, ISAM solves the inverse scattering problem for OCT [2]. An exact ISAM reconstruction would require manipulating the 3D Fourier space of the volumetric data to correct for blurring in both transverse axes. We will describe the 2D implementation of ISAM, which can be easily extended to 3D [21]. The processing steps for ISAM processing are shown in Fig. 14.8. ISAM is an extension of OCT processing with some additional steps shown in the shaded box that are required for the Fourier domain manipulation of the data. After the traditional OCT processing, the complex form of an OCT image is used for further ISAM processing, as ISAM requires access to both the amplitude and the phase of the data. 2D ISAM requires an

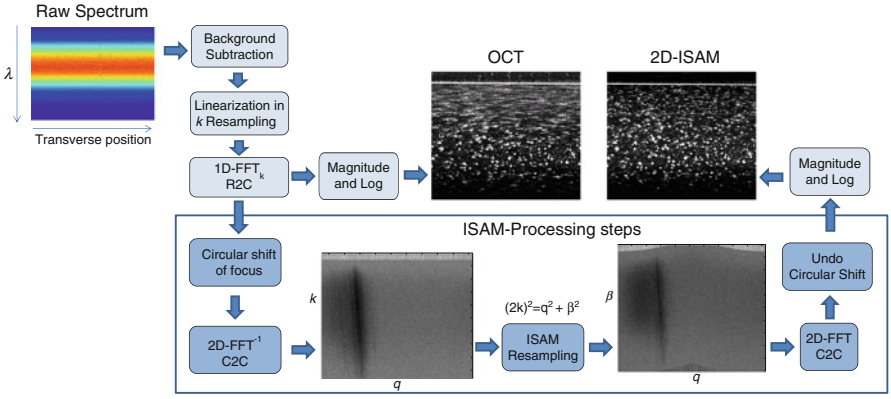

Fig. 14.8 Steps in the 2D ISAM signal chain. The shaded blocks are the additional processing steps required for ISAM. R2C is real-to-complex and C2C is complex-to-complex

inverse 2D FFT to move the data into the Fourier domain, resampling of the Fourier space, followed by another 2D FFT to bring back the data into the spatial domain. As the Fourier transforms and resampling operations are performed on the complex data, constraints are placed on the data sizes and the memory transfer overheads associated with moving the data in and out of the memory [15].

14.5.1 ISAM Dataflow

A 2D ISAM algorithm can be implemented as a sequence of 1D operations on the individual A-scans as shown in Fig. 14.9. The same general framework mentioned in Sect. 14.4 can be used for distributing the data among the cores and partitioning it further into patches to make use of the fast on-chip memory. Each patch containing multiple A-scans is then processed serially by a sequence of 1D operations. It is desirable to complete all the necessary operations while the data is residing in the internal memory. However, if the data size becomes too large, it would be inevitable to move it back to the external memory. Once each core operates on all the A-scans assigned to it, the A-scans are assembled back to a frame. The same procedure is repeated again until the ISAM processing is completed. A total of eight external and internal memory transfers were performed for the 2D ISAM implementation.

The two main building blocks for 2D ISAM are the 2D FFTs and the ISAM resampling. In the following sections these two modules are described in more detail.

14.5.2 Two-Dimensional FFT

The 2D FFT can be divided into a two-step process where 1D FFTs are taken along each of the dimensions alternatively. However, its implementation as a sequence of 1D FFTs would require transposing the data (as the data is accessed in the row-major order) prior to taking the 1D FFT along the second dimension. If the 1D FFT operations are performed on the data residing in the internal memory, the matrix transpose operation would require copying the data into either the shared RAM or the external memory to form another 2D frame with the dimensions now interchanged. Then, the data is again copied back to the internal memory to take the 1D-FFT along the orthogonal dimension.

14.5.3 ISAM Resampling

The ISAM resampling indices depend on the axial and transverse spatial frequency coverage of the imaging system and can be precomputed using the relationship $k = 0.5\sqrt{q^2 + \beta^2}$ where q is the transverse and β is the axial spatial frequency coordinate, respectively [20]. The resampling indices would, however, be different for every A-scan within the cross-sectional plane and once calculated and stored, can be used for every cross-sectional plane in the volume (they do not need to be

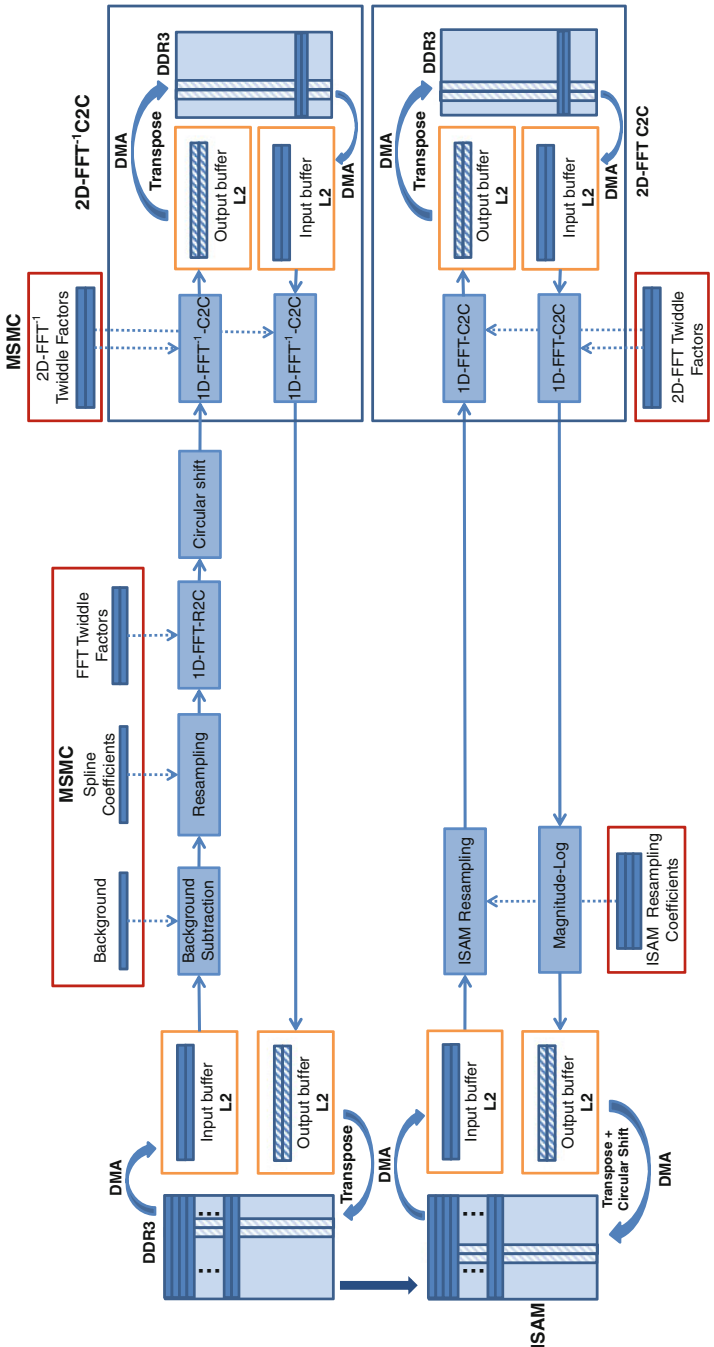

Fig. 14.9 2D ISAM implementation on the multi-core DSP

computed for each cross-sectional plane). These indices are then used to calculate the cubic spline parameters as described in Sect. 14.4.2.1. For each pixel in the image, four spline coefficients (bm0, bm1, bm2 and bm3) and an index need to be computed and stored in the memory. These spline coefficients will be heavily accessed using ISAM resampling; hence, it is desirable to store these in the MSMC RAM to make use of the fast access times. The large storage requirements and the memory access latencies make ISAM resampling consume a significant amount of processing time. The same resampling scheme mentioned in Sect. 14.4.2.1 can be applied individually to the real and imaginary part of the complex data. However, because of the complex nature of the data, the prefiltering was implemented by unrolling the causal and noncasual IIR filter equations up to one level, thereby computing two complex outputs per iteration.

14.6 Results

The volumetric datasets (1,024 × 512 × 512 pixels) corresponding to a field-of-view of 2.8 mm in depth and 1 mm × 1 mm in the transverse dimensions were acquired with a 1,300 nm spectral-domain OCT system operating at an A-scan rate of 91,912 kHz (with a line-scan array of 1,024 pixels). The data was transferred to the external memory on the DSP and was processed post-acquisition using single precision operations on the standard TMS320C6678 DSP evaluation module [22].

Figure 14.10 shows OCT and 2D ISAM cross-sectional planes processed using the DSP. The sample consisted of TiO_2 scattering particles embedded in a silicone matrix. The blurring outside the focal region is clearly evident in the OCT image, and after applying 2D ISAM on the cross-sectional plane, depth invariant transverse resolution is achieved.

The 2D ISAM applied to the cross-sectional planes can be extended to do a full 3D ISAM reconstruction by applying the same 2D ISAM reconstruction on the

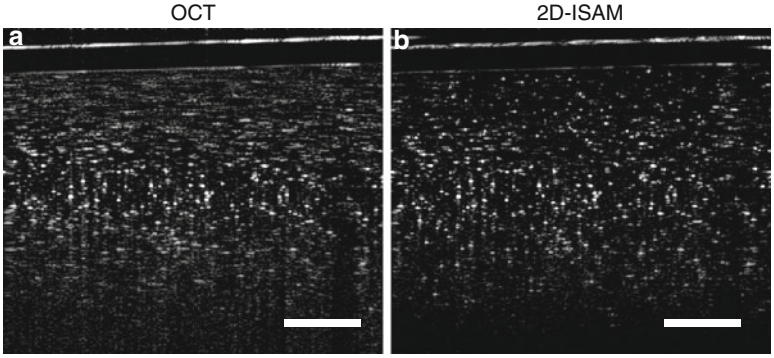

Fig. 14.10 Cross-sectional planes of a silicone phantom consisting of TiO_2 particles. Data processed using the DSP by (**a**) standard OCT processing (**b**) 2D ISAM processing. *Scale bars* represent 200 μm

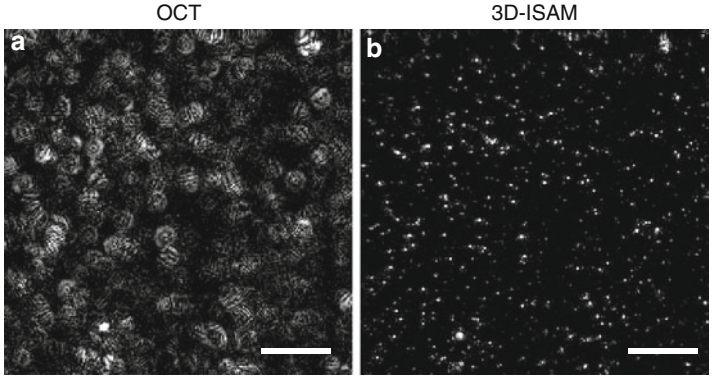

Fig. 14.11 En face plane 855 μm above the focus from a silicone phantom consisting of TiO_2 particles. Data processed using the DSP by (**a**) standard OCT processing (**b**) 3D ISAM processing. *Scale bars* represent 200 μm

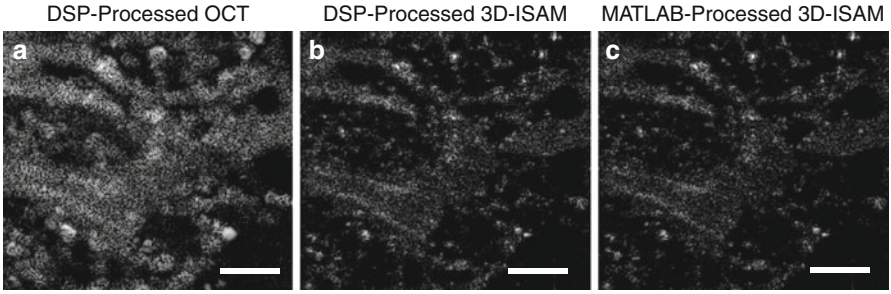

Fig. 14.12 En face plane at a distance of 850 μm above the focus from a mouse lung tissue volumetric dataset. The data is processed using a DSP by (**a**) standard OCT and (**b**) 3D ISAM, (**c**) 3D ISAM processed using MATLAB. *Scale bars* represent 200 μm

orthogonal cross-sectional planes in the volumetric dataset. Each frame, after undergoing 2D ISAM processing, was assembled back into a volume. Subsequently, the orthogonal axis frames were extracted from this volume and 2D ISAM was performed on these planes for a full 3D ISAM reconstruction [21]. 3D ISAM was performed on an output volume comprising of 512 × 512 × 512 pixels using the DSP. The en face plane taken at 855 μm above the focus in the tissue-mimicking phantom is shown in Fig. 14.11 where isotropic transverse resolution can be seen after applying 3D ISAM. Results using ex vivo mouse lung tissue are shown in Fig. 14.12. Significant improvements in the ISAM processed dataset can be seen, compared to the OCT processed dataset. A qualitative comparison between a DSP-based implementation of 3D ISAM (Fig. 14.12b) and a double precision implementation in Matlab (Fig. 14.12c) shows no visible differences in reconstruction quality.

Functions	Time	
	512 x 512	512 x 1024
Background subtraction	0.18 ms	0.37 ms
Pre-filtering and Resampling	0.81 ms	1.6 ms
FFT-1D-Real-to-Complex	0.49 ms	0.97 ms
Magnitude–Logarithm	1.25 ms	2.45 ms
TOTAL(OCT)	2.8 ms	5.6 ms

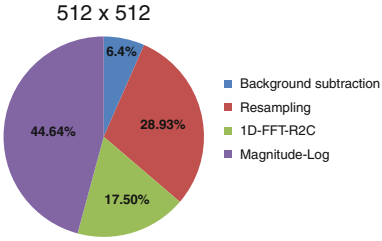

Fig. 14.13 OCT timing results. The pie chart shows processing speeds of the individual modules as a percentage of total processing time (does not include memory transfer overheads) (Adapted from Ref. [15])

Functions	Time	
	512 x 512	512 x 1024
Background subtraction	0.18 ms	0.37 ms
Pre-filtering and Resampling	0.81 ms	1.6 ms
FFT-1D-Real-to-Complex	0.49 ms	0.97 ms
Complex Circular Shift	0.12 ms	0.25 ms
2D-IFFT-Complex-to-Complex	0.98 ms	1.78 ms
ISAM Resampling	1.08 ms	4.34 ms
2D-FFT- Complex-to-Complex	0.86 ms	1.67 ms
Magnitude–Logarithm	1.25 ms	2.45 ms
TOTAL (ISAM)	**7 ms**	**15.4 ms**

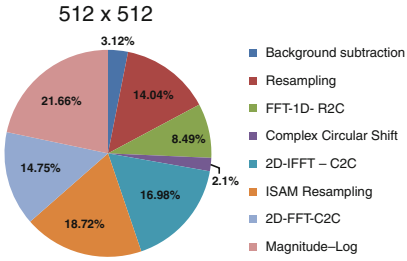

Fig. 14.14 ISAM timing results. The pie chart shows processing speeds of the individual modules as a percentage of total processing time (does not include memory transfer overheads) (Adapted from Ref. [15])

We also present timing results of our evaluation of OCT and 2D ISAM processing (Fig. 14.13 for the OCT signal chain and Fig. 14.14 for the ISAM signal chain) for output frame sizes of 512 × 512 and 512 × 1,024. These timing results show that 2D ISAM can be processed at 70,000 A-lines/sec and OCT at 180,000 A-lines/sec with the current implementation. The computation of magnitude (square root) and dynamic range compression (log) for visualization takes a considerable percentage of computational time in this implementation, especially for the OCT signal chain. We have used the full single precision accuracy for these computations. This computational time can be reduced considerably by using table-based dynamic range compression. Due to the parallel nature of computations, the processing rate can be scaled up by using multiple TMS320C6678 devices. For example, the quad/octal DSP PCI express board can be used to demonstrate full volume rate ISAM processing [23, 24]. The standard boards mentioned here can be used to quickly demonstrate the potential of DSP technology for OCT applications. However, an embedded system designed specifically for OCT applications will be preferred to take full advantage of the computational and power advantages of a DSP.

14.7 Conclusion

OCT systems have been steadily finding commercial applications in many medical and surgical areas including ophthalmology, optometry, cardiology, surgical oncology, gastroenterology, and dentistry. Many of these systems are currently based on desktop PC systems. As these systems evolve, the need for solutions based on embedded and scalable processing increases. This chapter discussed DSP technology, especially the multi-core version of this technology, and its potential use in OCT systems. As used in many other systems, DSP technology will help develop portable and handheld OCT systems. This will open new opportunities to bring OCT-based devices into point-of-care health-care systems.

Acknowledgment The contributions and helpful discussions with Fredrick South, Guillermo Monroy, Nathan Shemonski, Dr. Steven Adie, and Prof. Scott Carney from the University of Illinois at Urbana-Champaign are gratefully acknowledged. We would also like to thank Dan Wang at Texas Instruments, Inc. for the help provided in DSP implementation. This research was supported in part by a Bioengineering Research Partnership grant from the National Institutes of Health (R01 EB013723, S.A.B..) and a research agreement with Texas Instruments, Inc.

References

1. M. Wojtkowski, High-speed optical coherence tomography: basics and applications. Appl. Opt. **49**, D30–D61 (2010)
2. T.S. Ralston, D.L. Marks, P. Scott Carney, S.A. Boppart, Interferometric synthetic aperture microscopy. Nat. Phys. **3**, 129–134 (2007)
3. A.M. Rollins, S. Yazdanfar, J.K. Barton, J.A. Izatt, Real-time *in vivo* color Doppler optical coherence tomography. J. Biomed. Opt. **7**(1), 123–129 (2002)
4. B.R. White, M.C. Pierce, N. Nassif, B. Cense, B.H. Park, G.J. Tearney, B.E. Bouma, T.C. Chen, J.F. de Boer, *In vivo* dynamic human retinal blood flow imaging using ultra-high-speed spectral domain optical Doppler tomography. Opt. Express **11**(25), 3490–3497 (2003)
5. J.M. Schmitt, OCT elastography: imaging microscopic deformation and strain of tissue. Opt. Express **3**(6), 199–211 (1998)
6. E. Gotzinger, M. Pircher, B. Baumann, C. Ahlers, W. Geitzenauer, U. Schmidt-Erfurth, C.K. Hitzenberger, Three-dimensional polarization sensitive OCT imaging and interactive display of the human retina. Opt. Express **17**(5), 4151–4165 (2009)
7. K. Zhang, J.U. Kang, Real-time 4D signal processing and visualization using graphics processing unit on a regular nonlinear-k Fourier-domain OCT system. Opt. Express **18**, 11772–11784 (2010)
8. Y. Watanabe, T. Itagaki, Real-time display on Fourier domain optical coherence tomography system using a graphics processing unit. J. Biomed. Opt. **14**, 060506 (2009)
9. S. Van der Jeught, A. Bradu, A.G. Podoleanu, Real-time resampling in Fourier domain optical coherence tomography using a graphics processing unit. J. Biomed. Opt. **15**, 030511 (2010)
10. L.J. Karam, I. AlKamal, A. Getherer, G.A. Frantz, D.V. Anderson, B.L. Evans, Trends in multicore DSP platforms. IEEE Signal Proc. Mag. **26**(6), 38–49 (2009)
11. P.T. Yap, G. Wu, D. Shen, "DSPs see gains in their impact on new medical imaging designs," special report. IEEE Signal Proc. Mag. **27**(4), 6–134 (2010)
12. M. Nadeski, A. Gatherer, See the difference: DSPs in medical imaging, Texas Instruments Literature Number: SLYY019, (2008) [Online]. http://www.ti.com/lit/wp/slyy019/slyy019.pdf

13. TMS320C6678 multicore fixed and floating-point digital signal processor, Texas Instruments Literature Number: SPRS691E, [Online]. http://www.ti.com/lit/ds/symlink/tms320c6678.pdf Mar 2014
14. M. Ali, R. Parlapalli, Algorithms for optical coherence tomography on TMS320C64x+, Texas Instruments Literature Number: SPRABB7, (2008) [Online]. http://www.ti.com/litv/pdf/sprabb7
15. A. Ahmad, M. Ali, F. South, G. L. Monroy, S.G. Adie, N.D. Shemonski, P. S Carney, S. A. Boppart, Interferometric synthetic aperture microscopy implementation on a floating point multi-core digital signal processer, *Proc. SPIE* **8571**, 857134 (2013)
16. TMS320C66x DSP CPU and instruction set reference guide, Texas Instruments Literature Number: SPRUGH7, [Online]. http://www.ti.com/lit/ug/sprugh7/sprugh7.pdf Nov. 2010
17. TI Multicore Software Development Kits (MCSDK) [Online]. http://www.ti.com/tool/bioslinuxmcsdk
18. OpenMP [Online]. http://openmp.org/wp
19. S.R. Dooley, R.W. Stewart, T.S. Durrani, Fast on-line B-spline interpolation. Electron. Lett. **35**, 1130–1131 (1999)
20. T.S. Ralston, D.L. Marks, P.S. Carney, S.A. Boppart, Real-time interferometric synthetic aperture microscopy. Opt. Express **16**, 2555–2569 (2008)
21. A. Ahmad, N.D. Shemonski, S.G. Adie, H. Kim, W.-M.W. Hwu, P.S. Carney, S.A. Boppart, Real time in vivo computed optical interferometric tomography, Nature Photon **7**(6), 444–448 (2013)
22. TMS320C6678 Evaluation Modules [Online]. http://www.ti.com/tool/tmdsevm6678
23. DSPC-8681 [Online]. http://www.advantech.com/products/DSPC-8681/mod_A9314996-0022-4927-9AA4-6B1060D4E5E8.aspx
24. DSPC-8682 [Online]. http://www.advantech.com/products/DSPC-8682/mod_535C098D-21FC-4980-B06E-5C2AC152DE0F.aspx

OCT Motion Correction

15

Martin F. Kraus and Joachim Hornegger

Keywords
Motion correction • Motion artifacts • Registration • Regularizer • Multi-scale • Displacement field • Ophthalmology • Retinal imaging

15.1 Introduction

From the introduction of time domain OCT [1] up to recent swept source systems, motion continues to be an issue in OCT imaging. In contrast to normal photography, an OCT image does not represent a single point in time. Instead, conventional OCT devices sequentially acquire one-dimensional data over a period of several seconds, capturing one beam of light at a time and recording both the intensity and delay of reflections along its path through an object. In combination with unavoidable object motion which occurs in many imaging contexts, the problem of motion artifacts lies in the very nature of OCT imaging. Motion artifacts degrade image quality and make quantitative measurements less reliable. Therefore, it is desirable to come up with techniques to measure and/or correct object motion during OCT acquisition. In this chapter, we describe the effect of motion on OCT data sets and give an overview on the state of the art in the field of retinal OCT motion correction.

M.F. Kraus (✉) • J. Hornegger
Pattern Recognition Lab, University Erlangen–Nürnberg, Erlangen, Germany

School of Advanced Optical Technologies (SAOT), University Erlangen–Nürnberg, Erlangen, Germany
e-mail: martin.kraus@fau.de; joachim.hornegger@fau.de

© Springer International Publishing Switzerland 2015

W. Drexler, J.G. Fujimoto (eds.), *Optical Coherence Tomography*,
DOI 10.1007/978-3-319-06419-2_16

15.2 OCT Scanning

Both 2D and 3D OCT images are composed of a high number of 1D depth profiles of backscattered intensity along the beam of an OCT probe. Each of these axial scans or A-Scans is acquired at slightly different points in time. Usually, a pair of galvanometer mirrors is used to programmatically deflect the OCT beam along two principal directions x and y. These two directions are called transverse directions. Simultaneous transverse scanning of the beam using the mirrors while acquiring A-Scans is used to acquire multidimensional images in OCT. Since the basic unit of acquisition in OCT is 1D, additional spatial dimensions are encoded in time by scanning the beam over the object. To acquire a 2D OCT image or B-Scan, the OCT beam is swept in a linear trajectory while acquiring A-Scans. Similarly, 3D OCT volumes are acquired by raster scanning a grid of A-Scan sampling positions while acquiring A-Scans. In a raster scan, the grid of A-Scans is acquired as a series of linear B-Scans. After each B-Scan the mirrors are repositioned at the start of the next B-Scan. During this time, no acquisition takes place and a certain downtime called flyback time is incurred. Figure 15.1 shows a schematic overview of 1D, 2D, and 3D OCT imaging.

The direction that is rapidly scanned in each B-Scan is called transverse direction or the fast direction. In contrast, the orthogonal direction on the grid is scanned much slower, hence its name slow direction. The effect of the priority scanning in

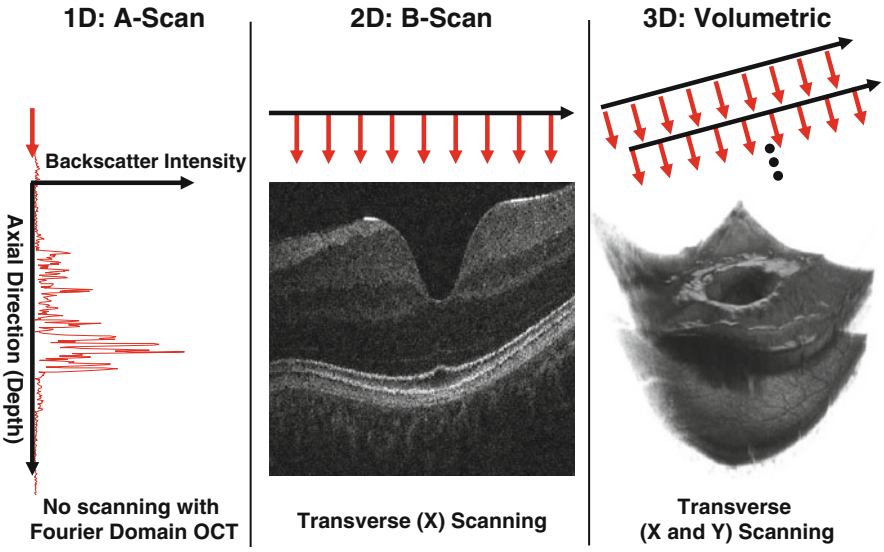

Fig. 15.1 OCT scanning and scanner coordinate system schematic. *Left*: 1D acquisition (A-Scan). A single depth profile is acquired which measures backscattered intensity vs. axial dimension (depth). *Middle*: 2D imaging (B-Scan). The OCT beam is scanned in a transverse direction while A-Scans (*red arrows*) are acquired. *Right*: 3D acquisition. Multiple B-Scans are acquired such that A-scans are sampled on a 2D grid in the transverse plane

one direction is that neighboring A-Scan samples on the grid along the slow scan direction are acquired much more apart from each other in time, compared to the fast scan direction.

OCT scanning takes place in a scan coordinate system that consists of x and y galvanometer mirror positions and axial depth along the light beam z. Given a static object that does not move relative to the OCT system, every set of galvanometer mirror positions maps to a certain beam path through the object. In combination with the axial coordinate z, a fixed relationship between scan coordinate system coordinates and positions on the object exists. However, especially in in vivo imaging, the relative position between the OCT system and the object can change over time. We can think of this as having another coordinate system called the object coordinate system that has a time-dependent relation to the scan coordinate system. Any relative motion between OCT system and imaged object changes this relationship.

OCT acquisition times in in vivo imaging can take as much as several seconds, due in part to the way spatial dimensions are encoded in time, the scan pattern used, and the speed of typical OCT systems. Object motion during this time leads to a deviation of the beam paths of individual A-Scans relative to the case of there being no motion. The deviation leads to the object being sampled at locations inconsistent with the time/space encoding and results in spatially distorted data. Motion can cause parts of the object to be imaged multiple times, while other parts might not be sampled at all. These effects cause errors in quantitative measurements on the OCT data that rely on the accurate measurement of spatial features of the object. If multiple spatial dimensions are encoded, we can expect that the potential distortion that is caused by motion is much larger in the direction that has the larger acquisition time difference between samples, i.e., the slow scan direction in a 3D raster scan pattern. Conversely, if the encoding is done very fast relative to the speed of the relative motion, the motion is effectively frozen out and the image shows no noticeable spatial distortion. This is, for example, the case for a 2D B-Scan image on a commercial Fourier domain OCT system of the current generation.

Motion correction approaches in OCT try to enforce that the individual A-Scans of a corrected acquisition show the expected locations, regardless of motion during the acquisition. In the following sections, we restrict ourselves to the motion problem and possible solutions in the context of OCT imaging of the retina. This is because retinal imaging is the most important in vivo application of OCT and the focus of most efforts in the area of motion correction.

15.3 Retinal Imaging

OCT is a standard of care for ophthalmologic examinations of the retina due to its high resolution and noninvasiveness. It has key applications in early detection and monitoring of common eye diseases such as glaucoma and age-related macular degeneration (AMD). As such, it is important for quantitative measurements that are extracted from retinal OCT data to be reliable and reproducible. However, when

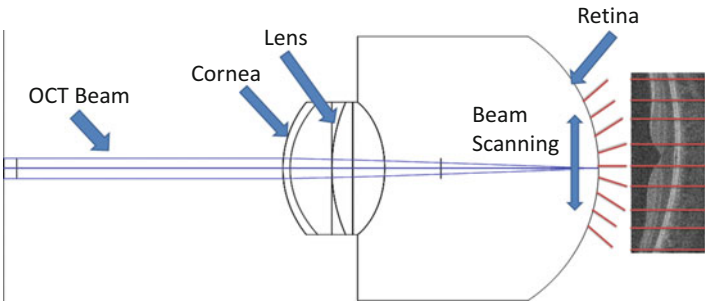

Fig. 15.2 Baseline situation of imaging an eye using OCT. A collimated beam originating from the OCT system passes through cornea and lens and is focused onto the retina. By changing the angle of incidence of the beam on the eye, the beam is scanned over the retina. During scanning, A-Scans are acquired (*red lines*). Because of the optics of the eye, the A-Scans are in a fanlike geometry. An OCT image is created by showing these A-Scans as parallel lines (*right image*)

imaging the eye in vivo, several sources of motion are not avoidable and motion artifacts occur that limit the reliability of quantitative measurements. In the following sections, we consider aspects of ophthalmologic imaging that are relevant to the motion correction problem.

15.3.1 Eye Optics/OCT Scanning

One peculiarity of retinal imaging is that the eye itself becomes part of the optics of the system, i.e., the combination of cornea and lens of the eye focuses the OCT beam onto the retina. This is different from an OCT microscope, for example, where all the optical elements such as lenses are fixed relative to the system. In retinal imaging, ideally the eye is aligned to the OCT system such that the scanning OCT beam is pivoted in a fixed point $\mathbf{P}_{pivot}$ in the center of the pupil of the eye. This minimizes vignetting of the beam by the pupil of the eye and enables imaging the largest possible area on the retina. Figure 15.2 shows a schematic view of the optics involved for imaging the retina. The OCT beam is collimated incident on the cornea which in combination with the lens focuses the beam onto the retina. Scanning of the retina is performed by changing the incident angles of the OCT beam relative to the optical axis using galvanometer mirrors. The eye optics maps the two incoming angles in x and y direction onto corresponding angles on the retina. Since the OCT beam is pivoted during scanning, the beam paths for each A-Scan during a linear scan create a fanlike pattern on the retina. This means that the beam paths of neighboring A-Scans are not actually parallel. When the OCT data is displayed though, the individual A-Scans are seen as parallel lines that form 2D and 3D images. Therefore, the OCT data is displayed as a 2D or 3D function of one or two galvanometer mirror positions and an axial depth. This representation maps approximately to Euclidian coordinates on the retina. However, for considering the possible effects of motion, it is important to consider the actual scan geometry.

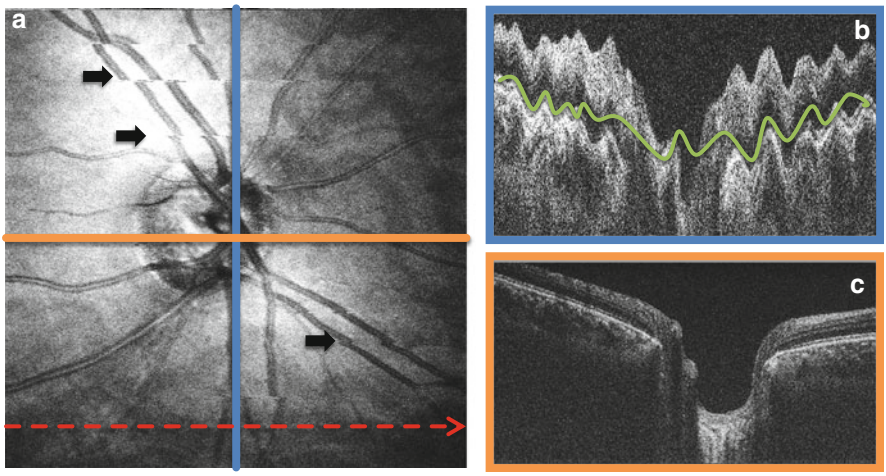

Fig. 15.3 Example of motion artifacts in a raster-scanned 3D OCT volume. The volume consists of 400 by 400 A-Scans sampled over 6 by 6 mm centered on the optic nerve head. The system was running at 90 kHz A-Scan rate, leading to a total acquisition time of approximately 2.5 s including flyback. (**a**) En face fundus projection of the volume. The *dotted red line* marks the fast scan direction of the volume. The *black arrows* indicate motion artifacts caused by transverse eye motion that create discontinuities in the vessel pattern. (**b**) Excerpt of the central slice of the volume along the slow scan direction (*blue line* in **a**). Axial motion leads to a wavy deformation of the retina in axial direction (*green curve*). (**c**): Excerpt of the central slice of the volume along the fast scan direction (*orange line* in **a**). The spatial structure of the retina remains intact along the fast scan direction

15.3.2 Motion Types/Effects

In eye motion, we can distinguish between transverse eye motion and axial eye motion. These names relate to the direction of displacement they cause within the scan coordinate system. Transverse eye motion is equivalent to a change in fixation of the subject. Here, muscles rotate the eyeball in the left/right and up/down directions. Transverse motion can further be subdivided into slow drifts of fixation and fast saccadic motion. Saccadic motion typically occurs up to two times a second and can lead to a change in fixation angle of up to 4° [2, 3]. The duration of saccadic motion itself can range from 20 ms to 100 ms and can be very fast with angular velocities of up to 300° per second [4]. The second fundamental type of eye motion is motion in the axial direction. This is equivalent to the eyeball and/or retina moving toward or away from the OCT system. Axial eye motion can be caused by changes in blood pressure caused by the heartbeat and by respiration. Compared to saccadic transverse motion, axial motion is slow and has low frequency. Figure 15.3 shows an example of the effect of different types of motion on a 3D-OCT data set.

Motion of the eye relative to the system causes two primary effects: For one, the angle of incidence of the OCT on the pivot point can change. The second effect is

that the *actual* pivot point of the combined system can deviate significantly from the ideal pivot point $\mathbf{p}_{pivot}$. Assuming that only the incident angles change about δx and δy and that the pivot point stays the same, this change in incident angle gets transformed to a change in angle within the coordinate system of the retina. The incident angle can also be changed using the galvanometer mirrors, though. Given the right correction on the mirror angles, the beam path can be the same as if there was no eye rotation. Therefore, if the beam always pivots a single point, transverse motion of the eye causes a transverse displacement of the beam on the retina that could also be reached by applying an offset to the incident galvanometer mirror positions.

If due to motion the actual pivot point is different from the reference pivot point $\mathbf{p}_{pivot}$, the light focuses at the same lateral position on the retina; however the optical path length changes. The dominant effect is a translation of the A-Scan content in the axial direction. This is usually seen as an axial tilt of the retina within the B-Scan. A secondary effect is that the incident angle of the A-Scan on a specific position on the retina changes with beam translation in the pupil plane. This means that the actual beam path through a certain point on the retina deviates from the beam path of a normally pivoted point. Both beams intersect in the same point on the retina, but due to the different angle of incidence, the beams do not sample the same transverse positions closer and farther down the axial dimension. If this effect were significant, it would mean that the effect of a change in pivot point could not be compensated by applying an offset on the galvanometer positions.

As an example for the size of this effect in a typical eye, a simulation using ZEMAX and an eye model was performed. A 2 mm translation of the beam in the pupil plane results in a change in the angle of incidence of the OCT beam on the retina of about 5°. Over the thickness of the retina of about 300 μm, the maximum deviation in the beam path which is caused by the change in pivot point is 13 μm. This is less than a typical spot size diameter of 20 μm. Also, this deviation is two orders of magnitude smaller than the effects of eye rotation. Assuming a typical pupil size of the eye of 4 mm and an OCT beam diameter of 2 mm incident on the pupil, any greater shift in beam position would already cause vignetting of the beam by the pupil, causing visible signal loss in the OCT data set. Furthermore, according to [2], the angular rotation induced by involuntary eye motion such as drifts and saccades does usually not exceed 4°. Using the simplifying assumption that the eye is spherical with a radius of about 11 mm and rotates around the center of the sphere, a 4° rotation corresponds to a lateral translation of the pupil with respect to the OCT beam of about 0.8 mm ($displacement = \sin(\alpha) radius$). This is well below the 2 mm shift for which the minimal change of the beam path was calculated and therefore leads to an even smaller effect.

In practice, both the incident angle and the pivot point position change because of motion. However, from these simplified sample calculations, we can conclude that in ophthalmologic imaging, the effects of eye motion in transverse and axial direction move the content of the A-Scan in a way that is consistent with applying a corresponding offset to the galvanometer positions and moving the content of the A-Scan in axial direction. Higher-order effects such as those resulting from

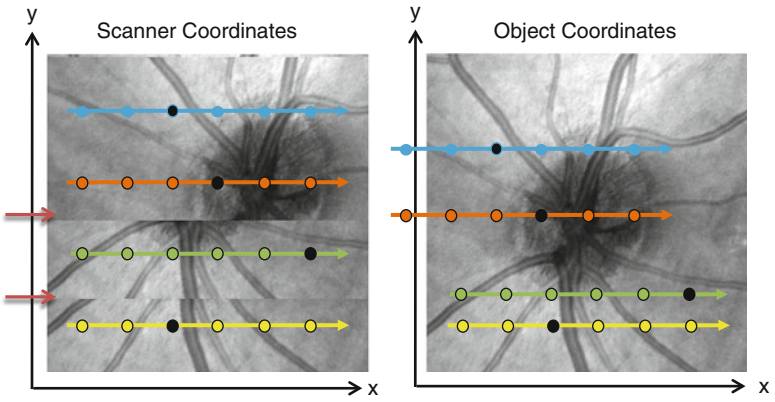

Fig. 15.4 Schematic showing relation between object and scanner coordinate system when affected by motion. *Left*: En face view in the scanner coordinate system. *Dotted colored arrows* indicate B-scans; *dots* indicate individual A-scans. The background shows an en face fundus projection as it would be acquired given motion. The two *red arrows* indicate discontinuities from motion. *Right*: En face view in the object coordinate system. Corresponding *color arrows* indicate where B-scans from the scanner coordinate system are located in the object coordinate system. The background shows an en face view of the object in the object coordinate system

a change in pivot position can be considered negligible for explaining the effects of normal eye motion. This is consistent with the effects that are due to motion and are observed in practice.

Figure 15.4 shows a schematic view of the relation between the scanner and object coordinates under the effects of motion. Due to saccadic motion of the eye, the relation in the transverse coordinates between the scan and object coordinate system changes rapidly. This leads to discontinuities in the acquired en face fundus projection. In addition, certain areas are missed during scanning, while others are imaged repeatedly. For a certain A-Scan, the difference in position between the two coordinate systems corresponds to the deviation in galvanometer mirror positions that was caused by motion at the time the A-Scan was acquired.

15.4 Motion Correction Approaches

Since motion artifacts constitute a serious issue, especially for retinal OCT imaging, considerable work has been performed by different groups to help solve the problem. In the following sections, we give an overview of the state of the art in OCT motion correction techniques.

One basic feature of a particular motion correction technique is whether it needs additional hardware support, i.e., the OCT system needs to be built with the motion correction technique in mind or additional imaging modalities need to be available. There are two basic ways to address the problem. Hardware-based methods try to avoid motion artifacts during the acquisition itself though a specific system design:

- Freeze out motion by improving the encoding of spatial dimensions in time, i.e., acquire the data set in a shorter time.
- Measure the deviations that originate from changes in relative position, and actively apply corrections to the galvanometer mirror positions during acquisition: tracking OCT.

Software-based methods on the other hand try to correct motion artifacts retrospectively using image processing:

- Use images from another modality that does not suffer from motion artifacts as OCT does as a reference to correct the OCT data.
- Correlate consecutively acquired data to filter out the effects of motion.
- Correct motion artifacts using additional OCT data with orthogonal fast scan axis.

In the following sections, we review selected state-of-the-art methods for each approach.

15.4.1 Hardware-Based Methods

15.4.1.1 High-Speed OCT

One fundamental way to alleviate the motion artifact problem in OCT is to increase the imaging speed of the OCT system, which continues to be important. Higher speed means that a higher number of A-Scans can be sampled per unit of time and that therefore a certain scan pattern can be sampled in less time. Since motion requires time to pass, short enough acquisition times can effectively be used to "freeze out" motion in parts or even in the whole OCT acquisition and minimize motion-induced spatial distortion.

Historically, the move from time domain to Fourier domain OCT [5] enabled an order of magnitude increase in acquisition speeds. This was mainly due to the inherent advantage of sensitivity of Fourier domain OCT [6]. In addition, the reference arm did not need to be scanned anymore during the acquisition of a single A-Scan. It is a reasonable assumption in time domain OCT that there is effectively no motion within an A-Scan. The higher speed of Fourier domain OCT systems allows current commercial systems to effectively disregard motion within a single 2D B-Scan, simply because the acquisition time is short enough compared to the speed and frequency of eye motion.

Within the realm of existing Fourier domain OCT technology, it has been shown that system speed can be improved tremendously with respect to standard commercial systems which operate at around 25 kHz A-Scan rate. Using Fourier domain mode locked (FDML) swept source lasers, retinal OCT operating at up to 6.7 MHz has been shown [7–9], albeit with reduced sensitivity and resolution compared to commercially available systems.

There is an inherent sensitivity loss associated with running faster than the maximally allowed light exposure on the eye, which is limited by safety standards. This puts an upper bound to the number of photons that can be collected per unit of time. Now, if one runs twice as fast, there are only half as many

photons available to be collected per A-Scan. All other things being equal, this means that one pays an increase in speed with a loss in sensitivity. Especially for clinical applications, where subjects might have bad eye optics, opacities, and floaters, system with sufficient sensitivity headroom is necessary for imaging.

Another issue is that one might want to use the high speed of a system not just to lower the overall acquisition time and motion artifacts. Instead one might choose to acquire more A-Scans in total, e.g., to sample more densely and/or to sample a larger area. This trade-off depends on the concrete data that one wants to collect.

Pending significant improvements in sensitivity, speed alone is unlikely to be the only solution to motion artifacts in OCT, at least as long as dense sampling of a clinically relevant area with good sensitivity and resolution is required. Such improvements might come from entirely alternative forms of OCT such as full-field OCT which has already been demonstrated for retinal imaging [10]. This technique illuminates the full field at once and does not require the scanning of the OCT beam. This helps in achieving high speeds and allows for a higher light exposure. However, as of now, low sensitivity and axial resolution as well as issues with cross talk and uniform image quality limit the practicality of the technique.

15.4.1.2 Tracking OCT

The approach of tracking OCT is to continuously measure the motion-induced deviation from a reference position and to apply a corresponding offset to the galvanometer mirrors and/or the reference arm mirror to cancel this deviation, effectively compensating for the deviation in scan position that is caused by object motion and therefore removing motion artifacts. Key factors in tracking OCT are the accuracy of measurement of the deviation and its correction and the update rate of the system, i.e., how fast the system can react to a motion-induced change in relative position.

Pircher et al. employed axial tracking of the eye motion in the context of retinal imaging using time domain en face OCT [11]. This modality acquires one en face plane of information at a time using rapid scanning. Therefore, it is very sensitive to axial motion even in the order of the axial resolution of the system. Axial deviation due to motion was measured by using a second Fourier domain channel at 1,300 nm that was used to continuously track the position of the cornea. The measured deviations in cornea position were used to generate a correction signal for a voice coil in the reference arm to rapidly change the reference arm length. This system achieved an update rate of 200 Hz.

Although there is some work on axial tracking, more commonly tracking in OCT is used to correct for transverse motion. Ferguson et al. used a secondary sensing beam that rapidly scans a circular area on the fundus, for example, around the optic nerve head [12–14]. The system extracts correction information from this secondary channel in a closed loop running at 1 kHz and applies the correction to the galvanometer mirrors. The reported accuracy of the technique is less than one spot diameter.

Transverse tracking is also employed in commercial OCT devices such as the Heidelberg Engineering Spectralis [15]. A scanning laser ophthalmoscope (SLO) is used to rapidly acquire 2D images of the fundus. These images are then registered to a reference SLO view. The shift between the two images corresponds to the deviation in scan angle. A correction signal is then applied to the galvanometer mirrors to compensate for this deviation. The use of this technique allows the system to acquire multiple 2D B-Scans at roughly the same location and average them in order to remove speckle noise and increase signal-to-noise ratio.

15.4.2 Software-Based Methods

The second fundamental class of motion correction methods is not relying on additional hardware, but instead motion correction of the OCT data is performed retrospectively in post-processing.

15.4.2.1 Use of Additional Modalities

This class of motion correction approach employs reference image data from a different modality that is not suffering from motion artifacts as OCT is. By registering the OCT data to the reference modality, image one can find corresponding locations between the two images. The OCT data can then be mapped into the space of the reference image. Since the reference image contains virtually no motion, the OCT data can be motion corrected if the mapping between the two images is accurate.

Two modalities that are used for retinal imaging and which are not suffering from OCT like motion artifacts are fundus camera photography and imaging using a scanning laser ophthalmoscope (SLO). Motion in fundus photography will lead to a blurring effect. However, typical exposures are short enough to prevent this problem. SLO is a scanning imaging modality that is similar to OCT in this respect. However, SLO typically scans much faster than OCT and can more effectively freeze out object motion. Capps et al. used an adaptive optics SLO that is running simultaneously with the OCT acquisition to estimate and correct for lateral motion [16]. After imaging, the OCT data is registered to the AO-SLO data in order to calculate the displacement caused by motion per A-Scan. Subsequently, the OCT data is resampled onto a regular grid. Ricco et al. registered the OCT fundus view to an SLO reference image in order to correct for motion [17]. The algorithm uses the vessel pattern visible in both modalities as features for the registration. After vessel detection, registration is performed in a two-step process: First, drift and tremor is corrected for by using an elastic registration technique that is based on patch-wise constant affine transformations between the two images. Over all pixels (x,y), the sum of the terms

$$\left(m_7 I^{SLO}(x,y) + m_8 - I^{OCT}(m_1 x + m_2 y + m_5, m_3 x + m_4 y + m_6)\right)^2 \qquad (15.1)$$

is minimized, where $I^{SLO}(x, y)$ and $I^{OCT}(x, y)$ are the two images and $\mathbf{m} = (m_1, \ldots, m_8)$ is the parameter vector. The same parameters $\mathbf{m}$ are shared over one patch. The second step attempts to correct discontinuities caused by microsaccades along the fast scan direction. The OCT en face pixels are treated as a time domain signal, and the best alignment with the reference image is found using dynamic time warping.

15.4.2.2 Consecutive Data Correlation

The underlying idea of consecutive data correlation algorithms is to assume that the imaged object is inherently smooth and densely sampled by the OCT scan pattern. Therefore, high-frequency spatial patterns in the data, i.e., jumps between consecutively acquired A-Scans or B-Scans, are induced by motion only. By correlating consecutive data and shifting it such that the smoothness of the result is maximized, the high-frequency artifacts that are induced by motion can be removed.

Early on Swanson et al. used 1D cross correlation between neighboring time domain OCT A-Scans within a 2D intensity B-Scan $I(x, z)$ to try to remove motion artifacts [18]. The axial shift $\delta z(x)$ between consecutive A-Scans that maximizes the cross correlation

$$\sum_z I(x, z) I(x + 1, z + \delta z(x)) \tag{15.2}$$

is calculated for every A-Scan. An absolute motion profile $motion_z(x)$ is calculated by cumulating the relative shifts such that $motion_z(x) = \sum_1^x \delta z(x)$. This 1D motion profile is subsequently filtered based on prior knowledge on the frequency distribution of axial motion. Specifically, the motion profile needs to be high-pass filtered; otherwise, the low-frequency curvature of the retina is removed. Finally, the filtered motion profile was applied to each A-Scan to remove axial motion.

A very widespread ability of current commercial clinical Fourier domain OCT systems is the ability to produce high-quality 2D B-Scans by repeated scanning of the same location, subsequent registration, and averaging of intensity values. This technique is implemented in all major commercial Fourier domain OCT systems in one form or another and is used in clinical practice [19, 20]. Motion during the repeated scans is likely to cause slightly different speckle patterns in each of the acquired B-Scans. By registering and averaging the subsequently acquired B-Scans, this change in speckle pattern is used to remove the speckle noise from the images and increase the signal-to-noise ratio of the B-Scan. To register two intensity B-Scans $I_1(x, z)$ and $I_2(x, z)$, a measure of similarity between two images as well as a parameterization of the degrees of freedom for the deviation in position between the two scans has to be chosen. A simple approach is to maximize the cross correlation while allowing a global 2D shift $(\delta x, \delta z)$ in position between the images. The objective function in this case becomes

$$\sum_x \sum_z I_1(x,z) I_2(x+\delta x, z+\delta z) \tag{15.3}$$

which can be effectively maximized using FFT. This simple approach does not model tilt in axial direction, which can result from transverse eye motion. By maximizing the function

$$\sum_x \sum_z \left(I_1(x,z) - I_2(x+\delta x, z+\delta z+m_z x)\right)^2 \tag{15.4}$$

according to $(\delta x, \delta z, m_z)$, tilt is also corrected. This objective function uses the sum of squared differences (SSD) measure as opposed to cross correlation. This function can be minimized using numerical optimization techniques [21]. Sub-pixel accurate registration can be obtained by making $I_2(x, y)$ interpolate values between image grid positions. In practice, more advanced methods are readily available for use, such as the StackReg plug-in [22] for the ImageJ software package.

In 3D volumetric imaging using raster scans, correlation and/or registration can similarly be used to estimate the motion-induced shift between consecutively scanned neighboring B-Scans within the volume. The registration of subsequent B-Scans in a volume is analogous to the repeated B-Scan case. Once consecutive B-Scans have been registered, the shifts can again be filtered in order to preserve low-frequency curvature of the scanned object. The underlying motion model assumes that motion only occurs in between B-Scans, i.e., that B-Scans themselves are rigid. Furthermore, the correlation of consecutive B-Scans can only correct for *in-plane* motion, which is motion that causes a shift of the image content in axial and/or in the direction of the fast scan direction of the raster scan. In reality however, transverse motion such as that caused by saccades can also take place in the direction of the slow raster scan direction. In this case, techniques that are based on subsequent B-Scan correlation produce inadequate results. Zawadski et al. used consecutive B-Scan registration, for example, [23]. Antony, et al. [24] corrected for axial motion artifacts in 3D raster scans using an approach based on layer segmentation and fitting of a thin-plate spline surface to the said segmentation followed by multiple steps of smoothing.

15.4.2.3 Orthogonal Scanning Based

The final class of motion correction algorithms applies to 3D volumetric imaging and employs orthogonal data. This means that one or more B-Scans are acquired with a fast scan axis that is orthogonal to the B-Scan direction of the 3D raster scan, which is to be corrected. In the extreme case, two or more full raster scans with orthogonal fast scan axis are acquired and all of them are corrected.

One idea of using orthogonal scans is to acquire a few orthogonal B-Scans in addition to a raster-scanned volume and use the orthogonal B-Scans as "guideposts" to which the raster-scanned volume is registered. It is assumed that no motion takes place during the acquisition of the guidepost scans. Within the context of these algorithms, they function as a motion-free reference. When the raster-scanned

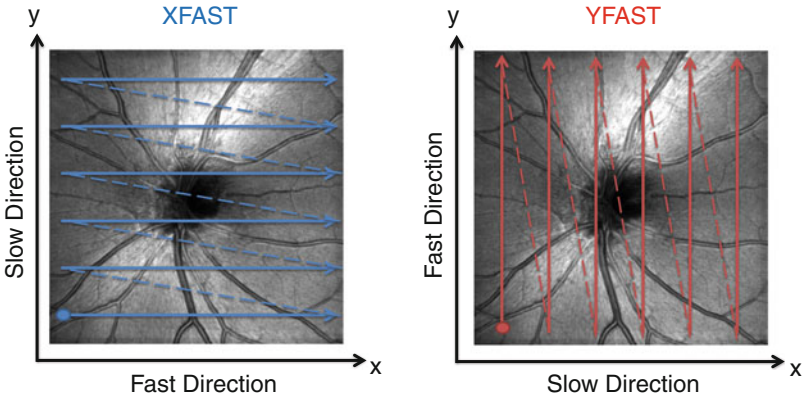

Fig. 15.5 Schematic of orthogonal raster scanning. The *full arrows* indicate B-Scans, and the *dotted arrows* indicate flyback. *Left*: XFAST type scan pattern. The X-direction is the fast scan direction, Y is slow. *Right*: YFAST-type scan pattern. The fast and slow scan directions are exchanged

volume can be accurately registered to the guidepost scans, it can be roughly motion corrected.

After consecutive B-Scan registration to remove axial and in-plane transverse motion, Zawadzki et al. used a single orthogonal guidepost B-Scan $I_{GP,x_{center}}(y,z)$ in the center of the volume (x coordinate x_{center}) to remove the flattening artifact that results from unfiltered correlation of B-Scans [23]. For each B-Scan along the slow scan axis with coordinate y, an A-Scan $I_{GP,x_{center}}(y,z)$ of the guidepost scan is associated with one A-Scan $I_{Vol}(x_{center}, y, z)$ of the raster-scanned volume. These matched A-Scans are again aligned by maximizing the correlation in dependence of an axial shift. The found shift is then applied to the corresponding B-Scan. This way reference information from the guidepost scan is used to try to accurately correct the flattening artifact and residual axial motion within the raster-scanned volume. Potsaid et al. extended this concept and used three instead of one guidepost scan [25]. This allows for increased robustness as instead of one pair of A-Scans, three pairs are correlated to find the axial motion profile.

A consequent extension of the guidepost concept is to acquire an additional orthogonal whole raster-scanned volume. Figure 15.5 shows a schematic of orthogonal raster scanning. The concept is that the fast direction of one scan can be used to correct the slow direction of the other and vice versa. We call these volume types XFAST and YFAST, respectively, or for brevity $I_x(x, y, z)$ and $I_y(x, y, z)$. The dense data that is available allows for unique opportunities to correct motion in all three directions, including out of plane motion.

Tolliver et al. used two orthogonal raster scans and an approach based on matching A-Scans from the two volumes to each other to estimate and recover motion in all three dimensions [26]. In a first step, each A-Scan is transformed into a feature vector using a shift invariant 1D Haar wavelet transform. Then a classifier

with the goal of assessing the probability whether two A-Scans are similar, i.e., they were sampled from close locations on the retina, is trained. Here, A-Scans that are on the same B-Scan and spatially close to a certain A-Scan are assumed to be similar for the purpose of training the classifier. The classifier is used to compute "pseudo-match probabilities" between A-Scans from both volumes. In a subsequent step, Bayesian smoothing is used to incorporate the prior knowledge of piecewise smooth eye motion. Instead of choosing the most likely matches given the classifier output, a less likely but piecewise smooth set of matches is favored. In addition, axial motion correction is performed.

Kraus et al. also uses multiple full orthogonal raster scans and can correct for motion in all three dimensions [27]. Two or more volumes with orthogonal scan patterns are each deformed using a dense 3D displacement field per A-Scan in order to register and motion correct them. Registration is performed by optimizing a global objective function that captures two ideas. First, after registration the set of volumes should be as similar as possible to each other. This is motivated by the fact that the same static object is imaged multiple times. Therefore, if the registration successfully maps corresponding anatomical locations onto each other, the resulting volumes should fundamentally be identical, discounting noise and other high-order effects. In the case of two orthogonal input intensity volumes $I_X(x, y, z)$ and $I_Y(x, y, z)$, we can express this goal using the similarity term

$$\begin{aligned} S = \sum_x \sum_y \sum_z & [I_X(x + \delta x_X(x,y), y + \delta y_X(x,y), z + \delta z_X(x,y)) \\ & - I_Y(x + \delta x_Y(x,y), y + \delta y_Y(x,y), z + \delta z_Y(x,y))]^2 \end{aligned} \tag{15.5}$$

that is parameterized using the two displacement fields $\mathbf{d}_X(x, y) = \{\delta x_x(x, y), \delta y_x(x, y), \delta z_x(x, y)\}$ and $\mathbf{d}_Y(x, y) = \{\delta x_Y(x, y), \delta y_Y(x, y), \delta z_Y(x, y)\}$.

The second part of the objective function captures the idea that within very short time spans, i.e., from one A-Scan to the next, we expect very little motion. This goal is incorporated by adding a term for each volume that penalizes changes in the value of the 3D displacement field over time. Based on the scan pattern for each volume, the time t is known from the 2D transverse A-Scan coordinate. Therefore the displacement functions can also be seen as functions in time $\mathbf{d}_X(t)$ and $\mathbf{d}_Y(t)$. The goal can be expressed as minimizing the term

$$R = \sum_t \left| \frac{d\mathbf{d}_X(t)}{dt} \right|^2 + \sum_t \left| \frac{d\mathbf{d}_Y(t)}{dt} \right|^2. \tag{15.6}$$

The complete objective function is a weighted combination of the two terms

$$F = S + \alpha R \tag{15.7}$$

with α being a positive number that is used to tune the relative importance of the two possibly conflicting goals. The registration is performed by employing a nonlinear

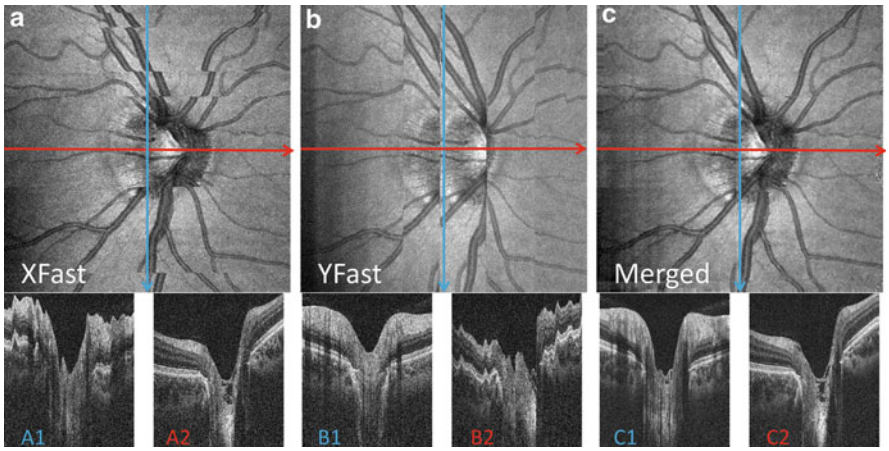

Fig. 15.6 Example of motion correction using orthogonal scan patterns [27]. (**a**, **b**) En face projections of input OCT volumes of the optic nerve head of a healthy subject with orthogonal fast scan axes captured with a 1,050 nm spectral/Fourier domain system at 47 kHz. 400 by 400 A-Scans were acquired in ~4 s each. Significant motion artifacts because of saccadic changes of the subject's fixation can be seen which completely destroy the topology of the object. (**c**) En face projection of registered and merged volume generated from **a** and **b**. *Lower row*: Cross-sectional slices of respective volumes at positions marked by the *red* and *blue arrows* in the en face views. No motion artifacts can be seen in (**c**), as opposed to **a** and **b**. Significant signal-to-noise ratio improvements are achieved by merging volumes

multi-resolution numerical optimization technique to minimize the objective function. Once optimization is finished, the resulting displacement functions are used to construct registered and motion corrected versions of each of the input volumes.

Given a set of registered and motion corrected 3D OCT volumes, it becomes possible to merge the data into a single volume. This is very useful as it allows averaging out speckle and other noise and leads to increased signal-to-noise ratio. Key to enabling merging without the loss of small details is accurate registration. This is enabled by allowing for 3D motion per A-Scan and for sub-pixel displacements.

The evaluation of registration performance and result stability as well as visual inspection shows that the algorithm can correct for motion in all three dimensions and on a per A-scan basis. Figure 15.6 shows an example case of the application of the algorithm.

15.5 Summary

Motion artifacts have been and continue to be a major issue in OCT imaging. They originate from the need to encode spatial dimensions in time, in combination with object motion. The most important application for OCT imaging is in imaging the retina in vivo. In this context, the effects of relative motion are consistent

with an axial displacement of the content of the A-Scan combined with the imaging of a different transverse position on the retina. A corresponding offset to the galvanometer mirror positions changes the transverse location to the same effect. Higher-order effects of motion do not play a significant role for normal eye motion.

We looked at a representative selection of approaches to perform motion correction in OCT. Approaches range from simply improving the system speed over the use of additional imaging modalities. Also, online tracking methods have been developed by various groups to solve the problem. In addition to hardware-based methods, a range of software-based post-processing methods have been presented. These range from maximizing the correlation of neighboring data to methods that employ orthogonal data. Initially orthogonal data was employed as a few "guide-post" B-Scans that acted as a reference to a dense raster-scanned volume. More recently advanced methods that employ two or more whole raster-scanned volumes have been developed. Given highly accurate motion correction and registration of multiple 3D-OCT volumes, the OCT data can also be merged to reduce speckle and increase SNR.

In the future, we expect motion correction in OCT to continue to play an important role. Accurate motion correction promises to increase to the reliability of quantitative measurements that are extracted from the OCT data. Also, multiple approaches can work together. For example, a system with high speed makes a software-based motion correction easier. On the other hand, the lower sensitivity of a high-speed system benefits a lot from accurate data merging that can be achieved using advanced post-processing-based motion correction algorithms. Likewise, a relatively low-accuracy, low-update-rate tracking system could be used as an initialization for a post-processing-based motion correction approach.

Acknowledgments The authors acknowledge support from National Institutes of Health R01-EY011289-25, R01-EY013178-11, R01-EY013516-09, R01-EY019029-03, R01-HL095717-03, R01-NS057476-05, Air Force Office of Scientific Research FA9550-10-1-0063 and Medical Free Electron Laser Program FA9550-10-1-0551. The authors also gratefully acknowledge funding of the Erlangen Graduate School in Advanced Optical Technologies (SAOT) by the German Research Foundation (DFG) in the framework of the German excellence initiative and DFG Training Group 1773 "Heterogeneous Image Systems" as well as grant DFG-HO-1791/11-1. The authors receive royalties from intellectual property licensed to Optovue, Inc. We would like to thank James G. Fujimoto, Ben Potsaid, Jonathan J. Liu, Chen D. Lu, Kenny Tao, Andreas Maier, Andre Aichert, Thomas Koehler, and Maria Polyanskaya for valuable discussions and assistance.

References

1. D. Huang, E.A. Swanson, C.P. Lin, J.S. Schuman, W.G. Stinson, W. Chang, M.R. Hee, T. Flotte, K. Gregory, C.A. Puliafito, J.G. Fujimoto, Optical coherence tomography. Science **254**, 1178–1181 (1991)
2. B. Povazay, B. Hofer, C. Torti, B. Hermann, A.R. Tumlinson, M. Esmaeelpour, C.A. Egan, A.C. Bird, W. Drexler, Impact of enhanced resolution, speed and penetration on three-dimensional retinal optical coherence tomography. Opt. Express **17**, 4134–4150 (2009)

3. R. Engbert, R. Kliegl, Microsaccades uncover the orientation of covert attention. Vision Res. **43**, 1035–1045 (2003)
4. A.T. Bahill, M.R. Clark, L. Stark, The main sequence, a tool for studying human eye movements. Math. Biosci. **24**, 191–204 (1975)
5. G. Hausler, M.W. Lindner, "Coherence radar" and "spectral radar"—new tools for dermatological diagnosis. J. Biomed. Opt. **3**, 21–31 (1998)
6. R. Leitgeb, C. Hitzenberger, A. Fercher, Performance of fourier domain vs. time domain optical coherence tomography. Opt. Express **11**, 889–894 (2003)
7. T. Klein, W. Wieser, R. Andre, T. Pfeiffer, C.M. Eigenwillig, R. Huber, Multi-MHz FDML OCT: snapshot retinal imaging at 6.7 million axial-scans per second. Opt. Coherence Tomogr. Coherence Domain. Opt. Methods. Biomed. Xvi **8213**, 6 (2012)
8. T. Klein, W. Wieser, C.M. Eigenwillig, B.R. Biedermann, R. Huber, Megahertz OCT for ultrawide-field retinal imaging with a 1050 nm Fourier domain mode-locked laser. Opt. Express **19**, 3044–3062 (2011)
9. W. Wieser, B.R. Biedermann, T. Klein, C.M. Eigenwillig, R. Huber, Multi-Megahertz OCT: high quality 3D imaging at 20 million A-scans and 4.5 GVoxels per second. Opt. Express **18**, 14685–14704 (2010)
10. T. Bonin, G. Franke, M. Hagen-Eggert, P. Koch, G. Hüttmann, In vivo Fourier-domain full-field OCT of the human retina with 1.5 million A-lines/s. Opt. Lett. **35**, 3432–3434 (2010)
11. M. Pircher, B. Baumann, E. Götzinger, H. Sattmann, C.K. Hitzenberger, Simultaneous SLO/OCT imaging of the human retina with axial eye motion correction. Opt. Express **15**, 16922–16932 (2007)
12. R.D. Ferguson, D. Hammer, L.A. Paunescu, S. Beaton, J.S. Schuman, Tracking optical coherence tomography. Opt. Lett. **29**, 2139–2141 (2004)
13. D.X. Hammer, R.D. Ferguson, J.C. Magill, L.A. Paunescu, S. Beaton, H. Ishikawa, G. Wollstein, J.S. Schuman, Active retinal tracker for clinical optical coherence tomography systems. J. Biomed. Opt. **10**, 024038–024038 (2005)
14. G. Maguluri, M. Mujat, B.H. Park, K.H. Kim, W. Sun, N.V. Iftimia, R.D. Ferguson, D.X. Hammer, T.C. Chen, J.F. de Boer, Three dimensional tracking for volumetric spectral-domain optical coherence tomography. Opt. Express **15**, 16808–16817 (2007)
15. H. Engineering. (2013, Feb 22). [SPECTRALIS Product Page – Heidelberg Engineering]. Available: http://www.heidelbergengineering.com/international/products/spectralis/
16. A. G. Capps, R. J. Zawadzki, Q. Yang, D. W. Arathorn, C. R. Vogel, B. Hamann, J. S. Werner, "Correction of eye-motion artifacts in AO-OCT data sets," pp. 78850D–78850D, 2011, Proc. SPIE 7885, Ophthalmic Technologies XXI, 78850D (February 11, 2011); doi:10.1117/12.874376
17. S. Ricco, M. Chen, H. Ishikawa, G. Wollstein, J. Schuman, Correcting motion artifacts in retinal spectral domain optical coherence tomography via image registration. Med. Image Comput. Comput. Assist. Intervent. Miccai Proceedings **5761**(Pt I), 100–107 (2009)
18. E.A. Swanson, J.A. Izatt, M.R. Hee, D. Huang, C.P. Lin, J.S. Schuman, C.A. Puliafito, J.G. Fujimoto, In vivo retinal imaging by optical coherence tomography. Opt. Lett. **18**, 1864–1866 (1993)
19. R.R. Pappuru, C. Briceno, Y. Ouyang, A.C. Walsh, S.R. Sadda, Clinical significance of B-scan averaging with SD-OCT. Ophthal. Surg. Lasers Imaging Off. J. Int. Soc. Imaging Eye **43**, 63 (2012)
20. A. Sakamoto, M. Hangai, N. Yoshimura, Spectral-domain optical coherence tomography with multiple B-scan averaging for enhanced imaging of retinal diseases. Ophthalmology **115**, 1071–1078 (2008)
21. J. Nocedal, S.J. Wright, *Numerical Optimization*, 2nd edn. (Springer, New York, 2006)
22. P. Thevenaz, U.E. Ruttimann, M. Unser, A pyramid approach to subpixel registration based on intensity. Image Proc. IEEE Trans. on **7**, 27–41 (1998)
23. R.J. Zawadzki, A.R. Fuller, S.S. Choi, D.F. Wiley, B. Hamann, J.S. Werner, Correction of motion artifacts and scanning beam distortions in 3D ophthalmic optical coherence tomography imaging – art. no. 642607. Ophthal. Technol. XVII **6426**, 42607–42607 (2007)

24. B. Antony, M.D. Abràmoff, L. Tang, W.D. Ramdas, J.R. Vingerling, N.M. Jansonius, K. Lee, Y.H. Kwon, M. Sonka, M.K. Garvin, Automated 3-D method for the correction of axial artifacts in spectral-domain optical coherence tomography images. Biomed. Opt. Exp. **2**, 2403–2416 (2011)
25. B. Potsaid, I. Gorczynska, V.J. Srinivasan, Y. Chen, J. Jiang, A. Cable, J.G. Fujimoto, Ultrahigh speed Spectral/ Fourier domain OCT ophthalmic imaging at70,000 to 312,500 axial scans per second. Opt. Express **16**, 15149–15169 (2008)
26. H. I. D. A. Tolliver, J. S. Schuman, G. L. Miller. An in-painting method for combining multiple SD-OCT scans with applications to Z-motion recovery, noise reduction and longitudinal studies, in *ARVO 2009* (Fort Lauderdale, 2009), p. 1100
27. M.F. Kraus, B. Potsaid, M.A. Mayer, R. Bock, B. Baumann, J.J. Liu, J. Hornegger, J.G. Fujimoto, Motion correction in optical coherence tomography volumes on a per A-scan basis using orthogonal scan patterns. Biomed. Opt. Exp. **3**, 1182–1199 (2012)

Image Processing in Intravascular OCT

16

Zhao Wang, David L. Wilson, Hiram G. Bezerra, and Andrew M. Rollins

16.1 Introduction

Coronary artery disease is the leading cause of death in the world [1]. Intravascular optical coherence tomography (IVOCT) [2] is rapidly becoming a promising imaging modality for characterization of atherosclerotic plaques [3, 4] and evaluation of coronary stenting [5]. OCT has several unique advantages over alternative technologies, such as intravascular ultrasound (IVUS), due to its better resolution and contrast. For example, OCT is currently the only imaging modality that can measure the thickness of the fibrous cap of an atherosclerotic plaque in vivo [6]. OCT also has the ability to accurately assess the coverage of individual stent struts by neointimal tissue over time [2, 5, 7, 8].

Figure 16.1 illustrates the major vascular features that can be visualized by IVOCT. The lumen boundary is the distinctive vessel inner boundary. A guide wire is commonly used during OCT imaging to guide the catheter through the coronary artery. It highly reflects light and creates a long dark shadow behind it in the image. Calcified plaque is a signal-poor region delineated by sharp boundaries [4]. It is associated with the extent and severity of atherosclerosis [9]. Superficial calcification also plays a determinant role in successful stent deployment [10]. The lipid plaque (necrotic core) is a signal-poor region delineated by diffuse boundaries [4]. It highly attenuates light, and therefore, the abluminal boundaries of the plaque are usually not visible in OCT images. Advanced lipid plaques are usually covered

Z. Wang • D.L. Wilson • A.M. Rollins (✉)
Department of Biomedical Engineering, Case Western Reserve University, Cleveland, OH, USA
e-mail: rollins@case.edu

H.G. Bezerra
Cardiovascular Imaging Core Laboratory, University Hospitals Case Medical Center, Cleveland, OH, USA

© Springer International Publishing Switzerland 2015

W. Drexler, J.G. Fujimoto (eds.), *Optical Coherence Tomography*,
DOI 10.1007/978-3-319-06419-2_17

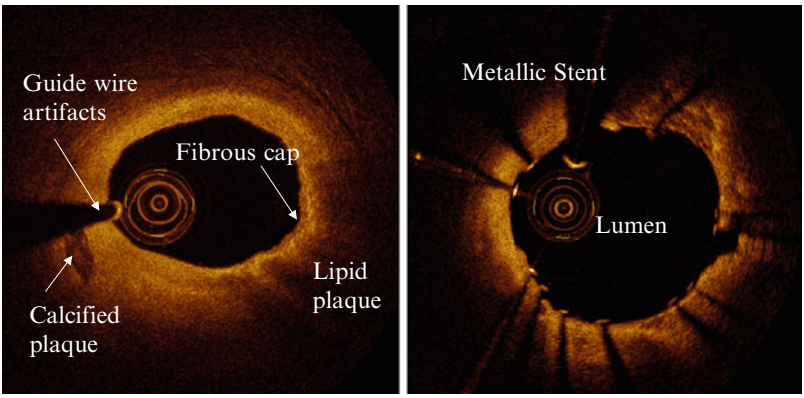

Fig. 16.1 Common vascular features in IVOCT images

by a fibrous cap infiltrated by macrophages. A fibrous cap appears as a signal-rich region. If the thickness of the fibrous cap is less than 65 μm, the plaque is often referred to as thin-cap fibroatheroma (TCFA). Rupture of TCFA has been considered the most frequent cause of acute coronary events including heart attack and sudden deaths [11]. Coronary stenting is the most common technique for coronary revascularization. The most commonly used stents are metallic stents. They strongly reflect light and manifest as bright reflections coupled with dark shadows in OCT images.

The typical speed for current IVOCT imaging is 50,000 lines/s and 100 frames/s (this is the specifications for C7-XRTM OCT Intravascular Imaging System, St. Jude Medical Inc., St. Paul, Minnesota, the current IVOCT system from Terumo Europe N.V. has higher speed, as will the next generation system from St. Jude Medical). The amount of image data and details generated by OCT can be overwhelming to the practicing clinician. Currently, analysis of OCT images has been typically conducted manually in an extremely time-consuming manner. For instance, for stent analysis, analysts need to manually mark every stent strut in a pullback. Based on our experience, it usually takes more than 7 h to analyze all the frames in a single pullback. In addition, many quantitative metrics of potential clinical diagnostic values are difficult to be generated by manual-based methods. Automated image analysis can (1) greatly alleviate the burdens of analysts, (2) provide more comprehensive metrics for diagnosis, (3) help reduce interobserver variability, and (4) be potentially used for live-time analysis during clinical procedures.

16.2 Image Display and Calibration

IVOCT images are naturally acquired in polar coordinates (Fig. 16.2). After logarithmic compression, images are typically converted from polar to Cartesian

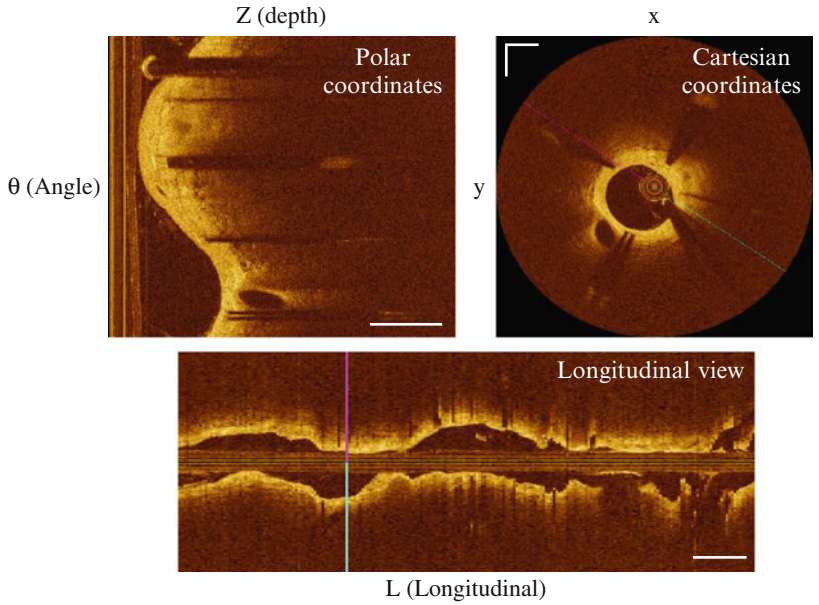

Fig. 16.2 Visualization modes of IVOCT images. Scale bar: 1 mm for the top panels; 5 mm for the bottom panel

coordinates for display. Notice that due to the helical scanning pattern during imaging, the cross-sectional plane is actually oblique with respect to the pullback direction. In commercial OCT systems, longitudinal view (L-mode) image is also used. It is obtained by combining all image pixels at the plane intersects the catheter center at one rotation angle (Fig. 16.2 bottom).

Before any image analysis, calibration must be performed to ensure accurate measurements [12]. Calibration is performed by adjusting the z-offset, which is the optical path length of the optical fiber within the catheter. In practice, cross-sectional images in Cartesian coordinates are adjusted to match the outer boundary of the catheter with the actual diameter. In the corresponding polar coordinates, adjusting the z-offset is equivalent to translating the image in the A-line direction. As the optical path length may change during a single pullback, the z-offset often needs to be adjusted multiple times during the analysis of a single pullback.

16.3 Segmentation, Detection, and Quantification Methods

Segmentation refers to partitioning an image into meaningful regions with different labels. It is fundamental for IVOCT image analysis and is the basis for quantification, plaque characterization, recognition, and 3-D visualization. Detection is to automatically detect meaningful features (e.g., stent struts) from original images and is often the basis for tissue quantification, recognition, and 3-D visualization.

16.3.1 Lumen Segmentation

Lumen segmentation is often the basis for more advanced plaque and stent analysis. In addition, lumen area itself is a direct indicator of vessel stenosis. In OCT images, luminal boundary is very distinctive, and it is likely that many image processing techniques can succeed in this task [13–16]. We describe two methods here, and both have been proved to be robust in practice. The first one is a 2-D optimization method using dynamic programming [17, 18], and the second one is a 3-D optimization method using closure graph and graph cut [19]. Later, one can see that the basic principles of the two methods can be easily extended to other applications.

16.3.1.1 2-D Dynamic Programming Method

Searching for the vessel luminal boundary in the polar coordinates of OCT images fits the graph search family of optimization problems naturally. The lumen boundary is unique and the accumulated optical intensity difference between the pixels from the vessel and luminal side along the contour is maximum. The globally optimal boundary can be efficiently found using a classic optimization method, dynamic programming (DP).

DP is a general technique used to solve certain optimization problems [20]. The basic concept is to find the globally optimal solution to the original problem by building on optimal solutions to subproblems. It is very robust in the presence of noise, and this is attractive to OCT image analysis because OCT images often suffer from speckle noise and various artifacts. Consider the OCT images in polar coordinates (θ, r) where θ is angle and r is depth. Suppose there are m A-lines in one image. We assign each pixel at row i and column j an objective function $f(i, j)$ favoring the characteristics of lumen boundary. Our goal is to search for a path from row 1 to row m with the optimal cost C. We can break the problem into subproblems such that the path to row i is always coming from the path to $i-1$ with some connectivity constraint. Therefore, we have the following recursive function:

$$\begin{aligned} C(i,j) &= \max_{j-n\le j^{*}\le j+n}\left\{C\left(i-1,j^{*}\right)\right\}+f(i,j) \qquad 1<i\le m \\ C(i,j) &= f(i,j) \qquad\qquad\qquad\qquad\qquad\qquad\qquad\qquad i=1 \end{aligned} \tag{16.1}$$

where $C(i, j)$ is the accumulated cost from row 1 to point (i, j), j^* is adjacent to j, and n specifies connectivity. The globally optimal boundary can be found by selecting the point in row m with the maximum accumulated cost and back tracking the path [17, 18]. $f(i, j)$ can be simply defined as the intensity difference between image pixels on the vessel side and the luminal side:

$$f(i,j)=\bar{I}(i,j\le j_{\alpha}\le j+w)-\bar{I}(i,j-w<j_{\alpha}<j) \tag{16.2}$$

where $\bar{I}$ refers to the average of pixel value and w is the length of the window for averaging. When the guide wire stays close to the lumen boundary, its bright reflections may obscure the lumen boundary and need to be excluded from lumen

segmentation. This can be achieved by guide wire segmentation introduced in Sect. 16.3.2. For image segmentation, the advantages of DP include its global optimum nature, simplicity, and stability. The limitation is that it is not easy to be generalized to 3-D or higher dimensional space.

16.3.1.2 3-D Method: Surface Segmentation Using Graph Cut

The 3-D lumen segmentation method is based on the surface segmentation method proposed by Li et al. [21]. It is worth mentioning that this method has been successfully applied to intraretinal layer segmentation in ophthalmic OCT images by Garvin et al. [22]. The main idea of the method consists of two steps [21]. First, the volumetric images are transformed into a closure graph, where the optimal closed set corresponds to the optimal surfaces in the original images. The second step is to search for the optimal closed set using graph cut algorithms. We next introduce the method.

We denote a voxel V in the IVOCT pullback as $V(z, \theta, l)$, where z, θ, l are the coordinate in the axial, lateral, and longitudinal direction, respectively. We first look at how we can transform the image stack into a closure graph according to the work by Wu et al. [23] and Li et al. [21]. Consider a directed graph $G = (V, E)$ with nodes V and edges E. Each node is formed by a voxel in the IVOCT pullback in polar coordinates. Each node is associated with a weight $c(z, \theta, l)$ (*node weight*) penalizing the probability of it being located on the lumen boundary, taking the form defined in Eq. 16.2.

We denote the farthest plane from the catheter in the IVOCT pullback as the *base layer* ($z = 0$). Then, the top plane (closest to the catheter) is represented by $z = \mathrm{N}-1$, where N is the number of points in each A-line. We change the *node weight* from $c(z, \theta, l)$ to $w(z, \theta, l)$ as follows:

$$w(z,\theta,l) = \begin{cases} c(z,\theta,l) & z = 0 \\ c(z,\theta,l) - c(z-1,\theta,l) & z > 0 \end{cases} \tag{16.3}$$

Each node $V(z, \theta, l)$ on layer $z = 1,\ldots\mathrm{N}-1$ has a direct edge linked to $V(z\text{-}1, \theta, l)$ We further denote θ_{adj} and l_{adj} as the sets of adjacent A-lines of θ and adjacent frames of l, respectively. We then make a direct edge linking V to the farthest node it could reach in every adjacent set under some smoothness hard constraint Δz:

$$E_V = \left\{V(z,\theta,l), V\left(\max(0, z-\Delta z), \theta_{adj}, l_{adj}\right)\right\} \tag{16.4}$$

Notice that we can incorporate the special helical scanning pattern of IVOCT into the neighborhood definition, i.e., the last A-line in frame i is adjacent to the first A-line in frame $i + 1$. These directed edges will be assigned infinite *edge weight*, and this ensures that the resulting surface intersects each A-line exactly once, and the surface is also smooth as defined by the smoothness hard constraint. In addition to the hard constraints, one can also add soft constraints between neighboring A-lines by assigning the edges finite *edge weights* [24, 25]. Soft constraints allow, but can penalize, the surface boundary deviating from predefined shape

priors [24]. Finally, we make the *base layer* strongly connected (every node in this layer is reachable from any other node) by making infinite edge links between the nodes in the layer such that this layer cannot be cut. Now, one can see that the optimal surface of the original IVOCT pullback corresponds to the optimal closed set (constituted by all the nodes on and below the surface) in the graph G [21, 23].

Searching for the optimal closed set in a graph can be efficiently solved using max-flow/min-cut algorithm, as shown by Picard in the 1970s [26]. Briefly, we construct a closure graph G^C from G by adding two special nodes source s and sink t. We create directed edges linking s to all the nodes with negative weights and edges connecting all nodes with positive weights to t, with the *edge weight* equal to the absolute value of the *node weight*. A cut in a graph partitions the graph into two disjoint sets containing s and t, respectively. The minimum cut is the cut where the sum of edges it severs is minimum. The minimum cut is also a finite cut and can only sever finite edges connected to s/t in G^C. One can easily prove that after a finite cut, the set containing s becomes a closed set and the optimal closed set corresponds to the minimum cut of this closure graph [26, 27].

The surface segmentation method presented above is ideal for robust 3-D lumen segmentation due to its global optimum nature. However, the time and space complexity of the method is huge. For typical IVOCT image stack consisting of 500*1,000*271 pixels, it takes several hours for state-of-the-art graph algorithms to compute the optimal surface, which is impractical for real applications. We can use a simple multi-resolution approach [28] to overcome this computation burden effectively. Consider a coarse level image stack obtained by downsampling the original image stack in axial and lateral directions. As the lumen boundary is very distinct, it still remains the globally optimal boundary although some details are lost in the coarse level. Hence, we can perform graph cut to obtain the optimal surface at this coarse level and then map it back to the original fine level. We know that the true optimal surface should be close to the mapped surface. Hence, we can perform the second round graph cut on the fine level, but only consider the voxels within a narrow band around the mapped surface. This allows the total computation time to be reduced to <1 min for a whole pullback (downsample by 8).

Examples of lumen segmentation results in challenging images are shown in Fig. 16.3.

Remark: distinction should be made between this surface segmentation method and the general graph cut method used for image segmentation proposed by Boykoy et al. [29, 30]. The major difference lies in the graph construction stage. The surface segmentation method uses closure graphs and strictly separates the nodes above the below the surface. Therefore, it is limited to terrain-like surfaces [21]. In comparison, general graph cut [29, 30] does not use closure graphs, and it allows for segmentation of contours/surfaces with arbitrary shape but typically requires user input of seed points indicating the foreground and background. Despite these differences, the same graph cut algorithm can be used in both methods. As IVOCT images are naturally acquired in polar coordinates, the surface segmentation method can guarantee an optimal terrain-like lumen

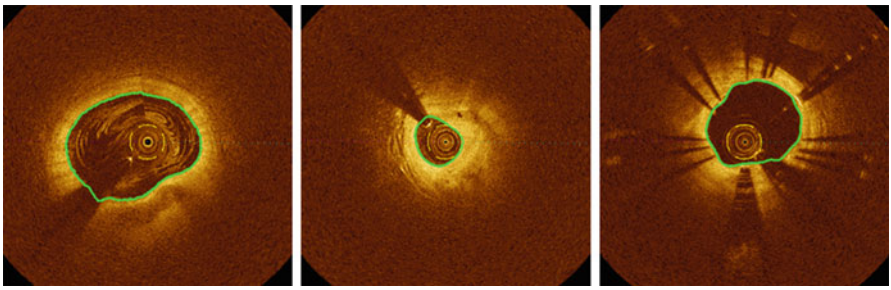

Fig. 16.3 Examples of lumen segmentation results in challenging images. *Left*: an image with significant luminal blood. *Middle*: an image showing severe stenosis. *Right*: an image from a stented vessel

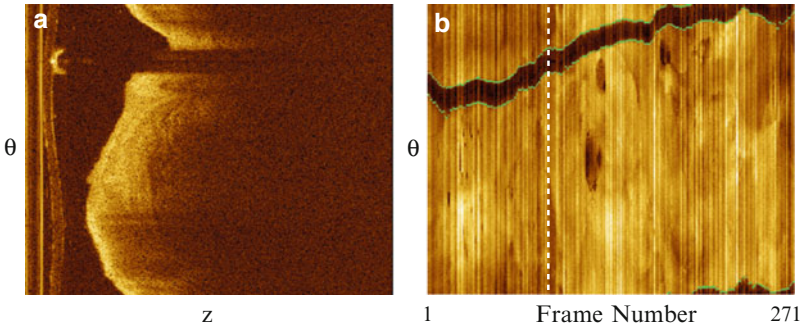

Fig. 16.4 Segmentation of guide wires using the *en face* projection view. (**a**) A cross-sectional image of a pullback showing the guide wire region with a long dark shadow. (**b**) The *en face* projection view showing the guide wire region as a continuous dark band traversing the whole pullback. The *white dotted line* illustrates the position of the frame (**a**) in the pullback. The guide wire positions of all frames can be simultaneously found by segmenting the two boundaries of the dark band. Modified from Wang et al. [17]

surface. However, it is important to note that the general graph cut is a powerful, globally optimal N-D segmentation method, with a wide range of applications in computer vision. More details of the method can be found in [29, 30]. For state-of-the-art graph cut algorithms, please refer to [30–33].

16.3.2 Guide Wire Segmentation

We describe a guide wire segmentation method that is able to extract the globally optimal guide wire positions of all the frames in the entire pullback at once [17, 18]. Briefly, we create an *en face* projection image where 2-D images of the pullback are projected to 1-D curves and combined into one image (Fig. 16.4b). The regions of the guide wire shadow become a continuous dark band. Similar to lumen

segmentation, an objective function of pixel value difference is applied to the two boundaries of the dark band but with different signs. DP is then applied twice to find the two boundaries. More robustly, the two coupled boundaries could also be found simultaneously using a multiple-surface segmentation technique in higher dimensions [21], or using higher-dimension DP [34], but at the expense of increased computation time. The above described method only applies to OCT pullbacks with a single guide wire. Sometimes, there could be more than one guide wire inserted in the same vessel. In such cases, the *en face* view image can be combined with other methods for guide wire segmentation.

16.3.3 Calcified Plaque Segmentation

16.3.3.1 Level Set Segmentation Method

Level set is a popular method used for image segmentation [35–37]. It tracks the object boundaries by minimizing an appropriately designed energy function on a continuous grid using partial differential equations. Instead of explicitly representing the evolving contours using parametric models like snakes [38], level set implicitly represents a contour using the zero level set of a higher dimension function and can treat topological changes such as contour break and merge easily. We define ϕ(t, x, y) (to simplify description, we use a 2-D grid, but level set can be easily generalized to higher dimensions) as the level set function in a higher dimension, and the zero level set $C = \{(x, y)|\phi = 0\}$ represents the evolving contour. Image segmentation using level sets begins with an initial contour and then evolves it in the normal direction based on the following general equation:

$$\frac{\partial \phi}{\partial t} = F|\nabla \phi| \tag{16.5}$$

where F is a speed function and is related to the image data.

For calcified plaque (CP) segmentation, we describe a level set approach combining the work of Li et al. [39] and Chan and Vese [40]. We define ϕ as a signed distance function (SDF) with its zero level curve represented by C. $\phi < 0$ if ϕ is outside C; $\phi > 0$ if ϕ is inside C. The initial contour C_0 is driven to the desired CP boundary by minimizing the following energy term:

$$\begin{aligned} E = \mu \int_\Omega \frac{1}{2}(\nabla \phi - 1)^2 dxdy + \lambda \int_\Omega g' \delta(\phi)|\nabla \phi| dxdy + \upsilon \int_\Omega g' H(-\phi) dxdy \\ + \kappa \left(\int_\Omega |I_0(x,y) - c_1|^2 H(\phi) dxdy + \int_\Omega |I_0(x,y) - c_2|^2 (1 - H(\phi)) dxdy \right) \end{aligned} \tag{16.6}$$

$\delta(\phi)$ is a 2-D smoothed Dirac function; H is the Heaviside function; I_0 is the original image; and $g' = 1/(1 + g)$, where g is the gradient image which is

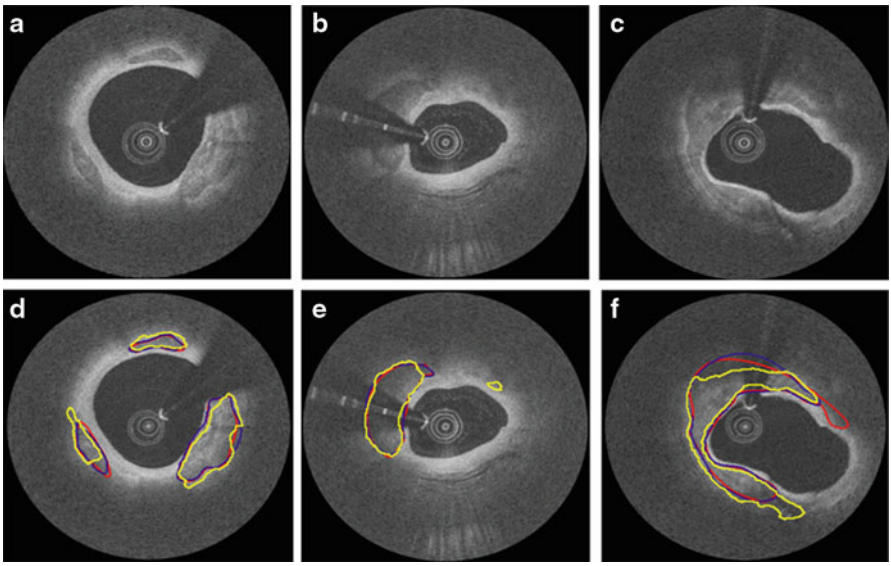

Fig. 16.5 Examples of calcified plaque segmentation results. (**a**–**c**) Original images. (**d**–**f**) Corresponding manual and automatic segmentation results. *Red*: observer 1; *blue*: observer 2; *yellow*: automatic method. Reprinted from Wang et al. [41]

determined by convolving the original image with different orientations of edge filters and selecting the maximum response for each point [41]. c_1 is the average intensity inside C; c_2 is the average intensity of an outer ring of thickness w surrounding C, μ, λ, ν; and κ are weighting terms. The first term is to keep ϕ as a SDF. The second term is a length term regulating the smoothness of the contour. The third term is an area term indicating whether the curve will grow or shrink. In our implementation, it was set positive to shrink the contour. The fourth term contains region-based intensity information. The minimization of E is based on the following gradient flow:

$$\frac{\partial \phi}{\partial t} = -\frac{\partial E}{\partial \phi} \tag{16.7}$$

The evolving contour is stopped if its speed is close to zero. In the discrete image space, all the terms in the above equations are numerically approximated. More details of the method can be found in [41]. The advantage of the level set method is its flexible topology for contour merge and break. The limitation is that it may find a local minimum instead of a global minimum. Therefore, the initial contour is often required to be placed close to the desired boundaries. Examples of automated CP segmentation results with comparison with human analysts are shown in Fig. 16.5. More details about level sets can be found in [35–37, 42].

16.3.3.2 Calcified Plaque Quantification

Based on the segmentation, the depth, area, volume, thickness, and angle fill fraction (AFF) of CP can be calculated automatically. The calculation of area is trivial. The volume of a lesion can be calculated from CP areas in individual frames using Simpson's rule. For depth and thickness, we typically use the rays radiating from the centroid of the lumen as the direction for calculation. AFF is simply the largest angle between the rays spanned across the CP [41].

16.3.4 Fibrous Cap Quantification

The conventional method to assess the fibrous cap (FC) thickness is to quantify only the minimum cap thickness (MCT). However, as FC is a 3-D structure, the single-point/single-frame representation is unable to capture the volumetric profile of FC. In addition, we have found that significant interobserver variations exist between different analysts in assessing the MCT [17]. Here, we describe a method that is able to quantify the volumetric morphology of FC and also the conventional MCT more accurately. In this method, users first select the circumferential boundaries (start and end angle) of FC, and the algorithm automatically determines the optimal FC boundaries in the radial dimension. Quantitative metrics can then be derived from the FC segmentation.

16.3.4.1 Fibrous Cap Segmentation

FC is delineated by a luminal boundary and an abluminal boundary. The luminal boundary coincides with the vessel lumen contour. The abluminal boundary is commonly described as the "diffuse border" created by the interface between the FC and the underlying lipid pool. In the polar coordinates, searching for the FC abluminal boundary can be treated as a similar graph search problem as lumen segmentation, but with different objective function. Essentially, the goal is to design an objective function such that its optimal value corresponds to the optimal boundary that best separates the FC from the underlying lipid plaque. The FC has been defined histologically as a distinct layer of connective tissue covering the lipid core and consists purely of smooth muscle cells in a collagenous-proteoglycan matrix, with varying degrees of infiltration by macrophages and lymphocytes [43]. The fibrous tissue appears bright by OCT and has a low attenuation coefficient, whereas the lipid pool appears dark and strongly attenuates the light [44, 45]. Therefore, the FC abluminal boundary has a high intensity difference between the FC and lipid pool and also a high gradient. Hence, we define the following objective function:

$$f_FC(i,j) = \bar{I}(i, j - d_l \le j_\alpha \le j) - \bar{I}(i, j < j_\alpha \le d_{\max}) - \lambda\mu \tag{16.8}$$

where d_l and $d_{\max}$ are predefined depths to calculate pixel intensity difference, μ is the slope of pixel value attenuation extracted from the A-line segment of length L across (i, j), and λ is a weighting term. The parameter values $d_l = 75$ μm, $d_{\max} = 0.38$ mm, $\lambda = 7$ and $L = 38$ μm are determined experimentally using

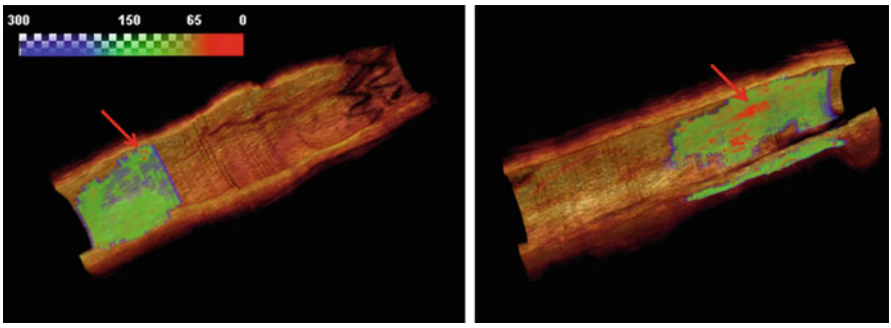

Fig. 16.6 Two coronary arteries used in the validation study with fibrous caps (*FC*) rendered in a continuous color map indicating the thickness. Both of the two lesions contain TCFA (*red arrows*) and similar minimum cap thickness. However, the plaque shown on the right panel contains a significantly larger surface area with thin cap as compared to the plaque in the left panel. Reprinted from Wang et al. [17]

training data [17]. With this objective function, the optimal FC abluminal boundary can be obtained using the same DP algorithm (Sect. 16.3.1) in the region bounded by the luminal boundary and $d_{\max}$ in the radial dimension and by the user-selected angle in the circumferential direction. Automation of the angle selection is possible but is presently hindered by the lack of a validated, reproducible criterion for FC circumferential boundaries.

16.3.4.2 Quantification and 3-D Visualization

With the fully segmented FC, we can quantify the thickness at each point of the FC luminal boundary, defined as the minimum distance from this point to the FC abluminal boundary. The conventional metric MCT can be accurately found from the pool of the thicknesses of all the points. In addition, volumetric metrics of the FC can be derived. The FC surface area (SA) of a lesion can be calculated as the product of the frame interval and the arc length of FC summed over involved frames. The absolute and fractional FC categorical surface area (ACSA and FCSA) of a lesion can be calculated as the absolute and relative FC area in a thickness category (e.g., <65 μm, 65–150 μm, and >150 μm). Other possible volumetric metrics can also be found in [17].

The segmented FC can be visualized in 3-D with a continuous color map indicating the FC thickness. Figure 16.6 illustrates two cases, both with TCFA, with FC thickness rendered in 3-D. If assessed using only the conventional methodology, the morphological differences between the cases would not be apparent. However, the 3-D visualization demonstrates dramatically different characteristics.

16.3.5 Stent Detection

Stent analysis is one of the most common tasks for IVOCT image analysis. Several automated stent detection methods have been reported [14–16, 46–49]. Due to

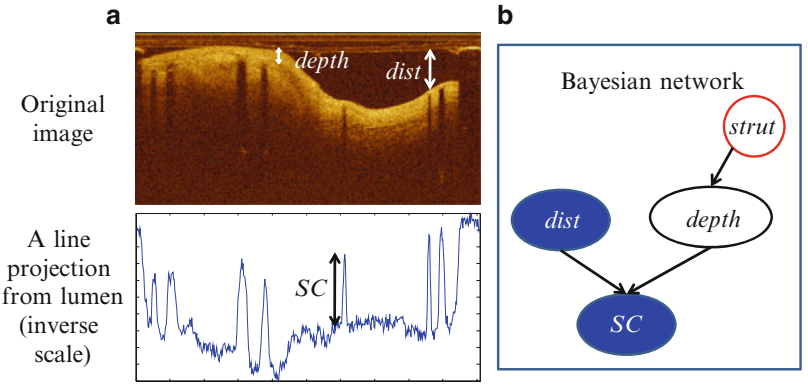

Fig. 16.7 The Bayesian network for inference of strut presence. (**a**) *Top*: original OCT image in polar coordinate. *Bottom*: by calculating the mean intensity of the A-line within a fixed depth from the lumen boundary, the 2-D image is projected into a 1-D curve (plotted in an inverse scale). Searching for strut locations is equivalent to searching for peaks in the 1-D curve. (**b**) A Bayesian network representation based on principles of OCT image formation

space constraint, we describe one method that has the advantage of having few empirical parameters and that has been validated using a large clinical dataset [50]. The method consists of two major steps, (1) probabilistic detection of strut positions and (2) simultaneous localization of all strut depths.

16.3.5.1 Probabilistic Detection of Strut Positions

As the metallic stent strongly reflects light, the struts cast clear shadows in intersecting A-lines. In comparison, surrounding tissues not covered by stents are free of strut shadows. Therefore, strut locations typically appear as extreme points in the 1-D projection, which is generated by taking the mean intensity of a fixed depth (1.5 mm) from the luminal boundary (Fig. 16.7).

We consider physical principles in the detection of struts in the 1-D projection curve. If we define the relative difference between the adjacent extreme peak and valley points to be shadow contrast (*SC*), it can be seen that real struts generate larger *SC* as compared to surrounding non-strut regions, but the size of *SC* depends on how far the lumen wall is from the catheter (represented by *dist*) and how deep the tissue is covering the strut (represented by *depth*). We can model these cause-effect relationships using a Bayesian network [51–53] as shown in Fig. 16.7b. It encodes the causal dependencies between variables and, more importantly, compactly represents the full joint probability distribution of the atomic event defined by all the variables. For example, the node *SC* encodes the conditional probability P(*SC*|*dist*,*depth*), i.e., probability of *SC* being a certain value given the observed values of *dist* and *depth*. For baseline cases where the OCT is performed immediately after stent implantation, the network can be simplified by not considering the strut depth.

In the stent detection problem defined in Fig. 16.7, our task is to query the probability of strut presence among all the peaks given our observations. Here, we can directly observe the values of *SC* and *dist*. We can also estimate the probabilities of P(*strut*) and P(*SC*|*dist*,*depth*) from manually analyzed training data. As *SC*, *dist*, and *depth* are continuous variables, we can discretize them into bins to generate the conditional probability tables (for *depth*, we include an additional variable, undefined, to make it compatible with presence of no strut). Note that the strut depth is still unknown at this point. According to probability theory, we can directly query P(*strut*|*SC*,*dist*) by marginally summing over all the possible depths a strut could occupy:

$$P(strut|SC, dist) = \frac{\sum_{depth} P(SC, dist, depth, strut)}{\sum_{strut}\sum_{depth} P(SC, dist, depth, strut)} \tag{16.9}$$

However, such an approach is noisy for non-strut and ambiguous strut positions. Instead, we adopt the following algorithm in which we first get a quick estimate of strut depth and then improve estimates of the probability of a strut and strut depth in subsequent steps.

Estimate-Strut-Presence

Step 1: Roughly estimate the strut depth bin for each of the peaks in the 1-D projection (i.e. suspected struts) using maximum likelihood estimation (MLE):

$$depth_{MLE} = \arg\max_{depth} P(SC|dist, depth) \tag{16.10}$$

Step 2: Estimate P(*strut*|*SC*,*dist*) and select only the peaks that are associated with high probability (e.g., 0.7) of strut presence. Notice that we can now treat strut depth as a deterministic variable by using the depth evidence from Step 1. Equation 16.9 can now be evaluated using equations below:

$$\begin{aligned} P(strut|SC, dist) &= \frac{P(SC, dist, depth_{MLE}, strut)}{\sum_{strut} P(SC, dist, depth_{MLE}, strut)} \\ &= \frac{P(SC|dist, depth_{MLE})P(dist)P(depth_{MLE}|strut)P(strut)}{\sum_{strut} P(SC|dist, depth_{MLE})P(dist)P(depth_{MLE}|strut)P(strut)} \\ &= \frac{P(SC|dist, depth_{MLE})P(depth_{MLE}|strut)P(strut)}{\sum_{strut} P(SC|dist, depth_{MLE})P(depth_{MLE}|strut)P(strut)} \end{aligned} \tag{16.11}$$

Step 3: Determine strut depths for high-confidence peaks found in Step 2 and then use these high-confidence depth locations to interpolate strut depths for other peaks in the 1-D projection curve. The refined strut depth is determined by searching the A-line for the point x^* that optimizes the objective function associated with strut features within the depth range found in Step 1. For a given point x, we use a linear objective function that models the strut presence by combining the features of bright strut reflection, low intensity of dark shadow, and high attenuation within the strut-shadow transition:

$$f_x = S_x + \mu I_x + \lambda M_x \tag{16.12}$$

where S_x is the slope of the A-line segment r_x (70 μm) following x. I_x is the intensity of x and M_x is the mean intensity of the A-line segment (500 μm long) after r_x, representing the intensity of the shadow. μ and λ are weighting terms and can be determined using a linear classifier using training data [54]. Interpolation uses the same method as used for stent area quantification. For those cases where there is not a high-confidence peak, Steps 3 and 4 are not executed, and the result from Eq. 16.11 will be directly used.

Step 4: Determine the final probability P(*strut*|*SC*,*dist*) using Eq. 16.11 with the updated depth information found in Step 3 for all peaks.

For baseline cases, P(*strut*|*SC*,*dist*) can be directly estimated without considering the strut depth. Once we have the probability map for all the peaks, we can simply classify strut locations using the Bayes decision rule, i.e., P(*strut*|*SC*,*dist*) > 0.5.

16.3.5.2 Simultaneous Localization of All Strut Depths

So far, we have identified A-lines containing stent struts. The next step is to determine the precise depth location of the strut in each A-line, with consideration to 3-D spatial information. We determine depths considering all struts in a pullback simultaneously making use of the spatial constraint between adjacent struts. Such an approach tends to be robust against outliers as the added spatial constraint forces the outlier to "come close" to the adjacent struts. A stent is a tubular structure which is expanded at implantation. Unless there is a rupture, a very rare event, the implanted stent will maintain its tubular shape with some deformations caused by resistance from the vessel, as in the presence of a calcification. This will be the case both at implantation and at follow-up. Choosing the centroid of the vessel lumen as the reference point, distances to struts are not likely to vary dramatically between adjacent struts. In fact, if we consider only the pixels in the A-lines containing stent struts (*strut lines*), all the struts in a pullback form a surface in the polar coordinates. If we associate each pixel with a cost penalizing the presence of strut-like features, given in Eq. 16.12, the problem becomes the optimal surface searching problem and can be efficiently solved using graph cut (Sect. 16.3.1).

This stent detection method has been shown to be robust in clinical images with different quality and artifacts. Some examples are shown in Fig. 16.8. The limitation of the method is that it is not effective for struts with very thick coverage where no shadow is present. For such cases, other methods may be considered, such as [46].

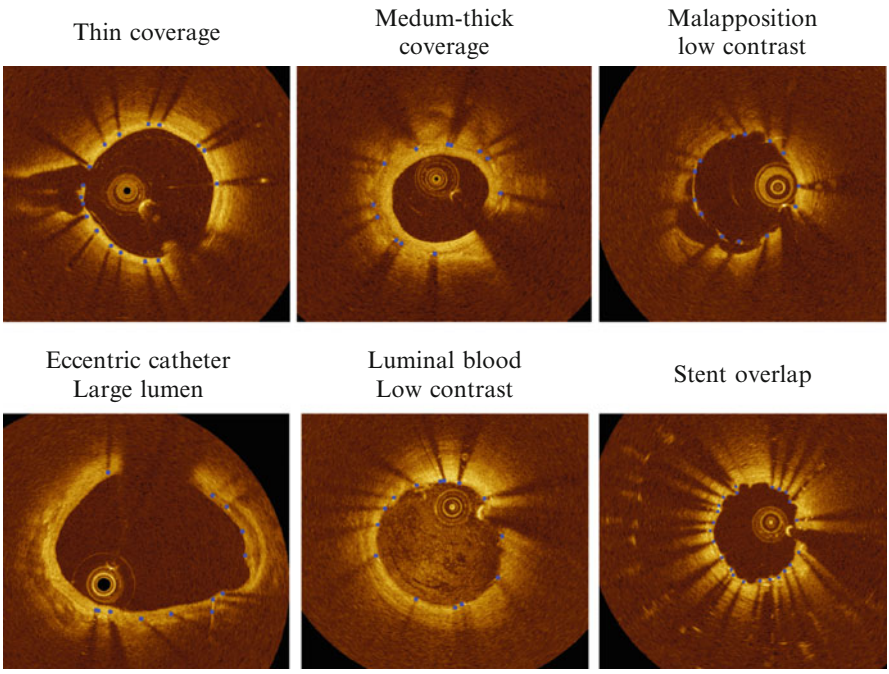

Fig. 16.8 Examples of automated stent strut detection in images with different thickness of strut coverage and diverse quality. *Blue dots* indicate the automatically detected struts

16.3.5.3 Area Quantification and Strut-Level Analysis

After identifying stent struts, we can make various clinically relevant area measurements, including *stent area*, *malapposition area*, and *neointima area* (*tissue coverage area*), as illustrated in Fig. 16.9. We can also perform *strut-level measurements*, including individual strut coverage thickness, malapposition distance, type (covered, malapposed, and apposed), etc. For a more complete list of possible quantitative metrics that can be derived from the image, please refer to [12]. Once all the stent struts and the luminal boundary of the vessel are detected, any quantitative metrics defined above can be computed. Specifically, all area measurements rely on obtaining a virtual stent contour, which is simply interpolated from the detected struts. In images where there are very few stent struts present, it may be challenging to reconstruct the stent contours accurately. Incorporating the strut information from neighboring slices for interpolation is therefore recommended.

16.4 Tissue Characterization, Classification, and Machine Learning

Tissue characterization means quantifying various tissue properties or features that can then be used for tissue classification. Tissue characterization is usually

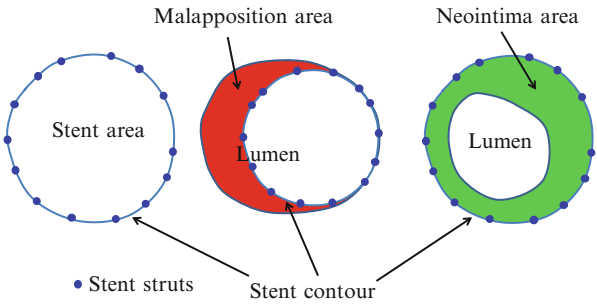

Fig. 16.9 Illustration of *stent area* (the area enclosed by the stent struts), *malapposition area* (the area enclosed by the lumen boundary and malapposed struts), and *neointima area* (the area enclosed by the lumen boundary and tissue covered stent struts)

performed first by establishing criteria for different tissue types by matching image features with a gold standard (typically histology). Then, when the features are validated, human experts can use these criteria to classify tissue types. Computers can also be used for tissue characterization. We can design algorithms to extract features with good correspondence with visual cues. Compared to human analysts, the advantages of automated tissue characterization methods are that they can extract quantitative features, are not subject to intra- nor interobserver variability, are repeatable, and can be fast. However, it is generally difficult for computers to utilize high-level knowledge, which is often key for tissue characterization and is being used by human analysts effortlessly and effectively all the time. After information-bearing image features are extracted, the computer algorithm can classify the tissue into appropriate categories using a variety of machine learning methods.

Here, we focus our discussions on automated or computer-assisted tissue characterization/classification (also called computer-aided diagnosis, CAD). For IVOCT, the most important and common task is to characterize/classify atherosclerotic plaques, namely, fibrous plaques, calcified plaques, and lipid plaques (necrotic cores) [4]. Other important tasks include characterization of coronary thrombosis [55], neointima hyperplasia [56], etc.

16.4.1 Tissue Characterization Using Optical Properties

Optical properties of tissues have been used to characterize and classify different tissue types in IVOCT. Xu et al. [45] proposed a single scattering model to extract the backscattering and attenuation coefficients of tissue. Consider a single A-line with $P(z)$ representing the power of the signal at depth z. The single scattering model can be represented as

$$\log(P(z)/P(z_0)) = \log(\mu_b/\mu_{b0}) - 2\mu_t z/n \tag{16.14}$$

where μ_b and μ_t are the backscattering and attenuation coefficients, respectively. $P(z_0)$ and μ_{b0} are measured from phantoms with negligible attenuation coefficient and are used to cancel light source-specific parameters. n is the refractive index of

the tissue. After the IVOCT image is logarithmically compressed, a straight line can be least squares fitted to the A-line profile, and the intercept and slope are related to the backscattering and attenuation coefficients, respectively. As both specular reflections and noise can affect the fitting, according to [45], the fit is restricted to region from 50 μm below the surface to the point where the signal is attenuated 1/e of the starting point. Results from this study demonstrate that fibrous plaques have high backscattering and low attenuation ($\mu_b = 18.4 \pm 6.4$ mm^{-1}, $\mu_t = 6.4 \pm 1.2$ mm^{-1}), calcified plaques have low backscattering and low attenuation ($\mu_b = 4.9 \pm 1.5$ mm^{-1}, $\mu_t = 5.7 \pm 1.4$ mm^{-1}), and lipid plaques have high backscattering and high attenuation ($\mu_b = 28.1 \pm 8.9$ mm^{-1}, $\mu_t = 13.7 \pm 4.5$ mm^{-1}). Therefore, plaques can be classified by combining both backscattering and attenuation coefficients. However, the above numbers are derived from transversal scanning OCT on paraffin-embedded sections, not radial scanning at the endothelial surface as used in clinical IVOCT. van Soest et al. [44] proposed a similar single scattering model and applied it to rotary IVOCT. The attenuation coefficient of every A-line was extracted, with additional considerations of tissue discontinuity. Similar attenuation coefficients were found for the major types of plaques. The entire image was then color coded with the attenuation map. More complex multiple scattering models have also been proposed [57, 58].

Tissue characterization using optical properties provides physical explanations of the image formation for various tissues, is easy to be interpreted by human analysts, and can be verified by experiments. However, directly applying the method to the original image is noisy, as only single A-line or averaged A-lines are used without considering the global properties of the image.

Other feature extraction methods have been employed for CAD in OCT imaging that make use of 2-D image properties. For example, texture analysis methods have been used for classification of dysplasia and cancer in Barrett's esophagus using catheter-based endoscopic OCT [59, 60].

Generally, selection of regions of interest for analysis is important. Segmentation methods (Sect. 16.3) can help constrain the feature extraction to single-type tissues or homogeneous regions and will help improve the performance of the methods. After segmentation and image feature extraction, machine learning methods can be employed for tissue classification (Sect. 16.4.2).

16.4.2 Machine Learning Methods for Tissue Classification

Machine learning refers to the ability of the system to improve its performance on the same task through experience [61]. In the context of IVOCT image analysis, we mainly focus our discussions on the tissue classification task. The inputs to the system are quantitative image features, and the performance measure of the task is how accurately the algorithm can classify a tissue type (by comparison to a gold standard, usually a human expert observer and/or histology). Further, we restrict ourselves to supervised learning, i.e., some training data with target's output are first provided to the system, and the system *learn*s to match the target during the training stage.

During the testing stage, the learned system can operate on unseen data. Notice that machine learning is not to simply memorize examples but to learn the underlying concept behind the examples, so the system can be generalized to new data.

Standard machine learning procedures typically include feature extraction (as introduced above), feature selection, and classification. Feature extraction is crucial to the final performance of the classification. During the feature extraction stage, various features are extracted from regions of interest. These features could include optical properties of tissues (Sect. 16.4.1), intensity features (e.g., pixel or region intensity), gradient features (e.g., edge strength and orientations, histogram of oriented gradients [62]), texture features (e.g., standard deviation and entropy of a region), shape descriptors, location information (e.g., distance to the lumen boundary), scale-invariant features (e.g., SIFT [63] and SURF features [64]), etc. Whether a feature is effective depends on the specific task. Irrelevant features do not contribute to prediction accuracy and may negatively affect the generalizability of the algorithm and increase the computation burden. Therefore, feature selection is important before classification and should result in a set of image features that are information rich, have strong contrast to tissue classes of interest, and are not redundant with each other. For more information on feature selection methods, we refer readers to [65–69].

Classification methods are broad and rich, and a detailed discussion is beyond the scope of this chapter. We provide a brief summary of the most commonly used classification methods as a practical guide (Table 16.1). For details, please refer to [61, 70]. It is important to note that there is no best learning algorithm for all cases [71]. In practice, the method that is best for a particular problem is usually the one that explores the most suitable hypotheses for that problem.

16.5 Interesting Topics and Future Directions

16.5.1 Macrophages

Macrophages (foam cells) are key players in the formation and progression of atherosclerotic plaques [72]. Macrophages can degrade the integrity of atherosclerotic plaques and make them more prone to rupture [73]. In OCT images, macrophages are strong scatters and often attenuate the light significantly. Tearney et al. [74] first suggested the ability of IVOCT to quantify the macrophage density. In this method, normalized standard deviation (NSD) within a region of interest (ROI) in the fibrous caps was quantified using linear OCT data for macrophage density estimation [74]. Another image analysis method has been proposed by Tahara et al. [75] to quantify the macrophage area in mouse aorta. This method considers both intensity and texture features at different scales for macrophage detection. In both methods, selection of ROI is important because macrophages should only be evaluated in the context of fibroatheroma [12]. The fibrous cap segmentation (Sect. 16.3.4) method may facilitate this task. It is important to note that whether current IVOCT systems can visualize individual macrophages is unknown [12].

Table 16.1 Commonly used machine learning methods

Method	Key concepts	Advantages	Disadvantages
Decision trees	Use tree structure, with internal nodes representing tests on features and leaves indicating class labels	Easy to interpret, simple to implement, widely used	Not very effective for continuous variables
	For learning, recursively select and remove the feature with the most predictive label, partition the training examples into disjoint sets until data are pure or no attributes are left	Good for nominal variables	Learning the optimal decision tree structure is NP-complete. Heuristic algorithms may lead to overfitting, often need post-pruning
	For classification, start from the root, check each feature test, move along the path until reaching the leaf	Can handle missing values	
Artificial neural networks	Mimic human brains using a large number of neurons, connect them with weighted edges	Can learn very complex hypotheses	Easy to overfit
	Can represent any Boolean function and continuous function using a network with one hidden layer, can represent any function in R^n using two hidden layers	Builds useful representations automatically	Typically require a large amount of data to train, slow training
	For learning, iteratively update weight parameters by minimizing the loss function through backpropagation starting from output neurons to hidden layers and to the input layer		Not very effective for nominal data
Support vector machines	Try to find a separating hyperplane with maximum margins between positive and negative instances	Powerful, elegant	Sensitive to noise with nonlinear kernels
	Implicitly represent high-dimensional features using kernels; kernel selection is flexible, can be linear or nonlinear	Robust to errors in data	Does not handle multi-class (>2) classification naturally
	Optimization can be performed in primal or dual space	Can handle high-dimensional and nonlinear features easily	Hard to implement
		Has "built-in" overfitting control	
		Good performance in a wide range of applications	

(*continued*)

Table 16.1 (continued)

Method	Key concepts	Advantages	Disadvantages
Bayesian networks	Directed acyclic graph with each node representing its conditional probability distribution given its parents	Powerful expressive representations, easy to incorporate real-world knowledge	Exact probabilistic inference in a general Bayesian network is #P-hard (harder than NP) but is easier in restricted structures (e.g., polytrees) and small networks
	Each variable is independent of its non-descendents given its parents. With this conditional independence, joint probability distributions can be compactly factorized	Probabilistic output, model uncertainty	If network structure is unknown, learning optimal network structure is NP-hard, heuristic optimization methods are often used to learn "good enough" structures
	For learning, estimate the conditional probabilities using training data	Can learn arbitrary shape of decision boundaries	
	For classification and inference, find the most probable class of a new example given the observations. There are both exact and approximate inference algorithms	Can encode causal relationships between variables	
		Can do inference both forward and backward. Inference can be facilitated by graph algorithms	
Ensemble methods	Combine a collection of classifiers (often called weak or base learners) and use some voting scheme for classification	Can be applied to any single classifier to improve its performance	The classification boundary of ensemble methods can be hard to interpret
	Most commonly used methods include bagging and boosting		
	Bagging – to generate replicates by uniformly sampling the training data with replacement and use majority voting for classification	Bagging can reduce the variance of noisy data, almost never hurt accuracy	The improvements of bagging over base learners are usually very small
	Boosting – one commonly used method is Adaboost. It works by maintaining a weighted training set and iteratively adjusting the weights of training examples based on the classification of the previous iteration. The classification is performed by a weighted vote	Boosting can reduce bias and can sometimes improve the performance of the base learner significantly. Can possibly maximize the margin and reduce the generalization error of the classifier	In most cases, boosting can outperform base classifiers; but it can also perform worse in some cases

16.5.2 Neointimal Hyperplasia

Drug-eluting stents (DES) are widely used clinically and can significantly reduce development of neointima hyperplasia (NIH) after stent implantation as compared to bare-metal stents. However, the potential risk of DES leading to late-stent thrombosis has become an important concern. Characterization of NIH and correlation of different NIH patterns with clinical events may provide insights on the safety of DES, as well as the underlying mechanisms of pathology, and therefore help future stent designs and potential treatment. Templin et al. [76] pioneered OCT characterization of fibrin vs. neointima coverage using a simple metric termed "optical density," defined as the pixel intensity of strut coverage normalized by the pixel intensity of struts. The method has been shown promising by correlation with scanning electron microscopy findings. More studies are needed to confirm and extend the findings.

16.5.3 Bioabsorbable Stents

Bioabsorbable stents [77, 78] use degradable polymers instead of metals and are likely to be the next generation stent designs. Under IVOCT, bioabsorbable stents exhibit very different characteristics from metallic stents. For instance, one type of bioabsorbable stent, BVS [77], presents as box-like shape at baseline and may change appearance thereafter before being fully absorbed by the tissue. Different bioresorbable stents may have different appearances. All automated stent detection methods proposed so far are for metallic stents. More studies on bioabsorbable stents are needed.

16.5.4 Stent Registration

The vascular response to stent implantation can be better understood if the IVOCT pullbacks at different time points can be registered at strut level. Ughi et al. [79] proposed a rigid registration method based on iterative closest point algorithm for registrations of IVOCT pullbacks at different time points. Promising results have been demonstrated. More research is needed in this area.

16.5.5 3-D Image Processing Methods

IVOCT images are intrinsically 3-D. As the longitudinal resolution of future IVOCT systems is expected to be further improved, 3-D image processing methods will play more and more important roles. Many segmentation, detection and classification tasks can be facilitated using neighboring frame information. As additional information is taken into account, 3-D methods are potentially more robust than 2-D methods. In addition, some feature morphology is better visualized in 3-D than in 2-D, such as side branches and stent fracture [80, 81]. Likewise, 3-D

quantification methods may provide additional clinically relevant metrics for diagnosis. However, very few studies so far have proposed 3-D image processing methods for IVOCT.

16.5.6 GPU-Accelerated Image Processing

A graphics processing unit (GPU) with hundreds of cores allows massively parallel computing and can significantly boost the performance of suitable algorithms. In many applications, GPU-based computing can be ten times faster more than its CPU equivalent. Recently, GPU processing has become popular in the OCT community and has been used in many tasks such as real-time OCT signal processing and volume rendering [82–85]. Most IVOCT image analysis methods involve the same processing operated on many A-lines or on many frames, and parallel computing can be naturally applied to these methods.

16.5.7 Image Understanding

Ideally, a fully automated tool to identify, segment, and quantify important vascular features (lumen, plaques, stents, thrombosis, etc.) could be very useful for real-time decision-making. This will require the algorithm to understand the IVOCT image content very well. This is a challenging task and may require combination of multiple image segmentation, detection, characterization, and classification methods, as well as expert medical knowledge into a meaningful hierarchical model. Without complicating the clinical task too much, some user input may be acceptable, and this will reduce the complexity of the problem significantly. High-level image understanding research is needed. The basis of human image understanding can be found in [86]. Some image understanding methods are introduced in [87, 88]. With the advance of IVOCT image analysis research, it is expected that more and more tasks can be automated towards this goal.

16.6 Conclusions

IVOCT image analysis is a relatively new area. The high resolution, superior image contrast, fast imaging speed, and volumetric profile of IVOCT make possible many high-impact image processing tasks. Significant advances have been made to automate various tasks, yet there are more to be explored. It can be expected that the research and development of IVOCT image analysis methods will have a direct impact on the diagnosis and treatment of coronary artery diseases.

Acknowledgements The authors thank Marco A. Costa, Hiram G. Bezerra, and all members of the Cardiovascular Imaging Core lab at the University Hospitals Case Medical Center (Cleveland OH); David L. Wilson, Michael Jenkins, David Prabbu, Hong Lu, and Madhusudhana Gargesha

from the Department of Biomedical Engineering, and Soumya Ray from the Department of Electrical Engineering and Computer Science at Case Western Reserve University; Joseph M. Schmitt, Chenyang Xu, and other technical support from St. Jude Medical Inc (St. Paul, Minnesota). Some research presented here was supported in part by grants R01 HL114406, R21 HL108263 and R01 HL095717 from the National Institutes of Health and in part by the American Heart Association Predoctoral Fellowship (#11PRE7320034).

References

1. V.L. Roger, A.S. Go, D.M. Lloyd-Jones, R.J. Adams, J.D. Berry, T.M. Brown, M.R. Carnethon, S. Dai, G. de Simone, E.S. Ford, C.S. Fox, H.J. Fullerton, C. Gillespie, K.J. Greenlund, S.M. Hailpern, J.A. Heit, P.M. Ho, V.J. Howard, B.M. Kissela, S.J. Kittner, D.T. Lackland, J.H. Lichtman, L.D. Lisabeth, D.M. Makuc, G.M. Marcus, A. Marelli, D.B. Matchar, M.M. McDermott, J.B. Meigs, C.S. Moy, D. Mozaffarian, M.E. Mussolino, G. Nichol, N.P. Paynter, W.D. Rosamond, P.D. Sorlie, R.S. Stafford, T.N. Turan, M.B. Turner, N.D. Wong, J. Wylie-Rosett, Heart disease and stroke statistics – 2011 update. Circulation **123**(4), e18–e209 (2011)
2. H.G. Bezerra, M.A. Costa, G. Guagliumi, A.M. Rollins, D.I. Simon, Intracoronary optical coherence tomography: a comprehensive review: clinical and research applications. JACC Cardiovasc. Interv. **2**(11), 1035–1046 (2009)
3. I.-K. Jang, B.E. Bouma, D.-H. Kang, S.-J. Park, S.-W. Park, K.-B. Seung, K.-B. Choi, M. Shishkov, K. Schlendorf, E. Pomerantsev, S.L. Houser, H.T. Aretz, G.J. Tearney, Visualization of coronary atherosclerotic plaques in patients using optical coherence tomography: comparison with intravascular ultrasound. J. Am. Coll. Cardiol. **39**(4), 604–609 (2002)
4. H. Yabushita, B.E. Bouma, S.L. Houser, H.T. Aretz, I.K. Jang, K.H. Schlendorf, C.R. Kauffman, M. Shishkov, D.H. Kang, E.F. Halpern, G.J. Tearney, Characterization of human atherosclerosis by optical coherence tomography. Circulation **106**(13), 1640–1645 (2002)
5. B.E. Bouma, G.J. Tearney, H. Yabushita, M. Shishkov, C.R. Kauffman, D. DeJoseph Gauthier, B.D. MacNeill, S.L. Houser, H.T. Aretz, E.F. Halpern, I.-K. Jang, Evaluation of intracoronary stenting by intravascular optical coherence tomography. Heart **89**(3), 317–320 (2003)
6. T. Kubo, T. Imanishi, S. Takarada, A. Kuroi, S. Ueno, T. Yamano, T. Tanimoto, Y. Matsuo, T. Masho, H. Kitabata, K. Tsuda, Y. Tomobuchi, T. Akasaka, Assessment of culprit lesion morphology in acute myocardial infarction: ability of optical coherence tomography compared with intravascular ultrasound and coronary angioscopy. J. Am. Coll. Cardiol. **50**(10), 933–939 (2007)
7. Y. Suzuki, F. Ikeno, T. Koizumi, F. Tio, A.C. Yeung, P.G. Yock, P.J. Fitzgerald, W.F. Fearon, In vivo comparison between optical coherence tomography and intravascular ultrasound for detecting small degrees of in-stent neointima after stent implantation. J. Am. Coll. Cardiol. Intv. **1**(2), 168–173 (2008)
8. M. Nakano, M. Vorpahl, F. Otsuka, M. Taniwaki, S.K. Yazdani, A.V. Finn, E.R. Ladich, F.D. Kolodgie, R. Virmani, Ex vivo assessment of vascular response to coronary stents by optical frequency domain imaging. J. Am. Coll. Cardiol. Img. **5**(1), 71–82 (2012)
9. L. Wexler, B. Brundage, J. Crouse, R. Detrano, V. Fuster, J. Maddahi, J. Rumberger, W. Stanford, R. White, K. Taubert, Coronary artery calcification: pathophysiology, epidemiology, imaging methods, and clinical implications: a statement for health professionals from the American Heart Association. Circulation **94**(5), 1175–1192 (1996)
10. I. Moussa, C. Di Mario, J. Moses, B. Reimers, L. Di Francesco, G. Martini, J. Tobis, A. Colombo, Coronary stenting after rotational atherectomy in calcified and complex lesions: angiographic and clinical follow-up results. Circulation **96**(1), 128–136 (1997)

11. E. Falk, Plaque rupture with severe pre-existing stenosis precipitating coronary thrombosis. Characteristics of coronary atherosclerotic plaques underlying fatal occlusive thrombi. Br. Heart J. **50**(2), 127–134 (1983)
12. G.J. Tearney, E. Regar, T. Akasaka, T. Adriaenssens, P. Barlis, H.G. Bezerra, B. Bouma, N. Bruining, J.-M. Cho, S. Chowdhary, M.A. Costa, R. de Silva, J. Dijkstra, C. Di Mario, D. Dudeck, E. Falk, M.D. Feldman, P. Fitzgerald, H. Garcia, N. Gonzalo, J.F. Granada, G. Guagliumi, N.R. Holm, Y. Honda, F. Ikeno, M. Kawasaki, J. Kochman, L. Koltowski, T. Kubo, T. Kume, H. Kyono, C.C.S. Lam, G. Lamouche, D.P. Lee, M.B. Leon, A. Maehara, O. Manfrini, G.S. Mintz, K. Mizuno, M.-A. Morel, S. Nadkarni, H. Okura, H. Otake, A. Pietrasik, F. Prati, L. Raber, M.D. Radu, J. Rieber, M. Riga, A. Rollins, M. Rosenberg, V. Sirbu, P.W.J.C. Serruys, K. Shimada, T. Shinke, J. Shite, E. Siegel, S. Sonada, M. Suter, S. Takarada, A. Tanaka, M. Terashima, T. Troels, S. Uemura, G.J. Ughi, H.M.M. van Beusekom, A.F.W. van der Steen, G.-A. van Es, G. van Soest, R. Virmani, S. Waxman, N.J. Weissman, G. Weisz, Consensus standards for acquisition, measurement, and reporting of intravascular optical coherence tomography studies: a report from the international working group for intravascular optical coherence tomography standardization and validation. J. Am. Coll. Cardiol. **59**(12), 1058–1072 (2012)
13. K. Sihan, C. Botha, F. Post, S. de Winter, N. Gonzalo, E. Regar, P.J.W.C. Serruys, R. Hamers, N. Bruining, Fully automatic three-dimensional quantitative analysis of intracoronary optical coherence tomography. Catheter. Cardiovasc. Interv. **74**(7), 1058–1065 (2009)
14. S. Gurmeric, G.G. Isguder, Carlier, G. Unal, A new 3-D automated computational method to evaluate in-stent neointimal hyperplasia in in-vivo intravascular optical coherence tomography pullbacks. Med. Image Comput. Comput. Assist. Interv. **12**(Pt 2), 776–785 (2009)
15. G. Ughi, T. Adriaenssens, K. Onsea, P. Kayaert, C. Dubois, P. Sinnaeve, M. Coosemans, W. Desmet, J. D'hooge, Automatic segmentation of in-vivo intra-coronary optical coherence tomography images to assess stent strut apposition and coverage. Int. J. Cardiovasc. Imaging **28**(2), 229–241 (2012)
16. S. Tsantis, G.C. Kagadis, K. Katsanos, D. Karnabatidis, G. Bourantas, G.C. Nikiforidis, Automatic vessel lumen segmentation and stent strut detection in intravascular OCT. Med. Phys. **39**(1), 503–513 (2012)
17. Z. Wang, D. Chamie, H.G. Bezerra, H. Yamamoto, J. Kanovsky, D.L. Wilson, M.A. Costa, A.M. Rollins, Volumetric quantification of fibrous caps using intravascular optical coherence tomography. Biomed. Opt. Express **3**(6), 1413–1426 (2012)
18. Z. Wang, H. Kyono, H.G. Bezerra, D.L. Wilson, M.A. Costa, A.M. Rollins, Automatic segmentation of intravascular optical coherence tomography images for facilitating quantitative diagnosis of atherosclerosis, *Proc. SPIE* (2011), p. 78890N
19. W.J. Cook, W.H. Cunningham, W.R. Pulleyblank, A. Schrijver, Combinatorial Optimization (John Wiley & Sons, New York, 1998)
20. P. F. Felzenszwalb, R. Zabih, Dynamic programming and graph algorithms in computer vision. IEEE Trans. Pattern. Anal. Mach. Intell **33**(4), 721–740 (2011)
21. K. Li, X. Wu, D.Z. Chen, M. Sonka, Optimal surface segmentation in volumetric images-A graph-theoretic approach. IEEE Trans. Pattern Anal. Mach. Intell. **28**(1), 119–134 (2006)
22. M.K. Garvin, M.D. Abramoff, R. Kardon, S.R. Russell, X. Wu, M. Sonka, Intraretinal layer segmentation of macular optical coherence tomography images using optimal 3-D graph search. IEEE Trans. Med. Imaging **27**(10), 1495–1505 (2008)
23. X. Wu, D. Chen, P. Widmayer, S. Eidenbenz, F. Triguero, R. Morales, R. Conejo, M. Hennessy, *Optimal Net Surface Problems with Applications, Automata, Languages and Programming*. Lecture Notes in Computer Science 2380 (Springer, Berlin, 2002), pp. 1029–1042
24. Q. Song, X. Wu, Y. Liu, M. Sonka, M. Garvin, Simultaneous searching of globally optimal interacting surfaces with shape priors, *Proc. Computer Vision and Pattern Recognition (CVPR), IEEE Conference on, IEEE* (2010), pp. 2879–2886

25. P.A. Dufour, L. Ceklic, H. Abdillahi, S. Schroder, S. De Dzanet, U. Wolf-Schnurrbusch, J. Kowal, Graph-based multi-surface segmentation of OCT data using trained hard and soft constraints. IEEE Trans. Med. Imaging **32**(3), 531–543 (2012)
26. J.C. Picard, Maximal closure of a graph and applications to combinatorial problems. Manag. Sci. **22**(11), 1268–1272 (1976)
27. D.S. Hochbaum, A new—old algorithm for minimum-cut and maximum-flow in closure graphs. Networks **37**(4), 171–193 (2001)
28. H. Lombaert, Y. Sun, L. Grady, C. Xu, A multilevel banded graph cuts method for fast image segmentation, *Proc. Computer Vision, 2005. ICCV 2005. Tenth IEEE International Conference on*, vol. 1, (2005), pp. 259–265
29. Y.Y. Boykov, M.P. Jolly, Interactive graph cuts for optimal boundary & region segmentation of objects in ND images, Computer Vision, 2001. ICCV 2001. Proceedings. Eighth IEEE International Conference on, **1**, 105–112 (2001)
30. Y. Boykov, V. Kolmogorov, An experimental comparison of min-cut/max-flow algorithms for energy minimization in vision, IEEE Trans. Pattern Anal. Mach. Intell. **26**(9), 1124–1137 (2004)
31. D.S. Hochbaum, The pseudoflow algorithm: a new algorithm for the maximum-flow problem. Oper. Res. **58**(4), 992–1009 (2008)
32. A.V. Goldberg, R.E. Tarjan, A new approach to the maximum-flow problem. J. ACM (JACM) **35**(4), 921–940 (1988)
33. R.K. Ahuja, T.L. Magnanti, J.B. Orlin, Some recent advances in network flows. SIAM Rev. **33**(2), 175–219 (1991)
34. M. Sonka, M.D. Winniford, S.M. Collins, Robust simultaneous detection of coronary borders in complex images. IEEE Trans. Med. Imaging **14**(1), 151–161 (1995)
35. V. Caselles, R. Kimmel, G. Sapiro, Geodesic active contours. Int. J. Comput. Vis. **22**(1), 61–79 (1997)
36. S. Osher, J.A. Sethian, Fronts propagating with curvature-dependent speed: algorithms based on Hamilton-Jacobi formulations. J. Comput. Phys. **79**(1), 12–49 (1988)
37. S. Osher, N. Paragios, *Geometric Level Set Methods in Imaging, Vision, and Graphics* (Springer-Verlag, New York, 2003)
38. M. Kass, A. Witkin, D. Terzopoulos, Snakes: active contour models. Int. J. Comput. Vis. **1**(4), 321–331 (1988)
39. C. Li, C. Xu, C. Gui, M.D. Fox, Level set evolution without re-initialization: a new variational formulation, *Proc. IEEE International Conference on Computer Vision and Pattern Recognition* (*CVPR*) (2005), pp. 430–436
40. T.F. Chan, L.A. Vese, Active contours without edges. IEEE Trans. Image Process. **10**(2), 266–277 (2001)
41. Z. Wang, H. Kyono, H.G. Bezerra, H. Wang, M. Gargesha, C. Alraies, C. Xu, J.M. Schmitt, D.L. Wilson, M.A. Costa, A.M. Rollins, Semi-automatic segmentation and quantification of calcified plaques in intracoronary optical coherence tomography images. J. Biomed. Opt. **15**(6), 061711 (2010)
42. S. Osher, R.P. Fedkiw, *Level Set Methods and Dynamic Implicit Surfaces* (Springer Verlag, New York, 2003)
43. R. Virmani, F.D. Kolodgie, A.P. Burke, A. Farb, S.M. Schwartz, Lessons from sudden coronary death: a comprehensive morphological classification scheme for atherosclerotic lesions. Arterioscler. Thromb. Vasc. Biol. **20**(5), 1262–1275 (2000)
44. G. van Soest, T. Goderie, E. Regar, S. Koljenovic, G. van Leenders, N. Gonzalo, S. van Noorden, T. Okamura, B.E. Bouma, G.J. Tearney, J.W. Oosterhuis, P.W. Serruys, Atherosclerotic tissue characterization in vivo by optical coherence tomography attenuation imaging. J. Biomed. Opt. **15**(1), 011105 (2010)
45. C. Xu, J.M. Schmitt, S.G. Carlier, R. Virmani, Characterization of atherosclerosis plaques by measuring both backscattering and attenuation coefficients in optical coherence tomography. J. Biomed. Opt. **13**(3), 034003–034003 (2008)

46. C. Xu, J.M. Schmitt, T. Akasaka, T. Kubo, K. Huang, Automatic detection of stent struts with thick neointimal growth in intravascular optical coherence tomography image sequences. Phys. Med. Biol. **56**(20), 6665 (2011)
47. G. Unal, S. Gurmeric, S.G. Carlier, Stent implant follow-up in intravascular optical coherence tomography images. Int. J. Cardiovasc. Imaging **26**(7), 809–816 (2010)
48. G.T. Bonnema, K.O.H. Cardinal, S.K. Williams, J.K. Barton, An automatic algorithm for detecting stent endothelialization from volumetric optical coherence tomography datasets. Phys. Med. Biol. **53**(12), 3083 (2008)
49. H. Lu, M. Gargesha, Z. Wang, D. Chamié, G.F. Attizani, T. Kanaya, S. Ray, M.A. Costa, A.M. Rollins, H.G. Bezerra, D.L. Wilson, Automatic stent detection in intravascular OCT images using bagged decision trees. Biomed. Opt. Express **3**(11), 2809–2824 (2012)
50. Z. Wang. (2013) *Intravascular Optical Coherence Tomography Image Analysis* (Doctoral dissertation), Case Western Reserve University, Cleveland OH
51. J. Pearl, *Probabilistic Reasoning in Intelligent Systems* (Morgan Kaufmann, San Francisco, 1988)
52. N. Friedman, D. Geiger, M. Goldszmidt, Bayesian network classifiers. Mach. Learn. **29**, 131–163 (1997)
53. D. Koller, N. Friedman, *Probabilistic Graphical Models Principles and Techniques* (The MIT Press, Cambridge, MA, 2009)
54. F. Rosenblatt, The perceptron: a probabilistic model for information storage and organization in the brain. Psychol. Rev. **65**(6), 386 (1958)
55. T. Kume, T. Akasaka, T. Kawamoto, Y. Ogasawara, N. Watanabe, E. Toyota, Y. Neishi, R. Sukmawan, Y. Sadahira, K. Yoshida, Assessment of coronary arterial thrombus by optical coherence tomography. Am. J. Cardiol. **97**(12), 1713–1717 (2006)
56. N. Tanaka, M. Terashima, S. Rathore, T. Itoh, M. Habara, K. Nasu, M. Kimura, T. Itoh, Y. Kinoshita, M. Ehara, E. Tsuchikane, K. Asakura, Y. Asakura, O. Katoh, T. Suzuki, Different patterns of vascular response between patients with or without diabetes mellitus after drug-eluting stent implantation: optical coherence tomographic analysis. J. Am. Coll. Cardiol. Intv. **3**(10), 1074–1079 (2010)
57. D. Levitz, L. Thrane, M. Frosz, P. Andersen, C. Andersen, S. Andersson-Engels, J. Valanciunaite, J. Swartling, P. Hansen, Determination of optical scattering properties of highly-scattering media in optical coherence tomography images. Opt. Express **12**(2), 249–259 (2004)
58. L. Thrane, H.T. Yura, P.E. Andersen, Analysis of optical coherence tomography systems based on the extended Huygens-Fresnel principle. J. Opt. Soc. Am. A **17**(3), 484–490 (2000)
59. X. Qi, M.V. Sivak, G. Isenberg, J.E. Willis, A.M. Rollins, Computer-aided diagnosis of dysplasia in Barrett's esophagus using endoscopic optical coherence tomography. J. Biomed. Opt. **11**(4), 044010 (2006)
60. X. Qi, Y. Pan, M.V. Sivak, J.E. Willis, G. Isenberg, A.M. Rollins, Image analysis for classification of dysplasia in Barrett's esophagus using endoscopic optical coherence tomography. Biomed. Opt. Express **1**(3), 825–847 (2010)
61. T.M. Mitchell, *Machine Learning. WCB* (WCB, McGraw-Hill Boston, 1997)
62. N. Dalal, B. Triggs, Histograms of oriented gradients for human detection, *Proc. Computer Vision and Pattern Recognition, CVPR,* vol. 881 (2005), pp. 886–893
63. D.G. Lowe, Object recognition from local scale-invariant features, *Proc. Computer Vision, 1999. The Proceedings of the Seventh IEEE International Conference on*, vol. 2 (1999), pp. 1150–1157
64. H. Bay, T. Tuytelaars, L. Van Gool, Surf: Speeded up robust features. *Computer Vision–ECCV 2006*(Springer Berlin Heidelberg, 2006), pp. 404–417
65. P.M. Narendra, K. Fukunaga, A branch and bound algorithm for feature subset selection. IEEE Trans. Comput. **100**(9), 917–922 (1977)

66. R. Kohavi, G.H. John, Wrappers for feature subset selection. Artif. Intell. **97**(1), 273–324 (1997)
67. I. Guyon, A. Elisseeff, An introduction to variable and feature selection. J. Mach. Learn. Res. **3**, 1157–1182 (2003)
68. F. Hussein, N. Kharma, R. Ward, Genetic algorithms for feature selection and weighting, a review and study, *Proc. Document Analysis and Recognition, 2001. Proceedings. Sixth International Conference on*, pp. 1240–1244
69. A.L. Blum, P. Langley, Selection of relevant features and examples in machine learning. Artif. Intell. **97**(1), 245–271 (1997)
70. C.M. Bishop, *Pattern Recognition and Machine Learning* (Springer, New York, 2006)
71. D.H. Wolpert, The lack of a priori distinctions between learning algorithms. Neural Comput. **8**(7), 1341–1390 (1996)
72. R.P. Choudhury, J.M. Lee, D.R. Greaves, Mechanisms of disease: macrophage-derived foam cells emerging as therapeutic targets in atherosclerosis. Nature **2**(6), 309–315 (2005)
73. C.L. Lendon, M.J. Davies, G.V.R. Born, P.D. Richardson, Atherosclerotic plaque caps are locally weakened when macrophages density is increased. Atherosclerosis **87**(1), 87–90 (1991)
74. G.J. Tearney, H. Yabushita, S.L. Houser, H.T. Aretz, I.-K. Jang, K.H. Schlendorf, C.R. Kauffman, M. Shishkov, E.F. Halpern, B.E. Bouma, Quantification of macrophage content in atherosclerotic plaques by optical coherence tomography. Circulation **107**(1), 113–119 (2003)
75. S. Tahara, T. Morooka, Z. Wang, H.G. Bezerra, A.M. Rollins, D.I. Simon, M.A. Costa, Intravascular optical coherence tomography detection of atherosclerosis and inflammation in murine aorta. Arterioscler. Thromb. Vasc. Biol. **32**(5), 1150–1157 (2012)
76. C. Templin, M. Meyer, M.F. Müller, V. Djonov, R. Hlushchuk, I. Dimova, S. Flueckiger, P. Kronen, M. Sidler, K. Klein, F. Nicholls, J.R. Ghadri, K. Weber, D. Paunovic, R. Corti, S.P. Hoerstrup, T.F. Lüscher, U. Landmesser. Coronary optical frequency domain imaging (OFDI) for in vivo evaluation of stent healing: comparison with light and electron microscopy. Eur Heart J. **31**(14): 1792–1801. (2010)
77. P.W. Serruys, J.A. Ormiston, Y. Onuma, E. Regar, N. Gonzalo, H.M. Garcia-Garcia, K. Nieman, N. Bruining, C. Dorange, K. Miquel-Hébert, S. Veldhof, M. Webster, L. Thuesen, D. Dudek, A bioabsorbable everolimus-eluting coronary stent system (ABSORB): 2-year outcomes and results from multiple imaging methods. Lancet **373**(9667), 897–910 (2009)
78. J.A. Ormiston, P.W. Serruys, E. Regar, D. Dudek, L. Thuesen, M.W. Webster, Y. Onuma, H.M. Garcia-Garcia, R. McGreevy, S. Veldhof, A bioabsorbable everolimus-eluting coronary stent system for patients with single de-novo coronary artery lesions (ABSORB): a prospective open-label trial. Lancet **371**(9616), 899–907 (2008)
79. G.J. Ughi, T. Adriaenssens, M. Larsson, C. Dubois, P.R. Sinnaeve, M. Coosemans, W. Desmet, J. D'hooge, Automatic three-dimensional registration of intravascular optical coherence tomography images. J. Biomed. Opt. **17**(2), 0260051–02600511 (2012)
80. D. Chamié, D. Prabhu, Z. Wang, H. Bezerra, A. Erglis, D. L. Wilson, A. M. Rollins, M. A. Costa, Three-dimensional Fourier-domain optical coherence tomography imaging: advantages and future development, Curr. Cardiovasc. Imaging Rep. **5**(4), 221–230 (2012)
81. T. Okamura, Y. Onuma, H.M. Garcia-Garcia, E. Regar, J.J. Wykrzykowska, J. Koolen, L. Thuesen, S. Windecker, R. Whitbourn, D.R. McClean, J.A. Ormiston, P.W. Serruys, 3-Dimensional optical coherence tomography assessment of jailed side branches by bioresorbable vascular scaffolds: a proposal for classification. J. Am. Coll. Cardiol. Intv. **3**(8), 836–844 (2010)
82. K. Zhang, J.U. Kang, Real-time 4D signal processing and visualization using graphics processing unit on a regular nonlinear-k Fourier-domain OCT system. Opt. Express **18**(11), 11772–11784 (2010)

83. K. Zhang, J.U. Kang, Graphics processing unit accelerated non-uniform fast Fourier transform for ultrahigh-speed, real-time Fourier-domain OCT. Opt. Express **18**(22), 23472–23487 (2010)
84. Y. Jian, K. Wong, M.V. Sarunic, Graphics processing unit accelerated optical coherence tomography processing at megahertz axial scan rate and high resolution video rate volumetric rendering. J. Biomed. Opt. **18**(2), 026002–026002 (2013)
85. W. Wieser, W. Draxinger, T. Klein, S. Karpf, T. Pfeiffer, R. Huber, High definition live 3D-OCT in vivo: design and evaluation of a 4D OCT engine with 1 GVoxel/s. Biomed. Opt. Express **5**(9), 2963–2977 (2014)
86. I. Biederman, Recognition-by-components: a theory of human image understanding. Psychol. Rev. **94**(2), 115 (1987)
87. M. Sonka, V. Hlavac, R. Boyle, Image processing, analysis, and machine vision (Brooks/Cole Publishing Company, USA, 1999)
88. R. Tadeusiewicz, M.R. Ogiela, Medical image understanding technology (Springer, Berlin, Heidelberg, 2004)

Superluminescent Diode Light Sources for OCT

17

Vladimir R. Shidlovski

Contrary to laser diodes, the way of superluminescent diodes (SLDs) to their wide use in practice was much longer. There was always a certain scientific interest to "superluminescent" light output from laser diode structures slightly below threshold that might be considerably enhanced by "damping" of laser resonator (e.g., by tilting of mesa structures) [1–3]. However, there was no considerable practical interest to such light sources until it was proved that SLDs are the real "light sources of choice" for fiber-optic gyroscopes [4]. Successful use of first SLDs in gyros in the early 1980s, as well as some overestimated market demand for gyros, had considerably intensified SLD design efforts. This resulted in the development of "first generation of SLDs" with gyro-rated output power, a few milliwatt or less in single-mode (or polarization maintain) fiber at 800–850 nm and 1,300–1,550 nm bands. Development of gyro-graded SLDs also gave some additional impetus to their usage as light sources in other prospective sensing systems, such as Faraday effect electric current sensors, distributed Bragg grating sensor systems, and some others.

The "second wave" of interest to SLDs as light sources came after successful demonstration of OCT technique and its advantages comparing with other probing techniques in medicine, as well as in other applications [5]. OCT required much more powerful SLDs than those existed in the earlier 1990s, particularly with output power of at least 10 mW from SM fiber with still wide and flat optical spectrum of few tens of nanometers. At the same time, other new applications for such SLDs appeared, for example, testing of fiber-optic telecom components (including WDM/DWDM). This additionally intensified design efforts, which resulted in the development of SLDs with outputs comparable to that of laser diodes, thus ensuring their successful usage in applications where high spatial but low temporal coherence is required.

Each application has its own specific requirements to SLD performance parameters, but OCT requirements are the most hard to meet. The main reason for this is

V.R. Shidlovski
Superlum Diodes Ltd., Moscow, Russia

© Springer International Publishing Switzerland 2015

W. Drexler, J.G. Fujimoto (eds.), *Optical Coherence Tomography*,
DOI 10.1007/978-3-319-06419-2_18

the fact that high optical power, very wide-spectrum, and negligible parasitic spectral modulation must be realized simultaneously. From this point of view, OCT may be considered as "the main driving vehicle" for significant improvement of SLD performance and for developing of new approaches to increase SLD power and decrease coherence length. We will overview and discuss the main principles of developing of powerful broadband SLDs and their performance parameters. Some important aspects of SLD use in practice will be discussed. We will also describe ultra-low-coherence light sources based on the combination of different SLD modules. Possibilities for further improvement of SLDs and SLD-based light sources will be discussed as well.

17.1 Main Principles of SLD Operation and SLD Spectrum Broadening

The unique property of superluminescent diodes is the combination of laser diode-like output power and brightness with broad, LED-like, optical spectrum. Such combination is allowed by high optical gain and wide gain spectrum in semiconductor laser materials.

In fact, any "ideal" SLD is optimized traveling wave semiconductor optical amplifier (SOA) with zero reflections from the ends of active channel ("end reflections" below). In every SLD, two counterpropagating beams of amplified spontaneous emission are traveling along the active region. For estimation of its output power, SLD may be described relatively well by a simple model that does not take into account spectral effects and considers uniform distribution of carriers' density in SLD active region [6, 7]. Stationary distributions of photon densities in each direction, carrier density, and driving current density are described by well-known rate equations of traveling wave laser diode amplifier [6, 7]:

$$c\frac{dS^+}{dz} = c(g-\alpha)S^+ + \beta\frac{N}{\tau_{sp}}, \tag{17.1}$$

$$-c\frac{dS^-}{dz} = c(g-\alpha)S^- + \beta\frac{N}{\tau_{sp}}, \tag{17.2}$$

$$Q(z) = N/\tau_{sp} + cg(S^+ + S^-), \tag{17.3}$$

where S^+ and S^- are photon densities of forward and backward propagated waves in active region, g is modal optical gain, α is non-resonant optical losses of waveguided mode, β is fraction of spontaneous emission coupled into guided mode, N is carrier density, τ_{sp} is spontaneous lifetime, Q is driving current density, and c is the velocity of light.

Equations 17.1–17.3 may be solved analytically assuming that carrier density is constant across the active region [6], that should be a good approximation in the

case of superluminescent diodes, at least with reasonable (1.5 mm or less) length of active region. In such a case, SLD output power $P^+(O)$ on the "output end" of active region of the length L and residual end-reflection coefficients R_{out} and R_b may be expressed from Eq. 17.1 as

$$P_{out}{}^+(O) \propto S^+(O) = R_b S^-(L)\exp[(g-\alpha)L] + \frac{\beta N}{c\tau_{sp}} \frac{\exp[(g-\alpha)L]}{g-\alpha} \tag{17.4}$$

and SLD power $P^-(L)$ on the back end of the active region may be expressed as

$$P_{back}{}^-(L) \propto S^-(L) = R_{out} S^+(O)\exp[(g-\alpha)L] + \frac{\beta N}{c\tau_{sp}} \frac{\exp[(g-\alpha)L]}{g-\alpha} \tag{17.5}$$

In case of "ideal SLD," end-reflection coefficients are zero and SLD output power is expressed as

$$P_{out}{}^+(L) = h\upsilon \Pi c S^+(L) = h\upsilon \Pi \frac{\beta N}{\tau_{sp}} \frac{\exp[(g-\alpha)L]-1}{g-\alpha}, \tag{17.6}$$

where Π is the cross-section of active region.

For simple estimations, linear dependence of modal gain on carrier density may be used, i.e.,

$$g(N) = \Gamma \frac{dg}{dN}(N - N_0), \tag{17.7}$$

where Γ is optical confinement factor.

Expressions (17.6) and (17.7) allow to estimate optical gain required to get high output powers. Particularly, considering SLD at 850 nm, carrier density $N = 2 \times 10^{19}$ cm^{-3}, transparency threshold $N_0 = 5 \times 10^{17}$ cm^{-3}, differential gain $dg/dN = 0.5 \times 10^{-16}$ cm^{-2}, optical confinement factor $\Gamma = 0.3$, spontaneous emission factor $\beta = 5 \times 10^{-4}$, $\tau_{sp} = 2$ ns, size of optical mode 0.3×5 μm, losses $\alpha = 5$ cm^{-1} and length of SLD active waveguide of 1 mm, net gain $G = exp[(g-\alpha)L]$ of ~30 dB is necessary to realize output power of 30–50 mW. Similar gain is required to make powerful SLDs at other wavelengths.

However, it is practically impossible to achieve zero reflections from the ends of semiconductor optical amplifiers due to high reflection coefficient of as-cleaved semiconductor crystals. Such residual reflections always result in parasitic Fabry-Perot modulation (so-called spectral ripple) with period and depth determined by length of amplifier, optical gain, losses, and reflection coefficients. This parasitic modulation results in so-called secondary coherence subpeaks in coherence function, as it is shown on Fig. 17.1. Averaged spectral modulation of 2–4 % usually results in intensity of correspondent secondary coherence subpeak of −25…−20 dB that may cause problems in OCT systems due to correspondent "ghost" images. In case of low modulation index, parasitic Fabry-Perot modulation depth of SLD spectrum may be expressed as [8, 9]

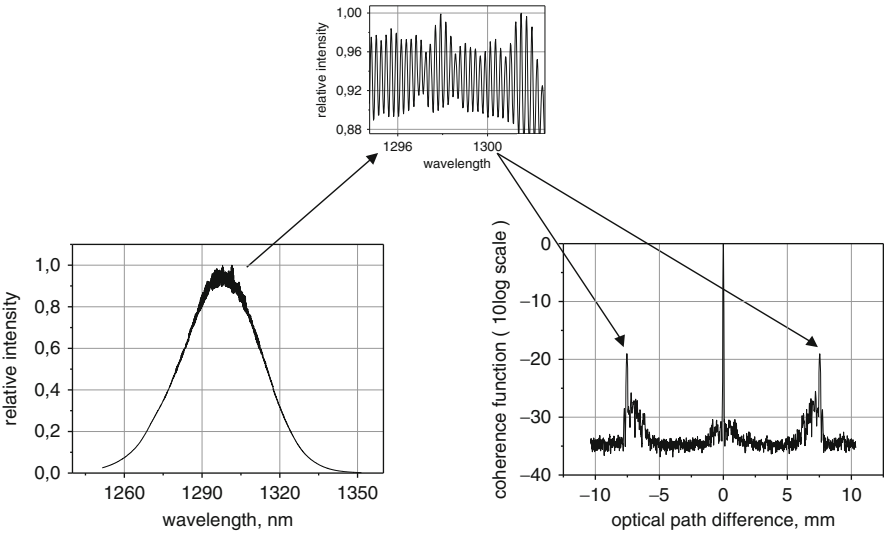

Fig. 17.1 Residual Fabry-Perot spectral modulation in SLD centered around 1,300 nm and correspondent secondary coherence subpeaks

$$m = 2G(R_{out}R_b)^{1/2}. \tag{17.8}$$

Comparison of (17.6) and (17.8) leads to one of the most important properties of SLD performance that is linear increasing of SLD spectral ripple with output power. In fact, both power and residual spectral modulation indices depend linearly on net gain G (6,8) because $N>>N_0$ (17.7) and $g>>\alpha$ in all high-power (i.e., high optical gain) SLDs.

Let us now estimate values of end reflections from SLD active region that are necessary to keep residual spectral modulation at low level. As it was pointed out above, net optical gain around 30 dB is required to produce output power of few tens of milliwatt per facet in single-transverse-mode SLDs. Therefore, product $R_{out}R_b$ must be as low as 10^{-10} (i.e., 10^{-5} per "reflective end") in order to keep residual spectral modulation in a range of 1–2 % in high-power SLDs.

This is very hard to do such low residual reflections in laser diode materials. Reflection coefficient of as-cleaved crystal facets in most of laser diode structures at 600–1,600 nm is around 0,35. Although a possibility for reaching of 10^{-5} residual reflection coefficient in AR-coated laser diode crystals was demonstrated in [10], in practice, all SLDs made by AR coating of laser diodes show very strong, 10 % and much higher, residual Fabry-Perot ripple starting some "low-to-moderate," 3–5 mW, output power per facet (see, e.g., [11, 12]; *to our knowledge*, *there are no reports about SLDs based on AR-coated lasers with better performance parameters*). Most probably, the reason for why it is impossible to do even "low-to-moderate" power low-rippled SLDs by simple antireflection coating of

laser diode crystals is that required residual reflection cannot be realized technologically on big lots due to minor lot-to-lot variations of center wavelength and far-field divergence in laser diode structures. The problem of high spectral ripple in SLDs based on AR-coated laser diodes resulted in the development of specific SLD geometries that allowed strong damping of residual "end reflections."

All low-rippled SLD geometries may be divided into two main categories: so-called "angled" (tilted, slanted) structures, where active waveguide is tilted to SLD crystal facet [2], and structures where ends of SLD active region are followed by relatively long "transparent window" regions and/or integrated absorbing region on the back side of SLD waveguide [7]. All modern powerful and low-rippled SLDs are based either on "tilted" or "transparent window" or "integrated absorber" designs, or on their combinations [see, e.g., 13–17].

But even after the problem of end reflections is solved on "design level" by appropriate SLD geometry, it is still necessary to apply antireflection coating on at least output facet of SLD crystal. Although "simple" AR coating may be used for medium-power SLDs, specific coating, that is not only antireflective but also protective, should be used in powerful diodes, especially in AlGaAs-based SLDs (AlGaAs is known for its relatively low catastrophic optical damage, COD, threshold). This problem may be solved by double-layer coating of output facet with the first layer working as protective layer and finishing layer optimized for best antireflection properties of resulted multilayer structure [18].

Let us now consider spectrum width of SLDs. Obviously, SLD spectrum is determined by the width of optical gain spectrum of active media. Optical spectrum width of the first SLDs, all based on bulk semiconductor heterostructures with relatively thick active layer, varied from (typical) 15–20 nm in 850 nm AlGaAs emitters to 30–40 nm in 1,300–1,550 nm InGaAsP SLDs. Although some exotic designs were proposed to broaden spectrum of "bulk" active layer SLD (particularly "stacked-layer-SLD" with two active layers with different material composition [19]), the real progress in SLD spectral broadening started after successful demonstration of quantum-well (QW) SLDs in [20].

Spectral broadening in QW SLDs is based on two main principles. The first one is a possibility for spectral broadening of optical gain due to very high density of states in QW structures with respect to bulk structures in case of the same driving current density [20]. Additional possibility for spectral broadening appears when transitions from different subbands in QW active layers are utilized to produce SLD output [21, 22]. Particularly, in single-quantum-well (SQW) AlGaAs laser structures, transitions from two, $n = 1$ (sometimes called "ground state") and $n = 2$ (sometimes called "excited state"), states in conductive band are possible [21]. While output power of only 3 mW and 50 nm spectrum width was realized in [20] for the first time from QW SLDs at 850 nm, it was shown in [22] that optimization of SLD active length and geometry allows additional spectral broadening by simultaneous amplification at $n = 1$ and $n = 2$ transitions and further increasing of SLD power; spectrum width of 70 nm was realized at 10 mW output power. Possibility for considerable spectral broadening by MQW (multiple-quantum-well) SLDs at longer wavelength (1,550 nm) was also demonstrated for the first time

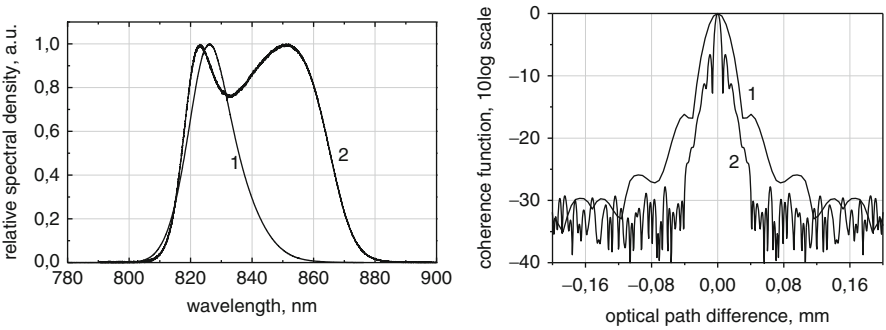

Fig. 17.2 Spectrum and coherence functions of bulk (*1*) and SQW (*2*) SLDs at 820 nm band. It is seen that unless SQW SLD coherence function is much narrower, sidelobes in main autocorrelation maximum of bulk SLD with Gaussian spectrum are well below –15 dB and are roughly 10 dB less than that of SQW SLD with "double-humped" spectrum

in [22]. Nowadays most of powerful and broad-spectrum SLDs at all spectral bands are based on SQW or MQW structure.

It should be pointed out, though, that SQW/MQW SLD spectrum width may depend on drive current much stronger than that of bulk SLD. Particularly, in bulk AlGaAs/GaAs heterostructures, spectrum width of optical gain is usually around 20 nm (around room ambient temperature; it may depend slightly on material composition and active layer doping, see, e.g., [23]). This is why all ever-reported bulk active region AlGaAs SLDs had spectrum width of 15–20 nm with weak dependence of spectrum width on drive current. In SQW/MQW SLD, spectrum width depends on drive current much stronger [21, 22]; particularly, it was broadened by 2–3 times in 820 nm and 1,550 nm SLDs reported in [21, 22] but became strongly non-Gaussian reaching its widest value at some "fixed" value of output power and driving current. Spectral shape of such SLDs is usually "double humped" due to energy separation between different subbands in quantum wells. Changing of driving current results in domination of one of the spectral maxima and narrowing of optical spectrum. Note also that complex form of spectrum may result in strong distortions of coherence function. Figure 17.2 shows main autocorrelation maxima of "bulk" and broadband SQW AlGaAs SLDs. Though some negligible distortions of coherence function due to spectrum asymmetry are seen in bulk SLD, they are much less than that of SQW SLD with very wide but double-humped spectrum.

During the last couple of few years, a possibility of further broadening of SLD spectrum by using quantum dot (QD) structures had been studied [24–26]. Principle of spectral broadening in QD structures is similar to that in QW structures. Considerable broadening is obtained when optical gains at "ground state" and "excited state" in QDs are equal. Additional broadening of entire spectrum is possible due to considerable fluctuation of dots size in today's QD structures. Electroluminescence covering almost 350 nm had been reported in QD structures centered at ~1,200 nm [27]. However, performance of QD SLDs reported so far (which will be reviewed below) is comparable with that of QW SLDs (in terms of

combination of high power and wide spectrum, although wider spectra were demonstrated at low levels of output power).

17.2 Reported SLD Performance Parameters

In this chapter we will review main achievements in development of very high-power and broad-spectrum SLDs at different spectral bands. The main attention will be paid to SLD output power and spectrum width, but some other issues like far-field, polarization, and noise will be discussed as well.

17.2.1 AlGaInP SLDs at 680 nm

Output power up to 4 mW was realized from bulk SLD [15]; output power was increased considerably, up to 50 mW, by using MQW active layer [28]. However, spectrum width of only 8–10 nm was reported in both publications. Commercially available SLDs have the same width of spectrum and output power of up to 5 mW from SM fiber.

17.2.2 AlGaAs SLDs at 780–870 nm Band

A lot of powerful SLDs at this spectral band had been reported. Output power of ~100 mW before COD was successively demonstrated in [18, 29]. It was also shown in [30] that COD threshold may be increased considerably by adding of short unpumped regions near SLD crystal facets. Free-space output power 250 mW per facet was realized by optimization of the length of such regions. SM fiber output power in excess of 100 mW was realized from such SLDs by coupling via cylindrical microlens on the fiber end. Such output power is comparable with powerful single-mode fiber-coupled laser diodes at this band.

In QW SLDs, output power up to 100 mW with 50 nm FWHM was realized by optimization of SLD structure and length of active region [28]. Commercially available SLDs at this spectral band now produce up to 30 mW output with up to 60 nm spectrum width. This spectrum width corresponds to coherence length in the air of less than 10 μm.

Possibilities to realize much broader spectrum in 820 nm SLDs were also demonstrated in [31, 32]. In [31], 100 nm averaged spectrum width was obtained by combined DC and pulse driving of SQW SLD. In [32], up to 90 nm spectrum width was obtained in SLDs with MQW active layer consisted of four layers with thickness varied from 2 to 12 nm. Though reaching of 100 nm spectrum width will allow ultrahigh-resolution OCT at 850 nm band by "single-SLD-emitter" light source, until now there are no commercially available powerful SLDs at 820 nm band with spectrum width exceeding 65 nm.

17.2.3 InGaAs SLDs at 920–1,060 nm Spectral Band

Very broad-spectrum and very high output power had been demonstrated for InGaAs SLDs at 920–980 nm, too. In [9, 28], output power in excess of 100 mW was reported for SLDs around 960–980 nm with bell-like spectrum with approximately 25–30 nm spectrum width and 70 nm wide spectrum with output power around 30 mW. Later, 100 nm spectrum width was realized from optimized QW SLD at 920 nm with free-space output power up to 30 mW (>10 mW ex SM fiber) [33]. Commercial SLDs emit up to 30 mW (SM fiber) output power with 50 nm wide bell-like spectrum and up to 100 nm wide spectrum and 10 mW SM fiber power.

It should be pointed out again that the most broadband and powerful SLDs at 780–1,000 nm have "double-humped" spectrum as simultaneous emission from different subbands of QW active region is used for spectral broadening. Figures 17.3 and 17.4 show spectrum of single-mode fiber-coupled SLD modules emitting

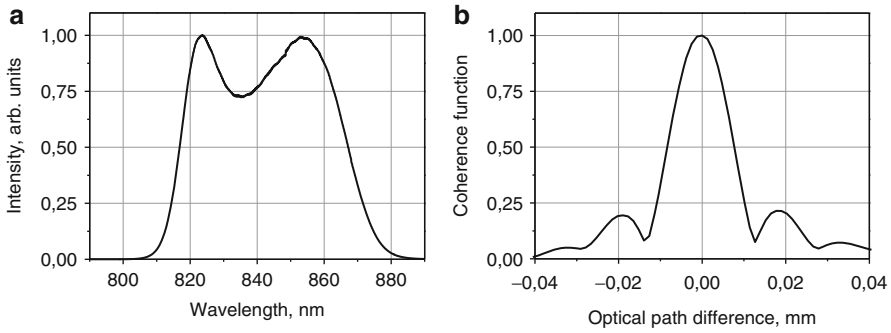

Fig. 17.3 Spectrum and coherence function of 35 mW SM fiber output power QW SLD module at 840 nm

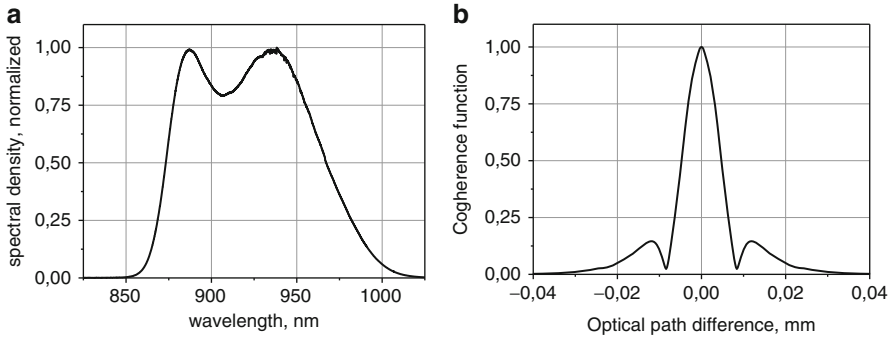

Fig. 17.4 Spectrum and coherence function of 10 mW SM fiber output power QW SLD module at 930 nm

35 mW at 840 nm with 50 nm spectral bandwidth and 10 mW at 930 nm with 100 nm spectral bandwidth and their coherence functions.

InGaAs/GaAs heterostructures were also used to make SLDs at 1,060 nm, the wavelength of growing interest for OCT [34, 35]. The first SLDs reported at this spectral band had output power less than 10 mW (less than 2 mW ex SM fiber [18]). Output power around 50 mW and spectrum width of 110 nm were demonstrated in SLDs centered at 1,030 nm later [36]. Currently, SLDs with spectrum width of ~50–60 nm (bell-shaped spectrum) and ~100 nm (double-humped spectrum) are commercially available.

A possibility of further improving of SLD output power and spectrum width in devices emitting around 1,000–1,060 nm was demonstrated by using of quantum dot (QD) structures. As mentioned above, such structures allow additional broadening of optical gain spectrum due to inhomogeneous dot size distribution in QD active layers. Being a disadvantage to do high-performance QD lasers such "QD dispersion" allows considerable broadening of SLD spectrum [37]. Very broad spectrum had been obtained in SLDs centered at 1,180 nm (up to 150 nm), but SLD power was below 100 μW in this case [38]. However, spectrum width became comparable with that possible by QW structures when shorter wavelengths were targeted. Particularly, free-space output power up to 200 mW with spectrum width around 60 nm was realized in such SLDs centered around 1,000 nm [39].

17.2.4 InGaAsP/InP SLDs at 1,300–1,600 nm Spectral Band

SLDs at this band, especially those centered around 1,300 nm, are very attractive for OCT due to better penetration into tissue. However, increasing of wavelength results in decreasing of coherence length proportionally to square of wavelength. This makes requirements to a long-wavelength SLDs more "stressed" as, for example, spectrum of 1,300 nm SLD must be at least 2.5 times broader with respect to 800 nm counterpart in order to get the same spatial resolution.

Numerous efforts had been put for the development of powerful and broadband SLDs at this spectral band, including optimization of quantum-well (usually multiple QWs) structures and QD structures [26, 39–45]. High output power and wide bell-shaped spectrum had been demonstrated at different center wavelengths. SLD modules with single-mode fiber output of 10–20 mW and spectrum width of up to 80 nm (bell-shaped) and 100 nm (double-hump) are now commercially available.

Let us now discuss briefly other important SLD performance parameters, starting from far-field pattern.

In principle, far field of any single-transverse-mode SLD should be similar to that of conventional single-transverse-mode laser diode (LD) as similar waveguide structures are used in both. However, analysis of SLD literature shows that in most of powerful SLDs active waveguide is tilted to crystal facets. Such tilting results in "crescent" structure of far field, like it is shown on Fig. 17.5 for SLD at 680 nm reported in [28]. Therefore, though conventional LD-graded optics may be used for collimation/focusing of SLD beams, additional optical elements may be required

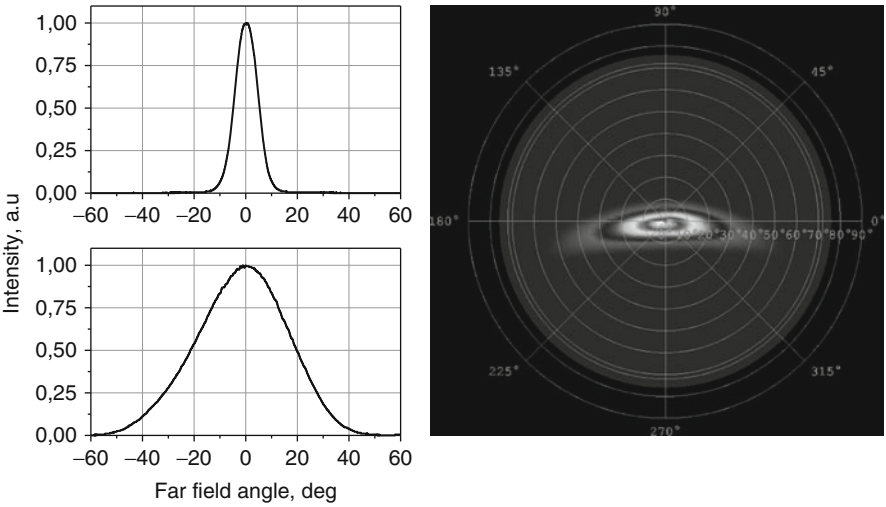

Fig. 17.5 Far-field distribution of angled waveguide SLD at 680 nm [24]

for focusing to diffraction-limited spots. As well, detailed study of spatial coherence [46] shows that even narrow active waveguide SLDs with far-field pattern similar to single-transverse-mode structure may be not 100 % spatially coherent, most probably due to additional high-order mode(s) of lower intensity. From this point of view, SM fiber-coupled SLDs may be more useful also for free-space OCT systems.

SLD polarization may be also important for OCT devices. Usually, there is no gain anisotropy in nonstressed bulk SLDs. Two main factors affecting bulk SLD polarization had been reported: different absorption of TE and TM polarized modes in upper metal contact layer [7] and stress-induced gain anisotropy [47] (residual stresses may be caused, e.g., by mounting SLD crystal onto carrier). Contrary to bulk counterparts, polarization-resolved spectrum of SQW and MQW SLDs may be considerably different to that "polarization non-resolved." In [48], different polarization of light correspondent to transitions from different subbands in AlGaAs SQW was obtained that resulted in considerable difference in spectrum of TE and TM modes. In [49], considerable (about 1.5 times) difference in spectral width of TE and TM polarized modes was obtained in MQW SLDs around 1,550 nm. Unfortunately, there are very few reports on the study of SLD polarization, so there are no more data available.

SLD noise parameters are also very important for OCT systems. The most common approach considers SLD as Gaussian light source with excess noise due to beating of independent spontaneously emitted photons, and spectral density of detector's current fluctuations is expressed as

$$<dI^2>= 2eI(1 + I/I_0), I_0 = e\mathrm{M}dv, \tag{17.9}$$

where e is elementary charge, I is photocurrent, dv is spectrum width, and M is coefficient that depends on polarization and number of modes. For polarized single-transverse-mode SLD at 830 nm with 50 mW output power and 0.4 A/W photoreceiver sensitivity, this model predicts relative intensity noise RIN = $<dI^2>/I^2$ of around –130 dB/Hz for 50 nm wide SLD and –127 dB/Hz for 20 nm wide SLD. Moreover, no any dependence of SLD noise on output power should be obtained accordingly to this model because second term in Eq. 17.9 exceeds shot noise limit $2eI$ by orders of magnitude starting SLD power of few milliwatts. However, different RIN values to those predicted by such model were obtained even in low power, 3 mW SLDs at 820 nm [45]. Moreover, SLD noise saturation was obtained in medium-power [14] and high-power [24] SLDs at 820 nm. In [28], reduction of RIN value by approximately ten times from –130 dB/Hz at 1 mW to –138 dB/Hz at 50 mW in 20 nm wide SLD at 820 nm was obtained, which cannot be explained by the abovementioned model of photon beat noise.

Another model of SLD quantum noise that takes into account amplifier nature of SLD was developed in [50]. Accordingly to this model, excess noise factor X over shot noise $2eI$ may be expressed in terms of transmission losses η, modal gain g, optical losses α, and net gain G as

$$X = e\eta(g + \alpha)(G - 1)/(g - \alpha), \tag{17.10}$$

or, assuming modal gain g much higher than non-resonant losses α,

$$X = e\eta(G - 1) \tag{17.11}$$

It is seen that within this model, excess noise factor is determined by optical gain in SLD. Gain saturates when SLD power increases, so this model may explain noise saturation in powerful SLDs. Good correspondence between results of SLD noise estimations and measurements was obtained in [45]; unfortunately there were no further detailed studies of SLD noise.

It should be pointed out that even in high-power SLDs, intensity noise is more than two orders of magnitude higher than shot noise limit $2eI$. So optimization of power in reference arm of interferometer for the best signal-to-noise ratio in OCT systems is necessary [51].

17.3 SLD Based Broadband and Powerful Light Sources

Previous section shows that a lot of powerful and wide-spectrum SLDs at different spectral bands have been successfully demonstrated. Moreover, further improvement of SLD performance should be possible including development of more powerful and broadband emitters. However, there is also other advantage of SLDs that allows further spectral broadening in SLD-based light sources, namely, easy variation of SLD wavelength by minor change of active layer composition and thickness.

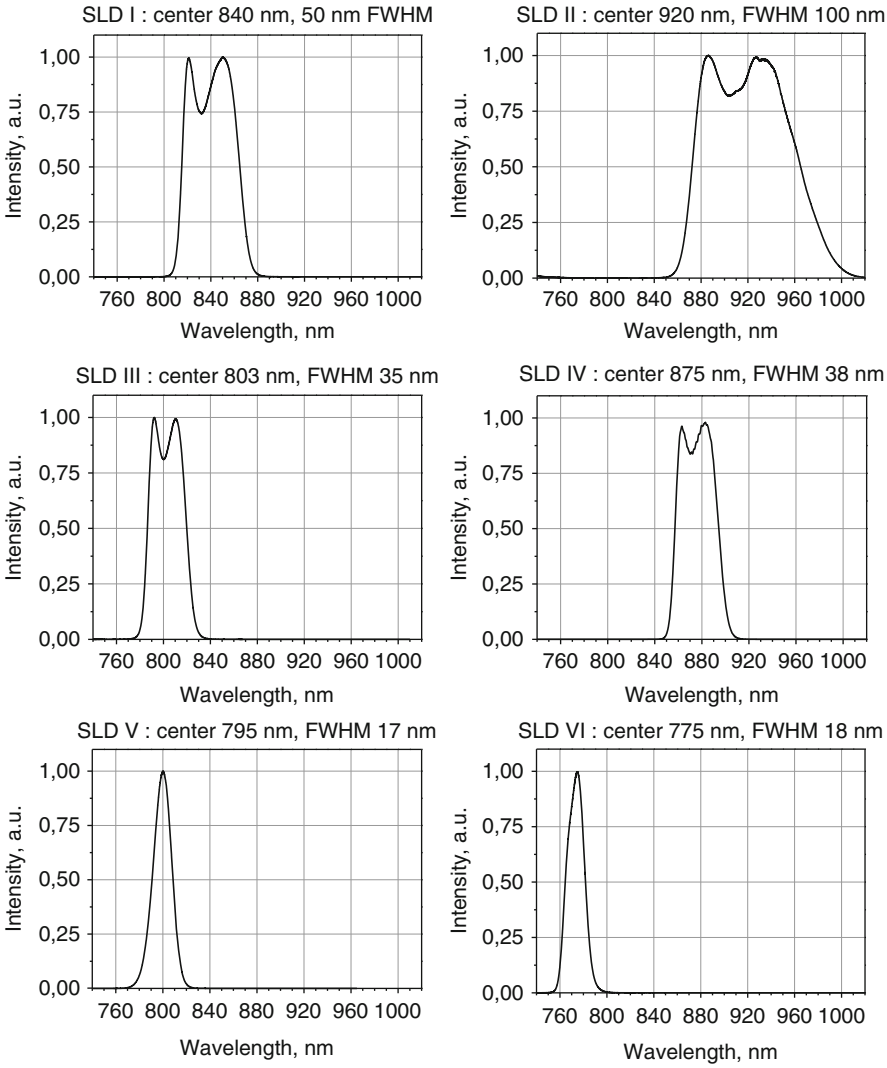

Fig. 17.6 Emission spectra of AlGaAs/GaAs and InGaAs/GaAs SLDs with different active layer composition and geometry

For example, Fig. 17.6 shows spectrum of different SLDs at 780–1,000 nm that were obtained by variation of active layer structure/composition in AlGaAs/GaAs and InGaAs/GaAs SLDs QWs [52, 53]. Most of SLDs had SM fiber-coupled power of 10 mW or more [53]. Combining of two and more of such SLDs by appropriate couplers may result in very broad optical spectrum.

Particularly, combining of "SLD I" and "SLD II" allows broadband light source with total 150 nm linewidth and output power of few milliwatts; see Fig. 17.7a. Images of human retina with 3.5 μm resolution and images of skin layers

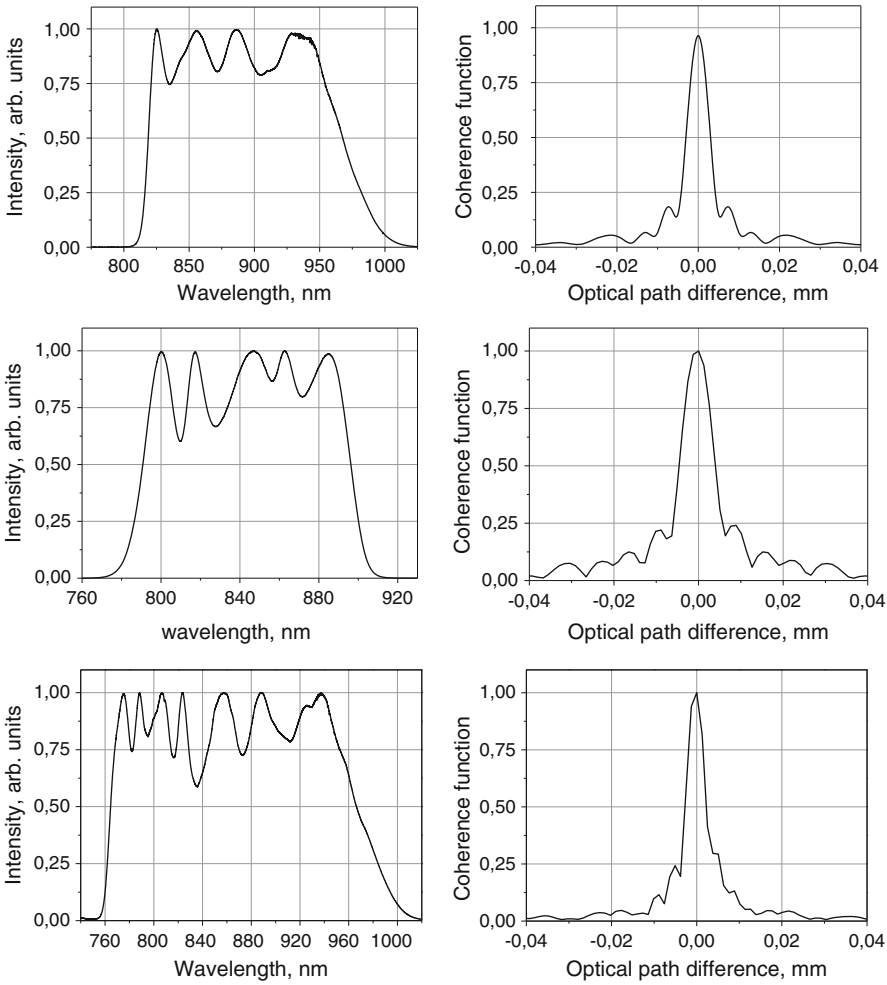

Fig. 17.7 (**a**) Spectrum and coherence function of 150 nm wide 2-SLD light source; coherence function FWHM 5,7 μm. (**b**) Spectrum and coherence function of 100 nm wide 3-SLD light source; coherence function FWHM 8,3 μm. (**c**) Spectrum and coherence function of 200 nm wide 4-SLD light source; coherence function FWHM 4,5 μm

with 2.3 μm resolution had been successively acquired using such light source [54]. This is nearly the same resolution as that obtained using femtosecond laser sources. More powerful and broadband "combined SLD light sources" at 800–1,000 nm range were developed in [55] by using of couplers with optimized coupling ratio and by varying of SLD operation conditions.

Figures 17.7a–c demonstrate spectra of broadband light sources based on different combinations of SLDs I–VI. Particularly, Fig. 17.7b demonstrates spectrum and coherence function of 18 mW 3-SLD light source with spectrum width exceeding 100 nm. Combination of four SLDs, Fig. 17.7c allowed 200 nm

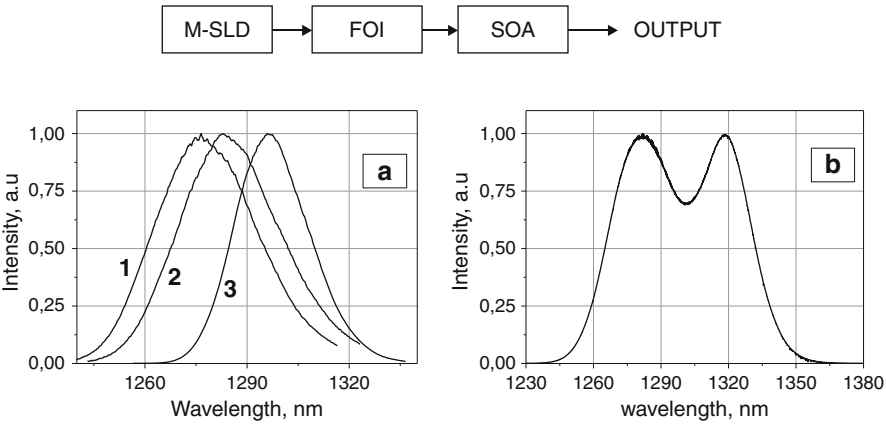

Fig. 17.8 (**a**, **b**) SLD-MOPA configuration and results. *M-SLD*: master SLD, *FOI* – optical isolator, *SOA* – amplifier. On the (**a**): *1*: SOA ASE spectrum; *2*: master SLD spectrum, *3*: resulted spectrum. Same amplifier was used to produce broad spectrum on (**b**) master SLD had center wavelength 1,318 nm in this case

wide light source centered around 890 nm with output power exceeding 5 mW from SM fiber.

Other possibility for improvement of performance of SLD-based light sources is so-called "SLD-MOPA (master oscillator power amplifier)" design. Feasibility of such an approach was first demonstrated by using of Er-doped fiber amplifier to increase output power of 1,550 nm SLD [56]; 20 mW output was obtained by amplifying of 1 mW output power SLD. Later, similar method had been used to do high-power SLD by integration of SLD and tapered MOPA in the same semiconductor chip. Output power in excess of 300 mW was obtained from 130 μm output aperture, integrated SLD-MOPA light emitters [57]. Possibility for considerable increase SLD output power and its spectral broadening by "SLD-MOPA" light source was demonstrated at 1,300 nm, too [58, 59]. Medium- to high-power master SLD at 1,300 nm and high gain SOA were used in experiments. Appropriate broadband optical isolator was placed between master SLD and SOA to exclude cross-coupling between them, like it is shown on the Fig. 17.8. When SLD with center wavelength close to spectral gain maximum of SOA was used as master source, output power up to 100 mW from SM fiber with 26 nm spectrum width was obtained on SOA's output (Fig. 17.8a). When SLD with "red-shifted" spectral center with respect to SOA spectral gain maximum was used as master oscillator, widening of output spectrum by a factor of two was obtained after SOA (Fig. 17.8b). Recently, up to 500 mW pulse power and 85 nm wide spectrum was demonstrated by QD SLD-MOPA device at 1,300 nm in [60].

SLD-MOPA configuration was also used successfully for increasing of SLD output power at 830 nm band. In particular, output power of 50 mW in single-mode fiber MOPA source had been obtained in [61], although with relatively narrow spectrum. Up to 500 mW had been obtained from a multimode design using tapered MOPA [62].

17.4 SLDs and Optical Feedback. Important Aspects of SLDs Use in Practice

It is well known that usage of semiconductor light sources similar to laser diodes requires essential practical experience. Particularly, such well-known problem as transient current/voltage surges in electronic drivers may be fatal to laser diodes and SLDs because of catastrophic or latent damage. However SLDs, especially high power ones, require additional safety measures due to their strong sensitivity to optical feedback and non-uniform distribution of drive current inside active region.

As it was pointed out above, 30 dB net optical gain is required to do powerful SLDs. It means that if there will be some optical feedback to SLD, reflected light will be amplified very effectively. Particularly, it is seen from Eq. 17.5 that if modal gain $G = \exp[(g-\alpha)L]$ is 30 dB then optical feedback of 10^{-3} will increase power of back-propagated light inside SLD by two times (assuming no gain saturation by this feedback; note real changes may be less because −30 dB feedback may already saturate optical gain in high-power SLD). This will also change output power and SLD spectrum considerably due to gain saturation effect. Most of OCT systems may result in optical feedback to SLD emitter due to "back-reflective" nature of Michelson interferometers with reflective mirror in reference arm. Of course, optical isolators may be good solution to protect SLDs from optical feedback, but usually this is hard to obtain broadband isolators with high optical isolation. As well, isolators at short (<1,000 nm) wavelength are still bulk and expensive. Let us discuss effects of optical feedback on SLD performance in more details.

Figure 17.9a shows the results on simulation of performance of powerful AlGaAs SLDs at 820 nm reported in [18] with mode size of 0.3 × 5 μm in free-running operation assuming zero end reflections in active region. Simulation of light-current characteristics was done using the most common parameters of

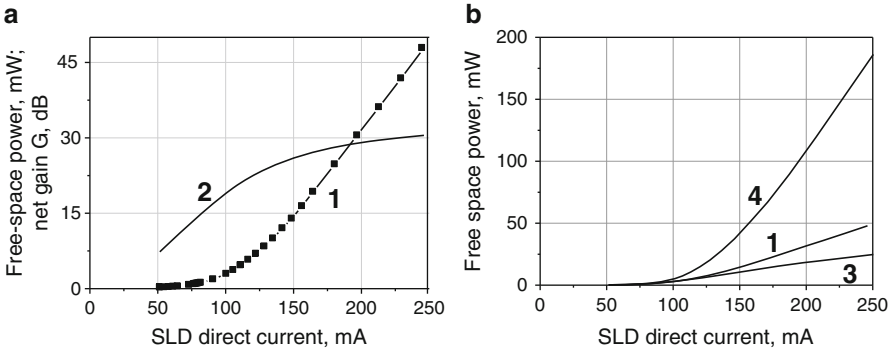

Fig. 17.9 (**a**) Light current characteristics (*1*) and net gain (*2*) of high-power AlGaAs SLD reported in [18], squares show measured power; (**b**) calculations in case of 1 % feedback, output facet (*3*) and back facet (*4*); "free-running" light-current characteristic is also shown for comparison. In case of 1 % feedback front output power decreases due to gain saturation effect

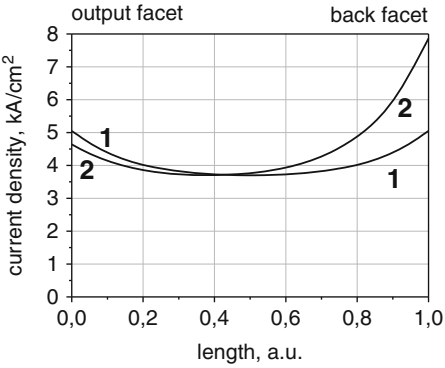

Fig. 17.10 Redistribution of driving current density in active region at 190 mA SLD current (30 mW free-space power); *1* – free-running, *2* – 1 % optical feedback

AlGaAs heterostructures similar to those mentioned above and described in details in [7]. Linear dependence of gain on carrier density Eq. 17.7 was used for calculations in low-power (<2 mW output power) operation mode. Differential gain $\Gamma dg/dN$ in Eq. 17.7 and spontaneous emission factor β were varied for the best fitting of measured SLD light-current characteristics in low-power area. At higher operation power, additional non-linear gain term was introduced for the best fitting of light-current characteristic.

Calculated light-current characteristics in case of 1 % optical feedback to the same SLD are shown on the Fig. 17.9b; dependence of optical gain on carrier density obtained by fitting of free-running light-current characteristic (curve 1) was used for calculations. It is seen that 1 % feedback deteriorates SLD performance considerably, resulting in increased back-propagated power and decreased output power. Distribution of driving current density inside the active region in case of free-running operation and 1 % feedback at 190 mA (30 mW free-space power in free-running mode) is shown on the Fig. 17.10. It is seen that optical feedback results in re-distribution of driving current density inside SLD active region. Current density near back facet becomes 1,5 times higher than "feedback-free" value. All these events (increased power of back-propagated light and increased driving current density at back SLD crystal facet) may have very strong impact on SLD performance in the system and result in fatal damage of COD-sensitive devices and decreased lifetime of SLDs based on materials sensitive to high driving current densities.

Experimental study on sensitivity of powerful SLDs to weak optical feedback was done in [63]. Changes of back facet SLD power of about 15–20 % at −30 dB optical feedback were obtained in 840 nm band SLDs emitted 50 mW of free-space power. This is less than estimations above because such a weak feedback already saturated optical gain in powerful SLDs. In addition to this, spectral changes due to feedback-induced gain saturation were obtained in powerful broad-spectrum QW SLDs starting −30 dB optical feedback (see also [63]).

Such a strong sensitivity to optical feedback requires special measures for SLD protection in optical systems. One of the main important problems arose is a possibility of catastrophic damage of SLD's back facet by optical feedback.

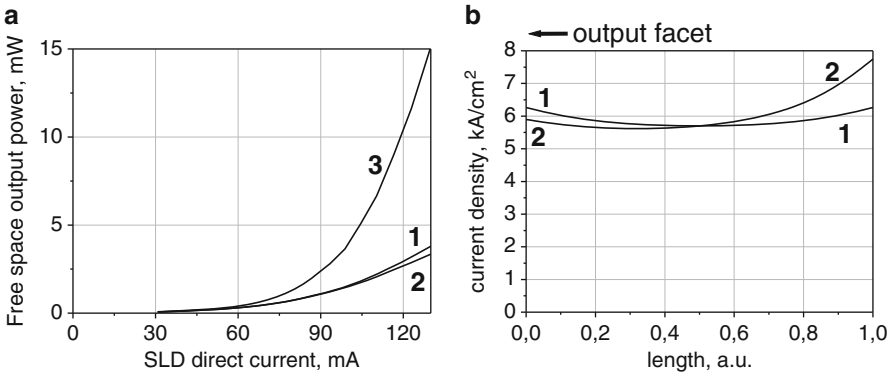

Fig. 17.11 (**a**) Light current characteristics of medium-power SLD (optical gain 19 dB at 130 mA in case of free-running operation), (*1*) – no feedback, (*2*) – output power, 5 % feedback, (*3*) – back facet power, 5 % feedback; (**b**) distribution of driving current density inside active region at 15 mW/130 mA, (*1*) – free-running, *2*–5 % feedback

Under certain circumstances, constant power (CP) driving mode by stabilizing of back facet power by monitor photodiode (when available) may be a good "protective measure" for SLDs in OCT systems without optical isolators. Feedback in OCT is usually relatively slow with respect to potential bandwidth of feedback loop via PD monitor (up to 1 MHz electrical feedback loop bandwidth via PD monitor should be possible when appropriate PD monitor is placed inside SLD module). However, it may be considered only as a "protection" of SLD against optical feedback (at least when optical feedback is relatively slow) and may result in a huge output power degradation in presence of any "essential" feedback. Particularly, in case of feedback-free operation at 160 mA (see Fig. 17.9), 1 % optical feedback will result in SLD drive current decreasing down to 110 mA in case of CP mode, with correspondent 4 times output power degradation form 20 mW to 5 mW. This may also result in very strong change of SLD spectrum [63].

Note that 1 % optical feedback may be applied to SLD easily. Particularly, coupling efficiency to single-mode optical fiber in powerful SLD modules is usually around 50 % (see, for example, [19]). Normal cleave of SM silica fiber results in 4 % reflection back to the fiber, thus in total 1 % back to SLD.

It should be pointed out that optical feedback may cause problems even in medium-power SLDs (see also [63] for experimental results). Figure 17.11a, b show estimations of feedback-induced changes of output power in "medium-power" SLD design for which high optical gain is not necessary. It is seen that for this SLD there are no considerable changes of output power in case of relatively strong, 5 %, feedback. However, it is also seen that driving current density near back facet increases by approximately 25 %, that may be the reason for SLD latent damage and shorter SLD lifetime. As well, strong decreasing of output power will be obtained if such SLD is driven in CP mode.

Unfortunately, influence of optical feedback on SLD performance and methods for decreasing of SLD sensitivity to optical feedback are not studied well enough so far. For example, increasing of spontaneous emission coupled to guided mode may be an effective way in decreasing of SLD reaction to feedback. As follows from Eq. 17.8 above, SLD power is proportional to the product of spontaneous emission coupled to guided mode and modal gain. If so, SLD with higher spontaneous emission will require lower gain for getting the same power. Therefore, such SLD should be less sensitive to feedback as the sensitivity is determined by optical gain, too. However, possibilities for considerable increasing of coupling of spontaneous emission to guided mode in SLDs have not been studied deeply until now. Some reduced sensitivity to feedback in single-mode fiber-coupled SLD modules had been reported in [64], however, physical reasons for observations had not been explained. Moreover, "weaker" sensitivity reported in [64] could be caused by relatively low coupling efficiency to single-mode fiber.

One effective method for increasing of SLD power and decreasing of its sensitivity to optical feedback is usage of SLD-MOPA configurations [61]. High gains are not required in power amplifiers, therefore sensitivity to feedback will be reduced. This design may be very useful for applications (including OCT) requiring powerful low coherent sources at wavelengths below 1,000 nm were broadband isolators with high enough isolation have relatively high insertion losses and are bulky and expensive.

17.5 Conclusions

Significant improvement of SLD performance parameters resulted in development of very high-power and broadband SLD-based light sources at different spectral bands from 680 to 1,600 nm. SLDs now have output power comparable with that of single-mode laser diodes and coherence length down to 10 μm and less, at least at some particular wavelengths. "Combined" SLD light sources on the base of two and more SLDs allowed ultrahigh, 2.5–3.5 μm, resolution OCT images of human eye and tissue, comparable with results obtained using bulky, noisy and expensive femtosecond laser light sources.

Further improving of SLD performance should be possible, too. Particularly, SLDs and SLD-based light sources with SM fiber output power of 100 mW and more were demonstrated at all wavelengths-of-OCT-interest, particularly at 800 nm and 1,300–1,600 nm spectral bands. The use of specially designed multi-quantum-well and quantum dot structures may allow SLDs with spectrum width of 100 nm and much broader, thus opening possibilities for OCT systems with 1–2 μm resolution basing on a single-SLD-emitter light source.

Acknowledgments Author highly appreciates help and valuable comments of Prof. Sergei Yakubovich, Dr. Dmitry Mamedov, and Vyatcheslav Prokhorov, Superlum Diodes, Ltd.

References

1. L.N. Kurbatov, S.S. Shakhidzhanov, L.V. Bystrova, V.V. Karpukhin, S.I. Kolenkova, Investigation of superluminescence emitted by a gallium arsenide diode. Sov. Phys. Semicond. **4**(11), 1739–1744 (1971)
2. C.A. Burrus, B.I. Miller, Small area double-heterostructure aluminium-gallium arsenide electroluminescent diode sources for optical-fiber transmission lines. Opt. Commun. **4**(4), 307–309 (1971)
3. V.A. Stupnikov, S.D. Yakubovich, Influence of configuration of injection superluminescent emitter on its performance parameters. Elekronnaya Technika, Seria 11, N 5, pp. 62–68, (1978) in Russian
4. C.C. Culter, S.A. Newton, H.J. Show, Limitation of rotation sensing by scattering. Opt. Lett. **5**, 488–490 (1980)
5. D. Huang, E.A. Swanson, C.P. Lin et al., Optical coherence tomography. Science **274**, 1178–1181 (1991)
6. A.T. Semenov, L.A. Rivlin, S.D. Yakubovich, Dynamics and spectra of semiconductor lasers. J. Sov. Laser Res. **7**(N2), 57–206 (1986). Plenum Publishing Corp., N.Y.-London
7. N.S.K. Kwong, K.-Y. Lau, N. Bar-Chaim, High-power, high-efficiency GaAlAs superluminescent diodes with integral absorber for lasing suppression. IEEE J. Quantum Electron. **QE-25**(4), 696–704 (1989)
8. B.D. Paterson, J.E. Epler, B. Graf, H.W. Lehamnn, H.S. Sigg, A superluminescent diode at 1,3 μm with very low spectral modulation. IEEE J. Quantum Electron. **QE-30**(3), 703–709 (1994)
9. G. Alphonse, Design of high power superluminescent diodes with low spectral modulation. Proc. SPIE **4648**, 125–138 (2002)
10. D.J. Gallant, M.L. Tilton, D.J. Bossert, J.D. Barrie, G.C. Dente, Optimized single-layer antireflection coatings for semiconductor lasers. IEEE Photon. Technol. Lett. **9**(N 3), 300–302 (1997)
11. C.S. Wang, W.H. Cheng, J. Hwang, W.K. Burns, R.P. Moeller, High-power low-divergence superradiance diode. Appl. Phys. Lett. **41**(7), 587–589 (1982)
12. N.K. Duta, P.P. Deimel, Optical properties of a GaAlAs superluminescent diode. IEEE J. Quantum Electron. **QE-19**(4), 496–498 (1983)
13. T.-P. Lee, C.A. Burrus, B.I. Miller, A Stripe-geometry double-heterostructure amplified-spontaneous-emission (superluminescent) diode. IEEE J. Quantum Electron. **QE-9**(8), 820–828 (1994)
14. S.A. Safin, A.T. Semenov, V.R. Shidlovski et al., High-power 0.82 μm superluminescent diodes with extremely low Fabry-Perot modulation depth. Electron. Lett. **28**(6), 530–532 (1993)
15. A.T. Semenov, V.R. Shidlovski, S.A. Safin, V.P. Konyaev, M.V. Zverkov, Superluminescent diodes for visible (670 nm) spectral range based on AlGaInP/GaInP heterostructures with tapered grounded absorber. Electron. Lett. **29**(6), 530–532 (1994)
16. Y. Kashima, M. Kobayashi, H. Takano, High output power GaInAP/InP superluminescent diode at 1.3 μm. Electron. Lett. **24**(24), 1507–1509 (1988)
17. H. Nagai, Y. Noguchi, S. Sudo, High-power, high-efficiency 1.3 μm superluminescent diode with buried bent absorbing guide structure. Appl. Phys. Lett. **54**(18), 1719–1721 (1989)
18. M.E. Lipin, V.E. Rafailov, A.T. Semenov, V.R. Shidlovski, Very high power superluminescent diodes as alternative to fluorescent fiber-doped light sources. Presented at: *Fiber Optic Sensors Conference*, *Photonics East'99, Boston, 19-22 Sept., 1999,* paper 3860–67; *Proc. SPIE*, vol. 3860, pp. 480–487 (1999)
19. O. Mikami, Y. Noguchi, H. Yasaka, Broader spectrum width InGaAsP stacked active layer superluminescent diodes. Appl. Phys. Lett. **56**(11), 987–989 (1990)
20. T.R. Chen, L. Eng, H. Zuang, A. Yariv, N.S. Kwong, P.C. Chen, Quantum well superluminescent diode with very wide emission spectrum. Appl. Phys. Lett. **56**(14), 1347–1348 (1990)

21. S. Kondo, H. Yasaka, Y. Noguchi, K. Magari, M. Sugo, O. Mikami, Very wide spectrum multiquantum well superluminescent diode at 1.5 μm. Electon. Lett. **28**(2), 132–134 (1992)
22. A.T. Semenov, V.R. Shidlovski, S.A. Safin, Wide-spectrum SQW superluminescent diodes at 0.8 μm with bent optical waveguide. Electron. Lett. **29**(10), 854–856 (1993)
23. H.C. Casey, M.B. Panish (eds.), *Heterostructure Lasers* (Academic, New York, 1978)
24. L.H. Li, M. Rossetti, A. Fiore, L. Occhi, C. Velez, Wide emission spectrum from superluminescent diodes with chirped quantum dot multilayers. Electron. Lett. **41**(1), 41–43 (2005)
25. E.V. Andreeva, A.E. Zhukov, V.V. Prokhorov, V.M. Ustinov, S.D. Yakubovich, Superluminescent InAs/AlGaAs/GaAs quantum dot heterostructure diodes emitting in the 1100—1230-nm spectral range. Quantum Electron. **36**(6), 527–531 (2006)
26. P.D.L. Greenwood, D.T.D. Childs, K. Kennedy et al., Quantum dot superluminescent diodes for optical coherence tomography: device engineering. IEEE J. Sel. Top. Quantum Electron. **16**(4), 1015–1022 (2010)
27. E.U. Rafailov, M.A. Cataluna, W. Sibbett, Mode-locked quantum-dot lasers. Nat. Photonics **1**, 395–401 (2007)
28. A.T. Semenov, V.R. Shidlovski, Very high power, broad and flat spectrum superluminescent diodes and fiber modules for OCT applications, *BIOS 2000*, *Photonics West '99, San-Jose, CA,* 24–26 Jan 2000, paper 3915–43
29. T. Tokayama, O. Imafuji, Y. Koichi et al., 100 mW high-power angle-stripe superluminescent diodes with new real refractive-index-guided self-aligned structure. IEEE J. Quantum Electron. **QE-32**(11), 1981–1987 (1996)
30. P.A. Lobintsov, D.S. Mamedov, V.V. Prohorov, A.T. Semenov, S.D. Yakubovich, Powerful superluminescent diodes with unpumped output sections. Quantum Electron. **34**(3), 209–212 (2004)
31. A.T. Semenov, V.K. Batovrin, I.A. Garmash et al., GalAlAs SQW superluminescent diodes with extremely low coherence length. Electron. Lett. **31**(4), 314–315 (1995)
32. C.-F. Lin, B.-L. Lee, Extremely broadband AlGaAs/GaAs superluminescent diodes. Appl. Phys. Lett. **71**(12), 1598–1600 (1997)
33. P.I. Lapin, D.S. Mamedov, S.D. Yakubovich, M. Wojtkowski, J.G. Fujimoto, Novel near-IR broad-band light sources for optical coherence tomography based on superluminescent diodes. Proc. SPIE-OSA Biomed. Opt. SPIE **5861**, 586108-2 (2005)
34. B. Považay, K. Bizheva, B. Hermann et al., Enhanced visualization of choroidal vessels using ultrahigh resolution ophthalmic OCT at 1050 nm. Opt. Express **11**, 1980–1986 (2003)
35. A. Unterhuber, B. Považay, B. Hermann, H. Sattmann, A. Chavez-Pirson, W. Drexler, In vivo retinal optical coherence tomography at 1040 nm – enhanced penetration into the choroids. Opt. Express **13**(9), 3252–3258 (2005)
36. P.I. Lapin, D.S. Mamedov, A.A. Marmaluk, A.A. Padalitsa, S.D. Yakubovich, Powerful and broadband SLDs at 1000–1100 nm. Quantum Electron. **36**(4), 315–317 (2006)
37. Z.Z. Sun, D. Ding, Q. Gong et al., Quantum-dot superluminescent diodes: proposal for an ultra-wide output spectrum. Opt. Quantum Electron. **31**, 1235 (1999)
38. E.V. Andreeva, P.I. Lapin, V.V. Prokhorov, S.D. Yakubovich, Quantum-dot superluminescent diodes with improved performance. Quantum Electron. **37**(4), 331–333 (2007)
39. Z.Z. Zhang, Z.G. Wang, B. Xu et al., High-performance quantum-dot superluminescent diodes. IEEE. Photon. Technol. Lett. **16**(1), 27–29 (2004)
40. S.H. Cho, I.K. Han, Y. Hu, J.H. Song et al., >90 mW CW superluminescent output power from single-angled facet-ridge waveguide diodes at 1.5 μm, in *Proc. Advanced Semiconductor Lasers and Their Applications*, vol. **31**, pp. 5–9 (2000)
41. D.S. Mamedov, V.V. Prokhorov, S.D. Yakubovich, Broad-band superluminescent diode based on multi quantum well (InGa)Pas heterostructure at 1550 nm, *CLEO/Europe-EQEC*

2003, Munich, Germany, 22–27 June, CC-Semiconductor Lasers, *Conf. Techn. Digest* Paper CC7W (2003)
42. T.-K. Ong, M. Yin, Z. Yu, Y.-C. Chang, Y.-L. Lam, High performance quantum well intermixed superluminescent diodes. Meas. Sci. Technol. **15**(8), 1591–1595 (2004)
43. J. Wang, L.T. Li, W. Xu et al., Ultrabroad-bandwidth and high-power superluminescent light-emitting diodes. Proc. SPIE **5690**, 531–539 (2005)
44. J.H. Song, S.H. Cho, I.K. Han et al., High-power broad-band superluminescent diode with low spectral modulation at 1,5 μm wavelength. IEEE Photon. Technol. Lett. **12**(7), 783–785 (2000)
45. W. Li, R. Ronkko, A. Rydefalk, P. Poyhonen, M. Pessa, Superluminescent diodes at 1.55 μm based on quantum-well and quantum-dot active regions. Proc. SPIE **5739**, 116–121 (2005)
46. C.K. Hitzenberger, M. Danner, W. Drexler, A.F. Fercher, Measurement of the spatial coherence of superluminescent diodes. J. Mod. Opt. **46**(12), 1763–1774 (1999)
47. P.D. Coldourne, D.T. Cassidy, Bonding stress measurements from the degree of polarization of facet emission of AlGaAs superluminescent diodes. IEEE J. Quantum Electon. **QE-27**(4), 914–920 (1991)
48. V.K. Batovrin, I.A. Garmash, V.M. Gelikonov et al., Superluminescent diodes based on single-quantum-well (GaAl)As-heterostructures. Quantum Electon. **23**(2), 113–118 (1996)
49. O. Mikami, Y. Noguchi, K. Magari, Y. Suzuki, Polarization-insensitive superluminescent diode at 1.5 μm with tensile-strained-barrier MQW. IEEE Photon. Technol. Lett. **4**(7), 703–705 (1991)
50. A.M. Yurek, H.F. Taylor, L. Goldberg, J.F. Weller, A. Dandridge, Quantum noise in superluminescent diodes. IEEE J. Quantum Electron. **QE-22**(4), 522–527 (1986)
51. W.V. Sorin, D.M. Baney, A simple intensity noise reduction technique for optical low-coherence reflectometry. IEEE Photon. Technol. Lett. **4**(12), 1404–1406 (1992)
52. A.A. Marmalyuk, D.R. Sabitov, A.V. Sukharev et al, Quantum well engineering for the broadband SLD heterostructures grown by MOCVD, *Proc. 11th European Workshop on MOVPE*, Lausanne 5–8 June 2005, pp. 297–298
53. M. Wojtkovski, P.I. Lapin, D.S. Mamedov, J.G. Fujimoto, S.D. Yakubovich, Multichannel extremely broadband near-IR radiation sources for optical coherence tomography. Quantum Electon. **35**(7), 667–669 (2005)
54. T.H. Ko, D. Adler, J.G. Fujimoto et al., Ultrahigh resolution optical coherence tomography imaging with broadband superluminescent diode source. Opt. Express **12**(10), 1212–1219 (2004)
55. P.I. Lapin, D.S. Mamedov, S.D. Yakubovich, M. Wojtkovski, J.G. Fujimoto, Novel near-IR broad-band light sources for optical coherence tomography based on superluminescent diodes. Proc. SPIE-OSA Biomed. Opt. SPIE **5861**, 586108-1 (2005)
56. N.S. Kwong, High-power, broad-band 1550 nm light source by tandem combination of a superluminescent diode and a Er-doped fiber amplifier. IEEE Photon. Technol. Lett. **4**(9), 996–999 (1992)
57. G. Du, C. Xu, Y. Liu, Y. Zhao, H. Wong, High-power integrated superluminescent light source. IEEE J. Quantum Electron. **39**(1), 149–153 (2003)
58. V.V. Prokhorov, D.S. Shavakov, S.D. Yakubovich, Broadband high-brightness light sources based on semiconductor optical amplifier and superluminescent diode. Proc. SPIE-OSA Biomed. Opt. SPIE **5861**, 5861OI-1 (2005)
59. V.V. Prokhorov, D.S. Shvakov, S.D. Yakubovich, Broadband highly bright radiation sources based on a superluminescent diode and a semiconductor optical amplifier. Quantum Electron. **35**(6), 504–506 (2005)
60. X. Li, P. Jin, A. Qi et al., A high-performance quantum dot SLD with a two-section structure. Nanoscale Res. Lett. **6**, 25 (2011). www.nanoscalereslett.com/content/6/1/625
61. V.R. Shidlovski, *Boosting of SLD power. Feedback insensitive, ultra high power MOPA SLD sources*, Application note, (2010) www.superlumdiodes.com/pdf/Ultra-High-Power-MOPA-SLD-Sources.pdf

62. Yu.O. Kostin, A.A. Lobintsov, S.D. Yakubovich, Novel SOA with tapered active channel, *Proc. of 5th Int. Conf. on Advanced Optoelectronics and Lasers* (*CAOL'2010*), Sevastopol, 2010, p. 175
63. E.V. Andreeva, M.V. Shramenko, S.D. Yakubovich, Feedback effect on output characteristics of QW SLDs. Quantum Electron. **37**(N 5), 443–445 (2007). in Russian
64. In: *Superluminescent Light Emitting Diodes with Reduced Sensitivity Against Optical Feedback: Isolator-Free Applications*, *Exalos White Papers*, www.exalos.com

SLEDs and Swept Source Laser Technology for OCT

18

Marcus Duelk and Kevin Hsu

18.1 Broadband SLEDs for OCT

Broadband and high-power superluminescent light-emitting diodes (SLEDs) can be fabricated at wavelengths ranging from 390 nm to 2700 nm. They can be realized in GaN (390–630 nm), GaAs (630–1,150 nm), InP (1,150–2,000 nm) or GaSb ([1], up to 2,700 nm). The vast majority of SLEDs used for OCT today is in the wavelength range of 800–900 nm and is employed in ophthalmic spectral-domain (SD) OCT systems. Broadband SLEDs at 1,300 nm have been used in time-domain (TD) OCT systems in industrial applications such as high-resolution thickness measurements. With the recent advent of high-speed InGaAs cameras having 2,048 pixels [2], SD-OCT systems at 1,060 nm or 1,300 nm may also be realized in the coming years for biomedical or other applications.

18.1.1 Coherence Function and Coherence Length

The coherence length l_{coh} and time τ_{coh} of a broadband light source is given by

$$l_{coh} = \gamma . \frac{2\ln 2}{\pi} . \frac{\lambda_0^2}{\Delta\lambda} \quad \tau_{coh} = \frac{l_{coh}}{c}$$

with λ_0 being the center wavelength and $\Delta\lambda$ being the 3-dB optical bandwidth. The factor γ accounts for the fact that many broadband SLEDs do not have a perfect Gaussian shape but rather a flat-top spectrum. For Gaussian-shaped SLEDs, this factor is unity ($\gamma = 1$), while for SLEDs with a flat-top spectrum, $\gamma = 1.186$ is typically used, i.e., there is almost a 20 % penalty in coherence length by deviating

M. Duelk (✉) • K. Hsu
EXALOS, Schlieren, Switzerland
e-mail: duelk@exalos.com

© Springer International Publishing Switzerland 2015

W. Drexler, J.G. Fujimoto (eds.), *Optical Coherence Tomography*,
DOI 10.1007/978-3-319-06419-2_19

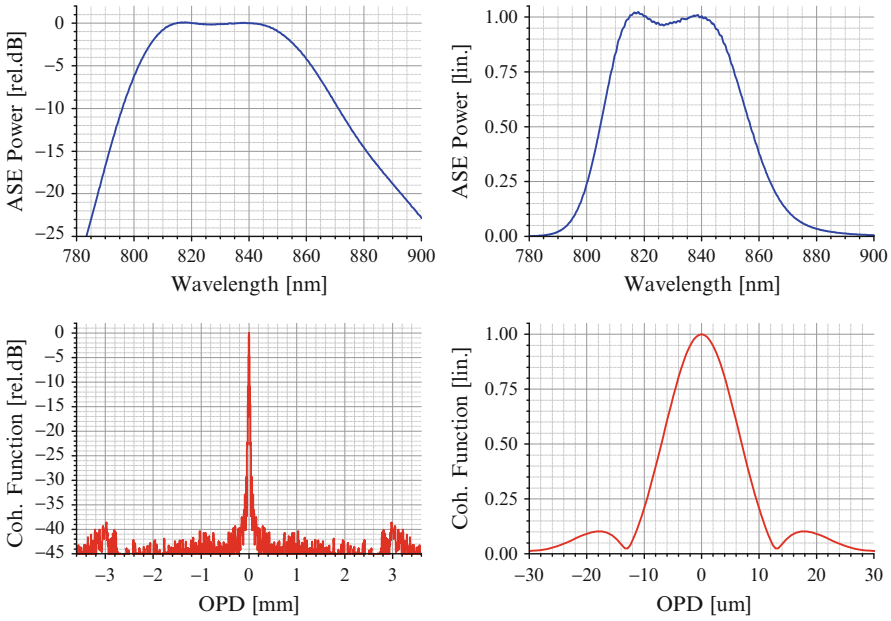

Fig. 18.1 ASE spectrum (*upper row*, in *blue*) of an 840-nm SLED with ~50-nm full width at half maximum (*FWHM*) optical bandwidth (EXS210022) and corresponding imaging or coherence function (*lower row*, in *red*) plotted versus optical path length difference (*OPD*). The half-width at half maximum (*HWHM*) of the coherence function shows a coherence length of 7–8 μm (in air)

from a perfect Gaussian shape. The coherence length of the SLED specifies the theoretical limit for the axial resolution of an OCT imaging system. For example, with $\lambda_0 = 840$ nm and $\Delta\lambda = 50$ nm, a coherence length $l_{coh} = 7.4$ μm is calculated when assuming a flat-top shape, as shown in Fig. 18.1.

The coherence function is equivalent to the autocorrelation function of an SLED, which is, according to the Wiener-Khinchin theorem, the Fourier transform of the ASE spectrum [3]. According to Parseval's theorem, the Fourier transform of a power spectrum represents again power, which means that the coherence or autocorrelation function represents optical power in the spatial domain. It is calculated by applying the FFT to the linear ASE spectrum that has been resampled with equidistant steps in the frequency domain. The magnitude of the FFT output is the linear coherence function, and its logarithmic counterpart is calculated by $10{\cdot}\log_{10}$ and not by $20{\cdot}\log_{10}$, as sometimes found as well. Since the ASE power spectrum is real-valued, the Fourier transform is Hermitian and hence symmetric in space or time, as shown in Fig. 18.1.

The drop-off of the coherence function from its maximum (at zero) to 50 % is the coherence length, i.e., the coherence length is the half width at half maximum (HWHM) and not the full width at half maximum, as sometimes referred to. This can be easily verified by the example given in Fig. 18.1.

The logarithmic coherence or imaging function plotted over a wide range may reveal *secondary coherence peaks* at a certain optical path length difference (OPD).

For the example shown in Fig. 18.1, secondary coherence peaks can be seen at an OPD of ~3 mm with a suppression of close to 40 dB. Typically, a secondary peak suppression ratio (SPSR) of 25–35 dB is needed in order to avoid OCT imaging artifacts like horizontal lines in a B-scan image. Such SPSR corresponds to a (peak-to-valley) ripple amplitude of the ASE spectrum in the range of 0.10–0.20 dB. This is achieved through an advanced SLED chip design and through high-performance antireflection coatings (ARC) at the chip facet.

The coherence function near the central peak (at zero) may reveal *sidelobes* when the ASE power spectrum deviates from a Gaussian shape. The example of Fig. 18.1 shows sidelobes with a suppression of ~10 dB (not considering any windowing prior to the FFT). The sidelobe suppression ratio (SLSR) is only given by the spectral shape of the SLED, and high SLSR values are needed particularly for TD-OCT systems where additional signal processing like spectral windowing is not implemented. Gaussian-shaped SLEDs have a high SLSR (i.e., no or little sidelobes), while SLEDs with a flat-top spectrum have a lower SLSR.

18.1.2 SLEDs at 400–500 nm

SLEDs in the blue-to-green spectral range are realized in the GaN material system [4]. The short emission wavelength may, in combination with broadband emission, allow for realizing SLEDs with a coherence length of 1–3 μm in air. However, due to very high absorption of blue light in hemoglobin, biomedical OCT for tissue diagnostic is rather unlikely. Instead, those sources may be deployed in nondestructive testing (NDT) or ultra-high-resolution optical coherence microscopy (OCM) systems [5]. Due to extensive work on the reliability of GaN SLEDs [6], blue SLEDs have been commercially available until very recently [7] such that OCT and OCM in this spectral region have not been explored yet. Figure 18.2 shows the electro-optic properties of high-power SLEDs in the wavelength range of 400 to 450 nm. The achievable output power and the slope efficiencies are nearly comparable with GaN single-mode laser diodes. The ASE emission spectra of the currently available SLEDs have a Gaussian shape with a typical 3-dB optical bandwidth of 4-5 nm. Similar to design efforts that were done for SLEDs at 800 to 900 nm, the ASE emission spectrum of such GaN SLEDs could be increased to achieve ultra-short coherence lengths or coherence times.

18.1.3 SLEDs at 840 nm

Most SD-OCT systems deployed today are used for retina imaging in ophthalmology and are based on an 840-nm SLED featuring a 3-dB (FWHM) optical bandwidth of 50 nm and a 10-dB bandwidth of 80 nm. Those SLEDs are used in combination with a spectrometer that spans 80 nm and a line camera with 2,048 pixels, resulting in a wavelength resolution of ~0.04 nm or a frequency resolution of ~17 GHz, which then translates into an axial resolution of 7–8 μm in air (without windowing) and an imaging depth of ~4.5 mm.

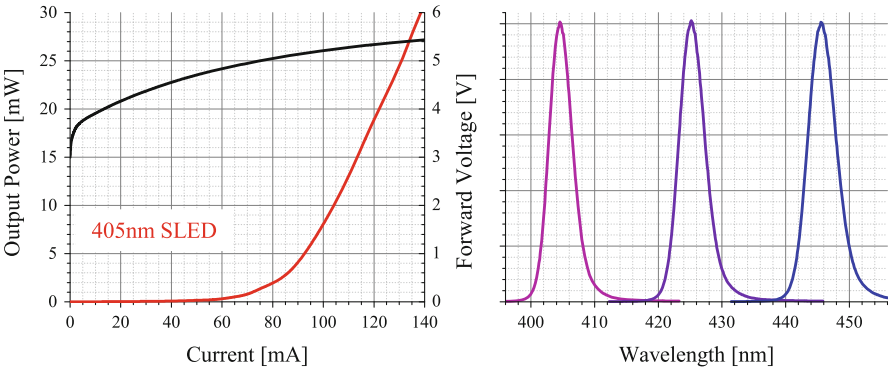

Fig. 18.2 Ex-facet output power and forward voltage of high-power single-mode 405-nm SLED as function of drive current (*left*). ASE emission spectra on a linear scale of SLEDs at 405, 425 and 445 nm with optical bandwidths of 4-5 nm (*right*)

The maximum permissible exposure (MPE) limit according to laser class 1 is ~750 μW at a wavelength of 840 nm [7]. Considering a 75:25 splitter in the OCT interferometer and an additional 2–3 dB loss in the optical train or delivery optics, the required output power of an 840-nm SLED is typically in the range of 2.5–4.5 mW.

Spectrometer-based OCT system may trade off resolution with imaging depth, for example, in anterior-chamber eye surgical systems where SD-OCT systems with an imaging depth of 8–10 mm are used. This is achieved by using a 2,048-pixel line camera in combination with a spectrometer that spans only 40 nm instead of 80 nm; hence, those systems typically use an SLED with a 3-dB optical bandwidth of 25 nm instead of 50 nm. Because of higher insertion losses in the optical train due to combining the diagnostic OCT system with the laser surgical system, SLEDs with an output power of 10–20 mW are typically needed. Similar considerations in terms of SPSR and SLSR apply here as well.

18.1.4 SLEDs at 1,060 nm

Cost-effective and high-speed InGaAs line cameras with a pixel count of 2,048, similar to silicon-based CMOS or CCD line cameras, may enable commercial SD-OCT systems based on broadband SLEDs. Due to deeper penetration into the choroid of the retina, the expected imaging range might be somewhat larger than in the 840-nm spectral range. Naturally, the axial resolution of such systems would be lower, requiring SLEDs with a 3-dB optical bandwidth of 60–70 nm and a 10-dB optical bandwidth of ~110 nm.

The class 1 MPE limit at 1,060 nm is ~2.0 mW and hence almost three times higher than at 840 nm. Therefore, higher power 1060-nm SLEDs (~10–15 mW) can be used to help increase sensitivity.

18.1.5 SLEDs at 1,300 nm

Broadband SLEDs at 1,300 nm are used for NDT or other type of industrial TD-OCT systems. State-of-the-art SLEDs achieve a 3-dB optical bandwidth of up to 120 nm from a single SLED chip with a low output power of 5 mW ex-fiber, or 90–100 nm with a medium output power of 10–15 mW, or 70–75 nm with a high output power of 20–30 mW. The class 1 MPD limit at 1,300 nm is ~15.6 mW; therefore, mainly high-power SLEDs with 20–30 mW are used in such OCT systems. As mentioned earlier, for TD-OCT systems, a good SLSR is typically required, which puts a preference on Gaussian-shaped SLEDs.

18.1.6 Combined Broadband Sources

For ultra-high-resolution SD-OCT systems, broadband light sources based on spectrally combined SLEDs are used. Those combined SLED sources are realized in the 750–900 nm range, for example, where a 3-dB optical bandwidth of 150–160 nm and a 10-dB optical bandwidth of 180 nm are achieved with a total output power of 5 mW. Such an ultra-broadband source has a coherence length of ~2.5 μm in air and hence less than 2 μm in tissue, achieving a similar axial resolution than a fs-pulsed laser with a pulse duration of 8–9 fs.

Similar broadband sources with a 3-dB optical bandwidth of 180–200 nm at a center wavelength of 1,060 nm or 1,300 nm can be realized [9].

18.1.7 Back-Reflection Immunity of SLEDs

SLEDs can be considered a broadband source of spontaneous emission that is connected to a high-power and high-gain optical amplifier, which then generates amplified spontaneous emission (ASE) in a single optical path, i.e., without any optical resonator like a laser. However, the on-chip high-gain amplifier amplifies ASE light not only in forward direction, i.e., towards the output facet of the SLED, but also in backward direction when light from is reflected back from an optical setup, for example. A good chip design prevents the SLED from being destroyed in the presence of back-reflections (BR); however, optical BR may reduce the amount of free carriers in the active region of the SLED, resulting in reduced output power and a reduction of optical bandwidth and in a redshift of the spectrum [10]. The amount of BR that can be tolerated depends on the application and on the SLED, i.e., high-power SLEDs will generally be more sensitive to BR than low-power SLEDs. Similarly, SLEDs with a flat-top optical spectrum will show stronger spectral changes due to BR than Gaussian-shaped SLEDs. Still, a negative impact of BR on the long-term reliability of SLEDs could not be found [10], and those findings have been confirmed by various lifetime experiments over several thousands of hours.

In order to avoid any kind of impact of BR on the SLED output performance, though, an optical return loss of less than −30 dB is recommended.

18.2 Broadband and High-Speed Swept Sources

High-speed wavelength-swept laser technology offers versatile applications in optical coherence tomography (OCT) [11–13], biochemical spectroscopy [14], and fiber-optic sensing [15]. Particularly in recent years, swept laser technology has been critical in advancing OCT applications in the field of biomedical imaging and industrial imaging, imparting the advantages of real-time in vivo diagnostics and high sensitivity. To realize real-time clinical imaging and broad-base commercial deployment, compact, small, and stable swept sources are of utmost importance. To meet such demands, wavelength-flexible swept sources between 400 and 1,700 nm with sweep rates from 1 to 200 kHz can be realized in a miniaturized optical butterfly package that also allows the integration of optical reference (k-clock) interferometers or other optical reference filters for spectral calibration [16]. The salient advantages of EXALOS' swept source technology include the following:

1. Wavelength flexibility: currently over various spectra from 800 to 1,650 nm; potentially reaching the visible spectrum near 400 nm or the near-infrared spectrum up to 2,500 nm
2. High phase stability: suitable for phase-sensitive applications such as Doppler OCT
3. Ultra-stable long-term operation: enables spectral calibration with fixed remapping vectors
4. Clean imaging performance: no secondary coherence peaks as well as sharp and narrow PSF peaks without sidelobes throughout the imaging range
5. Symmetric bidirectional sweeps: allows high duty cycle and efficiency
6. Customizable bidirectional or unidirectional operation
7. Small size: optical module in 26-pin butterfly package; packaged with electronics in hard disk drive (HDD) form factor

For biomedical OCT applications, different imaging system requirements would demand an optimum combination of spectral region, sweep range, sweep frequency, coherence length, average power, and frequency calibration (k-space remapping) methods.

18.2.1 Diverse Swept Source Requirements

In the following sections, we will discuss some key requirements of swept sources before explaining the EXALOS swept source architecture and demonstrating its performance characteristics.

18.2.1.1 Wavelength Region

The selection of the proper spectral region for OCT applications depends mainly on the scattering and absorption property of the targeted biological tissue. The 840-nm spectrum has been historically used for retinal imaging due to low water absorption through the entire eye length and high scattering in the retinal layers. The 1,060-nm

spectrum has been actively investigated in recent years due to a favorable combination of high penetration in retinal (choroidal) layers and better visualization in patients with hazy ocular media (e.g., cataract). The 1,310-nm spectrum is useful for imaging of the anterior chamber of the eye, for dermatology, for cardiology or for other areas due to its lower scattering and hence deeper tissue penetration. The 1,550-nm spectrum is more suitable for industrial imaging, e.g., NDT, or fiber-optic sensing but has also been investigated for the hope of deeper imaging in bone structures due to their lower water content.

To address higher-resolution SS-OCT applications with near-micrometer resolution, multiple sources can be spectrally combined in order to form an ultra-broadband swept source. The unique flexibility of the EXALOS laser architecture allows for tailored specifications at multiple wavelengths and for concatenating swept sources of different wavelengths in a synchronized master-and-slave sweep operation. Figure 18.3 shows optical spectra of five different lasers covering a wavelength range between 800 and 1,600 nm. As discussed in more detail in Sect. 18.3, the typical sweep spectrum has a rectangular shape with sharp spikes at the edges, which originates from the turning points of the resonant MEMS scanner. 10-dB sweep ranges as wide as 80 nm at 840 nm, 130 nm at 1,060 nm, 100 nm at 1,220 nm, 160 nm at 1,300 nm, and 200 nm at 1,550 nm, respectively, have been achieved.

18.2.1.2 Sweep Range and Axial Resolution

For Fourier domain OCT (FD-OCT), which includes both SS-OCT and SD-OCT, the spectral bandwidth defines the axial imaging resolution. Assuming a Gaussian shape for the spectral power distribution, the axial resolution (δz) is related to the 3-dB (FWHM) sweep range $\Delta\lambda$ through the relation 0

$$\delta z = \frac{2\ln 2}{\pi} \cdot \frac{\lambda_0^2}{\Delta\lambda}$$

with λ_0 being the center wavelength of the source. This is the same formula used to calculate the coherence length or axial resolution of SLEDs with $\Delta\lambda$ being the 3-dB bandwidth of the SLED. However, the sweep range of a swept source is typically specified as the range over which the spectral power drops to -10 dB relative to the peak value. For a Gaussian-shaped spectrum, the 10-dB optical bandwidth is 1.83 times larger than the 3-dB optical bandwidth, which needs to be considered when translating the sweep range of a swept source into axial resolution.

The sweep range is typically measured using an optical spectrum analyzer (OSA), which measures *average* optical power but does not capture the *instantaneous* output power of the swept source. For sources sweeping in a nonlinear fashion like sinusoidal swept sources, the optical spectrum is given by the convolution of the instantaneous output power of the source in the wavelength domain with the sweep characteristics in the time domain. It is therefore more appropriate to measure the optical sweep range and hence the axial resolution of a swept source in the time domain and, by means of a calibration, convert the time-domain signal into the wavelength domain.

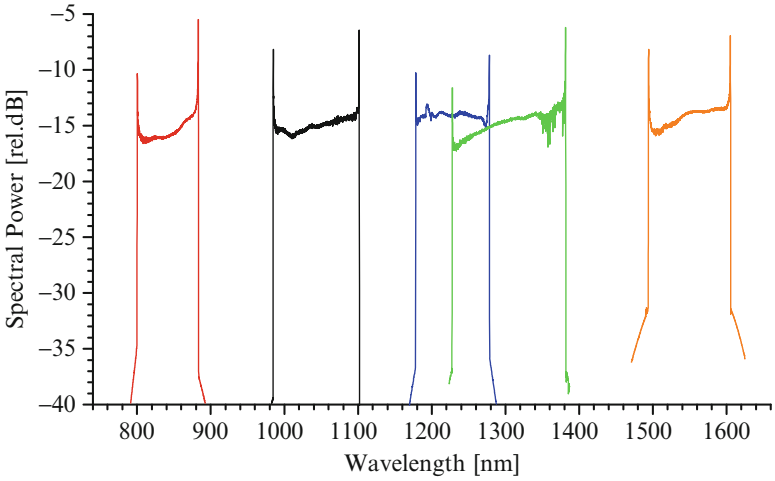

Fig. 18.3 Spectra of swept sources in different spectral regions

Generally, SS-OCT systems are expected to deliver an axial resolution that is comparable to SD-OCT systems based on SLEDs and spectrometers. In most cases, this means that the specified (10-dB) sweep range has to be larger than the specified (3-dB) optical bandwidth of SLEDs.

18.2.1.3 Coherence Length and Imaging Depth

In practical SS-OCT imaging implementations, the imaging depth is inherently governed by two parameters: the finite linewidth of the source $\delta\lambda$ in wavelength or δv in frequency $\left(\text{with } \delta\lambda = \frac{c}{v^2}\delta v\right)$, which leads to a sensitivity fall-off with imaging depth, and the spectral sampling interval (dk), which limits the observable imaging range. Assuming a Gaussian-shaped linewidth, the coherence length (l_c) is related to the dynamic or instantaneous linewidth through the relation [17]

$$l_c = \frac{2ln2}{\pi} \cdot \frac{\lambda_0^2}{\delta\lambda} = \frac{2ln2}{\pi} \cdot \frac{c}{\delta v}$$

Similar to SLEDs, the coherence length is defined as the optical path length difference (OPD) over which the coherence or autocorrelation function drops from its maximum to 50 %. Since OCT is a reflective interrogation technique, the so-called imaging depth captures the double path in the interferometer and is therefore half the coherence length of the source, i.e., a swept source with a coherence length of 10 mm has an imaging depth of 5 mm.

Optical and Electrical PSF

In many imaging applications and in the field of Fourier optics, the term "point spread function" (PSF) is being used. In analogy to RF systems, it can be thought of

the impulse response of an imaging system that is applied to an object through a convolution and that yields an image:

$$Image = PSF * Object$$

Applying this concept to OCT means that the OCT image (A-scan) can be thought of the convolution of the PSF of the light source with the object that is being scanned. Using an interferometer with zero OPD, the resulting image (A-scan) is the autocorrelation (coherence) function of the light source that is therefore equivalent to the "*optical PSF*" (PSF_o).

In the theoretical analysis of FD-OCT, the electrical currents and the electrical power signals that are generated through the detection of the optical fringe signals are considered [12], [18], 19], [29]. Therefore, to describe the imaging performance of an SD-OCT or SS-OCT system, it is common to calculate the square of the magnitude after the FFT [20] or to use 20·log10 [12] when plotting the "electrical PSF" (PSF_e) or when calculating the SNR and hence the system sensitivity. As a result, the coherence function or optical PSF will drop to 50% while the electrical PSF will drop by 6 dB over the specified coherence length.

To make it more challenging, the "coherence length" is a performance parameter of the source, while the "imaging depth" is a performance parameter of the SS-OCT imaging system. While most system vendors specify a minimum coherence length (amplitude fall-off) of the swept source, the imaging performance of the OCT system is given by the signal-to-noise ratio (SNR) fall-off behavior of the source and of the entire system, including linearization algorithms. It is commonly expected that the 6-dB SNR fall-off (imaging depth) is identical to the 6-dB amplitude fall-off of the source, which is most often not the case, though.

The imaging depth and hence the required coherence length or SNR fall-off is typically dictated by the application, e.g., retina OCT imaging requires an imaging depth of 3–4 mm, while anterior-chamber imaging needs an imaging depth of 7–8 mm, similar to endoscopic OCT applications where an imaging depth of 5–10 mm is often required.

In swept laser designs, many performance parameters are interrelated and may require trade-offs in order to optimize the most critical parameters. For example, a long photon lifetime is required to provide a large coherence length, and this is achieved by minimizing cavity loss and thus maximizing the number of cavity round trips for a given gain medium. A high spectral slew rate or sweep speed (expressed in nm/ns) can increase loss due to a fast-moving spectral filtering window and hence simultaneously reduce the photon lifetime, sweep range, and output power. For applications such as biometry where imaging depth is more critical than axial resolution, the sweep range or the sweep speed can be compromised to help increase the coherence length.

18.2.1.4 Secondary Peak Position and Suppression

Secondary peaks of the coherence function or PSF shall be well suppressed within the imaging range in order to not produce horizontal lines on a B-scan. A typical

SNR value of a swept source near the zero delay or zero OPD is 60 dB on a $20 \cdot \log_{10}$ scale. This means that, similar to SLEDs, a secondary peak suppression of 25–35 dB (50–70 dB on a $20 \cdot \log_{10}$ scale for the electrical PSF) within the imaging range is required.

18.2.1.5 Axial Scanning Frequency (Sweep Rate)

SS-OCT has the potential to deliver faster A-scan rates compared to camera-based SD-OCT systems and therefore allows addressing the needs for certain applications. For example, in high-resolution or wide-angle retinal OCT imaging, an A-scan rate of 100–200 kHz (or even more) is desired in order to avoid motion artifacts or to allow for imaging a larger area of the retina. For example, a 200-kHz swept source could enable B-scan imaging with a width of 1,000 A-scans and 8 times averaging with a video rate of 25 fps. In cardiovascular OCT applications, the maximum allowable time for flushing and the chosen artery length for imaging define the pullback rate of the catheter, which then defines the required A-scan rate of the swept source in order to maintain a certain spatial sampling resolution during the pullback. For such applications, A-scan rates in the range of 50–100 kHz are currently required.

The A-scan frequency of SS-OCT systems directly defines the spectral sweep frequency of the laser. In swept laser designs, an excessively high sweep frequency generally compromises the sweep range, the coherence length, and the output power in addition to imposing constraints on the sweep mechanisms whether mechanical or electronic.

Similar constraints may exist on system level as higher A-scan rates require faster and hence more expensive A/D converter (ADC), faster signal processing engines, and larger data throughput towards the host. Furthermore, faster electronics typically mean larger analog bandwidths and hence lower SNR performance, higher power consumption, and lower resolution. The A-scan rate and the imaging depth in conjunction with the linearity of the swept source define the required sampling rate of the ADC. A typical sampling rate for a 100-kHz A-scan rate is 500 MSPS that provides sufficient imaging depth for most sources.

Finally, for a given MPE level, faster A-scan rates will mean fewer photons per sweep (i.e., per A-scan) and therefore lower OCT system sensitivities.

18.2.1.6 Average and Instantaneous Output Power

The swept laser power is dependent on the cavity loss, the sweep frequency, and on the gain and saturation power of the optical gain chip. Furthermore, the average sweep power also depends on the sweep duty cycle. Because the average power directly affects the SNR, one often tries to maximize output power without exceeding the safety limits for biomedical imaging (after accounting for losses through the imaging system). Typically, the average output power of a swept source is specified. However, in case the MPE limit changes over the sweep range of the laser, the instantaneous spectral output power of the laser may need to be considered as well.

18.2.1.7 Relative Intensity Noise (RIN), SNR, and OCT Sensitivity

Noise in laser sources is generally characterized by relative intensity noise (RIN) and phase noise. Phase noise defines the laser linewidth (coherence length). RIN manifests itself in the SNR, the sensitivity, and in the dynamic range of a measurement system, which are critical parameters that determine image clarity against background noise in OCT imaging. Both SNR and OCT sensitivity quantify the minimum detectable reflected optical power for an ideal sample (metal mirror). Dynamic range describes the range of optical reflectivity values detectable in OCT imaging, i.e., the capability of detecting weak signals in presence of large-amplitude signals. Typical RIN values of both SLEDs and swept sources are in the range of −125 to −145 dBc/Hz. RIN of SLEDs is measured in the frequency domain using an electrical spectrum analyzer with a high sensitivity, while RIN of swept sources is typically measured in the time domain using sampling of consecutive sweeps over a certain period of time [21].

18.2.1.8 Sweep Linearity in Frequency

The ideal swept source for OCT applications has a constant sweep speed in the frequency domain, i.e., its sweep is linear in k. The corresponding k-clock signal will then have a constant frequency during the sweep. However, most high-speed swept sources exhibit some nonlinear sweep behavior with respect to optical frequency and therefore require a recalibration of the interferometric fringe patterns in k-space before the inverse Fourier transform can be applied in order to extract accurate spatial-domain (depth ranging) information. It is therefore useful to provide the k-clock signal as an integral part of the swept laser.

Nonlinear sweep in k also means that the sweep speed and hence the k-clock frequency varies over the sweep time of the laser. Depending on the amount of sweep nonlinearity, faster sampling rates of the ADCs and larger analog bandwidths of the receivers need to be considered. Additionally, fast-varying k-clock frequencies (strong frequency modulation) may challenge the acquisition electronics when direct k-clocking is employed.

18.2.1.9 Duty Cycle

In SS-OCT two types of duty cycles are of interest: the duty cycle of the swept source and the duty cycle for the OCT imaging. The duty cycle of the source describes the amount of time the laser spends for the wavelength sweep relative to the sweep period. The sinusoidal and bidirectional swept sources from EXALOS have a high duty cycle of 80–100 %, for example. Lower duty cycles translate into faster sweep times or slew rates and hence into higher fringe frequencies, which require faster sampling rates. The duty cycle for the OCT signal processing describes the percentage of the actual sweep time of the laser that is used for the generation of an A-scan. For example, the duty cycle of the laser might be 100 % but the duty cycle used for OCT signal processing is actually only 75 % of the sweep time because 25 % of the sweep time will be discarded for certain reasons.

18.3 Swept Source Architecture

EXALOS has developed a miniature external-cavity swept laser based on a micro-optic integrated platform that allows for compact embodiments, performance flexibility, field reliability, and economy of scale (Fig. 18.4). This laser architecture integrates a broadband semiconductor optical amplifier (SOA) gain chip, a high-speed resonant 1D micro-electro-mechanical system (MEMS) scanning mirror, and a proprietary diffraction grating on a temperature-controlled optical bench inside a 26-pin butterfly package (Fig. 18.5). In the category of longitudinal multimode lasers, this is a truly self-contained compact packaging. Contrary to monolithic devices such as the Vernier-tuned distributed Bragg reflector (VT-DBR) laser [22] and MEMS-tuned vertical-cavity surface-emitting laser (MEMS-VCSEL) [23], this hybrid platform offers realizing lasers in different spectral regions (from 400 to 2,500 nm) and at different sweep frequencies (currently 1–200 kHz).

Numerous design parameters for the critical components must be well-matched in order to generate a high-performance swept source. First, the high-performance SOAs are designed in-house for a wide spectral gain and linear behavior to enable long coherence sources in various spectral regions. Second, the wavelength scanning mechanism is based on a MEMS mirror. The long-term stability of the MEMS is extremely high as it is based on mono-crystalline electro-static MEMS scanners that do not degenerate or degrade over time. Changes in resonance frequency are mainly due to temperature effects (e.g., warm-up effects from light on/off) but are minimized by the temperature-controlled optical platform. The custom-designed MEMS scanners offer high mechanical stability (shock resistance >5,000 g), high phase stability, and low jitter. Novel diffraction gratings are designed for ultra-high effective resolvance to achieve narrow filtering and hence long coherence lengths while maintaining high diffraction efficiency over a wide spectral range. Optical retarders are used to achieve the right cavity length in order to optimize laser dynamics and minimize mode-hopping noise. A free-space k-clock interferometer followed by balanced detection simplifies post-processing in OCT systems. The A-scan trigger is directly derived from the MEMS clock and therefore is always in sync with the MEMS movement. The sweep is sufficiently stable such that one can create a remapping vector for initial calibration and continue to use the same remapping vector for hours of continuous use. The electronic A-scan trigger used in the swept source is derived from a crystal oscillator, which gives a timing jitter down to a few picoseconds. Due to the high Q factor, there is only little noise transferred from the electronics driver to the MEMS scanner.

The laser cavity is manufactured in a fully-automated micro-optic assembly station. This packaging platform offers highest flexibility, alignment accuracy, reproducibility, long-term stability, and high production rate. More details are given in Sect. 18.3.4.

The resultant wavelength-swept laser provides a bilateral and sinusoidal sweep operation driven by a resonant MEMS scanner. As illustrated in Fig. 18.6, the laser spectrum is continuously and repetitively tuned from short to long wavelengths (“up-sweep”) and from long to short wavelengths (“down-sweep”). The sweep duty

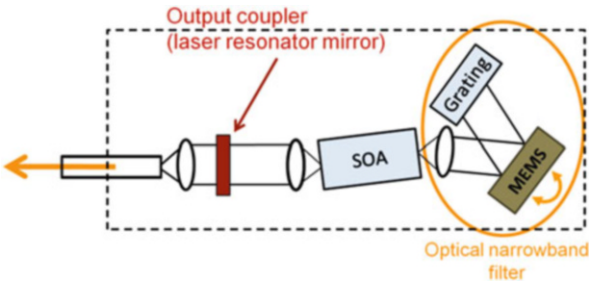

Fig. 18.4 Schematic of external-cavity swept laser with Littrow configuration. The dashed line represents the optical butterfly module, indicating that the entire laser cavity is contained inside the module

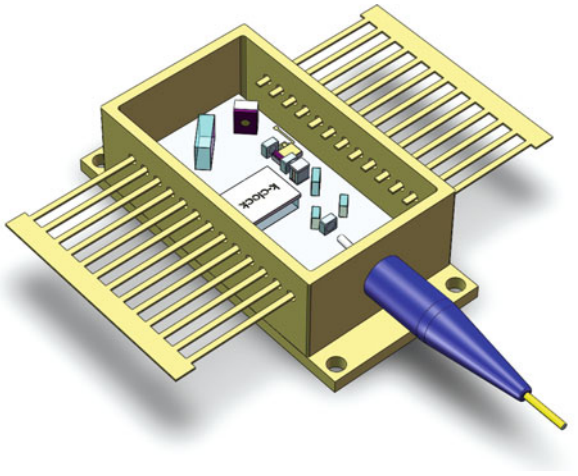

Fig. 18.5 3D model of the external-cavity swept laser in a butterfly package

cycle defines the relative portion of the sweep in either up- or down-sweep direction that can be used for the OCT scan. This duty cycle depends on a combination of the laser gain bandwidth, the scanning amplitude of the MEMS scanner, and the SOA modulation. The SOA modulation can be selected to turn off either the up-sweep or the down-sweep, thereby converting a bidirectional sweep operation into a unidirectional sweep operation.

Due to the harmonic oscillation of the resonant MEMS scanner, the sweep speed is reduced to nearly zero at the turning points of the sinusoidal movement. If the laser still has sufficient gain at the spectral edges of the sweep spectrum, it will remain on (100 % duty cycle). Consequently, the average optical output power at the edges of the spectrum will increase despite the fact that the instantaneous output power is lower than in the center of the sweep spectrum, resulting in a more rectangular shape of the optical spectrum of the swept sources with potentially pronounced spikes at the edges, as shown in Figs. 18.3 and 18.6.

For OCT signal processing, a typical duty cycle of 70–80 % of the sweep time of those sinusoidal lasers is used. However, a duty cycle of 80 %, for example, still

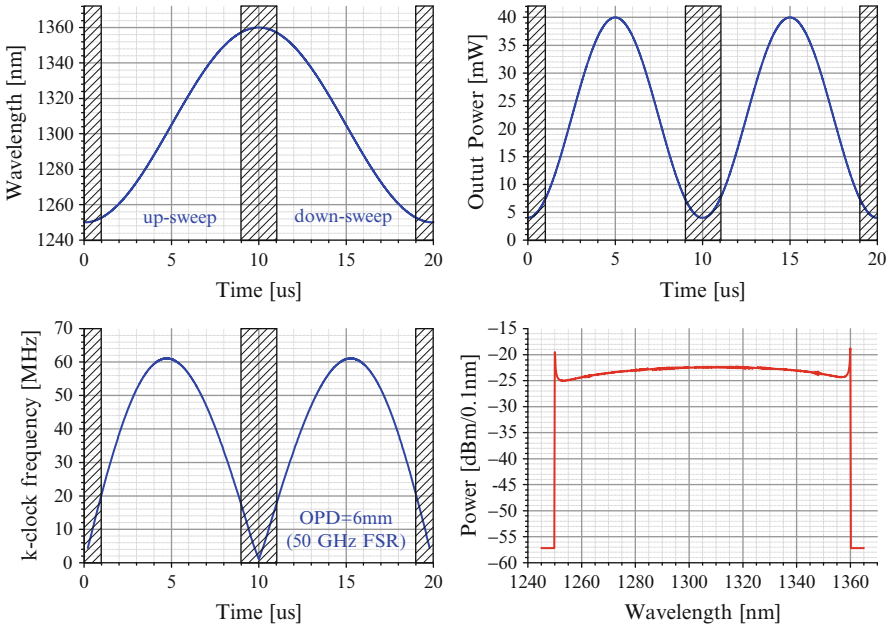

Fig. 18.6 Illustration of a 100-kHz bidirectional swept source with a sweep range of 1,250–1,360 nm and an average output power of 22 mW. The shaded areas indicate periods of time that will not be used for OCT imaging, i.e., the non-shaded areas represent the actual sampling periods with an 80 % duty cycle

covers 95 % of the sweep spectrum. Furthermore, as shown in Fig. 18.6, the 10 % that is ignored at the upper and lower edge of the sweep contains low-power sampling points that are typically outside the 6–7 dB bandwidth range; hence, the total loss in energy is below 10 % and the loss in axial resolution is in the range of 2 %.

18.3.1 Broadband Gain Chips

The semiconductor optical amplifier (SOA) gain chips are designed in-house and are fabricated using the same production and supply chain as SLED chips. Extensive device simulations that account for a variety of quantum-mechanical, carrier-transport, and thermal effects allow realizing SOA gain chips featuring wide spectral gain for high-resolution OCT, linear characteristics for long coherence lengths, fast carrier dynamics for fast tuning sources, high-power robustness for long-term reliability, and low noise for good image quality. Such SOA gain chips have been realized at various spectral regions (840, 1,060, 1,220, 1,310, 1,550 nm) using GaAs and InP material systems.

A good measure for broadband SOAs is the peak gain and the 10-dB gain bandwidth. For the latter, 1,060-nm gain chips with a 10-dB gain bandwidth of

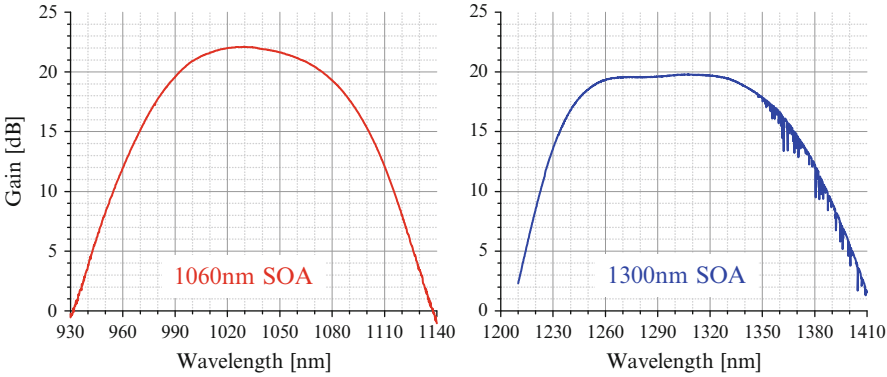

Fig. 18.7 Example of gain spectra of a broadband 1,060-nm (*left*) and a 1,310-nm (*right*) semiconductor optical amplifier (*SOA*). The 10-dB gain bandwidth is 960–1,110 nm (150 nm) and 1,220–1,390 nm (170 nm), respectively

150 nm have been realized, as shown in Fig. 18.7, as well as 1,310-nm gain chips with an equivalent bandwidth of 170 m.

18.3.2 MEMS Scanner

Based on a well-proven technology, the custom-designed MEMS scanner is a resonant structure made of mono-crystalline silicon (Fig. 18.8). Given its high Q factor (500–1,000) and high mechanical stability, it can provide an extremely deterministic oscillation behavior with high phase stability. The reflective metal coating provides an efficient reflectivity over a wide spectral range (visible to near-IR).

By design, this resonant scanner has a single operating frequency and hence a sinusoidal scan function at a fixed A-scan rate. For example, a MEMS scanner with a mechanical resonance frequency of 50 kHz and with a Q factor of 1,000 will perform (harmonic) oscillations only within an actuation frequency window of 50 Hz. Such a mirror could be used in a 100-kHz bidirectional source or a 50-kHz unidirectional source, for example.

Generally, there is a trade-off between scanning speed, mirror size, and scanning angle. A smaller mirror size is required for a higher scan frequency, which is one of the limiting factors for the filter bandwidth and hence for the coherence length of the laser. Practically, shorter-coherence (5–10 mm) swept sources can be realized with A-scan rates up to 200 kHz, and longer-coherence (10–30 mm) swept sources can be realized with A-scan rates up to 50 kHz. The sinusoidal wavelength dependence as a function of time demands careful considerations for the k-space recalibration. To synchronize with the MEMS scanner movement and the swept source spectrum, the A-scan trigger is directly derived from MEMS clock. Together with the highly stable resonant operation, one may use the same k-space recalibration vector for hours of continuous operation.

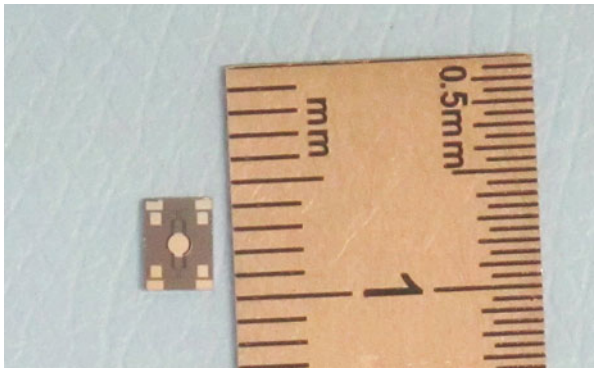

Fig. 18.8 Resonant MEMS scanner chip

18.3.3 Diffraction Gratings

The diffraction gratings are designed to have high dispersion and line densities for narrow band-pass filtering, as well as high diffraction efficiency over a wide spectral range. The resultant patented "grating optical engine" is fabricated with well-proven telecom-qualified processes.

As an example, to design for a spectral filter bandwidth of ~13 GHz (i.e., ~10 mm coherence length), the required grating effective resolvance (defined as the center wavelength divided by linewidth, equivalent to the number of illuminated grating lines in the first diffraction order) would need to be approximately 17,000. The effective spectral bandwidth also inevitably dictates the laser cavity length. For a swept source in which the lasing line structure is made of multiple longitudinal modes, it is important to have sufficient number of modes within the laser line profile to minimize the effect of mode-hopping noise in OCT applications. Therefore, given the spectral bandwidth of the filter and the minimum number of longitudinal modes required within, the minimum laser cavity length is subsequently defined.

18.3.4 Hybrid Optical Packaging Platform

An optical packaging platform is critical in the process of realizing the construction of complex optical system that can only exhibit the intended functionalities in a miniature embodiment. EXALOS has co-developed a unique hybrid optical packaging platform (HOPP) machine for (semi-)automated micro-optic assembly with unprecedented alignment accuracy (down to 50 nm or 1 arcsec) for free-space propagating beams. This HOPP machine has 21 motorized stages, six cameras, epoxy dispenser, machine vision, and custom programming interfaces and performs active or passive alignment of all optical elements inside the butterfly package. Advanced design rules are embedded into the process programming and machine training (alignment algorithms) for the laser cavity and its optical components to

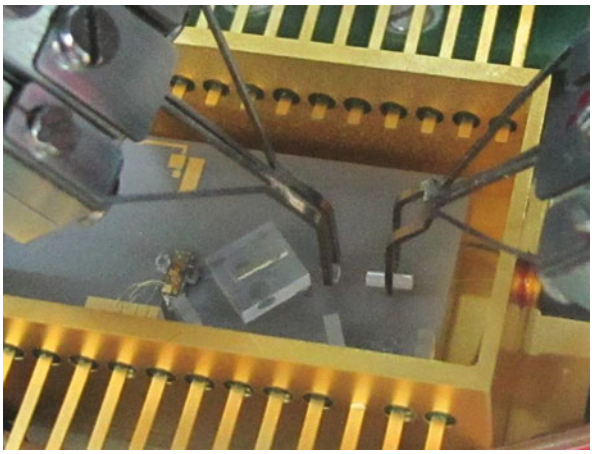

Fig. 18.9 Automated alignment process of optical components inside butterfly package

achieve required optical performance (low wavefront distortions, suppression of unwanted reflections, etc.). During the optical assembly process, the HOPP machine can perform active alignment of optical components, characterize each micro-optical component (size, flatness, optical axis, etc.), and measure optical near/far field and beam propagation through lenses, filters, etc. Once the machine has learned the alignment procedure, fabrication of swept source modules is highly repeatable.

The swept sources are operated while they are built on the HOPP machine, and certain target performance parameters like SNR or coherence fall-off can be used as active feedback signals to align critical components. This means that the laser performance is monitored throughout the whole manufacturing process, allowing high-yield manufacturing on module level.

18.3.5 Compact OEM Swept Source Module

The swept source optical modules (SSOMs) described above are assembled on electronic driver boards, as shown in Fig. 18.10. Those fiber-coupled turnkey swept sources are available either as a benchtop version or as an OEM module in 3.5″ HDD format (footprint 101.6 × 147.0 mm) that can be mounted inside a disk cage of a PC. The OEM module operates on 12 V or 24 V DC with a typical power consumption of 10 W.

18.4 Performance of Swept Sources

This chapter discusses some of the performance characteristics of EXALOS' swept sources at 1,060, 1,310, and 1,550 nm, including the instantaneous coherence length and its measurement, the fall-off amplitude (FOA), and the SNR.

Fig. 18.10 Swept source optical module (*SSOM*) mounted on a compact electronic driver board, enabling OEM swept sources (with metal case) in 3.5″ HDD form factor, as shown for comparison on the right side

18.4.1 Fall-off Measurements

For swept-wavelength lasers, the instantaneous linewidth tends to vary across the sweep spectrum because of a wavelength dependence of the laser dynamics and other certain cavity parameters. Due to the difficulty of characterizing the instantaneous linewidth of rapidly sweeping lasers and the need for accurately mapping the time–wavelength relation between successive sweeps, two indirect approaches are commonly adopted.

18.4.1.1 Time-Domain Analysis of Coherence Length

One method is to deduce the coherence length by measuring the interference fringe pattern of a Michelson or Mach–Zehnder interferometer for a set of varying OPD values. With a calibrated OPD value, the corresponding free-spectral range (FSR) of the interferometer can be calculated, (FSR = c/OPD), which is then used to convert the x-axis from time to relative frequency. Using an optical spectrum analyzer or absolute wavelength reference filters, an absolute frequency or wavelength scale can be calculated for the x-axis. At the same time, the decay of coherence with increasing OPD values is analyzed by comparing the amplitude values of the fringe envelope at certain time or spectral positions [24] (Fig. 18.11).

Therefore, for any wavelength position the particular OPD value can be determined at which the amplitude of the fringe envelope has dropped to 50 % of its initial value at an OPD close to zero. Typically, the reference position is an OPD value of 0.1–0.2 mm as the fringe pattern practically disappears at the exact zero path length difference.

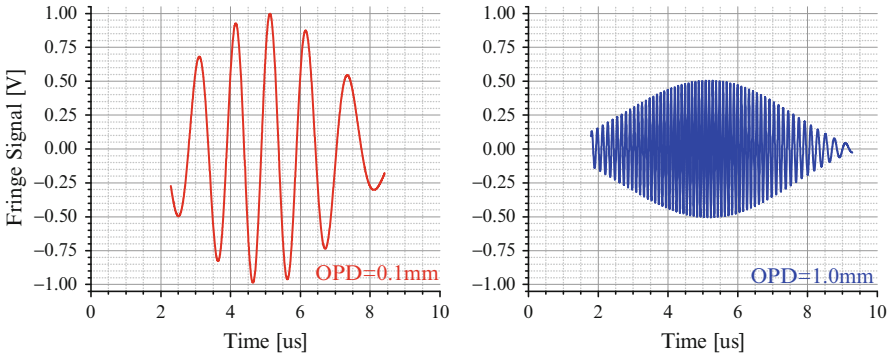

Fig. 18.11 Characterization of the instantaneous (spectral) coherence length by a time-domain measurement of the fringe amplitude fall-off after an interferometer. This example shows a 100-kHz swept source with a coherence length of 1.0 mm. The horizontal axis can be converted from time to wavelength

This time-domain approach allows characterizing the coherence length variation across the entire swept spectrum [24]. Note that due to laser cavity dynamics and alignment, the coherence characteristics may differ for the up-sweep and down-sweep direction [25] such that extra engineering effort is required to equalize the amplitude (and noise) fall-off for bidirectional swept sources.

18.4.1.2 Spatial-Domain Analysis of Coherence Length and SNR

Often it is more convenient and useful to provide an "average" coherence of the swept source that also accounts for phase fluctuations in the sweep. This average coherence length is derived by calculating the coherence or point spread functions (PSF) from the interference fringe pattern through an inverse Fourier transform at incremental OPD positions [17]. For swept sources that are not sweeping perfectly linear in the frequency domain and show a variation of the k-clock frequency across the sweep, the acquired fringe pattern in the time domain has to be resampled prior to the FFT, which means that the coherence length is not directly measured as in Sect. 18.4.1.1 but is calculated and extracted from the amplitude fall-off of the PSF in the spatial domain. Hence, the resulting coherence length also depends on the accuracy and effectiveness of the remapping algorithm that is used. The "average" coherence length is then expressed as the 50 % fall-off of the optical PSF amplitude PSF_o or the 6-dB fall-off of the electrical PSF amplitude (PSF_e).

The noise background of the electrical PSF (on a linear scale) is determined left and right of the PSF peak with a certain offset (e.g., five times the PSF width) and over a certain imaging depth (e.g., 100 sample points in space) where the RMS value and the standard deviation of the noise background are calculated. The corresponding SNR is then commonly given by

$$SNR[dB] = 20 \cdot \log_{10}\left(\frac{Magnitude(PSF_e) - RMS(Noise_e)}{StdDev(Noise_e)}\right)$$

The SNR of a swept source is typically determined with an adjustable interferometer where both arms of the interferometer have roughly the same insertion loss. High SNR values in the range of 50 dB to 65 dB, depending on the speed and the RIN of the swept source, are common near the "zero delay" (zero OPD) of the interferometer.

Many swept sources have higher-frequency noise contributions such that the noise floor increases slightly with increasing OPD values. This results in the 6-dB SNR fall-off being not as good as the 6-dB amplitude fall-off of the source. To describe just the performance of the source, both values are typically plotted as a function of OPD.

18.4.1.3 Sensitivity Fall-Off

For an OCT imaging system, the ultimate performance parameter is the sensitivity fall-off as a function of the imaging depth. To convert the x-axis to imaging depth, the OPD values are divided by two, as mentioned earlier. To measure the OCT system sensitivity, the adjustable interferometer is considered being constituted of a *reference arm* with higher optical power (typically 1.0–2.0 mW in front of the optical splitter used for balanced detection) and of a *sample arm* with lower optical power.

Depending on the wavelength and the class 1 allowable MPE level, the optical power in the sample arm is adjusted to a certain value (e.g., 1.5 mW at 1,060 nm) and then strongly attenuated by a certain value (typically 50–60 dB). In this condition, the SNR of the PSF (e.g., A-scan of a metal mirror) near the zero delay is measured and the OCT sensitivity is expressed as

$$Sensitivity[dB] = SNR[dB] + Sample\text{-}Attenuation[dB]$$

Sensitivity values of 95–105 dB are desired for commercial OCT systems. Consequently, with a sample attenuation of 60 dB, the measured SNR near the zero delay needs to be in the range of 35–45 dB.

Using a balanced interferometer with roughly similar insertion loss on both arms (see Sect. 18.4.1.2), an SNR of 52–62 dB is typically required to achieve such sensitivity values.

18.4.2 1,060-nm Swept Sources

Swept sources at the 1,060-nm spectral region are being considered for biometric, retinal, and whole-eye imaging. The benefits of this wavelength range comprise relatively low water absorption, lower scattering (compared to 800–900 nm) and hence better penetration into the retina or in patients with lens opacities (cataracts), truly invisible light for patients or higher laser safety power limits. For biometry, long coherence lengths are of primary importance, along with a desirable sweep range of 25–40 nm and an A-scan rate of 1–20 kHz. Figure 18.12 illustrates, for an A-scan rate of 20 kHz and a sweep range of 40 nm, an average coherence

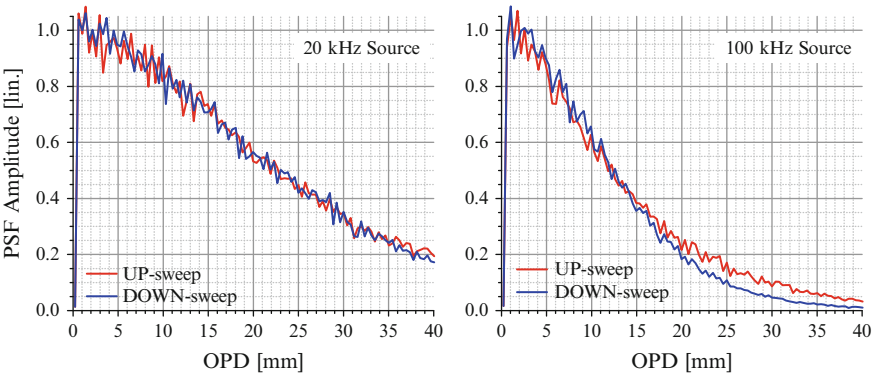

Fig. 18.12 PSF fall-off amplitude (*FOA*) for a 1,060-nm swept source with 40-nm sweep range: ~23 mm coherence length (50 % drop) at a 20-kHz sweep rate and ~12 mm coherence length at a 100-kHz sweep rate. This bidirectional source provides a symmetrical amplitude fall-off for both up- and down-sweep

length (50 % FOA) of ~23 mm. Furthermore, a coherence length of ~12 mm can be achieved at an A-scan rate of 100 kHz. The average output power for this source is 20 mW.

Retinal imaging experiments (Figs. 18.13 and 18.14) have been performed by using a 1,060-nm swept source with an A-scan frequency of 110 kHz. The laser is adjusted to a duty cycle of 100 % with a sweep range of 97 nm and center wavelength of 1,070 nm. Optical sweep power at the fiber output is ~10 mW. An instantaneous coherence of ~3–5 mm is obtained for up- and down-sweep with high sweep symmetry. The maximum SNR of this source near the zero delay is rather low (48 dB), which results in an OCT sensitivity of only 92 dB for a sample power of 1.5 mW. Figure 18.13 shows a tomogram without averaging (left) and with 5× averaging (right) of such source. The high degree of sweep symmetry is seen in the fact that the tomograms do *not* exhibit an alternating noise pattern for every second column (A-scan) considering the bidirectional sweep behavior.

Other retina measurements based on the same bidirectional swept source in combination with 20× averaging are shown in Fig. 18.14 and demonstrate that good penetration into the choroid of the retina can be achieved.

Analyzing not only the magnitude but also the phase of the Fourier transform, the temporal evolution of the phase of the PSF peak was investigated. Figure 18.15 shows such PSF phase variation over a longer period of time. The left graph shows three sets of measurements of ~4,300 consecutive A-scans in up-sweep direction only, each set spanning a time of nearly 80 ms. As can be seen, the phase of the PSF peak varies by ±3° over a longer period of time and shows some distinct pattern, which is an indication that in this source the low amount of *random* phase noise is overlaid by some slowly varying *patterned* phase noise that is coming from the drive electronics.

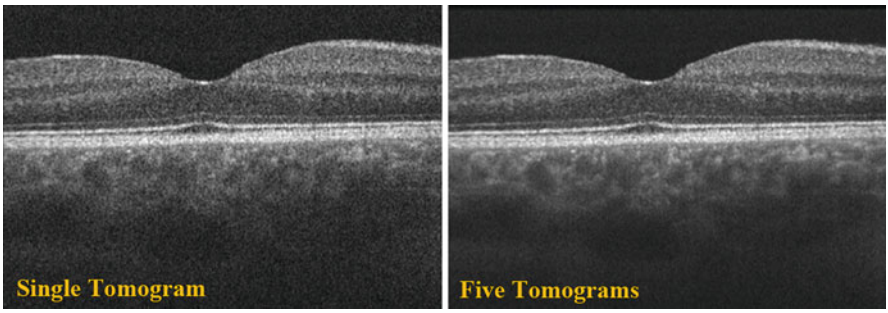

Fig. 18.13 ESS-1060/110 kHz: Retina measurements using a bidirectional swept source (Courtesy of Prof. Leitgeb's group, Medical University of Vienna, Nov. 2011)

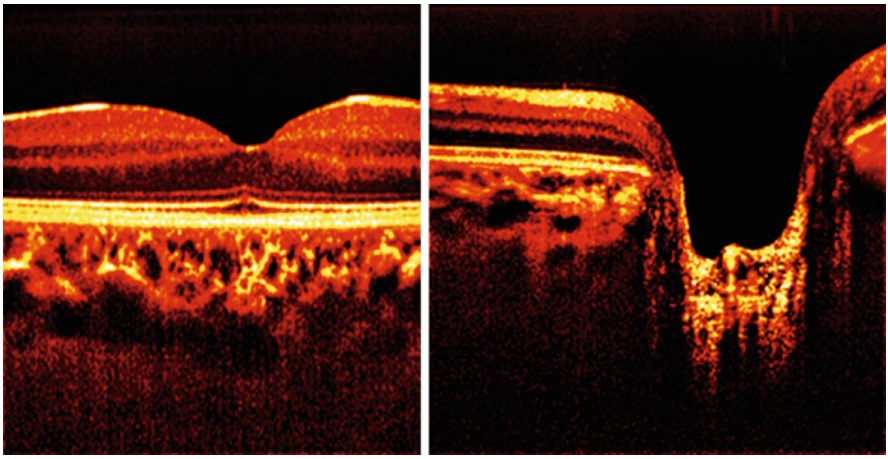

Fig. 18.14 ESS-1060/110 kHz: Retina measurements using both up-sweep and down-sweep of the source in combination with 20× averaging (Courtesy of Prof. Leitgeb's group, Medical University of Vienna, Nov. 2011)

The right graph of Fig. 18.15 shows ~8,600 consecutive bidirectional A-scans that are split into a set of ~4,300 up-sweeps and ~4,300 down-sweeps. This figure shows that the phase evolution in the down-sweep direction has the inverted pattern of the phase evolution in the up-sweep direction and that the phase difference between both sweep directions is within $\pm 1^\circ$ at all times. This level of phase noise is sufficiently small to perform Doppler measurements at full speed (bidirectional scanning).

The latest generation of drive electronics features significantly reduced timing jitter in operating the resonant MEMS scanners and will therefore further reduce the phase noise of such swept sources. Another contribution to an improved phase noise is coming from the fact that more recent swept sources are having a higher SNR, which scales inversely with the variance of the phase noise [26, 27].

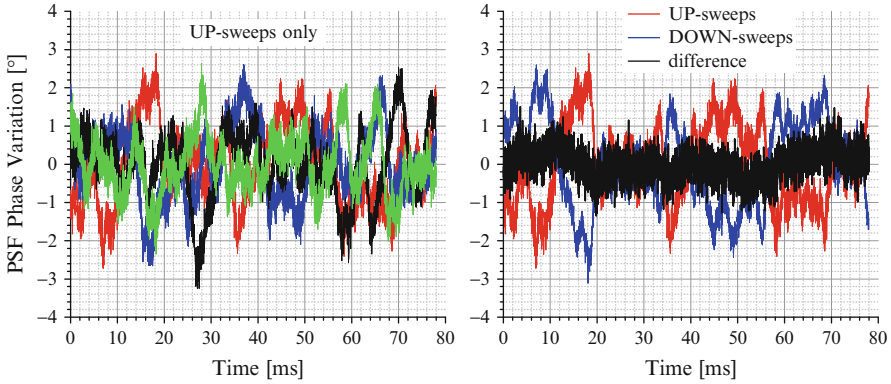

Fig. 18.15 ESS-1060/110 kHz: Temporal phase variation between different forward sweeps (Courtesy of Prof. Leitgeb's group, Medical University of Vienna, Nov. 2011)

18.4.3 1,310-nm Swept Sources

The measurement examples of Figs. 18.16, 18.17, and 18.18 are for a 1,310-nm swept source operating at an A-scan rate of 40 kHz (ESS-1310/40 kHz). The laser is adjusted to a duty cycle of 100 % with a sweep range of 100 nm and center wavelength of 1,310 nm, as shown in Fig. 18.16. Average optical sweep power at the fiber output is 20 mW with a peak power of ~40 mW. The laser shows high sweep symmetry with an instantaneous coherence of up to 10–12 mm for up- and down-sweep, as seen in the right graph of Fig. 18.16, which was generated using the time-domain analysis described in Sect. 18.4.1.1.

Using the spatial-domain analysis of Sect. 18.4.1.2 based on remapping and Fourier transform, the PSF fall-off graphs of Fig. 18.17 have been generated, showing that for both up-sweep and down-sweep directions, a clean imaging performance with narrow and sharp PSF peaks can be achieved. The 6-dB fall-off of the PSF_e magnitude occurs at an imaging depth of 5 mm. This is in agreement with the PSF_o amplitude fall-off graph in Fig. 18.18 that shows a 50 % drop at an OPD value of 10 mm. The maximum SNR of this 40-kHz source near the zero delay is ~63 dB, measured with a balanced interferometer as described in Sect. 18.4.1.2. This corresponds to an OCT sensitivity of ~105 dB for a power of 1.5 mW in the sample arm.

18.4.4 1,550-nm Swept Sources

For industrial OCT and certain sensor applications, swept sources in the 1,550-nm spectral range can provide distinct advantages, for example, reduced scattering coefficients that are useful for deeper imaging into scattering media with lower content of water (e.g., bones), non-destructive testing (NDT) of semiconductor devices that are more absorptive at shorter wavelengths, or industrial surface profiling.

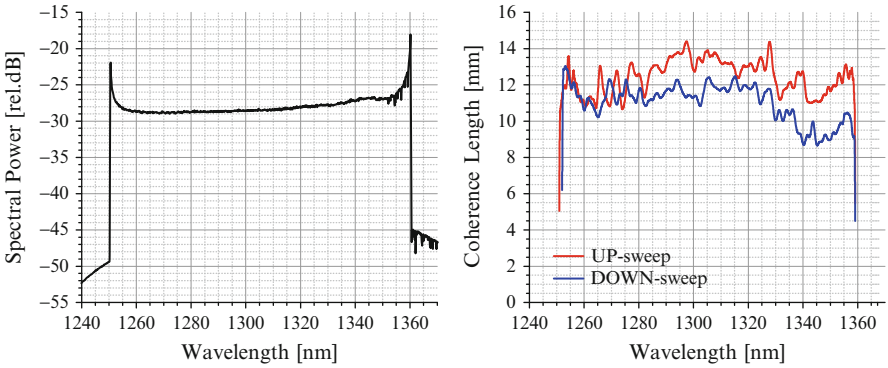

Fig. 18.16 ESS-1310/40 kHz: Sweep spectrum (*left*) and instantaneous coherence length for up- and down-sweep (*right*)

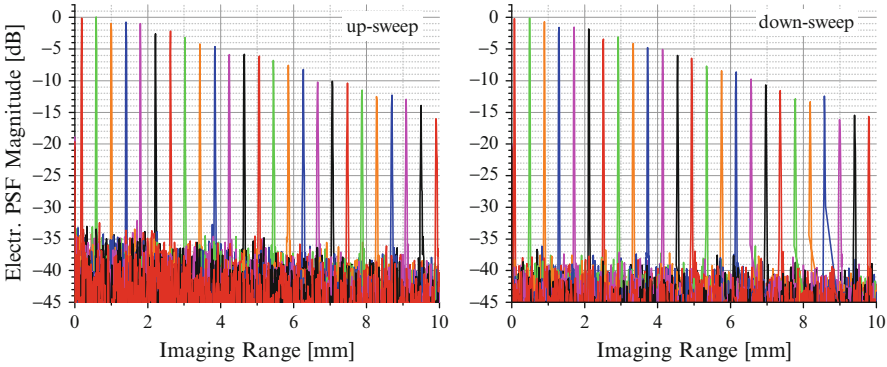

Fig. 18.17 ESS-1310/40 kHz: Electrical point spread function (PSF_e) for up- and down-sweep at various positions within the imaging range (imaging range is half of OPD)

Figure 18.19 shows two sweep profiles of the instantaneous output power of a 40-kHz (left) and a 150-kHz (right) swept source at 1,550 nm with a sweep range of 110 nm. As can be seen, these sources provide good symmetry in output power for the up- and down-sweep that does not significantly change in shape for sweep rates from 2 to 150 kHz. Those sources were adjusted for a 100 % duty cycle and exhibited a drop of instantaneous output power over the sweep range from ~100 to ~20 (factor 5 = 7 dB), as shown in Fig. 18.19.

The measured optical spectra of those sources, shown in Fig. 18.20, span a spectral range of ~1,505 nm to ~1,615 nm. The spectrum of the slower 2-kHz source shows a higher optical signal-to-noise ratio (OSNR) compared to the faster sources operating at 40 kHz or 150 kHz, still the shape of the spectrum being very similar. Figure 18.21 shows that the slower and faster sources also differ in their

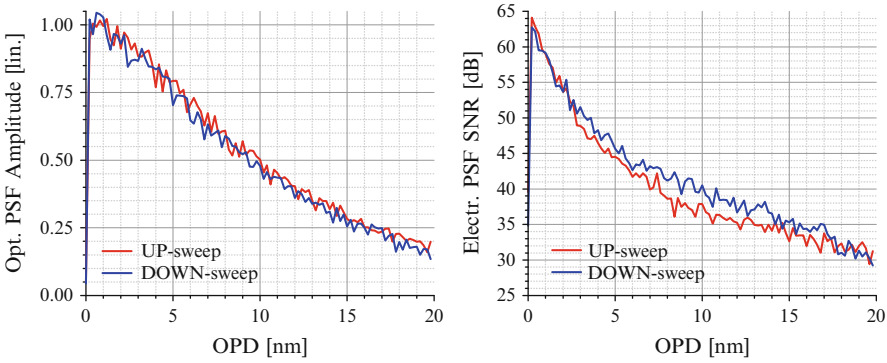

Fig. 18.18 ESS-1310/40 kHz: Amplitude fall-off of optical PSF (*left*) and SNR fall-off of electrical PSF (*right*) as function of the optical path length difference (*OPD*)

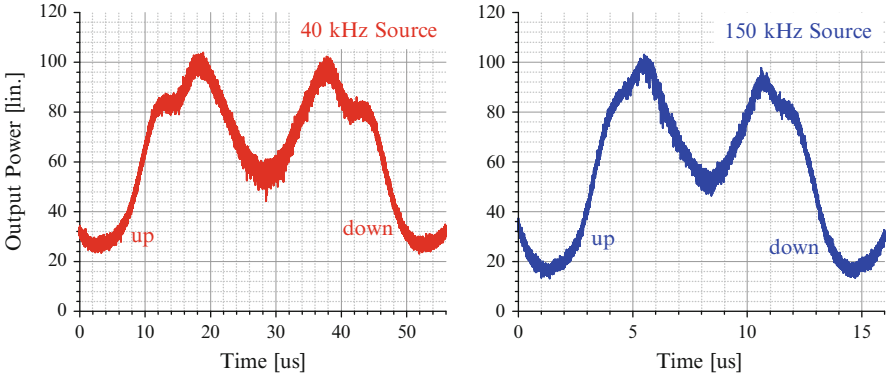

Fig. 18.19 ESS-1550: Temporal swept power profiles from 1,550-nm swept sources operating at 40 kHz (*left*) and 150 kHz (*right*). The turning points of the resonant MEMS scanners are at 3, 28, and 53 µs (*left*) and 1.3, 8.0, and 14.6 µs (*right*)

spectral coherence characteristics: While the 2-kHz source has an instantaneous coherence length of ∼14 mm (linewidth ∼75 pm), the faster 40-kHz source achieves a coherence length of ∼9 mm (linewidth ∼120 pm), which drops to ∼5 mm (linewidth ∼200 pm) at 150 kHz.

18.5 Detection and OCT Signal Processing

Proper optical and electrical detection in SS-OCT systems is as important as having a good swept source with sufficient imaging depth and low RIN. Besides highlighting a few technical considerations of the detection side, this chapter discusses real-time signal processing concepts for so-called OCT engines.

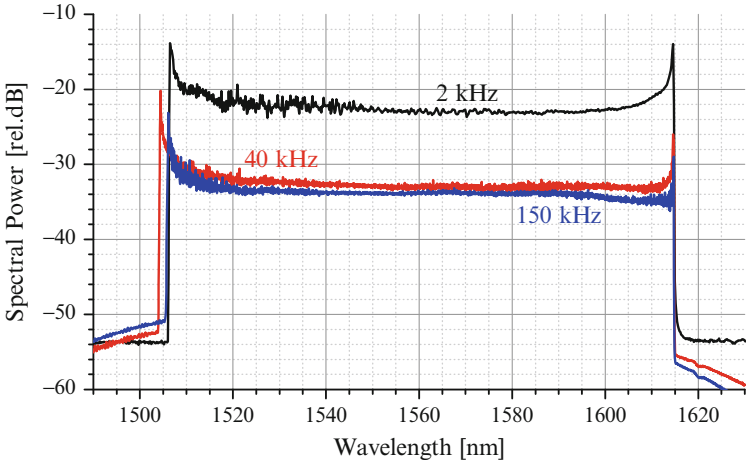

Fig. 18.20 ESS-1550: Optical spectra from 1,550-nm swept sources operating at 2 kHz (*black*), 40 kHz (*red*), and 150 kHz (*blue*). The sweep range is set to ~110 nm for all three lasers

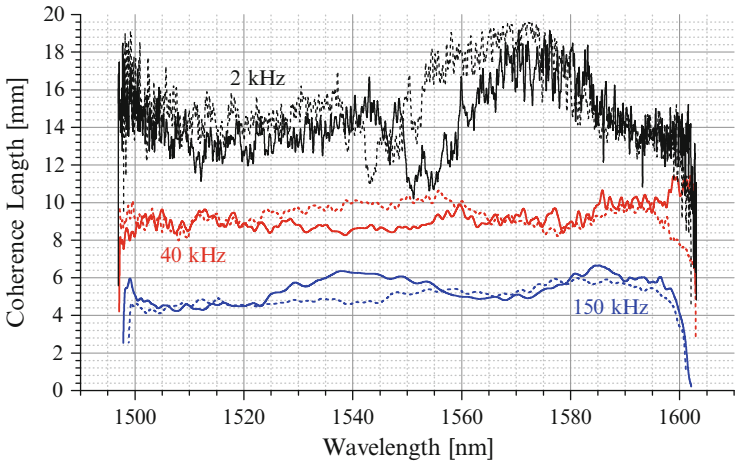

Fig. 18.21 ESS-1550: Instantaneous coherence length as a function of wavelength (*solid line*: up-sweep, *dashed line*: down-sweep) for 1,550-nm swept sources operating at 2 kHz (*black*), 40 kHz (*red*), and 150 kHz (*blue*)

18.5.1 Balanced Optical Detection

The promises of SS-OCT compared to SD-OCT include better sensitivity due to the fact that the OCT signal is received with a balanced optical receiver. As shown in Fig. 18.22, the OCT signal coming from the sample arm is interfering with light

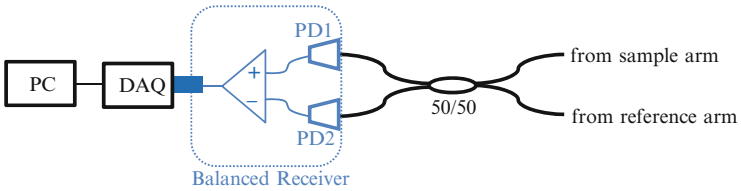

Fig. 18.22 Detection unit in a SS-OCT system, comprising of an optical 50:50 coupler in front of a balanced receiver that is connected to a data acquisition (*DAQ*) card

from the reference arm through a 50:50 optical coupler in front of the optical receiver. This balanced detection removes the DC component (common mode) of the light such that the relevant AC components of the fringe signal can be acquired with sensitivities near the shot-noise limit of the receiver.

In order to achieve a good SNR of the interference term and hence a good OCT system sensitivity, the power of the reference signal is increased to average values of 500–1,000 μW on each photodiode. At the same time, the common-mode rejection ratio (CMRR) of the whole detection unit needs to be high, which means that the optical power needs to be well balanced across the entire sweep range of the source [28].

Besides high CMRR, it is important for the balanced receiver to have a high gain but a low noise-equivalent power (NEP). The NEP is a measure of the receiver sensitivity and is the sum of the electrical shot noise, the thermal (Johnson or Nyquist) noise, and any other excess amplifier noise:

$$NEP.\sqrt{BW} = \sigma^2_{shot,el} + \sigma^2_{therm} + \sigma^2_{amp} = \sigma^2_{BR}$$

The total noise power of the balanced receiver, σ^2_{BR}, contributes to the noise of the electrical signal detected in SS-OCT [12, 19]:

$$\sigma^2_{OCT} = \sigma^2_{BR} + \sigma^2_{Shot,opt}\left(\alpha P_{ref}\right) + \sigma^2_{RIN,opt}\left(\alpha P^2_{ref}\right)$$

SS-OCT systems are operated in the shot-noise limit, which means that the optical power of the reference signal (P_{ref}) is adjusted such that the total noise is governed by the second term of the above equation and not by the RIN of the swept source (third term) or the receiver noise (first term). Also, due to the balanced optical detection, the RIN term is typically well suppressed if the CMRR of the receiver is high and the wavelength dependency of the 50:50 splitter in front of the receiver is small [28]. Consequently, the lower the NEP, the larger the dynamic shot-noise range, the higher the SNR of the OCT signal, and hence the better the system sensitivity.

EXALOS offers high-speed balanced receivers for SS-OCT with one of the lowest NEP values on the market [29], for example, a 380-MHz receiver with a high gain of 10,000 V/A and low NEP of 5 pW/√Hz (measured from DC to 100 MHz).

In general, the gain and the analog bandwidth of the balanced receiver shall be matched to the A-scan rate of the swept source, the imaging depth of the application, and the sampling rate of the data acquisition circuitry.

18.5.2 Data Acquisition and Digitization

Acquiring the analog fringe signals and converting them into digitized signals that can be processed in a field-programmable gate array (FPGA), a digital signal processor (DSP), a graphical or central processing unit (GPU/CPU) is an important task that decides upon the imaging performance of an OCT system. Key parameters of any DAQ card are sampling rate, voltage range, nominal resolution (Q), effective number of bits (ENOB), jitter, quantization error, and other parameters, such as the support for external clocking.

A general and typical architecture of a DAQ card is shown in Fig. 18.23. Here, two ADCs are clocked either from an internal clock (provided, e.g., by an on-board FPGA or by another clock source) or from an external clock, for example, the k-clock of the swept source (see Sect. 18.5.2.1). A second ADC might be needed in a polarization-diverse SS-OCT detection scheme, for example for endoscopic OCT with a highly-birefringent sample arm, or for polarization-sensitive OCT. It may be also needed to acquire the k-clock of the swept source in parallel to the OCT signal in order to perform real-time remapping (see Sect. 18.5.2.2). If the swept source is sufficiently stable over time, a fixed remapping vector could be used that was generated during a calibration procedure using the same ADC that is otherwise used for OCT signal detection (see Sect. 18.5.2.3).

Most DAQ cards feature an on-board FPGA anyway for various control tasks related to the data acquisition in the ADCs or related to the data exchange with the host, for example, through a PCIe bridge. Such an on-board FPGA can also be used to perform real-time OCT pre-processing and to transfer high-quality A-scans instead of raw data to the host PC (see Sects. 18.5.3 and 18.5.4). This FPGA may also be involved in the control of external peripherals such as optical scanners or other delivery optical systems.

18.5.2.1 ADC Resolution

Under certain conditions, a sampling resolution of 8 bits or less is sufficient for SS-OCT [30]. However, in order to support a larger dynamic range and to handle DC offsets through imperfect balancing, a nominal resolution of 12 bits or even more is used in many systems.

The resolution Q of an ADC determines the signal-to-quantization noise ratio (SQNR), which is equivalent to the maximum *theoretical* SNR that could be measured for a full-scale input sine wave [31]:

$$\max SNR_{\text{theo}}\ [dB] = 20 \cdot \log_{10}\left(2^{Q}\right) + 20 \cdot \log_{10}\left(\sqrt{\frac{3}{2}}\right) = 6.02 \cdot \mathrm{Q} + 1.76$$

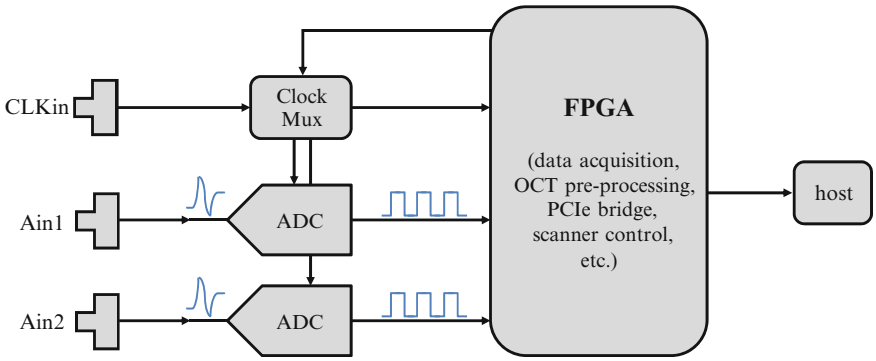

Fig. 18.23 Generic dual-channel DAQ card architecture with an onboard FPGA handling the data acquisition with the A/D converters and managing the data exchange to the host, for example, via an PCI Express bus. The DAQ card may support clocking of the ADCs through an external clock input

This means an 8-bit DAQ card could theoretically deliver a maximum SNR of 49.9 dB, while a 12-bit DAQ card could deliver a maximum SNR of 74.0 dB. However, due to signal distortions and other noise contributions besides the quantization noise, the maximum *effective* SNR that is measured with an ADC is always smaller than the theoretical value [32]:

$$\max SNR_{\text{eff}} \ [dB] = 6.02 \cdot ENOB + 1.76$$

For example, an 8-bit ADC achieving an SNR of 48.4 dB has an ENOB of 7.7 or a 12-bit ADC achieving an SNR of 65.4 dB has an ENOB of 10.7. The ENOB is dependent on the input frequency and is different for single-ended or differential detection.

18.5.2.2 Maximum SNR of PSF

It needs to be stressed that the maximum effective SNR is *not* describing the noise floor of the FFT and hence not the noise floor that the coherence function or PSF can have. This is because the FFT acts like an analog spectrum analyzer with a bandwidth proportional to the inverse of the number of FFT points N. The theoretical FFT noise floor is therefore $10 \cdot \log_{10}\left(\frac{N}{2}\right)$ dB below the quantization noise floor due to the processing gain of the FFT [31]. Some examples are given in Table 1.

The maximum SNR values that are practically achieved for a PSF are well below the theoretical limit due to various noise sources but also due to contributions from the OCT signal processing like an insufficient interpolation or resampling before the FFT.

18.5.2.3 ADC Sampling Rate

The required sampling rate (SR) of the DAQ card directly depends on the A-scan rate f_A and the duty cycle (DC) of the swept source, its sweep nonlinearity (ε),

Table 1 Maximum theoretical SNR of the PSF for DAQ cards with different resolutions as a function of the number N of FFT points

Resolution	$N = 2048$	$N = 4096$	$N = 8192$
6 bits	68.0 dB	71.0 dB	74.0 dB
8 bits	80.0 dB	83.0 dB	86.0 dB
10 bits	92.1 dB	95.1 dB	98.1 dB
12 bits	104.1 dB	107.1 dB	110.1 dB

the spectral sweep range in the frequency domain ($\Delta\nu$), and the targeted imaging depth (ID) of the application. It can be estimated as follows:

$$\mathrm{SR[MSPS]} \approx 6500 \cdot 2 \cdot \Delta\nu[\mathrm{THz}] \cdot \frac{(f_A)[\mathrm{kHz}]}{\mathrm{DC}} \cdot \varepsilon \cdot \mathrm{ID[mm]}$$

For example, a 100-kHz bidirectional sinusoidal swept source ($\varepsilon = 1.57$) with a sweep range of 1250–1360 nm ($\Delta\nu$ = 20 THz) and with a duty cycle of 100 % will require a DAQ card with a minimum sampling rate of ~408 MSPS for an imaging range of 10 mm. A 100-kHz linear swept source ($\varepsilon = 1.0$) with a 50 % duty cycle will require a minimum sampling rate of ~520 MSPS for the same imaging depth of 10 mm.

18.5.2.4 Direct k-Clocking

In this approach, the ADCs of the DAQ card are clocked directly from the k-clock of the swept source. However, most high-speed ADCs require continuous clocking operation, which means that an additional electrical circuitry has to generate a dummy clock for all periods of time at which the swept source does not provide a proper k-clock directly [33], for example, during a dark period of the laser or for a vanishing k-clock near the edges of the optical sweep spectrum. Furthermore, many high-speed swept sources exhibit nonlinear sweep characteristics with a k-clock that varies quickly in frequency. Such frequency-modulated external k-clock signals may cause dither and jitter problems in the ADCs, which can deteriorate the sampling performance. Finally, a lower-grade electrical k-clock signal may cause malfunction of the ADCs and may result in a complete A-scan loss.

18.5.2.5 Real-Time Resampling

In this approach the ADCs are clocked from an internal, continuous and fixed-rate clock that is provided by the DAQ card. The k-clock signal is acquired through a second ADC channel for every A-scan of the swept source and is used to generate in real time a calibration vector. This calibration vector is then used to resample the OCT signal prior to performing the FFT. Dynamic remapping is typically the method of choice to achieve the highest possible image quality with changing environmental influences or to get the highest degree of automation. On the other hand, dynamic calibration requires more hardware as well as more computing power than static calibration. Therefore, static calibration is typically used when hardware resources are limited. Nonetheless, dynamic and real-time remapping has been demonstrated for A-scan frequencies up to 100 kHz (further discussed in Sect. 18.5.4).

18.5.2.6 Resampling with Fixed Remapping Vector

In case the swept source is sufficiently stable over longer periods of time, a fixed remapping vector that is stored in memory may be used for linearization of the OCT signal. This remapping vector is generated through a calibration procedure where the fringe signal of a calibrated sample is recorded, typically using the same ADC channels that are otherwise used for OCT data acquisition. This method is least demanding in terms of detection hardware and processing infrastructure.

18.5.3 OCT Signal Processing Data Flow

Figure 18.24 shows the typical data flow used in SS-OCT signal processing based on remapping. This processing flow can be also realized in real-time OCT engines that perform signal processing in FPGA hardware (see Sect. 18.5.4). After acquisition of the OCT signal, a measured and stored background signal may be subtracted before the OCT signal is resampled using an interpolation algorithm (see Sect. 18.5.3.2). The resampling of the OCT signal is done through a calibration vector that is generated from the k-clock signal (see Sect. 18.5.3.1).

The inverse Fourier transform (FFT^{-1}) is applied to the resampled OCT signal that now has sample points being equidistant in k. The result of the FFT is an A-scan where typically the magnitude is plotted on a $20 \cdot \log_{10}$ scale. An optional final step of A-scan averaging may be implementing, as shown in Fig. 18.24. Furthermore, spectral windowing and dispersion compensation may be used prior to the FFT in order to improve the SNR of the A-scan.

18.5.3.1 Generation of Calibration Vector

Basically two approaches can be used to generate a calibration vector in order to resample the OCT signal.

The first approach relies on *amplitude detection* of the k-clock signal where certain reference points such as zero-crossings, peaks, or valleys are used to extract the timing positions of those points with an equidistant k-spacing.

The second approach relies on *phase unwrapping* through Hilbert transform. This Hilbert transform provides a phase rotation through a positive or negative 90° phase shift, which, in combination with a two-argument arc tangent operation, is used to extract the instantaneous phase of the k-clock signal, as shown in Fig. 18.25.

18.5.3.2 Interpolation and Resampling

The final step in the remapping process is the application of a linearization algorithm. The selection of an appropriate algorithm hinges on the balance between achieving a high-quality OCT tomogram and processing speed. In order to achieve high-performance remapping of nonlinear swept sources, it might be important to apply a nonlinear interpolation approach in real time unless the OCT signal is sufficiently oversampled (approximately by a factor 1.5–2). Several useful examples of signal processing methods to handle sweep nonlinearities in SS-OCT were reported in [20, 34, 35].

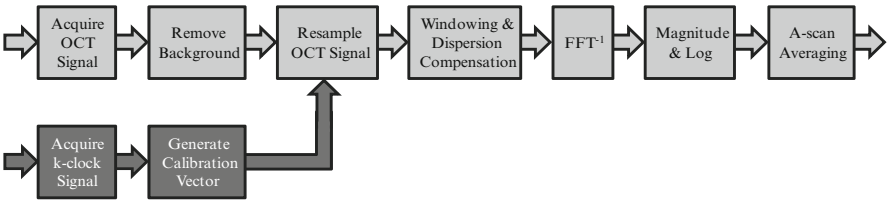

Fig. 18.24 Typical data flow of OCT signal processing based on remapping, here shown in a real-time architecture with acquisition of the k-clock reference signal in a parallel ADC port (*lower path*)

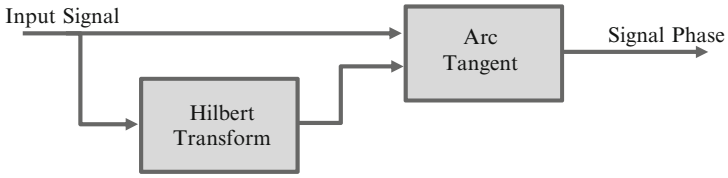

Fig. 18.25 Block diagram showing the use of Hilbert transform to extract the instantaneous phase information of the swept source

18.5.4 Real-Time OCT Engines

As mentioned in Sect. 18.5.2, real-time SS-OCT engines can be implemented on a variety of hardware platforms including FPGAs, DSPs, GPUs, or CPUs. In either of those choices, a DAQ card is needed that performs data acquisition and data transfer to the host PC. In many systems, an FPGA is employed anyway on the DAQ card such that the realization of an onboard real-time OCT engine inside the FPGA seems an interesting value proposition. In that approach, the DAQ card does not forward raw data to the host PC but preprocessed high-quality A-scans [36]. All the algorithms related to remapping and OCT signal processing are performed at real time on the DAQ card such that the host PC is mainly responsible for displaying of A-scan, B-scans, and C-scans and optional post-processing steps.

Such an FPGA-based SS-OCT engine for real-time linearization and remapping of nonlinear (e.g., sinusoidal) swept sources has been realized at A-scan frequencies of 40–100 kHz [37]. The two ADCs are clocked either at 250 MSPS for slower swept sources or at 500 MSPS for faster swept sources and feature a resolution of 12 bits. Real-time and unlimited generation of A-scans is performed using on-the-fly remapping in the FPGA. Each A-scan comprises 2,048 data points and could be extended to 4,096 data points to support longer imaging ranges. In addition, real-time A-scan averaging inside the FPGA is realized for

up to 32× averages. Video-rate B-scan displaying with 25 fps is supported on the host PC. OCT sensitivities of more than 100 dB (at a power of 1.5 mW in the sample arm) have been measured with a similar fall-off performance to off-line processing and spline interpolation. This platform is sufficient for 150 kHz swept sources and could be further extended to incorporate full-range imaging by using dispersion encoding or to a polarization-diverse detection scheme. By applying advanced real-time nonlinear interpolation algorithms, this system can be tailored to handle a wide variety of swept sources. This SS-OCT engine is also available as an OEM DAQ card to be integrated in a customer-specific system.

Acknowledgment The above-mentioned results are an outcome of a dedicated team of individuals working at EXALOS, namely, S. Gloor, A.H. Bachmann, M. Epitaux, T. von Niederhäusern, P. Vorreau, N. Matuschek, M. Rossetti, A. Hold, K. Brossi, and many others as well.

References

1. M.B. Wootten, J. Tan, Y.J. Chien, J.T. Olesberg, J.P. Prineas, "Broadband 2.4 μm superluminescent GaInAsSb/AlGaAsSb quantum well diodes for optical sensing of biomolecules", Semiconductor Science and Technology, **29**(11) (2014)
2. L. An, P. Li, G. Lan, D. Malchow, R.K. Wang, High-resolution 1050 nm spectral domain retinal optical coherence tomography at 120 kHz A-scan rate with 6.1 mm imaging depth. Biomed. Opt. Express **4**(2), 245–259 (2013)
3. J.M. Schmitt, Optical coherence tomography (OCT): a review. IEEE J. Sel. Top. Quantum. Electron. **5**(4), 1205–1215 (1999)
4. E. Feltin, A. Castiglia, G. Cosendey, L. Sulmoni, J.-F. Carlin, N. Grandjean, M. Rossetti, J. Dorsaz, V. Laino, M. Duelk, C. Velez, Broadband blue superluminescent light-emitting diodes based on GaN. Appl. Phys. Lett. 95(8) (2009)
5. S. Maliszewska, M. Wojtkowski, Broadband blue light for Optical Coherence Microscopy. Photonics. Lett. Pol. **3**(4), 138–140 (2011)
6. M. Rossetti, M. Duelk, C. Velez, A. Castiglia, J.-M. Lamy, L. Lahourcade, D. Martin, N. Grandjean, The reliability of GaN superluminescent diodes and laser diodes, *10th International Conference on Nitride Semiconductors ICNS*. Edinburgh, UK (2013)
7. EXALOS SLED modules (EXS), http://www.exalos.com/sled-modules/
8. Accessible emission limits (AEL) according to the international laser safety standard IEC-60825-1, edition 2.0 (2007.03) and ANSI Z136, Equipment classification and requirements, Table 4. p. 87, with Corrigendum 1 (2008–08)
9. EXALOS broadband light sources (EBS), http://www.exalos.com/broadband-light-sources/
10. M. Duelk, V. Laino, P. Navaretti, R. Rezzonico, C. Armistead, C. Vélez, Isolator-free 840-nm broadband SLEDs for high-resolution OCT, *Opt. Coherence Tomogr. Coherence Domain Opt. Methods BioMed. XIII, Proceedings SPIE* 7168 (2009)
11. S.R. Chinn, E.A. Swanson, J.G. Fujimoto, Optical coherence tomography using a frequency tunable optical source. Opt. Lett. **22**(5), 340–342 (1997)
12. M.A. Choma, M.V. Sarunic, C.H. Yang, J.A. Izatt, Sensitivity advantage of swept source and Fourier domain optical coherence tomography. Opt. Express **11**(18), 2183–2189 (2003)

13. S.H. Yun, G.J. Tearney, J.F. de Boer, N. Iftimia, B.E. Bouma, High-speed optical frequency-domain imaging. Opt. Express **11**(22), 2953–2963 (2003)
14. L.A. Kranendonk, X. An, A.W. Caswell, R.E. Herold, S.T. Sanders, R. Huber, J.G. Fujimoto, Y. Okura, Y. Urata, High speed engine gas thermometry by Fourier-domain mode-locked laser absorption spectroscopy. Opt. Express **15**(23), 15115–15128 (2007)
15. K. Hsu, T. Haber, J. Mock, J. Volcy, T.W. Graver, High-speed swept-laser interrogation system for vibration monitoring. Struct. Health Monit. 2003, DEStech Publications, pp. 1043–1050 (2003)
16. EXALOS swept sources (ESS), http://www.exalos.com/swept-sources/
17. E.A. Swanson, D. Huang, M.R. Hee, J.G. Fujimoto, C.P. Lin, C.A. Puliafito, High-speed optical coherence domain reflectometry. Opt. Lett. **17**(2), 151–153 (1992)
18. R. Leitgeb, C.K. Hitzenberger, A.F. Fercher, Performance of Fourier domain vs. time domain optical coherence tomography. Opt. Express. **11**(8), 889–894 (2003)
19. J.F. de Boer, B. Cense, B.H. Park, M.C. Pierce, G.J. Tearney, B.E. Bouma, Improved signal-to-noise ratio in spectral-domain compared with time-domain optical coherence tomography. Opt. Lett. **28**(21), 2067–2069 (2003)
20. A.E. Desjardins, B.J. Vakoc, M. Suter, S.-H. Yun, G.J. Tearney, B.E. Bouma, Real-time FPGA processing for high-speed optical frequency domain imaging. IEEE Trans. Med. Imaging **28**(9), 1468–1472 (2009)
21. B.R. Biedermann, W. Wieser, C.M. Eigenwillig, T. Klein, R. Huber, Dispersion, coherence and noise of Fourier domain mode locked lasers. Opt. Express **17**(12), 9947–9961 (2009)
22. B. George, D. Derickson, High-speed concatenation of frequency ramps using sampled grating distributed Bragg reflector laser diode sources for OCT resolution enhancement. *Opt. Coherence Tomogr. Coherence Domain Opt. Methods BioMed. XIV, Proceedings SPIE* 7554 (2010)
23. V. Jayaraman, J. Jiang, B. Potsaid, G. Cole, J.G. Fujimoto, A.E. Cable, Design and performance of broadly tunable, narrow line-width, high repetition rate 1310nm VCSELs for swept source optical coherence tomography. *Vertical-Cavity Surface-Emitting Lasers XVI, Proceedings SPIE* 8276 (2012)
24. T. von Niederhäusern, C. Meier, M. Duelk, P. Vorreau, Instantaneous coherence length measurement of a swept laser source using a Mach-Zehnder interferometer, *Opt. Coherence Tomogr. Coherence Domain Opt. Methods BioMed. XV, Proceedings SPIE* 7889 (2011)
25. A. Bilenca, S.H. Yun, G.J. Tearney, B.E. Bouma, Numerical study of wavelength-swept semiconductor ring lasers: the role of refractive-index nonlinearities in semiconductor optical amplifiers and implications for biomedical imaging applications. Opt. Lett. **31**(6), 760–762 (2006)
26. B.H. Park, M.C. Pierce, B. Cense, S.-H. Yun, M. Mujat, G.J. Tearney, B.E. Bouma, J.F. de Boer, Real-time fiber-based multi-functional spectral-domain optical coherence tomography at 1.3 μm. Opt. Express **13**(11), 3931–3944 (2005)
27. S.M.R. Motaghiannezam, D. Koos, S.E. Fraser, Differential phase-contrast, swept-source optical coherence tomography at 1060 nm for in vivo human retinal and choroidal vasculature visualization. J. Biomed. Opt. **17**(2), 026011 (2012)
28. Y. Chen, D.M. de Bruin, C. Kerbage, J.F. de Boer, Spectrally balanced detection for optical frequency domain imaging. Opt. Express **15**(25), 16390–16399 (2007)
29. EXALOS balanced receivers (EBR). http://www.exalos.com/balanced-receivers/
30. Z. Lu, D.K. Kasaragod, S.J. Matcher, Performance comparison between 8- and 14-bit-depth imaging in polarization-sensitive swept-source optical coherence tomography. Biomed. Opt. Express **2**(4), 794–804 (2011)
31. W. Kester, Taking the mystery out of the infamous formula 'SNR=6.02N+1.76dB' and why you should care. Analog Devices, Tutorial MT-001
32. W. Kester, Understand SINAD, ENOB, SNR, THD, THD+N, and SFDR so you don't get lost in the noise floor. Analog Devices, Tutorial MT-003

33. J. Xi, L. Huo, J. Li, X. Li, Generic real-time uniform K-space sampling method for high-speed swept-source optical coherence tomography. Opt. Express **18**(9), 9511–9517 (2010)
34. S. Vergnole, D. Lévesque, G. Lamouche, Experimental validation of an optimized signal processing method to handle non-linearity in swept-source optical coherence tomography. Opt. Express **18**(10), 10446–10461 (2010)
35. K.K.H. Chan, S. Tang, High-speed spectral domain optical coherence tomography using non-uniform fast Fourier transform. Biomed. Opt. Express **1**(5), 1309–1319 (2010)
36. V. Bandi, J. Goette, M. Jacomet, T. von Niederhäusern, A.H. Bachmann, M. Duelk, FPGA-based real-time swept-source OCT systems for B-scan live-streaming or volumetric imaging. *Opt. Coherence Tomogr. Coherence Domain Opt. Methods BioMed. XVII, Proceedings SPIE* 8571 (2013)
37. EXALOS OCT engine (EOE). http://www.exalos.com/oct-engine/

Broad Bandwidth Laser and Nonlinear Optical Sources for OCT

19

Angelika Unterhuber, Boris Považay, Aaron D. Aguirre, Yu Chen, Franz X. Kärtner, James G. Fujimoto, and Wolfgang Drexler

Keywords

Fibers • Lasers • Optical coherence tomography • Solid-state • Supercontinuum generation • Ultrafast lasers • Ultrafast technology

OCT achieves very high axial image resolutions independent of focusing conditions because the axial and transverse resolution are determined independently by different physical mechanisms. This implies that axial OCT resolution can be enhanced using broad bandwidth, low-coherence length light sources. The light source not only determines axial OCT resolution via its bandwidth and central emission wavelength but also determines the penetration in the sample (biological tissue), the contrast of the tomogram, and the OCT transverse resolution. A minimum output power with low amplitude noise is also necessary to enable high sensitivity and high-speed – real time – OCT imaging. Furthermore, ultrabroad bandwidth light sources emitting at different wavelength regions enable a potential extension of OCT, e.g., spectroscopic

A. Unterhuber (✉)
Center for Medical Physics and Biomedical Engineering, Medical University of Vienna, Vienna, Austria
e-mail: angelika.unterhuber@meduniwien.ac.at

B. Považay
Center for Medical Physics and Biomedical Engineering, Medical University of Vienna, Vienna, Austria

OptoLab, HuCe - Bern University of Applied Sciences (BUAS), Postfach, Biel/Bienne, Switzerland

A.D. Aguirre
Massachusetts General Hospital, Boston, MA, USA

Department of Electrical Engineering and Computer Science and Research Laboratory of Electronics, Massachusetts Institute of Technology, Cambridge, MA, USA

© Springer International Publishing Switzerland 2015

W. Drexler, J.G. Fujimoto (eds.), *Optical Coherence Tomography*,
DOI 10.1007/978-3-319-06419-2_20

OCT. Hence, it is obvious that the light source is *the* key technological parameter for an OCT system, and proper choice is imperative [1].

Several main criteria have to be considered when choosing a light source for OCT imaging. A light source and its usability for OCT can be characterized by:

- Center wavelength
- Bandwidth, spectral shape
- Power
- Noise
- Single transverse mode
- Stability

In principle, thermal light sources are capable of achieving high axial resolution because of their large spectral bandwidth, but their use for clinical OCT applications is limited by the low power contained in a single spatial mode which is necessary for high sensitivity, high-speed in vivo clinical OCT imaging. As stated previously, the depth resolution of OCT is defined as being equal to the coherence length of the light source.

Ti:sapphire lasers are excellent light sources for ultrahigh-resolution (UHR) OCT due to the extraordinary large gain bandwidth and high optical output power. With advanced mirror technology, dispersion control, and adapted cavity design, optical bandwidth of up to 300 nm at full width of half maximum (FWHM) centered at about 800 nm could be achieved resulting in sub-μm axial resolution OCT in tissue. Broad bandwidth Cr^{3+}:LiSGaF lasers are cost-effective, directly diode-pumped alternative solid-state light sources for OCT in the 800 nm wavelength region. Efforts also focused on developing broad bandwidth light sources in the 1,300 nm wavelength range permitting OCT micrometer-scale resolution along with millimeter range penetration depth. A laser spectrum covering the 1,230–1,580 nm wavelength region with an optical bandwidth of 250 nm (FWHM) was generated directly out of an all-solid-state Cr:forsterite laser. Cr^{4+}: YAG lasers have the ability to produce sub-20 fs pulses enabling broad optical bandwidth laser emission in the wavelength range from 1,300 to 1,600 nm. These

Y. Chen
Department of Electrical Engineering and Computer Science and Research Laboratory of Electronics, Massachusetts Institute of Technology, Cambridge, MA, USA

Biomedical Optics and Imaging Laboratory, Fischell Department of Bioengineering, University of Maryland, College Park, MD, USA

F.X. Kärtner
Center for Free-Electron Laser Science, DESY (Deutsches Elektronen-Synchrotron), Hamburg, Germany

J.G. Fujimoto
Department of Electrical Engineering and Computer Science and Research Laboratory of Electronics, Massachusetts Institute of Technology, Cambridge, MA, USA

W. Drexler
Center for Medical Physics and Biomedical Engineering, Medical University of Vienna, General Hospital Vienna, Vienna, Austria

lasers operate at room temperature, do not require a vacuum, and have larger gain bandwidths than Er-doped fiber lasers. Microstructured fibers (MF) have been investigated and explored in terms of nonlinear effects and corresponding supercontinuum generation over the past years. Different Ti:sapphire, Nd:Glass, and other ultrashort solid-state and fiber lasers have been adapted in respect of pulse duration (bandwidth), output power, and repetition rate and coupled to MFs and waveguides with varying parameters concerning diameter, length, and in case of waveguides doping and doping concentration. Supercontinua in the visible and near-infrared wavelength region can be generated.

19.1 Solid-State Lasers

The term solid-state laser is generally reserved for lasers that rely on a gain medium in crystalline or glass form having ions introduced as an impurity in an otherwise transparent dielectric host material (in crystalline or glass form). They have been of great research interest since the first ruby laser was invented by Maiman in 1960 [2]. This laser was based on an aluminum crystal (Al_2O_3) doped with Cr^{3+}. Several solid-state lasers provide optical gain over a broad frequency range, corresponding to that of ultrashort pulses. High output powers with ultrabroad bandwidth laser emission are achievable. The excess noise is higher than in conventional superluminescent diodes (SLDs) but comparable to multiplexed SLDs. Traditionally, the bandwidth of laser materials, $\Delta\lambda$, is defined as full width at half maximum (FWHM) of the gain cross-sectional spectrum in the wavelength domain. The bandwidth of the ultrashort optical pulse, $\Delta\nu$, is commonly defined at its intensity FWHM in the frequency domain. Finally, the pulse duration, $\Delta\tau$, is usually referred to as the FWHM of its intensity profile in the time domain. The uncertainty relation $\Delta\nu\Delta\tau \approx 1/\pi$ provides a measure of the minimum frequency bandwidth of the ultrashort pulse. The bandwidth $\Delta\lambda$ required from the amplifying medium depends on the central wavelength $\Delta\lambda \approx \Delta\nu\lambda^2/c$. On the contrary, the relative bandwidth $\Delta\lambda/\lambda$ provides a more convenient and natural bandwidth measure because it does not depend on the central wavelength, it is the same in wavelength and frequency domains, and it is directly connected to the number of cycles per pulse $(\Delta\lambda/\lambda)^{-1} \approx (\Delta\nu/\nu)^{-1} \propto N$.

Ions belonging to one of the series of transition elements of the Periodic Table, in particular rare earth (RE) or transition-metal (TE) ions, are generally used as the active impurities in lasers. These active ions are embedded in either oxides, e.g., Al_2O_3, or fluorides, e.g., $YLiF_4$. The Al^{3+} site is too small to accommodate RE ions, so it is generally used for transition-metal ions, while the Y^{3+} site can be used for RE ions. Also, $LiSrAlF_6$ (LiSAF) or $LiCaAlF_6$ (LiCAF) are used for transition metals – most common for Cr^{3+} ions. Oxides are very hard and offer good mechanical and thermomechanical properties. In contrast, fluorides are soft, but also have good thermo-optical properties (i.e., low thermal-induced birefringence and lensing). Glasses have a low melting temperature, so they can be produced very cheap, but they have a low thermal conductivity, thus bad thermomechanical and thermo-optical properties. We will only review transition-metal-doped materials,

since rare earth-doped materials offer bandwidths and wavelengths that have not typically been used for OCT.

19.1.1 Transition-Metal-Doped Materials

The electronic configuration of Cr can be written as (Ar)3d54s1, while those of Ti, Co, and Ni can be written in the general form (Ar)3dN4s2 (with $N = 2$ for Ti, 7 for Co, and 8 for Ni). By adding a chromium atom to an ionic crystal, the one electron belonging to its 4 s orbital and two 3d electrons are used for ionic binding, and Cr is found as a triply ionized ion with three electrons left in the 3d shell. In titanium, the two 4s electrons and one 3d electron are used for ionic binding, and Ti is again present as a triply ionized ion with only one electron left in the 3d shell. All absorption and emission features of transition-metal ions arise from 3d-3d transitions. The 3d states interact strongly with the crystal field of the host leading to the vibronic character of the corresponding transitions and to ultrabroad absorption and emission bands. Electric-dipole transitions within the 3d shell are parity forbidden. The crystal field is much stronger than in RE materials. As a result, the 3d-3d transitions are more readily allowed, and the lifetimes are significantly shorter (a few microseconds) than those of the 4f-4f transitions in RE ions. Doping of crystals or glasses with transition-metal ions supports a strong coupling of the electronic levels of the doped laser ion to the phonon relaxations of the host lattice leading to a good separation of absorption and emission spectra.

19.1.1.1 Ti:Sapphire

Since the reporting of laser action by Moulton in 1982 [3], the Ti:sapphire laser has been the subject of intensive investigations and has become the most widely used tunable solid-state laser and the medium of choice for ultrafast pulse generation because of the broad amplification bandwidth. Ti:sapphire systems provide a tuning range of about 400 nm (corresponding to $\Delta v_0 \approx 100$ THz) with a relatively large gain cross section centered at 800 nm, thus providing the largest bandwidth of any lasers shown to date. This large optical bandwidth has made Ti:Sapphire a medium of choice for UHR OCT in the NIR regime.

19.1.1.2 Alternative Solid-State Light Sources

Cr^{3+}:LiSAF and Cr^{3+}:LiCAF offer a wide tuning range, and the corresponding lasers can be either flash lamp pumped or diode-laser pumped. In both systems, Cr^{3+} ions replace some of the Al^{3+} ions in the lattice, and the impurity ion occupies the center of a (distorted) octahedral site surrounded by six fluorine ions. Due to its wider tuning range and higher n_2, Cr:LiSAF is generally preferred to Cr:LiCAF. Due to the large gain linewidth centered around 850 nm and the possibility of diode pumping with laser diodes at 670 nm wavelength, these media are also attractive for generating femtosecond pulses. Sub-10 fs pulses from diode-pumped Kerr-lens mode Cr-doped colquirite laser have been reported [4, 5], making these systems competitive with Ti:sapphire lasers in terms of performance. Other interesting broadband lasing materials include Cr:LiSGaF in the 800 nm regime, Cr^{4+}:$MgSiO_2$ in the

Table 19.1 Optical properties of broadband laser materials

Material	Pump band λ (μm)	Emission cross-section σ (10–19 cm^2)	Upper state lifetime τ (μs)	Absorption band λ (μm)
Ti^{3+}:sapphire	0.45–0.6	3.8	3.2	0.6–1.05
Cr^{3+}:LiSGaF	0.60–0.7	0.33	88	0.7–1.05
Cr^{4+}:forsterite	0.85–1.2	1.1	15	1.1–1.37
Cr^{4+}:YAG	0.88–1.1	8	4	1.35–1.65

1,350 nm regime, and Cr^{4+}:YAG in the 1,500 nm regime. Interesting lasing materials in the infrared are Cr^{2+}:ZnSe operating at 2.5 μm or Co^{2+}:MgF_2 centered at 2 μm. Table 19.1 compares the optical properties of these gain media.

19.1.2 Femtosecond Lasers

Ultrashort light pulses represent the shortest, controlled, and technically produced events. To put the time scale of the femtosecond pulse in context, consider that one femtosecond compared to a second is equivalent to 5 min compared to the age of the universe. Such short laser pulses are very attractive for two reasons: they concentrate a large amount of energy within a short time interval and offer a broad bandwidth coherent pulse spectrum. Femtosecond laser development to date has mainly concentrated on the temporal features of the pulses, which were often optimized to the detriment of the spectral shape. In OCT imaging, however, the spectral width and shape rather than the pulse duration is most important. Since shorter pulse width corresponds to broader spectrum, short pulses and broadband spectrum cannot be regarded as independent. They are connected via a time/frequency uncertainty relationship (time-bandwidth product). Short pulse duration allows for time-resolved studies of fast processes occurring on a time scale of the pulse width, while applications like OCT benefit from the broad coherent pulse spectrum.

However, unlike ultrafast femtosecond time-resolved measurements where special care must be exercised to maintain the short pulse duration, OCT measurements depend on field correlations rather than intensity correlations. Field correlation is preserved even if the pulse duration is long. Femtosecond mode-locked solid-state lasers can generate ultrabroad bandwidth, low-coherence light with a single spatial mode and high power, providing both high resolution and high brightness necessary for high-speed OCT imaging. These lasers can operate over a broad range of wavelengths that are desirable for ultrahigh-resolution as well as spectroscopic OCT imaging in tissue. Since the early days of OCT Ti:sapphire lasers have widely been used for in vitro and in vivo OCT imaging in nontransparent tissues [6].

19.1.3 Mode Locking

The ability to deliver high brightness, broadband light from solid-state lasers for OCT imaging is, in turn, intimately linked to the ability to generate ultrashort

optical pulses through mode-locking techniques. In a free-running laser, typically a large number of transverse and longitudinal modes are oscillating simultaneously without fixed mode-to-mode amplitude and phase relationships. The resulting laser output is a time-averaged statistical mean value. The formation of a mode-locked pulse train from noise starts with the selection of one peak fluctuation or at least a small number. By forcing the longitudinal modes to oscillate with some definite relation between their phases, the modes interfere and produce short pulses in the pico- or femtosecond regime which is referred to as mode-locked. In this case, very short pulses with high intensities can be generated, especially when the phase offset between different frequencies approaches zero. In the frequency domain, mode-locking corresponds to a frequency comb of equally spaced synchronized modes. A short pulse corresponds to a broad frequency comb. In the time domain, it corresponds to a light pulse traveling inside the laser cavity.

A large number of mode-locking techniques have been developed to generate short pulses in solid-state lasers:

- Active mode-locking – the longitudinal modes are locked by a phase or frequency modulator driven by an external source. An RF signal is applied to the modulator at exactly the frequency interval of the longitudinal modes.
- Passive mode-locking – the longitudinal modes are locked by an element that is not driven externally but instead exploits some nonlinear optical effect, such as saturation of a saturable absorber or a nonlinear refractive index change in a suitable material.

Nowadays, Kerr-lens mode-locking is the state-of-the-art method for sub-10 fs pulse generation directly from a mode-locked laser. In Kerr-lens mode-locking [7], strong nonlinear refraction at high peak intensities causes self-focusing of Gaussian beams. Since it relies on a nonresonant electronic nonlinearity, its response time is less than a femtosecond. The fast self-amplitude modulation of the pulses due to the Kerr effect can shape and stabilize extremely short pulses. The pulse propagates with the group velocity which can be expressed by

$$\frac{dvg}{dv} = -v_g^2 \beta'', \tag{19.1}$$

where β'' is the group dispersion of the medium. Materials in the visible region of the spectrum have positive or normal dispersion, i.e., $\beta'' > 0$. Therefore in a laser crystal, v_g decreases with increasing frequency. Longer wavelengths travel faster than shorter ones, causing a redshift of the pulse. High-intensity mode-locked pulses are redshifted due to self-phase modulation and normal dispersion. Positive self-phase modulation and positive group-velocity dispersion in the Kerr medium can be compensated for by a dispersive delay line based on prism pairs introducing negative dispersion into the resonator. Although the glasses of the prisms have normal dispersion, the geometry of the ray path can be arranged such that the blue components of the pulse pass the prisms in a shorter time than the red components. Although a number of prism arrangements can be devised, usually two prisms are used at minimum deviation and Brewster's angle incidence at each

surface. Also dispersive (chirped) mirrors are widely used for dispersion compensation.

Since the Kerr nonlinearity is usually not strong enough for the cw mode-locking process to self-start, usually a strong fluctuation must be induced by either perturbing the cavity or by adding nonlinearity to the system (saturable absorber). The simplest method to start KLM in a laboratory setup is to slightly tap one of the resonator mirrors. Disturbing the cavity mirrors will sweep the frequencies of competing longitudinal modes, and strong amplitude modulation due to mode beating will occur. The most intense mode-beating pulse will be strong enough to initiate mode locking.

19.1.4 Resonator Design

A resonator commonly employed for KLM is an astigmatically compensated cavity consisting of a pair of focusing mirrors and one or two flat mirrors. The laser crystal as a Kerr medium is inserted into a tightly focused section of the resonator for high nonlinearity. KLM can be established as a trade-off between output power, stability, and tolerance to the exact position of the components. An analytical treatment of nonlinear resonators has shown that for a given pump power and pump spot size, the most critical parameters are the distance of the two focusing mirrors and the location of the Kerr medium with respect to the mirrors [8].

In a basic oscillator-cavity configuration, the laser is pumped from a continuous-wave (cw) laser source, which is usually now an intracavity-doubled diode-pumped neodymium laser. Recently also compact frequency-doubled DBR-tapered diode lasers for direct pumping of Ti:sapphire lasers have been demonstrated [63]. This pump light is focused into a Brewster's angle cut crystal, collinearly with the laser axis, through the back side of one of the focusing mirrors and the fluorescent light (laser light) bounces between two concave focusing mirrors placed around it, several dispersive mirrors, and an output coupler. High doping concentration and reasonable lengths of laser crystals are necessary for efficient absorption of the pump radiation.

19.1.4.1 Cavity Dispersion in Femtosecond Mode-Locked Lasers

In the generation of ultrashort pulses, a key limitation poses the linear dispersion within the laser material itself, which causes a wavelength-dependant delay: long-wavelength components of the pulse spectrum propagate faster than the short-wavelength components.

For this reason, the concepts of phase velocity, group velocity, and group delay dispersion in a dispersive medium have to be reviewed.

The electric field $E(t,z)$ of a plane, linearly polarized, monochromatic electromagnetic wave traveling at a frequency ω in the z-direction in a transparent medium can be written as

$$E = A_0 \exp\ j(\omega t - \beta z) \tag{19.2}$$

with A_0 as a constant and β as the propagation constant which is a function of the angular frequency ω. In this case, the propagation constant $\beta = \beta(\omega)$ is a characteristic of the given medium, referred to as the dispersion relation of the medium. The total phase of the wave is now $\phi_t = \omega t - \beta z$. Elemental changes dt and dz of the temporal and spatial coordinates of the velocity of a given phase front must fulfill the condition $d\phi_t = \omega dt - \beta dz = 0$ giving

$$v_{ph} = \frac{dz}{dt} = \frac{\omega}{\beta} \tag{19.3}$$

where v_{ph} is the phase velocity of the wave.

Since a light pulse is generally traveling in the medium and ω_L is the center frequency and $\Delta\omega_L$ the width of the corresponding spectrum, the dispersion relation over the bandwidth $\Delta\omega_L$ can be approximated by a linear law

$$\beta = \beta_L + (d\beta/d\omega)_{\omega=\omega_L}(\omega - \omega_L) \tag{19.4}$$

with β_L as propagation constant corresponding to the frequency ω_L, where the electric field can be expressed as

$$E(t,z) = A\left[t - \left(z/v_g\right)\right]\exp[j(\omega_L t - \beta_L z)] \tag{19.5}$$

and A is the pulse amplitude, $\exp[j(\omega_L t - \beta_L z)]$ is the carrier wave, and v_g is the group velocity given by

$$v_g = \left(\frac{d\omega}{d\beta}\right)_{\beta=\beta_L} \tag{19.6}$$

Due to the fact that the pulse amplitude is a function of the variable t–(z/v_g), the pulse propagates at a speed v_g without changing its shape. After traversing the length l of the medium, the pulse experiences a time delay

$$\tau_g = \frac{l}{v_g} = l\left(\frac{d\beta}{d\omega}\right)_{\omega_L} = \phi'(\omega_L) \tag{19.7}$$

where the phase ϕ is dependent on the frequency ω

$$\phi(\omega - \omega_L) = \beta(\omega - \omega_L)l \tag{19.8}$$

and

$$\phi'(\omega_L) = [d\phi(\omega - \omega_L)/d\omega]_{\omega_L} \tag{19.9}$$

is referred to as the group delay of the medium at the frequency ω_L

When two pulses with bandwidths $\Delta\omega_1$ and $\Delta\omega_2$ centered at ω_1 and ω_2 travel in the medium ($\omega_2 > \omega_1$), the two pulses travel at different group velocities v_{g1} and v_{g2}. Thus, if the peaks of the two pulses enter the medium at the same time, then, after traversing the length l of the medium, they become separated in time by a delay

$$\Delta\tau_g = \phi'(\omega_2) - \phi'(\omega_1) \cong \phi''(\omega_1)(\omega_2 - \omega_1) \tag{19.10}$$

with

$$\phi''(\omega_1) = \left[d^2\phi/d\omega^2\right]_{\omega_1} \tag{19.11}$$

Light pulses with large bandwidths $\Delta\omega_L$ cannot any longer be described by the linear dispersion relation. Different spectral regions of the pulse travel with different group velocities resulting in a pulse broadening. Assuming that the dispersion relation within the bandwidth $\Delta\omega_L$ can be approximated by a parabolic law, the pulse broadening due to dispersion $\Delta\tau_d$ is given approximately by the difference in group delay between the fastest spectral component and the slowest one

$$\Delta\tau_d \cong |\phi''(\omega_L)|\Delta\omega_L \tag{19.12}$$

The quantity $\phi''(\omega_L)$ is referred to as the group delay dispersion (GDD) of the medium at frequency ω_L and is a measure for the pulse broadening per unit bandwidth of the pulse. It can also be written as

$$\Delta\tau_d \cong l\left|\left(\frac{d^2\beta}{d\omega^2}\right)_{\omega_L}\right|\Delta\omega_L \tag{19.13}$$

where the quantity group-velocity dispersion (GVD) at frequency ω_L is given

$$GVD = \left(\frac{d^2\beta}{d\omega^2}\right)_{\omega_L} = \left[\frac{d\left(1/v_g\right)}{d\omega}\right]_{\omega_L} \tag{19.14}$$

Its magnitude gives the pulse broadening per unit length of the medium and per unit bandwidth of the pulse. This concept for the GVD can only be applied for homogeneous media. For an inhomogeneous or multicomponent medium, GDD is differently to consider.

19.1.4.2 Introducing Negative Dispersion into the Laser Cavity: Dispersion Management

Since the laser crystal provides positive or normal dispersion, a suitable element providing negative or anomalous dispersion is required for the compensation of the cavity GDD. Advances in crystal growth have allowed for thinner and thinner

crystals with higher doping levels, but crystals ~2 mm thick are still required to achieve a reasonable gain. Compensation of the crystal's positive group delay dispersion with the opposite negative group delay dispersion introduced by an intracavity prism pair [9] ultimately led to fourth-order dispersion limited pulses of sub-10 fs duration.

A four-prism sequence allows for accurate dispersion compensation and low losses since all surfaces are at Brewster's angle to the beam path so that the GDD of the laser rod can be compensated for. The negative value of GDD can be coarsely changed by changing the separation l of the two prism pairs. By translating any one of the prisms along an axis normal to its base, the total length of the optical medium traversed by the beam can be changed. This motion introduces, in a finely controlled way, a positive (material) dispersion of adjustable size without altering the ray directions and hence the negative dispersion due to the geometry of the ray path. Since the transmitted beam is collinear with the incident beam, this facilitates inserting the four-prism sequence in an already aligned cavity. One of the drawbacks is that not only second-order dispersion but also third-order dispersion is introduced (fused quartz is one of the best optical materials with a very low ϕ'''/ϕ'' ratio). Simultaneous third-order dispersion (TOD) compensation is possible only at specific wavelengths depending on the rod and prism material. Therefore, limitations are due to the insufficient cancellation of higher-order dispersion terms (third, fourth, etc.) resulting in pulse duration of about 10 fs in Ti:sapphire oscillators. For Ti:sapphire lasers, simultaneous GDD and TOD compensation can be achieved in wavelengths ranges of a few nanometers around 800 nm with beryllium oxide (BeO) prisms, around 850 nm with fused silica and around 880 nm with BK7. Using solely fused silica prisms for the dispersion compensation, sub-10 fs pulses were reported for the first time directly from an oscillator [10]. These pulses showed M-shaped spectra owing to the fourth-order dispersion that was found to limit the achievable bandwidth. There exist compensation schemes with only one or more than two intracavity prisms, but none seems to allow for the intracavity dispersion compensation required for pulse durations below 8 fs. For even shorter pulse generation in the regime of one optical cycle, the development of dispersive high-reflective broad bandwidth mirrors is mandatory. Szipöcs [11, 12] set a new milestone in ultrashort pulse generation with the invention of chirped mirrors (CM). These first CM designs were obtained by computer optimization of "chirped" Bragg reflectors (cf. Fig. 19.1). Szipöcs reported a design consisting of 42 alternating layers of SiO_2 and TiO_2, which had a bandwidth of 200 nm at a center wavelength of 800 nm. Other than the geometric dispersion approaches, they allow for compensation of arbitrary higher-order dispersion. Several advances in laser technology with chirped and double-chirped mirrors have resulted in octave-spanning spectra.

19.2 Ti:Sapphire Laser Development

Recent advances in laser technology resulted in development of ultrafast solid-state lasers capable of emitting powerful spectra with bandwidths spanning several

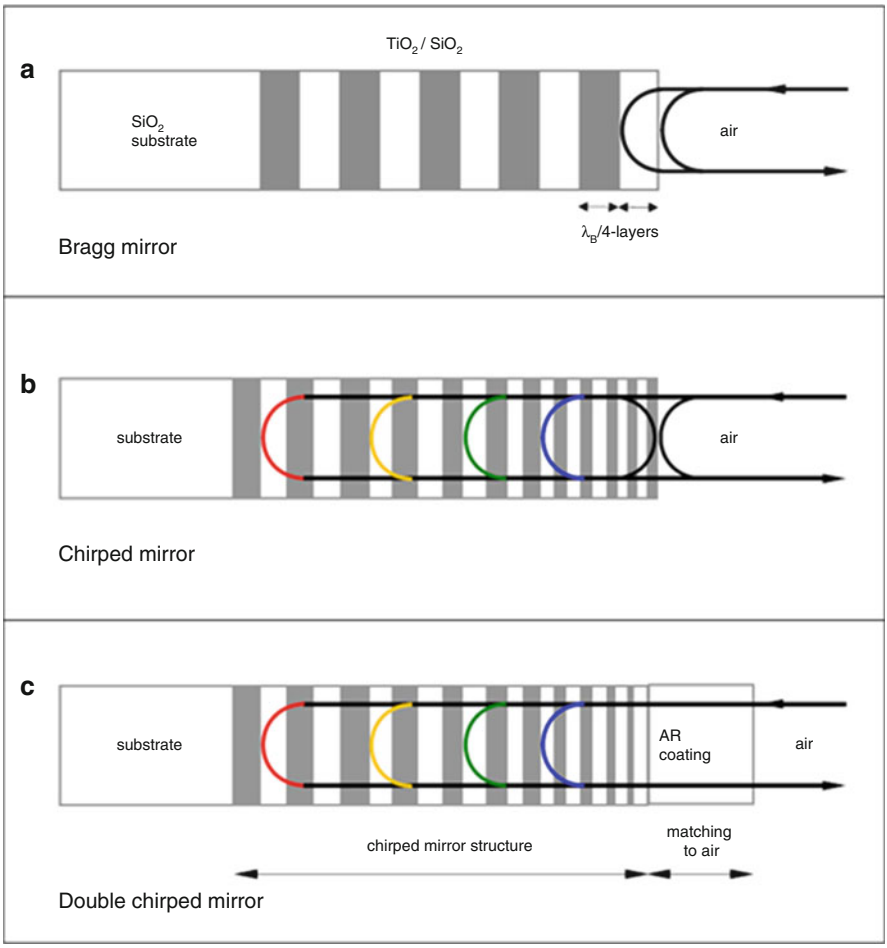

Fig. 19.1 *Mirror technology for Ti:sapphire lasers*. Comparison between Bragg mirror (**a**), chirped mirror (**b**), and double-chirped mirror (**c**)

hundred nanometer at full width at half maximum (FWHM) [13]. Pulses in the 8–10 fs range can easily be generated from prism-pair oscillators. Since pulse duration has been pushed towards the theoretical limit of one optical cycle, which is approximately three femtosecond, accurate dispersion control over a broad wavelength range is demanded, and dispersion effects have to be minimized in the design of these femtosecond lasers. The two major sources of dispersion in a mode-locked laser are self-phase modulation that is a part of the Kerr effect and normal dispersion in the laser crystal or any other optical component in the resonator.

Pulses significantly shorter than 10 fs could be generated from mirror-dispersion-controlled oscillators, whereas oscillators employing both prism pairs and chirped mirrors for dispersion control allowed the generation of sub-6 fs pulses. Moreover, external spectral broadening in special fibers, pumped by ultrashort

(picosecond to femtosecond) laser pulses, enabled the generation of so-called supercontinua (SC). While the bandwidth of a solid-state laser is limited by the gain spectrum of the laser crystal as well as the mirror technology, nonlinearly broadened light sources utilizing microstructured fibers like photonic crystal fibers (PCF) [14] or tapered fibers [15] do not exhibit such limitations. Spectra covering more than one octave or even more than two octaves are generally achievable. However, this kind of external broadening often results in significant power fluctuations, spectral modulations, and excess noise (in addition to the noise of the pump source) [16, 17] in the optical output, which limit clinical applications of OCT. Therefore, it is desirable to generate an ultrabroad spectrum directly from a compact solid-state laser. Octave-spanning (at the pedestal) Ti:sapphire lasers that use chirped mirrors in combination with prism pairs and some other intracavity elements such as a glass plate for enhanced self-phase modulation with a two-foci laser for broadening were demonstrated [18]. It was also demonstrated that a broad bandwidth optical output can be generated by self-phase modulation in a Ti:sapphire crystal in a prismless oscillator [19]; however, the spectra exhibited strong modulations, severely compromising applications where a clean temporal structure of the generated pulses or the first-order autocorrelation of the laser output is essential. The latter requirement applies to ultrahigh-resolution and spectroscopic OCT [20–22]. Further limitations of all these systems were the need of highly sophisticated, bulky, and very expensive pump sources and the lack of reliability and long-term stability. Each system represented a unique laboratory prototype with almost no chance of doubling. OCT imaging on a daily base was not feasible. With advanced mirror technology the generation of ultrabroad bandwidth ($>$277 nm at FWHM) and smooth spectra directly out of a prismless Ti:sapphire was reported [23].

19.2.1 Mirror Technology for Femtosecond Pulse Ti:Sapphire Lasers

Standard dielectric quarter-wave Bragg mirrors are inappropriate for the generation of sub-10 fs pulses because of their restricted high-reflectance bandwidth and the strong higher-order dispersion near the edges of the HR range. Metal mirrors do not experience these restrictions, but suffer from high insertion losses. Nevertheless, the first sub-10 fs pulses directly from an oscillator were achieved by using silver mirrors instead of dielectric mirrors and additional prism pair for dispersion control [10]. However, considerable residual higher-order dispersion prevented such lasers from producing pulses shorter than $\sim$8.5 fs. This restriction demanded alternative methods for dispersion compensation. Even for propagation in air, the group velocity of electromagnetic signals depends on the carrier frequency. Ultrashort pulses contain broad frequency spectra, and the varying propagation speed of the different spectral components will always cause the pulse to change its shape during propagation. Optimal performance can only be obtained if all spectral components arrive at the same time meaning that the spectral phase is the same for all frequency components. Such pulses are called “transform limited” because

they have a minimum root-mean-square time-bandwidth product. By introducing dispersive materials in the beam path, the resulting group delay between different spectral components will lead to a pulse whose instantaneous frequency (the derivative of the temporal phase with respect to time) depends on time. Such pulses are called "chirped." There are attributes like "down-chirped," "up-chirped," and "unchirped" for a pulse whose instantaneous frequency falls (blue-first, negative chirp) or rise (red-first, positive chirp) with time or remain constant ("transform limited"). Parallel to the standard design approach, chirped mirror technology allows minimizing the system complexity.

For ultrashort pulse generation, the round trip time τ_r in the resonator for all frequency components of the mode-locked pulse must be the same, i.e., $\tau_r = d\varphi/d\upsilon = \text{constant}$, where φ is the phase change after one round trip. Otherwise, frequency components that experience a cumulative phase shift no longer add constructively and are attenuated. This limits the bandwidth of the pulse and leads to pulse width broadening. The frequency-dependent phase shift of the pulse during one round trip can be expressed in a Taylor series about the center frequency v_0,

$$\frac{d\varphi}{dv} = \varphi'(v_0) + \varphi''(v_0)\Delta v + \frac{1}{2}\varphi'''(v_0)\Delta v^2,$$

with φ', φ'' and φ''' as the derivatives of the phase with respect to frequency. When φ'' is nonzero, the pulse will have a linear frequency chirp, while a nonzero third-order dispersion will induce a quadratic chirp on the pulse.

19.2.1.1 Quarter-Wave BRAGG Mirrors

Standard high-reflectance laser mirrors typically consist of quarter-wave stacks (cf. Fig. 19.1) and therefore are limited in the maximum reflectance which is given by the BRAGG wavelength λ_B that is twice the optical thickness of the unit cell defining the quarter-wave structure. It can be seen that in the stop band around the angular frequency $\omega_B = 2\pi c/\lambda_B$, the condition $(\cos\phi - r^2)/(1 - r^2) \leq -1$ holds, where $\phi = \pi\omega/\omega_B$ is the phase acquired after propagation through a layer pair and where Fresnel's reflectance for the index step is given by

$$r = (nH - nL)/(nH + nL) \tag{19.15}$$

The stop band covers the wavelength range between $\lambda_{St} = n\lambda_B/[2\pi - 2(\arccos(r))]$ and $\lambda_{St} = \pi\lambda_B/2\arccos(r)$ only in an ideal case when the wavelength dependence of the refractive index is neglected. Then its fractional width $\Delta\omega/\omega_B$ depends only on the index ratio between the high- and the low-index material:

$$\frac{\Delta\omega}{\omega_B} = \frac{4}{\pi}\arcsin(r) \tag{19.16}$$

For epitaxially grown semiconductor quarter-wave mirrors, all refractive indices are typically between 3.0 and 3.6, enabling bandwidths of about 10 %.

For amorphous coatings, typical materials with low indices are between MgF_2 ($n = 1.37$) and SiO_2 (n = 1.44), and high-index materials like Ta_2O_5 ($n = 2.1$) and TiO_2 ($n = 2.35$), which results in fractional bandwidths of about 30 %.

The maximum achievable reflectance in case of small absorption coefficients $\alpha_{H,L}$ for an infinite number of layers [24] is approximately given by $R(\lambda_B) = R_0(\lambda_B)$ $[1 - (\lambda_B/2)(\alpha_H + \alpha_L)n_l/(n_H^2 - n_L^2)]$. So the maximum reflectance of a quarter-wave mirror can be assumed for a lossless quarter-wave mirror and is given by

$$R_0(\lambda_B) = \left(\frac{1 - aqp^{m-1}}{1 + aqp^{m-1}}\right)^2 \tag{19.17}$$

It will already be approached for a limited number of layers. Assuming that the absorption in the mirror can be neglected which is especially valid for ion-beam sputtered coatings made of TiO_2 and SiO_2, the maximum reflectance will approach unity with increasing layer pairs. Since quarter-wave mirrors introduce significant amounts of negative dispersion for wavelengths $\lambda > \lambda_B$, they can be used for dispersion compensation over a small region of their high-reflectance bandwidth. Broadband mirrors can be designed by several quarter-wave sections whose stop bands overlap. Since such mirrors exhibit regions of extreme phase variations, they cannot be used for femtosecond or OCT applications.

19.2.1.2 Chirped Mirrors

UHR OCT demands for ultrabroad Gaussian-like stable spectra generated directly out of the Ti:sapphire. The proper choice of broad bandwidth dispersive mirrors is mandatory for accurate dispersion compensation in the spectral range approaching or even exceeding one optical octave (cf. Fig. 19.1). These mirrors have contributed significantly to enhancement of the performance, compactness, and reliability of femtosecond laser sources. The generation of sub-10 fs pulses directly from the oscillator can now be achieved routinely with CM dispersion-controlled oscillators. Progress in CM design and manufacturing in combination with advanced oscillator designs have permitted the direct generation of sub-6 fs pulses. Such extreme bandwidths create new challenges and difficulties making some of the small-bandwidth approaches ineffective and deserve special treatment.

CMs are custom-tailored multilayer dielectric mirrors, where the thickness of each layer is carefully chosen so that the whole system has special dispersion properties. The BRAGG wavelength is gradually decreased during deposition (at least in the initial design, which may be altered by subsequent computer optimization) so that the incident light is reflected with a wavelength-dependent group delay. The average group delay of such simple chirped mirrors can be increased with wavelength, but with the drawback of the superimposing of a strong wavelength-dependent dispersion oscillation [25]. The mirror consists of a large number (∼40) of alternating low- and high-refractive index layers whose thickness progressively increases going towards the substrate. Layers with

increasing thicknesses (e.g., quarter-wave layers with a gradually increasing local Bragg wavelength) are stacked such that longer wavelengths penetrate deeper into the mirror structure, producing negative group delay dispersion (GDD). Due to the chirp of the Bragg wavelength, the high-reflectivity bandwidth is larger compared to standard dielectric quarter-wave mirrors. Both features together allow for a more efficient compensation of higher-order dispersion over a broader spectral range. Interference of light waves reflected from different plane-parallel interfaces results in a certain frequency-dependent reflectance $R(\lambda)$ and phase shift $\varphi(\lambda)$ of the incident light, where $\varphi(\lambda)$ is directly connected to the group delay (GD) and the GDD introduced by the mirror:

$$\mathrm{GD}(\omega) = -\varphi'(\omega)$$

$$\mathrm{GDD}(\omega) = -\varphi''(\omega)$$

It is the same principle that works in the Bragg reflectors (stack of layers with a fixed optical thickness equal to $\lambda_0/4$). But CMs possess another very important property: they can be designed in such a way that the frequency-dependent phase shift $\varphi(\lambda)$ matches dispersion properties of materials common in laser systems (air, fused silica, or Ti:sapphire), which is essential for the generation of ultrashort pulses. A desirable dispersion can be achieved if optical layer thicknesses gradually change along the coating, so that a component with wavelength λ is reflected from the part of the stack, where the optical thickness of layers is close to $\lambda/4$. This gradual change of optical layer thicknesses is referred to as "chirping"; hence, this type of mirror is named "chirped mirror."

The GD of the reflected beam increases with decreasing values of ω, thus giving $\phi'' < 0$. One can obtain a value of ϕ'' that, within the bandwidth of interest, is approximately constant with frequency $\phi''' \cong 0$, but the GDD can also be designed to exhibit a slight linear variation with frequency and a slope suitable for compensating the TOD of other cavity components. GDD per bounce is in general $-50\ \mathrm{fs}^2$.

Of particular interest are the so-called double-chirped mirrors: an analytic approach based on the coupled-mode theory for multilayer interference coatings. In this approach, a chirped mirror is composed of Bragg cells, where each cell is characterized by a corresponding Bragg wavelength and the thickness of the high-refractive index layer. Both these parameters are chirped in order to achieve a smooth increase of the coupling coefficient, which was recognized as a prerequisite for suppression of GDD oscillations [26]. A perfect AR coating is assumed to match the impedance from air to the first low-index layer. Although the recently found improved implementations and the analytical predesign methods were essential for enhancing the performance of CMs, they did not obviate the need for efficient computer optimization techniques. On the one hand, the request for mirror designs with even larger bandwidth, which would permit the generation of nearly single-cycle pulses for scientific applications, makes the requirements for chirped mirrors extreme that even small improvements may play a crucial role. On the other hand, the high production cost of chirped mirrors demands designs

with reduced sensitivity to small discrepancies between the layer thicknesses of a calculated design and those of the manufactured mirror, especially if the mirror is designed for a broad spectral range.

Nevertheless, impedance matching with AR coatings or edge filters can only be achieved over a limited bandwidth. This drawback can be overcome by coating the CM on a thin wedged substrate and illuminating it from the substrate side. With this approach, the incident medium is glass (to which the multilayer can be perfectly impedance matched over an arbitrary broad bandwidth). The impedance mismatch will occur now at the substrate air interface, resulting in an additional reflected beam. This beam will not distort the GDD characteristic of the mirror because it cannot interfere with the main (useful) beam, having a different propagation direction. TFICM (tilted-front-interface chirped mirrors) [27] might allow enhancing the bandwidth of pulses emitted directly from the oscillator far beyond 300 nm.

19.2.2 Ultrabroad Bandwidth Ti:Sapphire

19.2.2.1 Sub-Two-Cycle Pulse Oscillator with Intracavity Prisms

In the early days of OCT a Ti:sapphire laser with 4 μm axial resolution has been used for in vitro OCT imaging in nontransparent tissues to improve OCT axial resolution [6]. Consequently, in preliminary UHR OCT studies, a system was developed and could be optimized to support 260 nm of optical bandwidth from a state-of-the-art Ti:sapphire laser [28] resulting in 1 μm axial resolution [20, 21]. This laser generated pulses of <5.5 fs duration corresponding to bandwidths of more than 350 nm at 800 nm center wavelength. This high performance was achieved using specially designed double-chirped mirrors with high-reflectivity bandwidth and controlled dispersion response. The resonator was a standard z-fold design, as shown in Fig. 19.2a. Figure 19.2b depicts the measured reflectivity of the DCM and the output-coupling mirror (OC) (top), the desired condition for perfect dispersion compensation, and the designed and the measured GDD of one bounce on the DCM (second from top), the measured spectrum behind the output coupler (third from top), as well as the measured intracavity spectrum with a silver mirror instead of the output coupler (bottom). An interferometric autocorrelation as shown in Fig. 19.2c was accomplished. A fit to the interferometric autocorrelation of a sech-shaped pulse would result in a pulse width of 4.3 fs FWHM, a fit to a Gaussian in 4.8 fs. The most conservative assumption for the pulse shape is the sinc function and results in 5.4 fs. The good agreement of the measured interferometric autocorrelation with those derived from the spectrum and the sinc function indicates a pulse width between 4.9 and 5.4 fs, which is shorter than two optical cycles at the center wavelength of 800 nm.

Necessary light source specifications for ultrahigh-resolution OCT include not only spatial coherence, ultrabroad bandwidth emission with enough output power, and good amplitude stability but also optimum spectral shape. Since the coherence length is defined as the full width at half maximum of the field autocorrelation measured by the OCT interferometer, the width and also the shape of the coherence

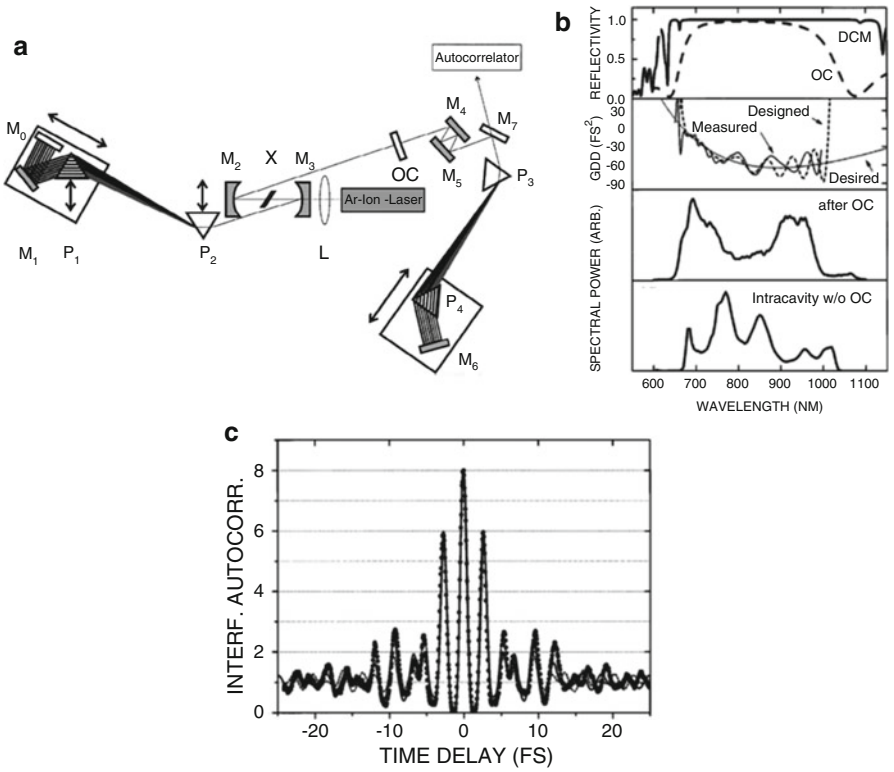

Fig. 19.2 *Sub-two-cycle pulses from a Kerr-lens mode-locked Ti:sapphire laser*. Cavity setup (**a**) with crystal X; curved mirrors M_2 and M_3; flat mirrors M_0, M_1, and M_4, M_7; output-coupling mirror OC; and prism sequence P_1, P_2. All double-chirped mirrors (*DCM's*) are *gray*; the other mirrors are silver mirrors. Lens L focuses the pump beam into the crystal. The prism sequence P_3, P_4 is necessary for extracavity dispersion compensation. (**b**) Depicts the measured reflectivity of the DCM and the output-coupling mirror (*OC*) (*top*), the desired condition for perfect dispersion compensation, and the designed and the measured GDD of one bounce on the DCM (second from *top*), the measured spectrum behind the output coupler (third from *top*), as well as the measured intracavity spectrum with a silver mirror instead of the output coupler (*bottom*). (**c**) Measured interferometric autocorrelation of the Ti:sapphire laser. The *dashed curve* is a fit of a sinc^2 function with a FWHM of 5.4 fs, and the *solid curve* is the calculation from the spectrum [28]

function of an OCT system are dependent on the spectral shape of the light source as well as on the transfer function of the OCT system. The latter one is mainly determined by the optical properties of the interferometer, e.g., wavelength-dependent losses and splitting ratios of beam splitter and lenses, as well as cutoff wavelength of employed single-mode fibers as well as the wavelength-dependent sensitivity of the employed photodetectors. The ideal spectrum for OCT would have Gaussian spectral shape, resulting in a Gaussian coherence function with no sidelobes. Large spectral modulations would reduce sensitivity and resolution, due to the presence of sidelobes in the fringe pattern that appear symmetrically to the coherence functions maximum. There are several possibilities to change the shape

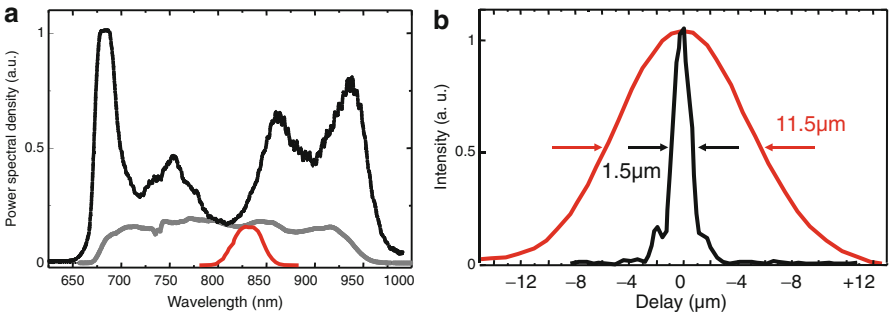

Fig. 19.3 *Ultrahigh-resolution OCT using a sub-two-cycle pulse Kerr-lens mode-locked Ti:sapphire laser*. Original spectrum from Ti:sapphire (**a**, *black*) and reshaped spectrum (**a**, *gray*) using wavelength-dependent attenuation compared to a spectrum from a standard superluminescent diode (**a**, *red*). (**b**) Demodulated OCT axial scan showing the axial resolution of OCT using this Ti:sapphire (*black*) versus a standard superluminescent diode SLD (*red*) light sources. Solid-state lasers enable almost a 10× improvement in resolution [21]

of the emission spectrum of the used light source. The easiest way is to introduce optical dichroic or interference filters that suppress certain wavelength regions. Another possibility is to spatially disperse the optical beam with prisms and to induce local and therefore wavelength-dependent losses by introducing razor blades or thin objects into the dispersed light beam. Figure 19.3a demonstrates the effect of this shaping method when applied to a strongly modulated spectrum of the sub-two-cycle pulses from the Kerr-lens mode-locked Ti:sapphire laser described above (cf. Fig. 19.2). It also shows a comparison of the spectra and resolution (Fig. 19.3b) of an OCT A-scan using a conventional superluminescent diode light source versus this femtosecond Ti:sapphire laser source. The ultrabroad bandwidths which are generated by the femtosecond laser enable the axial resolution of OCT to be improved by a factor of nearly 10× better than standard OCT technology.

19.2.2.2 All-Chirped Mirror Oscillator (ACM Oscillator)

An ultrabroad bandwidth complementary chirped mirrors pair, compensating for Ti:sapphire dispersion in the wavelength range 600–1,000 nm with maximal spectral intensity loss of 1 %, has been designed for an all-CM oscillator (cf. Fig. 19.4) [23].To design these mirrors, a suitable compromise between the bandwidth, dispersion, and reflectance has to be found. A major goal was to keep the dispersion fluctuations of each mirror as small as possible since we found that in this way, we can improve the manufacturing reproducibility of the design. Each of the mirrors consists of 63 layers. If the mirror is used in pair with the input coupler, the net GDD and the net reflectance are closer to their targets. The small positive second-order dispersion of the complementary mirror can be compensated with other chirped mirrors. For the implementation of CMs in an octave-spanning oscillator, the previously designed complementary pair of an input coupler (IC) and a chirped mirror (CM) has to be redesigned. The IC has transmission >99 % in the

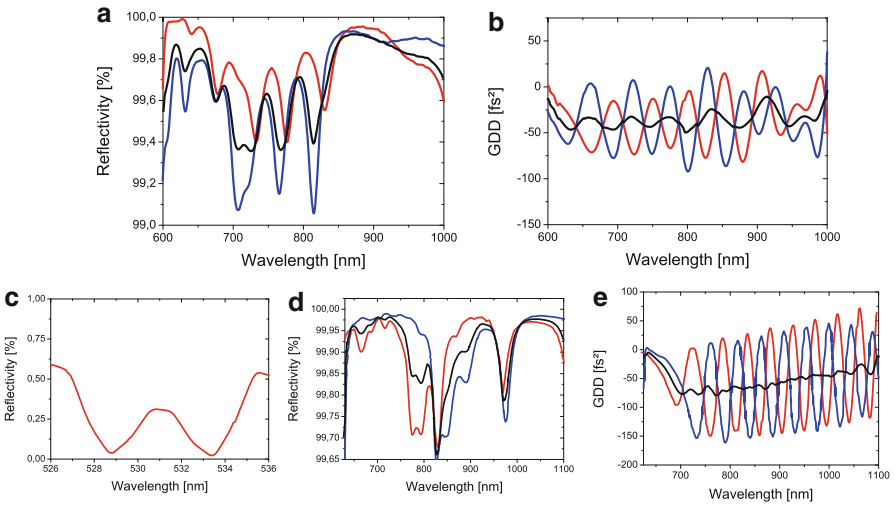

Fig. 19.4 *Chirped mirror technology for ultrabroad bandwidth Ti:sapphire lasers*. Reflectance (**a**) and GDD (**b**) of a chirped mirror pair. A broadband input coupler (**c**, **d**) and a complementary chirped mirror (**e**)

wavelength range 525–539 nm. Both IC and CM have reflectance >99.5 % in the range 625–1,110 nm, as well as a "smooth" dispersion in the range 700–1,100 nm.

Optimization of Ti:sapphire oscillators has resulted in lasers with short (few millimeters) highly doped active media – 2–3 mm in the experiments mentioned in the previous paragraphs. Consequently, the amount of positive dispersion to be compensated is limited and can be balanced by using 4–6 bounces of CMs. The total number of bounces of cavity mirrors is typically higher. One would thus be inclined to use a minimum number of CMs and employ the much cheaper and easier to manufacture standard Bragg mirrors (BMs) in addition. Although TiO_2/SiO_2 BMs exhibit high reflectance over ~200 nm at 800 nm (bandwidths that can support pulses with 120–140 nm at FWHM), the range within which GDD remains constant is smaller. Furthermore, deviations from GDD = 0 add up constructively, as all BMs have identical dispersion. In an oscillator employing both CMs and BMs, the bandwidth over which mode locking can be achieved is severely limited by the range within which the GDD of BMs remains constant. With accurate dispersion management, spectra slightly below 200 nm at FWHM are feasible. Nevertheless, a lot of effort is needed to obtain such spectra, and no reliable performance and reproducibility can be expected. In such laser cavities, BMs with enhanced transmittance at the pump wavelength have been widely used as input couplers because design and particularly manufacturing of dichroic CMs rise serious problems (mainly because of the high sensitivity of the dichroic CMs transmittance to manufacturing errors). However, comparing the dispersion and reflectance characteristics of BMs and dichroic CMs, the advantages of the latter are overwhelming. With the advent of highly accurate deposition methods

like magnetron sputtering tailored for CM coatings, manufacturing of dichroic CM has become possible. As the dichroic BM input coupler acted so far as a bottleneck on the bandwidth of the mode-locked pulsed lasers, there was no motivation to replace other BMs in the cavity with broader bandwidth CMs. Nevertheless a Ti:sapphire oscillator employing dichroic CMs enormously benefits in terms of bandwidth and pulse duration if all the other reflectors in the cavity are CMs.

Therefore, further increasing of the bandwidth using a compact oscillator design is feasible by replacing all high-reflecting mirrors by broadband dispersive mirrors and employing a single frequency 532 nm pump source on a platform of 600 × 400 mm. Ultrabroad bandwidth and smooth spectra from a prismless Ti:sapphire laser can be generated making additional external shaping not longer necessary.

Therefore, two main goals had to be followed in the development of dispersive dielectric multilayer coatings:

- One effort was the increasing of the bandwidth of chirped mirrors from 200 nm to as large as possible (>400 nm)
- Simultaneously search for a technology suitable for the accurate and reproducible high-yield production of CM in large quantities

Fulfilling these two criteria a laser formed by a standard x-folded resonator [29] composed of chirped, mirrors, a broadband output coupler, and a pair of wedges for fine tuning the dispersion in the cavity was built. The major benefit of the prismless laser is the compactness and stability of the cavity. The generated spectrum has a 277 nm bandwidth at FWHM and with only 2 dB spectral modulation. In addition, the spectral bandwidth is ~380 nm at −10 dB below its maximum, which is suitable for phase stabilization and frequency metrology based on interference of second- and third-harmonic light [30, 31]. The schematic of the laser cavity is shown in Fig. 19.5a. The laser is pumped by a diode-pumped, frequency-doubled Nd:YVO4 laser (Verdi, Coherent Inc.). The thickness and the absorption coefficient of the Ti:sapphire crystal are 2.5 mm and 5.0 cm^{-1}, respectively. The radius of curvature of the concave mirrors is $r = -50$ mm. All-chirped mirrors in the cavity were designed for minimal fluctuations and manufactured by Layertec GmbH. The transmission of the output coupler is 10 %. A pair of thin fused silica wedges is inserted at the Brewster's angle for intracavity dispersion control. The prismless laser generates an average output power of 250 mW for 3.65 W pump power and 64 MHz repetition rate.

The spectrum generated from the oscillator and measured with an optical spectrum analyzer with single monochromator mode is shown in Fig. 19.5b in linear (green) as well as logarithmic representations (red). The bandwidth of the spectrum is 277 nm (141 THz) at FWHM. The fine spectral modulations at long wavelengths are caused by vapor absorption and/or the structure of the reflectivity spectrum of the chirped mirrors in the cavity. On the logarithmic scale, spectral components can be observed at ~625 nm and 1,005 nm at −10 dB below maximum. Although the chirped mirrors and the output coupler only support a spectrum from 700 to 900 nm, the generated spectrum from the oscillator extends beyond this region. This means that most of the light at the wings of the spectrum is not generated through lasing but by self-phase modulation in the crystal, a phenomenon

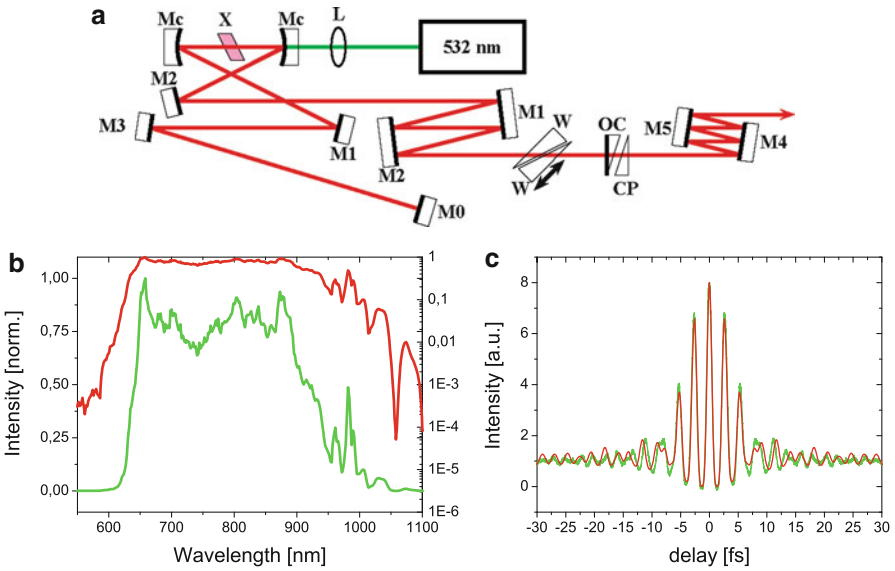

Fig. 19.5 *Ultrabroad bandwidth Ti:sapphire*. Schematic of prismless Ti:sapphire laser with extracavity dispersion control (**a**). *L* incoupling lens, *Mc* dichroic input coupler, *M1-5* dispersive mirrors, *W* wedge, *OC* output coupler, *CP* compensating plate. (**b**) Spectrum generated from the mirror-dispersion-controlled oscillator depicted on a logarithmic and linear scale. (**c**) Measured and reconstructed interferometric autocorrelation traces of the pulse. A phase-retrieval algorithm reveals a pulse width of 6.5 fs. The *red line* shows the retrieved IAC trace from the *Spider* measurement [23]

previously observed [32]. The output pulses are compressed by six reflections of the chirped mirrors, and the temporal characteristics of the pulses are measured using an interferometric autocorrelator designed for sub-10 fs pulse diagnostics (Femtometer, Femtolasers Produktions GmbH). The frequency-doubling crystal is a 10 μm thick BaB_2O_4 (BBO) crystal (type I, $\Theta = 29°$). Figure 19.5c shows the measured interferometric autocorrelation trace (IAC). The FWHM of the intensity envelope has been evaluated as 6.5 fs by using a phase-retrieval algorithm.

19.2.2.3 Ultrabroad Bandwidth Laser Sources with Modulations Below 3 dB

For UHR OCT imaging, a good compromise between high resolution and contrast has to be found. Especially the sharp spectral feature in the longer wavelength region is extreme prominent and would significantly impair OCT image quality. One possible solution to overcome these problems is the use of edge filters and to cut off this peak. Another possibility is to change the dispersion in the cavity. In a first trial, a slightly modified mirror arrangement with an edge filter could improve the spectral shape. An output power of 250 mW at 2.8 W pump power and a spectrum of 255 nm shown in Fig. 19.6a enabled 1.4 μm axial OCT resolution (Fig. 19.6b). Further investigations did not result in additional improvement neither

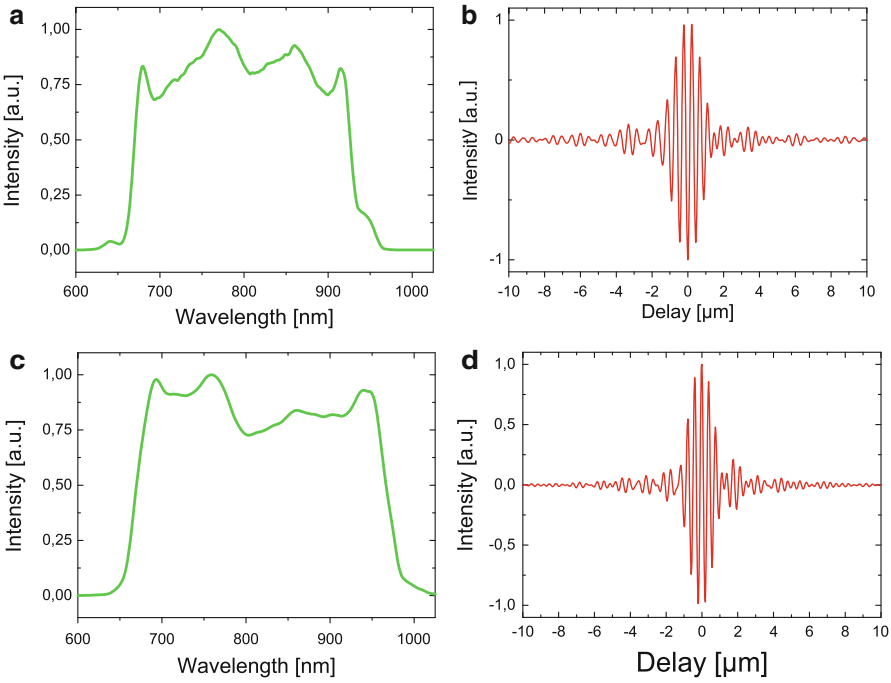

Fig. 19.6 *Ultrabroad bandwidth laser sources with modulations below 3 dB*. Typical output spectrum generated from the ultrabroad bandwidth all-chirped mirror oscillator with edge filter (**a**, 255 nm; **c**, 300 nm) and interference signal (**b**, **d**) corresponding to the spectrum resulting in a free-space axial resolution of 1.4 µm (**b**) and 1.3 µm (**d**), respectively

in terms of the spectral bandwidth or in the spectral shape. Therefore, ultrabroad bandwidth CMs were necessary. Insertion of one of the ultrabroad bandwidth CMs covering a wavelength range from ~600 to 1,000 nm allowed for a spectral bandwidth of 300 nm at FWHM with a nice spectral shape (Fig. 19.6c) enabling 1.3 µm axial OCT resolution (Fig. 19.6d). Careful balance of dispersion and reflectivity in the laser cavity plays a crucial role in the laser development. Oscillations in GDD and relative large losses in reflectivity produce large spectral ripples of more than 3 dB. Tilt and position of CMs have drastic effects and change the spectrum. By variation of the position of the CMs inside the laser cavity, the tilt can be changed. Hence, dispersion and reflectance characteristics can be improved and adapted to the demanded requirements. Slightly manufacturing errors in shifting the spectral wavelength of CMs can be balanced.

19.2.3 Low Pump Power Broad Bandwidth Laser Sources

State-of-the-art commercially available laser systems are producing sub-20 fs and sub-12 fs Ti:sapphire lasers for scientific applications (Femtolasers Produktions

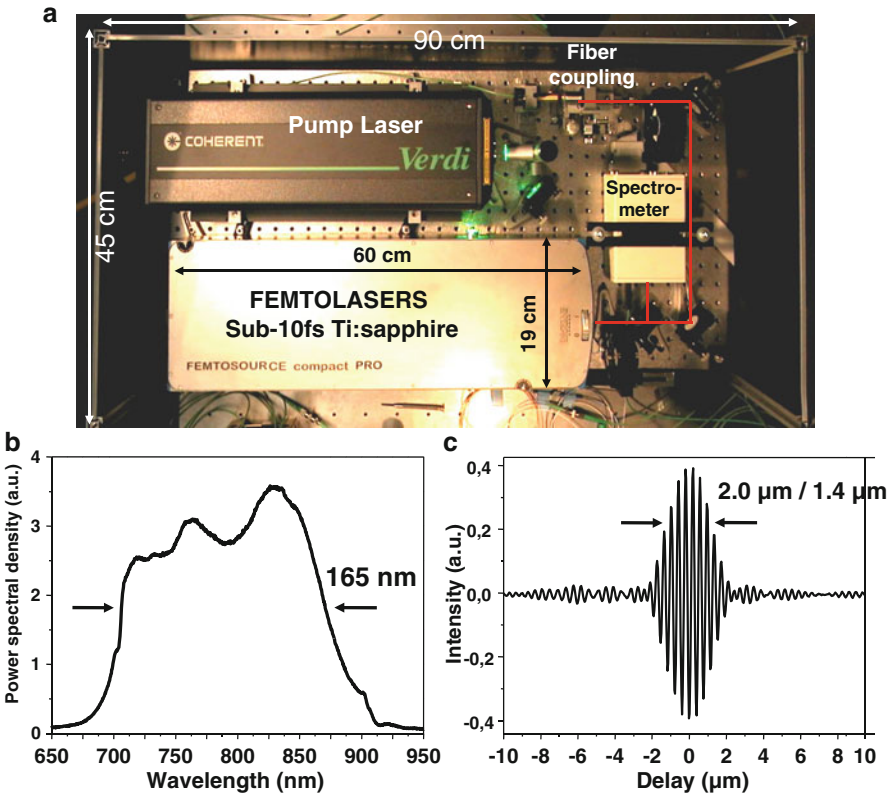

Fig. 19.7 *Ti:sapphire laser*. Schematic diagram (**a**) of a high power Ti:sapphire laser (FEMTOSOURCE COMPACT PRO, Femtolasers GmbH). Typical optical output power spectra of this Ti:sapphire laser (**b**) and corresponding interference signal (**c**) enabling a free-space axial resolution of 2 µm corresponding to 1.4 µm in biological tissue

GmbH). For a long time, the standard pump system for Ti:sapphire lasers has been the Argon:ion laser (cf. Fig. 19.7). This laser has an operating wavelength of 514 nm and suits the absorption maximum of Ti:sapphire. The Argon:ion laser, however, was expensive, bulky, and needed regular maintenance. These facts increased the complexity and susceptibility to faults. Nowadays, they are fully replaced by frequency-doubled diode-pumped lasers with neodymium as the active ion in a variety of hosts (YAG, YLF, etc.). These lasers operate at 532 nm. The pump sources are quite reliable, but bulky and extremely expensive. Since they are not operating at the absorption maximum of Ti:sapphire, they are less efficient. Nonetheless, they offer excellent beam quality and maintenance-free reliable operation. Clinical applications demand compact, user-friendly, cost-effective, and highly stable systems. Reducing the threshold of the laser system with newly developed low loss laser mirrors allows employment of cost-effective 1 W pump sources instead of expensive 5 W pump sources. A compact pump source in combination with an optimized cavity layout is

another prerequisite of increasing compactness and stability of the Ti:sapphire oscillator itself. This can be achieved with the elimination of prism pairs in the cavity, since chirped mirrors show a superior behavior in terms of performance as well as compactness and user-friendliness.

Development of state-of-the-art femtosecond laser technology that establishes a new generation of ultrabroad bandwidth, high-energy, compact, user-friendly light sources was achieved with a diode-pumped solid-state 1 W laser from Laser Quantum Ltd., namely, the *excel 1,000*. The *excel 1,000* was characterized in terms of its beam quality and stability. The *excel 1,000* was tested concerning its ability for pumping compact femtosecond Ti:sapphire oscillators. Nowadays the excel is a well established pump source for ultrabroad bandwidth Ti:sapphire lasers. For integration in a clinical viable system the laser has to meet some requirements concerning short- and long-term stability, reliability on a daily basis, and a reasonable price and size to transfer a high sophisticated ultrabroad bandwidth Ti:sapphire laser prototype from the optical bench to real-world applications.

The cavity of the compact, low-cost Ti:sapphire oscillator is a standard astigmatism compensated x-folded cavity with an incoupling lens with $f = 35$ mm, 50 mm folding mirrors, and a 3 mm thick Ti:sapphire laser crystal that has an absorption coefficient $\alpha = 5.0\ \mathrm{cm}^{-1}$ and where the pump source was implemented (cf. Fig. 19.8). Low-loss resonant dispersive "chirped" mirrors were designed to precisely compensate for second- and third-order dispersion of the laser crystal and air, keeping the reflectivity almost as high as for high-reflecting mirrors for a design bandwidth of about 200 nm. Two of these mirror pairs were implemented in the oscillator. The resonator is asymmetrical folded, and some mirrors are used in double pass for reducing the laser size. The laser can be mode locked without prisms. A compact low-cost frequency-doubled, diode-pumped Nd:vanadate laser has been used as a pump source, which emits as much as 1.5 W of pump power. The size of this pump source is 158 × 104 mm. The advantage of this prismless Ti:sapphire laser is that the cavity can be designed more compact and can act as a hands-off OCT laser source. Due to the compact size, the 1.5 W solid-state pump laser (158 × 104 × 45 mm) could be integrated into the resonator layout. The overall dimension of the setup is 500 × 200 mm including the pump laser. Kerr-lens mode-locking is starting by rapid translation of the end mirror which is mounted on a translation stage to induce intensity fluctuations. Due to the good beam quality of the pump source, the Ti:sapphire oscillator also shows satisfying beam quality in cw mode as well in the mode-locked regime. Since the laser beam has to be launched into a single-mode fiber to interface it to an OCT apparatus, good beam quality is an essential parameter for high-coupling efficiency and stable output power. The output power of the compact, low-cost Ti:sapphire laser was strongly dependent on the bandwidth of the laser and varied from 180 mW with 40 nm at full width at half maximum (FWHM) to 20 mW with 176 nm at FWHM [1, 33]. The cavity length varied between 1.8 and 2.4 m for fine tuning of the dispersion. This results in repetition rates between 62 and 83 MHz. The systems well-reproducible spectra and output power lead to high reliability on a day-to-day performance. Ex vivo OCT imaging was performed with the broadest possible bandwidth

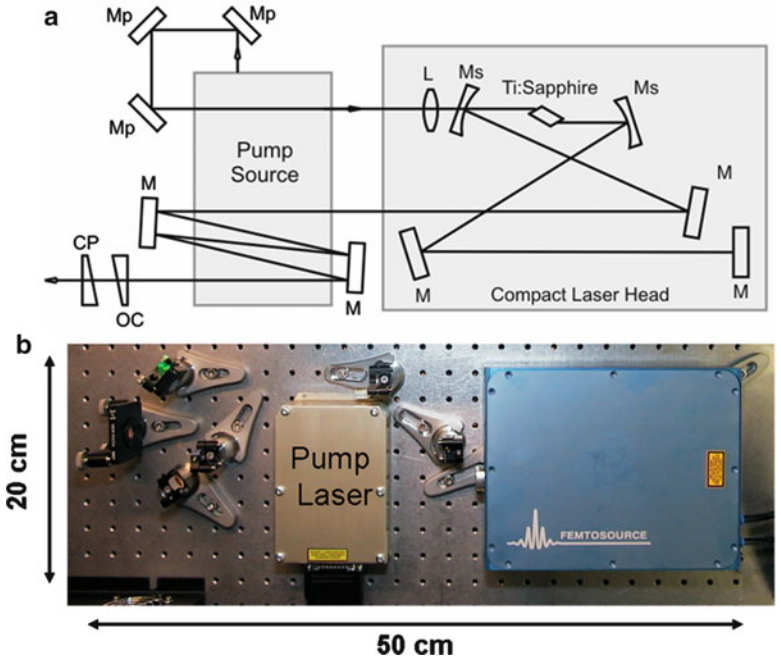

Fig. 19.8 *Low pump power broad bandwidth Ti:sapphire laser*. Schematic diagram (*top*) and a photograph (*bottom*) of the compact, low-cost Ti:sapphire laser. A commercially available compact (158 × 104 mm) 1.5 W pump source is used to pump a standard astigmatism compensated x-folded cavity. *Mp* pump mirror, *L* coupling lens, *Mc* 50 mm folding mirror, *M* mirror, *OC* output coupler, *CP* compensation plate [33]

(176 nm centered at 776 nm with 20 mW output power, cf. Fig. 19.9a, black line) enabling an axial resolution of 1.7 μm in free space corresponding to about 1.2 μm in tissue (cf. Fig. 19.9b). For ultrahigh resolution in vivo imaging in normals and patients, a less modulated, Gaussian-like spectrum with a bandwidth up to 135 nm at FWHM and 95 mW output power was used (Fig. 19.9a, gray line), enabling ∼3 μm axial resolution in the retina, similar to what has been achieved so far. The repetition rate of the compact low-cost Ti:sapphire laser was set to 72 MHz. The system shows extremely reproducible spectra, output power, and user-friendliness on a day-to-day performance. Stable operation for more than 12 h with less than 2 % power loss and less than 2–5 % loss in spectral bandwidth are usual.

Another demonstration of an ultralow-threshold Kerr-lens mode-locked Ti:sapphire laser pumped by the *excel 100* uses an extended cavity design shown in Fig. 19.10a [34]. The cavity is an astigmatically compensated, x-folded configuration with a 2 mm thick Ti:sapphire laser crystal. The focusing mirrors have 7.5-cm radii of curvature and transmit more than 95 % of the pump beam at 532 nm. The output coupler has a transmission of ∼1 % from 700 to 900 nm. All the mirrors are commercially available Bragg stacks with low dispersion. Because this laser uses commercially available mirrors and intracavity prisms rather than double-

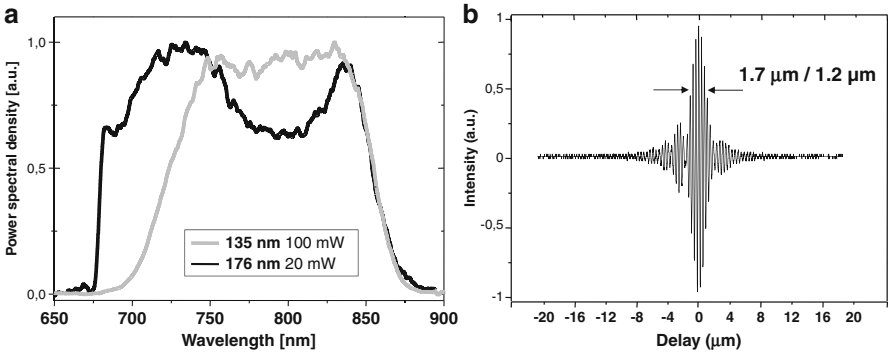

Fig. 19.9 *Specifications of a compact, low-cost Ti:sapphire laser*. Typical optical output power spectra of the compact, low-cost Ti:sapphire laser (*bottom*, *left*) and interference signal (*bottom*, *right*) corresponding to the spectrum indicated with the *solid black line* resulting a free-space axial resolution of 1.7 µm corresponding 1.2 µm in biological tissue [33]

chirped mirrors for dispersion compensation, third-order dispersion limits the pulse duration and bandwidth. Previous studies showed that third-order dispersion is minimized when the laser wavelength is shifted to longer wavelengths. A mirror set was chosen to shift the laser wavelength to be centered at approximately 840 nm. Intracavity dispersion compensation is accomplished with a pair of fused silica Brewster prisms separated by 45 cm. We tune the dispersion by varying prism insertion. Mode-locking thresholds as low as 156 mW were accomplished. Pulses with durations as short as 14 fs and bandwidths of 100 nm with output powers of ~15 mW at 50-MHz repetition rates were generated by only 200 mW of pump power (Fig. 19.10b, c).

Ultrastable diode-pumped, solid-state lasers with output powers from 2 up to 10 W are extremely expensive and dramatically increase the cost of a femtosecond Ti:sapphire laser. With pump power requirements of only 1–1.5 W, commercial available low-cost systems reduce the cost of a factor 5–6, but with still efficient output power for ultrahigh-resolution, spectroscopic OCT. The compact Ti:sapphire lasers presented here have sufficient output power and spectral bandwidth for ultrahigh-resolution and spectroscopic OCT. Total costs of the light source compared to commercial available state-of-the-art femtosecond Ti:sapphire laser could be reduced by a factor of 5–6 only by employing a 1.5 W pump source but achieving similar OCT performance as employing a 5 W single frequency-doubled, diode-pumped Nd:vanadate laser. This light source could be transferred from a laboratory prototype into the industrial environment. The result was a commercially available product from Femtolasers Produktions GmbH. This *Integral* poses an all-in-one system with integrated pump source, integrated diagnostics system, active stabilization of system parameters, >150 nm spectral bandwidth, >50 mW fiber-coupled output power, sealed cavity, low noise, and compact footprint (500 × 260 mm).

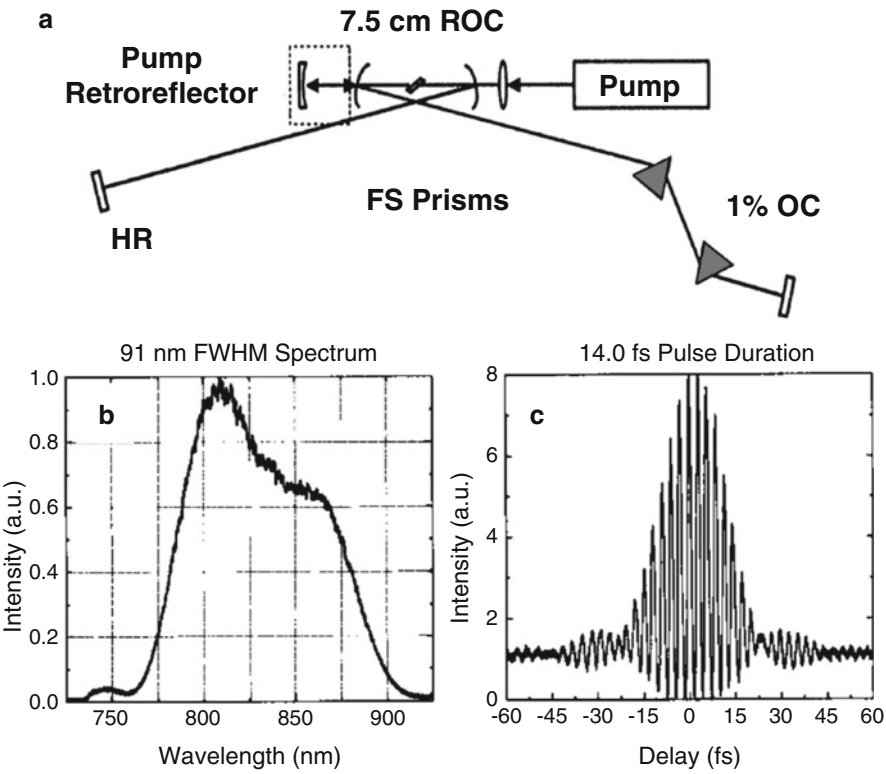

Fig. 19.10 *Ultralow-threshold Kerr-lens mode-locked Ti:sapphire laser*. (**a**) Schematic diagram of the ultralow-threshold Ti:sapphire laser. The pump lens has a 50 mm focal length, and the folding mirrors have 7.5-cm radii of curvature (*ROC*). The cavity is an astigmatically compensated x design, with arm lengths of 130 and 162 cm for the highly reflecting (*HR*) arm and the prism arm, respectively. A pair of fused silica (FS) prisms separated by 45 cm is used for compensating and tuning intracavity dispersion. (**b**) Output spectrum at 91 nm FWHM. (**c**) Corresponding interferometric autocorrelation measurement of a 14.0 fs pulse (assuming a sech2 fit) generated with 200 mW of pump power [34]

19.2.3.1 Ultrabroad Bandwidth Compact Laser Sources

Several approaches can be taken in improving solid-state laser sources for industrial and clinical applications. First, the length of the laser resonator can be reduced. The system can be realized on a smaller footprint with less mechanical components, but with a higher repetition rate at the expense of lower peak power. Second, the arms of the resonator can be folded more effectively. The all-chirped mirror designs with ultrabroad bandwidths facilitate this development of a compact user-friendly and extremely stable platform.

The technology of an ultrabroad bandwidth Ti:Sapphire laser could be transferred into a compact low pump power (<2 W) ultrastable design with more than 200 nm at FWHM. Pumping with an 1.9 W Nd:YVO_4 laser (*excel 1,000*, Laser Quantum Ltd.) resulted in a mode-locked output power of 95 mW and a bandwidth

of 240 nm at FWHM. With a cavity length of 2 m, a repetition rate of 75 MHz could be realized. The fiber output power was 56 mW. The resonator consisted of a standard x-folded cavity with a double pass in the long arm, a pair of wedges in the long arm, a 3 mm crystal, and a 5 % standard output coupler. Dispersive mirrors spanning from 640 to 920 nm were used in the cavity. This laser also enables ~1 μm axial OCT resolution in tissue and offers sufficient performance for real-time in vivo clinical UHR OCT applications.

Reliable mirror manufacturing technology combined with exact dispersion compensation in the cavity achieved with chirped mirrors and a pair of wedges reduces the overall modulations of the dispersion in the wavelength range between 640 and 950 nm to less than 70 fs^2 and thus permits generation of a smooth almost Gaussian-shaped output spectrum. Compared to state-of-the-art commercially available Ti:sapphire lasers with 140–160 nm bandwidth (FWHM), the use of this prototype Ti:sapphire laser results in twofold improvement of OCT axial resolution. With a slightly modified and reoptimized laser setup but almost the same parameters compared to the high-power all-chirped mirrors oscillator, an all-chirped mirrors oscillator was realized with a 1.8 W *excel* with the compact footprint of about 550 × 220 mm for the whole setup. Only the dispersive mirrors were adapted to the low pump power. With a repetition rate of 75 MHz, the mode-locked output power was in the range between 50 and 90 mW with 1–5 % out coupling efficiency. In the best case, 56 mW directly out of the fiber were achieved with a spectral bandwidth of 260 nm at FWHM. This bandwidth of 260 nm at 775 nm resulted in an axial resolution of 1.3 μm in air which corresponds to sub-μm resolution in biological tissue. Additional experiments with higher repetition rates resulted in no further improvements. These systems exhibited a much higher mode-locking threshold due to the reduced peak power. Bandwidths up to 300 nm at FWHM could be realized with low-loss RDMs (resonant dispersive mirrors) at repetition rates up to 200 MHz (Fig. 19.11). The system consists of seven chirped mirrors, a pair of wedges, and an output coupler. High mirror quality with low scattering is one important criteria to succeed. Otherwise, reliable operation at higher repetition rates might become more sensitive. The starting mechanism could become more difficult due to the low peak power and makes effective dispersion and reflectivity management essential. About 2.5 W of pump threshold with 200 nm and an output power of about 80 mW could be realized at the low pump power end and on the high pump power side 315 nm with 650 mW at 5.4 W pump power with repetition rates ranging between 150 and 200 MHz.

19.3 Cr^{3+}:LiCAF Laser Development

Diode-pumped, mode-locked colquiriite sources have been demonstrated to generate very broad spectra with bandwidth exceeding 150 nm and output powers on the order of tens of mW [4, 35, 36]. The Cr^{3+}:LiCAF laser developed for UHR OCT was pumped by the orthogonally polarized beams from two broad-area laser diodes (Coherent S-670-500C) with 500 mW optical power, each in an elliptical

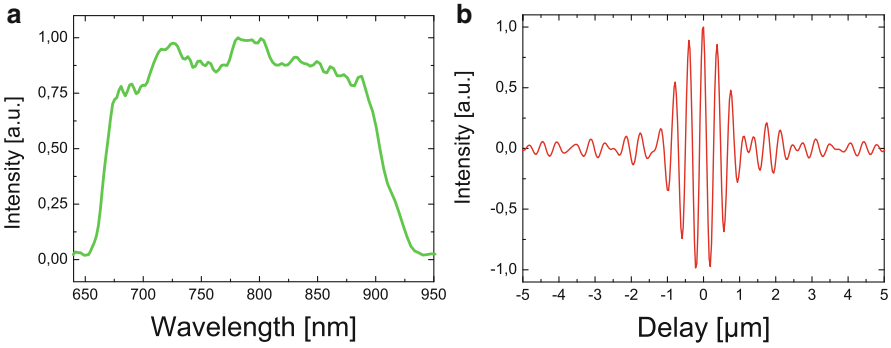

Fig. 19.11 *Ultrabroad bandwidth compact laser source*. Typical output spectrum of 300 nm (FWHM) generated from the compact *excel 100 l* (*1.5 W*) pumped ultrabroad bandwidth all-chirped mirror oscillator with mirrors with enhance bandwidth and reflectance (**a**) and interference signal (**b**) corresponding to the spectrum resulting in a free-space axial resolution of 1.3 μm

multimode beam. The emitter size of the diodes was 1 × 100 μm. Along the fast-diverging axis, the beam was close to diffraction limit, whereas it was multimode along the slow-diverging axis with a beam propagation M^2 factor of 15–18. Along the fast axis direction, a cylindrical fiber-collimating lens reduced the beam divergence. The collimation resulted in an elliptical pump beam with an aspect ratio of slow to fast axis about 4, where the ellipticity did not change as the beam is transformed by spherical optics. As a result of the collimation, the Rayleigh distances in both planes of the beam are equal, and they could be mode-matched simultaneously. The Cr^{3+}:LiCAF laser crystal was 2 mm long and had a nominal 10 % doping concentration that results in an absorption length of 0.7 mm for the pump light. High doping increased the small signal gain in a diode-pumped Cr^{3+}:LiCAF laser, where reabsorption did not affect the laser performance. The Rayleigh range of the pump beam was matched to half the absorption length by focusing the beam to a radius of 30 × 8 μm in the slow and fast axis, respectively. This was accomplished using a telescope consisting of achromatic doublet lenses of 100 mm and 50 mm focal lengths. The absorbed pump power was approximately 850 mW.

A schematic of the laser setup is shown in Fig. 19.12a. The laser was made compact by increasing the repetition rate to 165 MHz and by folding the z-design cavity twice more than previously reported layouts. The resonator eigenmode was focused into the laser crystal by two mirrors with 75 mm radius of curvature. Using this design, the laser size is 20 × 30 cm. The laser, the pump diodes and optics, and the fiber-coupling unit were integrated on a 30 × 60 cm optical board. In continuous-wave operation, the laser emitted up to 90 mW of power through a 0.8 % output coupler. The short absorption length in the highly Cr-doped crystal resulted in a high inversion density leading to strong gain guiding, which enhances the effect of the Kerr lens and the fast saturable absorber action [37]. The strongest Kerr-lensing occurred for resonator settings that are beyond the stability limits of the unpumped resonator without gain guiding. In this way, it was possible to exploit pure soft-aperture Kerr-lens modelocking in this diode-pumped laser, thus resulting

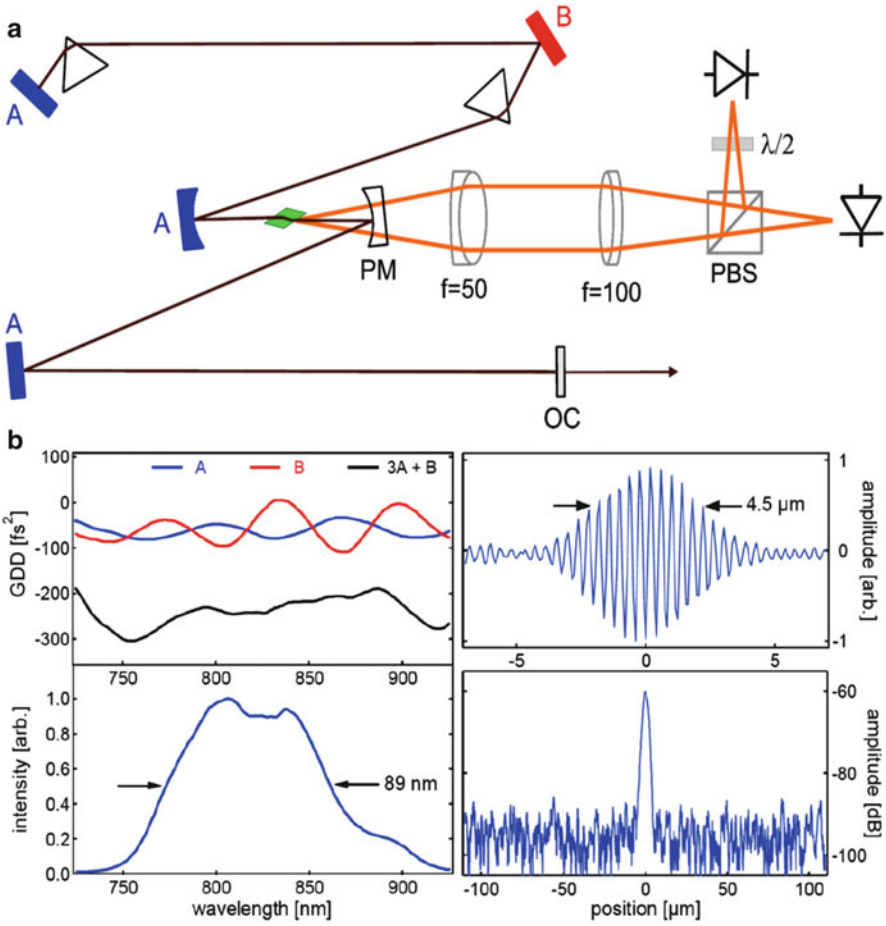

Fig. 19.12 *Broad bandwidth diode-pumped broadband Cr^{3+}:LiCAF laser*. (**a**) Schematic of the laser setup. *Blue* and *red* mirrors A and B are double-chirped mirrors (*DCM*), *PBS* polarizing beam splitter, *OC* output coupler, and *PM* pump mirror, *λ/2* half waveplate. (**b**) Dispersion characteristics of the double-chirped mirrors (*top left*), and mode-locked spectrum of the laser (*bottom left*), linear interferometric point spread function of the imaging system in air (*top right*), demodulated logarithmic point spread function of the OCT imaging system (*bottom right*). The resolution is 4.5 µm in air, which corresponds to 3.4 µm in biological tissue [36]

in stable pulsed operation. The laser was not self-starting, but mode-locked operation can be started by mechanically perturbing one of the laser mirrors, such as the output coupler. This starting mechanism was similar to that used in Ti:sapphire lasers. The dispersion compensation of the laser was carried out by a combination of double-chirped mirrors (DCMs), generating sufficient negative second-order dispersion, and a fused silica prism sequence for adjusting the second- and third-order dispersion (cf. Fig. 19.12b). Except for the pump mirror and the output coupler, which have low dispersion over the lasing bandwidth, all

mirrors are dispersion-compensating DCMs. The prisms are essential for higher-order dispersion compensation.

The dispersion of the mirrors as measured by white light interferometry is shown in Fig. 19.12b (top left). Mirror A has a dispersion oscillation magnitude of 45 fs^2, whereas oscillations of mirror B have a magnitude of 110 fs^2, with the oscillation out of phase with mirror A's oscillation. The dispersion of a combination of 3:1 reflections on the two different mirror sets is also shown in Fig. 19.12b (top left). Between 750 and 900 nm wavelengths, a near perfect cancellation of dispersion oscillations can be achieved. For practical reasons, 5:2 reflections on mirrors of type A and B are used instead of the optimum 6:2. This combination results in sufficiently flat dispersion characteristics so that broadband emission is obtained with a smooth mode-locked spectrum. The mode-locked spectrum in Fig. 19.12b (bottom left) is centered at 815 nm and has a modulation-free, nearly Gaussian shape with a full width at half maximum bandwidth of 89 nm. The output power of the mode-locked laser is 37 mW. The bandwidth is limited by higher-order dispersion terms of the intracavity prisms. The Cr^{3+}:LiCAF gain bandwidth enables the generation of an output bandwidth of well-above 130 nm. With further optimized DCM designs, which have more accurate dispersion compensation, prismless operation with broader bandwidths is achievable. The interferometric point spread function of the ophthalmic imaging system, shown in Fig. 19.12b top and bottom right, is determined by a calibrated measurement of the reflection from a mirror in the sample arm. The small asymmetry in the point spread function (PSF) is probably the result of wavelength dependence in the split ratio of the fiber couplers. The resolution is 4.5 μm in air, which corresponds to 3.4 μm in tissue.

19.4 Cr^{4+}:Forsterite Laser Development

A self-phase-modulated KLM Cr:forsterite laser has been used for in vivo OCT imaging in nontransparent tissues with 6 μm axial resolution [13]. Recent efforts were focused on developing even broader bandwidth light sources in the 1,300 nm wavelength range permitting OCT micrometer-scale resolution along with up to 2 mm penetration depth. A laser spectrum covering the 1,230–1,580 nm wavelength region with an optical bandwidth of 250 nm (FWHM) was generated directly out of an all-solid-state Cr:forsterite laser [38, 39]. A schematic of the laser is shown in Fig. 19.13a. The laser used a standard z-fold cavity design with 10-cm radius-of-curvature focusing mirrors. The Cr:forsterite crystal was a 5 mm × 5 mm × 5 mm Brewster cut crystal with an absorption coefficient of 2.4 cm^{-1} and was cooled to 263 K. A diode-pumped Nd:YAG laser was used as the pump, along with an optical isolator to prevent feedback. All mirrors in the cavity were double-chirped mirrors, except for the output coupler. To start mode locking, the prisms had to be scanned slightly. The beam path was enclosed by Plexiglas tubes, and the cavity was purged by fried nitrogen to avoid loss and dispersion from the water absorption band at 1.45 μm.

Since Cr:forsterite is a low-gain material, the mirrors must have high reflectivity and low loss. The reflectivity of the DCM's is greater than 0.998 from 1.1 to

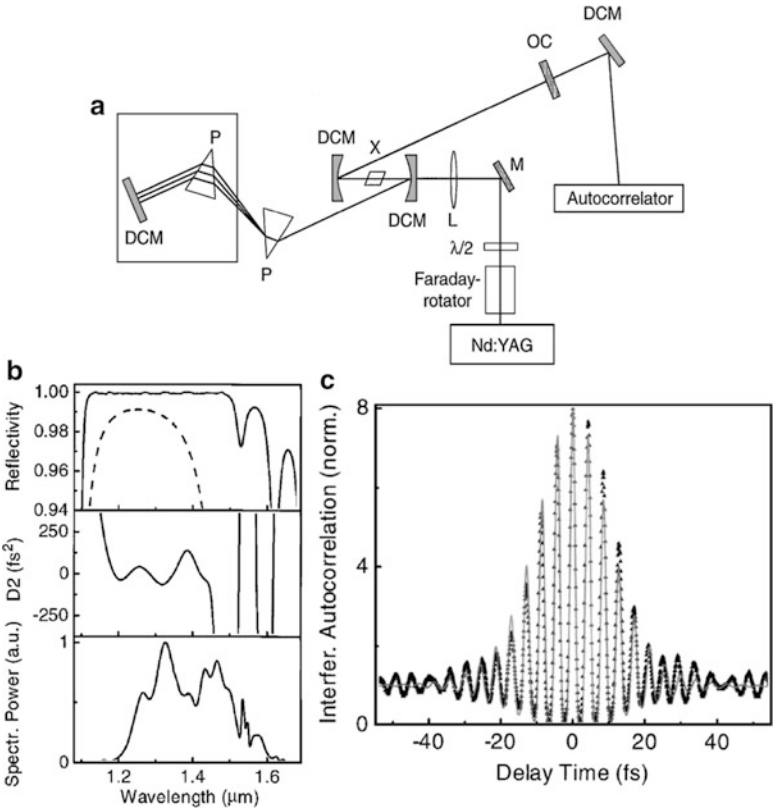

Fig. 19.13 *All-solid-state Cr:forsterite laser*. (**a**) Cr:forsterite laser with double-chirped mirrors (*DCM's*): *P's* PBH71 prisms, *X* crystal, *OC* output-coupling mirror, *L* focusing lens, *M* standard dielectric mirror, and l/2 half waveplate. (**b**) Measured reflectivity of the DCM's (*top, solid curve*) and the output-coupling mirror (*top, dashed curve*), total intracavity dispersion (*middle*), and laser output spectrum (*bottom*). (c) Interferometric autocorrelation measurement (*triangles*) and sech^2 fit assuming a 14 fs pulse duration [38]

1.5 mm, resulting in a bandwidth of 400 nm, as shown in Fig. 19.13b (top). At shorter wavelengths of <1.10 μm, the reflectivity decreases rapidly, permitting high transmission of the pump beam at 1.064 mm. To increase the gain of the Cr:forsterite, the crystal was cooled to 263 K. The reflectivity of the output-coupling mirror was centered at 1.25 μm and is greater than 0.98 over a 210 nm bandwidth. The pump thresholds for cw operation and Kerr-lens modelocking were 800 mW and 4 W, respectively. At 6 W pump power, the laser had an output power of 80 mW mode-locked and 100 mW cw. Figure 19.13b shows a comparison of the total cavity dispersion (middle) and the laser output spectrum (bottom). The DCM's in combination with the PBH71 prisms balance the dispersion over almost 300 nm. The laser spectrum spans wavelengths from 1,230 to 1,580 nm. The peaks in the output spectrum correspond with regions of net

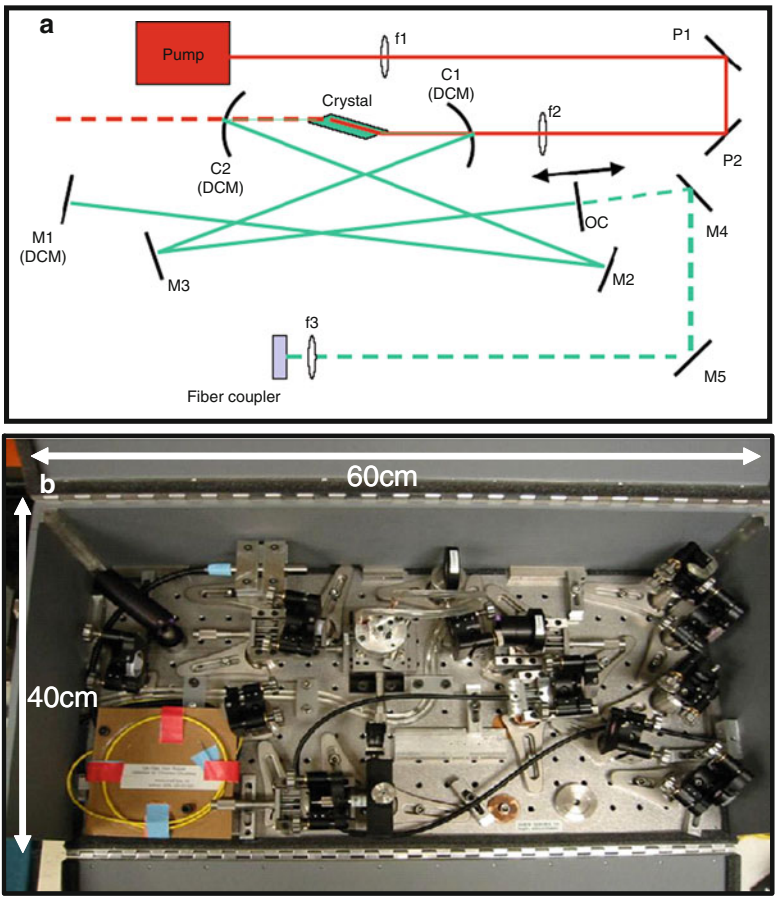

Fig. 19.14 *Compact Cr:forsterite laser for clinical imaging*. (**a**) Schematic of Cr:forsterite oscillator with double-chirped mirrors (*DCM's*). *C* curved mirrors, *OC* output-coupling mirror, *f* focusing lens, and *M* standard dielectric mirror; (**b**) portable Cr:forsterite laser packaged for use in clinical investigations outside the laboratory. The entire pump laser, oscillator, and nonlinear fiber assembly is contained on a 40 cm × 60 cm breadboard and surrounded by a safety enclosure

negative intracavity dispersion caused by the oscillations in the D2 of the DCM's. Figure 19.13c shows an interferometric autocorrelation of the laser output. The pulse duration is 14 fs with a sech^2 fit. This record pulse duration was achieved by use of specially designed DCM's for improved intracavity dispersion compensation in the 1.3 μm wavelength regime.

A compact, broadband prismless Cr^{4+}:forsterite laser was next constructed for use in clinical investigations. The laser was pumped with a compact Nd:YAG fiber laser at 1,064 nm, and the oscillator utilized only double-chirped mirrors to compensate intracavity dispersion. Figure 19.14a presents the system schematic for the laser. An x-cavity design was used for compactness, and the entire laser was

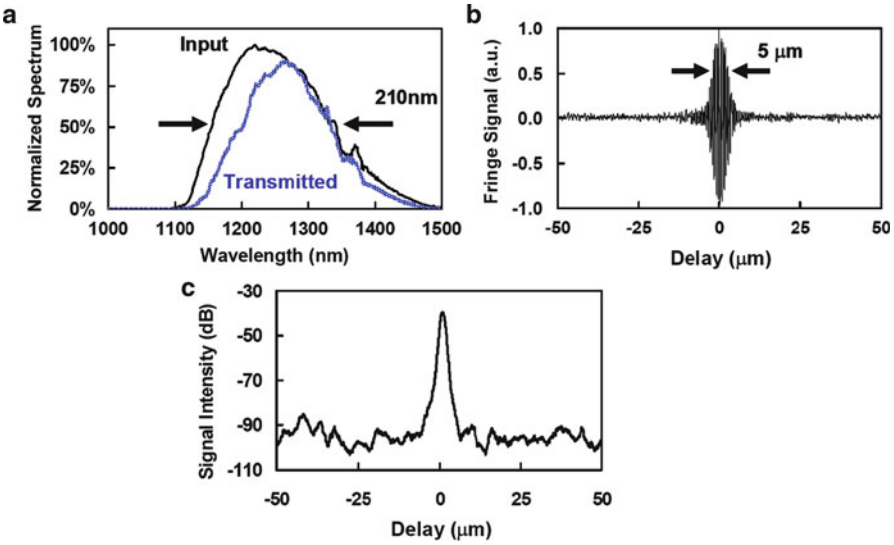

Fig. 19.15 *All-solid-state Cr:forsterite laser for ultrahigh-resolution OCT*. (**a**) Optical bandwidth of the Cr^{4+}:forsterite light source at the input to the OCT system (*black*) and transmitted through to the system (*blue*) enabling a threefold improvement in axial image resolution over standard endoscopic OCT systems using a superluminescent diode light source, (**b**) measured axial resolution of 5 μm in air, corresponding to 3.7 μm resolution in tissue, and (**c**) logarithmic point spread function shows low sidelobes in the point spread function [40]

built on a 40 cm × 60 cm breadboard. To provide optimal bandwidth for OCT imaging, the laser was coupled into a highly nonlinear Germanium-doped fiber, which resulted in spectral broadening to more than 200 nm. Figure 19.14b shows a photograph of the entire laser packaged for use outside the laboratory. The system produced fiber-coupled output power of 50 mW and bandwidth of 210 nm, which resulted in axial image resolution of 3.7 μm and system sensitivities of 102 dB for 10 mW sample power. Figure 19.15a shows the optical spectrum generated by the Cr^{4+}:forsterite laser and nonlinear fiber. Due to bandwidth limitations in the optical circulator, shorter wavelengths were attenuated and the transmitted spectrum was reduced to 150 nm bandwidth (also shown). The measured axial point spread function shown in Fig. 19.15b has a resolution of 5 μm in air, close to the calculated theoretical value of 4.6 μm for the transmitted bandwidth. This corresponds to an axial resolution of ∼3.7 μm in tissue, assuming an index of refraction of ∼1.37, and is a threefold improvement in resolution when compared to previous endoscopic OCT systems. Using the broadband Cr^{4+}:forsterite laser, in vivo ultrahigh-resolution endoscopic imaging of the rabbit gastrointestinal tract was demonstrated [40]. Human clinical investigations in the gastrointestinal tract were subsequently performed using this ultrahigh-resolution OCT system [41]. In a study of patients previously diagnosed with Barrett's esophagus, UHR OCT provided enhanced visualization of tissue architecture in Barrett's, dysplasia, and adenocarcinoma compared to prior standard resolution systems.

19.5 Cr^{4+}:YAG Laser Development

Mode-locked solid-state lasers are capable of generating ultrashort optical pulses with broad spectra and high peak intensities. Cr^{4+}:YAG lasers have the ability to produce such pulses in the wavelength range from 1,300 to 1,600 nm. These lasers operate at room temperature, do not require a vacuum, and have larger gain bandwidths than Er-doped fiber lasers. Ultrafast optical pulses shorter than 20 fs with 400-mW average power at a 110-MHz repetition rate have been generated by a Cr^{4+}:YAG laser with only double-chirped mirrors for dispersion compensation [42]. The corresponding pulse spectrum has a peak intensity at 1,450 nm and extends from 1,310 to 1,500 nm full width at half maximum (FWHM). These pulses, which are believed to be the shortest generated to date from a Cr^{4+}:YAG laser, are only four optical cycles within the FWHM intensity width. Figure 19.16a shows the schematic of the z-fold laser cavity. The laser crystal is 2 cm long with 3 mm diameter Brewster cut rod. Pump light at 1,064 nm with 11 W from a Nd:YVO_4 laser is focused by a 10 cm focal length lens in the crystal. The

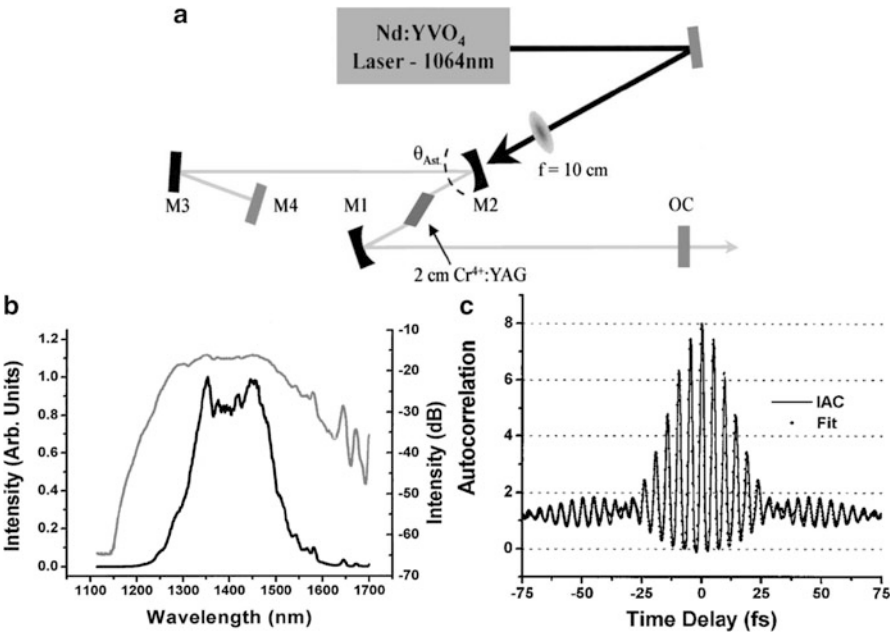

Fig. 19.16 *Broad bandwidth prismless Cr^{4+}:YAG laser*. (**a**) Schematic of the Cr^{4+}:YAG laser cavity: mirrors M1–M3 are *DCMs*, *M4* is a quarter-wave-stack high reflector, and *OC* is an output coupler. (**b**) Optical power spectrum of a Cr^{4+}:YAG pulse. The *darker curve* corresponds to a linear scale (left-hand axis) and the *lighter curve* corresponds to a logarithmic scale (right-hand axis). The FWHM is 190 nm, with a peak at 1,450 nm. (**c**) Measured autocorrelation function from an interferometric two-photon absorption autocorrelator (IAC) and fit by a pulse-retrieval algorithm. A pulse width of 19.5 fs is calculated by the pulse-retrieval algorithm, 18.3 fs by assumption of sech-shaped pulses, and 17.0 fs by assumption of Gaussian-shaped pulses [42]

latter one is cooled to 13 °C. All mirrors are double-chirped mirrors except one unchirped quarter-wave-stack high reflector. Mode-locking was initiated by tapping one of the end mirrors. The average power of the 110 MHz pulse train was 200-400 mW, depending on the alignment, for 9 W of absorbed pump. Water vapor in air introduced intracavity GDD and loss through a series of absorption lines from 1,300 to 1,500 nm. To remove this water vapor, the optical path was closed and purged with dry nitrogen gas. An example of the mode-locked pulse spectrum, measured with a calibrated optical spectrum analyzer, is shown on both linear and log scales in Fig. 19.16b. Significant spectrum was present above the noise floor within the wavelength range from 1,140 to 1,700 nm (the optical spectrum analyzer used has a long-wavelength limit of 1,700 nm) and had a full width at half maximum (FWHM) of 190 nm, from 1,310 to 1,500 nm. The spectrum was smooth, with a relatively flat top from 1,340 to 1,470 nm. The output coupler, which rolls off significantly at wavelengths smaller than 1,350 nm, enhanced the output spectrum at shorter wavelengths. The pulse width was measured by fringe-resolved autocorrelation. An autocorrelation trace is shown in Fig. 19.16c. The pulse width is estimated to be 18.3 fs for sech-shaped and 17.0 fs for Gaussian-shaped pulses. The retrieved pulse-intensity envelope had a width of 19.5 fs. A Fourier transform of the optical spectrum, assuming a flat phase profile, indicated a bandwidth-limited pulse width of 17.5 fs.

19.6 Supercontinuum Light Source Development

Spectra far broader than one optical octave can be produced via nonlinear propagation of laser pulses having only moderate energies of a few nJ in microstructured fibers. Photonic crystal fibers enable an emerging class of light sources emitting low time coherence but high space coherent light. Due to the geometry of these fibers, the cross section of the fundamental mode is unusually small, which enhances the peak power and thus nonlinearity [14, 15]. At the same time, the fiber dispersion can be engineered to avoid fast temporal spreading. Hence, photonic crystals offer many extraordinary features as easy dispersion management, single-mode behavior over many wavelengths, and useful nonlinear properties. They can easily be tailored for different needs with spectra at different wavelengths spanning several octaves. These spectral widths would never be accessible directly from a laser oscillator because it exceeds the fluorescence bandwidth of the active ions. Nevertheless, in order to avoid an excessively strong spectral modulation (inherent to the spectral broadening process), only moderated spectral broadening should result from the nonlinear fiber propagation, i.e., the initial bandwidth of the pulses emerging from the oscillator should be as broad as possible. Research in the field of photonic crystals was stimulated by the prediction of a photonic bandgap analogous to electronic bandgaps in semiconductors. Initially, the photonic bandgap was the only guiding mechanism considered for this new class of optical fibers. Now devices can be made by microstructuring and including air holes into the fiber applying the principle of total internal reflection.

19.6.1 Microstructured Fibers

The first demonstration of microstructured fibers (MFs) goes back to the 1970s [43]. Since that time, the technology of MFs has matured tremendously, especially during the last decade. Precise control of the fiber drawing process allows for production of a great variety of complex structures. A typical MF has a 2D cross-sectional structure with a solid pure silica core region providing very low losses at high power and temperature levels. It is surrounded by an array of microscopic air holes running along their entire length. These holes effectively lower the index of refraction, creating a step-index optical fiber and can vary according to the application. The large refractive-index step between silica and air allows light to be concentrated into a very small area, resulting in enhanced nonlinear effects. Moreover, because of the large waveguide contribution to their group-velocity dispersion, MFs can exhibit very unusual chromatic dispersion characteristics. They behave in many ways like standard step-index fibers (which are typically made of germanium-doped raised-index core surrounded by a pure silica cladding), but have a number of advantages.

The mode confinement is introduced by an air-hole structure which contains the beam by the strong index step between the silica core, typically between 1.5 and 4.0 μm, and the silica/air surroundings (size of structure elements is smaller than the guided wavelengths). Designers can manipulate the dispersion characteristics of MFs to create fibers having zero, low, or anomalous dispersion at visible wavelengths. The design flexibility is very large, and the fibers can be manipulated by

- Variation of dispersion
- Arrangement of air holes – many different air hole patterns may be applied
- Size of holes
- Nonlinearities
- Adjusting the effective area of the propagating modes

Although there has been tremendous progress in the fabrication of MFs in the last few years concerning loss, stability, and noise, they are still far away from being comparable with solid-state lasers. High-nonlinearity, air-silica microstructure fibers [14] or tapered fibers [15] have been used to generate an extremely broadband continuum using low energy femtosecond pulses. In the latter approach, a standard single-mode fiber is heated and then lengthened. The light is initially guided inside the fiber core, but in the tapered region, the light propagates through the cladding. As in the air hole fibers, the change of the index of refraction between the light-guiding region, the cladding in the tapered fibers, and the surrounding region, the air, is high. Depending on the cladding diameter, the zero-dispersion wavelength can be shifted. Both the air-hole fiber and the tapered fiber have been studied to find out optimum conditions for broadband continuum generation with minimum noise.

19.6.1.1 Generation of Super Continuum

One of the first applications of MFs has been supercontinuum generation (SC). Supercontinuum is a broadband coherent light source [44] that finds numerous applications in the fields of telecommunication, optical metrology, spectroscopy, and medical imaging. As we will discuss later in detail, the ultrabroad bandwidth

spectrum of a supercontinuum allows for submicron resolution in OCT [45–47]. One crucial point in this supercontinuum generation is the tight confinement. The mode can be confined into a small area, thus enhancing the strength of nonlinear processes that are responsible for supercontinuum generation. Mechanically, robust MFs with extremely small core size down to 1 μm can be fabricated.

Mechanisms leading to supercontinuum generation depend on both the parameters of the input pulses:

- Pulse duration
- Peak power
- Center wavelength

And the parameters of the MF:

- Dispersion profile
- Effective modal area
- Birefringence

These mechanisms include:

- Self-phase modulation (SPM)
- Cross-phase modulation (XPM)
- Four-wave mixing (FWM)
- Stimulated Raman scattering (SRS)

Fiber broadening in highly nonlinear microstructure fiber generating extremely broad bandwidth supercontinuum ranging from the visible to the near infrared by using femtosecond pulses is quite well explored. One reason lies in the waveguide dispersion characteristics of the fibers which shift the zero-dispersion wavelength to shorter wavelengths, and the small core diameters, which provide tight mode confinement. Since there was a rapid development in the design and fabrication of a variety of MFs in the last few years, broad bandwidth light generation from nonlinear optical fibers has also become an attractive method for UHR OCT. High-resolution OCT was achieved by broad bandwidth light generation with a highly nonlinear material-doped optical fiber [48]. Broad bandwidth light was generated at 1.55 μm by stimulated Raman scattering using an erbium-doped fiber [49]. Unfortunately, the generated light exhibited significant white amplitude noise. UHR OCT could be demonstrated achieving 2.5 μm axial resolution using a microstructure fiber [50]. Nevertheless, most of these systems exhibit highly unstable complicated fine structures which are extremely sensitive to the input pulse energy, which results in a poor signal-to-noise ratio (SNR) limiting their application in OCT. The instabilities [51, 52] are due to the fluctuations of the pump source and noise which is amplified during super continuum generation. Recently, it was shown that broad bandwidth light can be generated by coupling a fs Ti:sapphire laser into a single-mode optical fiber [53].

Supercontinuum is the result of a complex interplay of the nonlinear effects described above. The superposition of all these processes leads to its complex spectral shape. Supercontinuum generation by pumping a highly nonlinear fiber with femtosecond laser pulses is only efficient in the vicinity of the zero-dispersion wavelength (ZDW) of the fiber [44, 54] or in the normal dispersion area [55], since high dispersion value tends to limit the magnitude of the nonlinear processes. Supercontinuum generation in the vicinity of the ZDW usually generate very

broad spectra. Since the SC is generated by the excitation of unstable solitons, as described in Genty G., M. Lehtonen, H. Ludvigsen, J. Broeng, and M. Kaivola, *Spectral broadening of femtosecond pulses into continuum radiation in microstructured fibers*, Optics Express, 2002, **10**, 1083–1098, these light sources show large spectral modulation and a lot of noise. The anomalous dispersion region can generate a broad optical spectrum, but a complex interplay of nonlinear effects in this dispersion regime results in instabilities of the supercontinuum generation. Supercontinuum generation in the normal dispersion regime is mainly due to self-phase modulation and therefore creates nice and stable spectra. Investigation showed that the dynamic range of a broad bandwidth light source from a single-mode fiber can be 15 dB higher than with an MF source. No significant intensity noise amplification can be observed in these studies [47]. Nevertheless, SC based on SPM in conventional single-mode fibers generally results in small bandwidths with center wavelengths close to the pump wavelength [42]. Other attempts have been undertaken by pumping a PCF with two closely space ZDWs emitting at 800 nm and 1,300 nm [48, 56]. Although the SC generation of this light source is mainly due to SPM, the spectrum shows spectral modulations. Also a broad bandwidth SC light source with high-power, low-noise, and smooth spectrum centered at 1.15 μm was reported. The SC was generated by SPM using a compact 1.059 μm femtosecond laser pumping a novel photonic crystal fiber, which has a convex dispersion profile with no zero-dispersion wavelength W [50].

In addition, various MFs were employed for the investigation of broadband light generation with different Ti:sapphire oscillators. Light sources based on external broadening using MFs have been developed and utilized for UHR OCT. The fibers varied in terms of length (2–500 mm) and mode field diameter (1–2.4 μm) corresponding to zero-dispersion wavelengths between 650 and 950 nm. In fibers with small core diameter, light can be confined in a small area with high intensity, which increases the nonlinear broadening. Short fibers offered a much smoother spectrum than longer ones. The spectrum seemed to be less modulated, and also the gaps in the spectra could be removed. The stability increased also with the decrease in fiber length, since the bending of the fiber was not so dominant. In general, fibers from Crystal Fiber showed a higher efficiency than Bath fibers. About 800 mW before the objective resulted in 160 mW out of the fiber with 2 μm core diameter.

For all experiments, the laser beam was launched into the different MFs after passing a mirror compressor (cf. Fig. 19.17). Additionally, quarter-wave and/or half waveplates were used to change and adapt the polarization and shape the output spectrum. The focus length of the coupling lens was 3 mm, and the beam diameter was 2 mm before the lens. By matching the numerical aperture of the coupling system with that of the MF, up to 1.2 W linearly polarized pump radiation was launched into the different fibers. The broadband output of light was collimated by a 20× standard microscope objective and a numerical aperture of 0.8. The output spectrum is broadened gradually as the laser intensity increases to a certain threshold. Further increase of the input power only enhances modulations and the fine structure of the output spectrum.

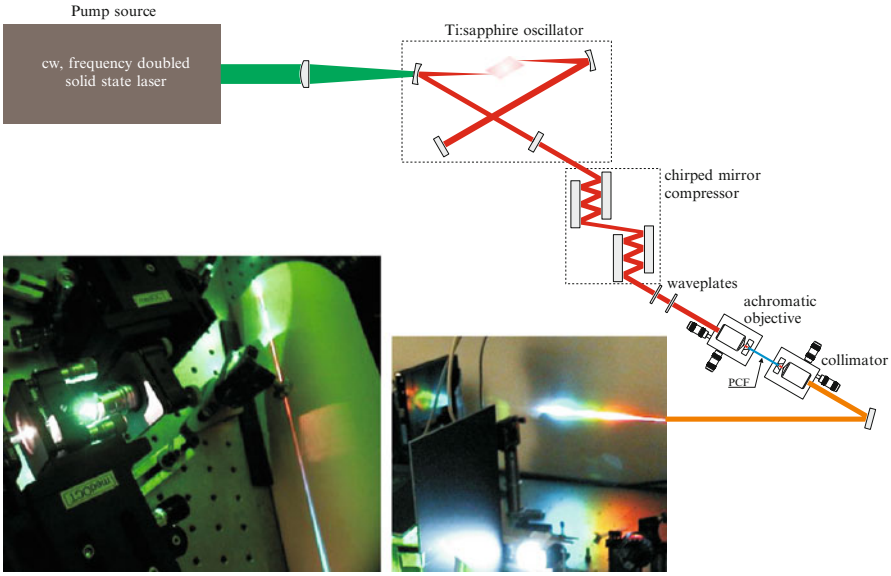

Fig. 19.17 *Supercontinuum light source setup*. The Ti:sapphire laser output is pre-compensated, polarization controlled, and then launched into a microstructured fiber

Different attempts concerning:

1. Ti:sapphire operation at different wavelengths, energies, and pulse durations (bandwidths)
2. Prechirp for precompensation: 16–28 bounces of ultrabroad bandwidth mirrors with $\sim$50 fs^2 GVD per bounce
3. Pair of wedges for fine tuning of the dispersion
4. Linear polarization control with $\lambda/2$ – waveplate
5. Rotational polarization control with $\lambda/4$ – waveplate
6. Achromatic lens or microscope objective as incoupling device
7. Fiber length
8. Core diameter determining the zero-dispersion wavelength
9. Short-/long-wavelength absorptive edge filters – to shape and cut the spectrum

Depending on the different input parameters, spectra in the visible and NIR could be achieved varying in the center frequency, bandwidth, spectral shape, output power, and noise behavior. Nevertheless, several parameters had to be watched very carefully for all these systems, when coupling the light into the microstructured fibers:

1. Exact overlap of the pump focus with the fiber core
2. Maximum energy applied on the fiber surface
3. Clean environment
4. Feedback from the fiber surface to the laser (cleaved angle/faraday rotator)
5. Overlap of the beam divergence at the waist to the acceptance angle of the fiber
6. Dispersion of the fiber and accurate precompensation to prevent pulse broadening and reduction in pulse energy

The setup (cf. Fig. 19.17) provided highly reproducible results (fibers have been used for several weeks without the need of realignment) without protective housing. The objective can be aligned by a 3-D stage with piezo driver (Thorlabs, PI) and actuators (manual, 2 mm; piezo, 150 μm). The influence of the NA of the focusing objective on the throughput was investigated. Several microscope objectives were introduced into the system, and an NA of more than 0.4 seemed to be appropriate for the setup. Even the higher dispersion introduced by the huge amount of glass and the larger chromatic aberrations were less significant than the stronger focusing. Standard microscope objectives with 20–40× magnification could be used as well as highly sophisticated achromatic lenses for fs pulses. Dispersion control should provide shortest pulses in any case and therefore highest energies in the active part of the fiber.

Commercial MFs obviously have a higher destruction threshold, better symmetry, and higher mechanical stability. Additionally, the zero-dispersion wavelength is better reproducible. A reliable quality over the whole fiber is guaranteed. In principle, the commercial fibers showed comparable behavior than the Bath fibers, though the stability was higher. The incident light was precompressed, and the polarization was controlled by half and quarter waveplates. Stable broadening up to 155 nm could be achieved in the yellow. Preliminary results in a free-space OCT system were acquired with a MF (2 μm core diameter, 770 nm ZDW, 4 mm length) with an output power of 24 mW and a SNR of 103 dB. When coupling a 1 W Ti:sapphire laser into the 2 μm or even shorter fiber with a ZDW of 770 nm spectra in the highly interesting 1,050 nm wavelength range (>160 nm bandwidth @ FWHM – in the best case about 250 nm (shorter wavelengths were cut off by a long-wave-pass filter) could be generated. The 22 mW of output power were reduced to ∼4 mW after collimation and recoupling to a 3 m fiber (for connection to the fiber optic OCT system, which is necessary for clinical imaging).

19.6.2 Spectral Broadening in the Visible

Spectral broadening in the visible can be achieved by coupling light from a Ti:sapphire oscillator into a MF with 2.3 μm core diameter and 6 mm length. The state-of-the-art Ti:sapphire pump source has a bandwidth of 120 nm (FWHM) with an average output power of 400 mW emitting sub-10 fs pulses with about 100 MHz repetition rate. By compensation for the positive chirp introduced by the air and the coupling elements with mirror pairs and matching the polarization to the main polarization axis of the fiber a stable, slightly modulated spectrum ranging from 550 to 950 nm can be generated. The SC spanning more than 325 nm (FWHM) with spectral modulations less than 1.5 dB, centered at 725 nm, and providing 27 mW of average output power (cf. Fig. 19.18a) results in 0.5 μm axial OCT resolution in tissue (cf. Fig. 19.18b) [47]. Hence, the spectrum can be successfully broadened by a factor of 3. The total output power from the optical fiber can be as high as 120 mW. The broad bandwidth of this light source also provides access to a spectral region covering the absorption bands of a number of biological

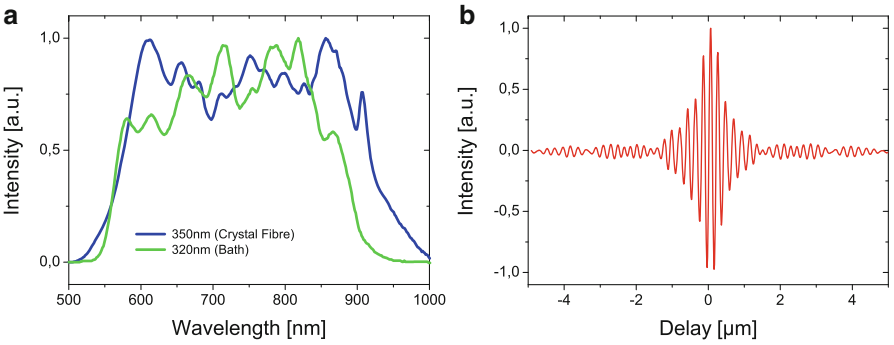

Fig. 19.18 *Supercontinuum light source*. Spectrum of supercontinuum (**a**) generated from a microstructured fiber with sub-µm axial resolution (**b**)

chromophores, thus it has great potential for spectroscopic OCT. This spectral region is interesting because of ultrahigh resolution of the OCT images (sub-µm resolution rather than several microns in the near infrared) with better image contrast as well as stronger absorption of biological chromophores. These three properties are extremely interesting for medical applications, since human cells with common sizes of some micrometers can only be properly investigated with sub-µm resolution for early cancer diagnosis. In addition, intra- and extracellular processes involve changes in optical properties in that special range of the optical spectrum and can be observed in real time, without additional staining.

19.6.3 Simultaneous Spectral Broadening in the Visible and NIR

19.6.3.1 Multiple Wavelengths, Ultrabroad Bandwidth Light Source

In addition to investigations of shorter wavelengths than the pump wavelength around 750–850 nm, also longer wavelengths are required for OCT. Applying 100 fs pulses to long pieces (>1,000 mm) of PCF have resulted in significant, broadening in the infrared wavelength region. For OCT, it is also of major interest if short pulses are also capable to produce light in the NIR at about 1,050 nm. This wavelength region is particularly attractive for ophthalmic OCT imaging due to reduced melanin and hemoglobin absorption in addition to lower scattering properties of biological tissue as compared to standard ophthalmic OCT imaging around 800 nm, which can result in significantly enhanced OCT image penetration below the retinal pigment epithelium into the choroid. Ocular media are still transparent enough in this wavelength region to enable optical access to the posterior pole of the eye. Visualization of subretinal layers have great clinical impact in the early diagnosis of several retinal pathologies, e.g., diabetic retinopathy or age-related macular degeneration. Also bandwidth light sources that cover wavelength regions for which scattering in human tissue decreases, based on SC emission generated by ultrashort pulses in fibers became available. In this study, the application of a source

with central emission wavelengths centered at the water absorption window at 1,060 nm that is utilized for OCT is reported and compared to the penetration properties of a state-of-the-art Ti:sapphire system.

Light sources emitting more than 100 nm bandwidth at full width at half maximum – depending on the central wavelength – are needed to accomplish ultrahigh axial resolution ($\leq$2 μm) OCT. Using full interferometric signal detection, also the spectral information can be extracted. Ultrabroad bandwidth, coherent light sources have enabled UHR OCT, which also gives access to metabolic tissue parameters since these light sources cover spectral regions of several diagnostically important biological chromophores, e.g., melanin or hemoglobin. Thus the combination of UHR OCT with spectroscopy has the potential to perform optical biopsy of biological tissue, i.e., the visualization of tissue morphology at the cellular resolution level, to enhance OCT tomogram contrast as well as to extract quantitative, spatially resolved spectroscopic tissue information over a broad wavelength region at high resolution in a single measurement. A triple band light source can simultaneously access several wavelength regimes for combining the advantages of each wavelength region in one light source and one measurement.

The spectra in the visible and NIR region are generated simultaneously by the means of nonlinear broadening in a MF pumped by a Ti:sapphire laser. The latter one is a commercially available oscillator formed by a standard x-folded resonator that is composed of chirped mirrors and high reflectors for dispersion compensation and pumped by 8 W of a diode-pumped, frequency-doubled Nd:YVO_4 laser. The oscillator provides sub-12 fs pulses with an average power of 1 W at 75 MHz repetition rate. The output spectrum is centered at 800 nm with 120 nm bandwidth at FWHM. According to our previous studies with MFs in combination with sub-20 fs pulses, only short fibers (a few millimeters in length) allow to generate broad spectra in the visible with minimal modulations and low pulse to pulse fluctuations of the spectrum.

Therefore, a 2 mm long fiber with core diameter of 2 μm is used. Since the fabrication process of MFs improved in the recent years, the throughput, the stability, and the noise behavior could be increased a lot. An achromatic objective with $f = 4$ mm and a numerical aperture of NA = 1.0 is used for focusing, providing smooth dispersion with minimal chromatic aberrations in the 700–900 nm wavelength range. Quarter and half waveplates designed for a central wavelength of 780 nm are used to optimize the polarization of the incident beam. Two pairs of chirped mirrors with a total number of 18 bounces are introduced mainly to precompensate the positive dispersion of the focusing objective and provide pulse duration of 14 fs in front of the fiber and 800 mW output power. An achromatic doublet lens designed for low chromatic aberration in the 600–1,000 nm wavelength range with an NA of 0.65 collimates the generated broad bandwidth output of the fiber.

An output spectrum covering the whole wavelength range from 500 to 1,400 nm has been realized in a single MF-based Ti:sapphire laser-pumped light source (cf. Fig. 19.19). The overall output power over the whole wavelength region is 360 mW. The short-wavelength part of the spectrum covers the visible wavelength range from 500 to 700 nm with a bandwidth of 140 nm at FWHM centered at

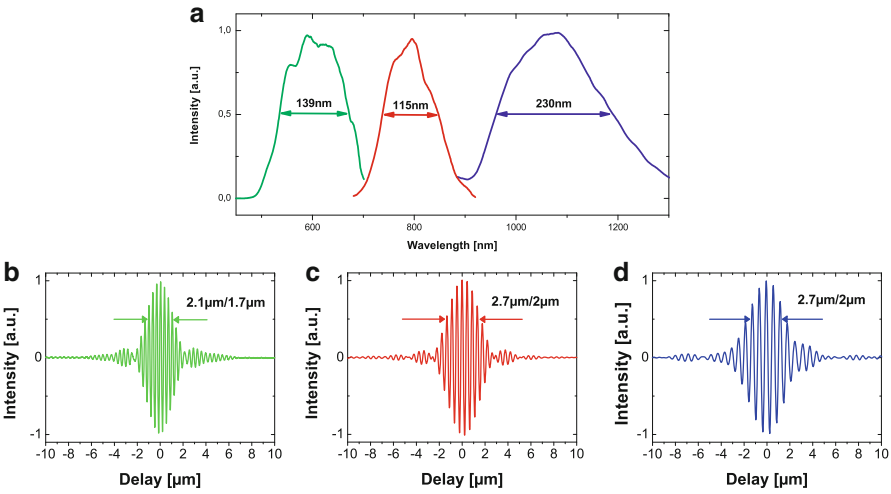

Fig. 19.19 *Multiple wavelengths, broad bandwidth light source*. The three wavelength regions of the light source and the corresponding autocorrelation fringes. Spectrum in *green* is centered at 600 nm achieving 1.7 µm axial resolution, the *red* spectrum is centered at 800 nm with 2 µm axial resolution, and the *blue* spectrum is paced in the so-called water window

602 nm with 40 mW output power. This region is especially interesting for several biological chromophores, i.e., hemoglobin, because the absorption compared to longer wavelength (around 800 nm) is significantly increased by a factor of 10. The central wavelength part spans from 700 to 900 nm at 800 nm with 120 nm bandwidth at FWHM and 160 mW output power. The longer wavelength part covers 950–1,350 nm centered at 1,060 nm with 230 nm bandwidth at FWHM and 35 mW output power. The latter one is the region of the zero-dispersion point of water, the so-called water window. The light source combines the advantages for spectroscopic OCT in the visible and 800 nm wavelength region enhancing the imaging contrast, permitting the differentiation of tissue pathologies by their spectroscopic properties or functional states (e.g., blood oxygenation) with enhanced penetration and cellular level resolution OCT imaging in the NIR region at 800 nm and 1,050 nm in a single optical instrument.

Low-noise broad bandwidth light for optical coherence tomography was also generated by a slightly different approach. A 70 cm long single-mode optical fiber (F-SPV, Newport) with a mode field diameter of 3.2 µm was pumped by a self-mode-locked Ti:sapphire laser [53]. The bandwidth of pump source could be broadened by a factor of 11 enabling a spectral output covering the range from 800 to 1,400 nm. A coherence length of 3.7 µm was achieved. Since the light was broadened by self-phase modulation, no noise amplification could be observed during the broadening process.

Ultrahigh-resolution optical coherence tomography was also demonstrated at 800 nm and 1,300 nm using continuum generation in a single photonic crystal fiber with a parabolic dispersion profile and two closely spaced zero-dispersion

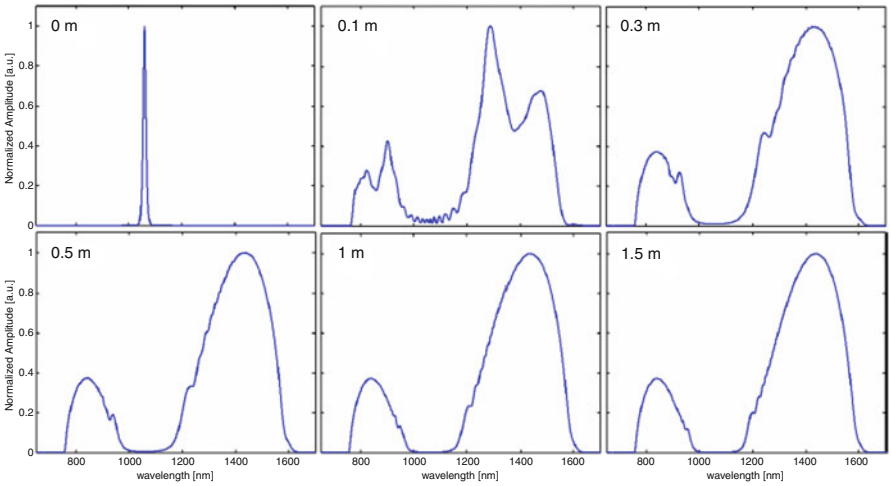

Fig. 19.20 *Numerical simulation for broad bandwidth light source development*. Computer modeling allows advance prediction of experimental results and optimization of nonlinear fiber parameters. Numerical simulations shown here demonstrate generation of dual-wavelength continuum in a photonic crystal fiber with two closely spaced zero-dispersion wavelengths centered at 1,050 nm. Using a pump wavelength of 1,060 nm, nearly complete depletion of the pump is observed along with creation of two high brightness main peaks centered at important OCT imaging wavelengths of 800 nm and 1,300 nm [57]

wavelengths centered around 1,050 nm [56]. The fiber was selected based on numerical simulation results, which demonstrated that relatively smooth spectral shape and sufficient power could be generated at both wavelengths simultaneously using a pump wavelength of 1,060 nm. Figure 19.20 presents the simulated results for spectral evolution as a function of fiber length for a 1,064 nm pump. Nearly complete depletion of the pump wavelength is observed along with creation of two high brightness main peaks centered at 800 nm and 1,300 nm. Results were generated experimentally using ~78 mW average power at 1,064 nm in a 52 MHz, 85 fs pulse train from a compact Nd:Glass oscillator. Continuum processes resulted in a double peak spectrum with >110 nm and 30 mW average power at 800 nm and >150 nm and 48 mW at 1,300 nm. OCT imaging with <5 μm resolution in tissue at 1,300 nm and <3 μm resolution at 800 nm was demonstrated [57]. Figure 19.21a, b compare the point spread function on a linear scale for both wavelengths. At 800 nm, 3.0 μm axial resolution was achieved in air, which for index of refraction in tissue of 1.38 provides ~2.2 μm in tissue. At 1,300 nm, 6.5 μm axial resolution in air provided ~4.7 μm in tissue. Both point spread functions were symmetric and correlate well to the Fourier transform interference bandwidths presented in Fig. 19.21e, f, indicating that dispersion mismatch was minimized. The interference bandwidths indicated that some spectral shaping in the OCT system resulted in reduction of optical bandwidth on the short-wavelength edges of the spectra. Spectral shaping likely resulted from wavelength dependent focusing aberration in the optics as well as some multimode leakage in long optical

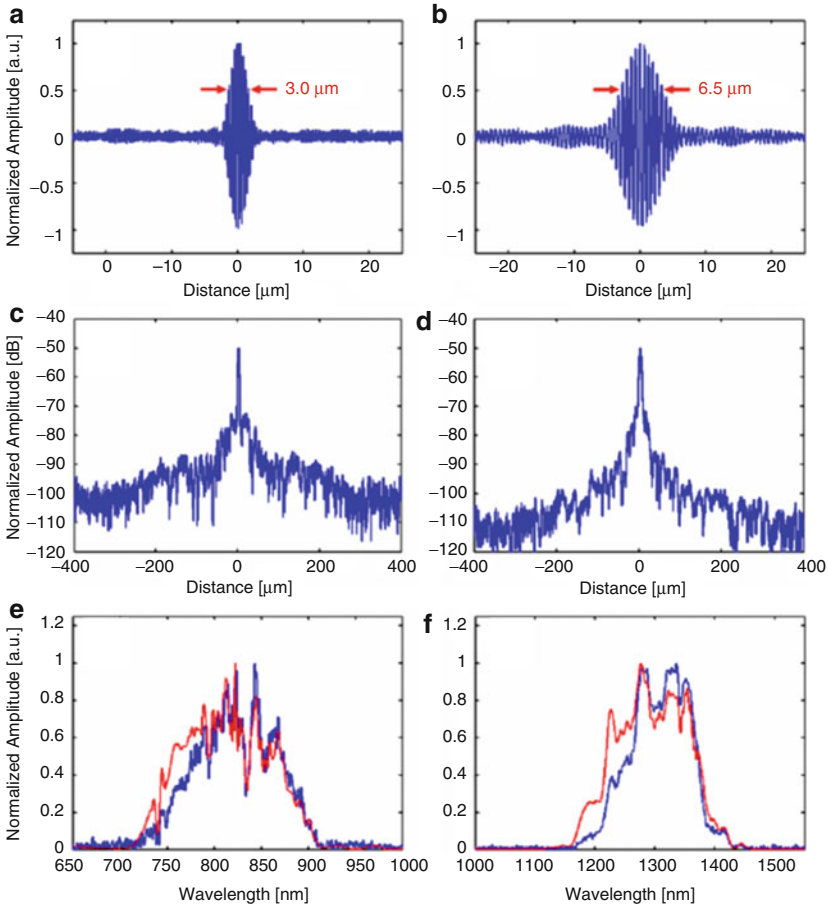

Fig. 19.21 *Dual-wavelength, broad bandwidth light source using a single PCF with parabolic dispersion profile*. Linear (**a**, **b**) and logarithmic (**c**, **d**) point spread functions are shown for both 800 nm (**a**, **c**) and 1,300 nm (**b**, **d**). The Fourier transform of the point spread functions in (**a**, **b**) are shown in *blue* in (**e**, **f**) to indicate the interference bandwidth. They are overlapped with the input source spectra shown in *red* [57]

fibers bringing light to the OCT system setup. Figures 19.21c, d present the logarithmically demodulated output signals for 800 nm and 1,300 nm, respectively. The traces have been normalized and scaled to reflect the 50 dB sample arm attenuation (2.5 OD filter, double pass) used to measure them. At both wavelengths, the sidelobe coherence artifacts on the point spread functions were present at ~25–30 dB. These results correlated well to the expected point spread function obtained by Fourier transforming the input optical bandwidths to the systems indicating that the source of the coherence artefact is the spectral modulation. In general sidelobe levels of 40–50 dB are desirable for OCT imaging.

Dual-band ultrahigh-resolution optical coherence tomography imaging has also been demonstrated simultaneously at 840 nm and 1,230 nm central wavelength using an off-the-shelf turnkey supercontinuum light source [58]. Spectral filtering of the light source emission resulted in a double peak spectrum with average powers exceeding 100 mW and bandwidths exceeding 200 nm for each wavelength band. A free-space OCT setup optimized to support both wavelengths in parallel was introduced. OCT imaging of biological tissue ex vivo and in vivo is demonstrated with axial resolutions measured to be <2 μm and <4 μm at 840 nm and 1,230 nm, respectively. This measuring scheme was used to extract spectroscopic features with outstanding spatial resolution enabling enhanced image contrast.

19.6.4 Spectral Broadening in the NIR

19.6.4.1 Supercontinuum Light Source in the 1,050 nm Region

Ultrahigh-resolution, real-time OCT imaging was demonstrated using a compact femtosecond Nd:Glass laser that is spectrally broadened in a high numerical aperture single-mode fiber [48]. A compact, commercially available diode-pumped femtosecond Nd:Glass laser (High Q Laser Production) generated pulses at 1,064 nm with 100–150 fs duration, 145 mW average power, and 75 MHz repetition rate. The laser employed measured only 53 cm × 20 cm, and even smaller lasers, measuring 18 cm × 10 cm, are now available. The Nd:Glass laser was pumped by two 1 W laser diodes and is soliton mode-locked using a semiconductor saturable absorber mirror (SESAM) for self-starting and intracavity prisms for dispersion compensation. To generate a continuum centered at 1 μm, the femtosecond pulses from the Nd:Glass laser were coupled into a 2 m long commercially available high numerical aperture (NA) single-mode fiber with a 2.75 mm focal length aspheric AR coated lens. The fiber had a germanium-doped core with a 2.5 μm mode field diameter to provide enhanced nonlinear effects. The fiber dispersion was approximately −125 ps/nm/km. Figure 19.22 shows a typical spectrum generated by the high numerical aperture fiber with 100 mW of average output power and a bandwidth of over 220 nm. This bandwidth should yield a theoretical axial resolution of 2.6 μm, as shown by the Fourier transform of the spectrum in Fig. 19.22c. The nearly symmetric broadening of the spectrum is the result of self-phase modulation in the normal, positive dispersion operating regime. A system resolution of <4.0 μm in air was achieved, as depicted in Fig. 19.22b. The difference from the theoretically predicted resolution values may be due to imperfect matching of the dispersion between the arms of the interferometer. Importantly, the relatively smooth spectral shape results in excellent sidelobe suppression on the point spread function, which is shown by the nearly −40 dB peak to sidelobe ratio in the log point spread function of Fig. 19.22d.

A similar approach has been reported using a broad bandwidth continuum light source with high-power, low-noise, and a smooth spectrum centered at 1.15 μm for ultrahigh-resolution optical coherence tomography [59]. The continuum was generated by self-phase modulation using a compact 1.059 μm femtosecond laser pumping

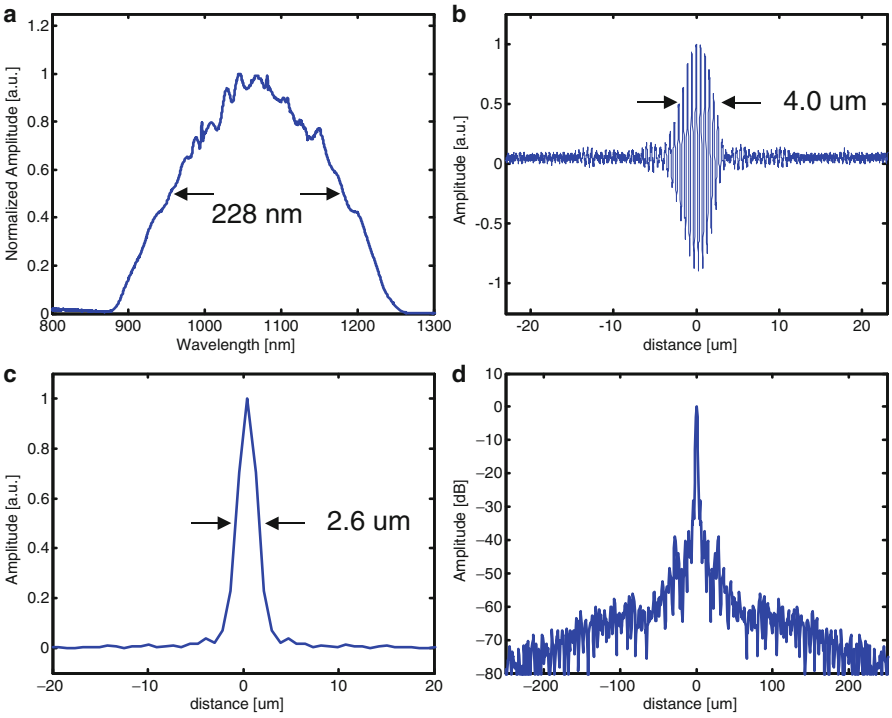

Fig. 19.22 *Broad bandwidth light source based on a compact Nd:Glass laser and a nonlinear fiber*. (**a**) Plot of the optical spectrum of the Nd:Glass laser broadened in the high numerical aperture (*NA*) single-mode fiber. (**b**) Linear point spread function measured in free space. (**c**) Theoretical point spread function computed by Fourier transform of the optical spectrum profile. (**d**) Measured point spread function on a log scale demonstrating excellent peak to sidelobe rejection for high-dynamic-range imaging [48]

a photonic crystal fiber, which had a convex dispersion profile with no zero-dispersion wavelengths. The emission spectrum was redshifted from the pump wavelength, ranges from 800 to 1,300 nm, and resulted in a measured axial resolution of ~2.8 μm in air, suggesting that PCFs with this type of dispersion profile are advantageous for generating SC as a light source for ultrahigh-resolution OCT.

Another supercontinuum source operating at 1.1 μm wavelength has been described accomplishing 372 nm optical bandwidth (FWHM) enabling 1.3 μm axial OCT resolution [45]. The pump source for the PCF was a Kerr-lens mode-locked Ti:sapphire laser. The total output laser power was greater than 700 mW, with a pulse duration of 110 fs and a repetition rate of 76 MHz. The laser output wavelength was 780 nm. The laser beam was then coupled into the PCF after a Faraday isolator to prevent interference of backreflected light. Nitrogen gas was slowly blown onto the coupling part to purge the fiber tip and prevent damage. A λ/2 waveplate after the Faraday isolator was used to adjust the polarization state of the light input to the fiber to optimize the spectrum.

The spectrum of light was broadened as it propagated through the fiber because of self-phase modulation and Raman scattering. The continuum output of light was collimated by a 4.5-mm focal length lens. The spectrum ranged from 800 to 1,430 nm. The total output power from the PCF could be as high as 100 mW, and the remaining power was approximately 50 mW after a long-pass filter.

19.6.4.2 Supercontinuum Light Source in the 1,300 nm–1,500 nm Region

The first development and application of PCF-based supercontinuum sources for UHR OCT was accomplished by launching 100 fs pulses generated by a commercial Kerr-lens mode-locked Ti:sapphire laser (Coherent Mira) pumped by a frequency-doubled Nd:vanadate laser (Spectra-Physics Millennia) into a 1 m length of microstructure fiber [50]. The beam was focused by a 3.5 mm focal length, 0.65 NA best-form lens into the fiber. Dramatic nonlinear effects allowed the generation of an extremely broadband continuum extending from 390 to 1,600 nm in the fiber. The pulse energy in the fiber was only ~2 nJ, corresponding

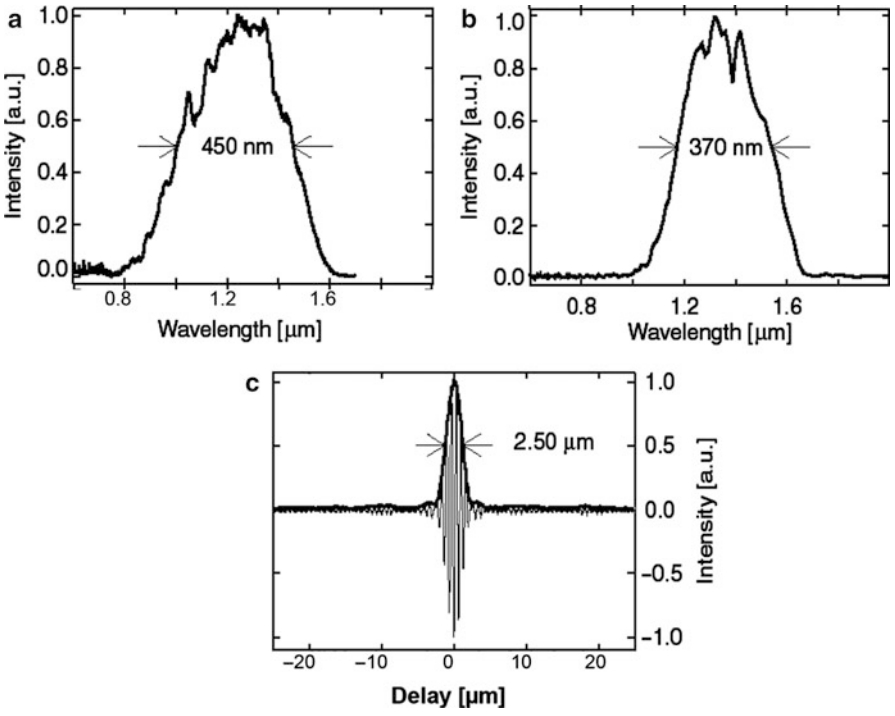

Fig. 19.23 *Supercontinuum light source at 1,300 nm.* (**a**) Typical spectrum of the light source after spectral filtering and coupling of the continuum in a single-mode fiber, measured at the entrance port of the second fiber coupler. (**b**) Detected optical spectrum obtained from the Fourier transform of the interferometric signal (**c**). (**c**) Interference fringes recorded by use of an isolated reflection. The FWHM was measured to be 2.5 μm [50]

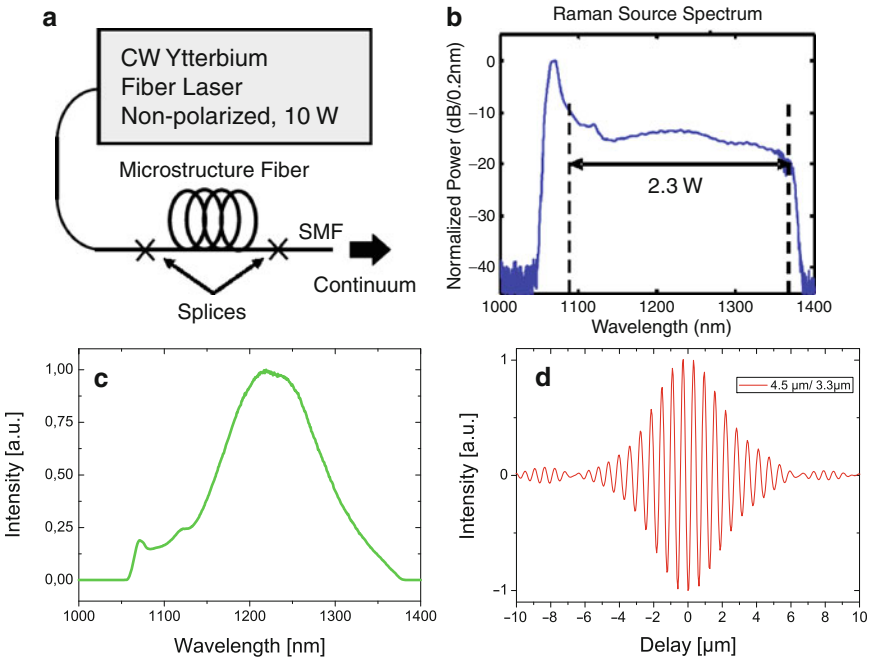

Fig. 19.24 *Broad bandwidth all-fiber Raman continuum light source at 1,300 nm.* (**a**) Fiber laser schematic including 100 m length of microstructure fiber for spectral broadening. (**b**) Light source spectrum before spectral shaping. (**c**) Gaussian-like spectrum in the 1,300 nm wavelength range achieved after filtering with WDM coupler. The output power after the coupler is about ~200 mW with a bandwidth of 140 nm at FWHM centered at 1,250 nm. (**d**) Sub-5 µm axial OCT resolution achieved with the Raman light source [51]

to an average power of 150 mW at 75 MHz repetition rate. Since the microstructured fiber was birefringent, a half waveplate was used to adjust the polarization of the light launched into the fiber to optimize the spectral properties of the continuum. The continuum out of the fiber is collimated by a 0.85-N.A. 603 microscope objective and focused by a 10-mm focal length, chromatically corrected, custom-designed 0.3-N.A. lens into the fiber-based OCT system. The spectrum of the light source at the entrance port of the second fiber coupler (cf. Fig. 19.23a) was measured by an optical spectrum analyzer and had a bandwidth of 450 nm centered at 1.2 um. The optimal interferometric signal is shown together with its envelope in Fig. 19.23c. The free-space axial OCT resolution of 2.5 µm was determined by measurement of the FWHM of the envelope. The detected optical spectrum (cf. Fig. 19.23b) was calculated by Fourier transformation of the interferometric signal. The detected spectral bandwidth was reduced to 370 nm. This reduction of the bandwidth occurred on the short-wavelength part of the spectrum and was probably caused by the low sensitivity of the InGaAs photodiodes at wavelengths shorter than 1 µm. In addition, the spectrally nonuniform-coupling ratio of the fiber couplers and the bending loss of the fibers, which are not single

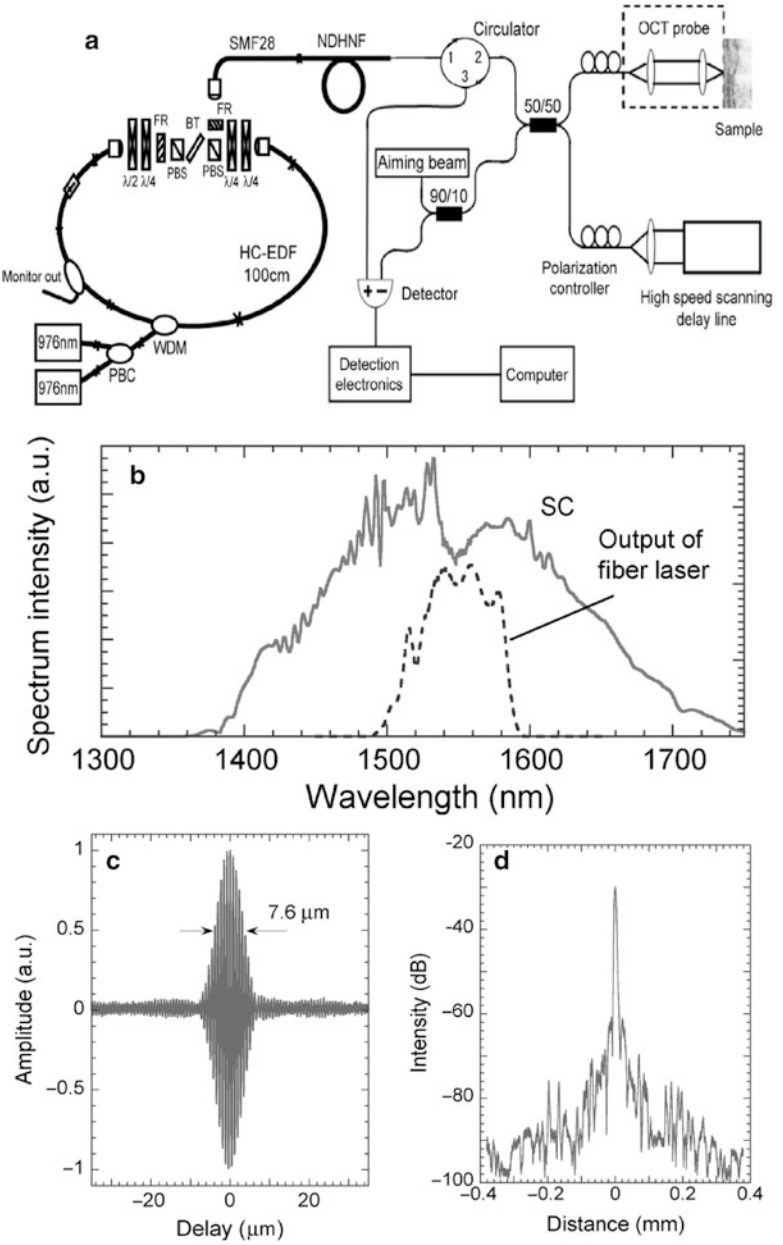

Fig. 19.25 *All-fiber, femtosecond fiber laser continuum at 1,500 nm.* (**a**) Fiber laser schematic. (**b**) Optical spectrum on a linear scale of the output from the fiber laser (*dashed*) and the supercontinuum generated in a high-nonlinearity fiber. (**c**) Interference signal point spread function and (**d**) logarithmically demodulated signal showing an axial resolution of 7.6 μm in air, corresponding to 5.5 μm in tissue [62]

mode for the short-wavelength part of the spectrum, may also cause this reduction in detected bandwidth.

A different approach based on a broadband all-fiber Raman continuum light source in the 1,300 nm region was also described recently using a high-power, continuous-wave, all-fiber pump light source. The turnkey broadband all-fiber Raman continuum light source is based on a 10 W cw, non-polarized, multimode diode-pumped, single-mode Yb-fiber laser directly spliced to an anomalously dispersive microstructure fiber, as shown in Fig. 19.24a. The microstructure fiber is 100 m long, has a dispersion of +35 ps nm^{-1} km^{-1}, a pitch of $\Lambda = 1.72$ µm, and an air-hole diameter of 0.65 µm. Figure 19.24b presents the measured Raman-soliton continuum. It contains 5.5 W of total power and a spectral width of 318 nm (at 20 dB). The spectrum covers the wavelength range from 1,090 to 1,370 nm with a flatness of ± 5 dB and 2.3 W of power. This output was filtered using a special WDM coupler to remove the pump wavelength and to achieve a smooth, Gaussian-like spectrum in the 1,300 nm wavelength range. The output power after the coupler is about ~200 mW with a Gaussian-shaped spectrum with a bandwidth of 140 nm at FWHM centered at 1,250 nm (cf. Fig. 19.24c) enabling sub-5 µm axial OCT resolution at 1,300 nm (Fig. 19.24d) [60, 61].

Real-time, ultrahigh-resolution optical coherence tomography (OCT) was demonstrated in the 1.4 to 1.7-µm wavelength region with a stretched-pulse, passively mode-locked, Er-doped fiber laser and highly nonlinear fiber [62]. The fiber laser, shown in Fig. 19.25a, generated 100 mW, linearly chirped pulses at a 51 MHz repetition rate. The pulses were compressed and then coupled into a normally dispersive, highly nonlinear fiber to generate a low-noise supercontinuum with a 180 nm FWHM bandwidth and 38 mW of output power. Figure 19.25b compares the spectrum of the fiber laser with that after spectral broadening. This light source was stable, compact, and broadband, permitting high-speed, real-time, OCT imaging with axial resolution of ~7.6 µm in air, corresponding to ~5.5 µm in tissue (Fig. 19.25c, d). In vivo high-speed OCT imaging of human skin was demonstrated.

19.7 Conclusion

Ultrabroad bandwidth light source technology has been developed enabling UHR OCT imaging in the visible and near-infrared wavelength region with unprecedented axial resolution. Subcellular structures were resolved with sub-micrometer axial resolution in human cancer and animal ganglion cells at shorter wavelengths, while the different contrast and improved penetration depth with increasing wavelength were demonstrated. Different medical fields such as ophthalmology, dermatology, neurology, gynecology, urology, laryngology, etc. impose various demands to the performance, size, and user-friendliness of UHR OCT systems. Since the OCT axial resolution scales with the center wavelength of the optical source, only relatively small bandwidths are required to achieve micrometer-scale resolution in the visible wavelength range. Here, the image contrast is enhanced due to stronger modulation of the backscattering profile of biological tissue. Major

limitations for UHR OCT in the visible wavelength range are the relatively low image penetration depth as well as the light source stability and inherent noise. Dispersion mismatch which deteriorates the imaging quality is more critical in the visible than in the near-infrared wavelength regime especially compared to 1,060 nm where the zero-dispersion point of water is located. The diversity in fiber-based light sources with respect to center wavelength, bandwidth, and output power makes them extremely attractive for UHR OCT applications. However, their excess noise is higher compared to Kerr-lens mode-locked lasers. It is not easy to find a light source for OCT which fulfills all technical and clinical requirements. On the one hand, there are low-noise, cheap, and nicely shaped SLDs covering a large wavelength range but with limited output power and bandwidth. By multiplexing of these SLDs ultrabroad bandwidth light sources can be generated at the cost of spectral shape and price. Alternatives are solid-state lasers which are capable of nice spectra spanning almost one octave. But these light sources are restricted to the fluorescence bands of the crystals. They have a complex architecture, which makes them expensive and not applicable for widespread industrial use. In the last decade, attempts have been made to make compact and cost-effective solid-state lasers by applying direct diode pumping or integrating of small and cheap pump sources in the optical platform. With this concept, ultrabroad bandwidth light could be generated direct out of a Ti: sapphire laser at reasonable cost with more than 300 nm bandwidth in the 800 nm regime. Nevertheless, they do not prevail the clinical daily routine until now.

MFs have become more and more important in generating ultrabroad bandwidth optical spectra in the visible and near-infrared wavelength range within the last decade. Advances in manufacturing processes allow for reliable operation of these light sources on a daily base. Constant quality is guaranteed from one fiber to the next. The noise behavior has also improved a lot in comparison to first-generation MFs. Especially short fibers and femtosecond pulses as demonstrated exhibit almost no amplification of the noise of the input pulse. OCT tomograms with sensitivities comparable to those acquired with Ti:sapphire lasers or SLDs could be obtained. Analytical treatment and simulation of the broadening process are extremely important to tailor MFs to the demanded wavelength regime and to the required low-noise pump sources. Complex fibers with one, two, or even no zero-dispersion wavelength can be designed and fabricated to fulfill special needs as large optical bandwidth and low noise. If the main broadening process is mainly due to self-phase modulation, no significant noise amplification is noticeable. So it is favorable to suppress all other broadening mechanisms like cross-phase modulation, four-wave mixing, and stimulated Raman scattering which generate a complex fine structure of the spectrum. The development in this direction is far not finished, and there are permanent attempts in this direction. Nevertheless the amplification of the noise especially with longer fibers combined with complex and expensive setups are still limiting factors and/or a handicap for OCT application.

Acknowledgements The authors would like to thank B. Herrmann, B. Hofer, and J.E. Morgan from the School of Optometry and Vision Science, Cardiff University; A.F. Fercher, R. Leitgeb, L. Schachinger, and H. Sattmann from the Centre of Biomedical Engineering and Physics, Medical

University of Vienna, Austria; K. Bizheva from the University of Waterloo, Canada; and A. Stingl, T. Le, G. Tempea, and V. Yakovlew from Femtolasers Produktions GmbH, Vienna, Austria.

The authors would also like to thank Desmond Adler, Stephan Bourquin, Iwona Gorczynska, Ingmar Hartl, Pei-Lin Hsiung, Robert Huber, Tony H. Ko, Jonathan Liu, Norihiko Nishizawa, Vivek J. Srinivasan, and Maciej Wojtkowski from the Department of Electrical Engineering and Computer Science at the Massachusetts Institute of Technology; James R. Taylor, Christiano J.S. de Matos, and Sergei V. Popov from the Imperial College; Valentin P. Gapontsev form IPG Photonics Corporation; Daniel Kopf, Wolfgang Seitz, and Max Lederer from High Q Laser Production, GmbH; and Vladimir Shidlovski and Sergei Yakubovich from Superlum Diodes, Ltd.

Financial support is acknowledged to Cardiff University, FP6-IST-NMP-2 STREPT (017128), the Christian Doppler Society, NP Photonics (Arizona, USA), FEMTOLASERS GmbH (Vienna, Austria), Carl Zeiss Meditec Inc. (Dublin, CA, USA), Maxon Computer GmbH (Friedrichsdorf, Germany); FWF P14218-PSY, FWF Y 159, CRAF-1999-70549, Christian Doppler Gesellschaft, FEMTOLASERS Produktions GmbH, Carl Zeiss Meditec Inc. This research was also supported at M.I.T. by the Air Force Office of Scientific Research and Medical Free Electron Laser Program FA9550-040-1-0046 and FA9550-040-1-0011, National Institutes of Health R01-EY011289-21, and R01-CA75289-10, and National Science Foundation ECS-0501478 and BES-0522845.

References

1. A. Unterhuber et al., Advances in broad bandwidth light sources for ultrahigh resolution optical coherence tomography. Phys. Med. Biol. **49**(7), 1235–1246 (2004)
2. T.H. Maiman, Stimulated optical radiation in ruby. Nature **182**, 493–494 (1960)
3. P.F. Moulton, Ti-doped sapphire: tunable solid-state laser. Opt. News **11**, 9 (1982)
4. P. Wagenblast et al., Diode-pumped 10-fs Cr3+:LiCAF laser. Opt. Lett. **28**(18), 1713–1715 (2003)
5. S. Uemura, K. Torizuka, Development of a diode-pumped Kerr-lens mode-locked Cr:LiSAF laser. IEEE J. Quantum Electron. **39**, 68–73 (2003)
6. B. Bouma et al., High-resolution optical coherence tomographic imaging using a mode-locked Ti-Al2O3 laser source. Opt. Lett. **20**(13), 1486–1488 (1995)
7. D.E. Spence et al., 60-fsec pulse generation from a self-modelocked Ti:sapphire laser. Opt. Lett. **16**(42), 42–44 (1991)
8. T. Brabec et al., Kerr lens mode locking. Opt Lett. **17**(18), 1292–1294 (1992)
9. R.L. Fork, O.E. Martinez, J.P. Gordon, Negative dispersion using pairs of prisms. Opt. Lett. **9**, 150–152 (1984)
10. J. Zhou et al., Pulse evolution is a broad-bandwidth Ti:sapphire laser. Opt. Lett. **19**, 1149–1151 (1994)
11. R. Szipöcz et al., Chirped multilayer coatings for broadband dispersion control in femtosecond lasers. Opt. Lett. **19**(3), 201–203 (1994)
12. R. Szipöcz, A. Kohazi-Kis, Theory and design of chirped dielectric laser mirrors. Appl Phys B **65**(2), 115–136 (1997)
13. B.E. Bouma et al., Self-phase-modulated Kerr-lens mode-locked Cr:forsterite laser source for optical coherence tomography. Opt. Lett. **21**(22), 1839–1841 (1996)
14. J.K. Ranka, R.S. Windeler, A.J. Stentz, Visible continuum generation in air-silica microstructure optical fibers with anomalous dispersion at 800 nm. Opt. Lett. **25**(1), 25–27 (2000)
15. T.A. Birks, W.J. Wadsworth, P.S.J. Russel, Generation of an ultra-broad supercontinuum in tapered fibers. Opt. Lett. **25**(19), 1415–1417 (2000)
16. N.R. Newbury et al., Noise amplification during supercontinuum generation in microstructured fibers. Opt. Lett. **28**, 944–945 (2003)
17. K.L. Corwin et al., Fundamental amplitude noise limitations to supercontinuum spectra generated in a microstructured fiber. Appl. Phys. B-Lasers Opt. **77**(2–3), 269–277 (2003)

18. R. Ell et al., Generation of 5-fs pulses and octave-spanning spectra directly from a Ti:sapphire laser. Opt. Lett. **26**, 373–375 (2001)
19. A. Bartels, H. Kurz, Generation of broadband continuum generation by a Ti:sapphire oscillator with a 1 GHz repetition rate. Opt. Lett. **27**, 1839–1841 (2002)
20. W. Drexler et al., Ultrahigh-resolution ophthalmic optical coherence tomography. Nat. Med. **7**(4), 502–507 (2001)
21. W. Drexler et al., In vivo ultrahigh-resolution optical coherence tomography. Opt. Lett. **24**(17), 1221–1223 (1999)
22. U. Morgner et al., Spectroscopic optical coherence tomography. Opt. Lett. **25**(2), 111–113 (2000)
23. T. Fuji et al., Generation of smooth, ultra-broadband spectra directly from a prism-less Ti: sapphire laser. Appl. Phys. B-Lasers Opt. **77**(1), 125–128 (2003)
24. D.I. Babic, S.W. Corzine, Analytic expression for the reflection delay, penetration depth, and absorptance of quarter-wave dielectric mirrors. IEEE J. Quantum Electron. **28**, 514–524 (1992)
25. P. Laporta, V. Magni, Dispersive effects in the reflection of femtosecond optical pulses from broadband dielectric mirrors. Appl. Opt. **24**, 2014–2020 (1985)
26. F.X. Kärtner et al., Design and fabrication of double-chirped mirrors. Opt. Lett. **22**(11), 831–833 (1997)
27. G. Tempea et al., Tilted-front-interface chirped mirrors. J. Opt. Soc. Am. B **18**, 1747–1750 (2001)
28. U. Morgner et al., Sub-two-cycle pulses from a Kerr-lens mode-locked Ti:sapphire laser. Opt. Lett. **24**(6), 411–413 (1999)
29. A. Stingl et al., Sub-10-fs mirror-dispersion-controlled Ti:sapphire laser. Opt. Lett. **20**, 602–604 (1995)
30. U. Morgner et al., Nonlinear optics with phase-controlled pulses in the sub-two-cycle regime. Phys. Rev. Lett. **86**(24), 5462–5465 (2001)
31. T.M. Ramond et al., Phase-coherent link from optical to microwave frequencies by means of the broadband continuum from a 1-GHz Ti:sapphire femtosecond oscillator. Opt. Lett. **27**(20), 1842–1844 (2002)
32. T.R. Schibli et al., *Continuum generation in a prism-less Ti:sapphire laser,* ed. by R.D. Miller, M.M. Murnsne, N.F. Scherer, A.M. Weinere. Ultrafast Phenomena XIII. *Chem. Phys.* pp. 131–133 (2002)
33. A. Unterhuber et al., Compact, low-cost Ti: Al2O3 laser for in vivo ultrahigh-resolution optical coherence tomography. Opt. Lett. **28**(11), 905–907 (2003)
34. A.M. Kowalevicz et al., Ultralow-threshold Kerr-lens mode-locked Ti:Al_2O_3 laser. Opt. Lett. **27**, 2037–2039 (2002)
35. P.C. Wagenblast et al., Generation of sub-10-fs pulses from a Kerr-lens mode-locked Cr 3+: LiCAF laser oscillator by use of third-order dispersion-compensating double-chirped mirrors. Opt. Lett. **27**, 1726–1728 (2002)
36. P.C. Wagenblast et al., Ultrahigh-resolution optical coherence tomography with a diode-pumped broadband Cr^{3+}: LiCAF laser. Opt. Express **12**(14), 3257–3263 (2004)
37. J. Herrmann, Theory of Kerr-lens mode-locking: role of self-focusing and radially varying gain. J. Opt. Soc. Am. B **11**, 498–512 (1994)
38. C. Chudoba et al., All-solid-state Cr:forsterite laser generating 14-fs pulses at 1.3 μm. Opt. Lett. **26**(5), 292–294 (2001)
39. R.P. Prasankumar et al., Self-starting mode locking in a Cr:forsterite laser by use of non-epitaxially-grown semiconductor-doped silica films. Opt. Lett. **27**(17), 1564–1566 (2002)
40. P.R. Herz et al., Ultrahigh resolution optical biopsy with endoscopic optical coherence tomography. Opt. Express **12**(15), 3532–3542 (2004)
41. Y. Chen et al., Ultrahigh resolution optical coherence tomography of Barrett's esophagus: preliminary descriptive clinical study correlating images with histology. Endoscopy **39**(7), 599–605 (2007)
42. D.J. Ripin et al., Generation of 20-fs pulses by a prismless Cr4+:YAG laser. Opt. Lett. **27**(1), 61–63 (2002)
43. P. Kaiser, E.A.J. Marcatili, S.E. Miller, A new optical fiber. Bell. Sys. Tech. J. **52**, 265–269 (1973)

44. S.L. Chin et al., The white light supercontinuum is indeed an ultrafast white light laser. Jpn. J. Appl. Phys. **38**(2), 126–128 (1999)
45. Y.M. Wang et al., Ultrahigh-resolution optical coherence tomography by broadband continuum generation from a photonic crystal fiber. Opt. Lett. **28**(3), 182–184 (2003)
46. D.L. Marks et al., Study of an ultrahigh-numerical-aperture fiber continuum generation source for optical coherence tomography. Opt. Lett. **27**(22), 2010–2012 (2002)
47. B. Považay et al., Submicrometer axial resolution optical coherence tomography. Opt. Lett. **27**(20), 1800–1802 (2002)
48. S. Bourquin et al., Ultrahigh resolution real time OCT imaging using a compact femtosecond Nd:glass laser and nonlinear fiber. Opt. Express **11**(24), 3290–3297 (2003)
49. K. Tamura et al., Broadband light generation by femtosecond pulse amplification with stimulated Raman scattering in a high power erbium-doped fiber amplifier. Opt. Lett. **20**, 1631–1633 (1995)
50. I. Hartl et al., Ultrahigh-resolution optical coherence tomography using continuum generation in an air-silica microstructure optical fiber. Opt. Lett. **26**(9), 608–610 (2001)
51. A.L. Gaeta, Nonlinear propagation and continuum generation in microstructured optical fibers. Opt. Lett. **27**, 924–926 (2002)
52. X. Gu et al., Frequency resolved optical gating and single shot spectral measurements reveal fine structure in microstructure-fiber-continuum. Opt. Lett. **27**, 1174–1176 (2002)
53. Y.M. Wang et al., Low-noise broadband light generation from optical fibers for use in high-resolution optical coherence tomography. J. Opt. Soc. Am. A-Opt. Imag. Sci. Vis. **22**(8), 1492–1499 (2005)
54. H. Lim et al., Ultrahigh-resolution optical coherence tomography with a fiber laser source at 1 mu m. Opt. Lett. **30**(10), 1171–1173 (2005)
55. G. Humbert et al., Supercontinuum generation system for optical coherence tomography based on tapered photonic crystal fibre. Opt. Express **14**(4), 1596–1603 (2006)
56. H. Wang, A.M. Rollins, Optimization of dual-band continuum light source for ultrahigh-resolution optical coherence tomography. Appl. Opt. **46**(10), 1787–1794 (2007)
57. A.D. Aguirre et al., Continuum generation in a novel photonic crystal fiber for ultrahigh resolution optical coherence tomography at 800 nm and 1300 nm. Opt. Express **14**(3), 1145–1160 (2006)
58. F. Spöler et al., Simultaneous dual-band ultra-high resolution optical coherence tomography. Opt. Lett. **15**(17), 10832–10841 (2007)
59. H. Wang, C.P. Fleming, A.M. Rollins, Ultrahigh-resolution optical coherence tomography at 1.15 15 μm mu;m using photonic crystal fiber with no zero-dispersion wavelengths. Opt. Express **15**(6), 3085–3092 (2007)
60. P.L. Hsiung et al., Optical coherence tomography using a continuous-wave, high-power, Raman continuum light source. Opt. Express **12**(22), 5287–5295 (2004)
61. K. Bizheva et al., Optophysiology: depth-resolved probing of retinal physiology with functional ultrahigh-resolution optical coherence tomography. Proc. Natl. Acad. Sci. U. S. A. **103**(13), 5066–5071 (2006)
62. N. Nishizawa et al., Real-time, ultrahigh-resolution, optical coherence tomography with an all-fiber, femtosecond fiber laser continuum at 1.5 microm. Opt. Lett. **29**(24), 2846–2848 (2004)
63. A. Müller, O.B. Jensen, A. Unterhuber, T. Le, A. Stingl, K-H. Hasler, B. Sumpf, G. Erbert, P.E. Andersen, P.M. Petersen, Frequency-doubled DBR-tapered diode laser for direct pumping of Ti: sapphire lasers generating sub-20 fs pulses. In: Optics Express. **19**(13), 12156–12163 (2011)

Wavelength Swept Lasers

20

Seok Hyun Yun and Brett E. Bouma

Keywords
Gain medium • Laser cavity • Sweep operation • Sweep techniques • Swept source

20.1 Introduction

In optical interferometric metrology, the wavelength of light serves as a reference for length. At a given optical wavelength, an interference signal varies as a sinusoidal function of distance with a period equal to the wavelength. Although this approach offers unrivaled precision, the periodic signal results in a 2π ambiguity for measurement of lengths greater than one wavelength. In optical coherence tomography (OCT), one wishes to determine light scattering distances and distribution within a sample, but without the ambiguity. To accomplish this, OCT is based on interferometry using many optical wavelengths, each serving as a "ruler" with different periodicities. OCT traditionally has used broadband light sources providing a wide range of wavelengths, all simultaneously. Alternatively, a tunable light source emitting one wavelength at a time, rapidly swept over a broad spectral range, can also be used to achieve the absolute ranging capability in OCT.

S.H. Yun (✉)
Partners Research Building, Wellman Center for Photomedicine, Cambridge, MA, USA

Wellman Center for Photomedicine, Massachusetts General Hospital, Harvard Medical School, Boston, MA, USA
e-mail: syun@hms.harvard.edu

B.E. Bouma
Wellman Center for Photomedicine, Massachusetts General Hospital, Harvard Medical School, Boston, MA, USA
e-mail: bouma@mgh.harvard.edu

© Springer International Publishing Switzerland 2015

W. Drexler, J.G. Fujimoto (eds.), *Optical Coherence Tomography*,
DOI 10.1007/978-3-319-06419-2_21

With such a wavelength-swept source, interference signals at individual wavelengths can be measured sequentially with high spectral resolution. This spectrally resolved data acquisition is central to frequency-domain ranging. This method offers significantly higher sensitivity than the time-domain ranging method used in conventional OCT. Furthermore, frequency-domain ranging does not require reference delay scanning and can therefore be applied to increase imaging speed. With a pressing need for high imaging speed in various applications, wavelength-swept sources, particularly rapidly tuned lasers, have developed substantially in recent years and have emerged as important and practical light sources for OCT.

In this chapter, we describe a technical overview of these new emerging light sources. We discuss general specifications of the sources in Sect. 20.2. Section 20.3 is devoted to basic fundamentals of laser and wavelength tuning. In Sect. 20.4, we discuss the principles of various techniques developed to date for high-speed and wide tuning range. Those who are not familiar with the principle of frequency-domain ranging and OCT system instrumentations are encouraged to read ▶ Chap. 7, "Optical Frequency Domain Imaging" before proceeding to the next section.

20.2 General Requirements

This section will review some current key specifications and requirements of swept lasers. The swept laser technology is rapidly progressing, driving and driven by continually expanding applications. Therefore, the following provides general guidelines rather than attempting to define the state of the art.

Output power. In theory [1], the signal-to-noise ratio (SNR) of imaging systems improves indefinitely with sample-arm optical power. In practice, however, various factors limit the dynamic range of SNR. As a result, an optimal power range depends upon the sample and system. For a highly reflecting sample, low sample power would be appropriate to avoid detector saturation ($<$100 μW) and to maximize SNR. The maximum permissible exposure level of the human retina is approximately 700 μW at 800 nm wavelength. Therefore, a source power of 10 mW would be sufficient for ophthalmic applications. Another tissue such as the skin can be exposed to $>$10 mW, so a powerful source with several tens of mW output is desired for deep tissue imaging applications.

Tuning curve. In Fig. 20.1a, a tuning curve shows the output wavelength varying over time. The exemplary curve shows a linear, unidirectional tuning from a short to long wavelength. Some lasers may produce nonlinear or bidirectional tuning curves. In frequency-domain ranging, depth is conjugate to wavenumber, $k = 2\pi/\lambda$. Ideally, the wavenumber, not wavelength, would be tuned linearly over time so that the interference signal can be sampled uniformly, directly Fourier transformed to yield a depth profile. In general, tuning k is nearly always nonlinear, requiring nonuniform sampling or interpolated processing. A highly nonlinear tuning curve is undesirable because it complicates the linearization process and consumes a larger detection bandwidth and sampling rate than is otherwise necessary.

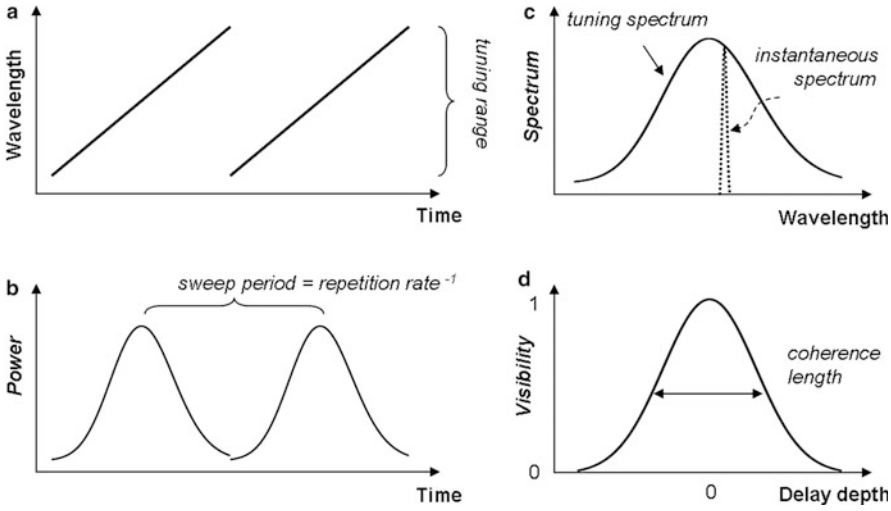

Fig. 20.1 Typical output properties of a swept laser. (**a**) Tuning curve. (**b**) Time trace. (**c**) Spectrum. (**d**) Coherence. The definition of each parameter is described in the text

Sweep repetition rate. Figure 20.1b illustrates an exemplary time trace of laser output power that corresponds to a Gaussian-like tuning spectrum shown in Fig. 20.1c. The sweep repetition rate, a reciprocal of sweep period, determines the A-line acquisition rate in OCT. A higher A-line rate can increase frame rate, reduce motion artifacts, and allow screening over a larger tissue surface in a limited time. For these reasons, A-line rates greater than 20 kHz would be required in most clinical applications. On the other hand, the limited bandwidth and data handling speed of currently available hardware put a practical limit on the maximum achievable A-line rate in a system. Depending on applications and system capability, the sweep repetition rate of a source may need to be between 20 and 200 kHz.

Center wavelength ($\boldsymbol{\lambda_0}$). The optimal center wavelength is somewhat dependent upon the sample and application. Longer wavelengths are less scattered and can penetrate deeper in tissue, but absorption, dominantly by water, has a strong wavelength dependence [2]. In general, there are two distinct spectral windows for imaging. The first window (650–900 nm) is suitable for retinal imaging because of low absorption in vitreous humor. This range can be extended to 1,100 nm where the penetration depth in the retina and choroid is increased. The second window in 1,100–1,360 nm permits even deeper tissue penetration and, therefore, is suitable for most non-ophthalmic imaging. Certainly, other wavelengths, such as visible or beyond 1,500 nm, have potential for specific applications, such as molecular contrast-based imaging or non-biological material with low water concentration.

Tuning range ($\boldsymbol{\Delta\lambda}$). Figure 20.1c depicts an exemplary output spectrum with a truncated Gaussian-like profile, typical of swept lasers. The spectral envelope is related to the point spread function through the Fourier transform, although windowing can be applied in data processing. The tuning range is defined from edge

to edge (full range), at –3 dB (full width at half maximum: FWHM), or at $1/e^2$ level. Assuming a Gaussian spectrum with $1/e^2$ width of $\Delta\lambda$, the axial resolution, defined as the FWHM of point spread function, is given by

$$\Delta z \approx 0.75 \frac{\lambda_0^2}{\Delta\lambda}, \tag{20.1}$$

As numerical examples, a tuning range of $\Delta\lambda = 127$ nm at $\lambda_0 = 1{,}300$ nm yields $\Delta z = 10$ μm; the same resolution is achieved with $\Delta\lambda = 48$ nm at $\lambda_0 = 800$ nm.

Instantaneous linewidth ($\delta\lambda$). The laser emits a narrowband spectrum instantaneously. The finite linewidth of the instantaneous output causes the visibility of interference to decrease with path length difference, as illustrated in Fig. 20.1d. The coherence function is related to the instantaneous spectrum through the Fourier transform, just like the point spread function is to the overall tuning spectral envelope. The coherence length is defined as the optical delay when interference visibility drops to 0.5. This corresponds to a full depth range with visibility greater than >0.5. Because SNR is proportional to the square of the visibility, longer coherence length is required in OCT. The coherence length, z_c, is related to the FWHM instantaneous linewidth, $\delta\lambda$, via

$$z_c \approx 0.44 \frac{\lambda_0^2}{\delta\lambda} \tag{20.2}$$

Most OCT applications require a depth range between 2 and 6 mm. Given that positive and negative depths are indistinguishable in normal OCT, a coherence length of 4–12 mm would be required. As a numerical example, $\delta\lambda = 0.1$ nm at $\lambda_0 = 1{,}300$ nm yields $z_c = 7.4$ mm; the same coherence length is obtained with $\delta\lambda = 0.038$ nm at $\lambda_0 = 800$ nm.

Intensity noise. Intensity fluctuations of laser output, if they have significant frequency components in the signal detection band, can degrade SNR and may produce image artifacts through frequency mixing with signals. Mechanical vibration and noisy pump sources are two primary sources for 1/f-type intensity noise. Mode partition noise or mode beating noise occurs at the fundamental frequency equal to the reciprocal of the cavity roundtrip time or its harmonics. In swept lasers, multiple path interference due to spurious back reflections in intracavity components or the gain chip can cause intensity modulation at frequencies corresponding to path differences. In OCT detection, the total intensity noise should be smaller than shot noise [3], given as $\langle \Delta P_r^2 \rangle < 2\, h\nu\, P_r$ where $\langle \Delta P_r^2 \rangle$ is the time-averaged intensity noise power per a 1 Hz bandwidth, $h\nu$ is a single photon energy (h is Planck's constant), and P_r is the average reference power. The noise power per bandwidth is conveniently characterized with relatively intensity noise (RIN) that is defined as

$$\mathrm{RIN} = \frac{< \Delta P^2 >}{P^2} \left[Hz^{-1} \right] \tag{20.3}$$

Therefore, the shot-noise limit condition is reduced to $\mathrm{RIN} < 2\, h\nu / P_r$. Typically, $P_r = 10$–100 μW, and therefore, RIN $< -135 - -145$ dB/Hz. This is achievable in

swept lasers. The RIN spectrum of a laser output can be measured with a photodiode and an electrical spectrum analyzer. In an OCT system, the effect of the laser RIN can be reduced by 15–30 dB using dual balanced detection.

Output polarization. Single polarization output is ideal. With a dual polarization source, polarization-dependent delay in the interferometer, such as polarization mode dispersion in a circulator, can cause blurry images. Even when the source output is singly polarized, the specific polarization state may vary as a function of wavelength in a swept laser, particularly if the cavity has strong birefringence. This wavelength dependence should be minimized, because it can lead to an intensity modulation through polarization-dependent loss or splitting ratio in the interferometer or probe optics, resulting in image artifacts.

Miscellaneous. A small-sized mechanically durable light source would be highly desirable if it is to be integrated into a compact, portable system for space-limited clinical environment. Long-term reliability and stability are highly desirable for clinical or industrial uses.

20.3 Fundamentals

A laser is an optical oscillator, coined after its underlying physical mechanism: light amplification by the stimulated emission of radiation. Central to laser instrumentation is a gain medium where light is amplified. Another fundamental component is an optical cavity that gives coherent optical feedback for laser oscillation. The optical cavity also provides space to insert other various optical components, such as lenses, nonlinear optical materials, and spectral filters. These intracavity components are used to condition temporal and spectral characteristics of laser light to specific purposes. For example, an intracavity tunable filter is widely used in a tunable laser. In this section, we describe some fundamentals of lasers and their wavelength sweep operation.

20.3.1 Gain Medium

A gain medium that is pumped to reach an electronic population inversion is able to amplify optical energy. Figure 20.2a illustrates this principle with regard to a semiconductor [4]. The valence and conduction bands serve as the ground and excited state. A positive bias is applied to the semiconductor so that injected electrons flow into the conduction band and populate it, whereas holes are created in the valence band. An incoming photon, if its energy is equal to the energy difference between the two bands, can trigger the transition of an excited electron to the valence band, where it is recombined with a matching hole. In this stimulated transition process, the energy difference is radiated optically, resulting in the emission of a new photon that has identical energy, phase, and propagation direction compared with the original photon. This process, called stimulated emission, is the fundamental

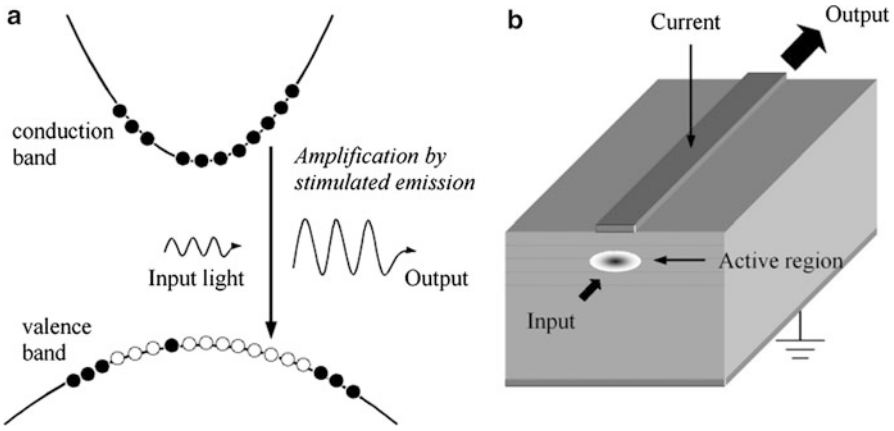

Fig. 20.2 Semiconductor optical amplifier. (**a**) The principle of light amplification in semiconductor. (**b**) A schematic of quantum-well amplifier. Light is guided and amplified in the active region

mechanism for coherent optical amplification. Other types of gain media, such as gas, dyes, crystals, and glass, are based on the same mechanism, although specifics of the transition levels of electrons and pumping methods are different. Gain saturation, or a decrease of gain due to the depletion of population inversion by strong optical intensity, is an intrinsic characteristic of gain media. In typical laser oscillation at the steady state, gain is saturated substantially to a level where the saturated gain is just enough to compensate for the loss in a laser cavity.

20.3.1.1 Semiconductor Optical Amplifier (SOA)

Figure 20.2b shows a schematic of an SOA. SOAs are one of the most widely used gain media for rapidly swept lasers for several reasons. First, the flexibility of semiconductors in making heterogeneous structures offers a wide range of gain center wavelengths. SOAs are typically made from group III–V compound semiconductors such as GaAs/$Al_xGa_{1-x}As$ ($\lambda_0 = 0.75$–0.9 μm) and $In_{1-x}Ga_xAs_{1-y}P_y$/InP ($\lambda_0 = 1.1$–1.6 μm).

Second, an SOA offers high gain with broad bandwidth. This gives a great flexibility in choosing a filter and cavity configuration for wide range and fast tuning. The high gain of an SOA, typically 20–35 dB, comes in part from its waveguide structure that ensures a long active region, typically 300–1,000 μm. Gain bandwidth, depending on the specific semiconductor materials, chip designs, and the inversion level, can be greater than 10 % of the center wavelength.

Third, the gain response time of an SOA is about 250 ps, much shorter than the micro- or millisecond timescale of other gain media, such as a titanium-sapphire and rare-earth-doped fibers. For fast sweep operation, the short gain response time is highly desirable to minimize the intensity noise of the laser output. With a slow gain medium, even a small magnitude of cavity loss modulation associated with

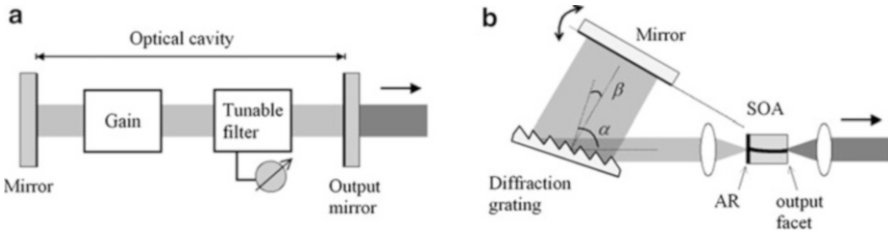

Fig. 20.3 Tunable laser. (**a**) Basic configuration. (**b**) A schematic of typical external-cavity semiconductor tunable laser. *AR* anti-reflection coating, *SOA* semiconductor optical amplifier

filter sweep can interplay resonantly with gain recovery and lead to self Q-switching or relaxation oscillation [5]. For solid-state gain media, this resonance is typically in the frequency range between 1 kHz and 1 MHz, which becomes a serious problem because it may overlap with the signal band used for imaging. A similar type of intensity modulation can arise in a semiconductor laser, but the modulation frequency is in the GHz range, and it can be easily removed electrically without affecting the signals.

20.3.2 Laser Cavity

A laser cavity is a resonator that gives phase-coherent optical feedback for regenerative amplification in the gain medium [5]. A variety of optical materials and components can be incorporated into a cavity to control and condition the characteristics of a laser. By its geometrical shape, a laser cavity can be categorized into a linear, ring, or hybrid (such as sigma) type. In a linear cavity, exemplified in Fig. 20.3a, intracavity light passes through a gain medium and a transmissive filter twice in each round trip. A ring cavity is often made unidirectional, ensured by a magneto-optic isolator with a direction-dependent insertion loss. The unidirectional ring cavity offers a distinct advantage that the backward reflected light from intracavity components is de-coupled from the main beam path and as a result, often produces more stable laser oscillation than a linear cavity. This advantage may not be evident, however, in most rapidly swept lasers that are less sensitive to the spurious feedback due to oscillation of multiple longitudinal modes.

Longitudinal cavity modes are a set of frequency components capable of oscillating resonantly in the cavity. Each mode satisfies the resonance condition that the total optical phase accumulated in one roundtrip propagation is equal to an integer multiple of 2π. The frequency difference between two adjacent modes, or the mode spacing f_m, is given by

$$f_m = 1/\tau = c/L, \tag{20.4}$$

where τ is the total propagation time of cavity roundtrip and L is the total optical length that includes group refractive indices of the cavity.

The laser output is obtained through an output coupler of the cavity. Large output coupling can extract larger optical energy from the cavity, thus resulting in a higher output power, but may decrease the tuning range due to resulting increased cavity loss. An optimum output coupling ratio can be chosen with some trade-off in performance, ranging from a few percent in low-gain lasers, such as a titanium-sapphire laser, to several tens of percents in high-gain lasers, such as a semiconductor or rare-earth-doped fiber laser.

20.3.3 Tunable Laser

Wavelength-tunable lasers have developed considerably since the mid-1960s and are now invaluable light sources for numerous scientific and industrial applications. Figure 20.3a represents a schematic of a tunable laser configuration consisting of a broadband gain media, an optical cavity, and a narrowband tunable filter. To illustrate the basic principle of a tunable laser, let us consider an extended-cavity semiconductor lasers, one of the most versatile and commercially successful tunable sources. Figure 20.3b depicts a representative schematic of the laser. One facet of a semiconductor gain chip serves as a partial reflector and output coupler of a laser cavity. Partial reflectance is normally achieved just by cleaving the facet perpendicular to the optic axis, yielding Fresnel reflection by 26–30 % for typical semiconductor materials. Optical reflection at the other facet of the chip is minimized to <0.001 % by anti-reflection dielectric coating ($R = 0.1$ %) and the curved active waveguide design. At the other end of the cavity, a diffraction grating and a mirror serve as a tunable wavelength selective filter. The angular position of the mirror determines the specific wavelength component that returns to the gain medium via [6]

$$\lambda = p \cdot (\sin\alpha + \sin\beta), \tag{20.5}$$

where p denotes the grating pitch, α is the angle between the grating normal and beam incidence axis, and β is the angle between the grating normal to the diffracted beam as determined by the angular position of the end mirror. The reflected spectrum of the grating filter has a narrowband Gaussian-like profile with a width approximately given by λ/N where N denotes the number of grooves illuminated by the optical beam on the grating.

Figure 20.4a depicts the resulting net-gain profile together with the spectrum of oscillating laser modes. The gain profile has a peak at the wavelength determined by Eq. 20.5. The net roundtrip gain becomes close to one in steady-state laser oscillation. Because of the strong gain discrimination by the filter, only the frequency mode closest to the gain peak is able to oscillate. Single-frequency oscillation offers a very narrow linewidth of <100 kHz and a long coherence length exceeding 10 km, typical of an extended-cavity semiconductor laser.

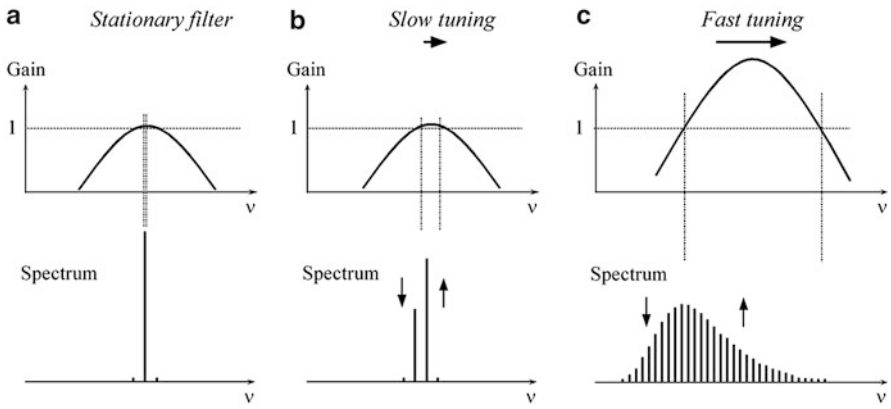

Fig. 20.4 Spectral dynamics in a tunable laser. The net-gain profile and oscillating mode spectrum are illustrated in three distinct cases: (**a**) fixed-wavelength filter and single-frequency oscillation, (**b**) slowly tuned filter and mode hopping, and (**c**) rapidly swept filter and multiple mode oscillation

20.3.4 Sweep Operation

By rotating the end reflector, the gain peak wavelength can be shifted continuously, and the output spectrum can be swept accordingly [7]. Figure 20.4b illustrates this situation in the case of slow adiabatic tuning where steady-state oscillation is reached at any given time. Here, the cavity length is assumed invariant so that the positions of cavity modes are stationary in the frequency domain. Under this condition, as the gain profile is continuously shifted by tuning, the laser spectrum steps from one mode to another – a process called mode hopping.

In some applications such as high-resolution atomic spectroscopy, truly continuous tuning without mode hopping is desirable. The extended-cavity tunable laser shown in Fig. 20.3b offers a simple way to achieve this feature. The underlying idea is to vary the cavity length in conjunction with tuning, such that the frequency of a cavity mode always coincides with the gain peak frequency. This can be achieved by placing the pivot point of the end mirror exactly at the output facet of the gain chip. Using this geometrical arrangement [8], commercial extended-cavity tunable lasers can produce a mode-hop-free sweep over several tens of nanometers. However, their tuning speeds currently are limited to <1 nm/ms, although the technique can work in principle at an arbitrary sweep speed.

Let us now consider high-speed tuning by a scanning filter. The cavity length is assumed invariant. This situation applies to swept lasers with a tuning speed of $>1{,}000$ nm/ms. When the gain profile is tuned so rapidly, it becomes impossible for any single-frequency mode to get amplified enough to reach the full optical power necessary to saturate the gain before the gain peak is shifted away. Then, stable laser

emission is only possible by simultaneously oscillating multiple modes. In this case, the envelope of the multimode spectrum is shifted continuously through the creation of new modes at the leading side of the spectrum and the extinction of modes at the trailing side, as illustrated in Fig. 20.4c. The peak net gain needs to be substantially greater than one in order to allow the new modes to build up. As a result, the peak of the laser spectrum lags behind the center frequency of the filter. It should be noted that the spectral offset and linewidth of the spectrum are dependent upon the magnitude of tuning per roundtrip rather than the absolute tuning speed (e.g., nm/ms) [9]. Therefore, for a given wavelength scan speed, a shorter cavity length can result in narrower output linewidth and higher output power (by reduced filter loss) than longer cavity lengths.

No phase relation would be expected between these multiple oscillating modes if they originated purely from spontaneous emission noise. This is not always the case for a semiconductor laser, because some degree of coherency between modes can be established through nonlinear effects in the gain medium, such as four-wave mixing and self-phase modulation. Although the propagation length in an SOA is short, typically <1 mm, strong nonlinear interactions can be generated efficiently, due to gain saturation and saturation-induced index gratings. Understanding the complicated spectral and temporal dynamics as a result of nonlinear coupling between oscillating modes requires numerical simulations [10]. Nevertheless, a great deal can be learned from the simple time-frequency domain picture, as illustrated in Fig. 20.4c.

A fiber laser is another example where strong nonlinear effects, particularly self-phase modulation, in intracavity optical fibers can generate coupling between oscillating modes. Self-phase modulation generates spectral broadening that provides seeds to newly growing modes under the scanning filter. This coherent process eventually can establish phase locking across the entire oscillating modes and leads to the generation of short pulses. This mechanism, termed sliding-frequency mode locking (SFM) [11], can be an effective method of producing wavelength-swept short pulses.

20.4 Techniques

Over the past few years, swept lasers have advanced rapidly, primarily driven by their applications to OCT. Using rapidly scanned intracavity filters, high wavelength sweep speeds exceeding 1,000 nm/ms have been realized in extended-cavity semiconductor lasers [12–14]. Inherent swept laser dynamics, such as self-frequency shift in semiconductor gain media [10], sliding-frequency mode locking [11], and resonant sweep matched to cavity roundtrip [15], have been used to improve the laser output performance. Furthermore, researchers have used various techniques, including broadband or super-continuum pulse chirping [16, 17], soliton self-frequency shift [18], and dispersive-cavity mode locking [19], to demonstrate an ultrafast sweep speed beyond 1,000 nm/μs at a high repetition rate up to several MHz. Early laser developments focused on 1,300 and 1,550 nm, but wideband high-gain semiconductor chips have become available at 1,060 nm [20]

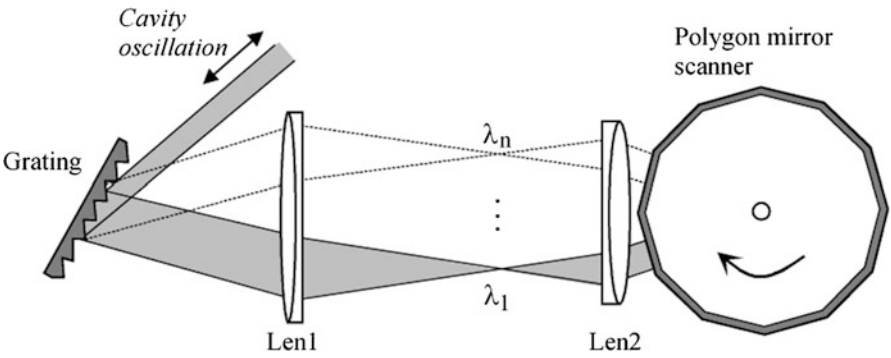

Fig. 20.5 Polygon scanner-based filter. As the polygonal mirror rotates, the center wavelength of narrowband spectrum returning back to the laser cavity is tuned continuously and repeatedly from λ_1 to λ_n

and 850 nm [21], where the output spectra are optimized for specific applications. Visible or infrared wavelengths would also be useful for other applications [22]. In this section, we describe the principles of some of these new technologies for an ultrafast wavelength sweep.

20.4.1 Scanning Filters

Grating and polygonal mirror. A polygon-based scanning filter was one of the first filters that was developed to achieve, simultaneously, a high sweep rate, a wide tuning range, and a narrow linewidth for OCT applications [12]. Figure 20.5 depicts a schematic of the filter, consisting of a diffraction grating, a telescope, and a polygonal mirror scanner. The telescope is constructed with two lenses in an infinite-conjugates configuration, with the grating at the front focal plane of lens 1 and the polygon spin axis at the back focal plane of lens 2. The telescope serves two distinct roles: it converts diverging angular dispersion from the grating into converging angular dispersion after the second lens and it controls the imaged beam size and convergence angle at the polygon. The principle of spectral selection and tuning is similar to that of the grating filter described in Sect. 20.3.3. The beam's orientation, incidence angle, and the rotation direction of the polygon mirror determine the direction of wavelength tuning. The arrangement in Fig. 20.5 produces a unidirectional positive (increasing wavelength) sweep that is advantageous over a negative (decreasing) sweep, because the nonlinear effects in an SOA transfer optical energy toward a long wavelength, resulting in higher output power and narrower linewidth.

The polygon filter can be incorporated into an extended-cavity semiconductor laser. Figure 20.6 shows the output characteristics of one of the first high-speed swept lasers with a 74 nm tuning range and a 16 kHz sweep repetition rate (1,200 nm/ms). The finesse of polygon filter, defined as the ratio of the tuning

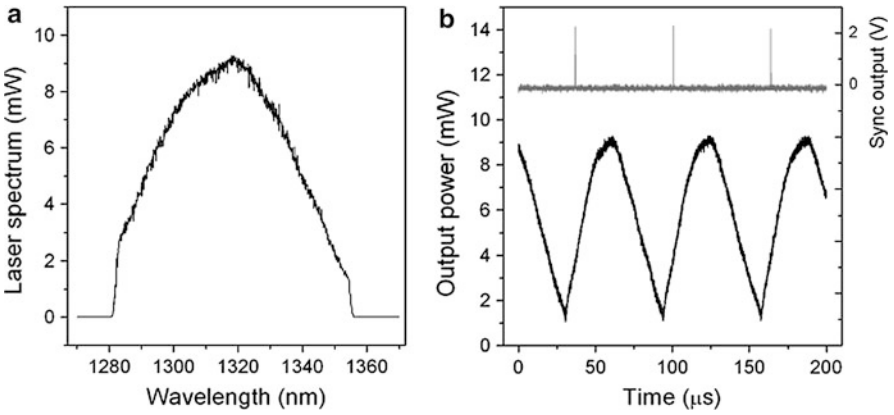

Fig. 20.6 Output characteristics of a polygon-scanned rapidly swept laser [12]. (**a**) Peak-hold spectrum and (**b**) time-domain oscilloscope trace of the laser output

range to the resolution, is typically 300–1,000. The resulting linewidth of the laser output was <0.1 nm, resulting in a coherence length of several mm. Using more optimized filter and cavity designs, much faster tuning rates of 115 kHz and wide ranges over 150 nm have been demonstrated [14]. One of the advantages of the polygon filter is the flexibility in changing varying tuning speed, range, resolution, or wavelength simply by controlling the rotational speed, grating angle, or the magnification of the telescope. A drawback, however, is that the polygonal mirror is a relatively bulky and moving part.

Fabry-Perot tunable etalon. A Fabry-Perot (FP) tunable etalon is constructed with a pair of high reflectivity mirrors separated by a distance that is variable with a piezoelectric actuator. A fiber-based small-mass etalon can be scanned over an entire free spectral range at high sweep repetition rates up to a few tens of kHz quasi-linearly [23] or up to hundreds of kHz using the mechanical resonance of the actuator [24]. The finesse of the etalon filter is determined by the reflectivity of the mirrors and easily can exceed 1,000. The etalon filter's relatively small size is an advantage, but its bidirectional and nonlinear tuning curve is a drawback for OCT applications.

Other filters. The grating filter shown in Fig. 20.3b can be modified to achieve high tuning speed, for example, by mounting the end mirror on a fast rotational actuator [25], such as resonant micro-electro-mechanical system (MEMS). This compact filter is potentially very attractive for commercialization because it can be integrated directly with a semiconductor gain chip to build a cm-scale compact light source. An acousto-optic tunable filter [26] does not have a mechanically moving part. However, currently available devices do not provide sufficiently high spectral resolution, and the tuning speed is typically much less than 100 nm/ms, even with a modest finesse of 100, because of the finite acoustic propagation time. Electro-optic tunable filters would be attractive because of their fast response time and nonmechanical actuation [27], but no practical designs with sufficient finesse have been developed to date.

20.4.2 Resonant Sweep

As briefly discussed in Sect. 20.3.4, intracavity spectral dynamics in a swept filter-based laser are largely affected by the finite buildup time of individual modes. As a result, the output linewidth and power can degrade significantly as the scan speed of the filter increases. One solution to this problem is to make the cavity length as short as possible to minimize the cavity buildup time. In this section, three different approaches are described, that are based on resonant laser dynamics and thereby capable of generating narrowband spectra without resorting to short cavities.

Dispersive mode locking. Active mode locking is a technique to generate short pulses from a laser by actively modulating cavity properties, such as loss, gain, and length (phase). Mode locking [5] occurs efficiently only when the modulation frequency is matched to the fundamental mode spacing frequency, given in Eq. 20.4, or with its harmonics precisely within $<10^{-5}$. Dispersive tuning is a technique applicable to an actively mode-locked laser with a highly dispersive cavity and in which the cavity length varies significantly as a function of wavelength. The resonant mode-locking frequency then becomes highly wavelength dependent. Therefore, a wavelength sweep is achieved by varying the modulation frequency over time. The cavity length and magnitude of dispersion need to be chosen carefully to optimize the output performance. Figure 20.7 illustrates this principle in a fiber-optic semiconductor ring laser employing a high-dispersion fiber. With this configuration, a wide sweep over 100 nm at repetition rates greater than 200 kHz has been demonstrated [19]. Here, harmonic mode locking was achieved by modulating the injection current to the SOA at a carrier frequency of 1 GHz, and the modulation frequency was swept over a couple of MHz corresponding to the amount of cavity dispersion. The electrical control of this technique is an advantage over other mechanical techniques. However, the lack of a direct filtering mechanism tends to make it difficult to obtain stable and narrowband output.

Cavity-resonance sweep. In this technique, the filter tuning period is matched to the cavity roundtrip time or its integer fraction [28]. The result is that a chirped wave is built up and circulates continuously in the cavity. Each wavelength component of this cavity-long chirped light passes the filter in successive roundtrips at the exact times when the filter's center wavelength coincides with the optical wavelength. Figure 20.8 illustrates the basic principle. This operation is reminiscent of active amplitude mode locking, in the sense that a phase relation is established between cavity modes so as to maximize the transmission through the filter (spectral vs. temporal) [15]. Some level of coherence is maintained among successive wavelength sweeps, unlike the previously described non-resonant filter-based techniques where individual sweeps start over from uncorrelated spontaneous emission. Using a resonant FP filter in a km-long fiber-optic cavity, this technique has produced high sweep rates up to 370 kHz with a >100 nm tuning range [29]. The chromatic dispersion of the cavity should be minimized to avoid wavelength walk off between the intracavity light and scanning filter. This resonant technique can

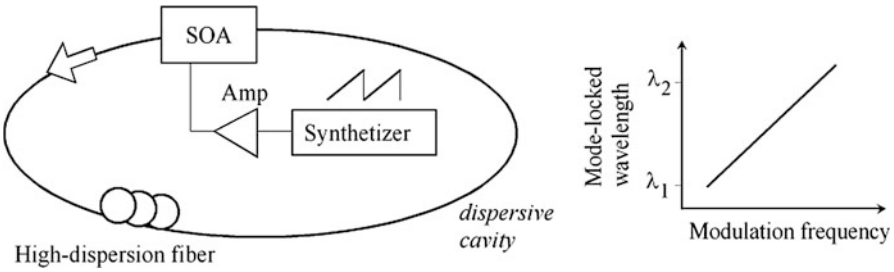

Fig. 20.7 Dispersive tuning in actively mode-locked laser. The output wavelength is tuned by sweeping the gain modulation frequency

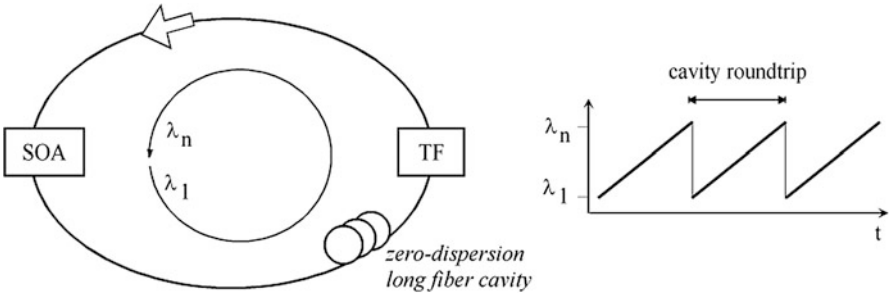

Fig. 20.8 Cavity-resonant sweep. The filter is scanned synchronously with the cavity round trip, resulting in an oscillation of cavity-long chirped pulse(s)

produce narrow linewidths of <0.01 nm, but requires precise sweep frequency control or cavity length stabilization within a precision much less than 10^{-5}, which is difficult to achieve in a km-long fiber cavity.

Frequency shifted feedback. A wavelength-swept operation combined with frequency-shifted feedback can lead to unique output characteristics. Consider a laser having a scanning filter and an acousto-optic frequency shifter in a cavity. On each roundtrip, the laser spectrum is shifted in frequency by f_{FS} and reshaped by a filter with its center frequency shifted by f_{filter} in one cavity roundtrip time. In this case, a simple model predicts that the linewidth of the oscillating laser spectrum is, approximately, proportional to $\delta\lambda \approx b^{2/3}\,|f_{FS} - f_{filter}|^{1/3}$ where b is the filter bandwidth [9]. Figure 20.9 depicts laser spectra of such lasers at three distinct cases. A narrow minimum linewidth is obtained by matching the filter sweep speed to the frequency shift, i.e., $f_{FS} = f_{filter}$. This resonant sweep has been demonstrated in a fiber laser employing an acousto-optic scanning filter. The experimental result in Fig. 20.9d clearly shows the linewidth narrowing at the resonant sweep rate of 270 Hz at which $f_{FS} = f_{filter} = 68$ MHz. This principle is applicable to the rapidly swept semiconductor lasers described in previous sections, but it requires a frequency shifter operating in the GHz range.

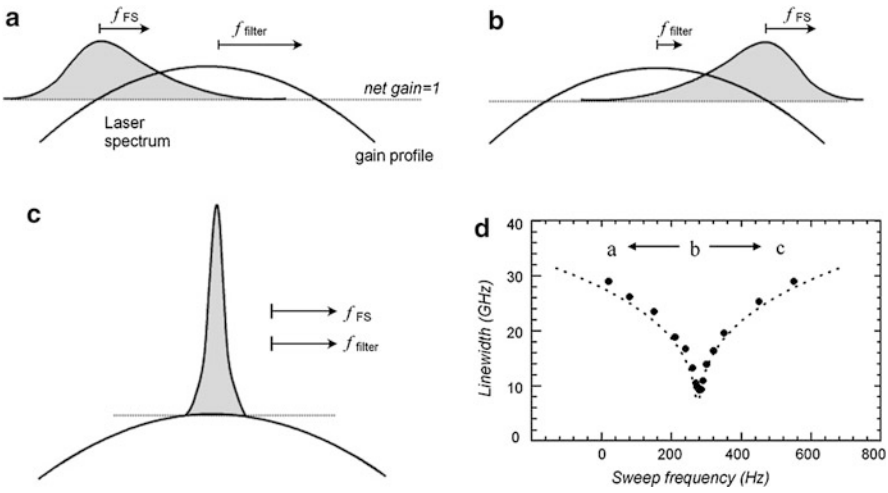

Fig. 20.9 Spectral dynamics in a swept laser with intracavity frequency shift for three cases: (**a**) $f_{filter} > f_{FS}$, (**b**) $f_{filter} < f_{FS}$, and (**c**) $f_{filter} = f_{FS}$. (**d**) Output linewidths (*circles*) of a frequency-shifted-feedback fiber laser [9], measured as a function of filter sweep rate (*dashed line*: numerical simulation)

20.4.3 Sliding Frequency Mode Locking (SFM)

As discussed in Sect. 20.3.4, a large number of cavity modes can oscillate simultaneously in a rapidly swept laser. If each of the modes originated from incoherent spontaneous emission, they would have a random relation with each other and lead to continuous-wave radiation. However, this situation can be completely changed if significant nonlinear broadening is present in the cavity. The nonlinearly generated spectral components can act as coherent seeds for newly developing modes, establish a defined phase relation among the oscillating modes, and, as a result, generate short pulses. This mode-locking mechanism, termed sliding-frequency mode locking (SFM), has been demonstrated in a rare-earth-doped fiber laser using self-phase modulation in optical fibers [11]. Figure 20.10a shows a schematic of the laser with an F-P scanning filter. Its output traces, shown in Fig. 20.10b, show a series of 100-ps pulses at a 12 MHz repetition rate corresponding to the cavity length. Their center wavelengths are scanned over 27 nm at 1,550 nm at a sweep rate of 250 Hz. Short swept pulses with duration of 10 ps to 100 fs may find applications in biomedical imaging based on multiphoton interactions in biological samples or time-resolved spectroscopy.

20.4.4 Stretched Chirped Pulses

In contrast to the laser-based approaches described so far, there are techniques capable of sweeping the wavelength outside a laser cavity. The simplest example is

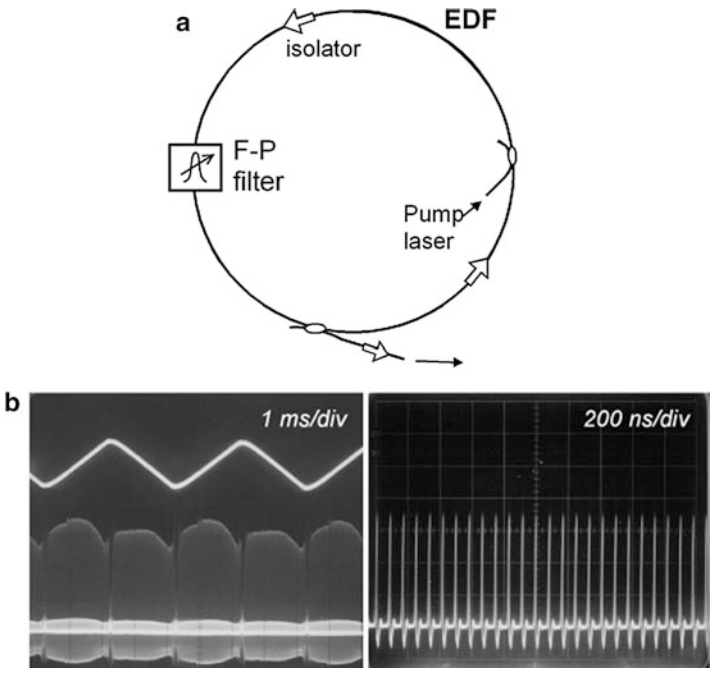

Fig. 20.10 Generation of wavelength-swept pulses. (**a**) Laser configuration. *EDF* erbium-doped fiber. (**b**) Time-domain oscilloscope traces of output pulses [11]

configured with a broadband source and a scanning filter that transmits only a narrowband spectrum of the broadband output at each time during a sweep. Although this approach is inefficient in terms of output power and spectral resolution, its operation is simple and it works with any type of broadband source, such as a super-continuum source. Another example is based on a combination of broadband pulse source and a high-dispersion fiber [30], schematically shown in Fig. 20.11. The light source can be a femtosecond mode-locked laser or sub-nanosecond super-continuum pulse source. The latter has been demonstrated with nonlinear fibers seeded by amplified, nanosecond gain-switched diode laser [17]. The width of each output pulse is stretched to 10–100 ns by a length of highly dispersive fiber. The typical dispersion of such fibers is about 10–100 ps/nm/km. To stretch a short pulse with 100-nm bandwidth to 100 ns, therefore, requires a relatively long fiber length of 10–50 km. The ratio of the initial pulse width to the final stretched value determines the finesse or the ratio of the spectral resolution to the total bandwidth. The repetition rate of the output pulses determines the A-line rate. High A-line rates of several MHz can be achieved easily with this passive tuning technique. The need for a broadband pulse source with low intensity noise and a long length of high-dispersion fiber for a high spectral resolution of <0.05 nm are two potential difficulties of the stretched pulse technique.

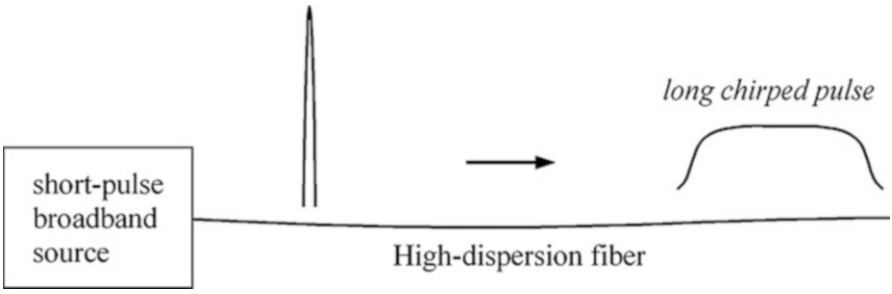

Fig. 20.11 Stretched-pulse swept source. The broadband short pulses from a laser source are stretched to long, typically an order of 100 ns, chirped pulses after propagating through a length of dispersive optical fiber

20.4.5 Wavelength Conversion

Laser-pumped wavelength conversion in nonlinear materials can be used to realize a wavelength-swept source. This section describes two techniques based on parametric conversion and soliton self-frequency shift.

Optical parametric oscillation (**OPO**). In a parametric conversion process in a nonlinear crystal, an intense pump wave is converted to two waves, idler and signal, with different or the same (degenerate) wavelengths. The frequency sum of the output waves is equal to the input wave frequency by phase matching. The efficiency of parametric conversion can be enhanced significantly by using a cavity oscillator resonant to the signal wave. With sufficient pump power, the gain provided by the nonlinear interaction can reach threshold and allow the signal wave to oscillate in the cavity, similarly to conventional laser operation. For a given pump wavelength, the output signal wavelength can be tuned continuously by changing the temperature or orientation of the crystal with respect to the pump beam. Much faster tuning can be achieved by sweeping the pump wavelength. To date, the tuning rate of OPOs has been limited to a few kHz, partly due to a lack of high-power rapidly swept pump lasers [22]. This approach is attractive for generating swept signal waves in the spectral range where conventional laser gain media are not available. Furthermore, a nonlinear optical crystal can be selected or designed such that a small change in pump wavelength leads to a wide tuning of the signal wavelength.

Soliton frequency shift. An optical fiber can support the propagation of soliton pulses through a balance between self-phase modulation and negative chromatic dispersion. When a short soliton pulse propagates through a long distance of optical fiber, stimulated Raman scattering in the optical fiber produces energy transfer within the pulse from short to long wavelength components, causing the pulse's center wavelength to increase constantly with propagation distance. This phenomenon, called soliton self-frequency shift, has been used to build a tunable source [18]. A typical configuration of the source is similar to that in Fig. 20.11, except that the pump source is a fixed-wavelength soliton laser, and the propagation fiber has an

appropriate dispersion and nonlinearity to guide quasi-soliton pulses. The magnitude of soliton frequency shift is sensitive to the input pulse intensity, so the output wavelength can be tuned by modulating the input power of the soliton pulses. A wide tuning range exceeding a few hundreds nm can be obtained easily. However, the need for short soliton pulses, typically with a width of 100–500 fs, makes it challenging to achieve high spectral resolution with this approach.

20.5 Outlook

This chapter covered a variety of techniques for wavelength-swept sources. The recent development of rapidly swept lasers resulted in dramatic improvements in imaging speed of OCT, opening up new applications such as comprehensive three-dimensional imaging in vivo [31]. ▶ Chapter 7, "Optical Frequency Domain Imaging" describes these remarkable advances in OCT technology and applications. We expect that swept laser technology will continue to advance and drive innovations in OCT. For an example, new ideas and engineering will broaden the tuning range to enhance spatial resolution to the cellular or subcellular level. Significant efforts to commercialize high-speed swept lasers have already begun. Compact, low-cost solutions will expedite the commercialization and, eventually, increase the availability and accessibility of swept-laser-based high-speed OCT systems to clinicians. The continuing development in wavelength-swept lasers will also benefit other application areas, including spectrally encoded confocal microscopy [32], sensing [16], and spectroscopy.

References

1. D. Derickson, *Fiber Optic Test and Measurement* (Prentice Hall PTR, Upper Saddle River, 1998)
2. T. Vo-Dinh, *Biomedical Photonics Handbook* (CRC Press, Boca Raton, 2003)
3. A. Yariv, P. Yeh, A. Yariv, *Photonics: Optical Electronics in Modern Communications* (Oxford University Press, New York, 2007)
4. B.E.A. Saleh, M.C. Teich, *Fundamentals of Photonics* (Wiley, New York, 1991)
5. A.E. Siegman, *Lasers* (University Science Books, Mill Valley, 1986)
6. E. Hecht, *Optics* (Addison-Wesley, Reading, 2002)
7. S.R. Chinn, E.A. Swanson, J.G. Fujimoto, Optical coherence tomography using a frequency-tunable optical source. Opt. Lett. **22**, 340–342 (1997)
8. K. Liu, M.G. Littman, Novel geometry for single-mode scanning of tunable lasers. Opt. Lett. **6**, 117–118 (1981)
9. S.H. Yun, D.J. Richardson, D.O. Culverhouse, B.Y. Kim, Wavelength-swept fiber laser with frequency shifted feedback and resonantly swept intra-cavity acoustooptic tunable filter. IEEE J. Sel. Top. Quant. Electron. **3**, 1087–1096 (1997)
10. A. Bilenca, S.H. Yun, G.J. Tearney, B.E. Bouma, Numerical study of wavelength-swept semiconductor ring lasers: the role of refractive-index nonlinearities in semiconductor optical amplifiers and implications for biomedical imaging applications. Opt. Lett. **31**, 760–762 (2006)

11. S.H. Yun, Mode locking of a wavelength-swept laser. Opt. Lett. **30**, 2660–2662 (2005)
12. S.H. Yun, C. Boudoux, G.J. Tearney, B.E. Bouma, High-speed wavelength-swept semiconductor laser with a polygon-scanner-based wavelength filter. Opt. Lett. **28**, 1981–1983 (2003)
13. R. Huber, M. Wojtkowski, J.G. Fujimoto, J.Y. Jiang, A.E. Cable, Three-dimensional and C-mode OCT imaging with a compact, frequency swept laser source at 1300 nm. Opt. Express **13**, 10523–10538 (2005)
14. W.Y. Oh, S.H. Yun, G.J. Tearney, B.E. Bouma, 115 kHz tuning repetition rate ultrahigh-speed wavelength-swept semiconductor laser. Opt. Lett. **30**, 3159–3161 (2005)
15. R. Huber, M. Wojtkowski, J.G. Fujimoto, Fourier domain mode locking (FDML): a new laser operating regime and applications for optical coherence tomography. Opt. Express **14**, 3225–3237 (2006)
16. S.T. Sanders, Wavelength-agile fiber laser using group-velocity dispersion of pulsed supercontinua and application to broadband absorption spectroscopy. Appl. Phys. B. Lasers Opt. **75**, 799–802 (2002)
17. S. Moon, D.Y. Kim, Ultra-high-speed optical coherence tomography with a stretched pulse supercontinuum source. Opt. Express **14**, 11575–11584 (2006)
18. J.W. Walewski, M.R. Borden, S.T. Sanders, Wavelength-agile laser system based on soliton self-shift and its application for broadband spectroscopy. Appl. Phys. B. Lasers Opt. **79**, 937–940 (2004)
19. S. Yamashita, M. Asano, Wide and fast wavelength-tunable mode-locked fiber laser based on dispersion tuning. Opt. Express **14**, 9299–9306 (2006)
20. E.C.W. Lee, J.F. de Boer, M. Mujat, H. Lim, S.H. Yun, In vivo optical frequency domain imaging of human retina and choroid. Opt. Express **14**, 4403–4411 (2006)
21. H. Lim et al., Optical frequency domain imaging with a rapidly swept laser in the 815–870 nm range. Opt. Express **14**, 5937–5944 (2006)
22. M.E. Klein et al., Rapidly tunable continuous-wave optical parametric oscillator pumped by a fiber laser. Opt. Lett. **28**, 920–922 (2003)
23. M.A. Choma, K. Hsu, J.A. Izatt, Swept source optical coherence tomography using an all-fiber 1300-nm ring laser source. J. Biomed. Opt. **10**, 044009 (2005)
24. R. Huber, M. Wojtkowski, K. Taira, J.G. Fujimoto, K. Hsu, Amplified, frequency swept lasers for frequency domain reflectometry and OCT imaging: design and scaling principles. Opt. Express **13**, 3513–3528 (2005)
25. B. Golubovic, B.E. Bouma, G.J. Tearney, J.G. Fujimoto, Optical frequency-domain reflectometry using rapid wavelength tuning of a Cr4+: forsterite laser. Opt. Lett. **22**, 1704–1706 (1997)
26. P.F. Wysocki, M.J.F. Digonnet, B.Y. Kim, Broad-spectrum, wavelength-swept, erbium-doped fiber laser at 1.55 μm. Opt. Lett. **15**, 879–881 (1990)
27. J.M. Telle, C.L. Tang, New method for electrooptical tuning of tunable lasers. Appl. Phys. Lett. **24**, 85–87 (1974)
28. J.M. Telle, C.L. Tang, Very rapid tuning of cw dye laser. Appl. Phys. Lett. **26**, 572–574 (1975)
29. R. Huber, D.C. Adler, J.G. Fujimoto, Buffered Fourier domain mode locking: unidirectional swept laser sources for optical coherence tomography imaging at 370,000 lines/s. Opt. Lett. **31**, 2975–2977 (2006)
30. J.W. Walewski, S.T. Sanders, High-resolution wavelength-agile laser source based on pulsed super-continua. Appl. Phys. B. Lasers Opt. **79**, 415–418 (2004)
31. S.H. Yun et al., Comprehensive volumetric optical microscopy in vivo. Nat. Med. **12**, 1429–1433 (2006)
32. C. Boudoux et al., Rapid wavelength-swept spectrally encoded confocal microscopy. Opt. Express **13**, 8214–8221 (2005)

Swept Light Sources

21

Bart Johnson, Walid Atia, Mark Kuznetsov, Christopher Cook, Brian Goldberg, Bill Wells, Noble Larson, Eric McKenzie, Carlos Melendez, Ed Mallon, Seungbum Woo, Randal Murdza, Peter Whitney, and Dale Flanders

Keywords

Axsun Technologies • Coherence • Coherence revival • Mode locking • Ophthalmic imaging • Swept laser • Swept source

21.1 Introduction

In the early to mid-2000s, it became apparent that swept-source optical coherence tomography (SS-OCT) offers significant advantages over both time-domain (TD-OCT) and spectral-domain OCT (SD-OCT). Since that time, significant academic and commercial effort has been focused on developing SS-OCT lasers and sources capable of enabling high-quality SS-OCT imaging. While there are many important components in an SS-OCT system, it can reasonably be argued that the swept source is the most critical as its properties form the basis for most of the major system performance metrics. The detection and data acquisition electronics, together with the source, ultimately define the SS-OCT system performance specifications such as imaging speed, SNR and sensitivity, axial resolution, and imaging depth.

In this chapter, we describe a commercially available 1,060 nm swept-source OCT "engine" developed at Axsun Technologies suitable for ophthalmic and other OCT imaging applications. The engine consists of a swept laser module, control electronics, k-clock, balanced receiver, and data acquisition board which samples on k-clock transitions. The OCT engine provides optical system performance for shot-noise-limited imaging. The engine is designed to simplify construction of OCT imaging systems; the final user provides the optical probe/interface, application

B. Johnson (✉) • W. Atia • M. Kuznetsov • C. Cook • B. Goldberg • B. Wells • N. Larson • E. McKenzie • C. Melendez • E. Mallon • S. Woo • R. Murdza • P. Whitney • D. Flanders
Axsun Technologies, Billerica, MA, USA
e-mail: bjohnson@axsun.com

© Springer International Publishing Switzerland 2015

W. Drexler, J.G. Fujimoto (eds.), *Optical Coherence Tomography*,
DOI 10.1007/978-3-319-06419-2_22

control electronics, computing, and specialized software. Axsun manufactures such optoelectronic swept-source OCT engines for a range of medical imaging applications.

Axsun's 1,060 nm laser with 110 nm tuning range and 100 kHz sweep speed is described in this chapter along with the associated engine electronics. This is just one design point in the Axsun design space; many other swept source and engine configurations are possible and have been realized using the Axsun technology platform. For example, swept sources with various sweep rates, tuning ranges, coherence lengths, and modes of operation have been manufactured in both 1,060 and 1,310 nm wavelength ranges.

This chapter begins with a general description of the Axsun laser design along with a theoretical description of the laser dynamics. Next, we use this theory to explain a recently discovered property of the Axsun swept laser known as coherence revival [12]. We then describe the OCT engine electronics and demonstrate shot-noise-limited performance with sensitivities greater than 103 dB at 1.9 mW sample power. Lastly, we show artifact-free images from both internal testing and Topcon Corporation, a leading supplier of ophthalmic OCT imaging systems.

21.2 Laser Operation

In general, a swept laser consists of a gain medium, a tunable wavelength selection filter, and a laser cavity that supports lasing over the desired wavelength range. The Axsun laser architecture is shown in Fig. 21.1 and contains a reflective MEMS tunable Fabry-Perot filter, a broadband 1,060 nm gain chip, and a fiber reflector that forms the other end of the laser cavity and serves as the output coupler [1]. The filter exhibits a tunable reflection peak due to the filter optical axis tilt with respect to the optical beam [1, 2], and filter tuning is accomplished by changing the drive voltage on the MEMS filter. The MEMS filter can be swept from DC up to several hundred kilohertz depending on the desired repetition rate. The fiber extension brings the equivalent air length of the cavity to 104 mm such that there are a handful of laser cavity modes underneath the filter at all times. The laser is constructed in a hermetically sealed butterfly package with a fiber-optic feed through and exhibits stable polarization due to the strong TE/TM gain asymmetry of the SOA gain chip.

Many rapidly swept lasers exhibit a preference for tuning short to long wavelength [4–6]. They have higher power and are more stable in that direction. This behavior has been attributed to four-wave mixing in the gain medium [6, 7] coupled

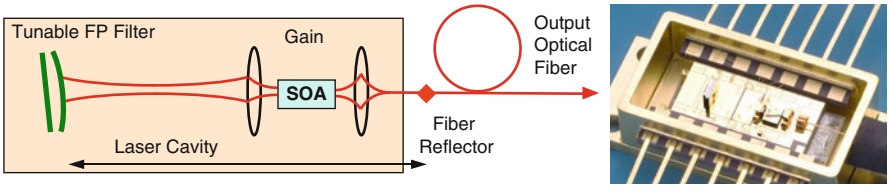

Fig. 21.1 External cavity laser with reflective Fabry-Perot MEMS tunable filter

with the Bogatov effect [8]. Computer simulations have predicted this red tuning behavior and laser pulsation under some conditions [7] and mode locking in some configurations [9]. We have shown both experimentally [3] and theoretically that sweeping the laser rapidly induces passive mode locking in the Axsun laser. Here we describe the basic dynamics of the laser.

Rapidly swept lasers tune too quickly for lasing to build up anew from spontaneous emission at each new wavelength [10]. A nonlinear optical mechanism is required to shift the wavelength of light circulating within the laser cavity to match the wavelength of the filter on successive round trips. In the case of the Axsun laser, a Doppler shift from the moving MEMS filter mirror does part of the job, although it is small compared to the wavelength shift required. Most of the shift comes from self-phase modulation induced by depletion of the gain as the mode-locked pulse travels through the semiconductor gain medium. Gain depletion is accompanied by a rise in refractive index. The coupling between the index and the power gain can be described using the linewidth enhancement factor, α, as

$$\Delta n = -\alpha \frac{\lambda}{4\pi} \Delta g$$

The mode-locking process is illustrated in Fig. 21.2. The SOA becomes optically longer as the pulse travels through, red shifting the light field. The laser does not tune continuously, but rather hops discretely to the next wavelength on each new pulse. The frequency hop for a SOA of length l is

$$\Delta v = -\frac{l}{\lambda} \frac{dn}{dt}$$

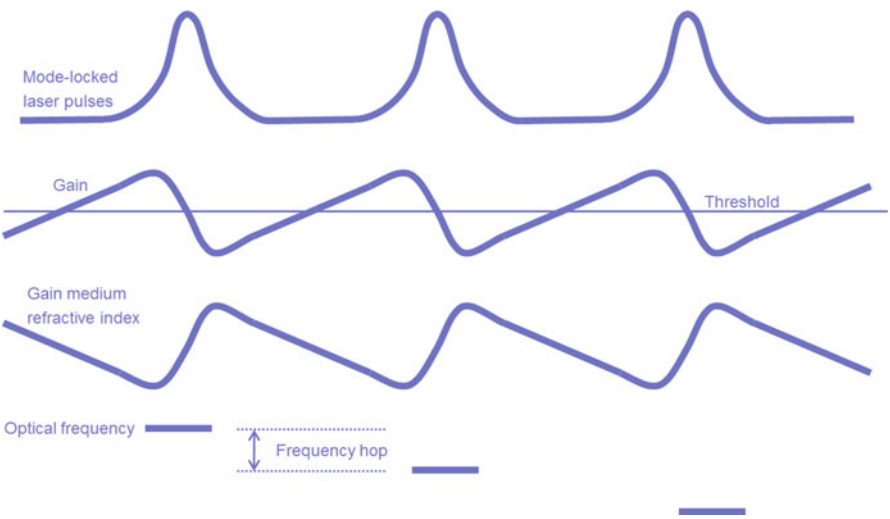

Fig. 21.2 Mode-locking and frequency hopping dynamics of a rapidly swept laser

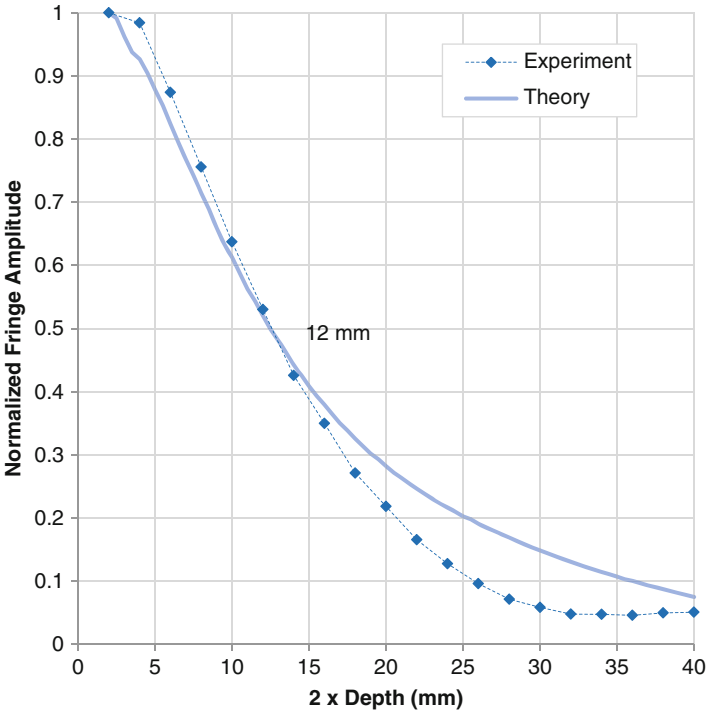

Fig. 21.3 Coherence length measurement compared with mode-locking model calculation

The pulse energy and width determine the magnitude of the frequency hop. The laser operates in this manner because the lowest threshold is obtained when the pulse frequency hops to follow the filter tuning. A feedback mechanism built into the laser dynamics naturally ensures the pulse hops to follow the filter. In the swept steady state, the pulses are tuned slightly to the long wavelength side of the filter and away from the reflection peak. If a pulse gets ahead of the filter (gets too red), it is attenuated by the filter and the lower power ensures the next pulse does not hop as far. Similarly, if a pulse falls behind (gets too blue), it becomes more powerful and catches up with the filter.

The filter line width and sweep rate play a critical role in ensuring proper mode-locking behavior throughout the sweep. The MEMS filter sweep is linearized to provide a nearly constant sweep rate during the tuning cycle. Stable passive mode-locking behavior can be maintained over the 100 nm data collection range of the laser with a total sweep range of 110 nm. This is essential for obtaining low relative intensity noise (RIN) and maintaining clean k-clocks for the optical engine.

We have developed a theory of these rapidly swept lasers, building on the mode-locking work by Haus [11]. This theory describes this mode-locking behavior in detail and can accurately predict a variety of laser characteristics, such as coherence lengths, as indicated in Fig. 21.3 below, and coherence revival properties, as discussed in the next section.

The upper limit of the coherence length of the mode-locked swept laser is determined by the pulse width. Theory predicts considerable chirp to the pulses, reducing the coherence lengths below this upper limit. The coherence length of these lasers is typically 12 mm, which ensures deep imaging capability required for many applications.

21.3 Coherence Revival

The 1,060 nm, 100 kHz laser operates with two pulses traveling in the cavity at once, with the two pulses separated by half the cavity roundtrip time. This can be seen with a high-speed detector and oscilloscope. Normally, an OCT interferometer is set up for short path mismatches, where laser pulses are interfering with themselves. With longer path mismatches, pulses can interfere with their neighbors, leading to the "coherence revival" phenomenon [12]. This behavior is shown in Fig. 21.4. The physical cavity length is 104 mm, but there is also interference at 52 mm due to the double pulsation. A pulse two away is an amplified copy of the first, whereas an adjacent pulse is not. There are two semi-independent pulse trains inside the cavity, leading to a 52 mm coherence function revival that is weaker than the revival at 104 mm.

Coherence revival is important because it can be a source of artifacts in an OCT system. An OCT interferometer needs to be carefully designed so that small stray reflections are not separated by intervals of half-cavity lengths, 52 mm, 104 mm, 156 mm . . . etc., where they can produce artifacts in the OCT image.

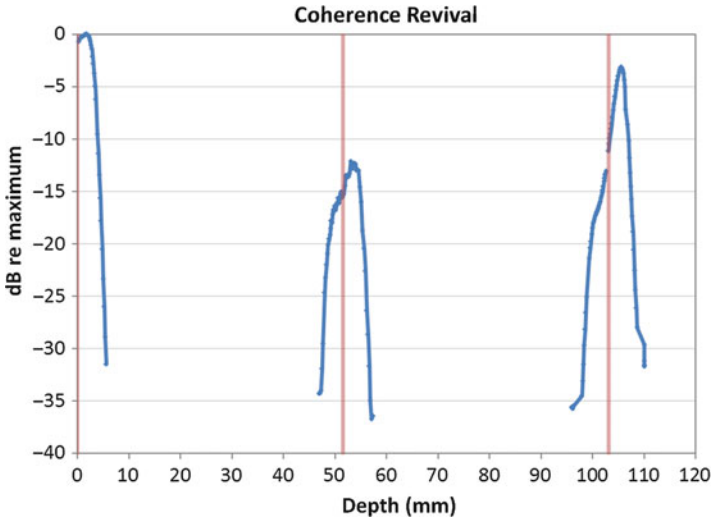

Fig. 21.4 Coherence function of the laser over a wide depth range showing the coherence revival phenomenon. The *red vertical lines* show the depths where the electrical signal frequency is zero. This measurement was made using an engine with a limited detector bandwidth, so the roll off of the curves reflects the detector bandwidth rather than the coherence length of the laser

Coherence revival has also been used to advantage to extend the imaging range of an OCT system [12]. Figure 21.4 shows that the 104 mm peak is displaced from the zero beat location. This means that the signal first goes up with depth before eventually rolling off. The imaging range, which normally is limited by the coherence length, is effectively doubled for this laser when operating at interferometer path mismatches near the 104 mm coherence revival peak. This coherence peak shift is a consequence of the pulse chirp and is a property of this particular laser design. By modifying the cavity design, it is possible to produce sources that do not have this behavior.

21.4 OCT Engine Design

The OCT engine consists of the swept laser module along with control electronics, a calibration k-clock, detection/receiver electronics, and a data acquisition board which samples on k-clock transitions. The engine is designed to simplify construction of OCT imaging systems; the end user provides the optical probe/interface, application control electronics, computing, and specialized software. Figure 21.5 shows a block diagram of the OCT engine.

The laser control board drives the SOA and MEMS tunable filter. The SOA current and filter drives are controlled through a file stored in flash memory. The control file specifies the SOA current and filter voltages as a function of time. In addition, the board contains two optical receivers. The first is for the calibration k-clock. The k-clock serves as an external clock input to the data acquisition (DAQ) board analog to digital (A2D) converter. A balanced receiver detects light from the main OCT imaging interferometer. The balanced receiver output, k-clock, and sweep trigger are differential signals for noise immunity and are run between the boards over SATA cables commonly used for disk drive interfaces.

In swept-source OCT, it is necessary to translate the raw OCT signal from one that is evenly spaced in time to one with data points evenly spaced in optical frequency, or k. This is often done through various software resampling approaches that interpolate the raw OCT signal. The resampling coefficients can be derived at predetermined intervals or on every A-line, depending on the stability of the swept source and the required imaging accuracy. Either way, the raw OCT signal must be resampled during each A-line.

An alternative approach, and the one used in the Axsun OCT engine, is to use a digital k-clock [13, 16]. The k-clock is derived from a fiber-based Mach-Zehnder interferometer (MZI) as shown in Fig. 21.5. As the laser source sweeps across its wavelength tuning range, the MZI receiver has zero-crossings that are evenly spaced in optical frequency. The MZI path length difference must be four times the maximum imaging depth (interference length $= 2 \times$ depth) in order to satisfy the Nyquist sampling limit. This approach speeds up data acquisition by eliminating the computing time for external resampling. However, this approach requires the A2D converter to handle a wide range of k-clock frequencies and duty cycles due to the nonlinear sweep dynamics of the laser.

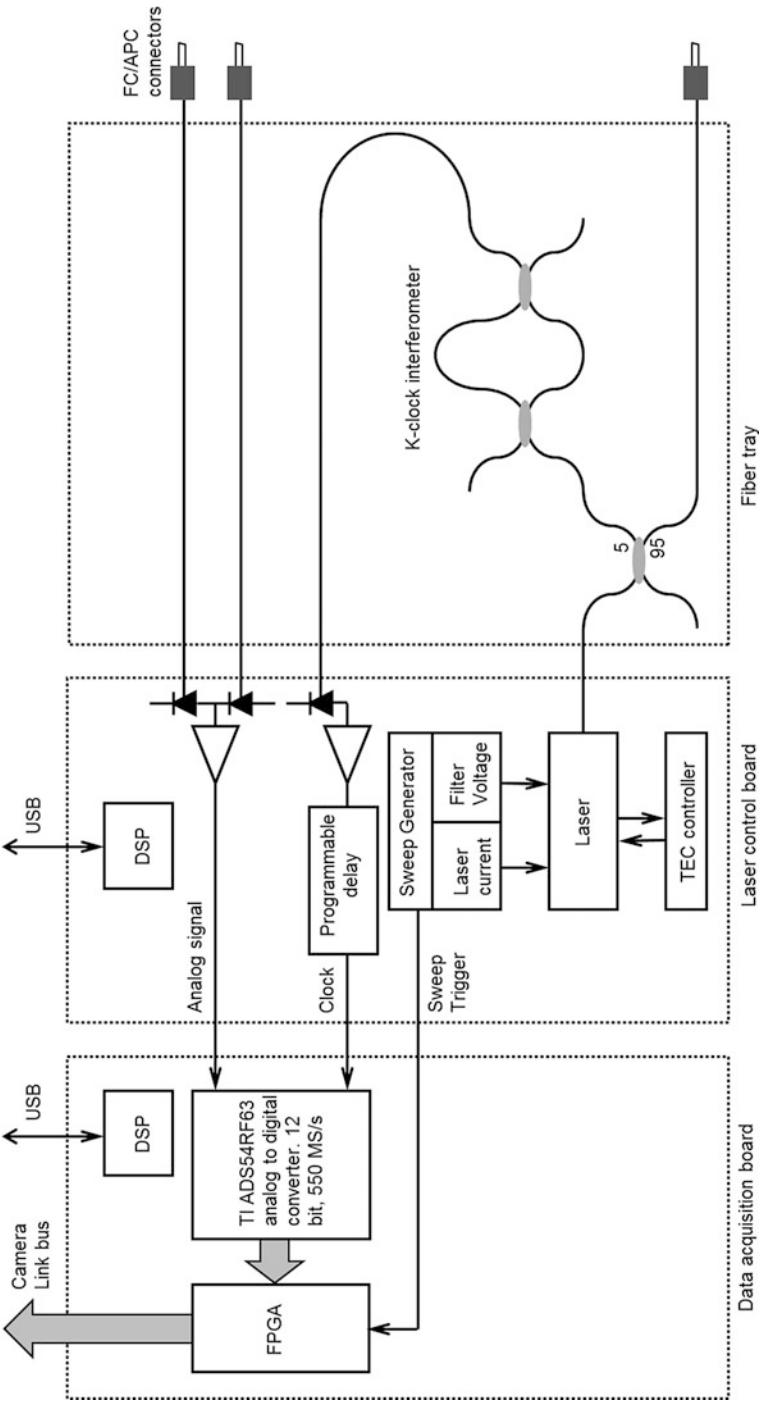

Fig. 21.5 Block diagram of the Axsun OCT engine

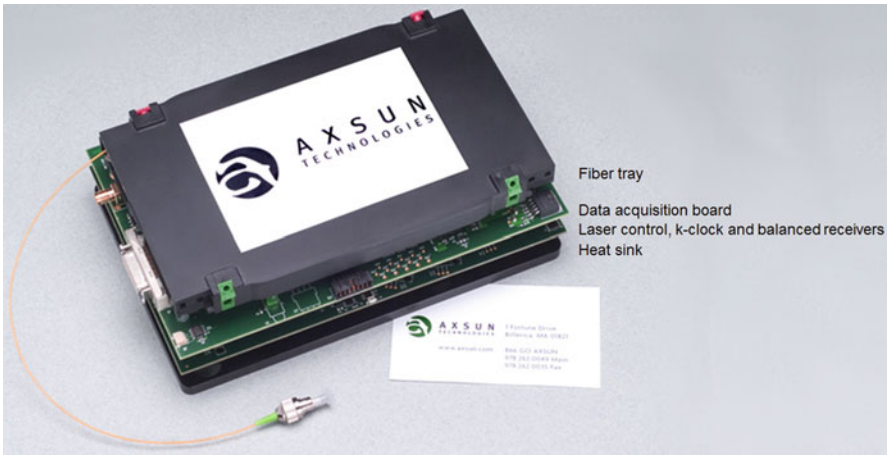

Fig. 21.6 Physical construction of the Axsun OCT engine

The data acquisition card in the Axsun OCT engine utilizes a 12-bit Texas Instruments ADS54RF63 analog to digital (A2D) converter. This chip is very tolerant of varying clock frequencies and duty cycles. Its clock specification is 40–550 MHz. We have verified that the DAQ card performs up to the limits of the chip. The FPGA presents the glue logic between the A2D converter and the Camera Link bus. The Camera Link bus can be set to run at 83.3, 41.7, 20.8, or 10.4 MHz. Two 12-bit samples are issued per clock cycle. There is no on-board data storage, but there is an FIFO buffer that mediates between the incoming variable data rate samples and the fixed rate Camera Link output samples. The engine must fill the FIFO faster than it is emptied and must not issue more samples than can be transferred between sweep trigger pulses. The system described in this chapter runs the Camera Link bus at 83.3 MHz. The laser is swept to keep the k-clock frequency greater than 167 MHz, so the FIFO is never empty. At the 100 kHz sweep rate, it transfers 1,376 out of a maximum of 1,670 samples.

The fiber Mach-Zehnder k-clock interferometer is located in the fiber tray. It is precisely cut and fusion spliced to set the maximum depth (Nyquist fold over distance) to an accuracy of ± 100 μm. Figure 21.6 shows a picture of the OCT engine stack.

Both laser control and DAQ boards can communicate with a personal computer via USB interfaces. A control program, OCTHost, is provided, but customer software can utilize a Windows .NET assembly for custom control.

21.5 System Performance

The Axsun OCT engine described in this chapter is set up for the scan plan in Fig. 21.7. The maximum imaging depth, set by the k-clock interferometer mismatch, is 3.7 mm. The laser sweeps over 110 nm at 100 kHz sweep rate. One thousand three hundred and seventy-six (1,376) samples are acquired, which

Parameter	Min	Value	Max	Units
Maximum scan depth in air		3.7		mm
FSR of clock interferometer		20.26		GHz
Sweep Frequency		100		kHz
Wavelength Range	985.0		1095.0	nm
Optical Frequency Range	273.783		304.358	THz
Data Range in wavelength	989.4		1089.6	nm
Data Range in optical frequency	275.144		302.997	THz
Sweep Range		110.0		nm
Sampled Range		100.2		nm
Maximum possible samples		1509		
Percent bandwidth used		91		%
Selected number of samples		1376		
Pixels in A-scan		688		
Data collection duty cycle		44		%
Estimated Clock Frequency		313		MHz

Window type	Resolution			
	3 dB	10 dB	20dB	Units
Cosine	6.4	11.0	14.6	μm
Hamming	7.0	12.4	16.6	μm
Hann	7.8	13.6	17.8	μm
Dolph-Chebyshev 60 dB	7.8	13.8	18.7	μm
Blackman	8.9	15.7	21.4	μm
Dolph-Chebyshev 80 dB	8.9	15.9	21.8	μm
Dolph-Chebyshev 100 dB	9.9	17.8	24.5	μm

Fig. 21.7 Scan plan for the 1,060 nm OCT engine. *Yellow* cells are inputs to the calculation. The Hann window is used in all of the measurements and calculations presented here

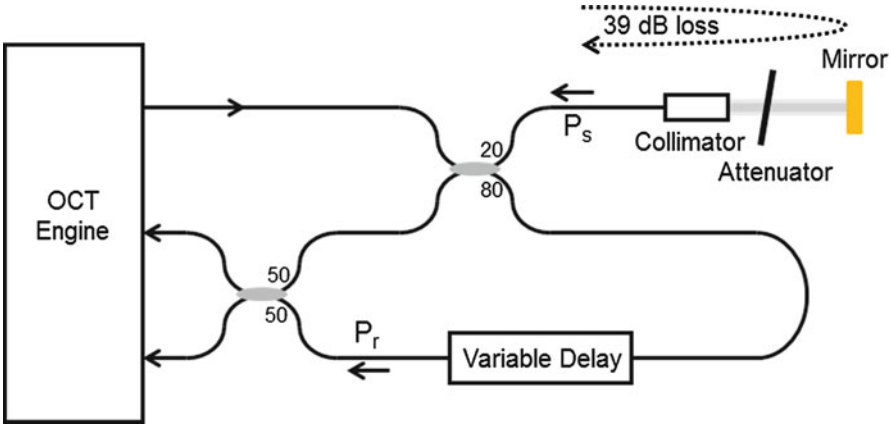

Fig. 21.8 Test interferometer

represents 100 nm of data out of the 110 nm sweep. Although the laser power output is not flat across the sweep, imaging depth resolutions very close to the limits imposed by the pre-FFT window function are obtained. All of the data presented here use a Hann window, though other windows can be chosen to trade resolution for side mode suppression. Calculated theoretical resolutions at 3, 10, and 20 dB from the point spread function peak are listed in the table.

System average output powers exceed 15 mW. The laser control board blanks the laser output power over the nonfunctional retrace portion of the laser frequency sweep. Given the roughly 50 % on/off duty cycle, the imaging power is roughly twice the average. This ensures high SNR while limiting average optical power, which is important, for example, in ophthalmic applications that have strict limits on the average optical power exposure to the eye.

Much of the OCT engine performance testing has been done with an interferometer configured as shown in Fig. 21.8. For imaging experiments, the attenuator and mirror are replaced by a galvo-scanner and imaging lens. Production systems are all tested in an automated test setup for sensitivity, resolution, imaging artifacts, and overall functionality. Most of the data presented here uses the setup of Fig. 21.8.

A calibration table defines the swept laser current and MEMS filter tuning voltage versus time. Each laser frequency sweep is calibrated separately, and a clock analysis similar to that in Fig. 21.9 verifies the calibration. At 100 kHz repetition rate, the filter is being driven well beyond its mechanical resonance, which limits the data collection duty cycle to around 45 % due to the resulting limitations in the linearization of the filter sweep. The red portion of the curves delimits the data collection region which proceeds for 1,376 clock pulses following the trigger. Power is measured with a wide bandwidth photodetector and a 2.5 GHz bandwidth oscilloscope. This is fast enough to see the mode-locked pulses. The wide bandwidth power trace is shown along with a 5 MHz low-pass filtered trace in red. The instantaneous powers are calibrated from an average power measurement made with a power meter.

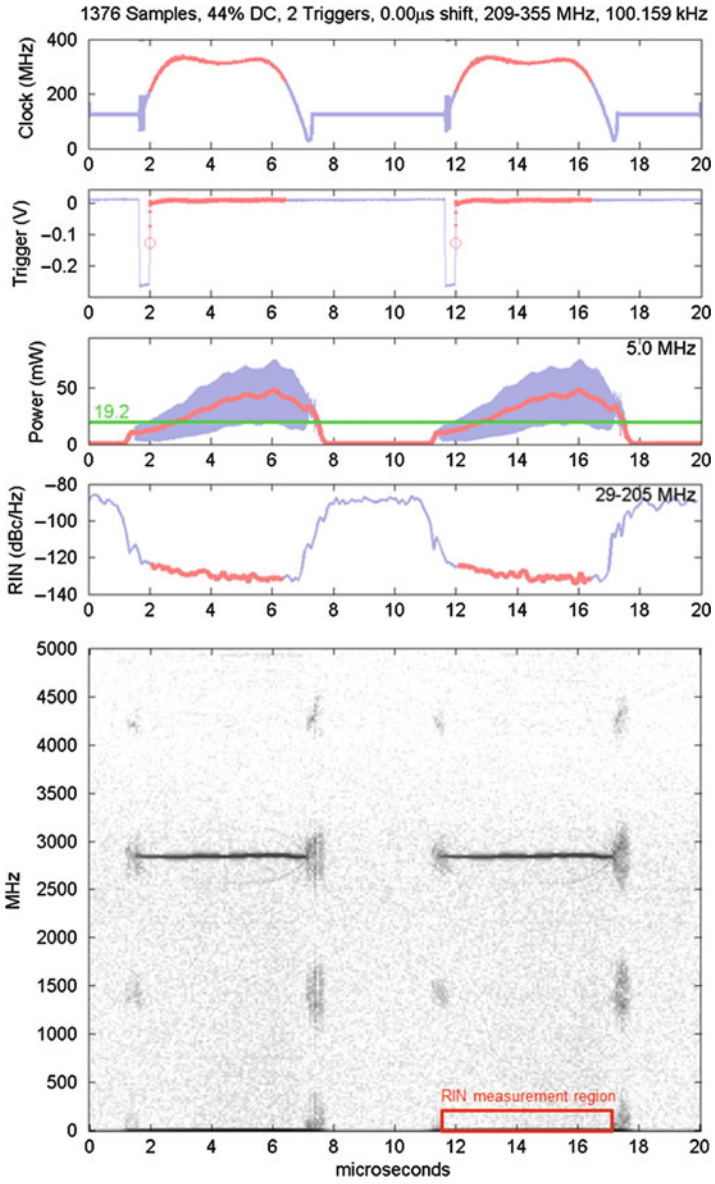

Fig. 21.9 Clock analysis, power, RIN, trigger, spectrogram

An RIN estimate is made from the wide bandwidth power data. It is based on the average noise between 29 and 209 MHz, which is approximately the bandwidth of the balanced receiver. Due to the laser pulsations, there are large RF signals outside this frequency range, but only the signals within the balanced receiver bandwidth are relevant. This high-speed measurement is routinely done to look for laser

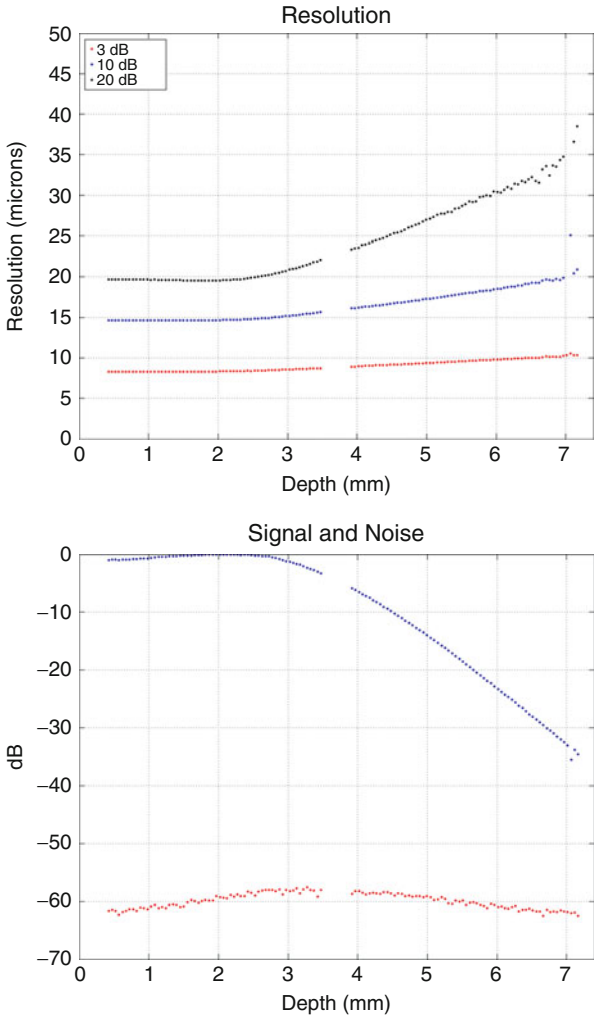

Fig. 21.10 Measured imaging depth resolution at 3, 10, and 20 dB below the point spread function peak. A Hann window was used in processing the data. Conditions: 1.2 mW reference power, 1.9 mW sample power, 46 dB loss. Signal and noise variations with depth are shown in the lower plot

instabilities. However, the RIN is too low to measure accurately by this method and only a rough estimate is obtained. In fact, high-performance telecommunication RIN test sets subtract out receiver noise and calculated shot noise when doing this type of test. Better RIN estimates can be obtained through measurements of system SNR as a function of reference power.

The bottom plot of Fig. 21.9 is a spectrogram of the wide bandwidth detector signal. It shows a strong signal at 2.9 GHz, indicating that the laser is pulsing twice per round trip in a 104 mm cavity. The clean spectrum between DC and 200 MHz indicates low RIN. The time-resolved nature of the spectrogram can reveal local laser instabilities where the laser is not cleanly mode locked.

Resolution and roll off measurements made on our automated test station are shown in Fig. 21.10. Resolution measurements generally match well to the

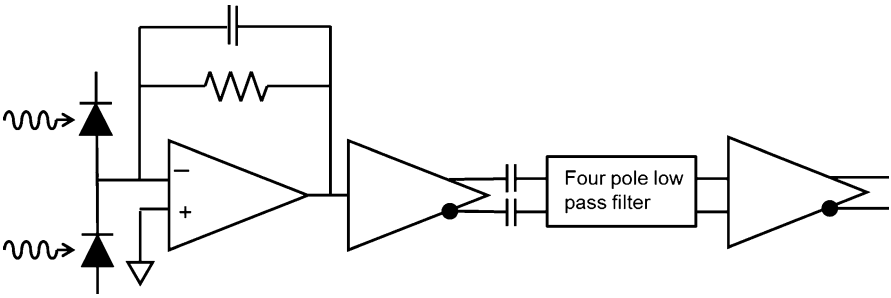

Fig. 21.11 Design of balanced receiver

calculations in the table of Fig. 21.7. These measurements were made through the depth range of 3.7 mm, and the aliased peaks beyond 3.7 mm were also tracked. Second- and third-order numeric dispersion compensation was used [14] and the sign of the compensation was flipped once the 3.7 mm Nyquist point was passed. An error in dispersion compensation broadens the point spread at all depths. It is also important to have the clock and balanced receiver signal time synchronized [15, 16]; otherwise, the resolution degrades with depth. System fiber lengths must be cut properly to achieve this. A programmable clock delay on the laser control board (see Fig. 21.5) can also be used to fine-tune the delay to minimize this effect.

Tracking roll off data past the 3.7 mm Nyquist depth shows the effectiveness of the antialiasing filters, which are located on the balanced receiver and the DAQ boards. The noise plotted is the noise level at the signal depth. It is nearly flat, as expected from shot-noise-limited operation. The test station uses a 1.2 mW reference power for these measurements.

The balanced receiver shown in Fig. 21.11 is a two-stage design followed by a differential output stage that drives the SATA cable connection to the data acquisition board. It has a transimpedance of 16 kohms and a frequency response shown in Fig. 21.12. It is AC coupled with a four-pole low-pass filter for antialiasing. It is thermal-noise limited at low frequency, but the noise is peaked at higher frequencies due to the operational amplifier input noise multiplied by the noise gain of the circuit [17]. This is an expected behavior for this type of receiver and means that the receiver noise is not flat versus depth.

The data acquisition system is another source of noise. The Axsun Camera Link DAQ card utilizes a Texas Instruments ADS54RF63 analog to digital converter. It is a 12 bit pipelined converter rated for a 40–550 MHz clock range. Axsun's own noise measurements with the card are shown in Fig. 21.13. The card is able to meet the ADS54RF63 noise specifications over the rated frequency range, but can also be under- or over-clocked with reduced performance. The converter translates ± 1.1 V differential signals into a 12 bit offset binary code. It achieves $\sigma = 0.9$ count RMS noise over much of its range. That translates to a maximum SNR of 64 dB and an ENOB of 10.4 bits, given the following expressions [18]:

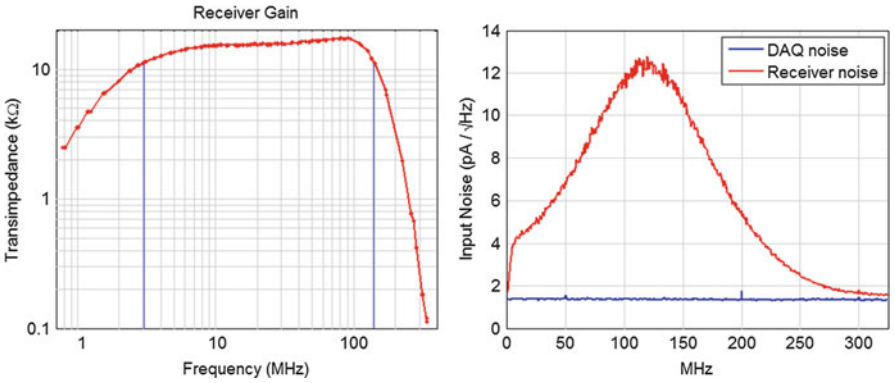

Fig. 21.12 Frequency response data for the balanced receiver. Transimpedance (*left*) and effective input current noise (*right*) are plotted

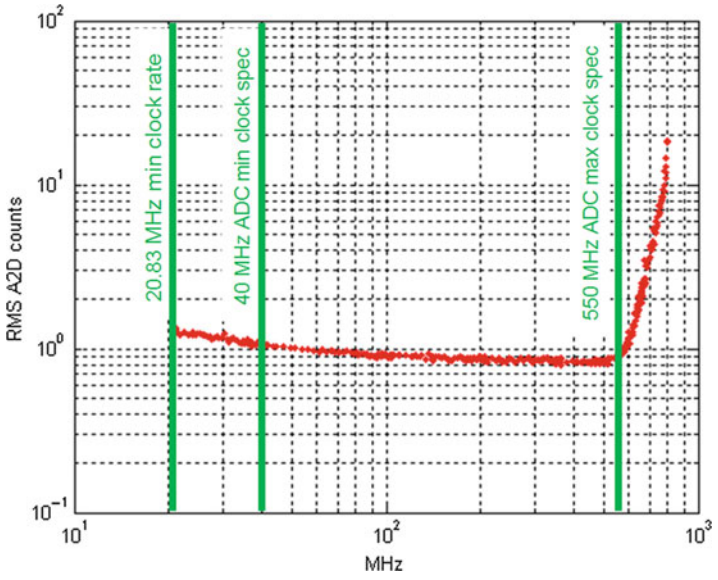

Fig. 21.13 Noise floor of data acquisition board

$$\mathrm{SNR} = \frac{\left(2^{N_{\mathrm{bits}}-1}\right)^2}{2\sigma^2}$$

$$\mathrm{SNR} = 6.02 \cdot \mathrm{ENOB} + 1.76\ \mathrm{dB}$$

Note that the 64 dB converter SNR limit is a broadband limit. FFT processing, which narrows the bandwidth, effectively averages OCT signals to much higher signal-to-noise ratios.

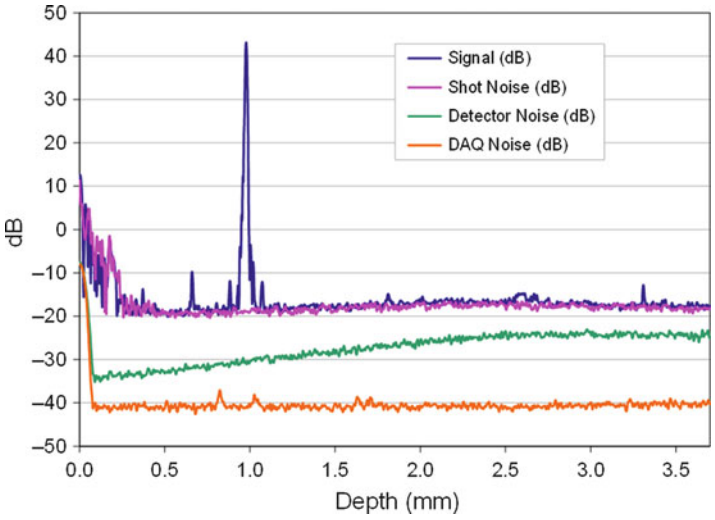

Fig. 21.14 Plot of signal and noise floor components versus depth. Conditions: 2.0 mW reference, 1.8 mW sample power, 39 dB attenuation

Figure 21.14 shows system noises versus depth along with the signal for a fixed reflector at 1 mm depth. It shows that the shot noise limit can be achieved throughout the imaging depth range. The traces are averages of 100 sweeps. Since the phase information is thrown away before averaging, the SNR is the same as for a single sweep, but the hash in the noise floor is reduced to give a better noise estimate. DAQ noise is not a limiting factor because the receiver noise is higher. The receiver noise is also not a limiting factor because the shot noise with 2 mW reference power is much higher. The shot noise is also flat because the transimpedance of the amplifier is flat up to the Nyquist frequency. The receiver noise is not flat, as pointed out earlier, because the noise gain of the receiver circuit is not flat. The useable depth range in this case is about 0.3–3.7 mm.

Figure 21.15 shows how the signal and noise behave as a function of reference power. Around 100 μW the shot noise becomes higher than the receiver noise. At this point the SNR becomes shot noise limited. Note that the SNR does not fall with further increases in reference power as expected from RIN-limited operation. The laser has very low noise. The data shown is limited to 2 mW, as measured on a power meter, which is getting close to the saturation limit of the balanced receiver.

The OCT engine's signal-to-noise behavior is modeled by the following expression, which is similar to that in reference [19]. Reference and sample powers, P_r and P_s, are defined in Fig. 21.8. The digital processing loss is 1.8 dB for a Hann window [20]. We estimate 2.2 dB miscellaneous loss:

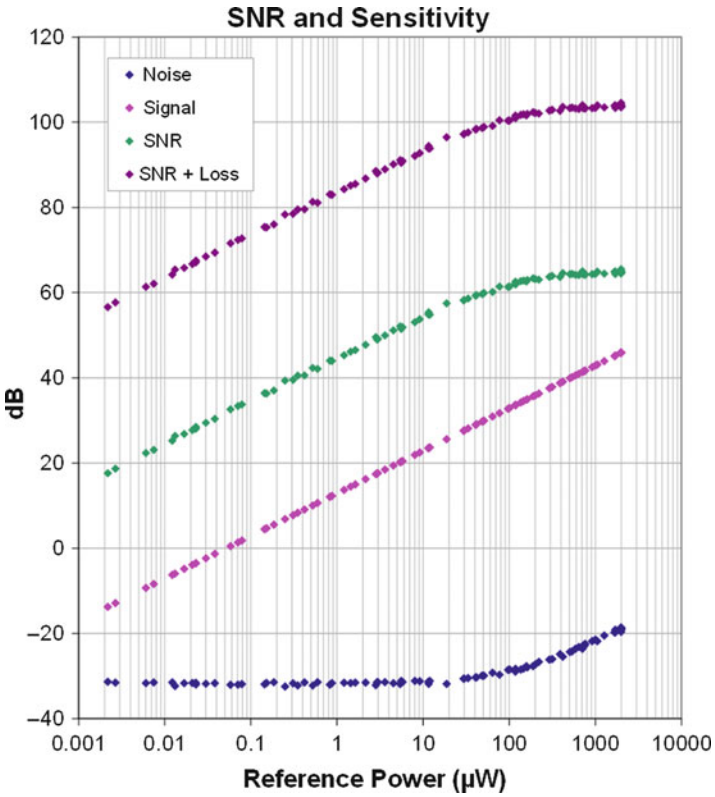

Fig. 21.15 Signal, noise, SNR, sensitivity versus reference power at 1 mm depth and 39 dB loss

$$\mathrm{SNR} = \frac{2\dfrac{T_{\mathrm{Misc}}T_{\mathrm{Coupler}}}{L_{\mathrm{Proc}}}\left(\dfrac{\eta q}{h\nu}\right)^2 P_r P_s}{\left[\left(\dfrac{\eta q}{h\nu}\right)^2 \mathrm{NEP}^2 + 2\dfrac{\eta q^2}{h\nu}P_r + \left(\dfrac{\eta q}{h\nu}\right)^2 \mathrm{RIN}\cdot\mathrm{CMRR}\cdot P_r^2\right]\dfrac{2B}{N}},$$

where

P_r = reference beam power
P_s = sample beam power
η = detector quantum efficiency
q = electronic charge
L_{Proc} = digital processing loss
T_{Coupler} = optical coupler power transmission
T_{Misc} = miscellaneous transmission reductions, such as connector and coupler loss

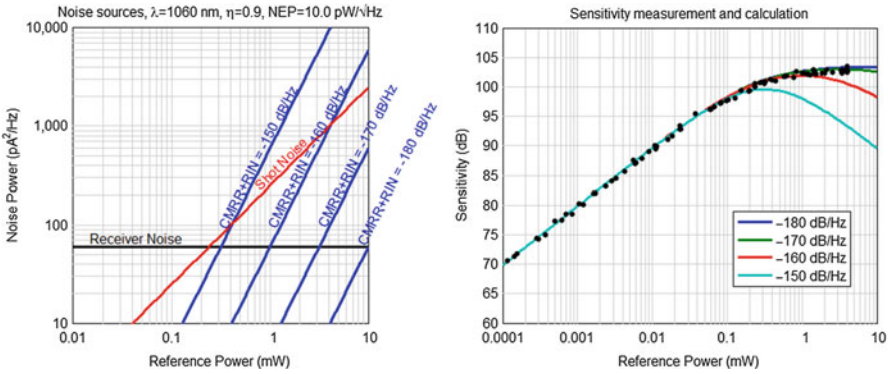

Fig. 21.16 Calculated noise powers (*left*) and comparison of experimental and theoretical sensitivities (*right*)

hν = photon energy
NEP = noise equivalent power of receiver
RIN = relative intensity noise
CMRR = common mode rejection ratio of balanced receiver
B = bandwidth of optical receiver (assumed 1/2 sampling rate)
N = number of samples

As pointed out in the discussion of the RIN measurement in Fig. 21.9, we believe that those numbers are pessimistic for the reasons illustrated in Fig. 21.16. We cannot determine the RIN directly from a measurement of SNR versus reference power, but we can get an estimate of CMRR+RIN (in dB/Hz). The left plot shows the noise floors for several values of CMRR+RIN. For shot noise to dominate, the RIN must be very low, because the CMRR will be poor given that the splitting ratios of fused 1,060 nm 3 dB couplers are not accurate and vary over wavelength. The right-hand plot of Fig. 21.16 shows no decrease in SNR at high reference power. It is likely that CMRR+RIN < -170 dB/Hz. We have not measured our CMRR, but it is probably around 20 dB. That would put the laser RIN in the neighborhood of -150 dB/Hz, much better than we can measure using the methods of Fig. 21.9. The laser has very low noise.

21.6 Images

The OCT engine described above, when coupled with a well-designed imaging interferometer and sample arm probe, is capable of delivering high-speed, high-resolution, high-sensitivity OCT images. The interferometer of Fig. 21.8 is well suited to ophthalmological applications where the average power to the eye is limited. An example image is shown in Fig. 21.17.

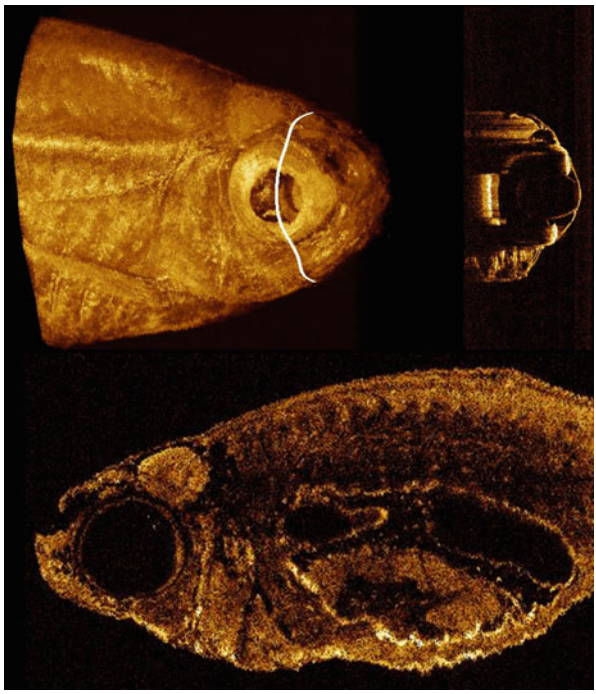

Fig. 21.17 Small aquarium fish imaged in the Axsun Technologies laboratories

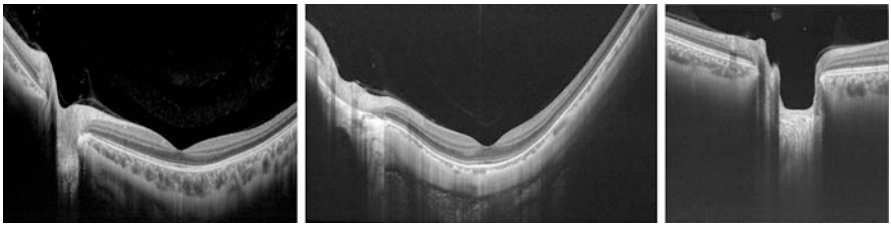

Fig. 21.18 Topcon DRI OCT-1 Atlantis system images of a healthy retina (*left*), a high myopia patient (*center*), and the optic nerve head (*right*) (Images courtesy of Topcon Corporation and Kyoto University)

High-quality retinal images in commercial equipment using the Axsun 1,060 nm OCT engine have also been produced. Figure 21.18 shows retinal images from a Topcon DRI OCT-1 Atlantis system. The 1,060 nm wavelength has several advantages over the current generation of 850 nm imaging systems. Reduced light scattering at longer wavelengths means that 1,060 nm light can penetrate deep into the choroid layer behind the retina. This wavelength also has superior penetration through cataracts. Another advantage is that the light is invisible to the patient, reducing eye motion from the patent's eyes natural tendency to follow the beam. The Axsun OCT engine also sweeps faster than current generation ophthalmic OCT systems and has shot-noise-limited performance, no fixed patterns, and low levels of ghost images.

21.7 Summary

In this chapter we described the design and performance of a 1,060 nm swept laser OCT imaging engine. In addition, we presented a new description of the passive mode-locking behavior of the Axsun swept laser. This deeper understanding of the swept laser dynamics is an important tool for many reasons. It enables modeling and rapid development of new lasers to meet the evolving needs of the OCT academic and commercial communities. In addition, the model allows us to better understand the design tolerance to changes in various key components, which is important for manufacturing these products with low cost.

The laser module, surrounding control and data acquisition electronics, produces an OCT engine that can accelerate commercial OCT system development. An OCT system manufacturer can concentrate on the application, the optical interface and software control. Axsun can provide high-speed shot-noise-limited system performance. This chapter shows one particular engine design useful for medical imaging, but Axsun has the ability to address other imaging and measurement problems with modifications to these systems. In particular, Axsun has both 1,310 and 1,060 nm band swept sources. They can be provided in a variety of sweep speeds, coherence lengths, and modes of operation.

References

1. M. Kuznetsov, W. Atia, B. Johnson, D. Flanders, Compact ultrafast reflective Fabry-Perot tunable lasers for OCT imaging applications. Proc. SPIE **7554**, 75541F-1 (2010)
2. D.C. Flanders, M.E. Kuznetsov, W.A. Atia, Laser with tilted multi spatial mode resonator tuning element, US Patent 7,415,049, issued 19 Aug 2008
3. B.C. Johnson, D.C. Flanders, Actively mode locked laser swept source for OCT medical imaging, US Patent application, Publication number US 2012/0162662 A1, 28 June 2012
4. S.H. Yun, B.E. Bouma, in *Optical Coherence Tomography*, ed. by W. Drexler, J.G. Fujimoto. Wavelength Swept Lasers, (Springer, ISBM 978-540-77549-2.), pp. 359–378
5. S.H. Yun, C. Boudoux, M.C. Pierce, J.F. de Boer, G.J. Tearney, B.E. Bouma, Extended-cavity semiconductor wavelength-swept laser for biomedical imaging. IEEE Photon. Technol. Lett. **16**, 293–295 (2004)
6. S.H. Yun, C. Boudoux, G.J. Tearney, B.E. Bouma, High-speed wavelength-swept semiconductor laser with a polygon-scanner-based wavelength filter. Opt. Lett. **28**, 1981–1983 (2003)
7. A. Bilenca, S.H. Yun, G.J. Tearney, and B.E. Bouma, Numerical study of wavelength-swept semiconductor ring lasers: the role of refractive-index nonlinearities in semiconductor optical amplifiers and implications for biomedical imaging applications, Opt. Lett. **31**, 760–762 (2006)
8. P. Bogatov, P.G. Eliseev, B.N. Sverdlov, Anomalous interaction of spectral modes in a semiconductor laser. IEEE J. Quantum Electron. **11**, 510–515 (1975)
9. E.A. Avrutin, L. Zhang, Dynamics of Semiconductor Lasers under Fast Intracavity Frequency Sweeping. 14th Int. Conf. on Transparent Optical Networks (ICTON), 1–4 (2012)
10. R. Huber, M. Wojtkowski, K. Taira, J.G. Fujimoto, Amplified, frequency swept lasers for frequency domain reflectometry and OCT imaging: design and scaling principles, Opt. Express **13**, 3513–3528 (2005)

11. H.A. Haus, Mode-Locking of Lasers, *IEEE Journal on Selected Topics in Quantum Electronics*, **6**, 1173–1185 (2000)
12. A. Dhalla, D. Nankivil, and J.A. Izatt, Complex conjugate resolved heterodyne swept source optical coherence tomography using coherence revival, Biomed. Opt. Express **3**, 633–649 (2012)
13. M.A. Choma, K. Hsu, J.A. Izatt, Swept source optical coherence tomography using an all-fiber 1300-nm ring laser source, J. Biomed. Opt. **10**, 044009 (2005)
14. M. Wojtkowski, V.J. Srinivasan, T.H. Ko, J.G. Fujimoto, A. Kowalczyk, J.S. Duker, Ultrahigh-resolution high-speed Fourier-domain optical coherence tomography and methods for dispersion compensation. Opt. Express **12**, 2404–2422 (2004)
15. E.D. Moore, R.R. McLeod, Correction of sampling errors due to laser tuning rate fluctuations in swept-wavelength interferometry, Opt. Express **16**, 13139–13149 (2008)
16. J. Xi, L. Huo, J. Li, X. Li, Generic real-time uniform K-space sampling method for high-speed swept-Source optical coherence tomography, Opt. Express **18**, 9511–9517 (2010)
17. J. Graeme, *Photodiode Amplifiers: Op Amp Solutions*, Chapter 5 – "Noise", McGraw Hill, ISBN 0-07-024247-X
18. W. Kester, Taking the Mystery out of the Infamous Formula, 'SNR = 6.02N + 1.76dB,' and Why You Should Care, Analog Devices MT-001 tutorial
19. S.H. Yun, G.J. Tearney, J.F. de Boer, N. Iftimia, B.E. Bouma, High-speed optical frequency-domain imaging, Opt. Express **11**, 2953–2963 (2003)
20. F. Harris, On the use of windows for harmonic analysis with the discrete Fourier transform. Proceedings of the IEEE **66**, 51–83 (1978)

VCSEL Swept Light Sources

22

Vijaysekhar Jayaraman, James Jiang, Benjamin Potsaid, Martin Robertson, Peter J. S. Heim, Christopher Burgner, Demis John, Garrett D. Cole, Ireneusz Grulkowski, James G. Fujimoto, Anjul M. Davis, and Alex E. Cable

Keywords

Tunable Laser • Swept Source • Optical Coherence Tomography • MEMS-VCSE

22.1 Background and Introduction

Wavelength-swept light sources are widely recognized as a critical enabling technology for swept source optical coherence tomography (SS-OCT) [1]. This fact has spurred a number of development efforts, employing varying approaches, aimed at creating the ideal SS-OCT tunable laser source. A few wavelength bands have

V. Jayaraman (✉) • M. Robertson • C. Burgner • D. John
Praevium Research, Inc., Santa Barbara, CA, USA
e-mail: vijay@praevium.com

J. Jiang • A.M. Davis
Thorlabs, Newton, NJ, USA

B. Potsaid
Department of Electrical Engineering and Computer Science and Research Laboratory of Electronics, Massachusetts Institute of Technology, Cambridge, MA, USA

Advanced Imaging Group, Thorlabs Inc., Newton, NJ, USA

P.J.S. Heim
Thorlabs Quantum Electronics (TQE), Jessup, MD, USA

G.D. Cole
Advanced Optical Microsystems, Mountain View, CA, USA

I. Grulkowski • J.G. Fujimoto
Department of Electrical Engineering and Computer Science and Research Laboratory of Electronics, Massachusetts Institute of Technology, Cambridge, MA, USA

A.E. Cable
Advanced Imaging Group, Thorlabs Inc., Newton, NJ, USA

© Springer International Publishing Switzerland 2015

W. Drexler, J.G. Fujimoto (eds.), *Optical Coherence Tomography*,
DOI 10.1007/978-3-319-06419-2_23

emerged as most important, including the 1,310 nm band for vascular, skin, and anatomic imaging and the 850 and 1,050 nm bands for ophthalmic imaging. The desired performance parameters of a swept source for SS-OCT include high maximum sweep rate, high output power, variable sweep rate, long dynamic source coherence length, and wide tuning range. High sweep rate is needed for real-time acquisition of large volumetric data sets [2], for reduced sensitivity to patient motion artifacts, and for imaging dynamically varying physiological processes. High output power enhances signal-to-noise and image quality, with 30–60 mW desirable for many 1,310 nm applications and 15–20 mW desirable for many 1,050 nm ophthalmic applications. Variable sweep rates are desirable, since detection bandwidth limits force tradeoffs between imaging range, axial resolution, and imaging speed, depending on the particular biological structure being imaged. Long coherence length is necessary for applications which require a long imaging range such as whole eye imaging and anatomic OCT. Wide tuning range is also critical, because the axial spatial resolution is inversely proportional to the laser tuning range [3].

In response to this diverse and challenging set of requirements, a large number of swept source laser configurations have been investigated in recent years. A comprehensive and up-to-date review of swept source options is found in table I of a recent publication on ophthalmic imaging [4]. It is not the purpose of this chapter to repeat this review, but we mention here briefly two leading swept source options, to illustrate some of the challenges and tradeoffs involved. These two leading candidates are commercial external cavity tunable lasers [5] and Fourier domain mode-locked (FDML) [6] lasers. A commercially available external cavity device at 1,060 nm uses a tunable Fabry-Perot mirror as the reflecting element, providing $\sim$100 nm tuning and axial scan rate up to 100 kHz [5]. Commercial 1,310 nm external cavity devices operating at 50 kHz are also used extensively in cardiovascular imaging. FDML lasers employ a fiber-based ring cavity with a tunable intracavity Fabry-Perot filter, in which the wavelength repetition period of the laser is matched to the round-trip delay time in the external cavity [6]. This allows the laser to operate in quasi-stationary configuration and circumvents the normal speed limitations associated with buildup of amplified spontaneous emission (ASE) to lasing operation [1]. In 2006, an FDML at 1,310 nm demonstrated 290 kHz fundamental axial line rate in conjunction with $>$100 nm tuning [7]. More recently, line rates of 400 kHz have been reported with the FDML [8]. Fiber-optic delay lines and multiple spots have been employed (as could be with other swept sources), to multiplex FDML rates into the multi-MHz range [9, 10].

Both the external cavity laser and FDML are multimode devices, a fact that ultimately limits dynamic coherence length and imaging range. An external cavity laser at 1,060 nm has shown 20 mm dynamic coherence length at 100 kHz operation [5], and the 1,310 nm FDML has shown $>$14 mm at 290 kHz line rate [7]. Both of these results represent impressive advancements over technology available before 2006. Nevertheless, the fact that both lasers operate with a cluster of modes, rather than a single mode, leads to a coherence length that is an order of magnitude or more smaller than single-mode semiconductor lasers. Multimode operation can also increase relative intensity noise (RIN). The FDML has a further limitation that it

must be operated at a fixed rate because of its fixed fiber external cavity length. In short, the external cavity laser and FDML suffer from limited or fixed sweep rate and limited dynamic coherence length due to multimode operation. These limitations are representative of not only these sources but also the majority of other swept sources developed in the last ~15 years [4].

In 2009, Praevium Research and commercial partner Thorlabs began developing a swept source based on amplified microelectromechanical systems tunable vertical-cavity surface-emitting lasers (MEMS-VCSELs). The purpose of this development was to create a truly single-mode swept source for OCT that was capable of variable sweep rates from the kHz range up to the MHz range. MEMS-VCSELs offered a potentially ideal solution to this problem. The short micron scale length of the VCSEL cavity promised single-mode operation and rapid buildup time to lasing [1], and the low mirror mass in previously demonstrated MEMS-VCSELs promised >1 MHz axial line rates [11]. In addition, initial short-cavity designs predicted a longitudinal mode spacing well exceeding 100 nm, suggesting the possibility of mode-hop-free continuous tuning over this range. Linewidths on the order of 3 MHz had been demonstrated in fixed wavelength VCSELs [12], corresponding to a coherence length of tens of meters at 1,310 nm. Previous MEMS-tunable VCSELs had shown larger linewidths up to several hundred MHz, due to additional mechanical chirp contributions associated with the suspended membrane [13], but this linewidth still corresponded to meter scale coherence length or more than an order of magnitude larger than leading competing SS-OCT sources. Lastly, the fully integrated structure of the VCSEL contrasted with the separation of gain and tuning elements present in external cavity lasers, suggesting both cost and performance benefits. By 2009, fixed wavelength VCSELs had established themselves as a low-cost wafer-scale laser technology, and a MEMS-tunable device promised to exploit these same advantages.

MEMS-VCSELs were first conceived in the mid-1990s [14], but development efforts in the field until 2009 were driven primarily by telecommunications [15] and narrow-tuning spectroscopic applications [16, 17]. Application of these devices to SS-OCT therefore posed a large number of uncertainties. As of 2009, no MEMS-VCSELs had been demonstrated at the desired OCT wavelength bands of 1,310 and 1,050 nm, though 1,550 nm devices had undergone advanced development for telecommunications [15]. Secondly, the widest tuning range $\Delta\lambda$ reported for any MEMS-VCSEL at any wavelength was 65 nm at $\lambda = 1{,}550$ nm, corresponding to a fractional wavelength tuning $\Delta\lambda/\lambda$ of 4.2 %. This is equivalent to 55 nm at 1,310 nm, or about half of what competing SS-OCT sources at the time offered. Thirdly, single-mode VCSEL output powers were limited to a few mW, short of the 30–60 mW required for 1,310 nm applications and the 15–20 mW required for 1,050 nm. Semiconductor-based optical amplification promised the required powers, but the quality of imaging obtainable with amplified VCSELs was unknown. Fourthly, although small signal and high-speed tuning had been demonstrated in MEMS-VCSELs [11], high speed in conjunction with wide tuning range had never been reported.

In the last 3 years, these challenges have been addressed through a large multi-disciplinary effort involving Praevium Research, Advanced Optical Microsystems,

Thorlabs, and the OCT Imaging Group at the Massachusetts Institute of Technology (MIT). Praevium Research has taken the lead on VCSEL device design and fabrication. Thorlabs has led manufacturing, packaging, commercialization, OCT imaging validation, and development of supporting electronics. MIT has developed and demonstrated the utility of the VCSEL in new imaging modes and applications. A few results of this effort include the first MEMS-VCSELs at 1,050 nm [18] and 1,310 nm [19]; record tuning ranges of 150 nm at 1,310 nm [19] and 100 nm at 1,050 nm [18]; whole eye imaging, anterior eye imaging, and retinal imaging with 1,050 nm VCSELs [4]; and additional high-quality skin and vascular images with both 1,310 and 1,050 nm VCSELs [20]. Record coherence length >100 mm and axial scan rates up to 1.2 MHz have been demonstrated [20]. Linearized drive waveforms at 200 kHz axial scan rates have also been shown [20].

As a consequence of the results described above, as of 2014, SS-OCT optimized MEMS-VCSELs have reached early commercialization. The sections below describe design, fabrication, and performance of these devices in detail, focusing on the laser source. Detailed discussion of OCT imaging with VCSELs is provided by other chapters of this book.

22.2 Widely Tunable 1,310 nm and 1,050 nm VCSEL Design

22.2.1 Overview of Device Structure

The first 1310 nm MEMS-VCSELs were reported by Praevium and collaborators in mid-2011 [21] and the first 1,050 nm devices in early 2012 [20]. Figure 22.1 illustrates a three-dimensional solid model of a 1,310 nm MEMS-VCSEL. The 1,310 nm epitaxial structure includes a wide-gain bandgap-engineered aluminum indium gallium arsenide (AlInGaAs) multi-quantum well (MQW) active region epitaxially grown on an indium phosphide (InP) substrate and joined by wafer bonding [22] to

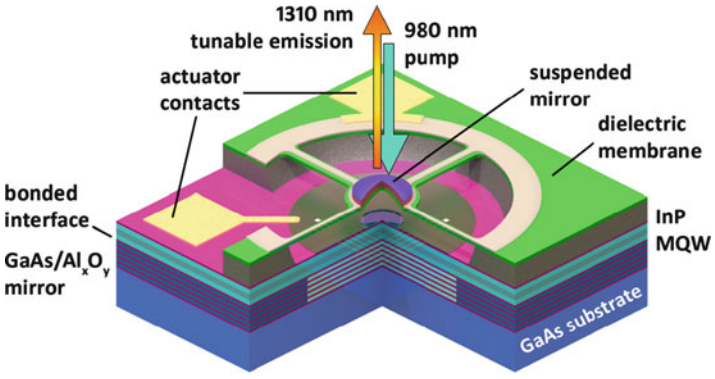

Fig. 22.1 Three-dimensional cutaway view of our 1,310 nm MEMS-VCSEL. InP gain region and GaAs mirror are integrated by wafer bonding. VCSEL is optically pumped at 980 nm (From Ref. [19])

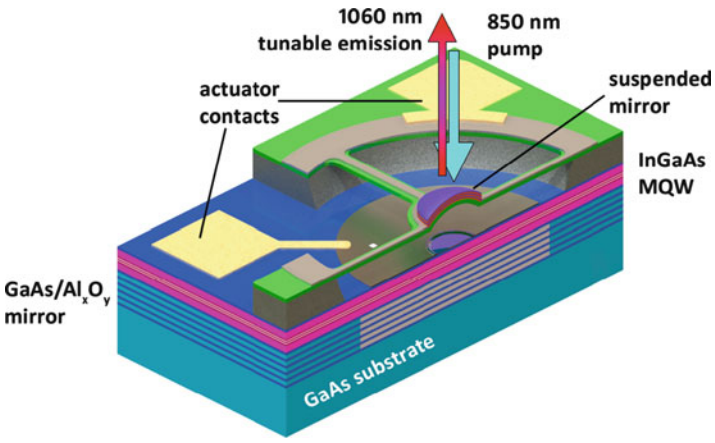

Fig. 22.2 Three-dimensional cutaway view of 1,050 nm MEMS-VCSEL. The structure is grown in one epitaxial step with no wafer bonding. VCSEL is optically pumped at 850 nm (From Ref. [18])

a wideband bottom gallium arsenide (GaAs)-based fully oxidized aluminum oxide (Al_xO_y)-GaAs bottom mirror [23]. Additional metal and dielectric layers on top of this "half-VCSEL" structure complete the optical cavity. This cavity includes a suspended top dielectric mirror, separated from the underlying half-VCSEL structure by an air gap, which can be contracted by electrostatic force as a voltage is applied between the two actuator contacts shown. The VCSEL is optically pumped at 980 nm through the top dielectric mirror, generating tunable 1,310 nm emission, which emerges from the top mirror and is fiber coupled and amplified by a low-noise semiconductor optical amplifier (SOA) before being sent to an OCT system.

Figure 22.2 illustrates a similar view of a 1,050 nm device. Here, the gain region employs compressively strained indium gallium arsenide (InGaAs) quantum wells integrated with a GaAs/Al_xO_y fully oxidized mirror. The structure requires no wafer bonding, since the InGaAs quantum wells are nearly lattice matched to the underlying GaAs and can be integrated by epitaxial growth with the GaAs-based mirror. In this case, the optical pump is at 850 nm, generating tunable 1,050 nm emission.

Implicit in the device structures of Figs. 22.1 and 22.2 are a number of design choices that are critical to obtaining wide tuning range. Below, we briefly describe those choices and the justification for each.

22.2.2 Optical Versus Electrical Pumping

This effort to date has focused on optically rather than electrically pumped devices. Though the ultimate low-cost device will be electrically pumped, optical pumping provides a number of performance advantages over electrical pumping, including enhanced tuning range and spectral purity, for a variety of reasons. First, the absence of electrically active dopants reduces absorption losses and thus reduces threshold gain, enabling lasing over a wider portion of the available gain spectrum.

Second, the absence of resistive heating associated with electrically pumped devices also increases available gain and again promotes wide tuning range. Third, optical pumping eliminates the need for thick intracavity current-spreading layers, which extends the overall cavity length, reducing the cavity free spectral range (FSR) and ultimately limiting the laser tuning range. The widest previously reported MEMS-VCSELs have had tuning range limited by (FSR) [15, 24]. Fourthly, optical pumping simplifies the use of resonant periodic gain structures, which are known to provide a maximal gain enhancement in a VCSEL cavity [25]. Lastly, a single-spatial-mode pump laser provides an optimal overlap between the pump area and the lowest order spatial mode of the VCSEL, which suppresses lasing of unwanted transverse modes. This enables very high side mode suppression ratio (SMSR) of >45 dB to be routinely achieved in properly designed optically pumped devices. This high SMSR has a favorable impact on SS-OCT imaging quality.

We also note that the highest power tunable VCSELs have been demonstrated by optical pumping, achieving an impressive peak power of 14 mW near 1,550 nm [15]. This falls short by a factor of 2–3 from that required for SS-OCT near 1,310 nm but is somewhat close to power levels required for ophthalmic imaging at 1,050 nm. Our design philosophy in this effort is to design the MEMS-VCSEL itself for wide tuning range, enabling improved axial resolution, rather than high output power. We then amplify the VCSEL emission with a semiconductor optical amplifier. The resulting widely tunable, high power emission is used as the source for OCT imaging and has resulted in excellent images, as discussed in Sect. 22.6 below and in additional publications. The previous high power result at 1,550 nm [15], however, suggests that further engineering of 1,050 nm MEMS-VCSELs may remove the need for amplification at this wavelength.

22.2.3 Mirror Design

Wide mirror reflectivity bandwidth is critically important for wide tuning range. A high refractive index contrast mirror with a short optical field penetration depth is also critical to reduce the overall effective cavity thickness and increase the FSR, which further increases tuning range. The fully oxidized mirror shown in Figs. 22.1 and 22.2 satisfies these requirements better than virtually any other mirror, with the possible exception of a hybrid metal/deposited dielectric mirror [24], which we discuss briefly below. Wide bandwidth is also provided by the recently proposed and demonstrated high contrast grating (HCG) [11]. The HCG provides a high reflectivity in a thin single layer structure that has a strong lateral refractive index perturbation. This provides very low mass and high mechanical resonance, but the calculated HCG bandwidth [26] falls short of the fully oxidized mirror, and the ability of the HCG to provide >30 nm tuning in a VCSEL structure remains unproven.

The fully oxidized mirror is realized by starting with an epitaxially grown stack of GaAs/AlAs, etching holes or mesas into the epilayer structure to access the underlying AlAs layers, and exposing the material to a steam atmosphere at elevated temperature [23]. This converts the AlAs layers to Al_xO_y layers with

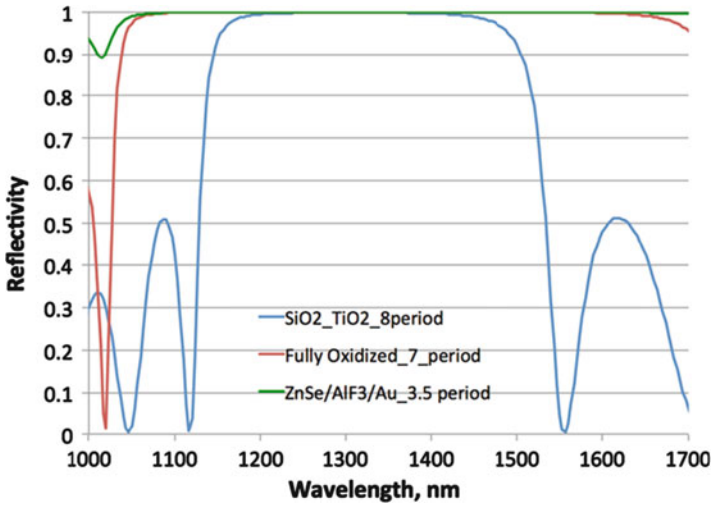

Fig. 22.3 Reflectivity of two candidate back mirrors (*red* and *green*) and one suspended mirror (*blue*)

a refractive index around 1.55, providing a large index contrast relative to the surrounding GaAs layers (index around 3.4). This enables the incorporation of a high reflectivity, wide bandwidth, and short penetration depth end mirror.

The use of the fully oxidized mirror at 1,050 nm is a natural choice, since it can be epitaxially grown with the GaAs gain region. Its use at 1,310 nm is less obvious, since this necessitates wafer bonding an InP-based gain region to a GaAs-based mirror region, as shown in Fig. 22.1. The choice of a heterogeneously integrated material structure stems from the fact that the InP material system provides no easily oxidized material-like AlAs or any other epitaxially grown high-index contrast mirror option [27]. In response to this challenge, previous MEMS-tunable work at 1,550 nm has employed deposited dielectric and/or metal/dielectric mirrors on both sides of the cavity [15, 24]. Similar approaches could be employed at 1,310 nm. Our choice of the wafer-bonded semiconductor mirror is related to mechanical robustness, manufacturability, and ease of handling, relative to a process that requires either backside vias [15] or gold bonding to a transfer substrate [24]. In addition, the transparency of the fully oxidized mirror enables coupling light out at either side of the cavity, to satisfy the needs of a variety of applications, while the metal/dielectric mirror can only function as a back mirror.

Figures 22.3 and 22.4 illustrate the reflectivity of three candidate mirrors for widely tunable MEMS-VCSELs centered at 1,300 nm, neglecting absorption and scattering losses. Reflectivity is calculated with respect to the antireflection (AR)-coated gain medium (i.e., looking from the gain medium outward to the respective mirrors), assuming that the pure dielectric mirror is suspended, and the fully oxidized or hybrid mirror is the fixed back mirror. Both the fully oxidized mirror ($GaAs/Al_xO_y$) and hybrid dielectric/gold mirror ($AlF_3/ZnSe/Au$) show a reflectivity bandwidth between first nulls of about 800 nm. The suspended

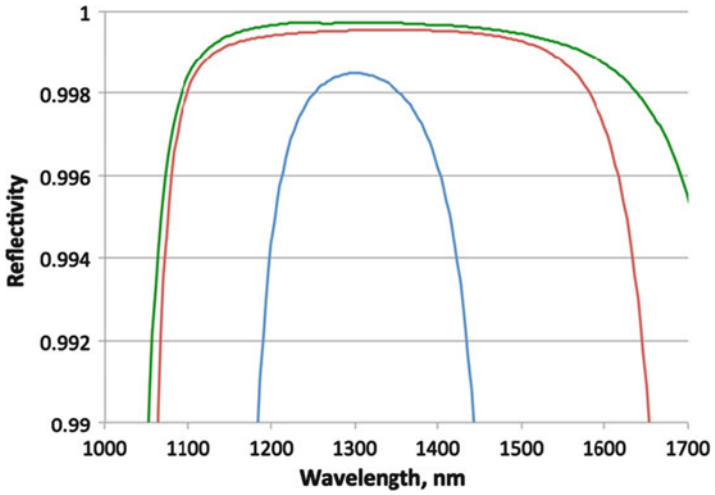

Fig. 22.4 Reflectivity in range > 99 %. Back mirrors (*red* and *green*) provide > 99.9 % over 400 nm. Suspended (*blue*) shows 99.5 % < R < 99.9 % over ~200 nm

dielectric mirror bandwidth between nulls is about half this value. The reflectivity plot of Fig. 22.4 shows the reflectivity spectrum of the same three mirrors over the same wavelength range but only for reflectivity above 99 %. Efficient top-emitting VCSELs require >99.9 % reflectivity on the back mirror. The fully oxidized and the hybrid dielectric/metal mirror both satisfy this requirement over >400 nm, with again the hybrid mirror exhibiting a slightly wider bandwidth. A lower reflectivity pure dielectric mirror, such as the SiO_2/TiO_2 combination calculated in Figs. 22.3 and 22.4, functions as the output coupler. Requirements on this output coupler are somewhat relaxed relative to the back mirror, with a required reflectivity in the range of about 99.5 % < R < 99.9 %. Reflectivity lower than 99.5 % increases the required threshold gain or inhibits wideband lasing, and reflectivity > 99.9 % can compromise output power as very little light is coupled out of the optical cavity. The SiO_2/TiO_2 combination shown in the figure satisfies this requirement over about 200 nm bandwidth, as do other commercially available and robust dielectric coatings such as SiO_2/Ta_2O_5 or SiO_2/Nb_2O_5.

A MEMS-VCSEL employing the dielectric mirror shown in Figs. 22.3 and 22.4 as an output coupler, and either of the back mirrors shown, can be expected to support lasing over 100–200 nm tuning range near 1,310 nm. Similar reflectivity plots can be generated near 1,050 nm and similar conclusions formed. The ultimate limit on tuning then becomes the cavity free spectral range (FSR) or the available gain bandwidth. In previous electrically pumped MEMS-VCSELs, FSR has often limited tuning range. In our optically pumped devices, we have pushed the FSR to 161 nm at 1,310 nm, achieving 150 nm tuning range as discussed below [19]. Achievement of this tuning range requires not only wide mirror bandwidth and large FSR but also proper engineering of the active region. We briefly discuss the active region material design in the next section.

22.2.4 Active Region Material Design

As discussed earlier, MEMS-VCSELs at both 1,050 and 1,310 nm employ compressively strained multi-quantum well (MQW) active regions, since compressive strain provides gain enhancements in quantum well gain for both GaAs-based (1,050 nm) and InP-based (1,310 nm) multi-quantum well active regions [28, 29]. Tensile strain has also been shown to provide superior edge-emitting laser performance for InGaAsP/InP MQW devices [30], but tensile strain enhances transverse magnetic (TM) gain (electric field perpendicular to quantum well plane) rather than transverse electric (TE) gain [29]. Since light propagation is perpendicular to the plane of the quantum well in VCSELs, the electric field will be in the plane of the quantum well and thus compressively strained wells can be employed.

MEMS-VCSELs at 1,050 nm employ InGaAs quantum wells with GaAs barriers as the gain region. This material is known to provide higher gain relative to lattice-matched quantum wells on GaAs [29], and incorporation of indium is necessary to increase the wavelength on GaAs beyond the ~870 nm achievable with lattice-matched materials. Compressively strained InGaAs quantum wells have been used for 980 nm fixed wavelength VCSELs since early in the history of VCSELs [31], and more recently, fixed wavelength devices at 1,100 nm using strained InGaAs quantum wells have also been demonstrated [32]. MEMS-VCSELs at 1,310 nm employ compressively strained AlInGaAs/InP quantum wells. Although the compressively strained InGaAsP/InP quantum wells have a longer history in edge-emitting lasers [30], the AlInGaAs/InP material system has provided superior temperature performance in edge-emitting lasers at 1,310 nm [33]. Other demonstrations in both 1,550 nm fixed wavelength [34] and 1,550 nm MEMS-VCSELs [35] have employed compressively strained AlInGaAs/InP multi-quantum well active regions. For tunable VCSELs, a lesser-known advantage of the AlInGaAs/InP material system is the wider gain spectrum relative to InGaAsP/InP. This width can be obtained by designing quantum wells to have two confined quantum states. State separation is wider in the AlInGaAs/InP material system relative to the InGaAsP/InP system, because of the larger conduction band offset [33], leading to wider gain spectra and higher output powers. This has been demonstrated in superluminescent diodes (SLED) developed by Praevium Research, an example spectrum of which is shown in Fig. 22.5. The InGaAs/GaAs system is also capable of wide dual-quantum state gain spectra, as shown in the SLED spectrum of Fig. 22.6.

22.2.5 MEMS Actuator Design

For SS-OCT operation, the ideal MEMS actuator should have a flat and wide bandwidth frequency response, enabling operation at arbitrary scan rates and linearization of drive waveforms through control of higher frequency dynamics. Note that here we focus exclusively on electrostatic rather than electrothermal [24] actuation, since the latter does not provide speeds appropriate for SS-OCT.

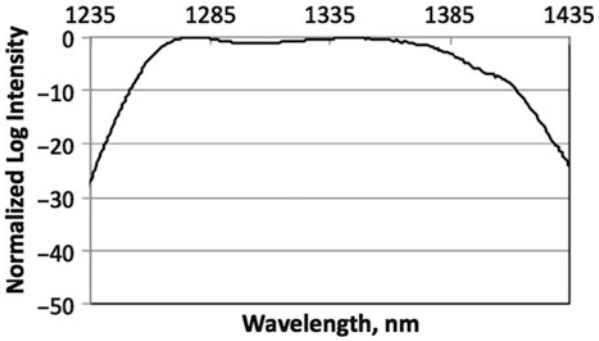

Fig. 22.5 Emission spectrum from a 1,310 nm superluminescent diode (*SLED*) using an AlInGaAs/InP MQW design with two quantum states. Width of SLED spectrum is indicative of width of the gain spectrum

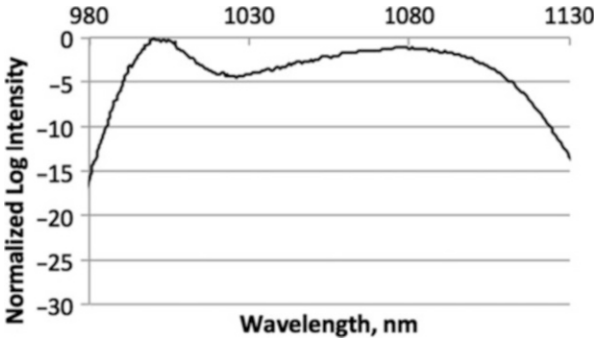

Fig. 22.6 Emission spectrum from 1,050 nm superluminescent diode (*SLED*) using an InGaAs/GaAs QW structure with two quantum states. Width of SLED spectrum is indicative of width of the gain spectrum

Numerous parameters associated with the actuator geometry affect the MEMS-VCSEL tuning frequency response. For the specific geometry of Figs. 22.1 and 22.2, using a central plate with a number of supporting arms, important parameters include the thickness and stress level of the membrane layer, the overall actuator area, the length and width of the supporting arms, the number of arms, the diameter of the central distributed Bragg reflector (DBR) mirror, and the initial air gap. These parameters affect resonant frequency, damping, resulting bandwidth, voltage required for a given wavelength shift, and maximum achievable wavelength span. Many of these factors must be traded off to achieve a commercially viable design. For example, increasing the thickness and stress of the membrane layer increases the resonant frequency but may require impractical voltages to achieve the full tuning range. Increasing the initial air gap thickness increases maximum achievable static deflection, because tuning beyond about one-third of the initial air gap causes electrostatic forces to overwhelm restoring forces, leading to "snapdown" of the actuator [36]. In dynamic operation, the peak voltage can exceed the snapdown voltage as long as the actuation frequency is sufficiently high. Nevertheless, a certain amount of static bias is required on all devices, and avoiding snapdown in electrostatic actuators therefore remains an important design consideration.

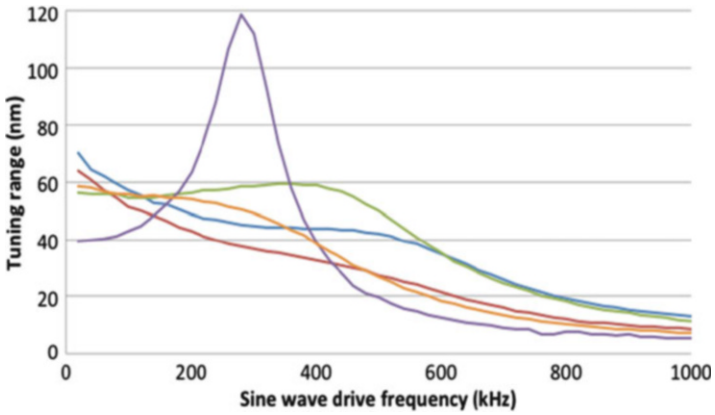

Fig. 22.7 Various frequency responses achieved through modification of the actuator geometry and membrane stress

However, increasing the initial air gap thickness also reduces the free spectral range, which reduces maximum achievable tuning range. Thus, an optimum initial air gap thickness must be chosen.

Diameters of the central DBR mirror and overall actuator area impact performance in a variety of ways. Minimizing DBR diameter increases resonant frequency through reduced mass, but diameter must be larger than the mode size to minimize sidewall scattering losses, accounting for lithographic fabrication tolerances on the alignment between the DBR and the central axis of the cavity. Increasing the overall area of the actuator can either increase or decrease resonant frequency, since increased mass is competing with increased spring stiffness. Lastly, increasing area increases squeeze-film damping through interaction with viscous air [37], which can reduce resonator Q and flatten frequency response, as long as the device is not overdamped.

Figure 22.7 illustrates the range of frequency responses experimentally measured, through variation of the parameters discussed above. As shown, resonant frequencies vary from about ~300 to ~500 kHz, and damping varies from highly under-damped to near critically damped. Peak voltages for full tuning over one FSR (see results in Sect. 22.4 below), for all designs shown, are under 85 V. The flatter responses with 300–500 kHz resonance are preferable for linearizing the wavelength tuning response, as discussed in Sect. 22.5 below. The highest resonance devices have led to record axial line rates of 1.2 MHz [20], when both forward and backward wavelength scans are employed.

The geometry of the MEMS actuator is sufficiently complex that the qualitative tradeoffs discussed above must be accurately modeled using a 3-D finite-element tool such as COMSOL™ to accurately predict frequency response and modal behavior. Finite-element modeling also identifies some subtle features such as the impact of higher order modes on the dynamic response of the actuator. Figure 22.8 illustrates example COMSOL™ modeling of a typical suspended mirror.

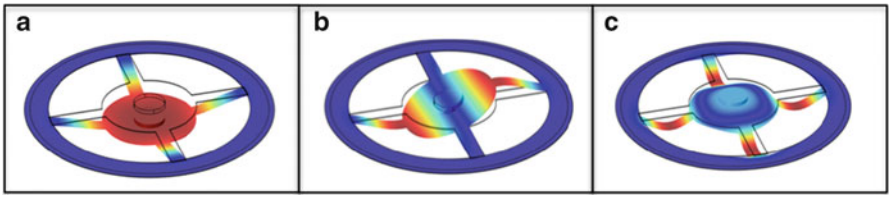

Fig. 22.8 COMSOL™ modeling of the three lowest order modes of a 4-arm actuator, illustrating piston mode (**a**), tilt mode (**b**), and higher order mode with minimal plate motion (**c**)

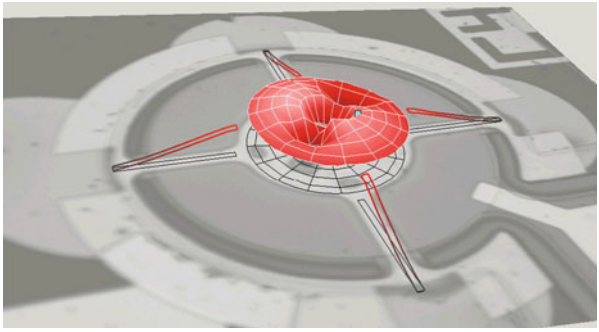

Fig. 22.9 Single frame of laser Doppler vibrometer (*LDV*) animation of actuator motion. Depressions in central plate are artifacts resulting from transparent portions of the membrane. The overall actuator motion is in the primary desired piston mode

The model reveals a lowest order "piston" mode, which is the primary peak seen in the responses of Fig. 22.7, and the motion desired for VCSEL tuning. Additionally shown is an undesirable tilting mode and another undesirable mode corresponding to movement of the actuator arms with minimal movement of the central plate. These higher order modes can be excited by fabrication imperfections or higher drive harmonics used for linearization, but their impact can be minimized by increasing the damping in the structure. Advanced MEMS characterization tools such as laser Doppler vibrometry (LDV) [38, 39] can help visualize actuator movement in real time, correlate with theoretical models, and adjust fabrication methods as necessary to achieve the desired movement. Figure 22.9 illustrates one frame of an LDV movie of actuator motion for a 4-arm device. Depressions in the central plate are measurement artifacts arising from transparent portions of the oscillating membrane. The primary value of the movie from which this frame is constructed is a demonstration that the actuator is moving primarily in the desired "piston mode," rather than in undesirable higher order modes.

22.3 Widely Tunable VCSEL Fabrication

Figures 22.10a–l illustrate key elements of the process flow used to fabricate the device structures illustrated in Figs. 22.1 and 22.2. Many elements of the process flow are derived from previous work [40]. The general process flow is essentially identical for 1,050 and 1,310 nm devices, with the exception that 1,310 nm devices

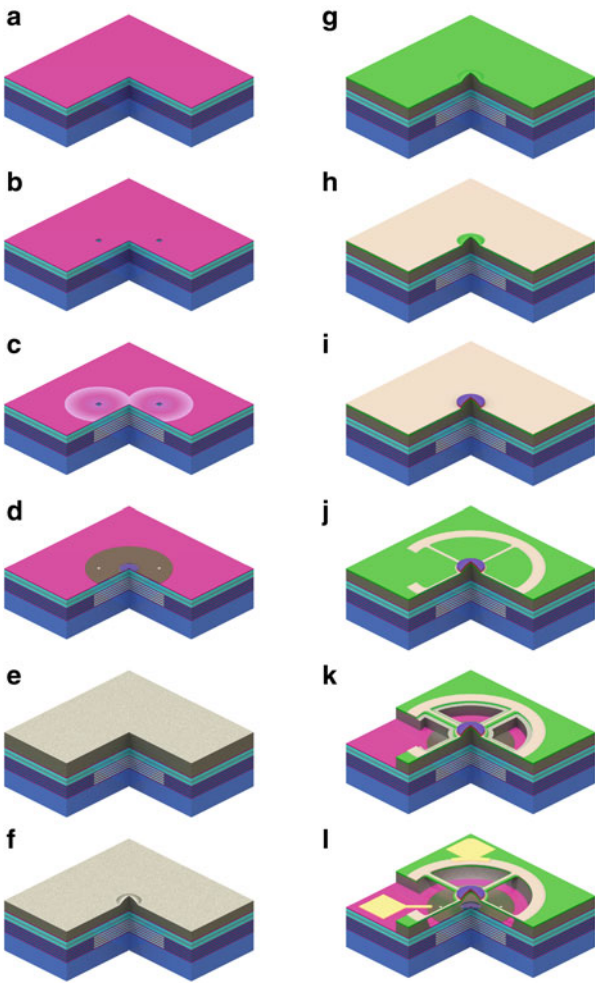

Fig. 22.10 MEMS-VCSEL fabrication. (**a**) Initial structure with gain region (*pink*) on top of the fixed bottom mirror. (**b**) Two etched oxidation vias. (**c**) The oxidized mirror layer region forms a figure 8 around the oxidation vias. (**d**) Deposited bottom contact (*brown disk*) and AR coating (*purple central film*). (**e**) Sacrificial layer (*gray top*) deposited over entire structure. (**f**) Curved surface etched in center of laser aperture. (**g**) Dielectric membrane (*green*) deposited over the entire sample. (**h**) *Tan top* metal deposited over membrane with central opening for light passage. (**i**) Dielectric top mirror (*purple*) deposited and patterned over central device area. (**j**) Actuator pattern wet-etched into *tan top* metal. (**k**) Actuator pattern is transferred to underlying layers. (**l**) Final structure including deposited contact pads (*yellow*) and undercut sacrificial layer creating a suspended membrane

additionally require wafer bonding to combine the InP-based epitaxial structure with the GaAs/Al_xO_y bottom mirror prior to beginning MEMS-VCSEL fabrication. In addition, thicknesses and composition of epitaxial layers and dielectric films are different for the two wavelengths.

For 1,310 nm devices, the process begins with wafer bonding of an epitaxially grown multi-quantum-well gain region on an InP wafer to an epitaxially grown stack of GaAs/AlAs layers on a GaAs wafer. After bonding, the InP substrate is chemically etched away, leaving an InP gain region integrated on a GaAs substrate. Wafer bonding is a well-known process in which lattice-mismatched semiconductors, such as GaAs and InP, can be joined through application of pressure and heat [41]. Wafer bonding for VCSELs was first demonstrated in the mid-1990s and led to some of the first demonstrations of 1,310 nm fixed wavelength VCSELs [42].

After bonding, 1,310 and 1,050 nm device processing proceeds identically as shown in Fig. 22.10a–l. Figure 22.10a shows the initial epitaxial structure, with gain region integrated on the GaAs/AlAs mirror layers. Figure 22.10b illustrates the formation of two oxidation via holes, which provide access to the underlying mirror layers for a subsequent oxidation step. The etched structure is then exposed to a steam atmosphere at elevated temperature, converting AlAs to AlxOy, creating a high contrast mirror in combination with the high-index GaAs layers. Figure 22.10c illustrates this mirror oxidation step, where the oxidized region expands radially around the etched holes, forming a figure 8 pattern. Deposition of the bottom contact layer proceeds after oxidation, containing an apertured central region with a broadband antireflection (AR) coating (Fig. 22.10d), through which intracavity light will pass into an air gap. Next, a sacrificial layer is deposited (Fig. 22.10e), the thickness of which determines the initial air gap and zero-bias device wavelength. In step (Fig. 22.10f), a curved surface is formed on the sacrificial layer through pattern transfer of a reflowed resist mesa. This curved surface contributes to the formation of a half-symmetric cavity in the final device. Figure 22.10g illustrates deposition of a dielectric membrane layer (green) on the sacrificial layer, followed by deposition of an apertured top actuator contact metal in Fig. 22.10h. The aperture serves to allow passage of light through the structure.

Deposition of the top dielectric DBR proceeds next, followed by etching of a post in the DBR (purple central region) to expose the top contact metal in the field (Fig. 22.10i). Wet chemical etching of the top contact metal creates the desired actuator shape, as shown in Fig. 22.10j. Further dry etching transfers this geometry downward through dielectric and sacrificial layers (Fig. 22.10k). After deposition of top and bottom wire bond pads, chemical undercutting of the sacrificial layer creates the final suspended structure shown in Fig. 22.10l.

22.4 1,310 nm and 1,050 nm VCSEL Static and Dynamic Tuning Results

22.4.1 Section Overview

This section describes the static and dynamic tuning range obtained with various generations of both 1,310 and 1,050 nm MEMS-VCSELs. Section 22.5 discusses additional laser properties relevant to OCT imaging, and Sect. 22.6 shows representative images obtained with these devices. Figure 22.11 illustrates a schematic of the optically pumped MEMS-VCSEL source used for OCT imaging, along with the supporting elements around the VCSEL source. An incoming optical fiber is coupled to the MEMS-VCSEL cavity, delivering incoming pump light at 980 nm for 1,310 nm MEMS-VCSEL operation and at 850 nm for 1050 nm MEMS-VCSEL operation. Isolators protect both the pump lasers and the MEMS-VCSELs from back reflections, ensuring low noise operating and enhancing laser lifetime. The pump fiber also collects the emitted tunable VCSEL radiation, and a subsequent

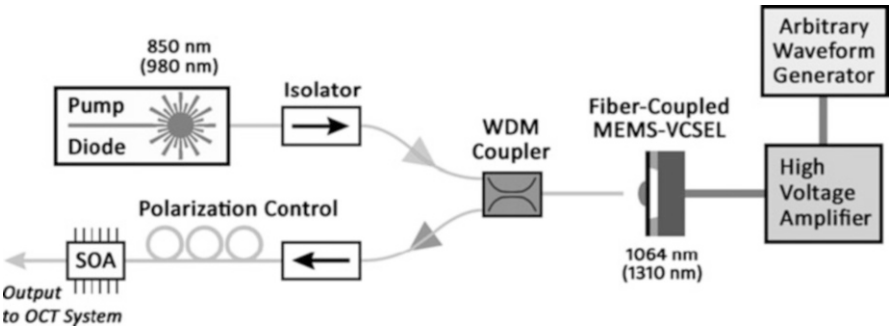

Fig. 22.11 Optically pumped MEMS-VCSEL source, illustrating various supporting elements around VCSEL. Pump laser emission passes through an isolator and WDM coupler before impinging on the VCSEL, which emits into same fiber and is separated to a different optical path by the WDM coupler. VCSEL emission also passes through a second isolator and a polarization controller before being amplified by the semiconductor optical amplifier (*SOA*) and sent to the OCT system. The tuning signal is supplied by an electrically amplified arbitrary waveform generator

WDM coupler separates the incoming pump light from the outgoing MEMS-VCSEL emission, with the latter sent to a semiconductor optical amplifier (SOA). The amplified VCSEL emission (output of the SOA) is sent to the OCT imaging system. As shown, the VCSEL output passes through a fiber polarization controller in order to align the polarization to the preferred orientation for maximum gain through the polarization-dependent SOA. Both pre-amplified and post-amplified VCSEL emissions are sent to an optical spectrum analyzer (not shown) to generate the tuning results below. Both static and high-speed time-dependent tuning voltages are applied via a high-voltage (HV) amplifier, which is driven by an arbitrary waveform generator.

22.4.2 First Generation Commercial 1,310 nm Devices

Our first generation commercial devices based on the structure described in the preceding sections demonstrate >100 nm tuning, with 110 nm being a typical value. Typical fiber-coupled power levels over the tuning range are 0.2–0.8 mW, prior to amplification, using pump power around 10 mW. Absorbed pump power is around half the incident pump power, or about 5 mW. These devices were first reported by Praevium and collaborators in mid 2011 [21]. Figure 22.12 shows these initial fiber-coupled tuning results, demonstrating 110 nm static tuning range with an applied bias of about 85 V. Initial devices also show MEMS resonance frequencies in the 300–400 kHz range with demonstrated axial scan rates of up to 760 kHz and excellent OCT images using amplified VCSEL output.

For commercial devices, the more relevant parameter is not static but dynamic tuning range, since devices will be operated under repetitive scanning at frequencies up to several hundred kHz. Furthermore, since amplification is employed prior

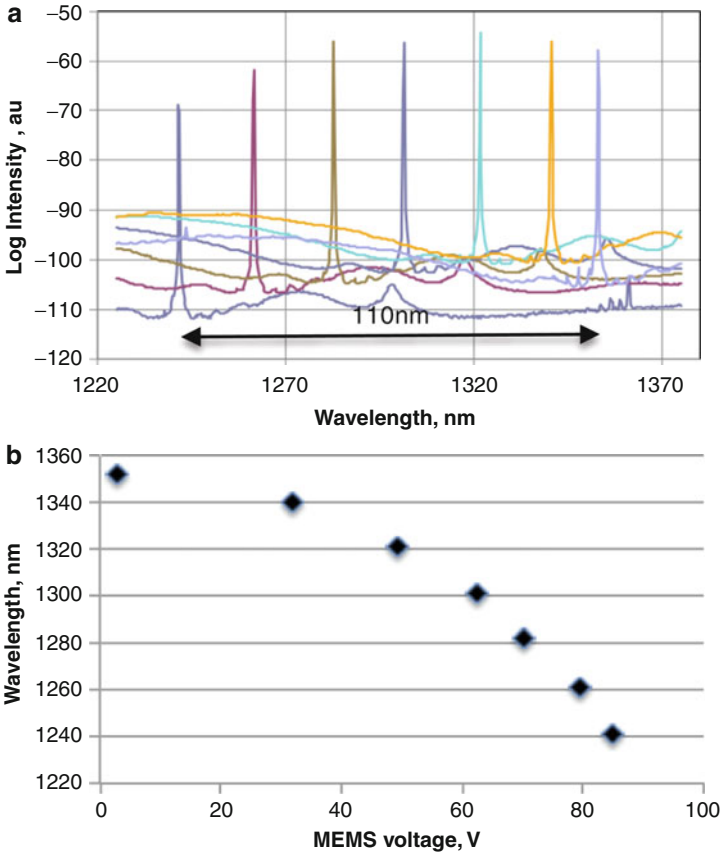

Fig. 22.12 Early tuning results from May 2011. 110 nm tuning (**a**) is achieved with about 85 V applied (**b**)

to OCT imaging, post-amplified dynamic spectral properties are the most critical. Figure 22.13 shows pre- and post-amplified time-averaged optical spectra under dynamic linearized sweeping at 200 kHz axial scan rate, on more recent devices based on a design similar to that used to obtain the results of Fig. 22.12. It is important to note that there is some spectral distortion in the time-averaged spectrum of Fig. 22.13, since the sweep is not perfectly linear and edges of the spectrum are emphasized more strongly as the suspended mirror slows before reversing direction. Nevertheless, Fig. 22.13 illustrates a significant improvement of 3-dB spectral bandwidth after amplification. Current devices show post-amplified 3-dB spectral bandwidth of up to 90 nm. The full tuning range is 110 nm and peak applied voltages are around 65 V. Amplified MEMS-VCSEL powers for these devices are typically >30 mW.

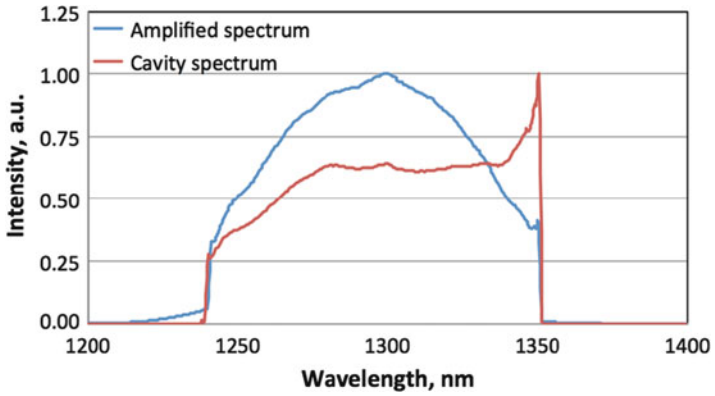

Fig. 22.13 Time-averaged pre-amplified (*red*) and post-amplified (*blue*) optical spectra under linearized wavelength scanning for devices with a design similar to that in Fig. 22.12. The post-amplified FWHM is near 90 nm

22.4.3 Next Generation Ultra-Broadband 1,310 nm Devices

Development progress since the first demonstration of >100 nm in 2011 has enabled expansion of the dynamic tuning range to 150 nm. These advancements have occurred as a result of increasing the cavity free spectral range and further optimization of the gain bandwidth and mirror reflectivity. This tuning range is close to that of the best external cavity lasers used in the research lab, such as the 160 nm reported for the FDML laser [2]. This result is significant, as prior to this demonstration, some questions remained as to the ability of VCSEL-based swept sources to compete with external cavity lasers on tuning range.

Figure 22.14 illustrates both the static and dynamic tuning properties of ultra-broadband VCSELs [19]. In Fig. 22.14a, the optical spectrum at an applied bias of ~12 V is shown as the right-most red spectrum in the figure. This spectrum shows laser emission at 1,372 nm along with a competing mode at 1,211 nm, yielding a 161 nm FSR for these devices. Application of a static voltage up to ~56 V pulls the mode across a stable and continuous static tuning range of 142 nm, illustrated by the overlaid spectra shown in Fig. 22.14a. Higher applied biases enable further tuning to 1,222 nm (covering a 148 nm range), though biases beyond ~56 V exceed the static snapdown voltage of the device. Figure 22.14b shows the theoretical and measured static wavelength as a function of the applied tuning voltage. The green curve of Fig. 22.14a shows the time-averaged optical spectrum under sinusoidal sweeping at 500 kHz, illustrating a 150 nm dynamic tuning range, which is the more relevant parameter for SS-OCT imaging. Note that this 500 kHz sweep rate enables bi-directional scanning at >1 MHz. These 150 nm devices can enable future VCSEL-based SS-OCT systems with improved axial resolution.

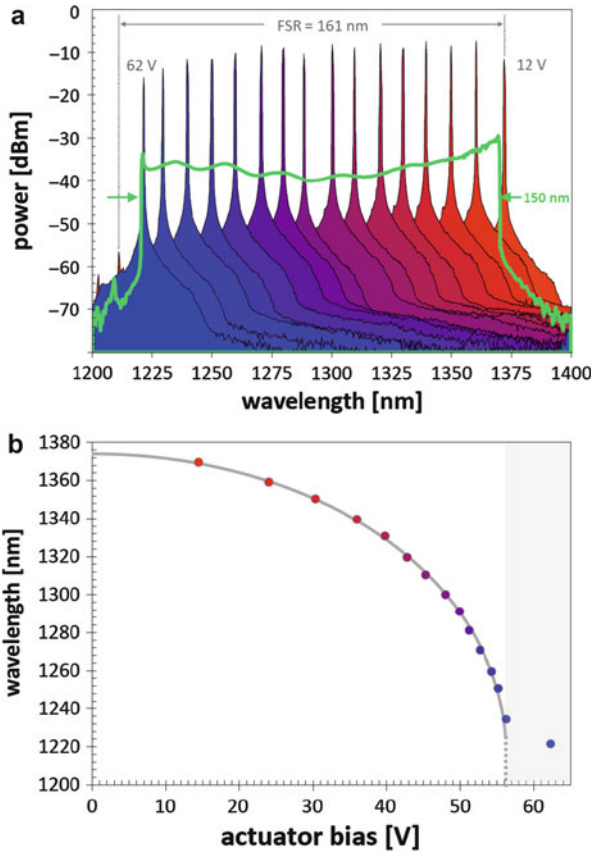

Fig. 22.14 (**a**) Static and dynamic tuning spectra of our ultrawidely tunable 1,310 nm MEMS-VCSEL. The long-wavelength (*red*) spectrum at 1,372 nm exhibits a competing mode at 1,211 nm, illustrating the 161 nm FSR of the cavity. The *green curve* represents the time-averaged spectrum under sinusoidal sweeping at 500 kHz. Both the static and dynamic spectra demonstrate continuous single-transverse and longitudinal mode lasing operation over a 150 nm span. The ripple in the integrated spectrum is due to the residual reflectance of the cleaved delivery fiber. (**b**) Emission wavelength vs. static tuning voltage corresponding to the spectra of (**a**). The shaded region beyond 56 V indicates the unstable regime for the actuator (Data reproduced with permission from Ref. [19])

22.4.4 1,050 nm Devices

The 1,310 nm devices reported first in mid-2011 were followed up by our report of the first 1,050 nm devices for ophthalmic imaging in early 2012 [20]. A subsequent publication [18] described device results in greater detail. Figure 22.2 illustrates the 1,050 nm device structure used for these devices. Figures 22.5a, b illustrate the tuning behavior of recent devices. The zero voltage emission wavelength occurs at 1,006 nm. Application of a small bias causes the device to switch to the longer wavelength mode at ~1,105 nm. Further increases in the applied voltage reduce the emission wavelength to ~1,010 nm before the snapdown instability at approximately 53 V inhibits further static tuning. Figure 22.15a illustrates an overlay of 11 spectra covering the >90 nm static tuning range, demonstrating single longitudinal and transverse mode operation over the entire span. A wavelength range of 100 nm, essentially equal to the free spectral range (FSR) of the cavity, can be accessed by dynamic tuning, as shown by the blue curve in Fig. 22.15a, which represents the time-averaged spectrum under repetitive sinusoidal sweeping at 200 kHz. This dynamic tuning range is, again, the relevant wavelength span for repetitively swept SS-OCT applications.

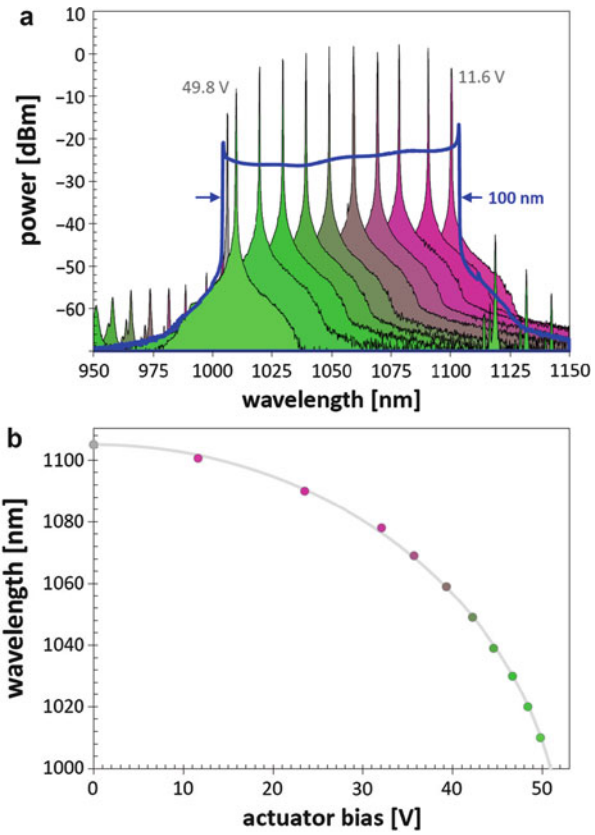

Fig. 22.15 (**a**) Eleven spectra at various actuator biases illustrate a >90 nm static tuning range, while the time-averaged (*blue*) spectrum illustrates a 100 nm dynamic tuning range, under 200 kHz sinusoidal sweeping, covering nearly one FSR. (**b**) Static emission wavelength as a function of the actuator voltage, corresponding to the spectra of (**a**) (Data reproduced with permission from Ref. [18])

The average fiber-coupled output power of 1,050 nm devices under full dynamic tuning is 0.5–1 mW, using pump powers from about 14 to 30 mW. Approximately 50 % of the pump power is absorbed, so absorbed powers are in the range of 7–15 mW. Similar devices have been integrated into ophthalmic imaging systems with collaborators at MIT, using optical amplification as in the 1,310 nm devices to boost the total output power into the ~20 mW range. Ophthalmic images obtained with these devices have demonstrated for the first time anterior eye, retinal, and whole eye imaging in a single SS-OCT instrument [4].

22.5 Additional OCT-Relevant Performance Parameters

22.5.1 Section Overview

The results of Sect. 22.4 demonstrated for the first time the ability of MEMS-VCSELs to access tuning ranges appropriate for SS-OCT at the relevant wavelengths. This demonstration of ~10 % fractional tuning range removed a primary

uncertainty with these devices, since prior to 2011, the maximum demonstrated fractional tuning range was 4.2 % and no MEMS-VCSELs of any sort existed at 1,050 and 1,310 nm. Demonstration of simultaneous high-speed and broadband tuning, at record axial scan rates in the MHz range, was also another significant achievement of these early efforts.

Validation of MEMS-VCSELs for SS-OCT, however, requires demonstration of a number of other stringent criteria not necessarily required for other applications. The ultimate validation of MEMS-VCSEL performance is the quality of OCT images obtained, which is the subject of other chapters of this book and briefly discussed in Sect. 22.6. In this section we touch on dynamic coherence length, transverse mode suppression, polarization stability, output power ripple, scan linearity, and variable speed operation, parameters that have a significant impact on OCT imaging quality.

22.5.2 Dynamic Coherence Length

The single-mode nature of MEMS-VCSELs suggests a very narrow static linewidth and long coherence length in the meter range. The fast cavity dynamics further suggest that this narrow linewidth can be maintained under dynamic operation. This fact is one of the most attractive motivations for applying MEMS-VCSELs in OCT.

Dynamic coherence length in OCT systems is typically measured by evaluating the system sensitivity as a function of imaging depth, as shown in the example measurement of Fig. 22.16. The dynamic coherence length is defined as twice the

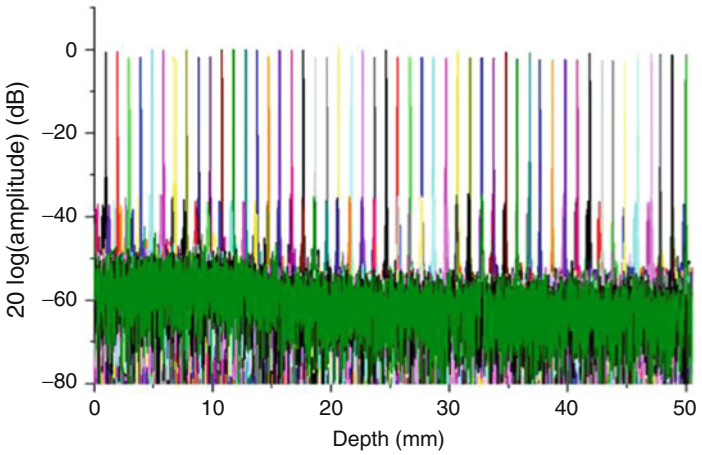

Fig. 22.16 OCT axial point spread function versus imaging depth in air, indicating minimal drop in sensitivity up to 50 mm depth. Measurement performed at 60 kHz uniaxial scan rate. The data shows that the coherence length is $\gg$10 cm. The measurement is detection bandwidth limited, and actual coherence length may be much larger for this device

imaging depth at which the signal sensitivity drops by a factor of 2, since light traverses the imaging depth twice upon reflection before being interfered with the reference beam. The measurement of dynamic coherence length is complicated by the need for increasingly high-speed detection electronics as sweep rate and coherence length is increased. Figure 22.16 shows a measurement using a swept MEMS-VCSEL with a 60 kHz unidirectional scan. As shown, negligible degradation of sensitivity is observed at 50 mm imaging depth in air, corresponding to $\gg$10 cm coherence length. The measurement of Fig. 22.16 remains detection limited, so the measured dynamic MEMS-VCSEL coherence length is even larger than measured. A more recent measurement of coherence length of the 1,060 nm MEMS-VCSEL source using different detection electronics has demonstrated >10 cm at up to 100 kHz axial scan rate [4]. This 10 cm value for 1,060 nm VCSELs compares with the 2 cm reported for a short external cavity 100 kHz swept source at 1,060 nm [5]. The long coherence length in our 1,050 nm MEMS-VCSELs has been validated in whole eye imaging [4]. Most recently, by reducing the axial scan rate and limiting tuning range to stay within the bandwidth of detection electronics, collaborators at MIT have demonstrated dynamic coherence length in excess of 1 m [43].

22.5.3 Transverse Mode Suppression and Output Power Ripple

MEMS-VCSELs, though they are single longitudinal mode devices, can have higher order transverse modes, which can create imaging artifacts. Current devices show >45 dB suppression over the tuning range. A minimum of ~40 dB is required for high-quality imaging, which is a requirement more stringent than many communications applications. The high SMSR in these devices is aided by optical pumping with a single-transverse mode pump beam.

Minimizing periodic output power variation or "ripple" is another critical OCT requirement, since ripple manifests itself as a spurious reflection plane in OCT images. Ripple arises from parasitic reflections in the laser or the package. Considerable development effort has been expended identifying and eliminating sources of ripple. This has resulted in recent commercial devices showing output power ripple values below 0.5 %.

22.5.4 Polarization Stability

Operation in a constant polarization state throughout the tuning range is ideal for commercial OCT-targeted VCSELs. Since our amplified MEMS-VCSELs use polarization-dependent amplification, polarization switching during tuning can lead to power dropouts and severe image degradation. Even in the case of polarization-independent amplification, multiple polarization states can create spectral broadening and degrade dynamic coherence length. The absence of

power dropouts in the amplified spectrum in Fig. 22.13, which used a polarization-dependent amplifier, demonstrates operation of devices in a constant polarization state throughout the tuning range. Another benefit of polarization stability is the ability to make polarization-sensitive OCT measurements [44].

Polarization control in tunable VCSELs has previously been addressed using a sub-wavelength grating [45] or intentionally induced stresses on the VCSEL chip to produce gain anisotropy [15]. Both of these methods have only been demonstrated over a limited tuning range, and suppression of switching in more widely tunable structures can present more challenges. Current state of the art devices show stable polarization over the entire 115 nm range. The factors affecting polarization in these new widely tunable structures are still under investigation, but we believe the combination of an optically pumped approach and internal stresses in the structure arising from local volume shrinkage in the fully oxidized mirror contribute to wideband polarization selection in current devices.

22.5.5 Scan Linearity and Variable Rate Scanning

Commercial OCT systems require linearized wavelength scanning to minimize the required detection bandwidth for a given axial scan rate and given tuning range. The electrostatic actuator used in our MEMS tuning structure is inherently nonlinear, since the suspended mirror displacement varies as the square of the applied voltage. However, the MEMS-VCSEL, like other MEMS-based tunable lasers, can be linearized through drive waveform pre-shaping. A variety of arbitrary drive waveforms have been investigated for scan linearization, and several successful waveforms have been designed. In addition to linearization, another desirable property for commercial OCT systems is the ability of a single source to be swept at a variety of scan rates and tuning ranges. OCT fringe frequency for a given scan rate increases with imaging range and tuning range, requiring faster fringe waveform sampling at long range. It is thus desirable to adjust scan rate and tuning range to tradeoff speed and resolution with depth for different imaging modes in one application with one laser source. Imaging of the human eye provides a good application example. Here, it is desirable to have ultrahigh axial scan rate up to >500 kHz for wide field retinal imaging and a lower axial scan rate of 50 kHz for whole eye imaging [4].

Figure 22.17 illustrates the capacity of a single 1,310 nm MEMS-VCSEL to operate over a wide variety of axial scan rates from 50 kHz to 1 MHz and to be linearized at 50–200 kHz rates. In this figure, the tuning range is held fixed at 115 nm, and a variety of drive waveforms are applied to achieve the desired wavelength trajectories. The top row of the figure illustrates the applied arbitrary waveform and the bottom row the wavelength response with time. The first three columns illustrate linearized scanning, including a unidirectional 100 kHz scan, a bi-directional 100 kHz scan, and a bi-directional 200 kHz scan, respectively. The final column illustrates sinusoidal scanning at 500 kHz, enabling bi-directional scanning at an axial scan rate of 1 MHz axial scan rate. More recent results have

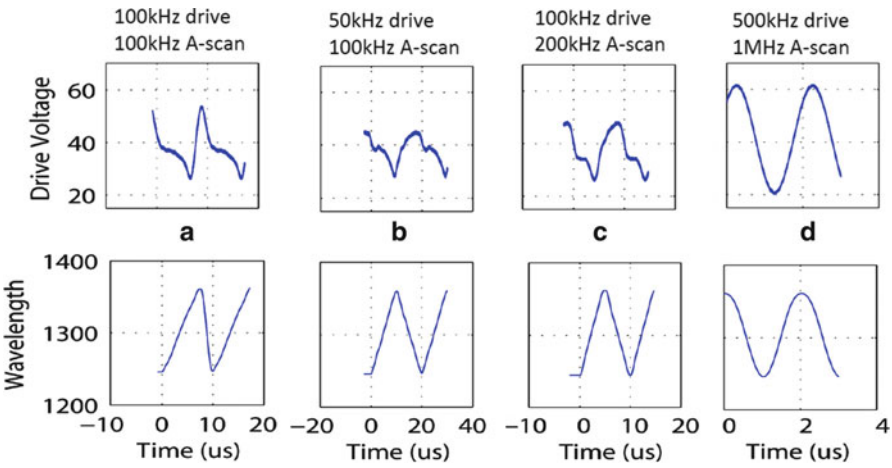

Fig. 22.17 Single VCSEL driven over 115 nm tuning range at a variety of axial scan rates. *Top row* of waveforms shows the applied arbitrary drive waveform, and the *bottom row* shows the measured wavelength response. Labels at *top* indicate the type of scanning achieved, including 100 kHz drive/100 kHz linearized uniaxial scan (**a**), 50 kHz drive/100 kHz linearized bi-directional scan (**b**), 100 kHz drive/200 kHz linearized bi-directional scan (**c**), and 500 kHz drive/1 MHz sinusoidal bi-directional scan (**d**)

extended this maximum axial scan rate to 1.2 MHz [20]. For the lower scan rates, one quantitative measure of linearity is the ratio of maximum slope in the wavelength scan to the ideal linear slope (excluding non-usable edges of the scan). For a sinusoid, this would yield a linearity of 1.57. Most recent linearized 1,310 nm MEMS-VCSELs can be driven to produce a typical linearity between 1.05 and 1.10 at 100 kHz axial scan rates.

22.6 Representative VCSEL-Based SS-OCT Images

The ultimate measure of the MEMS-VCSEL performance in an SS-OCT system is the quality of images produced. Other chapters of this book describe MEMS-VCSEL-based OCT system details and quantify imaging performance with VCSELs, and prior publications have shown a variety of images using 1,050 and 1,310 nm VCSELs operated at a variety of scan rates. These include retinal, anterior eye, and whole eye images using 1,050 nm MEMS-VCSELs at scan rates from 50 to 580 kHz [4] and anterior eye, finger, and leaf images using 1,310 nm MEMS-VCSELs [20].

Figures 22.18a–g show a representative sample of images obtained. Figures 22.18a–c [4] were obtained with a 1,050 nm MEMS-VCSEL-based system operating at 580 kHz axial scan rate. Figure 22.18a illustrates the long dynamic coherence length of the VCSEL in a single image capturing both the anterior eye and the retina. Figure 22.18b shows the volumetric image of the choroidal region from

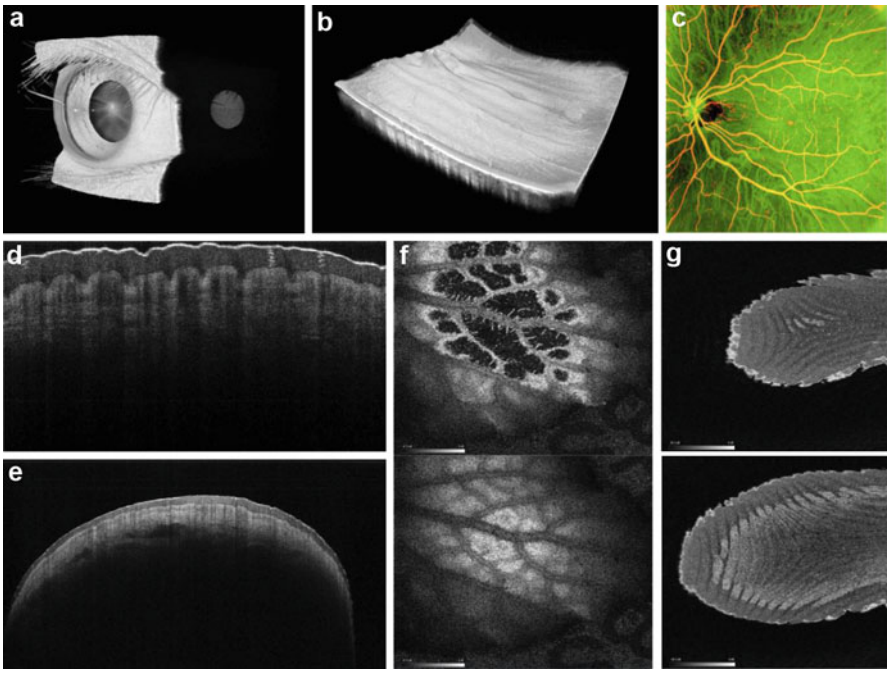

Fig. 22.18 Representative OCT images using 1,050 nm VCSEL (**a**–**c**) and 1,310 nm VCSEL (**d**–**g**). Full eye image showing anterior eye and retina in a single acquisition. (**b**) Volumetric image of choroidal region. (**c**) Choroidal and retinal vasculature superimposed and color coded, from the data of (**b**). (**d**) Finger cross section showing 4,096 axial scans over 5 mm depth at 1 MHz axial scan rate. (**e**) Finger cross section at 60 kHz uniaxial scan, showing blood vessel delineation. (**f**) En face plant leaf images using 300 × 340 axial scans over a field of 6 mm × 6 mm, acquired at 200 kHz axial scan rate. (**g**) OCT en face images of a finger pad consisting of 512 × 512 axial scans over 6.3 mm × 6.3 mm acquired at 400,000 axial scans per second

which the vascular cross section in Fig. 22.18c can be constructed. Figure 22.18c is a color-coded image representing an overlay of both retinal and choroidal vasculature systems and is similar to images obtained using ICG angiography but in a completely noninvasive MEMS-VCSEL-based OCT measurement requiring no injected dyes. Figures 22.18d–g illustrate images obtained with a 1,310 nm MEMS-VCSEL-based SS-OCT system. Figure 22.18d represents a human finger cross section consisting of 4,096 axial scans over 5 mm depth at 1 MHz axial scan rate. Figure 22.18e shows a finger cross section obtained at 60 kHz axial scan rate, showing clear delineation of blood vessels. Figure 22.18f illustrates en face images of a plant leaf using 300 × 340 axial scans over a field of 6 mm × 6 mm, acquired at 200 kHz axial scan rate. Figure 22.18g illustrates 512 × 512 axial scan en face images of a human finger pad over 6.3 × 6.3 mm, acquired at 400 kHz axial scan. The clarity, range, and resolution of these and other images acquired at a variety of scan rates provide the ultimate validation of MEMS-VCSEL technology for SS-OCT.

22.7 Conclusion

MEMS-VCSEL technology advances since 2011 have enabled unique gains in SS-OCT imaging performance, particularly in the achievable imaging speed and imaging range. VCSEL advances include the first demonstration of MEMS-VCSELs at the relevant OCT wavelength windows of 1,050 and 1,310 nm, the first demonstration of >100 nm tuning in MEMS-VCSELs at any wavelength, and the first demonstration of wide tuning in conjunction with several hundred kHz wavelength scanning operation. Integration of these devices into MEMS-VCSEL-based OCT systems has enabled >1 m imaging range, the first whole eye images of the human eye, and a 1.2 MHz axial line rate that is 3× faster than the fundamental un-buffered (no external fiber delays to copy the sweep) speed of the fastest competing swept sources with sensitivity high enough for imaging in vivo and ex-vivo [7, 8]. We note that an impressive 20 MHz axial scan rate has been obtained with the FDML laser using optical buffering and multiple spots [10], and similar approaches could be employed to further extend the axial scan rates of MEMS-VCSELs. The current maximum single-line sweep rate of the MEMS-VCSEL does not appear to be limited by laser dynamics, and higher speeds may be possible by changing MEMS actuator designs to increase mechanical resonance frequency to support higher frequency drive. Ultrahigh sweep rate operation will be especially important for applications which require en face OCT image generation because each en face pixel requires an axial scan. Aside from ophthalmic applications, long imaging range is also important for applications such as intravascular OCT, which requires imaging the entire circumference of arteries irrespective of catheter centration, and anatomic OCT, which involves profiling larger scale structures such as the upper airway.

A further advantage of the MEMS-VCSEL includes wavelength flexibility, and migration of the same technology to other wavelengths from 450 to 2,300 nm appears to be feasible. The recent demonstration of electrical [46] instead of optical pumping for VCSELs promises lower cost and miniaturization. Electrically pumped VCSELs have been demonstrated from wavelengths as short as 460 nm [47] to as long as 2,300 nm [48], suggesting extension of MEMS-VCSEL-based OCT to a wide variety of wavelengths limited only by the availability of semiconductor gain media.

The current tuning range of 150 nm at 1,310 nm is the largest reported for any MEMS-VCSEL and is comparable to the 160 nm reported for the FDML [2]. Further increase of tuning range to ~200 nm may be possible by increasing the number of quantum wells in the gain region, using a wider bandwidth top suspended mirror, and by further increasing the FSR. In addition, it should also be possible to multiplex two or more VCSELs with offset bandwidths in order to obtain increased sweep ranges and improve axial resolutions. Similar multiplexing approaches have been used with superluminescent diode light sources for OCT.

The MEMS-VCSEL continues to enable advances in imaging, including Doppler blood flow imaging [49], high-speed endoscopic imaging [50], hand-held retinal imaging [51], and chorio-capillaris and choroidal microvascular imaging with OCT

angiography [52]. These advances, coupled with lower cost and higher performance of emerging devices, suggest that the coming years may see an expanding array of new OCT applications.

Acknowledgment This work was supported by the National Cancer Institute grant R44CA101067, R01-CA075289-16; Air Force Office of Scientific Research contracts AFOSR FA9550-10-1-0063, FA9550-10-1-0551; and matching funds provided by Thorlabs. The content is solely the responsibility of the authors and does not necessarily represent the views of the Air Force or the National Cancer Institute of the National Institutes of Health.

References

1. R. Huber, M. Wojtkowski, K. Taira et al., Amplified, frequency swept lasers for frequency domain reflectometry and OCT imaging: design and scaling principles. Opt. Express **13**(9), 3513–3528 (2005)
2. D.C. Adler, Y. Chen, R. Huber et al., Three-dimensional endomicroscopy using optical coherence tomography. Nat. Photonics **1**(12), 709–716 (2007)
3. M.A. Choma, M.V. Sarunic, C.H. Yang et al., Sensitivity advantage of swept source and Fourier domain optical coherence tomography. Opt. Express **11**(18), 2183–2189 (2003)
4. I. Grulkowski, J.J. Liu, B. Potsaid et al., Retinal, anterior segment and full eye imaging using ultrahigh speed swept source OCT with vertical-cavity surface emitting lasers. Biomed. Opt. Express **3**(11), 2733–2751 (2012)
5. B. Potsaid, B. Baumann, D. Huang et al., Ultrahigh speed 1050 nm swept source/ Fourier domain OCT retinal and anterior segment imaging at 100,000 to 400,000 axial scans per second. Opt. Express **18**(19), 20029–20048 (2010)
6. R. Huber, D.C. Adler, J.G. Fujimoto, Buffered Fourier domain mode locking: unidirectional swept laser sources for optical coherence tomography imaging at 370,000 lines/s. Opt. Lett. **31**(20), 2975–2977 (2006)
7. R. Huber, M. Wojtkowski, J.G. Fujimoto, Fourier Domain Mode Locking (FDML): a new laser operating regime and applications for optical coherence tomography. Opt. Express **14**(8), 3225–3237 (2006)
8. W. Wieser, T. Klein, D.C. Adler et al., Extended coherence length megahertz FDML and its application for anterior segment imaging. Biomed. Opt. Express **3**(10), 2647–2657 (2012)
9. T. Klein, W. Wieser, C.M. Eigenwillig et al., Megahertz OCT for ultrawide-field retinal imaging with a 1050 nm Fourier domain mode locked laser. Opt. Express **19**(4), 3044–3062 (2011)
10. W. Wieser, B.R. Biedermann, T. Klein et al., Multi-megahertz OCT: high quality 3D imaging at 20 million A-scans and 4.5 GVoxels per second. Opt. Express **18**(14), 14685–14704 (2010)
11. M.C.Y. Huang, Y. Zhou, C.J. Chang-Hasnain, A nanoelectromechanical tunable laser. Nat. Photonics **2**(3), 180–184 (2008)
12. F.M. di Sopra, H.P. Zappe, M. Moser et al., Near-infrared vertical-cavity surface-emitting lasers with 3-MHz linewidth. IEEE Photon. Technol. Lett. **11**(12), 1533–1535 (1999)
13. H. Halbritter, C. Sydlo, B. Kogel et al., Linewidth and chirp of MEMS-VCSELs. IEEE Photon. Technol. Lett. **18**(17–20), 2180–2182 (2006)
14. M.S. Wu, E.C. Vail, G.S. Li et al., Tunable micromachined vertical cavity surface emitting laser. Electron. Lett. **31**(19), 1671–1672 (1995)
15. Y. Matsui, D. Vakhshoori, W. Peidong et al., Complete polarization mode control of long-wavelength tunable vertical-cavity surface-emitting lasers over 65-nm tuning, up to 14-mW output power. IEEE J. Quantum Electron. **39**(9), 1037–1048 (2003)
16. M. Lackner, M. Schwarzott, F. Winter et al., CO and CO_2 spectroscopy using a 60 nm broadband tunable MEMS-VCSEL at $\sim$1.55 μm. Opt. Lett. **31**(21), 3170–3172 (2006)

17. T. Svensson, M. Andersson, L. Rippe et al., VCSEL-based oxygen spectroscopy for structural analysis of pharmaceutical solids. Appl. Phys. B Lasers Opt. **90**(2), 345–354 (2008)
18. V. Jayaraman, G.D. Cole, M. Robertson et al., Rapidly swept, ultra-widely-tunable 1060 nm MEMS-VCSELs. Electron. Lett. **48**(21), 1331–1333 (2012)
19. V. Jayaraman, G.D. Cole, M. Robertson et al., High-sweep-rate 1310 nm MEMS-VCSEL with 150 nm continuous tuning range. Electron. Lett. **48**(14), 867–9 (2012)
20. B. Potsaid, V. Jayaraman, J.G. Fujimoto, et al., MEMS tunable VCSEL light source for ultrahigh speed 60kHz – 1MHz axial scan rate and long range centimeter class OCT imaging. Proc. SPIE Int. Soc. Opt. Eng. **8213**, 82130M (2012)
21. V. Jayaraman, J. Jiang, H. Li, et al., OCT imaging up to 760 kHz axial scan rate using single-mode 1310 nm MEMS-tunable VCSELs with >100 nm tuning range. CLEO: 2011 – Laser Science to Photonic Applications, pp. 1–2 (2011)
22. V. Jayaraman, T.J. Goodnough, T.L. Beam et al., Continuous-wave operation of single-transverse-mode 1310-nm VCSELs up to 115 degrees C. IEEE Photon. Technol. Lett. **12**(12), 1595–1597 (2000)
23. M.H. MacDougal, P.D. Dapkus, A.E. Bond et al., Design and fabrication of VCSELs with Al_xO_y-GaAs DBRs. IEEE J. Sel. Top. Quantum Electron. **3**(3), 905–915 (1997)
24. C. Gierl, T. Gruendl, P. Debernardi et al., Surface micromachined tunable 1.55 μm-VCSEL with 102 nm continuous single-mode tuning. Opt. Express **19**(18), 17336–17343 (2011)
25. S.W. Corzine, R.S. Geels, J.W. Scott et al., Design of Fabry-Perot surface-emitting lasers with a periodic-gain structure. IEEE J. Quantum Electron. **25**(6), 1513–1524 (1989)
26. C.J. Chang-Hasnain, High-contrast gratings as a new platform for integrated optoelectronics. Semicond. Sci. Technol. **26**(1), 11 (2011)
27. D.I. Babic, Y.C. Chung, N. Dagli et al., Modal reflection of quarter-wave mirrors in vertical-cavity lasers. IEEE J. Quantum Electron. **29**(6), 1950–1962 (1993)
28. S.W. Corzine, L.A. Coldren, Theoretical gain in compressive and tensile-strained InGaAs/InGaAsP quantum wells. Appl. Phys. Lett. **59**(5), 588–590 (1991)
29. S.W. Corzine, R.H. Yan, L.A. Coldren, Theoretical gain in strained InGaAa/AlGaAs quantum-wells including valence-band mixing effects. Appl. Phys. Lett. **57**(26), 2835–2837 (1990)
30. P.J.A. Thijs, L.F. Tiemeijer, J.J.M. Binsma et al., Progress in long-wavelength strained-layer InGaAsP quantum-well semiconductor-lasers and amplifiers. IEEE J. Quantum Electron. **30**(2), 477–499 (1994)
31. R.S. Geels, S.W. Corzine, L.A. Coldren, InGaAs vertical-cavity surface-emitting lasers. IEEE J. Quantum Electron. **27**(6), 1359–1367 (1991)
32. H. Hatakeyama, T. Anan, T. Akagawa et al., Highly reliable high-speed 1.1-mu m-range VCSELs with InGaAs/GaAsP-MQWs. IEEE J. Quantum Electron. **46**(6), 890–897 (2010)
33. C.E. Zah, R. Bhat, B.N. Pathak et al., High-performance uncooled 1.3-um Al(x)Ga(y)In(1-x-y)As/InP strained-layer quantum-well lasers for subscriber loop applications. IEEE J. Quantum Electron. **30**(2), 511–523 (1994)
34. A. Caliman, A. Mereuta, G. Suruceanu et al., 8 mW fundamental mode output of wafer-fused VCSELs emitting in the 1550-nm band. Opt. Express **19**(18), 16996–17001 (2011)
35. B. Kogel, K. Zogal, S. Jatta, et al., Micromachined tunable vertical-cavity surface-emitting lasers with narrow linewidth for near infrared gas detection. Proc. SPIE Int. Soc. Opt. Eng., **7266**, 72660O (2008)
36. C.J. Chang-Hasnain, Tunable VCSEL. IEEE J. Sel. Top. Quantum Electron. **6**(6), 978–987 (2000)
37. M. Bao, H. Yang, Squeeze film air damping in MEMS. Sensors Actuators A Phys **136**(1), 3–27 (2007)
38. K.L. Turner, P.G. Hartwell, N.C. MacDonald, Multi-dimensional MEMS motion characterization using laser vibrometry. *Digest of Technical Proceedings: transducers, '99: the 10th International Conference on Solid State Sensors and Actuators*, Sendai, Japan. pp. 1144–1147 (1999)
39. C. Rembe, R. Kant, R.S. Muller, Optical measurement methods to study dynamic behavior in MEMS. Proc. SPIE Int. Soc. Opt. Eng. **4400**, 127–137 (2001)

40. G.D. Cole, E. Behymer, T.C. Bond et al., Short-wavelength MEMS-tunable VCSELs. Opt. Express **16**(20), 16093–16103 (2008)
41. A. Black, A.R. Hawkins, N.M. Margalit et al., Wafer fusion: materials issues and device results. IEEE J. Sel. Top. Quantum Electron. **3**(3), 943–951 (1997)
42. J.J. Dudley, D.I. Babic, R. Mirin et al., Low-threshold, wafer fused long-wavelength vertical-cavity lasers. Appl. Phys. Lett. **64**(12), 1463–1465 (1994)
43. I. Grulkowski, J.J. Liu, B. Potsaid, et al., High-Precision, high-accuracy ultralong-range, swept source optical coherence tomography using vertical cavity surface emitting laser light source. Opt. Lett. **38**(5), 673–675 (2013)
44. B. Baumann, C. WooJhon, B. Potsaid et al.. Swept source/ Fourier domain polarization sensitive optical coherence tomography with a passive polarization delay unit. Opt. Express **20**(9), 10229–41 (2012)
45. M. Ortsiefer, M. Goerblich, Y. Xu et al., Polarization control in buried tunnel junction VCSELs using a birefringent semiconductor/dielectric subwavelength grating. IEEE Photon. Technol. Lett. **22**(1), 15–17 (2010)
46. V. Jayaraman, D.D. John, C. Burgner, et al., Recent Advances in MEMS-VCSELs for High Performance Structural and Functional SS-OCT Imaging. Proc. SPIE Int. Soc. Opt. Eng. 8934 (2014)
47. T.-C. Lu, C.-C. Kao, H.-C. Kuo et al., CW lasing of current injection blue GaN-based vertical cavity surface emitting laser. Appl. Phys. Lett. **92**(14), 141102 (2008)
48. G. Boehm, A. Bachmann, J. Rosskopf et al., Comparison of InP- and GaSb-based VCSELs emitting at 2.3 mu m suitable for carbon monoxide detection. J. Cryst. Growth **323**(1), 442–445 (2011)
49. C. WooJohn, B. Potsaid, V. Jayaraman, et al., Phase-sensitive swept source optical coherence tomography imaging of the human retina with a vertical cavity surface-emitting laser light source. Opt. Lett. **38**(3), 338–340 (2013)
50. T.H. Tsai, B. Potsaid, Y.K. Tao, et al., Ultrahigh speed endoscopic optical coherence tomography using micromotor imaging catheter and VCSEL technology. Biomed. Opt. Express **4**(7), 1119–1132 (2013)
51. C.D. Lu, M.F. Kraus, B. Potsaid et al., Handheld ultrahigh speed swept source optical coherence tomography instrument using a MEMS scanning mirror. Biomed Opt. Express **5**(1), 239–311 (2014)
52. W Choi, K.J. Mohler, B. Potsaid et al. Choriocapillaris and Choroidal Microvasculature Imaging with Ultrahigh Speed OCT Angiography. PLOS One **8**(12), e81499 (2013)

Akinetik Swept Sources

23

Michael Minneman, Jason Ensher, Michael Crawford, Marco Bonesi, Behrooz Zabihian, Paul Boschert, Erich Hoover, Dennis Derickson, Brian E. Applegate, Thomas Milner, and Wolfgang Drexler

Keywords

Akinetic • All-semiconductor • Coherence length • FDML • Insight • MEMS • OCT • Phase repeatability • Phase sensitive OCT • Phase stability • Power profile • Programmable laser • PS-OCT • RIN • Sliding RIN • Swept • Swept laser • Swept source • Trigger jitter • Tunable laser • VCSEL • Vernier tuned • Volumetric • VT-DBR

23.1 Introduction

Optical coherence tomography (OCT) [1, 2] is one of the fastest-growing medical imaging procedures. It has undergone three generations; the third and rapidly growing generation produces very high-quality images and to do so requires a swept-laser source at its core [3, 4].

M. Minneman (✉) • J. Ensher • M. Crawford • P. Boschert • E. Hoover
Insight Photonic Solutions, Lafayette, CO, USA
e-mail: mminneman@sweptlaser.com

M. Bonesi • B. Zabihian
Medical University of Vienna, Vienna, Austria

D. Derickson
California Polytechnic State University, San Luis Obispo, CA, USA

B.E. Applegate
Department of Biomedical Engineering, Texas A&M University, College Station, TX, USA

T. Milner
University of Texas, Austin, TX, USA

W. Drexler
Center for Medical Physics and Biomedical Engineering, Medical University of Vienna, General Hospital Vienna, Vienna, Austria

© Springer International Publishing Switzerland 2015

W. Drexler, J.G. Fujimoto (eds.), *Optical Coherence Tomography*,
DOI 10.1007/978-3-319-06419-2_4_24

An ideal swept-wavelength laser for OCT is intended to sweep over a wide wavelength range in a perfectly linear-in-frequency manner while maintaining low relative intensity noise (RIN), low side modes, and adequate coherence length—all at a speed that supports the imaging requirements without compromise [5]. A number of approaches have been utilized to build lasers for OCT, including ring lasers [6], grating-based Littman-Metcalf [7–10], MEMS [11–13], polygon mirror [14, 15] pump/VCSEL/MEMS/circulator/SOA [16, 17], crystal deflection [18], FDML [19, 20], DFB arrays [21], and resonant-sine lasers [22–24]. Mechanical movement of the optical filter elements to control the laser wavelength scan has been the basis of all commercial swept lasers, but this movement is often in direct opposition to these image quality goals due to the requisite creation and depletion of momentum and the hysteresis inherent to such mechanical systems. In addition, the resulting relatively long cavity lengths and the many optical elements often results in the cavity instability and vibration instability of typical mechanical systems and the potential for extraneous reflections. Development and implementation of all-semiconductor akinetic laser technology allows these limitations to be overcome.

The term "akinetic" describes absence of movement in a system. An all-semiconductor laser uses an integrated semiconductor optoelectronic design approach without the use of coupling to an external cavity—the only things moving are photons and electrons.

With the advent of akinetic all-semiconductor lasers, these example performance parameters are improved in most categories [25, 26]. The sweep flexibility of the akinetic laser is software driven. The superior line width and spectral performance is a natural outcome of the very short waveguide design. The all-semiconductor construction may allow for further advancements enabling improved OCT imaging and new swept-source OCT (SS-OCT) imaging methodologies.

The semiconductor wafer-scale production nature of the laser also foretells a day in the not-too-distant future where the cost of the laser drops by an order of magnitude [27–29], enabling implementation of OCT to a broader range of imaging and scientific applications [30].

This chapter describes the advantages and compromises of using all-electronic wavelength tuning in conjunction with a semiconductor chip implementation of a swept-wavelength OCT source.

23.2 History of All-Semiconductor Akinetic Lasers

Some of the first work to create a widely tunable all-semiconductor laser was by Professor Larry Coldren at the University of California Santa Barbara [31] in the late 1980s. After some years developing the technology at UCSB [32], Professor Coldren and his team founded the company Agility, which spent over $100 M US to develop widely tunable semiconductor laser technology which is now an indispensable building block for telecommunications [33]. No swept-wavelength products

were developed as a result of this effort, but the widely tunable products went on to dominate the telecommunications market for a long period. Work was being conducted by Syntune [34], Santur [35], and Oclaro [36] on similar semiconductor widely tunable lasers in a similar timeframe.

Professor Kohji Obayashi of Kitasato University did substantial work on adapting single-chip widely tunable lasers for wavelength sweeping. This work produced important results [37–41] and initial OCT images.

Companies such as Smart Fibres [42] were able to develop and commercialize slowly tuning swept lasers utilizing all-semiconductor technology. Additionally, Luna Technologies [43] and AXSUN Technologies [44] similarly adapted semiconductor technology, but these solutions were neither all-semiconductor nor were they akinetic.

Professor Dennis Derickson of California Polytechnic State University had been deeply involved in the development of traditional kinetic swept lasers at HP and then later at Agilent Technologies [45]. Dr. Derickson's work was the first to envision methodologies which would lead to the development and commercialization of all-semiconductor akinetic swept-wavelength lasers [46] with high repetition rates, narrow OCT system point spread functions (PSFs), and long coherence lengths. Working in conjunction with Insight Photonic Solutions, Professor Derickson had a strong role in developing essential techniques and approaches utilized for OCT applications of these akinetic laser designs.

The first commercial swept all-semiconductor akinetic source was developed and commercialized by Insight Photonic Solutions of Boulder, Colorado, USA, in 2012 [25, 26, 47].

Vertical cavity surface emitting laser (VCSEL)-based fixed lasers are all-semiconductor. However, because of the inclusion of a separate pump laser, external circulator, moving microelectromechanical (MEMS) tuning element, and necessary external amplifier with the VCSEL cavity for swept lasers, they do not comprise an all-semiconductor solution, are not akinetic, and will not be considered in this chapter.

23.3 Details of All-Semiconductor Akinetic Swept-Laser Technology

All-semiconductor akinetic laser technology has impacts on most aspects of performance of a swept source OCT system (SS-OCT). A conceptual OCT system diagram is shown in Fig. 23.1. Table 23.1 introduces some of the key performance parameters for the OCT swept source laser of Fig. 23.2 and provides a comparison to other common approaches.

In this section the akinetic laser's performance extant in early 2013 will be explored, and how the performance impacts OCT system performance will be discussed. It is anticipated that capabilities will continue to advance as the all-semiconductor laser design and implementation continues to mature.

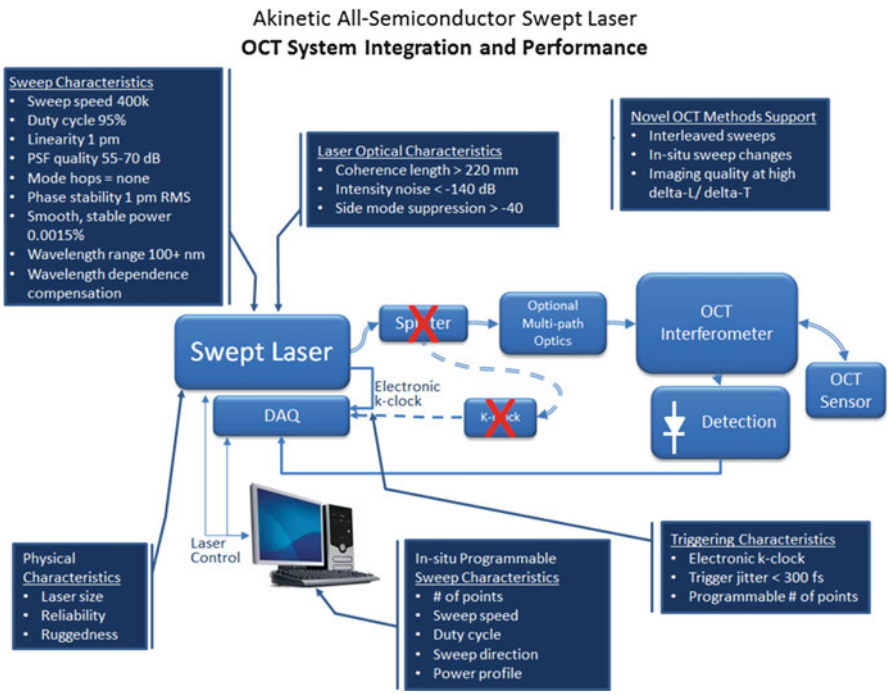

Fig. 23.1 Overall OCT system block diagram with akinetic all-semiconductor laser. Callouts note key system parameters of consideration when utilizing an all-semiconductor akinetic source. An all-semiconductor laser allows for simplification of the OCT system by providing a linear sweep, an electronic k-clock for triggering data acquisition, and programmability of system/laser parameters

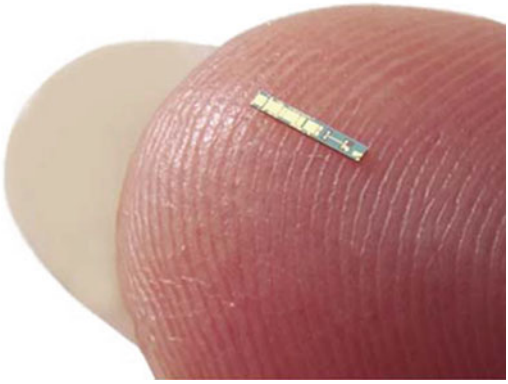

Fig. 23.2 The all-semiconductor akinetic approach promises small, inexpensive swept lasers enabling excellent image quality

Table 23.1 Comparison of characteristics of various swept laser approaches, including akinetic, mechanically tuned external cavity and MEMS-tuned external cavity

Swept laser technology characteristics			
Performance parameter	Akinetic monolithic cavity optoelectronic integrated design	Mechanically tuned external cavity	MEMS-tuned external cavity (micro-electromechanical)
Maximum sweep Repetition rate	Limited by laser diode resistance capacitance time constant product	Limited by mechanical factors and electrical drive interface	Limited by mechanical factors and electrical drive interface
Coherence length and associated spectral line width	Short optical cavity length results in single longitudinal mode operation and long coherence length	Most often multiple longitudinal mode due to long cavity length	Generally smaller cavity length and possible single longitudinal mode operation
Sweep repetition rate adjustability	Continuously adjustable	Typically fixed	Typically fixed
Power output	Moderate	Highly design dependent	Highly design dependent
Sweep to sweep power repeatability	Actively controlled, highly repeatable	Typically determined by gain profile of device	Typically determined by gain profile of device
Size	Diode laser package plus driver electronics	Typically needs to accommodate several packaged devices and interconnections	Typically has several packaged devices and interconnections
Sweep linearity	Controlled by accuracy of tuning tables and software algorithms	Sweep linearity often limited by momentum of mechanical tuning structure	Controlled by accuracy of tuning tables and software algorithms
Sweep drift over time	Controlled by long-term aging of semiconductor active region and internal system recalibration mechanism	Affected by mechanical wear and mechanical flexure aging	Effected by mechanical wear and mechanical flexure aging
Phase stability/ wavelength repeatability	Lack of kinetic movement with all-electronic control supports high repeatability	Mechanical hysteresis and acceleration limit repeatability	Mechanical hysteresis and acceleration and MEMS flexure non-idealities limit repeatability

23.3.1 Coherence Length/Imaging Depth Range

This section addresses achievable coherence length. In a later section on imaging depth range and multipath imaging, the application of longer coherence length on OCT will be investigated.

Long coherence length is a key factor in the following OCT conditions:

- Facilitating deep imaging, (such as anterior eye segment, full axial eye length OCT)

- Allowing for distance variation between the probe and the tissue (such as esophageal and lower GI imaging or in certain OCT-guided surgery applications)
- Enabling advanced OCT measurement techniques, such as superimposed multipath OCT, polarization-sensitive OCT [48], or phase-sensitive OCT [49]
- Accommodating differing length sensors or allowing less expensive sensors that are differing in length

Typical obstacles to long coherence length are finesse of the cavity and time-based shifting of the center wavelength [50]. The all-semiconductor laser cavity is short (~2 mm in length) and monolithically constructed within the semiconductor, minimizing the mechanical variation that might limit coherence length (Fig. 23.3).

The coherence length, z_c, is related to the full-width at half maximum (FWHM) instantaneous line width of a Gaussian profile laser, δλ, via [51].

$$z_c \approx 0.44 \frac{\lambda_0^2}{\delta\lambda} \tag{23.1}$$

The mirror penetration inherent in the all-semiconductor laser's distributed Bragg reflector (DBR)-like structure increases the finesse of the cavity by a factor of approximately nine times, resulting in a narrow line width. The small dimensions of the laser cavity, and the fact that the entire cavity is on a single rigid structure, substantially reduce cavity length variation.

23.3.1.1 Coherence Length Performance

An example coherence length measurement is shown in Fig. 23.4. The measurement shows the point spread function (PSF) as a function of imaging depth range Fig. 23.5.

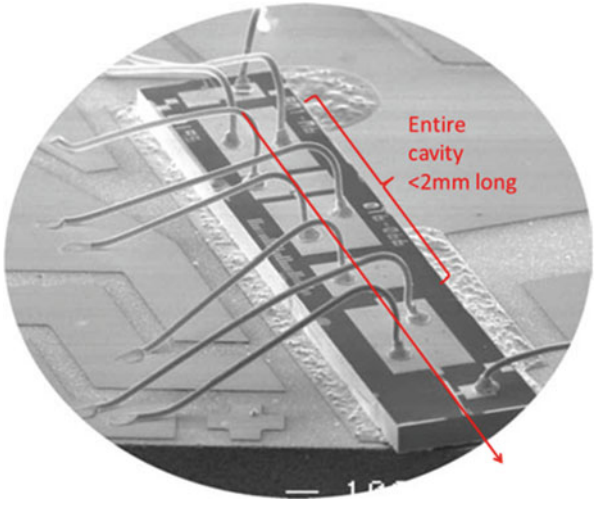

Fig. 23.3 SEM image of the bonded laser chip. The optical path is less than 2 mm long and in a single mechanical part, reducing cavity variation and leading to high coherence length, as well as eliminating the typical inter- and intracavity reflections that can create ghosting with other swept lasers

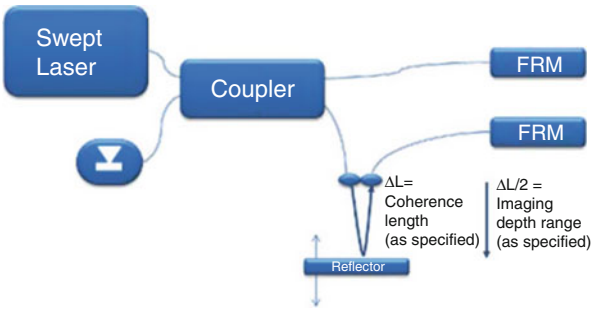

Fig. 23.4 Coherence length test apparatus. The swept wavelength laser is split into two beams with a fiber directional coupler. The two coupler output ports are coupled into Faraday rotation mirrors (FRM to reduce polarization dependency) [52]. One of the two arms consists of a movable reference reflector that allows for path length adjustment in this Michelson interferometer configuration. Finally the reflected beams are added together in the coupler and the combined beam is detected by a photodetector. The interference of the signal in the receiving photodetector is used to analyze coherence length [53]

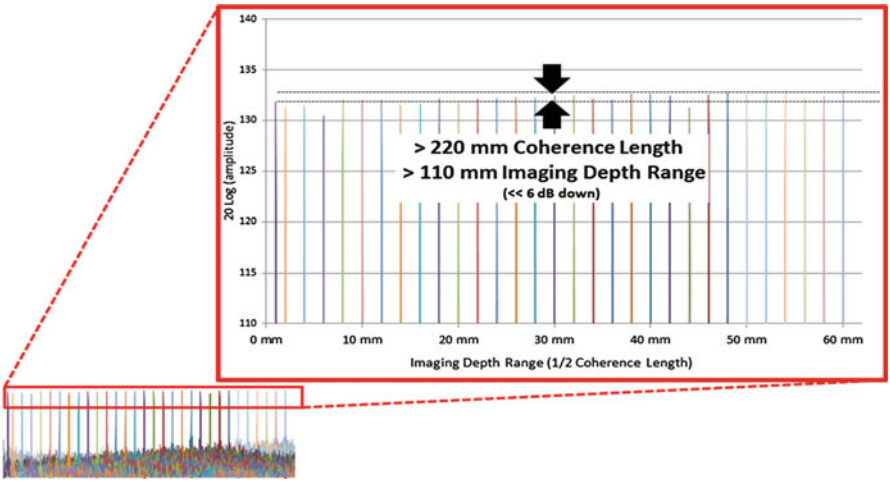

Fig. 23.5 Coherence length test data confirmed at least 220 mm at both 1,310 and 1,550 nm, 8 kHz to at least 320 kHz sweep rate

The PSF drops off very slowly with imaging depth. The resulting coherence length is in excess of 220 mm (~8.6 in., line width of 1.3 GHz, or 7.7 pm line width at 1,310 nm), even at sweep repetition rates up to at least 320 kHz.

The two most common ways to measure coherence length is to look for the −3 dB reduction of the amplitude of interferogram from a fixed reflector or to look for the −6 dB roll-off point of the point spread function (PSF) for the same signal [54, 55].

Another factor that can change coherence length in some lasers is the sweep rate. Typically, a faster sweep rate implies a lower coherence length. Due to the lack of

physical motion, sweep rate has only a weak effect on the coherence length of the all-semiconductor laser. As such, the same coherence length is obtained whether running at 4 k sweeps per second (sps) or to beyond 320 k sps.

23.3.1.2 Coherence Homogeneity in Different Wavelength Portions of the Sweep

Kinetic swept lasers often have a characteristic sweep rate that varies significantly over the duration of the sweep. This change in sweep rate and nonlinearity often leads to the nonhomogeneous coherence length across the sweep. However, no discernible difference in the coherence length at the beginning, middle, or ending portions of the sweep in the akinetic swept laser has been observed.

23.3.1.3 User-Adjusted Coherence Length

User-adjusted coherence length, an upcoming function for the akinetic laser, illustrates a unique characteristic of the laser: it is a software platform allowing detailed control over the laser's behavior. One of the implications of this control is that the coherence length can be adjusted with software. This capability can allow coherence length tuning to reduce unwanted signals in the OCT images caused by multiple reflections [56].

23.3.1.4 Imaging Depth Range Should Be Limited by Nyquist, Not Limited by the Laser

In high-speed systems with all-semiconductor swept lasers, it is increasingly likely that imaging depth range will be constrained by the Nyquist frequency limit of the detection of the interferogram [57] rather than by the long coherence length. One must also ensure that the detection amplifier bandwidth does not further limit the useful imaging depth range. Figure 23.6 shows imaging depth range as a function of sweep repetition rate for a 1,310 nm swept wavelength laser at various sweep conditions. These plots show that the imaging depth is often limited by the sampling rate of the receiver and not the coherence length of the swept laser. For longer coherence lengths at higher speeds, the sweep width is reduced to ensure the return frequencies were below the Nyquist limit.

23.3.2 Sweep Speed

There are a number of reasons that rapid laser sweep speed can be important for OCT. These include the following:

- Reducing blur from movement [58]
- Enabling high-resolution imaging
- Enabling 3D volumetric imaging [59–61]
- Higher time resolution in 4D imaging [62]
- Reducing measurement time needed, thus reducing patient impact

Experimental data shows that moving from any wavelength to an adjacent wavelength with the all-semiconductor laser takes ~2 ns. This measurement was

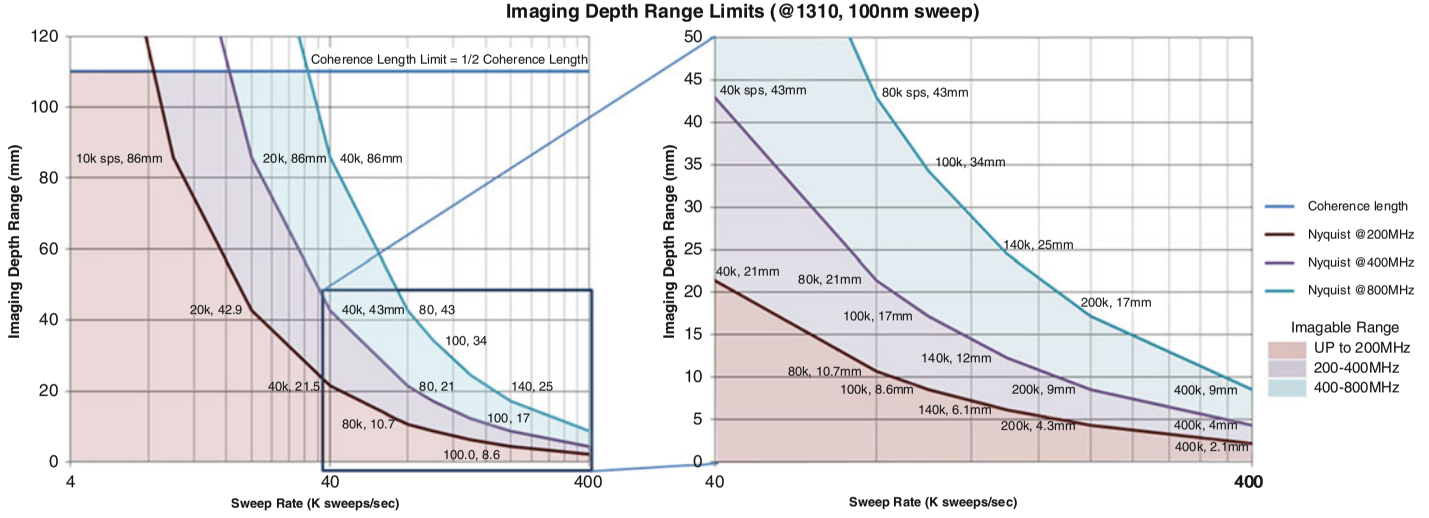

Fig. 23.6 A good laser will allow the imaging range to be limited by Nyquist, not the coherence length of the laser. The charts indicate the maximum imaging depth range due to Nyquist limits at different sweep rates, with curves for different measurement rates (different colored plots). Also shown is the coherence length limit. *Shaded* areas indicate combinations of measurement rate, sweep rate, and imaging depth range that are valid for imaging. The right-hand chart zooms in on short imaging depth range for clarity

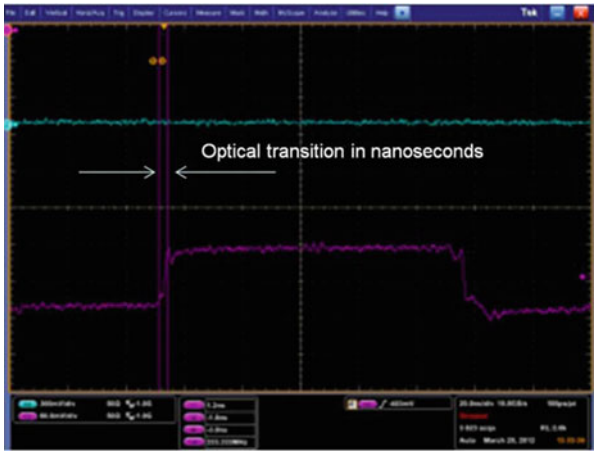

Fig. 23.7 High-speed oscilloscope trace showing full optical transition in <2.5 ns

obtained using a reference interferometer with known free spectral range as a frequency-to-amplitude converter. The resulting photo-detected signal was then measured with a high-speed oscilloscope. The measured time for the wavelength of the laser to change as a result of a step change in the control currents to the laser cavity is shown in Fig. 23.7. An amplitude change in the light transmitted through the interferometer corresponds to a wavelength change in the output of the laser. In the measurement shown, a step change in current occurring over 2.5 ns creates a step change in wavelength in approximately 2.5 ns.

Akinetic laser module designs in early 2013 can drive the laser up to 400,000,000 wavelength points per second. This can yield up to roughly 400,000 A-scans per second with 1,000 points per sweep or 2,000 points at 200,000 sweeps per second. Unlike some mechanically driven lasers, the speed is software controlled. The akinetic laser can be programmed for any speeds over a range from 4,000 to 400,000 sweeps per second. The low repetition rate value of 4,000 sweeps per second is not a fundamental limitation and could be made arbitrarily low.

In lab experiments, all-semiconductor lasers have been demonstrated at 1 million sweeps per second, thus ensuring a growth path with akinetic technology for faster future sweep rates to enable fast, high-resolution 3D imaging. For the longer term, it is believed that the akinetic technology can be pushed to roughly 2 million sweeps per second.

23.3.3 Duty Cycle

The akinetic semiconductor laser's fast tuning from any wavelength to any other wavelength means that the time from the end of a sweep to the beginning of a sweep is short, permitting a high duty cycle with little dead time between sweeps.

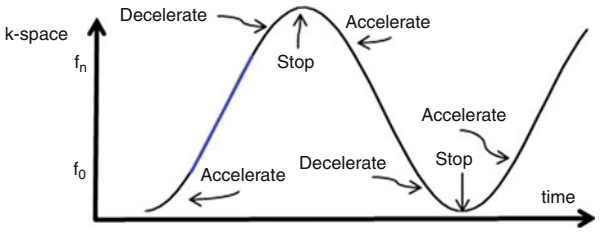

Fig. 23.8 Mechanically tuned lasers transition through accelerate/decelerate cycles, generating and dissipating momentum, that are not pertinent for akinetic lasers

Historically, achieving a sweep with a swept-wavelength laser required generating and dissipating momentum in a mechanical tuning mechanism [25]. Mechanically tuned lasers must start moving from an initial position of a physical tuning actuator, accelerate the actuator (building momentum), maintain the actuator tuning rate for the useful part of the sweep, decelerate the actuator, stop, reaccelerate, and so on (Fig. 23.8).

With some mechanical lasers, portions of this accelerate-decelerate cycle can be expedited but not eliminated [63], resulting in only a portion of the sweep that is actually useful for imaging. In the past, delays in the data acquisition system made this delay inconsequential because it took time to get the data transferred. In today's data acquisition, however, system measurement is virtually continuous. With these streaming-type data acquisition systems, high duty cycle afforded by the all-semiconductor laser increases total throughput and imaging speed (Fig. 23.9).

Because duty cycle is software controlled, it is adjustable. The duty cycle can be set to almost any value from 5 % to 95 %.

23.3.4 Linearity and k-Clock

23.3.4.1 Electronic k-Clock

Linear frequency (k-space) data is a requirement for swept source OCT applications. Mechanically tuned swept lasers often lack sufficient linearity of optical frequency versus time. Thus, most swept lasers require an external optical k-clock for variable-rate clocking of the data acquisition [6, 64] or require a similar k-clock signal that can be analyzed to properly resample the even-in-time data [65–67]. Figure 23.10 illustrates a typical external k-clock block diagram.

The all-semiconductor laser is inherently linear and does not require an external optical k-clock. The laser self-generates an internal electronic k-clock. The laser forces the wavelength to be correct at each of the evenly spaced clock transitions Fig. 23.11. The all-semiconductor laser does not need the extra cost of parts and integration of an optical k-clock and eliminates the challenges frequently associated with the nonuniform triggering that can occur with external optical k-clocks (where zero-level drift creates nonuniformity in the triggering periods and resulting degradation of trigger timing). The result is direct triggering of the data acquisition: No post-acquisition resampling, avoiding the potential of resulting ghosting [68, 69] and reducing computation time.

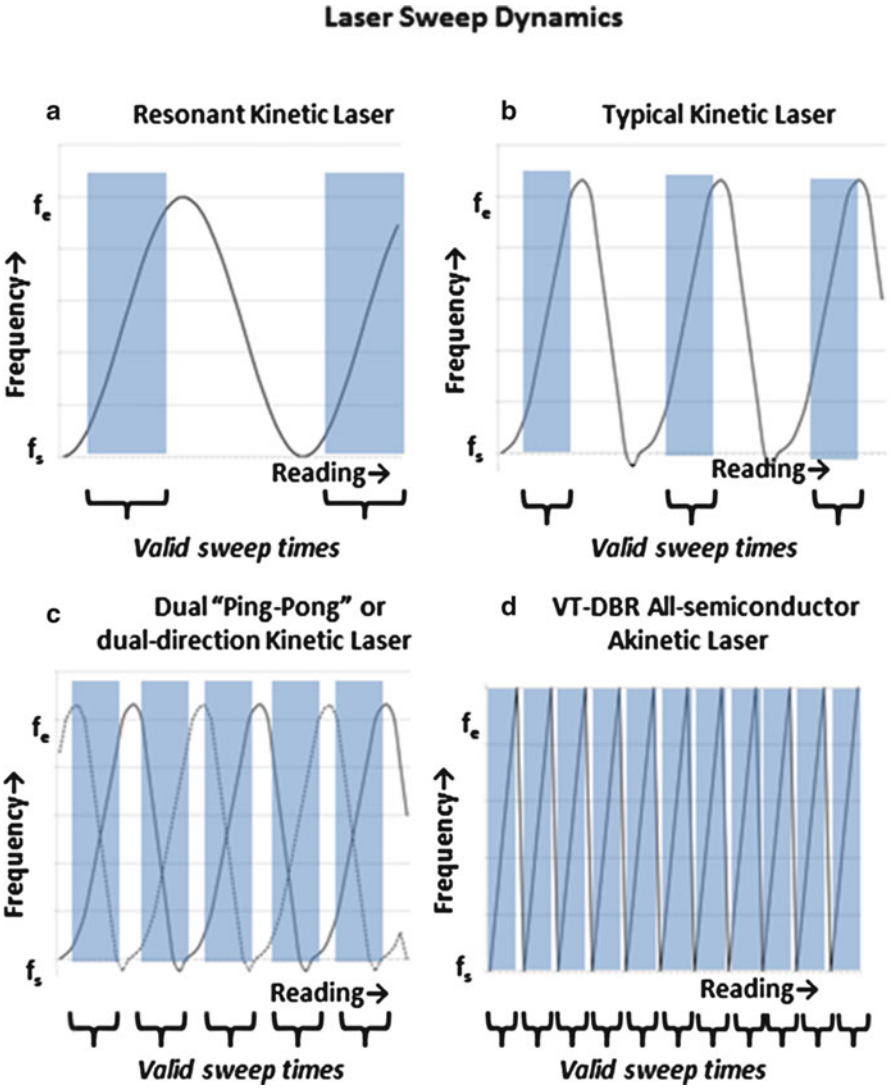

Fig. 23.9 Mechanically tuned lasers must move back from the end of the sweep to get to the beginning, taking time [63]. Akinetic lasers move directly from the end to the beginning, using only nanoseconds

In addition to the electronic k-clock, the akinetic laser also provides a sweep start trigger. This sweep start trigger is always deterministically aligned with the k-clock trigger, providing a pulse at a time just previous to the first valid k-clock, and thus ensuring that the ± 1 clock cycle error [49] that can exist in mechanically swept-laser systems where k-clock and sweep start are not deterministic.

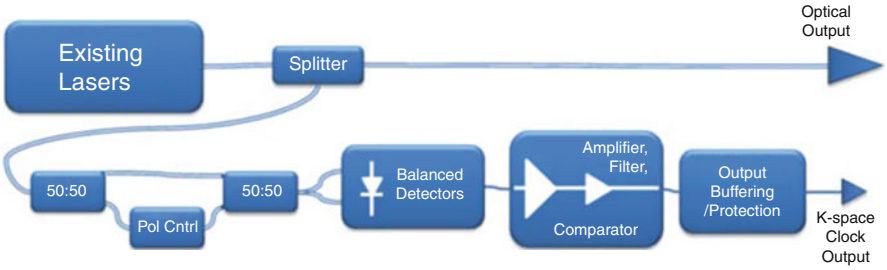

Fig. 23.10 Kinetic lasers generally lack sufficient linearity, requiring either resampling with an external k-clock, or triggering with one, leading to cost, trigger jitter, or the potential of artifacts. The 50:50 couplers and path length delay provides for a Mach-Zehnder filter that provides a repetitive passband filter with equal frequency steps. The interferometer output is detected and processed to provide electrical signal edges to trigger the data acquisition circuitry

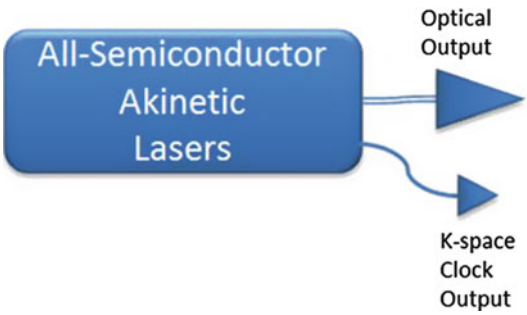

Fig. 23.11 Akinetic lasers can generate an extremely linear sweep, synchronized with an evenly spaced self-generated electronic k-clock. This simplifies receiver design

23.3.4.2 Inherent Linearity

The akinetic laser has typical RMS linearity of 0.0012 % at 200,000 sweeps per second (less than ±1 pm; ±0.2 GHz) and has a linearity span that is typically <±0.002 % (<±2 pm). This linearity produces uniform single-reflection interferograms and results in clean, low-artifact images. Figure 23.12 shows the example output of a Mach-Zehnder interferometer with ~42 GHz free spectral range operating at 1550 nm and Figure 23.13 shows similar performance for a laser operating at 1310 nm. The measurement shows that the spacing between zero crossings is uniform indicating a linear frequency versus time sweep.

23.3.4.3 Equally Spaced, 50 % Duty Cycle Trigger

To achieve high signal-to-noise ratio (SNR) and spurious-free dynamic range (SFDR) as well as the high-speed acquisition rates, most available data acquisition systems require uniform equally spaced 50 % duty cycle triggers. The akinetic laser has equally spaced clock triggers, allowing the system data acquisition hardware to achieve higher SNR. With external optical k-clocks with mechanically tuned lasers, ensuring exactly 50 % duty cycle can be difficult (Fig. 23.14).

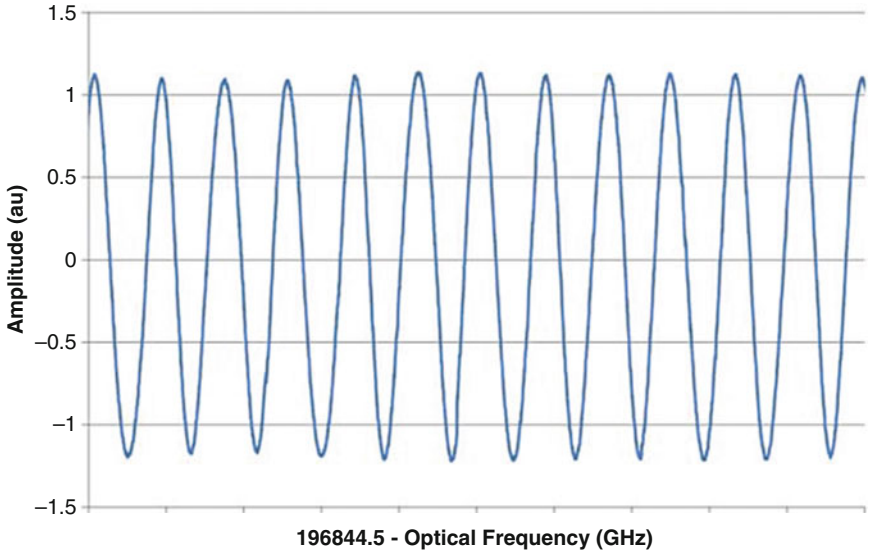

Fig. 23.12 Interferograms do not show the common "accordion" shape typical of mechanically tuned lasers [70]. This image is a short segment of a 1,550 nm laser, operating at 8 k sweeps per second to provide high-resolution interferogram using 400 MHz data acquisition

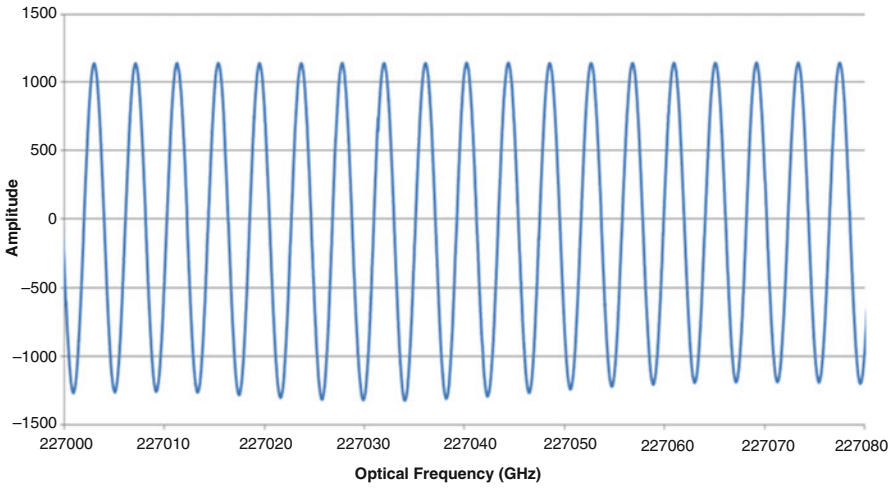

Fig. 23.13 Interferogram at 1,310 nm operating at 8 k sweeps per second to provide high-resolution interferogram using 400 MHz data acquisition

23.3.5 Point Spread Function (PSF) Quality

The axial PSF provides a measure of a fundamental limit on the quality of image possible with a swept laser in an SS-OCT system [4]. The PSF is the power

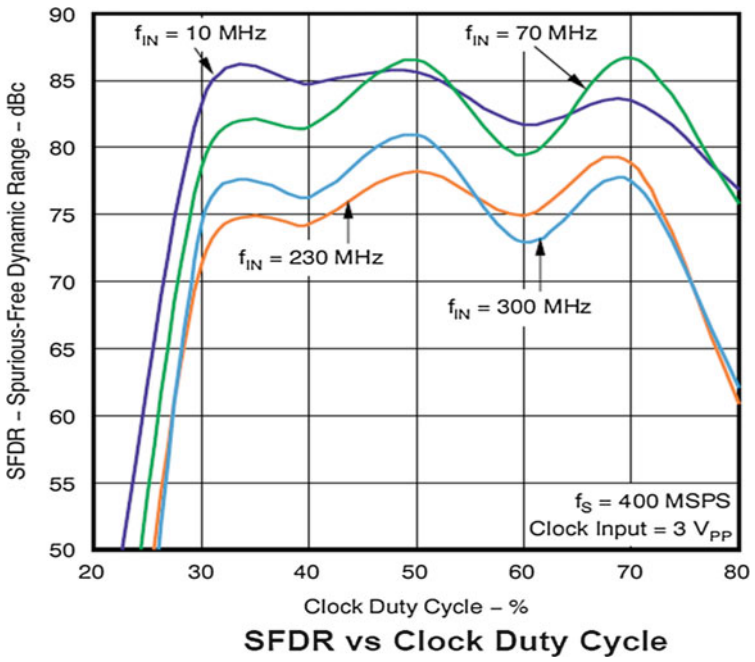

Fig. 23.14 This TI data sheet chart illustrates how a 10 % change in the duty cycle of the clocking can reduce SFDR by almost 10 dB at 300 Mhz [71]

spectrum of the interferogram produced by an OCT interferometer with a single reference reflector. A PSF with low side lobes and low background noise facilitates an image with low artifacts and high contrast and detail. Typical values for the akinetic laser PSF are 45–60 dB to the side lobes and 55–70 dB to the noise floor (defined as the variation of the background), as seen in Fig. 23.15 (the range of values is determined primarily by interferometer characteristics).

The PSF and image quality produced by the all-semiconductor laser will not degrade over time because the laser is constantly re-evaluating its own performance and making small adjustments to its drive signals. Maintaining sweep linearity over time can be a limitation for mechanical tuning lasers, primarily due to mechanical wear and mechanical changes with time and temperature.

23.3.6 Coherence Revival

Coherence revival is the effect where interference fringes are observed in an interferometer illuminated by a light source with a comb-like spectrum not only when the reference and sample arms are matched in delay but also when the two arms are mismatched at periodic intervals. These intervals can be several orders of magnitude longer than the source coherence length [50]. This occurs if a laser is simultaneously oscillating at multiple longitudinal

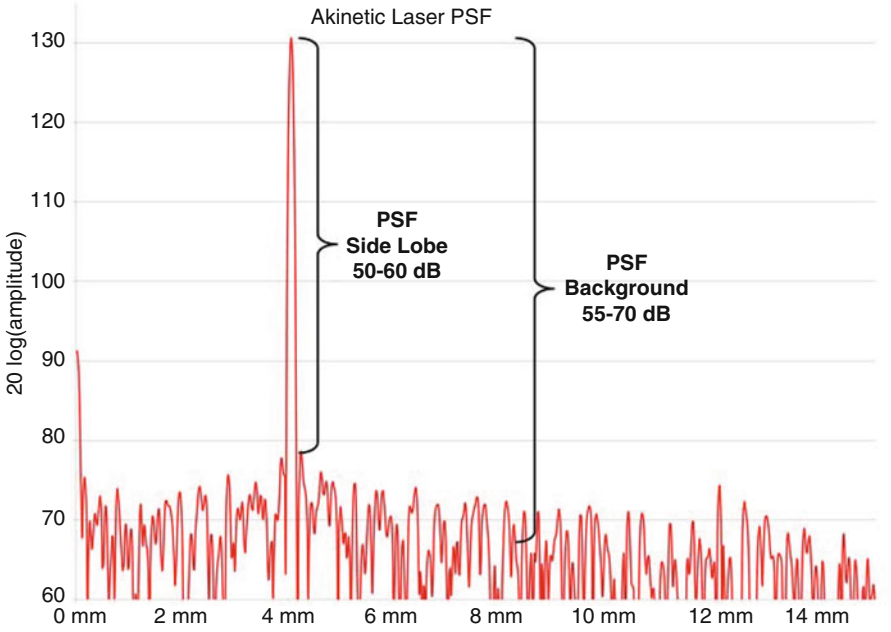

Fig. 23.15 This plot shows the PSF for a 153 kHz sweep. Deep side lobes and low background noise lead to low image artifacts and high image contrast and detail. These are due to the low trigger jitter, linearity, power stability, low RIN, and additional factors

modes of the cavity. The period of the interference fringes is equal to the reciprocal of the mode spacing (which equal to the roundtrip delay of the laser cavity) [50, 72]. These effects can create nonidealities such as ghosting in the OCT image [73].

Because the akinetic swept laser has a single longitudinal mode, the issues with coherence revival in mechanically tuned lasers are largely avoided.

23.3.7 Mode Hops

The all-semiconductor laser uses software control to constantly monitor and ensure that no mode hops occur. Long before the laser could even begin a mode hop, the control optimizes the sweep to ensure optimum side-mode-suppression ratio (SMSR) and guaranteeing no mode hops.

23.3.8 Phase Stability/Wavelength Repeatability

In phase-sensitive OCT applications, such as phase microscopy or Doppler OCT, it is beneficial to have wavelength sweeps of the laser starting at the same

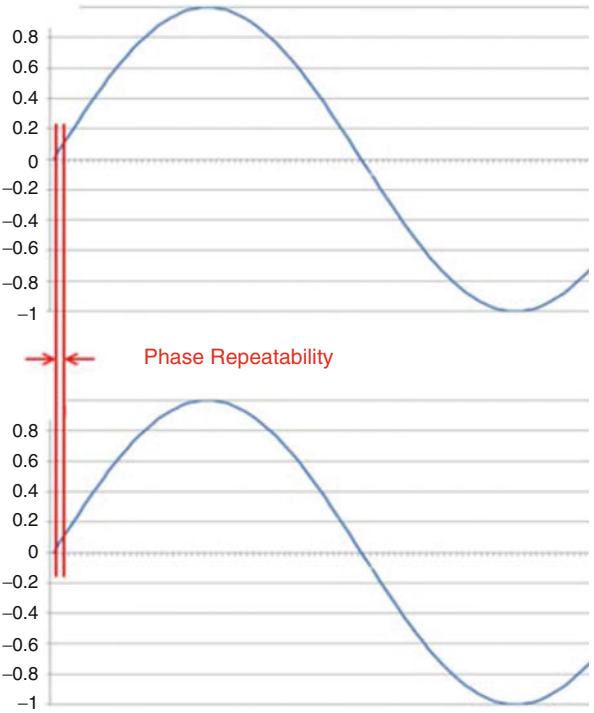

Fig. 23.16 Phase repeatability is typically defined as the repeatability from one sweep to another and is expressed either in picometers repeatability, in milliradians of a specified reflection, or in displacement sensitivity

wavelength and repeat the same wavelengths at all samples in an interferogram (Fig. 23.16). Wavelength repeatability of the laser contributes to phase stability in the resulting interferograms, directly affecting minimum phase sensitivity [49]. Phase sensitivity then determines displacement sensitivity and flow velocity resolution.

Wavelength repeatability of 0.5 pm standard deviation and ±2.5 pm span (peak amplitude) has been confirmed for the all-semiconductor laser. The following charts show the detailed test results (Figs. 23.17 and 23.18).

The displacement sensitivity of a phase-sensitive OCT system is obtained from

$$\delta z = \frac{\delta\phi\ \lambda}{4\pi\ n} + \frac{\delta\lambda}{\lambda} z \tag{23.2}$$

where $\delta\phi$ is the phase uncertainty in the interferogram measurement, $\delta\lambda$ is the wavelength repeatability, z is the nominal path length difference, n is the index of refraction, and λ is the center wavelength. The fundamental phase uncertainty of an OCT system is $1/\sqrt{SNR}$ [75, 76]. To achieve SNR-limited displacement sensitivity, variations in the wavelength repeatability must be minimized as shown in Eq. 23.2. Most phase-resolved OCT systems using mechanical swept sources require the use of a wavelength reference or phase reference to remove the effect of low

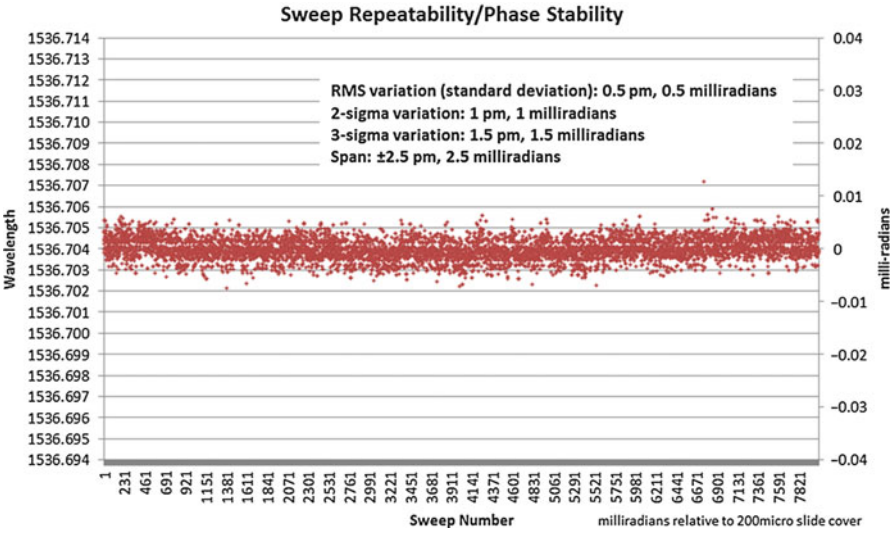

Fig. 23.17 Sweep phase repeatability in nanometers and milliradians. Peak variation is ±2.5 pm; standard deviation is 0.5 pm. A total of 8,040 sweeps were measured over a period of 30 min. Sweep rate was 118 KHz. Test consisted of measuring the wavelength of a feature from an $H^{13}CN$ gas absorption cell at 100 torr [74]. Repeatability was similar at various points along the sweep

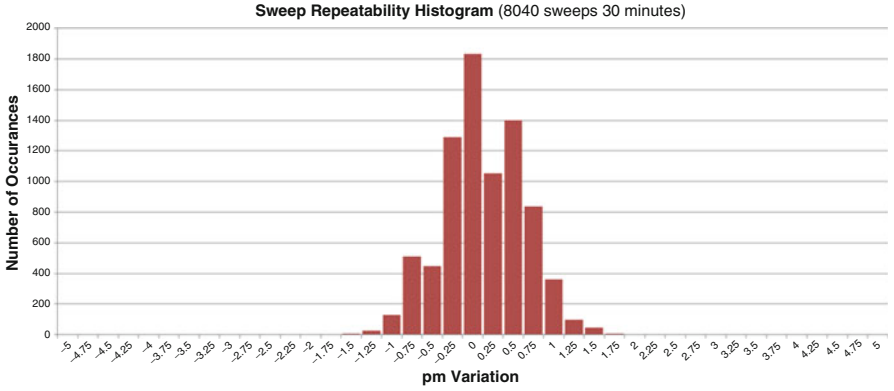

Fig. 23.18 A histogram of akinetic laser sweep wavelength variation in picometers. 0.25 pm is equivalent to 0.25 mrad

wavelength repeatability in sources based on polygon mirrors [49, 77], MEMS cavities [78], or MEMS VCSELs [79].

The predicted performance of the akinetic laser may be calculated in two ways. First, using Eq. 23.2, the measured wavelength repeatability of 0.5 pm and a center wavelength of 1,550 nm, the displacement sensitivity is 65 pm at the thickness of a slide cover of 0.2 mm (650 pm at 2 mm). Alternatively, the wavelength

repeatability term in Eq. 23.2 may be expressed as a depth-dependent phase error, given by

$$\delta\phi = \frac{4\pi\, n\, \delta\lambda\, z}{\lambda^2\, \delta\lambda} \tag{23.3}$$

In air, a wavelength repeatability of 0.5 pm produces a phase error of 0.5 mrad at 0.2 mm (5 mrad at 2 mm). The calculated phase errors for the akinetic laser meet or exceed results obtained from a number of swept-source phase-resolved OCT systems [77–84] without need of a wavelength reference or phase correction methodology [85, 86].

23.3.8.1 Phase Sensitivity Vis-à-Vis Alternatives

Comparing phase sensitivity among different systems with different light sources can be challenging. One typically would like to separate contributions from the source and detector from instabilities in the optics that constitute the interferometer. The most incontrovertible technique for achieving this separation is utilizing the front and back reflection from a glass plate, typically a microscope cover slip, as the reference and sample arm for phase stability analysis of the source and detector. A drawback to this technique is that there is little control over the reference power; hence, the measurement may not be under the appropriate conditions where near shot-noise limited detection may be achieved [87] and precludes the use of balanced detection. Nevertheless, this technique may be used to assess how closely the measured phase stability follows the ideal $1/\sqrt{\text{SNR}}$ relationship.

It is well known that spectrometer-based OCT systems typically have superior phase stability over swept-source-based systems [88] unless measures are taken to compensate for sweep to sweep variations in the swept-laser frequency [79]. This is commonly attributed to the lack of moving parts in spectrometer-based systems. The akinetic swept laser has a similar lack of moving parts; hence, one would expect similar phase stability without any compensation for sweep to sweep variability.

In order to test this conjecture, we have made a direct comparison between a spectrometer-based OCT system at 830 nm (±20 nm) described in detail in [89] with a 1,550 nm (±20 nm) akinetic swept-laser-based system using a glass microscope coverslip (#1,145 μm). The measured standard deviation of the phase noise based upon 10,000 a-lines was 2.28 mrad and 1.4 mrad at 54.8 dB SNR and 57.8 dB SNR for the 830 nm and 1,540 nm systems, respectively. In order to make a fair comparison, we need to ratio these results to the ideal case, i.e., $\sigma = 1/\sqrt{\text{SNR}}$. We can then see that under these conditions the phase noise is 126 % of ideal for the spectrometer-based system and 109 % of ideal for the akinetic swept-laser system. The wavelength repeatability of the akinetic swept laser enables phase stability on par with spectrometer-based systems without introducing compensatory absolute wavelength calibration (via, for instance, fiber Bragg grating).

The following table outlines published data on the phase stability for various laser technologies (note: there has been no effort to control for the different experimental

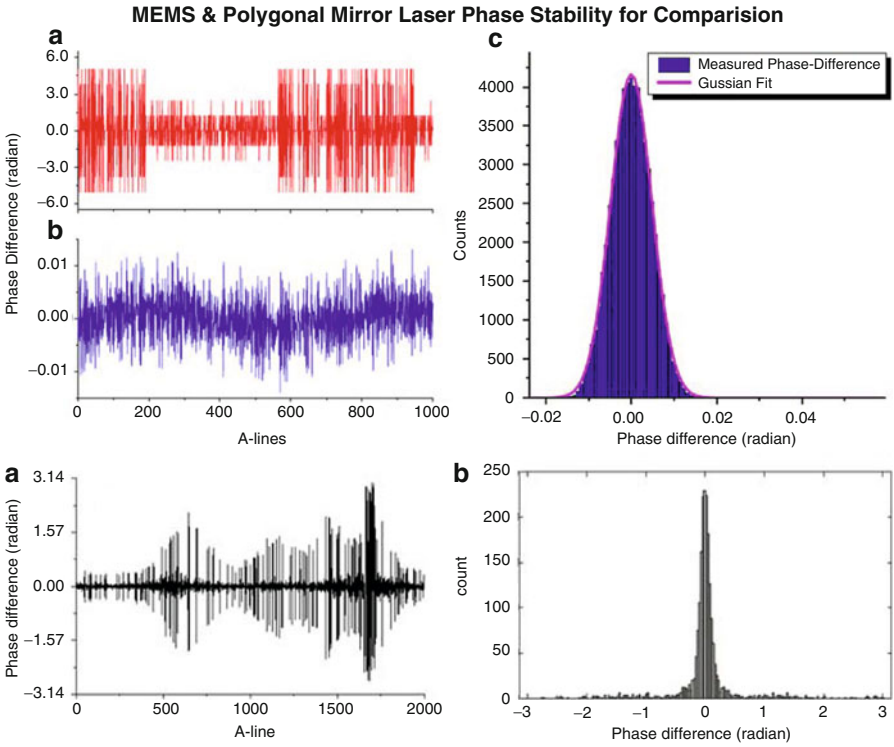

Fig. 23.19 MEMS laser phase stability of ~5,000 mrad peak (*left*) and ~3,000 mrad (*right*) compares to 0.01 mrad for the all-semiconductor akinetic laser. Even the corrected values, in which the researcher added a reference reflection to do corrections, are virtually identical to the uncorrected akinetic laser results (Courtesy of VU University, Amsterdam [78] and Beckman Laser Institute, California [81])

conditions, namely, the signal-to-noise ratio associated with the measurement; hence, ranges have been included where available) (Fig. 23.19 and Table 23.2).

Also pertinent to phase stability is the synchronization between sweep start and the k-clock. In mechanically tuned systems, these signals are typically not deterministic relative to one another, which results in the ±1 clock error issue [49]. Akinetic systems provide an electronic sweep start trigger which is synchronized with the electronic k-clock, eliminating the ±1 clock problem (Fig. 23.20).

23.3.9 Trigger Jitter

Trigger jitter in high-speed OCT systems can represent a key limitation that degrades the SNR [90]. As sweep speed increases, trigger jitter becomes a major factor in SNR and in the resulting image quality [91]. Even small triggering jitter reduces the PSF and image quality.

Table 23.2 Comparisons of phase stability/wavelength repeatability across different lasers [77–83]. Mechanical movement has meant swept-source systems had substantially lower stability. Akinetic lasers achieve results near or better than spectrometers and results much better than mechanically swept lasers

Laser technology	Typical wavelength repeatability	Phase stability (200 μm slide cover)
Akinetic swept laser	0.5 pm std. dev.,	0.5 mrad std. dev.,
	±2.5 pk-pk	2.6 mrad peak to peak
Spectral domain OCT (using spectrometer)	Not applicable	0.32–5.2 mrad std. dev.
		±17 mrad peak to peak
MEMS swept laser	294 pm peak to peak	4.8–3,000 mrad
Polygon mirror swept laser	18–600 pm	32 mrad std. dev.
FDML swept laser		0.76 mrad std. dev.
Crystal-based swept laser		
Littman-Metcalf swept laser	±1– ±20 pm peak to peak typical	
Pump/circulator/MEMS/VCSEL/SOA swept laser	±150 pm peak to peak	1.5 mrad

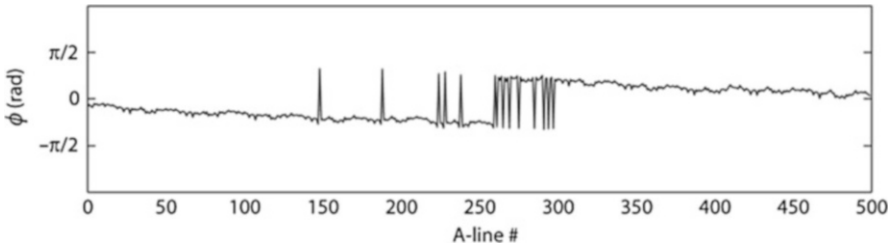

Fig. 23.20 Diagram illustrating the ±1 clock error problem typical with mechanically tuned lasers, where the k-clock and start sweep trigger are not deterministic. The akinetic laser eliminates this problem by providing an electronic start-sweep trigger that is synchronized and deterministic with the k-clock [49]

When utilizing an optical k-clock, it is difficult to achieve better than 18–50 ps jitter due to zero drift and other factors [85]. The akinetic all-semiconductor laser's internal electronic k-clock is designed to minimize trigger jitter and achieves a ±300 fs specification–roughly 10–100 times better than a typical external optical k-clock.

The SNR of a system with analog signal frequency $f_{\text{bandwidth}}$ and jitter $\Delta t_{\text{jitter RMS}}$ is as shown in the following equation [71, 90]:

$$\text{SNR} = \left[\frac{1}{(2\pi)\left(\Delta t_{\text{jitter RMS}}\right)\left(f_{\text{bandwidth}}\right)}\right]^2 \tag{23.4}$$

or expressed in dB

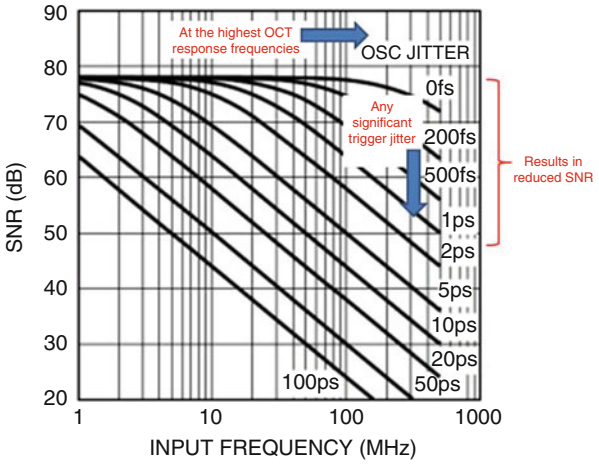

Fig. 23.21 Systematic OCT system SNR reduction with different trigger jitter specification [92]

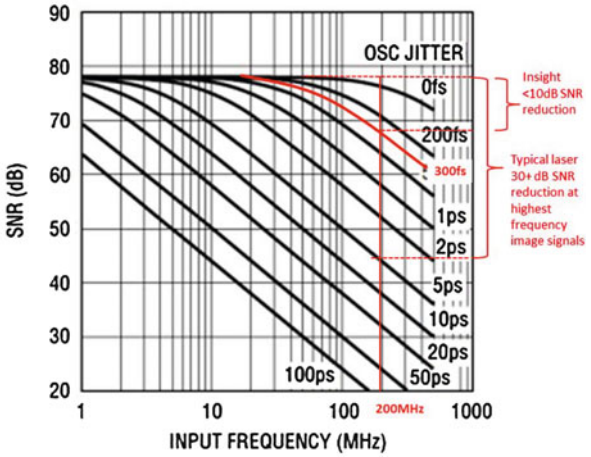

Fig. 23.22 Akinetic lasers can be designed to have low jitter; at 300 fs, SNR is still 65 dB for a 200 MHz signal (Nyquist for 400 MHz acquisition)

$$\mathrm{SNR_{dB}} = -20\log\left(2\pi f_{\mathrm{bandwidth}}\Delta t_{\mathrm{jiter\ RMS}}\right) \tag{23.5}$$

The following generic chart shows the relationship between trigger jitter and SNR [92] (Fig. 23.21).

Trigger jitter can become a significant issue at higher sweep speeds. A 6 mm imaging distance (12 mm round-trip distance) yields a signal of >100 MHz at 200,000 sweeps per second (100 nm width). The following chart shows that a jitter of 5 ps from an optical clock generates a >30 dB SNR reduction (Fig. 23.22).

23.3.10 Smooth, Stable, Controllable Power

The output power character of a sweeping laser can have a significant influence on the performance of an OCT system. Noise can reduce the image quality and sensitivity. Total power can be a limiting factor for penetration depth, and the overall shape of the power profile can limit resolution. In most mechanically tuned lasers, the output power varies substantially during the sweep [3, 5, 6, 11–13, 93], which can create image artifacts and affect the SNR. Precise control of the power profile over the sweep can accomplish the following:

- Smooth output power reduces image artifacts
- Selectable power allows tailoring to gain ranges of the receiver
- Custom profiles allow experimentation with and optimization of the PSF and resolution
- Higher average power across the band
- Flat, strong output power can reduce RIN trade-offs and improve penetration depth

Output power in the all-semiconductor akinetic laser is directly controlled on the chip with the same single-digit nanosecond timing that allows fast wavelength variation. The nominal output power of the laser can be selected from software.

23.3.10.1 Flatness

The all-semiconductor laser has direct control of output power during the sweep. The output power is automatically tailored to the desired output with conformance to ± 0.015 dB or about ± 0.3 % of the signal (Fig. 23.23).

Reduced amplitude variation can directly reduce spurious artifacts in the PSF, reducing ghosting or blurring of the image [94].

The importance of flatness is illustrated by the fact that amplitude variation is not eliminated by balanced detection—only the zero value is corrected [95, 96]. The varying amplitude envelope of other lasers remains in the interferogram, contaminating the image.

23.3.10.2 Selectable Power Profiles

Rather than having to accept the natural output power profile of the laser, the power profile can be selected to optimize image quality and overall system performance. Various research [97] has been inconclusive, with different studies demonstrating advantages of a power profile that is either flat, Gaussian, and cosine tapered Fig. 23.24 or even one with exaggerated power in the beginning and end of the sweep. With an akinetic laser, these and other exotic power profiles may be tried by the user, under program control, for application-specific optimization without any other changes to the system (Fig. 23.25).

Note that for resolution of an OCT image, a Gaussian profile creates a resolution reduction compared to flat top, but FFT artifacts affect the image through the dynamic range. A flat-top profile can be used as an alternative and the resulting interferogram windowed in the time domain for Gaussian or cosine tapered

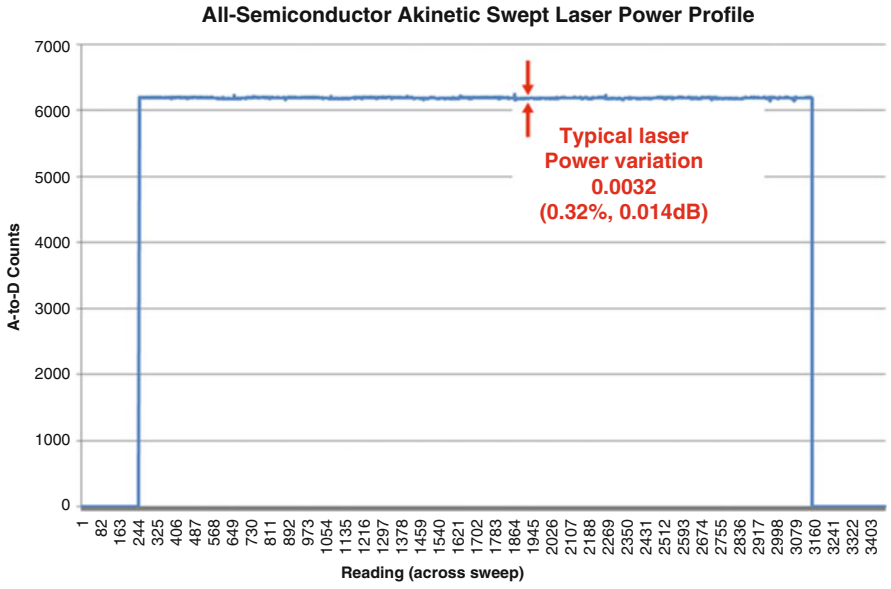

Fig. 23.23 Output power is controlled to ±0.015 dB, reducing power variation-driven image artifacts (Data taken at 108 kHz, 40 nm sweep)

(or other profile), allowing the advantage of the higher measurement SNR of the flat top while avoiding large FFT artifacts.

23.3.10.3 Higher Average Power

While many lasers are specified at peak power [11, 14], the edge-of-band power can be −3 dB, −6 dB, −10 dB, or even −20 dB down from the peak. Power specification for the all-semiconductor laser is flat power over the sweep, potentially yielding substantially higher average power.

23.3.10.4 Sweep Speed Effect on Power

There is no discernible change in output power with sweep speed.

23.3.11 Custom Power Profiles: Wavelength Dependence Compensation and Modulation

To potentially improve the PSF and the resulting image quality, an akinetic laser can auto-level the power profile across wavelength and can automatically preemphasize the optical signal to compensate for wavelength and polarization-dependent losses in the OCT interferometer. This compensation can be applied to the flat top, Gaussian or cosine-tapered profiles.

It is interesting to note that OCT practitioners often do not recognize that the wavelength dependence of the optics can play a strong role in artifact generation

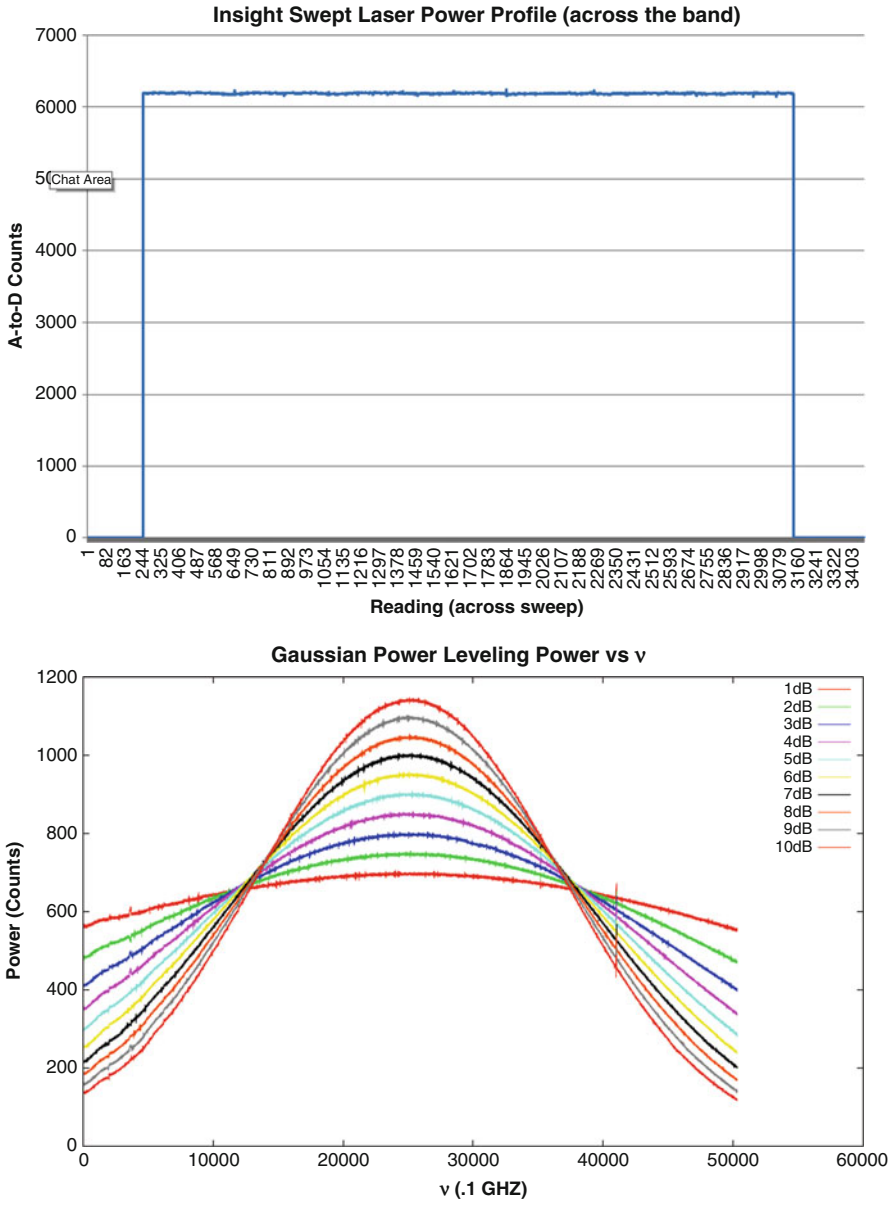

Fig. 23.24 The power profile is user-programmable to flat top, Gaussian, or cosine tapered

because the natural power profile from the mechanical laser is already so nonuniform that the optics wavelength dependency is masked.

In addition to compensating for wavelength dependence, a custom power profile can also be used to superimpose a modulation onto the optical signal amplitude.

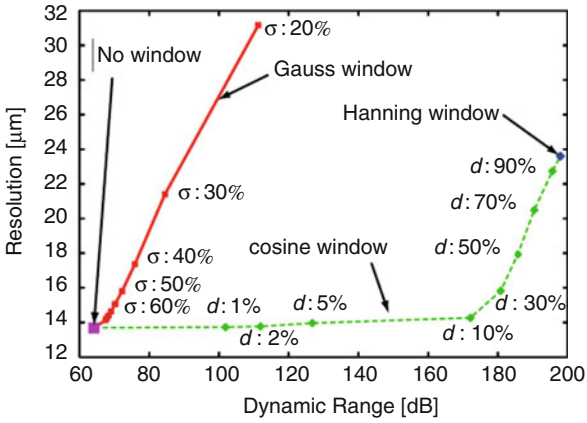

Fig. 23.25 Experimentation with different windows impacts both resolution and dynamic range limits (Chart courtesy Kitasato University [97])

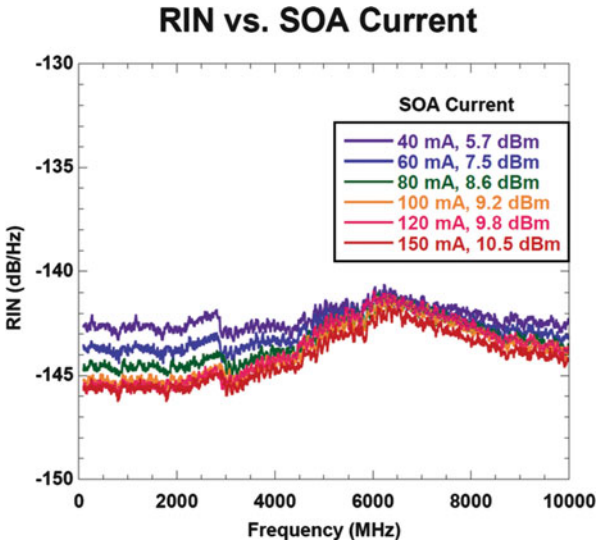

Fig. 23.26 Low RIN (< -140 dB/Hz) contributes to clean PSF and low-noise images

This modulation can be in the form of a sinusoid, a pulse, a repetitive pulse, or any other form of amplitude variation.

23.3.12 Intensity Noise

The static RIN of the laser chip in the all-semiconductor laser is shown in Fig. 23.26. The RIN is less than 140 dB/Hz and tends to be flat through the frequency range of interest to OCT measurements. RIN directly impacts image sensitivity [98, 99].

Integrating the akinetic laser RIN of -140 dB/Hz over a typical maximum 200 MHz bandwidth results in a total integrated 0.14 % noise.

Most OCT imaging systems use balanced detection to reduce the effect of RIN and improve the image sensitivity. Depending on the amount of RIN, the wavelength dependence of the imaging system, and the sensitivity required, sophisticated techniques of spectral balancing or normalization are required [100]. The low RIN of the akinetic laser, combined with the ability to shape the power vs. wavelength profile (see Sect. 23.3.10), should simplify achieving high-sensitivity images.

23.3.13 Side-Mode Suppression

Side-mode-suppression ratio (SMSR) is a measure of the amplitude of the optical side modes of the laser relative to the power of the strongest cavity mode of the laser. Laser side modes can degrade image quality by diminishing edge detail and reducing the sensitivity. The akinetic laser may be tuned such that the amplitudes of competing laser cavity modes are substantially suppressed. Side-mode-suppression ratios of 44–48 dB over the entire tuning range are typical with akinetic laser technology (see Figs. 23.27 and 23.28). By contrast, the mode selectivity of some mechanically tuned laser cavities (Fig. 23.29) may be lower (~30 dB), possibly limited by mechanical alignment tolerances of the laser cavity. The all-electronic control of the akinetic laser cavity allows the laser to operate in a single-longitudinal mode throughout a sweep. Evidence of the favorable SMSR during the sweep is the absence of coherence revivals in the coherence length measurement of Fig. 23.5. Coherence revivals – collapse and restoration of an interferogram – occur when a laser operates in multiple cavity modes [72]. The high dynamic range in PSFs measured with the akinetic laser (Fig. 23.15) also shows that the fringe contrast ratio remains high throughout the tuning range, which is also indicative of single-mode behavior.

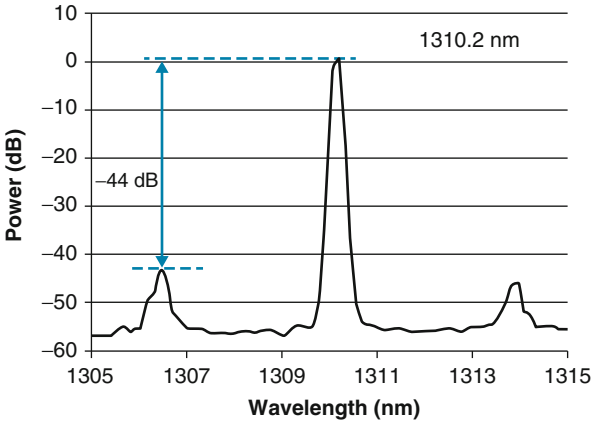

Fig. 23.27 Side modes for the akinetic laser are below −44 dB at 1,310 nm. Typical values for mechanical lasers vary between −15 and −40 dB, with many in the range of −25 to −35 dB

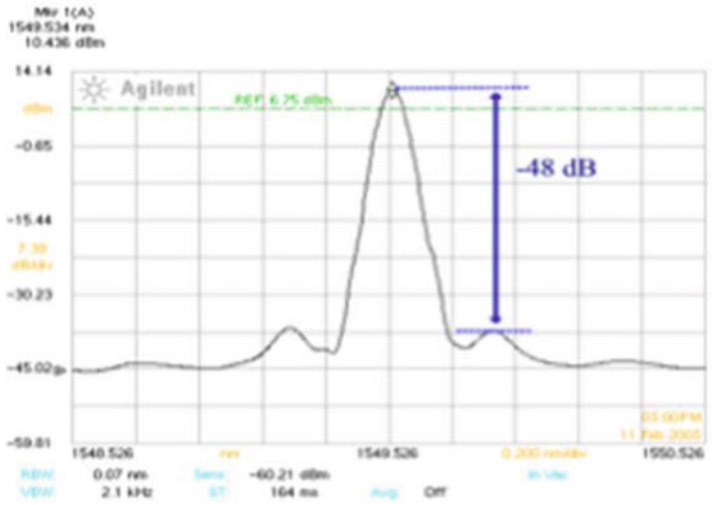

Fig. 23.28 Side-mode suppression at 1,550 nm is under −48 dB

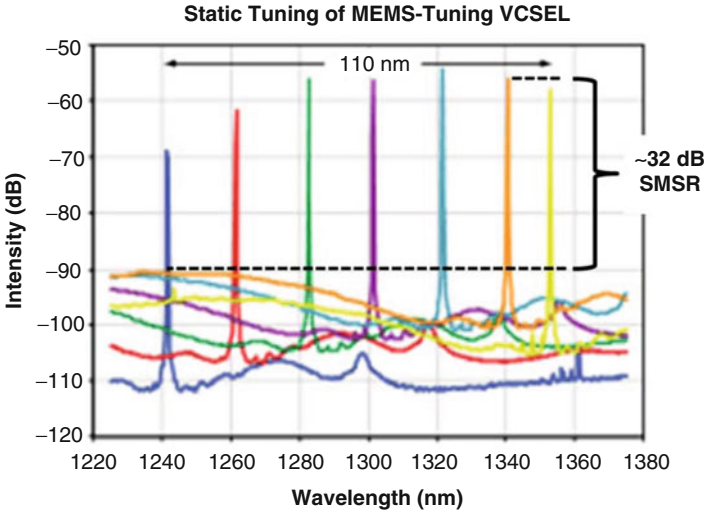

Fig. 23.29 It is not uncommon for other swept laser technologies to exhibit poor side-mode performance. As shown above, the VCSEL/MEMS/pump/circulator/SOA laser exhibits less than 33 dB of side-mode performance [17]

23.3.14 Wavelength Bands and Sweep Range

The initial all-semiconductor swept lasers were developed at 1,310 and 1,550 nm [101, 102]. Over the life of a laser, the center wavelength will only vary by approximately 80 pm based on life-test measurements taken on similar laser devices (Fig. 23.30).

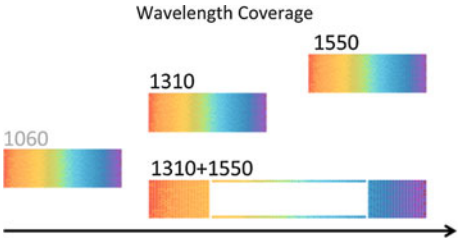

Fig. 23.30 Wavelength bands and sweep width. Dual wavelength band coverage from lower 1,310 to 1,550 nm is also planned

Initial availability of akinetic lasers was 40–50 nm at 1,550 nm, followed by both 100 nm at 1,550 nm and 40–50 nm at 1,310 nm. Full (~100 nm) wavelength coverage at 1,310 nm followed.

At the time of this writing, a consortium of companies is working with Insight Photonic Solutions to migrate the all-semiconductor approach to create a 1,060 nm akinetic swept laser, primarily for ophthalmic imaging applications [103]. The same technology (with a modified substrate) is employed for 1,060 nm. The electronic drive circuitry is identical for 1,310 nm, 1,550 nm, and 1,060 nm. It is also within the bounds of the technology to work with applications at 850 nm and above 1,640 nm. With appropriate frequency doubling, 430 nm may also be attainable.

The all-semiconductor technology will allow production lasers with wavelength coverage of ~140 nm and wider in the future.

23.3.15 Single Longitudinal Mode

The all-semiconductor laser, in contrast to typical mechanical lasers with longer cavity lengths, operates in a single longitudinal mode.

23.3.16 Polarization State Stability

Polarization state stability is critical for polarization-sensitive OCT [48, 104–109], but lack of stability also has negative effects on standard OCT [110].

- Polarization state wobble can impact image clarity and add artifacts through the impact it has on the OCT interferometer.
- Polarization state wobble makes polarization-sensitive OCT much less effective.
- Optional PM output provides flexibility for new avenues for research.

With some mechanically tuned swept lasers, it is common for the polarization state to vary substantially during a sweep [111]. Generally, this "polarization state wobble" is periodic with wavelength, typically with a period of oscillation of a few nanometers [112]. The wobble magnitude and period vary with the individual laser, but wobble of 5–23° is common, and periods from 3 to 7 nm are not unusual (Fig. 23.31).

Because the all-semiconductor akinetic laser is entirely in a single longitudinal mode, the polarization state wobble in the laser itself is very low and has been hard to measure. Optical elements inside and outside the laser cavity can create some wobble,

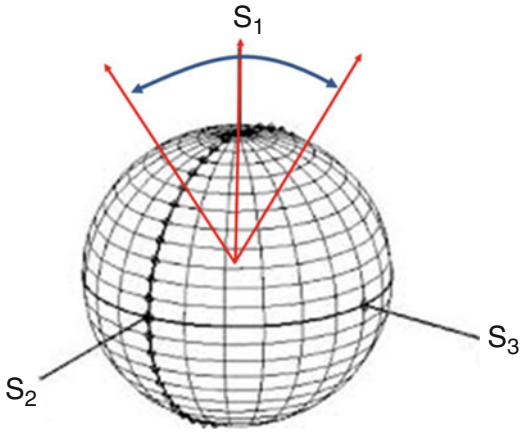

Fig. 23.31 Polarization state wobble is common in mechanical swept lasers and can be between 5 and 23°, creating image artifacts though the polarization dependency of OCT system components

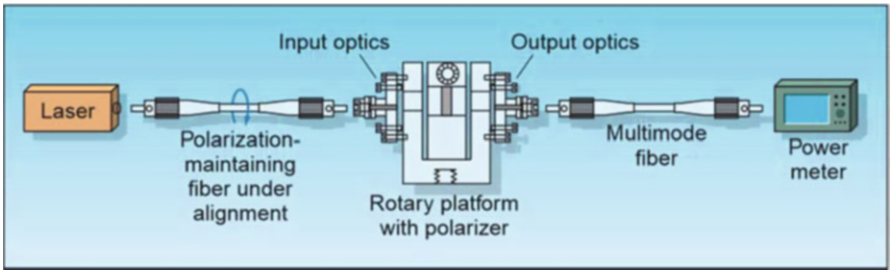

Fig. 23.32 Test configuration to characterize the polarization state wobble of a laser [113]. The polarizer is aligned or anti-aligned with the nominal output polarization of the laser (which can be SM or PM connected). The test shown above will characterize static wobble. To test dynamic inter-sweep wobble, the power meter is replaced with a photoreceiver and an oscilloscope

but the magnitude of such variations is low with the akinetic all-semiconductor approach. Figure 23.32 illustrates the measurement system that is used to characterize polarization state wander in swept lasers.

23.3.17 In-Situ Sweep Programmability

Most lasers can perform at only one speed with a prescribed duty cycle and power profile, and the only way to change the number of points is to change the optical k-clock hardware. With the all-semiconductor laser, each of these parameters is programmed and can be changed from experiment to experiment and imaging run to imaging run (Fig. 23.33).

The following table outlines the programmable parameters of the all-semiconductor laser (Table 23.3):

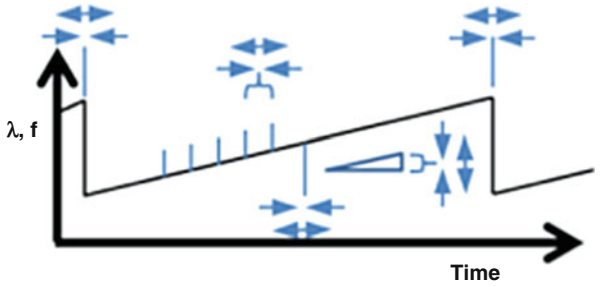

Fig. 23.33 With akinetic all-semiconductor lasers, the number of measurement points, sweep rate, sweep width, center wavelength, coherence length, sweep direction (increasing or decreasing frequency or wavelength), duty cycle, and whether the sweep is linear in frequency or wavelength are all programmable. A command to the laser over Ethernet and the laser uses the new settings for subsequent sweeps

Table 23.3 All-semiconductor, akinetic laser programmable parameters (at time of writing)

Parameter	Typical akinetic all-semiconductor
Programmable duty cycle	Yes: 5–95 %
Programmable sweep width	Yes: 10–140 nm
Programmable number of measurement points	Yes: 1–130,000
Programmable center wavelength	Yes
Programmable coherence length	Yes: 1–40 mm
Programmable sweep power profile	Yes: flat top, Gaussian, user defined
Programmable sweep speed	Yes: 2 k–200 k sweeps per second
Linear sweep parameter	Yes: linear in λ or linear in frequency
Programmable sweep direction	Yes: forward or backward in λ or frequency

Setting sweep parameters is accomplished through Ethernet using simple commands. Changing parameters can be done at any time. It takes a matter of seconds for the change to be fully implemented and the laser ready to run again.

Commands are simple, intuitive strings that control all of the lasers configurable options. As built-in measurement firmware and communications are added to the laser, the data will be available via gigabit Ethernet.

23.3.18 Bidirectional Forward and Backward Sweeps Without PSF Degradation

Probe movement is an issue for some OCT imaging applications and Doppler OCT. Providing interlaced forward and backward linear-in-frequency sweeps facilitates eliminating the effect of probe movement for certain applications.

The sweep linearity of the all-semiconductor laser and the resulting PSF is very nearly the same for forward and backward sweeps.

This was the first of the interlaced sweeps capabilities implemented in the all-semiconductor swept laser (see Sect. 23.3.23 for more discussion).

23.3.19 Imaging at Depth and Multipath Imaging

The coherence length of a swept source defines the maximum depth at which an image can be made (imaging depth range at which the PSF rolls off by 6 dB is one half of the coherence length). More generally, coherence length also sets the limit on the distance difference one can measure over between different arms of an interferometer, which impacts the design of multipath imaging systems and sensors (Fig. 23.34).

23.3.19.1 Imaging at Depth

In a single-path OCT imaging system application, there are a number of factors that can add to the needed coherence length. These are shown in the following equation:

$$\begin{aligned} CL_{\text{Needed}} = 2^{*}\Big(&\text{Depth}_{\text{imaging, desired}} + \Delta L_{\text{sensor-to-tissue movement during imaging}} \\ &+ \Delta L_{\text{sensor-to-sensor varitation}} \\ &+ \Delta L_{\text{sensor-to-tissue distance variation for 2D\&3D beam movement}}\Big) \end{aligned} \tag{23.6}$$

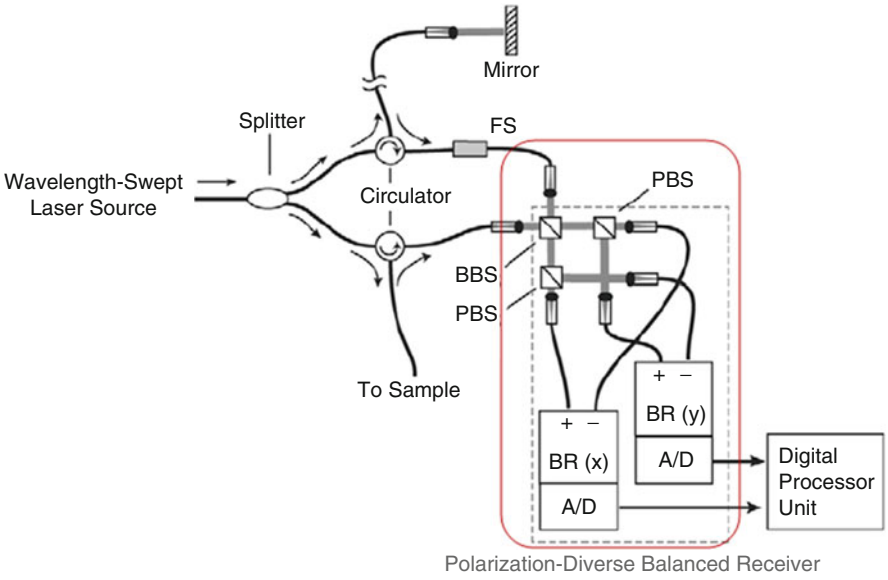

Fig. 23.34 Most existing multipath OCT systems use multiple detectors and data acquisition channels [115]. In some cases, these complications can be avoided by putting the different paths on the same fiber, delayed from one another, using the same detector. This is facilitated by the long coherence length afforded by akinetic lasers

where CL_{Needed} is the needed coherence length; $\text{Depth}_{\text{imaging, desired}}$ is the maximum imaging depth into the tissue; $\Delta L_{\text{sensor-to-tissue movement during imaging}}$ is the amount of movement of the sensor relative to the tissue due to patient movement, or sensor movement; $\Delta L_{\text{sensor-to-sensor varitation}}$ is the variation from one sensor to another, for example, due to fiber length differences; and $\Delta L_{\text{sensor-to-tissue distance - variation for 2D \&3D beam movement}}$ is the variation in the distance from the sensor to the tissue in scanning systems. For example, in endoscopic applications the endoscope is near one side of the esophagus and the light must penetrate the near-side tissue with no distance from the sensor and also penetrate the tissue at the other side of the esophagus 15–20 mm away.

23.3.19.2 Multipath OCT Coherence Requirements

In addition to the coherence requirements above, some approaches to accomplish multipath OCT imaging (i.e., polarization-discriminated OCT) in a single sensor, the effective delay for the multiple paths must be added to the coherence length requirement of the laser. For example, images using two different polarization states can be accomplished by using a polarization beam splitter in the source path and then delaying one of the states before recombining the signals. The measurement can be either polarization discriminating or not; in either case, the FFT is accomplished in the time window associated with each signal. The coherence length must be adequate to accommodate this longer time window, typically slightly over-doubling the coherence length requirement for two simultaneous signals or tripling for three.

Figure 23.43 shows images of a tooth taken at zero path length difference and images taken at 16 mm, 37 mm, and 13 cm (130 mm) path length differences. The similarity of the quality of the images helps illustrate the potential of utilizing the all-semiconductor laser's high coherence length to improve OCT imaging.

23.3.20 Laser Engine Size

- OCT systems can shrink substantially over time.
- Small form factor can enable portable systems.
- Small size can reduce system cost.

The initial size of the akinetic laser was roughly the same size as mechanical lasers [2–7] (Fig. 23.35). The initial development was optimized for performance, not size, leading to approximately 75 % of the volume of the laser package being air.

The first incarnation of the all-semiconductor laser comprised 23 ft^3 of instrumentation and took two lab benches to set up, as shown in Fig. 23.36.

The second incarnation shrank to approximately 7 ft^3. The first commercial unit is 1/8 ft^3. Future reductions in drive electronics and other changes will drive the laser through two major size reductions and lead to a laser about the size of a current smartphone (Fig. 23.37).

Fig. 23.35 Physical form factors for bench use (*left*) and OCT system build-in (*right*)

Fig. 23.36 The first incarnation of the laser comprised 23 ft^3 of space

Fig. 23.37 Laser size is anticipated to drop rapidly, with the laser evolving to be about the size of a smartphone by the end of the decade

23.3.21 Reliability and Ruggedness

Lasers have tended to be higher-mortality elements of an OCT system. Degradation over time of power or PSF leads to degradation in the image quality during the lifetime of an OCT system.

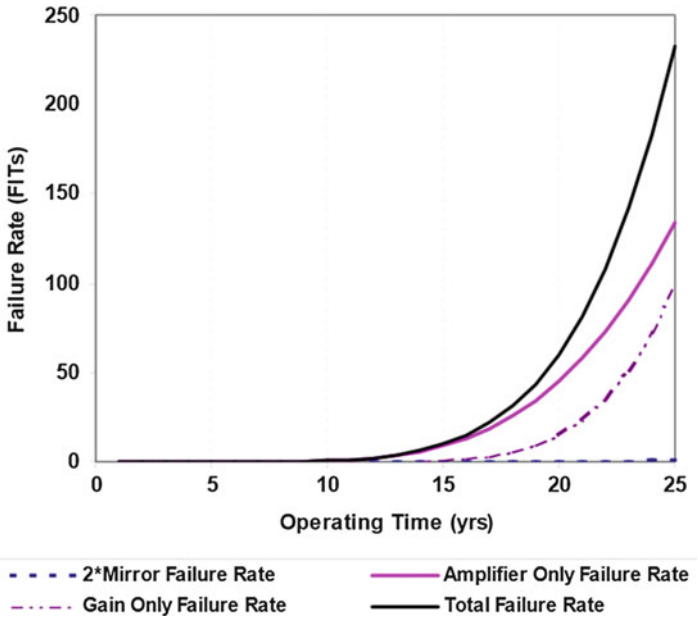

Fig. 23.38 FITs (failures per billion) of the semiconductor are minimal over 10 years and even at 15 years represent less than 20 failures per billion. The laser will likely succumb to a mechanical failure (e.g., connectors) before the laser reaches end of life. The lack of mechanical movement is a major reason for the long mean time to failure (*MTTF*)

The underlying technology that allowed invention of the all-semiconductor laser was originally developed for long-haul telecommunications [116, 117] where components are placed underground or underwater and require reliability over 30 years of operation from −40 °C to +70 °C [118] (Fig. 23.38).

23.3.21.1 Little Power Loss Over Time

Because the entire laser and tuning cavity are all on a single semiconductor chip, the all-semiconductor laser avoids the typical degradation of power over time due to cumulative misalignment losses when many discrete optical components are required [119]. There is a single alignment of fiber to laser within a sealed package, thus minimizing the drop in power over time.

23.3.21.2 Vibration Sensitivity

The same factors that lead to long life and low power loss over time contribute to low vibration sensitivity. The fiber itself is slightly vibration sensitive, but otherwise, the laser is relatively impervious to vibration. This vibration insensitivity applies to both reliability and to performance variation under vibration conditions.

23.3.22 Evolving Capabilities

23.3.22.1 Noncontiguous Sweeps

There have been suggestions that an outsized portion of the information in an OCT sweep is contained in the first and last portions of the sweep. If this concept can be exploited, utilizing the data from only these sections of the sweep may unlock new potential for very fast OCT (Fig. 23.39). Such sweeps can be performance with an akinetic laser without needing to measure faster at lower resolution and reducing the data processing bottlenecks that can exist for high-speed systems.

Since the all-semiconductor laser can produce coherent sweeps in different bands (e.g., 1,310 nm linked to 1,550 nm), implementing noncontinuous sweeps has the potential of creating a wider effective sweep, potentially increasing the resolution.

For a normal OCT sweep,

$$f(t) = f_0 + \frac{df}{dt}\,\Delta t \tag{23.7}$$

However, take two discontinuous segments can be used:

$$f(t) = \begin{cases} f_0 + \dfrac{df}{dt}|_0 \Delta t_0, t_0 < t < t_1 \\ f_1 + \dfrac{df}{dt}|_1 \Delta t_1, t_1 < t < t_n \end{cases} \tag{23.8}$$

23.3.22.2 Custom Wavelength Profiles

It may be that there is some advantage to utilizing a slightly nonlinear sweep to compensate for other system nonidealities. Since the sweep can be created in any increment, predetermined but nonlinear sweeps are possibilities in the future.

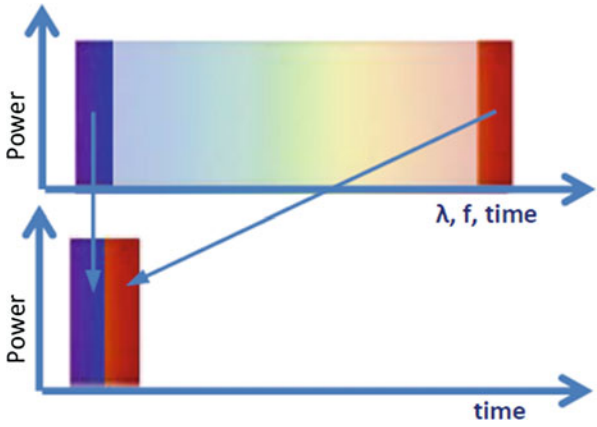

Fig. 23.39 Noncontiguous sweeps may speed imaging and reduce data communication and processing burden with manageable image quality degradation for some applications

23.3.22.3 Simultaneous Multiwavelength Sweeps

Because the all-semiconductor laser generates its own triggers and the wavelength is forced to be accurate at these equally spaced trigger points, the opportunity exists to run simultaneous multiwavelength sweeps. For example, two lasers may be linked to provide simultaneous 1,310 and 1,550 nm band sweeps. Since data from each of these bands provides different and complementary data for the image, combining the results from both bands can give physicians more and better diagnostic information [120–124]. A single fiber optic probe can carry both wavelength bands simultaneously [123, 125], but either time-delay multiplexing or wavelength division multiplexing can be used to separate the bands for data acquisition. In a time-delay multiplexing system, a single detector can be used to acquire both signals. Alternatively, in a wavelength division multiplexing system, dual-channel detection would be used.

23.3.23 Interlaced Sweeps

There is considerable research into new methodologies (Doppler and polarization-sensitive OCT are just two of many) to exploit OCT to derive more information from the tissue [100, 126–128]. The flexibility afforded by a truly software-controlled laser may enable new insights and innovations that were not previously thought possible.

23.3.23.1 Interleaved Coherence Sweeps

There is ongoing research into the potential of using the all-semiconductor laser's ability to interleave sweeps of differing coherence length to achieve advantageous image results, including the potential of speckle reduction and implementation of new analysis techniques.

23.3.23.2 Interlaced Differing Rate Sweeps

Kinetic lasers have limited ability to change sweep rate, while the sweep of the akinetic laser can be changed by the user at any time. In fact, it may be possible to interlace sweeps of differing sweep rates. Sweep repetition rates can be varied by a factor of 20. This capability may facilitate dual high-resolution/high-depth modes with a single laser semi-simultaneously.

23.3.23.3 Interlaced Number of Data Points

The number of data points in a sweep can affect certain characteristics of an image. Because the all-semiconductor laser opens the possibility to running interlaced sweeps with varying numbers of data points, this could help researchers develop ways to reduce more of the nonidealities in an image. With an external k-clock this could be problematic, but it becomes easy with the all-semiconductor laser's internal electronic k-clock.

23.4 OCT Images

Many images were made by various OCT companies over the last 2 years of the akinetic laser's development; however, these images had all been the proprietary property of the companies making the images. This changed in early 2013, when external and independent images were finally made public.

The following images suffer from being made at 1,550 nm and only for 40 nm range, but the resulting image quality from measurements made under these conditions was reasonable nonetheless (Figs. 23.40, 23.41, and 23.42, and 23.43).

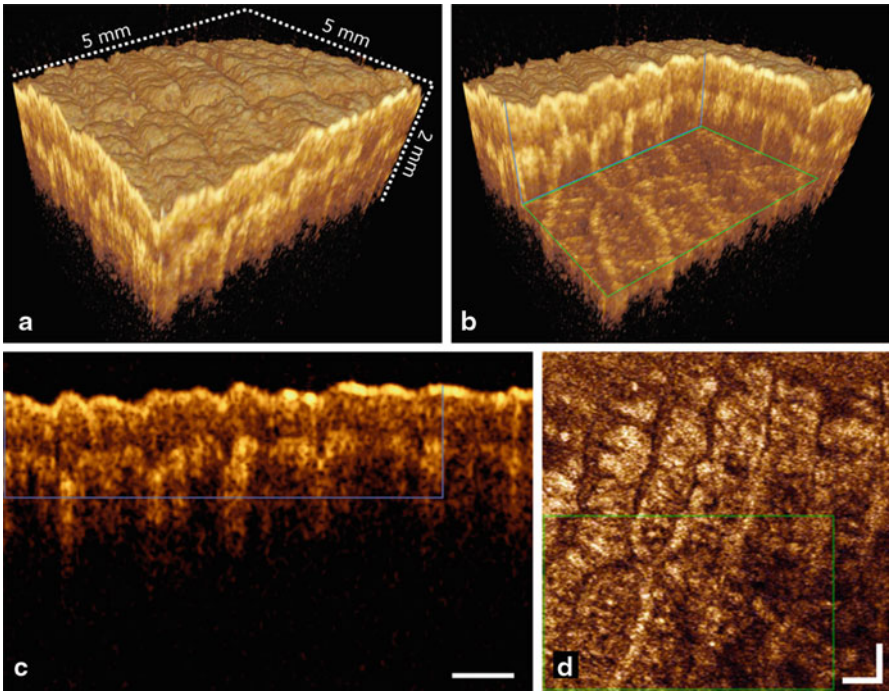

Fig. 23.40 In vivo human skin measurements at 1,550 nm with 20 μm isotropic resolution. (**a**) 3D reconstruction of the data set; (**b**) 3D reconstruction of the dataset with a portion of the data removed to reveal the internal structure of the skin; (**c**) cross-sectional tomography extracted from the 3D dataset, the data enclosed in the overlapped rectangle correspond to equivalent overlapped rectangle (*vertical plane, blue*) in (**b**); and (**d**) en-face view extracted from the 3D dataset, data enclosed in the overlapped rectangle correspond to equivalent overlapped rectangle (*horizontal plane, green*) in (**c**). Acquired volume dimensions were 5 × 5 × 5 mm^3, corresponding to 1,024 × 256 × 180 pixels (width × height × depth). Presented images were cropped along depth (*z*) to report only useful imaging area. *Scale bars* correspond to 0.50 mm (Courtesy Vienna Medical University [114])

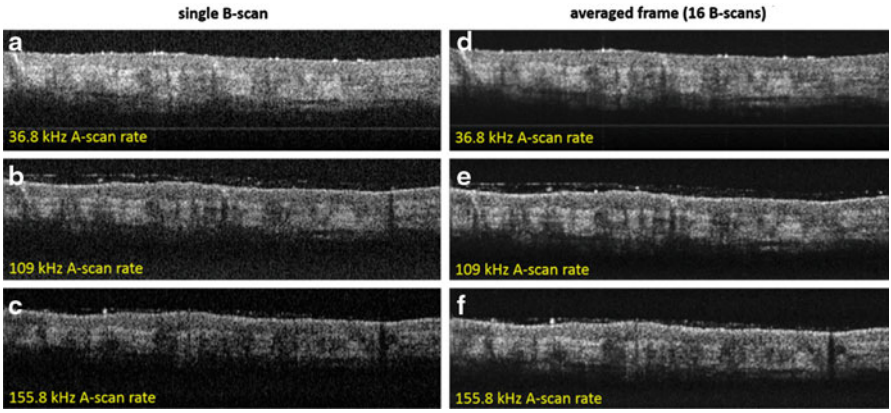

Fig. 23.41 Single-frame and averaged in vivo skin measurements acquired by the same akinetic laser, at different laser sweep rate, under program control. (**a**–**c**) single-frame measurements at 36.8 kHz, 109 kHz, and 155.8 kHz sweep rate, respectively; (**e**–**f**) average of 16 frames (M-scan), sweep rate similar to (**a**–**c**)**,** respectively. During the measurements, the coherence gate was located close to zero delay. Images dynamic range, from a to f, was 25.69, 24.18, 23.91, 35.12, 34.57, and 34.38 dB, respectively. Images area was 5 × 1.7 mm^2, corresponding to 1,024 × 60 pixels (hor. × vert.) (Courtesy Vienna Medical University [114])

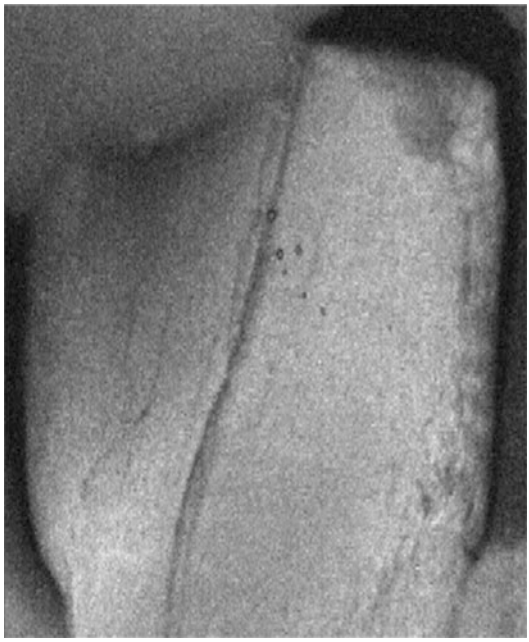

Fig. 23.42 En-face view of a tooth. Size 5 × 6 mm^2 (1,024 h × 256 v) [114]. The same tooth is imaged at different lengths in the subsequent Fig. 23.43

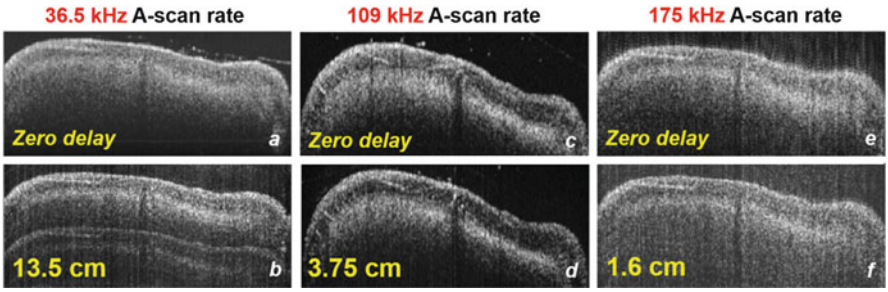

Fig. 23.43 To illustrate deep coherence, images of a tooth (including crack) with zero path length delay and then the same tooth with 16–135 mm of path length delay. Long akinetic laser coherence length may enable new OCT measurement approaches and techniques. Images were generated using 1,550 nm and 40 nm span. Courtesy of Vienna Medical University [114]

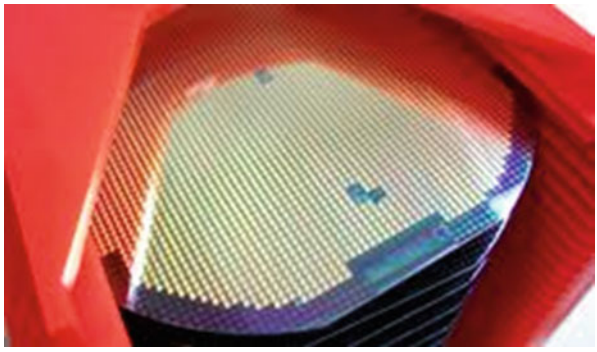

Fig. 23.44 A single wafer contains over 2,500 lasers, which creates a steep cost decline curve with time and volume

23.5 OCT Cost Reduction

Achieving lower cost is critical over time in commercial OCT imaging systems. Typically, the laser is the most expensive part of the OCT system and thus has a big impact on the profitability of OCT system suppliers and on the overall cost of OCT systems and the resulting ability of large markets to gain access to the technology.

Specifically, low pricing can have the following impacts:

- Reduce the development budget.
- Improve margins for OCT system suppliers.
- Allow OCT to penetrate into larger-volume, lower-cost applications.

An all-semiconductor laser can achieve cost advantage because:

- Wafer-scale laser manufacturing assures rapidly declining costs (Fig. 23.44).
- Internal electronics use high-volume telecom parts for continued declines in cost.

The initial cost of the all-semiconductor akinetic laser is near or lower than the cost of other OCT laser solutions. With hundreds of lasers per wafer, the entire laser

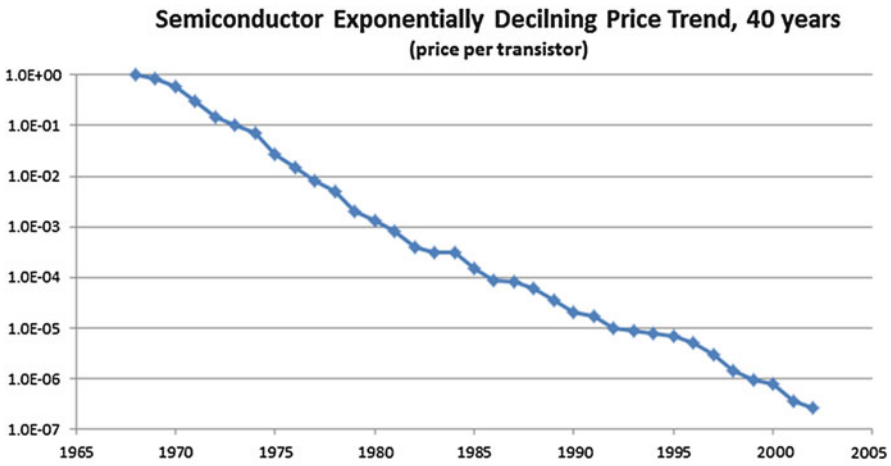

Fig. 23.45 Putting all of a device into semiconductor has been the key to improved performance and order-of-magnitude reductions in cost over time for the last 40 years [27–29]

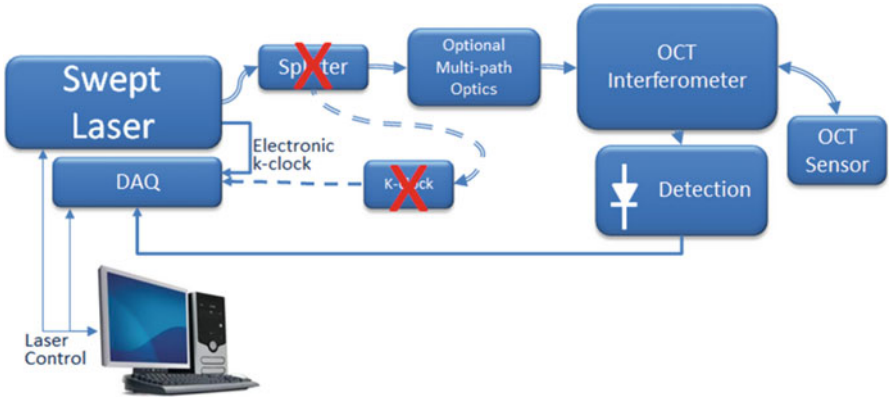

Fig. 23.46 Eliminating a separate k-clock further reduces system cost and assembly complexity

cavity is on the chip. Wafer-scale fabrication results in rapid declines in the cost of such systems [27–29]. The all-semiconductor laser should cost a tenth of existing laser solutions within just a few years (Fig. 23.45).

23.5.1 Reduce System Optics Cost

Because the all-semiconductor laser provides its own electronic k-clock, the system will not need the electronic and optical parts and integration cost of an external optical k-clock (Fig. 23.46).

23.5.2 Integrated High-Speed, High-Resolution Measurement

The all-semiconductor laser has integrated, high-speed, low-noise optical measurements which are used by the laser to ensure that its performance is always optimal. These same measurements can be dual purposed, thus eliminating the need for the additional cost of signal conditioning, analog-to-digital conversion, and related data processing. This can save substantial system cost.

The integrated measurement in the first incarnation of the all-semiconductor laser is 14 bit at 400 MHz, providing intrinsic high-resolution data at high speed, which can result in substantial reductions in overall OCT system cost.

The hardware for the data conversion is already part of the laser. Future versions of these lasers will include the built-in fast communications to transfer the data to the computing system (such as Thunderbolt or USB 3.1).

- Substantially reduce system cost
- Reduce development cost and time
- Reduce system size and complexity
- Provide faster time to market
- Serve as a complete OCT engine; just add the sensor and imaging visualization software
- Improve measurement performance
- Reduce cost of goods, improving margins or reducing price to increase market penetration

23.5.2.1 Dual-Purposed A/D Converter Mean System Cost Savings

The all-semiconductor laser uses high-speed A/D converters internally. The laser can dual-purpose those converters, giving access to data acquisition without much added cost. By adding high-speed 1 GB or 10 GB Ethernet communications and linkage through the built-in digital signal processor (DSP), the laser engine now provides both sourcing and measurement, at an overall system cost savings.

23.5.2.2 One, Two, or Three Converters

A single converter may be all that is necessary for traditional OCT. In multipath OCT applications, such as polarization-sensitive or multiangle or multifocal length, more than one converter can be advantageous (note that for some of these applications, when used with the all-semiconductor laser high coherence length, delay paths may be used to put the signals on a single fiber without the need for multiple converters).

23.5.2.3 14-Bit, 400 MHz High-Resolution Conversion

The quality optical signal and resulting PSF on akinetic lasers can then allow the effective use of higher resolution detection. This higher resolution can provide better image quality, SNR, and conversion at up to 400 MHz (at the time of this writing).

23.5.2.4 On-Board Signal Processing

Since the implementation of an all-semiconductor sweep laser already includes a high-performance field programmable gate array (FPGA), all of the core signal processing (including the FFT and windowing) can be accomplished inside the laser engine, if desired, with little additional cost.

23.6 Akinetic All-semiconductor Technology

23.6.1 Basic Tunable Laser Technology

Light in a tunable laser meets the following condition [129]:

$$m\frac{\lambda}{2} = \overline{n}L \tag{23.9}$$

where m is the mode number, λ is the wavelength, $\overline{n}$ is the effective index of refraction, and L is the effective cavity length.

Cavity-based lasers tune in relative wavelength λ by following the following conditions [129]:

$$\frac{\Delta\lambda}{\lambda} = \frac{\Delta\overline{n}}{n} + \frac{\Delta L}{L} - \frac{\Delta m}{m} \tag{23.10}$$

where $\frac{\Delta\overline{n}}{n}$ is tuned by the net cavity index change, $\frac{\Delta L}{L}$ is tuned by physical length change, and $\frac{\Delta m}{m}$ is tuned by mode selection filter (via index or grating angle).

23.6.2 All-Semiconductor Tuning Technology

The idea for an all-semiconductor tunable laser was first commercialized in the 1990s and 2000s, and over $100 M was spent developing the technology and making the technology manufacturable and reliable for demanding telecom applications. Today, hundreds of thousands of lasers based on this technology are shipped per year and are a mainstay of telecommunications systems worldwide.

The all-semiconductor laser is tuned through changes in the index of refraction of the semiconductor material, which is effected through carrier injection (via current applied to the segment of the semiconductor).

There are five tuning elements in the all-semiconductor swept laser (Fig. 23.47). Tuning occurs when current is applied to a segment of the laser. This current increases the carrier density in a specific region of the device thereby changing the index of refraction of the material. The change in the refractive index changes the effective path length of that specific segment of

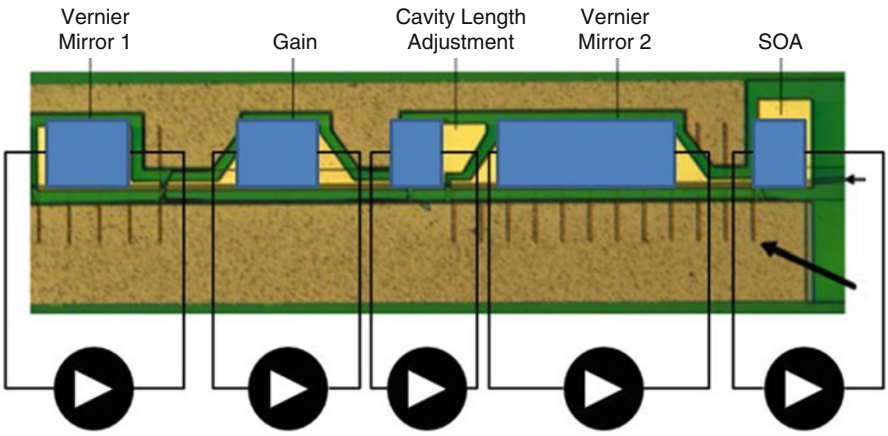

Fig. 23.47 Tuning is effected through changes to the index of refraction of the semiconductor material through carrier injection. This is a cross section of an akinetic all-semiconductor swept wavelength laser design. Each of the five sections of the laser diode is driven by a current source to control the power and wavelength of the laser. The gain section provides the amplification. The Vernier mirror 1 and Vernier mirror 2 provide wavelength-dependent feedback to select the lasing wavelength. The cavity length adjustment allows for small effective changes in the effective path length between the Vernier mirrors for fine wavelength adjustment and single-mode operation. The currents in the Vernier mirrors and cavity length adjustment sections can be coordinated in real time to create an electronically tuned swept wavelength laser. The semiconductor optical amplifier (SOA) boosts the output power of the laser

the laser, permitting precise adjustment of the cavity without moving any of its components.

Two of the tunable segments of the laser are mirror sections (the Vernier mirrors 1 and 2). By applying current and changing the index of the material, the effective mirror spacing is changed. Employing the Vernier-tuning effect, these two mirrors can be used in combination to select any wavelength across the tuning band.

The index change in the semiconductor material is [130]

$$\Delta\eta(N,P,E) = \frac{2ch}{e^2}\, P \int_0^{\infty} \frac{\Delta\alpha(N,P,E')}{E'^2 - E^2}\, dE' \tag{23.11}$$

where c is the speed of light, e is the electron charge, $E = h\omega$ is the photon energy, $\alpha = 4\pi k/\lambda$, and P indicates the principal value of the integral.

The phase section of the all-semiconductor laser is very similar to the mirror sections in that the index changes with the applied current, but instead of tuning a mirror, it is used to fine-tune the overall cavity length. This section is then adjusted in real time as the laser sweeps to ensure that at every point in the sweep, there is no chance of a mode hop.

For many reasons, it is important for the laser to be mode-hop free. Mode hops, or almost instantaneous jumps in wavelength, are a substantial obstacle in obtaining

quality images. In addition, the side-mode suppression is reduced near mode hops, also resulting in a reduction in image quality. In the Vernier-tuned distributed Bragg reflector (VT-DBR) laser, mode hops are avoided by rapidly adjusting the cavity length as the wavelength changes.

In the years since the all-semiconductor laser technology was developed, many groups and individuals around the world have tried to get the laser to sweep linearly over time. Some very capable people have made admirable progress, but none were able to get the laser to rapidly sweep linearly over both time and temperature to the extent required for OCT imaging applications. The first all-semiconductor lasers were built on their efforts.

The key obstacle to linear sweeping is the five different current-driven segments to the laser, each of which has an impact on the wavelength of the laser output. In addition, the temperature of the laser changes the wavelength substantially, and the laser inherently drifts slightly over time. In addition, there are rise and fall times of the signals and slightly differing path lengths for each segment. Compounding this situation, each of the currents has a direct impact on the wavelength through carrier concentration, but there is also an indirect affect on wavelength due to a slight temperature change in the segment. Further complicating this, when the temperature of one segment changes, it will also (with a time constant) change the adjacent segment and then (with a different time constant) change the next adjacent segment, and so on. Every change made to the system also has an effect on all the other variables with differing time constants, and these changes even change the relationship between the other control variables and the wavelength. This represents an imposing problem, indeed.

The first commercial all-semiconductor akinetic laser was developed by Insight Photonic Solutions of Boulder, Colorado, USA [25, 26]. They had spent over 6 years, millions of dollars and utilized the talents of over 35 development scientists and engineers and 20+ top industry technical advisors (including 15 professors and a Nobel Lauriat) to overcome these obstacles. The company claims many patents and patents pending.

23.6.3 Sweeping Tuning Paths

The sweep of the akinetic tunable is designed specifically for use in OCT systems and correlates sweep parameters to accommodate existing data acquisition systems. This includes trigger, clocking, settling times, signal propagation, linearity, and power requirements.

The nature of the VT-DBR laser utilized in swept sources is shown in simplified form in Fig. 23.48.

Tuning consists of the long linear drive current combinations that progress along path 1, then doing the same with path 2, path 3, and so on. The transitions from path to path take single digit nanoseconds.

The laser causes the wavelength at each evenly spaced time as defined by the electronic k-clock output to be correct, providing for linearity.

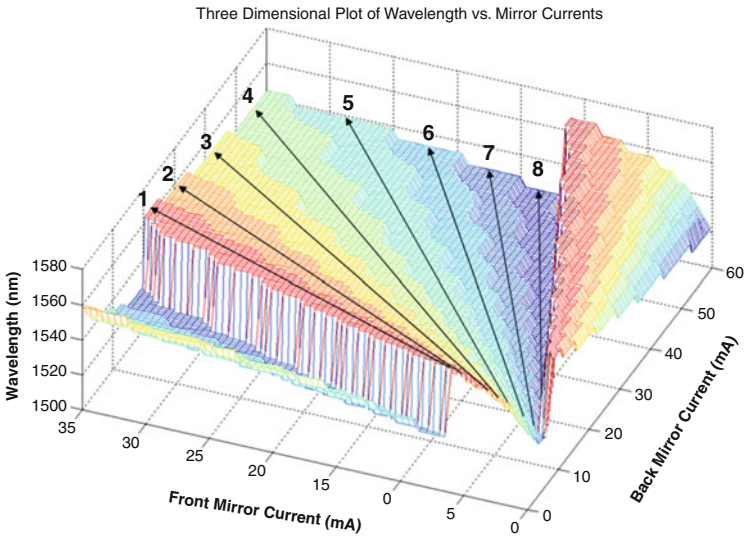

Fig. 23.48 All tuning is handled by the laser control circuitry; initiating a sweep just requires setting a hardware bit or sending a command to initiate the sweep

In the short times between these paths, the laser continues to output exactly evenly spaced-in-time trigger(s) to the data acquisition. After a predefined number of these "hold points," the laser will be back to the next evenly spaced in-frequency point to continue the sweep. The held points are simply removed in software (the laser can be queried for a vector of these hold points) or using a hardware signal ("data valid") which can be sent to the secondary channel of the data acquisition. One data acquisition company has already added this akinetic laser function to their onboard FPGA, eliminating the need for any user programming. Performing this process in software is very fast, as it is a vector function, and LabVIEW VIs are available to make software integration simple.

23.7 Limits of Akinetic All-Semiconductor Technology

Speed. As mentioned previously, maximum laser sweep repetition rate for existing semiconductor lasers and packaging is near 1 M sweeps per second (sps). With reconfigured lasers and packaging, 2 M sps should be attainable. This, though, is likely an upper limit based on today's technology.

Coherence Length. The nonactive coherence length of the all-semiconductor laser is in the 10s of meters. This is substantially higher coherence than the ~200 mm of currently available all-semiconductor lasers. While the nonactive limit may be difficult to achieve, improvement to the existing lasers is likely. In addition, new all-semiconductor topologies promise at least an order-of-magnitude improvement.

Wavelength, Wavelength Range. The materials and processes exist to produce all-semiconductor lasers at 850 nm, 1,060 nm, 1,310 nm, 1,550 nm, and perhaps up to 1,700 nm. Below these wavelengths it is not clear that the processes exist to produce tunable lasers, although frequency multiplication could support lasers in lower wavelength bands. It is believed that the wavelength range of an all-semiconductor system can be extended to roughly 140 nm. While it is possible to extend the range beyond this, cost could become a limiting factor. If the bifurcated wavelength band approach works, the effective range could be further extended. Each new wavelength band requires a semiconductor development, unlike other technologies that can use generally available gain chips. Once developed, chips are very inexpensive and the drive electronics are identical to that of other wavelength bands.

Cost. It seems reasonable to anticipate that the cost of all-semiconductor lasers will trend towards $1,000–2,000 over the next several years. It is not clear that pricing can drop below these levels, but these costs represent a substantial reduction from previous levels.

23.8 Conclusions

The akinetic all-semiconductor technology presents certain unique benefits for optical coherence tomography applications. These capabilities include the ability to perform uniform, linear sweeps while maintaining low RIN, a high SMSR, and sufficient coherence length to permit deep imaging depth range. Due to the novel all-semiconductor design of the akinetic swept laser, these features come without additional cost when compared to traditional mechanical lasers. While the technology is still young (as is OCT in general), akinetic lasers may be able to both respond to the OCT industry's growth and contribute to that growth.

Acknowledgements The writers would like to acknowledge the contributions of Jonathan Huber and Michael Maynard of Insight Photonic Solutions, Austin McElroy and Jordan Dwelle of the University of Texas, Austin; Professor Larry Coldren of the University of California Santa Barbara; Harald Sattmann and Rainer Leitgeb of the University of Vienna; and J.F. de Boer of Vrije Universiteit, Amsterdam.

References

1. E.A. Swanson, D. Huang, M.R. Hee, J.G. Fujimoto, C.P. Lin, C.A. Puliafito, High-speed optical coherence domain reflectometry. Opt. Lett. **17**(2), 151–153 (1992)
2. D. Huang, E.A. Swanson, C.P. Lin, J.S. Schuman, W.G. Stinson, W. Chang, M.R. Hee, T. Flotte, K. Gregory, C.A. Puliafito, Optical coherence tomography. Science **254**(5035), 1178–1181 (1991)
3. S.R. Chinn, E.A. Swanson, H.G. Fujimoto, Optical coherence tomography using a frequency-tunable optical source. Opt. Lett. **22**, 340–342 (1997)

4. E Swanson et al. *Method and apparatus for performing optical frequency domain reflectometry*. US Patent 6,169,826 (Dec 2000)
5. W. Drexler, J. Fujimoto, *Optical Coherence Tomography: Technology and Applications*, vol. 1 (Springer, Berlin, 2008). Chapter 11
6. M.A. Choma, K. Hsu, J.A. Izatt, Swept source optical coherence tomography using an all-fiber 1300 nm ring laser source. J. Biomed. Opt. **10**(4), 044009–044009 (2005)
7. T. Day, F. Michael, I-F. Brownell, Wu. Widely Tunable External Cavity Diode Lasers. *Photonics West'95. International Society for Optics and Photonic*s, http://spie.org/Publications/Proceedings/Paper/10.1117/12.208238, San Jose (1995)
8. K. Liu, M.G. Littman, Novel geometry for single-mode scanning of tunable lasers. Opt. Lett. **6**(3), http://www.opticsinfobase.org/ol/abstract.cfm?uri=ol-6-3-117, 117 (1981)
9. L.A. Kranendonk, R.J. Bartula, S.T. Sanders, Modeless operation of a wavelength-agile laser by high-speed cavity length changes. Opt. Express **13**(5), 1498–1507 (2005)
10. M. Wippich, K.L. Dessau, Tunable lasers enhance fiber sensors. Laser Focus World **39**, 89–94 (2003)
11. Santec data sheet, 50kHz high-speed, Wide range Swept Source, HSL-2100-HW, HSL-2100-HW-C-E/Ver.1.0 CODE-200907-TH-MT-CPY
12. AXSUN Technologies, High Speed 1310nm Swept Source for OCT, datasheet, (2011)
13. B.D. Goldberg, B. Johnson, D. Flanders, *200kHz a-line rate swept-source optical coherence tomography with a novel laser configuration*, AXSUN Technologies Inc. (USA), SPIE Photonics West, 7889–55, talk (2010, unpublished)
14. Santec Corporation, Inner Vision. Optical Coherence Tomography, 2010 volume 1.1, HSL application note 2010-E/Volume.1.1 201005-A4-TH-MT-print
15. S.H. Yun, C. Boudoux, G.J. Tearney, B.E. Bouma, High-speed wavelength-swept semiconductor laser with a polygon-scanner-based wavelength filter. Opt. Lett. **28**(20), 1981–1983 (2003)
16. V. Jayaraman, J. Jiang, H. Li, P. Heim, G. Cole, B. Potsaid, A. Cable, OCT imaging up to 760kHz axial scan rate using single-mode 1310nm MEMS-tunable VCSELs with >100nm tuning range. In *CLEO: Science and Innovations*. Optical Society of America (2011)
17. *Online Data sheet, Thor Labs, MEMS-VCSEL Swept Source OCT*, (2013)
18. Y. Okabe, Y. Sasaki, M. Ueno, T. Sakamoto, S. Toyoda, S. Yagi, M. Haruna, 200 kHz swept light source equipped with KTN deflector for optical coherence tomography. Electron. Lett. **48**(4), 201–220 (2012)
19. R. Huber, M. Wojtkowski, J.G. Fujimoto, Fourier Domain Mode Locking (FDML): a new laser operating regime and applications for optical coherence tomography. Opt. Express **14**(8), 3225–3237 (2006)
20. R. Huber, M. Wojtkowski, K. Taira, J.G. Fujimoto, K. Hsu, Amplified, frequency swept lasers for frequency domain reflectometry and OCT imaging: design and scaling principles. Opt. Express **13**(9), 3513–3528 (2005)
21. B. Pezeshki, E. Vail, J. Kubicky, G. Yoffe, S. Zou, J. Heanue, T. Razazan, 20-mW widely tunable laser module using DFB array and MEMS selection. IEEE Photon. Technol. Lett. **14**(10), 1457–1459 (2002)
22. R. Huber et al., Three-dimensional and C-mode OCT imaging with a compact, frequency swept laser source at 1300 nm. Opt. Express **13**(26), 10523–10538 (2005)
23. J. Lewandowski, D. Marcus, V. Christian, *Light source, and optical coherence tomography module*. WIPO Patent No. 2010111795. (2010)
24. V.J. Srinivasan, R. Huber, I. Gorczynska, J.G. Fujimoto, J. Jiang, P. Reisen, A.E. Cable, High-speed, high-resolution optical coherence tomography retinal imaging with a frequency-swept laser at 850 nm. Opt. Lett. **32**(4), 361–363 (2007)
25. M.P. Minneman, J. Ensher, M. Crawford, D. Derickson, All-semiconductor high-speed akinetic swept-source for OCT. Proc. SPIE **8311**, 831116 (2011)
26. J. Ensher, P. Boschert, K. Featherston, J. Huber, M. Crawford, M.P. Minneman, C. Chiccone, D. Derickson, Long coherence length and linear sweep without an external optical k-clock in

a monolithic semiconductor laser for inexpensive optical coherence tomography. Proc. SPIE **8213**(82130T) (2012)
27. J. Kilby, *Texas Instruments*, http://www.ti.com/corp/docs/kilbyctr/jackbuilt.shtml
28. G. E. Moore, Cramming More Components onto Integrated Circuits, *Electronics*, pp. 114–117 (1965)
29. R. Kurzweil, *The Singularity is Near: When Humans Transcent Biology*. (Viking Press, 2005)
30. Optical Coherence Tomography/General Medicine: Low-cost OCT probe targets primary care, developing countries, *Bioptics World*, 11/01/2012
31. L. A. Coldren, *Multi-section tunable laser with differing multi-element mirrors*. US Patent 4,896,325, issued (January 23, 1990)
32. *J. Sel. Top. Quant. Electron.* **6**(6), 988–999 (2000)
33. L.A. Coldren, G.A. Fish, Y. Akulova, J.S. Barton, L. Johansson, C.W. Coldren, Tunable semiconductor lasers: A tutorial. J. Light. Technol. **22**(1), 193 (2004)
34. R. Schatz, *Advances in Widely Tunable Lasers* (Laboratory of Photonics, Royal Institute of Technology)
35. B. Pezeshki, *Tunable optical device using a scanning MEMS mirror*. US Patent No. 6,791,694. (14 Sep. 2004)
36. A.J. Ward, D.J. Robbins, G. Busico, E. Barton, L. Ponnampalam, J.P. Duck, M.J. Wale, Widely tunable DS-DBR laser with monolithically integrated SOA: design and performance. Selected Topics in Quantum Electronics. IEEE J. Sel. Top. Quantum Electron. **11**(1), 149–156 (2005)
37. T. Amano, H. Hiro-Oka, D. Choi, H. Furukawa, F. Kano, M. Takeda, M. Nakanishi, K. Shimizu, K. Ohbayashi, Optical frequency-domain reflectometry with a rapid wavelength-scanning superstructure-grating distributed Bragg reflector laser. Appl. Optics **44**(5), 808–816 (2005)
38. N. Fujiwara, R. Yoshimura, K. Kato, H. Ishii, F. Kano, Y. Kawaguchi, Y. Kondo, K. Ohbayashi, H. Oohashi, 140-nm Quasi continuous fast sweep using SSG-DBR lasers. Photon. Technol. Lett. **18**, 1015–1017 (2008)
39. H. Kakuma, K. Ohbayashi, Y. Arakawa, Optical imaging of hard and soft dental tissues using discretely swept optical frequency domain reflectometry optical coherence tomography at wavelengths from 1560 to 1600 nm. J. Biomed. Opt. **13**(1), 0140121–0140126 (2008)
40. D. Choi, R. Yoshimura, H. Hiro-Oka, H. Furukawa, A. Goto, N. Satoh, K. Ohbayashi, Discretely swept optical coherence tomography system using super-structure grating distributed Bragg reflector lasers at 1561–1639nm. In *Proc. of SPIE* **8213**, 82132F-1) (2012)
41. H. Kakuma, D. Choi, H. Furukawa, H. Hiro-Oka, K. Ohbayashi, 24 mm depth range discretely swept optical frequency domain imaging in dentistry. In *SPIE BiOS: Biomedical Optics*. International Society for Optics and Photonics, Feb 2009, pp. 716208–716208
42. C. Doyle, et al. Chapter structural health monitoring using optical fibre strain sensing systems, in *Structural Health Monitoring 2003: From Diagnostics & Prognostics to Structural Health Management; Proceedings of the 4th International Workshop on Structural Health Monitoring, Stanford University, Stanford, CA, September 15–17, 2003*
43. Phoenix 1400 Tunable Laser Source brochure, 10/2012, LTPHO1400
44. M. Kuznetsov, W. Atia, B. Johnson, D. Flanders. Compact ultrafast reflective Fabry-Perot tunable lasers for OCT imaging applications. In *BiOS*. International Society for Optics and Photonics, (2010), pp. 75541F–75541F
45. D. Derickson, *Fiber Optic Test and Measurement* (Prentice Hall PTR, Upper Saddle River, 1998)
46. S. O'Connor, M. A. Bernacil, D. Derickson, Generation of high speed, linear wavelength sweeps using sampled grating distributed bragg reflector lasers *Proc. IEEE LEOS* (2008), pp. 147–148
47. *All-semiconductor akinetic swept laser technology background*, Insight Photonic Solutions, Inc, www.sweptlaser.com.

48. C.E. Saxer, J.F. de Boer, B.H. Park, Y. Zhao, Z. Chen, J.S. Nelson, High-speed fiber based polarization-sensitive optical coherence tomography of in vivo human skin. Opt. Lett. **25**(18), 1355–1357 (2000)
49. B.J. Vakoc, S.H. Yun, J.F. De Boer, G.J. Tearney, B.E. Bouma, Phase-resolved optical frequency domain imaging. Opt. Express **13**(14), 5483 (2005)
50. A.H. Dhalla, D. Nankivil, J.A. Izatt, Complex conjugate resolved heterodyne swept source optical coherence tomography using coherence revival. Biomed. Opt. Express **3**(3), 633 (2012)
51. D. Wolfgang, J. G. Fugimoto, *Optical Coherence Tomography: Technology and Applications* (Springer, New York, 2008), p. 377
52. M.J. Marrone, A.D. Kersey, A. Dandridge, *Fiber optic Michelson Array with Passive Elimination of Polarization Fading and Source Feedback Isolation. Optical Fiber Sensors* (Optical Society of America, Monterey, 1992)
53. D. Derickson, *Chapters 4 and 9 Fiber Optic Test and Measurement* (Prentice Hall PTR, Upper Saddle River, 1998)
54. Axsun Technologies, OCT Capabilities. *SPIE BIOS* (Jan 2010), p 11
55. D. Derickson, *Fiber Optic Test and Measurement* (Prentice Hall PTR, Upper Saddle River, 1998). Chapter 5
56. K. Jeehyun, D.T. Miller, E.K. Kim, S. Oh, J.H. Oh, E. Thomas, T.E. Milner, Optical coherence tomography speckle reduction by a partially spatially coherent source. J. Biomed. Opt. **10**(06), 064034 (2005)
57. B. Liu, M.E. Brezinski, Theoretical and practical considerations on detection performance of time domain, Fourier domain, and swept source optical coherence tomography. J. Biomed. Opt. **12**(4), 044007–044007 (2007)
58. G.J. Tearney, B.E. Bouma, S.A. Boppart, B.S.E.A. Golubovic, E.A. Swanson, J.G. Fujimoto, Rapid acquisition of in vivo biological images by use of optical coherence tomography. Opt. Lett. **21**(17), 1408–1410 (1996)
59. G.J. Tearney, S. Waxman, M. Shishkov, B.J. Vakoc, M.J. Suter, M.I. Freilich, A.E. Desjardins, W.-Y. Oh, L.A. Bartlett, M. Rosenberg, B.E. Bouma, Three-dimensional coronary artery microscopy by intracoronary optical frequency domain imaging. J. Am. Coll. Cardiol. Img. **2008**, 1752–1761 (2008). doi:10.1016/j.jcmg.2008.06.007
60. S.H. Yun, G.J. Tearney, B.J. Vakoc, M. Shiskov, W.Y. Oh, A.E. Desjardins, M.J. Suter, R.C. Chan, J.A. Evans, I.K. Jang, N.S. Nioshioka, J.F. de Boer, B.E. Bouma, Comprehensive volumetric optical microscopy in vivo. Nat. Med. **12**(12), 1429–1433 (2006)
61. D.C. Adler, Y. Chen, R. Huber, J. Schmitt, J. Connolly, J.G. Fujimoto, Three-dimensional endomicroscopy using optical coherence tomography. Nat. Photon. **1**, 709–716 (2007)
62. M.W. Jenkins, F. Rothenberg, D. Roy, V.P. Nikolski, Z. Hu, M. Watanabe, A.M. Rollins, 4D embryonic cardiography using gated optical coherence tomography. Opt. Express **14**(2), 736–748 (2006)
63. B. Goldberg, B. Johnson, D. Flanders, 200kHz a-line rate swept-source optical coherence tomography with a novel laser configuration, AXSUN Technologies Inc. (USA), SPIE Photonics West 2010, 7889–55, talk (2010, unpublished)
64. J. Xi, L. Huo, J. Li, X. Li, Generic real-time uniform K-space sampling method for high-speed swept-source optical coherence tomography. Opt. Express **18**(9), 9511 (2010)
65. Y. Yasuno, V.D. Madjarova, S. Makita, M. Akiba, A. Morosawa, C. Chong, T. Sakai, K.-P. Chan, M. Itoh, T. Yatagai, Three-dimensional and high-speed swept-source optical coherence tomography for in vivo investigation of human anterior eye segments. Opt. Express **13**(26), 10652 (2005)
66. R. Huber, M. Wojtkowski, K. Taira, J.G. Fujimoto, K. Hsu, Amplified, frequency swept lasers for frequency domain reflectometry and OCT imaging: design and scaling principles. Opt. Express **13**(9), 3513–3528 (2005)
67. S. Vergnole, D. Lévesque, G. Lamouche, Experimental validation of an optimized signal processing method to handle non-linearity in swept-source optical coherence tomography. Opt. Express **18**(10), 10446–10461 (2010)

68. A. M. Davis, M. A. Choma, J. A. Izatt, Heterodyne swept-source optical coherence tomography for complete complex conjugate ambiguity removal., *J. Biomed. Opt.* 0001;**10**(6):064005–064005-6
69. W. Tong, D. Zhihua, L. Wang, C. Minghui, Spectral phase based k-domain interpolation for uniform sampling in swept-source optical coherence tomography. Opt. Express **19**, 18430 (2011)
70. B.R. Washburn, R. Fox, N.R. Newbury, J.W. Nicholson, K. Feder, P.S. Westbrook, C.G. Jørgensen, Fiber-laser-based frequency comb with a tunable repetition rate. Opt. Express **12**(4999–5004), 10–15 (2004)
71. TI App Note Thomas Neu, Clock jitter analyzed in the time domain, Part 1, *Analog. Appl. J.*, **3**Q, 5–9 (2010)
72. S.-Y. Baek, O. Kwon, Y.-H. Kim, High-resolution mode-spacing measurement of the blue-violet diode laser using interference of fields created with time delays greater than the coherence time. Jpn. J. Appl. Phys. **46**(12), 7720–7723 (2007)
73. D. Piao, Q. Zhu, N.K. Dutta, S. Yan, L.L. Otis, Cancellation of coherent artifacts in optical coherence tomography imaging. Appl. Optics **40**(28), 5124–5131 (2001)
74. Model WA-1530-1560 spec sheet. dBmOptics.com. p 7. http://www.dbmoptics.com/downloads/brochures/WavelengthGasCells.pdf
75. B.H. Park, M.C. Pierce, B. Cense, S.H. Yun, M. Mujat, G.J. Tearney, B.E. Bouma, J.F. de Boer, Real-time fiber-based multi-functional spectral-domain optical coherence tomography at 1.3 μm. Opt. Express **13**, 3931–3944 (2005)
76. S. Yazdanfar, C.H. Yang, M.V. Sarunic, J.A. Izatt, Frequency estimation precision in Doppler optical coherence tomography using the Cramer-Rao lower bound. Opt. Express **13**, 410–416 (2005)
77. R.K. Manapuram, V.G.R. Manne, K.V. Larin, Phase-sensitive swept source optical coherence tomography for imaging and quantifying of microbubbles in clear and scattering media. J. Appl. Phys. **105**(10), 102040–102040 (2009)
78. J. Mo, L. Jianan , J. F. de Boer. Correction of phase-error for phase-resolved k-clocked optical frequency domain imaging. In *Proc. of SPIE Vol*, **8213**, 82132V-1. (2012)
79. W.J. Choi, B. Potsaid, V. Jayaraman, B. Baumann, I. Grulkowski, J.J. Liu, C.D. Lu, A.E. Cable, D. Huang, J.S. Duker, J.G. Fujimoto, Phase-sensitive swept-source optical coherence tomography imaging of the human retina with a vertical cavity surface-emitting laser light source. Opt. Lett. **38**(3), 338–340 (2013)
80. D.C. Adler, R. Huber, J.G. Fujimoto, Phase-sensitive optical coherence tomography at up to 370,000 lines per second using buffered Fourier domain mode-locked lasers. Opt. Lett. **32**(6), 626–628 (2007)
81. G. Liu, L. Chou, W. Jia, W. Qi, B. Choi, Z. Chen, Intensity-based modified Doppler variance algorithm: application to phase instable and phase stable optical coherence tomography systems. Opt. Express **19**(12), 11429 (2011)
82. J. Zhang, C. Zhongping, Quantitative phase imaging with spectral-domain optical coherence phase microscopy, in *Microscopy: Science, Technology, Applications and Education*, ed. by A. Méndez-Vilas, J. Díaz (Formatex Research Center, Badajoz, 2010), p. 1397
83. B. White, M. Pierce, N. Nassif, B. Cense, B. Park, G. Tearney, B. Bouma, T. Chen, J. de Boer, In vivo dynamic human retinal blood flow imaging using ultra-high-speed spectral domain optical coherence tomography. Opt. Express **11**(25), 3490–3497 (2003)
84. D. Wolfgang, J.G. Fugimoto, *Optical coherence tomography: technology and applications* (Springer, New York, 2008), 772pp
85. R.V. Kuranov, A.B.. McElroy, N. Kemp, S. Baranov, J. Taber, M.D. Feldman, T.E. Milner, Gas-cell referenced swept source phase sensitive optical coherence tomography. IEEE Photon. Technol. Lett. **22**(20), 1524–1526 (2010)
86. Z. Lu, D.K. Kasaragod, S.J. Matcher, Method to calibrate phase fluctuation in polarization-sensitive swept-source optical coherence tomography. J. Biomed. Opt. **16**(7), 070502–070502 (2011)

87. A.M. Rollins, J.A. Izatt, Optimal interferometer designs for optical coherence tomography. Opt. Lett. **24**, 1484–1486 (1999). <Go to ISI>://000083598000014
88. M.A. Choma, A.K. Ellerbee, C.H. Yang, T.L. Creazzo, J.A. Izatt, Spectral-domain phase microscopy. Opt. Lett. **30**, 1162–1164 (2005). <Go to ISI>://000229011800026
89. J. Park, J.A. Jo, S. Shrestha, P. Pande, Q. Wan, B.E. Applegate, A dual-modality optical coherence tomography and fluorescence lifetime imaging microscopy system for simultaneous morphological and biochemical tissue characterization. Biomed. Opt. Express **1**, 186–200 (2010)
90. Texas Instrument ADS5474 14-Bit, 400-MSPS Analog-to-Digital Converter data sheet. Revised Feb 2012, http://www.ti.com/lit/ds/symlink/ads5474.pdf
91. S.H. Yun, G.J. Tearney, J.F. de Boer, N. Iftimia, B.E. Bouma, High-speed optical frequency-domain imaging. Opt. Express **11**, 2953–2963 (2003)
92. D. Redmayne, E. Trelewicz, A. Smith, Understanding the effect of clock jitter on high speed ADCs, *linear technology design notes* 1013, Fig. 2. http://cds.linear.com/docs/en/design-note/dn1013f.pdf
93. S.H. Yun, C. Boudoux, M.C. Pierce, J.F. De Boer, G.J. Tearney, B.E. Bouma, Extended-cavity semiconductor wavelength-swept laser for biomedical imaging. IEEE Photon. Technol. Lett. **16**(1), 293–295 (2004)
94. W. Drexler, J.G. Fujimoto, *P411, Optical Coherence Tomography: Technology and Applications* (Springer, New York, 2008)
95. A.G. Podoleanu, Unbalanced versus balanced operation in an optical coherence tomography system. Appl. Optics **39**(1), 173–182 (2000)
96. M. Abtahi, S. Ayotte, J. Penon, L.A. Rusch, Intensity noise in balanced detection of correlated incoherent signals, in *Proc. IASTED Int. Conf. Wireless Opt. Commun*, Montreal, 204–209 (2007)
97. H. Hiro-Oka, D. Choi, H. Furukawa, R. Yoshimura, K. Ohbayashi, T. Wakabayashi, Use of cosine tapered window to improve dynamic range of OCT without loss of resolution. *Int. Biomedical Optics* (*BiOS*), International Society for Optics and Photonics (2008), pp. 68472C–68472C
98. JDSU, Relative Intensity Noise, Phase Noise, and Linewidth (application note) 1–8, (2006)
99. D. Wolfgang, J. G. Fugimoto, *Optical coherence tomography: technology and applications* (Springer, New York, 2008), p. 362
100. Y. Chen, D.M. de Bruin, C. Kerbage, J.F. de Boer, Spectrally balanced detection for optical frequency domain imaging. Opt. Express **15**(25), 16390–16399 (2007)
101. V.M. Kodach, J. Kalkman, D.J. Faber, T.G. Van Leeuwen, Quantitative comparison of the OCT imaging depth at 1300 nm and 1600 nm. Biomed. Opt. Express **1**(1), 176–185 (2010)
102. U. Sharman, E. Chang, S. Yun, Long-wavelength optical coherence tomography at 1.7 7 μm for enhanced imaging depth. Opt. Express **16**(24), 19712–19723 (2008)
103. M. Kaschke, S. Meyer, M. Everett, M. Grahl, Optical coherence tomography: a case study in medical imaging adoption. Optik Photonik **4**(4), 24–28 (2009)
104. M.R. Hee, D. Huang, E.A. Swanson, J.G. Fujimoto, Polarization-sensitive low-coherence reflectometer for birefringence characterization and ranging. J. Opt. Soc. Am. **B 9**(6), 903–908 (1992)
105. J.F. de Boer, T.E. Milner, M.J.C. van Gemert, J.S. Nelson, Two-dimensional birefringence imaging in biological tissue by polarization-sensitive optical coherence tomography. Opt. Lett. **22**(12), 934–936 (1997)
106. M.J. Everett, K. Schoenenberger, B.W. Colston Jr., L.B. Da Silva, Birefringence characterization of biological tissue by use of optical coherence tomography. Opt. Lett. **23**(3), 228–230 (1998)
107. B. Cense, T.C. Chen, B.H. Park, M.C. Pierce, J.F. de Boer, In vivo depth-resolved birefringence measurements of the human retinal nerve fiber layer by polarization-sensitive optical coherence tomography. Opt. Lett. **27**(18), 1610–1612 (2002)
108. B.H. Park, C. Saxer, S.M. Srinivas, J.S. Nelson, J.F. de Boer, In vivo burn depth determination by high-speed fiber-based polarization sensitive optical coherence tomography. J. Biomed. Opt. **6**(4), 474–479 (2001)

109. B. Elmaanaoui, B. Wang, J.C. Dwelle, A.B.. McElroy, S.S. Liu, H.G. Rylander III, T.E. Milner, Birefringence measurement of the retinal nerve fiber layer by swept source polarization sensitive optical coherence tomography. Opt. Express **19**(11), 10252 (2011)
110. J. Schmitt, *Methods and apparatus for swept-source optical coherence tomography*. WIPO Patent 2,008,086,017, issued (18 July 2008)
111. Model 4650 Swept Spectrometer technical brochure. *General purpose instrumentation*, dBm Optics Inc. (2008), http://www.dbmoptics.com/downloads/brochures/4650.pdf
112. Application Note, Agilent, polarization measurements of signals and components product note 8509–1
113. O. Sezerman, G. Best, Accurate alignment preserves polarization. Laser Focus World **33**(12), S27–S30 (1997)
114. B. Zabihian, M. Minneman, M. Bonesi, J. Ensher, H. Sattmann, S. Gray, R. Leitgeb, M. Crawford, and W. Drexler, "Akinetic swept-source technology for high speed OCT with unprecedented coherence length," in *Optics in the Life Sciences, OSA Technical Digest* (*online*), *paper BT3A.2*, (Optical Society of America, 2013)
115. B.E. Bouma, S.H. Yun, B.J. Vakoc, M.J. Suter, G.J. Tearney, Fourier-domain optical coherence tomography: recent advances toward clinical utility. Curr. Opin. Biotechnol. **20**(1), 111–118 (2009)
116. L.A. Coldren, Extended tuning range in sampled grating DBR lasers. Photon. Technol. Lett. IEEE **5**(5), 489–491 (1993)
117. Y.A. Akulova, G.A. Fish, P.C. Koh, C.L. Schow, P. Kozodoy, A.P. Dahl, L.A. Coldren, Widely tunable electroabsorption-modulated sampled-grating DBR laser transmitter. Sel. Top. Quantum Electron. IEEE J. **8**(6), 1349–1357 (2002)
118. *Generic Reliability Assurance Requirements for Optoelectronic Devices Used in Telecommunications Equipment*, Telcordia Document Number GR-468, Issue Number 2, Issue Date (Sep 2004)
119. A.-A. Abdul, *Fiber Optics: Principles and Practices*. Optical Science and Engineering Series (CRC Press, Boca Raton, 2006)
120. Y. Mao, S. Chang, E. Murdock, C. Flueraru, Simultaneous dual-wavelength-band swept source and dual-band common-path optical coherence tomography. Opt. Lett. **36**, 1990–1992 (2011)
121. S. Kray, F. Spoeler, M. Forst, H. Kurz, High-resolution simultaneous dual-band spectral domain optical coherence tomography. Opt. Lett. **34**(13), 1970–1972 (2009)
122. F. Spoeler, S. Kray, P. Grychtol et al., Simultaneous dual-band ultra-high resolution optical coherence tomography. Opt. Express **15**(17), 10832–10841 (2007)
123. S. Chang, Y. Mao, C. Flueraru, Dual-source swept-source optical coherence tomography reconstructed on integrated spectrum. Intl J Optics **2012**, 1–6 (2012)
124. D. Sacchet, J. Moreau, P. Georges, A. Dubois, Simultaneous dual-band ultra-high resolution full-field optical coherence tomography. Opt. Express **16**(24), 19434–19446 (2008)
125. Corning SMF-28e + ®*Photonic Optical Fiber datasheet*, doc M1100025 (March 2010), www.corning.com (2013), pp 33–36, http://www.corning.com/WorkArea/downloadasset.aspx?id=30931
126. D. Wolfgang, J.G. Fujimoto, *Chapter 21, optical coherence tomography: technology and applications* (Springer, New York, 2008)
127. D. Wolfgang, J.G. Fugimoto, *Chapter 6, optical coherence tomography: technology and applications* (Springer, New York, 2008)
128. D. Wolfgang, J.G. Fugimoto, *Chapter 22, optical coherence tomography: technology and applications* (Springer, New York, 2008)
129. L.A. Coldren, G.A. Fish, Y. Akulova, J.S. Barton, L. Johansson, C.W. Coldren, Tunable semiconductor lasers: a tutorial. J. Light. Technol. **22**, 193–202 (2004)
130. B.R. Bennett, R.A. Soref, J.A. Del Alamo, Carrier-induced change in refractive index of InP, GaAs and InGaAsP. IEEE J. Quantum Electron. **26**(1), 113–122 (1990)

FDML (incl. Parallelization)

24

Robert Huber

24.1 Introduction

24.1.1 History of Tunable Lasers and the OCT Challenge

Widely wavelength tunable lasers, i.e., laser where the emission wavelength can be changed in a desired, predefined way by several percent, have been known since the 1960s. For a long time, dye lasers have been the light sources of choice for applications that required wavelength tunable lasers [1, 2]. Later also bulk optics solid state systems, like cw-Ti:sapphire lasers [3, 4] or external cavity semiconductor lasers [5–7], became popular. Depending on their application, tunable lasers are often termed (a) *wavelength agile lasers*, in cases where the application demands fast changes in wavelength to arbitrary positions, (b) *tunable lasers* in cases where the laser is slowly tuned to a wavelength and is stabilized there for a longer time, and (c) *wavelength-swept lasers* in cases where an optical waveform is required that continuously changes wavelength.

In almost all SS-OCT/OFDI applications, ***wavelength-swept lasers*** are required. The wavelength ranges are centered around 800 nm [8, 9] or 1,050 nm [10, 11, 12] for retinal imaging and 1,300 nm [13, 14] or 1,550 nm [15] for highly scattering samples. The most important performance specifications required for OCT significantly differ from the ones typically needed in other tunable laser applications. Today a typical "100^3 performance" of an SS-OCT laser is (a) a wavelength sweep range of $\sim$100 nm, (b) a wavelength sweep repetition rate of $\sim$100 kHz, and (c) an instantaneous linewidth of $\sim$100 pm. The wavelength sweep range determines the axial resolution in OCT, and wider sweep operation results in better axial resolution. The sweep repetition rate directly translates to the OCT A-scan rate of

R. Huber
Institut für Biomedizinische Optik, Universität zu Lübeck, Lübeck
e-mail: Robert.Huber@BMO.Uni-Luebeck.DE

© Springer International Publishing Switzerland 2015

W. Drexler, J.G. Fujimoto (eds.), *Optical Coherence Tomography*,
DOI 10.1007/978-3-319-06419-2_25

the system. The instantaneous linewidth determines the inherent additional system's signal decay over ranging depth often called "sensitivity roll off." Whereas a linewidth below 100 pm has easily been achieved by tunable lasers long before their application to OCT, the combination of the required wide sweep range and fast sweep repetition rate was not available before the year 2000. A sweep operation of 100 nm at a center wavelength of 1 μm corresponds to 10 % relative wavelength tuning, about 30 THz optical frequency. Taking a 100 kHz sweep repetition rate, this is a frequency tuning speed of 3 THz/μs or 3e18 Hz/s.

24.1.2 The Limit of Standard Tunable Lasers: Cavity Buildup Dynamics

A standard tunable laser consists, like all lasers, of (a) a laser gain medium, which can simply be seen as light amplifier which increases the electric field of the incoming light, and (b) a resonator, i.e., the laser cavity, which feeds light from the output of the amplifier back to the input [14]. Resonators are, for example, two mirrors bouncing light forward and backward in a linear geometry or a piece of optical fiber guiding the amplifier output light back to the input. At some point in the resonator, a part of the light is extracted as the laser's output.

To make the laser tunable in wavelength, an additional filter element in the resonator acting as tunable optical bandpass is inserted. This filter transmits only a very narrow wavelength range, in OCT applications typically about 0.1 nm, thereby forcing the laser to operate at wavelengths within this passband (i.e., the transmission window) of the filter. This operation is sketched in Fig. 24.1 [14]. Now to operate a tunable laser as a wavelength-swept light source, the optical bandpass filter is controlled in a way such that it dynamically changes its passband, i.e., the transmitting wavelength window. Such a dynamic tuning causes the laser to operate in a nonstationary regime. This is depicted in Fig. 24.2 [14]. The figure shows the intensity over wavelength. The blue curve is the transmission window of the optical bandpass filter. Within this window, typically several so-called laser modes are active (here: ten red peaks under the blue filter curve). These laser modes are the only "allowed" discrete frequencies set by the laser resonator condition $f_n = n^* c/l$.

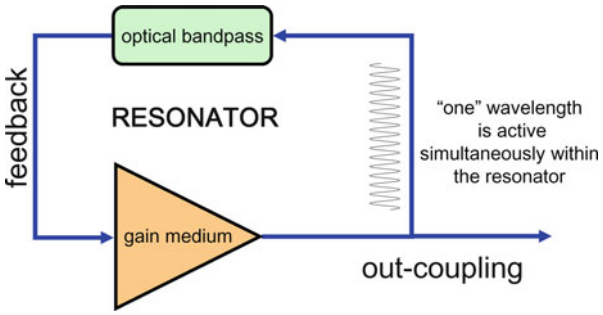

Fig. 24.1 Circuit diagram of a standard tunable laser/swept laser [14, 27]. A laser resonator/oscillator is an optical feedback loop. Inserting a tunable optical bandpass filter enables wavelength tuning [14]

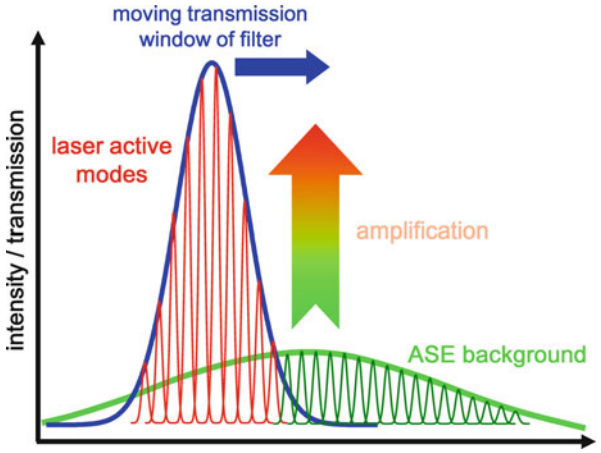

Fig. 24.2 Tunable laser buildup dynamics [14, 27]. The diagram shows the tuning operation of a standard wavelength-swept laser. As the transmission window of the optical bandpass filter (*blue line*) is moved in wavelength, the laser light field (*red lines*, laser modes) has to build up from amplified spontaneous emission (fluorescence) background (*green*). If the filter is tuned too fast, there is not enough time to build up saturated lasing – this effect limits the maximum achievable tuning speed

Where f_n is the *n*th optical frequency, *c* is the speed of light and *l* is the effective optical roundtrip length. Since these laser modes are circulating in the laser cavity and their light is amplified once per roundtrip, they have the highest intensity. The dynamic shift of the filter, indicated by the blue arrow in Fig. 24.2, will lead to increased loss of the active laser light, once the transmission maximum has substantially moved away from the spectral position. At the filter's new wavelength position, where initially there is no strong laser light, the intensity will slowly build up from amplified spontaneous emission (ASE) background by many amplification events in the laser gain medium. ASE is fluorescence that is amplified in the laser gain medium. Since the ASE intensity is typically many orders of magnitude smaller than the laser light intensity, several roundtrips of light in the laser cavity are required to achieve sufficient power. With the fact that light is amplified once per resonator roundtrip, it becomes clear that for fast tuning operation, a short resonator, which provides many roundtrips per second, in combination with a high amplification factor in the gain medium, so that a small number of amplification events are sufficient, is required.

Typical numbers of short cavity lasers are resonator roundtrip lengths of about 0.3 m, yielding ~1 GHz roundtrip frequency and an amplification factor in the gain medium of about a factor of 1,000×. If such a laser should be swept over a 100 nm wavelength range with 100 kHz sweep repetition rate (10 µs sweep repetition time) and a 0.1 nm wide spectral filter is used for tuning, light is only transmitted through the filter for about 0.1 nm/100 nm*10 µs = 10 ns. So light in a 1 GHz (0.3 m length) laser resonator can only perform ~10 roundtrips until it is blocked again. In this

configuration 1000 kHz sweep rate would be the absolute maximum frequency of the laser, since for faster tuning, light wouldn't even be able to finish a single roundtrip before the filter blocks the wavelength again. Strategies to further shorten the laser resonator lead to the problem that the resonator mode spacing, i.e., the optical frequency spacing of the "allowed" laser modes, spreads more and more, leading to a more stepwise, very coarse, and discrete frequency tuning characteristic [16]. The laser jumps from one mode to the next. For OCT application this is a major problem, because the maximum ranging depth of the OCT setup is directly linked to the spectral sampling density. When using classical tunable lasers for SS-OCT, the maximum imaging range cannot be longer than the laser's optical roundtrip length.

Recently, strategies have been demonstrated to solve the problem of the increasing spectral spread (coarse mode hopping operation) of laser modes when reducing the cavity length. One approach, followed in the "akinetic OCT laser source" [17], is to insert an additional active element, a "phase section," which allows to adjust the resonator length such that an "allowed" resonator frequency shifts synchronously with the laser tuning operation. The active synchronization requires complex electronic driving signals and repetitive resetting, blocking the source for ~10 ns every 1 nm tuning.

Another approach to solve the problem of the increasing spectral spread of laser modes when reducing the cavity length is vertical-external-cavity surface-emitting laser (VECSEL) or often just called vertical-cavity surface-emitting laser (VCSEL) [18–25] (▶ Chap. 22, "VCSEL Swept Light Sources", Jayaraman). In these lasers, the laser cavity acts as Fabry-Perot filter with a very wide free spectral range (optical frequency spacing between two laser modes) with the effect that the laser resonator modes are automatically always synchronously tuned to the laser sweep operation. Additionally, light in the laser resonator is Doppler shifted each time it is reflected from the moving laser end mirror; this solves the problem of the repeated buildup of laser light from ASE. The Doppler shift has always the right amount to match and synchronize to the tuning operation. A more detailed description of the intracavity Doppler shift and calculations is given by A. Siegman in the book *Lasers* [26].

24.2 Fourier Domain Mode Locking (FDML)

24.2.1 The Concept

The technique of Fourier domain mode locking (FDML) is one way to overcome the physical limitation of cavity buildup dynamics. The idea behind it is to synchronize the optical roundtrip time of light circulating in the laser cavity with the filter sweep operation period of the optical bandpass [14, 27, 28]. This means one tuning period of the laser takes exactly as long as the light needs to propagate through the laser cavity. In other words, light with a certain wavelength is transmitted through the optical bandpass filter and then propagates through a very long laser cavity, realized by an optical delay line. Meanwhile the optical bandpass filter

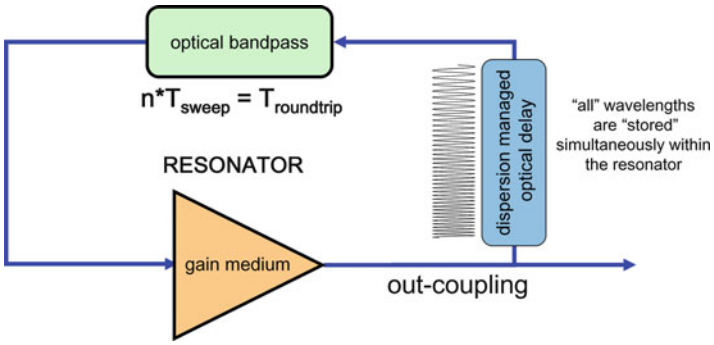

Fig. 24.3 Circuit diagram of an FDML laser [27]. An FDML laser consists of the same elements as a standard tunable laser plus an additional optical delay line (usually a km long fiber spool) to generate the long roundtrip times

is swept over one entire cycle, covering all desired wavelengths, and just when the light arrives back at the filter, the filter transmits this wavelength again, but now already for the next wavelength sweep. This means light does not have to build up from ASE background; it is still there from the last wavelength sweep. In other words, the entire wavelength sweep is optically stored inside the laser cavity. The setup of an FDML laser is identical to a regular swept laser, besides an additional very long optical delay line. Since sweep repetition rates of $f_{sweep} = \sim 100$ kHz require optical path length of $\Delta L = c/f_{sweep} = c/100{,}000\ \text{Hz} = 3$ km, usually a spool of optical single mode fiber is used. To make all wavelength components circulate at the same frequency, the chromatic dispersion of the fiber delay lines has to be compensated. The better the compensation, the higher the number of effective roundtrips of the photons inside the laser and the better the performance of the swept source [29, 30] (Fig. 24.3).

The synchronization condition of FDML operation leads to the effect that the light of a certain wavelength sees the spectral optical bandpass filter always in the same position (see Fig. 24.4, right), whereas in a standard tunable laser, light always is transmitted through a slightly changing filter (see Fig. 24.4, left). The fact the periodic operation makes the filter look "non-tuned" for the light results in a stationary operation of the FDML laser (see Fig. 24.4, right) [36].

24.2.2 Advantages of FDML

The system design and the fact that FDML is a stationary laser operating mode yield many advantages which dramatically improve the performance of the swept laser and, consequently, the OCT system specifications:

1. The high number of effective roundtrips leads to the effect of repetitive spectral filtering (mode competition) making the spectral linewidth of FDML laser much narrower than the one of standard tunable lasers with the same filter

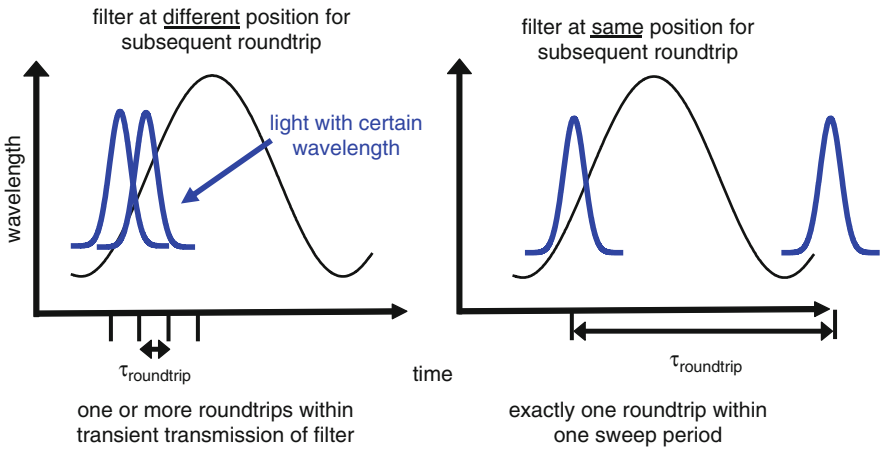

Fig. 24.4 Quasi-stationary filter in FDML operation. *Left*: Nonstationary operation of a standard tunable laser with a sinusoidally driven filter (*black line*). As light of a certain wavelength arrives at the filter after one roundtrip, the filter has changed its spectral position (*black line*). *Right*: In case of FDML the optical roundtrip time is increased so much that when light of a certain wavelength arrives back at the filter after one roundtrip, the periodically driven filter is at exactly the same position (but at the next cycle). This makes FDML a real stationary operation mode

width [27, 29–33]. The narrower linewidth improves the roll-off performance in OCT applications, resulting in a longer ranging depth [29, 30, 34, 35].

2. The fact that the laser light is seeded from the last roundtrip and that FDML is a real stationary laser operating regime reduces the relative intensity noise (RIN) of the laser [29, 32, 33, 36–38], which makes it much easier to design a high-speed OCT system that achieves shot noise-limited sensitivity [39].
3. The good saturation of the laser gain medium enables very high output powers of 100 mW and more, which improves the noise sensitivity in OCT applications where high-power incident on the sample is tolerable [40–43].
4. The separation of laser gain medium and filter element in FDML enables much more flexible system designs compared to VCSEL sources and standard tunable lasers. In both latter cases, the gain medium has to be very short, so typically only semiconductor media can be used. In FDML, almost all groups of laser gain media can be used with length up to meters, such as rare earth-doped fiber amplifiers, nonlinear Raman amplifiers, etc. [44–51]. This enables a much more flexible design of the target wavelengths; improves, as already mentioned, the achievable output power by orders of magnitude; and can dramatically reduce ASE background noise.
5. The high sweep to sweep reproducibility of FDML lasers with respect to their wavelength tuning operation renders hardware clocking in the OCT system unnecessary and reduces system cost [35, 43, 113].
6. Especially at 1,300 and 1,550 nm, FDML lasers are entirely built of standard telecom components [15, 27], which leads to very long lifetimes and high reliability.

24.2.3 The Name FDML and Other Lasers with Resonant Frequency Modulation

24.2.3.1 FDML Compared to Continuous Wave (CW) Lasers and Standard Mode-Locked Lasers

From a viewpoint of physics, FDML lasers are very different from other tunable lasers, because in FDML, the light field of the entire wavelength sweep is optically stored inside the laser resonator. So effectively, a wide range of laser modes is simultaneously active. In comparison, standard wavelength-swept lasers have only one or very few wavelength modes simultaneously active inside the resonator. The situation is sketched in Fig. 24.5. On the left and in the center, the two classical stationary laser operating regimes are shown. On the top is the emitted electric field and on the bottom the corresponding spectrum, which is essentially the squared amplitude of the Fourier transform of the field. A standard narrowband cw laser ideally has a harmonic wave output (Fig. 24.5, left top); the spectrum is a narrow peak (Fig. 24.5, left bottom). A classical mode-locked laser [52], like a femtosecond titanium sapphire laser, has an electric field output representing a train of short pulses (Fig. 24.5, center top), and the corresponding spectrum has a comblike structure with a wide spectral range (Fig. 24.5, center bottom). If this frequency comb is stabilized and the absolute position of each individual comb line is known, a wealth of applications in metrology and sensing can be realized [53]. An FDML laser has an almost constant output power (Fig. 24.5, top right) as the cw laser has;

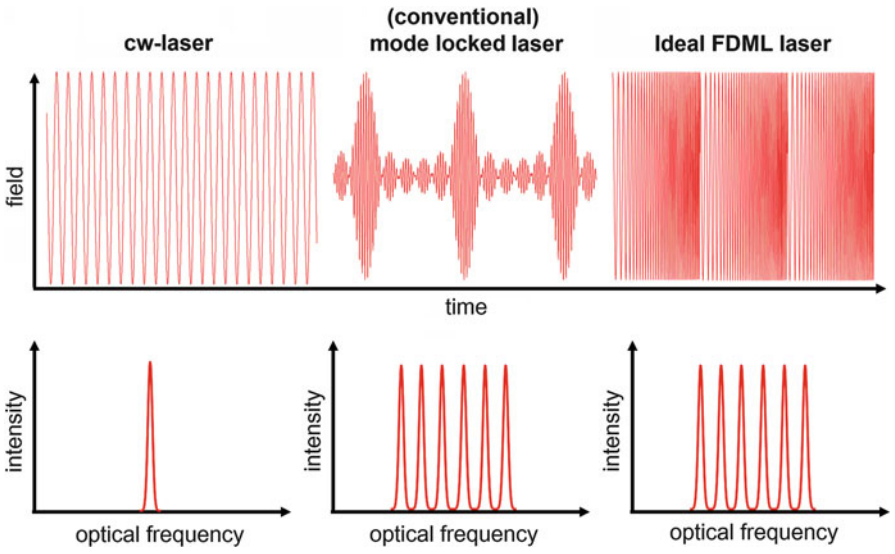

Fig. 24.5 The three stationary laser operating regimes. Electric fields (*top*) and spectra (*bottom*) of (*left*) a narrowband continuous wave (*cw*) laser, (*center*) a standard mode-locked laser, and (*right*) an FDML laser

Table 24.1 Comparison between standard mode locking [52] and FDML [27]. A comparison of the different elements in a standard mode-locked laser and an FDML laser shows that both operating regimes are complementary

	Standard mode locking	FDML
Modulation frequency	Synchronous to roundtrip time	Synchronous to roundtrip time
nature of modulation	Phase/amplitude	Spectrum
	Time domain	*Fourier domain*
Output	Short pulse	Long pulse (sweep)
	Minimum chirp	Maximum chirp
Instantaneous	Broad	Narrow
Phase relation	Fixed (*locked*) phase relation between modes and pulses	Fixed (*locked*), but different, phase relation between modes and pulses

however the output spectrum is broad and has, in the ideal case, a comblike structure. This can be understood, since the FDML wavelength sweep can be considered as highly chirped pulse [54].

Remark: It should be noted that the FDML output is in principle identical to the one of a so-called FM laser; however the experimental setup of both lasers is very different – the FM lasers [55] use ***NO*** filter and the intracavity element, which is a phase modulator, is driven ***OFF*** resonance.

The difference between the standard mode-locked laser and the FDML laser is that the phase of the individual modes with respect to each other is different. It should be noted at this point that currently it seems very difficult to measure the absolute position of the FDML comb line, so it cannot be expected that FDML lasers can be used for the same metrology and sensing applications like standard mode-locked lasers. However, the emission of an FDML laser spans 100 nm or more, proving that many individual modes are simultaneously active.

24.2.3.2 The Name "Fourier Domain Mode Locking"

Table 24.1 shows a comparison of FDML [27] to standard mode-locked lasers [52] which usually generate a train of ultrashort laser pulses. In standard mode-locked lasers, an active (e.g., an acousto-optic modulator) or a passive (e.g., transient Kerr lens, saturable absorber) amplitude or phase modulator modulates the intracavity light field synchronously to the optical roundtrip time. It acts like a shutter which transmits light only over a very short period of time, and only a short electromagnetic wave packet that arrives always at the modulator when the modulator has high transmission or low absorption can continuously circulate in the laser cavity. A time gate or a "time window" is applied. The output is a short pulse with minimum chirp. In FDML a "wavelength window" is applied, also synchronous to the roundtrip time, so it acts in the "Fourier domain" – actually the term "frequency domain" would be more accurate. The FDML output is, as described, a wavelength sweep, which is equivalent to an extremely chirped pulse. This equivalence has been shown by compressing the FDML sweep time [54]. The instantaneous spectrum of a standard mode-locked laser is wide, given by the time

bandwidth limit – in an FDML laser, the instantaneous spectrum is narrow. Because both types of laser emit a train of light fields where each pulse or sweep is a copy of the previous one, there is a more or less pronounced phase relation between the pulses or sweeps. So overall FDML has the same synchronization condition as standard mode-locked lasers; however the modulator does not operate in the time domain but in the Fourier (frequenc<) domain, physical quantities that are short in standard mode locking are long in FDML, and quantities that are wide in standard mode locking are narrow in FDML, so in most parameters the FDML characteristic resembles the Fourier transform of a standard mode-locked laser. FDML is complementary to standard mode locking "linked by Fourier transform."

24.2.3.3 Are the Modes in FDML Laser Locked?

The term mode locking in lasers is used, if there is a certain phase relation between the different cavity modes of the laser. For example, if thermal light or light from an amplified spontaneous emission (ASE) source is transmitted through a comb filter, like a Fabry-Perot, the output has also a comblike structure with multiple peaks, but with no phase relation between the different modes. If the spectrum of the light would be measured at a certain time, it would always contain all wavelength components. To generate a situation like in FDML, where at one certain point in time, only a very narrow range of wavelength can be measured, a phase relation between the different modes is required that generates destructive interference between all components, except the narrow range that is active at one moment in time. So already the fact that FDML lasers emit wavelength-swept light proves a certain phase relation between the different wavelength components.

A similar argument is analog to standard mode-locked lasers. In standard mode locking, the amplitude modulator, a type of "shutter," is operated ideally with a very short duty cycle of, e.g., 1 %. So 99 % of light with an arbitrary phase is absorbed when coupled into the modulator. Now if the modulator is used in a mode-locked laser, where it is driven synchronously to the optical roundtrip time, the cavity modes develop a phase relation amongst each other and almost 100 % of the circulating light field is transmitted. The same is true for typical FDML lasers. The optical bandpass filter has a typical transmission window of about 0,1 nm, and the emission is about 100 nm. If ASE light is coupled into the filter, 99.9 % is back reflected. In FDML operation, we observe at maximum only about ~10 % back reflection, because at each point in time, only modes within the transient spectral filter window interfere constructively.

So already the fact that the FDML laser emits wavelength sweeps and that the intracavity bandpass filter dissipates by orders of magnitude less light than its spectral fill factor proves that there is a certain phase relation between the different modes.

So there is a phase relation between the FDML cavity modes; however, how good this phase relation is, meaning how large the phase jitter between these modes is, is currently investigated. Theoretical models and numerical simulations provide access to the electric field [32, 33, 36–38]. Direct linewidth measurements in

comparison with the theoretical results prove the model of FDML as a stationary operation, because the theoretical models show that FDML lasers continue to operate even without ASE noise. Initially there was a problem numerically simulating FDML operation, because of the wide wavelength sweep range of about 20 THz and the close mode spacing of about 100 kHz which would require an enormous number of simulation points. However, the introduction of a simulation strategy using a sliding reference frame reduced the number of simulation points and enabled successful numerical models describing FDML [32, 33, 36–38].

Very recently, the successfully compression of light from an FDML laser also give access to the internal phase conditions [54]. Simulations with a complementary approach supported by experiments indicate that mainly dispersion in the FDML laser cavity deteriorates the phase relations, i.e., the "mode locking" [56].

24.2.3.4 Other Lasers with Frequency or Phase Modulation

There are other types of lasers that modulate the phase and frequency of the light field inside the laser cavity which are often confused with FDML. However, these lasers are technically very different to FDML. To avoid this confusion, the reader finds some explanations about these different technologies in the following.

FM Mode Locking

FM mode locking [57] is often confused with FDML because of the similar acronym. FM mode locking has been known since the 1970s, and it is used to generate short laser pulses, not wavelength sweeps. FM mode-locked lasers have a phase modulator and not an optical bandpass filter inside their cavity. The phase modulator is driven synchronously to the optical roundtrip time in the cavity. It is often discussed that a more accurate term for FM mode-locked lasers would be "phase mode-locked" lasers. Unlike an FDML laser, an FM mode locking laser does ***NOT*** have a tunable optical bandpass filter.

FM Lasers

An FM laser [55] is a laser with a setup identical to the FM mode-locked laser; however, the phase modulator is driven off resonance. By this strategy, transient wavelength sweeps can be generated. FM lasers generate one wavelength sweep per optical roundtrip time, similar to FDML; however FM lasers don't have an optical bandpass filter and their sweep range is usually limited to a few nm due to the lack of suppression of ASE. Also FM lasers usually exhibit a breathing of the spectrum. Unlike an FDML laser, an FM laser does ***NOT*** have a tunable optical bandpass filter.

Wavelength Tunable Laser with Resonant Frequency Shifting

FDML operation is also often confused with wavelength-swept lasers which incorporate an optical frequency shifter [58]. Such lasers have been demonstrated with sweep repetition rates up to ~1 kHz. The frequency shifter's purpose is to also

overcome the fundamental problem of the required repetitive buildup of lasing during sweep operation. The light inside the cavity is shifted exactly by the amount that is required to compensate the filter tuning operation. In other words, light which is transmitted through the filter is frequency shifted on its way through the cavity, and when it arrives back at the filter, the new wavelength matches exactly the new position of the optical bandpass filter. The problem with this design is that the amount of frequency shift achievable with current devices is hardly more than 1 GHz and it is therefore not sufficient for very fast tuning operation. Unlike an FDML laser, a resonant frequency shifting laser does ***NOT*** synchronize the optical roundtrip time with the filter tuning period of the optical bandpass filter.

Very Rapid Tuning of CW Dye Laser

In 1975 Telle and Tang [28] demonstrated a tunable laser using an electro-optical element acting as a type of optical bandpass filter. The concept of this approach is the same as in FDML; however, no narrowband wavelength filter was applied, and with a tuning range of 2 nm and a linewidth of 0.2 nm at a repetition rate of 100 MHz, this source cannot be used for OCT.

24.3 Milestones in FDML Development

24.3.1 The First Implementation of an FDML Laser

Figure 24.6 shows the first implementation of an FDML laser for OCT in 2005 [59]. The laser is implemented in a ring geometry using a fiber-based resonator. The laser gain medium is a fiber-pigtailed packaged semiconductor optical amplifier (SOA) from Inphenix, Inc. The tunable optical bandpass filter is a Fiber Fabry-Perot Tunable filter (FFP-TF) (Micron Optics, Inc.). A spool with 7 km standard single mode telecom fiber (Corning SMF 28e) provided the optical delay of 34 μs. Figure 24.7 shows the output power of the laser for different values of tuning frequency of the optical bandpass filter. It can be seen that only for a very narrow range of filter drive frequencies $f_{filterdrive}$, the FDML condition $f_{filterdrive} = c/l$ is fulfilled. The resonance has a width of about 7 Hz at a center of 29,015 Hz corresponding to a system finesse of 1/4,000.

As seen in Fig. 24.7, the laser resonator has an optical roundtrip frequency of 29 kHz. Since the Fabry-Perot Tunable filter is preferentially driven sinusoidally at such high speeds, two wavelength sweeps are generated for each drive cycle of the filter. So driving the filter with 29 kHz generates 29,000 forward (shorter to longer wavelength) sweeps and 29,000 backward sweeps per second. For OCT application, 58 kHz line rate is possible.

Obviously this laser can also be driven with higher harmonics, i.e., two or more sweeps are simultaneously active in the FDML laser. The laser has resonances at $2 \times 29 = 58$ kHz, at 3×29 kHz $= 87$ kHz, and so on. In the first demonstration in 2005, up to 290 kHz sweep rate had been demonstrated.

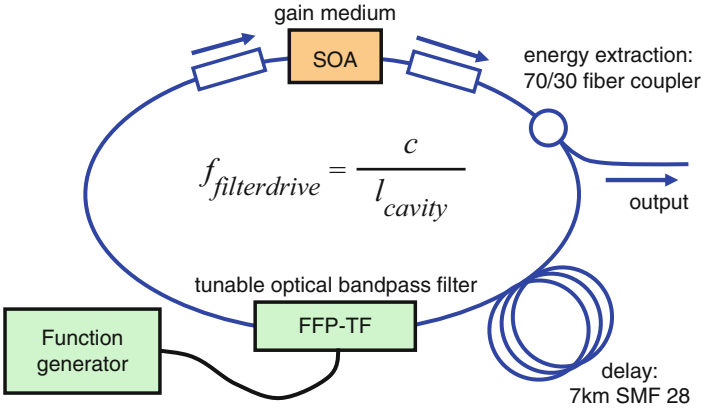

Fig. 24.6 Setup of first FDML laser [59]. *SOA* semiconductor optical amplifier. *FFP-TF* Fiber Fabry-Perot Tunable filter. *Arrows* Optical isolators, ensuring unidirectional lasing and blocking light that is back reflected from the FFP-TF. *SMF 28* Standard optical single mode fiber

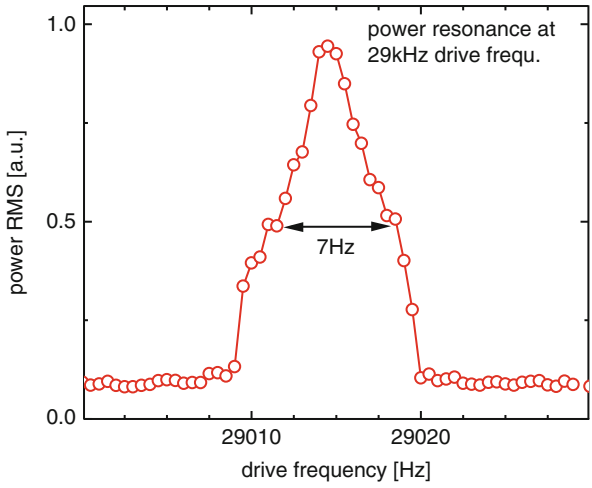

Fig. 24.7 FDML resonance [27, 59]. Output power over tuning frequency of the optical bandpass filter showing the sharp resonance when the FDML condition is fulfilled

24.3.2 Buffering: Increasing the Sweep Speed by Optical Time Multiplexing

Conceptionally, FDML lasers have no speed limit as long as the intracavity tunable bandpass filter supports the high sweep speeds. It actually turns out that FDML lasers are more stable at higher speed, because the required delay fiber length is shorter for higher frequencies. This reduces thermal drift effects and problems with unstable polarization [29, 60].

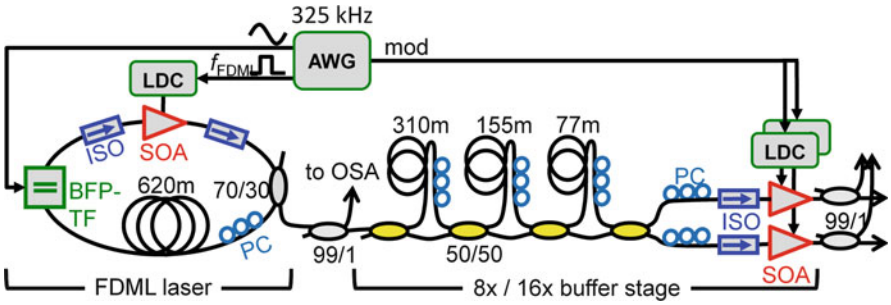

Fig. 24.8 Setup of a 2,600 kHz 8× buffered FDML laser [43]. Example of a buffering setup to multiply the sweep rate. The 2 × 325 kHz FDML is scaled to 2.6 MHz sweep repetition rate. The output is split, a part is delayed, and then the light is recombined

However, the availability of fast tunable optical bandpass filters with the required specifications is limited. The filters should have <0.15 nm passband, >120 nm free spectral range, and >40 dB out of band rejection. Currently, at sweep speeds of more than 100 kHz, only Fabry-Perot filters achieve this type of performance. Custom-built research devices achieve up to 2 × 419 kHz [61], and commercially available devices achieve 2 × 170 kHz (Lambdaquest, Inc.). This is typically the highest mechanical resonance ***frequency*** with sufficient response. However, the achievable tuning ***amplitude*** in these resonances is typically much larger than the lasing range, even larger than one free spectral range. So the total tuning speed measured in nm/μs can be increased by increasing the amplitude.

The technique of sweep buffering [62] can convert excess sweep amplitude to sweep frequency. It is used to convert lower filter sweep frequencies with a high amplitude to high sweep frequencies with lower amplitude. Figure 24.8 shows the setup of an 8× buffered FDML, and Fig. 24.9 shows the concept of sweep buffering in the case of 4× buffering. In the setup in Fig. 24.8, a 325 kHz FFP-TF is used. The filter is driven with such a high amplitude that the duty cycle of one forward sweep is only 12.5 %, and the rest of the time over one entire sweep cycle the SOA is switched off. The sweep output is now coupled into a cascade of splitters and recombiners, each with an additional length of fiber in one arm. The length of this arms is one half, one fourth, and one eight of the cavity length. This leads to multiple copies of the sweep, here 8. After the last coupler, there are two outputs, each with 8 × 325 kHz = 2,600 kHz sweep rate. Figure 24.9 shows the individual steps for a 4× buffered FDML with the steps of overdriving the FFP-TF, generating a short duty cycle, ON-OFF modulation of the SOA, copying and delaying the individual sweeps. It should be noted that sweep buffering is not limited to FDML lasers; it can be applied to all lasers that have excess tuning rate and short duty cycle [63].

The main reason for sweep buffering is to increase the repetition rate of FDML or standard swept lasers [30, 34, 62–71]. However, there are numerous additional advantages of buffering. The most important one is that there is an almost perfect

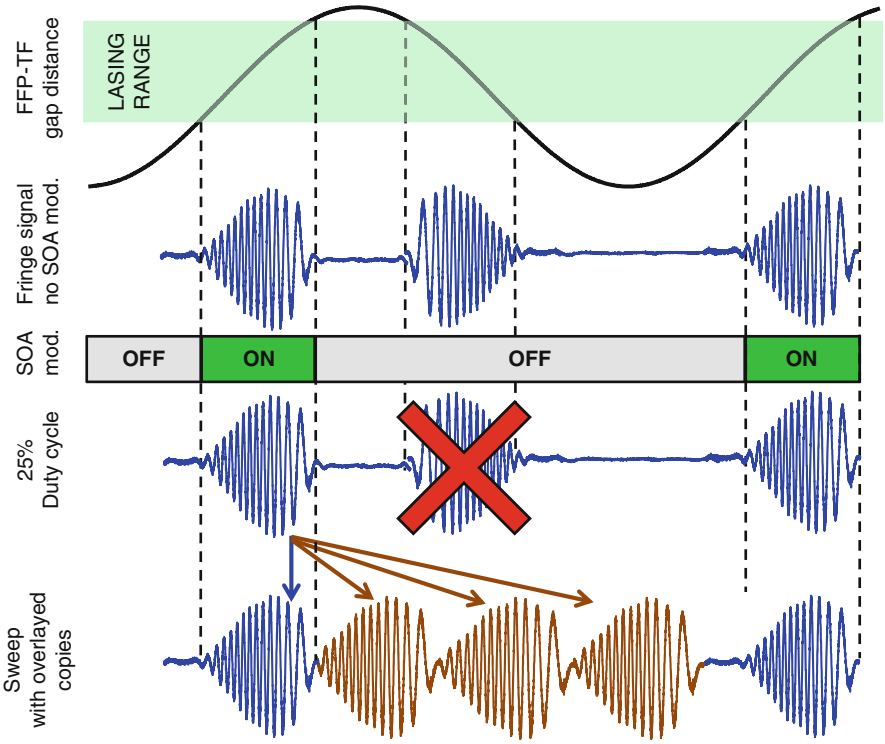

Fig. 24.9 The concept of buffering in case of an FFP-TF [62]. Here the situation for an FFP-TF filter buffering by a factor of 4× is shown. The sweep amplitude is increased to achieve a short duty cycle of the lasing operation, in this case 25 %. The laser gain SOA is switched off over 75 % of the time, and one sweep direction remains. The 75 % gap is filled with copies of the original sweep. The resulting sweeps have a 2× higher sweep rate and are unidirectional and highly linear in optical frequency and groups of four are almost mutually identical

optical phase relation between the different copies of the sweep, making them the ideal source for phase-sensitive and Doppler OCT imaging [68, 69].

Another advantage is that wavelength over time tuning characteristics and also the optical frequency over time tuning characteristics of the light sources' output is usually much more linear than in standard FDML lasers. The reason is that the FFP-TF filter in FDML lasers is usually driven in a mechanical resonance sinusoidally which leads to a very slow tuning operation near the turning points. On one hand, such a huge variation in filter sweep speed is problematic from an engineering viewpoint for an OCT system, because the resulting fringe frequencies span a very wide range of RF frequencies from the photo-receiver. This requires systems with a very flat electronic phase response. On the other hand, the very slow tuning speed at the turning points at a constant exposure level adds up to the total amount of optical power on the sample, but only very few data

points are collected right at the turning points, considering the equidistant optical frequency grid before FFT in SS-OCT/ODFI. This means a lot of energy is put on the sample, but very little information is acquired. So sweep buffering improves linearity which can simplify OCT system design and improve image quality.

A further advantage of sweep buffering is that the polarization state of the different sweeps can be passively controlled. For many PS-OCT applications, a sequence of wavelength sweeps with alternating polarization state is required [72, 73]. This is usually realized by active optical elements with the problem of synchronization, additional differential polarization-dependent group delay, and dispersion. With the technique of sweep buffering, different polarization states can be generated passively [60].

For these reasons, buffering stages are an integral element in many of the most advanced MHz FDML lasers.

24.3.3 The Second-Generation FDML Lasers: Dispersion Compensation

The idea of FDML is to synchronize the optical roundtrip time of light in the laser cavity with the filter tuning period. But this would require that all the different wavelength components of the FDML laser propagate with the same speed. Due to chromatic dispersion in the delay fiber, this is not the case which leads to a more or less pronounced miss synchronization for some wavelengths [29]. The first FDML lasers have been implemented at a center wavelength of ∼1,310 nm. This is the zero dispersion point of standard optical fiber, meaning in a narrow range around 1,310 nm, all wavelengths propagate at the same speed. However, zero dispersion point means only that there is no linear group velocity dispersion (GVD) (i.e., second-order dispersion), so no term measured in ps/(nm*km). However there still is remaining GVD slope measured in ps/(nm^{2}*km). And because typical OCT lasers sweep over a very wide spectral range of 100 nm or more, this has a significant effect on the roundtrip time. Figure 24.10 (left) shows the difference in roundtrip time for the various spectral components in a 100 kHz 1,300 nm FDML laser (2 km fiber).

It can be seen that light with 1,240 nm has a 550 ps longer propagation time through the cavity than light with 1,320 nm. At a roundtrip time of 10 μs, this is a synchronization error of 50 ppm (5e-5) which is small enough that it doesn't affect the output power of the FDML laser. However, it also means that light will not circulate in the FDML cavity forever; after a certain number of roundtrips, the timing offset will be large enough that the light is blocked by the filter. In the shown case, this reduces the number of roundtrips of the intracavity photons in the FDML laser to approximately 12 at the very edges of the spectrum [30]. This negatively affects the instantaneous linewidth of the FDML laser reducing the instantaneous coherence length. For this laser the practical single-sided OCT ranging depth is reduced to about 5 mm, i.e., the OCT depth range over which

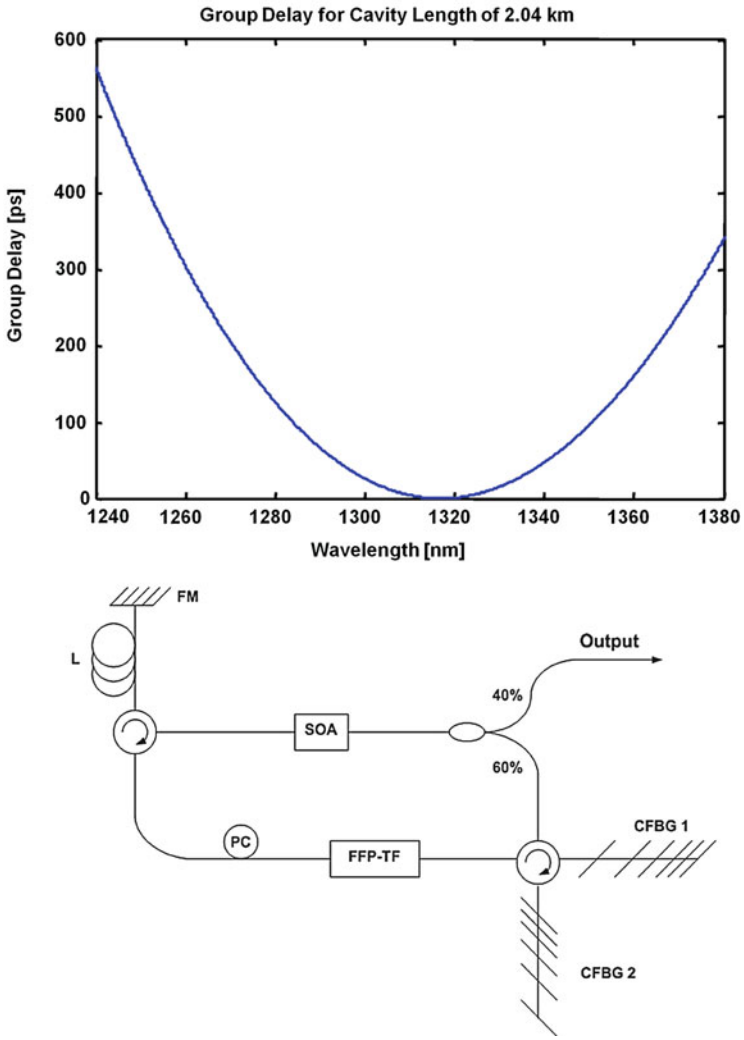

Fig. 24.10 Dispersion in FDML and compensation setup [30]. *Top*: Propagation time difference for the spectral components in a 100 kHz FDML laser cavity [30]. *Bottom*: Setup of an FDML laser with compensated chromatic dispersion. The laser uses two custom-designed chirped fiber Bragg gratings (*cFBG*) from Teraxion, Inc

almost no signal decay can be observed. The effect of chromatic dispersion is even more severe in FDML lasers at 1,050 nm as used for retinal imaging. There the chromatic dispersion of optical fiber has a substantial linear contribution of ∼40 ps/(nm*km).

The solution to this problem is to compensate the intracavity dispersion of the FDML. The different approaches that have successfully been demonstrated are

the use of a wideband zero dispersion photonics crystal fiber [64, 75], the use of a sequence of different fibers to cancel out the dispersion contributions of the individual pieces [29, 76], and most recently the application of chirped fiber Bragg gratings (cFBG) [30, 34, 35]. A cFBG is a piece of fiber with a periodic refractive index modulation where the period changes over length. This way, light with different wavelengths is reflected in different depths yielding a wavelength-dependent propagation time. The cFBGs can now be designed in a way that they exactly compensate the chromatic dispersion of the FDML cavity. Since usually cFBGs are preferred with a monotonic group delay over wavelength, a pair of matched cFBGs is used at 1,320 nm, because the dispersion zero of standard optical fiber leads to a minimum of propagation time. Figure 24.10 (right) shows the setup of a compensated 1,300 nm FDML, and a 4-port circulator is used in the light path to generate the two reflections from the cFBGs. The pair of cFBGs was designed and manufactured by TeraXion, Inc. (Quebec City, Canada). Figure 24.11 (left) shows the group delay of the two cFBGs and the total group delay. Starting from more than 200 ps timing error for the different wavelength components of a 100 nm range, less than 4 ps remain after compensation (Fig. 24.11 right); this is a reduction of more than 50×. The relative timing error of 4 ps compared to the 10 μs tuning period corresponds to a relative error of 400 ppb (4e-7). This value theoretically enables several 1,000 roundtrips of light in the cavity [30].

Because of this higher number, light is effectively filtered more often improving the instantaneous linewidth. The sensitivity roll off is reduced; the OCT system ranging depth improved to more than 10 mm (>21 mm 6 dB coherence length). Figure 24.12 shows the improvement; the point spread functions are plotted over OCT imaging depth. For the non-compensated FDML, a 6 dB roll off over 5 mm is observed. Using dispersion compensation this value is more than doubled. The measurements in Fig. 24.12 may have been limited by the detection electronics rather than by the laser linewidth properties, so the real roll-off performance of this laser can be even much better. This increase in total OCT imaging range is most important for applications in intravascular imaging, where a >5 mm range is usually desired to better image some anatomic features like arterial branches [30].

24.4 Different Variations and Implementations of FDML

Since in FDML both of the critical elements of a tunable laser are separated and because they can have substantial optical path length, FDML allows many different combinations of gain and filter media to specifically tailor them towards the application of interest.

Besides the typical SOA gain medium, FDML lasers has been built with Raman gain for extremely low ASE background noise [51], with rare earth-doped fiber amplifiers [44, 45, 47] for very high output powers, with nonlinear post conversion [77] or optical parametric amplification [47, 48, 78] for very flexible gain regions and with combinations of these different techniques.

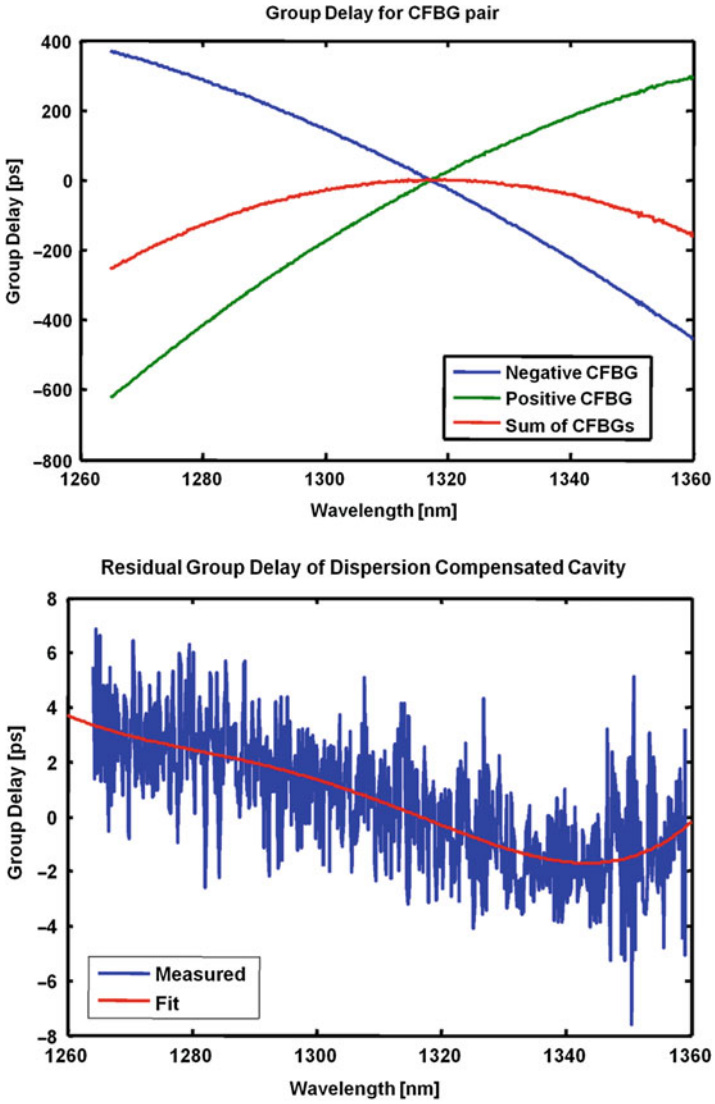

Fig. 24.11 Dispersion compensation with chirped fiber Bragg gratings (*cFBGs*) [30]. *Left*: A combination of two cFBGs can generate a net GVD slope value. *Right*: The dispersion is reduced by almost a factor 50

The tunable filters used for FDML lasers have been limited to very rapidly tunable ones. In most cases Fabry-Perot Tunable filters are used, but also polygon scanner-based systems are possible and have a number of advantages, like inherent unidirectional sweeping and very high-power handling capabilities [79].

Stabilization of FDML operation is usually performed by active or semi-passive mechanisms, solving the problem of drift in FDML.

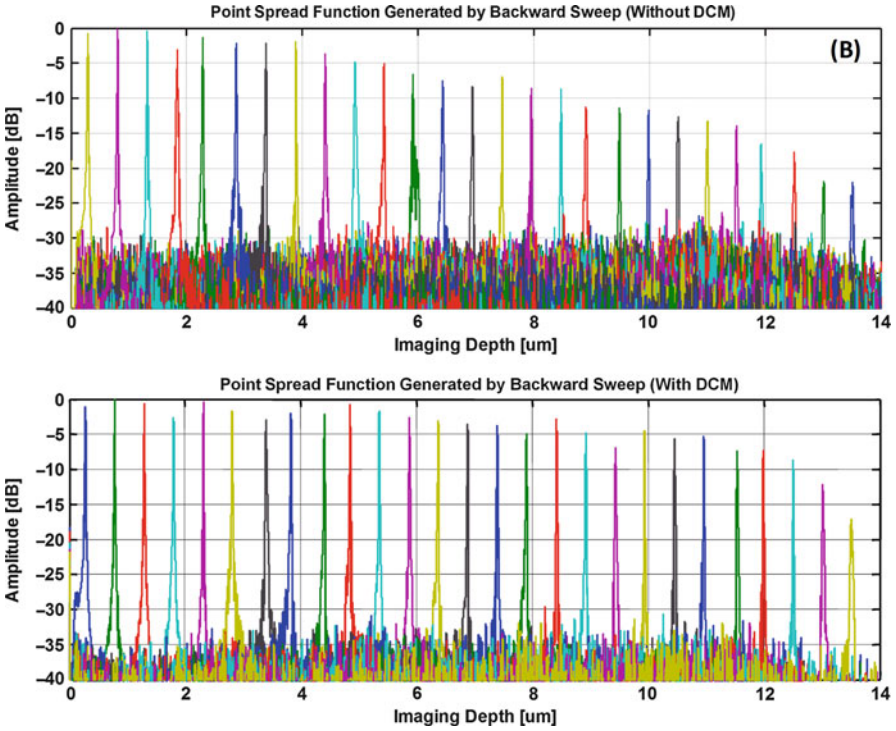

Fig. 24.12 Improved roll-off performance by dispersion compensation [30]. *Top*: Point spread function (*PSF*) over imaging depth for an OCT system using a standard 2 × 100 kHz 1,300 nm FDML laser. A 6 dB signal roll off over 5 mm can be seen. *Bottom*: Roll off for the same laser with additional dispersion compensation – the 6 dB signal roll off is extended to >10 mm

24.4.1 FDML with Raman Gain

Due to their setup with a long length of fiber, FDML lasers offer the ideal starting point for Raman amplification as laser gain process [46, 49–51]. Raman amplification in fibers is widely used, because the small mode field diameter in optical single mode fibers over a very long interaction length compensates for the very small Raman scattering cross section. The advantage of Raman gain is the potentially very flexible range of operating wavelengths and the good noise performance. It has also been used to study the photon life times and loss mechanisms in FDML lasers [51].

24.4.2 FDML with Erbium Fiber Gain

In the 1,550 nm wavelength range, which can also be used for OCT, especially if samples with low water concentration are imaged [15], an erbium-doped fiber amplifier (EDFA) can be used instead of an SOA as gain medium [47, 48]. EDFAs have also

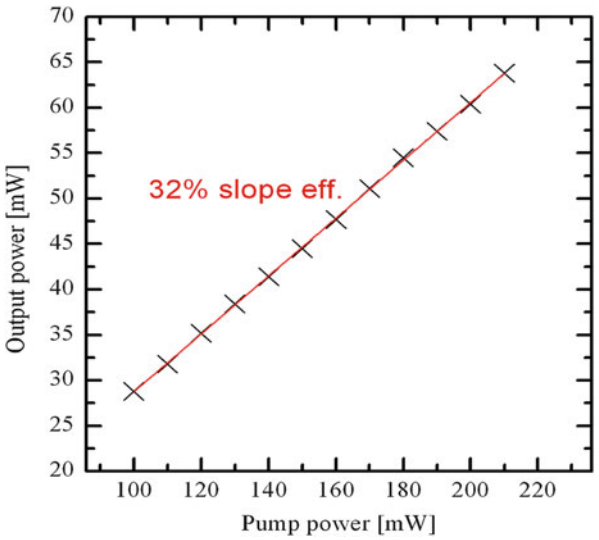

Fig. 24.13 Output power of 1,050 nm FDML using YDFA. The average output power of the FDML can easily exceed 60 mW. At duty cycles of 12.5 % for 8× buffering and a Hanning shaped spectrum, this corresponds to >400 mW peak power of the wavelength sweep

a better noise performance than SOAs, and they can achieve higher output powers. Disadvantages of EDFAs are the smaller amplification bandwidth and the tendency to Q-switch because of the long carrier lifetime of ~20 ms. If EDFAs are used for fast swept lasers and the sweep rate is increased, carrier relaxation oscillations get stronger and high output intensity fluctuations are observed. At some point the laser goes into Q-switching mode emitting a sequence of pulses. Due to the high power of such pulses, they can destroy the intracavity filter.

24.4.3 FDML with Ytterbium Fiber

At 1,050 nm an ytterbium-doped fiber amplifier (YDFA) can be used as amplification element [44–46]. In [45] this was used in combination with an SOA. YDFAs have the advantage of good noise performance and the capabilities for very high-power output. Their gain profile covers an extremely wide wavelength range of much more than 100 nm around 1,050 nm.

The output powers achievable with YDFAs are scalable into the Watt region. Figure 24.13 shows the case for an FDML laser used for retinal imaging. Considering the duty cycle of this laser, the peak power was larger 400 mW. Especially since in the 1,050 nm region swept laser sources often do not exhibit sufficient output power, YDFA-based FDML lasers appear very attractive.

24.4.4 FDML Polygon Scanner Filters

Even though in most cases FDML lasers are built with FFP-TFs, the FDML concept is not linked to a special type of optical bandpass. Leung, Liu, and Mao et al.

demonstrated an FDML laser using a grating filter based on a polygon scanner [40–42, 79]. The advantages of this device are unidirectional scanning operation and very good sweep linearity without buffering.

24.4.5 FDML with Regenerative Mode Locking

One problem of FDML operation, especially if an FFP-TF is used, is the control and automatic stabilization of the wavelength sweep filter. Sweep amplitude, offset, and frequency have to be controlled; thermal drift has to be compensated. Different active control loops have been demonstrated. A very interesting concept is the application of a regenerative mode locking concept [79]. The optical output of the FDML laser is used to control an electronic signal that drives the filter. This way, temperature-dependent changes in the optical roundtrip frequency are automatically compensated for, and the laser always finds the best frequency.

24.5 The Performance of FDML Lasers in Comparison to Other Light Sources

24.5.1 Competing Technologies

At the time of the first introduction in 2005, the performance of FDML lasers was quite unique, and hardly any other technology could achieve the combination of sweep speed, linewidth performance, and spectral sweep range. However, over the last few years, other swept source technologies have been developed that now approach and may even exceed FDML performance in some aspects. In the following sections the state of the art in the year 2013 will be shortly reviewed with respect to performance characteristics of these new sources compared to FDML. Currently there are many promising ideas and concepts for fast wavelength-swept light sources intended for use in OCT, but in several cases, it has not finally been proven, whether these sources can really achieve good imaging performance in biomedical applications [17, 80–82]. So here the focus lies only on three non-FDML techniques and light sources where OCT imaging has already been demonstrated at speeds in excess of 200 kHz, because the high sweep speed performance is the most outstanding characteristics of FDML laser.

The first class of high-speed swept light sources are lasers where the cavity length is reduced so far that the lasing buildup dynamics is fast enough to achieve high-speed tuning. Since this class of sources does not solve the problem of laser buildup dynamics, it can be expected that they are not arbitrarily scalable to higher speeds and probably only several 100 kHz sweep rates are possible, in case other typical OCT performance criteria are maintained. It should be noted that a reduction of the laser resonator cavity length in classic swept laser designs using a separated gain medium and an optical bandpass filter is only possible up to a certain amount. Since the cavity length defines the mode spacing of the laser resonator and this

mode spacing becomes larger as the laser resonator length is decreased, the possible spectral sampling density becomes coarser. In other words, if the cavity length of a linear laser resonator is, e.g., 5 mm, the optical mode spacing of the resonator modes is $\Delta f = c/2\ l = 30$ GHz. At 1,300 nm wavelength, this corresponds to 0.17 nm spectral separation which is, in OCT application, the best achievable spectral sampling density. This corresponds to an OCT imaging range of 2.5 mm. So with a standard laser, it is not possible to build an SS-OCT/OFDI system that has a single-sided ranging depth of more than the laser cavity length. In reality, the laser resonator length is typically chosen significantly longer to avoid beat noise between individual modes. Therefore highly integrated short cavity lasers have the laser end mirror outside the package in the fiber pigtail, resulting in typical cavity roundtrip lengths 30 cm, about 1 GHz optical mode spacing. According to the single roundtrip limit presented in [14], it can be expected that such lasers are limited to $<$300 kHz sweep rate if a 0.05 nm linewidth and 100 nm sweep range are chosen. The problem of discrete mode spacing may theoretically be overcome by advanced variable cavity designs or an active phase section in the laser resonator, as used in telecom applications [17]. However, the laser dynamics at fast sweep operation and the influence on OCT image quality have not been investigated yet. The most prominent examples of fast short cavity lasers are the ones from Oh et al. [63] as research systems and the ones from Axsun technologies [84] and Santec [85]. A more detailed discussion of this laser type can be found in .." reference to Bart Johnson (AXSUN), Bill Ahern chapter in this book.

The second class of successful high-speed tunable lasers are mechanically tunable vertical-external-cavity surface-emitting lasers (VECSEL) (see ▶ Chap. 22, "VCSEL Swept Light Sources"). These devices can achieve very fast tuning operation. It is often argued that the short cavity length of these devices promotes very rapid buildup. However, the most recent results showing meter long coherence lengths, equivalent to $>$10 ns coherence time, are not possible at the typical sweep rate of $>>$1 GHz/ns tuning if lasing is repetitively built up, since this would violate the time bandwidth product. So the reason for the good coherence performance at high tuning speed is that the Doppler shift caused by the reflection of light from the moving end mirror automatically adjusts the wavelength of the light field such that it always matches the resonance condition of the tuned laser cavity. The calculation can be found in [26]. For this reason, VECSELs have also no fundamental tuning speed limit.

The third class of light sources are non-laser sources, i.e., light sources without feedback [86, 93]. A sequence of filters is driven in a way to compensate propagation time effect of light in a pure feedforward configuration. These sources also inherently have no fundamental sweep speed limitation and are amongst the fastest swept sources.

The different sources have various strengths considering the important OCT imaging parameters. Today, sweep speed, achievable axial resolution, and output power are the most important ones. Previously, the instantaneous coherence length, which determines the roll-off performance and the maximum ranging depth of the OCT system, was also of interest. However, today almost all the sources mentioned

Table 24.2 Comparison – imaging speed (single spot)

	1,050 nm	1,300 nm
1. FDML	3,200 kHz [85]	5,200 kHz [43]
2. VCSEL	580 kHz [22]	1,200 kHz [22, 25]
3. ASE swept light source	340 kHz [86]	340 kHz [93]
4. Short cavity (Axsun)	200 kHz [94]	50 [83]

above can achieve more than 20 mm coherence length yielding more than 10 mm single-sided OCT ranging. VECSEL source can achieve even >50 mm. All these values are more than sufficient for almost all classical biomedical OCT applications.

24.5.2 Sweep Speed

One of the most crucial parameters of swept light sources for OCT imaging is the wavelength sweep repetition rate. Since each wavelength sweep results in one OCT A-scan, a faster sweep operation yields a faster OCT system. Today, the fastest swept light sources that have been used for biomedical OCT are FDML lasers, currently with a record speed of 5.2 MHz at 1,300 nm [43] and 3.2 MHz at 1,050 nm [86]. This is more than a factor of 5 faster than the fastest non-FDML source (Table 24.2).

24.5.3 Sweep Range and Axial Resolution

For many OCT applications, the achievable axial resolution is as or even more important than OCT imaging speed [87–90]. Currently and in the midterm future, it seems not likely that fast swept source OCT systems will achieve axial resolution as good as the values demonstrated with ultrahigh-resolution time domain or spectral domain systems [91, 92]. However, the sweep ranges that have been achieved with FDML lasers are still sufficient to allow for ∼3 μm axial resolution in tissue at 1,050 nm and ∼2.5 μm at 1,300 nm wavelength. Also very good values can be achieved with standard short cavity lasers and with the ASE swept light source. VCSEL light source has the inherent problem that the gain medium inside the Fabry-Perot laser resonator sets a lower limit for the cavity length, resulting in a reduced free spectral range and a reduced sweep range. But for many applications the achieved values are still sufficient (Table 24.3).

24.5.4 Output Power

Output power can be a critical parameter for OCT applications, because fast OCT systems require enough intensity on the sample to achieve sufficient signal levels. Usually OCT systems are designed to stay within the limits of a class one laser, but not dramatically below. For retinal imaging at 1,050 nm, up to 1.9 mW is often used and

Table 24.3 Comparison – sweep range and achievable resolution in biomedical OCT applications

	1,050 nm	1,300 nm
1. FDML	120 nm [85]	220 nm [92]
2. Short cavity (Axsun)	100 nm [94]	110 nm [83]
3. VCSEL	85 nm [22]	110 nm [22]
4. ASE swept light source	70 nm [86]	100 nm [93]

Table 24.4 Comparison – max output power

	1,050 nm	1,300 nm
1. FDML	>400 mW [45]	>100 mW [40–42]
2. ASE swept source	>40 mW [86]	>50 mW [93]
3. VCSEL	20 mW [22]	35 mW [25]
4. Short cavity (Axsun)	18 mW [94]	20 mW [83]

for imaging in highly scattering tissue 10 mW or more. Depending on the design of the OCT interferometers and on the inherent losses of the optical components, especially at 1,050 nm, often only 10–50 % of the light source output powers are incident on the sample. So ideally light sources at 1,050 nm should have 4–20 mW, and sources at 1,300 nm should have 20–100 mW. Table 24.4 shows the values for the different sources. The values include setups using an external booster to achieve sufficient power levels. A booster usually does not affect OCT imaging performance too much [14], only in the case of the ASE swept light source [86, 93] that the application of the final amplifier prevented the system from reaching shot noise-limited sensitivity. The good power values in Table 24.4 (Comparison – max output power) for the FDML laser are caused by the good saturation of the system and the high outcoupling value. Typically in FDML about 50 % of the light is extracted and in VECSELs about 0.1 %. The high value for the 1,050 FDML is caused by the application of an intracavity Yb fiber as gain medium, which allows up to Watt-level output.

24.6 OCT Imaging with FDML Lasers

FDML lasers have been applied to many different OCT imaging applications, in most cases because the application demanded fastest imaging speed. The applications range from developmental biology [67] over art conservations studies [114], profilometry with nanometer resolution [68, 69], sensing applications using fiber Bragg gratings [49, 96–100], photothermal imaging [100], deep field OCT imaging with special beam shaping optics [102], functional in vivo OCT imaging [61, 71, 103], ultrawide field retinal imaging [45, 85], intravascular imaging [30, 104], contrast-enhanced imaging with nanoparticles as contrast agents [100], and microangiography with an ultrawide field of view [61] to FDML lasers for noncontact detection of photoacoustic signals [103].

In the following chapter, some examples are chosen which represent some of the unique technical FDML features which, in the specific application, substantially improved the quality of the imaging result.

24.6.1 FDML for Developmental Biology

An early FDML application has been ultrafast OCT in developmental biology [67]. Here, the function and dynamics of the developing quail heart was studied, and the high imaging speed of 100 kHz possible with FDML enabled OCT at 195 frames per second. The resulting high time resolution enabled for the first time the direct detailed observation of the fast contraction phase of the heart. At a reduced line number, volumes with 200 × 60 lines per volume at a rate of 8.3 volumes per second have been acquired. A more detailed description of this application field is presented by Rollins and Jenkins in the "OCT Applications" part of this book in ▶ Chap. 65, "4-D OCT in Developmental Cardiology".

24.6.2 FDML for High-Speed Intravascular Imaging

Intravascular imaging is the second most important field of application in OCT. In 2006, the commercially available system M2 from LightLab Imaging (now a St. Jude Medical subsidiary) exhibited a 3.5 kHz A-scan rate at 15 frames per second. This slow A-scan rate leads to the risk of ischemia due to long pullback times [105], an additional step in the procedure and limited image quality caused by the low number of depth scans acquired during one catheter revolution. In 2006 LightLab Imaging developed their first swept source/OFDI system, which was based on an FDML laser [105].

Table 24.5 summarizes the performance of the LightLab FDML system compared to the pervious time domain M2. Figure 24.14 depicts some imaging results from the year 2006, clearly showing the improved image quality. Recently the potential of a further performance improvement of the LightLab C7XR intravascular FD-OCT system (LightLab Imaging, a St. Jude Medical subsidiary) has been evaluated. For this purpose a second-generation FDML (see Sect. 24.3.3) has been interfaced with the C7XR system and 100 kHz long-range OCT on phantoms was tested [29] (Fig. 24.15). Even though an even higher imaging speed would have been desired, the limitation was the maximum rotation speed of the catheter. with a new catheter, based on a design with a micro motor, the imaging speed could be increased by more than a factor ten. 3200 frames per second have been acquired [104].

24.6.3 FDML for Endomicroscopy

OCT has been extensively applied to gastrointestinal (GI) imaging. Whereas early time domain GI-OCT has usually been limited to single cross sections, the advent of

Table 24.5 LightLab FDML prototype compared to M2 [106]

	FDML-based OCT – prototype	LightLab M2
Line scan rate	45 KHz	3 KHz
Max frame rate	80 f/s (@562 lines/frame)	15.6 f/s (@200 lines/frame)
Scan diameter (in saline)	7 mm	6.8 mm
Signal-to-noise ratio (SNR)	~100 dB	~100 dB
Axial resolution (in tissue)	11–17 µm	15 µm

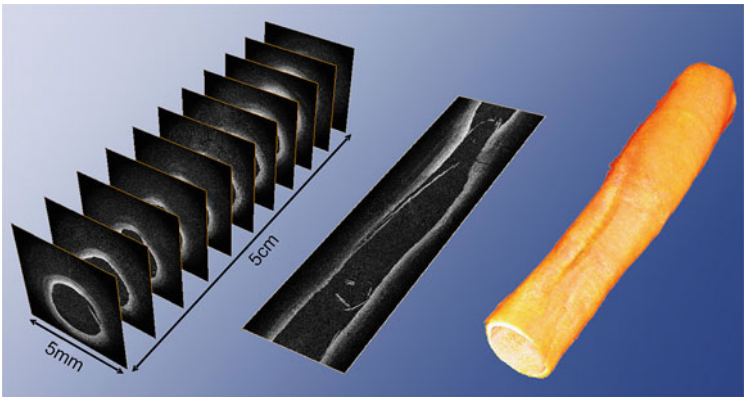

Fig. 24.14 Intravascular images with LightLab FDML prototype in 2006 [102]. Three-dimensional reconstruction of a 5 cm segment of an excised radial artery from a cadaver

fast swept source FD systems [13] enabled the acquisition of large areas as full three-dimensional volumes [106, 107]. Besides the advantage of having a very densely sampled data set, which reduces sampling errors and the probability of missing or overlooking pathology, the 3D volume provides also the possibility of reconstructing an en face visualization in a certain depth, which can be arbitrarily chosen after image acquisition. In combination with a high-resolution flying spot OCT endoscope, this can provide a new class of image representations for improved visualization of tissue morphology. Because an entire 3D data set is reduced to one image, each OCT A-scan yields only one image point. Consequently the A-scan rate has to be high enough, to keep procedure times acceptable.

Figure 24.16 shows endoscopic imaging results of rabbit colon; the data was acquired using an FDML system with 100 kHz line rate and 5 µm axial resolution. The steps of the endomicroscopy approach using OCT are shown. The individual OCT cross sections are fused to one 3D data set, they are flattened, and then a depth section is extracted. The comparison to histology shows that the characteristic crypt structure can clearly be identified in the OCT (Fig. 24.16, bottom).

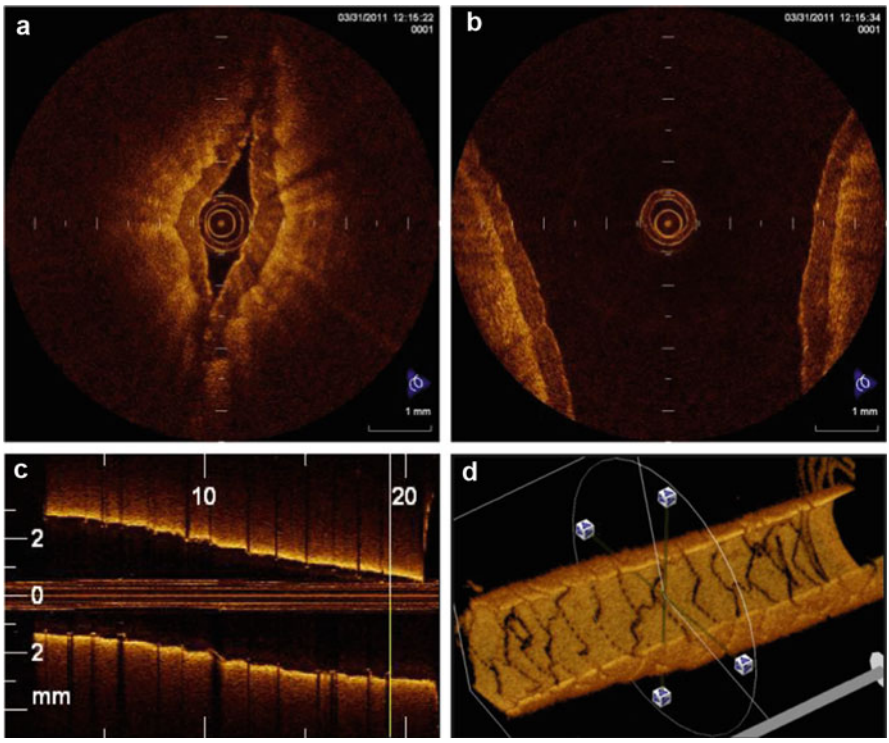

Fig. 24.15 100 kHz intravascular FDML images with a modified LightLab C7XR in 2012 [30]. Images of artery phantoms with 100 kHz second-generation FDML OCT

24.6.4 Buffered FDML for Phase-Sensitive OCT and Photothermal Imaging

In Sect. 24.3.2 the technique of buffering has been described. Buffering splits the output of the swept laser, delays one part of it, and recombines the two sweeps. The main application of buffering is to increase the sweep repetition rate. However, buffered lasers have also a very unique feature considering the stability of the OCT signal fringe phase stability. Usually frequency swept lasers are more prone to phase noise of the detected fringe signal than OCT systems using a spectrometer. This effect is less pronounced in FDML lasers, because each sweep is seeded by the previous one. However the amplification and the transmission through the optical bandpass filter generate some instabilities in the optical field which then cause phase fluctuations in the OCT fringe signal.

Buffered FDML lasers now exhibit a very unique feature, because they always emit, in the case of 2× buffering, pairs of almost identical optical waveforms. Because the FDML output is split and recombined, one of the two sweeps

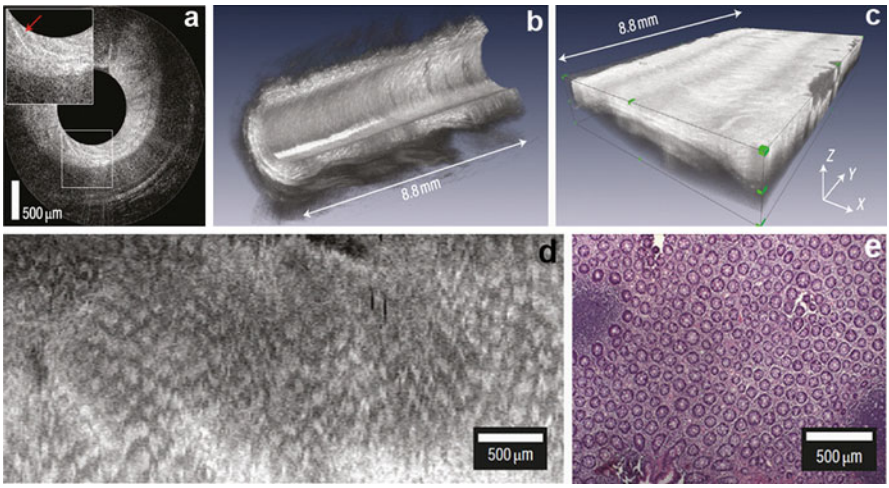

Fig. 24.16 Endomicroscopy of rabbit colon in vivo using FDML [107]. *Top* from *left*: Standard OCT cross section; 3D visualization of whole data set; flattened representation. *Bottom*: En face OCT (*left*) and histology (*right*) correspond well; the crypt structure can clearly be identified in the OCT

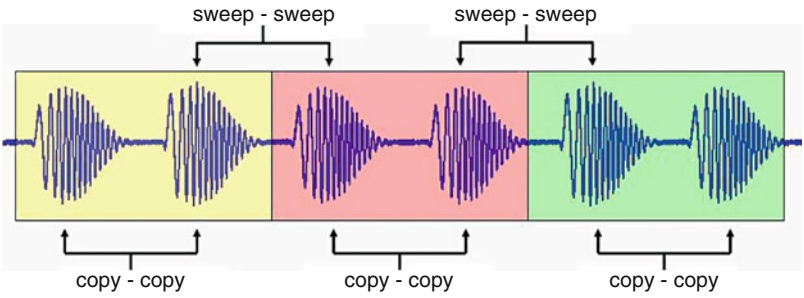

Fig. 24.17 Pairwise coherence of buffered FDML sweeps. FDML lasers with one buffering stage produce output sweeps in groups of two that are virtual optical copies of one another; they exhibit almost no phase noise

simply propagates through some more fiber. Because the fiber is completely passive, the electric field is hardly affected and only very little phase noise is added. A waveform change due to chromatic dispersion can easily be corrected by numerical resampling. The concept is shown in Fig. 24.17. The good coherence between the individual sweeps can now be used for many different phase-sensitive OCT imaging applications.

Figure 24.18 shows two examples of phase-sensitive OCT using a buffered FDML laser. On the left the buffered FDML is used for a phase-sensitive

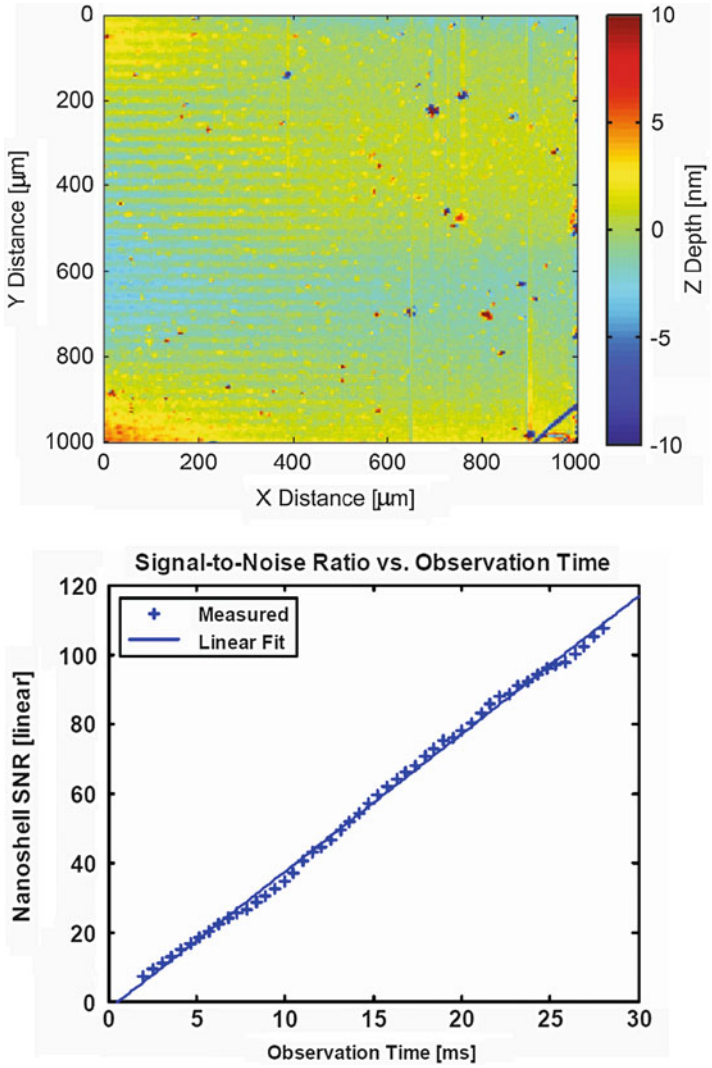

Fig. 24.18 Phase-sensitive OCT using buffered FDML [68, 100]. *Top*: Phase-sensitive profilometry of a glass plate; the overall angle/wedge effect has been subtracted. *Bottom*: Signal to noise achieved with FDML laser in photothermal OCT detection of gold nanoshells with potential use as contrast agent

profilometry OCT application. The image shows the surface of a glass plate with a sub-nanometer resolution (left) and the good signal to noise performance of buffered FDML lasers when used for the phase-sensitive photothermal detection of gold nanoshells as potential future OCT contrast agent (right).

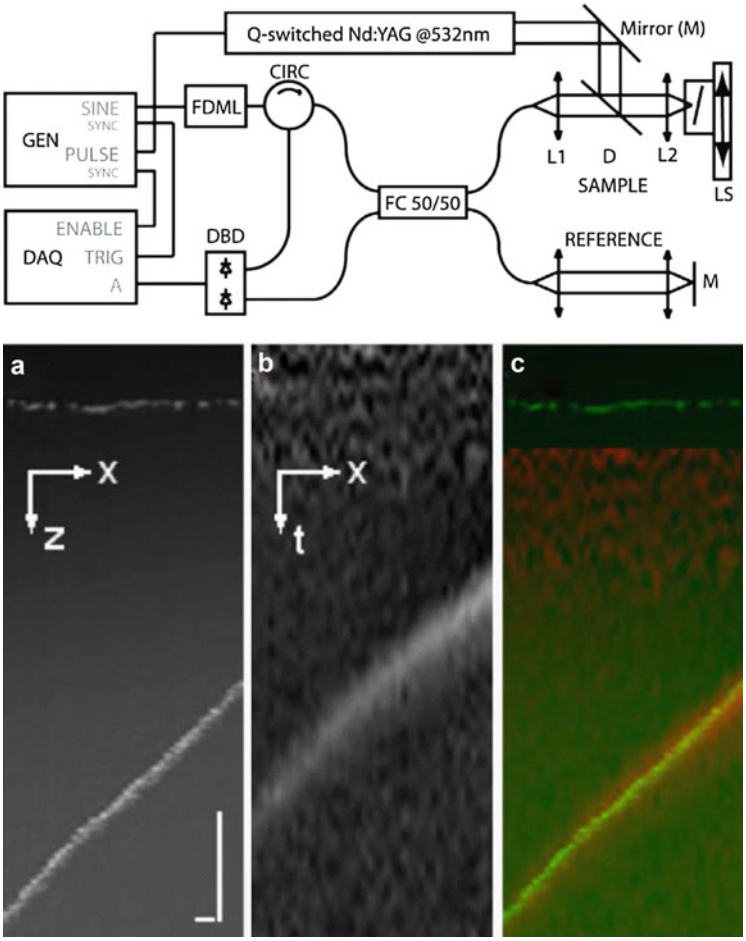

Fig. 24.19 FDML for contact less photoacoustic imaging [103]. *Top*: Setup for noncontact photoacoustic signal detection with an FDML-based OCT system. *Bottom*: (**a**) OCT contrast image, (**b**) photoacosutic contrast image, (**c**) combined contrast image of a phantom

24.6.5 FDML for Noncontact Photoacoustic Imaging

Another application that has been demonstrated by Blatter et al. [103] with an FDML laser makes use of the phase stability of FDML in combination with the high fringe frequency of the FDML OCT signal. The high fringe frequency and sweep speed of FDML-based OCT require high analog detection bandwidth and digital sampling rate. Because of this, the OCT system is capable of acquiring transients with nanosecond resolution making it sensitive to the transients which occur in photoacoustic imaging. Using an innovative analysis concept of the OCT fringe data, Blatter et al. could demonstrate the simultaneous detection of OCT and photoacoustic contrast in a phantom [103] (Fig. 24.19).

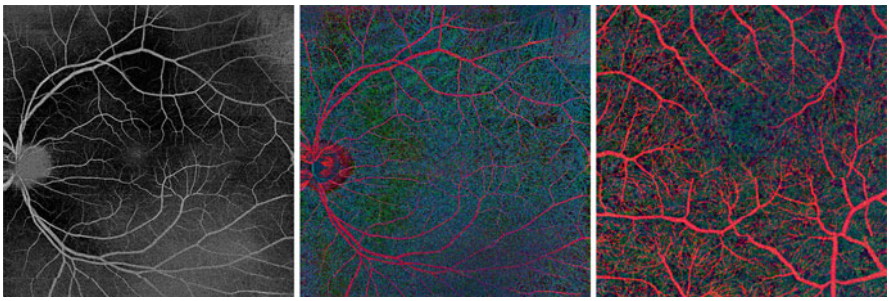

Fig. 24.20 Retinal ultrawide field microangiography with FDML [61]. *Left*: bw-contrasted wide field image. *Center*: Wide field image with color-coded depth. *Right*: Zoomed in view of foveal region

24.6.6 FDML for Functional Ultrawide Field Microangiography

The applications detailed above used the phase information mainly to acquire entirely new types of images with a contrast sensitive to contrast agent concentration or photoacoustic signal strength. However, the OCT phase information can also be used as a very powerful tool to add additional contrast to standard OCT images. Especially contrasting blood vessels appears to be a very important functional extension of OCT in the future. Microangiography using OCT has been demonstrated with different experimental setups that do not necessarily required FDML lasers [112]. However the increased imaging speed of FDML enables the acquisition of large fields of view at reasonable imaging time and without the need of mosaicing (Fig. 24.20).

24.7 Megahertz (MHz) and Multi-megahertz (Multi-MHz) OCT Using FDML

Imaging speed is one of the most important performance parameters in OCT. The 10× speed increase from ∼3 kHz A-scan rate of old time domain OCT systems to ∼30 kHz of spectral domain systems in 2003 triggered a paradigm shift in OCT imaging with respect to imaging protocols, averaging strategies, and data analysis approaches. A further 100× increase in imaging speed well into the megahertz (MHz) line rates can open many more entirely new fields of OCT applications. Live 3D surgical guidance, large area survey scans, functional OCT analysis, and many more are just a few applications where megahertz and multi-megahertz imaging speeds are mandatory. There have been a few demonstrations of concepts which are potentially capable of multi-MHz line rates [77–80]; however due to the challenging requirements of OCT, especially with respect to system sensitivity, it is not clear if such concepts can be used for biomedical OCT.

Table 24.6 Selected milestones in fast OCT with live 3D

	Year	Eff. line rate kHz	Vol. rate (Hz)	Data MS/s	Volume size depth x W x H	MV/s	Real-time visualization
Probst Hillmann [110]	2010	168	7	172	512 × 300 × 80	86	GPU
							CamLink
Sylwestrzak Szkulmowski [116]	2010	120	9	250	1,024 × 100 × 100	92	GPU
							2 CamLinks
Choi Hiro-Oka [108]	2012	1,020	12	419	160 × 256 × 256 (256 × 256 × 256)	122	20+ FPGA, GPU
						195	320 ADCs
Wieser Draxinger [113]	2013	2,656	26	2,050	400 × 320 × 320 (512 × 320 × 320)	1,069	2 GPUs
						1,368	2 ADCs

Only two techniques have achieved multi-MHz 3D OCT imaging of biomedical samples in vivo: (a) spectral domain SD OCT systems using arrayed waveguide technology [108, 109] and (b) FDML lasers as the only swept source-based OCT [43, 85]. The combination of performance parameters makes FDML a unique source for ultrahigh-speed megahertz OCT. The high sweep speed at a wide sweep range and very good output power performance make FDML the system of choice for many of the most demanding OCT imaging applications. To date there have been very few demonstrations of OCT systems with multi-MHz line rates, not only because of the limited availability of fast FDML laser sources but also because the extreme data stream generated with such fast OCT systems. The most recent systems which are capable of live processing and live 3D display without time limitation have to handle sustained data rates of >2 Gbytes/s [113] (Table 24.6).

At these speeds not only the data stream itself but also the processing poses a problem. Whereas early high-speed OCT systems often used FGPA processing, the advent of software development environments for standard PC graphics boards (GPU) for massively parallel processing leads to a paradigm shift in how to handle the large amounts of data. Today the record in real-time processing and 3D display is at 26 volumes/s, 2.65 million A-scans/s and 1.38 billion voxels/s [107]. The processing includes data transfer to the first GPU, cubic spline interpolation, data resampling, zero padding, Fourier transformation, data cropping, projection to logarithmic scale, transfer to second GPU, 3D volume display (ray cast) [113]. At the heart of the OCT system, a 3.2 MHz FDML laser enables these multi-MHz OCT line rates. The technology of multi-MHz FDML will be discussed in the following paragraphs.

24.7.1 MHz OCT at 1,300 nm

The initial FDML implementations in 2006 achieved sweep rates of up to 370 kHz [27, 59, 62]. Due to the demand for higher imaging speeds, a further scaling of sweep rate was necessary. To push the FDML speed well into the MHz range,

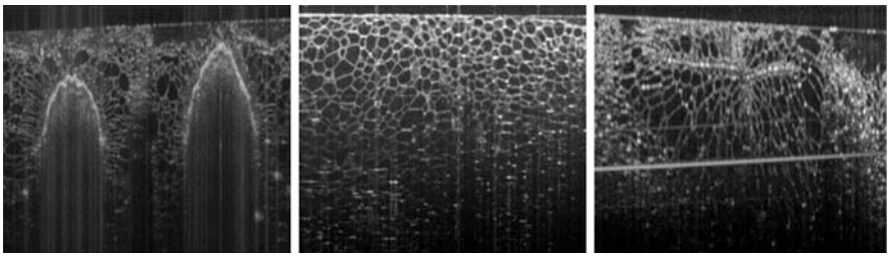

Fig. 24.21 MHz OCT imaging of low scattering samples [43]. MHz OCT images of Kiwi and cucumber 1 MHz (*left*), 2.6 MHz (*center*), and 5.2 MHz (*right*)

a combination of a fast FFP-TF drive frequency and extensive buffering has been applied. The laser design is described in detail in [43].

The most critical point in MHz OCT is the inevitable loss of image quality. On the one hand, the system sensitivity goes down, because at constant power levels on the sample, fewer photons are back reflected from the sample for each sweep, and thus the shot noise sensitivity limit drops. In theory, for many 1,300 nm imaging applications, this point should not be very critical, because the permitted power levels for various samples are often well above 10 mW enabling a sensitivity of ~100 dB even at multi-MHz imaging rates. In practice, it is increasingly difficult to really achieve this theoretical limit, because with the increase in sweep rate, also the OCT signal fringe frequencies are pushed well into the GHz range. For such wide electronic bandwidths, low noise electronics are difficult to implement, or fundamentally not possible. It turns out that the higher the OCT imaging speed, the lower noise the laser has to be to achieve shot noise-limited OCT detection [39]. So the most critical question is: "What OCT image quality can be achieved with multi-MHz FDML lasers?"

Figure 24.21 shows MHz OCT images of low scattering samples at 1 MHz, 2.6 MHz, and 5.2 MHz A-scan rate. Low scattering samples are good to assess the OCT system imaging performance with respect to artifacts, fixed pattern noise, ghost images, etc., because of the low signal levels in between the structures. It can be seen that at all these rates a reasonable image quality is possible. Only at 5.2 MHz the loss in resolution due to a narrower sweep bandwidth is noticeable.

Figure 24.22 shows MHz OCT images of highly scattering samples at A-scan rates of 1 MHz, 2.6 MHz, and 5.2 MHz. Highly scattering samples are good to assess the OCT dynamic range performance, because the high amount of total back reflected power generates high fringe signal levels. Because noise on fringe signals cannot be reduced by dual balanced detection schemes, highly scattering samples can reveal poor amplitude noise performance of the source. Again, it can be seen that at all these rates good overall image quality is possible, and the strong scattering does not generate extensive bands of background signal levels. Only at 5.2 MHz the increased speckle size due to the narrower sweep bandwidth is noticeable.

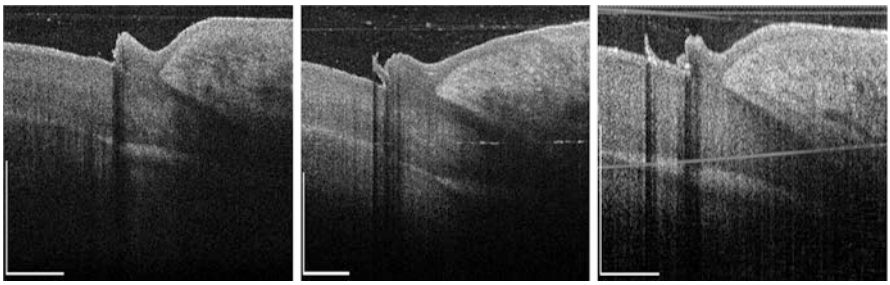

Fig. 24.22 MHz OCT imaging of highly scattering samples (nail bed) [43]. Direct comparison of imaging performance of 1 MHz (*left*), 2.6 MHz (*center*), and 5.2 MHz (*right*). The images show in vivo B-frames of human finger (nail bed). All three images are single non-averaged B-frames consisting of 1,250 A-scans each. The corresponding acquisition times were 1.3 ms, 480 μs, and 250 μs, respectively. Scale bars denote 1 mm in water

24.7.2 MHz OCT at 1,050 nm: Retinal Ultrawide Field OCT

The first multi-MHz FDML OCT imaging has been performed in the 1,300 nm region, because the typical 1,300 nm applications usually have higher permissible exposure levels on the sample. Much more challenging is in vivo retinal imaging, since there the typical OCT power levels are below 1.9 mW. This makes about 95 dB shot noise-limited sensitivity at 2 MHz axial scan rate. Another problem of 1,050 nm is specific to FDML, it is caused by the long fiber delay line. Whereas the linear GVD is zero at 1,320 nm for standard optical fiber, at 1,050 nm standard single mode fiber has about 40 ps/nm/km. Also the fiber and the optical components loss are higher, and active optical elements are less reliable and lower power.

In 2011, Klein et al. published the first swept source MHz 1,050 nm ultrawide field retinal OCT [45]. The high imaging speed allowed for the first time a single shot ultrawide field coverage of $\sim 70^\circ$ with dense isotropic sampling. Figure 24.23 (top) shows an OCT image acquired in 2012 with a newer 1.68 MHz system using a dispersion-compensated 1,050 nm FDML laser [85, 111]. A series of 3D OCT data sets consisting of 1,088 frames with 1,088 A-scans was acquired in 0.85 s each, i.e., a rate of 1.2 volumes/s sustained over 24 volumes. Despite the high speed, the quality is good, penetration well through the choroid is observed, and the long ranging depth without sensitivity roll off of the laser enables visualization of the entire nerve head structure. Figure 24.23 (bottom, left) shows a fundus projection, reconstructed from the 3D OCT data set. Because of the high sampling density in both directions, the quality approaches the quality of scanning laser ophthalmoscopic images, which enable a very accurate absolute registration of the scans for follow-up studies. Figure 24.23 (bottom, right) shows the additional advantage of ultrawide field OCT en face reconstruction over standard SLO, i.e., the depth resolved extraction of image contrast from different layers of the retina. The image shows a color-coded visualization.

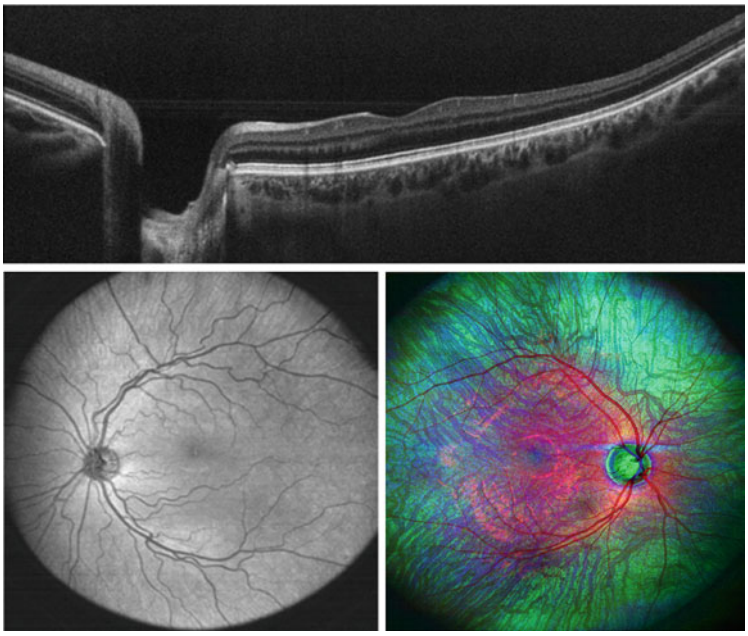

Fig. 24.23 Ultrawide field retinal MHz [45, 85, 111]. *Top*: Averaged cross section – 3D volumes consisting of 1,088 frames and 1,088 A-scans acquired in 0.85 s each or 1.2 volumes/s. *Bottom left*: High-definition reconstructed fundus view (1,900 × 1,900 data set). *Bottom right*: The densely sampled ultrawide field 3D data set enabled for the first time high-definition depth resolved en face projections and segmentations over a large part of the anterior pole

So in summary, FDML lasers have demonstrated the capability of OCT systems going well into the multi-MHz scan rate range. For many applications, the image quality is already sufficient. The results have triggered vibrant research efforts on other alternative laser designs, and currently several non-FDML lasers appear to be good candidates as the second multi-MHz OCT laser source. So it can be expected that in the future other swept sources also achieve MHz sweep rates which will make MHz and multi-MHz OCT applications more easily accessible for research groups.

24.8 Parallel Techniques: Multi-spot OCT Systems

24.8.1 The Problem of Low Sensitivity at MHz OCT Imaging Speed

The initial demonstrations of multi-MHz OCT have shown good image quality. However, especially at 1,050 nm, it should be considered that the data was acquired in a healthy volunteer. For routine imaging in clinical practice and in patients with cataract, the system sensitivity of the MHz OCT might not be sufficient.

Figure 24.24 shows a graph with the different values of shot noise-limited sensitivity for various MHz imaging speeds. It can be seen that with 1.4 mW on

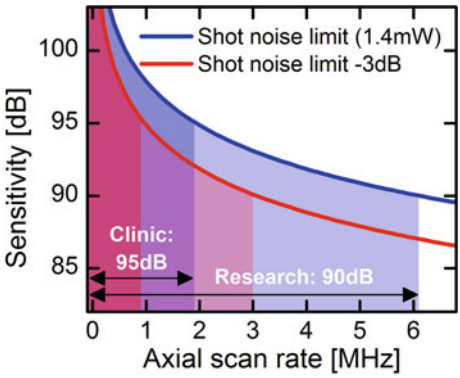

Fig. 24.24 Maximum possible MHz OCT speed for retinal imaging applications. The figure shows the theoretical shot noise limit and the sensitivity that can realistically be achieved (−3 dB) due to losses in the imaging setup. With a required sensitivity of more than 95 dB, this sets an upper OCT speed limit of ∼2 MHz line rate [85]

the sample, the imaging speed for clinical applications should not exceed 2 MHz. From a physical point of view, it could be argued that faster OCT imaging also leads to a lower amount of energy at each spot on the sample and that the power can be increased linearly. Indeed, the scanning operation is not considered in current OCT systems, so from a viewpoint of ANSI standards, more power could be applied in case the scanning operation is ensured. However, since in research very often multi-scan protocols are applied, where the OCT scans several times over the same sample spot, the situation would get very complex and the OCT system power would need to be changed depending on the imaging protocol. So it is preferred to find another solution.

24.8.2 Increasing the Sensitivity of MHz OCT I: Multi-spot OCT

The first solution is to apply several parallel OCT detection channels. The concept of multichannel OCT is used in the "multi-beam" OCT systems of Michelson Diagnostics, where four channels with different focusing increase the depth of field. However in this case, the total power on the sample is quadrupled at a single spot. Vitkin et al. [41] and Wieser et al. [43] demonstrated in 2010 a setup where the different spots are separated on the sample by a distance of several millimeters. Potsaid et al. [94] applied this concept to the human retina. Since this concept distributes the heat load on the sample caused by the OCT laser, more power can be applied. To distinguish this configuration from the four-beam incident on the same spot on the sample, the approach with separated spot is termed multi-spot OCT. Depending on the separation, each spot of the OCT system can have the same power as a single spot system. The ANSI standard usually defines a circular area over which the laser power has to be integrated to be considered in the exposure estimations.

Figure 24.25 shows the beam delivery optics for multi-spot detection. It should be noted here that multi-beam, multichannel, and multi-spot setups are usually more compatible with swept source OCT than with spectral domain systems. It is technically easier, cheaper, and more compact to use several photo-receivers and

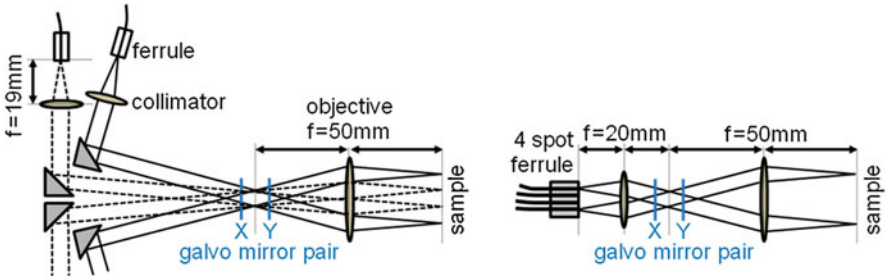

Fig. 24.25 Multi-spot beam delivery for multi-MHz OCT [43]. *Left*: Multi-beam setup with four individual collimators for reduced aberrations [43]. *Right*: More compact setup, but with increased lens aberrations [41]

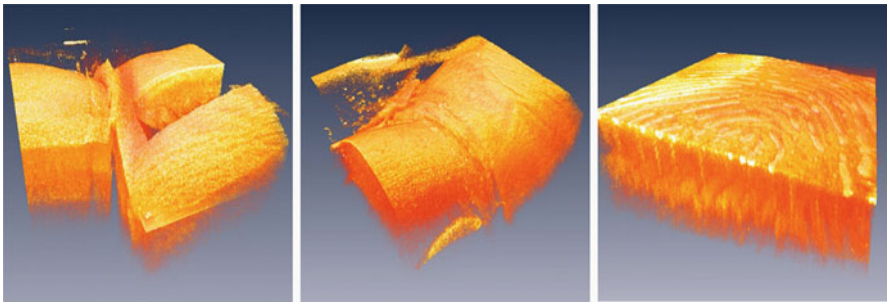

Fig. 24.26 Multi-spot MHz OCT images [43]. 4 × 1 MHz = 4 MHz (*left*), 4 × 2.6 MHz = 10.4 MHz (*center*), 4 × 5.2 = 20.8 MHz (*right*) – fastest 3D OCT to date

analog-to-digital converter channels than to build several spectrometers. Figure 24.26 shows 4-spot MHz OCT up to 20.8 million A-scans per second. With a rate of 4.5 billion voxels per second, this represents the fastest 3D OCT imaging to date. However, the data has not been processed and displayed live and in real time. The data was not streamed; only one volume could be acquired. But the data clearly shows the possibility of good image quality at 20 million OCT depth scans per second. A similar approach has been followed for retinal OCT imaging with MHz FDML lasers at 1,050 nm. In Ref. [85], Klein et al. investigated how well the different volumes from a multi-spot retinal OCT system can be aligned. The system ran at 2 × 3.35 = 6.7 MHz. Here the problem is non-reproducible aberrations caused by the lens of the human eye. For first investigations the system was operated at 2 × 800 μW, so half of the power is permissible for single spot. Figure 24.27 shows the results. It can be seen that both volumes can be fused very smoothly. However, the image quality of the individual spots exhibits very low signal levels. The combination of 3.35 MHz and 800 μW causes a sensitivity of only ~88 dB.

The concept of multi-beam approaches can significantly reduce the thermal stress on the sample and can increase the allowed power exposure levels according

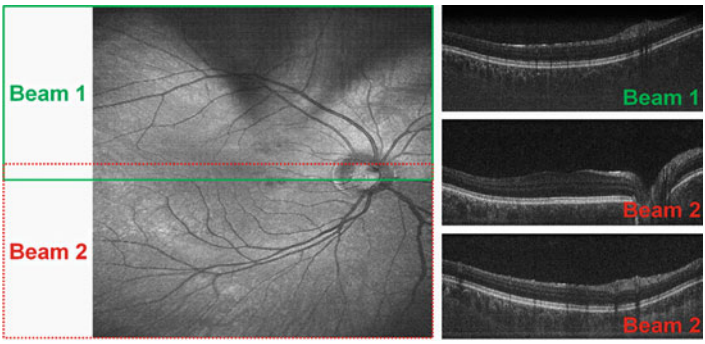

Fig. 24.27 6.7 MHz multi-spot OCT in human retina. Two volumes acquired with the different spots can be seamlessly fused. At 6.7 MHz A-scan rate, this is the fastest flying spot retinal 3D OCT to date [85]

to ANSI standard by splitting up the power to the different beams. However, as can be seen in Fig. 24.27 (left), an overlap region is required for numerical fine alignment and correction of potential image distortions caused by the lens aberrations. The overlap region is scanned twice which has to be considered calculating the power levels. A solution that can increase signal levels without increasing the total power will be presented in the next section.

24.8.3 Increasing the Sensitivity of MHz OCT II: Joint-Aperture OCT (JA-OCT)

A very recent technique in retinal MHz OCT is the so-called joint-aperture (JA) detection [111]. It is a multichannel OCT technique; however there is no multi-beam or multi-spot technique. JA-OCT is specifically tailored to ultrahigh-speed OCT systems. JA-OCT combines illumination from a standard active OCT channel with passive detection on a multitude of additional passive channels (Fig. 24.28, left). The active channel is equivalent to the single channel in a standard OCT system. However, no light is incident on the sample from the passive channels; they only collect light that is backscattered under an angle with respect to the beam from the active channel. This multiplexed approach combines the advantages of angle-resolved detection and does not sacrifice imaging speed. Additionally, the collection efficiency and thus the effective sensitivity of the OCT system are increased, and the quality of the OCT signal from the active beam is not compromised. As mentioned, both aspects are very important for ultrahigh-speed OCT systems, which already suffer from relatively low signal levels due to lower exposure time. Figure 24.28 (right) shows two possible layouts of a JA beam delivery system.

For JA-OCT the interferometer configuration is slightly different for the active and the passive channels. The layout of a JA-OCT system is shown in Fig. 24.29. The reference arms for the passive channels are Mach-Zehnder-type configurations,

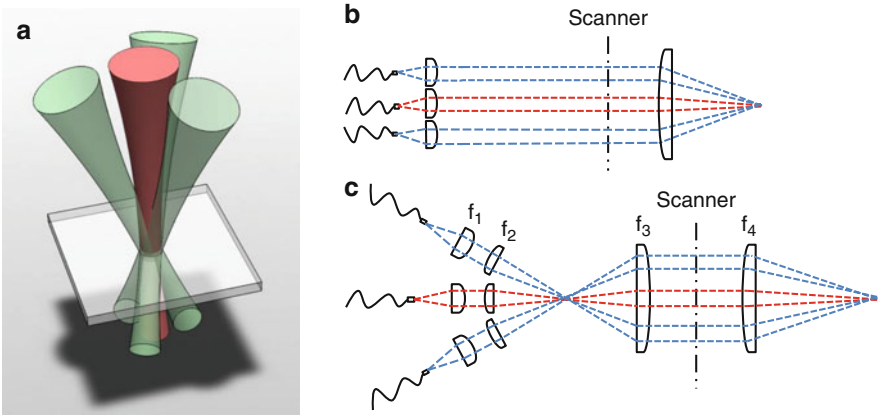

Fig. 24.28 Joint-aperture OCT [111]. *Left*: Concept of joint aperture. *Right*: Different implementations, without (**b**) and with (**c**) intermediate focus

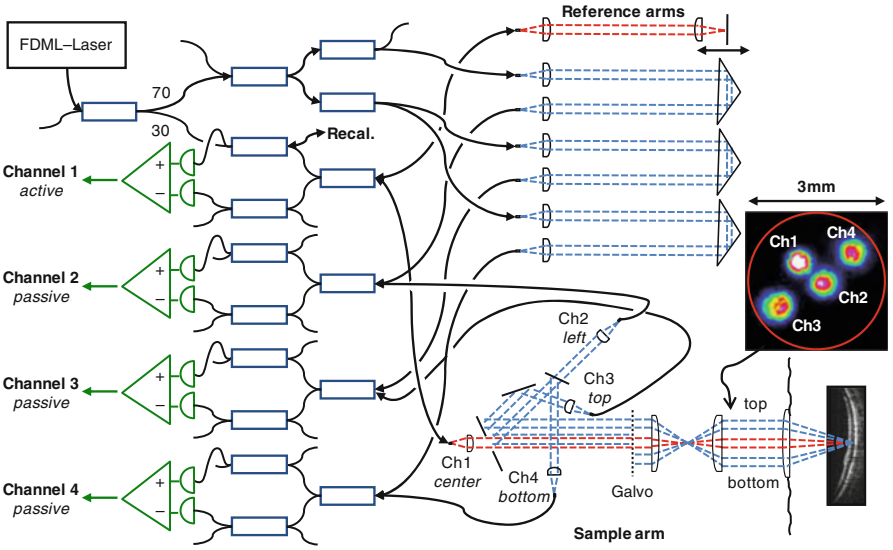

Fig. 24.29 JA-OCT interferometer [111]

and the one for the active channel a Michelson type. The beams, or in the case of the passive channels the beam paths, are combined via D-shaped mirrors and a mirror with a center hole. The losses due to clipping are several 10 %.

Figure 24.30 shows a comparison of image quality for standard OCT and JA-OCT at different levels of frame averaging. It can be seen that the image quality with respect to signal levels and especially with respect to speckle noise is significantly improved.

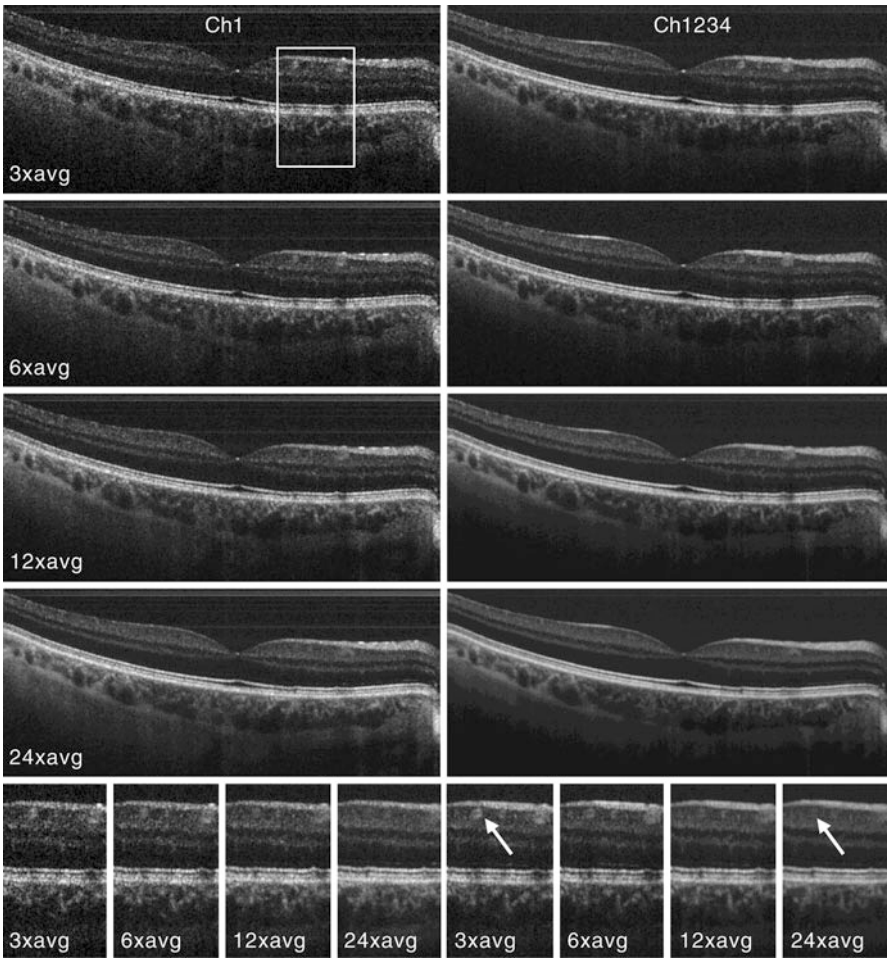

Fig. 24.30 Comparison of image quality of standard OCT and JA-OCT [113]. Averaging of adjacent frames in standard single-channel OCT (*left*) and JA-OCT (*right*). The image quality of the compounded JA-OCT images is always superior to single-channel imaging. *Bottom*: In the enlarged image sections, it can be clearly seen that averaging of frames spanning less than 100 μm distance already blurs out important image detail, such as the blood vessel indicated by the *arrow*. So the less averaging required in JA-OCT helps maintain image detail

24.9 Conclusion

So far, the main impact of FDML lasers has been the demonstration of OCT systems with dramatically higher imaging speed. The first versions have pushed the speed from several 10 KHz line rate which have been standard for the first FD-OCT systems to several 100 kHz, and later on FDML lasers have helped to break the barrier of 1 MHz line rate with swept sources. Besides the higher imaging speed, FDML lasers

have been proven useful for many different applications, where good phase stability, long coherence, low laser noise, or similar is required. Despite these many initial applications, only very few more applied or clinical studies using FDML have been published. The first reason is that commercial FDML lasers have only very recently become available. Also this may be attribute to the difficulty to build proper OCT systems that can handle the high imaging speed and with it the huge data rates generated by these multi-MHz OCT systems. It is interesting to see how the high-speed FDML results have triggered vibrant research efforts to realize non-FDML sources which can achieve similar performance. Currently in 2013 there are several promising candidates of swept laser sources with alternative technology. It can be expected that the availability of more than one swept laser technology for MHz OCT will spur research on applications to find out where MHz OCT imaging speeds are required. MHz imaging speeds may lead to even more applications of OCT as one of the most exciting optical imaging technologies in biomedical application today.

Acknowledgment The author would like to thank all people who contributed to the work on FDML lasers and their applications, especially Desmond Adler, Kenji Taira, Maciej Wojtkowski, James G. Fujimoto, Joseph Schmitt, Michael Jenkins, Andrew Rollins, Laura Kranendonk, Scott Sanders, Christoph Eigenwillig, Benjamin Biedermann, Gesa Palte, Wolfgang Wieser, Thomas Klein, Tom Pfeiffer, Sebastian Karpf, Raphael André, Cedric Blatter, Tilman Schmoll, Rainer Leitgeb, Sebastian Marschall, Aljoscha S. Neubauer, Lukas Reznicek, Anselm Kampik, Marcus Kernt, Armin Wolf, Antonius F. W. van der Steen, Gijs van Soest, Corinna Kufner, Matthias Eibl, Rainer Szalata, Jan Philip Kolb, Tianshi Wang, Yaokun Zhang, joerg raczkowsky, Thomas Klenzner, Erich Götzinger, Michael Pircher, Bernhard Baumann, Kathrin Mohler, Vivek Srinivasan, Aaron Aguirre, Peter Andersen, Teresa Torzicky, Marco Bonesi, Christoph Hitzenberger, Boris Hermann, Wolfgang Drexler, Sebastian Todor, and Christian Jirauschek. The author also acknowledges support from Wolfgang Zinth and Alfred Vogel and funding from the European Union (FP7 HEALTH, FUN-OCT, contract no. 201880; European Research Council, ERC Starting grant: FDML-Raman, contract no. 259158) and the German research foundation (Emmy Noether Programme: HU1006/2 and OCT-Labs: Hu1006/3).

References

1. F.P. Schafer, W. Schmidt, J. Volze, Organic dye solution laser. Appl. Phys. Lett. **9**(8), 306 (1966)
2. P.P. Sorokin, J.R. Lankard, Stimulated emission observed from an organic dye chloro-aluminum phthalocyanine. IBM J. Res. Dev. **10**(2), 162 (1966)
3. S.W. Chiow et al., 6 W, 1 kHz linewidth, tunable continuous-wave near-infrared laser. Opt. Express **17**(7), 5246–5250 (2009)
4. D. Haubrich, R. Wynands, A modified commercial Ti:Sapphire laser with 4 kHz rms linewidth. Opt. Commun. **123**(4–6), 558–562 (1996)
5. L.A. Coldren et al., Tunable semiconductor lasers: a tutorial. J. Light. Technol. **22**(1), 193–202 (2004)
6. R.W. Fox et al., The diode-laser as a spectroscopic tool. Spectrochim. Acta Rev. **15**(5), 291–299 (1993)
7. A. Mooradia, Tunable semiconductor lasers. IEEE J. Quantum Electron. **QE 8**(6), 574 (1972)

8. H. Lim et al., Optical frequency domain imaging with a rapidly swept laser in the 815–870 nm range. Opt. Express **14**(13), 5937–5944 (2006)
9. V.J. Srinivasan et al., High-speed, high-resolution optical coherence tomography retinal imaging with a frequency-swept laser at 850 nm. Opt. Lett. **32**(4), 361–363 (2007)
10. E.C.W. Lee et al., In vivo optical frequency domain imaging of human retina and choroid. Opt. Express **14**(10), 4403–4411 (2006)
11. Y. Yasuno et al., In vivo high-contrast imaging of deep posterior eye by 1-mu m swept source optical coherence tomography and scattering optical coherence angiography. Opt. Express **15**(10), 6121–6139 (2007)
12. R. Huber et al., Fourier domain mode locking at 1050 nm for ultra-high-speed optical coherence tomography of the human retina at 236,000 axial scans per second. Opt. Lett. **32**(14), 2049–2051 (2007)
13. S.H. Yun et al., High-speed optical frequency-domain imaging. Opt. Express **11**(22), 2953–2963 (2003)
14. R. Huber et al., Amplified, frequency swept lasers for frequency domain reflectometry and OCT imaging: design and scaling principles. Opt. Express **13**(9), 3513–3528 (2005)
15. B.R. Biedermann et al., Recent developments in Fourier domain mode locked lasers for optical coherence tomography: Imaging at 1310 nm vs. 1550 nm wavelength. J. Biophotonics **2**(6–7), 357–363 (2009)
16. S. Slepneva, B. O'Shaughnessy, B. Kelleher, S.P. Hegarty, A. Vladimirov, H.-C. Lyu, K. Karnowski, M. Wojtkowski, G. Huyet, Dynamics of a short cavity swept source OCT laser. Opt. Express **22**, 18177–18185 (2014). http://www.opticsinfobase.org/oe/abstract.cfm?URI=oe-22-15-18177
17. M.P. Minneman et al., All-semiconductor high-speed akinetic swept-source for OCT, in *Optical Sensors and Biophotonics Iii*, ed. by J. Popp et al. (Spie-Int Soc Optical Engineering, Bellingham, 2011)
18. L.M. Zinkiewicz, et al., 120-mw Vertical Cavity Surface-Emitting (vcse) Diode-Lasers. Institute of Physics Conference Series. (96) 567–570 (1989)
19. M. Maute et al., MEMS-tunable 1.55-mu m VCSEL with extended tuning range incorporating a buried tunnel junction. IEEE Photon. Technol. Lett. **18**(5–8), 688–690 (2006)
20. C. Gierl et al., Surface micromachined MEMS-tunable VCSELs with wide and fast wavelength tuning. Electron. Lett. **47**(22), 1243–1244 (2011)
21. T. Yano et al., Wavelength modulation over 500 kHz of micromechanically tunable InP-based VCSELs with Si-MEMS technology. IEEE J. Sel. Top. Quantum Electron. **15**(3), 528–534 (2009)
22. I. Grulkowski et al., Retinal, anterior segment and full eye imaging using ultrahigh speed swept source OCT with vertical-cavity surface emitting lasers. Biomed. Opt. Express **3**(11), 2733–2751 (2012)
23. V. Jayaraman, et al., OCT imaging up to 760 kHz axial scan rate using single-mode 1310nm MEMS-tunable VCSELs with >100nm tuning range. in *CLEO: 2011 – Laser Applications to Photonic Applications*, OSA Technical Digest (CD) (Optical Society of America, 2011), paper PDPB2. (2011). http://www.opticsinfobase.org/abstract.cfm?URI=CLEO_SI-2011-PDPB2
24. V. Jayaraman, J. Jiang, H. Li, P. Heim, G. Cole, B. Potsaid, J.G. Fujimoto, A. Cable, Design and performance of broadly tunable, narrow line-width, high repetition rate 1310nm VCSELs for swept source optical coherence tomography, in *Vertical-Cavity Surface-Emitting Lasers Xvi*, ed. by C. Lei, K.D. Choquette (SPIE, Bellingham, 2012)
25. B. Potsaid et al., MEMS tunable VCSEL light source for ultrahigh speed 60kHz-1MHz axial scan rate and long range centimeter class OCT imaging, in *Optical Coherence Tomography and Coherence Domain Optical Methods in Biomedicine Xvi*, ed. by J.A. Izatt, J.G. Fujimoto, V.V. Tuchin (SPIE, Bellingham, 2012)
26. A.E. Siegman, Lasers, in *Lasers (chapter 25.3 – Physical Interpretation: Linear Doppler Shift)*, ed. by A. Kelly (University Science, Sausalito, 1986), p. 986

27. R. Huber, M. Wojtkowski, J.G. Fujimoto, Fourier Domain Mode Locking (FDML): a new laser operating regime and applications for optical coherence tomography. Opt. Express **14**(8), 3225–3237 (2006)
28. J.M. Telle, C.L. Tang, Very rapid tuning of cw dye laser. Appl. Phys. Lett. **26**(10), 572–574 (1975)
29. B.R. Biedermann et al., Dispersion, coherence and noise of Fourier domain mode locked lasers. Opt. Express **17**(12), 9947–9961 (2009)
30. D.C. Adler et al., Extended coherence length Fourier domain mode locked lasers at 1310 nm. Opt. Express **19**(21), 20930–20939 (2011)
31. B.R. Biedermann et al., Direct measurement of the instantaneous linewidth of rapidly wavelength-swept lasers. Opt. Lett. **35**(22), 3733–3735 (2010)
32. S. Todor et al., Instantaneous line shape analysis of Fourier domain mode-locked lasers. Opt. Express **19**(9), 8802–8807 (2011)
33. S. Todor, C. Jirauschek, B. Biedermann, R. Huber, Linewidth optimization of Fourier domain mode-locked lasers. in *Conference on Lasers and Electro-Optics 2010*, OSA Technical Digest (CD) (Optical Society of America, 2010), paper CMW7. (2010). http://www.opticsinfobase.org/abstract.cfm?URI=CLEO-2010-CMW7
34. D.C. Adler et al., Coherence length extension of Fourier domain mode locked lasers, in *Optical Coherence Tomography and Coherence Domain Optical Methods in Biomedicine Xvi*, ed. by J.A. Izatt, J.G. Fujimoto, V.V. Tuchin (SPIE, Bellingham, 2012)
35. W. Wieser et al., Extended coherence length megahertz FDML and its application for anterior segment imaging. Biomed. Opt. Express **3**(10), 2647–2657 (2012)
36. C. Jirauschek, B. Biedermann, R. Huber, A theoretical description of Fourier domain mode locked lasers. Opt. Express **17**(26), 24013–24019 (2009)
37. C. Jirauschek, et al., Fourier Domain Mode Locking theory. *2008 Conference on Lasers and Electro-Optics & Quantum Electronics and Laser Science Conference*, Vols. 1–9, pp. 1403–1404 (2008)
38. S. Todor et al., Balance of physical effects causing stationary operation of Fourier domain mode-locked lasers. J. Opt. Soc. Am. B-Opt. Phys. **29**(4), 656–664 (2012)
39. Y.L. Chen et al., Spectrally balanced detection for optical frequency domain imaging. Opt. Express **15**(25), 16390–16399 (2007)
40. M.K.K. Leung et al., High-power wavelength-swept laser in Littman telescope-less polygon filter and dual-amplifier configuration for multichannel optical coherence tomography. Opt. Lett. **34**(18), 2814–2816 (2009)
41. M.K.K. Leung et al., Simultaneous 6-channel optical coherence tomography using a high-power telescope-less polygon-based swept laser in dual-amplifier configuration, in *Optical Coherence Tomography and Coherence Domain Optical Methods in Biomedicine Xiv*, ed. by J.A. Izatt, J.G. Fujimoto, V.V. Tuchin (SPIE, Bellingham, 2010)
42. G.Y. Liu et al., High power wavelength linearly swept mode locked fiber laser for OCT imaging. Opt. Express **16**(18), 14095–14105 (2008)
43. W. Wieser et al., Multi-megahertz OCT: high quality 3D imaging at 20 million A-scans and 4.5 GVoxels per second. Opt. Express **18**(14), 14685–14704 (2010)
44. M.K. Harduar et al., Dual core ytterbium doped fiber ring laser in Fourier domain mode locked operation for swept-source optical coherence tomography, in *Fiber Lasers Vii: Technology, Systems, and Applications*, ed. by K. Tankala, J.W. Dawson (SPIE, Bellingham, 2010)
45. T. Klein et al., Megahertz OCT for ultrawide-field retinal imaging with a 1050nm Fourier domain mode-locked laser. Opt. Express **19**(4), 3044–3062 (2011)
46. B. Vuong et al., Cascaded Raman fiber laser in Fourier domain mode lock operation, in *Fiber Lasers Vii: Technology, Systems, and Applications*, ed. by K. Tankala, J.W. Dawson (SPIE, Bellingham, 2010)
47. K.H.Y. Cheng et al., Wavelength-swept spectral and pulse shaping utilizing hybrid Fourier domain mode locking by fiber optical parametric and erbium-doped fiber amplifiers. Opt. Express **18**(3), 1909–1915 (2010)

48. K.H.Y. Cheng et al., Hybrid Fourier domain mode locked Laser utilizing a fiber optical parametric amplifier and an erbium doped fiber amplifier, in *Fiber Lasers Vii: Technology, Systems, and Applications*, ed. by K. Tankala, J.W. Dawson (Spie-Int Soc Optical Engineering, Bellingham, 2010)
49. S. Kim, O.J. Kwon, Y.G. Han, Long distance fiber Bragg grating strain sensor interrogation using high speed Raman-based Fourier domain mode-locked fiber laser with recycled residual Raman pump, in *22nd International Conference on Optical Fiber Sensors*, ed. by Y. Liao et al. (SPIE, Bellingham, 2012), pp. 1–3
50. H.S. Lee et al., Broadband wavelength-swept Raman laser for Fourier-domain mode locked swept-source OCT. J. Opt. Soc. Korea **13**(3), 316–320 (2009)
51. T. Klein et al., Raman-pumped Fourier-domain mode-locked laser: analysis of operation and application for optical coherence tomography. Opt. Lett. **33**(23), 2815–2817 (2008)
52. H.A. Haus, Mode-locking of lasers. IEEE J. Sel. Top. Quantum Electron. **6**(6), 1173–1185 (2000)
53. T. Udem, R. Holzwarth, T.W. Hansch, Optical frequency metrology. Nature **416**(6877), 233–237 (2002)
54. C.M. Eigenwillig, W. Wieser, S. Todor, B.R. Biedermann, T. Klein, C. Jirauschek, R. Huber, Picosecond pulses from wavelength-swept continuous-wave Fourier domain mode-locked lasers. Nat. Commun. **4**. doi:10.1038/ncomms2870 (2013)
55. A.E. Siegman, Lasers, in *Lasers (chapter 27.7 – FM laser operation)*, ed. by A. Kelly (University Science, Sausalito, 1986), p. 1095
56. S. Slepneva, B. Kelleher, B. O'Shaughnessy, S.P. Hegarty, A.G. Vladimirov, G. Huyet, Dynamics of Fourier domain mode-locked lasers. Opt. Express **21**, 19240–19251 (2013). http://www.opticsinfobase.org/oe/abstract.cfm?URI=oe-21-16-19240
57. A.E. Siegman, Lasers, in *Lasers (chapter 27.2 – FM Mode-Locking Behavior)*, ed. by A. Kelly (University Science, Sausalito, 1986), p. 1095
58. S.H. Yun et al., Wavelength-swept fiber laser with frequency shifted feedback and resonantly swept intra-cavity acoustooptic tunable filter. IEEE J. Sel. Top. Quantum Electron. **3**(4), 1087–1096 (1997)
59. R. Huber et al., Fourier domain mode locked lasers for OCT imaging at up to 290 kHz sweep rates, in *European Conference on Biomedical Optics*, ed. by W. Drexler (SPIE (Optical Society of America, 2005), Munich, 2005), p. PDA3
60. W. Wieser et al., Chromatic polarization effects of swept waveforms in FDML lasers and fiber spools. Opt. Express **20**(9), 9819 (2012)
61. C. Blatter et al., Ultrahigh-speed non-invasive wide field angiography. J. Biomed. Opt. **17**(7), 070705 (2012)
62. R. Huber, D.C. Adler, J.G. Fujimoto, Buffered Fourier domain mode locking: unidirectional swept laser sources for optical coherence tomography imaging at 370,000 lines/s. Opt. Lett. **31**(20), 2975–2977 (2006)
63. W.Y. Oh et al., 400 kHz repetition rate wavelength-swept laser and application to high-speed optical frequency domain imaging. Opt. Lett. **35**(17), 2919–2921 (2010)
64. S. Marschall et al., Broadband Fourier domain mode-locked laser for optical coherence tomography at 1060 nm, in *Optical Coherence Tomography and Coherence Domain Optical Methods in Biomedicine Xvi*, ed. by J.A. Izatt, J.G. Fujimoto, V.V. Tuchin (SPIE, Bellingham, 2012)
65. J. Zhang et al., Polarization maintaining buffered Fourier domain mode-locked swept source, in *Optical Coherence Tomography and Coherence Domain Optical Methods in Biomedicine Xvi*, ed. by J.A. Izatt, J.G. Fujimoto, V.V. Tuchin (SPIE, Bellingham, 2012)
66. J. Zhang et al., Polarization-maintaining buffered Fourier domain mode-locked swept source for optical coherence tomography. Opt. Lett. **36**(24), 4788–4790 (2011)
67. M.W. Jenkins et al., Ultrahigh-speed optical coherence tomography imaging and visualization of the embryonic avian heart using a buffered Fourier domain mode locked laser. Opt. Express **15**(10), 6251–6267 (2007)

68. D.C. Adler, R. Huber, J.G. Fujimoto, Phase-sensitive optical coherence tomography at up to 370,000 lines per second using buffered Fourier domain mode-locked lasers. Opt. Lett. **32**(6), 626–628 (2007)
69. D.C. Adler, R. Huber, J.G. Fujimoto, Phase sensitive optical coherence tomography using buffered Fourier Domain Mode Locked lasers at up to 370,000 scans per second – art. no. 64291L, in *Coherence Domain Optical Methods and Optical Coherence Tomography in Biomedicine XI*, ed. by J.G. Fujimoto, J.A. Izatt, V.V. Tuchin (SPIE, Bellingham, 2007), pp. L4291–L4291
70. D.C. Adler, R. Huber, J. G. Fujimoto, Optical coherence tomography phase microscopy using buffered Fourier Domain Mode Locked (FDML) Lasers at up to 370,000 lines per second. in *Conference on Lasers and Electro-Optics/Quantum Electronics and Laser Science Conference and Photonic Applications Systems Technologies*, OSA Technical Digest Series (CD) (Optical Society of America, 2007), paper CFL1. pp. 1658–1659 (2007). http://www.opticsinfobase.org/abstract.cfm?URI=CLEO-2007-CFL1
71. C. Blatter et al., High-speed functional OCT with self-reconstructive Bessel illumination at 1300 nm, in *Optical Coherence Tomography and Coherence Techniques V*, ed. by R.A. Leitgeb, B.E. Bouma (SPIE, Bellingham, 2011)
72. J.F. DeBoer et al., Two-dimensional birefringence imaging in biological tissue by polarization-sensitive optical coherence tomography. Opt. Lett. **22**(12), 934–936 (1997)
73. M. Yamanari, S. Makita, Y. Yasuno, Polarization-sensitive swept-source optical coherence tomography with continuous source polarization modulation. Opt. Express **16**(8), 5892–5906 (2008)
74. S. Marschall et al., FDML swept source at 1060 nm using a tapered amplifier, in *Optical Coherence Tomography and Coherence Domain Optical Methods in Biomedicine Xiv*, ed. by J.A. Izatt, J.G. Fujimoto, V.V. Tuchin (SPIE, Bellingham, 2010)
75. S. Marschall et al., Fourier domain mode-locked swept source at 1050 nm based on a tapered amplifier. Opt. Express **18**(15), 15820–15831 (2010)
76. R. Leonhardt et al., Nonlinear optical frequency conversion of an amplified Fourier Domain Mode Locked (FDML) laser. Opt. Express **17**(19), 16801–16808 (2009)
77. K.K.Y. Cheung et al., Fourier domain mode locking laser sweeping based on optical parametric amplification. *2010 Conference on Optical Fiber Communication Ofc Collocated National Fiber Optic Engineers Conference Ofc-Nfoec* (IEEE, New York, 2010)
78. Y. Mao et al., High-power 1300 nm FDML swept laser using polygon-based narrowband optical scanning filter, in *Optical Coherence Tomography and Coherence Domain Optical Methods in Biomedicine Xiii*, ed. by J.G. Fujimoto, J.A. Izatt, V.V. Tuchin (SPIE, Bellingham, 2009)
79. K. Murari et al., Self-starting, self-regulating Fourier domain mode locked fiber laser for OCT imaging. Biomed. Opt. Express **2**(7), 2005–2011 (2011)
80. K. Goda et al., High-throughput optical coherence tomography at 800 nm. Opt. Express **20**(18), 19612–19617 (2012)
81. S. Moon, D.Y. Kim, Ultra-high-speed optical coherence tomography with a stretched pulse supercontinuum source. Opt. Express **14**(24), 11575–11584 (2006)
82. S.B. Moon, D.S. Lee, D.Y. Kim, High-speed Fourier-domain optical coherence tomography using a chirped supercontinuum pulse source - art. no. 64291E, in *Coherence Domain Optical Methods and Optical Coherence Tomography in Biomedicine XI*, ed. by J.G. Fujimoto, J.A. Izatt, V.V. Tuchin (SPIE, Bellingham, 2007), p. E4291–E4291
83. I. Axsun Technologies. *Datasheet: high Speed 1310nm Swept Source for oct*. (2011)
84. Santec, *Datasheet (online): MEMS Based Swept Source, HSL-20*. (2013)
85. T. Klein, W. Wieser, L. Reznicek, A. Neubauer, A. Kampik, R. Huber, Multi-MHz retinal OCT. Biomed. Opt. Express **4**(10), 1890–1908 (2013)
86. C.M. Eigenwillig et al., Wavelength swept amplified spontaneous emission source for high speed retinal optical coherence tomography at 1060 nm. J. Biophotonics **4**(7–8), 552–558 (2011)

87. W. Drexler et al., In vivo ultrahigh-resolution optical coherence tomography. Opt. Lett. **24**(17), 1221–1223 (1999)
88. J.G. Fujimoto, Optical coherence tomography for ultrahigh resolution in vivo imaging. Nat. Biotechnol. **21**(11), 1361–1367 (2003)
89. I. Hartl et al., Ultrahigh-resolution optical coherence tomography using continuum generation in an air-silica microstructure optical fiber. Opt. Lett. **26**(9), 608–610 (2001)
90. N. Nassif et al., In vivo human retinal imaging by ultrahigh-speed spectral domain optical coherence tomography. Opt. Lett. **29**(5), 480–482 (2004)
91. M. Wojtkowski et al., Ultrahigh-resolution, high-speed, Fourier domain optical coherence tomography and methods for dispersion compensation. Opt. Express **12**(11), 2404–2422 (2004)
92. J. Zhang, G.J. Liu, Z.P. Chen, Ultra broad band Fourier domain mode locked swept source based on dual SOAs and WDM couplers, in *Optical Coherence Tomography and Coherence Domain Optical Methods in Biomedicine Xiv*, ed. by J.A. Izatt, J.G. Fujimoto, V.V. Tuchin (SPIE, Bellingham, 2010)
93. C.M. Eigenwillig et al., Wavelength swept amplified spontaneous emission source. Opt. Express **17**(21), 18794–18807 (2009)
94. B. Potsaid et al., Ultrahigh speed 1050nm swept source/ Fourier domain OCT retinal and anterior segment imaging at 100,000 to 400,000 axial scans per second. Opt. Express **18**(19), 20029–20048 (2010)
95. D. Chen, et al., Fiber Bragg grating interrogation for a sensing system based on a continuous-wave Fourier Domain Mode Locking fiber laser. *2008 Conference on Lasers and Electro-Optics & Quantum Electronics and Laser Science Conference*. Vols. 1–9 (2008), pp. 560–561
96. D. Chen, C. Shu, S. He, Multiple fiber Bragg grating interrogation based on a spectrum-limited Fourier domain mode-locking fiber laser. Opt. Lett. **33**(13), 1395–1397 (2008)
97. B.C. Lee, M.Y. Jeon, Remote fiber sensor based on cascaded Fourier domain mode-locked laser. Opt. Commun. **284**(19), 4607–4610 (2011)
98. B.C. Lee, et al., Dynamic and static strain fiber Bragg grating sensor interrogation with a 1.3 mu m Fourier domain mode-locked wavelength-swept laser. Meas. Sci. Technol. **21**(9), 094008 (2010)
99. Y. Wang et al., Quasi-distributed fiber Bragg grating sensor system based on a Fourier domain mode locking fiber laser. Laser Phys. **19**(3), 450–454 (2009)
100. D.C. Adler et al., Photothermal detection of gold nanoparticles using phase-sensitive optical coherence tomography. Opt. Express **16**(7), 4376–4393 (2008)
101. C. Blatter et al., Extended focus high-speed swept source OCT with self-reconstructive illumination. Opt. Express **19**(13), 12141–12155 (2011)
102. C. Blatter et al., Deep skin structural and microcirculation imaging with extended-focus OCT, in *Photonic Therapeutics and Diagnostics Viii, Pts 1 and 2*, ed. by N. Kollias et al. (SPIE, Bellingham, 2012)
103. C. Blatter et al., Intrasweep phase-sensitive optical coherence tomography for noncontact optical photoacoustic imaging. Opt. Lett. **37**(21), 4368–4370 (2012)
104. T. Wang, W. Wieser, G. Springeling, R. Beurskens, C.T. Lancee, T. Pfeiffer, A.F.W. van der Steen, R. Huber, G. van Soest, Intravascular optical coherence tomography imaging at 3200 frames per second. Opt. Lett. **38**, 1715–1717 (2013). http://www.opticsinfobase.org/ol/abstract.cfm?URI=ol-38-10-1715
105. E. Regar, P.W. Serruys, T.G. van Leeuwen, (eds.), *Optical Coherence Tomography in Cardiovascular (chapter 27 Limiting Ischemia by fast Fourier Domain Imaging)* (Informa Healthcare, Abington, 2007)
106. S.H. Yun et al., Comprehensive volumetric optical microscopy in vivo. Nat. Med. **12**(12), 1429–1433 (2006)
107. D.C. Adler et al., Three-dimensional endomicroscopy using optical coherence tomography. Nat. Photonics **1**(12), 709–716 (2007)

108. D.H. Choi et al., Spectral domain optical coherence tomography of multi-MHz A-scan rates at 1310 nm range and real-time 4D-display up to 41 volumes/second. Biomed. Opt. Express **3**(12), 3067 (2012)
109. D. Choi et al., Fourier domain optical coherence tomography using optical demultiplexers imaging at 60,000,000 lines/s. Opt. Lett. **33**(12), 1318–1320 (2008)
110. J. Probst et al., Optical coherence tomography with online visualization of more than seven rendered volumes per second. J. Biomed. Opt. **15**(2), 026014 (2010)
111. T. Klein, et al., Joint aperture detection for speckle reduction and increased collection efficiency in ophthalmic MHz OCT. Biomed. Opt. Express **4**, 619–634 (2013)
112. R.K. Wang et al., Depth-resolved imaging of capillary networks in retina and choroid using ultrahigh sensitive optical microangiography. Opt. Lett. **35**(9), 1467–1469 (2010)
113. W. Wieser, W. Draxinger, T. Klein, S. Karpf, T. Pfeiffer, R. Huber, High definition live 3D-OCT in vivo: design and evaluation of a 4D OCT engine with 1 GVoxel/s. Biomed. Opt. Express **5**(9), 2963–2977 (2014). http://dx.doi.org/10.1364/BOE.5.002963
114. W. Drexler et al., Ultrahigh-resolution ophthalmic optical coherence tomography. Nat. Med. **7**(4), 502–507 (2001)
115. D.C. Adler et al., Comparison of three-dimensional optical coherence tomography and high resolution photography for art conservation studies. Opt. Express **15**(24), 15972–15986 (2007)
116. M. Sylwestrzak et al., Real-time massively parallel processing of Spectral Optical Coherence Tomography data on Graphics Processing Units, in *Optical Coherence Tomography and Coherence Techniques*, ed. by V.R.A. Leitgeb, B.E. Bouma (Spie-Int Soc Optical Engineering, Bellingham, 2011)

Part III

Optical Coherence Microscopy

Time Domain Full Field Optical Coherence Tomography Microscopy

25

Fabrice Harms, Anne Latrive, and A. Claude Boccara

Keywords
Full field OCT • Full Field OCM • Signal to noise ratio • Endoscopy

25.1 Signal Introduction: OCT Acquisition and Multiplexing

For time- or frequency-encoded OCT systems samples, sections are obtained by quickly acquiring voxels along the optical axis of the imaging system [1–5]. More precisely the data is acquired along cylindrical sections of the samples that have roughly the length of the depth of field and then by scanning the beam along the sample surface. Differently, full-field OCM (FFOCM) [6–9] produces "en face" images (i.e., of a plane layer parallel to the sample surface) without scanning the light beam. FFOCM detects the interferometric signal across a plane section of the sample at a given depth and a 2D slice is thus obtained directly. When using this geometry, we can understand the main advantage of FFOCM over the competing OCT approaches: it allows the use of medium to large numerical aperture microscope objectives with a high transverse resolution of about one micrometer. For this reason in our first paper, we called it full-field optical microscopy (FFOCM) [10] and other authors did the same

F. Harms
LLTech SAS Pépinière Paris Santé Cochin, Paris, France

LLTech, Princeton, NJ, USA

A. Latrive
Institut Langevin, ESPCI ParisTech, Paris, France

LLTech SAS Pépinière Paris Santé Cochin, Paris, France

A.C. Boccara
LLTech SAS Pépinière Paris Santé Cochin, Paris, France

LLTech, Princeton, NJ, USA

Institut Langevin, ESPCI–ParisTech, Paris, France

© Springer International Publishing Switzerland 2015

W. Drexler, J.G. Fujimoto (eds.), *Optical Coherence Tomography*,
DOI 10.1007/978-3-319-06419-2_26

later [11], so we will continue here to use FFOCM because the microscopic resolution is more and more required for the various applications of this technique.

To record these images, the entire field is illuminated by a *spatially incoherent* source with low temporal coherence length (i.e., broadband) and is acquired on megapixel detectors such as CCD or CMOS cameras. The difference between FFOCM and OCM (see ▶ Chap. 26, "Assessment of Breast, Brain and Skin Pathological Tissue Using Full Field OCM" about OCM) is that OCM takes also "en face" images but uses a *single spatial mode optical source* (laser or SLD) that is focused by a microscope objective and scanned at the required depth [12, 13].

In the time-domain OCT approach, each voxel of the sample volume is scanned sequentially; a significant improvement has been achieved using spectroscopic or Fourier domain OCT that multiplexes the data by acquiring in parallel all the voxels along a line: typically a few hundred voxels are simultaneously acquired using a fast linear detector working in the kHz range. Typical values are of the order of megavoxels/s.

FFOCM allows millions of voxels acquisition in a few tens to thousand images/s range depending of the camera speed and the required signal-to-noise ratio. Here typical values are in the range of 100 megavoxels/s.

25.2 Full-Field Optical Coherence Microscopy

25.2.1 FFOCM: The Experimental Setup

In the case of full-field optical coherence microscopy, we combine an interferometer and a microscope. The experimental setup is shown schematically in Fig. 25.1.

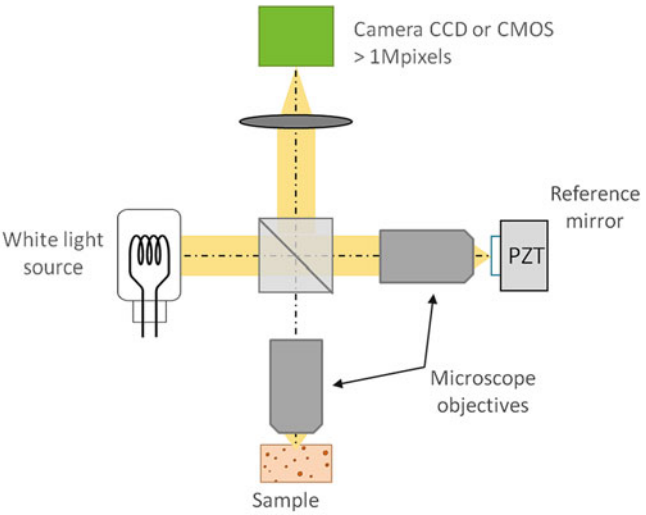

Fig. 25.1 Principle of the full-field OCM setup

This is a Michelson interferometer in the Linnik configuration where two identical microscope objectives are used in the object arm and in the reference arm.

Here we will describe the basic principles of the setup and the elementary signal processing.

The light source chosen for our system is a simple halogen lamp tungsten filament with a nominal power of 150 W that illuminates the interferometer via a Koehler illumination device that allows obtaining a homogeneous illumination of the sample. The emission spectrum of the source is very broad and can be modeled by that of a black body centered in the near infrared around 800 nm. This broadband incoherent source has a very short spatial and temporal coherence length leading to a sub-micrometer sectioning ability and avoiding cross talk.

The light beam emitted by the source is divided into the two arms of the interferometer through a broadband non-polarizing beamsplitter cube. The average power impinging the sample is of the order of 1 mW/mm^2.

The objectives that are mostly used for biomedical applications are immersion ones (oil or water) in order to reduce the surface reflection and to minimize the aberrations induced by the surface topographic irregularities. Routinely 10× water immersion objectives with a 0.3 numerical aperture (NA) are used but we have also used 20× (0.5 NA, water), 40× (0.8 NA, water), and 30× (1.05 NA, silicone oil) and a few more objectives working in air. The choice of two identical microscope objectives minimizes the path differences between the two arms and maximizes the overlap between the interfering wavefronts. The use of a sample immersion liquid (mostly buffer solutions) increases the duration of biological samples observation without damaging them under illumination.

Furthermore, using liquid immersion microscope objectives minimizes chromatic dispersion between the two arms when images are formed in depth.

25.2.1.1 Image Acquisition

The tomographic image intends to reveal the intensity reflected by a slice at a chosen depth; we call it $R_{obj}(x, y)$. The backscattered amplitude is calculated using the combination of two or four images obtained for two or for values of the phase ψ shifted by π or $\pi/2$, respectively. The recorded signal is given by

$$I(x,y,t) = \frac{I_0}{4}\left\{R_{inc}(x,y) + R_{ref}(x,y) + 2\sqrt{R_{obj}(x,y)R_{ref}(x,y)}\cos\left[\phi(x,y) + \psi\right]\right\}$$

where ϕ is the (unknown) phase difference between the reference signal and the object signal of the signal, ψ is the phase shift induced by the shift of the reference mirror, I_0 is the photon flux at the entrance of the interferometer, R_{ref} is the (rather uniform) reference mirror reflectivity, $R_{obj}(x, y)$ is the fraction of light reflected by the object that interferes with the reference beam, and $R_{inc}(x, y)$ is the fraction of light that does not interfere (light backscattered by the other slices of the sample, and the stray light of the interferometer). More precisely $R_{obj}(x, y)$ represents the reflectivity distribution of the sample structures contained in the coherence volume. $R_{obj}(x, y)$ thus corresponds to an en face tomographic image.

The two possible choices of two or four images need to be clarified:

- One can see easily that if R_{ref} is uniform over the field of view, four successive values of ψ (e.g., 0, π/2, π, 3π/2) allow to isolate the term $\sqrt{R_{obj}(x,y)R_{ref}(x,y)}$ that is proportional to $\sqrt{R_{obj}(x,y)}$ that is the amplitude of the backscattered signal intensity.
- OCT images always contain speckle because of the interference of the light backscattered by different tissue microstructures located inside the coherence volume. For this reason the amplitude and the phase of the recorded backscattered signals are random and we do not lose too much information by simply taking two images (instead of four) and rely on the absolute value of the real part of the complex signal (instead of the amplitude).

A software was developed to calculate and display the tomographic image in real time (at several tens of Hertz, depending on the camera frame rate and the computer speed).

By moving the sample step by step in the axial direction, one may acquire a stack of en face tomographic images. Once a three-dimensional data set is recorded, sections of arbitrary orientation can be extracted. Volume-rendering images can also be computed.

25.2.1.2 Full-Field OCM: Spatial Resolution and Sensitivity

As we mentioned earlier since conventional OCT produces axially oriented images, a depth of field equal to the axial extent of the images is required to avoid dynamic focusing as the coherence gate is scanned. Low-NA lenses are then used in order to obtain a large depth of field, which consequently limits the transverse resolution.

Full-field OCM produces en face tomographic images. In this configuration, microscope objectives with relatively high numerical aperture (NA) can be used. The transverse resolution of full-field OCM is that of a microscope, i.e., of the order of 1 μm.

Nevertheless as conventional OCT, full-field OCM has an axial resolution determined by the coherence length of the illumination source. In contrast to the spectrum of ultrashort femtosecond lasers, the spectrum of a thermal light source is very smooth. It does not contain spikes or emission lines that could cause side lobes in the coherence function and create artifacts in the images. In addition, the optical power is much more stable. The effective spectrum of the system is actually imposed above all by the spectral response of the detector. With our silicon-based CCD (e.g., DALSA), the effective spectrum is centered around $\lambda = 750$ nm, with width $\Delta\lambda = 300$ nm (FWHM). Using the usual formula that supposes a Gaussian shape spectrum:

$$\Delta z = \frac{2\ln 2}{n\pi}\left(\frac{\lambda^2}{\Delta\lambda}\right)$$

The theoretical axial resolution in a medium with refractive index $n = 1.33$ (water) is $\Delta z = 0.5$ μm. We have experimentally measured 0.7 μm as can be seen on Fig. 25.2.

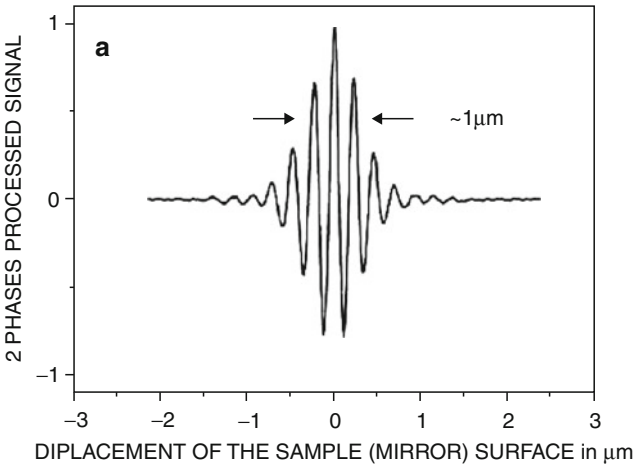

Fig. 25.2 Axial response of the Linnik interferometer (silicon camera, tungsten source)

If dispersion mismatch occurs in the two arms of the interferometer, the axial resolution is degraded. Since biological tissues are constituted mainly of water, the use of water immersion or silicone oil microscope objectives minimizes dispersion mismatch.

What Are the Parameters that Limit the FFOCM Sensitivity?

In general when using a standard tungsten halogen illuminators, we are not limited by the light level impinging the camera; indeed, we can work close to the saturation level for an optimum signal-to-noise ratio. More precisely the important parameter is the amount of electrons stored during the acquisition time. In order to get the maximum signal-to-noise ratio, one must optimize the following performances of the camera:

- The images close to the saturation level must be shot noise limited. The test for that is that the difference between two successive identical images must be much higher that the difference between two dark images (see Appendix).
- The full-well capacity W must be as high as possible (typically between 100,000 and 1,000,000 of charges for silicon cameras and around 1,000,000 for InGaAs cameras).
- Both for the signal-to-noise ratio and to be able to perform in vivo experiments, we need frame rate higher than $Fr = 150$ frames/s.
- The digitalization must be achieved with at least 10 bits in order to avoid sampling errors.
- The number N of pixels that we currently use today is one to four million for silicon cameras and 250,000–500,000 for InGaAs cameras.
- The camera must be equipped with an external trigger or at least an internal trigger in order to synchronize the image acquisition with the piezoelectric modulation of the path difference.

To summarize our overall quality factor Q for maximizing the signal-to-noise ratio, $\mathbf{Q} = \mathbf{W.Fr.N}$; it represents the amount of charges that can be stored during one second on the camera chip.

In order to increase the signal-to-noise ratio, the reference arm mirror must have a reflectivity that ensures a reference power equal or higher than all the incoherent light impinging the camera (light diffused by the sample that is function of the numerical aperture, or stray light of the setup).

As discussed in the Appendix, the images are mainly shot noise limited and one can show that a detection sensitivity of the order of 90 dB ($R_{\min} = 10^{-9}$) can be obtained by accumulating images during a full acquisition time of less than a second.

25.2.2 FFOCM: The LLTech Research Setup

In 2011, LLTech, an ESPCI ParisTech spin-off, has launched the first FFOCM system for clinical research applications (Fig. 25.3).

This system is based on the principle that we have described but it contains a number of improvements that are necessary in the framework of clinical research:

- It is a "plug-and-play" system, for instance, the zero path difference, which is often tricky to find in a Linnik configuration (1 μm position with 10 cm long arms!), is automatically positioned.
- The field of view that is required for pathology is typically of the order of 1″ (2.5 cm) in diameter whereas the standard field of view of the cameras using 10× objective is close to 1 mm. Stitching of elementary sub-images is then required to make such large images; because the transverse resolution is 1.4 μm (sampling 0.7 μm/pixel), it is possible to zoom in and out in these large images that are recorded in about 5 min.

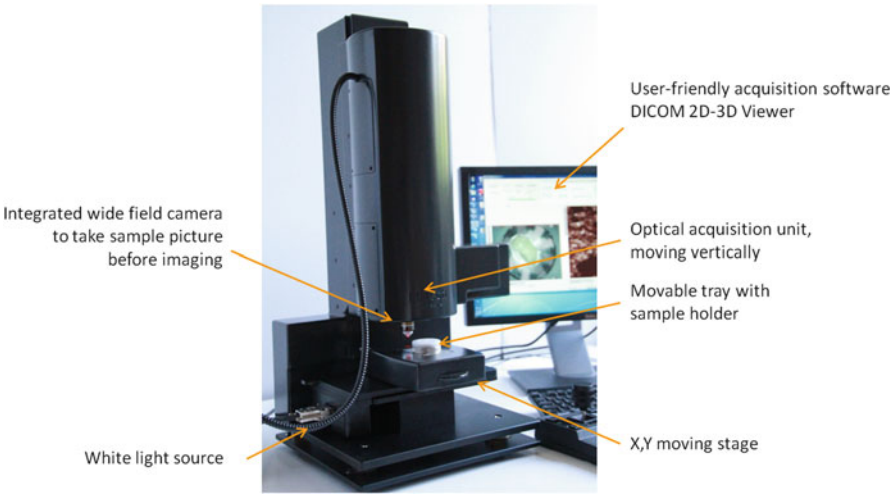

Fig. 25.3 Picture of the LLTech light CT scanner

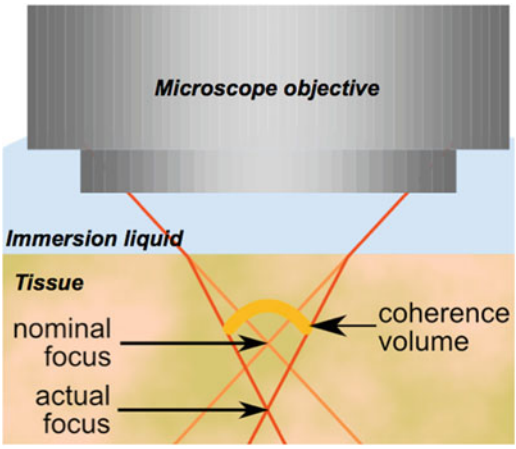

Fig. 25.4 The refractive index mismatch between the immersion liquid refractive index and the tissue refractive index induce a shift between the coherence volume and the focus (From Jonas Binding PhD defense, Paris 2012)

- For ex vivo experiments, the sample is placed in its sample holder and gently pressed against a transparent window. Incorporation of a liquid avoiding sample drying is ensured.
- When exploring a sample in depth, the following problem has to be solved: the refractive index of the tissue being generally different from the immersion liquid index, there is a shift between the focus and the zero path difference (coherence volume) as can be seen on Fig. 25.4 [14–16].

When this shift turns to be larger than the depth of field (e.g., 8 μm for 0.3 NA water immersion objectives), one can observe a reduction of the signal and a degradation of the image quality. The software that drives the system motors automatically compensates for this shift. For ex vivo or in vivo samples, at the end of the sample arm is the biological tissue to be imaged. It could be placed within a specific sample holder. Usually one explores either a large field of view obtained at a few depths or a stack of tomographic images of smaller lateral size.

Finally the LLTech system being designed to be placed in a research hospital environment, the images are available using DICOM data format that is a standard in medical imaging for handling, storing, printing, and transmitting information.

25.2.3 Improving the Available Depth Using InGaAs Cameras

In order to extend the capabilities of the full-field OCM technique and to improve the penetration, an infrared InGaAs FFOCM system has been developed [11, 17, 18]. Indeed in biological tissues there is a decrease in scattering coefficient with increasing wavelength.

For FFOCM tissue imaging systems, the camera detection sensitivity range is the limiting factor and silicon-based cameras are used to probe the 600–1,000 nm wavelength region. For wavelengths >1,000 nm, indium gallium arsenide (InGaAs) chips allow a detection range in the 900–1,700 nm band.

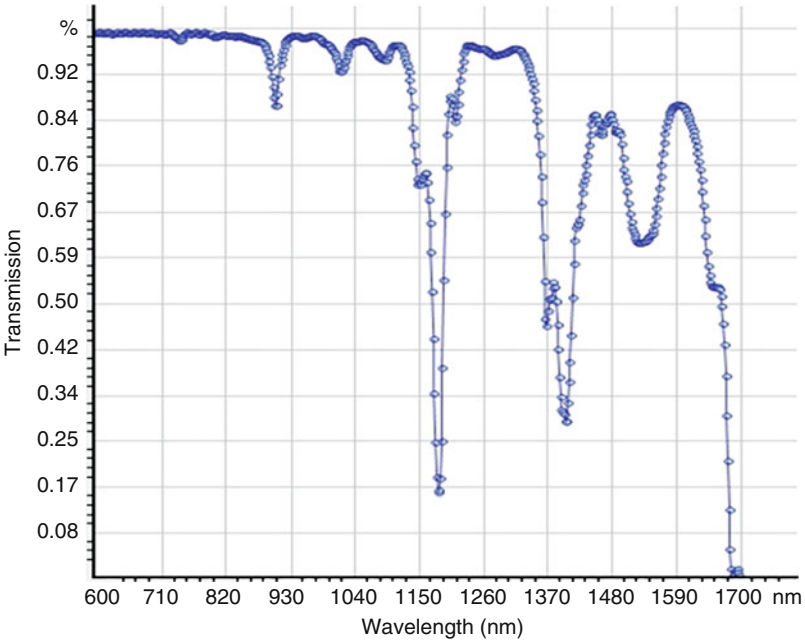

Fig. 25.5 Near-IR transmission of silicone oil (1 cm path)

Results presented here have been carried out using *silicone oil immersion* instead of water. This type of configuration has seemingly not been used in the past.

An infrared beamsplitter was used but microscope objectives were not optimized for this particular wavelength range: we only replaced Olympus 10× objectives by Zeiss 10× ones because their transmission is better above 1 µm. The InGaAs camera (Xeva-1.7-640c, Xenic, Leuven, Belgium) has been mounted onto the full-field OCT setup described on Fig. 25.1. This InGaAs camera full-well capacity (the largest charge that the camera can hold per pixel before saturation) is larger than two million e^- with and a frame rate of 25 Hz.

Water absorption spectrum is a major limitation when imaging at wavelengths higher than 1.25 µm (the working distance of the objective being about 3 mm, 6 mm of water has to be considered).

Silicone oil refractive index is about 1.41, which limits its usage to medium numerical aperture water immersion objectives (typically NA <0.35 unless spherical aberration would limit the transverse resolution). Nonetheless, it allows an almost full transmission from 0.9 up to 1.6 µm except for two absorption bands as shown on Fig. 25.5.

Indeed, the advantage of silicone oil can be appreciated by comparing the number of fringes observed on a mirror when measurements are performed in oil

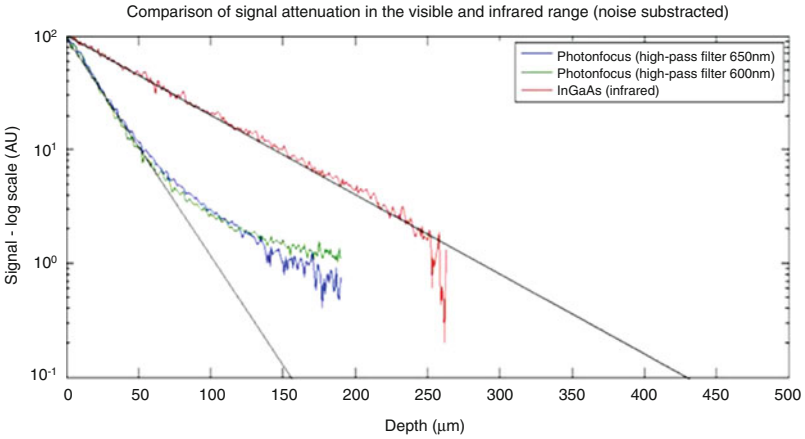

Fig. 25.6 Damping of the FFOCM signal (semilog scale) using a silicon camera (*red* and *green curves*) and InGaAs camera (*red curve*) [19]

immersion (about three periods, FWHM) for the near-infrared setup (InGaAs) in comparison to water immersion (about eight periods, FWHM).

In comparison to a configuration with silicone oil in the visible range (i.e., CMOS camera), the spectral bandwidth achieved by the InGaAs setup is significantly larger (i.e., $\sim$ 600 nm vs. 150–200 nm), but the central wavelength being about two times larger, the theoretical axial resolution is approximately similar to what we get using silicon cameras (around 1 μm). However, the gain lies in the effective spectrum achieved with silicone oil immersion and therefore a gain in penetration depth. The high absorption of water above 1,100 nm is thus drastically reduced by the oil immersion medium in both arms, allowing to fully benefit from the near-infrared part of the polychromatic light source. Recently, Dubois's group compared two similar FFOCM configurations (both silicon and InGaAs cameras) but within water as immersion medium showing limited or no gain in the near-infrared range [18].

As expected, a significant increase in photons' mean free path is observed with the InGaAs configuration (Fig. 25.6). The exponential attenuation shows an approximately threefold increase in penetration depth for the infrared system (red curve) in comparison to systems in the visible range (blue and green curves).

For this particular tissue (fibroadenoma), the multiple scattering shown by the departure from the exponential signal attenuation [7] is quasi absent from the infrared curve up to 250 μm in depth while it already occurs at around 70 μm for the two systems in the visible range. From this result, a power law expressing the wavelength dependence can be extracted. The broadness of both spectra require the use of each central spectrum resulting in a power law dependence scaling as λ^2 compatible with the Mie scattering regime. This result is confirmed by the direct image of this fibroadenoma breast tissue (Fig. 25.7).

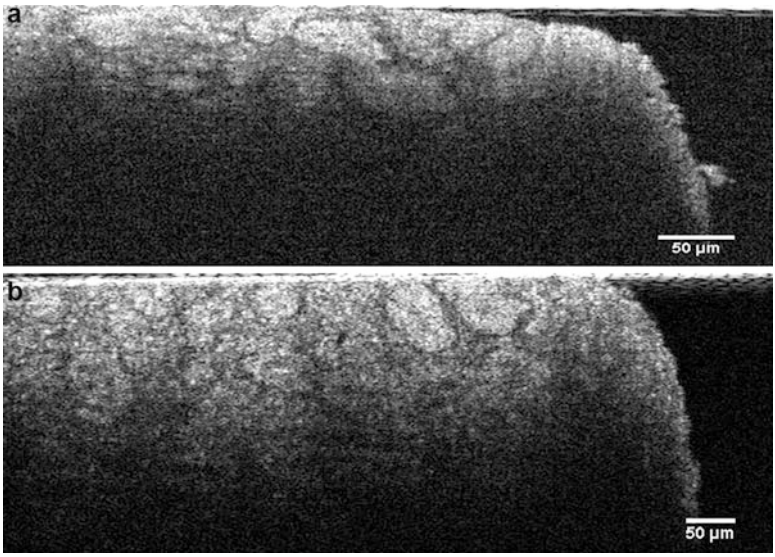

Fig. 25.7 Cross-sectional view of breast fibroadenoma imaged at (**a**) silicon camera, image depth: 200 µm (**b**) InGaAs camera image depth: 300 µm [19]

25.3 Clinical Research Applications of FFOCM

We have described in details the applications of FFOCM that have been performed in various hospitals in ▶ Chap. 26, "Assessment of Breast, Brain and Skin Pathological Tissue Using Full Field OCM" on clinical applications of full-field OCM. These studies include the breast (tumors and nodes), brain, and skin. Images of other organs can be found on http://www.lltechimaging.com/.

25.4 Nondestructive Evaluation and FFOCM: From Electro-optics to Art Materials

In these domains, the first range of applications deals with layered materials: one can control the thickness and the integrity of the various layers even if some of them scatter light (i.e., in solar cells) in a noncontact and nondestructive way. The very high sensitivity of FFOCM (90–100 dB) allows getting the scattering level map associated to a specific slice in a better way than usual scatterometers.

We also think that the submicron slicing ability of FFOCT matches the requirements of art materials. We have been able to reveal multiple layers even in highly scattering paints. As an example of layered and scattering materials, lacquers are easily imaged using FFOCT (Fig. 25.8).

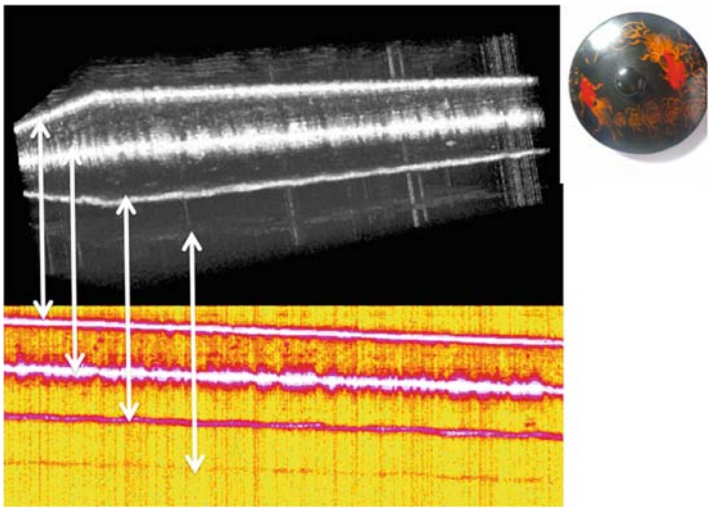

Fig. 25.8 3D FFOCM image of a Vietnamese lacquer and detail of a section (in *yellow*) [20]

25.5 Multimodal FFOCM: Fluorescence and Elasticity

Despite the good quality of the images, FFOCM provides a morphological contrast that could advantageously be completed by adding valuable complementary information.

As other OCT groups, we have worked in two directions in order to get new form of contrast.

25.5.1 FFOCM and Fluorescence Using Structured Illumination

One of the problems in cancer diagnosis is to be able to reveal the invasion of cancer cells and to identify these cells by the size of their nuclei. In FFOCM, the signals are dominated by the strong backscattering level of fibrous tissue that masks those of the nuclei that appear dark or are hidden under a strong background (see ▶ Chap. 26, "Assessment of Breast, Brain and Skin Pathological Tissue Using Full Field OCM").

As the sectioning cannot be obtained through the FFOCM signal, another method should be used to collect the fluorescence signal at the same depth that has been selected. Structured illumination is now a very popular approach to achieve fluorescence full-field sectioning with an axial resolution that is equivalent to what is achieved in confocal microscopy. Nevertheless, in order to get a sectioning of 1 μm, high numerical aperture must be used: we have chosen 1.05 NA silicone oil immersion objectives. Moreover, the camera dark noise must be reduced. The setup is represented on Fig. 25.9.

As an example, Fig. 25.10 shows the FFOCM image of a basal cell carcinoma where nuclei are not clearly visible and appear when using acridine orange as fluorophore.

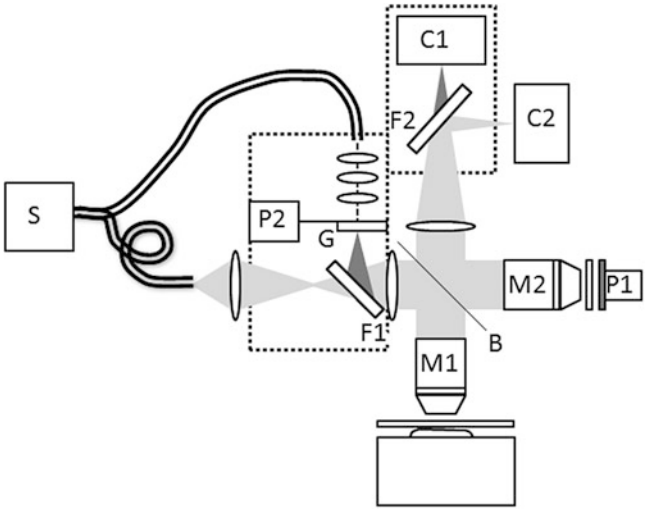

Fig. 25.9 Setup used for simultaneous recording of structured illumination and FFOCM. *S* Xenon Source, *C*1 Fluorescence camera, *C*2 FFOCT camera, *M*1, *M*2 microscope objectives, *P*1, *P*2 piezoelectric modulators, *F*1, *F*2 filters, *G* Ronchi grid, *B* beamsplitter [21]

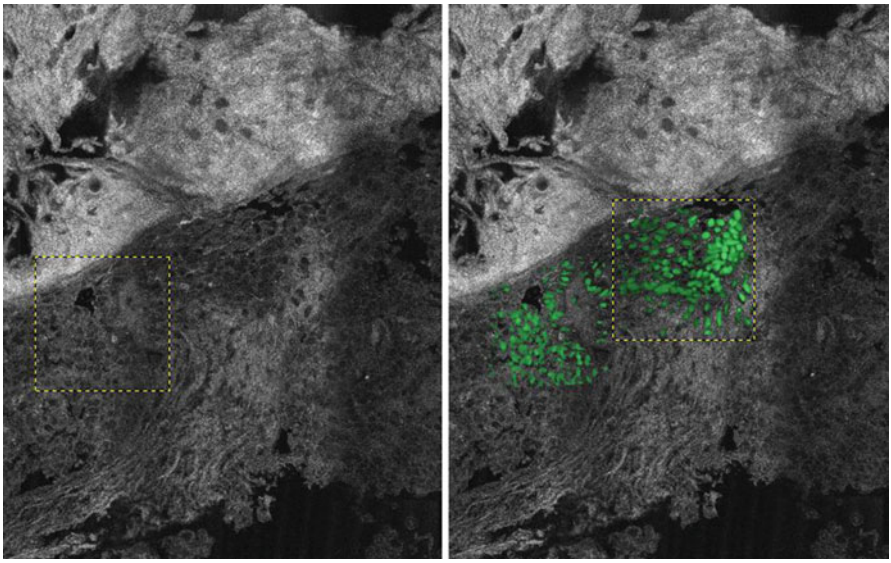

Fig. 25.10 Basal cell carcinoma (*BCC*). FFOCM image (*left*) and combined FFOCM/SIM image (*right*). The SIM image shows the increased density of nuclei due to cell proliferation. The upper part corresponds to the epidermis. The epidermis shows high contrast in FFOCT, compared to the BCC area, suggesting a significant refractive index change. FFOCM image size: 370 × 480 μm [21]

25.5.2 FFOCM Elasticity Map

Organ structures, tissues, and cells are characterized by their intrinsic mechanical properties. Moreover, the mechanical properties of cells are related to their structure and function: changes in those properties can reflect cellular healthy or pathological states. Adding this contrast to morphological images could be a powerful help for diagnosis. In this study, we add the elastographic contrast to FFOCM, and by combining it with elastography, one recreates a "virtual palpation" map at a micrometer scale.

We have used two static methods to add the elastographic contrast to FFOCM images. In the first method, we register a volumetric image before and after mechanical solicitation of the sample. From those two sets of images, we estimate the 2D and 3D strain maps inside the sample by using two different algorithms: one based on cross-correlations and one based on finite elements. We use this method not only with the custom LLTech setup but also with an endoscopic FFOCM setup (see below). In the second method, the sample is submitted to a low-amplitude periodical compression and using a phase-shifting modulation method derived from the one used earlier: so we are able to retrieve the local phase map modulation directly related to the local displacement. Those methods provide values of the local elastic properties along the compression axis. As an example, we have represented on Fig. 25.9 what we have obtained on a mouse ear that is a strongly heterogeneous sample in terms of their mechanical properties (Fig. 25.11).

25.6 Full-Field OCM for Endoscopy

All OCT systems have a limited maximum imaging depth in tissues of typically 1–2 mm due to absorption and scattering of light by the biological structures. For in situ and in vivo imaging of internal organs, a probe is thus required. The adaptation of the OCT technique into endoscopic setups [22, 23] allows the access to a variety of areas of the human body where high-resolution in-depth imaging is needed. Endoscopic OCT is now mainly used for intravascular imaging [24] where it is able to distinguish between different types of plaques. A second main domain of application is biopsy guidance with needlelike probes [25, 26]. However, the typical axial and transversal resolutions of such OCT systems lie between 5 and 30 μm, which is less than that of full-field OCM.

25.6.1 Principle: OCT Signal with Two Interferometers

A FFOCM system with probe has to address the problem of keeping the performances of FFOCM in a setup using a miniaturized, medically safe probe. Such systems with a probe rather use two coupled interferometers, as proposed in [27–29]. Indeed, integrating the probe as an arm of the Linnik interferometer could cause perturbations and damage the interference signal during in vivo use.

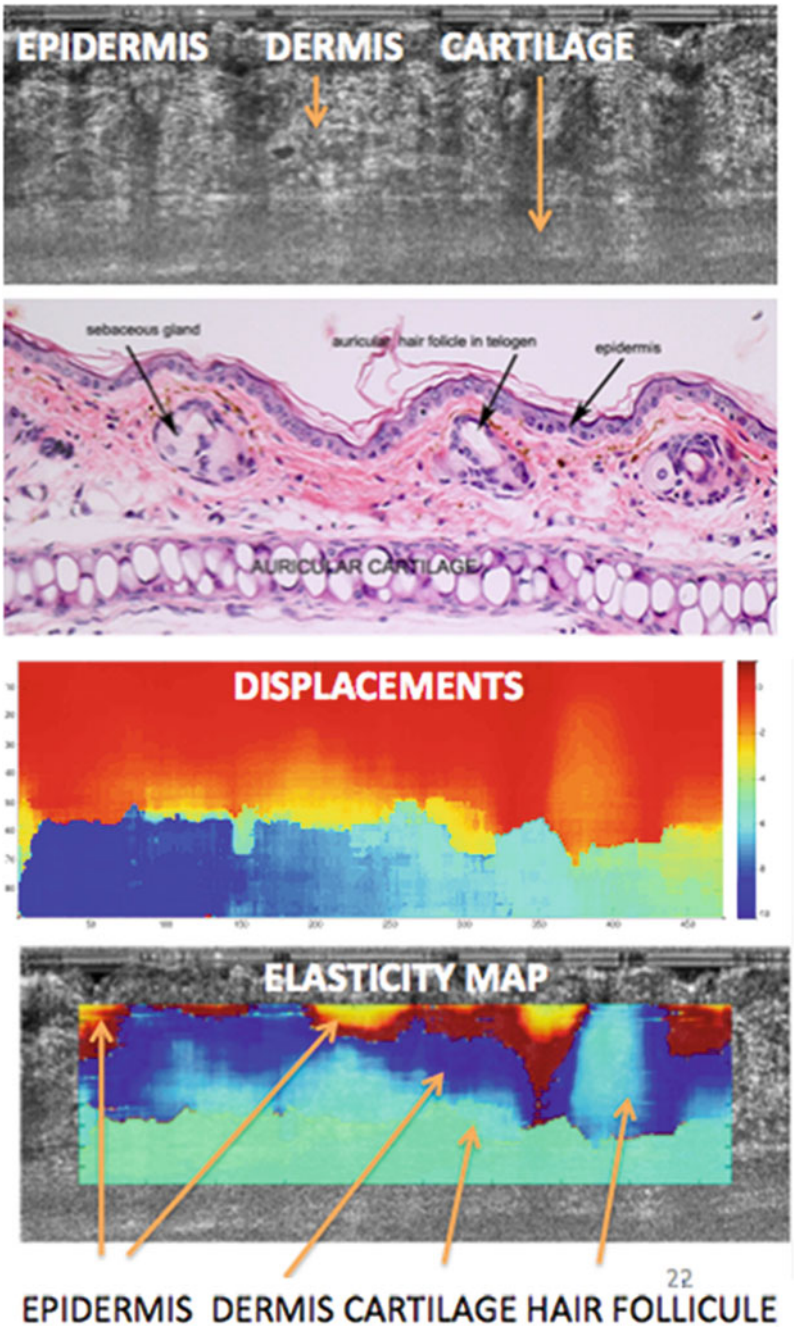

Fig. 25.11 FFOCM section of a mouse ear (*top left*), axial displacement map (*top right*) and elasticity map (*bottom right*) and typical H&E stain

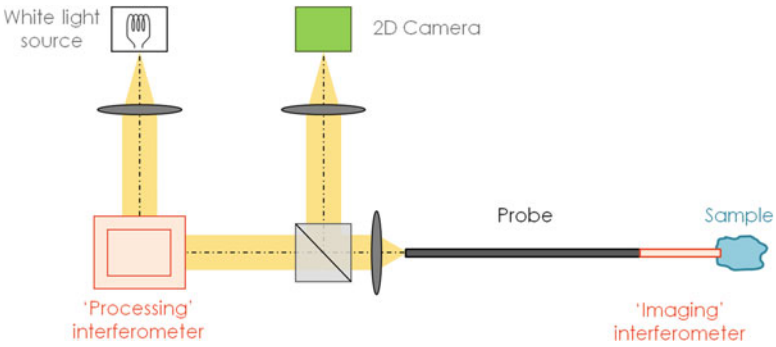

Fig. 25.12 Simplified principle of an endoscopic full-field OCM system with a common-path imaging interferometer

If the probe comprises an optical fiber or fiber bundle, bends and twists in the fibers will create differences between the states of polarization of light in the reference and object arms, thus distorting the signal. Moreover, it would also require to set identical probes in both arms of the Linnik interferometer, which would induce very large optical path lengths difficult to balance. On the contrary, in a system with two interferometers, the probe is not part of an interferometer arm and is only used to transport an image. It is thus entirely passive and insensitive to its environment. Such a system is to privilege for in situ imaging, where one needs a system able to image outer or inner parts of the body that are difficult to reach.

The main principle of endoscopic FFOCM systems is based on the coupling of two distinct interferometers: one is external to the probe, and one is placed at the distal end of the probe in contact with the tissue to image. The distal interferometer has to be kept simple for in situ imaging, for example, a common-path design is an adequate solution. It does not require any advanced miniaturized mechanical systems at the tip of the probe, which are likely to increase the diameter as well as the cost of the probe.

The principle of the system is described on Fig. 25.12 [30]. The broadband white light source is a Xenon arc lamp coupled to an optical fiber. This source spectrum is not as smooth as the one obtained with a thermal light source, e.g., a tungsten filament, but the luminance and the power level injected into the fiber are much higher. The use of a source with very low temporal coherence ensures a good axial resolution, whereas the spatial incoherence increases the sensitivity by decreasing cross-talk effects. It illuminates a Michelson-type processing interferometer, which modulates the spectrum at a frequency dependent on the path length difference. This spectrum is then injected into the probe to the distal imaging interferometer, which is common path: interferences occur between the reference beam reflected at the tip of the probe and light backscattered by structures at each depth within the tissue. The 2-D detector, a 1 megapixel camera such as a CCD or CMOS, detects the superposition of the modulated spectra coming from the processing interferometer and from the imaging interferometer. A maximum signal is detected only when both path length differences match, so that by setting the path length difference of the external interferometer, one

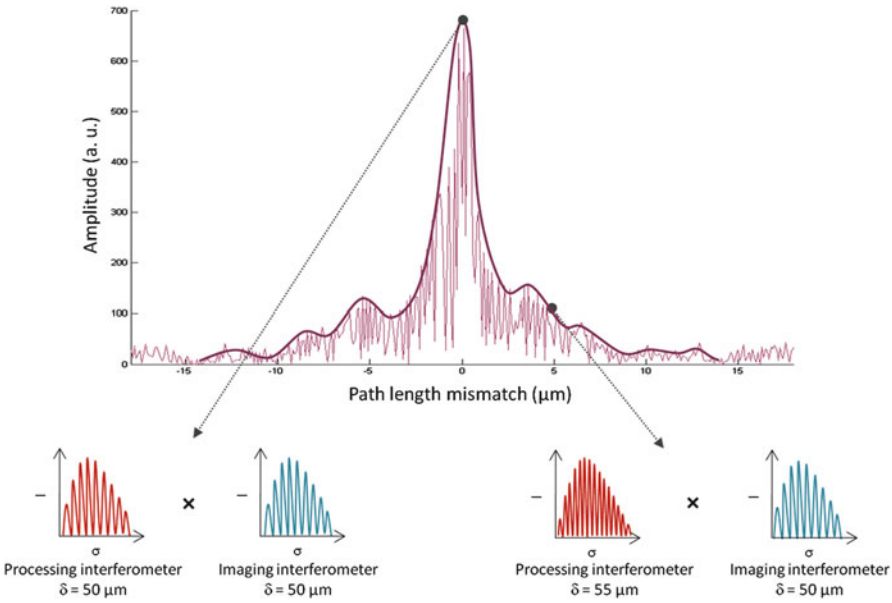

Fig. 25.13 Signal collected on one point of the 2-D detector showing interference fringes coming from a planar mirror placed at 25 μm ahead of the probe in air. The path length difference of the imaging interferometer is thus 50 μm. The path length difference of the processing interferometer is scanned from 30 to 70 μm using a step motor

sets the imaging depth within the sample. Furthermore, for extracting the interference signal from the background, we use a phase-shifting method with a piezoelectric modulation in the processing interferometer. A 3D image can be reconstructed by performing a one-dimensional depth scan using the processing interferometer.

Figure 25.13 shows, for example, the signal collected from a planar mirror as a function of the path length difference mismatch between both interferometers. The envelope of this signal gives an axial resolution of 1.8 μm.

Such a system can be used with different probes without changing the bulk setup to perform flexible or rigid endoscopy.

25.6.2 Flexible Endoscopy

A fiber bundle can be used as a flexible endoscope to transport a coherent image. Bundle as thin as 0.9 mm with as many as 30,000 optical fibers is available, which is suitable for biomedical applications. The use of a multimode fiber bundle degrades the image quality by the pixelation effect of the fibers and by additional artifacts. Indeed, cross talk resulting from coupling between adjacent cores in the bundle, and between propagation modes in one core, creates a ghost signal [31]. However, imaging of samples can still be achieved, as shown on Fig. 25.14. Transversal resolution is 4.9 μm and sensitivity is −70 dB.

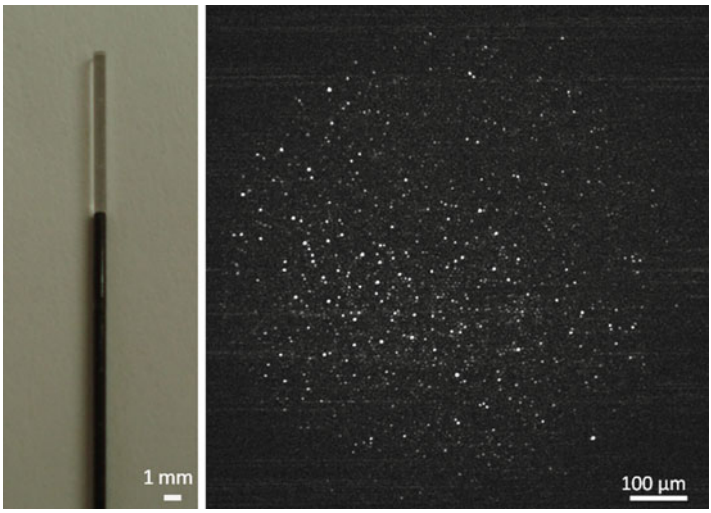

Fig. 25.14 Flexible probe composed of a fiber bundle and a graded refractive index (*GRIN*) lens (*left*). Image of a phantom (2 µm diameter TiO_2 beads embedded in a polyurethane matrix) (*right*)

25.6.3 Rigid Endoscopy

Graded refractive index (GRIN) lenses are thin lenses with a cylindrical shape that can be readily used as a rigid endoscope. For instance, two lenses can form a probe with a diameter of 2 mm and a length of 150 mm (GRINTECH, Germany), for a numerical aperture of 0.1. The transverse resolution is then 3.5 µm, for a sensitivity of −80 dB when averaging 20 images during about 1 s, which is enough to get signal from biological tissues. Figure 25.15 shows images taken with this probe on ex vivo samples.

The system can be used in vivo, as demonstrated on the skin (Fig. 25.16). The forward-viewing probe is applied in direct contact with the tissue and can image up to depths of 200 µm [30].

The rigid probe can also be used as a needlelike probe or be inserted inside a biopsy needle to image internal organs and perform biopsy guidance. Figure 25.17 shows examples on brain and kidney.

Appendix

FFOCM: Signals and Noises

(***The calculation is performed for a single pixel of the camera and the notations are indicated on the*** Fig. 25.18)

(a) Negligible incoherent and stray light level ($N_{\text{inch}} < \alpha N_0$)

Let a N_0 be the number of photoelectrons generated from the reference arm $\alpha N_0 \sim N_{\text{sat.}}$

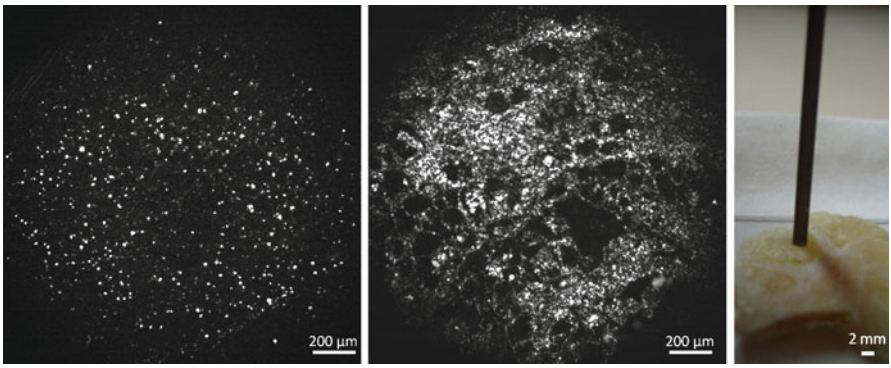

Fig. 25.15 Images of FFOCM with a rigid probe. *Left*: phantom. *Right*: ex vivo human breast sample

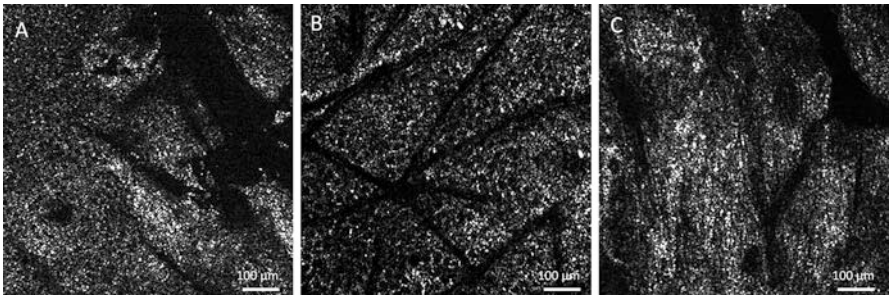

Fig. 25.16 Endoscopic FFOCM images on human skin in vivo, at depths of 30 µm under the surface, on the cheek (**a**), forearm (**b**), and mole (**c**). The epidermis shows epithelial cells

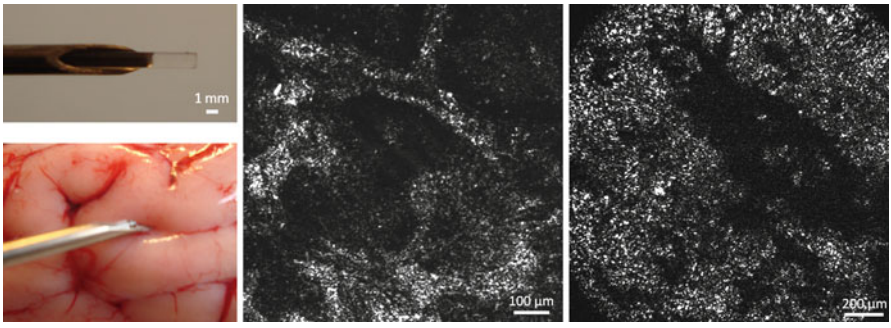

Fig. 25.17 Endoscopic FFOCM needlelike probe. Ex vivo images on human brain (*left*), and rat kidney (*right*) at depths of 20 µm ahead of the probe

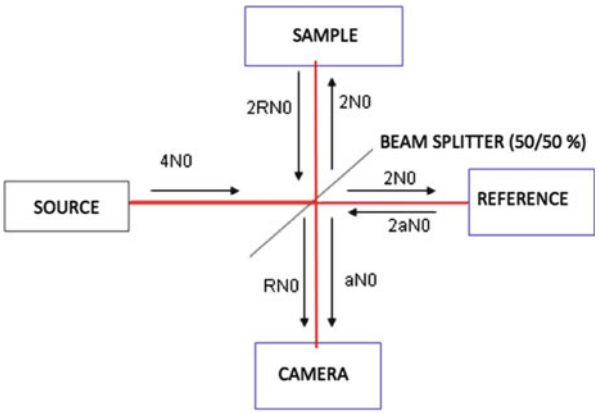

Fig. 25.18 Representation of the various light levels impinging the various parts of the interferometer

Let $R\,N_0$ be the number of photoelectrons generated from the object slice under examination ($R << \alpha$).

Let N_{inch} be the number of stray light- and incoherent light-induced photoelectrons ($N_{\text{inch}} << N_{\text{sat}}$).

For a π-shifted two-phase detection (+ or −),

$$I_+ = \alpha N_0 + RN_0 + N_{\text{inch}} + 2\sqrt{\alpha N_0 RN_0}\cos\varphi$$
$$I_- = \alpha N_0 + RN_0 + N_{\text{inch}} - 2\sqrt{\alpha N_0 RN_0}\cos\varphi$$

The measured signal is

$$\begin{aligned} S &= I_+ - I_- \\ &= 4\sqrt{\alpha N_0 RN_0}\cos\varphi \end{aligned}$$

We usually take its absolute value:

$$\begin{aligned} \langle|\cos\varphi|\rangle &= \left\langle\sqrt{\cos^2\varphi}\right\rangle \\ &= \left\langle\sqrt{\frac{1+\cos(2\varphi)}{2}}\right\rangle \\ &= 1/\sqrt{2} \end{aligned}$$

Please note that this is true for a random scattering sample and not for a mirror sample.

The signal is then

$$\begin{aligned} S &= 4\sqrt{\alpha N_0 RN_0/2} \\ &= 4\sqrt{N_{\text{sat}} RN_0/2} \end{aligned}$$

The shot noise being
$B = \sqrt{N_{\text{sat}}} = \sqrt{\alpha N_0}$ (the reference being the major signal)
The signal-to-noise ratio is

$$\begin{aligned} \text{S/B} &= 4\sqrt{RN_0/2} \\ &= 4\sqrt{RN_{\text{sat}}/2\alpha} \end{aligned}$$

The limit of detection (signal = noise) corresponds to $4\sqrt{R_{\min}N_{\text{sat}}/2\alpha} = 1$, so that

$$R_{\min} = \frac{\alpha}{8N_{\text{sat}}}$$

Typical numerical value
Using typical values of $\alpha = 0.16$ $N_{\text{sat}} = 200{,}000$ for silicon cameras, one gets
$R_{\min} = 10^{-7}$ or 70 dB for a two-image acquisition, 1 Mpixels, 75 processed images/s.
Averaging 100 images takes a few more than 1 s and leads to $\text{R}_{\min} = 10^{-9}$ or **90 dB**.

(b) Significant incoherent and stray light level ($N_{\text{inch}} =$ or $> \alpha N_0$)
We have then $\text{N}_{\text{sat}} = \alpha N_0 + N_{\text{inch}}$
The signal is

$$\begin{aligned} S &= 4\sqrt{\alpha N_0 RN_0/2} \\ &= 4\sqrt{(N_{\text{sat}} - N_{\text{inch}})RN_0/2} \end{aligned}$$

The shot noise is $B = \sqrt{N_{\text{sat}}}$
The signal-to-noise ratio is

$$\begin{aligned} \text{S/B} &= 4\sqrt{\frac{(N_{\text{sat}} - N_{\text{inch}})RN_0}{2N_{\text{sat}}}} \\ &= 4\sqrt{\frac{\alpha N_0 RN_0}{2N_{\text{sat}}}} \end{aligned}$$

The limit of detection (signal = noise) corresponds to $4\sqrt{\frac{(N\text{sat} - N_{\text{inch}})R_{\min}N_0}{2N_{\text{sat}}}} = 1$

$$R_{\min} = \frac{1}{8.(N_{\text{sat}} - N_{\text{inch}})} \cdot \frac{N_{\text{sat}}}{N_0}$$

$$R_{\min} = \frac{\alpha N_{\text{sat}}}{8.(N_{\text{sat}} - N_{\text{inch}})^2}$$

References

1. R. Leitgeb, C.K. Hitzenberger, A.F. Fercher, Performance of Fourier-domain vs. time-domain optical coherence tomography. Opt. Express **11**, 889–894 (2003)
2. M. Wojtkowski, R. Leitgeb, A. Kowalczyk, T. Bajraszewski, A.F. Fercher, In-vivo human retinal imaging by Fourier domain optical coherence tomography. J. Biomed. Opt. **7**, 457–463 (2002)
3. R. Leitgeb, W. Drexler, Unterhuber, B. Hermann, T. Bajraszewski, T. Le, A. Stingl, A. Fercher, Ultrahigh resolution Fourier domain optical coherence tomography. Opt. Express **12**(10), 2156–2165 (2004)
4. M.A. Choma, M.V. Sarunic, C.H. Yang, J.A. Izatt, Sensitivity advantage of swept source and Fourier domain optical coherence tomography. Opt. Express **11**, 2183–2189 (2003)
5. B.E. Yun, S.H. Tearney, G.J. de Boer, J.F. Iftimia, N. Bouma, High-speed optical frequency-domain imaging. Opt. Express **11**(22), 2953–2963 (2009)
6. L. Vabre, A. Dubois, A.C. Boccara, Thermal-light full-field optical coherence tomography. Opt. Lett. **27**, 530–532 (2002)
7. A. Dubois, L. Vabre, A.C. Boccara, E. Beaurepaire, High-resolution full-field optical coherence tomography with a Linnik microscope. Appl. Opt. **41**, 805–812 (2002)
8. A. Dubois, K. Grieve, G. Moneron, R. Lecaque, L. Vabre, A.C. Boccara, Ultrahigh-resolution full-field optical coherence tomography. Appl. Opt. **43**, 2874–2882 (2004)
9. A. Dubois, G. Moneron, K. Grieve, A.C. Boccara, Three-dimensional cellular-level imaging using full-field optical coherence tomography. Phys. Med. Biol. **49**, 1227–1234 (2004)
10. E. Beaurepaire, A.C. Boccara, M. Lebec, L. Blanchot, H. Saint-Jalmes, Full-field optical coherence microscopy. Opt. Lett. **23**(4), 244–246 (1998)
11. W.Y. Oh, B.E. Bouma, N. Iftimia, S.H. Yun, R. Yelin, G.J. Tearney, Ultrahigh-resolution full-field optical coherence microscopy using InGaAs camera. Opt. Express **14**, 726–735 (2006)
12. W. Drexler, U. Morgner, F.X. Kärtner, C. Pitris, S.A. Boppart, X.D. Li, E.P. Ippen, J.G. Fujimoto, In-vivo ultrahigh-resolution optical coherence tomography. Opt. Lett. **24**, 1221–1223 (1999)
13. K. Wiesauer, M. Pircher, E. Götzinger, S. Bauer, R. Engelke, G. Ahrens, G. Grützner, C. Hitzenberger, D. Stifter, En-face scanning optical coherence tomography with ultra-high resolution for material investigation. Opt. Express **13**, 1015–1024 (2005)
14. J. Fujimoto, G.G.J. Tearney, M.E. Brezinski, J.F. Souther, B.E. Bouma, M.R. Hee, Determination of the refractive index of highly scattering human tissue by optical coherence tomography. Opt. Lett. **20**(21), 2258–2260 (1995)
15. S. Labiau, G. David, S. Gigan, A.C. Boccara, Defocus test and defocus correction in full-field optical coherence tomography. Opt. Lett. **34**(10), 1576–1578 (2009)
16. J. Binding, J.B. Arous, J.-F. Léger, S. Gigan, C. Boccara, L. Bourdieu, Brain refractive index measured in vivo with high- NA defocus-corrected full-field OCT and consequences for two-photon microscopy. Opt. Express **19**(6), 4833–4847 (2011)
17. Dubois, G. Moneron, A.C. Boccara, Thermal-light full-field optical coherence tomography in the 1.2 mu m wavelength region. Opt. Commun. **266**(2), 738–743 (2006)
18. D. Sacchet, J. Moreau, P. Georges, A. Dubois, Simultaneous dual-band ultrahigh-resolution full-field optical coherence tomography. Opt. Express **16**, 19434 (2008)
19. A. Burcheri-Curatolo, *Avancées en Tomographie Optique Plein Champ pour des applications cliniques et biologie du développement*. PhD thesis, Paris VI; 2012
20. C. Boccara, in *French-Japanese Workshop, Science for Conservation of Cultural Heritage*, eds. by N. Kamba, M. Menu (E.D. Hermann, Paris, 2012)
21. F. Harms, E. Dalimier, P. Vermeulen, A. Fragola, A.C. Boccara, Multimodal full-field optical coherence tomography on biological tissue: toward all optical digital pathology. *Proc. SPIE* 8216, Multimodal Biomedical Imaging VII, 821609 (2012)
22. G.J. Tearney, M.E. Brezinski, B.E. Bouma, S.A. Boppart, C. Pitris, J.F. Southern, J.G. Fujimoto, In vivo endoscopic optical biopsy with optical coherence tomography. Science **276**, 2037–2039 (1997)

23. A.D. Aguirre, J. Sawinski, S.-W. Huang, C. Zhou, W. Denk, J.G. Fujimoto, High speed optical coherence microscopy with autofocus adjustment and a miniaturized endoscopic imaging probe. Opt. Express **18**, 4222–4239 (2010)
24. T.P.M. Goderie, G. van Soest, H.M. Garcia-Garcia, N. Gonzalo, S. Koljenović, G.J.L.H. van Leenders, F. Mastik, E. Regar, J.W. Oosterhuis, P.W. Serruys, A.F.W. van der Steen, Combined optical coherence tomography and intravascular ultrasound radio frequency data analysis for plaque characterization. Classification accuracy of human coronary plaques in vitro. Int. J. Cardiovasc. Imaging **26**, 843–850 (2010)
25. N.V. Iftimia, M. Mujat, T. Ustun, R.D. Ferguson, V. Danthu, D.X. Hammer, Spectral-domain low coherence interferometry/optical coherence tomography system for fine needle breast biopsy guidance. Rev. Sci. Instrum. **80**, 024302 (2009)
26. B.C. Quirk, R.A. McLaughlin, A. Curatolo, R.W. Kirk, P.B. Noble, D.D. Sampson, In situ imaging of lung alveoli with an optical coherence tomography needle probe. J. Biomed. Opt. **16**, 036009 (2011)
27. W.-Y. Oh, B.E. Bouma, N. Iftimia, R. Yelin, G.J. Tearney, Spectrally-modulated full-field optical coherence microscopy for ultrahigh-resolution endoscopic imaging. Opt. Express **14**, 8675–8684 (2006)
28. H.D. Ford, R.P. Tatam, Fibre imaging bundles for full-field optical coherence tomography. Meas. Sci. Technol. **18**, 2949–2957 (2007)
29. H.D. Ford, R. Beddows, P. Casaubieilh, R.P. Tatam, Comparative signal-to-noise analysis of fibre-optic based optical coherence tomography systems. J. Mod. Opt. **52**, 1965–1979 (2005)
30. Latrive, A.C. Boccara, In vivo and in situ cellular imaging full-field optical coherence tomography with a rigid endoscopic probe. Biomed. Opt. Express **2**(10), 2897–2904 (2011)
31. H.D. Ford, R.P. Tatam, Characterization of optical fiber imaging bundles for swept-source optical coherence tomography. Appl. Opt. **50**(5), 627–640 (2011)

Assessment of Breast, Brain and Skin Pathological Tissue Using Full Field OCM

26

Eugénie Dalimier, Osnath Assayag, Fabrice Harms, and A. Claude Boccara

The experiments described here have been performed in hospitals under the guidance of doctors [1] using the LLTech setup described in this chapter. We acknowledge doctors' efforts in evaluating our technology. In this chapter we have intentionally limited the field of applications to medical pathology of the breast, brain, and skin. The reader interested in other organs or in animal studies may find a large number of 2D or 3D images in the atlas [2].

> Let us underline that the technique used here takes "en face images" with a camera (full field: FF) and mixes interferometry (OCT) and microscopy (M); in order to point out its unique ability to reveal details at micron and sub-micron scales we will call it FFOCM rather than FFOCT.

The aim of this chapter is to assess whether the images of the breast, brain, and skin tissue obtained by FFOCM contain sufficient detail to allow pathologists to make a diagnosis of cancer and other pathologies comparable to what was obtained by *conventional* histological techniques. More precisely, it is necessary to verify on FFOCM images if it is possible to differentiate a healthy area from a pathological area.

E. Dalimier (✉) • F. Harms
LLTech SAS Pépinière Paris Santé Cochin, Paris, France

LLTech, Princeton, NJ, USA
e-mail: edalimier@lltech.fr

O. Assayag
Institut Langevin, ESPCI–ParisTech, Paris, France

A.C. Boccara
LLTech SAS Pépinière Paris Santé Cochin, Paris, France

LLTech, Princeton, NJ, USA

Institut Langevin, ESPCI–ParisTech, Paris, France

© Springer International Publishing Switzerland 2015

W. Drexler, J.G. Fujimoto (eds.), *Optical Coherence Tomography*,
DOI 10.1007/978-3-319-06419-2_27

26.1 Breast Cancer

Breast cancer is the most common cancer in women and is still the second leading cause of cancer mortality in women; however, breast cancer mortality has declined steadily since 1990. This decrease is due to more effective treatments and more systematic screening for detecting the presence of tumor at different stages earlier. For this type of injury, surgery techniques called conservative that remove only the tumor (lumpectomy) are preferred to the removal of the full breast (mastectomy). One of the difficulties of the procedure is to perform the lumpectomy excision of the tumor and to ensure that the surgical margins are good. Resection margins are healthy when the entire tumor and some healthy tissue surrounding it are removed.

Histological examination performed during surgery is called intraoperative examination; it consists in histological sections obtained by freezing the sample during the procedure to better orient surgery. However, it has emerged in recent years in the case of very small tumors (smaller than 1 cm) that the latter could be inappropriate to establish a diagnosis [3] and that in the evaluation of margins, it provides an overall sensitivity of only 73 % [4]. Moreover, part of the sample that is lost during cutting and freezing introduces artifacts [5–9].

It therefore appears that the improvement of the evaluation in terms of sensitivity and specificity of excision margins during surgery using a rapid, easy-to-use method, independent of the operator, which does not damage the tissue and provides a spatial resolution sufficient to enable pathologists to diagnose should be of paramount interest. As we have seen in the other chapters of this book, OCT, requiring no contrast agent and allowing making "virtual sections" in the sample surface, therefore seems appropriate. Indeed, several studies using OCT for imaging breast tissue and lymph nodes have been published in recent years [10–15]. One of the first studies showed that benign and malignant lesions could be differentiated by the criteria of comparison with histology using the technique called "ultrahigh-resolution 3D OCT" [11]. Another study, using spectral OCT, evaluated the surgical margins after excision of a breast tumor using diagnostic criteria based on "large scatterers" rather than on the morphology of the tissue at a microscopic level [12]. The techniques used in these two studies have limited spatial resolutions: the first has a transverse resolution of 6 μm and an axial resolution of 3.5 μm and the second transverse resolution of 35 μm and an axial resolution of 6 μm. In this resolution range, the OCT images appear blurry compared to traditional histology slides. Indeed, the alternative optical technique should allow reproducing the conditions used for the analysis of histology slides, i.e., an image area of the order of cm^2 and transverse resolution close to 1 μm.

We described in the FFOCM chapter that FFOCM acquisition of en face images offers the best lateral and axial resolution. Indeed, FFOCM can operate without the necessary depth of field of other types of OCT (time domain, spectral, or Fourier domain, swept source). For these types of OCT, the available depth should be about the depth of field of the lens, requiring objectives of low numerical aperture, which limits the lateral resolution of these systems typically to 5–40 μm. FFOCM offers

an isotropic resolution in the micrometer or submicrometer range. At this resolution, the comparison of images with histology is good enough to distinguish the different structures within and different lesions. Moreover, the en face acquisition geometry provided by FFOCM is intrinsically similar to the geometry of histology slides preparation, which facilitates the pathologist's assessment and eventually eases the adoption of the technique.

26.1.1 Breast Structure

The breast was the first organ studied because large amount of material can be made available for preclinical testing, firstly, on one hand, because of the high incidence of breast cancer in the population and secondly, on the other hand, in the case of mastectomy, because much of the tissue taken is not involved directly in the diagnosis and could be used in the first phase of this study.

Each milk duct channel is lined with epithelium which is a thick envelope and can penetrate deep into the breast. Interlobular channels undergo expansion forming the lactiferous sinus before terminating by groups of intralobular channels terminal. Each group constitutes a form of ovoid mammary lobule. The lobules contain from 10 to 100 cells (or acini) that are rounded cavities that constitute the secretory mammary gland. The supporting tissue of the breast is consisting essentially of fibrous tissue and fat and contains numerous muscular bundles. The breast is richly vascularized through three arteries (axillary, internal thoracic, and intercostal). The lymphatic breast system is composed of lymph vessels whose role is to fight infections.

26.1.2 Experimental Procedure

The process of paraffin embedding tissue samples in order to obtain histology slides, so-called slices for HES stained with hematoxylin-eosin-safran, takes place within four main steps in total lasting 2–5 days. A preliminary stage of this work has been performed to ensure the safety of the imaging procedure; thus, within ten samples (five pathological and five healthy), parts of mastectomy set and stored in the pathology department of Tenon's Hospital in Paris were imaged by FFOCM. Standard tests were performed on these samples and the results were compared with those obtained on samples from the same breast but that have not been imaged.

For H&E, immunohistochemistry with the markers usually involved in the evaluation of tumors were tested: estrogen receptors and progesterone (Cerb B2 (Her2/neu), ki-67, E-Cadherin). In the case of samples from healthy portions, the signals of the markers, such as cytokeratin (CK 7, 14, 18, 5/6) and vimentin, were measured and are given the same values as those obtained on not imaged samples. Extraction of DNA and RNA of nucleic and ribonucleic acids has been carried out on samples imaged in FFOCM. No changes have been noticed.

26.1.3 Optimization of the Imaging Protocol for FFOCM-Histology Comparison

The first part of the work was to make possible the comparison of histology slices samples with the images obtained in FFOCM. Iterative sequences of FFOCM imaging and comparison with corresponding HES slices were made to determine the most effective imaging protocol. Tissue samples were all chosen by pathologists from mastectomies or lumpectomies. Fresh tissue samples were preferred in this study: we found that images have a better contrast and the procedure is close to clinical conditions. After macroscopic evaluation of the tumor, at least four samples were collected for each patient: one in the tumor zone, one on the edge of the tumor, and, in the case of mastectomy, two samples areas appearing healthy. The selection of these three types of samples is intended to allow the identification of the three regions of interest of the breast tissue: normal breast tissue, cancerous breast tissue, and the area between the normal part and the pathological one in order to allow the evaluation of surgical margins.

Once selected, the tissue sample is placed in a sample holder and immersed in buffer type mineralized PBS (phosphate-buffered saline) to prevent its drying. This solution also has a refractive index close to that of water and hence the biological tissues. The sample was gently pressed against the silica window of the sample holder in order to obtain an imaging surface as flat as possible and to reduce optical aberrations.

26.1.4 Comparing FFOCM and Histology

One of the main difficulties in comparing the two types of images comes from the difference in orientation of the sample in the sample holder and into the paraffin block. It is therefore difficult to observe the same slice using FFOCM and HES. Thus, in the first step FFOCM images of the sample at different depths (surface: 20 μmm, 40 μmm, 60 μmm, and 80 μmm) were systematically recorded and HES slices at equivalent depths achieved.

The acquisition and processing time for 1.4×1.4 cm^2 field of view is about 5 min. All images presented were taken using direct (not reversed) LUT; structures with a high backscattering level appear white. At the end of the imaging procedure, the samples are placed in a cassette; the anonymity of patients is provided in accordance with the rules ethics relating to studies on human tissue.

Once the histology slides corresponding to FFOCM images are performed, the working sessions with the pathologist are organized to compare the two types of images. For this purpose, the images are observed without digital zooming and compared with histological images at low magnification, and recognition of structures is done on the two types of support by progressive zoom in and out.

By successive comparison of a large number of images of healthy breast tissues and pathologic ones, it was possible to highlight in the FFOCM images characteristics of normal breast tissue and their modification in case of cancer.

These structures are the lobules, ducts, fibrous tissue, the blood vessels, and the adipose tissue which are represented in Fig. 26.1.

In general, the structures containing spans of collagen (fibrous tissue and muscle) return an important backscattered signal (white on the FFOCM images). Instead, the epithelial structures (lobules and ducts) backscatter less and appear gray. Lobules structures (A) appear as dark gray and rounded. Longitudinal sections of mammary channels (B) appear as dark gray elongated structures with epithelial membrane of variable thickness. Their clear gray level in the thick elastic surrounding membrane distinguishes these glands, tangentially sectioned by FFOCM (C). We can also note the presence of calcifications that appear very white. Blood vessels in tangential section (D) do not have the thick epithelial membrane of ducts but are also distinguished by the presence of a thin elastic membrane. Adipocytes (E) are not backscattering features and appear as black rounded structures that differ only by the presence of the membrane that is more diffusive and appears white. The honeycomb structure characterizing adipose tissue is very well reproduced on the FFOCM images. Normal fibrous tissue (G) has a grainy and moderately backscattering level. In an area of cancerous stroma, fibrous tissue appears very different; it is composed of fine highly backscattering structures that appear white. In scar area (F) fibrous tissue is made of thick and wide spans that induce a low level of backscattering.

During a routine histological examination of a mastectomy, the nipple was excised and analyzed for the presence of Paget disease.

The FFOCM image of a nipple is shown in Fig. 26.2 with the corresponding histological image. The elongated structures are milk ducts cut transversely (E), and one can recognize their white elastic membrane. Sebaceous glands (D and F) are rounded structures along the nipple; they correspond to rounded structures on histology and scored on GS (B). The outer edge of the nipple is a layer of skin where one recognizes the dermoepidermal border by its reticulated appearance (C).

When imaging pathological tissues:

- *Malignant tumors* can invade and destroy adjacent structures. A malignant tumor can spread through remote metastasis (cells detached from the original tumor to proliferate at a distance). Infiltrating cancer is when the proliferation of cancer cells exceeds specific limits histological and if metastatic cells spread to other organs by lymphatic channels.
- *Benign tumors* are localized tumors. If cancer cells are contained within well-defined limits, the structure is called carcinoma in situ. However, such a tumor can develop into malignancy, which may be fatal if not treated.

Tumors that develop from glandular epithelial structures are called adenocarcinoma: If the spread is within a lobule and without exceeding the limits, we speak of in situ lobular carcinoma (often benign). If the tumor develops from a milk duct, it is called ductal adenocarcinoma; this tumor is malignant in most cases. The presence of a tumor in the breast results in the case of invasive cancer is revealed by a change in the appearance of breast tissue and of a structure having a stellar or nodular shape.

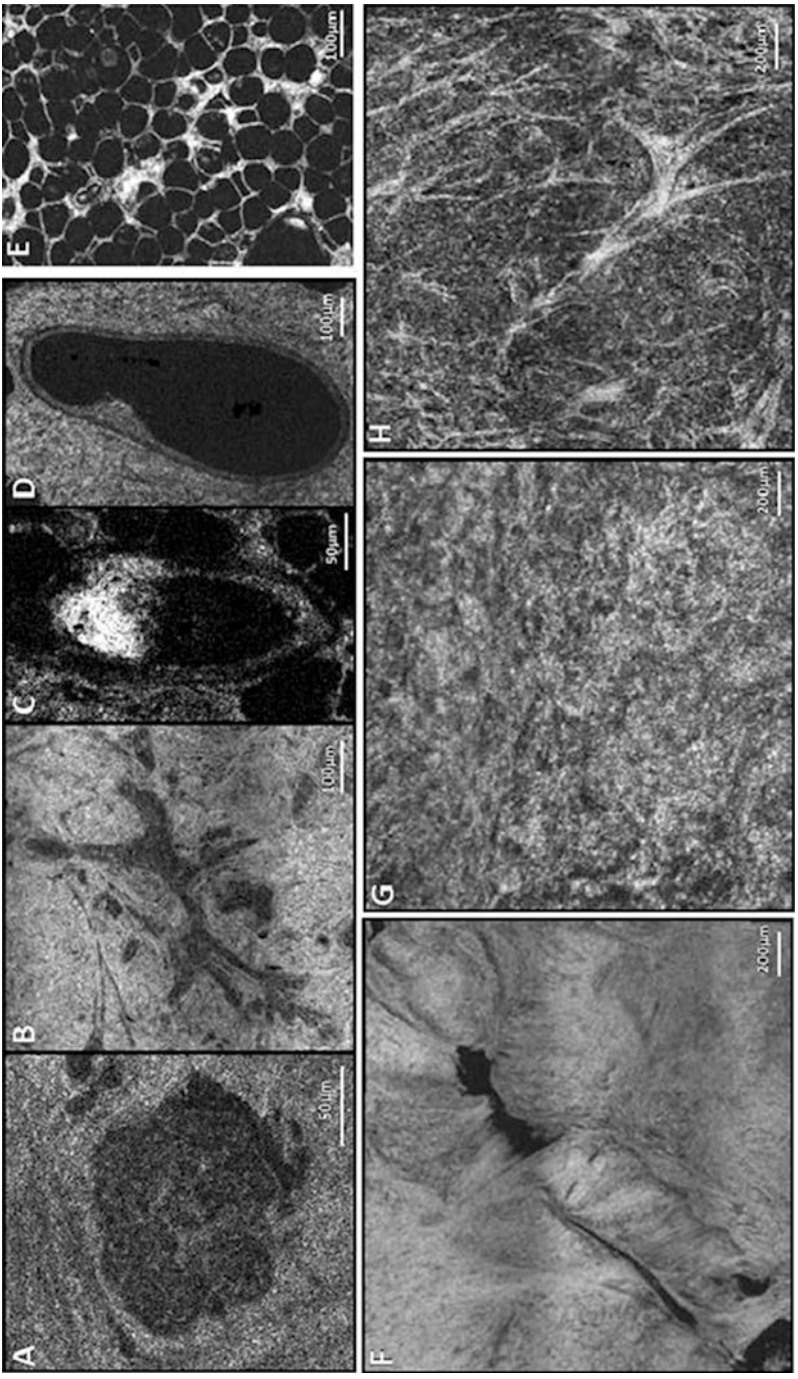

Fig. 26.1 Basic structures of breast tissue: lobule (**a**), milk duct (**b**), cutting cross milk duct with calcification (**c**), blood vessel (**d**), adipocytes (**e**), scar fibrous tissue (**f**), normal fibrous tissue (**g**), fibrous tissue surrounding carcinomatous cells in tumorous stroma (**h**)

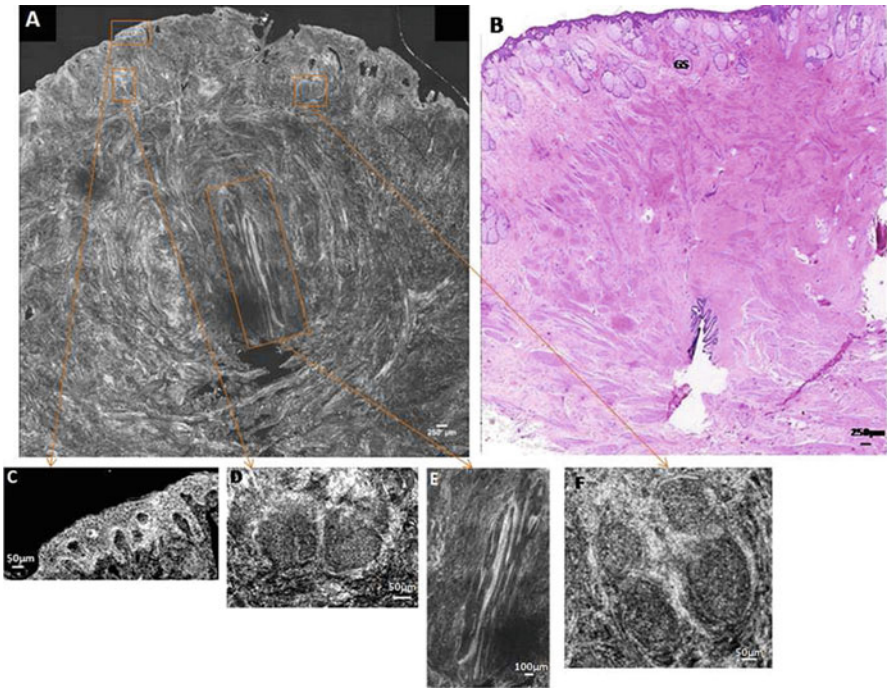

Fig. 26.2 Nipple: dermoepidermal junction of the outer skin layer (**c**), sebaceous glands (**d**) and (**f**), milk duct transected (**e**)

Examples of invasive cancers are represented in Figs. 26.3 and 26.4. Figure 26.3 is a tumor called stellar and Fig. 26.4 one nodular tumor. In both cases the fibrous and adipose tissue are separated; in the case of the stellar tumor, stroma tends to invade the adipose tissue (Fig. 26.3c). Fibrous tissue has a characteristic appearance of fine highly scattering spans (Fig. 26.3c, d), which is distinct from normal fibrous tissue (Fig. 26.4d). Adipocytes at the edge of the stroma (Fig. 26.3e) appear smaller and less rounded in form than in healthy tissue. In the case of nodular tumor, adipose tissue surrounds cancer cells that form a dense region of dark gray.

The difference in appearance of the fibrous web can be used to mark the margins of the tumor. A circular channel dilated with secretions in the lumen is visible in the center of the sample. These changes in appearance of the fibrous tissue and the shape of the adipocytes are highly visible on the images FFOCM, while it does not appear clearly on the histological images. These characteristics are used as criteria for classification of breast tissue by the FFOCM imaging technique.

There are also cases where invasive cancer and carcinoma in situ are simultaneously developed for a patient, as in the example of Fig. 26.5. Ductal carcinoma in situ is characterized by channels extended by the presence of cancer cells in the interior (D). Invasive ductal carcinoma components result in the presence of fine highly scattering

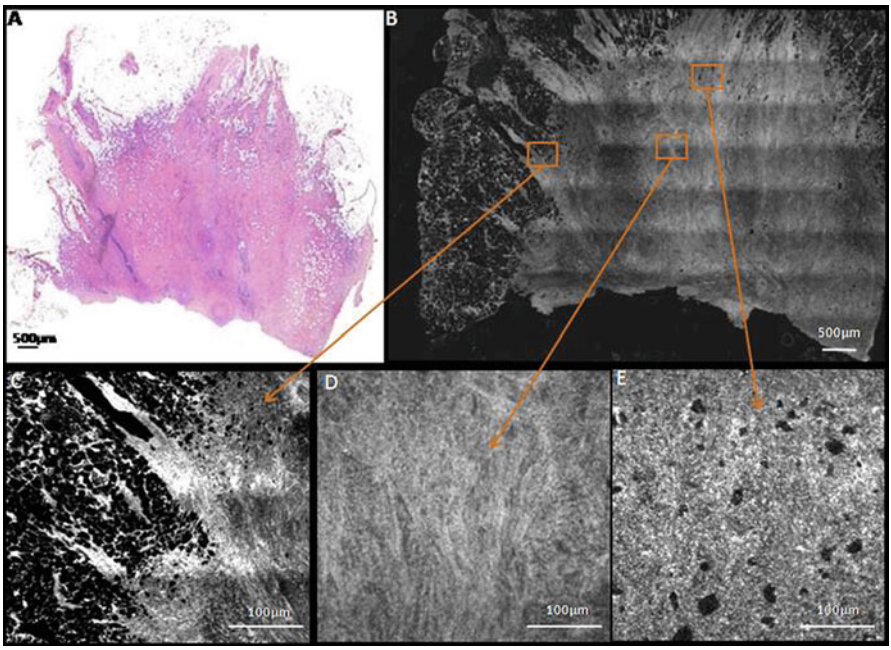

Fig. 26.3 Infiltrating carcinoma: stellar tumor (**a**, **b**). Invasion of adipose tissue (**c**), fibrous tissue tumor (**d**), small adipocytes, and deformed (**e**)

fibrous tissue (B) and foci of darker grey carcinoma cells (D). Ductal in situ components are recognisable by enlarged ducts and lobules filled with cancer cells.

A fibroadenoma is represented in Fig. 26.6. This lesion is characterized by the presence of dilated ducts called tubular easily recognizable in the FFOCM image (B).

Lobular carcinoma in situ is shown in Fig. 26.7, it is characterized by a proliferation of small cells widely dilated acini of lobules (C). This lesion is benign; however, in the example shown here, a milk duct (D) has at its center proliferation that is a sign of malignancy.

Upon an analysis based on FFOCM images, it is possible to start a classification breast tissue. This approach is described in detail in [16].

26.1.5 FFOCM and Lymph Nodes

In this section, we intend to discuss the usefulness of FFOCM as a tool for classification of lymph nodes in order to assess whether this imaging technique could help surgical ablation of lymph more efficiently. Surgical treatment of breast malignancy is based on the removal of the primary tumor and the axillary dissection that involves the removal of more than half of the lymph nodes in the armpit on the same side. This process of removal of lymph is still considered

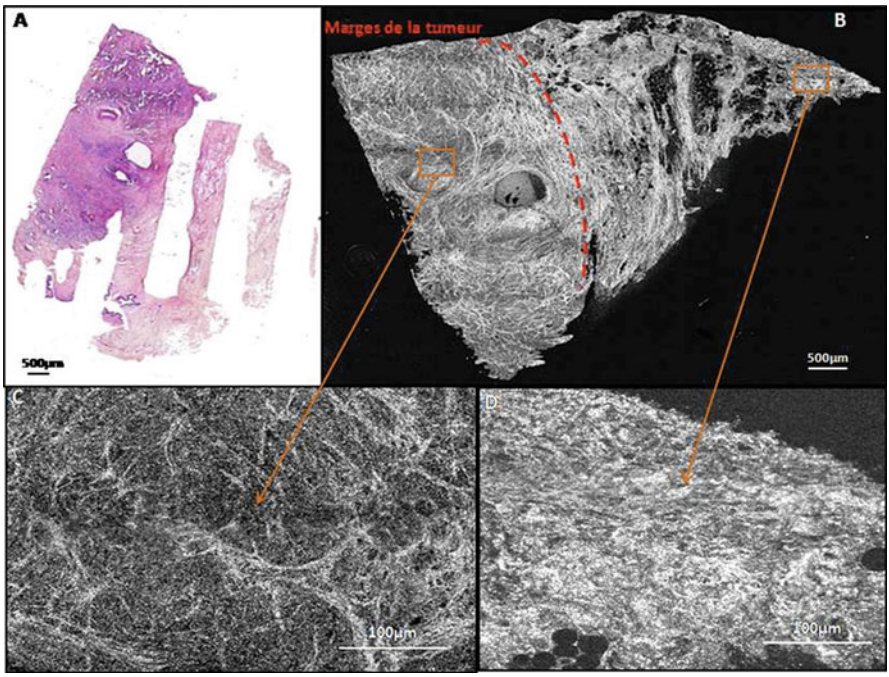

Fig. 26.4 Infiltrating carcinoma: tumor nodule (**a**, **b**). Fibrous tissue surrounding cancer cells (**c**), normal fibrous tissue (**d**)

as the standard even if it has several drawbacks. In fact, it often induces complications in the arm such as the decrease in the sensitivity of touch, pain in the upper arm on the operated side, a reduction in the function of the shoulder joint, or lymphedema of the arm in 80 % of cases [17]. In addition, it was shown for T1 tumors (tumor size less or equal to 2 cm) that the percentage of invaded axillary lymph nodes is 23 %, which means that 77 % of axillary dissection are unnecessary [18]. To limit the number of dissections, axillary sentinel node technique was introduced in 1998 [19]. The sentinel lymph node is a lymph node in the armpit. It is anatomically the closest to the breast tumor and, accordingly, will be the first node receiving lymphatic drainage from a tumor. If it is invaded, axillary dissection is performed; however if it appears not invaded, lymph nodes in the area are not removed.

The results of sentinel nodes analysis are used to determine the type of treatment to administer after surgery but are only available until several days after the operation, once achieving complete histology slides. It would be useful to the surgeon to have a quick picture of lymph to assess their invasion during the operation. It is in this spirit that FFOCM lymph nodes images have been made in order to estimate if this imaging technique is able to distinguish invaded lymph from healthy ganglions.

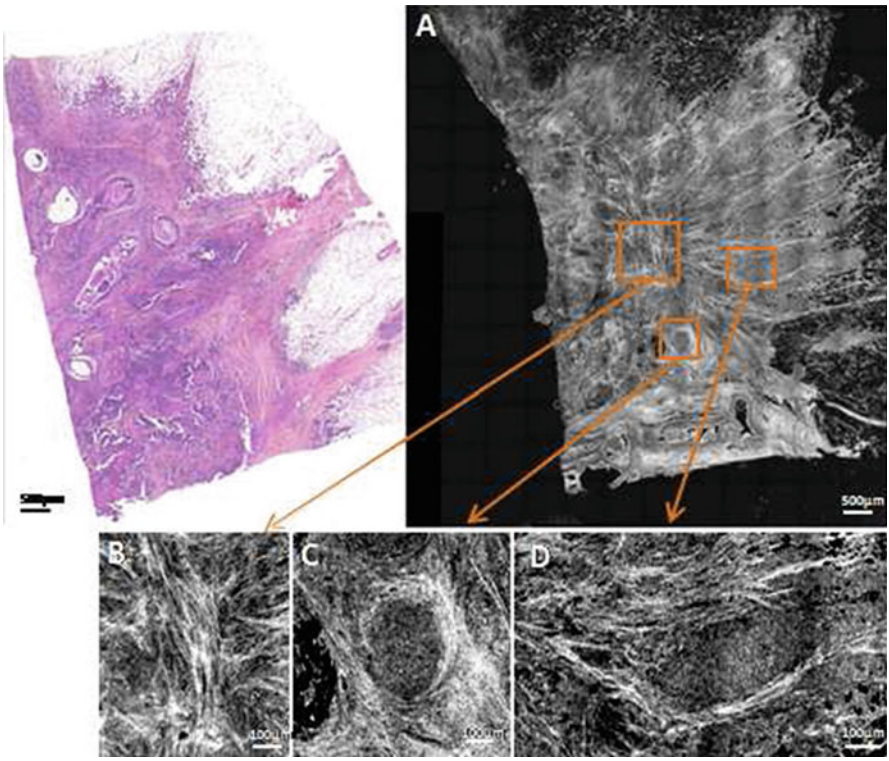

Fig. 26.5 Ductal adenocarcinoma with ductal in situ component: fibrous tissue finely spans highly diffusive (**c**), recognizable by its enlarged channel membrane elastic (**c**), fibrous tissue (*white*) surrounding cancer cells (*dark gray*) (**d**)

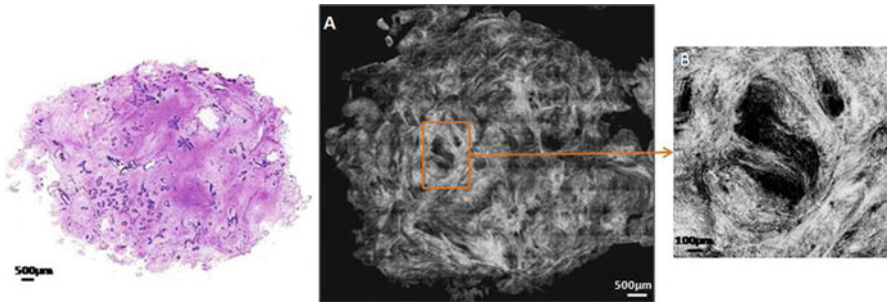

Fig. 26.6 Fibroadenoma (**a**) with characteristic enlarged channel (**b**)

An initial study using the elastic scattering spectroscopy (ESS) showed the usefulness of intraoperative analysis lymph nodes [20], but this study provides only macroscopic information and not microscopic architectures. Normal breast node tissues are seen in Fig. 26.8: one can see dense fibrous tissue and spans (D)

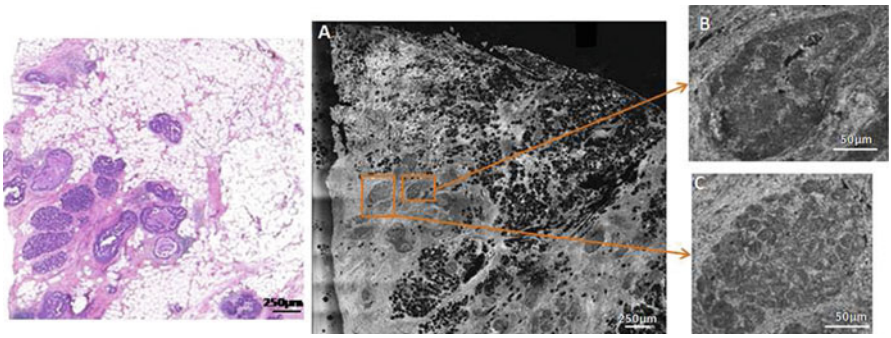

Fig. 26.7 Lobular carcinoma in situ (**a**) channel with expanded cellular proliferation in the center (**b**), with expanded lobule with visible acini (**c**)

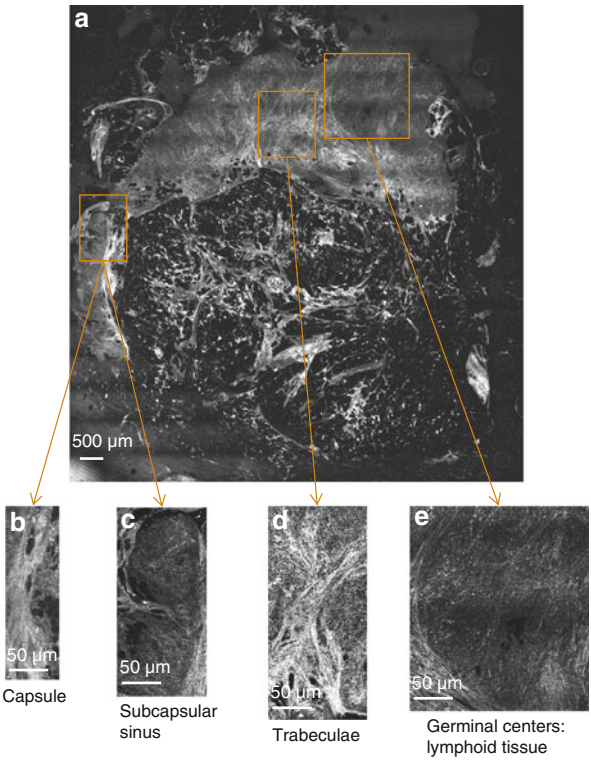

Fig. 26.8 Normal lymph node FFOCM images

that appear white. Subcapsular sinus (C) stands below the capsule, while terminal centers (E) appear as areas gray rounded.

The tumor lymph nodes are as recognizable in Fig. 26.9 as the structure of the ganglion is no longer respected and cell invasion within a zone lymphoid appears as

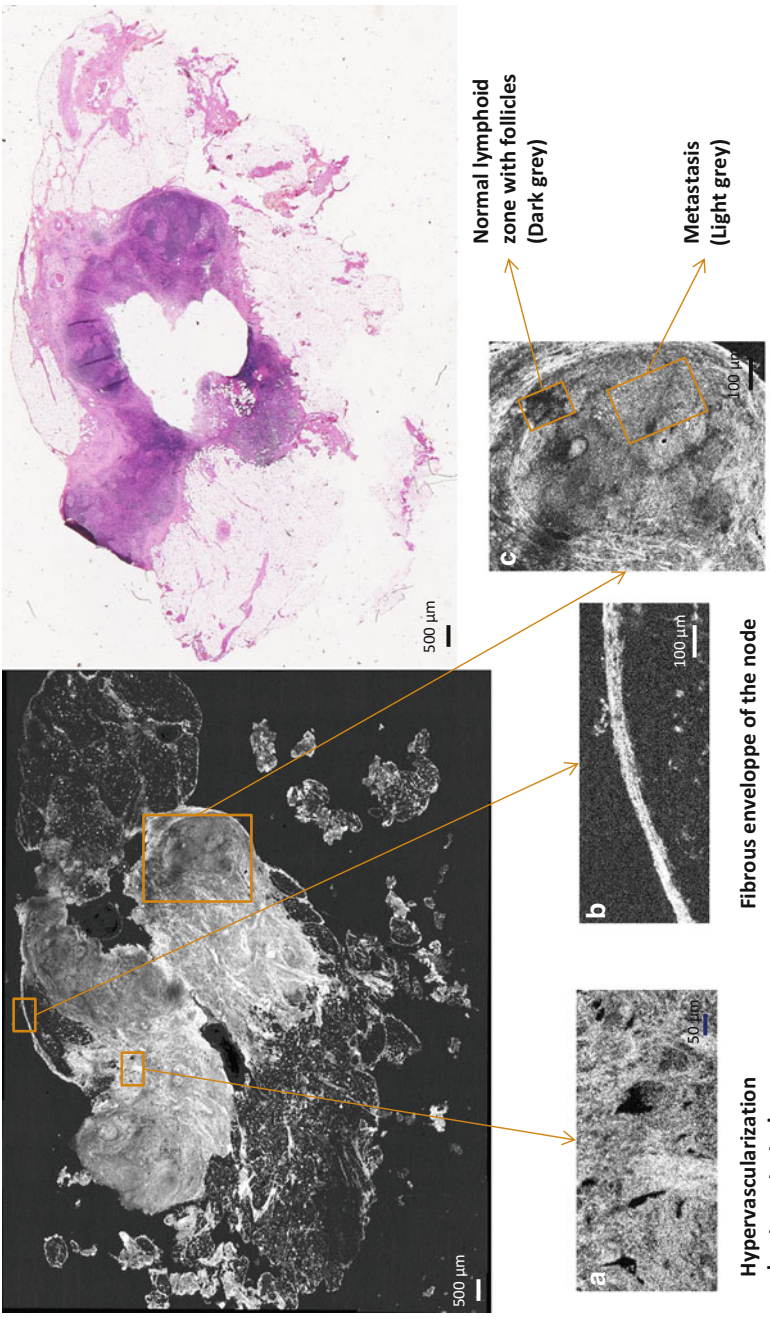

Fig. 26.9 Invaded lymph node FFOCM images

light gray areas. These zones correspond to purple regions on the HES slice that are clusters of cancer cells (C bottom); healthy lymphoid appears very dark gray (C top). Also, by zooming in the FFOCM image, we note the presence of many vessels reflecting hypervascularity characteristic of the presence of metastases (A).

26.2 FFOCM Study of Brain Tissue

26.2.1 Specificity of Brain Tissue Surgery

The encouraging results on breast tissue prompted us to test full-field OCT diagnostic of the brain where resection is difficult and risky. In this section we offer a preliminary phase of preclinical evaluation with FFOCM as an intraoperative tool of brain tumor surgery. Despite significant progress in the diagnosis and treatment of tumors, the survival rate for malignant tumors of the central nervous system (CNS) remains low [21]. Awake surgery technique, which was developed in the 1990s by Professor Mitchell Berger at UCSF, has improved the quality of resection of tumors located near the functional areas of the brain. This surgery intends to avoid language disorders or sensorimotor functions penalties. However, when removing a tumor, the neurosurgeon should be able to identify the nature of the tissue that is removed. Current tools for the identification of tissue include intraoperative MRI, the use of a surgical microscope, the fluorescence-guided resection, and finally extemporaneous histological analysis.

Intraoperative MRI provides low-resolution images of the surgical field and complete section of the brain that are sufficient for a rough estimate of the abnormal tissue excised but offers low acquisition resolution (ranging typically between 0.5 and 1 mm) and artifacts occur at the air-tissue interface. Using an operating microscope illuminated by a xenon lamp gives a clear vision of the operative field but is limited by the low capacity of discrimination of white light. Fluorescence-guided resection allows a more accurate assessment of the tumor region with the specific binding of fluorophores on cancer cells and therefore allows a better selection of pathological tissues than the white-light operating microscope. However, this technique requires the absorption of an exogenous fluorophore by the patient before the operation and is only sensitive to solid tumors with a low sensitivity to detect infiltration of the brain parenchyma by cancer cells.

The results that we will show in this section are, to the best of our knowledge, the only large images with a resolution sufficient to distinguish microstructural cerebral parenchyma. The first published study using OCT for the study of brain tissue was performed with a surgical probe OCT system [22]. This in vivo system has axial and lateral resolutions limited to 16 and 30 μm, respectively, and is focused on a single sample of excised brain. Nevertheless, it was possible to recognize a melanoma and an artery. Later, SD-OCT systems have been favored for their better resolution (4/8 μm, transverse/axial) allowing distinguishing areas of solid tumors, areas

invaded by the tumor and normal tissue [23] through the depth attenuation of signals. More recently, a study involving more patients with gliomas (9 in all) and using a TD-OCT system with 15 μm axial and transverse resolution was used to classify samples as malignant or benign with a good correlation with the histopathological diagnosis [24]. However, in this case too, the differentiation was based on the attenuation of the signal returned by the tumor zones relative to the healthy areas. The classification does not lead to the recognition of microscopic structures of the brain parenchyma in contrast to what we will show with FFOCM. A study published in 2005 showed images of brain microstructures using an ultrafast laser providing axial/lateral resolution of 1.3/3 μm, respectively. Thus, it was possible to differentiate malignant tissue from healthy tissue by the presence of blood vessels, microcalcifications, and cysts in the tumor tissue [25]. However, the images obtained are small (2×1 mm^2), and they have only been performed on fixed tissue and require a femtosecond laser whose cost is high and size is rather large limiting its implementation under clinical conditions.

Our imaging technique presented here and described in ▶ Chap. 25, "Time Domain Full Field Optical Coherence Tomography Microscopy" combines several advantages; their large sizes are comparable to those of samples embedded in paraffin for histological analysis, thus facilitating images analysis by physicians. The imaging system is compact, can be placed in the operating room, and provides a sufficient resolution (1 μm axial and lateral) for distinguishing brain tissue microstructures.

The histological and immunohistochemical analysis of excised tissues (from stereotactic biopsies or samples excised during surgery) is the only reliable method to analyze tissues and cellular level architectures. However, this method requires the use of paraffin and staining of tissue, which cannot be obtained during surgery. The extemporaneous examinations are poorly made during the surgical resection of a brain tissue tumor, as the brain parenchyma limit is very difficult to section and to color selectively.

For these reasons there exists a need for a rapid and reliable method that would bring information to neurosurgeons during the operation for guiding the surgical procedure. The objective of this preliminary study is to ensure that healthy and pathologic brain structures are recognizable through FFOCM images.

26.2.2 Nervous System Tumors

There are benign and malignant brain tumors. Neurons are postmitotic cells and cannot produce purely neuronal tumor. Glial cells, in contrast, can produce cancers called gliomas, which are primary most common brain tumors, although still rare in the world's population [21]. Some are benign gliomas such as astrocytoma, the most common, while others, such as glioblastoma, are malignant.

Among benign brain tumors, there are meningioma and papilloma choroid plexus. Microscopically, meningioma is composed of spans cells organizing themselves in vortex of concentric spheres.

26.2.3 Brain Tissue FFOCM Imaging

All images in this study were performed on brain tissue samples from the neurosurgery department of Pr. Devaux, Hospital Sainte-Anne. Agreement of the patients was obtained following the standard procedure for consent patients undergoing biopsy or surgery in this hospital. This study was conducted with samples of fresh tissue from the tumors surgically excised. Immediately after surgical ablation, the sample was sent to the pathology department. The total surface of the sample was imaged. Once imaged, the sample was immediately fixed in formalin-zinc. Then, the pathology department followed the standard histology process. Samples from diseased tissue were observed. For this study, 20 samples from 11 different patients were included. The results have been published in an article [26].

26.2.4 Cortex and Hippocampus

Samples of cortex and hippocampus were obtained from patients treated for surgery of epilepsy. On these samples containing no cancer cells, we have verified that it was possible to recognize different areas of brain parenchyma or morphologically. Indeed Fig. 26.10 shows a cross section of a brain parenchyma.

The gray and white matter differ significantly: in fact we recognize the cell body of neurons in the cortex and the beams leading to the axon white matter. The cell bodies of neurons appear as black dots with a triangular shape. Cortex does not contain myelin; it appears dark gray. Myelin fibers are strong backscatters [25, 27] and appear white in the images (C). Capillaries are distinguished by a thin collagen membrane which appears gray or white (D). It is important to note that on a single FFOCM image, these three types of structures appear (cell body, axon, vessels), whereas classical HES staining of myelin fibers do not appear clearly and it is necessary to make special staining of the paraffin block by Bodian-Luxol.

The hippocampus consists of two parts: Ammon's horn and the dentate gyrus consist of gray matter. It is a very complex structure folded upon itself and formed by a single layer of neurons. The hippocampus comprises a plurality of anatomical regions or fields named CA1, CA2, CA3, and CA4 (Ammon's horn 1, 2, 3, and 4). Regions of the hippocampus are recognizable in the FFOCM image (Fig. 26.11). More precisely there are CA1 field and stratum radiatum, CA4 field, the crack of the hippocampus, the dentate gyrus, the hippocampal alveus, and the furrow. Other structures appear by zooming in the FFOCM image: large pyramidal neurons of CA4 that are responsible for memory and granule neurons and smaller and more rounded neurons that form the granular layer of dentate gyrus are visible.

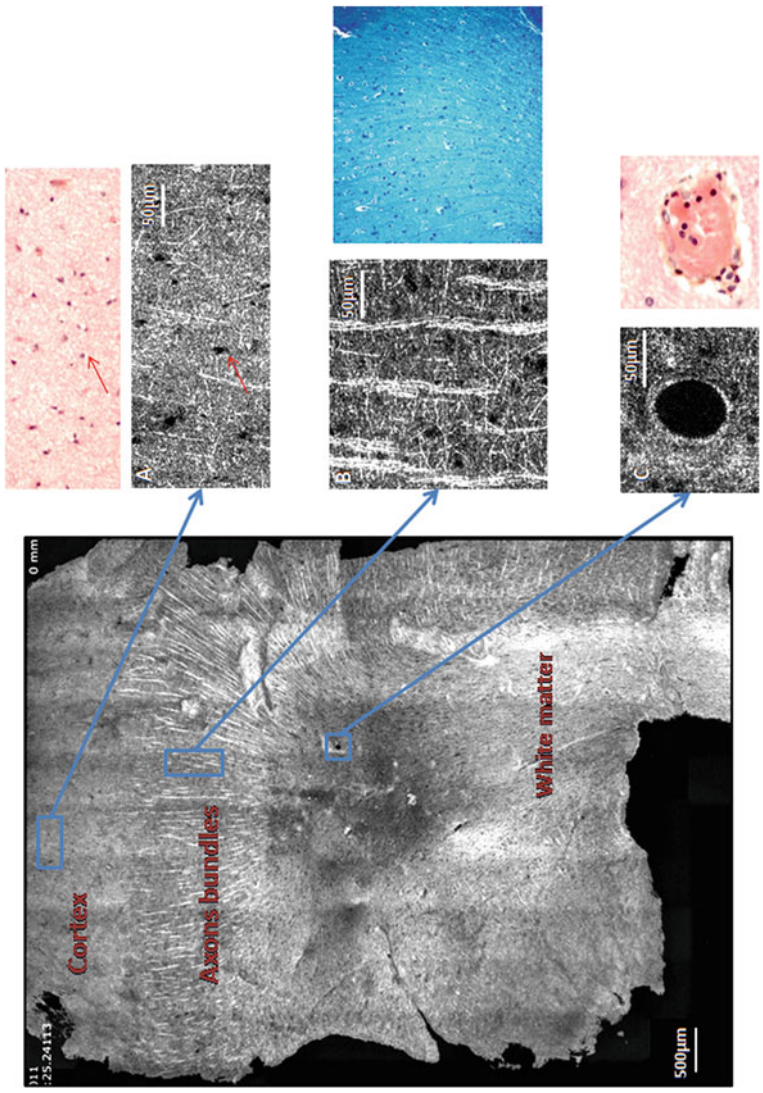

Fig. 26.10 FFOCM image of a sagittal section of the brain parenchyma: cell bodies neurons (**b**), myelin fibers (**c**), capillary (**d**)

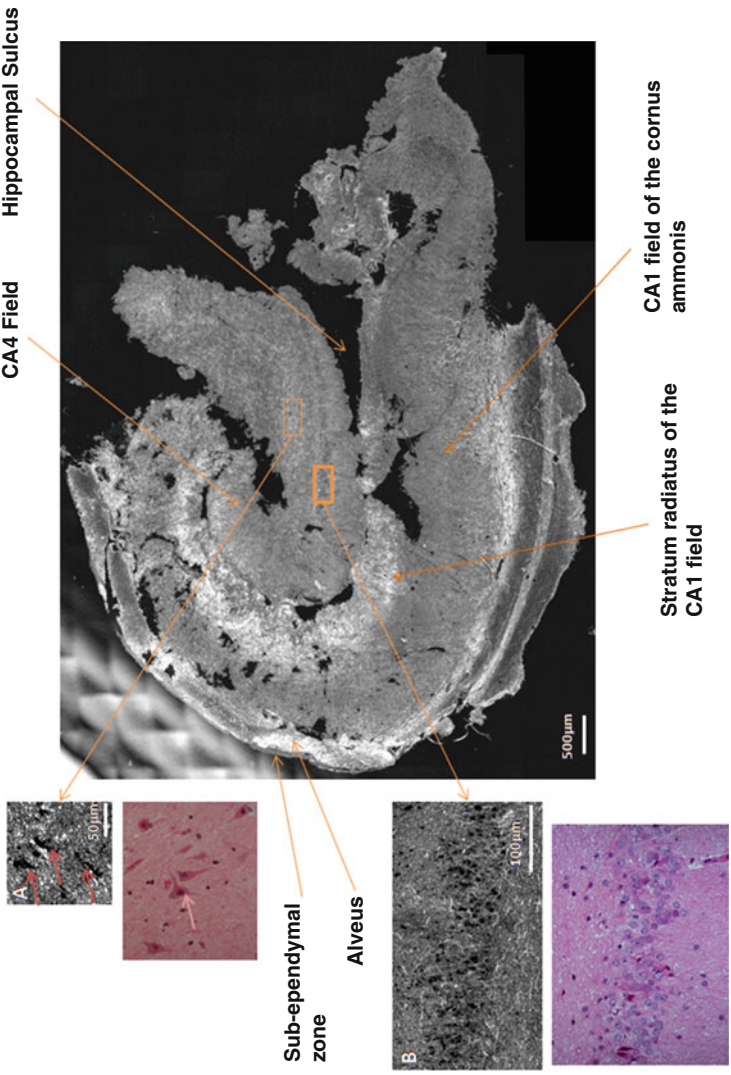

Fig. 26.11 FFOCM image a coronal section of hippocampus

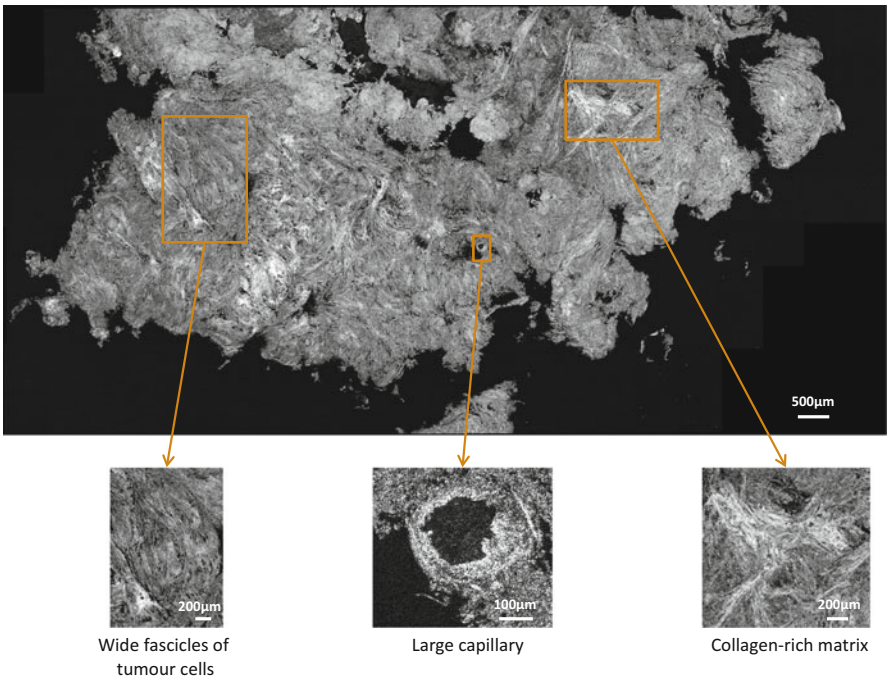

Fig. 26.12 FFOCM image a fibroblastic meningioma grade I

26.2.5 Meningiomas

Meningiomas are tumors developed at the expense of the meninges (grade I tumors) and three variants for each of grade II and grade III meningiomas. The most common subtypes are meningotheliomatous, transitional or mixed type, fibrous, and psammomatous. The stroma is often rich in collagen and reticulin and the tumor is often richly vascularized. An example of meningioma is shown in Fig. 26.12. The morphological characteristics of the tumor found in FFOCM image are large clusters of cancer cells (A), the matrix rich in collagen (C), and the presence of large capillaries surrounded by a white elastic membrane (B) characterizing tumor vasculature.

26.2.6 Choroidal Plexus Papilloma

Choroid plexus papillomas grow at the expense of the choroid plexus. The choroid plexus are papillary formations, which form the cerebrospinal fluid. They consist of connective tissue covered with epithelial cells forming papillae. These lesions have a very particular form of words in "cauliflower." This architecture is easily recognized as can be seen in Fig. 26.13. Papillae filled with blood differ significantly;

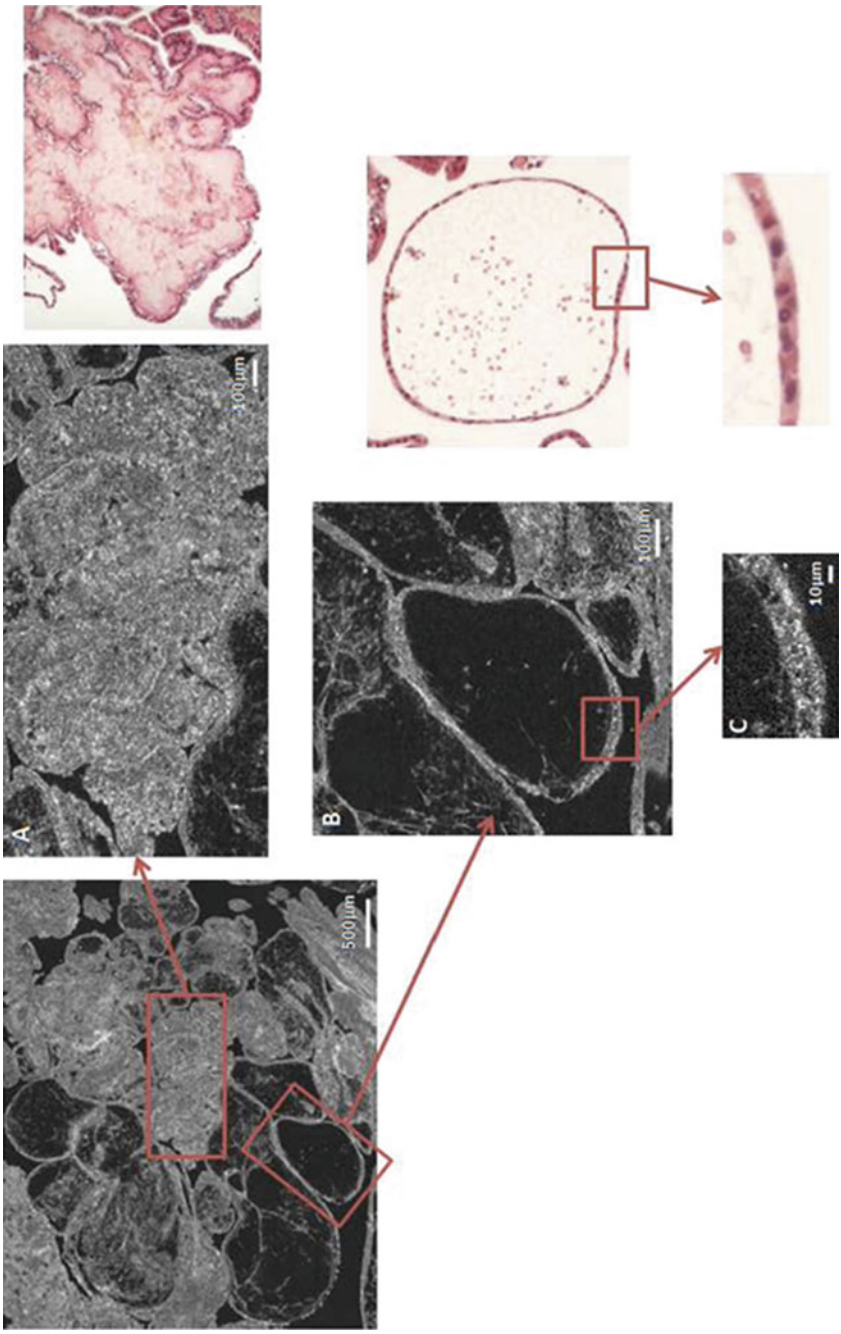

Fig. 26.13 Choroid plexus papillomas FFOCM and histology

by zooming in the image, we can acknowledge the good comparison with histology. Similarly, on a papilla, information at the cellular level is visible; there are the layers of epithelial cells that are connective tissue-like clusters.

26.3 Skin Tissue

26.3.1 FFOCM Study of Skin Tissue

The skin is the organ most readily accessible. Yet its clinical examination is limited nowadays to either the low-resolution, superficial analysis given by the dermatoscope or the high-resolution diagnostic allowed by histology, to the expense of an invasive and tedious procedure. This hampers the possibilities of an early diagnosis of skin cancer that could be decisive regarding the chance of cure of the patient. This is particularly critical as skin cancer is currently the most frequent cancer, with about 3.5 million new cases every day. As FFOCM can provide virtual sections of the tissue noninvasively and without the need for a contrast agent, it appears well suited for the analysis of skin pathological tissues. The usefulness of such a technique can also be highlighted for the analysis of margins in skin surgery. Basal cell carcinoma (BCC), the most frequent skin cancer, mostly affects facial areas; therefore, it is desired that excision surgeries remain as minimally invasive as possible. In that context, Mohs micrographic surgery is a commonly employed treatment for BCC. In Mohs protocol, excised tissue is examined during the surgery using frozen section histology as in breast surgery, as detailed above. An alternative technique such as FFOCM can prove preferable as it is simpler, noninvasive, occupying a small footprint, and operator independent.

Several studies have been published on the use of OCT imaging techniques on skin, and in particular to assess its capacity to discriminate cancerous tissue [28–34]. The results showed that the altered architecture of cancerous areas could be visualized and matched to the histological or light microscopy analysis. The OCT systems used however had a lower resolution (5–10 μm axial and transverse) than that allowed by FFOCM. It is therefore very relevant to examine the capacities offered by FFOCM on the analysis of skin pathological tissues.

26.3.1.1 Skin Structure

Skin is made of three separate layers. On top, the epidermis contains the stratum corneum, the stratum granulosum, the stratum spinosum, and the stratum basale that makes the junction with the dermis. The dermis mostly contains collagen and blood vessels, among which adnexal structures such as pilosebaceous structures or sweat glands can be found. Finally, adipocytes lay in the hypodermis.

26.3.1.2 Skin Tissue FFOCM Imaging

Skin tissues used for this study were obtained from the Hopitaux Universitaires de Genève, in collaboration with Dr Salomon and with informed consent from the patients. Fresh and formaldehyde fixed tissues were examined ex vivo, before being processed as histology slides.

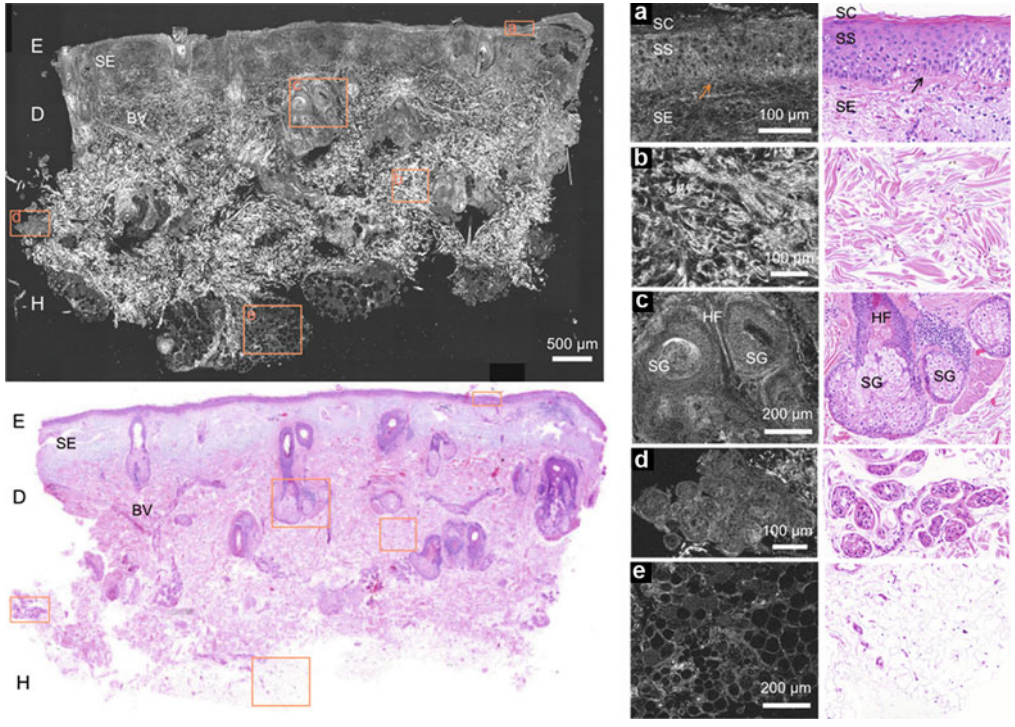

Fig. 26.14 FFOCM image of a normal aged skin and the corresponding histological slide. The three layers of the skin, epidermis (*E*), dermis (*D*), hypodermis (*H*), as well as a solar elastosis region (*SE*) and blood vessels (*BV*) are clearly distinguished. At high magnification, the stratum corneum (*SC*) can be differentiated from the stratum spinosum (*SS*) (inset 2**a**) and the enlargement of the nuclei from the basal layer (*arrows*) to the upper spinous layer is highly visible. The elastotic superficial dermis (SE in 2**a**) contrasts with the highly refractive collagen fibers of the dermis (2**b**). A pilosebaceous unit with hair follicle (HF) and sebaceous glands (SG) (2**c**), a sweat gland unit (2**d**) and adipocytes with their bright cell membranes (2**e**) are identified

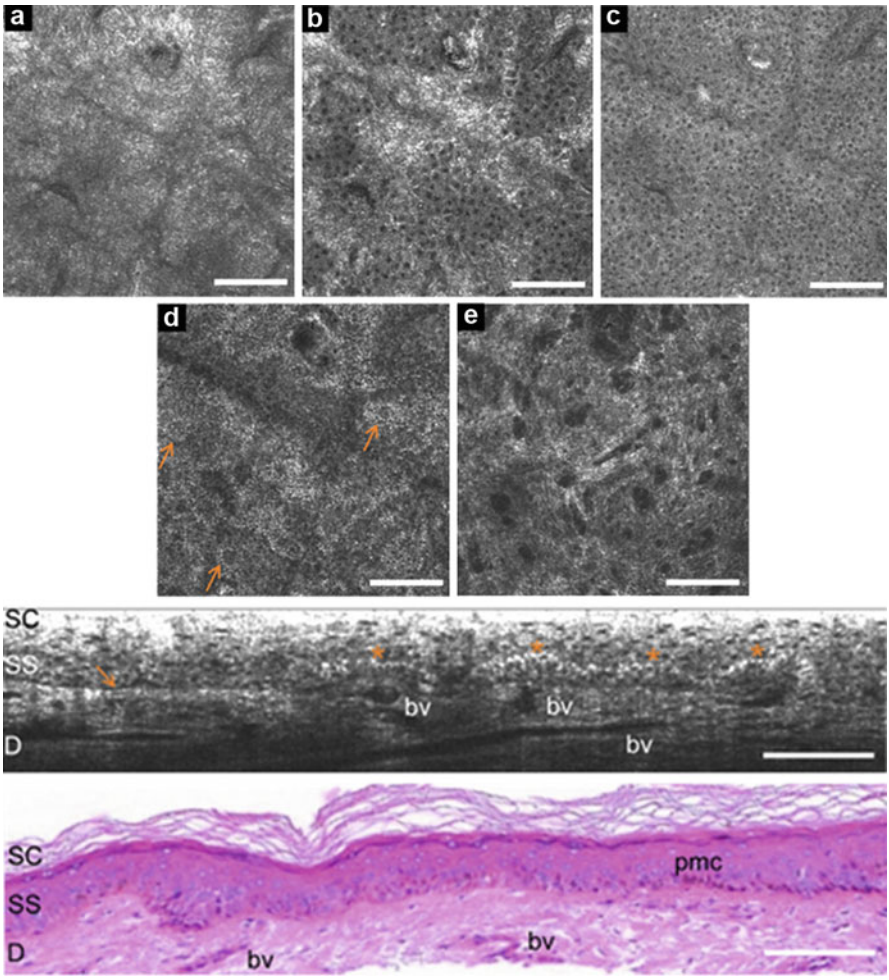

Fig. 26.15 *Left*, tangential images of skin fresh excision. (**a**) Stratum corneum (depth 10 μm); (**b**) stratum granulosum (depth 25 μm); (**c**) stratum spinosum (depth 35 μm); (**d**) stratum basale where *arrows* point at some papillaries (depth 60 μm); (**e**) dermis (depth 100 μm). Scale bar represents 200 μm. *Right*, vertical reconstruction and histological corresponding slide. Visible layers: stratum corneum (*S*), stratum spinosum (*SS*), dermis (*D*). The basement membrane (*arrow*) and melanin caps (stars) are visible. Blood vessels (*bv*) can also be identified. Scale bar is 100 μm

26.3.1.3 Normal Skin

As shown in Fig. 26.14, the main skin layers and structures can be easily identified and compared to histology in a vertical excision. Tangential imaging of the skin, allowing vertical reconstruction, is also possible as demonstrated in Fig. 26.15.

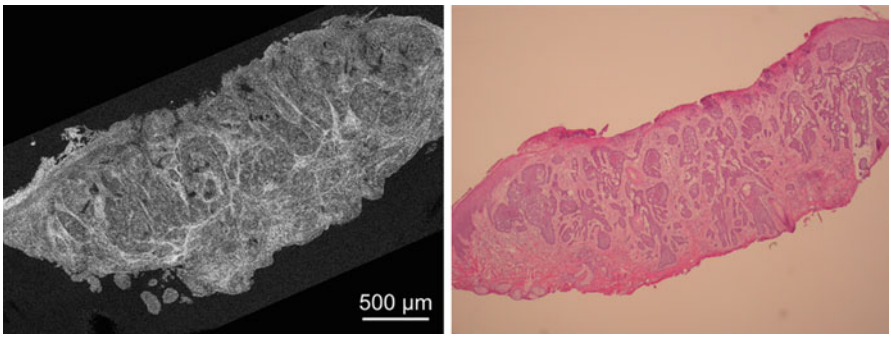

Fig. 26.16 Comparison of the FFOCM image of a vertical skin fresh excision with nodular basal cell carcinoma, with the corresponding histological slide

26.3.1.4 Cancerous Skin

An example of BCC lesion is shown in Fig. 26.16. The BCC nodules, surrounded by dense peritumoral stroma, are clearly distinguished from normal tissue, and this is confirmed by the histological slide. A closer analysis on another sample shows that the tumorous cell aggregations are visible on OCT images as black spots densely arranged (Fig. 26.17).

A more extensive description of the capacities of FFOCM in skin imaging for clinical and cosmetics applications is presented in publications [34, 35].

In conclusion, these studies, the first that we have conducted in a clinical hospital environment using FFOCM, open a critical door in the process of assisting and replacing cryogenic sections when many are impossible to perform cryogenic sections as intraoperative diagnostic tools. Although the contrast of the image is not able to provide the chemical or biological signature used by the pathologists, this nondestructive endogenous technique brings a large number of valuable informations dealing with the tumor malignancy, the margins, etc.

The expected field of application of FFOCM is clearly tissue selection and identification:

- Needle core biopsy in the operating room, where the aim is to validate the tissue sample "quality" for further chemical and biological analysis; studies have already started [36–39].
- Biobanking is another field where tissue selection is critical; a first trial using FFOCM is underway.
- Tissue selection in the grossing room could be performed in order to identify the optimal sample for further histology/immunohistochemistry.
- Intraoperative assessment of surgical margins in various organs such as the prostate, breast, etc. could be performed in order to optimize the resection process [37, 38].

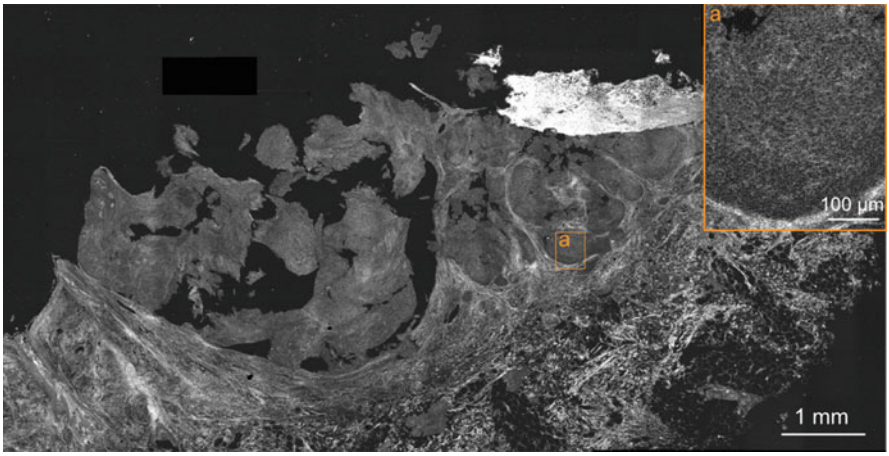

Fig. 26.17 Basal cell carcinoma in a skin vertical excision. Inset sows zoom of region *a*

Finally we hope that the endoscopic FFOCM approach described in ▶ Chap. 25, "Time Domain Full Field Optical Coherence Tomography Microscopy" will become a useful tool in the surgeon's hands for an in situ and in vivo diagnostic.

References

1. The hospitals involved in FF-OCT studies are: curie and tenon hospitals in Paris, MD Anderson (Texas), Cornell Weill (New York) and Hôpitaux Universitaires de Genève
2. http://www.lltechimaging.com/image-gallery/atlas-of-images/
3. M.J. Silverstein, A. Recht, M.D. Lagios, I.J. Bleiweiss, P.W. Blumencranz, T. Gizienski, S.E. Harms, J. Harness, R.J. Jackman, V.S. Klimberg, R. Kuske, G.M. Levine, M.N. Linver, E. Rafferty, H. Rugo, K. Schilling, D. Tripathy, F. Vicini, P.W. Whitworth, S.C. Willey, Special report: consensus conference III. Image-detected breast cancer: state-of-the-art diagnosis and treatment. J. Am. Coll. Surg. **209**(4), 504–520 (2009)
4. T.P. Olson, J. Harter, A. Muñoz, D.M. Mahvi, T. Breslin, Frozen section analysis for intraoperative margin assessment during breast-conserving surgery results in low rates of re-excision and local recurrence. Ann. Surg. Oncol. **14**(10), 2953–2960 (2007)
5. K. Ishak, Benign tumors and pseudotumors of the liver. PubMed. J. Article Appl. Pathol. **6**(2), 82–104 (1988)
6. J.B. Taxy, Frozen section and the surgical pathologist: a point of view. Arch. Pathol. Lab. Med. **133**(7), 1135–1138 (2009). *Références* 93
7. A. Sienko, T.C. Allen, D.S. Zander, P.T. Cagle, Frozen section of lung specimens. Arch. Pathol. Lab. Med. **129**(12), 1602–1609 (2005)
8. N. Nagasue, H. Akamizu, H. Yukaya, I. Yuuki, Hepatocellular pseudo tumor in the cirrhotic liver: report of three cases. Cancer **54**(11), 2487–2494 (1984)
9. E. Weinberg, C. Cox, E. Dupont, L. White, M. Ebert, H. Greenberg, N. Diaz, V. Vercel, B. Centeno, A. Cantor, S. Nicosia, Local recurrence in lumpectomy patients after imprint cytology margin evaluation. Am. J. Surg. **188**(4), 349–354 (2004)
10. S.A. Boppart, W. Luo, D.L. Marks, K.W. Singletary, Optical coherence tomography: feasibility for basic research and image-guided surgery of breast cancer. Breast Cancer Res. Treat. **84**(2), 85–97 (2004)

11. P.-L. Hsiung, D.R. Phatak, Y. Chen, A.D. Aguirre, J.G. Fujimoto, J.L. Connolly, Benign and malignant lesions in the human breast depicted with ultrahigh resolution and three-dimensional optical coherence tomography. Radiology **244**(3), 865–874 (2007)
12. F.T. Nguyen, A.M. Zysk, E.J. Chaney, J.G. Kotynek, U.J. Oliphant, F.J. Bellafiore, K.M. Rowland, P. Johnson, S. Boppart, Intraoperative evaluation of breast tumor margins with optical coherence tomography. Cancer Res. **69**(22), 8790–8796 (2009)
13. A.M. Zysk, S. Boppart, Computational methods for analysis of human breast tumor tissue in optical coherence tomography images. J. Biomed. Opt. **11**(5), 054015 (2006)
14. W. Luo, F.T. Nguyen, A.M. Zysk, T.S. Ralston, J. Brockenbrough, D.L. Marks, A.L. Oldenburg, S. Boppart, Optical biopsy of lymph node morphology using optical coherence tomography. Technol. Cancer Res. Treat. **4**(5), 539–548 (2005)
15. F.T. Nguyen, A.M. Zysk, E.J. Chaney, S.G. Adie, J.G. Kotynek, J. Uretz, F.J. Bellafiore, K.M. Rowland, P.A. Johnson, A. Stephen, Optical coherence tomography: the intraoperative assessment of lymph nodes in breast cancer. IEEE Eng. Med. Biol. Mag. **29**(2), 63–70 (2010)
16. O. Assayag, M. Antoine, B. Sigal-Zafrani, M. Riben, F. Harms, A. Burcheri, K. Grieve, E. Dalimier, B. Le Conte de Poly, C. Boccara, Large field, high resolution full field optical coherence tomography: a pre-clinical study of human breast tissue and cancer assessment. Accepted in technology in cancer research and treatment. TCRT: Express **1**(1), 21–34 (2013)
17. K.D. Beitsch, D. Weaver, T. Ashikaga, F. Moffat, V.S. Klimberg, C. Shriver, S. Feldman, R. Kusminsky, M. Gadd, J. Kuhn, S. Harlow, P. Beitsch, The sentinel node in breast cancer. A multicenter validation study. N. Engl. J. Med. **339**(14), 941–946 (1998)
18. P.H. Spruit, S. Siesling, M.G. Elferink, E.J. Vonk, C.J.M. Hoekstra, Regional radiotherapy versus an axillary lymph node dissection after lumpectomy: a safe alternative for an axillary lymph node dissection in a clinically uninvolved axilla in breast cancer. A case control study with 10 years follow up. Radiat. Oncol. **2**, 40 (2007)
19. D. Weaver, D. Krag, T. Ashikaga, S. Harlow, Development of sentinel node targeting technique in breast cancer patients. Breast J. **4**(2), 67–74 (1998)
20. M.R.S. Keshtgar, D.W. Chicken, M.R. Austwick, S.K. Somasundaram, C. Mosse, Y. Zhu, I.J. Bigio, S.G. Bown, Optical scanning for rapid intraoperative diagnosis of sentinel node metastases in breast cancer. Br. J. Surg. **97**(8), 1232–1239 (2010)
21. D. Ricard, A. Idbaih, F. Ducray, M. Lahutte, K. Hoang-Xuan, J.-Y. Delattre, Primary brain tumours in adults. Lancet **379**(9830), 1984–1996 (2012)
22. S.A. Boppart, M.E. Brezinski, C. Pitris, J.G. Fujimoto, Optical coherence tomography for neurosurgical imaging of human intracortical melanoma. Neurosurgery **43**(4), 834–841 (1998)
23. H.J. Böhringer, D. Boller, J. Leppert, U. Knopp, E. Lankenau, E. Reusche, G. Hüttmann, A. Giese, Time-domain and spectral-domain optical coherence tomography in the analysis of brain tumor tissue. Lasers Surg. Med. **38**(6), 588–597 (2006)
24. H.J. Böhringer, E. Lankenau, F. Stellmacher, E. Reusche, G. Hüttmann, A. Giese, Imaging of human brain tumor tissue by near-infrared laser coherence tomography. Acta Neurochir. **151**(5), 507–517 (2009)
25. K. Bizheva, A. Unterhuber, B. Hermann, B. Povazay, H. Sattmann, A.F. Fercher, W. Drexler, M. Preusser, H. Budka, A. Stingl, T. Le, Imaging ex vivo healthy and pathological human brain tissue with ultra-high-resolution optical coherence tomography. J. Biomed. Opt. **10**(1), 11006 (2005)
26. O. Assayag, K. Grieve, B. Devaux, F. Harms, J. Pallud, F. Chretien, C. Boccara, P. Varlet, Imaging of non-tumorous and tumorous human brain tissues with full-field optical coherence tomography. NeuroImage: Clinical **2**, 549–557 (2013)
27. J. Binding, J.B. Arous, J.-F. Léger, S. Gigan, C. Boccara, L. Bourdieu, Brain refractive index measured in vivo with high-NA defocus-corrected full-field OCT and consequences for two-photon microscopy. Opt. Express **19**(6), 4833–4847 (2011)
28. J.B. Arous, J. Binding, J.-F. Léger, M. Casado, P. Topilko, S. Gigan, A.C. Boccara, L. Bourdieu, Single myelin fiber imaging in living rodents without labeling by deep optical coherence microscopy. J. Biomed. Opt. **16**(11), 116012 (2011). doi:10.1117/1.3650770

29. T. Hinz, L.K. Ehler, H. Voth, I. Fortmeier, T. Hoeller, T. Hornung, M.H. Schmid-Wendtner, Assessment of tumor thickness in melanocytic skin lesions: comparison of optical coherence tomography, 20-MHz ultrasound and histopathology. Dermatology **223**, 161–168 (2011)
30. T. Gambichler, P. Regeniter, F.G. Bechara, A. Orlikov, R. Vasa, G. Moussa, M. Stücker, P. Altmeyer, K. Hoffmann, Characterization of benign and malignant melanocytic skin lesions using optical coherence tomography in vivo. J. Am. Acad. Dermatol. **57**, 629–637 (2007)
31. T. Gambichler, A. Orlikov, R. Vasa, G. Moussa, K. Hoffmann, M. Stücker, P. Altmeyer, F.G. Bechara, In vivo optical coherence tomography of basal cell carcinoma. J. Dermatol. Sci. **45**, 167–173 (2007)
32. J.M. Olmedo, K.E. Warschaw, J.M. Schmitt, D.L. Swanson, Optical coherence tomography for the characterization of basal cell carcinoma in vivo: a pilot study. J. Am. Acad. Dermatol. **55**, 408–412 (2006)
33. R. Pomerantz, D. Zell, G. McKenzie, D.M. Siegel, Optical coherence tomography used as a modality to delineate basal cell carcinoma prior to Mohs micrographic surgery. Case Rep. Dermatol. **3**, 212–218 (2011)
34. E. Dalimier, D. Salomon, Full-field optical coherence tomography: a new technology for high-resolution skin imaging. Dermatology **224**, 84–92 (2012)
35. J.R. Durkin, J.L. Fine, H. Sam, M. Pugliano-Mauro, J. Ho, Imaging of Mohs micrographic surgery sections using full-field optical coherence tomography: a pilot study. Dermatologic Surgery 40(3), 266–274 (2014)
36. M. Jain, N. Narula, B. Salamoon, M.M. Shevshuk, A. Aggarwal, N. Altorki, B. Stiles, C. Boccara, S. Mukherjee, Full-field optical coherence tomography for the analysis of fresh unstained human lobectomy specimens. J Pathol Inform **4**, 1–26 (2013)
37. F. Beuvon, E. Dalimier, F. Cornud, N. Barry Delongchamps, Full field optical coherence tomography of prostate biopsies: a step towards pre-histological diagnosis? Progrès en Urologie **24**, 22630 (2014)
38. F. De Leeuw, A. Latrive, O. Casiraghi, M. Ferchiou, F. Harms, C. Boccara, C. Laplace-Builhé, Optical biopsy and head and neck tissue using full-field OCT: a pilot study. Proc SPIE 8926–892626 (2014). doi:10.1117/12.20369959
39. K. Grieve, L. Palazzo, E. Dalimier, P. Vielh, M. Fabre, A feasibility study of full-field optical coherence tomography for rapid evaluation of EUS-guided microbiopsies. Gastrointestinal Endoscopy, in press

Digital Holoscopy

27

Dierck Hillmann, Gesa Franke, Christian Lührs, Peter Koch, and Gereon Hüttmann

27.1 Introduction

Optical coherence tomography (OCT) images three-dimensional biological tissues with micrometer resolution. While time-domain OCT required axial scanning of the imaging plane or the specimen, Fourier-domain OCT enabled parallel detection of all depths, which allowed to increase the acquisition speed by several orders of magnitude. When increasing the numerical aperture (NA) for achieving microscopic resolution, the advantage of Fourier-domain over time-domain OCT is lost. The resolution and sensitivity of FD-OCT imaging is only optimal within the Rayleigh range. Both degrade outside of the focal region, which shrinks with the square of the NA. The sensitivity is lost due to the confocal gating as photons from out-of-focus layers do not even reach the detector.

In full-field swept-source OCT, a parallel illumination and detection and the abandoning of the confocal gating allowed to maintain sensitivity over larger measurement depths [1, 2].

In digital holography (DH) entire wave fields, including their phase and amplitude, are captured, and the image information is calculated from the interference pattern. This allows for numerical refocusing in order to obtain images of the specimen over a larger measurement depth than provided by the focal depth [3–5]. But DH does not provide tomographic imaging, as no cross-sectional images are obtained.

D. Hillmann (✉) • C. Lührs
Thorlabs GmbH, Lübeck, Germany

G. Franke • P. Koch • G. Hüttmann
Institute of Biomedical Optics, University of Lübeck, Lübeck, Germany

Medical Laser Center GmbH, Lübeck, Germany

© Springer International Publishing Switzerland 2015

W. Drexler, J.G. Fujimoto (eds.), *Optical Coherence Tomography*,
DOI 10.1007/978-3-319-06419-2_28

Finally, by combining digital holography and full-field swept-source OCT, tomographic images are obtained, with optimal sensitivity and resolution spanning regions much larger than the focal range. Using numerical algorithms, comparable to the ones first shown in interferometric synthetic aperture microscopy (ISAM, [6–10]) and inverse scattering for full-field OCT [8, 11], the depth of focus can be extended, and thus, a depth-independent resolution and sensitivity can be obtained.

The combination of digital holography with time-domain and Fourier-domain OCT was shown by several groups. Massatsch et al. [12] demonstrated the combination of time-domain OCT with digital holography. However, when using time-domain OCT, axial scanning is still required. First optical sectioning using digital holography with multiple wavelengths was shown by Kim in 1999 [13], but cumbersome and inefficient reconstruction algorithms were used, and imaging quality was not comparable to OCT. The limitations were mostly due to the small number of wavelengths used. Later work used OCT technology to obtain better images, but in the applied reconstruction algorithms, the focus was fixed to a single layer, and thus, the principal advantage of digital holography – virtual refocusing – was not used [14, 15]. An efficient reconstruction using simulated full-field OCT data was shown using inverse scattering techniques but not demonstrated experimentally [8, 11]. Finally, a consequent combination of digital holography with full-field swept-source OCT was shown in holoscopy [16–18, 23]. The extended depth of focus in terms of sensitivity and resolution compared to standard confocal scanning OCT was demonstrated, and images were shown that demonstrate an imaging quality comparable to full-field swept-source OCT.

27.1.1 Sensitivity Improvement of Holoscopy

In FD-OCT the imaging depth resulting in optimal images is limited to the focus region, which extends over two Rayleigh lengths z_R. The Rayleigh length at the Numerical Aperture (NA) is given by

$$z_R = \frac{\lambda}{\pi \mathrm{NA}^2},$$

with λ being the wavelength. Therefore, for the total measurement depth d, only a ratio of $2z_R/d$ of the B-scan shows optimal sensitivity and resolution. This motivates the definition of a photon efficiency of confocal OCT η_{confocal} by

$$\eta_{\mathrm{confocal}} = \frac{2z_R}{d} = \frac{2\lambda}{\pi d \mathrm{NA}^2}.$$

The photon efficiency for various measurement depths, ranging from 0.3 to 3 mm, at a central wavelength of 823.5 nm is shown in Fig. 27.1. The photon efficiency drops rapidly with increasing NA, and for microscopic NA around 1.0, it is several orders of magnitude smaller than the optimal value $\eta_{\mathrm{confocal}} = 1$.

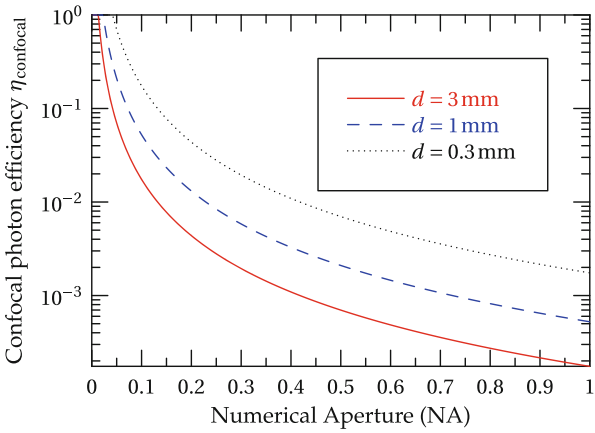

Fig. 27.1 Photon efficiency $\eta_{\text{confocal}} = 2z_R/d$ for a confocal FD-OCT. The photon efficiency describes the relative amount of backscattered photons that can be used for imaging with optimal diffraction limited resolution and sensitivity

In holoscopy all photons backscattered within the NA are detected and provide optimal resolution when refocused to the plane in which they were scattered. Holoscopy thus allows in principle an optimal photon efficiency of $\eta_{\text{holoscopy}} \approx 1$. It is therefore more efficient than FD-OCT and allows either to increase the sensitivity and imaging speed or to reduce the light intensity on the specimen.

27.2 Digital Holography

In digital holography, a wave field $O(x, y)$ of light scattered or reflected by the object is captured by recording the interference pattern of $O(x, y)$ with a well-known reference wave $R(x, y)$. The interference pattern $I(x, y)$ can be described by

$$\begin{aligned} I(x,y) &= \gamma |O(x,y) + R(x,y)|^2 \\ &= \gamma \Big(|O|^2(x,y) + |R|^2(x,y) + (O^* R)(x,y) + (O R^*)(x,y) \Big), \end{aligned}$$

where γ is a factor considering camera sensitivity and scaling between squared field strength and measured intensity values and x and y denote coordinates of the camera pixels. With a known reference wave $R(x, y)$, the wave field $O(x, y)$ can be computed by multiplying with $R/|R|^2$:

$$\left(\frac{R}{|R|^2} I \right)(x,y) = \gamma \left(\underbrace{\frac{R|O|^2}{|R^2|}(x,y) + R(x,y)}_{\text{Autocorrelation and DC term}} + \underbrace{\frac{O^* R^2}{|R|^2}(x,y)}_{\text{Conjugated signal}} + \underbrace{O(x,y)}_{\text{Signal term}} \right)$$

As in FD-OCT additional terms appear. Here, the autocorrelation term denotes the interference of the sample with itself. The DC term describes an offset to the entire

image, created by object and sample wave fields. The signal term is the wave field that was captured from the object, and the conjugated signal is proportional to the complex-conjugated object wave field.

In digital holography the reference illumination on the camera is in most cases applied under an angle to the object wave (off-axis holography), resulting in a separation of all three terms after a two-dimensional Fourier transform of the acquired interference pattern $I(x, y)$. In Fourier space the signal term can then be filtered, and disturbance of the non-signal terms can be minimized (see, e.g., [5]).

In FD-OCT similar terms arise in the spectral interference pattern, which disturb the final A-scan.

27.2.1 Propagation

Having obtained the object wave field $O(x, y)$ does in general not give any information about the structures of the object itself, as the object field from a deep volume cannot be focused onto the camera, i.e., for large parts of the sample volume, only an unfocused image is obtained. To solve this issue, one can propagate the wave field numerically by computing its diffraction pattern in the appropriate plane. One effective way to do this is the angular spectrum approach (see, e.g., [4, 5, 19]).

Using this approach the wave field $O(x, y)$ is first two-dimensionally Fourier transformed to obtain its angular spectrum, i.e., it is decomposed to plane waves propagating in different directions:

$$\tilde{O}\left(k_x, k_y\right) = \mathcal{F}[O(x,y)] = \int \mathrm{d}x\,\mathrm{d}y\;\; O(x,y)\mathrm{e}^{-\mathrm{i}\left(k_x x + k_y y\right)},$$

The original field $O(x, y)$ is then expressed as a superposition of plane waves $\exp(\mathrm{i}(k_x x + k_y y))$, each propagating in direction given by (k_x, k_y) and with amplitude $\tilde{O}\left(k_x, k_y\right)$

$$O(x,y) = \frac{1}{(2\pi)^2}\int \mathrm{d}k_x, k_y\;\; \tilde{O}\left(k_x, k_y\right)\mathrm{e}^{+\mathrm{i}\left(k_x x + k_y y\right)}.$$

Each plane wave

$$\tilde{O}\left(k_x, k_y\right)\mathrm{e}^{+\mathrm{i}\left(k_x x + k_y y\right)}$$

can be propagated in z-direction by multiplication with the phase factor

$$e^{+\mathrm{i}k_z z}, \;\text{ with }\; k_z = \sqrt{k^2 - k_x^2 - k_y^2}.$$

Thus, the propagation of the entire wave field $O(x, y)$ is achieved by propagating the plane waves it is composed of. Mathematically the propagation of the diffracted field from a known wave position can be described by an operator, called propagator $\mathcal{P}_{k,\,z}$.

The propagator is defined as

$$\mathcal{P}_{k,z}[O(x,y)] = \mathcal{F}^{-1}\left[\mathrm{e}^{+ik_z z}\mathcal{F}[O(x,y)]\right], \tag{27.1}$$

where k is the wavenumber and z denotes the propagation distance. The propagator yields results identical to the first Rayleigh-Sommerfeld diffraction integral [20].

27.3 Theory of Holoscopy

Holoscopy contains two critical steps: acquiring scattered object fields at multiple wavelengths by a camera and efficiently processing of the data to obtain tomographic images, which incorporates the reconstruction principles known from digital holography.

27.3.1 Basic Setups of Holoscopy

Setups that can be used for holoscopy are similar to the setups used in digital holography. Both techniques are based on the interference of a wave that is scattered or reflected by the sample and a well-known – usually spherical or plane – reference wave. The sample is illuminated with an extended, usually collimated, beam. The backscattered light is superimposed with the reference beam, and the resulting interference pattern is recorded. In contrast to digital holography, this is done in holoscopy for many wavenumbers using a swept-source laser and is thus comparable to swept-source OCT.

In general, no imaging optics are required for either technique, but the achievable lateral resolution is limited without using imaging optics. Digital holography and holoscopy can be used lensless or with microscope objectives to achieve high-resolution holoscopy. Schematic drawings of possible holoscopy setups are shown in Fig. 27.2a, b.

27.3.2 The Acquired Images

In holoscopy, the interference image $I(x, y, k)$, which is caused by a superposition of a reference wave field $R(x, y, k)$ and a sample wave field $O(x, y, k)$ on the camera, is dependent on the wavenumber k. We assume that the fields R and O have been acquired for the entire plane, i.e., for all (x, y). In practice this is never the case,

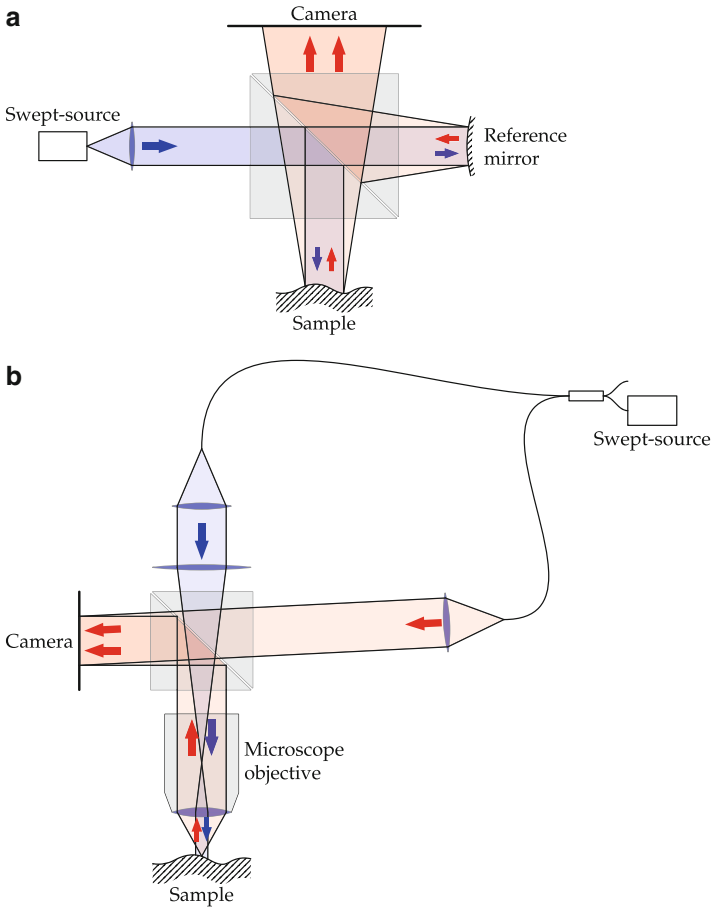

Fig. 27.2 (**a**) Schematic drawing of a lensless holoscopy setup. Coherent light of a known reference beam and light scattered from the sample are superimposed and digitized for many wavelengths. (**b**) Mach-Zehnder-type setup of a high-resolution holoscope

and limitations of the camera size will result in a limited resolution and/or lateral field of view. The only difference compared to digital holography (as shown in Sect. 27.2) is that the wavenumber k is now an additional variable as data are acquired for multiple wavenumbers. Additionally, it is assumed that the camera lies in the $z = z_0$ plane. The interference pattern in this plane is given by

$$\begin{aligned} I(x,y,k) &= \gamma |R(x,y,k) + O(x,y,k)|^2 \\ &= \gamma \Big(|R(x,y,k)|^2 + |O(x,y,k)|^2 + (R^* O)(x,y,k) + (R O^*)(x,y,k) \Big). \end{aligned} \tag{28.2}$$

The meaning of the terms is identical compared to the case of digital holography: the term $|R(x,y,k)|^2$ describes the absolute value of the reference field, which contributes mostly to the DC part of the recorded interference pattern. The term $|O(x,y,k)|^2$ describes the interference of the object wave with itself (autocorrelation). Finally, $2\mathrm{Re}(R^*O)(x, y, k)$ is the real cross-correlation term and contains the information of interest.

The reference wave is usually a plane or spherical wave, described by

$$R(x,y,k) = A_C(k)A_R \cdot \exp[i\boldsymbol{k} \cdot \boldsymbol{x} + i\phi_0(k)]|_{\boldsymbol{x}=(x,y,z_0)}, \tag{28.3}$$

where $\boldsymbol{k}$ is the wave vector, which defines wavelength and propagation direction of the wave, z_0 is the camera plane, $A_C(k)$ is the relative amplitude spectrum, and A_R describes the overall amplitude of the reference wave. $\phi_0(k)$ is the initial phase in the reference plane, in which the path length in the sample arm is the same as the one in the reference arm. In this plane, both reference and sample waves, have the same phase for all wavenumbers k. For on-axis imaging geometry, the reference wave is propagating perpendicular to the camera. To reduce spatial fringe frequencies on the camera, a spherical reference wave can be used similar to digital holography (see, e.g., [4]).

In case of the Michelson-type setup, as shown in Fig. 27.2a, the spherical wave can be created by subjecting a plane wave to a reference mirror with a given focal length f. In a Mach-Zehnder-type setup, a spherical wave can be created by focusing the light with a suitable lens. The following will describe the Michelson setup. Adjusting the formalism for a Mach-Zehnder-type setup is straightforward, as the introduction of a spherical reference wave in our computations is equivalent to introducing a numerical lens. Both lead to identical phase factor multiplications [19].

Let the distance from the reference mirror to the camera be denoted z_0. Then the reference field is given by

$$R(x,y,k) = A_C(k)A_R \cdot \mathrm{e}^{\mathrm{i}k\sqrt{x^2+y^2+(z_0+f)^2}-ikf+i\phi_0(k)}. \tag{27.4}$$

This describes a spherical wave originating at a distance f behind the reference plane (Fig. 27.3).

The fraction of light backscattered from the sample at a transversal position (x, y) at a distance z from the reference plane is given by the scattering potential $\eta(x, y, z)$, thereby neglecting any angular dependence of the backscattering. The collimated light enters the sample, moves a distance z to the scatterer, is backscattered, and then is propagated by a distance $z + z_0$ to the camera. Assuming the validity of the first-order Born approximation [21], which assumes single scattering and a constant incident wave field throughout the volume, the object field $O(x, y, k)$ and its angular spectrum $\tilde{O}_{xy}(k_x, k_y, k)$ in the camera plane are just a superposition of the fields generated by the backscattering in each depth, i.e.,

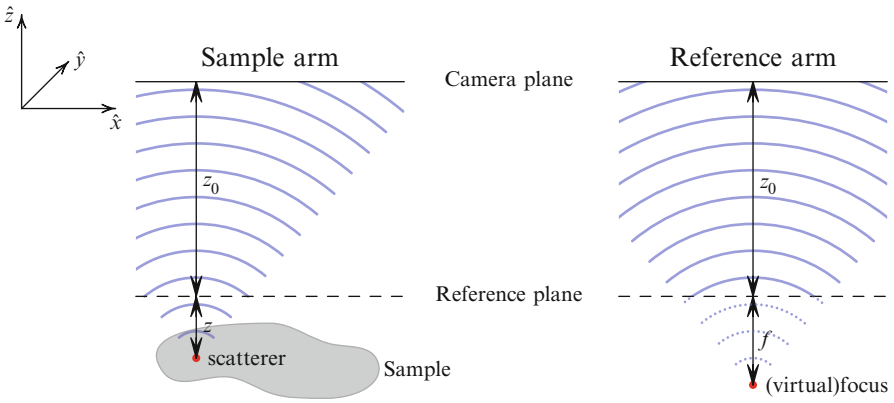

Fig. 27.3 Coordinate as used in the computation of the sample (*left*) and reference (*right*) wave field. The sample is made of several point scatterers whose fields are superimposed in the camera plane. In this case, the reference wave is a spherical wave with a (virtual) origin behind the reference plane. The configuration can be achieved by using a spherical reference mirror as shown in Fig. 27.2a

$$\begin{aligned} O(x,y,k) &= A_O A_C(k) \cdot \int \mathrm{d}z\, \mathcal{P}_{k,z_0+z}\left[\eta(x,y,z)\mathrm{e}^{\mathrm{i}kz}\mathrm{e}^{\mathrm{i}\phi_0(k)}\right], \\ \tilde{O}_{xy}\left(k_x,k_y,k\right) &= A_O A_C(k) \cdot \int \mathrm{d}z\, \mathrm{e}^{\mathrm{i}k_z(z+z_0)+\mathrm{i}kz} \cdot \mathrm{e}^{\mathrm{i}\phi_0(k)} \cdot \widetilde{\eta}_{xy}\left(k_x,k_y,z\right). \end{aligned} \tag{27.5}$$

The coordinate system as used for reference and object field is illustrated in Fig. 27.3.

27.3.3 The Phase-Corrected Propagator and Object and Reference Field

Propagating a wave field by the propagator $\mathcal{P}_{k,z}[\cdot]$ will change the overall phase of the field. In OCT, depth information is contained in the phase of the wave field, and thus, arbitrarily changing the phase will destroy this depth encoding. If a wave is propagated by a distance z by the propagator $\mathcal{P}_{k,z}[\cdot]$, its overall phase will change by $\mathrm{e}^{\mathrm{i}kz}$. For focusing of the object without changing the phase information, and thus without changing the depth encoding, the propagator needs to be adapted accordingly. This motivates the definition of a phase-corrected propagator

$$\mathcal{P}^0_{k,z}[\cdot] \equiv \mathrm{e}^{-\mathrm{i}kz}\mathcal{P}_{k,z}[\cdot].$$

The phase-corrected propagator is just a mathematical construct. Physical propagation of the wave field in free space will inevitably change the phase of the wave. Nevertheless, computations simplify significantly when introducing the phase-corrected propagator.

The reference as well as the object wave field, given by Eqs. 27.4 and 27.5, travel the same optical path length from the light source to the reference plane and have an identical time-dependent phase term $\phi_0(k)$, and common phase factors occur in reference and sample that need to be taken into account during reconstruction. In general, changing the overall phase of the two fields in exactly the same manner does not change the measurable quantity $I(x, y, k)$. For the following computations, it is therefore advantageous to redefine and simplify the phases of object and reference field, instead of using the previously obtained and physically motivated formulas, similar to the way the phase-corrected propagator replaces the propagator Eq. 27.1.

The phase-corrected reference wave field is therefore introduced by

$$\begin{aligned} R_0(x,y,k) &\equiv R(x,y,k)\cdot \mathrm{e}^{-\mathrm{i}\phi_0(k)}\cdot \mathrm{e}^{-\mathrm{i}kz_0} \\ &= A_R A_C(k)\mathrm{e}^{\mathrm{i}k\sqrt{x^2+y^2+(z_0+f)^2}-\mathrm{i}k(z_0+f)}. \end{aligned} \tag{27.6}$$

For $f \to 0$ the origin of the reference wave goes to the reference plane. Holograms of this kind are also referred to as Fourier holograms as they can be reconstructed in paraxial approximation by means of a simple Fourier transform (see, e.g., [4]).

The phase-corrected object wave field is accordingly defined by

$$\begin{aligned} O_0(x,y,k) &\equiv O(x,y,k)\cdot \mathrm{e}^{-\mathrm{i}\phi_0(k)}\cdot \mathrm{e}^{-\mathrm{i}kz_0} \\ &= A_O A_C(k)\int \mathrm{d}z\, \mathcal{P}^0_{k,\,z_0+z}\left[\eta(x,y,z)\mathrm{e}^{\mathrm{i}2kz}\right]. \end{aligned} \tag{27.7}$$

It is worthwhile to note the similarity to the standard FD-OCT cross-correlation term, except for the phase-corrected propagator $\mathcal{P}^0_{k,\,z_0+z}[\cdot]$. If the effect of the propagator can be reverted, images can be reconstructed similar to FD-OCT reconstruction by a Fourier transform. The effect of a propagator also arises in standard FD-OCT, but its influence is neglectable since FD-OCT works near the focal plane.

27.3.4 Obtaining the Phase-Corrected Object Wave Field

Interference of the phase-corrected object and reference wave gives the same intensity distribution as real physical waves:

$$I(x,y,k) = \gamma|R(x,y,k)+O(x,y,k)|^2 = \gamma|R_0(x,y,k)+O_0(x,y,k)|^2$$

and consequently also Eq. 27.2 still holds, if R and O are replaced by R_0 and O_0, respectively. Hence, the phase-corrected object wave field can be calculated from the acquired interference patterns.

27.3.4.1 On-Axis Geometry

The measured intensity $I(x, y, k)$ contains two conjugated parts $R_0^* O_0$ and $(R_0^* O_0)^*$, which are referred to as twin images in holography.

In FD-OCT the two conjugated terms cause the inability to distinguish negative from positive time delays and halve the effective measurement depth. They are usually separated by ensuring that all parts of the object are on one side of the reference plane. In this case, the complex signal is be obtained by removing all negative frequency components, i.e., by performing a Hilbert transform $\mathcal{H}_k[\cdot]$ with respect to the k-axis:

$$I^{\mathcal{H}}(x, y, k) = I(x, y, k) + \mathrm{i}\mathcal{H}_k[I(x, y, k)]. \tag{27.8}$$

$$\approx \gamma(R_0{}^* O_0)(x, y, k) + \gamma\Big(|O_0|^2(x, y, k) + \mathrm{i}\mathcal{H}_k\Big[|O_0|^2(x, y, k)\Big]\Big). \tag{27.9}$$

The phase-corrected object field can be approximately obtained by simply dividing the intensity Eq. 27.8 by the complex-conjugated phase-corrected reference field from Eq. 27.6:

$$O_0(x, y, k) \approx \frac{I^{\mathcal{H}}(x, y, k)}{\gamma R_0^*(x, y, k)} + \text{DC term} + \text{autocorrelation term}. \tag{27.10}$$

27.3.4.2 Off-Axis Geometry

In digital holography, off-axis reference illumination is commonly used to separate the twin images, the DC, and the autocorrelation term. This is also possible for holoscopy with a similar setup (Fig. 27.2b). The reference wave is not aligned perpendicular to the camera plane. This introduces a carrier frequency as illustrated in Fig. 27.4, which allows a separation of the terms after a two-dimensional Fourier transform.

With a suitable filter function $w(k_x, k_y)$, the object field can be isolated:

$$I_{\text{filtered}}(x, y, k) = \mathcal{F}_{xy}^{-1}\left[w\left(k_x, k_y\right)\mathcal{F}_{xy}[I(x, y, k)]\right].$$

The filter function $w(k_x, k_y)$ will act as computational aperture, and the lateral PSF in position space is determined by the filter function.

The resulting signal after this spatial filter can be approximated by the object wave field which can be determined approximately from the filtered intensity of the interference pattern by

$$O_0(x, y, k) = \frac{\gamma\left(R_0^* O_0\right)(x, y, k)}{\gamma R_0^*(x, y, k)} \approx \frac{I^{\text{filtered}}(x, y, k)}{\gamma R_0^*(x, y, k)}.$$

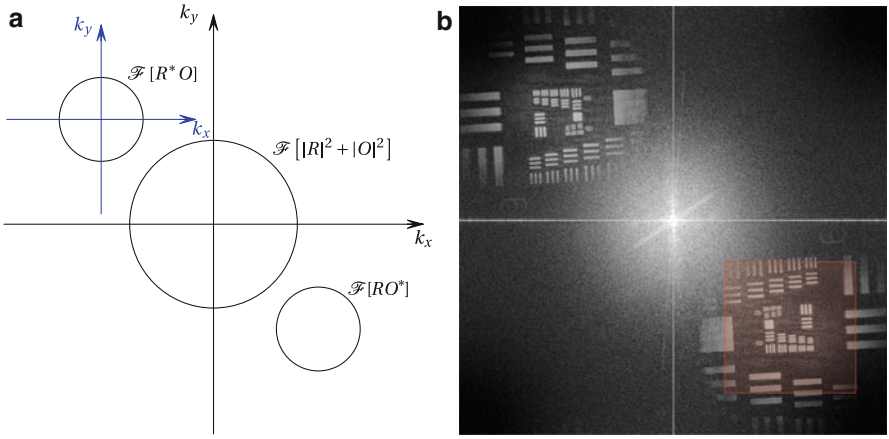

Fig. 27.4 (**a**) Off-axis separation of the different terms in frequency space. Suitable filtering and an inverse Fourier transform can isolate the appropriate wave field. The exact filter function is wavelength dependent, and thus, a suitable phase shift needs to be added to compensate for this effect. (**b**) Fourier transform of a hologram of a US Air Force (*USAF*) test chart acquired at 867.5 nm and the respective filtering window is shown

The autocorrelation object term $|O_0(x, y, t)|^2$ and the complex-conjugated wave field $O_0^*(x, y, k)$ are removed, which is not possible with the on-axis geometry. The autocorrelation terms add additional coherence noise, especially in the upper areas of the reconstructed volume. Filtering of the complex-conjugated signal resolves also the complex-conjugate ambiguity entirely similar to full-range OCT.

27.4 Reconstruction

27.4.1 Reconstruction Within One Rayleigh Length

To reconstruct the scatterer distribution of the specimen, the corrected object wave field $O_0(x, y, k)$ is propagated back for all wavenumbers to a common plane within the volume of interest by applying the phase-corrected propagator. The propagation reverts the effect of the phase-corrected propagator in Eq. 27.7 for the chosen reconstruction distance. The focus of the reconstruction lays in the chosen common plane of the volume. The data obtained after propagation are equivalent to measured full-field FD-OCT data. A Fourier transform along the k-axis is performed analogous to FD-OCT processing, to achieve the depth sectioning. The reconstructed volume will have diffraction limited resolution in the common propagation plane. The other planes will have degraded lateral resolution as observed with imaging optics.

With a distance z_P of the common plane to the reference plane, the reconstructed object is obtained by

$$\begin{aligned}\mathcal{P}^0_{k,\,-z_0-z_P}[O_0(x,y,k)] &= A_O A_C(k) \int \mathrm{d}z\, \mathcal{P}^0_{k,\,-z_0-z_P} \mathcal{P}^0_{k,\,z_0+z} \left[\eta(x,y,z)\mathrm{e}^{2\mathrm{i}kz}\right] \\ &= A_O A_C(k) \int \mathrm{d}z\, \mathcal{P}^0_{k,\,z-z_P} \left[\eta(x,y,z)\mathrm{e}^{2\mathrm{i}kz}\right],\end{aligned}$$

where the property $\mathcal{P}^0_{k,z_1}\mathcal{P}^0_{k,z_1}[\cdot] = \mathcal{P}_{,k,z_1+z_2}[\cdot]$ has been used to combine the operators. Performing a Fourier transform then gives the scattering potential:

$$\tilde{A}_C(z) * \eta_{z_P}(x,y,z) = \frac{1}{\pi A_O} \int \mathrm{d}k \exp(-\mathrm{i}2kz) \mathcal{P}^0_{k,\,-z_0-z_P}[O_0(x,y,k)], \tag{27.11}$$

where $*$ denotes the convolution operation with respect to the z-axis and $\tilde{A}_C(z)$ is the point spread function obtained by Fourier transforming the spectrum. Due to $\mathcal{P}^0_{k,0}[\cdot] = \mathrm{id}[\cdot]$ being the identity operator, the scattering potential is only reconstructed without aberrations for the layer $z = z_P$.

27.4.2 One-Step Reconstruction

27.4.2.1 Reconstruction in Free Space

For a complete depth-independent reconstruction of the volume data, single reconstructions for different reconstruction depths z_P as outlined in Sect. 27.4.1 are needed so that the propagator vanishes for all layers. In order to achieve this, one needs to set $z_P = z$ in Eq. 27.11 which gives

$$\tilde{A}_C(z) * \eta(x,y,z) = \frac{1}{\pi A_O} \int \mathrm{d}k\, \mathrm{e}^{-\mathrm{i}2kz} \mathcal{P}^0_{k,\,-z_0-z_P}[O_0(x,y,k)] \Big|_{z_P=z}.$$

For the angular spectrum, the respective equation reads

$$\tilde{A}_C(z) * \tilde{\eta}_{xy}(k_x,k_y,z) = \frac{1}{\pi A_O} \int \mathrm{d}k\, \mathrm{e}^{-\mathrm{i}2kz} \mathrm{e}^{-\mathrm{i}(k_z-k)(z_0+z_P)} \left[\tilde{O}_0(k_x,k_y,k)\right] \Big|_{z_P=z}.$$

The convolution operation $*$ only affects the z-axis and thus remains untouched from the change to the angular spectrum. Finally, setting effectively $z_P = z$ gives

$$= \frac{1}{\pi A_O} \int \mathrm{d}k\, \mathrm{e}^{-\mathrm{i}(k+k_z)z} \mathrm{e}^{-\mathrm{i}(k_z-k)z_0} \left[\tilde{O}_0(k_x,k_y,k)\right].$$

Going back to spatial space gives

$$\tilde{A}_C(z) * \eta(x,y,z) = \frac{1}{\pi A_O} \mathcal{F}_{xy}^{-1} \left[\int \mathrm{d}k \, \mathrm{e}^{-\mathrm{i}(k+k_z)z} \mathrm{e}^{-\mathrm{i}(k_z-k)z_0} \mathcal{F}_{xy}[O_0(x,y,k)] \right]. \quad (27.12)$$

With this transformation all layers are reconstructed with diffraction limited resolution. However, this relation is only valid if the applied free-space propagator is correct. Lenses in between sample and camera or a sample with refractive index larger than one ($n > 1$) need a different propagator.

27.4.2.2 Reconstruction in a Medium

In a medium with index of refraction n, the wavenumber k will be increased by a factor n. Assuming that entry and exit to the medium are parallel to the camera plane, the lateral components of $\boldsymbol{k}$ will remain unchanged, as they must not change abruptly when entering or leaving the medium (see, e.g., [21]). Therefore, for propagation in the medium, the wave vector needs to be changed according to

$$\boldsymbol{k}' = \begin{pmatrix} k_x \\ k_y \\ k_z' \end{pmatrix} = \begin{pmatrix} k_x \\ k_y \\ \sqrt{n^2k^2 - k_x^2 - k_y^2} \end{pmatrix},$$

and it follows

$$\|\boldsymbol{k}'\| = nk,$$

where $\boldsymbol{k}'$ denotes the wave vector in the medium. In the one-step reconstruction by Eq. 27.12, the kernel needs to be modified by replacing k and k_z by nk and k'_z, respectively. However, assuming that z_0 describes the propagation distance to focus the reference plane, which is in a medium not equal to the physical distance, the phase factor does not need to be modified. The reconstruction is then given by

$$\tilde{A}_C(z) * \widetilde{\eta}(k_x,k_y,z) = \frac{1}{\pi A_O} \times \int \mathrm{d}(nk) \underbrace{\exp\left(-\mathrm{i}\left(k_z' + nk\right)z\right)}_{\text{kernel}} \underbrace{\exp(-\mathrm{i}(k_z-k)z_0)}_{\text{phase}} \tilde{O}_0(k_x,k_y,k). \quad (27.13)$$

This integral transform with the modified kernel can also be calculated by a Fourier transform on non-equidistant data points (NFFT, [22]). By using $\sqrt{1-x^2} \approx 1 - x^2/2$

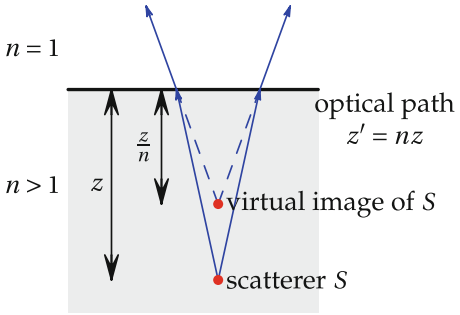

Fig. 27.5 After an optical interface to a medium with different index of refraction the apparent focus position of the virtual image is reduced by a factor 1/n whereas the optical path length is increased by a factor of n

a simplification is possible for low to moderate NA: in paraxial approximation the term for k_z can be expanded and rewritten to

$$\exp\left(+\mathrm{i}\left(k_z' + nk\right)z\right) \approx \exp\left(+\mathrm{i}\left(2nk + \frac{1}{n}\left(k_z - k\right)\right)z\right).$$

By introducing the optical path length $z' = nz$, the kernel is modified to

$$= \exp((+\mathrm{i}(2-\zeta)k + \zeta k_z)z'), \tag{27.14}$$

with

$$\zeta = \frac{1}{n^2}. \tag{27.15}$$

ζ describes the proportionality constant between imaging distance and optical path length as illustrated in Fig. 27.5. The complete reconstruction formula is then

$$\tilde{A}_C\left(z'\right) * \tilde{\eta}\left(k_x, k_y; z'\right) = \frac{1}{\pi A_O}\int \mathrm{d}k \underbrace{\mathrm{e}^{-\mathrm{i}((2-\zeta)k+\zeta k_z)z'}}_{\text{kernel}} \underbrace{\mathrm{e}^{-\mathrm{i}(k_z-k)z_0}}_{\text{phase}} \tilde{O}_0\left(k_x, k_y; k\right). \tag{27.16}$$

For $\zeta = 0$, Eq. 27.16 reduces to Eq. 27.11 with $z_P = 0$, i.e., the chosen reconstruction distance is the reference plane. For increasing n the parameter ζ tends to zero; thus, the higher the refractive index of the sample, the better the approximation by Eq. 27.11. In fact, for $\zeta < 0.5$ the reconstruction by Eq. 27.11 yields better results than the reconstruction by Eq. 27.12, which assumes free space. In case the paraxial approximation of Eq. 27.14 is not valid, the more general formula Eq. 27.13 needs to be used.

If n of the medium is not exactly known, an approximate solution of the reconstruction can be used for a fast experimental determination of ζ. By first

Fourier transforming the object waves $O_0(x, y; k)$ with respect to the k-axis, i.e., using FD-OCT depth discrimination on the unprocessed holograms and only afterwards performing holographic refocusing with the center wavenumber for at least two different depths, the focus positions and the optical path lengths of these layers can be determined. A linear regression of these points gives ζ and the reference propagation length z_0.

27.4.2.3 The Complete Reconstruction Integral

The reconstruction described by Eq. 27.16 can be evaluated by a variable substitution. Introducing

$$\kappa_\zeta(k_x, k_y; k) = (2-\zeta)k + \zeta k_z = (2-\zeta)k + \zeta\sqrt{k^2 - k_x^2 - k_y^2}$$

and substituting the integral variable simplifies the reconstruction integral to

$$\tilde{A}_C(z') * \tilde{\eta}(k_x, k_y; z') = \frac{1}{\pi A_O}\int \mathrm{d}\kappa_\zeta \frac{\mathrm{d}k}{\mathrm{d}\kappa_\zeta} \mathrm{e}^{-\mathrm{i}\kappa_\zeta z}\mathrm{e}^{-\mathrm{i}(k_z-k)z_0}\tilde{O}_0(k_x, k_y; k), \qquad (27.17)$$

where $\mathrm{d}k/\mathrm{d}\kappa_\zeta$ is neglectable and only results in a different weighting of frequencies in the dataset. As κ_ζ depends on the lateral frequencies k_x and k_y, evaluation of the integral in Eq. 27.17 requires an interpolation of the dataset in frequency space. In practice, the integration is performed over the range between a minimum and maximum of κ_ζ,

$$\kappa_{\zeta,\min} = 2k_{\min}$$
$$\kappa_{\zeta,\max} = (2-\zeta)k_{\max} + \zeta\sqrt{k_{\max}^2 - (k_x)_{\max}^2 - (k_y)_{\max}^2},$$

which are obtained from the minimum and maximum wavenumber ($k_{\min}$, $k_{\max}$) during the sweep and the NA of the setup (maximal k_x and k_y) as indicated in Fig. 27.6 and shown in more detail in [23]. For low to moderate NA this leads to a reduction of the axial frequency range and thus a loss in axial resolution, since samples below $\kappa_{\zeta,\min}$ and above $\kappa_{\zeta,\max}$ have to be discarded. For high NA imaging and high axial resolution the distortion in frequency space becomes too large for this reconstruction to be effective. Integrating from $\kappa_{\zeta,\min}$ to $\kappa_{\zeta,\max}$ will miss a large portion of the sampled data and sampling density in the κ_ζ, k_x and k_y space varies considerably, which makes interpolation imprecise. Suitable algorithms need to be developed and applied for high NA holoscopy.

27.4.3 Resolution

27.4.3.1 Axial Resolution

The axial resolution is determined by the sweep range of the swept-source laser and the spectral shape, after spectral apodization of the acquired signals. The resolution

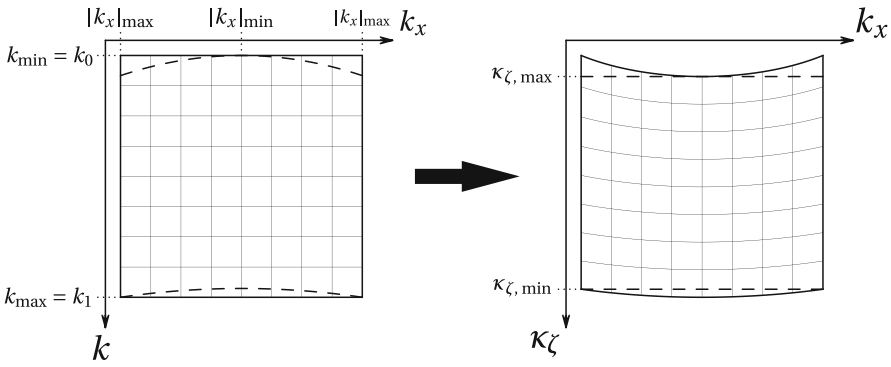

Fig. 27.6 Coordinate transformation that is required for the one-step reconstruction

will thus be approximately the OCT resolution using an identical light source [24]. However, applying the complete reconstruction, the interpolation variable κ_ζ is determining the axial resolution instead of the original wavenumber k. As some parts of the $\boldsymbol{k}$-space cannot be used for reconstruction, it will thus be slightly decreased. The discretization of the interpolated reconstruction integral yields the spacing of subsequent A-scan data points to

$$\Delta z = \frac{2\pi}{N\Delta\kappa_\zeta}.$$

Assuming a Hann-apodized spectrum, the axial resolution will thus be twice as large [25], resulting in

$$\sigma_z = \frac{4\pi}{\left|\kappa_{\zeta,\max} - \kappa_{\zeta,\min}\right|}.$$

27.4.3.2 Lateral Resolution

The lateral resolution is determined by the numerical aperture of the setup in analogy to classical imaging systems.

In lensless holoscopy the aperture is given by the sensor area. The NA can be computed from the distance of the camera to the sample (see also Fig. 27.7). However, distance cannot be decreased arbitrarily to increase NA, as interference fringe frequencies become higher and can no longer be resolved and physically the space between camera and sample needs to be sufficiently large to allow superposition with the reference wave.

For the setup using imaging optics (Fig. 27.2b), the resolution is determined by the circular aperture of the objective.

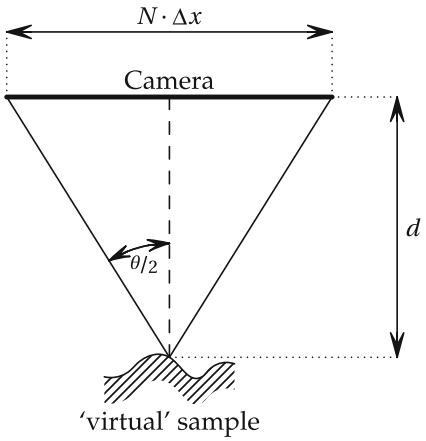

Fig. 27.7 Definition of the numerical aperture of a lensless holoscopy setup

27.4.4 Numerical Complexity and Execution Speed

For one focal volume the simple reconstruction by Eq. 27.11 requires the propagation of each acquired hologram to a certain depth. For a single propagation of an image array of size $N_X \times N_Y$, two 2D Fourier transforms of size $2N_X \times 2N_Y$ are required, if zero padding is applied to prevent circular convolution artifacts. One transform is needed to go from position space to Fourier space and one to go back. Consequently, for N holograms at different wavelengths, a total of $2N$ two-dimensional Fourier transforms of size $2N_X \times 2N_Y$ are required. For each lateral position, a one-dimensional Fourier transform of size N needs to be performed afterwards to gain depth information, i.e., additional $N_X \times N_Y$ Fourier transforms calculate the final data. In total, $2N$ Fourier transforms of $2N_X \times 2N_Y$ arrays plus $N_X \times N_Y$ one-dimensional Fourier transforms of N data points are needed for each focal volume. The overall time complexity C_{SL} of a simple reconstruction with a single focus layer is of the order of

$$C_{SL} \sim \mathcal{O}(8NN_XN_Y \cdot \log(4N_XN_Y) + NN_XN_Y \cdot \log N).$$

The one-step reconstruction of the complete volume by Eq. 27.16 reduces the computational complexity significantly. It also requires N two-dimensional Fourier transforms of size $2N_X \times 2N_Y$ to bring the images to Fourier space and $2N_X \times 2N_Y$ one-dimensional Fourier transforms of size N to gain depth information. For the complete volume, this is $4\times$ more than for the reconstruction of only one focal volume by propagation and Fourier transform, because the Fourier transform to get the depth information is performed on the spatial frequency spectrum and not in the position space of the refocused planes. Because of the Hermitian symmetry, i.e., the same information content in positive and negative frequencies,

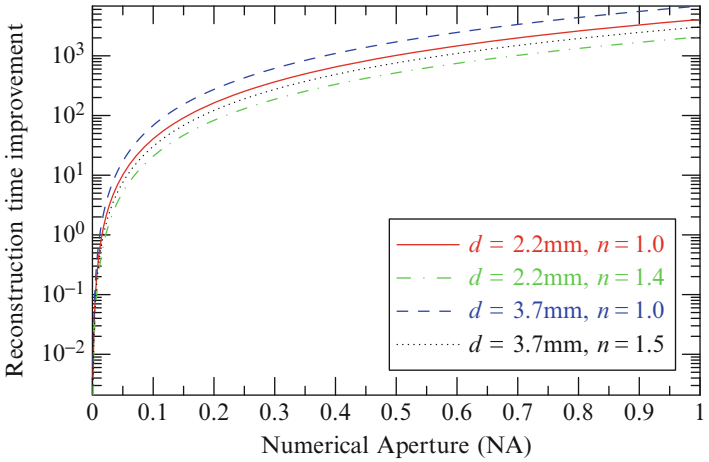

Fig. 27.8 Approximate increase of the reconstruction speed by using the one-step algorithm of Eq. 27.16 instead of sequentially applying Eq. 27.11 for multiple focal volumes. The increase of speed depends on measurement depth d and the refractive index n of the sample

the inverse transform from 2D Fourier space to position space only requires $N/2 + 1$ two-dimensional Fourier transforms of size $2N_X \times 2N_Y$, which is about half the amount required for the propagation and Fourier transform approach. The overall time complexity C_{FV} of the one-step reconstruction for the full volume can thus be written as

$$C_{FV} \sim \mathcal{O}(6NN_XN_Y \cdot \log(4N_XN_Y) + 4NN_XN_Y \cdot \log N).$$

On a quad-CPU Opteron 6150, a reconstruction of a dataset of 1,024 holograms with 1,024 × 1,024 pixel by Eq. 27.11 of one focal volume took about 22 s, whereas a reconstruction of the complete volume by Eqs. 27.12 or 27.16 took about 40 s, i.e., about twice the time required for the reconstruction of the focal volume. For the lensless setup with 0.05 NA shown in Fig. 27.2a, the confocal parameter (i.e., twice the Rayleigh length) was $2z_R = 220$ µm and the measurement depth of 3.7 mm was achieved (see Fig. 27.9). Thus, a data set would need 17 reconstructions of different focal volume for an overall diffraction limited resolution in air. Hence, the one-step reconstruction of the complete volume offered a speedup of about 8.5 times for this low NA setup. For the scattering sample in Fig. 27.9 with refractive index $n = 1.5$ this speedup is reduced by a factor $\zeta = 1/n^2 \approx 0.44$, because the focal range is increased by a factor n and the effective total measurement depth is the optical depth which is reduced by a factor $1/n$. The full reconstruction is still about three to four times faster in this case.

For the high NA measurements shown in Fig. 27.12 in the next chapter, the confocal parameter was reduced to about $2z_R = 30$ µm and the measurement depth

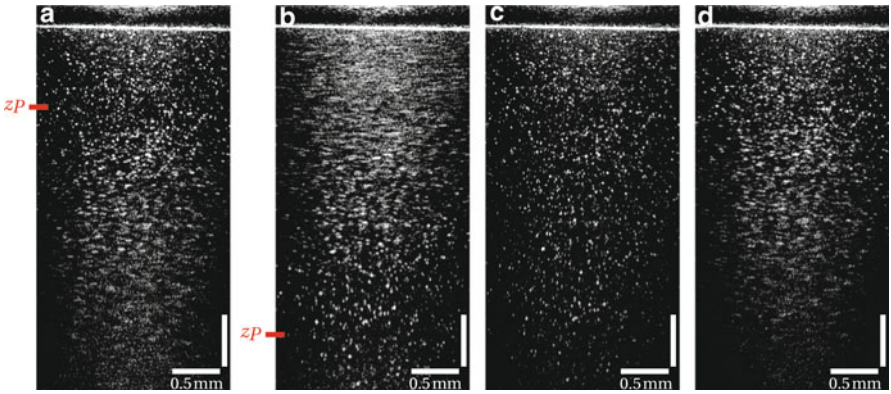

Fig. 27.9 B-scans from a reconstructed volume of a scattering phantom [26] consisting of multiple point scatterers. (**a**) and (**b**) result from reconstructions of the focal volume according to Eq. 27.11 at two different propagation depths z_P, which correspond to virtual numerical foci of the reconstruction. Outside the focal regions the lateral resolution is degraded. The confocal parameter was 220 µm. (**c**) One-step reconstruction of the complete volume by Eq. 27.16 with the correct refractive index $n = 1.5$ ($\zeta = 0.44$). No lateral resolution degradation is visible. The loss of intensity in depth is caused only by a sensitivity roll-off due to the limited instantaneous coherence length of the laser source. (**d**) One-step reconstruction of the complete volume by Eq. 27.12 without correcting for the increased index of refraction in the sample volume (i.e., $n = 1.0$ and thus $\zeta = 1$). Focus degradation is worse than in the reconstruction for a single focal volume. This is due to the fact that the former corresponds to $\zeta = 1$ and the latter to $\zeta = 0$. The correct value of $\zeta = 0.44$ is thus closer to the reconstruction of a single plane by Eq. 27.11

was about 2.2 mm. Therefore, in air about 70 reconstructions are required with Eq. 27.11. With a refractive index of about $n = 1.4$, the volume can be reconstructed about 15 times faster using the one-step reconstruction.

For higher lateral resolution, this factor will increase further. The actual gain of time for the reconstruction depends on the ratio of confocal parameter $2z_R$ to the measurement depth d of the system and the refractive index n of the sample. The expected improvements in reconstruction speed are shown in Fig. 27.8. At high NAs near unity, the one-step reconstruction is expected to be about three orders of magnitude faster.

27.5 Examples of Holoscopy

27.5.1 Lensless Holoscopy

Holoscopic imaging of a scattering sample which contains $300 - 800$ nm sized iron oxide nanoparticles embedded in polyurethane resin [26] demonstrated the effectiveness of the technique. The images shown in Fig. 27.9 were acquired at NA 0.05 using a Mikrotron EoSens CMOS camera and a Superlum Broadsweeper BS840 with a tuning range of 50 nm centered at 848.5 nm. It demonstrates the

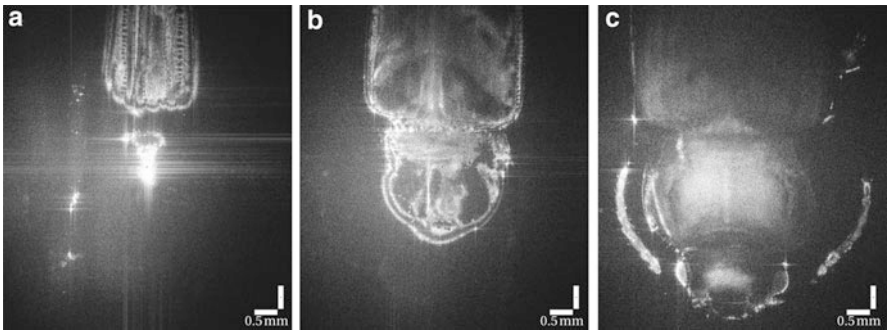

Fig. 27.10 En face tomographic images of a bug at three different layers. The image cube was acquired by holoscopy. For reconstruction the one-step algorithm described by Eq. 27.16 was used. Internal structures of the bug can clearly be seen

simple reconstruction according to Eq. 27.11, which propagates the object field from the camera plane to one depth in the sample first and then applies the axial Fourier transform. This gave high lateral resolution only in the focal range around the reconstruction depth z_P (Fig. 27.9a, b). Applied to the same dataset, the one-step reconstruction by Eq. 27.16 obtained a volume which images the nanoparticles sharply in all layers spanning a depth of more than 30 Rayleigh lengths (Fig. 27.9c). However, the index of refraction of the sample volume needs to be incorporated correctly. A one-step reconstruction of a complete volume when falsely assuming an index of refraction of air (see Eq. 27.12) reconstructed only a limited depth range correctly (Fig. 27.12d). In this phantom, having a refractive index of about $n = 1.5$, the simple reconstruction shows better results than the one-step reconstruction with $n = 1.0$, as the actual $\zeta = 1/n^2 = 0.44$ is closer to 0 than to 1.0.

Holoscopy has also been demonstrated for more complex biological structures. In Fig. 27.10 en face images of a bug at three different depths are shown. The image quality of structures from within the bug is degraded because of refraction on the outer shell, caused by its nonhomogeneous refractive index. The outer shell of the bug however is sharply imaged within all depth layers.

In vivo images of a fingertip have been acquired at an acquisition rate of about 7×10^6 A - scans/s, which is comparable to the fastest OCT measurements up to date. The results are shown in Fig. 27.11. Imaging quality is sufficient to clearly visualize the ducts of the sweat glands.

27.5.2 High-Resolution Holoscopy

The advantage of holoscopy becomes more significant for higher NA since the Rayleigh length drops quadratically with the NA. So far, holoscopy has been demonstrated with NA of up to 0.14 using a 5× Mitutoyo Plan-IR microscope

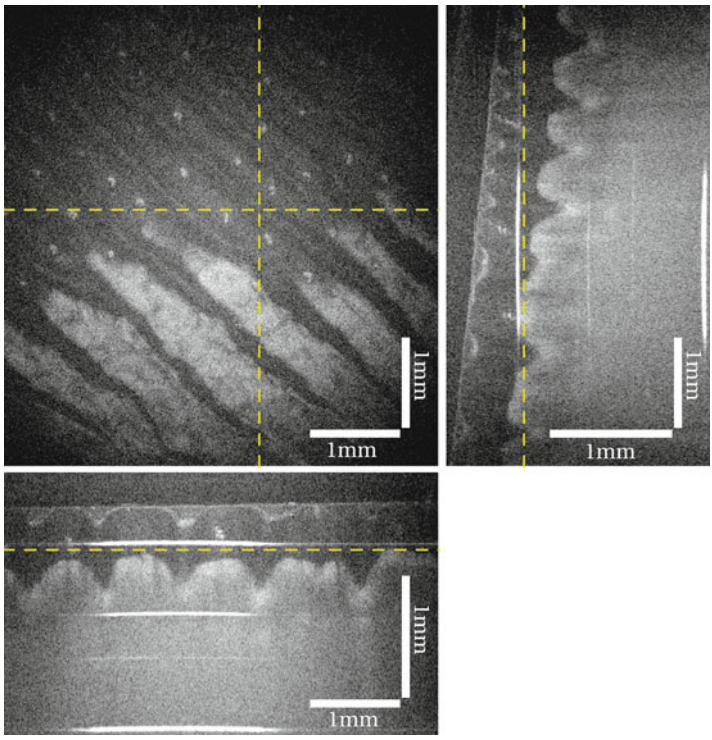

Fig. 27.11 Volumetric measurement of a fingertip acquired using holoscopy. The acquisition speed of 7, 000 frames/s corresponds to about 7×10^6A - scans/s

objective, a Basler ACE acA2040-180 km camera, and a Superlum Broadsweeper BS840-1 with a tuning range of 82 nm centered at 841 nm. A Mach-Zehnder Interferometer as shown Fig. 27.2b was used. B-scans from reconstructed volumes demonstrated that also for more complex structures at NA 0.14 a one-step reconstruction by Eq. 27.16 is possible while maintaining lateral resolution over the depth (Fig. 27.12). However, additional artifacts were introduced by reflections of the microscope objective.

27.5.3 Artifacts in Holoscopic Imaging

Due to the lack of a confocal gating, holoscopic imaging suffers from numerous artifacts, either because of additional light reaching the detector which cannot be filtered properly or because the reconstruction process is not capable to re-obtain the actual scattering structures. Some artifacts occur for both, confocal and scanning OCT, but effect the images differently. Other artifacts are restricted to either one of the two imaging technologies.

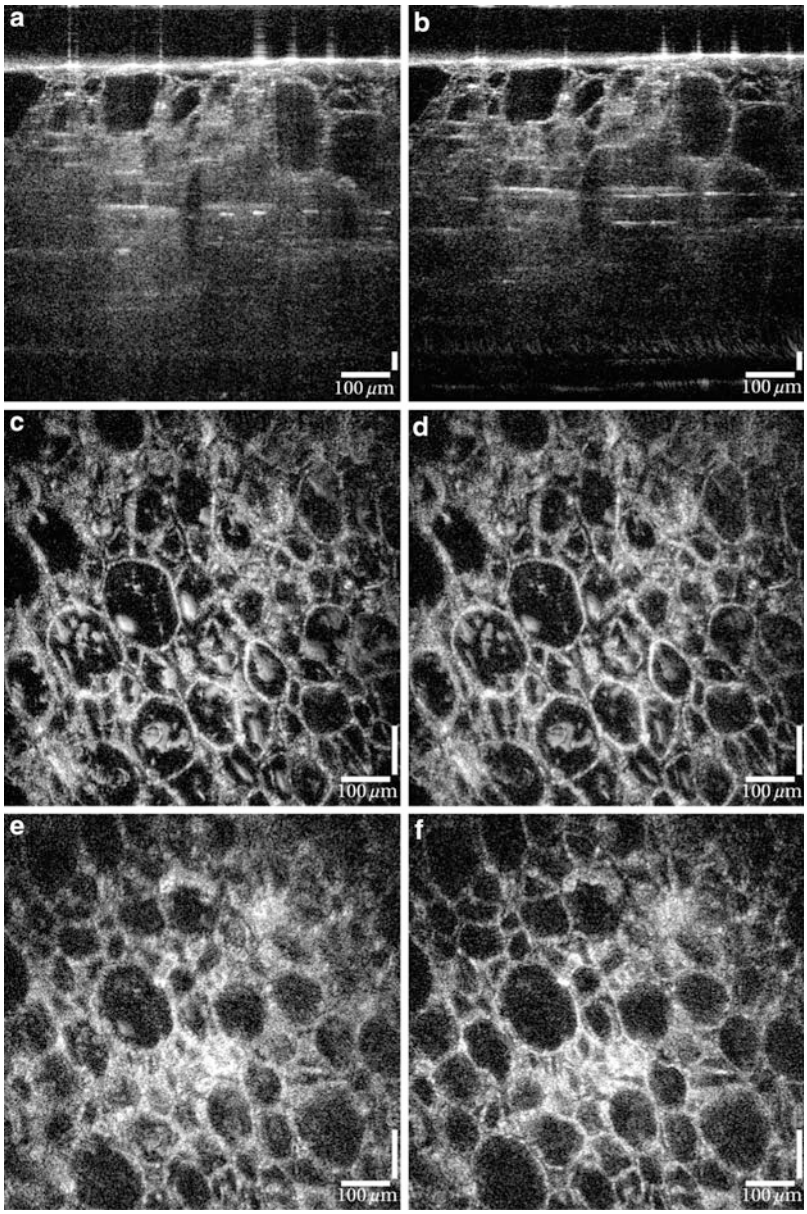

Fig. 27.12 Holoscopic images of a grape acquired at 0.14 NA using the Mach-Zehnder interferometer with additional microscope objective. Simple reconstruction by propagating the field to one focal plane (*left column*) is compared with the one-step reconstruction of the complete volume (*right column*). (**a**) B-scan of the simple reconstruction of a focal volume according to Eq. 27.11. (**b**) B-scan of the one-step reconstruction according to Eq. 27.16. (**c**) En face image of the focal plane of the simple reconstruction. (**d**) En face image of the same plane in the one-step reconstruction. (**e**) En face image of the simple reconstruction in an optical distance of about 160 µm

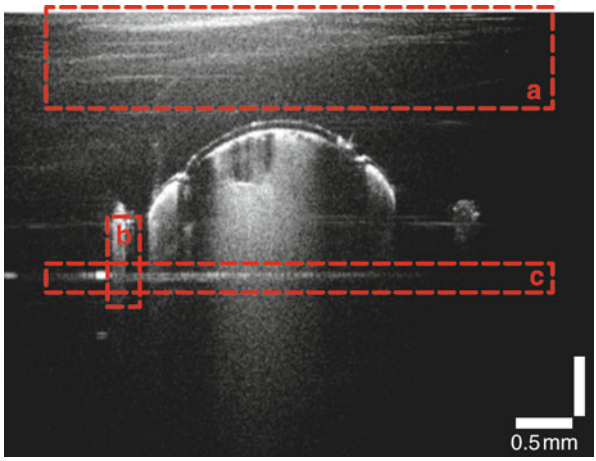

Fig. 27.13 B-scan of the bug shown in Fig. 27.10 with artifacts caused by holoscopic imaging. Autocorrelation terms create an increased noise floor in the upper part of the image (**a**). Multiple scattering of photons causes wrong depth assignment of the structures resulting in a bright shadow beneath strongly scattering surfaces (**b**). Reflecting or scattering parallel surface from within the setup causes horizontal lines in the B-scans (**c**)

27.5.3.1 Autocorrelation Artifacts

Interference of sample radiation originating from various depths within the sample (autocorrelation terms) causes additional signals in the tomographic data as shown in the area (*A*) of Fig. 27.13. In off-axis holoscopy (Fig. 27.2b), these artifacts can be filtered. Since the ratio between sample and reference light cannot be adjusted arbitrarily in on-axis, lensless holoscopy, autocorrelation artifacts can be quite dominant. The autocorrelated signals are not to be imaged sharply, making them appear mostly as an additional noise floor with speckles. This is in contrast to FD-OCT where the imaging structures are often clearly identified as twin images.

27.5.3.2 Multiple Scattering

Multiple scattering is a major problem in holoscopy. For the images shown, artifacts of multiply scattered photons are rather neglectable. In a single focus layer reconstruction as described in Sect. 27.4.1, the multiple scattered photons will in most scenarios be assigned to a higher depth, but their lateral origin will be correct. This can be seen in Fig. 27.13 in the area marked by (*B*) which shows a bug's antenna. Strongly scattering structures therefore appear to have a shadowlike vertical structure below them.

27.5.3.3 Horizontal Lines

In Fig. 27.13 a horizontal line (*C*) is shown, which originates from reflecting interfaces within the setup. To minimize these effects, parallel plates and surfaces perpendicular to the optical axis should be avoided, and the number of optical

Fig. 27.12 (continued) from the virtual focus shows deteriorated resolution (**f**) En-face image of a one-step reconstruction of the same layer. No degradation of the lateral resolution is observed. The confocal parameter was 28 µm. Remaining artifacts arose because of reflections from within the setup

components in the setup should be kept small. Tilting of optical components and using an off-axis holoscopy suppress these artifacts significantly.

27.6 Conclusion

Holoscopy enables an increased depth of focus in terms of uncompromised sensitivity and resolution. So far, measurements with an extension of the focal region by a factor of about 15 were demonstrated, without reaching the theoretical limit. The benefits of holoscopy become especially visible at high NA, as it allows to preserve the Fourier-domain SNR advantage even in this range.

Current implementations of holoscopy face many challenges: reduced image quality caused by artifacts, incoherent background and multiple scattered photons, and lack of cameras and suitable tunable light sources. If these problems are solved, higher sensitivity and acquisition speed will make holoscopy a clinically useful alternative to full-field time-domain OCT (see, e.g., [27–29]), extended focus optical coherence microscopy (OCM) [30, 31], and μOCT [32].

References

1. B. Považay, A. Unterhuber, B. Hermann, H. Sattmann, H. Arthaber, W. Drexler, Full-field time-encoded frequency-domain optical coherence tomography. Opt. Express **14**, 7661–7669 (2006)
2. T. Bonin, G. Franke, M. Hagen-Eggert, P. Koch, G. Hüttmann, In vivo Fourier-domain full-field OCT of the human retina with 1.5 million A-lines/s. Opt. Lett. **35**, 3432–3434 (2010)
3. D. Gábor, *Holography, 1948-1971: in Nobel Lectures in Physics (1971–1980)*. World Scientific Publishing Co. Pte. Ltd, Singapore, 1992)
4. U. Schnars, W. Jueptner, *Digital Holography: Digital Hologram Recording, Numerical Reconstruction, and Related Techniques* (Springer, Berlin Heidelberg, 2010)
5. M. Kim, *Digital Holographic Microscopy: Principles, Techniques, and Applications*. Springer Series in Optical Sciences (Springer, New York, 2011)
6. T.S. Ralston, D.L. Marks, P. Scott Carney, S.A. Boppart, Interferometric synthetic aperture microscopy. Nat. Phys. **3**, 129–134 (2007). doi:10.1038/nphys514
7. P.S. Carney, B.J. Davis, D.L. Marks, T.S. Ralston, S.A. Boppart, Interferometric synthetic aperture microscopy, in *Adaptive Optics: Analysis and Methods/Computational Optical Sensing and Imaging/Information Photonics/Signal Recovery and Synthesis Topical Meetings on CD-ROM* (Optical Society of America, 2007), p. CTuC2
8. D.L. Marks, T.S. Ralston, S.A. Boppart, P.S. Carney, Inverse scattering for frequency-scanned full-field optical coherence tomography. J. Opt. Soc. Am. A **24**, 1034–1041 (2007)
9. T.S. Ralston, D.L. Marks, P.S. Carney, S.A. Boppart, Real-time interferometric synthetic aperture microscopy. Opt. Express **16**, 2555–2569 (2008)
10. S.A. Boppart, T.S. Ralston, D.L. Marks, P.S. Carney, Interferometric synthetic aperture microscopy, in *Optical Fiber Communication Conference and Exposition and the National Fiber Optic Engineers Conference* (Optical Society of America, 2008), p. OThV1
11. B.J. Davis, D.L. Marks, T.S. Ralston, P.S. Carney, S.A. Boppart, Interferometric synthetic aperture microscopy: computed imaging for scanned coherent microscopy. Sensors **8**, 3903–3931 (2008)

12. P. Massatsch, F. Charrière, E. Cuche, P. Marquet, C.D. Depeursinge, Time-domain optical coherence tomography with digital holographic microscopy. Appl. Opt. **44**, 1806–1812 (2005)
13. M.K. Kim, Wavelength-scanning digital interference holography for optical section imaging. Opt. Lett. **24**, 1693–1695 (1999)
14. A.V. Zvyagin, Fourier-domain optical coherence tomography: optimization of signal-to-noise ratio in full space. Opt. Commun. **242**, 97–108 (2004). doi:10.1016/j.optcom.2004.07.060
15. D.V. Shabanov, G.V. Geliknov, V.M. Gelikonov, Broadband digital holographic technique of optical coherence tomography for 3-dimensional biotissue visualization. Laser Phys. Lett. **6**, 753–758 (2009)
16. D. Hillmann, C. Lührs, T. Bonin, P. Koch, G. Hüttmann, Holoscopy—holographic optical coherence tomography. Opt. Lett. **36**, 2390–2392 (2011)
17. G.L. Franke, D. Hillmann, T. Claussen, C. Luhrs, P. Koch, G. Huttmann, High resolution holoscopy. Proc. SPIE **8213**, 821324 (2012)
18. D. Hillmann, G. Franke, C. Lührs, P. Koch, G. Hüttmann, Efficient holoscopy image reconstruction. Opt. Express **20**, 21247–21263 (2012)
19. J. Goodman, *Introduction to Fourier Optics*. (Roberts & Co., Englewood, 2005)
20. G.C. Sherman, Application of the convolution theorem to Rayleigh's integral formulas. J. Opt. Soc. Am. **57**, 546–547 (1967)
21. M. Born, E. Wolf, A. Bhatia, P. Clemmow, D. Gábor, A. Stokes, A. Taylor, P. Wayman, W. Wilcock, *Principles of Optics: Electromagnetic Theory of Propagation, Interference and Diffraction of Light* (Cambridge University Press, Cambridge, 2010)
22. D. Potts, G. Steidl, M. Tasche, Fast Fourier transforms for nonequispaced data: a tutorial, in *Modern Sampling Theory: Mathematics and Applications*, ed. by J. Benedetto, P.J.S.G. Ferreira (Birkhäuser, Boston, 2001), pp. 247–269. chap. 12
23. D. Hillmann, *Holoscopy* (Springer Vieweg, Wiesbaden, 2014)
24. W. Drexler, J. Fujimoto, *Optical Coherence Tomography: Technology and Applications*. Biological and Medical Physics, Biomedical Engineering (Springer, Berlin, 2008)
25. F.J. Harris, On the use of windows for harmonic analysis with the discrete Fourier transform. Proc. IEEE **66**, 51–83 (1978)
26. P.D. Woolliams, R.A. Ferguson, C. Hart, A. Grimwood, P.H. Tomlins, Spatially deconvolved optical coherence tomography. Appl. Opt. **49**, 2014–2021 (2010)
27. A. Dubois, L. Vabre, A.-C. Boccara, E. Beaurepaire, High-resolution full-field optical coherence tomography with a Linnik microscope. Appl. Opt. **41**, 805–812 (2002)
28. A. Dubois, K. Grieve, G. Moneron, R. Lecaque, L. Vabre, C. Boccara, Ultrahigh-resolution full-field optical coherence tomography. Appl. Opt. **43**, 2874–2883 (2004)
29. K. Grieve, A. Dubois, M. Simonutti, M. Paques, J. Sahel, J.-F.L. Gargasson, C. Boccara, In vivo anterior segment imaging in the rat eye with high speed white light full-field optical coherence tomography. Opt. Express **13**, 6286–6295 (2005)
30. R.A. Leitgeb, M. Villiger, A.H. Bachmann, L. Steinmann, T. Lasser, Extended focus depth for Fourier domain optical coherence microscopy. Opt. Lett. **31**, 2450–2452 (2006)
31. L. Liu, C. Liu, W.C. Howe, C.J.R. Sheppard, N. Chen, Binary-phase spatial filter for real-time swept-source optical coherence microscopy. Opt. Lett. **32**, 2375–2377 (2007)
32. L. Liu, J.A. Gardecki, S.K. Nadkarni, J.D. Toussaint, Y. Yagi, B.E. Bouma, G.J. Tearney, *Imaging the subcellular structure of human coronary atherosclerosis using micro-optical coherence tomography*, Nat. Med. 17, 1010–1014 (2011)

Optical Coherence Microscopy

28

Aaron D. Aguirre, Chao Zhou, Hsiang-Chieh Lee,
Osman O. Ahsen, and James G. Fujimoto

Keywords
Optical coherence microscopy • Cellular imaging • Endoscopy • Confocal microscopy • Femtosecond laser

28.1 Introduction

Cellular imaging of human tissues remains an important advance for many clinical applications of optical coherence tomography (OCT). Current diagnosis and management of many human diseases, including cancers and various inflammatory and autoimmune conditions, depend upon biopsy and histopathologic analysis of cellular and subcellular features. Imaging cells with traditional OCT methods, however, has not been routinely possible due to the limited transverse resolution of such techniques.

The term optical coherence microscopy (OCM) refers to optical coherence tomography methods with high transverse spatial resolution. OCM techniques use higher numerical aperture focusing than conventional OCT and therefore typically generate *en face* rather than cross sectional images in order avoid the depth of field

A.D. Aguirre (✉)
Massachusetts General Hospital, Boston, MA, USA

Department of Electrical Engineering and Computer Science and Research Laboratory of Electronics, Massachusetts Institute of Technology, Cambridge, MA, USA
e-mail: aaguirre@alum.mit.edu

C. Zhou
Department of Electrical Engineering and Computer Science and Research Laboratory of Electronics, Massachusetts Institute of Technology, Cambridge, MA, USA

Department of Electrical and Computer Engineering, Lehigh University, Bethlehem, PA, USA

H.-C. Lee • O.O. Ahsen • J.G. Fujimoto
Department of Electrical Engineering and Computer Science and Research Laboratory of Electronics, Massachusetts Institute of Technology, Cambridge, MA, USA

© Springer International Publishing Switzerland 2015

W. Drexler, J.G. Fujimoto (eds.), *Optical Coherence Tomography*,
DOI 10.1007/978-3-319-06419-2_29

limitation in the cross-sectional plane. Combining high transverse resolution with coherence-gated detection, OCM enables cellular imaging in human tissues without the use of extrinsic contrast agents. Coherence gating dramatically reduces detection of unwanted scattered light, improving image contrast and enabling imaging to greater depths than possible with confocal microscopy. This has made OCM a promising approach for cellular resolution imaging of human pathologies without the need for conventional tissue staining and histologic processing. Coherence gating in OCM also enables the use of lower numerical aperture focusing than required for classic confocal microscopy, which makes OCM a key technology to enable cellular level, internal body imaging in endoscopic applications. Beyond biological specimens, OCM techniques have also found application for imaging of novel materials, which require non-invasive, non-destructive high resolution microscopic analysis.

Two general approaches for OCM have been described. The point-scanning, or "flying spot," approach is based directly upon the principle of confocal microscopy where the scattering medium is illuminated at a single point, which is subsequently relay imaged to a pinhole point detector. The pinhole imposes a spatial gate on photons returning from the sample and serves to preferentially reject light from outside the focal plane. Two-dimensional *en face* images are created by raster scanning the point focus. Traditional fiber-optic OCT systems are inherently confocal and implement the point-scanning technique. As the transverse spot size is reduced in the OCM limit, the confocal axial response becomes comparable to the axial coherence gate and the combined confocal and coherence gating creates both important advantages and challenges. In contrast to point-scanning OCM systems, the second approach to OCM involves full-field illumination and detection. The full-field technique is similar to conventional white-light interference microscopy and produces *en face* images using parallel illumination and detection. Full-field OCM/OCT techniques typically use CCD based detection and have achieved impressive image quality. The full-field methods have the advantage of simplicity and highly parallel data acquisition, but because of their inherent sensitivity to motion, in vivo imaging is challenging. The full-field approaches are covered in detail in other chapters in this book.

This chapter focuses on point-scanning, confocal OCM implementations, and this approach to optical coherence microscopy is henceforth assumed. The chapter provides an overview of OCM image formation and discusses several of the challenges and advantages of the technique. In addition, system design approaches for high resolution OCM are covered, with a focus on enabling technological developments. Examples of cellular level imaging in human tissues are presented. The capability to visualize cellular structure promises to have important implications for many clinical applications, including optical biopsy and the detection of neoplastic changes.

28.2 Confocal Microscopy

Confocal microscopy was first proposed by Marvin Minsky in the late 1950s [1]. Imaging can be performed in reflectance or fluorescence modes, depending on

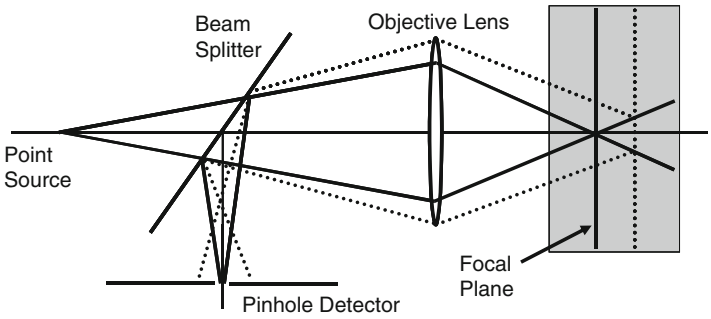

Fig. 28.1 Schematic illustrating the principle of reflectance confocal microscopy

the specific application. Figure 28.1 illustrates the basic principle of confocal microscopy in reflection geometry. A point source illuminates a sample plane through a focusing objective lens. The backscattered light from the focal plane is recollected by the objective lens and focused through a pinhole detector. Unwanted scattered light from outside the focal plane is also collected by the objective, but this light is defocused at the detector and is therefore rejected. The spatial discrimination against out of focus scattered light is known as confocal gating. The combination of focused illumination and spatially filtered detection reduces blurring, increases effective resolution, and improves contrast through improved signal to noise ratio [2]. The single point transverse resolution of a confocal microscope is typically defined as the width of the transverse point spread function. For a focused Gaussian beam, the transverse spot dx can be characterized by the $1/e^2$ radius of the transverse response [3], which is given as

$$dx = \frac{0.46\lambda}{NA} \tag{28.1}$$

The axial response of a confocal microscope to a perfectly reflecting plane at the focus under Gaussian beam assumptions can similarly be described as

$$dz = \frac{1.4n\lambda}{NA^2} \tag{28.2}$$

where dz represents the FWHM of the axial irradiance [4]. As shown, the transverse resolution varies inversely with the numerical aperture (NA) of the objective lens, while the axial resolution or axial sectioning capability of the confocal microscope varies inversely with the square of the NA. Hence, image quality in scattering objects requires the use of high magnification, high-NA objectives. With such high NA lenses, typically NA 0.7–1.2, confocal microscopy systems can achieve 3–5 um axial sectioning capability and better than 1 um transverse resolution [5].

To generate an image in two dimensions, several scanning approaches have been demonstrated, including sample scanning, objective scanning, and beam scanning [3]. The use of laser sources marked a major development in confocal microscopy [6, 7] and enabled high speed, high resolution point scanning systems at multiple wavelengths. Typically, the confocal scanning laser microscope (CLSM) samples an *en face* scan plane by rapidly raster scanning the beam on tissue.

Confocal laser scanning microscopy was demonstrated for in vivo cellular imaging of human tissues at visible wavelengths [4]. Advances in instrumentation and design led to the development of video-rate reflectance systems capable of reliable imaging in clinical applications [4, 8, 9]. These systems offer high power illumination and extension to deeper penetrating wavelengths in the near infrared. Operating at wavelengths of 800 nm and 1,064 nm, the systems provide transverse resolution of 0.5–1 um and axial sectioning capacity of 3–5 um. Confocal reflectance imaging of human skin [9–13], oral mucosa [14], and cervix [15] has demonstrated the capability to image normal and pathologic cellular features in vivo with impressive correlation of confocal images with histology. Commercial versions of the CLSM imaging system now offer new tools for clinical diagnostic applications in dermatology and other specialties where open access to tissue specimens is possible. In addition, endoscope compatible reflectance confocal microscopes are being developed [16, 17].

Using exogenous fluorescence dyes to provide contrast, fluorescence confocal endoscopy has been developed for clinical application in the gastrointestinal tract [4, 18–24]. Excellent in vivo image quality has generated excitement about this technology and has set a standard for reflectance-based endoscopic methods to match. Because excitation of fluorophores is typically performed with visible wavelengths, however, fluorescence confocal imaging has limited penetration depth. In addition, exogenous dyes can have toxicities, which may limit clinical applicability. Reflectance-based, endoscopic confocal or optical coherence microscopy methods that can provide comparable image quality at greater depths, but without the need for exogenous contrast, would therefore be an important advance.

28.3 High Transverse Resolution in Optical Coherence Tomography

Compared with confocal microscopy, conventional optical coherence tomography systems work in the opposite focusing limit. In OCT, the focal spot size is comparatively large because of the need to use relatively low NA lenses in order to preserve a sufficient depth of field for cross sectional imaging. As the NA of the OCT optics increases, the depth of field decreases and signal loss occurs at depths away from the focus. Figure 28.2 compares these focusing limits and their implications for OCT image formation. Images are acquired by setting the focus to a defined position in the tissue and detecting light from different depths by coherence gating, either in the time domain or in the frequency domain. In confocal

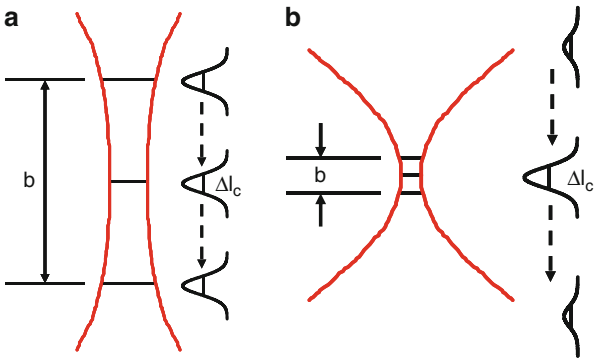

Fig. 28.2 Focusing limits for OCT imaging. Use of a low numerical aperture lens (**a**) preserves depth of field across the entire depth scan while a higher aperture lens (**b**) leads to restricted confocal parameter and signal loss at the edges of the depth scan. Confocal parameter, *b*; Coherence length l_c

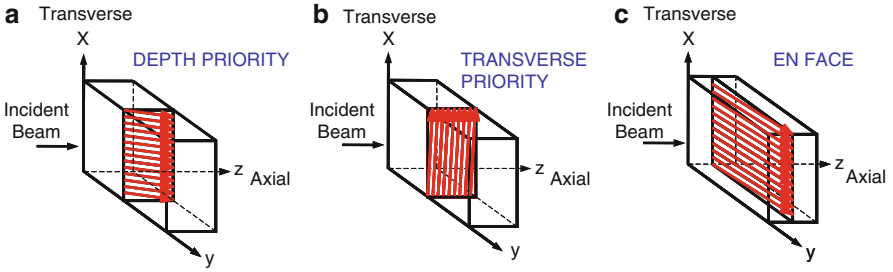

Fig. 28.3 Image scanning protocols for optical coherence tomography

microscopy, the goal is precisely to use high NA focusing to restrict the depth of field, such that light outside of the focal plane is rejected. *En face* images are then formed by rapidly raster scanning the beam.

Several solutions to overcome the depth of field restriction in OCT have been demonstrated in the literature. These methods can be classified into three types according to the image acquisition scan protocol, as illustrated in Fig. 28.3. Depth priority methods maintain the cross-sectional imaging plane of conventional OCT by rapidly acquiring along the depth axis while scanning the transverse beam position at the image frame rate. Transverse priority OCT techniques also scan a cross-sectional plane. In contrast, however, the transverse beam position is scanned to rapidly acquire the transverse axis, while varying the depth axis at the frame rate. The third option is to acquire an *en face* image plane analogous to confocal laser scanning microscopy.

28.3.1 Depth Priority Techniques

One strategy for maintaining high transverse resolution across the image using depth priority scanning is to coordinate the optical focus depth with the depth of the

coherence gate. This approach has been termed focus tracking in the literature and has been used by Schmitt et al. to generate high quality cross-sectional images of human skin with 3 um transverse resolution [25]. Coherence depth scanning was synchronized with focus depth scanning by mounting the reference reflector and the focusing objective on a single translation stage. The disadvantage of this setup is the relatively limited axial scan rates that can be achieved using mechanical translation of the objective. Image acquisition required nearly 30 s for 256 lines. Lexer et al. devised a different scheme for high speed focus tracking based on a novel microscope design that shifts the beam focus through the object without changing the reference path length [26]. Images were acquired of an in vitro human cornea specimen in approximately 1 s with 5 um transverse resolution. The ability to scan the focus without translating the optical path required careful choice of the microscope magnification, which limits overall design flexibility. Other groups have investigated fast focus adjustment using a variable focus micromachined mirror [27, 28] or liquid lens [4, 29, 30].

Typical focus tracking approaches are not readily compatible with high speed, Fourier domain detection OCT techniques. In Fourier domain OCT, backscattered or backreflected light is acquired from all depths simultaneously in the frequency or Fourier domain and axial scan information is subsequently reconstructed using a Fourier transform. Fourier domain OCT methods have been shown to have a significant speed and sensitivity advantage compared with time-domain OCT [31–33]. Two basic Fourier domain implementations have been demonstrated. Spectral/Fourier domain OCT uses a broadband light source and a spectrometer with a line scan camera in the detection arm. Swept source/Fourier domain OCT uses a frequency swept laser source and individual photodiode detectors. In either implementation, depth scanning of the coherence gate is not performed, and it is therefore impossible to perform classic focus-tracking to extend depth of field. The increases in speed and sensitivity, however, have made Fourier domain detection the method of choice for most OCT imaging applications, such as ophthalmology and intravascular imaging [4, 34–36]. Strategies for improving the transverse resolution that are compatible with both time and Fourier domain detection are therefore desirable.

One technique for improving transverse resolution that works for all OCT implementations has been termed C-mode scanning in analogy to ultrasound. This method was demonstrated for OCT by Drexler et al. using an ultrahigh resolution OCT system with 1 um axial $\times$ 3 um transverse resolution [37]. Figure 28.4 presents the concept of C-mode scanning. Multiple OCT images with high axial and transverse resolution were acquired with the focal position set at different depths. The individual images in Fig. 28.4a clearly demonstrate the limited depth of focus. These images were overlapped and fused in Fig. 28.4b to form a single image with extended depth of field. Cellular and subcellular structures in the Xenopus laevis tadpole are visualized. C-mode scanning and image fusion techniques have also been demonstrated for Fourier domain OCT [38, 39]. Like focus-tracking, C-mode scanning still requires translation of the focal position in depth, albeit at a much slower rate. The number of images required scales inversely with the desired transverse resolution. As the focal spot and depth

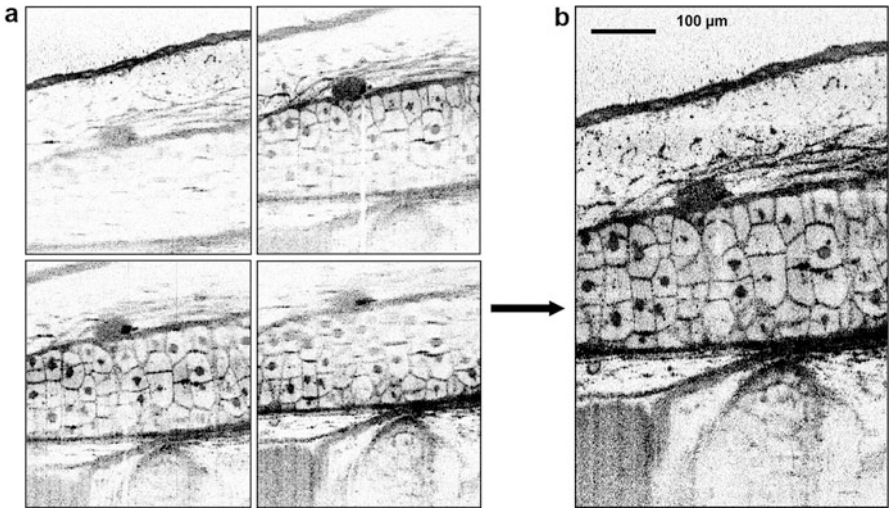

Fig. 28.4 C-mode scanning in optical coherence tomography. Acquisition of individual images with high transverse resolution but restricted depth of field can be reconstructed to form a single image with extended depth of field (Images are reproduced from Drexler et al. [37])

of field for an individual image is reduced, more images are required, which reduces the overall frame rate that can be achieved in the composite image. To address this limitation, Yang et al. developed a multi-focus fiber probe capable of simultaneously generating images at different depths in tissue [40]. In the initial demonstration, four simultaneous images were acquired while maintaining a spot diameter of 9–14 um.

Other techniques are being developed to increase the image depth of field without requiring focus translation or offset. Ding et al. proposed the use of an axicon lens in the OCT probe to generate a long focal volume [41]. In phantom imaging experiments, a 6 mm focusing depth range with 10 um transverse resolution was demonstrated. Axicons produce a cylindrical Bessel beam field distribution with an extended central lobe lying along the optical axis of the lens and are typically used in the form of refracting cone lenses. Unfortunately, there is a trade-off between signal intensity and focusing range since the axicon distributes the focal energy along the focusing range and the central lobe of the Bessel field carries only a fraction of the total power compared with a focused Gaussian beam. In double pass reflection geometry, the squared signal loss limits the utility for high sensitivity imaging in biological tissues. Leitgeb et al. has improved upon the initial axicon demonstration by using the improved sensitivity of spectral domain detection in combination with a modified confocal detection scheme [42]. Transverse resolution of $\sim$1.5 um was maintained over 200 um image range with a sensitivity of 105 dB. Liu et al. have used sample beam apodization as an alternative means to achieve longer depth of field while preserving lateral resolution. In a method they have termed micro-optical coherence tomography (µOCT), a custom designed microscope using beam

apodization is combined with a high speed, ultrahigh resolution spectral/Fourier domain OCT system to achieve resolution of 2 um × 2 um × 1 um with 16 kHz axial scan rate [43]. Striking cellular resolution images of human coronary arteries and human trachea ex vivo have been demonstrated [43, 44]. Techniques such as these are compelling for high speed, cross-sectional cellular imaging and will undoubtedly be the subject of further research and development.

Another approach for increasing transverse resolution without focus adjustment is the use of post-processing algorithms. Image processing is attractive for increasing resolution since the algorithms require minimal to no modifications to existing OCT setups and can be applied offline to large volumes of data. Advanced image processing approaches are enabled by the enhanced phase stability of Fourier domain OCT methods. Ralston et al. have introduced synthetic aperture inverse scattering methods for reducing transverse blurring in OCT images [45]. Depth of field and resolution improvement was demonstrated in scattering phantoms and selected human breast specimens [46]. Adie et al. subsequently showed that computational aberration correction can be combined with synthetic aperture techniques to further image enhancement [47]. The development of high speed processing strategies for real-time imaging [48] and further investigation of these methods in the high NA limit has promise for cellular imaging.

28.3.2 Transverse Priority and En Face Imaging

Transverse priority image acquisition requires rapid transverse scanning of the beam on tissue and slow depth scanning, as illustrated in Fig. 28.3b. Podoleanu et al. suggested transverse priority scanning for performing OCT imaging of the retina and skin [49]. As in C-mode scanning, transverse-priority acquisition enables a slow translation of the focus in tissue at the image frame rate. If focus-tracking is implemented to coordinate the depth scan and focus translation, then no image fusion is required and data collection is very efficient. Cobb et al. demonstrated continuous focus tracking to achieve in vitro OCT images of excised rabbit esophagus at 1 frame/s with transverse resolution of 10.5 um [50]. Transverse scanning was performed at 1.37 kHz using a miniaturized probe, and the reference path length was adjusted to compensate for index of refraction path length shifts produced by the air-tissue interface.

To date, *en face* imaging has proven to be the most robust approach for achieving fine enough transverse resolution for cellular imaging in scattering tissues. In the *en face* plane, the position of the coherence gate can be matched to the position of the optical focus while the beam is raster scanned in two transverse dimensions on the sample. In this manner, high speed focus tracking methods are not required and the image acquisition rate is limited only by the speed of the XY scanner. Furthermore, high NA can be used to achieve high axial and transverse resolutions, in the confocal limit. The implementation of *en face* optical coherence microscopy was first demonstrated by Izatt and colleagues [51], although it has a history in the development of confocal interference microscopes [52–56]. Izatt and others

demonstrated that broadband coherence gating can significantly enhance the imaging depth of conventional confocal microscopy [51, 57, 58]. Subsequently, Izatt et al. showed that *en face* OCM could generate high quality images of cellular features deep below the surface in human gastrointestinal tissues [59]. In vivo *en face* optical coherence tomography was implemented for imaging in the skin and retina, although systems were limited to relatively low transverse resolution and were not capable of visualizing cellular features [49, 60]. In comparison, the development of *en face* optical coherence microscopy for in vivo cellular imaging applications has been relatively slow. In part, this is related to the numerous exciting developments in OCT imaging, which have spread the efforts of researchers across many fronts. In addition, however, OCM technology development for cellular imaging presents unique challenges and requires additional complexity compared with other OCT methods. The remainder of this chapter is devoted to discussing the challenges and the advantages of *en face* OCM imaging and to describing progress toward in vivo cellular imaging applications.

28.3.3 *En Face* Imaging in the Time and Fourier Domain

En face OCM systems based on time domain and Fourier domain detection techniques have both been developed and will be detailed in this chapter. Given the dramatic speed advantages of Fourier domain versus time domain OCT for cross-sectional imaging, it is worth discussing the relative performance of the two approaches for *en face* imaging. For imaging in the *en face* plane, time domain detection approaches can actually have an advantage in terms of imaging speed compared with Fourier domain detection. This results from precisely the same property of Fourier domain detection that creates the sensitivity advantage for cross-sectional imaging. Using spectral/Fourier domain detection or swept-source/Fourier domain detection, signals from multiple depths are detected simultaneously. In order to acquire an *en face* image, an entire three-dimensional volume must effectively be acquired. This places a tremendous demand upon the Fourier-domain OCT system axial line rate and data processing capabilities in order to achieve high frame rates in the *en face* plane. For a typical image of 500 × 500 pixels, acquisition speeds of 8 frames/s require an axial scan rate of two million axial lines per second. This is beyond the specifications of standard spectral/Fourier domain or swept source/Fourier domain systems reported in the literature. For spectral/Fourier domain systems with line rate of 29 kHz [34], acquisition of a 500 × 500 scan volume would take over 8 s. Similarly, swept source/Fourier domain systems operating at 15–20 kHz [38, 61, 62] would require 12–17 s for the same volume.

By contrast, time domain OCT imaging systems acquire signals from only a single *en face* plane. Rather than scanning in depth to generate a Doppler frequency for detection, *en face* imaging systems use phase modulation in the reference arm to provide an external carrier [59]. The reference path is set to the focus depth such that only one depth is sampled at any given transverse position. Image acquisition rate is then determined by signal to noise constraints and by the

maximum speed of the XY scanners. In addition, the intrinsic sensitivity advantage of Fourier domain detection vanishes when only a single *en face* plane is of interest. For a given image acquisition time, the increase in line rate required for sampling a three-dimensional volume in Fourier domain detection cancels the sensitivity advantage compared with sampling a single *en face* plane in time domain.

There are, however, significant advantages to performing *en face* OCT and OCM imaging using Fourier domain detection. Sampling of an entire volume can be quite powerful. Within the depth of field allowed by the confocal parameter of the optics, arbitrary *en face* planes can be displayed from the volume or structures can be rendered in three dimensions. In addition, Fourier domain detection provides greatly increased phase stability compared with time domain detection. Choma et al. [63] and Joo et al. [64] demonstrated this property and implemented spectral/Fourier domain phase microscopy using common path interferometer designs. Other OCT/OCM methods including numerical dispersion compensation [65] and spectroscopic OCM [66] have also shown to have advantages in the spectral/Fourier domain.

Importantly, the volumetric nature of the Fourier domain data makes possible computational approaches for aberration correction and compensation of path length variations between reference and sample arm, which are critically important for fiber-optic microscope and endoscope configurations. In addition, the majority of commercial laser scanning confocal microscopes have a variation of the optical path length as the beam is scanned over the field of view. This delay variation with scanning is caused by optical designs which use paired galvanometer scan mirrors, where the mirrors are not located precisely at the telecentric scan planes. This has prevented the integration of OCM using time domain detection with widely available commercial microscopes, since it is difficult to match the coherence and confocal gates across the field of view as the beam is scanned. In addition, with fiber-optic sample arm probes, manipulation and stretching of the fiber leads to small path length changes that can degrade signal. Fourier domain OCM systems, which acquire a volumetric image around the zero path delay, can allow pixel-by-pixel optimization of path-delay variation over the field of view.

Ultrahigh imaging speeds for Fourier domain OCM are also becoming available, particularly for swept source/Fourier domain imaging. Axial line rates of up to 5.2 MHz have been demonstrated using Fourier-domain modelocked (FDML) lasers [67] and up to 1 MHz using vertical cavity surface emitting lasers (VCSEL) [68, 69]. As imaging speeds for *en face* Fourier domain OCM continue to improve, the advantages of these methods over time domain techniques will become more important for future in vivo imaging applications.

28.4 Combined Confocal and Coherence Gating in OCM

OCM utilizes high NA optics together with broadband light sources to reject unwanted scattered light using both confocal gating and coherence gating. To understand how these two mechanisms interact, consider the detected heterodyne signal in a typical time domain OCM system. An equivalent derivation can also be

shown for Fourier domain systems. In the time domain system, light from the low coherence light source is split between a reference arm and a sample arm. The reference and sample reflectivities are denoted R_r and R_s, respectively. A wavelength dependent phase delay ϕ (ω,t) can be imparted by a reference phase modulator. Light returning from the sample and the reference path interferes at a photodetector. Ignoring the transverse dependence of the interfering electric fields, the time averaged photocurrent at the detector can be written as [70]

$$i_D = \left\langle \frac{\eta e}{h\nu} \frac{|E_R + E_S|^2}{2\eta_f} \right\rangle \tag{28.3}$$

where η is the detector quantum efficiency, e is the electronic charge, $h\nu$ is the photon energy and η_f is the intrinsic impedance of the fiber core material. The detector response time is taken to be much longer than the coherence time for a low-coherence source but much shorter than the heterodyne signal beat oscillations. For a polychromatic, low-coherence source, the oscillating component of the heterodyne signal depends on the sum of the interference due to monochromatic plane waves and can be determined by integration of the cross-spectral interference term over the bandwidth of the light source. Ignoring the sample arm confocal response and assuming pure phase delay scanning from the reference arm modulator, the heterodyne photocurrent can then be written in terms of the optical frequency ω and center frequency ω_0 as

$$\begin{aligned} i_D(\Delta l) &\propto R_R R_S \left\{ F^{-1}[S_o(\omega)] \right\} \cos\left(\omega_o \Delta t_p\right) \\ &= R_R R_S G_o \left(\frac{2\Delta l}{v_g}\right) \cos\left[\frac{2\omega_o \Delta l}{v_p} + \phi(\omega_o, t)\right] \end{aligned} \tag{28.4}$$

where

$$v_p = \frac{2\Delta l}{\Delta \tau_p} \tag{28.5}$$

and

$$v_g = \frac{2\Delta l}{\Delta \tau_g} \tag{28.6}$$

describe the phase velocity v_p and group velocity v_g in terms of the phase delay $\Delta\tau_p$, group delay $\Delta\tau_g$, and the difference in path length $\Delta l = l_S - l_R$ between the sample and reference arms. The source power spectrum $S_o(\omega)$ is related to the autocorrelation $G_o(\Delta\tau_g)$ by the Fourier transform with respect to the group delay. The autocorrelation is a measure of the degree of temporal coherence of the source. Using the concept of the time-bandwidth product in Fourier transform theory, it is

clear that the width of the interference signal envelope decreases for larger bandwidth or shorter coherence length light sources. In the case of a Gaussian light source spectral distribution, the full width at half maximum (FWHM) of the interference signal in free space can be shown to relate to the center wavelength λ_0 and spectral bandwidth $\Delta\lambda$ as [70]

$$\Delta l_{FWHM} = \frac{2\ln 2}{\pi}\left(\frac{\lambda_0^2}{\Delta\lambda}\right) \tag{28.7}$$

This expression is typically used for the specification of the coherence gate or axial resolution of a low-coherence interferometry system.

Izatt et al. described the heterodyne signal in OCM by incorporating a sample reflection in confocal geometry [59]. The influence of the sample arm confocal microscope is determined by the convolution of the field reflectivity function $R_S(x, y, z)$ with the confocal impulse response $[h_I(x, y, z)]^2$. The appropriate confocal point spread function for a fiber-based microscope has been described by Gu et al. [71]. For an axially distributed reflectivity that is present in scattering media, the heterodyne signal can be written as an integral over the sample arm path length l_S. Replacing R_S in Eq. 28.4 with the confocal response and integrating over the sample path, the heterodyne current becomes

$$i_D(\Delta l) \propto \int_{-\infty}^{\infty} dl_S R_R \left[R_S(l_S) \otimes [h_I(l_S)]^2\right] G_o\left(\frac{2\Delta l}{v_g}\right) \cos\left[\frac{2\omega_o \Delta l}{v_p} + \phi(\omega_o, t)\right] \tag{28.8}$$

where the (x,y) dependence of R_s and h_I have been ignored for simplicity. The heterodyne component is the convolution of the sample arm confocal response with the carrier dependent source autocorrelation term. For a single scatterer at a depth location l_{s0} with reflectivity $R_s(l_{s0})$, the heterodyne current reduces to [59]

$$i_D(\Delta l) \propto R_R R_S(l_{S0}) \sqrt{I_C(l_{S0})} G_o\left(\frac{2(l_{S0} - l_R)}{v_g}\right) \cos\left[\frac{2\omega_o(l_{S0} - l_R)}{v_p} + \phi(\omega_o, t)\right] \tag{28.9}$$

where I_c represents the confocal intensity response and, by definition, $l_s = 0$ corresponds to the position of the focus.

From Eq. 28.9 it is evident that control of the positions and widths of the confocal and coherence gates are decoupled. The confocal gate width is determined by the NA of the focusing objective and its position is set by the focus position. For the coherence gate, the width is determined by the light source bandwidth, and, for fixed focus position, the depth location is set by the reference arm path length l_R. The maximum heterodyne signal occurs when the reference and sample arm path lengths match $l_{S0} = l_R$ such that the coherence and confocal gates overlap. The sensitivity of the heterodyne signal to the relative position of the gates scales with the NA of the objective lens. For high NA, the confocal parameter b as shown in

Fig. 28.2b is quite small and results in a small depth of field for imaging. When the reference path length is set to the microscope focus, $l_R = 0$, the heterodyne amplitude is subject to the multiplication of the coherence and confocal gate point spread functions.

28.5 Advantages of OCM

For imaging in scattering media, combined confocal and coherence gating can have advantages compared with confocal gating alone. Coherence and confocal gating reject unwanted out of focus scattered light using distinct mechanisms. The confocal gate rejects light based on spatial imaging constraints, while the coherence gate rejects photons based on the path length they travel in tissue. The multiplicative effect of the two gates can be stronger than either gate individually, achieving greater image contrast and image penetration in scattering tissue. Moreover, as Wang et al. point out, the typical Gaussian coherence gate has a functional response which is not only more effective than the confocal gate but also more effective than the exponential extinction of incident light in tissue [72]. Figure 28.5 compares measured point spread functions on a log scale from an early OCM demonstration [51]. At depths of several tens of micrometers from the focus, the coherence gate rejects scattered light with orders of magnitude better efficiency than the confocal

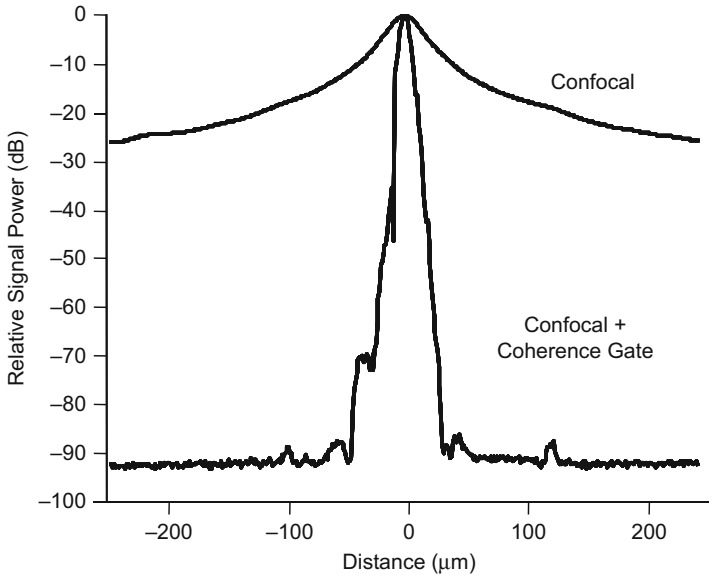

Fig. 28.5 Measured confocal and coherence-gated axial resolutions for a typical OCM imaging system. Data is presented on a log scale and demonstrates the improved rejection of out of focus scattered light using combined confocal and coherence-gating compared with confocal gating alone (Figure is reproduced from Izatt et al. [51])

gate alone. In addition, the confocal axial response is affected by aberrations when focusing into tissue, which causes broadening of the peak of the point spread function and increases the wings of the response [73]. Combined coherence and confocal gating can help to minimize reductions in contrast due to loss of confocal axial resolution.

Image penetration depth limits in confocal microscopy and their enhancement using coherence gating have been studied by several investigators [51, 58, 74–76]. Using single scattering theory, and signal to background noise considerations, Izatt et al. estimated the confocal penetration limit to be in the range of 5–8 mean free paths (MFP) [51]. Schmitt et al. used Monte Carlo simulations to investigate the role of multiple scattering and concluded that penetration depth is actually limited to the range of 2–4 MFP [75, 76]. Smithpeter et al. subsequently used experimental measurements to predict a similar penetration depth of about 3–4 MFP in amelanotic tissue [74]. Coherence gating has been shown to enhance image penetration by rejecting multiply scattered light, particularly from superficial depths. Based on the shot-noise quantum detection limit, initial estimates of imaging depth improvement were placed at 2–3 times compared with confocal gating alone [51]. As researchers became more aware of the sensitivity of coherence-gating methods to multiple scattering, these expectations were tempered. In highly scattering media, contrast in OCT and OCM images is limited by the ratio of single scattered to multiple scattered light, not by the quantum sensitivity limit [77]. Furthermore, the system sensitivity to multiple scattering is a function of both the optical properties of the tissue as well as the system design parameters, including the numerical aperture. Given these constraints, precise quantification of the image depth enhancement will depend upon the specifics of the application. Nonetheless, several initial studies in human tissues have demonstrated significant improvement using coherence gating. In one study, imaging of cellular features in colonic crypts was possible at depths of 500 um [59]. Another study imaging human oral mucosa demonstrated an average depth improvement of 33 % [78].

Since image quality is dependent upon both contrast and resolution, the question of resolution degradation in OCM images deep in scattering media is closely linked to the notion of imaging depth in OCM. Bizheva and Boas studied these questions using both simulation and experiment over a range of typical OCM parameters for scattering anisotropy and imaging NA [79]. Their results indicate relatively small changes in axial resolution at both low and high NA when imaging in media with low scattering anisotropy of 0.2. However, in media of high scattering anisotropy of 0.9, axial resolution degradation is quite rapid after 3–4 MFP. Moreover, degradation is more pronounced at lower NA compared with higher NA. With respect to transverse resolution, their results show no significant change up to seven MFP for either low or high anisotropy and some resolution degradation after seven MFP. Further studies such as these will be important to determine optimal parameters for deep cellular imaging in highly scattering tissues.

Combined coherence and confocal gating can have additional advantages beyond imaging depth improvement. One such advantage lies in the ability to use

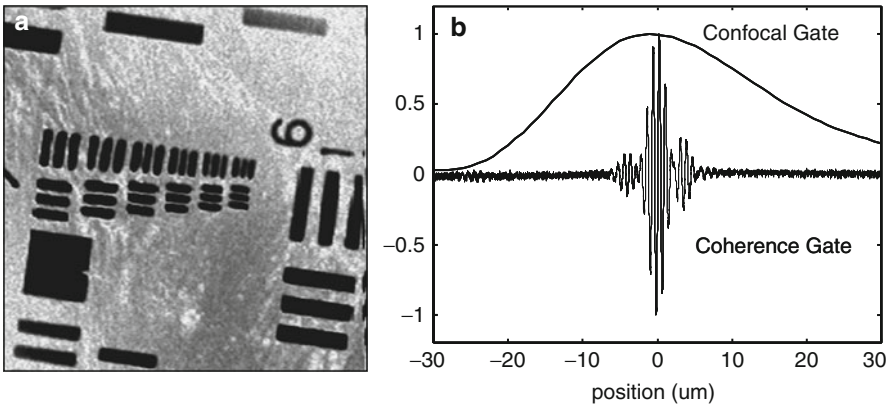

Fig. 28.6 Optical coherence microscopy using a femtosecond laser source. High transverse resolution of <2 um allows visualization of even the smallest elements of the USAF 1951 resolution target (**a**). This transverse resolution was achieved with a reduced numerical aperture compared with that typically used for confocal microscopy, resulting in a confocal axial resolution of only ~30 um. A short coherence gate of ~3 um was then used to compensate for the lower confocal resolution (Images reproduced from Aguirre et al. [80])

ultrahigh axial resolutions provided by very broad bandwidth light sources. Results from confocal microscopy in human skin demonstrate that achieving an axial resolution of <5 um is important for high contrast imaging of cellular features [4]. Such an optical slice axial thickness is similar to the conventional section thickness used in histopathology. Because the axial resolution depends inversely on the square of the NA ($1/NA^2$), achieving a 5 um axial resolution with confocal microscopy alone requires high NA objectives, typically in the range of 0.7–1.2 NA. Most OCM systems to date have operated in this limit, using the confocal axial section as the dominant gating method with the coherence gate acting mostly to reduce the background from out of focus scattered light.

The development of ultrahigh resolution OCT techniques opened the possibility of using the coherence gate rather than the confocal gate to set the optical section thickness [37]. Transverse resolution of 1–2 um can be maintained with much lower NA, since the transverse spot size only scales inversely with the NA ($1/NA$). This implies that OCM with ultrahigh axial coherence resolution can achieve high contrast cellular imaging with significantly reduced NA compared with confocal microscopy. Figure 28.6 demonstrates this operating limit. A confocal microscope with an axial resolution of ~30 um was combined with a broad bandwidth modelocked Ti:Al_2O_3 solid-state laser light source and an OCM system with a broadband phase modulator [80]. The coherence gate measures ~3 um and provides most of the optical sectioning power of this microscope. The effective NA of the microscope was only ~0.22. Figure 28.6a shows that high transverse resolution is still maintained. The smallest elements measuring 2.2 um in width on the USAF 1951 resolution target can be visualized. Figure 28.7 demonstrates that high contrast cellular images in human tissue can be achieved, despite the low

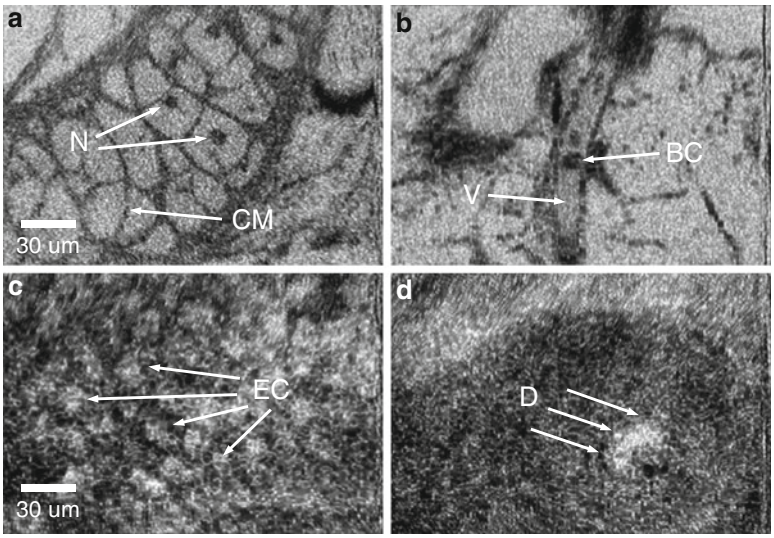

Fig. 28.7 In vivo cellular imaging with optical coherence microscopy. Images of Xenopus laevis tadpole (**a**, **b**) show cell membranes (*CM*), cell nuclei (*N*), and individual blood cells (*BC*) in a vessel (*V*). Epidermal cells (*EC*) and a duct (*D*) structure are also in images of human skin (**c**, **d**) (Images reproduced from Aguirre et al. [80])

confocal axial resolution. Figure 28.7a, b present images from the Xenopus laevis tadpole, a commonly used model organism in developmental biology specimens. Cell nuclei and membranes as well as small vessels and blood cells are visible. Figure 28.7c, d show images of human skin in vivo. Epidermal cells and the lumen of a sweat duct can be clearly identified.

The ability to image with reduced NA makes OCM an enabling technology for endoscopic imaging. Miniaturization of high NA objectives is a challenging optical design problem [81]. Using a broad bandwidth light source to provide ultrahigh axial coherence resolutions can reduce the numerical aperture requirement, therefore allowing smaller and simpler probe designs. Figure 28.8 further highlights this advantage. Confocal axial and transverse resolutions are plotted versus numerical aperture. OCM can achieve sufficient transverse resolutions in the range of 0.2–0.5 NA and lower, despite the rapid degradation of the axial resolution seen in confocal microscopy.

Figure 28.9 further illustrates the advantage of OCM for cellular imaging at lower numerical aperture compared to confocal microscopy. These images were acquired using a Fourier domain/swept source OCM system operating at 1.3 um center wavelength [82] and described in further detailed later in this chapter. Figure 28.9a, b demonstrate OCM images of colonic crypts and goblet cells taken with 10×/0.3 NA and 20×/0.4 NA lenses, respectively. For comparison, Fig. 28.9c, d are simulated confocal images generated from stacks of OCM images taken at the same magnifications and at the same tissue location. The image stacks have been summed over all depths, which simulates an effective axial resolution

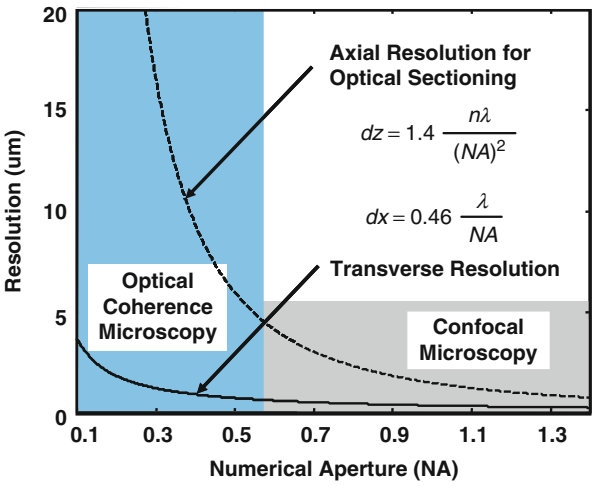

Fig. 28.8 Operating ranges for optical coherence microscopy compared with confocal microscopy

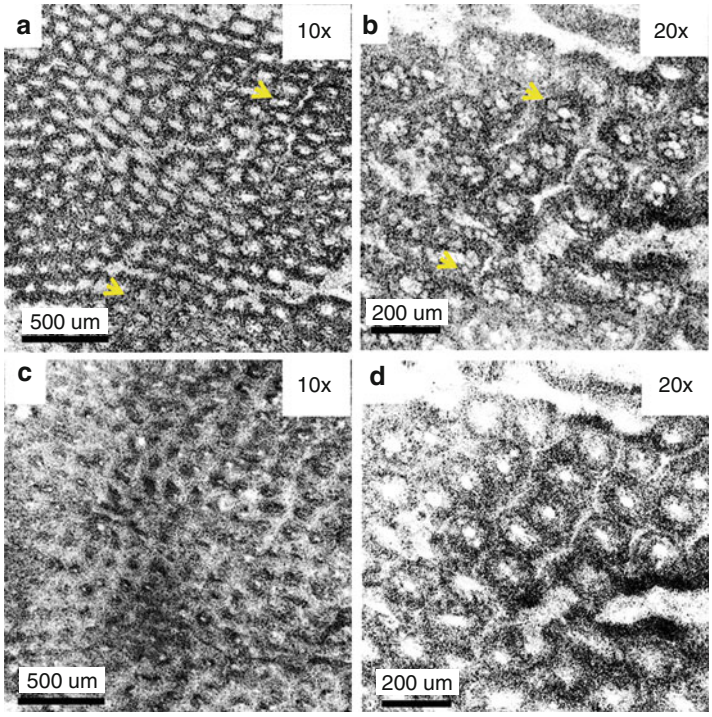

Fig. 28.9 Comparison of OCM and confocal images of human colon. OCM images at 10× (**a**) and 20× magnification (**b**) exhibit high contrast and high resolution compared to the confocal images at similar magnification 10× (**c**) and 20× (**d**). Confocal images were formed from summing over all depths in a volumetric OCM image acquired using Fourier domain OCM (Images reproduced from Ahsen et al. [82])

provided from only the confocal gate. Cellular features in the OCM images are clearly visible, however there is loss of resolution and contrast for cellular features in the simulated confocal images.

An added advantage of OCM using lower NA lenses with lower magnification is the ability to achieve larger fields of view, large depth of field and longer working distance compared with confocal microscopy. Improved field of view allows the user to survey larger regions of tissue and helps to provide context to the microscopic features visualized with OCM. Furthermore, the larger confocal axial resolution affords the possibility of acquiring multiple depth sections around the location of the focal plane. This may be useful for applications such as characterizing the three dimensional shape and size of cells in a particular tissue layer. This type of imaging cannot be performed with confocal microscopy without translating the focus.

28.6 Technology for OCM

Cellular imaging with OCM comes at the cost of increased system complexity compared with conventional OCT as well as confocal microscopy. System designs must incorporate the core features of a confocal microscope, including a two-axis scanner and reasonably high NA lens, in addition to the heterodyne interferometer and detection electronics necessary in OCT. To achieve ultrahigh coherence axial resolutions, very broadband light sources must be used. Furthermore, optical interferometer and microscope designs capable of supporting these large spectral bandwidths must be developed. For in vivo imaging, the imaging speed is also a critical parameter. Visualization of cellular and subcellular features requires sufficient speed to eliminate motion artifacts and transverse blurring. Based on work with confocal microscopy, a speed of ~8 frames per second is desirable, even with the use of contact tissue stabilization schemes [4]. This necessitates fast raster scanning and either high speed phase modulation methods in the time domain or ultrahigh speed axial rate systems in the Fourier domain. High speed imaging also requires high power light sources to overcome signal loss due to reduced pixel dwell times. At near-infrared wavelengths, permissible tissue exposures for high speed imaging are in the range of 10–20 mW. Including coupler loss and optical transmission loss, typical system throughput can be quite low, however, and this can substantially increase the light source output power requirements to obtain sufficient tissue illumination. Finally, an OCM system must have some mechanism to ensure overlap of the confocal and coherence gates in scattering tissue. This section reviews progress on technology for OCM that will enable high speed in vivo imaging.

28.6.1 Broadband Light Sources

Light source requirements for OCM essentially parallel the requirements for OCT. Near infrared wavelengths between 800 and 1,300 nm are desirable to take advantage of lower absorption and scattering in tissue compared with visible

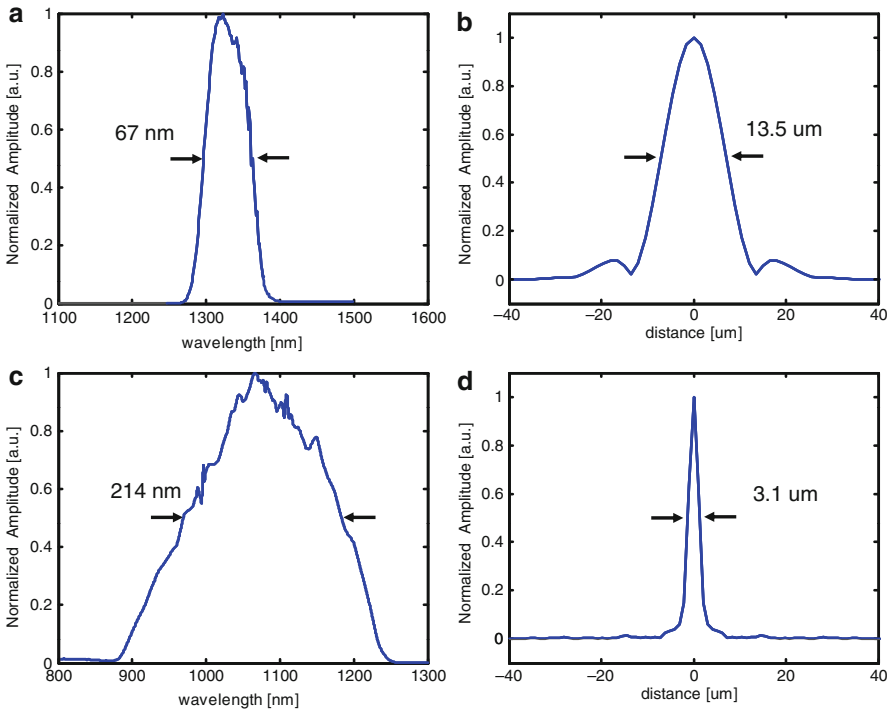

Fig. 28.10 Comparison of light sources for optical coherence microscopy. A typical superluminescent diode source provides a spectrum of around 70 nm (**a**), which corresponds to an axial resolution of about 14 um (**b**). State of the art femtosecond lasers and continuum generation can provide much broader spectra and higher axial resolution. Shown here are results achieved using a compact Nd:Glass oscillator. Spectral bandwidth (**c**) measures over 200 nm, corresponding to an axial resolution of about 3 um (**d**)

wavelengths. Within this range, the shorter wavelengths near 800 nm provide increased contrast and better resolution for a fixed optical bandwidth compared with the longer wavelengths near 1,300 nm. Nonetheless, the increased penetration depth at longer near infrared wavelengths is attractive for imaging below the surface in scattering tissues. For time-domain or spectral/Fourier domain implementations of OCM, broadband superluminescent diode light sources or modelocked femtosecond solid state lasers are utilized. Superluminescent diode light sources have typical bandwidths in the range of 40–80 nm and output powers between 1 and 20 mW. Figure 28.10a presents a measured spectrum from a typical superluminescent diode at 1,300 nm. The coherence gate can be computed from the autocorrelation of the spectrum and has a width of 13.5 um, as shown in Fig. 28.10b. Superluminescent diodes offer compact, stable, turnkey solutions and have been widely applied in clinical studies with OCT. Femtosecond lasers have enabled ultrahigh resolution OCT with coherence gates of less than 5 um. These systems offer superior performance in terms of bandwidth and output power compared with the SLD's, but they are typically expensive as well as complex to

build and operate. The use of supercontinuum generation in highly nonlinear fibers has enabled the application of commercially available femtosecond lasers for OCT. Such commercial laser sources can be made highly stable and compact, compared with research prototypes, which allows the development of portable systems for clinical investigations outside of the research laboratory. Figure 28.10c, d present the measured spectrum and the computed coherence gate for a laser light source of this type [83]. Using a compact Nd: Glass oscillator coupled into a Germanium-doped, high numerical aperture, nonlinear fiber, an optical spectrum of over 200 nm centered at 1,060 nm was generated using self phase modulation nonlinearity. This enables resolutions of $\sim$3 um in air. Moreover, the average power was $>$100 mW, enabling high speed imaging. The wavelength range around 1,060 nm is compelling for use in scattering tissues because it offers both increased penetration compared with the 800 nm region and improved resolution compared with 1,300 nm. Some studies suggest that this wavelength window is an optimum choice for ultrahigh resolution imaging [84], and continuous wave lasers around 1,060 nm have been extensively used for confocal imaging [4, 85]. Fully-integrated, turn-key supercontinuum generation systems utilizing photonic crystal fibers are also now available and have been used by several groups for optical coherence imaging [43, 86].

Swept source/Fourier domain OCM systems require wavelength swept laser sources with ultrahigh sweep speeds. As previously mentioned, recent novel laser designs to achieve high scan speeds include the Fourier domain modelocked (FDML) laser [67, 87] and the vertical cavity surface emitting laser (VCSEL) [68, 69]. Figure 28.11 demonstrates the characterization of a state of the art VCSEL laser used for OCM imaging [82]. The laser operates at 1,310 nm with 117 nm sweep bandwidth and sweeps at 280 kHz, providing a bidirectional axial scan rate of 560 kHz. Figure 28.11 shows the spectrum and characterization of this light source. The VCSEL is wavelength scanned using a microelectromechanical (MEMS) tunable cavity, and has the unique feature of a micron-scale cavity length allowing single mode lasing with an extremely narrow instantaneous linewidth, which supports a long coherence range for imaging. Figure 28.11d shows the minimal roll-off in image signal as a function of depth, consistent with long instantaneous coherence length during the sweep.

28.6.2 Time Domain Phase Modulation Schemes

For time domain OCM systems, broadband and high speed phase modulators are required. The basic goal is to provide a phase delay to the reference arm light, without imparting significant group delay that would cause the coherence gate to shift relative to the confocal gate. The first OCM system demonstrated by Izatt et al. used a piezo-electric fiber stretcher to dither the reference path length by a fraction of a wavelength [51]. A similar approach employs a piezo-electric stack to vibrate the reference mirror [59, 78, 88]. This method uses a relatively simple interferometer design that supports broad optical bandwidth but is limited to relatively slow modulation rates and therefore does not allow real-time imaging.

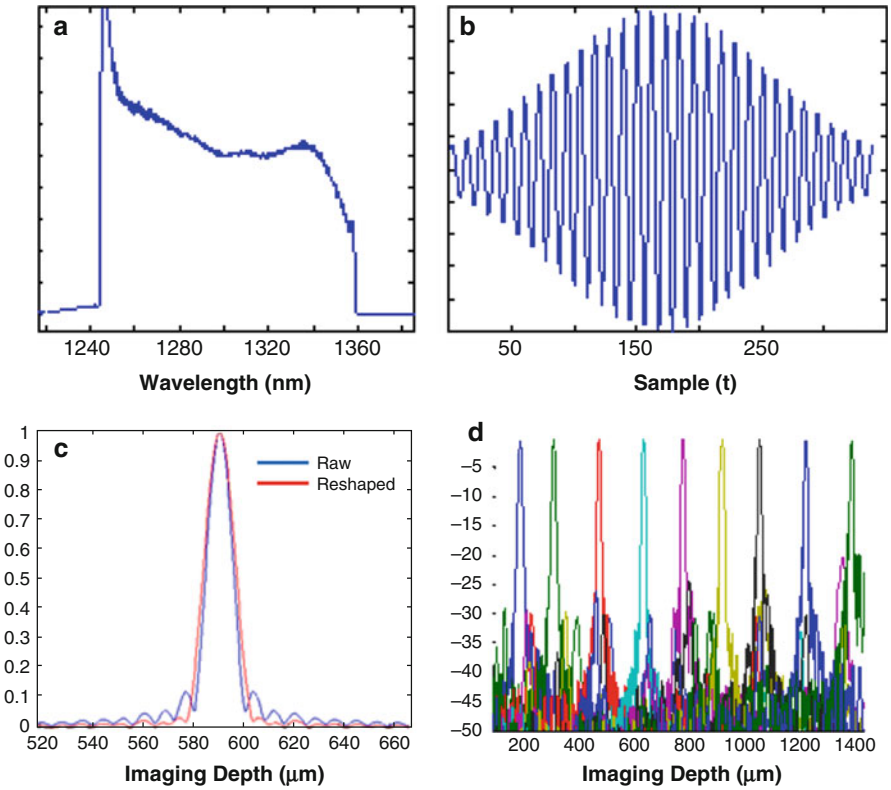

Fig. 28.11 Vertical cavity surface emitting laser (*VCSEL*) for high speed swept source OCM. (**a**) Spectrum of the VCSEL showing 117 nm tuning range. (**b**) Interferometric fringe signal after spectral reshaping and numerical dispersion compensation. (**c**) Axial point spread function after Fourier transformation of the raw acquired fringe data (*blue curve*) and the fringes after spectral reshaping (*red curve*). (**d**) Sensitivity fall-off of the VCSEL swept source as a function of depth showing no significant change in the sensitivity over the imaging range (Figure reproduced from Ahsen et al. [82])

An alternative approach to reference arm phase modulation involves the use of a rapid scanning optical delay line (RSOD) similar to those designed for OCT [89, 90]. The RSOD uses a grating and lens combination to perform an optical Fourier transform. A scanning mirror in the Fourier plane of the delay line imparts a wavelength dependent phase shift which, when passing back through the lens-grating combination, produces a group delay scan in the time domain. In addition, offsetting the optical beam from the scanning mirror center axis allows the generation of a phase delay scan, which adds a Doppler frequency shift to the heterodyne signal. Zvyagin et al. demonstrated that, with proper choice of grating, lens, and offset parameters, the RSOD can also be set to generate phase delay without group delay [91]. Aguirre et al. utilized this approach in an all-reflective configuration to construct a broadband optical phase modulator for OCM imaging [80].

The reflective design eliminates chromatic aberration encountered with lens geometries. Using resonant galvanometer scanners, RSOD modulators such as this are capable of producing modulation frequencies in the MHz range [90]. An OCM system utilizing an RSOD modulator has been used for in vivo cellular imaging at 4 frames per second, as shown previously in Fig. 28.7.

Acousto-optic (AO) and electro-optic (EO) modulators are excellent solutions for high speed modulation. Several investigators have used EO modulators in OCT to provide a highly phase stable Doppler shift at 1,300 nm wavelength [92–94]. Electro-optic modulators can be driven at very high modulation rates in the GHz range, well beyond what would be needed for even the fastest OCM system. Linear, broadband EO phase modulators are not widely available at wavelengths outside of the standard telecommunications band encompassing 1,300–1,500 nm. Moreover, typical $LiNbO_3$ crystals used in EO modulators are highly birefringent. For unpolarized superluminescent diode sources, this does not present a significant problem. However, with polarized broadband laser sources that have complex polarization evolution in the fiber, the polarization dependence of EO modulators can make them difficult to use and potentially necessitate polarization control or diversity approaches.

Acousto-optic modulators have also been applied for cross-sectional, transverse-priority and *en face* OCT imaging [50, 95, 96]. AO modulators are available at many wavelengths and provide a pure frequency shift rather than a phase modulation, but typical frequency shifts are in the tens of MHz range. To reduce the frequency shift to a lower value more suitable for OCT or OCM imaging, a modified approach can be used in which a pair of AO modulators is cascaded with opposite frequency shifts offset in magnitude by a small amount. For example, Xie et al. used AO modulators with frequencies of +55 MHz and −54 MHz giving a round-trip, double pass net frequency shift of 2 MHz [95]. This approach requires the added complexity of two separate modulators and drive electronics, but like the EO modulation schemes, it can provide a highly stable modulation. In addition, AO modulators are generally polarization insensitive.

Dispersion compensation is another important challenge in using either an EO or AO modulators with broadband OCT or OCM systems. The optical materials used in modulators introduce large amounts of dispersion in the reference arm that must be balanced or compensated in order to preserve the axial point spread function. This issue has been addressed primarily by using rapid scanning optical delay lines (RSODs) to remove second order dispersion [93, 97]. An RSOD alone, however, cannot remove higher order dispersion terms. One approach that enables compensation of high order dispersion is to place identical optical materials as are used in the reference arm modulator in the sample arm. Wiesauer et al. used this strategy to achieve <3 um axial resolution in a free-space *en face* OCT system [98]. However, this approach is undesirable for use in endoscopy or other applications using fiber-optic sample probes, since it would require free space coupling out of and into the fiber in order to introduce the dispersion compensation material. Chen et al. demonstrated a simple and elegant modification to the RSOD compensation technique which allows dispersion management up to third order by using a length

of single-mode optical fiber in the sample arm [99]. This technique was theoretically analyzed and experimentally demonstrated for EO as well as AO modulators and a resolution of ~2.8 um was achieved with an AO modulator at 800 nm wavelength. The same group subsequently developed a technique for optimization of the spectral throughput of AO modulators which supports more than 200 nm bandwidth at 800 nm [100]. With the development of suitably broadband dispersion compensation approaches, AO and EO modulators promise to be widely used for high speed in vivo OCM imaging in the future.

Two interesting approaches to *en face* imaging have been demonstrated which do not require modulators in the reference arm. The first approach makes use of the inherent modulation imparted by raster scanning the beam with a galvanometer mirror. In the case when the scan field in the sample arm is curved, a sampling function based on Newton rings can be used [101]. Alternately, an offset of the beam on the galvanometer scanner mirror can be used to produce a parallel fringe sampling function [102]. A second approach uses homodyne detection based on 3 × 3 optical couplers [103]. The homodyne method takes advantage of the inherent phase shifts between the ports of the coupler to obtain amplitude and phase information. Images of a *Xenopus* tadpole were demonstrated with sensitivity of ~90 dB and transverse resolution of 9.4 um. OCM schemes that do not require modulation can result in simpler system designs and are therefore promising for further study.

28.6.3 Microscope Scanner Designs

Microscope design principles for OCM imaging are similar to those for confocal microscopy in epi-reflection mode. The microscope consists of three basic subsystems: (1) an XY scanning apparatus, (2) collimation and relay optics, (3) a focusing objective. The XY scanner should ideally maintain the same optical path length to the focus across the entire scan field in order to ensure overlap of the confocal and coherence gates. The most direct way to do this is would be to mechanically scan the microscope and sample with respect to each other using translation stages. For high speed imaging, however, beam steering is the preferred method. Galvanometer mirror scanners have been widely used for OCM, because rotating polygon scanners typically used for video rate confocal microscopes [4] introduce an unwanted path length shift across the scan. Resonant scanning galvanometers can offer fast axis scan rates, as high as 10–15 kHz, which are sufficient for video rate imaging with high line density per image.

Collimation and relay optics are typically composed of multiple-element achromatic lenses designed and coated for use at near-infrared wavelengths. Focusing objectives are generally chosen to provide field flatness, which aids in reference path length matching across the field of view. Furthermore, water immersion lenses are often used for imaging in biological tissue to minimize aberrations from refractive index mismatch. However, high quality focusing objectives designed for the near infrared are not widely available, and therefore most systems

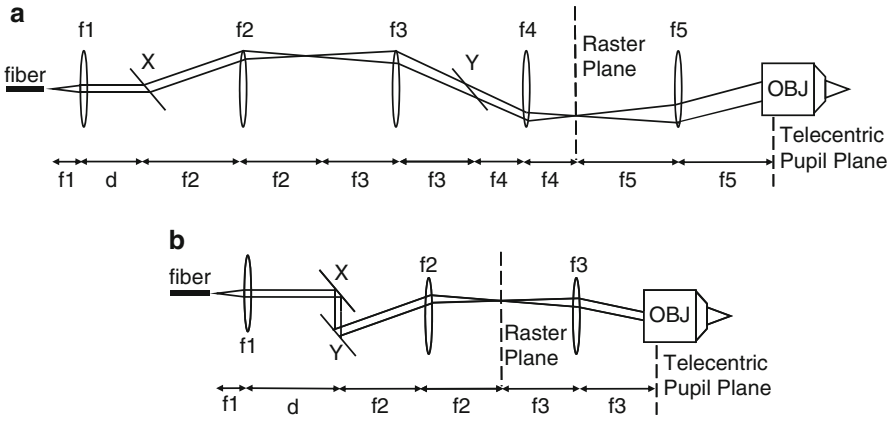

Fig. 28.12 Fiber-optic confocal microscope designs typically used for OCM. A true telecentric design (**a**) separates the transverse scanners and precisely images the points of angular scan on each axis to the telecentric plane of the objective. An approximate geometry (**b**) which uses a pair of closely spaced galvanometer scanners can also work well but introduces aberration

have used lenses designed for visible wavelengths. This leads to poor optical throughput as well as focusing aberrations. As near IR imaging methods, including multiphoton and harmonic microscopies as well as OCT, become more established, it can be expected that near IR objective lenses will become more readily available.

Figure 28.12 illustrates two examples of benchtop OCM microscope designs for use with galvanometer scanners and an infinity corrected objective lens. The design in Fig. 28.12a is a true telecentric design. The beam from the fiber is collimated and directed onto the center of the first galvanometer scanner. The center point of this galvanometer is then relay imaged to the center point of the second scanner by lenses f2 and f3. A final telescope, formed by lenses f4 and f5, then images the scanners to the telecentric pupil plane in the objective lens. This design offers true telecentricity in that the beam can be made to pivot on both axes about the telecentric plane and there is negligible path length delay variation with scanning. The disadvantage of this design is that it requires several lenses and a relatively large optical path. A second design, shown in Fig. 28.12b, uses a closely-spaced pair of galvanometers after the collimator. The center point between the mirrors is imaged by a single telescope to the telecentric pupil plane. This configuration can provide only approximate telecentricity, since neither of the pivoting mirrors can be exactly imaged to the correct pupil plane in the objective. The spacing between the galvanometers should be minimized to reduce the degree of scan induced path length delay that results. This design offers compactness, and is more amenable to use with handheld imaging devices.

The development of miniaturized microscopes for endoscopic confocal and OCM imaging is a critical enabling step necessary for widespread application of these techniques for human clinical imaging. Two separate challenges must be

overcome: design of small diameter, high NA objective lenses and development of miniaturized, fast two-axis scanners. These issues have been the topic of significant research efforts in recent years. Ideally, the device diameter would be a maximum of 3–4 mm in order to enable its use through the accessory ports of clinical endoscopes. As described above, OCM has the important advantage that it can image with lower NA compared with confocal microscopy, which facilitates the development the small diameter objective lenses required. Several approaches for developing compact endoscopic scanning devices have been investigated. Some groups are pursuing fiber imaging bundles for confocal [16, 19, 104–107] and optical coherence imaging [108]. Fused coherent fiber bundles consist of thousands of individual fibers which preserve spatial relationship between proximal and distal ends. Each fiber in the bundle serves as an image pixel, and scanning can be performed at the proximal end of the fiber bundle using conventional galvanometer scanners. Fiber bundles tend to have poor optical efficiency, however, and image pixelation as well as fiber cross talk can degrade resolution and contrast. In addition, phase differences between individual fiber paths can present problems for phase sensitive heterodyne detection methods.

Single-mode fiber scanners have much better optical efficiency, but require miniaturized scanners located at the distal tip of the fiber optic probe. Two-dimensional scanning of the input fiber tip has been used by several groups for endoscopy, confocal microscopy and multiphoton microscopy [109–112]. Piezo-electric devices typically require resonance drives to achieve sufficient deflection, which limits their ability to scan arbitrary XY scan patterns. Two axis resonant piezo scanners can scan a two dimensional plane using a Lissajous scan pattern [109] or a spiral scan pattern [113, 114]. The scanner from Wu et al. utilized a tubular four quadrant piezo actuator, and is particularly promising for endoscopy due to is small diameter of 2.4 mm and capability for rapid imaging at 3.3 frames/s [114]. Sawinski and colleagues developed a novel non-resonant piezolever fiber scanner (PLFS) capable of scanning arbitrary patterns with independent X and Y axes [115, 116]. This device was subsequently incorporated into an endoscope with a custom designed objective lens and demonstrated for cellular resolution OCM imaging [117]. Figure 28.13 shows a schematic and photo of the device with diameter of 8 mm used for imaging. Imaging was performed with 600 Hz drive on the fast axis and up to 4 Hz on slow axis to scan a raster pattern. Images of human colon ex vivo and human skin in vivo are demonstrated with <2 um transverse resolution and <4 um axial resolution.

Two-axis micro-electro-mechanical systems (MEMS) may also enable a wide range of fiber optic endoscope devices for OCT and OCM. Two-axis MEMS scanning mirrors have been demonstrated for confocal microscopy applications [118] and one and two axis scanners have been designed for optical coherence tomography applications [4, 119–127]. Figure 28.14 illustrates an example implementation of a two-axis MEMS scanning catheter used for 3D and *en face* ultrahigh resolution OCT imaging. The scanner, shown in the scanning electron micrograph in Fig. 28.14a, has a large 1 mm diameter mirror for high resolution imaging. It uses angular vertical comb (AVC) drive actuators on the mirror and on the outer gimbal

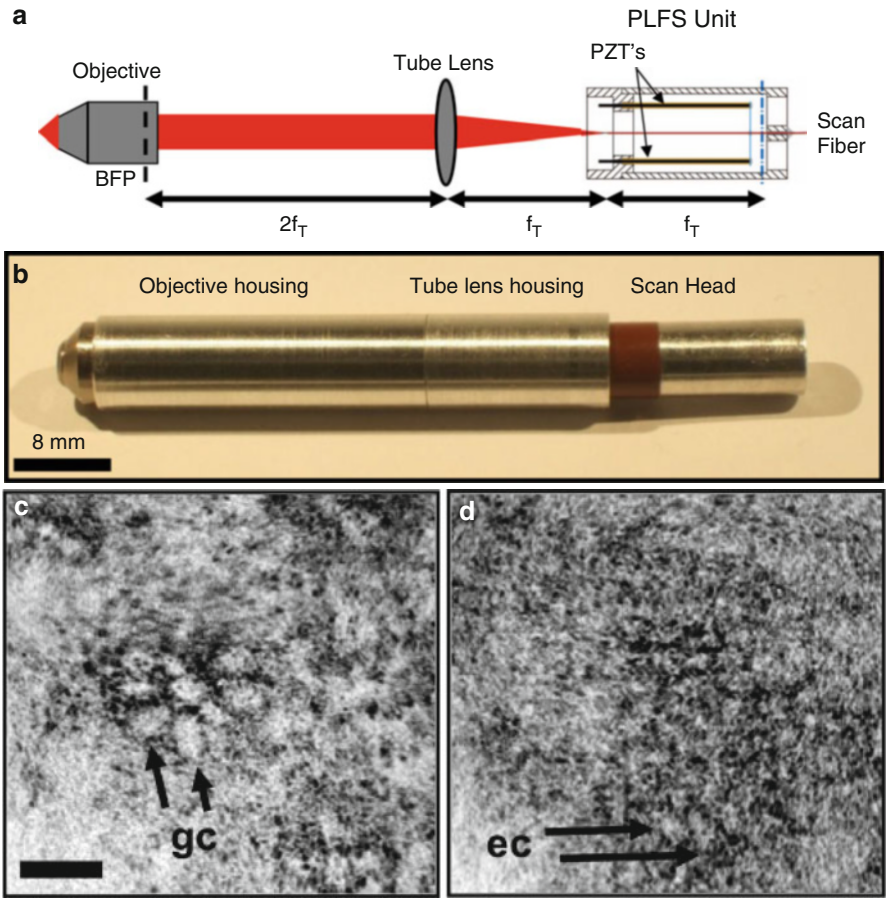

Fig. 28.13 Piezo-electric scanning endoscope for OCM imaging. (**a**) Endoscope design showing a non-resonant piezolever fiber scanner (*PLFS*) incorporated into a forward looking microscope configuration with a miniaturized objective lens. Piezoelectric benders *PZT's*, Tube lens focal length f_T, Back focal plane *BFP*. (**b**) Packaged endoscope design measuring 8 mm in diameter. (**c**, **d**) In vivo cellular images of human skin acquired with the endoscope. Scale bar, 50 um (Figure modified from Aguirre et al. [117])

to actuate in two dimensions over large angles of >8° with only ~50 V applied bias [123, 128]. The mirror and gimbal axes can achieve high resonance frequencies of over 1 kHz for high speed imaging. The mirror was incorporated into a small diameter catheter, as shown in Fig. 28.14b. The device consists of an outer aluminum housing with maximum diameter of ~5 mm. A fiber collimator delivers light to an achromatic objective lens (not visible in the schematic), which focuses the beam. The MEMS scanner is used in a post-objective scanning configuration with the focused beam reflected at 90° out of the device for side-view imaging. Figure 28.14c shows a three-dimensional rendering of hamster cheek pouch

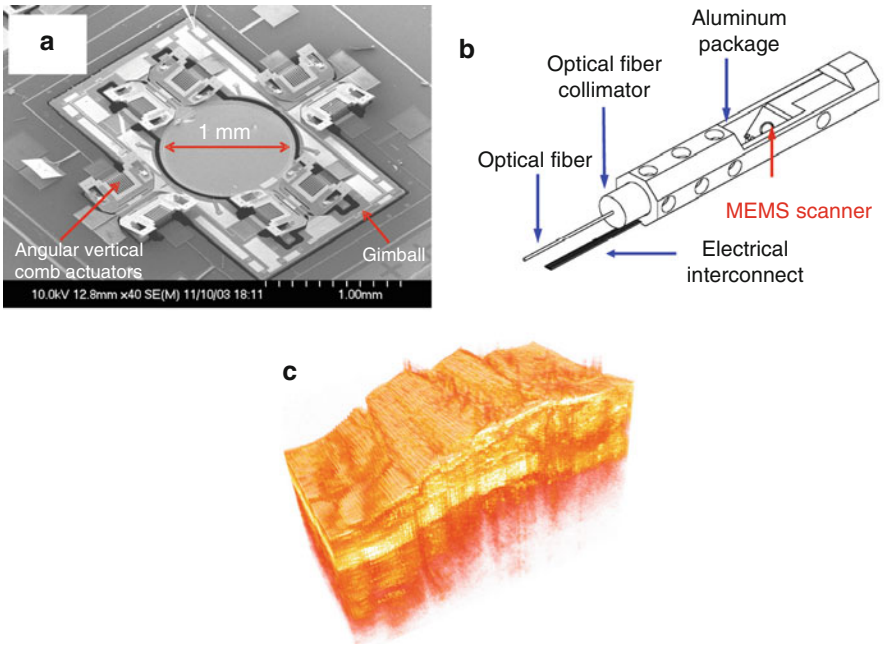

Fig. 28.14 Two-axis MEMS scanning catheter endoscope for three-dimensional and *en face* imaging. A large 1 mm diameter MEMS mirror (**a**) was integrated into a 5 mm diameter catheter package (**b**). Three-dimensional imaging was demonstrated in vitro of the hamster oral mucosa (Figure reproduced from Aguirre et al. [128])

acquired in vitro with the miniaturized catheter. While catheter designs such as this are continuing to advance, other challenges such as focus adjustment and tissue stabilization remain to be addressed. Therefore, in vivo endoscopic confocal and OCM imaging remains a difficult problem.

28.6.4 Controlling the Overlap of Coherence and Confocal Gating

OCM is critically sensitive to the overlap of the confocal and coherence gates determined by matching of the reference and sample arm optical path lengths. Focusing into a sample with a change in index of refraction leads to a reduction in heterodyne amplitude and loss of resolution because the confocal and coherence gates shift relative to each other. Optical path length (OPL) is defined as

$$OPL = nl \tag{28.10}$$

If the reference and sample refractive indices are matched, $n_S = n_R$, the reference arm OPL remains equal to the sample arm OPL as the focus is translated deeper into the sample. This does not hold true when the refractive index of the sample is

different from that of the reference arm. In this case, a physical thickness of δl over which $n_S \neq n_R$ produces an OPL mismatch of

$$\Delta L_{OPL} = (n_S - n_R)\delta l = \Delta n \delta l. \tag{28.11}$$

The index mismatch is particularly important when using dry objectives and can be minimized by the use of water immersion objectives. Given the variations in index of refraction in tissue [129], path length mismatch cannot be insured in general by matching the reference path to the microscope focus outside of tissue. Furthermore, fiber optic imaging probes such as catheters or handheld microscopes are subject to path length shifts between the reference and sample arms produced by stretching and bending of the optical fiber as the probe is positioned for in vivo imaging. The sensitivity to path length changes between the reference and sample arms is exacerbated when the confocal and coherence gates are both very small. Using broadband laser sources to provide ultrahigh coherence axial resolutions, as in Fig. 28.10, allows the confocal gate to be longer than in standard confocal microscopy. This helps to make the gate overlap less sensitive to index variations.

To ensure optimum image quality in highly scattering tissue, some form of overlap alignment between the confocal and coherence gates is desirable. This is most easily done by adjusting the reference arm path length. Schmitt et al. used a focus-tracking scanner with the reference mirror and the sample objective mounted on the same translation scanner [25]. As the objective was translated by a distance Δz toward the sample, the optical pathlength in the reference arm increased by an amount $2\Delta l$. Since focus tracking requires a change of $\Delta l = n^2 \Delta z$ and $n^2 \approx 2$ for biological tissues, this technique provided approximate overlap alignment of the confocal and coherence gates across the depth scan. This approach does not work for fiber optic systems with separate reference and sample paths. Most investigators have instead used manual adjustment of the reference path length with a translation stage. The position of the focus was determined using image intensity as the metric. For in vivo imaging applications, high speed adjustment is required. Aguirre et al. used a galvanometer scanner in the reference path to quickly scan depth and provide a depth profile of image intensity [117]. The focal position could then be determined and the DC offset to the depth scanner adjusted to ensure overlap of confocal and coherence gates. This method is essentially an autofocusing technique, analogous to the autofocus methods used in digital cameras. The ability to rapidly and automatically align overlap for OCM in tissue is important to ensure optimum image quality at different depths.

In the Fourier domain, minor path length mismatch between reference and sample arms can be computationally corrected. Fourier domain OCM images are extracted from a volumetric dataset, with each point in the *en face* image taken from an entire axial depth scan. If the confocal gate and depth of field of the microscope optics are sufficiently long, then the *en face* image can be optimized at each point by finding the point of maximal overlap of the confocal and coherence gates within each axial scan. Such corrections can also be applied to compensate for microscope path length delay scanning and focusing aberrations that limit performance in time domain interferometric microscopes. Graf et al. demonstrated methods for

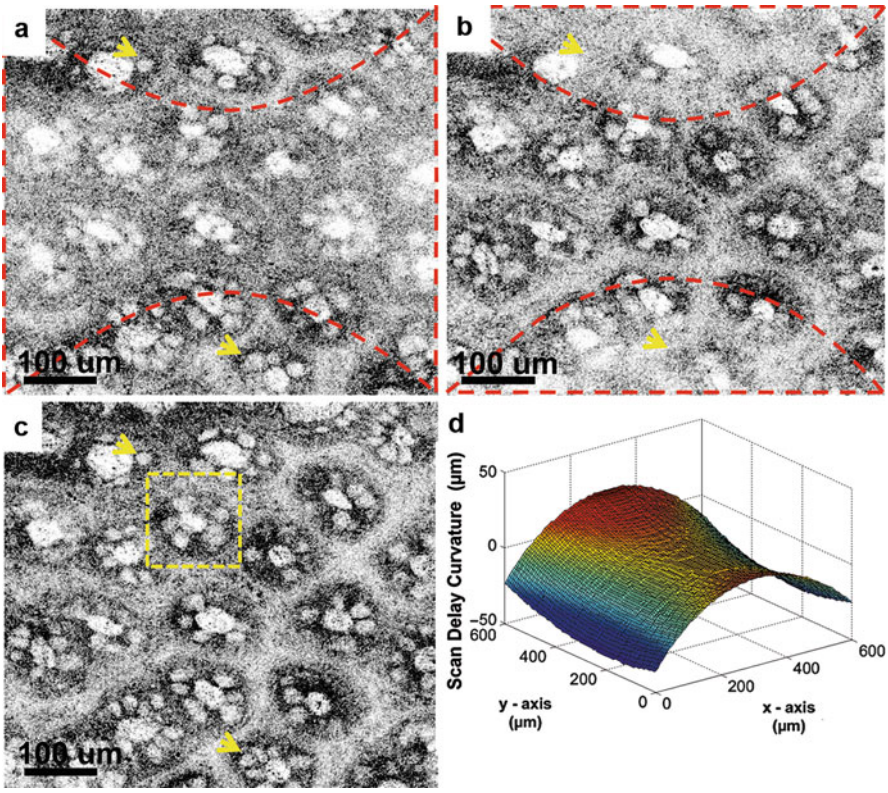

Fig. 28.15 Correction of optical path delay variation with scanning. (**a**, **b**) OCM images acquired at two distinct depths. (**c**) Corrected image after using volumetric Fourier domain OCM data set to optimize the image at every point along the field of view. (**d**) Plot of scan delay curvature measured from a coverslip (Figure reproduced from Ahsen et al. [82])

correction of coherence gate delay curvature from scanning induced path length variations [130]. Lee et al. [131] and Ahsen et al. [82] have also incorporated algorithms for removing scan delay curvature artifacts introduced by the beam scanners to enable *en face* image optimization in tissue. Figure 28.15 demonstrates this concept for correction of scan delay variation introduced by closely spaced galvanometer scanners, as shown in Fig. 28.15b. A calibration method was first used to extract the delay curvature of the scan and then applied to correct the individual axial scans and produce a delay flattened scan.

28.6.5 State of the Art High Speed OCM System Designs

High speed implementations of OCM for cellular imaging have been developed using both time and Fourier domain detection. Aguirre et al. developed an ultrahigh resolution time domain system at 1,060 nm for imaging at 5 Hz frame rate with

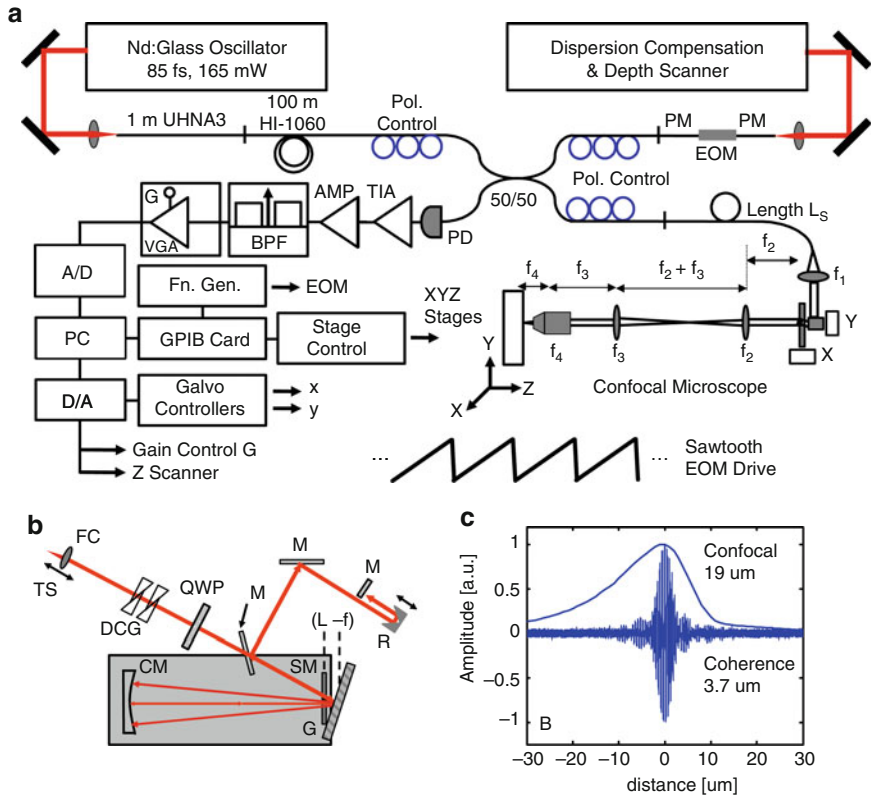

Fig. 28.16 High speed time domain OCM. (**a**) System diagram. The system operates at 1,060 nm center wavelength using a broadband electro-optic waveguide phase modulator. *TIA* transimpedance amplifier, *BPF* bandpass filter, *PD* photodiode, *VGA* variable-gain amplifier, *A/D* analog-to-digital converter, *PC* personal computer, *D/A* digital-to-analog converter, *PM* polarization- maintaining, *EOM* electro-optic modulator. (**b**) Schematic of the reference arm optical delay line used for dispersion compensation and path length scanning. *FC* fiber collimator, *DCG* dispersion compensating glass, *QWP* quarter waveplate, *M* mirror, *R* retroreflector, *CM* curved mirror, *SM* stationary mirror, *G* grating. (**c**) Axial resolution measurements demonstrating a coherence gate of 3.7 um and confocal gate of 19 um (Figure modified from Aguirre et al. [117])

resolutions of <4 um axial and <2 um transverse [117]. This system was demonstrated for in vivo imaging of human skin using a miniaturized endoscopic probe and has been subsequently used extensively for pathology laboratory studies of multiple tissue types [117, 132–135]. Figure 28.16 demonstrates the time domain system design and characterization.

A Nd:Glass femtosecond laser generating 85 fs pulses with >165 mW output power was spectrally broadened by self-phase modulation in a high NA optical fiber to generate >200 nm optical bandwidth centered at 1,060 nm, as shown previously in Fig. 28.10 [83]. A 50/50 fiber optic coupler divided the light between a reference arm and a sample arm, both of which also contained polarization controllers to achieve an

optimized interference point spread function. The reference arm used an electro-optic waveguide phase modulator designed for 1,060 nm center wavelength. After the modulator, reference-arm light passed into a grating optical delay line used for dispersion compensation. The delay line also contained a rapid-depth scanning galvanometer to adjust the coherence gate position. The optical delay line used for dispersion compensation and depth scanning is shown in Fig. 28.16b. The delay line was an all-reflective geometry modified from rapid scanning optical delay (RSOD) line configurations previously used for OCT and OCM [80]. The grating-lens delay was used here only to compensate dispersion, but not to generate group and phase delay, and an additional linear scanning galvanometer was used for depth scanning. In addition, a quarter-wave retarder compensated for wavelength dependent polarization properties of the source. Figure 28.16c demonstrates the measured confocal gate of 19 um and the coherence gate of 3.7 um. A fiber optic confocal microscope with achromatic lenses provided transverse optical resolution of <2 um. This system has been applied for in vivo imaging of human skin, and is readily compatible with endoscopic imaging devices. Figure 28.13 shown previously demonstrates results using this system together with a probe to perform in vivo imaging.

Imaging engines for high speed Fourier domain OCM systems are shown in Fig. 28.17a, b. Lee et al. demonstrated high speed spectral/Fourier domain OCM using a superluminescent diode light source and a fast, low noise charge coupled device (CCD) line scan camera capable of acquiring 210 kHz axial scan rate [131]. The SLD output of $\sim$100 nm bandwidth at 840 nm center wavelength was split between sample and reference arms by a 50/50 coupler and the interfering light was dispersed onto the CCD using a transmission holographic grating. The raw output signal from the CCD was processed using spline interpolation followed by numerical dispersion compensation and fast Fourier transformation (FFT) to reconstruct axial scans. Axial resolution measured 4.2 um and the total axial imaging range was 470 um.

Swept source/Fourier domain OCM was demonstrated by Huang and colleagues using a swept source configuration operating at 42 kHz axial scan rate with image resolution of 1.6 um transverse and 8 um axial [136]. Ahsen et al. extended these results using a high speed VCSEL MEMS tunable laser operating at 1,310 nm capable of 560 kHz axial scan rate, the characteristics of which are shown in Fig. 28.11 [82]. The imaging engine for ultrahigh speed swept source OCM is shown in Fig. 28.17b. An optical clocking method utilizing a Mach-Zehnder interferometer to generate a sampling frequency that drives a high speed data acquisition card allowed sampling of the interference fringes linearly in wavenumber, which eliminates the need for computational resampling and interpolation in post-processing. The system provided axial resolution of 8.1 um in tissue.

The microscopes used in both of the Fourier domain OCM systems (not shown) are inherently similar to the one used in the time domain system inf Fig. 28.16. The Fourier domain systems have an important advantage of allowing dispersion compensation using computational algorithms in post-processing. The lower phase stability and lack of direct access to the measured phase in the time domain makes numerical dispersion compensation much more difficult with time domain systems. As a result, interchange between objective lenses in a time domain system

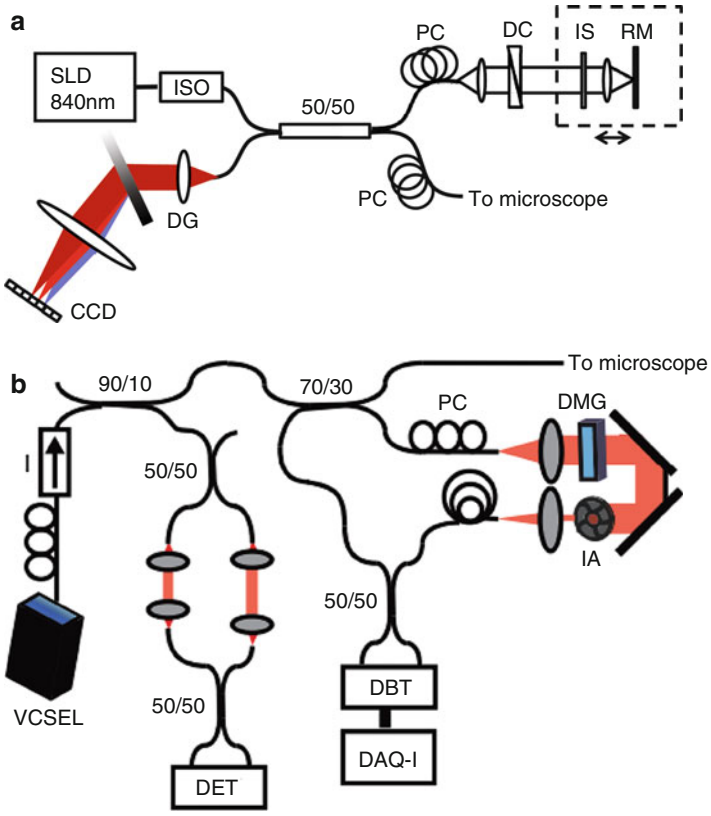

Fig. 28.17 High speed Fourier domain OCM system designs. (**a**) Spectral/Fourier domain OCM system. *PC* polarization controller, *DC* dispersion compensation, *IS* iris, *RM* reference mirror, *GS* galvanometer scanner pair, *OBJ* objectives, *S* sample, *DG* diffraction grating, *CCD* line scan camera, *ISO* isolator. (**b**) VCSEL based swept source/Fourier domain OCM system. *DAQ* Data acquisition card, *DAQ-C* External clock channel, *DAQ-I* Acquisition channel, *DMG* Dispersion matching glass, *IA* Iris attenuator, *DBT* Dual balanced detector, *PS* Pulse shaper, *I* Isolator, *PC* Polarization controller (**a** modified from Lee et al. [131] and **b** modified from Ahsen et al. [82])

requires manual adjustment of dispersion compensation in the system optics. With Fourier domain systems, however, seamless interchange between different objective lenses and imaging with variable magnification can be performed with subsequent computational dispersion compensation.

In a current era where Fourier domain OCT has nearly completely replaced time domain approaches for cross-sectional imaging, time domain methods remain relevant for high speed, ultrahigh resolution OCM. As Fourier domain OCM imaging speeds continue to increase, however, spectral and swept source OCM techniques will likely be the methods of choice for most future investigations. The ease of integration with Fourier domain OCT, as well as the ability to seamlessly switch sample arm optics while incorporating numerical dispersion compensation

and optimization algorithms to minimize optical path length variations, all contribute to systems that are both flexible and reliable for clinical use. Spectral domain OCM has the advantage of offering ultrahigh resolution through use of state of the art broadband laser sources. Swept source OCM, on the other hand, has not yet achieved the coherence gated axial resolution realized with time domain and spectral domain systems, but it has tremendous promise for continued improvement in imaging speeds.

28.7 Cellular Imaging Applications of OCM

As mentioned earlier, investigation of OCM imaging applications has generally lagged behind similar studies with OCT and confocal microscopy, in part because of the technical challenges. Early work developing technology has demonstrated imaging of plants [137], developmental biology specimens [80, 138], human skin [80], and human colonic mucosa [59]. Of the human imaging studies, to date, only imaging of human skin has been performed in vivo [117]. However, the promise of minimally invasive imaging at the cellular level in vivo will undoubtedly push these applications forward in the future as endoscopic microscopy imaging probes emerge. One of the most critical areas of investigation is likely to be early cancer detection. Excisional biopsy and histology are the time-tested gold standards for disease assessment at the tissue and cellular levels, and they continue to be the dominant method used for the diagnosis, staging, and management of many neoplasms. Biopsy and histology, however, can be subject to high false negative rates due to sampling errors, and can pose risks to the patient, such as bleeding, which also limit the ability to screen large areas. Optical imaging technology that provides real-time, high-resolution screening of vulnerable areas with resolution at or near that of histopathology could significantly improve clinicians' capabilities to identify malignancies at curable stages. The ability to visualize the histologic hallmarks of cancer at the tissue architectural and cellular levels, including alterations in glandular or stromal morphology, presence of abnormal mitoses and increased nuclear-to-cytoplasm ratio, in situ and in real time, without the need for tissue excision and processing, would be a major advance in cancer diagnostics.

Studies have now been published investigating OCM for imaging human malignant pathologies in multiple tissues, including the oral mucosa [78], gastrointestinal tract [132], thyroid [134], breast [133], and kidney [135]. Aguirre and colleagues developed a portable, high speed time domain OCM system (system diagram shown in Fig. 28.16) and performed ex vivo imaging of specimens in the hospital pathology laboratory. Imaging at the point of care allowed access to fresh tissue and to samples that could not otherwise be removed from the laboratory. Images were acquired in vitro with transverse resolution of <2 um and axial coherence gated resolution of <5 um over a field of view of up to 400 um square. Figures 28.18 and 28.19 present representative images of the gastrointestinal tract [132]. The image in Fig. 28.18a illustrates the characteristic pattern of squamous cells in the esophagus. Corresponding histology is shown in Fig. 28.18b. In the OCM images as well as

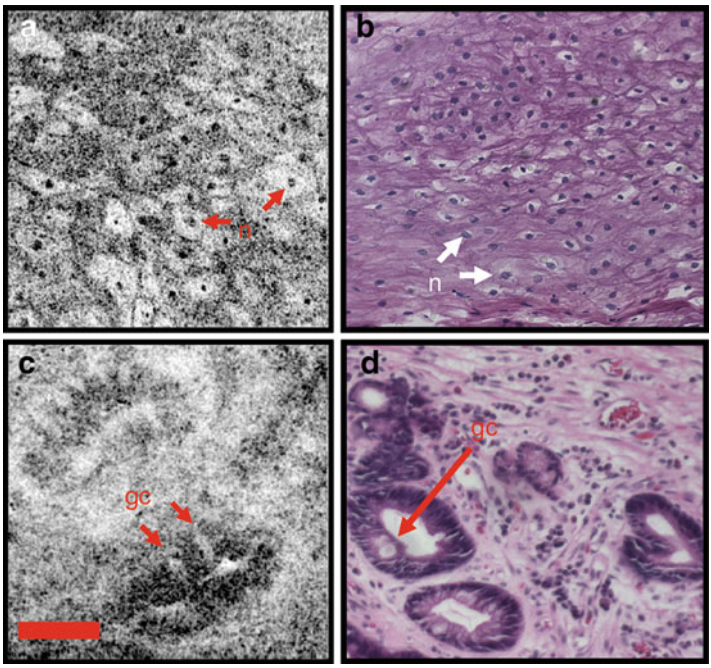

Fig. 28.18 OCM images and histology of normal squamous esophagus and Barrett's esophagus in vitro. Normal squamous mucosa (**a**, **b**) exhibits a characteristic pattern of squamous cells with centrally-located, highly scattering nuclei (*n*). Images of Barrett's epithelium exhibit the presence of intestinalized glands with hallmark barrel-shaped goblet cells (*gc*). Scale bar, 100 um, pertains to all images

histology, cell nuclei can be clearly differentiated from the surrounding cytoplasm and individual membranes which delineate cell boundaries. Figure 28.18c, d show example images of Barrett's esophagus. Barrett's esophagus is a condition in which chronic gastrointestinal reflux leads to a metaplastic change in the esophageal mucosa from the normal squamous architecture to a columnar architecture with similar features to gastric mucosa. The presence of Barrett's metaplasia is a predisposing risk factor for the development of dysplasia and adenocarcinoma of the esophagus. The hallmark histopathologic feature of Barrett's is the presence of barrel-shaped goblet cells. OCM identifies the glandular architecture of the Barrett's mucosa as well as the presence of goblet cells in the columnar epithelium.

Figure 28.19 shows a comparison of OCM images of normal and dysplastic colonic mucosa. The normal colonic mucosa shown in the OCM images and histology of Fig. 28.19a, b, respectively, exhibits a regular pattern of round crypts with numerous goblet cells and nuclei restricted to the basal aspect of the columnar epithelium. In contrast, Fig. 28.19c, d present images and histology from a tubular adenoma with low-grade dysplasia. Glands in the adenoma are larger and exhibit significant eccentricity compared with the small round crypts present in normal

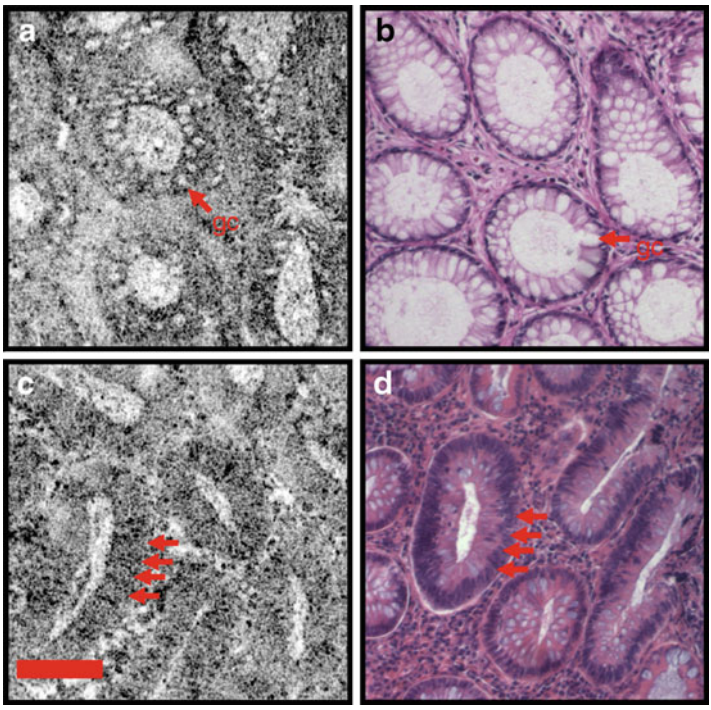

Fig. 28.19 OCM images and histology of normal and dysplastic colon in vitro. Normal colonic mucosa (**a**, **b**) shows the presence of round crypts with goblet cells (*gc*) and basally situated nuclei. Adenomatous dysplastic crypts (**c**, **d**) have increased eccentricity and exhibit characteristic cigar-shaped nuclei (*arrows*) in an epithelium which appears thickened. Scale bar, 100 um

mucosa. In addition, the adenomatous glands show the presence of cigar-shaped nuclei extending beyond the basal third of the columnar epithelium. OCM images correlate well with histology and demonstrate the ability to identify key histologic features of normal and pathologic tissues.

Figure 28.20 shows OCM imaging of malignant conditions of the breast [133]. The figure illustrates distinguishing features between carcinoma in situ and invasive carcinoma visualized with OCM. Lobular carcinoma in situ (LCIS), shown in A, and ductal carcinoma in situ (DCIS), shown in B, appear well circumscribed with a defined contour that is identifiable within the surrounding stroma. Invasive carcinoma, shown in C, destroys the normal stromal architecture with infiltration of tumor cells. The ability to aid in guiding core needle biopsy of breast lesions or in surgical resection margin assessment would be an important advance in the management of breast malignancies.

OCM achieves high resolution in three-dimensions for visualization of cellular and subcellular morphology. However, due to the high magnification of the objective lens, the field of view in OCM is generally restricted to the range of 500 um. From a clinical perspective, OCM is essentially a point-sampling technique and will

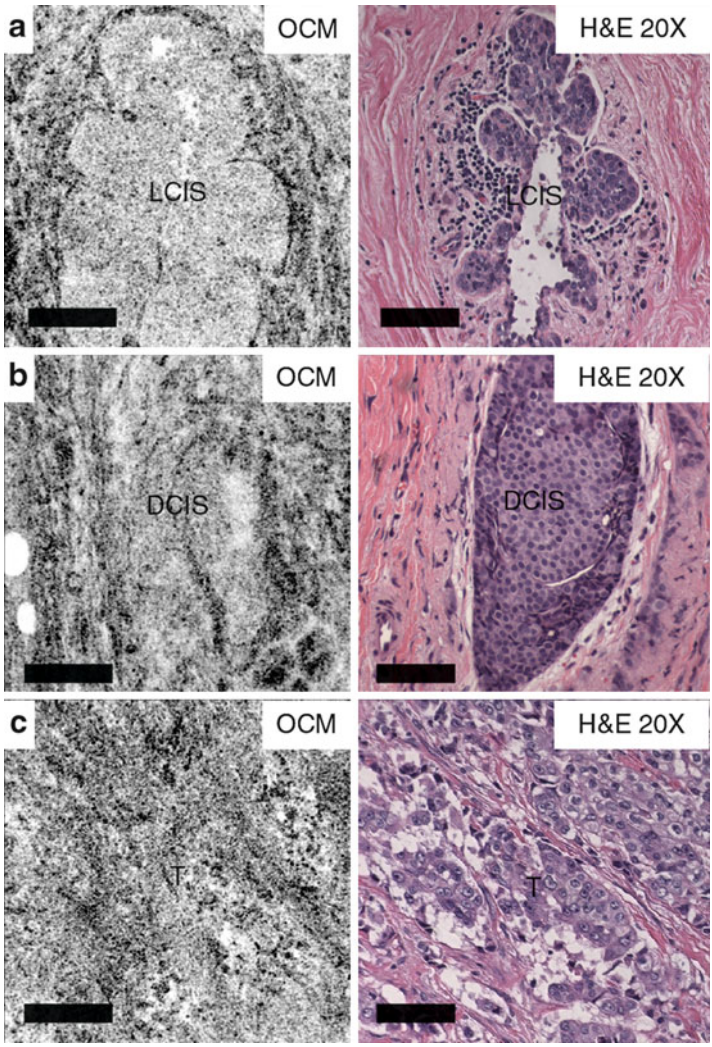

Fig. 28.20 OCM images and histology of neoplastic breast tissue in vitro. (**a**) Lobular carcinoma in situ, LCIS, and (**b**) ductal carcinoma in situ, DCIS, appear well circumscribed with a defined contour that is identifiable within the surrounding stroma. Invasive carcinoma (**c**) destroys the normal stromal architecture with infiltration of tumor cells, T Scale bars, 100 um (Images reproduced from Zhou et al. [133])

therefore suffer from sampling error in screening and diagnostic applications. One solution to this limitation involves the combination of OCM with conventional OCT imaging. Figure 28.21 presents an example data set to illustrate this point. The data was acquired with a combined OCT and OCM microscope with an adjustable objective lens magnification [117]. The microscope allowed precise registration of *en face* OCM images to OCT cross sectional image data. Figure 28.21a shows an

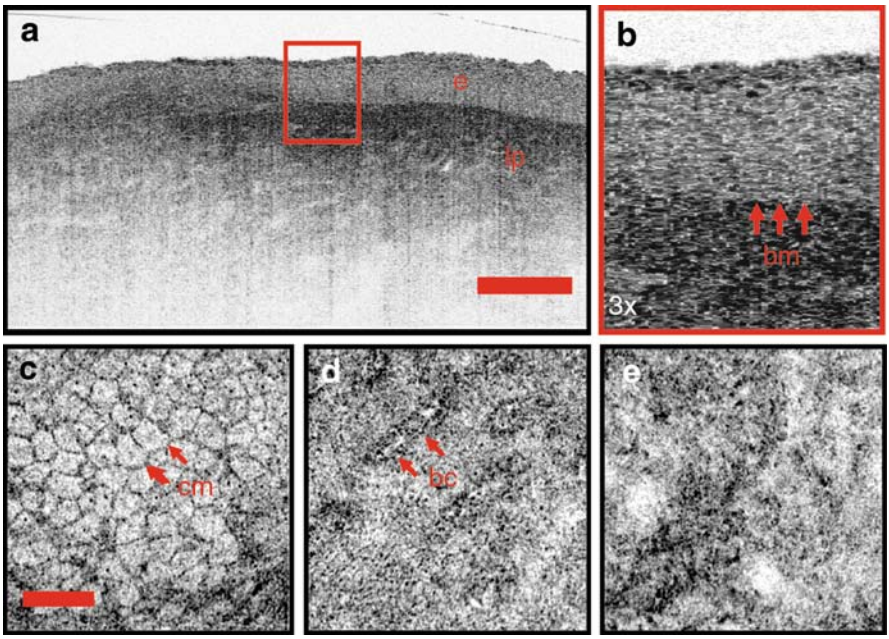

Fig. 28.21 Co-registered OCT and OCM imaging of normal cervix. Ultrahigh resolution OCT (**a**, **b**) clearly identifies the layers of the cervical mucosa and delineates the basement membrane (*bm*) separating the epithelium from the underlying lamina propria. OCM images at progressive depths identify cell membranes (*cm*) in the upper epithelium (**c**) as well as the rim of basal cells (*bc*) surrounding the ridges of lamina propria (**d**). OCM can image deep into the lamina propria, shown here by an image of the loose connective tissue at 400 um depth (**e**). Scale bars, (**a**) 500 um, (**c**) 100 um (Figure modified from Aguirre et al. [117])

ultrahigh resolution OCT image of squamous mucosa of the cervix. Transverse resolution was measured to be ~12 um with axial resolution of <3 um, and the field of view was 3 mm in length. OCT provides cross-sectional visualization of the epithelial layer thickness, with clear delineation of the basement membrane and underlying lamina propria. The lamina propria appears highly scattering compared with the stratified squamous epithelium. As shown by the 3× zoom view in Fig. 28.21b, OCT cannot clearly delineate cellular structure due to its limited transverse resolution. *En face* OCM images of the same region delineated by this zoom view allows cellular resolution with <2 um resolution over a restricted field of view. Figure 28.21c, d, e were obtained at imaging depths of 60 um, 150 um, and 400 um below the surface, respectively. The regular pattern of squamous cells is evident in Fig. 28.21c, while Fig. 28.21d shows the ridges of lamina propria projecting through the lower epithelial layers. A highly scattering rim of basal cells can be seen surrounding the islands of lamina propria. Figure 28.21e shows the disorganized loose connective tissue deep below the tissue surface.

The concept of imaging over multiple fields of view to allow visualization of tissue architecture at varying resolutions is a promising approach in clinical

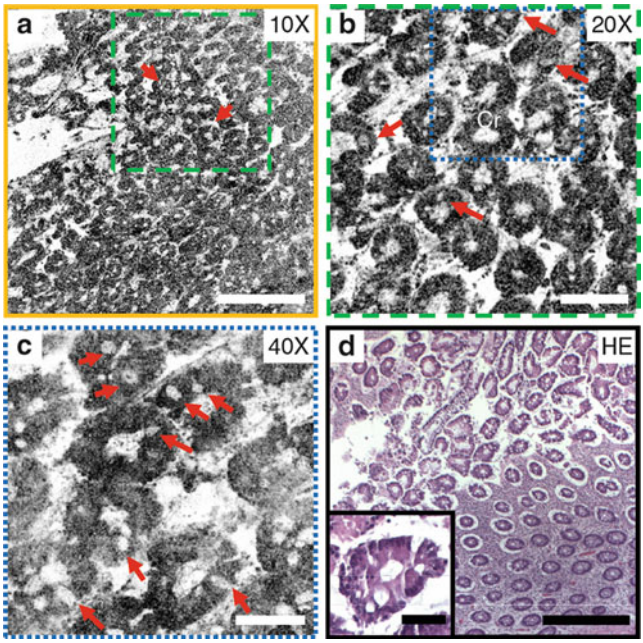

Fig. 28.22 Multi-scale OCM images of human colon, ex vivo. Coregistered images are acquired with (**a**) 10×, (**b**) 20×, and (**c**) 40× objectives. (**d**) Corresponding H&E histology image showing normal crypts in human colon. Scale bars: 10×: 500 um; 20×: 200 um; 40×: 100 um; HE: 500 um; Inlet: 50 um. Crypts, Cr. Goblet cells, *red arrows* (Images reproduced from Lee et al. [131])

applications such as endoscopic surveillance for dysplasia or resection of tumor margins. In these scenarios a clinically useful imaging solution should provide both high resolution to enable visualization of important architectural and cellular features as well as broad area coverage to avoid sampling error and excessive false negative rates. With high imaging speeds that are now available using OCT with Fourier domain detection techniques, it is becoming possible to survey large areas of tissue in vivo, which allows the user to identify areas of interest for closer inspection [139, 140]. OCM could then be used to look directly at cellular and glandular features in these focal regions. This mode of operation would be similar to the approach used by pathologists when viewing conventional histopathology slides. A lower magnification is first used to gain an appreciation for the overall tissue architecture including layers and glandular organization. Then a high magnification is used to investigate cellular features. Both views provide important information used for making a diagnosis. OCT and OCM can function as complementary imaging methods in an analogous way. OCT can survey large areas of tissue architectural morphology in a cross-sectional view, while OCM can provide high, cellular level resolution in an *en face* view.

Figure 28.22 shows a series of co-registered OCM images of human colon taken with varying magnifications using a spectral/Fourier domain OCM system to illustrate

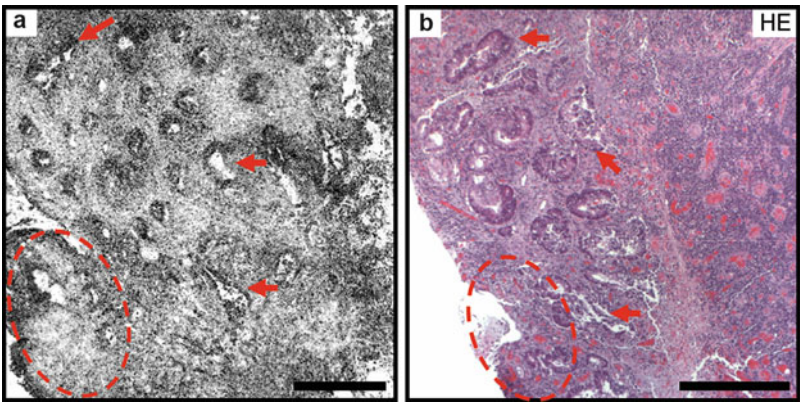

Fig. 28.23 Mosaicked OCM image of the human colon specimen with ulcerative colitis. (**a**) Nine individual 900 × 900 um images taken with a 20× objective are combined to create a mosaicked image with enhanced field of view of 2.1 × 2.1 mm^2. (**b**) Corresponding H&E histology image. Scale bars, 500 um. Crypts, *red arrows* (Images reproduced from Lee et al. [131])

this point [131], At lower magnification (10×) the organization of crypt structure can be appreciated, while use of higher magnification (20× and 40×) allows analysis of cellular features, including individual goblet cells. Miniaturized OCM imaging probes using zoom lens technology may in the future allow users to seamlessly change magnification and to flip between cross-sectional and *en face* views as needed to analyze tissue morphology in vivo during endoscopic or surgical procedures.

The field of view can also be extended in OCM utilizing mosaicking techniques, as has been done in confocal microscopy [141]. Figure 28.23 presents an example of mosaicking using OCM. Nine individual en face OCM images, each with 900 × 900 um field of view and acquired with a 20× objective lens, were assembled with an overlap ratio of 33 % to generate the mosaicked OCM image over a large imaging area (2.1 × 2.1 mm^2) [131]. Comparative histology is also shown. Compared to wide field acquisition of images at lower magnification, mosaicking approaches require longer acquisition time but can offer composite high definition images with both very high resolution and large field of view.

28.8 Summary and Future Prospects

This chapter has reviewed several important developments in optical coherence microscopy during the past 20–25 years. Techniques are progressing rapidly and new system designs and technology are becoming available for high-speed imaging. Miniaturized two-axis scanning devices are also being developed for endoscopic and laparoscopic applications. In addition, ex vivo tissue imaging studies are establishing the validity of OCM imaging in various organ systems. OCM undoubtedly represents an important advance in OCT imaging generally, but its ultimate clinical utility remains to be determined. OCM has several important advantages compared with confocal

microscopy, but the imaging technology is generally more complex. However, the development of high speed Fourier domain detection techniques is an important advance because it will enable OCM to be integrated with existing confocal scanning microscopes. The ability of OCM to provide variable magnifications and fields of view in microscopy, image tissue without the need for exogenous contrast, and integrate with endoscopic imaging devices, promises to provide powerful new approaches to make real-time, in situ, cellular-resolution optical biopsy a clinical reality.

Acknowledgments We would like to acknowledge scientific discussions and contributions from Drs. Yu Chen, James Connolly, Shu-Wei Huang, Robert Huber, Desmond Adler, Norihiko Nishizawa, Joseph Schmitt. This research was sponsored in part by the National Institutes of Health R01-CA75289, R01-EY11289, and R01-CA178636; the Air Force Office of Scientific Research FA9550-040-1-0011 and F∼9550-12-1-0499.

References

1. M. Minsky, *Microscopy Apparatus*, (U.S.A., 1961)
2. D.R. Sandison, W.W. Webb, Background rejection and signal-to-noise optimization in confocal and alternative fluorescence microscopes. Appl. Opt. **33**, 603–615 (1994)
3. T. Corle, G. Kino, *Confocal Scanning Optical Microscopy and Related Imaging Systems* (Academic, San Diego, 1996)
4. M. Rajadhyaksha, R.R. Anderson, R.H. Webb, Video-rate confocal scanning laser microscope for imaging human tissues in vivo. Appl. Opt. **38**, 2105–2115 (1999)
5. M. Rajadhyaksha, S. Gonzalez, J.M. Zavislan, R.R. Anderson, R.H. Webb, In vivo confocal scanning laser microscopy of human skin II: advances in instrumentation and comparison with histology. J. Investig. Dermatol. **113**, 293–303 (1999)
6. P. Davidovits, M.D. Egger, Scanning laser microscope. Nature **223**, 831 (1969)
7. P. Davidovits, M.D. Egger, Scanning laser microscope for biological investigations. Appl. Opt. **10**, 1615–1619 (1971)
8. M. Rajadhyaksha, M. Grossman, D. Esterowitz, R.H. Webb, R.R. Anderson, In vivo confocal scanning laser microscopy of human skin: melanin provides strong contrast. J. Invest. Dermatol. **104**, 946–952 (1995)
9. M. Rajadhyaksha, S. Gonzalez, J.M. Zavislan, R.R. Anderson, R.H. Webb, In Vivo confocal scanning laser microscopy of human skin II: advances in instrumentation and comparison with histology. J. Invest. Dermatol. **113**, 293–303 (1999)
10. M. Rajadhyaksha, G. Menaker, T. Flotte, P. Dwyer, S. Gonzalez, Confocal examination of nonmelanoma cancers in thick skin excisions to potentially guide mohs micrographic surgery without frozen histopathology. J. Invest. Dermatol. **117**, 1137–1143 (2001)
11. M. Huzaira, F. Rius, M. Rajadhyaksha, R. Anderson, S. Gonzalez, Topographic variations in normal skin, as viewed by in vivo reflectance confocal microscopy. J. Invest. Dermatol. **116**, 846–852 (2001)
12. R. Langley, M. Rajadhyaksha, P. Dwyer, A. Sober, T. Flotte, R. Anderson, Confocal scanning laser microscopy of benign and malignant melanocytic skin lesions in vivo. J. Am. Acad. Dermatol. **45**, 365–376 (2001)
13. S. Gonzalez, Characterization of psoriasis in vivo by confocal reflectance microscopy. J. Med. **30**, 337–356 (1999)
14. W.M. White, M. Rajadhyaksha, R.L. Fabian, R.R. Anderson, Noninvasive imaging of human oral mucosa in vivo by confocal reflectance microscopy. Laryngoscope **109**, 1709–1717 (1999)
15. R.A. Drezek, T. Collier, C.K. Brookner, A. Malpica, R. Lotan, R.R. Richards-Kortum, M. Follen, Laser scanning confocal microscopy of cervical tissue before and after application of acetic acid. Am. J. Obstet. Gynecol. **182**, 1135–1139 (2000)

16. K.B. Sung, C. Liang, M. Descour, T. Collier, M. Follen, R. Richards-Kortum, Fiber-optic confocal reflectance microscope with miniature objective for in vivo imaging of human tissues. IEEE Trans. Biomed. Eng. **49**, 1168–1172 (2002)
17. C. Pitris, B.E. Bouma, M. Shiskov, G.J. Tearney, A GRISM-based probe for spectrally encoded confocal microscopy. Opt. Express **11**, 120–124 (2003)
18. A.L. Polglase, W.J. McLaren, S.A. Skinner, R. Kiesslich, M.F. Neurath, P.M. Delaney, A fluorescence confocal endomicroscope for in vivo microscopy of the upper- and the lower-GI tract. Gastrointest. Endosc. **62**, 686–695 (2005)
19. A.R. Rouse, A. Kano, J.A. Udovich, S.M. Kroto, A.F. Gmitro, Design and demonstration of a miniature catheter for a confocal microendoscope. Appl. Opt. **43**, 5763–5771 (2004)
20. P.M. Delaney, M.R. Harris, R.G. King, Fiberoptic laser-scanning confocal microscope suitable for fluorescence imaging. Appl. Opt. **33**, 573–577 (1994)
21. R. Kiesslich, J. Burg, M. Vieth, J. Gnaendiger, M. Enders, P. Delaney, A. Polglase, W. McLaren, D. Janell, S. Thomas, B. Nafe, P.R. Galle, M.F. Neurath, Confocal laser endoscopy for diagnosing intraepithelial neoplasias and colorectal cancer in vivo. Gastroenterology **127**, 706–713 (2004)
22. M. Bajbouj, M. Vieth, T. Rosch, S. Miehlke, V. Becker, M. Anders, H. Pohl, A. Madisch, T. Schuster, R.M. Schmid, A. Meining, Probe-based confocal laser endomicroscopy compared with standard four-quadrant biopsy for evaluation of neoplasia in Barrett's esophagus. Endoscopy **42**, 435–440 (2010)
23. P. Sharma, A.R. Meining, E. Coron, C.J. Lightdale, H.C. Wolfsen, A. Bansal, M. Bajbouj, J.P. Galmiche, J.A. Abrams, A. Rastogi, N. Gupta, J.E. Michalek, G.Y. Lauwers, M.B. Wallace, Real-time increased detection of neoplastic tissue in Barrett's esophagus with probe-based confocal laser endomicroscopy: final results of an international multicenter, prospective, randomized, controlled trial. Gastrointest. Endosc. **74**, 465–472 (2011)
24. M.B. Sturm, C. Piraka, B.J. Elmunzer, R.S. Kwon, B.P. Joshi, H.D. Appelman, D.K. Turgeon, T.D. Wang, In vivo molecular imaging of Barrett's esophagus with confocal laser endomicroscopy. Gastroenterology **145**, 56–58 (2013)
25. J.M. Schmitt, S.L. Lee, K.M. Yung, An optical coherence microscope with enhanced resolving power in thick tissue. Opt. Commun. **142**, 203–207 (1997)
26. F. Lexer, C.K. Hitzenberger, W. Drexler, S. Molebny, H. Sattmann, M. Sticker, A.F. Fercher, Dynamic coherent focus OCT with depth-independent transversal resolution. J. Mod. Opt. **46**, 541–553 (1999)
27. B. Qi, A.P. Himmer, L.M. Gordon, X.D.V. Yang, L.D. Dickensheets, I.A. Vitkin, Dynamic focus control in high-speed optical coherence tomography based on a microelectromechanical mirror. Opt. Commun. **232**, 123–128 (2004)
28. V.X. Yang, Y. Mao, B.A. Standish, N.R. Munce, S. Chiu, D. Burnes, B.C. Wilson, I.A. Vitkin, P.A. Himmer, D.L. Dickensheets, Doppler optical coherence tomography with a micro-electro-mechanical membrane mirror for high-speed dynamic focus tracking. Opt. Lett. **31**, 1262–1264 (2006)
29. A. Divetia, T.H. Hsieh, J. Zhang, Z.P. Chen, M. Bachman, G.P. Li, Dynamically focused optical coherence tomography for endoscopic applications. Appl. Phys. Lett. **86**, 103902 (2005)
30. S. Murali, K.P. Thompson, J.P. Rolland, Three-dimensional adaptive microscopy using embedded liquid lens. Opt. Lett. **34**, 145–147 (2009)
31. R. Leitgeb, C.K. Hitzenberger, A.F. Fercher, Performance of Fourier domain vs. time domain optical coherence tomography. Opt. Express **11**, 889–894 (2003)
32. M.A. Choma, M.V. Sarunic, C.H. Yang, J.A. Izatt, Sensitivity advantage of swept source and Fourier domain optical coherence tomography. Opt. Express **11**, 2183–2189 (2003)
33. J.F. de Boer, B. Cense, B.H. Park, M.C. Pierce, G.J. Tearney, B.E. Bouma, Improved signal-to-noise ratio in spectral-domain compared with time-domain optical coherence tomography. Opt. Lett. **28**, 2067–2069 (2003)

34. N. Nassif, B. Cense, B.H. Park, S.H. Yun, T.C. Chen, B.E. Bouma, G.J. Tearney, J.F. de Boer, In vivo human retinal imaging by ultrahigh-speed spectral domain optical coherence tomography. Opt. Lett. **29**, 480–482 (2004)
35. M. Wojtkowski, T. Bajraszewski, P. Targowski, A. Kowalczyk, Real-time in vivo imaging by high-speed spectral optical coherence tomography. Opt. Lett. **28**, 1745–1747 (2003)
36. H.C. Lowe, J. Narula, J.G. Fujimoto, I.K. Jang, Intracoronary optical diagnostics current status, limitations, and potential. JACC Cardiovasc. Interv. **4**, 1257–1270 (2011)
37. W. Drexler, U. Morgner, F.X. Kartner, C. Pitris, S.A. Boppart, X.D. Li, E.P. Ippen, J.G. Fujimoto, In vivo ultrahigh-resolution optical coherence tomography. Opt. Lett. **24**, 1221–1223 (1999)
38. R. Huber, M. Wojtkowski, J.G. Fujimoto, J.Y. Jiang, A.E. Cable, Three-dimensional and C-mode OCT imaging with a compact, frequency swept laser source at 1300 nm. Opt. Express **13**, 10523–10538 (2005)
39. J.P. Rolland, P. Meemon, S. Murali, K.P. Thompson, K.S. Lee, Gabor-based fusion technique for optical coherence microscopy. Opt. Express **18**, 3632–3642 (2010)
40. V.X. Yang, N. Munce, J. Pekar, M.L. Gordon, S. Lo, N.E. Marcon, B.C. Wilson, I.A. Vitkin, Micromachined array tip for multifocus fiber-based optical coherence tomography. Opt. Lett. **29**, 1754–1756 (2004)
41. Z. Ding, H. Ren, Y. Zhao, J.S. Nelson, Z. Chen, High-resolution optical coherence tomography over a large depth range with an axicon lens. Opt. Lett. **27**, 243–245 (2002)
42. R.A. Leitgeb, M. Villiger, A.H. Bachmann, L. Steinmann, T. Lasser, Extended focus depth for Fourier domain optical coherence microscopy. Opt. Lett. **31**, 2450–2452 (2006)
43. L.B. Liu, J.A. Gardecki, S.K. Nadkarni, J.D. Toussaint, Y. Yagi, B.E. Bouma, G.J. Tearney, Imaging the subcellular structure of human coronary atherosclerosis using micro-optical coherence tomography. Nat. Med. **17**, 1010–U1132 (2011)
44. L. Liu, K.K. Chu, G.H. Houser, B.J. Diephuis, Y. Li, E.J. Wilsterman, S. Shastry, G. Dierksen, S.E. Birket, M. Mazur, S. Byan-Parker, W.E. Grizzle, E.J. Sorscher, S.M. Rowe, G.J. Tearney, Method for quantitative study of airway functional microanatomy using micro-optical coherence tomography. PLoS One **8**, e54473 (2013)
45. T.S. Ralston, D.L. Marks, F. Kamalabadi, S.A. Boppart, Deconvolution methods for mitigation of transverse blurring in optical coherence tomography. IEEE Trans. Image Process. **14**, 1254–1264 (2005)
46. T.S. Ralston, D.L. Marks, P.S. Carney, S.A. Boppart, Interferometric synthetic aperture microscopy. Nat. Phys. **3**, 129–134 (2007)
47. S.G. Adie, B.W. Graf, A. Ahmad, P.S. Carney, S.A. Boppart, Computational adaptive optics for broadband optical interferometric tomography of biological tissue. Proc. Natl. Acad. Sci. U. S. A. **109**, 7175–7180 (2012)
48. A. Ahmad, N.D. Shemonski, S.G. Adie, H.S. Kim, W.M.W. Hwu, P.S. Carney, S.A. Boppart, Real-time in vivo computed optical interferometric tomography. Nat. Photonics **7**, 445–449 (2013)
49. A.G. Podoleanu, J.A. Rogers, D.A. Jackson, S. Dunne, Three dimensional OCT images from retina and skin. Opt. Express **7**, 292–298 (2000)
50. M.J. Cobb, X. Liu, X. Li, Continuous focus tracking for real-time optical coherence tomography. Opt. Lett. **30**, 1680–1682 (2005)
51. J.A. Izatt, M.R. Hee, G.M. Owen, E.A. Swanson, J.G. Fujimoto, Optical coherence microscopy in scattering media. Opt. Lett. **19**, 590–592 (1994)
52. T. Sawatari, Optical heterodyne scanning microscope. Appl. Opt. **12**, 2768–2772 (1973)
53. D.K. Hamilton, C.J.R. Sheppard, A confocal interference microscope. Optica Acta **29**, 1573–1577 (1982)
54. M. Gu, C.J.R. Sheppard, Fiberoptic confocal scanning interference microscopy. Opt. Commun. **100**, 79–86 (1993)
55. M. Gu, C.J.R. Sheppard, Experimental investigation of fiberoptic confocal scanning microscopy – including a comparison with pinhole detection. Micron **24**, 557–565 (1993)

56. H. Zhou, C.J.R. Sheppard, M. Gu, A compact confocal interference microscope based on a four-port single-mode fibre coupler. Optik **103**, 45–48 (1996)
57. M. Kempe, W. Rudolph, Analysis of heterodyne and confocal microscopy for illumination with broad-bandwidth light. J. Mod. Opt. **43**, 2189–2204 (1996)
58. M. Kempe, W. Rudolph, E. Welsch, Comparative study of confocal and heterodyne microscopy for imaging through scattering media. J. Opt. Soc. Am.Opt. Image Sci. Vis. **13**, 46–52 (1996)
59. J.A. Izatt, M.D. Kulkarni, H.-W. Wang, K. Kobayashi, M.V. Sivak Jr., Optical coherence tomography and microscopy in gastrointestinal tissues. IEEE J. Sel. Top. Quantum Electron. **2**, 1017–1028 (1996)
60. A.G. Podoleanu, M. Seeger, G.M. Dobre, D.J. Webb, D.A. Jackson, F.W. Fitzke, Transversal and longitudinal images from the retina of the living eye using low coherence reflectometry. J. Biomed. Opt. **3**, 12–20 (1998)
61. S.H. Yun, G.J. Tearney, J.F. de Boer, N. Iftimia, B.E. Bouma, High-speed optical frequency-domain imaging. Opt. Express **11**, 2953–2963 (2003)
62. R. Huber, M. Wojtkowski, K. Taira, J.G. Fujimoto, K. Hsu, Amplified, frequency swept lasers for frequency domain reflectometry and OCT imaging: design and scaling principles. Opt. Express **13**, 3513–3528 (2005)
63. M.A. Choma, A.K. Ellerbee, C. Yang, T.L. Creazzo, J.A. Izatt, Spectral-domain phase microscopy. Opt. Lett. **30**, 1162–1164 (2005)
64. C. Joo, T. Akkin, B. Cense, B.H. Park, J.F. de Boer, Spectral-domain optical coherence phase microscopy for quantitative phase-contrast imaging. Opt. Lett. **30**, 2131–2133 (2005)
65. M. Wojtkowski, V.J. Srinivasan, T.H. Ko, J.G. Fujimoto, A. Kowalczyk, J.S. Duker, Ultrahigh-resolution, high-speed, Fourier domain optical coherence tomography and methods for dispersion compensation. Opt. Express **12**, 2404–2422 (2004)
66. C. Xu, C. Vinegoni, T.S. Ralston, W. Luo, W. Tan, S.A. Boppart, Spectroscopic spectral-domain optical coherence microscopy. Opt. Lett. **31**, 1079–1081 (2006)
67. W. Wieser, B.R. Biedermann, T. Klein, C.M. Eigenwillig, R. Huber, Multi-megahertz OCT: high quality 3D imaging at 20 million A-scans and 4.5 GVoxels per second. Opt. Express **18**, 14685–14704 (2010)
68. V. Jayaraman, G.D. Cole, M. Robertson, A. Uddin, A. Cable, High-sweep-rate 1310 nm MEMS-VCSEL with 150 nm continuous tuning range. Electron. Lett. **48**, 867–868 (2012)
69. T.H. Tsai, B. Potsaid, Y.K. Tao, V. Jayaraman, J. Jiang, P.J.S. Heim, M.F. Kraus, C. Zhou, J. Hornegger, H. Mashimo, A.E. Cable, J.G. Fujimoto, Ultrahigh speed endoscopic optical coherence tomography using micromotor imaging catheter and VCSEL technology. Biomed. Opt. Express **4**, 1119–1132 (2013)
70. M. Hee, Optical coherence tomography: theory, in *Handbook of Optical Coherence Tomography*, ed. by B. Bouma, G. Tearney (Marcel Dekker, New York, 2002)
71. M. Gu, C.J.R. Sheppard, X. Gan, Image-formation in a fiberoptic confocal scanning microscope. J. Opt. Soc. Am.Opt. Image Sci. Vis. **8**, 1755–1761 (1991)
72. H.-W. Wang, J. Izatt, M. Kulkarni, Optical coherence microscopy, in *Handbook of Optical Coherence Tomography*, ed. by B. Bouma, G. Tearney (Marcel Dekker, New York, 2002), pp. 275–298
73. C.J.R. Sheppard, M. Gu, K. Brain, H. Zhou, Influence of spherical-aberration on axial imaging of confocal reflection microscopy. Appl. Opt. **33**, 616–624 (1994)
74. C.L. Smithpeter, A.K. Dunn, A.J. Welch, R. Richards-Kortum, Penetration depth limits of in vivo confocal reflectance imaging. Appl. Opt. **37**, 2749–2754 (1998)
75. J.M. Schmitt, K. BenLetaief, Efficient monte carlo simulation of confocal microscopy in biological tissue. J. Opt. Soc. Am.Opt. Image Sci. Vis. **13**, 952–961 (1996)
76. J.M. Schmitt, A. Knuttel, M. Yadlowsky, Confocal microscopy in turbid media. J. Opt. Soc. Am. A Opt. Image Sci. Vis. **11**, 2226–2235 (1994)
77. J.M. Schmitt, A. Knuttel, Model of optical coherence tomography of heterogeneous tissue. J. Opt. Soc. Am. A Opt. Image Sci. Vis. **14**, 1231–1242 (1997)

78. A.L. Clark, A. Gillenwater, R. Alizadeh-Naderi, A.K. El-Naggar, R. Richards-Kortum, Detection and diagnosis of oral neoplasia with an optical coherence microscope. J. Biomed. Opt. **9**, 1271–1280 (2004)
79. K. Bizheva, *Low Coherence Interferometry in Turbid Media: The Effect of Multiply Scattered Light Detection on Image Quality* (Department of Physics and Astronomy, Tufts University, Boston, 2001), p. 168
80. A.D. Aguirre, P. Hsiung, T.H. Ko, I. Hartl, J.G. Fujimoto, High-resolution optical coherence microscopy for high-speed, in vivo cellular imaging. Opt. Lett. **28**, 2064–2066 (2003)
81. C. Liang, K.B. Sung, R.R. Richards-Kortum, M.R. Descour, Design of a high-numerical-aperture miniature microscope objective for an endoscopic fiber confocal reflectance microscope. Appl. Opt. **41**, 4603–4610 (2002)
82. O.O. Ahsen, Y.K. Tao, B.M. Potsaid, Y. Sheikine, J. Jiang, I. Grulkowski, T.H. Tsai, V. Jayaraman, M.F. Kraus, J.L. Connolly, J. Hornegger, A. Cable, J.G. Fujimoto, Swept source optical coherence microscopy using a 1310 nm VCSEL light source. Opt. Express **21**, 18021–18033 (2013)
83. S. Bourquin, A.D. Aguirre, I. Hartl, P. Hsiung, T.H. Ko, J.G. Fujimoto, T.A. Birks, W.J. Wadsworth, U. Bunting, D. Kopf, Ultrahigh resolution real time OCT imaging using a compact femtosecond Nd: glass laser and nonlinear fiber. Opt. Express **11**, 3290–3297 (2003)
84. Y.M. Wang, J.S. Nelson, Z.P. Chen, B.J. Reiser, R.S. Chuck, R.S. Windeler, Optimal wavelength for ultrahigh-resolution optical coherence tomography. Opt. Express **11**, 1411–1417 (2003)
85. K.B. Sung, C. Liang, M. Descour, T. Collier, M. Follen, A. Malpica, R. Richards-Kortum, Near real time in vivo fibre optic confocal microscopy: sub-cellular structure resolved. J. Microsc. **207**, 137–145 (2002)
86. F.E. Robles, C. Wilson, G. Grant, A. Wax, Molecular imaging true-colour spectroscopic optical coherence tomography. Nat. Photonics **5**, 744–747 (2011)
87. R. Huber, M. Wojtkowski, J.G. Fujimoto, Fourier Domain Mode Locking (FDML): a new laser operating regime and applications for optical coherence tomography. Opt. Express **14**, 3225–3237 (2006)
88. B.M. Hoeling, A.D. Fernandez, R.C. Haskell, D.C. Petersen, Phase modulation at 125 kHz in a Michelson interferometer using an inexpensive piezoelectric stack driven at resonance. Rev. Sci. Instrum. **72**, 1630–1633 (2001)
89. G.J. Tearney, B.E. Bouma, J.G. Fujimoto, High-speed phase- and group-delay scanning with a grating-based phase control delay line. Opt. Lett. **22**, 1811–1813 (1997)
90. A.M. Rollins, M.D. Kulkarni, S. Yazdanfar, R. Ung-arunyawee, J.A. Izatt, In vivo video rate optical coherence tomography. Opt. Express **3**, 219–229 (1998)
91. A.V. Zvyagin, D.D. Sampson, Achromatic optical phase shifter-modulator. Opt. Lett. **26**, 187–189 (2001)
92. V. Westphal, S. Yazdanfar, A.M. Rollins, J.A. Izatt, Real-time, high velocity-resolution color Doppler optical coherence tomography. Opt. Lett. **27**, 34–36 (2002)
93. J.F. de Boer, C.E. Saxer, J.S. Nelson, Stable carrier generation and phase-resolved digital data processing in optical coherence tomography. Appl. Opt. **40**, 5787–5790 (2001)
94. Y. Zhao, Z. Chen, C. Saxer, S. Xiang, J.F. de Boer, J.S. Nelson, Phase-resolved optical coherence tomography and optical Doppler tomography for imaging blood flow in human skin with fast scanning speed and high velocity sensitivity. Opt. Lett. **25**, 114–116 (2000)
95. T.Q. Xie, Z.G. Wang, Y.T. Pan, High-speed optical coherence tomography using fiberoptic acousto-optic phase modulation. Opt. Express **11**, 3210–3219 (2003)
96. M. Pircher, E. Goetzinger, R. Leitgeb, C.K. Hitzenberger, Transversal phase resolved polarization sensitive optical coherence tomography. Phys. Med. Biol. **49**, 1257–1263 (2004)
97. T.Q. Xie, Z.G. Wang, Y.T. Pan, Dispersion compensation in high-speed optical coherence tomography by acousto-optic modulation. Appl. Opt. **44**, 4272–4280 (2005)

98. K. Wiesauer, M. Pircher, E. Gotzinger, S. Bauer, R. Engelke, G. Ahrens, G. Grutzner, C.K. Hitzenberger, D. Stifter, En-face scanning optical coherence tomography with ultra-high resolution for material investigation. Opt. Express **13**, 1015–1024 (2005)
99. Y.C. Chen, X.D. Li, Dispersion management up to the third order for real-time optical coherence tomography involving a phase or frequency modulator. Opt. Express **12**, 5968–5978 (2004)
100. Y.C. Chen, X.M. Liu, M.J. Cobb, M.T. Myaing, T. Sun, X.D. Li, Optimization of optical spectral throughput of acousto-optic modulators for high-speed optical coherence tomography. Opt. Express **13**, 7816–7822 (2005)
101. A.G. Podoleanu, G.M. Dobre, D.J. Webb, D.A. Jackson, Coherence imaging by use of a Newton rings sampling function. Opt. Lett. **21**, 1789–1791 (1996)
102. A.G. Podoleanu, G.M. Dobre, D.A. Jackson, En-face coherence imaging using galvanometer scanner modulation. Opt. Lett. **23**, 147–149 (1998)
103. Z. Yaqoob, J. Fingler, X. Heng, C. Yang, Homodyne en face optical coherence tomography. Opt. Lett. **31**, 1815–1817 (2006)
104. J. Knittel, L. Schnieder, G. Buess, B. Messerschmidt, T. Possner, Endoscope-compatible confocal microscope using a gradient index-lens system. Opt. Commun. **188**, 267–273 (2001)
105. P.M. Lane, A.L.P. Dlugan, R. Richards-Kortum, C.E. MacAulay, Fiber-optic confocal microscopy using a spatial light modulator. Opt. Lett. **25**, 1780–1782 (2000)
106. Y.S. Sabharwal, A.R. Rouse, L. Donaldson, M.F. Hopkins, A.F. Gmitro, Slit-scanning confocal microendoscope for high-resolution in vivo imaging. Appl. Opt. **38**, 7133–7144 (1999)
107. A.F. Gmitro, D. Aziz, Confocal microscopy through a fiberoptic imaging bundle. Opt. Lett. **18**, 565–567 (1993)
108. T. Xie, D. Mukai, S. Guo, M. Brenner, Z. Chen, Fiber-optic-bundle-based optical coherence tomography. Opt. Lett. **30**, 1803–1805 (2005)
109. F. Helmchen, M.S. Fee, D.W. Tank, W. Denk, A miniature head-mounted two-photon microscope: high-resolution brain imaging in freely moving animals. Neuron **31**, 903–912 (2001)
110. L.D. Swindle, S.G. Thomas, M. Freeman, P.M. Delaney, View of normal human skin in vivo as observed using fluorescent fiber-optic confocal microscopic imaging. J. Investig. Dermatol. **121**, 706–712 (2003)
111. E.J. Seibel, Q.Y.J. Smithwick, Unique features of optical scanning, single fiber endoscopy. Lasers Surg. Med. **30**, 177–183 (2002)
112. X. Liu, M.J. Cobb, Y. Chen, M.B. Kimmey, X. Li, Rapid-scanning forward-imaging miniature endoscope for real-time optical coherence tomography. Opt. Lett. **29**, 1763–1765 (2004)
113. M.T. Myaing, D.J. MacDonald, X.D. Li, Fiber-optic scanning two-photon fluorescence endoscope. Opt. Lett. **31**, 1076–1078 (2006)
114. Y. Wu, Y. Leng, J. Xi, X. Li, Scanning all-fiber-optic endomicroscopy system for 3D nonlinear optical imaging of biological tissues. Opt. Express **17**, 7907–7915 (2009)
115. J. Sawinski, W. Denk, Miniature random-access fiber scanner for in vivo multiphoton imaging. J. Appl. Phys. **102**, 034701 (2007)
116. J. Sawinski, D.J. Wallace, D.S. Greenberg, S. Grossmann, W. Denk, J.N. Kerr, Visually evoked activity in cortical cells imaged in freely moving animals. Proc. Natl. Acad. Sci. U. S. A. **106**, 19557–19562 (2009)
117. A.D. Aguirre, J. Sawinski, S.W. Huang, C. Zhou, W. Denk, J.G. Fujimoto, High speed optical coherence microscopy with autofocus adjustment and a miniaturized endoscopic imaging probe. Opt. Express **18**, 4222–4239 (2010)
118. D.L. Dickensheets, G.S. Kino, Silicon-micromachined scanning confocal optical microscope. J. Microelectromech. Syst. **7**, 38–47 (1998)
119. Y. Pan, H. Xie, G.K. Fedder, Endoscopic optical coherence tomography based on a microelectromechanical mirror. Opt. Lett. **26**, 1966–1968 (2001)

120. J.M. Zara, S. Yazdanfar, K.D. Rao, J.A. Izatt, S.W. Smith, Electrostatic micromachine scanning mirror for optical coherence tomography. Opt. Lett. **28**, 628–630 (2003)
121. J.T.W. Yeow, V.X.D. Yang, A. Chahwan, M.L. Gordon, B. Qi, I.A. Vitkin, B.C. Wilson, A.A. Goldenberg, Micromachined 2-D scanner for 3-D optical coherence tomography. Sensors Actuators A Phys. **117**, 331–340 (2005)
122. A. Jain, A. Kopa, Y.T. Pan, G.K. Fedder, H.K. Xie, A two-axis electrothermal micromirror for endoscopic optical coherence tomography. IEEE J. Sel. Top. Quantum Electron. **10**, 636–642 (2004)
123. W. Piyawattanametha, P.R. Patterson, D. Hah, H. Toshiyoshi, M.C. Wu, Surface- and bulk-micromachined two-dimensional scanner driven by angular vertical comb actuators. J. Microelectromech. Syst. **14**, 1329–1338 (2005)
124. J. Sun, S. Guo, L. Wu, L. Liu, S.W. Choe, B.S. Sorg, H. Xie, 3D in vivo optical coherence tomography based on a low-voltage, large-scan-range 2D MEMS mirror. Opt. Express **18**, 12065–12075 (2010)
125. K.H. Kim, B.H. Park, G.N. Maguluri, T.W. Lee, F.J. Rogomentich, M.G. Bancu, B.E. Bouma, J.F. de Boer, J.J. Bernstein, Two-axis magnetically-driven MEMS scanning catheter for endoscopic high-speed optical coherence tomography. Opt. Express **15**, 18130–18140 (2007)
126. J. Su, J. Zhang, L. Yu, Z. Chen, In vivo three-dimensional microelectromechanical endoscopic swept source optical coherence tomography. Opt. Express **15**, 10390–10396 (2007)
127. D. Wang, L. Fu, X. Wang, Z. Gong, S. Samuelson, C. Duan, H. Jia, J.S. Ma, H. Xie, Endoscopic swept-source optical coherence tomography based on a two-axis microelectromechanical system mirror. J. Biomed. Opt. **18**, 86005 (2013)
128. A.D. Aguirre, P.R. Hertz, Y. Chen, J.G. Fujimoto, W. Piyawattanametha, L. Fan, M.C. Wu, Two-axis MEMS scanning catheter for ultrahigh resolution three-dimensional and en face imaging. Opt. Express **15**, 2445–2453 (2007)
129. J.M. Schmitt, G. Kumar, Turbulent nature of refractive-index variations in biological tissue. Opt. Lett. **21**, 1310–1312 (1996)
130. B.W. Graf, S.G. Adie, S.A. Boppart, Correction of coherence gate curvature in high numerical aperture optical coherence imaging. Opt. Lett. **35**, 3120–3122 (2010)
131. H.-C. Lee, J.J. Liu, Y. Sheikine, A.D. Aguirre, J.L. Connolly, J.G. Fujimoto, Ultrahigh speed spectral-domain optical coherence microscopy. Biomed. Opt. Express **4**, 1236–1254 (2013)
132. A.D. Aguirre, Y. Chen, B. Bryan, H. Mashimo, Q. Huang, J.L. Connolly, J.G. Fujimoto, Cellular resolution ex vivo imaging of gastrointestinal tissues with optical coherence microscopy. J. Biomed. Opt. **15**, 016025 (2010)
133. C. Zhou, D.W. Cohen, Y.H. Wang, H.C. Lee, A.E. Mondelblatt, T.H. Tsai, A.D. Aguirre, J.G. Fujimoto, J.L. Connolly, Integrated optical coherence tomography and microscopy for ex vivo multiscale evaluation of human breast tissues. Cancer Res. **70**, 10071–10079 (2010)
134. C. Zhou, Y.H. Wang, A.D. Aguirre, T.H. Tsai, D.W. Cohen, J.L. Connolly, J.G. Fujimoto, Ex vivo imaging of human thyroid pathology using integrated optical coherence tomography and optical coherence microscopy. J. Biomed. Opt. **15**, 016001 (2010)
135. H.C. Lee, C. Zhou, D.W. Cohen, A.E. Mondelblatt, Y.H. Wang, A.D. Aguirre, D.J. Shen, Y. Sheikine, J.G. Fujimoto, J.L. Connolly, Integrated optical coherence tomography and optical coherence microscopy imaging of ex vivo human renal tissues. J. Urol. **187**, 691–699 (2012)
136. S.W. Huang, A.D. Aguirre, R.A. Huber, D.C. Adler, J.G. Fujimoto, Swept source optical coherence microscopy using a Fourier domain mode-locked laser. Opt. Express **15**, 6210–6217 (2007)
137. J.W. Hettinger, M. de la Pena Mattozzi, W.R. Myers, M.E. Williams, A. Reeves, R.L. Parsons, R.C. Haskell, D.C. Petersen, R. Wang, J.I. Medford, Optical coherence microscopy. A technology for rapid, in vivo, non-destructive visualization of plants and plant cells. Plant Physiol. **123**, 3–16 (2000)

138. B.M. Hoeling, A.D. Fernandez, R.C. Haskell, E. Huang, W.R. Myers, D.C. Petersen, S.E. Ungersma, R.Y. Wang, M.E. Williams, S.E. Fraser, An optical coherence microscope for 3-dimensional imaging in developmental biology. Opt. Express **6**, 136–146 (2000)
139. S.H. Yun, G.J. Tearney, B.J. Vakoc, M. Shishkov, W.Y. Oh, A.E. Desjardins, M.J. Suter, R.C. Chan, J.A. Evans, I.K. Jang, N.S. Nishioka, J.F. de Boer, B.E. Bouma, Comprehensive volumetric optical microscopy in vivo. Nat. Med. **12**, 1429–1433 (2006)
140. D.C. Adler, Y. Chen, R. Huber, J. Schmitt, J. Connolly, J.G. Fujimoto, Three-dimensional endomicroscopy using optical coherence tomography. Nat. Photonics **1**, 709–716 (2007)
141. D.S. Gareau, Y. Li, B. Huang, Z. Eastman, K.S. Nehal, M. Rajadhyaksha, Confocal mosaicing microscopy in Mohs skin excisions: feasibility of rapid surgical pathology. J. Biomed. Opt. **13**, 054001 (2008)

OCM with Engineered Wavefront

29

Rainer A. Leitgeb, Theo Lasser, and Martin Villiger

29.1 Introduction

The promise of optical coherence microscopy (OCM) is to combine the high sensitivity and imaging speed of optical coherence tomography with the high spatial resolution of confocal microscopy, thereby providing cellular and subcellular resolution compatible with in vivo measurements. Thanks to the coherent amplification, OCT approaches the shot-noise limit. The resulting outstanding sensitivity is needed for imaging thick scattering tissues, such as skin, at depths up to 2 mm, and providing high acquisition speeds necessary for imaging large fields of view. This substantiated the hope to develop a diagnostic tool to perform optical biopsy, by measuring tissue in situ and in vivo and thereby overcoming the randomness and invasiveness of conventional tissue biopsies and histopathology [1]. To meet this goal it is important to significantly enhance resolution power, as many pathological features indicative of disease manifest on a subcellular scale. An isotropic resolution of approximately 1 μm would be highly desirable; ideally without compromising the acquisition speed, the sensitivity, or the imaging depth.

Much of the success of OCT resides on the decoupling of the lateral resolution from the axial resolution: the first is given by the numerical aperture (NA) of the

R.A. Leitgeb (✉)
Center for Medical Physics and Biomedical Engineering, Medical University of Vienna, Vienna, Austria
e-mail: rainer.leitgeb@meduniwien.ac.at

T. Lasser
Laboratoire d'Optique Biomedicale, Ecole Polytechnique Federal de Lausanne, Lausanne, Switzerland

M. Villiger
Wellman Center for Photomedicine, Massachusetts General Hospital, Harvard Medical School, Boston, MA, USA

© Springer International Publishing Switzerland 2015

W. Drexler, J.G. Fujimoto (eds.), *Optical Coherence Tomography*,
DOI 10.1007/978-3-319-06419-2_30

detection optics, whereas axial resolution is only defined by the spectral properties of the employed light source. Using the coherence gate rather than the confocal gate for depth sectioning proved extremely advantageous, as it replaced complex sample optics with sophisticated light sources. The central theorem is the Wiener-Khintchin theorem that states that the temporal coherence function can be expressed as Fourier transform of the spectral power density. As a consequence, axial resolution given by the width of the envelope of the temporal coherence function $\delta z = \Delta\tau c$ and spectral bandwidth $\Delta\lambda$ are inversely proportional: $\delta z \propto \lambda_c^2/\Delta\lambda$, with λ_c the central wavelength of the light source. Higher axial resolution requires light sources with larger bandwidths or shorter central wavelengths. Early efforts to increase resolution in OCT have focused on the axial direction, spurred by continuous advancements in light source technology. First implementations of ultrahigh-resolution OCT have been presented already in the framework of time domain OCT (TDOCT), employing femtosecond Ti:Sapphire lasers [2]. The main challenge was the dispersion management in order to avoid loss of axial resolution due to chromatically unbalanced optical path lengths between the interferometer arms. Besides spatially coherent laser sources, thermal sources exhibit very large bandwidths and have the additional advantage of being low cost. Due to their limited spatial coherence, they are incompatible with traditional, scanned focus OCT, but provide the ideal light source for full-field OCT. They offer excellent axial resolution, and the low spatial coherence acts as confocal gate, providing high lateral resolution and little cross talk. Up to now, some of the most impressive high-resolution OCM images have been demonstrated with this kind of full-field OCT [3]. On the other hand, ultrabroad bandwidth sources based on nonlinear spectral broadening in photonic crystal fibers offer not only high power spectral densities but also interesting wavelength bands outside the usual therapeutic window at 800 nm, both in the visible as well as at longer wavelength range around 1,300 nm [4, 5]. Their drawback, so far, is high spectrally dependent random intensity noise due to the nature of the light generation itself.

Improving the lateral resolution proved more challenging. For a conventionally focused beam, the lateral resolution and the confocal gate are directly linked. Whereas the lateral resolution scales linearly with 1/NA, the confocal gate scales quadratically with $1/NA^2$. For an improved lateral resolution, the confocal gate ultimately limits the available imaging range, or depth of field (DOF), for OCT imaging. Different strategies have been adapted to overcome the restrictions imposed on the DOF for OCM. In TDOCT one can apply dynamic focusing, a method that coordinates the reference arm scanning with scanning the focus position such that the confocal and the coherence gate always coincide [6]. This method is very powerful in combination with en face OCT. For en face OCT the scanning priority is in the transverse plane, whereas the axial direction is scanned slowly [7, 8]. The first en face OCM system, introducing the OCM terminology, has been demonstrated already in 1994 [9]. The coherence gate significantly enhances the imaging depth of conventional confocal microscopy, whereas the confocal gate suppresses multiply scattered out of focus light. Hence their combination seems to be ideal for revealing subsurface cellular details [10]. Dynamic focusing cannot directly be applied, however, in case of FDOCT. It is nevertheless possible to use

a C-mode technique by recording several tomograms focused at different depths and merge the in focus regions in post-processing [11]. A similar solution using axially displaced multifoci has been successfully integrated into a commercial system. Other strategies involve signal processing techniques for digitally refocusing the scattered field distribution, measured by the complex-valued OCT signal, to recover an extended DOF [13–15].

An alternative strategy is to specifically engineer an illumination and a detection beam that directly provide an extended DOF. Diffraction obviously embodies the limiting factor, but it is possible to significantly improve upon the situation with a conventional Gaussian-like focal volume. In principle, the illumination and detection beam can be independently tailored by defining appropriate wavefronts in the illumination and detection paths, respectively. An interesting example is to impose a conical wavefront onto a collimated Gaussian beam, which results in a Bessel-like beam [16]. Bessel-like beams have the extraordinary property of propagating over significant lengths without apparent diffraction. Airy beams are another example of such diffraction-less beams that have attracted a lot of attention and are currently extensively investigated. A Bessel-like beam consists of a central lobe, surrounded by a large number of concentric side lobes. The apparent defeat of the laws of diffraction can be understood by considering that all side lobes roughly carry the same amount of energy as the central lobe. Indeed, although the central lobe stands out in intensity, the energy is distributed over a relatively large area.

Ding et al. were the first to replace the conventional objective lens in front of the sample with an axicon lens [17], illuminating the sample with a Bessel pattern and defining an identical detection mode. Although the large optical bandwidth used in OCT can help to reduce the side lobes if refractive axicons are used, the resulting tomograms featured many such side lobes and suffered from the sensitivity critical double pass through the axicon. The coupling of light from a single scattering site into the detection fiber through the axicon is inherently inefficient and can readily induce a signal penalty of 20 dB. On the illumination side, the spread of the energy over the various side lobes can be partly compensated by increasing the source power.

Using identical paths for illumination and detection is very attractive, because it reduces system complexity and can be implemented into an endoscope. Fiber probes using micro-axicon lenses, or conically etched fiber tips, have been demonstrated [18, 19] but suffer from similar limitations. The helical scanning usually performed with endoscopes is well suited for such fiber probes. Using a conical sample lens in a bench-top configuration is more limiting, however, as it precludes normal beam scanning.

This can be helped with an additional relay system with integrated scanning mirrors. The axicon-type illumination results in an annular illumination in the back aperture of the sample lens. This offers an alternative view: A similar Bessel-like illumination pattern could be defined with a simple annular intensity mask, suffering from very little throughput. Using a pure phase mask, instead, illuminated with a collimated Gaussian beam, would provide far better transmission. Most flexibility for such a wavefront shaping is offered by Spatial Light Modulators (SLM). They are limited by the finite pixel width and cross talk between the elements. This drawback

is, however, outweighed by the attractive possibility to dynamically adapt the wavefront, e.g., compensating for additional sample-induced aberrations and achieve better imaging penetration. A simpler approach to shape the wavefront involves tailored phase masks. There exists already a multitude of designs for binary phase masks with different advantages for resolution and contrast. Probably, their most important advantage for biomedical imaging is the cheap and small footprint [20].

Systems with symmetric illumination and detection wavefronts offer interesting performance for both intensity [21] and phase masks [22] if only a moderate gain of DOF is attempted. For more significant extended DOFs, however, we found that decoupling the illumination and detection paths offers more flexibility and results in better performance [12]. Using an axicon for creating an annular illumination pattern in the back aperture of the sample objective provides an efficient way of illuminating the sample over an extended axial range. Decoupling the detection path avoids the critical double pass through the axicon. Defining instead a Gaussian detection mode with a lower NA provides an interesting compromise between axial imaging range, lateral resolution, and sensitivity. Importantly, the decoupled scheme allows for efficient scanning of the Bessel and the detection beam across the sample using appropriate relay optics and a 2D scanner with a single pivot point. Rapid scanning is indispensable for most in vivo applications to overcome respiratory and other movement artifacts. This extended focus scheme fully benefits from the parallel signal acquisition along depth characteristic of FDOCT without the time-consuming need to readjust the focus position.

Besides the benefits of an extended DOF, the combination of Bessel illumination with Gaussian detection also provides a very advantageous dark field effect. The imaging system is more sensitive to light scattered from small structures and suppresses specular reflections. This results in excellent contrast from many biological structures and enables the suppression of strong reflections that often limit the dynamic range. The Bessel beam further profits from a self-regeneration property that helps to look behind light shading obstacles. Extended focus configurations have been implemented for OCM at 800 nm central wavelength, but were also successfully applied at 1,300 nm for skin imaging.

The present chapter aims at providing an in-depth understanding of extended focus schemes and demonstrates interesting applications of Bessel-shaped illumination beams for optical coherence microscopy and tomography. As already alluded to, decoupled extended focus schemes feature specific characteristics that have particular advantages for imaging of biological tissue with Fourier domain OCM and OCT. We first introduce a theoretical framework to describe the OCM signal and understand the mechanism of the limited DOF using the formalism of the coherent transfer function (CTF). Implications on resolution, contrast, and sensitivity for specific realizations of the CTF are then discussed. In the subsequent section we demonstrate examples for high-resolution biomedical imaging with extended focus OCM and OCT. A unique feature of OCT and OCM as interferometric techniques is the availability of phase information. This enables important functional extensions such as the quantitative assessment of blood flow and

depth-resolved imaging of tissue microvasculature free of any contrast agent. Moreover, recent developments for contrast-enhanced OCM show great potential for adding structural and molecular specific contrast that is of paramount importance in biomedical imaging. The chapter concludes with a short outlook on future developments, in particular for contrast enhancement techniques, and applications of extended focus imaging as well as wavefront engineered OCM.

29.2 Theoretical Framework

Here we present a theoretical framework for image formation in OCT that encompasses both the coherence and the confocal gate. This framework enables to investigate the detrimental effect of the confocal gate on OCT and provides a toolset to devise possible remedies. This section follows closely the work [23].

Most imaging methods can be cast in a linear, shift invariant formalism, in which the final image is expressed as the convolution of the original object with the system response function, i.e., the point spread function (PSF). Whereas this view can be adopted for OCT in the case of low NA [24], the shift invariance in the axial direction is lost for a higher NA. Instead of reasoning in the spatial domain, looking at image formation in the spatial frequency domain provided interesting insights, both for OCT in general and the problem of extended depth of field in particular.

The object that is imaged can be described in terms of its susceptibility $\chi(\mathbf{r}) = \mathrm{n}(\mathbf{r})^2 - \mathrm{n}_0{}^2$. $\mathrm{n}(\mathbf{r})$ is the refractive index of the sample as function of the spatial coordinate $\mathbf{r}$, and n_0 is the average refractive index. Bold type indicates a vector quantity. Seeking an expression within the limits of the first-order Born approximation, both the incident and the scattered light propagate as if in a homogenous background with index n_0. Taking the inverse Fourier transform of this sample function, expressed in lateral coordinates $\boldsymbol{\rho} = [x, y]$ and z, and their corresponding spatial frequencies $\mathbf{q} = [q_\mathrm{x}, q_\mathrm{y}]$ and s, the OCT signal can be expressed as

$$\tilde{P}(\mathbf{q},k) \approx \underbrace{kA(k)}_{\text{source spectrum}} \int_s \underbrace{\mathrm{CTF}(\mathbf{q},s,k)}_{\text{filter function}} \underbrace{\tilde{\tilde{\boldsymbol{\chi}}}(\mathbf{q},s)}_{\text{object spectrum}} ds. \tag{29.1}$$

$\tilde{P}(\mathbf{q}, k)$ is one of the two complex conjugate terms of the interference signal, recorded as a function of wavenumber k in spectrometer-based or swept-source OCT, and lateral spatial frequency $\mathbf{q}$. $\mathbf{q}$ is obtained by inverse Fourier transformation of the signal along the lateral scanning position $\boldsymbol{\rho}$. The two tildes indicate the Fourier transformation along the lateral and the axial spatial coordinates. CTF($\mathbf{q}$, s, k) is the coherent transfer function of wavenumber k, depending on all spatial frequencies [25]. A(k) is the power spectral density of the light source, which is weighted by the wavenumber k, a remnant of the k^2 factor in the commonly used scattering potential $k^2\chi(\mathbf{r})$. The origin of the z coordinate is placed in the focal plane of the imaging optics, and the reference arm length is assumed matched to this position. An additional linear phase term would otherwise have to be added. The same formalism

obviously also holds for time domain OCT, except that $\tilde{P}(\mathbf{q}, k)$ does not directly correspond to any measured signal. Also, experimental limitations such as instantaneous coherence length, spectrometer resolution, or wavenumber linearization are ignored.

The CTF is defined through the illumination and the detection optics. Indeed, both parts play an equal role in OCT. The illumination optics defines the focal volume that scans over the sample. Part of this illumination light is scattered back by the sample susceptibility and then finally filtered by the detection optics that rejects any contribution that does not match the detection mode. The concept of the generalized aperture is convenient to express the illumination and detection modes, as it also holds for higher NA, and could be extended to vector notation [26]. The generalized aperture describes the electromagnetic field in the focal volume as the three-dimensional Fourier transformation of its plane wave decomposition. These components lie, by definition, on a spherical shell of radius k, and their angular distribution corresponds, within the limits of the Debye approximation, to the field distribution in the spherical output principle plane of the imaging objective with a radius corresponding to the focal length of this lens. And the radial distribution in this principle output plane corresponds, in turn, to the distribution in the flat input principle plane.

In spatial coordinates, the signal recorded for each wavenumber corresponds to the convolution in the lateral direction of the product of the illumination and the detection mode with the sample susceptibility, weighted by the power spectral density. No scanning in the axial direction is performed. The corresponding situation in the spatial frequency domain is the product of the sample spatial frequency spectrum (SSFS) with the convolution along all spatial frequencies of the illumination and detection modes, i.e., their generalized apertures, which defines the CTF. To take account of the absence of axial scanning, the integral along the axial spatial frequency s is taken to find expression (29.1). The integral along s is equivalent to a Fourier transformation back to the spatial domain, evaluated only at the position $z = 0$.

Hence, the CTF is defined as the convolution of the two spherical shells, m_{ill} and m_{det}, as represented in Fig. 29.1a:

$$\mathrm{CTF}(\mathbf{q}, s, k) = 1/2 \iint_{\mathbf{q}', s'} m_{\mathrm{ill}}(\mathbf{q}', s', k) m_{\mathrm{det}}(\mathbf{q} - \mathbf{q}', s - s', k) d\mathbf{q}' ds'. \tag{29.2}$$

The field distribution on the shells is entirely defined by the illumination and detection modes at the principle input plane of the sample objective. Panel (b) of Fig. 29.1 displays the resulting CTFs for three wavenumbers for a system with Gaussian illumination and detection modes, whose waists fill 70% of the aperture of the sample objective with NA = 0.5. Due to geometry, the CTF has an outer rim defined by a sphere of radius $2k$. For the Gaussian CTF, the transmission values are highest at this rim and then decay for smaller s. A change in wavenumber has the effect of scaling the CTF around the origin of the spatial frequencies with a scaling factor $2k$. Due to the limited bandwidth of the light sources used, usually limited to less than one

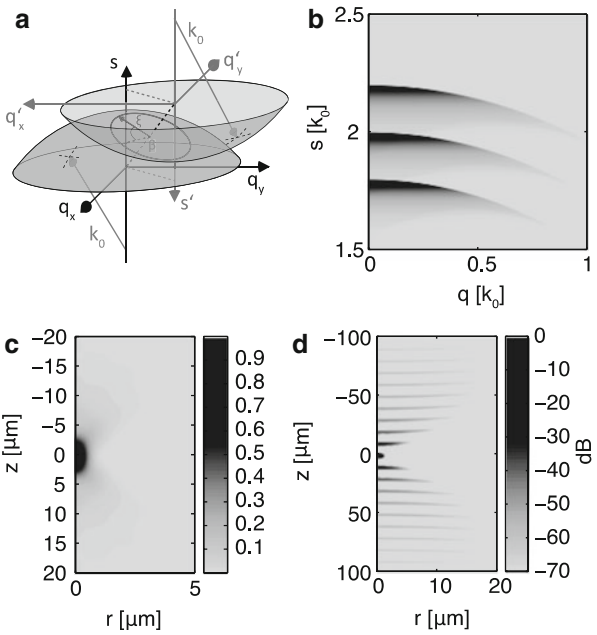

Fig. 29.1 (**a**) The convolution of the illumination and detection generalized apertures defines the CTF. (**b**) The CTF scales about the origin with the wavenumber. (**c**) The 3D FT of the CTF at a given wavenumber defines the corresponding focal volume. (**d**) Simulated tomogram of individual point-like scatterers aligned along the axial direction at 10 um intervals for a Gaussian illumination mode with an NA of 0.5

fifth of the central wavenumber, it is possible to ignore this scaling effect and simply assume that the CTF at a given wavenumber is a shifted copy of the CTF at the central wavenumber $\mathrm{CTF}(\mathbf{q}, s, k) \approx \mathrm{CTF}(\mathbf{q}, s, k_c) \bigotimes \boldsymbol{\delta}(s - 2(k - k_c))$. As usual, to reconstruct the tomogram, the inverse Fourier transformation from k to z is computed:

$$T(\mathbf{q}, z) \approx \int_k \tilde{P}(\mathbf{q}, k) \mathrm{e}^{i2kz} dk = \int_k kA(k) \mathrm{e}^{i2kz} \int_s \mathrm{CTF}(\mathbf{q}, s - 2(k - k_c), k_c) \widetilde{\widetilde{\boldsymbol{\chi}}}(\mathbf{q}, s) ds\, dk. \tag{29.3}$$

In this view, the tomogram can be pictured as the Fourier transform of the SSFS convolved with the central wavenumber CTF along s and weighted with the power spectral density of the employed light source. Panel (c) of Fig. 29.1 displays the focal volume corresponding to the central wavenumber's CTF. And panel (d) represents the tomogram of point-like scatterers, aligned along the axial direction at 10 μm intervals. This clearly illustrates the limited depth of field for a CTF with such a high NA. Only a single in focus scatterer appears clearly resolved. The signal of the out of focus scatterers drops rapidly in intensity and is blurred in the lateral direction. Although the coherence gating still works and clearly locates the signal at a single depth, this depth changes with the lateral scanning position.

Having revealed how the CTF impacts the final tomogram, it is possible to devise an ideal CTF: It should be separable along $\mathbf{q}$ and s, approach a Dirac function along the axial spatial frequency, and feature a smooth envelope along the lateral spatial frequencies. Along the axial spatial frequency, the CTF acts as the sampling

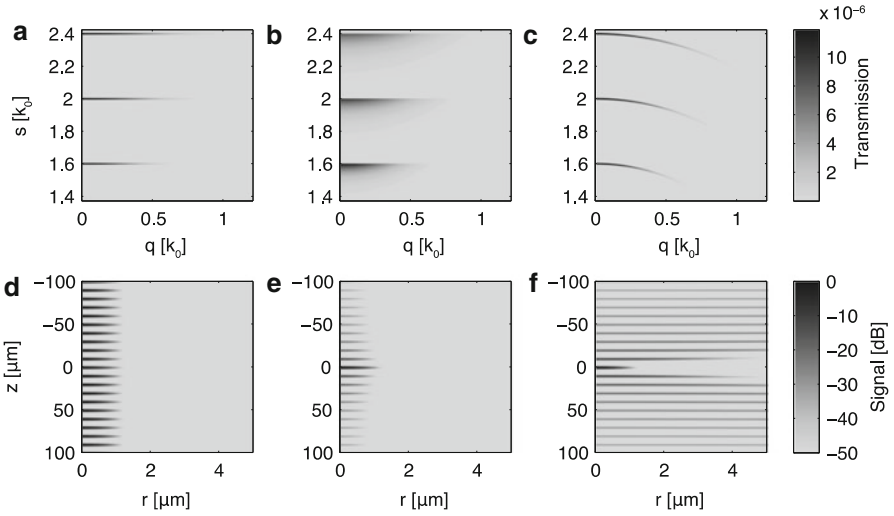

Fig. 29.2 (**a**) Hypothetical ideal CTF with very narrow support along s and no curvature. (**b**) Hypothetical CTF without curvature but finite support along s. (**c**) Hypothetical CTF with narrow support, but curvature. (**d**–**f**) Simulated tomograms of point-like scatterers resulting from the CTFs in (**a**–**c**)

function of the Fourier domain detection, mapping an axial spatial frequency to a specific wavenumber. The range of this mapping is imposed by the spectral bandwidth and defines the resulting axial resolution. In the lateral direction, the envelope of the CTF simply apodizes the higher lateral spatial frequencies, defining the lateral resolution.

This hypothetical situation of this idealized CTF is depicted in Fig. 29.2a, d and results in the expected ideal tomogram. A real CTF usually differs in two ways from this ideal CTF: Its width along *s* and the separability of the CTF along **q** and s. Most CTFs exhibit a curved shape, making the position of the window along *s* dependent on **q**. Figure 29.2b, e demonstrate the effect of a hypothetical CTF that still consists of two separable windows along **q** and *s*, but with an increased window width along *s*. Although the signal of the out of focus scatterers does not experience any blurring, their signal intensity drops rapidly with increasing out of focus distance. On the other hand, panels (c) and (f) show the effect of a very narrow window along *s*, but with a spherical curvature along **q**. In this case, defocused scatterers become extremely blurred. The integrated intensity over the blurs of the scatterers does not decrease with out of focus distance; it is simply spread over a larger area. The on axis signal, however, decreases at the same rate as in case of the previous CTF of Fig. 29.2b.

The defocusing mechanism can be understood by recognizing that the axial position of the scatterer location translates to a phase slope in the spatial frequency domain, for all but the in focus signals. Although the SSFS amplitude of a small scattering component can be assumed nearly constant over the spatial frequency range covered by the CTF, the curved shape of the CTF results in a sampling of

nonconstant axial spatial frequencies, and hence a spherical phase term, responsible for the observed blurring. ISAM [27] attempts to numerically compensate for this second effect by resampling the recorded signal in the spatial frequency domain.

If, instead of imaging individual scatterers, a tissue-like sample with many scatterers, spaced on a subresolution scale, were measured, a speckle pattern would result. In this case, the CTF of Fig. 29.2b would still result in a similar intensity decay as already observed for the single scatterers. The CTF of Fig. 29.2c, however, would result in constant signal intensity along depth. Although the resolution is lost, the signal energy is not. As is well known, speckle is resistant to defocusing.

This suggests the definition of two independent measures for the DOF: the first related to the width of the CTF along s, limiting the signal energy of out of focus structure, and the second related to the curvature of the CTF, resulting in a blurring of out of focus structure.

The CTFs depicted in Fig. 29.2 are hypothetical and cannot be engineered in practice. Certainly, a very low NA system approaches the ideal CTF, but limits the achievable lateral resolution. Striving for higher NA, the definition of the CTF as the convolution of the illumination and detection aperture severely constrains the solution space of realizable CTFs. With identical Gaussian-like illumination and detection modes, the curvature and the s-width of the CTF are directly linked and provide an identical definition of DOF. Using decoupled illumination and detection apertures provides more flexibility in engineering of a CTF, and the two criteria for the DOF will in general differ. Besides the two DOF criteria, it is also important to consider the third criterion of an ideal CTF: its lateral envelope, which should be wide and smooth to provide high lateral resolution without imaging artifacts.

29.3 Contrast and Contrast Enhancement

Imaging a scattering, semitransparent, three-dimensional object with a low coherent imaging system such as OCT and OCM is best described in terms of spatial frequencies and the concept of the CTF (see preceding section). Ignoring for the current discussion the limitations imposed on the depth of field and restricting the reasoning to the in focus region, Eq. 29.1 can be further simplified to

$$\tilde{P}(\mathbf{q},k) \approx kA(k)\mathrm{sCTF}(\mathbf{q})\tilde{\tilde{\boldsymbol{\chi}}}(\mathbf{q},s=2k), \tag{29.4}$$

where sCTF is in principle the envelope of the CTF along $\mathbf{q}$ or more precisely its projection along s:

$$\mathrm{sCTF}(\mathbf{q}) = \int \mathrm{CTF}(\mathbf{q},s,k)ds. \tag{29.5}$$

In this case, OCM imaging reduces to a linear, shift-invariant system and can be described in Fourier space as a filtering process. In the spatial frequency domain,

the sample or object spectrum is directly related to the image spectrum, simply weighted by this filter function.

Defined by the NA of the sample lens, the sCTF has an upper cutoff q_{cutoff}. The inverse Fourier transform of the sCTF defines the lateral PSF, and depending on the precise shape of the sCTF, the exact width of the PSF can vary.

In the axial direction, the resolution is entirely defined by the coherence length, i.e., the spectral span of the light source in the spatial frequency space. Along the axial direction, an OCM system always acts as a band-pass system, transmitting only the axial spatial frequencies in the band accessible by the light source, stretching from $s = 2k_{min}$ to $s = 2k_{max}$, where k_{min} and k_{max} are the minimum and maximum wavenumbers of the light source. Only object structure with axial spatial frequencies in that range can be imaged by OCM.

Besides spatial resolution, high contrast is of paramount importance for the visual impression of a tomogram. In terms of pure spatial frequencies, the contrast can be directly defined as the visibility of the image of a pure spatial frequency, i.e., a sinusoidal variation of the square of the refractive index along a defined direction, which is entirely defined through Eq. 29.4 by $kA(k)$ and sCTF($\mathbf{q}$).

More relevant in an experimental image is the contrast between various structures within the tissue. Figure 29.3a shows a schematic object spectrum, indicating different spatial frequency bands. The low frequency band is dominated by specular reflection (s-band). This contribution is caused by surface reflections, glass slides supporting cell samples, or other well-defined interfaces perpendicular to the optical axis. Such interfaces have a very broad axial spatial frequency spectrum (along s) mainly determined by the coherence length, but very low lateral spatial frequencies ($\mathbf{q}$).

The adjacent frequency band (tissue band) contains the macroscopic features of tissue morphology. The higher frequency (cell band) contains information of the subcellular structures. Figure 29.3b shows the sCTF of the instrumental counterpart. The diagram indicates several cases: First, the sCTF of a low NA imaging system, with a low cutoff frequency $q^{(1)}_{cutoff}$, i.e., a moderate lateral resolution; second, the sCTF of a higher NA OCM system with an increased cutoff frequency $q^{(2)}_{cutoff}$, i.e., an improved lateral resolution; and third, the sCTF of a dark field OCM system with an identical NA (when compared to the high NA OCM system), but suppressed lower spatial frequencies. This dfOCM system prevents the specular frequency band from being detected and privileges the structural bands.

Assuming two types of tissue, that both have similar spectra in the tissue band, but one of them has far more content in the cell band, would be imaged with varying contrasts with these three imaging systems. The low NA system would hardly be able to tell them apart. The higher NA system would provide sufficient contrast to distinguish the two, but only the dark field configuration would really allow a stronger differentiation of cell structures, i.e., resulting in a further contrast enhancement for all signal content in the cell band.

The integral contributions over different spectral bands are indicated by the boxes in Fig. 29.3a. A targeted selection of these contributions translates into an

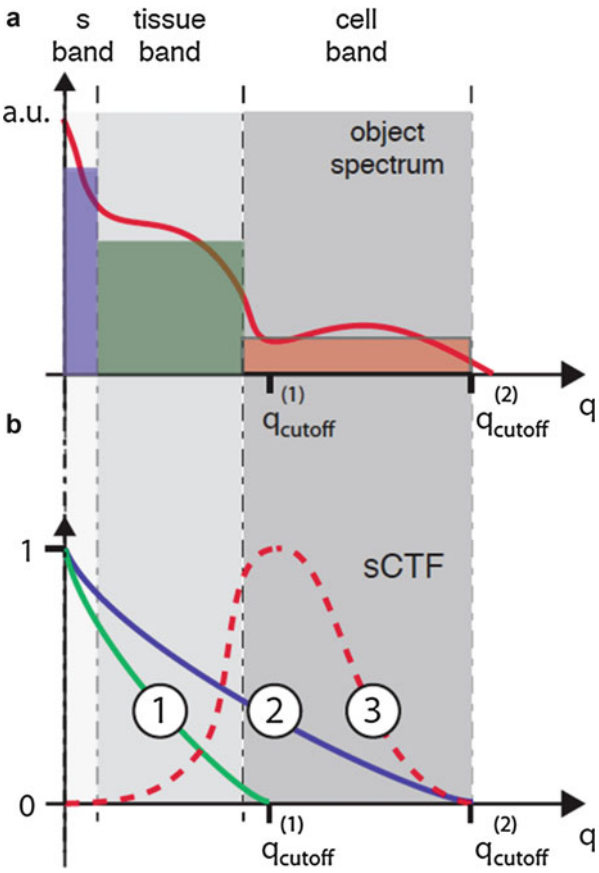

Fig. 29.3 (**a**) Object spectrum overlayed with the integral signal per k-band. (**b**) sCTF of a low NA OCM system (*1*), a high NA OCM system (*2*), and a dark field OCM (*3*) with identical NA as system (*2*)

intrinsic contrast enhancement, an important feature in OCM especially when aiming for structural and dynamic cell imaging.

The schematic and qualitative classification of the object spectrum into different frequency bands can be substantiated for instance with works by Schmitt et al. [28], who measured the power spectrum of index variations of biological tissue by analyzing light scattered by cell samples. The cell-associated index variations follow a power-law and show a fractal index structure within a particular band of spatial frequencies. These findings have been advanced in further studies [29, 30] indicating a fractal order for light scattering in cell clusters over a large span of spatial frequencies.

In OCM the generation of adequate contrast is as important as providing sufficient resolution when imaging small features of a specimen. Imaging almost transparent cells that only slightly differ from their surrounding in their refractive index, their absorbance, or the amount and polarization of the light they scatter increases the request for enhanced or specifically tailored contrast. This demand becomes even more challenging for the observation of dynamic cell processes.

Besides the contrast between different tissues or structure, the sensitivity Σ, the signal-to-noise ratio (SNR), and the dynamic range (DR) are important key factors. The SNR is given as a ratio between the signal and the sum of all noise contributions. The sensitivity is defined as the reciprocal of the smallest reflectivity that can be resolved. The SNR and the sensitivity are principally defined through the noise present in the system. The absolute value of the CTF has, however, likewise an influence. It acts as a filter that reduces the signal and, thus, can limit these characteristics. A sensitivity of 100 dB is typical for a well-designed OCM system which for a SNR = 1 corresponds to a minimum reflectivity of $R_{smin} = 10^{-10}$.

However the available dynamic range is limited well below the sensitivity of an OCM system.

In spectrometer-based FDOCT the signal contains a strong DC (reference) and weaker AC (interference) contribution. For a single line detector with N discretization levels and the DC part γ filling a major part of the quantum well capacity, only a minor part α of the full well capacity is available for the interference signal.

At the saturation level of the detector, the strongest possible signal α is given by $\alpha = \left(1 - \sqrt{\gamma}\right)^2$. Neglecting all noise contributions and an interference amplitude of $2\sqrt{\alpha\gamma}$, we obtain for the dynamic range DR

$$\mathrm{DR} = 2\sqrt{\gamma}(1 - \sqrt{\gamma})M \tag{29.6}$$

where the smallest interference contribution has been set to one discretization level $1/M$. For a typical setting with $\gamma = 0.75$ and $M = 2{,}048$ (11 bits), the resulting DR is typically 50 dB.

This argument is of paramount importance when detecting small signals next to very strong signals originating from specular reflection. To avoid the detection from saturating, the reference signal frequently has to be reduced at the cost of sensitivity. In dfOCM, the specular reflections are sufficiently suppressed to maximize system sensitivity and use the available dynamic range for detection of the small scattering signal of the sample (see Fig. 29.3c).

In swept-source systems, the commonly employed dual-balanced receivers improve the DR, but specular reflections maintain the capability to saturate the detection.

The issue of low frequency band suppression with dark field configuration is nicely demonstrated in Fig. 29.4a, b. Figure 29.4a is obtained with a standard OCT system and shows an en face intensity image of a USAF resolution test target. As expected, highly reflective lines appear bright, and low reflective areas are dark. Figure 29.4b on the other hand is obtained with a dark field OCT configuration (see Sect. 29.4.3). The resulting image is obviously a band-pass filtered version of the resolution test target pattern. Interestingly, the contrast of the small numbers labeling the test patterns, which presumably have a relatively broad frequency content, appears much enhanced in the dark field image.

Figure 29.4c, d demonstrates the effect of efficient exploitation of the system dynamic range for the structural signal, when using a dark field system. In this case the sample is skin, covered by a glass plate commonly applied for better stabilization. Again Fig. 29.4c is obtained with a standard OCT system. The strong reflex from the glass interface drives the camera load close to saturation, and only a small portion of

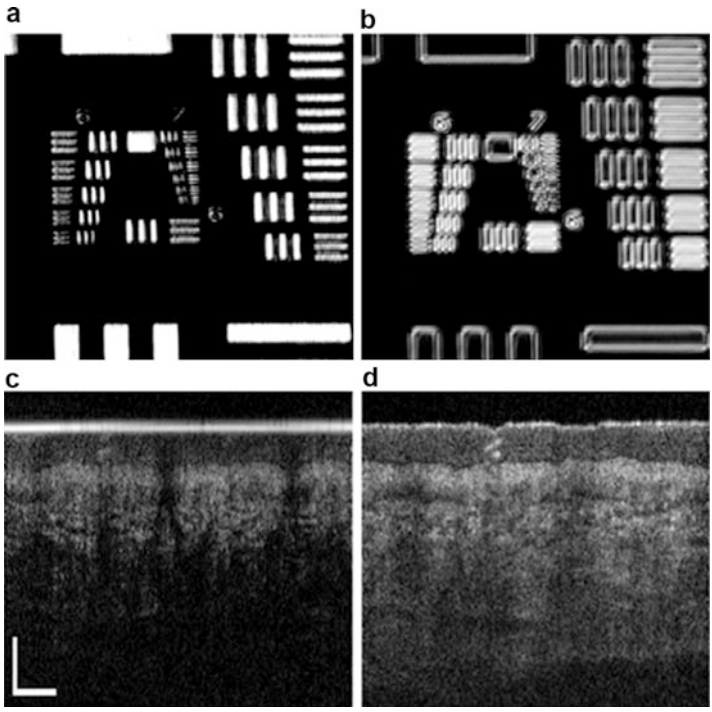

Fig. 29.4 (**a**–**b**) En face projections of a USAF resolution test target obtained with standard OCT and the xfOCT system, respectively, displaying the dark field effect. (**c**–**d**) Tomograms from skin with a glass plate on top. The glass surface is almost perpendicular to the optical axis, with the reference power adjusted to avoid saturation. Standard OCT in (**c**) is missing sensitivity due to the strong reflex from the glass interface. xfOCT in contrast does not suffer from the reflection and exhibits thus better sensitivity and depth penetration for the skin structures. Scale bar denotes 250 μm [57]

the dynamic range is left for the structure of interest, resulting in poor contrast. The situation is different for the dark field configuration as shown in Fig. 29.4d. The reflection is suppressed, and the full dynamic range is available for the actual structure, providing excellent contrast of various tissue structures. The imaging depths are likewise enhanced, due to the combined effect of the optimized sensitivity and the extended DOF that comes in hand with the dark field effect (see Sect. 29.4).

29.4 Extended Focus Optical Coherence Microscopy: Configurations and Applications

So far we presented a general theoretical framework to understand and investigate how specific illumination and detection modes define the CTF and influence the available DOF. Further, the meaning of contrast and specific regions of interest in the sample spatial frequency spectrum were discussed. As a reminder, the goal is to

design a system providing high spatial resolution in all three dimensions without compromising the parallel acquisition unique to Fourier Domain OCT. If speed is not a critical parameter, performing a confocal scan in all three dimensions will undoubtedly provide the best image quality. Here, instead, a compromise between image quality and imaging speed is pursued. The particular physics of Bessel beams makes this class of beams a strong candidate to help in such a compromise, and it is tempting to replace the conventional imaging lens with an axicon-like lens. The generalized aperture of the resulting focal spot is defined by a thin annulus. The CTF resulting from a symmetric system with identical illumination and detection modes is defined by the convolution of two such annuli. Indeed, this results in a narrow and flat CTF, approaching two of the three criteria of an ideal CTF. Unfortunately, the transmission values feature very strong variations. The CTF can be pictured as a ring of twice the diameter of the annulus of the generalized aperture and a strong, very narrow central peak, connected to the outer annulus with very low transmission values. In the tomogram, this results in very strong side lobes and a very poor imaging of edge-like structures. As discussed in the introduction, for a moderate gain of DOF, such a configuration does offer a valuable configuration with the benefit of simple physical implementation, as shown for instance by Liu et al. [21] and Lorenser et al. [22].

In the attempt of realizing a more substantial gain in DOF, decoupling of the illumination and detection aperture has shown better performance. A Bessel-like mode is still used to deliver the light into the sample and illuminate the sample with an axially extended light needle. The detection volume, however, is defined as a lower NA Gaussian mode. In the following, three specific implementations of this combination and their corresponding benefits for biological applications are discussed.

29.4.1 Extended Focus Optical Coherence Microscopy: xfOCM

This first realization of extended focus OCM (xfOCM) provided a near isotropic resolution of 1.3 μm in the lateral and 2 μm in the axial direction, over an axial range of 300 μm, corresponding to a more than tenfold increase in the DOF of a Gaussian system with identical lateral resolution. An axicon lens was used to generate a Bessel-like beam, which was relayed through a scanning system and finally projected into the sample space with a microscope objective of NA = 0.3. The decoupled detection was defined by the Gaussian-like fiber mode, relayed in a way to define an NA slightly below the illumination NA. The excellent axial resolution was achieved with an Ti:Sapphire laser centered at 800 nm. Figure 29.5 displays the schematic layout; details are provided in [12, 23].

The theoretical CTF corresponding to this configuration is shown in panel (b). For comparison, the CTF of a system with symmetric Gaussian-like illumination and detection resulting in a comparable lateral resolution is also depicted. The projections of these CTFs along s, i.e., their sCTFs, are plotted in the bottom part of the same figure. Due to the Gaussian detection, the CTF of the xfOCM

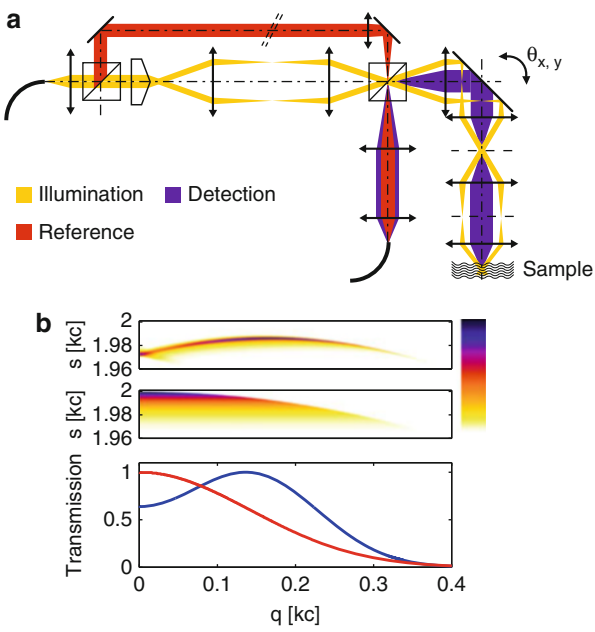

Fig. 29.5 (**a**) Schematic layout of the xfOCM, evidencing the decoupling of the illumination and the detection paths (not drawn to scale). (**b**) *Top*: CTF of the xfOCM configuration. *Middle*: CTF of a confocal Gaussian-like system with similar lateral resolution as the xfOCM. *Bottom*: Projections of the CTFs along *s*

configuration is curved along **q** and will eventually induce a defocusing for out of focus structure. Due to the Bessel-like illumination, the width of the CTF along *s* is very limited and provides a strong intensity signal over a significantly extended depth range. The Gaussian CTF, in contrast, features a much wider width along *s*, paired with a stronger curvature, resulting in a very short DOF.

The preferential selection of higher lateral spatial frequencies of the xfOCM scheme is clearly visible in the sCTF plots. The contrast is best for a spatial frequency range that is above the specular reflection band and contains valuable sample information.

Importantly, this configuration allowed efficient and rapid scanning of the extended focus beam over the sample. This is crucial to benefit from the advantage of the extended focus scheme and necessary for in vivo imaging to overcome movement artifacts.

29.4.1.1 Imaging of Langerhans Islets

We used this configuration for imaging of islets of Langerhans in mice [31, 32]. These agglomerations of insulin-producing beta cells are scattered throughout the pancreas and exhibit an excellent contrast when imaged with xfOCM. They are strongly vascularized and sense the blood glucose level to release, in response, insulin and achieve glucose homeostasis. Destruction of these islets due to an autoimmune attack results in type I diabetes. Using a mouse model of this type of diabetes, we were able to prove the capability of xfOCM to image islets down to a size corresponding to a cluster of only a few beta cells and perform quantitative analysis of their size distribution. Also, although access to the

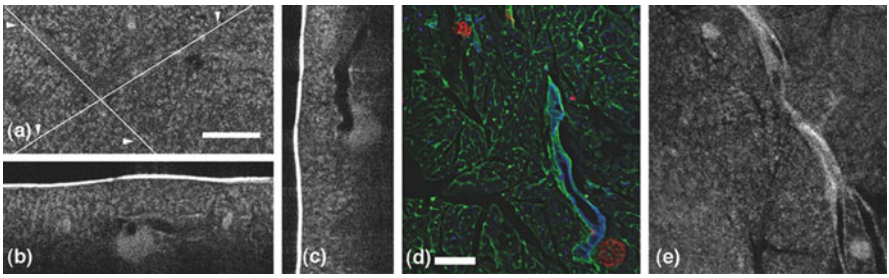

Fig. 29.6 In vivo imaging of murine pancreas with islets of Langerhans. En face view (**a**) and tomographic sections (**b**, **c**), indicated by the *white lines*. Scale bar 200 μm, applied to (**a**, **b**, **c**). Comparison with immunohistology. (**d**) Histological section labeled for insulin (*red*), PECAM (*green*) and DBA lectin (*blue*). (**e**) Corresponding xfOCM en face view. Scale bar 200 μm, applies to (**d**, **e**)

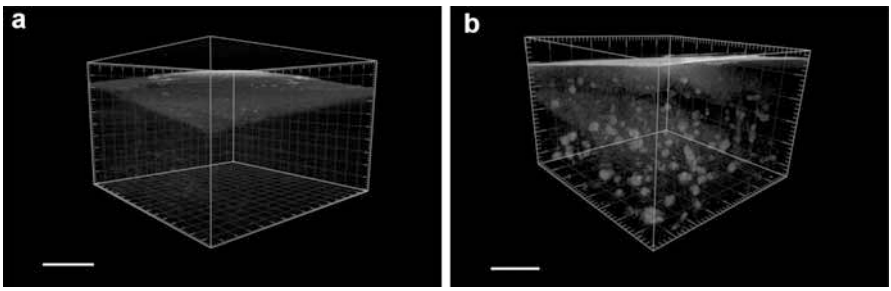

Fig. 29.7 Three-dimensional rendering of an ex vivo xfOCM image of the parietal cortex of the transgenic mouse brain. (**a**) 1 month-old pre-depositing brain sample. (**b**) 3 month-old brain sample showing amyloid plaque deposits. Scalebar 200 μm

pancreas involved surgery and is invasive, repeated imaging for longitudinal studies is possible. Analyzing the size distribution of islets during the onset of diabetes could help advance our understanding of this disease (Fig. 29.6).

29.4.1.2 Imaging of Cerebral Beta-Amyloidosis in Alzheimer's Disease

In a recent study, xfOCM has been applied in neuroscience to investigate Alzheimer's disease (AD) [33]. The pathology of AD is characterized by the accumulation of amyloid-β (Aβ) peptides in cerebral plaques and blood vessels. The APPPS1 mouse model of AD used in the study develops cerebral plaques consisting of human amyloid at the age of 2 months [34]. Three-dimensional xfOCM images of the AD brain structure clearly revealed Aβ plaques both ex vivo and in vivo without exogenous contrast agents, as shown in Fig. 29.7. By imaging brain samples simultaneously with xfOCM and confocal fluorescence, the structures observed with xfOCM were confirmed to be Aβ plaques. The image contrast was sufficient to allow segmentation of Aβ plaques and to analyze Aβ plaque volume in function of age, as well as other statistics. Furthermore, in vivo Aβ plaque formation was

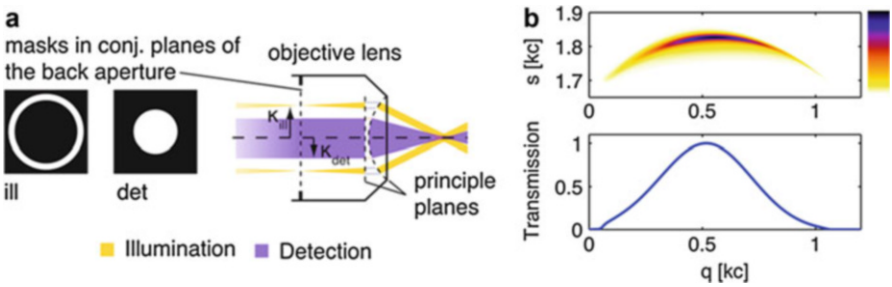

Fig. 29.8 (**a**) Illumination and detection modes for dfOCM, defined by masks in conjugate planes to the sample objectives back aperture. (**b**) *Top*: CTF for dfOCM. *Bottom*: Projection of CTF along *s*

monitored through a cranial window during a 1-month longitudinal study. To precisely re-localize the same region of brain tissue at several time points, image registration using the vascular network as a reference was employed.

29.4.2 Dark Field Optical Coherence Microscopy: dfOCM

A dark field configuration with its intrinsic contrast enhancement is particularly well suited for cell imaging. Analogous to xfOCM, the dfOCM illumination is based on a Bessel beam. To improve the annular illumination pattern in the back focal plane of the objective lens, it is filtered with a mask in a conjugate plane, blocking any light outside a thin annulus. Similarly, the light backscattered by the sample is filtered with a complementary mask, accepting only light within the non-overlapping inner portion of the ring illumination. This results in a strong suppression of specular reflection originating from flat interfaces, such as the microscope slide, i.e., contributions from low spatial frequency structures are eliminated to a large extent. In consequence, the sensitivity of dfOCM for very small intensities of backscattered light is highly improved. The overall interferometric setup of dfOCM [35] is very similar to xfOCM [12], and the major modifications are an increased numerical aperture of the objective lens ($NA_{eff} = 0.68$) ensuring an improved lateral resolution of <0.6 µm with a reduced DOF of approximately 45 µm. Figure 29.8 shows the illumination and detection modes at the sample objective and the amplitude masks positioned in planes conjugate to the Fourier plane of the objective. The corresponding sCTF defines a clear band-pass filter, centered on the cell frequency band and strongly suppressing the specular reflection band. Due to the high NA, the CTF features a significant curvature.

The resulting contrast enhancement is particularly interesting for the imaging of cells, subcellular structures, and dynamics of cell processes. The available DOF is sufficient for such samples and still provides the speed advantage of parallel imaging along depth inherent to detection in the Fourier domain.

For demonstrating the performance of dfOCM, Fig. 29.9 displays en face views and B-scans of individual cells of four different cell lines. The high sensitivity of

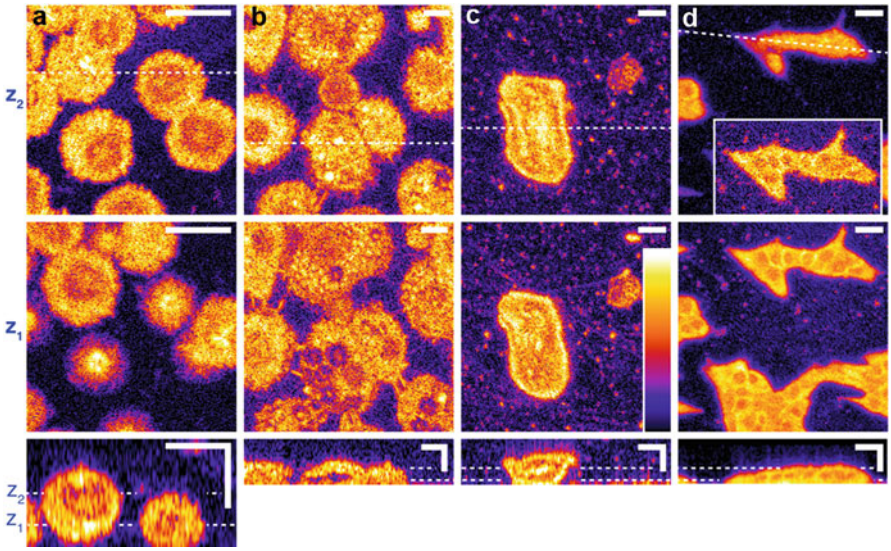

Fig. 29.9 dfOCM tomograms of four different types of living cells. For each tomogram, two en face views were extracted from the depths z_1 and z_2, indicated by the dashed lines in the respective B-scans. The *dashed line* in the en face view z_2 indicates the position of the displayed B-scan. (**a**) Chinese hamster ovary (*CHO*) cells in suspension. (**b**) Differentiated mouse fibroblasts (NIH-3T3) in suspension. (**c**) Cheek cell in suspension. (**d**) Pancreatic beta cells (INS-1) adhering to the glass slide, with ten-frame averaging for improved contrast. The inset shows a single frame for comparison. Scale bars: 20 μm. Dynamic range of *color bar*: 45 dB

dfOCM to weak scattering signals reveals distinct backscattering signal from these near-transparent objects. Significant differences between the various cell types are observed, pointing to fundamental differences in their internal organization. In this particular setting of the dfOCM imaging instrument, the specular reflections have been suppressed by more than 34 dB.

29.4.3 Extended Focus Optical Coherence Tomography xfOCT

The Bessel beam configuration has not only distinct advantages for microscopic imaging but can equally be applied to tissue imaging. In case of scattering tissue such as the skin, the optimal wavelength is 1,300 nm, where scattering becomes less prominent and water absorption has a local minimum. For this wavelength range the most promising OCT technology is based on wavelength-swept light sources. Recent developments of Fourier Domain Mode Locking (FDML) sources allowed for up to then unimaginable imaging speeds of several MHz A-scan rate [36]. High-speed tissue imaging is of particular importance for in vivo applications to keep motion artifacts small and measurement times short such as in endoscopy or for microcirculation imaging (see next section). Wavelength tuning sources are ideally launched

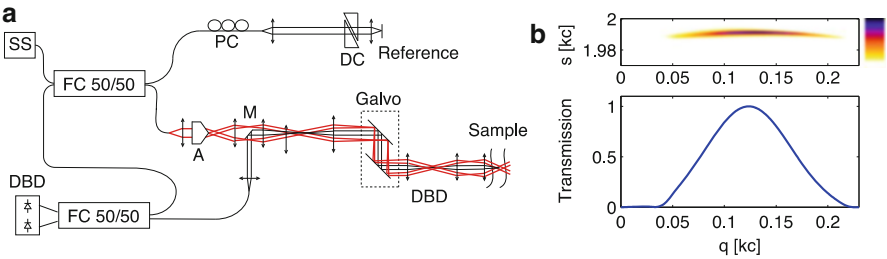

Fig. 29.10 (**a**) Optical setup of SS-OCT system employing a dark field xfOCM scheme via mirror *M*, A-axicon, *SS* swept source, *FC* fiber coupler, *PC* polarization control, *DC* dispersion compensating prisms, *DBD* dual balancing detector. (**b**) Theoretical spatial frequency picture for the configuration in [Blatter 2010] and CTF according to Eq. 29.2. Note the suppressed low frequency part for s(kc) characteristic for a dark field configuration

through single-mode fibers. A setup for extended focus imaging at 1,310 nm with swept-source (SS) OCT is depicted in Fig. 29.10 (lhs). Details can be found in Blatter et al. [37, 38]. The central element of this configuration is a small mirror M that serves both as spatial filter for the illumination Bessel mode through the axicon A, as well as central mirror for the Gaussian detection mode, basically exhibiting the filter characteristics of the masks in the dfOCM setup in Fig. 29.6 of the previous section. The images in the following are obtained with an FDML laser centered at 1,310 nm with a 140 nm full bandwidth, giving an axial resolution of 12 µm in air at 220 kHz A-scan rate. The lateral resolution can be evaluated from its $1/e^2$ lateral extent to be of ∼15 µm, constant over an axial distance of ∼500 µm. With such a configuration a sensitivity of better than 100 dB was achieved.

The setup has a detection NA of 0.06 and an effective illumination NA of 0.13. The calculated CTF is displayed in Fig. 29.10 (rhs). Due to the lower NA, the curvature in the CTF is reduced. But the dark field effect is obvious, with the characteristic suppression of the low spatial frequencies. This has been discussed in Sect. 29.3 and nicely demonstrated in Fig. 29.4.

Another important property of Bessel beams is the so-called self-healing effect. This is basically due to the conical illumination that manages to illuminate structures beneath obstacles, because they do not cast a clear shadow along the optical axis. This effect is clearly visible in case of skin hairs that produce shadows along the optical axis and reduce the signal from the underlying structure for standard OCT configurations (Fig. 29.11a, c). Almost no shadowing results for the xfOCT configuration (Fig. 29.11b, d). The spurious shadow is due to the decoupled Bessel beam illumination and axial Gaussian detection. Clearly the effect depends on the size of the obstacle and its position along the axis.

The performance for imaging of healthy human skin in vivo is well visible from Fig. 29.12a–c. Apart from pure structural imaging, OCT has also important functional imaging capabilities. The following section is dedicated to the advantages of xfOCT for label-free microvascular imaging.

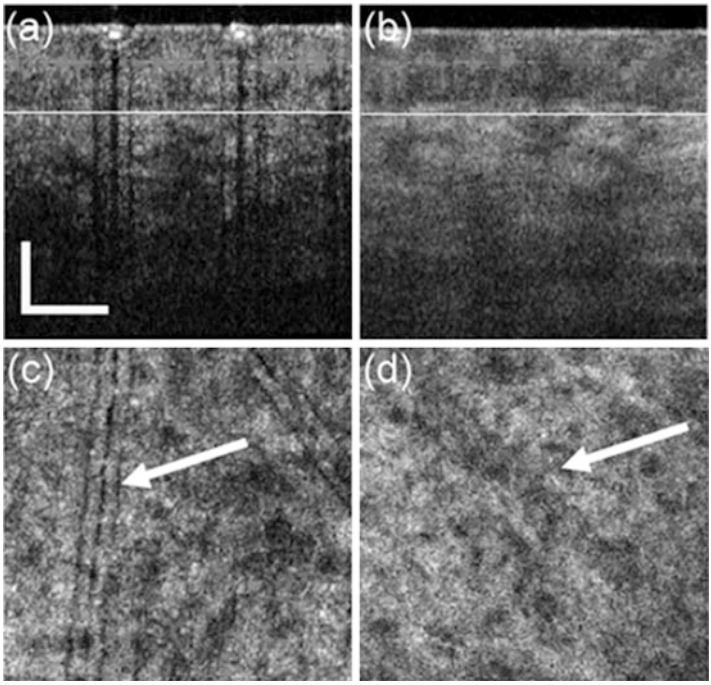

Fig. 29.11 Self-regeneration of Bessel beams: shadowing of skin hair along the depth. (**a**, **c**) Standard. (**b**, **d**) xf-configuration. (**a**, **b**) Tomograms. (**c**, **d**) En face projection views at depth indicated by the *white line* in the tomograms showing remaining shadowing in the standard OCT setup whereas only slight signal reduction is seen in xfOCT (*white arrows*). Tomograms are taken at different but close locations of the skin. Scale bar denotes 250 μm in every picture

29.4.4 Extended Focus Microcirculation Imaging

Since the first implementations of OCT, functional extensions of OCT have been extensively investigated [39–41]. They promise to compensate the intrinsically missing molecular contrast as provided, for example, by confocal fluorescence microscopy. A unique position among these techniques has Doppler OCT, as it allows not only to contrast blood flow in a fully noninvasive and label-free way but also to quantify flow within individual vessels in tissue. This is due to the fact that OCT is an interferometric technique with the possibility to track changes of the optical path length by fractions of the center wavelength.

Especially the availability of high-speed OCT technology based on Fourier domain detection boosted the development of highly sensitive optical angiography techniques. Clearly blood flow and tissue blood supply is a key information for understanding tissue health, as well as for effective treatment monitoring. Insight into capillary structure, its integrity, and perfusion would create new diagnostic capabilities in clinical practice and research.

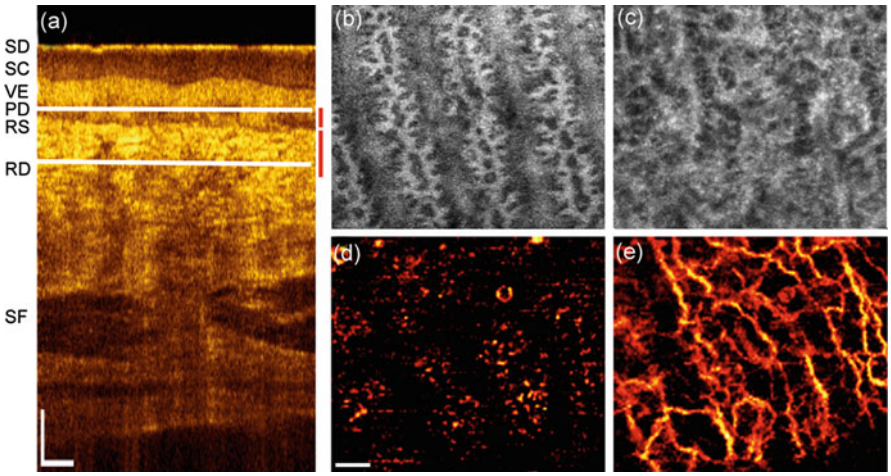

Fig. 29.12 Healthy skin of the palm. (**a**) OCT tomogram. *Red bars* indicate depth range for (**b**) and (**c**), respectively. *SD* stratum disjunctum, *SC* stratum corneum, *VE* viable epidermis, *PD* Papillary dermis, *RS* rete subpapillare, *RD* reticular dermis, *SF* subcutaneous fat. (**b**, **c**) 2 × 2 mm en face mean projection over depth range indicated in (**a**). *Scale bars* indicate 250 μm in each picture. (**d**–**e**) OCT angiography for en face cross section of (**b**–**c**), respectively. (**d**) Shows cross sections of small capillary loops that perfuse the *upper* skin layers. (**e**) Shows preferentially flat vessel beds with larger vessels in the dermis [38]

In the following we review the implementation of intensity-based Doppler OCT on the dark field swept-source OCT platform operating at 1,300 nm center wavelength characterized in the previous section. We demonstrate examples for label-free high-resolution angiography in the human skin both healthy and diseased, including cases of nonmelanoma skin cancer.

The vascular contrasting method is based on calculating logarithmically scaled intensity differences between successive tomograms [42–47]. Ideally, the tomograms are taken at the same lateral position in order to keep speckle decorrelation signatures of static tissue low. Using the intensity information instead of the phase is easily implemented and better suited to high-speed FDML laser sources regarding trigger jitter between successive tomograms. An angiographic image P, contrasting flow against static tissue, is obtained by calculating the squared intensity difference between successive tomograms:

$$P(x, y_i, z) = \left(I(x, y_i, z) - I\left(x, y_{i+1}, z\right)\right)^2 \tag{29.7}$$

where $I(x, y, z) = 20 \cdot \log[|FFT\{I(x, y, k)\}|]$, x, y, z are the spatial pixel coordinates corresponding to fast and slow scanning and depth coordinate, respectively, and k is the wavenumber. Motion artifacts give rise to high intensity difference signatures; thus, a simple thresholding can help to exclude those images. This method is more robust against motion artifacts than a variance analysis over the full tomogram

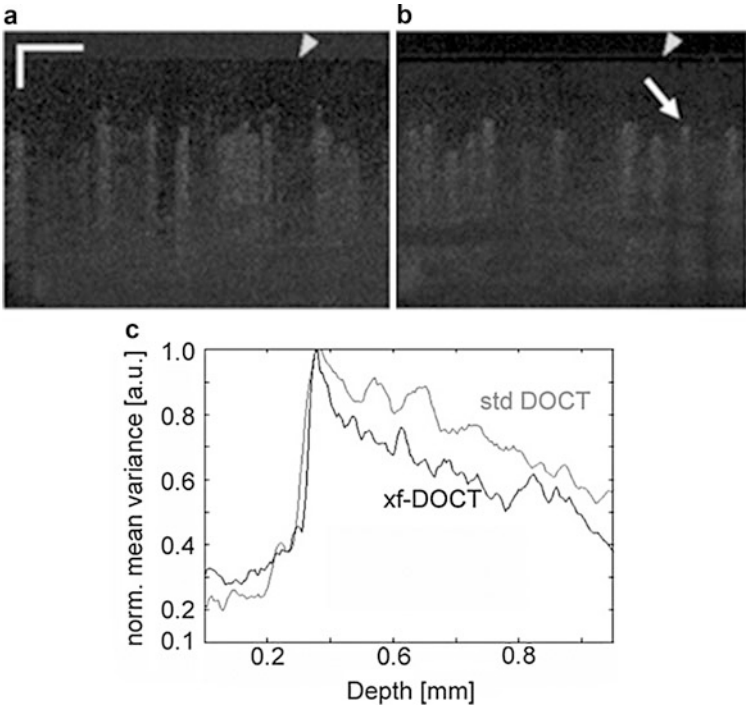

Fig. 29.13 Result of intensity difference tomograms. The static tissue appears *dark*, while motion is represented by *bright* values. Blood vessels are visible; however, their axial extend determination is limited by decorrelation. (**a**) Standard (*std*) DOCT mean intensity difference plot. (**b**) Extended focus (*xf*) DOCT. *Arrows* point at the skin surface in contact with a glass plate. *Long white arrow* points at vessel cross section. Scale bar denotes 250 μm. (**c**) Normalized mean depth profile through vessel showing a better defined vessel axial size and a steeper decrease of the signal with the xfDOCT scheme [37]

series acquired at the same position, since pictures with strong decorrelation are rejected. Furthermore, the difference is only calculated between successive tomograms, thus reducing the time interval over which correlation is required. This improves further the stability with respect to motion artifacts. Figure 29.12 below shows the vascular structure for healthy skin.

The en face images of Fig. 29.12d, e are obtained by adding the mean intensity difference values $P(x, y, z)$ (Eq. 29.7) along the axial extent indicated in Fig. 29.12a by the red bars. The visible small dots in Fig. 29.12d represent cross sections of small capillary loops in the uppermost skin layers, whereas deeper vasculature is characterized by flat vessel beds with increased vessel diameter (Fig. 29.12e).

Despite the high sensitivity to even capillary flow, such contrast methods have in common that they lead to axial signal decorrelation artifacts below blood vessels. They are due to multiple scattering as well as the refractive index change over time of intrinsically inhomogeneous blood. Figure 29.13 demonstrates this effect for an

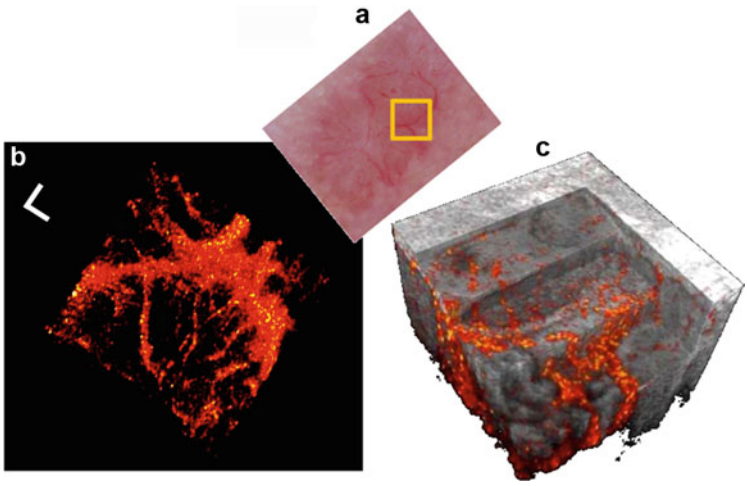

Fig. 29.14 BCC on the forehead. (**a**) Dermoscopy image with square indicating the OCT FOV. (**b**) Doppler OCT (DOCT) angiography using the xfOCT configuration. *Scale bars* indicate 250 μm. (**c**) Volume rendered overlay of microcirculation (*red*) on structural information (*gray scale*) [38]

intensity difference tomogram for a dark field xfOCT configuration as well as for a standard OCT configuration. The vessel tails are clearly visible in both cases.

However, by taking an average axial profile, it becomes visible that xfOCT suffers slightly less from these artifacts as shown in Fig. 29.13 (right). The extended focus curve exhibits an axially better defined vessel size and a steeper decrease of the variance signal. This can be attributed to the conical illumination of the Bessel beam illuminating structures below the vessel without actually crossing the vessel. Of course the effect is reduced by the standard axial Gaussian detection. It can be expected that the decorrelation tails would be better suppressed by configurations with Bessel illumination and detection (see above) at the expense of overall detection sensitivity.

Depth-resolved visualization of microvasculature is already a powerful tool for characterizing lesions [38, 48, 49]. Figure 29.14 shows the microvascular pattern of a basal cell carcinoma (BCC), a nonmelanoma skin cancer, assessed in vivo and in situ.

The standard tool in dermatology is the dermascope (Fig. 29.14a). It provides high contrast visual inspection and documentation, but is restricted to the surface alone. Deep structural and microvascular details are accessible through xfOCT as shown in Fig. 29.14b, c. Figure 29.14c shows a volume-rendered vascular contrast image together with the intensity information in gray scale that allows for better correlation between structure and vasculature. In combination with complementary optical methods for assessing metabolite concentrations or tissue oxygenation, the label-free microcirculation imaging modality could give unique insight into the metabolic demand of tissue.

29.5 Conclusion and Outlook

This work has given an overview of how beam engineering can enhance the imaging capabilities and performance of OCM by reviewing the current state of research. First, a theoretical description of image formation in OCM, based on the concept of the CTF, was presented. Next, implications of the CTF on image resolution and the depth of field, as well as the resulting contrast of biological tissue, were discussed. Engineering of a specific CTF can be aimed at extending the DOF or at achieving a dark field configuration to improve imaging contrast.

The various implementations of the described extended focus, and dark field modalities have demonstrated their potential in a wide range of applications, spanning from cell and small animal imaging to dermatology. The benefits in resolution, speed, and contrast enabled to address relevant questions in important research areas such as diabetes, Alzheimer's, or microcirculation. The extended focus concepts yield furthermore distinct advantages for mesoscopic resolution OCT and for its functional extension with Doppler OCT.

All the presented configurations rely on decoupling of the illumination from the detection aperture. While this is the fundamental concept that enabled the engineering of the reported CTFs, it adds significant system complexity and has limited its use to bench-top settings. The development of a fiber probe that achieves decoupling of the illumination and detection paths in an elegant and simple way would make the advantages of extended DOF and dark field accessible to an endoscopic setting. Clinical, catheter-based applications would greatly benefit from the gained resolution and contrast.

Although beam engineering can improve the contrast for imaging of biological samples, this signal is entirely defined by the structure, i.e., the refractive index, of the sample. The possibility to add contrast with molecular specificity remains a long-lasting goal and would expand the possibilities of OCM and open up new applications. In a recent effort, the high sensitivity of the dfOCM configuration to small backscattered signals was extended with a photothermal optical lock-in detection (poliOCM) [50]. The photothermal response [51, 52] provided a highly sensitive and specific extrinsic contrast mechanism. In poliOCM an external pump source modulated beyond 100 kHz induced time-varying changes of the refractive index in the close vicinity of strongly absorbing particles. Gold nanoparticles (AuNP) were used as small, point-like absorption centers, down to a size of only 6 nm. Tuning the pumping wavelength to the plasmon resonance of these AuNPs resulted in a strong local absorption and efficient heating of the AuNPs' immediate surroundings. AuNPs are interesting markers, as they offer good biocompatibility without any adverse bleaching, known from the widely used fluorescent labels. Modulating the reference signal with a phase variation locked to the pump modulation suppressed the signal from static structure, providing a selective image of the AuNPs. Turning off the reference arm modulation provided a conventional dfOCM tomogram. poliOCM still benefits from the parallel acquisition speed advantage and offers and interesting alternative to the much slower confocal microscopy,

especially for studies of cell dynamics, where both the biocompatibility of the probes and the imaging speed are crucial.

An alternative way to add the missing molecular contrast to OCM is to combine different imaging modalities with complementary contrast mechanisms into a multimodal platform. In case of thin samples, OCM can easily be combined with fluorescence and fluorescence lifetime microscopy. The most promising candidate for thick tissue imaging is photoacoustics (PA) as it combines high resolution with high absorption sensitivity [53]. A drawback of PA is the missing absorption contrast to the embedding tissue that would often be required for proper image interpretation. In that, it is fully complementary to the structural imaging provided by OCM. The combination of PA and OCM would therefore allow for more complete characterization of tissue structure and metabolism [46, 54–56]. In a recent work, an elegant combination of xfOCM and PA in a fully optical way using the same detection optics was shown [57, 58].

The framework of beam engineering presented in this chapter is limited to scalar expressions, ignoring the vectorial nature of light and the resulting polarization effects. Also, the aperture functions were assumed to be rotationally symmetric. Breaking this symmetry would offer additional parameters and offer more flexibility in designing a specific system CTF. Deformable mirrors and spatial light modulators, well known from adaptive optics, could provide a convenient toolset to explore more advanced beam engineering modalities. These wavefront manipulation devices were developed to correct for optical aberrations and help to recover a tightly focused spot, and more recently even to refocus light deep inside scattering samples, correcting for multiple scattering [59]. They could also serve to dynamically redefine the system CTF, test different regions of the sample spatial frequency spectrum, and vary the extension of the depth of field. This would enable to adapt contrast, resolution, and acquisition speed for the specific sample under investigation and would optimize the information content gained on the imaged tissue.

Acknowledgements We would like to acknowledge the contributions of Cedric Blatter, Branislav Grajciar, Alex Aneesh, Wolfgang Drexler, Hubert Pehamberger, and Jessica Weingast from the Medical University Vienna (Austria); Tristan Bolmont, Arno Bouwens, Christophe Pache, and Corinne Berclaz from the Ecole Polytechnique Fédérale de Lausanne (Switzerland); Robert Huber from the Ludwig Maximillian University in Munich (Germany); as well as the following financial support: European Commission FP7-HEALTH (grant 201880, FUN OCT), Austrian Christian Doppler Association, Swiss National Fonds (SNF grant 205321-10974, 203321L-135353(MCOCM)), SCIEX-NMS(533006), CTI(13964.1PFLS-LS (AIM)), and EU-Funding (222980 BetaImage).

References

1. J.G. Fujimoto, M.E. Brezinski, G.J. Tearney, S.A. Boppart, B. Bouma, M.R. Hee, J.F. Southern, E.A. Swanson, Optical biopsy and imaging using optical coherence tomography. Nat. Med. **1**, 970–972 (1995)

2. W. Drexler, U. Morgner, F.X. Kartner, C. Pitris, S.A. Boppart, X.D. Li, E.P. Ippen, J.G. Fujimoto, In vivo ultrahigh-resolution optical coherence tomography. Opt. Lett. **24**, 1221–1223 (1999)
3. L. Vabre, A. Dubois, A.C. Boccara, Thermal-light full-field optical coherence tomography. Opt. Lett. **27**, 530–532 (2002)
4. B. Povazay, K. Bizheva, A. Unterhuber, B. Hermann, H. Sattmann, A.F. Fercher, W. Drexler, A. Apolonski, W.J. Wadsworth, J.C. Knight, P.S.J. Russell, M. Vetterlein, E. Scherzer, Submicrometer axial resolution optical coherence tomography. Opt. Lett. **27**, 1800–1802 (2002)
5. S. Kray, F. Spöler, M. Först, H. Kurz, High-resolution simultaneous dual-band spectral domain optical coherence tomography. Opt. Lett. **34**, 1970–1972 (2009)
6. J.M. Schmitt, S.L. Lee, K.M. Yung, An optical coherence microscope with enhanced resolving power in thick tissue. Opt. Commun. **142**, 203–207 (1997)
7. A.G. Podoleanu, G.M. Dobre, D.A. Jackson, En-face coherence imaging using galvanometer scanner modulation. Opt. Lett. **23**, 147–149 (1998)
8. C. Hitzenberger, P. Trost, P.-W. Lo, Q. Zhou, Three-dimensional imaging of the human retina by high-speed optical coherence tomography. Opt. Express **11**, 2753–2761 (2003)
9. J.A. Izatt, M.R. Hee, G.M. Owen, E.A. Swanson, J.G. Fujimoto, Optical coherence microscopy in scattering media. Opt. Lett. **19**, 590–592 (1994)
10. M. Pircher, B. Baumann, E. Götzinger, H. Sattmann, C.K. Hitzenberger, Phase contrast coherence microscopy based on transverse scanning. Opt. Lett. **34**, 1750–1752 (2009)
11. R. Huber, M. Wojtkowski, J.G. Fujimoto, J.Y. Jiang, A.E. Cable, Three-dimensional and C-mode OCT imaging with a compact, frequency swept laser source at 1300 nm. Opt. Express **13**, 10523–10538 (2005)
12. R.A. Leitgeb, M. Villiger, A.H. Bachmann, L. Steinmann, T. Lasser, Extended focus depth for Fourier domain optical coherence microscopy. Opt. Lett. **31**, 2450–2452 (2006)
13. T.S. Ralston, D.L. Marks, P.S. Carney, S.A. Boppart, Inverse scattering for optical coherence tomography. J. Opt. Soc. Am. A **23**, 1027–1037 (2006)
14. A. Kumar, W. Drexler, R.A. Leitgeb, Numerical focusing methods for full field OCT: a comparison based on a common signal model. Opt. Express **22**, 16061–16078 (2014)
15. Y. Yasuno, Y. Sando, J.I. Sugisaka, T. Endo, S. Makita, G. Aoki, M. Itoh, T. Yatagai, In-focus Fourier-domain optical coherence tomography by complex numerical method. Opt. Quant. Electron. **37**, 1185–1189 (2005)
16. R.M. Herman, T.A. Wiggins, Production and uses of diffractionless beams. J. Opt. Soc. Am. A Opt. Image Sci. Vis. **8**, 932–942 (1991)
17. Z.H. Ding, H.W. Ren, Y.H. Zhao, J.S. Nelson, Z.P. Chen, High-resolution optical coherence tomography over a large depth range with an axicon lens. Opt. Lett. **27**, 243–245 (2002)
18. K.S. Lee, L.P. Rolland, Bessel beam spectral-domain high-resolution optical coherence tomography with micro-optic axicon providing extended focusing range. Opt. Lett. **33**, 1696–1698 (2008)
19. K.M. Tan, M. Mazilu, T.H. Chow, W.M. Lee, K. Taguchi, B.K. Ng, W. Sibbett, C.S. Herrington, C.T.A. Brown, K. Dholakia, In-fiber common-path optical coherence tomography using a conical-tip fiber. Opt. Express **17**, 2375–2384 (2009)
20. L.B. Liu, C. Liu, W.C. Howe, C.J.R. Sheppard, N.Q. Chen, Binary-phase spatial filter for real-time swept-source optical coherence microscopy. Opt. Lett. **32**, 2375–2377 (2007)
21. L. Liu, J.A. Gardecki, S.K. Nadkarni, J.D. Toussaint, Y. Yagi, B.E. Bouma, G.J. Tearney, Imaging the subcellular structure of human coronary atherosclerosis using micro-optical coherence tomography. Nat. Med. **17**, 1010–1014 (2011)
22. D. Lorenser, X. Yang, D.D. Sampson, Ultrathin fiber probes with extended depth of focus for optical coherence tomography. Opt. Lett. **37**, 1616–1618 (2012)
23. M. Villiger, T. Lasser, Image formation and tomogram reconstruction in optical coherence microscopy. J. Opt. Soc. Am. A **27**, 2216–2228 (2010)

24. J.M. Coupland, J. Lobera, Holography, tomography and 3D microscopy as linear filtering operations. Meas. Sci. Technol. **19**, 12 (2008)
25. C.J.R. Sheppard, M. Gu, X.Q. Mao, 3-dimensional coherent transfer-function in a reflection-mode confocal scanning microscope. Opt. Commun. **81**, 281–284 (1991)
26. C.W. McCutchen, Generalized aperture + 3-dimensional diffraction image. J. Opt. Soc. Am. **54**, 240 (1964)
27. T.S. Ralston, D.L. Marks, P.S. Carney, S.A. Boppart, Interferometric synthetic aperture microscopy. Nat. Phys. **3**, 129–134 (2007)
28. J.M. Schmitt, G. Kumar, Turbulent nature of refractive-index variations in biological tissue. Opt. Lett. **21**, 1310–1312 (1996)
29. M. Xu, R.R. Alfano, Fractal mechanisms of light scattering in biological tissue and cells. Opt. Lett. **30**, 3051–3053 (2005)
30. C.J.R. Sheppard, Fractal model of light scattering in biological tissue and cells. Opt. Lett. **32**, 142–144 (2007)
31. M. Villiger, J. Goulley, M. Friedrich, A. Grapin-Botton, P. Meda, T. Lasser, R.A. Leitgeb, In vivo imaging of murine endocrine islets of Langerhans with extended-focus optical coherence microscopy. Diabetologia **52**, 1599–1607 (2009)
32. C. Berclaz, J. Goulley, M. Villiger, C. Pache, A. Bouwens, E. Martin-Williams, D. Van de Ville, A.C. Davison, A. Grapin-Botton, T. Lasser, Diabetes imaging-quantitative assessment of islets of Langerhans distribution in murine pancreas using extended-focus optical coherence microscopy. Biomed. Opt. Express **3**, 1365–1380 (2012)
33. T. Bolmont, A. Bouwens, C. Pache, M. Dimitrov, C. Berclaz, M. Villiger, B.M. Wegenast-Braun, T. Lasser, P.C. Fraering, Label-free imaging of cerebral beta-amyloidosis with extended-focus optical coherence microscopy. J. Neurosci. **32**, 14548–14556 (2012)
34. R. Radde, T. Bolmont, S.A. Kaeser, J. Coomaraswamy, D. Lindau, L. Stoltze, M.E. Calhoun, F. Jäggi, H. Wolburg, S. Gengler, C. Haass, B. Ghetti, C. Czech, C. Hölscher, P.M. Mathews, M. Jucker, Abeta42-driven cerebral amyloidosis in transgenic mice reveals early and robust pathology. EMBO Rep. **7**, 940–946 (2006)
35. M. Villiger, C. Pache, T. Lasser, Dark-field optical coherence microscopy. Opt. Lett. **35**, 3489–3491 (2010)
36. W. Wieser, B.R. Biedermann, T. Klein, C.M. Eigenwillig, R. Huber, Multi-megahertz OCT: high quality 3D imaging at 20 million A-scans and 4.5 GVoxels per second. Opt. Express **18**, 14685–14704 (2010)
37. C. Blatter, B. Grajciar, C.M. Eigenwillig, W. Wieser, B.R. Biedermann, R. Huber, R.A. Leitgeb, Extended focus high-speed swept source OCT with self-reconstructive illumination. Opt. Express **19**, 12141–12155 (2011)
38. C. Blatter, J. Weingast, A. Alex, B. Grajciar, W. Wieser, W. Drexler, R. Huber, R.A. Leitgeb, In situ structural and microangiographic assessment of human skin lesions with high-speed OCT. Biomed. Opt. Express **3**, 2636–2646 (2012)
39. W. Drexler, J.G. Fujimoto (eds.), *Optical Coherence Tomography – Technology and Applications* (Springer, Berlin, 2008)
40. W. Drexler, R.A. Leitgeb, C.K. Hitzenberger, New developments in optical coherence tomography technology, in *Medical Retina*, ed. by R.F. Spaide (Springer, Berlin, 2009)
41. R.A. Leitgeb, Current technologies for high-speed and functional imaging with optical coherence tomography, in *Advances in Imaging and Electron Physics*, ed. by P.W. Hawkes, vol. 168 (Elsevier Academic Press, San Diego, 2011), pp. 109–192
42. A. Mariampillai, B.A. Standish, E.H. Moriyama, M. Khurana, N.R. Munce, M.K.K. Leung, J. Jiang, A. Cable, B.C. Wilson, I.A. Vitkin, V.X.D. Yang, Speckle variance detection of microvasculature using swept-source optical coherence tomography. Opt. Lett. **33**, 1530–1532 (2008)
43. L. Conroy, R.S. DaCosta, I.A. Vitkin, Quantifying tissue microvasculature with speckle variance optical coherence tomography. Opt. Lett. **37**, 3180–3182 (2012)

44. L. An, J. Qin, R.K. Wang, Ultrahigh sensitive optical microangiography for in vivo imaging of microcirculations within human skin tissue beds. Opt. Express **18**, 8220–8228 (2010)
45. G. Liu, A.J. Lin, B.J. Tromberg, Z. Chen, A comparison of Doppler optical coherence tomography methods. Biomed. Opt. Express **3**, 2669–2680 (2012)
46. E.Z. Zhang, B. Povazay, J. Laufer, A. Alex, B. Hofer, B. Pedley, C. Glittenberg, B. Treeby, B. Cox, P. Beard, W. Drexler, Multimodal photoacoustic and optical coherence tomography scanner using an all optical detection scheme for 3D morphological skin imaging. Biomed. Opt. Express **2**, 2202–2215 (2011)
47. D.Y. Kim, J. Fingler, J.S. Werner, D.M. Schwartz, S.E. Fraser, R.J. Zawadzki, In vivo volumetric imaging of human retinal circulation with phase-variance optical coherence tomography. Biomed. Opt. Express **2**, 1504–1513 (2011)
48. B.J. Vakoc, R.M. Lanning, J.A. Tyrrell, T.P. Padera, L.A. Bartlett, T. Stylianopoulos, L.L. Munn, G.J. Tearney, D. Fukumura, R.K. Jain, B.E. Bouma, Three-dimensional microscopy of the tumor microenvironment in vivo using optical frequency domain imaging. Nat. Med. **15**, 1219–1223 (2009). U1151
49. T. Schmoll, A.S.G. Singh, C. Blatter, S. Schriefl, C. Ahlers, U. Schmidt-Erfurth, R.A. Leitgeb, Imaging of the parafoveal capillary network and its integrity analysis using fractal dimension. Biomed. Opt. Express **2**, 1159–1168 (2011)
50. C. Pache, N.L. Bocchio, A. Bouwens, M. Villiger, C. Berclaz, J. Goulley, M.I. Gibson, C. Santschi, T. Lasser, Fast three-dimensional imaging of gold nanoparticles in living cells with photothermal optical lock-in optical coherence microscopy. Opt. Express **20**, 21385–21399 (2012)
51. D. Boyer, P. Tamarat, A. Maali, B. Lounis, M. Orrit, Photothermal imaging of nanometer-sized metal particles among scatterers. Science **297**, 1160–1163 (2002)
52. D.C. Adler, S.-W. Huang, R. Huber, J.G. Fujimoto, Photothermal detection of gold nanoparticles using phase-sensitive optical coherence tomography. Opt. Express **16**, 4376–4393 (2008)
53. L.V. Wang, Multiscale photoacoustic microscopy and computed tomography. Nat. Photonics **3**, 503–509 (2009)
54. S. Jiao, M. Jiang, J. Hu, A. Fawzi, Q. Zhou, K.K. Shung, C.A. Puliafito, H.F. Zhang, Photoacoustic ophthalmoscopy for in vivo retinal imaging. Opt. Express **18**, 3967–3972 (2010)
55. L. Li, K. Maslov, G. Ku, L.V. Wang, Three-dimensional combined photoacoustic and optical coherence microscopy for in vivo microcirculation studies. Opt. Express **17**, 16450–16455 (2009)
56. Y. Wang, C. Li, R.K. Wang, Noncontact photoacoustic imaging achieved by using a low-coherence interferometer as the acoustic detector. Opt. Lett. **36**, 3975–3977 (2011)
57. C. Blatter, B. Grajciar, B. Hermann, R. Huber, W. Drexler, R.A. Leitgeb, Simultaneous dark-bright field swept source OCT for ultrasound detection, Proc. SPIE Int. Soc. Opt. Eng. **82131M** (2012)
58. C. Blatter, B. Grajciar, P. Zou, W. Wieser, A.J. Verhoef, R. Huber, R.A. Leitgeb, Intrasweep phase-sensitive optical coherence tomography for noncontact optical photoacoustic imaging. Opt. Lett. **37**, 4368–4370 (2012)
59. R. Fiolka, K. Si, M. Cui, Complex wavefront corrections for deep tissue focusing using low coherence backscattered light. Opt. Express **20**, 16532–16543 (2012)

Holographic Optical Coherence Imaging 30

David D. Nolte, Kwan Jeong, John Turek, and Paul M. W. French

30.1 Introduction

Holographic optical coherence imaging (HOCI) is a wide-field imaging approach that acquires en face images from a fixed depth inside scattering media by using low-coherence off-axis holography as a coherence gate [1]. There are two forms of holographic recording in optical coherence imaging: (1) dynamic holography in photorefractive media and (2) digital holography on pixel-array detectors.

Photorefractive holographic OCI uses a holographic real-time film (most commonly a photorefractive quantum well structure [2]) to provide the coherent demodulation that extracts information-bearing light from the multiply scattered statistically incoherent background. The photorefractive effect responds to the gradient in intensity, rather than to direct intensity, and records low-coherence light interfering with a reference wave. The hologram is read out by diffracting a reconstruction beam into a video camera. The diffracted image is "background-free" because the nominally uniform background is not recorded. The real-time character of the holographic film makes it possible to interrogate tissue interactively by viewing on a video monitor without computed tomography or reconstruction.

D.D. Nolte (✉)
Department of Physics, Purdue University, West Lafayette, IN, USA

Department of Basic Medical Sciences, Purdue University, West Lafayette, IN, USA
e-mail: nolte@purdue.edu

K. Jeong
Physics Department, Korean Military Academy, Soeul, South Korea

J. Turek
Department of Basic Medical Sciences, Purdue University, West Lafayette, IN, USA

P.M.W. French
Imperial College, London, UK

© Springer International Publishing Switzerland 2015

W. Drexler, J.G. Fujimoto (eds.), *Optical Coherence Tomography*,
DOI 10.1007/978-3-319-06419-2_31

The real-time character makes it adaptive and enables it to compensate mechanical motions in the optical system.

Digital holographic OCI uses a digital pixel array (either CCD or CMOS camera chip) placed at the recording plane, and the hologram is read out electronically to a computer. The speckle hologram is typically recorded on a Fourier plane, with interference fringes between the signal and reference modulated by the speckle envelope. The image is reconstructed using a fast Fourier transform (FFT) algorithm that generates an image and its phase conjugate. The pixel spacing of the array determines the smallest fringe spacing that can be supported by the Nyquist sampling theorem and hence sets the reconstruction spatial resolution.

This chapter gives an overview of the principles of holographic OCI. It begins with a description of off-axis holography as spatial heterodyne detection and continues with the origin and role of speckle in multichannel illumination of tissue. Image-domain holography (IDH) and Fourier-domain holography (FDH) are described. Holography in the Fourier domain has the capability for phase-contrast imaging that can acquire small sub-wavelength displacements despite long coherence length. The trade-offs between photorefractive and digital holography are discussed. The chief biological target is multicellular spheroids, specifically rat osteogenic sarcomas that are grown in vitro. After describing the physiological and optical properties of these spheroids, results from holographic OCI are presented using both photorefractive and digital holography.

30.2 Development and Applications of Holographic OCI

Holography is a wide-field 2-D coherent recording technique, making it an obvious choice as a coherence-gating method to image through turbid media [3]. It was with holography that Stetson first showed the principle of coherence gating for imaging through a fog-like medium [4]. In 1989 light-in-flight (LIF) holography was demonstrated, exploiting the finite coherence length of the light source to facilitate depth-resolved imaging of three-dimensional objects [5], including through optical diffusers. However, photographic film was used as the holographic recording medium, and each image acquisition had to be chemically developed before being reconstructed. Subsequent research has concentrated on using real-time methods to perform the holographic recording and reconstruction, focusing mainly on two techniques: “electronic” or “digital” holography [6, 7] and photorefractive holography [8]. These “off-axis holography” techniques are closely related to wide-field OCT, sharing many of the strengths and drawbacks. Perhaps the key advantage of the holographic approach is that the coherent detection is in the spatial domain, rather than the temporal, and so can provide a full-field sectioned image in “single-shot” acquisition, making it less sensitive to motion artifacts. Wide-field techniques may also employ sources of low spatial coherence, such as thermal sources [9] or LEDs [10], which provide short coherence lengths and reasonable average powers – usually with lower cost than the spatially coherent laser sources required for single-channel OCT. The chief drawback of wide-field coherence-gated

imaging is the lack of the strong spatial filter employed by conventional OCT systems and hence significant scattered backgrounds and speckle.

Photorefractive holography offers an opportunity to realize high-speed coherence-gated imaging *without* the scattered light background, and the dynamic range is not directly limited by the CCD camera but by the photorefractive material [11]. In 1993 Mamaev et al. [12] showed that a photorefractive crystal of strontium barium niobate (SBN) could be used to image through a suspension of milk in real time. This demonstrated the utility of photorefractive holography for coherence-gated imaging, albeit using narrowband c.w. radiation and imaging in transmission. In 1995 Hyde et al. demonstrated real-time 2-D/3-D imaging through a scattering solution of polystyrene spheres with both c.w. and ultrashort pulsed near-infrared radiation using rhodium-doped barium titanate (Rh-Ba:TiO_3) as the photorefractive recording medium [13]. This approach permitted a weak ballistic image to be recorded in the presence of an incoherent background 10^6 times higher [14], demonstrating that photorefractive holography is not sensitive to a uniform background of multiply scattered diffuse light. This reflects the *unique* behavior of photorefractive media that are sensitive, not to the incident intensity but to the *spatial derivative of the incident intensity distribution* – in contrast to all other wide-field imaging detectors.

A typical low-coherence photorefractive holography setup is nearly the same as for conventional or (image plane) digital holography except that the CCD in the holographic recording plane is replaced by a photorefractive medium. A holographic image formed by the coherent (ballistic) light is recorded and read out using a laser that may be at a different wavelength from the broadband source. Using Rh-Ba:TiO_3 as the photorefractive medium, wide-field 3-D imaging through scattering media of up to 16 MFP (round trip) thickness was demonstrated for the first time with sub-100 μm depth and transverse spatial resolution [13], albeit with a long ($\sim$300 s) integration time owing to the relatively slow response of Rh-Ba:TiO_3. To obtain both high-speed and near infrared sensitivity, the most promising candidates are semiconductor media and the highest sensitivities and fastest responses have been obtained from semi-insulating photorefractive MQW devices exploiting the transverse-field Franz Keldysh effect [15]. This approach permits rapid 3-D imaging through turbid media with NIR radiation and depth-resolved image acquisition with integration times shorter than 0.4 ms [16]. Thus, real-time 3-D imaging may be implemented with image acquisition direct to a videocassette recorder, without recourse to a digital frame grabber [17]. Using a high-speed CCD camera, photorefractive holography using PRQW devices realized depth-resolved imaging at 476 frames/s [18], By using a (spatially incoherent) LED source, PRQW holography provides sub-10 μm depth resolution [10] and speckle-free images through static turbid media including sandstone [19] and biological tissue [20]. The imaging depth range for OCI is approximately 0.7 mm [21] for imaging epithelial layers or 1 mm for tumor spheroids in reflection [22]. The axial resolution of OCI achieved 14 μm using short-coherence sources [23], and the lateral resolution is typically 10 μm [24] although this is determined solely by the optics and the magnification.

The first application of holographic OCI to living tissue was imaging into rat osteogenic tumor spheroids [22, 24]. The tumor spheroids are roughly spherical in

shape and have a differentiated structure with a 100–200 μm thick shell of proliferating cells surrounding a necrotic core. This tumor morphology was captured by holographic OCI as an average intensity dependence on radius [25]. Time-dependent changes in speckle intensities were also found to correlate with the metabolic health of the spheroids [26].

The early work on holographic OCI was performed using image-domain holograms for which the hologram plane was at or near the image plane of the imaging optics. Better performance was attained by using Fourier-domain holograms for which the hologram plane was at or near the Fourier plane of the imaging optics. This was especially important for reduction of light scattered to the CCD camera by imperfections in the holographic film. The Fourier-domain system [27] has a dynamic range approaching −100 dB. This system improvement enabled volumetric imaging of detail within mouse eye as well as tumor spheroids and demonstrated robust repeatability [28]. Phase-contrast imaging of tissue with sensitivity to surface topology down to 200 nm was also demonstrated in the Fourier system [29].

The direct capture of interference fringes on electronic pixel-array detectors had a long nascent period beginning with work by Joseph Goodman in the first decade after the invention of the laser [30, 31] and extending through the early 1990s [32–34]. The first use of digital holography (also called electronic holography) to image through living issue was by Emmet Leith's group in 1994 [35]. Progress in digital holography mirrored progress in CCD cameras, which became increasingly more powerful as well as inexpensive in the late 1990s, driven by consumer electronics markets. Breakthroughs in applications of digital holography had a cusp in the years 1994–1998 [36–40] after which many improvements and advances were made by many groups.

There was an early interest in low-coherence digital holography [33, 41] merged with full-field optical coherence tomography [9, 42–45] that employed in-line phase-shifting low-coherence interferometric imaging, which is the subject of several other chapters in this volume. Off-axis digital holography, on the other hand, employs spatial heterodyne detection on the pixel array without the need for phase shifting [46–49], which simplifies the image reconstruction, but with a trade-off in hologram resolution limited by the pixel pitch of the pixel-array detectors. The first application of low-coherence digital off-axis holography to living tissue was to multicellular tumor spheroids [50]. Living tissue exhibits highly dynamic speckle that is captured by the digital holography [51, 52] and has been used to derive a new form of functional imaging called motility contrast imaging (MCI) which is the topic of ▶ Chap. 37, "Motility Contrast Imaging and Tissue Dynamics Spectroscopy" in this volume.

30.3 System Architecture and Performance

30.3.1 Speckle Holography and Spatial Heterodyne

Speckle arises from the simultaneous illumination of an optically heterogeneous target by multiple optical modes. Fully developed speckle has a Poissonian intensity distribution for which the root variance of the intensity equals the mean intensity.

This speckle carries no structural information, but can contain statistical information related to the tissue. On the other hand, partially developed speckle with a mean intensity larger than the root-variance does carry partial structural information.

Whether speckle is fully or partially developed, it can remain coherent with respect to a reference wave. Holograms written between the speckle field and the reference wave are called speckle holograms. The basis of holographic OCI is the recording of speckle holograms, either from fully or partially developed speckle, in the presence of a statistically incoherent speckle background. In this sense, there are different types of speckle: (1) information-bearing speckle carrying statistical or structural information; (2) multiply scattered background speckle that is spatially and temporally coherent with the reference, but which represents channel cross talk and does not carry any spatial structural information from the target; and (3) statistically incoherent speckle that is outside the spatial or temporal envelopes of the reference. This last form of speckle does not generate holograms, while the first two do. Of these two, only the first carries explicit information about the target. The purpose of holographic OCI is to select only the information-bearing speckle, while attempting to suppress the noninformation-bearing (but still coherent) speckle by controlling spatial coherence and using statistical time averaging.

Off-axis speckle holograms consist of bright and dark spatial interference fringes within each speckle. The fringes define a spatial carrier wave that is modulated by the speckle envelope. Therefore, holography is based on spatial heterodyne detection that is the spatial analog to temporal heterodyne. The coherent field at the hologram recording plane is

$$E = E_s\left(\vec{r}\right)e^{i\vec{k}_s\cdot\vec{r}}e^{i\phi\left(\vec{r}\right)} + E_0 e^{i\vec{k}_0\cdot\vec{r}} \tag{30.1}$$

where $E_s\left(\vec{r}\right)$ is the speckle field amplitude that varies spatially and $\phi\left(\vec{r}\right)$ is the speckle phase that also varies spatially. The optic axis of the speckle field is defined by the direction of the scattered k-vector $\vec{k}_s$, although this vector also varies spatially. The reference field amplitude is E_0 and the k-vector of the reference is k_0. The coherent speckle hologram intensity is

$$I = |E|^2 = I_s\left(\vec{r}\right) + I_0 + 2\sqrt{I_s\left(\vec{r}\right)I_0}\cos\left(\vec{K}\cdot\vec{r} + \phi\left(\vec{r}\right)\right) \tag{30.2}$$

where the grating vector is $\vec{K} = \vec{k}_s - \vec{k}_0$ and the position vector $\vec{r}$ is in the hologram plane. The first term is the speckle intensity and the second term is the reference intensity. The third term is the coherent interference between the speckle and the reference fields, i. e., the hologram with interference fringes of fringe spacing Λ with $|K| = \frac{2\pi}{\Lambda}$. The hologram amplitude is modulated by the speckle intensity into regions of randomly distributed bright speckles, and the phase of each speckle is independent of each other. However, for off-axis hologram recording, the fringe orientation and spacing Λ are the same for every speckle. This is the spatial heterodyne term that allows coherent detection of depth-resolved scattered light.

30.3.2 Image-Domain Versus Spatial Fourier-Domain OCI

Holographic OCI was initially performed using image-domain OCI, in which a photorefractive film was located at or near the image plane of the imaging optics. However, dust and other imperfections on the device can produce highly localized scatter in the reconstructed images [25]. These background problems were almost eliminated by conversion of image-domain OCI to Fourier-domain OCI, in which the holographic film is located at the Fourier plane [27]. The key to this conversion is the recognition that diffuse targets such as tissue produce relatively uniform intensity distributions at the Fourier plane (unlike specular test charts that are commonly used for system alignment characterization) permitting uniform hologram recording in the photorefractive film.

The optical configurations for photorefactive holography are shown in Fig. 30.1 for both image-domain and Fourier-domain holography. In Fourier-domain photorefractive OCI, the background scattered from a defect on the holographic film is uniformly distributed at the CCD plane, while it forms a replica of the defect (strong background) in image-domain OCI. In Fourier-domain OCI, in addition to the removal of strong spot background, the total background in the images is reduced and hence the dynamic range is extended. The amount of scattered light that is collected depends on the square of the numerical aperture, where the numerical aperture is proportional to the diameter, D, of the imaging lens in image-domain OCI but size, L, of the imaging CCD chip in Fourier-domain OCI. The ratio of the total background collected in images in image-domain OCI to those for Fourier-domain OCI is $(D/L)^2$. Therefore, Fourier-domain holography enables OCI to become background free in practice, and the signal-to-background ratio in Fourier-domain OCI improved by over 30 dB relative to image-domain OCI and hence allowed the imaging of weaker or thicker objects.

The full optical system for both photorefractive holography and digital holography is shown in Fig. 30.2. The low-coherence light source is either a mode-locked titanium-sapphire laser (nominal 100 fsec) or a superluminescent diode operating near 840 nm. This is passed through a half-wave plate and a polarizing beam splitter (PBS) to create the signal and reference arms of the Mach-Zehnder interferometer. The intensity ratio of the signal to reference arms is typically 10:1. The signal beam passes through a beam expander and illuminates the biological sample through a second polarizing beam splitter and quarter-wave plate. The returned signal is relayed to an image plane and is then Fourier transformed by lens L4 to the holographic plane. When a PRQW device is at the hologram plane, a physical hologram is recorded and the reconstruction is achieved through diffraction of the reference beam and Fourier transformation by lens L6 to the image plane of a digital camera. Alternatively, the digital camera can be placed at the hologram plane and reconstructed numerically.

A specialized capability for photorefractive holography using photorefractive quantum well (PRQW) devices is in speckle reduction. This is achieved by controlling the spatial coherence using a diffuser plate in the beam expander of Fig. 30.2. The diffuser and the steering mirror are vibrated by a piezo-stack at

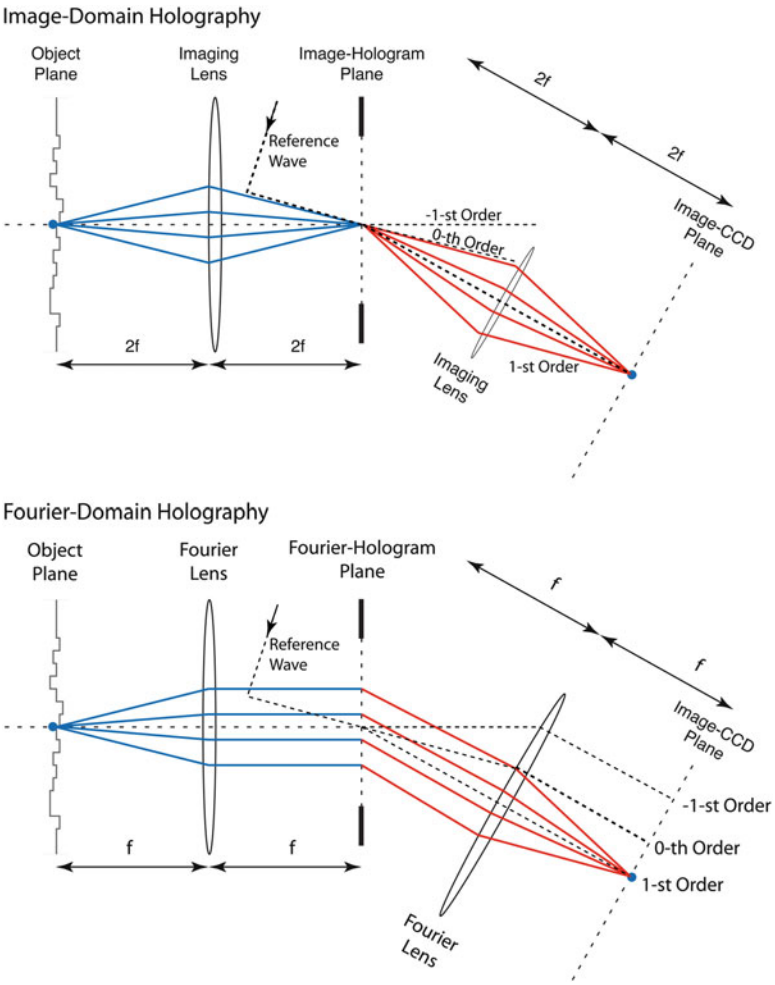

Fig. 30.1 Image-domain holography (*IDH*) vs. Fourier-domain holography (*IDH*). Image-domain holography places the holographic film at or near the image plane, while Fourier-domain holography places the holographic film at or near the Fourier plane (Note: FDH is based on spatial Fourier techniques and is not to be confused with spectral techniques)

a frequency near 100 Hz. The high-speed photorefractive device tracks the moving hologram fringes in real time, maintaining the diffraction that is the basis of the coherence gating, while the vibrating mirror and vibrating diffuser reduce speckle effects by time-averaging the holographic readout on the camera. These eliminate stray speckle and reduce channel cross talk [53]. Digital holography, on the other hand, cannot use these vibrating mirror or diffuser techniques because the fringes would wash out during the fringe motion. Therefore, photorefractive optical coherence imaging has the advantage of imaging internal structure over digital

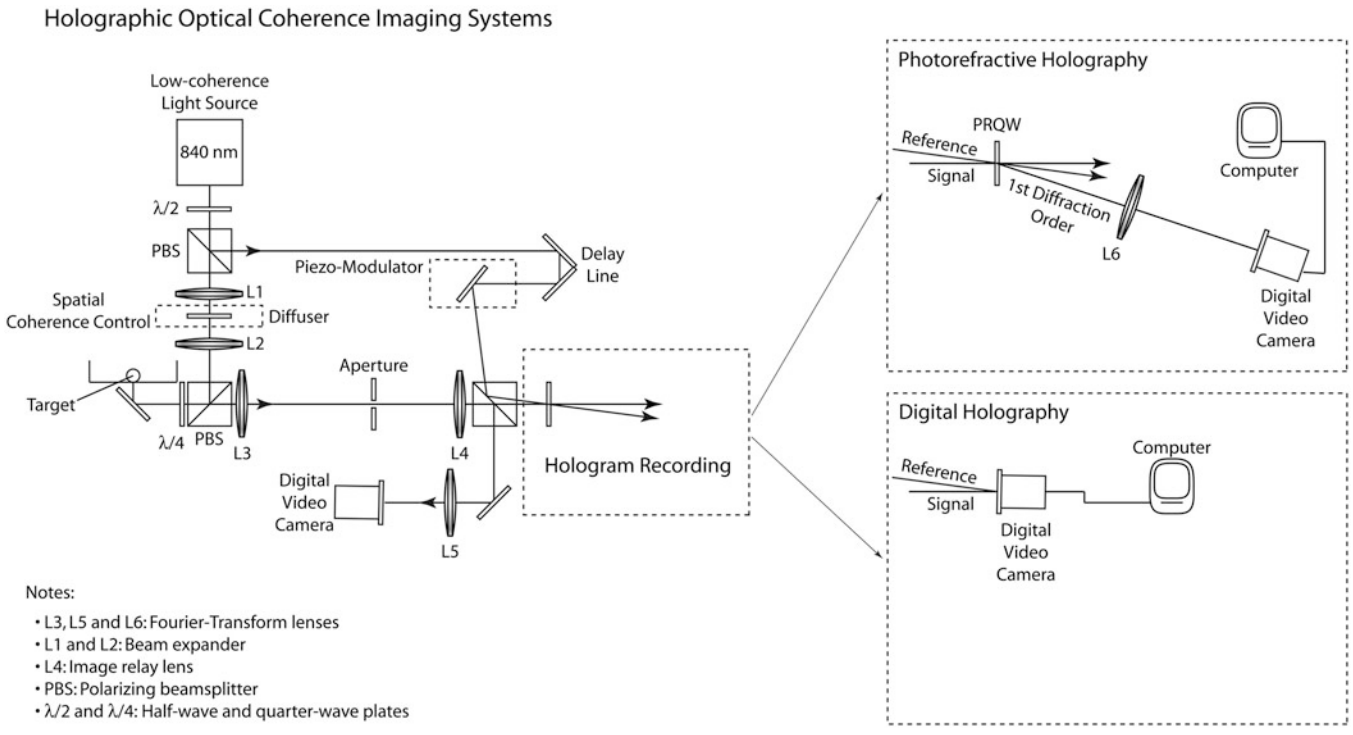

Fig. 30.2 Experimental schematic of the Fourier-domain holography system for photorefractive holography and digital holography. The holographic plane is at the Fourier plane of lens L4. The photorefractive quantum well (*PRQW*) records a physical hologram that is reconstructed by diffraction to a camera. Alternatively, a CCD chip records a digital hologram that is reconstructed by a FFT algorithm

holographic optical coherence imaging. Digital holography, on the other hand, has an advantage for dynamic speckle studies. Therefore, these two approaches to optical coherence imaging trade off between imaging structure and imaging dynamics.

30.3.3 Photorefractive Holography

Holographic OCI was initially developed using bulk photorefractive crystals and volume holograms [8], which were replaced with photorefractive semiconductor quantum well (PRQW) devices [16] because of their high sensitivity [2, 54]. These devices use molecular beam semiconductor growth processes to produce semiconductor structures that have enhanced optical properties based on quantum localization of electrons in very thin layers (7.5 nm). The enhanced optical properties make these devices sensitive dynamic holographic materials, with interferometric and imaging applications in laser-based ultrasound detection, femtosecond pulse processing, and interferometric bioassays, among others [16, 55–58].

Holographic OCI with PRQW devices uses the same short-coherence light sources as conventional OCT, including either pulsed laser sources or superluminescent diodes. For the PRQW devices, the probe wavelength of the source is at the absorption-edge wavelength of the semiconductor, which is typically $\lambda \approx 840$ nm.

The key performance parameters of the photorefractive quantum wells that are relevant for the OCI application are the minimum writing intensity, the fringe-spacing dependence, and the spectral bandwidth of the quantum well diffraction spectrum. The PRQW devices record fully developed holograms using intensities of only 10–20 $\mu W/cm^2$. The intensity dependence of wave mixing in a PRQW device is shown in Fig. 30.3a. The data are from two-wave mixing [15], showing fully developed gratings above 20 $\mu W/cm^2$. The fringe-spacing dependence is shown in Fig. 30.3b. The diffraction efficiency from four-wave mixing increases rapidly above a 5 μm fringe spacing. In speckle holography, a minimum of three fringes are needed per speckle to ensure a well-defined spatial carrier frequency. The 5 μm cutoff places a minimum speckle diameter at around 15 μm. Although speckle size is related to the lateral spatial resolution of the imaging optics, they are not identical, and in the case of Fourier-domain holography, they have an inverse relationship. The bandwidth of the diffraction spectrum is set by the inhomogeneous width of the quantum-confined excitons which is approximately 5 nm. Broader widths are possible through bandgap engineering, but Coulomb correlation effects prevent significantly broader bandwidths to be attained [59, 60].

30.3.4 Digital Holography

The discreteness of the pixels of a CCD or CMOS array sets limits on the resolution of off-axis digital holography. The interference fringes need to be well sampled by the

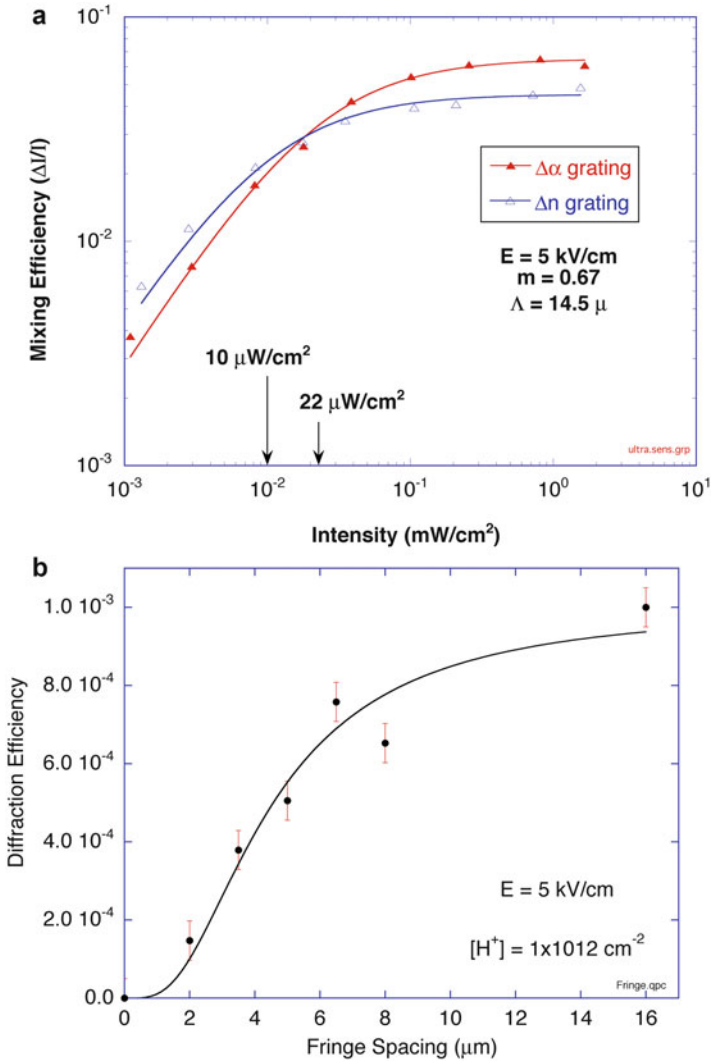

Fig. 30.3 Demonstration of the sensitivity of the holographic film in (**a**) shows a fully saturated holographic grating for an intensity of only 10–20 μW/cm^2. The fringe-spacing dependence in (**b**) shows a cutoff of 5 μm

discrete pixels, as shown in Fig. 30.4. Full resolution is predicted using Nyquist sampling theory, with two pixels per fringe spacing Λ and two fringes per speckle. However, a general rule of thumb for practical implementation is three pixels per fringe and three fringes per speckle. In other words, at the sensor plane, the condition

$$a_{speck} \approx 3\Lambda \approx 3\left(3\Delta x_{pix}\right) = 9\Delta x_{pix} \tag{30.3}$$

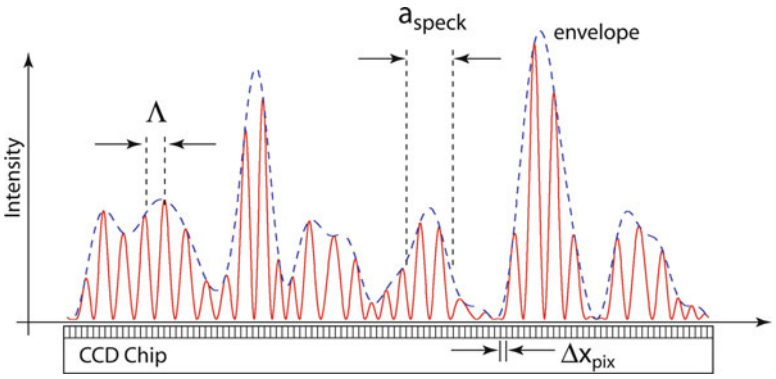

Fig. 30.4 Spatial variation of interference fringes and speckle envelope across a CCD chip. Optimum digital holography performance uses three interference fringes per speckle and three digital pixels per fringe

is nominal. These parameters are evaluated on the Fourier plane for Fourier-domain holography. The condition of the speckle size at the camera gives the magnification by lens L4 in Fig. 30.2 to be

$$M = \frac{9\Delta x_{pix}}{\frac{f_{Obj}\lambda}{D_{tum}}} \tag{30.4}$$

where f_{Obj} is the focal length of the objective lens and D_{tum} is the diameter of the tumor. The maximum angle that can be detected is set by the size of the CCD chip, placing a condition on the diameter of the camera detector area and the marginal aperture of the objective lens, through $D_{cam} = MD_{lens}$, giving another requirement for the magnification

$$M = \frac{D_{cam}}{D_{lens}} \tag{30.5}$$

Equating the two magnifications gives a resolution

$$\begin{aligned} \mathbb{R} &= 2\lambda \cdot f/\# \\ &= 18\Delta x_{pix}\frac{D_{tum}}{D_{cam}} \end{aligned} \tag{30.6}$$

where the resolution is independent of the characteristics of the objective lens.

30.4 Multicellular Tumor Spheroids

In vitro monitoring of tissue response to drugs is an area of strong interest to pharmaceutical companies [61]. Although the in vitro environment is artificial, the biochemistry, metabolism, and cell signaling response of cells grown as 3D constructs closely simulates in vivo tissue because three-dimensional cell cultures have active 3D intercellular signaling pathways that are often absent in 2D dish cultures. Therefore, in vitro experiments are a validated (and inexpensive) surrogate for in vivo response. The most common in vitro tissue cultures are multicellular spheroids. Multicellular spheroids of normal cells or neoplastic cells (tumor spheroids) are balls of cells that may be easily cultured up to 1 mm in size in vitro [62–67]. The spheroids can be used to simulate the optical properties of a variety of tissues such as the epidermis and various epithelial tissues and may be used to simulate the histological and metabolic features of small nodular tumors in the early avascular stages of growth [67]. Since the introduction of the concept of multicellular tumor spheroids in the early 70s [68], 3-D aggregates of permanent cell lines have offered a reliable model for systematic study of tumor response to therapy [65, 69].

Beyond a critical size (about 100 μm), most spheroids develop a necrotic core surrounded by a shell of viable, proliferating cells, with a thickness varying from 100 to 300 μm. The development of necrosis has been linked to deficiencies in the metabolites related to energy generation and transfer. The limiting factor for necrosis development is oxygen – the oxygen consumption and oxygen transport reflecting the status of the spheroid [63, 70]. Early work [71] launched the study of therapeutic strategies for cancer. The response to drug therapy was quantified from analysis of spheroid volume growth delay, increase in the necrotic area, and change in survival capacity. This work focused on hypoxia and its induction by chemical agents [72].

Tumor spheroids are cultured in a rotating bioreactor (Synthecon, Houston, TX) where they were maintained in suspension. The spheroids may be grown up to several mm in diameter and are thus large enough to simulate the thickness of different mammalian tissue (skin epidermis is 70–120 μm thick over most of the human body). An advantage to using this continuous culture model is that fresh spheroids of varying size are easily prepared on a daily basis. Overall, the tumor spheroids provide a reasonable tissue model that does not require special handling of animal subjects.

Electron microscopy sections of two types of tumor embedded in Toluidine-blue-stained epoxy resin and sectioned at 1 μm thickness are shown in Fig. 30.5. The tumors are nearly a millimeter in diameter, and each shares a common morphology. The outermost layers of the tumors have healthy, proliferating cells that form a shell from 100 to 200 μm thick. These cells are in close proximity to the nutrients and oxygen of the growth medium. This layer is structurally homogeneous and is optically homogeneous as well. Deeper inside the tumors, the cells become apoptotic because of nutrient deprivation and oxidative stress from the diffusion

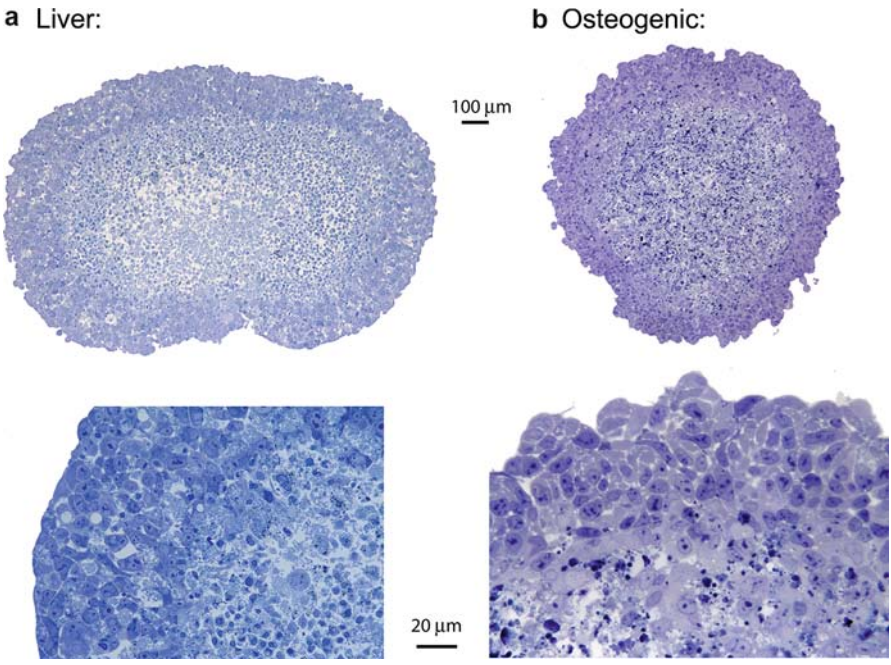

Fig. 30.5 Cross-sectional TEM micrographs of multicellular tumor spheroids consisting of (**a**) human liver and (**b**) rat osteogenic cells. The spheroids have an outer shell of healthy proliferating cells around a necrotic core. The higher magnifications at the *bottom* show the transitions from the shells to the cores

limitation of nutrients and oxygen into these avascular spheroids. The apoptotic cells give way, deeper in the tumor spheroids, to necrotic regions characterized by voids of extracellular debris or by microcalcifications, which are especially pronounced in the osteogenic spheroids. The core is structurally heterogeneous and is optically heterogeneous as well. Therefore the tumor spheroids have the general morphology of a healthy outer shell that tends to be homogeneous and a core of necrotic regions that are spatially heterogeneous.

Experimentally measured reduced scattering coefficients μ' of rat osteogenic tumor spheroids are on the order of 8 mm^{-1} to 15 mm^{-1}. There is a weak tumor size dependence to the extinction coefficient with decreasing extinction with increasing tumor size. The phase function for two tumors of slightly different diameter is shown in Fig. 30.6a. A tumor with a diameter of 416 μm is fit best with an anisotropy factor of $g = 0.9$, and a slightly larger tumor with a diameter of 484 μm is fit with a smaller factor of $g = 0.85$. Therefore, the rat osteogenic tumor spheroids are relatively translucent tumors with strong forward scattering. Maps of the optical densities of several tumors are shown in Fig. 30.6b, obtained using coherent heterodyne transmission interferometry.

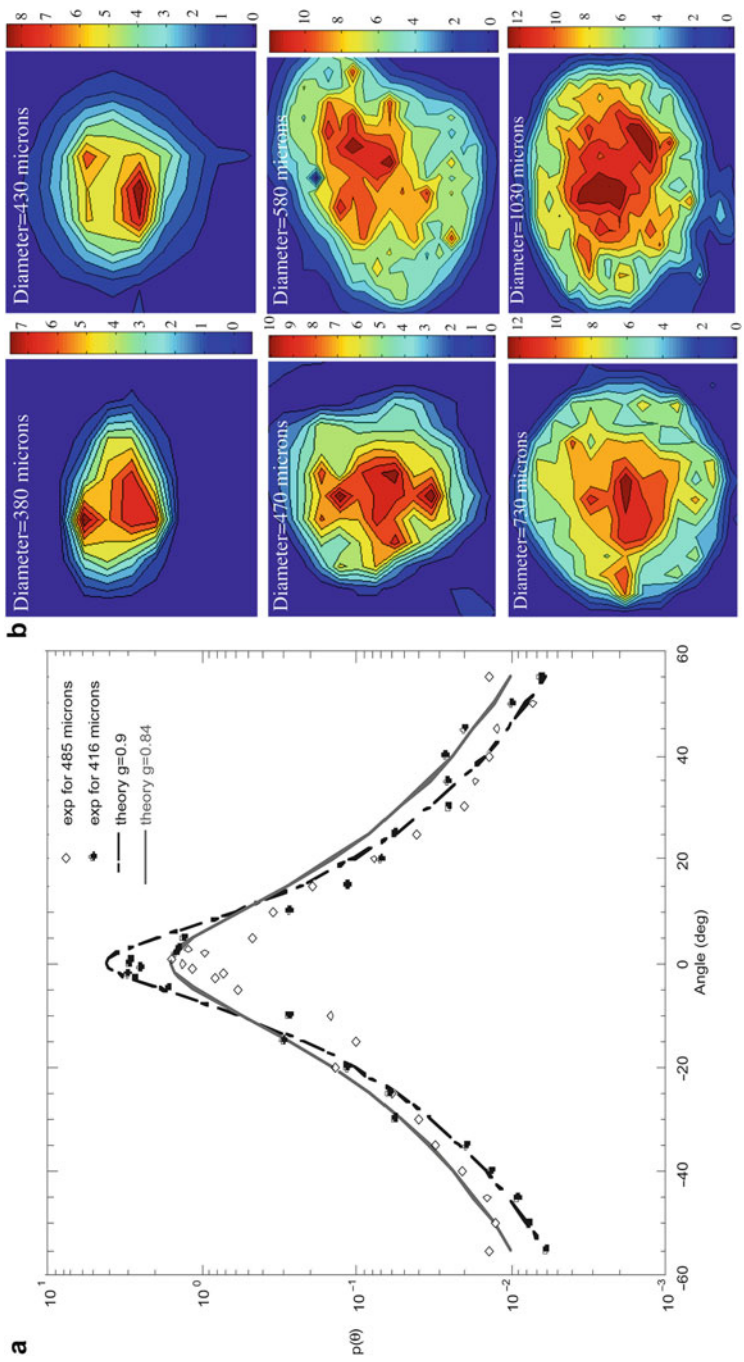

Fig. 30.6 Henyey-Greenstein phase function (**a**) and optical density maps (**b**). The HG functions were obtained using incoherent illumination in a forward-scattering arrangement. The optical densities were measured using coherent heterodyne detection of transmitted light

30.5 Photorefractive OCI of Tumor Spheroids

The principal acquisition mode for holographic imaging of tumor spheroids is called a "fly-through". In this mode, the reference mirror is stepped by 10 μm, several successive images are averaged on the CCD camera and downloaded to the computer, the mirror steps again, and the process reiterates. The raw data are stored in a volumetric data cube of en face sections at successive depths from the top of the tumor through the bottom of the tumor (that usually sits on the surface of a Petri dish). Selected en face (called XY) sections of a 400 μm diameter tumor are shown in (Fig. 30.7a) separated by 23 μm (approximately equal to the longitudinal coherence length). The top of the tumor is at frame 15, and the Petri dish appears in frame 66. The tissue gray scale is logarithmic in a range from −50 to −85 dB. Alternatively, the data cube can be viewed laterally, giving pseudo-B-scans (called YZ sections), shown in (Fig. 30.7b) for the same tumor on logarithmic scale. The Petri dish is at the bottom of each YZ section. The distance between the selected sections is 26 μm (approximately equal to the transverse optical resolution for this data). The reflected intensities are brightest in the necrotic core, with relatively weak reflections arising from the homogeneous healthy tissue shell.

The data for this tumor are visualized volumetrically in Fig. 30.8 for two selected threshold values of the isosurfaces. The left-hand figure has a low threshold and displays the full tumor volume with the Petri dish at the bottom. The right-hand figure has a high threshold to display only the brightest reflections from the tumor. The brightest features reside toward the center of the tumor, which is consistent with the necrotic core of the tumor spheroids. The necrotic core contains relatively large (10–20 μm) necrotic voids with extracellular debris as well as microcalcifications that are fairly pronounced in these osteogenic tumor spheroids. The heterogeneity of these internal structures are the likely source of the bright reflections that are localized internally to the tumor.

The dynamic range of holographic OCI is illustrated by selecting a set of A-scans from the volumetric data. These are shown in Fig. 30.9 on a logarithmic scale. The peak tissue reflectance is approximately −50 dB, and the noise floor is approximately −95 dB, providing a dynamic range through the tissue of 45 dB. The high reflection of the Petri dish is observed in these data at the depth of 400 μm. The initial rise of reflectance with increasing depth to about 150 μm, followed by a nearly linear (exponential) decrease with increasing depth, is consistent with an optically homogeneous healthy outer shell that produces weak reflectances, but with the strongest reflectances arising from the necrotic core. The absence of signal below the Petri dish is a signature of low channel cross talk. Multiply scattered light would appear to originate from greater depths. Therefore, if channel cross talk were significant in these tumors, a diffuse tail would have been present at depths below the Petri dish. This confirms the relatively low extinction and low multiple scattering of these osteogenic tumors.

A striking feature of the cross-section images in Fig. 30.7 is the speckled quality and the absence of specific structure. Fully developed speckle can arise

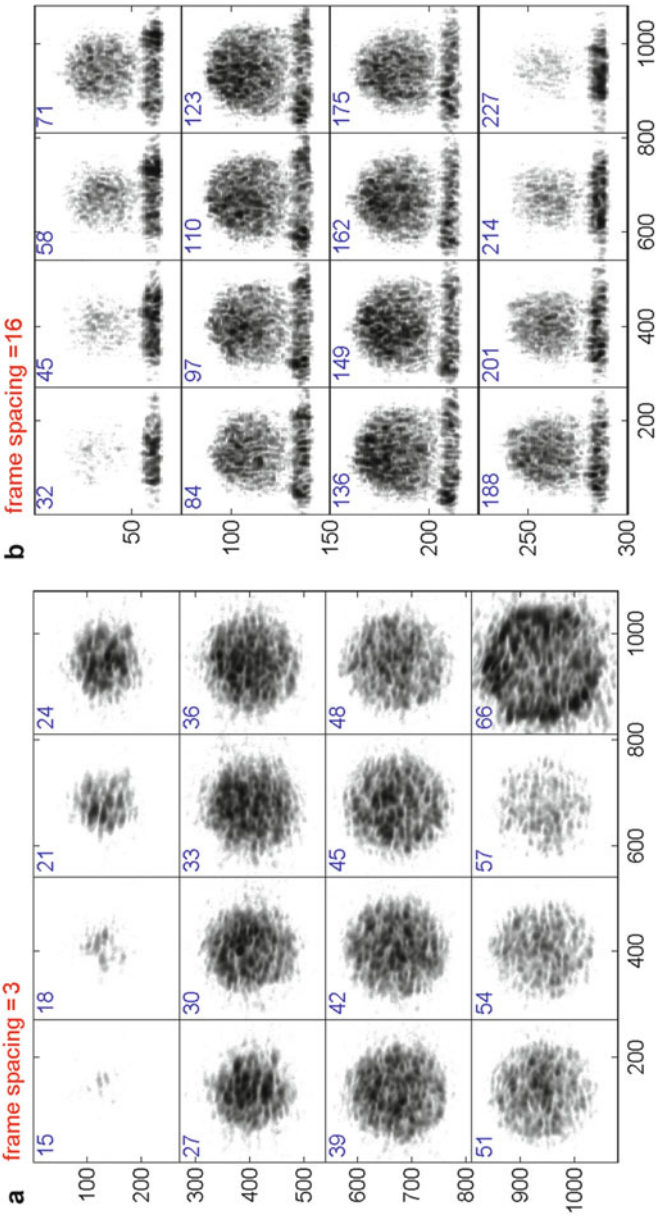

Fig. 30.7 Sections from a healthy rat tumor. Selected xy en face sections are shown in (**a**), and pseudo-B scans are shown in (**b**). The Petri dish reflection appears in frame 66 of the en face sections and at the *bottom* of the B-scan sections. The exposure time per frame was 0.5 s

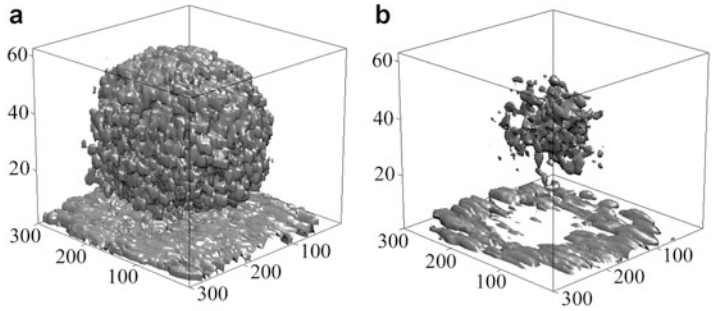

Fig. 30.8 Volumetric rendering of a tumor on a Petri dish. The image in (**a**) is the full isosurface, while in (**b**) a higher isosurface is shown. This illustrates the increasing intensity of reflections from the core of the tumor

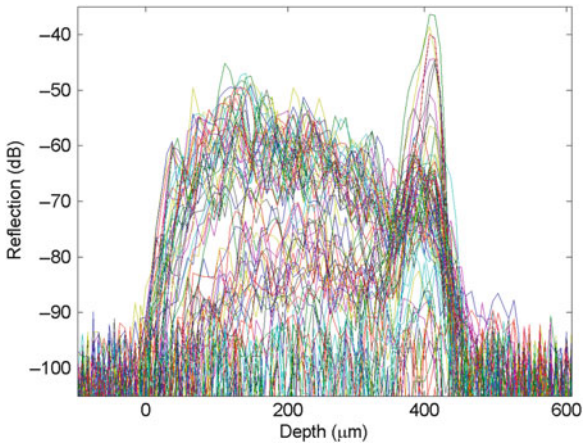

Fig. 30.9 Numerous A-scans of a tumor on a dB scale. The Petri reflection is at the *right*. The dynamic range of reflectivities from tissue is approximately 45 dB, showing the noise floor near −95 dB. The exposure time per frame was 2.5 msec

when the density of scatterers per modal volume is large, leading to a characteristic Poisson distribution of intensities with a speckle contrast of unity. Histograms of the intensity at several selected depths for a 560 μm diameter rat tumor are shown in Fig. 30.10. The histogram at a depth of 180 μm exhibits nearly perfect Poisson behavior, while the distributions from greater depths show a peak in the intensity probability. A fit of the 180 μm depth data to the Poisson distribution is shown in the inset of Fig. 30.10. The fit is good over two orders of magnitude and deviates only at the lowest intensities. Therefore, the intensity distribution at a depth of 180 μm shows fully developed speckle and hence no identifiable structure. On the other hand, the intensity distributions at deeper levels do show deviations, with well-defined maximum probabilities. This is indicative of specific structure, possibly arising from necrotic voids or microcalcifications within the core.

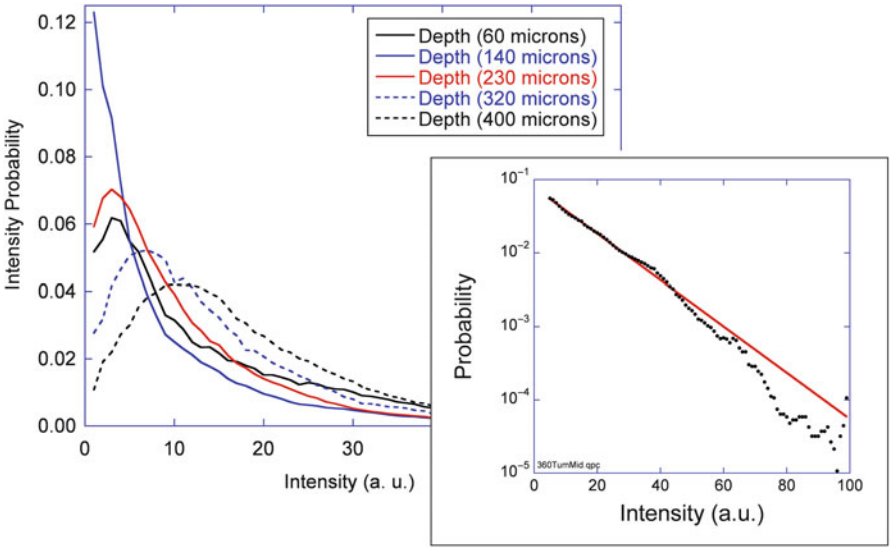

Fig. 30.10 Histograms of intensity distributions for increasing depth. The average intensity increases with depth. The inset is a log plot of the histogram from a depth of 180 μm, showing classic Poisson distribution behavior, signifying fully developed speckle from the healthy top shell of the tumor

30.6 Digital Holographic Optical Coherence Imaging

Digital holograms are captured on the Fourier plane with a small crossing angle between the optic axis of the signal arm and the reference beam. The acquisition exposure time is 10 msec. An example of a digital hologram of a tumor spheroid is shown in Fig. 30.11. The entire hologram is in Fig. 30.11a, and a magnification of a small area is shown in Fig. 30.11b with speckle modulating interference fringes. A line section is shown in Fig. 30.11c in which the interference fringes are difficult to distinguish from the speckle modulation. There is a high background, but these are outside the coherence envelope and do not generate periodic fringes. Because the holograms are acquired on the Fourier plane, a fast Fourier transform algorithm is sufficient to do the image reconstruction. A line section through the reconstruction is shown in Fig. 30.11d on a logarithmic scale. There is a DC spike and a zero-order ungated image at the center and two side bands that are the reconstructed coherence-gated images – a direct image and a phase conjugate.

Optical sections of a large millimeter diameter tumor spheroid are shown in Fig. 30.12 with a color scale in dB from −60 to −90 dB. Optical sections are taken every 10 μm, and only every eighth section is shown in the figure in steps of 80 μm. These data were taken with the illumination beam incident from the bottom of the transparent sample holder, and the coherence gate is moved successively higher into the spheroid. The midsection is around frame 64, showing high intensity

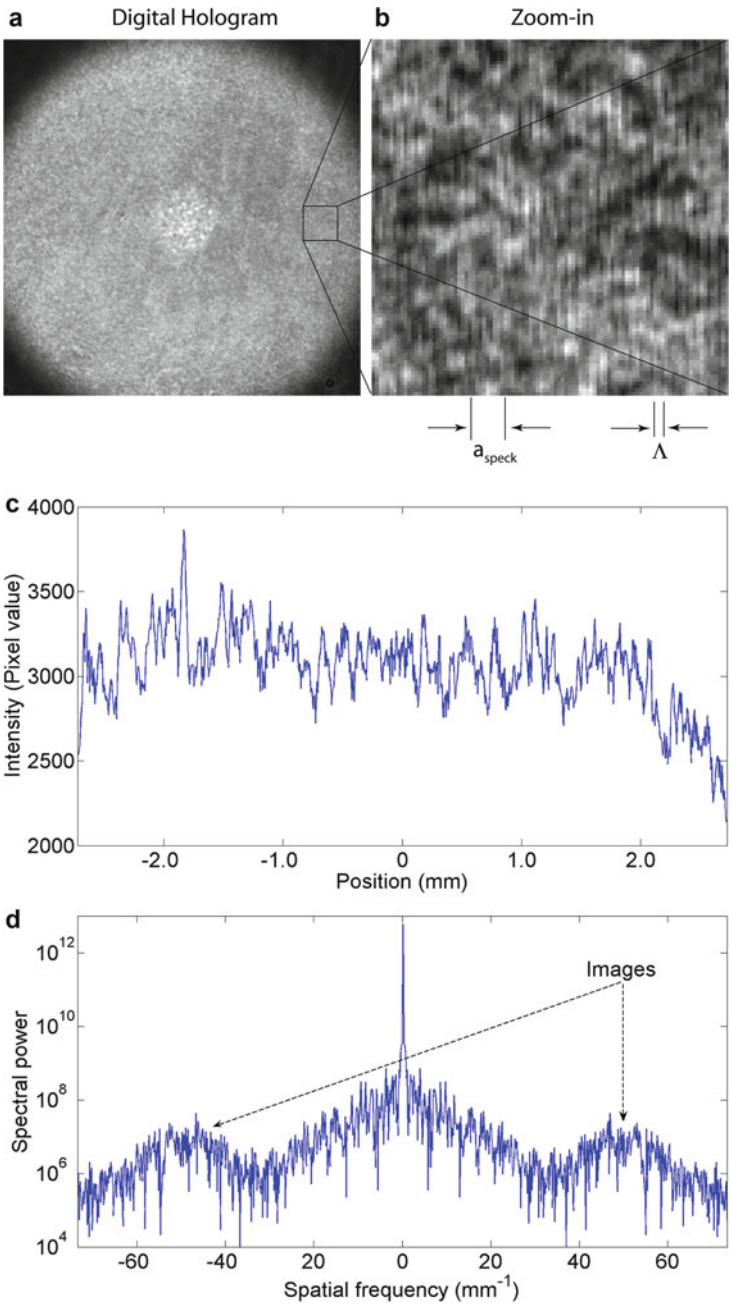

Fig. 30.11 (**a**) A full digital hologram. (**b**) a magnification of one region showing fringes modulated by speckle. (**c**) A line section through the hologram. (**d**) A line section through the Fourier reconstruction showing the image sidebands

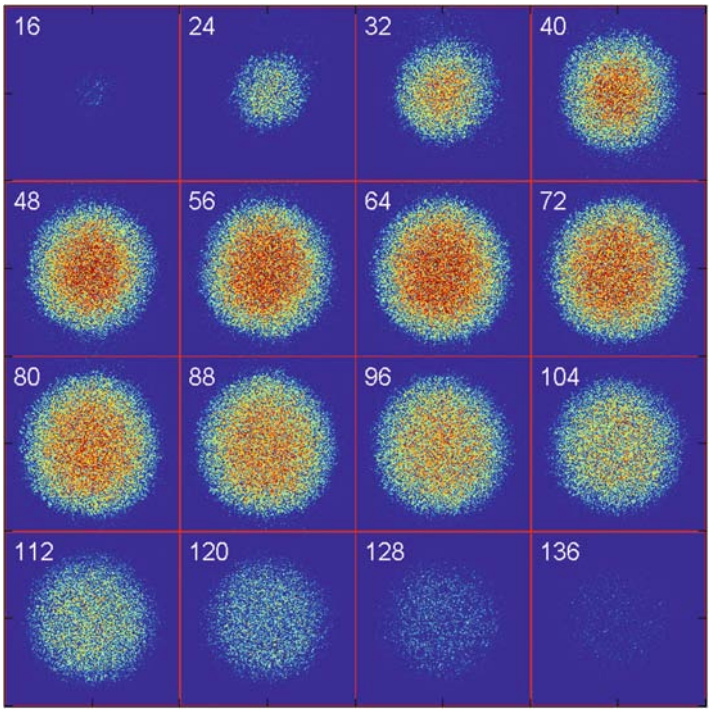

Fig. 30.12 Selected optical sections of large millimeter diameter tumor spheroid with a color scale in dB from −60 to −90 dB. The depth separation between each frame is 80 μm

reflectances from the core and relatively weaker reflectances from the proliferating shell that is more optical homogeneous. The data in Fig. 30.12 have a much finer speckle than the corresponding photorefractive data in Fig. 30.7. The broader applicability of digital holographic optical coherence imaging is demonstrated for a mouse eye in Fig. 30.13. The cornea, the iris, and the lens in the mouse eye are all discernable in the section that was extracted from a stack of en face sections [50].

Photorefractive and digital holography applied to optical coherence imaging are both en face coherence-gated formats. The relative advantages between photorefractive holography and digital holography trade off between biological structure and ease of use. The high-speed updating of photorefractive quantum wells allows the use of vibrating diffusers and reference mirrors to reduce spatial coherence (and hence reduce channel cross talk) and to time-average the reconstructed speckle (speckle reduction). Photorefractive holography also has the advantage that no computed reconstruction is needed. Digital holography, on the other hand, is simple and has become relatively inexpensive with improving performance of digital cameras at decreasing cost. However, typical frame speeds currently prevent the use of vibrating elements in the optical system, and digital holography of biological tissues is highly speckled. Although high-contrast speckle

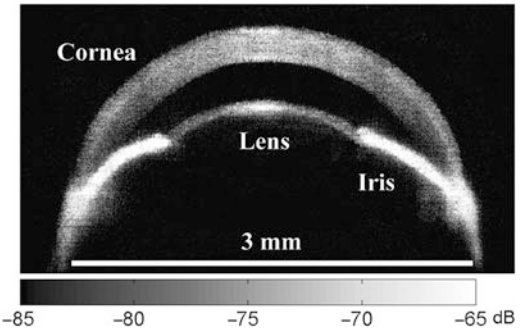

Fig. 30.13 Section of a mouse eye that is constructed from a stack of en face sections acquired with digital holography

carries little structural information of tissue, it does carry a high information content related to the dynamics within the tissue, leading to optical coherence imaging applications that use intracellular motions as a novel form of imaging contrast [51, 52, 73–75], which is the topic of ▶ Chap. 37, "Motility Contrast Imaging and Tissue Dynamics Spectroscopy" in this volume.

Acknowledgements The authors gratefully acknowledge support from NSF1263753-CBET and NIH NIBIB 1R01EB016582-01.

Bibliography

1. D.D. Nolte, Holography of tissues, Chap. 12, in *Optical Interferometry for Biology and Medicine* (Springer, New York, 2012), pp. 307–333
2. D.D. Nolte, Semi-insulating semiconductor heterostructures: optoelectronic properties and applications. J. Appl. Phys. **85**, 6259–6289 (1999)
3. C. Dunsby, D. Mayorga-Cruz, I. Munro, Y. Gu, P.M.W. French, D.D. Nolte, M.R. Melloch, High-speed wide-field coherence-gated imaging via photorefractive holography with photorefractive multiple quantum well devices. J. Opt. A Pure Appl. Opt. **5**, S448–S456 (2003)
4. K.A. Stetson, Holographic fog penetration. J. Opt. Soc. Am. **57**, 1060–1061 (1967)
5. K.G. Spears, J. Serafin, N.H. Abramson, X. Zhu, H. Bjelkhagen, Chrono-coherent imaging for medicine. IEEE Trans. Biomed. Eng. **36**, 1210–1214 (1989)
6. H. Chen, Y. Chen, D. Dilworth, E. Leith, J. Lopez, J. Valdmanis, Two-dimensional imaging through diffusing media using 150-fs gated electronic holography techniques. Opt. Lett. **16**, 487 (1991)
7. P. Massatsch, F. Charriere, E. Cuche, P. Marquet, C.D. Depeursinge, Time-domain optical coherence tomography with digital holographic microscopy. Appl. Opt. **44**, 1806–1812 (2005)
8. S.C.W. Hyde, R. Jones, N.P. Barry, J.C. Dainty, P.M.W. French, K.M. Kwolek, D.D. Nolte, M.R. Melloch, Depth-resolved holography through turbid media using photorefraction. IEEE J. Sel. Top. Quantum Electron. **2**, 965–975 (1996)
9. L. Vabre, A. Dubois, A.C. Boccara, Thermal-light full-field optical coherence tomography. Opt. Lett. **27**, 530–532 (2002)
10. M. Tziraki, R. Jones, P. French, D. Nolte, M. Melloch, Short-coherence photorefractive holography in multiple-quantum-well devices using light-emitting diodes. Appl. Phys. Lett. **75**, 363–365 (1999)
11. C. Dunsby, P.M.W. French, Techniques for depth-resolved imaging through turbid media including coherence-gated imaging. J. Phys. D Appl. Phys. **36**, R207–R227 (2003)

12. A.V. Mamaev, L.L. Ivleva, N.M. Polozkov, V.V. Shkunov, Photorefractive visualisation through opaque scattering media, in *Conference on Lasers and Electro-Optics* (Optical Society of America, Washington, DC, 1993), p. CFK6
13. S.C.W. Hyde, N.P. Barry, R. Jones, J.C. Dainty, P.M.W. French, Sub-100 micron depth-resolved holographic imaging through scattering media in the near-infrared. Opt. Lett. **20**, 2330–2332 (1995)
14. N.P. Barry, R. Jones, S.C.W. Hyde, J.C. Dainty, P.M.W. French, High background holographic imaging using photorefractive barium titanate. Electron. Lett. **33**, 1732–1733 (1997)
15. Q.N. Wang, R.M. Brubaker, D.D. Nolte, M.R. Melloch, Photorefractive quantum wells: transverse Franz-Keldysh geometry. J. Opt. Soc. Am. B **9**, 1626–1641 (1992)
16. R. Jones, S.C.W. Hyde, M.J. Lynn, N.P. Barry, J.C. Dainty, P.M.W. French, K.M. Kwolek, D.D. Nolte, M.R. Melloch, Holographc storage and high background imaging using photorefractive multiple quantum wells. Appl. Phys. Lett. **69**, 1837 (1996)
17. R. Jones, N.P. Barry, S.C.W. Hyde, P.M.W. French, K.M. Kwolek, D.D. Nolte, M.R. Melloch, Direct-to-video holographic readout in quantum wells for 3-D imaging through turbid media. Opt. Lett. **23**, 103 (1998)
18. Z. Ansari, Y. Gu, J. Siegel, D. Parsons-Karavassilis, C.W. Dunsby, M. Itoh, M. Tziraki, R. Jones, P.M.W. French, D.D. Nolte, W. Headley, M.R. Melloch, High-frame-rate, 3-D photorefractive holography through turbid media with arbitrary sources and photorefractive structured illumination. Sel. Top. Quantum Electron. **7**, 878–886 (2001)
19. P. Yu, M. Mustata, D. Chen, L.J. Pyrak-Nolte, D.D. Nolte, Holographic 3-D laser imaging into sandstone. Geophys. Res. Lett. **29**, 49-1–49-4 (2002)
20. M. Tziraki, R. Jones, P.M.W. French, M.R. Melloch, D.D. Nolte, Photorefractive holography for imaging through turbid media using low coherence light. Appl. Phys. B Lasers Opt. **70**, 151–154 (2000)
21. R. Jones, N.P. Barry, S.C.W. Hyde, M. Tziraki, J.C. Dainty, P.M.W. French, D.D. Nolte, K.M. Kwolek, M.R. Melloch, Real-time 3-D holographic imaging using photorefractive media including multiple-quantum-well devices. IEEE J. Sel. Top. Quantum Electron. **4**, 360–369 (1998)
22. P. Yu, M. Mustata, J.J. Turek, P.M.W. French, M.R. Melloch, D.D. Nolte, Holographic optical coherence imaging of tumor spheroids. Appl. Phys. Lett. **83**, 575–577 (2003)
23. Z. Ansari, Y. Gu, J. Siegel, D. Parsons-Karavassilis, C.W. Dunsby, M. Itoh, M. Tziraki, R. Jones, P.M.W. French, D.D. Nolte, W. Headley, M.R. Melloch, High frame-rate, 3-D photorefractive holography through turbid media with arbitrary sources, and photorefractive structured illumination. IEEE J. Sel. Top. Quantum Electron. **7**, 878–886 (2001)
24. P. Yu, M. Mustata, W. Headley, D.D. Nolte, J.J. Turek, P.M.W. French, Optical coherence imaging of rat tumor spheroids, in *Coherence Domain Optical Methods in Biomedical Science and Clinical Applications VI*, ed. by SPIE, vol. 4619 (SPIE, Bellingham, 2002)
25. P. Yu, M. Mustata, L.L. Peng, J.J. Turek, M.R. Melloch, P.M.W. French, D.D. Nolte, Holographic optical coherence imaging of rat osteogenic sarcoma tumor spheroids. Appl. Optics **43**, 4862–4873 (2004)
26. P. Yu, L. Peng, M. Mustata, J.J. Turek, M.R. Melloch, D.D. Nolte, Time-dependent speckle in holographic optical coherence imaging and the state of health of tumor tissue. Opt. Lett. **29**, 68–70 (2004)
27. K. Jeong, L. Peng, D.D. Nolte, M.R. Melloch, Fourier-domain holography in photorefractive quantum-well films. Appl. Opt. **43**, 3802–3811 (2004)
28. K. Jeong, L. Peng, J.J. Turek, M.R. Melloch, D.D. Nolte, Fourier-domain holographic optical coherence imaging of tumor spheroids and mouse eye. Appl. Opt. **44**, 1798–1805 (2005)
29. K. Jeong, J.J. Turek, D.D. Nolte, Phase-contrast optical coherence imaging of tissue, in *Progress in Biomedical Optics and Imaging - Coherence Domain Optical Methods and Optical Coherence Tomography in Biomedicine IX* (2005)
30. J.W. Goodman, R.W. Lawrence, Digital image formation from electronically detected holograms. Appl. Phys. Lett. **11**, 77 (1967)

31. T.S. Huang, Digital holography. Proc. Inst. Electr. Electron. Eng. **59**, 1335 (1971)
32. T. Kreis, Digital holographic interference-phase measurement using the fourier-transform method. J. Opt. Soc. Am. A Opt. Image Sci. Vis. **3**, 847–855 (1986)
33. H. Chen, Y. Chen, D. Dilworth, E. Leith, J. Lopez, J. Valdmanis, 2-dimensional imaging through diffusing media using 150-Fs gated electronic holography techniques. Opt. Lett. **16**, 487–489 (1991)
34. E. Leith, H. Chen, Y. Chen, D. Dilworth, J. Lopez, R. Masri, J. Rudd, J. Valdmanis, Electronic holography and speckle methods for imaging through tissue using femtosecond gated pulses. Appl. Optics **30**, 4204–4210 (1991)
35. H. Chen, M. Shih, E. Arons, E. Leith, J. Lopez, D. Dilworth, P.C. Sun, Electronic holographic imaging through living human tissue. Appl. Optics **33**, 3630–3632 (1994)
36. U. Schnars, Direct phase determination in hologram interferometry with use of digitally recorded holograms. J. Opt. Soc. Am. A Opt. Image Sci. Vis. **11**, 2011–2015 (1994)
37. T.M. Kreis, W.P.O. Juptner, Suppression of the dc term in digital holography. Opt. Eng. **36**, 2357–2360 (1997)
38. I. Yamaguchi, T. Zhang, Phase-shifting digital holography. Opt. Lett. **22**, 1268–1270 (1997)
39. B. Nilsson, T.E. Carlsson, Direct three-dimensional shape measurement by digital light-in-flight holography. Appl. Opt. **37**, 7954–7959 (1998)
40. T. Zhang, I. Yamaguchi, Three-dimensional microscopy with phase-shifting digital holography. Opt. Lett. **23**, 1221–1223 (1998)
41. F. Dubois, L. Joannes, J.C. Legros, Improved three-dimensional imaging with a digital holography microscope with a source of partial spatial coherence. Appl. Opt. **38**, 7085–7094 (1999)
42. E. Beaurepaire, A.C. Boccara, M. Lebec, L. Blanchot, H. Saint-Jalmes, Full-field optical coherence microscopy. Opt. Lett. **23**, 244–246 (1998)
43. A. Dubois, L. Vabre, A.C. Boccara, Sinusoidally phase-modulated interference microscope for high-speed high-resolution topographic imagery. Opt. Lett. **26**, 1873 (2001)
44. A. Dubois, L. Vabre, A.C. Boccara, E. Beaurepaire, High-resolution full-field optical coherence tomography with a Linnik microscope. Appl. Opt. **41**, 805–812 (2002)
45. A. Dubois, K. Grieve, G. Moneron, R. Lecaque, L. Vabre, C. Boccara, Ultrahigh-resolution full-field optical coherence tomography. Appl. Opt. **43**, 2874–2883 (2004)
46. E. Cuche, P. Marquet, C. Depeursinge, Simultaneous amplitude-contrast and quantitative phase-contrast microscopy by numerical reconstruction of Fresnel off-axis holograms. Appl. Opt. **38**, 6994–7001 (1999)
47. E. Cuche, P. Marquet, C. Depeursinge, Spatial filtering for zero-order and twin-image elimination in digital off-axis holography. Appl. Opt. **39**, 4070–4075 (2000)
48. E. Umetsu, K.P. Chan, N. Tanno, Non-scanning optical coherence tomography using off-axis interferometry with an angular-dispersion imaging scheme. Opt. Rev. **9**, 70–74 (2002)
49. M. Gross, M. Atlan, E. Absil, Noise and aliases in off-axis and phase-shifting holography. Appl. Opt. **47**, 1757–1766 (2008)
50. K. Jeong, J.J. Turek, D.D. Nolte, Fourier-domain digital holographic optical coherence imaging of living tissue. Appl. Opt. **46**, 4999–5008 (2007)
51. K. Jeong, J.J. Turek, D.D. Nolte, Imaging motility contrast in digital holography of tissue response to cytoskeletal anti-cancer drugs. Opt. Express **15**, 14057–14064 (2007)
52. K. Jeong, J.J. Turek, D.D. Nolte, Speckle fluctuation spectroscopy of intracellular motion in living tissue using coherence-domain digital holography. J. Biomed. Opt. **15**, 030514 (2010)
53. K. Jeong, J.J. Turek, M.R. Melloch, D.D. Nolte, Multiple-scattering speckle in holographic optical coherence imaging. Appl. Phys. B Lasers Opt. **95**, 617–625 (2009)
54. D.D. Nolte, T. Cubel, L.J. Pyrak-Nolte, M.R. Melloch, Adaptive beam combining and interferometry using photorefractive quantum wells. J. Opt. Soc. Am. B **18**, 195–205 (2001)
55. I. Lahiri, L.J. Pyrak-Nolte, D.D. Nolte, M.R. Melloch, R.A. Kruger, G.D. BAcher, M.B. Klein, Laser-based ultrasound detection using photorefractive quantum wells. Appl. Phys. Lett. **73**, 1041–1043 (1998)

56. Y. Ding, R.M. Brubaker, D.D. Nolte, M.R. Melloch, A.M. Weiner, Femtosecond pulse shaping by dynamic holograms in photorefractive multiple quantum wells. Opt. Lett. **22**, 718–721 (1997)
57. Y. Ding, D.D. Nolte, M.R. Melloch, A.M. Weiner, Time-domain image processing using dynamic holography. IEEE J. Sel. Top. Quantum Elect. **4**, 332–341 (1998)
58. Y. Ding, A.M. Weiner, M.R. Melloch, D.D. Nolte, Adaptive all-order dispersion compensation of ultrafast laser pulses using dynamic spectral holography. Appl. Phys. Lett. **75**, 3255 (1999)
59. M. Dinu, K. Nakagawa, M.R. Melloch, A.M. Weiner, D.D. Nolte, Broadband low-dispersion diffraction of femtosecond pulses from photorefractive quantum wells. J. Opt. Soc. Am. B **17**, 1313–1319 (2000)
60. M. Dinu, D.D. Nolte, M.R. Melloch, Electroabsorption spectroscopy of effective-mass AlGaAs/GaAs Fibonacci superlattices. Phys. Rev. B **56**, 1987 (1997)
61. C.A. Tyson, J.M. Frazier (eds.), *In Vitro Toxicity Indicators*. Methods in Toxicology (Academic, San Diego, 1994)
62. L. de Ridder, Autologous confrontation of brain tumor derived spheroids with human dermal spheroids. Anticancer Res. **17**, 4119–4120 (1997)
63. K. Groebe, W. Mueller-Klieser, On the relation between size of necrosis and diameter of tumor spheroids. Int. J. Radiat. Oncol. Biol. Phys. **34**, 395–401 (1996)
64. R. Hamamoto, K. Yamada, M. Kamihira, S. Iijima, Differentiation and proliferation of primary rat hepatocytes cultured as spheroids. J. Biochem. (Tokyo) **124**, 972–979 (1998)
65. G. Hamilton, Multicellular spheroids as an in vitro tumor model. Cancer Lett. **131**, 29–34 (1998)
66. P. Hargrave, P.W. Nicholson, D.T. Delpy, M. Firbank, Optical properties of multicellular tumour spheroids. Phys. Med. Biol. **41**, 1067–1072 (1996)
67. L.A. Kunz-Schughart, M. Kreutz, R. Knuechel, Multicellular spheroids: a three-dimensional in vitro culture system to study tumour biology. Int. J. Exp. Pathol. **79**, 1–23 (1998)
68. R. Sutherland, W. Inch, J. McCredie, J. Kruuv, Int. J. Radiat. Biol. Relat. Stud. Phys. Chem. Med. **18**, 491–495 (1970)
69. L.A. Kunz-Schughart, Multicellular tumor spheroids: intermediates between monolayer culture and in vivo tumor. Cell Biol. Int. **23**, 157–161 (1999)
70. W. Mueller-Klieser, Biophys. J. **46**, 343–348 (1984)
71. J.P. Freyer, P.L. Schor, K.A. Jarrett, M. Neeman, L.O. Sillerud, Cellular energetics measured by phosphorus nuclear-magnetic-resonance spectroscopy are not correlated with chronic nutrient deficiency in multicellular tumor spheroids. Cancer Res. **51**, 3831–3837 (1991)
72. W. Mueller-Klieser, Three-dimensional cell cultures: from molecular mechanisms to clinical applications. Am. J. Physiol. **273**, 1109–1123 (1997)
73. D.D. Nolte, R. An, J.J. Turek, K. Jeong, Tissue dynamics spectroscopy for phenotypic profiling of drug effects in three-dimensional culture. Biomed. Opt. Express **3**, 2825–2841 (2012)
74. D.D. Nolte, R. An, J. Turek, K. Jeong, Tissue dynamics spectroscopy for three-dimensional tissue-based drug screening. JALA **16**, 431–442 (2011)
75. K. Jeong, J.J. Turek, M.R. Melloch, D.D. Nolte, Functional imaging in photorefractive tissue speckle holography. Opt. Commun. **281**, 1860–1869 (2008)

Interferometric Synthetic Aperture Microscopy (ISAM)

31

Steven G. Adie, Nathan D. Shemonski, Tyler S. Ralston, P. Scott Carney, and Stephen A. Boppart

Keywords

Interferometric synthetic aperture microscopy • Computational adaptive optics • Computed optical imaging • Adaptive optics • Wavefront shaping • Aberrations • Inverse Problem

31.1 Introduction

The trade-off between transverse resolution and depth-of-field, and the mitigation of optical aberrations, are long-standing problems in optical imaging. The deleterious impact of these problems on three-dimensional tomography increases with numerical aperture (NA), and so they represent a significant impediment for real-time cellular resolution tomography over the typical imaging depths achieved with OCT. With optical coherence microscopy (OCM) [1], which utilizes higher-NA optics than OCT, the depth-of-field is severely reduced [1, 2], and it has been

S.G. Adie
Department of Biomedical Engineering, Cornell University, Ithaca, NY, USA

N.D. Shemonski • P.S. Carney
Beckman Institute for Advanced Science and Technology, University of Illinois at Urbana-Champaign, Urbana, IL, USA

T.S. Ralston
Biophotonics Imaging Laboratory, Beckman Institute for Advanced Science and Technology, University of Illinois at Urbana-Champaign, Urbana, IL, USA

S.A. Boppart (✉)
Biophotonics Imaging Laboratory, Beckman Institute for Advanced Science and Technology, University of Illinois at Urbana-Champaign, Urbana, IL, USA

Departments of Bioengineering, Electrical and Computer Engineering, and Medicine, University of Illinois at Urbana-Champaign, Urbana, IL, USA
e-mail: boppart@illinois.edu

© Springer International Publishing Switzerland 2015

W. Drexler, J.G. Fujimoto (eds.), *Optical Coherence Tomography*,
DOI 10.1007/978-3-319-06419-2_32

postulated that aberrations play a major role in reducing the useful imaging depth in OCM [3]. Even at lower transverse resolution, both these phenomena produce artifacts that degrade the imaging of fine tissue structures. Early approaches to the limited depth-of-field problem in time-domain OCT utilized dynamic focusing [4]. In spectral-domain OCT, this focus-shifting approach to data acquisition leads to long acquisition times and large datasets [5]. Adaptive optics (AO) has been utilized to correct optical aberrations, in particular for retinal OCT [6–8], but in addition to requiring elaborate and expensive setups, the real-time optimization requirements at the time of imaging, and the correction of spatially varying effects of aberrations throughout an imaged volume, remain as significant challenges. This chapter presents computed imaging solutions for the reconstruction of sample structure when imaging with ideal and aberrated Gaussian beams. These post-acquisition methods are based on the ability of an OCT system to infer the complex scattered field and make use of a physics-based forward model to describe the "imaging operation" and thus connect the measured signal to the sample structure. Inversion of this forward model to recover the object structure is referred to as inverse scattering.

The complexity of the solution to the inverse scattering problem for OCT is increased by the fact that data acquisition is typically performed using 2D (rather than 3D) beam scanning. When 3D scanning of the point spread function is performed over the object volume,[1] such as in the case of OCT with dynamic focusing [4], a quantitative (band limited) reconstruction of the object can be obtained through straightforward 3D deconvolution. In practice, due to time constraints on data acquisition, only two-dimensional (transverse) beam scanning is performed, i.e., with the focus depth fixed. Consequently, the acquired three-dimensional signal can be written as a two-dimensional (transverse) convolution of the point spread function with the object structure, with a third dimension that is indexed by optical wavenumber.

Interferometric synthetic aperture microscopy (ISAM) [9–12] is a solution to the inverse scattering problem for OCT that utilizes Fourier-domain resampling of the signal. The ISAM Fourier resampling provides a band-pass filtered version of the 3D Fourier transform of the sample structure. This solution to the inverse scattering problem was called *ISAM* in recognition of the similarities between far-from-focus OCT and synthetic aperture radar (SAR).[2] Given these similarities, it is not surprising that object reconstruction in ISAM can be performed via the method of aperture synthesis in SAR.[3]

Computational adaptive optics (CAO) provides post-acquisition aberration correction through a connection between the aberrated forward model and the

[1] Similar to acquisition of a *z*-stack in confocal microscopy

[2] Both measure time of flight while sequentially illuminating the object over a range of angles (see Section 31.2.3 for further details relating an illumination wave vector to the wave vector of the collected scattering).

[3] The ISAM Fourier-domain resampling relationship is known in SAR as the Stolt mapping.

pupil function modified by hardware-based AO [13]. The presence of aberrations modifies the forward model utilized for ISAM reconstruction. In particular, certain aberrations require spatially dependent reconstruction, such as the depth-dependent artifacts introduced by spherical aberration [13]. The solution of this more general forward model requires additional computation for full-volume reconstructions. Computational AO can be utilized with OCT processing to correct aberrations near the optical focus, or it can be combined with ISAM to extend the aberration-corrected reconstruction far from focus.

This chapter is divided into two main parts: the first deals exclusively with ISAM (Sects. 31.2 and 31.3), and the second deals with CAO for OCT and ISAM (Sect. 31.4). In addition to summarizing key theoretical aspects and the experimental validation of these methods, the key ISAM resampling result is understood within the context of the Ewald sphere formalism used in diffraction tomography (Sect. 31.2.2). Furthermore, ISAM and CAO are compared to other related techniques (Sect. 31.5), such as numerical refocusing in digital holographic microscopy. This section also discusses the general applicability of these computed imaging methods to other system geometries, such as in holoscopy, that acquire interferometric data over a broad optical bandwidth. In the latter sections, the phase stability requirements and practical limitations are discussed (Sects. 31.6 and 31.7). Finally, a summary and outlook is presented discussing the impact that these computed imaging techniques hold for the future of broadband optical interferometric tomography.

31.2 ISAM Theory

31.2.1 Forward Model

This section provides a summary of the derivation of ISAM for the far-from-focus regime where the effects of defocus are most significant. This is derived for a standard OCT imaging geometry based on Cartesian beam scanning [9, 14]. The near-focus result is included in the final forward model at the end of this section without proof. The near-focus forward model contains relatively minor differences from the far-from-focus model, and the reader is referred to Ref. [15] for further details of the derivation. Although the treatment below is presented for scalar optical fields, the theoretical framework of ISAM is also valid for large numerical aperture setups where the vector nature of optical fields is significant [15].

We begin with the three-dimensional dispersion-corrected complex analytic signal, $S(x, y; k)$, acquired through two-dimensional transverse scanning of the incident focused beam along the x- and y-axes, with the third dimension indexed by optical wavenumber k. This signal can be written as a convolution of the (complex) system point-spread function (PSF), $h(x, y, z; k)$, with the scattering potential $\eta(x, y, z)$ [15, 16]

$$S(x, y; k) = \iiint h(x - x', y - y', z'; k)\eta(x', y', z')\ dx'dy'dz'. \tag{31.1}$$

Due to a double-pass (reflection imaging) geometry in OCT, the system PSF, $h(x, y, z; k) = \mu_r k^2 |P(k)|^2 g^2(-x, -y, z; k)$ [15], is defined in terms of a product of the complex incident and (identical) collection beam $\sqrt{\mu_r} k |P(k)| g(x, y, z; k)$. The optical power spectral density is denoted by $|P(k)|^2$ and μ_r determines the interferometric (power) splitting ratio. Without loss of generality, the axial coordinate origin $z = 0$ is set at the nominal (aberration-free) beam focus, with the z-axis oriented in the propagation direction of the incident beam. (The physical significance of the *transverse* coordinate inversion in the definition of $h(x, y, z; k)$ in terms of $g(-x, -y, z; k)$ is related to the 3D (vector) spatial frequency support of the instrument, $\mathbf{Q}_{\text{range}}$, such that $\mathbf{Q}_{\text{range}} \subseteq -2\mathbf{k}_{\text{range}}$, where $\mathbf{k}_{\text{range}}$ is the range of optical wave vector components of the focused beam. A coordinate inversion along the *axial* dimension can be found in Eqs. 31.6 and 31.9 below. The relationship between the incident optical wave vector $\mathbf{k}$ and the detected object spatial frequency $\mathbf{Q}$ is also discussed in Sect. 31.2.3.) By invoking the convolution theorem, we can write Eq. 31.1 in the transverse spatial frequency domain as

$$\tilde{S}(Q_x, Q_y; k) = \int \tilde{h}(Q_x, Q_y, z'; k) \; \tilde{\eta}(Q_x, Q_y, z') \; dz', \tag{31.2}$$

where the tilde (˜) denotes the two-dimensional (2D) transverse Fourier transform and $\tilde{h}(Q_x, Q_y, z; k)$ encodes the (depth-dependent) transverse band-pass response of the effective PSF.

In order to simplify Eq. 31.2, let us consider a plane wave decomposition of the focused optical beam [15, 17] and write

$$g(x, y, z; k) = \frac{-i}{2\pi} \iint \frac{G(Q_x, Q_y; k)}{k_z(Q_x, Q_y)} \exp\{i[Q_x x + Q_y y + k_z(Q_x, Q_y) z]\} \; dQ_x dQ_y, \tag{31.3}$$

where $G(Q_x, Q_y; k)$ is the pupil function of the beam (see Sect. 31.4.2 for further details). The integration limits are over the aperture of the objective lens, but since the optical field is taken to be zero outside this aperture, the limits of the integration can be extended to infinity, and the above equation can be equated with an inverse Fourier transform. The complex exponential term is written in terms of the optical wave vector $\mathbf{k} = (k_x, k_y, k_z)$ corresponding to each plane wave component, where $k_x = Q_x$, $k_y = Q_y$, and $k_z(Q_x, Q_y) = \sqrt{k^2 - Q_x^2 - Q_y^2}$. For an ideal Gaussian beam, $G(Q_x, Q_y; k)$ is a real Gaussian weighting. Computing the transverse Fourier transform of Eq. 31.3 results in

$$\tilde{g}(Q_x, Q_y, z; k) = -i2\pi \frac{G(Q_x, Q_y; k)}{k_z(Q_x, Q_y)} \exp[ik_z(Q_x, Q_y) z]. \tag{31.4}$$

The complex exponential term can be recognized as the angular spectrum propagator [18] that can be utilized to propagate the optical field by a given distance z.

Substitution of $z = 0$ provides the plane wave coefficients of the optical field at the beam focus. Notice the constant phase factor of $-i$ relating $\tilde{g}(Q_x, Q_y, 0; k)$, the angular spectrum at focus, to the pupil function $G(Q_x, Q_y; k)$. This can be attributed to the Gouy phase shift associated with a focused beam [19], which results in a $\pi/2$ phase retardation of the focused beam (relative to a plane wave) upon propagation from the objective lens to the beam focus.

Taking into account the double-pass detection geometry, we can make use of Eq. 31.4 and the convolution theorem to express the (transverse) transfer function of the system PSF in Eq. 31.2 as

$$\tilde{h}(-Q_x, -Q_y, z; k) = -4\pi^2 \mu_r k^2 |P(k)|^2 \iint \frac{G\left(Q'_x, Q'_y; k\right)}{k_z\left(Q'_x, Q'_y\right)} \frac{G\left(Q_x - Q'_x, Q_y - Q'_y; k\right)}{k_z\left(Q_x - Q'_x, Q_y - Q'_y\right)} \times \exp\left\{-i\left[k_z\left(Q'_x, Q'_y\right) + k_z\left(Q_x - Q'_x, Q_y - Q'_y\right)\right] z\right\} dQ'_x \, dQ'_y. \tag{31.5}$$

This form for $\tilde{h}(-Q_x, -Q_y, z; k)$ allows us to make an approximation for the far-from-focus case. When $|k_z|$ is large, the integrand in Eq. 31.5 rapidly oscillates due to the complex exponential term. The method of stationary phase [20] can be used to approximate the right-hand side of Eq. 31.5 at the stationary points of the oscillating phase. Using the stationary point at $(Q'_x, Q'_y) = (Q_x/2, Q_y/2)$ [15], the method of stationary phase gives

$$\tilde{h}(-Q_x, -Q_y, z; k) \approx \frac{i4\pi}{-z} \mu_r k |P(k)|^2 G^2\left(\frac{Q_x}{2}, \frac{Q_y}{2}; k\right) \exp\left[-i2k_z\left(\frac{Q_x}{2}, \frac{Q_y}{2}\right) z\right]. \tag{31.6}$$

Note that this expression, derived for large $|k_z|$, decouples the amplitude and phase contributions to the transverse transfer function of the system. A coordinate inversion over the axial and transverse dimensions is evident from inspection of the expressions for the system PSF and the optical beam (cf. Eqs. 31.6 and 31.4). Apart from a slowly varying factor of $-1/z$, which represents the signal decay with distance from focus, the characteristic depth dependence of the system PSF is captured by the complex exponential term. Most importantly, it is the *phase* variation across the transverse frequency bandwidth that is responsible for the apparent degradation of resolution with increasing distance from focus.

The usefulness of the far-from-focus approximation in Eq. 31.6 becomes apparent when substituted into the forward model in Eq. 31.2:

$$\tilde{S}_F(Q_x, Q_y; k) = H_F(-Q_x, -Q_y; k) \int \frac{\tilde{\eta}(Q_x, Q_y, z')}{-z'} \exp\left[-i2k_z\left(\frac{Q_x}{2}, \frac{Q_y}{2}\right) z'\right] dz'$$
$$\text{with} \qquad H_F(-Q_x, -Q_y; k) = i4\pi\mu_r k |P(k)|^2 G^2(Q_x/2, Q_y/2; k), \tag{31.7}$$

where $H_F(-Q_x, -Q_y; k)$ is the far-from-focus band-pass response of the instrument, and we have used the fact that $k_z(-Q_x/2, -Q_y/2) = k_z(Q_x/2, Q_y/2)$. Note that the forward model is now in the form of a Fourier transform with space and frequency variables of z' and $2k_z(Q_x/2, Q_y/2)$, respectively.

In order to provide a forward model applicable to both near- and far-from-focus regimes, we note that a separate near-focus approximation results in a forward model that has the same form as Eq. 31.7, but with a slightly different (near-focus) band-pass response $H_N(Q_x, Q_y; k)$ and without the $-1/z'$ attenuation factor in the integrand [15]. The main difference between $H_F(Q_x, Q_y; k)$ and $H_N(Q_x, Q_y; k)$ is a factor of i resulting from the Gouy phase shift and a slowly varying real (amplitude-only) function of the arguments Q_x, Q_y, and k (see Eqs. 42 and 43 in Ref. [15] for the full expressions). For utility in evaluation, an *attenuated scattering potential* can be defined as

$$\widetilde{\eta}'(Q_x, Q_y, z) = \rho(z)\widetilde{\eta}(Q_x, Q_y, z), \tag{31.8}$$

where $\rho(z) = -1/z$ when far from focus and $\rho(z) = 1$ when near focus, where the transition point between the two regimes occurs at one Rayleigh range [15]. This now allows us to write the forward model for both the near- and far-from-focus regimes in the frequency domain as

$$\begin{aligned} \tilde{S}(Q_x, Q_y; k) &= H(-Q_x, -Q_y; k)\widetilde{\widetilde{\eta}}'(Q_x, Q_y, Q_z), \\ \text{with} \quad Q_z &= -2k_z\left(\frac{Q_x}{2}, \frac{Q_y}{2}\right) = -2\sqrt{k^2 - (Q_x/2)^2 - (Q_y/2)^2}, \end{aligned} \tag{31.9}$$

where $\widetilde{\widetilde{\eta}}'(Q_x, Q_y, Q_z)$ is the 3D Fourier transform of the attenuated scattering potential. The instrument transfer function is then $H(Q_x, Q_y; k) = H_N(Q_x, Q_y; k)$ when within one Rayleigh range of the focus, and $H(Q_x, Q_y; k) = H_F(Q_x, Q_y; k)$ otherwise. Note that this reduces the many-to-one mapping in Eq. 31.2 to a one-to-one mapping between the Fourier (spatial frequency) domain of the object and the Fourier domain of the signal. Inherent in this mapping is the coordinate warping relating the Fourier coordinates of the object, (Q_x, Q_y, Q_z), to the Fourier coordinates of the signal, $(Q_x, Q_y; k)$. Also note that for an ideal Gaussian beam, the instrument transfer function is symmetrical, i.e., $H(-Q_x, -Q_y; k) = H(Q_x, Q_y; k)$. The functional form of the required coordinate warping $Q_z = -2k_z(Q_x/2, Q_y/2)$ was originally developed in the field of geophysics [12, 21] and is known as the Stolt mapping.

Before we discuss the inverse scattering procedure, it is worth pointing out the operator description of the forward model [22]:

$$\tilde{S}(Q_x, Q_y; k) = K\ \widetilde{\widetilde{\eta}}'(Q_x, Q_y, Q_z), \tag{31.10}$$

where the operator K maps from the vector space representation of the object to the vector space of the signal. The observed (discrete) signal will generally be noisy and band limited, resulting in an inverse problem that is ill-conditioned and possibly ill-posed. Since the inverse K^{-1} is not expected to exist, it is appropriate to compute the solution $\tilde{\tilde{\eta}}^{+}\left(Q_x, Q_y, Q_z\right)$ that minimizes $\left\|\tilde{S} - K\,\tilde{\tilde{\eta}}^{+}\right\|$, where $\| \bullet \|$ denotes the $l_2(\mathbb{R}^2)$ norm. This solution can be written as

$$\tilde{\tilde{\eta}}^{+} = (K^{*}K)^{-1}K^{*}S = K^{+}S, \tag{31.11}$$

where K^{+} is the pseudoinverse of K, K^{*} is the adjoint of K, $K^{*}K$ is the normal operator, and $(K^{*}K)^{-1}$ is the inverse of $K^{*}K$ restricted to the orthogonal complement to the null space. The operators K and K^{*} affect the coordinate transformation in Eq. 31.9, i.e., between the coordinate systems $(Q_x, Q_y; k) \leftrightarrow (Q_x, Q_y, Q_z)$, and the normal operator acts as a space-invariant filter.

31.2.2 Inverse Scattering Procedure

The following provides a procedure for inverting the signal model in Eq. 31.9. These steps include the full procedure to obtain a quantitatively accurate reconstruction of the scattering potential. In practice, however, it is common to omit steps 2 and 5 below since they do not produce a significant qualitative improvement to the reconstruction. In this problem the normal operator is approximately diagonal, and so it is useful to compute the *unfiltered* solution $\eta_A = K^{*}S$. The advantage of this approach using the adjoint operator is that stable solutions are obtained (without the need for regularization). The full pseudoinverse (with appropriate regularization) is more susceptible to noise, but results in a more localized PSF with reduced width. The required steps for ISAM (corresponding to the unfiltered solution η_A) are highlighted in bold:

1. **Take the transverse Fourier transform of the complex interferometric (phase stable) signal** $S(x, y; k)$**, to get the Fourier-domain data** $\tilde{S}\left(Q_x, Q_y; k\right)$.
2. Apply a linear filter, i.e., Fourier-domain multiplication of $\tilde{S}\left(Q_x, Q_y; k\right)$ and a transfer function, in order to compensate for the (ideal spatially invariant) transfer function of the instrument $H(Q_x, Q_y; k)$. In practice, the slowly varying effects of the instrument band-pass response obtained when imaging with an ideal Gaussian beam are usually ignored, i.e., $H(Q_x, Q_y; k)$ is set to unity.
3. **Remap the coordinate space of** $\tilde{S}\left(Q_x, Q_y; k\right)$ **according to the Stolt mapping in Eq. 31.9. This crucial step is the basis of the computational efficient reconstruction provided by ISAM and can be performed through resampling** k **to** Q_z**, i.e., by evaluating** $\tilde{S}\left(Q_x, Q_y; k\right)$ **at the desired values of** Q_z **using** $k = \frac{1}{2}\sqrt{Q_x^2 + Q_y^2 + Q_z^2}$. This resampling "rephases" the transverse spatial frequencies (for each given value of Q_z) to produce constructive

interference across the bandwidth simultaneously for all depths (see the ISAM resampling curve in Fig. 31.6).
4. **Take the inverse Fourier transform to recover $\rho(z)\eta(x, y, z)$, the attenuated scattering potential.**
5. A quantitatively accurate map of the scattering potential $\eta(x, y, z)$ can be computed by dividing by $\rho(z)$ to compensate for signal loss away from the focus. This step is commonly omitted or replaced with other depth normalization methods.

Note that it may also be necessary to add preprocessing steps to account for material dispersion and to compensate for phase instabilities in the instrument. See Sect. 31.6.1 for the requirements on phase stability.

31.2.3 Relationship to Diffraction Tomography

Similarities between the OCT forward model and diffraction tomography[4] have been recognized in the comprehensive review paper by Fercher et al. [23]. In this section, we will see how these commonalities can be used to determine the ISAM resampling relationship in Sect. 31.2.1, Eq. 31.9.

Figure 31.1 shows the geometry of a far-from-focus scattering event, where $\mathbf{k}_{in}$ and $\mathbf{k}_{out}$ are the wave vectors of the plane wave components of the incident and scattered field, respectively. Recall from Eq. 31.3 that an arbitrary field can be expressed as a superposition of plane wave components. These wave vectors satisfy the scattering vector relationship:

$$\mathbf{Q} = \mathbf{k}_{out} - \mathbf{k}_{in}, \tag{31.12}$$

where $\mathbf{Q}$ is the three-dimensional spatial frequency of the sample that is probed. This vector relationship is a consequence of momentum conservation. For a given $\mathbf{k}_{in}$, the (far-field) placement of the detector in diffraction tomography provides access to spatial frequencies that lie on a sphere with radius k, known as the *Ewald sphere of reflection* [24].

For an OCT system, the angular relationship between the incident and scattered wave vectors is governed by the specific imaging geometry. Consider scattering from the far-from-focus scatterer in Fig. 31.1, i.e., in the regime where the correction of defocus is required most. Figure 31.1c presents a simple geometrical optics argument describing why the angular detection range of scattering vectors is constrained to a narrow solid angle centered about the $-\mathbf{k}_{in}$ direction. This acceptance angular range of the OCT imaging geometry reduces with increasing distance from focus, so that in the far-from-focus limit,

$$\mathbf{k}_{out} = -\mathbf{k}_{in}. \tag{31.13}$$

[4]Through the basic theorem of diffraction tomography

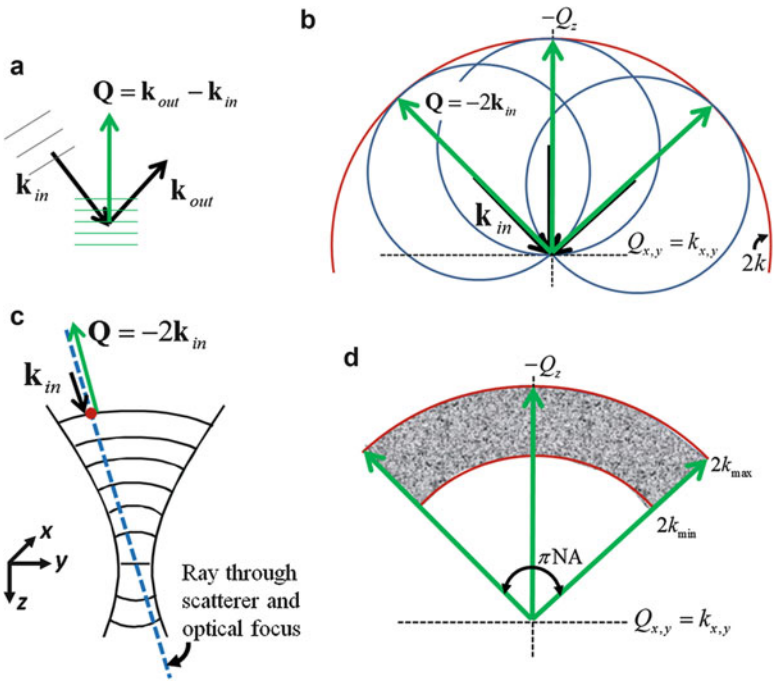

Fig. 31.1 Description of scattering in the far-from-focus regime using the Ewald sphere formalism utilized in diffraction tomography, and the resulting spatial frequency bandwidth of the instrument. (**a**) Scattering geometry showing the relationship between object spatial frequency Q (*green vector*) and the optical wave vectors k_{in} and k_{out} (*black vectors*) for the plane wave components of the incident and scattered fields, respectively. (**b**) Ewald spheres (*blue circles* with radius *k*) corresponding to three different incident wave vectors (*black vectors*), showing the spatial frequency coverage resulting from the detection of all scattering angles as well as the particular spatial frequency detected through the measurement of direct backscattering (*green vectors*). The spatial frequency coverage resulting from the measurement of direct backscattering is given by the limiting Ewald sphere (*red circle* with radius 2*k*). (**c**) Geometrical optics argument limiting the collection of scattered light from far-from-focus scatterers to direct backscattering. (**d**) Far-from-focus spatial frequency coverage of an OCT system. Note that although the bandwidth limits of the instrument are drawn as sharp cutoffs, the magnitude of the instrument transfer function is better approximated along each dimension by a Gaussian-shaped function

Consequently, as the beam is scanned transversally along the *x*- and *y*-axes during data acquisition, the angle of the effective illumination wave vector (which is perpendicular to the incident wavefront of the illumination beam) is scanned, resulting in the sequential acquisition of sample spatial frequencies from far-from-focus object structure. In contrast, for a scatterer at the optical focus, the full range of scattering angles is detected simultaneously.

The essential physics of the far-from-focus ISAM resampling result can thus be captured by substituting Eq. 31.13 into Eq. 31.12:

$$\mathbf{Q} = -2\mathbf{k}_{in}, \tag{31.14}$$

with $|\mathbf{Q}| = 4\pi/\lambda$. This implies that the sample spatial frequencies that are acquired by varying the angle of the illumination lie on a sphere of radius $2k$, known as the *Ewald limiting sphere* [24]. Note that Eq. 31.14 is equivalent to Eq. 2.10 in the paper by Fercher et al. [23]. However, rather than restricting the discussion to direct backscattering that is parallel to the z-axis (i.e., one-dimensional low-coherence interferometry (LCI), with $Q_z = -2k$ and $Q_x = Q_y = 0$), the ISAM result becomes accessible by considering the detection of backscattering corresponding to all illumination angles within the NA of the imaging system, i.e., where $\mathbf{k}_{in}$ spans over the solid angle of illumination. Maintaining this angular diversity in the incident (and antiparallel backscattered) wave vectors, calculation of the magnitude squared of the vectors in Eq. 31.14 yields $Q_x^2 + Q_y^2 + Q_z^2 = 4k^2$, which can be rearranged to give

$$Q_z = -2\sqrt{k^2 - (Q_x/2)^2 - (Q_y/2)^2}, \tag{31.15}$$

which is the ISAM coordinate mapping in Eq. 31.9. Note that the negative sign of the square root was chosen to be consistent with the direction of the backscattering vector $-\mathbf{k}_{in}$ (see Fig. 31.1c). The coordinate mapping in Eq. 31.15 which relates the frequency coordinate of the signal, k, to axial spatial frequency of the object, Q_z, is the basis of the key resampling step in Sect. 31.2.2 for reconstructing far-from-focus object structure with ISAM.

31.3 Experimental Demonstration and Validation

31.3.1 Resolution Phantom

Tissue phantoms consisting sub-resolution "point" scatterers provide a sample for the investigation of resolution in OCT and ISAM. Three-dimensional imaging was performed on a silicone tissue phantom laced with titanium dioxide scatterers, with mean diameter of 1 μm. Imaging was conducted using an 800 nm spectral-domain (SD)-OCT system with 100 nm bandwidth, at an $NA \sim 0.05$ (confocal parameter of 239 μm). Figure 31.2 shows a side-by-side visualization of the OCT and ISAM reconstructions obtained from the same raw dataset. The OCT dataset begins to show transverse blurring at a distance of 240 μm from focus, with increased blurring with distance from focus. In contrast, the ISAM reconstruction provides spatially invariant transverse resolution over a depth exceeding nine Rayleigh ranges. These results provided the first experimental demonstration that ISAM was able to correct defocus simultaneously for all depths.

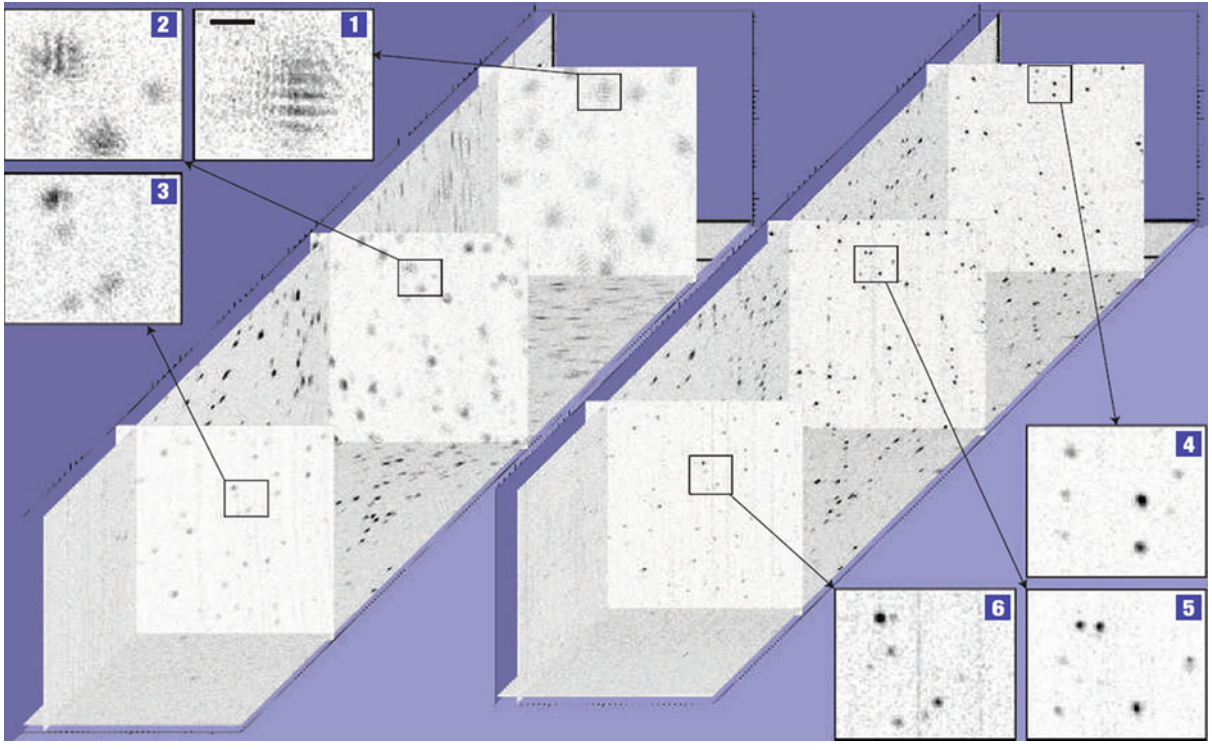

Fig. 31.2 Three-dimensional OCT (left) and ISAM (right) images of a silicone phantom containing titanium dioxide microparticles. The three en face planes in each dataset correspond to (*1*) $z = 1{,}100$ μm, (*2*) $z = 475$ μm, and (*3*) $z = -240$ μm, where $z = 0$ μm is the focal plane. The images were generated from a single 3D dataset acquired using an 800 nm SD-OCT system at an imaging NA of 0.05 (From [9])

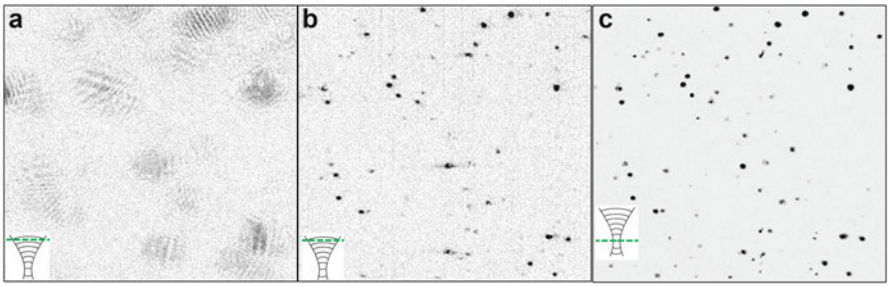

Fig. 31.3 Cross-validation of ISAM and in-focus OCT in a silicone phantom containing titanium dioxide microparticles. (**a**) En face OCT from 3.75 Rayleigh ranges above the focus and (**b**) the same en face plane extracted from the 3D ISAM reconstruction. (**c**) In-focus OCT obtained by shifting the beam focus to the same depth as in (**a**) and (**b**). The inset in the *lower left* of each panel shows the relative depths of the displayed en face planes with respect to the beam focus. The two datasets were acquired using an 800 nm OCT system with an $NA \sim 0.05$ (Adapted from [25])

31.3.2 Cross-Validation with OCT

It is obvious from Sect. 31.3.1 that ISAM provides significant improvements in resolution in the far-from-focus regime. But does three-dimensional ISAM accurately reconstruct the object structure? This question was addressed by comparing specific en face planes extracted from 3D ISAM reconstructions to in-focus OCT images of the same plane. In a sparse tissue phantom (see Fig. 31.3), the resolution and scatterer positions in an en face ISAM image are in excellent agreement to in-focus OCT of the same plane, demonstrating that ISAM provides an accurate reconstruction of the object. It should be noted that the signal-to-noise ratio (SNR) of the in-focus OCT is higher. This can be attributed to the increased light collection efficiency at the focal plane of the optical system, due to the $1/|z|$ depth dependence in the forward model describing the away-from-focus signal (see Eqs. 31.8 and 31.9). The improved signal collection at focus is the reason to place the object near the focus. In practice, the focus is positioned at approximately 50–75 % of the maximum imaging depth in a given sample.

For biomedical imaging applications it is important to confirm the reconstruction accuracy of ISAM in biological tissue. Figure 31.4 presents results of rat mammary tissue, once again comparing a specific en face plane extracted from 3D ISAM reconstructions to the in-focus OCT image of the same plane. Close agreement between structural features of tissue is seen between the far-from-focus ISAM reconstruction and the in-focus OCT. As with the phantom results, the in-focus OCT demonstrates higher SNR, resulting in better definition of structural features with weak signals. Additionally, since the acquisition rate was relatively low (0.6 frames/s), uncorrected phase instabilities may also result in degraded definition of weak signals. Sections 31.6 and 31.7 discuss the relevant data acquisition requirements, limitations of ISAM, and practical methods to address these limitations.

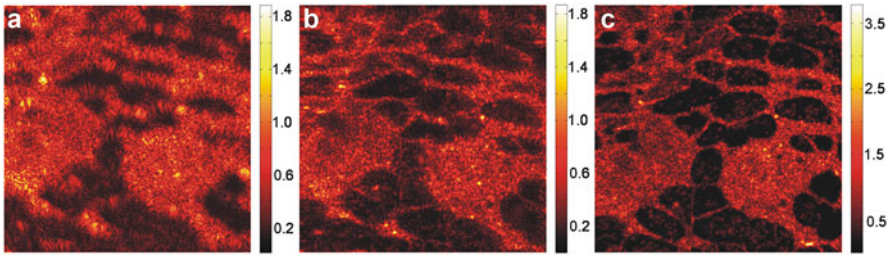

Fig. 31.4 Cross-validation of ISAM and in-focus OCT in rat mammary tissue. (**a**) En face OCT from eight Rayleigh ranges above the focus and (**b**) the same en face plane extracted from the 3D ISAM reconstruction. (**c**) In-focus OCT obtained by shifting the beam focus to the same depth as in (**a**) and (**b**). The datasets were acquired using an 800 nm OCT system with $NA \sim 0.1$ (From [25])

31.3.3 Validation of ISAM with Histology

Histological analysis is the gold standard for diagnosing the pathological status of tissue. Thus, in order to test the accuracy of reconstruction in tissue, ISAM of resected human breast tissue was performed and compared to histology. Imaging was performed using an OCT system with 800 nm central wavelength and 100 nm bandwidth, with a focused beam numerical aperture of 0.05. Figure 31.5 shows a volumetric ISAM rendering and selected en face sections from near- and far-from-focus regions. The en face ISAM sections clearly provide improved resolution compared to OCT, over an extended depth-of-field. Tissue structure reconstructed by ISAM shows a close correspondence to histology, demonstrating that ISAM provides anatomically accurate reconstructions of biological tissue. This suggests that ISAM could be applied for high-resolution "optical biopsy" over a large imaging depth, as compared to OCM.

31.4 Computational Adaptive Optics

31.4.1 Aberrated Forward Model

The forward model in Eq. 31.9, which forms the basis of ISAM, is essentially space invariant. Apart from a gradual depth-dependent amplitude variation (the main contribution being the $1/z$ signal decay with distance from focus), and a gradual through-focus variation of the (Gouy) phase, the transfer function of the instrument, $H(Q_x, Q_y; k)$,[5] is space invariant. Spatially invariant resolution has been clearly demonstrated for ISAM reconstructions of data acquired with (near ideal) Gaussian

[5]The minus signs on the coordinates (Q_x, Q_y) have been dropped, since, for an ideal Gaussian beam, the instrument transfer function $H(-Q_x, -Q_y; k) = H(Q_x, Q_y; k)$. For the aberration correction filter in Section 31.4.2, Hermitian symmetry applies, i.e., $H_{AC}(Q_x, Q_y; k) = H^*_{AC}(-Q_x, -Q_y; k)$.

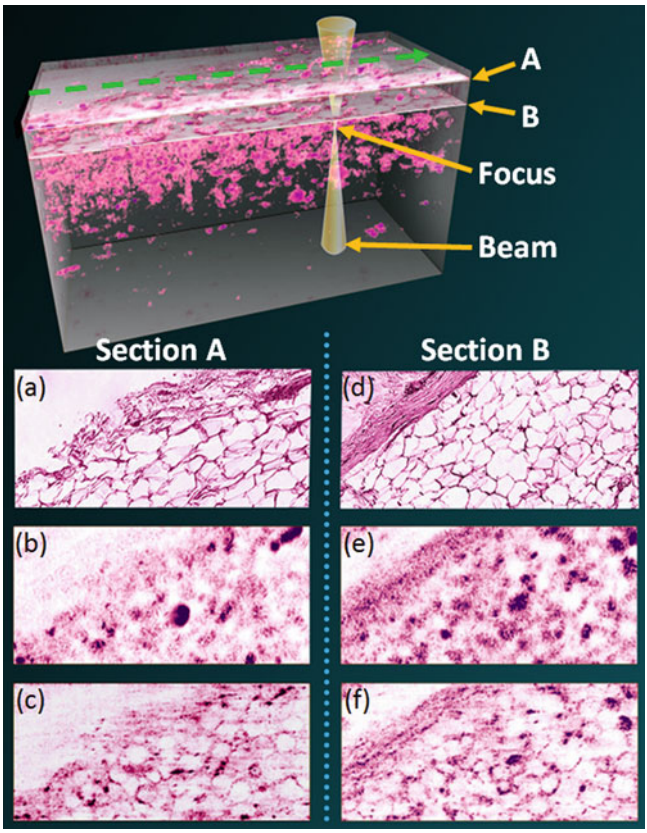

Fig. 31.5 Three-dimensional ISAM of resected human breast tissue compared with histology. En face images are shown for depths located at 643 μm (Section A) and 591 μm (Section B) above the focal plane. (**a**, **d**) Histological sections show comparable features with respect to the (**b**, **e**) OCT data and (**c**, **f**) the ISAM reconstructions. The ISAM reconstructions resolve features in the tissue which are not decipherable from the OCT data. To acquire this 3D dataset, the beam was raster scanned in the geometry shown at the *top* (*dashed green arrow*) (Adapted from [9])

beams [9, 15, 16, 25]. However, for an aberrated Gaussian beam, the ISAM reconstruction can produce a spatially varying point spread function, as seen, for example, by the asymmetry about the focus that is introduced by spherical aberration [13].

The effect of aberrations can be incorporated through a generalization of the forward model in Eq. 31.9. This approach considers the impact of aberrations as an extra (space-variant) filtering step in the forward model. In the general case, the effect of aberrations can have a dependence on all three spatial coordinates. This coupling between the space and frequency domains leads to an aberrated forward model that is defined in a piecewise manner over the spatial domain. This three-dimensional space-dependent imaging operation was considered by Frieden, who

introduced the concept of an *isotome* [26], or volume of stationarity $V(x_0, y_0, z_0)$ centered at position (x_0, y_0, z_0). The term isotome is a generalization of the term *isoplanatic patch* used in astronomical adaptive optics to denote the angular range over which a wavefront correction with hardware-based adaptive optics is valid [27]. The *isotomic volume* is then the region of space over which the 3D imaging operation can be considered space invariant. When restricted to one such isotome, the aberrated forward model can be written as

$$\tilde{S}_A(Q_x, Q_y; k)\big|_{V(x_0, y_0, z_0)} = H_A(Q_x, Q_y, x_0, y_0, z_0; k) H(Q_x, Q_y; k) \widetilde{\widetilde{\eta}}'(Q_x, Q_y, Q_z), \tag{31.16}$$

where $H_A(Q_x, Q_y, x, y, z; k)$ represents the extra (space-dependent) filtering step and $\widetilde{\widetilde{\eta}}'(Q_x, Q_y, Q_z)$ is the axial Fourier transform of the modified scattering potential defined in Eq. 31.8. In the general case, a different forward model of the signal may be required to describe the signal at different spatial locations.

In practice, space invariance in the transverse dimension is achieved over a relatively wide field of view, and Eq. 31.16 can be written for a slab volume geometry, $V(z_0)$, centered at depth z_0 as

$$\tilde{S}_A(Q_x, Q_y; k)\big|_{V(z_0)} = H_A(Q_x, Q_y, z_0; k) H(Q_x, Q_y; k) \widetilde{\widetilde{\eta}}'(Q_x, Q_y, Q_z). \tag{31.17}$$

For the special case when the effects of particular aberrations are space invariant, $V(x_0, y_0, z_0)$ is equal to the complete volume acquired, and Eq. 31.16 reduces to

$$\tilde{S}_A(Q_x, Q_y; k) = H_A(Q_x, Q_y; k) H(Q_x, Q_y; k) \widetilde{\widetilde{\eta}}'(Q_x, Q_y, Q_z), \tag{31.18}$$

where $H_A(Q_x, Q_y; k)$ is an additional filtering step in the ISAM forward model of Eq. 31.9. When imaging with an ideal Gaussian beam, the instrument transfer function, $H(Q_x, Q_y; k)$, is slowly varying and can be ignored in practice. However, the phase distortions that aberrations induce across the bandwidth of the signal cannot be ignored since they can result in severe broadening of the point spread function or modify its functional form (i.e., to exhibit non-Gaussian structure).

31.4.2 The Computed Pupil and Hardware-Based AO

Computational adaptive optics is based on the Fourier optics result connecting the objective lens pupil function that is physically modified by hardware-based AO systems to the Fourier transform of the complex optical field at the nominal (aberration-free) focus. The objective lens pupil function, $P(x, y)$, describes the

deviation of the aberrated optical wavefront from an ideal spherical wavefront. It is related to the focal-plane transverse frequency response of the illumination beam according to [18]

$$\tilde{g}\left(Q_x, Q_y, 0; k\right) = P\left(\frac{-2\pi z_f Q_x}{k}, \frac{-2\pi z_f Q_y}{k}\right), \tag{31.19}$$

where z_f is the (object-side) focal length of the objective lens and the coordinate change $(x, y) = (-2\pi z_f Q_x/k, -2\pi z_f Q_y/k)$ provides the mapping between transverse spatial frequency and the spatial coordinates of the objective lens pupil. As done in Ref. [18], a prefactor of $2\pi A z_f/k$ in the right-hand side of Eq. 31.19 has been set to unity. The pupil phase aberration, Φ_g, is included in the generalized pupil function [18]

$$P(x, y) = P_{\text{ideal}}(x, y)\exp\left[ik\Phi_g(x, y)\right], \tag{31.20}$$

where $P_{\text{ideal}}(x, y)$ for a typical OCT system is a real Gaussian envelope. Since the ideal beam focus is the impulse response of the (single-pass) imaging system, $\tilde{g}\left(Q_x, Q_y, 0; k\right)$ can be regarded as the (transverse) amplitude transfer function [18]. Making use of Eqs. 31.4 and 31.19, the transverse Fourier domain of the aberrated OCT PSF may be written in terms of the objective lens pupil function as

$$\tilde{g}\left(Q_x, Q_y, z; k\right) = i2\pi P\left(\frac{-2\pi z_f Q_x}{k}, \frac{-2\pi z_f Q_y}{k}\right)\exp\left[ik_z\left(Q_x, Q_y\right)z\right], \tag{31.21}$$

where the phase of the pupil function, Φ_g (x, y), can conveniently be expressed as a sum of Zernike polynomials [14, 28], as is commonly done to represent aberrations in optical systems.[6]

Due to the double-pass (epi-illumination) imaging geometry, the OCT PSF is related to the square of the optical beam [15, 16]. A *computed pupil* is defined here as the convolution of the pupil functions (see Eq. 31.5) that are physical modified by hardware-based AO. Note that this definition of the computed pupil uses the exact expression for the PSF, i.e., before the asymptotic approximations made by ISAM. This is important since the convolution operation (of phase-only pupil functions) can produce depth-dependent amplitude and phase structure in the transverse Fourier domain that is not preserved after the asymptotic approximations, such as that far-from-focus approximation in Eq. 31.6. In particular, depth-dependent amplitude structure in the transverse Fourier domain of the PSF, $\tilde{h}_A\left(Q_x, Q_y, z; k\right)$, was found to contribute to the asymmetry about the beam focus when imaging with a beam that has spherical aberration [13].

[6]Since the Zernike polynomials are defined on a unit circle, *normalized* spatial coordinates are employed.

Aberrations of the computed pupil are described by an aberration filter, $H_A(Q_x, Q_y; k)$, which are calculated as the deviation of the computed pupil function from its ideal functional form:

$$H_A(Q_x, Q_y, z_0; k) = \frac{\tilde{h}_A(Q_x, Q_y, z_0; k)\tilde{h}^*(Q_x, Q_y, z_0; k)}{\left|\tilde{h}(Q_x, Q_y, z_0; k)\right|^2 + \alpha} = \frac{\left[\tilde{g}_A(Q_x, Q_y, z_0; k) \bigotimes_{\|} \tilde{g}_A(Q_x, Q_y, z_0; k)\right]\left[\tilde{g}(Q_x, Q_y, z_0; k) \bigotimes_{\|} \tilde{g}(Q_x, Q_y, z_0; k)\right]^*}{\left|\tilde{g}(Q_x, Q_y, z_0; k) \bigotimes_{\|} \tilde{g}(Q_x, Q_y, z_0; k)\right|^2 + \alpha}, \tag{31.22}$$

where $\bigotimes_{\|}$ denotes a convolution over the transverse spatial frequency coordinates, the asterisk $(*)$ denotes the complex conjugate, α is a regularization constant, and the transverse Fourier transform of the aberrated optical field, $\tilde{g}_A(Q_x, Q_y, z_0; k)$, can be evaluated using Eqs. 31.20 and 31.21. Intuitively, this definition provides the deviation of the actual phase fronts of the OCT PSF from the ideal (unaberrated) phase fronts. In addition, it should be noted that due to the Fourier-domain amplitude structure that can result from the convolution operation mentioned in the paragraph above, in general $\left|\tilde{h}_A(Q_x, Q_y, -z; k)\right| \neq \left|\tilde{h}(Q_x, Q_y, -z; k)\right|$. An aberration correction filter can be calculated by inverting the effects of $H_A(Q_x, Q_y, z_0; k)$. Although this calls for a (potentially space-variant) regularized inverse, this step can be approximated through the use of a simpler phase-only aberration correction filter [14]:

$$H_{\mathrm{AC}}(Q_x, Q_y; k) = \exp\left[-ik\Phi_h\left(-2\pi z_f Q_x/k, -2\pi z_f Q_y/k\right)\right], \tag{31.23}$$

where the PSF phase aberration $\Phi_h(x, y)$, defined here in the spatial coordinate system of the objective lens pupil, can be calculated from a convolution of the pupil functions as

$$\Phi_h\left(\frac{-2\pi z_f Q_x}{k}, \frac{-2\pi z_f Q_y}{k}\right) = \arg\left\{\left[P\left(\frac{-2\pi z_f Q_x}{k}, \frac{-2\pi z_f Q_y}{k}\right) \otimes_{\|} P\left(\frac{-2\pi z_f Q_x}{k}, \frac{-2\pi z_f Q_y}{k}\right)\right]\right\}. \tag{31.24}$$

Equations 31.23 and 31.24 thus provide the connection between the objective lens pupil function $P(x, y)$, the phase of which is physically modified in hardware AO, and the filtering operation used to correct aberration effects at the nominal focal plane of an OCT tomogram. For correction of the depth-dependent aberration effects implied in Eqs. 31.17 and 31.22, see the space-variant aberration correction steps shown in Fig. 31.6.

The aberration correction filter $H_{\mathrm{AC}}(Q_x, Q_y; k)$ is based on the concept of a generalized 3D pupil [29] and so can correct both monochromatic and chromatic aberration [15, 30]. Correcting chromatic aberration is relevant to broadband

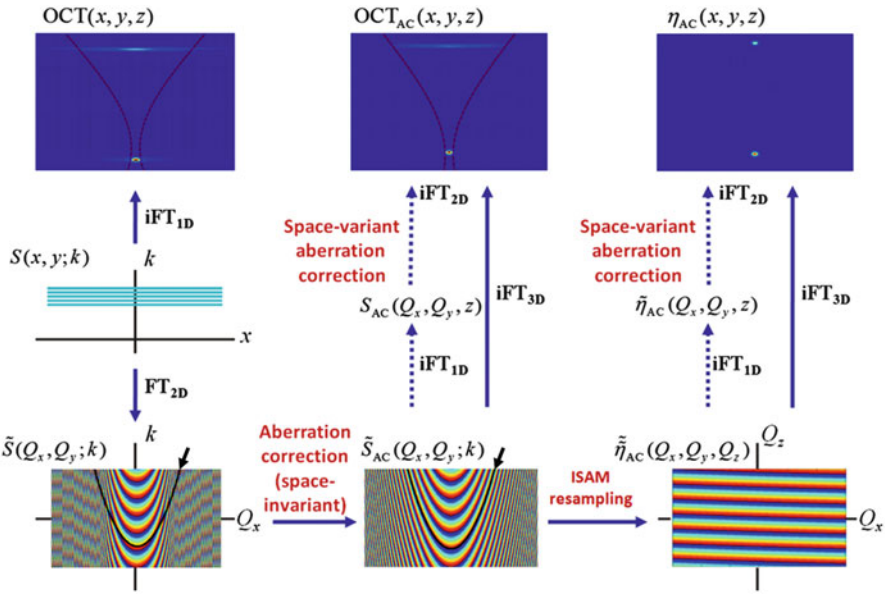

Fig. 31.6 Overview of CAO processing for OCT or ISAM. *Bolded blue arrows* denote processing steps for space-invariant aberration correction, while the *dashed blue arrows* indicate the steps enabling space-variant aberration correction (i.e., at specific en face depths). See the text for definition of the variables. The *dashed red curves* in the $\mathrm{OCT}(x, y, z)$ and $\mathrm{OCT}_{\mathrm{AC}}(x, y, z)$ images represent one transverse scan position of the incident optical beam with respect to the two-scatterer sample. Frequency domain images in the bottom row represent the phase profiles associated with the out-of-focus scatterer, with an ISAM resampling curve (corresponding to a fixed value of Q_z) superimposed in *black* and highlighted by *black arrows* (From [14])

imaging systems since it manifests both as longitudinal (along the z-axis) and transverse blurring. In the absence of chromatic aberration, the k-dependence of the 3D aberration correction filter is a simple scaling of the monochromatic aberration function. The presence of chromatic aberration however results in more complex 3D pupil phase functions. This filtering operation which corrects chromatic aberration is a generalization of numerical dispersion correction in OCT [31, 32]. Numerical dispersion correction in OCT is a one-dimensional correction applied independently to each A-scan, whereas chromatic aberration also has a dependence on the transverse pupil coordinate [30].

31.4.3 Computational AO for Broadband Interferometric Tomography

This section provides an overview of how CAO can be utilized. The reference to *broadband interferometric tomography* is intended to indicate the general applicability of CAO for correcting aberrations in the numerous imaging

geometries and system designs that acquire interferometric data over a broad optical bandwidth, for the purposes of tomography, such as spectral-domain OCT, swept-source OCT, full-field OCT, and holoscopy [33]. In particular, the connection between aberrations of the objective lens pupil (the phase of which is physically adjusted using AO hardware) and deviations from the ideal instrument response in the Fourier domain of the tomogram is generally applicable to broadband interferometric data. The main requirement of phase stability is discussed in Sect. 31.6.1.

Figure 31.6 presents an overview of how CAO can be combined with OCT to correct aberrations near the optical focus, or how it can be combined with ISAM to extend the aberration-corrected reconstruction far from focus. ISAM is based on the fact that defocus in the spatial domain manifests as a coordinate warping in the Fourier domain of the signal. This result, governed by the physics of data acquisition, relates the 3D FT of the complex OCT tomogram to the 3D FT of the object structure through the Stolt mapping. Reconstruction via ISAM resampling (see black curve superimposed in the Fourier domain corresponding to a given value of Q_z) corrects defocus by restoring constructive interference across the transverse bandwidth for all depths simultaneously.

Aberrations disrupt the ideal phase behavior in the Fourier domain, and the ISAM resampling does not result in constructive interference across the transverse bandwidth (see ISAM resampling curve in the bottom left image of Fig. 31.6). The effects of the aberrations can be deconvolved using the aberration correction filter, to restore the expected phase profile across the transverse band (see ISAM resampling curve in the central image at the bottom row of Fig. 31.6). The aberration correction filter $H_{\mathrm{AC}}(Q_x, Q_y; k)$ in Eq. 31.24 provides a space-invariant correction throughout the volume. In general, the effects of aberrations will be depth-dependent and can be corrected using the space-invariant aberration correction pathways in Fig. 31.6, by making use of two-dimensional aberration correction filters $H_{\mathrm{AC}}(Q_x, Q_y; z_0)$ at a given depth of z_0. This can be accounted for in computational AO by performing separate corrections for the space-invariant and space-variant effects.

31.4.4 Resolution Phantom Results

Figure 31.7 shows volumetric data from a silicone phantom laced with titanium dioxide microparticles. The 3D dataset was acquired with a highly astigmatic beam. Astigmatism was generated with a plano-convex cylindrical lens, of focal length f = 1,000 mm, positioned between the collimator and galvanometers of the sample arm. The nominal aberration-free optics in the sample arm had an $NA \sim 0.1$. Because of this astigmatism, the microparticles do not look like points in the OCT volume, but demonstrate two orthogonal and axially separated line foci, with the plane-of-least-confusion between them. The computed pupil correction was calculated from Eqs. 31.23 and 31.24, i.e., as the convolution of astigmatic pupil functions. The phase aberration of the pupil function, Φ_{g}, was expressed as a linear

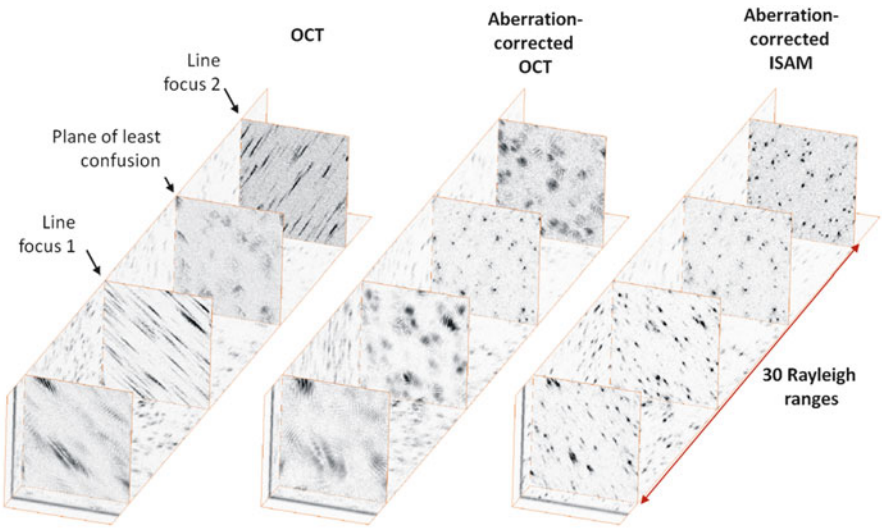

Fig. 31.7 Computational aberration correction of astigmatism in a silicone phantom containing titanium-dioxide microparticles. These renderings were generated from a single 3D dataset that was acquired with a highly astigmatic illumination beam. The OCT reconstruction highlights the plane-of-least-confusion and the two en face (x-y) planes with the best line foci, located 300 μm above and 300 μm below it. The aberration-corrected OCT and aberration-corrected ISAM reconstructions show en face planes corresponding to the same depths as the OCT rendering. Dimensions of the rendered 3D dataset are 256 × 256 × 1,230 μm ($x \times y \times z$), where the units of the z-axis denote optical path length (Adapted from [14])

combination of the Zernike polynomials Z_5 and Z_6 describing astigmatism at 45° and 0°, respectively [28]. Notice that, after the correction of astigmatism, the plane-of-least-confusion is restored as the focal plane, and the planes previously showing line symmetry now show circular symmetry. The subsequent application of ISAM reconstructs the entire volume with focal-plane resolution over a depth range greater than 30 Rayleigh ranges (see Sect. 31.4.7 for quantitative analysis of the resolution).

31.4.5 Tissue Results

Figure 31.8 shows CAO for 3D imaging of highly scattering muscle tissue. The dataset was collected with a 1,330 nm SD-OCT system, but with an astigmatic beam ($NA = 0.09$, defined at the $1/e^2$ level). Astigmatism, a common aberration in retinal or catheter-based OCT, was emulated through the insertion of cylindrical lenses in an otherwise standard OCT sample arm design. The effects of the astigmatism on the reconstruction were found in practice to be well corrected using a single (space-invariant) aberration correction filter. This data provides evidence that the condition of space invariance can be satisfied when imaging in highly scattering tissue and therefore for the validity of the signal model approximations in Eqs. 31.17 and 31.18.

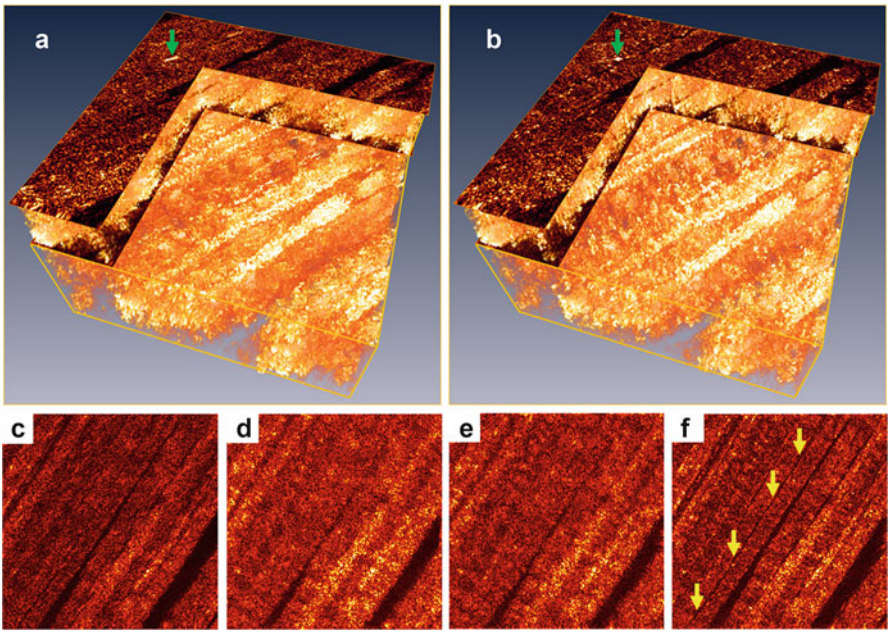

Fig. 31.8 Three-dimensional reconstructions of a rabbit muscle tissue dataset that was acquired with an astigmatic optical system. (**a**) OCT processing and (**b**) CAO-ISAM reconstruction of the complete volume. The displayed volumes span 1 × 1 × 1 mm (optical depth). An en face plane extracted from 110 μm below the tissue surface is shown for (**c**) OCT, (**d**) CAO-OCT, (**e**) ISAM, and (**f**) CAO-ISAM. The *green arrow* in (**a**) shows that the long axis of the astigmatic point spread function is aligned approximately parallel to the muscle fiber bundles, and the *yellow arrows* in (**f**) highlight previously unresolved fine tissue structure that is clearly resolved after CAO-ISAM. The midpoint between the axially separated astigmatic line foci is 600 μm below the tissue surface

31.4.6 Methods to Optimize the Aberration Correction

In hardware-based AO there are generally two methods to optimize the pupil correction. The first is the use of so-called guide-stars [27]. Since in astronomical imaging distant stars present as point sources of light, they have been used in astronomical AO for wavefront sensing.[7] Natural guide-stars are stars that are present near the region of interest [27]. However, when no suitable star is present, an artificial guide-star can be generated by focusing a high-power laser in the upper atmosphere [34]. In AO-OCT the guide-star can be generated by the focused imaging beam itself [6, 8] or by a separate static beam that is focused into the sample [7, 35]. The aberration correction in optical microscopy can also be optimized through the use of image metrics such as the peak amplitude of signals, or the

[7] A point source of light generates approximately planar wave fronts far from the source.

spatial frequency content of images. Since this method does not require the use of a wavefront sensor, it is known as sensor-less AO [36–38].

Image metrics have been utilized in CAO to guide the aberration correction in tissue phantoms while using Zernike polynomials to correct the pupil aberrations [14]. A drawback with this approach is that when high-order aberrations are present, the correction requires a large number of Zernike polynomials, potentially requiring computationally expensive optimization. In addition, it has been shown that the more general (non-Zernike) correction using the segmented pupil approach is preferred when imaging in biological samples [39].

Guide-star-based CAO has also been demonstrated in silicone resolution phantoms and in scattering biological tissue by making use of point-like scatterers as guide-stars [30]. By isolating the signal from a guide-star, aberrations of the computed pupil[8] can be detected. The guide-star signal can be isolated via windowing in the spatial domain, and the phase component of the computed pupil aberration can be digitally conjugated in the Fourier domain of the tomogram. Ideally, the window should be large enough to capture all the aberrated signal of the PSF; however, if it is too large, the signal from neighboring scatterers will be included, and the quality of the pupil measurement will be compromised. In a sample with many scatterers, this motivates an iterative approach and the use of a window size sufficient to capture the majority of the aberration-free signal. With each iteration the size of the aberrated PSF reduces, thus bringing more of the PSF signal within the window and resulting in the correction of increasingly higher-order aberrations. The guide-star-based correction is valid over an isotome (or isotomic volume), which is the volumetric extension of the term isoplanatic patch in astronomical AO.

31.4.7 Advantageous Use of Aberrated Optics

In order to determine the effectiveness of CAO and ISAM, it is worth quantifying the depth-dependent resolution and signal-to-noise ratio. Figure 31.9 presents quantitative analysis of these parameters for the data presented in Fig. 31.7, acquired with an astigmatic imaging beam. Notice that the resolution of aberration-corrected OCT exhibits Gaussian-like behavior, whereas aberration-corrected ISAM shows spatially invariant resolution equivalent to that at the aberration-corrected focus. For comparison, the ISAM resolution for imaging with a standard Gaussian beam (i.e., without the cylindrical lens) is seen to be similar to that of ISAM with the astigmatic optical system.

Figure 31.9b shows the depth-dependent signal-to-noise ratio (after ISAM), comparing imaging with the astigmatic system to that of a standard Gaussian beam. The astigmatic system is seen to have a flatter depth-dependent SNR. The

[8] Aberrations of the computed pupil correspond to deviations from the ideal (complex) PSF, $h(x, y, z_f)$, in the objective lens pupil plane, i.e., at depth $z = -z_f$.

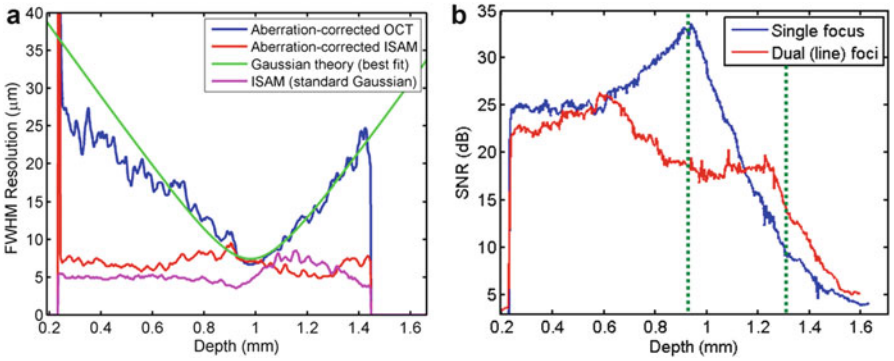

Fig. 31.9 Depth-dependent resolution and signal-to-noise ratio when imaging with an astigmatic beam. Analysis of a 3D dataset of a silicone tissue phantom containing titanium dioxide microparticles, showing (**a**) depth-dependent resolution (along the *x*-axis) vs. depth for the aberration-corrected OCT and ISAM and (**b**) signal-to-noise ratio after ISAM reconstruction, comparing the cylindrical lens setup producing two axially separated line foci to a standard single-focus setup (Figure generated from data presented in [14])

SNR at the focal plane is reduced, but deep in the sample where SNR is low, the signal is boosted. The flatter depth-dependent response can be attributed to preferential light collection from the two axially separated confocal gates.

These results suggest an interesting prospect for high-resolution optical tomography. Since CAO can circumvent the resolution penalty associated with optical aberrations, then it can actually be preferable, from a signal collection perspective, to image with an aberrated optical system. Specifically, the advantage of this CAO signal collection scheme is that it reduces the dynamic range between all imaging planes. A lower dynamic range allows for a system to achieve relatively uniform SNR for all depths. Lower dynamic range can be especially beneficial when measuring with a photodetector having a single integration time for light from multiple acquisition depths. In this integrated approach to interferometric optical tomography, traditional optical hardware and computational techniques play synergistic roles.

31.5 Comparison to Related Techniques and Acquisition Geometries

CAO and ISAM as described above take advantage of the fact that the data available are coherent. That is, the measurement provides a means to infer the complex optical field at the detector. This is important as the fundamental laws of physics describe the behaviors of fields, but do not uniquely determine the behavior of intensities. While intensities may always be computed from fields, the converse is not generally true. Access to the fields not only allows us to do in

post-processing many things normally done with physical optical elements, but also things impossible with physical optical elements, for example, the reconstructions in ISAM with in-principle unlimited depth-of-field. Below some related techniques are discussed.

31.5.1 Holographic Reconstruction and Aberration Correction

Digital holography provides access to the complex optical field in the plane of measurement. This allows for the calculation of the field that would have been measured in any other plane separated from the measurement plane by free-space. Moreover, it allows the calculation of the field that would result from the insertion of additional optical elements such as lenses, all accomplished in post-processing [40, 41]. For example, the field may be refocused to bring into focus planes that were defocused at the expense of defocusing planes that had been in-focus. Without further information to section the sample in three dimensions, the signals from the in-focus plane and the out-of-focus planes appear in superposition in the resultant image (traditional digital holography does not employ low-coherence depth discrimination). However, the focal plane can be thus scanned through the object and, under certain assumptions about the sample,[9] can numerically provide an extended depth of focus [42].

Holoscopy is a broadband digital holographic technique that utilizes a swept laser source to record multiple holograms over a broad optical bandwidth [33]. Three-dimensional object structure is encoded in the 3D data (which can be written as a function of two transverse dimensions and wavenumber), much as in wide-field OCT. Here the data are sufficient to distinguish the signals arising from different planes in the sample, and so numerical refocusing can bring into focus the structure of the sample in one plane without corruption of the image by superposed defocused images from other planes. In 3D tomographic imaging, holographic refocusing can be described as the numerical analog of a z-stack, such as in confocal microscopy, where the focus is physically translated through the sample. Spatially invariant resolution can be achieved in holoscopy by synthesizing a z-stack reconstruction by combining separate sequentially numerically focused planes.

It has been recognized that a SD-OCT system can be thought of as a system for digital holographic tomography [43]. Spectral-domain OCT instrumentation, however, combines this aspect of (broadband) holography with the advantages of confocal-type transverse beam scanning to obtain high-quality tomographic images of scattering biological tissue [1, 44]. The use of confocal beam scanning makes OCT well suited to imaging in scattering biological tissues because of its ability to

[9]Holographic reconstructions of solid 3D objects are possible from a 2D holographic dataset since the surface (or *boundary*) of a 3D object is 2D. A 3D dataset is required for 3D reconstruction of the internal structure of scattering samples such as biological tissue.

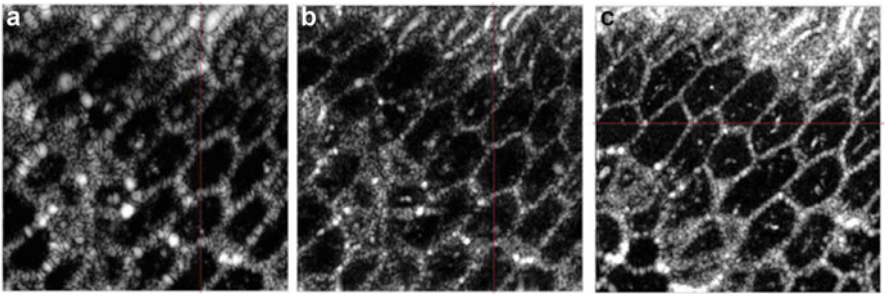

Fig. 31.10 Numerical refocusing of OCT data from an onion. (**a**) En face plane from outside the focal region. (**b**) The same en face after numerical refocusing. (**c**) A representative plane from the focal region (Figure adapted from [47])

reduce cross talk (which is present with spatially coherent full-field illumination) and reject out-of-focus multiple scattering.

The connection between broadband/swept-source holography and SD-OCT is highlighted in [43], the only difference being that SD-OCT data is acquired via point beam scanning over two spatial dimensions. Thus, just as in digital holography and holoscopy, numerical refocusing can be applied to OCT data [45–48], and the focus of the acquired dataset can then be freely adjusted in post-processing. Figure 31.10 shows an onion sample being brought into focus numerically. In Fig. 31.10a, an en face plane outside the focal region suffers from defocus; Fig. 31.10b shows the same en face after numerical refocusing. The optimal reconstruction was determined using entropy as an image metric. Finally, Fig. 31.10c shows a representative en face plane from the focal region.

It should be stressed that ISAM is not a refocusing technique. Rather, it is a reconstruction technique that is an implementation of the solution of the inverse scattering problem for OCT and directly computes sample structure, not the data that would be collected with a different optical system. It may be easily misinterpreted as a method with extended depth-of-field or infinite focal depth. In fact, the notion of a focus has little to do with the reconstruction except as the size of the focal spot pertains to the spatial bandwidth of the system. Nonetheless, for the end user, the main practical difference between ISAM and numerical refocusing techniques in digital holography is that ISAM provides a simultaneous reconstruction at all depths within the tomogram and is thus significantly more efficient (faster). With numerical focusing, a given shift of the focus (corresponding to a given propagation distance) produces optimal resolution at only a single plane, whereas the ISAM resampling step removes defocus for all depths without the need for multiple numerical focus-shifting operations.

Numerical correction of optical aberrations has also been demonstrated in digital holography [41, 49–52]. Compensation of spherical aberration and astigmatism has been shown for imaging in thin biological samples such as a single cell [49]. However, the benefits of numerical aberration correction have not been demonstrated for

holographic tomography in scattering tissue. This is likely due to cross talk problems, occurring with full-field illumination using spatially coherent illumination [53], that impede progress toward high-quality digital holographic tomography of tissue. Although the majority of the work on holographic aberration correction was performed using monochromatic laser sources, numerical correction of aberrations has also been demonstrated in nonbiological samples at a small number of discrete wavelengths [54, 55] and for broadband holography [56].

31.5.2 Full-Field and Rotational Imaging Geometries

The full-field swept-source imaging geometry is of interest for its potential for rapid data acquisition, where interferometric data is acquired in parallel from the entire sample volume while the illumination wavelength is scanned. An additional benefit is that full-field detection does not result in signal decay with distance from focus inherent to imaging with beam-scanning OCT systems. The solution of the inverse scattering problem via Fourier space resampling has been described for full-field ISAM (FF-ISAM) using swept-source illumination and demonstrated through simulations [57]. This theoretical work has also been extended to the use of optical sources for partially (spatially) coherent illumination [53].

Although the methods of FF-ISAM had been explored theoretically, until recently its experimental implementation remained open. Mimicking the techniques of digital holography, holoscopy was initially performed using numerical refocusing where several independent refocusing steps were applied, and for each step, a small volume of data which was deemed in-focus was extracted.

In order to improve the efficiency of numerical refocusing in holoscopy, a Fourier-domain coordinate warping very similar to FF-ISAM was derived and demonstrated experimentally [58]. By utilizing coordinate warping rather than refocusing, the computational complexity of the reconstruction was significantly reduced, and the full reconstruction can be performed in a single computationally efficient step. Figure 31.11 demonstrates holoscopy on a grape using an effective NA of 0.14. Digital refocusing is computationally expensive, and thus for practical considerations, each en face plane was not individually brought into focus. Instead, $\sim$15 virtual focal planes were used throughout the tomogram, and regions around each virtual focus were chosen to approximate the local neighbourhood, but each refocused volume still suffers from residual defocus (Fig. 31.11c). With the one-step reconstruction, every plane is brought into focus simultaneously, providing a higher-quality reconstruction than refocusing (Fig. 31.11f). With increasing NA, the depth of focus decreases, meaning that for the numerical refocusing method, many more virtual foci are required. In contrast, using a Fourier-domain coordinate warping similar to ISAM, the reconstruction requires the same computation regardless of the NA or depth of focus. Figure 31.12 shows the time improvement of the one-step coordinate warping scheme over numerical refocusing. It shows that at high NAs, the one-step reconstruction can be up to three orders of magnitude faster than 3D object reconstruction via digital refocusing.

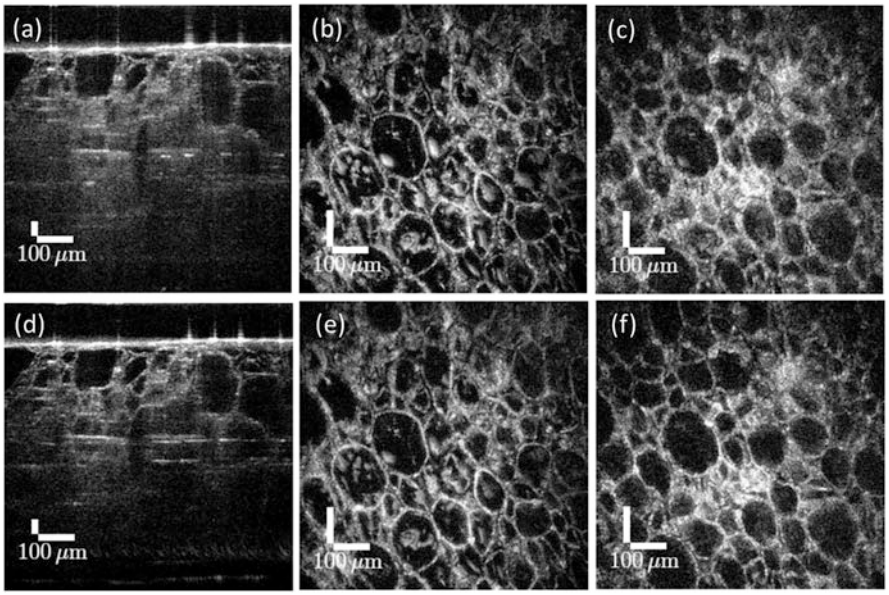

Fig. 31.11 Holographic reconstruction of a grape comparing refocusing to the one-step reconstruction. (**a**) Cross section from the refocused volume. (**b**) En face plane at the virtual focus. (**c**) En face plane 160 μm above the virtual focus. Since each plane is not separately brought into focus, defocus is still visible away from each virtual focus. (**d**) Cross section from the one-step reconstruction. (**e**) En face plane at same location as (**b**). (**f**) En face plane at same location as (**c**). The section does not suffer from defocus since the one-step reconstruction simultaneously brings every plane into focus. The NA was 0.14 (confocal parameter of 28 μm) (Figure adapted from [58])

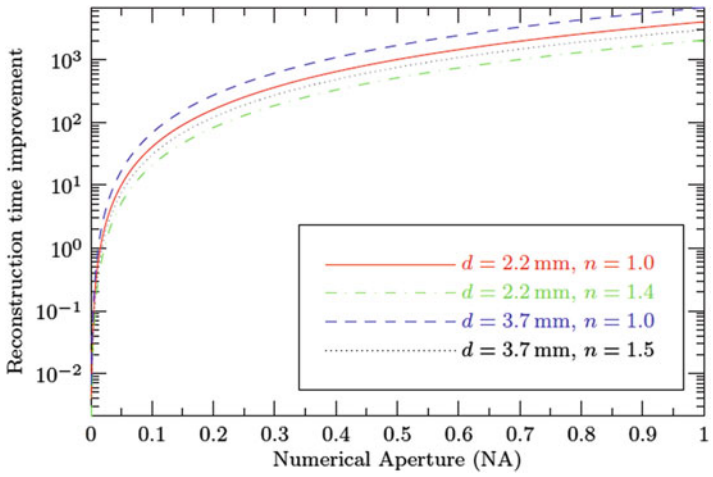

Fig. 31.12 Speed increase of the one-step Fourier-domain coordinate warping over numerical refocusing. The speed of a numerical refocusing reconstruction depends on the depth of focus in the sample and thus depends on both NA and refractive index (From [58])

Another important geometry is the catheter-based or rotational imaging geometry, used for gastrointestinal and cardiovascular OCT applications. The inverse problem for this imaging geometry has been investigated in theory and simulations, where the inversion utilizes the Radon transform and the projection-slice theorem to convert between the polar and Cartesian representation of the Fourier-domain signals [16]. Further work is needed to experimentally demonstrate ISAM and to incorporate CAO, especially since the optical systems utilizing this imaging geometry are known to suffer from astigmatism [59–61].

31.5.3 Fourier Migration Techniques in Other Imaging Fields

The Fourier resampling method in ISAM is similar to the well-known migration-by-Fourier-transform technique introduced by Stolt in 1978 in the field of geophysics [21, 62]. Researchers in many other branches of imaging have adopted a similar approach.

In ultrasound imaging, 3D phase shift migration is a method for implementing a synthetic aperture focusing technique (SAFT) [63]. While the technique can be performed in the time domain with a delay-and-sum approach, the Fourier-domain implementation allows for fast and efficient reconstructions. SAFT originates from a method developed in the 1970s and 1980s from ultrasonic nondestructive testing (NDT) called synthetic aperture imaging (SAI). Some authors have framed the SAFT methods in the context of computed tomography, diffraction tomography, and holography [64, 65]. Others have characterized the transverse and longitudinal resolutions in SAFT [66].

While synthetic aperture radar (SAR) has been developing since the 1960s, the digital processing algorithms were developed later. In the 1980s, a full computer-aided tomographic formulation of spotlight-mode SAR related these algorithms to those developed for medical x-ray computed tomography [67]. Subsequently, a method called the range migration algorithm (RMA) based on the seismic migration theory was developed first for strip map radar and then spotlight-mode radar systems [68–70]. The RMA method utilizes the Stolt transform in the processing chain [71].

31.6 Phase Stability Considerations

31.6.1 Phase Stability Requirements for ISAM and CAO

The ISAM forward model requires that several things are specified or assumed such as a Gaussian beam profile, focus location, and sampling spacing (both transverse and axial) that are necessary. As discussed above, deviations from a Gaussian beam can be taken into account by use of CAO, and the location of the focus can, in principle, be determined through an iterative approach using image metrics to optimize the reconstruction quality [47]. Even if these two assumptions are not completely satisfied or are not fully taken into account, reasonable reconstructions are still

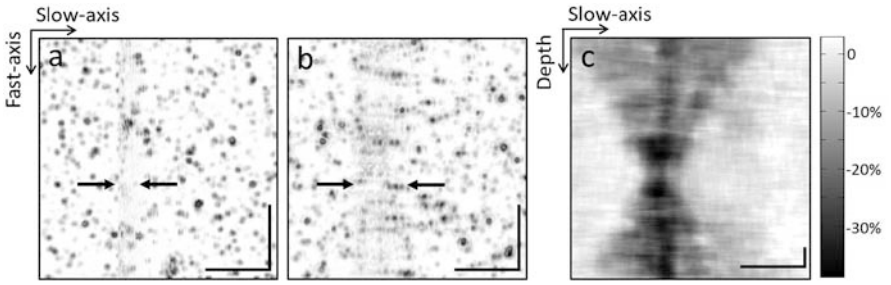

Fig. 31.13 Depth-dependent phase stability requirements. A silicone tissue phantom with sub-resolution titanium dioxide microparticles is used to investigate an ISAM reconstruction following a localized disturbance (a tap to the mounting stage) during image acquisition. (**a**) An en face plane near the optical focus. The effect of the disturbance remains localized (width along the slow axis is approximated by *black arrows*). (**b**) An en face plane 135 μm above optical focus. The blurring due to the localized disturbance now has a larger lateral extent (width along the slow axis is approximated by *black arrows*). (**c**) An image-based representation of the percent change in SNR comparing reconstructions obtained with and without the disturbance. The region which experiences a drop in SNR traces out the optical beam profile and demonstrates the depth-dependent local interrogation time. Scale bar represents 100 μm (Adapted from [74])

possible and may be sufficient for the end application. Ensuring a known relationship between A-scans, though, proves to be more difficult and warrants specific consideration when designing a high-resolution ISAM/CAO system. Often referred to as "phase stability" [72, 73] because of the scale to which it is required (often measured in radians), this term encapsulates many factors such as galvanometer jitter (in 1D or 2D point scanning techniques), wavelength variability (in swept-source techniques), sample and system motion, and environmental vibrations (especially in non-common-path interferometry) which can contribute to the degradation of reconstruction quality in computed imaging techniques such as ISAM and CAO.

As a guideline, a system can be considered locally phase stable if the measurements do not deviate by more than $\lambda/4$ over the specified "local interrogation time." The local interrogation time is defined as the time over which a small region or point in 3D space is probed by the imaging beam [74]. Notice that stability over the local interrogation time will have different implications for different OCT imaging geometries or systems such as swept source, spectral domain, time domain, full field, etc. In a spectral-domain point-scanned geometry, the stability requirements vary as a function of depth (see depiction of beam profile scanning in Fig. 31.13). This is because the local interrogation time will vary depending on the magnitude of the correction desired and thus should be directly proportional to the shape of the blurred or aberrated PSF. In Fig. 31.13, the depth-dependent stability requirement is demonstrated experimentally with an SD-OCT system with central wavelength at 1,330 nm and a bandwidth of 105 nm. Using a silicone-based tissue phantom with sub-resolution TiO_2 scatterers, Fig. 31.13a demonstrates that near the focus, a localized disturbance (in this case a tap to the mounting stage) affects the ISAM reconstruction over a small lateral range. Data collected further from

the focus (135 μm above), as shown in Fig. 31.13b, reveals that the local disturbance affects an extended lateral range. By measuring the local SNR across the slow axis, the region affected by the disturbance (manifested as a drop in SNR when compared to a non-perturbed reconstruction) traces out the imaging beam profile, shown in Fig. 31.13c. This means that when an ISAM reconstruction in a spectral-domain, point-scanned OCT system many Rayleigh ranges from the focus is desired (or if strong aberrations are to be corrected with CAO), local stability over a larger area (longer interrogation time) is required. Interestingly, this also suggests that the stability requirements can also be different for each scanning axis in the presence of an asymmetric PSF, such as is the case with astigmatism.

31.6.2 Obtaining Phase-Stable Data

When designing a high-resolution ISAM/CAO system, both the hardware and software play important roles in obtaining and processing phase-stable data. Phase stability is affected by several major factors: galvanometer jitter, swept-source variability, sample and system (beam-delivery instrument) motion, and environmental vibrations. Discussed here are hardware considerations and post-processing techniques which, together, can overcome these factors to provide the best possible ISAM and CAO reconstructions.

31.6.2.1 Hardware Methods

Dual galvanometer mirrors are typically used in OCT for lateral beam scanning in a raster pattern. The physical construction and mechanical operation of galvanometers make them inherently subject to imperfections and noise. Assuming precise synchronization between mirror scanning and acquisition hardware, the scanned beam pattern for each frame can be divided into two parts, one which is repeatable and common to all frames and the other which represents noise and varies randomly for each frame. Although not required, the repeatable portion is typically made as linear as possible. The second term (the noise) should be made minimal by choice of low-jitter galvanometers. This design choice will also present trade-offs between speed, accuracy, and jitter. In catheter/endoscopic setups [16, 72], a cylindrical coordinate system is used, and thus instead, smooth and reliable motor rotation and pullback methods need to be considered.

In swept-source systems, extra phase instability is associated with the difficulty of repeatedly linearizing the acquired spectrum in wavenumber (though groups have successfully performed other phase-sensitive imaging modalities like Doppler OCT with swept-source systems [75]). Hardware triggers using fiber Bragg gratings have been used to generate a reliable trigger indicating a reference around which the acquired spectrum can be linearized in wavenumber [76].

Sample and beam-delivery system motion likely presents the greatest challenge to computed imaging techniques such as ISAM and CAO. Without the possibility for in vivo use, clinical applications may be very limited. Sample and system

motion can be addressed with hardware in two major ways. First, if possible, the sample movement can be restricted by use of sample-specific mounting stages. However, in many cases (such as when imaging the human eye), either contact with the sample is not possible or motion is involuntary and inevitable. Second, by scanning faster or imaging a smaller region, it may be possible to retain phase stability. For a spectral-domain system, this means a faster line-scan camera which can reach speeds faster than 90,000 A-scans/second [30, 77]. For a swept-source system, speeds are typically limited by the swept laser source, which can achieve MHz rates [78, 79]. However, because of the physical motion of swept-source elements (e.g., scanning Fabry-Perot filters or rotating polygon mirrors), faster scanning may also be associated with greater mechanical (and therefore phase) instability. Faster scanning, in general, results in shorter exposure times and thus can result in a trade-off between imaging sensitivity and speed.

Finally, environmental factors can lead to instability in the acquired data. In many OCT/ISAM/CAO setups, separate paths are used for the sample and reference arms. Therefore, any slight change to one arm and not the other such as fiber bending, air currents, or mechanical vibrations that modulate the optical path difference will affect the phase stability. Optical path difference fluctuations are a special case of phase instability where, as opposed to sample motion or galvanometer jitter, the effect is entirely in the axial dimension. To mitigate this effect, a common-path setup can be used where both the sample and reference beams overlap (and thus are subject to the same environmental factors) for nearly their entire propagation distance. In the next section, an alternative software or hardware/software combination, which can be used to address this issue, is discussed.

31.6.2.2 Software Methods

For a non-common-path system, a phase reference can be used to remove any optical path difference fluctuations throughout the full 3D dataset. Previously, a coverslip has been used to provide a clean, flat surface along which there should be little phase fluctuations [73, 80]. Mathematically, the phase fluctuations of the acquired data are written as a function of the wavenumber and expanded to the first two terms using a Taylor series expansion around the central wavenumber, k_0:

$$\phi'(x,y;k) = \phi'(x,y;k_0) + (k-k_0)\frac{\partial\phi'}{\partial k}\bigg|_{k=k_0} + \ldots \tag{31.25}$$

By performing a linear fit along the unwrapped phase, the $\phi'(x, y; k_0)$ and $\frac{\partial\phi'}{\partial k}\Big|_{k=k_0}$ can be determined and applied to the acquired data, $S(x, y, k)$, as $S'(x,y;k) = S(x,y;k)e^{-i\phi'(x,y;k)}$. Figure 31.14 shows an experimental validation of this method. Three-dimensional imaging was performed over 800 × 800 μm (transverse) ×2,000 μm (axial) at 4 B-mode frames/s, on a system with 800 nm central wavelength and 100 nm bandwidth and a sample arm NA of 0.05. First, in

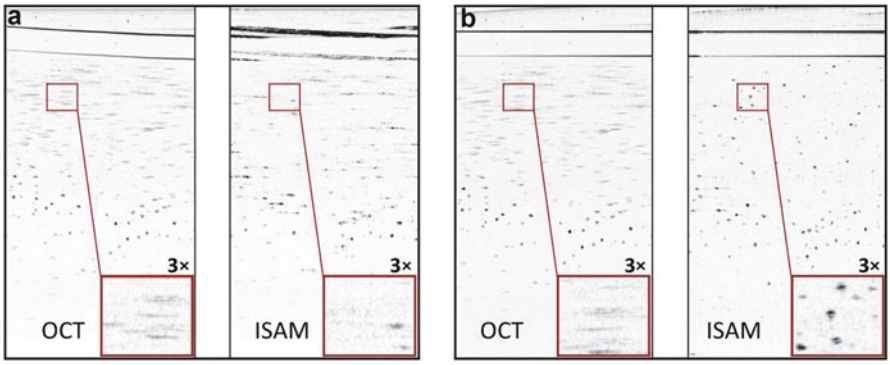

Fig. 31.14 Silicone-based tissue phantom demonstrating the use of phase correction. (**a**) Far from focus, even after ISAM has been applied, point scatterers still remain blurred and are not well resolved. (**b**) After using a coverslip for phase correction, full constructive interference is recovered and point scatterers are well defined. The images shown were extracted from a 3D dataset. Phase correction was applied to the entire 3D dataset and the cross-sectional frames shown are oriented along the slow-scanning axis. Image dimensions are 800 μm (transverse) ×2,000 μm (depth) (From [81])

Fig. 31.14a, ISAM was performed without phase correction. Far from focus, full constructive interference was not obtained. After phase correction using a surface coverslip as a phase reference (Fig. 31.14b), the sub-resolution scatterers are fully revealed along the entire imaging depth.

With the addition of a fiber stretcher (or similar phase modulator) to induce a desired optical path change, axial phase disturbances have also been corrected using an iterative "phase equalization" method [48]. For more generalized phase correction, both axial and transverse movements need to be compensated. Post-acquisition, cross-correlation algorithms have previously been utilized in various averaging techniques [82] and have also been shown to correct for transverse motion or instabilities between acquired frames [14].

Common to many of these techniques, though, is a required high spatial overlap between A-scans. Ensuring a large oversampling factor, though, either greatly reduces the acquired field of view or increases the acquisition time (thus making the data inherently more susceptible to phase noise). Care should be taken to balance all the benefits and drawbacks of each method.

31.7 Practical Limitations and Opportunities

The phase stability requirements outlined in Sect. 31.6.1 can determine the reconstruction quality of dynamic samples or of static samples measured at slower acquisition rates. The first case presents the more serious limitation. Sample or system motion on the order of the interrogation time can disrupt the expected phase

relationship during the sequential or multiplexed acquisition of transverse spatial frequencies in the away-from-focus regime (see Fig. 31.13). For a given set of scanning parameters (A-scan rate, transverse sampling period, and range), the imaging NA and overall depth of reconstruction cannot be chosen arbitrarily. There is a trade-off between the imaging NA and the absolute distance from focus that can be reconstructed without degradation resulting from phase instabilities. This is because at a given distance from focus, the interrogation time is directly proportional to the synthetic aperture length, which in turn is proportional to the imaging NA. For the measurement of dynamic samples, this places an upper bound on the imaging NA for a given set of scanning parameters. An increase of the imaging speed (A-scan rate) by a factor β will reduce the interrogation time by a factor of $1/\beta$ and thereby increase the upper bound on NA by a factor β. Preliminary work suggests that with the recent developments in high-speed acquisition, in vivo ISAM and CAO are feasible.

The reduction in signal collection with increasing distance from focus becomes a serious problem for cellular resolution tomographic reconstruction over the typical imaging depth ranges in OCT. This is a natural consequence of the reduction in the width of the axial confocal gate with increasing NA, and for a given NA, it limits the overall depth range of the reconstruction. The decay of signal strength with distance away from focus has a $1/|z|$ dependence [15], resulting in an increase of the required dynamic range of the instrument as imaging NA and distance from focus increase. For example, at 1 mm away from the focus with an imaging NA of 0.4, the signal collection relative to the focus is attenuated by five orders of magnitude (see Fig. 6 in [15]). Therefore, in order to image the highest scattering signals at the focus as well as weak scattering signals at a depth of 1 mm (assuming a 40 dB dynamic range of signals from typical tissues), the dynamic range of the instrument is required to be on the order of 90 dB. If the NA is reduced to 0.05, the dynamic range requirement reduces to 70 dB (see Fig. 6 in [15]). One method to equalize the signal collection vs. depth is to acquire multiple datasets, each with a different focus depth (these datasets may be separated by many Rayleigh ranges from each other). This solution comes at the expense of increased acquisition time, which could lead to motion artifacts between volumetric datasets. Another method is to strategically position the focus deep within the sample to enhance the collection of weak signals from greater depths within the sample. This solution also counteracts the exponential attenuation that the incident light already experiences with increasing depth into the sample, effectively reducing the required dynamic range. Finally, exploiting synergistic roles between aberrated optics and computational methods (see Sect. 31.4.7) can also reduce the dynamic range requirements without affecting the imaging NA or resolution.

Multiple scattering and/or sample-induced aberrations are the major limiting factors on imaging depth in OCT. In OCM, which can achieve cellular transverse resolution through the use of higher-NA optics, it is thought that aberrations represent a more severe limitation to imaging depth than that imposed by multiple scattering [3]. The assumption of single scattering, i.e., the first Born approximation, is used to linearize the inverse scattering problem [24]. When this assumption breaks down,

the accuracy of both ISAM and OCT is degraded, leading to an imaging depth that is limited by the collection of multiple scattering [23, 83, 84]. Although ISAM and CAO share the multiple scattering limitation with OCT/OCM, recent work in hardware-based wavefront control suggests that pupil corrections based on generalized segmented pupil approaches can utilize the turbidity of the medium to provide sub-diffraction resolution [85–87] and enable improved focusing deep into tissue [88]. The phase conjugation of wavefront aberrations, shown to be equivalent to a time reversal operation [89], has been demonstrated for imaging or focusing in optics and ultrasonics [89–93]. These approaches to hardware-based wavefront control provide promising future areas of investigation for CAO.

Finally, a limitation that is not obvious at an imaging NA below about 0.2 is that of vignetting. Scatterers near the edge of the transverse field of view are probed by a truncated synthetic aperture, which results in a reduction of signal amplitude and an attenuation of high lateral spatial frequency components. This problem becomes apparent further away from focus and nearer to the edge of the lateral field of view. Vignetting can be addressed by increasing the transverse field of view by half the maximum synthetic aperture length (this should be done for the synthetic aperture length at the maximum distance from focus that is desired in the reconstruction).

31.8 Summary and Future Outlook

ISAM and CAO enable computational reconstruction of sparse and highly scattering samples in broadband optical interferometric tomography. ISAM is a solution to the inverse scattering problem that utilizes Fourier space resampling to reconstruct areas typically regarded as out of focus in OCT, overcoming the perceived trade-off between transverse resolution and depth of focus. CAO provides post-acquisition correction of optical aberrations for OCT imaging near the optical focus or for far-from-focus ISAM reconstructions. The underlying theory behind ISAM was connected to the principles of diffraction tomography. In particular, ISAM resampling is now understood from the Ewald sphere description of the process of optical scattering and signal detection in OCT. A general signal model was also presented for the case where severe optical aberrations can restrict the volumes of stationarity (or space invariance) in 3D tomography. Approximations were presented for specific situations where 2D or 3D space invariance holds, since these situations can readily be (approximately) achieved in practice. Methods for the optimization of aberrations in CAO, based on previous approaches in hardware wavefront control that utilized guide-stars or image metrics, were presented.

Results in tissue phantoms demonstrated the correction of astigmatism with CAO and the correction of defocus with ISAM over a depth range spanning tens of Rayleigh ranges. Cross-validation of ISAM with OCT in phantoms and biological tissue demonstrated that ISAM can provide similar resolution as “in-focus” OCT. The anatomical reconstruction accuracy of ISAM was validated in human breast tissue through a comparison with the corresponding histology. The validity of space-invariant approximations was demonstrated with CAO and ISAM

reconstructions of tissue phantoms and biological tissue. Related work by other groups in OCT and holography was highlighted, and experimental results were presented to demonstrate the phase stability requirements of ISAM and CAO.

The combination of ultrahigh axial resolution [94] with ISAM and CAO presents an opportunity for unprecedented 3D visualization of tissue. Traditional diagnosis of neoplastic changes is based on cellular features such as atypia of cell nuclei, accelerated rate of growth, and local invasion. This motivates the pursuit of isotropic cellular-level resolution over a large depth-of-field. The development of high-NA instrumentation to achieve this presents both challenges and opportunities for ISAM and CAO.

Imaging applications where high isotropic resolution over a large depth-of-field could add significant value include optical biopsy, image-guided surgery, and the study of tumorigenesis. One of the important capabilities for clinical applications of ISAM and CAO is the ability to perform real-time tomography in vivo. Current work is aimed at real-time in vivo ISAM and parallelization of 3D ISAM algorithms using GPU-based hardware architectures. In addition to the enhanced diagnostic value of high isotropic resolution, real-time 3D reconstruction of cellular-scale tissue structure could translate the diagnostic functions currently available in the pathology lab toward real-time point-of-care scenarios. Isotropic cellular resolution could also provide valuable insights on the fundamental question of how tumors grow and spread, both in cell cultures and scaffolds in vitro, as well as in animal models in vivo. In contrast to histopathology, where tissue excision provides a "snapshot" of tissue, ISAM with CAO could be used to monitor tumor development in three dimensions within the same animal.

The impact of computational methods in high-resolution optical tomography is expanding. The work reported in this chapter provides evidence that optical imaging science is moving toward an integrated approach where optical hardware and computation play synergistic roles. An interesting possibility with CAO and ISAM is that imaging systems can now be designed to optimize signal collection over an extended volume rather than minimizing aberrations at a given depth. The computed pupil in CAO provides the flexibility of a large number of independent segments, allowing the correction of large phase gradients without the limiting requirement of having to determine the phase correction at the time of imaging.

Future work will investigate CAO for correcting space-variant and sample-induced aberrations and the potential advantages of using a computed pupil for phase conjugation (time reversal) imaging deep into turbid media. These investigations will be able to quantify the dimensions of isotomic volumes in tissue and help to understand the relative impact of multiple scattering and aberrations on imaging depth in high-resolution tomography. The pursuit of isotropic cellular resolution over the depth ranges typically achieved in OCT is a challenging and open area for the application of ISAM and CAO. An application area that could significantly benefit from CAO is retinal OCT (e.g., the imaging of rods/cones). Further work is also needed to enable ISAM and CAO for catheter- and needle-based OCT applications, e.g., for the computational correction of astigmatism typically encountered with these imaging geometries. Ultimately, studies on the improvement of sensitivity and

specificity to diagnose diseases, and/or the ability to longitudinally track disease progression, will determine the role of ISAM and CAO in biomedicine.

Acknowledgments We thank all our colleagues for their contributions to the research presented in this chapter. Recent studies and results presented here were funded in part by grants from the US National Institutes of Health (R01 EB012479 and R01 EB013723, S.A.B..). Additional information can be found at http://biophotonics.illinois.edu and http://optics.beckman.illinois.edu.

References

1. J.A. Izatt, M.R. Hee, G.M. Owen, E.A. Swanson, J.G. Fujimoto, Optical coherence microscopy in scattering media. Opt. Lett. **19**, 590–592 (1994)
2. S.A. Boppart, B.E. Bouma, C. Pitris, J.F. Southern, M.E. Brezinski, J.G. Fujimoto, In vivo cellular optical coherence tomography imaging. Nat. Med. **4**, 861–865 (1998)
3. C. Zhou, D.W. Cohen, Y.H. Wang, H.C. Lee, A.E. Mondelblatt, T.H. Tsai, A.D. Aguirre, J.G. Fujimoto, J.L. Connolly, Integrated optical coherence tomography and microscopy for ex vivo multiscale evaluation of human breast tissues. Cancer Res. **70**, 10071–10079 (2010)
4. M.J. Cobb, X.M. Liu, X.D. Li, Continuous focus tracking for real-time optical coherence tomography. Opt. Lett. **30**, 1680–1682 (2005)
5. V.J. Srinivasan, H. Radhakrishnan, J.Y. Jiang, S. Barry, A.E. Cable, Optical coherence microscopy for deep tissue imaging of the cerebral cortex with intrinsic contrast. Opt. Express **20**, 2220–2239 (2012)
6. B. Hermann, E.J. Fernandez, A. Unterhuber, H. Sattmann, A.F. Fercher, W. Drexler, P.M. Prieto, P. Artal, Adaptive-optics ultrahigh-resolution optical coherence tomography. Opt. Lett. **29**, 2142–2144 (2004)
7. Y. Zhang, J.T. Rha, R.S. Jonnal, D.T. Miller, Adaptive optics parallel spectral domain optical coherence tomography for imaging the living retina. Opt. Express **13**, 4792–4811 (2005)
8. Y. Zhang, B. Cense, J. Rha, R.S. Jonnal, W. Gao, R.J. Zawadzki, J.S. Werner, S. Jones, S. Olivier, D.T. Miller, High-speed volumetric imaging of cone photoreceptors with adaptive optics spectral-domain optical coherence tomography. Opt. Express **14**, 4380–4394 (2006)
9. T.S. Ralston, D.L. Marks, P.S. Carney, S.A. Boppart, Interferometric synthetic aperture microscopy. Nat. Phys. **3**, 129–134 (2007)
10. T.S. Ralston, G.L. Charvat, S.G. Adie, B.J. Davis, P.S. Carney, S.A. Boppart, Interferometric synthetic aperture microscopy: microscopic laser radar. Opt. Photon. News **21**, 32–38 (2010)
11. T.S. Ralston, D.L. Marks, P.S. Carney, S.A. Boppart, Real-time interferometric synthetic aperture microscopy. Opt. Express **16**, 2555–2569 (2008)
12. B.J. Davis, D.L. Marks, T.S. Ralston, P.S. Carney, S.A. Boppart, Interferometric synthetic aperture microscopy: computed imaging for scanned coherent microscopy. Sensors **8**, 3903–3931 (2008)
13. S.G. Adie, B.W. Graf, A. Ahmad, B. Dabarsyah, S.A. Boppart, P.S. Carney, The impact of aberrations on object reconstruction with interferometric synthetic aperture microscopy, in *Proceedings of the SPIE* (*Photonics West*), San Francisco, 2011, p. 78891O (8 pp)
14. S.G. Adie, B.W. Graf, A. Ahmad, P.S. Carney, S.A. Boppart, Computational adaptive optics for broadband optical interferometric tomography of biological tissue. Proc. Natl. Acad. Sci. U. S. A. **109**, 7175–7180 (2012)
15. B.J. Davis, S.C. Schlachter, D.L. Marks, T.S. Ralston, S.A. Boppart, P.S. Carney, Nonparaxial vector-field modeling of optical coherence tomography and interferometric synthetic aperture microscopy. J. Opt. Soc. Am. A **24**, 2527–2542 (2007)
16. D.L. Marks, T.S. Ralston, P.S. Carney, S.A. Boppart, Inverse scattering for rotationally scanned optical coherence tomography. J. Opt. Soc. Am. A **23**, 2433–2439 (2006)

17. B. Richards, E. Wolf, Electromagnetic diffraction in optical systems. II. Structure of the image field in an aplanatic system. Proc. R. Soc. Lond. Ser. A **253**, 358–379 (1959)
18. J.W. Goodman, *Introduction to Fourier Optics*, 2nd edn. (McGraw-Hill, San Francisco, 1996)
19. S.M. Feng, H.G. Winful, Physical origin of the Gouy phase shift. Opt. Lett. **26**, 485–487 (2001)
20. L. Mandel, E. Wolf, *Optical Coherence and Quantum Optics* (Cambridge University Press, Cambridge, MA, 1996)
21. R.H. Stolt, Migration by Fourier-transform. Geophysics **43**, 23–48 (1978)
22. T.S. Ralston, D.L. Marks, P.S. Carney, S.A. Boppart, Inverse scattering for optical coherence tomography. J. Opt. Soc. Am. A **23**, 1027–1037 (2006)
23. A.F. Fercher, W. Drexler, C.K. Hitzenberger, T. Lasser, Optical coherence tomography – principles and applications. Rep. Prog. Phys. **66**, 239–303 (2003)
24. M. Born, E. Wolf, *Principles of Optics: Electromagnetic Theory of Propagation, Interference and Diffraction of Light*, 7th edn. (Cambridge University Press, New York, 1999)
25. T.S. Ralston, S.G. Adie, D.L. Marks, S.A. Boppart, P.S. Carney, Cross-validation of interferometric synthetic aperture microscopy and optical coherence tomography. Opt. Lett. **35**, 1683–1685 (2010)
26. B.R. Frieden, Optical transfer of the three-dimensional object. J. Opt. Soc. Am. **57**, 56–66 (1967)
27. J.M. Beckers, Adaptive optics for astronomy – principles, performance, and applications. Annu. Rev. Astron. Astrophys. **31**, 13–62 (1993)
28. D. Malacara, *Optical Shop Testing*, 3rd edn. (Wiley, Hoboken, 2007)
29. C.W. McCutchen, Generalized aperture and the three-dimensional diffraction image. J. Opt. Soc. Am. **54**, 240–244 (1964)
30. S.G. Adie, N.D. Shemonski, B.W. Graf, A. Ahmad, P.S. Carney, S.A. Boppart, Guide-star-based computational adaptive optics for broadband interferometric tomography. Appl. Phys. Lett. **101**, 221117 (2012)
31. A.F. Fercher, C.K. Hitzenberger, M. Sticker, R. Zawadzki, B. Karamata, T. Lasser, Numerical dispersion compensation for partial coherence interferometry and optical coherence tomography. Opt. Express **9**, 610–615 (2001)
32. D.L. Marks, A.L. Oldenburg, J.J. Reynolds, S.A. Boppart, Autofocus algorithm for dispersion correction in optical coherence tomography. Appl. Opt. **42**, 3038–3046 (2003)
33. D. Hillmann, C. Luhrs, T. Bonin, P. Koch, G. Huttmann, Holoscopy-holographic optical coherence tomography. Opt. Lett. **36**, 2390–2392 (2011)
34. C.E. Max, S.S. Olivier, H.W. Friedman, K. An, K. Avicola, B.V. Beeman, H.D. Bissinger, J.M. Brase, G.V. Erbert, D.T. Gavel, K. Kanz, M.C. Liu, B. Macintosh, K.P. Neeb, J. Patience, K.E. Waltjen, Image improvement from a sodium-layer laser guide star adaptive optics system. Science **277**, 1649–1652 (1997)
35. E.J. Fernandez, B. Hermann, B. Povazay, A. Unterhuber, H. Sattmann, B. Hofer, P.K. Ahnelt, W. Drexler, Ultrahigh resolution optical coherence tomography and pancorrection for cellular imaging of the living human retina. Opt. Express **16**, 11083–11094 (2008)
36. M.J. Booth, Wave front sensor-less adaptive optics: a model-based approach using sphere packings. Opt. Express **14**, 1339–1352 (2006)
37. D. Debarre, M.J. Booth, T. Wilson, Image based adaptive optics through optimisation of low spatial frequencies. Opt. Express **15**, 8176–8190 (2007)
38. D. Debarre, E.J. Botcherby, T. Watanabe, S. Srinivas, M.J. Booth, T. Wilson, Image-based adaptive optics for two-photon microscopy. Opt. Lett. **34**, 2495–2497 (2009)
39. N. Ji, D.E. Milkie, E. Betzig, Adaptive optics via pupil segmentation for high-resolution imaging in biological tissues. Nat. Methods **7**, 141–147 (2010)
40. U. Schnars, W.P.O. Juptner, Digital recording and numerical reconstruction of holograms. Meas. Sci. Technol **13**, R85–R101 (2002)
41. T. Colomb, F. Montfort, J. Kuhn, N. Aspert, E. Cuche, A. Marian, F. Charriere, S. Bourquin, P. Marquet, C. Depeursinge, Numerical parametric lens for shifting, magnification, and

complete aberration compensation in digital holographic microscopy. J. Opt. Soc. Am. A **23**, 3177–3190 (2006)
42. T. Colomb, N. Pavillon, J. Kuhn, E. Cuche, C. Depeursinge, Y. Emery, Extended depth-of-focus by digital holographic microscopy. Opt. Lett. **35**, 1840–1842 (2010)
43. L.F. Yu, Z.P. Chen, Digital holographic tomography based on spectral interferometry. Opt. Lett. **32**, 3005–3007 (2007)
44. W. Drexler, J.G. Fujimoto, *Optical Coherence Tomography: Technology and Applications* (Springer, New York, 2009)
45. L.F. Yu, B. Rao, J. Zhang, J.P. Su, Q. Wang, S.G. Guo, Z.P. Chen, Improved lateral resolution in optical coherence tomography by digital focusing using two-dimensional numerical diffraction method. Opt. Express **15**, 7634–7641 (2007)
46. Y. Yasuno, J.I. Sugisaka, Y. Sando, Y. Nakamura, S. Makita, M. Itoh, T. Yatagai, Non-iterative numerical method for laterally superresolving Fourier domain optical coherence tomography. Opt. Express **14**, 1006–1020 (2006)
47. G.Z. Liu, Z.W. Zhi, R.K.K. Wang, Digital focusing of OCT images based on scalar diffraction theory and information entropy. Biomed. Opt. Express **3**, 2774–2783 (2012)
48. A.A. Moiseev, G.V. Gelikonov, D.A. Terpelov, P.A. Shilyagin, V.M. Gelikonov, Digital refocusing for transverse resolution improvement in optical coherence tomography. Laser Phys. Lett. **9**, 826–832 (2012)
49. L. Miccio, D. Alfieri, S. Grilli, P. Ferraro, A. Finizio, L. De Petrocellis, S.D. Nicola, Direct full compensation of the aberrations in quantitative phase microscopy of thin objects by a single digital hologram. Appl. Phys. Lett. **90**, 041104 (2007)
50. S.T. Thurman, J.R. Fienup, Phase-error correction in digital holography. J. Opt. Soc. Am. A **25**, 983–994 (2008)
51. S.T. Thurman, J.R. Fienup, Correction of anisoplanatic phase errors in digital holography. J. Opt. Soc. Am. A **25**, 995–999 (2008)
52. A.E. Tippie, A. Kumar, J.R. Fienup, High-resolution synthetic-aperture digital holography with digital phase and pupil correction. Opt. Express **19**, 12027–12038 (2011)
53. D.L. Marks, B.J. Davis, S.A. Boppart, P.S. Carney, Partially coherent illumination in full-field interferometric synthetic aperture microscopy. J. Opt. Soc. Am. A **26**, 376–386 (2009)
54. P. Ferraro, S. Grilli, L. Miccio, D. Alfieri, S. De Nicola, A. Finizio, B. Javidi, Full color 3-D imaging by digital holography and removal of chromatic aberrations. J. Disp. Technol. **4**, 97–100 (2008)
55. S. De Nicola, A. Finizio, G. Pierattini, D. Alfieri, S. Grilli, L. Sansone, P. Ferraro, Recovering correct phase information in multiwavelength digital holographic microscopy by compensation for chromatic aberrations. Opt. Lett. **30**, 2706–2708 (2005)
56. A.S.G. Singh, T. Schmoll, B. Javidi, R.A. Leitgeb, In-line reference-delayed digital holography using a low-coherence light source. Opt. Lett. **37**, 2631–2633 (2012)
57. D.L. Marks, T.S. Ralston, S.A. Boppart, P.S. Carney, Inverse scattering for frequency-scanned full-field optical coherence tomography. J. Opt. Soc. Am. A **24**, 1034–1041 (2007)
58. D. Hillmann, G. Franke, C. Lührs, P. Koch, G. Hüttmann, Efficient holoscopy image reconstruction. Opt. Express **20**, 21247–21263 (2012)
59. J.F. Xi, L. Huo, Y.C. Wu, M.J. Cobb, J.H. Hwang, X.D. Li, High-resolution OCT balloon imaging catheter with astigmatism correction. Opt. Lett. **34**, 1943–1945 (2009)
60. D. Lorenser, X. Yang, R.W. Kirk, B.C. Quirk, R.A. McLaughlin, D.D. Sampson, Ultrathin side-viewing needle probe for optical coherence tomography. Opt. Lett. **36**, 3894–3896 (2011)
61. W. Jung, W. Benalcazar, A. Ahmad, U. Sharma, H. Tu, S.A. Boppart, Numerical analysis of gradient index lens-based optical coherence tomography imaging probes. J. Biomed. Opt. **15**, 066027 (2010)
62. R. Graebner, C. Wason, H. Meinardus, Three-dimensional methods in seismic exploration. Science **211**, 535–540 (1981)
63. A. Barkefors, *3D Synthetic Aperture Technique for Ultrasonic Imaging*, Masters, Signals and Systems Group, Uppsala University, 2010

64. K.J. Langenberg, M. Berger, T. Kreutter, K. Mayer, V. Schmitz, Synthetic aperture focusing technique signal-processing. NDT Int. **19**, 177–189 (1986)
65. K. Mayer, R. Marklein, K.J. Langenberg, T. Kreutter, Three-dimensional imaging-system based on Fourier-transform synthetic aperture focusing technique. Ultrasonics **28**, 241–255 (1990)
66. R.N. Thomson, Transverse and longitudinal resolution of the synthetic aperture focusing technique. Ultrasonics **22**, 9–15 (1984)
67. D.C. Munson, J.D. Obrien, W.K. Jenkins, A tomographic formulation of spotlight-mode synthetic aperture radar. Proc. IEEE **71**, 917–925 (1983)
68. F. Rocca, C. Cafforio, C. Prati, Synthetic aperture radar – a new application for wave-equation techniques. Geophys. Prospect. **37**, 809–830 (1989)
69. C. Cafforio, C. Prati, E. Rocca, SAR data focusing using seismic migration techniques. IEEE Trans. Aerosp. Electron. Syst. **27**, 194–207 (1991)
70. C. Cafforio, C. Prati, F. Rocca, Full resolution focusing of SEASAT SAR images in the frequency-wave number domain. Int. J. Remote Sens. **12**, 491–510 (1991)
71. W.G. Carrara, R.M. Majewski, R.S. Goodman, *Spotlight Synthetic Aperture Radar: Signal Processing Algorithms* (Artech House, Norwood, 1995)
72. C. Sun, F. Nolte, K.H.Y. Cheng, B. Vuong, K.K.C. Lee, B.A. Standish, B. Courtney, T.R. Marotta, A. Mariampillai, V.X.D. Yang, In vivo feasibility of endovascular Doppler optical coherence tomography. Biomed. Opt. Express **3**, 2600–2610 (2012)
73. T.S. Ralston, D.L. Marks, P.S. Carney, S.A. Boppart, Phase stability technique for inverse scattering in optical coherence tomography, in *Biomedical Imaging: Nano to Macro, 2006. 3rd IEEE International Symposium on*, 2006, p. 578–581
74. N.D. Shemonski, S.G. Adie, Y-Z Liu, F.A. South, P.S. Carney, S.A. Boppart, Stability in computed optical interferometric tomography (Part I): Stability requirements. Opt. Express 22, 19183–19197 (2014)
75. G. Liu, L. Chou, W. Jia, W. Qi, B. Choi, Z. Chen, Intensity-based modified Doppler variance algorithm: application to phase instable and phase stable optical coherence tomography systems. Opt. Express **19**, 11429–11440 (2011)
76. T. Meng-Tsan, L. Ya-Ju, Y. Yung-Chi, K. Che-Yen, C. Feng-Yu, J.D. Lee, Quantitative phase imaging with swept-source optical coherence tomography for optical measurement of nanostructures. Photon. Technol. Lett. IEEE **24**, 640–642 (2012)
77. W. Choi, B. Baumann, J.J. Liu, A.C. Clermont, E.P. Feener, J.S. Duker, J.G. Fujimoto, Measurement of pulsatile total blood flow in the human and rat retina with ultrahigh speed spectral/Fourier domain OCT. Biomed. Opt. Express **3**, 1047–1061 (2012)
78. W. Wieser, T. Klein, D.C. Adler, F. Trépanier, C.M. Eigenwillig, S. Karpf, J.M. Schmitt, R. Huber, Extended coherence length megahertz FDML and its application for anterior segment imaging. Biomed. Opt. Express **3**, 2647–2657 (2012)
79. K. Goda, A. Fard, O. Malik, G. Fu, A. Quach, B. Jalali, High-throughput optical coherence tomography at 800 nm. Opt. Express **20**, 19612–19617 (2012)
80. C. Yang, A. Wax, M.S. Hahn, K. Badizadegan, R.R. Dasari, M.S. Feld, Phase-referenced interferometer with subwavelength and subhertz sensitivity applied to the study of cell membrane dynamics. Opt. Lett. **26**, 1271–1273 (2001)
81. S.G. Adie, B.J. Davis, T.S. Ralston, D.L. Marks, P.S. Carney, S.A. Boppart, Interferometric synthetic aperture microscopy, in *Biomedical Applications of Light Scattering*, ed. by A. Wax, V. Backman (McGraw-Hill, New York, 2009), pp. 77–111
82. P.H. Tomlins, R.K. Wang, Digital phase stabilization to improve detection sensitivity for optical coherence tomography. Meas. Sci. Technol. **18**, 3365–3372 (2007)
83. Y.T. Pan, R. Birngruber, R. Engelhardt, Contrast limits of coherence-gated imaging in scattering media. Appl. Opt. **36**, 2979–2983 (1997)
84. M.J. Yadlowsky, J.M. Schmitt, R.F. Bonner, Multiple-scattering in optical coherence microscopy. Appl. Opt. **34**, 5699–5707 (1995)
85. I.M. Vellekoop, A. Lagendijk, A.P. Mosk, Exploiting disorder for perfect focusing. Nat. Photonics **4**, 320–322 (2010)

86. Y. Choi, T.D. Yang, C. Fang-Yen, P. Kang, K.J. Lee, R.R. Dasari, M.S. Feld, W. Choi, Overcoming the diffraction limit using multiple light scattering in a highly disordered medium. Phys. Rev. Lett. **107**, 023902 (2011)
87. E.G. van Putten, D. Akbulut, J. Bertolotti, W.L. Vos, A. Lagendijk, A.P. Mosk, Scattering lens resolves sub-100 nm structures with visible light. Phys. Rev. Lett. **106**, 193905 (2011)
88. R. Fiolka, K. Si, M. Cui, Complex wavefront corrections for deep tissue focusing using low coherence backscattered light. Opt. Express **20**, 16532–16543 (2012)
89. M. Fink, D. Cassereau, A. Derode, C. Prada, P. Roux, M. Tanter, J.L. Thomas, F. Wu, Time-reversed acoustics. Rep. Prog. Phys. **63**, 1933–1995 (2000)
90. Z. Yaqoob, D. Psaltis, M.S. Feld, C.H. Yang, Optical phase conjugation for turbidity suppression in biological samples. Nat. Photonics **2**, 110–115 (2008)
91. M. Cui, C.H. Yang, Implementation of a digital optical phase conjugation system and its application to study the robustness of turbidity suppression by phase conjugation. Opt. Express **18**, 3444–3455 (2010)
92. A.P. Mosk, A. Lagendijk, G. Lerosey, M. Fink, Controlling waves in space and time for imaging and focusing in complex media. Nat. Photonics **6**, 283–292 (2012)
93. G. Montaldo, M. Tanter, M. Fink, Time reversal of speckle noise. Phys. Rev. Lett. **106**, 054301 (2011)
94. W. Drexler, Ultrahigh-resolution optical coherence tomography. J. Biomed. Opt. **9**, 47–74 (2004)

Part IV

Contrast Enhanced, Functional and Multimodal OCT

Optical Coherence Elastography

32

Brendan F. Kennedy, Kelsey M. Kennedy, Amy L. Oldenburg, Steven G. Adie, Stephen A. Boppart, and David D. Sampson

Keywords

Elastography • Optical elastography • Tissue mechanics • Biomechanics • Cell mechanics • Soft tissue

32.1 Introduction

Manual probing (palpation) of a suspicious region is one of the most basic diagnostic tools used by physicians to identify disease. Palpation is sensitive to variations in the mechanical properties (e.g., stiffness) of soft tissue. These properties are determined

B.F. Kennedy (✉) • K.M. Kennedy
Optical+Biomedical Engineering Laboratory, School of Electrical, Electronic and Computer Engineering, The University of Western Australia, Crawley, WA, Australia
e-mail: Brendan.Kennedy@uwa.edu.au

A.L. Oldenburg
Department of Physics and Astronomy and the Biomedical Research Imaging Center, University of North Carolina at Chapel Hill, Chapel Hill, NC, USA

S.G. Adie
Department of Biomedical Engineering, Cornell University, Ithaca, NY, USA

S.A. Boppart
Biophotonics Imaging Laboratory, Beckman Institute for Advanced Science and Technology, University of Illinois at Urbana-Champaign, Urbana, IL, USA

Departments of Bioengineering, Electrical and Computer Engineering, and Medicine, University of Illinois at Urbana-Champaign, Urbana, IL, USA

D.D. Sampson
Optical+Biomedical Engineering Laboratory, School of Electrical, Electronic and Computer Engineering, The University of Western Australia, Crawley, WA, Australia

Centre for Microscopy, Characterisation and Analysis, The University of Western Australia, Crawley, WA, Australia

© Springer International Publishing Switzerland 2015

W. Drexler, J.G. Fujimoto (eds.), *Optical Coherence Tomography*,
DOI 10.1007/978-3-319-06419-2_33

by the composition and organization of the structural components of tissue, including elastin, collagen, and the extracellular matrix and cytoskeletons of cells, as well as its fluid content [1]. Tissue pathologies are accompanied by changes in one or more of these factors, which often leads to a palpable disease state.

Despite its utility, palpation is limited by its subjectivity, low spatial resolution, and poor sensitivity. Over the last 20 years, a diagnostic imaging technique known as elastography has emerged that addresses these issues. In elastography, images (elastograms) are generated based on a tissue's mechanical properties [2]. A range of different approaches has been adopted, generally sharing three key steps.

1. A mechanical load is applied to a tissue.
2. Tissue displacement in response to the load is determined.
3. A mechanical property of tissue is estimated from the measured displacement.

Initially, elastography was developed using ultrasound [3] or magnetic resonance imaging (MRI) [4] as the underlying imaging modalities. A number of pathologies have been targeted, most notably, breast cancer [5], liver fibrosis [6], and prostate cancer [7]. Clinical results have demonstrated improved diagnostic capabilities. For example, in a multicenter study of ultrasound elastography in breast cancer involving more than 750 patients, improved specificity (89.5 %) and positive predictive value (86.6 %) compared with standard ultrasound (76.1 % and 77.2 %) were reported [8]. Both ultrasound and magnetic resonance elastography are commercially available, including from Echosens, General Electric, Hitachi, Philips, Siemens, Supersonic, Toshiba, and Ultrasonix.

The use of optical coherence tomography (OCT) as the underlying imaging modality in elastography, known as optical coherence elastography (OCE), was first demonstrated by Schmitt in 1998 [9]. Closely related optical elastography techniques based on laser speckle imaging [10, 11], ultrasound-modulated optical tomography [12, 13], and digital holography [14, 15] have also been demonstrated. OCE has a number of distinctive aspects in comparison to ultrasound and magnetic resonance elastography or OCT, including.

Spatial resolution: OCE has the potential to provide a spatial resolution of 1–10 μm, much higher than for (clinical) ultrasound and MR elastography. Such resolution provides information on length scales not previously studied, with the potential to resolve mechanical heterogeneity in diseases such as cancer.

Acquisition speed: OCE provides for 2D image acquisition rates exceeding 1 kHz – generally much higher than for ultrasound or magnetic resonance elastography. Such high speed promises 3D in vivo application without motion artifact.

Sensitivity: Sub-nanometer (possibly tens of picometer) displacement sensitivity enables the measurement of smaller changes in mechanical properties than other forms of elastography. This sensitivity has the potential to better differentiate subtle changes, e.g., between benign and malignant tumors.

Contrast: The Young's modulus of soft tissue varies from Pa to MPa, whereas the scattering coefficient of such tissues (largely determining contrast in OCT) is typically in the range 2–20 mm^{-1}. Thus, there is an apparent advantage in the dynamic range of mechanical over optical contrast.

Imaging penetration: OCE penetrates only millimeters from the probe, which is much less than for ultrasound and MR elastography. This limitation is overcome by exploiting fiber optics in endoscopic and interstitial probes, which expands the applications of OCE, e.g., to the assessment of atherosclerotic plaques in coronary arteries.

The landscape of OCE is rapidly changing. OCT technology has matured to the point that sub-nanometer displacement sensitivity and rapid image acquisition speeds are enabling, for the first time, the generation of high-resolution, high-contrast elastograms. Commercial and clinical successes in ultrasound and magnetic resonance elastography promise to pave the way for OCE. Current research efforts are focusing on the key advances needed to enable clinical OCE, i.e., quantitative and repeatable measurements, practical imaging probes integrated with loading mechanisms, and convincing demonstrations of contrast in pathological tissue.

In this chapter, we review the basic principles and development of OCE. We begin by describing the mechanical principles of tissue deformation. We then describe how deformation has been measured and review OCE techniques proposed so far. We discuss the development of imaging probes and the fidelity of contrast in elastograms before presenting an outlook for OCE. Throughout, we touch on applications of OCE, which are in their infancy.

32.2 Tissue Deformation

Fundamentally, elastography is a method for mapping the mechanical properties of tissue from a set of displacement measurements. First, let us consider the physical principles that govern tissue deformation. We use the conventional quantities defined in continuum mechanics to link tissue displacement, deformation, load, and elasticity [16]. We describe the load applied to tissue and the resulting deformation using stress and strain tensors. A constitutive equation is then used to define the elasticity by relating these tensors. In this analysis, we describe tissue as a linearly elastic solid, allowing us to derive a number of elastic properties that characterize its mechanical behavior, including those properties that most closely describe the variations in stiffness that are sensed by manual palpation. It should be recognized that the assumption of linear elasticity is generally not valid for the majority of soft tissues, which are more accurately described as nonlinear viscoelastic materials [1]. However, in elastography, these assumptions are often made to simplify the analysis. Similar analyses have been used to describe tissue deformation in ultrasound and magnetic resonance elastography [17, 18].

32.2.1 Stress Tensor

The application of a mechanical load results in stress acting throughout a tissue. To analyze the stress, we consider a volume, subject to an arbitrary number of external forces, $\mathbf{F}_m$, as illustrated in Fig. 32.1a. These external forces give rise to internal forces distributed throughout the volume. To define the corresponding

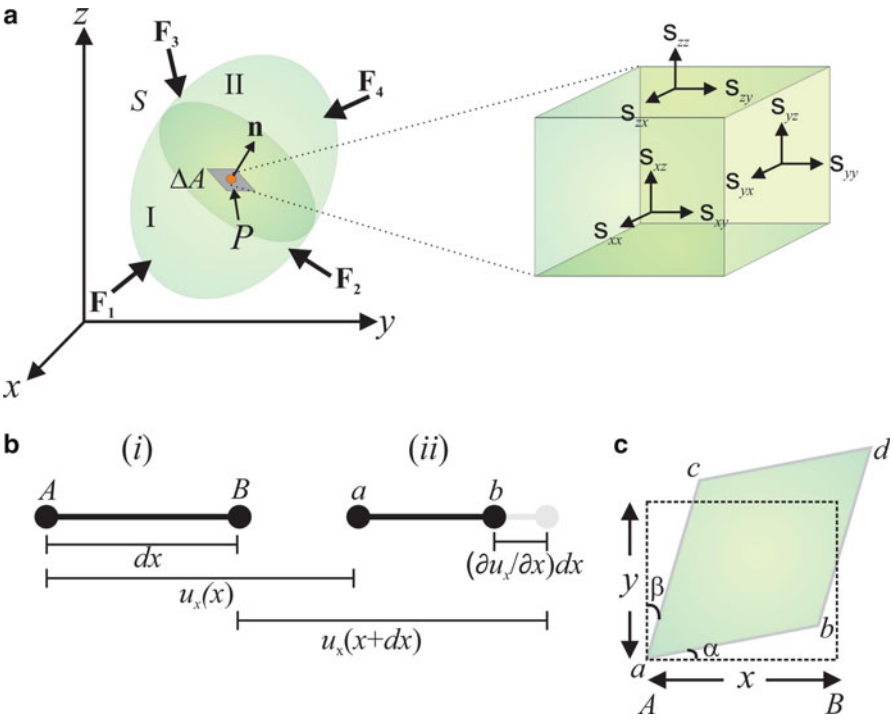

Fig. 32.1 (**a**) Stress components acting at the point *P* located within a deformable body under load. (**b**) Normal strain along the *x*-axis of the cube in (*a*) *(i)* before and *(ii)* after compressive deformation. The *gray line* in *(ii)* represents the initial length. (**c**) Shear strain: *xy*-plane of the cube in (*a*) after shear deformation. The *dashed rectangle* represents the *xy*-plane before deformation

stress, we divide the volume into two portions (I and II), using the plane *S* which passes through an arbitrary point, *P*, with unit normal vector, **n**. Considering I, we assume this portion is in equilibrium under the action of the external forces $\mathbf{F}_1$ and $\mathbf{F}_2$ and the internal forces distributed over the plane *S* representing the actions of II on I. To obtain the stress acting in the small area ΔA in the plane *S* containing *P*, we assume that the forces acting in this area can be reduced to a resultant force $\Delta\mathbf{F}$, where the limiting direction of $\Delta\mathbf{F}$ is perpendicular to *S*. The stress vector, $\boldsymbol{\sigma}_\mathbf{n}$, acting at this point is defined as

$$\boldsymbol{\sigma}_\mathbf{n} = \lim_{\Delta A \to 0} \frac{\Delta \mathbf{F}}{\Delta A}. \tag{32.1}$$

The S.I. unit of stress is the Pascal, equivalent to Nm^{-2}. Equation 32.1 defines the particular case where the direction of the resultant force, $\Delta\mathbf{F}$, is also the direction of the stress vector. More generally, the direction of the stress vector is inclined to ΔA and is described by two components: a normal stress perpendicular

to ΔA and a shear stress acting in the plane of ΔA. Consider the infinitesimal cubic element located at the point P, shown in Fig. 32.1a, with faces parallel to the coordinate axes. Each component of stress acting on the cube is highlighted in Fig. 32.1a. Two subscripts are used for each component. The first indicates the direction of the normal to the plane and the second indicates the direction of the stress component. The total stress acting on the cube is described by a second-order tensor:

$$\boldsymbol{\sigma} = \begin{bmatrix} \sigma_{xx} & \sigma_{xy} & \sigma_{xz} \\ \sigma_{yx} & \sigma_{yy} & \sigma_{yz} \\ \sigma_{xz} & \sigma_{yz} & \sigma_{zz} \end{bmatrix}. \tag{32.2}$$

32.2.2 Strain Tensor

The strain tensor describes each component of the deformation resulting from an applied load. Consider the x-axis of the infinitesimal cube presented in Fig. 32.1a. In Fig. 32.1b, this axis is shown (*i*) before and (*ii*) after compressive deformation. The component u_x describes the displacement at the point A. The initial length along the x-axis, $|AB|$, is given by dx. After deformation, this length ($|ab|$ in Fig. 32.1b) is given by $dx + \frac{\partial u_x}{\partial x} dx$. The normal strain is defined as the unit elongation/contraction:

$$\varepsilon_{xx} = \frac{|ab| - |AB|}{|AB|} = \frac{\partial u_x}{\partial x}. \tag{32.3}$$

The same analysis holds for the normal strain in the y- and z-axes, ε_{yy} and ε_{zz}, defined as $\frac{\partial u_y}{\partial y}$ and $\frac{\partial u_z}{\partial z}$, respectively. In OCE, the strain defined in Eq. 32.3 is often referred to as the local strain [19]. As the strain is a ratio of lengths, it is dimensionless. By convention, tensile strains are positive and compressive strains are negative. Following this convention, the quantity $\frac{\partial u_x}{\partial x} \partial x$ in Fig. 32.1b is negative, and therefore, the compressive strain ε_{xx} is also negative. Analogously to stress, the strain has both normal and shear components. The xy-plane of the cube in Fig. 32.1a is illustrated in Fig. 32.1c. After deformation, the area $dxdy$ takes the form of a parallelogram in the general case. The shear strain is defined as the change in angle between two axes that were originally orthogonal. From Fig. 32.1c, the shear strain, ε_{xy}, is given by $\alpha + \beta$. For small displacement gradients, we have $\alpha = \frac{\partial u_y}{\partial x}$ and $\beta = \frac{\partial u_x}{\partial y}$, where u_y is the displacement along the y-axis at the point A, allowing the shear strain, ε_{xy}, to be defined as $\frac{\partial u_y}{\partial x} + \frac{\partial u_x}{\partial y}$. By interchanging x and y and u_x and u_y, it can be demonstrated that $\varepsilon_{xy} = \varepsilon_{yx}$. Shear strain components in the xz and yz planes can be defined in a similar manner. The infinitesimal strain tensor describing each component of strain can then be expressed as

$$\varepsilon = \begin{bmatrix} \varepsilon_{xx} & \varepsilon_{xy} & \varepsilon_{xz} \\ \varepsilon_{yx} & \varepsilon_{yy} & \varepsilon_{yz} \\ \varepsilon_{zx} & \varepsilon_{zy} & \varepsilon_{zz} \end{bmatrix}$$

$$= \begin{bmatrix} \dfrac{\partial u_x}{\partial x} & 0.5\left(\dfrac{\partial u_x}{\partial y} + \dfrac{\partial u_y}{\partial x}\right) & 0.5\left(\dfrac{\partial u_x}{\partial z} + \dfrac{\partial u_z}{\partial x}\right) \\ 0.5\left(\dfrac{\partial u_y}{\partial x} + \dfrac{\partial u_x}{\partial y}\right) & \dfrac{\partial u_y}{\partial y} & 0.5\left(\dfrac{\partial u_y}{\partial z} + \dfrac{\partial u_z}{\partial y}\right) \\ 0.5\left(\dfrac{\partial u_z}{\partial x} + \dfrac{\partial u_x}{\partial z}\right) & 0.5\left(\dfrac{\partial u_z}{\partial y} + \dfrac{\partial u_y}{\partial z}\right) & \dfrac{\partial u_z}{\partial z} \end{bmatrix}, \tag{32.4}$$

where the shear components are scaled by 0.5, as $\varepsilon_{xy} = \varepsilon_{yx}$, $\varepsilon_{xz} = \varepsilon_{zx}$, and $\varepsilon_{yz} = \varepsilon_{zy}$. It should also be noted that in dynamic elastography techniques, the strain rate is often measured. Strain rate is defined as the rate of change of strain with time [1] and is easily obtained from the expressions defined in Eq. 32.4.

32.2.3 Constitutive Equation for a Linearly Elastic Solid

Having defined the load applied to tissue using the stress tensor and the resulting deformation using the strain tensor, a constitutive equation relating the two is used to define tissue elasticity. In elastography, the most commonly used constitutive equation is that of a linearly elastic (or Hookean) solid in which the relationship between stress and strain is linear and strain is independent of the rate at which the load is applied. The constitutive equation for a linearly elastic solid is

$$\sigma_{ij} = C_{ijkl}\varepsilon_{kl}, \tag{32.5}$$

where i, j, k, and l define each tensor component. As σ and ε are second-order tensors, C is a fourth-order tensor, consisting of 81 elastic constants, referred to as the elasticity tensor. To simplify the analysis, it is frequently assumed that the elasticity is isotropic, i.e., elasticity can be described without reference to direction. This imposes maximum symmetry on the tensor, reducing the 81 elastic constants to two and resulting in the isotropic linear elastic constitutive equation, defined as

$$\sigma_{ij} = \lambda\varepsilon_{kk}\delta_{\mathrm{ij}} + 2\mu\varepsilon_{ij}, \tag{32.6}$$

where λ and μ are the elastic constants, also known as the Lamé constants, and δ_{ij} is the Kronecker delta (equal to 1 if $i = j$ and 0 otherwise). As ε is dimensionless, the unit for λ and μ is that of stress, i.e., the Pascal. It should be noted that constitutive equations that more accurately model the nonlinear viscoelastic response of soft

tissue to loading have also been proposed [20]. However, their complexity has restricted their use in OCE.

32.2.4 Elastic Properties

A number of descriptors may be derived from the Lamé constants for a material's elastic properties. In this section, we define these descriptors, namely, Young's modulus, shear modulus, bulk modulus, and Poisson's ratio and describe their relevance to OCE.

Young's modulus, E, characterizes the elasticity of a material subjected to uniaxial stress, i.e., only one normal stress component in Eq. 32.2 is nonzero. Uniaxial stress is generally a good approximation for the loads applied in OCE. For a load acting along z, E is defined as $\sigma_{zz}/\varepsilon_{zz}$, i.e., the ratio of normal (axial) stress to normal (axial) strain. In terms of the Lamé constants, it is expressed as $\frac{\mu(3\lambda+2\mu)}{(\lambda+\mu)}$. E has the same unit as stress, i.e., the Pascal.

Shear modulus, G, is the ratio of shear stress to shear strain, e.g., $\sigma_{xz}/\varepsilon_{xz}$. It is equal to the Lamé constant, μ, and its unit is the Pascal.

Bulk modulus, K, is defined as the ratio of hydrostatic pressure, σ, to unit volume change, $\Delta v/v$. Hydrostatic pressure describes the situation when all shear stress components are zero and the normal stress components are equal, i.e., $\sigma_{xx} = \sigma_{yy} = \sigma_{zz}$. K is a measure of the compressibility of a material and defined as $\lambda + \frac{2}{3}\mu$, and its unit is the Pascal. Its unit of measurement is the Pascal.

Poisson's ratio, ν, is defined as the ratio of the normal strain along the axis of stress to the normal strain in each orthogonal axis. In compression, it is the ratio of elongation per unit breadth to contraction per unit length, e.g., $-\varepsilon_{xx}/\varepsilon_{zz}$, where the negative sign results from the division of a tensile normal strain, ε_{xx}, by a compressive normal strain, ε_{zz}. It is defined in terms of the Lamé constants as $\frac{\lambda}{2(\lambda+\mu)}$. As it is a ratio of two strains, it is dimensionless.

The Lamé constants, Young's modulus, shear modulus, bulk modulus, and Poisson's ratio are related. Only two of these parameters are independent for an isotropic, linearly elastic material, and thus, measurement of any two determines the other parameters. For soft tissue, the high water content results in the near conservation of volume upon compression. As a result, the bulk modulus of soft tissue has been reported to vary by less than 15 % from that of water [17]. The incompressibility of soft tissue also results in a Poisson's ratio of very close to but not exceeding 0.5. As these properties do not vary significantly for soft tissues, the goal of most OCE techniques is to estimate Young's modulus or shear modulus, which has a much larger dynamic range. These moduli also correspond most closely to what is sensed by manual palpation of the tissue. In soft tissue, it is readily shown that $E \approx 3G$, under the assumption that $\nu \approx 0.5$ [16]. Therefore, Young's modulus is the most common single property used to characterize tissue elasticity and the most commonly probed property in OCE. The value of Young's

modulus of soft tissues extends from tens of Pascals, in very soft tissues such as adipose [21], to hundreds of kPa to MPa, as in hard tumors [22].

32.2.5 Equations of Motion

In some OCE techniques, as well as in some ultrasound and magnetic resonance elastography techniques, a dynamic (sinusoidal) load is applied to the sample. In this case, inertia must be taken into account. The constitutive equation of motion for a linearly elastic solid is given by Navier's equation as [16]

$$\rho_0 \frac{\partial^2 \mathbf{u}}{\partial t^2} = (\lambda + \mu)\nabla(\nabla \cdot \mathbf{u}) + \mu \nabla^2 \mathbf{u}, \tag{32.7}$$

where ρ is the density of the tissue and $\mathbf{u}$ is the displacement vector. Transverse and longitudinal waves can propagate independently in the material: S (shear) waves and P (pressure) waves, respectively. For shear wave propagation, there is no volume change in the material. The dilatation term ($\nabla \cdot \mathbf{u}$) is therefore zero and Eq. 32.7 becomes

$$\nabla^2 \mathbf{u} = \frac{1}{c_s^2}(\lambda + \mu)\nabla(\nabla \cdot \mathbf{u}) + \mu \nabla^2 \mathbf{u}, \tag{32.8}$$

where c_s, the shear wave speed, is defined as $\sqrt{\mu/\rho}$. Pressure waves are irrotational, i.e., $\nabla \times \mathbf{u} = 0$, allowing $\mathbf{u}$ to be written in terms of a potential, ψ, such that $\mathbf{u} = \nabla\psi$. The wave equation then becomes

$$\nabla^2(\nabla\psi) = \frac{1}{c_p^2}(\lambda + \mu)\nabla(\nabla \cdot \mathbf{u}) + \mu \nabla^2 \mathbf{u}, \tag{32.9}$$

where the P-wave speed, c_p, is defined as $\sqrt{\frac{\lambda+2\mu}{\rho}}$.

For soft tissues, the pressure wave speed, typically several thousand m/s, is orders of magnitude faster than the shear wave speed, typically several m/s [18]. The focus in dynamic OCE to date has mainly been to measure elasticity from the shear wave properties [23–26]. There are several reasons for this: firstly, as the P-wave speed depends on variations of the bulk modulus, it has a much lower dynamic range in tissue than S-waves; secondly, the high speed of P-waves makes their detection challenging.

An advantage of dynamic OCE is that it should enable the complex dynamic mechanical response of a sample to be measured, providing information about both its elastic and viscoelastic properties. OCE techniques that have been used to measure viscoelastic properties of tissue are discussed in more detail in Sect. 32.4.4. Dynamic OCE is also potentially more suitable for in vivo measurements, as it enables loading in a frequency range not affected by sample motion, e.g., due to breathing.

32.3 Measuring Displacement in OCE

The accuracy and dynamic range of the displacement measured in response to a load has a major impact on elastogram quality. In this section, we describe three techniques to measure the displacement: speckle tracking, phase-sensitive detection, and use of the Doppler spectrum.

32.3.1 Speckle Tracking

Speckle is the phenomenon of fine-scale, apparently random, fluctuating light and dark intensity present in all coherent imaging systems. In OCT, it is generated by the summation of the multiple backscattered optical wavefields arising from the sub-resolution sample scatterers. The wavefields may be represented as a summation of complex phasors, which determines the intensity and phase of the detected signal. A detailed analysis of OCT speckle can be found elsewhere [27].

Speckle tracking may be considered to be a sub-branch of the much broader field of speckle metrology, developed since the late 1960s [28, 29]. The utility of speckle for tracking motion in OCE arises because each speckle realization, far from being random, is dependent upon the precise location of backscatterers within the sample. As the backscatterers translate, within a certain range, so does the speckle pattern associated with them. Under the assumption that the relative positions of sub-resolution scatterers remain fixed while they translate, any variation of the speckle pattern between successive acquisitions, or equivalently, of its second-order temporal statistics, can be used to measure sample motion. This is shown in Fig. 32.2, in which a small portion of an OCT speckle pattern acquired from a homogeneously scattering phantom under compressive load (applied from above) is shown in false color. The pattern is shown for four increments in load, increasing from Fig. 32.2a–d. Translation of a single bright speckle is highlighted by a black outline in each figure part. Evident in Fig. 32.2 is the gradual decorrelation of the speckle pattern with load, a major limitation of the technique. This decorrelation is caused by the reorganization of the positions of the sub-resolution scatterers due to loading. It limits the maximum measurable displacement to considerably less than the OCT resolution.

The speckle shift is typically evaluated by calculating the cross-correlation of a portion of B-scans acquired at two time points during compression [9]. Consider a point scatterer embedded in a transparent medium at position (x, z). When the sample is placed under load, the scatterer is displaced to a new location, $(x + \Delta x, z + \Delta z)$. The normalized cross-correlation between the OCT signal before, $I_1(x, z)$, and after loading, $I_2(x, z)$, within a predefined window of dimensions $X \times Z$, is given by

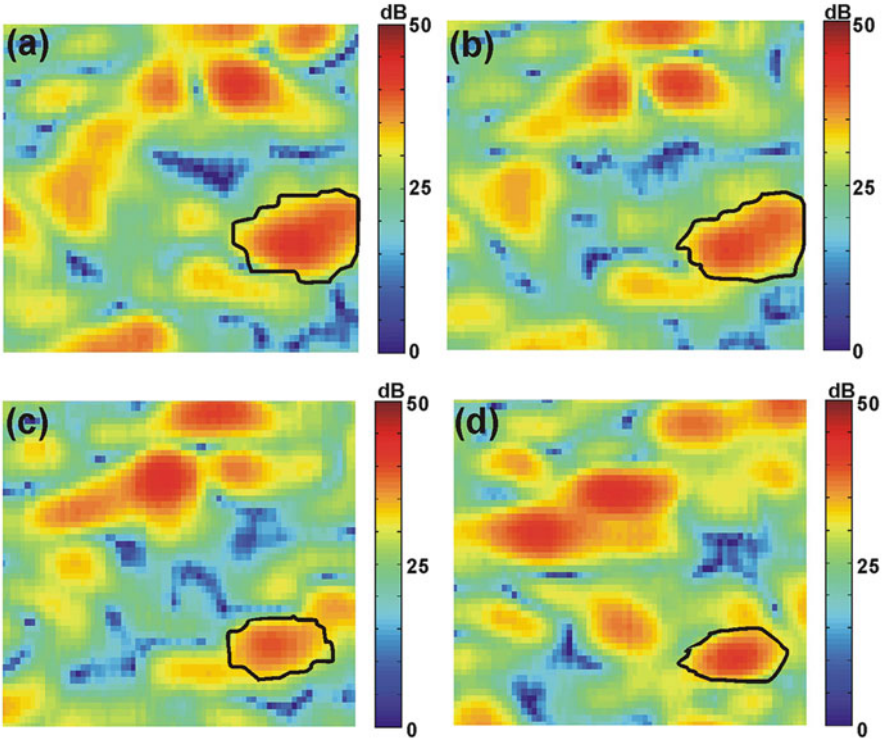

Fig. 32.2 Speckle pattern of a silicone phantom (logarithmic intensity scale) under increasing compressive load (applied from above) from (**a**–**d**). Image dimensions 50 × 50 μm. *Black outline* highlights the evolution of an individual speckle

$$\rho(x',z') = \frac{\int_{-Z/2}^{Z/2}\int_{-X/2}^{X/2} I_1(x,z)I_2(x-x',z-z')dxdz}{\sqrt{\int_{-Z/2}^{Z/2}\int_{-X/2}^{X/2} I_1^2(x,z)dxdz \int_{-Z/2}^{Z/2}\int_{-X/2}^{X/2} I_2^2(x-x',z-z')dxdz}}. \quad (32.10)$$

The relative displacement, between the acquisition of $I_1(x, z)$ and $I_2(x, z)$, in the x and z directions can then be determined from

$$\Delta u_x = \max[(\rho(x',z'))] \text{ for } z' = 0, -X/2 \le x' \le X/2, \quad (32.11)$$

and

$$\Delta u_z = \max[(\rho(x',z'))] \text{ for } x' = 0, -Z/2 \le z' \le Z/2. \quad (32.12)$$

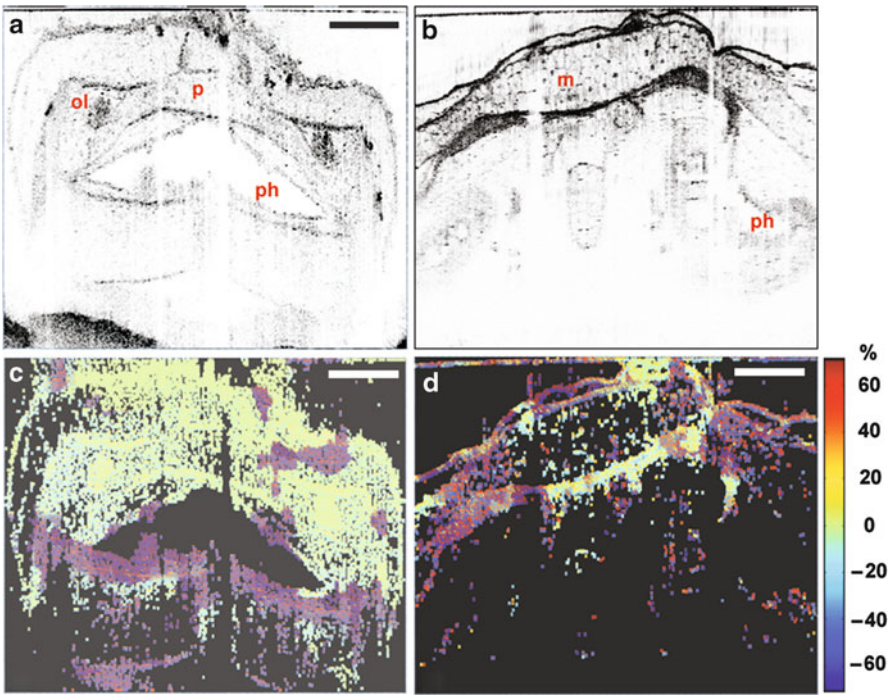

Fig. 32.3 OCT images and strain maps of a *Xenopus laevis* tadpole at different life cycle stages. (**a**, **c**) Representative structural OCT and OCE relative (local) strain maps, respectively, for stage 42 (3 -day-old). (**b**, **d**) Representative structural OCT and OCE relative (local) strain maps for Stage 50 (15 -day-old). Scale bar = 300 μm (adapted from [34])

From Eqs. 32.10–32.12, ρ is maximum for $x' = \Delta x$ and $z' = \Delta z$, respectively. Correlation-based speckle tracking was used in early OCE research [9, 30–34] and has been commonly used in ultrasound elastography [3]. Early examples of OCE elastograms obtained using correlation-based speckle tracking, along with the corresponding OCT images, acquired from a *Xenopus laevis* tadpole at different stages of development are shown in Fig. 32.3.

The minimum measurable displacement obtainable with speckle tracking is determined by the spatial sampling in the underlying OCT system, assuming an adequate OCT SNR. For cross-correlation techniques that use a central difference approach to evaluate Eq. 32.10, this corresponds to 0.5 pixels [10]. Displacements as small as 0.1 pixels can be measured using parametric techniques, such as the maximum likelihood estimator [11, 35]. However, these estimators result in intolerably large errors for displacements >0.8 pixels.

The maximum measurable displacement using the cross-correlation method is set by speckle decorrelation, as mentioned, which depends on the sample elasticity as well as on the size range, density, and arrangement of the sub-resolution scatterers. In a study on a silicone phantom containing titanium dioxide particles,

the maximum displacement was reported to be ~0.5 times the resolution of the OCT system [35]. Low OCT SNR also results in decorrelation between successive B-scans [35], reducing the accuracy of displacement measurements with increasing depth in the sample.

The above limits imply a severely limited dynamic range for speckle tracking. Consider an OCT system with spatial resolution of 10 × 10 × 10 μm and spatial sampling such that the axial pixel size is 3 μm and the lateral pixel size is 1 μm. Use of a smaller pixel size either imposes restrictions on the field of view (for fixed pixel count) or increases in the acquisition time (for more pixels). Using cross-correlation, minimum and maximum measurable displacements of ~1.5 and ~5 μm (from the example in [36]), respectively, might be reasonably expected and correspond to a dynamic range of ~3.3, with the same range applying to the measurable elasticity in OCE.

An additional limitation is that the displacement is calculated within a predefined window ($X \times Z$ in Eq. 32.10). The window sets the imaging spatial resolution of each displacement measurement, lowering it relative to the OCT image resolution, typically by a factor of 5–10 [9, 31].

An important further consideration when using speckle tracking is the avoidance of decorrelation caused by changes in the tissue configuration not related to its elastic properties, such as bulk motion, Brownian motion, or blood flow. This implies an acquisition speed high enough to ensure the speckles remain correlated between successive scans.

An advantage of speckle tracking is that motion can be tracked in more than one spatial dimension. Speckle tracking in OCE has been performed in only one or two dimensions, but 3D tracking has been proposed in ultrasound [37]. 3D tracking would provide the opportunity to measure shear strain in addition to normal strain (see Eq. 32.4) and to remove the otherwise necessary assumption of isotropic mechanical behavior. This may provide additional OCE contrast in anisotropic tissues, such as skin and muscle, as has already been demonstrated in ultrasound [38] and magnetic resonance elastography [39]. Indeed, 3D information is routinely obtained in magnetic resonance elastography.

32.3.2 Phase-Sensitive Detection

Speckle tracking utilizes changes in the *intensity* of an OCT image with loading. In Fourier-domain (FD) OCT, after performing a Fourier transform on the detected spectral fringes, the depth-resolved complex signal is obtained. This provides the opportunity to analyze the *phase* of the detected signal. OCT phase is generally random in soft tissue; however, it is temporally invariant if the sample is stationary. If a sample is subjected to mechanical loading, its axial displacement, Δu_z, between two A-scans, acquired from the same lateral position, results in a phase shift, $\Delta\phi$ [40]. The displacement, Δu_z, along the axis of the incident beam is defined as

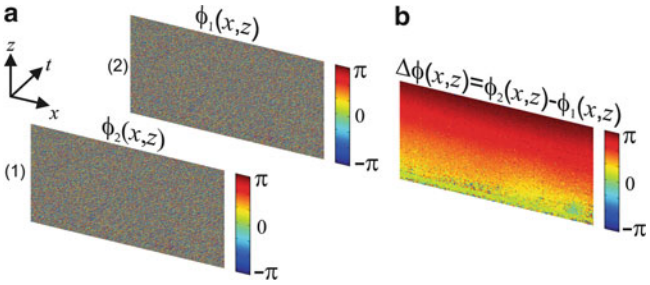

Fig. 32.4 Schematic illustration of phase-sensitive detection with experimental data from a mechanically homogeneous silicone phantom. (**a**) The phase of OCT B-scans acquired at the same lateral position before (*1*) and after (*2*) sample loading. (**b**) Phase difference between the B-scans shown in (**a**). As the load was applied from the *top*, the phase difference is maximum in this position, reducing to near zero at large depths

$$\Delta u_z(z,t) = \frac{\Delta\phi(z,t)\lambda}{4\pi n}, \tag{32.13}$$

where λ is the mean wavelength of the source and n is the average refractive index along the beam path. The phase difference is calculated either between two successive A-scans in a B-scan (requiring high lateral sampling density) [40] or between two A-scans acquired in the same lateral position in successive B-scans [41]: the latter is illustrated in Fig. 32.4 with experimental data acquired from a uniformly scattering silicone phantom. Phase-sensitive detection was initially developed for Doppler flow velocity measurement in OCT [42]. Indeed, the phase-sensitive technique is based on the Doppler shift; thus, unlike speckle tracking, only the axial component of the displacement can be detected. If we assume that the maximum measurable displacement is set by the maximum unambiguous phase difference, i.e., 2π, then this corresponds to half the source center wavelength (in the sample medium). The minimum measurable displacement, $\sigma_{\Delta u_z}$, is determined by the phase sensitivity of the OCT system [43], which, in the shot-noise limited regime, is related to the OCT signal-to-noise ratio (SNR) and is approximated as

$$\sigma_{\Delta\phi} = \frac{1}{\sqrt{SNR}}, \quad SNR >> 1. \tag{32.14}$$

Park et al., in their work on flow imaging [44], demonstrated good agreement between Eq. 32.14 and experimental results for OCT SNR >30 dB. It is important to emphasize, however, that this approximation is only valid for large OCT SNR.

Another source of phase noise is introduced under the successive A-scans scenario if the temporally displaced beams are not precisely overlapped in space. The phase noise introduced due to lateral beam motion, Δx, between successive A-scans is given by [44]

$$\sigma_{\Delta x} = \sqrt{\frac{4}{3}\left\{1 - \exp\left[-2\left(\frac{\Delta x}{w}\right)^2\right]\right\}}, \tag{32.15}$$

where w is the $1/e^2$ beam width at the focus. In practice, to minimize phase noise due to scanning, dense sampling is performed along the axis used to calculate the phase difference. As an example, consider a typical OCT system with a $1/e^2$ beam width of 25 μm at the focus. Acquiring A-scans in 1 μm lateral steps ensures that the phase noise due to scanning is <0.05 rad, within a factor of 5 of the limiting phase noise for OCT SNR = 40 dB. A further source of phase noise, σ_{mech}, is introduced by mechanical instabilities in the system, such as jitter in the scanning mirrors. Combining Eqs. 32.14 and 32.15 and including mechanical instabilities, considering each of these processes to be additive and Gaussian, the total phase noise, σ_{Tot}, is given by

$$\sigma_{Tot} = \sqrt{\sigma_{\Delta\phi}^2 + \sigma_{\Delta x}^2 + \sigma_{mech}^2}. \tag{32.16}$$

To minimize σ_{Tot}, both $\sigma_{\Delta\phi}$ and σ_{mech} must be negligible and the OCT SNR must be maximized (see Eq. 32.14). Under these conditions, displacement sensitivity of ~20 pm has been reported [45]. The minimization of σ_{mech} has been discussed in detail in relation to optical coherence microscopy (see ▶ Chap. 28, "Optical Coherence Microscopy" for more details). Techniques employed to minimize σ_{mech} include the use of a common-path interferometer and a reference reflector within the sample arm. In practice, $\sigma_{\Delta\phi}$ is often appreciable due to the requirement to laterally scan across the sample, such that typical displacement sensitivities lie in the range 0.1–1 nm.

A key advantage of phase-sensitive detection over speckle tracking is its larger dynamic range. If we consider the phase difference between two A-scans acquired using an OCT system with mean wavelength of 1300 nm and minimum OCT SNR of 30 dB, the displacement dynamic range in air is >60, almost 20-fold larger than that achievable using the cross-correlation method for speckle tracking described in Sect. 32.3.1.

A major limitation is imposed by phase wrapping, one which invalidates the assumption of a linear relationship between phase difference and displacement (Eq. 32.13). Phase jumps of 2π not only occur when the desired phase difference is close to the 2π limit but also arise due to noise when the OCT SNR is low. In the case of dynamic loading, phase wrapping due to noise can be mitigated by faster acquisition. An alternative means of mitigation is intensity thresholding and weighting, which gives preference to the phase difference estimated from pixels with high SNR. On the other hand, robust algorithms to correctly unwrap phase may enable significant increases in the dynamic range of phase-sensitive OCE, e.g., successfully unwrapping one such event would lead to a 3 dB improvement in dynamic range. However, it must be emphasized that all phase-unwrapping algorithms break down in the presence of high noise.

Phase-sensitive detection possesses several advantages over speckle tracking, including the larger dynamic range, lower computational complexity, and higher displacement sensitivity. Also, the spatial resolution of displacement measurements is matched to that of the underlying OCT system: the displacement is not estimated in an $X \times Z$ window, as is the case in speckle tracking.

The above discussion has not explicitly considered determining the displacement by phase measurement under dynamic mechanical loading. Liang et al. [46] developed a technique to measure displacement under dynamic loading using phase-sensitive detection. The vibration amplitude is calculated from the displacement and used to estimate the strain rate. A related technique has also been presented for measuring vibration within the ear [45]. In the next section, we consider a recently introduced improvement over these phase-sensitive methods for detecting vibration amplitude.

32.3.3 Doppler Spectrum

A major limitation of phase-sensitive detection is the large drop-off in accuracy with decreasing SNR (Eq. 32.14). Recently, with the goal of reducing this drop-off, a new technique has been proposed for extracting the displacement from the measured intensity under dynamic mechanical loading. Joint spectral- and time-domain optical coherence elastography (STdOCE) improves vibration amplitude measurement in dynamic OCE [47] by adapting the technique previously proposed for Doppler flow imaging [48]. STdOCE provides more accurate vibration amplitude measurements than the phase-sensitive technique in the case of low OCT SNR ($<$20 dB), thereby extending the depth range of accurate dynamic OCE measurements.

Dynamic loading results in an amplitude spectrum of frequency tones described by Bessel functions of the first kind. In STdOCE, a Fourier transform is performed in the time domain, i.e., across multiple A-scans. If the A-scan rate is much higher than the loading rate, the result is a Doppler spectrum containing frequency tones, which can be used to extract the vibration amplitude at each depth in the sample.

STdOCE is closely related to a previously reported dynamic OCE technique based solely on time-domain (TD) OCT [19, 49]. The bandwidth of the frequency tones in TD-OCT increases with both the bandwidth of the source and the A-scan velocity, which causes them to overlap in frequency and restricts measurements to only the first few tones. This limits the accuracy and requires the use of a very slow A-scan acquisition rate ($\sim$1 Hz). Nonetheless, this technique was capable of being used to demonstrate the first in vivo dynamic OCE measurements [49].

In STdOCE, the increased number of tones in the Doppler spectrum provided by spectral-domain (SD) OCT allows a signal processing technique proposed in ultrasound elastography to be employed [50], in which the vibration amplitude is determined from the variance or spectral spread of frequency tones in the Doppler spectrum. Figure 32.5 shows the data acquisition and processing procedure for

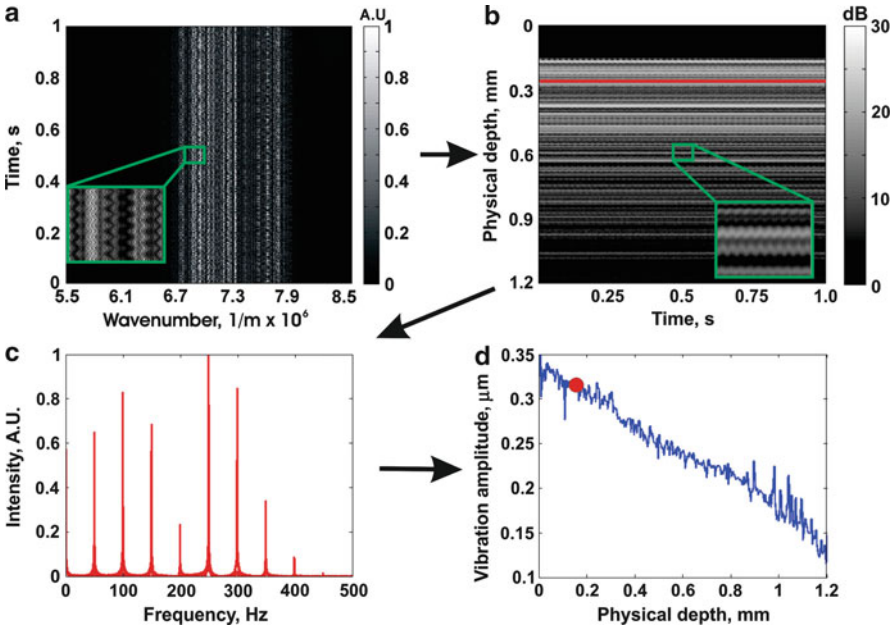

Fig. 32.5 Data processing procedure for STdOCE: (**a**) 2,000 spectral interferograms; (**b**) A-scans obtained after Fourier transform in *k*-space; (**c**) Doppler spectrum after Fourier transform in time, performed at depth indicated by the *red line* in (**b**); and (**d**) vibration amplitude (peak) calculated using the spectral spread algorithm. The *red dot* in (**d**) corresponds to the vibration amplitude calculated from the Doppler spectrum in (**c**) (reproduced from [47])

STdOCE. In Fig. 32.5a, 2,000 successive spectral interferograms acquired from the same lateral position in a homogeneous phantom are shown. In Fig. 32.5b, the corresponding depth-resolved A-scans, after Fourier transformation in *k*-space, are shown. In Fig. 32.5c, the Doppler spectrum obtained after performing a second Fourier transform in the time domain at the depth indicated by the red line in Fig. 32.5b is shown, with nine overtones in evidence. Having calculated the Doppler spectrum, the spectral spread algorithm is used to calculate the vibration amplitude. The vibration amplitude calculated from the spectrum in Fig. 32.5c is indicated by the red dot in Fig. 32.5d. This procedure is repeated for each depth in the sample, allowing a vibration amplitude plot (blue line in Fig. 32.5d) to be generated.

Figure 32.6 demonstrates the superiority of STdOCE over a representative technique for phase-sensitive detection [45]. In Fig. 32.6a, a structural OCT image of a soft phantom containing a stiff inclusion is shown. The inclusion is located in the center of the image and is indicated by the labeled arrow. Below the inclusion, a shadow artifact, corresponding to a region of low OCT SNR, is also labeled. A plot of the OCT SNR, at the lateral position indicated by the vertical red arrow in Fig. 32.6a, is shown in Fig. 32.6d. Vibration amplitude images generated using STdOCE and phase-sensitive OCE are shown in Fig. 32.6b, f, respectively. In both

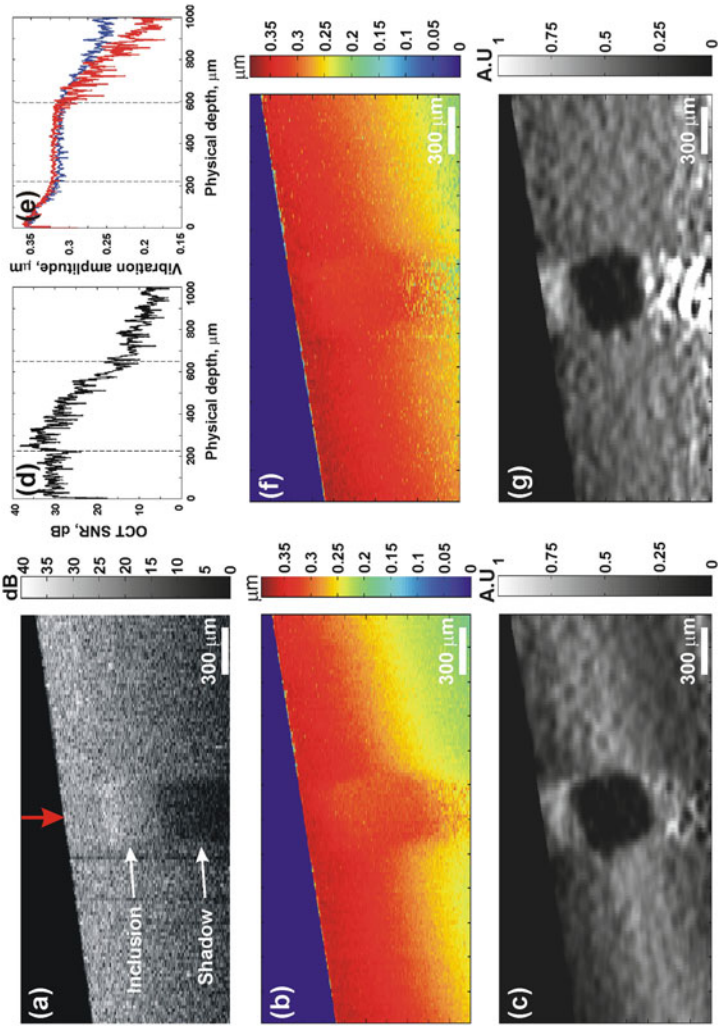

Fig. 32.6 Soft phantom containing a stiff inclusion: (**a**) OCT structural image; (**b**) vibration amplitude image; (**c**) elastogram for STdOCE; (**d**) OCT A-scan; (**e**) vibration amplitude plots for STdOCE (*blue*) and phase-sensitive OCE (*red*) at the lateral position indicated by the *red arrow* in (**a**), where the *dashed lines* in (**d**) and (**e**) indicate the boundaries between the soft bulk and hard inclusion; (**f**) vibration amplitude image; and (**g**) elastogram for phase-sensitive OCE [47]

Table 33.1 Comparison of different methods to measure displacement in OCE

	Minimum displacement	Maximum displacement	Axial resolution	Lateral resolution	Dimension of elasticity measured	Minimum data required
Speckle tracking	~0.1 × pixel size	~0.5 × OCT resolution	5–10 × OCT resolution	5–10 × OCT resolution	1D, 2D, 3D	2 A-scans
Phase-sensitive	~20 pm	~0.5 × source wavelength	OCT resolution	OCT resolution	1D	2 A-scans
Doppler spectrum	~10 nm	~0.5 × OCT axial resolution	OCT resolution	OCT resolution	1D	>10 A-scans

images, the stiff inclusions are denoted by the lower rate of change in vibration amplitude with depth, i.e., lower strain. Vibration amplitude plots generated using both techniques, at the lateral position indicated by the red arrow in Fig. 32.6a, are shown in Fig. 32.6e. Both plots match well until a depth of ~600 μm. At depths >600 μm, the decrease in vibration amplitude is higher for the phase-sensitive technique (red). This is caused by an underestimation of the vibration amplitude in the low OCT SNR region below the inclusion. In comparison, the decrease in vibration amplitude with depth measured with STdOCE below the inclusion is the same as that above the inclusion, as expected for these mechanically uniform regions. The strain elastograms corresponding to Figs. 32.6b and f are shown in Figs. 32.6c and g, respectively. The artificially high strain in the phase-sensitive elastogram (Fig. 32.6g) is clearly visible below the inclusion. As the elastogram is used as a surrogate for elasticity, this leads to errors in the interpretation of elastograms.

In this section, we described the two main techniques used to measure the displacement in OCE: the technique used in early OCE papers, speckle tracking, and the most commonly used technique in recent papers, phase-sensitive OCE. A recent improvement on phase-sensitive OCE that applies to dynamic displacement, STdOCE, based on the analysis of the Doppler spectrum, was also described. As discussed, each technique has its advantages and disadvantages, and these are summarized in the table below. It is expected that phase-sensitive techniques will continue to be prominent, as they enjoy a significantly larger dynamic range than speckle tracking and require the acquisition of much less data than STdOCE (Table 32.1).

32.4 OCE Techniques

In this section, we consider the wide variety of techniques that have been used to estimate elasticity from the measured displacement, as categorized by the nature and dynamics of the loading mechanism. We divide OCE techniques into five categories: compression, surface acoustic wave, acoustic radiation force, magnetomotive, and spectroscopic.

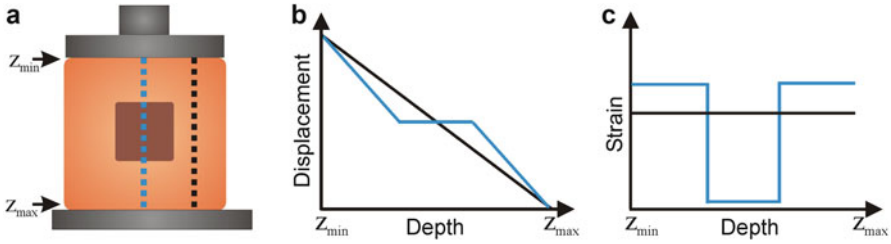

Fig. 32.7 (**a**) Illustration of an external load applied to a tissue sample, (**b**) tissue displacement versus depth for the positions indicated by the *blue* and *black lines* in (**a**), and (**c**) corresponding strain versus depth

32.4.1 Compression

In compression OCE, a step load is introduced externally to a sample between acquisitions (of either A-scans or B-scans) and the strain is estimated from the change in measured displacement with depth. This technique was used by Schmitt et al. in the first demonstration of OCE [9]. Compression elastography is the most straightforward to implement and is also the most mature in ultrasound elastography [3, 5]. In compression OCE, a number of assumptions are commonly made: (1) the stress is uniformly distributed throughout the sample, allowing the strain to be used as a surrogate for elasticity; (2) the sample is linearly elastic; and (3) it compresses uniaxially. These assumptions are also made in a number of dynamic OCE techniques [19, 49, 51], with one notable exception [52]. The adequacy and appropriateness of these assumptions is discussed in detail in Sect. 33.6.

The basic principle of compression OCE is illustrated in Fig. 32.7. A soft material containing a stiff inclusion, resting on a rigid, immovable surface, is subjected to a step load by an external compression plate. The displacement versus depth introduced at the positions indicated by the black and blue lines in Fig. 32.7a is shown in Fig. 32.7b. The displacement in the homogeneous region of the sample (black line) decreases linearly to zero at z_{max}, i.e., the sample undergoes uniform compression. The displacement through the center of the sample (blue curve) shows a local deviation in the displacement in the region corresponding to the stiff inclusion. Assuming the inclusion has a Young's modulus much larger than the background material, it can be considered to displace as a bulk, i.e., the displacement at each position in the inclusion is equal.

In Fig. 32.7b, the presence of the inclusion can be readily distinguished from the displacement. However, the difference in slope would be less visible if the stiffness of the inclusion approached that of the bulk medium. Furthermore, displacement alone cannot be used to quantify stiffness, as the displacement at a given depth in the sample is also dependent on the distance from the load. To overcome these issues, the uniaxial local strain, i.e., $\partial u_z/\partial z$ in the strain tensor (Eq. 32.4), may be plotted. The local strain corresponding to the displacement plots in Fig. 32.7b is plotted in Fig. 32.7c. The homogeneous region (black line) undergoes constant strain versus depth, whereas the hard inclusion undergoes a locally reduced strain

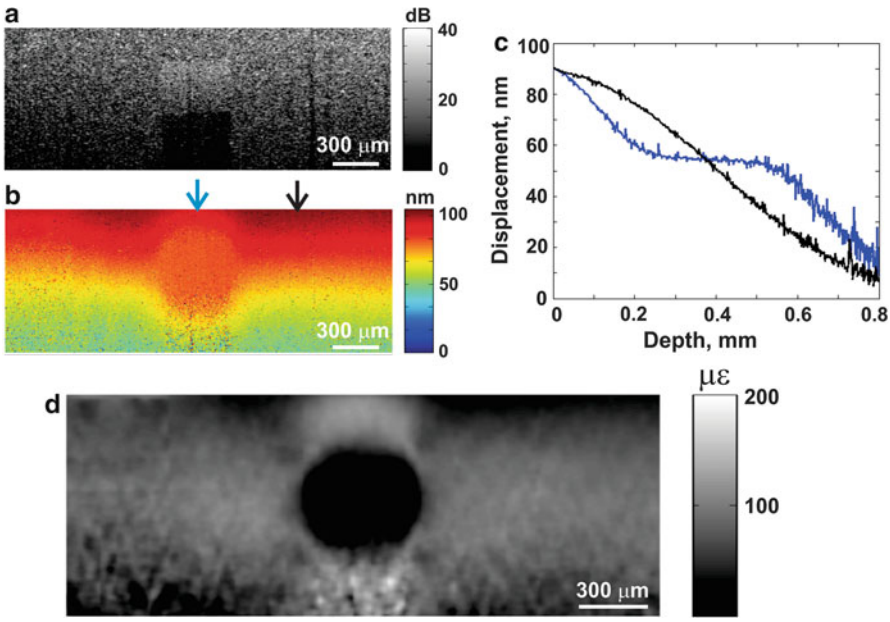

Fig. 32.8 (**a**) OCT image of a soft phantom containing a stiff inclusion, (**b**) displacement map generated for a load similar to that shown in Fig. 32.7a, (**c**) displacement plots corresponding to the positions indicated by the *blue* and *black* arrows in (**b**), and (**d**) elastogram generated from the displacement map in (**b**)

(zero strain in the ideal case of bulk motion of the inclusion shown here). It should also be noted that because the total change in displacement from z_{max} to z_{min} is the same in both regions, the strain above and below the inclusion is higher than that in the homogeneous region.

Experimental phase-sensitive compression OCE results from a phantom similar to the sample illustrated in Fig. 32.7, i.e., a stiff inclusion embedded in a soft surrounding material, are presented in Fig. 32.8. In Fig. 32.8a, the OCT image is shown. The inclusion is visible in the center of this image. The displacement map calculated from the phase difference between B-scans is shown in Fig. 32.8b and the displacement plots, similar to those illustrated in Fig. 32.7b, are presented in Fig. 32.8c at the lateral positions indicated by the arrows in Fig. 32.8b. In Fig. 32.8d, the corresponding strain image is presented. Each pixel in this image corresponds to the local strain estimated at that spatial location. The local strain is presented in $\mu\varepsilon$, signifying microstrain. As expected, the stiff inclusion has lower strain than the surrounding soft material. The strain is estimated as the change in displacement, Δu_z, over a depth increment, Δz, which, in turn, defines the strain axial resolution [53]. This estimation results in an inherent loss of spatial (axial) resolution in compression OCE. For the results shown in Fig. 32.8d, Δz was 75 μm, while the axial resolution of the OCT system was ~8 μm. Although it is a qualitative measurement of elasticity (in the sense that local strain cannot be

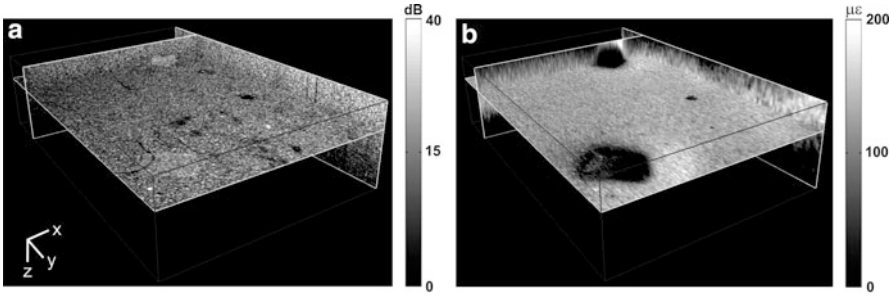

Fig. 32.9 3D-OCT (**a**, **b**) compression 3D-OCE images of the same soft phantom with two stiff inclusions visible, showing enhanced mechanical over scattering contrast for the chosen values of scattering strength and stiffness. Scale bars represent 200 μm

used to determine modulus because the local stress is not known), we define the strain image as an elastogram.

The two major factors in determining the strain measurement accuracy are the displacement measured from the OCT data and the method used to calculate strain from the measured displacement. The techniques used to measure displacement were discussed in detail in Sect. 32.3. Four estimation methods have been used to determine strain in compression OCE: finite difference, ordinary least squares, weighted least squares, and Gaussian smoothed weighted least squares (GS-WLS) [53]. In order to compare these methods, strain imaging parameters have been defined. The strain sensitivity, S_ε, is defined as the standard deviation of the strain estimate, σ_ε, and the strain SNR, SNR_ε, is defined as the ratio of the mean to the standard deviation of the strain estimate, $\mu_\varepsilon/\sigma_\varepsilon$. The GS-WLS method has been shown to provide an improvement in both sensitivity and SNR of 3 dB compared with weighted least squares, 7 dB compared with ordinary least squares, and 12 dB compared with finite difference. For all methods, strain spatial resolutions <40 μm did not provide accurate strain estimation [53].

3D visualizations of an OCT image and the corresponding elastogram, generated using GS-WLS strain estimation, are presented in Fig. 32.9. The sample is a soft silicone phantom containing two stiff inclusions. The elastogram axial resolution is 75 μm, and the lateral resolution is 10 μm. The inclusions are more readily visible in the elastogram than in the OCT image, demonstrating the potential of compression OCE to provide additional contrast in comparison with OCT. The subject of strain contrast in compression OCE will be discussed in greater detail in Sect. 32.6.

32.4.2 Surface Acoustic Wave

In recent years, a number of OCE techniques based on the measurement of the velocity of waves propagating along the sample surface have emerged [14, 15, 25, 54–57]. The shear modulus can be extracted from this velocity measurement using

inverse methods. Proposed techniques have used phase-sensitive detection in SD-OCT [54, 55], swept-source OCT [25, 57], and digital holography [14, 15]. In this subsection, we focus on the technique employing holographic detection.

Digital holographic imaging (DHI) is in many ways similar to OCT, as it is an interferometric technique that provides both the amplitude and phase of light scattered from an object. As such, it is similarly sensitive to tissue displacements, on the order of a fraction of the light wavelength. The primary difference is that DHI typically uses a long-coherence length light source that does not provide depth-resolved imaging. At the same time, DHI more naturally provides tissue surface displacement imaging over wide areas, ranging from imaging of vibrations on an eardrum [58], to induced vibrations over the whole human body [59]. Because DHI provides such comprehensive surface displacement data, it is helpful to look toward other areas of science where surface data have been employed for elasticity measurements. In fact, nondestructive testing has been widely employed to analyze the integrity of structural materials, where inversion of vibration data to produce a quantitative elastogram is treated as a boundary value problem [60, 61]. On a much larger scale, seismology is concerned with the analysis of the earth's surface movements (e.g., from earthquakes), which has been used to produce maps of the stiffness within the interior of the earth [62].

In seismology, the depth-dependent stiffness of, e.g., layers of rock, is often found by analysis of Rayleigh waves (also known as surface acoustic waves or SAWs) [63]. The ability to depth-resolve elasticity using SAWs is due to two key features of the waves: (1) SAWs propagate laterally with a penetration depth proportional to their wavelength and, thus, are only "sensitive" to materials within this characteristic depth, and (2) the wave velocity depends upon the material's Young's modulus E within this sensitive region (which we will define as our sensitivity kernel) according to $c_R \approx \frac{0.87+1.12\nu}{1+\nu}\sqrt{\frac{E}{2\rho(1+\nu)}}$, where ν is Poisson's ratio and ρ is mass density (both of which vary only slightly in tissue). As illustrated in Fig. 32.10, we can therefore measure SAW velocity versus frequency and use this to infer the depth-dependent elasticity. A stiff surface layer with an underlying soft layer will appear as a positive dispersion in the SAWs (i.e., wave speed increasing with frequency) because higher frequency waves "feel" only the stiffer surface material, resulting in higher velocity. Conversely, a soft surface layer with stiff underlying layer is negatively dispersed.

By using an appropriate model for the sensitivity kernel of the SAWs, one can construct a linear system relating a measurement of the SAW velocity dispersion, $c_R(f)$, to the 1D depth-dependent Young's modulus of the sample, $E(z)$. This inverse method was first demonstrated in soft materials using a single-point optical vibrometer scanned away from a point source actuator [64, 65]. It was subsequently translated to DHI, where depth-resolved elasticity was measured in 2-layer phantoms up to 55 mm deep (Fig. 32.10 panels e, f) [15]. The advantage of using DHI to perform SAW elastography is the capability for real-time imaging of SAWs across the entire tissue surface, extending the 1D measurement of E into three dimensions. Importantly, this could have applications in performing whole-breast elastography,

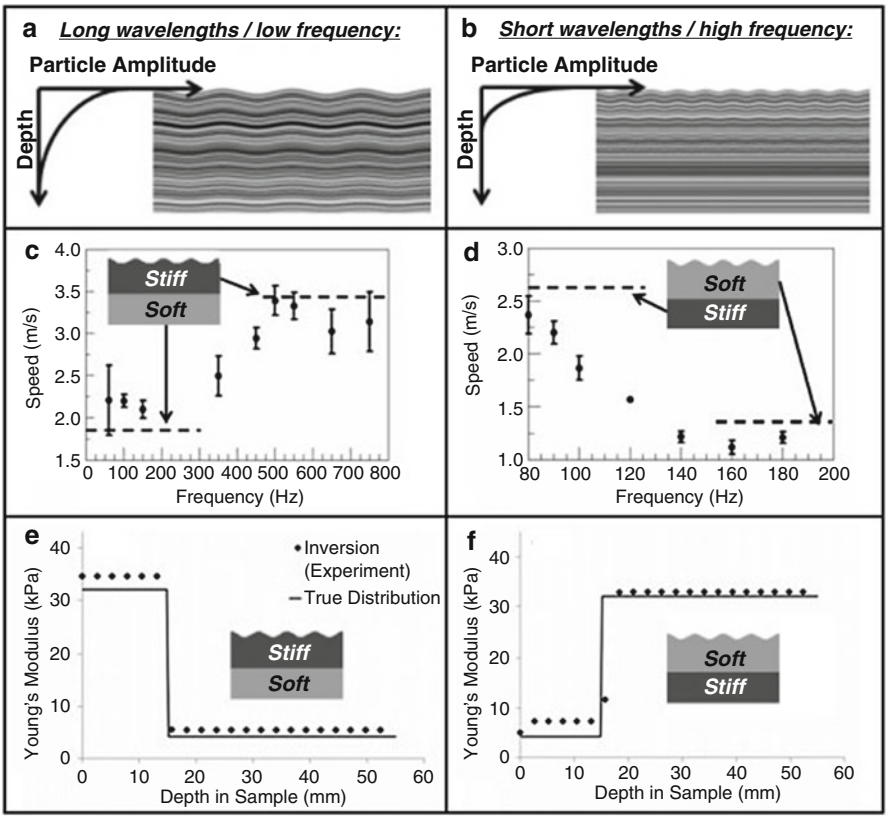

Fig. 32.10 Relationship between velocity dispersion of SAWs and depth-dependent stiffness. (**a**, **b**) Schematic illustration of SAWs versus depth showing how frequency affects the depth of penetration. (**c**, **d**) SAW velocity dispersion curves obtained using DHI in 2-layer tissue phantoms (data reprinted from [14]). (**e**, **f**) Reconstructed elastic depth profile in 2-layer phantoms is consistent with the actual phantom stiffness (Data reprinted from [15])

as a quantitative method to replace manual palpation currently used in breast cancer screening. In materials of similar elasticity as the human breast, SAW frequency sweeps from 20 to 600 Hz would be expected to provide elastograms over depths from nominally 5–50 mm. Currently, it has been qualitatively shown that DHI can detect perturbations in SAWs propagating over a 5 mm tumor-like inclusion embedded 9 mm deep in a breast tissue phantom [15] and that SAWs on real tissues appear well behaved when visualized with DHI (Fig. 32.11).

The visualization of SAWs using DHI deserves some attention here. There are several standard techniques employed in DHI for dynamic displacement measurement, which typically include off-axis holography and either Fourier transformation or spatial phase-shifting of the resulting fringe pattern [66, 67]. Interestingly, SAW elastography only requires measurement of the SAW phase velocity under a condition of a priori knowledge of the SAW frequency. Using this advantage, a method was recently

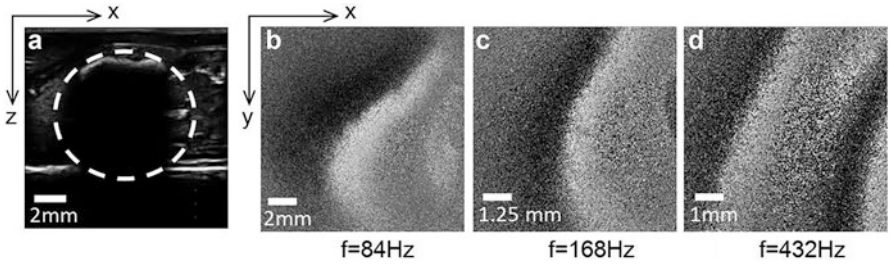

Fig. 32.11 Imaging SAWs in chicken thigh. (**a**) B-mode ultrasound showing the depth position of the thigh bone (*dashed circle*). (**b**–**d**) Corresponding DHI phase maps of SAWs propagating on the surface as a function of frequency. While low-frequency SAWs are strongly perturbed by the presence of the bone, well-behaved SAWs at high frequencies suggest that the softer tissue above the bone is relatively elastically homogeneous (Reprinted from [15])

developed to extract SAW phase (modulo π) using an on-axis DHI system without any phase modulation [14]. This method circumvents the limitation to the maximum spatial frequency of fringes imposed by off-axis holography, with the trade-off that one cannot readily extract the amplitude of the SAWs (only the phase). Example SAW phase maps obtained from chicken tissue are displayed in Fig. 32.11, revealing apparent wave "crests" corresponding to where the SAW phase wraps from π back to zero, which is a very intuitive way of visualizing the SAW wave fronts.

In summary, DHI-based elastography is a promising method for quantitative elastography that exploits the depth-penetrating property of SAWs to provide elastography several centimeters into tissues. Importantly, it is not limited by the shallow depth penetration of light but trades off overall spatial resolution. While standard elastography requires 3+1D (spatial+temporal) data collection, SAW-based elastography requires only 2+1D (spatial+frequency) data collection with the use of an appropriate model for SAWs to solve the boundary value problem. Future emphasis in this area will be on extending the current quantitative 1D elastography method to 3D.

32.4.3 Acoustic Radiation Force

In acoustic radiation force impulse (ARFI) imaging, a focused ultrasound pulse creates a localized mechanical load within a sample and the resulting deformation is measured using imaging techniques. Its initial development was based on ultrasound detection [68], with continuing clinical and commercial interest [69, 70]. More recently, OCT-based ARFI has been proposed, allowing smaller displacements to be measured with improved spatial resolution [23, 26, 71, 72].

Consider an acoustic wave, propagating in tissue generated using an ultrasound transducer. A unidirectional force is applied to absorbing or reflecting targets in the propagation path of the acoustic wave. This force results from a transfer of momentum from the acoustic wave to the tissue. Under the assumption of plane

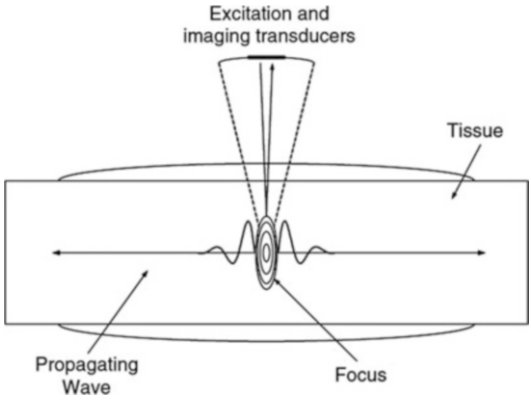

Fig. 32.12 Illustration of shear wave propagation caused by a focused ultrasound pulse (Reproduced from [2])

wave propagation, the acoustic body force (i.e., force per unit volume) applied to tissue at a given location due to local absorption is given by $F = \frac{2\alpha I}{c}$, where F has units of kg/(s^{2}cm^2), c is the speed of sound (m/s) in the tissue, α is the tissue absorption coefficient (m^{-1}), and I is the average intensity of the acoustic beam (W/cm^2) at the given location.

On-off modulation of the acoustic wave results in a corresponding on-off modulation of the local force and, hence, displacement, which can be measured directly or through the generation of an accompanying shear wave propagating in the direction perpendicular to the direction of the focused ultrasound beam, as illustrated in Fig. 32.12. The goal in ARFI imaging has primarily been to measure the sub-surface shear wave speed, c_s, which is directly related to the sample's shear modulus, μ, by $c_s = \sqrt{\mu/\rho}$, where ρ is the density of the tissue. Both speckle tracking [71] and phase-sensitive detection [23, 26] have been used to measure the shear wave speed in ARF-OCE. Axial displacement has also been measured in an ARF-OCE technique [72].

A related ARFI technique known as transient optoelastography has also been proposed [12, 73]. This technique is based on ultrasound-modulated optical tomography (UMOT) [13]. Detection of variations in laser speckle patterns recorded on the surface of a sample due to acoustic stimulation at depths up to several centimeters is possible, providing information from much greater depths than possible using OCE. However, the spatial resolution is determined by that of the ultrasound beam and is, therefore, much lower than that of OCE.

In all ARFI techniques, it should be considered that the high-intensity acoustic pulses used can be potentially harmful and above the safe limits set by, e.g., the U.S. Food and Drug Administration (FDA) [68]. However, this may prove not to be a major concern in ARF-OCE, as much smaller tissue displacements are required than when using ultrasound detection. Another noteworthy issue is the use of water or gel to couple the transducer and sample required to achieve acoustic impedance matching. Furthermore, same-side optical imaging and acoustic loading requires use of an annular or off-axis acoustic transducer.

32.4.4 Magnetomotive

Magnetomotive OCE (MM-OCE) utilizes an external magnetic field to induce magnetomotion within a sample of interest and OCT to detect displacements within the sample on the order of tens to hundreds of nanometers. Magnetomotion can be produced via internal excitation through the use of magnetic nanoparticles (MNPs) distributed within the sample [74–76], through a magnetic implant embedded in a sample [77], or via external excitation, e.g., through the use of a metallic slab transducer placed in contact with the sample [78]. MM-OCE can perform optical rheology of viscoelastic materials by measuring the dynamic response of a sample, either to a step excitation [74] or to a frequency sweep [75, 78]. The natural resonant frequencies of the sample can be connected to elastic and viscous moduli through an appropriate mechanical model.

The use of step excitation for optical rheology of tissue phantoms is shown in Fig. 32.13. These measurements were carried out in silicone phantoms doped with titanium dioxide particles to provide optical scattering and iron oxide MNPs to provide internal magnetomotive forces. Motion-mode (M-mode) measurements show an under-damped response to the (broadband) step excitation, where the dominant relaxation frequency is the natural resonance of the sample. The Young's modulus of the samples was varied over a range from 0.4 to 140 kPa, as calibrated using a commercial indentation instrument. The resonant frequency of the sample showed a linear dependence versus the square root of the Young's modulus, which is consistent with the behavior of a Voigt model, as previously adopted to model the mechanical response of bulk tissue [52].

Magnetomotive resonant acoustic spectroscopy (MRAS) is another magnetomotive technique to measure tissue elasticity [75]. MRAS utilizes a frequency sweep to measure the natural resonant frequencies of tissue-mimicking phantoms and biological samples. This approach provides improved signal-to-noise ratio compared to the step excitation, due to the increased measurement time of the sweep. Experiments in tissue-mimicking phantoms confirmed that the longitudinal vibration modes (natural resonant frequencies of the sample) depended on both sample viscoelastic properties as well as the geometrical dimensions (cylinder aspect ratio). For known sample geometry, Young's modulus and the viscous damping coefficient of the samples were determined by fitting the data to a viscoelastic mechanical model. In this model, Young's modulus was proportional to the square of the resonant frequency, while the viscous damping coefficient was proportional to the Lorentzian-shaped linewidth (related to the quality factor Q) of the resonant peak.

With biological tissue, where the geometry of the sample is not well controlled, MRAS has shown the ability to track relative changes in Young's modulus of the sample. Figure 32.14a shows measurements of the complex mechanical spectrum of rat liver undergoing formalin fixation. The increase in the resonant frequency with time can be seen in both the amplitude and phase of the mechanical response. Over a period of 147 min, the resonant frequency of the tissue undergoing fixation increased by a factor of 2, which suggests an increase in Young's modulus by a factor of 4.

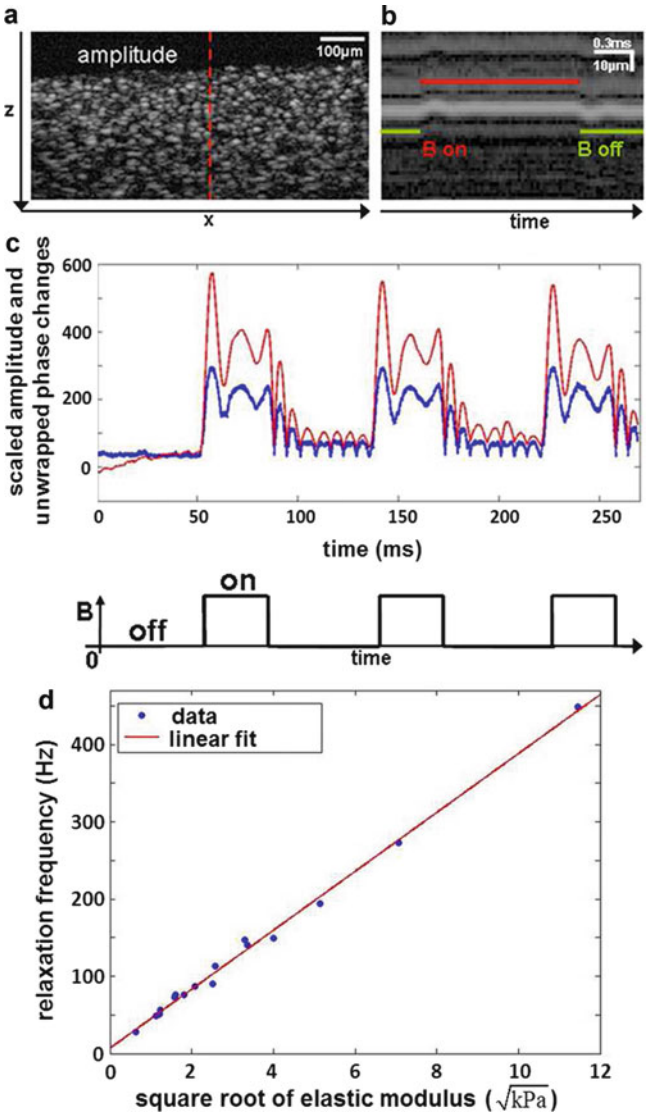

Fig. 32.13 Optical rheology of tissue phantoms based on a step magnetic excitation. (**a**) Cross-sectional OCT image. (**b**) M-mode image at the transverse position denoted by the *dashed red line* in (**a**). (**c**) Average scatterer response showing the amplitude (*blue*) and phase (*red*) characteristics of the magnetomotion from the excitation profile shown directly below (**c**). (**d**) The natural resonance frequency of phantoms of varying stiffness (adapted from [74])

MRAS was utilized in a subsequent study to evaluate the dependence of the resonant frequency of fibrin clots vs. fibrinogen concentration [78]. The viscoelastic properties of fibrin networks are important in bleeding and clotting disorders. Clots were formed with controlled geometry in custom-printed rectangular wells, and in

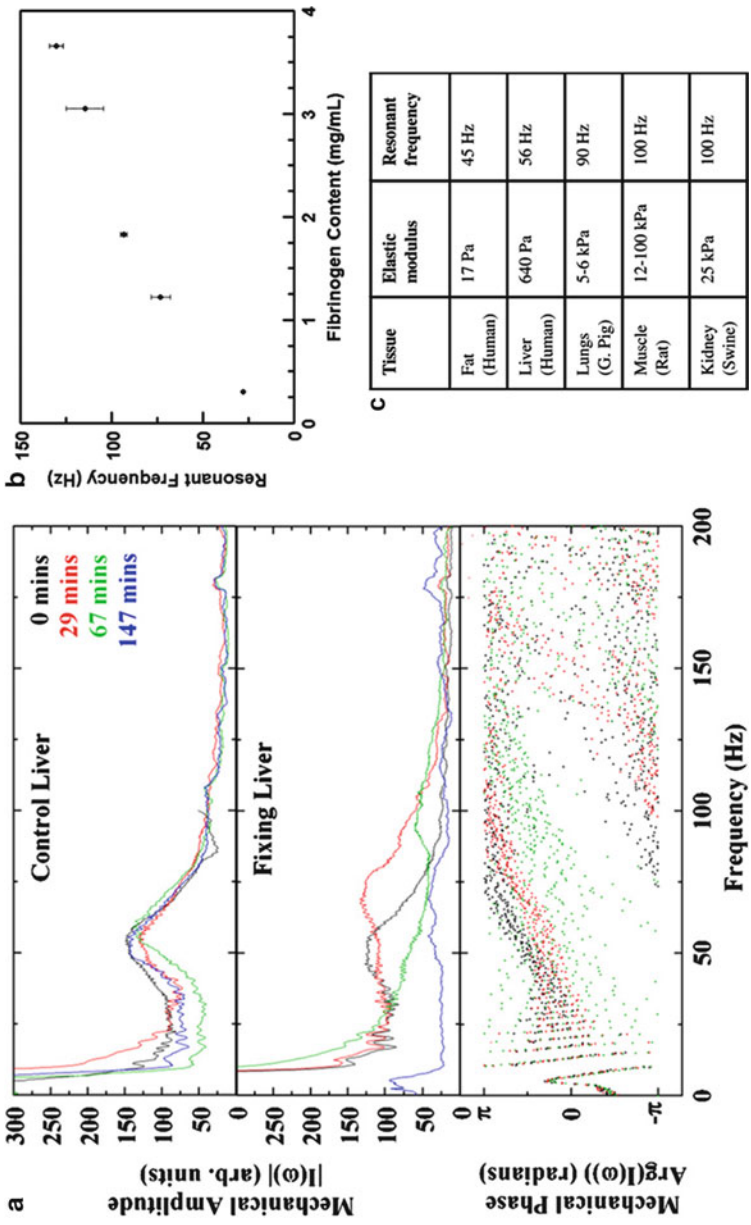

Tissue	Elastic modulus	Resonant frequency
Fat (Human)	17 Pa	45 Hz
Liver (Human)	640 Pa	56 Hz
Lungs (G. Pig)	5-6 kPa	90 Hz
Muscle (Rat)	12-100 kPa	100 Hz
Kidney (Swine)	25 kPa	100 Hz

Fig. 32.14 MRAS of biological samples. (**a**) Longitudinal tracking of rat liver tissue undergoing formalin fixation ex vivo (from [75]), (**b**) resonant frequency of fibrin clots prepared in custom-printed rectangular wells (From [78]), and (**c**) table of natural resonant frequencies for different tissues (From [79]). Magnetomotion was produced via internal iron-oxide MNPs in (**a**) and (**c**), but with an external microtransducer in (**b**)

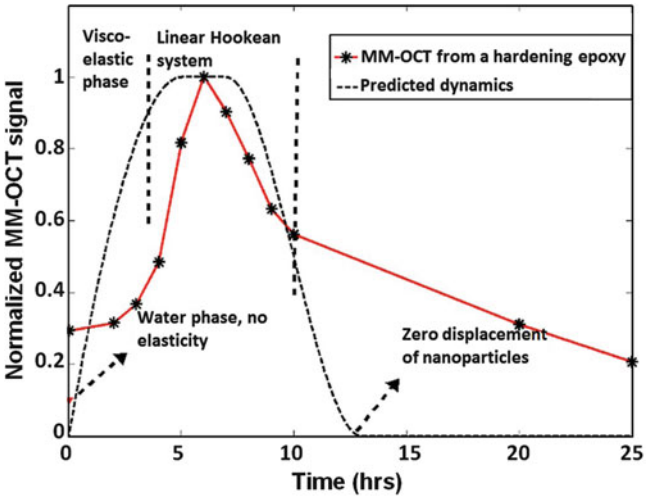

Fig. 32.15 Magnetomotive response of an epoxy sample undergoing transition from a viscous liquid state to a rigid solid (Adapted from [79])

this study an external microtransducer was used in order to avoid embedding the clots with MNP nanotransducers. Figure 32.14b presents results from M-mode measurements, showing that the resonant frequency increases monotonically with fibrinogen concentration. The Young's modulus is proportional to the square of the resonant frequency. Figure 32.14c presents measurements of the natural vibration frequencies for different types of tissues [79].

The magnetomotion facilitated by MNPs has been investigated in a wide range of viscoelastic conditions [79], experimentally simulated through the hardening process of epoxy from a viscous liquid to its final hardened state (see Fig. 32.15). The epoxy had a characteristic setting time of 12 h at a temperature of 90 °C. The low initial MM-OCT signal shows that initially the MNPs are not bound within the viscous fluid and so experience virtually no elastic restoring forces. Since the direction of the magnetic gradient force is the same regardless of polarity of the magnetic field [75], the oscillating magnetic field simply results in unidirectional displacements in addition to the Brownian motion of the particles in the liquid. Since the signal processing detects only sinusoidal motion, the liquid phase regime does not generate an appreciable MM-OCT signal. As the epoxy sets, it enters the regime of a linear Hookean system, where the MNPs that are now bound to the matrix experience elastic restoring forces. Finally, as the epoxy hardens the MNPs become tightly bound to the medium (which now has a significantly increased elastic constant), and the magnetomotion tends to zero. Ongoing work with a dual coil setup will enable bipolar forces on the magnetic particles, to extend the regime of applicability of MM-OCE to highly viscous samples [80].

Further work on MM-OCE will investigate the contributions of tissue geometry to the complex mechanical spectra and the extraction of quantitative mechanical properties. Finite element modeling, discussed in detail in Sect. 32.6, can simulate

deformation due to magnetomotive forces in irregularly shaped samples and help disentangle the impact of biomechanical heterogeneity on the bulk natural vibration modes of the sample. Extending these M-mode MM-OCE measurements to perform B-mode (or volumetric) imaging has the potential to provide spatially localized information on the mechanical properties of heterogeneous samples.

32.4.5 Spectroscopic

Mechanical spectroscopic imaging of tissue was first reported in landmark papers on ultrasound-stimulated vibro-acoustography [81, 82]. Vibro-acoustography utilizes the radiation force of focused ultrasound (see Sect. 32.4.3) within tissue to excite sinusoidal motion in the kHz regime and a sensitive hydrophone to detect the amplitude and phase of the resulting acoustic emission. Instead of pulsed ultrasound considered in Sect. 32.4.3, local excitation in the kHz regime was achieved through the use of two confocal ultrasonic transducers (each operating at ~3 MHz) to generate at their difference frequency a kHz oscillation of the ultrasonic energy density at the overlap of the foci. These overlapped foci were raster scanned within the sample to record an image of the object motion. Mechanical spectroscopy was performed by tuning the difference (beat) frequency between the transducers. Vibro-acoustic spectrography of human iliac arteries ex vivo demonstrated clear differences between stiffer calcified regions and nearby normal regions of the artery, at an excitation frequency of 6 kHz. These differences were observed in both the (mechanical) amplitude and phase images [81].

Motivated by the success of ultrasound vibro-acoustography [83–86], mechanical spectroscopic imaging has also been developed for OCE [87]. Utilizing a spectral-domain OCT platform for phase-sensitive B-mode imaging during external mechanical excitation [32, 46], 2D B-mode images were recorded over a wide range of excitation frequencies (20–1,000 Hz). Signal processing steps were developed to extract the (spatially localized) complex mechanical displacement. Figure 32.16 shows spectroscopic OCE in rat mammary tissue consisting of tumor adjacent to adipose. Peaks in the mechanical spectra at 83 and 385 Hz were attributed to adipose and tumor regions of the tissue, respectively. Contrast between mechanically distinct regions of the tissue can be seen in both the amplitude and mechanical phase response images corresponding to 83 Hz excitation. In particular, the mechanical phase image highlighted an oval region of the sample, with a mechanical phase shift of $+\pi$ that is characteristic behavior above resonance. The distinction of this region from its surroundings was seen over a wide frequency range (25–83 Hz, and at 125 and 167 Hz), suggesting a relatively low resonant frequency. Appearing as oval-shaped structures in the histology image, this feature was attributed as a fluid-dense follicle or vacuole.

Spectroscopic OCE is at an early stage of development and several areas require further investigation. As discussed in Sect. 32.4.4, the impact of tissue geometry,

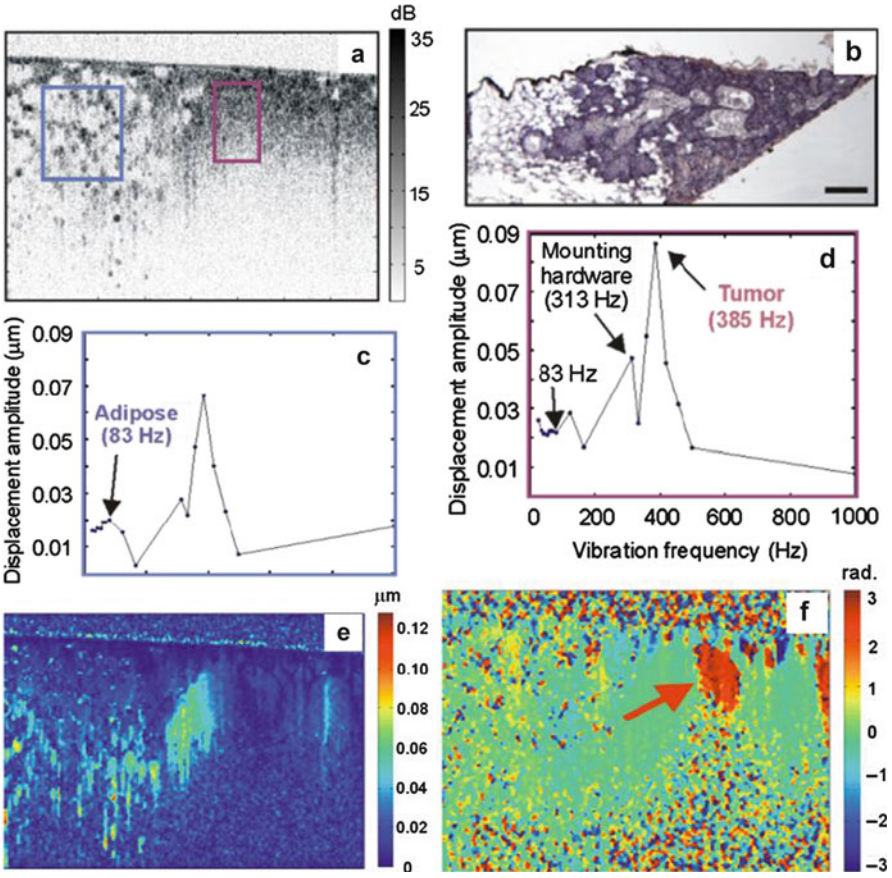

Fig. 32.16 Spectroscopic OCE of rat mammary tumor adjacent to adipose tissue. (**a**) B-mode OCT image, (**b**) corresponding nearby histology, (**c**) mechanical amplitude spectrum for adipose (spatial average over *blue box* in (**a**)), (**d**) mechanical amplitude spectrum for tumor (spatial average over *magenta box* in (**a**)), (**e**) displacement amplitude image at excitation frequency of 83 Hz, and (**f**) displacement phase image at excitation frequency of 83 Hz (Adapted from [87])

heterogeneity, and the natural vibration modes of the mechanical mounting hardware on the complex mechanical response measured in the sample needs to be determined. Further work on theoretical modeling and simulation (see Sect. 32.6) could provide a method to invert the complex displacement maps in order to extract the elastic and viscous properties of the sample. These simulations could also investigate the role of mechanical coupling on the spatial resolution of the inversion process. ARF-OCE (see Sect. 32.4.3) is a promising approach to address potential resolution limitations with external (bulk) mechanical excitation [23]. Further work is required to adapt ARF-OCE for B-mode or volumetric spectroscopic imaging. Finally, it would be interesting to extend the excitation frequency range into the kHz regime (as in ultrasound-stimulated vibro-acoustography). Ultimately, the

success of spectroscopic OCE will depend on characterizing the appropriate frequency ranges (or specific excitation frequencies) that maximize contrast between regions of tissue with distinct biomechanical properties.

32.5 Implementation

Translation of OCE techniques to clinical use requires further development of practical probes that enable simultaneous loading and imaging of tissue. This section reviews initial efforts to implement OCE in vivo, using probes suitable for superficial tissues such as skin and catheter-based and needle-based probes suitable for use within the body.

32.5.1 Imaging Superficial Tissues

Most initial OCE studies performed imaging and loading of small samples from opposite sides [40, 49, 52]. While this configuration may be sufficient for imaging small ex vivo tissue samples or phantoms, imaging and loading from the same side are essential for in vivo imaging. In the first OCE paper [9], loading and imaging were performed from the same side using an annular piezoelectric actuator, but an A-scan rate of 11 Hz and decorrelation of speckle due to sample movement limited the in vivo capabilities of this setup. A same-side OCE setup was later proposed using a similar design [19], as shown in Fig. 32.17. An annular piezoelectric transducer is fixed to an imaging window and coupled directly to the sample, enabling simultaneous, concentric actuation and imaging of the tissue. This ring

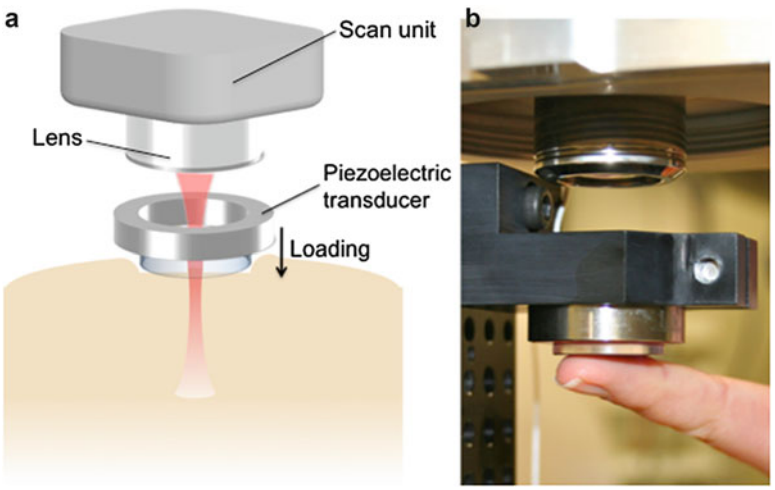

Fig. 32.17 Ring actuator design for in vivo OCE of superficial tissues. (**a**) Probe schematic and (**b**) photograph of implementation for skin imaging

actuator design can be used to apply pico- to microscale displacements to tissue over a wide range of frequencies and has been used in compression and spectroscopic OCE studies [51, 87], including the first in vivo 3D OCE measurements, which used human skin as the target tissue [51].

To perform ARF-OCE or SAW-OCE requires either an impulse load or vibrational load applied to the tissue. Implementation of these dynamic loading techniques requires careful synchronization of the actuation and imaging, but they have the practical advantage that the tissue loading may be performed adjacent to the imaging, eliminating the need to combine actuation and imaging capabilities into a single device. SAW-OCE on skin in vivo has been achieved using a mechanical shaker coupled directly to the tissue [54]. The mechanical shaker employed a piezoelectric element to introduce an impulse load to the tissue, and the resulting surface waves were measured by the adjacent OCT probe. For applications where direct contact of the probe with tissue is not desirable, such as imaging of the cornea, a noncontact implementation of SAW-OCE has also been proposed using a remote laser pulse to generate surface waves [88].

Other loading techniques for superficial tissues have included an air puff system for measuring the elastic response of the cornea [89, 90] as well as an annular suction device which applies a suction force concentric with the OCT imaging to measure elasticity of skin in tension [32].

32.5.2 Catheter-Based OCE

Implementation of OCE using miniaturized, fiber-based probes for endoscopic and intravascular imaging presents new challenges for developing loading schemes that can be deployed in such confined spaces. One natural approach to overcoming this issue is to use physiological deformation of the tissue as the "loading" mechanism. This is especially suitable for tissues that undergo regular changes in luminal pressure, such as airways and blood vessels. This concept has been used for measurement of the elastic properties of the airway wall using anatomical OCT (*a*OCT), a long-range OCT technique for profiling of hollow organs [91]. Here, changes in airway dimensions versus pressure were measured in patients with and without obstructive lung diseases to investigate the correspondence of airway wall compliance with pathology.

Luminal pressure changes have also been proposed as a loading technique for performing intravascular OCE [92, 93]. Although physiological deformation of tissue is convenient to measure, quantitative measurement of mechanical properties requires controlled loading of the tissue. An OCT imaging catheter that achieves this has been proposed for applying acoustic radiation force at localized points deep in the body [94]. A catheter design incorporating a piezoelectric ultrasound transducer into the distal probe head has the advantage that direct contact with the tissue is not required, as the acoustic radiation force may be focused to induce a tissue "push" at a desired distance from the probe. Such a probe design, shown in Fig. 32.18, has been realized for combined OCT and ultrasound structural imaging

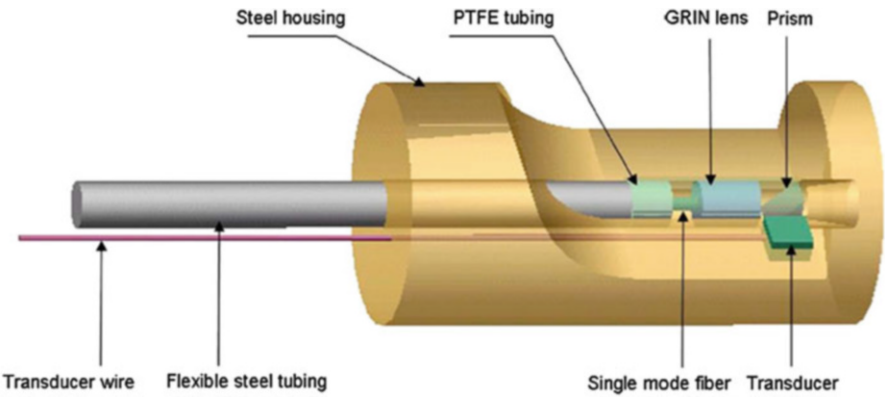

Fig. 32.18 Schematic of combined ultrasound and OCT probe that may be suitable for performing catheter-based ARF-OCE. *PTFE* polytetrafluoroethylene, *GRIN* graded-index (Adapted from [94])

of arteries [94], but not yet been used to perform elastographic measurements. Another proposed technique for catheter-based OCE incorporates a small palpation device in the distal end of the probe, which may consist of a controlled liquid jet or mechanical indenter for compressing adjacent tissues [95]. Despite the several proposed embodiments of catheter-based OCE, results acquired using such a probe have yet to be reported.

32.5.3 Needle-Based OCE

The recent development of three-dimensional OCT needle probes has allowed imaging deep within solid tissues, extending potential OCT applications to include, e.g., biopsy and surgical guidance and monitoring of interstitial procedures [96, 97]. When needles are inserted into soft tissue, the needle exerts a force on the tissue ahead of the tip, as well as a shear force on the surrounding tissue due to friction. Measurement of this needle-induced deformation has been used to perform the first needle-based OCE measurements [98]. These measurements used a forward-facing probe design and phase-sensitive displacement measurement to capture 1D deformation ahead of the needle during insertion. The deformation caused by a flat end-faced needle, such as the one employed in these studies, can be approximated as compression of a column of tissue ahead of the needle [99]. Therefore, changes in the displacement with depth, i.e., the strain, indicate changes in mechanical properties.

Results from needle insertion into excised pig airway wall, consisting of layers of varying stiffness, are shown in Fig. 32.19. The displacement plot shows three distinct slopes, indicating the locations of tissue boundaries, as well as providing a measure of their relative stiffness. The displacement curve is in agreement with the corresponding histology acquired along the path of needle insertion, which shows layers of mucosa, submucosa, and smooth muscle.

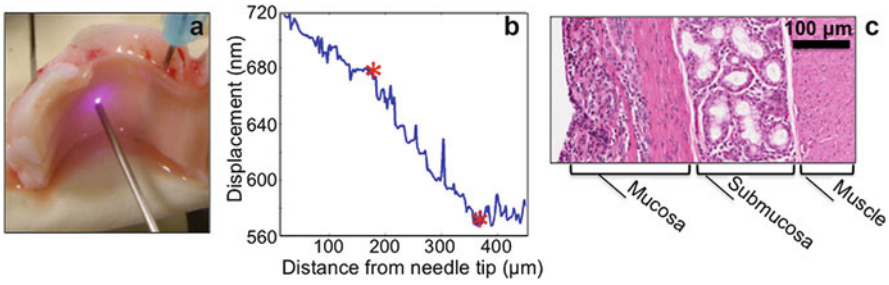

Fig. 32.19 Needle OCE of excised pig airway wall. (**a**) Photograph of OCE needle probe insertion into sample; (**b**) measured tissue displacement ahead of the *needle tip* shows changes in slope at the positions of the *red stars*, indicating different tissue types; and (**c**) corresponding histology validates the presence of three tissue types (Reproduced from [98])

32.6 Fidelity of OCE: Comparison to Models of Tissue Deformation

In this section, we discuss artifacts that can arise in OCE and limit the accuracy with which elastograms represent the underlying elastic properties of tissue. We present initial efforts to use modeling of tissue deformation to investigate the impact of parameters such as tissue geometry and boundary conditions on the resulting contrast in elastograms. We also review initial efforts in OCE to produce more reliable, quantitative elastograms by approaching elasticity reconstruction as an inverse problem.

32.6.1 Limitations on the Mechanical Fidelity of Elastograms

In OCE, constructing a map of elasticity from measured displacements requires some assumptions to be made about the tissue, such that its observed behavior and mechanical properties may be linked through a mathematical model. The most common of these assumptions, which underlie image formation in compression, ARF, and SAW techniques described in Sect. 32.4, are (1) tissue is linear elastic, which allows stress and strain to be related linearly through elastic constants, and (2) tissue is isotropic (properties are direction independent), which reduces the fourth-order elasticity tensor to two elastic constants for describing the mechanical behavior of tissue (as described in Sect. 32.2.3). Magnetomotive and spectroscopic techniques (Sects. 32.4.4 and 32.4.5) have employed a more advanced model of tissue behavior, accounting for viscoelastic properties, but image formation and quantitative measurements in these techniques rely on assumptions about the tissue geometry and mechanical coupling of tissue regions.

Use of such assumptions simplifies the characterization of tissue, facilitates the development of OCE methods, and may in some cases prove sufficient for producing clinically useful images. However, tissue behavior in general is much more complex, exhibiting varying degrees of nonlinearity, viscoelasticity, poroelasticity,

anisotropy, and geometric complexity. When simple assumptions break down in the presence of such complexities, the resulting elastograms contain mechanical artifacts, limiting their fidelity to the underlying tissue properties and, ultimately, their potential clinical utility.

For OCE to advance toward clinical implementation, it is necessary to test the validity of assumptions employed in the various techniques, understand where they break down, and quantify the impact of artifacts on image contrast and reliability. Such quantitative assessment requires comparison of the measured tissue deformation in OCE to that predicted by mechanical models. Discrepancies between the two will highlight sources of mechanical artifacts and allow their effects on image contrast to be assessed. In addition to serving as an investigative tool, modeling of tissue deformation may also be used as part of an iterative elasticity reconstruction process to produce quantitative elastograms.

Accurate modeling of tissue deformation involves solving for complex geometries and heterogeneous elasticity fields, and therefore, numerical methods are preferred over analytical methods for accurate representation of tissue deformation. The predominant numerical method for modeling tissue deformation is the finite element method (FEM). In FEM, the tissue geometry is divided into a mesh of individual elements, and the governing equations of motion are solved for each element. FEM has been used in OCE to validate new methods for estimating velocity and strain [30], to validate new loading techniques for generating elastographic contrast [77, 100], and to estimate stress and strain fields in artery walls under luminal pressure [92], but has not yet been used to evaluate the limitations of mechanical artifacts on image contrast. Such investigations have been performed extensively in ultrasound elastography [101–104]. However, the impact of mechanical artifacts on image contrast in OCE will differ from those in ultrasound elastography due to different limits on measurable displacement and an increased sensitivity to boundary conditions, as images are generally limited to the first few millimeters of tissue. In the next section, we report on early efforts in using FEM to investigate sources of mechanical artifacts and evaluate their effects on image contrast for the particular case of compression elastography.

32.6.2 Modeling of Compression OCE

In compression elastography, strain is measured and used to represent elasticity. Interpreting strain elastograms as one-to-one representations of modulus assumes a uniform stress distribution within the sample. This assumption is invalid for samples with heterogeneous mechanical properties or when stress concentrations arise at tissue boundaries. Stress distribution beyond the sample surface cannot be measured directly, but FEM allows us to simulate the stress distribution for a given sample and investigate sources of its nonuniformity. In the case study described here, FEM is employed to simulate sample deformation in compression OCE of tissue-mimicking phantoms. The effect of feature geometry and boundary

conditions on mechanical artifacts and the resulting image contrast are investigated in both FEM and experiments.

Careful fabrication of phantoms with known geometry and mechanical properties was essential for input to the model and fair comparison of the simulated and measured sample deformation. Silicone was used, as its optical and mechanical properties can be controlled over a wide range, and it can be readily molded into complex shapes [105]. Two types of phantoms were fabricated: mechanically homogeneous phantoms and phantoms comprising a hard inclusion (Young's modulus 450 MPa) in soft bulk (Young's modulus 23 kPa). The mechanical behavior of the silicones was measured independently using compression tests, providing stress-strain curves for each material from which moduli were estimated. Compression OCE was performed using a ring actuator setup as described previously [51]. A phase-sensitive technique [40] was used to measure sample displacement, and weighted least squares (WLS) strain estimation [53] was used to generate elastograms.

A linear elastic, axisymmetric 3D model was employed, and the phantom geometry and material behavior from the compression tests were used as inputs to the simulations. FEM produced simulations of sample displacement and strain fields, which were compared to that produced experimentally for validation. Once agreement was obtained between the measured and simulated displacements and strain, the simulated stress distributions could also be analyzed to aid interpretation of mechanical artifacts in the elastograms. Two prevalent sources of stress nonuniformity in the compression experiments are discussed here: friction and stress concentrations at feature boundaries.

Friction: For a homogeneous sample undergoing uniaxial compression, the strain and stress are expected to be uniform throughout the sample. For nearly incompressible materials such as soft tissues, axial compression is coupled to lateral expansion in order to conserve volume, as discussed in Sect. 32.2.4. If friction is present between the sample and the compressor, this restricts lateral motion of the sample at the boundary, resulting in lower strain, and, as a result, a region of apparently higher stiffness in the elastogram. To demonstrate the effect of friction on the resulting elastogram, two OCE measurements of a 0.8 mm thick, homogeneous silicone phantom were acquired with different boundary conditions. The results are shown in Fig. 32.20. In the first experiment, a lubricant was applied at both surfaces to allow slipping of the sample boundary against the compression plate. In the second, no lubricant was used on either surface. In the resulting elastograms shown in Fig. 32.20, the lubricated case shows a homogeneous strain field, as expected, while in the non-lubricated case, the effect of friction manifests as two bands of low strain at the top and bottom surfaces. These experiments were also simulated with FEM, using the two extreme boundary conditions of frictionless and no-slip at the surface, respectively. The representative plots (taken from the center of the sample) of displacement versus depth in Fig. 32.20 show good agreement between the measured and simulated displacements. This example demonstrates the importance of considering boundary conditions both when acquiring and interpreting elastograms in compression OCE.

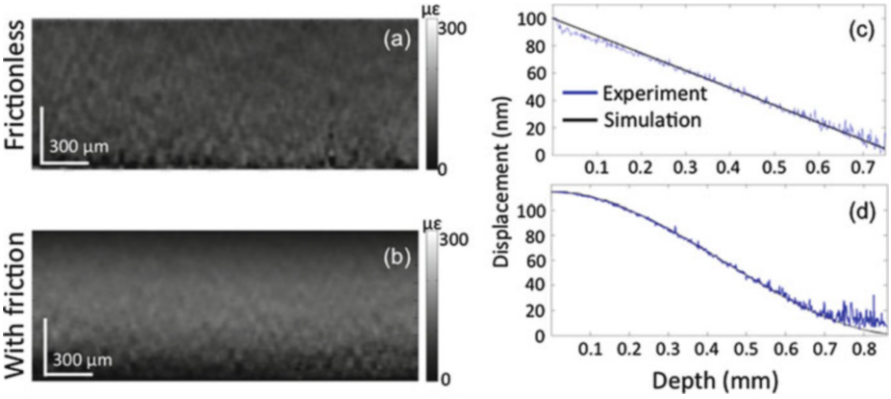

Fig. 32.20 (**a**, **b**) Experimental strain elastograms and (**c**, **d**) comparison of measured and simulated displacement plots for the cases of (**a**) and (**c**) frictionless and (**b**) and (**d**) no-slip conditions at the boundaries

Stress Concentrations at Feature Boundaries: When a lesion of higher stiffness than that of the background is present, this creates a region of low strain in the elastogram, as expected. However, stress concentrations also arise above, below, and at the sides of the lesion, resulting in regions of higher strain at these locations. Thus, the assumption of stress uniformity does not hold for this geometry; if the strain image were interpreted directly as elasticity, the regions of higher strain about the inclusion would erroneously be interpreted as regions of low stiffness. The magnitude of this artifact increases for increasing modulus contrast between the lesion and the background material and also depends on the position in depth of the lesion. To demonstrate the presence of these artifacts and the nonuniform stress field for the case of a stiff lesion, compression OCE was performed on a soft phantom with a hard inclusion embedded. The resulting experimental elastogram, simulated strain, and simulated stress fields are shown in Fig. 32.21. The experimental and simulated strain both show the regions of higher and lower strain around the inclusion, and the simulated stress field allows analysis of where the stress uniformity assumption fails.

Although a linear elastic FEM was employed in this initial study, the silicone materials used exhibit nonlinear behavior, as do many tissues. This results in a nonlinear relationship between the strain introduced to the sample and the resulting strain contrast; i.e., the elastogram contrast changes as a function of stress on the sample. This was observed to cause discrepancies between the model, for which a single modulus value was assigned to each material, and the experiments, in which the effective stiffness of each material varied depending on the applied stress. Although tissue may be assumed to behave linearly at strains <0.1 [22], remaining in this linear regime is not always feasible when performing elastography of tissue, as large local deformations are common in the body; e.g., arteries undergo physiological strains of up to 0.2 [93]. This highlights a need to employ more advanced models of tissue to enable more accurate construction of elastograms.

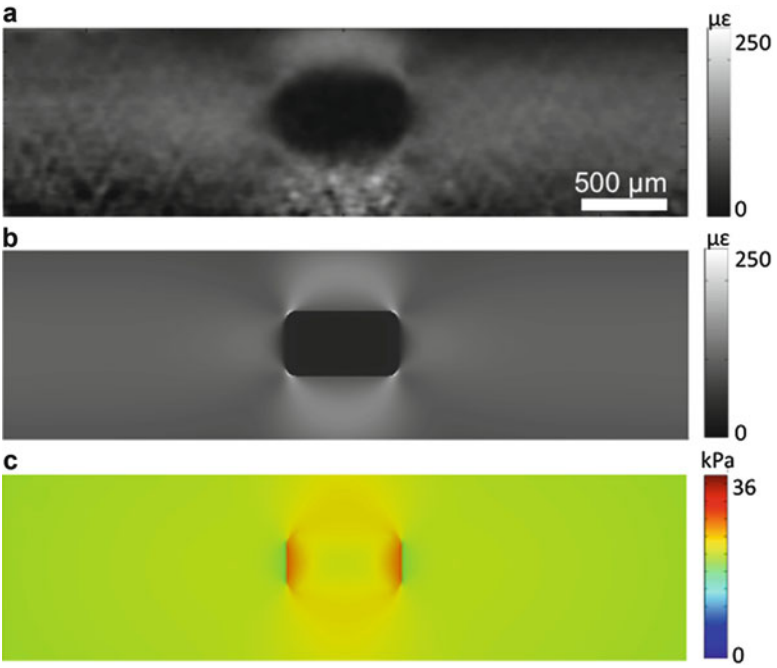

Fig. 32.21 (**a**) Measured strain, (**b**) simulated strain, and (**c**) simulated stress of a phantom comprising a stiff inclusion in soft bulk, demonstrating regions of high strain due to stress concentrations about the inclusion

32.6.3 Model-Based Elastography: Inverse Methods for Quantitative Elastograms

As seen in the preceding example of compression elastography, elastograms constructed based on simplified models of tissue deformation do not always accurately represent tissue elasticity. In ultrasound and magnetic resonance elastography, several techniques have aimed to produce quantitative, reliable elastograms by approaching elastography as an inverse problem [106]. The forward problem in elastography can be formulated as follows: given a distribution of mechanical properties and boundary conditions, calculate the displacements resulting from an applied load, as described in Sect. 32.6.2. The inverse problem for elastography, then, attempts to calculate the distribution of mechanical properties from a distribution of measured displacements. Reconstructing elasticity images using inverse methods has been an active area of research in ultrasound and magnetic resonance elastography for several years [106], but only a few studies in OCE have begun to approach this problem. The earliest of these studies were toward the application of OCE for assessment of atherosclerotic plaque vulnerability [93, 107, 108]. These studies proposed an iterative approach to solving the inverse problem using FEM, in which the mechanical parameters in the model are optimized to produce the best match to

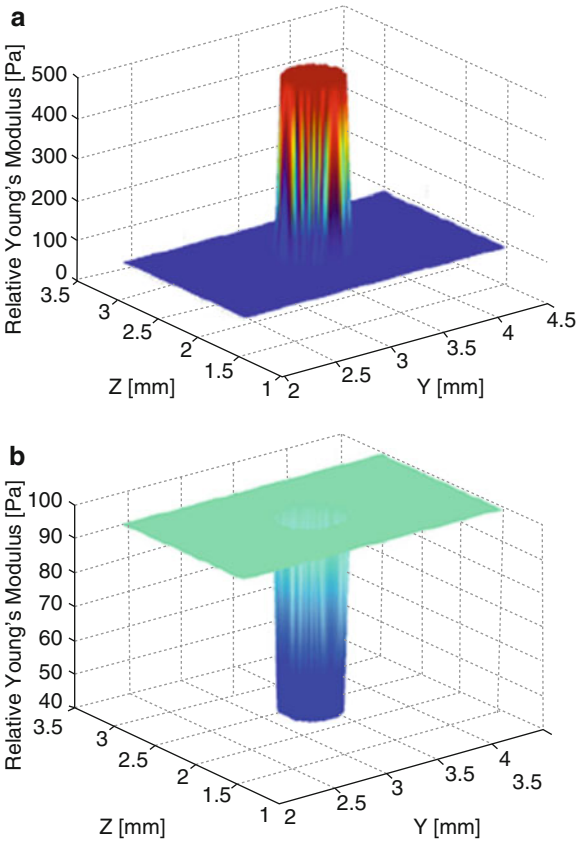

Fig. 32.22 Estimated distribution of elasticity for (**a**) a hard inclusion in a soft bulk, simulating a calcified nodule in an artery wall, and (**b**) a soft inclusion in a stiffer bulk, simulating a lipid pool in an artery wall, as determined by an iterative solution to the inverse problem using simulated OCE data as an input to a finite element model of tissue (Modified from [108])

the measured displacements using OCT. Images of the resulting elasticity distributions for a hard and soft inclusion embedded in a bulk material of constant stiffness are shown in Fig. 32.22. These studies showed promising results in simulations of OCT-derived displacements of tissue, but would be very computationally intensive to implement and may be prone to error in the presence of experimental system noise.

Quantitative, model-based OCE has also been achieved by measuring sample response to a mechanical waveform, then fitting the measured response to an analytical model for motion in a viscoelastic material [52]. Although it provides quantitative maps of Young's modulus, this method requires solving the wave equation for each pixel, a computationally intensive and slow process. More recent studies have moved toward quantification of Young's modulus by implementing transient loading techniques in which the shear modulus may be extracted directly from the velocity of shear waves in the sample [23, 26, 56]. However, these quantitative techniques come at a loss of resolution, as they assume tissue homogeneity for the length over which shear wave speed is calculated [56, 57]. This assumption may not be suitable for imaging organs with heterogeneous, complex structures, such as the breast.

32.7 Outlook

Since its first demonstration in 1998, over 200 papers on OCE and related techniques have been published, accumulating over 500 citations in 2012 alone. As the technical development of OCT reaches maturity, the scope and capacity for the development of OCE is increasing. Indeed, over the last 2 years, the number of groups publishing in OCE has doubled. Comparison of the published literature suggests that OCE is at a similar stage of development to that of ultrasound elastography in the late 1990s, and thus, continued rapid development is expected in the coming years. In the following, we predict the key developments needed to enable the technique to flourish.

Imaging Probes: The majority of OCE results have been demonstrated on excised tissue when in vivo imaging is the intended application. However, the clinical applicability of many current implementations is limited. A key requirement is the development of probes incorporating both imaging optics and loading mechanisms. In recent years, as discussed in Sect. 32.5, this has been recognized, and an increasing number of OCE probe implementations have been proposed [19, 72, 98, 109]. This is a key enabling technology required for clinical OCE imaging, and substantial further work is required.

Displacement Measurement: Measurement of mechanical properties over a large range and with high sensitivity is ultimately limited by the measurable displacement. Using cross-correlation in speckle tracking, the dynamic range of measurable strain is limited to $\sim$3.3. In phase-sensitive compression OCE, the measurable displacement range enables a strain dynamic range of $>$60 and the minimum measurable displacement in phase-sensitive detection is in the sub-nanometer range [45]. In both speckle tracking and phase-sensitive methods, there is significant scope for improvement. In speckle tracking, there is a scope for parametric algorithms to provide sub-pixel displacement sensitivity, and in phase-sensitive methods, phase unwrapping algorithms will enable maximum displacements beyond the 2π limit.

Elastogram Fidelity: Contrast in elastograms depends not only on the true elastic contrast within the tissue being probed but also on the accuracy of the employed mechanical model of tissue behavior. As illustrated in Sect. 32.6 for the particular case of compression OCE, erroneous assumptions about tissue mechanics, such as the assumption of uniform stress distribution, result in significant artifacts in elastograms, degrading their fidelity to the true underlying elastic properties. This and other common assumptions, such as that of linear elastic tissue behavior or tissue homogeneity over the acoustic wavelength in wave-based techniques, allow for straightforward estimation of the distribution of elastic properties and may in many cases prove sufficient for providing clinically useful contrast. However, the validity of employed assumptions must be assessed for each technique and proposed application. Finite element modeling is expected to remain an essential tool for validating the contrast generated using various OCE techniques and for analyzing how variables such as geometry, heterogeneity, boundary conditions, and loading rate impact on contrast.

Applications: Until now, the reported results of applying OCE to tissue have largely served to demonstrate a particular technique or implementation. In so doing,

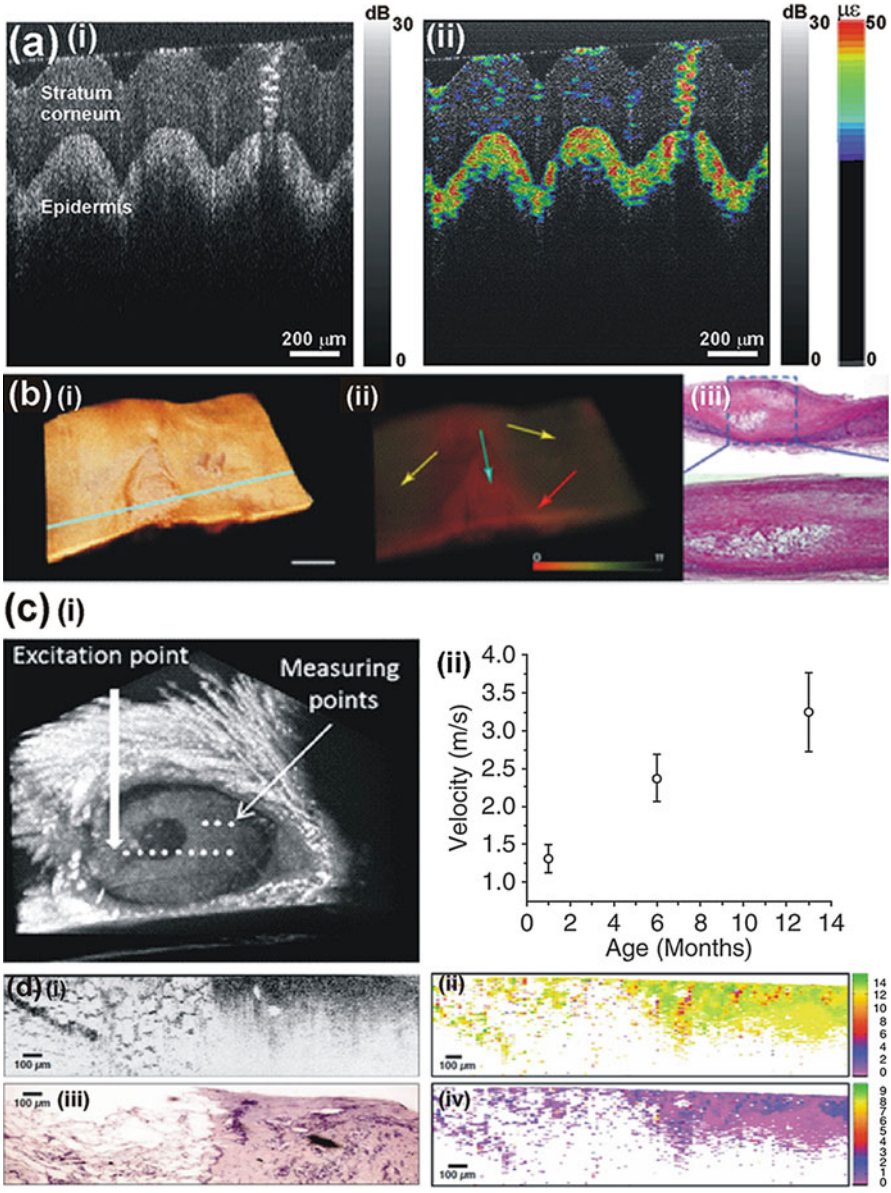

Fig. 32.23 Example images from potential OCE clinical applications. (**a**) Dermatology, (Adapted from [51]), (**b**) cardiology [72], (**c**) ophthalmology [57], and (**d**) breast cancer [52]

such reports have highlighted a number of potential applications, including in dermatology (Fig. 32.23a) [11, 19, 24, 32, 51], cardiology (Fig. 32.23b) [30, 31, 72, 92, 107, 108, 110], ophthalmology (Fig. 32.23c) [57, 89, 90, 111], and breast cancer (Fig. 32.23d) [15, 52, 112]. As well as human in vivo applications, there is

opportunity for clinical ex vivo applications, e.g., as an intraoperative tumor margin assessment in freshly resected tumor masses and as a tool in studying animal models of disease.

Although various applications show promise or appear attractive, there is a need to *prove* the ability of OCE to provide additional contrast (particularly over standard OCT) through baseline ex vivo studies, co-registered with histology, of diseased and non-diseased tissue. To date, there have been no reports focused on the systematic application of OCE to multiple cases of a particular pathology. As discussed above, enabling such studies also depends on the further development of imaging probes.

OCE is undoubtedly at an early stage of development, especially when compared with the closely related fields of ultrasound and magnetic resonance elastography. The recent increase in activity in the field and the acceleration of progress suggest there is good cause to expect future clinical applications of this emerging technique.

Note: Since submitting this manuscript in April 2013, many works in this field, including our own, have been published. For a more recent review, see B. F. Kennedy et al., "A Review of Optical Coherence Elastography: Fundamentals, Techniques and Prospects" IEEE J. Sel. Top. Quantum Electron. 20, 7101217 (2014)

Acknowledgments BFK, KMK, and DDS acknowledge funding from the Australian Research Council, the National Health and Medical Research Council, the Raine Medical Research Foundation, and the University of Western Australia. They thank their colleagues and coworkers Prof Mark Bush, Mr Lixin Chin, Dr Chris Ford, and Dr Robert McLaughlin.

References

1. Y.C. Fung, *Biomechanics: Mechanical Properties of Living Tissues* (Springer, New York, 1981)
2. K.J. Parker, M.M. Doyley, D.J. Rubens, Imaging the elastic properties of tissue: the 20 year perspective. Phys. Med. Biol. **56**, R1 (2011)
3. J. Ophir, I. Cespedes, H. Ponnekanti, Y. Yazdi, X. Li, Elastography: a quantitative method for imaging the elasticity of biological tissues. Ultrason. Imaging **13**, 111–134 (1991)
4. R. Muthupillai, D.J. Lomas, P.J. Rossman, J.F. Greenleaf, A. Manduca, R.L. Ehman, Magnetic resonance elastography by direct visualization of propagating acoustic strain waves. Science **269**, 1854–1857 (1995)
5. B.S. Garra, E.I. Cespedes, J. Ophir, S.R. Spratt, R.A. Zuurbier, C.M. Magnant, M.F. Pennanen, Elastography of breast lesions: initial clinical results. Radiology **202**, 79–86 (1997)
6. J. Foucher, E. Chanteloup, J. Vergniol, L. Castéra, B. Le Bail, X. Adhoute, J. Bertet, P. Couzigou, V. de Lédinghen, Diagnosis of cirrhosis by transient elastography (FibroScan): a prospective study. Gut **55**, 403–408 (2006)
7. D.L. Cochlin, R.H. Ganatra, D.F.R. Griffiths, Elastography in the detection of prostatic cancer. Clin. Radiol. **57**, 1014–1020 (2002)
8. S. Wojcinski, A. Farrokh, S. Weber, A. Thomas, T. Fischer, T. Slowinski, W. Schmidtand, F. Degenhardt, Multicenter study of ultrasound real-time tissue elastography in 779 cases for the assessment of breast lesions: improved diagnostic performance by combining the BI-RADS – US classification system with sonoelastography. Ultraschall Med. **31**, 484–491 (2010)
9. J.M. Schmitt, OCT elastography: imaging microscopic deformation and strain of tissue. Opt. Express **3**, 199–211 (1998)

10. D.D. Duncan, S.J. Kirkpatrick, Processing algorithms for tracking speckle shifts in optical elastography of biological tissues. J. Biomed. Opt. **6**, 418–426 (2001)
11. S.J. Kirkpatrick, R.K. Wang, D.D. Duncan, M. Kulesz-Martin, K. Lee, Imaging the mechanical stiffness of skin lesions by in vivo acousto-optical elastography. Opt. Express **14**, 9770–9779 (2006)
12. K. Daoudi, A.C. Boccara, E. Bossy, Detection and discrimination of optical absorption and shear stiffness at depth in tissue-mimicking phantoms by transient optoelastography. Appl. Phys. Lett. **94**, 154103 (2009)
13. D.S. Elson, R. Li, C. Dunsby, R. Eckersley, M.X. Tang, Ultrasound-mediated optical tomography: a review of current methods. J. R. Soc. Interface Focus **1**, 632–648 (2011)
14. S. Li, K.D. Mohan, W.W. Sanders, A.L. Oldenburg, Toward soft-tissue elastography using digital holography to monitor surface acoustic waves. J. Biomed. Opt. **16**, 116005–116005 (2011)
15. K.D. Mohan, A.L. Oldenburg, Elastography of soft materials and tissues by holographic imaging of surface acoustic waves. Opt. Express **20**, 18887–18897 (2012)
16. W. Michael Lai, D. Rubin, E. Krempl, *Introduction to Continuum Mechanics* (Butterworth-Heinemann, Oxford, 2010)
17. J.F. Greenleaf, M. Fatemi, M. Insana, Selected methods for imaging elastic properties of biological tissues. Annu. Rev. Biomed. Eng. **5**, 57–78 (2003)
18. K.J. Parker, L.S. Taylor, S. Gracewski, D.J. Rubens, A unified view of imaging the elastic properties of tissue. J. Acoust. Soc. Am. **117**, 2705–2712 (2005)
19. B.F. Kennedy, T.R. Hillman, R.A. McLaughlin, B.C. Quirk, D.D. Sampson, In vivo dynamic optical coherence elastography using a ring actuator. Opt. Express **17**, 21762–21772 (2009)
20. S.J. Kirkpatrick, D.D. Duncan, Optical assessment of tissue mechanics, in *Handbook of Optical Biomedical Diagnostics*, ed. by V.V. Tuchin (SPIE-The International Society for Optical Engineering, Bellingham, 2002), pp. 1037–1084
21. S. Abbas, B. Jonathan, L. Chris, B.P. Donald, Measuring the elastic modulus of ex vivo small tissue samples. Phys. Med. Biol. **48**, 2183 (2003)
22. T.A. Krouskop, T.M. Wheeler, F. Kallel, B.S. Garra, T. Hall, Elastic moduli of breast and prostate tissues under compression. Ultrason. Imaging **20**, 260–274 (1998)
23. X. Liang, M. Orescanin, K.S. Toohey, M.F. Insana, S.A. Boppart, Acoustomotive optical coherence elastography for measuring material mechanical properties. Opt. Lett. **34**, 2894–2896 (2009)
24. X. Liang, S.A. Boppart, Biomechanical properties of in vivo human skin from dynamic optical coherence elastography. IEEE Trans. Biomed. Eng. **57**, 953–959 (2010)
25. R. Manapuram, S. Aglyamov, F.M. Menodiado, M. Mashiatulla, S. Wang, S.A. Baranov, J. Li, S. Emelianov, K.V. Larin, Estimation of shear wave velocity in gelatin phantoms utilizing PhS-SSOCT. Laser Phys. **22**, 1439–1444 (2012)
26. M. Razani, A. Mariampillai, C. Sun, T.W.H. Luk, V.X.D. Yang, M.C. Kolios, Feasibility of optical coherence elastography measurements of shear wave propagation in homogeneous tissue equivalent phantoms. Biomed. Opt. Express **3**, 972–980 (2012)
27. A. Curatolo, B.F. Kennedy, D.D. Sampson, T.R. Hillman, Speckle in optical coherence tomography, in *Advanced Biophotonics: Tissue Optical Sectioning*, ed. by R.K. Wang, V.V. Tuchin (Taylor & Francis, London, 2013)
28. E. Archibald, A.E. Ennos, P.A. Taylor, A laser speckle interferometer for the detection of surface movements and vibrations, in *Optical Instruments and Techniques*, ed. by J.H. Dickson (Oriel, Newcastle upon Tyne, 1969), p. 265
29. J.A. Leendertz, Interferometric displacement measurement on scattering surfaces utilizing speckle effect. J. Phys. E Sci. Instrum. **3**, 214 (1970)
30. R. Chan, A. Chau, W. Karl, S. Nadkarni, A. Khalil, N. Iftimia, M. Shishkov, G. Tearney, M. Kaazempur-Mofrad, B. Bouma, OCT-based arterial elastography: robust estimation exploiting tissue biomechanics. Opt. Express **12**, 4558–4572 (2004)

31. J. Rogowska, N. Patel, J. Fujimoto, M. Brezinski, Optical coherence tomographic elastography technique for measuring deformation and strain of atherosclerotic tissues. Heart **90**, 556–562 (2004)
32. F.M. Hendriks, D. Brokken, C.W. Oomens, D.L. Bader, F.P. Baaijens, The relative contributions of different skin layers to the mechanical behavior of human skin in vivo using suction experiments. Med. Eng. Phys. **28**, 259–266 (2006)
33. S.J. Kirkpatrick, R.K. Wang, D.D. Duncan, OCT-based elastography for large and small deformations. Opt. Express **14**, 11585–11597 (2006)
34. H.J. Ko, W. Tan, R. Stack, S.A. Boppart, Optical coherence elastography of engineered and developing tissue. Tissue Eng. **12**, 63–73 (2006)
35. D. Duncan, S. Kirkpatrick, Performance analysis of a maximum-likelihood speckle motion estimator. Opt. Express **10**, 927–941 (2002)
36. B.F. Kennedy, T.R. Hillman, A. Curatolo, D.D. Sampson, Speckle reduction in optical coherence tomography by strain compounding. Opt. Lett. **35**, 2445–2447 (2010)
37. J. Meunier, Tissue motion assessment from 3D echographic speckle tracking. Phys. Med. Biol. **43**, 1241 (1998)
38. S. Gahagnon, Y. Mofid, G. Josse, F. Ossant, Skin anisotropy in vivo and initial natural stress effect: a quantitative study using high-frequency static elastography. J. Biomech. **45**, 2860–2865 (2012)
39. J.-L. Gennisson, S. Catheline, S. Chaffai, M. Fink, Transient elastography in anisotropic medium: application to the measurement of slow and fast shear wave speeds in muscles. J. Acoust. Soc. Am. **114**, 536–541 (2003)
40. R.K. Wang, Z. Ma, S.J. Kirkpatrick, Tissue Doppler optical coherence elastography for real time strain rate and strain mapping of soft tissue. Appl. Phys. Lett. **89**, 144103-144103-144103 (2006)
41. R.K. Wang, S. Kirkpatrick, M. Hinds, Phase-sensitive optical coherence elastography for mapping tissue microstrains in real time. Appl. Phys. Lett. **90**, 164105 (2007)
42. Y. Zhao, Z. Chen, C. Saxer, S. Xiang, J.F. de Boer, J.S. Nelson, Phase-resolved optical coherence tomography and optical Doppler tomography for imaging blood flow in human skin with fast scanning speed and high velocity sensitivity. Opt. Lett. **25**, 114–116 (2000)
43. J.W. Goodman, *Statistical Optics* (Wiley, New York, 1985)
44. B. Park, M.C. Pierce, B. Cense, S.-H. Yun, M. Mujat, G. Tearney, B. Bouma, J. de Boer, Real-time fiber-based multi-functional spectral-domain optical coherence tomography at 1.3 μm. Opt. Express **13**, 3931–3944 (2005)
45. R.K. Wang, A.L. Nuttall, Phase-sensitive optical coherence tomography imaging of the tissue motion within the organ of Corti at a subnanometer scale: a preliminary study. J. Biomed. Opt. **15**, 056005–056005 (2010)
46. X. Liang, S.G. Adie, R. John, S.A. Boppart, Dynamic spectral-domain optical coherence elastography for tissue characterization. Opt. Express **18**, 14183–14190 (2010)
47. B.F. Kennedy, M. Wojtkowski, M. Szkulmowski, K.M. Kennedy, K. Karnowski, D.D. Sampson, Improved measurement of vibration amplitude in dynamic optical coherence elastography. Biomed. Opt. Express **3**, 3138–3152 (2012)
48. M. Szkulmowski, A. Szkulmowska, T. Bajraszewski, A. Kowalczyk, M. Wojtkowski, Flow velocity estimation using joint spectral and time domain optical coherence tomography. Opt. Express **16**, 6008–6025 (2008)
49. S.G. Adie, B.F. Kennedy, J.J. Armstrong, S.A. Alexandrov, D.D. Sampson, Audio frequency in vivo optical coherence elastography. Phys. Med. Biol. **54**, 3129 (2009)
50. S.-R. Huang, R.M. Lerner, K.J. Parker, On estimating the amplitude of harmonic vibration from the Doppler spectrum of reflected signals. J. Acoust. Soc. Am. **88**, 2702–2712 (1990)
51. B.F. Kennedy, X. Liang, S.G. Adie, D.K. Gerstmann, B.C. Quirk, S.A. Boppart, D.D. Sampson, In vivo three-dimensional optical coherence elastography. Opt. Express **19**, 6623–6634 (2011)
52. X. Liang, A.L. Oldenburg, V. Crecea, E.J. Chaney, S.A. Boppart, Optical micro-scale mapping of dynamic biomechanical tissue properties. Opt. Express **16**, 11052–11065 (2008)

53. B.F. Kennedy, S.H. Koh, R.A. McLaughlin, K.M. Kennedy, P.R.T. Munro, D.D. Sampson, Strain estimation in phase-sensitive optical coherence elastography. Biomed. Opt. Express **3**, 1865–1879 (2012)
54. C. Li, G. Guan, R. Reif, Z. Huang, R.K. Wang, Determining elastic properties of skin by measuring surface waves from an impulse mechanical stimulus using phase-sensitive optical coherence tomography. J. R. Soc. Interface **9**, 831–841 (2011)
55. C. Li, Z. Huang, R.K. Wang, Elastic properties of soft tissue-mimicking phantoms assessed by combined use of laser ultrasonics and low coherence interferometry. Opt. Express **19**, 10153–10163 (2011)
56. C. Li, G. Guan, X. Cheng, Z. Huang, R.K. Wang, Quantitative elastography provided by surface acoustic waves measured by phase-sensitive optical coherence tomography. Opt. Lett. **37**, 722–724 (2012)
57. R.K. Manapuram, S.R. Aglyamov, F.M. Monediado, M. Mashiatulla, J. Li, S.Y. Emelianov, K.V. Larin, In vivo estimation of elastic wave parameters using phase-stabilized swept source optical coherence elastography. J. Biomed. Opt. **17**, 100501–100501 (2012)
58. M. del Socorro Hernández-Montes, C. Furlong, J.J. Rosowski, N. Hulli, E. Harrington, J.T. Cheng, M.E. Ravicz, F.M. Santoyo, Optoelectronic holographic otoscope for measurement of nano-displacements in tympanic membranes. J. Biomed. Opt. **14**, 034023–034023 (2009)
59. M. Leclercq, M. Karray, V. Isnard, F. Gautier, P. Picart, Quantitative evaluation of skin vibration induced by a bone-conduction device using holographic recording in a quasi-time-averaging regime, in *Digital Holography and Three-Dimensional Imaging* (Optical Society of America, 2012), paper DW1C
60. G. Eskin, J. Ralston, On the inverse boundary value problem for linear isotropic elasticity. Inverse Probl. **18**, 907 (2002)
61. B.A. Auld, General electromechanical reciprocity relations applied to the calculation of elastic wave scattering coefficients. Wave Motion **1**, 3–10 (1979)
62. E.R. Engdahl, R. van der Hilst, R. Buland, Global teleseismic earthquake relocation with improved travel times and procedures for depth determination. Bull. Seismol. Soc. Am. **88**, 722–743 (1998)
63. F.-C. Lin, M.P. Moschetti, M.H. Ritzwoller, Surface wave tomography of the western United States from ambient seismic noise: Rayleigh and Love wave phase velocity maps. Geophys. J. Int. **173**, 281–298 (2008)
64. T.J. Royston, H.A. Mansy, R.H. Sandler, Excitation and propagation of surface waves on a viscoelastic half-space with application to medical diagnosis. J. Acoust. Soc. Am. **106**, 3678–3686 (1999)
65. X. Zhang, J.F. Greenleaf, Estimation of tissue's elasticity with surface wave speed. J. Acoust. Soc. Am. **122**, 2522–2525 (2007)
66. G. Pedrini, S. Schedin, H.J. Tiziani, Pulsed digital holography combined with laser vibrometry for 3D measurements of vibrating objects. Opt. Lasers Eng. **38**, 117–129 (2002)
67. L. Mertz, Real-time fringe-pattern analysis. Appl. Opt. **22**, 1535–1539 (1983)
68. K.R. Nightingale, M.L. Palmeri, R.W. Nightingale, G.E. Trahey, On the feasibility of remote palpation using acoustic radiation force. J. Acoust. Soc. Am. **110**, 625–634 (2001)
69. Y. Takuma, K. Nouso, Y. Morimoto, J. Tomokuni, A. Sahara, N. Toshikuni, H. Takabatake, H. Shimomura, A. Doi, I. Sakakibara, K. Matsueda, H. Yamamoto, Measurement of spleen stiffness by acoustic radiation force impulse imaging identifies cirrhotic patients with esophageal varices. Gastroenterology **144**, 92–101 (2013)
70. http://www.medical.siemens.com/webapp/wcs/stores/servlet/PSGenericDisplay~q_catalogId~e_-1~a_langId~e_-1~a_pageId~e_110950~a_storeId~e_10001.htm
71. G. van. Soest, R. R. Bouchard, F. Mastik, N. de. Jong, A. F. W. van der Steen, Robust intravascular optical coherence elastography driven by acoustic radiation pressure, in *Optical Coherence Tomography and Coherence Techniques III* (Optical Society of America, 2007), paper 66270EE

72. W. Qi, R. Chen, L. Chou, G. Liu, J. Zhang, Q. Zhou, Z. Chen, Phase-resolved acoustic radiation force optical coherence elastography. J. Biomed. Opt. **17**, 110505–110505 (2012)
73. E. Bossy, A.R. Funke, K. Daoudi, A.-C. Boccara, M. Tanter, M. Fink, Transient optoelastography in optically diffusive media. Appl. Phys. Lett. **90**, 174111–174113 (2007)
74. V. Crecea, A.L. Oldenburg, X. Liang, T.S. Ralston, S.A. Boppart, Magnetomotive nanoparticle transducers for optical rheology of viscoelastic materials. Opt. Express **17**, 23114–23122 (2009)
75. A.L. Oldenburg, S.A. Boppart, Resonant acoustic spectroscopy of soft tissues using embedded magnetomotive nanotransducers and optical coherence tomography. Phys. Med. Biol. **55**, 1189–1201 (2010)
76. A.L. Oldenburg, F.J.J. Toublan, K.S. Suslick, A. Wei, S.A. Boppart, Magnetomotive contrast for in vivo optical coherence tomography. Opt. Express **13**, 6597–6614 (2005)
77. A. Grimwood, L. Garcia, J. Bamber, J. Holmes, P. Woolliams, P. Tomlins, Q.A. Pankhurst, Elastographic contrast generation in optical coherence tomography from a localized shear stress. Phys. Med. Biol. **55**, 5515 (2010)
78. A.L. Oldenburg, G. Wu, D. Spivak, F. Tsui, A.S. Wolberg, T.H. Fischer, Imaging and elastometry of blood clots using magnetomotive optical coherence tomography and labeled platelets. IEEE J. Sel. Top. Quantum Electron. **18**, 1100–1121 (2012)
79. R. John, E.J. Chaney, S.A. Boppart, Dynamics of magnetic nanoparticle-based contrast agents in tissues tracked using magnetomotive optical coherence tomography. IEEE J. Sel. Top. Quantum Electron. **16**, 691–697 (2010)
80. J. Kim, A. Ahmad, S.A. Boppart, Dual-coil magnetomotive optical coherence tomography for contrast enhancement in liquids. Opt. Express **21**, 7139–7147 (2013)
81. M. Fatemi, J.F. Greenleaf, Ultrasound-stimulated vibro-acoustic spectrography. Science **280**, 82–85 (1998)
82. M. Fatemi, J.F. Greenleaf, Vibro-acoustography: an imaging modality based on ultrasound-stimulated acoustic emission. Proc. Natl. Acad. Sci. U. S. A. **96**, 6603–6608 (1999)
83. M.W. Urban, A. Alizad, W. Aquino, J.F. Greenleaf, M. Fatemi, A review of vibro-acoustography and its applications in medicine. Curr. Med. Imaging Rev. **7**, 350–359 (2011)
84. J. Greenleaf, M. Fatemi, Vibro-acoustography: speckle free ultrasonic imaging. Med. Phys. **34**, 2527–2528 (2007)
85. J.F. Greenleaf, M. Fatemi, M. Belohlavek, Ultrasound stimulated vibro-acoustography. Lect. Notes Comput. Sci. **3117**, 1–10 (2004)
86. M. Fatemi, L.E. Wold, A. Alizad, J.F. Greenleaf, Vibro-acoustic tissue mammography. IEEE Trans. Med. Imaging **21**, 1–8 (2002)
87. S.G. Adie, X. Liang, B.F. Kennedy, R. John, D.D. Sampson, S.A. Boppart, Spectroscopic optical coherence elastography. Opt. Express **18**, 25519–25534 (2010)
88. C. Li, G. Guan, Z. Huang, M. Johnstone, R.K. Wang, Noncontact all-optical measurement of corneal elasticity. Opt. Lett. **37**, 1625–1627 (2012)
89. D. Alonso-Caneiro, K. Karnowski, B.J. Kaluzny, A. Kowalczyk, M. Wojtkowski, Assessment of corneal dynamics with high-speed swept source optical coherence tomography combined with an air puff system. Opt. Express **19**, 14188–14199 (2011)
90. S. Wang, J. Li, R.K. Manapuram, F.M. Menodiado, D.R. Ingram, M.D. Twa, A.J. Lazar, D.C. Lev, R.E. Pollock, K.V. Larin, Noncontact measurement of elasticity for the detection of soft-tissue tumors using phase-sensitive optical coherence tomography combined with a focused air-puff system. Opt. Lett. **37**, 5184–5186 (2012)
91. J.P. Williamson, R.A. McLaughlin, W.J. Noffsinger, A.L. James, V.A. Baker, A. Curatolo, J.J. Armstrong, A. Regli, K.L. Shepherd, G.B. Marks, Elastic properties of the central airways in obstructive lung diseases measured using anatomical optical coherence tomography. Am. J. Respir. Crit. Care Med. **183**, 612–619 (2011)
92. A. Chau, R. Chan, M. Shishkov, B. MacNeill, N. Iftimia, G. Tearney, R. Kamm, B. Bouma, M. Kaazempur-Mofrad, Mechanical analysis of atherosclerotic plaques based on optical coherence tomography. Ann. Biomed. Eng. **32**, 1494–1503 (2004)

93. R. Karimi, T. Zhu, B.E. Bouma, M.R. Kaazempur Mofrad, Estimation of nonlinear mechanical properties of vascular tissues via elastography. Cardiovasc. Eng. **8**, 191–202 (2008)
94. J. Yin, H.C. Yang, X. Li, J. Zhang, Q. Zhou, C. Hu, K.K. Shung, Z. Chen, Integrated intravascular optical coherence tomography ultrasound imaging system. J. Biomed. Opt. **15**, 010512 (2010)
95. J. Sliwa, Y. Liu, *Optical coherence tomography catheter for elastographic property mapping of lumens utilizing micropalpation*, U.S. Patent 20,120,265,062, 2012
96. X. Li, C. Chudoba, T. Ko, C. Pitris, J.G. Fujimoto, Imaging needle for optical coherence tomography. Opt. Lett. **25**, 1520–1522 (2000)
97. R.A. McLaughlin, B.C. Quirk, A. Curatolo, R.W. Kirk, L. Scolaro, D. Lorenser, P. Robbins, B. Wood, C. Saunders, D. Sampson, Imaging of breast cancer with optical coherence tomography needle probes: feasibility and initial results. IEEE J. Sel. Top. Quantum Electron. **18**, 1184–1191 (2012)
98. K.M. Kennedy, B.F. Kennedy, R.A. McLaughlin, D.D. Sampson, Needle optical coherence elastography for tissue boundary detection. Opt. Lett. **37**, 2310–2312 (2012)
99. O.A. Shergold, N.A. Fleck, Experimental investigation into the deep penetration of soft solids by sharp and blunt punches, with application to the piercing of skin. J. Biomech. Eng. – T. ASME **127**, 838 (2005)
100. C. Li, S. Li, G. Guan, C. Wei, Z. Huang, R.K. Wang, A comparison of laser ultrasound measurements and finite element simulations for evaluating the elastic properties of tissue mimicking phantoms. Opt. Laser Technol. **44**, 866–871 (2012)
101. M. Bilgen, Target detectability in acoustic elastography. IEEE T. Ultrason. Ferroelectr. **46**, 1128–1133 (1999)
102. F. Kallel, M. Bertrand, J. Ophir, Fundamental limitations on the contrast-transfer efficiency in elastography: an analytic study. Ultrasound Med. Biol. **22**, 463–470 (1996)
103. H. Ponnekanti, J. Ophir, Y. Huang, I. Cespedes, Fundamental mechanical limitations on the visualization of elasticity contrast in elastography. Ultrasound Med. Biol. **21**, 533–543 (1995)
104. T. Varghese, J. Ophir, An analysis of elastographic contrast-to-noise ratio. Ultrasound Med. Biol. **24**, 915–924 (1998)
105. G. Lamouche, B.F. Kennedy, K.M. Kennedy, C.-E. Bisaillon, A. Curatolo, G. Campbell, V. Pazos, D.D. Sampson, Review of tissue simulating phantoms with controllable optical, mechanical and structural properties for use in optical coherence tomography. Biomed. Opt. Express **3**, 1381–1398 (2012)
106. M. Doyley, Model-based elastography: a survey of approaches to the inverse elasticity problem. Phys. Med. Biol. **57**, R35 (2012)
107. A.H. Chau, R.C. Chan, M. Shishkov, B. MacNeill, N. Iftimia, G.J. Tearney, R.D. Kamm, B.E. Bouma, M.R. Kaazempur-Mofrad, Mechanical analysis of atherosclerotic plaques based on optical coherence tomography. Ann. Biomed. Eng. **32**, 1494–1503 (2004)
108. A.S. Khalil, R.C. Chan, A.H. Chau, B.E. Bouma, M.R.K. Mofrad, Tissue elasticity estimation with optical coherence elastography: toward mechanical characterization of in vivo soft tissue. Ann. Biomed. Eng. **33**, 1631–1639 (2005)
109. L.M. Peterson, M.W. Jenkins, S. Gu, L. Barwick, M. Watanabe, A.M. Rollins, 4D shear stress maps of the developing heart using Doppler optical coherence tomography. Biomed. Opt. Express **3**, 3022–3032 (2012)
110. G. van Soest, F. Mastik, N. de Jong, A.F.W. van der Steen, Robust intravascular optical coherence elastography by line correlations. Phys. Med. Biol. **52**, 2445 (2007)
111. M.R. Ford, J.W.J. Dupps, A.M. Rollins, A.S. Roy, Z. Hu, Method for optical coherence elastography of the cornea. J. Biomed. Opt. **16**, 016005–016005 (2011)
112. A. Srivastava, Y. Verma, K.D. Rao, P.K. Gupta, Determination of elastic properties of resected human breast tissue samples using optical coherence tomographic elastography. Strain **47**, 75–87 (2011)

Polarization Sensitive Optical Coherence Tomography

33

B. Hyle Park and Johannes F. de Boer

Keywords
Polarization sensitive OCT • PS-OCT • Jones vector • Mueller matrix • Stokes parameter • Poincaré sphere

Optical coherence tomography (OCT) is an interferometric technique capable of noninvasive high-resolution cross-sectional imaging by measuring the intensity of light reflected from within tissue [1]. This results in a noncontact imaging modality that provides images similar in scale and geometry to histology. Just as different stains can be used to enhance the contrast in histology, various extensions of OCT allow for visualization of features not readily apparent in traditional OCT. For example, optical Doppler tomography [2] can enable depth-resolved imaging of flow by observing differences in phase between successive depth scans [3–5]. This chapter will focus on polarization-sensitive OCT (PS-OCT), which utilizes depth-dependent changes in the polarization state of detected light to determine the light-polarization changing properties of a sample [6–11]. These properties, including birefringence, dichroism, and optic axis orientation, can be determined directly by studying the depth evolution of Stokes parameters [7–10, 12–16] or indirectly by using the changing reflected polarization states to first determine Jones or Mueller matrices [11, 17–21]. PS-OCT has been used in a wide variety of applications, including correlating burn depth with a decrease in birefringence [14], measuring the birefringence of the retinal nerve fiber layer [22, 23], and monitoring the onset and progression of caries lesions [24].

B.H. Park (✉)
Department of Bioengineering, UC Riverside, Riverside, CA, USA
e-mail: hylepark@engr.ucr.edu

J.F. de Boer
Department of Physics and Astronomy, LaserLaB Amsterdam, Vrije Univ Amsterdam, Amsterdam, The Netherlands

© Springer International Publishing Switzerland 2015

W. Drexler, J.G. Fujimoto (eds.), *Optical Coherence Tomography*,
DOI 10.1007/978-3-319-06419-2_34

33.1 Theory

Waves can generally be categorized as either longitudinal or transverse. Sound traveling through air is a classic example of a longitudinal wave. In this case, the wave propagates by compression and rarefaction of air. These local oscillations are constrained to occur in the same direction as the wave itself. A longitudinal wave traveling in a particular direction can be characterized completely by its amplitude, frequency, and phase (for propagation through a given medium). The same cannot be said for transverse waves. In contrast to longitudinal waves, local oscillations for transverse waves are oriented perpendicular to the direction of wave propagation. The three parameters that completely describe a longitudinal wave are not adequate for a transverse wave, while the amplitude, frequency, and phase of two transverse waves might be identical, they can differ by the direction of their local oscillations. For monochromatic light propagation in the z-direction, the electric field component can oscillate in the x-direction, y-direction, or any arbitrary combination of the two. This extra degree of freedom is described by its state of polarization.

Following the notation of Bohren and Huffman [25], consider a homogeneous monochromatic electromagnetic wave propagating in the z-direction with angular frequency $\omega = 2\pi c/\lambda$ and wave number $k = \omega N/c$, where $N = n + i\kappa$ represents the complex refractive index and λ and c are the wavelength and the speed of light, respectively, *in vacuo*. This wave can be described by its complex electric field $\mathbf{E}_C(z, t)$, given by

$$\mathbf{E}_C(z,t) = \mathbf{E}\, e^{i(kz-\omega t)} \tag{33.1}$$

where $\mathbf{E} = \mathbf{A} + i\mathbf{B}$ represents a vector of complex amplitude that lies in the xy-plane. In a particular plane, say $z = 0$ for convenience, the tip of the electric field traces out a curve known as the vibrational ellipse, given by

$$\mathbf{E}_{vib}(t) = \mathrm{Re}\{\mathbf{E}_C(z=0,t)\} = \mathbf{A}\cos\omega t + \mathbf{B}\sin\omega t \tag{33.2}$$

If the real vector $\mathbf{A} = 0$ (or $\mathbf{B} = 0$), the vibrational ellipse collapses to a straight line and the wave is said to be linearly polarized along the direction of $\mathbf{B}$ (or $\mathbf{A}$). If $|\mathbf{A}| = |\mathbf{B}|$ and $\mathbf{A} \cdot \mathbf{B} = 0$, the vibrational ellipse is a circle and the wave is said to be circularly polarized. In general, a monochromatic wave of the form in Eq. 33.2 is elliptically polarized (Fig. 33.1).

The effect of light propagation through a material with a complex index of refraction, $N = n + i\kappa$, can be seen through expansion of Eq. 33.1 to yield

$$\mathbf{E}_C(z,t) = \mathbf{E}\, e^{-(\omega\kappa/c)z}\, e^{i((\omega n/c)z-\omega t)} \tag{33.3}$$

It can be inferred that the imaginary part of the complex refractive index, κ, determines the attenuation of the wave as it propagates through the medium and that the real part, n, determines the phase velocity. There are a wide variety of media in which the index of refraction is independent of the polarization state of light.

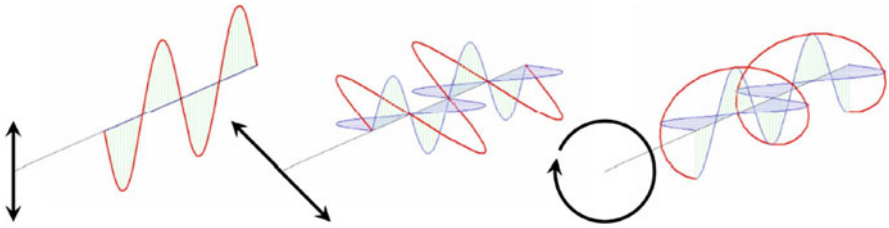

Fig. 33.1 Vibrational ellipses (from *left* to *right*) for vertically linear polarized light, linear polarized light oriented at 45° with respect to the vertical and horizontal orientations, and circularly polarized light

In these cases, light can propagate with no change of its polarization state. However, there are also many materials for which this is not the case. The goal of PS-OCT is to ascertain these light-polarization changing properties of a sample.

A material is said to be birefringent if the real part of its refractive index is polarization state dependent. Calcite is a classic example of a crystal with uniaxial birefringence; the difference in the real part of the refractive index of calcite causes light traveling through it to decompose into two beams that travel at different speeds. The orientation of this decomposition depends on that of the crystal and will be along and orthogonal to the material optic axis. Assuming a difference in refractive index of Δn, the two beams will experience a phase retardation, η, given by

$$\eta = \frac{2\pi \Delta n x}{\lambda} \tag{33.4}$$

where x is the distance traveled through the birefringent material. This phase retardation leads to an alteration of the resultant polarization state of the wave. Organized linear structures can exhibit form birefringence. This includes a variety of biological tissues, such as tendon, muscle, nerve, bone, cartilage, and teeth.

A difference in the imaginary portion of the refractive index leads to a differential attenuation of polarization states. Materials exhibiting this quality are termed dichroic. The differential attenuation experienced by light traveling through a dichroic material can be quantified by an amount of diattenuation, d, given by the ratio [26, 27]

$$d = \frac{P_1^2 - P_2^2}{P_1^2 + P_2^2} \tag{33.5}$$

where P_1 and P_2 are the electric field amplitude attenuation ratios for light polarized along and orthogonal to the optic axis of the material. These amplitude attenuation ratios, P_i, can be derived directly from the corresponding imaginary portion of refractive index, κ_i, according to the relation

$$P_i = e^{-2\pi \kappa_i x/\lambda} \tag{33.6}$$

where x is the distance traveled through the dichroic material. It should be noted that, unlike phase retardation, neither the amplitude attenuation ratios nor diattenuation scale linearly with the distance traveled through the tissue. While similar measures such as biattenuance [28, 29], defined simply as the difference in the imaginary portions of the refractive index of a dichroic material, have been recently introduced, diattenuation remains the more commonly used measure of differential attenuation.

33.1.1 Jones Formalism I

The Jones formalism provides a convenient mathematical description of polarized light and polarization effects [30]. In this section, an introduction to this calculus will be followed by its application to a simplified analysis of early PS-OCT systems.

33.1.1.1 Jones Vectors

In the previous discussion of vibrational ellipses, the complex vector **E** was described in terms of its real and imaginary parts, **A** and **B**. A somewhat more useful decomposition can be done in terms of a pair of orthonormal basis vectors to yield

$$\mathbf{E} = E_{\parallel}\hat{\mathbf{e}}_{\parallel} + E_{\perp}\hat{\mathbf{e}}_{\perp}E_{\parallel} = a_{\parallel}e^{-i\delta_{\parallel}}E_{\perp} = a_{\perp}e^{-i\delta_{\perp}} \tag{33.7}$$

where $\hat{\mathbf{e}}_{\parallel}$ and $\hat{\mathbf{e}}_{\perp}$ are unit vectors along the horizontal and vertical, respectively. In this case, the vibrational ellipse can be reformulated as

$$\mathbf{E}_{vib}(t) = a_{\parallel}\cos\left(\omega t + \delta_{\parallel}\right)\hat{\mathbf{e}}_{\parallel} + a_{\perp}\cos\left(\omega t + \delta_{\perp}\right)\hat{\mathbf{e}}_{\perp}. \tag{33.8}$$

The overall irradiance, or intensity, of the beam of light then can be expressed as the scalar quantity

$$I = a_{\parallel}^2 + a_{\perp}^2 \tag{33.9}$$

It is worth noting that while the overall irradiance of a beam is not dependent on its polarization state, it is possible to measure irradiance along a particular orientation (e.g., the intensity of a beam in the horizontal direction).

Linear polarization states occur for phase differences $\Delta\delta = \delta_{\parallel} - \delta_{\perp} = m\,\pi$, where $m \in \mathbb{Z}$, as the vibrational ellipse collapses to a line described by

$$\mathbf{E}_{vib}(t) = \left(a_{\parallel}\hat{\mathbf{e}}_{\parallel} + (-1)^m a_{\perp}\hat{\mathbf{e}}_{\perp}\right)\cos\left(\omega t + \delta_{\parallel}\right). \tag{33.10}$$

The orientation of the linear polarization state depends on the ratio of amplitudes $a_{\parallel}$ and $a_{\perp}$. The polarization state of light is horizontal or vertical when $a_{\perp} = 0$ or

$a_{\parallel} = 0$, respectively, and oriented at $\pm 45^{\circ}$ if $|a_{\parallel}| = |a_{\perp}|$. An orientation angle θ can then be defined according to the relations:

$$\begin{aligned} a_{\parallel} &= a\cos\theta \qquad a_{\perp} = a\sin\theta \\ a &= \sqrt{a_{\parallel}^2 + a_{\perp}^2} \quad \theta = \tan^{-1}\frac{a_{\parallel}}{a_{\perp}} \end{aligned} \tag{33.11}$$

where α can be thought of as an overall amplitude of the electric field and $\Delta\delta = 0$.

Circular polarization states are obtained when $|a_{\parallel}| = |a_{\perp}|$ and $\Delta\delta = \frac{\pi}{2} + n\pi$, which is evident through the form of the resultant vibrational ellipse:

$$\mathbf{E}_{vib}(t) = a_{\parallel}\big(\cos\left(\omega t + \delta_{\parallel}\right)\hat{\mathbf{e}}_{\parallel} \pm \sin\left(\omega t + \delta_{\parallel}\right)\hat{\mathbf{e}}_{\parallel}\big). \tag{33.12}$$

This describes a circle, the handedness (left or right circular) of which is determined by the sign between the orthogonal components. Circular polarization states differ only in their phase difference compared to linearly polarized light at 45°, and so the phase difference $\Delta\delta$ between orthogonal electric field components reflects the ratio between circular and linear components of the polarization state.

The electric field decomposition in Eq. 33.7 can be rewritten as a complex 2-vector such that

$$\mathbf{E} = \begin{bmatrix} E_{\parallel} \\ E_{\perp} \end{bmatrix} = \begin{bmatrix} a_{\parallel}e^{-i\delta_{\parallel}} \\ a_{\perp}e^{-i\delta_{\perp}} \end{bmatrix} = a\,e^{-i\delta_{\parallel}} \begin{bmatrix} \cos\theta \\ e^{i\,\Delta\delta}\sin\theta \end{bmatrix}. \tag{33.13}$$

While the time-invariant electric field vector $\mathbf{E}$, also known as a Jones vector, does depend on the amplitude and exact phase of the electric field components, it should be noted that the polarization state itself is completely determined by the orientation angle θ and the phase difference $\Delta\delta$.

33.1.1.2 Jones Matrices

Just as two vectors of length n can be related using a matrix of dimension $n \times n$, two polarization states can be related using a complex 2×2 matrix known as a Jones matrix. The polarization properties of any non-depolarizing optical system can be described using a Jones matrix. The transmitted polarization state $\mathbf{E}'$ as a result of an optical system represented by a Jones matrix $\mathbf{J}$ acting on an incident polarization state $\mathbf{E}$ can be determined by

$$\mathbf{E}' = \begin{bmatrix} E'_{\parallel} \\ E'_{\perp} \end{bmatrix} = \begin{bmatrix} J_{11} & J_{12} \\ J_{21} & J_{22} \end{bmatrix} \begin{bmatrix} E_{\parallel} \\ E_{\perp} \end{bmatrix} = \mathbf{J}\,\mathbf{E}. \tag{33.14}$$

Subsequent transmission of $\mathbf{E}'$ through an optical system $\mathbf{J}'$ results in a polarization state $\mathbf{E}'' = \mathbf{J}'\ \mathbf{E}' = \mathbf{J}'(\mathbf{J}\ \mathbf{E}) = \mathbf{J}'\mathbf{J}\ \mathbf{E}$. As a result, the combined polarization effect of a cascade of optical elements, $\mathbf{J}_1, \mathbf{J}_2, \cdots, \mathbf{J}_n$, can be described by the product $\mathbf{J} = \mathbf{J}_n \cdots \mathbf{J}_2\mathbf{J}_1$.

The Jones matrix for a birefringent material that induces a phase retardation η between electric field components parallel and orthogonal to a polarization state characterized by an orientation angle θ and a circularity related to ϕ is given by [31]

$$\mathbf{J}_b = \begin{bmatrix} e^{i\eta/2}C_\theta^2 + e^{-i\eta/2}S_\theta^2 & \left(e^{i\eta/2} - e^{-i\eta/2}\right)C_\theta S_\theta e^{-i\phi} \\ \left(e^{i\eta/2} - e^{-i\eta/2}\right)C_\theta S_\theta e^{i\phi} & e^{i\eta/2}S_\theta^2 + e^{-i\eta/2}C_\theta^2 \end{bmatrix}, \tag{33.15}$$

where $C_\theta = \cos\,\theta$ and $S_\theta = \sin\,\theta$. The Jones matrix of a dichroic material with attenuation ratios of P_1 and P_2 for electric field components parallel and orthogonal, respectively, to a polarization state given by an orientation angle Θ and a circularity Φ has the form [31]

$$\mathbf{J}_d = \begin{bmatrix} P_1C_\Theta^2 + P_2S_\Theta^2 & (P_1 - P_2)C_\Theta S_\Theta e^{-i\Phi} \\ (P_1 - P_2)C_\Theta S_\Theta e^{i\Phi} & P_1S_\Theta^2 + P_2C_\Theta^2 \end{bmatrix}. \tag{33.16}$$

33.1.1.3 Early Bulk-Optic PS-OCT Systems

Prior to 1992, the emphasis in OCT was the reconstruction of two-dimensional maps of tissue reflectivity while neglecting the polarization state of light. Hee et al. then presented an OCT system able to measure the changes in the polarization state of light reflected from a sample [6]. Using an incoherent detection technique, they demonstrated birefringence-sensitive ranging in a wave plate, an electro-optic modulator, and calf coronary artery. In 1997, the first two-dimensional images of birefringence were presented using a similar system, and the effect of laser-induced thermal damage on tissue birefringence in bovine tendon was demonstrated [7], followed in 1998 by a demonstration of the birefringence in porcine myocardium [8]. In 1999, phase-sensitive detection was implemented to determine the phase relation between the interference fringes in orthogonal polarization channels, which allowed for calculation of the Stokes parameters (Sect. 33.1.2.1) of the reflected light with a single measurement. Hitzenberger et al. used the phase relation in 2001 to determine the optic axis orientation of a birefringent sample [12].

The underlying theory behind extraction of the reflectivity and birefringence of a sample using these three bulk-optic PS-OCT systems will be discussed in the context of the Michelson interferometer presented by Hee et al. [6]. A schematic diagram of this early bulk-optic system is shown in Fig. 33.2. Collimated light with a short coherence length passes through a polarizer (Pol) to select a pure linear horizontal input state and is split into reference and sample arms by a polarization-insensitive beam splitter (BS). Light in the reference arm passes through a zero-order quarter-wave plate (QWP) oriented at 22.5°. Light in the sample arm passes through a QWP oriented at 45° and through focusing optics, producing circularly polarized light incident on the sample. Reflected light from the sample, in an arbitrary (elliptical) polarization state determined by the optical properties of the sample, returns through the focusing optics and the QWP. After recombination with light from the reference arm, the light in the detector arm is split into its horizontal

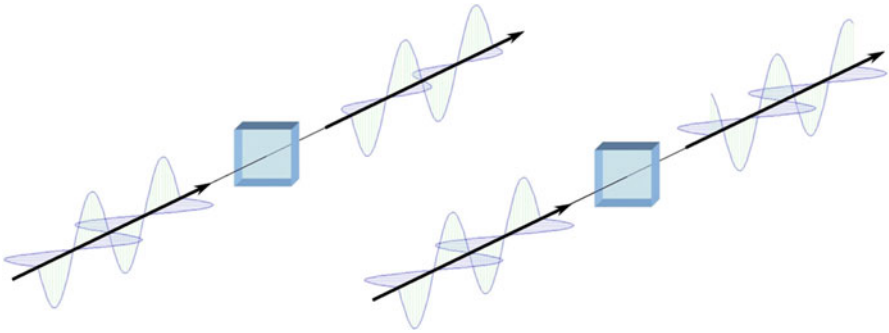

Fig. 33.2 Illustration of diattenuation (*left*) and birefringence (*right*). For diattenuation, the horizontal electric field component is attenuated more than the vertical component. The birefringent material on the right creates a phase delay between the horizontal and vertical electric field components

and vertical components by a polarizing beam splitter (PBS) and detected separately (Fig. 33.3).

The intensity detected in each polarization channel can be described by a two-dimensional intensity vector **I**, where the two components describe the horizontal and vertical polarized intensities. The intensities at the detectors are given by

$$\langle \mathbf{I}(\Delta z) \rangle = \left\langle \begin{bmatrix} E_{r\|} E_{r\|}^* \\ E_{r\perp} E_{r\perp}^* \end{bmatrix} \right\rangle + \left\langle \begin{bmatrix} E_{s\|} E_{s\|}^* \\ E_{s\perp} E_{s\perp}^* \end{bmatrix} \right\rangle + \left\langle \begin{bmatrix} E_{r\|} E_{s\|}^* \\ E_{r\perp} E_{s\perp}^* \end{bmatrix} \right\rangle + \left\langle \begin{bmatrix} E_{s\|} E_{r\|}^* \\ E_{s\perp} E_{r\perp}^* \end{bmatrix} \right\rangle, \tag{33.17}$$

where $\mathbf{E}_r = \begin{bmatrix} E_{r\|}, & E_{r\perp} \end{bmatrix}^T$ and $\mathbf{E}_s = \begin{bmatrix} E_{s\|}, & E_{s\perp} \end{bmatrix}^T$ are the Jones vector representations of light returning from the reference and sample arms, respectively, $*$ represents the complex conjugate, T is the transpose operation, and the angular brackets ($\langle \cdots \rangle$) denote time averaging. The last two terms of Eq. 33.17 correspond to the interference between reference and sample arm light.

The polarizer in the source arm allows for full transmission of only horizontally polarized light and can therefore be parameterized with attenuation ratios $P_1 = 1$ and $P_2 = 0$ along and orthogonal to an orientation $\theta = 0$. After the polarizer, horizontally polarized source light is described by the Jones vector

$$\mathbf{E}(z) = E(z) \begin{bmatrix} 1 \\ 0 \end{bmatrix}, \tag{33.18}$$

where $E(z) = \int \tilde{e}(k) e^{-ikz} dk$ represents the integrated overall complex electric field amplitude of field amplitudes $\tilde{e}(k)$. From the Wiener–Khintchine theorem, it follows that

$$\langle \tilde{e}^*(k) \tilde{e}(k') \rangle = S(k) \delta(k - k'), \tag{33.19}$$

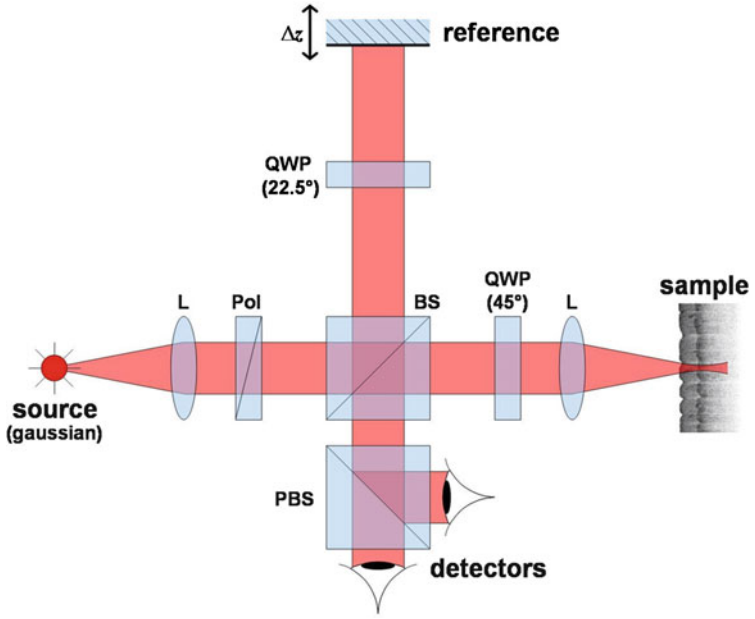

Fig. 33.3 Schematic of the bulk-optic PS-OCT system. The output of a source with a Gaussian spectrum is linearly polarized and split using a nonpolarizing beam splitter into sample and reference arms. The reference arm is composed of a quarter-wave plate (*QWP*) oriented at 22.5° and a mirror. The sample arm uses a QWP at 45° and a lens to focus light onto a sample. The reflected light from both arms is recombined and the resulting interference pattern is split using a polarizing beam splitter (*PBS*) onto two separate detectors. Individual axial scans are generated by translation of the reference arm mirror, and images are formed by combining axial scans for different lateral positions of the beam on the sample

which defines $\tilde{e}(k)$ in terms of the source power spectral density $S(k)$. The beam splitter divides the incident light by amplitude evenly between the sample and reference arms of the interferometer such that the Jones vectors describing the light entering each arm is given by

$$\mathbf{E}_{si}(z) = \mathbf{E}_{ri}(z) = \frac{E(z)}{\sqrt{2}}\begin{bmatrix}1\\0\end{bmatrix}. \tag{33.20}$$

The polarization state of light reflected from the reference arm can be calculated by multiplying $\mathbf{E}_{ri}$ (z) by the Jones matrices of the optical elements in the reference optical path. A QWP aligned at 22.5° can be characterized by $\mathbf{J}_b$ with $\eta = \pi/2$, $\eta = \pi/8$, and $\phi = 0$, and so the reflection reference polarization state is given by

$$\mathbf{E}_r(z_r) = \mathbf{J}_b\left(\frac{\pi}{2}, \frac{\pi}{8}, 0\right)\mathbf{J}_b\left(\frac{\pi}{2}, \frac{\pi}{8}, 0\right)\mathbf{E}_{ri} = \frac{1}{2}E(2z_r)\begin{bmatrix}1\\1\end{bmatrix}, \tag{33.21}$$

where z_r is the single-pass length of the reference arm. The horizontal and vertical components of the electric field have equal amplitude and phase. The polarization state of light returning from the sample arm can be computed similarly. In this case, the orientation of the QWP is $\theta = \frac{\pi}{4}$. Dichroism can generally be neglected for biological tissue, and the round-trip nature of light propagation in OCT cancels the effect of any circular birefringence. The measurable Jones matrix for a biological sample can then be modeled as a linearly birefringent material and can be written in the form $\mathbf{J}_S = \sqrt{R(z)}e^{i2kz\overline{n}}\mathbf{J}_b(2kz\Delta n, \alpha, 0)$, with $R(z)$ and $kz\overline{n}$ representing the scalar reflectivity and average phase delay of a wave propagating to some depth z, $\overline{n}$, and Δn representing the average and difference of the refractive indices along the parallel and orthogonal to the orientation of the material, α. The Jones vector of the light reflected from the sample arm is then given by

$$\begin{aligned}\mathbf{E}_s(z_s + z) &= \mathbf{J}_b(\tfrac{\pi}{2}, \tfrac{\pi}{4}, 0)\mathbf{J}_S\mathbf{J}_b(\tfrac{\pi}{2}, \tfrac{\pi}{4}, 0) \\ &\propto \sqrt{R(z)}\int \tilde{e}(k)e^{-2ik(z_s+z\overline{n})}\begin{bmatrix} e^{2i\alpha}\sin(kz\Delta n) \\ \cos(kz\Delta n)\end{bmatrix}dk\end{aligned} \tag{33.22}$$

where z_s is the optical length of the arm up to the sample surface. Using the Wiener–Khintchine theorem, the interference terms in the horizontally and vertically polarized channels are

$$\begin{aligned}A_H(z,\Delta z) &= E^*_{rx}E_{sx} + E_{rx}E^*_{sx} \propto \sqrt{R(z)}\int \sin(kz\Delta n)\cos(2k\Delta z + 2\alpha)S(k)dk \\ A_V(z,\Delta z) &= E^*_{ry}E_{sy} + E_{ry}E^*_{sy} \propto \sqrt{R(z)}\int \cos(kz\Delta n)\cos(2k\Delta z)S(k)dk\end{aligned} \tag{33.23}$$

with z the depth in the tissue and $\Delta z = z_r - s_s - z\overline{n}$ the optical path length difference between sample and reference arms. A Gaussian power spectral density is assumed for the source

$$S(k) \propto \exp\left(-\left(\frac{k-k_0}{\kappa}\right)^2\right) \tag{33.24}$$

with a full width at half maximum (FWHM) spectral bandwidth given by $\kappa 2\sqrt{\ln 2}$. The integration over k in Eq. 33.23 can be performed analytically and, in the approximation $\kappa z\Delta n \ll 1$, simplifies to

$$\begin{aligned}A_H(z,\Delta z) &\propto \sqrt{R(z)}\sin(k_0 z\Delta n)\cos(2k_0\Delta z + 2\alpha)e^{-(\Delta z/\Delta l)^2} \\ A_V(z,\Delta z) &\propto \sqrt{R(z)}\cos(k_0 z\Delta n)\cos(2k_0\Delta z)e^{-(\Delta z/\Delta l)^2}\end{aligned} \tag{33.25}$$

with the FWHM of the interference fringe envelope given by $\Delta l 2\sqrt{\ln 2}$ where

$$\Delta l = \frac{1}{\kappa} = \frac{\lambda_0^2\sqrt{\ln 2}}{\pi\Delta\lambda} \tag{33.26}$$

and $\Delta\lambda$ is the spectral FWHM of the source in wavelength.

Demodulation of the signals eliminates the $\cos(2k_0\Delta z)$ terms in Eq. 33.25 to yield intensities in the horizontal and vertical polarization channels proportional to

$$\begin{aligned} I_H(z) &= |A_H(z)|^2 \propto R(z)\sin^2(k_0 z\Delta n) \\ I_V(z) &= |A_V(z)|^2 \propto R(z)\cos^2(k_0 z\Delta n) \end{aligned} \tag{33.27}$$

The total reflected intensity and phase retardation as functions of depth are given by

$$\begin{aligned} I_T(z) &= I_H(z) + I_V(z) \propto R(z) \\ \eta(z) &= \tan^{-1}\left(\sqrt{\frac{I_V(z)}{I_H(z)}}\right) = k_0 z\Delta n \end{aligned} \tag{33.28}$$

Examination of Eq. 33.25 reveals that $A_H(z, \Delta z)$ and $A_V(z, \Delta z)$ differ in phase by 2α. Hitzenberger et al. [12] took advantage of this fact by using phase-sensitive detection to then additionally extract the sample optic axis orientation.

33.1.2 Mueller–Stokes Formalism

There are two weaknesses of the Jones formalism: the inability to describe partially polarized light and the inability to describe the processes that lead to depolarization. These shortcomings are addressed by Stokes parameters and Mueller matrices [25], which are quantities based on irradiance, a measure of the energy per unit area and time of a light beam. If two or more quasi-monochromatic beams propagating in the same directions are superposed incoherently, that is to say, there is no fixed relationship among the phases of the separate beams; the total irradiance is merely the sum of the individual beam irradiances. This property of irradiance makes it particularly attractive as a basis for an alternative way to describe polarization phenomena.

33.1.2.1 Stokes Parameters

Following the treatment in Bohren and Huffman [25], consider the following experimental setup to determine a set of irradiance measurements by which a polarization state can be completely characterized: a monochromatic beam, a set of perfect polarizers, and a detector capable of measuring irradiances regardless of polarization state. The simplest measurement is the overall irradiance of the beam. With no polarizer, the irradiance of the beam, ignoring the factor $k/2\omega\mu_0$, is given by $E_\parallel E_\parallel^* + E_\perp E_\perp^*$. The simplest polarization characterization is to use horizontal and vertical linear polarizers to determine the difference in the irradiances of the horizontally and vertically polarized components of the beam given by $E_\parallel E_\parallel^* - E_\perp E_\perp^*$. While these measurements immediately reveal the fraction of the overall beam irradiance due to horizontally and vertically polarized light, it reveals nothing regarding the phase between these elements. This can be overcome using linear polarizers oriented at +45° and −45° to measure $E_+E_+^* - E_-E_-^*$, where

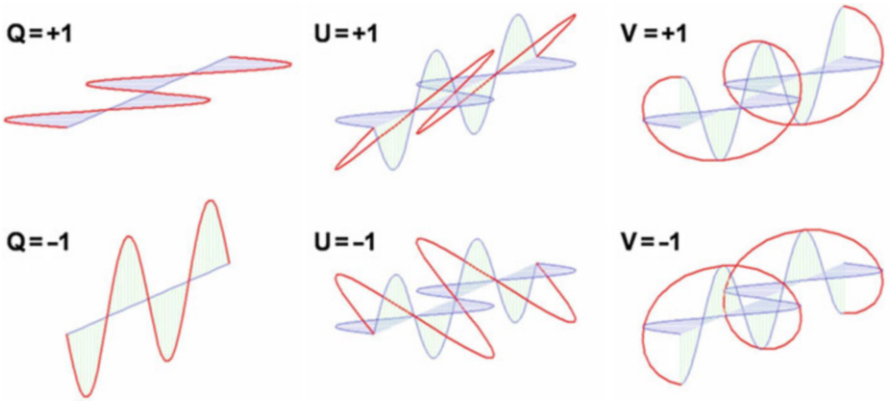

Fig. 33.4 Electric field components for various polarization states corresponding to the different Stokes parameters

$E_+ = \frac{\sqrt{2}}{2}\left(E_\parallel + E_\perp\right)$ and $E_- = \frac{\sqrt{2}}{2}\left(E_\parallel - E_\perp\right)$ are the complex electric field component amplitudes in a basis spanned by light at +45° and –45° as defined by $\hat{\mathbf{e}}_+ = \frac{\sqrt{2}}{2}\left(\hat{\mathbf{e}}_\parallel + \hat{\mathbf{e}}_\perp\right)$ and $\hat{\mathbf{e}}_- = \frac{\sqrt{2}}{2}\left(\hat{\mathbf{e}}_\parallel - \hat{\mathbf{e}}_\perp\right)$. Between these measurements, any completely linearly polarized beam can be fully characterized; however, light with any circularity cannot be characterized. Using circular polarizers to measure $E_R E_R^* - E_L E_L^*$ then rounds out the characterization, where $E_R = \frac{\sqrt{2}}{2}\left(E_\parallel - iE_\perp\right)$ and $E_L = \frac{\sqrt{2}}{2}\left(E_\parallel + iE_\perp\right)$ are the complex electric field component amplitudes in a basis spanned by right and left circularly polarized light as defined by $\hat{\mathbf{e}}_R = \frac{\sqrt{2}}{2}\left(\hat{\mathbf{e}}_\parallel + i\hat{\mathbf{e}}_\perp\right)$ and $\hat{\mathbf{e}}_L = \frac{\sqrt{2}}{2}\left(\hat{\mathbf{e}}_\parallel - i\hat{\mathbf{e}}_\perp\right)$. These measurements can be summarized as follows:

$$\begin{aligned} I_m &= E_\parallel E_\parallel^* + E_\perp E_\perp^* \\ Q_m &= E_\parallel E_\parallel^* - E_\perp E_\perp^* \\ U_m &= E_+ E_+^* - E_- E_-^* = E_\parallel E_\perp^* + E_\perp E_\parallel^* \\ V_m &= E_R E_R^* - E_L E_L^* = i\left(E_\parallel E_\perp^* - E_\perp E_\parallel^*\right) \end{aligned} \tag{33.29}$$

The polarization state of any monochromatic beam can be described using these four parameters (Fig. 33.4).

The Stokes parameters can be used to describe a nearly monochromatic, or quasi-monochromatic, beam by simply taking time averages over an interval long compared with the period, such that

$$\begin{aligned} I &= \left\langle E_\parallel E_\parallel^* + E_\perp E_\perp^* \right\rangle \\ Q &= \left\langle E_\parallel E_\parallel^* - E_\perp E_\perp^* \right\rangle \\ U &= \left\langle E_\parallel E_\perp^* + E_\perp E_\parallel^* \right\rangle \\ V &= \left\langle i\left(E_\parallel E_\perp^* - E_\perp E_\parallel^*\right) \right\rangle \end{aligned} \tag{33.30}$$

These quantities can be described by the notation s_j, where $s_0 = I$, $s_1 = Q$, $s_2 = U$, and $s_3 = V$. Algebraic manipulation of the Stokes parameters leads to $I^2 = Q^2 + U^2 + V^2 + 4(\langle a_{\|}^2\rangle\langle a_{\perp}^2\rangle - \langle a_{\|}a_{\perp}e^{i\delta}\rangle\langle a_{\|}a_{\perp}e^{-i\delta}\rangle) \geq Q^2 + U^2 + V^2$. Equality holds if the light is purely polarized; if the light is unpolarized, $Q = U = V = 0$. The degree of polarization P can now be defined by

$$P = \sqrt{\frac{Q^2 + U^2 + V^2}{I^2}} \tag{33.31}$$

The degree of polarization of a beam of light can range from unity for purely polarized light to zero for unpolarized light.

Determination of Stokes Parameters in PS-OCT

The most direct method for measuring the Stokes parameters for light in a PS-OCT system is with a complete set of irradiance measurements (e.g., $E_{\|}E_{\|}^*$, $E_{\perp}E_{\perp}^*$, $E_{+}E_{+}^*$, etc.). This can be implemented with a set of polarizers and wave plates in the detection arm of an OCT interferometer. However, characterization of a polarization state would then require a multitude of measurements from any particular region of tissue. While sufficient for determining the polarization properties of a crystalline sample, this can be problematic for biological samples, especially for in vivo and clinical settings. Motion artifacts and other time constraints dictate that practical implementation of PS-OCT uses a minimum of measurements from any single location.

In 1999, de Boer et al. demonstrated a PS-OCT system that used phase-sensitive detection to determine the phase relation between the interference fringes in orthogonal polarization channels, which allowed for calculation of the Stokes parameters of the reflected light with a single measurement [10]. It is evident from Eq. 33.30 that all four Stokes parameters can be derived from phase-sensitive measurement of $E_{\|}$ and $E_{\perp}$ for light returning from a sample (as opposed to their corresponding irradiances). Using a system similar to that illustrated in Fig. 33.3, de Boer et al. utilized phase-sensitive detection of the interference fringe intensity for each polarization component to determine the complete Stokes parameters of light in a single measurement according to the relation [10]

$$s_j(z_s) = \frac{(8\pi)^2 \int \left|\tilde{\mathbf{I}}(z_s, 2k)\right| dk}{P_0} \int \frac{\tilde{\mathbf{I}}^*(z_s, 2k)\sigma_j \tilde{\mathbf{I}}(z_s, 2k)}{\left|\tilde{\mathbf{I}}(z_s, 2k)\right|} dk, \tag{33.32}$$

where $\tilde{\mathbf{I}}(z_s, 2k)$ is a complex 2-vector representation of the components for positive k of the Fourier transform of the measured interference fringe intensities, σ_0 is the 2×2 identity matrix, and σ_1, σ_2, and σ_3 are the Pauli spin matrices.

It should be noted that an interferometric gating technique such as OCT measures only the light reflected from the sample arm that does interfere with the

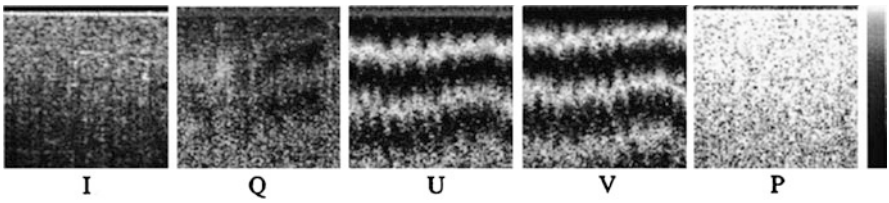

Fig. 33.5 PS-OCT images of ex vivo rodent muscle, 1 × 1 mm, pixel size 10 × 10 μm. From *left* to *right*: the Stokes parameters (**I**); normalized parameters (**Q**, **U**, **V**) in the sample frame for right circularly polarized incident light; and the degree of polarization (**P**). The *gray scale* to the right gives the magnitude of the signal, 35 dB range for I, from 1 (*white*) to –1 (*black*) for **Q**, **U**, and **V**, and from 1 (*white*) to 0 (*black*) for **P** (Reprinted from Fig. 2 of Ref. [10] with permission of the Optical Society of America)

reference arm light. On first inspection, this suggests that the degree of polarization will always be unity, since only the coherent part of the reflected light is detected [17]. A closer inspection of Eq. 33.32 reveals that the Stokes parameters of each spectral component of the source are determined with a spectral resolution inversely proportional to the interval over which the Fourier transform was taken. Integration over the wave number k sums the Stokes parameters of each spectral component with a weight proportional to the power spectral density $S(k)$. The larger the Δz interval and the higher the resolution in k-space, the more Stokes parameters of incoherently superposed beams are summed. When the Stokes parameters of reflected light do not vary over the source spectrum (the polarization state does not vary), the Stokes parameters add without changing the degree of polarization. However, when the Stokes parameters vary over the source spectrum, the sum of Stokes parameters over the spectral necessarily leads to an overall degree of polarization less than unity.

Rodent muscle was mounted in a chamber filled with saline solution and covered with a thin glass lip so that the muscle was not dehydrated during measurements. Figure 33.5 shows images of the four Stokes parameters in the sample frame for right circularly polarized incident light. Several periods of S_2 and S_3, cycling back and forth between 1 and -1, can be observed in the muscle.

33.1.2.2 Mueller Matrices

The Stokes parameters can be written as a real 4-vector $\mathbf{S} = [I, \quad Q, \quad U, \quad V]^T$, where $I, Q, U, V \in \mathbb{R}$. This allows for characterization of an optical system with a real 4×4 matrix $\mathbf{M}$, known as a Mueller matrix, that relates an incident Stokes vector $\mathbf{S}$ to a transmitted Stokes vector $\mathbf{S}'$ such that

$$\mathbf{S}' = \begin{bmatrix} I' \\ Q' \\ U' \\ V' \end{bmatrix} = \begin{bmatrix} M_{11} & M_{12} & M_{13} & M_{14} \\ M_{21} & M_{22} & M_{23} & M_{24} \\ M_{31} & M_{32} & M_{33} & M_{34} \\ M_{41} & M_{42} & M_{43} & M_{44} \end{bmatrix} \begin{bmatrix} I \\ Q \\ U \\ V \end{bmatrix} = \mathbf{MS} \tag{33.33}$$

Since Stokes vectors can be used to describe depolarized and partially polarized light, Mueller matrices have the advantage over Jones matrices of being able to describe depolarization effects.

Vector and matrix quantities in the Jones formalism can be converted into Stokes parameters and Mueller matrices using the relations [25]

$$\begin{aligned}\mathbf{S} &= \langle \mathbf{U}(\mathbf{E} \bigotimes \mathbf{E}^*)\rangle \\ \mathbf{M} &= \mathbf{U}(\mathbf{J} \bigotimes \mathbf{J}^*)\mathbf{U}^{-1} \\ \mathbf{U} &= \begin{bmatrix} 1 & 0 & 0 & 1 \\ 1 & 0 & 0 & -1 \\ 0 & 1 & 1 & 0 \\ 0 & i & -i & 0 \end{bmatrix}\end{aligned} \tag{33.34}$$

where $\otimes$ represents the Kronecker tensor product. The Mueller matrix for a partial polarizer (a dichroic material) $\mathbf{M}_P$ can be formed from Eq. 33.16 to yield

$$\mathbf{M}_P = \begin{bmatrix} q_1 & q_2 C_{2\theta} & q_2 S_{2\theta} C_\phi & q_2 S_{2\theta} S_\phi \\ q_2 C_{2\theta} & q_3 + (q_1 - q_3) C_{2\theta}^2 & (q_1 - q_3) C_{2\theta} S_{2\theta} C_\phi & (q_1 - q_3) C_{2\theta} S_{2\theta} S_\phi \\ q_2 S_{2\theta} C_\phi & (q_1 - q_3) C_{2\theta} S_{2\theta} C_\phi & q_3 + (q_1 - q_3) S_{2\theta}^2 C_\phi^2 & (q_1 - q_3) S_{2\theta}^2 C_\phi S_\phi \\ q_2 S_{2\theta} S_\phi & (q_1 - q_3) C_{2\theta} S_{2\theta} S_\phi & (q_1 - q_3) S_{2\theta}^2 C_\phi S_\phi & q_3 + (q_1 - q_3) S_{2\theta}^2 S_\phi^2 \end{bmatrix}, \tag{33.35}$$

where $q_1 = \frac{1}{2}\left(P_1^2 + P_2^2\right)$, $q_1 = \frac{1}{2}\left(P_1^2 - P_2^2\right)$, and $q_3 = P_1 P_2$. The Mueller matrix for a retarder (a birefringent material) $\mathbf{M}_R$ is given by

$$\mathbf{M}_b = \begin{bmatrix} 1 & 0 & 0 & 0 \\ 0 & C_\eta + \left(1 - C_\eta\right) C_{2\Theta}^2 & -S_\eta S_{2\Theta} S_\Phi + \left(1 - C_\eta\right) C_{2\Theta} S_{2\Theta} C_\Phi & S_\eta S_{2\Theta} C_\Phi + \left(1 - C_\eta\right) C_{2\Theta} S_{2\Theta} S_\Phi \\ 0 & S_\eta S_{2\Theta} S_\Phi + \left(1 - C_\eta\right) C_{2\Theta} S_{2\Theta} C_\Phi & C_\eta + \left(1 - C_\eta\right) S_{2\Theta}^2 C_\Phi^2 & -S_\eta C_{2\Theta} + \left(1 - C_\eta\right) S_{2\Theta}^2 C_\Phi S_\Phi \\ 0 & -S_\eta S_{2\Theta} C_\Phi + \left(1 - C_\eta\right) C_{2\Theta} S_{2\Theta} S_\Phi & S_\eta C_{2\Theta} + \left(1 - C_\eta\right) S_{2\Theta}^2 C_\Phi S_\Phi & C_\eta + \left(1 - C_\eta\right) S_{2\Theta}^2 S_\Phi^2 \end{bmatrix} \tag{33.36}$$

Mueller Matrix Determination in PS-OCT

Yao et al. [11] and Jiao et al. [17] have presented a method by which the full Mueller matrix of a biological sample can be obtained. Their systems used variable wave plates and polarizers to sequentially obtain the four irradiance measurements $I_H = \langle E_\parallel E_\parallel^* \rangle$, $I_V = \langle E_\perp E_\perp^* \rangle$, $I_P = \langle E_+ E_+^* \rangle$, and $I_R = \langle E_R E_R^* \rangle$. Since the overall intensity of light has the property $I = \langle E_\parallel E_\parallel^* \rangle + \langle E_\perp E_\perp^* \rangle = \langle E_+ E_+^* \rangle + \langle E_- E_-^* \rangle = \langle E_R E_R^* \rangle + \langle E_L E_L^* \rangle$, the Stokes parameters will be given by

$$\mathbf{S} = \begin{bmatrix} I_H + I_V \\ I_H - I_V \\ 2I_P - (I_H + I_V) \\ 2I_R - (I_H + I_V) \end{bmatrix} \tag{33.37}$$

Acquisition of the reflected Stokes parameters for incident polarization states characterized by $\hat{\mathbf{e}}_{\parallel}$, $\hat{\mathbf{e}}_{\perp}$, $\hat{\mathbf{e}}_{+}$, and $\hat{\mathbf{e}}_R$ then yields sufficient information to completely determine the Mueller matrix of a sample. One disadvantage is that determination of a Mueller matrix requires a relatively large number of sequential measurements from any location in a sample. More importantly, this mathematically complete characterization can be difficult to interpret; decomposition of a given Mueller matrix [26, 27, 31] to yield useful parameterization of polarization effects can be difficult to obtain.

A number of subsequent publications have also determined the Mueller matrix for a sample using faster systems with a more traditional two-channel detection scheme similar to that shown in Fig. 33.3 [19, 20, 32]. However, these studies compared the Jones vectors for light incident on and reflected back from a sample to first determine the sample Jones matrix, which is used to derive a corresponding Mueller matrix. The coherent detection of OCT and the nature of Jones vectors necessarily dictates that the degree of polarization be unity. Unless these calculations are performed in a wavelength-dependent manner, any resultant Mueller matrices can be used to only determine the non-depolarizing polarization properties of a sample, negating any potential advantage of the otherwise difficult-to-interpret Mueller matrix.

33.1.2.3 Poincaré Sphere

The Poincaré sphere is a three-dimensional representation of polarization states that allows for a more intuitive depiction of polarization phenomena. The Q-, U-, and V-components of the Stokes parameters are sufficient to describe the polarization state of light. For a partially polarized beam, the I-Stokes parameter additionally provides only the degree of polarization. In the case of a fully polarized beam, $I^2 = Q^2 + U^2 + V^2$. Thus, an explicit parameter to describe only the intensity of a beam is unnecessary, and the Stokes parameters can be expressed as a real 3-vector of the form

$$\vec{S} = \begin{bmatrix} Q \\ U \\ V \end{bmatrix} \tag{33.38}$$

Such vectors can be pictured in a three-dimensional space known as a Poincaré sphere [33]. In the conventional Poincaré sphere notation, the direction of a polarization state is described by a vector $\vec{S} = [q, \quad u, \quad v]^T$, where $q = Q/I$, $u = U/I$, and $v = V/I$. The radius of the sphere itself is unity, and the magnitude of a polarization state vector is defined by its degree of polarization. However, in discussions of purely polarized light, a modified Poincaré sphere can be more

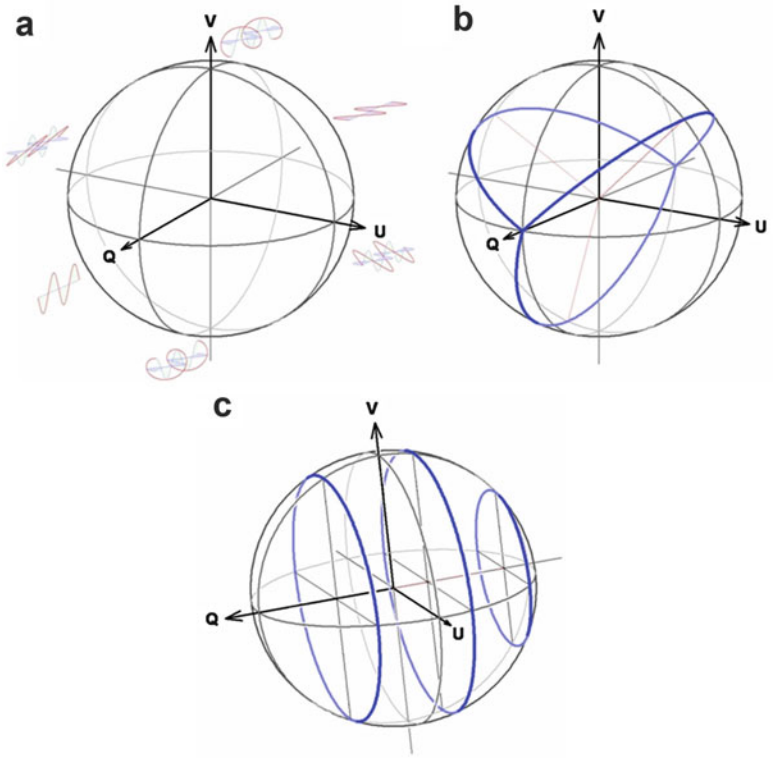

Fig. 33.6 (**a**) The Poincaré sphere with illustrations of the electric field representations of the major axes. (**b**, **c**) Poincaré spheres showing arcs of equal phase difference and equal amplitude ratio, respectively, between orthogonal electric field components

useful, where the Q-, U-, and V-parameters map to the x-, y-, and z-coordinates of a three-dimensional space. The radius of the sphere will be defined by I, and the degree of polarization will be ignored. It should be noted that the degree of polarization of light detected with optical coherence tomography can be less than unity [34]. The Poincaré sphere representation provides a convenient framework for visualizing polarization phenomenon by using the Q-, U-, and V-parameters as the x-, y-, and z-coordinates of a three-dimensional space (Fig. 33.6).

Polarization states with equal amplitude ratios and equal phase differences between orthogonal electric field components follow well-defined arcs in a Poincaré sphere representation. Using the definitions in Eq. 33.7, the Stokes 3-vector simplifies to

$$\vec{S} = \begin{bmatrix} a_{\parallel}^2 - a_{\perp}^2 \\ 2a_{\parallel}a_{\perp}C_{\Delta\delta} \\ 2a_{\parallel}a_{\perp}S_{\Delta\delta} \end{bmatrix} = \left(a_{\parallel}^2 + a_{\perp}^2\right) \begin{bmatrix} C_{\alpha} \\ S_{\alpha}C_{\Delta\delta} \\ S_{\alpha}S_{\Delta\delta} \end{bmatrix} \tag{33.39}$$

where α is governed by the amplitude ratio such that $C_\alpha = (a_\parallel^2 - a_\perp^2)/(a_\parallel^2 + a_\perp^2)$ and $S_\alpha = 2a_\parallel a_\perp/(a_\parallel^2 + a_\perp^2)$. It becomes evident that polarization states of equal amplitude ratio and equal phase difference between orthogonal electric field components trace latitude and longitude lines, respectively, where the Q -axis of the Poincaré sphere is treated as the pole.

The Jones matrices describing diattenuation and birefringence both fit the general form

$$\mathbf{J} = \begin{bmatrix} XC_\theta^2 + YS_\theta^2 & (X-Y)C_\theta S_\theta e^{-i\phi} \\ (X-Y)C_\theta S_\theta e^{i\phi} & XS_\theta^2 + YC_\theta^2 \end{bmatrix} \tag{33.40}$$

where X and Y are parameters defining the magnitude of polarization effects about an optic axis defined by θ and ϕ. For diattenuation, the general parameters take the form $X = P_1$ and $Y = P_2$, and in the case of birefringence, $X = e^{i\eta/2}$ and $Y = e^{-i\eta/2}$. For simultaneous birefringence and diattenuation about a common axis, $X = P_1 e^{i\eta/2}$ and $Y = P_2 e^{-i\eta/2}$. The transmitted state $\mathbf{S}' = [I', \quad Q', \quad U', \quad V']^T$ is the product of the equivalent Mueller matrix $\mathbf{M}$ and the incident polarization state $\mathbf{S} = [I, \quad Q, \quad U, \quad V]^T$. If no depolarization takes place, all such transformations can be completely described by the lower-right 3 × 3 sub-matrix of $\mathbf{M}$. This reduction of the Mueller matrix allows for examination of the 3-vector equivalents of the transmitted and incident states, $\vec{S}'$ and $\vec{S}$, in terms of polarization parameters X and Y and optic axis $\vec{A} = [C_{2\theta}, \quad S_{2\theta}C_\phi, \quad S_{2\theta}S_\phi]^T$, yielding the relation [35]

$$\vec{S}' = \frac{1}{2}\left((X^*Y + XY^*)\vec{S} + i(X^*Y - XY^*)\left(\vec{S} \times \vec{A}\right) + \left((X^*X + YY^*)I + (X-Y)(X^* - Y^*)\left(\vec{S}\cdot\vec{A}\right)\right)\vec{A}\right) \tag{33.41}$$

This expression allows for visualization of polarization effects in the Poincaré sphere.

For diattenuation, Eq. 33.41 simplifies to

$$\vec{S}' = q_3\vec{S} + \left(q_2 I + (q_1 - q_3)\left(\vec{S}\cdot\vec{A}\right)\right)\vec{A}. \tag{33.42}$$

Since this expression is a linear sum of $\vec{S}$ and $\vec{A}$, $\vec{S}'$ must be coplanar with $\vec{S}$ and $\vec{A}$. Furthermore, for $d = 1$, $q_1 = q_2 = \frac{1}{2}$ and $q_3 = 0$, and $\vec{S}' = \frac{1}{2}\left(I + \vec{S}\cdot\vec{A}\right)\vec{A}$. Since $\left|\vec{S}\cdot\vec{A}\right| \le I$, the transmitted polarization state is not only parallel to $\vec{A}$ but must be in the same direction as well. On the other extreme, if $d = -1$, then $q_1 = \frac{1}{2}$, $q_2 = -\frac{1}{2}$, and $q_3 = 0$, resulting in a transmitted polarization state $\vec{S}' = -\frac{1}{2}\left(I - \vec{S}\cdot\vec{A}\right)\vec{A}$. In this case, the transmitted polarization state is parallel to $\vec{A}$ but lies in the opposite direction. Thus, positive diattenuation can be visualized as a "pulling" of the polarization toward the optic axis, and a negative diattenuation value implies a "pushing away," as illustrated in Fig. 33.7a.

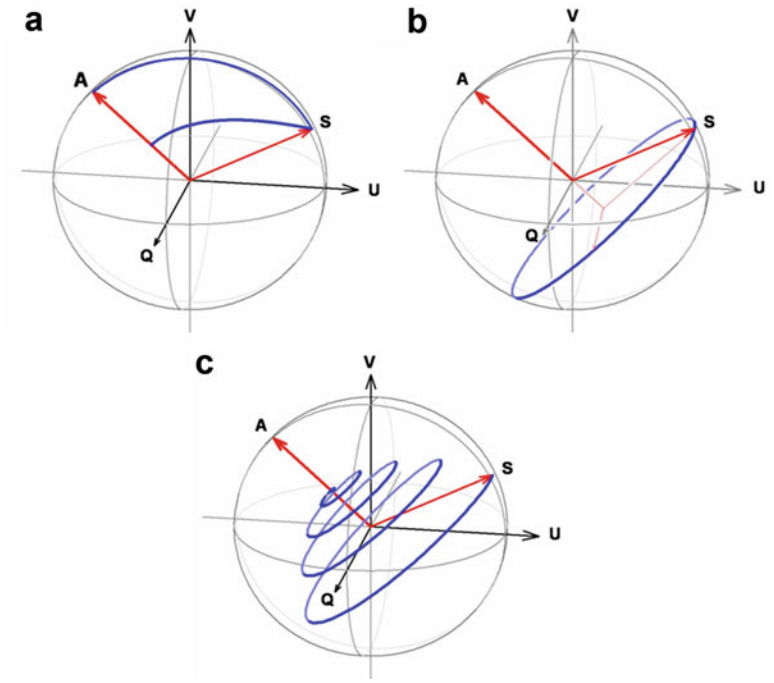

Fig. 33.7 Poincaré sphere representations of the effects of (**a**) diattenuation, (**b**) birefringence, and (**c**) the combined effect about a common optic axis A on a polarization state S. The "pulling" effect of diattenuation is evident from the trace (*inner arc*) of the transmitted polarization state as diattenuation increases (the normalized trace along the surface of the sphere is also shown). Birefringence is equivalent to a rotation in the Poincaré sphere. The combined effect has the appearance of a spiral

In the case of birefringence,

$$\vec{S'} = \left(\vec{S}\cdot\vec{A}\right)\vec{A} + C_\eta\left(\vec{S} - \left(\vec{S}\cdot\vec{A}\right)\vec{A}\right) + S_\eta\left(\vec{S}\times\vec{A}\right) \tag{33.43}$$

The first portion, $\left|\left(\vec{S}\cdot\vec{A}\right)\vec{A}\right| = \left|\vec{S}\right|\cos\theta_{\vec{S},\vec{A}}$, is the portion of $\vec{S}$ that lies along $\vec{A}$. Examination of the other vector components show that $\left|\vec{S} - \left(\vec{S}\cdot\vec{A}\right)\vec{A}\right| = \left|\vec{S}\times\vec{A}\right| = \left|\vec{S}\right|\sin\theta_{\vec{S},\vec{A}}$ and $\left(\vec{S} - \left(\vec{S}\cdot\vec{A}\right)\vec{A}\right) \perp \left(\vec{S}\times\vec{A}\right)$, which represent a decomposition of $\vec{S}$ along orthogonal directions in the plane perpendicular to $\vec{A}$. Thus, birefringence represents a rotation of $\vec{S}$ about the optic axis $\vec{A}$ in a Poincaré sphere representation.

The more general equation for the combined effect about a common optic axis is given by

$$\vec{S'} = q_3 C_\eta \vec{S} + q_3 S_\eta\left(\vec{S}\times\vec{A}\right) + \left(q_2 I + \left(q_1 - q_3 C_\eta\right)\left(\vec{S}\cdot\vec{A}\right)\right)\vec{A} \tag{33.44}$$

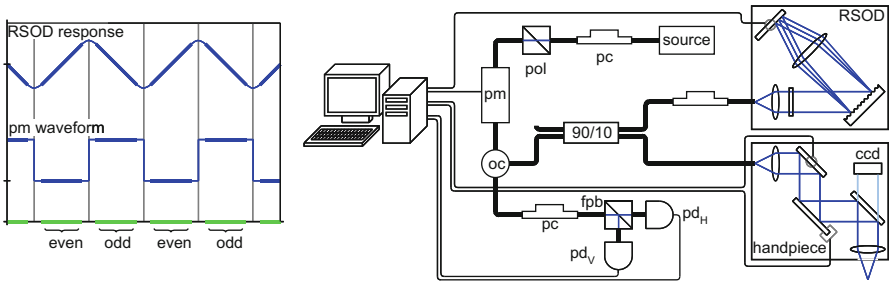

Fig. 33.8 Diagram of a fiber-based PS-OCT system and driving waveforms. The RSOD and phase modulator are driven by a rounded sawtooth and a step function, respectively, both at approximately 1 kHz. A phase delay is introduced such that the RSOD galvo response is in phase with the polarization modulator. The system processes the central 80 % of the positive and negative sloping regions of the RSOD response, yielding even and odd A-lines. (*pol* polarizer, *pc* passive polarization controller, *pm* electro-optic polarization modulator, *oc* optical circulator, *RSOD* rapid scanning optical delay line, *fpb* fiber polarizing beam splitter, *pd* fiber-pigtailed photodiodes, *ccd* charge-coupled device camera) (Reprinted from Fig. 1 of Ref. [37] with permission of the Optical Society of America)

Although direct analysis of this vector equation is more complicated, the combined trace on a Poincaré sphere is of a simultaneous pulling in toward and a rotation about the optic axis. It is worth noting that vector expressions for polarization effects have been formulated in a differential geometry as well [36].

Stokes Vector-Based Analysis for Fiber-Based PS-OCT

The previous PS-OCT systems were air-spaced interferometers that used bulk optical components that permitted precise control over the polarization state of light in the sample and reference arms. The incident polarization state does not vary and can be controlled so that it is circular. This insures insensitivity to the direction of the optic axis of the sample, which, for birefringent materials, must be constrained to the *QU*-plane in a Poincaré sphere representation. In this case, the change in the polarization state can be completely determined from the difference between the known incident polarization state and that reflected or backscattered from a particular point in the scan. Fiber-based interferometers offer distinct advantages in terms of system alignment and handling but pose design problems owing to polarization changes induced in optical fibers. To understand the problem posed by fiber-based PS-OCT [13–15], consider the schematic of a fiber-based PS-OCT drawn in Fig. 33.8. Assuming lossless transmission through optical fiber, diattenuation can be ignored; the main polarization effect of optical fiber in a system is birefringence. Since the amount and orientation of fiber birefringence in the system is an unknown quantity, it is clear that determination of sample polarization properties becomes quite complicated: the incident polarization state is no longer known and that the overall direction of the optic axis (from the combination of sample and fibers) is no longer constrained to the *QU*-plane.

Further, even if the birefringence in the fiber could be completely characterized at all times, it is entirely possible that the polarization state incident on the sample becomes aligned parallel or orthogonal to the optic axis of the sample. In this case, the incident polarization state remains unchanged upon reflection from the sample, and thus the amount or orientation of any sample polarization properties cannot be determined by examination of the reflected polarization state. It becomes clear that fiber-based PS-OCT must overcome two main difficulties: being able to compensate for an unknown amount of fiber birefringence to extract sample polarization properties only and to avoid the problem of the incident polarization state being aligned with or orthogonal to the optic axis of the sample.

Both these problems are solved by using multiple incident polarization states and by comparison of reflected light from the surface to that from some depth. The detected polarization state in a fiber-based PS-OCT system reflects the overall birefringence of both the sample and the fiber of the system. The fiber birefringence affects the polarization state reflected from the surface of the sample in the same way it affects light returning from some depth below the surface. Since orthogonality between states is preserved in a lossless system, the difference between these polarization states is due to the sample only. Comparison of at least two incident polarizations can be used to insure that polarization states will return information regarding the sample polarization properties, even if a polarization state becomes aligned parallel to the optic axis of the sample.

The optimal choice of two incident polarization states is dependent on the acquisition scheme. In earlier systems, the incident polarization state alternated during acquisition of successive depth profiles. The fact that these depth profiles were acquired separately makes it difficult to determine the absolute phase relationship between reflected polarization states. The optimal choice for recovery of tissue birefringence in this case is incident states that are perpendicular in a Poincaré sphere representation [13–15, 21, 22, 37].

Simultaneous acquisition of two polarization states, e.g., by modulating the polarization state within a single A-line (depth profile) in TD-OCT [38], SD-OCT [39], or swept-source OCT [40, 41], allows determination of the absolute phase relationship between reflected polarization states, which changes the optimal choice of the incident polarization states. In these cases, the optimal choice for incident polarization states becomes two states separated by 180° in a Poincaré sphere representation due to the fact that the phase relationship between reflected polarization states is available [42]. A brief rationale for this is given later at the end of Sect. 33.1.3 of this chapter.

The following discussion makes no assumption regarding the phase relationship between the two reflected polarization state depth profiles. The incident polarization state will be toggled between two different states in adjacent depth profiles such that all even A-lines have the same incident polarization state perpendicular to the incident state in a Poincare sphere representation of all odd A-lines. Let the intensity and polarization state of light at the sample surface be denoted by the scalar quantity I_j and normalized polarization 3-vector $\vec{I}_j = \left[Q_j, \quad U_j, \quad V_j \right]^T$,

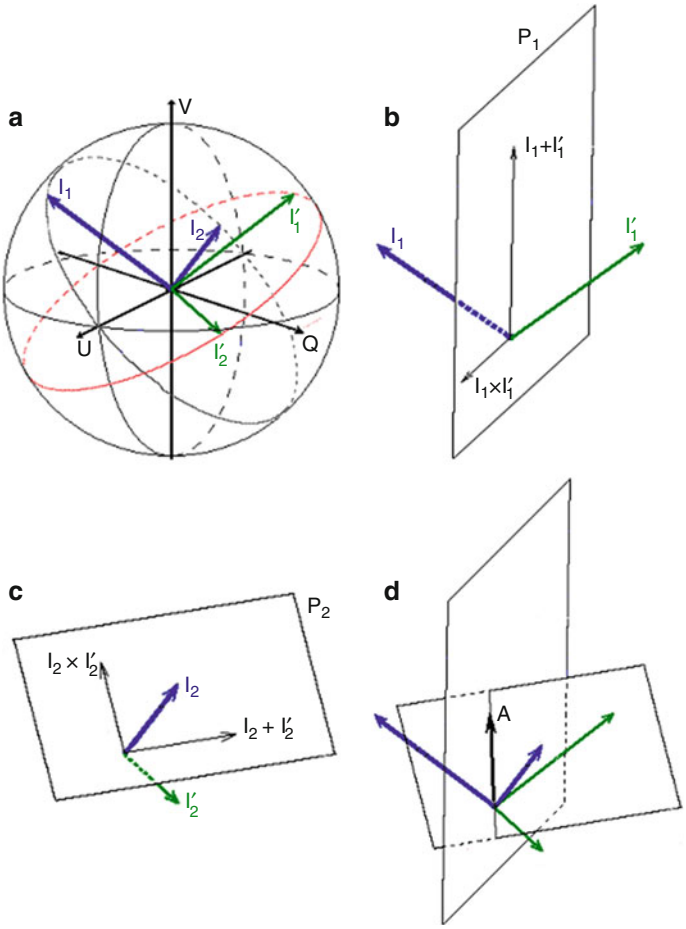

Fig. 33.9 Birefringence calculation illustrating (**a**) the surface states, I_1 and I_2, in *blue* and the reflected states, I'_1 and I'_2, in *green*, (**b**, **c**) the planes P_1 and P_2 that span all possible rotation axes, and (**d**) the intersection of the planes resulting in determination of the optic axis (Reprinted from Fig. 2 of Ref. [14] with permission from the International Society of Optical Engineering)

where $j = 1$ indicates even A-lines and $j = 2$ off A-lines. The sample polarization properties at a depth z computed from an adjacent pair of A-lines may then be calculated in the following way (Fig. 33.9). Let the intensity and polarization state at depth z be represented by I'_j and $\vec{I'}_j$, respectively. The plane P_j containing all possible axes that can rotate the surface polarization state, $\vec{I}_j$, to the normalized reflected polarization state at a depth z, $\vec{I'}_j$, is spanned by their sum and cross products. The intersection of the two planes P_1 and P_2 determines a single axis of rotation $\vec{A}$ capable of rotating both sets of polarization states simultaneously. The relative optic axis of the sample is then given by

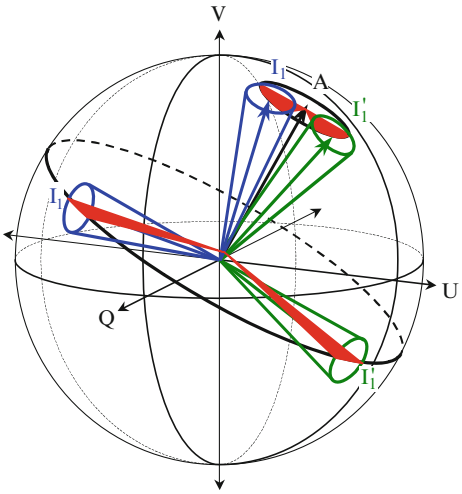

Fig. 33.10 Effect of noise on the calculated rotation angle. For a given optic axis $\vec{A}$, two pairs of $\vec{I}_1$ and $\vec{I'}_1$ are shown, one with large $\theta\vec{A}, \vec{I}_1$ and the other with small $\theta\vec{A}, \vec{I}_1$. The *cones* represent the uncertainty in orientation of the polarization states due to noise. The *red* areas show the variation in rotation angle θ_1 due to the uncertainty introduced by noise, demonstrating the increased uncertainty involved in determining θ_1 when the polarization state of incident light is closely aligned with the optic axis (Reprinted from Fig. 5 of Ref. [37] with permission of the Optical Society of America)

$$\vec{A} \parallel \left(\left(\vec{I'}_1 + \vec{I}_1\right) \times \left(\vec{I'}_1 \times \vec{I}_1\right)\right) \times \left(\left(\vec{I'}_2 + \vec{I}_2\right) \times \left(\vec{I'}_2 \times \vec{I}_2\right)\right)$$
$$\parallel \left(\vec{I'}_1 - \vec{I}_1\right) \times \left(\vec{I'}_2 - \vec{I}_2\right) \tag{33.45}$$

The final step in the analysis is determining the degree of phase retardation over this optic axis. θ_1 may be defined as the degree of rotation about $\vec{A}$ that takes $\vec{I}_1$ to $\vec{I'}_1$, and θ_2 is defined analogously. The expectation is that the two rotation angles are equal; however, in practice they differ slightly due to noise. The overall phase retardation is taken as the intensity-weighted average of the two angles. However, the effect of noise on the value of θ_j ($j = 1, 2$) increases as the angle between the rotation axis $\vec{A}$ and either Stokes states $\vec{I}_1$ or $\vec{I'}_1$ decreases. This may be illustrated by defining $\theta\vec{A}, \vec{I}_j$ and $\theta\vec{A}, \vec{I}_j$ as the angles between $\vec{A}$ and $\vec{I}_j$ and $\vec{I'}_j$, respectively, where $\sin\theta\vec{A}, \vec{I}_j = \left|\vec{A} \times \vec{I}_j\right| / \left(\left|\vec{A}\right|\left|\vec{I}_j\right|\right)$ and $\sin\theta\vec{A}, \vec{I}'_j = \left|\vec{A} \times \vec{I}'_j\right| / \left(\left|\vec{A}\right|\left|\vec{I}'_j\right|\right)$. In the absence of noise, the rotation angle required to rotate both incident polarization states to the reflected polarization states at depth z will be identical, such that $\theta\vec{A}, \vec{I}_j = \theta\vec{A}, \vec{I}'_j$. As illustrated in Fig. 33.10, the effect of noise on the polarization state of detected light can be modeled in the Poincaré sphere by adding a randomly

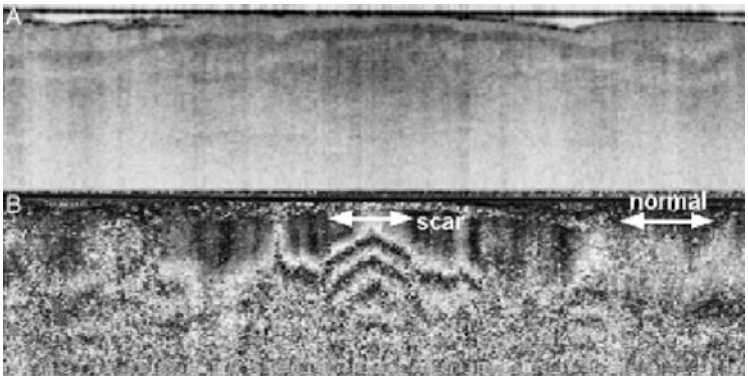

Fig. 33.11 PS-OCT images of scar tissue in vivo. Structural (**a**) and polarization-sensitive (**b**) images from a region of scar tissue on the hand, 5 mm wide by 1.2 mm deep. Labeled *arrows* in (**b**) indicate clinically determined regions of scar tissue and adjacent normal skin (Reprinted from Fig. 4 of Ref. [72] with permission of the Society of Investigative Dermatology)

oriented vector of a length proportional to the magnitude of the noise to the polarization state of the light. Since cross products are linear, $\vec{A} \times \left(\vec{I} + \vec{N}\right) = \vec{A} \times \vec{I} + \vec{A} \times \vec{N}$. As $\theta\vec{A}, \vec{I}_j$ decreases, the contribution to θ_j due to the signal decreases while that due to noise is unchanged. This means the calculated rotation angle θ_j becomes more susceptible to noise for small $\theta\vec{A}, \vec{I}_j$. To account for this, we additionally weight the calculated angles by the product of the sines of the angles between the axis of rotation and the polarization states. The degree of phase retardation is then given by

$$\theta = \frac{\left(I_1 I_1' \sin\theta\vec{A}, \vec{I}_1 \sin\theta\vec{A}, \vec{I}_1'\right)\theta_1 + \left(I_2 I_2' \sin\theta\vec{A}, \vec{I}_2 \sin\theta\vec{A}, \vec{I}_2'\right)\theta_2}{\left(I_1 I_1' \sin\theta\vec{A}, \vec{I}_1 \sin\theta\vec{A}, \vec{I}_1'\right) + \left(I_2 I_2' \sin\theta\vec{A}, \vec{I}_2 \sin\theta\vec{A}, \vec{I}_2'\right)} \tag{33.46}$$

These values can be encoded on a gray scale with black and white representing rotation of 0 and π radians, respectively, as shown in the images of scar tissue in vivo displayed in Fig. 33.11.

33.1.3 Jones Formalism II

As birefringence seems to be the primary polarization property exhibited by biological tissue, most PS-OCT analysis methods concentrate on determination of phase retardation. Schoenenberger et al. [43] analyzed system errors introduced by the extinction ratio of polarizing optics and chromatic dependence of wave retarders and errors due to dichroism. System errors can be kept small by careful

design of the system with achromatic elements but can never be completely eliminated. In principle, dichroism is a more serious problem when interpreting results as solely due to birefringence. However, Mueller matrix ellipsometry measurements have shown that the error due to dichroism in the eye is relatively small [44, 45], and earlier PS-OCT work shows that dichroism is of minor importance in rodent muscle [10]. Despite this, a method for simultaneous determination of sample birefringence and dichroism is desirable, especially one that can be applied to systems with the unrestricted use of optical fiber and fiber components.

The non-depolarizing polarization properties of an optical system can be completely described by its complex Jones matrix, $\mathbf{J}$, which transforms an incident polarization state described by a complex electric field vector, $\mathbf{E} = [H, \quad V]^T$, to a transmitted state, $\mathbf{E}' = [H', \quad V']^T$, and can be decomposed in the form $\mathbf{J} = \mathbf{J}_R\mathbf{J}_P = \mathbf{J}_{P'}\mathbf{J}_{R'}$ [31]. Birefringence, described by $\mathbf{J}_R$, can be parameterized by three variables: a degree of phase retardation η about an axis defined by two angles, γ and δ. Diattenuation, described by $\mathbf{J}_P$, is defined as $d = (P_1^2 - P_2^2)/(P_1^2 + P_2^2)$ and can be parameterized by four variables, where P_1 and P_2 are the attenuation coefficients parallel and orthogonal, respectively, to an axis defined by angles Γ and Δ. These seven independent parameters, along with an overall common phase $e^{i\Psi}$, account for all four complex elements of a general Jones matrix $\mathbf{J}$. Assuming that birefringence and diattenuation arise from the same fibrous structures in biological tissue and thus share a common axis ($\delta = \Delta$ and $Y = \Gamma$) [19], the number of independent parameters is reduced by two. An incident and reflected polarization state yield three relations involving the two orthogonal amplitudes and the relative phase between them [10]. Therefore, it is possible to use the six relationships defined by two unique pairs of incident and reflected polarization states to exactly solve for the Jones matrix of a sample.

In general terms, a PS-OCT system sends polarized light from a broadband source into the sample and reference arms of an interferometer, and reflected light from both arms is recombined and detected. Define $\mathbf{J}_{in}$ as the Jones matrix representing the optical path from the polarized light source to the sample surface, $\mathbf{J}_{out}$ as that going from the sample surface to the detectors, and $\mathbf{J}_S$ as the round-trip Jones matrix for light propagation through a sample [21]. This nomenclature can be applied to all PS-OCT systems, ranging from bulk-optic systems [6, 7, 9–12] to those with fibers placed such that they are traversed in a round-trip manner [20] to time-domain [13, 15] (Fig. 33.12) and spectral-domain [16] PS-OCT systems with the unrestricted use of optical fiber and non-diattenuating fiber components, and even for retinal systems [22], where the polarization effects of the cornea can be included in $\mathbf{J}_{in}$ and $\mathbf{J}_{out}$. The electric field of light reflected from the sample surface, $\mathbf{E}$, can be expressed as $\mathbf{E} = e^{i\psi}\mathbf{J}_{out}\mathbf{J}_{in}\mathbf{E}_{source}$, where Ψ represents a common phase and $\mathbf{E}_{source}$ represents the electric field of light coming from the polarized source. Likewise, the electric field of light reflected from some depth within the tissue may be described by $\mathbf{E}' = e^{i\psi'}\mathbf{J}_{out}\mathbf{J}_S\mathbf{J}_{in}\mathbf{E}_{source}$. These two measurable polarization states

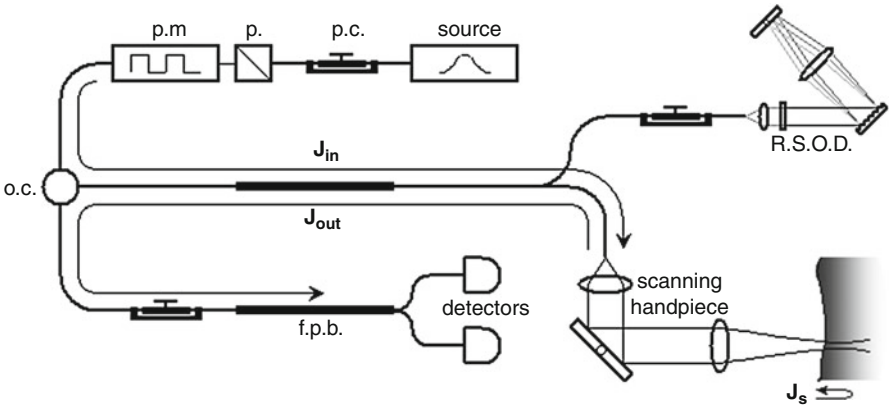

Fig. 33.12 Schematic of the fiber-based PS-OCT system (*p.c.* polarization controller, *p* polarizer, *pm* polarization modulator, *oc* optical circulator, *RSOD* rapid scanning optical delay, *fpb* fiber polarizing beam splitter). Jin, Jout, and JS are the Jones matrix representations for the one-way optical path from the polarization modulator to the scanning handpiece, the one-way optical path back from the scanning handpiece to the detectors, and the round-trip path through some depth in the sample, respectively (Reprinted from Fig. 1 of Ref. [21] with permission of the Optical Society of America)

can be related to each other such that $\mathbf{E}' = e^{i\Delta\psi}\mathbf{J}_T\mathbf{E}$, where $\mathbf{J}_T = \mathbf{J}_{out}\mathbf{J}_S\mathbf{J}_{out}^{-1}$ and $\Delta\psi = \psi' - \psi$.

If the optical system representing $\mathbf{J}_{out}$ is non-diattenuating, $\mathbf{J}_{out}$ can be treated as a unitary matrix with unit determinant after separating out a common attenuation factor. $\mathbf{J}_S$ can be decomposed into a diagonal matrix $\mathbf{J}_C = \begin{bmatrix} P_1 e^{i\eta/2}, & 0; & 0, & P_2 e^{-i\eta/2} \end{bmatrix}$, containing complete information regarding the amount of sample diattenuation and phase retardation, surrounded by unitary matrices $\mathbf{J}_A$ with unit determinant that define the sample optic axis. $\mathbf{J}_T$ can be reformed such that $\mathbf{J}_T = \mathbf{J}_{out}\mathbf{J}_S\mathbf{J}_{out}^{-1} = \mathbf{J}_{out}(\mathbf{J}_A\mathbf{J}_C\mathbf{J}_A^{-1})\mathbf{J}_{out}^{-1} = \mathbf{J}_U\mathbf{J}_C\mathbf{J}_U^{-1}$, where $\mathbf{J}_U = \mathbf{J}_{out}\mathbf{J}_A$. Since unitary matrices with unit determinant form the special unitary group SU(2) [46], $\mathbf{J}_U$ must also be a unitary matrix with unit determinant by closure and can be expressed in the form

$$\mathbf{J}_U = e^{i\beta}\begin{bmatrix} C_\theta e^{i(\phi-\varphi)} & -S_\theta e^{i(\phi+\varphi)} \\ S_\theta e^{-i(\phi+\varphi)} & C_\theta e^{-i(\phi-\varphi)} \end{bmatrix} \tag{33.47}$$

An alternative formulation for $\mathbf{J}_T$ can be obtained by combining information from two unique incident polarization states: $\begin{bmatrix} H_1', & H_2'; & V_1', & V_2' \end{bmatrix} = e^{i\Delta\psi_1}\mathbf{J}_T\begin{bmatrix} H_1, & e^{i\alpha}H_2; & V_1, & e^{i\alpha}V_2 \end{bmatrix}$, where $\alpha = \Delta\psi_2 - \Delta\psi_1$. The polarization properties of interest can be obtained by equating the two expressions for $\mathbf{J}_T$ to yield

$$e^{i\Delta\psi_1}\begin{bmatrix} P_1 e^{i\eta/2} & 0 \\ 0 & P_2 e^{-i\eta/2} \end{bmatrix} = \begin{bmatrix} C_\theta & S_\theta \\ -S_\theta & C_\theta \end{bmatrix}\begin{bmatrix} e^{-i\phi} & 0 \\ 0 & e^{i\phi} \end{bmatrix}\begin{bmatrix} H_1' & H_2' \\ V_1' & V_2' \end{bmatrix} \begin{bmatrix} H_1 & e^{i\alpha}H_2 \\ V_1 & e^{i\alpha}V_2 \end{bmatrix}^{-1}\begin{bmatrix} e^{i\phi} & 0 \\ 0 & e^{-i\phi} \end{bmatrix}\begin{bmatrix} C_\theta & -S_\theta \\ S_\theta & C_\theta \end{bmatrix} \tag{33.48}$$

In principle, parameters θ, ϕ, and α can be solved for with the condition that the off-diagonal elements of the matrix product on the right-hand side of Eq. 33.48 are equal to zero. In practice, real solution cannot always be found, as measurement noise can induce nonphysical transformations between incident and transmitted polarization states. To account for this, Eq. 33.48 can be solved by optimizing parameters θ, ϕ, and α to minimize the sum of the magnitudes of the off-diagonal elements. In principle, this can be achieved using two unique incident polarization states to probe the same volume of a sample. However, when two orthogonal incident polarization states are used [20], birefringence cannot be retrieved under all circumstances [47]. A better choice is to use two incident polarization states perpendicular in a Poincaré sphere representation to guarantee that polarization information can always be extracted [13–16, 22, 37]. The degree of phase retardation can easily be extracted through the phase difference of the resulting diagonal elements and the diattenuation by their magnitudes. It should be noted that these phase retardation values range from $-\pi$ to π and can therefore be unwrapped to yield overall phase retardations in excess of 2π.

As a control measurement, a series of OCT intensity images with varying single linear incident polarization states were acquired from chicken tendon and muscle tissue. The orientations for which the reflected polarization states from within the tissue varied minimally as a function of depth were chosen as those where the incident state was aligned parallel or orthogonal to the sample optic axis. The corresponding intensity profiles described attenuation parameters P_1 and P_2, from which depth-resolved control diattenuation plots were derived. PS-OCT scans were then acquired of the same tissue regions. After correcting for slight imbalances between the gains for the two orthogonal detectors, depth-resolved plots of both diattenuation and phase retardation were calculated. The resulting single-pass diattenuation plots are shown in Fig. 33.13. Numerical simulation revealed that the average angular displacement of a polarization state on the Poincaré sphere for a small diattenuation d is approximately (40d)°. Given that the a standard deviation of the order of 5° for individual polarization states reflected from the surface was found, the control and PS-OCT-derived diattenuation per unit depth of chicken muscle, 0.0380 ± 0.0036/mm versus 0.0622 ± 0.0533/mm, and tendon, 0.5027 ± 0.0353/mm versus 0.3915 ± 0.0365/mm, were within reasonable agreement. These diattenuation values correspond to angular displacement on the order of 1.5 − 2.5°/mm and 15 − 20°/mm for muscle and tendon, respectively. The slopes of the respective phase retardation plots, 179.7°/mm and 1,184.4°/mm for tendon, are well within expected parameters. The angular displacement of the Stokes vectors as a result of diattenuation are negligible compared with those due to birefringence in both cases, implying that for these samples, birefringence can be

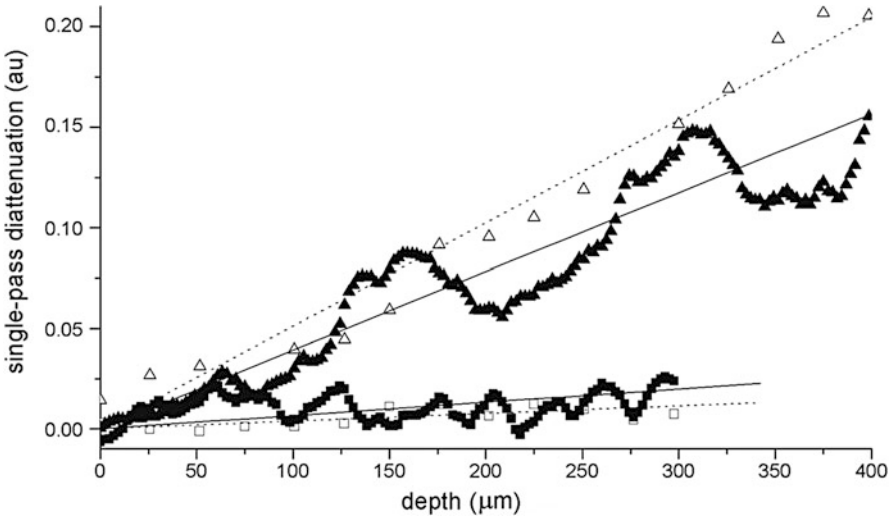

Fig. 33.13 Single-pass diattenuation as a function of depth. The open *triangles* and *squares* represent control diattenuation values of chicken tendon and muscle, respectively, calculated from comparison of the reflectivity profiles for linear incident polarization states along and orthogonal to the fiber direction. The *solid triangles* and *squares* are diattenuation values derived from PS-OCT images acquired from the same tissues. Linear least-squares fits are shown for all plots (Reprinted from Fig. 3 of Ref. [21] with permission of the Optical Society of America)

determined with accuracy even ignoring diattenuation. This was confirmed by applying the Stokes vector-based analysis presented in Sect. 33.1.2.3, which yielded similar slopes of 211.9°/mm and for muscle and tendon, respectively.

A relative optic axis can be derived from ϕ and θ, given in Stokes parameter form by $\mathbf{A} = [\,1, \quad C_{2\phi}C_{2\theta}, \quad C_{2\phi}S_{2\theta}, \quad S_{2\phi}\,]^T$. However, determination of this relative optic axis in a fiber-based system has a fundamental ambiguity. All members of the SU(2) group can be mapped to rotations in SO(3), and so $\mathbf{J}_{out}$, $\mathbf{J}_A$, and $\mathbf{J}_U$ all represent rotations in a Poincaré sphere representation. This means that $\mathbf{J}_C$, $\mathbf{J}_S$, and $\mathbf{J}_T$ are related by unitary transforms and are equivalent except for their respective coordinate systems. Therefore, the amount of phase retardation and diattenuation in $\mathbf{J}_C$, $\mathbf{J}_S$, and $\mathbf{J}_T$ is the same. The three matrices differ only in their eigenvectors and their optic axis equivalents in a well-defined manner dictated by $\mathbf{J}_{out}$. In other words, the optic axis of $\mathbf{J}_T$ is the product of the sample optic axis defined by $\mathbf{J}_A$ and the fiber transformations represented by $\mathbf{J}_{out}$.

Due to the round-trip nature of detected light propagation in tissue, the circular components of birefringence and diattenuation in the sample cancel. Only the linear components of these properties can be measured using PS-OCT. In mathematical terms, the optic axes of $\mathbf{J}_S$, defined by its eigenvectors, can represent only linear birefringence and diattenuation; the V-component (describing circular polarization effects) of the equivalent Stokes vector must equal zero. Therefore, all possible

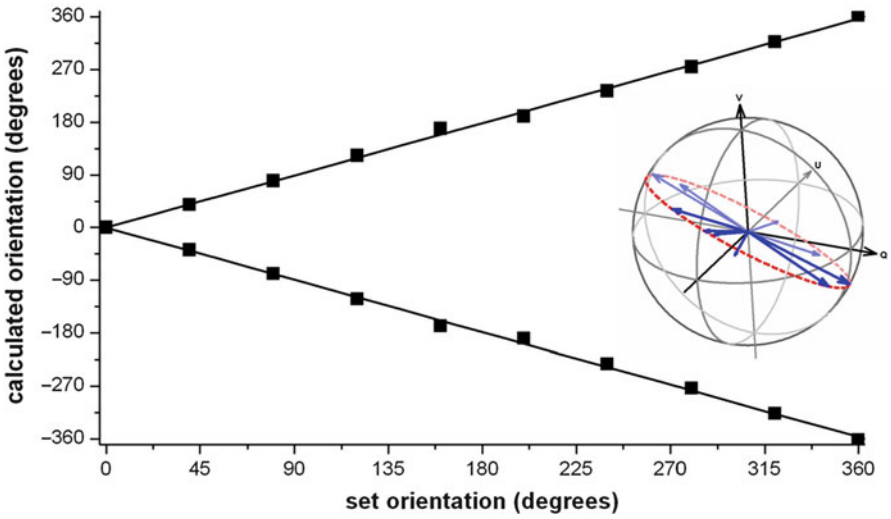

Fig. 33.14 Calculated optic axis orientation as a function of set orientation relative to 0° (*squares*, measured orientation; *lines*, linear fit to the data). As a result of the π-ambiguity (see text), the measured orientation can have both a positive and a negative slope with equal likelihood. Inset, Poincaré sphere representation of the calculated optic axes (*arrows*) for various set orientations of the tissue sample optic axis. The plane (*dashed circle*) in which these optic axes lie was determined by least-squares fitting (Reprinted from Fig. 1 of Ref. [48] with permission from the Optical Society of America)

optic axes for $\mathbf{J}_S$ lie on the QU-plane of a Poincaré sphere. Since $\mathbf{J}_T$ and $\mathbf{J}_S$ differ only by an overall rotation of their coordinate systems, the plane of all possible optic axes for $\mathbf{J}_T$ can be rotated off the QU-plane to some arbitrary plane passing through the origin. The optic axes of $\mathbf{J}_T$ can then have circular components that are entirely due to rotations of the coordinate system arising from system fiber. To verify this analysis, PS-OCT images were taken of a chicken muscle sample, its surface oriented orthogonal to the incident beam and rotated in 40° increments to span a full 360°. Details of the fiber-based PS-OCT system, capable of imaging at 2,048 depth scans per second, were presented by Pierce et al. [15]. It should be noted that the sample itself was rotated and that the fibers in the system were left untouched. Two different analysis methods, the vector-based method and the Jones matrix-based method, were used to analyze the data, providing nearly identical results. The resulting optic axes, along with a plane determined by least-squares fitting, are shown in the inset of Fig. 33.14. The rotation away from the QU-plane is evident, as is the coplanarity of the calculated optic axes.

One method of determining optic axis orientation is to simply determine the orientation as an angle on this tilted plane, as shown in Fig. 33.14. The resulting orientations, relative to that at 0°, are plotted as a function of the set orientation and show that the relative optic axis orientation can be recovered accurately. A second method is to rotate the calculated plane of optic axes back down onto the QU-plane

of the Poincaré sphere. The change in coordinate system due to optical fibers in the system can be decomposed into two parts: a rotation within the plane of possible measured optic axes and a tilting of the plane about some arbitrary axis in the QU-plane. The rotation within the plane causes an overall offset in the calculated orientation that has been discussed in previous publications [14, 20, 47, 48] and implies that only relative orientation angles, not absolute angles, can be determined from a fiber-based PS-OCT system. The tilting of the plane leads to what can be termed a π-ambiguity, or an indeterminacy in the sign of the orientation angle [48].

One proposed method to compensate for this tilting uses the reflection from the surface of a sample to determine the rotation needed to tilt the plane back onto the QU-plane by solving $\mathbf{E} = e^{i\psi}\mathbf{J}_{in}^{T}\mathbf{J}_{in}\mathbf{E}_{source}$, where $\mathbf{J}_{in}$ represents the sample arm fiber only [20]. Four possible solutions to $\mathbf{J}_{in}$ can be found that map to two unique rotations in SO(3) corresponding to common phase factors Ψ differing by π. In geometrical terms, this is the equivalent of the fact that there are two ways to rotate the plane of measured optic axes onto the QU-plane of the Poincaré sphere (faceup and facedown). This results in an ambiguity in the sign of the orientation angle. In other words, as the set optic axis orientation of a sample rotates in one direction, the measured optic axis orientation, depending on the correction chosen, could move in either direction. Thus, the sign of the orientation angle cannot be determined explicitly, only the absolute value, or magnitude, of change from one location to the next. The slope of Fig. 33.14, relating the calculated orientation to the set orientation for a set of data where the same correction could be used throughout, could be positive or negative with equal validity. This π-ambiguity is inherent to all fiber-based PS-OCT systems and implies that although the relative optic axis within an image can be determined, the direction of change in optic axis orientation cannot be compared from image to image absolutely without a priori knowledge.

The case where the information for the two polarization states are acquired simultaneously will now be briefly examined. In this situation, there is no ambiguity in phase between the reflected polarization states, and so $\alpha = \Delta\psi_2 - \Delta\psi_1 = 0$. The polarization properties of a sample can now be *analytically* determined by a simple diagonalization of the right-hand side of Eq. 33.48. The significance of knowledge of the absolute phase relation between the reflected states can also be appreciated by examination of the problem when an incident polarization state is aligned with or orthogonal to the optic axis of a sample. While the Stokes vector for a reflected polarization state might not differ from the incident state, the complex electric field will become shifted by $e^{i\eta/2}$ or $e^{-i\eta/2}$ if it is aligned with or orthogonal to the optic axis, respectively. The amount of birefringence can now be determined in this situation by examination of the overall phase shift between the incident and reflected complex electric fields. Therefore, simultaneous acquisition of the two reflected polarization states makes it possible to *always* recover birefringence using any two unique incident polarization states. In this case, the optimal choice for the two incident polarization states is given when they are separated by 180° in a Poincaré sphere representation, as this is ideal for determination of diattenuation.

33.2 Applications

PS-OCT has been applied to a wide variety of clinical problems, including in vivo examination of the polarization properties of the retinal nerve fiber layer [10, 22, 23, 49–55], the detection and monitoring of caries lesion progression and treatment [24, 56–63], and examination of articular cartilage for detection of osteoarthritis [64–71]. Rather than detail these myriad studies, this section will concentrate on dermatological and ophthalmic studies for illustrative purposes.

33.2.1 Dermatology

OCT and its variants have been applied to a wide variety of dermatological problems [72]. One of the first clinical applications of PS-OCT in particular was for the assessment of burn depth. Burns are classified by depth into first-, second-, and third-degree injuries. First-degree burns cause redness and pain (e.g., sunburn). Second-degree burns are marked by blisters (e.g., scald by hot liquid). In third-degree burns, both the epidermis and dermis are destroyed and the underlying tissue may also be damaged. A second-degree burn will heal if given proper care. However, a third-degree burn will not heal and requires a skin graft. Making the distinction between the two is difficult; a burn surgeon will often observe the injury over the course of several days before making an educated guess regarding burn depth [73]. Initial studies [14] have indicated the potential for PS-OCT to solve this problem by taking advantage of the fact that skin contains collagen, a birefringent material [7, 9]. At temperatures between 56 °C and 65 °C, collagen begins to denature and lose its birefringence [8, 74]. It should be expected that normal and burned skin differ in their natural collagen content and leads to a reduction in the ability of burned skin to alter the polarization state of light that has passed through and been reflected back from some depth.

The computationally efficient Stokes vector method [14–16, 37] described in Sect. 33.1.2.3 was used to correlate birefringence derived from data acquired with a fiber-based PS-OCT instrument [13] versus burn depth as determined by histological analysis for 22 burn sites in a rat model [14]. Figure 33.15 shows examples of normal, unburned rat skin and skin burned for 30 s at 75 °C, respectively. Figure 33.15a and e are histological sections, and comparison between the two highlights the damage to the adnexal structures, the contrast in H&E staining color, and the presence of hyalinization that are associated with thermal injury. Normal skin in Fig. 33.15a has a fairly uniform density of collagen fibers through the dermis that is not visible in the upper regions of Fig. 33.15e due to collagen coagulation. The effects of thermal injury are also readily apparent in the PS-OCT scans. In the burned tissue, the darker region extends to a visibly greater depth than in normal skin, indicating a lesser degree of birefringence in that tissue. This difference is quantified in the phase retardation plots. The degree of phase retardation depends on two factors: distance through the tissue that the light has traveled and the density of natural collagen. The variation with distance is evident in the first 300–500 μm in

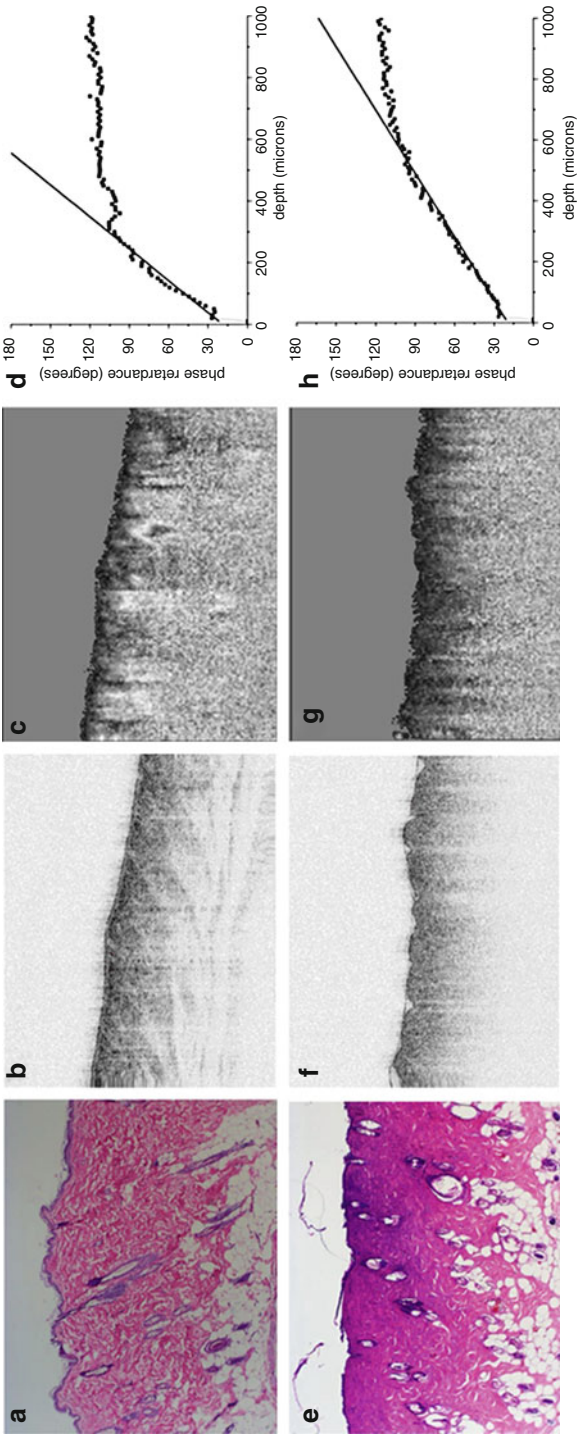

Fig. 33.15 Normal and burned rat skin, respectively, (**a**, **e**) histology, (**b**, **f**) OCT image, (**c**, **g**) phase retardation image, and (**d**, **h**) plot of phase retardance versus depth. The thermal injury was for 30 s at 75 °C. The dimensions of the histological images and phase maps are 3.2 mm by 2 mm, and depths in the graphs are measured from the tissue surface. The absence of speckle above the sample surface is due to the fact that calculation of the phase map was only performed below the surface (Reprinted from Figs. 3 and 4 of Ref. [14] with permission of the International Society for Optical Engineering)

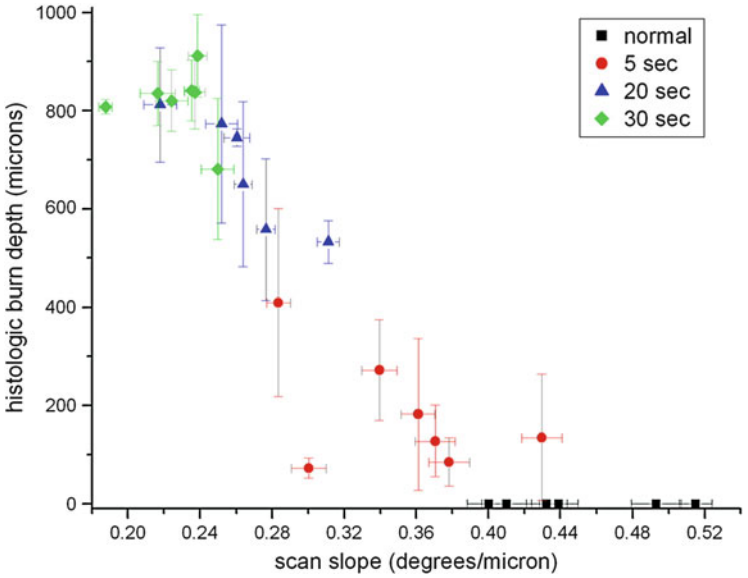

Fig. 33.16 Overall graph of burn depth determined by histological analysis as a function of phase retardation from PS-OCT by burn duration. The A-lines in an image are averaged to generate a graph of degree of phase retardation versus depth into the tissue. The slopes of the roughly linear portions of these graphs are determined by least-squares fitting and the slope and error reported as a measure of phase retardation (scan slope)

depth in the PS-OCT scans; as the depth increases, the degree of phase retardation increases. After this initial depth, the graphs asymptotically approach approximately 115°, which can be attributed to depolarization due to scattering as confirmed by Monte Carlo simulation of the phase retardation measured by randomized polarization states returning from tissue.

Figure 33.16 summarizes the results of the 22 burn sites grouped as normal skin and in three exposure durations of 5, 20, and 30 s at 75 °C. The thermal injury results in skin with lowered fractions of natural collagen. Comparing areas burned for 5 and 30 s, respectively, light that that has traveled a certain depth in the less burned skin will be retarded more than light traveling through the same depth in the tissue with more collagen denaturation. This correlation is clear in Fig. 33.16, where the degree of phase retardation per unit depth decreases with increasing burn depth.

While similar studies in animals have been performed that demonstrate a similar correlation between PS-OCT-derived birefringence and histologically determined burn depth [32, 75], such animal studies are far from the only clinical application of PS-OCT in dermatology. A good deal of work has been done toward establishing baselines for the polarization properties of normal human skin as PS-OCT technology has progressed [13, 72, 76–78]. This work has helped pave the way toward

assessment of burns in humans [79], identification and delineation of basal cell carcinoma [80] and dermal photoaging [81].

33.2.2 Ophthalmology

Ophthalmological application of OCT has arguably driven a great deal of its development and probably represents the most researched clinical application of the technology to date. PS-OCT in particular has been used to measure the birefringence of the human retinal nerve fiber layer in vivo [6, 22, 23, 50–52] for potential early detection of glaucoma, the world's second leading cause of blindness.

Glaucoma causes damage to the retinal ganglion cells, resulting in a thinning of the retinal nerve fiber layer (RNFL). In addition, nerve fiber layer tissue loss may be preceded by changes in birefringence as ganglion cells become necrotic and axons in the RNFL are replaced by a less organized and amorphous tissue composed of glial cells. When glaucoma is detected at an early stage, further loss of vision can be prevented by treatment. The visual field test is the current standard method of detecting loss of peripheral vision in glaucoma. However, measurements show that up to 40 % of nerves are irreversibly damaged before loss of peripheral vision can be clinically detected. PS-OCT has the potential to detect changes to the RNFL at an earlier time point through changes in its birefringence and thickness.

Ophthalmic studies can be performed using systems similar to that used by Cense et al. [22], in which a slit lamp has been adapted for use with PS-OCT. Figure 33.17 is a typical example of a structural-intensity time-domain OCT image of the retina in the left eye of a healthy volunteer obtained with a circular scan with a radius of 2.1 mm around the optic nerve head (ONH). The image measures 13.3 mm wide and 0.9 mm deep and is shown at an expanded aspect ratio in depth for clarity. Structural layers such as the RNFL, the interface between the inner and outer segments of the photoreceptors, and the retinal pigmented epithelium can be seen.

The addition of polarization sensitivity allows for localized quantitative assessment of the thickness and birefringence of the RNFL. Figure 33.18 shows two examples of combined thickness and birefringence measurements, one of a region temporal to the ONH and the other of a region superior to the ONH. The depth of the RNFL can be determined by a decrease in backscattered intensity from the RNFL to the inner plexiform layer. The birefringence of the RNFL can then be estimated from a linear least-squares fit of the measured double-pass phase retardation through the determined depth. Two main observations can be drawn from such graphs: the retinal layers directly below the RNFL are minimally birefringent and that the thickness and birefringence of the RNFL are not constant. These observations can also be seen in Fig. 33.19, which overlays the thickness and birefringence determined as in Fig. 33.18 on a circular scan across the ONH. The plots indicate that the RNFL is thickest and most birefringent superiorly and inferiorly to the ONH.

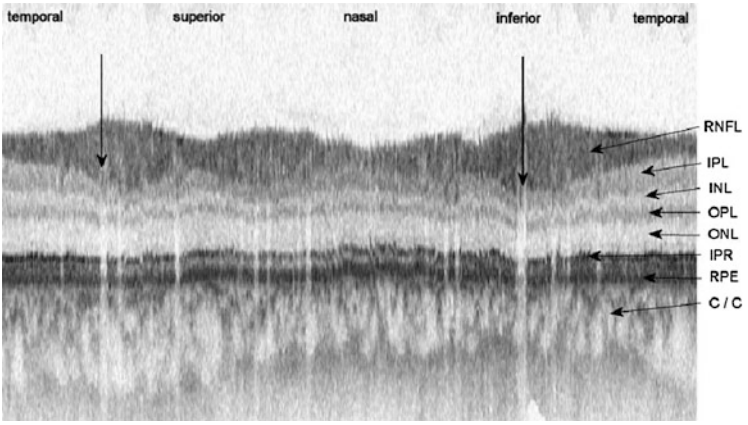

Fig. 33.17 A realigned OCT intensity image created with a 2.1-mm radius circular scan around the ONH. The dynamic range of the image is 36 dB. *Black* pixels represent strong reflections. The image measures 13.3 mm wide and 0.9 mm deep. Visible structures: retinal nerve fiber layer (*RNFL*), inner plexiform layer (*IPL*), inner nuclear layer (*INL*), outer plexiform layer (*OPL*), outer nuclear layer (*ONL*), interface between the inner and outer segments of the photoreceptor layer (*IPR*), retinal pigmented epithelium (*RPE*), and choriocapillaris and choroid (*C/C*). *Vertical arrows*: locations of the two largest blood vessels. Other smaller blood vessels appear as vertical white areas in the image (Reprinted from Fig. 3 of Ref. [23] with permission from the Association for Research in Vision and Ophthalmology)

En-face maps of RNFL thickness and birefringence can be generated from data obtained with recently developed spectral-domain ophthalmic PS-OCT systems [82]. A three-dimensional volume ($4.24 \times 5.29 \times 1.57$ mm^3) of the retina of a normal volunteer (right eye) was scanned at a rate of 29 fps with 1,000 A-lines/frame and contains 190 frames (B-scans) acquired in 6.5 s. The integrated reflectance, birefringence, and retinal nerve fiber layer (RNFL) thickness maps are shown in Fig. 33.20, confirming previous findings that the RNFL birefringence is not uniform across the retina. Superior, nasal, inferior, and temporal areas of the retina around the ONH are indicated by the letters S, N, I, and T. The integrated reflectance map, obtained by simply integrating the logarithmic depth profiles, illustrates the blood vessel structure around the ONH. The RNFL thickness map is scaled in microns (color bar on the top of the image) indicating an RNFL thickness of up to 200 mm. The central dark-blue area corresponds to the position of the ONH that was excluded from both the thickness and the birefringence maps. A typical bow-tie pattern can be seen for the distribution of the RNFL thickness around the ONH, showing a thicker RNFL superior and inferior to the ONH. The birefringence map illustrates a variation of the birefringence values between 0 and 5.16×10^{-4}, and it clearly demonstrates that the RNFL birefringence is not uniform across the retina; it is smaller nasally and temporally and larger superiorly and inferiorly to the ONH.

Given that measurements of the thickness and birefringence of the RNFL can be acquired with the speed and accuracy demonstrated, further research into changes

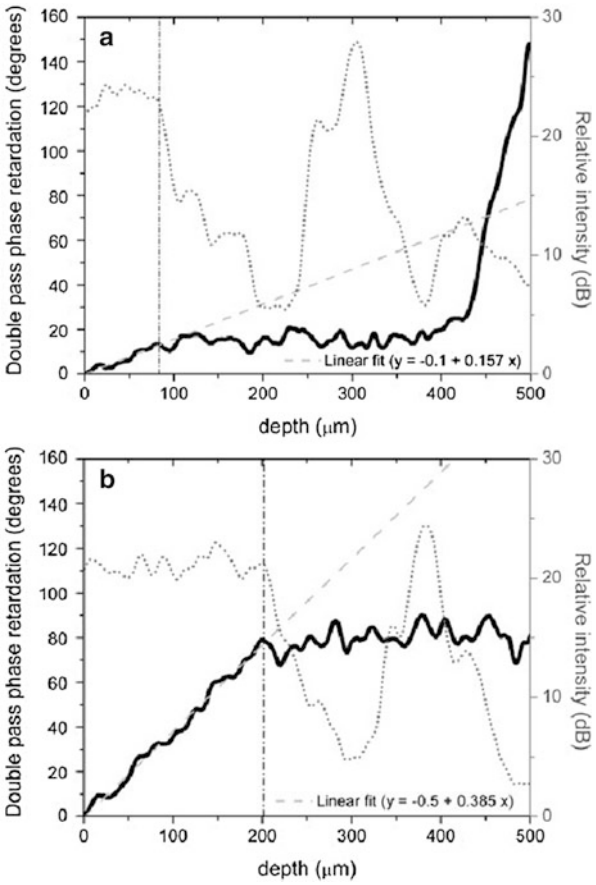

Fig. 33.18 Thickness (*dotted line*) and birefringence (*solid line*) plots of an area temporal (**a**) and superior (**b**) to the ONH. DPPR data belonging to the RNFL is fit with a least-square linear fit. The slope in the equation represents the DPPR/UD or birefringence. The *vertical line* indicates the boundary of the RNFL, as determined from the intensity and DPPR data. In (**a**), the increase in DPPR at a depth beyond 450 μm is caused either by a relatively low signal-to-noise ratio or by the presence of a highly birefringent material – for instance, collagen in the sclera (Reprinted from Fig. 2 of Ref. [23] with permission of the Association for Research in Vision and Ophthalmology)

in these parameters with glaucoma can be performed. Experiments – for instance, a longitudinal study with PS-OCT on patients at high risk for development of glaucoma – will either confirm of reject the hypothesis. In addition, PS-OCT can enhance the specificity in determining RNFL thickness in structural OCT images by using changes in tissue birefringence to determine the border between the RNFL and the ganglion cell layer.

33.3 Future Directions

33.3.1 Fourier-Domain OCT

In traditional or time-domain OCT (TD-OCT), a depth profile is obtained by scanning the length of the reference arm of an interferometer [1]. Alternatively, depth information can be retrieved by detecting the interference signal as a function

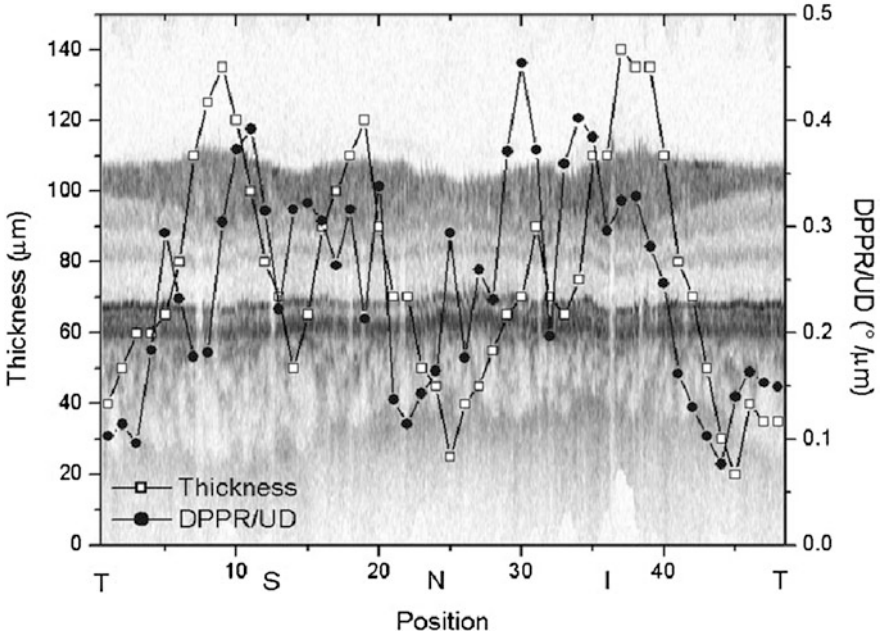

Fig. 33.19 A typical example of combined RNFL thickness and birefringence measurements along a circular scan around the ONH. The intensity image is plotted in the background. The RNFL is relatively thicker superiorly (*S*) and inferiorly (*I*). A similar development can be seen in the birefringence plot. The birefringence is relatively higher in the thicker areas, whereas it is lower in the thinner temporal (*T*) and nasal (*N*) areas (Reprinted from Fig. 4 of Ref. [23] with permission from the Association for Research in Vision and Ophthalmology)

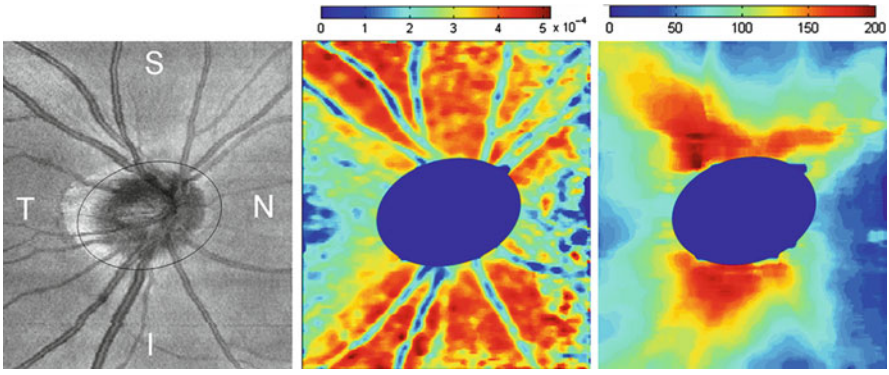

Fig. 33.20 OCT scan (4.24 × 5.29 mm^2) of the retina of a normal volunteer, centered on the ONH. (**a**) An integrated reflectance map showing a normal temporal crescent (*white* area temporal to the ONH), (**b**) birefringence map, and (**c**) RNFL thickness map (*color bar* scaled in microns). The *circle* on the *left* indicates the excluded area in the birefringence and thickness maps as corresponding to ONH. (*S* superior, *N* nasal, *I* inferior, *T* temporal) (Reprinted from Fig. 8 of Ref. [82] with permission of the International Society for Optical Engineering)

of wavelength. In spectral-domain OCT (SD-OCT), this is achieved with a broadband source and a spectrometer in the detector arm [83–85]. Optical frequency domain imaging (OFDI) uses a swept source and point detectors to acquire the same information [86]. The main advantage of these schemes, collectively known as Fourier-domain OCT, is a marked increase in sensitivity [87–91] that can be translated into increased imaging speed. SD-OCT [16, 39, 52, 76] and OFDI [92] systems with polarization sensitivity have been reported.

In both paradigms, the recorded interference signal can be converted into a depth profile by Fourier transform, which relates physical distance with wave number k. A proper depth profile is only obtained after remapping the interference signal evenly in k-space [85], requiring accurate assessment of the wavelength corresponding to each spectral element of the recorded signal. This accuracy becomes even more important with polarization-sensitive measurements. Even a slight mismatch of the wavelength mapping between the two analysis channels can give rise to an artificial appearance of birefringence [16]. While this is typically not the case with OFDI, alignment and calibration of polarization-sensitive SD-OCT systems to remove this artifact is critical for accuracy and has been reported by several groups [16, 39, 52, 82].

Since TD-OCT does not suffer from any such artifact, direct comparison of TD- and SD-OCT results can be used to verify the accuracy of the remapping procedure and removal of birefringence artifacts. Using a polarization-sensitive SD-OCT system [16], images were taken of a chicken muscle sample, its surface oriented orthogonal to the axis of the incident beam and rotated in 20° increments about this axis, spanning a full 360°. Data from orientations with signal saturation were ignored. The same sample was then imaged with the same geometry with a TD-OCT system capable of imaging at 2,048 depth scans per second [15, 37]. A more computationally intensive Jones matrix-based analysis capable of providing unwrappable phase retardations (in excess of 360°) was used to analyze both sets of data [21]. The data from the Jones matrix-based approach is displayed. Representative data acquired with both systems are displayed in Fig. 33.21. Average double-pass phase retardation slopes of $0.919 \pm 0.031°$/mm and $0.885 \pm 0.069°$/mm for time domain and spectral domain, respectively, are in excellent agreement. The resulting optic axes, along with a plane determined by least-squares fitting, as well as their corresponding orientation angles on that plane, are shown in Fig. 33.22. The calculated orientation shows good agreement with the set orientation angle of the tissue sample. These results demonstrate the accuracy of the system to determine sample polarization properties, such as phase retardation and optic axis orientation.

33.3.2 Noise Analysis

Assessment of its accuracy has developed as PS-OCT has evolved. In its earliest conception, Everett et al. [9] gave an analysis of the systematic error in the phase retardation due to background noise for the amplitude-based PS-OCT detection

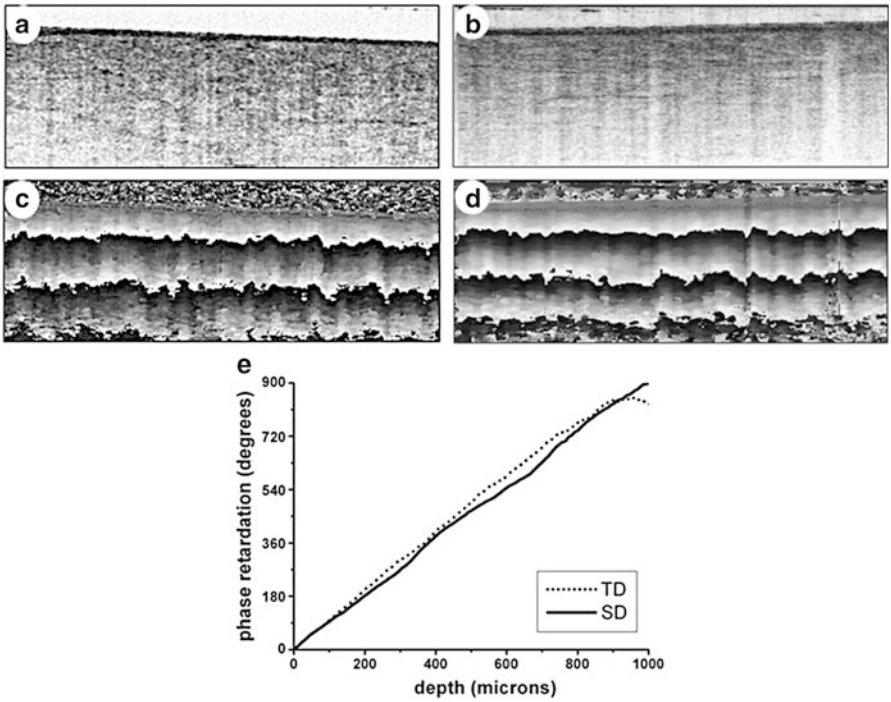

Fig. 33.21 Representative TD- and SD-OCT images of the same chicken breast muscle sample. The width of the images was 4.0 mm, and the depth was 1.2 and 1.4 mm for the TD- and SD-OCT images, respectively. Each set of images (TD,SD) are composed of an intensity image (**a**, **c**) and phase retardation image (**b**, **d**). The unwrapped phase retardation profiles were averaged over the full width of the image (**e**). Intensity images are gray-scaled encoded over the dynamic range of the image, and phase retardation images are gray-scaled from *black* to *white*, representing phase retardations from $-\pi$ to π radians, respectively (Reprinted from Fig. 8 of Ref. [16] with permission of the Optical Society of America)

scheme. They showed that for phase retardations close to 0° or 90°, the background noise on the detectors introduces a significant and systematic error. However, determination of the Stokes parameters of reflected light [10] reduces this error by calculating the Stokes parameters Q, U, and V based on the amplitude *and* phase relation between interference fringes [34]. The remaining variance in the computed Stokes vectors of reflected light (excluding polarization effects) can largely be attributed to a combination of multiple scattering, shot noise (in an optimized system), and speckle.

Multiple scattering will scramble the polarization mainly in a random manner. This offers some means to distinguish it from polarization effects. However, an optic axis that varies with depth will give changes in the polarization state that can make it difficult to distinguish from the random manner of multiple scattering. While a number of studies have demonstrated an ability to determine localized

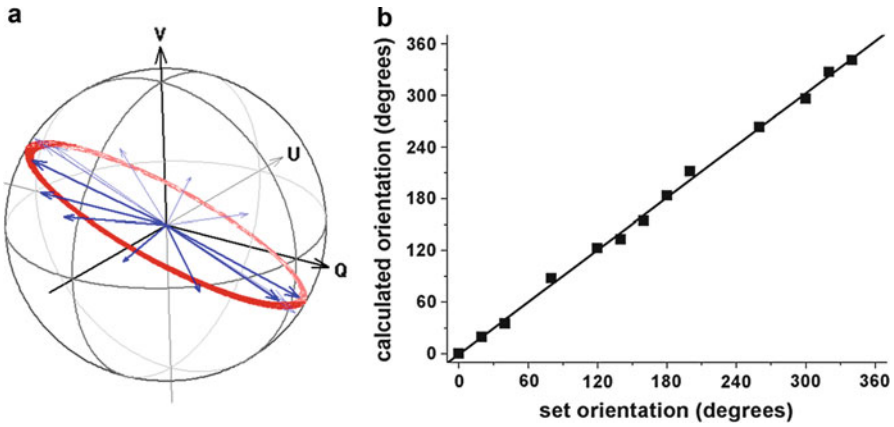

Fig. 33.22 (**a**) Optic axis orientation in a Poincaré sphere representation of the calculated optic axes (*arrows*) for various set orientations of the tissue sample optic axis. The plane (*dotted circle*) in which these optic axes lie was determined by least-squares fitting. (**b**) Calculated optic axis orientation as a function of set orientation relative to 0°. *Squares*: Measured orientation. *Line*: Linear fit to the data (Reprinted from Fig. 9 of Ref. [16] with permission of the Optical Society of America)

sample polarization properties, including depth-resolved changes in optic axis orientation [28, 93, 94], more research is necessary to truly solve this complex problem.

Since calculation of any sample polarization properties is dependent on determination of the polarization state of light measured with PS-OCT, the accuracy of these polarization properties is highly dependent on the accuracy of polarization state determination. One such fundamental limitation in a shot noise-limited system arises from errors in phase determination as a function of the signal-to-noise ratio (SNR) of a measurement [16, 95]. To quantify this effect, 1,024 consecutive depth profiles at a single point on a glass slide were obtained at different SNRs using a variable neutral density filter in the sample arm of a spectral-domain PS-OCT system [16]. The polarization state reflected from the surface of the slide was determined, and the average angular deviation of these polarization states from their mean, as illustrated in the inset of Fig. 33.23, was calculated. The resulting data, plotted as a function of SNR in Fig. 33.23, demonstrate a decreasing average angular standard deviation with increasing SNR. The theoretical curve was generated based on a simple additive noise model. The standard deviation of a complex electric field can be estimated from the vector sum of a random complex vector to a complex electric field vector, where the relative length of the two vectors is determined by SNR [16]. This can be translated into an angular standard deviation, $\Delta\theta$, in a Poincaré sphere representation of a measured polarization states such that $\Delta\theta = \sqrt{2/SNR}$. It should be noted that this relation takes into account amplitude variations between orthogonal electric field components. The experimental results

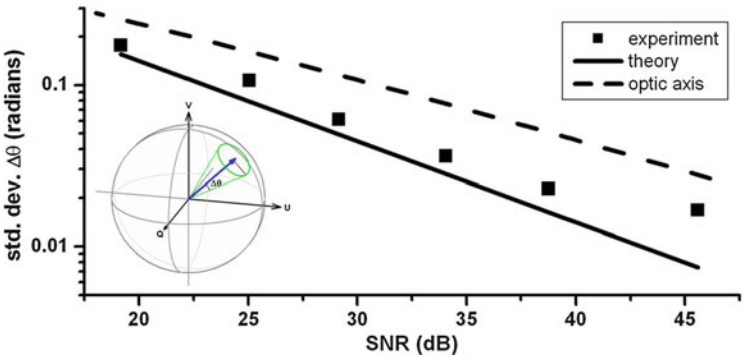

Fig. 33.23 Angular standard deviation in the Poincaré sphere, $\Delta\theta$, as a function of signal-to-noise ratio on a log–log scale for polarization state (*squares*, standard deviation over 1,024 measurements; *solid line*, theoretical curve; see text) and optic axis determination (*dashed line*, simulated prediction; see text). Inset, Poincaré sphere illustrating a probability distribution as indicated by a cone defined by the standard deviation, $\Delta\theta$ (Reprinted from Fig. 2 of Ref. [48] with permission of the Optical Society of America)

show good agreement with predicted theory, except at 45 dB, where the combined power of the sample and reference arms was outside the shot noise-limited range of the system. Clearly, this relation will affect the accuracy of any resulting sample polarization properties. To calculate the effect on optic axis determination accuracy, numerical simulations were performed for a range of SNR values. Figure 33.23 shows the resulting prediction of the mean angular standard deviations for optic axis determination as a function of SNR.

Speckle introduces noise on the Stokes parameters by the large fluctuations in the interference fringes that could be uncorrelated in the orthogonal detection channels. Kemp et al. have introduced quantifications of this effect in the notions of polarimetric speckle noise [96], or the standard deviation of a polarization state on the Poincaré sphere, and polarimetric signal-to-noise ratio [29], which estimates the ability of PS-OCT to estimate polarization parameters in the presence of polarimetric speckle noise. A great deal of work has been done with various speckle reduction techniques in OCT [97–108], the application of which reduces this noise as does averaging the Stokes parameters over distances larger than the coherence length. Speckle remains one of the principle problems in the development of OCT.

33.3.3 Other Developments

PS-OCT continues to develop and find application in ever expanding ways. For example, Ugryumova et al. have developed a system that uses variable incident angles to determine the three-dimensional sample optic axis [109]. Among the other recent applications of PS-OCT are studies of endoscopic OCT [110], examination

of collagen content in coronary plaque [111–115], and even detection of ultrastructural changes in murine muscle during exercise [116]. These novel fields of research show that, just as the field has evolved and grown since its inception, PS-OCT continues to advance rapidly and find application in clinical medicine and biological research.

Acknowledgements This research was supported in part by funding from the National Institutes of Health (1R24 EY12877, R01 EY014975, and RR19768, K99/R00 EB007241), the Department of Defense (F4-9820-01-1-0014), the Center for Integration of Medicine and Innovative Technology, and a gift from Dr. and Mrs. J.S. Chen to the Optical Diagnostics Program at the Wellman Center for Photomedicine. The authors would like to thank a number of graduate students and postdoctoral research fellows that have contributed to the results presented in this chapter: Mark Pierce, PhD, Barry Cense, PhD, and Mircea Mujat, PhD. We would also like to acknowledge the contributions of Dr. Teresa Chen, MD, of the Massachusetts Ear and Eye Infirmary.

References

1. D. Huang, E.A. Swanson, C.P. Lin, J.S. Schuman, W.G. Stinson, W. Chang, M.R. Hee, T. Flotte, K. Gregory, C.A. Puliafito, J.G. Fujimoto, Optical coherence tomography. Science **254**(5035), 1178–1181 (1991)
2. X.J. Wang, T.E. Milner, J.S. Nelson, Characterization of fluid-flow velocity by optical Doppler tomography. Opt. Lett. **20**(11), 1337–1339 (1995)
3. Y.H. Zhao, Z.P. Chen, C. Saxer, S.H. Xiang, J.F. de Boer, J.S. Nelson, Phase-resolved optical coherence tomography and optical Doppler tomography for imaging blood flow in human skin with fast scanning speed and high velocity sensitivity. Opt. Lett. **25**(2), 114–116 (2000)
4. Y.H. Zhao, Z.P. Chen, C. Saxer, Q.M. Shen, S.H. Xiang, J.F. de Boer, J.S. Nelson, Doppler standard deviation imaging for clinical monitoring of in vivo human skin blood flow. Opt. Lett. **25**(18), 1358–1360 (2000)
5. V. Westphal, S. Yazdanfar, A.M. Rollins, J.A. Izatt, Real-time, high velocity-resolution color Doppler optical coherence tomography. Opt. Lett. **27**(1), 34–36 (2002)
6. M.R. Hee, D. Huang, E.A. Swanson, J.G. Fujimoto, Polarization-sensitive low-coherence reflectometer for birefringence characterization and ranging. J. Opt. Soc. Am. B Opt. Phys. **9**(6), 903–908 (1992)
7. J.F. de Boer, T.E. Milner, M.J.C. van Gemert, J.S. Nelson, Two-dimensional birefringence imaging in biological tissue by polarization-sensitive optical coherence tomography. Opt. Lett. **22**(12), 934–936 (1997)
8. J.F. de Boer, S.M. Srinivas, A. Malekafzali, Z.P. Chen, J.S. Nelson, Imaging thermally damaged tissue by polarization sensitive optical coherence tomography. Opt. Express **3**(6), 212–218 (1998)
9. M.J. Everett, K. Schoenenberger, B.W. Colston, L.B. Da Silva, Birefringence characterization of biological tissue by use of optical coherence tomography. Opt. Lett. **23**(3), 228–230 (1998)
10. M.G. Ducros, J.F. de Boer, H.E. Huang, L.C. Chao, Z.P. Chen, J.S. Nelson, T.E. Milner, H.G. Rylander, Polarization sensitive optical coherence tomography of the rabbit eye. IEEE J. Sel. Top. Quantum Electron. **5**(4), 1159–1167 (1999)
11. G. Yao, L.V. Wang, Two-dimensional depth-resolved Mueller matrix characterization of biological tissue by optical coherence tomography. Opt. Lett. **24**(8), 537–539 (1999)
12. C.K. Hitzenberger, E. Gotzinger, M. Sticker, M. Pircher, A.F. Fercher, Measurement and imaging of birefringence and optic axis orientation by phase resolved polarization sensitive optical coherence tomography. Opt. Express **9**(13), 780–790 (2001)

13. C.E. Saxer, J.F. de Boer, B.H. Park, Y.H. Zhao, Z.P. Chen, J.S. Nelson, High-speed fiber-based polarization-sensitive optical coherence tomography of in vivo human skin. Opt. Lett. **25**(18), 1355–1357 (2000)
14. B.H. Park, C. Saxer, S.M. Srinivas, J.S. Nelson, J.F. de Boer, In vivo burn depth determination by high-speed fiber-based polarization sensitive optical coherence tomography. J. Biomed. Opt. **6**(4), 474–479 (2001)
15. M.C. Pierce, B.H. Park, B. Cense, J.F. de Boer, Simultaneous intensity, birefringence, and flow measurements with high-speed fiber-based optical coherence tomography. Opt. Lett. **27**(17), 1534–1536 (2002)
16. B.H. Park, M.C. Pierce, B. Cense, S.H. Yun, M. Mujat, G.J. Tearney, B.E. Bouma, J.F. de Boer, Real-time fiber-based multi-functional spectral-domain optical coherence tomography at 1.3 mu m. Opt. Express **13**(11), 3931–3944 (2005)
17. S.L. Jiao, G. Yao, L.H.V. Wang, Depth-resolved two-dimensional stokes vectors of backscattered light and Mueller matrices of biological tissue measured with optical coherence tomography. Appl. Opt. **39**(34), 6318–6324 (2000)
18. S.L. Jiao, L.H.V. Wang, Jones-matrix imaging of biological tissues with quadruple-channel optical coherence tomography. J. Biomed. Opt. **7**(3), 350–358 (2002)
19. S.L. Jiao, L.H.V. Wang, Two-dimensional depth-resolved Mueller matrix of biological tissue measured with double-beam polarization-sensitive optical coherence tomography. Opt. Lett. **27**(2), 101–103 (2002)
20. S.L. Jiao, W.R. Yu, G. Stoica, L.H.V. Wang, Optical-fiber-based Mueller optical coherence tomography. Opt. Lett. **28**(14), 1206–1208 (2003)
21. B.H. Park, M.C. Pierce, B. Cense, J.F. de Boer, Jones matrix analysis for a polarization-sensitive optical coherence tomography system using fiber-optic components. Opt. Lett. **29**(21), 2512–2514 (2004)
22. B. Cense, T.C. Chen, B.H. Park, M.C. Pierce, J.F. de Boer, In vivo depth-resolved birefringence measurements of the human retinal nerve fiber layer by polarization-sensitive optical coherence tomography. Opt. Lett. **27**(18), 1610–1612 (2002)
23. B. Cense, T.C. Chen, B.H. Park, M.C. Pierce, J.F. de Boer, Thickness and birefringence of healthy retinal nerve fiber layer tissue measured with polarization-sensitive optical coherence tomography. Invest. Ophthalmol. Vis. Sci. **45**(8), 2606–2612 (2004)
24. D. Fried, J. Xie, S. Shafi, J.D.B. Featherstone, T.M. Breunig, C. Le, Imaging caries lesions and lesion progression with polarization sensitive optical coherence tomography. J. Biomed. Opt. **7**(4), 618–627 (2002)
25. C.F. Bohren, D.R. Huffman, *Absorption and Scattering of Light by Small Particles* (Wiley, New York, 1983)
26. R.A. Chipman, Polarization analysis of optical systems. Opt. Eng. **28**, 90–99 (1989)
27. S.Y. Lu, R.A. Chipman, Interpretation of Mueller matrices based on polar decomposition. J. Opt. Soc. Am. A **13**, 1106–1113 (1996)
28. M. Todorovic, S.L. Jiao, L.V. Wang, Determination of local polarization properties of biological samples in the presence of diattenuation by use of Mueller optical coherence tomography. Opt. Lett. **29**(20), 2402–2404 (2004)
29. N.J. Kemp, H.N. Zaatari, J. Park, H.G. Rylander, T.E. Milner, Form-biattenuance in fibrous tissues measured with polarization-sensitive optical coherence tomography (PS-OCT). Opt. Express **13**(12), 4611–4628 (2005)
30. R.C. Jones, A new calculus for the treatment of optical systems I. Description and discussion of the calculus. J. Opt. Soc. Am. A **31**(7), 488–493 (1941)
31. J.J. Gil, E. Bernabeu, Obtainment of the polarizing and retardation parameters of a non-depolarizing optical system from the polar decomposition of its Mueller matrix. Optik **76**(2), 67–71 (1987)
32. S.L. Jiao, W.R. Yu, G. Stoica, L.H.V. Wang, Contrast mechanisms in polarization-sensitive Mueller-matrix optical coherence tomography and application in burn imaging. Appl. Opt. **42**(25), 5191–5197 (2003)

33. W.A. Shurcliff, S.S. Ballard, *Polarized Light* (Van Nostrand, New York, 1964)
34. J.F. de Boer, T.E. Milner, Review of polarization sensitive optical coherence tomography and Stokes vector determination. J. Biomed. Opt. **7**(3), 359–371 (2002)
35. B.H. Park, Fiber-based polarization-sensitive optical coherence tomography, in *Physics and Astronomy* (University of California, Irvine, 1995)
36. J. Park, N.J. Kemp, H.N. Zaatari, H.G. Rylander, T.E. Milner, Differential geometry of normalized stokes vector trajectories in anisotropic media. J. Opt. Soc. Am. A Opt. Image Sci. Vis. **23**(3), 679–690 (2006)
37. B.H. Park, M.C. Pierce, B. Cense, J.F. de Boer, Real-time multi-functional optical coherence tomography. Opt. Express **11**(7), 782–793 (2003)
38. S.L. Jiao, M. Todorovic, G. Stoica, L.H.V. Wang, Fiber-based polarization-sensitive Mueller matrix optical coherence tomography with continuous source polarization modulation. Appl. Opt. **44**(26), 5463–5467 (2005)
39. M. Yamanari, S. Makita, V.D. Madjarova, T. Yatagai, Y. Yasuno, Fiber-based polarization-sensitive Fourier domain optical coherence tomography using B-scan-oriented polarization modulation method. Opt. Express **14**(14), 6502–6515 (2006)
40. M. Yamanari, S. Makita, Y. Yasuno, Polarization-sensitive swept-source optical coherence tomography with continuous source polarization modulation. Opt. Express **16**(8), 5892–5906 (2008)
41. W.Y. Oh, S.H. Yun, B.J. Vakoc, M. Shishkov, A.E. Desjardins, B.H. Park, J.F. de Boer, G.J. Tearney, E. Bouma, High-speed polarization sensitive optical frequency domain imaging with frequency multiplexing. Opt. Express **16**(2), 1096–1103 (2008)
42. K.H. Kim, B.H. Park, Y. Tu, T. Hasan, B. Lee, J. Li, J.F. de Boer, Polarization-sensitive optical frequency domain imaging based on unpolarized light. Optics Express **19**(2), 552–561 (2011)
43. K. Schoenenberger, B.W. Colston, D.J. Maitland, L.B. Da Silva, M.J. Everett, Mapping of birefringence and thermal damage in tissue by use of polarization-sensitive optical coherence tomography. Appl. Opt. **37**(25), 6026–6036 (1998)
44. G.J. van Blokland, Ellipsometry of the human retina in vivo: preservation of polarization. J. Opt. Soc. Am. A **2**, 72–75 (1985)
45. H.B.K. Brink, G.J. van Blokland, Birefringence of the human foveal area assessed in vivo with Mueller-matrix ellipsometry. J. Opt. Soc. Am. A **5**, 49–57 (1988)
46. W.K. Tung, *Group Theory in Physics* (World Scientific, Philadelphia, 1985)
47. B.H. Park, M.C. Pierce, J.F. de Boer, Comment on "optical-fiber-based Mueller optical coherence tomography". Opt. Lett. **29**(24), 2873–2874 (2004)
48. B.H. Park, M.C. Pierce, B. Cense, J.F. de Boer, Optic axis determination accuracy for fiber-based polarization-sensitive optical coherence tomography. Opt. Lett. **30**(19), 2587–2589 (2005)
49. M.G. Ducros, J.D. Marsack, H.G. Rylander, S.L. Thomsen, T.E. Milner, Primate retina imaging with polarization-sensitive optical coherence tomography. J. Opt. Soc. Am. A Opt. Image Sci. Vis. **18**(12), 2945–2956 (2001)
50. B. Cense, H.C. Chen, B.H. Park, M.C. Pierce, J.F. de Boer, In vivo birefringence and thickness measurements of the human retinal nerve fiber layer using polarization-sensitive optical coherence tomography. J. Biomed. Opt. **9**(1), 121–125 (2004)
51. M. Pircher, E. Gotzinger, R. Leitgeb, H. Sattmann, O. Findl, C.K. Hitzenberger, Imaging of polarization properties of human retina in vivo with phase resolved transversal PS-OCT. Opt. Express **12**(24), 5940–5951 (2004)
52. E. Gotzinger, M. Pircher, C.K. Hitzenberger, High speed spectral domain polarization sensitive optical coherence tomography of the human retina. Opt. Express **13**(25), 10217–10229 (2005)
53. O.K. Naoun, V.L. Dorr, P. Alle, J.C. Sablon, A.M. Benoit, Exploration of the retinal nerve fiber layer thickness by measurement of the linear dichroism. Appl. Opt. **44**(33), 7074–7082 (2005)

54. H.G. Rylander, N.J. Kemp, J.S. Park, H.N. Zaatari, T.E. Milner, Birefringence of the primate retinal nerve fiber layer. Exp. Eye Res. **81**(1), 81–89 (2005)
55. L.M. Zangwill, C. Bowd, Retinal nerve fiber layer analysis in the diagnosis of glaucoma. Curr. Opin. Ophthalmol. **17**(2), 120–131 (2006)
56. B.W. Colston, U.S. Sathyam, L.B. DaSilva, M.J. Everett, P. Stroeve, L.L. Otis, O.C.T. Dental, Opt. Express **3**(6), 230–238 (1998)
57. X.J. Wang, T.E. Milner, J.F. de Boer, Y. Zhang, D.H. Pashley, J.S. Nelson, Characterization of dentin and enamel by use of optical coherence tomography. Appl. Opt. **38**(10), 2092–2096 (1999)
58. A. Baumgartner, S. Dichtl, C.K. Hitzenberger, H. Sattmann, B. Robl, A. Moritz, Z.F. Fercher, W. Sperr, Polarization-sensitive optical coherence tomography of dental structures. Caries Res. **34**(1), 59–69 (2000)
59. B.T. Amaechi, S.M. Higham, A.G. Podoleanu, J.A. Rogers, D.A. Jackson, Use of optical coherence tomography for assessment of dental caries: quantitative procedure. J. Oral Rehab. **28**, 1092–1093 (2001)
60. D. Fried, J. Xie, S. Sahar, J.D.B. Featherstone, T.M. Breunig, C. Le, Imaging of early caries lesions and lesion progression using an all fiber 1310-nm polarization sensitive OCT system. J. Dent. Res. **81**, A386–A386 (2002)
61. B.T. Amaechi, A.G. Podoleanu, S.M. Higham, D.A. Jackson, Correlation of quantitative light-induced fluorescence and optical coherence tomography applied for detection and quantification of early dental caries. J. Biomed. Opt. **8**, 1297–1304 (2003)
62. R.S. Jones, M. Staninec, D. Fried, Imaging artificial caries under composite sealants and restorations. J. Biomed. Opt. **9**(6), 1297–1304 (2004)
63. P. Ngaotheppitak, C.L. Darling, D. Fried, Measurement of the severity of natural smooth surface (interproximal) caries lesions with polarization sensitive optical coherence tomography. Lasers Surg. Med. **37**(1), 78–88 (2005)
64. J.M. Herrmann, C. Pitris, B.E. Bouma, S.A. Boppart, C.A. Jesser, D.L. Stamper, J.G. Fujimoto, M.E. Brezinski, High resolution imaging of normal and osteoarthritic cartilage with optical coherence tomography. J. Rheumatol. **26**(3), 627–635 (1999)
65. W. Drexler, D. Stamper, C. Jesser, X.D. Li, C. Pitris, K. Saunders, S. Martin, M.B. Lodge, J.G. Fujimoto, M.E. Brezinski, Correlation of collagen organization with polarization sensitive imaging of in vitro cartilage: implications for osteoarthritis. J. Rheumatol. **28**(6), 1311–1318 (2001)
66. Y.T. Pan, Z.G. Li, T.Q. Xie, C.R. Chu, Hand-held arthroscopic optical coherence tomography for in vivo high-resolution imaging of articular cartilage. J. Biomed. Opt. **8**(4), 648–654 (2003)
67. C.W. Han, C.R. Chu, N. Adachi, A. Usas, F.H. Fu, J. Huard, Y. Pan, Analysis of rabbit articular cartilage repair after chondroctye implantation using optical coherence tomography. Osteoarthritis Cartilage **11**, 111–121 (2003)
68. C.R. Chu, D. Lin, J.L. Geisler, C.T. Chu, F.H. Fu, Y.T. Pan, Arthroscopic microscopy of articular cartilage using optical coherence tomography. Am. J. Sports Med. **32**, 699–709 (2004)
69. X.D. Li, S. Martin, C. Pitris, R. Ghanta, D.L. Stamper, M. Harman, J.G. Fujimoto, M.E. Brezinski, High-resolution optical coherence tomographic imaging of osteoarthritic cartilage during open knee surgery. Arthritis Res. Ther. **7**(2), R318–R323 (2005)
70. N.A. Patel, J. Zoeller, D.L. Stamper, J.G. Fujimoto, M.E. Brezinski, Monitoring osteoarthritis in the rat model using optical coherence tomography. IEEE Trans. Med. Imag. **24**(2), 155–159 (2005)
71. J.I. Youn, G. Vargas, B.J.F. Wong, T.E. Milner, Depth-resolved phase retardation measurements for laser-assisted non-ablative cartilage reshaping. Phys. Med. Biol. **50**(9), 1937–1950 (2005)
72. M.C. Pierce, J. Strasswimmer, B.H. Park, B. Cense, J.F. de Boer, Advances in optical coherence tomography imaging for dermatology. J. Investig. Dermatol. **123**(3), 458–463 (2004)
73. P.A. Brigham, E. McLoughlin, Burn incidence and medical care use in the United States: estimates, trends, and data sources. J. Burn Care Rehabil. **17**, 95 (1997)

74. D.J. Maitland, J.T. Walsh, Quantitative measurements of linear birefringence during heating of native collagen. Lasers Surg. Med. **20**, 310 (1997)
75. S.M. Srinivas, J.F. de Boer, H. Park, K. Keikhanzadeh, H.E.L. Huang, J. Zhang, W.Q. Jung, Z.P. Chen, J.S. Nelson, Determination of burn depth by polarization-sensitive optical coherence tomography. J. Biomed. Opt. **9**(1), 207–212 (2004)
76. Y. Yasuno, S. Makita, Y. Sutoh, M. Itoh, T. Yatagai, Birefringence imaging of human skin by polarization-sensitive spectral interferometric optical coherence tomography. Opt. Lett. **27**(20), 1803–1805 (2002)
77. M.C. Pierce, J. Strasswimmer, B.H. Park, B. Cense, J.F. de Boer, Birefringence measurements in human skin using polarization-sensitive optical coherence tomography. J. Biomed. Opt. **9**(2), 287–291 (2004)
78. M. Pircher, E. Goetzinger, R. Leitgeb, C.K. Hitzenberger, Three dimensional polarization sensitive OCT of human skin in vivo. Opt. Express **12**(14), 3236–3244 (2004)
79. M.C. Pierce, R.L. Sheridan, B.H. Park, B. Cense, J.F. de Boer, Collagen denaturation can be quantified in burned human skin using polarization-sensitive optical coherence tomography. Burns **30**(6), 511–517 (2004)
80. J. Strasswimmer, M.C. Pierce, B.H. Park, V. Neel, J.F. de Boer, Polarization-sensitive optical coherence tomography of invasive basal cell carcinoma. J. Biomed. Opt. **9**(2), 292–298 (2004)
81. T. Kuwahara, J. Strasswimmer, J. de Boer, R. Anderson, Noninvasive measurements of the photodamaged human skin in vivo by polarization-sensitive optical coherence tomography. J. Am. Acad. Dermatol. **52**(3), P163–P163 (2005)
82. M. Mujat, B.H. Park, B. Cense, T.C. Chen, J.F. de Boer, Auto-calibration of spectral-domain optical coherence tomography spectrometers for in vivo quantitative retinal nerve fiber layer birefringence determination. J. Biomed. Opt. **12**(4):041205 (2007). doi: 10.1117/1.2764460
83. A.F. Fercher, C.K. Hitzenberger, G. Kamp, S.Y. Elzaiat, Measurement of intraocular distances by backscattering spectral interferometry. Opt. Commun. **117**(1–2), 43–48 (1995)
84. G. Hausler, M.W. Lindner, "Coherence Radar" and "Spectral Radar" – new tools for dermatological diagnosis. J. Biomed. Opt. **3**(1), 21–31 (1998)
85. M. Wojtkowski, R. Leitgeb, A. Kowalczyk, T. Bajraszewski, A.F. Fercher, In vivo human retinal imaging by Fourier domain optical coherence tomography. J. Biomed. Opt. **7**(3), 457–463 (2002)
86. S.H. Yun, G.J. Tearney, J.F. de Boer, N. Iftimia, B.E. Bouma, High-speed optical frequency-domain imaging. Opt. Express **11**(22), 2953–2963 (2003)
87. P. Andretzky, M.W. Lindner, J.M. Hermann, A. Schultz, M. Konzog, F. Kiesewetter, G. Hausler, Optical coherence tomography by spectral radar: dynamic range estimation and in vivo measurements of skin. Proc. SPIE **3567**, 78–87 (1998)
88. T. Mitsui, Dynamic range of optical reflectometry with spectral interferometry. Japan. J. Appl. Phys. 1-Reg. Pap. Short Notes Rev. Pap. **38**(10), 6133–6137 (1999)
89. R. Leitgeb, C.K. Hitzenberger, A.F. Fercher, Performance of Fourier domain vs. time domain optical coherence tomography. Opt. Express **11**, 889–894 (2003)
90. J.F. de Boer, B. Cense, B.H. Park, M.C. Pierce, G.J. Tearney, B.E. Bouma, Improved signal-to-noise ratio in spectral-domain compared with time-domain optical coherence tomography. Opt. Lett. **28**(21), 2067–2069 (2003)
91. M.A. Choma, M.V. Sarunic, C.H. Yang, J.A. Izatt, Sensitivity advantage of swept source and Fourier domain optical coherence tomography. Opt. Express **11**, 2183–2189 (2003)
92. J. Zhang, W.G. Jung, J.S. Nelson, Z.P. Chen, Full range polarization-sensitive Fourier domain optical coherence tomography. Opt. Express **12**(24), 6033–6039 (2004)
93. S.G. Guo, J. Zhang, L. Wang, J.S. Nelson, Z.P. Chen, Depth-resolved birefringence and differential optical axis orientation measurements with fiber-based polarization-sensitive optical coherence tomography. Opt. Lett. **29**(17), 2025–2027 (2004)
94. N.J. Kemp, H.N. Zaatari, J. Park, H.G. Rylander, T.E. Milner, Depth-resolved optic axis orientation in multiple layered anisotropic tissues measured with enhanced

polarization-sensitive optical coherence tomography (EPS-OCT). Opt. Express **13**(12), 4507–4518 (2005)
95. S. Yazdanfar, C.H. Yang, M.V. Sarunic, J.A. Izatt, Frequency estimation precision in Doppler optical coherence tomography using the Cramer-Rao lower bound. Opt. Express **15**, 410–416 (2004)
96. N.J. Kemp, J. Park, H.N. Zaatari, H.G. Rylander, T.E. Milner, High-sensitivity determination of birefringence in turbid media with enhanced polarization-sensitive optical coherence tomography. J. Opt. Soc. Am. A Opt. Image Sci. Vis. **22**(3), 552–560 (2005)
97. J.M. Schmitt, Array detection for speckle reduction in optical coherence microscopy. Phys. Med. Biol. **42**(7), 1427–1439 (1997)
98. J.M. Schmitt, S.H. Xiang, K.M. Yung, Speckle in optical coherence tomography. J. Biomed. Opt. **4**(1), 95–105 (1999)
99. M. Bashkansky, J. Reintjes, Statistics and reduction of speckle in optical coherence tomography. Opt. Lett. **25**(8), 545–547 (2000)
100. M.A. Sapia, D.C. Colosi, L.L. Otis, Reduction of speckle noise in OCT images. J. Dent. Res. **79**, 550–550 (2000)
101. N. Iftimia, B.E. Bouma, G.J. Tearney, Speckle reduction in optical coherence tomography by "path length encoded" angular compounding. J. Biomed. Opt. **8**(2), 260–263 (2003)
102. D.C. Adler, T.H. Ko, J.G. Fujimoto, Speckle reduction in optical coherence tomography images by use of a spatially adaptive wavelet filter. Opt. Lett. **29**(24), 2878–2880 (2004)
103. J.H. Kim, J.W. Oh, D.T. Miller, T.E. Milner, Speckle reduction in OCT using mode averaging. Lasers Surg. Med. 8–8 (2004)
104. B.H. Park, M.C. Pierce, B. Cense, J.F. de Boer. *S*peckle averaging for optical coherence tomography. SPIE Photon. West. (2004)
105. J. Kim, D.T. Miller, E. Kim, S. Oh, J. Oh, T.E. Milner, Optical coherence tomography speckle reduction by a partially spatially coherent source. J. Biomed. Opt. **10**(6), 064034 (2005)
106. D.L. Marks, T.S. Ralston, S.A. Boppart, Speckle reduction by I-divergence regularization in optical coherence tomography. J. Opt. Soc. Am. A Opt. Image Sci. Vis. **22**(11), 2366–2371 (2005)
107. A.E. Desjardins, B.J. Vakoc, G.J. Tearney, B.E. Bouma, Speckle reduction in OCT using massively-parallel detection and frequency-domain ranging. Opt. Express **14**(11), 4736–4745 (2006)
108. B.H. Park, B. Cense, M.C. Pierce, J.F. de Boer, *A novel technique for speckle reduction with multi-functional optical coherence tomography*. SPIE Photon. West. (2006)
109. N. Ugryumova, S.V. Gangnus, S.J. Matcher, Three-dimensional optic axis determination using variable-incidence-angle polarization-optical coherence tomography. Opt. Lett. **31**(15), 2305–2307 (2006)
110. M.C. Pierce, M. Shishkov, B.H. Park, N.A. Nassif, B.E. Bouma, G.J. Tearney, J.F. de Boer, Effects of sample arm motion in endoscopic polarization-sensitive optical coherence tomography. Opt. Express **13**(15), 5739–5749 (2005)
111. B. Stanford, D.L. Stamper, P.R. Herz, S.D. Giattina, S.B. Adams, A.L. Robertson, T.H. Ko, M.J. Roberts, N.D. Joshi, J.G. Fujimoto, P.J. Fitzgerald, M.E. Brezinski, Polarization sensitive optical coherence tomography imaging in coronary arteries for enhanced identification of vascular lesion components. Circulation **110**(17), 524–524 (2004)
112. S. Nadkarni, M. Pierce, H. Park, J. deBoer, S. Houser, J. Bressner, B. Bouma, G. Tearney, Polarization-sensitive optical coherence tomography for the analysis of collagen content in atherosclerotic plaques. Circulation **112**(17), U679–U679 (2005)
113. S.K. Nadkarni, M. Pierce, H. Park, J. deBoer, S. Houser, J. Bressner, B. Bouma, G. Tearney, Analysis of collagen birefringence in atherosclerotic plaques using polarization sensitive optical coherence tomography. Am. J. Cardiol. **96**(7A), 111H–111H (2005)

114. S. Shortkroff, S.D. Giattina, B.K. Courtney, P.R. Herz, D.L. Stamper, J.J. Fugimoto, M.E. Brezinski, Collagen content of coronary plaque measured by polarization sensitive optical coherence tomography (PS-OCT). J. Am. Coll. Cardiol. **47**(4), 121A–121A (2006)
115. S.K. Nadkarni, M.C. Pierce, B.H. Park, J.F. de Boer, P. Whittaker, B.E. Bouma, J.E. Bressner, E. Halpern, S.L. Houser, G.J. Tearney, Measurement of collagen and smooth muscle cell content in atherosclerotic plaques using polarization-sensitive optical coherence tomography. J. Am. Coll. Cardiol. **49**(13), 1474–1481 (2007)
116. J.J. Pasquesi, S.C. Schlachter, M.D. Boppart, E. Chaney, S.J. Kaufman, S.A. Boppart, In vivo detection of exercise-induced ultrastructural changes in genetically-altered murine skeletal muscle using polarization-sensitive optical coherence tomography. Opt. Express **14**(4), 1547–1556 (2006)

MUW Approach of PS OCT

34

Christoph K. Hitzenberger and Michael Pircher

Keywords
Polarization sensitive OCT • Birefringence • Depolarization • Retina • Glaucoma • Age related macular degeneration

34.1 Introduction

Since its first introduction more than two decades ago [1], optical coherence tomography (OCT) has revolutionized retinal diagnostics [2]. Especially the paradigm shift from the early time domain instruments to spectral domain (SD) technology [3–5] was paramount for the enormous progress and success of OCT in recent years. The massively parallel approach of SD OCT provides a huge sensitivity advantage [6–8] and enabled improvements of imaging speeds by several orders of magnitude. While presently available commercial retinal OCT scanners can operate at speeds of several tens of kA-lines/s, speeds in the multi-100 kHz range and even beyond a MHz have been reported recently [9–12].

Despite their great success, all these intensity-based OCT systems still have a considerable drawback: they cannot directly differentiate between different tissues. Especially in ocular diseases where retinal layers are damaged, distorted, displaced, disrupted, or vanished, it is often very difficult to identify specific layers based just on backscattered intensity. This, however, is mandatory for correct diagnosis, monitoring, and follow-up. To overcome this and other limitations, additional information beyond signal intensity is required. One method to gain such additional information is to exploit the light's polarization state. This can be achieved by polarization-sensitive (PS) OCT [13, 14], the topic of this chapter.

C.K. Hitzenberger (✉) • M. Pircher
Center for Medical Physics and Biomedical Engineering, Medical University of Vienna, Vienna, Austria
e-mail: christoph.hitzenberger@meduniwien.ac.at

© Springer International Publishing Switzerland 2015

W. Drexler, J.G. Fujimoto (eds.), *Optical Coherence Tomography*,
DOI 10.1007/978-3-319-06419-2_35

PS-OCT measures, in addition to intensity, the polarization state of light and draws advantage from the fact that some tissues can change the polarization state of the probing light beam. Different mechanisms of light-tissue interaction can change the polarization state: birefringence, diattenuation, and depolarization. While diattenuation is regarded to be negligible in biologic tissue [15–17], the other two interaction mechanisms were demonstrated in various ocular tissues: e.g., birefringence was found in the corneal stroma [18, 19], the sclera [20, 21], ocular muscles and tendons [21], trabecular meshwork [20], the retinal nerve fiber layer (RNFL) [22, 23], Henle's fiber layer [24, 25], and scar tissue [26]. Depolarization was demonstrated in melanin-containing tissue like the retinal pigment epithelium (RPE) [25, 27, 28], the iris pigment epithelium [29], choroidal nevi and melanoma [30], but also in accumulations of pigment-loaded macrophage and – to a smaller amount – in the choroid [28, 31].

There is now already a large body of literature on PS-OCT in general and on applications of PS-OCT for ocular imaging. Reviews on these topics can be found, e.g., in [32, 33]. In this chapter, we will provide an overview of polarization changing light-tissue interactions found in the eye, of the theoretic and technical principles used in our own work (which forms the basis of the results reported here); a description of the use of PS-OCT to segment retinal layers and lesions based on their intrinsic, tissue-specific contrast; and various applications of PS-OCT to image healthy and diseased human retina. We would like to point out that this chapter does not contain a comprehensive description of all aspects and methods of PS-OCT. More information on other aspects and variants of this interesting functional extension of OCT can be found in ▶ Chaps. 33, "Polarization Sensitive Optical Coherence Tomography" and ▶ 35, "Jones Matrix Based Polarization Sensitive Optical Coherence Tomography" of this book.

34.2 Polarization Changing Light-Tissue Interactions

As mentioned above, three different light-tissue interactions may alter the polarization state of the incident light: birefringence, depolarization, and diattenuation. While the latter can be neglected in biological tissue [15, 16], the former two interaction types allow accessing tissue-specific properties. In order to describe changes in the polarization state, Jones or Mueller formalism may be used. Jones matrix formalism [34], which is limited to fully polarized light, is already sufficient for most scenarios in OCT because OCT is a coherent imaging technique. Therefore, only fully polarized light components from the sample may interfere with the light from the reference arm and will contribute to the OCT signal. Nevertheless, the more general formulation of Mueller calculus [35] which includes the description of partially polarized (or even depolarized) light is frequently used for the description of PS-OCT [36, 37].

Birefringence is caused by anisotropy of the material or tissue. In this case the refractive index is dependent on the polarization state of light and the direction of light propagation. We want to emphasize that our description presented here refers to linear materials where the polarization vector is linearly proportional to the

electric field [38]. In tissue this differing refractive index can be caused by a compounding of at least two different rather homogeneous dielectric materials. However, in order to observe a net birefringence, these materials have to be arranged in an organized manner which is then referred to as form birefringence [38]. This type of birefringence is typically found in tissue where fibrils of one refractive index are surrounded by material of a slightly different index, as is observed, for example, in the retinal nerve fiber layer [22] or Henle's fiber layer [24]. The propagation of light through a birefringent medium causes a time delay between two orthogonal polarization states (one state is parallel to the slow birefringent axis; the other state is parallel to the fast axis of the sample). This delay is equivalent to a phase retardation. The phase retardation remains unambiguous as long as the accumulated phase retardation remains below the wavelength period of the light. In the case of larger phase retardations, delays corresponding to multiples of the wavelength cannot be distinguished leading to a banding structure in the images. These banding structures may already be observed in the intensity images of "standard" OCT instruments and may cause misinterpretations of the underlying tissue. The second light-tissue interaction affecting the polarization state of light is scattering. Multiple scattering is known to depolarize the incident polarization state of light as even small changes of the polarization state arising from a single scattering event accumulate [39]. However, the dominating signal in retinal OCT originates from single scattered light. In this case the preservation of the incident polarization state depends on the size and shape of the scattering particle as well as on the direction and polarization state of the incident light [32, 40].

34.3 Principles of PS-OCT

Several different variants of PS-OCT have been reported in literature. They differ by the used basic OCT technique (time or spectral domain), by optical technology used (bulk or fiber optic), by interferometer arrangement, by incident polarization states, and by the number of measurements required per sample location. Furthermore, they differ by the calculus used to extract polarization parameters (Jones or Mueller calculus). Based on the different complexities of the used methods, the number of accessible polarization parameters varies, ranging from simple retardation measurements to fully characterized Jones and Mueller matrices. A comprehensive description of all these methods and techniques is beyond the scope of this chapter. Instead, we will restrict our description to methods used in our own work that provide access to those parameters that seem of greatest relevance for retinal imaging: parameters that characterize birefringent and depolarizing tissues.

34.3.1 Basic Setup

Figure 34.1 shows a generic sketch of a basic PS-OCT instrument of the type used in our own work. It is based on the original concept first reported by Hee et al. [13]

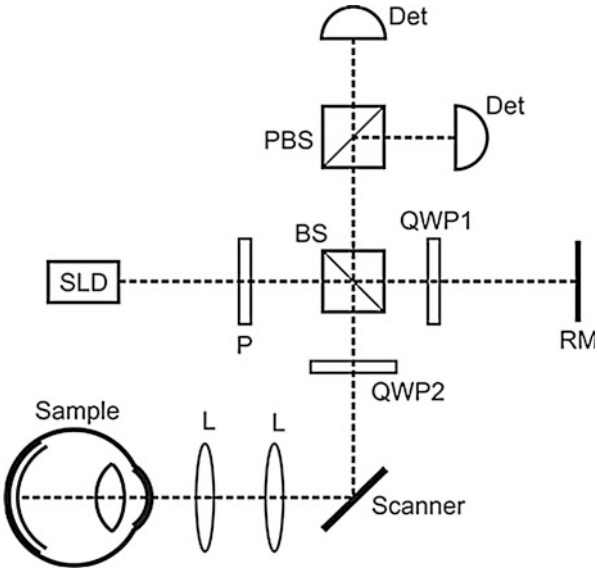

Fig. 34.1 Sketch of basic PS-OCT setup. *BS* beam splitter, *Det* detector, *P* polarizer, *PBS* polarizing beam splitter, *QWP* quarter wave plate, *RM* reference mirror, *SLD* super luminescent diode

in a time domain version. However, different variants and extensions of this instrument, bulk and fiber optic, time domain, and spectral domain, were later reported and used for various applications.

A broadband super luminescent diode (SLD) emits a light beam that is vertically polarized before it illuminates a Michelson interferometer. At the non-polarizing beam splitter BS, the light is split in a reference and a sample beam. The reference beam traverses a quarter wave plate QWP1 oriented at 22.5° to the vertical. After reflection at the reference mirror and back propagation through QWP1, the light is linearly polarized at 45° to the horizontal, providing equal reference power in both orthogonal polarization channels. The sample beam traverses QWP2 oriented at 45°, providing circularly polarized light to the sample. This ensures that the measured retardation of a birefringent sample is independent of its optic axis orientation. An x-y scanner and a scanning optics are used to scan the sample beam over the sample (eye/retina). After backscattering at the sample and back propagation through QWP2, the sample beam is usually in an elliptical polarization state that carries the information on the sample's polarization characteristics. This elliptical polarization state is to be measured and analyzed.

Sample and reference beams are recombined at the interferometer beam splitter BS where they interfere. In the detection arm of the interferometer, a polarizing beam splitter PBS splits the interfering beam into two orthogonal polarization states that are measured separately by two detectors, one for the horizontal and one for the vertical polarization state. The detectors convert the light intensity into electric signals that are amplified and recorded by frame grabbers or a data acquisition board and stored in a computer.

From the interferometric signals acquired in the two channels, information on various parameters can be derived. As we will show in Sect. 34.3.2, some basic information (reflectivity, retardation) can be obtained from the amplitude of the signals while other parameters (Stokes vectors, axis orientation) require also phase information. While the access to phase information with time domain systems required either computationally extensive methods like analytic signal continuation by a Hilbert transform [41] or more complicated experimental methods like signal demodulation [29], SD OCT methods directly provide a complex valued signal by Fourier transform of the real-valued spectral intensity data. From these complex valued signals, amplitude and phase information can readily be retrieved.

34.3.2 Calculation of Polarization States and Polarization Parameters

To illustrate how the birefringent properties of a sample can be characterized by a PS-OCT system as depicted in Fig. 34.1, we will now calculate the evolution of the polarization states of the beams within the interferometer. We will use the Jones formalism [34] which is best suited for calculation of polarization states of fully polarized beams and assume that the sample is a homogenous linear retarder. The calculation follows a similar path as used in our previous work [41, 42].

The beam incident on the Michelson interferometer, after passing the polarizer, is in a linear, vertical polarization state. Its Jones vector can be written as:

$$\tilde{\boldsymbol{E}} = \tilde{E}\begin{pmatrix} 0 \\ 1 \end{pmatrix}. \tag{34.1}$$

$\tilde{\boldsymbol{E}}$ is the electric field vector, with $\tilde{E} = E_0 \exp(i\omega t)$ the scalar electric field, E_0 the field amplitude, ω the angular frequency, and t the time. The upper and lower components of the vector in Eq. 34.1 correspond to the horizontal and vertical components of the electric field vector, respectively. For the sake of simplicity, we ignore the oscillating term $\exp(i\omega t)$ and set $E_0 = 1$ in the following.

The Jones vector of a beam after passing an optical element can be found by multiplying the Jones vector of the incident beam by the Jones matrix corresponding to the optical element. The Jones matrix is a 2×2 matrix consisting of – usually complex – elements. If more than one optical element is traversed, the input Jones vector has to be multiplied by the Jones matrices of all elements, in the order they are transmitted by the beam.

The beam described by Eq. 34.1 enters the Michelson interferometer where it is split by a non-polarizing beam splitter into a reference and a sample beam of equal field amplitudes. The reference beam passes both, the beam splitter and the quarter wave plate QWP1, twice. The effect of the beam splitter is simply to reduce the intensity of the reference beam by a factor of 2 at every pass, leading to a total intensity reduction of a factor of 4, equivalent to a reduction in field amplitude by

a factor of 2. The Jones matrix of a general retarder of retardation δ and fast axis orientation θ is [43]:

$$\mathbf{M}(\delta,\theta) = \begin{bmatrix} \cos^2(\theta) + \sin^2(\theta)\cdot\exp(-i\delta) & \cos(\theta)\cdot\sin(\theta)\cdot(1-\exp(-i\delta)) \\ \cos(\theta)\cdot\sin(\theta)\cdot(1-\exp(-i\delta)) & \cos^2(\theta)\cdot\exp(-i\delta) + \sin^2(\theta) \end{bmatrix}. \tag{34.2}$$

For QWP1, $\delta = \pi/2$ and $\theta = 3\pi/8$. The Jones vector of the reference beam, after double passing QWP1 (and the beam splitter) is:

$$\mathbf{E}_r(z_r) = \frac{1}{2}\mathbf{M}_{QWP1}\cdot\mathbf{M}_{QWP1}\cdot\begin{pmatrix}0\\1\end{pmatrix} = \frac{1}{2\sqrt{2}}\begin{pmatrix}1\\1\end{pmatrix}\cdot\exp(-i2k_0z_r), \tag{34.3}$$

where z_r is the (optical) length of the reference arm and k_0 the center wave vector of the source emission spectrum. This is a linearly polarized beam with its polarization axis oriented at 45°. It provides equal reference intensity for both, the horizontal and the vertical polarization component, which are separated by the polarizing beam splitter PBS of the detection unit. Furthermore, no phase shift occurs between the two polarization components (this would cause at least one of the vector components to have an imaginary part). Therefore, the reference beam influences neither the intensity ratio nor the phase of the interference signals recorded in the two detection channels.

The sample beam passes the beam splitter QWP2 and the sample (reflectivity: R) twice each. Again, the effect of the beam splitter is simply to reduce the field amplitude by a factor of 2. QWP2 has retardation and axis values of $\delta = \pi/2$ and $\theta = \pi/4$, respectively. Assuming that the polarizing properties of the sample can be described by a homogenous retarder (Jones matrix $\mathbf{M}_{sample}$, retardation δ_s(z), fast axis orientation θ_s (constant with depth)), the Jones vector of the sample beam, after exiting the interferometer towards the detection arm, is [41, 44]:

$$\begin{aligned}\mathbf{E}_s(z) &= \frac{1}{2}\mathbf{M}_{QWP2}\cdot\mathbf{M}_{sample}(\delta_s(z),\theta_s)\cdot\sqrt{R(z)}\cdot\mathbf{M}_{sample}(\delta_s(z),\theta_s)\cdot\mathbf{M}_{QWP2}\cdot\begin{pmatrix}0\\1\end{pmatrix} \\ &= \frac{\sqrt{R(z)}}{2}\cdot\begin{pmatrix}\cos(\delta_s(z))\exp(-i\delta_s(z))\\ \sin(\delta_s(z))\exp(i(\pi-\delta_s(z)-2\theta_s))\end{pmatrix}\cdot\exp(-i2k_0z\overline{n}),\end{aligned} \tag{34.4}$$

where z is the geometrical distance from the interferometer beam splitter to a sample reflection site, $\overline{n}$ is the mean refractive index of ordinary and extraordinary beam, and $\delta_s(z) = \Delta n\cdot z\cdot k_0$ (Δn is the refractive index difference between ordinary and extraordinary beam; for simplicity, no air gap has been assumed between beam splitter and sample surface).

After recombination at the beam splitter BS, reference and sample beams interfere. The recombined beams travel towards the polarization-sensitive detection unit where they are split by polarizing beam splitter PBS into horizontal and vertical polarization components. The interference terms $A_{H,V}$ at the detectors, corresponding to the horizontal and vertical polarization channels, respectively, are:

$$A_{H,V}(z,\Delta z) = A_{0;H,V}(z,\Delta z)\cdot \cos\left[\Phi_{H,V}(\Delta z)\right] \tag{34.5}$$

with

$$A_{0;H}(z,\Delta z) = \frac{\sqrt{R(z)}}{2\sqrt{2}}\cdot \cos\left[\delta_s(z)\right]\cdot\left|\gamma(\Delta z)\right| \tag{34.6a}$$

$$A_{0;V}(z,\Delta z) = \frac{\sqrt{R(z)}}{2\sqrt{2}}\cdot \sin\left[\delta_s(z)\right]\cdot\left|\gamma(\Delta z)\right| \tag{34.6b}$$

and

$$\Phi_H(\Delta z) = 2k_0\Delta z \tag{34.7a}$$

$$\Phi_V(\Delta z) = 2k_0\Delta z + \pi - 2\theta_s, \tag{34.7b}$$

where $A_{0;H,V}$ describe the envelopes of the interferometric signals caused by a single reflective site in the sample, $\Phi_{H,V}$ are the corresponding phase functions of the interferometric fringes, $\Delta z = z_r - z\cdot\overline{n}$ is the optical path length difference between reference and sample arms, and $|\gamma(\Delta z)|$ is the modulus of the complex degree of coherence of the interfering beams which describes the width of the interferometric signal (the axial point spread function). In Eqs. 34.7a and 34.7b an unimportant common phase term has been omitted.

The terms $\cos(\delta_s(z))$ and $\sin(\delta_s(z))$ in Eqs. 34.6a and 34.6b oscillate slowly with depth z, if a sample with constant birefringence Δn is assumed, giving rise to intensity oscillations in the horizontal and vertical polarization channels which are $\pi/2$ out of phase. The cosine term in Eq. 34.5 oscillates rapidly with path difference Δz and describes the fringes of the interferometric signals, as typically observed in time domain OCT. The fringes of the horizontal and vertical components have a phase difference of $\pi - 2\theta_s$.

34.3.2.1 Quantification of Birefringence-Related Parameters

To calculate sample reflectivity $R(z)$ and retardation $\delta_s(z)$, we only need the envelopes of the interferometric signals $A_{0;H,V}$. For simplicity, we assume

a coherence function of infinitesimal width (i.e., a nonzero amplitude only for $\Delta z = 0$) and can therefore omit the Δz dependence in the following equations:

$$R(z) \propto A_{0;H}(z)^2 + A_{0;V}(z)^2 \tag{34.8}$$

$$\delta_s(z) = \arctan\left(\frac{A_{0;V}(z)}{A_{0;H}(z)}\right). \tag{34.9}$$

A closer look at the phase terms $\Phi_{H,V}$ (Eqs. 34.7a and 34.7b) reveals that the information on the optic axis orientation θ_s of the sample is encoded entirely in the phase difference $\Delta\Phi = \Phi_H - \Phi_V$ of the two signals:

$$\theta_s = (\pi - \Delta\Phi)/2 \tag{34.10}$$

The unambiguous ranges of retardation and axis orientation, as provided by Eqs. 34.9 and 34.10, are 90° and 180°, respectively.

In time domain PS-OCT, amplitude and phase information can be retrieved, e.g., by lock-in demodulation [29] or by analytic continuation of the fully recorded fringe signals by a Hilbert transform [41]. In spectral domain PS-OCT, the inverse Fourier transform of the real-valued spectral interference signals directly yields complex valued signals of the form:

$$FT^{-1}\{I_{H,V}(k)\} \rightarrow A_{0;H,V}(z)\exp\left[i\Phi_{H,V}\right], \tag{34.11}$$

with $I_{H,V}(k)$ being the intensity as a function of wave number k in the horizontal and vertical polarization channel, respectively. For simplicity, the DC, autocorrelation, and mirror terms were omitted in Eq. 34.11. From these signals, amplitude and phase values can be directly taken and inserted into the corresponding parameters of Eqs. 34.8, 34.9, and 34.10 (it should be mentioned that the absolute phase values $\Phi_{H,V}$ in Eq. 34.11 have no physical relevance; however, their difference provides the sample axis orientation via. Eq. 34.10).

As an example for imaging a birefringent structure in the human eye, Fig. 34.2 shows a circumpapillary scan recorded with a SD PS-OCT system in a healthy volunteer [45]. In this area, the RNFL forms rather thick bundles in the quadrants superior and inferior to the optic nerve head which are birefringent. Figure 34.2a shows a generic fundus photo illustrating the measured area: the scan was recorded approximately along the circular white line. Figure 34.2b shows the cross-sectional reflectivity (intensity) image. The increased thickness of the superior and inferior RNFL bundles is clearly visible. Figure 34.2c shows the retardation image, where the increased retardation caused by these nerve fiber bundles is clearly observed (color change from blue to green). Figure 34.3d shows the axis

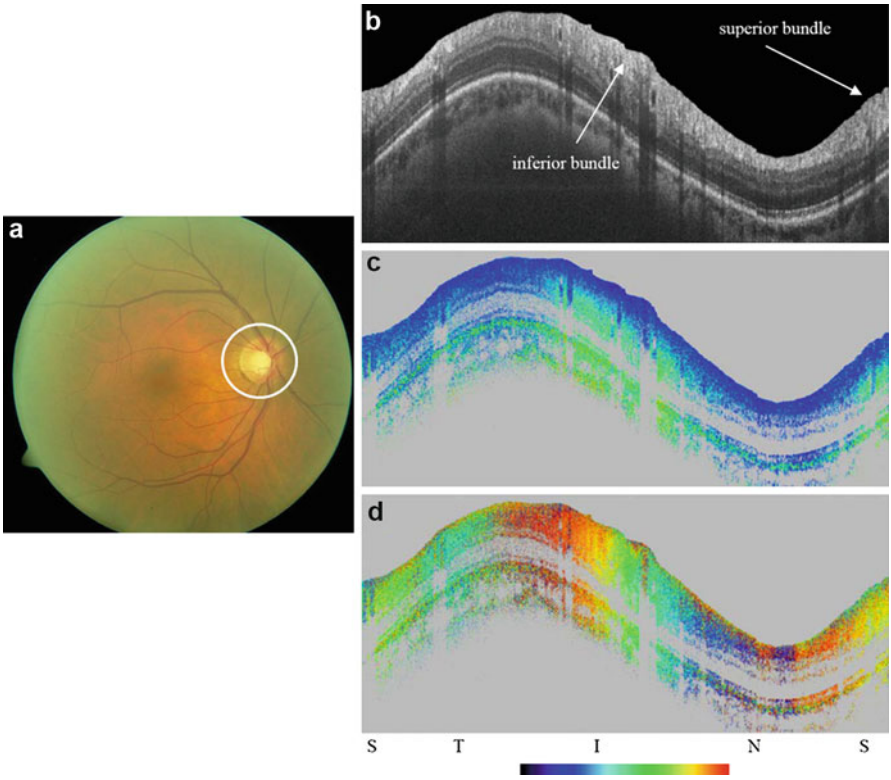

Fig. 34.2 Circumpapillary PS-OCT scan from healthy human retina. (**a**) Generic fundus photo illustrating scan geometry; the *white circle* indicates the approximate position of the scan line. (**b–d**): Circumpapillary B-scans. Scan diameter: ∼10° (corresponds to a circumference of ∼9.4 mm, equal to horizontal image width; optical image depth: 1.8 mm). (**b**) reflectivity (log scale); (**c**) retardation (color bar: 0–90°); (**d**) optic axis orientation (color bar: 0–180°). Orientation of scan from *left* to *right*: (*S*)uperior, (*T*)emporal, (*I*)nferior, (*N*)asal, (*S*)uperior (Reproduced from Götzinger et al. [45] by permission of the Optical Society of America)

orientation image, where the two full color oscillations from left to right indicate the radial orientation of the nerve fibers (360° rotation of axis orientation).

34.3.2.2 Quantification of Depolarization

Since OCT is based on a coherent detection method, the degree of polarization (DOP) known from classical polarization optics cannot be directly measured. The light corresponding to a single speckle is always fully polarized, i.e., its DOP = 1 [37]. However, PS-OCT can obtain information on depolarization by analyzing the local distribution of polarization states among neighboring speckles. In case of a depolarizing tissue, polarization states of adjacent speckles will be uncorrelated, i.e., the polarization states vary randomly, while in other tissues

(polarization maintaining or birefringent), the relation will be well defined. Therefore, depolarization is manifested by a scrambling of polarization states in PS-OCT images. To quantify this effect, we introduced a new parameter, the degree of polarization uniformity (DOPU), that has a strong formal relationship to DOP [28]. To quantify DOPU, we first calculate the Stokes vector $\boldsymbol{S}$ for each pixel in the PS-OCT image:

$$\mathbf{S} = \begin{pmatrix} I \\ Q \\ U \\ V \end{pmatrix} = \begin{pmatrix} {A_{0;H}}^2 + {A_{0;V}}^2 \\ {A_{0;H}}^2 - {A_{0;V}}^2 \\ 2A_{0;H}A_{0;V}\cos\Delta\Phi \\ 2A_{0;H}A_{0;V}\sin\Delta\Phi \end{pmatrix}, \tag{34.12}$$

where I, Q, U, V denote the four Stokes vector elements. Then we average Stokes vectors over adjacent pixels by calculating the mean value of each Stokes vector element within a rectangular evaluation window (kernel) and derive DOPU:

$$\mathrm{DOPU} = \sqrt{Q_m^2 + U_m^2 + V_m^2}, \tag{34.13}$$

where the indices m indicate mean Stokes vector elements. DOPU can be regarded as a spatially averaged DOP and is closely related to the apparent degree of polarization obtained by temporal averaging [37] and to the quantity $\overline{\zeta}$ that was used to describe the local correlation of polarization states for detection of multiple scattered light by OCT [46].

In case of a polarization preserving or birefringent tissue, the value of DOPU should be close to 1; in case of a depolarizing layer, DOPU is lower than 1. In a typical application, the use of DOPU to segment the depolarizing RPE in PS-OCT images of the retina, a threshold value of $\mathrm{DOPU_{thr}} = 0.7 - 0.8$ is used. All image areas where $\mathrm{DOPU} < \mathrm{DOPU_{thr}}$ are classified as depolarizing.

Figure 34.3 shows an example of imaging a depolarizing structure in the human retina, obtained by a high-resolution SD PS-OCT system [45]. Figure 34.3a shows a cross-sectional reflectivity image (B-scan) through the fovea of a healthy human eye. In the posterior retina, four boundaries are marked: the external limiting membrane (ELM), the boundary between inner and outer photoreceptor segments (IS/OS), the end tips of the photo receptors (ETPR), and the RPE. Figure 34.3b, c show a zoom-in of retardation and axis orientation data into the posterior three of these layers. While the top two boundaries show rather constant color values (indicative of low retardation and constant axis orientation in this area of the retina), the bottom layer shows a striking difference: the color values are scrambled, i.e., more or less random. The DOPU image (Fig. 34.3d) demonstrates this difference even better: while the IS/OS and the ETPR show DOPU values close to 1 (red color), the RPE is strongly depolarizing (green to blue colors, $\mathrm{DOPU} < 0.7$).

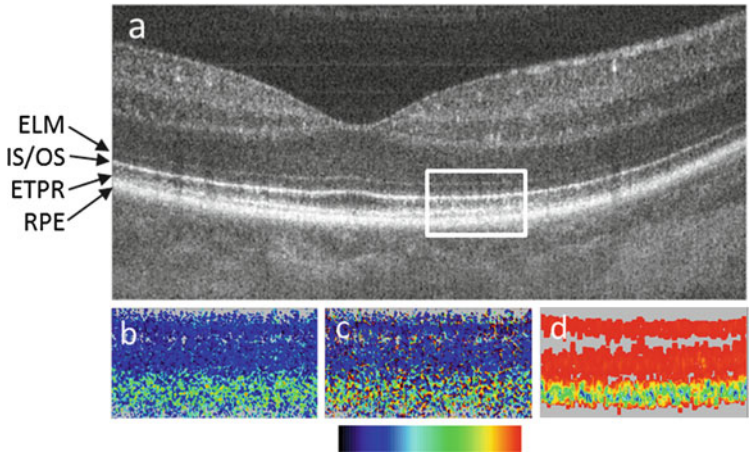

Fig. 34.3 PS-OCT B-scan of a healthy human fovea. (**a**) Reflectivity (log scale), the *white rectangle* shows approximate areas of the zoom-ins (**b**)–(**d**); **b** retardation (color bar: 0–90°); (**c**) optic axis orientation (color bar: 0–180°); (**d**) DOPU (color bar: 0–1). *ELM* external limiting membrane, *IS*/*OS* boundary between inner and outer photoreceptor segments, *ETPR* end tips of photoreceptors, *RPE* retinal pigment epithelium (Reproduced from Götzinger et al. [45] by permission of the Optical Society of America)

34.3.3 Spectral Domain and Fiber-Optic Implementations

Several variants of the basic setup described in Sect. 34.3.1 have been reported. While the initial work was based on time domain technology in various forms [13, 14, 29, 41], spectral domain variants gained more attraction after the discovery of their huge sensitivity advantage. Bulk optic [21, 47] and fiber-optic [45] setups were reported, employing either a two-channel spectrometer with a single line scan camera [21] or two separate spectrometers, each equipped with its own camera [47]. Spectrometer-based SD PS-OCT systems require either a nearly perfect pixel-to-pixel correspondence of the spectrometers recording the two channels (otherwise, depth-dependent artifacts of mainly the axis orientation can occur [47]) or an additional post-processing step that corrects for the spectral mismatch (this is mandatory for single camera systems [21]). These spectrometer type systems typically operate in the 840 nm wavelength regime.

A related variant is based on swept source (SS) technology which is preferred at the longer wavelength centered around 1,050 nm. This technique has the advantage of improved imaging depth beyond the RPE, down to the choroid and sclera [48–51], however, is presently more expensive. Different versions of PS-OCT at this wavelength have been reported for retinal imaging, employing single [52] and multiple [53] input polarization states.

Bulk optic PS-OCT setups have the advantage that the optical components used are very stable with respect to their polarization properties. Once aligned, they can

be used without recalibration over extended periods of time. However, for commercial instruments, fiber-optic systems are preferred since they can be quite robust and need little optical alignment. The use of normal single-mode (SM) fibers (that are commonly used for intensity-based OCT), however, causes a problem for PS-OCT: the fiber is birefringent, and the exact amount of birefringence varies with environmental influences like bending and temperature. Therefore, it is neither easily possible to achieve a constant polarization state (e.g., circular) at the sample nor to maintain the polarization state of the light beam passing the fiber. Therefore, SM fiber-based PS-OCT systems usually require to probe the sample with more than one polarization state and retrieve the sample's polarizing properties by differential measurements and elaborate algorithms that compensate for possible changes of the light's polarization state within the fiber [54].

A solution to this problem is the use of polarization-maintaining (PM) fibers [45, 55, 56]. PM fiber-based PS-OCT systems can employ the same principles as described in Sect. 34.3.2. The amplitudes of the two orthogonal light components are well preserved throughout the PM fibers, enabling a direct calculation of sample reflectivity and retardation. However, due to the different propagation velocities of the two orthogonal modes in the PM fiber, the phase relation between the modes is lost, destroying the original elliptic polarization state backscattered from the sample. The phase difference, however, is needed to calculate axis orientation and Stokes vector. To solve this problem, the lengths of the PM fibers in the sample and reference arms have to be carefully matched. In this case, the phase differences in the two arms cancel each other. A remaining phase difference caused, e.g., by imperfect fiber length matching can be compensated in a post-processing step [45]. This method provides correct relative axis orientations; to obtain the absolute axis orientation, a calibration measurement is needed.

As an example of a state-of-the-art PS-OCT retinal scanner, Fig. 34.4 shows a sketch of one of our newest instruments. More than 200 patients with various diseases have been imaged with this device and several of the images presented in this chapter were recorded with the system. It is a PM fiber-based SD PS-OCT instrument employing a two-channel spectrometer with a single camera. An SLD emits a light beam centered at ~840 nm whose polarization state is matched by a polarization controller (paddle) PC to the orientation transmitted by the PM fiber polarizer. A 90:10 splitter directs 10 % of the beam to the sample and 90 % to the reference mirror. After passing the QWP, the sample light is in a circular polarization state and raster scanned via the galvanometer scanner and a telescope (lenses L1 and L2) over the retina. In the reference arm, a QWP ensures equal reference power in both polarization states, as described above. After recombination at the 90:10 splitter (90 % of the sample beam power is transmitted into the detection arm), the beams interfere and are guided to the polarizing beam splitter which separates the horizontal and the vertical state. The two polarization states are spectrally dispersed by a diffraction grating and imaged adjacent to each other onto a high-speed CMOS line scan camera (Basler sprint, 4,096 pixels).

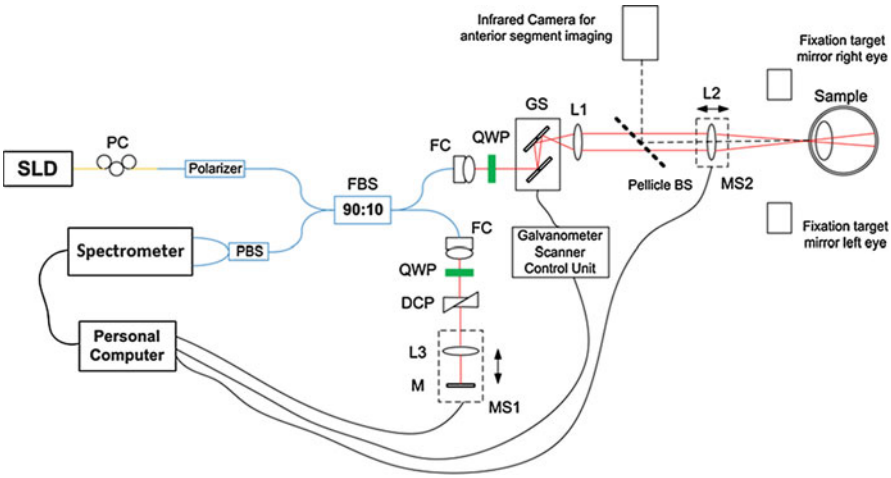

Fig. 34.4 Sketch of wide-field SD PS-OCT system. *SLD* super luminescent diode, *PC* polarization controller, *FBS* fiber non-polarizing beam splitter, *PBS* fiber polarizing beam splitter, *FC* fiber collimator, *QWP* quarter wave plate, *DCP* dispersion-compensating prisms, *L* lens, *MS* motorized stage, *GS* galvanometer scanner, *M* mirror, *Pellicle BS* pellicle beam splitter; *yellow lines*, single-mode fibers; *red lines*, free space beam paths; *blue lines*, polarization-maintaining fiber; *black lines*, cable connection (Reproduced from Zotter et al. [57] by permission of the Optical Society of America)

The camera is operated at a line rate of 70 kHz. With a light power of 730 μW at the cornea, a maximum sensitivity of 98 dB is obtained, with a roll-off of 8 dB over an imaging depth of 1.8 mm. The axial resolution is 7.8 μm in air or ∼5.7 μm in tissue (assuming a group index of ∼1.38). The maximum scan field size of the instrument is 40° × 40°. Various scan patterns, ranging from 512(x) × 125(y) up to 1,024 × 250 A-scans, are available. More details on the instrument can be found in ref. [57].

The processing of data acquired with this system comprises the following steps: the two adjacent spectra provided by the camera are separated and numerically resampled to achieve a pixel-to-pixel correspondence (this step is equivalent to squeezing/compressing one spectrum until it fits the width of the other one). Afterwards, standard post-processing steps (subtraction of the mean spectrum, rescaling from wavelength to wavenumber space, inverse Fourier transform) are performed. Then, amplitude and phase difference data are calculated, from which retardation, axis orientation, Stokes vectors, and DOPU values are obtained as described in detail above. Since the birefringence-related data of retinal structures are obtained by a measurement through the birefringent cornea, the influence of the cornea has to be compensated for. This is performed by retrieving the polarization state at the retinal surface (which corresponds to the influence exerted by the cornea) and subsequently compensating the polarization state distortions caused by the cornea by a software-based algorithm [58].

34.4 Applications of PS-OCT to Retinal Imaging

34.4.1 Imaging of the Macular Region

The macula represents the most precious location on the retina because it contains the fovea, which represents, in the healthy eye, the spot with the best vision. A variety of different diseases (e.g., age-related macula degeneration (AMD) and diabetic retinopathy (DR)) may alter the normal structure in the macular region, and in recent years, OCT has become an indispensable clinical tool for an accurate determination of these changes.

PS-OCT provides additional contrast that is not accessible with standard OCT. Figure 34.5 shows imaging examples obtained in a healthy volunteer recorded at 840 nm with a large field of view scan [57]. Within the DOPU images (e, j), the RPE can be easily outlined because it contains particles (e.g., pigments) that scramble the polarization state of the backscattered light. Birefringence introduced by Henle's fiber layer causes an increased retardation in the macula area (c.f. increased retardation at the junction between inner and outer segments of photoreceptors (IS/OS) and end tips of photoreceptors (ETPR) indicated by arrows in Fig. 34.5c, h). Note that because of the orientation of the fibers in Henle's fiber layer, no increase in retardation can be observed in the fovea centralis (c.f. dark blue color at the IS/OS junction). The instrument operates at an imaging speed of 70 kHz. This high speed enables, in order to reduce speckle noise and enhance the signal to noise ratio, recording and averaging of several B-scans at the same location resulting in high-quality scans shown in Fig. 34.5g–j.

In order to illustrate the similarities between different wavelength regions, Fig. 34.6 shows averaged PS-OCT images recorded at 1,040 nm with a swept source system [52]. Essentially the same polarization characteristics as with the 840 nm system can be observed within the anterior layers, the photoreceptor layers, and the RPE. However, the longer wavelength region provides a better penetration into choroid and sclera. The sclera is known to be highly birefringent which can directly be observed in Fig. 34.6b by the strong increase of retardation within this layer. This specific characteristic of the sclera can be used in order to segment the posterior boundary of the choroid based on PS-OCT data [59, 60].

If we take a closer look at the DOPU image recorded at the longer wavelength, we will observe lower DOPU values in the choroid than in the anterior retinal layers. These lower values are probably caused by pigments embedded within the choroid leading to a random polarization state for part of the backscattered light. Nevertheless, the images clearly show that the interaction between light and RPE scrambles (depolarizes) only the backscattered light while the polarization state of the transmitted light is preserved. While the basic polarization effects observed in the two wavelength regimes are qualitatively similar, a thorough quantitative comparison between the wavelengths is still missing.

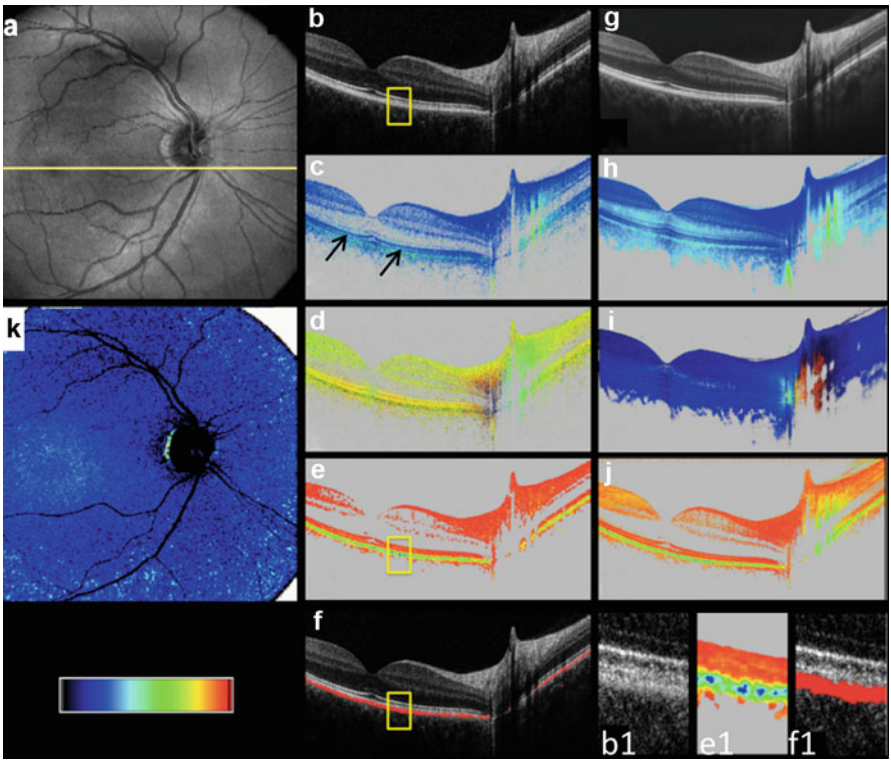

Fig. 34.5 PS-OCT measurement results recorded from a healthy human volunteer (scan angle: 40 × 40°, 1,024 × 250 A-scans). (**a**) Depth integrated OCT en face view, *yellow line* indicates the location of the corresponding B-scans. (**b**) Intensity B-scan on logarithmic gray scale. *Yellow rectangle* indicates magnified area that is shown in **b1**. (**c**) Retardation image (color scale 0–90°). The *arrows* indicate increased retardation at the IS/OS junction caused by Henle's fiber layer. (**d**) Optic axis orientation (color scale 0–180°). (**e**) DOPU image (color scale 0–1). *Yellow rectangle* indicates magnified area shown in **e1**. (**f**) Segmented depolarizing material (*red*) overlaid with the intensity image. *Yellow rectangle* indicates magnified area shown in **f1**. (**g**) Average of 50 intensity B-scans recorded at the same position. (**h**) Average retardation image. (**i**) Average optic axis orientation image. (**j**) DOPU image calculated from a temporal window over 50 B-scans. (**k**) Depth summation of the number of depolarizing pixels along each A-scan within the 3-D data set (color scale 0–100 μm). Areas with low signal quality are displayed in *white* (Reproduced from Zotter et al. [57] by permission of the Optical Society of America)

34.4.1.1 Age-Related Macular Degeneration

In order to quantify changes caused by retinal diseases, accurate and automated segmentation algorithms are needed. While this is difficult to achieve when relying solely on the data provided by standard OCT intensity images, PS-OCT offers complementary information. As pointed out in the previous chapter, the OCT signal from the RPE is in a random polarization state. This effect is clearly visible in the DOPU images (c.f. Figs. 34.5e, j and 34.6d), and within these images, the location

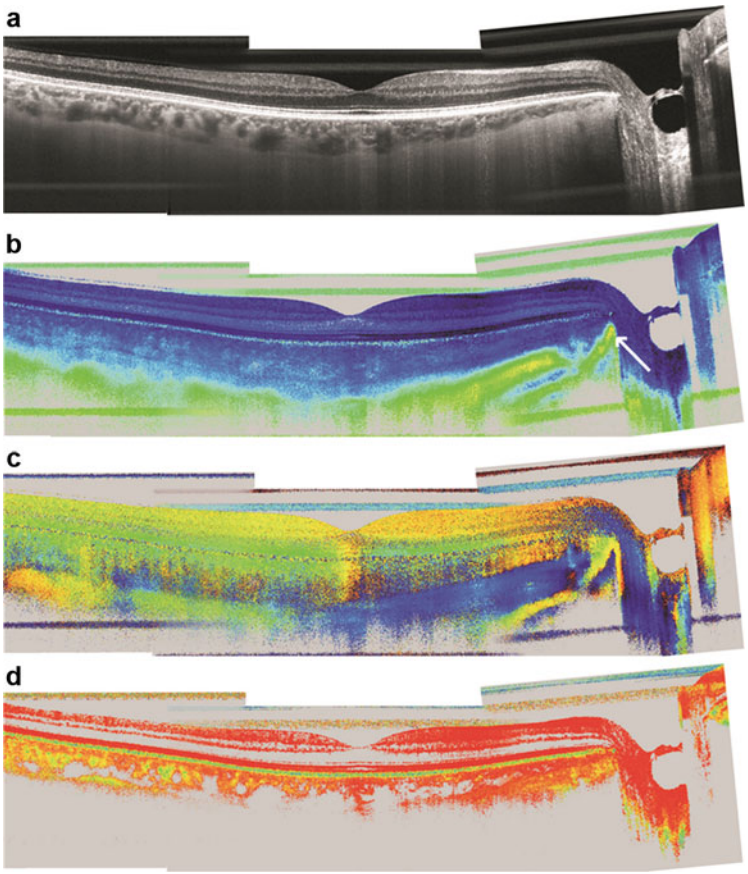

Fig. 34.6 Averaged PS-OCT images recorded at 1,040 nm with a swept source system. (**a**) Intensity, (**b**) phase retardation (*arrow* indicates the location of the sclera rim), (**c**) axis orientation, (**d**) DOPU (Same color scale as in Fig. 34.5) (Reproduced from Torzicky et al. [52] by permission of the American Academy of Optometry)

of the RPE can be determined quite easily because, in the healthy eye, other anterior retinal layers do not contain depolarizing tissue. In order to segment this layer automatically, the introduction of a simple threshold is already sufficient [28]. The segmented RPE can then be used as a backbone for other segmentation procedures.

The integrity of the RPE is of specific interest in AMD patients because it plays a fundamental role in the metabolism of the overlying photoreceptors. Currently, AMD can be regarded as the leading cause of blindness in the developed world [61]. Hence, improved diagnosis or a better treatment control is of social importance.

One of the first clinical indicators of this disease are drusen. In OCT drusen can be recognized by localized elevations of the normal RPE structure and represent

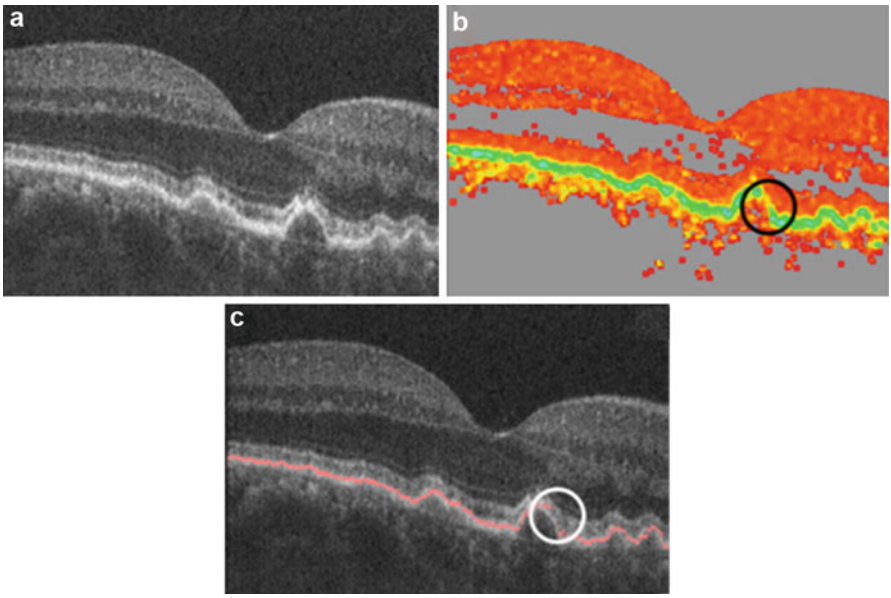

Fig. 34.7 B-scan images of a patient with drusen. (**a**) Intensity image, (**b**) DOPU image showing a small atrophic area (indicated by the *circle*) within the pigment epithelium, (**c**) segmented RPE overlaid to the intensity image (Reproduced from Ahlers et al. [63] by permission from the Association for Research in Vision and Ophthalmology)

a major risk factor for further disease progression. The evolution of the disease not only depends on several drusen parameters as size, area, and volume but also on the type of drusen [62]. Figure 34.7 shows exemplary PS-OCT B-scans recorded from a drusen patient [63]. Within the DOPU image (c.f. Fig. 34.7b), the localized elevation of the RPE can be clearly observed. In the intensity image, the RPE appears continuous; however the DOPU image shows a small focal skip lesion indicating a possible local destruction of this layer. Figure 34.7c shows the segmented RPE (thresholded DOPU image) overlaid to the intensity image. Together with an algorithm that searches for the "normal" RPE location (equivalent to the position of Bruch's membrane), [31] the drusen area and volume can be quantified. The reproducibility of drusen area and volume measurements using PS-OCT data showed a variability of only $\sim$7 % [31]. Motion artifacts occurring during the volume scan mainly account for this residual variability which therefore can be further reduced using, e.g., active eye tracking. Schlanitz et al. compared the automated drusen segmentation using PS-OCT with manual segmentation by expert readers and found excellent agreement between both methods [64].

Besides the segmentation capabilities, PS-OCT is able to provide additional information on the drusen and the underlying tissue which might be of importance in order to judge on the further development of these structures. Of specific interest is the continuity of the RPE throughout the druse which is regarded as an important indicator of a starting transition into the next stage of the disease

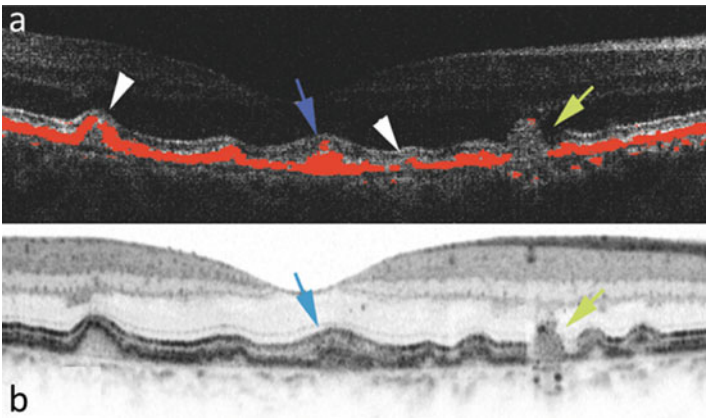

Fig. 34.8 Different appearance of drusen in PS-OCT data. (**a**) Segmented depolarizing tissue overlaid to the intensity image; (**b**) averaged intensity B-scan of a commercially available instrument. The *blue arrows* indicate a druse filled with depolarizing material; the *yellow arrows* indicate a drusenoid structure with complete absence of RPE. The *white arrowheads* indicate small atrophic lesions (Reproduced from Schlanitz et al. [64] by permission from the Association for Research in Vision and Ophthalmology)

(e.g., geographic atrophy). Figure 34.8 shows a comparison of segmented PS-OCT data with an intensity image recorded with a commercial instrument. From the information provided by the intensity image (c.f. Fig. 34.8b), only the disruption at the druse at the right hand of the image can be detected. On the other hand, the segmentation provided by PS-OCT (c.f. Fig. 34.8a) shows in addition discontinuities of the RPE roughly in the center of the image and on the druse at the left-hand side of the image. Moreover, PS-OCT can differentiate material underneath drusen: the center druse is filled with depolarizing material while the druse on the left-hand side of the image does not contain depolarizing material. However, the causes and the consequences of this difference with respect to the further development of the druse need further investigations.

As the disease progresses, atrophic zones may develop. These zones may already be visible in the en face intensity projection of OCT data (c.f. Fig. 34.9a). However, the en face map generated by a summation of depolarizing pixels along the A-scan direction using PS-OCT DOPU data shows increased contrast of the atrophic zone in comparison to the surrounding region (cf. Fig. 34.9b). Note that the contrast provided by PS-OCT has a similar appearance as that of autofluorescence (AF) imaging (c.f. Fig. 34.9c). In order to automatically segment the atrophic zones, the depth information provided by OCT is used in order to exclude image pixels that contribute to the en face map from other depths (e.g., from the choroid) than that of the "normal" location of the RPE [31]. After this exclusion a simple thresholding algorithm can be applied to segment the atrophic zones and to measure the corresponding area. Although the measured area is again influenced by motion artifacts, the variability of this measurement is only ~9 % [31].

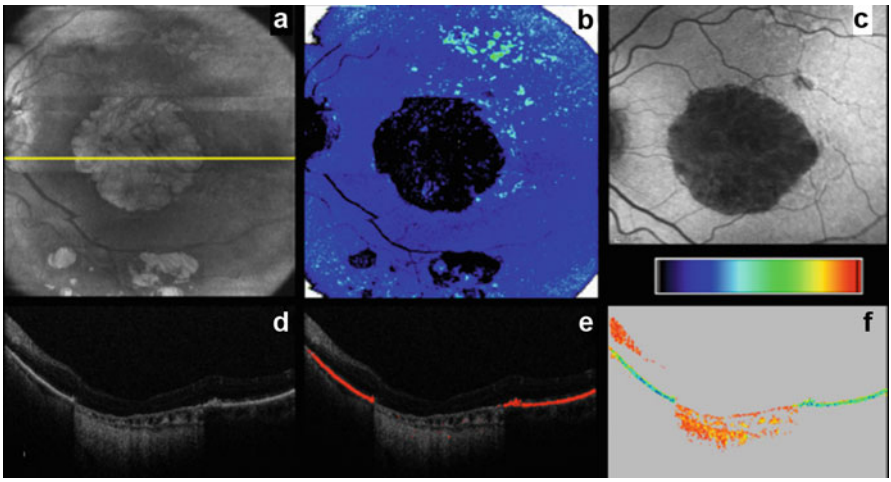

Fig. 34.9 PS-OCT images of a patient with geographic atrophy. (**a**) Pseudo SLO image; *yellow line* indicates the position of the corresponding B-scans. (**b**) Depolarizing material thickness map (color scale 0–160 μm). (**c**) Autofluorescence image for comparison. (**d**) Intensity B-scan, (**e**) RPE segmentation B-scan, and (**f**) DOPU image (Reproduced from Zotter et al. [57] by permission of the Optical Society of America)

The neovascular form of AMD (nAMD) is in general associated with severe loss of visual acuity. Recent developments in therapy aim to prohibit vascular growth in order to reduce leakages into the neurosensory retina and in order to restore the retinal structure. Although the retinal thickness approaches normal values, visual acuity does not necessarily improve. Figure 34.10 shows an example of PS-OCT data recorded in nAMD. The elevation of the RPE and subretinal fluid are clearly observable. Although the RPE appears continuous in the intensity image, the DOPU image shows an atrophic area on the right-hand side of the lesion. The development of previously undetected RPE atrophies in nAMD might be responsible for the poor correlation between retinal thickness and visual acuity [63]. In the late stage of AMD fibrotic scars are frequently observed. The organized structure of collagen fibrils in these scars leads to form birefringence that can be detected using PS-OCT [26] as is shown in Fig. 34.11. The retardation image (c.f. Fig. 34.11b) clearly shows strong birefringence in the scar area. The information provided by the axis orientation (c.f. Fig. 34.11c) may be used in order to determine the fibril orientation. A quantitative analysis of the birefringence may be used as an indicator for the underlying consistency of these scars.

34.4.1.2 Other Diseases Affecting the Macula

The capability of PS-OCT to detect depolarizing tissue makes this technology well suited for any disease associated with pigmentation changes. One example is Stargardt's disease which affects, similar to GA, the RPE [65]. Figure 34.12 shows an example of PS-OCT measurements in comparison with AF imaging [57].

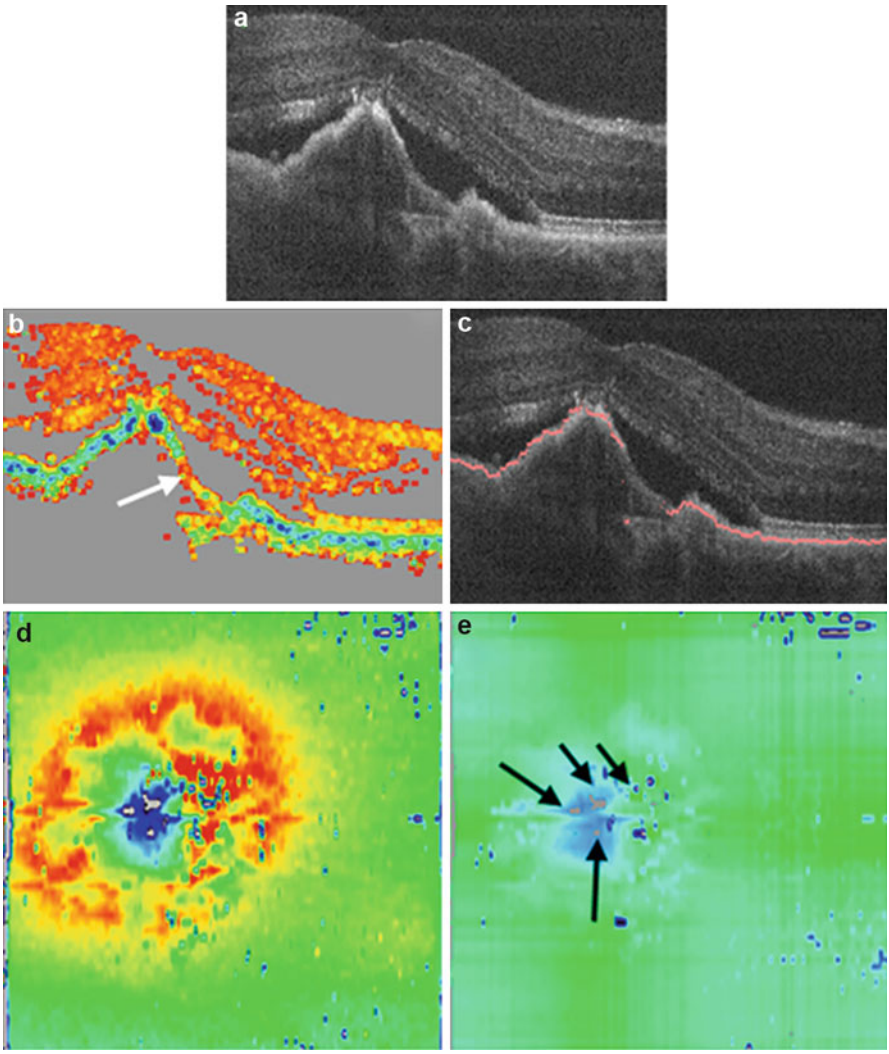

Fig. 34.10 PS-OCT images of a patient with nAMD. (**a**) Intensity image; (**b**) DOPU image (*white arrow* points to local RPE atrophy); (**c**) segmented depolarizing tissue overlaid to the intensity image; (**d**) retinal thickness map (Bruch's membrane to inner limiting membrane); (**e**) retinal thickness map (RPE to inner limiting membrane. Zones of RPE atrophy are displayed as gray pixels in (**d**) and are in addition marked with *arrows* in (**e**) (Reproduced from Ahlers et al. [63] by permission from the Association for Research in Vision and Ophthalmology)

Interestingly, the en face depolarizing tissue thickness map (Fig. 34.12b) shows more depolarizing tissue within the lesion than outside. This is contrary to the observation in most of the GA patients. The corresponding PS-OCT B-scans (Fig. 34.12e, f) show that the depolarization originates from the choroid. In contrast,

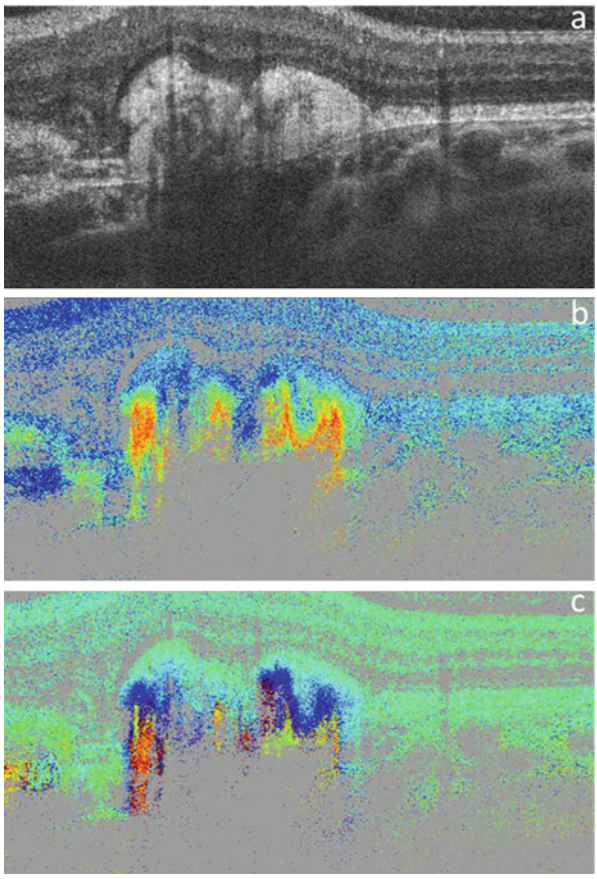

Fig. 34.11 PS-OCT images of a patient with fibrosis in the end stage of nAMD. (**a**) Intensity B-scan; (**b**) retardation image; (**c**) axis orientation image (Reproduced from Michels et al. [26] by permission from the British Journal of Ophthalmology)

the AF image (c.f. Fig. 34.12c) shows hypo-fluorescence within the atrophic lesion indicating that the structures within the choroid that give rise to depolarization are not fluorescent.

Idiopathic juxtafoveal telangiectasia (IJT), a disease that is associated with changes in the pigmentation, represents another example where PS-OCT is able to provide additional, clinically relevant information [66]. Here PS-OCT can be used in order to differentiate between morphological changes and to automatically segment deposits within the inner retina. The latter PS-OCT capability is of great interest in diabetic retinopathy [67]. The detection and quantification of deposits or hard exudates as a result of macula edema may be very valuable for monitoring disease progression and treatment control.

34.4.1.3 Retinal Pigmentation

One question remains on the origin of the depolarizing effect within the RPE. The RPE cells consist of regular constituents like cell nuclei and other organelles and

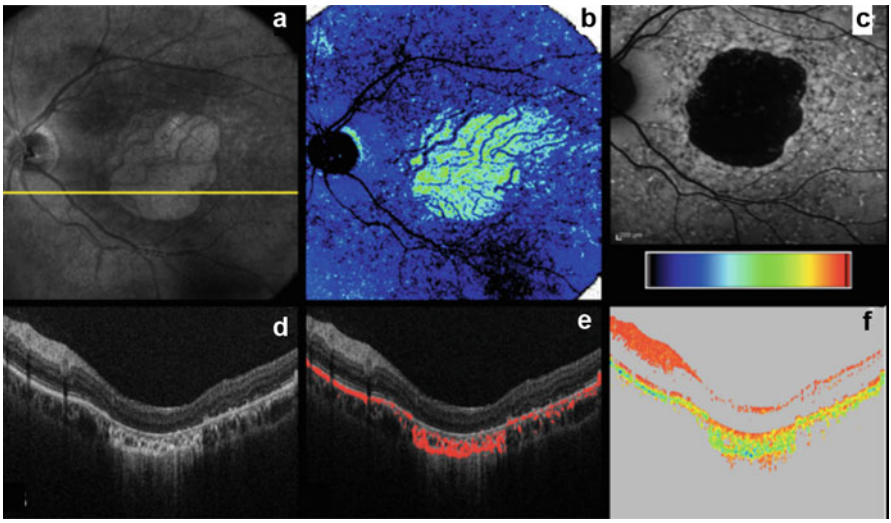

Fig. 34.12 PS-OCT images of a patient with Stargardt's disease (pathologic mutations in the ABCA4 gene). (**a**) Pseudo SLO image; *yellow line* indicates the position of the corresponding B-scan. (**b**) Depolarizing material thickness map (color scale 0–160 μm). (**c**) Autofluorescence image for comparison. (**d**) Intensity B-scan at the position of the *yellow line* in (**a**). (**e**) Segmented depolarizing material overlaid to intensity B-scan. (**f**) DOPU image (Reproduced from Zotter et al. [57] by permission of the Optical Society of America)

additionally contain pigments as melanin and lipofuscin. Pigments are large nonspherical particles that may cause depolarization [40]. A first PS-OCT study investigated the amount of depolarization caused by melanin as a function of melanin concentration in phantoms [68]. This study found a logarithmic decrease of DOPU values with melanin concentration and represents a first evidence that melanin is one cause of depolarization introduced by the RPE. Furthermore, this dependence allows estimating the melanin concentration within the RPE based on the measured DOPU value. In the healthy eye, the DOPU value measured in the RPE is lowest within the macula region and increases with eccentricity from the fovea [69]. A similar behavior can be found for the melanin concentration (using, e.g., autofluorescence imaging) which is further evidence that the depolarization in the healthy eye is mainly caused by melanin.

In order to test this assumption, patients with ocular albinism were imaged. This disease results in a significant decrease of retinal melanin. Depending on the amount of residual pigments present in the RPE, we expect to observe less depolarization in these patients. Figure 34.13 shows an example of PS-OCT measurements in a patient with ocular albinism [57]. The DOPU image (c.f. Fig. 34.13d) clearly shows the expected low depolarization (higher DOPU values as compared to the healthy eye, cf. Fig. 34.5e) at the level of the RPE. It is noticeable that the RPE does not appear as diffuse layer within the intensity image, as observed in normal eyes. In addition to the three bright layers (IS/OS, ETPR, RPE) that are normally

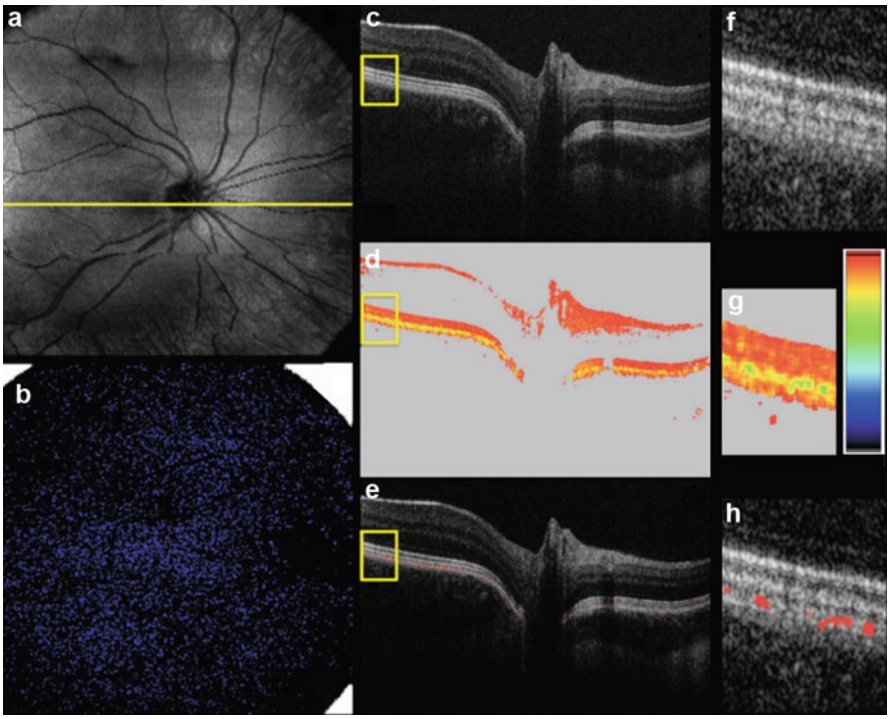

Fig. 34.13 PS-OCT images of a patient with albinism. (**a**) Pseudo SLO image; *yellow line* indicates the position of the corresponding B-scan. (**b**) Depolarizing material thickness map (color scale 0–100 μm). (**c**) Intensity B-scan. (**d**) DOPU image. (**e**) Segmentation of depolarizing material overlaid to the intensity image. The *yellow boxes* in (**c**–**e**) mark the position of the enlarged areas of (**f**–**h**) (Reproduced from Zotter et al. [57] by permission of the Optical Society of America)

visible in the OCT intensity images, a fourth layer can be observed (the bottom layer is split into two layers; c.f. enlargements in the B-scans of Fig. 34.13f–h) [57, 68]. This additional bottommost layer might be associated with Bruch's membrane that is otherwise obscured by the diffusive broadening of the RPE, probably caused by multiple scattering in this layer.

34.4.2 Imaging in the Nerve Head and Peripheral Regions

The main tissue of interest for PS-OCT imaging in the region of the optic nerve head (ONH) is the birefringent RNFL. This layer is damaged by glaucoma, one of the leading causes of blindness in the world. A thinning of the RNFL can be observed before visual field loss is detected [70, 71]. Untreated, this thinning leads to irreversible vision loss and finally to blindness. An early detection of RNFL thinning is therefore imperative to prevent further progression of glaucoma.

Based on these considerations, scanning laser polarimetry (SLP) [22, 72] has been introduced as a tool to measure the RNFL thickness via its birefringence: if a constant RNFL birefringence is assumed, the retardation observed between two orthogonally polarized components of a sampling laser beam is directly proportional to the thickness of the RNFL. SLP is based on a confocal scanning laser ophthalmoscope with an integrated ellipsometer; it measures the retardation in the area of the ONH and calculates RNFL thickness maps that can be used for glaucoma diagnosis.

However, SLP has some shortcomings which are essentially caused by the fact that it is a 2-D imaging technique: since no depth information is available, the total birefringence of the ocular fundus is integrated in depth. This causes artifacts in subjects where the beam penetrates deeper, down to the birefringent sclera [73]. These artifacts are known as atypical GDx scans and occur in a considerable subset of healthy and glaucomatous eyes [74–77]. In these cases, a reliable diagnosis is not warranted. Furthermore, a constant birefringence is assumed to convert retardation into RNFL thickness maps. Since birefringence of the RNFL varies around the ONH [23], these thickness maps are distorted.

Since PS-OCT provides 3-D information, it can solve these problems. PS-OCT provides retardation and thickness information simultaneously and therefore also enables a direct measurement of tissue birefringence. This is illustrated in Fig. 34.14 [78]. A 3-D PS-OCT data set was recorded with the instrument shown in Fig. 34.4. The data set covers an area of 27°(x) × 24°(y), centered at the ONH. Figure 34.14a shows a pseudo SLO en face projection of reflectivity data. The horizontal yellow line indicates the position of the extracted B-scan shown in Fig. 34.14b (intensity), c (retardation). The topmost, brightly reflecting layer of Fig. 34.14b is the RNFL; its birefringence is revealed by the color change from blue to green in the retardation image (Fig. 34.14c) (best seen in the area around the thickest RNFL bundle, i.e., around the vertical yellow line). Figure 34.14d shows the reflectivity image with superimposed segmentation lines: the red lines show the boundaries of the RNFL (found by an intensity-based algorithm); the layers between the green lines correspond to the photoreceptors. These lines are obtained by first segmenting the RPE based on its depolarization and then generating a band of fixed width anterior to the RPE [78]. The vertical yellow lines in Fig. 34.14b, c correspond to the location of the extracted A-scan values plotted in Fig. 34.14e. This graph shows the extracted intensity (black dots) and retardation (red dots) values along a single A-scan. One can clearly see that, within the RNFL, the retardation linearly increases with depth due to the birefringence of the RNFL. The birefringence within the RNFL along this A-scan is obtained by fitting a straight line (black) to the red points located within the RNFL (marked by short red lines on the x-axis).

From the data presented in Fig. 34.14, three different types of quantitative en face maps can be generated: (i) RNFL retardation maps, retardation data are taken from within the band between the green segmentation lines of Fig. 34.14d (the photoreceptor layers provide the strongest signals and therefore the least noisy retardation data; since there are no birefringent layers between the RNFL and the photoreceptors around the ONH area, the retardation measured at the

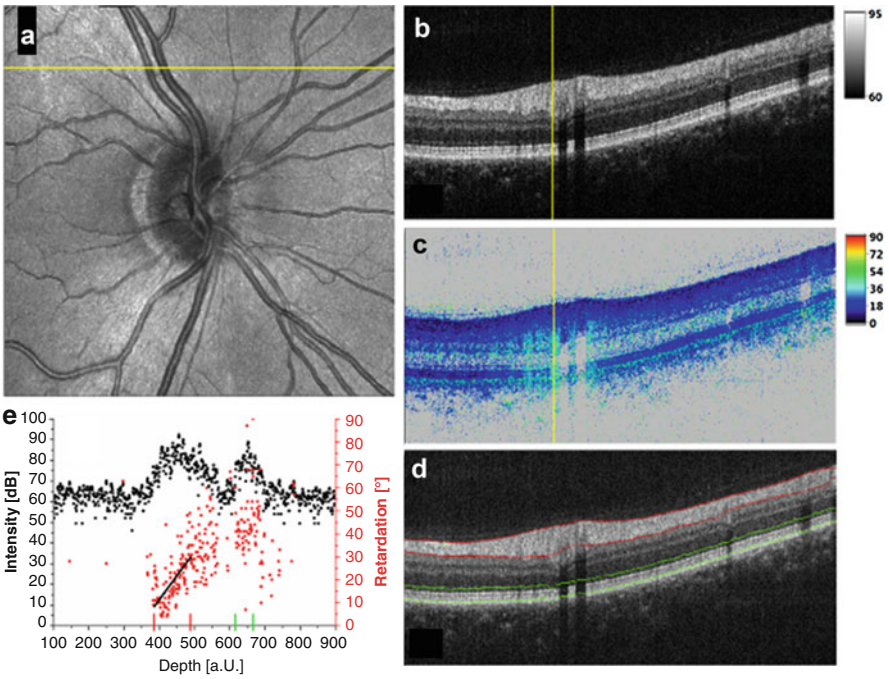

Fig. 34.14 3-D PS-OCT scan (scan angle 27 × 24°, sampling 1,024 × 250 A-scans). (**a**) Pseudo SLO en face image. *Yellow line* indicates the position of the B-scans shown in (**b**)–(**d**). (**b**) Exemplary reflectivity B-scan (log scale). *Yellow line* indicates the position of the extracted A-scan values presented in (**e**). (**c**) Corresponding retardation B-scan. Areas below a certain intensity threshold are displayed in gray (color scale: deg). (**d**) Intensity B-scan overlaid with segmented anterior and posterior boundary of the RNFL (*red lines*) and window indicating the area from which retardation is derived (between *green lines*). (**e**) Extracted intensity (*black dots*) and retardation (*red dots*) values for a single A-scan marked as *yellow line* in (**b**) and (**c**). Segmented RNFL is marked by red lines on the x-axis. Window indicating the area from which retardation is derived is marked by *green lines* on the x-axis. Linear regression fit of the retardation values within the RNFL is indicated by a *solid black line* (Reproduced from Zotter et al. [78] by permission of the Association for Research in Vision and Ophthalmology)

photoreceptors is equal to that at the posterior side of the RNFL); (ii) RNFL thickness maps (showing the vertical distance between the red segmentation lines depicted in Fig. 34.14d); and (iii) RNFL birefringence maps (depicting the slope of the retardation vs. depth linear fit of Fig. 34.14e as a function of x-y position of the recorded A-scan).

Figure 34.15 shows examples of the three quantitative en face maps [78]. The maps are averages from five data sets recorded in the same healthy eye. Figure 34.15a is a retardation map, showing the typical retardation pattern known from SLP: strong retardation along the superior and inferior RNFL bundles and low retardation on the temporal and nasal side. The RNFL thickness map of Fig. 34.15b shows a similar distribution (it is somewhat smoothed because some areal

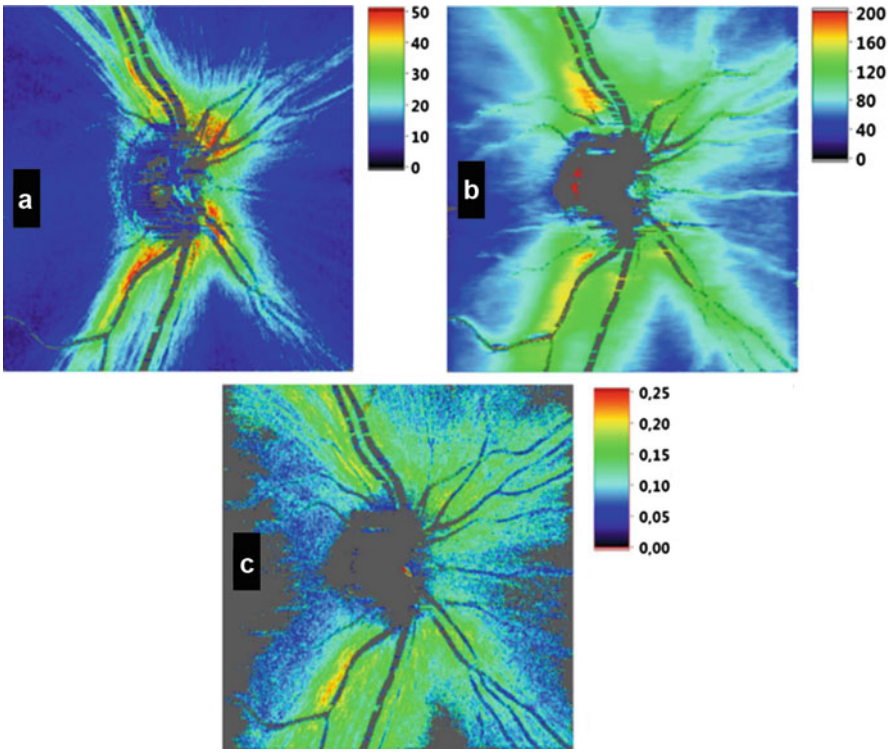

Fig. 34.15 Averaged 2-D en face maps calculated from five 3-D PS-OCT data sets recorded in the optic nerve head area of a healthy human eye. (**a**) RNFL retardation map (color scale: deg). (**b**) RNFL thickness map (color scale: μm). (**c**) RNFL birefringence map (color scale: deg/μm) (Reproduced from Zotter et al. [78] by permission of the Association for Research in Vision and Ophthalmology)

averaging is performed prior to calculating the thickness map). Finally, the birefringence map of Fig. 34.15c shows that the birefringence of the RNFL is not uniform. Especially on the nasal and temporal side, a lower birefringence is observed.

Figure 34.16 shows a comparison of retardation maps obtained by PS-OCT (Fig. 34.16a) and SLP (Fig. 34.16b) in the same eye. The SLP image was obtained by a commercial instrument (GDx VCC, Carl Zeiss Meditec). While the general patterns are in good agreement, the PS-OCT map shows a much better resolution, revealing thin nerve fiber bundles that are not resolved by the SLP instrument.

Figure 34.17 summarizes results obtained in ten healthy eyes. These TSNIT curves show the circumpapillary (azimuthal) distribution of RNFL retardation (Fig. 34.17a), thickness (Fig. 34.17b), and birefringence (Fig. 34.17c), measured along a circle around the ONH, starting at the temporal (T) position and going over the superior (S), the nasal (N), the inferior (I), and back to the temporal (T) position.

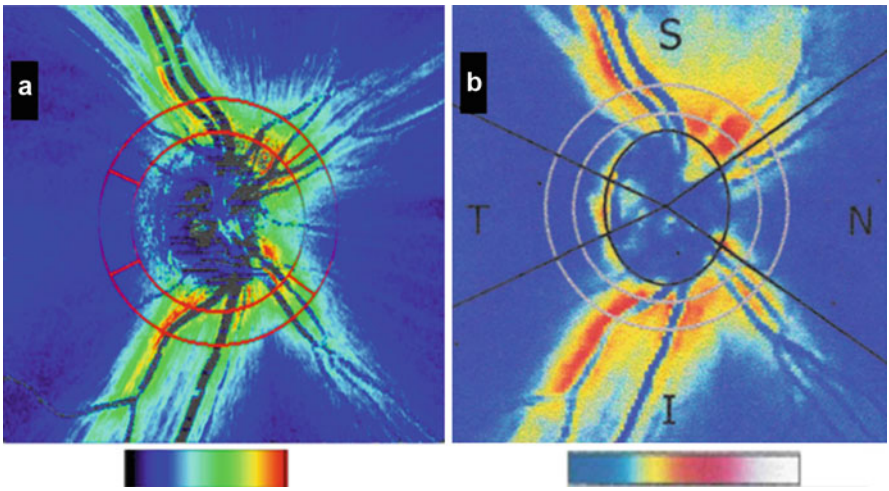

Fig. 34.16 Comparison between PS-OCT and SLP recorded within the same eye. (**a**) Averaged retardation map from Fig. 34.6a (color scale: 0–50°). *Red lines* indicate the region for the circumpapillary evaluation. (**b**) GDx VCC en face retardation map (color scale: 0–61°) (Reproduced from Zotter et al. [78] by permission of the Association for Research in Vision and Ophthalmology)

The data are taken from within the area marked by two red circles in Fig. 34.16a. The black curves show the mean values found for the ten eyes; the red curves indicate the position of mean ± standard deviation. For glaucoma diagnostics by SLP, deviations from a similar retardation standard curve (taken from a normative database) are analyzed. Since PS-OCT provides three different types of TSNIT curves, improved sensitivity and specificity can be expected.

Figure 34.18 shows a comparison of wide-field (40 × 40°) retardation maps obtained in a healthy (Fig. 34.18a) and a glaucomatous eye (Fig. 34.18b). The glaucomatous eye clearly shows a nerve fiber bundle defect in the superior hemisphere.

Apart from glaucoma diagnostics by analyzing RNFL birefringence in the ONH area, other applications of PS-OCT in the peripheral retina are conceivable, though not yet explored in greater detail. An example of a possible application is imaging of choroidal nevi and melanoma based on the depolarization caused by the melanin they contain. The contrast mechanism is similar to that reported for the RPE contrast in Sect. 34.3.2.2. Figure 34.19 shows an example of a 3-D data set obtained from an eye with a choroidal nevus [30]. Figure 34.19a–c show intensity, retardation, and DOPU images, respectively (each image contains sub-images of volume rendering, transverse scan, and horizontal and vertical B-scan). Figure 34.19d, e show different aspects of a volume-rendered DOPU data set, clearly visualizing the extension of the nevus (blue-green color). Figure 34.19f shows a corresponding color fundus photo. A limitation of these PS-OCT images is that the strong scattering and absorption of the melanin prevents the measurement of total thickness of the pigmented tumors; PS-OCT at 1,050 nm might overcome that limitation.

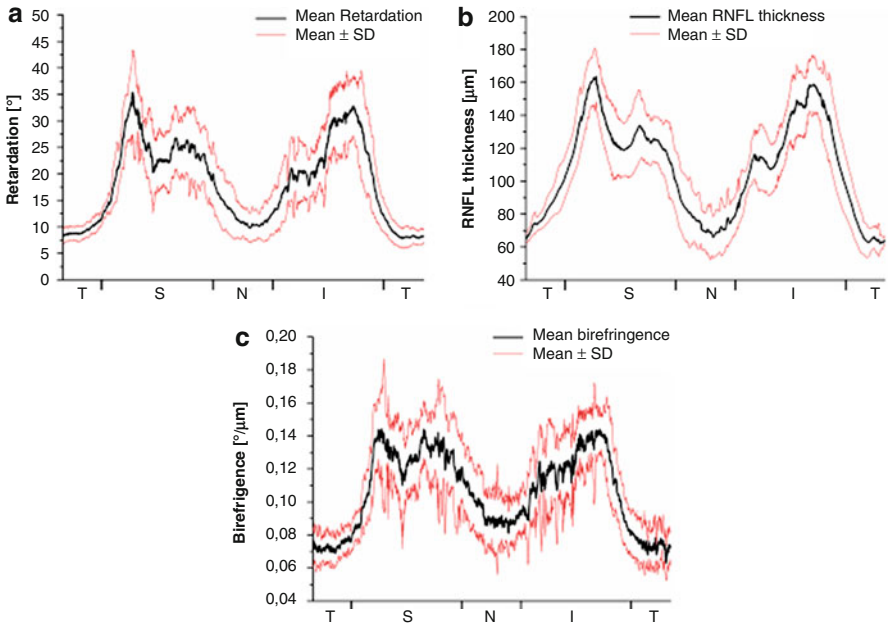

Fig. 34.17 Averaged RNFL retardation (**a**), thickness (**b**), and birefringence (**c**) circumpapillary plots ± standard deviation calculated from the measurement results of ten healthy eyes. The respective quantity is plotted as a function of the azimuth angle around the optic nerve head. The area from which the data of the circumpapillary plots are taken is indicated by two red rings in Fig. 34.16 (Reproduced from Zotter et al. [78] by permission of the Association for Research in Vision and Ophthalmology)

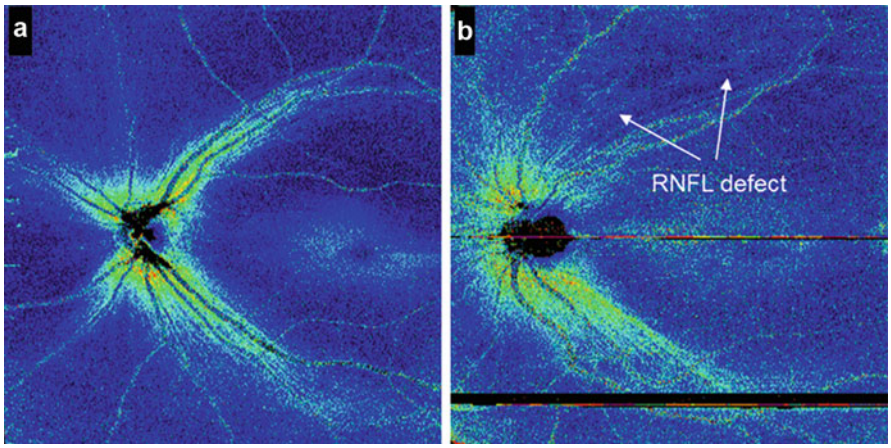

Fig. 34.18 Wide-field (40 × 40°) RNFL retardation maps obtained by PS-OCT in a healthy eye (**a**) and in a glaucomatous eye (**b**) (Reproduced from Zotter et al. [57] by permission of the Optical Society of America)

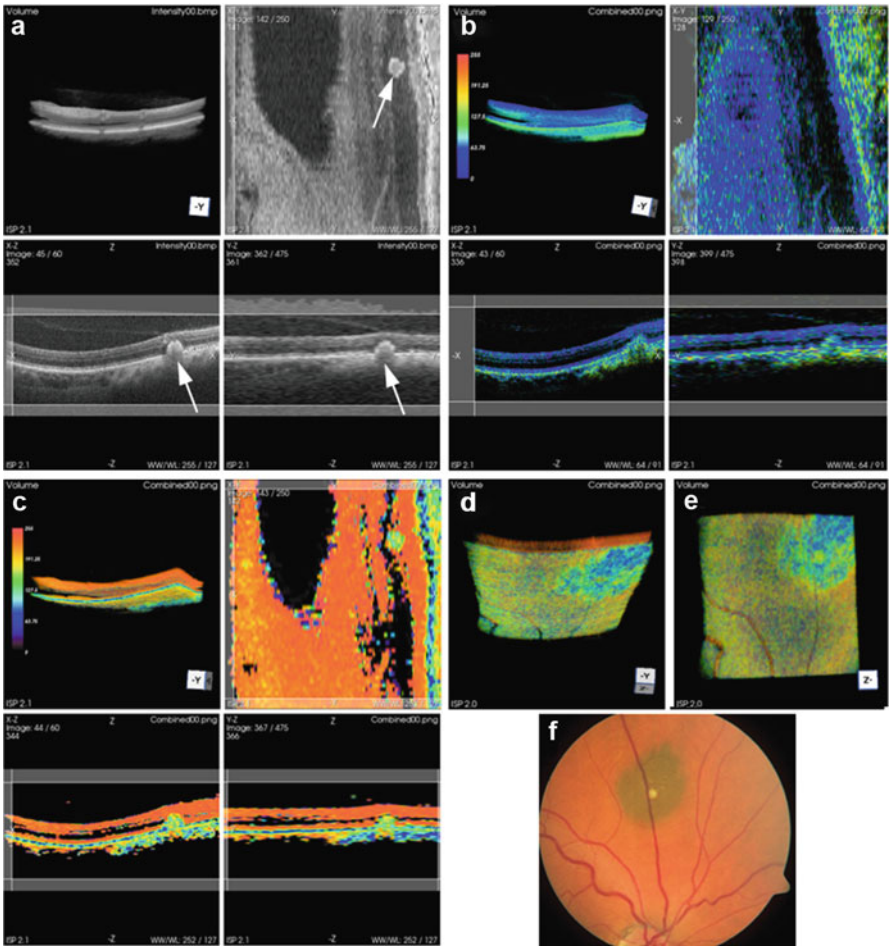

Fig. 34.19 3-D PS-OCT data set of the retina of a patient with a choroidal nevus. (**a**) Reflectivity; (**b**) retardation (color bar: 0 = 0°, 255 = 90°); (**c**) DOPU (color bar: 0 = 0, 255 = 1). Sub-figure arrangement: *top left*, volume rendering; *top right*, en face section; *bottom left*, horizontal B-scan; *bottom right*, vertical B-scan. (**d, e**) Additional views of the volume-rendered DOPU data set: (**d**) inclined upwards and (**e**) upwards. For better comparison with the fundus photo (**f**), these reverse-direction images are mirrored. Image size of OCT images: ~14.25°(x) × 15°(y) × 1.5 mm (z, in air) (Reproduced from Götzinger et al. [30] by permission of the Optical Society of America)

34.5 Conclusions

PS-OCT is a functional extension of OCT that provides intrinsic, tissue-specific contrast and thereby overcomes some of the limitations of conventional, intensity-based OCT. The eye contains several tissues that can change the light's polarization state. Therefore, PS-OCT has several applications in ocular imaging. Presently, the

most promising applications are glaucoma diagnostics via the birefringence of the RNFL and the automated segmentation of the RPE and of lesions that are associated with changes of the RPE, as found, e.g., in age-related macular degeneration.

Since PS-OCT is an extension of standard OCT techniques, essentially all new developments made for intensity-based OCT can be transferred to PS-OCT. Therefore, we expect that improvements in light source and camera technology that recently have led to ultrahigh-speed OCT systems will also further improve the imaging speed of PS-OCT. Furthermore, the integration of retinal trackers that are already available in some commercial OCT scanners will lead to motion-artifact free PS-OCT images that should further improve the precision of quantitative PS-OCT imaging.

Acknowledgments We thank B. Baumann, M. Bonesi, E. Götzinger, T. Torzicky, and S. Zotter, Center for Medical Physics and Biomedical Engineering, Medical University of Vienna, and C. Ahlers, M. Bolz, J. Lammer, S. Michels, M. Ritter, P. Roberts, F. Schlanitz, C. Schütze, C. Vass, and U. Schmidt-Erfurth, Department of Ophthalmology, Medical University of Vienna, for cooperation. Part of this work was financially supported by the Austrian Science Fund (grants P16776 and P19624), by the European Commission (project FUN OCT, FP7 HEALTH, contract no. 201880), and by Canon Inc., Tokyo.

References

1. D. Huang, E.A. Swanson, C.P. Lin, J.S. Schuman, W.G. Stinson, W. Chang, M.R. Hee, T. Flotte, K. Gregory, C.A. Puliafito, J.G. Fujimoto, Optical coherence tomography. Science **254**, 1178–1181 (1991)
2. W. Drexler, J.G. Fujimoto, State-of-the-art retinal optical coherence tomography. Prog. Retin. Eye Res. **27**, 45–88 (2008)
3. A.F. Fercher, C.K. Hitzenberger, G. Kamp, S.Y. Elzaiat, Measurement of intraocular distances by backscattering spectral interferometry. Opt. Commun. **117**, 43–48 (1995)
4. G. Häusler, M.W. Lindner, "Coherence radar" and "spectral radar" – new tools for dermatological diagnosis. J. Biomed. Opt. **3**, 21–31 (1998)
5. M. Wojtkowski, R. Leitgeb, A. Kowalczyk, T. Bajraszewski, A.F. Fercher, In vivo human retinal imaging by Fourier domain optical coherence tomography. J. Biomed. Opt. **7**, 457–463 (2002)
6. R. Leitgeb, C.K. Hitzenberger, A.F. Fercher, Performance of Fourier domain vs. time domain optical coherence tomography. Opt. Express **11**, 889–894 (2003)
7. J.F. de Boer, B. Cense, B.H. Park, M.C. Pierce, G.J. Tearney, B.E. Bouma, Improved signal-to-noise ratio in spectral-domain compared with time-domain optical coherence tomography. Opt. Lett. **28**, 2067–2069 (2003)
8. M.A. Choma, M.V. Sarunic, C.H. Yang, J.A. Izatt, Sensitivity advantage of swept source and Fourier domain optical coherence tomography. Opt. Express **11**, 2183–2189 (2003)
9. B. Potsaid, I. Gorczynska, V.J. Srinivasan, Y.L. Chen, J. Jiang, A. Cable, J.G. Fujimoto, Ultrahigh speed spectral/Fourier domain OCT ophthalmic imaging at 70,000 to 312,500 axial scans per second. Opt. Express **16**, 15149–15169 (2008)
10. V.J. Srinivasan, D.C. Adler, Y. Chen, I. Gorczynska, R. Huber, J.S. Duker, J.S. Schuman, J.G. Fujimoto, Ultrahigh-speed optical coherence tomography for three-dimensional and en face imaging of the retina and optic nerve head. Invest. Ophthalmol. Vis. Sci. **49**, 5103–5110 (2008)
11. T. Klein, W. Wieser, C.M. Eigenwillig, B.R. Biedermann, R. Huber, Megahertz OCT for ultrawide-field retinal imaging with a 1050 nm Fourier domain mode-locked laser. Opt. Express **19**, 3044–3062 (2011)

12. L. An, P. Li, T.T. Shen, R.K. Wang, High speed spectral domain optical coherence tomography for retinal imaging at 500,000 A-lines per second. Biomed. Opt. Express **2**, 2770–2783 (2011)
13. M.R. Hee, D. Huang, E.A. Swanson, J.G. Fujimoto, Polarization-sensitive low-coherence reflectometer for birefringence characterization and ranging. J. Opt. Soc. Am. B Opt. Phys. **9**, 903–908 (1992)
14. J.F. de Boer, T.E. Milner, M.J.C. van Gemert, J.S. Nelson, Two-dimensional birefringence imaging in biological tissue by polarization-sensitive optical coherence tomography. Opt. Lett. **22**, 934–936 (1997)
15. B.H. Park, M.C. Pierce, B. Cense, J.F. de Boer, Jones matrix analysis for a polarization-sensitive optical coherence tomography system using fiber-optic components. Opt. Lett. **29**, 2512–2514 (2004)
16. M. Todorovic, S.L. Jiao, L.V. Wang, Determination of local polarization properties of biological samples in the presence of diattenuation by use of Mueller optical coherence tomography. Opt. Lett. **29**, 2402–2404 (2004)
17. N.J. Kemp, H.N. Zaatari, J. Park, H.G. Rylander, T.E. Milner, Form-biattenuance in fibrous tissues measured with polarization-sensitive optical coherence tomography (PS-OCT). Opt. Express **13**, 4611–4628 (2005)
18. L.J. Bour, Polarized light and the eye, in *Visual Optics and Instrumentation*, ed. by W.N. Charman (CRC Press, Boca Raton, 1991), pp. 310–325
19. E. Götzinger, M. Pircher, M. Sticker, A.F. Fercher, C.K. Hitzenberger, Measurement and imaging of birefringent properties of the human cornea with phase-resolved, polarization-sensitive optical coherence tomography. J. Biomed. Opt. **9**, 94–102 (2004)
20. M. Yamanari, S. Makita, Y. Yasuno, Polarization-sensitive swept-source optical coherence tomography with continuous source polarization modulation. Opt. Express **16**, 5892–5906 (2008)
21. B. Baumann, E. Götzinger, M. Pircher, C.K. Hitzenberger, Single camera based spectral domain polarization sensitive optical coherence tomography. Opt. Express **15**, 1054–1063 (2007)
22. R.N. Weinreb, A.W. Dreher, A. Coleman, H. Quigley, B. Shaw, K. Reiter, Histopathologic validation of Fourier-ellipsometry measurements of retinal nerve-fiber layer thickness. Arch. Ophthalmol. **108**, 557–560 (1990)
23. B. Cense, T.C. Chen, B.H. Park, M.C. Pierce, J.F. de Boer, Thickness and birefringence of healthy retinal nerve fiber layer tissue measured with polarization-sensitive optical coherence tomography. Invest. Ophthalmol. Vis. Sci. **45**, 2606–2612 (2004)
24. H.B. Klein Brink, G.J. van Blokland, Birefringence of the human foveal area assessed in vivo with Mueller-matrix ellipsometry. J. Opt. Soc. Am. A Opt. Image Sci. Vis. **5**, 49–57 (1988)
25. M. Pircher, E. Götzinger, R. Leitgeb, H. Sattmann, O. Findl, C.K. Hitzenberger, Imaging of polarization properties of human retina in vivo with phase resolved transversal PS-OCT. Opt. Express **12**, 5940–5951 (2004)
26. S. Michels, M. Pircher, W. Geitzenauer, C. Simader, E. Gotzinger, O. Findl, U. Schmidt-Erfurth, C.K. Hitzenberger, Value of polarisation-sensitive optical coherence tomography in diseases affecting the retinal pigment epithelium. Br. J. Ophthalmol. **92**, 204–209 (2008)
27. M. Pircher, E. Götzinger, O. Findl, S. Michels, W. Geitzenauer, C. Leydolt, U. Schmidt-Erfurth, C.K. Hitzenberger, Human macula investigated in vivo with polarization-sensitive optical coherence tomography. Invest. Ophthalmol. Vis. Sci. **47**, 5487–5494 (2006)
28. E. Götzinger, M. Pircher, W. Geitzenauer, C. Ahlers, B. Baumann, S. Michels, U. Schmidt-Erfurth, C.K. Hitzenberger, Retinal pigment epithelium segmentation by polarization sensitive optical coherence tomography. Opt. Express **16**, 16410–16422 (2008)
29. M. Pircher, E. Goetzinger, R. Leitgeb, C.K. Hitzenberger, Transversal phase resolved polarization sensitive optical coherence tomography. Phys. Med. Biol. **49**, 1257–1263 (2004)

30. E. Götzinger, M. Pircher, B. Baumann, C. Ahlers, W. Geitzenauer, U. Schmidt-Erfurth, C.K. Hitzenberger, Three-dimensional polarization sensitive OCT imaging and interactive display of the human retina. Opt. Express **17**, 4151–4165 (2009)
31. B. Baumann, E. Götzinger, M. Pircher, H. Sattman, C. Schutze, F. Schlanitz, C. Ahlers, U. Schmidt-Erfurth, C.K. Hitzenberger, Segmentation and quantification of retinal lesions in age-related macular degeneration using polarization-sensitive optical coherence tomography. J. Biomed. Opt. **15**, 061704 (2010)
32. J.F. de Boer, T.E. Milner, Review of polarization sensitive optical coherence tomography and Stokes vector determination. J. Biomed. Opt. **7**, 359–371 (2002)
33. M. Pircher, C.K. Hitzenberger, U. Schmidt-Erfurt, Polarization sensitive optical coherence tomography in the human eye. Prog. Retin. Eye Res. **30**, 431–451 (2011)
34. R.C. Jones, A new calculus for the treatment of optical systems. I. Description and discussion of the calculus. J. Opt. Soc. Am. **31**, 488–493 (1941)
35. H. Mueller, *Memorandum on the polarization optics of the photoelastic shutter*, (Report No. 2 of the OSRD project OEMsr-576, 1943)
36. G. Yao, L.V. Wang, Two-dimensional depth-resolved Mueller matrix characterization of biological tissue by optical coherence tomography. Opt. Lett. **24**, 537–539 (1999)
37. S.L. Jiao, G. Yao, L.H.V. Wang, Depth-resolved two-dimensional Stokes vectors of backscattered light and Mueller matrices of biological tissue measured with optical coherence tomography. Appl. Optics **39**, 6318–6324 (2000)
38. R.C. Haskell, F.D. Carlson, P.S. Blank, Form birefringence of muscle. Biophys. J. **56**, 401–413 (1989)
39. M.I. Mishchenko, J.W. Hovenier, Depolarization of light backscattered by randomly oriented nonspherical particles. Opt. Lett. **20**, 1356–1358 (1995)
40. J.M. Schmitt, S.H. Xiang, Cross-polarized backscatter in optical coherence tomography of biological tissue. Opt. Lett. **23**, 1060–1062 (1998)
41. C.K. Hitzenberger, E. Götzinger, M. Sticker, M. Pircher, A.F. Fercher, Measurement and imaging of birefringence and optic axis orientation by phase resolved polarization sensitive optical coherence tomography. Opt. Express **9**, 780–790 (2001)
42. A.F. Fercher, C.K. Hitzenberger, Optical coherence tomography. Prog. Opt. **44**, 215–302 (2002)
43. A. Gerrard, J.M. Burch, *Introduction to Matrix Methods in Optics* (Wiley, London, 1975)
44. K. Schoenenberger, B.W. Colston, D.J. Maitland, L.B. Da Silva, M.J. Everett, Mapping of birefringence and thermal damage in tissue by use of polarization-sensitive optical coherence tomography. Appl. Optics **37**, 6026–6036 (1998)
45. E. Gotzinger, B. Baumann, M. Pircher, C.K. Hitzenberger, Polarization maintaining fiber based ultra-high resolution spectral domain polarization sensitive optical coherence tomography. Opt. Express **17**, 22704–22717 (2009)
46. S.G. Adie, T.R. Hillman, D.D. Sampson, Detection of multiple scattering in optical coherence tomography using the spatial distribution of Stokes vectors. Opt. Express **15**, 18033–18049 (2007)
47. E. Götzinger, M. Pircher, C.K. Hitzenberger, High speed spectral domain polarization sensitive optical coherence tomography of the human retina. Opt. Express **13**, 10217–10229 (2005)
48. A. Unterhuber, B. Povazay, B. Hermann, H. Sattmann, A. Chavez-Pirson, W. Drexler, In vivo retinal optical coherence tomography at 1040 nm-enhanced penetration into the choroid. Opt. Express **13**, 3252–3258 (2005)
49. Y. Yasuno, Y.J. Hong, S. Makita, M. Yamanari, M. Akiba, M. Miura, T. Yatagai, In vivo high-contrast imaging of deep posterior eye by 1-mu m swept source optical coherence tomography and scattering optical coherence angiography. Opt. Express **15**, 6121–6139 (2007)
50. E.C.W. Lee, J.F. de Boer, M. Mujat, H. Lim, S.H. Yun, In vivo optical frequency domain imaging of human retina and choroid. Opt. Express **14**, 4403–4411 (2006)
51. P. Puvanathasan, P. Forbes, Z. Ren, D. Malchow, S. Boyd, K. Bizheva, High-speed, high-resolution Fourier-domain optical coherence tomography system for retinal imaging in the 1060 nm wavelength region. Opt. Lett. **33**, 2479–2481 (2008)

52. T. Torzicky, M. Pircher, S. Zotter, M. Bonesi, E. Gotzinger, C.K. Hitzenberger, High-speed retinal imaging with polarization-sensitive OCT at 1040 nm. Optom. Vis. Sci. **89**, 585–592 (2012)
53. M. Yamanari, Y. Lim, S. Makita, Y. Yasuno, Visualization of phase retardation of deep posterior eye by polarization-sensitive swept-source optical coherence tomography with 1-mu m probe. Opt. Express **17**, 12385–12396 (2009)
54. B.H. Park, C. Saxer, S.M. Srinivas, J.S. Nelson, J.F. de Boer, In vivo burn depth determination by high-speed fiber-based polarization sensitive optical coherence tomography. J. Biomed. Opt. **6**, 474–479 (2001)
55. D.P. Dave, T. Akkin, T.E. Milner, Polarization-maintaining fiber-based optical low-coherence reflectometer for characterization and ranging of birefringence. Opt. Lett. **28**, 1775–1777 (2003)
56. M.K. Al-Qaisi, T. Akkin, Polarization-sensitive optical coherence tomography based on polarization-maintaining fibers and frequency multiplexing. Opt. Express **16**, 13032–13041 (2008)
57. S. Zotter, M. Pircher, T. Torzicky, B. Baumann, H. Yoshida, F. Hirose, P. Roberts, M. Ritter, C. Schutze, E. Gotzinger, W. Trasischker, C. Vass, U. Schmidt-Erfurth, C.K. Hitzenberger, Large-field high-speed polarization sensitive spectral domain OCT and its applications in ophthalmology. Biomed. Opt. Express **3**, 2720–2732 (2012)
58. M. Pircher, E. Götzinger, B. Baumann, C.K. Hitzenberger, Corneal birefringence compensation for polarization sensitive optical coherence tomography of the human retina. J. Biomed. Opt. **12**, 041210 (2007)
59. L. Duan, M. Yamanari, Y. Yasuno, Automated phase retardation oriented segmentation of chorio-scleral interface by polarization sensitive optical coherence tomography. Opt. Express **20**, 3353–3366 (2012)
60. T. Torzicky, M. Pircher, S. Zotter, M. Bonesi, E. Gotzinger, C.K. Hitzenberger, Automated measurement of choroidal thickness in the human eye by polarization sensitive optical coherence tomography. Opt. Express **20**, 7564–7574 (2012)
61. R.D. Jager, W.F. Mieler, J.W. Miller, Medical progress: age-related macular degeneration. N. Engl. J. Med. **358**, 2606–2617 (2008)
62. M. Rudolf, M.E. Clark, M.F. Chimento, C.M. Li, N.E. Medeiros, C.A. Curcio, Prevalence and morphology of druse types in the macula and periphery of eyes with age-related maculopathy. Invest. Ophthalmol. Vis. Sci. **49**, 1200–1209 (2008)
63. C. Ahlers, E. Gotzinger, M. Pircher, I. Golbaz, F. Prager, C. Schutze, B. Baumann, C.K. Hitzenberger, U. Schmidt-Erfurth, Imaging of the retinal pigment epithelium in age-related macular degeneration using polarization-sensitive optical coherence tomography. Invest. Ophthalmol. Vis. Sci. **51**, 2149–2157 (2010)
64. F.G. Schlanitz, B. Baumann, T. Spalek, C. Schutze, C. Ahlers, M. Pircher, E. Gotzinger, C.K. Hitzenberger, U. Schmidt-Erfurth, Performance of automated Drusen detection by polarization-sensitive optical coherence tomography. Invest. Ophthalmol. Vis. Sci. **52**, 4571–4579 (2011)
65. R. Allikmets, N.F. Shroyer, N. Singh, J.M. Seddon, R.A. Lewis, P.S. Bernstein, A. Peiffer, N.A. Zabriskie, Y.X. Li, A. Hutchinson, M. Dean, J.R. Lupski, M. Leppert, Mutation of the Stargardt disease gene (ABCR) in age-related macular degeneration. Science **277**, 1805–1807 (1997)
66. C. Schutze, C. Ahlers, M. Pircher, B. Baumann, E. Gotzinger, F. Prager, G. Matt, S. Sacu, C.K. Hitzenberger, U. Schmidt-Erfurth, Morphologic characteristics of idiopathic juxtafoveal telangiectasia using spectral-domain and polarization-sensitive optical coherence tomography. Retina **32**, 256–264 (2012)
67. J. Lammer, M. Bolz, B. Baumann, E. Götzinger, M. Pircher, C. Hitzenberger, U. Schmidt-Erfurth, Automated detection and quantification of hard exudates in diabetic macular edema using polarization sensitive optical coherence tomography, *ARVO abstract* **4660/D935** (2010)

68. B. Baumann, S.O. Baumann, T. Konegger, M. Pircher, E. Gotzinger, F. Schlanitz, C. Schutze, H. Sattmann, M. Litschauer, U. Schmidt-Erfurth, C.K. Hitzenberger, Polarization sensitive optical coherence tomography of melanin provides intrinsic contrast based on depolarization. Biomed. Opt. Express **3**, 1670–1683 (2012)
69. B. Baumann, E. Gotzinger, M. Pircher, C.K. Hitzenberger, Measurements of depolarization distribution in the healthy human macula by polarization sensitive OCT. J. Biophotonics **2**, 426–434 (2009)
70. H.A. Quigley, E.M. Addicks, W.R. Green, Optic-nerve damage in human glaucoma. 3. Quantitative correlation of nerve-fiber loss and visual-field defect in glaucoma, ischemic neuropathy, papilledema, and toxic neuropathy. Arch. Ophthalmol. **100**, 135–146 (1982)
71. H.A. Quigley, Number of people with glaucoma worldwide. Br. J. Ophthalmol. **80**, 389–393 (1996)
72. A.W. Dreher, K. Reiter, R.N. Weinreb, Spatially resolved birefringence of the retinal nerve-fiber layer assessed with a retinal laser ellipsometer. Appl. Optics **31**, 3730–3735 (1992)
73. E. Götzinger, M. Pircher, B. Baumann, C. Hirn, C. Vass, C.K. Hitzenberger, Analysis of the origin of atypical scanning laser polarimetry patterns by polarization sensitive optical coherence tomography. Invest. Ophthalmol. Vis. Sci. **49**, 5366–5372 (2008)
74. H. Bagga, D.S. Greenfield, W.J. Feuer, Quantitative assessment of atypical birefringence images using scanning laser polarimetry with variable corneal compensation. Am. J. Ophthalmol. **139**, 437–446 (2005)
75. C. Bowd, F.A. Medeiros, R.N. Weinreb, L.M. Zangwill, The effect of atypical birefringence patterns on glaucoma detection using scanning laser polarimetry with variable corneal compensation. Invest. Ophthalmol. Vis. Sci. **48**, 223–227 (2007)
76. T.A. Mai, N.J. Reus, H.G. Lemij, Structure-function relationship is stronger with enhanced corneal compensation than with variable corneal compensation in scanning laser polarimetry. Invest. Ophthalmol. Vis. Sci. **48**, 1651–1658 (2007)
77. M. Sehi, S. Ume, D.S. Greenfield, A.I.G.S. Grp, Scanning laser polarimetry with enhanced corneal compensation and optical coherence tomography in normal and glaucomatous eyes. Invest. Ophthalmol. Vis. Sci. **48**, 2099–2104 (2007)
78. S. Zotter, M. Pircher, E. Götzinger, T. Torzicky, H. Yoshida, F. Hirose, S. Holzer, J. Kroisamer, C. Vass, U. Schmidt-Erfurt, C.K. Hitzenberger, Measuring retinal nerve fiber layer birefringence, retardation, and thickness using wide-field, high-speed polarization sensitive spectral domain OCT. Invest. Ophthalmol. Vis. Sci. **54**, 72–84 (2013)

Jones Matrix Based Polarization Sensitive Optical Coherence Tomography

35

Yoshiaki Yasuno, Myeong-Jin Ju, Young Joo Hong, Shuichi Makita, Yiheng Lim, and Masahiro Yamanari

Keywords
Polarization sensitive OCT • PS-OCT • Jones matrix • Birefringence • Retardation • Diattenuation • Optic-axis

35.1 Introduction

Polarization-sensitive optical coherence tomography (PS-OCT) is an extension of OCT and is capable of measuring the polarization properties of biological tissues, such as phase retardation, diattenuation, and optic-axis orientation. It is known that several types of biological tissues possess microscopic fibrous structures including collagen fibers and nerve fibers. Since these microscopic structures are smaller than the resolution of OCT, standard OCT is not capable of assessing them. However, these microscopic structures are known to possess birefringence, and PS-OCT is capable of assessing these microscopic tissue properties by measuring its polarization property.

PS-OCT has been applied to several biological and clinical investigations such as the examination of burn depth of skin [1–5], corneal integrity [6, 7], retinal disorders including macular diseases [8–10], glaucoma surgery [11], quantification of the retinal nerve fiber layer [12–14] and choroidal thickness [15, 16], assessments of caries [17–19], and cardiovascular plaques [20, 21].

PS-OCT modalities are classified into several subtypes. One of the most widely utilized methods is the circular polarization-based method, which was first demonstrated by Hee et al. [22] and later widely investigated by Hitzenberger and his

Y. Yasuno (✉) • M.-J. Ju • Y.J. Hong • S. Makita • Y. Lim • M. Yamanari
Computational Optics Group, University of Tsukuba, Tsukuba, Ibaraki, Japan
e-mail: yasuno@optlab2.bk.tsukuba.ac.jp

© Springer International Publishing Switzerland 2015

W. Drexler, J.G. Fujimoto (eds.), *Optical Coherence Tomography*,
DOI 10.1007/978-3-319-06419-2_36

associates [6, 8, 23]. In this chapter, this method is denoted as the Hee-Hitzenberger method. The Hee-Hitzenberger method determines the phase retardation and the optic-axis orientation of a sample by using a circularly polarized probe beam. Since this method uses only the intensity of OCT and does not use its phase to determine the phase retardation, this method is robust and stable. On the other hand, since the probe beam should be circularly polarized, the interferometer should be a bulk interferometer or built with a polarization-maintaining fiber. Another property of this method is its insensitivity to diattenuation. Although no particular utility was found for a diattenuation measurement of biological tissues, this limitation should be noted to understand the differences among several PS-OCT methods.

Stokes parameter-based PS-OCT has also been widely investigated [24]. This method is capable of determining the phase retardation and optic-axis orientation of a sample. As with the Hee-Hitzenberger method, the Stokes method is also not capable of measuring the diattenuation of a sample. One of the advantages of this method against Hee-Hitzenberger method is its ability to be implemented with a single-mode fiber, which is widely utilized for OCT [25–27]. The optic-axis orientation measured by this method is an absolute orientation if the system is implemented with a bulk interferometer and is a relative axis orientation if it is implemented with a flexible single-mode fiber. One drawback of this method is its requirement for an active optical device that alters the polarization state of a probe beam, typically an electro-optic modulator.

Mueller matrix-based PS-OCT has also been demonstrated [28, 29]. This method determines the Mueller matrix of a sample, and hence, it provides all of the polarization properties of the sample including the phase retardation, axis orientation, and the diattenuation except depolarization. The depolarization cannot be measured because of a fundamental limitation of a coherent imaging modality such as OCT [30]. Mueller matrix PS-OCT uses only the intensity signal of OCT, and hence, it could be robust in principle. However, this method requires relatively large numbers of measurements, and hence, the measurement time is relatively long. This long measurement time would deteriorate the polarization measurement accuracy of an in vivo measurement.

Among several subtypes of PS-OCT, Jones matrix-based PS-OCT, or Jones matrix OCT in short, is a method that determines the polarization properties of a sample by measuring the double-pass Jones matrix of a sample or its similar matrix [31–34]. This method can be implemented both with a bulk interferometer or a single-mode fiber-based interferometer. With the bulk interferometer, this method can provide a round-trip Jones matrix of the sample. On the other hand, with the single-mode fiber interferometer, a similar matrix of the round-trip Jones matrix of the sample is obtained. From the round-trip Jones matrix or its similar matrix, the phase retardation, the diattenuation, and the relative optic-axis orientation are obtained.

This chapter is dedicated to describing the principles and implementations of Jones matrix OCT.

35.2 General Principle

The objective of Jones matrix OCT is to obtain the tomographies of the round-trip phase retardation, diattenuation, relative optic-axis orientation, and backscattering intensity of a sample. To obtain these polarization parameters, Jones matrix OCT first determines the Jones matrix or its similar matrix at each location in the sample. Since a matrix and its similar matrix have the same eigenvalues, the phase retardation, namely, the phase difference between two eigenvalues, and the diattenuation, namely, the contrast of the squared power of the eigenvalues, are determined from the similar matrix. The axis orientation is determined as the directions of the eigenvectors of the round-trip Jones matrix of the sample. Since a matrix and its similar matrix do not always possess the same eigenvectors, the absolute axis orientation is not obtained from the similar matrix. However, Jones matrix OCT still provides a relative axis orientation from the similar matrix. The backscattering tomography can be obtained by several means from the Jones matrix as described later in this chapter.

35.2.1 Basic Principle of Jones Matrix Measurement

Although various implementations of the Jones matrix OCT exist, almost all of them share a similar concept. Namely, Jones matrix OCT determines a Jones matrix by measuring Jones vectors of two backscattered probe beams $\vec{E}_{out}^{(1)}(x,y,z)$ and $\vec{E}_{out}^{(2)}(x,y,z)$, which correspond to two different incident polarization states, $\vec{E}_{in}^{(1)}$ and $\vec{E}_{in}^{(2)}$, where x, y is the transversal position and z is the position in depth. The Jones vectors of $\vec{E}_{out}^{(1)}(x,y,z)$ and $\vec{E}_{out}^{(2)}(x,y,z)$ are measured by a polarization-diversity OCT detection scheme, by which two OCT images of two orthogonal polarization components, typically the horizontal and vertical components, are obtained. One of the OCTs represents the first entry of the Jones vector, and the other represents the second entry. The details of the polarization-diversity detection are described in Sect. 35.3.2. Owing to the three-dimensional resolution of OCT, $\vec{E}_{out}^{(1)}(x,y,z)$ and $\vec{E}_{out}^{(2)}(x,y,z)$ are spatially resolved, that is, they are functions of space, while the incident polarization states $\vec{E}_{in}^{(1)}$ and $\vec{E}_{in}^{(2)}$ are constants.

By denoting a Jones matrix of interest as $\mathbf{J}(x, y, z)$, the Jones vectors of incident and backscattered light are associated as

$$\begin{cases} \vec{E}_{out}^{(1)}(x,y,z) &= \mathbf{J}(x,y,z)\vec{E}_{in}^{(1)} \\ \vec{E}_{out}^{(2)}(x,y,z) &= \mathbf{J}(x,y,z)\vec{E}_{in}^{(2)} \end{cases}. \tag{35.1}$$

This set of equations corresponds to two measurements of OCT with different incident polarization states. By calculating $\vec{E}_{out}^{(1)}(x,y,z)\,[1 \quad 0\,] + \vec{E}_{out}^{(2)}(x,y,z)\,[0 \quad 1\,]$, these two equations are unified as

$$\mathbf{E}_{out}(x,y,z) = \mathbf{J}(x,y,z)\mathbf{E}_{in} \tag{35.2}$$

where $\mathbf{E}_{out}(x, y, z)$ and $\mathbf{E}_{in}$ are the Jones vector matrices of $\mathbf{E}_{out}(x,y,z) \equiv \left[\vec{E}^{(1)}_{out}(x,y,z) \quad \vec{E}^{(2)}_{out}(x,y,z)\right]$ and $\mathbf{E}_{in} \equiv \left[\vec{E}^{(1)}_{in} \quad \vec{E}^{(2)}_{in}\right]$. By using Eq. 35.2, the spatially resolved Jones matrix, i.e., Jones matrix tomography, is obtained from the measured Jones vectors matrix $\mathbf{E}_{out}(x, y, z)$ and predefined Jones vectors matrix $\mathbf{E}_{in}$ as

$$\mathbf{J}(x,y,z) = \mathbf{E}_{out}(x,y,z)\mathbf{E}_{in}^{-1} \ . \tag{35.3}$$

Since this equation contains the inverse matrix of $\mathbf{E}_{in}$, $\mathbf{E}_{in}$ should be a non-singular matrix. In other words, the two incident light beams should not be parallel, namely, $\vec{E}^{(1)}_{in} \neq \zeta \vec{E}^{(2)}_{in}$, where ζ is an arbitrary complex constant.

As represented by Eq. 35.3, the basic principle of Jones matrix OCT is very simple. However, there are still fundamental issues such as the effect of birefringence of the OCT system and the determination of $\mathbf{E}_{in}$. The following section describes an extended principle of Jones matrix OCT by which the system birefringence is canceled. In addition, the extended principle enables a determination of $\mathbf{J}(x, y, z)$ without any knowledge of $\mathbf{E}_{in}$.

35.2.2 Extended Principle of Jones Matrix Optical Coherence Tomography

The Jones vectors of incident and backscattered light in the previous section had been defined at just before and after the sample. However, in general, the optical components utilized in OCT have specific polarization properties. In particular, optical fiber, which is commonly utilized in an OCT interferometer, has birefringence, and this fiber birefringence is altered by several factors including mechanical stress and temperature. Hence, especially with single-mode fiber-based Jones matrix OCT, it is rarely possible to determine the Jones vector of the real incident light to the sample and also to measure the Jones vector of the backscattered light.

To first mathematically describe this issue and then provide its solution, we introduce a modified model of the Jones matrix measurement. Figure 35.1 shows a simplified schematic Jones matrix measurement by Jones matrix OCT. $\mathbf{J}_{in}$ and $\mathbf{J}_{out}$ represent Jones matrices of illumination and collection optics that may include the optical fiber, and $\mathbf{J}_s(x, y, z)$ is a single-trip Jones matrix of a sample. Note that, in this scheme, $\vec{E}^{(1)}_{in}$, $\vec{E}^{(2)}_{in}$ and $\vec{E}^{(1)}_{out}(x,y,z)$, $\vec{E}^{(2)}_{out}(x,y,z)$ are the Jones vectors of the light incident to and output from the system, respectively, not to and from the sample. The incident point can be arbitrarily defined and does not affect the final measurement results except for axis orientation as discussed later in this section. The output polarization is typically defined as that at a detection unit.

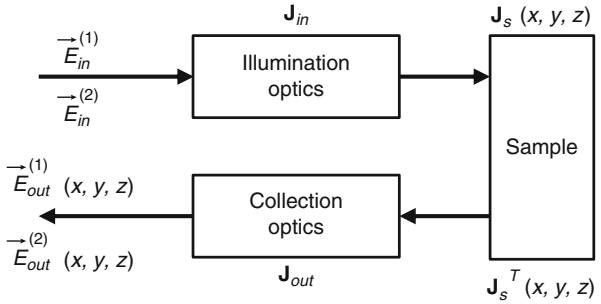

Fig. 35.1 A conceptual scheme of polarization properties of Jones matrix OCT. $\vec{E}_{in}^{(1)}$ and $\vec{E}_{in}^{(2)}$ are the Jones vectors of the incident light to the OCT system, $\vec{E}_{out}^{(1)}$ and $\vec{E}_{out}^{(2)}$ are the those of output light from the system, $\mathbf{J}_{in}$ and $\mathbf{J}_{out}$ are Jones matrices of illumination and detection optics, and $\mathbf{J}_s$ is a single-trip Jones matrix of the sample

In this scheme, the entire Jones matrix of the system and the sample becomes

$$\mathbf{J}_{all}(x, y, z) = \mathbf{J}_{out}\,\mathbf{J}_s^T(x, y, z)\mathbf{J}_s(x, y, z)\mathbf{J}_{in} \tag{35.4}$$

where $\mathbf{J}_s^T\,\mathbf{J}_s$ is a round-trip Jones matrix of the sample [32]. According to the similar discussion with Sect. 35.2.1, $\mathbf{J}_{all}, \mathbf{E}_{in} \equiv \left[\vec{E}_{in}^{(1)} \quad \vec{E}_{in}^{(2)}\right]$ and $\mathbf{E}_{out} \equiv \left[\vec{E}_{out}^{(1)} \quad \vec{E}_{out}^{(2)}\right]$ are associated as

$$\mathbf{J}_{all}(x, y, z) = \mathbf{E}_{out}(x, y, z)\mathbf{E}_{in}^{-1}. \tag{35.5}$$

Note that the output Jones vector matrix $\mathbf{E}_{out}(x, y, z)$ can be measured and the incident polarization state $\mathbf{E}_{in}$ is arbitrarily selected.

The objective of the Jones matrix OCT measurement is to determine the phase retardation, diattenuation, and optic-axis orientation of the round-trip Jones matrix of the sample $\mathbf{J}_s^T(x, y, z)\ \mathbf{J}_s\ (x, y, z)$. For this purpose, $\mathbf{J}_s^T(x, y, z)\ \mathbf{J}_s\ (x, y, z)$ or its similar matrix should be obtained. This similar matrix at a position of (x, y, z) can be obtained by using $\mathbf{J}_{all}\ (x, y, z)$ and $\mathbf{J}_{all}\ (x, y, z_{surf})$ where z_{surf} is the position of the surface of the sample [33]. According to Eq. 35.4, the product of $\mathbf{J}_{all}\ (x, y, z)$ and the inverse of $\mathbf{J}_{all}\ (x, y, z_{surf})$ is expressed as

$$\mathbf{J}_{all}(z)\mathbf{J}_{all}\left(z_{surf}\right)^{-1} = \mathbf{J}_{out}\,\mathbf{J}_s^T(z)\mathbf{J}_s(z)\mathbf{J}_{in}\,\mathbf{J}_{in}^{-1}\mathbf{J}_s^T\left(z_{surf}\right)^{-1}\mathbf{J}_s\left(z_{surf}\right)\mathbf{J}_{out}^{-1} \tag{35.6}$$

where the variables of x and y are omitted for simplicity. By using the fact that $\mathbf{J}_s\ (z_{surf})$ is a unit matrix, Eq. 35.6 is simplified to be

$$\mathbf{J}_{all}(z)\mathbf{J}_{all}\left(z_{surf}\right)^{-1} = \mathbf{J}_{out}\,\mathbf{J}_s^T(z)\mathbf{J}_s(z)\mathbf{J}_{out}^{-1}. \tag{35.7}$$

On the other hand, by using the relationship of Eq. 35.5, the same product of $\mathbf{J}_{all}(z)\mathbf{J}_{all}(z_{surf})^{-1}$ is also expressed as

$$\begin{aligned}\mathbf{J}_{all}(z)\mathbf{J}_{all}\left(z_{surf}\right)^{-1} &= \mathbf{E}_{out}(z)\mathbf{E}_{in}^{-1}\mathbf{E}_{in}\mathbf{E}_{out}^{-1}\left(z_{surf}\right) \\ &= \mathbf{E}_{out}(z)\mathbf{E}_{out}{}^{-1}\left(z_{surf}\right).\end{aligned} \tag{35.8}$$

By combining Eqs. 35.7 and 35.8, the key equation of Jones matrix OCT

$$\mathbf{J}_{out}\,\mathbf{J}_{s}^{T}(z)\mathbf{J}_{s}(z)\mathbf{J}_{out}^{-1} = \mathbf{E}_{out}(z)\mathbf{E}_{out}^{-1}\left(z_{surf}\right) \tag{35.9}$$

is obtained. The left-hand side is a similar matrix of the round-trip Jones matrix of the sample, while the right-hand side consists of only measurable values.

In general, a matrix and its similar matrix possess the same eigenvalues. Therefore, the eigenvalues of the matrix obtained by Eq. 35.9 provide the round-trip phase retardation and the diattenuation of the sample. It is also noteworthy that this equation does not consist of $\mathbf{E}_{in}$. It indicates the selection of two polarization states of the two incident light beams $\vec{E}_{in}^{(1)}$ and $\vec{E}_{in}^{(2)}$ is arbitrary as far as $\mathbf{E}_{in}$ is a non-singular matrix (see also Sect. 35.2.1).

35.2.3 Phase Retardation, Diattenuation, and Relative Optic-Axis Orientation

After determining the similar matrix of the round-trip Jones matrix by using Eq. 35.9, its eigenvalues and eigenvectors are obtained through one of the general numerical eigenvalue algorithms, for instance, which are described in Ref. 33. Such eigenvalue algorithms [35] are frequently available in standard programming libraries/languages for numerical computation, such as LAPACK (for Fortran 90 and C), MATLAB, and LabVIEW. The eigenvalues can also be obtained by the following equation

$$\lambda_{1,2} = \frac{T}{2} \pm \sqrt{\frac{T^2}{4} - D} \tag{35.10}$$

where T and D are the trace and the determinant of the similar matrix, respectively.

The phase retardation, diattenuation, and relative optic-axis orientation are then determined by these eigenvalues and eigenvectors as described in the following subsections.

35.2.3.1 Phase Retardation

The phase retardation δ is determined by the phase difference between two eigenvalues as

$$\delta \equiv \mathrm{Arg}[\lambda_1/\lambda_2] = \arctan\left[\frac{\mathrm{Im}(\lambda_1/\lambda_2)}{\mathrm{Re}(\lambda_1/\lambda_2)}\right]. \tag{35.11}$$

Although it is omitted for simplicity, δ, λ_1, and λ_2 are the functions of (x, y, z), such that a tomography of double-path phase retardation is obtained. In addition, the phase retardation measured at a particular position in the sample is affected by its anterior tissue. Thus, this phase retardation is a cumulative double-path phase retardation from the surface of the sample to the depth position being measured.

It should be noted that the selection of λ_1 and λ_2 from the two numerically obtained eigenvalues is arbitrary; the phase-retardation value has an ambiguity of π rad. For practical Jones matrix OCT, the phase retardation is aliased into a 0 to π rad range as

$$\delta' \equiv \begin{cases} \delta & : \quad 0 \le \delta < \pi \\ 2\pi - \delta & : \quad \pi \le \delta < 2\pi. \end{cases} \tag{35.12}$$

where δ' is the aliased double-path phase retardation.

35.2.3.2 Diattenuation

The diattenuation d is defined as the contrast of the amplitudes of the eigenvectors as

$$d \equiv \frac{\left||\lambda_1|^2 - |\lambda_2|^2\right|}{|\lambda_1|^2 + |\lambda_2|^2}. \tag{35.13}$$

Since λ_1 and λ_2 are the functions of (x, y, z), d is also a function of (x, y, z) and represents the tomography of diattenuation.

35.2.3.3 Relative Optic-Axis Orientation

The relative optic-axis orientation is defined as the direction of an eigenvector, which is a Jones vector of a characteristic polarization state of the similar matrix, on the equatorial plane of the Poincaré sphere. It should be noted that this eigenvector is not an eigenvector of the round-trip Jones matrix of the sample but that of the similar matrix. Hence, the optic-axis orientation obtained by this method is not identical to that of the sample but only a relative axis orientation.

Although this relative axis orientation is not a direct property of the sample, it would provide useful information to the extent that $\mathbf{J}_{out}$ is constant. In addition, a calibration technique of Jones matrix OCT that enables the absolute optic-axis orientation has recently been presented [36].

35.2.3.4 Degree of Polarization Uniformity

In addition to the abovementioned fundamental polarization properties, Jones matrix tomography can also be utilized to obtain the secondary polarization property of the sample, the so-called degree of polarization uniformity (DOPU) [37, 38]. DOPU measurement by PS-OCT was independently proposed by

Lee et al. [37] and Götzinger et al. [38]. DOPU is known to be associated with melanin concentration in the sample [39] and has been utilized for the segmentation of the retinal pigment epithelium [38].

DOPU is defined by spatially averaged Stokes parameters of the backscattered probe beam as

$$\mathrm{DOPU} = \sqrt{\overline{Q}^2 + \overline{U}^2 + \overline{V}^2} \tag{35.14}$$

where $\overline{Q}$, $\overline{U}$, and $\overline{V}$ are the normalized Stokes parameters defined as

$$\left(\overline{Q}, \overline{U}, \overline{V}\right) = \left(\sum_i \frac{Q_i}{I_i}, \sum_i \frac{U_i}{I_i}, \sum_i \frac{V_i}{I_i}\right). \tag{35.15}$$

$[I_i\ Q_i\ U_i\ V_i]^T$ is a Stokes vector of the ith pixel in a spatial kernel of the averaging. Since OCT is a coherence imaging modality, it is not possible to measure the degree of polarization [30]. However, DOPU is regarded as a spatial analogy of the degree of polarization.

Although DOPU is defined from the Stokes parameters, Jones matrix OCT can also provide DOPU from the Jones matrix by assuming a virtual incident beam and its resulting virtual output Stokes vector. For example, by assuming the incident polarization state of $[1\ 0]^T$, the virtual Stokes parameters are defined as

$$\begin{bmatrix} I \\ Q \\ U \\ V \end{bmatrix} \equiv \begin{bmatrix} |J_{11}|^2 + |J_{12}|^2 \\ |J_{11}|^2 - |J_{12}|^2 \\ J_{11}J_{12}^* + J_{11}^* J_{12} \\ i\left(J_{11}J_{12}^* - J_{11}^* J_{12}\right) \end{bmatrix} \tag{35.16}$$

where J_{11} and J_{12} are the upper-left and lower-left entries of the similar matrix $\mathbf{J}_{all}(z)\mathbf{J}_{all}(z_{surf})^{-1} = \mathbf{E}_{out}(z)\mathbf{E}_{out}^{-1}(z_{surf})$.

The DOPU is also directly calculated from $\mathbf{E}_{out}(z)$ by substituting $J_{11} = E_{out,11}$ and $J_{12} = E_{out,12}$ into Eq. 35.16, where $E_{out,11}$ and $E_{out,12}$ are the upper-left and lower-left entries of the Jones vector matrix $\mathbf{E}_{out}(z)$, respectively. Note that, in this case, the assumed virtual incident polarization state is $\mathbf{E}_{out}\left(z_{surf}\right)[1 \quad 0]^T$.

35.3 Implementation Theory

As we discussed in Sect. 35.2, Jones matrix OCT relies on two incident polarization states and Jones vector measurement of the backscattered beam. The former is realized by one of the polarization multiplexing mechanisms, and the latter is typically realized by a polarization-diversity detection scheme. This section is dedicated to providing a brief review of these methods.

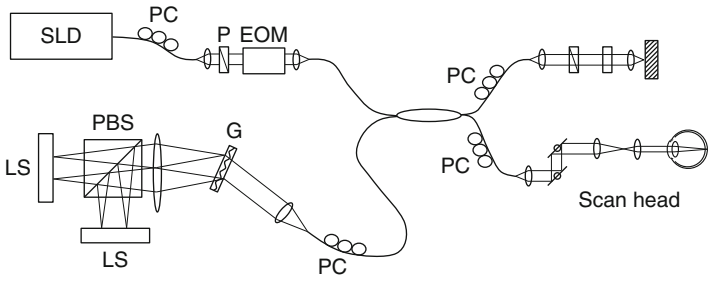

Fig. 35.2 Example of the optical scheme for polarization modulation along the transversal scan. *SLD* is a superluminescent diode light source, *PCs* are polarization controllers, *LPs* are linear polarizers, *ND* is neutral density filter, and *EOM* is an electro-optic modulator. This modulation scheme is particularly suitable for the SD-OCT scheme, and this example is equipped with a polarization-diversity spectrometer consisting of a grating (*G*), a polarization beam splitter (*PBS*), and two line scan CCD cameras

35.3.1 Multiplexing of Incident Polarization States

As is evident from Eq. 35.1, Jones matrix OCT relies on two incident polarization states. These two polarization states are multiplexed by several means in Jones matrix OCT measurement including time-division multiplexing [33], polarization modulation along the transversal scan (mainly for spectral domain (SD-)OCT) [40] or along the wavelength scan (only for swept-source (SS-)OCT) [41], frequency shifting [42], and time delay-based multiplexing [43, 44].

35.3.1.1 Time-Division Multiplexing

In the time-division multiplexing scheme, two polarization states of the incident beam are sequentially switched for A-line by A-line [33]. This method is the most straightforward implementation of incident polarization multiplexing.

35.3.1.2 Polarization Modulation Along the Transverse Scan

In this multiplexing scheme, the phase of a polarization component of incident light is modulated by a sinusoidal function along the transversal scanning direction. By this modulation, two incident beams with two polarization states are multiplexed such that one is modulated in phase and the other is not. After OCT detection, these two multiplexed components are demultiplexed by spatial frequency filtering based on a numerical Fourier transform along the transversal direction [40].

The modulation is typically performed by an electro-optic (EO) modulator as shown in Fig. 35.2. The EO modulator is configured to modulate the relative phase of the polarization component of a probe beam that oriented to one of the axes of the modulator (so denoted as EO-modulation axis) in respect to the phase of the OCT reference beam, while the relative phase of the polarization component oriented to the other EO axis (EO-non-modulation axis) is not modulated. The frequency of the modulation is defined in respect to the A-line frequency of the OCT detection so that it is several fractions of the A-line frequency. An example of the modulation

frequency was 9.23 kHz, which is one-third of the A-line frequency of 27.7 kHz [40]. Consequently, the modulation frequency of this method is around ten few kHz.

With the phase modulation depth of 2.405 rad, the theoretical modulation efficiency in the EO-modulation axis, which is the ratio of the total optical power of the modulated beam including those of high-order harmonics over non-modulated optical power in the EO-modulation axis, is 100 %. Under this condition, the polarization states of the non-modulated incident beam, which would be $\vec{E}_{in}^{(1)}$, and the modulated incident beam $\vec{E}_{in}^{(2)}$ are orthogonal to each other, and the maximum robustness of phase-retardation measurement is obtained [45].

Because of several kinds of turbulences, such as temperature drift, and imperfection of the EO modulator, the accurate modulation depth of 2.405 rad is hard to achieve in practice. Under non-ideal modulation conditions, $\vec{E}_{in}^{(1)}$ and $\vec{E}_{in}^{(2)}$ are no longer orthogonal to each other. However, it is noteworthy that the extended principle of Jones matrix OCT also holds its validity for this non-ideal case because it does not rely on the orthogonality of the incident polarization states.

35.3.1.3 Polarization Modulation Along the Wavelength Scan

This scheme is a variation of the abovementioned polarization modulation method and is specifically applicable to SS-OCT. The phase modulation is performed by an EO modulator with a similar optical scheme to that in Fig. 35.2 but along the wavelength scan. Similar to the modulation along the transversal scan, the two incident polarization states are demultiplexed by frequency filtering but based on a numerical Fourier transform along the wavelength scan [41].

This scheme requires a typical modulation frequency of one-third or slightly less than half of the sampling frequency of wavelength sampling. A typical modulation frequency is 33.3 MHz [41] or 40 MHz [46] for a sampling frequency of 100 MHz. Therefore, the modulation frequency of this scheme is around a few 10 MHz and is higher than that of modulation along the transversal scan by a magnitude greater than 1,000. This high-frequency operation requires a resonant EO modulator [41] or a wave guide-based miniature EO modulator [7]. These EO modulators could be a potential limitation of the implementation of this method. On the other hand, similar to the transversal modulation scheme, the incident polarization states are not necessarily orthogonal. This fact relaxes the requirement for the implementation.

An advantage of this method over the transversal modulation is that $\vec{E}_{in}^{(1)}$ and $\vec{E}_{in}^{(2)}$ are simultaneously obtained at exactly the same location in the sample. In the transversal modulation scheme, the probe locations on the sample corresponding to the two incident polarizations are slightly displaced to each other because the EO modulator alters the incident polarization state for each A-line. This small displacement results in a structural decorrelation between two OCT signals associated with the two incident polarization states, and it finally degrades the sensitivity of the Jones matrix measurement. This issue raises an additional requirement of the transversal modulation scheme, i.e., the A-lines should be dense enough in space so that the separation between adjacent A-lines is less than a fraction of the transversal optical resolution. The wide-range and high-speed measurements are in contradiction to each other with the transversal modulation scheme.

On the other hand, in the wavelength scan-oriented modulation scheme, the OCT signals associated with two incident polarization states are obtained at exactly the same time and location. Hence, the structural decorrelation does not occur. This property makes the wavelength-oriented modulation scheme suitable for high-speed wide-range measurements.

35.3.1.4 Shifting Frequency-Based Multiplexing

This scheme is for SS-OCT and has recently been demonstrated by Kim et al. [42]. In this scheme, the frequencies of the two incident beams with orthogonal polarization states are frequency shifted by two frequency shifter with different shifting frequency (20 MHz and 40 MHz). Namely, two incident polarization states are multiplexed in its frequency. This multiplexed incident beams would have different carrier frequency after interference with a reference beam, and these beams are demultiplexed by numerical Fourier transform.

To avoid unwanted interference, this scheme is equipped with an unpolarizer, which is a polarization-dependent delay unit generating a path length difference more than the instantaneous coherence length of the light source between the two polarization states.

35.3.1.5 Delay-Based Incident Polarization Multiplexing

If the coherence length of a light source in SS-OCT or the spectral resolution of a spectrometer in SD-OCT is high and hence the depth measurement range of the OCT is sufficiently long, the two incident polarizations can also be multiplexed at two different depths.

This polarization-dependent spectral delay can be implemented, for example, by two PBSs and two Dove prisms as depicted in Fig. 35.3a [43] or by the combination of a PBS and two quarter-wavelength plates (QWPs) as depicted in Fig. 35.3b [44]. Since the OCT images associated with two incident polarization states appear at different depths as depicted in Fig. 35.3c, it can be easily demultiplexed by cropping specific portions of the OCT images.

The relatively low extinction ratio of the reflection beam of PBS and the wavelength dependency of QWP would degrade the orthogonality of two incident polarization states. However, this issue is negligible because of a reason similar to that with the polarization modulation-based multiplexing methods, i.e., the orthogonality of the two incident polarization states is not required.

Since this scheme does not require any active optical components, such as an EO modulator, it is stable, and the sequential control of this type of Jones matrix OCT would be simpler than of those using polarization modulation schemes.

35.3.2 OCT-Based Jones Vector Detection

In Jones matrix OCT, the Jones vector of the backscattered probe beam after the collection optics, i.e., $\vec{E}_{out}^{(1)}$ and $\vec{E}_{out}^{(2)}$ of Fig. 35.1, is measured by a polarization-diversity detection unit. In the polarization-diversity detection unit, two orthogonal

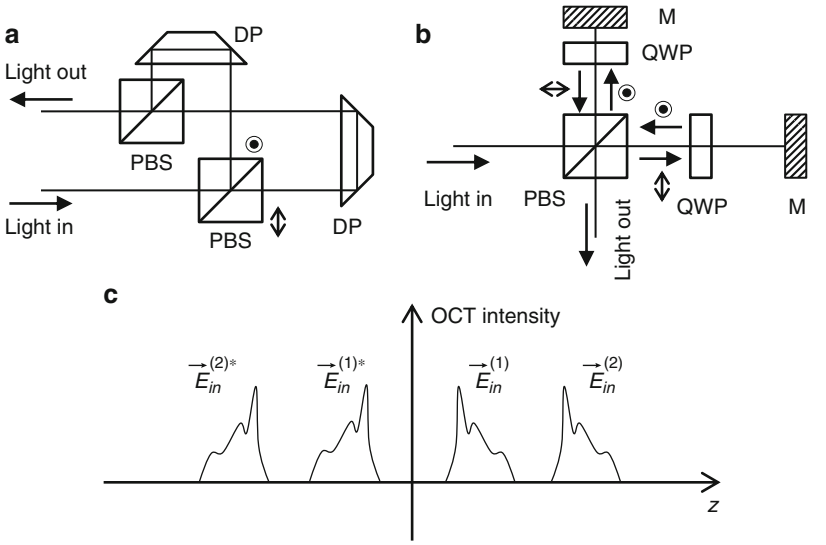

Fig. 35.3 (**a**, **b**) The optical schemes for delay-based input polarization multiplexing. *PBSs* are polarizing beam splitters, *DPs* are Dove prisms, *QWPs* are quarter-wavelength plates, and Ms are flat mirrors. (**c**) A schematic figure of demultiplexing two incident polarization components. The OCT images associated with two incident polarization states appear at different depths

polarization components, typically horizontal and vertical, of the probe and reference beams are split by a PBS or a Wollaston prism and detected by two detectors, except for some sophisticated polarization-diversity detection units that use a single detector. In this section, some examples of polarization-diversity detection units and the principle of OCT-based Jones vector measurement are presented.

35.3.2.1 Implementation Examples of Polarization-Diversity Detection Unit

A polarization-diversity spectrometer is a detection unit specifically utilized for SD-OCT. Although there are some variations, all of them split two orthogonal polarization components after combining the reference and probe beams in an interferometer.

Figure 35.4a is a straightforward implementation of a polarization-diversity spectrometer, which was originally developed for a Hee-Hitzenberger-type PS-OCT [23]. In this scheme, the probe and reference beams are combined in an OCT interferometer and then introduced into the polarization-diversity spectrometer unit. In this spectrometer unit, the horizontal and vertical polarization components of the beams are split by a fiber PBS and detected by two independent spectrometers. This polarization-diversity spectrometer is a straightforward implementation and is hence easy to design. On the other hand, it requires two whole spectrometers and thus results in double the implementation cost. In addition, it is sometimes difficult to obtain a fiber PBS with sufficient quality for some wavelength bands.

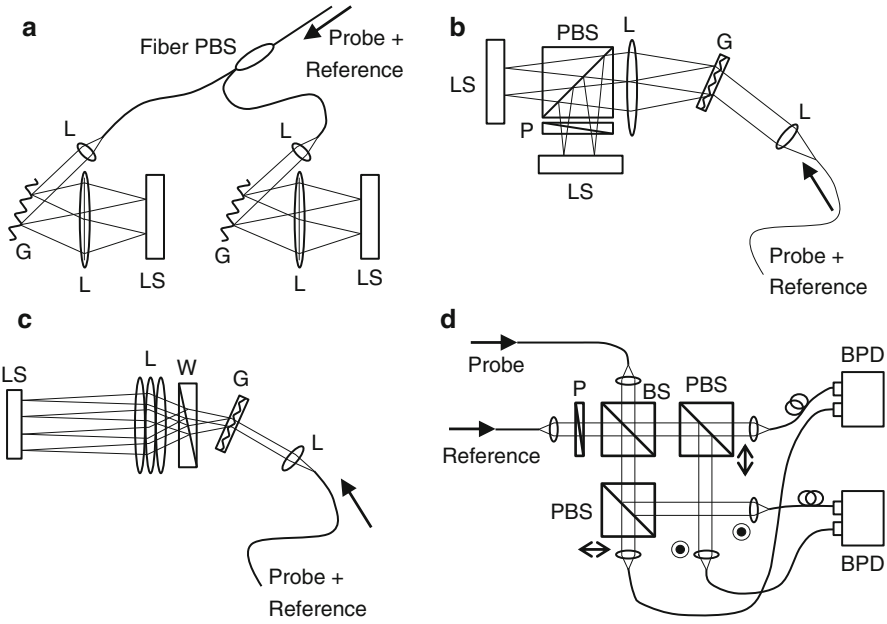

Fig. 35.4 Examples of polarization-diversity spectrometers (**a**–**c**) and polarization-diversity balanced detection unit (**d**). *L* lenses, *G* grating, *LS* line sensors grating, *PBS* polarizing beam splitter, *P* polarizer, *W* Wollaston prism, *BS* non-polarizing beam splitter, and *BPD* balanced photodetector

Figure 35.4b is a polarization-diversity spectrometer using only one diffraction grating [26, 40]. The vertical and horizontal polarization components are resolved into its spectral components by a single diffraction grating and then split into two polarization components by a PBS. Two polarization components are then detected by two line sensors.

The purity of polarization of a reflected beam by PBS is relatively low. To improve the purity and the accuracy of Jones vector measurement, a polarizer after reflection, a so-called cleanup polarizer, can be utilized. However, as discussed in Sect. 35.5.2, this relatively low purity of polarization and its resulting polarization cross talk would have no significant effect on the final result. As a result, the cleanup polarizer is optional.

This PS spectrometer is relatively easy to design, but it sometimes requires a large PBS to cover the whole area of the line sensors.

Figure 35.4c shows one of the sophisticated designs of polarization-diversity spectrometer using only one line sensor that was originally developed for Stokes parameter-based PS-OCT [27] and Hee-Hitzenberger method [47]. In this scheme, two polarization components are displaced relative to each other by a Wollaston prism, and two spectra corresponding to the two polarization components illuminate different areas of a single line sensor. This scheme requires fewer optical

components than the other schemes and can be compact. On the other hand, it requires more careful optical design to suppress aberrations to in turn obtain high spectral resolutions for both of the polarization components.

Figure 35.4d shows a balanced polarization-diversity detection unit for SS-OCT [41, 48]. The probe and reference beams are introduced into this detection unit through two independent fiber ports. Two beams are combined by a non-polarized beam splitter (BS) and then decomposed into its polarization components by two PBSs. Each of polarization components is then detected by two balanced photodetectors. Similar to the configuration shown in Fig. 35.4b, the purity of the polarization can be improved using cleanup polarizers, although this is optional. The polarizer at the input port of the reference beam is to balance the optical powers of the reference beam between two detection channels.

35.3.2.2 Principle of OCT-Based Jones Vector Measurement

To determine the Jones vector of the backscattered probe beam, the amplitudes and the relative phase of the electric fields of the horizontal and vertical polarization components should be measured. In Jones matrix OCT, this complex measurement is achieved by using an interferometric detection scheme through the polarization-diversity detection unit.

By annotating the Jones vectors of the backscattered probe beam and the reference beam at the polarization-diversity detection unit as $\vec{E}_{out}$ and $\vec{E}_{ref}$, the interference signal becomes

$$\left\|\vec{E}_{out}+\vec{E}_{ref}\right\|^2=\left\|\vec{E}_{out}\right\|^2+\left\|\vec{E}_{ref}\right\|^2+\vec{E}_{out}\circ\vec{E}^*_{ref}+\vec{E}^*_{out}\circ\vec{E}_{ref} \tag{35.17}$$

where $\|\|^2$ and $\circ$ denote the absolute-square and multiplication operations for each entry of the vector, respectively. The polarization-diversity OCT signal corresponds to the third term of the right-hand side of this equation:

$$\vec{E}_{out}\circ\vec{E}^*_{ref}=\begin{bmatrix}E^{(H)}_{out}E^{(H)^*}_{ref}\\E^{(V)}_{out}E^{(V)^*}_{ref}\end{bmatrix} \tag{35.18}$$

where the superscripts of (H) and (V) denote the horizontal and vertical components of the Jones vectors, respectively. The horizontal and vertical components of Eq. 35.17 are detected by two detectors, and the component described by Eq. 35.18 is selected through OCT image reconstruction. By configuring the optical setup to $E^{(H)}_{ref}=E^{(V)}_{ref}$, i.e., make the reference beam linear with 45° polarization, the polarization-diversity OCT signal becomes

$$\vec{E}_{out}\circ\vec{E}^*_{ref}\propto\begin{bmatrix}E^{(H)}_{out}\\E^{(V)}_{out}\end{bmatrix} \tag{35.19}$$

and the Jones vector of the backscattered probe beam is given.

In a practical optical setup, it is hard to accurately achieve the abovementioned condition of $E_{ref}^{(H)} = E_{ref}^{(V)}$. However, this condition is not required in practice as will be discussed in Sect. 35.5.1.

35.4 Implementation Examples

35.4.1 Schematics

To conclude the presentation of the principle and implementation of Jones matrix OCT, an example of one of the Jones matrix OCT systems is described in this section. The system is a swept-source Jones matrix OCT using the delay-based polarization multiplexing unit, which is similar to the systems described by Lim et al. [43] and Baumann et al. [44].

The schematic of the Jones matrix OCT is depicted in Fig. 35.5. The light source is a wavelength-scanning laser with a center wavelength of 1.06 μm, a scan range of 120 nm, and a −3-dB bandwidth of 100 nm (AXSUN Technologies Inc., NJ, USA). The scanning frequency of the light source is 100 kHz, and it results in an A-line rate of the Jones matrix OCT of 100,000 A-lines/s. The probe arm consists of a delay-based polarization multiplexer. This multiplexer gives a different delay to $\vec{E}_{in}^{(1)}$ and $\vec{E}_{in}^{(2)}$, so OCT signals corresponding to these incident polarization states

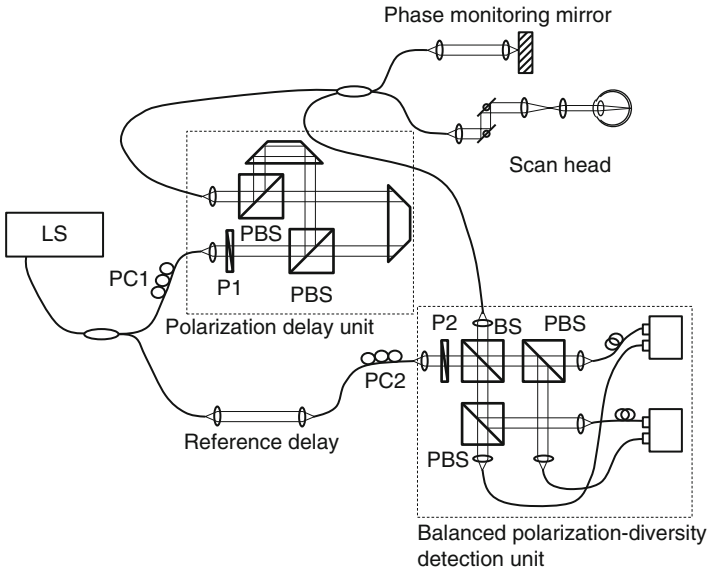

Fig. 35.5 Example of an optical scheme of Jones matrix OCT, which is based on a delay-based polarization multiplexer and a balanced polarization-diversity detection unit. *PC* polarization controller, *P* polarizer, and *PBS* polarizing beam splitter, *BS* non-polarizing beam splitter

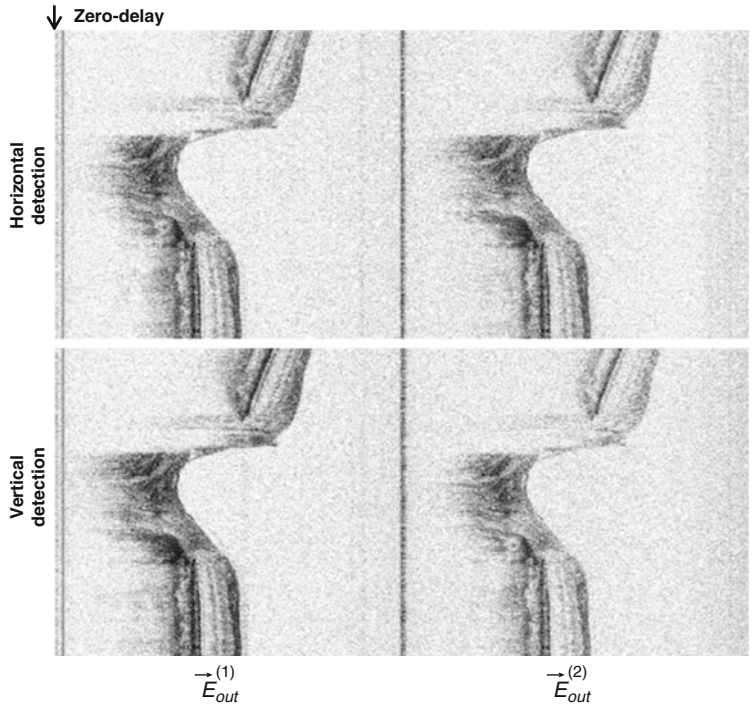

Fig. 35.6 Raw OCT images measured by the PD detection unit. The *upper image* is of horizontal detector, and the *lower image* is of vertical detector. Each image consists of two OCT images which correspond to the first and the second incident polarization states

appear at different depths in the OCT image. Since $\vec{E}_{in}^{(1)}$ and $\vec{E}_{in}^{(2)}$ signals appear at different depths, these two signals have different phase offsets. However, this difference in phase offset does not affect the Jones matrix measurement owing to the properties of Eqs. 35.8 and 35.9.

The OCT signals are detected by a balanced polarization-diversity detection unit that consists of a BS, two PBSs, and two InGaAs balanced photodetectors (350 MHz, PDB430C, Thorlabs Inc., NJ, USA).

The detected signals are digitized by a data acquisition board (DAQ, ATS9350, Alazar Tech, QC, Canada) with a sampling speed of 500 MHz after passing a high-pass filter (1.5 MHz Chebyshev) and a low-pass (250 MHz Chebyshev) filter.

Two of the spectra detected by two detection channels of the DAQ are resampled into the k-domain and Fourier transformed to obtain depth-resolved OCT signals. As shown in Fig. 35.6, each OCT image corresponding to each detection channel is composed of two OCT cross sections at two different depths that correspond to the two incident polarization states. Since each of the two detection channels provides two OCT signals, four OCT signals are acquired simultaneously. These four OCTs are the entries of the output Jones vector matrix $\mathbf{E}_{out}(x, y, z)$ discussed in Sect. 35.2.2.

In this particular implementation, the spectral sampling spacing after the rescaling was 0.402 cm^{-1}, and it results in a depth measurement range of 2.94 mm for a single incident polarization state. The depth resolution was 8.5 μm in air.

A phase monitoring mirror is utilized to stabilize the phase of the SS-OCT signal, which is particularly important to phase-sensitive OCT detection such as Doppler OCT [49, 50, 51].

The surface of the sample is segmented and $\mathbf{E}_{out}$ at the sample surface is obtained at each transversal position. This $\mathbf{E}_{out}$ is then averaged over x or (x, y) by complex Jones matrix averaging methods (described in Sect. 35.5.4) to have a single constant $\mathbf{E}_{out}(z_{surf})$. This $\mathbf{E}_{out}(z_{surf})$ is then utilized with Eqs. 35.9 to obtain a similar matrix to the round-trip Jones matrix of the sample. Finally, the methods described in Sect. 35.2.3 provide a phase-retardation image and a DOPU image.

The intensity OCT can be created by several means such as averaging squared intensities of the entries of the Jones matrix. In this particular example, the maximum intensity composite of all entries of the similar matrix is utilized as the intensity OCT.

35.4.2 Polarization Alignment

This Jones matrix OCT uses three polarization controllers (PCs) and two polarizers (POLs) that should be aligned properly.

POL1 and PC1 are used to balance the powers of the two incident polarization states. Since, in principle, the incident polarization states including its power and phase offset do not affect the polarization measurement as suggested by Eq. 35.8, the alignment of PC1 and POL1 fundamentally does not affect the Jones matrix measurement. However, under a constant amount of probe light power, equal signal-to-noise ratios (SNRs) of the OCT signals of the two polarization states would provide the robustness for phase-retardation measurement [45]. Hence, one possible optimal alignment of POL1 and PC1 is to have the same signal levels of two OCT signals associated with two incident polarization states that are obtained with a non-birefringent sample, such as a mirror. For this alignment, the OCT signals of each polarization states appearing at different depths are monitored; the orientation of POL1 is properly aligned to have an equal signal power to the two signals. Then, PC1 is aligned to have the maximum OCT signal strength, i.e., the maximum probe power. Once this alignment is done, realignment is not requires as far as the fiber birefringence between the light source and the delay-based polarization multiplexing unit is stable. Hence, frequent alignment is not required for POL1 and PC1.

POL2 and PC2 are to have optimal balance between the horizontal and vertical polarization components of the reference beam for the horizontal and vertical detection channels. POL2 is aligned to have the identical optical power to the transmitted and reflected light of PBS by monitoring the optical power with an optical power meter. PC2 is then aligned to optimize the reference power by which the sensitivity of OCT is maximized. The alignment of POL2 is associated with the condition of $E_{ref}^{(H)} = E_{ref}^{(V)}$, which was utilized to derive Eq. 35.19. In addition, as

will be discussed in Sect. 35.5.1, this condition is loosened for practical measurements (see Sect. 35.5.1), and hence, the required accuracy of this alignment is relatively low. The realignment of POL2 and PC2 is not required as far as the output power of the light source and the fiber birefringence of the source arm and the reference arm are stable.

PC3 is then aligned to have roughly equal OCT signals for two incident polarization states. PC3 only alters the birefringence of the collection path, $\mathbf{J}_{out}$, without harming its unitarity. As suggested by Eq. 35.9, $\mathbf{J}_{out}$ and hence PC3 have no fundamental influence to determine the polarization properties of the sample. However, when the noise property of phase-retardation measurements was taken into account, equally distributed OCT signals for two incident polarization states would provide high robustness for phase-retardation measurements [45]. The signal ratio between the two incident polarization states is not only affected by $\mathbf{J}_{out}$ but also by the birefringence of the optic media located before the sample, such as the cornea for retinal measurements, and the birefringence of the optic media varies among subjects. It is therefore recommended to realign PC3 for each measurement session.

35.4.3 In Vivo Measurement of the Posterior Eye

Examples of in vivo polarization-sensitive measurement of the human optic nerve head are shown in Fig. 35.7. The intensity image (Fig. 35.7a) is created as the maximum intensity composite of four entries of $\mathbf{E}_{out}$. The pore structure of a lamina cribrosa is visible at the deep region as indicated by an arrow.

Figure 35.7b is a tomography of double-path cumulative phase retardation. Rapid alteration of the phase retardation along the depth is observed at the myopic conus as indicated by a circle. This rapid alteration is an indicator of strong birefringence.

Figure 35.7c is a DOPU image, which was calculated from $\mathbf{E}_{out}$ by assuming the virtual incident beam of $\mathbf{E}_{out}\left(z_{surf}\right)\left[\begin{array}{cc}1 & 0\end{array}\right]^{T}$. Namely, the DOPU image is obtained only from the left two images of Fig. 35.6. In this image, moderately low DOPU value (yellow to green) is observed at the retinal pigment epithelium and lower part of the choroid. It would indicate the existence of melanin at these regions [39].

35.5 Advanced Issues

35.5.1 The Effect of Phase and Amplitude Unbalance of the Reference Beam

In the practical implementation of Jones OCT, it is sometimes hard to exactly balance the phase and amplitude of two reference beams for polarization-diversity detection. As indicated by Eq. 35.18, the unbalance between the reference beams will result in a failure to obtain accurate measurements of the Jones vector of the probe beam. And hence in the previous section, it had been assumed to be balanced as $E_{ref}^{(H)} = E_{ref}^{(V)}$.

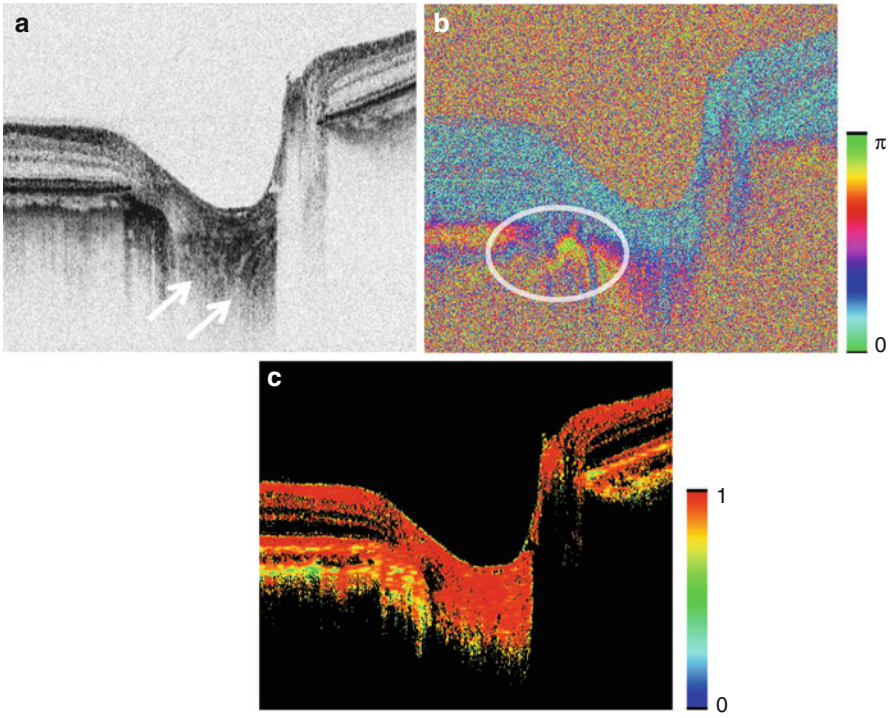

Fig. 35.7 Examples of tomography of an in vivo human optic nerve head. (**a**) Intensity images created as a maximum intensity composite of four elements of $\mathbf{E}_{out}$, (**b**) phase-retardation image, and (**c**) DOPU image

However, in practice, the extended principle of Jones matrix OCT, described in Sect. 35.2.2, provides correct polarization properties of the sample even without this condition of $E_{ref}^{(H)} = E_{ref}^{(V)}$. The detailed reason for this robustness is described below.

By using a complex constant $\eta \equiv E_{ref}^{(V)*}/E_{ref}^{(H)*}$, the measured Jones vector described by Eq. 35.18 becomes

$$\vec{E}_{out} \circ \vec{E}_{ref}^{*} = E_{ref}^{(H)^*} \begin{bmatrix} E_{out}^{(H)} \\ \eta E_{out}^{(V)} \end{bmatrix}. \tag{35.20}$$

The reference unbalanced Jones vector matrix obtained by this reference unbalanced measurement is

$$\mathbf{E}'_{out} = E_{ref}^{(H)^*} \begin{bmatrix} E_{out}^{(1)\,(H)} & E_{out}^{(2)\,(H)} \\ \eta E_{out}^{(1)\,(V)} & \eta E_{out}^{(2)\,(V)} \end{bmatrix} \tag{35.21}$$

where the superscripts of (35.1) and (35.2), respectively, indicate the first and second incident polarization states. By ignoring the global constant $E_{ref}^{(H)*}$ and by decomposing $\mathbf{E}'_{out}$ into a correct Jones vector matrix of the backscattered probe $\mathbf{E}_{out}$ and a matrix representing the reference unbalance $\boldsymbol{\eta}$, Eq. 35.21 becomes

$$\mathbf{E}'_{out} = \boldsymbol{\eta}\mathbf{E}_{out} \tag{35.22}$$

with

$$\begin{aligned} \boldsymbol{\eta} &= \begin{bmatrix} 1 & 0 \\ 0 & \eta \end{bmatrix} \\ \mathbf{E}_{out} &= \begin{bmatrix} E_{out}^{(1)(H)} & E_{out}^{(2)(H)} \\ E_{out}^{(1)(V)} & E_{out}^{(2)(V)} \end{bmatrix} = \begin{bmatrix} \vec{E}_{out}^{(1)} & \vec{E}_{out}^{(2)} \end{bmatrix}. \end{aligned} \tag{35.23}$$

This $\mathbf{E}'_{out}$ is a Jones vector matrix measured by a polarization-diversity detection unit with an unbalanced reference beam, while $\mathbf{E}_{out}$ is that measured with an accurately adjusted reference beam, which is identical to that of Sect. 35.2.2.

It should be recalled that since $\mathbf{E}_{out}$ and $\mathbf{E}'_{out}$ are obtained through OCT measurement, they are in practice the functions of space. By denoting $\mathbf{E}'_{out}(z)$ as a Jones vector matrix measured at a particular point of interest and $\mathbf{E}'_{out}(z_{surf})$ as measured at the surface of the sample, a similar calculation with Eq. 35.9 is defined as

$$\mathbf{E}'_{out}(z)\,\mathbf{E}'^{-1}_{out}(z_{surf}) = \boldsymbol{\eta}\mathbf{E}_{out}(z)\mathbf{E}^{-1}_{out}(z_{surf})\boldsymbol{\eta}^{-1} = \boldsymbol{\eta}\mathbf{J}_{out}\mathbf{J}_s^T(z)\mathbf{J}_s(z)\mathbf{J}^{-1}_{out}\boldsymbol{\eta}^{-1}. \tag{35.24}$$

As evidently shown in this equation, $\mathbf{E}'_{out}(z)\,\mathbf{E}'^{-1}_{out}(z_{surf})$ is a similar matrix of the round-trip Jones matrix of the sample. Hence, the principle described in Sect. 35.2.2 provides correct polarization properties of the sample by also using $\mathbf{E}'_{out}$ as an alternative to $\mathbf{E}_{out}$.

35.5.2 Polarization Cross Talk in the Polarization-Diversity Detection Unit

Some of the polarization-diversity detection units use PBS to split the horizontal and vertical polarization components. In general, the polarization purity of a reflection beam of PBS is low. This low purity would result in cross talk between two polarization detection channels.

One of the solutions to this issue is to use a cleanup polarizer as described in Sect. 35.3.2. However, a cleanup polarizer is only optionally required because of the intrinsic robustness of Jones matrix OCT to the polarization cross talk.

By using cross-talk coefficients of χ_1 and χ_2, the measured Jones vector matrix $\mathbf{E}''_{out}$ is expressed as

$$\mathbf{E}''_{out} = \begin{bmatrix} E^{(1)(H)}_{out} + \chi_1 E^{(1)(V)}_{out} & E^{(2)(H)}_{out} + \chi_1 E^{(2)(V)}_{out} \\ E^{(1)(V)}_{out} + \chi_2 E^{(1)(H)}_{out} & E^{(2)(V)}_{out} + \chi_2 E^{(2)(H)}_{out} \end{bmatrix}. \tag{35.25}$$

By considering that $\mathbf{E}''_{out}$ is actually a function of space and by using a matrix representation of the cross-talk coefficients of $\boldsymbol{\chi} = [\,1 \quad \chi_1;\, \chi_2 \quad 1\,]$, Eq. 35.25 is rewritten as

$$\mathbf{E}''_{out}(z) = \boldsymbol{\chi}\mathbf{E}_{out}(z) \tag{35.26}$$

where $\mathbf{E}_{out}(z)$ is an ideal Jones vector matrix of the backscattered probe beam identical to those in Sects. 35.2.2 and 35.5.1. By using $\mathbf{E}''_{out}(z)$ and $\mathbf{E}''_{out}(z_{surf})$, a similar calculation with Eq. 35.9 becomes

Evidently, $\mathbf{E}''_{out}(z)\,\mathbf{E}''^{-1}_{out}(z_{surf})$ is also a similar matrix to the round-trip Jones matrix of the sample $\mathbf{J}^T_s(z)\mathbf{J}_s$. Thus, the Jones matrix OCT method provides the correct polarization parameters of the sample even with the polarization cross talk of the polarization-diversity detection unit.

35.5.3 Unbalance in the OCT Signals of Two Incident Polarization States

The evenness of amplitudes and phases of OCT signals between two incident polarization states is corrupted for several reasons. For example, in a delay-based multiplexing scheme, depth-dependent signal decay and phase offset of OCT results in uneven amplitude and phase, respectively. Jones matrix OCT also has intrinsic robustness to this unevenness between OCTs of two incident polarization states.

By considering this unevenness, a measured Jones vector matrix becomes

$$\mathbf{E}'''_{out} = \begin{bmatrix} E^{(1)(H)}_{out} & \alpha E^{(2)(H)}_{out} \\ E^{(1)(V)}_{out} & \alpha E^{(2)(H)}_{out} \end{bmatrix} \tag{35.27}$$

where α is a complex constant representing the unauthorized difference in magnification of amplitude and the phase between OCTs of two incident polarization states. By using a matrix $\boldsymbol{\alpha} \equiv [\,1 \quad 0;\, 0 \quad \alpha\,]$ and an ideal Jones vector matrix of the backscattered probe beam $\mathbf{E}_{out}(z)$, $\mathbf{E}'''_{out}$ is decomposed as

$$\mathbf{E}'''_{out} = \mathbf{E}_{out}\boldsymbol{\alpha}. \tag{35.28}$$

By using $\mathbf{E}'''_{out}(z)$ and $\mathbf{E}'''_{out}(z_{surf})$, a similar calculation with Eq. 35.9 provides

$$\mathbf{E}'''_{out}(z)\mathbf{E}'''^{-1}_{out}(z_{surf}) = \mathbf{E}_{out}(z)\boldsymbol{\alpha}\boldsymbol{\alpha}^{-1}\mathbf{E}^{-1}_{out}(z_{surf}) = \mathbf{E}_{out}(z)\mathbf{E}^{-1}_{out}(z_{surf}). \tag{35.29}$$

As evidently seen in this equation, unevenness between OCTs of two incident polarization states is canceled and does not affect the final results.

By combining the discussions in Sects. 35.5.1 through 35.5.3, practically measured Jones matrix vector would be expressed as $\hat{\mathbf{E}}_{out}(z) = \boldsymbol{\chi}\boldsymbol{\eta}\mathbf{E}_{out}(z)\boldsymbol{\alpha}$, and Eq. 35.9 is altered to

$$\hat{\mathbf{E}}_{out}(z)\hat{\mathbf{E}}^{-1}_{out}(z_{surf}) = \boldsymbol{\chi}\boldsymbol{\eta}\mathbf{J}_{out}\mathbf{J}^{T}_{s}(z)\mathbf{J}_{s}(z)\mathbf{J}^{-1}_{out}\boldsymbol{\eta}^{-1}\boldsymbol{\chi}^{-1}. \tag{35.30}$$

This matrix is still similar to the round-trip Jones matrix of the sample. Hence, cross talk in a polarization-diversity detection unit, unbalance of the reference beams, and unevenness of OCTs of two incident polarization states do not affect the final result.

35.5.4 Jones Matrix/Jones Vector Matrix Averaging

Jones matrix OCT relies on the measured value of $\mathbf{E}_{out}(z_{surf})$. Since the error of phase-retardation measurement is severely affected by the SNR of $\mathbf{E}_{out}(z_{surf})$ [45], it would be good to enhance the SNR by averaging several $\mathbf{E}_{out}(z_{surf})$ obtained at several transversal positions. However, $\mathbf{E}_{out}(z_{surf})$ obtained at each transversal position have random global phase due to the interference among scatters in a coherence volume. So simple complex averaging of $\mathbf{E}_{out}(z_{surf})$ is not be utilized because it cancels not only the noise but also the OCT signal.

A solution for this issue is Jones matrix/Jones vector matrix averaging method [7]. In this matrix averaging method, at first, a relative global phase of two complex 2×2 matrices is conjectured as

$$\Delta\varphi^{(2,1)} \equiv \mathrm{Arg}\left[\sum_{i=1}^{2}\sum_{j=1}^{2}\frac{1}{\left|M^{(1)}_{i,j}\right|^{-1} + \left|M^{(2)}_{i,j}\right|^{-1}}\exp i\left(\varphi^{(2)}_{i,j} - \varphi^{(1)}_{\mathrm{i,j}}\right)\right] \tag{35.31}$$

where the complex matrices $\mathbf{M}^{(1)}$ and $\mathbf{M}^{(2)}$ are

$$\mathbf{M}^{(1),(2)} = \begin{bmatrix} \left|M^{(1),(2)}_{1,1}\right|\exp\left(i\varphi^{(1),(2)}_{1,1}\right) & \left|M^{(1),(2)}_{1,2}\right|\exp\left(i\varphi^{(1),(2)}_{1,2}\right) \\ \left|M^{(1),(2)}_{2,1}\right|\exp\left(i\varphi^{(1),(2)}_{2,1}\right) & \left|M^{(1),(2)}_{2,2}\right|\exp\left(i\varphi^{(1),(2)}_{2,2}\right) \end{bmatrix} \tag{35.32}$$

and $\Delta\varphi^{(2,1)}$ is the relative global phase of $\mathbf{M}^{(2)}$ respect to $\mathbf{M}^{(1)}$.

The Jones matrix/Jones vector matrix averaging is then defined as complex averaging of complex matrices in which the global phase of each matrix is defined by Eq. 35.32 in respect to a particular reference matrix and canceled out before performing the complex averaging.

The utility of this matrix averaging is not only limited to the averaging $\mathbf{E}_{out}(z_{surf})$. The signal-to-noise ratio of the measured Jones matrix of the sample can also be enhanced by averaging several Jones matrices measured at a small region of interest, i.e., averaging kernel.

35.6 Conclusion

The principle and implementation of Jones matrix OCT was presented in this chapter, and the high intrinsic robustness of this technique was discussed. Owing to this robustness, the requirement for calibration of Jones matrix measurement is very low. Thus, Jones matrix OCT would provide a robust and stable platform to determine the polarization properties of biological samples.

This chapter was organized to provide an insight into and comprehensive overview of Jones matrix OCT, and hence, a more detailed description of practical implementations would be not enough. To better understand the implementation details of Jones matrix OCT, the reader is encouraged to explore the literature, for example, Refs. [7, 31, 39–43, 45, 46, 50]. This chapter hopefully provides the reader with the foundation necessary to achieve a deep understanding of Jones matrix OCT presented in these individual research articles.

References

1. J. De Boer, S. Srinivas, A. Malekafzali, Z. Chen, J. Nelson, Imaging thermally damaged tissue by polarization sensitive optical coherence tomography. Opt. Express **3**, 212–218 (1998)
2. K. Schoenenberger, B.W. Colston, D.J. Maitland, L.B. Da Silva, M.J. Everett, Mapping of birefringence and thermal damage in tissue by use of polarization-sensitive optical coherence tomography. Appl. Opt. **37**, 6026–6036 (1998)
3. S. Jiao, W. Yu, G. Stoica, L.V. Wang, Contrast mechanisms in polarization-sensitive Mueller-matrix optical coherence tomography and application in burn imaging. Appl. Opt. **42**, 5191–5197 (2003)
4. M.C. Pierce, J. Strasswimmer, B.H. Park, B. Cense, J.F. de Boer, Advances in optical coherence tomography imaging for dermatology. J. Invest. Dermatol. **123**, 458–463 (2004)
5. S.M. Srinivas, J.F. de Boer, H. Park, K. Keikhanzadeh, H.L. Huang, J. Zhang, W.Q. Jung, Z. Chen, J.S. Nelson, Determination of burn depth by polarization-sensitive optical coherence tomography. J. Biomed. Opt. **9**, 207 (2004)
6. E. Götzinger, M. Pircher, M. Sticker, A.F. Fercher, C.K. Hitzenberger, Measurement and imaging of birefringent properties of the human cornea with phase-resolved, polarization-sensitive optical coherence tomography. J. Biomed. Opt. **9**, 94–102 (2004)
7. Y. Lim, M. Yamanari, S. Fukuda, Y. Kaji, T. Kiuchi, M. Miura, T. Oshika, Y. Yasuno, Birefringence measurement of cornea and anterior segment by office-based polarization-sensitive optical coherence tomography. Biomed. Opt. Express **2**, 2392–2402 (2011)

8. M. Pircher, E. Götzinger, O. Findl, S. Michels, W. Geitzenauer, C. Leydolt, U. Schmidt-Erfurth, C.K. Hitzenberger, Human macula investigated in vivo with polarization-sensitive optical coherence tomography. Invest. Ophthalmol. Vis. Sci. **47**, 5487–5494 (2006)
9. M. Miura, M. Yamanari, T. Iwasaki, A.E. Elsner, S. Makita, T. Yatagai, Y. Yasuno, Imaging polarimetry in age-related macular degeneration. Invest. Ophthalmol. Vis. Sci. **49**, 2661–2667 (2008)
10. M. Pircher, C.K. Hitzenberger, U. Schmidt-Erfurth, Polarization sensitive optical coherence tomography in the human eye. Prog. Retin. Eye Res. **30**, 431–451 (2011)
11. Y. Yasuno, M. Yamanari, K. Kawana, T. Oshika, M. Miura, Investigation of post-glaucoma-surgery structures by three-dimensional and polarization sensitive anterior eye segment optical coherence tomography. Opt. Express **17**, 3980–3996 (2009)
12. B. Cense, T.C. Chen, B.H. Park, M.C. Pierce, J.F. de Boer, Thickness and birefringence of healthy retinal nerve fiber layer tissue measured with polarization-sensitive optical coherence tomography. Invest. Ophthalmol. Vis. Sci. **45**, 2606–2612 (2004)
13. M. Yamanari, M. Miura, S. Makita, T. Yatagai, Y. Yasuno, Phase retardation measurement of retinal nerve fiber layer by polarization-sensitive spectral-domain optical coherence tomography and scanning laser polarimetry. J. Biomed. Opt. **13**, 014013 (2008)
14. E. Götzinger, M. Pircher, B. Baumann, C. Hirn, C. Vass, C.K. Hitzenberger, Retinal nerve fiber layer birefringence evaluated with polarization sensitive spectral domain OCT and scanning laser polarimetry: a comparison. J. Biophotonics **1**, 129–139 (2008)
15. L. Duan, M. Yamanari, Y. Yasuno, Automated phase retardation oriented segmentation of chorio-scleral interface by polarization sensitive optical coherence tomography. Opt. Express **20**, 3353–3366 (2012)
16. T. Torzicky, M. Pircher, S. Zotter, M. Bonesi, E. Götzinger, C.K. Hitzenberger, Automated measurement of choroidal thickness in the human eye by polarization sensitive optical coherence tomography. Opt. Express **20**, 7564 (2012)
17. A. Baumgartner, S. Dichtl, C.K. Hitzenberger, H. Sattmann, B. Robl, A. Moritz, A.F. Fercher, W. Sperr, Polarization-sensitive optical coherence tomography of dental structures. Caries Res. **34**, 59–69 (2000)
18. Y. Chen, L. Otis, D. Piao, Q. Zhu, Characterization of dentin, enamel, and carious lesions by a polarization-sensitive optical coherence tomography system. Appl. Opt. **44**, 2041–2048 (2005)
19. D. Fried, J. Xie, S. Shafi, J.D.B. Featherstone, T.M. Breunig, C. Le, Imaging caries lesions and lesion progression with polarization sensitive optical coherence tomography. J. Biomed. Opt. **7**, 618–627 (2002)
20. S.K. Nadkarni, M.C. Pierce, B.H. Park, J.F. de Boer, P. Whittaker, B.E. Bouma, J.E. Bressner, E. Halpern, S.L. Houser, G.J. Tearney, Measurement of collagen and smooth muscle cell content in atherosclerotic plaques using polarization-sensitive optical coherence tomography. J. Am. Coll. Cardiol. **49**, 1474–1481 (2007)
21. W.-C. Kuo, M.-W. Hsiung, J.-J. Shyu, N.-K. Chou, P.-N. Yang, Assessment of arterial characteristics in human atherosclerosis by extracting optical properties from polarization-sensitive optical coherence tomography. Opt. Express **16**, 8117–8125 (2008)
22. M.R. Hee, D. Huang, E.A. Swanson, J.G. Fujimoto, Polarization-sensitive low-coherence reflectometer for birefringence characterization and ranging. J. Opt. Soc. Am. B **9**, 903–908 (1992)
23. E. Götzinger, M. Pircher, C.K. Hitzenberger, High speed spectral domain polarization sensitive optical coherence tomography of the human retina. Opt. Express **13**, 10217–10229 (2005)
24. J.F. de Boer, T.E. Milner, J.S. Nelson, Determination of the depth-resolved Stokes parameters of light backscattered from turbid media by use of polarization-sensitive optical coherence tomography. Opt. Lett. **24**, 300–302 (1999)
25. C.E. Saxer, J.F. de Boer, B.H. Park, Y. Zhao, Z. Chen, J.S. Nelson, High-speed fiber based polarization-sensitive optical coherence tomography of in vivo human skin. Opt. Lett. **25**, 1355–1357 (2000)

26. B. Park, M.C. Pierce, B. Cense, S.-H. Yun, M. Mujat, G. Tearney, B. Bouma, J. de Boer, Real-time fiber-based multi-functional spectral-domain optical coherence tomography at 1.3 μm. Opt. Express **13**, 3931–3944 (2005)
27. B. Cense, M. Mujat, T.C. Chen, B.H. Park, J.F. de Boer, Polarization-sensitive spectral-domain optical coherence tomography using a single line scan camera. Opt. Express **15**, 2421–2431 (2007)
28. G. Yao, L.V. Wang, Two-dimensional depth-resolved Mueller matrix characterization of biological tissue by optical coherence tomography. Opt. Lett. **24**, 537–539 (1999)
29. Y. Yasuno, S. Makita, Y. Sutoh, M. Itoh, T. Yatagai, Birefringence imaging of human skin by polarization-sensitive spectral interferometric optical coherence tomography. Opt. Lett. **27**, 1803–1805 (2002)
30. S. Jiao, G. Yao, L.V. Wang, Depth-resolved two-dimensional stokes vectors of backscattered light and Mueller matrices of biological tissue measured with optical coherence tomography. Appl. Opt. **39**, 6318–6324 (2000)
31. S. Jiao, L.V. Wang, Two-dimensional depth-resolved Mueller matrix of biological tissue measured with double-beam polarization-sensitive optical coherence tomography. Opt. Lett. **27**, 101–103 (2002)
32. S. Jiao, W. Yu, G. Stoica, L. Wang, Optical-fiber-based Mueller optical coherence tomography. Opt. Lett. **28**, 1206–1208 (2003)
33. B.H. Park, M.C. Pierce, B. Cense, J.F. de Boer, Jones matrix analysis for a polarization-sensitive optical coherence tomography system using fiber-optic components. Opt. Lett. **29**, 2512–2514 (2004)
34. Y. Yasuno, S. Makita, T. Endo, M. Itoh, T. Yatagai, M. Takahashi, C. Katada, M. Mutoh, Polarization-sensitive complex Fourier domain optical coherence tomography for Jones matrix imaging of biological samples. Appl. Phys. Lett. **85**, 3023–3025 (2004)
35. W.H. Press, S.A. Teukolsky, W.T. Vetterling, B.P. Flannery, *Numerical Recipes*. The Art of Scientific Computing, 3rd edn. (Cambridge University Press, Cambridge, 2007)
36. Z. Lu, S.J. Matcher, Absolute fast axis determination using non-polarization-maintaining fiber-based polarization-sensitive optical coherence tomography. Opt. Lett. **37**, 1931–1933 (2012)
37. S.-W. Lee, J.-H. Kang, J.-Y. Yoo, M.-S. Kang, J.-T. Oh, B.-M. Kim, Quantification of scattering changes using polarization-sensitive optical coherence tomography. J. Biomed. Opt. **13**, 054032 (2008)
38. E. Götzinger, M. Pircher, W. Geitzenauer, C. Ahlers, B. Baumann, S. Michels, U. Schmidt-Erfurth, C.K. Hitzenberger, Retinal pigment epithelium segmentation by polarization sensitive optical coherence tomography. Opt. Express **16**, 16410–16422 (2008)
39. B. Baumann, S.O. Baumann, T. Konegger, M. Pircher, E. Götzinger, F. Schlanitz, C. Schütze, H. Sattmann, M. Litschauer, U. Schmidt-Erfurth, C.K. Hitzenberger, Polarization sensitive optical coherence tomography of melanin provides intrinsic contrast based on depolarization. Biomed. Opt. Express **3**, 1670–1683 (2012)
40. M. Yamanari, S. Makita, V.D. Madjarova, T. Yatagai, Y. Yasuno, Fiber-based polarization-sensitive Fourier domain optical coherence tomography using B-scan-oriented polarization modulation method. Opt. Express **14**, 6502–6515 (2006)
41. M. Yamanari, S. Makita, Y. Yasuno, Polarization-sensitive swept-source optical coherence tomography with continuous source polarization modulation. Opt. Express **16**, 5892–5906 (2008)
42. K.H. Kim, B.H. Park, Y. Tu, T. Hasan, B. Lee, J. Li, J.F. de Boer, Polarization-sensitive optical frequency domain imaging based on unpolarized light. Opt. Express **19**, 552–561 (2011)
43. Y. Lim, Y.-J. Hong, L. Duan, M. Yamanari, Y. Yasuno, Passive component based multifunctional Jones matrix swept source optical coherence tomography for Doppler and polarization imaging. Opt. Lett. **37**, 1958–1960 (2012)

44. B. Baumann, W. Choi, B. Potsaid, D. Huang, J.S. Duker, J.G. Fujimoto, Swept source/Fourier domain polarization sensitive optical coherence tomography with a passive polarization delay unit. Opt. Express **20**, 10229–10241 (2012)
45. S. Makita, M. Yamanari, Y. Yasuno, Generalized Jones matrix optical coherence tomography: performance and local birefringence imaging. Opt. Express **18**, 854–876 (2010)
46. M. Yamanari, Y. Lim, S. Makita, Y. Yasuno, Visualization of phase retardation of deep posterior eye by polarization-sensitive swept-source optical coherence tomography with 1-μm probe. Opt. Express **17**, 12385–12396 (2009)
47. B. Baumann, E. Götzinger, M. Pircher, C.K. Hitzenberger, Single camera based spectral domain polarization sensitive optical coherence tomography. Opt. Express **15**, 1054–1063 (2007)
48. W.Y. Oh, S.H. Yun, B.J. Vakoc, M. Shishkov, A.E. Desjardins, B.H. Park, J.F. de Boer, G.J. Tearney, B.E. Bouma, High-speed polarization sensitive optical frequency domain imaging with frequency multiplexing. Opt. Express **16**, 1096–1103 (2008)
49. B. Vakoc, S. Yun, J. de Boer, G. Tearney, B. Bouma, Phase-resolved optical frequency domain imaging. Opt. Express **13**, 5483–5493 (2005)
50. Y.-J. Hong, S. Makita, F. Jaillon, M.J. Ju, E.J. Min, B.H. Lee, M. Itoh, M. Miura, Y. Yasuno, High-penetration swept source Doppler optical coherence angiography by fully numerical phase stabilization. Opt. Express **20**, 2740–2760 (2012)
51. M. Yamanari, S. Makita, Y. Lim, Y. Yasuno, Full-range polarization-sensitive swept-source optical coherence tomography by simultaneous transversal and spectral modulation. Opt. Express **18**, 13964–13980 (2010)

Spectroscopic Low Coherence Interferometry

36

Nienke Bosschaart, T. G. van Leeuwen, Maurice C. Aalders, Boris Hermann, Wolfgang Drexler, and Dirk J. Faber

Keywords

Absorption • Chromophores • Low coherence interferometry • Spectroscopy, spectroscopic

36.1 Introduction

Optical coherence tomography provides cross-sectional images of tissues at micrometer scale resolution up to several millimeters deep. Within these volumes information on the physiological function of tissues can be derived, such as flow and perfusion as discussed in ▶ Chap. 21, "Swept Light Sources". Assessment of nanoscale organization of tissue, assessed through elastic light scattering properties, is demonstrated in ▶ Chap. 27, "Digital Holoscopy" and will be elaborated below. Given the large optical bandwidths involved in low coherence interferometry (LCI), the development of spectroscopic LCI modalities seems almost straightforward. In this chapter, the combination of spatial and spectroscopic information from these low-coherent signals is discussed. With spectroscopic OCT (SOCT) [1–9] and low-coherence spectroscopy (LCS) [10–13], localized absorption and/or (back)scattering spectra of tissue can be measured. The spectroscopic content of the

N. Bosschaart (✉) • T.G. van Leeuwen • M.C. Aalders • D.J. Faber
Department of Biomedical Engineering and Physics, Academic Medical Center, University of Amsterdam, The Netherlands
e-mail: n.bosschaart@amc.uva.nl

B. Hermann
Center for Medical Physics and Biomedical Engineering, Medical University of Vienna, Vienna, Austria

W. Drexler
Center for Medical Physics and Biomedical Engineering, Medical University of Vienna, General Hospital Vienna, Vienna, Austria

© Springer International Publishing Switzerland 2015

W. Drexler, J.G. Fujimoto (eds.), *Optical Coherence Tomography*,
DOI 10.1007/978-3-319-06419-2_37

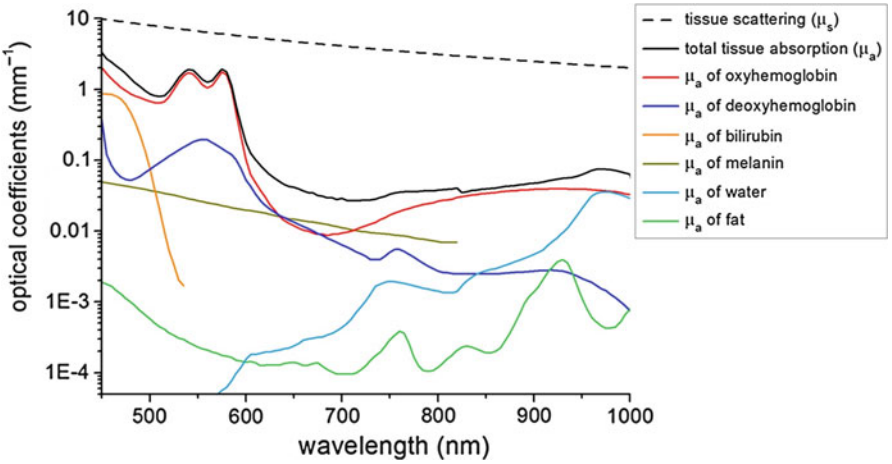

Fig. 36.1 Absorption spectra of common chromophores in human tissue, total tissue absorption, and tissue scattering for biologically normal concentrations (Data obtained from Ref [44]). Scattering is assumed to follow power-law dependence on wavelength $\mu_s = a\lambda^{-b}$

SOCT signal can be used for contrast enhancement, but our focus will be on quantification of depth-resolved spectra to retrieve the concentration of tissue chromophores (e.g., hemoglobin and bilirubin) and characterize tissue light scattering. One promising application is measurement of hemoglobin and bilirubin levels to monitor anemia and jaundice in neonates, which is currently only possible by frequent, invasive heel pricks [14]. Figure 36.1 shows the absorption spectra of the most common chromophores in tissue, as well as the general trend of wavelength-dependent scattering.

Roughly, the scattering coefficient μ_s shows an inverse power-law dependence on wavelength $\mu_s = a\lambda^{-b}$, from which the parameters (a,b) depend on the size distribution, concentration, and relative refractive index of the scattering volume elements (e.g., cell membranes, collagen fibers, mitochondria). A light scattering experiment thus provides information on the structural organization of the probed tissue. A demonstration of this paradigm was given by Van der Meer et al. [15] by determining the attenuation coefficient μ_{LCI} (see Sect. 36.2.2, Eq. 36.8) averaged over the bandwidth of an 800 nm OCT system, of cells forced into apoptosis and necrosis. Both apoptosis, programmed cell death, and necrosis, accidental cell death, are processes that are known to follow a cascade of morphological changes at the (sub)cellular level. The experiment shown in Fig. 36.2 demonstrates that, even though OCT does not have sufficient resolution-to directly image processes at the subcellular level, it is still sensitive to the associated morphological changes through changes in light scattering.

A major application of spectroscopic LCI is the quantification of spatially localized hemoglobin concentration and oxygen saturation which, combined with local perfusion measurements, can have significant impact on cancer care.

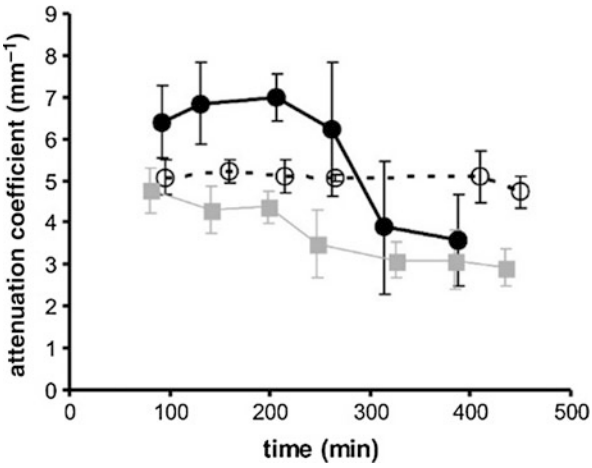

Fig. 36.2 The measured attenuation coefficient for 800 nm light in pelleted human fibroblasts, as a function of time. Time was measured in minutes from the point that the cells forced into necrosis (*filled squares*) or apoptosis (*filled dots*). Untreated control cells show no change in scattering (*open circles*)

A tumor's local oxygen status, specifically hypoxia, is considered one of the "hallmarks of cancer" predicting progression and response to therapy. The potential of spectroscopic LCI may be further enhanced by quantification of changes in tissue morphology during disease progression based on spectrally resolved scattering properties. The potential of this method is illustrated in Fig. 36.3, showing in panel A and B in vivo obtained volume rendering resp. individual B-scans of vulvar intraepithelial neoplasia (VIN), a precursor of cancer. Panel C sketches how the signal decay with depth is quantified though the attenuation coefficient μ_{LCI}, a procedure that is detailed in Sect. 36.2.2. Panel D indicates the potential of discriminating between normal and premalignant tissue using μ_{LCI} [16]. Similar results were obtained discriminating between normal kidney tissue and kidney cancer [17, 18].

Despite this application potential, clinical studies have been reported where the measurement of only one parameter (e.g., the value of μ_{LCI} averaged over the bandwidth of an OCT system) was not sufficient to differentiate between different grades (pathologists' assessment of tumor aggressiveness) of urothelial carcinoma of the bladder [19]. As we discuss in the next sections, spectroscopic LCI provides the possibility of retrieval of not only $\mu_{LCI}(\lambda)$ but also of backscattering coefficients $\mu_b(\lambda)$ which shows large sensitivity to morphology.

This chapter starts with outlining the theory of spectroscopic LCI, describing methods to quantitatively obtain localized spectra. This includes computational and instrumental considerations such as proper correction for point spread functions of the LCI equipment. We then discuss the retrievable optical property spectra, e.g., absorption and scattering spectra that can be derived from these measurements and their interpretation in terms of physiologically relevant tissue characteristics. We conclude by presenting clinical examples of spectroscopic LCI.

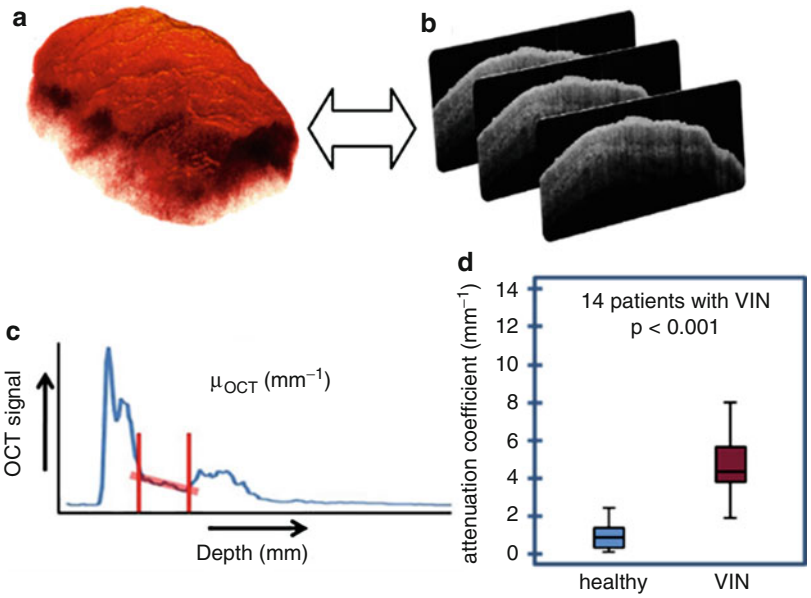

Fig. 36.3 (**a**) 3D image obtained in the clinic from a lesion suspected for vulvar intraepithelial neoplasia (*VIN*), a precursor of cancer. (**b**) Constituting 2D-OCT images of this lesion. (**c**) The decay of the OCT signal versus depth in a region of interest selected from the images of panel (**a**) or (**b**) is determined by fitting a mathematical model of the OCT signal to this data (after careful calibration of the system). (**d**) Results demonstrating the capability of differentiating between normal and VIN tissues by the attenuation coefficient μ_{LCI} [16]

36.2 Theory

The general form of the detected LCI interferogram is written as:

$$i_D = |E_s + E_R|^2 = |E_s|^2 + |E_R|^2 + 2\{E_s E_R^* \cos(k2d)\} \tag{36.1}$$

where E_S and E_R are the fields returning from sample and reference arm, respectively, with wave number $k = 2\pi/\lambda$ with λ the wavelength. Further, $2d$ is the optical path length difference so that d is the assigned depth location in the tissue. Wave number k and optical path length difference $2d$ form the fundamental Fourier pair in LCI data analysis. Classic time domain detection receives all wavelengths at once, while modulating $2d$ using a moving reference arm (effectively integrating Eq. 36.1 over k), whereas in Fourier domain OCT, the signal is obtained as function of k, integrating over $2d$. The goal of spectroscopic LCI modalities is to obtain information in k and d domains simultaneously, with high resolution in both domains.

Both 2d-domain and k-domain descriptions of the OCT signal i_D are equivalent and are related by Fourier transformation:

$$i_D(2d) = |\Im\{i_D(k)\}| \tag{36.2}$$

where $\mathfrak{I}$ denotes the Fourier transform. Since the wave number k is directly related to wavelength λ, wavelength dependent spectra $i_D(\lambda)$ can be obtained from the backscattered LCI signal. We drop the factor "2" going onward and use the concepts "spatial domain" and "depth domain" interchangeably.

36.2.1 Localized Spectroscopic Information

Time-frequency analysis – Due to wavelength-dependent scattering and absorption by the different structures in tissue, the spectral content of the OCT signal changes with depth. Therefore direct application of the Fourier transform on either spatial or spectral domain detected signal Eq. 36.2 is not appropriate to obtain localized spectroscopic information because the depth resp. wave number varying information will be lost. Instead, spectral analysis methods, conventionally called time-frequency (TF) [20] analysis must be used (or, for the present context, depth-wavelength analysis). In most studies, the preferred method has been to use short-time Fourier transforms (STFT):

$$STFT(k, d; w) = \int_{-\infty}^{\infty} i_D(d')w(d - d'; \Delta d)e^{-ikd'}d(d') \tag{36.3}$$

where w is an analysis window confined in space around d with spatial width Δd, for example, a Gaussian function. The multiplication with a relatively short window effectively suppresses the signal outside the analysis point $d \pm \Delta d$. Physically, the STFT can be considered as the result of passing a signal through an array of band-pass filters with linearly increasing center frequency and constant bandwidth which is inversely proportional to Δd. Thus, there is an inherent trade-off between spectral and spatial resolution. A window with short spatial width Δd will localize the signal well in space but will have reduced k-resolution; conversely a signal with long width will be less well localized in space with the benefit of increased spectral resolution. For a Gaussian window, a spatial domain width Δd will yield a spectral resolution of $\Delta k = 1/(2\Delta d)$.

The wavelet transform was introduced to partially overcome this trade-off by adjusting the window size to the frequency being considered. The basic difference between the wavelet transform and the STFT is that the duration and the bandwidth of the wavelet are both changed (while shape remains the same). Physically, the wavelet transform can also be seen as an array of band-pass filters with constant relative bandwidth with respect to the center frequency. In contrast with the STFT, which uses a single analysis window, the wavelet transform uses short windows at high frequencies and long windows at low frequencies. Again, there is a trade-off between time and frequency resolutions. However, these resolutions depend on frequency: the frequency (resp. time) resolution becomes poorer (resp. better) with increasing analysis frequency.

The wavelet transform projects a signal on a family of functions deduced from a (complex) window function w, the "mother wavelet," by translations and dilations:

$$WT(\kappa, d; w) = \int_{-\infty}^{\infty} i_D(d') w\left(\frac{d - d'}{\kappa}\right) d(d') \tag{36.4}$$

The variable κ is the scale factor, dilating ($|\kappa| > 1$) or compressing ($|\kappa| < 1$) the wavelet w. When mother wavelets are used that are well localized around a wave number k_0, then a time-frequency interpretation is possible through $k = k_0/\kappa$.

Bilinear TF distributions do not suffer from the resolution trade-off between both domains. The most important member of this class is the Wigner distribution:

$$WD(k, d) = \int i_D(d + d') i_D{}^*(d - d') \exp(ikd') d(d') \tag{36.5}$$

The Wigner distribution is the Fourier transform of an autocorrelation measure of the signal $i_D(d)$. Whereas in conventional autocorrelation computations, the result is a function of lag only, here the functional dependence on d is maintained. In concordance with the Wiener-Khinchine theorem, the straightforward interpretation of the WD is as a localized power spectral density of the detector signal.

The drawback of the WD lies in its quadratic nature: whereas the STFT of two signals X and Y yields $STFT_x(k, d) + STFT_y(k, d)$, the WD will contain interference terms, e.g., $WD_{x+y}(k, d) = WD_x(k, d) + WD_y(k, d) + 2\mathrm{Re}[WD_{x,y}(k, d)]$. Even though the interference term contains information on the separation of X and Y (e.g., in space), when it overlaps with the signal terms, interpretation of the WD becomes challenging. In practice (like with the STFT), the signal is analyzed using a window w. This pseudo-WD effectively smoothens the time-frequency distribution, suppressing the interference terms. However, a short smoothing window will be narrow in time and wide in frequency, leading to a good time resolution but bad frequency resolution and vice versa. It is possible to add a degree of freedom by considering a separable smoothing function $\Pi(k, d) = w_1(k, \Delta k) w_2(d, \Delta d)$ that allows independent control in both time and frequency of the smoothing applied to the WVD; Δk and Δd denote the width of the window functions in the spectral and spatial domain, respectively. The STFT compromise between time and frequency resolution is now replaced by a compromise between the joint time-frequency resolution and the level of suppression of the interference terms. Robles et al. showed that the pseudo-WD can also be obtained by STFT analysis using two k-domain window sizes $\Delta k_1 >> \Delta k_2$. The result $STFT_1(k, d) \times STFT_2(k, d)$ is mathematically equivalent to a pseudo-WD with window widths of $W_1(k, \Delta k = k_2/2)$ in the spectral domain and window $W_2(d, \Delta d = 1/(2\ k_1))$ in the spatial domain. As for the WD, any remaining interference terms may carry information, for example, on average spatial scatterer separation [7–9].

Xu et al. [21] also define a third class of time-frequency distributions, based on the presumed known spectral profiles of the laser source and the sample. This allows for fitting the obtained OCT signal to this model equation, thereby retrieving the sought spectral properties. In practice, there may exist an optimal time-frequency analysis depending on the application. For example, the STFT is completely free of artifacts such as introduced by the quadratic analysis of the energy distributions. The poor depth resolution resulting from the requirement of a high spectral resolution may not be a problem at all when analyzing relatively large tissue structures, where a spatially averaged spectrum over the entire tissue structure is required. For example, a spectral resolution of 6 nm in LCS corresponds to a depth resolution of 22 μm, which is sufficient to measure hemoglobin concentrations from optical property spectra in distinct regions of the epidermis and the dermis [12] (see Sect. 36.3.2).

Hardware-based approaches and considerations – For proper quantification of local spectra, signal attenuating factors caused by the LCI system need to be accounted for. The two dominating factors are the confocal point spread function (e.g., loss of sensitivity away from the focal region) and the sensitivity roll-off in depth for spectral domain LCI, caused by the finite resolution of the spectrometer (or the finite instantaneous bandwidth of the swept source).

Confocal point spread function – The confocal point spread function (PSF) for a single-mode fiber-based OCT system was derived in [22] and validated experimentally in [23]. It can be directly imaged using OCT on a highly diluted (e.g., negligible scattering) sample.

An example of this procedure is shown in Fig. 36.4 for LCS, in a weakly scattering medium (0.038 vol.% of ø198 polystyrene spheres, $\mu_s << 1\ \mathrm{mm}^{-1}$). The PSF is then given by

$$T\left(d_{focus} - d\right) = \frac{\alpha}{\left(\frac{d_{focus}-d}{2Z_R}\right)^2 + 1} \tag{36.6}$$

where α is a scaling factor, d_{focus} is the geometrical position of the focus in the sample, and Z_R is the Rayleigh length of the system (Fig. 36.4b). From Z_R, the beam waist can be computed as $\omega = (Z_R\lambda/2\pi)^{1/2}$, and from that the NA can be derived, using $NA = \sin(\theta) \approx \sin(\lambda/(\pi\ \omega))$. In the preceding definitions, $Z_R\ \omega$ and NA are defined in the medium, e.g., $Z_R = nZ_0$ where Z_0 is the Rayleigh length of the system measured in air and n is the refractive index. Clearly, the PSF is therefore wavelength dependent. When possible the calibration should be performed wavelength resolved (Fig. 36.4).

The confocal PSF can also be exploited to optimize the trade-off between spatial and spectral resolution by restricting the spatial extent of the collected data region. Xu et al. used high-numerical-aperture optics, geometrically restricting the spatial extent of the signal while using long analysis windows to extract high-resolution spectral information [24].

Sensitivity roll-off – SOCT suffers, when using spectral domain detection (▶ Chaps. 5, "Spectral/Fourier Domain Optical Coherence Tomography", ▶ 6, "Complex and Coherence-Noise Free Fourier Domain Optical Coherence

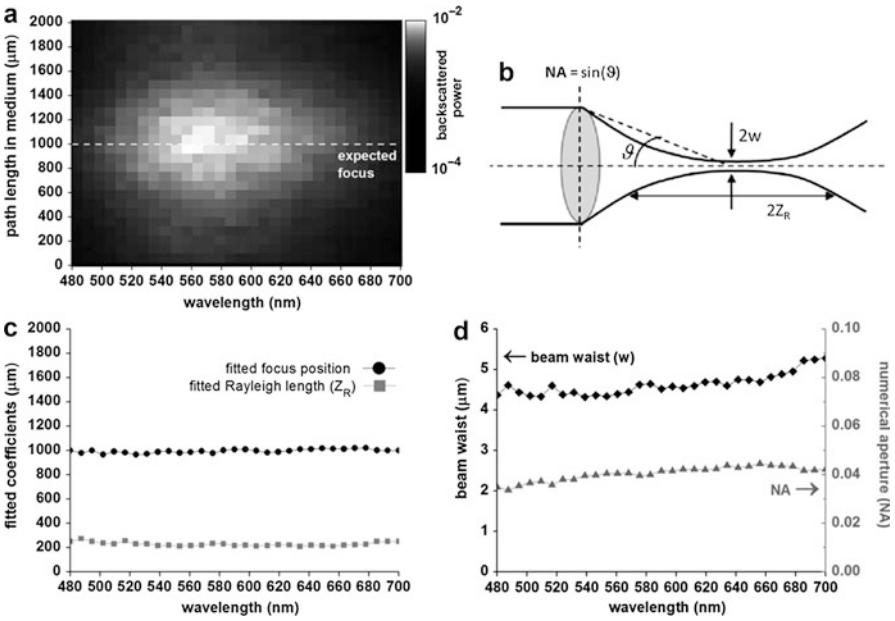

Fig. 36.4 (**a**) Point spread function measurement (*PSF*) on a weakly scattering sample of ø198 spheres (0.038 vol.%), (**b**) schematic illustration of focus geometry, (**c**) fitted focus position (d_{focus}) and Rayleigh length (Z_R) on the measured PSF, (**d**) calculated beam waist (ω) and numerical aperture (*NA*). The parameters Z_R, ω, and NA are defined within the medium ($n = 1.35$)

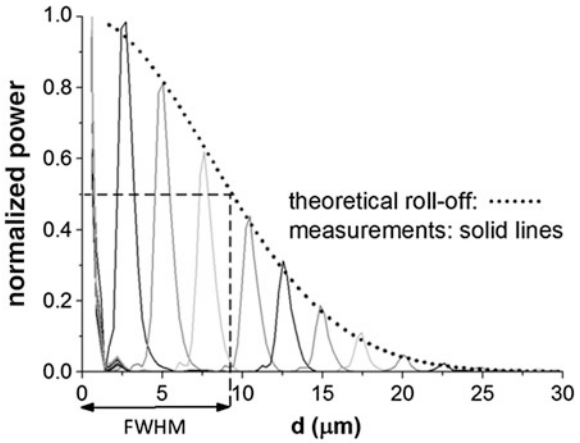

Fig. 36.5 Theoretical and measured sensitivity roll-off of a spectral domain LCS setup using an Ocean Optics USB4000 spectrometer

Tomography", and ▶ 7, "Optical Frequency Domain Imaging"), from the inherent loss of sensitivity with depth due to the finite resolution of the detecting spectrometer (or the finite instantaneous bandwidth/sampling time in swept-source implementations). This causes unwanted signal attenuation that can, similarly to the confocal PSF correction, be accounted for in post-processing.

Here too, the effect can be turned to advantage by limiting the spatial extent of the collected data. Figure 36.5 shows the theoretical and measured roll-off of an LCS system based on a commercially available Ocean Optics USB4000 spectrometer. The "low" spectral resolution of 8 nm of this device results in roll-off function with full width at half maximum of FWHM ~10 μm, so that meaningful interference signals are only collected in a window of approximately 20 μm around the equivalent position of the reference arm in the sample. Details of spectral domain LCS can be found in [13].

36.2.2 Quantitative Determination of Optical Properties

Retrievable properties using spectroscopic low-coherence interferometry – In general, all methods described above result in a wavelength-resolved power spectrum $\boldsymbol{S}$ acquired within a depth window Δd around a depth d in the sample. We will indicate all wavelength-dependent parameters in the remainder of this chapter by a bold-faced character. The following theory assumes validity of the 1st Born approximation, e.g., the illuminating field is much stronger than the scattered field. Under this assumption, the LCI signal is formed by single backscattering, so that the amplitude of $\boldsymbol{S}(d)$ decreases exponentially with measurement depth and the attenuation coefficient $\boldsymbol{\mu_{LCI}}$ of the sample. Hence, we can describe $\boldsymbol{S}(d)$ using Beer's law:

$$\boldsymbol{S}(d) = \boldsymbol{\zeta} \cdot \boldsymbol{\mu}_{b,NA} e^{-\boldsymbol{\mu}_{LCI} 2d} \tag{36.7}$$

The factor 2 in Eq. 36.7 accounts for round-trip attenuation to and from depth d. We note that if the amplitude $\mathbf{E}(d)$ of the LCI signal is considered, rather than backscattered power, this factor drops from Beer's law since $\mathbf{E}(d)$ is proportional to the square root of $\boldsymbol{S}(d)$. We also assume that the influence of the PSF and sensitivity roll-off have been accounted for in preprocessing. The LCI-attenuation coefficient $\boldsymbol{\mu_{LCI}}$ is given by

$$\boldsymbol{\mu_{LCI}} = \boldsymbol{\mu_t} \equiv \boldsymbol{\mu_s} + \boldsymbol{\mu_a} \tag{36.8}$$

with $\boldsymbol{\mu_t}$ the attenuation coefficient, defined as the sum of the scattering coefficient $\boldsymbol{\mu_s}$ and the absorption coefficient $\boldsymbol{\mu_a}$. The latter 3 parameters are formally defined in textbooks, e.g. [25], and are discussed in more detail below. We introduce the LCI-attenuation coefficient $\boldsymbol{\mu_{LCI}}$ (the experimental outcome) because in practice, even when correction for PSF and roll-off is not (optimally) performed, and/or when the first Born approximation does not hold, a single exponential decay model Eq. 36.7 is often suitable for fitting the OCT system [23]. In these cases, the simple relation of Eq. 36.8 breaks down, i.e., $\boldsymbol{\mu_{LCI}} \neq \boldsymbol{\mu_t}$. However, the $\boldsymbol{\mu_a}$ can still be retrieved because absorption takes place *along the photon's path* (regardless of its trajectory), but values for "$\boldsymbol{\mu_s}$" should be interpreted with caution in this case.

The parameters $\boldsymbol{\zeta}$ and $\boldsymbol{\mu_{b,\ NA}}$ determine the amplitude of $\boldsymbol{S}(d)$ at $d = 0$. The system-dependent parameters are defined by $\boldsymbol{\zeta} = \boldsymbol{S_0}\cdot\boldsymbol{T}\cdot 2\Delta d$, with $\boldsymbol{S_0}$ the source power spectrum incident on the sample and $\boldsymbol{T}$ the axial point spread function Eq. 36.6. The backscattering coefficient $\boldsymbol{\mu_{b,\ NA}}$ is a sample-dependent parameter, which is defined as the product of the scattering coefficient $\boldsymbol{\mu_s}$ and the scattering phase function $\boldsymbol{p}(\theta)$, integrated over the numerical aperture ($\boldsymbol{NA}$) of the detection optics:

$$\boldsymbol{\mu_{b,NA}} = \boldsymbol{\mu_s}\cdot 2\pi\int_{\pi-\boldsymbol{NA}}^{\pi}\boldsymbol{p}(\theta)\sin\theta\, d\theta \tag{36.9}$$

To quantitatively determine the $\boldsymbol{\mu_{b,\ NA}}$ of the sample using Eq. 36.8, knowledge of $\boldsymbol{\zeta}$ is required. A method to determine $\boldsymbol{\zeta}$ is by a separate calibration measurement on a sample with a known $\boldsymbol{\mu_{b,\ NA}}$, e.g., using Mie theory on well-defined scattering particles [11].

To determine $\boldsymbol{\mu_{LCI}}$ the same calibration measurement may be used, although it is not always necessary since $\boldsymbol{\mu_{LCI}}$ can be obtained directly from the slope of the exponential decay between two or more chosen depths d (according to Eq. 36.7, see also Fig. 36.3c). As a consequence, $\boldsymbol{\mu_{LCI}}$ can be determined in any depth region of interest. The sample's attenuation is composed of the losses due to both scattering and absorption. When correcting $\boldsymbol{S}(d)$ for the attenuation, also the $\boldsymbol{\mu_{b,\ NA}}$ can be determined at any depth of interest.

Interpretation of measured properties – The absorption coefficient $\boldsymbol{\mu_a}$ is directly related to the individual absorption spectra and concentrations of chromophores (e.g., water, hemoglobin, bilirubin) present in the probed volume. The diagnostic value of $\boldsymbol{\mu_s}$ measurements depends on its relation to tissue morphology and organization. Ideally, tissue classification based on $\boldsymbol{\mu_s}$ would be highly correlated with classification by the pathologist based on microscopic evaluation. The classic approach is to model tissue as an ensemble of spherical scatterers with an effective size to match the experiment. The scattering cross section $\boldsymbol{\sigma_s}$ and phase function $\boldsymbol{p}(\theta)$ are then obtained, e.g., by Mie theory [25]. The scattering coefficient follows from

$$\boldsymbol{\mu_s} = \frac{f_v}{V}\boldsymbol{\sigma_s}\left[2\pi\int_0^{\pi}\boldsymbol{S_{P-Y}}(f_v,\theta)\boldsymbol{p}(\theta)\sin\theta\, d\theta\right] \tag{36.10}$$

where f_v is the volume fraction of the particles with volume V and $\boldsymbol{S_{P\text{-}Y}}$ is the Percus-Yevick structure factor [26] accounting for interparticle correlations at high volume fractions (but still assuming validity of the 1st Born approximation). The term between square brackets evaluates to unity for low concentrations and decreases with increasing f_v. The expression for $\boldsymbol{\mu_{b,\ NA}}$ is analogous to Eqs. 36.9 and 36.10. This approach is attractive because model systems consisting of well-defined particle sizes and size distributions can be readily constructed for system calibration and evaluation of measurement accuracy. The drawback is that all complexity of tissue scattering is reduced to a single effective scatterer, which makes it tempting to interpret scattering data only in terms of tissue structures of approximately equal size.

Alternatively, we start with the work of Fercher (▶ Chap. 4, "Inverse Scattering and Aperture Synthesis in OCT") where the scattering potential $\boldsymbol{m}'(r)^2$-1 is introduced, with $\boldsymbol{m}'$ is the relative complex refractive index at location $\boldsymbol{r}$ in the sample (with respect to the average refractive index $\boldsymbol{m_0}$). The scattering coefficient is obtained as

$$\boldsymbol{\mu_s} = \frac{1}{dV}\int_{4\pi}\left|\Im_r\left\{\boldsymbol{m}'(r)^2 - 1\right\}\right|^2 d\Omega \tag{36.11}$$

For example, the scattering coefficient of a volume element dV is obtained by integrating the squared magnitude of the Fourier transform of the scattering potential over solid angle. By a form of the Gladstone-Dale relation, the scattering potential is related to the spatial distribution of mass density ρ(r) [27]:

$$\boldsymbol{m}'(r)^2 - 1 = \frac{2\boldsymbol{\alpha}}{\boldsymbol{m}_0}\rho(r) \tag{36.12}$$

where $\boldsymbol{\alpha}$ is a tissue-specific proportionality factor. Equations 36.11 and 36.12 form the desired link between tissue scattering and architecture. However, the spatial mass density cannot be resolved from a scattering measurement directly. It is therefore more appropriate to evaluate the statistics of the spatial refractive index/mass density fluctuation by means of their correlation functions. For the case of spectroscopic OCT, Yi and Backman [28] used a Whittle-Matern refractive index correlation function $\boldsymbol{C_m}(r)$ to arrive at the following approximate expression for the scattering coefficient:

$$\boldsymbol{\mu_s} \approx 2\left[\boldsymbol{\sigma_m^2}\right]\sqrt{\pi}\Gamma\left(1 - \frac{b}{2}\right)\boldsymbol{k}^2\boldsymbol{l}_{corr,\,m} \tag{36.13}$$

where $\Gamma(\cdot)$ is the gamma function, $\boldsymbol{\sigma_m^2}$ is the variance of the refractive index fluctuation, b is a power law coefficient (see Sect. 36.2.3) assumed <2, and $\boldsymbol{l_{corr,m}}$ is the correlation length of the refractive index fluctuation. Interpretation of tissue scattering in terms of the (statistics of) mass density distribution is attractive because it directly relates to the assessment of tissue slices by a pathologist. The drawback is the difficulty in creating samples with well-controlled and verifiable $\boldsymbol{\sigma_m^2}$, b, and $\boldsymbol{l_{corr,m}}$ for calibration and validation experiments.

36.2.3 Separation of μ_s and μ_a

To quantitatively measure the scattering and absorption coefficient spectra of the sample, their individual contributions to the measured $\boldsymbol{\mu_{LCI}}$ need to be separated (Eq. 36.8). Several methods have been described to achieve this, which will be discussed in this section.

Least squares fitting [12, 29] – This method models the scattering dependence on wavelength with a power law: $\boldsymbol{\mu_s} = a{\cdot}\lambda^{-b}$, with scaling factor a and scatter power b.

The absorption coefficient spectrum is modeled as the sum of the absorption spectra $\boldsymbol{\mu_{a,\,i}}$ of all present chromophores i with contribution c_i: $\boldsymbol{\mu_a} = \sum_i (c_i \cdot \boldsymbol{\mu_{a,\,i}})$. Next, least squares fitting of the model $\boldsymbol{\mu_t} = a \cdot \lambda^{-b} + \sum_i (c_i \cdot \boldsymbol{\mu_{a,\,i}})$ to the measured $\boldsymbol{\mu_t}$ with fit parameters a, b, and c_i results in the individual contributions of $\boldsymbol{\mu_s}$ and $\boldsymbol{\mu_a}$ (scattering is modeled by inverse power-law dependence on wavelength $\mu_s = a \cdot \lambda^{-b}$). In addition, this method directly provides the concentrations c_i of the present chromophores. A restriction of this method is that all present chromophores and their literature absorption spectra need to be known. A similar approach was developed by Xu et al. in Ref [29].

Calibration measurement [11, 24, 30] – The $\boldsymbol{\mu_a}$ of a scattering sample can be obtained by subtracting the $\boldsymbol{\mu_s}$ of that sample from the measured $\boldsymbol{\mu_t}$, if this $\boldsymbol{\mu_s}$ is known from a separate calibration measurement without absorption but with equal $\boldsymbol{\mu_s}$. This is a straightforward method for in vitro experiments, but for in vivo experiments, it requires the assumption that tissue scattering is equal for absorbing and non-absorbing tissue regions, which is likely to induce errors in the $\boldsymbol{\mu_a}$ determination.

Kramers-Kronig (KK) relations [31–33] – For certain applications, it may be feasible to separate scattering and absorption based on the physical ties between the real and imaginary part of the complex refractive index $\boldsymbol{m}$ as a function of frequency $\boldsymbol{\omega} = c \times \mathbf{k}$ where c is the speed of light: $\boldsymbol{m(\omega)} = \boldsymbol{n(\omega)} + i\boldsymbol{\kappa(\omega)}$. By the principle of causality, $\boldsymbol{n(\omega)}$ and $\boldsymbol{\kappa(\omega)}$ are related through the Kramers-Kronig relations,

$$\boldsymbol{n(\omega)} - 1 = \frac{2}{\pi} P \int_0^\infty \frac{\omega' \boldsymbol{\kappa(\omega')}}{(\omega^2 - \omega'^2)} d\boldsymbol{\omega'} \tag{36.14}$$

and the inverse transform given by

$$\boldsymbol{\kappa(\omega)} = \frac{2\omega}{\pi} P \int_0^\infty \frac{\boldsymbol{n(\omega')} - 1}{(\omega^2 - \omega'^2)} d\omega' \tag{36.15}$$

where P denotes the Cauchy principal value of the integral. The imaginary part of the refractive index is related to the absorption coefficient through

$$\boldsymbol{\kappa(\omega)} = \frac{c\boldsymbol{\mu_a}(\omega)}{2\omega} \tag{36.16}$$

Robles et al. used the KK relations to separate the contributions of $\boldsymbol{\mu_a}$ and $\boldsymbol{\mu_s}$, from $\boldsymbol{\mu_t}$ [33]. Their method relies on the determination of the $\boldsymbol{\mu_a}$ from the real part $\boldsymbol{n(\omega)}$ of the refractive index Eqs. 36.15 and 36.16, which is obtained from the nonlinear dispersion phase term of the low-coherent interferometric signal. Subsequently, the $\boldsymbol{\mu_a}$ is subtracted from the measured $\boldsymbol{\mu_t}$ to determine $\boldsymbol{\mu_s}$. Currently, this method has only been applied in vitro.

36.2.4 Accuracy of SOCT and LCS

The accuracy of the optical property spectra determination in SOCT and LCS is limited by:

1. The size and number of averages in the investigated region of interest (ROI): the size (in depth) determines the depth/spectral resolution, depending on the analysis method chosen as discussed above in Sect. 36.2.1. The number of lateral averages is of importance since a single (S)OCT measurement essentially returns a speckle pattern, with standard deviation to intensity ratio of 0.52 (for fully developed speckle). This value reduces with the square root of the number of independent A-scans in the averaging, which can either be performed spatially (increasing the ROI width) or temporally (increasing the measurement time).
2. Sample homogeneity in the ROI: clearly, if volumes with different spectral signatures are present in the ROI, e.g., a vessel and a substantial surrounding region, the fidelity of the localized spectra assigned to the vessel is reduced.
3. The optical density ($\boldsymbol{OD} = \boldsymbol{\mu_t} \times \mathrm{d}$) of the tissue covering the ROI: because it directly influences the optical power available for local signal formation.
4. The localized sensitivity of the system, which for SOCT is determined by the sensitivity roll-off in depth and the decrease in sensitivity away from the focus determined by the confocal point spread function.

The accuracy of SOCT to quantify spatially localized absorption profiles of chromophores embedded in weakly scattering media with a single measurement over the full spectral bandwidth of the light source was investigated Hermann et al. [34]. The precision of the method as a function of the chromophore absorption, the sample thickness, and the different parameters related to the measurement procedure were evaluated both theoretically and experimentally in single and multilayered phantoms (Fig. 36.6). It was demonstrated that in weakly scattering media, SOCT is able to extract $\boldsymbol{\mu_a}$ as small as 0.5 mm^{-1} from 450 μm thick phantoms with a precision of ~2 % in the central and ~8 % at the edges of the used wavelength region. As expected, in phantoms with the same absorption properties and thickness ~180 μm, the precision of SOCT decreases to >10 % in the central wavelength region. Similar results were obtained for LCS absorption measurements [10]. However, when measuring in large ROIs, the accuracy may be improved to <0.5 mm^{-1} by spatial averaging.

The limitation in the accuracy of the $\boldsymbol{\mu_a}$ determination directly influences the accuracy of chromophore concentration measurements by SOCT and LCS. When measuring in the NIR wavelength region around 800 nm, the absorption coefficient of most tissue chromophores is relatively low compared to tissue scattering (Fig. 36.1). As a consequence, it is challenging to use the method for the accurate quantification of absorption in the presence of scattering. In addition, the spectral features of the tissue chromophores are only moderately distinct, which hampers the distinction between, e.g., oxyhemoglobin and deoxyhemoglobin by SOCT (Fig. 36.7). Current applications of SOCT and LCS therefore focus on the visible wavelength region, where absorption is substantially higher and the chromophores

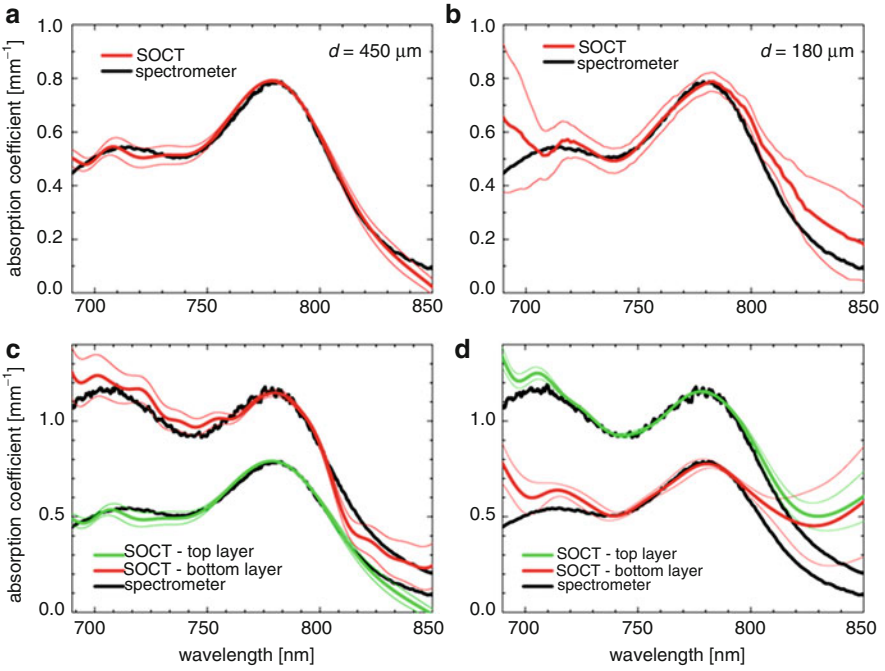

Fig. 36.6 Absorption profiles of measured from 450 µm- (**a**) and 180 µm thick (**b**) single-layered as well as double-layered (**c**, **d**) gel phantoms doped with indocyanine green using SOCT (*red* and *green lines*) and control measurements with a spectrometer (*black lines*). (**c**) Low absorption layer on top (∼490 µm) and high absorption layer below (∼530 µm). (**d**) High absorption layer (∼560 µm) on top of a low absorption layer (∼510 µm). *Thin red lines* indicate the standard deviation for 200 SOCT measurements [34]

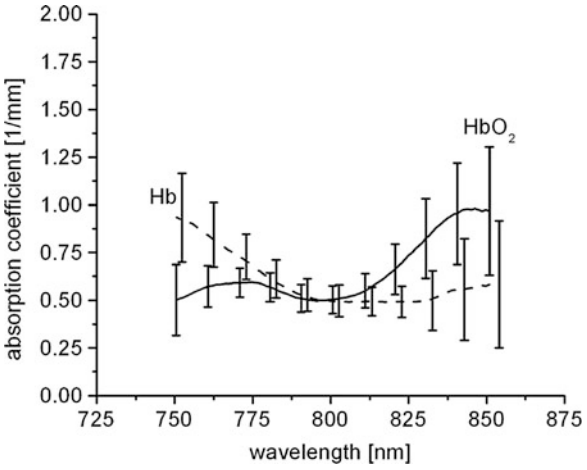

Fig. 36.7 Absorption spectra of hemoglobin (*dashed line*) and oxygenated (*solid line*) hemoglobin measured by spectroscopic optical coherence tomography. Spectral resolution was 1 nm. The *plotted lines* are the average of 1,000 absorption spectra; the *error bars* correspond to the standard deviation (not all error bars are plotted for clarity) [5]

exhibit more distinct absorption features. In this wavelength region, an accuracy of 0.5 mm^{-1} for the determination of $\boldsymbol{\mu_a}$ will be sufficient to, e.g., measure a 6 % oxygenation change or a 2 % change in hemoglobin concentration for whole blood. The imaging depth in the visible wavelength range is lower than for the NIR due to higher tissue scattering and absorption, but is at least 0.5 mm in adult human skin.

36.3 Applications

36.3.1 Contrast Enhancement

The spectroscopic content of the OCT signal can be used to enhance contrast in the OCT image, based on either endogenous or exogenous contrast agents. This application does not require quantitative determination of optical property spectra with high spectral resolution, but can rely on approaches that ensure good depth resolution such as shifting of the spectral center of gravity [4, 35, 36], spectral triangulation [37], and spectral autocorrelation analysis [38]. For SOCT systems that operate in the NIR, the outcome of the spectral analysis is commonly mapped to a false color scale, which is combined with the high-resolution OCT image that shows the spatial distribution of the contrast agent. When operating in the visible wavelength range, the spectral information can be mapped to a color scale that "matches" our visual perception, as was shown by Robles et al. for endogenous contrast agents in Fig. 36.8 [9] and by Li et al. for exogenous contrast agents [30] using the dual window method described in Sect. 36.2.1. The lower panels of Fig. 36.8 quantifying optical spectra within the true-color image are discussed in Sect. 36.3.2.

A relatively unexplored application is OCT speckle reduction using "frequency compounding," e.g., by averaging OCT images obtained at different wavelength bands [39–41]. Averaging N different realizations of the speckle patterns (e.g., OCT images) improves the speckle contrast by $\sqrt{N}$.

36.3.2 Localized Measurements of Optical Properties

Supported by the structural tissue information of an OCT image, SOCT and LCS offer the possibility to accurately and simultaneously quantify a unique set of optical wavelength-resolved properties ($\boldsymbol{\mu_t}$, $\boldsymbol{\mu_a}$, $\boldsymbol{\mu_s}$, and $\boldsymbol{\mu_{b,\,NA}}$) and, derived from that, tissue chromophore concentrations within a very confined and controllable tissue volume of choice. As a consequence, SOCT and LCS can solve several methodological problems related to conventional reflectance spectroscopy, e.g., assumptions on photon path lengths, probing volume, and homogeneity of the investigated tissue. This offers new opportunities for tissue diagnostic applications. This section describes the current applications of SOCT and LCS for localized measurements of optical properties.

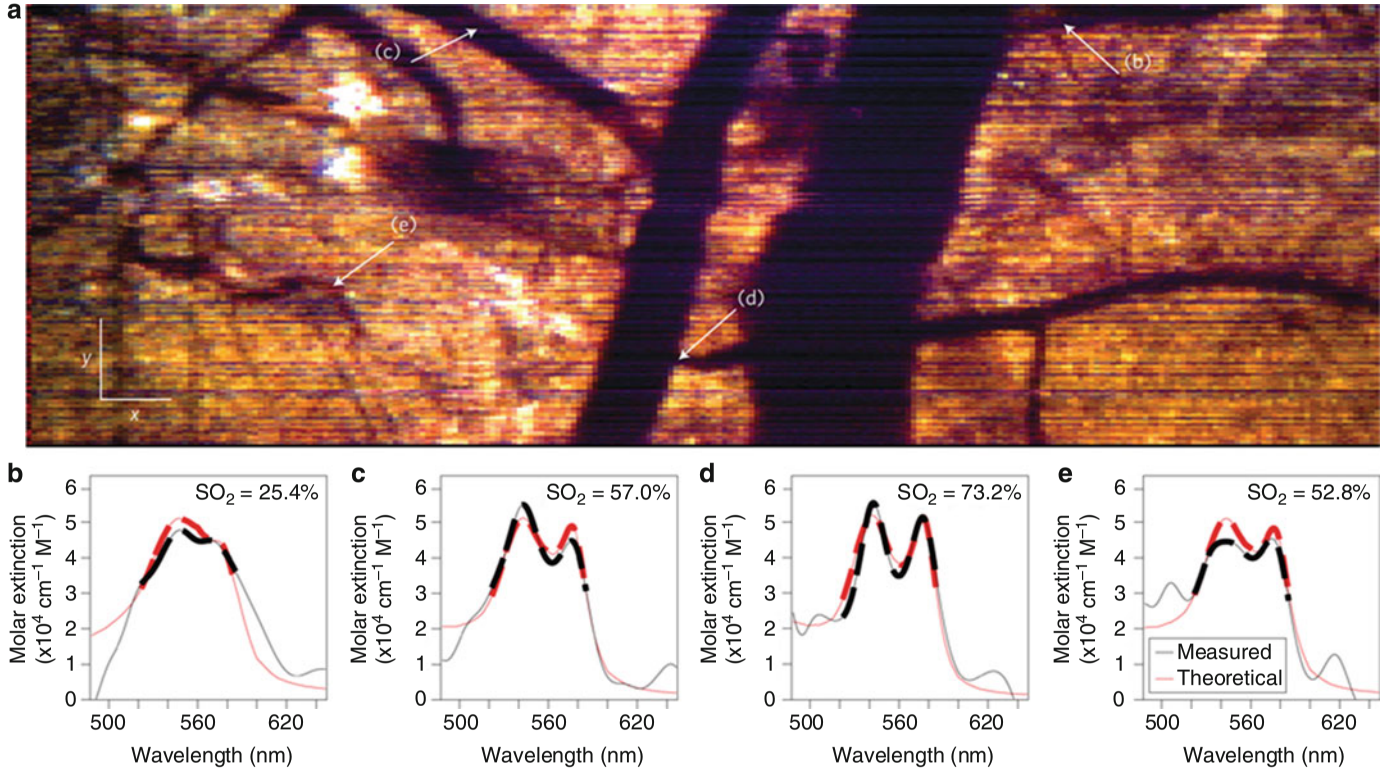

Fig. 36.8 (**a**) En face true-color OCT image with *arrows* indicating points where the spectra in panels (**b**–**e**) are quantified. *White x* and *y scale bars*, 100 μm. (**b**–**e**) Spectral profiles from points (**b**–**e**) in (**a**) measured spectral profiles (*black*) are superposed with the theoretical hemoglobin molar extinction coefficients (*red*). The *dashed* portion of the curves outlines the region used to determine SO_2 levels. All spectra were selected from depths immediately below each corresponding vessel [9]

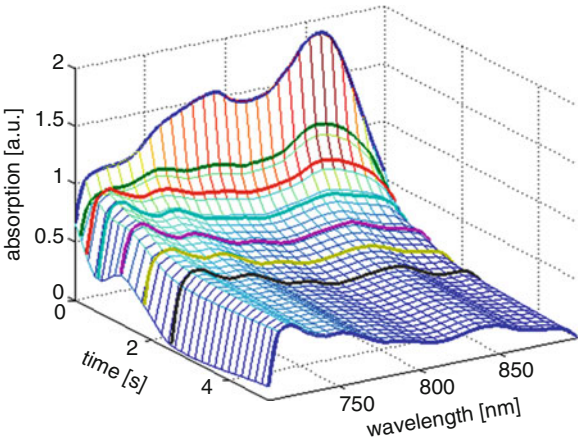

Fig. 36.9 Time evolution of spectral absorption for a non-scattering, absorbing ICG phantom. Photobleaching caused by the measurement light leads to time-dependent changes of the absorption profile. *Thick lines* indicate measured time points [42]

Absorption-based applications – The first absorption coefficient spectra measurements by SOCT were performed in vitro on homogeneous media in the absence of scattering, among others described in [2, 5, 7, 8]. Using the methods discussed in Sect. 36.2.3, these experiments were followed by in vitro validation studies on absorbing turbid media in homogeneous configurations for SOCT and LCS [11, 13, 33] and also in layered configurations for weakly scattering and absorbing media for SOCT [29, 34, 42]. The high acquisition speed of frequency domain OCT enables dynamic spectroscopic measurements. Figure 36.9 shows the absorption dynamics of indocyanine green (ICG) in a non-scattering phantom in the near-infrared wavelength region measured with LCS [42]. The bleaching effect of the light incident on the sample leads to a temporal change of its absorption characteristic.

The full potential of low-coherent interferometry techniques to do both *quantitative* and *localized* measurements of optical property measurements for applications in tissue has been shown using layered, more densely scattering and absorbing media [12].

The absorption coefficient spectrum of tissue is composed of the relative contributions of the present tissue chromophores. Hence, decomposition of the measured $\boldsymbol{\mu_a}$ by SOCT and LCS results in the individual chromophore concentrations.

A particularly interesting tissue chromophore is hemoglobin, since its absolute concentration is related to clinical parameters such as the blood content of the investigated tissue volume and the hematocrit of whole blood. In addition, the ratio between oxyhemoglobin and deoxyhemoglobin provides the oxygen saturation of the investigated tissue volume, which is related to the oxygen supply and consumption of the tissue. The first localized in vivo measurements of hemoglobin concentrations and oxygen saturations were performed by LCS in combination with least squares fitting, which are shown in Fig. 36.10 and are described in Ref [12]. Figure 36.10 shows that the total hemoglobin concentration differs substantially between a vessel poor (3.0 ± 0.5 g/L, region 2) and a vessel rich region (7.8 ± 1.2 g/L, region 3) in the human

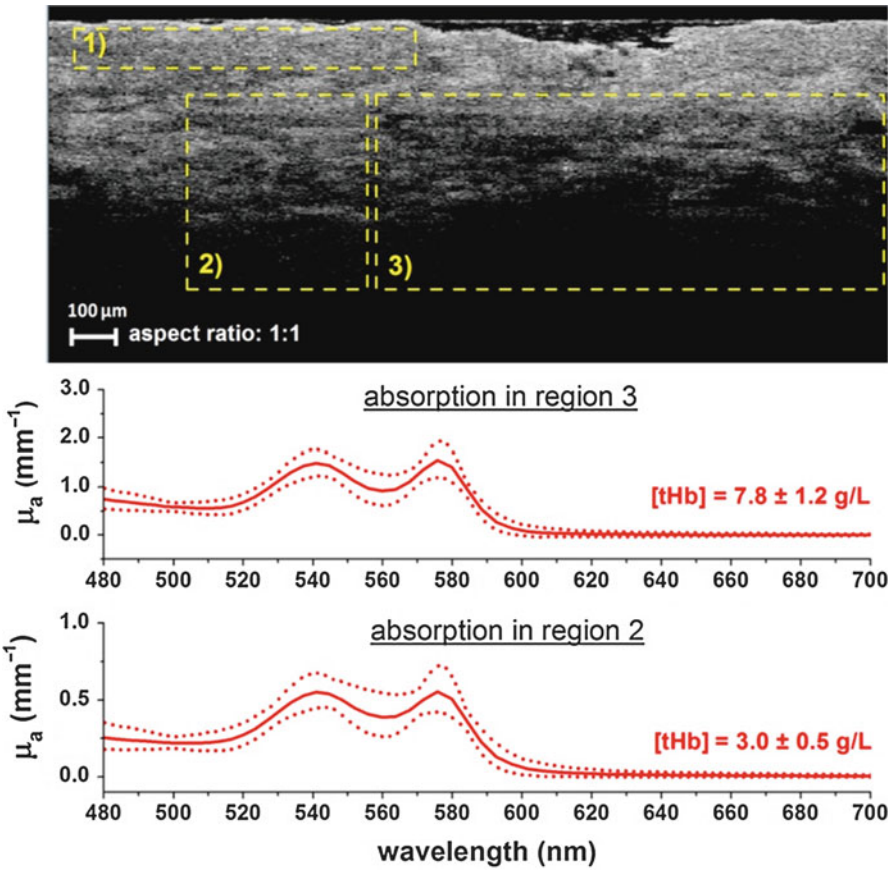

Fig. 36.10 In vivo LCS measurement on the skin of the palmar side of a human finger joint, supported by an OCT B-scan. The absorption spectra (*solid lines*) and their confidence intervals (*dotted lines*) are shown for the selected regions 2 and 3 in the dermis. From the absorption spectra, the total hemoglobin concentration [tHb] and oxygen saturation were determined. The attenuation spectrum in the epidermal region 1 did not exhibit any absorption features, as is expected from the absence of blood vessels in this skin layer (data not shown) [12]

dermis of the finger, corresponding to normal dermal blood volume fractions of 2 % and 5 %, respectively. Due to error propagation in the ratio of oxy- and deoxyhemoglobin, the oxygen saturation was determined with less accuracy, accounting for 81 ± 34 % and 100 ± 31 % for regions 2 and 3, respectively. Tissue attenuation in the epidermal layer (region 1) only exhibited the contribution of scattering (not shown), which agrees with the expected absence of blood vessels in this skin layer. Localized measurements of tissue oxygen saturation were also shown in a mouse model by Robles et al. using METRICS OCT (lower panels of Fig. 36.8) [9].

Although currently not yet investigated, other tissue chromophores have potential to be quantified by SOCT and LCS as well, depending on the investigated wavelength region (Fig. 36.1). As addressed in Ref [14], a valuable application of LCS and/or SOCT would be the noninvasive determination of bilirubin concentrations inside blood vessels for jaundiced neonates.

Scattering-based applications – The possibility to combine elastic scattering spectroscopy with OCT is discussed in ▶ Chap. 27, "Digital Holoscopy" and was explored in numerical simulations in [43]. This section focuses on the scattering property measurements that can be obtained using the theory described in Sect. 36.2.2, which result in scattering $\boldsymbol{\mu_s}$ and backscattering $\boldsymbol{\mu_{b,\ NA}}$ coefficient spectra. This offers the unique possibility for a combination of simultaneous, quantitative, and spectrally resolved measurements of $\boldsymbol{\mu_s}$ and $\boldsymbol{\mu_{b,\ NA}}$ [11]. This combination of optical properties is characteristic for particle or tissue type and therefore offers new opportunities for tissue and/or particle characterization studies. For these studies, the measurement of both $\boldsymbol{\mu_s}$ and $\boldsymbol{\mu_{b,\ NA}}$ may assist in better differentiation, because low contrast in $\boldsymbol{\mu_s}$ can be accompanied by high contrast in $\boldsymbol{\mu_{b,\ NA}}$. The latter is illustrated in Fig. 36.11 for LCS measurements on polystyrene spheres of various sizes (Ø 409, 602, 799, and 1,004 nm). Whereas the $\boldsymbol{\mu_s}$ spectra are similar for all spheres at these concentrations, the $\boldsymbol{\mu_{b,\ NA}}$ spectra differ substantially both in absolute value and in spectral features, i.e., sphere size-dependent oscillations as a function of wavelength. Note that the measurements (dots) agree well with the expected values (solid lines) from Mie calculations. Another encouraging result is that, although the $\boldsymbol{\mu_s}$ spectra are similar, LCS succeeds in distinguishing the samples based on subtle differences in scatter power b. Further demonstrating the potential of this method, Yi et al. [28] extracted scatter power and correlation length of the refractive index (e.g., analysis based on Eq. 36.13).

Figure 36.12 shows that accurate agreement with Mie calculations is obtained also for a wider range of sphere concentrations and sizes, i.e., more densely scattering media. For clarity reasons, only the values at $\lambda = 700$ nm have been displayed. This suggests the absence of the influence of multiple scattering and/or dependent scattering (presence of a large non-unity structure factor $\boldsymbol{S}(\theta)$) on the LCS signal for these measurements. If present, these effects will result in an underestimation of $\boldsymbol{\mu_s}$ and an overestimation of $\boldsymbol{\mu_{b,\ NA}}$ (Sect. 36.2.2). These effects have been observed for densely scattering media at shorter wavelengths [11]. Hence, the quantitative interpretation of scattering property measurements on tissue should be made with caution, although the absolute measured value of $\boldsymbol{\mu_s}$ and $\boldsymbol{\mu_{b,\ NA}}$ can still contain tissue-specific information. We repeat that multiple and/or dependent scattering does not affect the absolute measurement of $\boldsymbol{\mu_a}$, since absorption always takes place along the (known) photon path in LCS and SOCT. Although the spectra in Figs. 36.11 and 36.12 were measured in the absence of absorption, quantitative $\boldsymbol{\mu_s}$ spectra agreeing with Mie calculations have also been measured in the presence of absorption by both time domain and spectral domain LCS [13].

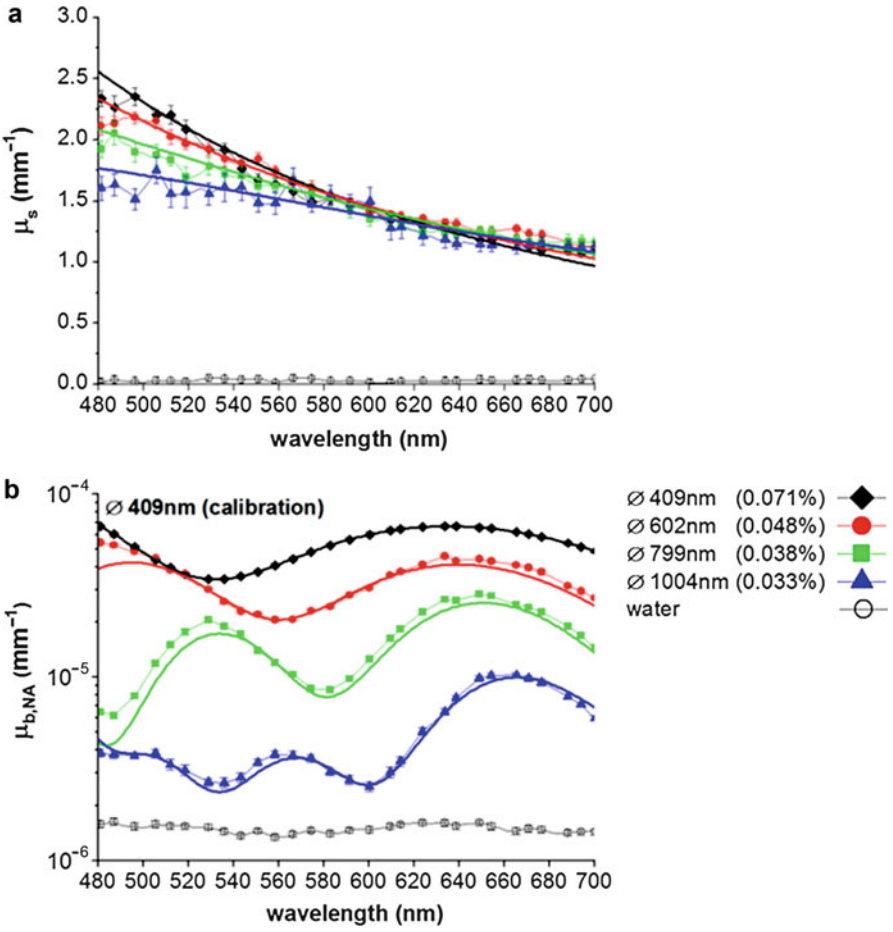

Fig. 36.11 LCS (*dots*) and Mie (*thick solid lines*) results for (**a**) scattering coefficients $\boldsymbol{\mu_s}$, and (**b**) backscattering coefficients $\boldsymbol{\mu_{b,NA}}$ for four aqueous suspensions of different sized polystyrene spheres, and water. *Error bars*, representing the 95 % confidence intervals of the fitted values, may fall behind data points. The $\boldsymbol{\mu_{b,NA}}$ were calibrated using the 409 nm sample and the procedure described in Sect. 36.2.2 [11]

36.4 Recent advances in the field of Spectroscopic Low-Coherence Interferometry

Since the acceptance for publication of this chapter in 2012, some interesting advances have been made in the field of Spectroscopic Low-Coherence Interferometry. For the completeness of this chapter, these advances will be briefly described here. The application of in vivo oximetry by SOCT has been demonstrated and validated in individual vessels of the retina and the skin [45, 46]. Although the probing depth for most applications of SOCT and LCS is limited to

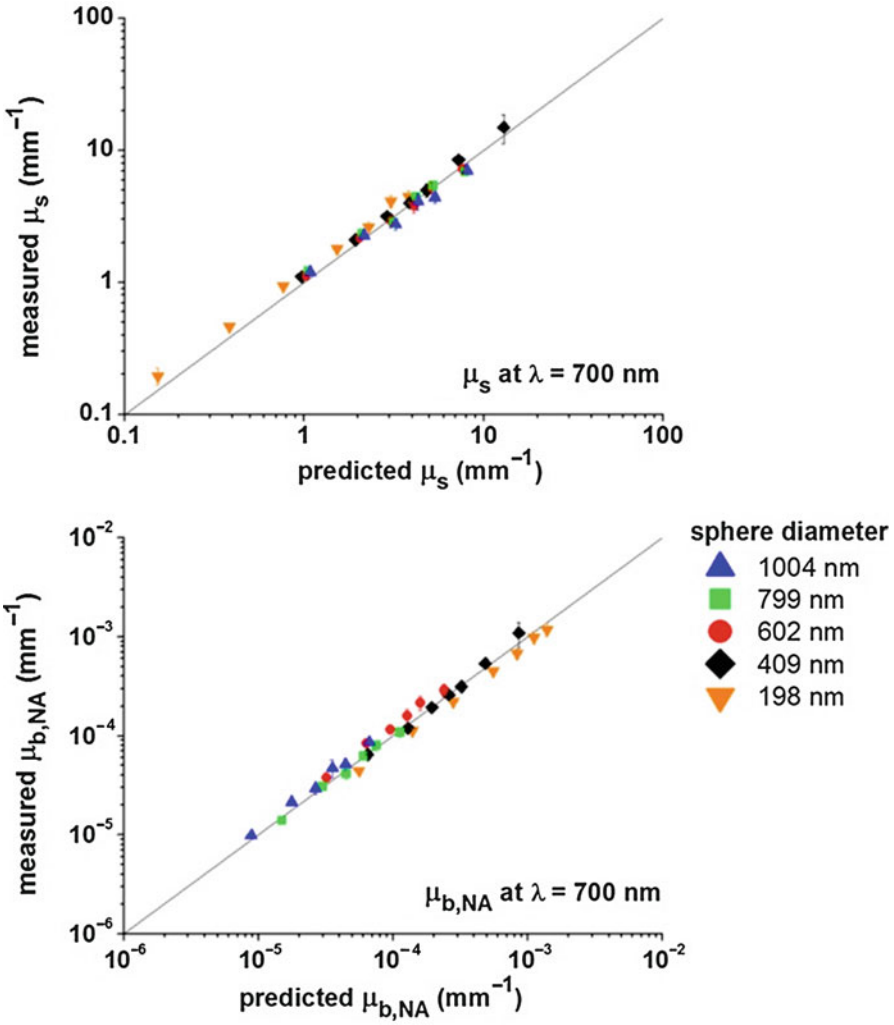

Fig. 36.12 Measured (LCS) versus predicted (Mie theory) values of $\boldsymbol{\mu_s}$ and $\boldsymbol{\mu_{b,NA}}$ for different-sized polystyrene spheres and various concentrations. For clarity reasons, only the values at $\lambda = 700$ nm have been displayed

$\sim$1 mm in tissue due to the analysis of single scattered photons, the probing depth can be increased considerably by also analyzing multiple scattered photons – at the expense of spatial resolution. Refs [47, 48] show how to retrieve spatially resolved spectroscopic information from larger depths using this principle. A more comprehensive and validated comparison of the time-frequency analysis methods for SOCT and LCS described in this chapter is described in Refs [49–51]. Other analysis methods for the visualization of spectroscopic information in SOCT images are compared in Ref [52].

36.5 Conclusion

Spectroscopic low-coherence interferometry groups modalities that quantify spatially resolved spectral properties. The best known to date are spectroscopic OCT and low-coherence spectroscopy. Spatially resolved measurement of absorption spectra allows retrieval of local chromophore concentrations such as (oxy)hemoglobin and bilirubin which has various potential applications ranging from determination of oxygen saturation in small tissue (tumor) volumes to monitoring jaundice in neonates while preventing invasive heal pricks. Similarly, the spectra of scattering properties such as the scattering coefficient and backscattering coefficient hold a wealth of information on tissue organization. The potential of this method is yet to be explored, but "non-spectroscopic" results (e.g., averaged over the LCI systems wavelength bandwidth) are promising.

This chapter starts by describing time-frequency (or "depth-wavelength") analysis to obtain localized spectra from LCI data. We discuss the most common form, short-time Fourier transform, and its inherent trade-off between spatial and spectral resolution. We proceed to discuss methods to meet that challenge, based on the wavelet transform and on the pseudo-Wigner distribution. Intriguingly, a convenient way to perform the latter analysis is through dual-window STFT analysis.

Signal decay with depth caused by instrumental factors can both be a problem and an asset. In the former case, we present calibration methods to account for the axial confocal point spread function and the sensitivity roll-off in depth. In the latter case, these effects are maximized, e.g., by using very large NA optics and/or spectrometers with spectral resolution in the order over several nanometers, thus highly localizing the detected interference signal in the spatial domain while leaving room for sufficient spectral resolution.

We proceed to describe the LCI signal in terms of depth-resolved absorption and (back)scattering coefficients and discuss approaches to separate the contributions of absorption and scattering to the total signal attenuation. We briefly touch on the possible diagnostic significance of scattering measurements by seeking direct theoretical relations between light scattering properties and (statistical) descriptors of tissue organization.

After discussing the spectroscopic accuracy of spectroscopic OCT and low-coherence interferometry, we discuss clinical and experimental applications: in vivo measurements of local hemoglobin concentrations and oxygen saturation are discussed as well as in vitro validation of quantitative measurements of scattering and backscattering spectra.

Concluding, low-coherence interferometry continues to have significant diagnostic potential as it not only allows high-resolution volumetric imaging but also provides localized measurement of parameters describing the physiological status. As other chapters in this book demonstrate, measurement of flow and perfusion has spectacularly improved in recent years. In this chapter, we highlighted the opportunities and challenges of localized spectroscopy within these tissue volumes.

References

1. M.D. Kulkarni, J.A. Izatt, *CLEO'96. Summaries of Papers Presented at the Conference on Lasers and Electro Optics*, Anaheim, CA, USA 9 (96CH35899) 59–60 (1996)
2. R. Leitgeb, M. Wojtkowski, A. Kowalczky, C.K. Hitzenberger, M. Sticker, A.F. Fercher, Spectral measurement of absorption by frequency domain optical coherence tomography. Opt. Lett. **25**, 820–822 (2000)
3. J.M. Schmitt, S.H. Xiang, K.M. Yung, Differential absorption imaging with optical coherence tomography. J. Opt. Soc. Am. A **15**, 2288–2296 (1998)
4. U. Morgner, W. Drexler, F.X. Kärtner, X.D. Li, C. Pitris, E.P. Ippen, J.G. Fujimoto, Spectroscopic optical coherence tomography. Opt. Lett. **2**, 111–113 (2000)
5. D.J. Faber, E. Mik, M. Aalders, T. van Leeuwen, Light absorption of (oxy-) hemoglobin assessed by spectroscopic optical coherence tomography. Opt. Lett. **28**, 1436–1438 (2003)
6. D.J. Faber, E. Mik, M. Aalders, T. van Leeuwen, Toward assessment of blood oxygen saturation by spectroscopic optical coherence tomography. Opt. Lett. **30**, 1015–1017 (2005)
7. F. Robles, R.N. Graf, A. Wax, Dual window method for processing spectroscopic optical coherence tomography signals with simultaneously high spectral and temporal resolution. Opt. Express **17**, 6799–6811 (2009)
8. F.E. Robles, S. Chowdhury, A. Wax, Assessing hemoglobin concentration using spectroscopic optical coherence tomography for feasibility of tissue diagnostics. BioMed. Opt. Express **1**, 310–317 (2010)
9. F.E. Robles, C. Wilson, G. Grant, A. Wax, Molecular imaging true-colour spectroscopic optical coherence tomography. Nat. Photonics **5**, 744–747 (2011)
10. N. Bosschaart, M.C.G. Aalders, D.J. Faber, J.J.A. Weda, M.J.C. van Gemert, T.G. van Leeuwen, Quantitative measurements of absorption spectra in scattering media by low-coherence spectroscopy. Opt. Lett. **34**, 3746–3748 (2009)
11. N. Bosschaart, D.J. Faber, T.G. van Leeuwen, M.C.G. Aalders, Measurements of wavelength dependent scattering and backscattering coefficients by low-coherence spectroscopy. J. BioMed. Opt. **16**, 030503 (2011)
12. N. Bosschaart, D.J. Faber, T.G. van Leeuwen, M.C.G. Aalders, In vivo low-coherence spectroscopic measurements of local hemoglobin absorption spectra in human skin. J. BioMed. Opt. **16**, 100504 (2011)
13. N. Bosschaart, M.C.G. Aalders, T.G. van Leeuwen, D.J. Faber, Spectral domain detection in low-coherence spectroscopy. BioMed. Opt. Express **3**, 2263–2272 (2012)
14. N. Bosschaart, J.H. Kok, A.M. Newsum, D.M. Ouweneel, R. Mentink, T.G. van Leeuwen, M.C.G. Aalders, Limitations and opportunities of transcutaneous bilirubin measurements. Pediatrics **129**, 689–694 (2012)
15. F.J. van der Meer, D.J. Faber, M.C.G. Aalders, A.A. Poot, I. Vermes, T.G. van Leeuwen, Apoptosis- and necrosis-induced changes in light attenuation measured by optical coherence tomography. Lasers Med. Sci. **25**(2), 259–267 (2010)
16. R. Wessels, D.M. de Bruin, D.J. Faber, H.H. van Boven, A.D. Vincent, T.G. van Leeuwen, M. van Beurden, T.J.M. Ruers, Optical coherence tomography in vulvar intraepithelial neoplasia. J. Biomed. Opt. **17**(11), 116022 (2012)
17. K. Barwari, D.M. de Bruin, E.C.C. Cauberg, D.J. Faber, T.G. van Leeuwen, H. Wijkstra, J. de la Rosette, M. Pilar Laguna, Advanced diagnostics in renal mass using optical coherence tomography: a preliminary report. J. Endourol. **25**(2), 311–315 (2012)
18. K. Barwari, D.M. de Bruin, D.J. Faber, T.G. van Leeuwen, J.J. de la Rosette, M. Pilar Laguna, Differentiation between normal renal tissue and renal tumors using functional optical coherence tomography, a Phase I study in-vivo human". Br. J. Urol. **110**, E415–E420 (2012)
19. E.C.C. Cauberg, D.M. de Bruin, D.J. Faber, T.M. de Reijke, M. Visser, J.J.M.C.H. de la Rosette, T.G. van Leeuwen, Quantitative measurement of attenuation coefficients of bladder

biopsies using optical coherence tomography for grading urothelial carcinoma of the bladder. J. BioMed. Opt. **15**, 066013 (2010)
20. R. Carmona, W. Hwang, B. Torresani, *Practical Time-Frequency Analysis* (Academic, San Diego, 1998)
21. C. Xu, F. Kamalabadi, S. Boppart, Comparative performance analysis of time-frequency distributions for spectroscopic optical coherence tomography. Appl. Opt. **44**, 1813–1822 (2005)
22. T.G. van Leeuwen, D.J. Faber, M.C. Aalders, Measurement of the axial point spread function in scattering media using single-mode fiber-based optical coherence tomography. IEEE J. Sel. Top. Quantum Electron. **9**(2), 227 (2003)
23. D.J. Faber, F.J. van der Meer, M.C.G. Aalders, T.G. van Leeuwen, Quantitative measurement of attenuation coefficients of weakly scattering media using optical coherence tomography. Opt. Express **12**(19), 4353–4365 (2004)
24. C. Xu, C. Vinegoni, T.S. Ralston, W. Luo, W. Tan, S.A. Boppart, Spectroscopic spectral-domain optical coherence microscopy. Opt. Lett. **31**, 1097–1081 (2006)
25. H.C. van de Hulst, *Light Scattering by Small Particles* (Dover, New York, 1981)
26. V. Duc Nguyen, D.J. Faber, E. van der Pol, T.G. van Leeuwen, J. Kalkman, Dependent and multiple scattering in transmission and backscattering optical coherence tomography. Optics Express (**21**)24, 29145–29156 (2013)
27. A. Wax, V. Backman (eds.), *Biomedical Applications of Light Scattering* (McGraw Hill, New York, 2010)
28. J. Yi, V. Backman, Imaging a full set of optical scattering properties of biological tissue by inverse spectroscopic optical coherence tomography. Opt. Lett. **37**(21), 4443 (2012)
29. C. Xu, D. Marks, M. Do, S. Boppart, Separation of absorption and scattering profiles in spectroscopic optical coherence tomography using a least-squares algorithm. Opt. Express **12**, 4790–4803 (2004)
30. Y.L. Li, K. Seekell, H. Yuan, F.E. Robles, A. Wax, Multispectral nanoparticle contrast agents for true-color spectroscopic optical coherence tomography. BioMed. Opt. Express **3**, 1914–1923 (2012)
31. D.J. Faber, M.C.G. Aalders, E.G. Mik, B.A. Hooper, M.J.C. van Gemert, T.G. van Leeuwen, Oxygen saturation-dependent absorption and scattering of blood. Phys. Rev. Lett. **93**, 028102 (2004)
32. V. Lucarni, J.J. Saarinen, K.-E. Peiponen, E.M. Vartiainen, *Kramers-Kronig Relations in Optical Materials Research* (Springer, Berlin/Heidelberg, 2010)
33. F.E. Robles, A. Wax, Separating the scattering and absorption coefficients using the real and imaginary parts of the refractive index with low-coherence interferometry. Opt. Lett. **35**, 2843–2845 (2010)
34. B. Hermann, K. Bizheva, A. Unterhuber, B. Považay, H. Sattmann, L. Schmetterer, A. Fercher, W. Drexler, Precision of extracting absorption profiles from weakly scattering media with spectroscopic time-domain optical coherence tomography. Opt. Express **12**, 1677–1688 (2004)
35. C. Xu, J. Ye, D. Marks, S. Boppart, Near-infrared dyes as contrast-enhancing agents for spectroscopic optical coherence tomography. Opt. Lett. **29**, 1647–1649 (2004)
36. A. Dubois, J. Moreau, C. Boccara, Spectroscopic ultrahigh-resolution full-field optical coherence microscopy. Opt. Express **16**, 17082–17091 (2008)
36. C. Yang, L. McGuckin, J. Simon, M. Choma, B. Applegate, J. Izatt, Spectral triangulation molecular contrast optical coherence tomography with indocyanine green as the contrast agent. Opt. Lett. **29**, 2016–2018 (2004)
38. D. Adler, T. Ko, P. Herz, J. Fujimoto, Optical coherence tomography contrast enhancement using spectroscopic analysis with spectral autocorrelation. Opt. Express **12**, 5487–5501 (2004)
39. F. Spöler, S. Kray, P. Grychtol, B. Hermes, J. Bornemann, M. Först, H. Kurz, Simultaneous dual-band ultra-high resolution optical coherence tomography. Opt. Express **15**(17), 10832 (2007)

40. S. Kray, F. Spöler, M. Först, H. Kurz, High resolution simultaneous dual-band spectral domain optical coherence tomography. Opt. Lett. **34**(13), 1970 (2009)
41. P. Cimally, J. Walther, M. Mehner, M. Cuevas, E. Koch, Simultaneous dual band optical coherence tomography in the spectral domain for high resolution in vivo imaging. Opt. Express **17**(22), 19486 (2009)
42. B. Hermann, B. Hofer, C. Meier, W. Drexler, Spectroscopic measurements with dispersion encoded full range frequency domain optical coherence tomography in single- and multilayered non-scattering phantoms. Opt. Express **17**(26), 24162 (2009)
43. C. Xu, P. Carney, S. Boppart, Wavelength-dependent scattering in spectroscopic optical coherence tomography. Opt. Express **13**(14), 5450 (2005)
44. Data tabulated from various sources compiled by S. Prahl, http://omlc.ogi.edu/spectra
45. J. Yi, Q. Wei, W. Liu, V. Backman, H.F. Zhang, Visible-light optical coherence tomography for retinal oximetry. Opt. Lett. **38**, 1796–1798 (2013)
46. J. Yi, S. Chen, V. Backman, H.F. Zhang, In vivo functional microangiography by visible-light optical coherence tomography. Biomed. Opt. Express **5**, 3603–3612 (2014)
47. T.E. Matthews, M.G. Giacomelli, W.J. Brown, A. Wax, Fourier domain multispectral multiple scattering low coherence interferometry. Applied Opt. **52**, 8220–8228 (2013)
48. T.E. Matthews, M. Medina, J.R. Maher, H. Levinson, W.J. Brown, A. Wax, Deep tissue imaging using spectroscopic analysis of multiply scattered light. Optica **1**, 105–111 (2014)
49. N. Bosschaart, T.G. van Leeuwen, M.C.G. Aalders, D.J. Faber, Quantitative comparison of analysis methods for spectroscopic optical coherence tomography. Biomed. Opt. Express **4**, 2570–2584 (2013)
50. M. Kraszewski, M. Trojanowski, M.R. Strąkowski, Quantitative comparison of analysis methods for spectroscopic optical coherence tomography: comment. Biomed. Opt. Express **5**, 3023–3033 (2014)
51. N. Bosschaart, T.G. van Leeuwen, M.C.G. Aalders, D.J. Faber, Quantitative comparison of analysis methods for spectroscopic optical coherence tomography: reply to comment, Biomed. Opt. Express **5**, 3034–3035 (2014)
52. V. Jaedicke, S. Agcaer, F.E. Robles, M. Steinert, D. Jones, S. Goebel, N.C. Gerhardt, H. Welp, M.R. Hofmann, Comparison of different metrics for analysis and visualization in spectroscopic optical coherence tomography. Biomed. Opt. Express. **4**, 2945–2961 (2013)

Motility Contrast Imaging and Tissue Dynamics Spectroscopy

37

David D. Nolte, Ran An, and John Turek

Keywords
Dynamic light scattering • Digital holography • Optical coherence tomography • Drug discovery • Phenotypic profiling • Three-dimensional tissue

37.1 Introduction: Biological Relevance of Intracellular Motion

Motion is the defining physiological characteristic of living matter. If we are interested in how things *function*, then the way they *move* is most informative. Motion provides an endogenous and functional suite of biomarkers that are sensitive to subtle changes that occur under applied pharmacological doses or cellular stresses. This chapter reviews the application of biodynamic imaging to measure cellular dynamics in three-dimensional tissue culture for drug screening applications. Nanoscale and microscale motions are detected through statistical fluctuations in dynamic speckle across an ensemble of cells within each resolution voxel. Tissue dynamics spectroscopy generates drug-response spectrograms that serve as phenotypic fingerprints of drug action and can differentiate responses from heterogeneous regions of tumor tissue.

Motion occurs across broad spatial and temporal scales. At one extreme, molecules executing Brownian diffusion cross nanometers in microseconds. At the other extreme, metastatic crawling cells cross microns in hours. Spanning these scales, different functional processes take place: molecular diffusion, molecular

D.D. Nolte (✉)
Department of Physics, Purdue University, West Lafayette, IN, USA

Department of Basic Medical Sciences, Purdue University, West Lafayette, IN, USA
e-mail: nolte@purdue.edu

R. An • J. Turek
Department of Basic Medical Sciences, Purdue University, West Lafayette, IN, USA

© Springer International Publishing Switzerland 2015

W. Drexler, J.G. Fujimoto (eds.), *Optical Coherence Tomography*,
DOI 10.1007/978-3-319-06419-2_38

polymerization or depolymerization of the cytoskeleton, segregation of enzymes into vesicles, exocytosis and endocytosis, shepherding of vesicles by molecular motors, active transport of mitochondria, cytoskeletal forces pushing and pulling on the nucleus, undulations of the cell membrane, push and pull at cell-to-cell adhesions, deformation of the cell, cell division, and ultimately to movement of individual cells through tissue. All of these very different types of cellular dynamics are active and useful indicators of the functioning behavior of cells in tissue.

Imaging motion in three-dimensional tissue is simpler than imaging structure or performing molecular imaging in 3D, because motion modulates coherent light through phase modulation that is detected by interferometry [1]. Anytime light scatters from a displacing object, the phase of the light is modified. If the light has coherence, then the motion-induced phase shifts of one light path interfere with the phase shifts of other light paths. Even light that is multiply scattered in tissue carries a record of the different types of motions that the light encounters. By measuring the fluctuating phase of light scattered from living tissue, different types of motion across different space and time scales can be measured.

This article reviews the principles of low-coherence dynamic imaging of three-dimensional tissue that uses low-coherence digital holography to spatially isolate optical signals that return from specific depths inside tissue, as in optical coherence tomography (OCT) [2–5]. Digital holographic optical coherence imaging is ideally suited to dynamic imaging because of the well-developed speckle and high signal-to-noise of dynamic speckle. For drug screening in three-dimensional tissues, tissue dynamics spectroscopy (TDS) produces drug-response spectrograms that serve as fingerprints of tissue responding to different applied drugs [6, 7]. These drug-response fingerprints capture the phenotypic similarities and differences among different drugs and cell types and can be used to build a phenotypic database that can serve as a dynamic classifier of new compounds.

37.2 Dynamic Light Scattering from Cells and Tissue

Dynamic light scattering is a characterization tool for remotely extracting dynamic information, such as internal displacements, diffusivities, and velocities [8, 9], from inside media. In the dilute limit, in which light is scattered once, dynamic light scattering is called quasi-elastic light scattering (QELS) [10]. In biological applications, QELS is useful for optically thin systems, such as cell monolayer cultures, and it provides information on diffusion and directed motion in the cytosol [11, 12], nucleus [13], and undulations of the plasma membrane [14–18]. However, as the optical thickness of a sample increases beyond one optical transport length, multiple scattering becomes significant, and the diffusive character of light begins to dominate [19–21]. In this multiple scattering limit, diffusing-wave spectroscopy (DWS) [22] and diffuse correlation spectroscopy (DCS) [23–25] continue to carry motional signatures from inside tissue in the field and intensity fluctuations of the scattered light.

Dynamic light scattering (DLS) is a fundamental process by which light scattered from displacing scatterers experiences phase shifts related to the

magnitude and direction of displacement [8]. Living tissue is a dense collection of scatterers that are executing many different types of motion, leading to a rich collection of phase shifts. For the slow motions inside a cell (microns per second and slower), the phase drift associated with displacements is equivalent to an ultra-low-frequency (ULF) Doppler shift in the light frequency. The Doppler frequency offsets are too small to measure directly, but by using interferometry (such as digital holography), the phase modulation is measured as a heterodyne intensity fluctuation signal. The fluctuating intensities of the backscattered speckle contain the motional information of the scatterers.

Fluctuation analysis begins with the autocorrelation function of the intensity fluctuations. The autocorrelation is defined by

$$A_I(\tau) = \langle I(0)I(\tau)\rangle = V_I F(\tau) + \langle I\rangle^2 \tag{37.1}$$

where the intensity variance is $V_I = (\langle I^2\rangle - \langle I\rangle^2)$, and the delay-dependent function $F(\tau)$ is a decorrelation function that has contributions from many different dynamic processes in the cells and tissue. In the case of single scattering (QELS), it can be defined as a sum of independent exponential decorrelations as [26]

$$F(\tau) = \sum_n f_n \exp\left(-q^2 \Delta x_n^2(\tau)\right) \tag{37.2}$$

where $\Delta x_n^2(\tau)$ is the mean-squared displacement (MSD) of moving scatterers inside the cells and tissue [8] and $q = 2\,k$ is the backscattering vector where $k = 2\pi/\lambda$. The index n represents the n-th process or n-th set of cellular constituents that contribute to the mean-squared displacement, and f_n is the fractional contribution of the n-th process to the total variance. The high-content information of dynamic imaging originates from the summation over the different types of processes. If these processes have widely distributed characteristic times, then their contributions can be separated and isolated, enabling their quantification as they are affected by applied drugs.

Typical time scales for scattering are related to the scattering vector and to the motion of the scatterer. For particles diffusing with a diffusion coefficient D, or drifting with a drift velocity v, the characteristic decorrelation times are

$$\tfrac{1}{\tau}\big|_{Diff} = q^2 D \qquad \tfrac{1}{\tau}\big|_{drift} = qv \tag{37.3}$$

respectively, where the expression for drift is also equal to the Doppler frequency shift. Motions in living cells are not fast. Even molecules executing Brownian motion are hindered by the crowded molecular constituents of the cytoplasm [27]. Therefore, characteristic decorrelation times for light scattered from tissue range from many milliseconds to as slow as hundreds of seconds. This time frame is easily accessible with frame rates of common digital cameras.

When there are many processes that have characteristic times that are similar, the decorrelation function of Eq. 37.2 becomes difficult to separate into

isolated contributions. It is then more convenient to work in the frequency domain by taking the Fourier transform of the dynamic imaging decorrelation function in Eq. 37.1. The mean-squared displacement of processes in biological systems is rarely by simple diffusion and commonly displays the signature of anomalous diffusion. Deviation from free diffusion is described phenomenologically through the relation

$$\Delta r^2 = D^* \left(\frac{t}{t_0} \right)^{\beta} \tag{37.4}$$

where D^* is a time-independent coefficient and t_0 is a characteristic time. The exponent for normal Fickian diffusion is $\beta = 1$. If $\beta < 1$, the diffusion is called subdiffusive, while if $\beta > 1$, the diffusion is called superdiffusive. Superdiffusive behavior occurs if there is persistent and correlated motion of the particle, as in the active transport of organelles. On the other hand, subdiffusive behavior is the most commonly encountered case when motion is constrained or impeded in some way, such as diffusion of molecules through the crowded cytosol.

Even in the presence of multiple scattering, dynamic light scattering information can still be extracted [28, 29] using diffusing wave spectroscopy (DWS) [30, 31] and an equivalent formulation of multi-scattering dynamic light scattering called diffuse correlation spectroscopy (DCS) [23, 25, 32, 33]. For multiple scattering in thick tissue, the effective squared scattering vector is

$$q_{eff}^2 = 4k^2 \left[1 + \frac{z}{l_s}(1 - g) \right] \tag{37.5}$$

where g is the anisotropy factor (typically $g \approx 0.9$ in tissue), z is the coherence-gated depth in the tissue, and l_s is the mean-free scattering length of a photon (typically $l_s \approx 20$ μm). Multiple scattering causes the effective squared scattering vector to increase linearly with depth from the value set by single backscattering. This has the effect of "speeding up" the light fluctuations from increasing depths.

In biological applications, DCS has been used to monitor tissue response to burns [34], brain activity [35], blood flow [24, 25] and tissue structure [36]. DCS uses high-coherence laser sources and measures the temporal diffusing field autocorrelation function. The primary uses have been for macroscopic measurements of blood flow, which has been validated through comparisons with Doppler flowmetry and ultrasound [37–39]. A technique related to DCS, but that more directly uses speckle imaging, is speckle contrast imaging (SCI) [24]. This technique is used primarily for imaging of vasculature in vivo because the fast motions of blood cells blur the speckle contrast in images acquired with a long exposure time [40].

Optical coherence tomography (OCT) forms images by scanning and rastering. Speckle in OCT has long been considered an unwanted side effect of the coherent imaging, and many approaches have been explored to reduce speckle [41–43]. However, speckle decorrelation also can be studied in OCT data to provide similar

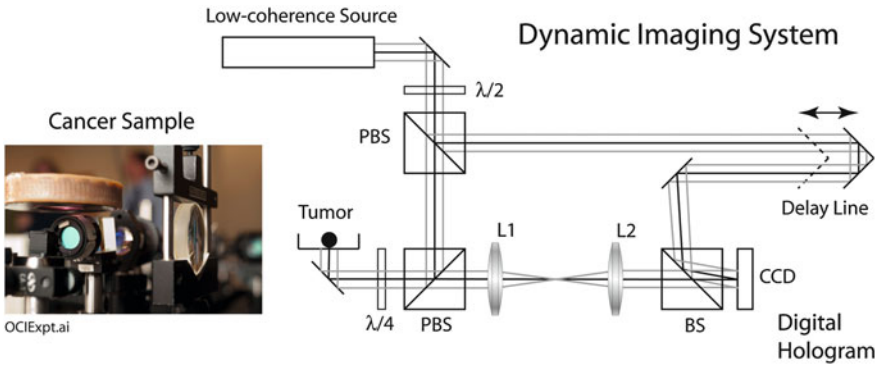

Fig. 37.1 Biodynamic imaging experimental setup that uses off-axis digital holography to capture dynamic speckle from a living tissue sample

information as provided by DCS. This has been used to measure intracellular rheology [12] and diffusion [44] and to find dynamic signatures of apoptosis [45] and motion of mucosa [46]. OCT is used in a Doppler mode for blood flow detection [47, 48]. Motility contrast imaging (MCI) is a related tissue-scale functional imaging technique that uses subcellular motion as the imaging contrast [49–51]. Motility contrast imaging of live tissue is based on two principles: dynamic light scattering from the motions of the constituents of living cells and coherence-gated depth resolution [52] that isolates the motional signals from specific depths.

37.3 Motility Contrast Imaging of Living Tissue

In biodynamic imaging, the coherence gate is formed by a low-coherence light source detected by digital holography on a CCD camera chip [53] (see ▶ Chap. 31, "Interferometric Synthetic Aperture Microscopy (ISAM)"). Light scattered from a selected depth is recorded in the digital hologram. When dynamic light scattering and coherence gating are combined, intracellular motion can be measured volumetrically up to 1 mm deep inside tissue with a spatial resolution of tens of microns. The basic optical configuration for an optical coherence imaging (OCI) system is shown in Fig. 37.1. Low-coherence light is split at a beam splitter into a signal arm that illuminates the sample and a reference arm that has a variable-delay retroreflector. Light scattered from the sample intersects with the reference beam at the plane of the CCD electronic chip [54] with a small crossing angle of about two degrees. The selected depth is defined by the path length from the beam splitter to the CCD plane. The low-coherence light source is either a 100 fsec Ti:sapphire laser or a Superlum superluminescent diode, both operating at a center wavelength of 840 nm. The hologram is recorded on the CCD chip and is "read-out" by a digital Fourier transform algorithm, which is stored as a layer in a volumetric data set.

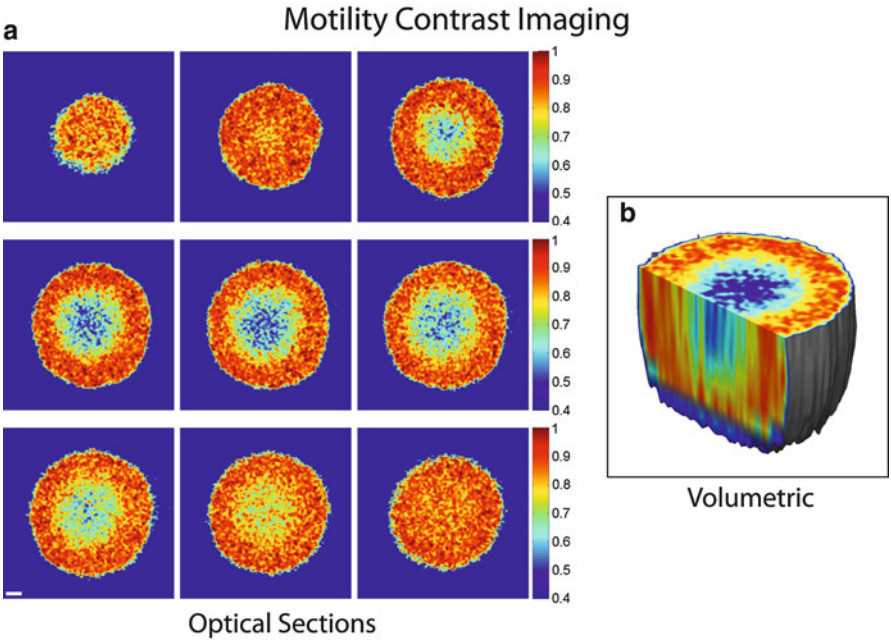

Fig. 37.2 (**a**) False-color motility contrast image of an 800 μm-diameter tumor spheroid, showing the proliferating shell (*red*) and the necrotic core (*blue*). (**b**) Volumetric motility contrast image

A motility metric captures the general activity level of a living sample. The simplest motility metric is the normalized standard deviation (NSD) of fluctuating time-dependent speckle, which is also the temporal contrast

$$NSD = \sqrt{\frac{\langle I^2 \rangle - \langle I \rangle^2}{\langle I \rangle^2}} = \frac{\sqrt{V_I}}{\langle I \rangle} \tag{37.6}$$

The NSD(x,y,z) motility metric is volumetric, with depth defined by the digital holographic coherence gate and the (x, y) coordinates of the image defined by reconstruction. An example of motility contrast imaging of a three-dimensional multicellular tumor spheroid is shown in Fig. 37.2 [50]. The spheroid is approximately 0.8 mm in diameter. The data are color coded according to the motility metric, with red signifying a high degree of motion and blue signifying a low degree of motion. For a spheroid of this size, the core is hypoxic and necrotic. The 200 μm thick proliferating shell is clearly discernible surrounding the less active core. The proliferating shell has high motility (red), and the necrotic core has low motility (blue).

Biodynamic imaging is a general imaging technique because it is responsive to intracellular motions, which occur in all living samples. Therefore, there are many

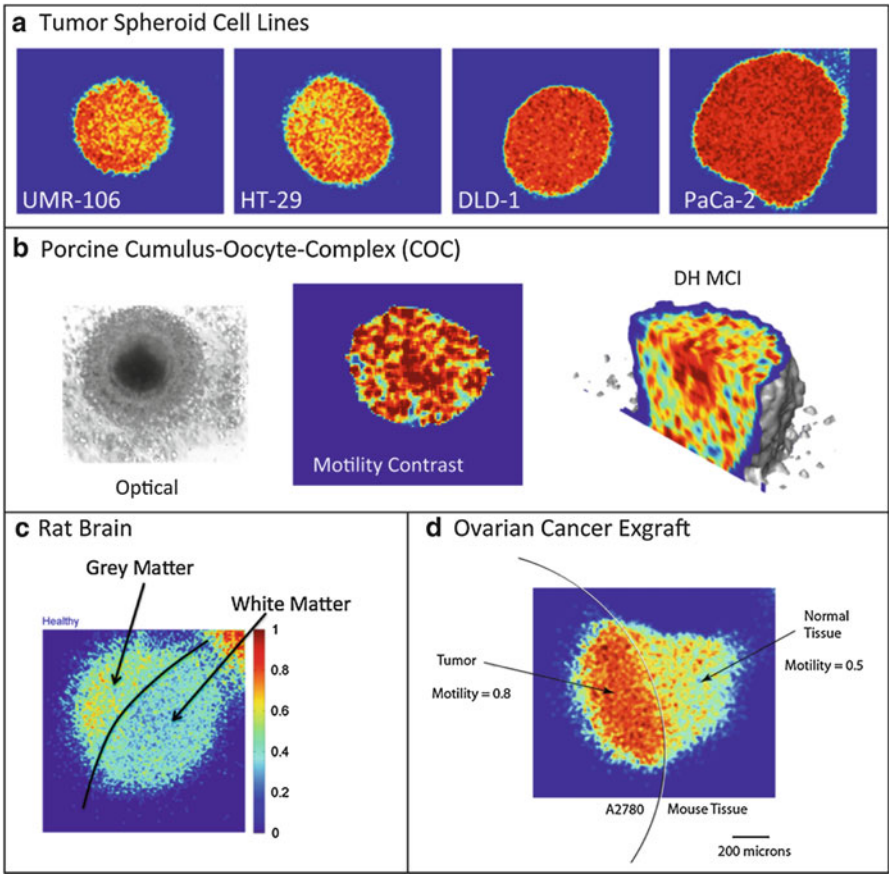

Fig. 37.3 Motility contrast images of (**a**) multicellular tumor spheroids derived from several different cell lines, (**b**) porcine cumulus-oocyte complexes, (**c**) *white* and *gray* matter of excised rat brain, and (**d**) cancer and normal tissue in a mouse ovarian cancer exgraft

potential applications for this new form of dynamic and functional imaging. Several of these are illustrated in Fig. 37.3. In (Fig. 37.3a) MCI is used to measure the activity of tissues from different cell lines, showing increasing activity from UMR-106 (rat osteogenic sarcoma), HT-29, and DLD-1 (human adenocarcinomas) to PaCa-2 (human pancreatic). A possible application in artificial reproductive technologies would be viability assessment of eggs and embryos prior to implantation in in vitro fertilization clinics. The motility activity of the central oocyte inside a cumulus-oocyte-complex (COC) is shown in Fig. 37.3b. MCI has been applied to tissue ex vivo as well, extending applications beyond purely in vitro culture. For instance, Fig. 37.3c shows the motility contrast between excised rat brain gray and white matter. Gray matter contains the cell bodies and is more dynamically active, while white matter consists primarily of axons. Figure 37.3d

shows the margin between normal tissue and cancerous tissue in a mouse exgraft in which the cancerous tissue is more dynamically active than the normal tissue.

37.4 Tissue Dynamics Spectroscopy and Drug-Response Spectrogram Fingerprints

The information received from coherence-gated light scattered from tissue relates to the many different types of motion that occur within cells across broad frequency ranges. It is possible to extend motility contrast imaging to tissue dynamics spectroscopy (TDS) by performing fluctuation spectroscopy to separate these motion contributions into partially overlapping frequency bands related to the different types of motion [55]. Tissue dynamics spectroscopy provides a label-free and noninvasive probe of cellular function and provides a functional assessment of drug candidates as a unique and new form of phenotypic profiling [7].

The Fourier transform of Eq. 37.1 under conditions of anomalous diffusion takes the form

$$S(\omega) = FT(A_I(\tau)) = \frac{V_I}{\pi}\sum_n \left[\frac{4}{(3-\beta_n)}\frac{f_n\omega_n^{\beta_n}}{\left(\omega_n^{1+\beta_n}+\omega^{1+\beta_n}\right)}\right] \tag{37.7}$$

where β_n is an anomalous diffusion exponent that is usually in the range $\beta_n \approx 0.7$–1.3.

Equation 37.7 retains the summation over the different dynamic processes taking place inside living tissue, and each process has a characteristic frequency ω_n given by $\omega_n = \sqrt[\beta]{q^2 D_n^*/t_n}$. Because most motions in living cells are stochastic, even if they are actively driven by molecular motors consuming ATP, they can be described in terms of an effective (active) diffusion coefficient D_n^* that describes different types of motion, such as vesicle or nucleus motion.

An example of a fluctuation power spectrum from a tumor spheroid grown from the DLD-1 adenocarcinoma cell line is shown in Fig. 37.4. The baseline spectrum shows a knee frequency around 0.1 Hz with a slope around $\beta \approx 1$. Two hours after 50 μM valinomycin is applied (a mitochondrial decoupler), the knee has shifted to 0.03 Hz with a smaller slope $\beta < 1$. Nine hours after the dose is applied, the spectrum has no clear knee frequency, and the slope is noticeably subdiffusive. Valinomycin reduces the mitochondrial membrane polarization (MMP) and suppresses the generation of ATP, thus significantly slowing the cellular metabolism. The shift of the spectrum to lower frequencies reflects this reduced metabolic activity, and the more subdiffusive slope may reflect a broader range of motional contributions.

The power spectrum of Eq. 37.7 changes as a function of time through the shift in the parameters $\Delta\omega_n(t)$, $\Delta f_n(t)$, and $\Delta\beta_n(t)$. The changes can be small, which suggests the use of a differential spectral response defined by

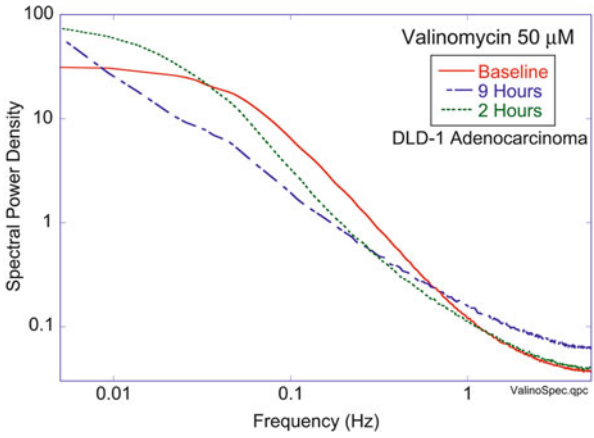

Fig. 37.4 Power spectrum of DLD-1 adenocarcinoma tumor spheroid responding to 50 µM valinomycin. The spectra 2 h and 9 h after the dosing is compared to the baseline spectrum. The spectrum has three orders of magnitude of dynamic range and spans three decades of frequency from 0.005 to 5 Hz

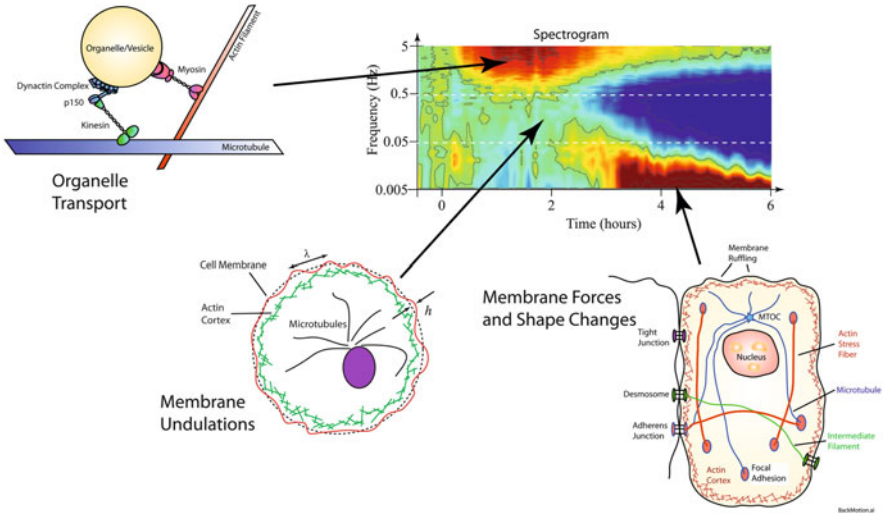

Fig. 37.5 The origin of spectroscopic motional signatures in a tissue-response spectrogram. The highest frequencies (around 5 Hz) relate to organelle transport, the mid-frequencies (around 0.5–0.05 Hz) to membrane undulations, and the lowest frequencies (around 0.005 Hz) to membrane forces and shape changes

$$D(\omega,t) = \frac{S(\omega,t) - S(\omega,0)}{S(\omega,0)} \tag{37.8}$$

This relative differential spectrogram captures the changes in spectral content as a function of time after a dose or a condition is applied. Tissue contains a wide range of characteristic frequencies producing complicated differential spectrograms.

An example of a tissue-response spectrogram is shown in Fig. 37.5 for pH 9 applied to rat UMR-106 osteogenic sarcoma tumor spheroids. The two-dimensional

representation of the differential response is presented as relative frequency content change as a function of time. The treatment is applied at $t = 0$, and the tumor spheroids are monitored over 6 h. The times preceding the treatment show the system baseline. The spectrogram shows an initially high-frequency enhancement that decays over several hours. There is a sudden enhancement of low frequencies around 3 h after the change in pH.

The mechanistic interpretation of the tissue-response spectrogram is facilitated by considering the backscattering frequencies from dynamic intracellular processes. The general relationship for single backscattering under heterodyne (holographic) detection is $q^2D = \omega_D$ for diffusion, and $qv = \omega_d$ for directed transport, where D is the diffusion coefficient, and v is a directed speed. The ranges in the parameters for directed transport and diffusion, respectively, are $0.006 < v < 2$ μm/s and $4 \times 10^{-4} < D < 0.1$ μm^2/s, set by the lowest and highest frequencies of 0.005–5 Hz. These are well within the range of intracellular motion in which molecular motors move organelles at speeds of microns per second [13, 56–59], although diffusion of very small organelles, as well as molecular diffusion, is too fast to be resolved by a frame rate of 10 fps. Membrane undulations are a common feature of cellular motions, leading to the phenomenon of flicker [60–64], and the characteristic frequency for light scattering from membrane undulations is in the range around 0.01–0.1 Hz [58, 61, 65]. The very low frequencies below 0.01 Hz relate to cellular rheology and the response of the cells to their local force environment, possibly including blebbing or the release of apoptotic bodies.

37.5 Phenotypic Profiling Based on Drug-Response Spectrograms

Cellular systems are highly complex, with high redundancy and dense cross talk among signaling pathways [66]. Biochemical target-based high-content screening can isolate single mechanisms in important pathways, but often fails to capture integrated system-wide responses. Phenotypic profiling, on the other hand, presents a systems-biology approach that has more biological relevance by capturing multimodal influence of therapeutics [67]. Ironically, phenotypic profiling is anachronistic, harking back to the days before genomics provided isolated targets. Nonetheless, it remains today one of the most successful approaches for the discovery of new drugs [68].

Most phenotypic profiling continues to be performed on two-dimensional culture, even though two-dimensional monolayer culture on flat hard surfaces does not respond to applied drugs in the same way as cells in their natural three-dimensional environment. This is in part because genomic profiles are different in primary monolayer cultures [69–71]. Several studies have tracked the expression of genes associated with cell survival, proliferation, differentiation, and resistance to therapy that are expressed differently in 2D cultures relative to three-dimensional culture. For example, three-dimensional culture display expression profiles more like those from tumor tissues than when grown in 2D [72–77].

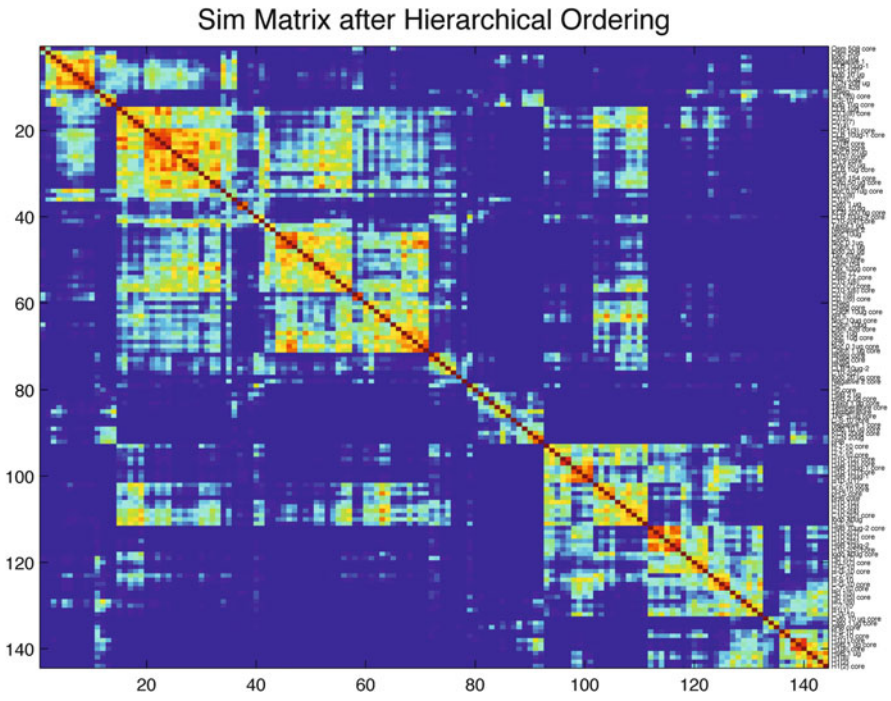

Fig. 37.6 A clustered similarity matrix among 144 different drugs, doses, and cell lines. The nearly block-diagonal structure after hierarchical ordering shows the quasi-orthogonality among the different groups of drug response

In addition, the three-dimensional environment of 3D culture presents different pharmacokinetics than 2D monolayer culture and produces differences in cancer drug sensitivities [78–81].

A drug-response spectrogram acts like a fingerprint, showing a distinct pattern in response to an applied drug or condition that is unique for that drug and cell line. To apply bioinformatic algorithms to the drug-response spectrograms, it is first necessary to convert the two-dimensional data format of the drug-response spectrograms into a quantitative feature vector [82]. Feature recognition and extraction is not a unique process, but a simple approach defines frequency response ranges across multiple time frames. The resulting feature vectors are N-dimensional representations of the specific response of the tissue cell line to the drug and dose. A similarity matrix is constructed from the correlation coefficients among the many pairs of feature vectors for different drugs and cell lines. A similarity matrix for 144 different drugs, doses, and cell lines is shown in Fig. 37.6 after unsupervised hierarchical clustering [83]. The drugs consist of nocodazole, colchicine, taxol, cytochalasin D, iodoacetate, TNF, cycloheximide, KCN, changes in pH and osmolarity, and several RAF inhibitors. The cell lines are UMR-106 rat osteogenic sarcoma as well as human HT-29 and DLD-1 adenocarcinomas. The clustering algorithm orders the tissue-response spectrograms of the different drugs and cell lines into groups based

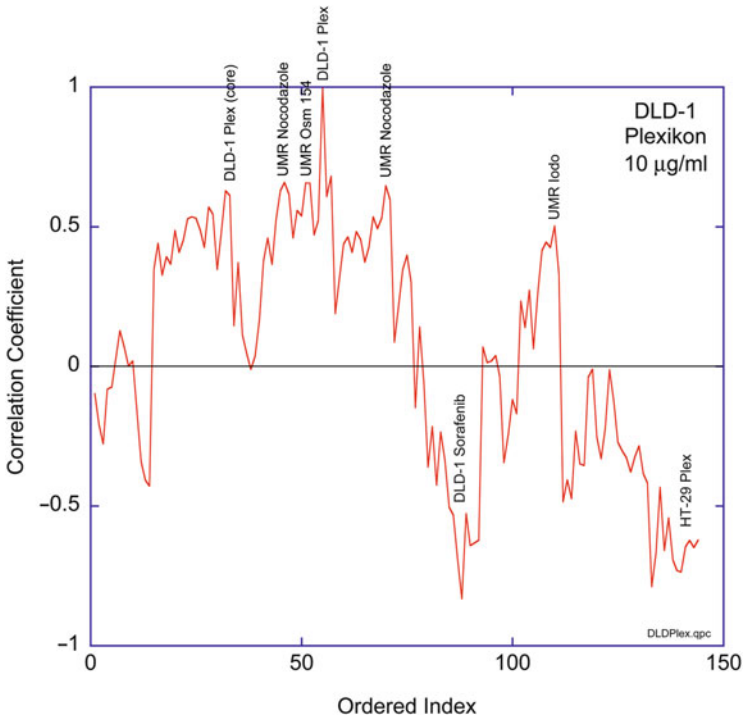

Fig. 37.7 Correlation graph as the cross-section of Fig. 37.6 centered on the response of DLD-1 shell to the PLX-4032 RAF inhibitor. The response of the related HT-29 adenocarcinoma (with a KRAS mutation) is anticorrelated to the same RAF inhibitor

on the similarity of their response. The similarity matrix shows strong block-diagonal structure, indicating that groups with high similarity have little overlap with other groups. By comparing a feature vector with in the groupings, it is possible to assign physiological attributes to the different groups. For instance, on the right of the similarity matrix, the groups are assigned enhanced or suppressed properties such as membrane motions, mechanical responses, and effective temperatures. This quasi-orthogonality among the groups provides the basis of a phenotypic classification scheme in which a new lead compound of unknown mechanism may be compared against a reference compound library of dynamic tissue response spectrograms that have known mechanisms of action.

An example of a correlation comparison is shown in the graph in Fig. 37.7 for the RAF inhibitor PLX-4032 at 10 µg/ml applied against the DLD-1 adenocarcinoma cell line that has a BRAF mutation. The graph is the cross section of the similarity matrix in Fig. 37.6 centered on the DLD-1 PLX-4032 response in the shell of the tumor spheroid. The same RAF inhibitor applied against the similar HT-29 cell line leads to an anticorrelation (shown on the far right of the graph). The HT-29 cell line has a KRAS mutation that the DLD-1 cell line does not share. There is also a strong anticorrelation between DLD-1 spheroids treated with Plexikon compared with

sorafenib, which is another RAF inhibitor that has a different mechanism of action. This is just an illustrative sample, showing the potential for phenotypic comparisons among different cell types and different applied drugs.

37.6 Future Directions in Biodynamic Imaging

Using intracellular motion as suite of functional biomarkers is a new concept that is in its infancy. In this review, dynamic light scattering imaging and spectroscopy were described in the context of applications to drug discovery. Drugs have a wide range of mechanisms of action which can be partially matched by the wide range of different types of cellular motions that may be affected by specific drugs. Metabolic activity of cells is clearly observed in the dynamic light scattering, and hence the effect of drugs on cell metabolism, and in particular cellular toxicity, is a prime target for dynamic imaging. Cell proliferation is another sensitive measure of the effect of a drug, and dynamic imaging is well suited to interrogate cellular proliferation and to monitor how proliferation is affected by applied drugs.

An attractive application for dynamic imaging is in the field of personalized medicine. Cancers are heterogeneous both genetically and phenotypically. Choosing the correct therapy for a patient is often a long process of trial and error, and sometimes a prescribed chemotherapy has no benefit, while carrying severe side effects. By applying dynamic imaging to heterogeneous biopsies from a cancer patient, there is an opportunity to apply combinations and sequences of drugs to the tumor samples to find which are most effective for treating that specific patient. This approach would go far beyond the current paradigm of only a small number of therapies applied to broad populations of patients, many of whom fail to respond.

Going beyond drug screening, the ubiquity of motion in all living tissue suggests that the generality of this approach is broad. For instance, there is significant motion involved in developmental biology, as stem cells differentiate into cells of different identities and move through morphogenic fields in the developing embryo. Metastatic cancer cells move by amoeboid crawling motions through tissue across millimeters. Mitosis and cytokinesis are large-amplitude and energetic processes with relatively high speeds, but with low probability per cell per time. Pixel-based interrogation of light scattered from proliferating tissue is likely to uncover distinct frequency signatures of these processes. Neurological processes in the brain involve high synaptic activity with the emission and absorption of synaptic vesicles, and action potentials are energetic processes that require active cellular metabolism to sustain membrane depolarization. In the arena of artificial reproductive technologies, the assessment of viable oocytes and developing embryos is essential for effective in vitro fertilization. These examples illustrate just some of the many possible applications of dynamic imaging.

Acknowledgements This work was supported by NSF1263753-CBET and NIH NIBIB 1R01EB016582-01.

References

1. D.D. Nolte, *Optical Interferometry for Biology and Medicine*, vol. 1 (Springer, New York, 2012)
2. D. Huang, E.A. Swanson, C.P. Lin, J.S. Schuman, W.G. Stinson, W. Chang, M.R. Hee, T. Flotte, K. Gregory, C.A. Puliafito, J.G. Fujimoto, Optical coherence tomography. Science **254**, 1178–1181 (1991)
3. J.M. Schmitt, Optical coherence tomography (OCT): a review. IEEE J. Sel. Top. Quantum Electron. **5**, 1205–1215 (1999)
4. A.F. Fercher, W. Drexler, C.K. Hitzenberger, T. Lasser, Optical coherence tomography – principles and applications. Rep. Prog. Phys. **66**, 239–303 (2003)
5. M.A. Choma, M.V. Sarunic, C.H. Yang, J.A. Izatt, Sensitivity advantage of swept source and Fourier domain optical coherence tomography. Opt. Express **11**, 2183–2189 (2003)
6. D.D. Nolte, R. An, J.J. Turek, K. Jeong, Tissue dynamics spectroscopy for phenotypic profiling of drug effects in three-dimensional culture. Biomed. Opt. Express **3**, 2825–2841 (2012)
7. D.D. Nolte, R. An, J. Turek, K. Jeong, Tissue dynamics spectroscopy for three-dimensional tissue-based drug screening. JALA **16**, 431–442 (2011)
8. B.J. Berne, R. Pecora, *Dynamic Light Scattering: With Applications to Chemistry, Biology, and Physics* (Dover, Mineola, 2000)
9. D.A. Weitz, D.J. Pine, Chap. in *Dynamic Light Scattering: The Method and Some Applications*, vol. 49, ed. by W. Brown, (Oxford: Oxford University Press, 1993), pp. 652–720
10. V.A. Bloomfield, Quasi-elastic light-scattering applications in biochemistry and biology. Annu. Rev. Biophys. Bioeng. **10**, 421–450 (1981)
11. T.G. Mason, D.A. Weitz, Optical measurements of frequency-dependent linear viscoelastic moduli of complex fluids. Phys. Rev. Lett. **74**, 1250–1253 (1995)
12. C. Joo, C.L. Evans, T. Stepinac, T. Hasan, J.F. de Boer, Diffusive and directional intracellular dynamics measured by field-based dynamic light scattering. Opt. Express **18**, 2858–2871 (2010)
13. M. Suissa, C. Place, E. Goillot, E. Freyssingeas, Internal dynamics of a living cell nucleus investigated by dynamic light scattering. Eur. Phys. J. E **26**, 435–448 (2008)
14. L. Kramer, Theory of light scattering from fluctuations of membranes and monolayers. J. Chem. Phys. **55**, 2097-& (1971)
15. R. Hirn, T.M. Bayer, J.O. Radler, E. Sackmann, Collective membrane motions of high and low amplitude, studied by dynamic light scattering and micro-interferometry. Faraday Discuss. **111**, 17–30 (1998)
16. M.A. Haidekker, H.Y. Stevens, J.A. Frangos, Cell membrane fluidity changes and membrane undulations observed using a laser scattering technique. Ann. Biomed. Eng. **32**, 531–536 (2004)
17. M.S. Amin, Y. Park, N. Lue, R.R. Dasari, K. Badizadegan, M.S. Feld, G. Popescu, Microrheology of red blood cell membranes using dynamic scattering microscopy. Opt. Express **15**, 17001–17009 (2007)
18. R.B. Tishler, F.D. Carlson, A study of the dynamic properties of the human red-blood-cell membrane using quasi-elastic light-scattering spectroscopy. Biophys. J. **65**, 2586–2600 (1993)
19. A. Wax, C.H. Yang, R.R. Dasari, M.S. Feld, Path-length-resolved dynamic light scattering: modeling the transition from single to diffusive scattering. Appl. Optics **40**, 4222–4227 (2001)
20. R. Carminati, R. Elaloufi, J.J. Greffet, Beyond the diffusing-wave spectroscopy model for the temporal fluctuations of scattered light. Phys. Rev. Lett. **92**, 213903-1–213903-4 (2004)
21. P.A. Lemieux, M.U. Vera, D.J. Durian, Diffusing-light spectroscopies beyond the diffusion limit: the role of ballistic transport and anisotropic scattering. Phys. Rev. E **57**, 4498–4515 (1998)
22. D.J. Pine, D.A. Weitz, J.X. Zhu, D.J. Durian, A. Yodh, M. Kao, Diffusing-wave spectroscopy and interferometry. Macromol. Symp. **79**, 31–44 (1994)
23. D.A. Boas, L.E. Campbell, A.G. Yodh, Scattering and imaging with diffusing temporal field correlations. Phys. Rev. Lett. **75**, 1855–1858 (1995)
24. D.A. Boas, A.K. Dunn, Laser speckle contrast imaging in biomedical optics. J. Biomed. Opt. **15**, 011109-1–011109-12 (2010)

25. T. Durduran, R. Choe, W.B. Baker, A.G. Yodh, Diffuse optics for tissue monitoring and tomography, Rep. Prog. Phys. **73**, (2010) 076701 (43pp)
26. D.D. Nolte, Speckle and spatial coherence. Chap. 3, in *Optical Interferometry for Biology and Medicine* (Springer, New York, 2012), pp. 95–121
27. K. Luby-Phelps, Cytoarchitecture and physical properties of cytoplasm: volume, viscosity, diffusion, intracellular surface area, in *International Review of Cytology – A Survey of Cell Biology*, vol. 192 (Academic, London, 2000), pp. 189–221
28. G. Maret, P.E. Wolf, Multiple light-scattering from disordered media – the effect of brownian-motion of scatterers. Zeitschrift Fur Physik B-Condensed Matter **65**, 409–413 (1987)
29. M.J. Stephen, Temporal fluctuations in wave-propagation in random-media. Phys. Rev. B **37**, 1–5 (1988)
30. D.J. Pine, D.A. Weitz, P.M. Chaikin, E. Herbolzheimer, Diffusing-wave spectroscopy. Phys. Rev. Lett. **60**, 1134–1137 (1988)
31. G. Maret, Diffusing-wave spectroscopy. Curr. Opin. Colloid Interface Sci. **2**, 251–257 (1997)
32. B.J. Ackerson, R.L. Dougherty, N.M. Reguigui, U. Nobbmann, Correlation transfer – application of radiative-transfer solution methods to photon-correlation problems. J. Thermophy. Heat Transf. **6**, 577–588 (1992)
33. R.L. Dougherty, B.J. Ackerson, N.M. Reguigui, F. Dorrinowkoorani, U. Nobbmann, Correlation transfer – development and application. J. Quant. Spectrosc. Radiat. Transf. **52**, 713–727 (1994)
34. D.A. Boas, A.G. Yodh, Spatially varying dynamical properties of turbid media probed with diffusing temporal light correlation. J. Opt. Society Am. a-Opt. Image Sci. Vis. **14**, 192–215 (1997)
35. J. Li, G. Dietsche, D. Iftime, S.E. Skipetrov, G. Maret, T. Elbert, B. Rockstroh, T. Gisler, Noninvasive detection of functional brain activity with near-infrared diffusing-wave spectroscopy. J. Biomed. Opt. **10**, 044002-1–044002-12 (2005)
36. D.A. Zimnyakov, V.V. Tuchin, Optical tomography of tissues. Quantum Electron. **32**, 849–867 (2002)
37. C. Menon, G.M. Polin, I. Prabakaran, A. Hsi, C. Cheung, J.P. Culver, J.F. Pingpank, C.S. Sehgal, A.G. Yodh, D.G. Buerk, D.L. Fraker, An integrated approach to measuring tumor oxygen status using human melanoma xenografts as a model. Cancer Res. **63**, 7232–7240 (2003)
38. G.Q. Yu, T. Durduran, C. Zhou, H.W. Wang, M.E. Putt, H.M. Saunders, C.M. Sehgal, E. Glatstein, A.G. Yodh, T.M. Busch, Noninvasive monitoring of murine tumor blood flow during and after photodynamic therapy provides early assessment of therapeutic efficacy. Clin. Cancer Res. **11**, 3543–3552 (2005)
39. E.M. Buckley, N.M. Cook, T. Durduran, M.N. Kim, C. Zhou, R. Choe, G.Q. Yu, S. Shultz, C.M. Sehgal, D.J. Licht, P.H. Arger, M.E. Putt, H. Hurt, A.G. Yodh, Cerebral hemodynamics in preterm infants during positional intervention measured with diffuse correlation spectroscopy and transcranial Doppler ultrasound. Opt. Express **17**, 12571–12581 (2009)
40. A.K. Dunn, T. Bolay, M.A. Moskowitz, D.A. Boas, Dynamic imaging of cerebral blood flow using laser speckle. J. Cereb. Blood Flow Metab. **21**, 195–201 (2001)
41. J.M. Schmitt, S.H. Xiang, K.M. Yung, Speckle in optical coherence tomography. J. Biomed. Opt. **4**, 95–105 (1999)
42. N. Iftimia, B.E. Bouma, G.J. Tearney, Speckle reduction in optical coherence tomography by "path length encoded" angular compounding. J. Biomed. Opt. **8**, 260–263 (2003)
43. M. Bashkansky, J. Reintjes, Statistics and reduction of speckle in optical coherence tomography. Opt. Lett. **25**, 545–547 (2000)
44. J. Kalkman, R. Sprik, T.G. van Leeuwen, Path-length-resolved diffusive particle dynamics in spectral-domain optical coherence tomography, Phys. Rev. Lett. **105**, 198302 (2010)
45. G. Farhat, A. Mariampillai, V.X.D. Yang, G.J. Czarnota, M.C. Kolios, Detecting apoptosis using dynamic light scattering with optical coherence tomography. J. Biomed. Opt. **16**, 070505 (2011)
46. A.L. Oldenburg, R.K. Chhetri, D.B. Hill, B. Button, Monitoring airway mucus flow and ciliary activity with optical coherence tomography. Opt. Express **3**, 1978–1992 (2012)

47. R.A. Leitgeb, L. Schmetterer, W. Drexler, A.F. Fercher, R.J. Zawadzki, T. Bajraszewski, Real-time assessment of retinal blood flow with ultrafast acquisition by color Doppler Fourier domain optical coherence tomography. Opt. Express **11**, 3116–3121 (2003)
48. A.M. Rollins, S. Yazdanfar, J.K. Barton, J.A. Izatt, Real-time in vivo colors Doppler optical coherence tomography. J. Biomed. Opt. **7**, 123–129 (2002)
49. P. Yu, L. Peng, M. Mustata, J.J. Turek, M.R. Melloch, D.D. Nolte, Time-dependent speckle in holographic optical coherence imaging and the state of health of tumor tissue. Opt. Lett. **29**, 68–70 (2004)
50. K. Jeong, J.J. Turek, D.D. Nolte, Imaging motility contrast in digital holography of tissue response to cytoskeletal anti-cancer drugs. Opt. Express **15**, 14057–14064 (2007)
51. K. Jeong, J.J. Turek, M.R. Melloch, D.D. Nolte, Functional imaging in photorefractive tissue speckle holography. Opt. Commun. **281**, 1860–1869 (2008)
52. Y. Pan, E. Lankenau, J. Welzel, R. Birngruber, R. Engelhardt, Optical coherence gated imaging of biological tissues. IEEE J. Sel. Top. Quantum Electron. **2**, 1029 (1996)
53. G. Indebetouw, P. Klysubun, Imaging through scattering media with depth resolution by use of low-coherence gating in spatiotemporal digital holography. Opt. Lett. **25**, 212–214 (2000)
54. K. Jeong, J.J. Turek, D.D. Nolte, Fourier-domain digital holographic optical coherence imaging of living tissue. Appl. Opt. **46**, 4999–5008 (2007)
55. D.D. Nolte, R. An, J. Turek, K. Jeong, Holographic tissue dynamics spectroscopy. J. Biomed. Opt. **16**, 087004–13 (2011)
56. X.L. Nan, P.A. Sims, X.S. Xie, Organelle tracking in a living cell with microsecond time resolution and nanometer spatial precision. Chemphyschem **9**, 707–712 (2008)
57. K.J. Karnaky, L.T. Garretson, R.G. Oneil, Video-enhanced microscopy of organelle movement in an intact epithelium. J. Morphol. **213**, 21–31 (1992)
58. N.A. Brazhe, A.R. Brazhe, A.N. Pavlov, L.A. Erokhova, A.I. Yusipovich, G.V. Maksimov, E. Mosekilde, O.V. Sosnovtseva, Unraveling cell processes: interference imaging interwoven with data analysis. J. Biol. Phys. **32**, 191–208 (2006)
59. B. Trinczek, A. Ebneth, E. Mandelkow, Tau regulates the attachment/detachment but not the speed of motors in microtubule-dependent transport of single vesicles and organelles. J. Cell Sci. **112**, 2355–2367 (1999)
60. F. Brochard, J.F. Lennon, Frequency spectrum of flicker phenomenon in erythrocytes. J. Phys. **36**, 1035–1047 (1975)
61. H. Strey, M. Peterson, Measurement of erythrocyte-membrane elasticity by flicker eigenmode decomposition. Biophys. J. **69**, 478–488 (1995)
62. A. Zilker, M. Ziegler, E. Sackmann, Spectral-analysis of erythrocyte flickering in the 0.3-4-Mu-M-1 regime by microinterferometry combined with fast image-processing. Phys. Rev. A **46**, 7998–8002 (1992)
63. M.A. Peterson, H. Strey, E. Sackmann, Theoretical and phase-contrast microscopic eigenmode analysis of erythrocyte flicker – amplitudes. J. Phys. II **2**, 1273–1285 (1992)
64. Y.Z. Yoon, H. Hong, A. Brown, D.C. Kim, D.J. Kang, V.L. Lew, P. Cicuta, Flickering analysis of erythrocyte mechanical properties: dependence on oxygenation level, cell shape, and hydration level. Biophys. J. **97**, 1606–1615 (2009)
65. J. Evans, W. Gratzer, N. Mohandas, K. Parker, J. Sleep, Fluctuations of the red blood cell membrane: relation to mechanical properties and lack of ATP dependence. Biophys. J. **94**, 4134–4144 (2008)
66. C. Ainsworth, Networking for new drugs. Nat. Med. **17**, 1166–1168 (2011)
67. C.T. Keith, A.A. Borisy, B.R. Stockwell, Multicomponent therapeutics for networked systems. Nat. Rev. Drug Discov. **4**, 71–U10 (2005)
68. D.C. Swinney, J. Anthony, How were new medicines discovered? Nat. Rev. Drug Discov. **10**, 507–519 (2011)
69. P. Hamer, S. Leenstra, C.J.F. Van Noorden, A.H. Zwinderman, Organotypic glioma spheroids for screening of experimental therapies: how many spheroids and sections are required? Cytometry A **75A**, 528–534 (2009)

70. J. Poland, P. Sinha, A. Siegert, M. Schnolzer, U. Korf, S. Hauptmann, Comparison of protein expression profiles between monolayer and spheroid cell culture of HT-29 cells revealed fragmentation of CK18 in three-dimensional cell culture. Electrophoresis **23**, 1174–1184 (2002)
71. K. Dardousis, C. Voolstra, M. Roengvoraphoj, A. Sekandarzad, S. Mesghenna, J. Winkler, Y. Ko, J. Hescheler, A. Sachinidis, Identification of differentially expressed genes involved in the formation of multicellular tumor spheroids by HT-29 colon carcinoma cells. Mol. Ther. **15**, 94–102 (2007)
72. N.A.L. Cody, M. Zietarska, A. Filali-Mouhim, D.M. Provencher, A.M. Mes-Masson, P.N. Tonin, Influence of monolayer, spheroid, and tumor growth conditions on chromosome 3 gene expression in tumorigenic epithelial ovarian cancer cell lines, BMC Med. Genet, **1**, 1755–8794 (2008)
73. M. Zietarska, C.M. Maugard, A. Filali-Mouhim, M. Alam-Fahmy, P.N. Tonin, D.M. Provencher, A.M. Mes-Masson, Molecular description of a 3D in vitro model for the study of epithelial ovarian cancer (EOC). Mol. Carcinog. **46**, 872–885 (2007)
74. T.T. Chang, M. Hughes-Fulford, Monolayer and spheroid culture of human liver hepatocellular carcinoma cell line cells demonstrate distinct global gene expression patterns and functional phenotypes. Tissue Eng. Part A **15**, 559–567 (2009)
75. M. Shimada, Y. Yamashita, S. Tanaka, K. Shirabe, K. Nakazawa, H. Ijima, R. Sakiyama, J. Fukuda, K. Funatsu, K. Sugimachi, Characteristic gene expression induced by polyurethane foam/spheroid culture of hepatoma cell line, Hep G2 as a promising cell source for bioartificial liver. Hepatogastroenterology **54**, 814–820 (2007)
76. Y. Yamashita, M. Shimada, N. Harimoto, S. Tanaka, K. Shirabe, H. Ijima, K. Nakazawa, J. Fukuda, K. Funatsu, Y. Maehara, cDNA microarray analysis in hepatocyte differentiation in Huh 7 cells. Cell Transplant. **13**, 793–799 (2004)
77. L. Gaedtke, L. Thoenes, C. Culmsee, B. Mayer, E. Wagner, Proteomic analysis reveals differences in protein expression in spheroid versus monolayer cultures of low-passage colon carcinoma cells. J. Proteome Res. **6**, 4111–4118 (2007)
78. A. Frankel, R. Buckman, R.S. Kerbel, Abrogation of taxol-induced G(2)-M arrest and apoptosis in human ovarian cancer cells grown as multicellular tumor spheroids. Cancer Res. **57**, 2388–2393 (1997)
79. L.A. Hazlehurst, T.H. Landowski, W.S. Dalton, Role of the tumor microenvironment in mediating de novo resistance to drugs and physiological mediators of cell death. Oncogene **22**, 7396–7402 (2003)
80. I. Serebriiskii, R. Castello-Cros, A. Lamb, E.A. Golemis, E. Cukierman, Fibroblast-derived 3D matrix differentially regulates the growth and drug-responsiveness of human cancer cells. Matrix Biol. **27**, 573–585 (2008)
81. L. David, V. Dulong, D. Le Cerf, L. Cazin, M. Lamacz, J.P. Vannier, Hyaluronan hydrogel: an appropriate three-dimensional model for evaluation of anticancer drug sensitivity. Acta Biomater. **4**, 256–263 (2008)
82. D.D. Nolte, R. An, K. Jeong, J. Turek, Holographic Motility Contrast Imaging of Live Tissues, in *Biomedical Optical Phase Microscopy and Nanoscopy*, ed. by N.T. Shaked, Z.Zalevskey, L. Satterwhite, (Elsevier, 2012), Academic Press, Oxford, UK
83. B. Andreopoulos, A.J. An, X.G. Wang, M. Schroeder, A roadmap of clustering algorithms: finding a match for a biomedical application. Brief. Bioinform. **10**, 297–314 (2009)

Elastic Scattering Spectroscopy and Optical Coherence Tomography

38

Adam Wax, Michael Giacomelli, and Francisco Robles

38.1 Introduction

Elastically scattered light contains information about the scattering medium with which it has interacted. The elastic scattering process can be interpreted as a change in the momentum of light due to its interaction with a scattering object. By analyzing this change in momentum, structural information such as the size, shape, and organization of scattering objects can be recovered. Recently, light-scattering techniques have been developed for examining biological cells and tissues both in the laboratory and the clinic. These techniques are broadly termed elastic scattering spectroscopy (ESS).

In order to implement an effective ESS method for probing cells and tissues, it is important to isolate the component of returned light which has undergone a single scattering process. This is complicated by the fact that only a small fraction of light exits the scattering medium after a single scattering event. The majority of the returned light exits the tissue having undergone multiple interactions with various scattering components, creating an overall background of diffuse light. ESS methods aim to distinguish the singly scattered light from the diffusive background, often relying on polarization gating or modeling. As an alternative approach, the

A. Wax (✉)
Department of Biomedical Engineering and Medical Physics, Duke University, Durham, NC, USA
e-mail: a.wax@duke.edu

M. Giacomelli
Department of Electrical Engineering and Computer Science and Research Laboratory of Electronics, Massachusetts Institute of Technology, Cambridge, MA, USA

F. Robles
Department of Chemistry, Duke University, Durham, NC, USA

© Springer International Publishing Switzerland 2015

W. Drexler, J.G. Fujimoto (eds.), *Optical Coherence Tomography*,
DOI 10.1007/978-3-319-06419-2_39

use of coherence gating, which is responsible for depth resolution in optical coherence tomography (OCT), offers a powerful method for suppressing the detection of diffuse light.

In this chapter, the development of cell and tissue analysis methods based on the combination of ESS and OCT is discussed. Background information consisting of an overview of the advantages of ESS is presented first. This is followed by a survey of ESS schemes which employ coherence gating to isolate photons which have scattered once. Finally, a review of recent experimental results which use combinations of ESS and OCT methods is presented, including basic validation experiments, studies of in vitro cells, preclinical studies of animal and human tissues, and ultimately an in vivo clinical study.

38.2 Elastic Scattering Spectroscopy

Many clinical and laboratory studies seek to determine the structure of cells and biological tissues. The most widespread approach is based on traditional pathology analysis, which relies on examining histological slides of fixed and stained specimens using a light microscope. While histopathology is the current gold standard for clinical diagnosis of disease, it limits the knowledge of cell structure by the artifacts it introduces in preparing tissue samples for study. Tissue processing requires fixation, sectioning, and often the addition of exogenous staining agents which alter the structure of the cells in nontrivial ways. In addition, this approach can only reveal a snapshot of the evolution of an individual cell and must rely on statistical studies of large ensembles of cells to assess their development in time. ESS methods offer the opportunity to study living cells in situ by providing a noninvasive means of measuring cellular structure without the need for exogenous contrast agents. In addition, since light scattering does not perturb the structure or function of cells, ESS techniques permit studies of the development, formation, and function of cellular structures through examination of the properties of the *same* cells at extended intervals.

In this section, the two basic approaches for deducing structure based on light scattering are discussed. In one approach, the wavelength dependence of scattered light is examined for a fixed angular collection. In the other, the wavelength is fixed and the angular dependence of the scattered intensity is examined. Both approaches recover structural information by assessing the change in the momentum of light due to elastic scattering but are implemented differently. For each approach, the section below will present a brief overview of its theoretical basis, the experimental schemes used to implement it, and clinical and laboratory results obtained using light-scattering techniques for measuring cellular structure and organization.

38.2.1 ESS Using Spectral Analysis

Light incident on a scattering particle can be used to deduce its structure by examining the wavelength dependence of the scattered light [1]. Spectral ESS

approaches have been developed as biomedical diagnostic methods for identifying diseased tissue by probing cellular structure. One complication in application of spectral ESS is that in general, single scattering events cannot be directly measured in biological tissue [2]. Three basic approaches have been implemented to overcome this challenge. The first is to use an analytic method to model coarse features of the measured spectrum which are then removed, leaving the residual for analysis. The second approach is polarization gating, which can be employed to discriminate low-order scattering from the diffusive background. These approaches were used in experiments with various models of living tissues as well as ex vivo and in vivo human tissues [3, 4]. Analysis of these data can be accomplished using Mie theory or Fourier transform-based analysis, where periodic variations in spectral ESS signals are related to spatial correlations over specific length scales. The Fourier transform-based method for analyzing periodic variations in spectral ESS signals has been used to measure the size distribution of cell nuclei in clinical studies [5–7] but was later found to be vulnerable to corruption by absorption features [8]. As an alternative, coherence gating, the depth sectioning method employed in OCT, can also be employed to detect singly scattered light for ESS analysis. This approach avoids the limitations of the other approaches, including avoiding the influence of absorption due to hemoglobin in underlying layers. The combination of spectral ESS and OCT is discussed further below.

38.2.2 ESS Using Angular Features

Another ESS method which can be used to determine the structure of a scattering object is analysis of the angular distribution of scattered light. Angular ESS methods rely on deducing scatterer size by measuring the differential cross section or a portion of it. This approach obtains similar information to that obtained with spectral ESS methods but possesses its own considerations for implementation. Both approaches examine the momentum transferred to the light during elastic scattering and both must isolate the contribution of single scattering for analysis. However, angular ESS methods are not vulnerable to the effects of absorption, which does not vary appreciably with scattering angle. In order to determine structure by analysis of angular ESS signals, a theoretical basis of the angular dependence of scattering is needed.

A straightforward approach is to use the Born approximation to relate the scattered field with fluctuations in density and in turn the dielectric properties in the sample. Spatial correlations in the density of the sample can be obtained through Fourier transform of the measured angular distribution within the small angle approximation [9]:

$$\mathcal{I}\left[\left|E\left(\vec{\theta}\right)\right|^2\right] \propto \left\langle \partial\rho\left(\vec{r}_\perp{}'\right)\partial\rho\left(\vec{r}_\perp{}' + r\hat{\theta}\right)\right\rangle \equiv \Gamma_\rho(r). \tag{39.1}$$

In this expression, the mean squared field, E, as a function of scattering angle, θ, is related to the two-point density correlation function, $\Gamma_\rho(r)$, of the sample as a function of separation, r, along the direction given by the scattering angle θ.

An alternative to analytic approaches is to numerically solve Maxwell's equations for a range of scattering geometries and then compare a measured distribution to a database of simulated values. Frequently, Mie theory has been used because it can rapidly produce exact scattering solutions for spherical scatterers and approximately correct solutions for nearly spherical scatterers. Surprisingly, even moderately aspherical objects such as the nuclei of many types of cells can show relatively good agreement with Mie theory [10], allowing application to a variety of biological scatterers.

A more sophisticated approach to modeling scattering is to use the T-matrix method, also referred to as the extended boundary condition method (EBCM), a generalization of Mie theory to arbitrarily shaped objects that reduces to Mie theory in the spherical case [11]. Because most cell nuclei are approximately spheroidal rather than spherical, the T-matrix is a more widely applicable alternative to Mie theory that can provide more accurate solutions. Furthermore, the T-matrix method enables simulation of the effects of parameters beyond the size and refractive index of cell nuclei, including the extent to which scatterers are elongated (aspect ratio) and the orientation of scatterers [12, 13].

Unfortunately, generating comprehensive databases of T-matrix solutions is computationally challenging, both because nonspherical solutions are more computationally complex and because the range of biologically interesting geometries is much larger than in Mie theory [14]. This disadvantage is partially offset by the availability of very efficient FORTRAN codes that implement recent advances in T-matrix modeling [15].

Experimentally, detection of angular ESS signals has been demonstrated with Fourier plane imaging. In this approach, the detection element is located in a Fourier transform conjugate plane [16] to the scattering sample such that the spatial distribution of light in the Fourier plane corresponds to light scattered at a particular angle by the sample. Thus, a spatially selective detection scheme such as an aperture can be used to detect light scattered over a range of angles. In one implementation of an angular ESS scheme, the input slit of an imaging spectrograph was placed in a Fourier plane of scattering samples, enabling both spectral and angular scattering to be observed simultaneously [17]. This approach, termed elastic light-scattering fingerprinting, was used to study early carcinogenesis events in ex vivo rat colon [18]. In another implementation, angular ESS information has been obtained using Fourier plane imaging in a microscopy scheme [19]. This method has been applied to study scattering changes associated with apoptosis [20]. A third approach uses holographic methods to record angular scattering due to localized particles [21]. These approaches offer the advantages that scattering data are collected in parallel rather than serially; they are compatible with broadband light sources and permit detection of light scattered near the backscattering direction which is important for probing the structure of larger structures, such as cell nuclei.

38.3 Angle-Resolved Low-Coherence Interferometry: Combining ESS and OCT for Detecting Precancerous Cells

Angle-resolved low-coherence interferometry (a/LCI) has been developed as an angular ESS method for probing the structure and organization of cells and their components. The a/LCI technique is unique among angular ESS approaches in that it uses coherence gating, the mechanism employed in optical coherence tomography (OCT) to achieve depth resolution, in order to isolate the component of returned light due to single scattered photons. While a/LCI and OCT share the ability to selectively probe subsurface layers, conventional OCT implementations lack the resolution and contrast to quantitatively assess changes in subcellular features. In contrast, because a/LCI uses elastic scattering spectroscopy to assess structure, it can detect changes in subcellular structure. Early efforts to combine the ESS and OCT methods sought to perform a/LCI using a Michelson interferometer [9, 22, 23] to measure depth-resolved scattered fields as a function of scattering angle. In a/LCI, the transverse component of the momentum transfer associated with the light-scattering process is detected by using Fourier plane imaging concepts with interferometry where the reference field is tailored to select specific transverse momenta, i.e., angles of propagation for detection. This section presents the optical design and evolution of a/LCI schemes and the theoretical basis which permits structural information to be extracted from the scattering distributions.

38.3.1 Optical Design of a/LCI Systems

There have been three implementations of a/LCI systems for detecting the angle-resolved scattering distribution using low-coherence interferometry. These include the Michelson interferometer-based a/LCI prototype; a second-generation a/LCI system based on a Mach–Zehnder interferometer, which records depth-resolved data in the time domain; and, the most recent, clinical a/LCI implementation based on spectral-domain interferometry. The primary driving force behind the evolution of a/LCI systems has been to improve the speed of data acquisition while also providing low-noise, high-fidelity measurements, to enable clinical application to detecting dysplasia in human epithelial tissues based on measuring the size of cell nuclei.

The first a/LCI systems used time-domain interferometry in Michelson geometry similar to time-domain OCT. Depth scanning was accomplished by translating the sample [23] or reference [22] arms, while measurement of the angular distribution was accomplished by translating a lens perpendicular to the beam pass to scan the angular distribution across a photodiode. However, this approach suffered from limited sensitivity due to the use of a kHz Doppler shift to separate the interferometric signal from the DC background. Combined with the very low intensity per angle of typical scattered fields, these systems required long scan times of greater than 30 min to acquire sufficiently high sensitivity measurements.

Following the demonstration of time-domain a/LCI, an improved implementation based on a Mach–Zehnder interferometer (MZI) was developed to address these limitations [24, 25]. The MZI implementation improved sensitivity by separating the collection optics from the angle scanning optics and introducing acousto-optic modulators with balanced heterodyne detection. The resulting system demonstrated higher angular resolution and sensitivity combined with faster scan times of less than 5 min and enabled a number cellular [26] and ex vivo tissue studies [27].

Recent advances in OCT have shown that improvements in signal-to-noise and reductions in data acquisition time are possible by recording the depth scan in the Fourier (or spectral) domain [28–30]. These advances were leveraged to implement Fourier-domain a/LCI [31]. In this approach, measurement is again performed using a Mach–Zehnder interferometer, but the reference arm is fixed and a spectrometer is used to read out a spectral interferogram as in Fourier-domain OCT. Furthermore, by using an imaging spectrometer, angle scanning optics are obviated by rapid parallel detection along the spatial channel of the spectrometer.

By combining the Fourier-domain a/LCI scheme with a coherent fiber bundle, angle-resolved measurements can be performed endoscopically, enabling in vivo applications. Figure 38.1a depicts an endoscopic a/LCI system using a coherent fiber bundle [32]. The system again consists of a Mach–Zehnder interferometer, now implemented using fiber-optic components to minimize space. Light from a superluminescent diode (SLD) is divided into a sample (90 %) and reference (10 %)

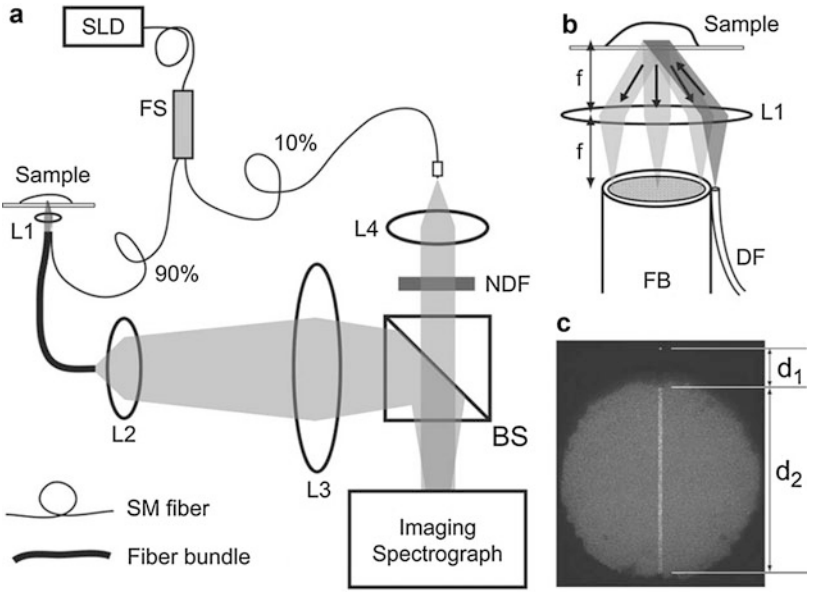

Fig. 38.1 Fiber-based Fourier-domain a/LCI system taken from [32]. (**a**) Diagram of the endoscopic interferometer. (**b**) Detailed view of the sample optics. (**c**) Photograph of the fiber bundle face

arms by a fiber splitter (FS). The sample arm light is delivered by a polarization-maintaining delivery fiber (DF) and grin lens L1 onto the sample (Fig. 38.1b). The use of a separate delivery fiber is essential because it ensures the illumination angle and polarization state are precisely controlled, an essential feature for accurately determining cell morphology [33].

Light scattered from the tissue surface is collected by lens L1 and relayed to the distal face of the fiber bundle. By positioning the face of the fiber bundle in the Fourier plane of L1, each channel of the bundle receives light scattered at a particular angle. The light relayed by the bundle is imaged onto the entrance slit of an imaging spectrometer along with the overlapped reference field. The imaging spectrometer slit is positioned along the center of the fiber bundle (Fig. 38.1c) with approximately 130 fibers imaged onto the slit in order to capture a comparable angular range as used in previous a/LCI systems. By carefully determining the magnification so that individual fibers are adequately sampled, cross talk between adjacent angular channels can be minimized. Although the fibers are not single mode, coherence gating effectively rejects any contribution from higher-order modes which experience a much greater optical path length [34].

An alternative collection method to using a coherent fiber bundle is to use a single-mode optical fiber combined with mechanical scanning to obtain scattering measurements. This approach was implemented in the fiber-optic interferometric two-dimensional scattering (FITS) system to perform polarization-resolved one- or two-dimensional scattering measurements by translating a single-mode fiber across the back focal plane of a collection lens [35]. Polarization selectivity is obtained using a novel hybrid Michelson–Sagnac hybrid interferometer implemented in fiber. By mixing the scattered field and reference field inside of an optical fiber, the polarization state of the detected field can be precisely measured. Furthermore, as the reference and sample arms propagate along common single-mode fibers, the system is relatively insensitive to dispersion, even in very long fiber probes. Although the FITS system forgoes the sensitivity advantage of parallel detection, it was the first a/LCI system capable of 2D measurement of scattered fields.

38.3.2 Processing a/LCI Distributions to Obtain Structural Information

As discussed above, a/LCI signals must be processed and then analyzed in order to determine structural features from measurements of angle-resolved scattering. In frequency-domain a/LCI, light at each scattering angle is detected as a function of wavelength such that the detected signal can be related to the signal and reference fields (E_s, E_r) by [36]

$$I(\lambda_m, \theta_n) = \left\langle |E_r(\lambda_m, \theta_n)|^2 \right\rangle + \left\langle |E_s(\lambda_m, \theta_n)|^2 \right\rangle + 2\mathrm{Re}\left\langle E_s(\lambda_m, \theta_n) E_r^*(\lambda_m, \theta_n) \cos(\phi) \right\rangle, \tag{38.2}$$

where ϕ is the phase difference between the two fields, the indices (m, n) correspond to a particular pixel, and $\langle\rangle$ denotes a temporal average.

In order to process the raw pixel data to produce depth-resolved scattering measurements, the data are processed as described in [37], in a process similar to Fourier-domain processing of OCT signals. First, the average intensities of the sample and reference beams are measured independently and then subtracted from I. Second, at each scattering angle, the spectrum in wavelength (λ) is converted into a linear function of wavenumber (using $k = 2\pi/\lambda$), using a cubic spline interpolation. At this point, any chromatic dispersion in the system is corrected numerically using empirical parameters. Finally, at each scattering angle, the spectrum as a function of wavenumber is 1D Fourier transformed to generate a signal which is a function of optical path length (or depth in the sample).

This processed signal is analyzed to determine structural information, typically the size of cell nuclei in a tissue sample. First, the angular distribution is divided by the normalized reference field, which varies smoothly from 0.5 to 1, to produce a signal that is linear in the scattered field. The scaled data are then squared to yield scattered intensity versus angle and path length. These data are further processed to remove high-frequency noise by binning the angular data. The angular data for a particular depth (optical path length) are then compared to database of theoretical predictions which have been calculated previously. Chi-squared values are calculated as the mean square difference between the data and each theoretical prediction for a range of scatterer diameters. The minimum chi-squared value is determined by searching through all values generated and the corresponding size is reported as the best fit. The uncertainty in these measurements is given as the change in structure diameters where the minimum chi-squared value is doubled.

Although this procedure is generally applicable, additional steps must be taken for the specific case of analyzing scattering due to cell nuclei. As discussed in detail in [33], accurate size determination can be complicated by other structures if the angular data are compared directly to the predictions of Mie theory. First, one must consider that Mie theory predicts scattering by a homogenous dielectric sphere while, for most cells, the nucleus is not a sphere but rather a spheroid. In addition, the presence of inhomogeneities in and around the nucleus can also complicate interpretation of the angular-scattering distribution.

The a/LCI analysis algorithm for extracting nuclear size information from cells and tissues consists of four steps. First, data from a particular region of interest are selected, usually corresponding to a particular tissue layer. The data are then filtered to remove high-frequency oscillations, as described above. Since the angular distribution is Fourier transform related to the two-point correlation function (Eq. 38.1), removing these oscillations over fine angular scales corresponds to suppressing scattering arising from long correlation distances. Physically, this step removes the contribution to angular scattering arising from coherent scattering by neighboring cell nuclei which are necessarily spaced at distances greater than the cell size. This effect was examined in a previous study [38] which systematically varied cell spacing to demonstrate that this process permitted accurate size determinations in the presence of coherent scattering by adjacent cell nuclei.

An additional filtering step is then implemented, which uses a second-order polynomial to remove the background trend from the processed data. This step is important to enable fitting using chi-squared minimization and serves to isolate the oscillatory component of the angular scattering due to diffraction, as described in [39]. The final step of the analysis is to compare the processed angular distribution to theoretical distributions which have also had their background trend removed. For determining the size of cell nuclei, a database of calculated distributions will include a Gaussian distribution of scatterer sizes, characterized by a mean diameter (d) and a standard deviation (δd) in the size parameter, a range of refractive indices of the nuclei ($n_{nucleus}$), and a range of refractive indices of the cytoplasm ($n_{cytoplasm}$).

As a final note, when fitting data for cell nuclei, whether in isolated cells or from tissue, criteria that establish a unique fit are needed. The a/LCI processing typically employs two checks, including a comparison with scattering that is constant versus angle and demanding that the chi-squared value for the best fit is at least 10 % greater than the next best value to ensure a unique fit.

Processing of a/LCI data can be readily generalized to two-dimensional, solid angle-resolved fields resulting in more accurate measurement of size and shape. In this case, the database of theoretical scattering solutions is constructed with scattered field intensities recorded over two dimensions. The scattering simulations and the 2D measurement coordinates are coregistered by comparing measurements from known scattering samples to the simulated values. During this step, effects such as field curvature can be removed if present. After coregistration, low-pass filtering is implemented similar to the 1D process by using a 2D filter kernel and second-order polynomial subtraction. The processed measurement data is then compared on an angle per angle basis to generate a χ^2 error value for each database entry. As in the 1D case, the simulation with the lowest χ^2 value indicates the scattering geometry.

38.4 Applications of a/LCI

A number of studies have employed a/LCI to investigate structure through depth-resolved angular-scattering measurements. These include validation experiments with polystyrene microspheres and in vitro cells which have served to demonstrate various aspects and capabilities of the technique. Further experiments have applied a/LCI to examine the nuclear morphology of epithelial cells in tissues drawn from animal models of carcinogenesis. Finally, a clinical implementation of a/LCI has been developed which introduces an endoscopic fiber-optic probe that is compatible with standard endoscopes. This section concludes with ex vivo and in vivo studies which apply the new fiber probe to detect precancerous changes in human epithelial tissues.

38.4.1 a/LCI Validation Experiments

Validation of the a/LCI approach was first achieved by measuring the scattering distribution of polystyrene microspheres [22]. Upon realizing Fourier-domain a/LCI,

it became much easier to acquire scattering data and a study was undertaken to demonstrate the capability of the system across a range of clinically relevant-sized polystyrene microspheres of sizes 6.0, 8.0, 9.7, 12.0, and 15.0 μm [37]. The results showed that a/LCI-determined mean diameter agreed very well with the corresponding NIST traceable mean diameters, producing an r^2 value of 0.9997.

While polystyrene microspheres are suitable targets for developing light-scattering systems, measurement of cell nuclear morphology is a more challenging target due to the lower refractive index compared to the surrounding medium. The first application of a/LCI to measurement of nuclear morphology was accomplished using monolayers of cultured HT29 epithelial cells [9], a line of human tumor cells. This study demonstrated sub-wavelength precision and accuracy by comparing the light-scattering results to quantitative image analysis (QIA). This first application also developed the signal-processing methods to account for the nonspherical and inhomogeneous nature of cell nuclei. Significantly, this work identified a power law correlation function that described the residual light-scattering signal once the nuclear contribution was removed. A more comprehensive study of scattering by in vitro cells was completed by Pyhtila et al. [33], which explored the role of polarization in analyzing light-scattering signals from cell nuclei. A comprehensive list of a/LCI nuclear morphology data for in vitro cells can be found in *Biomedical Applications of Light Scattering* [40].

The first use of the T-matrix method for assessing the size of cell nuclei using with a/LCI was demonstrated using cultured MCF-7 breast cancer cells [12]. In these experiments, 37 a/LCI measurements were taken with 48 angles per measurement from six cell monolayers prepared on coverslips. Cells were then imaged using DAPI fluorescence and QIA to determine nuclear diameter. Analysis was enabled by a T-matrix database that contained simulated scattering for nuclei from 7.5 to 12.5 μ diameter in increments of 40 nm, spheroidal aspect ratio from 0.56 to 1 (prolate to spherical) in increments of 0.01, background index of refraction 1.35 and 1.36, and scatterer index of refraction 1.42 and 1.43, all with a 10 % standard deviation normal size distribution. Both methods provided nearly identical answers, with QIA yielding an EVD of 9.52 μm (95 % standard error = 0.44 μm) and an aspect ratio of 0.70 ± 0.026 and a/LCI with T-matrix determining an EVD of 9.51 ± 0.34 μm with an aspect ratio of 0.69 ± 0.032 determined. These results confirmed the ability of a/LCI to measure both the size and shape of living cell nuclei with extremely high accuracy.

Following the demonstration of T-matrix-based analysis in a/LCI, the technique was generalized to 2D using and the FITS system to analyze scattering from stretched polystyrene microspheres [41]. In these experiments, small numbers of microspheres were mixed into transparent plastic, heated beyond their melting point, and then allowed to cool under tension. The resulting phantoms had a nearly perfect spheroidal geometry of known size and shape. A database was prepared using the T-matrix method to simulate the complex polarization state of the 2D angle-resolved fields over 360° of azimuth angle and 30° of polar angle (corresponding to the range achieved in 1D a/LCI). In total, 10,250 unique scatterer geometries were simulated with equal volume diameters ranging from 8 to 18 μm in

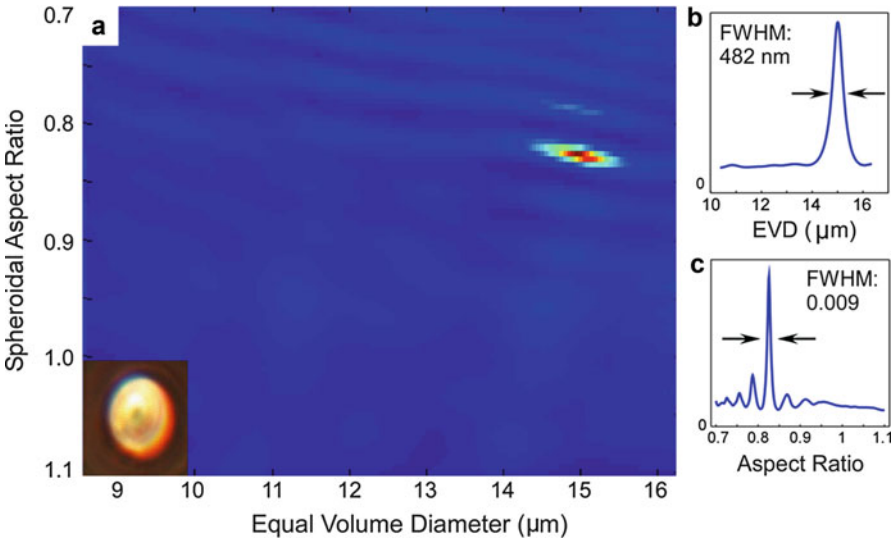

Fig. 38.2 (**a**) χ^2 error plotted against equal volume diameter and aspect ratio for a single 0.82 (determined by QIA) 15 μm stretched microsphere (see inset). (**b**) Plot of χ^2 compared to diameter. (**c**) χ^2 error compared to aspect ratio (Adapted from [41])

80 nm increments and aspect ratios between 0.7 (prolate spheroidal) and 1.1 (oblate spheroidal) in steps of 0.005 [42].

Individual stretched microspheres were selected and scanned using the FITS system and then analyzed using a T-matrix database. Measurements were presented for three representative samples of microspheres with a diameter of 15.02 μm +/− 80 nm prior to stretching [43]. In the spherical geometry, a/LCI measured an equal volume diameter (EVD) of 15.00 ± 0.24 μm and an aspect ratio of 0.995 ± 0.04. For a slightly stretched (QIA aspect ratio = 0.93) spheroid, a/LCI measured an EVD of 14.95 ± 0.33 μm and an aspect ratio of 0.925 ± 0.01. Finally, for a moderately stretched (QIA aspect ratio = 0.82) spheroid, an a/LCI measured an EVD of 15.00 ± 0.24 μm and an aspect ratio of 0.825 ± 0.005 (Fig. 38.2). This analysis demonstrated that 2D a/LCI size and shape determinations are unique even over very large parameter spaces.

38.4.2 Application of a/LCI in Cell Biology

The ability of a/LCI to noninvasively measure changes in cell nuclei with wavelength accuracy has been applied to measurement of cell dynamics in several experiments. In the first of these, subtle changes in the volume of cell nuclei with changes in osmolarity were measured with Mie theory [44]. This study also showed that changes in cell nucleus shape due to a substrate texture could be measured with a/LCI but required multiple measurements with different orientations of the sample.

With the development of T-matrix-based fitting for the measurement of both size and shape, a/LCI was extended to measure deformation of cell nuclei in response to nanopatterned substrates within a single measurement [13]. These results demonstrated that real-time quantitative measurement of changes in live cells in response to environmental stimuli was possible without the use of exogenous contrast agents.

The improved accuracy enabled by T-matrix-based fitting was subsequently used to investigate the onset of apoptosis in breast cancer [45]. In these experiments, cells were treated with one of two chemotherapeutic agents at levels sufficient to initiate apoptosis. Treated cells were then measured at regular intervals with a/LCI and the size and shape determined with T-matrix-based processing. The T-matrix fit was then subtracted from the angular-scattering data and Fourier transformed to obtain a residual signal correlation function. While the size and shape data did not appreciably change due to treatment, analysis of the residual signal using a fractal dimension formalism did produce statistically significant results, showing a dramatic change 3 h after treatment with paclitaxel (Fig. 38.3a) and doxorubicin (Fig. 38.3b). Subsequently, time courses demonstrated a statistically significant change after just 90 min (Fig. 38.3c), demonstrating that angle-resolved light scattering can detect pre-apoptotic changes in nuclear organization.

38.4.3 Application of a/LCI to Detecting Precancerous Lesions in Animal Tissues

The first application of a/LCI to assessing structure within tissues was in quantitative studies of the nuclear morphometry of epithelial cells in a rat model of esophageal carcinogenesis [46, 47]. Changes in the size and texture of cell nuclei due to neoplastic transformation were observed in situ via quantitative measurements of basal epithelial cell nuclei, approximately 50–100 μm beneath the tissue surface. In the first study, a/LCI measurements, made on freshly excised tissue samples without using exogenous contrast agents or tissue fixation, were compared to traditional histopathological images to establish a correlation with the degree of neoplastic transformation [47]. The grading criteria from this initial study were then used to detect neoplastic transformation in a prospective study [46].

The rat esophagus studies focus on two morphological parameters: the mean nuclear size and the fractal dimension. The a/LCI measurements of these parameters from the first study are presented graphically in Fig. 38.4. The measurements are grouped by histological classification: normal epithelium, low-grade dysplasia (LGD), high-grade dysplasia (HGD), epithelium with vacuolated cells, or epithelium with apoptotic cells. The latter two classifications were seen in tissues treated with prospective chemopreventive agents. The observations of vacuolization and apoptosis using a/LCI are important findings as it illustrates a potential application of the technique for assessing the efficacy of chemopreventive agents or the toxic effects of chemicals on tissue health.

In this first study [47], the mean nuclear size was found to be a powerful indicator of neoplastic progression, resulting in 80 % sensitivity and 100 %

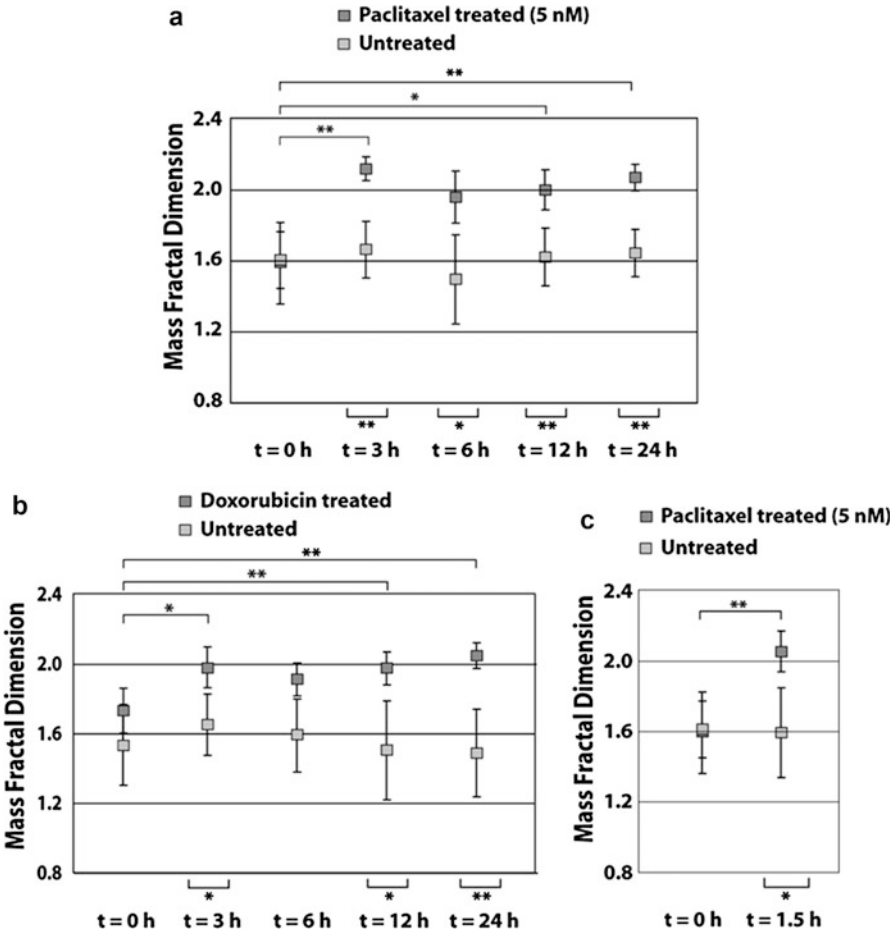

Fig. 38.3 a/LCI T-matrix-measured fractal dimension of chemotherapy-treated cells. (**a**) Fractal dimension after 0, 3, 6, 12, and 24 h after paclitaxel treatment demonstrating a rapid increase in fractal dimension following the initiation of apoptosis. (**b**) Previous results repeated for doxorubicin. (**c**) Paclitaxel treatment after 90 min (Taken from [45])

specificity in distinguishing normal from dysplastic tissues. In addition, apoptotic cells could be easily distinguished via nuclear size distribution. The fractal dimension measurements did not improve the diagnostic capability of a/LCI for classifying neoplasia, but fractal dimension measurements were later found to offer utility in assessing therapy [45].

In a second prospective study of the rat esophagus carcinogenesis model [46], the tissue classifications established in the initial study were used to grade tissue samples. Freshly excised esophageal tissues were examined using a/LCI at time points of 8, 12, and 20 weeks following treatment with N-nitrosomethylbenzylamine (NMBA). The degree of neoplastic transformation

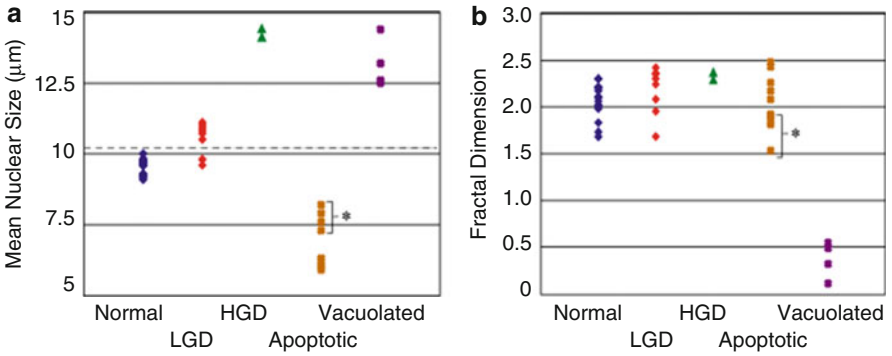

Fig. 38.4 (**a**) Average cell nuclei size from intact excised rat esophagus tissues as determined with a/LCI. The *dashed line* represents a decision line between normal and dysplastic cells. (**b**) Fractal dimensions of subcellular components measured using a/LCI. There is a significant difference ($p < 0.05$) between normal and dysplastic (LGD+HGD) populations (From Ref [47])

was assessed by measuring the average diameter of the cell nuclei in the basal layer and comparing to the grading criteria established previously. This prospective study showed that a/LCI successfully identified 58 of 60 normal tissue sites (97 % specificity) and 20 of 22 dysplastic tissue sites (91 % sensitivity) upon comparison to traditional histopathology. In addition, this study further reinforced the use of a/LCI for assessing the efficacy of chemopreventive agents, by comparing the modulation in incidence of neoplastic change due to addition of difluoromethylornithine (DFMO) to the diet of the animals. The a/LCI data showed no difference in incidence at 8 weeks but that DFMO was effective in reducing the incidence of dysplasia at 12 and 20 weeks post-NMBA treatment. Traditional tumor metrology measurements confirmed the observation of modulation in incidence at 20 weeks but could not detect it at earlier times, suggesting that a/LCI can provide greater sensitivity than traditional methods.

38.4.4 Application of a/LCI to Human Tissues

The first demonstration of the clinical utility of a/LCI was shown with measurements on ex vivo human tissue samples from three patients with dysplastic Barrett's esophagus (BE) who underwent esophagogastrectomies [48]. The tissue was opened longitudinally and data was taken within 2 h of resection. These studies showed a high sensitivity and specificity for distinguishing dysplastic BE tissue from healthy columnar tissue (Fig. 38.5), as would be found in the gastric epithelium. No non-dysplastic BE tissue was encountered. A follow-up study was conducted using the first portable a/LCI system in the pathology clinic, enabling data to be taken within 1 h of resection [36]. This study employed a handheld optical probe, allowing precise selection of the location for each data point and enabling better coregistration. Three types of tissue from a single specimen were probed.

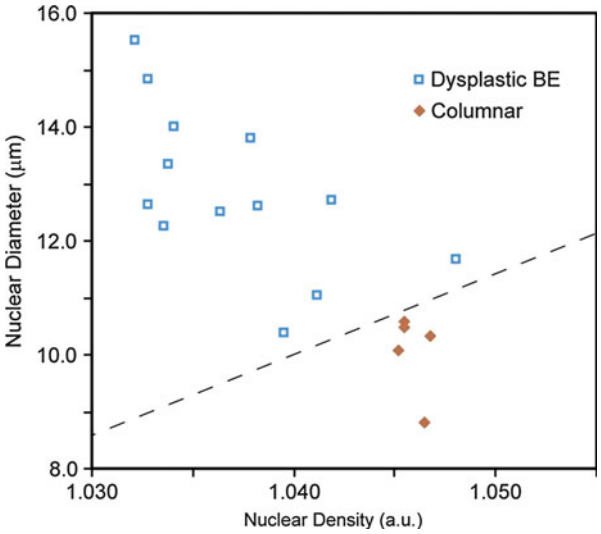

Fig. 38.5 Scatter plot of pathological tissue classification versus mean nuclear diameter and mean relative refractive index over superficial 150 μm of tissue. *Dashed line* indicates potential decision line for identifying dysplastic tissue in Barrett's esophagus (From [48], with permission)

Data were acquired from normal squamous tissue from the esophagus, from the normal-appearing gastric tissue from the stomach, and from Barrett's tissue in the esophagus which appeared normal but was later classified as low-grade dysplasia in the pathology report. As with the previous ex vivo study, no non-dysplastic BE tissue was observed. These data showed good sensitivity (100 %; 6/6) for the superficial 150 μm of the epithelium using a similar decision line used in the previous study; however, the specificity was lower (56 %; 5/9). When the analysis was extended to include a deeper segment of tissue, which contained the basal layer, there was again excellent sensitivity (100 %; 6/6) but also improved specificity (78 %; 7/9). This result indicated that the deep basal layer might provide the greatest insight into the disease state of the tissue as measured by a/LCI.

Upon completion of the clinical a/LCI system, the first-in-man pilot study was conducted [49]. This study included 46 patients undergoing routine upper endoscopy for BE at two endoscopy centers. The study design compared a/LCI data from three to six tissue sites per patient with a coregistered standard biopsy for each. Upon pathological classification of these biopsies, the a/LCI measurements were correlated with the disease state to evaluate the diagnostic ability of a/LCI.

In total, this study included 172 coregistered optical and physical biopsies. For analysis, these biopsies were classified as either "dysplastic" ($n = 13$) or "non-dysplastic" ($n = 159$) according to their pathological state. For dysplastic tissues, a statistically significant ($P < 0.001$) increase in nuclear diameter in the deep epithelial layer (200–300 μm beneath the tissue surface) was observed compared with non-dysplastic tissues, consistent with previous a/LCI studies. To evaluate the diagnostic capacity of a/LCI-measured nuclear size in the basal layer, a receiver-operating characteristic (ROC) was developed. This metric showed good overall performance, producing an area under the curve (AUC) of 0.91, and identified an

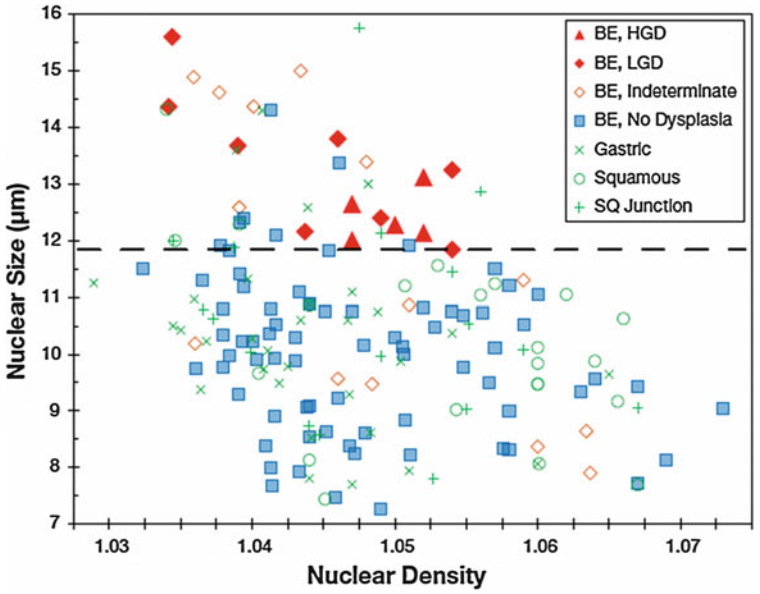

Fig. 38.6 Scatter plot of optical biopsies from pilot a/LCI in vivo clinical study. Data points are colored according to pathological diagnosis. *Dashed black line* indicates optimal decision line (Taken from [49])

optimal decision line at 11.91 μm for the classification of dysplasia. This decision line (Fig. 38.6) yielded a sensitivity of 100 % (13/13), a specificity of 84 % (134/159), an overall accuracy of 86 % (147/172), and positive and negative predictive values of 34 % (13/38) and 100 % (134/134), respectively. This pilot in vivo study represented a significant step in the development of an a/LCI-based clinical diagnostic of dysplasia in the esophagus and provides proof-of-concept for future trials.

The most recent application of a/LCI in a clinical study used the approach to evaluate dysplasia in colonic epithelium [50]. In this study, tissues from 27 patients undergoing partial colonic resection surgery were examined with the a/LCI technique in the pathology lab. As in previous studies, a/LCI measurements of nuclear morphology were compared to traditional histopathology. The results showed a statistically significant correlation ($P < 0.0001$) between increased nuclear size in the basal layer of the epithelium, at a depth of 200–300 μm beneath the tissue surface, and the presence of dysplasia. In addition, the nuclear density, a metric that compares the refractive index of the cell nuclei to the surrounding cytoplasm, showed a statistically significant *decrease* with the presence of dysplasia. Combining these two metrics, an ROC analysis was conducted, producing an AUC of 0.91, and used to construct a decision line (Fig. 38.7). By using this decision line, which

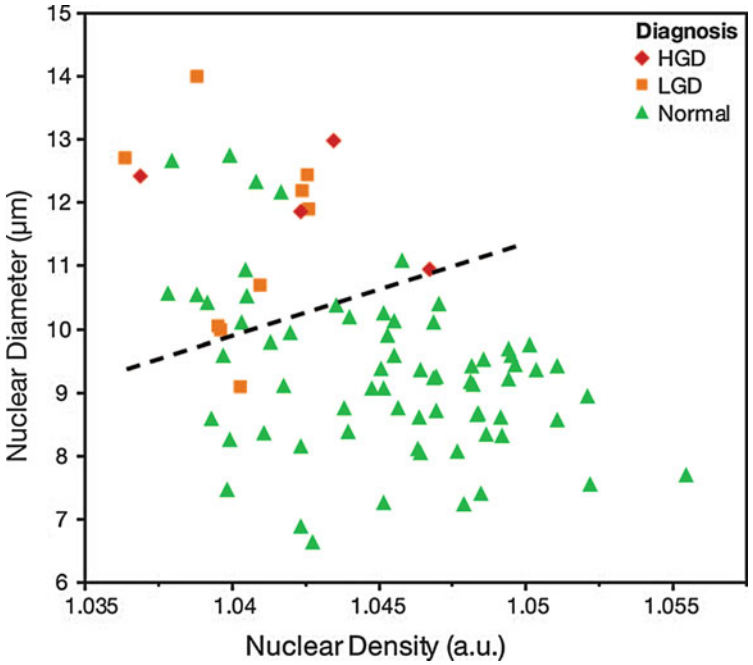

Fig. 38.7 Scatter plot showing a/LCI measurements of nuclear size (micrometer) and nuclear density for the depth segment 200–300 μm beneath the surface of colonic epithelium sorted by pathological diagnosis. The *dashed black line* was determined using an ROC analysis, providing an ideal decision line for the prediction of dysplasia [50]

is nearly identical to that previously determined by Pyhtila et al. [48] (see Fig. 38.4 above), a sensitivity of 92.9 % (13/14), a specificity of 83.6 % (56/67), and an overall accuracy of 85.2 % (69/81) are achieved. The corresponding negative predictive value of 98.2 % (56/57) is comparable to that found in previous a/LCI studies. This preliminary demonstration of applicability of a/LCI to evaluating colonic epithelium serves as motivation to pursue in vivo clinical studies in this organ site.

The use of a/LCI to evaluate dysplasia in BE and other sites was considered in a recent review article that compared the technique to the capabilities of other developing advanced imaging modalities including OCT [51]. It was identified that not only is discrimination of dysplasia important but that other factors such as ease of use, reliability, and cost, particularly related to the economics of surveillance, must be considered. Thus, while several technologies have demonstrated proof of principle, there is a need for data that substantiates improved clinical outcomes. Further work with a/LCI is underway via commercial development by Oncoscope, Inc. (Durham, NC) to establish improved outcomes compared to standard of care as well as to gain regulatory approval.

38.5 Combination of Spectral ESS and OCT Methods

Recently, there has been increased interest in using spatially resolved spectroscopic methods, such as spectroscopic OCT (SOCT), to detect spectral features for ESS [52]. In SOCT, depth-resolved spectral profiles are obtained by processing LCI signals using a window filter [53], which results in decreased axial resolution but provides some information regarding the spatially resolved, spectral dependence of the scattered light. Fourier-domain low-coherence interferometry (fLCI) uses SOCT methods to obtain structural information by analyzing the spectral modulation of white light due to elastic scattering. The fLCI approach has advanced significantly in the past few years by incorporating a novel processing scheme that avoids the resolution trade-off between depth resolution and spectral features, named the dual-window (DW) processing method. This section describes the fLCI technique and the DW method, along with application to probing morphological features for early cancer diagnosis. Results from phantoms and ex vivo tissue studies are reviewed.

38.5.1 Fourier-Domain Low-Coherence Interferometry and Dual-Window Method

The general principle behind fLCI is illustrated in Fig. 38.8a. Light scattered from a spherical object with diameter d, such as a microsphere or cell nucleus, will contain two components that interact with each another, one originating from the front surface and another from the back surface. This interaction produces periodic oscillations in the spectrum with a frequency given by the optical path length difference of the two components, and is related to the diameter of the object by $2 \cdot n \cdot d$, where n is the refractive index (RI) of the object. It is important to understand that these local oscillations are found in the vicinity of the scatterer, and hence, fLCI necessitates high spectral *and* spatial resolution.

To obtain the local oscillations via fLCI, a parallel frequency-domain OCT (pfdOCT) system is used (Fig. 38.8b). The light source consists of a xenon arc lamp (250W Thermo Oriel), which provides a spectral bandwidth ($\sim$250 nm) wide enough to observe the spectral ESS features of interest. This source, however, presents some challenges due to its low spatial coherence. Thus, the pfdOCT system is designed to minimize the detrimental effects of the thermal light source by using a 4f interferometer [56] and by collimating the light onto the sample, which reduces the number of spatial modes illuminating each diffraction-limited spot [57].

To obtain depth-resolved spectroscopic information and gain access to the local oscillations, the DW method is used [58]. This method consists of processing each interferogram using two short-time Fourier transforms (STFTs) and then multiplying the results. Each STFT involves sweeping a window across the interferometric data while simultaneously taking a FT at each step. This process yields a map,

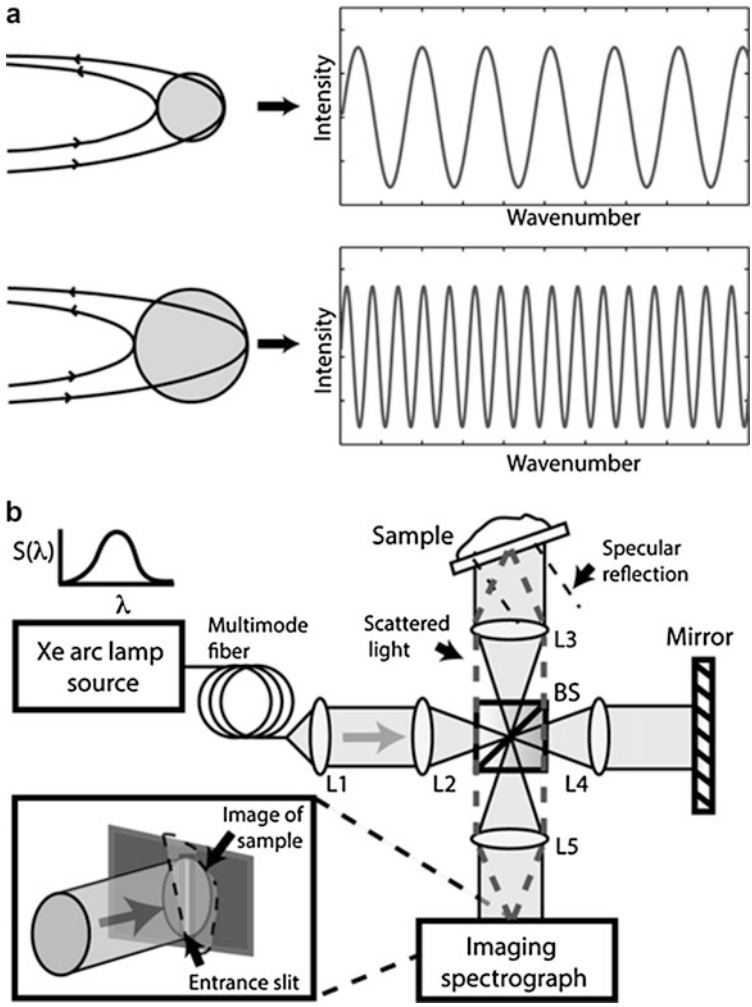

Fig. 38.8 (**a**) General principle of fLCI: scattering from a spheroidal object produces periodic spectral oscillations, proportional to the diameter (Taken from [54]). (**b**) pdfOCT system consists of a modified 4f Michelson interferometer geometry (Taken from [55])

known as a time–frequency distribution (TFD), which describes the localized backscattered spectra. Note, however, that the windowing process in STFTs introduces an inherent trade-off between the spectral and spatial resolutions, and while this method is routinely applied in SOCT, it is inadequate for fLCI. The DW method, on the other hand, utilizes the high spectral resolution of a STFT using a narrow window, and the high spatial resolution of a STFT using a wide window to avoid the deleterious effects of the time–frequency trade-off. Mathematically, this may be described as

$$DW(k,z) = STFT_1(k,z) \cdot STFT_2^*(k,z) = \iint 4E_S^*(k_1)E_s(k_2) \cdot \cos(k_1 \cdot d)\cos(k_2 \cdot d) \cdot e^{\frac{(k_1-k)^2}{2a^2}} \cdot e^{\frac{(k_2-k)^2}{2b^2}} \cdot e^{-(k_1-k_2)^2} dk_1 dk_2, \quad (38.3)$$

where d is the path length difference and a and b are independent parameters that set the widths of the windows.

While implementation of the DW method is relatively simple, the use of two STFTs has significant implications on the resulting TFDs. Specifically, the DW TFD may be considered a bilinear distribution, which, in general, provides a representation of the time–frequency space that does not suffer from the resolution trade-off. In fact, when a is small compared to b, the DW TFD simplifies to

$$DW(k,z) = 4b\sqrt{\pi}\iint Ws(\Omega,\zeta) \cdot e^{-2\frac{(\Omega-k)^2}{b^2}} \cdot e^{-2(d+\zeta+z)^2 a^2} \cdot \cos(2\Omega \cdot d) d\Omega d\zeta, \quad (38.4)$$

where $\Omega = (k_1 + k_2)/2$ and $q = k_1 - k_2$ represent a change in the coordinate system, $W_S(\Omega, \zeta)$ is the Wigner distribution of the sample filed, and ζ is the conjugate space of Ω. The Wigner distribution is a bilinear distribution that has been extensively studied [59]. Equation 38.4 shows that the DW method is equivalent to probing the Wigner TFD of the sample field with two orthogonal windows that independently tune the spatial and spectral resolutions. Thus, like the Wigner distribution, the DW also avoids the trade-off that hinders STFTs. If, however, the windows are chosen inadequately, for example, using a narrow window with a width of a single pixel and a wide window that spans the full spectral range, undesirable artifacts associated with other types of bilinear distributions will pollute the results [59].

38.5.2 Experimental Results

38.5.2.1 Phantom Studies

The capabilities of fLCI were first demonstrated using a 2-dimensional phantom consisting of polystyrene microspheres (1.55 μm mean diameter, 3 % variance) attached to a glass coverslip [52]. The results from this work showed that the size of scatterers could in fact be determined with sub-wavelength accuracy ($d = 1.65$ +/− 0.33 μm). Later, fLCI was shown to be capable of sizing cell nuclei in vitro (T84 epithelial cells in a monolayer), further confirming the methods' ability to evaluate this important biomarker [60]. In a subsequent study, a more complex, 3-dimensional, scattering phantom was considered to assess the potential of quantifying nuclear morphology in tissue. The phantom in Ref [61] consisted of two layers containing polystyrene beads (with RI $n_b = 1.59$) of different sizes suspended in a mixture of agar (2 % by weight) and water, with RI $n_a = 1.35$.

Data were acquired with the pfdOCT system and processed with the DW method. Representative processed spectra from two microspheres, one from the front layer

and another from the back layer (blue solid lines in Figs. 38.9a, b), show two important features: The low-frequency spectral oscillations (dotted green line) represent the scattering cross section of the microspheres as a function of wavenumber and are theoretically described by Mie theory ($\sigma(k)$, red dashed line) [1]. This spectrally dependent backscattering behavior has been analyzed previously by various groups using light-scattering spectroscopy (LSS) [4], confocal light absorption and scattering spectroscopy [62], and also SOCT [63]; however, analysis of these features is highly sensitive to the RI of the medium and scatterer, which need to be known a priori. The other important feature of the DW processed spectrum is the high-frequency, local oscillations (i.e., the fLCI measurement). After subtracting the low-frequency component, a FT of the local oscillations reveals a correlation function with a peak corresponding to the diameter of the microspheres (Fig. 38.9c, d). Note that this measurement is independent of the RI of the medium.

Results from the entire phantom are shown in Fig. 38.9e, where the fLCI results (color) are overlaid with the OCT image. Here, the top layer shows scatterers with a yellow hue corresponding to an average size of 3.82 +/−0.67 μm, and the bottom layer shows a red/purple hue corresponding to an average size of 6.55+/−0.47 μm. Both measurements are in good agreement with the expected size (4.00 ± 0.033 μm and 6.98 ± 0.055 μm, respectively) and with the results from the low-frequency component (LSS measurement). These results demonstrated that fLCI can determine the size of scatterers with sub-wavelength accuracy in thick, turbid samples, such as intact tissue.

38.5.2.2 Animal Studies

The ability of fLCI to detect structural changes associated with neoplastic transformation was tested using two animal models. The first study employed a hamster cheek pouch carcinogenesis model where neoplastic (precancerous) changes are induced by topical treatment with 7,12-dimethylbenz[a]anthracene (DMBA). In this study, each tissue sample was harvested and examined using a pfdOCT system with a white light source [57]. The data were analyzed using the DW method and the local oscillations were examined to determine the average nuclear size in the basal layer of the epithelium. Based on these results, the tissues treated with DMBA showed an increased average nucleus size that was significantly ($p < 0.0001$) greater than that seen for the untreated animals. In this small proof-of-principle study, complete separation between the treated and untreated samples was realized with a simple, nuclear size-based decision line.

The second fLCI study employed the azoxymethane (AOM) rat carcinogenesis model [64], a well-characterized and well-established model for colon cancer research and drug development [65]. The progression of this model is similar to that seen in humans and is a good surrogate for human colon cancer development. In this study, tissues from 40 animals were analyzed with 30 receiving AOM treatment and the remainder serving as an untreated control. Tissues were examined at 4, 8, and 12 weeks after the AOM dosing using the pfdOCT system and the fLCI measurements were compared to the observed number of aberrant crypt foci (ACF), preneoplastic lesions that are biomarkers of neoplastic transformation in this model [66].

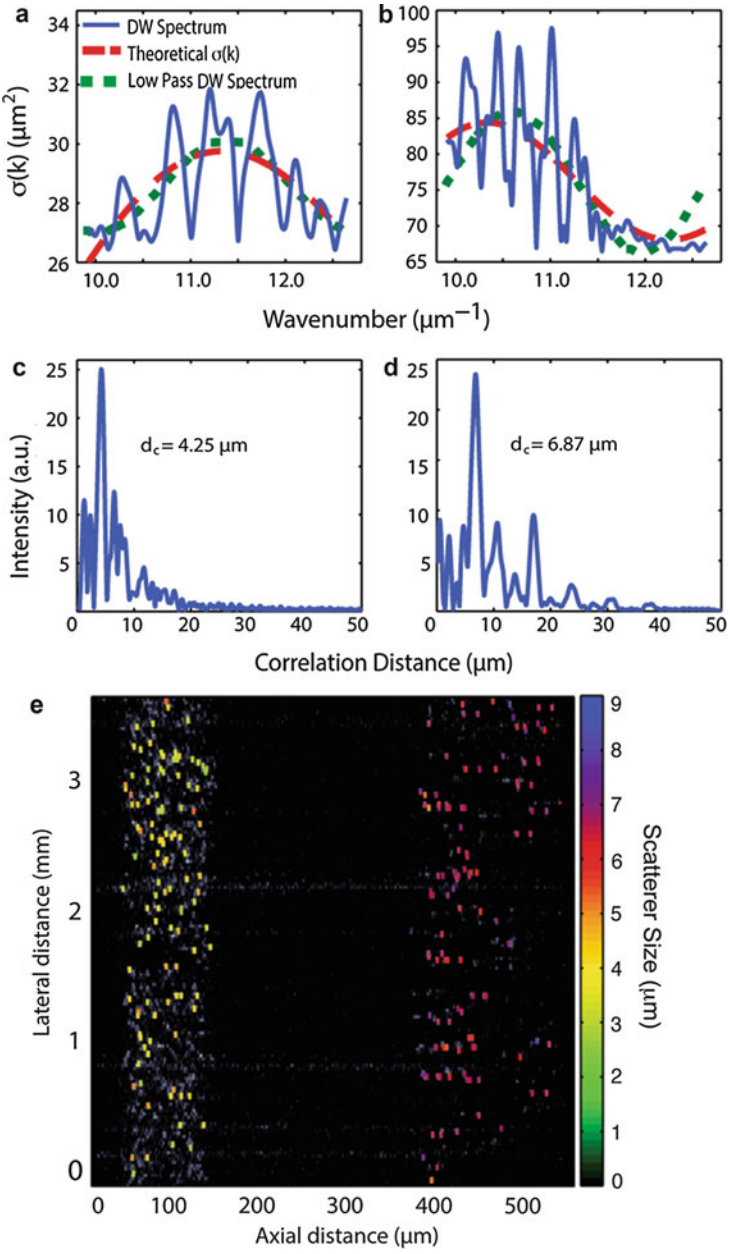

Fig. 38.9 (**a**, **b**) Representative depth-resolved spectra from the front layer and back layer, respectively, of the scattering phantom with microspheres of 4.00 ± 0.033 μm and 6.98 ± 0.055 μm in diameter in each layer. (**c**, **d**) Correlation function from (**a**) and (**b**), respectively, with a peak corresponding to the diameter of the scatterer. (**e**) Functional fLCI map, with the color indicating the scatterer size, overlaid with the OCT image of the phantom (Adapted from [61])

Again, data were acquired with the pfdOCT system and the depth-resolved spectra were generated using the DW method. For this study, a lateral resolution of 10 μm and an axial resolution of ~1.1 μm were achieved, a RI of $n = 1.38$ was used to convert the optical path length to physical axial distance in tissue, and a constant nuclear RI of $n_n = 1.395$ was used for the fLCI analysis [67]. For the generation of the DW TFDs, the window standard deviations used were $a = 0.029\ \mu m^{-1}$ and $b = 0.804\ \mu m^{-1}$, resulting in TFDs with an axial resolution of 3.45 μm and spectral resolution of 1.66 nm. Three different tissue sections were analyzed based on their depth from the tissue surface: surface section 0–25 μm, midsection 22.5–47.5 μm, and low section 37.5–62.5 μm. Here, the OCT images were used to contour the surface of the tissue to permit consistent analysis of the same depth in tissue.

A representative OCT image of an AOM-treated rat tissue sample is shown in Fig. 38.10a, where the dotted line delineates an averaged region from the mid depth

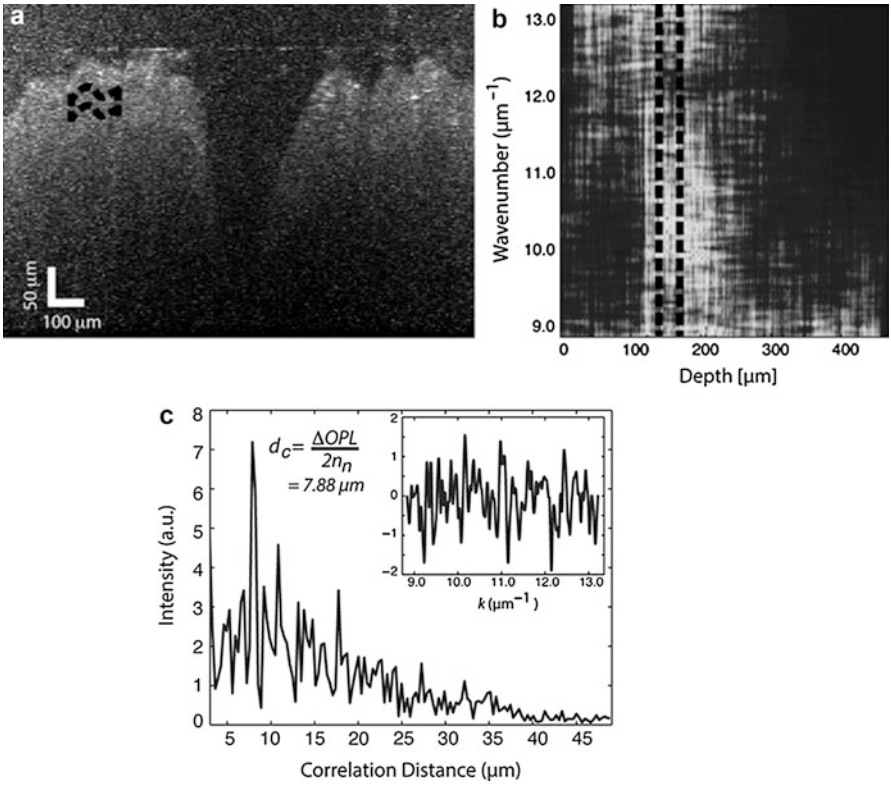

Fig. 38.10 (**a**) pfdOCT image of an ex vivo, AOM-treated rat colon sample. (**b**) DW TFD of average region (after alignment and averaging laterally), (**c**) Correlation plot from the averaged region in the dotted region of (**a**) where the peak reveals the average nuclear diameter (7.88 μm). Inset shows the average local oscillations from the region between the *dotted lines* in (**b**) (Adapted from [64])

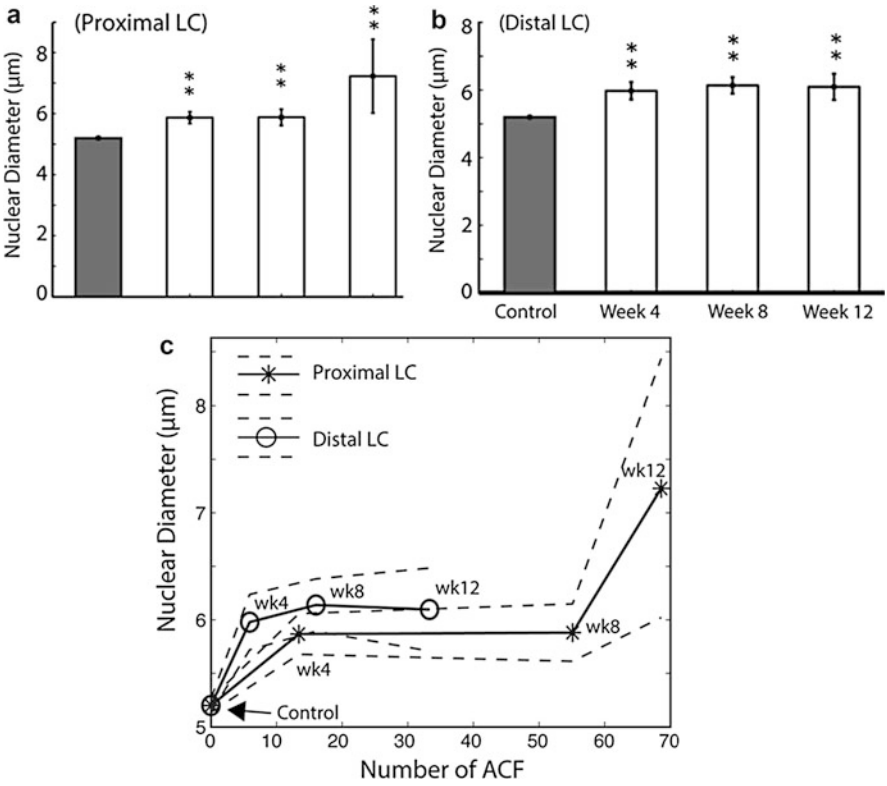

Fig. 38.11 Results by colon length segments. Highly statistical differences (*p value* $<10^{-4}$ **) were observed between the control group and treated groups for the proximal LC (**a**) and distal LC (**b**). (**c**) Plots of the measured cell nuclear diameter as a function of the number of ACF. For clarity, the time of measurement is noted next to each point (*wk* week) (Taken from [64])

section. The corresponding DW TFD (after alignment and averaging laterally) is shown in Fig. 38.10b, c showing the average correlation function for that section (corresponding local oscillations are shown in the inset).

The nuclear diameters of the treated groups were found to be significantly different from the control group (*p-values* $<10^{-4}$ **) for all time points and for both the proximal and distal sections of the left colon (LC). Further, a close inspection of the results (Fig. 38.11) revealed a plateau region in the increase of the nuclear diameter, for both the distal and proximal LC, that is initially independent of the number of ACF. This behavior strongly suggests that the field effect of carcinogenesis, which ubiquitously affects the tissue, can also be observed by measuring changes in nuclear morphology. The data also show that once the number of ACF increased to the maximum value observed in this study (∼70), the measured increase of the nuclear diameter was specific to the region manifesting more advanced neoplastic development, supporting the hypothesis that fLCI can locate more aggressive cancerous development.

Other groups have used OCT and spectral ESS features for imaging and tissue analysis. For example, Adler et al. have used a similar approach that analyzes the local oscillations near zero frequency (a method known as spectral autocorrelation) to provide functional contrast of scatterers [68]. Bosschaart et al. have used low-coherence spectroscopy to assess wavelength dependence of scattering coefficients [69], building on previous work by Faber et al. [70]. Recently, Tay et al. have optimized the spectral autocorrelation approach by using the dual-window method and have shown promising results using ex vivo human palatine tonsil samples [71].

This section has demonstrated the capabilities of fLCI for assessing structure in strongly scattering media by using a combination of spectral ESS and low-coherence interferometry. The results summarized here also demonstrate the ability of fLCI to quantitatively distinguish between tissues that are normal and those that exhibit early precancerous development, including signs of the field effect of carcinogenesis. Further development of this approach could lead to a modality for in vivo, noninvasive clinical screening.

38.6 Conclusions

The combination of ESS and OCT methods can provide unique methods for probing the properties of scattering samples. The depth resolution achieved via coherence gating in OCT can be exploited to obtain scattering signals for ESS analysis. Information for analyzing the structure of scattering objects can be obtained by observing the wavelength or angular dependence of elastic scattering. However, the component of light which has been scattered a single time is most useful. The desired signal can be isolated from the diffuse background due to multiply scattered light using coherence gating in a similar manner as in OCT.

In this chapter, methods for combining angular and spectral ESS methods with the depth resolution of coherence gating have been presented. The a/LCI technique examines angular-scattering distributions to assess structure while using coherence gating to obtain depth resolution, similar to the method used in OCT. As a complimentary method, fLCI has been developed as a synthesis of spectral ESS and spectroscopic OCT methods. This new method has been applied to detect nuclear morphology in animal models and is expected to be further developed for clinical applications.

By combining ESS and OCT methods, a/LCI can provide a viable means for detecting nuclear morphology in situ which cannot be accomplished by current OCT technology, which lacks the ability to observe subcellular features in all but the most advanced research systems. Nuclear morphology measurements can serve as biomarkers of disease progression, particularly as indicators of precancerous tissue states. The key difference between a/LCI and OCT is that the beam input to the sample is collimated rather than focused. In OCT, a focused beam, typically a few microns across, is used to obtain lateral resolution. However, a focused beam necessarily contains a broad angular distribution. When this broad angular distribution is incident on a scattering particle, the angular-scattering pattern from the particle is convolved with the angular distribution of the incident light.

The convolution process serves to smooth out the features in the measured angular distribution. In a/LCI, the incident light is a pencil beam (~0.5 mm diameter), with a very narrow angular distribution determined by the diffraction angle of the collimated beam (angular resolution = 1–2 mrad). This narrow angular resolution permits accurate measurement of the scattered angular distribution.

The a/LCI technique has been applied to study nuclear morphology in cultured cells as well as intact tissue specimens. After validation experiments with in vitro cells and animal tissues, the a/LCI technique has been advanced to study human epithelial tissues, including an in vivo study of the approach for detecting precancerous lesions in the esophageal epithelium.

References

1. H.C. Van de Hulst, *Light Scattering by Small Particles* (Dover, New York, 1957)
2. A. Yodh, B. Chance, Spectroscopy and imaging with diffusing light. Phys. Today **48**, 34 (1995)
3. V. Backman, R. Gurjar, K. Badizadegan, L. Itzkan, R.R. Dasari, L.T. Perelman, M.S. Feld, Polarized light scattering spectroscopy for quantitative measurement of epithelial cellular structures in situ. IEEE J. Sel. Top. Quantum Electron. **5**(4), 1019–1026 (1999)
4. V. Backman, M.B. Wallace, L.T. Perelman, J.T. Arendt, R. Gurjar, M.G. Muller, Q. Zhang, G. Zonios, E. Kline, T. McGillican, S. Shapshay, T. Valdez, K. Badizadegan, J.M. Crawford, M. Fitzmaurice, S. Kabani, H.S. Levin, M. Seiler, R.R. Dasari, I. Itzkan, J. Van Dam, M.S. Feld, Detection of preinvasive cancer cells. Nature **406**(6791), 35–36 (2000)
5. I. Georgakoudi, B.C. Jacobson, J. Van Dam, V. Backman, M.B. Wallace, M.G. Muller, Q. Zhang, K. Badizadegan, D. Sun, G.A. Thomas, L.T. Perelman, M.S. Feld, Fluorescence, reflectance, and light-scattering spectroscopy for evaluating dysplasia in patients with Barrett's esophagus. Gastroenterology **120**(7), 1620–1629 (2001)
6. I. Georgakoudi, E.E. Sheets, M.G. Muller, V. Backman, C.P. Crum, K. Badizadegan, R.R. Dasari, M.S. Feld, Trimodal spectroscopy for the detection and characterization of cervical precancers in vivo. Am. J. Obstet. Gynecol. **186**(3), 374–382 (2002)
7. M.B. Wallace, L.T. Perelman, V. Backman, J.M. Crawford, M. Fitzmaurice, M. Seiler, K. Badizadegan, S.J. Shields, I. Itzkan, R.R. Dasari, J. Van Dam, M.S. Feld, Endoscopic detection of dysplasia in patients with Barrett's esophagus using light-scattering spectroscopy. Gastroenterology **119**(3), 677–682 (2000)
8. C. Lau, O. Šćepanović, J. Mirkovic, S. McGee, C.C. Yu, S. Fulghum, M. Wallace, J. Tunnell, K. Bechtel, M. Feld, Re-evaluation of model-based light-scattering spectroscopy for tissue spectroscopy. J. Biomed. Opt. **14**(2), 024031-024031-8 (2009)
9. A. Wax, C.H. Yang, V. Backman, K. Badizadegan, C.W. Boone, R.R. Dasari, M.S. Feld, Cellular organization and substructure measured using angle- resolved low-coherence interferometry. Biophys. J. **82**(4), 2256–2264 (2002)
10. K.J. Chalut, M. Giacomelli, A. Wax, Application of Mie theory to assess structure of spheroidal scattering in backscattering geometries. J. Opt. Soc. Am. A **25**(8), 1866–1874 (2008)
11. M.I. Mishchenko, L.D. Travis, A.A. Lacis, *Scattering, Absorption, and Emission of Light by Small Particles* (Cambridge University Press, New York, 2002), pp. 119–126
12. M.G. Giacomelli, K.J. Chalut, J.H. Ostrander, A. Wax, Application of the T-matrix method to determine the structure of spheroidal cell nuclei with angle-resolved light scattering. Opt. Lett. **33**, 2452 (2008)
13. K.J. Chalut, K. Kulangara, M.G. Giacomelli, A. Wax, K.W. Leong, Deformation of stem cell nuclei by nanotopographical cues. Soft Matter **6**, 1675 (2010)

14. M.G. Giacomelli, K.J. Chalut, J.H. Ostrander, A. Wax, Review of the application of T-Matrix calculations for determining the structure of cell nuclei with angle-resolved light scattering measurements. IEEE J. Sel. Top. Quantum Electron **16**(4), 900–908 (2010)
15. M.I. Mishchenko, L.D. Travis, Capabilities and limitations of a current FORTRAN implementation of the T-matrix method for randomly oriented, rotationally symmetric scatterers. J. Quant. Spectrosc. Radiat. Transf. **60**, 309–324 (1998)
16. J.W. Goodman, *Introduction to Fourier Optics*, vol. 2 (McGraw-Hill, New York, 1968)
17. Y.L. Kim, Y. Liu, R.K. Wali, H.K. Roy, M.J. Goldberg, A.K. Kromin, K. Chen, V. Backman, Simultaneous measurement of angular and spectral properties of light scattering for characterization of tissue microarchitecture and its alteration in early precancer. IEEE J. Sel. Top. Quantum Electron. **9**(2), 243–256 (2003)
18. H.K. Roy, Y. Liu, R.K. Wali, Y.L. Kim, A.K. Kromine, M.J. Goldberg, V. Backman, Four-dimensional elastic light-scattering fingerprints as preneoplastic markers in the rat model of colon carcinogenesis. Gastroenterology **126**(4), 1071–1081 (2004)
19. J.-Y. Zheng, R.M. Pasternack, N.N. Boustany, Optical scatter imaging with a digital micromirror device. Opt. Express **17**(22), 20401–20414 (2009)
20. R.M. Pasternack, J.-Y. Zheng, N.N. Boustany, Optical scatter changes at the onset of apoptosis are spatially associated with mitochondria. J. Biomed. Opt. **15**(4), 040504 (2010)
21. T. Gutzler, T.R. Hillman, S.A. Alexandrov, D.D. Sampson, Three-dimensional depth-resolved and extended-resolution micro-particle characterization by holographic light scattering spectroscopy. Opt. Express **18**(24), 25116–25126 (2010)
22. A. Wax, C. Yang, V. Backman, M. Kalashnikov, R.R. Dasari, M.S. Feld, Determination of particle size using the angular distribution of backscattered light as measured with low-coherence interferometry. J. Opt. Soc. Am. A. **19**, 737–744 (2002)
23. A. Wax, C.H. Yang, R.R. Dasari, M.S. Feld, Measurement of angular distributions by use of low-coherence interferometry for light-scattering spectroscopy. Opt. Lett. **26**(6), 322–324 (2001)
24. J.W. Pyhtila, R.N. Graf, A. Wax, Determining nuclear morphology using an improved angle-resolved low coherence interferometry system. Opt. Express **11**, 3473–3484 (2003)
25. J.W. Pyhtila, A. Wax, Improved interferometric detection of scattered light with a 4f imaging system. Appl. Optics **44**, 1785–1791 (2005)
26. J.W. Pyhtila, A. Wax, Improved interferometric detection of scattered light with a 4f imaging system. Appl. Optics **44**(10), 1785–1791 (2005)
27. A. Wax, J.W. Pyhtila, R.N. Graf, R. Nines, C.W. Boone, R.R. Dasari, M.S. Feld, V.E. Steele, G.D. Stoner, Prospective grading of neoplastic change in rat esophagus epithelium using angle-resolved low-coherence interferometry. J. Biomed. Opt. **10**(5), 051604–051610 (2005)
28. M.A. Choma, M.V. Sarunic, C.H. Yang, J.A. Izatt, Sensitivity advantage of swept source and Fourier domain optical coherence tomography. Opt. Express **11**(18), 2183–2189 (2003)
29. J.F. de Boer, B. Cense, B.H. Park, M.C. Pierce, G.J. Tearney, B.E. Bouma, Improved signal-to-noise ratio in spectral-domain compared with time-domain optical coherence tomography. Opt. Lett. **28**(21), 2067–2069 (2003)
30. R. Leitgeb, C.K. Hitzenberger, A.F. Fercher, Performance of Fourier domain vs. time domain optical coherence tomography. Opt. Express **11**(8), 889–894 (2003)
31. J.W. Pyhtila, A. Wax, Rapid, depth-resolved light scattering measurements using Fourier domain, angle-resolved low coherence interferometry. Opt. Express **12**(25), 6178–6183 (2004)
32. J.W. Pyhtila, K.J. Chalut, J.D. Boyer, J.D. Boyer, T.A. D'Amico, J.D. Keener, M. Gottfried, F. Gress, A. Wax, Fourier-domain angle-resolved low coherence interferometry through an endoscopic fiber bundle for light-scattering spectroscopy. Opt. Lett. **31**, 772–774 (2006)
33. J.W. Pyhtila, A. Wax, Polarization effects on scatterer sizing accuracy analyzed with frequency-domain angle-resolved low-coherence interferometry. Appl. Optics **46**(10), 1735–1741 (2007)
34. T.Q. Xie, D. Mukai, S.G. Guo, M. Brenner, Z.P. Chen, Fiber-optic-bundle-based optical coherence tomography. Opt. Lett. **30**(14), 1803–1805 (2005)

35. Y. Zhu, M.G. Giacomelli, A. Wax, Fiber-optic interferometric two-dimensional scattering-measurement system. Opt. Lett. **35**, 1641–1643 (2010)
36. W.J. Brown, J.W. Pyhtila, N.G. Terry, K.J. Chalut, T. D'Amico, T.A. Sporn, J.V. Obando, A. Wax, Review and recent development of angle-resolved low coherence interferometry for detection of pre-cancerous cells in human esophageal epithelium. IEEE J. Sel. Top. Quantum Electron. **14**, 88–97 (2008)
37. J.W. Pyhtila, J.D. Boyer, K.J. Chalut, A. Wax, Fourier-domain angle-resolved low coherence interferometry through an endoscopic fiber bundle for light-scattering spectroscopy. Opt. Lett. **31**(6), 772–774 (2006)
38. J.W. Pyhtila, H. Ma, A.J. Simnick, A. Chilkoti, A. Wax, Analysis of long range correlations due to coherent light scattering from in-vitro cell arrays using angle-resolved low coherence interferometry. J Biomed Opt **11**, 034022 (2006)
39. J.W. Pyhtila, R.N. Graf, A. Wax, Determining nuclear morphology using an improved angle-resolved low coherence interferometry system. Opt. Express **11**(25), 3473–3484 (2003)
40. A. Wax, Y. Zhu, N.G. Terry, Angle-resolved low coherence interferometry: depth-resolved light scattering for detecting neoplasia, in *Biomedical Applications of Light Scattering*, ed. by A. Wax, V. Backman (McGraw Hill, New York, 2010), pp. 313–339
41. M.G. Giacomelli, Y. Zhu, J. Lee, A. Wax, Size and shape determination of spheroidal scatterers using two-dimensional angle resolved scattering. Opt. Express **18**, 14616–14626 (2010)
42. M. Giacomelli, K. Chalut, J. Ostrander, A. Wax, Light-cell and light-tissue interactions review of the application of T-matrix calculations for determining the structure of cell nuclei with angle-resolved light scattering measurements. IEEE J. Sel. Top. Quantum Electron. **16**(4), 900 (2010)
43. M. Giacomelli, Y. Zhu, J. Lee, A. Wax, Size and shape determination of spheroidal scatterers using two-dimensional angle resolved scattering. Opt. Express **18**(14), 14616–14626 (2010)
44. K.J. Chalut, S. Chen, J.D. Finan, M.G. Giacomelli, F. Guilak, K.W. Leong, A. Wax, Label-free, high-throughput measurements of dynamic changes in cell nuclei using angle-resolved low coherence interferometry. Biophys. J. **94**(12), 4948–4956 (2008)
45. K.J. Chalut, J.H. Ostrander, M.G. Giacomelli, A. Wax, Light scattering measurements of subcellular structure provide noninvasive early detection of chemotherapy-induced apoptosis. Cancer Res. **69**, 1199–1204 (2009)
46. A. Wax, J.W. Pyhtila, R.N. Graf, R. Nines, C.W. Boone, R.R. Dasari, M.S. Feld, V.E. Steele, G.D. Stoner, Prospective grading of neoplastic change in rat esophagus epithelium using angle-resolved low-coherence interferometry. J. Biomed. Opt. **10**(5), 051604 (2005)
47. A. Wax, C.H. Yang, M.G. Muller, R. Nines, C.W. Boone, V.E. Steele, G.D. Stoner, R.R. Dasari, M.S. Feld, In situ detection of neoplastic transformation and chemopreventive effects in rat esophagus epithelium using angle-resolved low-coherence interferometry. Cancer Res. **63**(13), 3556–3559 (2003)
48. J.W. Pyhtila, K.J. Chalut, J.D. Boyer, J. Keener, T. D'Amico, M. Gottfried, F. Gress, A. Wax, In situ detection of nuclear atypia in Barrett's esophagus using angle-resolved low coherence interferometry. Gastrointest. Endosc. **65**, 487–491 (2007)
49. N.G. Terry, Y. Zhu, M.T. Rinehart, W.J. Brown, S.C. Gebhart, S. Bright, E. Carretta, C.G. Ziefle, M. Panjehpour, J. Galanko, R.D. Madanick, E.S. Dellon, D. Trembath, A. Bennett, J.R. Goldblum, B.F. Overholt, J.T. Woosley, N.J. Shaheen, A. Wax, Detection of dysplasia in Barrett's esophagus with in vivo depth-resolved nuclear morphology measurements. Gastroenterology **140**(1), 42–50 (2011)
50. N. Terry, Y. Zhu, J.K.M. Thacker, J. Migaly, C. Guy, C.R. Mantyh, A. Wax, Detection of intestinal dysplasia using angle-resolved low coherence interferometry. J. Biomed. Opt. **16**(10), 106002–106006 (2011)
51. A. Wax, N.G. Terry, E.S. Dellon, N.J. Shaheen, Angle-resolved low coherence interferometry for detection of dysplasia in Barrett's esophagus. Gastroenterology **141**(2), 443–447.e2 (2011)

52. A. Wax, C. Yang, J. Izatt, Fourier-domain low-coherence interferometry for light-scattering spectroscopy. Opt. Lett. **28**(14), 1230–1232 (2003)
53. U. Morgner, W. Drexler, F. Kärtner, X. Li, C. Pitris, E. Ippen, J. Fujimoto, Spectroscopic optical coherence tomography. Opt. Lett. **25**(2), 111–113 (2000)
54. R. Graf, F. Robles, X. Chen, A. Wax, Detecting precancerous lesions in the hamster cheek pouch using spectroscopic white-light optical coherence tomography to assess nuclear morphology via spectral oscillations. J. Biomed. Opt. **14**, 064030 (2009)
55. F.E. Robles, *Light Scattering and Absorption Spectroscopy in Three Dimensions Using Quantitative Low Coherence Interferometry for Biomedical Applications*, PhD Thesis in Medical Physics Program, Duke University: Durham, 2011
56. A. Wax, C.H. Yang, R.R. Dasari, M.S. Feld, Path-length-resolved dynamic light scattering: modeling the transition from single to diffusive scattering. Appl. Optics **40**(24), 4222–4227 (2001)
57. R. Graf, W. Brown, A. Wax, Parallel frequency-domain optical coherence tomography scatter-mode imaging of the hamster cheek pouch using a thermal light source. Opt. Lett. **33**(12), 1285–1287 (2008)
58. F. Robles, R.N. Graf, A. Wax, Dual window method for processing spectroscopic optical coherence tomography signals with simultaneously high spectral and temporal resolution. Opt. Express **17**(8), 6799–6812 (2009)
59. L. Cohen, Time frequency-distributions – a review. Proc. IEEE **77**, 941–981 (1989)
60. R. Graf, A. Wax, Nuclear morphology measurements using Fourier domain low coherence interferometry. Opt. Express **13**(12), 4693–4698 (2005)
61. F. Robles, A. Wax, Measuring morphological features using light-scattering spectroscopy and Fourier-domain low-coherence interferometry. Opt. Lett. **35**(3), 360–361 (2010)
62. I. Itzkan, L. Qiu, H. Fang, M.M. Zaman, E. Vitkin, I.C. Ghiran, S. Salahuddin, M. Modell, C. Andersson, L.M. Kimerer, P.B. Cipolloni, K.-H. Lim, S.D. Freedman, I. Bigio, B.P. Sachs, E.B. Hanlon, L. Perelman, Confocal light absorption and scattering spectroscopic microscopy monitors organelles in live cells with no exogenous labels. Proc. Natl. Acad. Sci. U. S. A. **104**(44), 17255–17260 (2007)
63. J. Yi, J. Gong, X. Li, Analyzing absorption and scattering spectra of micro-scale structures with spectroscopic optical coherence tomography. Opt. Express **17**(15), 13157–13167 (2009)
64. F. Robles, Y. Zhu, J. Lee, S. Sharma, A. Wax, Detection of early colorectal cancer development in the azoxymethane rat carcinogenesis model with Fourier domain low coherence interferometry. Biomed. Opt. Express **1**, 736 (2010)
65. B. Reddy, Studies with the azoxymethane-rat preclinical model for assessing colon tumor development and chemoprevention. Environ. Mol. Mutagen. **44**(1), 26–35 (2004)
66. E. McLellan, R. Bird, Aberrant crypts: potential preneoplastic lesions in the murine colon. Cancer Res. **48**(21), 6187 (1988)
67. A. Zysk, S. Adie, J. Armstrong, M. Leigh, A. Paduch, D. Sampson, F. Nguyen, S. Boppart, Needle-based refractive index measurement using low-coherence interferometry. Opt. Lett. **32**(4), 385–387 (2007)
68. D. Adler, T. Ko, P. Herz, J. Fujimoto, Optical coherence tomography contrast enhancement using spectroscopic analysis with spectral autocorrelation. Opt. Express **12**(22), 5487–5501 (2004)
69. N. Bosschaart, D.J. Faber, T.G. van Leeuwen, M.C.G. Aalders, Measurements of wavelength dependent scattering and backscattering coefficients by low-coherence spectroscopy. J. Biomed. Opt. **16**(3), 030503-030503-3 (2011)
70. D. Faber, F. van der Meer, M. Aalders, T. van Leeuwen, Quantitative measurement of attenuation coefficients of weakly scattering media using optical coherence tomography. Opt. Express **12**(19), 4353–4365 (2004)
71. B.C.-M. Tay, T.-H. Chow, B.-K. Ng, T.K.-S. Loh, Dual-window dual-bandwidth spectroscopic optical coherence tomography metric for qualitative scatterer size differentiation in tissues. IEEE Trans. Biomed. Eng. **59**(9), 2439–2448 (2012)

Nonlinear Interferometric Vibrational Imaging (NIVI) with Novel Optical Sources

39

Stephen A. Boppart, Matthew D. King, Yuan Liu, Haohua Tu, and Martin Gruebele

39.1 Introduction

Optical imaging is essential in medicine and in fundamental studies of biological systems. Although many existing imaging modalities can supply valuable information, not all are capable of label-free imaging with high-contrast and molecular specificity. The application of molecular or nanoparticle contrast agent may adversely influence the biological system under investigation. These substances also present ongoing concerns over toxicity or particle clearance, which must be properly addressed before their approval for in vivo human imaging. Hence there is an increasing appreciation for label-free imaging techniques. It is of primary importance to develop imaging techniques that can indiscriminately identify and quantify biochemical compositions to high degrees of sensitivity and specificity through only the intrinsic optical response of endogenous molecular species.

Multiphoton coherent Raman scattering techniques, such as coherent anti-Stokes Raman scattering (CARS) and stimulated Raman scattering (SRS), have drawn considerable attention due to many distinct advantages over other imaging modalities [1–3]. Raman scattering processes provide chemical contrast during imaging of materials by exploiting the vibrational "fingerprints" of the molecules contained within the sample. In addition to its label-free imaging capabilities, there are many

S.A. Boppart (✉)
Biophotonics Imaging Laboratory, Beckman Institute for Advanced Science and Technology, University of Illinois at Urbana-Champaign, Urbana, IL, USA

Departments of Bioengineering, Electrical and Computer Engineering, and Medicine, University of Illinois at Urbana-Champaign, Urbana, IL, USA
e-mail: boppart@illinois.edu

M.D. King • Y. Liu • H. Tu • M. Gruebele
Beckman Institute for Advanced Science and Technology, University of Illinois at Urbana-Champaign, Urbana-Champaign, USA

© Springer International Publishing Switzerland 2015

W. Drexler, J.G. Fujimoto (eds.), *Optical Coherence Tomography*,
DOI 10.1007/978-3-319-06419-2_40

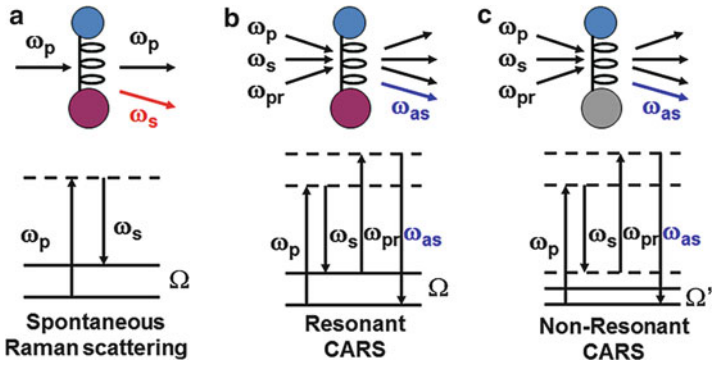

Fig. 39.1 Comparison of (**a**) spontaneous Raman scattering, (**b**) resonant CARS, and (**c**) nonresonant CARS. Optical frequencies of pump, probe, Stokes, and anti-Stokes photons are related by $\omega_{as} = \omega_p - \omega_s + \omega_{pr}$

other notable advantages to CARS imaging. The blue shifting of the generated signal makes it easily separable from the excitation sources and the strong fluorescence background emission of biological samples. In addition, the phase matching requirements of the nonlinear CARS process permit high-resolution three-dimensional imaging [4, 5]. The CARS process is also a much more efficient process than spontaneous Raman scattering, allowing for high-speed image acquisition [6, 7].

In CARS excitation, Raman-active molecular vibrations are coherently driven to generate a strong anti-Stokes Raman signal. The wave-mixing process requires a pump, Stokes, and probe excitation fields to produce the higher-frequency anti-Stokes signal (Fig. 39.1). The pump frequency at ω_p and the Stokes frequency at ω_s induce a vibrational coherence when $\omega_p - \omega_s$ coincides with a molecular vibrational frequency, Ω_R. The subsequent probe frequency at ω_{pr} generates the anti-Stokes signal at $\omega_{as} = \omega_{pr} + \omega_p - \omega_s = \omega_{pr} + \Omega_R$. Under these conditions, there is significant enhancement in the resonant CARS signal. When $\omega_p - \omega_s$ is of resonance, the electronic response of the material produces a nonresonant CARS signal. By isolating the resonant contribution to the collected CARS signal, detailed molecular information can be obtained.

Conventional CARS imaging uses narrowband nanosecond or picosecond sources with frequencies tuned to selectively excite a single Raman resonance. However, this approach is limited in that the obtainable spectral information is not sufficient to discriminate between different biomolecules, or to determine their relative concentrations in unknown samples containing molecules with overlapping Raman bands. These limitations can be overcome by using a broadband Stokes pulse to cover a larger bandwidth of vibrational excitations in what is referred to as multiplex CARS [8–12]. The additional structural information made available by multiplex methods allows for quantitative molecular imaging of unknown samples. However, one disadvantage of multiplex CARS comes with the higher peak field intensities of the ultrafast broadband laser sources compared to narrowband sources, leading to a large nonresonant contribution to

the overall signal due to the increased electronic response. The nonresonant CARS often dominates the collected signal and can easily mask any low-intensity resonant spectral features. The interference between the resonant and nonresonant signals poses additional problems as this leads to distortion of the retrieved Raman line shapes, which makes it difficult to measure molecular concentrations quantitatively. The presence of this undesirable nonresonant contribution has led to a variety of approaches aimed at suppressing the background signal in order to make multiplex CARS methods feasible for sensitive biomedical imaging applications [13].

The most widely used approach to suppress nonresonant CARS signal is the introduction of a local oscillator, or reference beam, for phase-sensitive interferometric detection [5, 6, 14–24]. Spectral interferometry acts to simultaneously enhance the resonant signal while eliminating the nonresonant contribution. Many variations in interferometric detection schemes have been introduced, including time-resolved interferometry [14], vibrational phase-contrast [17, 18], phase-cycling [19], and spectral-domain heterodyne CARS [6, 24]. While there are advantages to each approach, there are also significant disadvantages that can limit their applicability for quantitative high-speed imaging techniques. Time-resolved methods, such as Fourier-transform CARS [14, 15], rely on temporal scanning of the excitation pulses in order to retrieve spectral information. Likewise, phase-cycling schemes require scanning of the excitation phase to obtain the Raman spectrum [19, 20]. These methods are largely devised to overcome the constraints to spectral resolution resulting from the implementation of broadband excitation sources, but conversely impose limitations on imaging speed due to the temporal- or phase-scanning requirements. Phase-contrast CARS does not suffer these limitations and can provide much faster acquisition rates using a single-beam experimental setup [17]. However, this technique is restricted by the associated difficulties with quantitative spectral reconstruction. The most promising methods use heterodyne interferometry in a spectral-domain OCT-like scheme, which combines imaging speed, chemical sensitivity, and high spectral resolution [6, 24]. In such methods, the sensitivity increase comes from the interference of the generated CARS signal with a stable local oscillator, resulting in a possible sensitivity gain up to 1,000-fold [19]. The amplification occurs for both the resonant CARS signal and the nonresonant background, followed by the computational recovery of the phase-sensitive resonant contribution.

Nonlinear interferometric vibrational imaging (NIVI) [21] takes advantage of the speed and sensitivity of the spectral-domain detection while eliminating the dominant nonresonant background, allowing for quantitative reconstruction of Raman line shapes. This method differs from other heterodyne schemes in that spectral inteferometry enables full characterization of the CARS signal field. In the time domain, the resonant and nonresonant contributions can then be separated easily [25–27]. NIVI employs a two-pulse excitation scheme with a transform-limited Stokes pulse and a time-delayed chirped broadband pulse to probe the resonant CARS vibrational excitations. The high-resolution Raman spectrum can then be computationally reconstructed from the interferogram generated from

the spectral-domain interference of the CARS signal with a reference pulse [21, 28]. This results in the amplification of the resonant component and provides quantitative molecular detection with reliable reconstruction of the Raman spectrum.

The important attributes of NIVI over other interferometric CARS-based techniques are that it simultaneously implements heterodyne amplification [29, 30], time-resolved resonant signal isolation [25], and spectral-domain interferometric field reconstruction [21]. The technique has been demonstrated in the quantitative analysis of lipid samples [31] and with molecular imaging of biological samples, including skin domains [32] and rat mammary tumor margins [33]. NIVI was capable of differentiating normal and tumor tissues with >99 % confidence and of detecting the molecular tumor margin within 100 μm. It was shown that the NIVI spectra of biomolecules are equivalent to the corresponding Raman spectra and can be acquired up to 1,000 times faster than with spontaneous Raman microscopy, at comparable signal-to-noise ratios [31, 34]. In the following sections, the theory, experimental setup, and demonstrated results of NIVI are covered in detail. Also discussed are the future directions for extending the imaging capacity of this technique into the Raman fingerprint region (500–1,800 cm^{-1}) using ultrabroadband fiber continuum sources.

39.2 Theory

Conventional multiplex CARS measurements utilize a narrowband pump/probe pulse and a broadband Stokes pulse. However, methods using broadband pulses originating from a single femtosecond source have been devised by implementing a positively chirped pump/probe pulse [21, 28]. In doing so, the probe field is able to interact with the resonant coherent excitation over the extended vibrational time decay, whereas the nonresonant contribution due to the instantaneous electronic response only occurs for the duration of the transform-limited Stokes pulse. NIVI takes advantage of this increase in resonant CARS signal produced by the chirped excitation pulse and recovers the complex Raman spectra through an interferometric detection scheme. The resulting CARS signal has an identical chirp as the excitation pulse, and by measuring the cross-correlation of the signal with a known reference signal, the time-resolved resonant contribution can be extracted. By this method, an accurate Raman spectrum can be retrieved while eliminating the dominant nonresonant signal.

CARS is a wave-mixing process that involves the interaction of three photons to generate a fourth anti-Stokes photon at higher frequency than the incident photons. The CARS process using two broadband pulses, E_p and E_s, corresponding to the pump/probe and Stokes pulses, respectively, can be described in the frequency domain by the equations

$$A(\Omega) = \chi^{(3)}(\Omega) \int_0^\infty E_p(\omega + \Omega) E_s(\omega)^* d\omega \tag{39.1}$$

$$P^{(3)}(\omega) = \int_0^\infty A(\Omega) E_P(\omega - \Omega)^* d\Omega \tag{39.2}$$

where $A(\Omega)$ is the Raman transition amplitude, $\chi^{(3)}$ is the third-order nonlinear susceptibility of the material, $P^{(3)}$ is the third-order hyperpolarizability, and Ω is the resonant molecular vibrational frequency. The two equations give the two-step time evolution of a CARS process involving many possible simultaneous Raman-active vibrations. By Eq. 39.1, a molecule is put into a coherent vibrationally excited state by the pump frequency ω_p and Stokes frequency ω_s that are separated by the vibrational frequency $\Omega = \omega_p - \omega_s$. Using a broadband Stokes pulse enables the simultaneous excitation of vibrational modes over a wide range of frequencies. The generation of anti-Stokes radiation is described by Eq. 39.2, in which the molecule is stimulated from the coherently excited vibrational state by the probe frequency ω_1 to produce the higher energy photon at $\omega_{AS} = \omega_p + \Omega = 2\omega_p - \omega_s$. For broadband excitation, the anti-Stokes signal must be summed over all probe frequencies. The Raman response of the sample is contained in the nonlinear susceptibility, $\chi^{(3)}(\Omega)$ which contains resonant and nonresonant contributions, $\chi^{(3)}(\Omega) = \chi^{(3)}_{NR} + \chi^{(3)}_R(\Omega)$.

For CARS using a chirped pump/probe pulse, the spectrum can be expressed by the equation

$$E_p(\omega) = E_0 \exp\left[-i(\omega - \omega_0)^2/2\alpha\right] \tag{39.3}$$

where α is the chirp rate of the pulse. From the stationary phase approximation for a small α, the time-domain signal can be written as

$$E_p(t) = \alpha^{-1/2} E_0(\alpha t + \omega_0) \exp[i(\alpha t/2 + \omega_0)t]. \tag{39.4}$$

The Stokes pulse spectrum $E_S(\omega)$ is transform limited and centered about $t = 0$ such that $E_S(\omega)$ is real. Because of this, the instantaneous frequency of the pump/probe pulse at $t = 0$ is ω_0, which can be approximated as a δ function. With these representations of the pump/probe and Stokes pulses, the nonlinear polarizability expressed in Eq. 39.2 can be approximated as

$$P^{(3)}(\Omega) = \chi^{(3)}(\Omega) \int_0^\infty \alpha^{-1/2} E_0(\omega_0) \delta(\omega + \Omega - \omega_0) E_s(\omega)^* d\omega \tag{39.5}$$

$$= \chi^{(3)}(\Omega) \alpha^{-1/2} E_0(\omega_0) E_s(\omega_0 + \Omega).$$

The anti-Stokes pulse in the time domain $E_{AS}(t)$ can be calculated by Eq. 39.2, yielding

$$E_{AS} = \alpha^{-1/2} E_0(\alpha t + \omega_0) \exp[i(\alpha t/2 + \omega_0)t] \frac{1}{2\pi} \int_0^\infty d\Omega \chi^{(3)}(\Omega) E_s(\omega_0 - \Omega) E_0(\omega_0) \exp(i\Omega t). \tag{39.6}$$

The chirp of the probe can be removed by multiplying the anti-Stokes pulse by the conjugate phase $\exp[-i(\alpha t/2 + \omega_0)t]$. Then, the inverse Fourier transform of this product produces $\chi^{(3)}(\Omega)$, weighted by the Stokes spectrum, which is the estimation of the Raman spectrum.

NIVI is implemented experimentally by reconstructing the complex CARS field from the interferometric cross-correlation of the anti-Stokes and reference fields, retrieving amplitude and phase information of the anti-Stokes field. The interferogram is generated by mixing the CARS field with a transform-limited reference pulse. The measured interferogram, $I(\omega)$, is described by the equation

$$I(\omega) = |E_{AS}(\omega)|^2 + \left|E_{ref}(\omega)\right|^2 + 2\mathrm{Re}\left[E_{AS}(\omega)E_{ref}(\omega)^* \exp(-i\omega\tau)\right] \tag{39.7}$$

where $E_{AS}(\omega)$ and $E_{ref}(\omega)$ are the anti-Stokes and reference fields, respectively, and τ is the time delay between the two pulses (Fig. 39.2a). The spectral interferogram contains DC components from the CARS and reference fields and the phase-sensitive cross-term that contains the NIVI signal. The DC reference term can be removed by the subtraction of the known reference spectrum. The remaining terms can be separated in the time domain, wherein the DC component of the CARS field can be rejected, leaving only the phase-sensitive components (Fig. 39.2b). Substituting $\chi(\omega) = E_{AS}(\omega)E_{ref}(\omega)^*$ and taking the inverse Fourier transform of $I(\omega)$ yields

$$FT^{-1}(I(\omega)) = FT^{-1}(\mathrm{DC}) + \chi(t-\tau) + \chi(-t-\tau). \tag{39.8}$$

The first term is a slowly varying DC component symmetric about $t = 0$, while the last two terms are time reversed from each other. As it is known that there is no CARS signal prior to the vibrational coherence induced by the Stokes pulse, the time origin can be shifted to be the center of the Stokes pulse, thereby isolating the $\chi(t - \tau)$ term (Fig. 39.2c). The Fourier transform of the remaining term results in $\chi(\omega) = \chi^{(3)}(\omega)^* E_s(\omega - \Omega)E_{ref}(\omega)^*$. The nonresonant CARS signal is real and can be rejected by discarding the real part of $\chi^{(3)}$. The NIVI spectrum is represented by the imaginary part of $\chi^{(3)}$ and is analogous to the spontaneous Raman spectrum (Fig. 39.2d).

39.3 Instrumentation

The experimental NIVI setup is shown in Fig. 39.3. A mode-locked Ti:Sa oscillator (Coherent, MIRA, 82 MHz) is used to seed a regenerative amplifier (Coherent, RegA-9000). The 380-mW, 82-MHz Ti:Sa output is amplified to 1.1 W at a 250-kHz repetition rate, resulting in microjoule pulse energies. The amplifier output is split through a 90:10 beam splitter, sending 90 % of the light to pump an optical parametric amplifier (Coherent, OPA-9450), which generates the Stokes pulse at 1,060 nm and the reference pulse at 655 nm, corresponding to the idler and signal pulses generated from the OPA, respectively. The remaining 10 % of the amplifier output is used as the probe beam. The probe pulses are linearly chirped to ~6 ps by passing the beam through an 85-cm bar of BK7 glass. A delay line is

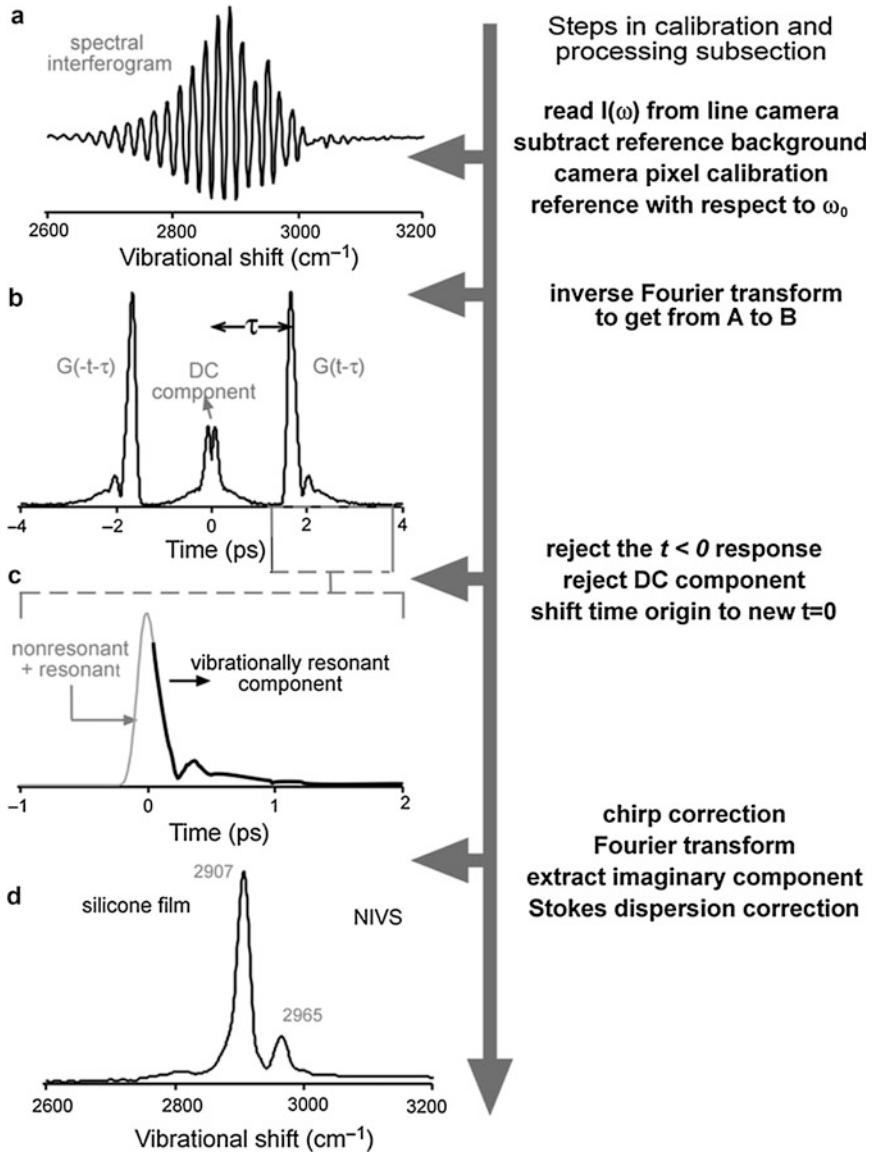

Fig. 39.2 Working principle of Fourier-transform spectral interferometry is demonstrated by extracting the NIVI spectrum of a silicone film starting from the interferogram acquired on the line camera. (**a**) Wavelength calibrated spectral interferogram referenced to the pump wavelength. The reference power spectrum is subtracted. (**b**) Modulus of the time-domain polarization obtained by inverse Fourier transforming the interferogram in (**a**). (**c**) The $t > 0$ response, identifying the short-time nonresonant (follows the Stokes pulse shape) and long-time resonant (vibrational dephasing) components. The temporal chirp of the pump can be corrected here. (**d**) NIVI spectrum of a silicone film obtained as the imaginary part by Fourier transforming the time response in (**c**), and Stokes dispersion is corrected (Adapted from [31], with permission)

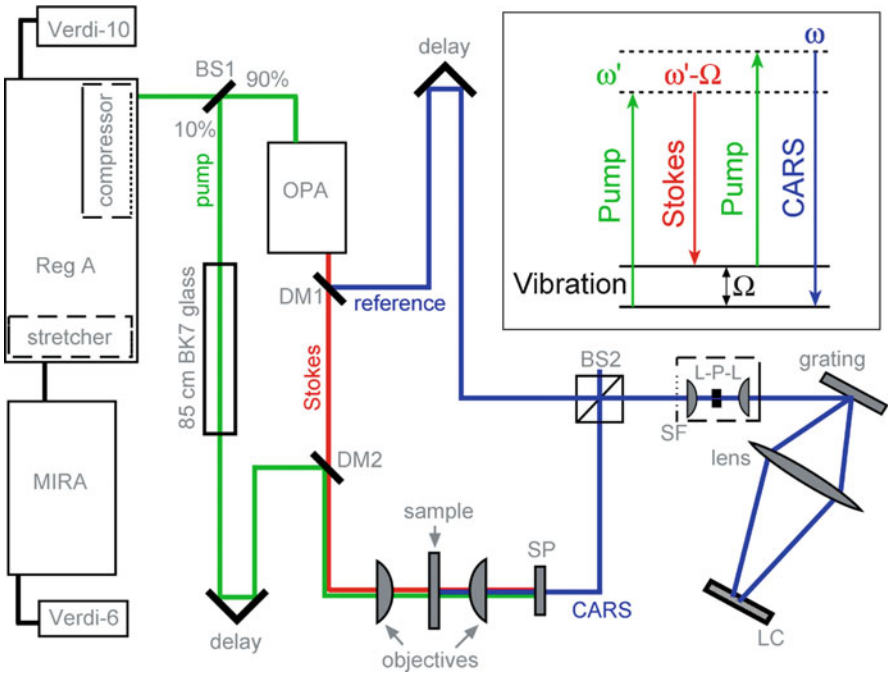

Fig. 39.3 Experimental setup for nonlinear interferometric vibrational imaging (*NIVI*). MIRA–Ti:sapphire oscillator; *Reg A* regenerative amplifier, *OPA* optical parametric amplifier, *DM* dichroic mirrors, *BS* beam splitter, *SP* short-pass filter, *SF* spatial filter, *LC* line camera (Figure adapted from [31] and used with permission)

placed in the beam path to control the temporal delay of the probe and, therefore, the instantaneous pump wavelength. The probe and Stokes beams are recombined using a dichroic mirror and delivered to the sample in a collinear geometry. The wavelengths of the pump and Stokes pulses were tuned to target the spectral range of 2,800−3,000 cm^{-1}, corresponding to the C−H stretching vibrational region. The power of the excitation pulses varied depending on the application, i.e., higher powers are needed for imaging of biological samples, which are highly scattering and contain low concentrations of the specific target molecules.

The probe and Stokes pulses were focused onto the sample with parallel polarization using a high-NA objective. Tight focusing of these excitation beams relaxes the phase matching conditions required for four-wave-mixing processes [2]. The nonlinear interaction of the excitation fields produces the CARS signal at a higher frequency than the incident radiation. The forward-generated CARS signal is collected by a second objective. A high-pass filter is used to remove the excitation wavelengths, transmitting only the blue-shifted CARS signal. The CARS and reference beams were combined at a 50:50 cube beam splitter for collinear detection by spectral interferometry which requires precise spatial and temporal overlap. The combined beams were spatially filtered at a 30-μm pinhole to improve beam

and interference quality. They were subsequently dispersed by a grating (1,200 grooves/mm), and the spectral interferogram was acquired on a 2,048-pixel line camera (DALSA P2) at a 1-kHz line rate. The implementation of spectral interferometry allows for a significant increase in image acquisition speed, signal-to-noise ratio, and signal stability.

39.4 Quantitative Analysis of Lipids

The quantitative capabilities of NIVI for bioanalytical and biomedical imaging applications were demonstrated by measuring the relative degree of unsaturation of different lipid samples [31]. NIVI was shown to be comparable to spontaneous Raman scattering in the ability to distinguish subtle vibrational spectral features, however, with data collection approximately 200 times faster for comparable signal-to-noise ratio. The interferometric technique allows for the spectra to be reconstructed with the same $\chi^{(3)}$ line shape as Raman spectroscopy, without the nonresonant line shape distortions typically obtained from CARS measurements. Quantitative measurements are straightforward because the NIVI signal is linear in analyte concentration. Combining the spectral quality of spontaneous Raman and the high speed of CARS imaging techniques provides a powerful tool for quantitative label-free biomedical imaging.

The comparison of NIVI and spontaneous Raman spectra for six various lipid samples in the spectral range (2,700−3,050 cm^{-1}) containing the C−H stretching vibrational bands is shown in Fig. 39.4. In this spectral region, there is significant overlap of methyl, methylene, and =CH− stretching bands, which makes spectral analysis quite challenging. The presence of unsaturated C=C bonds within the lipids is evident in the intensity of the small spectral feature centered at 3,010 cm^{-1}. The relative intensity of this peak with those of the saturated C−H stretching modes at 2,856 and 2,885 cm^{-1} provides quantitative information as to the degree of unsaturation. A singular value decomposition algorithm to extract the principal spectral components was applied to assess the accuracy of NIVI with Raman spectroscopy. The number of C=C double bonds per unit volume ($N_{C=C}$/mL) was determined for each measurement (Fig. 39.4b). Both spectroscopic techniques produced excellent linear fits when plotted against data obtained from a standard chemical assay, verifying the quantifiable information content of the NIVI spectra.

39.5 Biological Imaging with NIVI

In addition to the chemical bonding probed in lipid samples, other biological compounds, such as proteins and nucleic acids, contain characteristic bonding motifs that produce unique spectral structures that can be used to identify and quantify the presence of such molecules in complex media by NIVI. The ability to evaluate relative molecular concentrations from the spectral profile in the C−H stretching region and to use this information to map the molecular composition

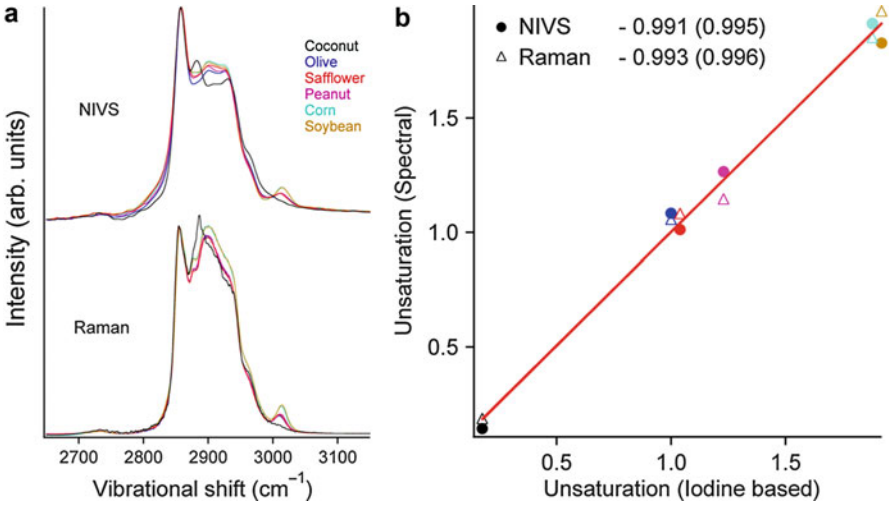

Fig. 39.4 (**a**) Comparison of polarized NIVI and isotropic Raman spectra of various cooking oils. Relative variations are expected due to the polarization sensitivity of NIVI and Raman depolarization ratios of different vibrational mode symmetries. (**b**) Relative $N_{C=C}$/mL derived from NIVI and Raman spectra plotted against unsaturation data obtained from an iodine assay. The slopes of the linear fits are listed with the correlation coefficients in parentheses (Figure adapted from [31] and reproduced with permission)

of complex biological tissues was demonstrated in the imaging of ex vivo porcine skin (Fig. 39.5) [32]. It was shown that the probed C−H spectral region was adequate to distinguish the stratum corneum, epidermis, dermal stroma, and the collagen and adipose domains of the subcutaneous tissue.

Distinct spectroscopic domains arising from the relative lipid and protein concentrations provide the contrast in the images. Evident in the spontaneous Raman spectra in Fig. 39.5c, three primary vibrational bands could be used to decompose the broadband NIVI spectra. The dermis and epidermis show higher concentrations of CH_3 symmetric stretches, and the stratum corneum exhibits comparable amplitudes of the CH_2 and CH_3 symmetric stretching modes. The higher signal of the CH_2 band results from the higher relative concentrations of lipids in the stratum corneum compared with the dermis and epidermis. An image showing the resonant CARS signal over the entire probed bandwidth is provided in Fig. 39.5a. The color-coded molecular map resulting from the molecular-specific decomposition is shown in Fig. 39.5b. A NIVI composite image can be generated by modulation of the molecular map by the intensity map (Fig. 39.5d). Each color in the composite image represents a molecular vibration appropriate for tissue identification and allows for the spatial differentiation of the prevalent molecular species. Comparison of the NIVI composite image with a corresponding H&E-stained tissue section shows that the individual skin domains can be clearly discriminated. However, the NIVI image contains the added benefit of molecule-specific information made available in an instantaneous label-free manner without the need for histological staining

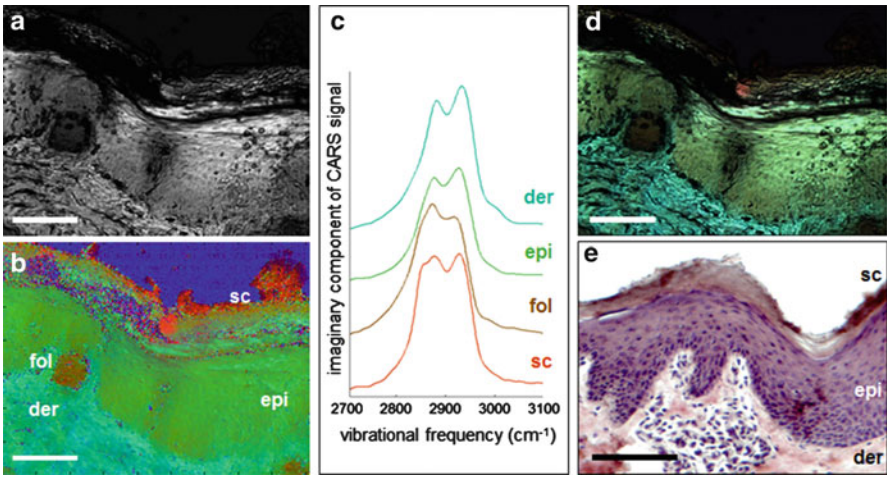

Fig. 39.5 Molecular imaging of cutaneous tissue. (**a**) Intensity image (total integrated spectral power). (**b**) NIVI composite showing discrimination of stratum corneum (*sc*), epidermis (*epi*), dermis (*der*), and hair follicle (*fol*). (**c**) NIVI spectra for each domain in (**b**), as obtained by cluster analysis: each spectrum is the result of averaging the spectra of the members of most prevalent cluster in regions of 20 × 20 pixels^2 within each domain. (**d**) NIVI image showing both structural and molecular compositions. (**e**) H&E histology of a section from the same region. The scale bar is 100 μm in every image (Adapted from [32], with permission)

procedures. Such advantages make NIVI a promising diagnostic technique for quantitative histological and cytological measurements.

The combination of quantitative chemical accuracy and fast image acquisition speed provides reliable tissue characterization suitable for differentiating normal and cancerous tissues. To translate this technique into a robust approach for the reliable distinction of pathologic tissue states, several key factors were addressed. It has been demonstrated that the NIVI signal is linear to the biochemical composition, which permits proper analysis of the tissue composition. In addition, rapid imaging of histological sections, resected tissue specimens, and in situ tissue is permitted by the millisecond spectral acquisition. Lastly, the reduction of complex spectral information to a simple visual code allows for a clear and accurate diagnosis.

We have used NIVI to study mammary tissues from a carcinogen-induced rat mammary tumor model [33]. Earlier Raman studies revealed that the ratio between relative fat and collagen concentrations was the key diagnostic parameter between normal and malignant tumor tissues [35, 36]. Normal tissues rich in lipids exhibit Raman signatures corresponding to $C-H_2$ and $C=C-H$ stretches observed at approximately 2,850 and 3,020 cm^{-1}. These bonding motifs are not as abundant in protein chemical structures, and the Raman signal is therefore decreased as the fat-to-protein ratio is reduced. Figure 39.6 shows the comparison of the NIVI spectra for normal and tumor tissues, as well as those for the reference spectra of collagen (protein) and methyl oleate (lipid). The differences in the Raman spectral

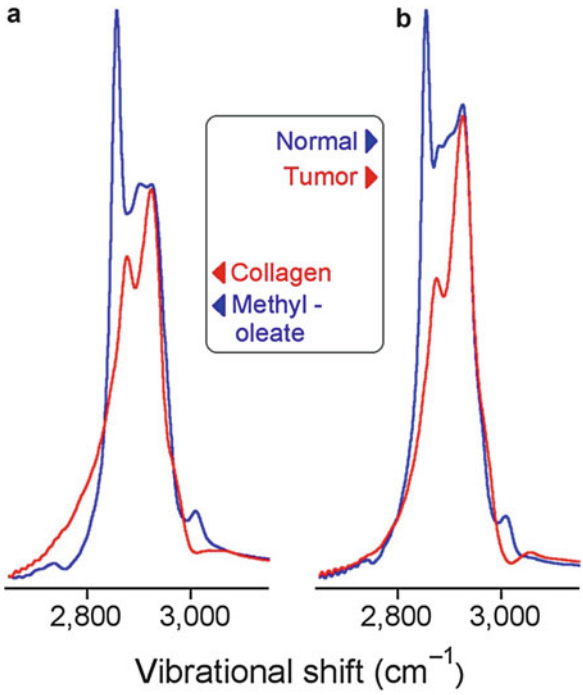

Fig. 39.6 Comparison of NIVI spectra for (**a**) reference spectra of collagen and methyl oleate, and (**b**) normal versus tumor tissues (Adapted from [33] and used with permission)

profiles are evident, and from these NIVI spectra, normal and tumor tissues can easily be accurately distinguished.

The NIVI spectra acquired from different tissue pathologies are sufficient for classifications to be made by comparing the relative intensities of C−H peaks arising from lipids and proteins. Figure 39.7 shows a number of NIVI images of normal and tumor tissues that were differentiated in this manner. The determination of major spectral components can be achieved through a variety of multivariate statistical techniques. The diagnostic algorithm developed in these studies combined principle component analysis (PCA) with logistic regression and reduces the spectral decomposition to only the most significant chemical components contributing to the acquired spectra. For the analysis, the spectra were digitized at 1,000 frequency data points in the range of 2,420–3,320 cm^{-1}. A singular value decomposition (SVD) algorithm was then used to extract the principal components of this data matrix. The three most significant principal components account for >99 % of the variance in the data. The segregation of the normal and tumor spectra is apparent in the two-dimensional subspace of the principal components C_2 and C_3, as shown in Fig. 39.7. A logistic regression could then be used to draw a decision line between the normal and tumor tissues. Figure 39.8 also shows the 99 % confidence intervals for the normal and tumor categories, based on a student's *t* test on the sample set. Images that contained both normal and tumor tissues lie near the decision line from the logistic regression. However, through visual inspection of these images, the normal and tumor tissues can be spatially resolved to less than 100 μm.

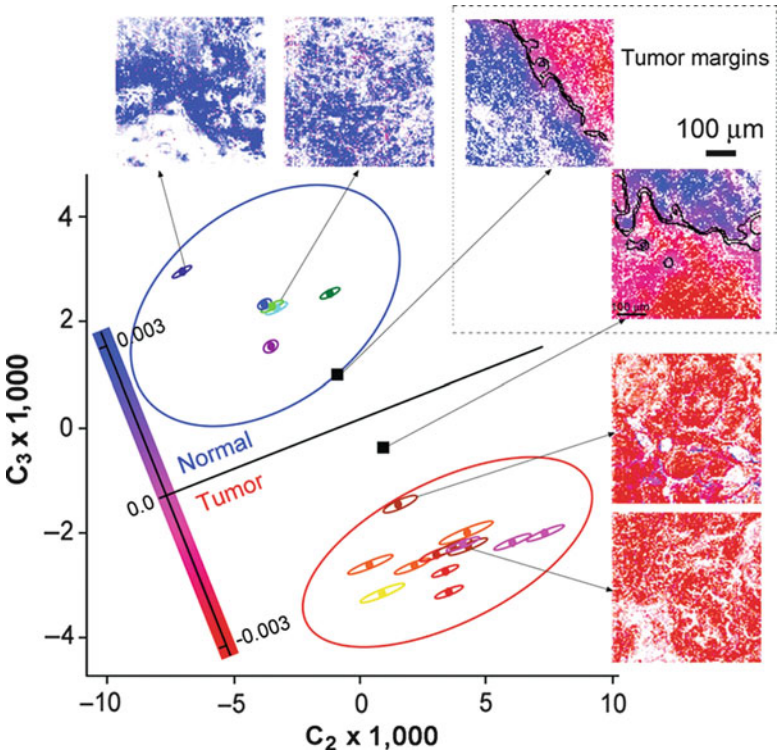

Fig. 39.7 Two-dimensional subspace showing clear differentiation between normal and tumor tissues based on SVD coefficients C_2 and C_3 of the spectral basis functions. Automated tumor margin identification is represented as *black curves* overlaid on the top-right NIVI images. The two boundaries of the margin demarcate normal and tumor domains at greater than the 99 % confidence interval. Tumor margins are readily resolved to 100 μm (Adapted from [33] with permission)

Automated detection of tumor margins can be achieved at the 100-μm scale (Fig. 39.7). The tumor margins were detected in less than a few seconds at the 99 % confidence interval. The images for margin detection again show the optimum linear combination of the spectral coefficients C_2 and C_3. A clean margin (1–2 pixels wide) demarcating the tumor and normal domains can be obtained, with the double band representing the 99 % confidence ellipses near the decision line. The margins are depicted in the upper-right images in Fig. 39.7.

39.6 NIVI with Novel Optical Sources

Although NIVI has been demonstrated as a high-performance multiplex CARS technique, three critical limitations largely limit its clinical translation. First, the inevitable alignment drift between the two collinear incident beams forbids

long-term imaging. Second, the cost and complexity of the amplified ultrafast laser system prohibit widespread application. Third, the narrow acquisition range of Raman frequency (2,700–3,100 cm^{-1}) is insufficient to differentiate biomolecules, which are more distinguishable in the fingerprint region (500–1,800 cm^{-1}). All these limitations can be overcome by integrating the advanced features of coherently controlled single-beam multiplex CARS into the current NIVI instrumentation, using a coherent fiber continuum source [37] based on a regular femtosecond (~100 fs) laser oscillator, rather than the broadband (<20 fs) solid-state laser employed in a typical single-beam multiplex CARS. The single-beam NIVI might be treated as if the spectral gaps among Stokes beam, pump/probe beam, and reference beam would disappear, so that the Stokes, pump, probe, and reference photons could be supplied by one broadband beam (pulse). Because the new features of single-beam setup, coherent control, and fiber continuum source are compatible with the key features of NIVI (i.e., heterodyne signal amplification and field reconstruction, time-resolved resonant signal isolation, and high spectral-resolution broadband interferometry) [16, 38, 39], all advantages of NIVI can be retained.

Due to broad bandwidth, the single-beam NIVI relies on precise shaping of the excitation pulses by a pixelated 4-*f* pulse shaper [40] to maximally stimulate molecular vibration signals that can be interferometrically detected. The importance of pulse shaping in imaging can be appreciated by comparing the performance of two-pulse shapers in two-photon excitation fluorescence microscopy (TPEF) and second-harmonic generation (SHG) microscopy, two nonlinear optical imaging techniques similar to NIVI. The pixelated pulse shaper significantly outperforms the common prism pair-based pulse shaper in resolving the microstructure of biological tissues (Fig. 39.8a). For largely the same reason, the pixelated pulse shaper-incorporated NIVI outperforms regular multiplex CARS (with prism pair-based pulse shaping or no pulse shaping) in resolving the Raman spectrum of biomolecules. The operation of the pixelated pulse shaper had been notoriously difficult until the invention of the multiphoton intrapulse interference phase scan (MIIPS) (see reviews in [41, 42]). MIIPS is a computerized procedure performed in the pixelated pulse shaper that automates the pulse measurement and shaping at targeted sample location and is therefore considered as a highly enabling technology in the ultrafast laser industry. Assuming automatic pulse shaping by MIIPS, we have proposed a "matched filter" pulse shaping method to selectively image a target molecule by NIVI [43]. Figure 39.8b demonstrates that specifically shaped pulses can selectively excite DNA over RNA, even though the two have very similar Raman spectra. This capability will be useful if a biomarker molecule can be identified for a particular human cancer.

In single-beam NIVI, the coherent fiber continuum [44] (Fig. 39.8c) is preferred over the broadband (<20 fs) solid-state laser because of several noticeable advantages: (1) environmental stability of passive extracavity spectral broadening compared to active intracavity broadband mode locking, (2) the absence of a trade-off between broad bandwidth and stable operation, and (3) intrinsic compatibility with alignment-free fiber-based components. Fiber continuum sources have been employed to perform single-frequency CARS [45] and multiplex CARS [46].

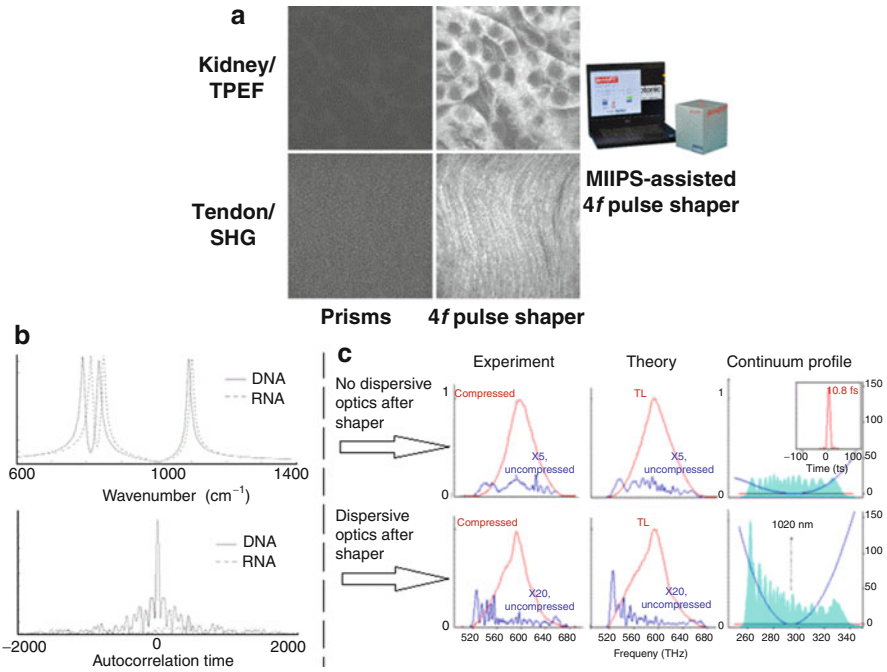

Fig. 39.8 (**a**) TPEF images of stained mouse kidney and SHG images of rat tendon using 12-fs laser pulses shaped by a prism pair, or an MIIPS-assisted pixelated 4-*f* pulse shaper. (**b**) *Top*: Raman spectra of phosphodiester modes of DNA (*solid line*) and RNA (*dashed line*). *Bottom*: time-domain autocorrelation signals for the pulse designed to selectively excite DNA. The signal from RNA (*dashed line*) is negligible in comparison to that from DNA (*solid line*) (Adapted with permission from [43]). (**c**) Adaptive pulse shaping and compression by MIIPS-assisted pixelated 4-*f* pulse shaper with or without dispersive optics after the shaper, as indicated by the agreement of SHG results between experiment and theory (Adapted with permission from [44])

Unfortunately, few known fiber continuum sources have sufficient coherence, bandwidth, or power for coherent control. We have developed an Yb laser-pumped fiber continuum [44, 47, 48], with broad bandwidth (880–1,180 nm), high average power (361 mW), and excellent coherence (Fig. 39.9a, b). These properties represent a significant improvement over the existing coherently controllable fiber continuum sources [38, 39] and have the potential for many future improvements [49, 50]. For the first time, both the spectrum and the spectral phase (i.e., full optical field) of fiber continuum can be simultaneously predicted with high accuracy (Fig. 39.9b). This degree of predictability and controllability allows us to compress and arbitrarily shape the fiber continuum using an MIIPS-assisted 4-*f* pulse shaper (Fig. 39.9c) [48] and to conduct multimodal multiphoton imaging on biological samples. Also, MIIPS adaptively compensates for the transmission optics and microscope objective after the shaper (Fig. 39.8c) [51], implying that the free-space NIVI optics can be fiber coupled externally.

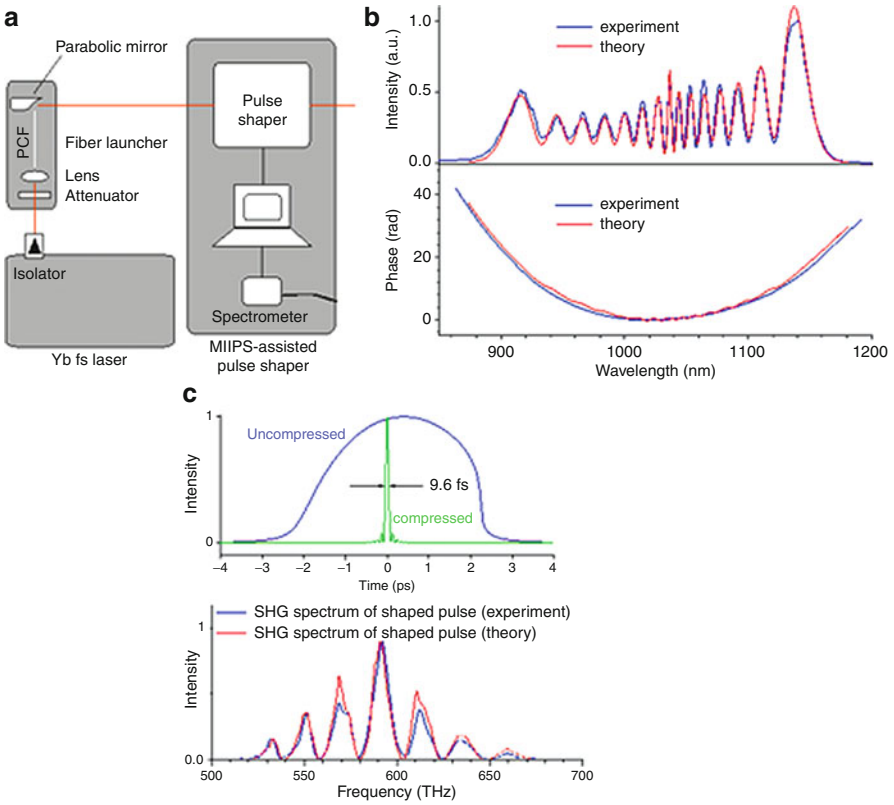

Fig. 39.9 (**a**) Schematic of fiber continuum source incorporating an MIIPS-assisted 4-*f* pulse shaper (Adapted with permission from [44]). (**b**) Comparison of the spectrum (*top panel*) and phase (*low panel*) of the fiber continuum between the experiment based on MIIPS-assisted 4-*f* pulse shaper (*blue curves*) and the theory based on generalized nonlinear Schrödinger equation (*red curves*) (Adapted with permission from [47, 48]). (**c**) *Top*: compression of fiber continuum pulse to transform-limited width of 9.6 fs by MIIPS-assisted 4-*f* pulse shaper. *Bottom*: comparison of the second-harmonic generation spectrum of a specifically shaped pulse of the fiber continuum (Adapted with permission from [48])

These preliminary results suggest the possibility for replacing the existing free-space lab NIVI system with a fiber-based clinical NIVI system. The key for this clinical translation is to replace the bulky amplified Ti:sapphire laser system or the solid-state laser-based fiber continuum source with a compact monolithic fiber continuum laser. The confinement of light to optical fibers eliminates the need for precise alignment of mirrors and other bulk-optical elements, making the optical system resistant to mechanical and thermal disturbances. In the future, the newly designed system will likely have reduced size, cost, complexity, and environmental instability, allowing NIVI to be performed by clinical personnel just as standard spectral-domain OCT is used by clinical personnel today.

39.7 Conclusions

We have described the theory, instrumentation, and demonstrated experimental results for imaging and spectroscopy with the technique of nonlinear interferometric vibrational imaging (NIVI). High-resolution Raman spectra were obtained using spectral interferometry to isolate resonant CARS signals generated from material samples and highly scattering biological tissues. The quantitative capacity of NIVI was demonstrated by the accurate determination of the degree of saturation in lipid samples. NIVI was also successfully used to map molecular constituents in skin domains and to differentiate between normal and tumor tissues in a rat mammary tumor model. Spectral-domain detection has been demonstrated, which allows for significant increases in image acquisition speed, signal-to-noise ratio, and signal stability.

In the future, increasing the spectral range into the Raman fingerprint region by increasing the Stokes bandwidth is expected to further enhance the sensitivity of NIVI for differentiating normal from tumor tissue, as well as permit detailed investigations into local biochemical compositions and dynamics. Novel application of supercontinuum sources will not only broaden the applicability of NIVI but will also advance the instrumentation towards compact all-fiber-based systems. The intrinsically complicated beam geometry of the NIVI instrument described in this chapter can be considerably simplified using compressible coherent continuum sources suitable for single-beam CARS excitation. NIVI, through continuing development as a highly sensitive and promising new real-time imaging modality, will be capable of addressing a greater range of fundamental biological studies and diagnostic clinical challenges.

Acknowledgments We thank all of our former colleagues, students, and researchers who have contributed to the development and application of this technology. Animals used for this research were handled and cared for under a protocol approved by the Institutional Animal Care and Use Committee (IACUC) at the University of Illinois at Urbana-Champaign. Since its inception, NIVI was supported in parts by grants for the US National Institutes of Health (NIH) and the US National Aeronautics and Space Administration (NASA). Ongoing research is being supported in part by an NIH Academic-Industry Partnership grant (R01 CA166309, S.A.B.). Additional information can be found at http://biophotonics.illinois.edu.

References

1. J.-X. Cheng, X.S. Xie, Coherent anti-stokes Raman scattering microscopy: instrumentation, theory, and applications. J. Phys. Chem. B **108**, 827 (2003)
2. A. Zumbusch, G.R. Holtom, X.S. Xie, Three-dimensional vibrational imaging by coherent anti-stokes Raman scattering. Phys. Rev. Lett. **82**, 4142 (1999)
3. C.W. Freudiger, W. Min, B.G. Saar, S. Lu, G.R. Holtom, C. He, J.C. Tsai, J.X. Kang, X.S. Xie, Biomedical imaging with high sensitivity by stimulated Raman scattering microscopy. Science **322**, 1857 (2008)
4. R.D. Schaller, J. Ziegelbauer, L.F. Lee, L.H. Haber, R.J. Saykally, Chemically selective imaging of subcellular structure in human hepatocytes with coherent anti-stokes Raman scattering (CARS) near-field scanning optical microscopy (NSOM). J. Phys. Chem. B **106**, 8489 (2002)

5. J. Sung, B.-C. Chen, S.-H. Lim, Fast three-dimensional chemical imaging by interferometric multiplex coherent anti-stokes Raman scattering microscopy. J. Raman Spectrosc. **42**, 130 (2011)
6. C.L. Evans, E.O. Potma, X.S. Xie, Coherent anti-stokes Raman scattering spectral interferometry: determination of the real and imaginary components of nonlinear susceptibility $\chi^{(3)}$ for vibrational microscopy. Opt. Lett. **29**, 2923 (2004)
7. C.L. Evans, X.S. Xie, Coherent anti-stokes Raman scattering microscopy: chemical imaging for biology and medicine. Annu. Rev. Anal. Chem. **1**, 883 (2008)
8. J.-X. Cheng, A. Volkmer, L.D. Book, X.S. Xie, Multiplex coherent anti-stokes Raman scattering microspectroscopy and study of lipid vesicles. J. Phys. Chem. B **106**, 8493 (2002)
9. S.H. Parekh, Y.J. Lee, K.A. Aamer, M.T. Cicerone, Label-free cellular imaging by broadband coherent anti-stokes Raman scattering microscopy. Biophys. J. **99**, 2695 (2010)
10. G.W.H. Wurpel, J.M. Schins, M. Müller, Chemical specificity in three-dimensional imaging with multiplex coherent anti-stokes Raman scattering microscopy. Opt. Lett. **27**, 1093 (2002)
11. M. Okuno, H. Kano, P. Leproux, V. Couderc, J.P.R. Day, M. Bonn, H.-O. Hamaguchi, Quantitative CARS molecular fingerprinting of single living cells with the use of the maximum entropy method. Angew. Chem. Int. Ed. **49**, 6773 (2010)
12. H.A. Rinia, M. Bonn, M. Müller, E.M. Vartiainen, Quantitative CARS spectroscopy using the maximum entropy method: the main lipid phase transition. Chem. Phys. Chem. **8**, 279 (2007)
13. J.P.R. Day, K.F. Domke, G. Rago, H. Kano, H.-O. Hamaguchi, E.M. Vartiainen, M. Bonn, Quantitative coherent anti-stokes Raman scattering (CARS) microscopy. J. Phys. Chem. B **115**, 7713 (2011)
14. J.P. Ogilvie, E. Beaurepaire, A. Alexandrou, M. Joffre, Fourier-transform coherent anti-stokes Raman scattering microscopy. Opt. Lett. **31**, 480 (2006)
15. M. Cui, J. Skodack, J.P. Ogilvie, Chemical imaging with fourier transform coherent anti-stokes Raman scattering microscopy. Appl. Opt. **47**, 5790 (2008)
16. T.W. Kee, H. Zhao, M.T. Cicerone, One-laser interferometric broadband coherent anti-stokes Raman scattering. Opt. Express **14**, 3631 (2006)
17. S.-H. Lim, A.G. Caster, S.R. Leone, Single-pulse phase-control Interferometric coherent anti-stokes Raman Scattering spectroscopy. Phys. Rev. A **72**, 041803 (2005)
18. G. Marowsky, G. Lüpke, CARS-background suppression by phase-controlled nonlinear interferometry. Appl. Phys. B **51**, 49 (1990)
19. B. von Vacano, T. Buckup, M. Motzkus, Highly sensitive single-beam heterodyne coherent anti-stokes Raman scattering. Opt. Lett. **31**, 2495 (2006)
20. B. Li, W.S. Warren, M.C. Fischer, Phase-cycling coherent anti-stokes Raman scattering using shaped femtosecond laser pulses. Opt. Express **18**, 25825 (2010)
21. G.W. Jones, D.L. Marks, C. Vinegoni, S.A. Boppart, High-spectral-resolution coherent anti-stokes Raman scattering with interferometrically detected broadband chirped pulses. Opt. Lett. **31**, 1543 (2006)
22. A. Wipfler, T. Buckup, M. Motzkus, Multiplexing single-beam coherent anti-stokes Raman spectroscopy with heterodyne detection. Appl. Phys. Lett. **100**, 071102 (2012)
23. K. Orsel, E.T. Garbacik, M. Jurna, J.P. Korterik, C. Otto, J.L. Herek, H.L. Offerhaus, Heterodyne interferometric polarization coherent anti-stokes Raman scattering (HIP-CARS) spectroscopy. J. Raman Spectrosc. **41**, 1678 (2010)
24. E.O. Potma, C.L. Evans, X.S. Xie, Heterodyne coherent anti-stokes Raman scattering (CARS) imaging. Opt. Lett. **31**, 241 (2006)
25. D.L. Marks, C. Vinegoni, J.S. Bredfeldt, S.A. Boppart, Interferometric differentiation between resonant coherent anti-stokes Raman scattering and nonresonant four-wave-mixing processes. Appl. Phys. Lett. **85**, 5787 (2004)
26. D. Pestov, R.K. Murawski, G.O. Ariunbold, X. Wang, M. Zhi, A.V. Sokolov, V.A. Sautenkov, Y.V. Rostovtsev, A. Dogariu, Y. Huang, M.O. Scully, Optimizing the Laser-Pulse configuration for coherent Raman spectroscopy. Science **316**, 265 (2007)

27. A. Volkmer, L.D. Book, X.S. Xie, Time-resolved coherent anti-stokes Raman scattering microscopy: imaging based on Raman free induction decay. Appl. Phys. Lett. **80**, 1505 (2002)
28. K.P. Knutsen, J.C. Johnson, A.E. Miller, P.B. Petersen, R.J. Saykally, High Spectral resolution multiplex CARS spectroscopy using chirped pulses. Chem. Phys. Lett. **387**, 436 (2004)
29. D.L. Marks, S.A. Boppart, Nonlinear interferometric vibrational imaging. Phys. Rev. Lett. **92**, 123905 (2004)
30. C. Vinegoni, J.S. Bredfeldt, D.L. Marks, S.A. Boppart, Nonlinear optical contrast enhancement for optical coherence tomography. Opt. Express **12**, 331 (2004)
31. P.D. Chowdary, W.A. Benalcazar, Z. Jiang, D.L. Marks, S.A. Boppart, M. Gruebele, High speed nonlinear interferometric vibrational analysis of lipids by spectral decomposition. Anal. Chem. **82**, 3812 (2010)
32. W. Benalcazar, S.A. Boppart, Nonlinear interferometric vibrational imaging for fast label-free visualization of molecular domains in skin. Bioanal. Chem. **400**, 2817 (2011)
33. P.D. Chowdary, Z. Jiang, E.J. Chaney, W.A. Benalcazar, D.L. Marks, M. Gruebele, S.A. Boppart, Molecular histopathology by spectrally reconstructed nonlinear interferometric vibrational imaging. Cancer Res. **70**, 9562 (2010)
34. W.A. Benalcazar, P.D. Chowdary, Z. Jiang, D.L. Marks, E.J. Chaney, M. Gruebele, S.A. Boppart, High-speed nonlinear interferometric vibrational imaging of biological tissue With comparison to Raman microscopy. IEEE J. Sel. Top. Quantum **16**, 824 (2010)
35. K.E. Shafer-Peltier, A.S. Haka, M. Fitzmaurice, J. Crowe, J. Myles, R.R. Dasari, M.S. Feld, Raman Microspectroscopic model of human breast tissue: implications for breast cancer diagnosis in vivo. J. Raman Spectrosc. **33**, 552 (2002)
36. A.S. Haka, K.E. Shafer-Peltier, M. Fitzmaurice, J. Crowe, R.R. Dasari, M.S. Feld, Diagnosing breast cancer by using Raman spectroscopy. Proc. Natl. Acad. Sci. U. S. A. **102**, 12371 (2005)
37. J.M. Dudley, G. Genty, S. Coen, Supercontinuum generation in photonic crystal fiber. Rev. Mod. Phys. **78**, 1135 (2006)
38. B. von Vacano, M. Motzkus, Time-resolved two color single-beam CARS employing supercontinuum and femtosecond pulse shaping. Opt. Commun. **264**, 488 (2006)
39. B. von Vacano, W. Wohlleben, M. Motzkus, Actively shaped supercontinuum from a photonic crystal fiber for nonlinear coherent microspectroscopy. Opt. Lett. **31**, 413 (2006)
40. A.M. Weiner, Femtosecond Pulse shaping using spatial light modulators. Rev. Sci. Instrum. **71**, 1929 (2000)
41. Y. Coello, V.V. Lozovoy, T.C. Gunaratne, B. Xu, I. Borukhovich, C.-H. Tseng, T. Weinacht, M. Dantus, Interference without an interferometer: a different approach to measuring, compressing, and shaping ultrashort laser pulses. J. Opt. Soc. Am. B **25**, A140 (2008)
42. B. Xu, J.M. Gunn, J.M.D. Cruz, V.V. Lozovoy, M. Dantus, Quantitative investigation of the multiphoton intrapulse interference phase scan method for simultaneous Phase Measurement and compensation of femtosecond laser pulses. J. Opt. Soc. Am. B **23**, 750 (2006)
43. D.L. Marks, J.B. Geddes III, S.A. Boppart, Molecular identification by generating coherence between molecular normal modes using stimulated Raman scattering. Opt. Lett. **34**, 1756 (2009)
44. H. Tu, Y. Liu, D. Turchinovich, S.A. Boppart, Compression of fiber supercontinuum pulses to the fourier-limit in a high-numerical-aperture focus. Opt. Lett. **36**, 2315 (2011)
45. H.N. Paulsen, K.M. Hilligse, J. Thøgersen, S.R. Keiding, J.J. Larsen, Coherent anti-Stokes Raman scattering microscopy with a photonic crystal fiber based light source. Opt. Lett. **28**, 1123 (2003)
46. T.W. Kee, M.T. Cicerone, Simple Approach to One-laser, Broadband coherent anti-stokes Ramanscattering microscopy. Opt. Lett. **29**, 2701 (2004)
47. H. Tu, Y. Liu, J. Lægsgaard, U. Sharma, M. Siegel, D. Kopf, S.A. Boppart, Scalar generalized nonlinear Schrödinger equation-quantified continuum generation in an all-normal dispersion photonic crystal fiber for broadband coherent optical sources. Opt. Express **18**, 27872 (2010)

48. H. Tu, Y. Liu, J. Lægsgaard, D. Turchinovich, M. Siegel, D. Kopf, H. Li, T. Gunaratne, S.A. Boppart, Cross-validation of theoretically quantified fiber continuum generation and absolute pulse measurement by MIIPS for a broadband coherently controlled optical source. Appl. Phys. B Lasers Opt. **106**, 379 (2012)
49. Y. Liu, H. Tu, S.A. Boppart, Wave-breaking-extended fiber supercontinuum generation for high compression ratio transform-limited pulse compression. Opt. Lett. **37**, 2172 (2012)
50. H. Tu, Y. Liu, X. Liu, D. Turchinovich, J. Lægsgaard, S.A. Boppart, Nonlinear polarization dynamics in a weakly birefringent all-normal dispersion photonic crystal fiber: toward a practical coherent fiber supercontinuum laser. Opt. Express **20**, 1113 (2012)
51. Y. Liu, H. Tu, W.A. Benalcazar, E.J. Chaney, S.A. Boppart, Multimodal nonlinear microscopy by shaping a fiber supercontinuum from 900 to 1160 nm. IEEE J. Sel. Top. Quantum **18**, 1209 (2012)

Ultrasensitive Phase-Resolved Imaging of Cellular Morphology and Dynamics

40

Michael A. Choma, Audrey Ellerbee, and Joseph A. Izatt

Keywords

Phase contrast • Quantitative phase microscopy • Phase retrieval • Interferometric phase microscopy • Cellular morphology • Cellular motion

40.1 Introduction

40.1.1 Phase Contrast Microscopy

Microscopy is an important imaging tool in modern clinical medicine and basic biomedical research. Although microscopy is centuries old, cutting-edge research in techniques such as confocal microscopy, fluorescence microscopy, and quantitative phase microscopy continues at a rapid pace. The retrieval of phase information from microscopic samples has a long history [1] initiated by the development of the phase contrast microscope. Phase contrast microscopy is routinely employed for live visualization of cells since it enhances subcellular contrast. This technique exploits the fact that optically thin samples such as cells diffract light secondary to local variations in optical index. A phase plate and matching phase annulus added to the light train of a standard compound microscope can be used to interfere

M.A. Choma (✉)
Departments of Diagnostic Radiology, Pediatrics, Biomedical Engineering, and Applied Physics, Yale University, New Haven, CT, USA
e-mail: michael.choma@yale.edu

A. Ellerbee
Ginzton Laboratory and Department of Electrical Engineering, Stanford University, Palo Alto, CA, USA

J.A. Izatt
Fitzpatrick Institute for Photonics and Departments of Biomedical Engineering and Ophthalmology, Duke University Medical Center, Durham, NC, USA

© Springer International Publishing Switzerland 2015

W. Drexler, J.G. Fujimoto (eds.), *Optical Coherence Tomography*,
DOI 10.1007/978-3-319-06419-2_41

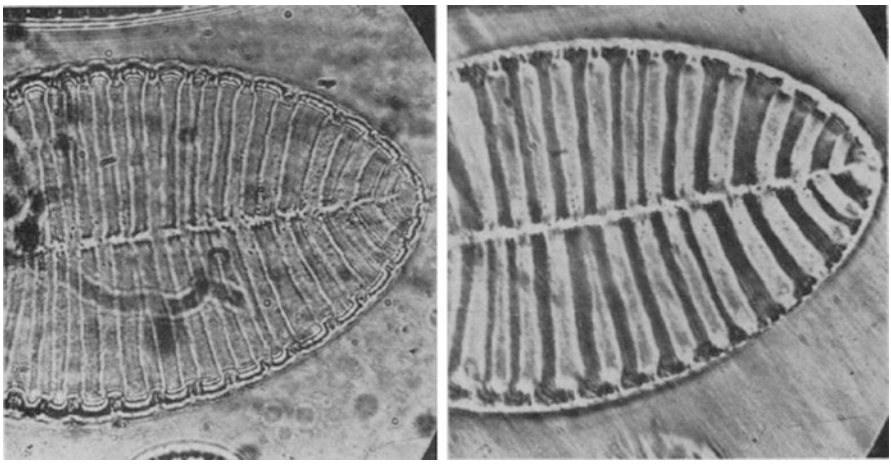

Fig. 40.1 Phase contrast microscopy. Brightfield (*left*) and phase contrast (*right*) images of a diatom. These are the oldest phase contrast micrographs from Zernike and were taken in 1932 (Figure from Zernike [1])

diffracted and undiffracted light. The degree of interference is manifest in the amplitude of the detected image. In this way, even unstained cells become distinguishable from their surroundings (Fig. 40.1). Frits Zernike was awarded the Nobel Prize for Physics in 1953 for this development.

Phase contrast microscopy has had an immeasurable impact by allowing the user to qualitatively visualize small, subcellular variations in optical index. Quantitative phase microscopy seeks to build upon the principles of Zernike to extract information relating to optical index, birefringence, motion, and flow. In addition to highlighting subcellular detail in unstained cells, quantitative phase techniques can measure small cell motions, small changes in cell index, and cytoplasmic flow.

Because of its sensitivity to phase and its ability to reliably quantify and track changes in coherent wavefronts, interferometry has recently gained momentum as a technique for the implementation of quantitative phase microscopy. This chapter seeks to review several of these interferometric techniques, with an emphasis on broadband interferometric techniques which exploit the principles of OCT. Both the underlying theory as well biological applications are discussed. Although this chapter gives particular focus to biologically relevant applications, the methods are readily extendable for other, nonbiological applications.

40.1.2 Definition of Interferometric Phase

When discussing coherent wavefields, it is usual to represent the wavefield as a complex function $\Psi(\mathbf{r}) = \sqrt{\mathrm{I}(\mathbf{r})}\exp(j\varphi(\mathbf{r}))$, where $\mathbf{r}$ is a vector representing three-dimensional position, $\mathrm{I}(\mathbf{r})$ is the intensity of the wave, and $\varphi(\mathbf{r})$ the phase of the field [2]. This representation is convenient for several reasons. The surfaces of constant

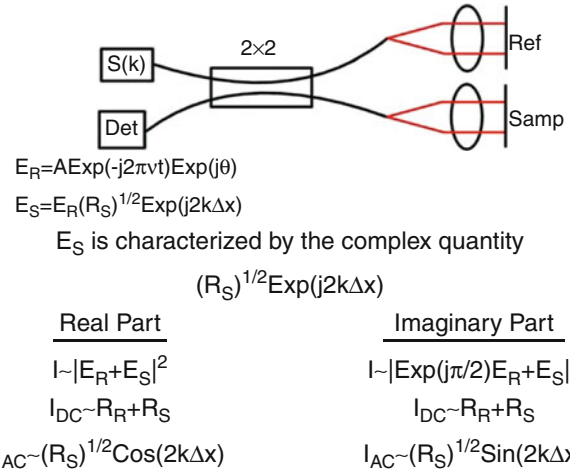

Fig. 40.2 Definition of the complex interferometric signal illustrated in a 2 × 2 50/50 Michelson topology. S(k) represents a monochromatic source. The free-space path length difference between the reference and sample arms is Δx. At the detector the reference electric field is characterized by an amplitude A which incorporates the reference arm reflectivity R_R and the double-pass attenuation in the 2 × 2, a time-varying component (v, optical frequency), and a phase θ which incorporates the initial phase of the light out of the source and phase accumulated in the interferometer. The sample field is an attenuated and phase-shifted version of the reference field. It is attenuated by the square root of the sample reflectivity and phase shifted by twice the product of the path length difference Δx between the reference and sample reflectors and the optical wavenumber k. When mixed at a square-law detector, the real (cosinusoidal) part of the complex interferometric electric field is measured. One method to gain access to the imaginary (sinusoidal) part of the field is to phase shift the reference field by π/2 rad with respect to the sample field

$\varphi(\mathbf{r})$ represent wavefronts, while $\nabla\varphi(\mathbf{r})$ describes the free-space propagation direction [2]. This definition decouples temporal and spatial variation in the field: the time-varying wavefunction is given by $\exp(j2\pi\nu t)\Psi(\mathbf{r})$, where ν is the frequency of the field. If $\Psi(\mathbf{r})$ is a one-dimensional wave propagating in a medium of uniform index n, $\varphi(\mathbf{r})$ can be represented as $\varphi(x) = nkx + \varphi_o$, where k is the free-space wavenumber ($2\pi/\lambda$; λ = free-space wavelength), x is the spatial coordinate in the direction of propagation, and φ_o is the initial or reference phase of the field. φ_o is analogous to a reference electrical potential insofar as both phase and potential are relative measurements.

Interferometry is a powerful, although by no means the only [2], technique for retrieving the phase of coherent wavefields. The interferometric signal is complex in nature and can be related to the linear difference between the sample and reference arm phase functions $\varphi_S(x)$ and $\varphi_R(x)$. If both arms are free space (i.e., $n = 1$), then $\varphi_S(x) - \varphi_R(x)$ reduces to $2k\Delta x$, where Δx is the free-space path length difference between the two arms (Fig. 40.2). One insight that can be drawn from this representation is that small displacements of the sample reflector can be monitored by holding the reference arm fixed and measuring the phase of the interferometric signal versus time. This is a powerful technique limited by the stability of the reference reflector.

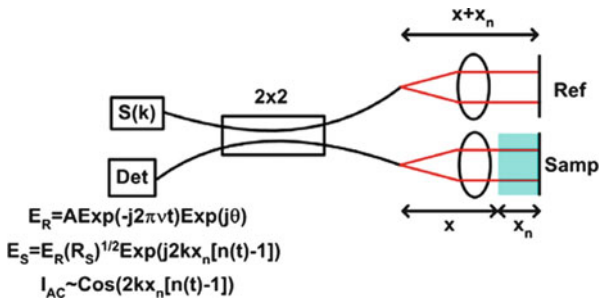

Fig. 40.3 Relationship of interferometric phase to changes in optical index

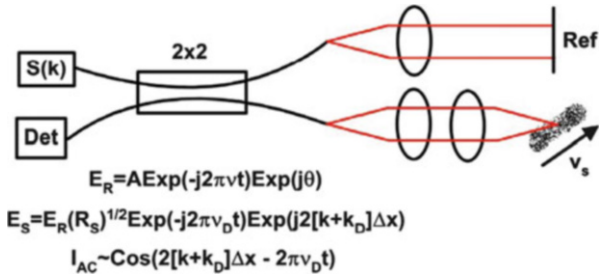

Fig. 40.4 Interferometric phase and scatterer-induced Doppler shift

The phase of the interferometric signal is sensitive to changes in optical index as well. Consider the setup in Fig. 40.3. The free-space path length of both arms are identical, but the sample arm has two compartments: one free-space compartment of path length x and another compartment of length x_n with a time-varying index n(t). The interferometric phase $\varphi_S(x) - \varphi_R(x)$ is now related to the index by $2kx_n$[n(t)−1]. Since the index of an aqueous solution is proportional to its osmolarity, this suggests a method for monitoring changes in solution osmolarity by tracking the interferometric phase.

Just as changes in index and in path length can be monitored by measuring interferometric phase, changes in sample arm wavenumber can likewise be monitored. The sample field frequency can be changed by reflection from a moving reflector or scatterer. This is the familiar Doppler shift that leads the field frequency v and wavenumber k to be changed by the quantities v_D and k_D, respectively (Fig. 40.4). Time variations in phase manifest in the beat term exp(−j2π$v_D t$). It should be noted that the effect of displacement, changing index, and Doppler shifting is inseparable. For example, if the sample reflector in Fig. 40.4 were moving as the index was changing, it would be impossible to establish the relative contribution of each term to the phase measurement.

40.2 Review of Prior Techniques

40.2.1 Monochromatic Interferometric Techniques

Monochromatic phase-sensitive interferometric techniques in cell biology predate their broadband counterparts by approximately half a decade. These monochromatic techniques are not able to perform depth sectioning and effectively integrate phase content along the optical axis. Nonetheless, their ability to measure cell volumes has yielded impressive results.

The maintenance of cell volume and osmolarity are basic homeostatic functions. As such, there is a keen interest in developing techniques that can quantify the response of various epithelial and endothelial cell types to osmotic and/or pharmacologic challenge. Monochromatic interferometry is an attractive candidate for measuring changes in cell volume because the phase of an optical field that is reflected from (or transmitted through) a cell responds linearly to changes in the thickness or optical index of that cell.

This principle was elegantly demonstrated by Farinas and Verkman in 1996 [3]. They performed full-field and single-point monochromatic Mach-Zehnder interferometry in which the reference optical field was mixed with a sample beam transmitted through a single-layer epithelial cell layer (Fig. 40.5). Since the interferometer was monochromatic, this technique is unable to coherently gate phase information at the cell-perfusate interface from that at other interfaces. Farinas and Verkman cleverly circumvented this problem by placing cells in a perfused flow chamber (Fig. 40.5). If it is assumed that the cell acts as a perfect osmometer (i.e., the product of cell volume and cell osmolarity is constant), it then follows that cell expansion (contraction) results from the influx (outflux) of free water into (out of) the cell, leading to a commensurate decrease (increase) in cell osmolarity. Given that the optical index is proportional to osmolarity, and since cell osmolarity is inversely proportional to cell volume per the perfect osmometer assumption, changes in interferometric phase shift are unambiguously related to changes in cell volume. This relationship is qualified with the assumption that the cell thickness scales linearly with cell volume.

The major drawback to this technique was in the retrieval of the interferometric phase data. The setup in Fig. 40.5 is a homodyne detection system insofar as both the reference and sample arm phase velocities are zero. As such, both non-interferometric and interferometric information reside at baseband, precluding the use of various hardware and software time-domain phase-sensitive retrieval techniques. Farinas and Verkman used a nontraditional technique that involved taking the inverse cosine of the data after it was normalized to have values ranging from -1 to $+1$. Normalization was aided by fringes generated from a spatial phase gradient placed in the reference arm. This inverse cosine operation yields the interferometric phase, but the sensitivity of this technique is limited by the accuracy of the normalization process. As interferometric images were acquired by the use of a CCD camera, imaging speed matched that of the camera frame acquisition rate ($\sim$1 s).

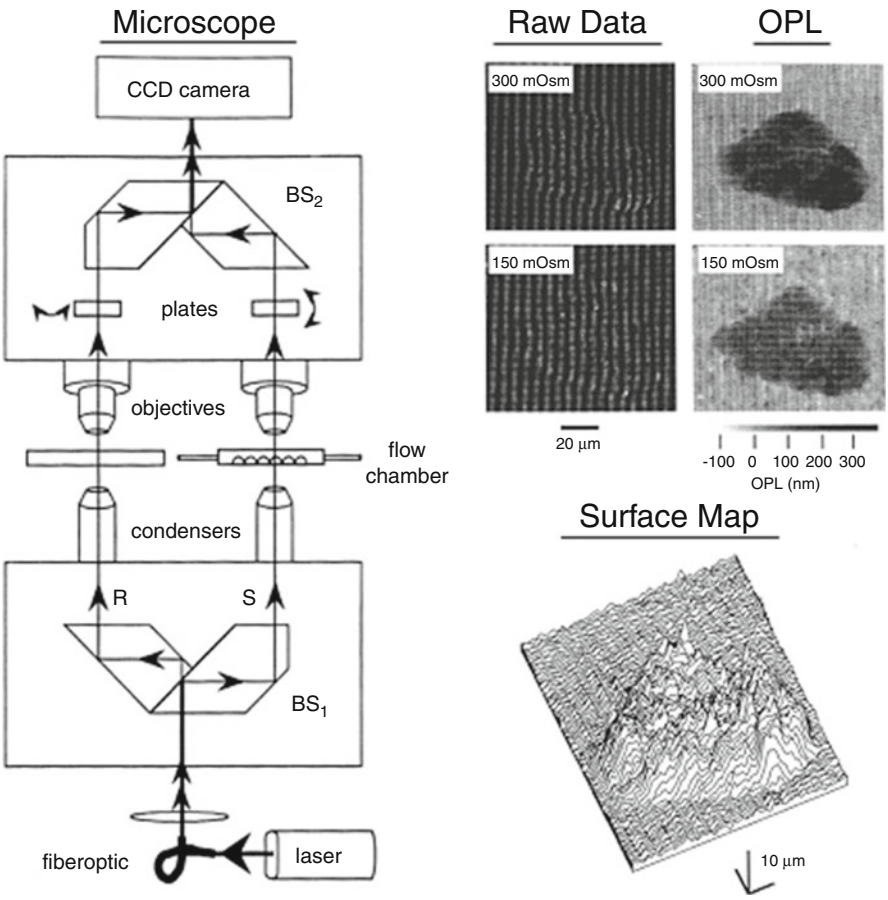

Fig. 40.5 Full-field Mach-Zehnder cell volume interferometer (Images are from Farinas and Verkman [3])

As expected, cells swell in response to a decrease in perfusate tonicity (Fig. 40.5). Since changes in optical index are small compared to the concurrent changes in path length, the change in phase never exceeded 2π. Since zero phase can be defined at the perfusate-coverslip interface, this technique avoids the commonly encountered 2π ambiguity problem that renders phase measurements relative as opposed to absolute.

The approach used by Farinas and Verkman was revisited in 2005 by M. Feld and colleagues [4, 5]. The setup uses a tilted reference arm to generate spatially varying fringes. Two other advances were introduced. First, Hilbert transformation was used to more directly retrieve the complex spatial interferometric signal. Second, a high-speed CCD camera which acquired 480×640 pixel images at a 291 Hz frame rate was used. The imaging speed of these systems is compatible with many cell dynamic applications (Fig. 40.6). Nonetheless, the monochromatic sources used prevent depth-selective isolation of the sample behavior.

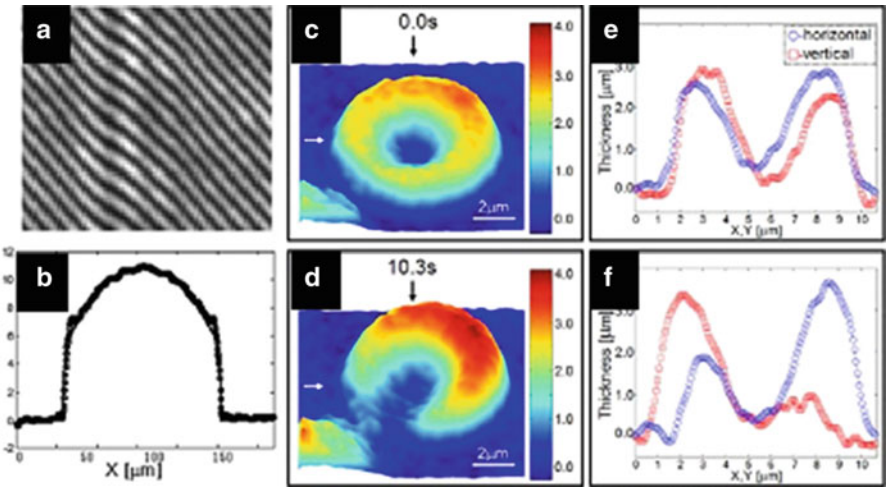

Fig. 40.6 Hilbert phase microscopy applied to static and dynamic objects. *Top left*: The spatial fringe pattern generated by a tilted reference arm on this image of a bare fiber core has a similar effect to the parallel plates used by Farinas et al. *Bottom left*: Transverse profile of a fiber core used as a phase object. Rightmost panel of images is the time-varying deformation of a red blood cell recorded using a high-speed version of the technique. (**a**–**b**) Are from Ikeda et al. [4] and (**c**–**f**) are from Popescu et al. [5]

40.2.2 Broadband Time-Domain Techniques

The use of phase-sensitive detection to extract nonpolarization-based functional information from the interferometric OCT signal was first demonstrated with color Doppler OCT [6, 7]. In CD-OCT, depth-resolved flow information is extracted from the complex-valued signal through a variety of time-frequency analyses. One conceptually straightforward analysis is to calculate the instantaneous Doppler frequency as the derivative of the phase with respect to time. This definition of Doppler shift provides an intuitive understanding of the relationships among phase, Doppler frequency, particle position, and particle velocity. The Doppler frequency (i.e., the derivative of phase with respect to time) is proportional to particle velocity (i.e., derivative of position with respect to time). The phase, which can be viewed as the integral of Doppler frequency, is proportional to the particle position, which is the integral of the particle velocity. Defining phase and position in terms of the integral of Doppler frequency and particle velocity, respectively, has the mathematical convenience of equating the unknown constant of integration with the unknown zero-phase point that generally renders phase, and consequently position, measurements relative as opposed to absolute.

It was in this framework that Yang et al. developed a phase-referenced interferometry (PRI) technique for the measurement of changes in cell diameter in response to an osmotic challenge (Fig. 40.7) [8]. This technique has two advantages over that of Farinas and Verkman [3]. First, because PRI employs a broadband light source,

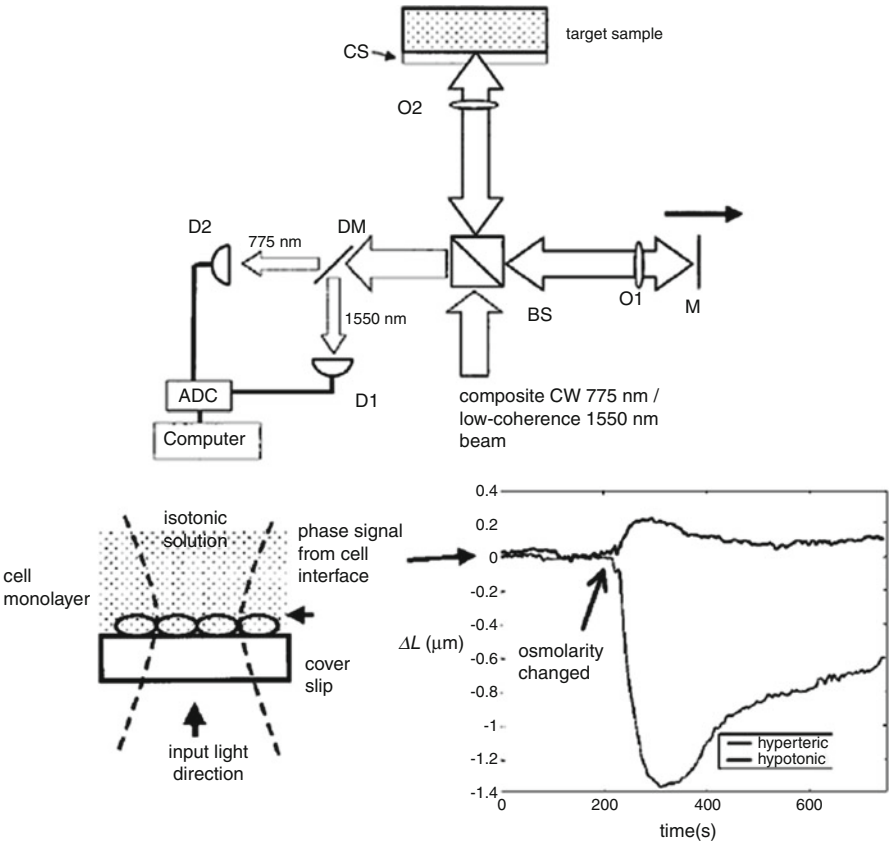

Fig. 40.7 Phase-referenced interferometry (Figures are from Yang et al. [8]

it is able to section via coherence gating signal from interfaces of interest (e.g., cell-perfusate interface) and reject signal from others. Second, since PRI uses a scanning delay line, the interferometric signal was encoded with a characteristic heterodyne beat frequency which allowed for the straightforward extraction of phase by Hilbert transformation of the data. PRI uses a CW source that is harmonically related to the broadband source center wavelength to measure and correct for interferometer jitter introduced by the scanning delay line. This correction was not required in Farinas and Verkman's full-field setup because data was acquired at a single point in time as opposed to over the course of several seconds. One disadvantage of this setup is that it acquires data pointwise and not in a full-field, parallel manner.

Yang et al. measured the average change in cell thickness of a few cells in response to a moderate hypo- and hypertonic challenge (Fig. 40.7). The reported system sensitivity was 3.6 nm, and the temporal resolution was several hertz. The cells underwent a two-step response to alterations in perfusate tonicity. Upon an increase (decrease) in tonicity, the cells contracted (swelled) for ~100 s. After this initial response, the cells gradually swelled (contracted) towards a new steady-state thickness.

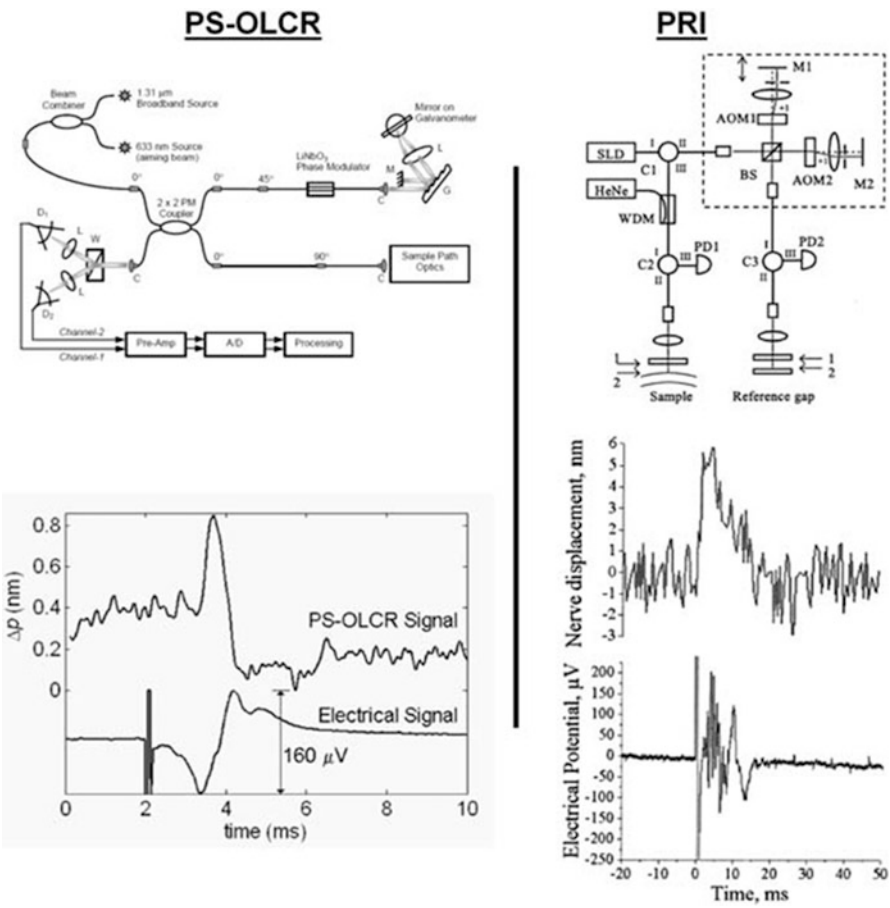

Fig. 40.8 Broadband, time-domain interferometer designs for detection of nanoscale neuronal activity associated with action potential generation. PS- OLCR figures from Akkin et al. [14] (PRI images from Fang-Yen et al. [13])

It is a well-established phenomenon that electrical action potentials in a neuron are associated with temporally correlated changes in neuron thickness, birefringence, and optical scattering [9–12]. Fang-Yen et al. [13] employed an improved heterodyne version of the phase-referenced interferometer to visualize such changes in neuron thickness. Rather than using a continuous-wave reference source, this setup employed an additional Michelson interferometer as a phase reference (Fig. 40.8). Phase differences taken between the interrogated sample and a passive reference gap mitigated the effects of phase noise introduced by the added interferometer.

Akkin et al. [14] employed polarization-sensitive optical low-coherence reflectometry (PS-OLCR) to detect action potential-related nerve swelling. The PS-OLCR system (Fig. 40.8) uses two decorrelated polarization channels within

a single-mode fiber. Optical path length changes were measured with respect to a selected depth along the optical axis. Longitudinal separation of orthogonal polarization components was achieved by placement of birefringent wedges in path of the sample illuminating light. In the detection arm, the optical phase associated with each polarization was separately detected and determined with the Hilbert transform. The differential phase mitigated common mode noise and provided the relative phase, and therefore path length, change between the two spatially separated polarization channels. Results obtained for electrical stimulation of a crayfish nerve bundle demonstrate subnanometer resolution capabilities of this system (Fig. 40.8).

40.3 Theoretical Limits to Phase Stability in Interferometry

OCT was first demonstrated by Huang et al. in 1991 [15]. Two key insights from this first demonstration were (1) the use of time-domain (TD) low-coherence interferometry techniques developed in telecommunications [16] to obtain depth-reflectivity profiles in biological tissue and (2) the use of laterally scanning sample arm optics to generate two-dimensional optical reflectivity profiles of tissue. It was quickly realized that phase-based information could be extracted from the interferometric OCT signal [6, 7, 17] and that this information could be used to characterize biological tissue.

There are two types of phase information which have been extracted from interferometric OCT signals. The first type is polarization-based phase, which describes the differential propagation of orthogonal polarization states in biological tissue. This technique is not the focus of this chapter and is discussed extensively elsewhere in this book. The second type of phase information is discussed in Sect. 40.1.1 and is referred to here as interferometric phase. This interferometric phase is sensitive to sample motion, Doppler shift, and changes in optical index. For example, in TDOCT, in the absence of sample arm motion and interferometer jitter, the real interferometric phase is proportional to $\cos(2k_o[x_R - x_S])$, where k_o is the source center wavenumber, x_R is the linearly swept reference arm path length, and x_S is the location of a sample reflector of interest. In the setting of sample motion δx, the signal is proportional to $\cos(2k_o[\Delta x - x_o + \delta x])$. If the interferometric phase is measured over successive scans, the relative (but not absolute) position of a reflector can be tracked.

In the early 2000s, it was demonstrated that spectral domain OCT techniques have a substantial amplitude sensitivity advantage over their time-domain techniques [18–20]. This prompted a shift in technology development for amplitude and phase imaging using OCT. With respect to phase imaging, the interferometric phase information is available in the native spectral domain (spectrally but not spatially resolved) or in the time domain (spatially but not spectrally resolved). Data processing to obtain displacement and Doppler data is substantially similar for both TD and SD-OCT. From a practical perspective, SD-OCT holds an advantage over TD-OCT in measuring interferometric phase since SD-OCT systems employ

few, if any, moving parts. Additionally, in SD-OCT a common path or coaxial interferometer topology can be employed [21, 22]. This approach has the advantage of forcing virtually all phase noise to be common mode between the reference and sample optical fields. From a theoretical perspective, the phase stability of SD-OCT holds an intrinsic advantage over TD-OCT. This advantage comes from the fact that phase stability is a straightforward function of amplitude stability. This relationship is explored in this section, in the context of SD-OCT. Experimental results that exploit the phase stability of spectral domain techniques are presented later in the chapter.

40.3.1 Phase and Doppler Sensitivity of Spectral Domain OCT

The complete spectral domain photocurrent in SD-OCT may be written as [18]

$$i(k) = \frac{1}{2}\rho S(k)\delta k\left[R_R + \sum_n R_n + 2\sqrt{R_r}\sum_n \sqrt{R_n}\cos\left(2k[\Delta x_n + \delta x_n]\right)\right]. \quad (40.1)$$

Here, S(k) is the source power spectral density, k is wavenumber (radians per meter), δk is the spectral channel bandwidth, ρ is the detector responsivity, R_R is the reference arm reflectivity, and R_n is the reflectivity of the nth sample reflector. The quantity $\Delta x_n + \delta x_n$ is the position of the nth reflector. Δx_n is an integer multiple of the discrete sampling interval in the x-domain, given by $m\pi/\Delta k$, where Δk is the total optical bandwidth interrogated and m is any positive or negative integer. δx_n accounts for subresolution deviations in reflector position away from $m\pi/\Delta k$. δx_n is an important quantity because it primarily manifests in the phase of $i(k)$. Note that n and m are distinct and separate variables: n indexes discrete reflectors in the sample, while m indexes elements in the one-dimensional x-domain A-scan array.

In swept-source OCT, $i(k)$ is directly measured, whereas in spectrometer- based Fourier domain OCT, $i(k)$ is integrated over the A-scan acquisition time in a charge-coupled device (CCD) or similar charge-accumulation detector. In either case, after Fourier transformation of the k-domain signal, the complex-valued x-domain signal and shot noise is given by, respectively,

$$I_{\text{signal}}(2\Delta x_n) = \frac{\rho S_o\sqrt{R_R R_n}}{2ef_{\text{ascan}}}E(2\delta x_n)\exp(jk_o 2\delta x_n). \quad (40.2)$$

$$I_{\text{noise}}(2\Delta x_n) = \sqrt{\frac{\rho S_o R_R}{ef_{\text{ascan}}}}\exp(j\phi_{\text{rand}}). \quad (40.3)$$

Here, E(·) is the unity-amplitude x-domain autocorrelation function, S_o is the total sample illumination power (i.e., $\int S(k)dk$), k_o is the source center wavenumber, and ϕ_{rand} is the random phase of the shot noise. f_{ascan} is the rate, in Hz, at which A-scans were acquired. In situations where the detector integration time is less than

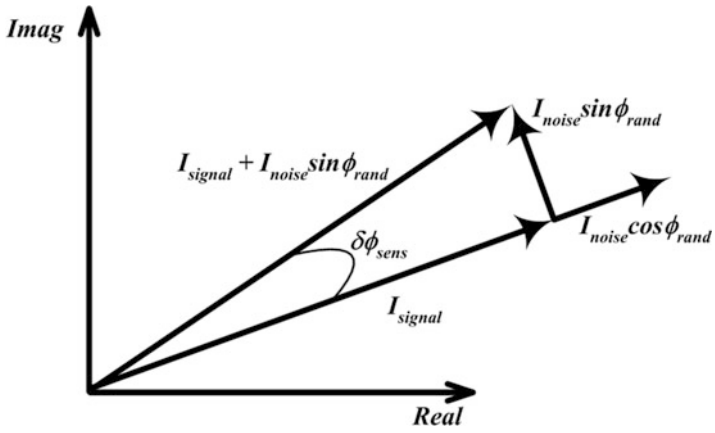

Fig. 40.9 Phase stability of spectral domain phase microscopy. In the x-domain, the signal and noise are complex-valued signals that add in a vectoral manner. If the phase of the noise is defined to be zero when I_{noise} is parallel to I_{signal}, then the error in the phase of I_{signal} is given by the component of I_{noise} that is perpendicular to I_{signal} (i.e., $I_{\text{noise}}sin_{\phi\text{rand}}$). The average rotation of I_{signal} caused by $I_{\text{noise}}sin_{\phi\text{rand}}$ taken over all ϕ_{rand} defines the phase stability

the interval between acquired A-scans, f_{ascan} is the numerical inverse of the integration time. It is assumed that $R_R >> R_n$. The amplitude signal-to-noise ratio of the nth reflector is given by the square of the ratio of the amplitudes of Eqs. 40.2 and 40.3. The shot noise-limited phase stability of the nth reflector signal is limited by the phase angle $\delta\phi_{\text{sens}}$ between $I_{\text{signal}}(2\Delta x_n)$ and $I(2\Delta x_n) = I_{\text{signal}}(2\Delta x_n) + I_{\text{noise}}(2\Delta x_n)$. The issue can be generally approached by considering the average value of the phase angle between $I_{\text{signal}}(2\Delta x_n)$ and $I(2\Delta x_n)$ over all values of ϕ_{rand}. This is given by (Fig. 40.9)

$$\delta\phi_{\text{sens}} = \frac{2}{\pi}\int_0^{\pi/2} \tan^{-1}\left(\frac{|I_{\text{noise}}|}{|I_{\text{signal}}|}\sin\phi_{\text{rand}}\right) d\phi_{\text{rand}}. \tag{40.4}$$

Equation 40.4 is derived in part from the representation of signal and noise in Fig. 40.9. At any particular instant, the signal vector (I_{signal}) and the noise vector (I_{noise}) have a random angular orientation with respect to each other. Since the phase of *Isignal* is not random, the phase of I_{noise} (i.e. ϕ_{rand}) can be conveniently defined with respect to I_{signal}. I_{noise} can be decomposed into components that are parallel ($I_{\text{noise}}\cos\phi_{\text{rand}}$) and orthogonal ($I_{\text{noise}}\sin\phi_{\text{rand}}$) to the signal vector. The parallel component contributes to amplitude sensitivity, while the orthogonal component contributes to the phase sensitivity. The phase noise of I_{signal} is defined by the magnitude of the rotation of I_{signal} by $I_{\text{noise}}\sin\phi_{\text{rand}}$. The phase noise also defines the phase sensitivity ($\delta\phi_{\text{sens}}$) since the smallest observable change in the phase of the signal vector is determined by the phase noise. In other words, an observable change in the signal phase must be larger than the phase noise.

If $|I_{noise}| \ll |I_{signal}|$, which is the usual case, then I_{signal}, $I_{noise}\sin\phi_{rand}$, and $I_{signal} + I_{noise}\sin\varphi_{rand}$ form a right triangle, and $\delta\phi_{sens}$ is the angle opposite $I_{noise}\sin\phi_{rand}$. $\delta\phi_{sens}$ is defined by the argument of the integral in Eq. 40.4, while the integral itself takes the average value of $\delta\phi_{sens}$ over all possible random values of ϕ_{rand}. This integral assumes that ϕ_{rand} has a uniform distribution. If it is assumed that $|I_{noise}| \ll |I_{signal}|$, then the arctangent function can be approximated by the value of its argument. The integral in Eq. 40.4 then simplifies to the mean value of the sine function over a quarter period, yielding

$$\delta\phi_{sens} = \frac{2}{\pi}\sqrt{\frac{1}{SNR(S_o, R_n, f_{ascan})}}. \tag{40.5}$$

where SNR(S_o, R_n, f_{ascan}) is the signal-to-noise ratio of the nth reflector.

Because the phase of $I(2\Delta x_n)$ is proportional to δx_n, displacements in a sample reflector can be tracked over time by tracking the phase over time. This is the basic principle of spectral domain phase microscopy (SDPM). SDPM may be extended to velocimetry measurements by noting that the instantaneous velocity of a reflector is given by the difference of δxn or two successive A-scans divided by the temporal sampling interval, which is equivalent to defining the instantaneous Doppler shift as the derivative of the phase with respect to time. This gives

$$v(t) = \frac{\lambda_o}{2\cos\theta} f_{dopp} = \frac{\lambda_o}{4\pi\cos\theta} f_{ascan}\left(\angle I(2\Delta x_n, t) - \angle I\left(2\Delta x_n, t - f_{ascan}^{-1}\right)\right) \tag{40.6}$$

Here, $\angle$ is the phase operator, λ_o is the source center wavelength, f_{dopp} is Doppler frequency shift, and θ is the Doppler angle between the optical axis and the direction of motion. The phase error in $v(t)$ is $\sqrt{2}$ times higher than the phase error in $\angle I(2\Delta x_n, t_o)$. The factor of $\sqrt{2}$ arises because velocity is proportional to the numerical difference between two successive phase measurements. As such, the uncertainty in difference (i.e., velocity) must be larger than the individual data points in the difference (i.e., phase). We assume that the summation of N random data points with identical standard deviations (or errors) has an error that is $N^{1/2}$ times larger than the error of each data point. The velocity sensitivity is thus (Fig. 40.10).

$$v_{sens} = \frac{\lambda_o}{2\sqrt{2}\pi\cos\theta}\delta\phi_{sens} f_{ascan} \frac{\lambda_o f_{ascan}}{\sqrt{2}\pi^2\cos\theta\sqrt{SNR(S_o, R_n, f_{ascan})}} \tag{40.7}$$

Equation 40.7 is consistent with the Cramer-Rao lower bound for a model-based velocity estimator [23], which has been previously verified in time-domain OCT [23]. In Doppler OCT imaging, it has been suggested that the minimum observable Doppler shift is related to the inverse of the observation period, which yields a velocity sensitivity of $\lambda_o f_{ascan}/2$ [24, 25]. The basis for this Fourier-limited assumption is that at least one cycle of the Doppler-induced electronic beat frequency must be

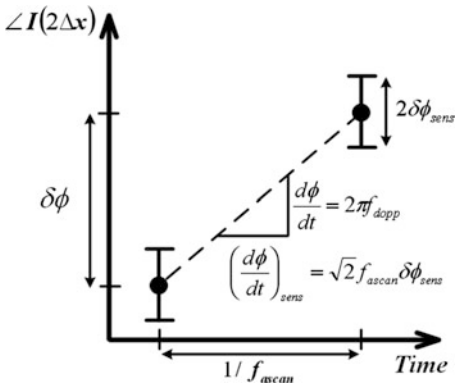

Fig. 40.10 Velocity sensitivity of Doppler flow imaging. dϕ/dt is experimentally calculated by taking the numerical derivative of the phase with respect to time. f_{dopp}, Doppler frequency shift

sampled in order to detect the motion of a reflector. If we define instantaneous Doppler shift (or velocity) as being the derivative of the phase (or position), it is clear the Fourier limit is overly restrictive. For example, if a reflector is moving at a constant velocity, the phase of the interferometric signal increases linearly over time. The accuracy of the phase difference between two sequential points, which is directly proportional to the instantaneous Doppler shift, is limited only by the phase noise on each individual point (Fig. 40.10). In this light, there is no clear need to sample an entire fringe of the Doppler-induced electronic beat frequency in the detector photocurrent.

40.4 SDPM Imaging Systems: Design, Characterization, and Validation

Spectral domain phase microscopy (SDPM) is being vigorously developed by several research groups for two main reasons. First, as discussed in Sect. 40.2, interferometry is a powerful technique for quantitative phase microscopy. Second, as discussed in Sect. 40.3, SD-OCT offers practical and theoretical advantages over TD-OCT in terms of phase stability. In this section, we describe several different SDPM topologies. We start with a detailed system characterization and validation of SDPM systems built by our group at Duke University. This discussion builds on the theoretical description of Sect. 40.3. The section closes with a discussion of more advanced topologies.

Figure 40.11 shows two spectral domain detection systems adapted to two types of sample arm optics. Both the swept-source and Fourier domain setup were adapted to tabletop imaging optics on a floated optical table, while the Fourier domain setup was additionally adapted to a Zeiss Axiovert 200 inverted microscope for the simultaneous acquisition of SDPM data and real-time video microscopy.

The insets to Fig. 40.11 illustrate experimental measurements from a clean glass coverslip for displacement sensitivity of 53 pm for the Fourier domain system (with ~9 μW incident on the coverslip) and 780 pm for the swept-source system (with ~3 mW incident on the coverslip). Despite these exquisite sensitivities, the experimental values are significantly higher (by a factor of 6 and 7×10^4,

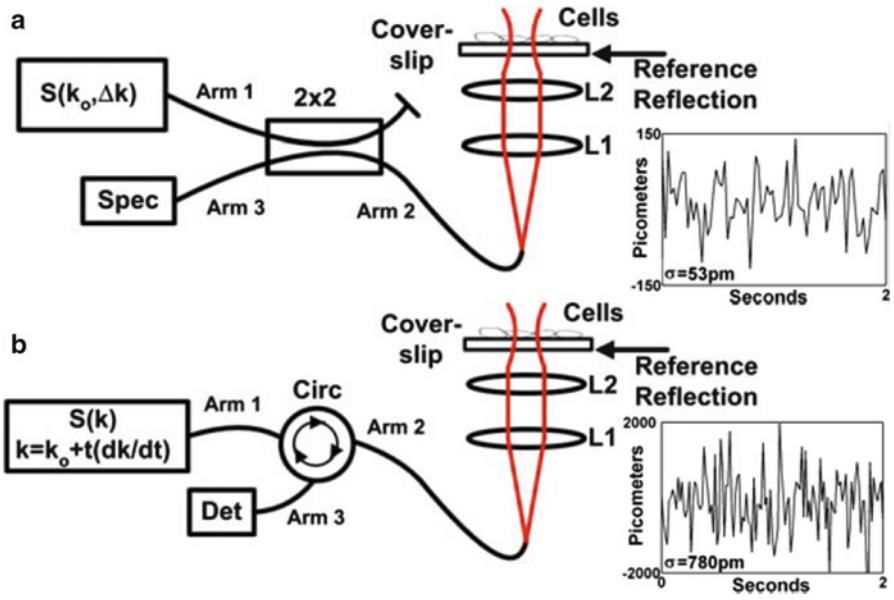

Fig. 40.11 Common-path spectral domain interferometers (**a**) Fourier domain SDPM interferometer. The source is a ~5 mW SLD with a center wavelength and 3 dB bandwidth of 830 nm and 45 nm, respectively. The spectrometer (Spec) has 25 ms readout rate and a 5 ms integration time. (**b**) Swept-source SDPM interferometer. The narrow linewidth source is swept through a 130 nm bandwidth over 5 ms with a center wavelength of 1,310 nm and an average power of ~3 mW (Micron Optics, Inc. [18]). The insets show the displacement signals recorded from a clean coverslip. The standard deviation of this signal defines the displacement stability at a particular sample reflectivity and sample illumination power. With ~3 mW incident on the coverslip, the swept-source displacement stability was 780 pm. With ~9 μW incident on the coverslip, the Fourier domain displacement stability was 53 pm (Figure is from Choma et al. [22])

respectively, for Fourier domain and swept-source interferometers) than theoretically predicted by Eq. 40.7.

The lower displacement sensitivity exhibited by the swept-source system is likely due to variability in the starting sweep wavelength. In other words, the first wavelength emitted by the swept source at the start of the wavelength sweep varies on the order of 780 pm sweep-to-sweep. This is an important design specification to consider given the increased interest in swept laser sources for spectral domain OCT. Possible limitations in the Fourier domain system include the presence of 1/f contamination in the sub-kilohertz bandwidth signal and any mechanical jitter in the sample arm optics which was not mitigated by the common path topology.

Equation 40.7 implies that the magnitude of the displacement stability noise floor is related to the square root of the reciprocal of the detector integration time. This is in contrast to amplitude sensitivity, which is a linear function of detector integration time. To test this model, we measured as a function of spectrometer integration time the displacement stability of the Fourier domain interferogram generated by a clean coverslip. Equation 40.7 predicts that the slope of $\log(\delta x_{\text{sens}})$

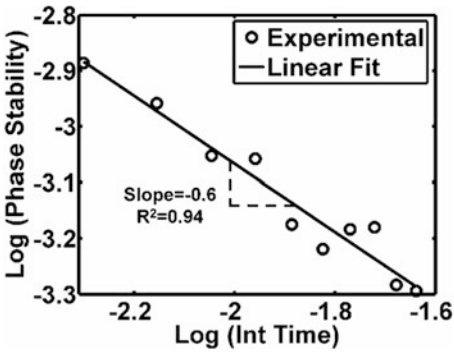

Fig. 40.12 Power (inverse square root) relationship between phase stability and detector integration time (Figure is from Choma et al. [22])

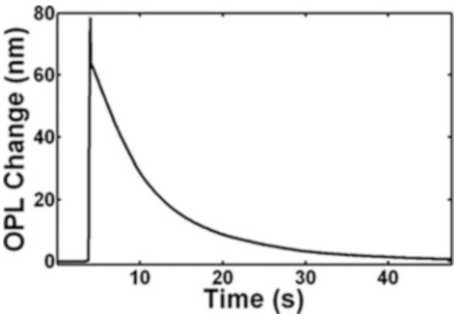

Fig. 40.13 Thermal expansion and contraction of a glass coverslip. The upswing corresponds to the application of a flame to the coverslip, and the downswing corresponds to cooling down to room temperature. The inset highlights the expansion of the coverslip

versus $\log(\Delta t)$ is -0.5. The experimental line has a slope of -0.6, which is consistent with the theory (Fig. 40.12).

Equation 40.7 predicts that the velocity sensitivity in spectral domain Doppler imaging is limited by phase stability. To test this prediction, we used SDPM to measure the velocity of thermal expansion of an uncoated glass coverslip transiently heated by a butane flame. The change in the optical path length (OPL) of the coverslip during heating and cooling was tracked by recording the phase of the x-domain interference signal at a depth corresponding to the thickness of the coverslip.

The rapid expansion and slow contraction of the coverslip is shown in Fig. 40.13. The baseline phase stability of the interference signal immediately before placing the flame near the coverslip was 0.4 mrad (18 pm). The phase stability is defined as the standard deviation of the x-domain interference phase at the depth corresponding to the coverslip thickness. The instantaneous velocity of expansion and contraction was calculated by numerically differentiating the OPL on sequential successive A-scans and multiplying that quantity by the line rate.

Figure 40.14 shows the instantaneously calculated velocity while the coverslip cooled off after flame removal. The yellow curve is a smoothed estimate of the actual velocity generated by low-pass filtering the phase data before calculation of

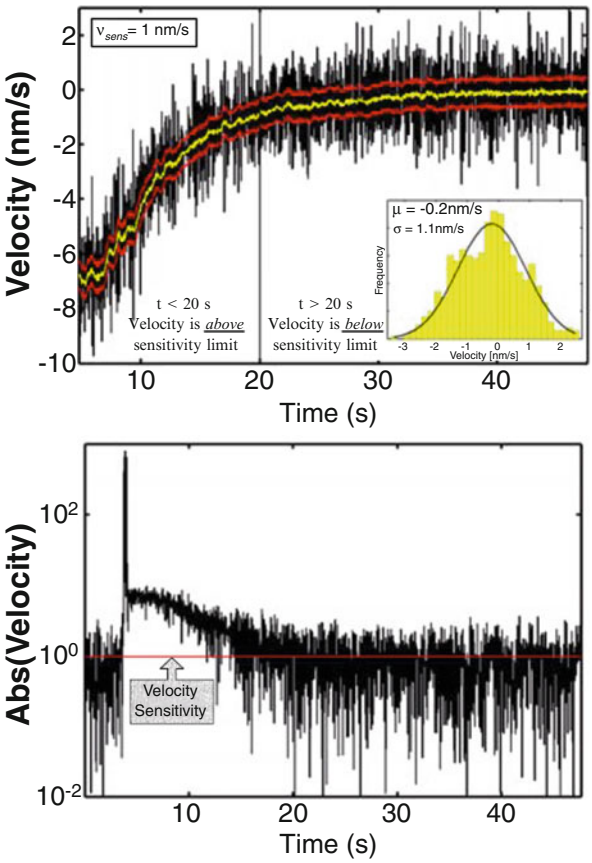

Fig. 40.14 Velocity sensitivity of SDPM. *Top*: Velocity of thermal contraction of glass coverslip ($t = 4.8$–48 s). The *black curve* is generated by taking the numerical derivative of the data in Fig. 40.13. The *yellow* line is the velocity estimated by low-pass filtering the raw data in *black*. The *red lines* are the velocity estimate plus/minus one-half of the predicted velocity sensitivity of 1 nm/s. The inset shows a histogram (*yellow bars*) of the velocity values measured for $t > 20$ s. The mean (μ) and standard deviation (σ) of the measured data are shown. The black curve is a Gaussian distribution with the measured μ and σ. *Bottom*: Absolute value of the velocity of expansion and contraction calculated from Fig. 40.13 and plotted on a log scale (From Choma et al. [26])

the Doppler shift. The red curves represent the estimated velocity plus/minus half of the velocity sensitivity calculated using Eq. 40.7. The black vertical line at $t = 20$ s represents the approximate time at which the magnitude of the velocity fell below the sensitivity of 1 nm/s. The inset to Fig. 40.14 (top) shows a histogram of the measured velocity values for $t > 20$ s. This data distribution, which is approximately Gaussian, has a standard deviation of 1.1 nm/s, consistent with the predicted velocity sensitivity of 1 nm/s.

Figure 40.14 (top) illustrates two points. First, the experimental velocity data were bound by a range defined by the actual velocity (estimated by low-pass filtering the velocity data) and the predicted velocity. This supports Eq. 40.7 as a valid expression for the noise and uncertainty in a Doppler calculation given a level of phase stability. Second, it demonstrates that the magnitude of the velocity must be greater than the velocity sensitivity in order to be resolved from zero velocity. In other words, when the velocity magnitude is equal to the velocity sensitivity, the "velocity signal-to-noise ratio" is unity, rendering the velocity measurement indistinguishable from zero velocity. Figure 40.14 (bottom) shows the absolute value of the expansion and contraction velocity on a log scale.

The predicted velocity sensitivity is shown as a horizontal red line. This figure draws an analogy with amplitude sensitivity for OCT in that the level of the "height" of the noise floor on a log plot is determined by the measurement sensitivity.

Phase-sensitive spectral domain interferometry has also been extended to collect multidimensional data. Towards this end, two distinct techniques have been demonstrated. Joo et al. [27] demonstrated a technique which they termed spectral domain optical coherence phase microscopy (SDOCPM) in which raster scanning was employed to acquire two-dimensional en face phase images of samples (Fig. 40.15). This system had a line scan rate of 29 kHz and a free-space axial resolution of $\sim$8 mm. Unwrapping the phase along transverse axes for a given axial depth yielded very sensitive information about the spatial dependence of the optical path length generated by the sample.

An alternate approach to full-field phase imaging builds on full-field parallel setups demonstrated for OCT [29, 30], and optical coherence microscopy [31] Sarunic et al. [28] demonstrated full-field SDPM images using a swept-source interferometer topology (Fig. 40.15). Interferograms acquired over the duration of the source sweep were collected simultaneously for all spatial positions during the integration time of a two-dimensional CCD camera. Phases unwrapped in space mapped out the surfaces of the samples of interest. Imaging speed for this particular demonstration was limited by the minimum integration time and duty cycle rate of the CCD used.

40.4.1 Applications in Cell Biology

The reductionist drive to describe living organisms in terms of complex interactions of basic building blocks and functional units (e.g., molecules, organelles, cells, tissues, organs) has been greatly facilitated by numerous imaging modalities (e.g., optical microscopy, ultrasound, magnetic resonance imaging). Elucidating in vivo structure and function in the cellular and subcellular regimes is a critical component of this drive. In these regimes, optical techniques hold great promise owing to their speed, spatial resolution, and nondestructive nature. In this section, several demonstrations of SDPM in cell biology are shown. It is hoped that these results motivate the development of SDPM as an important imaging tool in the cellular and subcellular regimes.

40.4.2 Characterizing Cardiomyocyte Contractility

The ability of SDPM systems to characterize dynamic cellular events was demonstrated on spontaneously beating 2-day-old isolated chick embryo cardiomyocytes (Fig. 40.16). A detailed description of the isolation and culture method can be found elsewhere [32]. Briefly, after decapitation of the embryo, the heart was removed, the atria and great vessels were trimmed away, and the ventricles were cleaned of connective tissue. Ventricular cardiomyocytes were dissociated by digestion of the

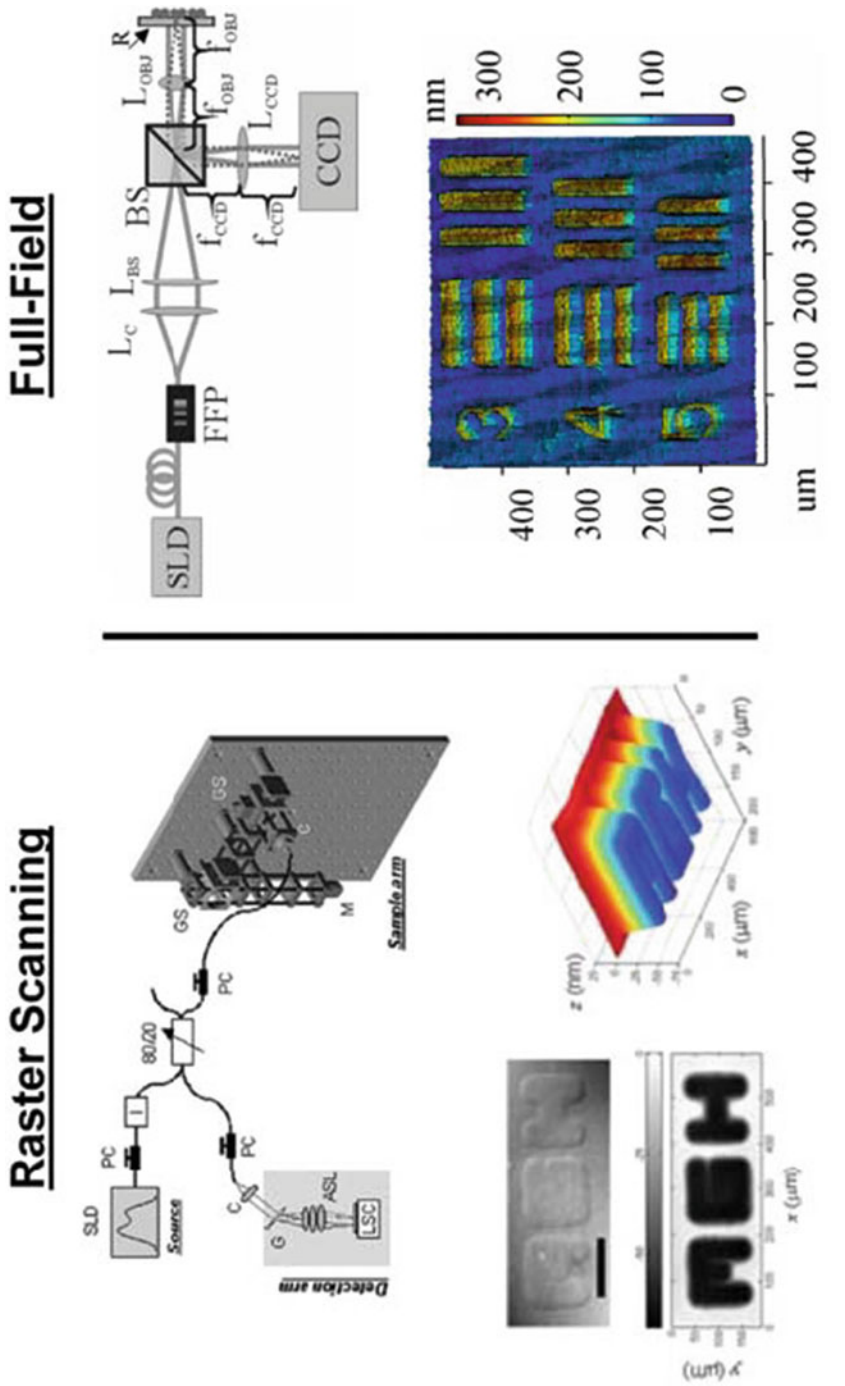

Fig. 40.15 Multidimensional SDPM images on the *left* are from Joo et al. [27] (Images on the *right* are from Sarunic et al. [28])

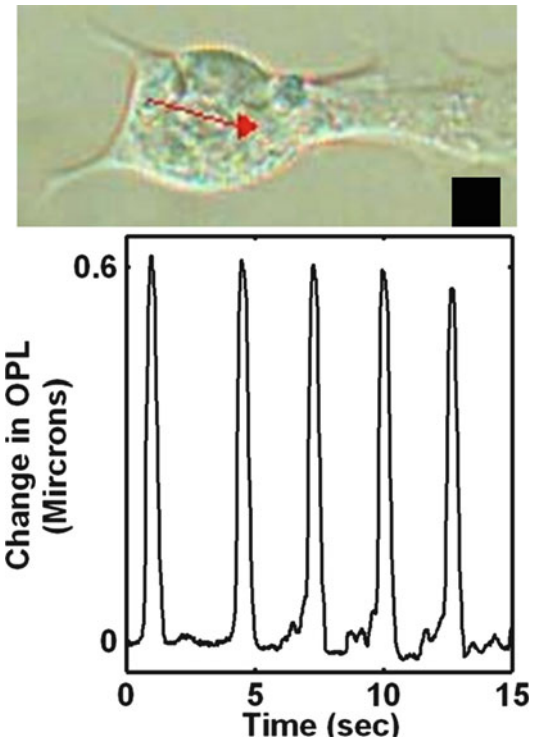

Fig. 40.16 Embryonic cardiomyocyte dynamics measured using SDPM. *Top*: Photomicrograph of an isolated ventricular cardiomyocyte from a 2-day-old chick embryo. The tip of the *red arrow* denoted the location of the SDPM beam. The *black box* is 10 × 10 μm. *Bottom*: Change in thickness of spontaneously beating cardiomyocyte measured using SDPM (Figure is from Choma et al. [22])

ventricle with DNAse and collagenase at 37 °C. Cells were cultured in DeHaan's 21,212 medium on glass coverslips and used within 24 h of enzymatic dissociation. During SDPM experiments, the cells were maintained at 37 °C using a heated microscope stage. At 37 °C the ventricular cardiomyocytes spontaneously beat via electromechanical coupling.

Using SDPM, we measured changes in cell thickness associated with cardiomyocyte contraction (Fig. 40.16). The cardiomyocyte depicted was spontaneously beating at ∼0.3 Hz. The dynamics of contraction were well represented in the SDPM trace.

40.4.3 Characterizing Cytoplasmic Flow in an Individual Cell

Cytoplasmic flow is central to a variety of cellular processes, including the development of neuronal polarity [33], cell migration [34], a-p axis formation in embryos [35], and amoeboid motion [36–47]. For in vivo Doppler imaging of cytoplasmic flow in *Amoeba proteus* [26], cellular measurements, an SDPM setup was relayed into a Zeiss Axiovert 200 using a documentation port as illustrated in Fig. 40.17. Simultaneous acquisition of SDPM and visible light microscopy video was achieved by placement of an 80/20 beamsplitter in the microscope optical path.

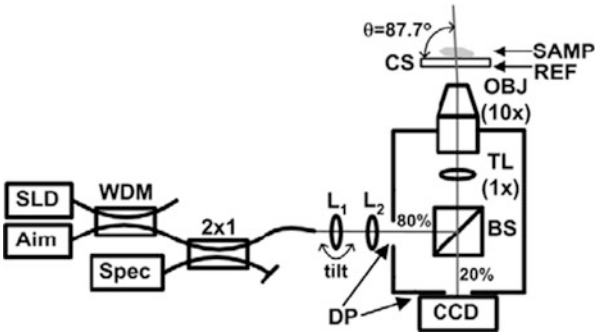

Fig. 40.17 SDPM setup adapted to Zeiss Axiovert 200 inverted microscope with simultaneous acquisition of SDPM and video light microscopy. A 635 nm aiming beam (*Aim*) is combined with an 840 nm superluminescent diode (*SLD*) (50 nm FWHM bandwidth) with a wavelength division multiplexing (*WDM*) fiber coupler. The combined light enters a 2 × 1 50/50 fiber coupler whose output fiber core is imaged via lenses (*L*) one and two onto a documentation port (*DP*) of the microscope with a magnification of $L_2/L_1 = 22$. The image formed at the documentation port is then relayed onto the sample (*SAMP*) with magnification of 1/10. The sample also is imaged onto a documentation port CCD. *CS* coverslip, *OBJ* microscope objective, *REF* reference reflection, *Spec* spectrometer, *TL* tube lens (From Choma et al. [26])

There was thus real-time display of video and A-scan data. The SDPM spot size (1/e diameter) on the sample was estimated from the magnification factor of the coupler fiber core being imaged onto the sample. This factor was (L2/L1) × (TL/OBJ), giving a calculated spot size of 12 μm and a calculated depth of focus of 1 mm. (L_n, nth lens, TL, tube lens, OBJ, objective lens; see Fig. 40.17 for more detail). The ration OBJ/TL is specified by the manufacturer as the effective or net magnification of a sample object onto the documentation port. The reflection from an uncoated coverslip surface proximal to the SDPM interferometer acted as the reference reflection.

Several amoebas (species *Amoeba proteus*) were placed on the other coverslip surface in a springwater solution. Since cytoplasmic streaming in these cells is nominally parallel to the coverslip surface, lens 1 (L1) was tilted to make a Doppler angle of $\theta = 87.7°$ between the SDPM light and the streaming. This Doppler angle represents a compromise between recoupling efficiency of the reference beam (highest at 90°) and optimal Doppler angle (optimal at 0°). The angle was verified through image analysis of the position of the aiming beam on the video image taken at calibrated displacements of the objective lens along the optical axis. With respect to recoupling efficiency of the reference beam, it should be noted that standard OCT sensitivity expressions here and in the literature are typically independent of reference arm power provided that (a) reference power is much greater than sample power and (b) the system operates in the shot noise limit.

A visible light microscopic image selected from a video recording of an extruding *A. proteus* is in Fig. 40.18. SDPM data were recorded from the location marked with the white triangle. This location was identified with a 635 nm aiming bean that was turned off after the acquisition window was marked with the triangle. The aiming

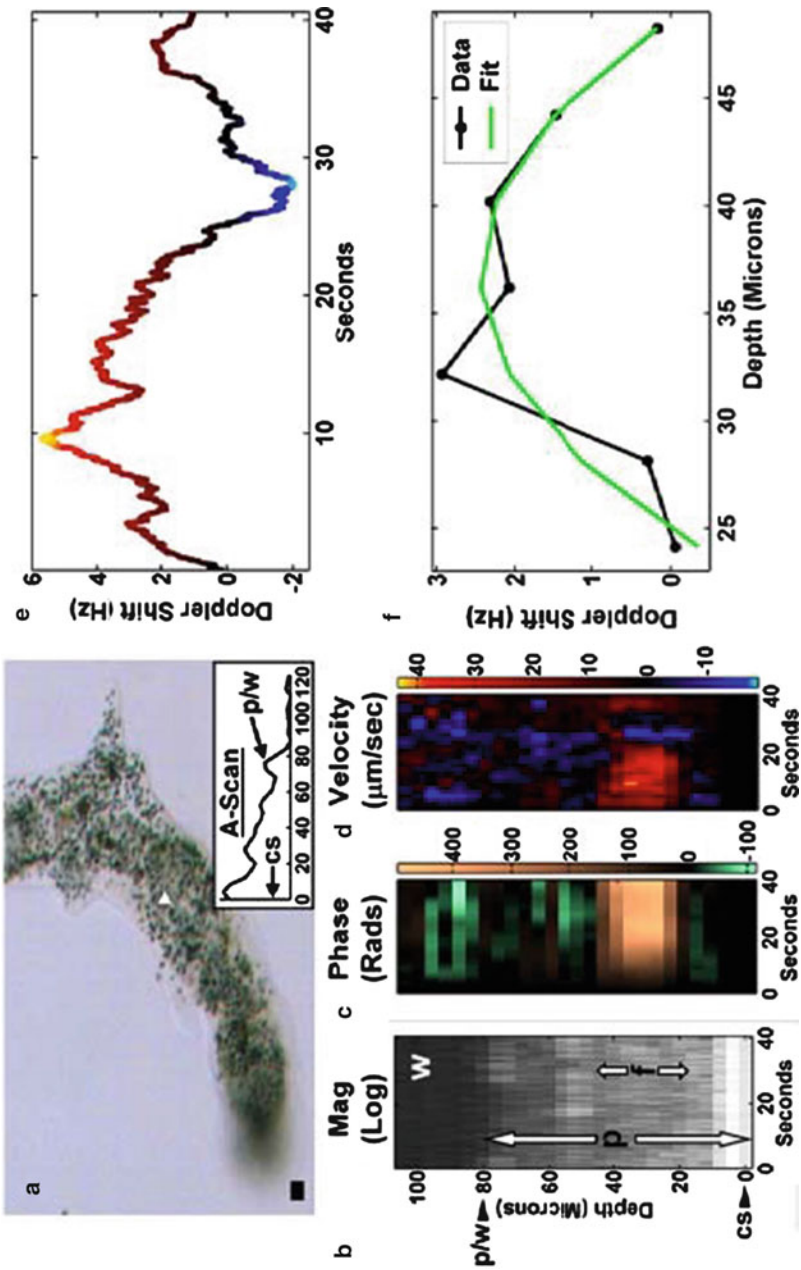

Fig. 40.18 (continued)

beam was turned off to avoid contamination of the data by photophobic reflex in A. proteus. M-mode recordings (repeated recordings at a given spatial location) of magnitude, phase, and derived Doppler images are in Fig. 40.18b–d. M-mode images have a vertical axis with units of depth, horizontal axis with units of time, and image intensity proportional to the measurement of interest (e.g., reflectivity, velocity). Between $t = 18-20$ s, several drops of a 50 mM $CaCl_2$ solution were added to the springwater solution. This triggered a slowdown and subsequent reversal in the cytoplasmic flow. The flow reversal is manifest as a decrease in accumulated phase (Fig. 40.18c) and as a change in the sign of the Doppler shift (Fig. 40.18d–e). The flow reversed again at t $\approx$ 35 s. Overall, measured flow rates were consistent with previously reported values for *A. proteus* [48].

Low-pass filtering of the Doppler data was performed to mitigate the influence of SNR variations due to speckle on the calculation of Doppler shift. Since speckle is multiplicative noise imposed on $I(2\Delta x)$ (i.e., $I = I_{\text{speckle}} \times [I_{\text{signal}} + I_{\text{noise}}]$), SNR($S_o$,$R_n$,$f_{\text{ascan}}$) is modulated by this multiplicative noise as well. Additionally, the "nulls" of the speckle pattern have a phase SNR of zero since there is zero signal. These nulls give the false impression that there is zero flow in an otherwise flowing sample. Likewise, SNR is maximum at the "peaks" of the speckle pattern, and the Doppler shift at these peaks presumably will most accurately represent the sample flow velocity. The Doppler data in Fig. 40.18 were low-pass filtered with a moving average filter with a time constant (or width) of 3,459 ms. This relatively longer time constant was chosen to emphasize changes in flow over the course of a few seconds. Figure 40.19 shows the Doppler shift recorded at a depth of 36 μm that was low-pass filtered with time constants ranging from 0 to 3,459 ms. The Doppler data is clearly interpretable with little to no filtering.

Visual inspection of the extruding *A. proteus* pseudopod on light microscopy indicates that the cytoplasm flows within a channel delineated on either side by non-flowing cytoplasm (the so-called gel, in contrast to the flowing "sol"). The gel has high viscosity and acts as a stationary conduit, while the sol, which has much lower viscosity, flows within that conduit. Flow is generated by active (i.e., ATP-dependent) cytoskeletal and cytoplasmic processes. In the absence of turbulence, which would be difficult to generate owing to the viscosity of

Fig. 40.18 Cytoplasmic flow in Amoeba proteus. (**a**) Photomicrograph of *A. proteus* pseudopod (*p*). The *white triangle* marks location of data collection, and *black box* in *lower left* is 10 × 10 μm. The inset to (**a**) shows an A-scan of the pseudopod (*abscissa* has units of depth in micrometers; ordinate has units of reflectivity in dB). The coverslip (*cs*) on which the pseudopod sits is located at zero displacement. The pseudopod/water (p/w) interface is clearly identified near 80 μm by a reflectivity peak followed by the decreased reflectivity of water. (**b**) M-mode magnitude image of *Amoeba proteus* pseudopod. (**c**, **d**) are M-mode phase and Doppler image, respectively. The *arrows* marked with "f" in **b** demarcate the flowing portion of the cytoplasm as determined from the phase and Doppler data in **c** and **d**, respectively. (**e**) Doppler shift versus time at a depth of 36 μm. (**f**) Doppler shift versus depth at $t = 20$ s. The *green line* is a least-squares parabolic fit of the flow profile ($R^2 = 80$ %) (From Choma et al. [26])

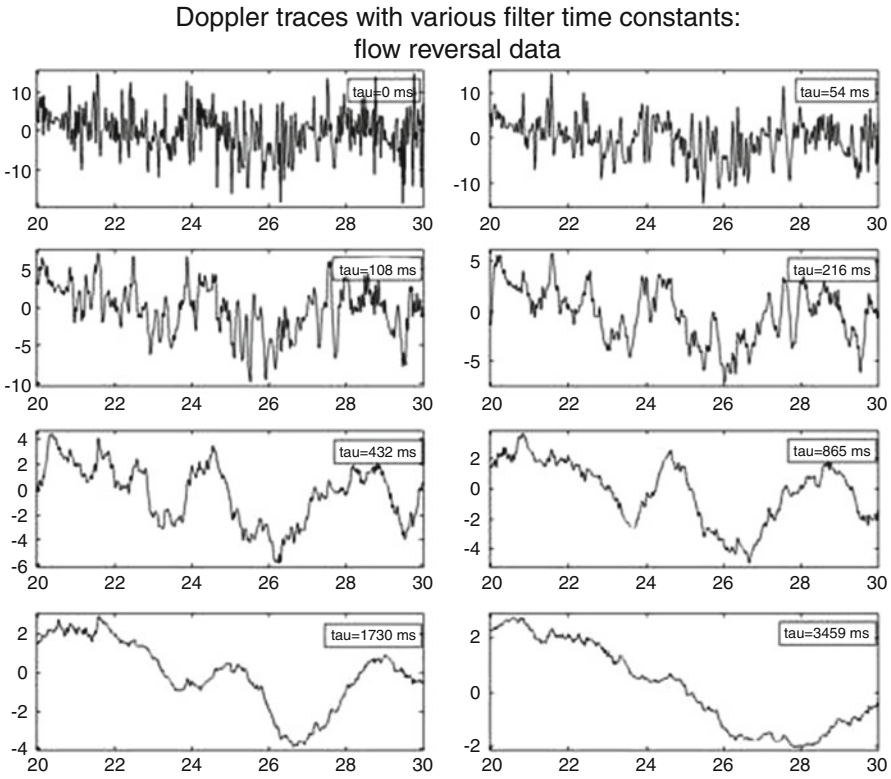

Fig. 40.19 Filtering of Doppler SDPM data Doppler shift versus time at a depth of 36 μm after processing with moving-average filters of various time constants (tau). Data points corresponding to flow reversal that occurs between 20 and 30 s are shown. *Abscissa* has units of time in seconds; ordinate, Doppler shift in Hz (From Choma et al. [26])

cytoplasm, the amplitude of the flow is expected to follow a parabolic profile as a function of depth. Figure 40.18f, which shows the Doppler frequency as a function of depth at $t = 20$ s, supports this laminar flow hypothesis. This measured flow profile matches that of an ideal parabolic flow profile with an R^2 value of 80 %. The laminar flow profile also is suggested from the plot of the flow-induced Doppler shift against both depth and time in a 3-D surface plot (Fig. 40.20).

Depth-resolved Doppler SDPM has been extended to obtain cross sections of *A. proteus* flow. Phase for all depths is unwrapped in time and in space, resulting in movies of cytoplasmic flow in a single cell. Representative frames from one such movie are shown in Fig. 40.21. There is the suggestion of antiparallel channels of flow within the pseudopod. Given the angle ambiguity presented by Doppler imaging, further investigation is needed to elucidate the origin of oppositely signed Doppler shifts from within the pseudopod.

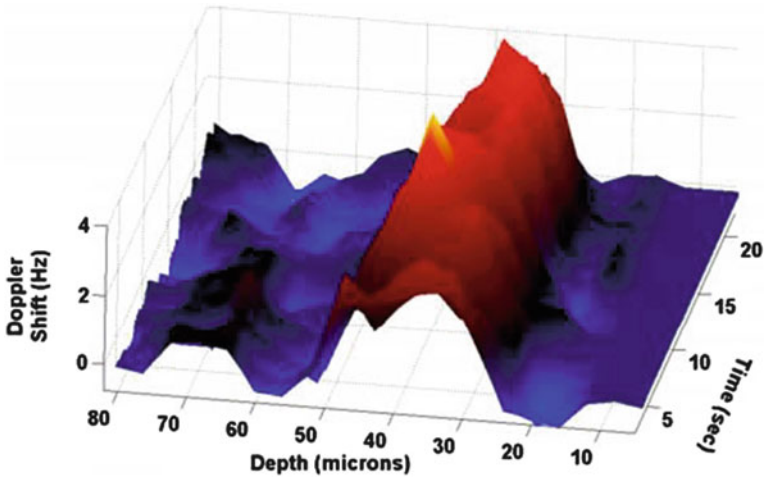

Fig. 40.20 Surface plot of flow-induced Doppler shift as a function of time and depth. Laminar (parabolic) cytoplasmic flow is suggested (From Choma et al. [26])

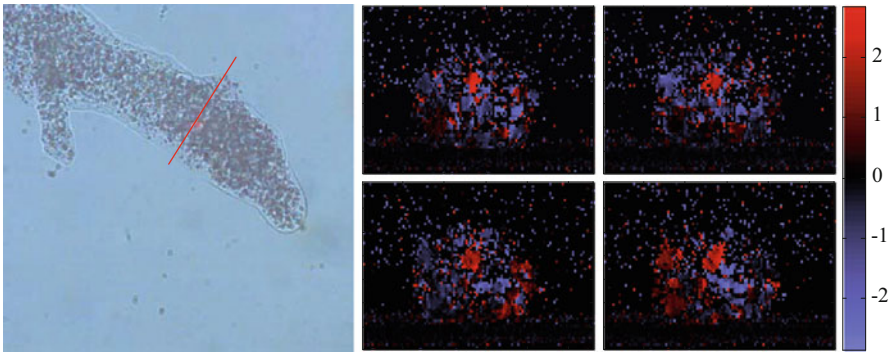

Fig. 40.21 Detection of cytoplasmic flow across the lateral plane of *A. proteus*. *Left*: CCD image of Amoeba cell with *line* denoting lateral acquisition plane. *Right*: Snapshots of time-sequential (Frames 13–16) B-mode phase difference images for flowing pseudopodium taken at 13.3 Hz. Flow direction is out of the page, and the lateral scan range is 153 mm. *Color bar* indicates mapping for phase differences (radians)

40.4.4 Characterizing Mechanical Properties of the Cytoskeleton Using Magnetic Tweezers and SDPM

Widespread interest in cellular motility, particularly as relates to cancer metastasis, has motivated extensive study of the mechanical properties of the cytoskeleton. The structural components of the cytoskeleton are responsible for coordinating cellular transport, locomotion, as well as internal signal transduction and gene expression.

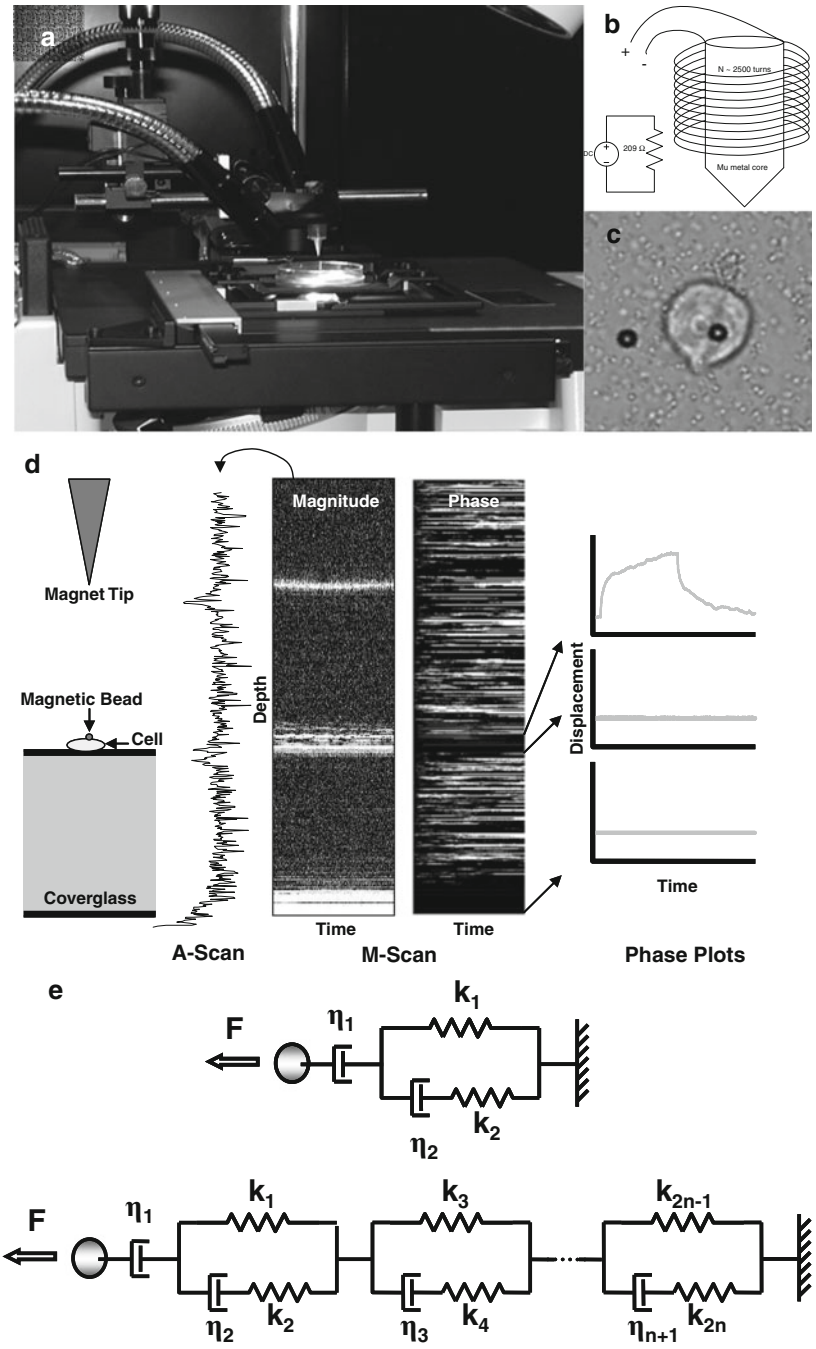

Fig. 40.22 Cellular mechanics measured with magnetic trapping and SDPM. Magnetic probe positioned above cell culture dish on inverted microscope stage (**a**). Schematic of electromagnet

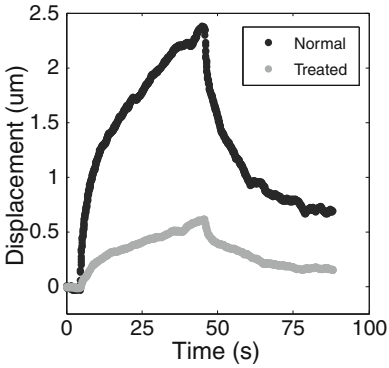

Displacement after 40 s

	Normal	Treated
Avg.	0.57 μm	2.40 μm
Std. Dev.	0.35 μm	1.86 μm

Fig. 40.23 Mechanical deformation of cancer cells measured with SDPM. Average vertical displacement and recovery profile for untreated MCF-7 human breast cancer cell (*black line*) as well as those treated with cytochalasin D (*gray line*). A statistically significant ($p < 0.05$) increase in cell displacement was seen after 30 min of treatment. McDowell et al. [49]

Given the extraordinary sensitivity of SDPM systems to morphological changes in cellular samples, McDowell et al. [49] used this system to investigate the rheological properties of cancer cells, demonstrating the versatility of the SDPM technique and its ability to be complement standard methods practiced in well-established fields like cell biology.

McDowell et al. designed a calibrated magnetic trap to study the viscoelastic response of breast cancer cells to applied forces. Ferromagnetic beads attached to the cell surface served as handles with which the trap could pull on the cell; SDPM was used to measure the resulting change in cell thickness in the vertical direction (Fig. 40.22), distinguishing this experiment from previous works that probed lateral morphological changes in cells [50–53]. It was hypothesized that the magnitude of the cell thickness change related to the viscous properties of the cell. The quantitative data acquired with SDPM permitted fitting measured deformation to various proposed viscoelastic models. Fitting to these models allows for the extraction of quantitative constants that could be used to compare across cells in various experimental conditions. It was demonstrated that cells treated with cytochalasin D (an agent that depolymerizes actin, an important cytoskeletal component) have statistically significant different rheological properties than untreated cells (Fig. 40.23).

Fig. 40.22 (continued) (**b**). Photomicrograph of magnetic bead adherent to an MCF-7 human breast cancer cell (**c**). The SDPM system outputs a complex-valued M-scan, providing depth information over time (**d**). The magnitude of the M-scan gives a series of A-scans or depth profiles. The phase of the M-scan carries information about small changes in reflector position over time, seen in the plots on the *right*. Common-used models of cytoskeletal mechanics (**e**)

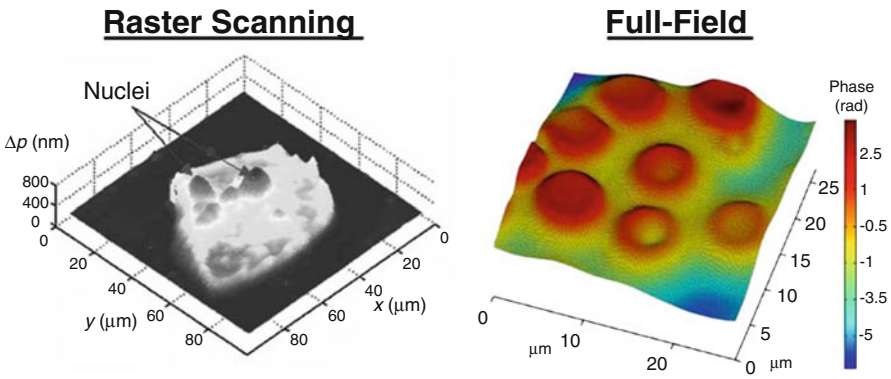

Fig. 40.24 Whole-cell imaging using SDPM. *Left* image is of a cheek cell and is from Joo et al. [27]. *Right* image is of several red blood cells and is from Sarunic et al. [28]

40.4.5 Whole-Cell Imaging Using SDPM

As previously discussed, SDPM has been extended to multidimensional imaging using raster scanning or full-field imaging. Representative images of cells obtained with these techniques are shown in Fig. 40.24. In both images, the source bandwidth was not adequate to obtain depth-indexed information. Since optical path length is an integrative term that accumulates in depth, the phase content at the furthermost reflective surface of the sample is comparable to the quantitative information obtained from the monochromatic techniques discussed earlier.

40.5 Conclusion

Over the past decade, quantitative phase imaging has made significant advances. These advances retain the original advantage of qualitative phase microscopy first described by Zernike (i.e., enhanced contrast) and augment this seminal technique with information regarding subcellular function and motion. These quantitative techniques were first demonstrated with monochromatic interferometry. These techniques can now image cellular dynamics at rates in excess of video rate. In parallel, phase-sensitive OCT techniques have been refined to detect cellular dynamics. Spectral domain phase microscopy (SDPM) is a functional extension of OCT which grew out of the increased phase stability available in SDOCT systems. SDPM allows for the depth-dependent measurement of cellular motions and dynamics with sensitivities in the picometer to nanometer regimes. This sensitivity has a lower limit defined by the image signal-to-noise ratio. In this chapter several initial demonstrations of the ability of SDPM to quantify cellular morphology and subcellular dynamics have been shown.

There are several technical advances to be made in SDPM over the next several years. The use of ultrabroadband sources with potentially hundreds of nanometers

of bandwidth will allow for better localization of phase information within cells. This will be important for the imaging of eukaryotic cells, which have nominal thicknesses of ~1–10 μm. It also will be important to push SDPM line rates into the hundreds of kilohertz regime. Several different cell types, most notable neurons and myocytes, have dynamics in the kHz regime. Detailed volumetric imaging of these cell types will require line rates at a considerable multiple of the detection bandwidth required for the detection of electrical action potentials.

Multimodal imaging that incorporates SDPM promises to be a powerful tool. From an OCT perspective, simultaneous acquisition of phase, polarization, and spectroscopic data in a depth-indexed manner can yield a tremendous amount of data about dynamic cell function. This data can be augmented with the simultaneous acquisition of molecular- or ion-specific fluorescent microscopic information. With this data in hand, the whole-cell and intracellular dynamics of several different key processes, ranging from excitation-contraction coupling to cell migration, can be studied with remarkable detail.

References

1. F. Zernike, How I discovered phase contrast. Science **121**(3141), 345–349 (1955)
2. K.A. Nugent, D. Paganin, T.E. Gureyev, A phase odyssey. Phys. Today **2001**, 27 (2001)
3. J. Farinas, A.S. Verkman, Cell volume and plasma membrane osmotic water permeability in epithelial cell layers measured by interferometry. Biophys. J. **71**(6), 3511–3522 (1996)
4. T. Ikeda, G. Popescu, R.R. Dasari, M.S. Feld, Hilbert phase microscopy for investigating fast dynamics in transparent systems. Opt. Lett. **30**(10), 1165–1167 (2005)
5. G. Popescu, T. Ikeda, C.A. Best, K. Badizadegan, R.R. Dasari, M.S. Feld, Erythrocyte structure and dynamics quantified by Hilbert phase microscopy. J. Biomed. Opt. **10**(6), 060503 (2005)
6. J.A. Izatt, M.D. Kulkami, S. Yazdanfar, J.K. Barton, A.J. Welch, In vivo bidirectional color Doppler flow imaging of picoliter blood volumes using optical coherence tomography. Opt. Lett. **22**(18), 1439–1441 (1997)
7. Z.P. Chen, T.E. Milner, D. Dave, J.S. Nelson, Optical Doppler tomographic imaging of fluid flow velocity in highly scattering media. Opt. Lett. **22**(1), 64–66 (1997)
8. C. Yang, A. Wax, M.S. Hahn, K. Badizadegan, R.R. Dasari, M.S. Feld, Phase-referenced interferometer with subwavelength and subhertz sensitivity applied to the study of cell membrane dynamics. Opt. Lett. **26**(16), 1271–1273 (2001)
9. I. Tasaki, Rapid structural changes in nerve fibers and cells associated with their excitation processes. Jpn. J. Physiol. **49**(2), 125–138 (1999)
10. I. Tasaki, P.M. Byrne, The origin of rapid changes in birefringence, light-scattering and dye absorbency associated with excitation of nerve-fibers. Jpn. J. Physiol. **43**, S67–S75 (1993)
11. L.B. Cohen, B. Hille, R.D. Keynes, Changes in axon birefringence during the action potential. J. Physiol. **211**(2), 495–515 (1970)
12. L.B. Cohen, R.D. Keynes, B. Hille, Light scattering and birefringence changes during nerve activity. Nature **218**, 438–441 (1968)
13. C. Fang-Yen, M.C. Chu, H.S. Seung, R.R. Dasari, M.S. Feld, Noncontact measurement of nerve displacement during action potential with a dual-beam low-coherence interferometer. Opt. Lett. **29**(17), 2028 (2004)
14. T. Akkin, D.P. Dave, T.E. Milner, H.G. Rylander, Detection of neural activity using phase-sensitive optical low-coherence reflectometry. Opt. Express **12**(11), 2377–2386 (2004)
15. D. Huang, E.A. Swanson, C.P. Lin, J.S. Schuman, W.G. Stinson, W. Chang, M.R. Hee, T. Flotte, K. Gregory, C.A. Puliafito, Optical coherence tomography. Science **254**(5035), 1178–1181 (1991)

16. R.C. Youngquist, S. Carr, D.E.N. Davies, Optical coherence- domain reflectometry: a new optical evaluation technique. Opt. Lett. **12**(3), 158–160 (1987)
17. M.R. Hee, D. Huang, E.A. Swanson, J.G. Fujimoto, Polarization- sensitive low-coherence reflectometer for birefringence characterization and ranging. J. Opt. Soc. Am. B Opt. Phys. **9**(6), 903–908 (1992)
18. M.A. Choma, M.V. Sarunic, C. Yang, J.A. Izatt, Sensitivity advantage of swept-source and Fourier-domain optical coherence tomography. Opt. Express **11**(18), 2183–2189 (2003)
19. R. Leitgeb, C.K. Hitzenberger, A.F. Fercher, Performance of fourier domain vs. time domain optical coherence tomography. Opt. Express **11**(8), 889–894 (2003)
20. J.F. de Boer, Signal to noise gain of spectral domain over time domain optical coherence tomography, presented at the Photonics West, San Jose, Jan 2004
21. A.F. Fercher, C.K. Hitzenberger, G. Kamp, S.Y. Elzaiat, Measurement of intraocular distances by backscattering spectral interferometry. Opt. Commun. **117**(1–2), 43–48 (1995)
22. M.A. Choma, A.K. Ellerbee, C.H. Yang, T.L. Creazzo, J.A. Izatt, Spectral-domain phase microscopy. Opt. Lett. **30**(10), 1162–1164 (2005)
23. S. Yazdanfar, C.H. Yang, M.V. Sarunic, J.A. Izatt, Frequency estimation precision in Doppler optical coherence tomography using the Cramer-Rao lower bound. Opt. Express **13**(2), 410–416 (2005)
24. M.D. Kulkarni, T.G. van Leeuwen, S. Yazdanfar, J.A. Izatt, Velocity-estimation accuracy and frame-rate limitations in color Doppler optical coherence tomography. Opt. Lett. **23**(13), 1057–1059 (1998)
25. Y.H. Zhao, Z.P. Chen, C. Saxer, S.H. Xiang, J.F. de Boer, J.S. Nelson, Phase-resolved optical coherence tomography and optical Doppler tomography for imaging blood flow in human skin with fast scanning speed and high velocity sensitivity. Opt. Lett. **25**(2), 114–116 (2000)
26. M.A. Choma, A.K. Ellerbee, S.Y. Yazdanfar, J.A. Izatt, Doppler flow imaging of cytoplasmic streaming using spectral domain phase microscopy. Journal of Biomedical Optics 11: 024014, 2006.
27. C. Joo, T. Akkin, B. Cense, B.H. Park, J.F.D. Boer, Spectral- domain optical coherence phase microscopy for quantitative phase- contrast imaging. Opt. Lett. **30**(16), 2131–2133 (2005)
28. M.V. Sarunic, S.H. Weinberg, J.A. Izatt, Full field swept source phase microscopy. Opt. Lett. (Doc. ID 67182) (2006 in press)
29. S. Bourquin, P. Seitz, R.P. Salathé, Optical coherence tomography based on a two-dimensional smart detector array. Opt. Lett. **26**, 512–514 (2001)
30. B. Grajciar, M. Pircher, A.F. Fercher, R.A. Leitgeb, Parallel Fourier domain optical coherence tomography for in vivo measurement of the human eye. Opt. Express **13**, 1131–1137 (2005)
31. E. Beaurepaire, A.C. Boccara, M. Lebec, L. Blanchot, H. Saint- Jalmes, Full-field optical coherence microscopy. Opt. Lett. **23**, 244–246 (1998)
32. T.L. Creazzo, J. Burch, R.E. Godt, Calcium buffering and excitation-contraction coupling in developing avian myocardium. Biophys. J. **86**(2), 966–977 (2004)
33. F. Bradke, C.G. Dotti, Neuronal polarity: vectorial cytoplasmic flow precedes axon formation. Neuron **19**(6), 1175–1186 (1997)
34. A.J. Ridley, M.A. Schwartz, K. Burridge, R.A. Firtel, M.H. Ginsberg, G. Borisy, J.T. Parsons, A.R. Horwitz, Cell migration: integrating signals from front to back. Science **302**(5651), 1704–1709 (2003)
35. S.N. Hird, J.G. White, Cortical and cytoplasmic flow polarity in early embryonic cells of Caenorhabditis elegans. J. Cell Biol. **121**(6), 1343–1355 (1993)
36. D.L. Taylor, J.R. Blinks, G. Reynolds, Contractile basis of amoeboid movement. VII. Aequorin luminescence during amoeboid movement, endocytosis, and capping. J. Cell Biol. **86**(2), 599–607 (1980)
37. D.L. Taylor, Y.L. Wang, J.M. Heiple, Contractile basis of ameboid movement. VII. The distribution of fluorescently labeled actin in living amebas. J. Cell Biol. **86**(2), 590–598 (1980)
38. S.B. Hellewell, D.L. Taylor, The contractile basis of ameboid movement. VI. The solation-contraction coupling hypothesis. J. Cell Biol. **83**(3), 633–648 (1979)

39. D.L. Taylor, J.A. Rhodes, S.A. Hammond, The contractile basis of ameboid movement. II. Structure and contractility of motile extracts and plasmalemma-ectoplasm ghosts. J. Cell Biol. **70**(1), 123–143 (1976)
40. D.L. Taylor, J.S. Condeelis, P.L. Moore, R.D. Allen, The contractile basis of amoeboid movement. I. The chemical control of motility in isolated cytoplasm. J. Cell Biol. **59**(2 Pt 1), 378–394 (1973)
41. J.S. Condeelis, D.L. Taylor, The contractile basis of amoeboid movement. V. The control of gelation, solation, and contraction in extracts from Dictyostelium discoideum. J. Cell Biol. **74**(3), 901–927 (1977)
42. D.L. Taylor, The contractile basis of amoeboid movement. IV. The viscoelasticity and contractility of amoeba cytoplasm in vivo. Exp. Cell Res. **105**(2), 413–426 (1977)
43. D.L. Taylor, J.S. Condeelis, J.A. Rhodes, The contractile basis of amoeboid movement III. Structure and dynamics of motile extracts and membrane fragments from Dictyostelium discoideum and Amoeba proteus. Prog. Clin. Biol. Res. **17**, 581–603 (1977)
44. L.W. Janson, D.L. Taylor, In vitro models of tail contraction and cytoplasmic streaming in amoeboid cells. J. Cell Biol. **123**(2), 345–356 (1993)
45. S.W. Oh, K.W. Jeon, Characterization of myosin heavy chain and its gene in Amoeba proteus. J. Eukaryot. Microbiol. **45**(6), 600–605 (1998)
46. H. Miyoshi, Y. Kagawa, Y. Tsuchiya, Chaotic behavior in the locomotion of Amoeba proteus. Protoplasma **216**(1–2), 66–70 (2001)
47. M. Dominik, W. Klopocka, P. Pomorski, E. Kocik, M.J. Redowicz, Characterization of Amoeba proteus myosin VI immunoanalog. Cell Motil. Cytoskeleton **61**(3), 172–188 (2005)
48. R.D. Allen, Biophysical aspects of pseudopodia, in *The Biology of Amoeba*, ed. by K.W. Jeon (Academic, New York, 1973)
49. E.J. McDowell, A.K. Ellerbee, M.A. Choma, B.E. Applegate, J.A. Izatt, Spectral domain phase microscopy for local measurements of cytoskeletal rheology in single cells. (2006 in revision)
50. F.J. Alenghat, B. Fabry, K.Y. Tsai, W.H. Goldmann, D.E. Ingber, Analysis of cell mechanics in single vinculin-deficient cells using a magnetic tweezer. Biochem. Biophys. Res. Commun. **27**, 93–99 (2000)
51. A.R. Bausch, F. Ziemann, A.A. Boulbitch, K. Jacobson, E. Sackmann, Local measurements of viscoelastic parameters of adherent cell surfaces by magnetic bead microrheometry. Biophys. J. **75**, 2038–2049 (1998)
52. M. Keller, J. Schilling, E. Sackmann, Oscillatory magnetic bead rheometer for complex fluid microrheometry. Rev. Sci. Instrum. **72**, 3626–3634 (2001)
53. F. Ziemann, J. Radler, E. Sackmann, Local measurements of viscoelastic moduli of entangled actin networks using an oscillating magnetic bead micro-rheometer. Biophys. J. **66**, 2210–2216 (1994)

Doppler Optical Coherence Tomography

41

Zhongping Chen and Jun Zhang

Keywords
Blood flow • Doppler • Doppler OCT • Microcirculation • Ocular flow • Ophthalmology

41.1 Introduction

Optical coherence tomography (OCT) is a recently developed imaging modality based on coherence-domain optical technology [1–4]. OCT uses coherence gating of backscattered light for tomographic imaging of tissue structure. Variations in tissue scattering due to inhomogeneities in the optical index of refraction provide imaging contrast. However, in many instances and especially during early stages of disease, the change in tissue scattering properties between normal and diseased tissue is small and difficult to measure. One of the great challenges for extending clinical applications of OCT is to find more contrast mechanisms that can provide physiological information in addition to morphological structure. A number of extensions of OCT capabilities for functional imaging of tissue physiology have been developed. Doppler OCT, also named optical Doppler tomography (ODT), combines the Doppler principle with OCT to obtain high-resolution tomographic images of tissue structure and blood flow simultaneously [5–13]. Spectroscopic OCT combines spectroscopic analysis with

Z. Chen (✉)
Department of Biomedical Engineering, Beckman Laser Institute, University of California Irvine, Irvine, CA, USA

The Edwards Life Sciences Center for Advanced Cardiovascular Technology, Beckman Laser Institute, Irvine, CA, USA
e-mail: z2chen@uci.edu

J. Zhang
Department of Biomedical Engineering, The Beckman Laser Institute, University of California Irvine, Irvine, CA, USA

© Springer International Publishing Switzerland 2015

W. Drexler, J.G. Fujimoto (eds.), *Optical Coherence Tomography*,
DOI 10.1007/978-3-319-06419-2_42

OCT to obtain depth-resolved tissue absorption spectra [14, 15]. Polarization-sensitive OCT (PS-OCT) combines polarization-sensitive detection with OCT to determine tissue birefringence [16–20]. Second harmonic optical coherence tomography combines second harmonic generation with coherence gating to obtain images with molecular contrast [21]. These functional extensions of OCT provide clinically important information on tissue physiology, such as tissue blood perfusion, oxygen saturation, hemodynamics, and structural remodeling. Each provides several potential clinical applications, such as vasoactive drug screening, tissue viability and burn depth determination, tumor angiogenesis studies and cancer diagnosis, bleeding ulcer management, and ocular pathology evaluation [10, 11, 19, 22–24]. This chapter reviews the principle and clinical applications of Doppler OCT.

Noninvasive techniques for imaging in vivo blood flow are of great value for biomedical research and clinical diagnostics [25] where many diseases have a vascular etiology or component. In dermatology, for example, the superficial dermal plexus alone is particularly affected by the presence of disease (e.g., psoriasis, eczema, scleroderma), malformation (e.g., port-wine stain, hemangioma, telangiectasia), or trauma (e.g., irritation, wound, burn). In these situations, it would be most advantageous to the clinician if blood flow and structural features could be isolated and probed at user-specified discrete spatial locations in either the superficial or deep dermis. In ophthalmology, many ophthalmic diseases may involve disturbances in ocular blood flow, including diabetic retinopathy, low tension glaucoma, anterior ischemic optic neuritis, and macular degeneration. For example, in diabetic retinopathy, retinal blood flow is reduced and the normal autoregulatory capacity is deficient. Ocular hemodynamics is altered in patients with glaucoma, and severe loss of visual function has been associated with reduced macular blood flow. Simultaneous imaging of tissue structure and blood flow could provide critical information for early diagnosis of ocular diseases. Finally, three-dimensional mapping of microcirculation may also provide important information for the diagnosis and management of cancers.

Doppler OCT combines the Doppler principle with OCT to obtain high-resolution tomographic images of static and moving constituents simultaneously in highly scattering biological tissues [5–7]. The first use of coherence gating to measure localized flow velocity was reported in 1991 where the one-dimensional velocity profile of the flow of particles in a duct was measured [26]. In 1997, the first two-dimensional in vivo Doppler OCT imaging was reported using the spectrogram method [5–7]. The spectrogram method uses a short time fast Fourier transformation (STFFT) or wavelet transformation to determine the power spectrum of the measured fringe signal [5–8, 10, 11]. Although spectrogram methods allow simultaneous imaging of in vivo tissue structure and flow velocity, the velocity sensitivity is limited for high-speed imaging. It was not until 2000 when phase-resolved D-OCT (PR-D-OCT) was developed that Doppler OCT was applied for imaging vasculature in clinical studies [12, 22, 27]. Phase-resolved D-OCT uses the phase change between sequential A-line scans for velocity image reconstruction [12, 27–29]. Phase-resolved D-OCT decouples spatial resolution and velocity sensitivity in flow images and increases imaging speed by more than two orders of magnitude without compromising spatial resolution and velocity sensitivity [12, 28].

The significant increase in scanning speed and velocity sensitivity makes it possible to image in vivo tissue microcirculation in human skin [12, 22, 28]. A real-time PR-D-OCT system that uses polarization optics to perform Hilbert transformation was demonstrated [29]. A number of real-time, PR-D-OCT systems using hardware and software implementations of a high-speed processor have also been reported [30, 31]. Phase-resolved D-OCT was first demonstrated with time domain OCT systems [12, 22, 27]. Recently, the development of Fourier-domain OCT (FD-OCT) has significantly increased imaging speed and sensitivity [32–34]. Combination of FD-OCT with the phase-resolved method has been demonstrated by a number of groups [35–39]. Because the dynamic range of the phase-resolved Doppler OCT depends on the speed of the line scans, Fourier-domain Doppler OCT has an advantage over the time-domain method in terms of imaging speed and velocity dynamic range.

One of the limitations in using the Doppler shift to study blood flow is that the Doppler shift is only sensitive to the flow velocity parallel to the probing beam. However, in many biological cases where flow direction is not known, Doppler shift measurement alone is not enough to fully quantify the flow. Furthermore, there are many clinical applications, such as ocular blood flow, where vessels are in the plane perpendicular to the probing beam. A method to measure transverse flow velocity using the bandwidth (standard deviation) of the Doppler spectrum was reported in 2002 [13]. The advantage of this technique is that a single measurement of the Doppler spectrum will provide both transverse and longitudinal flow velocities [22, 27, 28, 40–43].

Recently, several groups have successfully extended a number of similar methods for mapping blood vessel networks. Ren et al. demonstrated a power Doppler angiography method by using a band-pass-filtered intensity image for imaging the moving scatterer in tissue [44]. Barton et al. proposed a method based on the speckle of conventional amplitude optical coherence tomography images [45]. Mariampillai et al. used speckle variance in a small 3D volume to image blood vessels [46]. The logarithmic intensity variance and differential logarithmic intensity variance for mapping vasculatures were also demonstrated [47]. Yasuno et al. used the intensity threshold binarization-based method for retinal and choroidal blood vessel imaging [48–50]. Jonathan et al. used a two-dimensional correlation map based on OCT intensity images for blood vessel extraction [51]. Jia et al. developed a split-spectrum amplitude-decorrelation angiography method [52]. Wang et al. proposed a method called optical microangiography to separate the static and moving signals with a modified Hilbert transform that remove low frequency static signals [53–55]. Liu et al. have demonstrated an intensity-based method that used an algorithm derived from a modified Doppler variance algorithm [43].

Owing to its exceptionally high spatial resolution and velocity sensitivity, Doppler OCT has a number of applications in biomedical research and clinical medicine. Several clinical applications of Doppler OCT have been demonstrated in our laboratory, such as screening vasoactive drugs, monitoring changes in image tissue morphology and hemodynamics following pharmacological intervention and photodynamic therapy, evaluating the efficacy of laser treatment in port wine stain patients, assessing the depth of burn wounds, and mapping cortical hemodynamics for brain

research [10–12, 22, 27, 28, 40, 41, 56, 57]. In addition, applications of Doppler OCT in ophthalmology [35, 36, 40, 43, 54, 56, 58–62] and in the gastrointestinal tract [63, 64] were demonstrated. Furthermore, the high resolution and high sensitivity of Fourier-domain D-OCT has enabled this technique to become a powerful tool for imaging and quantifying vascular hemodynamics for brain research and tumor angiogenesis studies [41, 65–67]. Recently, optical coherence elastography (OCE) that uses phase-resolved D-OCT to evaluate elastic properties of tissue was reported [68]. Phase-resolved D-OCT has also been extended to other applications where nm resolution of the phase-resolved method is required, for example, photothermal imaging [69] and extraction of photoacoustic signal [70].

41.2 Principles of Doppler OCT

Doppler OCT combines the Doppler principle with OCT to obtain high-resolution tomographic images of static and moving constituents in high scattering media. When light backscattered from a moving particle interferes with the reference beam, a Doppler frequency shift f_D occurs in the interference fringe:

$$f_D = \frac{1}{2\pi}(\mathbf{k}_s - \mathbf{k}_i) \bullet \mathbf{v}, \tag{41.1}$$

where $\mathbf{k}_i$ and $\mathbf{k}_s$ are wave vectors of incoming and scattered light, respectively, and $\mathbf{v}$ is the velocity vector of the moving particle (Fig. 41.1). Since Doppler OCT measures the backscattered light, assuming the angle between flow and sampling beam is θ, the Doppler shift equation is simplified to

$$f_D = \frac{2V \cos\theta}{\lambda_0}, \tag{41.2}$$

where λ_0 is the vacuum center wavelength of the light source.

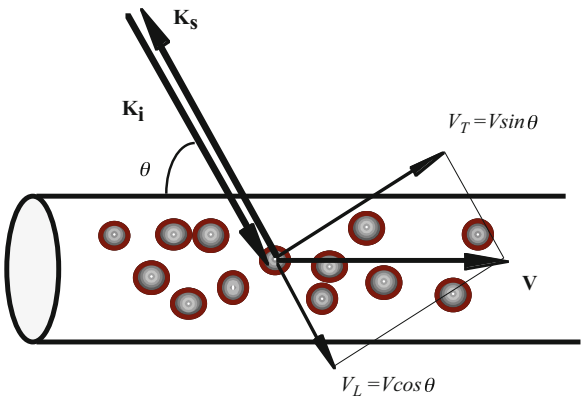

Fig. 41.1 Schematic of flow direction and probe beam angle

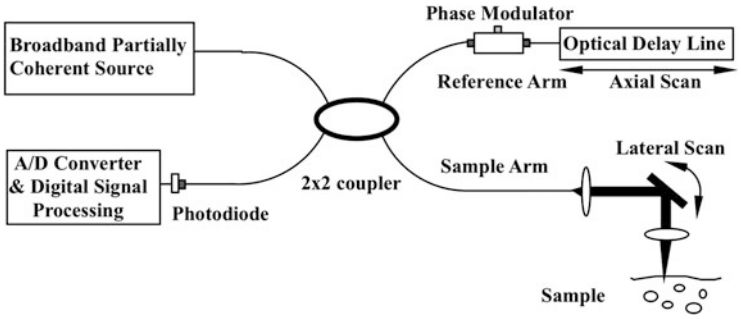

Fig. 41.2 Schematic of OCT system consisting of a fiber-based Michelson interferometer with a partially coherent light source

The optical system of Doppler OCT is similar to that of OCT. The primary difference is in signal processing. Figure 41.2 illustrates a Doppler OCT instrument that uses a fiber-optic Michelson interferometer with a broadband light as a source. Light from a broadband partially coherent source is coupled into a fiber interferometer by a 2×2 fiber coupler and then split equally into reference and sample arms of the interferometer. Light backscattered from the turbid sample is coupled back into the fiber and forms interference fringes with the light reflected from the reference arm. A rapid-scanning optical delay line is used for group delay and axial scanning. Because this delay line can decouple the group delay from the phase delay, an electro-optical phase modulator is introduced to produce a stable carrier frequency. The interference fringe intensity signal is amplified, band pass filtered, and digitized with a high-speed analog-to-digital converter. The signal processing is carried out at the same time as data is transferred to the computer, and real-time display can be accomplished by use of a digital signal processing board.

To understand the signal processing of Doppler OCT, let us look at the fringe signal due to the moving particles. If we denote $U(t)$ as a complex-valued analytic signal of a stochastic process representing the field amplitude emitted by a low coherent light source and $\overline{U}(v)$ as the corresponding spectral amplitude at optical frequency v, the amplitude of a partially coherent source light coupled into the interferometer at time t is written as a harmonic superposition

$$U(t) = \int_0^\infty \overline{U}(v) e^{2\pi i v t} dv. \tag{41.3}$$

Because the stochastic process of a partially coherent light source is stationary, the cross-spectral density of $\overline{U}(v)$ satisfies

$$\left\langle \overline{U}^*(v) \overline{U}(v') \right\rangle = S_o(v) \delta(v - v'), \tag{41.4}$$

where $S_o(v)$ is the source power spectral density and $\delta(v - v')$ is the Dirac delta function. Assuming that light couples equally into the reference arm and sample

arm with spectral amplitude of $\overline{U}_o(\nu)$, the light coupled back to the detector from the reference, $\overline{U}_r(\nu)$, and sample, $\overline{U}_s(\nu)$, are

$$\overline{U}_r(\nu) = e^{2\pi i\nu(2L_r+L_d)/c}K_r(\nu)e^{i\alpha_r(\nu)}\overline{U}_o(\nu) \tag{41.5}$$

and

$$\overline{U}_s(\nu) = e^{2\pi i\nu(2L_s+L_d)/c}K_s(\nu)e^{i\alpha_s(\nu)}\overline{U}_o(\nu), \tag{41.6}$$

where L_r and L_s are the optical pathlengths from the beam splitter to the reference mirror and sample, respectively; L_d is the optical pathlength from the beam splitter to the detector; and $K_r(\nu)e^{i\alpha r(\nu)}$ and $K_s(\nu)e^{i\alpha s(\nu)}$ are the amplitude reflection coefficients of light backscattered from the reference mirror and turbid sample, respectively.

The total power detected at the interferometer output is given by a time-average of the squared light amplitude

$$P_d(\tau) = \left\langle |U_s(t) + U_r(t+\tau)|^2 \right\rangle, \tag{41.7}$$

where τ is the time delay between light traveled in the sample and reference arms. Combining harmonic expansions for $U_s(t)$ and $U_r(t)$ and applying Eq. 41.4 when calculating the time-average, total power detected is a sum of three terms representing reference I_r, sample I_s, and the interference fringe intensity $\Gamma_{ODT}(\tau)$,

$$P_d(\tau) = \int_0^\infty (P_r(\nu) + P_s(\nu) + P_{ODT}(\nu))d\nu = I_r + I_s + \Gamma_{ODT}(\tau), \tag{41.8}$$

with

$$P_r(\nu) = S_o(\nu)|K_r(\nu)|^2, \tag{41.9}$$

$$P_s(\nu) = S_o(\nu)|K_s(\nu)|^2, \tag{41.10}$$

$$P_{ODT}(\nu) = 2S_o(\nu)K_r(\nu)K_s(\nu)\cos\left[2\pi\nu(\Delta_d/c + \tau) + \alpha_s(\nu) - \alpha_r(\nu)\right], \tag{41.11}$$

$$I_r = \int_0^\infty P_r(\nu)d\nu, \tag{41.12}$$

$$I_s = \int_0^\infty P_s(\nu)d\nu, \tag{41.13}$$

and

$$\Gamma_{ODT}(\tau) = \int_0^\infty P_{ODT}(v)dv. \tag{41.14}$$

When there is a moving particle, light scattered from a moving particle is equivalent to a moving phase front; therefore, Δ_d in Eq. 41.11 can be written as

$$\Delta_d = \Delta + 2\overline{n}V_z t, \tag{41.15}$$

where Δ is the optical pathlength difference between light in the sample and reference arms, V_z is the velocity of a moving particle parallel to the probe beam, and $\overline{n}$ is the refractive index of flow media.

To simplify the computation, we assume α_s and α_r are constants over the source spectrum and can be neglected. The spectral domain fringe signal, $P_{ODT}(v)$, is simplified to

$$P_{ODT}(v) = 2S_o(v)K_r(v)K_s(v)\cos\left[2\pi v((\Delta + 2\overline{n}V_z t)/c + \tau)\right]. \tag{41.16}$$

The corresponding time domain signal, $\Gamma_{ODT}(\tau)$, is given by

$$\Gamma_{ODT}(\tau) = 2\int_0^\infty S_o(v)K_r(v)K_s(v)\cos\left[2\pi v((\Delta + 2\overline{n}V_z t)/c + \tau)\right]dv. \tag{41.17}$$

A comparison of Eqs. 41.16 and 41.17 shows that there is a Fourier transformation relation between spectral domain and time domain signals. Consequently, there are two methods to acquire the Doppler OCT signal: the time-domain method and the Fourier-domain method.

In the time-domain method, a delay line is incorporated in the reference arm to generate a delay. A spectrogram analysis or phase-resolved algorithm is then used to determine the Doppler frequency shift. In the Fourier-domain method, the reference mirror is fixed, and there is no depth scan (τ = constant). The Fourier-domain fringe signal, $P_{ODT}(v)$, is obtained either by a spectrometer at the detection arm or by a frequency sweeping light source. The time domain signal, $\Gamma_{ODT}(\tau)$, is determined from the Fourier-domain signal by a Fourier transformation.

41.2.1 Phase-Resolved Doppler OCT Method

The first two-dimensional in vivo Doppler OCT imaging was reported using the spectrogram method [6, 7]. Researchers used the spectrogram method based on either short time fast Fourier transformation (STFFT) or wavelet transformation to determine the power spectrum of the measured fringe signal [5–7, 11, 71]. Although spectrogram methods allow simultaneous imaging of in vivo tissue structure and

flow velocity, the velocity sensitivity is limited for high-speed imaging. When STFFT or wavelet transformation is used to calculate flow velocity, the resolution is determined by the window size of the Fourier transformation for each pixel. The minimum detectable Doppler frequency shift, f_D, varies inversely with the STFFT window size. Because pixel acquisition time is proportional to the STFFT window size, the image frame rate is limited by velocity resolution. Furthermore, spatial resolution is also proportional to the STFFT window size. Therefore, a large STFFT window size increases velocity resolution while decreasing imaging speed and spatial resolution. This coupling between velocity sensitivity, spatial resolution, and imaging speed prevents the spectrogram method from achieving simultaneously both high imaging speed and high velocity sensitivity which are essential for measuring flow in small blood vessels where flow velocity is low.

Phase-resolved Doppler OCT overcomes the compromise between velocity sensitivity and imaging speed by using the phase change between sequential scans to construct flow velocity images [12]. The phase information of the fringe signal can be determined from the complex analytical signal $\widetilde{\Gamma}(t)$, which is determined through analytic continuation of the measured interference fringe function, $\Gamma(t)$, using a Hilbert transformation [10]:

$$\widetilde{\Gamma}(t) = \Gamma(t) + \frac{i}{\pi} P \int_{-\infty}^{\infty} \frac{\Gamma(\tau)}{\tau - t} d\tau = A(t) e^{i\phi(t)}, \tag{41.18}$$

where P denotes the Cauchy principle value, i is the complex number, and $A(t)$ and $\phi(t)$ are amplitude and phase term of $\widetilde{\Gamma}(t)$, respectively. Because the interference signal $\Gamma(t)$ is quasi-monochromatic, the complex analytical signal can be determined by

$$\widetilde{\Gamma}(t) = 2 \int_0^{+\infty} \int_0^{+\tau} \Gamma(t') \exp(-2\pi i v t') dt' \exp(2\pi i v t) dv, \tag{41.19}$$

where τ is the time duration of the fringe signal in each axial scan.

The Doppler frequency shift f_n at n'th pixel in the axial direction is determined from the average phase shift between sequential A-scans. This can be accomplished by calculating the phase change of sequential scans from the individual analytical fringe signal:

$$f_n = \frac{\Delta\phi}{2\pi T} = \frac{1}{2\pi T} \sum_{m=(n-1)M}^{nM} \sum_{j=1}^{N} \left[\tan^{-1}\left(\frac{\mathrm{Im}\widetilde{\Gamma}_{j+1}(t_m)}{\mathrm{Re}\widetilde{\Gamma}_{j+1}(t_m)} \right) - \tan^{-1}\left(\frac{\mathrm{Im}\widetilde{\Gamma}_{j}(t_m)}{\mathrm{Re}\widetilde{\Gamma}_{j}(t_m)} \right) \right]. \tag{41.20}$$

Alternatively, the phase change can also be calculated by the cross-correlation method:

$$f_n = \frac{1}{2\pi T}\tan^{-1}\left(\frac{\mathrm{Im}\left[\sum_{m=(n-1)M}^{nM}\sum_{j=1}^{N}\widetilde{\Gamma}_j(t_m)\cdot\widetilde{\Gamma}^*_{j+1}(t_m)\right]}{\mathrm{Re}\left[\sum_{m=(n-1)M}^{nM}\sum_{j=1}^{N}\widetilde{\Gamma}_j(t_m)\cdot\widetilde{\Gamma}^*_{j+1}(t_m)\right]}\right), \tag{41.21}$$

where $\widetilde{\Gamma}_j(t_m)$ and $\widetilde{\Gamma}^*_j(t_m)$ are the complex signals at axial time t_m corresponding to the j'th A-scan and its respective conjugate, $\widetilde{\Gamma}_{j+1}(t_m)$ and $\widetilde{\Gamma}^*_{j+1}(t_m)$ are the complex signals at axial time t_m corresponding to the next A-scan and its respective conjugate, M is an even number that denotes the window size in the axial direction for each pixel, N is the number of sequential scans used to calculate the cross correlation, and T is the time duration between A-scans. Because T is much longer than the pixel time window within each scan used in the spectrogram method, high velocity sensitivity can be achieved.

In addition to the local velocity information, the standard deviation of the Doppler spectrum gives the variance of local velocity and can be determined from the measured analytical fringe signal:

$$\sigma^2 = \frac{\int_{-\infty}^{\infty}(f-f_D)^2P(f)df}{\int_{-\infty}^{\infty}P(f)df} = \frac{1}{(2\pi T)^2}\left(1-\frac{\left|\sum_{m=(n-1)M}^{nM}\sum_{j=1}^{N}\widetilde{\Gamma}_j(t_m)\cdot\widetilde{\Gamma}^*_{j+1}(t_m)\right|}{\frac{1}{2}\sum_{m=(n-1)M}^{nM}\sum_{j=1}^{N}\left[\widetilde{\Gamma}_j(t_m)\cdot\widetilde{\Gamma}^*_j(t_m)+\widetilde{\Gamma}_{j+1}(t_m)\cdot\widetilde{\Gamma}^*_{j+1}(t_m)\right]}\right), \tag{41.22}$$

where $P(f)$ is the Doppler power spectrum and f_D is the centroid value of the Doppler frequency shift. The σ value depends on the flow velocity distribution. Variations in flow velocity will broaden the Doppler frequency spectrum and result in a large σ value. Thus, the Doppler variance image can be an indicator of flow variations and can be used to study flow turbulences. In addition, Doppler variance imaging can also be used to map microvasculature because it is less sensitive to the random direction and the pulsatile nature of blood flow in small vessels [22, 28]. Finally, standard deviation imaging can also be used to determine the transverse flow velocity [13].

Phase-resolved Doppler OCT decouples spatial resolution and velocity sensitivity in flow images and increases imaging speed by more than two orders of magnitude without compromising spatial resolution and velocity sensitivity. In addition, because two sequential A-line scans are compared at the same location, speckle modulations in the fringe signals cancel each other and, therefore, will not affect the phase difference calculation. Consequently, the phase-resolved method reduces the speckle noise in the velocity image.

41.2.2 Fourier-Domain Phase-Resolved Doppler OCT Method

Compared with conventional time domain OCT, which is based on a scanning optical delay line, Fourier-domain OCT measures interference fringes in the spectral domain to reconstruct a tomographic image. Modulation of the interference fringe intensity in the spectral domain is used to determine the locations of all scattering objects along the beam propagation direction by a Fourier transformation. Two methods have been developed to employ the Fourier-domain technique: a spectrometer based system that uses a high-speed line-scan camera [72, 73] and a swept laser source-based system that uses a single detector [74–78]. Fourier-domain phase-resolved Doppler OCT combines Fourier-domain OCT with the phase-resolved method and has the advantage of high-sensitivity, fast imaging speed, and large velocity dynamic range [35–39].

A schematic diagram of a swept source-based Fourier-domain Doppler OCT system is shown in Fig. 41.3. The output light from the swept light source is split into reference and sample arms by a 1 × 2 coupler. Two circulators were used in both reference and sample arms to redirect the back-reflected light to a 2 × 2 fiber coupler (50/50 split ratio) for balanced detection. In the reference arm, an EO phase modulator was used to generate a stable carrier frequency for elimination of the Fourier transform generated mirror image and low frequency autocorrelation noise [76].

The complex analytical depth-encoded signal was converted from the detected time fringe signal by the digital approach shown in the following block diagram [38] (Fig. 41.4), where FFT denotes the fast Fourier transform, FFT^{-1} denotes the inverse fast Fourier transform, and H(f) is the Heaviside function given by

$$H(f) = \begin{cases} 0 & f < 0 \\ 1 & f \geq 0 \end{cases}. \tag{41.23}$$

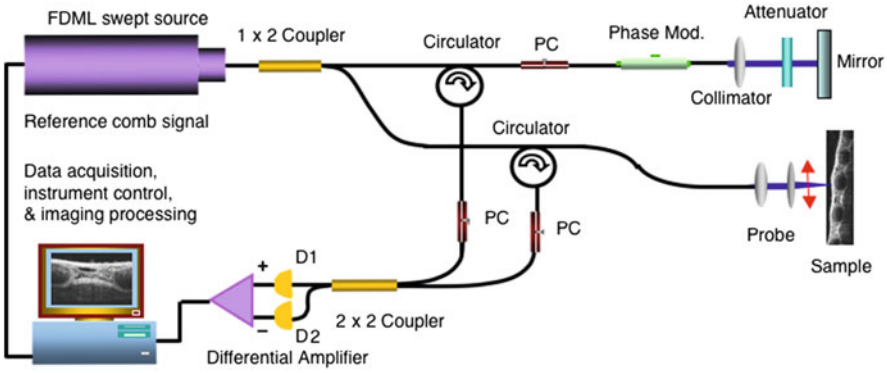

Fig. 41.3 Schematic of a swept source-based Fourier-domain Doppler OCT system

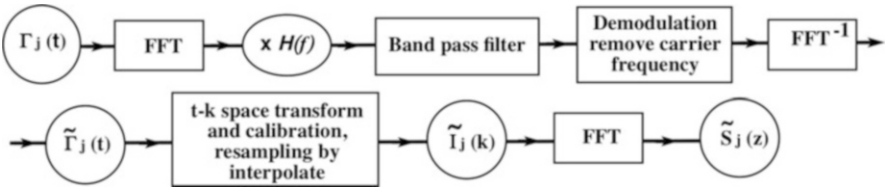

Fig. 41.4 Signal processing diagram for processing Doppler signals in swept source-based Fourier-domain Doppler OCT (From [38])

The time fringe signal $\Gamma(t)$ acquired with wavelength scanning is firstly transformed from time to frequency space by FFT. Multiplication of $H(f)$ selects the positive term of the Fourier transformed signal. The signal is then band-pass filtered to remove the low frequency and DC noises. The subsequent demodulation step shifts the center frequency of the filtered interference term from the carrier frequency to zero. The frequency fringe signal is then converted back to time space by inverse FFT. To cancel the distortion originating from nonlinearities in the wave number function $k(t)$, the data are numerically remapped from uniform time to uniform wave number space based on the function of $k(t)$, which is determined by the spectra calibration process provided by calibration comb signals generated from a fiber Fabry-Perot interferometer. Dispersion calibration is also performed at this step by adding a wave number-dependent phase term. The last FFT performed in k space retrieves the complex depth-encoded fringe signal $\tilde{S}(z) = A(z)e^{i\phi(z)}$, which contains both the amplitude $A(z)$ and phase $\phi(z)$ terms.

Using the phase-resolved method, the Doppler frequency shift and Doppler variance can be determined from the depth-encoded complex fringe signal $\tilde{S}(z)$ [38]:

$$f_n = \frac{1}{2\pi T}\tan^{-1}\left(\frac{\mathrm{Im}\left[\sum_{m=(n-1)M}^{nM}\sum_{j=1}^{N}\tilde{S}_j(z_m)\cdot\tilde{S}_{j+1}^{*}(z_m)\right]}{\mathrm{Re}\left[\sum_{m=(n-1)M}^{nM}\sum_{j=1}^{N}\tilde{S}_j(z_m)\cdot\tilde{S}_{j+1}^{*}(z_m)\right]}\right) \tag{41.24}$$

and

$$\sigma^2 = \frac{1}{(2\pi T)^2}\left(1 - \frac{\left|\sum_{m=(n-1)M}^{nM}\sum_{j=1}^{N}\tilde{S}_j(z_m)\cdot\tilde{S}_{j+1}^{*}(z_m)\right|}{\frac{1}{2}\sum_{m=(n-1)M}^{nM}\sum_{j=1}^{N}\left[\tilde{S}_j(z_m)\cdot\tilde{S}_j^{*}(z_m) + \tilde{S}_{j+1}(z_m)\cdot\tilde{S}_{j+1}^{*}(z_m)\right]}\right). \tag{41.25}$$

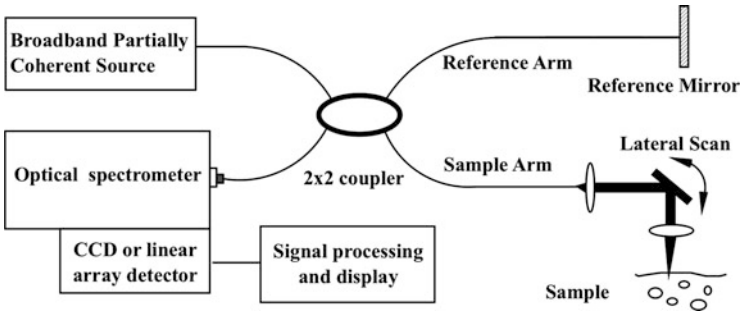

Fig. 41.5 Schematic of a spectrometer based Fourier-domain Doppler OCT system

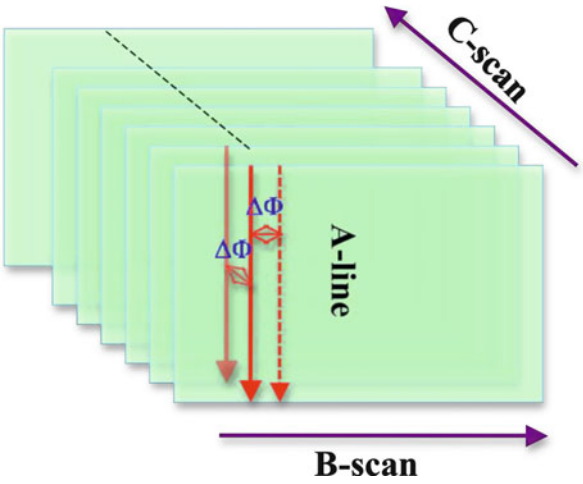

Fig. 41.6 Schematic signal processing diagram for the phase-resolved D-OCT system

A spectrometer based Fourier-domain Doppler OCT is shown in Fig. 41.5 [37]. The signal from the Michelson interferometer is directly coupled to a spectrometer that records the spectral fringe pattern, $P_{Doppler\ OCT}(\nu)$. The temporal interference fringe can be calculated by a Fourier transformation of the spectral fringe pattern (Eq. 41.17). The Doppler shift and variance can then be determined using phase-resolved Doppler OCT algorithms (Eqs. 41.21 and 41.22).

Phase-resolved D-OCT using cross-correlation between A-lines decouple velocity sensitivity, spatial resolution, and imaging speed. The development of FD-OCT greatly increased imaging speed, which enables cross-correlation not only between sequential A-lines in B-scan but also sequential A-lines in C-scan (Fig. 41.6) [12, 79]. For sequential A-lines in B-scan, T is the inter-A-line time. For sequential A-lines in C-scan, T is the inter-frame time. Therefore, a large velocity dynamical range can be achieved since the T can be increased by several orders of magnitude, which makes it possible to image and quantify flow in the capillary level [79].

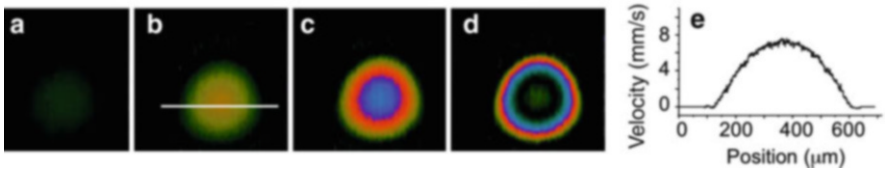

Fig. 41.7 PR-D-OCT images of a flow phantom which is pumped at different speeds: (**a**) 0.1 μl/min, (**b**) 0.3 μl/min, (**c**) 0.6 μl/min, and (**d**) 1.1 μl/min. (**e**) Velocity profile along a horizontal cross section passing through the center of the tube in (**b**)

Figure 41.7 shows the PR-D-OCT images of a flow phantom pumped at different speeds using a swept source-based FD-OCT system with an A-line rate of 50 kHz. Figure 41.7a–d are PR-D-OCT images of the flow phantom pumped at, respectively, 0.1 μl/min, 0.3 μl/min, 0.6 μl/min, and 1.1 μl/min. It should be noted that the phase is wrapped in Fig. 41.7c, d, which can be unwrapped [27]. The increase of Doppler frequency shift with the increase of pumping speed can be clearly seen from the PR-D-OCT images. Figure 41.7e shows the velocity profile along a horizontal cross section passing through the center of the tube in Fig. 41.7b.

41.2.3 Doppler Variance, Transverse Flow Velocity, and Doppler Angle Determination

One of the limitations of using Doppler shift to determine the flow is that the technique is only sensitive to longitudinal flow velocity (Fig. 41.1). If one knows the flow direction, Doppler shift measurement can fully quantify the flow. However, in many biological cases where flow direction is not known, Doppler shift measurement alone is not enough to fully quantify the flow. Furthermore, there are many clinical cases, such as ocular blood flow, where vessels are in the plane perpendicular to the probe beam. When flow direction is perpendicular to the probe beam, the Doppler shift is not sensitive to transverse flow V_T. Therefore, a method to measure transverse flow velocity is essential.

Doppler variance can be used to determine the transverse flow. The technique is based on the fact that Doppler OCT imaging uses a relatively large numeric aperture lens in the sample arm. The beam from different sides of the edges will produce different Doppler shifts, f_1 and f_2, as indicated in Fig. 41.8. Consequently, the Doppler spectra will be broadened by the transverse flow. If the incident beam has a Gaussian spectral profile and contributions from Brownian motion and other sources that are independent of the macroscopic flow velocity are included, a linear relation between standard deviation of the Doppler spectra and transverse flow velocity, $V_T = V\sin\theta$, can be written as [13]

$$\sigma = \frac{\pi V \sin\theta NA_{eff}}{8\lambda} + b, \tag{41.26}$$

where b is a constant and NA_{eff} is the effective numeric aperture.

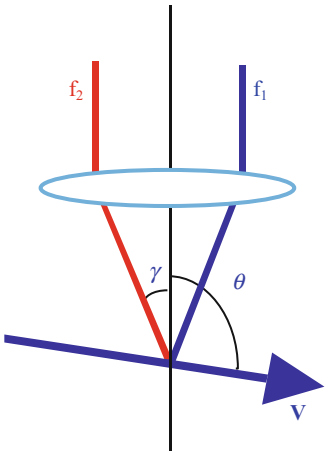

Fig. 41.8 Effect of numerical aperture and transverse flow velocity on Doppler bandwidth

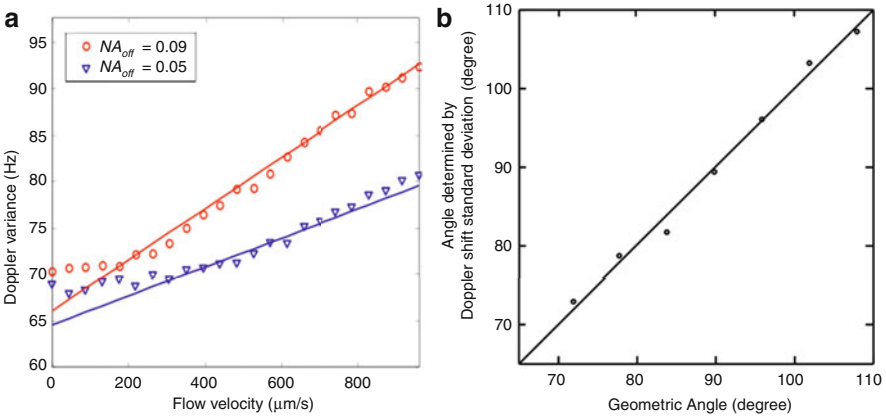

Fig. 41.9 (**a**) Doppler variance as a function of flow velocity for two different numeric apertures (From [13]). (**b**) Flow velocity angles measured by phase-resolved Doppler OCT as a function of geometric angles. The solid line shows a linear fit (From [82])

The Doppler variance can be determined from the measured analytical fringe signal using Eq. 41.22. We have measured the σ value as a function of the transverse flow velocity (Fig. 41.9a) [13]. As predicted, the Doppler bandwidth is a linear function of transverse flow velocity above a certain threshold level. The effective numerical aperture of the optical objective in the sample arm determines the slope of this dependence. This result indicates that standard deviation can be used to determine the transverse flow velocity. Since both longitudinal and transverse flow velocities (V_L and V_T) can be measured by the Doppler shift and standard deviation, respectively, flow direction can be determined from a single measurement of the Doppler fringe signal [80–82]. Figure 41.9b shows the comparison of angle determined by phase-resolved Doppler OCT and the geometric angle [82].

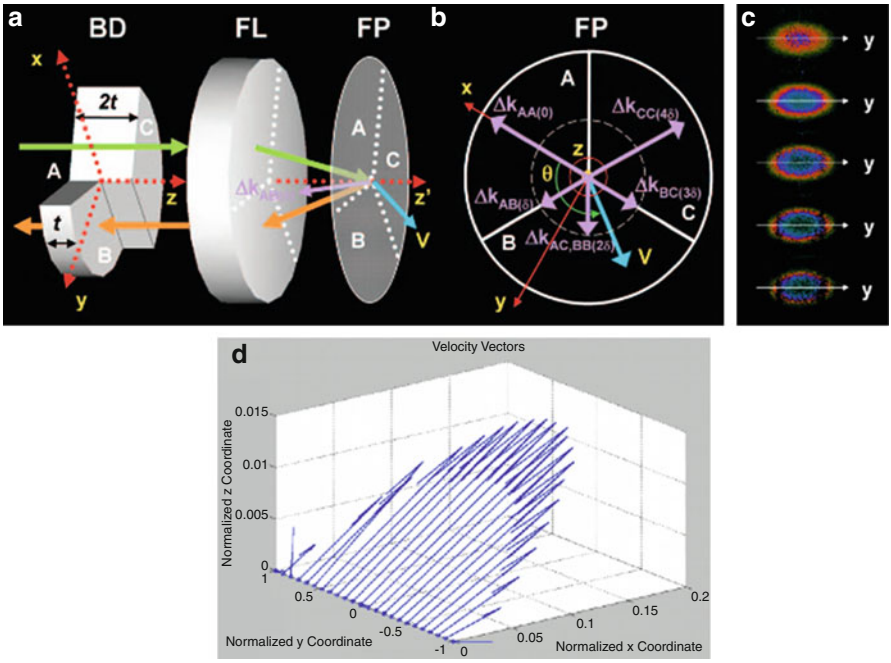

Fig. 41.10 The beam divider (**a**) that generates five independent $\Delta\mathbf{k}$ with different pathlength delays (**b**). Velocity vector field measured by the multi-angle Doppler OCT along the diameter of the microtube. Velocity vectors shown in (**d**) were determined from the five Doppler images in (**c**) (From [83])

We have demonstrated that an arbitrary velocity vector can be determined from a single measurement by generating multiple $\Delta\mathbf{k}$ vectors with different pathlength delays simultaneously [83]. A beam divider which has three parts with different thicknesses of 0, t, and 2 t was inserted in the sample arm as shown in Fig. 41.10a. After passing through the focusing lens, the divider produced five independent $\Delta\mathbf{k}$s and divided a probe beam to have five independent view points and path length delays (Fig. 41.10b). Figure 41.10c shows Doppler images of a scattering fluid flowing through a microtube from a single scan. The five Doppler images correspond to five different $\Delta\mathbf{k}$ with different pathlengths. The velocity vector field can be quantified by solving a three-dimensional minimization problem from five Doppler images. The results are shown in Fig. 41.10d and have good agreement with the actual values [83].

In addition to the phase-resolved Doppler variance (PR-DV) method, methods that are dependent on the intensity or amplitude fluctuation can also be used for mapping vascular networks [43, 45, 46, 51, 84]. Recently, we have developed an intensity-based Doppler variance (IB-DV) method that uses an algorithm derived from a modified phase-resolved Doppler variance algorithm [43]:

$$\sigma_{IB}{}^2 = \frac{1}{(2\pi T)^2}\left(1 - \frac{\sum_{m=(n-1)M}^{nM}\sum_{j=1}^{N}\left|\tilde{S}_j(z_m)\cdot\tilde{S}_{j+1}^*(z_m)\right|}{\frac{1}{2}\sum_{m=(n-1)M}^{nM}\sum_{j=1}^{N}\left[\tilde{S}_j(z_m)\cdot\tilde{S}_j^*(z_m)+\tilde{S}_{j+1}(z_m)\cdot\tilde{S}_{j+1}^*(z_m)\right]}\right). \quad (41.27)$$

IB-DV is not sensitive to gradient phase changes and can be used without bulk motion correction for in vivo imaging [43]. The IB-DV method can minimize the artifact from the phase instability [43].

41.2.4 Qualitative and Quantitative Microvascular Imaging and Optical Microangiogram

PR-D-OCT and Doppler variance (DV) imaging provide complementary information. While PR-D-OCT is most sensitive when the flow direction is along the probing beam, PR-DV and IB-DV can be used to measure the flow when the flow direction is near perpendicular to the probing beam. The sensitivity and dynamic range of these methods are limited by the time interval T between A-lines [79]. Figure 41.11 shows measured PR-DV and IB-DV values as a function of transverse flow speed [79]. At low speed regions up to 100 mm/s, the curve shows a linear relationship between the flow speed and the variance values. At higher flow speed regions, the curve shows saturation of the variance value.

There are many applications where mapping of microvascular network is essential for diagnosis and management of diseases that have a vascular etiology. Although PR-D-OCT provides high-sensitivity measurement of flow velocity, the technology is very sensitive to phase stability of the OCT system, the motion artifact, and orientation of the vasculature. In applications where absolute flow velocity is less important than vessel distribution, Doppler variance has the advantage of being less sensitive to the pulsatile nature of the blood flow and the complex variation of incident angle and provides an excellent method for optical angiogram

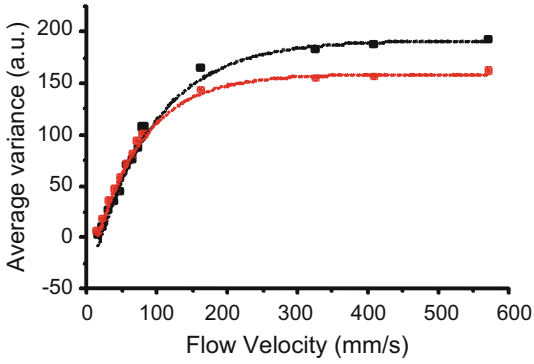

Fig. 41.11 The dependence of IB-DV and PR-DV values on the flow rate with a 50 kHz swept source-based FD-OCT (From [79])

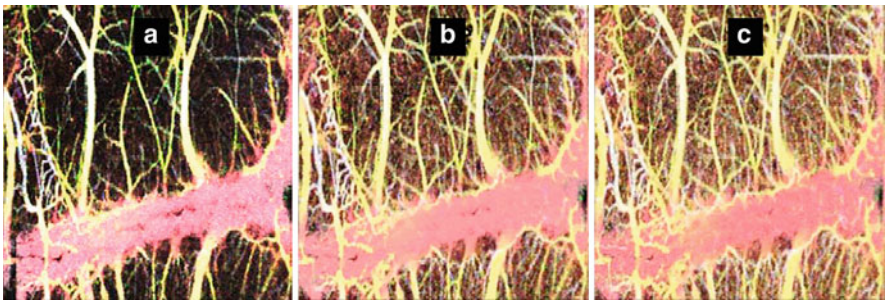

Fig. 41.12 Optical angiogram of mouse brain with intact skull. (**a**) PR-D-OCT image, (**b**) PR-DV image, and (**c**) IB-DV image. The depth information is color coded in these images. Scale bar: 1 mm (From [79])

[22, 27, 28, 40–43]. Figure 41.12 shows cerebrovascular circulations in mice obtained by a swept source OCT system. PR-D-OCT, PR-DV, and IB-DV images are shown in Fig. 41.12a–c, respectively. Both of the variance methods are able to detect the capillary vessels with high sensitivity and high contrast. PR-D-OCT is also sensitive for capillary vessel detection. However, the contrast of the PR-DV and IB-DV images is better than that of an PR-D-OCT image, especially in regions with smaller blood vessels.

41.3 Applications of Doppler OCT

Due to its exceptionally high spatial resolution and velocity sensitivity, several clinical applications of Doppler OCT have been demonstrated, including screening vasoactive drugs, monitoring changes in image tissue morphology and hemodynamics following pharmacological intervention and photodynamic therapy, evaluating the efficacy of laser treatment in port wine stain (PWS) patients, assessing the depth of burn wounds, imaging tumor microenvironment, mapping cortical hemodynamics for brain research, imaging ocular blood flow, and mapping blood flow in gastrointestinal tracts. Furthermore, applications of phase-resolved Doppler OCT have been extended to other fields, such as optical coherence elastography (OCE) that uses the phase-resolved method to map the mechanical property of the tissue and optical coherence phase microscopy that extracts high-resolution phase information to retrieve nanometer or sub-nanometer scale displacement variation of a sample.

41.3.1 Drug Screening

Noninvasive drug screening is essential for the rapid development of new drugs. Doppler OCT can be used for in vivo blood flow monitoring after pharmacological intervention. The effects of nitroglycerin (NTG) on the CAM artery and vein have

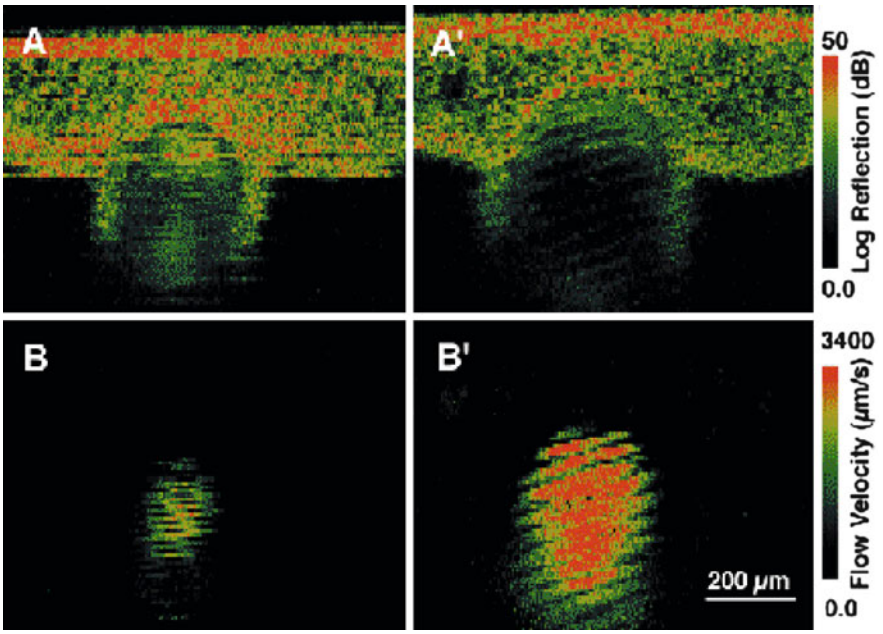

Fig. 41.13 Effects of topical NTG on blood flows in CAM artery (I). Doppler structural and velocity images, respectively, before (**a**, **b**) and after (**a′**, **b′**) drug application (From [11])

been investigated [11]. Changes in arterial vascular structure and blood flow dynamics are shown in Fig. 41.13, where Figs. 41.13a, b are structural and velocity images, respectively, before and Fig. 41.13a′, b′ are after topical application of NTG. The arterial wall can be clearly identified and dilation of the vessel after nitroglycerin application is observed in the structural images. Although velocity images appear discontinuous due to arterial pulsation (Fig. 41.13b, b′), enlargement of the cross-sectional area of blood flow is evident. Peak blood flow velocity at the center of the vessel increased from 3,000 to 4,000 μm/s after NTG application.

41.3.2 In Vivo Blood Flow Monitoring During Photodynamic Therapy (PDT)

Doppler OCT can be used to monitor changes in in vivo blood flow during PDT [11, 85, 86]. Changes in in vivo blood flow in rodent mesentery after benzoporphyrin derivative (BPD) injection and laser irradiation were imaged (Fig. 41.14) [11]. Doppler OCT structural and velocity images, respectively, were recorded before laser irradiation (Fig. 41.14a, a′), 16 (Fig. 41.14b, b′) and 71 min after laser irradiation (Fig. 41.14c, c′). The results indicate that the artery goes into vasospasm after laser exposures and compensatory vasodilatation occurs in response to PDT-induced tissue hypoxia.

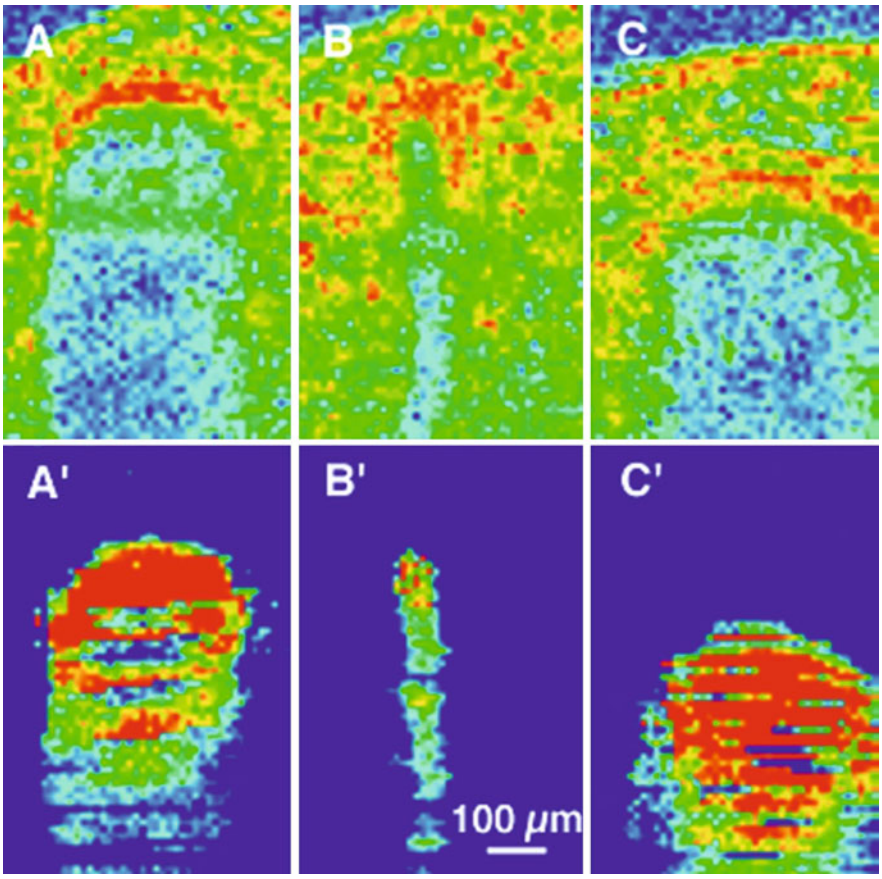

Fig. 41.14 Vessel structure and blood flow dynamics in rodent mesenteric artery after PDT. Doppler OCT structural and velocity images, respectively, prior to laser irradiation (**a**, **a′**), 16 min (**b**, **b′**), and 71 min (**c**, **c′**) after laser irradiation (From [11])

The pharmacokinetics of the PDT drug can also be studied with Doppler OCT. Doppler OCT images were taken at different intervals between photosensitizer injection and laser irradiation [11]. Rodents were given a PDT sensitizing drug 20 min, 4 h, and 7 h before mesenteric laser irradiation, and the changes in arterial diameter and flow were calculated from Doppler OCT images (Fig. 41.15). The results indicate that the effects of PDT are strongly dependent on the time interval between drug injection and light irradiation. For a drug-light time interval of 20 min, the arterial diameter (Fig. 41.15a) decreased by 80 % after light irradiation followed by a rebound with vasodilative overshoot. Mesenteric arterial flow (Fig. 41.15b) mirrored changes in diameter with an initial reduction with a subsequent rebound. These effects were significantly reduced with longer postinjection times due to progressive diffusion of the photosensitizer out of the vasculature.

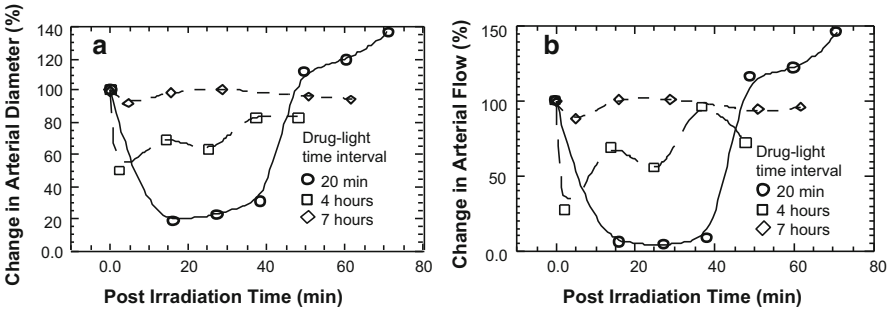

Fig. 41.15 Changes in relative arterial diameter (**a**) and flow rate (**b**) in rodent mesentery following PDT as a function of post-irradiation time (From [11])

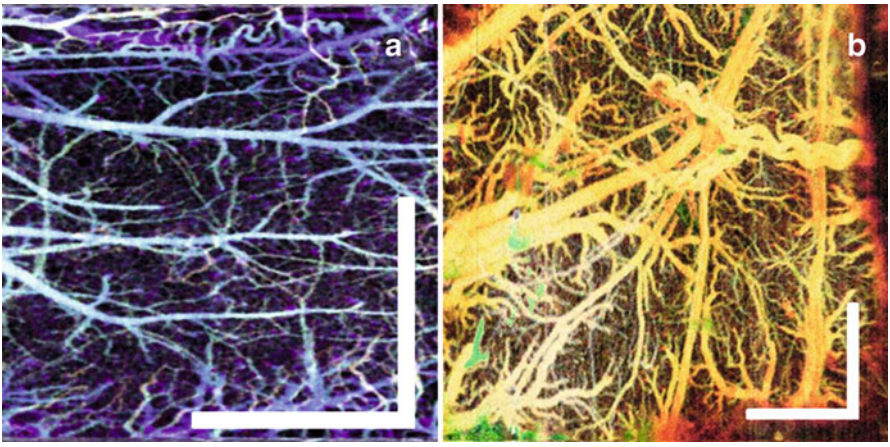

Fig. 41.16 Doppler OCT imaging of microvasculature. (**a**) Microvasculature of mouse cerebral cortex. (**b**) Microvasculature of rat cerebral cortex. Scale bar: 1 mm

41.3.3 Imaging Brain Hemodynamics

Doppler OCT has also been used to image brain hemodynamics in the cerebral cortex of the brain. The first in vivo imaging of blood flow in the rat cerebral cortex was reported in 2000 [10]. Recent development of Doppler OCT with an interframe scheme has greatly improved the velocity sensitivity, which makes it possible to map microvasculature of the brain cortex [48, 65, 87–89]. Figure 41.16a shows the *en-face* maximum intensity projection (MIP) microvasculature of mouse cerebral cortex with intact skull. Figure 41.16b shows the *en-face* MIP microvasculature of rat cerebral cortex with thinned skull. Doppler OCT shows great promise in brain research for imaging the entire depth of the cortex. Doppler OCT can be used to measure stimulus-induced changes in blood flow [10] and to evaluate and monitor brain ischemia and trauma [41, 90].

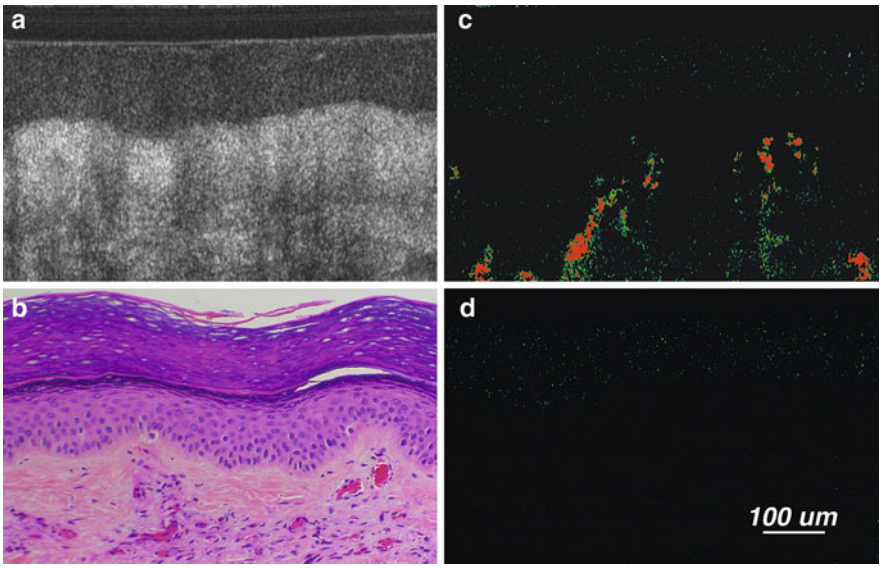

Fig. 41.17 Doppler OCT images taken in situ from PWS human skin. (**a**) Structural image, (**b**) histological section, (**c**) image before laser treatment, and (**d**): image after laser treatment (From [22])

41.3.4 In Vivo Monitoring of the Efficacy of Laser Treatment of Port Wine Stains

The first clinical application of Doppler OCT was the in vivo monitoring of the efficacy of laser treatment of PWS [12, 22, 28]. PWS is a congenital, progressive vascular malformation of capillaries in the dermis of human skin that occurs in approximately 0.7 % of children. Histopathological studies of PWS show an abnormal plexus of layers of dilated blood vessels located 150–750 μm below the skin surface in the dermis, having diameters varying on an individual patient basis, and even from site to site on the same patient, over a range of 10–150 μm. The pulsed dye laser can selectively coagulate PWS vessels by inducing microthrombus formation within the targeted blood vessels. However, currently there is no technique to evaluate efficacy of therapy immediately after laser treatment. Phase-resolved Doppler OCT provides a means to evaluate the efficacy of laser therapy in real time.

Figure 41.17 shows Doppler OCT structural and flow velocity images of a patient with PWS before and after laser treatment, respectively. The vessel locations from the Doppler OCT measurement and histology agree very well. Furthermore, the destruction of the vessel by laser can be identified since no flow appears on the Doppler flow image after laser treatment. This result indicates that Doppler OCT can provide a fast, semiquantitative evaluation of the efficacy of PWS laser therapy in situ and in real time.

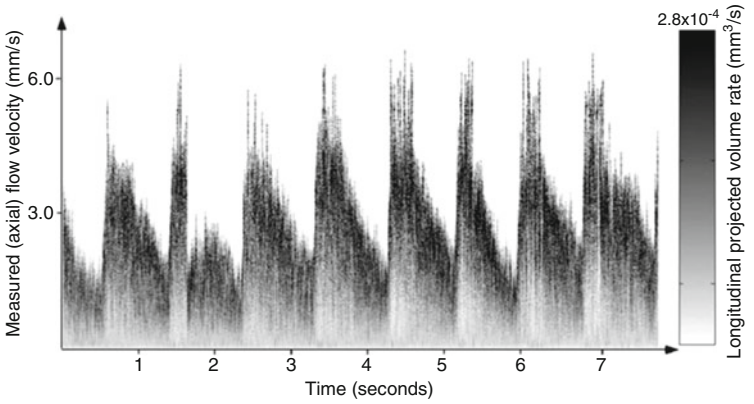

Fig. 41.18 Spectral Doppler wave forms that show the change of axial velocity and flow volume rate within a time span of 7.9 s. The right grayscale bar is used to represent the volume-rate contribution for a given velocity bin (From [56])

41.3.5 In Vivo Imaging and Quantification of Ocular Blood Flow

Doppler OCT has also been applied to imaging and quantifying the pulsatile nature of human retinal blood flow, detecting blood flow within the choroid and retinal capillaries, and providing information on the cardiac cycle [35, 36, 40, 43, 54, 56, 58–62]. Accurate knowledge of retinal blood flow dynamics is important in not only the treatment of but also understanding the pathophysiology of many diseases, such as glaucoma, diabetic retinopathy, and age-related macular degeneration [35, 36, 40, 43, 54, 56, 58–62].

The development of high-speed Fourier-domain Doppler OCT allows fast scanning of a single blood vessel multiple times over a cardiac cycle. Spectral Doppler waveforms can be obtained by performing spectral analysis of the time sequences of Doppler images [56]. In this method, repeated Doppler OCT scans across a few selected vessels were performed to get Doppler flow maps of a certain time period, which provides an accurate estimation of 2D flow dynamics across the vessels. Spectral Doppler analysis of continuous Doppler images demonstrates how the velocity components and longitudinally projected flow volume rate change over time for scatters within the imaging volume using spectral Doppler waveforms. Figure 41.18 shows spectral Doppler wave forms for a retinal blood vessel [56]. Various velocity envelope curves can be derived from spectral Doppler waveforms and used to extract the corresponding pulsatility index, resistance index (RI), and several other indices that can provide interpretable Doppler-angle-independent information needed to quantify the pulsatile nature of blood flow [56].

In addition to quantitative imaging, another important application of Doppler OCT is optical angiogram, which maps the human retina and choroid microvascular network. In contrast to traditional angiography methods, such as fluorescein angiography (FA) and indocyanine green angiography (ICGA), Doppler OCT is a label-free technique and has three-dimensional imaging capability.

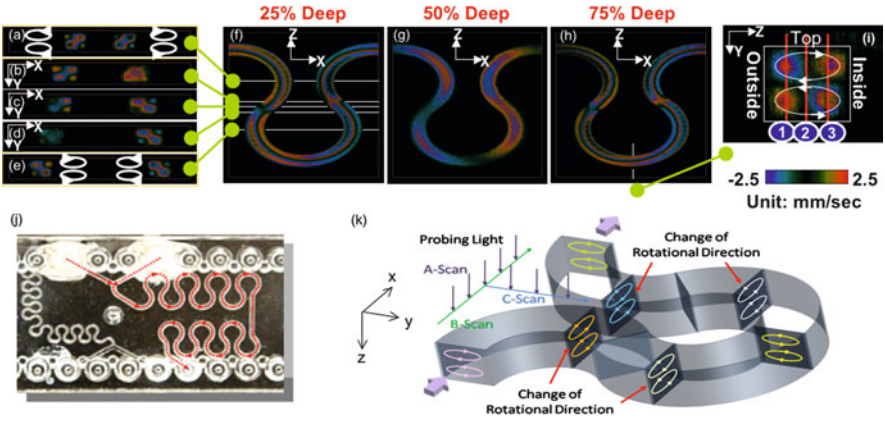

Fig. 41.19 Three-dimensional D-OCT images of secondary flow along the out-of-plane velocity (y direction). The out-of-plane velocity fields sectioned by x-y planes (**a**–**e**), by x-z planes (**f**–**h**), and by the y-z plane (i). The velocity field shows a pair of counterrotating vortices (**a**–**e**). Since the curvature is alternating, the rotational direction of the vortices is also alternating (**a**–**e**). Alternating flow direction of the secondary flow at different depths in the X-Z plane can be clearly visualized (**f**–**h**) (From [91]

By extracting the *en-face* images from the 3D image volume, FA- or ICGA-like angiography images can be obtained. In addition, the projection images can be obtained by summing up the *en-face* images at different depths [35, 36, 40, 43, 54, 56, 58, 61, 62].

41.3.6 Imaging and Quantifying the Flow Characteristics in a Micro-channel

Doppler OCT can provide cross-sectional imaging of channel geometry and flow velocity within a microfluidic channel with a spatial resolution on the order of a micrometer and a velocity sensitivity of 1 μm/s. Doppler OCT has been used to quantify the secondary flow, which plays a critical role in mixing in micro-channels [91]. A Y branch device of a meandering micro-channel with a square cross section is shown in Fig. 41.19. Aqueous suspension of polystyrene beads with a diameter of 0.2 μm and concentration of 20.5 mg/cm^3 was injected into both inlets of the device. The device was imaged with a spectrometer-based Doppler OCT system. The probe beam of the Doppler OCT was adjusted to be approximately perpendicular to the plane of the micro-channel (x-z plane) so that only the secondary flow along the y-direction would contribute to the Doppler signal [91]. The y-component of the secondary flow velocity $V_y(x,y,z)$ was imaged and quantified with Doppler OCT. Counterrotating vortices and alternating flow direction of the secondary flow at different depths in the x-z plane can be clearly visualized. This result clearly demonstrates that D-OCT can be used to image and quantify secondary flow.

41.3.7 Phase Imaging with Spectral Domain Optical Coherence Phase Microscopy

High-sensitivity phase measurement to detect nm or sub-nm scale displacement is an important technique for application on subcellular dynamics. The recent application of spectral domain phase microscopy, which is an extension of phase-resolved Doppler OCT, shows its capability of excellent phase stability, high sensitivity, and imaging speed for quantitative phase measurement [92–95].

In phase measurement with spectral domain phase microscopy, the phase information is extracted from the complex depth-resolved profile, which is obtained by Fourier transformation of the spectral fringes generated by the optical path difference (OPD) between the reference and sample arms. Since the phase oscillates 2π radians at every shift of half a wavelength of the OPD, an ultrahigh accurate measurement of the OPD can be achieved with high-sensitivity phase measurement of the fringes.

One limitation of spectral domain phase microscopy for phase measurement is the limited dynamic range of OPD detection due to the 2π ambiguity. Phase unwrapping algorithms are needed to measure OPD longer than half a wavelength. A spectral domain phase microscopy technique that is capable of high dynamic range quantitative phase-contrast imaging by overcoming the limitation of 2π ambiguity was recently reported [93]. Unlike conventional spectral domain phase microscopy, this technique retrieves phase information in the spectral domain instead of the depth domain by Hilbert transformation of the detected fringe signal to convert the discontinuous phase change in the depth domain to a gradually varying phase shift in the spectral domain. The spectral fringe was transformed from wave number to depth space by fast Fourier transformation. The process of narrow band pass filtering was adopted to select the positive term of the complex depth function and reject the noise from DC term and multiple reflections. With the phase retrieval approach performed in wave-number space, the spectral domain phase microscopy system could measure a large range of displacements, ranging from the minimum measurable displacement of 34 pm to the maximum measurable displacement of 2.0 mm, which is the imaging range of the system and determined by the spectral resolution of the spectrometer [93].

Figure 41.20a shows phase imaging of a resolution target with a spectrometer-based phase microscopy system [93]. The image covers a sample area of 1,000 × 1,000 μm. To demonstrate the performance of the system in cell imaging, living human neonatal dermal keratinocyte cells were used as samples. Figure 41.20b shows two-dimensional quantitative phase imaging of the cells. The image covering a sample area of 150 × 150 μm was acquired in 0.3 s [93].

We have used quantitative phase microscopy to image and quantify dynamic changes of phase during the process of laser microsurgery of cells in real time, which enables absolute quantification of localized alteration/damage to transparent phase objects, such as the cell membrane or intracellular structures, being exposed to the laser microbeam [96]. An example of quantitative phase images of red blood cell before and after laser microsurgery is shown in Fig. 41.21.

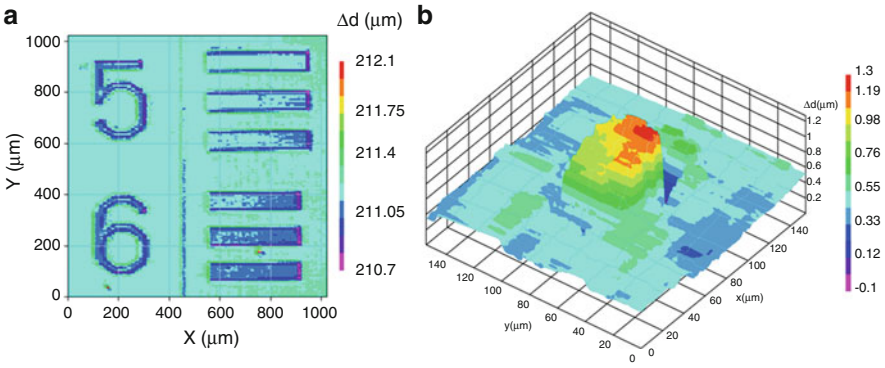

Fig. 41.20 OCT quantitative phase microscopic images: (**a**) resolution target and (**b**) human neonatal dermal keratinocyte cells (From [93])

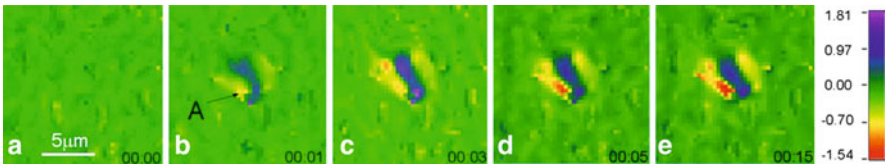

Fig. 41.21 Time-lapse (in seconds) phase images showing dynamic changes of phase variation during laser microsurgery of RBC. (**a**) Before laser microbeam irradiation; (**b**) 1 s, (**c**) 3 s, (**d**) 5 s, and (**e**) 15 s after laser microbeam irradiation (From [96])

41.3.8 Phase-Resolved Doppler OCT to Evaluate Elastic Properties of Tissue

Many diseases involve change in the biomechanical properties of tissue, and there is a close correlation between tissue elasticity and pathology. Elastography, which enable imaging and quantifying biomechanical properties such as elasticity and viscosity of soft tissue, has become a powerful technique to distinguish healthy and diseased tissues, particularly in tumor and cardiovascular research. Optical coherence elastography (OCE) uses OCT to map the mechanical property of the tissue. In OCE, an external force (or load) is usually applied to the sample to excite tissues for a certain deformation which is then quantified with OCT. The first demonstration of OCE utilized a tissue compressor consisting of a piezoelectric actuator with a circular glass cover slip glued to its ring-shaped head [97]. Phase-resolved Doppler OCT was used as an approach of elastography to characterize tissue mechanical properties such as Young's modulus and shear modulus by measuring the phase shift between sequential A-scans [98, 99]. The applications of OCE have been demonstrated in ophthalmology, dermatology, cardiology, and oncology [100]. However, adoption of these methods to in vivo real-time imaging is limited by low cycling frequency of external forces.

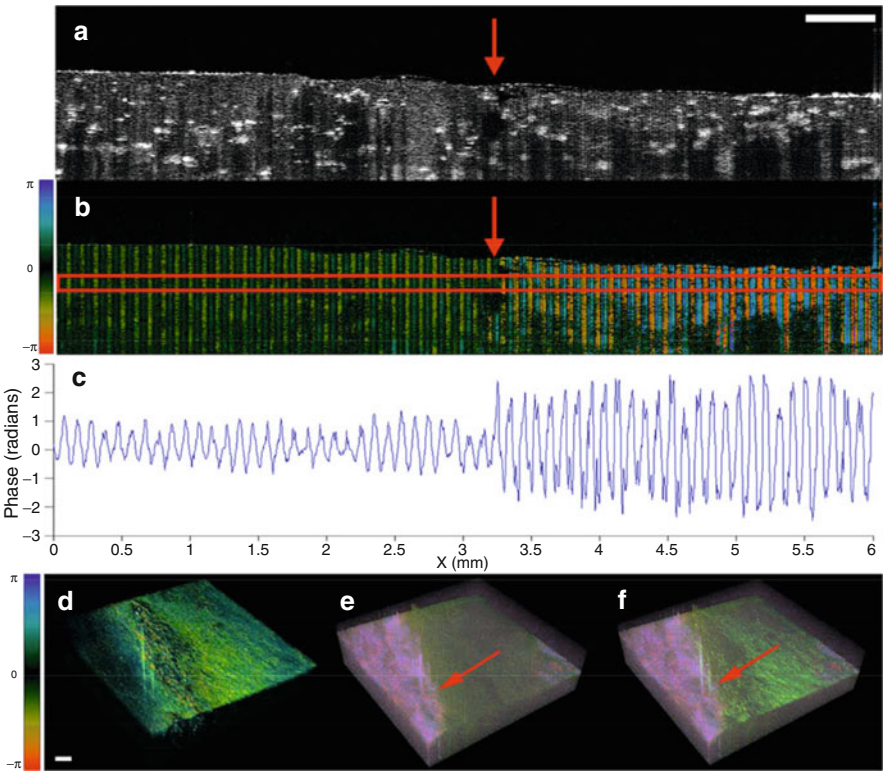

Fig. 41.22 ARF-OCE images of a tissue phantom consisting of a thin film made of agarose with two different concentrations (7 % and 3.5 %) side by side. (**a**) OCT intensity image, (**b**) ARF-OCE image under 4 MHz with 500 Hz AM modulation ARF excitation, (**c**) phase amplitude averaged over the depth of tissue, (**d**) 3D OCT imaging, (**e**) 3D ARF-OCE image, and (**f**) fused 3D OCT and PR-ARF-OCE image. *Red arrow* indicates the boundary between two sides of 7 % and 3.5 % agarose film. Scale bars: 1 mm (From [68])

Recently, we developed dynamic phase-resolved acoustic radiation force optical coherence elastography (ARF-OCE), which is capable of high-speed, high-spatial-resolution, point-by-point elastogram mapping in an axial direction [68]. This method utilizes chirped acoustic radiation force to produce excitation along the sample's axial direction, and phase-resolved Doppler OCT is used to measure the vibration of the sample. Results from a tissue phantom consisting of a thin film made of agarose with two different concentrations side by side are shown in Fig. 41.22. The concentration of agarose is 7 % and 3.5 % for each side, respectively. The OCT image of the phantom is shown in Fig. 41.22a, from which the two sides of agarose film with different concentrations cannot be clearly distinguished. The phase change map of the OCE image for the agarose film under ARF from an ultrasound transducer, driven at RF frequency of 4 MHz and AM modulation of 500 Hz, is shown in Fig. 41.22b. The phase change amplitude averaged over depth

is shown in Fig. 41.22c. The boundary (red arrow) between the two sides of the phantom with different concentrations can be clearly visualized in Fig. 41.22b, c. Figure 41.22d-f shows 3D OCT, ARF-OCE, and fused OCT/ARF-OCE imaging of the tissue phantom. The 3D ARF-OCE image (Fig. 41.22e) clearly delineates the two materials with different stiffness. The ratio of Young's moduli between the 7 % and 3.5 % agarose material within the two sides of the phantom measured by phase shifts is consistent with the value measured using a standard compression test. This result clearly shows that ARF-OCE combines high-speed excitation of ARF with high sensitive displacement measurement of the phase-resolved method and has great potential to quantitatively characterize tissue mechanical properties and thereby delineate diseased tissue from normal tissue.

41.4 Summary

Doppler OCT is a rapidly developing imaging technology with many potential applications. The development of the phase-resolved method and Fourier-domain method has enabled high-speed and high-sensitivity Doppler imaging in 3D. New developments in all components of an OCT system can be integrated to a Doppler OCT system, including new light sources for high resolution and high speed, new scanning endoscopic probes, and new processing algorithms. Integration of Doppler OCT with other functional OCT, such as polarization-sensitive OCT, spectroscopic OCT, and second harmonic OCT, can greatly enhance the potential applications of this technology. Given its noninvasive nature and exceptionally high spatial resolution and velocity sensitivity, functional OCT that can simultaneously provide tissue structure, blood perfusion, birefringence, and other physiological information has great potential for basic biomedical research and clinical medicine.

Acknowledgments We would like to thank many of our colleagues who have contributed to the Doppler OCT project at the Beckman Laser Institute and Department of Biomedical Engineering at UCI, particularly the students and postdoctoral fellows. Dr. Chen also wants to acknowledge grants support from the National Institutes of Health (R01EB-10090, R01EY-021529, R01HL-105215, R01HL-125084, and P41EB-015890), Air Force Office of Scientific Research (FA9550-04-0101), and the Beckman Laser Institute Endowment.

References

1. D. Huang, E.A. Swanson, C.P. Lin, J.S. Schuman, W.G. Stinson, W. Chang, M.R. Hee, T. Flotte, K. Gregory, C.A. Puliafito, J.G. Fujimoto, Optical coherence tomography. Science **254**(5035), 1178–1181 (1991)
2. B.E. Bouma, G.J. Tearney, *Handbook of Optical Coherence Tomography* (Marcel Dekker, New York, 2002)
3. A.F. Fercher, C.K. Hizenberger, Optical coherence tomography, in *Progress in Optics*, ed. by E. Wolf, vol. 44 (Elsevier, North-Holland, 2002), p. 215

4. Z. Chen, Functional optical coherence tomogoraphy, in *Frontiers in Biomedical Engineering*, ed. by N.H.C. Hwang, S.L.-Y. Woo (Kluwer Academic/Plenum, New York, 2003), pp. 345–364
5. Z. Chen, T.E. Milner, D. Dave, J.S. Nelson, Optical Doppler tomographic imaging of fluid flow velocity in highly scattering media. Opt. Lett. **22**, 64–66 (1997)
6. Z. Chen, T.E. Milner, S. Srinivas, X.J. Wang, A. Malekafzali, M.J.C. van Gemert, J.S. Nelson, Noninvasive imaging of in vivo blood flow velocity using optical Doppler tomography. Opt. Lett. **22**, 1119–1121 (1997)
7. J.A. Izatt, M.D. Kulkarni, S. Yazdanfar, J.K. Barton, A.J. Welch, In vivo bidirectional color Doppler flow imaging of picoliter blood volumes using optical coherence tomography. Opt. Lett. **22**, 1439–1441 (1997)
8. M.D. Kulkarni, T.G. van Leeuwen, S. Yazdanfar, J.A. Izatt, Velocity-estimation accuracy and frame-rate limitations in color Doppler optical coherence tomography. Opt. Lett. **23**, 1057–1059 (1998)
9. S. Yazdanfar, M.D. Kulkarni, J.A. Izatt, High resolution imaging of in vivo cardiac dynamics using color Doppler. Opt. Express **1**, 424 (1997)
10. Z. Chen, Y. Zhao, S.M. Srinivas, J.S. Nelson, N. Prakash, R.D. Frostig, Optical Doppler tomography. IEEE J. Sel. Top. Quant. Electron. **5**(4), 1134–1141 (1999)
11. Z. Chen, T.E. Milner, X.J. Wang, S. Srinivas, J.S. Nelson, Optical Doppler tomography: imaging in vivo blood flow dynamics following pharmacological intervention and photodynamic therapy. Photochem. Photobiol. **67**, 56–60 (1998)
12. Y. Zhao, Z. Chen, C. Saxer, S. Xiang, J.F. de Boer, J.S. Nelson, Phase-resolved optical coherence tomography and optical Doppler tomography for imaging blood flow in human skin with fast scanning speed and high velocity sensitivity. Opt. Lett. **25**, 114–116 (2000)
13. H. Ren, M.K. Breke, Z. Ding, Y. Zhao, J.S. Nelson, Z. Chen, Imaging and quantifying transverse flow velocity with the Doppler bandwidth in a phase-resolved functional optical coherence tomography. Opt. Lett. **27**, 409–411 (2002)
14. U. Morgner, W. Drexler, X.D. Kartner, C. Piltris, E.P. Ippen, J.G. Fujimoto, Spectroscopic optical coherence tomography. Opt. Lett. **25**, 111–113 (2000)
15. J.M. Schmitt, S.H. Xiang, K.M. Yung, Differential absorption imaging with optical coherence tomography. J. Opt. Soc. Am. **A15**, 2288 (1998)
16. M.R. Hee, D. Huang, E.A. Swanson, J.G. Fujimoto, Polarization-sensitive low-coherence reflectometer for birefringence characterization and ranging. J. Opt. Soc. Amer. B **9**, 903–908 (1992)
17. J.F. de Boer, S.M. Srinivas, A. Malekafzali, Z. Chen, J.S. Nelson, Imaging thermally damaged tissue by polarization sensitive optical coherence tomography. Opt. Express **3**, 212–218 (1998)
18. H. Ren, Z. Ding, Y. Zhao, J. Miao, J.S. Nelson, Z. Chen, Phase-resolved functional optical coherence tomography: simultaneous imaging of *in situ* tissue structure, blood flow velocity, standard deviation, birefringence, and the Stokes vectors in human skin. Opt. Lett. **27**, 1702–1704 (2002)
19. C.E. Saxer, J.F. de Boer, B. Hyle Park, Y. Zhao, Z. Chen, J.S. Nelson, High-speed fiber-based polarization-sensitive optical coherence tomography of in vivo human skin. Opt. Lett. **25**, 1355–1357 (2000)
20. S. Jiao, L.V. Wang, Two-dimensional depth-resolved Mueller matrix of biological tissue measured with double-beam polarization-sensitive optical coherence tomography. Opt. Lett. **27**, 101–103 (2002)
21. Y. Jiang, I. Tomov, Y. Wang, Z. Chen, Second harmonic optical coherence tomgoraphy. Opt. Lett. **29**, 1090–1092 (2004)
22. J.S. Nelson, K.M. Kelly, Y. Zhao, Z. Chen, Imaging blood flow in human port-wine stain in situ and in real time using optical Doppler tomography. Arch. Dermatol. **137**(6), 741–744 (2001)

23. J.F. de Boer, S.M. Srinivas, B.H. Park, T.H. Pham, C. Zhongping, T.E. Milner, J.S. Nelson, Polarization effects in optical coherence tomography of various biological tissues. IEEE J. Sel. Top. Quant. Electron. **5**(4), 1200–1204 (1999)
24. M.G. Ducros, J.F. de Boer, H. Huai-En, L.C. Chao, Z. Chen, J.S. Nelson, T.E. Milner, H.G. Rylander III, Polarization sensitive optical coherence tomography of the rabbit eye. IEEE J. Sel. Top. Quant. Electron. **5**, 1159–1167 (1999)
25. E. Yamada, M. Matsumura, S. Kyo, R. Omoto, Usefulness of a prototype intravascular ultrasound imaging in evaluation of aortic dissection and comparison with angiographic study, transesophageal echocardiography, computed tomography, and magnetic resonance imaging. Am. J. Cardiol. **75**, 161–165 (1995)
26. V. Gusmeroli, M. Martnelli, Distributed laser Doppler velocimeter. Opt. Lett. **16**, 1358–1360 (1991)
27. Y. Zhao, Z. Chen, Z. Ding, H. Ren, J.S. Nelson, Three-dimensional reconstruction of in vivo blood vessels in human skin using phase-resolved optical Doppler tomography. IEEE J. Sel. Top. Quant. Electron. **7**, 931–935 (2001)
28. Y. Zhao, Z. Chen, C. Saxer, Q. Shen, S. Xiang, J.F. de Boer, J.S. Nelson, Doppler standard deviation imaging for clinical monitoring of in vivo human skin blood flow. Opt. Lett. **25**, 1358–1360 (2000)
29. Z. Ding, Y. Zhao, H. Ren, S.J. Nelson, Z. Chen, Real-time phase resolved optical coherence tomography and optical Doppler tomography. Opt. Express **10**, 236–245 (2002)
30. V.X. Yang, M.L. Gordon, A. Mok, Y. Zhao, Z. Chen, R.S.C. Cobbold, B.C. Wilson, I.A. Vitkin, Improved phase-resolved optical Doppler tomography using the Kasai velocity estimator and histogram segmentation. Opt. Commun. **208**, 209–214 (2002)
31. V. Westphal, S. Yazdanfar, A.M. Rollins, J.A. Izatt, Real-time, high velocity-resolution color Doppler optical coherence tomography. Opt. Lett. **27**(1), 34–36 (2002)
32. R. Leitgeb, C.K. Hitzenberger, A.F. Fercher, M. Kulhavy, Performance of fourier domain vs. time domain optical coherence tomography. Opt. Express **11**, 889–894 (2003)
33. J.F. de Boer, B. Cense, B.H. Park, M.C. Pierce, G.J. Tearney, B.E. Bouma, Improved signal-to-noise ratio in spectral-domain compared with time-domain optical coherence tomography. Opt. Lett. **28**, 2067–2069 (2003)
34. M.A. Choma, M.V. Sarunic, C. Yang, J.A. Izatt, Sensitivity advantage of swept source and Fourier domain optical coherence tomography. Opt. Express **11**, 2183–2189 (2003)
35. R.A. Leitgeb, L. Schmetterer, W. Drexler, A.F. Fercher, R.J. Zawadzki, T. Bajraszewski, Real-time assessment of retinal blood flow with ultrafast acquisition by color Doppler Fourier domain optical coherence tomography. Opt. Express **11**, 3116–3121 (2003)
36. B.R. White, M.C. Pierce, N. Nassif, B. Cense, B.H. Park, G.J. Tearney, B.E. Bouma, T.C. Chen, J.F. de Boer, In vivo dynamic human retinal blood flow imaging using ultra-high speed spectral domain optical Doppler tomography. Opt. Express **25**, 3490–3497 (2003)
37. L. Wang, Y. Wang, M. Bachaman, G.P. Li, Z. Chen, Frequency domain Phase-resolved optical Doppler and Doppler variance tomography. Opt. Commun. **242**, 345–347 (2004)
38. J. Zhang, Z. Chen, In vivo blood flow imaging by a swept laser source based Fourier domain optical Doppler tomography. Opt. Express **13**, 7449–7457 (2005)
39. B. Vakoc, S. Yun, J.F. de Boer, G. Tearney, B.E. Bouma, Phase-resolved optical frequency domain imaging. Opt. Express **13**, 5483–5493 (2005)
40. L. Yu, Z. Chen, Doppler variance imaging for three-dimensional retina and choroid angiography. J. Biomed. Opt. **15**(1), 016029 (2010)
41. L. Yu, E. Nguyen, G. Liu, B. Choi, Z. Chen, Spectral Doppler optical coherence tomography imaging of localized ischemic stroke in a mouse model. J. Biomed. Opt. **15**(6), 066006 (2010)
42. G. Liu, M. Rubinstein, A. Saidi, W. Qi, A. Foulad, B. Wong, Z. Chen, Imaging vibrating vocal folds with a high speed 1050 nm swept source OCT and ODT. Opt. Express **19**(12), 11880–11889 (2011)

43. G. Liu, W. Qi, L. Yu, Z. Chen, Real-time bulk-motion-correction free Doppler variance optical coherence tomography for choroidal capillary vasculature imaging. Opt. Express **19**(4), 3657–3666 (2011)
44. H. Ren, Y. Wang, J. S. Nelson and Z. Chen, Power optical Doppler tomography imaging of blood vessel in human skin and M-mode Doppler imaging of blood flow in chick chorioallantoic membrane, Proc. SPIE. (2003, unpublished)
45. J. Barton, S. Areomaki, Flow measurement without phase information in optical coherence tomography. Opt. Express **13**, 5483–5493 (2005)
46. A. Mariampillai, B.A. Standish, E.H. Moriyama, M. Khurana, N.R. Munce, M.K. Leung, J. Jiang, A. Cable, B.C. Wilson, I.A. Vitkin, V.X. Yang, Speckle variance detection of microvasculature using swept-source optical coherence tomography. Opt. Lett. **33**(13), 1530–1532 (2008)
47. Reza Motaghiannezam, S. Fraser, Logarithmic intensity and speckle-based motion contrast methods for human retinal vasculature visualization using swept source optical coherence tomography. Biomed. Opt. Express **3**, 503–521 (2012)
48. S. Makita, Y. Hong, M. Yamanari, T. Yatagai, Y. Yasuno, Optical coherence angiography. Opt. Express **14**(17), 7821–7840 (2006)
49. Y. Hong, S. Makita, M. Yamanari, M. Miura, S. Kim, T. Yatagai, Y. Yasuno, Three-dimensional visualization of choroidal vessels by using standard and ultra-high resolution scattering optical coherence angiography. Opt. Express **15**(12), 7538–7550 (2007)
50. Y. Yasuno, Y. Hong, S. Makita, M. Yamanari, M. Akiba, M. Miura, T. Yatagai, In vivo high-contrast imaging of deep posterior eye by 1-microm swept source optical coherence tomography and scattering optical coherence angiography. Opt. Express **15**(10), 6121–6139 (2007)
51. E. Jonathan, J. Enfield, M.J. Leahy, Correlation mapping method for generating microcirculation morphology from optical coherence tomography (OCT) intensity images. J. Biophotonics **4**(9), 583–587 (2010)
52. Y. Jia, O. Tan, J. Tokayer, B. Potsaid, Y. Wang, J.J. Liu, M.F. Kraus, H. Subhash, J.G. Fujimoto, J. Hornegger, D. Huang, Split-spectrum amplitude-decorrelation angiography with optical coherence tomography. Opt. Express **20**(4), 4710–4725 (2012)
53. L. An, R.K. Wang, In vivo volumetric imaging of vascular perfusion within human retina and choroids with optical micro-angiography. Opt. Express **16**(15), 11438–11452 (2008)
54. R.K. Wang, L. An, P. Francis, D.J. Wilson, Depth-resolved imaging of capillary networks in retina and choroid using ultrahigh sensitive optical microangiography. Opt. Lett. **35**(9), 1467–1469 (2010)
55. R.K. Wang, L. An, S. Saunders, D.J. Wilson, Optical microangiography provides depth-resolved images of directional ocular blood perfusion in posterior eye segment. J. Biomed. Opt. **15**(2), 020502 (2010)
56. B. Rao, L. Yu, H.K. Jiang, L.C. Zacharias, R.M. Kurtz, B.D. Kuppermann, Z. Chen, Imaging pulsatile retinal blood flow in human eye. J. Biomed. Opt. **5**, 040505 (2008)
57. X. Xu, L. Yu, Z. Chen, Effect of erythrocyte aggregation on hematocrit measurement using spectral-domain optical coherence tomography. IEEE Trans. Biomed. Eng. **55**(12), 2753–2758 (2008)
58. S. Yazdanfar, A.M. Rollins, J.A. Izatt, Imaging and velocimetry of the human retinal circulation with color Doppler optical coherence tomography. Opt. Lett. **25**, 1448–1450 (2000)
59. Y. Wang, A. Fawzi, O. Tan, J. Gil-Flamer, D. Huang, Retinal blood flow detection in diabetic patients by Doppler Fourier domain optical coherence tomography. Opt. Express **17**(5), 4061–4073 (2009)
60. Y. Wang, B.A. Bower, J.A. Izatt, O. Tan, D. Huang, In vivo total retinal blood flow measurement by Fourier domain Doppler optical coherence tomography. J. Biomed. Opt. **12**(4), 041215 (2007)
61. R.K. Wang, L. An, Doppler optical micro-angiography for volumetric imaging of vascular perfusion in vivo. Opt. Express **17**(11), 8926–8940 (2009)

62. D.Y. Kim, J. Fingler, J.S. Werner, D.M. Schwartz, S.E. Fraser, R.J. Zawadzki, In vivo volumetric imaging of human retinal circulation with phase-variance optical coherence tomography. Biomed. Opt. Express **2**(6), 1504–1513 (2011)
63. V.X. Yang, M.L. Gordon, S. Tang, N.E. Marcon, G. Gardiner, B. Qi, S. Bisland, E. Seng-Yue, S. Lo, J. Pekar, B.C. Wilson, I.A. Vitkin, High speed, wide velocity dynamic range Doppler optical coherence tomography (part III): in vivo endoscopic imaging of blood flow in the rat and human gastrointestinal tracts. Opt. Express **11**, 2416–2424 (2003)
64. V.X. Yang, S.J. Tang, M.L. Gordon, B. Qi, G. Gardiner, M. Cirocco, P. Kortan, G.B. Haber, G. Kandel, I.A. Vitkin, B.C. Wilson, N.E. Marcon, Endoscopic Doppler optical coherence tomography in the human GI tract: initial experience. Gastrointest. Endosc. **61**, 879–890 (2006)
65. B.J. Vakoc, R.M. Lanning, J.A. Tyrrell, T.P. Padera, L.A. Bartlett, T. Stylianopoulos, L.L. Munn, G.J. Tearney, D. Fukumura, R.K. Jain, B.E. Bouma, Three-dimensional microscopy of the tumor microenvironment in vivo using optical frequency domain imaging. Nat. Med. **15**(10), 1219–1223 (2009)
66. V.J. Srinivasan, S. Sakadzic, I. Gorczynska, S. Ruvinskaya, W. Wu, J.G. Fujimoto, D.A. Boas, Quantitative cerebral blood flow with optical coherence tomography. Opt. Express **18**(3), 2477–2494 (2010)
67. G. Liu, Z. Chen, Optical coherence tomography for brain imaging, in *Optical Methods and Instrumentation in Brain Imaging*, ed. by S.J. Madsen (Springer, New York, 2013), pp. 157–172
68. W. Qi, R. Chen, L. Chou, G. Liu, J. Zhang, Q. Zhou, Z. Chen, Phase-resolved acoustic radiation force optical coherence elastography. J. Biomed. Opt. **17**(11), 110505 (2012)
69. C. Zhou, T.H. Tsai, D.C. Adler, H.C. Lee, D.W. Cohen, A. Mondelblatt, Y. Wang, J.L. Connolly, J.G. Fujimoto, Photothermal optical coherence tomography in ex vivo human breast tissues using gold nanoshells. Opt. Lett. **35**(5), 700–702 (2010)
70. C. Blatter, B. Grajciar, P. Zou, W. Wieser, A.J. Verhoef, R. Huber, R.A. Leitgeb, Intrasweep phase-sensitive optical coherence tomography for noncontact optical photoacoustic imaging. Opt. Lett. **37**(21), 4368–4370 (2012)
71. Z. Chen, J. Zhang, Doppler optical coherence tomography, in *Optical Coherence Tomography: Technology and Applications*, ed. by W. Drexler, J.G. Fujimoto (Springer, Berlin, 2008), pp. 621–649
72. M. Wojtkowski, V.J. Srinivasan, T. Ko, J.G. Fujimoto, A. Kowalczyk, J.S. Duker, Ultrahigh-resolution high speed Fourier domain optical coherence tomography and methods for dispersion compensation. Opt. Express **12**, 2404–2422 (2004)
73. B. Cense, N. Nassif, T.C. Chen, M.C. Pierce, S.H. Yun, B.H. Park, B.E. Bouma, G.J. Tearney, J.F. de Boer, Ultrahigh-resolution high-speed retinal imaging using spectral-domain optical coherence tomgoraphy. Opt. Express **12**, 2435–2447 (2004)
74. S.H. Yun, G.J. Tearney, J.F. de Boer, N. Iftimia, B.E. Bouma, High speed optical frequency domain imaging. Opt. Express **11**, 2593–2563 (2003)
75. S.H. Yun, C. Boudoux, G.J. Tearney, B.E. Bouma, High-speed wavelength-swept semiconductor laser with a polygon-scanner-based wavelength filter. Opt. Lett. **28**, 1981–1983 (2003)
76. J. Zhang, J.S. Nelson, Z. Chen, Removal of mirror image and enhancement of signal to noise ratio in Fourier domain optical coherence tomography using an electro-optical phase modulator. Opt. Lett. **30**, 147–149 (2005)
77. J. Zhang, J.S. Nelson, Z. Chen, Full range polarization-sensitive Fourier domain optical coherence tomography. Opt. Express **12**, 6033–6039 (2004)
78. M.V. Sarunic, M.A. Choma, C. Yang, J.A. Izatt, Instantaneous complex conjugate resolved spectral domain and swept-source OCT using 3×3 fiber couplers. Opt. Express **13**, 957–967 (2005)
79. G. Liu, A.J. Lin, B.J. Tromberg, Z. Chen, A comparison of Doppler optical coherence tomography methods. Biomed. Opt. Express **3**(10), 2669–2680 (2012)

80. D. Piao, L.L. Otis, Q. Zhu, Doppler angle and flow velocity mapping by combine Doppler shift and Doppler bandwidth measurements in optical Doppler tomography. Opt. Lett. **28**, 1120 (2003)
81. S. Proskurin, Y. He, R. Wang, Determination of flow velocity vector based on Doppler shift and spectrum broadening with optical coherence tomography. Opt. Lett. **28**, 1227 (2003)
82. L. Wang, *Development of phase-resolved optical Doppler tomography for imaging and quantifying microflow dynamics and particle size in microfluidic channels*, Ph.D. Thesis, University of California, Irvine, 2004
83. Y.-C. Ahn, W. Jung, Z. Chen, Quantification of a three-dimensional velocity vector using spectral-domain Doppler optical coherence tomography. Opt. Lett. **32**, 1587–1589 (2007)
84. V.J. Srinivasan, J.Y. Jiang, M.A. Yaseen, H. Radhakrishnan, W. Wu, S. Barry, A.E. Cable, D.A. Boas, Rapid volumetric angiography of cortical microvasculature with optical coherence tomography. Opt. Lett. **35**, 43–45 (2010)
85. H. Li, B.A. Standish, A. Mariampillai, N.R. Munce, Y. Mao, S. Chiu, N.E. Marcon, B.C. Wilson, I.A. Vitkin, V.X.D. Yang, Feasibility of interstitial Doppler optical coherence tomography for in vivo detection of microvascular changes during photodynamic therapy. Lasers Surg. Med. **38**, 754–761 (2006)
86. M.C.G. Aalders, M. Triesscheijn, M. Ruevekamp, M. de Bruin, P. Baas, D.J. Faber, F.A. Stewart, Doppler optical coherence tomography to monitor the effect of photodynamic therapy on tissue morphology and perfusion. J. Biomed. Opt. **11**, 044011 (2006)
87. A. Mariampillai, M.K. Leung, M. Jarvi, B.A. Standish, K. Lee, B.C. Wilson, A. Vitkin, V.X. Yang, Optimized speckle variance OCT imaging of microvasculature. Opt. Lett. **35**(8), 1257–1259 (2010)
88. G. Liu, W. Jia, V. Sun, B. Choi, Z. Chen, High-resolution imaging of microvasculature in human skin in-vivo with optical coherence tomography. Opt. Express **20**, 7694–7705 (2012)
89. L. An, H.M. Subhush, D.J. Wilson, R.K. Wang, High-resolution wide-field imaging of retinal and choroidal blood perfusion with optical microangiography. J. Biomed. Opt. **15**(2), 026011 (2010)
90. Y. Jia, M.R. Grafe, A. Gruber, N.J. Alkayed, R.K. Wang, In vivo optical imaging of revascularization after brain trauma in mice. Microvasc. Res. **81**(1), 73–80 (2010)
91. Y.-C. Ahn, W. Jung, Z. Chen, Optical sectioning for microfluidics: secondary flow and mixing in a meandering microchannel. Lab Chip **8**, 125–133 (2008)
92. M.A. Choma, A.K. Ellerbee, C. Yang, T.L. Creazzo, J.A. Izatt, Spectral-domain phase microscopy. Opt. Lett. **30**(10), 1162–1164 (2005)
93. J. Zhang, B. Rao, L. Yu, Z. Chen, High-dynamic-range quantitative phase imaging with spectral domain phase microscopy. Opt. Lett. **34**(21), 3442–3444 (2009)
94. C. Joo, T. Akkin, B. Cense, B.H. Park, J.F. de Boer, Spectral-domain optical coherence phase microscopy for quantitative phase-contrast imaging. Opt. Lett. **30**(16), 2131–2133 (2005)
95. D.C. Adler, R. Huber, J.G. Fujimoto, Phase-sensitive optical coherence tomography at up to 370,000 lines per second using buffered Fourier domain mode-locked lasers. Opt. Lett. **32**(6), 626–628 (2007)
96. L. Yu, S. Mohanty, G. Liu, S. Genc, Z. Chen, M.W. Berns, Quantitative phase evaluation of dynamic changes on cell membrane during laser microsurgery. J. Biomed. Opt. **13**(5), 050508 (2008)
97. J.M. Schmitt, OCT elastography: imaging microscopic deformation and strain of tissue. Opt. Express **3**(6), 199–211 (1998)
98. R.K. Wang, Z. Ma, S.J. Kirkpatrick, Tissue Doppler optical coherence elastography for real time strain rate and strain mapping of soft tissue. Appl. Phys. Lett. **89**(19), 144103 (2006)
99. S.J. Kirkpatrick, R.K. Wang, D.D. Duncan, OCT-based elastography for large and small deformations. Opt. Express **14**(24), 11585–11597 (2006)
100. C. Sun, B. Standish, V.X.D. Yang, Optical coherence elastography: current status and future applications. J. Biomed. Opt. **16**(4), 043001 (2011)

Doppler Fourier Domain Optical Coherence Tomography for Label-Free Tissue Angiography

42

Rainer A. Leitgeb, Maciej Szkulmowski, Cedric Blatter, and Maciej Wojtkowski

Keywords
Angiography • Blood Flow • Doppler OCT • Functional OCT • OCT Angiography • Optical Microangiography • Vascular Imaging

42.1 Introduction

Information about tissue perfusion and the vascular structure is certainly most important for assessment of tissue state or personal health and the diagnosis of any pathological conditions. It is therefore of key medical interest to have tools available for both quantitative blood flow assessment as well as qualitative vascular imaging. The strength of optical techniques is the unprecedented level of detail even for small capillary structures or microaneurysms and the possibility to combine different techniques for additional tissue spectroscopy giving insight into tissue metabolism. Still the gold standard for retinal vascular imaging is fluorescein or indocyanine green (ICG) angiography, again with the need to administer contrast agents. ICG absorbs in the infrared region where tissue scattering is lower and allows therefore deeper vessels in the choroid to be imaged, whereas fluorescein is applied for contrasting retinal vessels. This outlines already another important demand: to distinguish flow signatures of different vascular beds in depth. A noncontact and label-free method for tissue perfusion assessment is Laser Doppler Imaging (LDI). This method uses coherent laser illumination and detects

R.A. Leitgeb (✉) • C. Blatter
Center for Medical Physics and Biomedical Engineering, Medical University of Vienna, Vienna, Austria
e-mail: rainer.leitgeb@meduniwien.ac.at

M. Szkulmowski • M. Wojtkowski
Faculty of Physics, Astronomy and Informatics, Institute of Physics, Nicolaus Copernicus University, Toruń, Poland

© Springer International Publishing Switzerland 2015

W. Drexler, J.G. Fujimoto (eds.), *Optical Coherence Tomography*,
DOI 10.1007/978-3-319-06419-2_43

the beating frequency between light scattered by moving blood cells that experience a Doppler shift and that scattered from static tissue. Fourier analysis of the beating frequencies gives relative quantitative information about flow and particle concentration. Alternatively, speckle fluctuations can be used in LDI as fast indicator of blood flow, allowing vascular contrast. Laser Doppler velocimetry (LDV) is a related method that retrieves tissue perfusion parameters from diffusion theory [1]. For focal assessment of flow in selected vessels bidirectional Laser Doppler Flowmetry has been successfully applied, which like LDI is analyzing the beating frequency spectrum. Several studies based on Laser Doppler techniques outlined that blood flow changes are a precursor of major retinal diseases such as glaucoma, diabetes, or age-related macular degeneration [4–6]. Precise quantitative assessment of ocular flow in small retinal vessels opened the door for tissue-sensitive pharmacological studies. Investigations shed, for example, light on the role of endothelial cells and its release of vasoactive substances such as NO for perfusion regulation [7, 8]. Despite the success of those methods, they suffer from missing depth localization capability for moving scatterers. Hence, there is an immediate diagnostic and pharmacological demand for high-resolution, label-free, tissue angiography and flow assessment that in addition allow for precise depth gating of flow information. The most promising candidate is Doppler optical coherence tomography (DOCT) which shares the advantage with LDI of being noncontact, label free, and without employing hazardous radiation. However, in contrary to LDI, DOCT provides fully quantitative volumetric information about blood flow together with the vascular and structural anatomy [9, 10]. Segmentation and visualization of blood vessels from OCT measurements, called also as “OCT angiography,” acts directly on the standard OCT data sets. It is only a matter of post-processing in combination with dedicated scanning patterns whether one reconstructs the OCT intensity or angiography images. Having both intensity and angiography information available with the same data set potentially reduces the shortcoming of DOCT being only sensitive to blood at motion, not sensing static leakage sites that are, for example, signs of retinal diseases. Also, systemic and vascular diseases should be visible through studying the integrity [11] and perfusion properties of vasculature networks. For example, the irregular vascular network of tumor tissue has been imaged and characterized with an impressive level of detail [12]. DOCT has furthermore great potential for treatment monitoring, e.g., during photodynamic therapy, or for analyzing tissue grafts. Because of the huge potential of DOCT for diagnosis, the last years saw a rapid increase of publications in this field with many different approaches.

42.2 Vascular Contrasting and Doppler Techniques

First implementations of DOCT based on TDOCT were capable of real-time quantitative perfusion imaging in the retina and skin [13, 14]. High velocity sensitivity has been achieved by calculating OCT signal phase differences along the A-scan [17]. The velocity sensitivity has been further enhanced using spectral

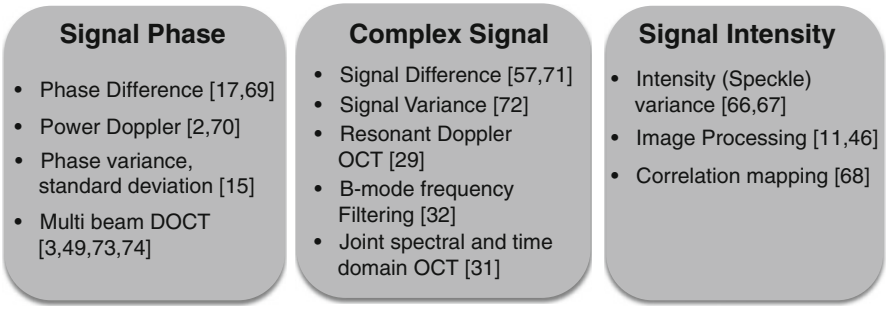

Fig. 42.1 Classification of methods for DOCT and optical angiography

referencing that revealed slow cell dynamics during osmotic changes [16]. Flow contrasting has been demonstrated by calculating the standard deviation of the motion-induced phase fluctuations [15]. Since OCT senses blood flow depth resolved within the tissue, a three-dimensional angiographic map may be calculated. Still, TDOCT suffers from low temporal resolution, and the sensitivity is critically decreasing at higher A-scan rates. Therefore FdOCT is gradually replacing time domain OCT due to its intrinsic sensitivity and speed advantage [18–22, 25]. Its ability for in vivo 3D imaging due to its outstanding high-speed performance [23, 24] paved the way for noninvasive comprehensive volumetric angiography and the quantitative assessment of pulsatile flow. The intrinsic phase stability of the method supports functional extensions of OCT that use phase information for enhanced sensitivity, such as measurement of blood flow, or polarization-sensitive OCT [2, 26–28]. High-speed data recording maintaining high image quality offered large flexibility, which resulted in novel signal processing schemes, supported by dedicated scanning patterns. We have today a rich variety of DOCT methods available for both quantitative perfusion assessment and for flow contrasting down to the level of individual capillaries. Apart from phase-sensitive flow detection as in time domain OCT, recent developments include speckle and phase-variance imaging, resonant Doppler imaging [29], optical microangiography [30], joint spectral and time domain OCT [31], and other different flow filtering methods [32, 33] to characterize and contrast perfusion of tissue volumes. Figure 42.1 tries to categorize those methods based on whether they involve only the OCT signal phase, only the intensity, or the full complex OCT signal.

42.3 Theory

42.3.1 Phase-Sensitive DOCT

In Fourier domain optical coherence tomography (FDOCT), the Fourier transformation of the spectral interferometric fringe signal measured by a single exposure of the line scan light detector creates one line of a structural

cross-sectional image (A-scan). In order to assess the velocity of a moving interface, most known methods require at least two spectral fringes acquired at the same or nearly the same lateral position [17, 69] of a sampling light beam. This allows the calculation of the initial phase difference between the two spectral fringe signals; this difference is directly linked to the optical path change between the reference mirror and a moving reflecting or scattering object within the sample. In general, a higher number of spectra can be acquired over time to increase the accuracy of the velocity estimation. The acquired set of spectral fringes can be described as a function of the wavenumber k and time t according to the following equation:

$$I(k,t) = I_0(k)\left(\sum_l R_l + R_r + 2\sum_l \sqrt{R_l R_r}\cos\left(2z_l(t)\cdot k\right)\right), \tag{42.1}$$

where $I(k, t)$ is the spectral fringe signal; $I_0(k)$ is the spectral density of the light source; R_l and R_r denote the reflectivity of the sample and reference mirrors, respectively; and $z_l(t)$ denotes the optical path difference between the reference mirror and the *l-th* interface in the sample. The optical path difference is time dependent due to the movement of the reference mirror and/or the displacement of the interfaces within the sample. This displacement is caused either by the movement of the entire sample or of the specific interface z_l within the sample. If we assume that both the reference mirror velocity and the velocities in the sample are constant during the acquisition of the spectral fringes, see Eq. 42.1, then the time-dependent position of the *l-th* interface, $z_l(t)$, can be expressed as:

$$z_l(t) = z_l + \delta z(t) = z_l + v_l \cdot t. \tag{42.2}$$

In this relation, z_l is the depth position of the *l-th* interface when data acquisition begins, and v_l is the difference between the velocity of the reference mirror and an axial component of the velocity of the *l-th* interface (parallel to the direction of the probing beam propagation). One can rewrite Eq. 42.1 making use of Eq. 42.2:

$$I(k,t) = I_0(k)\left(\sum_l R_l + R_r + 2\sum_l \sqrt{R_l R_r}\cos\left(2(z_l + \Delta z_l(t))\cdot k\right)\right) \tag{42.3}$$

$$I(k,t) = I_0(k)\left(\sum_l R_l + R_r + 2\sum_l \sqrt{R_l R_r}\cos\left(2z_l\cdot k + \omega_l\cdot t\right)\right) \tag{42.4}$$

Although the above equations represent the same interference pattern, they emphasize different properties. The phase of the oscillatory component present in Eq. 42.3 is a function of the wavenumber, and its modulation frequency depends on the static position z_l of the *l-th* interface, and a small additional change δz that occurs if the *l-th* interface is moving. Equation 42.4 highlights the time dependence of the interferometric fringes and shows that the signal is modulated in time with

frequency ω_l. This beat frequency is caused by a Doppler effect that arises for each *l-th* interface along the time axis. The frequency depends on the velocity v_l and is different for each wavenumber k:

$$\omega_l = 2v_l k \tag{42.5}$$

The phase-resolved methods [17] for estimating velocity use the signals' phase differences as described by Eqs. 42.3 and 42.5:

$$v_l = \frac{\Delta\Phi_l}{2k\Delta t} = \frac{\lambda}{4\Delta t}\frac{\Delta\Phi}{\pi} \tag{42.6}$$

Here, $\Delta\Phi$ is the phase difference between successively recorded depth profiles at the same location of the probing beam:

$$\Delta\Phi_l = 2\Delta z_l k = 2v_l \Delta t k, \tag{42.7}$$

The time between the acquisitions of successive profiles, Δt, is approximately equal to the exposure time of the detector; therefore, $1/\Delta t$ is the frame rate of an array detector (or equivalently, the "A-scan" rate). It is important to ensure that $|\Delta\Phi|$ is less than π.

42.3.2 Optical Angiography

In the following chapter, we will focus on the DOCT modalities for noninvasive tissue angiography. In general, all methods can be realized with either spectrometer-based FdOCT or swept source OCT (SSOCT). SSOCT has particular advantages for motion sensing as it does not suffer from fringe washout and keeps high sensitivity even for several hundred kHz A-scan rates, due to its higher dynamic range than CCD or CMOS-based FdOCT and the option of dual-balanced detection. In the present chapter, we would like to demonstrate applications of tissue angiography in ophthalmology and dermatology. Those have been obtained with intensity-based DOCT, which is well adapted to swept source OCT, because it is independent from any acquisition timing problems such as trigger jitter. Also the fact that it does not require bulk motion correction alleviates the post-processing effort as compared to other techniques. An angiographic image volume $P(x, y, z)$, contrasting flow against static tissue, is obtained by calculating the squared intensity difference between successive tomograms [35]:

$$P(x, y_i, z) = \left(I(x, y_i, z) - I\left(x, y_{i+1}, z\right)\right)^2, \tag{42.8}$$

where $I(x, y, z) = 20 \cdot log[FFT(I(x, y, k))]$, (x, y, z) are the spatial pixel coordinates corresponding to fast and slow scanning and depth coordinate, respectively, and

k is the wavenumber. Such method requires good correlation for static tissue over successive tomograms. This is obtained by driving the slow axis scanner with a multiple-step function. It allows for measuring N tomograms at the same position y. A calculation of the intensity squared difference mean value at each position permits to detect decorrelation, caused by motion artifact, and to potentially reject that picture for further processing by setting manually a threshold T. The value of T is chosen such as to obtain visually optimal vessel contrast. The pictures representing the same location can be averaged to increase SNR. The number of pictures averaged at each position can be formally written as:

$$M(y) = \sum_{i=0}^{N-1} \left(\left[\sum_{x,z} P(x, y_i, z) \right] < T \right). \tag{42.9}$$

The logic operation in the brackets yields 1 or 0 for TRUE or FALSE, respectively. Finally, the motion contrast volume V is obtained by averaging only over the remaining M intensity squared difference tomograms P:

$$V(x, y, z) = \frac{1}{M(y)} \sum_{i=0}^{N-1} \left(\left[\sum_{x,z} P(x, y_i, z) \right] < T \right) \cdot P(x, y_i, z). \tag{42.10}$$

This method is more robust against motion artifacts than a variance analysis over the full tomogram series acquired at the same position, since pictures with strong decorrelation are rejected. Furthermore, the difference is only calculated between successive tomograms, thus reducing the time interval over which correlation is required. This improves further the stability with respect to motion artifacts.

In principle, one could replace the intensity difference in Eq. 42.8 by the difference of the full complex signal or by the phase difference only. The phase has the advantage of being insensitive to changing backscattering intensity. To be precise, the phase noise will scale with the SNR as is outlined also in the next chapter. Phase-sensitive contrasting of flowing blood seems to perform also better in case of strongly scattering embedding tissue, whereas intensity-based techniques are particularly well suited in case the embedding tissue scatters less than blood. Using the full complex signal is therefore a good compromise.

42.3.3 Noise in DOCT

In view of the importance of phase, it is therefore worth investigating the factors that determine phase fluctuations. In a scanning OCT system, phase fluctuations have two to three contributions [2] depending on the modality. Shot noise causes phase fluctuations that depend on the SNR as $\Delta\varphi_{SNR} = 1/\sqrt{SNR}$. In the case of shot

noise limited detection the distributions of the OCT signal phase and amplitude can be found using the formalism presented by Goodman [36].

The probability density function for the phase can be described by the following expression:

$$p(\Phi) = \begin{cases} \dfrac{e^{-{\kappa_{zt}}^2/2}}{2\pi} + \dfrac{\kappa_{zt}\cos\Phi}{\sqrt{2\pi}} \exp\left[-\dfrac{{\kappa_{zt}}^2 \sin^2\Phi}{2}\right] \Omega(\kappa_{zt}\cos\Phi) & -\pi < \Phi \le \pi \\ 0 & \text{otherwise} \end{cases}, \tag{42.11}$$

where function $\Omega(b) = \frac{1}{\sqrt{2\pi}} \int_{-\infty}^{b} e^{-y^2/2} \mathrm{d}y$, $\kappa_{zt} = s_{zt}/\sigma$ is the signal-to-noise ratio (SNR) of the OCT signal dependent on time, s_{zt} is the amplitude of the signal, and σ is the standard deviation of the noise in the real and imaginary parts of the complex-valued time-dependent A-scans. With increasing κ_{zt}, the density function narrows, and it converges toward a Dirac delta function centered at $\Phi = 0$. When the signal s decreases to zero ($\kappa_{zt} \to 0$), the distribution converges to a uniform distribution as seen in Fig. 42.2a. Since the phase-resolved FdOCT requires phase subtraction, the width of the final distribution becomes broader. As the distribution broadens, more random wrapped phase differences are detected, and in turn, the averaged value of the phase differences moves closer to zero.

The probability density function of the amplitude of a time-dependent OCT signal is given by a Rician density function:

$$p(a) = \begin{cases} \dfrac{a}{\sigma^2} \exp\left[-\dfrac{a^2 + {s_{z\omega}}^2}{2\sigma^2}\right] I_0\left(\dfrac{a s_{z\omega}}{\sigma^2}\right) & a > 0 \\ 0 & \text{otherwise} \end{cases}, \tag{42.12}$$

Where $I_0(\cdot)$ is a modified Bessel function of the first kind and zeroth order, $\kappa_{z\omega} = s_{z\omega}/\sigma$ is the SNR of time-dependent A-scan, $s_{z\omega}$ is the amplitude of the signal, and σ is the standard deviation of the noise in the real and imaginary parts of the complex-valued time-dependent A-scan. As the signal $s_{z\omega}$ increases, the shape of the density function $p_A(a)$ changes from that of a Rayleigh density to approximately that of a Gaussian density with a mean equal to $s_{z\omega}$, as shown in Fig. 42.2b. Due to the Fourier transform linking the time-dependent interferometric fringe signal with optical frequency-dependent one, the signal-to-noise ratio is increased for the latter $\kappa_{z\omega} = \sqrt{M}\kappa_{zt}$, where M is the number of spectra being transformed.

Another factor influencing accuracy of DOCT is lateral scanning across a scattering surface. This gives rise to another contribution that depends on the lateral sampling according to $\Delta\varphi_{scan} = \sqrt{(4\pi/3)\left(1 - \exp\left(-2(\Delta x/d)^2\right)\right)}$ where

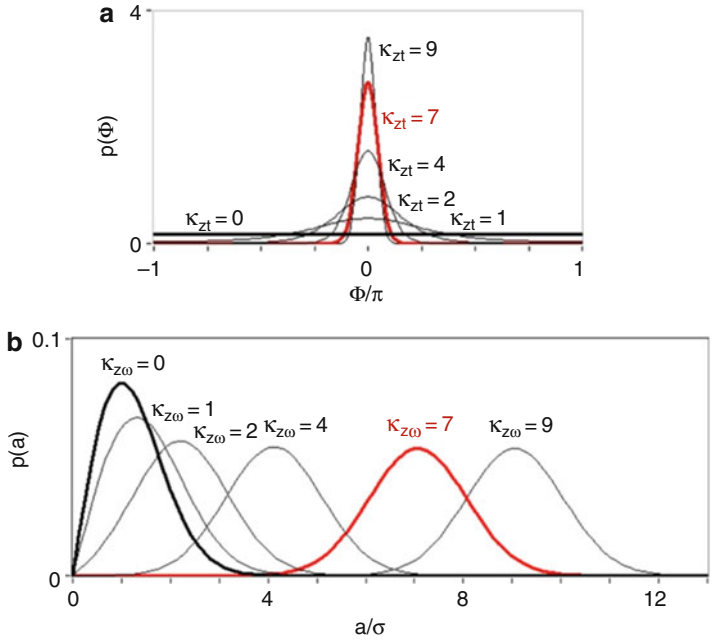

Fig. 42.2 (**a**) Phase distributions for various values of the κ_{zt} parameter. (**b**) The probability density functions for the amplitude at different values of parameter $\kappa_{z\omega}$. The *black curve* corresponds to the distributions of amplitude for pure noise ($\kappa_{z\omega} = 0$), and the *red curve* is for a signal with a critical value ($\kappa_{z\omega} = 7$) that assures the correct recovery of the velocity in DOCT [36]

d is the $1/e^2$ is the Gaussian beam waist in the focus, and Δx is the lateral displacement between successive A-scans [2]. The quotient $d/\Delta x$ defines the lateral oversampling (Fig. 42.3). The third contribution in SSOCT systems is trigger jitter for starting an A-scan, or B-scan, depending on the post-processing scheme [37]. Any time offset of the A-scan or B-scan causes increasing phase error in depth, as the associated fringe period becomes smaller. This can be avoided by fast and precise phase-locked loops (PLL) or by cutting A-scans in post-processing.

In most cases, the phase fluctuation due to scanning across a scattering sample is most critical and dominating. Nevertheless, by increasing the lateral oversampling factor one eventually hits the boundary set by SNR (Fig. 42.3). Phase noise determines the lower boundaries of phase-sensitive methods, in particular the minimum resolvable or contrastable speed in Doppler OCT.

For a given phase noise, the minimal resolvable velocity is determined as

$$v_{min} = {}^{\lambda}/_{4\pi T \Delta\varphi_{noise}}. \tag{42.13}$$

Apart from the dependence on the phase noise, it also depends on the time interval between the signals that are used for velocity analysis. Higher sensitivity can thus be achieved by using long time intervals. If one increases the A-scan period time,

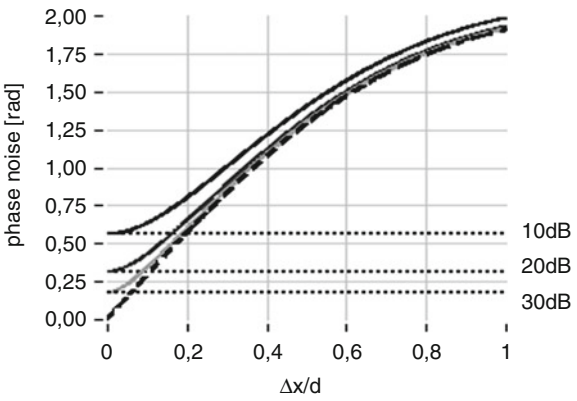

Fig. 42.3 Phase noise depending on lateral displacement and SNR

the total measurement time will increase, which results in strong motion artifacts. Using two B-scans immediately allows for larger time intervals and hence higher velocity sensitivities without sacrificing total recording time. For the first time, it was possible to contrast tissue capillaries with great detail. Modern DOCT angiography techniques measure the signal decorrelation due to flow. This needs long time intervals and even higher sensitivities in order to achieve an optimal effect also for small capillaries. The high sensitivity to optical path length changes comes however at a price: flowing blood gives rise to signal decorrelation shadows below vessels. This is seen in Fig. 42.4b. Those artifacts can be reduced by weighting or even masking the vascular contrast image with the intensity image or a binarized intensity image, respectively. Those artifacts might be problematic for studying axial vasculature. They are not visible in fundus projections of DOCT angiography images. In Fig. 42.4a, another typical artifact of B-scan-based techniques is visible: horizontal stripes. They are due to increased variance or difference values in the presence of motion artifacts. They can be reduced by using a thresholding procedure as outlined in the previous chapter and by applying Fourier band-pass filtering along the direction normal to the B-scans.

42.3.4 Joint Spectral and Time Domain OCT

Another approach for extracting the velocity is to use the Fourier transform to detect the time-dependent frequency of the signal given in Eq. 42.4. This idea underlies the joint spectral and time domain OCT technique (STdOCT), [31] as it uses only Fourier transforms to analyze the data in the wavenumber and time domains simultaneously.

To explain the principle of the technique, it is convenient to present the data processing on a so-called STdOCT diagram (Fig. 42.5). Each of the diagram's four panels present data connected via Fourier transforms. The transition in the horizontal direction transforms the data from the wavenumber domain to an in-depth position domain, while the vertical transitions transform the data from the time domain to the Doppler frequency domain.

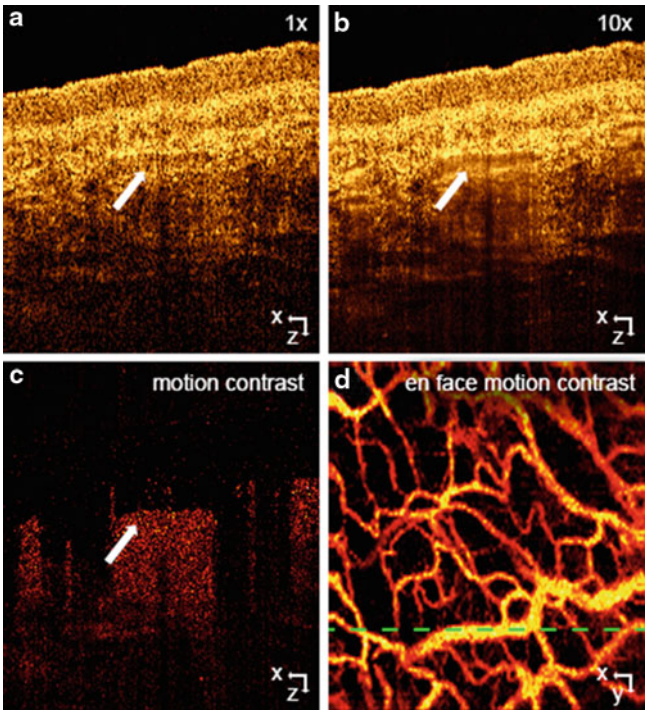

Fig. 42.4 Amplitude speckle decorrelation for blood flow imaging in skin. (**a**) Skin tomogram, (**b**) average of ten tomograms taken at the same lateral location with reduce speckle contrast at the vessel location (*white arrow*), (**c**) amplitude squared difference resolving motion in *red* against static tissue in *black*, (**d**) en-face mean projection of the motion data set. *Green dashed line* indicates the position of the (**a**), (**b**), and (**c**)

Two STdOCT diagrams are shown in Fig. 42.5. Figure 42.5a shows a diagram for the data acquired in a simple OCT experiment where a mirror is driven with a constant speed, and Fig. 42.5b shows a diagram for data obtained from imaging a laminar flow in a glass capillary phantom. Here, we discuss the data visible on all of the panels of the diagram.

k-t plane. Rows of the interferogram presented in this panel are simply interferometric spectra acquired by the FdOCT device that underwent standard FdOCT preprocessing (consisting of background removal, resampling to the wavenumber domain, and dispersion compensation [38]). The number of spectra is equal to the number desired to create one line of the final tomogram.

z-t plane. Data in this panel are obtained by a Fourier transform of each row from the k-t plane. Each complex-valued row in this data set is a so-called optical A-scan. Standard FdOCT processing uses these A-scans to find a line of the structural tomogram by averaging the amplitudes of the A-scans or by using phase differences between consecutive A-scans to find the Doppler shift as

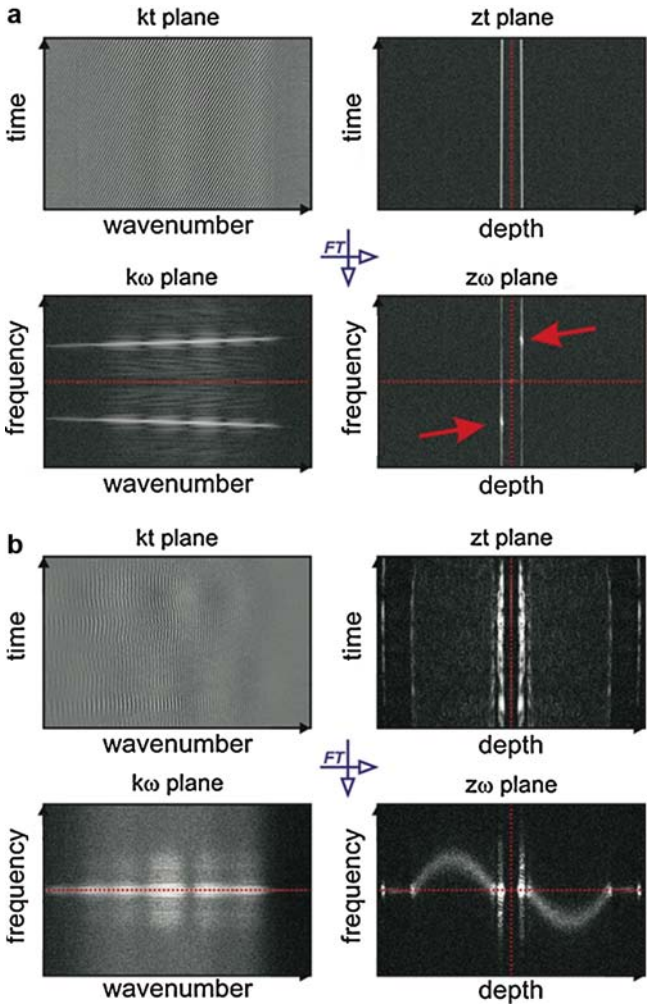

Fig. 42.5 STdOCT diagrams. Vertical transitions are accomplished by a Fourier transform along the wavenumber axis and horizontal transitions by a Fourier transform along the time axis. The amplitude of the complex signal is displayed for visualization purposes. In the zω-domain, complex conjugate images are symmetrical with respect to the central point of the plot (zero position, zero velocity). (**a**) Moving mirror experiment in which two points (*red arrows*) represent two complex conjugate images of the mirror; each of the points gives simultaneously information about the position and velocity of the moving mirror with respect to the reference mirror. (**b**) Laminar flow of intralipid solution in a glass capillary. Two complex conjugate images of a parabolic flow distribution are visible [65]

shown in Eq. 42.6. The signal in this plane is symmetrical with respect to the zero path delay (marked by the red dotted line).

k-ω plane. Data in this panel are obtained by Fourier transforming the data in the k-t panel with respect to time. It can be seen from Eq. 42.4 that information

about the depth position of the scatterer is encoded only in the non-time-dependent component of the spectral fringe phase. Therefore, the time-dependent Fourier transform does not provide information about the in-depth localization of scatterers. However, it does provide information about the distribution of Doppler frequencies as a function of wavenumber. For the moving mirror experiment, when there is only one component in such a spectrum, its velocity can be recovered from the Doppler frequency ω_l according to Eq. 42.5. For each k, the velocity can be calculated separately. Therefore, this representation of the data can be used to find the exact relationship between the wavenumbers and pixels in an array detector and can also be used to very accurately calibrate the spectrometer. This idea was proposed by Szkulmowski et al. [31] and discussed in detail by Faber and van Leeuwen [39]. For more complicated sample structures, it can be difficult to extract any useful information, but it is possible to filter the data to remove any undesired components of the Doppler spectrum before further processing. The optical microangiography (OMAG) technique [30] used to quantitatively visualize capillary networks uses a similar idea. The signal in this plane is symmetrical with respect to the zero velocity (marked by the red dotted line).

z-ω plane. This panel shows the result of a two-dimensional Fourier transform of the set of M spectral fringes. The coordinates of the displayed signals link the positions of all measured interfaces with their corresponding velocities. Each interface z_l is represented by two symmetrical points appearing with respect to the zero path delay and zero velocity. The sign of the velocity indicates a forward or backward direction. The point localized symmetrically with respect to the zero delay and zero velocity is the complex conjugate image of the scattering particle. The data in this panel can be regarded as a distribution of the Doppler spectrum of the signal as a function of depth, and as such, there is equivalence of the techniques developed for the time domain OCT [40–42]. It has been shown that the spread of the Doppler spectrum along the ω – axis depends on the optical parameters of the setup, such as the numerical aperture of the imaging objective, the spectral width of the light source, and the axial and transversal velocities of the imaged scattering particles. This Doppler distribution is visible in images of laminar flow as presented in Fig. 42.5b, where the distribution along the frequency axis is broadened in the center of the capillary lumen where the velocity components have their highest values in both the axial and transverse directions.

There are two ways to estimate the value of velocity component along the direction of beam propagation (Doppler component) using the STdOCT technique: maximum projection approach [31] and center of gravity approach [43]. In the first method, the velocity value is measured by finding the signal with maximum amplitude. This approach was proposed in the initial work by Szkulmowski et al. [31]. In 2011, Walther et al. [43] proposed alternative way of velocity estimation by calculating the center of gravity of the Doppler spectrum. Since the detectable Doppler frequencies are limited to half of the OCT sampling frequency, the center of gravity is calculated as the mean value of a circular

distribution of amplitude. This is achieved by weighting the amplitudes by complex vectors with phases equally distributed from 0 to 2π.

$$\Psi_l(f_D) = B_l(f_D) \cdot \exp\left[-i\frac{2\pi l}{N}\right] \quad \text{with} \quad l = 1, 2, \ldots, N \tag{42.14}$$

Here, N is the number of A-scans, and $B_l(f_D)$ is the amplitude of the *l-th* point Doppler frequency distribution. Finally, the center of gravity is calculated by averaging the modified complex value $\Psi_l(f_D)$ and determining the argument for each depth z as shown in Eq. 42.15, where f_D is the read-out rate for a single interference spectrum:

$$f_D(z) = \arg\left\{\frac{1}{N}\sum_{l=1}^{N}\Psi_l(f_D)\right\}. \tag{42.15}$$

The above estimator is compared to the velocity estimator proposed in 2009 by Vakoc et al. [12], which extended the standard phase-resolved approach. Here, the noise of the phase shift is more effectively reduced by considering the amplitudes $A_l(z)$ of the complex-valued A-scans $\Gamma_l(z)$, instead of averaging the absolute value of the phase differences $\Delta\Phi_l$. This is because the values with a high signal have a larger weight.

$$\overline{\Delta\varphi(z)} = \arg\left\{\frac{1}{N-1}\sum_{l=1}^{N-1}\Gamma_{l+1}(z)\Gamma_l^*(z)\right\}, \quad \text{where} \quad \Gamma_l(z) = A_l(z) \cdot \exp[-i\varphi_l(z)] \tag{42.16}$$

Experiments with intralipid emulsion flowing throughout glass capillary phantoms showed that the two above estimators are equivalent and have smaller variance than does the STdOCT with maximum amplitude detection (Fig. 42.6).

42.4 Qualitative and Quantitative Blood Flow Visualization with DOCT

42.4.1 Intensity Variance Ocular Angiography

Assessment of the retinal and choroidal vascularization is of important diagnostic benefit for major ocular diseases that affect the vascular network already at an early state. The visualization of the microvasculature yields an easy accessible and intuitive way to assess its integrity. During the last years, a number of strategies for contrasting

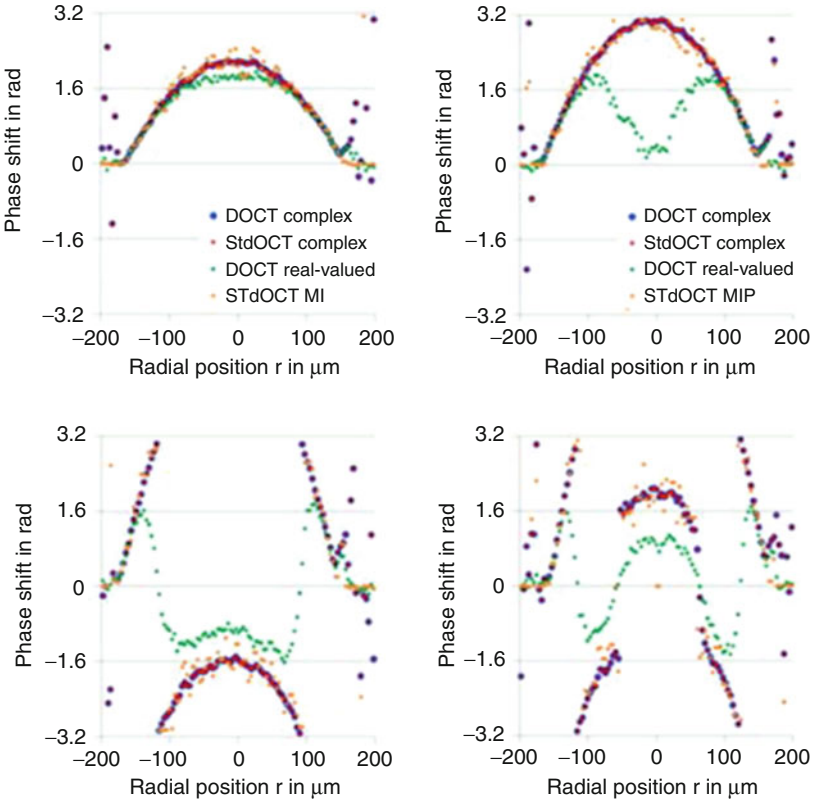

Fig. 42.6 Averaged flow profiles by STdOCT (STdOCT MIP – f_D by the maximum intensity signal, STdOCT complex – f_D by the center of gravity via complex $\Psi(f_D)$) and phase-resolved DOCT (DOCT complex, averaging the complex $\Gamma(z) \cdot \Gamma^*(z)$, DOCT real-valued, averaging the absolute value of $\Delta\varphi$), respectively [43]

microvasculature based on FdOCT have been introduced. The gold standards for their visualization are fluorescein angiography (FA) and indocyanine green angiography. They are commonly used in clinical practice for diagnosis of vascular occlusions, diabetic retinopathy, and choroidal neovascularization, usually a cause of age-related macular degeneration. The invasiveness of these techniques together with undesirable side effects, through the injection of a fluorescent dye, limits the screening capabilities for large populations. Therefore DOCT angiography is an attractive alternative as it is noninvasive, label-free, and easy to operate. The availability of both intensity information and vascular contrast with the same OCT data set might soon establish this technique for patient screening, as well as for treatment monitoring. The data recording takes only a few seconds, which further improves the patient comfort.

As has been outlined above, B-scan-based analysis yields contrast even for small retinal capillaries. However, if the B-scan rate is too low, motion artifacts are more likely to cause unwanted signal decorrelation, reducing the contrast between static

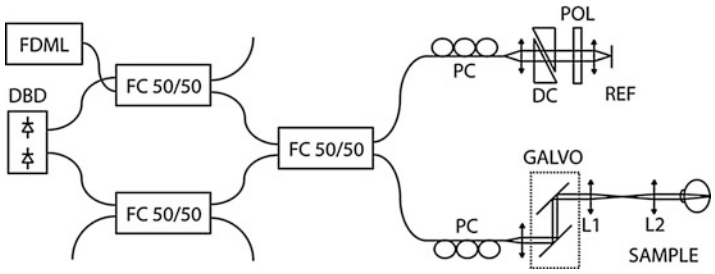

Fig. 42.7 Experimental setup for ultrahigh-speed posterior segment imaging. *FC* fiber coupler, *PC* polarization control, *DC* dispersion control, *POL* polarizer, *GALVO* scanning system, *L* lenses, and *DBD* dual-balanced detector [48]

tissue and flow. The increase of B-scan rate should however be limited so that high sensitivity for small capillary flow is preserved. Recent demonstrations applied B-scan rates of several hundred Hz [44]. Generally, the demonstration of these techniques was restricted to small FOV because of limited acquisition speed. It was partially solved by stitching small volumes together [44]. A critical point, however, concerning the clinical acceptance of this technique, is certainly the associated total long measurement time because of fixation change and the recording of redundant overlap areas required for registration. The development of ultrahigh-speed OCT techniques based on Fourier domain mode-locked (FDML) lasers for SSOCT allowed for A-scan rates beyond 1 MHz [45]. Recent results showed that ultrahigh speed is a prerequisite for flexible and comprehensive vascular contrast imaging with DOCT over a large field of view (FOV). Ultrahigh-speed FdOCT is therefore a promising candidate to compete with the FOV and resolution of fluorescein angiography, since a large patch can be covered by a single recording in a few seconds. Retinal and choroidal imaging with this technology at ultrahigh speed was demonstrated at a center wavelength of 1,060 nm [46, 47]. Posterior segment OCT imaging in that water window has the advantage to provide increased penetration into the choroid compared to common 850 nm region because of reduced scattering. It allows for a better assessment of choroidal vasculature that is particularly important for ocular diagnosis, its network being the main oxygen and nourishment supplier of the retina.

Figure 42.7 shows a setup for SSOCT with dual-balanced detection [45, 48].

The light source is an FDML laser with its Fabry-Perot filter driven at ~419 kHz. The so-called buffering technique of time multiplexing is later used to increase the sweep rate by a factor of 4 leading to 1.68 MHz A-scan rate. The spectrum is centered at 1,060 nm with a 72 nm sweep range. It produces a ~14 μm axial resolution in air. Shot noise limited sensitivity of ~91 dB with 1.7 mW power at the cornea is achieved, thanks to the symmetrical detection using matched fiber coupler (FC) to ensure a proper balancing. The slow axis scanner is driven by a multiple-step function. It permits measuring successive B-scans at the same vertical position y, giving an almost perfect correlation for static tissue. We measure $N = 5$ B-scans at 800 vertical positions. The fast axis driving function is a ramp of ~70 % duty cycle and a frequency of 560 Hz. Each B-scan constitutes of 2,060 A-scans.

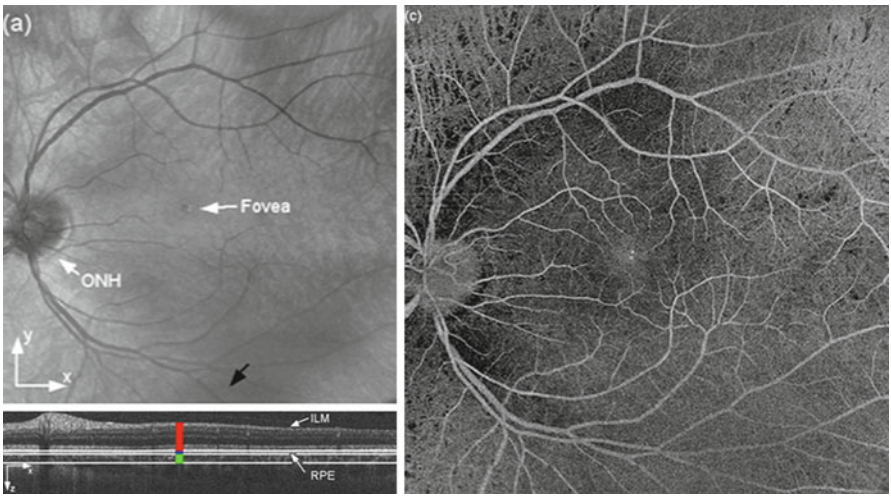

Fig. 42.8 (**a**) Pseudo-SLO fundus obtained by en-face mean projection of the intensity data set. *ONH* optic nerve head. *Black arrow*: low signal region (**c**) 48° widefield angiogram, en-face mean projection of the intensity variance 3D data set calculated from (**a**). (**b**) Fivefold averaged tomogram after flattening to the retinal pigment epithelium (*RPE*) [48]

This leads to an effective volume sampling of 2,060 × 800 × 460 (xyz). The scan amplitude is set to produce a ∼48° FOV on the retina. The total acquisition time for the full FOV is only 7 s.

Figure 42.8a shows the en-face mean projection of the intensity data set of the retina of a healthy volunteer acquired over a wide FOV of ∼48°. Large retinal and choroidal vessels are already visible; however, smaller vessels lack contrast. They are on the other hand well appreciated in the high-contrast en-face mean projection of the calculated 3D intensity variance set (Fig. 42.8c). The FOV of our label-free and noninvasive widefield angiography can be well compared to that of standard FA. An important advantage of our technique as compared to previous noninvasive methods based on OCT is the small acquisition time for such image obtained in a single recording. The depth resolution of OCT allows differentiating the retinal and choroidal vasculature network for further investigation. For this task, the intensity tomograms were first flattened by detection of the retinal pigment epithelium (RPE) layer (Fig. 42.8b). In a second step, the position of the inner limiting membrane (ILM) was determined. The corresponding coordinates were used for segmented en-face projection of the intensity variance 3D set. The first segment consisted of the region from ILM to the RPE layer; the second segment comprises the vascular structures down to about 50 μm below the RPE. Large choroidal vessels are finally segmented in a third layer. For the retinal layer, the intensity variance 3D data set was multiplied by a manually thresholded copy of the intensity data set. It reduces background noise, so that high backscattered blood vessels are better visible. The segmentation of the RPE is not possible in the ONH region; hence, the ONH vasculature is attributed to the upper layer.

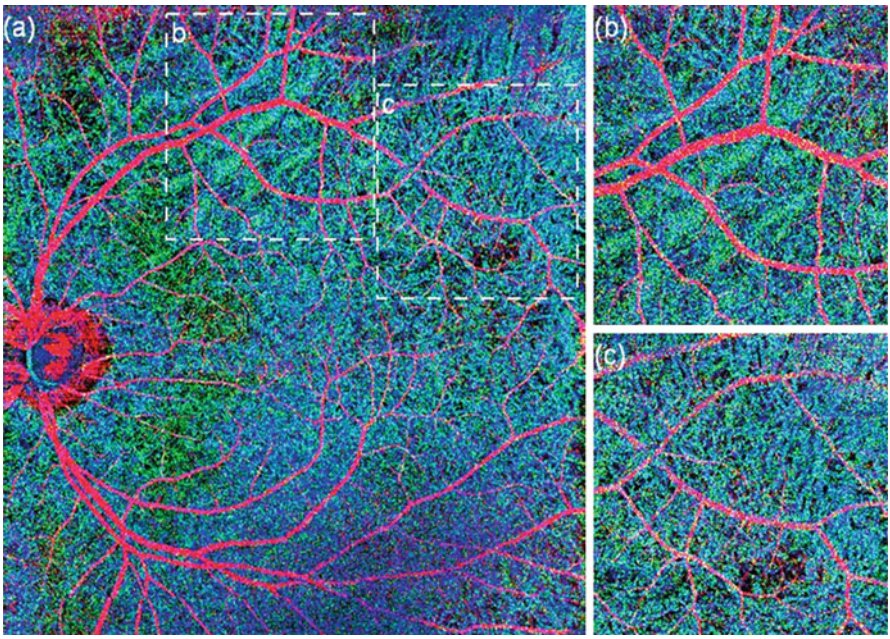

Fig. 42.9 (Color online) color-coded en-face mean projection of the retinal and choroidal vasculature. (**a**) ∼48° depth-resolved angiogram. (**b** and **c**) Zoom showing large choroidal vessels and fine vasculature [48]. The colors code depth ranges as indicated in Fig. 42.8 (**b**)

Figure 42.9 shows a color-coded combined representation of the segmented en-face mean projections for the retina and choroid according to Fig. 42.8b. It is possible to resolve simultaneously retinal and choroidal vessels. The high lateral sampling allows revealing also small vessels and fine network as shown in Fig. 42.9c. The choroid exhibits different kinds of vessels along depth. Close below the RPE, a dense network of small choroidal vessels is visible (Fig. 42.9c). In deeper regions, the vessel size increases (Fig. 42.9b). The low contrast region in the picture lower part is the result of low signal in the original intensity tomograms due to iris shading (cf. Fig. 42.9a, black arrow).

Small retinal capillaries, particularly in the parafoveal region, are only weakly visible. This is due to the coarse sampling. Nevertheless, the current protocol would provide a first widefield overview that can then be used as guide to focus on a suspicious area or a region of interest. Figure 42.14 shows a ∼12° FOV centered on the fovea acquired with the same parameters as for the large FOV. The lateral resolution is obviously sufficient to contrast also small parafoveal capillaries efficiently (Fig. 42.10b, c) in the en-face mean projection of the intensity variance data set while absent of the intensity projection (Fig. 42.10a). Furthermore, choroidal vessels are well appreciated (Fig. 42.10d). It is however difficult to resolve single choroidal vessels in the fovea region due to the dense vascular network directly underneath the RPE. The latter also shades the variance signatures of deeper

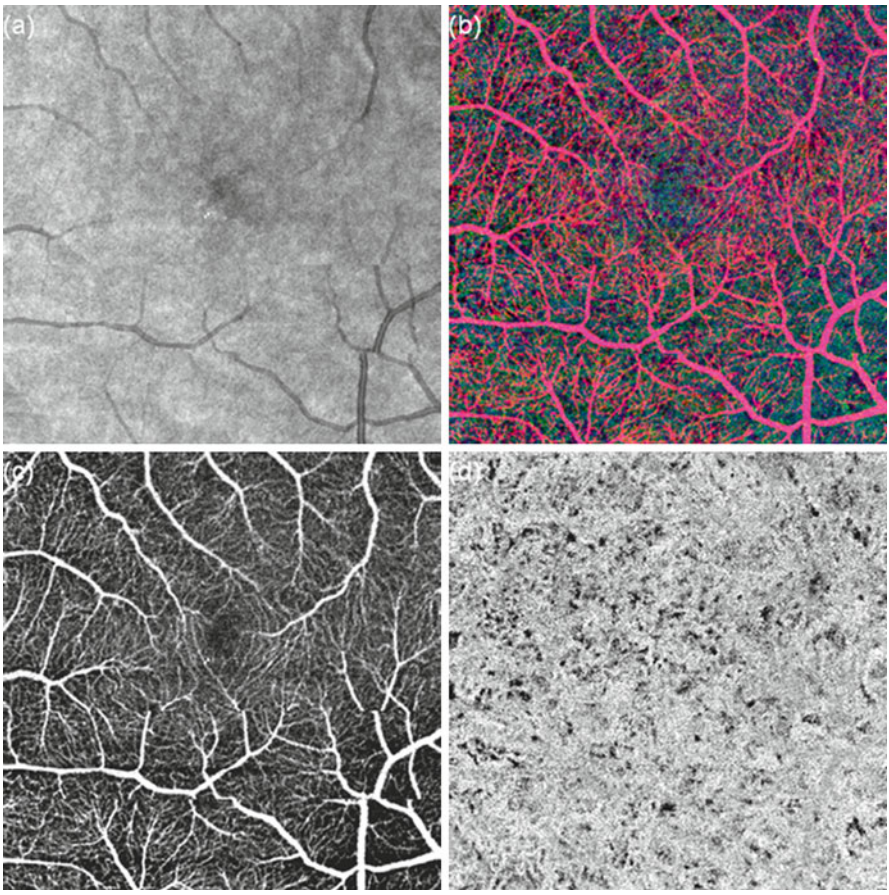

Fig. 42.10 (Color online) ∼12° FOV centered at the fovea. (**a**) Pseudo-SLO fundus obtained by en-face mean projection of the intensity data set. (**b**) Color-coded en-face mean projection of the retinal and choroidal vasculature. (**c**) Retinal vasculature. (**d**) Choroidal vasculature [48]

choroidal vessels in the en-face view. Faster B-scan rates could decrease the variance signal of the choriocapillary layer and enhance the contrast of larger vessels underneath. This has been demonstrated employing a dual-beam technique [49, 50].

Given the quality and level of detail of DOCT angiography images, this technique could be a natural candidate for replacing fluorescein and ICG fundus angiography. Being fully noninvasive, it could serve to screen large populations which would help early diagnosis of ocular diseases. It also allows frequent disease and treatment monitoring of the same patient and does not require especially qualified personnel. This would further significantly cut down social costs, and patients could be treated early on, avoiding in many cases critical degeneration of neural tissue.

42.4.2 Ocular Doppler Imaging with Joint STdOCT

In 2009, Szkulmowska et al. [51] presented quantitative and qualitative visualizations of retinal vessels in the human eye based on the STdOCT approach. A scanning protocol, shown in Fig. 42.11a, permitted the acquisition of 100 B-scans with 2,200 A-scans each.

This enabled the development of a 3D data set containing 100 tomograms with 546 lines each, using the sliding window technique for selecting the spectra for STdOCT processing, shown in Fig. 42.11b. Both structural and velocity profiles were obtained using the STdOCT approach as described above. Two sampling densities were applied and led to either a 5×5 mm or a 3×2 mm imaging area as shown in Fig. 42.11c. One of the most important limitations of Doppler measurements in vivo is the presence of involuntary object motion – so-called bulk motion. Because the shape of the Doppler spectrum for the bulk motion (offset of the Doppler spectrum) is usually different than the one for the blood flow (continuously varying profile), those two components are easily distinguishable by STdOCT approach (Fig. 42.12). Therefore, STdOCT enables a straightforward way of bulk motion removal by simple identification of the offset in the Doppler profile and numerical correction of the OCT signals.

Figures 42.13a–c show the morphological image with the bulk motion compensation, the axial velocity Doppler maps, and angiographic cross sections, respectively. In order to obtain the improvement of contrast in visualization of the blood vessels (Fig. 42.13c), we used a binary mask (obtained by thresholding of the modulus of the velocity value) and applied the mask to the morphological cross-sectional image.

These three types of signal processing give comprehensive 3D visualization of the blood vessel network and enable the creation of quantitative and qualitative maps of retinal vasculature (Fig. 42.14).

Another important constraint in Doppler OCT imaging is limitation in detectable Doppler bandwidth once the OCT signal is detected with classical raster scanning pattern. This shortcoming can be overcome by using smart scanning protocols with sinusoidal trajectory (Fig. 42.15) of the light beam on the sample applied to STdOCT by Grulkowski et al. in 2009 [52]. Since the maximal detectable velocity is inversely proportional to the time span between the A-scans used for Doppler analysis, this allowed for simultaneous estimation of blood flow velocity in two velocity ranges from the same data set. Figure 42.15a shows an example of application of the smart scanning protocol to retinal imaging – in the proximity of the nerve head. The use of such scanning protocols allows for quantitative measurement of axial velocity component in large retinal vessels in Fig. 42.15c and small capillaries, Fig. 42.15d, when small velocity range is chosen for calculations.

In the same publication, authors demonstrated a visualization of a retinal capillary network with small velocity range detection [52]. Five A-scans from adjacent B-scans were selected for the STdOCT analysis. This allowed the observation of

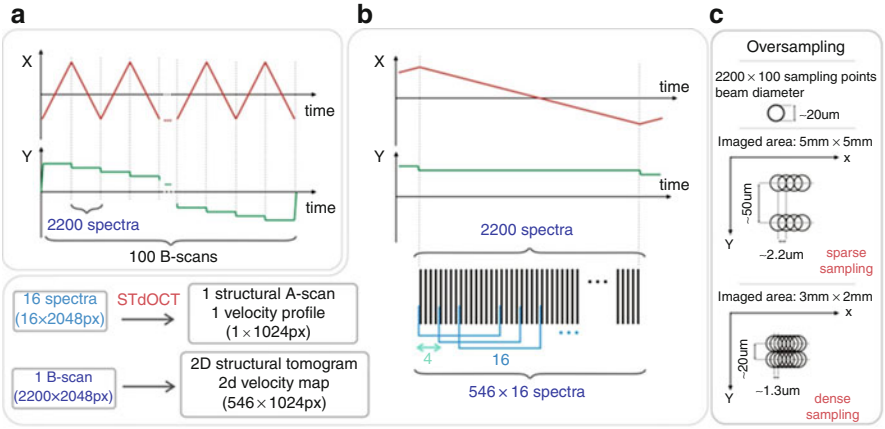

Fig. 42.11 Scanning protocol. (**a**) 3D imaging with driving signals for X and Y scanners. (**b**) The procedure for generating a 2D velocity map from a single B-scan. (**c**) Two types of sampling depending on the size of the imaged area [51]

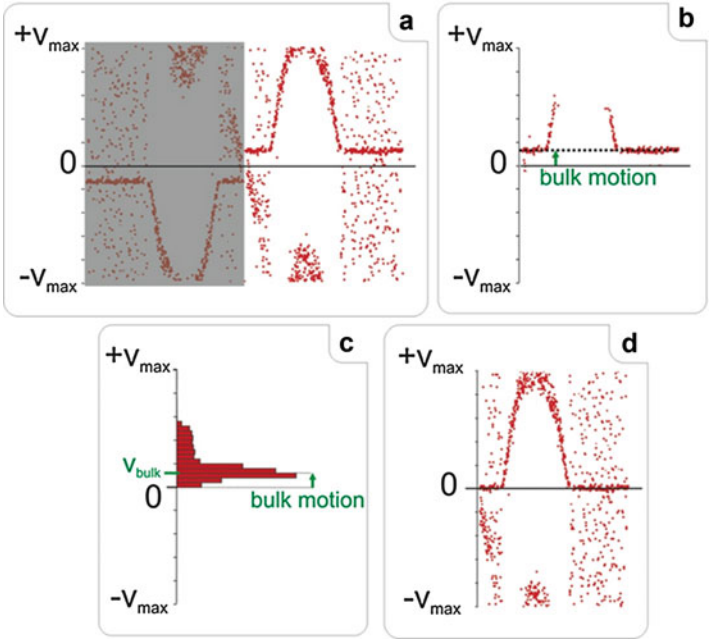

Fig. 42.12 Pictorial representation of the bulk motion correction algorithm. (**a**) Raw velocity profile with a bulk motion artifact. The complex conjugation of the image is marked by the gray background and is not considered. (**b**) Velocity profile plotted for signals that exceed a certain intensity threshold. (**c**) Histogram of velocity values corresponding to (**b**). (**d**) Corrected velocity profile [51]

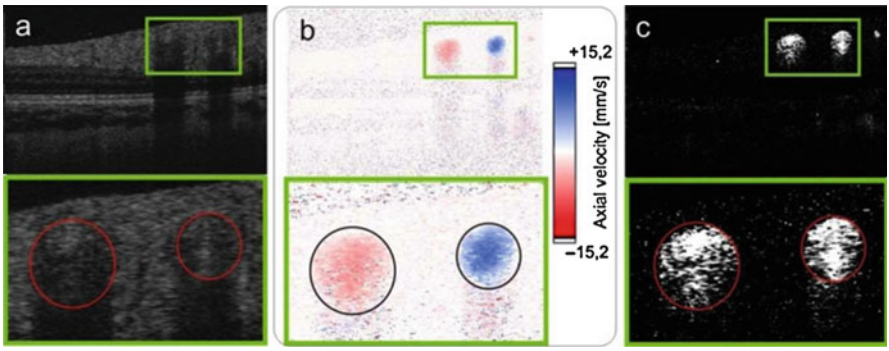

Fig. 42.13 Results of the bulk motion correction and segmentation of blood vessels by STdOCT. (**a**) Standard structural image. (**b**) Velocity map used in a further segmentation procedure. (**c**) Structural image of the segmented vessels (details are zoomed with 8.5× magnification) [51]

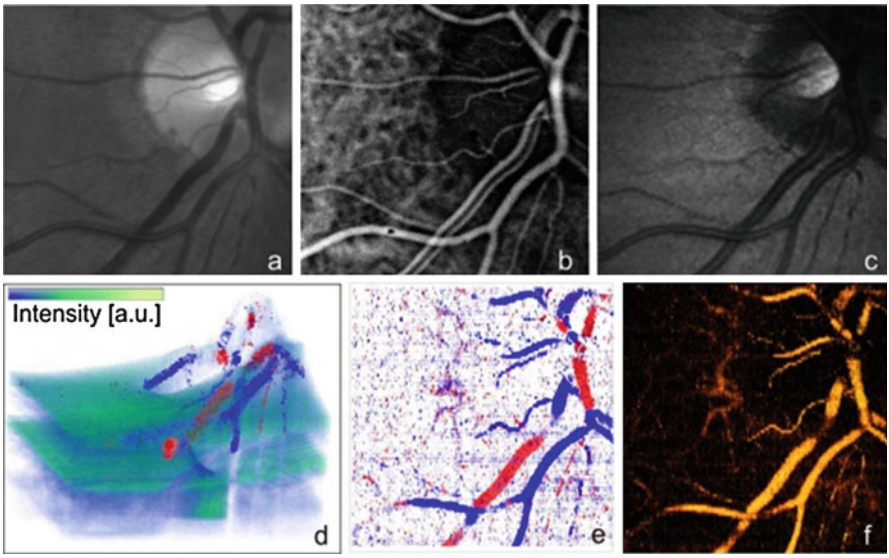

Fig. 42.14 Imaging of retinal blood vessels in the region of the optic nerve head (5 mm × 5 mm, exposure time 12 μs, maximum value of the axial velocity ±15 mm/s, measurement time <3 s). (**a**) Red-free fundus photography. (**b**) ICG angiography. (**c**) FdOCT fundus view. (**d**) Reconstructed 3D velocity image overlaid onto structural FdOCT data. (**e**) Velocity en-face map created from 3D STdOCT data. (**f**) En-face view of segmented vessels. None of presented images required filtering, smoothing, or manual segmentation [51]

flows with an axial velocity smaller than 220 μm/s in an area of 1.2 × 1.2 mm. A 3D visualization of the capillaries allowed the creation of qualitative angiographic maps, seen in Fig. 42.16a–c, along with quantitative axial velocity maps, depicted in Fig. 42.16d–f from different retinal layers.

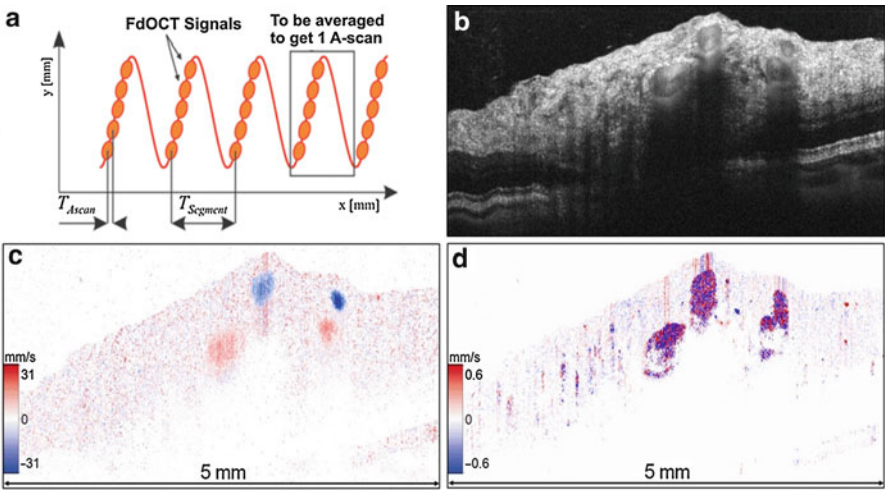

Fig. 42.15 Smart OCT Doppler analysis of retinal vasculature in the vicinity of optic disc: (**a**) illustration of STdOCT smart scanning protocol, (**b**) structural images with averaged A-scans measured for the beam deflected slightly in orthogonal direction (with significant oversampling), (**c**) Doppler map for velocities ranging between ± 30mm/s, and (**d**) Doppler map for velocities ranging between ±0.6 mm/s [52]

42.4.3 Application of DOCT to Dermatology

The application of OCT to dermatology is generating raising interest because of the previously mentioned advantages. Several studies have already been conducted to investigate inflammatory skin diseases, such as dermatitis, or skin cancer, such as basal cell carcinoma [53]. They were however limited to analysis of structural changes assessed from OCT intensity pictures alone. The capability of OCT to visualize also the vascular network has the capacity to provide complementary information related to the important metabolic tissue demand.

We have seen several techniques using OCT to contrast blood vessels in ▶ Chap. 2, "Theory of Optical Coherence Tomography", but few were applied to human skin microvasculature imaging in vivo. Although first 2D and 3D images of single vessels section have been presented already with time domain OCT [17, 54], the limited acquisition speed prevented the measurement of larger vasculature patches. The development of Fourier domain OCT brought a dramatic increase in sensitivity, which made in vivo full volume measurement with short acquisition time possible [18, 19]. Human skin microcirculation imaging based on Fourier domain OCT was demonstrated by calculating the intensity-based Doppler variance [55]. An enhanced field of view (FOV) of up to 8 × 7 mm was shown by correlation mapping OCT [56]. Based on the method of ultrahigh-sensitive optical microangiography (UHS OMAG) [57], differences in the blood vessel network between normal skin and psoriatic skin conditions have been resolved [58].

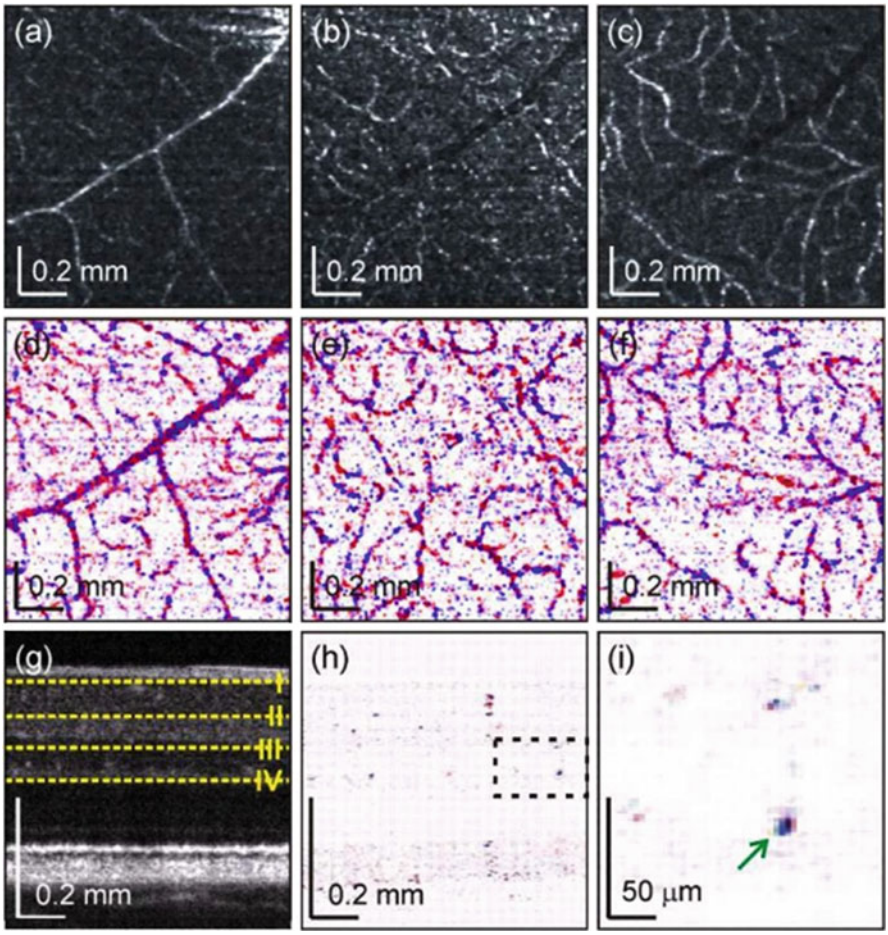

Fig. 42.16 STdOCT imaging of retinal capillaries. (**a**–**c**) The projection of OCT fundus images generated for depth ranges between boundaries I–II, II–III, and III–IV, respectively. These are shown as *yellow dashed lines* in panel (**g**). (**d**–**f**) The flow maps at the depth ranges visualized in the projection OCT fundus images. (**g**) Cross-sectional OCT image; the *dashed yellow lines* indicate boundaries of depth ranges used for projection OCT fundus imaging. (**h**) Example cross-sectional flow image extracted from the 3D data at a location indicated by the *dashed line* in panel (**f**). (**i**) Enlarged image of capillaries indicated by the *dashed rectangle* in panel (**h**); the *green arrow* points to a capillary with colors encoding the velocity value and direction ranging from *blue* to *red*. The *scale bars* in images (**a**–**h**) indicate lengths 200 μm by 200 μm and in image (**i**), 50 μm by 50 μm [52]

In the following, label-free angiography of skin using an extended focus OCT (xf-OCT) system [59] is demonstrated. xf-OCT that is based on Bessel beam illumination provides an enhanced depth of focus as compared to standard Gaussian illumination. This system operates further at a center wavelength of 1,300 nm for optimal penetration into skin tissue [60]. It is based on swept source OCT and

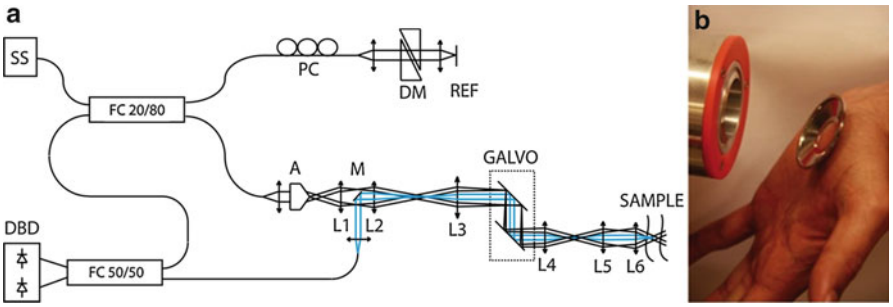

Fig. 42.17 (**a**) Optical setup of the xf-OCT system. *Blue*: detection path. *SS* Swept source, *FC* fiber coupler, *PC* polarization control, *DM* dispersion matching, *A* axicon, *M* mirror, *L1 to L6* lenses, *Galvo* scanning mirrors, *DBD* dual-balanced detector. (**b**) Adapter plate, containing a cover glass window, taped on a hand palm, in front of the mating ring that surrounds the objective lens on the *left* [35]

provides high-speed imaging by employing a Fourier domain mode-locked (FDML) laser [61]. The optical setup (Fig. 42.17a) for extended focus OCT imaging is the same as the one previously published [62]. An axicon lens creates a Bessel intensity distribution that is relayed on the beam steering device and further in the objective back focal plane to produce a Bessel beam illumination on the sample. Backscattered light is collected by a path-decoupled Gaussian mode. The lateral point spread function of the system is thus a Gaussian apodized version of the Bessel beam. The lateral resolution can be evaluated from its $1/e^2$ lateral extend to be of ~6 μm, constant over an axial distance of ~500 μm. For skin imaging, an adapter plate containing a cover glass window of 150 μm thickness is centered on the lesion and then taped on the skin. The adapter plate is then fixed via a mating ring in front of the sample objective (L6) keeping the region of interest centered to the scanning beam (Fig. 42.17b).

Microcirculation imaging was performed over a 2 × 2 mm FOV by acquiring $N = 10$ tomograms at 100 different vertical positions. The number of 10 tomograms is an empirical value selected such as to have on the one hand high microcirculation contrast and on the other hand enough data for motion contrast analysis after rejection of patient motion affected tomograms. In addition, we aimed at keeping the measurement time as short as possible. Each tomogram contains 800 A-scans. The acquisition was performed at 220kA-scans/s leading to a measurement time of about 4 s. In a second step, a highly sampled volume consisting of 800 tomograms, without any redundancy, was acquired.

The microvascularization of the palm of a healthy volunteer is used for indication of a normal condition. Figure 42.18a is a representative tomogram of the referred location visualizing the characteristic layers of a glabrous skin. Figure 42.18b, c show the en-face microvascularization for two different depth ranges, 300–350 μm and 350–450 μm, respectively. A mean projection is calculated over successive axial ranges in order to resolve two different kinds of vasculature: capillary loops feeding the living part of the epidermis and a deeper

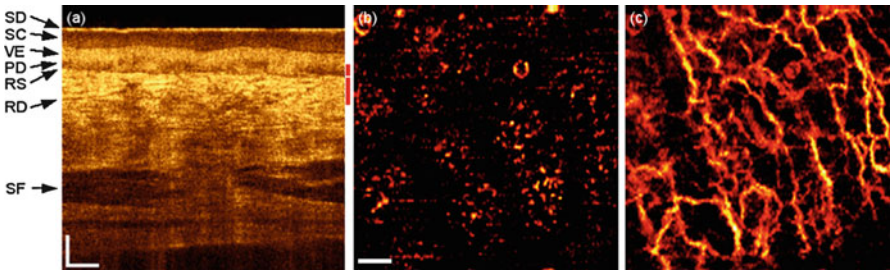

Fig. 42.18 Healthy skin of the palm. (**a**) OCT tomogram. *Red bars* indicate depth range for (**b**) and (**c**), respectively. *SD* stratum disjunctum, *SC* stratum corneum, *VE* viable epidermis, *PD* papillary dermis, *RS* rete subpapillare, *RD* reticular dermis, and *SF* subcutaneous fat. (**b** and **c**) 2 × 2 mm en-face mean projection over depth range indicated in (**a**) *scale bars* indicate 250 μm in every picture [48]

planar vascular network that supports the capillary vessels. The vasculature images are thresholded to reduce the background noise. This may however lead to missing signals visible as discontinuities along the contrasted vascular network.

The vascular pattern is visually different for pathological conditions. The case presented in Fig. 42.19 is an allergy-induced eczema on the forearm. A dermascope is used to acquire a reflectance picture of the lesion over a large FOV. Figure 42.19a shows the lesion and indicates the FOV of OCT. Dilated vessels and scaly patches are visible; however, the resolution does not permit to resolve the finer vascular network. Furthermore, no depth information is available. The OCT tomogram in Fig. 42.19b shows increased perfusion and vasculature visible through increased shadowing artifacts as compared to the healthy case. An en-face mean projection of the highly sampled intensity volume is displayed in Fig. 42.19c. Complementary information is provided by the OCT angiograms obtained with the squared intensity difference method. Figure 42.19d shows a microvasculature en-face mean projection image of the dermoepidermal junction, displaying cross sections of superficial vertical capillary loops. The perfusion signatures of those capillaries are larger in diameter than those of the healthy control due to increased perfusion in the inflammation region. Relative change of perfusion can be inferred by our technique from visible vessel size changes. Also, the inflammation causes an alteration of the tissue structure that obviously leads to larger lateral distances between the capillary loops. The red areas in the dermoscopy image are diagnosed as subcutaneous bleeding caused by scratching. It is expected that the blood visible with the dermascope should also be visible in the OCT tomogram because of the intrinsic stronger backscattering of blood. We observe in fact that the red areas of subcutaneous bleeding in the dermoscopy image correlate well with the regions of enhanced backscattering seen in the OCT tomograms and marked with the asterisk in Fig. 42.19b. Those areas do not appear in the motion contrast angiogram, since the subcutaneous blood is basically static. Figure 42.19e shows an overlay of the microcirculation on the structural information. Note that both pieces of information are extracted from the same data set, resulting in a perfect registration.

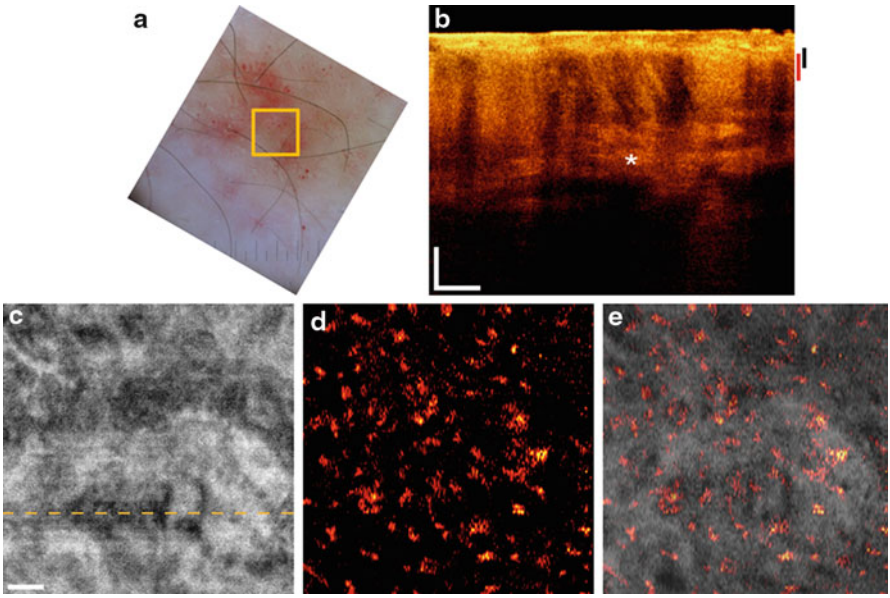

Fig. 42.19 Eczema on the forearm. (**a**) Dermoscopy image with square indicating the OCT FOV. (**b**) OCT tomogram. *Black* and *red bars* indicate depth range for (**c**) and (**d**), respectively. (**c**) Intensity en-face mean projection for depth range in (**b**), *dashed line* indicates the tomogram position. (**d**) 2 × 2 mm en-face view of angiography. (**e**) Overlay of microcirculation on structural information. *Scale bars* indicate 250 μm in every picture [48]

The presented case is a nice example of how complementary information given by structural as well as angiographic method helps for a better interpretation and understanding of the tissue pathology.

Finally, a case of nonmelanoma skin cancer is presented – basal cell carcinoma (BCC) on the forehead. Dermoscopy (Fig. 42.20a) reveals characteristic arborizing vessels, which are seen in 50–70 % of BCCs [64]. The tomogram has a different signature, particularly in the epidermis region resembling the rolled border of the tumor caused by tumor cell aggregations surrounded by fibrous stroma (Fig. 42.20b). The dark areas in the deeper regions visible in the OCT tomogram are possibly necrotic or cystic regions. The OCT microvasculature imaging reveals a dense network of unorganized vessels (Fig. 42.20d). Furthermore, large vessels are abnormally present close to the surface. The large vessels branch out to provide the perfusion support through the smaller secondary vessels to the tumor sites with high metabolic demand.

Due to our additional completely noninvasive motion contrast modality, we obtain further complementary information on the angiographic properties of the skin diseases. The measurements performed on different pathological conditions clearly indicate abnormal and characteristic signatures of the vasculature (see Table 42.1).

Noninvasive vascular imaging has certainly large potential for treatment monitoring by providing, for example, information on antivascular treatment effectiveness, in case of photodynamic therapy. This imaging technique could also be used to assess the

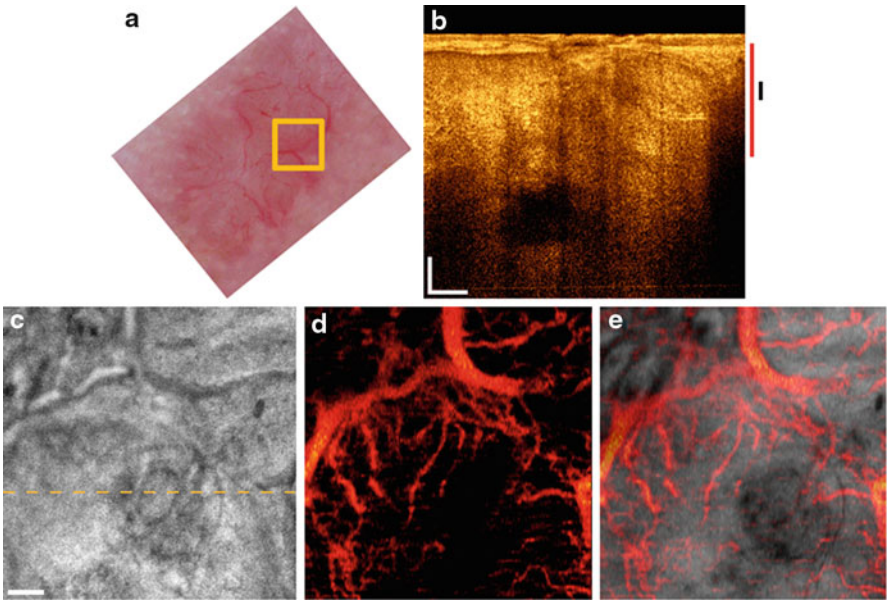

Fig. 42.20 BCC on the forehead. (**a**) Dermoscopy image with *square* indicating the OCT FOV. (**b**) OCT tomogram. *Black* and *red bars* indicate depth range for (**c**) and (**d**), respectively. (**c**) Intensity en-face mean projection for depth range in (**b**), *dashed line* indicates the tomogram position. (**d**) 2 × 2 mm en-face fly through the microvasculature starting from surface (media 4). (**e**) Overlay of microcirculation on structural information. *Scale bars* indicate 250 μm in every picture [35]

Table 42.1 Comparison between the different pathological conditions [35]

Condition	Effect on microcirculation
Healthy	Organized flat vessels beds with smaller capillary vessels in the upper layers and increased vessel size in deeper skin tissue
Inflammation	Enlarged blood vessels, in particular capillaries that indicate increased perfusion
Basal cell carcinoma	Denser network of unorganized vessels with chaotic branching, larger vessels even close to the skin surface, capillary structure less pronounced and visible

stage of the disease not only qualitatively but also quantitatively. Analysis on vessel density or the fractal dimension of the vascular tree can potentially give more precise information about the severity and progression of the disease [11, 12, 64].

42.5 Outlook

In the present chapter, we aimed at providing a brief summary of Doppler FdOCT applied to vascular contrasting with examples of ophthalmic and dermatology OCT

imaging. Future directions in ophthalmology will certainly include OCT intensity information in order to complement the dynamic flow contrasting also with static information. Tracking systems as well as smart registration algorithms will further improve the quality of flow contrast images by reducing motion artifacts. Also in case of dermatology, the access to functional perfusion data will enhance the diagnostic capabilities of current OCT scanners. Perfusion is an important biomarker for tissue health and can therefore be applied for assessing wound healing and treatment progression. Apart from the skin and the eye, DOCT is extensively used for brain imaging. Further applications of DOCT can be envisioned in the field of endoscopy. Finally, new light source and detector technology might open the door for novel DOCT methods that allow for even faster vascular imaging over larger field of views.

Acknowledgements We would like to thank Leopold Schmetterer, Wolfgang Drexler, Amardeep Singh, Branislav Grajciar, Tilman Schmoll, Rene Werkmeister, Alex Aneesh, Michael Binder, and Jessica Weingast from the Medical University of Vienna; Andrzej Kowalczyk, Anna Szkulmowska, and Ireneusz Grulkowski from the Nicholas Copernicus University in Torun, Poland; and Robert Huber, Wolfgang Wieser, and Thomas Klein from the LMU Munich, Germany. We acknowledge funding from the EU FP7 program (FUN OCT, grant no. 201880), funding by the Austrian Christian Doppler Association and EURYI grant/award funded by the European Heads of Research Councils (EuroHORCs) together with the European Science Foundation (ESF – EURYI 01/2007PL) operated by the Foundation for Polish Science.

References

1. R. Bonner, R. Nossal, Model for laser Doppler measurements of blood flow in tissue. Appl. Optics **20**, 2097–2107 (1981)
2. B.H. Park, M.C. Pierce, B. Cense, S.H. Yun, M. Mujat, G. Tearney, B. Bouma, J. de Boer, Real-time fiber-based multi-functional spectral-domain optical coherence tomography at 1.3 μm. Opt. Express **13**, 3931–3944 (2005)
3. S. Zotter, M. Pircher, T. Torzicky, M. Bonesi, E. Götzinger, R.A. Leitgeb, C.K. Hitzenberger, Visualization of microvasculature by dual-beam phase-resolved Doppler optical coherence tomography. Opt. Express **19**, 1217–1227 (2011)
4. E. Friedman, A hemodynamic model of the pathogenesis of age-related macular degeneration. Am. J. Ophthalmol. **124**, 677–682 (1997)
5. L. Schmetterer, M. Wolzt, Ocular blood flow and associated functional deviations in diabetic retinopathy. Diabetologia **42**, 387–405 (1999)
6. C.E. Riva, S.D. Cranstoun, J.E. Grunwald, B.L. Petrig, Choroidal blood flow in the foveal region of the human disc. Invest. Ophthalmol. Vis. Sci. **35**, 4273–4281 (1994)
7. R.F. Furchgott, J.V. Zawadzki, The obligatory role of endothelial cells in the relaxation of arterial smooth muscle by acetylcholine. Nature **288**, 373–376 (1980)
8. M. Lie, O.M. Sejersted, F. Kiil, Local regulation of vascular cross section during changes in femoral arterial blood flow in dogs. Circ. Res. **27**, 727–737 (1970)
9. W. Drexler, R.A. Leitgeb, C.K. Hitzenberger, New developments in optical coherence tomography technology, in *Medical Retina*, ed. by R.F. Spaide (Springer, Berlin, 2009), p. 277
10. R.A. Leitgeb, Current technologies for high-speed and functional imaging with optical coherence tomography, in *Advances in Imaging and Electron Physics*, ed. by P.W. Hawkes, vol. 168 (Elsevier Academic, San Diego, 2011), pp. 109–192

11. T. Schmoll, A.S.G. Singh, C. Blatter, S. Schriefl, C. Ahlers, U. Schmidt-Erfurth, R.A. Leitgeb, Imaging of the parafoveal capillary network and its integrity analysis using fractal dimension. Biomed. Opt. Express **2**, 1159–1168 (2011)
12. B.J. Vakoc, R.M. Lanning, J.A. Tyrrell, T.P. Padera, L.A. Bartlett, T. Stylianopoulos, L.L. Munn, G.J. Tearney, D. Fukumura, R.K. Jain, B.E. Bouma, Three-dimensional microscopy of the tumor microenvironment in vivo using optical frequency domain imaging. Nat. Med. **15**, 1219–1223 (2009)
13. S. Yazdanfar, A.M. Rollins, J.A. Izatt, Imaging and velocimetry of the human retinal circulation with color Doppler optical coherence tomography. Opt. Lett. **25**, 1448–1450 (2000)
14. S. Yazdanfar, A.M. Rollins, J. Izatt, In vivo imaging of human retinal flow dynamics by color Doppler optical coherence tomography. Arch. Ophthalmol. **121**, 235–239 (2003)
15. Y. Zhao, Z. Chen, C. Saxer, Q. Shen, S. Xiang, J.F. de Boer, J.S. Nelson, Doppler standard deviation imaging for clinical monitoring of in vivo human skin blood flow. Opt. Lett. **25**, 1358–1360 (2000)
16. C. Yang, A. Wax, M.S. Hahn, K. Badizadegan, R.R. Dasari, M.S. Feld, Phase-referenced interferometer with subwavelength and subhertz sensitivity applied to the study of cell membrane dynamics. Opt. Lett. **26**, 1271–1273 (2001)
17. Y. Zhao, Z. Chen, C. Saxer, S. Xiang, J.F. de Boer, J.S. Nelson, Phase-resolved optical coherence tomography and optical Doppler tomography for imaging blood flow in human skin with fast scanning speed and high velocity sensitivity. Opt. Lett. **25**, 116 (2000)
18. A.F. Fercher, C.K. Hitzenberger, G. Kamp, S.Y. Elzaiat, Measurement of intraocular distances by backscattering spectral interferometry. Opt. Commun. **117**, 43–48 (1995)
19. R. Leitgeb, C.K. Hitzenberger, A.F. Fercher, Performance of Fourier domain vs. time domain optical coherence tomography. Opt. Express **11**, 889–894 (2003)
20. J.F. de Boer, B. Cense, B.H. Park, M.C. Pierce, G.J. Tearney, B.E. Bouma, Improved signal-to-noise ratio in spectral-domain compared with time-domain optical coherence tomography. Opt. Lett. **28**, 2067–2069 (2003)
21. M.A. Choma, M.V. Sarunic, C. Yang, J. Izatt, Sensitivity advantage of swept source and Fourier domain optical coherence tomography. Opt. Express **11**, 2183–2189 (2003)
22. M. Wojtkowski, R. Leitgeb, A. Kowalczyk, T. Bajraszewski, A.F. Fercher, In vivo human retinal imaging by Fourier domain optical coherence tomography. J. Biomed. Opt. **7**, 457–463 (2002)
23. M. Wojtkowski, V. Srinivasan, J.G. Fujimoto, T. Ko, J.S. Schuman, A. Kowalczyk, J.S. Duker, Three-dimensional retinal imaging with high-speed ultrahigh-resolution optical coherence tomography. Ophthalmology **112**, 1734–1746 (2005)
24. U. Schmidt-Erfurth, R.A. Leitgeb, S. Michels, B. Povazay, S. Sacu, B. Hermann, C. Ahlers, H. Sattmann, C. Scholda, A.F. Fercher, W. Drexler, Three-dimensional ultrahigh-resolution optical coherence tomography of macular diseases. Invest. Ophthalmol. Vis. Sci. **46**, 3393–3402 (2005)
25. N. Nassif, B. Cense, B.H. Park, S.H. Yun, T.C. Chen, B.E. Bouma, G.J. Tearney, J.F. de Boer, In vivo human retinal imaging by ultrahigh-speed spectral domain optical coherence tomography. Opt. Lett. **29**, 480–482 (2004)
26. R.A. Leitgeb, L. Schmetterer, C.K. Hitzenberger, A.F. Fercher, F. Berisha, M. Wojtkowski, T. Bajraszewski, Real-time measurement of in vitro flow by Fourier-domain color Doppler optical coherence tomography. Opt. Lett. **29**, 171–173 (2004)
27. B.R. White, M.C. Pierce, N. Nassif, B. Cense, B.H. Park, G.J. Tearney, B.E. Bouma, T.C. Chen, J.F. de Boer, In vivo dynamic human retinal blood flow imaging using ultra-high-speed spectral domain optical Doppler tomography. Opt. Express **11**, 3490–3497 (2003)
28. T. Schmoll, C. Kolbitsch, R.A. Leitgeb, Ultra-high-speed volumetric tomography of human retinal blood flow. Opt. Express **17**, 4166–4176 (2009)
29. A.H. Bachmann, M.L. Villiger, C. Blatter, T. Lasser, R.A. Leitgeb, Resonant Doppler flow imaging and optical vivisection of retinal blood vessels. Opt. Express **15**, 408–422 (2007)

30. L. An, R.K. Wang, In vivo volumetric imaging of vascular perfusion within human retina and choroids with optical micro-angiography. Opt. Express **16**, 11438–11452 (2008)
31. M. Szkulmowski, A. Szkulmowska, T. Bajraszewski, A. Kowalczyk, M. Wojtkowski, Flow velocity estimation using joint spectral and time domain optical coherence tomography. Opt. Express **16**, 6008–6025 (2008)
32. Y.K. Tao, A.M. Davis, J.A. Izatt, Single-pass volumetric bidirectional blood flow imaging spectral domain optical coherence tomography using a modified Hilbert transform. Opt. Express **16**, 12350–12361 (2008)
33. C. Kolbitsch, T. Schmoll, R.A. Leitgeb, Histogram-based filtering for quantitative 3D retinal angiography. J. Biophotonics **2**, 416–425 (2009)
34. R.A. Leitgeb, L. Schmetterer, W. Drexler, A.F. Fercher, R.J. Zawadzki, T. Bajraszewski, Real-time assessment of retinal blood flow with ultrafast acquisition by color Doppler Fourier domain optical coherence tomography. Opt. Express **11**, 3116–3121 (2003)
35. C. Blatter, J. Weingast, A. Alex, B. Grajciar, W. Wieser, W. Drexler, R. Huber, R.A. Leitgeb, In situ structural and microangiographic assessment of human skin lesions with high-speed OCT. Biomed. Opt. Express **3**, 2636–2646 (2012)
36. J.W. Goodman, *Statistical Optics* (Wiley, New York, 2000)
37. B.J. Vakoc, S.H. Yun, J.F. De Boer, G.J. Tearney, B.E. Bouma, Phase-resolved optical frequency domain imaging. Opt. Express **13**, 5483–5493 (2005)
38. M. Gora, K. Karnowski, M. Szkulmowski, B.J. Kaluzny, R. Huber, A. Kowalczyk, M. Wojtkowski, Ultra high-speed swept source OCT imaging of the anterior segment of human eye at 200 kHz with adjustable imaging range. Opt. Express **17**, 14880–14894 (2009)
39. D.J. Faber, T.G. van Leeuwen, Doppler calibration method for spectral domain OCT spectrometers. J. Biophotonics **2**, 407–415 (2009)
40. D.Q. Piao, Q. Zhu, Quantifying Doppler angle and mapping flow velocity by a combination of Doppler-shift and Doppler-bandwidth measurements in optical Doppler tomography. Appl. Optics **42**, 5158–5166 (2003)
41. D.Q. Piao, L.L. Otis, Q. Zhu, Doppler angle and flow velocity mapping by combined Doppler shift and Doppler bandwidth measurements in optical Doppler tomography. Opt. Lett. **28**, 1120–1122 (2003)
42. S.G. Proskurin, Y. He, R.K. Wang, Determination of flow velocity and spectrum broadening with vector based on Doppler shift optical coherence tomography. Opt. Lett. **28**, 1227–1229 (2003)
43. J. Walther, E. Koch, Enhanced joint spectral and time domain optical coherence tomography for quantitative flow velocity measurement. Opt. Coherence Tomogr. Coherence Tech. V **8091**, 22 (2011)
44. D.Y. Kim, J. Fingler, J.S. Werner, D.M. Schwartz, S.E. Fraser, R.J. Zawadzki, In vivo volumetric imaging of human retinal circulation with phase-variance optical coherence tomography. Biomed. Opt. Express **2**, 1504–1513 (2011)
45. T. Klein, W. Wieser, C.M. Eigenwillig, B.R. Biedermann, R. Huber, Megahertz OCT for ultrawide-field retinal imaging with a 1050 nm Fourier domain mode-locked laser. Opt. Express **19**, 3044–3062 (2011)
46. Y. Yasuno, Y. Hong, S. Makita, M. Yamanari, M. Akiba, M. Miura, T. Yatagai, In vivo high-contrast imaging of deep posterior eye by 1-um swept source optical coherence tomography and scattering optical coherence angiography. Opt. Express **15**, 6121–6139 (2007)
47. A. Unterhuber, B. Povazay, B. Hermann, H. Sattmann, A. Chavez-Pirson, W. Drexler, In vivo retinal optical coherence tomography at 1040 nm – enhanced penetration into the choroid. Opt. Express **13**, 3252–3258 (2005)
48. C. Blatter, T. Klein, B. Grajciar, T. Schmoll, W. Wieser, R. Andre, R. Huber, R.A. Leitgeb, Ultrahigh-speed non-invasive widefield angiography. J. Biomed. Opt. **17**, 070505 (2012)
49. F. Jaillon, S. Makita, Y. Yasuno, Variable velocity range imaging of the choroid with dual-beam optical coherence angiography. Opt. Express **20**, 385–396 (2012)

50. F. Jaillon, S. Makita, E.-J. Min, B.H. Lee, Y. Yasuno, Enhanced imaging of choroidal vasculature by high-penetration and dual-velocity optical coherence angiography. Biomed. Opt. Express **2**, 1147–1158 (2011)
51. A. Szkulmowska, M. Szkulmowski, D. Szlag, A. Kowalczyk, M. Wojtkowski, Three-dimensional quantitative imaging of retinal and choroidal blood flow velocity using joint spectral and time domain optical coherence tomography. Opt. Express **17**, 10584–10598 (2009)
52. I. Grulkowski, I. Gorczynska, M. Szkulmowski, D. Szlag, A. Szkulmowska, R.A. Leitgeb, A. Kowalczyk, M. Wojtkowski, Scanning protocols dedicated to smart velocity ranging in spectral OCT. Opt. Express **17**, 23736–23754 (2009)
53. T. Gambichler, V. Jaedicke, S. Terras, Optical coherence tomography in dermatology: technical and clinical aspects. Arch. Dermatol. Res. **303**, 457–473 (2011)
54. Y.H. Zhao, K.M. Brecke, H.W. Ren, Z.H. Ding, J.S. Nelson, Z.P. Chen, Three-dimensional reconstruction of in vivo blood vessels in human skin using phase-resolved optical Doppler tomography. IEEE J. Sel Top. Quant. Electron. **7**, 931–935 (2001)
55. G. Liu, W. Jia, V. Sun, B. Choi, Z. Chen, High-resolution imaging of microvasculature in human skin in-vivo with optical coherence tomography. Opt. Express **20**, 7694–7705 (2012)
56. J. Enfield, E. Jonathan, M. Leahy, In vivo imaging of the microcirculation of the volar forearm using correlation mapping optical coherence tomography (cmOCT). Biomed. Opt. Express **2**, 1184–1193 (2011)
57. L. An, J. Qin, R.K. Wang, Ultrahigh sensitive optical microangiography for in vivo imaging of microcirculations within human skin tissue beds. Opt. Express **18**, 8220–8228 (2010)
58. J. Qin, J. Jiang, L. An, D. Gareau, R.K. Wang, In vivo volumetric imaging of microcirculation within human skin under psoriatic conditions using optical microangiography. Lasers Surg. Med. **43**, 122–129 (2011)
59. R.A. Leitgeb, M. Villiger, A.H. Bachmann, L. Steinmann, T. Lasser, Extended focus depth for Fourier domain optical coherence microscopy. Opt. Lett. **31**, 2450–2452 (2006)
60. A. Alex, B. Povazay, B. Hofer, S. Popov, C. Glittenberg, S. Binder, W. Drexler, Multispectral in vivo three-dimensional optical coherence tomography of human skin. J. Biomed. Opt. **15**, 026025 (2010)
61. W. Wieser, B.R. Biedermann, T. Klein, C.M. Eigenwillig, R. Huber, Multi-megahertz OCT: high quality 3D imaging at 20 million A-scans and 4.5 GVoxels per second. Opt. Express **18**, 14685–14704 (2010)
62. C. Blatter, B. Grajciar, C.M. Eigenwillig, W. Wieser, B.R. Biedermann, R. Huber, R.A. Leitgeb, Extended focus high-speed swept source OCT with self-reconstructive illumination. Opt. Express **19**, 12141–12155 (2011)
63. D. Altamura, S.W. Menzies, G. Argenziano, I. Zalaudek, H.P. Soyer, F. Sera, M. Avramidis, K. DeAmbrosis, M.C. Fargnoli, K. Peris, Dermatoscopy of basal cell carcinoma: morphologic variability of global and local features and accuracy of diagnosis. J. Am. Acad. Dermatol. **62**, 67–75 (2010)
64. J.W. Baish, R.K. Jain, Fractals and cancer. Cancer Res. **60**, 3683–3688 (2000)
65. M. Szkulmowski, I. Grulkowski, D. Szlag, A. Szkulmowska, A. Kowalczyk, M. Wojtkowski, Flow velocity estimation by complex ambiguity free joint spectral and time domain optical coherence tomography. Opt. Express **17**, 14281–14297 (2009)
66. A. Mariampillai, B.A. Standish, E.H. Moriyama, M. Khurana, N.R. Munce, M.K.K. Leung, J. Jiang, A. Cable, B.C. Wilson, I.A. Vitkin, V.X.D. Yang, Speckle variance detection of microvasculature using swept-source optical coherence tomography. Opt. Lett. **33**, 1530–1532 (2008)
67. J. Barton, S. Stromski, Flow measurement without phase information in optical coherence tomography images. Opt. Express **13**, 5234–5239 (2005)
68. E. Jonathan, J. Enfield, M.J. Leahy, Correlation mapping method for generating microcirculation morphology from optical coherence tomography (OCT) intensity images. J. Biophotonics **4**, 583–587 (2011)

69. R. Leitgeb, L. Schmetterer, M. Wojtkowski, C. Hitzenberger, M. Sticker, A. Fercher, Flow velocity measurements by frequency domain short coherence interferometry. SPIE Proc. **4619**, 16–21 (2002)
70. V. Yang, M. Gordon, B. Qi, J. Pekar, S. Lo, E. Seng-Yue, A. Mok, B. Wilson, I. Vitkin, High speed, wide velocity dynamic range Doppler optical coherence tomography (Part I): system design, signal processing, and performance. Opt. Express **11**, 794–809 (2003)
71. T. Schmoll, I.R. Ivascu, A.S.G. Singh, A. Unterhuber, R.A. Leitgeb, Intra-and Inter-Frame Differential Doppler Imaging, in *Optical Coherence Tomography and Coherence Techniques*, ed. by V.R.A. Leitgeb, B.E. Bouma (SPIE, Bellingham, 2011)
72. L. Yu, Z. Chen, Doppler variance imaging for three-dimensional retina and choroid angiography. J. Biomed. Opt. **15**, 016029–016029 (2010)
73. R.M. Werkmeister, N. Dragostinoff, M. Pircher, E. Götzinger, C.K. Hitzenberger, R.A. Leitgeb, L. Schmetterer, Bidirectional Doppler Fourier domain optical coherence tomography for measurement of absolute flow velocities in human retinal vessels. Opt. Lett. **33**(24), 2967–2969 (2008)
74. C.J. Pedersen, D. Huang, M.A. Shure, A.M. Rollins, Measurement of absolute flow velocity vector using dual-angle, delay-encoded Doppler optical coherence tomography. Opt. Lett. **32**(5), 506–508 (2007)

Dual Beam Doppler Optical Coherence Angiography

43

Yoshiaki Yasuno, Shuichi Makita, and Franck Jaillon

Keywords
Optical coherence angiography • OCA • Dual-beam • Doppler • Vasculature • Circulation • Ophthalmology

43.1 Introduction

The ocular vasculature and circulation play a crucial role in the development of several eye diseases including glaucoma [1], diabetic retinopathy [2], and exudative macular diseases [3]. Modalities that are capable of investigating the ocular vasculature and circulation are important for both understanding the mechanisms of the diseases and diagnosing these diseases.

The current chief modality for this purpose is angiographies including fluorescein angiography (FA) and indocyanine green angiography (ICGA) [4]. In these angiographies, ocular vessels are contrasted using the fluorescence of dyes injected into a vein. The fluorescent dye utilized in FA is sodium fluorescein and that of ICGA is indocyanine green. Since the excitation wavelength of indocyanine green is relatively longer than that of sodium fluorescein, ICGA is commonly used for the investigation of choroidal vasculature, while FA is used to investigate abnormalities of the retinal vasculature and retinal pigment epithelium (RPE). Although the utility is very high, these modalities are invasive and have some adverse reactions. For instance, the skin will be colored in yellow by the fluorescein dye. Furthermore, moderate adverse effects, such as nausea and vomiting, occur with frequencies of less than 1 % and 10 %, respectively, for FA [5] and 0.15 % for ICGA [6]. In addition, although it is rare, severe adverse effects such as anaphylaxis also occur.

Y. Yasuno (✉) • S. Makita • F. Jaillon
Computational Optics Group, University of Tsukuba, Tsukuba, Ibaraki, Japan
e-mail: yasuno@optlab2.bk.tsukuba.ac.jp

© Springer International Publishing Switzerland 2015

W. Drexler, J.G. Fujimoto (eds.), *Optical Coherence Tomography*,
DOI 10.1007/978-3-319-06419-2_44

In addition to angiography methods that are used to investigate the ocular vasculature, there are several noninvasive blood flow assessment techniques that use lasers. Laser Doppler velocimetry (LDV) measures the blood flow velocity, and it has been applied to human retinal vessels [7, 8]. Microcirculation in the optic nerve head (ONH) [9] and the choroidal blood flow [10] of the human eye have been investigated with laser Doppler flowmetry (LDF) [11], which acquires the volume, flux, and average velocity of the red blood cells in the small vessels surrounded by the scattering tissues. Two-dimensional perfusion mapping of blood flow can be obtained using scanning laser Doppler flowmetry (SLDF) [12, 13], laser speckle photography [14], and laser speckle flowgraphy [15]. Although these techniques are useful for investigating the ocular circulation, they demonstrate no or poor ability to resolve the depth structure. SLDF, which is based on scanning laser ophthalmoscopy, exhibits depth-resolving power inherently due to the confocal effect; however, its axial resolution is limited to around 300 μm due to the limited numerical aperture and the aberrations of the eye.

Doppler optical coherence tomography (Doppler OCT), which is also denoted as optical Doppler tomography, is an extension of OCT [16, 17]. Doppler OCT measures the Doppler shift of the probe beam in OCT and enables depth-resolved cross-sectional flow imaging of in vivo tissues [18–22] and has also been applied for the investigation of retinal vessels. Among several variations of Doppler OCT, phase-resolved Fourier domain (FD) Doppler OCT [23–25] has become the most commonly used Doppler OCT technique, because of the recent success of FD-OCT. Phase-resolved FD Doppler OCT provides high-resolution, high-speed, and three-dimensional (3-D) imaging of retinal blood flow [26–28].

The phase-resolved FD Doppler OCT has been utilized for both quantification of ocular circulation [29–31] and structural imaging of ocular vasculatures [32]. The latter is sometimes denoted as optical coherence angiography (OCA) or OCT angiography. OCA is an OCT-based alternative to standard angiography including FA and ICGA. Although its contrast mechanism is not the same as FA and ICGA, OCA images have shown high similarity with FA and ICGA [33]. In contrast to FA and ICGA, OCA is totally noninvasive. Hence, it can be utilized not only for standard clinical diagnosis but also for mass screening. In addition, the depth resolution of OCA enables separate retinal and choroidal angiograms and three-dimensional examination of the ocular vasculature.

In order to enhance the flow sensitivity of Doppler OCT and hence to investigate the fine vasculature with OCA, several extended Doppler measurement protocols have been presented. In the most standard phase-resolved FD Doppler OCT measurement, the Doppler shift signal is given as the phase difference between adjacent A-lines in a single OCT cross-section [24]. Since the Doppler shift of the probe beam is proportional to this phase difference, the phase difference of the OCT cross-section provides a cross-sectional Doppler OCT image. In this process, the phase difference is not only in proportion to the Doppler shift but also the time interval between the two A-lines.

Hence, a larger time interval provides a larger phase difference even with an identical Doppler shift. Since the phase noise of the OCT is not a function of the time interval, a larger time interval between adjacent A-lines provides a higher Doppler sensitivity for OCA.

However, there is another factor that degrades the Doppler sensitivity. Since Doppler OCT is a scanning imaging modality, the larger time interval between adjacent A-lines results in larger spatial separation between the A-lines. It causes large structural decorrelation between the A-lines and degrades the Doppler sensitivity. Therefore, the ideal scanning protocol for high-sensitive OCA imaging is a method that scans the same location of the sample twice with a large time interval.

Dual-beam Doppler OCA (DB-OCA) is a solution to enable this ideal scanning protocol [34–38]. DB-OCA uses two probe beam spots, where one spot follows the other spot during a retinal scan. Hence, a single location on the retina is scanned twice with a particular time interval that is in proportion to the spatial separation of the two probe spots. Subsequently, the Doppler phase difference is defined as a phase difference between the two A-lines obtained by the two spots. In this scheme, the time interval can be configured to be very large, while the spatial decorrelation can be kept very small or even negligible, because the two A-lines were obtained at the same location on the retina. Owing to this property, DB-OCA provides very high-sensitive Doppler imaging of the human eye in vivo.

This chapter describes the principle, implementation, and applications of DB-OCA. Among several implementations of DB-OCA, a standard spectral domain DB-OCA using polarized multiplexed dual-probe beams at 840 nm is described. As examples of the application, fine vasculature imaging of a normal macula and a case of abnormal vasculature, i.e., polypoidal choroidal vasculopathy, are presented. The standard DB-OCA is known to suffer from an artifact that occurs with the birefringence of the sample. An extension of DB-OCA, which is free from this artifact, is also described in detail.

Finally, a short summary of several extensions of DB-OCA is provided with pointers to references. The extensions include another multiplexing method for probe beams, high-penetration imaging by using a 1-μm wavelength probe, and a DB-OCA system with variable detectable flow velocity.

43.2 Principle and Implementation

43.2.1 Phase-Resolved Doppler Optical Coherence Tomography

The detailed principles of standard phase-resolved Doppler OCT exceed the scope of this chapter and have been extensively described elsewhere [23–25]. Hence, here we describe only the essential principles of phase-resolved Doppler FD-OCT, which are crucial for understanding DB-OCA.

In phase-resolved Doppler FD-OCT, the Doppler frequency shift is computed from the phase difference between two A-lines that have been acquired at nearly the same location of the sample but with a time interval of τ. Therefore, the mean Doppler frequency shift at a given sample location (x, y, z) between time t and $t+\tau$ is given by

$$\Delta f(x,y,z,t) = \frac{1}{2\pi\tau}\mathrm{Arg}\left[\Gamma_1(x,y,z,t)\Gamma_2^*(x+\Delta x,y,z,t+\tau)\right] \tag{43.1}$$

where $\Delta f(x, y, z)$ is the mean Doppler frequency shift between time t and $t+\tau$ and at a sample location of x (fast scan direction), y (slow scan direction), and z (depth). $\Gamma_1(x, y, z, t)$ and $\Gamma_2(x + \Delta x, y, z, t + \tau)$ are the complex OCT signals of the first and second A-lines. Δx is the spatial displacement between the two A-lines and is now assumed to be negligibly small in comparison to the transversal resolution of OCT. The subscript of * indicates a complex conjugate.

The Doppler frequency shift $\Delta f(x, y, z, t)$; Doppler phase shift $\Delta\varphi(x, y, z, t)$, i.e. the phase difference between the two A-lines $\mathrm{Arg}[\Gamma_1(x, y, z, t)\Gamma_2^*(x + \Delta x, y, z, t + \tau)]$; and the sample velocity are related as

$$\Delta\phi(x,y,z,t) = 2\pi\tau\Delta f(x,y,z,t) \tag{43.2}$$

$$\Delta\phi(x,y,z,t) = \frac{4\pi n\tau}{\lambda_0}v_z \tag{43.3}$$

where n is the refractive index of the sample, λ_0 is the center wavelength of the probe beam, and $v_z = v\cos\theta$ is the axial component of the velocity of the sample with the sample velocity of v and the angle between the probe beam and the direction of the motion θ. Equation 43.2 indicates that, even with a same velocity, the Doppler phase shift $\Delta\varphi(x, y, z)$ becomes larger with a lager τ. Hence, a larger τ provides a better signal-to-noise ratio for Doppler phase detection and consequent higher Doppler sensitivity when the phase noise of the OCT is constant in respect to τ.

However, in standard OCT implementation, the phase noise is not constant in τ. In the discussions above, we have assumed the spatial separation of two A-lines, Δx, is negligibly small. Meanwhile, in standard Doppler OCT, Δx and τ are related as $\Delta x = v_s\tau$ with v_s of the transversal scanning velocity of a probe spot on the sample. Hence, the assumption of a small Δx is no longer valid with a large τ. The larger Δx is known to increase the phase noise [39, 40]. As a result, a large τ enhances the Doppler phase shift but also increases the phase noise.

This property of Doppler OCT suggests that a possible Doppler OCT system that enables a large τ with a small Δx would be an ideal system to provide high Doppler sensitivity. DB-OCA described in this chapter is an extension of Doppler OCT, which provides this condition and hence enables very high Doppler sensitivity.

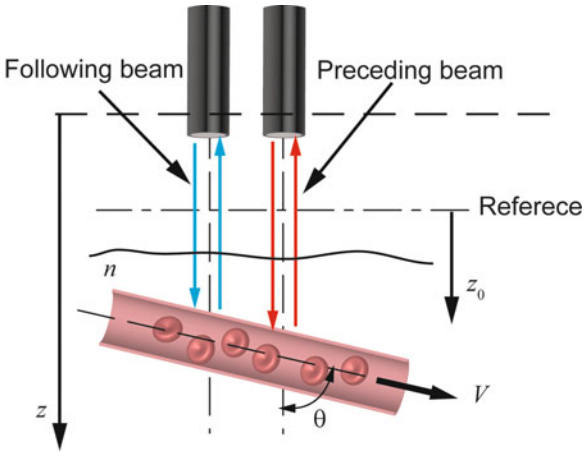

Fig. 43.1 The detection scheme of DB-OCA

43.2.2 Principle of Dual-Beam Doppler Optical Coherence Tomography

DB-OCA utilizes a Doppler detection scheme measuring the single Doppler frequency shift from two backscattered lights associated with two probe beams. The two probe beams have the same scanning speed and are spatially separated on the sample in the scanning direction as depicted in Fig. 43.1. Through the scanning of probes over the sample, the electric fields of lights, $E_p(x, y, z, t_p)$ and $E_f(x, y, z, t_f)$, are backscattered from a position (x, y, z) in the sample and are collected at different times, t_p and t_f, where the subscripts of p and f denote preceding and following probes, respectively. Spectrally resolved interference signals between collected lights and the reference light are detected and Fourier transformed into complex OCT signals, $\Gamma_p(x, y, z, t_p)$ and $\Gamma_f(x, y, z, t_f)$ [23]. Since the motion of the sample causes a Doppler frequency shift $\Delta f(x, y, z)$, it modulates the complex OCT signals as

$$\Gamma_p(x, y, z, t_p) = \Gamma'_p(x, y, z)\exp\left[i2\pi\Delta f(x, y, z)t_p\right] \tag{43.4}$$

$$\Gamma_f(x, y, z, t_f) = \Gamma'_f(x, y, z)\exp\left[i2\pi\Delta f(x, y, z)t_f\right] \tag{43.5}$$

where $\Gamma'_f(x, y, z)$ and $\Gamma'_f(x, y, z)$ are the time-independent components of the preceding and following probes, respectively. Using the same wavelength for the two probes, we can assume $\Gamma'_f(x, y, z) = \Gamma'_f(x, y, z)$. Under this circumstance, the Doppler frequency shift is obtained by calculating the phase difference between $\Gamma_p(x, y, z, t_p)$ and $\Gamma_f(x, y, z, t_f)$ as

$$\Delta f(x, y, z) = \frac{1}{2\pi\tau}\mathrm{Arg}\left[\Gamma_p(x, y, z, t_p)\Gamma_f^*(x, y, z, t_f)\right] \tag{43.6}$$

where the time interval $\tau \equiv t_f - t_p$. When the spatial separation of the two probes on the sample is d and the scan speed of the probe is v_s, τ is configured to be $\tau = d/v_s$. Since d can be arbitrarily configured using a proper optical design, τ can also be arbitrarily selected. By selecting a large τ, as suggested by Eq. 43.3, we can enlarge the Doppler phase shift value. In addition, two OCT signals utilized in the Doppler calculation in Eq. 43.6 were obtained at the same location in the sample. Namely, Δx that appears in the standard Doppler OCT equation (Eq. 43.1) becomes zero. Hence, phase noise elevation with a large Δx does not occur. Due to these properties, DB-OCA enables extremely high-sensitive Doppler OCT detection.

43.2.3 Implementation of Dual-Beam Doppler OCA

DB-OCA can be implemented by several means including Wollaston prism-based polarization multiplexing [34], polarization multiplexing with a polarization beam splitter [38], and an interferometer multiplexing method [35]. In this section, we describe the Wollaston-based polarization multiplexing method as the simplest examples. Some of the other implementations and extensions of DB-OCA are described in a later section.

43.2.3.1 Hardware Implementation

The instrumentation diagram of DB-OCA is presented in Fig. 43.2. In this setup, two probing beams are multiplexed in two orthogonal polarization states. The light source is a superluminescent diode (SLD-37-HP, Superlum Diodes Ltd., Ireland, in this example) with a center wavelength of 840 nm and spectral bandwidth of 50 nm (full width at half-maximum: FWHM). The beam from the light source propagates in a single-mode (SM) fiber and passes through an isolator and then a polarization controller. The light is split into the fast and slow modes in the polarization-maintaining (PM) fiber. The interferometer consists of a PM fiber coupler. In this particular example, the splitting ratio of the coupler is 80/20 with 20 % going to the sample arm.

Two polarization modes are separated by a Wollaston prism in the probing arm. The separation angle of the Wollaston prism is 0.35°. Two polarization modes independently propagate in the system. The separation of two modes on the cornea becomes 0.684°. After passing the eye optics, the two polarization modes form two probe light spots on the retina and are backscattered. The backscattered lights are combined again by the Wollaston prism and introduced to a polarization-sensitive spectrometer through a PM fiber. The two backscattered lights from the sample are independently detected by a polarization-sensitive spectrometer [41]. In this spectrometer, a polarization beam splitter divides the two polarization modes, and two-line scan cameras (AViiVA M2 CL 2014, e2V) detect each mode. The acquisition rate of the camera is 27, 778 lines/s.

The polarization controller in the SM fiber regulates the polarization state at the connection between the SM and PM fibers to ensure identical optical powers in each mode and the same sensitivity in both polarization channels. The optical

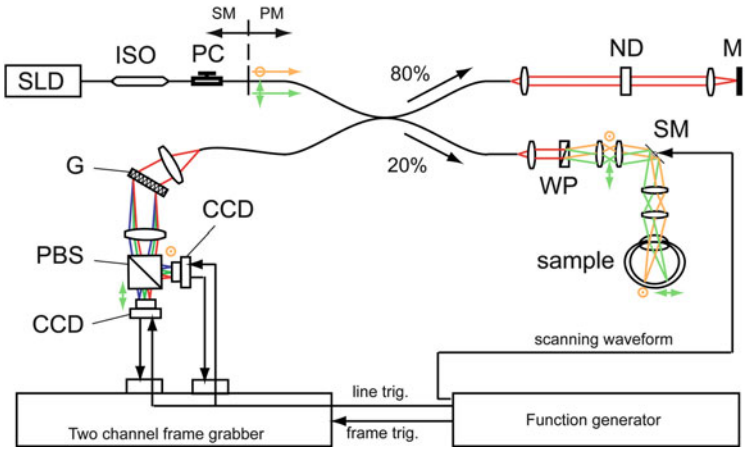

Fig. 43.2 Instrumentation scheme of DB-OCA based on spectral domain optical coherence tomography uses a superluminescent diode (*SLD*). Orthogonal polarization states are separated and independently propagated inside a polarization-maintaining (*PM*) fiber 80/20 coupler. They are separated spatially on the sample using a Wollaston prism (*WP*) and scanned by a scanning mirror module (*SM*). Reference beams are attenuated by a neutral density filter (*ND*) and reflected by a mirror (*M*). The reference arm should exhibit no birefringence to avoid crosstalk between the two channels. Interference signals of each polarization state are detected by a polarization-sensitive spectrometer consisting of a grating (*G*), polarization beam splitter (*PBS*), and two-line scan CCD cameras (*CCD*). The cameras are synchronously driven by the same trigger from a function generator through a frame grabber

power on a sample is 370 μW for each polarization mode. The total power is 740 μW, which is lower than the safe exposure limit according to the ANSI standard (Z136.1) [42].

In this particular example, the predicted shot-noise-limited sensitivity is 100 dB with an integration time of 34.8 μs. The sensitivity was measured as 94 dB and 93 dB for each channel, which was approximately 6 dB lower than the shot-noise-limited sensitivity. This is reasonable since the optical power loss of the system was measured as 6.5 dB, which may be due to the loss at fiber re-coupling, polarization crosstalk in optical components, and the alignment error of the mirror sample for sensitivity measurement because of the difficulty in aligning the mirror for both separated sampling beams. The beam diameter at $1/e^2$ on the cornea is about 820 μm. The beam spot diameter on the retina is around 13 μm (FWHM). The axial resolution of approximately 8 μm (FWHM) in air is achieved.

43.2.3.2 Processing of Flow Signal

In the signal processing procedure, the two OCT signals obtained by the preceding and following probes are accurately co-registered and aligned to each other. The lateral alignment is performed by accounting the time interval between the two probe beams. A fiber length mismatch between the sample and reference arms and the resulting group delay mismatch between the two polarization channels

of the PM fiber cause axial displacement between the two OCT signals. The variance of the phase difference of two OCT signals, which takes its minimum when the axial displacement is canceled, is utilized for the axial alignment. The axial displacement was determined during the system calibration process by minimizing the phase variance of OCT signals obtained from a static turbid phantom. The axial displacement of two OCT images of a real sample, e.g., a retina, is then numerically canceled according to this predefined amount of axial displacement.

After the alignment process, the Doppler phase shift between these two OCT images is obtained using the Kasai autocorrelation with complex averaging as

$$\Delta\phi\left(x_i, z_j\right) = \mathrm{Arg}\left[\sum_{k=1}^{M}\sum_{l=1}^{N}\Gamma_f\left(x_{i+k+m}, z_{j+l}\right)\Gamma_p^*\left(x_{i+k}, z_{j+l}\right)\right] \tag{43.7}$$

where Γ_p and Γ_f are complex OCT signals obtained with the preceding and following probes, respectively. i and j are lateral and axial indices of pixels, m is the number of axial scans acquired in the time interval between the two probes τ, and M and N are lateral and axial window sizes, respectively.

43.2.3.3 Image Processing for Angiographic Visualization

One important post-image process to generate an OCA image is removing the low signal region. Since the low signal-to-noise ratio exhibits a random phase distribution, it disturbs flow images and significantly degrades the clinical utility of OCA.

In order to enhance the signal-to-noise ratio of OCA, the Doppler phase shift at the pixels that have lower average autocorrelation amplitudes $g(x_i, z_j)$ is masked out and set to zero, where $g(x_i, z_j)$ is defined as

$$g\left(x_i, z_j\right) \equiv \frac{1}{MN}\left|\sum_{k=1}^{M}\sum_{l=1}^{N}\Gamma_f\left(x_{i+k+n}, z_{j+l}\right)\Gamma_p^*\left(x_{i+k}, z_{j+l}\right)\right| \tag{43.8}$$

In the random noise region, the complex signals at the pixels in the averaging window cancel each other, and $g(x_i, z_j)$ approaches zero. On the other hand, in the region with significant signal strength, $g(x_i, z_j)$ takes a relatively large value. Hence, by applying a low threshold value, the noise region and signal region are effectively classified.

As for additive white noise, SD-OCT noise is a zero-mean circular Gaussian variable in a complex plane. On the other hand, its amplitude is no longer a Gaussian variable but a random Rayleigh variable. In contrast, Eq. 43.8 contains an amplitude of product of an OCT signal and the complex conjugate of another OCT signal, and hence its noise distribution becomes a double-Rayleigh distribution [43]. According to the statistical property of OCT amplitude, the mean and standard deviation of the amplitude of the auto-correlation at the noise region are $\mu_a = \pi\sigma^2/4$ and $\sigma_a = \sqrt{16 - \pi^2}\sigma^2/4$, respectively, where σ is the standard deviation

of amplitude noise in the OCT signal. Using μ_a and σ_a, the pixels to be masked are determined as:

$$\Delta\phi'(x_i, z_j) = \begin{cases} \Delta\phi(x_i, z_j) & : \quad g(x_i, z_j) \geq \dfrac{\mu_a + \alpha\sigma_a}{\sqrt{MN}} \\ 0 & : \quad \text{otherwise} \end{cases} \tag{43.9}$$

where α is a constant factor and set as 4 or 6 in for the cases described in Sect. 43.3.

A squared Doppler phase shift is calculated from the result of Eq. 43.9 and is used for qualitative vasculature imaging. Projection images, i.e., *en face* OCA, are created by integrating the squared phase shift along the depth. By applying a retinal layer segmentation algorithm [32], two en face OCAs are created for the retina and the choroid. Stereograms, which are pairs of projections from slightly different angles, also can be created to provide a three-dimensional distribution of the vasculature.

43.3 Application to the Human Eye In Vivo

In this section, the clinical utility of DB-OCA is demonstrated by imaging normal pathologic cases. DB-OCA was used to investigate the retina and choroid in three dimensions with a resolution of approximately 15 × 30 × 6 μm (horizontal sampling separation × vertical sampling separation × and coherence length).

43.3.1 Capillary Imaging

To demonstrate the capability of DB-OCA for fine capillary imaging, juxtafoveal regions of normal eyes without marked posterior disorder were investigated. The eyes of three healthy subjects were scanned over a 1.9 × 1.9 mm^2 area with 512 × 256 points. A relatively slow transversal scanning speed was selected to enable a very long time interval between the preceding and following probes of $\tau = 1.58$ ms.

Retinal capillaries around the fovea were visualized in three dimensions with a stereogram. The three-dimensional complex and dense capillary network of the macula is shown in Fig. 43.4a. A volume rendering [44] with a depth-encoded color map (Fig. 43.4b) shows that retinal capillaries comprise roughly three layers (yellow, orange, and purple vessels). The depth-segmented projections (Fig. 43.3) show different patterns of the retinal capillary network at each depth. These appearances are consistent with histological findings [45]. The relatively thick retinal vessels at the anterior retina appeared through all depth segments, which may because of the shadowing effect of Doppler OCT [18].

A region without vasculature is found at the center of the fovea, which is known as a foveal avascular zone (FAZ). Because expansion of the FAZ is known to be an indicator of diabetic retinopathy [46–48], the capability of visualizing the FAZ is clinically significant. The FAZ was manually outlined as indicated by the yellow line in Fig. 43.4, and the perimeter and area of the FAZ were measured as 1.59 mm

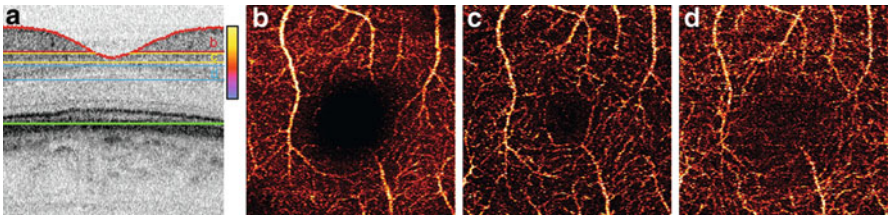

Fig. 43.3 Retinal capillary networks at different depths. (**a**) An OCT cross-section at the fovea. The color map on the *right* denotes the colors assigned to various depths, as shown in Fig. 43.6b. Integrated projections of blood flow volume at (**b**) the ganglion cell layer and (**c**) from the inner plexiform layer to the inner nuclear layer. (**d**) From the inner nuclear layer to the outer plexiform layer. Different capillary networks are observed at these three depth regions (This figure is reproduced from Ref. [34])

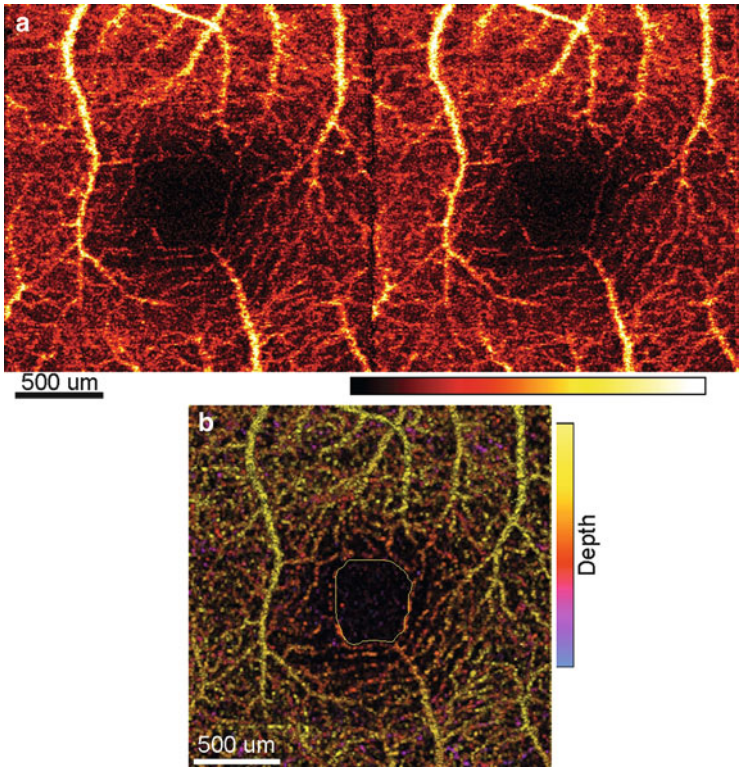

Fig. 43.4 Three-dimensional retinal capillary imaged by DB-OCA. (**a**) A stereo view showing the retinal capillaries and (**b**) the projection image of the retinal capillary with color to encode depth. The foveal avascular zone was outlined manually (*yellow closed line*). The scan size is $7.9 \times 7.9°$ (512×256 lines), and the acquisition took 5 s (This figure is reproduced from Ref. [34])

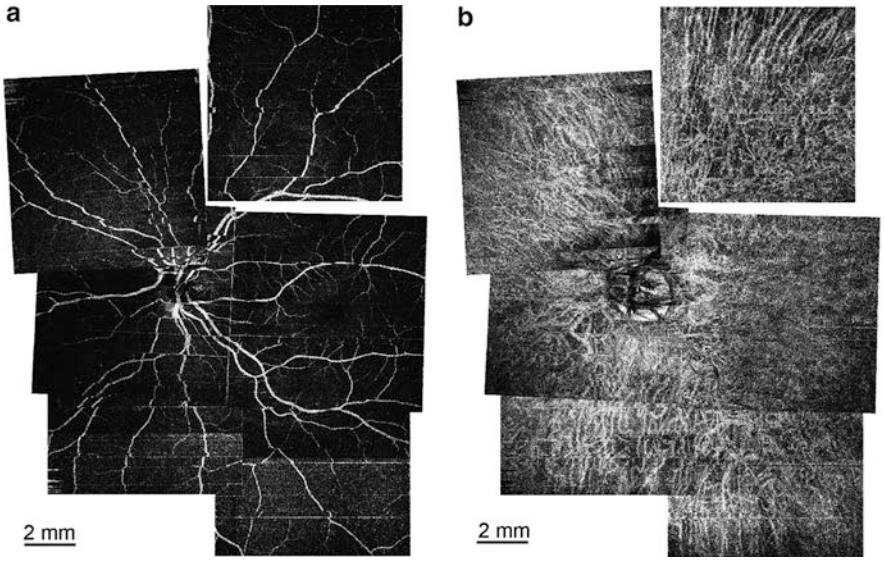

Fig. 43.5 Wide-field DB-OCA created by stitching 6 DB-OCA volumes. (**a**) and (**b**) represent retinal and choroidal vessels, respectively (This figure is reproduced from Ref. [34])

and 0.179 mm^2, respectively, in this particular case. The results from three subjects ranged between 1.59–2.42 mm in the perimeter and 0.177–0.339 mm^2 on the surface. These results are consistent with a study conducted with FA [48]. Noninvasive, detailed, high-speed imaging of the microvasculature by DB-OCA will be suitable for screening and monitoring of vascular diseases.

43.3.2 Wide-Field Imaging

More wide-field angiography is enabled by stitching several DBA-OCAs. In the example depicted in Fig. 43.5, six sections of a retina were scanned to compose wide-field images. The mosaic of vasculature images at the retina and the choroid is shown in Fig. 43.5a, b. Each section was acquired in 5 s and covered an approximate 7.8 × 7.8 mm^2 area. The total acquisition time was 30 s, and the mosaic image covered approximately 16 × 20 mm^2. Owing to the high-resolution three-dimensional imaging, two overlaid vasculatures, the retina and the choroid, could be discriminated. Major retinal vessels around the ONH and the macula are shown in Fig. 43.5a. Fine branches around the fovea were also clearly visualized. In Fig. 43.5b, the fine choroidal vasculature of the peripapillary region was well contrasted. It shows macroscopic structural properties of the vasculatures in the posterior eye.

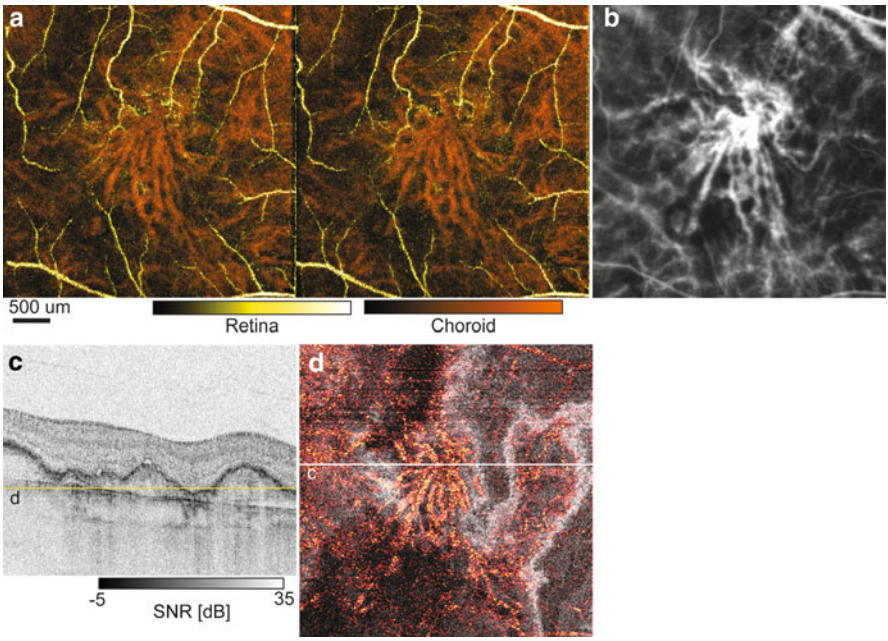

Fig. 43.6 A case of polypoidal choroidal vasculopathy. (**a**) Stereogram of volume rendering of D-OCA where *yellow* indicates the retinal vasculature and *red* indicates the choroidal vasculature, (**b**) corresponding ICGA, (**c**) cross-sectional OCT at a pigment epithelial detachment indicated by a *white line* in (**d**), and (**d**) OCA overlapped en face OCT cross-section. The depth location of (**d**) is indicated by a *yellow line* in (**c**) (This figure is reproduced from Ref. [34])

43.3.3 A Pathologic Case

Abnormal choroidal vasculature imaging is one of the significant applications for DB-OCA. Figure 43.6 demonstrates a DB-OCA application to a case of polypoidal choroidal vasculopathy (PCV). The pathologic region of the retina was scanned over a 3.9 × 3.9 mm^2 area with 512 × 256 A-lines. The time interval for Doppler detection was 792 μs.

The depth-resolved vasculatures are visualized by a stereogram shown in Fig. 43.6a. There is a thick abnormal vascular network under the RPE at the fovea. It was also found that the network is located above the surrounding choroidal vessels. Retinal vessels undulated in the longitudinal direction since the retina was elevated. In PCV, polyp-like lesions with pigment epithelium detachment (PED) occurred around the abnormal vascular network, which was clearly visualized by DB-OCA.

By comparison with ICGA (Fig. 43.6b), it was found that the remarkable abnormal vasculature generated a similar pattern in both OCA and ICGA images. The depth-resolved structure of the vascular network could be identified by cross-sectional tomography of the eye, as shown in Fig. 43.6c. Severe retinal pigment

detachments are clearly visible. According to the en face cross-section of the blood flow image overlaid on the OCT image (Fig. 43.6d), the abnormal vasculature was found to exist at the space between the detached RPE and Bruch's membrane.

Although the origin of these abnormal vessels is controversial, DB-OCA will provide new insight on the debate about this pathology.

43.4 Advanced Issue: Birefringence Artifact

The DB-OCA system presented in previous sections uses polarization to multiplex two probe beams. This method implicitly assumes the sample to be measured exhibits no birefringence. However, the eye consists of several birefringent tissues including the cornea, sclera, nerve fibers, and lamina cribrosa. Hence, this assumption is not always validated. The birefringence in the sample results in a pseudo-Doppler phase shift and disturbs flow measurements.

In this section, initially, the formulation of DB-OCA is extended using the Jones matrix in order to account for the birefringence issues. Subsequently, a modified DB-OCA system, which is free from the birefringence artifact, is described.

43.4.1 Jones Matrix Formulation of Dual-Beam Doppler Optical Coherence Angiography

By denoting the single-trip Jones matrix of a sample as $\mathbf{J}_s$, the round-trip Jones matrix of the sample is defined as

$$\mathbf{J}(\mathbf{r}) = \mathbf{J}_s^T(\mathbf{r})\mathbf{J}_s(\mathbf{r}) \equiv \begin{bmatrix} j_{11}(\mathbf{r}) & j_{12}(\mathbf{r}) \\ j_{21}(\mathbf{r}) & j_{22}(\mathbf{r}) \end{bmatrix} \tag{43.10}$$

where $j_{12} = j_{21}$, because $\mathbf{J}$ is transpose symmetric [49]. Using this round-trip Jones matrix, Γ_p and Γ_f of Eq. 43.6 are described as

$$\begin{aligned} \Gamma_p(\mathbf{r}, t) &= \mathbf{E}_{out}^{p\dagger}\mathbf{J}(\mathbf{r})\mathbf{E}_{in}^{p} \\ \Gamma_f(\mathbf{r}, t+\tau) &= \mathbf{E}_{out}^{f\dagger}\mathbf{J}(\mathbf{r})\mathbf{E}_{in}^{f}\exp[i\Delta\phi_m(\mathbf{r})] \end{aligned} \tag{43.11}$$

where $\mathbf{r} = (x, y, z)$ are the spatial coordinates, $\mathbf{E}_{in}$ and $\mathbf{E}_{out}$ are Jones vectors of incident and detected polarization states of the probe beams, respectively, $\Delta\phi_m(\mathbf{r})$ is the Doppler phase shift due to the spatially distributed axial motion of the sample, and the subscripts and superscripts of p and f indicate preceding and following probe beams, respectively.

In the DB-OCA setup described in Fig. 43.2, both the incident and detected polarization states are linear polarization, and they are parallel to each other, while the polarization states of the preceding and the following beams are orthogonal to each other. Hence, the polarization states can be assumed as $\mathbf{E}_{in}^{p} \parallel \mathbf{E}_{out}^{p} \parallel [1 \quad 0]^T$ and $\mathbf{E}_{in}^{f} \parallel \mathbf{E}_{out}^{f} \parallel [0 \quad 1]^T$. Under this condition, Γp and Γ_f are expressed as

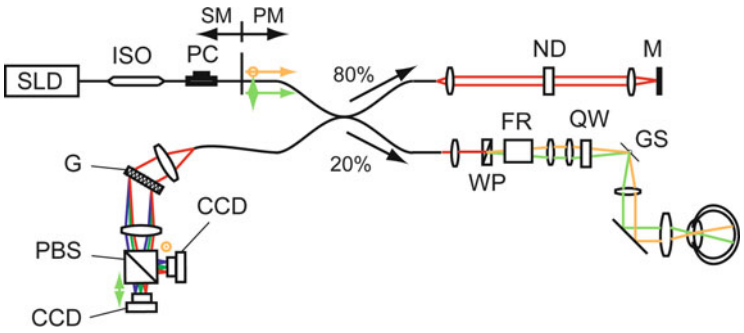

Fig. 43.7 Optical scheme of modified DB-OCA which is free from phase artifact occurred by the birefringence of the sample. SM and PM represent single-mode and multimode fibers, *ISO* isolator, *ND* neutral density filter, *M* mirror, *G* grating, *PBS* polarization beam splitter, *GS* galvanometric scanner, *WP* Wollaston prism, *FR* Faraday rotator, and *QW* quarter wavelength plate. The *green* and *yellow lines* represent two probe beams with orthogonal polarization states

$$\begin{aligned} \Gamma_p(\mathbf{r},t) &= C\ j_{11}(\mathbf{r}) \\ \Gamma_f(\mathbf{r},t) &= C\ j_{22}(\mathbf{r})\exp[i\Delta\phi_m(\mathbf{r})] \end{aligned} \tag{43.12}$$

where C is a constant of proportion. By substituting Eq. 43.12 into Eqs. 43.6 and 43.3, the Doppler phase shift measured by DB-OCA is found to be

$$\Delta\phi(\mathbf{r}) = \Delta\phi_m(\mathbf{r}) + \Delta\phi_b(\mathbf{r}) \tag{43.13}$$

where $\Delta\phi_b(\mathbf{r})$ is the phase difference between j_{11} and j_{22}, which is defined as $\Delta\phi_b = \mathrm{Arg}[j_{22}(\mathbf{r})j_{11}^*(\mathbf{r})]$.

It is evident that the measured Doppler phase shift reflects not only the Doppler phase shift due to the motion in the sample, $\Delta\phi_m(\mathbf{r})$, but is biased by the phase difference between j_{11} and j_{22}, $\Delta\phi_b$, which is not zero if the sample is birefringent. Hence, $\Delta\phi_b(\mathbf{r})$ is a phase artifact in DB-OCA measurement and causes pseudo-flow in a DB-OCA image.

43.4.2 Modified Dual-Beam Optical Coherence Angiography System

By using a modified version of DB-OCA, the phase artifact can be canceled [37]. Figure 43.7 shows the optical scheme of the modified DB-OCA. This system is nearly identical to the original DB-OCA except for a Faraday rotator (FR) and a quarter wavelength plate (QW) located between the Wollaston prism (WP) and a galvanometric scanner (GS). The rotation angle of the Faraday rotator is 45°.

The round-trip Jones matrix of the combination of the Faraday rotator, quarter wavelength plate, and the sample is

$$\mathbf{M}(\mathbf{r}) = \mathbf{R}(\pi/4)\mathbf{Q}^T\mathbf{J}(\mathbf{r})\mathbf{Q}\,\mathbf{R}(\pi/4) = \frac{i}{2}\begin{bmatrix} j_{11}(\mathbf{r}) + j_{22}(\mathbf{r}) & j_{11}(\mathbf{r}) - i2j_{12}(\mathbf{r}) - j_{22}(\mathbf{r}) \\ -[j_{11}(\mathbf{r}) - i2j_{12}(\mathbf{r}) - j_{22}(\mathbf{r})] & -[j_{11}(\mathbf{r}) + j_{22}(\mathbf{r})] \end{bmatrix} \tag{43.14}$$

where $\mathbf{R}(\theta)$ is a rotation matrix with an rotation angle of θ, which represents the effect of the Faraday rotator, and $\mathbf{Q}$ is the Jones matrix of the quarter wavelength plate. Here, the optic axis of the quarter wavelength plate is assumed to be aligned vertically. The definition of the optic axis, i.e., slow or fast axis, is not a matter of concern. In both cases, the effect is the same. Note that the diagonal elements of the matrix $\mathbf{M}(\mathbf{r})$ differ only in their signs.

By replacing $\mathbf{J}(\mathbf{r})$ in Eq. 43.12 with $\mathbf{M}(\mathbf{r})$, the Γ_p and Γ_f are altered to be

$$\begin{aligned} \Gamma_p(\mathbf{r}, t) &= C\frac{1}{2}[j_{11}(\mathbf{r}) + j_{22}(\mathbf{r})] \\ \Gamma_f(\mathbf{r}, t+\tau) &= -C\frac{1}{2}[j_{11}(\mathbf{r}) + j_{22}(\mathbf{r})]\exp[i\Delta\phi_m(\mathbf{r})] \end{aligned} \tag{43.15}$$

By substituting the Γ_p and Γ_f in Eq. 43.6 and subsequently in Eq. 43.2, the measured Doppler phase shift becomes the following:

$$\Delta\phi(\mathbf{r}) = \mathrm{Arg}\left[\Gamma_f(\mathbf{r})\Gamma_p^*(\mathbf{r})\right] = \Delta\phi_m + \pi \tag{43.16}$$

Although this measured Doppler phase is biased with a constant phase of π, it evidently expresses the Doppler phase shift due to the localized motion in the sample. Since the constant phase bias can be canceled by a common bulk motion correction method for Doppler OCT, e.g., the methods described in Refs. [28] or [32], this modified DB-OCA provides the Doppler phase shift value due to the motion in the sample without artifacts due to the sample birefringence.

It is also noteworthy that the role of the quarter wavelength plate is not to cancel the birefringence artifact but to maximize the probe light efficiency. Furthermore, the orientation of the quarter wavelength plate has no impact on the measured Doppler phase shift value. More detailed discussion about this issue can be found in Ref. [36].

43.4.3 Optic Nerve Head Imaging by Modified Dual-Beam Optical Coherence Angiography

Since the cornea consists of collagen and is birefringent, the birefringence artifact always has some negative impact on the imaging of the posterior eye. The impact is significant especially for ONH imaging because several birefringent tissues, including nerve fibers and lamina cribrosa, exist at the ONH.

Figure 43.8 demonstrates the comparison of OCA images of an eye taken by the original and the modified DB-OCA devices. All images were obtained from a

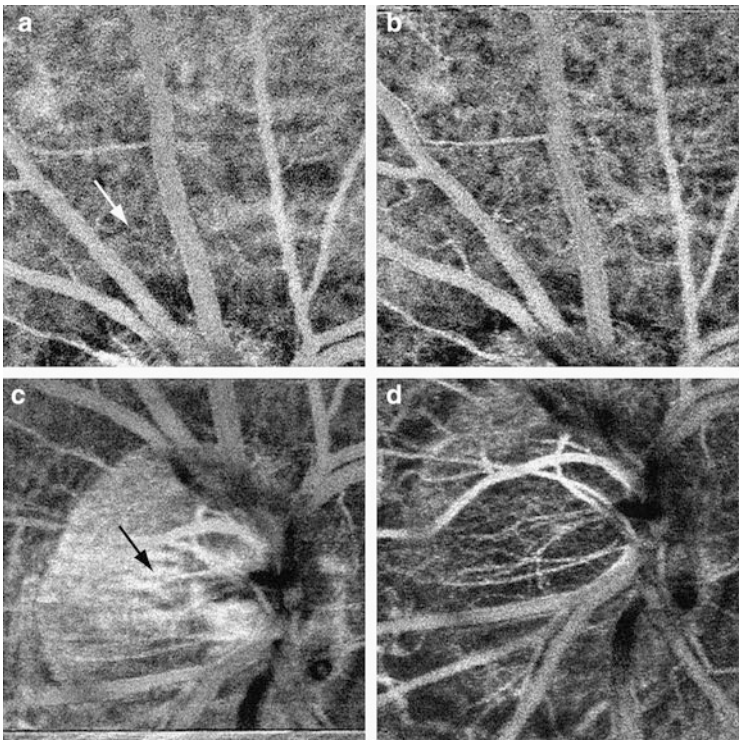

Fig. 43.8 DB-OCA of in vivo human ONH. (**a**) and (**c**) were taken by an original DB-OCA system, while (**b**) and (**d**) were taken by a modified DB-OCA system which is free from birefringence artifacts (This figure is reproduced from Ref. [37])

single subject. Figure 43.8a, c was taken by an original DB-OCA configuration, while Fig. 43.8b, d was taken by the modified DB-OCA. Both retinal and choroidal vessels are visualized in these images. Figure 43.8a, b is the images obtained at the superior region to the ONH. Because of scleral birefringence, the contrast of the fine vessels is low in Fig. 43.8a, as exemplified by an arrow. In contrast, fine vessels are clearly visualized in the image obtained by the modified DB-OCA system, as shown in Fig. 43.8a.

Figure 43.8c shows a very strong OCA signal in the ONH region. This strong signal was generated by the strong birefringence of a lamina cribrosa. By using the modified DB-OCA, this strong birefringence artifact was perfectly canceled, and fine vessels are visualized within the ONH.

43.5 Conclusions and Further Topics

This chapter presented the basics of DB-OCA and its modified version, which is free from birefringence artifacts. With DB-OCA, extremely high sensitivity of Doppler

OCT measurement was achieved. With this high sensitivity, DB-OCA enabled clear visualization of the fine vasculature in the retina. More examples of retinal imaging using DB-OCA and modified DB-OCA can be found in Refs. [33, 37].

Although this chapter is sufficient for understanding the principles of DB-OCA, there are several issues that should be carefully considered to implement DB-OCA. Especially for modified DB-OCA, the quarter wavelength plate should be aligned with a particular optimization strategy. The details of this issue are described in Ref. [37].

In addition to the two implementations of DB-OCA described in this chapter, there are several other implementations and extensions of DB-OCA. For example, Zotter et al. have demonstrated DB-OCA, which is denoted as dual-beam phase-resolved Doppler OCT in their terminology, with interferometer multiplexing [35]. In this system, the two probe beams were created using two independent interferometers.

Jaillon et al. demonstrated DB-OCA with a 1-μm probe wavelength and visualized high-sensitive Doppler imaging of the choroidal vasculature [36]. This 1-μm DB-OCA system was further extended to have a variable velocity range [38]. In this extended system, the measurable flow velocity can be selected by rotating a particular mirror in its scanning optics.

The clinical utility of DB-OCA is still not evaluated in detail. With further technical development, comprehensive and systematic clinical studies will make DB-OCA a very powerful tool for ophthalmic diagnosis in the future.

References

1. J. Flammer, S. Orgül, V.P. Costa, N. Orzalesi, G.K. Krieglstein, L.M. Serra, J.-P. Renard, E. Stefánsson, The impact of ocular blood flow in glaucoma. Prog. Retin. Eye Res. **21**, 359–393 (2002)
2. V. Patel, S. Rassam, R. Newsom, J. Wiek, E. Kohner, Retinal blood flow in diabetic retinopathy. BMJ **305**, 678–683 (1992)
3. E. Friedman, A hemodynamic model of the pathogenesis of age-related macular degeneration. Am. J. Ophthalmol. **124**, 677–682 (1997)
4. J.D.M. Gass, *Stereoscopic Atlas of Macular Diseases: Diagnosis and Treatment*, 4th edn. (Mosby, St. Louis, 1997)
5. L.A. Yannuzzi, K.T. Rohrer, L.J. Tindel, R.S. Sobel, M.A. Costanza, W. Shields, E. Zang, Fluorescein angiography complication survey. Ophthalmology **93**, 611–617 (1986)
6. M. Hope-Ross, L.A. Yannuzzi, E.S. Gragoudas, D.R. Guyer, J.S. Slakter, J.A. Sorenson, S. Krupsky, D.A. Orlock, C.A. Puliafito, Adverse reactions due to indocyanine green. Ophthalmology **101**, 529–533 (1994)
7. G.T. Feke, C.E. Rivat, Laser Doppler measurements of blood velocity in human retinal vessels. J. Opt. Soc. Am. **68**, 526–531 (1978)
8. C.E. Riva, G.T. Feke, B. Eberli, V. Benary, Bidirectional LDV system for absolute measurement of blood speed in retinal vessels. Appl. Opt. **18**, 2301–2306 (1979)
9. C.E. Riva, S. Harino, B.L. Petrig, R.D. Shonat, Laser Doppler flowmetry in the optic nerve. Exp. Eye Res. **55**, 499–506 (1992)
10. C.E. Riva, S.D. Cranstoun, J.E. Grunwald, B.L. Petrig, Choroidal blood flow in the foveal region of the human ocular fundus. IOVS **35**, 4273–4281 (1994)

11. R. Bonner, R. Nossal, Model for laser Doppler measurements of blood flow in tissue. Appl. Opt. **20**, 2097–2107 (1981)
12. G. Michelson, B. Schmauss, M.J. Langhans, J. Harazny, M.J. Groh, Principle, validity, and reliability of scanning laser Doppler flowmetry. J. Glaucoma **5**, 99–105 (1996)
13. G. Michelson, B. Schmauss, Two dimensional mapping of the perfusion of the retina and optic nerve head. Br. J. Ophthalmol. **79**, 1126–1132 (1995)
14. J.D. Briers, A.F. Fercher, Retinal blood-flow visualization by means of laser speckle photography. IOVS **22**, 255–259 (1982)
15. Y. Tamaki, M. Araie, E. Kawamoto, S. Eguchi, H. Fujii, Noncontact, two-dimensional measurement of retinal microcirculation using laser speckle phenomenon. IOVS **35**, 3825–3834 (1994)
16. Z. Chen, T.E. Milner, S. Srinivas, X. Wang, A. Malekafzali, M.J.C. van Gemert, J.S. Nelson, Noninvasive imaging of in vivo blood flow velocity using optical Doppler tomography. Opt. Lett. **22**, 1119–1121 (1997)
17. X. Wang, T.E. Milner, Z. Chen, J.S. Nelson, Measurement of fluid-flow-velocity profile in turbid media by the use of optical Doppler tomography. Appl. Opt. **36**, 144–149 (1997)
18. Y. Zhao, Z. Chen, C. Saxer, S. Xiang, J.F. de Boer, J.S. Nelson, Phase-resolved optical coherence tomography and optical Doppler tomography for imaging blood flow in human skin with fast scanning speed and high velocity sensitivity. Opt. Lett. **25**, 114–116 (2000)
19. Y. Zhao, Z. Chen, C. Saxer, Q. Shen, S. Xiang, J.F. de Boer, J.S. Nelson, Doppler standard deviation imaging for clinical monitoring of in vivo human skin blood flow. Opt. Lett. **25**, 1358–1360 (2000)
20. V. Westphal, S. Yazdanfar, A.M. Rollins, J.A. Izatt, Real-time, high velocity-resolution color Doppler optical coherence tomography. Opt. Lett. **27**, 34–36 (2002)
21. Z. Ding, Y. Zhao, H. Ren, J. Nelson, Z. Chen, Real-time phase-resolved optical coherence tomography and optical Doppler tomography. Opt. Express **10**, 236–245 (2002)
22. V.X.D. Yang, M. Gordon, E. Seng-Yue, S. Lo, B. Qi, J. Pekar, A. Mok, B. Wilson, I. Vitkin, High speed, wide velocity dynamic range Doppler optical coherence tomography (part II): imaging in vivo cardiac dynamics of Xenopus laevis. Opt. Express **11**, 1650–1658 (2003)
23. R.A. Leitgeb, L. Schmetterer, W. Drexler, A.F. Fercher, R.J. Zawadzki, T. Bajraszewski, Real-time assessment of retinal blood flow with ultrafast acquisition by color Doppler Fourier domain optical coherence tomography. Opt. Express **11**, 3116–3121 (2003)
24. B.R. White, M.C. Pierce, N. Nassif, B. Cense, B.H. Park, G.J. Tearney, B.E. Bouma, T.C. Chen, J.F. de Boer, In vivo dynamic human retinal blood flow imaging using ultra-high-speed spectral domain optical coherence tomography. Opt. Express **11**, 3490–3497 (2003)
25. R.A. Leitgeb, L. Schmetterer, C.K. Hitzenberger, A.F. Fercher, F. Berisha, M. Wojtkowski, T. Bajraszewski, Real-time measurement of in vitro flow by Fourier-domain color Doppler optical coherence tomography. Opt. Lett. **29**, 171–173 (2004)
26. B. Baumann, B. Potsaid, M.F. Kraus, J.J. Liu, D. Huang, J. Hornegger, A.E. Cable, J.S. Duker, J.G. Fujimoto, Total retinal blood flow measurement with ultrahigh speed swept source/Fourier domain OCT. Biomed. Opt. Express **2**, 1539–1552 (2011)
27. A. Bassi, L. Fieramonti, C. D'Andrea, M. Mione, G. Valentini, In vivo label-free three-dimensional imaging of zebrafish vasculature with optical projection tomography. J. Biomed. Opt. **16**, 100502 (2011)
28. Y.-J. Hong, S. Makita, F. Jaillon, M.J. Ju, E.J. Min, B.H. Lee, M. Itoh, M. Miura, Y. Yasuno, High-penetration swept source Doppler optical coherence angiography by fully numerical phase stabilization. Opt. Express **20**, 2740–2760 (2012)
29. H. Wehbe, M. Ruggeri, S. Jiao, G. Gregori, C.A. Puliafito, W. Zhao, Automatic retinal blood flow calculation using spectral domain optical coherence tomography. Opt. Express **15**, 15193–15206 (2007)
30. Y. Wang, B.A. Bower, J.A. Izatt, O. Tan, D. Huang, Retinal blood flow measurement by circumpapillary Fourier domain Doppler optical coherence tomography. J. Biomed. Opt. **13**, 064003–064009 (2008)

31. S. Makita, T. Fabritius, Y. Yasuno, Quantitative retinal-blood flow measurement with three-dimensional vessel geometry determination using ultrahigh-resolution Doppler optical coherence angiography. Opt. Lett. **33**, 836–838 (2008)
32. S. Makita, Y. Hong, M. Yamanari, T. Yatagai, Y. Yasuno, Optical coherence angiography. Opt. Express **14**, 7821–7840 (2006)
33. Y.-J. Hong, M. Miura, S. Makita, M.-J. Ju, B.H. Lee, Y. Yasuno, Non-invasive vascular imaging of exudative macular disease by high penetration Doppler optical coherence angiography. ARVO Meet. Abstr. **53**, 1152 (2012)
34. S. Makita, F. Jaillon, M. Yamanari, M. Miura, Y. Yasuno, Comprehensive in vivo micro-vascular imaging of the human eye by dual-beam-scan Doppler optical coherence angiography. Opt. Express **19**, 1271–1283 (2011)
35. S. Zotter, M. Pircher, T. Torzicky, M. Bonesi, E. Götzinger, R.A. Leitgeb, C.K. Hitzenberger, Visualization of microvasculature by dual-beam phase-resolved Doppler optical coherence tomography. Opt. Express **19**, 1217–1227 (2011)
36. F. Jaillon, S. Makita, E.-J. Min, B.H. Lee, Y. Yasuno, Enhanced imaging of choroidal vasculature by high-penetration and dual-velocity optical coherence angiography. Biomed. Opt. Express **2**, 1147–1158 (2011)
37. S. Makita, F. Jaillon, M. Yamanari, Y. Yasuno, Dual-beam-scan Doppler optical coherence angiography for birefringence-artifact-free vasculature imaging. Opt. Express **20**, 2681–2692 (2012)
38. F. Jaillon, S. Makita, Y. Yasuno, Variable velocity range imaging of the choroid with dual-beam optical coherence angiography. Opt. Express **20**, 385–396 (2012)
39. B. Park, M.C. Pierce, B. Cense, S.-H. Yun, M. Mujat, G. Tearney, B. Bouma, J. de Boer, Real-time fiber-based multi-functional spectral-domain optical coherence tomography at 1.3 μm. Opt. Express **13**, 3931–3944 (2005)
40. B.J. Vakoc, G.J. Tearney, B.E. Bouma, Statistical properties of phase-decorrelation in phase-resolved Doppler optical coherence tomography. IEEE Trans. Med. Imaging **28**, 814–821 (2009)
41. M. Yamanari, S. Makita, V.D. Madjarova, T. Yatagai, Y. Yasuno, Fiber-based polarization-sensitive Fourier domain optical coherence tomography using B-scan-oriented polarization modulation method. Opt. Express **14**, 6502–6515 (2006)
42. American National Standard Institute, *American National Standard for the Safe Use of Lasers ANSIZ 136.1−2000* (American National Standards Institute, 2000)
43. J. Salo, H.M. El-Sallabi, P. Vainikainen, The distribution of the product of independent Rayleigh random variables. IEEE Trans. Antennas Propag. **54**, 639–643 (2006)
44. M. Levoy, Display of surfaces from volume data. IEEE Comput. Graph. Appl. **8**, 29–37 (1988)
45. D. Toussaint, T. Kuwabara, D.G. Cogan, Retinal vascular patterns: part II. Human retinal vessels studied in three dimensions. Arch. Ophthalmol. **65**, 575–581 (1961)
46. G.H. Bresnick, R. Condit, S. Syrjala, M. Palta, A. Groo, K. Korth, Abnormalities of the foveal avascular zone in diabetic retinopathy. Arch. Ophthalmol. **102**, 1286–1293 (1984)
47. O. Arend, S. Wolf, F. Jung, B. Bertram, H. Pöstgens, H. Toonen, M. Reim, Retinal microcirculation in patients with diabetes mellitus: dynamic and morphological analysis of perifoveal capillary network. Br. J. Ophthalmol. **75**, 514–518 (1991)
48. J. Conrath, R. Giorgi, D. Raccah, B. Ridings, Foveal avascular zone in diabetic retinopathy: quantitative vs qualitative assessment. Eye **19**, 322–326 (2005)
49. S. Jiao, L.V. Wang, Jones-matrix imaging of biological tissues with quadruple-channel optical coherence tomography. J. Biomed. Opt. **7**, 350 (2002)

Optical Microangiography Based on Optical Coherence Tomography

44

Roberto Reif and Ruikang K. Wang

Keywords
Optical microangiography • Optical coherence tomography • Vascular diseases

44.1 Introduction

Proper homeostasis regulation of in vivo biological systems requires microvascular blood perfusion, which is the process of delivering blood into the tissue's capillary beds. Abnormal tissue vascularization has been associated with various disorders such as cancer, diabetes, neurological disorders, wounds, and inflammation. Understanding the changes in the vascular network or microangiography will have an important role in determining the causes and developing potential treatments for these diseases.

The ability to noninvasively image the blood flow within microcirculatory tissue beds will have potential applications in several basic research and clinical settings. Currently, there are several noninvasive methods for providing spatial and temporal maps of blood flow in both animal models and humans. These techniques include magnetic resonance imaging [1] and positron emission tomography [2]; however, these techniques have poor spatial and temporal resolutions.

Other techniques have mostly been used in animal models for basic research applications, such as two-photon microscopy [3], which has been used to estimate the transverse velocity and linear density of red blood cells. This procedure requires determining the flow profile and vessel orientation, which can be challenging.

R. Reif
Department of Bioengineering, University of Washington, Seattle, WA, USA

R.K. Wang (✉)
Department of Automation Engineering, Northeastern University at Qinhuangdao, Hebei, Peoples' Republic of China

Department of Bioengineering, University of Washington, Seattle, WA, USA
e-mail: wangrk@uw.edu

© Springer International Publishing Switzerland 2015

W. Drexler, J.G. Fujimoto (eds.), *Optical Coherence Tomography*,
DOI 10.1007/978-3-319-06419-2_45

Laser speckle contrast imaging [4, 5] is an imaging technique that has been used to obtain images of the relative changes of blood flow with high spatial and temporal resolution. This method is based on analyzing the speckle decorrelation time, which is inversely related to the mean blood flow velocities. This method cannot provide depth information and its resolution cannot discern the small vessels, such as the capillaries.

Other methods have only been applicable for animal studies given their invasiveness. For example, autoradiography is a gold standard method which has been used for studying blood flow. This technique consists of using a tracer which is administered over a short period of time, followed by cardiac arrest and quick freezing. Autoradiography of these frozen sections provides a representation of the radioactivity levels in the different tissue layers. This information is then converted to blood flow by incorporating the time course of arterial blood radioactivity. Although this method provides three-dimensional spatial information, it does not provide the temporal information of the blood flow change [6], given that the sample is damaged. Therefore, studies of disease progression or response to treatment within the same animal cannot be performed.

In summary, microvascular imaging has been challenging due to the high spatial and temporal resolution requirements. A system with high sensitivity for imaging small diameter capillaries and slow blood flow velocities is needed. Also, contact techniques alter the optical properties of the tissue, which affect the data analysis [7]. Therefore, a method which can provide noninvasive, noncontact, label-free, three-dimensional, spatially resolved blood flow measurements with capillary resolution would be beneficial for the diagnosis and treatment of several tissue pathologies.

Optical coherence tomography (OCT) is a noninvasive method for imaging three-dimensional biological tissues with high resolution ($\sim$10 μm) and without requiring the use of contrast agents [8]. OCT can image up to a depth of several millimeters, at speeds of up to 500 kHz of line scan rate [9]. Currently, there are two type of OCT systems, the time-domain OCT (TD-OCT) [10] and the Fourier-domain OCT, which is divided into spectral domain (SD-OCT) [11] and swept source (SS-OCT) [12]. Fourier-domain OCT has demonstrated higher sensitivity and imaging speed compared to its time-domain counterpart. The high speed of the Fourier-domain systems has enabled it to image not only structural images but also functional parameters which provide information about the blood flow velocities and vessel microangiography.

In this chapter we will review several techniques for using Fourier-domain OCT to determine blood flow velocities and the vessel morphology. Different techniques will be discussed with a brief explanation of their limitations. Also, methods for quantifying these images will be presented, as well as the depiction of several applications. Finally, examples of the combination of different imaging modalities will be highlighted.

44.2 OCT Angiography Methods

The first commercial OCT systems developed were based on time domain and were used for ophthalmology applications. In TD-OCT a reference mirror, which is constantly moving through mechanical scanning, is used to alter the location of

the coherence gate. The location of the coherence gate allows for the detection of the scattering structures at different depths within the biological tissues. The mechanical scanning of the reference mirror has limited repeatability and gives rise to motion artifacts due to its mechanical jitters. As a result, the quality of the OCT image deteriorates, especially at the higher acquisition speeds.

Fourier-domain OCT has enabled considerable improvements in image acquisition speed and image resolution compared to its TD-OCT counterpart. In Fourier-domain OCT, the reference mirror is stationary and the OCT signal collected is a function of the wavenumber ($k = 2\pi/\lambda$), where λ is the wavelength. Fourier-domain OCT is based on the principle of transforming the OCT time-varying signal along the optical axis (A scan) into the frequency domain. In SD-OCT, the light source is a broadband source and the signal is acquired with a spectrometer as a detector, which measures the recombined broadband spectra returning from the sample and reference mirror. The image acquisition speeds have reached up to 500,000 A-lines per second [9], which reduces the vulnerability from motion artifacts and allows for highly dense tissue sampling. In SS-OCT, a light source in which the emission wavelength is tuned rapidly through time over a broad wavelength range is used [13], and the signal is detected using a single photo detector. Since SD-OCT and SS-OCT are mathematically identical, the discussion below assumes the case of the SD-OCT, unless otherwise stated.

The detected interference spectrum in a Fourier OCT system is given by

$$I(t,k_j) = 2S(k_j)E_R\left[\int_{-\infty}^{\infty} a(z,t)\cos\left(2k_j n(t)z\right)dz + a(z_1)\cos\left[2k_j n(t)(z_1 - vt)\right]\right] \tag{44.1}$$

where j is the pixel number index of the CCD camera in the spectrometer, t is the timing when an A-line is captured, E_R is the light reflected from the reference mirror, $S(k)$ is the spectral density of the light source used, n is the refractive index of the tissue, z is the depth coordinate within the sample, $a(z, t)$ is the amplitude of the back scattered light, and v is the velocity of moving particles such as blood cells in a blood vessel, which is located at a depth z_1.

To extract the depth information from a Fourier-domain OCT system, a Fourier transform (FT) is used on the interference contributions of all the pathlength differences from each wavenumber, which is given by

$$I(z) = FT[I(k)] = M(z)e^{i\varphi(z)} \tag{44.2}$$

The result of the Fourier transformation is a complex valued signal that has a phase ($\varphi(z)$) and a magnitude ($M(z)$) terms.

The analysis of $M(z)$ enables the reconstruction of the OCT structural image, which is commonly used on most OCT applications. Often, this refers to anatomical OCT, because it provides information about the microstructural features about the sample. For example, commercial OCT eye imaging systems analyze the thickness of the different

retinal layers with micrometer resolution. The anatomical OCT is limited to providing morphological information; however, it does not provide functional information.

The value of $\varphi(z)$ is a random phase caused by the microstructures located at the depth z. The analysis of the dynamic changes in the phase signal has been used for measuring tissue movement, which has allowed for the quantification of several tissue properties, such as the displacement of the trabecular meshwork in the anterior segment of the eye [14], the skin elastic properties [15], and the tissue photothermal responses [16]. The phase information has also been used to analyze the Doppler effect that is caused by the scattering of light from a moving object. This analysis enables the quantification of the axial velocity of moving particles such as red blood cells inside patent blood vessels. However, this technique is limited to fast flow velocities and is unable to quantify the blood flow velocities within capillary tissue beds.

By analyzing the dynamic changes in the magnitude, phase, or both, it is possible to extract the three-dimensional location of the patent blood vessels within the biological tissue, thus recreating the blood vessel microangiography. In the following sections we provide an overview of several techniques that have been previously used to extract the vessel microangiography.

44.2.1 Phase-Based Methods

Phase-based methods are established by analyzing the dynamic changes in the phase term ($\varphi(z)$) of the OCT signal. The axial displacement of a moving scatterer, such as a red blood cell, adds a Doppler shift to the carrier frequency, which can be measured by an OCT system through its phase. The disadvantage of these methods is that they are sensitive to the OCT system's phase noise and the tissue's bulk-motion artifacts.

44.2.1.1 Doppler Method

Doppler optical coherence tomography (DOCT) is an extension of OCT which combines the Doppler principles with OCT. The method was first used for analyzing the frequency shift due to the Doppler effect [17]. DOCT provides in vivo images of blood vessels, blood flow direction, and blood flow velocity, with good sensitivity [18]. This method is sensitive to the phase term; therefore, the phase stability of the OCT system is critical for obtaining high-quality images.

The phase difference is calculated between two A-lines captured at the same or at highly overlapping spatial locations [19]. The axial blood flow velocity (V_z) depends on the time interval (Δt) between the captured A-lines, which is given by

$$V_z = \frac{\lambda \Delta \varphi}{4\pi n \Delta t} \tag{44.3}$$

where λ is the wavelength of the light, $\Delta\varphi$ is the phase difference between the time points, and n is the index of refraction of the sample. The maximum resolvable

velocity is limited by the 2π ambiguity of the phase measurements; therefore, the phase changes are constrained by π and $-\pi$. The minimum velocity that can be resolved by this method is dictated by the system's phase stability and the bulk tissue motions. As a result, this method has difficulty in determining the slow flow velocities from small blood vessels, such as capillaries.

Measurement of the absolute blood flow velocity (V) is important in several studies, such as retinal imaging, since it allows for the evaluation of the blood flow dynamics within individual vessels. To obtain the absolute velocity, it is important to determine the angle (Φ) between the flow velocity vector and the vector of the incident OCT light, also known as the Doppler angle. The Doppler angle may be determined by using the three-dimensional OCT data set and the following equation [20]:

$$\Phi = \pi - \arccos\left(\frac{dz}{\sqrt{(dx^2 + dy^2 + dz^2)}}\right) \tag{44.4}$$

where dx, dy, and dz are the directional components of the blood vessel. The calculation of the total blood flow velocity can be obtained from

$$V = \left|\frac{V_z}{\cos\Phi}\right| \tag{44.5}$$

The total blood flow within a vessel is then calculated by multiplying the total velocity times the cross-sectional area of the vessel. Another method that has been proposed to calculate the total blood flow, which does not require the calculation of the Doppler angle, is to integrate the axial velocity in the xz plane (*en face*) [21], a method borrowed from Doppler ultrasound imaging. Given that the surface normal is parallel to the components of the velocity that is measured, the following expression can be used:

$$F = -\iint_{xy\ plane} v_z(x, y)dxdy \tag{44.6}$$

Averaging the phase differences between several A-lines causes a systematic error which is dependent on both the signal-to-noise ratio and the proximity of the measured velocity to the limits of the velocity range [22]. An improvement has been devised by using an extension of the Kasai autocorrelation algorithm [23], which can obtain the phase difference ($\Delta\varphi$) given by

$$\Delta\varphi(z, t) = \tan^{-1}\left[\frac{\sum_{m=1}^{N} Im[I(z, t_n) \times I^*(z, t_{n-1})]}{\sum_{m=0}^{N} Re[I(z, t_n) \times I^*(z, t_{n-1})]}\right] \tag{44.7}$$

where N is the number of phase differences that are going to be averaged together and * indicates the complex conjugate.

44.2.1.2 Phase-Resolved Doppler Variance

Phase-resolved Doppler variance [24–26] methods have been developed to detect small phase variations from microvascular flow and are based on using the bandwidth of the Doppler frequency spectrum. These methods have the advantages of being less sensitive to the pulsatile nature of the blood flow and the incident angle, as well as the capability of being able to monitor transverse flow velocities [27]. Several Doppler variance algorithms have previously been compared [28]; however, they are based on the autocorrelation principles:

$$\sigma^2 = \frac{1}{\Delta T^2}\left[1 - \frac{\left|\sum_{j=1}^{J}\sum_{z=1}^{N}\left(I_{j,z}I_{j+1,z}{}^{*}\right)\right|}{\sum_{j=1}^{J}\sum_{z=1}^{N}\frac{1}{2}\left(I_{j,z}I_{j,z}{}^{*} + I_{j,z+1}I_{j,z+1}{}^{*}\right)}\right] \tag{44.8}$$

where J is the number of A-lines that are averaged and N is the number of depth points that are averaged. The averaging along the lateral and depth direction can reduce the background noise and improve the image quality although it may degrade the spatial resolution. The chosen values for J and N will depend on the specific biological tissue application. One drawback of the phase-resolved Doppler variance methods is their lost ability to provide the values of flow velocity.

44.2.2 Magnitude-Based Methods

In many applications, such as in imaging the retinal blood vessels, the direction of the vessels are nearly perpendicular to the OCT beam. As a result the axial velocity is small which yields a low-signal-to-noise ratio on the phase data. In other cases, there is low phase stability in the OCT system, such as in the application of several swept source OCT systems, where a source of phase noise is introduced from the cycle-to-cycle tuning and timing variability [29]. For these cases, the use of the phase information is highly susceptible to error. Therefore, methods have been developed that can obtain the angiography of the blood vessels based only on the temporal changes in the magnitude of the OCT signals. Such methods have less dependence on the beam incident angle, system phase stability, and small sample motion, thus are attractive in some of the applications in which only vascular morphology is of interests.

44.2.2.1 Autocorrelation Methods

Autocorrelation methods have been developed to quantitatively map the transverse particle-flow velocities. The method is based on analyzing the statistical nature of the intensity fluctuations of the backscattered light, which is modulated by flowing particles [30]. For example, Fig. 44.1 shows the magnitude of the detected OCT signal obtained from a flow phantom with different velocities, as well as the autocorrelation curves. The slope of the normalized autocorrelation function is proportional to the transverse velocities (Fig. 44.1d), as demonstrated in Fig. 44.2.

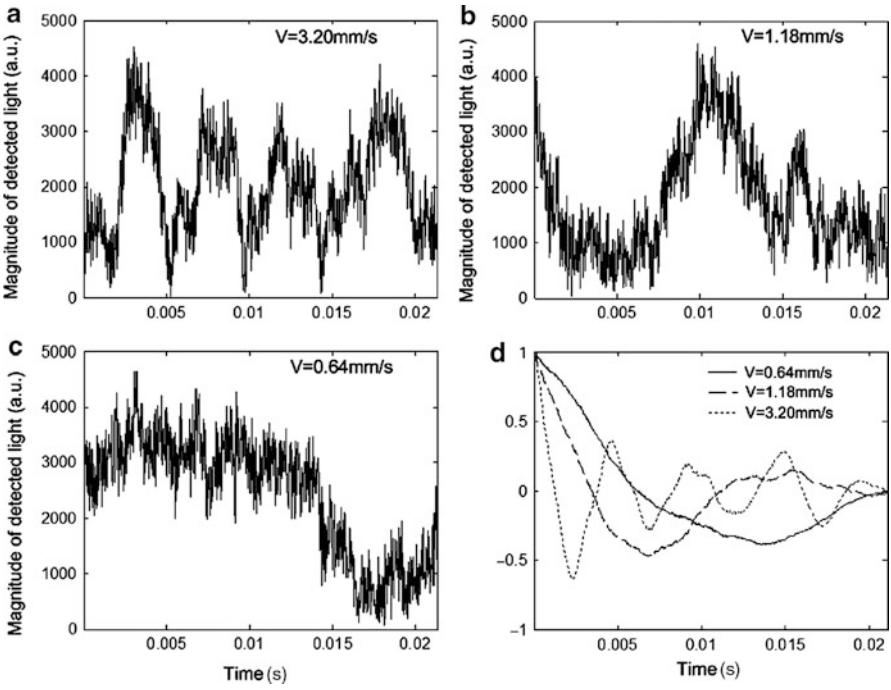

Fig. 44.1 Magnitude of the detected light which was modulated by intralipid flowing particles through a syringe pump phantom at the velocities of (**a**) 3.20 mm/s, (**b**) 1.18 mm/s, and (**c**) 0.64 mm/s. (**d**) Normalized autocorrelation function (Modified figure reprinted with permission from Ref. [30])

44.2.2.2 Correlation Methods

Another method that has been widely used is analyzing the correlation among B scans. This method consists of determining the average correlation (D) value between several pairs of OCT frames at the same cross section. The average correlation can be expressed by

$$D(x,z) = \frac{1}{N-1}\sum_{n=1}^{N-1} \frac{M_n(x,z)M_{n+1}(x,z)}{\left|\frac{M_n(x,z)^2}{2} + \frac{M_{n+1}(x,z)^2}{2}\right|} \tag{44.9}$$

where N is the total number of frames at the same cross section and $M_n(x, z)$ and $M_{n+1}(x, z)$ are the amplitude signal from adjacent frames. Methods have been devised to minimize noise such as using a window of several pixels instead of a single pixel; however, this produces a reduction in its spatial resolution. The value of $|D|$ varies between 0 and 1, where 0 indicates no correlation and 1 indicates high correlation. Therefore, static tissues have high absolute correlation values, while noise pixels and pixels that contain blood vessels have low

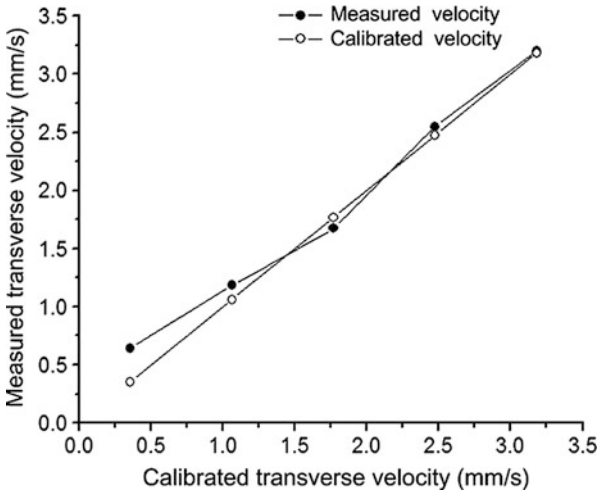

Fig. 44.2 Measured transverse velocities (*line with solid circles*) and calibrated velocities (*line with open circles*) (Modified figure reprinted with permission from Ref. [30])

absolute correlation values. For this reason, typically a structural mask is used over the cross-correlation map in order to eliminate the noise pixels, which adds an additional layer of complexity to this approach.

This technique has previously been used for correlation mapping OCT (cmOCT) [31, 32], split-spectrum amplitude-decorrelation angiography (SSADA) [33], and a variation has been also used for intensity-based Doppler variance algorithm [34].

44.2.2.3 Speckle Variance

Speckle variance OCT (svOCT) is a functional extension of OCT, which can yield three-dimensional vascular images by analyzing the Fourier transform of the temporal variation of the speckle [35] or by calculating the interframe variance (SV_{ijk}) of N consecutive B-mode OCT structural intensity (M_{ijk}) images. By analyzing each individual pixel within the image and using N frames for the analysis, the variance is calculated with the following expression [36]:

$$SV_{ijk} = \frac{1}{N} \sum_{i=1}^{N} \left(M_{ijk} - M_{mean} \right)^2 \tag{44.10}$$

Given that the vascular regions decorrelate faster compared to their static counterparts, the speckle patterns produced yield an endogenous contrast that is used for extracting the blood microangiography.

44.2.3 Complex-Based Methods

Up to this point, we have determined ways of extracting the vessel microangiography using the magnitude or the phase information obtained from

the OCT measurements. The phase-based methods are sensitive to the movements of the scatterers in the axial direction, while the magnitude-based methods are sensitive to the movements in both the lateral and the axial directions. Given that the OCT signal is a complex value, it is possible to take advantage of both the magnitude and phase information simultaneously to extract the vessel microangiography.

44.2.3.1 Optical Microangiography (OMAG)

Optical microangiography (OMAG) is a recently developed imaging technique that produces three-dimensional images of dynamic blood perfusion within microcirculatory tissue beds [37, 38]. OMAG was initially based on full range complex Fourier-domain OCT [39, 40], in which a high-pass filtering of the real valued signal is essentially employed to extract the blood flow signal from the static background signal. In OMAG, Wang et al. used a high-pass filter over the complex signal, to take advantage of both the magnitude and phase information. This process allows for the isolation of the positive and negative blood flow velocities [37].

OMAG analyzes the spatial frequency of the time-varying spectral interferograms. This analysis enables OMAG to separate the signal that is backscattered by static particles, such as bulk tissue, from moving particles, such as blood cells. There have been two generations of OMAG. The first generation consisted of introducing a carrier frequency by adding a phase delay to each A scan using a moving reference mirror or an off-pivot scanning beam. However, this technique is dependent on the precise synchronization of the reference arm modulation and the B-scan acquisition. As a result, it requires expensive modulators and is unable to detect bi-directional flow within a single B scan. The second generation overcame this limitation by using an algorithm which included a modified Hilbert transform that is used without the need of a spatial frequency modulation. This new algorithm is applicable for both the spectral domain and swept source OCT, provided that they both have comparable B-scan acquisition rates. The second generation OMAG requires only one B scan to obtain both the positive and negative flow.

The theory of OMAG is based on the depth-encoded spectral interferogram, which is captured by the linear detector as a real function $B(z, t)$, and can be expressed as

$$B(z,t) = A(z)cos\,(k_0 z + 2\pi ut) \tag{44.11}$$

where $A(z)$ is the reflective coefficient of the scatterer, k_0 is the wave vector of the detected light, and z relates to the detecting path. To simplify the expression we have ignored the random phase arising from the refractive index and assume that $A(z)$ is constant along the B-direction, t is the B-scan time that corresponds to the different lateral positions, and u is the modulation frequency generated by the flow speed. The Fourier transform of the spectral signal $B(z, t)$ is expressed by

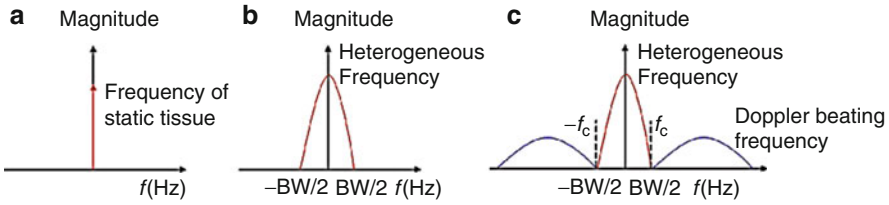

Fig. 44.3 Diagram of frequency components for different tissue sample: (**a**) an ideal tissue sample (optically homogeneous sample) with no moving particles, (**b**) a real tissue sample (optically heterogeneous sample) with no moving particles, and (**c**) a real tissue sample (optically heterogeneous sample) with moving particles (Modified figure reprinted with permission from Ref. [38])

$$
\begin{aligned}
H(z,u) &= \frac{A(z)}{T_0}\int_{t_0-\frac{\tau_0}{2}}^{t_0+\frac{\tau_0}{2}} cos\left(k_0 z + 2\pi u t\right)e^{-i2\pi u_0 t}dt \\
&= \frac{A(z)e^{ik_0 z}sin\left[\pi\tau_0(u-u_0)\right]}{2T_0\pi(u-u_0)}e^{-i2\pi(u-u_0)t_0} \\
&\quad + \frac{A(z)e^{-ik_0 z}sin\left[\pi\tau_0(u+u_0)\right]}{2T_0\pi(u+u_0)}e^{-i2\pi(u+u_0)t_0}
\end{aligned}
\tag{44.12}
$$

Based on the above equation, the nonmoving scatterers will be centered at the zeroth frequency (DC) region, and the moving scatterers will be shifted away from the zeroth frequency. Figure 44.3 presents examples of a frequency analysis using OMAG. If the tissue is completely homogeneous, which is an ideal case scenario, the frequency response would be a delta function centered at 0. However, a broadening of the spectra is observed when the tissue is inhomogeneous, which is a real case scenario. If there are moving particles within the inhomogeneous tissue, a higher frequency component will be observed. The shifting distance is directly related to the velocity u_0. The dynamic signal can be recreated by using a high-pass filter and then performing an inverse Fourier transform. The parameters that affect the flow signal detection include the flow velocity, the number and size of the moving scatterers, and the sampling line density.

By first using the OMAG method, it is possible to then apply the Doppler analysis method (Eq. 44.7), also known as Doppler OMAG (DOMAG). The key advantage of OMAG is that only the signals backscattered by the moving scatterers are obtained, and the static signal is filtered out. Therefore, the Doppler signal obtained in DOMAG is free of artifact induced noise. After the OMAG algorithm is applied, the correlation between adjacent A scans within the static tissue region is lost, which leads to a signal with high noise. However, this limitation is overcome by digitally reconstructing an ideal static background tissue which is optically homogeneous. This background tissue replaces the original heterogeneous tissue sample; therefore, creating correlated adjacent A-lines. Figure 44.4 presents a flowchart that highlights the algorithm used for the OMAG and DOMAG calculation.

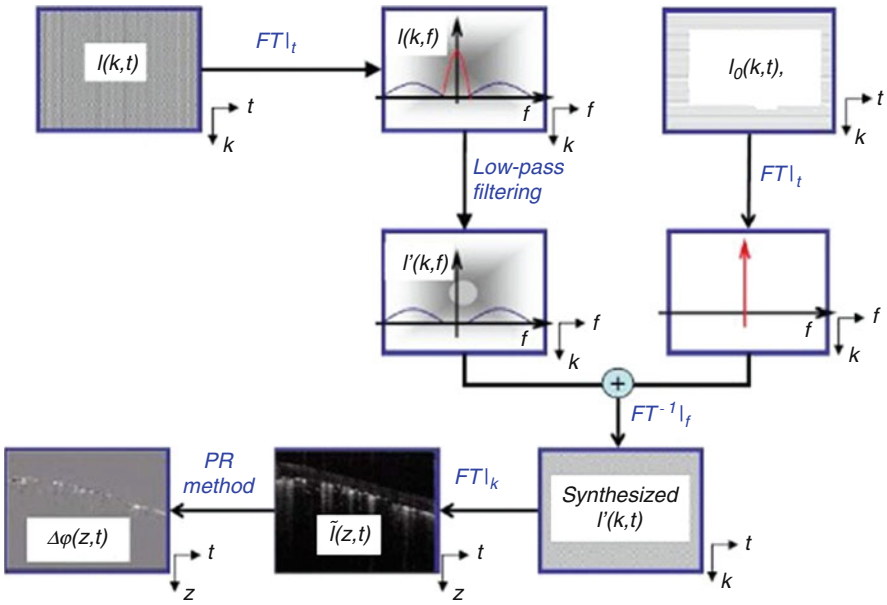

Fig. 44.4 Flow chart showing the steps for DOMAG to evaluate the velocities of blood flow from a B-scan data set, $I(k, t)$. The data coordinates are indicated in the *lower right* corner of each data block, where t is the time variable of probe beam scanning over a sample, k is the wavenumber, f is the spatial frequency, and z is the imaging depth. $\mathbf{FT|_t}$ represents the Fourier transform (FT) against the time variable t in the B scan; $\mathbf{FT^{-1}}\,|_\mathbf{f}$ indicates the inverse FT against the spatial frequency, f; and $\mathbf{FT|k}$ is FT against the wavenumber k (Modified figure reprinted with permission from Ref. [38])

DOMAG has been demonstrated to be more sensitive to the phase velocities than simple Doppler analysis as in phase-resolved Doppler OCT [38]. Figure 44.5 presents a comparison of both methods.

Figure 44.6 presents an example of a cross-sectional cut (B scan) obtained from a mouse brain with an intact skull. The location of the vessels and the Doppler signal can be observed.

OMAG has been applied in both the fast axis (B scan) and slow axis (C scan), for imaging fast and slow flows, respectively. Given that the time interval between A-lines in the slow axis is larger, this method allows higher sensitivity to capillary flow [41]. However, the high sensitivity requires removal of bulk-motion artifacts by resolving the Doppler phase shift.

44.2.3.2 Joint Spectral and Time-Domain OCT

A variation of OMAG is the joint spectral- and time-domain OCT (STdOCT). STdOCT requires the acquisition of a high number of repeated A scans at the same lateral position which increases the imaging time [42, 43]. The method consists on processing the interferograms along both the spectral and the time domain. This is done by applying two-dimensional Fourier transforms which converts the

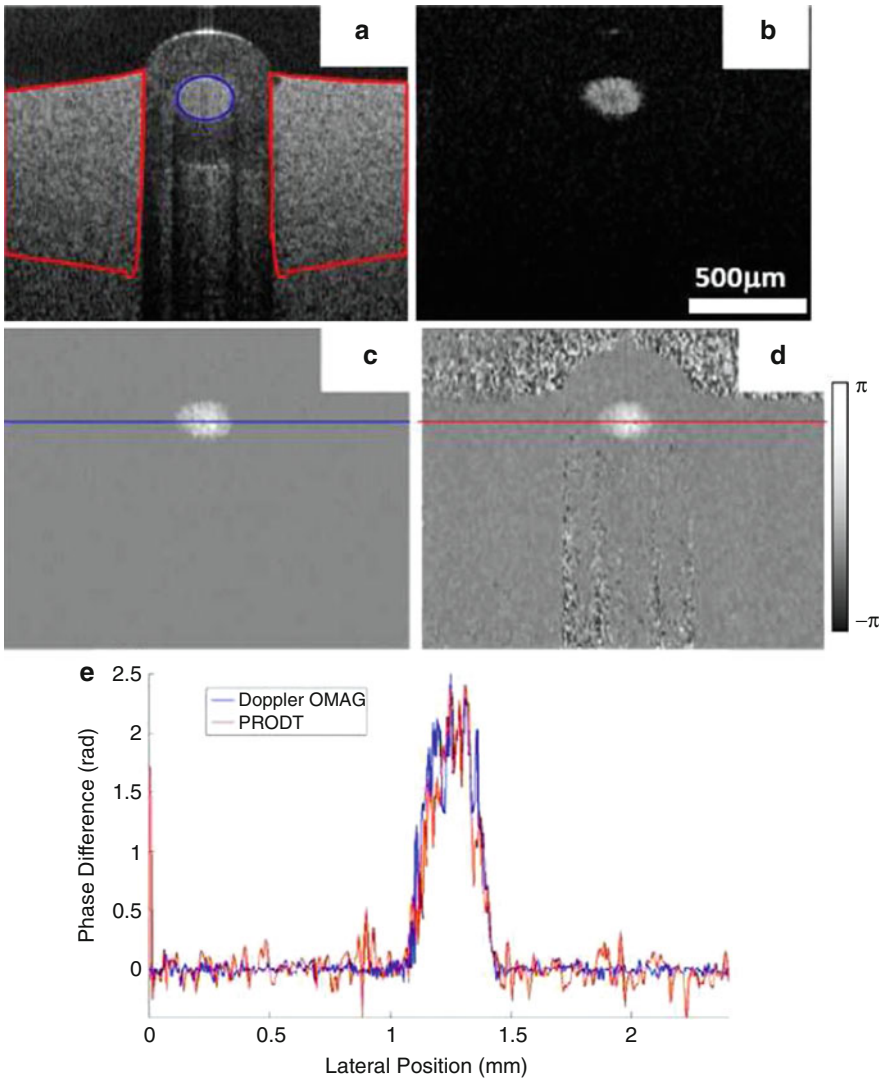

Fig 44.5 Flow phantom experiment results. (**a**) OMAG structural image, (**b**) OMAG flow image, (**c**) DOMAG velocity image, (**d**) PRDOCT velocity image, and (**e**) flow signal profiles extracted from the positions marked in (**c**) and (**d**) (Modified figure reprinted with permission from Ref. [38])

data from "wavenumber – time" domain to "in-depth position – beat frequency" domain. In this method, the squared maximum of the highest peak is proportional to the reflectivity of the scattering particle, and the position of the highest peak along the beat frequency axis ends up being proportional to the velocity.

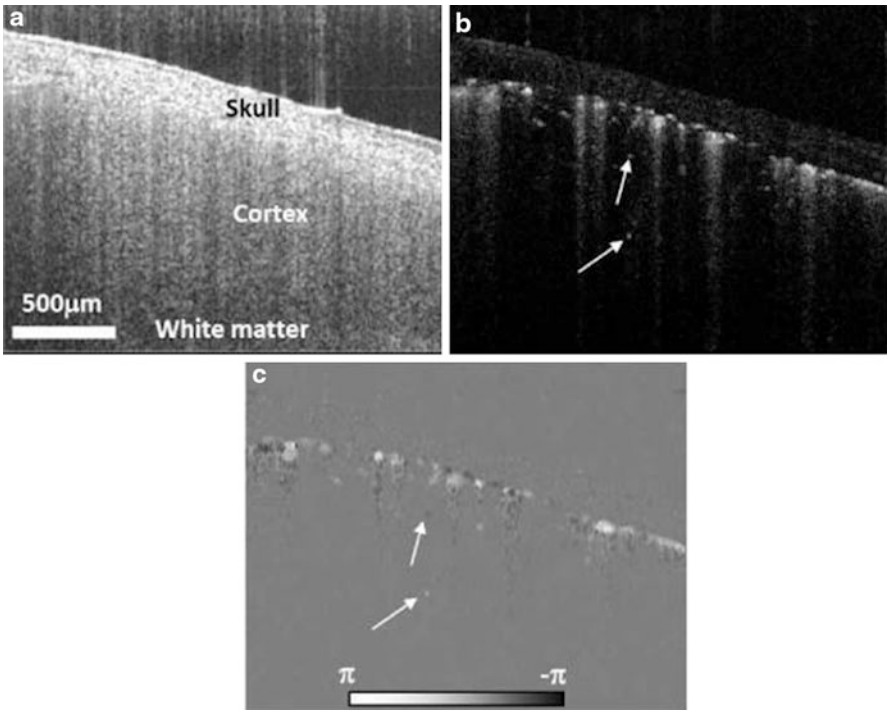

Fig. 44.6 In vivo OMAG image from a typical B scan of a mouse brain with the skull left intact. (**a**) OMAG image of the microstructures, identical to conventional spectral domain OCT image; (**b**) the corresponding OMAG image of blood flow; and (**c**) the corresponding DOMAG image of axial velocities of the blood flow (Modified figure reprinted with permission from Ref. [38])

44.3 Sources of Noise

There are several sources of noise for obtaining microvascular information from the OCT systems. The sources of noise are divided into system and sample noise. System noise relates to all the sources that come from the OCT system itself. These include the shot noise and the jitters caused by the scanners that move the probe beam spot over the sample. Shot noise has been previously studied, and the minimum measureable phase shift (assuming a zero-mean, complex Gaussian) is given by $\frac{1}{\sqrt{SNR}}$, where SNR is the signal-to-noise ratio [44–46]. The sample noise relates to the physiological motion artifacts, such as the heart and respiration rates, as well as vibrations that are mostly minimized by the use of floating tables. A crucial problem in imaging microcirculation is that the blood flow velocities can be lower than typical physiological or bulk tissue motion. Therefore, rejection of the tissue motion artifacts becomes critical.

The effects of noise can be separated into axial and lateral properties. In the axial direction, the effects can cause phase shift and decorrelation. Axial motion

compensation algorithms, such as the use of a histogram method, can correct phase shifts smaller [47] and larger [41] than $\lambda/4$, given that every axial position in an A-line experiences the same shift. A lateral shift can also cause decorrelation [48], which is usually not corrected due to its complicated nature; however, some methods have been derived [49].

A challenge in imaging at capillary level is that a large Δt between A-lines is required to allow for slow flow decorrelation; however, this duration is prone to higher motion artifacts.

44.4 Applications

Several diseases have been related to the changes in the vascular network of the tissues. In this section various examples of applications for studying vessel microangiography in different biological tissues are presented. The illustrations used in this section have been previously obtained using the OMAG technique; however, all of the techniques described above may be used based on their own advantages and drawbacks.

One of the most common applications for OCT, which has gained wide commercial acceptance, is the imaging of the human retina. OCT has been used to evaluate macular holes, assess vitreoretinal interface, diagnose macular edema, assess age-related macular degeneration, and others. Currently, fluorescein angiography is the gold standard for vascular imaging of the retina. However, fluorescein angiography is invasive and time consuming and presents side effects [50]. OMAG has allowed the imaging of the retinal microvasculature without using contrast agents, as shown in Fig. 44.7. An advantage of using OMAG is that it is possible to obtain both the structural and microvascular images. The different tissue layers such as the ganglion cell layer, inner plexiform layer, and outer plexiform layer can be segmented from the structural image, and this can then be applied on the three-dimensional microvascular image itself to separate the vascular networks within landmarked layers.

There has also been interest in imaging the anterior segment of the eye around the corneoscleral limbus. This area is important given that the aqueous outflow system, which regulates the intraocular pressure of the eye, must work properly to maintain a healthy physiological pressure within the eye. Changes in the tissue perfusion and vascularization may affect the behavior of the aqueous outflow system, causing a deregulation of the intraocular pressure which may lead to diseases such as glaucoma. Figure 44.8 presents an example of images obtained from the anterior segment of the eye.

Several skin diseases, such as psoriasis, have also been related to changes in the microvasculature of the tissue. Figure 44.9 presents an example of microvascular images obtained from different skin layers, such as the papillary dermis, reticular dermis, and hypodermis. The vessel morphology has different patterns for each tissue layer.

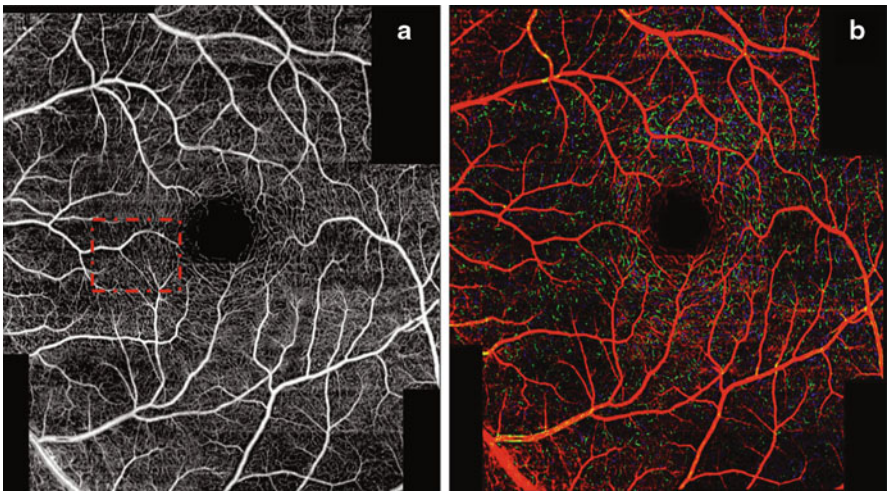

Fig. 44.7 Projection view image of (**a**) retinal microvasculature maps within a large field of view and (**b**) the corresponding color depth-encoded retinal vasculature map (the *red*, *green* and *blue colors* represent the ganglion cell layer, inner plexiform layer, and outer plexiform layer, respectively) (Modified figure reprinted with permission from Ref. [41])

The mouse brain has been a great model for neurological disorders, such as stroke and traumatic brain injury. OMAG is well applicable for imaging this tissue [21] and has the advantage of not requiring the removal of the skull, which makes the procedure highly noninvasive. Figure 44.10, presents an example of an image of the mouse brain.

Cochlear blood flow has been related to several hearing disorders such as noise-induced hearing loss, age-related hearing loss, sensorineural hearing loss, tinnitus, and Ménière's disease. OMAG has recently been used to image the vessels in the cochlea [51–54] and study several hearing disorders that are related to cochlear blood flow. Figure 44.11 presents an image of the vessels from a mouse cochlea, including the scalae which were extracted from the structural image.

44.5 Angiography Quantification

The analysis of the tissue vasculature is an important biomarker for determining the health of tissues. It has been demonstrated that the changes in retinal vessels is an early indicator of coronary heart disease [55] and stroke [56]. Microangiography images enable the visualization of blood vessels and capillaries in biological tissues. These images are usually interpreted qualitatively by an expert reviewer [57]; however, they lack of quantitative information and the analysis has large variability among reviewers. Some methods provide quantitative information from these images such as the blood vessel diameter [58] and the distance between

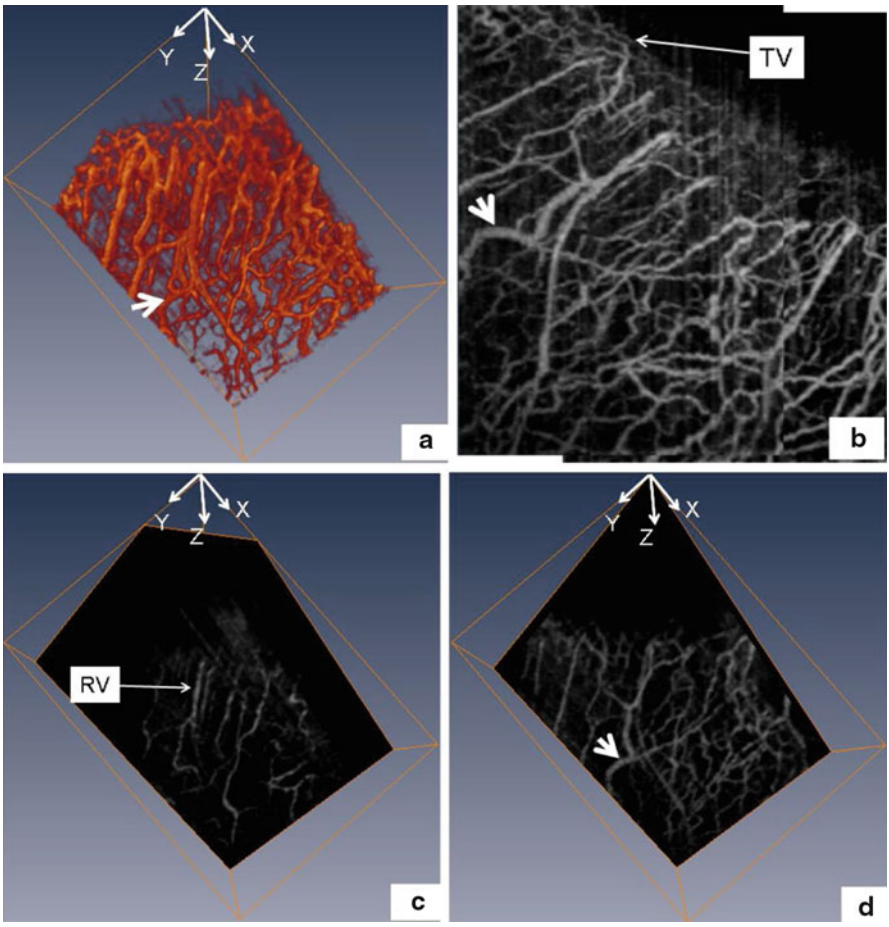

Fig. 44.8 In vivo 3D blood flow imaging of the human corneoscleral limbus from a temporal location. (**a**) 3D rendering of the flow images, (**b**) projection view (x-y) from the 3D blood flow image, (**c**) oblique slice of (**a**) within the conjunctival layer, and (**d**) oblique slice of (**a**) in the scleral area. *Bold white arrow* indicates the episcleral vein; *TV* terminal vessel, *RV* recurrent vessel. The physical image size was 5.5 × 4.0 × 3.0 (x-y-z) mm^3 (Modified figure reprinted with permission from Ref. [64])

blood vessels [59]. Other parameters that have been quantified include the vessel area density (a relative value which represents the area of the vessels), vessel length fraction (a relative value which represents the length of the vessels), and the fractal dimension (a relative value which represents the tortuosity of the vessels) [60].

Although there are several methods for analyzing angiography images, they all contain a vessel segmentation algorithm. The analysis is usually done over two- or three-dimensional images [61]. Given that the OCT signal exponentially degrades with depth due to the scattering and absorption attenuation of the light (Beer-Lambert law), it is commonly preferred to analyze a two-dimensional projection

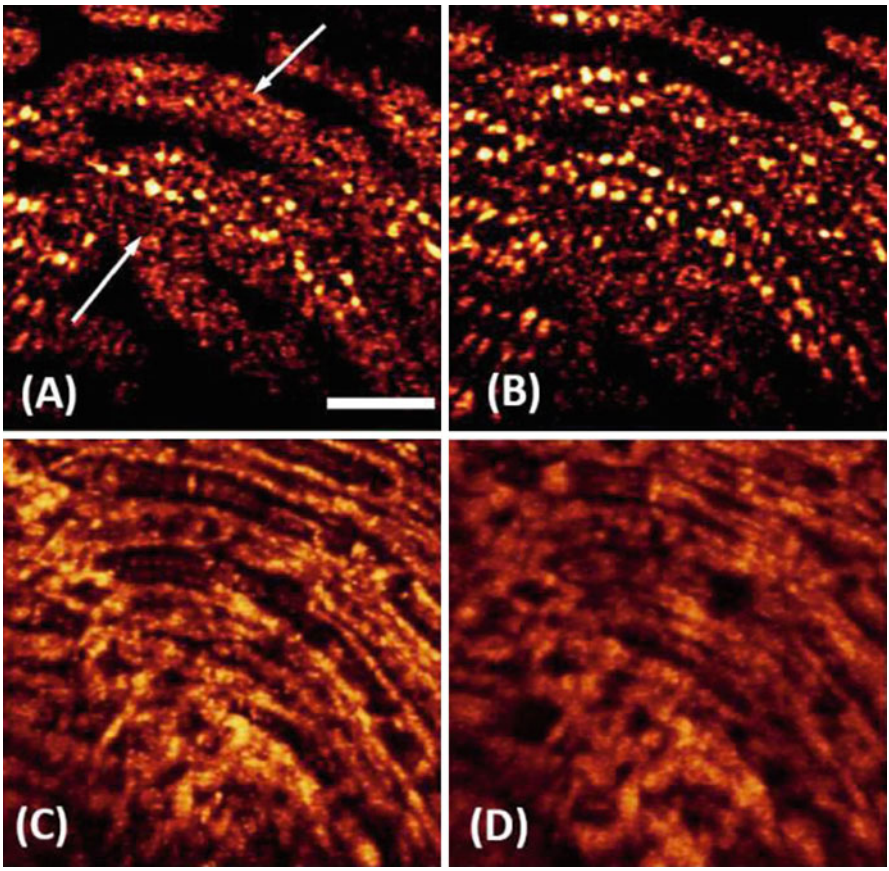

Fig. 44.9 Detailed projection view of microcirculation network at different depths of skin obtained from (**a**) 400–450 μm (closely representing papillary dermis), (**b**) 450–650 μm, (**c**) 650–780 μm (closely representing reticular dermis), and (**d**) 780–1,100 μm (part of hypodermis), respectively. The strength of reflectance signals in the images is displayed within a range between 20 (*dark*) and 50 dB (*bright*) (Modified figure reprinted with permission from Ref. [65])

view of the three-dimensional image. In several cases the images are also skeletonized to show the backbone of these vessels. Figure 44.12 presents an example of the binarization and skeletonization of a section of a two-dimensional projection view image of a mouse ear.

In Fig. 44.13 a projection view image of the vascularization of a large area of a mouse ear is presented. The fractal dimension calculated throughout the mouse ear is also depicted. There are regions with highly tortuous vessel which contain higher fractal dimension values (orange/red areas) compared to the smoother vessels which present a lower fractal dimension value (yellow/green areas). Two regions of interest were selected with high and low tortuosity, and the mean and

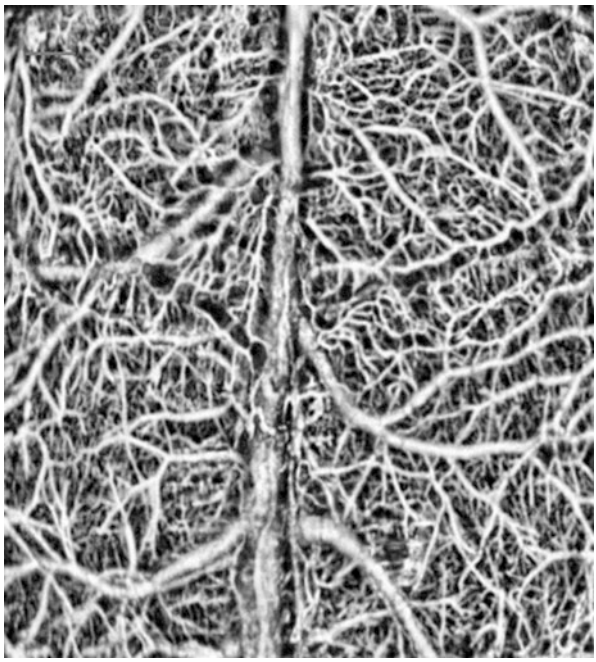

Fig. 44.10 Projection view image of the vessels located in the mouse brain with an intact skull. Scale bar: 500 μm (Modified figure reprinted with permission from Ref. [66])

standard deviation of these regions have been presented in Fig. 44.13c. This type of quantitative analysis may be applicable for the diagnosis and development of treatments for several vascular diseases.

44.6 Integrated Imaging Modalities

Integrated imaging modalities have been used to extract a wider range of information from biological tissues. Each imaging modality is sensitive to a different set of parameters; therefore, the advantage of combining them offers the ability to extract a larger amount of information. The parameters obtained from several imaging modalities can be taken together to provide a greater picture about the physiological properties of the tissue. In this section we briefly highlight a few of these combined imaging techniques.

Photoacoustic microscopy is an imaging modality that can detect changes in the concentration of oxyhemoglobin and deoxyhemoglobin within small vessels. Photoacoustic microscopy has been previously combined with the Doppler OCT to determine the metabolic rate of oxygen [62]. The metabolic rate of oxygen can be obtained by integrating the hemoglobin oxygen saturation and vessel diameter information obtained with photoacoustic microscopy, with the blood flow velocity obtained with Doppler OCT.

Dual-wavelength laser speckle contrast imaging has previously been combined with OMAG. Dual-wavelength laser speckle contrast imaging is a simple technique

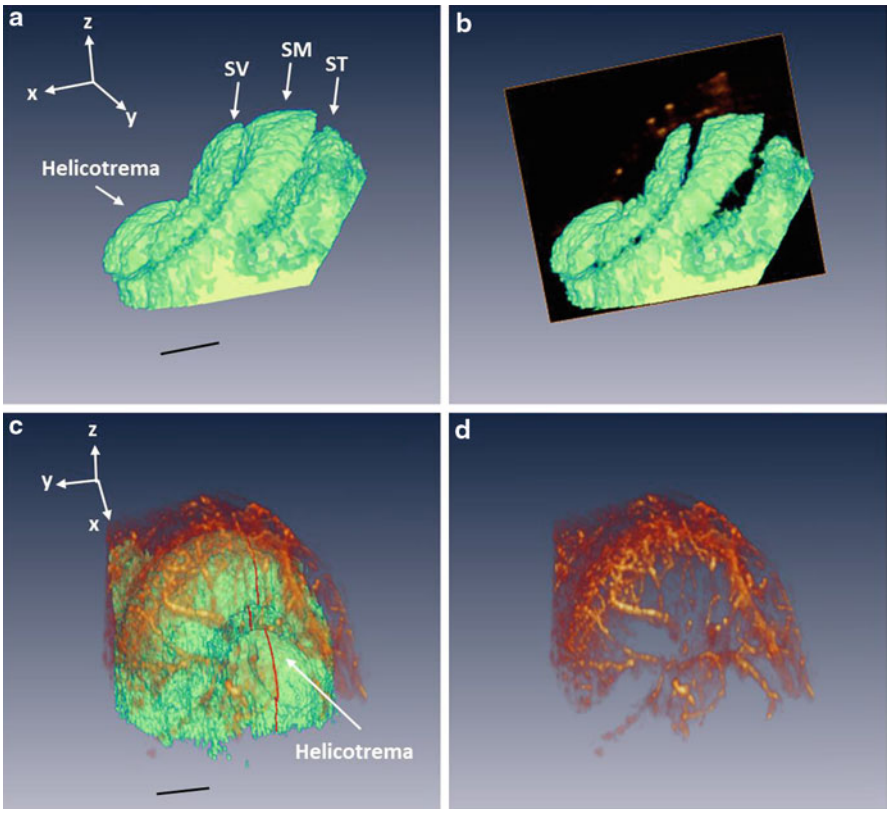

Fig. 44.11 (**a**) Three-dimensional side view of the scala media (*SM*), tympani (*ST*), and vestibuli (*SV*), (**b**) with a cross section showing the blood vessels obtained with OMAG. The cross section cuts through the apical turn close and far away from the helicotrema. The OCT light is incident in the z direction. (**c**) Apex view of the three-dimensional overlap of the cochlear scalae and the blood vessels. (**d**) Blood vessels alone. The *red line* through the center plane in (**c**) corresponds to the same cross-sectional area depicted by the *black square* in (**b**). The *black line* in (**a**) and (**c**) represents 250 μm (Modified figure reprinted with permission from Ref. [51])

which enables the extraction of the changes in the concentrations of oxyhemoglobin, deoxyhemoglobin, and total hemoglobin [63]. Figure 44.14 presents an overlap of an image obtained with both the OMAG and laser speckle contrast imaging system from a mouse ear after a burn injury. It can be noted that the middle circle presents the burn area where there are no vessels that can be observed and there is a decrease in blood flow.

In the commercial area, newer devices are being incorporated into the Fourier-domain OCT machines. For example, they have been combined with scanning laser ophthalmoscope technology, OCT with indocyanine angiography, and polarization-sensitive OCT using the birefringent characteristics of the retinal nerve fiber layer to better evaluate its thickness.

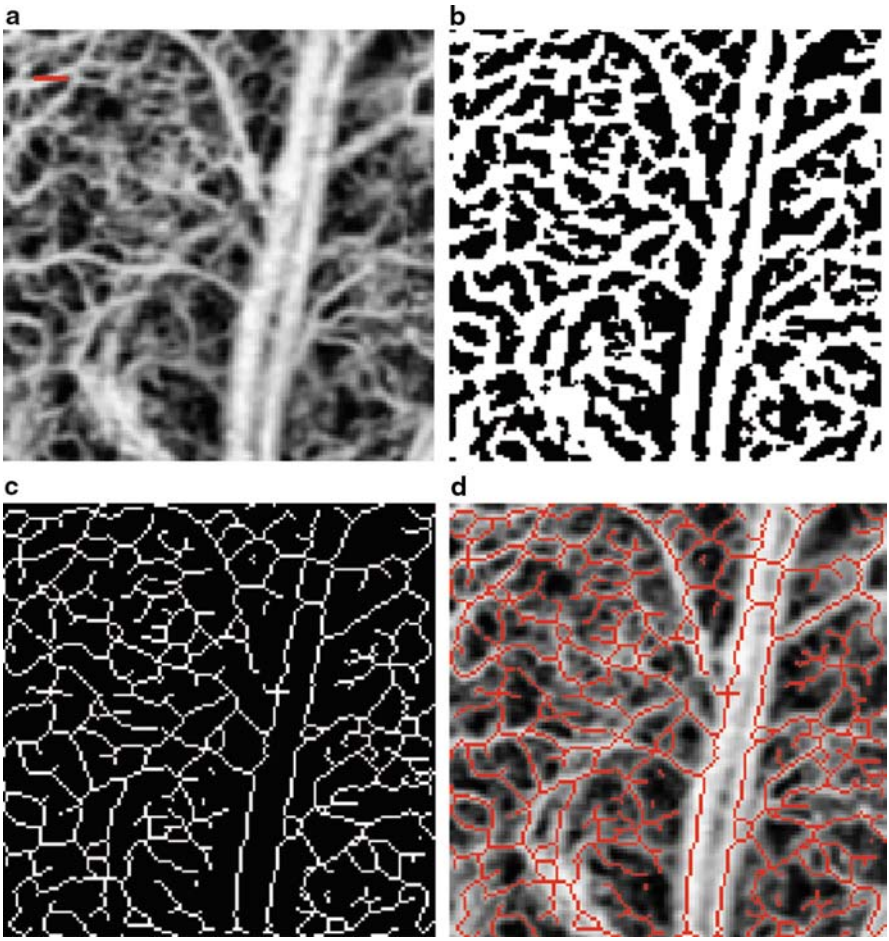

Fig. 44.12 (**a**) OMAG image obtained from a mouse ear. Scale bar is 0.1 mm. (**b**) *Black* and *white* segmented image of (**a**). (**c**) Skeletonization of the segmented image (**b**). (**d**) Overlay of (**c**) and (**a**) (Modified figure reprinted with permission from Ref. [60])

44.7 Summary

This chapter has reviewed the use of OCT for extracting the three-dimensional microvascular angiography from biological tissues in vivo. We have explored different methods of using the OCT system and described the advantages and disadvantages from each method as well as the overall general challenges. Several existing application for the microvascular angiography have been described; however, new applications are constantly being conceived. Methods for quantitatively analyzing these images have been described, and applications of combined imaging systems have been characterized.

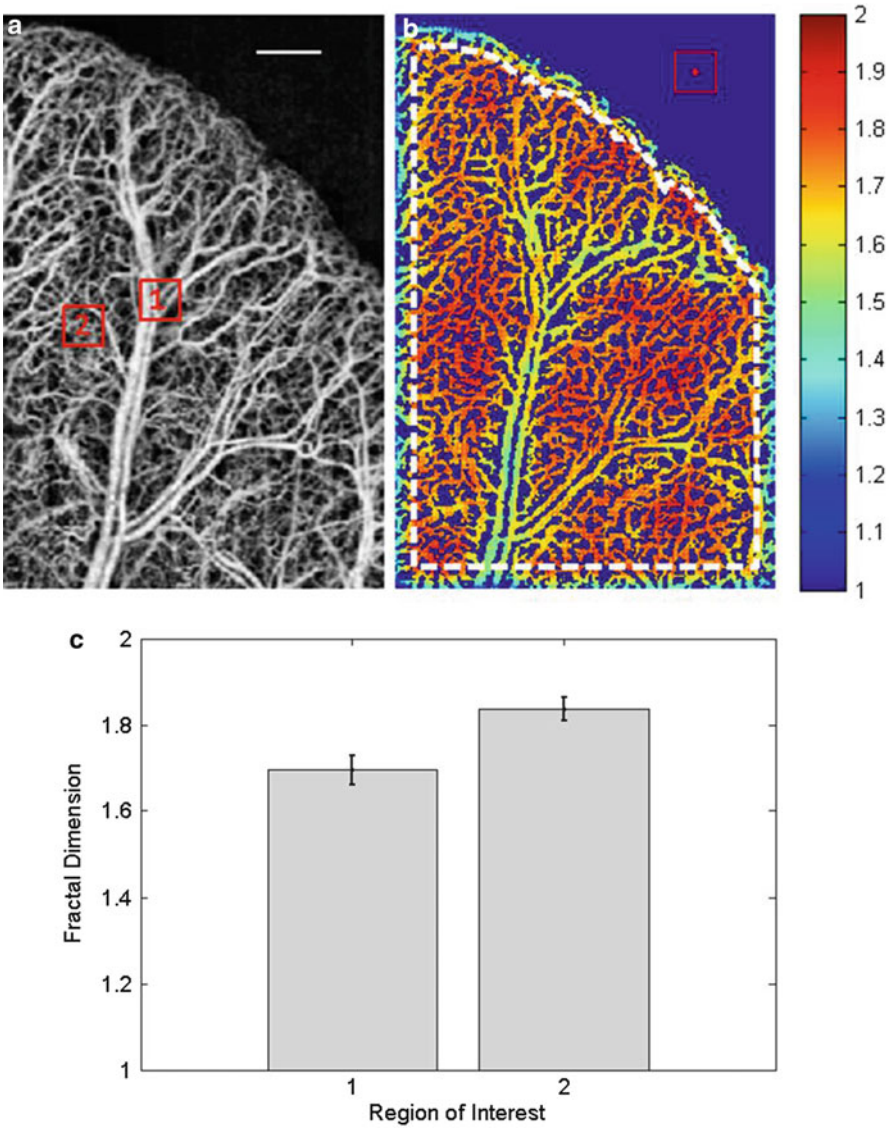

Fig. 44.13 (**a**) OMAG images obtained from the mouse ear. Scale bar is 0.5 mm. (**b**) *Black* and *white* segmented image multiplied by the fractal dimension. (**c**) Mean and standard deviation of the fractal dimension for the two regions of interest in (**a**) (Modified figure reprinted with permission from Ref. [60])

Fourier-domain OCT systems are a promising imaging device for several clinical applications, based on their rapid acquisition time and high resolution and sensitivity. However, while high acquisition speeds of A scans minimize the effects of motion artifacts in a single frame, the three-dimensional data sets are still subject

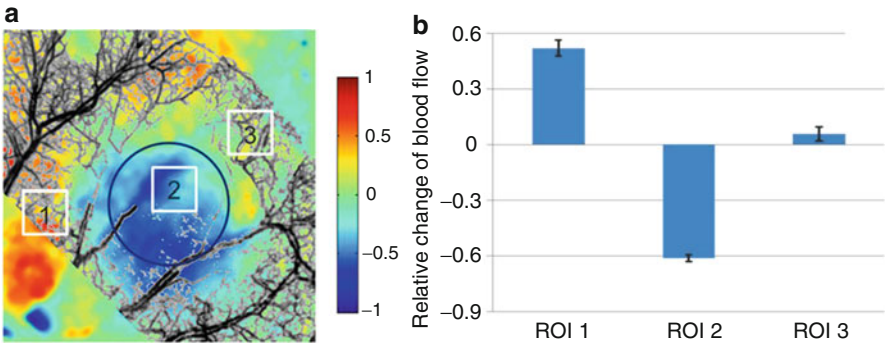

Fig. 44.14 (**a**) Co-registered image of the change in blood flow with the projection view image of the blood vessel network obtained by the OMAG method after the injury. (**b**) Mean and standard deviation of the relative change in blood flow from the three regions of interest in (**a**) (Modified figure reprinted with permission from Ref. [63])

to movements, as they are acquired over a few seconds. Further improvements in readout rates and pixel densities of CCD cameras in the case of SD-OCT may overcome much of these limitations.

Acknowledgements Some of the results presented in this chapter were made possible with research grants awarded by the National Institutes of Health (R01HL093140, R01HL093140S, R01EB009682, and R01DC01201), the American Heart Association (0855733G), and the W.H. Coulter Foundation Translational Research Partnership Program. Dr Wang is a recipient of Research to Prevent Blindness Innovative Research Award. The content is solely the responsibility of the authors and does not necessarily represent the official views of grant-giving bodies.

References

1. F. Calamante, D.L. Thomas, G.S. Pell, J. Wiersma, R. Turner, Measuring cerebral blood flow using magnetic resonance imaging techniques. J. Cereb. Blood Flow Metab. Off. J. Int. Soc. Cereb. Blood Flow Metab. **19**(7), 701–735 (1999)
2. W.D. Heiss, R. Graf, K. Wienhard, J. Löttgen, R. Saito, T. Fujita, G. Rosner, R. Wagner, Dynamic penumbra demonstrated by sequential multitracer PET after middle cerebral artery occlusion in cats. J. Cereb. Blood Flow Metab. Off. J. Int. Soc. Cereb. Blood Flow Metab. **14**(6), 892–902 (1994)
3. D. Kleinfeld, P.P. Mitra, F. Helmchen, W. Denk, Fluctuations and stimulus-induced changes in blood flow observed in individual capillaries in layers 2 through 4 of rat neocortex. Proc. Natl. Acad. Sci. U. S. A. **95**(26), 15741–15746 (1998)
4. A.F. Fercher, J.D. Briers, Flow visualization by means of single-exposure speckle photography. Opt. Commun. **37**(5), 326–330 (1981)
5. A.K. Dunn, H. Bolay, M.A. Moskowitz, D.A. Boas, Dynamic imaging of cerebral blood flow using laser speckle. J. Cereb. Blood Flow Metab. Off. J. Int. Soc. Cereb. Blood Flow Metab. **21**(3), 195–201 (2001)
6. O. Sakurada, C. Kennedy, J. Jehle, J.D. Brown, G.L. Carbin, L. Sokoloff, Measurement of local cerebral blood flow with iodo [14C] antipyrine. Am. J. Physiol. **234**(1), H59–H66 (1978)

7. R. Reif, M.S. Amorosino, K.W. Calabro, O. A'Amar, S.K. Singh, I.J. Bigio, Analysis of changes in reflectance measurements on biological tissues subjected to different probe pressures. J. Biomed. Opt. **13**(1), 010502 (2008)
8. D. Huang, E. Swanson, C. Lin, J. Schuman, W. Stinson, W. Chang, M. Hee, T. Flotte, K. Gregory, C. Puliafito, Optical coherence tomography. Science **254**(5035), 1178–1181 (1991)
9. L. An, P. Li, T.T. Shen, R. Wang, High speed spectral domain optical coherence tomography for retinal imaging at 500,000 A-lines per second. Biomed. Opt. Express **2**(10), 2770–2783 (2011)
10. R. Leitgeb, C. Hitzenberger, A. Fercher, Performance of fourier domain vs time domain optical coherence tomography. Opt. Express **11**(8), 889 (2003)
11. A.F. Fercher, C.K. Hitzenberger, G. Kamp, S.Y. El-Zaiat, Measurement of intraocular distances by backscattering spectral interferometry. Opt. Commun. **117**(1–2), 43–48 (1995)
12. S.R. Chinn, E.A. Swanson, J.G. Fujimoto, Optical coherence tomography using a frequency-tunable optical source. Opt. Lett. **22**(5), 340 (1997)
13. M.E.J. van Velthoven, D.J. Faber, F.D. Verbraak, T.G. van Leeuwen, M.D. de Smet, Recent developments in optical coherence tomography for imaging the retina. Prog. Retin. Eye Res. **26**(1), 57–77 (2007)
14. P. Li, R. Reif, Z. Zhi, E. Martin, T.T. Shen, M. Johnstone, R.K. Wang, Phase-sensitive optical coherence tomography characterization of pulse-induced trabecular meshwork displacement in ex vivo nonhuman primate eyes. J. Biomed. Opt. **17**(7), 076026 (2012)
15. C. Li, G. Guan, R. Reif, Z. Huang, R.K. Wang, Determining elastic properties of skin by measuring surface waves from an impulse mechanical stimulus using phase-sensitive optical coherence tomography. J. R. Soc. Interface R. Soc. **9**(70), 831–841 (2012)
16. G. Guan, R. Reif, Z. Huang, R.K. Wang, Depth profiling of photothermal compound concentrations using phase sensitive optical coherence tomography. J. Biomed. Opt. **16**(12), 126003 (2011)
17. Z. Chen, T.E. Milner, D. Dave, J.S. Nelson, Optical Doppler tomographic imaging of fluid flow velocity in highly scattering media. Opt. Lett. **22**(1), 64–66 (1997)
18. Y. Zhao, Z. Chen, C. Saxer, S. Xiang, J.F. de Boer, J.S. Nelson, Phase-resolved optical coherence tomography and optical Doppler tomography for imaging blood flow in human skin with fast scanning speed and high velocity sensitivity. Opt. Lett. **25**(2), 114 (2000)
19. B.J. Vakoc, S.H. Yun, J.F. de Boer, G.J. Tearney, B.E. Bouma, Phase-resolved optical frequency domain imaging. Opt. Express **13**(14), 5483–5493 (2005)
20. Z. Zhi, W. Cepurna, E. Johnson, T. Shen, J. Morrison, R.K. Wang, Volumetric and quantitative imaging of retinal blood flow in rats with optical microangiography. Biomed. Opt. Express **2**(3), 579–591 (2011)
21. V.J. Srinivasan, S. Sakadžić, I. Gorczynska, S. Ruvinskaya, W. Wu, J.G. Fujimoto, D.A. Boas, Quantitative cerebral blood flow with optical coherence tomography. Opt. Express **18**(3), 2477 (2010)
22. A. Szkulmowska, M. Szkulmowski, A. Kowalczyk, M. Wojtkowski, Phase-resolved Doppler optical coherence tomography – limitations and improvements. Opt. Lett. **33**(13), 1425 (2008)
23. V.X. Yang, M.L. Gordon, A. Mok, Y. Zhao, Z. Chen, R.S. Cobbold, B.C. Wilson, I. Alex Vitkin, Improved phase-resolved optical Doppler tomography using the Kasai velocity estimator and histogram segmentation. Opt. Commun. **208**(4–6), 209–214 (2002)
24. J. Fingler, R.J. Zawadzki, J.S. Werner, D. Schwartz, S.E. Fraser, Volumetric microvascular imaging of human retina using optical coherence tomography with a novel motion contrast technique. Opt. Express **17**(24), 22190 (2009)
25. L. Yu, Z. Chen, Doppler variance imaging for three-dimensional retina and choroid angiography. J. Biomed. Opt. **15**(1) (2010)
26. Y. Zhao, Z. Chen, C. Saxer, Q. Shen, S. Xiang, J.F. de Boer, J.S. Nelson, Doppler standard deviation imaging for clinical monitoring of in vivo human skin blood flow. Opt. Lett. **25**(18), 1358 (2000)

27. H. Ren, K.M. Brecke, Z. Ding, Y. Zhao, J.S. Nelson, Z. Chen, Imaging and quantifying transverse flow velocity with the Doppler bandwidth in a phase-resolved functional optical coherence tomography. Opt. Lett. **27**(6), 409 (2002)
28. G. Liu, L. Chou, W. Jia, W. Qi, B. Choi, Z. Chen, Intensity-based modified Doppler variance algorithm: application to phase instable and phase stable optical coherence tomography systems. Opt. Express **19**(12), 11429 (2011)
29. M.-T. Tsai, T.-T. Chi, H.-L. Liu, F.-Y. Chang, C.-H. Yang, C.-K. Lee, C.-C. Yang, Microvascular imaging using swept-source optical coherence tomography with single-channel acquisition. Appl. Phys. Express **4**(9), 097001 (2011)
30. Y. Wang, R. Wang, Autocorrelation optical coherence tomography for mapping transverse particle-flow velocity. Opt. Lett. **35**(21), 3538 (2010)
31. J. Enfield, E. Jonathan, M. Leahy, In vivo imaging of the microcirculation of the volar forearm using correlation mapping optical coherence tomography (cmOCT). Biomed. Opt. Express **2**(5), 1184–1193 (2011)
32. E. Jonathan, J. Enfield, M.J. Leahy, Correlation mapping method for generating microcirculation morphology from optical coherence tomography (OCT) intensity images. J. Biophotonics **4**(9), 583–587 (2011)
33. Y. Jia, O. Tan, J. Tokayer, B. Potsaid, Y. Wang, J.J. Liu, M.F. Kraus, H. Subhash, J.G. Fujimoto, J. Hornegger, D. Huang, Split-spectrum amplitude-decorrelation angiography with optical coherence tomography. Opt. Express **20**(4), 4710 (2012)
34. G. Liu, A.J. Lin, B.J. Tromberg, Z. Chen, A comparison of Doppler optical coherence tomography methods. Biomed. Opt. Express **3**(10), 2669 (2012)
35. J.K. Barton, S. Stromski, Flow measurement without phase information in optical coherence tomography images. Opt. Express **13**(14), 5234 (2005)
36. A. Mariampillai, B.A. Standish, E.H. Moriyama, M. Khurana, N.R. Munce, M.K.K. Leung, J. Jiang, A. Cable, B.C. Wilson, I.A. Vitkin, V.X.D. Yang, Speckle variance detection of microvasculature using swept-source optical coherence tomography. Opt. Lett. **33**(13), 1530 (2008)
37. R.K. Wang, S.L. Jacques, Z. Ma, S. Hurst, S.R. Hanson, A. Gruber, Three dimensional optical angiography. Opt. Express **15**(7), 4083 (2007)
38. R.K. Wang, L. An, Doppler optical micro-angiography for volumetric imaging of vascular perfusion in vivo. Opt. Express **17**(11), 8926–8940 (2009)
39. R.K. Wang, In vivo full range complex Fourier domain optical coherence tomography. Appl. Phys. Lett. **90**(5), 054103 (2007)
40. R.K. Wang, Fourier domain optical coherence tomography achieves full range complex imaging in vivo by introducing a carrier frequency during scanning. Phys. Med. Biol. **52**(19), 5897–5907 (2007)
41. L. An, T.T. Shen, R.K. Wang, Using ultrahigh sensitive optical microangiography to achieve comprehensive depth resolved microvasculature mapping for human retina. J. Biomed. Opt. **16**(10), 106013 (2011)
42. M. Szkulmowski, A. Szkulmowska, T. Bajraszewski, A. Kowalczyk, M. Wojtkowski, Flow velocity estimation using joint spectral and time domain optical coherence tomography. Opt. Express **16**(9), 6008 (2008)
43. M. Szkulmowski, I. Grulkowski, D. Szlag, A. Szkulmowska, A. Kowalczyk, M. Wojtkowski, Flow velocity estimation by complex ambiguity free joint spectral and time domain optical coherence tomography. Opt. Express **17**(16), 14281 (2009)
44. M.A. Choma, A.K. Ellerbee, C. Yang, T.L. Creazzo, J.A. Izatt, Spectral-domain phase microscopy. Opt. Lett. **30**(10), 1162–1164 (2005)
45. B. Park, M.C. Pierce, B. Cense, S.-H. Yun, M. Mujat, G. Tearney, B. Bouma, J. de Boer, Real-time fiber-based multi-functional spectral-domain optical coherence tomography at 1.3 microm. Opt. Express **13**(11), 3931–3944 (2005)
46. S. Yazdanfar, C. Yang, M. Sarunic, J. Izatt, Frequency estimation precision in Doppler optical coherence tomography using the Cramer-Rao lower bound. Opt. Express **13**(2), 410–416 (2005)

47. S. Makita, Y. Hong, M. Yamanari, T. Yatagai, Y. Yasuno, Optical coherence angiography. Opt. Express **14**(17), 7821–7840 (2006)
48. B.J. Vakoc, G.J. Tearney, B.E. Bouma, Statistical properties of phase-decorrelation in phase-resolved Doppler optical coherence tomography. IEEE Trans. Med. Imaging **28**(6), 814–821 (2009)
49. J. Lee, V. Srinivasan, H. Radhakrishnan, D.A. Boas, Motion correction for phase-resolved dynamic optical coherence tomography imaging of rodent cerebral cortex. Opt. Express **19**(22), 21258–21270 (2011)
50. Frequency of adverse systemic reactions after fluorescein angiography. Results of a prospective... – Abstract – UK PubMed Central [Online]. Available: http://ukpmc.ac.uk/abstract/MED/1891225. Accessed 25 Sept 2012
51. S. Dziennis, R. Reif, Z. Zhi, A.L. Nuttall, R.K. Wang, Effects of hypoxia on cochlear blood flow in mice using Doppler optical microangiography. J. Biomed. Opt. **17**(10), 106003 (2012)
52. H.M. Subhash, V. Davila, H. Sun, A.T. Nguyen-Huynh, X. Shi, A.L. Nuttall, R.K. Wang, Volumetric in vivo imaging of microvascular perfusion within the intact cochlea in mice using ultra-high sensitive optical microangiography. IEEE Trans. Med. Imaging **30**(2), 224–230 (2011)
53. H.M. Subhash, V. Davila, H. Sun, A.T. Nguyen-Huynh, A.L. Nuttall, R.K. Wang, Volumetric in vivo imaging of intracochlear microstructures in mice by high-speed spectral domain optical coherence tomography. J. Biomed. Opt. **15**(3), 036024 (2010)
54. N. Choudhury, F. Chen, X. Shi, A.L. Nuttall, R.K. Wang, Volumetric imaging of blood flow within cochlea in gerbil in vivo. IEEE J. Sel. Top. Quantum Electron. **16**(3), 524–529 (2010)
55. G. Liew, P. Mitchell, E. Rochtchina, T.Y. Wong, W. Hsu, M.L. Lee, A. Wainwright, J.J. Wang, Fractal analysis of retinal microvasculature and coronary heart disease mortality. Eur. Heart J. **32**(4), 422–429 (2011)
56. N. Cheung, G. Liew, R.I. Lindley, E.Y. Liu, J.J. Wang, P. Hand, M. Baker, P. Mitchell, T.Y. Wong, Retinal fractals and acute lacunar stroke. Ann. Neurol. **68**(1), 107–111 (2010)
57. Y. Zhou, K.G. Sheets, E.J. Knott, C.E. Regan, J. Tuo, C.-C. Chan, W.C. Gordon, N.G. Bazan, Cellular and 3D optical coherence tomography assessment during the initiation and progression of retinal degeneration in the Ccl2/Cx3cr1-deficient mouse. Exp. Eye Res. **93**(5), 636–648 (2011)
58. D. Goldenberg, U. Soiberman, A. Loewenstein, M. Goldstein, Heidelberg spectral-domain optical coherence tomography findings in retinal artery macroaneurysm. Retina **32**, 990–995 (2011)
59. J.W. Baish, T. Stylianopoulos, R.M. Lanning, W.S. Kamoun, D. Fukumura, L.L. Munn, R.K. Jain, Scaling rules for diffusive drug delivery in tumor and normal tissues. Proc. Natl. Acad. Sci. U. S. A. **108**(5), 1799–1803 (2011)
60. R. Reif, J. Qin, L. An, Z. Zhi, S. Dziennis, R.K. Wang, Quantifying optical microangiography images obtained from a spectral domain optical coherence tomography system. Int. J. Biomed. Imaging **509783**, 11 (2012)
61. L. Conroy, R.S. DaCosta, I.A. Vitkin, Quantifying tissue microvasculature with speckle variance optical coherence tomography. Opt. Lett. **37**(15), 3180 (2012)
62. T. Liu, Q. Wei, J. Wang, S. Jiao, H.F. Zhang, Combined photoacoustic microscopy and optical coherence tomography can measure metabolic rate of oxygen. Biomed. Opt. Express **2**(5), 1359–1365 (2011)
63. J. Qin, R. Reif, Z. Zhi, S. Dziennis, R. Wang, Hemodynamic and morphological vasculature response to a burn monitored using a combined dual-wavelength laser speckle and optical microangiography imaging system. Biomed. Opt. Express **3**(3), 455–466 (2012)
64. P. Li, L. An, R. Reif, T.T. Shen, M. Johnstone, R.K. Wang, In vivo microstructural and microvascular imaging of the human corneo-scleral limbus using optical coherence tomography. Biomed. Opt. Express **2**(11), 3109–3118 (2011)
65. J. Qin, J. Jiang, L. An, D. Gareau, R.K. Wang, In vivo volumetric imaging of microcirculation within human skin under psoriatic conditions using optical microangiography. Lasers Surg. Med. **43**(2), 122–129 (2011)
66. R. Reif, R.K. Wang, Label-free imaging of blood vessel morphology with capillary resolution using optical microangiography. Quant. Imaging Med. Surg. **2**(3), 207–212 (2012)

Optical Coherence Tomography in Cancer Imaging

45

Ahhyun Stephanie Nam, Benjamin Vakoc, David Blauvelt, and Isabel Chico-Calero

Keywords

Cancer • intravital microscopy • OCT • angiography • angiogenesis • mouse models of cancer • Doppler OCT

Investigations into the biology of cancer and novel cancer therapies rely on preclinical mouse models and traditional histological endpoints. Historically, tumor growth and disease progression were monitored by periodic caliper measurements and by endpoint measurements of weight or volume in preclinical models. Drawbacks of this approach included the difficulty in assessing cell viability and the effect of therapeutics on tumor vasculature, a limit in the number of time points for evaluation, and an increased number of animals per study [1].

The adoption of imaging modalities that allow for noninvasive, serial imaging represented a breakthrough in the field. Cancer investigators were able to employ simple-to-use, scientifically reliable technology which translated into more accurate results and simplified experimental workload. Preclinical versions of radiological tools [2] such as magnetic resonance imaging (MRI) and positron-emission tomography (PET) are commonly available as core instruments to many cancer investigators. Optical fluorescence and multiphoton microscopy [3] have also been adopted into cancer investigations to enable high-resolution imaging with molecular contrast and to validate in vitro studies with fluorescently labeled cells. Together, these tools have accelerated the pace of discovery in cancer biology and drug development and advanced our understanding of complex biological processes.

By contrast with fluorescence confocal and nonlinear microscopy, OCT has seen a more rapid integration into clinical diagnostic medicine [4] than into basic or preclinical research. This was driven by the unique capabilities of OCT to image

A.S. Nam • B. Vakoc (✉) • D. Blauvelt • I. Chico-Calero
Wellman Center for Photomedicine, Massachusetts General Hospital and Harvard Medical School, Boston, MA, USA
e-mail: bvakoc@mgh.harvard.edu

© Springer International Publishing Switzerland 2015

W. Drexler, J.G. Fujimoto (eds.), *Optical Coherence Tomography*,
DOI 10.1007/978-3-319-06419-2_46

rapidly, to probe deeper into tissue, and to operate without the need for labels or contrast agents [5]. Recent works, however, demonstrate that OCT has the potential to become a key player in intravital preclinical imaging in cancer research [6]. This is especially evident in vascular studies where OCT-based angiography offers new capabilities to characterize and monitor the process of angiogenesis and the response of tumor vessels to therapy.

To date, OCT has contributed to cancer research in a variety of ways [6]: OCT has been used to monitor tumor burden [7], to reveal wide-field tumor vascular morphology, to noninvasively monitor lymphangiogenesis and lymph vessel dysfunction, and to differentiate viable and nonviable tumor compartments during tumor growth and anticancer drug therapy. Here, examples where OCT serves as a valuable tool for preclinical cancer research are summarized.

45.1 Angiography

Angiogenesis is a crucial step by which a tumor develops its own de novo blood vessels [8]. Tumor cells secrete angiogenic factors to induce the creation of new vascularization. Unlike physiological angiogenesis, tumor angiogenesis is a seemingly chaotic process that results in the development of a largely dysfunctional vascular network [9]. Given the central role that angiogenesis plays in tumor biology, it is a much sought-after target for therapeutic intervention. Many antiangiogenic molecules have been developed, such as VEGFR inhibitors, and some are being used clinically [10–12]. However, despite the discovery of very potent antiangiogenic molecules, and their promising results in preclinical models, these drugs have translated poorly into the clinic, often offering minimal improvement upon existing therapies [13].

Intravital imaging has played an important role in the study of tumor angiogenesis and antiangiogenic treatment during the past decades. Commonly used methods to visualize blood vessels in vivo include Doppler ultrasound [14], micro-magnetic resonance imaging (μMRI) [2], μCT [15], photoacoustic tomography [16–19], and fluorescence microscopy [20]. The nonoptical methods (Doppler ultrasound, μMRI, and μCT) are limited by their relatively low resolutions, which make it difficult to visualize single vessels. By contrast, fluorescence microscopy has sufficiently high resolution to resolve individual vessels, but are often limited in their depth penetration and field of view. Furthermore, fluorescence methods require systemic vascular labeling with exogenous contrast, which can accumulate in tissues in longitudinal studies [21]. Because OCT has a larger field, deeper penetration, and images without exogenous labels, it can be used in angiographic applications where the drawbacks of fluorescence microscopy are significant.

OCT-based angiography is based on dynamic changes in optical scattering induced by moving scatterers in the blood. Many approaches for detecting these changes have been used, and each has specific benefits and limitations. Originally, Doppler processing techniques revealed the optical frequency shift of induced by upward or downward flowing blood [22–24]. Later, approaches that cue in on

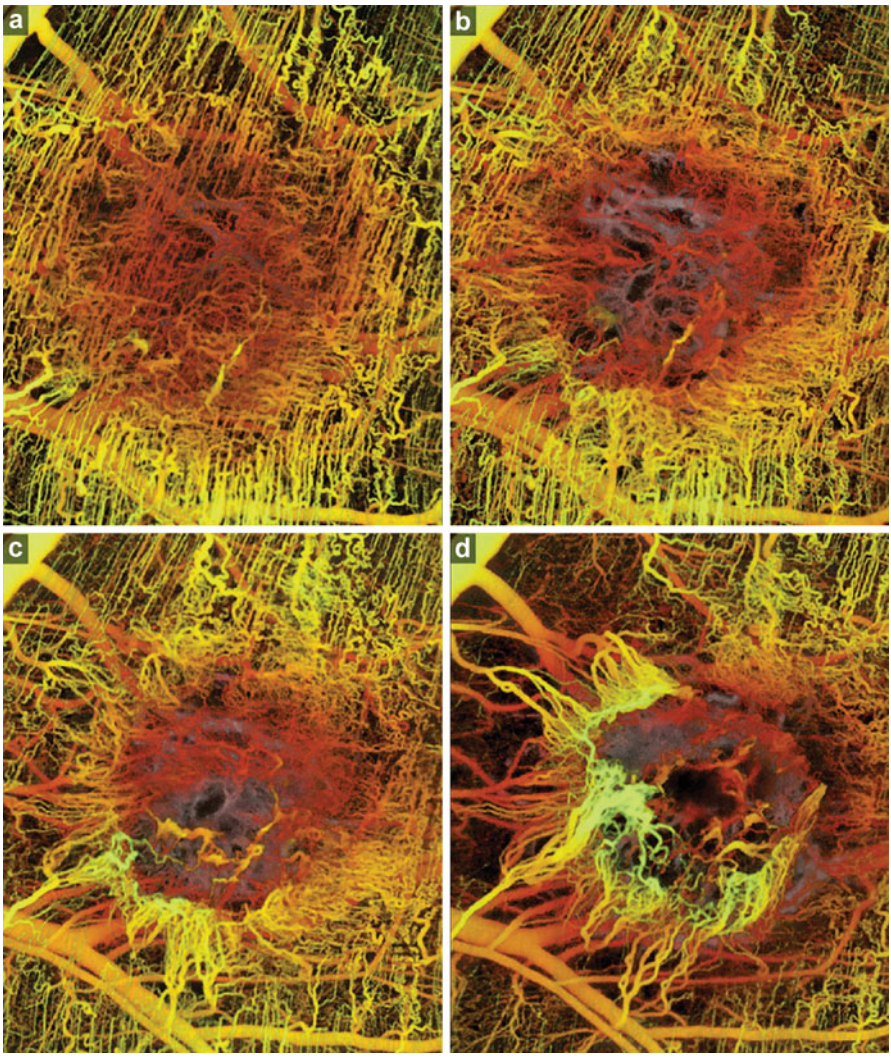

Fig. 45.1 Longitudinal OCT-based vascular imaging of a breast cancer (MCaIV) tumor growing in a dorsal skinfold chamber (angiography). *Color* is used to encode vessel depth in these projections of the three-dimensional angiographic dataset. Relative imaging times: (**a**) d0; (**b**) d2; (**c**) d6; (**d**) d10

the intensity fluctuations induced by flowing blood were used [25, 26]. Currently, there are algorithms in use that are entirely phase based [27–29], intensity based [30–32], or combine both intensity and phase [6, 33–35]. An example of OCT-based angiography is shown in Fig. 45.1. Here, OCT was used to monitor tumor vascularization longitudinally over a wider field and to deeper depths than is possible using alternative optical microscopies. Note the ability of wide-field OCT

angiography to visualize the aggressive vascularization of the tumor and the modulation of host vessels to support this vascularization.

To detect OCT signal dynamics, at least two measurements of nominally the same location are compared. Original approaches used adjacent depth scans (A-lines) for these measurements and slowed the transverse beam scanning to ensure sufficient beam overlap between the measurements [22–24]. While this approach is straightforward to implement, the time separation between measurements was relatively small and dropped as OCT A-line rates increased. This resulted in relatively poor flow sensitivity, yielding patchwork angiographic datasets characterized by frequent missing vessels and vessel segments. The sensitivity of OCT-based angiography to smaller and slower flowing vessels increased dramatically when angiographic imaging adopted beam scanning sequences that decoupled the time difference between repeated measurements from the system A-line rate. This could be done as simply as comparing between frames (thereby linking measurement timing to the frame rate) [26, 27, 30, 36] or by designing more complex scan patterns that separate both the frame rate and the A-line rate from the measurement timing [6, 29, 37].

Animal motion is a persistent challenge for preclinical angiographic imaging. Bulk physiological motion from animal respiration or cardiac cycles can induce submicron displacements which are easily detectable by OCT and can obscure vascular signals. Two strategies are combined to limit bulk motion degradation: mechanical stabilization and algorithm design. Mechanical approaches simply limit the magnitude of physiological motion. These include the stable fixture of window frames (dorsal or mammary fat-pad window models [21]) to the microscope, or a secure holding of the animal head when imaging in the brain. Imaging in the skin and with subcutaneous (non-window) models typically requires some level of mechanical stabilization; otherwise, respiratory motion often dominates vascular signals. Adhesive fixtures [30] or inverted microscope designs can be used in these studies. However, when immobilizing the imaging area, it is important to control the pressure in order to maintain blood flow and avoid possible occlusions. The second strategy to combat bulk motion is algorithmic in nature. Many of the most successful angiographic algorithms are designed to be inherently robust to sub-pixel axial displacements induced by environmental fluctuations and animal motion. While automated measurement and removal of this motion is possible in some applications, robust deployment in large biological studies benefits from a more fail-proof method to limit bulk motion sensitivity. Eliminating OCT signal phase [30–32], or specifically tailoring how phase data is included in angiographic processing [6], has yielded algorithms that are intrinsically insensitive to sub-resolution axial bulk motion.

45.2 Tumor Margins

Tumor margins are extremely important not only in cancer investigation but also in the clinic. The boundaries between healthy and tumor tissue are often blurred and, in most cases, difficult to distinguish in vivo with current imaging diagnostics without the need for a biopsy. In recent years, the study and characterization of the

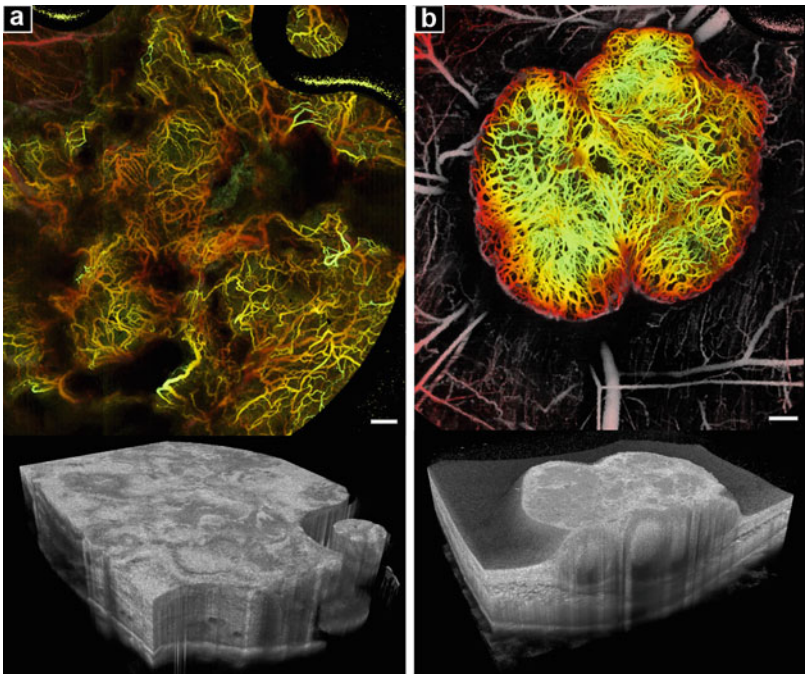

Fig. 45.2 OFDI angiography across tumor types and sites. (**a**) A human breast cancer cell line (MDA-MB-361HK) growing in the mammary fat pad window chamber model of a female SCID mouse. Large avascular regions are notable in the vascular image (*top*) and reflected in the topographically diffuse tumor microstructure (*bottom*). (**b**) Tumor vasculature of a human colorectal adenocarcinoma (LS174T) implanted in the dorsal skinfold chamber of a SCID mouse (*top*). Nonviable tissue is evident within the tumor nodules on cross section (*lighter regions*) in the tissue scattering intensity image (*bottom*). Scale bars 500 μm (Adopted from Ref. [6])

tumor microenvironment and the delicate, complex dialogue between tumor cells, host cells, and inflammatory agents has become one of the epicenters of cancer investigations. Delineating the tumor margin is of paramount importance for tumor resection in the operating room, characterization of tumor progression, and/or remission under drug therapy in the clinic and to better understand the molecular pathways and drug targets involved in the tumor microenvironment [20].

Gross measurements using calipers are the primary method for preclinical measure of tumor size or volume. This method suffers from obvious inaccuracies and cannot be used longitudinally in many sites such as the brain. Because OCT benefits from relatively high soft tissue contrast, three-dimensional OCT can often be used to delineate tumor from host tissue at near cellular resolution. This use of OCT to probe tumor volume and boundaries is especially attractive in studies when OCT is also being used to probe another measure such as the tumor vasculature (Fig. 45.2). Here, because OCT structural images are obtained simultaneously with angiographic imaging, the overall imaging procedure does not need to be

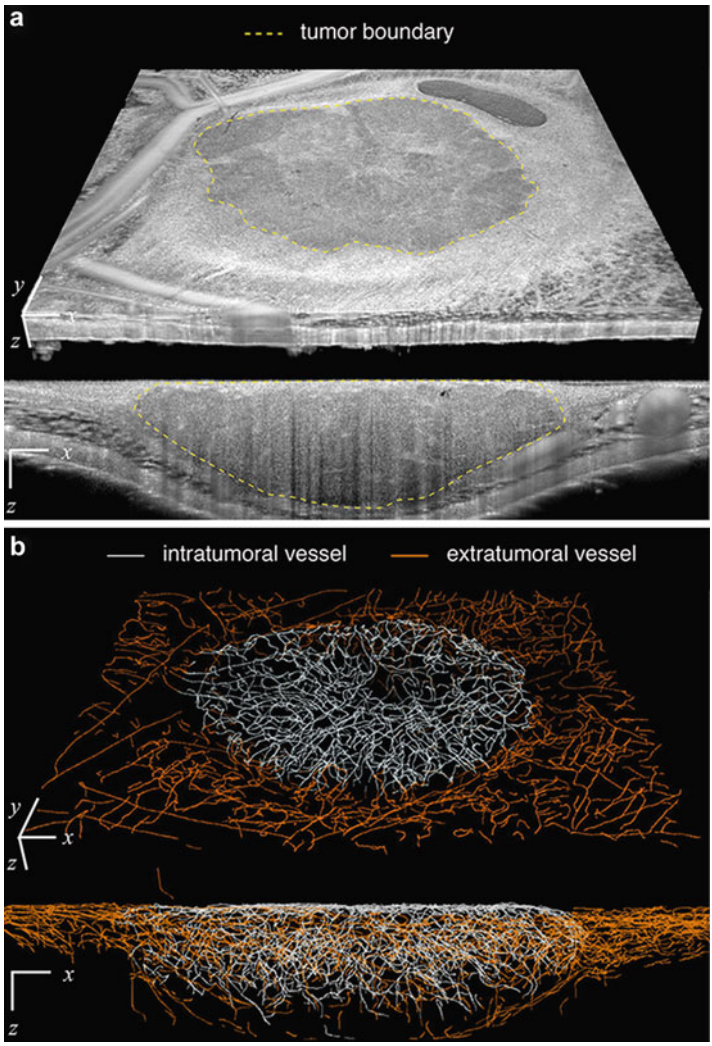

Fig. 45.3 Vascular tracing and structural correlation. (**a**) Microanatomical display showing tumor boundary definition in a three-dimensional tissue volume. (**b**) Skeletonized traced vessels differentiated between intratumoral and extratumoral for the tumor depicted in (**a**). Transverse extent in (**a**, **b**) 5 mm (x), 4.4 mm (y) (Adopted from Ref. [6])

lengthened, and the additional information on tumor size and the ability to define intra- and extra-tumoral vessels is often valuable (Fig. 45.3). One drawback of OCT is that it is limited by its depth penetration; OCT can only image soft tissue up to a depth of 2 mm. Thus, larger tumors cannot be comprehensively imaged using OCT. However, OCT can probe more superficial segments of the tumor and often reveal growth/regression trends for this segment (Fig. 45.4).

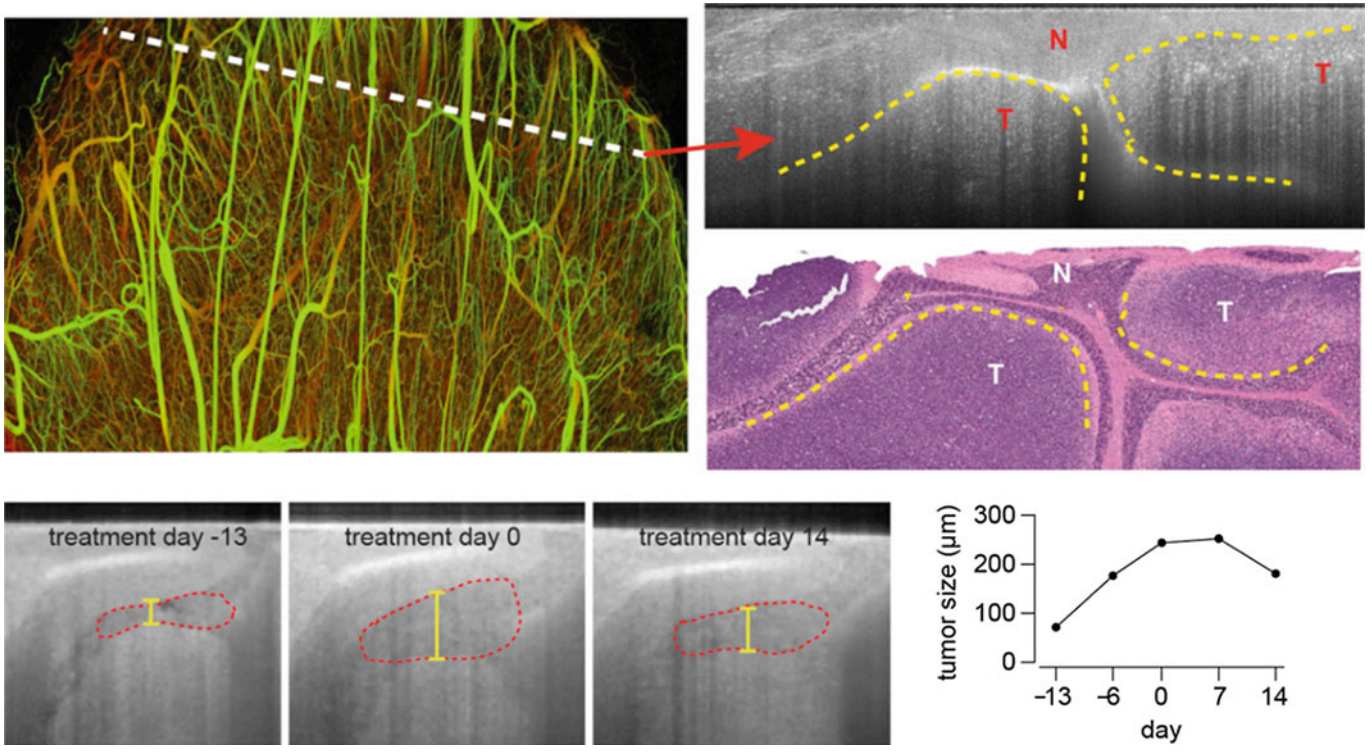

Fig. 45.4 Monitoring medulloblastoma growth using OCT. OCT images (*top right*) show distinct regions that can be correlated with normal (*N*) and tumor (*T*) tissues in histology (*middle right*). *Longitudinal imaging* shows growth and tumor regression with αPlGF treatment (*bottom left*). The *red dotted line* represents the tumor area observed with OCT, and the *yellow line* is the tumor diameter that was quantified during treatment (*bottom right*) (Reprinted from Ref. [7])

45.3 Tissue Viability Imaging

In addition to size, OCT signals can be used to differentiation between regions of viable and nonviable tissue within tumors. Tumors will commonly contain pockets of necrotic tissue due to insufficient perfusion. In addition, treatments often affect the tumor in a spatially heterogeneous manner, leading to differential viability. Viability imaging is typically done using micro-positron-emission tomography (μPET) using ^{18}F-fluorodeoxyglucose (^{18}F-FDG) as a radiographic contrast agent [2]. However, μPET has limited spatial resolution, usually greater than 1 mm. Fluorescence microscopy has also been used to monitor viability. Fluorescent deoxyglucose analogues have been used to study cell viability in cell culture as well as in vivo and may offer an alternative to PET imaging [38–41]. In addition, tumors expressing stable fluorescent proteins, such as the green fluorescent protein (GFP), will cease to produce the fluorescent protein upon cell death [42–44]. GFP has a half-life of 36 h, but its expression can be used as a crude measure of tissue viability. Both of these methods, however, are limited in their imaging field size and depth. In addition, they require exogenous agents to report viability.

It has been shown that OCT-detected tissue scattering magnitudes are dependent in some tumor models on the viability status of that tissue and that viable and nonviable tissues can be differentiated by analysis of the magnitude of associated OCT scattering signals [6, 45] (Fig. 45.5). Again, as with microstructural imaging, this viability contrast is derived directly from the microstructural images and can be combined with vascular and tumor margin measures. However, since the underlying cause of this increased scattering has not yet been elucidated, it is important to evaluate increased scattering in the context of other indications of viability. This is especially critical because increased scattering is not specific for viability changes.

45.4 Lymphangiography

The lymphatic system is partly responsible for fluid homeostasis and protein transport in the body and plays an important role in the development of a tumor [46]. As a tumor grows locally, it begins to shed cells into the lymph. Some of these cells travel through the lymphatic vessels to new sites, thus making the lymphatic system a critical component of tumor metastasis. In addition, the growth of a tumor can cause lymphatic compression, which can affect convective drug transport [47]. Finally, the lymphatics are a critical component of the immune system. Thus, the functionality of the lymphatic vessels can determine the effectiveness of the immune response to cancer. For these reasons, the ability to image the lymphatics is important if we are to broadly understand the processes driving tumor development and treatment resistance.

Generally, intravital lymphangiography is more challenging than angiography. While contrast can be introduced intravenously for imaging the blood vessels, accessing the lymphatic system surrounding a tumor site is considerably more

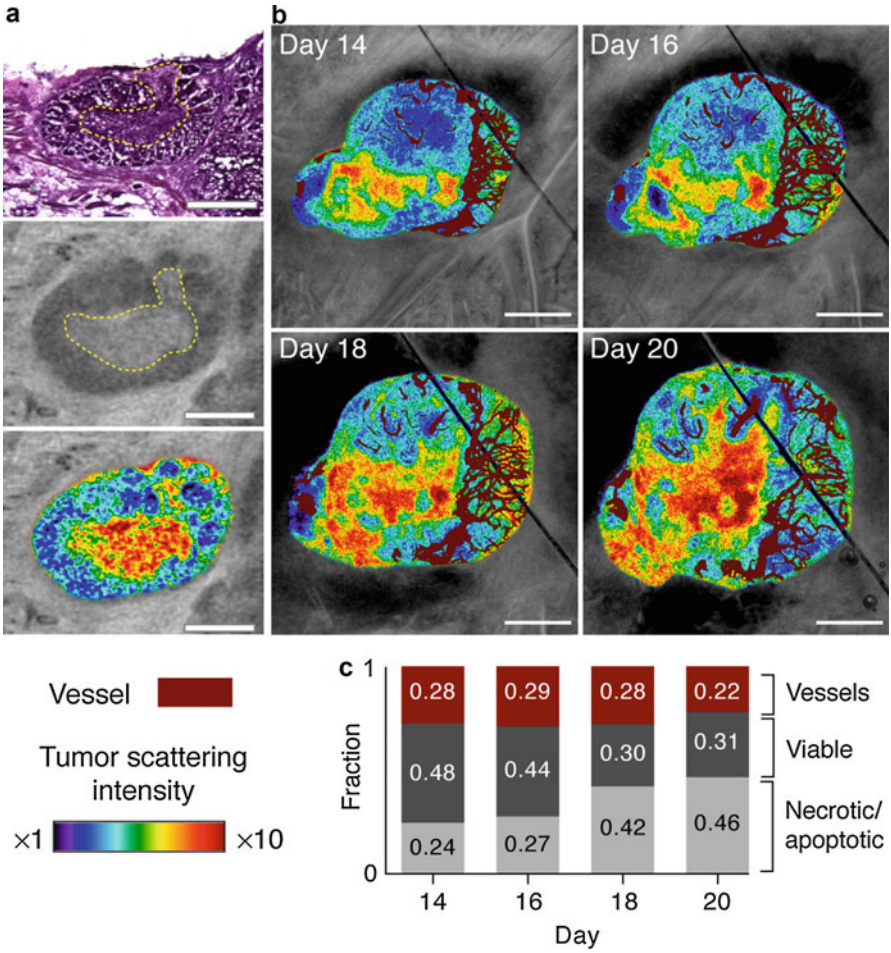

Fig. 45.5 Imaging tissue viability. (**a**) Comparison of standard hematoxylin and eosin staining (*top*) with OFDI (*middle*) reveals association of tissue necrosis with highly scattering regions. Viable and necrotic regions within the same tumor highlighted by color gradients indicating scattering intensity (*lower*). (**b**) Scattering properties correlated with the microvasculature during tumor progression illustrate the expansion of necrotic/apoptotic regions in areas with minimal vascular supply. Within the viable tissue, the mean distance to the nearest vessel was ~65 μm throughout progression. (**c**) Quantitative analysis of tissue viability and vascular regions in vivo revealed an increase in the fraction of necrotic/apoptotic tissue from ~24 % to ~46 % during tumor progression. Scale bars (**a**) 500 μm; (**b**) 1.0 mm (Adopted from Ref. [6])

difficult. The most common method involves injecting a tracer locally into the tumor and waiting for the draining lymphatic vessels to take up the contrast [48]. However, lymphatic uptake can be heterogeneous, so this technique often only allows imaging of a partial lymphatic network. Furthermore, local injection of contrast can disrupt the tumor microenvironment, including the lymph.

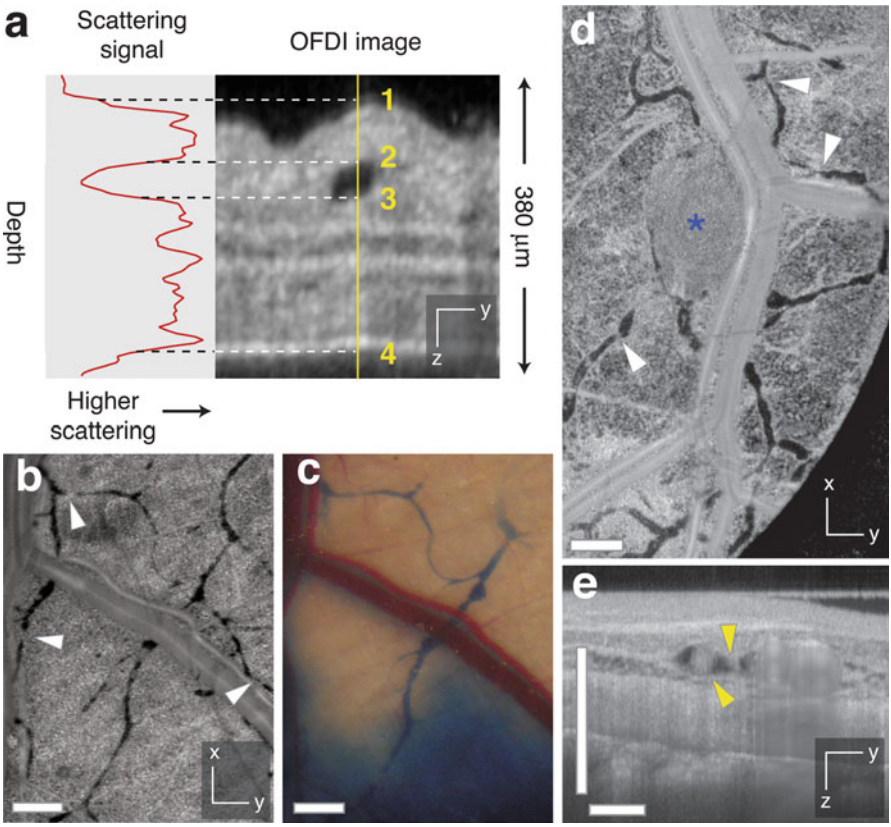

Fig. 45.6 Contrast-free lymphangiography using OCT. (**a**) The scattering signal along a single depth scan within an OFDI image of a mouse ear, showing the reduced scattering between the upper (*2*) and lower (*3*) boundaries of a patent lymphatic vessel. Scattering within the vessel is similar to background levels above the upper surface of the ear (*1*) or below the lower surface (*4*). (**b**, **c**) In addition to the lymphatic vessels revealed by traditional cutaneous injection of Evan's blue dye imaged by wide-field transillumination with a CCD camera (**c**), OCT lymphangiography (**b**) was able to detect numerous additional vessels in the normal dorsal skin and resolve the lymphatic valves found between individual lymphangions (*white arrowhead*). (**d**) OCT lymphangiography showing hyperplastic lymphatics associated with HSTS26T tumor (*blue asterisk*). (**e**) Cross-sectional presentations of OFDI lymphangiography showing cellular masses in a lymphatic vessel (*yellow arrowhead*) located near the tumor in (**d**). Scale bars, 500 µm (Adopted from Ref. [6])

Lymphangiography with OCT is possible due to the optical transparency of lymph fluid [6, 49]. The lymphatic fluid does not significantly scatter incident light, which is in stark contrast to the surrounding highly scattering soft tissue. Thus, in an OCT image, the lymphatic vessels appear hypoechoic when filled with lymph (Fig. 45.6). In addition, the lymphatic vessels have a unique valve and lymphangion morphology, allowing easy identification of lymphatic structures. A notable limitation of this method is that the lymphatic vessels are not always expanded and filled with fluid. This can sometimes make comprehensive

visualization of the lymphatic networks difficult. However, this limitation may be overcome with the use of higher-resolution OCT systems. OCT lymphangiography in the study of cancer has been performed in both ear models and dorsal skinfold chamber models. In recent work, OCT lymphangiography was used to track single lymphatic vessels longitudinally, where it demonstrated the presence of lymphatic hyperplasia in the peri-tumor environment.

45.5 Conclusions

In recent years, the scope of OCT imaging has expanded considerably in preclinical and basic science settings. The reason for this expansion can be found in its unique capabilities relative to alternative techniques. OCT is a truly noninvasive, high-resolution imaging modality that provides histological cross-sectional tomographic images and allows highly sensitive imaging of microvascular structures. One of the advantages of employing OCT is that it does not need administration of exogenous contrast agents or cell engineering for stable labeling with fluorescent or bioluminescent tags. In comparison with many other preclinical imaging modalities (such as MRI or PET), acquisition speed is faster. In addition, OCT can be successfully combined with other modalities (such as fluorescence confocal) for co-registration and complementary studies for data validation [6].

While much progress has been made in OCT, the possibilities for future improvements remain vast. Current work in polarization-sensitive OCT may allow monitoring of tumor interactions with stromal tissues [50–53]. Another area of interest is the efficient use of OCT signal dynamics to enable wide-field and large-dynamic range quantification of blood flow within the tumor. Finally, all of the contrast modes discussed here are intrinsically generated from tissue scattering; differing digital post-processing techniques are used to highlight each scattering feature. With the development of appropriate biological probes and exogenous labels, it may become possible to augment these intrinsic measurements with molecular sensing, opening opportunities for to study tumor structures and vasculature alongside measure of tumor hypoxia or pH.

References

1. D.M. Euhus, C. Hudd, M.C. LaRegina, F.E. Johnson, Tumor measurement in the nude mouse. J. Surg. Oncol. **31**(4), 229–234 (1986)
2. J. Condeelis, R. Weissleder, In vivo imaging in cancer, Cold Spring Harb. Perspect. Biol. **2**(12), 1–22 (2010)
3. E. Brown, R. Campbell, Y. Tsuzuki, L. Xu, P. Carmeliet, D. Fukumura, R.K. Jain, In vivo measurement of gene expression, angiogenesis and physiological function in tumors using multiphoton laser scanning microscopy. Nat. Med. **7**(7), 864–868 (2001)
4. B.E. Bouma, S.-H. Yun, B.J. Vakoc, M.J. Suter, G.J. Tearney, Fourier-domain optical coherence tomography: recent advances toward clinical utility. Curr. Opin. Biotechnol. **20**(1), 111–118 (2009)

5. B.J. Vakoc, D. Fukumura, R.K. Jain, B.E. Bouma, Cancer imaging by optical coherence tomography: preclinical progress and clinical potential. Nat. Rev. Cancer **12**(5), 363–368 (2012)
6. B.J. Vakoc, R.M. Lanning, J.A. Tyrrell, T.P. Padera, L.A. Bartlett, T. Stylianopoulos, L.L. Munn, G.J. Tearney, D. Fukumura, R.K. Jain, B.E. Bouma, Three-dimensional microscopy of the tumor microenvironment in vivo using optical frequency domain imaging. Nat. Med. **15**(10), 1219–1223 (2009)
7. M. Snuderl, A. Batista, N.D. Kirkpatrick, C. Ruiz De Almodovar, L. Riedemann, E.C. Walsh, R. Anolik, Y. Huang, J.D. Martin, W. Kamoun, E. Knevels, T. Schmidt, C.T. Farrar, B.J. Vakoc, N. Mohan, E. Chung, S. Roberge, T. Peterson, C. Bais, B.H. Zhelyazkova, S. Yip, M. Hasselblatt, C. Rossig, E. Niemeyer, N. Ferrara, M. Klagsbrun, D.G. Duda, D. Fukumura, L. Xu, P. Carmeliet, R.K. Jain, Targeting placental growth factor/neuropilin 1 pathway inhibits growth and spread of medulloblastoma. Cell **152**(5), 1065–1076 (2013). Cell Press
8. R.K. Jain, P. Carmeliet, SnapShot: tumor angiogenesis. Cell **149**(6), 1408–1408.e1 (2012)
9. S.M. Weis, D.A. Cheresh, Tumor angiogenesis: molecular pathways and therapeutic targets. Nat. Med. **17**(11), 1359–1370 (2011)
10. D. Hanahan, R. Weinberg, Hallmarks of cancer: the next generation. Cell **144**(5), 646–674 (2011). Cell Press
11. P. Carmeliet, R.K. Jain, Molecular mechanisms and clinical applications of angiogenesis. Nature **473**(7347), 298–307 (2011)
12. M. Potente, H. Gerhardt, P. Carmeliet, Basic and therapeutic aspects of angiogenesis. Cell **146**(6), 873–887 (2011). Cell Press
13. M.W. Kieran, J. Folkman, J. Heymach, Angiogenesis inhibitors and hypoxia. Nat. Med. **9**(9), 1104–1105 (2003). 1104–author reply
14. M. Jugold, M. Palmowski, J. Huppert, E. Woenne, M. Mueller, W. Semmler, F. Kiessling, Volumetric high-frequency Doppler ultrasound enables the assessment of early antiangiogenic therapy effects on tumor xenografts in nude mice. Eur. Radiol. **18**(4), 753–758 (2008)
15. C.T. Badea, M. Drangova, D.W. Holdsworth, G.A. Johnson, In vivo small-animal imaging using micro-CT and digital subtraction angiography. Phys. Med. Biol. **53**(19), R319 (2008)
16. S. Hu, L.V. Wang, Photoacoustic imaging and characterization of the microvasculature. J. Biomed. Opt. **15**(1), 011101–011115 (2010)
17. L.V. Wang, Multiscale photoacoustic microscopy and computed tomography. Nat. Photonics **3**(9), 503–509 (2009)
18. J.L. Su, B. Wang, K.E. Wilson, C.L. Bayer, Y.-S. Chen, S. Kim, K.A. Homan, S.Y. Emelianov, Advances in clinical and biomedical applications of photoacoustic imaging. Expert Opin. Med. Diagn. **4**(6), 497–510 (2012)
19. M.-L. Li, J.-T. Oh, X. Xie, G. Ku, W. Wang, C. Li, G. Lungu, G. Stoica, L.V. Wang, Simultaneous molecular and hypoxia imaging of brain tumors in vivo using spectroscopic photoacoustic tomography. Proc. IEEE **96**(3), 481–489 (2008)
20. D. Fukumura, D.G. Duda, L.L. Munn, R.K. Jain, Tumor microvasculature and microenvironment: novel insights through intravital imaging in pre-clinical models. Microcirculation **17**(3), 206–225 (2010)
21. E. Brown, L.L. Munn, D. Fukumura, R.K. Jain, In vivo imaging of tumors. Cold Spring Harb. Protoc. **2010**(7), 5452 (2010). pdb.prot
22. J.A. Izatt, M.D. Kulkarni, S. Yazdanfar, J.K. Barton, A.J. Welch, In vivo bidirectional color Doppler flow imaging of picoliter blood volumes using optical coherence tomography. Opt. Lett. **22**(18), 1439–1441 (1997)
23. Z. Chen, T.E. Milner, D. Dave, J.S. Nelson, Optical Doppler tomographic imaging of fluid flow velocity in highly scattering media. Opt. Lett. **22**(1), 64–66 (1997)
24. Y. Zhao, Z. Chen, C. Saxer, S. Xiang, J.F. de Boer, J.S. Nelson, Phase-resolved optical coherence tomography and optical Doppler tomography for imaging blood flow in human skin with fast scanning speed and high velocity sensitivity. Opt. Lett. **25**(2), 114–116 (2000)

25. J. Barton, S. Stromski, Flow measurement without phase information in optical coherence tomography images. Opt. Express **13**(14), 5234–5239 (2005)
26. A. Mariampillai, B. Standish, E. Moriyama, M. Khurana, N. Munce, M. Leung, J. Jiang, A. Cable, B. Wilson, I. Vitkin, V. Yang, Speckle variance detection of microvasculature using swept-source optical coherence tomography. Opt. Lett. **33**(13), 1530–1532 (2008)
27. J. Fingler, D. Schwartz, C. Yang, S.E. Fraser, Mobility and transverse flow visualization using phase variance contrast with spectral domain optical coherence tomography. Opt. Express **15**(20), 12636–12653 (2007)
28. S. Makita, Y. Hong, M. Yamanari, T. Yatagai, Y. Yasuno, Optical coherence angiography. Opt. Express **14**(17), 7821–7840 (2006)
29. B. Braaf, K.A. Vermeer, K.V. Vienola, J.F. de Boer, Angiography of the retina and the choroid with phase-resolved OCT using interval-optimized backstitched B-scans. Opt. Express **20**(18), 20516–20534 (2012)
30. C. Blatter, J. Weingast, A. Alex, B. Grajciar, W. Wieser, W. Drexler, R. Huber, R.A. Leitgeb, In situ structural and microangiographic assessment of human skin lesions with high-speed OCT. Biomed. Opt. Express **3**(10), 2636–2646 (2012)
31. G. Liu, L. Chou, W. Jia, W. Qi, B. Choi, Z. Chen, Intensity-based modified Doppler variance algorithm: application to phase instable and phase stable optical coherence tomography systems. Opt. Express **19**(12), 11429–11440 (2011)
32. R. Motaghiannezam, S. Fraser, Logarithmic intensity and speckle-based motion contrast methods for human retinal vasculature visualization using swept source optical coherence tomography. Biomed. Opt. Express **3**(3), 503–521 (2012)
33. Y. Zhao, Z. Chen, C. Saxer, Q. Shen, S. Xiang, J.F. de Boer, J.S. Nelson, Doppler standard deviation imaging for clinical monitoring of in vivo human skin blood flow. Opt. Lett. **25**(18), 1358–1360 (2000)
34. R.K. Wang, S.L. Jacques, Z. Ma, S. Hurst, S.R. Hanson, A. Gruber, Three dimensional optical angiography. Opt. Express **15**(7), 4083–4097 (2007)
35. V. Yang, M. Gordon, B. Qi, J. Pekar, S. Lo, E. Seng-Yue, A. Mok, B. Wilson, I. Vitkin, High speed, wide velocity dynamic range Doppler optical coherence tomography (part I): system design, signal processing, and performance. Opt. Express **11**(7), 794–809 (2003)
36. G. Liu, W. Jia, V. Sun, B. Choi, Z. Chen, High-resolution imaging of microvasculature in human skin in-vivo with optical coherence tomography. Opt. Express **20**(7), 7694–7705 (2012)
37. I. Grulkowski, I. Gorczynska, M. Szkulmowski, D. Szlag, A. Szkulmowska, R.A. Leitgeb, A. Kowalczyk, M. Wojtkowski, Scanning protocols dedicated to smart velocity ranging in spectral OCT. Opt. Express **17**(26), 23736–23754 (2009)
38. K. Yoshioka, H. Takahashi, T. Homma, M. Saito, K. Oh, Y. Nemoto, H. Matsuoka, A novel fluorescent derivative of glucose applicable to the assessment of glucose uptake activity of Escherichia coli. Biochim. Biophys. Acta **1289**, 5–9 (1996)
39. R. O'Neil, L. Wu, N. Mullani, Uptake of a fluorescent deoxyglucose analog (2-NBDG) in tumor cells. Mol. Imaging Biol. **7**(6), 388–392 (2005)
40. R.A. Sheth, L. Josephson, U. Mahmood, Evaluation and clinically relevant applications of a fluorescent imaging analog to fluorodeoxyglucose positron emission tomography. J. Biomed. Opt. **14**(6), 064014–064018 (2009)
41. N. Nitin, A.L. Carlson, T. Muldoon, A.K. El-Naggar, A. Gillenwater, R. Richards-Kortum, Molecular imaging of glucose uptake in oral neoplasia following topical application of fluorescently labeled deoxy-glucose. Int. J. Cancer **124**(11), 2634–2642 (2008)
42. P. Corish, C. Tyler-Smith, Attenuation of green fluorescent protein half-life in mammalian cells. Protein Eng. **12**(12), 1035–1040 (1999)
43. G. Elliott, J. McGrath, E. Crockett-Torabi, Green fluorescent protein: a novel viability assay for cryobiological applications. Cryobiology **40**(4), 360–369 (2000)
44. C. Baumstark-Khan, M. Palm, J. Wehner, M. Okabe, M. Ikawa, G. Horneck, Green Fluorescent Protein (GFP) as a marker for cell viability after UV irradiation. J. Fluoresc. **9**(1), 37–43 (1999)

45. G. Farhat, A. Mariampillai, V.X.D. Yang, G.J. Czarnota, M.C. Kolios, Detecting apoptosis using dynamic light scattering with optical coherence tomography. J. Biomed. Opt. **16**(7), 070505-3 (2012)
46. J. Hagendoorn, R. Tong, D. Fukumura, Q. Lin, J. Lobo, T.P. Padera, L. Xu, R. Kucherlapati, R.K. Jain, Onset of abnormal blood and lymphatic vessel function and interstitial hypertension in early stages of carcinogenesis. Cancer Res. **66**(7), 3360–3364 (2006)
47. R.K. Jain, Taming vessels to treat cancer. Sci. Am. **298**(1), 56–63 (2008)
48. N. Isaka, T. Padera, J. Hagendoorn, D. Fukumura, R.K. Jain, Peritumor lymphatics induced by vascular endothelial growth factor-C exhibit abnormal function. Cancer Res. **64**, 4400–4404 (2004)
49. Z. Zhi, Y. Jung, R.K. Wang, Label-free 3D imaging of microstructure, blood, and lymphatic vessels within tissue beds in vivo. Opt. Lett. **37**(5), 812–814 (2012)
50. J. de Boer, T. Milner, Review of polarization sensitive optical coherence tomography and Stokes vector determination. J. Biomed. Opt. **7**(3), 359–371 (2002)
51. E.Z. Zhang, W.-Y. Oh, M.L. Villiger, L. Chen, B.E. Bouma, B.J. Vakoc, Numerical compensation of system polarization mode dispersion in polarization-sensitive optical coherence tomography. Opt. Express **21**(1), 1163–1180 (2013)
52. M. Villiger, E.Z. Zhang, S. Nadkarni, W.-Y. Oh, B.E. Bouma, B.J. Vakoc, Artifacts in polarization-sensitive optical coherence tomography caused by polarization mode dispersion. Opt. Lett. **38**(6), 923–925 (2013)
53. E.Z. Zhang, B.J. Vakoc, Polarimetry noise in fiber-based optical coherence tomography instrumentation. Opt. Express **19**(18), 16830–16842 (2011)

Clinical Applications of Doppler OCT and OCT Angiography

46

Ou Tan, Yali Jia, Eric Wei, and David Huang

46.1 Introduction

Doppler optical coherence tomography (OCT) is a functional extension of OCT that allows for the visualization and measurement of blood flow [1, 2]. Phase-resolved Doppler OCT has become a standard algorithm for measuring Doppler shift with Fourier-domain (FD)-OCT because of its high velocity sensitivity [3]. In ophthalmology, several methods have been developed to measure in vivo retinal blood flow using this algorithm. Since Doppler OCT measures only the velocity component parallel to the OCT probe beam, additional information is needed to calculate absolute velocity and volumetric flow rate. One method is to employ two OCT beams with a fixed offset in incidence angles [4, 5]. However, this approach requires special hardware and is not compatible with commercial single-beam OCT systems. Another approach is to use special scan patterns to measure the Doppler angle (angle between the OCT beam and the blood vessel). Some groups used concentric scan patterns [6, 7], while other groups used raster scan patterns [8, 9]. Finally, Srinivasan et al. developed en face Doppler OCT for cerebral blood flow calculation, which obviated the need for Doppler angle estimation [10]. Bauman et al. adapted the method for total retinal blood flow (TRBF) calculation with ultrafast swept-source OCT [11]. In this chapter, we focus our attention on the double-circular scan pattern developed in our research group, which has been used in a number of clinical studies for preliminary demonstration of utility.

Although Doppler OCT is able to image and measure blood flow in larger blood vessels [12, 13], it has difficulty distinguishing the slow flow in small blood vessels

O. Tan (✉) • Y. Jia • E. Wei
Casey Eye Institute, Oregon Health and Science University, Portland, OR, USA
e-mail: tano@ohsu.edu

D. Huang
Center for Ophthalmic Optics and Lasers, Casey Eye Institute and Department of Ophthalmology, Oregon Health and Science University, Portland, OR, USA

© Springer International Publishing Switzerland 2015

W. Drexler, J.G. Fujimoto (eds.), *Optical Coherence Tomography*,
DOI 10.1007/978-3-319-06419-2_47

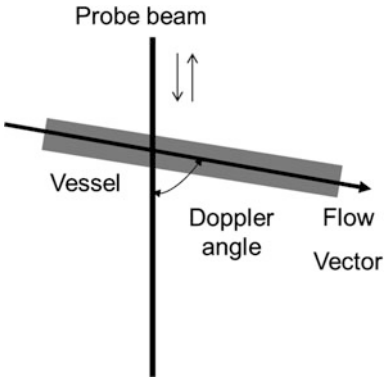

Fig. 46.1 In OCT, a probe beam is reflected from a sample. In a moving sample such as cells in a blood vessel, the frequency of reflected light is Doppler shifted in proportion to the component of the flow velocity in the direction of beam propagation

from tissue bulk motion [14, 15]. In the imaging of retinal blood vessels, Doppler OCT faces the additional constraint that most vessels are nearly perpendicular to the OCT beam, and therefore the detectability of the Doppler shift signal depends critically on the beam incident angle [16, 17]. Thus other techniques that do not depend on beam incidence angle are particularly attractive for retinal and choroidal angiography. To measure local microcirculation, we recently developed the split-spectrum amplitude-decorrelation angiography (SSADA) algorithm that provides high-quality three-dimensional (3D) angiography using ultrahigh-speed OCT [18]. Because SSADA is based on the variation of reflectance amplitude, it is sensitive to motion and flow in all directions. This omnidirectional nature allows it to detect perfusion in a way that is independent of beam incidence angle [18]. Therefore SSADA may be a good basis for quantitative angiography of the ocular microcirculation. The principle and clinical applications of this new angiography algorithm are also covered in this chapter.

46.2 Total Retinal Blood Flow Measurement with Doppler OCT

46.2.1 Doppler Principle

Doppler optical coherence tomography (Doppler OCT) is based on the principle that moving particles such as red blood cells inside a blood vessel cause a Doppler frequency shift (Δf) (Fig. 46.1) to the scattered light according to

$$\Delta f = \frac{1}{2\pi}\left(\vec{k}_s - \vec{k}_i\right) \bullet V \tag{46.1}$$

where $\boldsymbol{k_i}$ and $\boldsymbol{k_s}$ are wave vectors of incident and scattered light, respectively, and $\boldsymbol{V}$ is the velocity vector of the moving particles. Given the Doppler angle θ between the probe beam and the vessel vector, the velocity vessel can be estimated as

$$V = \frac{\lambda_0 \Delta f}{2n\ \cos\theta} \tag{46.2}$$

where λ_0 is the center wavelength of the light source and n is the refractive index of the medium.

In FD-OCT, this frequency shift Δf will introduce a phase shift in the spectral interference pattern that is captured by the line camera. With fast Fourier transform (FFT), the transformation result is a complex function characterized by amplitude and phase. The phase difference between sequential axial scans at each pixel is calculated to determine the Doppler shift [3]. One limitation of phase-resolved flow measurement is an aliasing phenomenon caused by 2π ambiguity in the arctangent function. This phenomenon limits the maximum determinable Doppler shift to $\Delta f = 1/(2\tau)$, where τ is the time difference between sequential axial lines. Thus, the maximum detectable speed is $V = \lambda_0/(4n\tau \cos\theta)$.

Using Eq. 46.2 to determine real flow speed V, the Doppler angle θ must be determined. Therefore, we needed at least two locations on a same vessel to decide the vessel vector.

46.2.2 Circumpapillary Double-Circular Scan

In the circumpapillary double-circular scan pattern, the OCT sampling beam scans two circles around the optic disc (Fig. 46.2), which ensures we sample at least two points for any main vessel around the optic disc. With a 26 kHz FD-OCT, the frame rate was six frames per second. Each scan contained 12 circles and was recorded over consecutive 2-s intervals (Fig. 46.2a).

Figure 46.2b shows the three dimensional diagram of the scan pattern in the rectangular region of Fig. 46.2a. The two positions of the blood vessel segment on the two scanning circles have coordinates $P_1(r_1, \alpha_1, z_1)$ and $P_2(r_2, \alpha_2, z_2)$, respectively. The vector of the blood vessel can be expressed as $\mathbf{r_b}(\Delta x = r_1 \cos\alpha_1 - r_2 \cos\alpha_2, \Delta y = r_1 \sin\alpha_1 - r_2 \sin\alpha_2, \Delta z = z_1 - z_2)$. For OCT scans at radius r, when the probe beam scans to the angle α, the vector of the scanning beam is $\mathbf{s}$ ($r\cos\alpha$, $r\sin\alpha$, $-h$), where h is the distance from the nodal point to the retina. With vector $\mathbf{s}$ and $\mathbf{r_b}$, the Doppler angle θ between the OCT probe beam and vessel can be calculated.

46.2.3 Correction for Sampling Density Effect

In phase-resolved Doppler OCT, the phase difference between sequential axial scans is calculated to determine Doppler frequency shift. If the sampling locations are not negligibly small relative to the beam diameter, phase decorrelation results in a decrease in the measured Doppler shift. For example, in the dual circular scan pattern, there are 4,000 axial lines for each circle. At a scanning radius of 1.8 mm, the sampling step is about 2.8 μm. For the FD-OCT with laser beam of 20 μm focus spot size, a calibrated factor of 0.8 is needed to correct the measured flow result.

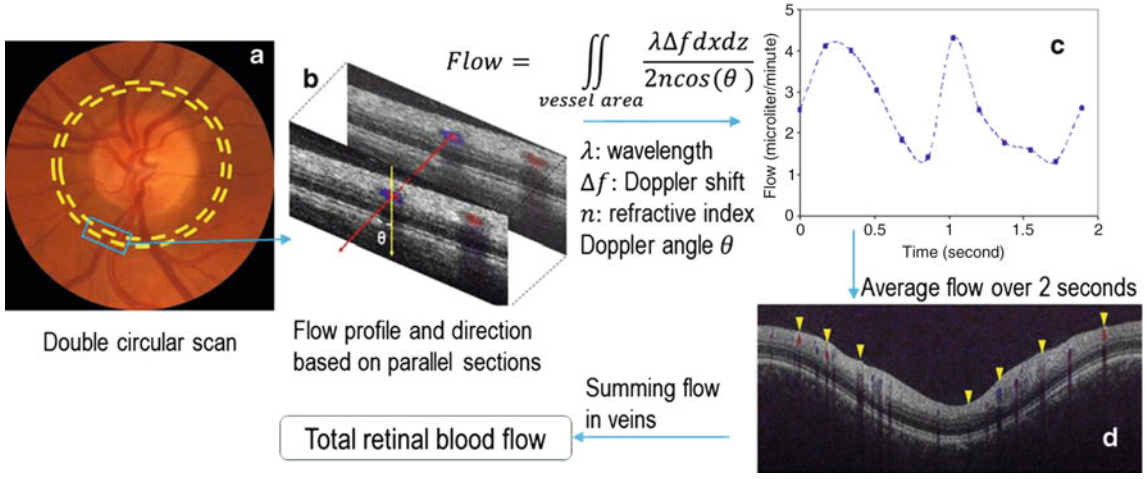

Fig. 46.2 Measurement of retinal blood flow using double-circular Doppler scan. (**a**) Two concentric circular scans transect all retinal blood vessels emanating from the optic nerve head (ONH). (**b**) The blood vessels are identified by Doppler frequency shift within the lumen as shown by blue and red color Doppler displays. By comparing the lumen positions in the two concentric sections, the vessel orientation relative to the OCT beam is measured. Velocity is calculated using the Doppler shift and Doppler angle. Volumetric blood flow rate is calculated by integrating velocity within the lumen area. (**c**) Flow measurements are averaged from 12 circular scans recorded over 2 s. (**d**) Total retinal blood flow (*TRBF*) is calculated by summing flow from all detected veins

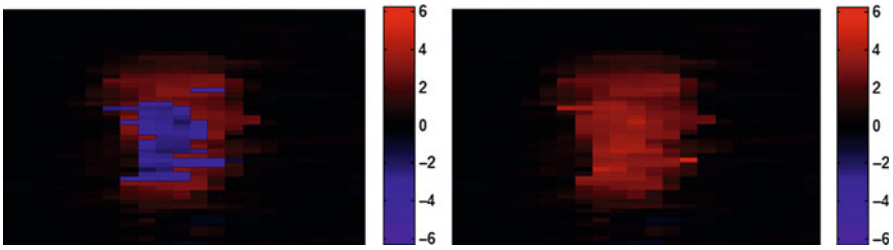

Fig. 46.3 Phase unwrapping in a single vessel. *Left*: Doppler shift with phase wrapping. *Right*: Doppler shift after phase unwrapping

46.2.4 Correction of Bulk Motion

The Doppler information contains artifacts from the motion of the eye and the OCT system. To obtain the Doppler frequency shift induced by actual blood flow, the artifacts must be identified and subtracted. The eye and OCT motion artifacts induce constant Doppler shift for whole axial scan (A-scan). Therefore, most bulk motion correction methods calculate the constant phase term of each a-scan and subtract it from the Doppler shift [19–21].

Our study showed that bulk motion is equivalent to the average Doppler signal between the inner limiting membrane and the top vessel boundary for each a-scan. This value represents the Doppler signal due to local tissue motion and is subtracted from the Doppler signal in the whole a-scan to get the net signal induced by blood flow.

46.2.5 Correction of Phase Wrapping

For FD-OCT systems with 840 nm laser source and 26 kHz scan rate, the maximum measurable axial velocity component in the eye is 4.2 mm/s. On the other hand, a typical average velocity in the main vein is about 18 mm/s and the velocity in the center of the vein is about 36 mm/s. In order to detect Doppler shifts without phase wrapping, the Doppler angle needs be above 82°. In order to allow measurement of vessels with smaller Doppler angles, a phase-unwrapping algorithm is needed. Figure 46.3 shows the Doppler signal with onefold phase wrapping (maximum Doppler shift was between π and 2π) and after phase unwrapping for a vessel.

However, only onefold of phase unwrapping is practical. Multiple phase unwrapping is difficult in practice because of noise. Therefore, it is difficult to get accurate measurements of arteries with high velocities. In our study, the total TRBF is measured from only from veins.

46.2.6 Reduce Eye Motion Error for Doppler Angle Estimation

The measured position of vessels contains noise from eye motion. Variance is doubled when we use two positions for vessel vector estimation, and this dominates the variance of the Doppler angle measurement and flow calculation. To reduce the eye motion artifact for vessel position, the circles are registered in transverse direction based on vessel pattern matching. Vessel vectors between consecutive circles are then averaged to reduce the eye motion error.

46.2.7 Correction for Pulsation

In a cardiac cycle, the flow velocity changes with pulsation. In order to get an average flow velocity, it is necessary to average flow at different time points. In CDCS, the Doppler shift in a vessel is averaged from the 12 frames, which corresponds to 12 time points in 2 s.

46.2.8 Semiautomated Doppler OCT Grading Software

We developed a software, which we named "Doppler OCT of retinal circulation," or DOCTORC, to include all the above ideas for measuring TRBF [22]. DOCTORC can automatically detect vessels on all circles and calculate the Doppler angle and TRBF. It can also provide total vessel area and average vessel velocity measurements. In the event of incorrect vessel detection, DOCTORC allows for human input to manually correct the error.

DOCTORC identifies blood vessels based on both Doppler and reflectance OCT images. The distinction between veins and arteries is based on both OCT images and fundus photographs. Vessel diameter (D) is measured by computing caliper on the cross-sectional Doppler OCT images which is used to compute lumen area ($\pi D^2/4$). The venous cross-sectional areas for all branch vessels around the optic disc are summed to obtain the total venous area for the eye. The Doppler angle between the vessel and OCT beam is measured by the relative position of each vessel in two concentric OCT images.

The effect of eye motion on the calculation of Doppler angle is small due to the short time interval between the inner and outer circular scans (0.16 s). This error is further minimized by averaging the Doppler angle estimates from concentric circular scans. Flow velocity can be computed from the Doppler shift and Doppler angle, with steps to account for the effect of background retinal motion and transverse scan step size [23]. When the peak axial Doppler shift is between π and 2π (or $-\pi$ and -2π) at the center of the vessel, the phase-unwrapping algorithm previously described is automatically applied to allow valid flow measurements [24].

Veins are identified by the flow direction toward the optic disc. The volumetric blood flow rate for each pixel is calculated by multiplying the velocity by vessel area.

Table 46.1 Visual field and Doppler OCT measurements in normal and glaucoma subjects

Parameter	Normal	Glaucoma	*p*-value
Visual field			
Mean deviation (dB)	0.16 ± 1.00	−4.39 ± 4.14	<0.0001
Pattern standard deviation (dB)	1.61 ± 0.39	6.54 ± 4.45	<0.0001
Total retinal blood flow (μl/min)	45.5 ± 9.5	34.9 ± 8.5	<0.001
Arterial area (mm^2)	0.033 ± 0.0077	0.028 ± 0.0074	0.006
Venous area (mm^2)	0.047 ± 0.012	0.041 ± 0.0086	0.01
Arterial velocity (mm/sec)	23.9 ± 7.2	21.8 ± 7.3	0.22
Venous velocity (mm/sec)	16.3 ± 2.8	14.5 ± 3.7	0.03

Flow within a vein is calculated by summing the flow in the pixels over lumen cross section. Flow measurements are averaged over each 2-s recording. Measurements from all valid scans are averaged. Total retinal blood flow is calculated by summing flow from all detectable veins. Retinal blood flow in arteries and veins should have an equal sum because inflow must equal outflow in any steady state system that obeys the law of conservation of mass. This has been confirmed by actual measurements of retinal arterial and venous flows with a number of techniques [25]. Thus, measuring total venous flow alone is sufficient to quantify the total retinal blood flow. Average venous velocities are obtained by dividing the total retinal flow by the total venous areas.

46.2.9 Blood Flow Measurement for Normal and Glaucoma with Doppler OCT

We performed a study comparing blood flow measurements obtained with Doppler OCT between glaucoma patients and normal subjects. A total of 47 consecutive eyes of 42 patients with glaucoma were age-matched with 27 normal eyes of 27 patients [23]. There were no significant differences in age, systemic hypertension, and diabetes mellitus between the two groups. However, the mean intraocular pressure was lower in glaucoma eyes ($p = 0.03$), which were all undergoing treatment.

Traditional measures of function and structure were consistent with expected findings for glaucoma eyes (Table 46.1). Glaucoma eyes demonstrated visual field loss with lower mean deviation (MD) values and higher pattern standard deviation (PSD) values compared to normal eyes ($p < 0.0001$). Structural evaluation identified loss of disc rim area, GCC thickness, and RNFL thickness in glaucoma eyes relative to normal eyes ($p < 0.0001$).

Total retinal blood flow was significantly reduced in glaucoma eyes with decreased vessel area and venous velocity compared to normal eyes (Table 46.1). Blood flow reduction was correlated with visual field loss, but had no correlation or paradoxical correlation with structural loss of neural tissue as measured by optic disc rim area, peripapillary nerve fiber layer (NFL) thickness, or macular ganglion

cell complex (GCC) thickness ($p \geq 0.23$). Univariate analysis demonstrated that each dB decrease in blood flow resulted in a 1.91 dB decreased in MD ($p < 0.001$). Multivariate analysis confirmed a largely independent relationship between reduced blood flow and visual field loss, even after accounting for structural loss of rim area and NFL thickness.

46.2.10 Blood Flow Measurement in Diabetic Retinopathy and Optic Neuropathy Eyes with Doppler OCT

The Doppler OCT and algorithms were also applied to nine eyes with nonarteritic ischemic optic neuropathy (AION), five eyes with proliferative diabetic retinopathy (PDR, after treatment with pan-retinal photocoagulation), and two eyes with branch retinal vein occlusion (BRVO) [26]. All diseases caused significant reduction of total blood flow compared to normal (AION, 28.2 ± 8.2 μl/min; PDR, 15.8 ± 10.1 μl/min; BRVO, 26.7 ± 5.7 μl/min).

46.3 OCT Angiography

Several OCT-based techniques have been successfully developed to image microvascular networks in human eyes in vivo [9, 24, 25, 27–32]. One example is optical microangiography (OMAG), which works by using a modified Hilbert transform to separate the scattering signals from static and moving scatters [33]. By applying the OMAG algorithm along the slow scanning axis, high-sensitivity imaging of capillary flow can be achieved [34]. However, the high sensitivity of OMAG requires precise removal of bulk motion by resolving the Doppler phase shift [35]. Thus, it is susceptible to artifacts from system or biological phase instability. Other related methods such as phase variance [25] and Doppler variance [31] have been developed to detect small phase variations from microvascular flow. These methods do not require non-perpendicular beam incidence and can detect both transverse and axial flow. They have also been successful in visualizing retinal and choroidal microvascular networks. However, these phase-based methods require precise removal of background Doppler phase shifts due to the axial movement of bulk tissue. Artifacts can also be introduced by phase noise in the OCT system and transverse tissue motion, and these also need to be removed. In order to circumvent these issues, our research group has investigated the use of amplitude-based OCT signal analysis, which in this context may be advantageous for ophthalmic microvascular imaging.

46.3.1 Principles of OCT Angiography

The speckle decorrelation phenomenon has previously been applied to techniques including ultrasound and laser speckle to detect optical scattering from moving

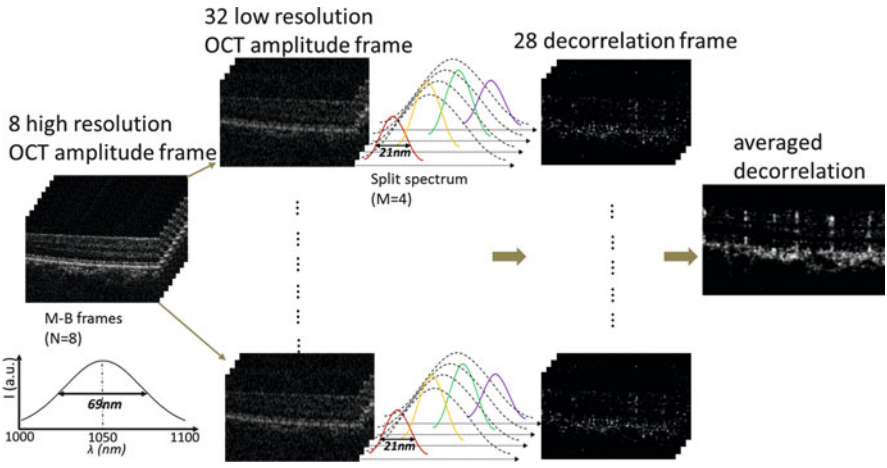

Fig. 46.4 Flow chart detailing the basic steps of the SSADA algorithm. Eight OCT M-B frames were scanned consecutively at the same spatial location to produce eight spectral interferograms and eight standard-resolution cross-sectional images. Using SSADA, each full spectral interferogram was split into four spectral bands creating 32 low-resolution interferograms. B-scan decorrelation of each split band yielded 28 decorrelation frames which were averaged to produce one final decorrelation-based flow cross section with improved quality (Reprinted with permission from Jia et al. in *Biomedical Optics Express* [39])

particles such as red blood cells [36–38]. This phenomenon is also clearly observed in real-time OCT reflectance images where the scattering pattern of blood flow varies rapidly over time due to the flow stream that drives randomly distributed blood cells through the imaging volume. This results in decorrelation of the received backscattered signals that are a function of scatterer displacement over time, creating a contrast between decorrelated blood flow and nondecorrelated static tissue that can be used to extract flow signals for angiography.

In contrast to Doppler and other phase-based approaches in Fourier-domain OCT, amplitude-decorrelation measurements are sensitive to transverse flow and immune to phase noise. However, amplitude-decorrelation measurements are very sensitive to pulsatile bulk motion noise in the axial direction due to the high axial resolution of OCT. In the fundus, ocular pulsation occurs primarily along the axial direction and is driven by the retrobulbar orbital tissue in line with cardiac activity. This results in high sensitivity in the axial direction results that produce unacceptable signal-to-noise ratio (SNR). To overcome this limitation, we created SSADA based on the decorrelation of OCT signal amplitude due to flow.

The basic procedures of SSADA are shown in Fig. 46.4. The key step of SSADA is splitting the raw full spectrum into a new spectrum with multiple narrow bands. Rather than using the high-resolution OCT amplitude frames (M-B frames) transformed by the full spectrum for amplitude-decorrelation computation, new bandwidth is intentionally created to limit the OCT axial resolution. The creation of a modified isotropic resolution cell minimizes noise along the axial direction and

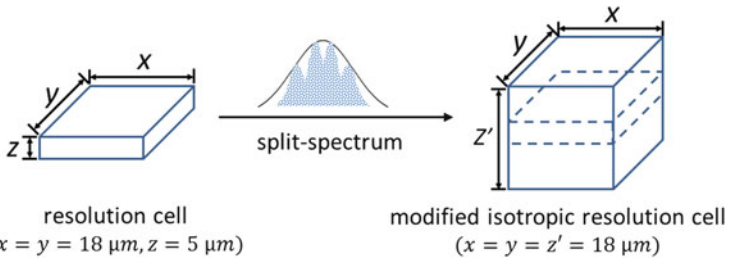

Fig. 46.5 Diagram of the modification of the OCT imaging resolution cell using the split-spectrum method. The resolution cell ($x = y > z$) in the current configuration can be modified into a new resolution cell ($x = y = z$') (Reprinted with permission from the *En Face OCT Atlas* [40])

optimizes flow detection along the transverse direction (Fig. 46.5). After the new narrow spectrums are Fourier transformed, the resultant low-resolution OCT amplitude frames are used to calculate decorrelation. Inter-B-scan decorrelation can be determined at each of the narrow spectral bands independently and subsequently averaged. Recombining the decorrelation images from the spectral bands yields angiograms that utilize the full information in the entire OCT spectral range. Our work has shown that such images produce significant improvement of SNR for both flow detection and connectivity of microvascular networks when compared to other amplitude decorrelation techniques [18]. Furthermore, the creation of isotropic resolution cells with equal sensitivity to axial and transverse flow can be useful for quantifying flow. As a result of the flow value generated by the isotropic resolution being a function of the flow velocity regardless of direction, OCT angiography can be used to extract flow information that can be further processed for quantification.

46.3.2 System and Scan Pattern

OCT angiography requires a high-speed OCT system for image acquisition. The system we used in our OCT angiography studies is an ultrahigh-speed swept-source OCT device built by our group at the Massachusetts Institute of Technology [41]. The instrument operates at a speed of 100 kHz axial scan rate using a short cavity laser centered at a wavelength of 1,050 nm with a 100 nm tuning range.

Each OCT angiography scan set contains four individual scans comprised of two x-fast scans and two y-fast scans. For each x-fast scan, a 3 mm × 3 mm image is obtained by sampling 200 axial scans across a 3 mm line along the x-axis to obtain a single B-scan. Each B-scan is repeated seven more times to obtain a total of eight B-scans at a single y-position. Upon completion, the scan probe moves the next y-position where eight more B-scans are acquired along the x-axis. A total of 200 y-positions covering 3 mm are sampled amounting to a total of 1,600 B-scans acquired per scan to form a 3D data cube. With a B-scan frame rate of

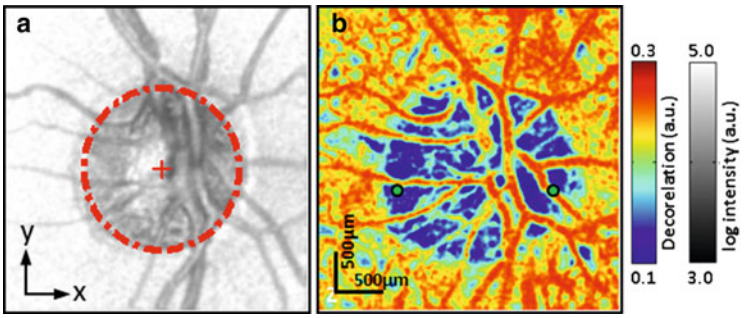

Fig. 46.6 SSADA reflectance intensity (**a**) and angiogram (**b**) of the retinal and ONH circulations of a normal subject. *Red circle* in (**a**) shows the boundary of the *disc*

500 frames per second, each scan takes approximately 3.4 s to complete. Y-fast scans are performed in the same manner as x-fast scans with the exception that B-scans are obtained along the y-axis rather than along the x-axis.

46.3.3 OCT Angiography for Normal and Glaucoma Eyes

SSADA can be used to monitor blood flow changes in the optic nerve head associated with glaucoma. While the traditional mechanical theory for the pathogenesis of glaucoma suggests that an acute rise in intraocular pressure causes the lamina cribrosa to deform and disrupt axonal bundles of the optic nerve, there is a growing body of evidence that implicates vascular dysfunction to the pathogenesis of glaucoma [42]. In studies of normal-tension glaucoma, disease progression was observed in 20 % of eyes despite greater than 30 % reductions in IOP [43, 44]. The vascular theory attributes glaucoma to insufficient blood supply resulting from either an increase in IOP or other risk factors that reduce ocular blood flow [45]. Furthermore, the hypothesis that localized damage occurs due to a breakdown in the autoregulation of ocular perfusion pressure is supported by studies indicating low ocular perfusion pressure as a risk factor for glaucoma [46–48].

The 3D volumetric data set from OCT angiography provides both reflectance intensity and decorrelation (angiography) images. From the ONH scan in Fig. 46.6, the en face maximum projection of reflectance intensity shows major retinal blood vessels and second-order branches, but finer branches and the microcirculation of the retina, choroid, and optic disc are not visible (Fig. 46.6a). In contrast, the en face maximum decorrelation projection angiogram shows not only the same major retinal and second-order branches but also finer branches and the microcirculation of the retina, choroid, and optic disc that were not visible in the en face maximum projection of reflectance intensity (Fig. 46.6b).

SSADA can also be used to demonstrate en face ONH angiography at different tissue depths. Figure 46.7 shows single slice angiograms within the retina, choroid, and lamina cribrosa that can be used to separately visualize microcirculation within

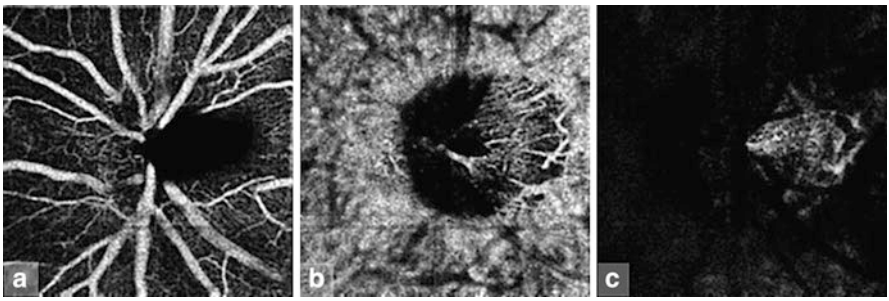

Fig. 46.7 En face ONH angiograms separately showing the microcirculation at a single slice within the retina (**a**), choroid (**b**), and lamina cribrosa (**c**)

each layer. In the retinal slice, disc surface vessels and retinal vessels are clearly visible (Fig. 46.7a). In the choroidal slice (Fig. 46.7b), a near confluent choriocapillaris is visible around the optic disc, along with a network of large arteries and veins of Haller's layer. Within the disc itself, a dense vascular network is seen temporally. Within the scleral slice, there is no visible circulation outside the disc (Fig. 46.7c). Due to the tilt of the disc, the nasal portion of the lamina cribrosa is overshadowed by the RPE and the choroid, and the superior and inferior poles are overshadowed by major retinal vessels. But in the temporal quadrant, deep ONH circulation in the lamina cribrosa can be visualized. To our knowledge, this is the first time that the disc microcirculation has been visualized noninvasively in such a comprehensive manner.

In a pilot study, we used OCT angiography to measure the difference in ONH blood flow between three preperimetric glaucoma eyes and three normal controls. Four angiography scans were obtained in one session. While normal eyes and glaucoma eyes appeared similar in disc photographs (Fig. 46.8a, c), OCT angiography images revealed a visible reduction in ONH perfusion for glaucoma eyes (Fig. 46.8). This reduction can be seen within the whole disc marked by the red solid line and most noticeably in the temporal ellipse region marked by yellow dashed lines that exclude major branch retinal vessels (Fig. 46.8b, d). To quantify the difference in perfusion, we used SSADA to measure flow index rates in the whole disc and the temporal ellipse. Glaucoma eyes showed a significant reduction of flow index in both the whole disc ($P = 0.040$) and the temporal ellipse ($P = 0.010$). In comparison to normal eyes, glaucoma eyes showed a 35 % reduction of flow index in the whole disc and a 57 % reduction in the temporal ellipse. We calculated the coefficient of variation (CV) for intravisit repeatability to be 6.8 % in the whole disc and 9.0 % in the temporal ellipse within one session.

46.4 Summary and Conclusions

Doppler OCT and OCT angiography are complementary to each other. The multicircular Doppler OCT is more difficult to process due to the need to calculate

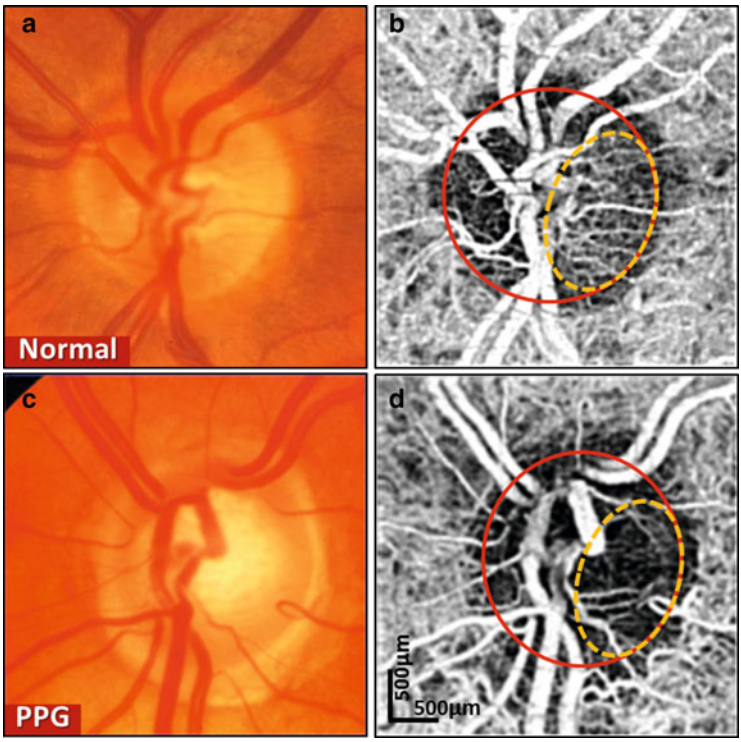

Fig. 46.8 Disc photographs (**a**, **c**) and en face OCT angiograms (**b**, **d**) of ONHs in representative normal (**a**, **b**) and preperimetric glaucoma (PPG) subjects (**c**, **d**). In (**b**) and (**d**), the *solid circles* indicate the discs, and the *dash circles* indicate the temporal ellipses. A dense microvascular network was visible on the OCT angiography of the normal disc (**b**). This network was greatly attenuated in the glaucomatous disc (**d**) (Reprinted with permission from Jia et al. in *Biomedical Optics Express* [39])

Doppler angles for each vessel, but it has the advantage of being able to provide absolute measurements of total retinal blood flow in units of μl/min. This technique does not require the use of an ultrahigh-speed OCT system and can be performed with spectral domain OCT systems with scan rates as low as 20 kHz. It can also provide the velocity and vessel area measurement for main veins and arteries in the optic disc and peripapillary region. These measurements of total retinal blood flow have been found to be well correlated to visual field function for glaucoma patients. For faster OCT systems, the en face Doppler approach [11] to the measurement of total retinal blood flow may have the advantage of simpler processing and greater reliability.

OCT angiography provides flow index which is related to perfusion. It is more robust than Doppler OCT because it is omnidirectional and measurements are not affected by beam incidence angle. Although OCT angiography is capable of measuring blood flow in large retinal vessels, its significance lies in the ability to

obtain blood flow measurements in microcirculatory networks that cannot be picked up by Doppler OCT. This allows for the ability to detect and pinpoint focal damage and give insight to local ischemia. Measurements of ONH microcirculation with OCT angiography have revealed a significant reduction of blood flow in glaucoma eyes, and these measurements were also well correlated with visual field function. The main caveat to OCT angiography is that it is not able to provide absolute volumetric flow in μl/min, rather yielding flow index on an arbitrary scale. Additionally, use of an ultrafast OCT system (above 70 kHZ) is required for the technique.

Doppler OCT and OCT angiography goes beyond traditional structural OCT and measures tissue function. Functional OCT is in an early stage of development and is not yet used clinically. However, because leading causes of blindness such as age-related macular degeneration (AMD), diabetic retinopathy, and glaucoma all involve reduced or abnormal ocular circulation, the potential clinical applications are vast. Doppler OCT has already been used to detect reduced retinal blood flow in diabetic retinopathy, glaucoma, and other optic neuropathies. OCT angiography has been used to demonstrate reduced ONH perfusion in glaucoma. OCT angiography may also be useful in assessing capillary dropout and macular ischemia, visualizing retinal neovascularization in diabetic retinopathy, and visualizing choroidal neovascular membrane in AMD. The potential applications of functional OCT may be as wide as structural OCT.

References

1. Z. Chen, T.E. Milner, D. Dave, J.S. Nelson, Optical Doppler tomographic imaging of fluid flow velocity in highly scattering media. Opt. Lett. **22**, 64–66 (1997)
2. J.A. Izatt, M.D. Kulkarni, S. Yazdanfar, J.K. Barton, A.J. Welch, In vivo bidirectional color Doppler flow imaging of picoliter blood volumes using optical coherence tomography. Opt. Lett. **22**, 1439–1441 (1997)
3. Y. Zhao et al., Phase-resolved optical coherence tomography and optical Doppler tomography for imaging blood flow in human skin with fast scanning speed and high velocity sensitivity. Opt. Lett. **25**, 114–116 (2000)
4. R.M. Werkmeister et al., Bidirectional Doppler Fourier-domain optical coherence tomography for measurement of absolute flow velocities in human retinal vessels. Opt. Lett. **33**, 2967–2969 (2008)
5. C.J. Pedersen, D. Huang, M.A. Shure, A.M. Rollins, Measurement of absolute flow velocity vector using dual-angle, delay-encoded Doppler optical coherence tomography. Opt. Lett. **32**, 506–508 (2007)
6. Y. Wang, B.A. Bower, J.A. Izatt, O. Tan, D. Huang, In vivo total retinal blood flow measurement by Fourier domain Doppler optical coherence tomography. J. Biomed. Opt. **12**, 041215 (2007)
7. H. Wehbe et al., Automatic retinal blood flow calculation using spectral domain optical coherence tomography. Opt. Express **15**, 15193–15206 (2007)
8. S. Makita, T. Fabritius, Y. Yasuno, Quantitative retinal-blood flow measurement with three-dimensional vessel geometry determination using ultrahigh-resolution Doppler optical coherence angiography. Opt. Lett. **33**, 836–838 (2008)

9. Y.K. Tao, K.M. Kennedy, J.A. Izatt, Velocity-resolved 3D retinal microvessel imaging using single-pass flow imaging spectral domain optical coherence tomography. Opt. Express **17**, 4177–4188 (2009)
10. V.J. Srinivasan et al., Quantitative cerebral blood flow with optical coherence tomography. Opt. Express **18**, 2477–2494 (2010)
11. B. Baumann et al., Total retinal blood flow measurement with ultrahigh speed swept source/ Fourier domain OCT. Biomed. Opt. Express **2**, 1539–1552 (2011)
12. R. Leitgeb et al., Real-time assessment of retinal blood flow with ultrafast acquisition by color Doppler Fourier domain optical coherence tomography. Opt. Express **11**, 3116–3121 (2003)
13. B. White et al., In vivo dynamic human retinal blood flow imaging using ultra-high-speed spectral domain optical coherence tomography. Opt. Express **11**, 3490–3497 (2003)
14. R.K. Wang, Z. Ma, Real-time flow imaging by removing texture pattern artifacts in spectral-domain optical Doppler tomography. Opt. Lett. **31**, 3001–3003 (2006)
15. R.K. Wang, L. An, Doppler optical micro-angiography for volumetric imaging of vascular perfusion in vivo. Opt. Express **17**, 8926–8940 (2009)
16. Y. Wang, B.A. Bower, J.A. Izatt, O. Tan, D. Huang, Retinal blood flow measurement by circumpapillary Fourier domain Doppler optical coherence tomography. J. Biomed. Opt. **13**, 064003 (2008)
17. Y. Wang, A. Fawzi, O. Tan, J. Gil-Flamer, D. Huang, Retinal blood flow detection in diabetic patients by Doppler Fourier domain optical coherence tomography. Opt. Express **17**, 4061–4073 (2009)
18. Y. Jia et al., Split-spectrum amplitude-decorrelation angiography with optical coherence tomography. Opt. Express **20**, 4710–4725 (2012)
19. R.K. Wang, S. Hurst, Mapping of cerebro-vascular blood perfusion in mice with skin and skull intact by Optical Micro-AngioGraphy at 1.3 mum wavelength. Opt. Express **15**, 11402–11412 (2007)
20. S. Makita, Y. Hong, M. Yamanari, T. Yatagai, Y. Yasuno, Optical coherence angiography. Opt. Express **14**, 7821–7840 (2006)
21. V.X.D. Yang, et al., Improved phase-resolved optical Doppler tomography using the Kasai velocity estimator and histogram segmentation. Opt. Commun. 6, 209–214 (2002)
22. O. Tan et al., Doppler optical coherence tomography of retinal circulation. J. Vis. Exp. **67**, e3524 (2012)
23. J.C. Hwang et al., Relationship among visual field, blood flow, and neural structure measurements in glaucoma. Invest. Ophthalmol. Vis. Sci. **53**, 3020–3026 (2012)
24. I. Grulkowski et al., Scanning protocols dedicated to smart velocity ranging in Spectral OCT. Opt. Express **17**, 23736–23754 (2009)
25. J. Fingler, R.J. Zawadzki, J.S. Werner, D. Schwartz, S.E. Fraser, Volumetric microvascular imaging of human retina using optical coherence tomography with a novel motion contrast technique. Opt. Express **17**, 22190–22200 (2009)
26. Y. Wang et al., Pilot study of optical coherence tomography measurement of retinal blood flow in retinal and optic nerve diseases. Invest. Ophthalmol. Vis. Sci. **52**, 840–845 (2011)
27. Y. Yasuno et al., In vivo high-contrast imaging of deep posterior eye by 1-um swept source optical coherence tomography and scattering optical coherence angiography. Opt. Express **15**, 6121–6139 (2007)
28. Y. Hong et al., Three-dimensional visualization of choroidal vessels by using standard and ultra-high resolution scattering optical coherence angiography. Opt. Express **15**, 7538–7550 (2007)
29. L. An, R.K. Wang, In vivo volumetric imaging of vascular perfusion within human retina and choroids with optical micro-angiography. Opt. Express **16**, 11438–11452 (2008)
30. R.K. Wang, L. An, P. Francis, D.J. Wilson, Depth-resolved imaging of capillary networks in retina and choroid using ultrahigh sensitive optical microangiography. Opt. Lett. **35**, 1467–1469 (2010)

31. L. Yu, Z. Chen, Doppler variance imaging for three-dimensional retina and choroid angiography. J. Biomed. Opt. **15**, 016029 (2010)
32. G. Liu, W. Qi, L. Yu, Z. Chen, Real-time bulk-motion-correction free Doppler variance optical coherence tomography for choroidal capillary vasculature imaging. Opt. Express **19**, 3657–3666 (2011)
33. R.K. Wang et al., Three dimensional optical angiography. Opt. Express **15**, 4083–4097 (2007)
34. R.K. Wang, L. An, Multifunctional imaging of human retina and choroid with 1050-nm spectral domain optical coherence tomography at 92-kHz line scan rate. J. Biomed. Opt. **16**, 050503 (2011)
35. J.W. Cho et al., Relationship between visual field sensitivity and macular ganglion cell complex thickness as measured by spectral-domain optical coherence tomography. Invest. Ophthalmol. Vis. Sci. **51**, 6401–6407 (2010)
36. I.A. Hein, W.R. O'Brien, Current time-domain methods for assessing tissue motion by analysis from reflected ultrasound echoes-a review. IEEE Trans. Ultrason. Ferroelectr. Freq. Control **40**, 84–102 (1993)
37. A.P. Hoeks, T.G. Arts, P.J. Brands, R.S. Reneman, Comparison of the performance of the RF cross correlation and Doppler autocorrelation technique to estimate the mean velocity of simulated ultrasound signals. Ultrasound Med. Biol. **19**, 727–740 (1993)
38. Dainty JC, (ed), Laser speckle and related phenomena, second ed. New York: Springer-Verlag, 1984
39. Y. Jia, et al., Quantitative OCT angiography of optic nerve head blood flow. Biomed. Opt. Express 3, 3127–3137 (2012)
40. Y. Jia, D. Huang, J.G. Fujimoto, J. Hornegger, M.F. Kraus, in *Eye Disease "En face" OCT Atlas* eds. by B. Lumbroso, D. Huang, M. Rispoli, A. Romano, G. Coscas. En face angiography of the retinal, choroidal, and optic nerve head circulation with ultrahigh speed OCT. (Jaypee Brothers Medical Publishers, New Delhi, in press) (2013)
41. B. Potsaid et al., Ultrahigh speed 1050nm swept source/Fourier domain OCT retinal and anterior segment imaging at 100,000 to 400,000 axial scans per second. Opt. Express **18**, 20029–20048 (2010)
42. D.B. Yan et al., Deformation of the lamina cribrosa by elevated intraocular pressure. Br. J. Ophthalmol. **78**, 643–648 (1994)
43. Collaborative Normal-Tension Glaucoma Study Group.The effectiveness of intraocular pressure reduction in the treatment of normal-tension glaucoma. Am. J. Ophthalmol. **126**, 498–505 (1998)
44. Collaborative Normal-Tension Glaucoma Study Group.Comparison of glaucomatous progression between untreated patients with normal-tension glaucoma and patients with therapeutically reduced intraocular pressures. Am. J. Ophthalmol. **126**, 487–497 (1998)
45. J. Flammer, The vascular concept of glaucoma. Surv. Ophthalmol. **38**(Suppl), S3–S6 (1994)
46. M.C. Leske, Open-angle glaucoma – an epidemiologic overview. Ophthalmic Epidemiol. **14**, 166–172 (2007)
47. M.C. Leske et al., Predictors of long-term progression in the early manifest glaucoma trial. Ophthalmology **114**, 1965–1972 (2007)
48. L. Bonomi et al., Vascular risk factors for primary open angle glaucoma: the Egna-Neumarkt Study. Ophthalmology **107**, 1287–1293 (2000)

Molecular Optical Coherence Tomography Contrast Enhancement and Imaging

47

Amy L. Oldenburg, Brian E. Applegate, Jason M. Tucker-Schwartz, Melissa C. Skala, Jongsik Kim, and Stephen A. Boppart

47.1 Introduction

Histochemistry began as early as the nineteenth century, with the development of synthetic dyes that provided spatially mapped chemical contrast in tissue [1]. Stains such as hematoxylin and eosin, which contrast cellular nuclei and cytoplasm, greatly aid in the interpretation of microscopy images. An analogous development is currently taking place in biomedical imaging, whereby techniques adapted for MRI, CT, and PET now provide in vivo molecular imaging over the entire human body, aiding in both fundamental research discovery and in clinical diagnosis and treatment monitoring. Because OCT offers a unique spatial scale that is intermediate between microscopy and whole-body biomedical imaging, molecular contrast

A.L. Oldenburg (✉)
Department of Physics and Astronomy and the Biomedical Research Imaging Center, University of North Carolina at Chapel Hill, Chapel Hill, NC, USA
e-mail: aold@physics.unc.edu

B.E. Applegate
Department of Biomedical Engineering, Texas A&M University, College Station, TX, USA

J.M. Tucker-Schwartz • M.C. Skala
Department of Biomedical Engineering, Vanderbilt University, Nashville, TN, USA

J. Kim
Department of Electrical and Computer Engineering, Bioengineering, Medicine, and the Beckman Institute for Advanced Science and Technology, University of Illinois at Urbana-Champaign, Champaign, IL, USA

S.A. Boppart
Biophotonics Imaging Laboratory, Beckman Institute for Advanced Science and Technology, University of Illinois at Urbana-Champaign, Urbana, IL, USA

Departments of Bioengineering, Electrical and Computer Engineering, and Medicine, University of Illinois at Urbana-Champaign, Urbana, IL, USA

© Springer International Publishing Switzerland 2015

W. Drexler, J.G. Fujimoto (eds.), *Optical Coherence Tomography*,
DOI 10.1007/978-3-319-06419-2_48

OCT (MCOCT) also has great potential for providing new insight into in vivo molecular processes. The strength of MCOCT lies in its ability to isolate signals from a molecule or contrast agent from the tissue scattering background over large scan areas at depths greater than traditional microscopy techniques while maintaining high resolution.

MCOCT involves the use of OCT image acquisition and/or processing techniques to generate image contrast using endogenous molecular species or exogenous molecular probes of interest [2]. It should be noted that several other chapters in this book cover techniques that provide information about tissue composition that will not be repeated here, including nonlinear interferometric vibrational imaging (NIVI), second harmonic generation OCT, and optical coherence elastography. This chapter does address spectroscopic OCT (SOCT) in the context of chromophore and probe detection, while the reader should refer to related SOCT chapters in this book for greater detail on SOCT processing methods.

This chapter is structured according to the physical mechanisms used for contrast, starting from direct schemes whereby probes add to or subtract from the optical backscattering spectrum that comprises the OCT signal (i.e., scattering- and absorption-based contrast, respectively), then covering methods that indirectly modulate the OCT signal (i.e., pump-probe, magnetomotive, and photothermal OCT). It should be noted that any scheme developed for MCOCT must be compatible with interferometric detection, which precludes the use of several physical mechanisms such as fluorescence emission. In this chapter, imaging technology development will be emphasized and presented with selected examples of biomedical applications. Interestingly, many endogenous and exogenous probes can be sensed by more than one method. For example, photothermal contrast relies upon absorption, and therefore, the same agents provide contrast in both photothermal and spectroscopic OCT. The development of exogenous imaging probes (or contrast agents) that enable MCOCT is also a rich and varied topic that poses particular challenges in materials science and targeted delivery. Here we introduce a variety of molecular probes in the context of specific MCOCT imaging strategies, while the reader is referred elsewhere [3–6] for detailed information about probe development.

47.2 Scattering-Based Contrast

The native "contrast" observed in OCT is light that has been coherently backscattered. All MCOCT methods are based upon modifying this backscattering signal in a way that can provide additional, molecular information about the sample. One of the most straightforward strategies is to increase the OCT signal directly with a probe particle that exhibits high backscattering. Analogous methods include the use of positive T_1 contrast agents in MRI and echogenic microbubbles in ultrasound. In fact, microbubbles also happen to have reasonably high light scattering and were one of the first types of contrast agents studied with OCT [7]. Oil-filled protein microspheres were subsequently found to offer flexibility in loading the shell or core with nanoparticles to further increase the optical

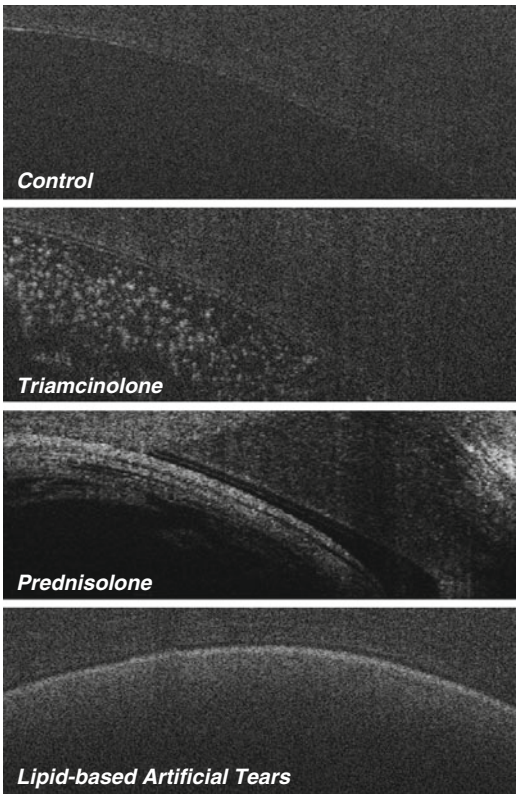

Fig. 47.1 OCT images of fresh, ex vivo porcine eyes after intra-cameral injection of contrast agents. From *top* to *bottom*: Control, triamcinolone acetonide 40 mg/mL, prednisolone acetate 1 %, and lipid-based artificial tears. The agents provide positive contrast within the anterior chamber that has a different pattern depending on the type of agent used. These differences are expected because the agents are comprised of varying particulate or oil-in-water suspensions, with differing mean particle sizes, reflectivities, and diffusivities

scattering [8], and variants of these are in continued use with magnetomotive OCT, as discussed below [9]. It is important to note, however, that any new contrast agent must undergo thorough safety and efficacy testing before it can be used on humans, such as that required by the Food and Drug Administration in the United States. As such, the study of agents already approved for human use can more readily lead to clinical translation. Interestingly, it was recently found that several commonly used ophthalmic medications provide scattering-based OCT contrast [10]. As shown in Fig. 47.1, OCT reveals the diffusion of several medications within the anterior chamber after administration. They were also shown to enhance the visibility of corneal incisions postoperatively, which may provide a method for assessing wound integrity. Future adaptations of molecularly targeted agents may further broaden the functionality of OCT in ophthalmology.

While scattering-based contrast agents are readily visible within the highly transparent anterior segment of the eye, the ability to detect these types of agents endoscopically or on the skin is more challenging, as they must be distinguishable against the already high optical scattering of the tissue. Mie theory provides exact solutions for light scattering from spherical particles, shelled spheres, and spheroids [11]. As a general rule, there is a rapid increase in scattering with particle size (scattering cross section, $\sigma_s \propto d^6$) in the Rayleigh regime ($d << \lambda$) and a rapid increase in

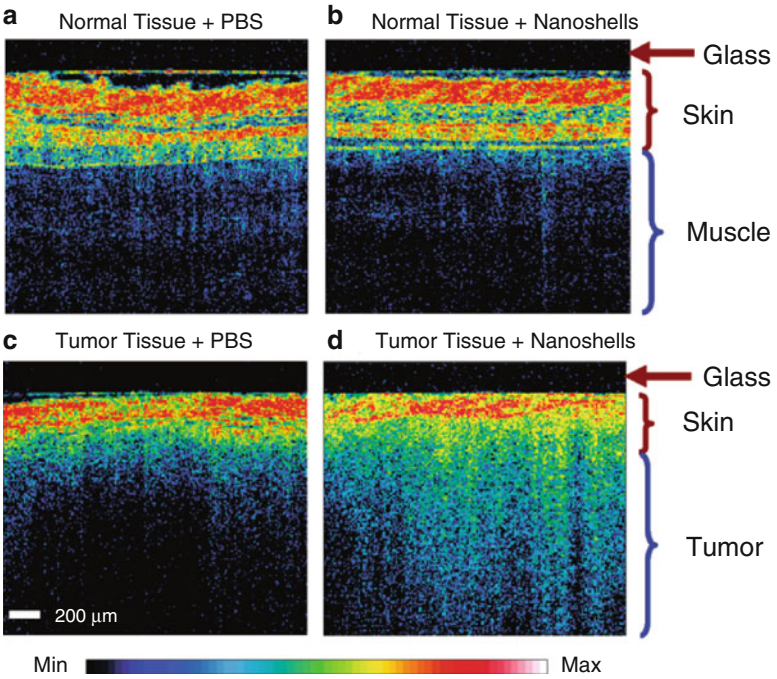

Fig. 47.2 OCT images of tissues from mice with subcutaneous tumors systemically treated with phosphate-buffered saline (*PBS*) as a control (**a**, **c**) and multifunctional nanoshells (**b**, **d**). Enhanced retention of nanoshells in the tumor in panel (**d**) provides better delineation of tumor borders, as well as subsequent tumor-specific photothermal ablation (Reprinted with permission from Ref. [13]. Copyright 2007 American Chemical Society)

scattering as the material refractive index is different (higher or lower) than that of the (typically aqueous) medium. At the same time, one must weigh the choice of the material and the particle size against the biocompatibility and the ability for the probes to access their target, respectively, for the needed application.

One of the most useful types of OCT contrast agents, which will be discussed many times throughout this chapter, is plasmonic gold nanoparticles in their various forms (nanospheres, nanoshells, nanorods, etc.). This is because gold is highly unreactive and consequently relatively biocompatible, while at the same time providing a surface plasmon resonance (SPR) effect at the red and near-infrared wavelengths used in OCT [12]. This SPR is evident as either a strong absorption or scattering spectral peak, with a transition from predominantly absorbing (low albedo) to predominantly scattering behavior (high albedo) as the particle size is increased; for spheres, the transition occurs at $d \approx 80$ nm [12]. Nanoshells in particular have been highly developed for scattering-based OCT contrast [13–15]. They are comprised of a silica core and gold shell and offer spectral tunability by adjusting the core diameter and shell thickness [3]. Figure 47.2 displays a demonstration of enhanced OCT contrast in the tumors of mice systemically intravenously

injected with nanoshells [13]. These results highlight the enhanced permeation and retention (EPR) effect, whereby the permeable vasculature of tumors acts to trap particles, providing selective targeting [16]. Importantly, EPR further enables site-targeted treatment; in this example, the nanoshells were designed to be nearly equally light scattering and absorbing, providing both imaging contrast (via scattering) and photothermal therapy (via absorption).

It should also be noted that, in cases where the SPR is narrow compared to the bandwidth of the light used in OCT, it may be possible to employ spectroscopic OCT (SOCT) techniques to distinguish the SPR signature, providing enhanced specificity against the tissue scattering background. While this idea has been explored [17], a confounding factor that makes this method challenging is the highly modulated backscattering spectrum typically obtained from Mie scatterers ($d \sim \lambda$) within the tissue. In current practice, SOCT techniques are much more commonly employed to detect absorption-based contrast agents, which is the focus of the following section.

47.3 Absorption-Based Contrast

Light absorption is a very attractive molecular process to exploit for contrast, both because of the potential signal strength and because essentially all molecular species have the capacity to absorb light. The imaging light used in OCT is spectrally broad, and hence, the backscattered spectrum may be utilized to identify the absorption spectrum of endogenous or exogenous species present within the tissue. The group of techniques designed to extract this information are collectively referred to as spectroscopic optical coherence tomography (SOCT) [18].

The different algorithms developed for SOCT diverge in how they deal with the trade-off between spatial and spectral resolution. One approach is to use multiple light sources to collect independent OCT images with different center wavelengths. Relatively straightforward algorithms such as spectral triangulation [19] may then be implemented to extract the depth-resolved backscattered spectrum. A judicious choice of center wavelengths can facilitate the detection of highly peaked spectral features with limited spectral resolution. This approach has largely been used to detect dyes such as indocyanine green (ICG) [19].

An alternate approach is to directly utilize the broad spectral bandwidth of the light source and use the short-time Fourier transform (STFT) to gain spectral resolution at the expense of spatial resolution [20]. This approach has the advantage that it is entirely a post-processing technique; hence, it can be tailored to maximize contrast to a target contrast agent. Likewise, the time-frequency distribution (TFD) need not be limited to the STFT but may optimized as well to maximize the spatial and spectral resolution [21]. Wax and coworkers [22] have recently developed an algorithm that incorporates two STFTs, one with a narrow spectral window and one with a broad spectral window. The two TFDs are multiplied point by point to generate a TFD with both high spatial and spectral resolution.

Exogenous chromophores for SOCT are largely repurposed, commercially available fluorescent dyes. Utilizing these dyes carries with it the advantage of

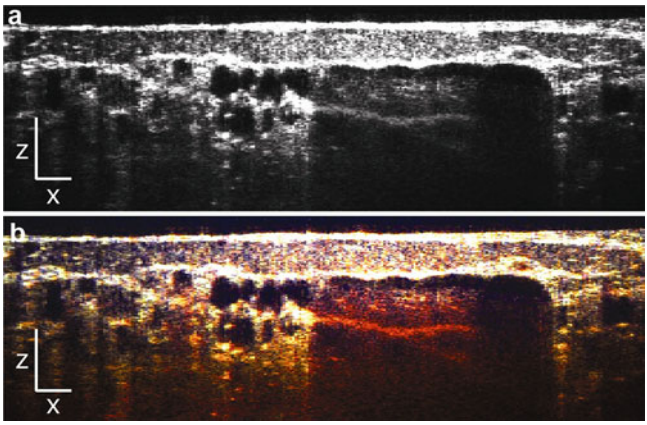

Fig. 47.3 Conventional OCT (**a**) and METRiCS OCT (**b**) images, located above point (**e**) in the en face (*x*–*y*) image in Fig. 47.4. *White x* and *z* scale bars, 100 μm (Reprinted with permission from Ref. [22]. Copyright 2011 Macmillan)

a wealth of biological and chemical research aimed toward targeting particular disease states of tissue, chemical species, or morphologies. Some examples include ICG [23], photodynamic therapy-related dyes [24], and fluorescent microspheres [25]. Dyes typically also have strongly peaked spectra which enable detection via fairly simple methodologies. For instance, a commercial NIR absorbing dye (H.W. Sands, ADS7460) which exhibits a sharp absorption peak at 740 nm was used to produce contrast in an 800 nm OCT system by effectively clipping the shorter wavelengths, resulting in a redshift of scattered light [26].

The major endogenous chromophore is hemoglobin. Detection of hemoglobin absorption with SOCT has been explored as a method to measure blood oxygen saturation [27]. Wax and coworkers [22] recently measured the oxygen saturation along with fluorescein dye injected into the bloodstream in a mouse window chamber model using METRiCS OCT which uses the two TFD methods noted above along with OCT imaging at nontraditional wavelengths. Their imaging bandwidth spans the 455-695 nm range which overlaps strong peaks in the oxy- and deoxyhemoglobin spectrum. Selected results from this work demonstrating the endogenous and exogenous tissue contrast as well as SO_2 measurements are shown in Figs. 47.3 and 47.4.

Plasmonic gold nanoparticles have also been widely employed for absorption-based contrast, where the SPR peaks are tuned within the OCT imaging band by varying the size of specific geometrical features of the nanoparticles. For instance, light-absorbing gold nanorods are tuned by varying their aspect ratio (length over width) while maintaining a length typically $<$100 nm to favor absorption over scattering. Many of the different particle geometries have been explored for contrast in SOCT, including gold nanospheres [28], gold nanorods [28, 29], and gold nanocages [30]. For example, gold nanorods were imaged after injection into excised human breast carcinoma tissue [29]. As mentioned above, light-absorbing

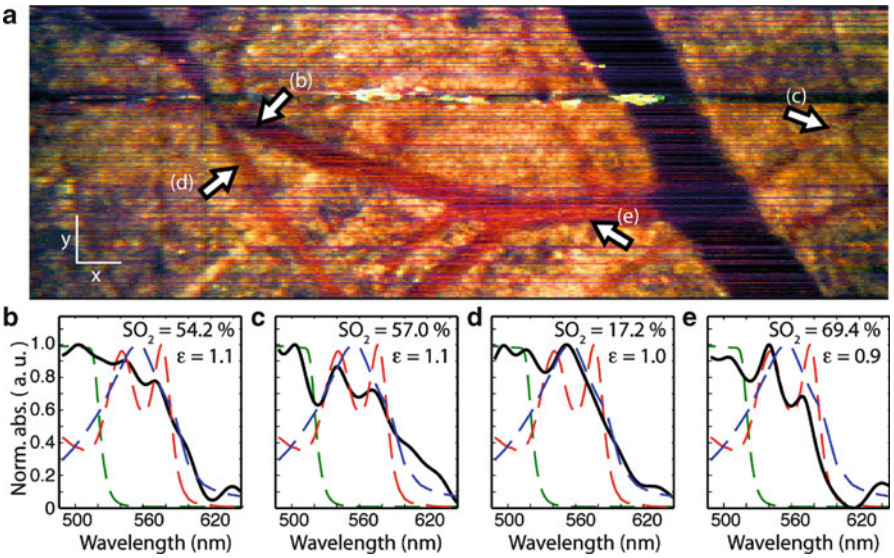

Fig. 47.4 (**a**) En face METRiCS OCT image with *arrows* indicating points where the spectra are extracted. *White x* and *y* scale bars, 100 μm. (**b–e**) Spectral profiles from corresponding points in (**a**). Measured spectral profiles (*black*) are superposed with the theoretical oxy- (*dashed red*) and deoxy- (*dashed blue*) hemoglobin normalized extinction coefficients, and normalized absorption of NaFS (*dashed green*). Also shown are the SO_2 levels and the relative absorption of NaFS with respect to total hemoglobin (ε ≡ NaFS/Hb). All spectra were selected from depths immediately below each corresponding vessel (Reprinted with permission from Ref. [22]. Copyright 2011 Macmillan)

gold nanoparticles are, at the same time highly effective for photothermal cancer therapy, where a high power laser is used to irradiate particle-laden tumors [31]. The synergy between imaging and therapy, which allows us to monitor permeation and diffusion of SPR particles into tissues before treatment, aids in particle development for improved delivery and informs the design of more effective treatment protocols.

47.4 Pump-Probe OCT

Pump-probe optical coherence tomography (PPOCT) is fundamentally the fusion of optical coherence tomography with pump-probe absorption spectroscopy. Spatially resolving the pump-probe interaction can provide molecular contrast for absorbing agents in a tissue sample similar to SOCT. The major advantages of PPOCT are that contributions to the OCT light attenuation due to scattering and absorption are easily separated and there is no compromise between spatial and spectral resolution. The disadvantages are that the optical setup is more complicated and typically requires pulsed light sources. Only under special circumstances could PPOCT be accomplished with a swept OCT laser source or superluminescent diode.

A typical PPOCT system has the following features: The probe is the light in the sample arm of the OCT interferometer, i.e., the same light used for OCT imaging serves as the probe light. A separate pump beam co-propagates with the OCT light in the sample arm. The pump is typically amplitude modulated at frequency f_0. Transfer of the modulation onto the backscattered probe (OCT) signal at f_0 is then evidence of absorption of the probe light by some tissue absorber. In time-domain OCT implementations, the PPOCT signal appears as sidebands on the Doppler carrier frequency, $f_D \pm f_0$ [32]. In spectral-domain OCT, the PPOCT signal can be extracted from an M-scan by Fourier transformation along the time axis (at each depth) and filtering around f_0. For the process to work, absorption of the pump by the contrast agent must change the absorption/scattering properties at the probe wavelength.

The first experimental realization of PPOCT [33] demonstrated imaging of methylene blue, a dye used for chromoendoscopy [34]. The specific physical mechanism leading to PPOCT signal from methylene blue is well understood and therefore serves as a germane example, where the energy level diagram is illustrated in Fig. 47.5a. The pump light drives a transition from the singlet ground state (S_0) to the first excited electronic state (S_1). Molecular population in the excited singlet state is transferred to the triplet state via a particularly efficient [35] spontaneous process ($S_1 \rightarrow T_1$, $\tau_{1\text{-}1}$). Methylene blue in its triplet state has a resonant transition peaked at 830 nm ($T_1 \rightarrow T_2$). When the pump is on, an 830 nm probe can be absorbed by methylene blue, but when the pump is off, there is no probe absorption. In reality the excited triplet state has a finite lifetime (analogous to fluorescence lifetime) that is a function of the oxygen level in its local environment, but varies from ~200 ns to over 1 μs. Consequently, the pump and probe need not be incident on the sample at the same time, but may be delayed in time by some fraction of the excited state lifetime. Measurement of this characteristic lifetime may be used to help differentiate among multiple chromophores. An example decay for methylene blue is in Fig. 47.5b. The average decay time (lifetime) from T_1 to S_0 (τ_{0-1}) was calculated to be 247 ns via $\tau_{avg} = \sum S \cdot t / \sum S$, where S is the PPOCT signal at delay time t [36]. In addition to the lifetime, the absorption spectrum at the pump or probe may be measured by recording the PPOCT signal as a function of the pump or probe wavelength, respectively.

Several molecular species in addition to methylene blue have been imaged using PPOCT. Phytochrome A, a naturally occurring molecular switch which may be reversibly optically pumped from one isomeric state to another, was imaged in a tissue phantom [37]. Hemoglobin was measured in the gill filament arteries of a zebrafish (*Brachyrerio danio*) using a time-domain 532 nm PPOCT system with a 532 nm pump [32]. The same system was also used to image the fluorescent protein DsRed in a transgenic zebrafish. Melanin was imaged in the first spectral-domain PPOCT system in a phantom made from human hair embedded in chicken breast tissue [38]. Melanin has also been imaged using a time-domain optical coherence microscopy system [39]. Recent work [36] has demonstrated volumetric imaging of microvasculature in *Xenopus laevis* using a two-color (532 nm pump, 830 nm probe) PPOCT system. Representative PPOCT cross sections overlain on the OCT cross sections are shown in Fig. 47.6 along with volumetric

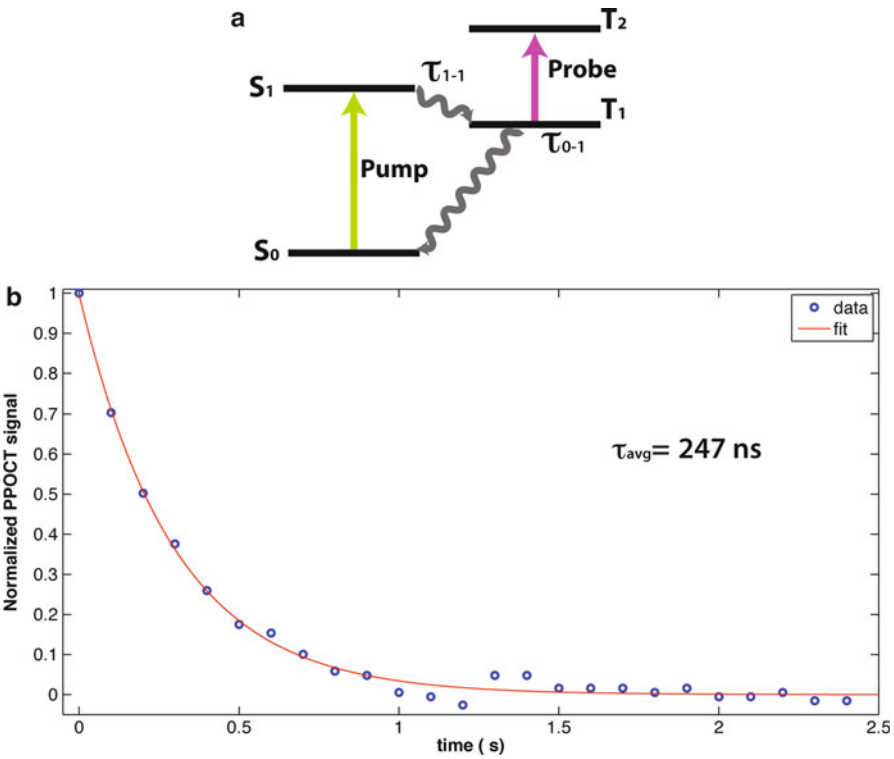

Fig. 47.5 (**a**) Molecular energy level diagram for the methylene blue PPOCT mechanism. Driven transitions are indicated by *straight arrows* and spontaneous transitions as *zigzag arrows*. (**b**) Measured normalized decay of the PPOCT signal due to methylene blue as a function of delay between the pump and probe pulse. The decay has a characteristic average lifetime of 247 ns (Modified and reprinted with permission from Ref. [36]. Copyright 2013)

reconstructions of the vasculature measured with PPOCT. They have also demonstrated the use of the characteristic lifetime to differentiate PPOCT signals from two different chromophores.

Figure 47.7 shows a pair of capillary tubes loaded with methylene blue/microspheres and bovine whole blood in heparin. The top panel (a) is the standard OCT image showing similar signal from both capillary tubes. A PPOCT image with 2 ns pump-probe delay (Fig. 47.7b) appears very similar to the OCT image. However, when the pump-probe delay is increased to 24.8 μs, the signal from the methylene blue/microsphere-loaded capillary tube decays, leaving only signals from the blood-filled capillary. Taking advantage of the difference in lifetime between two chromophores is an effective strategy for imaging multiple chromophores with PPOCT.

Future research in PPOCT may lead in several directions. There is a clear potential for imaging vasculature. While Doppler-based OCT can also measure vasculature, a major advantage of PPOCT is that the signal is independent of the angle of flow, while the Doppler signal approaches zero when the illumination is orthogonal to

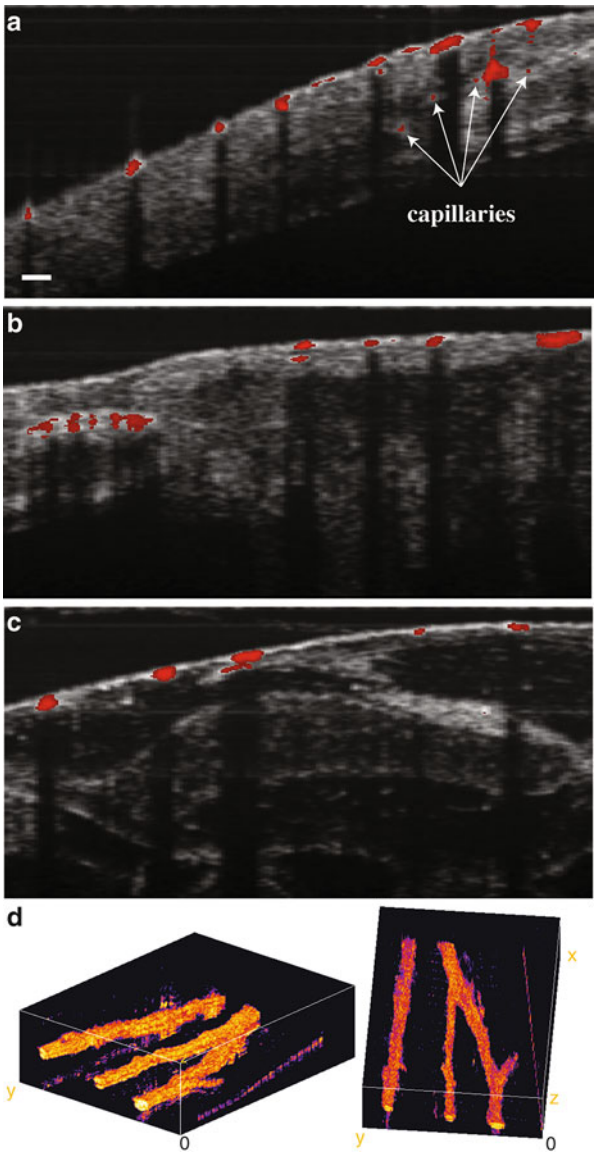

Fig. 47.6 (**a**–**c**) PPOCT B-scans overlaid on the corresponding co-registered OCT B-scans. *Xenopus laevis* vasculature is clearly depicted. *Arrows* in (**a**) point to capillaries that were not visible in conventional OCT. (**d**) Volumetric reconstructions of the microvasculature (Modified and reprinted with permission from Ref. [36]. Copyright 2013)

the flow. The PPOCT signal is also molecularly specific, so it may be possible to differentiate oxy- and deoxyhemoglobin and develop a PPOCT-based measure of blood oxygen saturation. Furthermore, the imaging of exogenous contrast agents such as methylene blue could potentially be used to tag and image specific molecular species that are otherwise invisible to OCT. Such applications hinge on the demonstration of sufficient sensitivity either with methylene blue or some other discovered or engineered contrast agent.

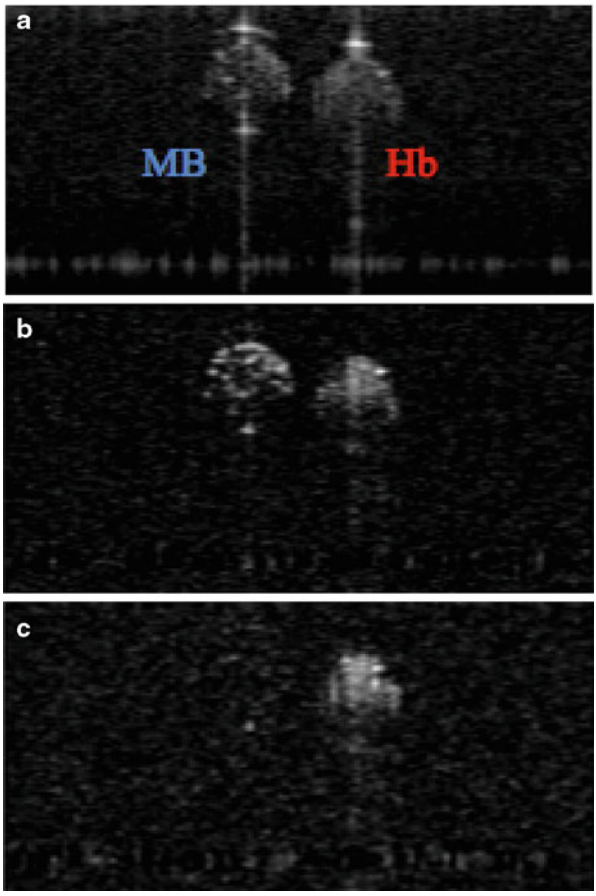

Fig. 47.7 (**a**) OCT B-scan of methylene blue (*MB*) and hemoglobin (*Hb*) in acrylic capillary tubes. (**b**) Corresponding PPOCT B-scans with a pump-probe delay of 3 ns. (**d**) Corresponding PPOCT B-scan with a pump-probe delay of 24.8 μs. The absence of the MB tube demonstrates the potential for using the lifetime as an effective method for differentiating multiple chromophores

47.5 Magnetomotive OCT

47.5.1 Theory and Instrumentation

Magnetomotive OCT (MMOCT) is a method for contrasting the distribution of magnetic particles based on their induced motion within a temporally modulated, magnetic field gradient [40]. Figure 47.8 illustrates the mechanism of MMOCT, showing how magnetic particles inside the imaging volume are mechanically pulled toward an electromagnet placed in the imaging arm of an OCT system. Typically, phase-sensitive OCT is then used to track the motion of light scattering tissue structures that are mechanically coupled to the particles [41]. Modulation of the electromagnet thus leads to phase modulation that can be band-pass filtered at the modulation frequency to detect the magnetomotion. Because human tissues are only very weakly magnetic (magnetic susceptibility $|\chi| < 10^{-5}$),

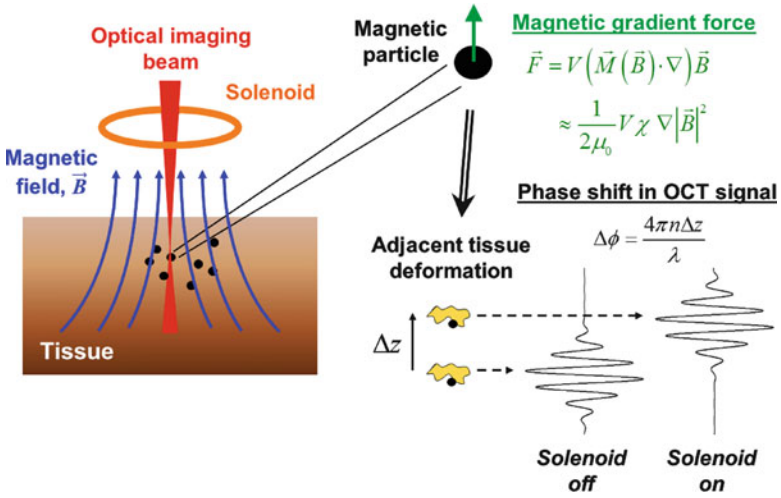

Fig. 47.8 Mechanism of magnetomotive contrast in OCT. A solenoid placed in the imaging arm of an OCT system provides a magnetic gradient force, $\vec{F}$, on magnetic particles inside tissue according to the gradient of the magnetic field, $\nabla \vec{B}$, and the magnetization and volume of the particles, $\vec{M}$ and V, respectively. The resultant elastic displacement of mechanically coupled light scattering structures, Δz, is sensed as a phase shift in the OCT interferogram, $\Delta\phi$. χ is the particle magnetic susceptibility, μ_0 is the vacuum permeability, and n is the tissue refractive index at the imaging beam wavelength, λ

MMOCT provides high specificity against the tissue background, on the order of 10^5 when using probes of $\chi \approx 1$ [42].

A class of biomedical imaging probes currently used in MRI, called superparamagnetic iron oxides (SPIOs), are ideal for MMOCT because they are designed to exhibit large χ, avoid irreversible aggregation that is associated with ferromagnetic agents, and are composed of iron oxide which has a proven safety profile. FDA-approved MR liver contrast agents such as Feridex™, for example, have been shown to provide excellent MMOCT contrast [43]. Another type of MMOCT probe is protein microspheres encapsulating SPIO-containing ferrofluid, which then offer flexibility in adding targeting ligands and therapeutic payloads [44].

Implementing MMOCT on an existing phase-sensitive OCT system is relatively straightforward. A small electromagnet can be placed on either the same side (as shown in Fig. 47.8) or opposite side of the tissue to provide a magnetic field gradient oriented along the imaging axis. Somewhat counterintuitively, the strength of the magnetic field should only be on the order of 0.1T; higher fields will typically saturate the magnetic particles and reduce the detection sensitivity [41, 43]. The absolute sensitivity of MMOCT can be determined by considering the balance of forces between the diamagnetic tissue, which is pushed away from the magnet, and from the paramagnetic particles, which are pulled toward the magnet.

For a typical SPIO particle, the minimum particle concentration needed to tip this force balance in favor of motion toward the magnet is on the order of 10 μg Fe/g. Another important consideration is the elastic property of the tissue medium. Magnetic particles in liquid do not undergo a restoring force during magnetic field modulation, moving only in one direction, and exhibit little contrast by conventional band-pass-filtered MMOCT. In a solid medium, the compliance of the tissue dictates the amount of displacement Δz, resulting in MMOCT contrast that is weighted by both the local particle concentration and the local tissue stiffness. Owing to the nanoscale displacement sensitivity afforded by phase-sensitive OCT systems, the tissue stiffness is typically of little detriment to the overall MMOCT sensitivity, and sensitivities as low as 27 μg Fe/g have been reported in optomechanical tissue phantoms [41]. The high sensitivity and specificity afforded by MMOCT have recently led to several new molecular imaging application areas, which will be reviewed below.

47.5.2 MMOCT of Atherosclerosis

Atherosclerosis is a disease in which an arterial vessel wall thickens as a result of the accumulation of fatty materials, including macrophages. Atherosclerosis is promoted by low-density lipoproteins (LDL) and cholesterol (crystals) and results in calcification in advanced lesions [45]. Standard intravascular OCT imaging has been extensively investigated for applications in cardiology such as imaging intraluminal 3D structure and function at high resolution, evaluating arterial stents, and visualizing atherosclerotic plaque [46–51]. The addition of contrast agents for use with intravascular OCT can enable site-specific molecular cardiovascular imaging, just as has been shown for ultrasound imaging using gas-filled microbubbles [52]. Targeted contrast agents may enable the early detection and localization of atherosclerotic lesions which may not be clearly evident in structural OCT imaging or in other imaging modalities. Therefore, the combination of intravascular OCT and targeted molecular contrast enhancement with MMOCT can potentially improve the sensitivity of early atherosclerotic lesion detection. Figure 47.9 shows representative MMOCT images from an ex vivo hyperlipidemic rabbit aorta. The RGD (arginine-glycine-aspartic acid)-functionalized protein microspheres [44] were fabricated to target the $\alpha_V\beta_3$ integrin overexpressed in atherosclerotic lesions [53]. These microspheres were loaded with SPIOs and a fluorescent dye, enabling multimodal imaging using MMOCT, MRI, ultrasound, and fluorescence imaging. The ex vivo aorta sample was perfused in a custom-designed flow chamber at physiologically relevant pulsatile flow rates and pressures. The functionalized microspheres have been successfully targeted to fatty streaks present during early-stage atherosclerosis. The future development of a MMOCT catheter or a new solenoid configuration for current commercial intravascular OCT systems may enable in vivo MMOCT imaging of atherosclerosis-targeted magnetic probes.

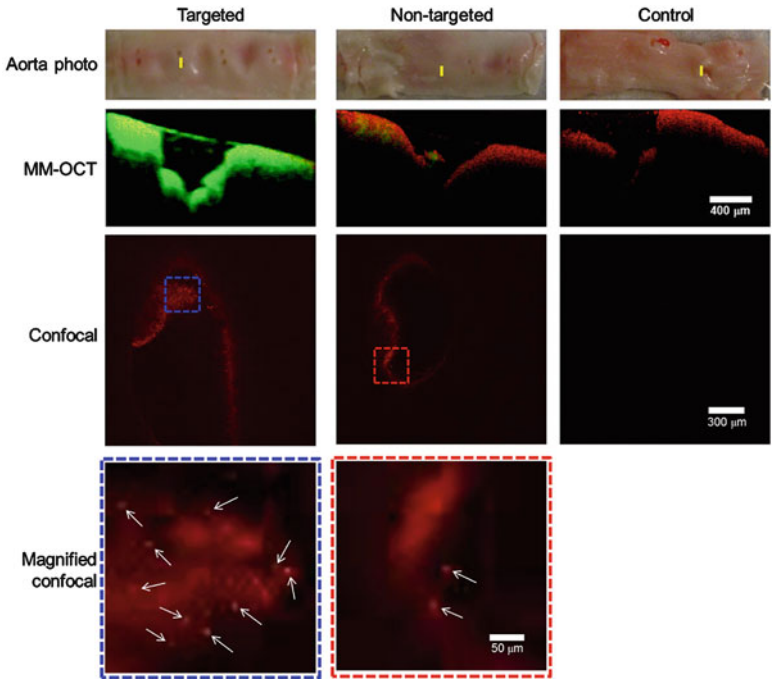

Fig. 47.9 Representative MMOCT and corresponding fluorescence confocal microscopy images of hyperlipidemic rabbit aortas after administration of RGD microspheres. Parametric MMOCT images are displayed showing the magnetomotive signal in *green* and the OCT signal in *red*. The MMOCT signal in the targeted microsphere group was statistically significantly higher ($p < 0.01$) than the nontargeted and control groups. *Yellow lines* in the aorta photos correspond to the imaging locations. The *dotted blue* and *red boxes* are magnified to show the presence of individual microspheres (*white arrows*). Scale bars are consistent across each row

47.5.3 MMOCT of Breast Cancer

Breast cancer is one of the most commonly occurring cancers in women and has a widespread effect on our society [54, 55]. Like other diseases, early detection is the key in the treatment of breast cancer. Breast cancer screening methods include manual clinical and self-breast exams, mammography, genetic screening, ultrasound, and MRI. Breast cancer cells often overexpress $\alpha_V\beta_3$ integrin and HER-2/neu receptors which are considered to be biomarkers for targeted cancer treatment [56]. Figure 47.10 shows an important step in breast cancer diagnosis using MMOCT to contrast HER-2/neu-targeted SPIOs [57]. In this study, the authors used a nitroso-methyl-urea (MNU) carcinogen-induced rat mammary tumor model. In vivo MMOCT images of tumors from rats injected with targeted SPIOs, nontargeted SPIOs, and saline exhibit an accumulation of SPIOs only in the tumors of rats injected with targeted MNPs.

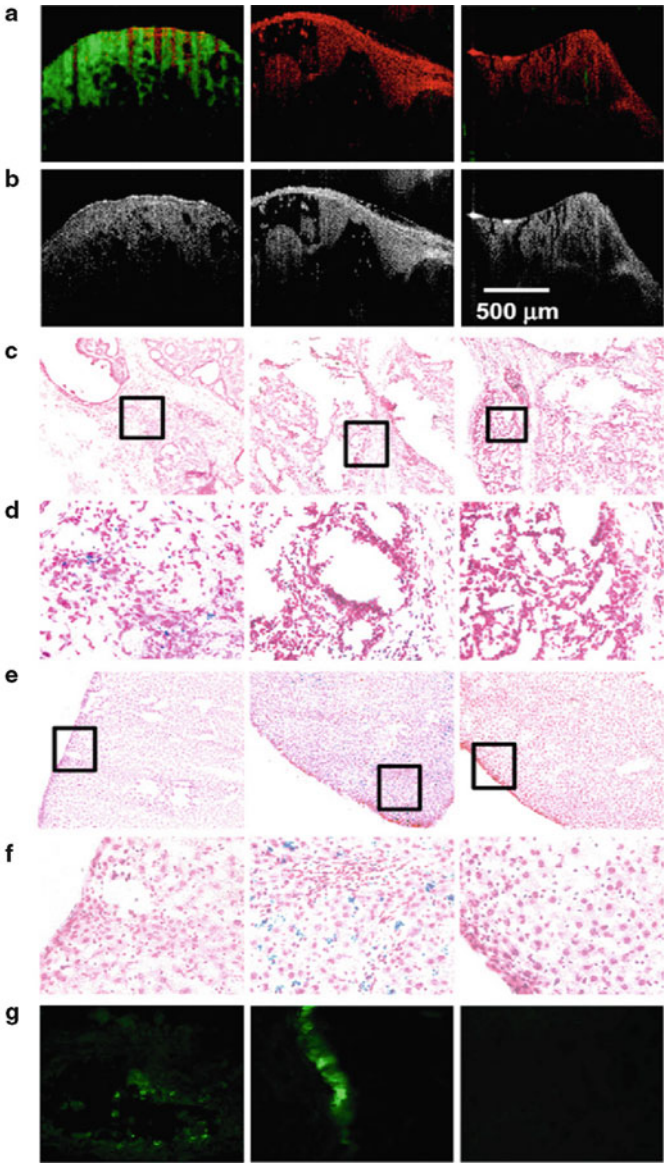

Fig. 47.10 In vivo (**a**) MMOCT and (**b**) OCT of rat mammary tumors. The magnetomotive signal (*green*) is superposed on the OCT (*red*) in MMOCT images. Prussian blue (*PB*) sections of (**c**, **d**) tumors and (**e**, **f**) livers from rats after injection with (left) targeted SPIOs, (center) nontargeted SPIOs, and (right) saline. PB sections in (**d**, **f**) at 40× from boxed regions in (**c**, **e**), at 10×. (**g**) Immunohistochemical-stained sections of (left) tumor from a targeted SPIO injected rat, (center) tail injection site from a targeted SPIO injected rat, and (right) tumor from a saline injected rat (Reprinted with permission from Ref. [57]. Copyright 2010 National Academy of Sciences)

Furthermore, $\alpha_V\beta_3$ integrin is also overexpressed in cancer cells [58]. As in the previous section on atherosclerosis, the protein shell of microspheres can be functionalized with the RGD tripeptide to target the $\alpha_V\beta_3$ integrin. A recent study reported MMOCT imaging of a rat mammary tumor containing RGD-targeted magnetic protein microspheres [9]. MMOCT imaging was performed ex vivo on the tumor approximately 4 h post injection of RGD-functionalized protein microspheres. It was found that the $\alpha_V\beta_3$ integrin-targeted microspheres preferentially accumulated in the tumor.

These preliminary results demonstrate the feasibility of using targeted magnetic nanoparticles and microspheres to detect breast cancer in OCT images. In addition, the liquid-core protein microspheres can potentially also be used to deliver a drug payload, such as the anticancer drug Taxol [59].

47.5.4 Platelets as Functional MMOCT Contrast Agents for Thrombosis

Another way of achieving molecular specificity is to label cells with imaging agents in vitro and to subsequently monitor the activity of the cells after in vivo administration. Platelets are cellular fragments present in blood that are responsible for primary hemostasis (plug formation) as part of the blood clotting process [60]. Platelets respond to factors expressed when the blood vessel endothelium is damaged, such as during trauma and atherosclerosis [61]. Therefore, platelets labeled with SPIOs can be considered novel contrast agents for targeting localized endothelial damage.

Interestingly, platelets have a unique method for nanoparticle uptake, dubbed "covercytosis" [62], which is thought to be part of the body's native immune mechanism. As such, they avidly take up particles at levels reaching hundreds [63], if not thousands [64], of femtograms of iron per platelet. Platelets harvested from blood can also be partially fixed and lyophilized to allow for long-term storage; these are known as rehydratable, lyophilized (RL) platelets [65].

To date, in vitro and ex vivo studies have demonstrated the potential for MMOCT to provide targeted imaging of reactive vascular sites using SPIO-labeled RL platelets [43, 63]. In an ex vivo study, pig arteries were cannulated and flowed with whole blood containing both native platelets and SPIO-RL platelets at equal concentrations [43]. The endothelium of one set of arteries was lightly injured, resulting in blood clotting at the injury sites. As shown in Fig. 47.11, subsequent MMOCT of the luminal wall of these arteries revealed specific magnetomotive contrast to injured artery only, due to the incorporation of SPIO-RL platelets into the clots. These findings may be broadly translatable for assessing internal bleeding and a broad spectrum of cardiovascular diseases such as atherosclerosis.

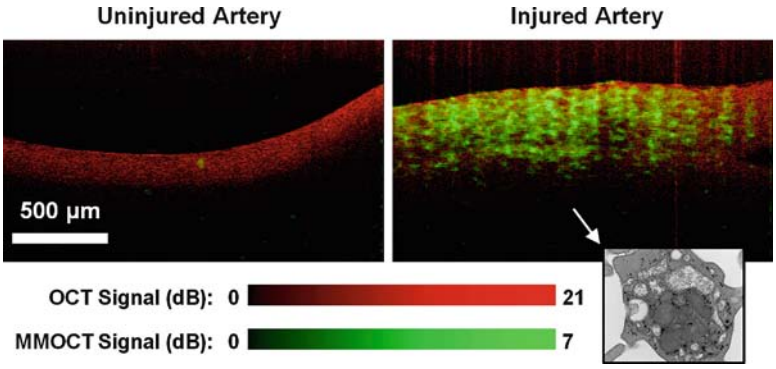

Fig. 47.11 Representative MMOCT images of ex vivo porcine arteries after exposure to SPIO-labeled RL platelets in a flow chamber, revealing specific contrast to injured vascular endothelium. Arteries were subsequently longitudinally cut and are imaged with the luminal wall facing upward. Inset: TEM image of an SPIO-labeled platelet containing hundreds of SPIOs in its surface-connected open canalicular system

47.6 Photothermal OCT

Photothermal OCT (PTOCT) provides sensitivity and specificity of OCT to absorbers in a sample through active detection of photothermal heating. Photon absorption by an endogenous chromophore or exogenous contrast agent leads to a temperature rise in the surrounding environment. These local temperature changes cause thermoelastic expansion of the sample and shifts in the local index of refraction [66, 67], which in turn cause changes in the local optical path length. These small, typically nanometer-scale, local optical path length changes can be resolved with phase-sensitive OCT. Unlike fluorescence-based imaging modalities, most absorption-based contrast agents do not undergo photobleaching, allowing for constant PTOCT signal over time, even at high irradiance.

47.6.1 Theory and Instrumentation

In PTOCT, a separate laser source for photothermal heating is incorporated into the sample arm of the OCT system, either via direct, free beam coupling at the sample arm optics or through shared sample arm fiber optics. The heating laser wavelength is chosen to match the peak absorption of the desired imaging target. In most applications of PTOCT, square or sine wave amplitude modulation of the heating beam (e.g., using a mechanical optical chopper or acousto-optical modulator) is performed during temporal sampling (M-mode scanning) of each spot. An example PTOCT instrumentation diagram can be seen in Fig. 47.12, with the incorporation of an amplitude-modulated 808 nm laser into the sample arm of a spectral-domain

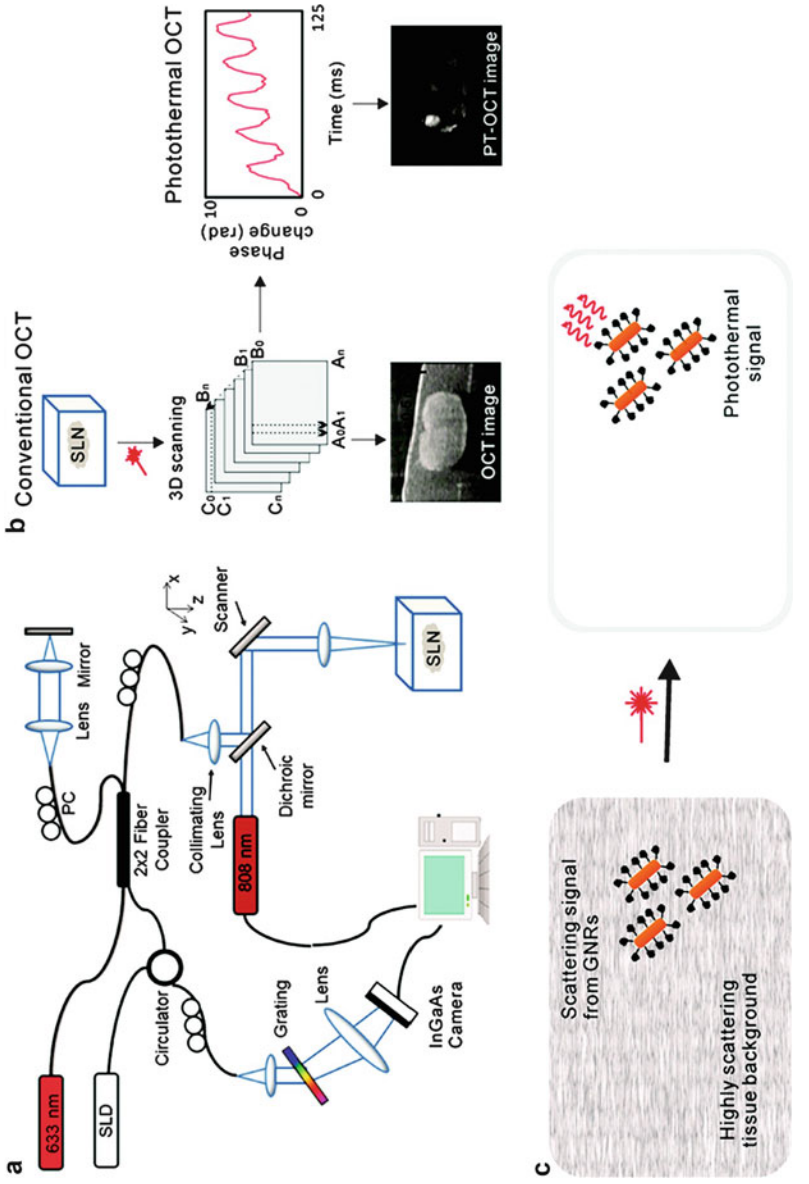

Fig. 47.12 (**a**) Experimental setup of the PTOCT system, where PC denotes the polarization controller. (**b**) Diagram of the data processing method used to image sentinel lymph nodes with PTOCT (Adapted with permission from Ref. [68]. Copyright 2011 American Chemical Society)

OCT system [68]. Amplitude modulation of the heating beam allows for digital lock-in techniques to be used during signal processing, which can detect and isolate the active heating dynamics from the passive scattering signal. Modulation frequencies as low as 25 Hz [69] and as high as 120 kHz [70] have been reported in PTOCT and PTOCM applications.

In PTOCT, the signal is isolated from an oversampled M-mode scan by obtaining the Fourier transform (in the time dimension) of the OCT phase data at each point in depth. The PTOCT signal is then defined as the magnitude of this Fourier-transformed phase data at the modulation frequency. More complex signal processing considerations are often taken into account to remove artifacts, including fifth- [69] or sixth- [71] order polynomial background subtraction of the phase data to minimize $1/f$ noise, baseline subtraction of nearby frequency components in the FFT data to account for the additive noise floor in the signal [69, 71–73], and averaging of overlapping short-time Fourier transforms over the M-mode scan to better estimate the noise floor [73]. Previous investigations into the PTOCT imaging parameters have demonstrated that the PTOCT signal increases linearly with both absorber concentration [67–69, 72–75] and photothermal laser power [69, 73, 74], decreases logarithmically with increased amplitude modulation frequency [73], and has a constant mean value but increased noise level in the presence of weak reflections in the sample [73].

47.6.2 PTOCT Applications

PTOCT has been demonstrated in vitro, ex vivo, and in vivo both with endogenous and exogenous forms of contrast. The most common use of PTOCT is to visualize ultralow concentrations of highly absorptive contrast agents in tissue and in vitro. In particular, PTOCT can exploit the rapidly advancing field of nanotechnology to image contrast agents with strong, wavelength-tunable absorption peaks.

Gold nanoparticles are the most common PTOCT contrast agents due to their biocompatibility and well-established surface modification chemistry, which can allow for specific imaging of molecular targets. In vitro molecular imaging of 60 nm diameter epidermal growth factor receptor (EGFR)-targeted gold nanospheres has been performed in agarose phantoms using a 532 nm heating laser at 25 Hz modulation, where EGFR+ cells exhibited a 300 % increase in PTOCT signal compared to EGFR cells [69]. This study also demonstrated a sensitivity of 14 ppm (*w*/*w*) to gold nanospheres within a scattering background. Although this is the only demonstration of true molecularly targeted imaging using PTOCT to date, a number of applications have used nontargeted NIR-resonant nanoparticles in systems ranging from phantoms to in vivo. Early investigations into PTOCT were performed with gold nanoshells having an SPR tuned to the near-infrared [67]. In subsequent studies with ex vivo human breast tissues, direct injections of 120 nm silica core and 16 nm gold shell nanoshells at a 5×10^9/mL concentration were visible 300–600 μm deep into the tissue using PTOCT with an 808 nm laser modulated at frequencies from 5 to 20 kHz, with 22 mW of power on the sample [71]. Gold nanorods have also generated

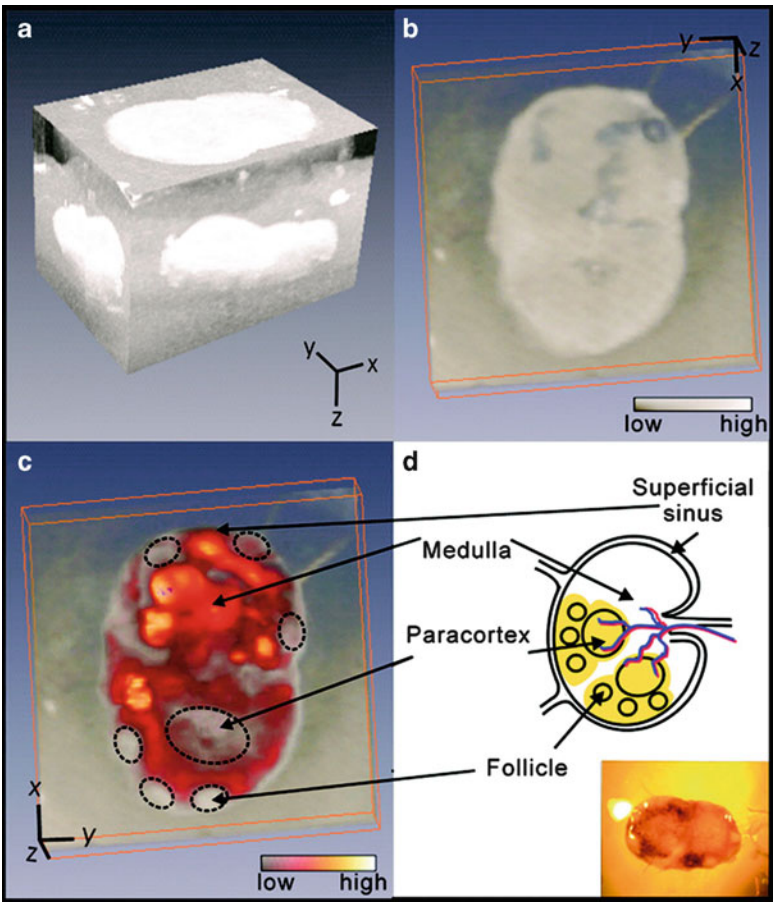

Fig. 47.13 (**a**) Three-dimensional OCT projection image of a dissected sentinel lymph node (*SLN*) at 48 h after gold nanorod injection. (**b**) 3D OCT view of SLN morphology with a cross-sectional cut at a depth of 240 μm below the top surface. (**c**) 3D PTOCT view of SLN corresponding to the cross-sectional cut displayed in (**b**) reveals structures within the SLN. (**d**) Schematic diagram and photograph of a dissected SLN. (Volume size = 2.5 × 2.5 × 2.0 mm (*x*–*y*–*z*)) (Adapted with permission from Ref. [68]. Copyright 2011 American Chemical Society)

interest as PTOCT contrast agents due to their tunability (based on the aspect ratio) and particularly narrow SPR peak. Gold nanorods coated in poly(ethylene glycol) (PEG) were found to have a significantly enhanced PTOCT signal at as low as 1 pM concentration using 50 Hz modulation of an 808 nm laser interfaced with a 1,310 nm OCT system [68]. The same system was used to image nonspecific uptake of gold nanorods in sentinel lymph nodes (SLN). After injection with PEG-coated gold nanorods, SLNs were dissected at varying time points from sacrificed mice and imaged ex vivo after being embedded in 1 % agar gel. PTOCT was able to identify the accumulation of nanorods within several SLN structures (Fig. 47.13, [68]).

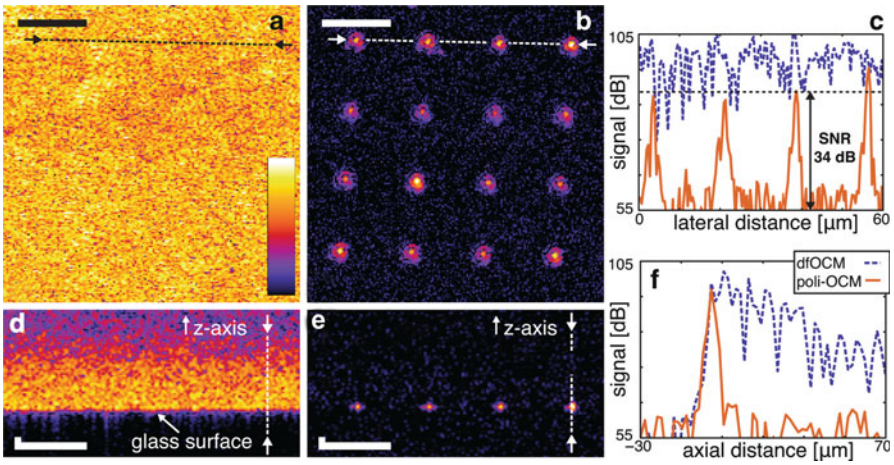

Fig. 47.14 Demonstration of the contrast selective to gold nanoparticles offered by poli-OCM, as compared to dfOCM. A square lattice of isolated 40 nm gold particles on a glass surface immersed in intravenous perfusion fluid, imaged with dfOCM (**a**), and poli-OCM (**b**). (**d**, **e**) correspond to cross sections along the *lines* indicated in (**a**, **b**). Graph (**c**) depicts the signal along the lines in (**a**, **b**), while (**f**) corresponds to the axial signal along the *line* highlighted in (**d**, **e**). Scale bars: 10 μm (Adapted with permission from Ref. [70]. Copyright 2012 Optical Society of America)

A separate study was able to image, in vivo, picomolar concentrations of PEG-coated gold nanorods directly injected into a mouse ear [73].

Applications of PTOCT are not limited to gold nanoparticles, but include any targets that have strong absorption at the wavelength of the heating laser. PTOCT has also been demonstrated using carbon nanotubes [72], indocyanine green encapsulated poly(lactic-co-glycolic) acid nanoparticles [76], gold-iron oxide nanoroses [75], and iron oxide-silica-gold multifunctional nanoprobes [77]. PTOCT has also been used to characterize hemoglobin oxygen saturation using dual-wavelength approaches to probe the absorption differences of oxy- and deoxyhemoglobin in vitro and in vivo [78, 79].

47.6.3 Recent PTOCT Advances

Recent advances in the field of PTOCT have been working toward providing quantitative molecular imaging. First, measurements of the local slope in the axial dimension of a PTOCT image has found some success in correcting for phase accumulation in PTOCT [74]. Second, a method to perform photothermal optical lock-in optical coherence microscopy (poli-OCM) has been developed for real-time photothermal imaging [70]. In poli-OCM, one creates phase modulations in the reference arm that are matched to the amplitude modulation frequency of the heating beam, resulting in a demodulated photothermal signal of the absorbers in the sample. The signal due to scatterers is then isolated from the photothermal

signal by setting the CCD integration time to a multiple of the modulation period. This provides real-time photothermal imaging without the need for temporal (M-mode) sampling or extensive digital processing. Pache et al. demonstrated single particle detection of gold nanoparticles using poli-OCM with modulation frequencies of 120 kHz while rejecting the scattering signal captured from their dark-field optical coherence microscopy (dfOCM) system (Fig. 47.14, [70]). Photothermal optical lock-in has yet to be demonstrated with a traditional OCT system, but the underlying principles remain the same.

PTOCT is a promising imaging technique for isolating absorbers in a scattering sample and thus provides specific and sensitive molecular imaging of both endogenous and exogenous contrasts. With recent advances in PTOCT optimization, demonstrations in ex vivo and in vivo samples, and incorporation of optical lock-in techniques, PTOCT promises to be not only sensitive and specific, but also a fast method for imaging absorptive contrast agents in tissue.

47.7 Conclusion

It should be evident to the reader that MCOCT can be accomplished by a wide variety of methods that each offer unique advantages, all of which should be weighed when considering a specific biomedical application. All of the methods presented here are in continued development, and we can expect to see continued progress (greater sensitivity, specificity, imaging speeds, and higher resolution) in the years to come. Also, new methods continue to emerge, such as imaging thermal diffusion of micro- and nanoprobes [80, 81], which may allow one to sense the local macromolecule concentration in bodily fluids such as mucus and blood. Fundamentally, OCT provides a unique and flexible platform for exploring new concepts in molecular imaging. Tying these imaging technology advances with concomitant advances in nanotechnology and targeted delivery makes this a rapidly changing field with many new opportunities for scientific discovery.

Acknowledgments We wish to thank our many colleagues and collaborators conducting research in this area and apologize that, due to length restrictions, we were unable to highlight more results. We acknowledge Justis Ehlers at the Cole Eye Institute, Cleveland Clinic, for aiding in Fig. 47.1. Some of the studies reported in this chapter were supported in part by a grant from the US National Institutes of Health (R01 EB009073, S. A. B.).

References

1. E.K.W. Schulte, Standardization of biological dyes and stains: pitfalls and possibilities. Histochem. Cell Biol. **95**, 319–328 (1991)
2. C. Yang, Molecular contrast optical coherence tomography: a review. Photochem. Photobiol. **81**, 215–237 (2005)
3. S.J. Oldenburg, R.D. Averitt, S.L. Westcott, N.J. Halas, Nanoengineering of optical resonances. Chem. Phys. Lett. **288**, 243–247 (1998)

4. S.A. Boppart, A.L. Oldenburg, C. Xu, D.L. Marks, Optical probes and techniques for molecular contrast enhancement in coherence imaging. J. Biomed. Opt. **10**, 41208 (2005)
5. K. Chen, Y. Liu, G. Ameer, V. Backman, Optimal design of structured nanospheres for ultrasharp light-scattering resonances as molecular imaging multilabels. J. Biomed. Opt. **10**, 024005 (2005)
6. M. Hu, J. Chen, Z.-Y. Li, L. Au, G.V. Hartland, X. Li, M. Marquez, Y. Xia, Gold nanostructures: engineering their plasmonic properties for biomedical applications. Chem. Soc. Rev. **35**, 1084–1094 (2006)
7. J.K. Barton, J.B. Hoying, C.J. Sullivan, Use of microbubbles as an optical coherence tomography contrast agent. Acad. Radiol. **9**(Suppl 1), S52–S55 (2002)
8. T.M. Lee, A.L. Oldenburg, S. Sitafalwalla, D.L. Marks, W. Luo, F.J. Toublan, K.S. Suslick, S.A. Boppart, Engineered microsphere contrast agents for optical coherence tomography. Opt. Lett. **28**, 1546–1548 (2003)
9. R. John, F.T. Nguyen, K.J. Kolbeck, E.J. Chaney, M. Marjanovic, K.S. Suslick, S.A. Boppart, Targeted multifunctional multimodal protein-shell microspheres as cancer imaging contrast agents. Mol. Imaging Biol. **14**, 17–24 (2012)
10. J.P. Ehlers, P.K. Gupta, S. Farsiu, R. Maldonado, T. Kim, C.A. Toth, P. Mruthyunjaya, Evaluation of contrast agents for enhanced visualization in optical coherence tomography. Invest. Ophthalmol. Vis. Sci. **51**, 6614–6619 (2010)
11. C.F. Bohren, D.R. Huffman, *Absorption and Scattering of Light by Small Particles* (Wiley, New York, 1983)
12. N.G. Khlebtsov, L.A. Dykman, Optical properties and biomedical applications of plasmonic nanoparticles. J. Quant. Spectrosc. Radiat. Transf. **111**, 1–35 (2010)
13. A.M. Gobin, M.H. Lee, N.J. Halas, W.D. James, R.A. Drezek, J.L. West, Near-infrared resonant nanoshells for combined optical imaging and photothermal cancer therapy. Nano Lett. **7**, 1929–1934 (2007)
14. J.C.Y. Kah, T.H. Chow, B.K. Ng, S.G. Razul, M. Olivo, C.J.R. Sheppard, Concentration dependence of gold nanoshells on the enhancement of optical coherence tomography images: a quantitative study. Appl. Opt. **48**, D96–D108 (2009)
15. M. Kirillin, M. Shirmanova, M. Sirotkina, M. Bugrova, B. Khlebtsov, E. Zagaynova, Contrasting properties of gold nanoshells and titanium dioxide nanoparticles for optical coherence tomography imaging of skin: Monte Carlo simulations and in vivo study. J. Biomed. Opt. **14**, 021017 (2009)
16. H. Maeda, The enhanced permeability and retention (EPR) effect in tumor vasculature: the key role of tumor-selective macromolecular drug targeting. Adv. Enzym. Regul. **41**, 189–207 (2001)
17. C. Xu, P.S. Carney, S.A. Boppart, Wavelength-dependent scattering in spectroscopic optical coherence tomography. Opt. Express **13**, 5450–5462 (2005)
18. U. Morgner, W. Drexler, F.X. Kärtner, X.D. Li, C. Pitris, E.P. Ippen, J.G. Fujimoto, Spectroscopic optical coherence tomography. Opt. Lett. **25**, 111–113 (2000)
19. C.H. Yang, L.E.L. McGuckin, J.D. Simon, M.A. Choma, B.E. Applegate, J.A. Izatt, Spectral triangulation molecular contrast optical coherence tomography with indocyanine green as the contrast agent. Opt. Lett. **29**, 2016–2018 (2004)
20. A.L. Oldenburg, C. Xu, S.A. Boppart, Spectroscopic optical coherence tomography and microscopy. Sel. Top. Quant. Electron. IEEE J. **13**, 1629–1640 (2007)
21. C. Xu, F. Kamalabadi, S.A. Boppart, Comparative performance analysis of time-frequency distributions for spectroscopic optical coherence tomography. Appl. Opt. **44**, 1813–1822 (2005)
22. F.E. Robles, C. Wilson, G. Grant, A. Wax, Molecular imaging true-colour spectroscopic optical coherence tomography. Nat. Photonics **5**, 744–747 (2011)
23. B. Hermann, K. Bizheva, A. Unterhuber, B. Povazay, H. Sattmann, L. Schmetterer, A. Fercher, W. Drexler, Precision of extracting absorption profiles from weakly scattering media with spectroscopic time-domain optical coherence tomography. Opt. Express **12**, 1677–1688 (2004)

24. T. Støren, A. Røyset, L.O. Svaasand, T. Lindmo, Functional imaging of dye concentration in tissue phantoms by spectroscopic optical coherence tomography. J. Biomed. Opt. **10**, 024037 (2005)
25. J. Yi, J. Gong, X. Li, Analyzing absorption and scattering spectra of micro-scale structures with spectroscopic optical coherence tomography. Opt. Express **17**, 13157–13167 (2009)
26. C. Xu, J. Ye, D.L. Marks, S.A. Boppart, Near-infrared dyes as contrast-enhancing agents for spectroscopic optical coherence tomography. Opt. Lett. **29**, 1647–1649 (2004)
27. D.J. Faber, E.G. Mik, M.C.G. Aalders, T.G. van Leeuwen, Toward assessment of blood oxygen saturation by spectroscopic optical coherence tomography. Opt. Lett. **30**, 1015–1017 (2005)
28. Y.L. Li, K. Seekell, H.K. Yuan, F.E. Robles, A. Wax, Multispectral nanoparticle contrast agents for true-color spectroscopic optical coherence tomography. Biomed. Opt. Express **3**, 1914–1923 (2012)
29. A.L. Oldenburg, M.N. Hansen, T.S. Ralston, A. Wei, S.A. Boppart, Imaging gold nanorods in excised human breast carcinoma by spectroscopic optical coherence tomography. J. Mater. Chem. **19**, 6407–6411 (2009)
30. H. Cang, T. Sun, Z.Y. Li, J.Y. Chen, B.J. Wiley, Y.N. Xia, X.D. Li, Gold nanocages as contrast agents for spectroscopic optical coherence tomography. Opt. Lett. **30**, 3048–3050 (2005)
31. X. Huang, I.H. El-Sayed, M.A. El-Sayed, *Applications of Gold Nanorods for Cancer Imaging and Photothermal Therapy*. vol. 624, ed. by S.R. Grobmyer, B.M. Moudgil (Humana Press, New York, 2010), pp. 343–357
32. B.E. Applegate, J.A. Izatt, Molecular imaging of endogenous and exogenous molecular chromophores with ground state recovery pump-probe optical coherence tomography. Opt. Express **14**, 9142–9155 (2006)
33. K.D. Rao, M.A. Choma, S. Yazdanfar, A.M. Rollins, J.A. Izatt, Molecular contrast in optical coherence tomography by use of a pump-probe technique. Opt. Lett. **28**, 340–342 (2003)
34. M.I. Canto, Methylene blue chromoendoscopy for Barrett's esophagus: coming soon to your GI unit? Gastrointest. Endosc. **54**, 403–409 (2001)
35. C. Tanielian, C. Wolff, Determination of the parameters controlling singlet oxygen production via oxygen and heavy-atom enhancement of triplet yields. J. Phys. Chem. **99**, 9831–9837 (1995)
36. O. Carrasco-Zevallos, R.L. Shelton, W. Kim, J. Pearson, B.E. Applegate, In vivo pump-probe optical coherence tomography imaging in Xenopus laevis. J. Biophoton. (2013) doi:10.1002/jbio.201300119
37. C.H. Yang, M.A. Choma, L.E. Lamb, J.D. Simon, J.A. Izatt, Protein-based molecular contrast optical coherence tomography with phytochrome as the contrast agent. Opt. Lett. **29**, 1396–1398 (2004)
38. D. Jacob, R.L. Shelton, B.E. Applegate, Fourier domain pump-probe optical coherence tomography imaging of melanin. Opt. Express **18**, 12399–12410 (2010)
39. Q. Wan, B.E. Applegate, Multiphoton coherence domain molecular imaging with pump-probe optical coherence microscopy. Opt. Lett. **35**, 532–534 (2010)
40. A.L. Oldenburg, J.R. Gunther, S.A. Boppart, Imaging magnetically labeled cells with magnetomotive optical coherence tomography. Opt. Lett. **30**, 747–749 (2005)
41. A.L. Oldenburg, V. Crecea, S.A. Rinne, S.A. Boppart, Phase-resolved magnetomotive OCT for imaging nanomolar concentrations of magnetic nanoparticles in tissues. Opt. Express **16**, 11525–11539 (2008)
42. A.L. Oldenburg, F.J-J. Toublan, K.S. Suslick, A. Wei, S.A. Boppart, Magnetomotive contrast for in vivo optical coherence tomography. Opt. Express **13**, 6597–6614 (2005)
43. A.L. Oldenburg, C.M. Gallippi, F. Tsui, T.C. Nichols, K.N. Beicker, R.K. Chhetri, D. Spivak, A. Richardson, T.H. Fischer, Magnetic and contrast properties of labeled platelets for magnetomotive optical coherence tomography. Biophys. J. **99**, 2374–2383 (2010)
44. F.J. Toublan, S.A. Boppart, K.S. Suslick, Tumor targeting by surface-modified protein microspheres. J. Am. Chem. Soc. **128**, 3472–3473 (2006)

45. R. Ross, Atherosclerosis – an inflammatory disease – reply. N. Engl. J. Med. **340**, 1929–1929 (1999)
46. S.K. Nadkarni, B.E. Bouma, J. de Boer, G.J. Tearney, Evaluation of collagen in atherosclerotic plaques: the use of two coherent laser-based imaging methods. Lasers Med. Sci. **24**, 439–445 (2009)
47. E. Regar, T.G.V. Leeuwen, P.W. Serruys, *Optical Coherence Tomography in Cardiovascular Research* (Informa Healthcare, Oxon, 2007)
48. M.J. Suter, S.K. Nadkarni, G. Weisz, A. Tanaka, F.A. Jaffer, B.E. Bouma, G.J. Tearney, Intravascular optical imaging technology for investigating the coronary artery. J. Am. Coll. Cardiol. Img. **4**, 1022–1039 (2011)
49. G.J. Tearney, S.A. Boppart, B.E. Bouma, M.E. Brezinski, N.J. Weissman, J.F. Southern, J.G. Fujimoto, Scanning single-mode fiber optic catheter-endoscope for optical coherence tomography. Opt. Lett. **21**, 543–545 (1996)
50. Z. Wang, D. Chamie, H.G. Bezerra, H. Yamamoto, J. Kanovsky, D.L. Wilson, M.A. Costa, A.M. Rollins, Volumetric quantification of fibrous caps using intravascular optical coherence tomography. Biomed. Opt. Express **3**, 1413–1426 (2012)
51. H. Yoo, J.W. Kim, M. Shishkov, E. Namati, T. Morse, R. Shubochkin, J.R. McCarthy, V. Ntziachristos, B.E. Bouma, F.A. Jaffer, G.J. Tearney, Intra-arterial catheter for simultaneous microstructural and molecular imaging in vivo. Nat. Med. **17**, 1680–1684 (2011)
52. S. Peng, Y. Xiong, K. Li, M. He, Y. Deng, L. Chen, M. Zou, W. Chen, Z. Wang, J. He, L. Zhang, Clinical utility of a microbubble-enhancing contrast ("SonoVue") in treatment of uterine fibroids with high intensity focused ultrasound: a retrospective study. Eur. J. Radiol. **81**, 3832–3838 (2012)
53. O. Dormond, L. Ponsonnet, M. Hasmim, A. Foletti, C. Ruegg, Manganese-induced integrin affinity maturation promotes recruitment of alpha V beta 3 integrin to focal adhesions in endothelial cells: evidence for a role of phosphatidylinositol 3-kinase and Src. Thromb. Haemost. **92**, 151–161 (2004)
54. R.C. Richie, J.O. Swanson, Breast cancer: a review of the literature. J. Insur. Med. **35**, 85–101 (2003)
55. J. Sariego, Breast cancer in the young patient. Am. Surg. **76**, 1397–1400 (2010)
56. A. Ocana, A. Pandiella, Targeting HER receptors in cancer. Curr. Pharm. Des. **19**(5), 808–817 (2012)
57. R. John, R. Rezaeipoor, S.G. Adie, E.J. Chaney, A.L. Oldenburg, M. Marjanovic, J.P. Haldar, B.P. Sutton, S.A. Boppart, In vivo magnetomotive optical molecular imaging using targeted magnetic nanoprobes. Proc. Natl. Acad. Sci. U. S. A. **107**, 8085–8090 (2010)
58. W. Cai, X. Chen, Anti-angiogenic cancer therapy based on integrin $\alpha_V\beta_3$ antagonism. Anticancer Agents Med. Chem. **6**, 407–428 (2006)
59. O. Grinberg, M. Hayun, B. Sredni, A. Gedanken, Characterization and activity of sonochemically-prepared BSA microspheres containing taxol – an anticancer drug. Ultrason. Sonochem. **14**, 661–666 (2007)
60. N. Mackman, R.E. Tilley, N.S. Key, Role of the extrinsic pathway of blood coagulation in hemostasis and thrombosis. Arterioscler. Thromb. Vasc. Biol. **27**, 1687–1693 (2007)
61. M. Gawaz, H. Langer, A.E. May, Platelets in inflammation and atherogenesis. J. Clin. Invest. **115**, 3378–3384 (2005)
62. J.G. White, Platelets are covercytes, not phagocytes: uptake of bacteria involves channels of the open canalicular system. Platelets **16**, 121–131 (2005)
63. A.L. Oldenburg, G. Wu, D. Spivak, F. Tsui, A.S. Wolberg, T.H. Fischer, Imaging and elastometry of blood clots using magnetomotive optical coherence tomography and labeled platelets. Sel. Top. Quant. Electron. IEEE J. **18**, 1100–1109 (2012)
64. K. Aurich, M.-C. Spoerl, B. Fürll, R. Sietmann, A. Greinacher, N. Hosten, W. Weitschies, Development of a method for magnetic labeling of platelets. Nanomedicine: Nanotechnol. Biol. Med. **8**, 537–544 (2012)

65. M.S. Read, R.L. Reddick, A.P. Bode, D.A. Bellinger, T.C. Nichols, K. Taylor, S.V. Smith, D.K. McMahon, T.R. Griggs, K.M. Brinkhous, Preservation of hemostatic and structural properties of rehydrated lyophilized platelets: potential for long-term storage of dried platelets for transfusion. Proc. Natl. Acad. Sci. U. S. A. **92**, 397–401 (1995)
66. J. Kim, J. Oh, T.E. Milner, Measurement of optical path length change following pulsed laser irradiation using differential phase optical coherence tomography. J. Biomed. Opt. **11**, 041122 (2006)
67. D.C. Adler, S.W. Huang, R. Huber, J.G. Fujimoto, Photothermal detection of gold nanoparticles using phase-sensitive optical coherence tomography. Opt. Express **16**, 4376–4393 (2008)
68. Y. Jung, R. Reif, Y.G. Zeng, R.K. Wang, Three-dimensional high-resolution imaging of gold nanorods uptake in sentinel lymph nodes. Nano Lett. **11**, 2938–2943 (2011)
69. M.C. Skala, M.J. Crow, A. Wax, J.A. Izatt, Photothermal optical coherence tomography of epidermal growth factor receptor in live cells using immunotargeted gold nanospheres. Nano Lett. **8**, 3461–3467 (2008)
70. C. Pache, N.L. Bocchio, A. Bouwens, M. Villiger, C. Berclaz, J. Goulley, M.I. Gibson, C. Santschi, T. Lasser, Fast three-dimensional imaging of gold nanoparticles in living cells with photothermal optical lock-in optical coherence microscopy. Opt. Express **20**, 21385–21399 (2012)
71. C. Zhou, T.H. Tsai, D.C. Adler, H.C. Lee, D.W. Cohen, A. Mondelblatt, Y.H. Wang, J.L. Connolly, J.G. Fujimoto, Photothermal optical coherence tomography in ex vivo human breast tissues using gold nanoshells. Opt. Lett. **35**, 700–702 (2010)
72. J.M. Tucker-Schwartz, T. Hong, D.C. Colvin, Y.Q. Xu, M.C. Skala, Dual-modality photothermal optical coherence tomography and magnetic-resonance imaging of carbon nanotubes. Opt. Lett. **37**, 872–874 (2012)
73. J.M. Tucker-Schwartz, T.A. Meyer, C.A. Patil, C.L. Duvall, M.C. Skala, In vivo photothermal optical coherence tomography of gold nanorod contrast agents. Biomed. Opt. Express **3**, 2881–2895 (2012)
74. G.Y. Guan, R. Reif, Z.H. Huang, R.K.K. Wang, Depth profiling of photothermal compound concentrations using phase sensitive optical coherence tomography. J. Biomed. Opt. **16**, 126003 (2011)
75. A.S. Paranjape, R. Kuranov, S. Baranov, L.L. Ma, J.W. Villard, T.Y. Wang, K.V. Sokolov, M.D. Feldman, K.P. Johnston, T.E. Milner, Depth resolved photothermal OCT detection of macrophages in tissue using nanorose. Biomed. Opt. Express **1**, 2–16 (2010)
76. H.M. Subhash, H. Xie, J.W. Smith, O.J.T. McCarty, Optical detection of indocyanine green encapsulated biocompatible poly (lactic-co-glycolic) acid nanoparticles with photothermal optical coherence tomography. Opt. Lett. **37**, 981–983 (2012)
77. Y.R. Jung, G.Y. Guan, C.W. Wei, R. Reif, X.H. Gao, M. O'Donnell, R.K.K. Wang, Multifunctional nanoprobe to enhance the utility of optical based imaging techniques. J. Biomed. Opt. **17**, 016015 (2012)
78. R.V. Kuranov, S. Kazmi, A.B.. McElroy, J.W. Kiel, A.K. Dunn, T.E. Milner, T.Q. Duong, In vivo depth-resolved oxygen saturation by dual-wavelength photothermal (DWP) OCT. Opt. Express **19**, 23831–23844 (2011)
79. R.V. Kuranov, J.Z. Qiu, A.B.. McElroy, A. Estrada, A. Salvaggio, J. Kiel, A.K. Dunn, T.Q. Duong, T.E. Milner, Depth-resolved blood oxygen saturation measurement by dual-wavelength photothermal (DWP) optical coherence tomography. Biomed. Opt. Express **2**, 491–504 (2011)
80. J. Kalkman, R. Sprik, T.G. van Leeuwen, Path-length-resolved diffusive particle dynamics in spectral-domain optical coherence tomography. Phys. Rev. Lett. **105**, 198302 (2010)
81. R.K. Chhetri, K.A. Kozek, A.C. Johnston-Peck, J.B. Tracy, A.L. Oldenburg, Imaging three-dimensional rotational diffusion of plasmon resonant gold nanorods using polarization-sensitive optical coherence tomography. Phys. Rev. E Stat. Nonlinear Soft Matter Phys. **83**, 040903 (2011)

Optical Tissue Clearing to Enhance Imaging Performance for OCT

48

Ruikang K. Wang and Valery V. Tuchin

Keywords

Imaging contrast • Imaging depth • Optical clearing • Optical coherence tomography • Osmotically active chemical agents • Tissue scattering

48.1 Introduction

Over the last decade, noninvasive or minimally invasive spectroscopy and imaging techniques have witnessed widespread and exciting applications in biomedical diagnostics. Optical techniques that use the intrinsic optical properties of biological tissues, such as light scattering, absorption, polarization, and fluorescence, have many advantages over the conventional *x*-ray computed tomography, MRI, and ultrasound imaging in terms of safety, costs, contrast, and resolution features. Time-resolved, phase-resolved, and frequency-resolved optical techniques are capable of deep imaging of the tissues that could provide information of tissue macrostructures and oxygenation states and detect brain and breast tumors [1, 2], whereas confocal microscopy and multiphoton excitation imaging have been used to show cellular and subcellular details of superficial living tissues [3, 4]. However,

R.K. Wang (✉)
Department of Automation Engineering, Northeastern University at Qinhuangdao, Hebei, Peoples' Republic of China

Department of Bioengineering, University of Washington, Seattle, WA, USA
e-mail: wangrk@uw.edu

V.V. Tuchin
Research–Educational Institute of Optics and Biophotonics, Saratov State University, Saratov, Russia

Laboratory of Laser Diagnostics of Technical and Living Systems, Institute of Precise Mechanics and Control RAS, Saratov, Russia

Optoelectronics and Measurement Techniques Laboratory, University of Oulu, Oulu, Finland

© Springer International Publishing Switzerland 2015

W. Drexler, J.G. Fujimoto (eds.), *Optical Coherence Tomography*,
DOI 10.1007/978-3-319-06419-2_49

most biological tissues strongly scatter the probing light within the visible and near-infrared range, i.e., the therapeutic and/or diagnostic optical window. The multiple scattering of light is detrimental to imaging contrast and resolution, which limits the effective probing depth to several hundred micrometers for the confocal microscopy and multiphoton excitation imaging techniques. However, some clinical applications, such as early cancer diagnosis, require the visualization of intermediate depth range of the localized anatomical structures with micron-scale resolution.

We have seen from the previous chapters that optical coherence tomography (OCT) fills a nice niche in this regard. Briefly, it uses low-coherence interferometer to image internal tissue structures to the depth up to 2 mm with micron-scale resolution [5–9]. Although its first applications in medicine were reported less than a decade ago [10–13], it stems from the early work on white-light interferometry where the primary purpose was the development of optical coherence-domain reflectometry (OCDR), a one-dimensional optical ranging technique [14]. OCDR was inspired originally for finding faults in fiber-optic cables and network components and measuring distances in metrology [15]. Because it is sensitive to the discontinuity of refractive index interfaces, it was soon realized that such technique is able to probe the microstructures of the eye [16–18] and other biological tissues [19]. Perhaps, the biggest advantage of this technique for the applications in biomedicine is its superb axial resolution, which is achieved by exploiting the short temporal coherence of a broadband light source. Migrated the basic concepts from ultrasound imaging and recently developed confocal microscopy, OCDR was quickly extended to section the biological tissues [5] through the raster scanning of the focused beam spot, which was subsequently termed as optical coherence tomography. OCT enables microscopic structures in biological tissue to be visualized at a depth beyond the reach of conventional confocal microscopes. Probing depth exceeding 2 cm has been reported for transparent tissues, including the eye [20] and frog embryo [21]. To date, successful stories of in vitro and in vivo OCT applications in medicine have been delivered in a wide branch of areas, for example, ophthalmology [22], gastrointestinal tract [23–27], dental [28], dermatology [29–31], etc. Please refer to the other chapters in this book for these aspects of OCT applications.

Although exciting when screening the OCT developments and applications to date, its fundamental limitation of imaging depth has somehow hindered its broader applications in biomedicine and other applications. This is because OCT relies on the penetration and backscattering of light into tissue to construct cross-sectional, tomographic images. It collects the backscattered photons that have experienced less scattering, i.e., ballistic or least-scattered photons. However, unlike the transparent ocular organs where OCT found its most successful applications [20], there is no evidence that an OCT imaging depth beyond 2 mm for opaque biological tissues is possible [32]. This is largely due to the multiple scattering inherent in the interactions between the probing light and the targeted tissue, which limits light penetration into the tissue and, therefore, prevents the imaging of deep microstructures. Furthermore, the multiple scattering of photons inside the tissue tends to blur the targeted tissue boundaries, leading to the degradation of the imaging contrast of

the resulted OCT images. Thus, it is reasonable to state that the multiple scattering could degrade signal attenuation and localization, leading to an image artifact that reduces the imaging depth and degrades the signal localization, i.e., the image contrast. To improve the imaging capabilities, the multiple scattering of tissue must be, therefore, reduced.

Tissue as a scattering medium shows all optical effects that are characteristic to turbid physical system. It is well known that the turbidity of a dispersive physical system can be effectively controlled using immersion effect matching of refractive indices of the scatters and the ground material [33–35]. The living tissue allows one to control its optical (scattering) properties using various physical and chemical actions such as compression, stretching, dehydration, coagulation, UV irradiation, exposure to low temperature, and impregnation by chemical solutions, gels, and oils [36–49]. Such methods of controlling optical properties of tissue have been explored to enhance the optical imaging capabilities of OCT [27, 50–56]. The possible mechanisms of enhancing OCT imaging depth and contrast have been suggested [27, 50–62].

This chapter is designed to introduce the effects of light scattering on OCT and discuss how multiple scattering of tissue would an impact on the OCT imaging performances. We then elucidate the developments of techniques in reducing the overwhelming multiple scattering effects and improving imaging capabilities by the use of immersion techniques.

48.2 Theoretical Aspects

Although it has been described in detail in the previous chapters, it is necessary here to revisit briefly the theoretical treatments of OCT sensing the biological tissue and its relevant aspects on the light scattering in tissue that produces the imaging contrast and depth in OCT.

48.2.1 Low-Coherence Interferometry

OCT is an interferometric technique, relying on interference between a split and later recombined broadband optical field. We consider a conventional time domain OCT device based on a Michelson interferometer setup, as shown in Fig. 48.1. In this setup, the depth profile is provided by the scanning of optical delay between the reference and sample arm (or A-scan) that is usually achieved by the scanning of a mirror mounted in the reference arm. The transversal information is obtained by recording A-scans at several adjacent sample positions. In this section we discuss only the depth scans.

A low coherent light source, e.g., an SLD, emits a light beam with short coherence length towards the Michelson interferometer, where it is first split by a beam splitter. The split field travels in a reference path, reflecting from a reference mirror, and also in a sample path where it is reflected from multiple layers within a sample. Due to

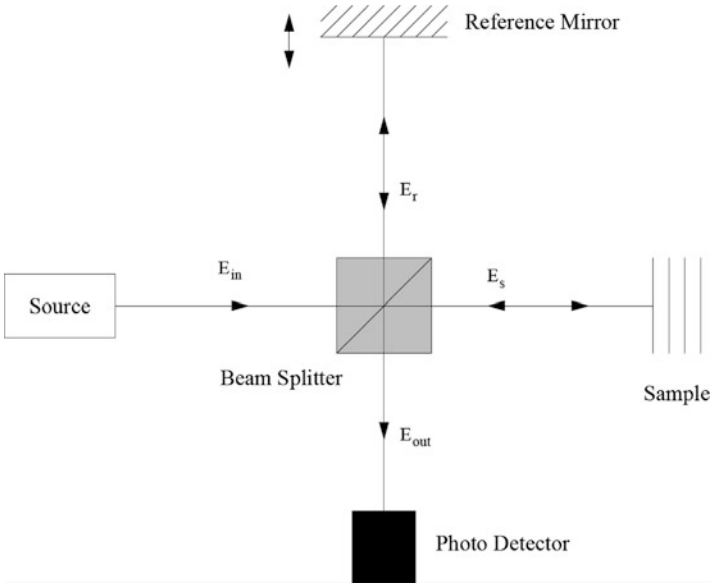

Fig. 48.1 Low-coherence Michelson interferometer

the broadband nature of the light, interference between the optical fields is only observed when the reference and sample arm optical lengths are matched to within the coherence length of the light. Therefore, the depth (axial) resolution of an OCT system is determined by the temporal coherence of the light source. Sharp refractive index variations between layers in the sample medium manifest themselves as corresponding peaks in the interference pattern.

To describe OCT mathematically, it is useful to express the electric field $E(\omega, t)$ as a complex exponential.

$$E(\omega, t) = s(\omega)\exp[-i(\omega t + kz)]. \tag{48.1}$$

This is a plane-polarized solution to the wave equation, with source field amplitude spectrum $s(\omega)$, frequency ω, and time variation t. The second term in the exponential, in terms of wave number k and distance z, simply accounts for phase accumulated throughout the interferometer. Since the input phase is arbitrary and the interferometer only measures the relative output phase between the two optical paths, the phase term can be dropped from the input electric field. The field in each part of the interferometer is denoted by subscripts as follows: E_{out}, E_{r}, and E_{s} corresponding to the input, output, and reference and sample arm optical fields, respectively. The sample has a frequency-domain response function $H(\omega)$ that describes its internal structure and accounts for phase accumulation therein. Optical detectors are square law intensity detection devices, where the recorded intensity is proportional to a time average over the electric field multiplied by its complex

conjugate. Assume that the interferometer operates in air, then the output from the detector is

$$I(\omega, \Delta z) = \left\langle E_{\text{out}}(\omega, t, \Delta z) E^{*}_{\text{out}}(\omega, t, \Delta z) \right\rangle. \tag{48.2}$$

The angled brackets denote a time average, given by

$$I(\omega, \Delta z) = \lim_{T \to \infty} \frac{1}{2T} \int_{-T}^{T} E_{\text{out}}(\omega, t, \Delta z) E^{*}_{\text{out}}(\omega, t, \Delta z) dt. \tag{48.3}$$

It can be shown that the intensity is a sum of three terms

$$I(\omega, \Delta z) = \left\langle E_r E_r^{*} \right\rangle + \left\langle E_s E_s^{*} \right\rangle + 2\Re\left\{ \left\langle E_s E_r^{*} \right\rangle \right\}. \tag{48.4}$$

Here, $\Delta z = \Delta t c / n_{\text{air}}$ is the mismatch distance between the reference and sample arm. The first two terms can be identified as "self-interference" that is not relevant to the OCT imaging and therefore is dropped in the following treatment. The last term is the real part (denoted by $\Re$) of the complex "cross-interference" that is the interest of concern. Making the relevant mathematical operations and substituting for the field spectrum $s(\omega)$ a corresponding intensity spectrum $S(\omega) = |s(\omega)|^2$, the frequency and path difference-dependent intensity is given by

$$I(\omega, \Delta z) = \Re\{S(\omega) H(\omega) \exp[-i\phi(\Delta z)]\} \tag{48.5}$$

where $\phi(\Delta z)$ is the phase accumulated in translating the reference mirror by a geometric distance Δz, $\phi(\Delta z) = 2\omega n_{\text{air}} \Delta z / c$. The sample response function $H(\omega)$ describes the overall reflection from all structures distributed in the z direction within the sample and is given by

$$H(\omega) = \int_{-\infty}^{\infty} r(\omega, z) e^{i2n(\omega, z)\omega z / c} dz. \tag{48.6}$$

The function $n(\omega, z)$ is the frequency-dependent, depth-varying group refractive index and $r(\omega, z)$ is a function of the reflected photons escaped from the sample at depth z that bears the structure features of the sample. The exponential term accounts for phase accumulated by the multiple optical paths within the sample.

From Eq. 48.6 it is evident that information about the optical structure of the sample can be obtained from measurements in both the time and frequency domains. Clearly the imaging depth and contrast are related to the function $r(\omega,z)$. Assuming that the sample is transparent consisting of N multiple layers that do not absorb and scatter the incoming light, $r(\omega, z)$ can be simplified as the

reflectivity of each layer, r_j (j = 1,2,..., N), that can be determined by the application of Fresnel's equations:

$$r_j = \frac{n_{j+1} - n_j}{n_{j+1} + n_j}. \tag{48.7}$$

Thus, for such a simple multilayered sample, the sample response function can be modeled as a summation over N individual layers and assuming negligible dispersion [9]

$$H(\omega) = \sum_{1}^{N} r_j(\omega) \exp\left\{ i2\frac{\omega}{c} \sum_{i=1}^{j} (n_i z_i) \right\} \tag{48.8}$$

Here, z_i is the thickness of the ith layer with a group refractive index n_i. However, it will never be the case for the biological tissues where there are almost no planar boundaries, i.e., the interfaces distinguished by the refractive index. And more important, there are other optical properties of tissue that are detrimental to the OCT imaging of microstructures inside the tissue. The most notable optical properties that are responsible for degrading the imaging depth and contrast are the absorption and scattering. It is reasonable to consider that biological tissue has depth-varying distribution of absorption and scattering. Thus, the sample response function will be modulated by the local optical properties. For the case of only one scatter within the coherence volume, the sample response function from this particular scatter at the depth z can be expressed as the multiplication of backscattering profile $r_b(\omega, z)$ and the accumulated attenuation $r_a(\omega, z)$ along the optical path in the sample before that scatter, such that

$$r(\omega, z) = r_a(\omega, z) r_b(\omega, z). \tag{48.9}$$

The accumulated attenuation $r_a(\omega, z)$ along the optical path has both scattering and absorption contributions. In simple cases, it follows Beer's law:

$$r_a(\omega, z) = \exp\left\{ -2\int_0^z \left[\mu_a(\omega, x) + \mu_s(\omega, x) dx \right\} \right. \tag{48.10}$$

Here, $\mu_a(\omega, z)$ and $\mu_s(\omega, z)$ are wavelength dependent and spatially varying absorption and scattering coefficients of the biological sample, respectively. The backscattering coefficient at depth z, $r_b(\omega, z)$ is determined by the local refractive index variation that gives the imaging contrast of the final OCT image. Therefore, the sample response function at depth z can now be expressed by

$$H(\omega, z) = r_b(\omega, z) \exp\left\{ -2\int_0^z \left[\mu_a(\omega, x) + \mu_s(\omega, x) dx \right\} \exp\left\{ i2\frac{\omega}{c} \int_0^z n(\omega, x) x dx \right\}. \right. \tag{48.11}$$

Thus, the explanation of OCT imaging contrast and depth can be decoupled from the above equation, where the imaging contrast is provided by the local backscattering coefficient, $r_b(\omega, z)$, and the imaging depth is determined by the attenuation coefficient of the targeted sample. In particular, the imaging contrast at a certain depth z is severely affected by the accumulated light attenuation before the depth z. That is to say, if there is no attenuation of light before the depth z, theoretically the imaging depth z can approach infinity while the imaging contrast is provided by the true local reflectivity of the sample. However, as we are dealing with the biological tissue which is highly scattering in nature, the imaging depth would be determined by the point at which the light is attenuated to the limit of the system noise floor. Thus, the weaker the light attenuation before the depth z, the higher the imaging contrast at the depth z and the further the light can reach beyond z.

48.2.2 Light Scattering in Tissue

As explained in the previous section, the OCT imaging depth and contrast are affected by the total spectral-dependent attenuation coefficient of the sample. That is to say, the depth of penetration for the light into a biological tissue depends on the scattering characteristics and absorptivity of the tissue. To simplify the discussion, here we assume that the absorption and scattering coefficient of the sample are not wavelength dependent. Further, as the OCT imaging is usually performed in the near-infrared region of spectrum, compared to the scattering effect the absorption is relatively small and is therefore not discussed in the following sections. However, this is by no means to say that the absorption is not a factor in influencing OCT imaging performance. Please refer to the other chapters in this book, particularly the spectroscopic OCT, for details of exciting usage of OCT to sense the absorption in tissue, thereby the molecular-sensitive detection.

Optically, tissue can be described as a spatial distribution of refractive index on the microscopic scale that could be classified into those of the extracellular and intracellular components [63–65]. The local refractive index within the tissue can vary from anywhere within the background refractive index, i.e., 1.34 and 1.50 depending on what type of soft tissue is concerned. It is this variation of refractive index distribution within the tissue that causes a strong light scattering. Figure 48.2 shows a hypothetical index profile formed by measuring the refractive index along a line in an arbitrary direction through a volume of tissue and corresponding to the statistical mean index profile. The widths of the peaks in the actual index profile are proportional to the diameters of the elements, and their heights depend on the refractive index of each element relative to that of its surroundings. This is the origin of the tissue-discrete particle model. In accordance with this model, the index variations may be represented by a statistically equivalent volume of discrete particles having the same index but different sizes.

To describe theoretically the optical scattering in tissues, attempts have been made using the particle model with some success [63, 64]. Based on the model,

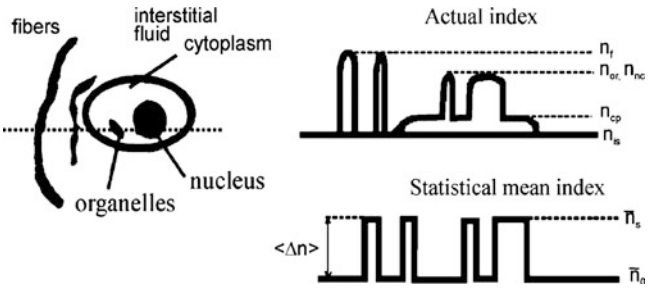

Fig. 48.2 Spatial variations of the refractive index of a soft tissue. A hypothetical index profile through several tissue components is shown, along with the profile through a statistically equivalent volume of homogeneous particles. The indices of refraction labeling of the profile are defined in the text [63, 66]

the biological tissue is treated as that consisting of the discrete scattering centers with different sizes randomly distributed in the background media. According to the Rayleigh-Gans approximation, the reduced scattering, $\mu_s' = \mu_s(1 - g)$, of turbid media is related to the reduced cross section, σ_s', and the total number of scattering particles per unit volume, i.e., number density, ρ:

$$\mu_s' = \sum_{i=1}^{n} \rho_i \sigma_{si}' = \sum_{i=1}^{n} \frac{3\varphi_i}{4\pi a_i^3} \sigma_{si}' \tag{48.12}$$

and

$$\sigma_{si}' = \frac{9}{256\pi} \left| \frac{m_i^2 - 1}{m_i^2 + 2} \right|^2 \left(\frac{\lambda}{n_0} \right)^2 \int_0^{\pi} (\sin u_i - u_i \cos u_i)^2 \frac{(1 + \cos^2\theta) \sin \theta (1 - \cos\theta)}{\sin^6(\theta/2)} d\theta \tag{48.13}$$

where $u_i = 2(2\pi a_i n_0/\lambda)\sin(\theta/2)$, $m_i = n_{si}/n_0$ with n_{si} and n_0 being the refractive indices of the ith scattering centers and background medium, φ_i the volume fraction of the ith particles, and a_i the radius of the ith scatterer. This equation is valid for non-interacting Mie scatterers, $g > 0.9$, $5 < 2\pi a/\lambda < 50$, and $1 < m < 1.1$.

It can be seen that the reduced scattering coefficient of the scattering medium is dependent on both the refractive index ratio, m_i, and the size of the scattering centers. A study by Schmitt and Kumar [66] reveals that the spectrum of index variation exhibits a power law behavior for spatial frequencies from 0.5 to 5 μm^{-1}. In other words, they found evidence for a broad distribution of scatters in tissue cells with sizes ranging from 0.2 to 2 μm. Studies by Beauvoit et al. [40] and Mourant et al. [67] revealed that the size of scattering centers varies in radius from less than 0.2 μm to more than 1 μm. Thus, the particles inside the tissue with sizes in microscopic scale are mainly responsible for the light scattering.

The refractive indices of tissue structure elements, such as fibrils, interstitial medium, nuclei, cytoplasm, organelles, and the tissue itself can be derived using the law of Gladstone and Dale, which states that the resulting value represents an average of the refractive indices of the components related to their volume fractions

$$\overline{n} = \sum_{1}^{n} n_i f_i, \qquad \sum_{i} f_i = 1 \tag{48.13}$$

where n_i and f_i are the refractive index and volume fraction of the individual components, respectively, and N is the number of components. The statistical mean index profile in Fig. 48.1 illustrates the nature of the approximation implied by this model. According to Eq. 48.13, the average background index is defined as the weighted average of the refractive indices of the cytoplasm and the interstitial fluid, n_{cp} and n_{is}, as

$$\overline{n}_0 = f_{cp} n_{cp} + \left(1 - f_{cp}\right) n_{is} \tag{48.14}$$

where f_{cp} is the volume fraction of the fluid in the tissue contained inside the cells. For the human soft tissues, the total fluid occupies approximately 60 % of the body weight, of which 40 % is the intracellular component and 20 % the extracellular component. As a result, approximately 70 % of the total fluid in the soft tissue is contained in the intracellular compartment and 30 % in the extracellular compartment. Estimated from the dissolved fractions of proteins and carbohydrates in the intracellular and extracellular fluids, refractive indices of the extracellular fluid, ne, and the intracellular fluid, ni, are found to be approximately 1.34 and 1.36, respectively [6]. The average background refractive index of a soft tissue can thus be estimated from the weighted refractive indices of ne and ni as

$$n_0 = f n_e + (1 - f) n_i \tag{48.15}$$

where f is the fraction of the fluid in tissue contained in between the cells. Therefore, it follows from Eq. 48.15 that $n_0 = 0.3 \times 1.34 + 0.7 \times 1.36 = 1.354$.

Figure 48.3 illustrates the reduced scattering coefficient of the turbid medium, predicted by the Rayleigh-Gans approximation, against the refractive index of background medium for the wavelengths at 800 nm and 1,300 nm, respectively. The parameters taken for scattering centers in the numerical evaluation were the refractive index $n_s = 1.46$, the volume fraction $\varphi = 0.3$, and the radius a = 1 μm. It is clear from Fig. 48.3 that the reduced scattering of the tissue is dramatically reduced with the increase of refractive index of the background medium. The reduction rate is approximately the same for both the wavelength applied, with 800 nm being a little bit faster than that of 1,300 nm. At least threefold reduction is expected if the refractive index of the background medium is changed from $n_0 = 1.354$ to $n_0 = 1.4$.

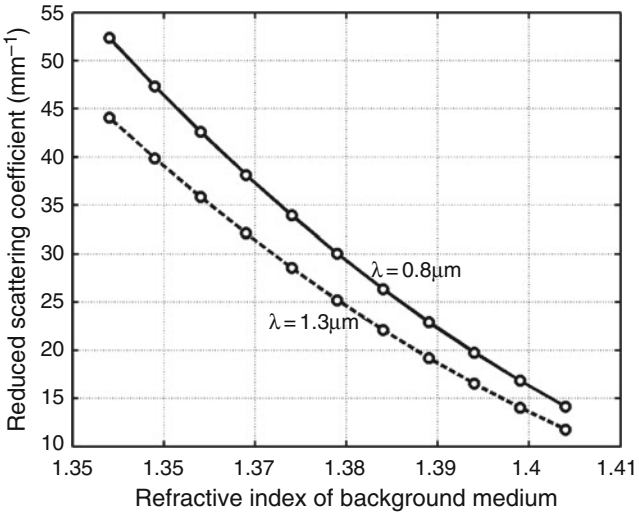

Fig. 48.3 Reduced scattering coefficient calculated from Rayleigh-Gans approximation as a function of the refractive index of the background medium for the wavelength at 800 and 1,300 nm, respectively. Please see the text for the parameters used in the numerical evaluation [54]

It is possible to achieve a marked impairment of scattering by means of the intratissue administration of appropriate chemical agents. Conspicuous experimental optical clearing in human and animal sclera; human, animal, and artificial skin; human gastrointestinal tissues; and human and animal cartilage and tendon in the visible and NIR wavelength ranges induced by the administration of x-ray contrast agents (Verografin, Trazograph, and Hypaque-60), glucose, propylene glycol, polypropylene glycol-based polymers (PPG), polyethylene glycol (PEG), PEG-based polymers, glycerol, and other solutions as has been described in Refs. [27, 34–62].

With the connection from the last section, such effect of reduction of scattering in biological tissue can be explored in the OCT to enhance its imaging performance, aspects which will be discussed in the following sections.

48.3 Monte Carlo Simulations

To illustrate how the multiple scattering has the effect on the OCT imaging performance, recently, Wang [32] used the Monte Carlo simulation technique (refer to ref [68] for details of Monte Carlo techniques) to systematically simulate such effects with an emphasis on the effects on imaging depth, resolution degradation, and signal localization. Generally from the results, it was found that signal localization and attenuation are dependent on the optical properties of tissue. The high scattering coefficient and the low degree of forward scattering are the primary causes for the degradation of signal localization and attenuation, leading to

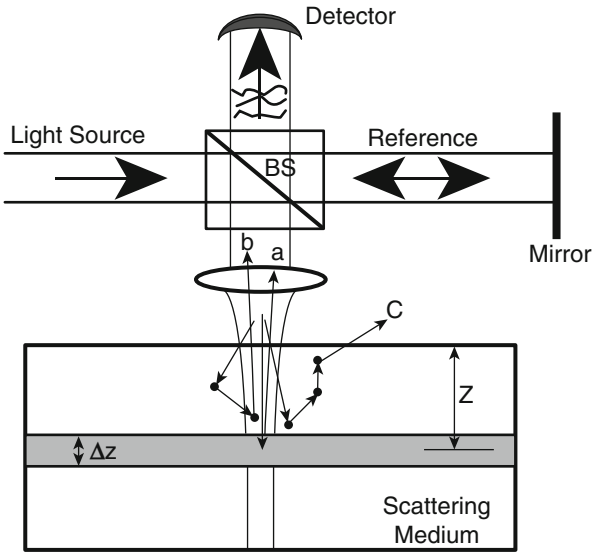

Fig. 48.4 Simple schematic of OCT system showing scattering interactions between a probing beam and biological tissue. Three types of interactions are backscattered from within the tissue: single scatter a, small-angle scatter b, and wide-angle scatter c. A layer with a thickness Δz at the depth of z is the expected layer for OCT localization

complication of interpretation of the measured OCT signals. More importantly, it was found that the imaging resolution is a function of the probing depth within the medium, as opposed to the claimed OCT system resolution. This fact has been overlooked recently in the OCT imaging applications. The imaging resolution is greatly reduced with increasing depth; this case is even more severe for the highly scattering medium. Therefore, attention must be paid to this fact when applying the OCT to human organs because of the high scattering nature of tissue.

Let us revisit the OCT system by looking closely at the backscattering light from the high scattering medium that has the possibility to contribute to the interference signal. A simple schematic of OCT system when probing the highly scattering medium is illustrated in Fig. 48.4, where the sample beam progressively loses its spatial coherence as it penetrates a turbid biological tissue. This loss of coherence results from the scattering by a variety of cellular structures with sizes ranging from less than one wavelength (e.g., cellular organelles) to several hundreds of micrometers (e.g., the length of a collagen fiber). As illustrated in Fig. 48.4, the dominant scattering interaction of the probing beam in the turbid medium can be categorized into three types [32, 69]: single backscatter **a**, small-angle forward scatter **b**, and extinction by absorption or wide-angle scatter **c** (i.e., light scattered out of the view of the interferometric receiver). The detector will only receive the first two categories of scatters because of the heterodyne detection characteristics of the OCT system. Furthermore, the low-coherence light source used, as stated in Sect. ▶ 12.2, provides a time gate to enable the detector to receive only those photons that traveled beneath the tissue surface with their optical path lengths matching the optical path length of the reference arm to within coherence length of the light source. Consequently, the OCT system in reality plays a role to sieve all the backscattering photons that emerged at the detector

according to their arrival times or equivalently the optical path lengths that the photons have traveled. Therefore, to enable the detector to produce the signal, the following criteria must be fulfilled:

$$\left|L_p - 2nz\right| < \frac{L_c}{2} \tag{48.16}$$

where L_p is the optical path length that the photon has traveled within the tissue, n is the refractive index of the medium, and z is the depth of a layer whose distance from the tissue surface matches the scanning distance of the mirror, nz, in the reference arm. For signal localization, we normally expect that the detected photons would be backscattered from the layer whose thickness is determined by

$$2n\Delta z = L_c. \tag{48.17}$$

However, because of the multiple scattering, there are possibilities for those photons contributing to the detected signal that are not backscattered from the expected layer, z, but fulfill the criteria of Eq. 48.17. As a consequence, these photons degrade the signal attenuation, localization, and resolution because they are not from the desired layer, leading to a signal artifact complicating the interpretation of the OCT image. The author in the paper [32] termed the photons that satisfy Eq. 48.17 as the least-scattered photons (LSP) and otherwise as the multiple-scattered photons (MSP). It is clear that the MSP comes solely from the interaction type **b**, while the LSP includes the interaction type **a** and part of type **b** because the photons backscattered from the desired layer might be subject to multiple scattering but with very small angle scattering. A distinct advantage of MC simulation technique is its ability to sort the LSP and MSP according to their optical path lengths, thereby enabling the investigation of their influence on the OCT signal attenuation and localization. Signal localization can be investigated systematically by means of the point spread function (PSF) at the specific depth for different optical properties to illustrate how the LSP and MSP contribute to signal localization.

With these conventions in mind, we now turn to looking at some results of how multiple scattering affects the OCT imaging performances by the use of the Monte Carlo simulation technique. For details, refer to the reference [32].

Figure 48.5 gives typical examples of depth point spread function (zPSF) at different probing depths for the turbid media representing moderate scattering in the left column ($\mu_s = 10\ \text{mm}^{-1}$) and highly scattering in the right ($\mu_s = 67\ \text{mm}^{-1}$). The figures were obtained for $g = 0.7$, 0.9, and 0.98 from top to bottom, respectively, to allow us to scrutinize the influence of the anisotropic parameter of the medium on the signal localization. The depths monitored are indicated in each figure. The filled symbol curves are the actual PSFs that are the summation of LSP and MSP signals from a specific depth. However, to investigate the effects of LSP and MSP signals separately on the PSFs, the signals from the LSP alone are plotted in each case, represented by the hollow symbol curves. Firstly, it is obvious that the worst case is from the medium with the highest scattering coefficient and lowest degree of forward scattering, i.e., $\mu s = 67\ \text{mm}^{-1}$ and $g = 0.7$ in this case (see the top right figure), where

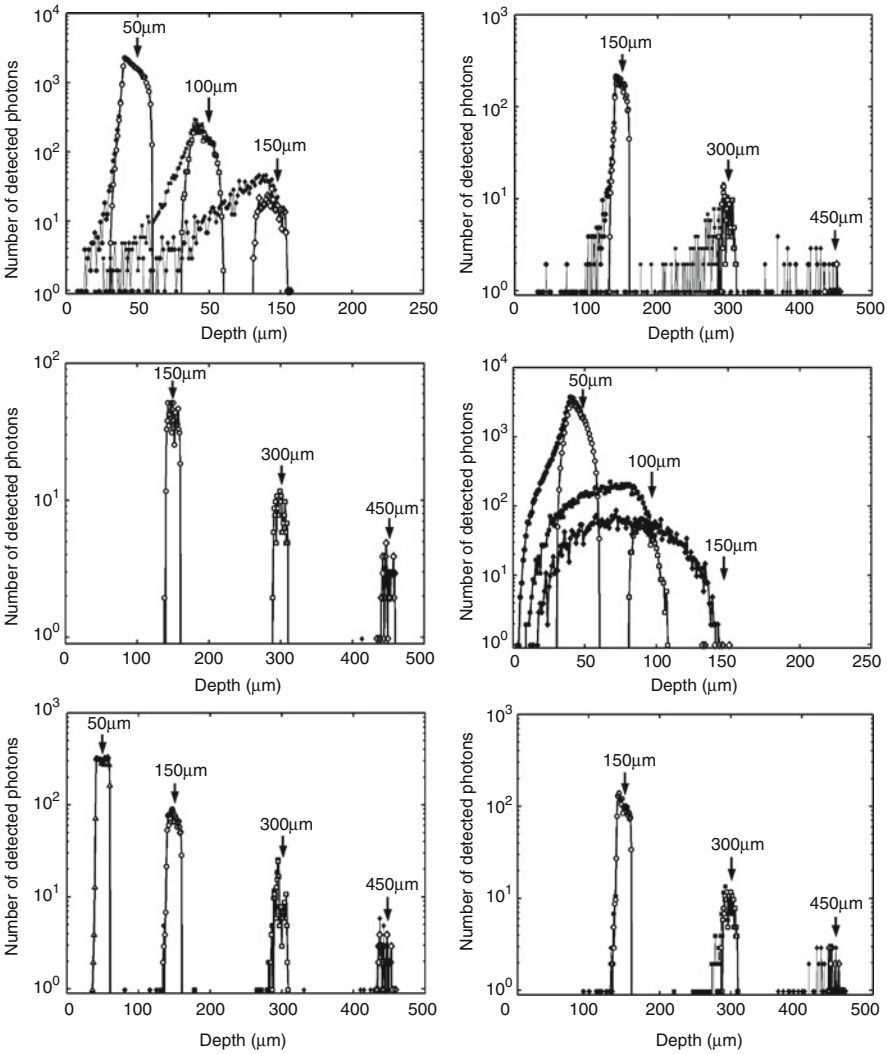

Fig. 48.5 Depth point spread functions (*solid symbol curves*) at different probing depths as indicated for the turbid media representing moderate scattering ($\mu s = 10\ \mathrm{mm}^{-1}$) in the left column and high scattering ($\mu s = 67\ \mathrm{mm}^{-1}$) in the right. From top to bottom, $g = 0.7$, 0.9, and 0.98, respectively. The LSP photons are plotted as the *curves* with hollow symbols [32]

signal localization is merely discerned at a depth of 50 μm. Even at this depth, the contribution from an MSP signal is big enough to degrade the signal localization, where it can be seen that the PSF curve is skewed towards the nominal probing depth, indicating that the photons multiply scattered within the medium before this depth have more chances of surviving to reach the detector. Moreover, the photons backscattered from a very shallow depth at approximately 5 μm still survive the

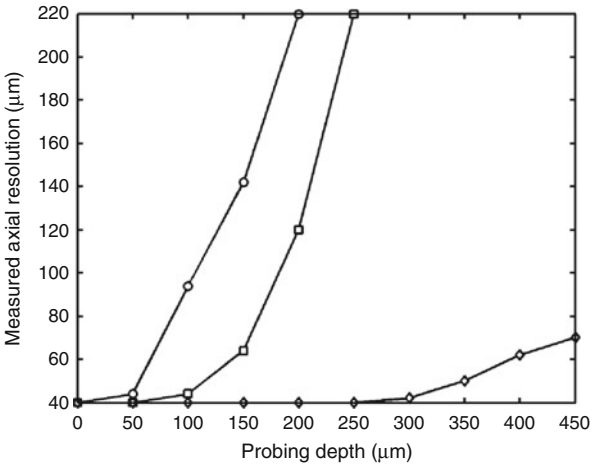

Fig. 48.6 The measured axial resolution from the simulation results plotted as a function of the probing depth for (μs, g) = (67 mm^{-1}, 0.7) (*circle*), (67 mm^{-1}, 0.9) (*square*), and (10 mm^{-1}, 0.9) (*diamond*), respectively [32]

scattering to meet the criterion of Eq. 48.17 for depth localization at 50 μm. With an increase in probing depth to 150 μm, the PSF is overwhelmed by the MSP signal with only a few photons belonging to the LSP category. At this depth the signal localization is totally lost for OCT imaging. Furthermore, the axial resolution and imaging contrast are greatly reduced. The claim of high-resolution optical imaging of OCT is therefore questionable for highly scattering biological tissues. The axial resolution of OCT imaging is dependent on the optical properties of tissue and is a function of depth.

Figure 48.6 illustrates the measured axial resolution from the simulation results as a function of depth for the cases of (μs, g) = (67 mm^{-1}, 0.7), (67 mm^{-1}, 0.9), and (10 mm^{-1}, 0.9), respectively. The axial resolution of the OCT system is merely kept up to the depth of 50 μm for the case of (μs, g) = (67 mm^{-1}, 0.7). After this depth, the actual axial resolution degrades exponentially with the increase of depth, where it becomes approximately 220 μm at the depth of 200 μm as opposed to the system resolution of 40 μm. With the increase of g to 0.9, this performance has been improved, with system resolution retained up to a depth of 100 μm. If in the meantime the scattering coefficient of the medium is reduced, for example, to μs = 10 mm^{-1} in this case, the probing depth at which imaging resolution is retained to the theoretical value would dramatically improve. This result is particularly welcome for the optical clearing of tissues with the purpose of enhancing the imaging depth of OCT which will be discussed in the next section.

With the reduction of the scattering coefficient (compare the left and right columns in Fig. 48.5), signal localization improves with the lesser MSP signal contributing to the depth of PSFs. This indicates that the low-scattering medium offers the more localized signal at any probing depth, which alternatively implies that the light penetration depth, i.e., optical imaging depth, is enhanced with less deterioration of the imaging resolution as stated above. On the other hand, it can be clearly seen from Fig. 48.5 that with increasing g, the signal localization at any depth for the scattering medium improves dramatically, where the highly forward-scattering medium, i.e., $g = 0.98$, offers the best signal localization for all the cases

investigated, see the bottom two figures for $\mu_s = 10$ mm^{-1}and $\mu_s = 67$ mm^{-1}, respectively. In these cases, only a few photons from the MSP category survive the scattering to contribute to the final PSF at a depth of up to 600 μm.

From these results, the advantage of reduction of scattering in the tissue in the enhanced OCT imaging performance is clearly seen. Here, we also see the importance of g factor in the OCT imaging for which the detailed investigation still remains to be explored.

48.4 Enhancement of Light Transmittance

Optical clearing effect on the reduction of multiple scattering through the use of biocompatible chemical agents has been experimentally investigated by a number of groups. The impregnation of the sclera, skin, human gastrointestinal tissues, cartilage, and tendon with x-ray contrast agents (Verografin, Trazograph, and Hypaque-60), glucose, propylene glycol, polypropylene glycol-based polymers (PPG), polyethylene glycol (PEG), PEG-based polymers, glycerol, etc. [27, 34–62], all shows the optical clearing effect in the visible and NIR wavelength ranges. A number of studies used near-infrared spectroscopic technique to quantitatively assess the light transmittance and scattering after the application of chemical agents [54–58]. With the use of Varian Cary 500 spectrophotometer with an internal integrating sphere, Fig. 48.7a, b gives an example of the measurement of the shift of transmittance and diffuse reflectance spectra, respectively, over the range of 800–2,200 nm as a function of time when the native porcine stomach pyloric mucosa specimen was applied with 80 % glycerol. The curves shown in the Figure were obtained at the time intervals of 0, 5, 10, 20, and 30 min, respectively, from bottom to top for transmittance (Fig. 48.7a) and from top to bottom for reflectance (Fig. 48.7b). It can be seen from Fig. 48.7 that, over the whole wavelength range investigated, the transmittance was increased with time. Diffuse reflectance was decreased over the range of 800–1,370 nm. The greatest increase in transmittance was at 1,278 nm, and the greatest decrease in reflectance was at 1,066 nm.

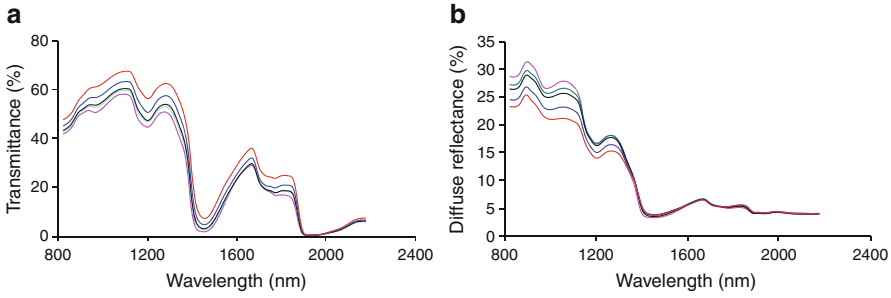

Fig. 48.7 Optical changes for porcine stomach pyloric mucosa before and after application of 80 % glycerol over the range from 800 to 2,200 nm measured by spectrophotometer. (**a**) Transmittance after application of the agent at the time intervals of 0, 5, 10, 20, and 30 min (from *bottom* to *top*), respectively. (**b**) Diffuse reflectance at the time intervals the same as in (**a**) (from *top* to *bottom*) [56, 58]

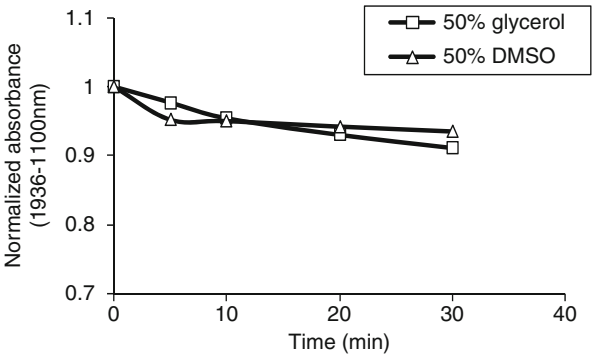

Fig. 48.8 Correlation between the NIR absorbance (measured at 1,936–1,100 nm) and time of application of 50 % glycerol and 50 % DMSO, respectively [56, 58]

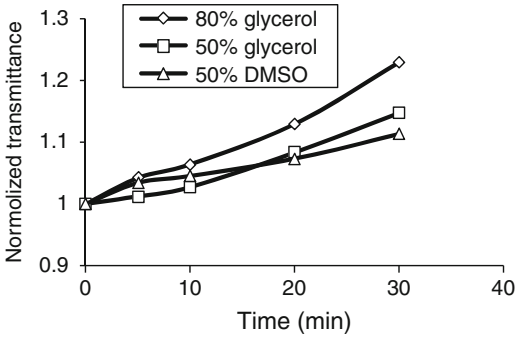

Fig. 48.9 Changes in transmittance at 1,278 nm against time for porcine stomach pyloric mucosa treated with 80 %, 50 % glycerol or 50 % DMSO [56, 58]

It is found that there is a strong correlation between optical clearing and water desorption [55–58]. The measured water activities for 80 % glycerol and 50 % DMSO give 0.486 and 0.936, respectively. Figure 48.8 gives the water content measurements at 30 min after the treatment, where 80 % glycerol caused 15 % water loss, whereas 50 % glycerol and 50 % DMSO caused 9 % and 7 %. The patterns of optical clearing are similar to those of water desorption.

Because most OCT systems use the light source with a central wavelength of 1,300 nm, Fig. 48.9 gives experimental results of the transmittance enhancement at about 1,300 nm after application of different chemical agent solutions, where it is seen that transmittance was increased by approximately 23 % at 30 min after the application of 80 %, while 15 % and 11 % were received after the treatment with 50 % glycerol and 50 % DMSO, respectively.

48.5 Enhancement of OCT Imaging Capabilities

In the last section, we clearly see that the administration of chemical agents in the tissue would increase light transmittance through the tissue, the effect of which would no doubt increase the imaging depth for OCT. Such results have been

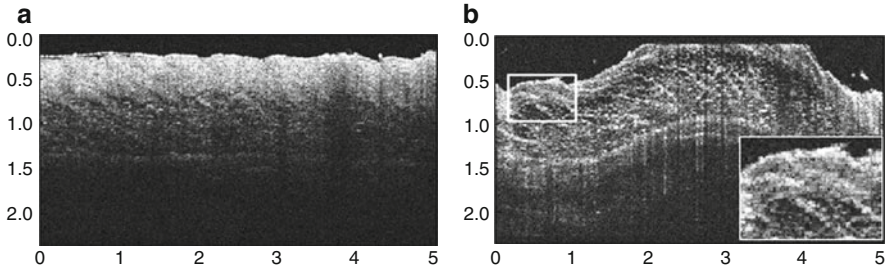

Fig. 48.10 OCT images of an adult rat through skin (**a**) without and (**b**) with topical application of glycerol solution. The insert in (**b**) is the enlargement of the marked area. Units presented are in millimeters, and the vertical axis presents the imaging depth [51]. Unit = mm

demonstrated by the administration of glycerol, propylene glycol, DMSO, oleic Acid, etc., on in vitro and in vivo skin [50, 51, 53–55] and GI tract tissues [27, 56, 58]. The tested wavelength in the OCT included 820 and 1,310 nm, the two most popular wavelength employed in the OCT imaging to date. Wang et al. was the first to investigate the enhancement of OCT imaging performance by the optical clearing approach. With the use of 820 nm wavelengths in their OCT system, Fig. 48.10 shows the OCT images of ex vivo rat skin (a) before and (b) after the application of glycerol solution, respectively, where a significant improvement of the imaging depth and contrast is clearly evident. The sharp differentiation of layered structures and features are visualized including the epidermis (E), papillary dermis (PD), reticular dermis (RD), hypodermis (HD), muscles (M), fascia, hair follicles (HF), and hairs in Fig. 48.10b, where the fascia is sandwiched between layers of muscle. Whereas these structures are quite vague in Fig. 48.10a where the transitional zones for dermal-epidermis and dermal-hypodermis cannot be distinguished. Far more detailed structures are clearly delineated in the hypodermis, which appeared to be an interwoven structure apart from the hair follicles and hair cortex. Such interwoven structures are well correlated with the adipose cells within the hypodermis. Compared with Fig. 48.10a, the imaging depth is improved by about 0.5 mm as the lower muscle layer can now be identified in the bottom of Fig. 48.10b. It should be noted that the tissue deformation in Fig. 48.10b was due to (1) the tissue shrinkage after applying the glycerol and (2) the optical path length difference induced by the uneven liquid solution thickness applied onto the skin surface.

In vitro studies of optical clearing of gastrointestinal tissues, such as the stomach, esophagus, and colonic mucosa, were recently performed using OCT imaging technique [27, 51, 54–56, 58]. Figure 48.11 shows two OCT images of intact and treated by 80 % propylene glycol solution normal, fresh human stomach tissue (fundus). A clearer image with the excellent differentiation of the epithelium, isthmus, lamina propia, and muscular tissue is achieved through the action of the agent [27].

The authors argued that such imaging depth and imaging contrast enhancements in OCT are attributed to the diffusion of the biocompatible agents applied to the skin. The diffusion of the chemicals into the tissue would reduce the refractive

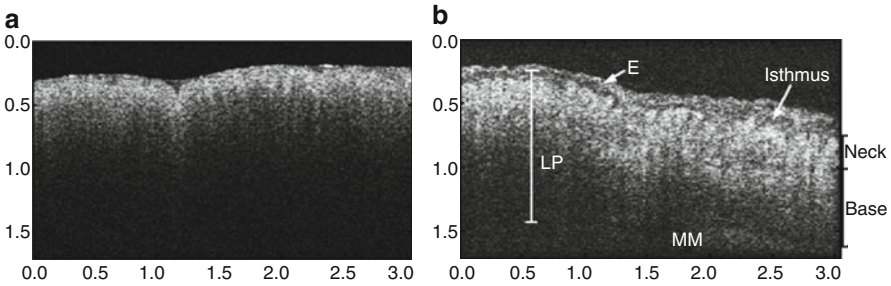

Fig. 48.11 OCT images of a normal, fresh human stomach tissue (fundus): (**a**) without and (**b**) with topical application of 80 % propylene glycol solution. *E* epithelium, *LP* lamina propia, *MM* muscularis mucosae [27]

index mismatch, leading to the reduction of scattering and therefore the increase of the imaging depth. However, the chemical diffusion in the tissue depends on the physical properties of the chemicals used, for example, the size of the molecules and the osmolarity of the environment induced by the chemicals. It also depends on the physical properties of the tissue targeted, for example, whether there is proper channel for the chemical to diffuse within. It is a very complicated process, and the exact mechanism still remains to be explored. Therefore, different chemicals would possess different diffusion rate in different types of tissues. It is reasonable to believe that due to the speed of chemical diffusion, the outmost layers would be optically cleared first. This enables more photons to penetrate into the tissue, thus increases the OCT signals from deeper layers, which otherwise is either blurred or blocked by the outer layers because of the high scattering. With the time elapses, the optical clearing effect gradually takes over the bulk tissue. From this point on, the OCT imaging contrast would disappear, and the only effect left is the imaging depth enhancement. This approach can be explained by the theory presented in Sect. ▶ 30.2.1. The dynamic process of OCT imaging performance enhancement through the application of the optical clearing agents has been reported in a number of studies on the human and animal skin [50, 51, 53, 58], stomach [55–58], esophagus [27] and blood [52, 62].

Figure 48.12 shows dynamic OCT structural images of porcine stomach with the topical application of 50 % glycerol solution, which was recorded at the time intervals of 0, 10, 20, 30, 40 and 50 min, respectively. A metal needle was inserted into the tissue approximately 1 mm beneath the surface. The signals reflecting back from the needle surface were used to suggest improvement of back reflectance signal caused by the chemical clearing. The OCT image of the porcine stomach without the administration of glycerol has a visualization depth of approximately 1.0 mm as shown in Fig. 48.12a. It can be seen that a significant improvement of the imaging depth is clearly demonstrated after the topical application of glycerol. The penetration depth has increased to about 2.0 mm after 50 min application of glycerol as shown in Fig. 48.12f. Tissue shrinkage occurs after the administration of the agents to tissue, see Fig. 48.12b–f. The needle embedded in the tissue

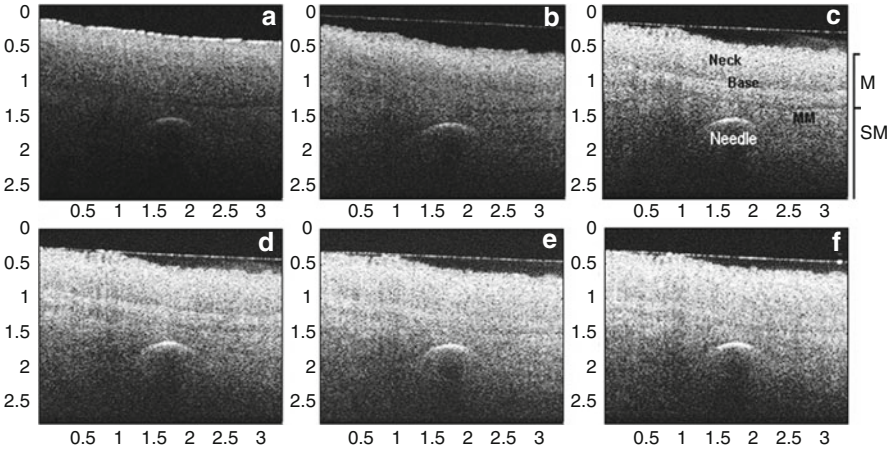

Fig. 48.12 Dynamic OCT images obtained at the time (**a**) 0, (**b**) 10, (**c**) 20, (**d**) 30, (**e**) 40, and (**f**) 50 min after the topical application of 50 % glycerol solution onto the porcine stomach tissue. Note central wavelength used in the experiment was 1,310 nm [55]. Unit = mm

becomes brighter and brighter with the increase of the time duration, see Fig. 48.12b–f. The imaging contrast of Fig. 48.12c, d is also greatly improved, for example the features of lamina propria (LP) and muscularis mucosae (MM). The neck, base, and MM layers of the tissue could be differentiated after 20–30 min application of glycerol. The reflection from the needle surface is also sharp within this period of time. With further increase of time, the imaging contrast improvement disappears gradually, as shown in Fig. 48.11e, f. The analogous results were also received from the ex vivo rat skin [51].

To see the different diffusion rates for different chemicals in the tissue, Fig. 48.13 illustrates the M-mode OCT images obtained from the repeated A-scans of the porcine stomach with the application of (a) glycerol and (b) DMSO. It was noted that because the system used required to re-localize the tissue surface manually after topical application of agents, the registration of OCT signal starts at about 0.5 min after the agent application. From the image obtained with glycerol application, it is clearly seen that the penetration depth increases gradually with the increase of time duration. However, from Fig. 48.13b, a significant depth improvement appears at the time immediately after the application of DMSO. This indicates that DMSO could fulfill tissue clearing within a very short time period. There is a slope of the surface of the tissue. The downward trend of the tissue surface is attributed to the tissue dehydration induced by the chemical agents.

Figure 48.14 shows an even more convincing case for the action of glycerol and propylene glycol to the tissue in vivo where the OCT imaging depth and contrast are dramatically improved when comparing the images before and after the application of agents.

The OCT images captured from the skin site of the volunteer at hyperdermal injection of 40 % glucose allowed one to estimate the total attenuation coefficient,

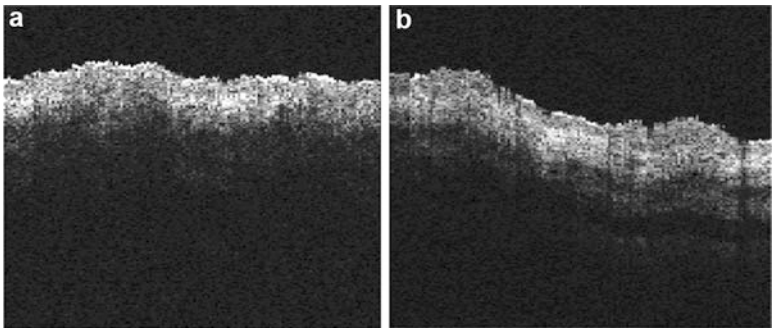

Fig. 48.13 OCT images captured from human forearm in vivo (**a**) without and (**b**) with 50 % topical application of propylene glycol solution. Image sizes: 1.8 × 1.6 mm [54]

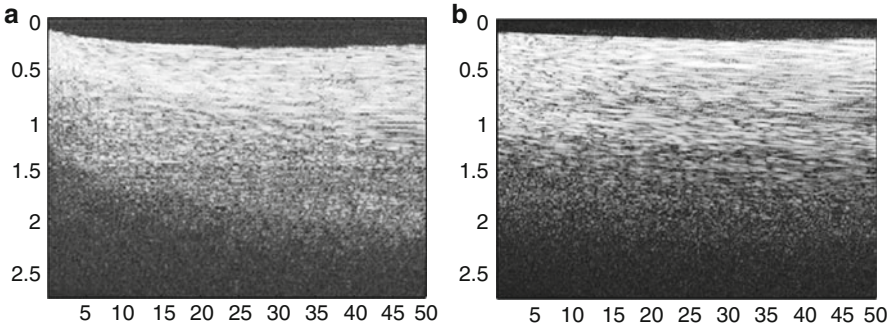

Fig. 48.14 Comparison of the time course of repeated A-scans of the porcine stomach tissue with the application of (**a**) glycerol and (**b**) DMSO, respectively. The horizontal and vertical axes present the time (min) and the imaging depth (mm), respectively [55]

see Eq. 48.10 [54]. The attenuation initially goes down and then goes up with the time course. Such behavior well correlates with the in vivo spectral measurements and reflects the index matching induced by the glucose injection. The light beam attenuation in tissue, $I/I_0 \sim \exp(-\mu_t)$, for intact skin (0 min) was found from OCT measurements as $I/I_0 \cong 0.14$ and for immersed skin at 13 min $I/I_0 \cong 0.30$, i.e., intensity of transmitted light increased 2.1-folds. That value also well correlates with the independent spectral measurements [36–38]. It should be noted that high sensitivity of OCT signal to immersion of living tissue by glucose allows one to monitor its concentration in the skin at a physiological level [70–73].

Although glycerol and glucose are effective optical clearing agents when injected into the dermis, [50, 54] normally they do not penetrate so well into intact skin. In recent OCT experiments with human skin in vivo at topical application during 90–120 min of the combined lipophilic polypropylene glycol-based prepolymers (PPG) and hydrophilic polyethylene glycol (PEG)-based prepolymers, both with indices of refraction of 1.47 that closely match that of skin scattering

components in SC, epidermis, and dermis, it was shown that polymer mixture can penetrate intact skin and improve OCT images to see dermal vasculature and hair follicles more clearly [74]. This composition may have some advantages in skin optical clearing due to the hydrophilic component which may more effectively diffuse within living epidermis and dermis; less osmotic strength also may have some advantages, but the optical clearing depth could not be improved radically in comparison with topical application of other clearing agents, such as glycerol, glucose, x-ray contrast, and propylene glycol, because of principle limitations of chemical agent diffusion through intact cell layers. Thus, to provide fast and effective optical clearing of skin, the appropriate well known or newly developed methods of enhanced agent delivery should be applied.

Thus far, we have used the examples to illustrate that the impregnation of tissue with the biocompatible chemical can enhance OCT imaging capabilities through the optical clearing and chemical mass transport upon diffusion mechanisms. However, such imaging capability enhancement is agent selectable, particularly for the imaging contrast enhancement. The mechanisms for light penetration enhancement have been well established, i.e., in the framework of refractive index matching approach, which can improve the OCT imaging depth and resolution. The explanations for imaging contrast enhancement, thereby the improvement of OCT localization capability, are based on the dehydration induced by the chemicals and chemical mass transport characteristics. The exact mechanism behind the contrast enhancement still remains to be explored.

48.6 OCT Glucose Sensing

Recently, OCT technique has been proposed for noninvasive assessment of glucose concentration in tissues [70–73, 75–77]. High resolution of the OCT technique may allow high sensitivity, accuracy, and specificity of glucose concentration monitoring due to precise measurements of glucose-induced changes in the tissue optical properties from the layer of interest (dermis). Unlike diffuse reflectance method, OCT allows to provide depth-resolved qualitative and quantitative information about tissue optical properties of the three major layers of human skin: stratum corneum of epidermis, epidermis and dermis. Dermis is the only layer of the skin containing developed blood microvessel network. Since glucose concentration in the interstitial fluid is closely related to the blood glucose concentration, one can expect glucose-induced changes in OCT signal detected from the dermis area of the skin. Two methods of OCT-based measurement and monitoring of tissue glucose concentration were proposed: (1) monitoring of tissue scattering coefficient, μ_s, as a function of blood glucose concentration using standard OCT [71–73] and (2) measurement of glucose-induced changes in refractive index, Δn, using novel polarization maintaining fiber-based dual channel phase-sensitive optical low-coherence reflectometer (PS-OLCR) [75].

The experiments were performed with a portable OCT system with the central wavelength of 1,300 nm, power of 0.5 mW, and coherence length and lateral

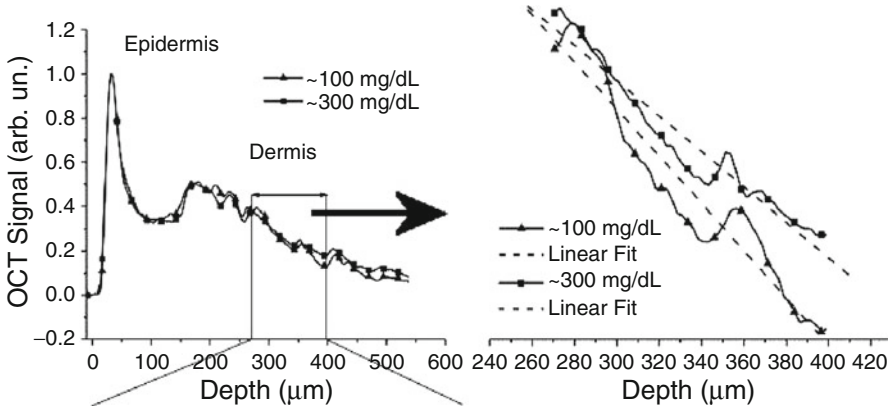

Fig. 48.15 Representative OCT signals obtained from Yucatan micropig skin during glucose clamping experiment at low and high blood glucose concentration (*top*) and a part of the OCT signal in the dermis area with the linear fit of the OCT signals in this layer (*right*) [73]

resolution of approximately 14 and 12 μm, respectively [71–73, 77]. The authors reported results obtained from phantom, animal, and human studies. OCT images were obtained from skin (ear of the rabbits, dorsal area of the micropigs, and arm of the volunteers). The slopes of the OCT signals were calculated at a depth of 150–900 μm. Glucose administration was performed using (1) intravenous bolus injections for rapid increase of blood glucose concentration and (2) intravenous clamping technique for slow, controlled changes of the blood glucose concentration in animal studies and (3) standard oral glucose tolerance test (OGTT) in human studies.

First an OCT image of the layers of skin was taken, and the OCT signal as a function of depth was evaluated. The slope of the portion of the plot in the dermis layer was used to calculate μ_s. In an anesthetized animal skin experiment OCT images demonstrate that glucose affects the refractive index mismatch in skin and decreases μ_s [77]. The slope of the OCT signal versus depth line is determined and is correlated with the concentration of blood glucose (Fig. 48.15).

Typical results obtained in the clinical studies are shown in Fig. 48.16. OCT images and blood samples (for monitoring of glucose concentration in blood) were taken from left and right forearm, respectively. Good correlation between increase of the blood glucose concentration and decrease of the smoothed OCT signal slope has been observed at the depth of 200–600 μm during OGTT. Measurements performed in layers of epidermis and upper dermis either did not show changes in the OCT signal slope at variations of blood glucose concentration or the changes were very weak. Most likely it is due to a gradient of glucose concentration from dermal blood micro-vessels to the SC. Thus, sensitivity and accuracy of the OCT measurements of blood glucose concentration would be maximal in the regions of developed blood microvessel network (that is dermis area).

A question of specificity of the OCT technique to monitor blood glucose concentration in tissues has been addressed. The experimental and theoretical

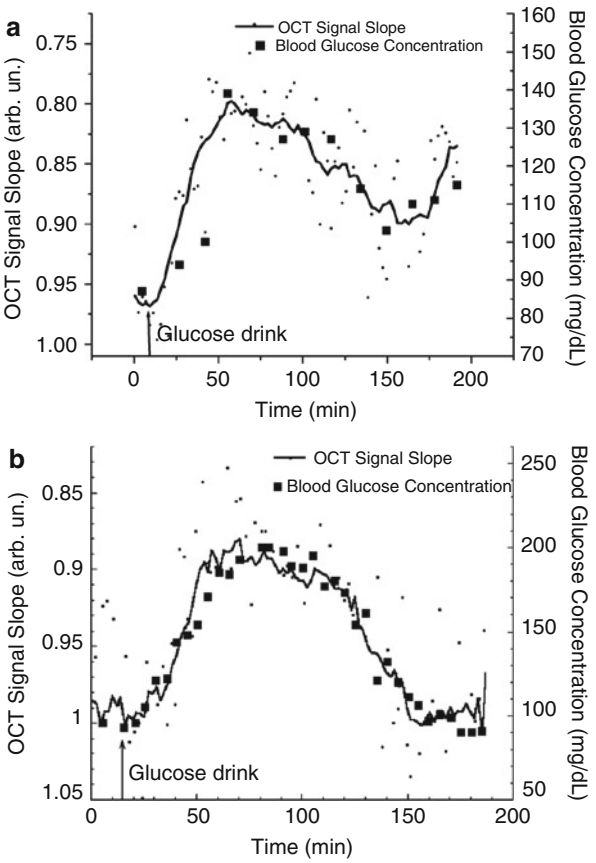

Fig. 48.16 Slope of OCT signal and blood glucose concentration vs. time. OCT images and blood samples were taken from a human skin of (**a**) *left* and (**b**) *right* forearm during OGTT [72]

analysis of influence of several physical and physiological parameters (such as altering the refractive index mismatch between the interstitial fluid and scattering centers and structural modifications in tissue due to changes in glucose concentration) on the OCT signal slope was performed. Obtained results demonstrate that (1) several body osmolytes may change the refractive index mismatch between the interstitial fluid and scattering centers in tissue; however, the effect of the glucose is approximately one to two orders of magnitude higher; (2) an increase of the interstitial fluid glucose concentration in the physiological range (3–30 mM) may decrease the scattering coefficient by 0.22 %/mM due to cell volume change; (3) stability of the OCT signal slope is dependent on tissue heterogeneity and motion artifacts; and (4) moderate skin temperature fluctuations (± 1 °C) do not decrease accuracy and specificity of the OCT-based glucose sensor; however, substantial skin heating or cooling (several °C) significantly changes the OCT signal slope. These results suggest that the OCT technique may provide blood glucose concentration monitoring with sufficient specificity under normal physiological conditions.

A new differential phase contrast OCT-based method (PS-OLCR) of monitoring glucose-induced changes in tissue optical properties has been also proposed [75]. While conventional OCT uses the detection and analysis of intensity of backscattered optical radiation, phase-sensitive OCT utilizes the phase information obtained by probing a sample simultaneously with two common path low-coherence beams. Variations in the sample refractive index will be exhibited in the phase difference, $\Delta\varphi$, between these two beams. The PS-OLCR technique is capable of measuring Angstrom/nanometer scale path length change between the beams (associated with the phase difference as $(\lambda/4\pi)\Delta\varphi$) in clear and scattering media. The theoretical and experimental pilot studies on application of PS-OLCR for noninvasive, sensitive, and accurate monitoring of analyte concentration were reported by authors of Ref. [78]. It was demonstrated that the effect of glucose concentration change on refractive index is approximately one to four orders of magnitude greater than that of the other analytes at the physiological concentrations.

Like other scattering techniques, the detected phenomenon in OCT is the effect of glucose on the refractive index of the interstitial fluid. Unlike the spatially resolved back reflectance and frequency-domain methods that use larger measuring volume and spans multiple layers in tissues [41, 47, 70, 78, 79], OCT offers certain advantage, as it limits sampling depth to the upper dermis without unwanted signal from other layers. Precise sampling is very important at glucose monitoring in tissue, because glucose uptake is different in different tissue layers being lowest in connective tissue and smooth muscle and highest in adipose tissue and skeletal muscle [80].

48.6.1 Imaging Through Blood

As it follows from the above discussions and other chapters in this book, OCT is a powerful technique for study of structure and dynamics of highly scattering tissues and blood, including imaging of vascular system for the diagnosis of atherosclerotic lesions. In vitro studies performed on human aorta have shown that OCT is able to identify structural features such as lipid collections, thin intimal caps, and fissures characteristic of plaque vulnerability [81–84]. In in vivo OCT imaging of the rabbit aorta through a catheter, a vascular structure was defined, but saline infusion was required during imaging since blood led to significant attenuation of the optical signal [81]. Eliminating the need of saline or minimization its concentration would represent a substantial advance for intravascular OCT imaging.

Refractive index mismatch between erythrocyte cytoplasm and blood plasma causes strong scattering of blood that prevents to get high quality images of intravascular structures through a whole blood. The refractive index of erythrocyte cytoplasm is mostly defined by hemoglobin concentration (blood hematocrit) [85]. The scattering properties of blood are also dependent on erythrocytes volume and shape, which are defined by blood plasma osmolarity [86, 87], and aggregation or disaggregation ability [62, 88, 89]. Recently the feasibility of index matching as a method to overcome the limited penetration through blood for getting of OCT

tissue images has been demonstrated [52, 62, 89]. Glucose, low and high molecular dextrans, *x*-ray contrasting, glycerol, and some other biocompatible agents were used to increase the refractive index of blood plasma closer to that of the erythrocyte cytoplasm to improve penetration depth of OCT images.

The 1,300 nm OCT system was used for taking images of the reflector through circulated blood in vitro [52]. The total intensity of the signal off the reflector was used to represent penetration. As immersion substances dextran (group refractive index –1.52) and IV contrast (group refractive index –1.46) were taken. Both dextran and IV contrast were demonstrated to increase penetration through blood: 69 ± 12 % for dextran and 45 ± 4 % for IV contrast.

Studies of blood scattering reduction by the immersion technique using various osmotically active solutions, which are biocompatible with blood, like saline, glucose, glycerol, propylene glycol, trazograph (*x*-ray contrasting substance for intravenous injection), and dextran were also described [62, 89]. The 820 and 1,310 nm OCT systems were applied for taking images of the reflector through a 1 mm layer of un-circulating fresh whole blood. It was shown that for un-circulating blood the sedimentation plays an important role in blood clearing using immersion technique and OCT allows for precise monitoring of blood sedimentation and aggregation.

The result of the OCT study is the measurement of optical backscattering or reflectance, $R(z)$, from the RBCs versus axial ranging distance, or depth, z. The reflectance depends on the optical properties of blood, i.e., the absorption (μ_a) and scattering (μ_s) coefficients, or total attenuation coefficient (μ_t), $\mu_t = \mu_a + \mu_s$. For optical depths less than four, reflected power can be approximately proportional to $-2\mu_t z$ in exponential scale according to the single scattering model [62, 89], but due to interferential signal detection in OCT [89, 90], it is finally proportional to $-\mu_t z$, i.e.,

$$R(z) = I_0 \alpha(z) \exp(-\mu_t z). \tag{48.18}$$

Here I_0 is the optical power launched into the blood sample and $\alpha(z)$ is the reflectivity of the blood sample at the depth of z.

Optical clearing (enhancement of transmittance) ΔT by an agent application can be estimated using the following expression

$$\Delta T = \left[\left(R_{\text{agent}} - R_{\text{saline}}\right)/R_{\text{saline}}\right] \times 100\% \tag{48.19}$$

where R_{agent} is the reflectance from the backward surface of the vessel within a blood sample with an agent, and R_{saline} is that with a control blood sample (whole blood with saline).

The OCT system used yields 12 μm axial resolution in free space. This determines the imaging axial resolution which is comparable with the dimensions of red blood cells (RBCs) or small aggregates. A few different glass vessels of 0.2–2 mm of thickness were used as blood sample holders. For some holders to enhance reflection from the bottom interface, a metal reflector was applied. The sample holder was mounted on a translation stage at the sample arm and was placed

Table 48.1 Influence of dextrans (2.43 gdl^{-1}) on light attenuation property of the sample containing 65 % blood and 35 % saline [89]

Agent	μt (mm − 1)	ΔT (%)
Saline	3.71	–
Dextran10	3.82	11.9
Dextran70	2.97	100.1
Dextran500	3.12	86.7

perpendicular to the probing beam. The amplitude of reflected light as a function of depth at one spatial point within the sample was obtained. The result is the measurement of optical backscattering or reflectance, $R(z)$, from the RBCs versus axial ranging distance, or depth, z, described by Eq. 48.18. Optical clearing (enhancement of transmittance) ΔT by an agent application was estimated using Eq. 48.19. Averaging for a few tenths of z-scans were employed.

Venous blood was drawn from healthy volunteers and stabilized by K2E EDTA K2. For example, blood samples containing dextrans were prepared immediately after blood taking by gently mixing blood and dextran-saline solution with low rate manual rotating for 1 min before each OCT measurement. Four groups of the blood samples with various hematocrit values were investigated in this study [89]. The dextrans used in the experiments were D × 10, D × 70 and D × 500 with the molecular weights (MW) at 10,500, 65,500 and 473,000, respectively.

Table 48.1 gives the results from 65 % blood (from a 24 years old male volunteer) with 35 % dextran-saline solution. The concentration of dextrans used was 2.43 gdl^{-1}. The measurement started immediately after the addition of dextran. It can be seen from Table 48.1 that D × 500 and D × 70 are effective agents to decrease the light attenuation of blood compared to the saline control, with the total attenuation coefficient decreased from 3.71 mm^{-1} for the saline control to 3.12 mm^{-1} and 2.97 mm^{-1}, respectively. The optical clearing capability ΔT was approximately 90 % and 100 % for D × 500 and D × 70, respectively.

Interesting that D × 500 providing a higher refraction had less effect than that of D × 70 at the same concentration. Moreover, the increase in concentration (refraction power) cannot always achieve higher optical clearance. 0.5 gdl^{-1} D × 500 had a stronger effect than 5 gdl^{-1} D × 500 in 20 % blood with 80 % saline samples. The changes in scattering property brought above by the addition of dextran solution may first be explained by the refractive index matching hypothesis [51]. It can be seen that scattering can be reduced when the refractive index of plasma is increased.

The refractive index of dextran-saline solution was increased with concentration in all molecular weight groups. The measured indices of blood samples with dextrans were in good agreement with the theoretical values calculated according to the equation $n = c_b n_b + (1 - c_b) n_s$, where c_b is the volume fraction (20 %) of whole blood in the diluted sample and n_s is the index of saline with or without dextrans. As expected, the refractive index of blood with dextran increases as the concentration of the added dextran increases due to an increase of the index of the ground matter of the sample.

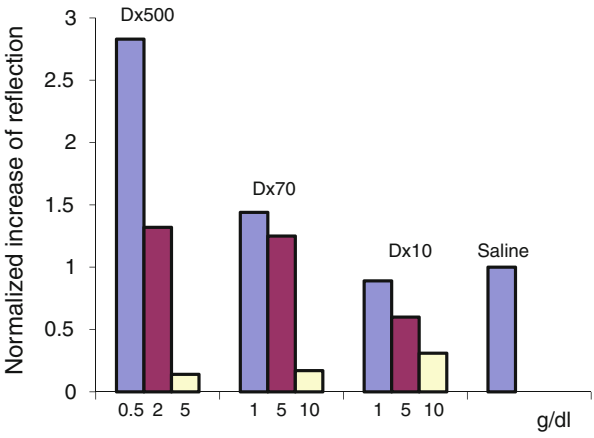

Fig. 48.17 A summary of effects of dextrans compared to that of the saline control on light transmission after 10 min sedimentation. Lower concentration Dextran500 and Dextran70 had significant effects in enhancing light transmission. Efficiency of higher concentration dextrans was much lower than that of the saline control [89]

Blood optical property can be altered by dextrans-induced refractive index matching between RBCs and plasma. However, refractive index matching is not the only factor affecting blood optical properties. Obviously, this discrepancy resulted from the assumption of only refractive index influence. Thus other factors should be taken into account, particularly, the cellular aggregation effect induced by dextrans [89].

As the aggregation process is time-dependent, the blood sample was allowed 10 min sedimentation in this study after the measurement at the beginning stage of the addition of dextrans. Figure 48.17 shows the summary of the effect of dextrans compared to the saline control on light transmission for the sample with 20 % blood and 80 % saline after 10 min sedimentation. It can be seen from Fig. 48.17 that the influence of dextran on the light transmission was different compared to that at the beginning of mixing dextrans in blood. The lower concentration (0.5 gdl^{-1}) D × 500 still had the strongest effect on reducing the scattering of light in blood, with a 2.8-fold stronger effect than that of the saline control. However, enhancement by the highest concentration of D × 500 (5 gdl^{-1}) and D × 70 (10 gdl^{-1}) was dramatically lower than that of the saline control. At the beginning, they both had a very high blood optical clearing capability with 67.5 % and 76.8 % ΔT, respectively. In addition, the effect was decreased with the increase of dextran in blood within all three groups, contrary to the expectation of the refractive index matching hypothesis.

The decreased aggregation capability of dextran with concentration explained well that light transmission decreased less with the increase of dextran for both types (mid-molecular and large-molecular). Over a range of concentrations, D × 500 and D × 70 induced RBC aggregation. However, dextrans have been known to exert a biphasic effect on RBC aggregation; they induce aggregation at low concentration, and disaggregation at high concentration [88]. For example, with D × 70, the maximal aggregation size is obtained at approximately 3 %, above which the size decreases. In our OCT measurements, 2 gdl^{-1} D × 500 and 5 gdl^{-1}

D × 70 in 20 % blood with 80 % saline appeared to be the critical concentration to affect RBC aggregation. Their aggregation parameters became smaller than those of 0.5 gdl^{-1} D × 500 and 1 gdl^{-1} D × 70. When the concentration increased to 5 gdl^{-1} for D × 500 and 10 gdl^{-1} for D × 70, they played a role of disaggregation. That is the reason why the cells are much less packed than with the saline control, accounting for the reduced light transmission. Although refractive index matching suggested a higher light transmission, it can be seen that the aggregation-disaggregation effects are now dominant.

The behavior of red blood cells (RBC) in flow is dependent on the processes of aggregation-disaggregation, orientation and deformation. Increased RBC aggregability has been observed in various pathological states, such as diabetes and myocardial infarction, or following trauma. The aggregation and disaggregation properties of human blood can be used for the characterization of the hemorheological status of patients suffering different diseases [87]. Our work suggests that OCT may be a useful noninvasive technique to investigate rheology for diagnosis together with its additional advantage of monitoring blood sedimentation [62].

48.7 Summary

To summarize, we have discussed in this chapter the basic principles of enhancing the OCT imaging performances. The human tissue is highly scattering in nature to the near-infrared light that is usually used to illuminate the OCT systems. In this chapter it was shown that multiple scattering of tissue is a detrimental factor that limits the OCT imaging performances, for example, the imaging resolution, depth, localization, and contrast. In order to improve the imaging capabilities for OCT systems, the multiple scattering of tissue must be reduced. We then introduce the optical clearing technique, mainly concentrated on the use of the biocompatible and osmotically active chemical agent to impregnate the tissue, to enhance the OCT imaging performances through the tissue. The mechanisms for such improvements, for example, imaging depth and contrast, were discussed, primarily through the experimental examples. It is assumed that when chemical agents are applied onto the targeted sample, there are two approaches concurrently applied to the tissue. The imaging depth, or light penetration depth, is enhanced by the refractive index matching of the major scattering centers within the tissue with the ground material induced by the chemical agents, usually through the diffusions of the interstitial liquids of tissue and the chemical agents. Whereas, the imaging contrast enhancement is caused by the tissue dehydration due to the high osmotic characteristics of the chemical agents, which is also dependent on the mass transport of chemical agents within tissue.

Optical clearing technology for OCT needs is a growing field of investigations and biomedical applications. A few special issues of journals, book chapters, and overview papers discussing results and perspectives of this method for biomedical imaging and in-depth monitoring of molecular diffusion were recently published [91–97].

Not only the benefits of the method but also the drawbacks and toxicity issues were discussed [95]. Recent original publications demonstrate innovative approaches in the assessment of tissue optical clearing as a function of glucose concentration using OCT [98], testing of novel effective mixtures of optical clearing agents (OCAs) [99], enhanced optical clearing of skin in vivo and OCT in-depth imaging [100], and enhanced OCT imaging of embryonic tissue [101]. One of the important applications of OCT in combination with optical clearing is the differentiation of normal tissue from benign/malignant tumor tissue using strong differences in spatial and temporal kinetics of OCT images for these types of tissues [102–105].

The depth-resolved monitoring of glucose, other metabolites, and drug molecule diffusion in different tissues by using OCT is one of the prospective applications of this technology [102–127]. Different types of tissues from soft to hard, in normal and pathology, and in in vitro and in vivo states, such as animal and human skin, ocular tissues, breast tissue, esophagus, atherosclerotic vascular tissues, tooth dentin, and others, were studied [102–127].

Blood optical clearing technique, which is well discussed in this chapter, received its further development in discovery and direct experimental prove of concept of blood "self-clearing" at local blood hemolysis in the vicinity of OCT endoscopic probe within vessel lumen [128, 129]. Safety and usefulness of this non-occlusive OCT image acquisition technique based on usage of such OCA as a low-molecular-weight dextran were demonstrated [130, 131].

Besides immersion optical clearing using exogenous liquids, mechanical compression as a method for increasing the informative value of OCT due to enhanced light penetration and involvement of specific elastic properties of tissues is of great interest at the moment [132–136].

Acknowledgements Some of the results presented in this chapter were made possible with the financial supports received from the Engineering and Physical Science Research Council, UK, for the projects GR/N13715, GR/R06816, and GR/R52978; the North Staffordshire Medical Institute, UK; Keele University Incentive Scheme; Cranfield University; Oregon Health and Science University, and the Royal Society for a joint project between Cranfield University and Saratov State University; as well as grants RFBR 11-02-00560-a, 11-02-12248-ofi-m, and 12-02-92610-RS_a; 224014 Photonics4Life of FP7-ICT-2007-2; 1.4.09 of RF Ministry of Education and Science; RF Governmental contracts 11.519.11.2035, 14.B37.21.0728, and 14.B37.21.0563; FiDiPro, TEKES Program (40111/11), Finland; SCOPES EC, Uzb/Switz/RF, Swiss NSF, IZ74ZO_137423/1; RF President's grant "Supporting of Scientific Schools," 1177.2012.2.

References

1. A. Yodh, B. Chance, Phys. Today **48**, 34–40 (1995)
2. D. Delpy, Phys. World **7**, 34–39 (1994)
3. D.W. Piston, B.R. Masters, W.W. Webb, J. Microsc. **178**, 20–27 (1995)
4. M. Rajadhyaksha, M. Grossman, D. Esterowitz, R. Webb, R. Anderson, J. Invest. Dermatol. **104**, 946–952 (1995)
5. D. Huang, E.A. Swanson, C.P. Lin, J.S. Schuman, W.G. Stinson, W. Chang, M.R. Hee, T. Flotte, K. Gregory, C.A. Puliafito, J.G. Fujimoto, Science **254**, 1178–1181 (1991)

6. V.V.Tuchin (ed.), *Coherent-Domain Optical Methods: Biomedical Diagnostics, Environmental Monitoring and Material Science*. Vols. 1&2, 2nd edn. (Springer-Verlag, Berlin, Heidelberg, N.Y., 2013)
7. A.F. Fercher, J. Biomed. Opt. **1**, 157–173 (1996)
8. J.M. Schmitt, IEEE J. Sel. Top. Quant. Electron. **5**, 1205–1215 (1999)
9. P.H. Tomolins, R.K. Wang, J Phys. D Appl. Phys. **38**, 2519–2535 (2005)
10. A.F. Fercher, C.K. Hitzenberger, W. Drexler, G. Kamp, H. Sattmann, Am. J. Ophthalmol. **116**, 113–114 (1993)
11. J.M. Schmitt, A. Knüttel, M. Yadlowsky, R.F. Bonner, Phys. Med. Biol. **42**, 1427–1439 (1994)
12. J.G. Fujimoto, M.E. Brezinski, G.J. Tearney, S.A. Boppart, B.E. Bouma, M.R. Hee, J.F. Southern, E.A. Swanson, Nature Med. **1**, 970–972 (1995)
13. G.J. Tearney, M.E. Brezinski, B.E. Bouma, S.A. Boppart, C. Pitris, J.F. Southern, J.G. Fujimoto, Science **276**, 2037–2039 (1997)
14. R.C. Youngquist, S. Carr, D.E.N. Davies, Opt. Lett. **12**, 158–160 (1987)
15. K. Takada, I. Yokohama, K. Chida, J. Noda, Appl. Opt. **26**, 1603–1606 (1987)
16. A.F. Fercher, K. Mengedoht, W. Werner, Opt. Lett. **13**, 1867–1869 (1988)
17. C.K. Hitzenberger, W. Drexler, A.F. Fercher, Invest. Ophthalmol. Vis. Sci. **33**, 98–103 (1992)
18. J.A. Izatt, M.R. Hee, E.A. Swanson, C.P. Lin, D. Huang, J.S. Schuman, C.A. Puliafito, J.G. Fujimoto, Arch. Ophthalmol. **112**, 1584–1589 (1994)
19. W. Clivaz, F. Marquis-Weible, R.P. Salathe, R.P. Novak, H.H. Gilgen, Opt. Lett. **17**, 4–6 (1992)
20. M.R. Hee, J.A. Izatt, E.A. Swanson, D. Huang, C.P. Lin, J.S. Schuman, C.A. Puliafito, J.G. Fujimoto, Arch. Ophthalmol. **113**, 326–332 (1995)
21. S.A. Boppart, M.E. Brezinsk, B.E. Boump, G.J. Tearney, J.G. Fujimoto, Dev. Biol. **177**, 54–64 (1996)
22. C.A. Puliafito, M.R. Hee, C.P. Lin, J.G. Fujimoto, Ophthalmology **102**, 217–229 (1995)
23. C. Pitris, C. Jesser, S.A. Boppart, D. Stamper, M.E. Brezinski, J.G. Fujimoto, J. Gastroenterol. **35**, 87–92 (2000)
24. S. Brand, J.M. Poneros, B.E. Bouma, G.J. Tearney, C.C. Compton, N.S. Nishioka, Endoscopy **32**, 796–803 (2000)
25. B.E. Bouma, G.J. Tearney, C.C. Compton, N.S. Nishioka, Gastrointest. Endosc. **51**, 467–574 (2000)
26. S. Jackle, N. Gladkova, F. Feldchtein, A. Terentieva, B. Brand, G. Gelikonov, V. Gelikonov, A. Sergeev, A. Fritscher-Ravens, J. Freund, U. Seitz, S. Schroder, N. Soehendra, Endoscopy **32**, 743–749 (2000)
27. R.K. Wang, J.B. Elder, Lasers Surg. Med. **30**, 201–208 (2002)
28. B.W. Colston, M.J. Everett, L.B. Da Silva, L.L. Otis, P. Stroeve, H. Nathel, Appl. Opt. **37**, 3582–3585 (1998)
29. J.M. Schmitt, M. Yadlowsky, R. Bonner, Dermatology **191**, 93–98 (1995)
30. N.D. Gladkova, G.A. Petrova, N.K. Nikulin, S.G. Radenska-Lopovok, L.B. Snopova, Y.P. Chumakov, V.A. Nasonova, V.M. Geilkonov, G.V. Geilkonov, R.V. Kuranov, A.M. Sergeev, F.I. Feldchtein, Skin Res. Technol. **6**, 6–16 (2000)
31. R.K. Wang, J.B. Elder, Laser Phys. **12**, 611–616 (2002)
32. R.K. Wang, Phys. Med. Biol. **47**, 2281–2299 (2002)
33. V.V. Tuchin, Phys. Usp. **40**, 495–515 (1997)
34. V.V. Tuchin, I.L. Maksimova, D.A. Zimnyakov, I.L. Kon, A.H. Mavlutov, A.A. Mishin, J. Biomed. Opt. **2**, 401–417 (1997)
35. V.V. Tuchin, J. Biomed. Opt. **4**, 106–124 (1999)
36. V.V. Tuchin, *Optical Clearing of Tissues and Blood*, vol. PM 154 (SPIE Press, Bellingham, 2006)
37. V.V. Tuchin, J. Phys. D Appl. Phys. **38**, 2497–2518 (2005)
38. V.V. Tuchin, Laser Phys. **15**, 1109–1136 (2005)

39. V.V. Tuchin (ed.), *Handbook of Optical Biomedical Diagnostics*, **PM107** (SPIE Press, Bellingham, 2002)
40. B. Beauvoit, T. Kitai, B. Chance, Biophys. J. **67**, 2501–2510 (1994)
41. J.T. Bruulsema, J.E. Hayward, T.J. Farrell, M.S. Patterson, L. Heinemann, M. Berger, T. Koschinsky, J. SandahlChristiansen, H. Orskov, Opt. Lett. **22**, 190–192 (1997)
42. E.K. Chan, B. Sorg, D. Protsenko, M. O'Neil, M. Motamedi, A.J. Welch, IEEE J. Sel. Top. Quant. Electron. **2**, 943–950 (1996)
43. B. Chance, H. Liu, T. Kitai, Y. Zhang, Anal. Biochem. **227**, 351–362 (1995)
44. I.F. Cilesiz, A.J. Welch, Appl. Opt. **32**, 477–487 (1993)
45. M. Kohl, M. Esseupreis, M. Cope, Phys. Med. Biol. **40**, 1267–1287 (1995)
46. H. Liu, B. Beauvoit, M. Kimura, B. Chance, J. Biomed. Opt. **1**, 200–211 (1996)
47. J.S. Maier, S.A. Walker, S. Fantini, M.A. Franceschini, E. Gratton, Opt. Lett. **19**, 2062–2064 (1994)
48. X. Xu, R.K. Wang, A. El Haj, Eur. Biophys. J. **32**, 355–362 (2003)
49. V.V. Tuchin, A.N. Bashkatov, E.A. Genina, Y.P. Sinichkin, N.A. Lakodina, Tech. Phys. Lett. **27**, 489–490 (2001)
50. G. Vargas, E.K. Chan, J.K. Barton, H.G. Rylander III, A.J. Welch, Lasers Surg. Med. **24**, 133–141 (1999)
51. R.K. Wang, X. Xu, V.V. Tuchin, J.B. Elder, J. Opt. Soc. Am. **B18**, 948–953 (2001)
52. M. Brezinski, K. Saunders, C. Jesser, X. Li, J. Fujimoto, Circulation **103**, 1999–2003 (2001)
53. G. Vargas, K.F. Chan, S.L. Thomsen, A.J. Welch, Lasers Surg. Med. **29**, 213–220 (2001)
54. R.K. Wang, V.V. Tuchin, J. X-Ray Sci. Tech. **10**, 167–176 (2002)
55. Y. He, R.K. Wang, J. Biomed. Opt. **9**, 200–206 (2004)
56. R.K. Wang, X. Xu, Y. He, J.B. Elder, IEEE J. Sel. Top. Quant. Electron. **9**, 234–242 (2003)
57. X. Xu, R.K. Wang, Med. Phys. **30**, 1246–1253 (2003)
58. X. Xu, R.K. Wang, J.B. Elder, J. Phys. D Appl. Phys. **36**, 1707–1713 (2003)
59. J.Y. Jiang, R.K. Wang, Phys. Med. Biol. **49**, 5283–5294 (2004)
60. J. Jiang, R.K. Wang, J. X-Ray Sci. Tech. **13**, 149–159 (2005)
61. A.N. Bashkatov, E.A. Genina, Y.P. Sinichkin, V.I. Kochubey, N.A. Lakodina, V.V. Tuchin, Biophys. J. **85**, 3310–3318 (2003)
62. V.V. Tuchin, X. Xu, R.K. Wang, Appl. Opt. **41**, 258–271 (2002)
63. J.M. Schmitt, G. Kumar, Appl. Opt. **37**, 2788–2797 (1998)
64. R.K. Wang, J. Modern Opt. **47**, 103–120 (2000)
65. R.K. Wang, Z. Ma, Opt. Lett. **31**, 3001–3003 (2006)
66. J.M. Schmitt, G. Kumar, Opt. Lett. **21**, 1310–1312 (1996)
67. J.R. Mourant, J.P. Freyer, A.H. Hielscher, A.A. Eick, D. Shen, T.M. Johnson, Appl. Opt. **37**, 3586–3593 (1998)
68. L.H. Wang, S.J. Jacques, L.Q. Zheng, Comput. Methods Program. Biomed. **47**, 131–146 (1995)
69. G. Yao, L.V. Wang, Phys. Med. Biol. **44**, 2307–2320 (1999)
70. O. Khalil, Diabetes Technol. Ther. **6**, 660–697 (2004)
71. R.O. Esenaliev, K.V. Larin, I.V. Larina, M. Motamedi, Opt. Lett. **26**, 992–994 (2001)
72. K.V. Larin, M.S. Eledrisi, M. Motamedi, R.O. Esenaliev, Diabetes Care **25**, 2263–2267 (2002)
73. K.V. Larin, M. Motamedi, T.V. Ashitkov, R.O. Esenaliev, Phys. Med. Biol. **48**, 1371–1390 (2003)
74. M.H. Khan, B. Choi, S. Chess, K.M. Kelly, J. McCullough, J.S. Nelson, Lasers Surg. Med. **34**, 83–85 (2004)
75. K.V. Larin, T. Akkin, M. Motamedi, R.O. Esenaliev, T.E. Millner, Appl. Opt. **43**, 3408–3414 (2004)
76. M. Essenpreis, A. Knüttel, D. Boecker, inventors; Boehringer Mannheim GmbH, US patent 5,710,630, January 20, 1998.
77. K.V. Larin, I.V. Larina, M. Motamedi, V. Gelikonov, R. Kuranov, R.O. Esenaliev, Proc. SPIE **4263**, 83 (2001)
78. M. Kohl, M. Cope, M. Essenpreis, D. Böcker, Opt. Lett. **19**, 2170–2172 (1994)

79. L. Heinemann, U. Kramer, H.M. Klotzer, M. Hein, D. Volz, M. Hermann, T. Heise, K. Rave, Diabetes Technol. Ther. **2**, 211–220 (2000)
80. D.W. Schmidtke, A.C. Freeland, A. Heller, R.T. Bonnecaze, Proc. Natl. Acad. Sci. U. S. A. **95**, 294–299 (1998)
81. M.E. Brezinski, G.J. Tearney, B.E. Bouma, J.A. Izatt, M.R. Hee, E.A. Swanson, J.F. Southern, J.G. Fujimoto, Circulation **93**, 1206–1213 (1996)
82. M.E. Brezinski, G.J. Tearney, N.J. Weissman, S.A. Boppart, B.E. Bouma, M.R. Hee, A.E. Weyman, E.A. Swanson, J.F. Southern, J.G. Fujimoto, Heart **77**, 397–403 (1997)
83. J.G. Fujimoto, S.A. Boppart, G.J. Tearney, B.E. Bouma, C. Pitris, M.E. Brezinski, Heart **82**, 128–133 (1999)
84. P. Patwari, N.J. Weissman, S.A. Boppart, C.A. Jesser, D. Stamper, J.G. Fujimoto, M.E. Brezinski, Am. J. Card. **85**, 641–644 (2000)
85. A. Roggan, M. Friebel, K. Dorschel, A. Hahn, G. Mueller, J. Biomed. Opt. **4**, 36–46 (1999)
86. S.Y. Shchyogolev, J. Biomed. Opt. **4**, 490–503 (1999)
87. A.V. Priezzhev, O.M. Ryaboshapka, N.N. Firsov, I.V. Sirko, J. Biomed. Opt. **4**, 76–84 (1999)
88. S.M. Bertoluzzo, A. Bollini, M. Rsia, A. Raynal, Blood Cell Mol. Dis. **25**, 339–349 (1999)
89. X. Xu, R.K. Wang, J.B. Elder, V.V. Tuchin, Phys. Med. Biol. **48**, 1205–1221 (2003)
90. Y. Yang, T. Wang, N.C. Biswal, X. Wang, M. Sanders, M. Brewer, Q. Zhu, J. Biomed. Opt. **16**(9), 090504-1–3 (2011)
91. R.K. Wang, V.V. Tuchin, in *Coherent-Domain Optical Methods: Biomedical Diagnostics, Environmental Monitoring and Material Science*. V. 2/ed. by V.V. Tuchin. 2nd ed. (Springer, Berlin, 2012), pp. 665–742
92. V.V. Tuchin, IEEE J. Sel. Top. Quant. Electr. **13**(6), 1621–1628 (2007)
93. V.V. Tuchin, R.K. Wang, A.T. Yeh, Special issue on optical clearing of tissues and cells. J. Biomed. Opt. **13**, 021101–1 (2008)
94. V.V. Tuchin, M. Leahy, D. Zhu, eds., Special issue on optical clearing for biomedical imaging in the study of tissues and biological fluids. J. Innov. Opt. Health Sci. **3**(3), 147–219 (2010)
95. E.A. Genina, A.N. Bashkatov, V.V. Tuchin, Expert Rev. Med. Devices **7**(6), 825–842 (2010)
96. E.A. Genina, A.N. Bashkatov, K.V. Larin, V.V. Tuchin, in *Laser Imaging and Manipulation in Cell Biology*, ed. by F.S. Pavone (Wiley-VCH Verlag GmbH & Co. KGaA, Weinheim, 2010), p. 657
97. K.V. Larin, M.G. Ghosn, A.N. Bashkatov, E.A. Genina, N.A. Trunina, V.V. Tuchin, IEEE J. Sel.. Top. Quant. Electr. **18**, 1244–1259 (2012)
98. N. Sudheendran, M. Mohamed, M. Ghosn, V.V. Tuchin, K.V. Larin, J. Innov. Opt. Health Sci. **3**, 169–176 (2010)
99. J. Wang, Y. Liang, S. Zhang, Y. Zhou, H. Ni, Y. Li, Biomed. Opt. Express **2**(8), 2329–2338 (2011)
100. X. Wen, S.L. Jacques, V.V. Tuchin, D. Zhu, J. Biomed. Opt. **17** (2012)
101. I.V. Larina, E.F. Carbajal, V.V. Tuchin, M.E. Dickinson, K.V. Larin, Laser Phys. Lett. **5**, 476–480 (2008)
102. H.Q. Zhong, Z.Y. Guo, H.J. Wei, C.C. Zeng, H.L. Xiong, Y.H. He, S.H. Liu, Laser Phys. Lett. **7**(4), 315–320 (2010)
103. Q.L. Zhao, J.L. Si, Z.Y. Guo, H.J. Wei, H.Q. Yang, G.Y. Wu, S.S. Xie, X.Y. Li, X. Guo, H.Q. Zhong, L.Q. Li, Laser Phys. Lett. **8**(1), 71–77 (2011)
104. Q. Zhao, Z. Guo, H. Wei, H. Yang, S. Xie, Quant. Electr. **41**(10), 950–955 (2011)
105. Z. Zhu, G. Wu, H. Wei, H. Yang, Y. He, S. Xie, Q. Zhao, X. Guo, J. Biophotonics **5**(5–6), 1–8 (2012). doi:10.1002/jbio.201100106
106. M. Ghosn, V.V. Tuchin, K.V. Larin, Opt. Lett. **31**, 2314–2316 (2006)
107. M.G. Ghosn, V.V. Tuchin, K.V. Larin, Invest. Ophthalmol. Vis. Sci. **48**, 2726–2733 (2007)
108. M.G. Ghosn, E.F. Carbajal, N. Befrui, V.V. Tuchin, K.V. Larin, J. Biomed. Opt. **13**, 021110-1–6 (2008)
109. K.V. Larin, V.V. Tuchin, Quant. Electr. **38**, 551–556 (2008)

110. K.V. Larin, V.V. Tuchin, in *Handbook of Optical Sensing of Glucose in Biological Fluids and Tissues*, ed. by V.V. Tuchin (CRC Press, Taylor & Francis Group, London, 2009), pp. 623–656
111. A.N. Bashkatov, E.A. Genina, V.V. Tuchin, in *Handbook of Optical Sensing of Glucose in Biological Fluids and Tissues*, ed. by V.V. Tuchin (CRC Press, Taylor & Francis Group, London, 2009), pp. 587–621
112. E.A. Genina, A.N. Bashkatov, V.V. Tuchin, in *Handbook of Optical Sensing of Glucose in Biological Fluids and Tissues*, ed. by V.V. Tuchin (CRC Press, Taylor & Francis Group, London, 2009), pp. 657–692
113. K.V. Larin, M.G. Ghosn, V.V. Tuchin, in *Handbook of Photonics for Biomedical Science*, ed. by V.V. Tuchin (CRC Press, Taylor & Francis Group, London, 2010), pp. 410–428
114. E.A. Genina, K.V. Larin, A.N. Bashkatov, V.V. Tuchin, in *Handbook of Biophotonics*, ed. by J. Popp, V. Tuchin, A. Chiou, S.H. Heinemann. Photonics for Health Care, vol. 2 (Wiley-VCH Verlag GmbH & Co. KGaA, Weinheim, 2011), pp. 835–853
115. M. Kinnunen, R. Myllylä, T. Jokela, S. Vainio, Appl. Opt. **45**(10), 2251–2260 (2006)
116. M. Kinnunen, R. Myllylä, S. Vainio, J. Biomed. Opt. **13**(2), 021111-1–7 (2008)
117. A. Popov, A. Bykov, S. Toppari, M. Kinnunen, A. Priezzhev, R. Myllylä, IEEE J. Sel. Tops Quant. Electr. **18**, 1335–1342 (2012)
118. M. Ghosn, E.F. Carbajal, N. Befrui, V.V. Tuchin, K.V. Larin, Opt. Lasers Eng. **46**, 911–914 (2008)
119. E.A. Genina, A.N. Bashkatov, V.V. Tuchin, M. Ghosn, K.V. Larin, T.G. Kamenskikh, Quant. Electr. **41**, 407–413 (2011)
120. M. Ghosn, N. Sudheendran, M. Wendt, A. Glasser, V.V. Tuchin, K.V. Larin, J. Biophotonics **3**, 25–33 (2010)
121. K.V. Larin, M.G. Ghosn, S.N. Ivers, A. Tellez, J.F. Granada, Laser Phys. Lett. **4**, 312–317 (2007)
122. M.G. Ghosn, E.F. Carbajal, N. Befrui, A. Tellez, J.F. Granada, K.V. Larin, J. Biomed. Opt. **13**, 010505-1–3 (2008)
123. M.G. Ghosn, S.H. Syed, N.A. Befrui, M. Leba, A. Vijayananda, N. Sudheendran, K.V. Larin, Laser Phys. **19**, 1272–1275 (2009)
124. M.G. Ghosn, M. Mashiatulla, M.A. Mohamed, S.H. Syed, F. Castro-Chavez, J.D. Morrisett, K.V. Larin, Biochim. Biophys. Acta **1810**, 555–560 (2011)
125. M.G. Ghosn, M. Mashiatulla, S.H. Syed, M.A. Mohamed, K.V. Larin, J.D. Morrisett, J. Lipid Res. **52**(7), 1429–1434 (2012)
126. N.A. Trunina, V.V. Lychagov, V.V. Tuchin, SPIE Proc. **7563**, 75630U-1–7 (2010)
127. N.A. Trunina, V.V. Lychagov, V.V. Tuchin, Opt. Spectrosc. **109**(2), 162–168 (2010)
128. V.V. Tuchin, D.M. Zhestkov, A.N. Bashkatov, E.A. Genina, Opt. Express **12**, 2966–2971 (2004)
129. G. Popescu, T. Ikeda, C.A. Best, K. Badizadegan, R.R. Dasari, M.S. Feld, J. Biomed. Opt. **10**(6), 060503-1–3 (2005)
130. H. Kataiwa, A. Tanaka, H. Kitabata, T. Imanishi, T. Akasaka, Circ. J. **72**, 1536–1537 (2008)
131. Y. Ozaki, H. Kitabata, H. Tsujioka, S. Hosokawa, M. Kashiwagi, K. Ishibashi, K. Komukai, T. Tanimoto, Y. Ino, S. Takarada, T. Kubo, K. Kimura, A. Tanaka, K. Hirata, M. Mizukoshi, T. Imanishi, T. Akasaka, Circ. J. 76 (2012); released online Feb. 3, 2012, doi:10.1253/circj.CJ-11-1122
132. P.D. Agrba, M.Y. Kirillin, A.I. Abelevich, E.V. Zagaynova, V.A. Kamensky, Opt. Spectosc. **107**, 853–858 (2009)
133. C. Drew, T.E. Milner, C.G. Rylander, J. Biomed. Opt. **14**, 064019 (2009)
134. A.A. Gurjarpadhye, W.C. Vogt, Y. Liu, C.G. Rylander, Int. J. Biomed. Image **2011**, 817250 (2011)
135. M.Y. Kirillin, P.D. Agrba, V.A. Kamensky, J. Biophotonics **3**, 752–758 (2010)
136. E.I. Galanzha, V.V. Tuchin, A.V. Solovieva, T.V. Stepanova, Q. Luo, H. Cheng, J. Phys. D Appl. Phys. **36**, 1739–1746 (2003)

Second Harmonic OCT and Combined MPM/OCT

49

Zhongping Chen and Shuo Tang

Keywords
MPM • Multimodal imaging • Multiphoton microscopy • Second harmonic • Second harnomic OCT • SH-OCT

49.1 Introduction

Although medicine has evolved rapidly with advances in biotechnology, many therapeutic procedures still require diagnosis of disease at an early stage to enable effective treatment and prevent irreversible damage. Direct visualization of cross-sectional tissue anatomy and physiology provides important information for the diagnosis, staging, and management of disease. Optical coherence tomography (OCT) is a promising noninvasive, noncontact imaging modality that uses coherence gating to obtain cross-sectional images of tissue microstructure with micrometer spatial resolution [1]. OCT was first used clinically in ophthalmology for the imaging and diagnosis of retinal disease [2]. Recently, it has been applied to image subsurface structure in skin, vessels, and oral cavities, as well as respiratory, urogenital, and gastrointestinal tracts.

Despite its advantages, one limitation of OCT is the relatively low imaging contrast. In OCT, imaging contrast originates from the inhomogeneities of sample scattering properties that are linearly dependent on sample refractive indices. In many instances,

Z. Chen (✉)
The Edwards Life Sciences Center for Advanced Cardiovascular Technology, Beckman Laser Institute, Irvine, CA, USA

Department of Biomedical Engineering, Beckman Laser Institute, University of California Irvine, Irvine, CA, USA
e-mail: z2chen@uci.edu

S. Tang
Department of Electrical and Computer Engineering, University of British Columbia, Vancouver, BC, Canada

© Springer International Publishing Switzerland 2015

W. Drexler, J.G. Fujimoto (eds.), *Optical Coherence Tomography*,
DOI 10.1007/978-3-319-06419-2_50

changes in sample linear scattering properties are small and difficult to measure. Multiphoton microscopy (MPM), on the other hand, is based on multiphoton-excited fluorescence and/or harmonic generation and provides molecular contrast and specificity. Fluorescent signals, for example, give exceptional insights into the biophysical and biochemical interactions of biological tissue with molecular specificity and sensitivity. Second harmonic generation (SHG) signals reveal orientation, organization, and local symmetry of biomolecules. Since the first demonstration of MPM in 1990 [3], MPM has been widely used to image morphology and function of various cells and tissues [4]. For the past few years, deep-tissue and in vivo MPM imaging has been reported [5–7]. MPM has found wide applications in neurobiology and developmental biology to monitor calcium dynamics, image neuronal plasticity, and evaluate neurodegenerative disease in animal models. MPM has also been shown to be a valuable tool to study angiogenesis and metastasis and to characterize cell/extracellular matrix interactions in cancer research [4]. There are a number of advantages using MPM for in vivo tissue imaging. First, nonlinear interaction provides intrinsic sectioning capability. Second, use of near-infrared light reduces scattering and enables deep penetration depth. Third, the excitation volume for MPM is limited to the focus region, which minimizes photodamage. Finally, the large separation between excitation, fluorescence, and second harmonic spectra allows highly sensitive detection. Combining nonlinear optical contrast with OCT will greatly enhance clinical applications of these imaging modalities.

In this chapter, we describe multimodal MPM/OCT systems that allow imaging of complementary contrasts and field of views (FOVs) in biological tissues [8–13]. In addition, we present an SH-OCT system that combines the nonlinear optical effect of SHG and coherence gating of OCT to produce highly contrasting cross-sectional images of biological tissues [14–19].

49.2 Combined MPM/OCT System

Combined MPM/OCT is a multimodal imaging technique that combines high-resolution imaging techniques derived from complementary signals to provide simultaneous structural and functional imaging of tissues. It integrates the advantages of MPM and OCT while overcoming the limitations of each other.

MPM and OCT have complementary contrasts [20, 21]. The primary contrasts of MPM include two-photon-excited fluorescence (TPEF) and SHG. TPEF derives from intrinsic sources (e.g., cofactors, proteins) and exogenous fluorophores, while strong SHG comes from non-centrosymmetric molecules, such as collagen, a common structural protein. OCT contrast is backscattered light from refractive index discontinuities that occur between tissues of different structures or compositions. The different contrasts are all related to the induced polarization, the response of a medium to an electromagnetic field,

$$P = \varepsilon_0\left(\chi^{(1)}E + \chi^{(2)}EE^* + \chi^{(3)}EE^*E + \cdots\right), \tag{49.1}$$

where E is the applied electric field, ε_0 is the permittivity of free space, $\chi^{(1)}$ is the linear susceptibility, $\chi^{(n)}$ is the nth-order nonlinear susceptibility (for $n > 1$) [21–23].

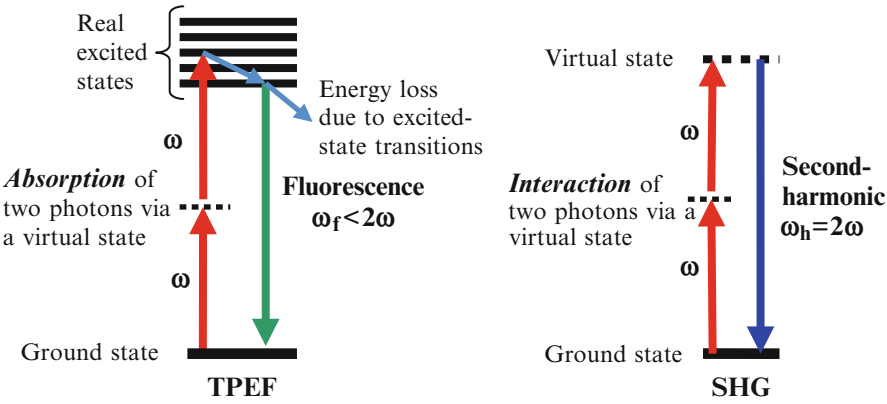

Fig. 49.1 Energy diagrams of TPEF and SHG

Linear effects including absorption and scattering relate to the linear susceptibility $\chi^{(1)}$, whereas nonlinear effects depend upon the higher-order susceptibilities $\chi^{(n)}$. Specifically, scattering is related to $\chi^{(1)}$, SHG to $\chi^{(2)}$, and TPEF to $\chi^{(3)}$, respectively. Due to the nonlinear effects, both the SHG and TPEF intensities depend quadratically on the incident laser power [3, 24, 25].

The energy diagrams of TPEF and SHG are illustrated in Fig. 49.1. In TPEF, a susceptible molecule absorbs two photons simultaneously and is excited from ground state to a real excited state. When the molecule returns to the ground state, it emits a fluorescence photon that has $\omega_f < 2\omega$, where ω is the angular frequency of the incident light. In SHG, a molecule interacts with two photons simultaneously and is excited to a virtual excited state. When the molecule returns to the ground state, it emits an SHG photon which has $\omega_h = 2\omega$. In OCT, the scattering signal is at the same frequency as the incident beam, which has $\omega_s = \omega$. Therefore, the three contrast signals in MPM/OCT have different frequencies and can be separated using dichroic mirrors and filters.

The TPEF signal derives from intrinsic sources, such as elastin, NADH, and flavins, and exogenous fluorophores, such as various fluorescent dyes conjugated to molecular probes. Intrinsic TPEF signals have been observed from cells, collagen, and elastin fibers. Using exogenous probes, TPEF can image targeted subcellular structures and specific proteins. The generation of SHG signals requires a non-centrosymmetric molecular structure. SHG imaging has been primarily applied to collagen fibers, a common structural extracellular matrix protein. Therefore, MPM contrasts are of high biochemical specificity. Meanwhile, OCT detects backscattered light from refractive index discontinuities in cells and tissues. OCT contrast lacks the biochemical specificity.

Furthermore, MPM and OCT are also complementary in imaging resolution, speed, and FOV. MPM provides a sub-micrometer resolution over an FOV of a few hundred micrometers, while OCT has an FOV over a few millimeters at a resolution of ~10 μm. Imaging speed of MPM is typically ~1 fps, while spectral-domain OCT can be as fast

as ~100 fps. Because of their complementary characteristics, MPM and OCT are especially suitable for developing multimodal imaging for clinical applications.

Compared to traditional MPM and OCT, multimodal MPM/OCT can provide multiple complementary contrasts and FOVs and thus is very important for label-free imaging to obtain a sufficient set of parameters for reliable sample analysis. When combined into a single platform, their multiple contrasts can be acquired simultaneously. The sensitivity of MPM to cells and extracellular matrix and of OCT to interfaces can enable observations of cell-cell and cell-matrix interactions during the development of neovasculature, cell migration, and extracellular matrix remodeling. These events are fundamentally important to nearly all biological processes, from growth and development to cancer, wound healing, aging, and diabetes. Furthermore, integrating MPM with OCT can provide multi-scale FOVs, covering a large area for screening and a high-resolution zoom-in for molecular identification. With benefits from both MPM and OCT, the combined system can provide a powerful imaging tool that has both sensitivity and specificity to detect precancerous and cancerous lesions.

While traditional OCT provides a cross-sectional view of layered tissue structures, optical coherence microscopy (OCM), a variation of OCT, provides high-resolution en face view of tissue microstructures. In the following, two types of multimodal MPM/OCT systems will be presented: the MPM/OCM and the multi-scale MPM/OCT systems. The MPM/OCM is a microscopy technique that is able to acquire multiple contrasts, including SHG, TPEF, and scattering simultaneously. The multi-scale MPM/OCT is capable of both tissue level and cellular level imaging, where OCT images layered tissue structures and MPM images cells and extracellular matrix.

49.2.1 MPM/OCM System and Applications

By combining MPM with OCM, the multiple contrasts, including scattering, TPEF, and SHG, can be imaged simultaneously from the same spatial scale. The OCM contrast is scattering from refractive index discontinuities at tissue interfaces. The MPM contrasts include TPEF and SHG. TPEF originates from autofluorescence of tissue or exogenous fluorophores. Endogenous fluorophores in tissue include NADH in cell cytoplasm and elastin fibers, etc. SHG comes mainly from collagen fiber which is the most abundant extracellular matrix. Therefore, the multimodality system can acquire more information about tissues than a single modality alone. In MPM/OCM, high-resolution MPM and OCM images can be acquired from the same FOV of a few hundred micrometers, simultaneously.

MPM/OCM systems have been reported by several groups [8–11, 13, 26, 27]. Beaurepaire et al. [8] and Yazdanfar et al. [13] used ~100 fs Ti:sapphire lasers for combining MPM with OCM. In these systems, the coherence length of the light sources could not match with the MPM axial resolution. To improve depth resolution, a pinhole was needed in front of the OCM detector, which largely limited the system sensitivity. Recently, a fiber-based MPM/OCM system was developed using a femtosecond fiber laser that also had a long coherence length of 16.1 μm [26].

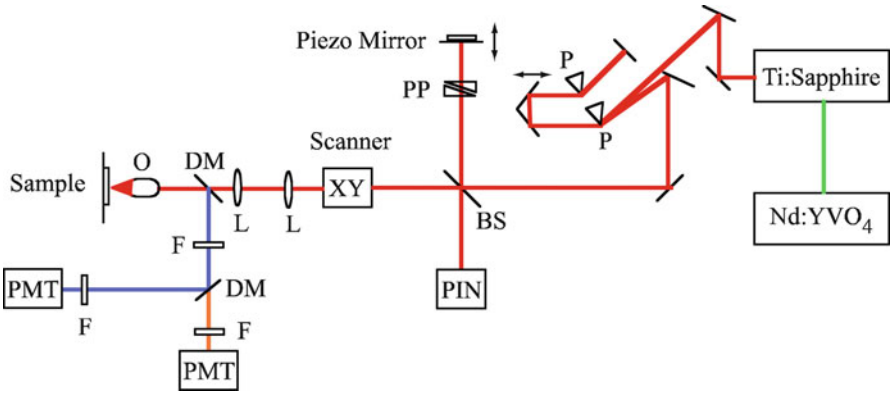

Fig. 49.2 Schematics of the multimodal MPM/OCM system. *BS* beam splitter, *DM* dichroic mirror, *F* filter, *L* lens, *O* objective, *P* prism, *PP* prism pair, *PMT* photomultiplier tube (From Ref. [9])

We have developed a co-registered MPM/OCM system using a 12 fs Ti:sapphire laser [9, 10]. The axial resolution of OCM determined by the coherence length of the laser source was directly matched with the MPM axial resolution of ~1.5 μm. Details about this system are presented in the following.

49.2.1.1 System Configuration

The schematic of the co-registered MPM/OCM system is shown in Fig. 49.2 [9]. A femtosecond Ti:sapphire laser (Femtolasers) is pumped by an Nd:YVO_4 laser (Coherent). The center wavelength of the Ti:sapphire is 800 nm. The laser beam passes through a dispersion precompensation unit composed of two prisms. Afterwards, the laser beam is split by a beam splitter into two arms: the sample arm and the OCM reference arm. In the sample arm, the laser beam is raster scanned by two galvanometer mirrors in an en face mode. The TPEF and SHG signals are collected by the same objective lens in a backward direction and separated from the excitation source by a dichroic mirror (675DCSP, Chroma). The TPEF and SHG are separated by a second dichroic mirror (475DCLP, Chroma), selected by bandpass filters, and detected by two photomultiplier tubes (PMTs). For OCM imaging, a time-domain system was developed. The backscattered fundamental light is reflected by the beam splitter to a PIN detector where it is mixed with the reference beam. In the OCM reference arm, a scanning piezoelectric mirror generates a 5 kHz carrier frequency for OCM detection. OCM interference fringes are received by the PIN detector and processed by envelope detection. Three channels can simultaneously detect TPEF, SHG, and OCM signals. En face imaging is achieved by raster scanning the two galvanometer mirrors. For Z scanning, the sample is vertically scanned by a linear translation stage. The image size is 256 × 256 pixels. The pixel dwell time is ~100 μs which is limited by the carrier frequency of the OCM interference fringe.

TPEF and SHG are nonlinear processes which depend quadratically on the incident laser power [3, 24, 25]. For MPM/OCM imaging, a femtosecond laser

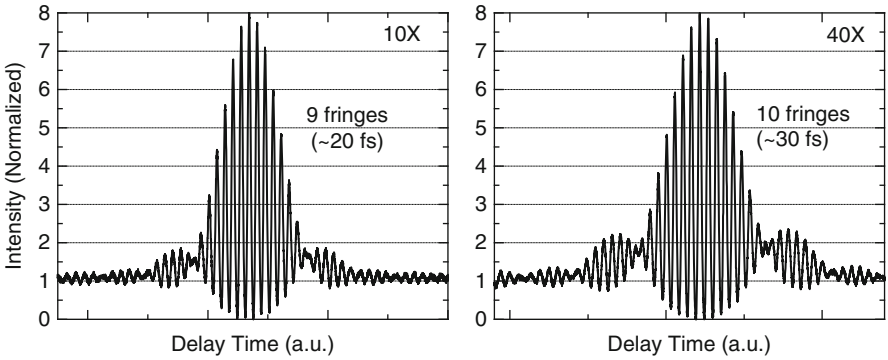

Fig. 49.3 Autocorrelation traces showing 20 fs and 30 fs pulses obtained at the focal plane of a 10× and a 40× objective lens, respectively

with a broad bandwidth is desirable, which provides short pulses (high peak power) for MPM imaging and a short coherence length for OCM imaging. However, for short pulses with broad bandwidth, pulse broadening due to dispersion is significant. Therefore, dispersion precompensation needs to be applied in order to compress the pulses to the femtosecond regime at the sample location [28, 29]. Dispersion precompensation can be achieved using two prisms. In the MPM/OCM system as shown in Fig. 49.2, the laser has a 12 fs pulse duration and 100 nm bandwidth. The laser output passes through a pair of fused silica Brewster prisms. The prism pair precompensates the dispersion from the objective lens and other optics in the beam path. Autocorrelation traces in Fig. 49.3 show 20 fs and 30 fs pulses obtained at the focal plane of a 10× and a 40× objective lens, respectively, after applying the dispersion precompensation. The 100 nm bandwidth is maintained as the short pulses propagate.

49.2.1.2 Co-registration

In a multimodality imaging system such as the MPM/OCM, co-registration is a critical issue. We need to ensure that the different modalities have matched resolutions in three dimensions, and the multichannel images are acquired from the same sampling volume. Due to their quadratic dependence on the incident laser power, TPEF and SHG signals are excited and confined within the focal volume of the objective lens. The MPM transverse and axial resolutions are determined by the focal diameter and the focal depth of the objective lens, respectively. For an objective lens with a numerical aperture of NA, the focal diameter (transverse resolution) is

$$R = 0.61 \frac{\lambda_0}{\mathrm{NA}}, \tag{49.2}$$

and the focal depth (axial resolution) is

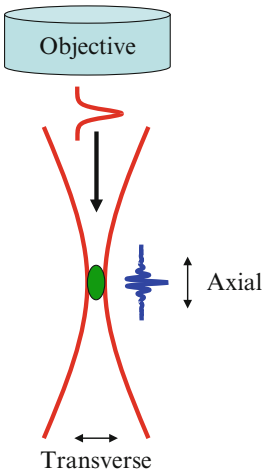

Fig. 49.4 Illustration of the axial and transverse resolutions of MPM and OCM

$$d = \frac{\lambda_0 n}{\mathrm{NA}^2} \tag{49.3}$$

where λ_0 is the illumination light wavelength and n is the refractive index of the immersion medium.

In OCM imaging, the transverse resolution is similarly determined by the focal diameter of the objective lens. However, its axial resolution comes from a different mechanism which is the coherence gating defined by the coherence length of the light source. For a light source with a Gaussian spectral shape, the coherence length is

$$l_c = \frac{2\ln 2}{\pi}\frac{\lambda_0^2}{\Delta\lambda} = 0.44\frac{\lambda_0^2}{\Delta\lambda}, \tag{49.4}$$

where $\Delta\lambda$ is the bandwidth of the light source [30].

In MPM imaging, a high NA objective lens is usually used in order to focus the laser beam to a small volume to achieve high efficiency of nonlinear excitation. To match the resolutions, especially the axial resolutions, between MPM and OCM, the coherence length of the light source needs to match with the focal depth of the objective lens. Figure 49.4 illustrates how the coherence length should be matched with the focal depth.

In the MPM/OCM system as shown in Fig. 49.2, a water immersion achroplan 63× objective lens (Carl Zeiss) of 0.95 NA is used. The theoretically estimated focal diameter is ~0.5 μm, and the focal depth is ~1.3 μm. The Ti:sapphire laser has a pulse width of 12 fs, a center wavelength of 800 nm, and a bandwidth of 100 nm. The bandwidth corresponds to a coherence length of 2.8 μm in free space or 1.87 μm in tissue (assuming $n = 1.5$). Therefore, with the ultrafast Ti:sapphire laser, the MPM and OCM resolutions can be matched closely.

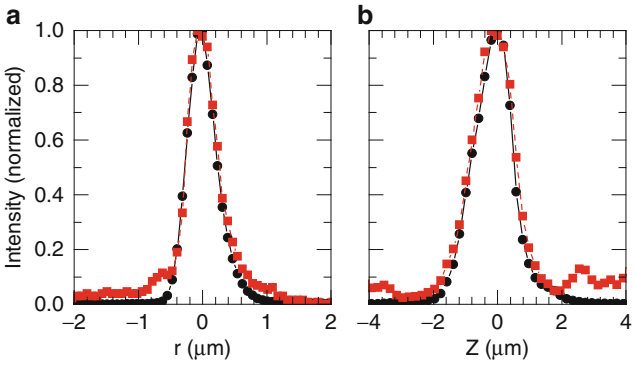

Fig. 49.5 Measured transverse (**a**) and axial (**b**) point spread functions of MPM and OCM. The *circles* are for MPM, and the *squares* are for OCM (From Ref. [9])

Figure 49.5 shows the measured transverse and axial point spread functions (PSFs) of the system. The transverse PSFs from the MPM and OCM match closely and the full width at half maximum (FWHM) is measured to be ~0.5 μm. The axial PSFs for MPM and OCM are also matched with a measured axial resolution of ~1.5 μm.

49.2.1.3 Applications

The multimodal MPM/OCM system has been applied to study cell-cell and cell-matrix interactions. Figure 49.6 shows MPM/OCM images of an organotypic RAFT tissue model [9]. The RAFT model consists of a basic polymerized collagen gel made up of type I rat-tail collagen and primary human dermal fibroblasts. The SHG image shows the organization of the collagen matrix, the TPEF image shows the autofluorescence from a fibroblast, and OCM shows the morphology of the RAFT including the extracellular collagen matrix and the cell. The combination of the three channels provides a more complete picture of the tissue with both structural and compositional information.

The MPM/OCM system has been applied to study the origin of OCM contrast in cells as shown in Fig. 49.7 [10]. Single glioblastoma cells embedded in 3D matrigel are imaged, where the OCM channel shows the scattering locations and the TPEF channel shows the identification of the subcellular structures by specific fluorescence labeling. Figure 49.7a–c shows an unlabeled cell. The TPEF signal is the autofluorescence that is known to be mainly from the cytoplasm due to mitochondrial fluorescence. The weakly fluorescent nuclear region matches with the low-scattering area in the center of the cell. The bright autofluorescence region in the cytoplasm matches with the bright scattering cluster area. The bright scattering pattern in the outer ring (possibly plasma membrane region) does not have a corresponding autofluorescence signature. Cells labeled with DAPI are imaged to identify the nuclear area as shown in Fig. 49.7d–f. The area of DAPI fluorescence matches well with the dark area of low light scattering in OCM. This confirms that the low-scattering area coincides with the nuclear core area. To identify what

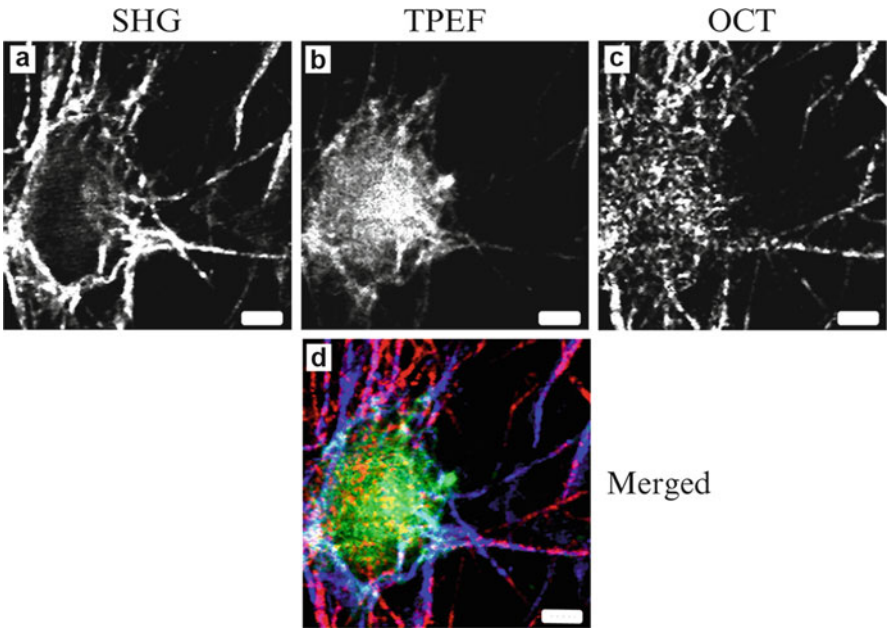

Fig. 49.6 MPM/OCM images of an organotypic RAFT tissue model. (**a**) SHG from collagen matrix; (**b**) TPEF from fibroblasts; (**c**) OCM from scattering interfaces; (**d**) Merged image with SHG, TPEF, and OCM signals in *blue*, *green*, and *red*. The scale bar is 5 μm (From Ref. [9])

generates the bright scattering in the cytoplasm, Fig. 49.7g–i shows a cell labeled with a mitochondrial vital dye, rhodamine 123. The bright scattering area in the cytoplasm matches well with the mitochondrial distribution. Figure 49.7j–l shows images of a cell stained with PKH67 membrane dye. Along the plasma membrane region, bright scattering signals are observed. Figure 49.7m–o shows images of a cell stained with Alexa Fluor 488 conjugated to phalloidin particularly targeting actin filaments. It is observed that the distribution of actin filaments is co-localized with the bright scattering on the cell surface within the resolution of the system. This study shows that strong scattering is mainly from mitochondria, plasma membrane, actin filaments, and the boundary between cytoplasm and nucleus, where there is low scattering from inside the nuclear core.

The MPM/OCM system has also been applied to study the wound-healing process using engineered tissues. The organotypic RAFT model is an engineered tissue model commonly used for studying the wound-healing process. An artificial wound is created by removing part of the RAFT tissue. MPM/OCM imaging is applied to monitor the migration of fibroblasts and remodeling of the collagen matrix. Figure 49.8 shows the MPM/OCM image of the RAFT tissue. The OCM image indicates the boundary between the intact and the wounded areas of the tissue. The SHG shows the collagen matrix, and the TPEF shows a fibroblast that aligns in parallel with the boundary of the wounded area.

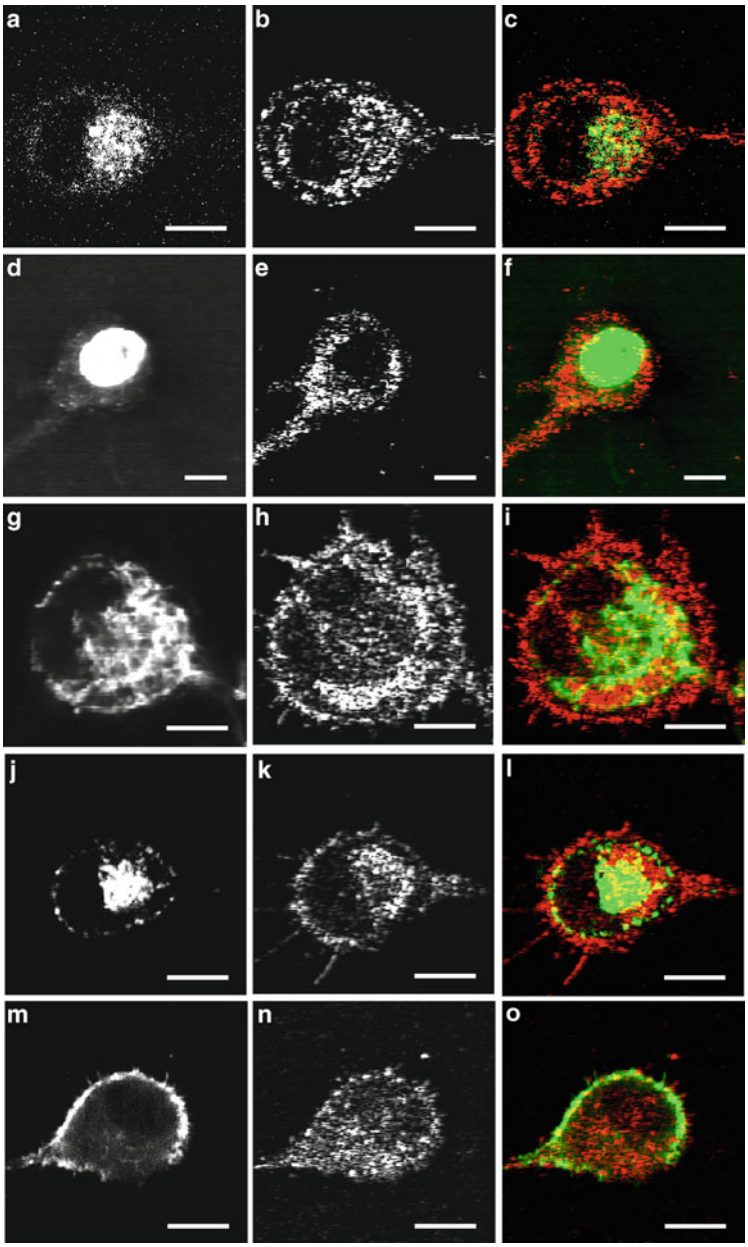

Fig. 49.7 Single-cell imaging with MPM/OCM. TPEF (*left*), OCM (*middle*), and merged (*right*) images of single cells. Single cell without labeling (**a**–**c**); with DAPI labeling for nuclei (**d**–**f**); with rhodamine 123 labeling for mitochondria (**g**–**i**); with PKH67 labeling for plasma membrane (**j**–**l**); and with Alexa Fluor 488 conjugated to phalloidin for actin filaments (**m**–**o**). Pseudo color: TPEF (*green*) and OCM (*red*). The scale bar is 10 μm (From Ref. [10])

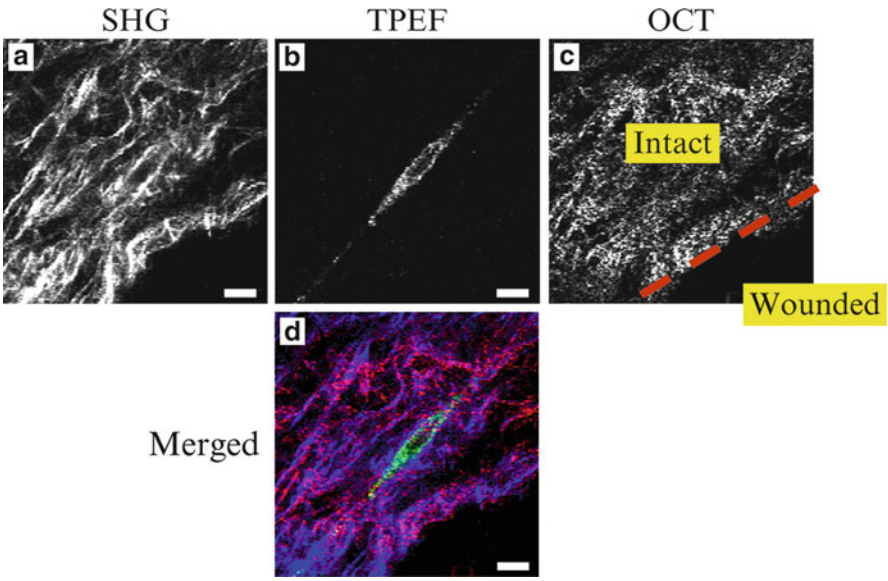

Fig. 49.8 MPM/OCM images of an organotypic RAFT tissue model for studying wound healing. (**a**) SHG image shows collagen matrix. (**b**) TPEF image shows a fibroblast. (**c**) OCM image shows the boundary between intact and wounded areas. (**d**) Merged image of the above three channels. Pseudo color: SHG (*blue*), TPEF (*green*), and OCM (*red*). The scale bar is 10 μm

These results demonstrate that MPM/OCM is a microscopy system that can acquire multiple contrasts simultaneously with pixel level co-registration. The multiple contrasts have different mechanisms and thus can provide complementary information about tissues.

49.2.2 Multi-scale MPM/OCT System and Applications

While the MPM/OCM takes the advantages of the complementary contrasts from MPM and OCT, the multi-scale MPM/OCT is able to take additional advantages from their complementary FOV and speed [31–33]. In multi-scale MPM/OCT, the OCT mode can image a large FOV for assessing overall tissue structures, and the MPM mode can provide a high-resolution zoom-in imaging for identifying cellular level structures. A multi-scale MPM/OCT system is reported by Jeong et al. by utilizing the effective NA of a single objective lens [31]. Different beam spot sizes were shined on the objective to achieve a high NA for MPM and low NA for OCT imaging, respectively. The system used separate laser sources and beam scanners which required critical alignment for registration. We have developed a multi-scale MPM/OCT system using a single sub-10 fs Ti:sapphire laser [32, 33]. The laser source provided a short coherence length which was comparable with the MPM

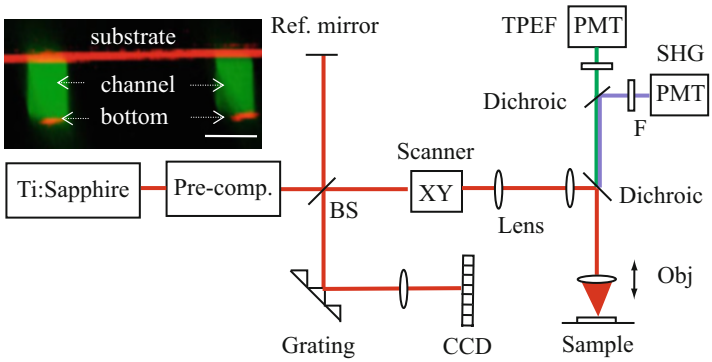

Fig. 49.9 Schematics of the multi-scale MPM/OCT system. The insertion shows co-registered MPM (*green*) and OCT (*red*) images of microfluidic channels. *BS* beam splitter, *F* filter, *Obj* objective *PMT* photomultiplier tube. Scale bar is 40 μm (From Ref. [32])

axial resolution. Two objectives were used: a high NA objective for MPM and a low NA objective for OCT. Because the MPM and OCT shared the same laser source and scanners, co-registration was ensured between the MPM and OCT imaging regions. Details about this system are presented below.

49.2.2.1 System Configuration

The schematic of the multi-scale MPM/OCT system is shown in Fig. 49.9 [32]. A sub-10 fs Ti:sapphire laser (Fusion PRO 400, Femtolasers) is the source for both the MPM and OCT imaging. The laser has a center wavelength of 800 nm, a bandwidth of 120 nm, and a coherence length of 2.3 μm in air. The system is similar to the setup for the multi-contrast MPM/OCM as shown in Fig. 49.2 except that the OCT detection is changed to a spectral-domain OCT. For OCT imaging, the interference signal between the reflected sample and reference light is detected by a custom-built spectrometer. The spectrometer consists of a 1,200 lines/mm transmission grating (Wasatch Photonics), a compound focusing lens composed of two 75 mm focus achromatic doublets back to back with an effective focal length of 37.5 mm, and a 1,024 pixels linescan CCD camera (AViiVA SM2 CL, E2V). A water immersion 40× objective (LUMPlanFL N, Olympus) of 0.8 NA is used for the high-resolution MPM imaging, and a 4× objective (Plan N, Olympus) of 0.1 NA is used for the OCT imaging. The two objectives can be switched without touching the sample. The same XY galvo scanners control the transverse beam scanning for both MPM and OCT. The axial scan of MPM is achieved by a piezo objective scanner (MIPOS 500, Piezosystem Jena). The spectral-domain OCT requires no depth scanning.

The MPM lateral resolution is ~0.6 μm, and axial resolution is ~1.5 μm, respectively. The OCT lateral resolution is ~5 μm, and axial resolution is ~3.3 μm in air. The MPM acquires en face view images with an FOV up to ~300 × 300 μm^2 and speed of 0.4 fps. The OCT acquires cross-sectional view images with an FOV of up to ~3 mm in lateral and ~0.6 mm in depth at a speed of ~100 fps.

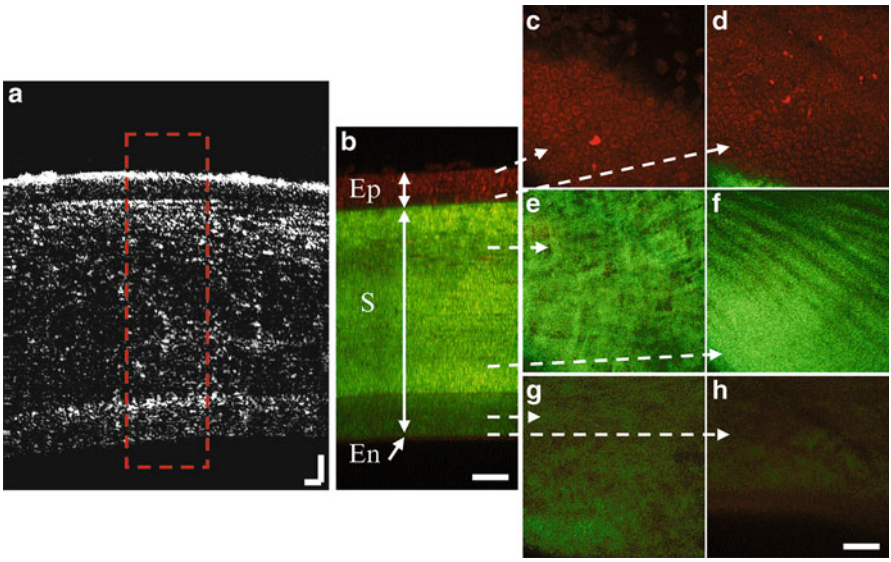

Fig. 49.10 Multi-scale MPM/OCT images of fish cornea. (**a**) Cross-sectional view of OCT. (**b**) Reconstructed cross-sectional view of MPM. (**c**)–(**h**) MPM en face view at depths 5, 25, 80, 220, 275, and 290 μm below the surface. The MPM imaging region is indicated by the *dashed box* in the OCT image. *Ep* epithelium, *S* stroma, *En* endothelium. Pseudo color: SHG (*green*) and TPEF (*red*). Scale bars are 40 μm (From Ref. [32])

49.2.2.2 Co-registration

In the multi-scale MPM/OCT, OCT images a large FOV, while MPM provides zoom-in imaging on a region of interest. Therefore, the co-registration is on the regional level where the MPM FOV is a smaller region that can be localized on the OCT image. This co-registration is achieved by sharing the same laser source and scanning components. The insertion in Fig. 49.9 shows the cross-sectional (XZ) view of two fluorescent dye-filled channels on a microfluidic chip. OCT (red) shows the substrate of the chip and the bottom of the channels, while MPM (green) shows the body of the channels. The locations of the channels are matched in the MPM and OCT images, which indicate the co-registration of the imaging regions.

49.2.2.3 Applications

The multi-scale MPM/OCT imaging is demonstrated in Fig. 49.10 on fish cornea [32]. Figure 49.10a shows the OCT image (XZ view) of the fish cornea. The full thickness of the cornea is detected in a single scan. The image size is 800 μm in lateral and 600 μm in axial direction. In the OCT image, three layers can be detected. However, the identity of the three layers cannot be confirmed. Figure 49.10c–h shows a series of MPM images (XY view) acquired at depths from 5, 25, 80, 220, 275, to 290 μm below the surface, respectively. In Fig. 49.10c, cells are clearly visible in the TPEF channel where the contrast is autofluorescence from the cell cytoplasm, which is an indication of epithelium.

Figure 49.10d shows the junction between the cellular and collagen layers. From Fig. 49.10e–g, the images show mainly SHG contrast from collagen fibers with different structures and densities, which is an indication of stroma. Figure 49.10h is near the bottom of the cornea, where we can still see a weak collagen signal in the SHG channel. Although endothelium cells are not resolved, a thin layer with weak autofluorescence is observed below the end of the collagen layer, which is an indication of endothelium. Therefore, from the TPEF and SHG imaging, the epithelium, stroma, and endothelium layers can be identified in the cornea. Figure 49.10b shows the cross-sectional view of the cornea reconstructed from a MPM stack. It clearly shows the epithelium, stroma, and endothelium layers by looking at the cellular and collagen structures. The different layers identified in the MPM image match well with the layers observed in the OCT image. With the information from the MPM imaging, the three layers observed in the OCT image can be identified to be the epithelium and the two sub-layers of stroma.

Figure 49.11 shows the multi-scale MPM/OCT imaging of a human tooth [33]. In Fig. 49.11a, the OCT shows a large FOV cross-sectional image of the tooth that covers a region of 2 mm in lateral and 0.6 mm in axial directions. The image is acquired near the junction between the crown and the root of the tooth. Two layers are clearly observed: the enamel and the dentin layers. Next, en face MPM images are acquired from a smaller FOV but with higher resolution at multiple depths. The MPM imaging region is co-registered with the center of the OCT imaging region. Specific TPEF and SHG contrasts are observed from the enamel and dentin layers, respectively. Figure 49.11c shows a typical enamel layer where mineralized enamel rods are shown to have bright TPEF contrast. Figure 49.11d shows the boundary between the enamel and dentin layers. The enamel rods are shown to form parallel aggregates in columns. From deeper position of tissue in Fig. 49.11e, the SHG channel shows bright signal from collagen in the dentin layer. The dentin tubules are observed as small holes in the collagen mesh. A stack of 150 frames of the en face MPM images are acquired. The volume data are processed, and a cross-sectional view is displayed in Fig. 49.11b. Compared with the OCT cross-sectional view, the MPM cross-section view covers a smaller region at the center of the OCT FOV. Two distinct layers with TPEF and SHG contrasts, respectively, are distinguishable in Fig. 49.11b which corresponds to the enamel and dentin layers identified by their specific structure and biochemical composition imaged by the MPM. The MPM and OCT cross-sectional images match well with each other.

In the multi-scale MPM/OCT system, a large FOV is provided by the OCT mode, and high-resolution imaging is provided by the MPM mode. Thus, the multi-scale MPM/OCT is both a tissue and cellular level imaging system, where OCT shows layered tissue structures and MPM shows cellular and extracellular matrix structures of each tissue layer. The MPM/OCT system provides a powerful tool which can be used for screening over a large tissue area and for disease diagnosis with high-resolution zoom-in imaging.

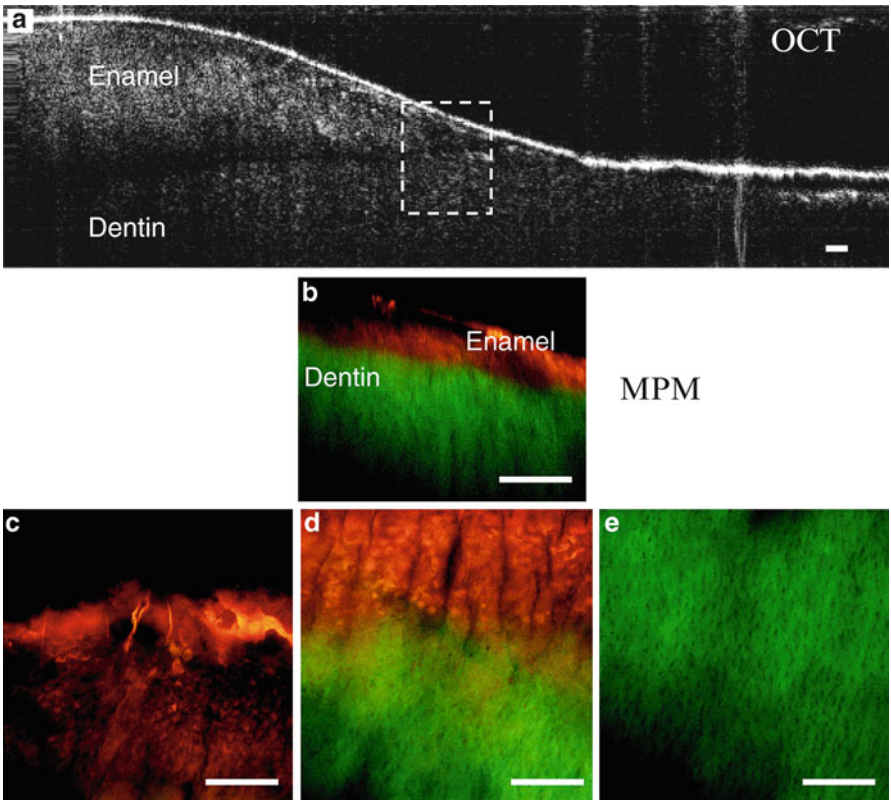

Fig. 49.11 Multi-scale MPM/OCT imaging of a human tooth. (**a**) Cross-sectional view of OCT. (**b**) Reconstructed cross-sectional view of MPM. (**c**)–(**e**) MPM en face view at depths ~30, 60, and 100 μm below the surface, respectively. The MPM imaging region is indicated by the *dashed box* in the OCT image. Pseudo color: SHG (*green*) and TPEF (*red*). Scale bars are 50 μm (From Ref. [33])

49.2.3 Fiber-Based Integrated OCT/MPM System

Although bench top and free-space microscopic-based combined OCT/MPM has many applications for in vitro imaging, it has limitations for in vivo animal and clinical imaging. A fiber-based system reduces system complexity and minimizes the requirement of optical alignment. More importantly, development of a miniature probe can extend the technology to endoscopic imaging for in vivo animal and clinical studies. Although fiber-based systems have been widely used in OCT systems, and fiber-based MPM systems have also been reported by several groups [34–38], there are significant challenges to integrated OCT/MPM in an all-fiber implementation. Recently, our group has developed a fiber-based combined OCM/MPM system that integrates a fiber laser, a fiber combiner, and

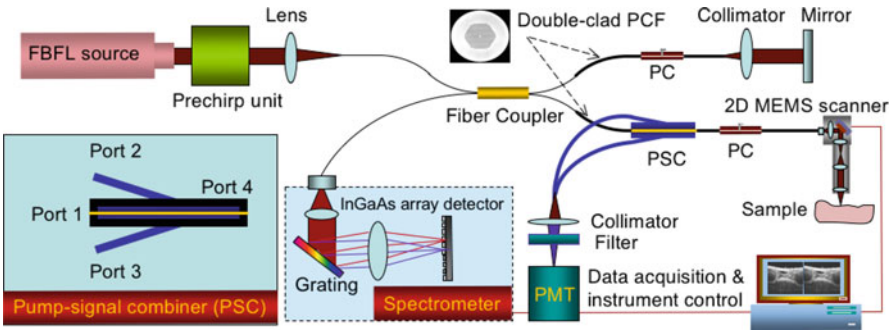

Fig. 49.12 Schematic diagram of the fiber-based combined MPM/OCT system. *FBFL* fiber-based femtosecond laser, *DCF* double-clad fiber, *PSC* pump/signal combiner, *PC* polarization controller. The schematic diagram of a (2 + 1):1 PSC is inserted in the *low left side*

a double-cladding fiber device [26]. Integration of a femtosecond fiber laser as the source for combined OCT/MPM provides more flexibility and lower cost, which will greatly enhance the translation potential of imaging modalities for in vivo animal and clinical studies [37, 39].

49.2.3.1 System Configuration

The fiber-based combined OCM/MPM system is schematically illustrated in Fig. 49.12. A fiber-based femtosecond laser (FBFL), developed in collaboration with Dr. Frank Wise of Cornell University, was used as the light source for both OCM and MPM [26, 39]. The FBFL delivers a sub-100 fs pulse with an average power of more than 1 W and a repetition rate of 76 MHz [26, 39]. The FWHM spectrum bandwidth of the output spectrum is 29 nm which gives an axial resolution of 16.1 μm in air for the OCM [26].

The laser output is sent to a grating pair dispersion-compensation stage and then focused into one arm of a single-mode (SM) 2 × 2 fiber coupler. In the sample arm, the SM fiber of the coupler is fused with one end of a DCF-based pump/signal combiner (PSC). Another end of the PSC is angle cleaved to reduce the reflection. The DCF of the PSC is terminated with a SMA connector and connected with a handheld probe. The handheld probe includes two axial galvo-mirror scanners, a scanning lens, a relay lens, and an objective. The pulse width at the sample side is 300 fs after dispersion compensation. In the reference arm, a DCF with a core size of 10 μm is spliced to the SM fiber of the coupler in order to match the property (dispersion, nonlinear effect, etc.) of the reference arm. A prism pair is used to match the dispersion induced by lenses and objective in the sample arm. The interference signal between the reference arm and sample backscattering or back reflection signal is sent to a home-built spectrometer using a grating with 1,200 grooves per millimeter and an InGaAs detection array with 1,024 pixels. A liner interpolation is used to transform the spectrum from a linear wavelength array to a linear optical frequency array.

A PSC is used for the purpose of delivering the OCM and MPM excitation lights and collection of the OCM and MPM signals. A (2 + 1):1 pump/signal combiner includes two multimode fibers (ports 2 and 3 in Fig. 49.12) fused with one DCF. In the experimental setup, port 1 of the combiner is fused with the sample arm of the fiber coupler. The backscattered excitation light will be collected by both the core and the inner clad of the DCF through port 4. However, only the backscattered excitation light in the core is finally sent to interfere with the OCM reference signal and detected by the spectrometer. The MPM signal will also be collected by both the core and the inner clad of the DCF through port 4. Because the signal collected by the core of the PCF is much less than the one collected by the inner clad of the PCF, only the portion of the signal collected by the clad of the DCF will finally be detected by the PMT. The detectable portion of the collected MPM signal is the portion that goes through the multimode fibers (ports 2 & 3). This portion of the MPM signal is finally detected by the PMT after passing through a band-pass filter. It should be pointed out that the amount of signals that could be sent for detection in this scheme is dependent on the number of multimode fibers used. The amount of detectable signal can be increased by fusing more multimode fibers with the PCF. With a (6 + 1):1 and even (19 + 1):1 pump/signal combiner, detecting more than 50 % of the totally collected power is possible with PSC.

49.2.3.2 Co-registered OCM/MPM Images

We have tested the fiber-based combined OCM/MPM system for imaging biological samples. Figure 49.13a, b shows OCM and MPM images of a thin slice of fixed rabbit heart tissue stained with hematoxylin and eosin. MPM contrast originates from the TPEF of the eosin, which is a pinkish-red dye which has a typical one-photon absorption peak around 527 nm. The MPM image (Fig. 49.13b) shows clear structure of the thin slice. However, the OCM image (Fig. 49.13a) shows that the thin slice has a quite uniform scattering property. Figures 49.13c, d demonstrate the capability of our system to produce simultaneous OCM and MPM images on unstained rat-tail tendon. The MPM image (Fig. 49.13d) originates its contrast from the SHG signal of the collagen fibrils. However, the collagen fibrils are not obvious in the OCM image (Fig. 49.13c). The result shows the complementary nature of OCM and MPM technology.

49.3 Second Harmonic OCT

SHG is a powerful contrast mechanism in nonlinear optical microscopy [4, 40]. SHG microscopy is known for its capability of high-resolution optical 3D sectioning of the sample because signals only arise from the focal area of the objective lens with sufficient peak power. Because SHG is a coherent process, the scattering beam is highly forward directed. The directionality of SHG depends on the distribution and orientation of the induced dipoles within the focal volume and has been investigated [41, 42]. However, because transmission images are difficult to acquire

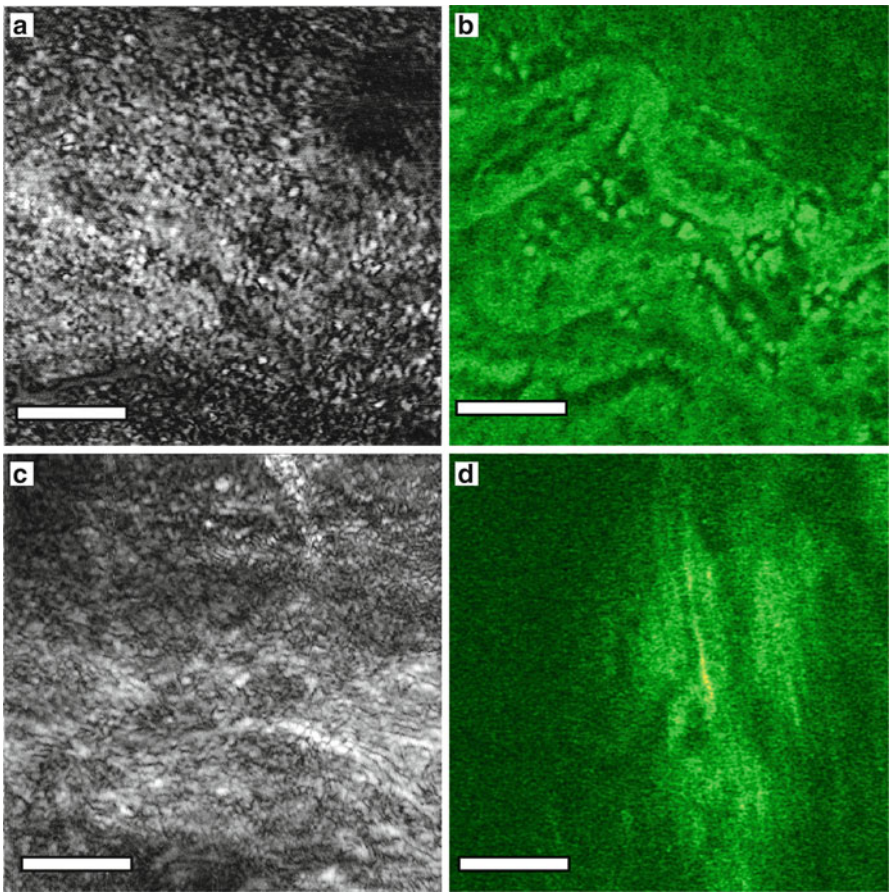

Fig. 49.13 (**a**) OCM and (**b**) SHG images of a thin slice of fixed rabbit heart stained with hematoxylin and eosin. (**c**) OCM and (**d**) SHG images of a rat tail tendon. Scale bar: 50 μm (From Ref. [26])

in thick samples or in vivo studies, SHG microscopy that uses backscattered light has been demonstrated [4]. SHG enables direct imaging of anisotropic biological structures, such as membranes [42], structure proteins [20, 43], and microtubule ensembles [44]. Besides successfully producing high-contrast images of tissue morphology [5, 20, 22, 42–46], SHG microscopy has also been applied recently to study dynamics in tissue physiology, such as monitoring collagen modification in tumors growing in mice [47–49], and optically recording the action potentials change in neuron cells [50]. SHG is emerging as a powerful nonlinear optical imaging modality for biomedical research.

Because SHG signal intensity depends on the square of the excitation laser power, 3D sectioning of the sample is possible with a high numeric aperture objective. However, in a high-scattering turbid tissue sample, such as the skin, scattering reduces the spatial confinement of the SH signal. The detected SHG

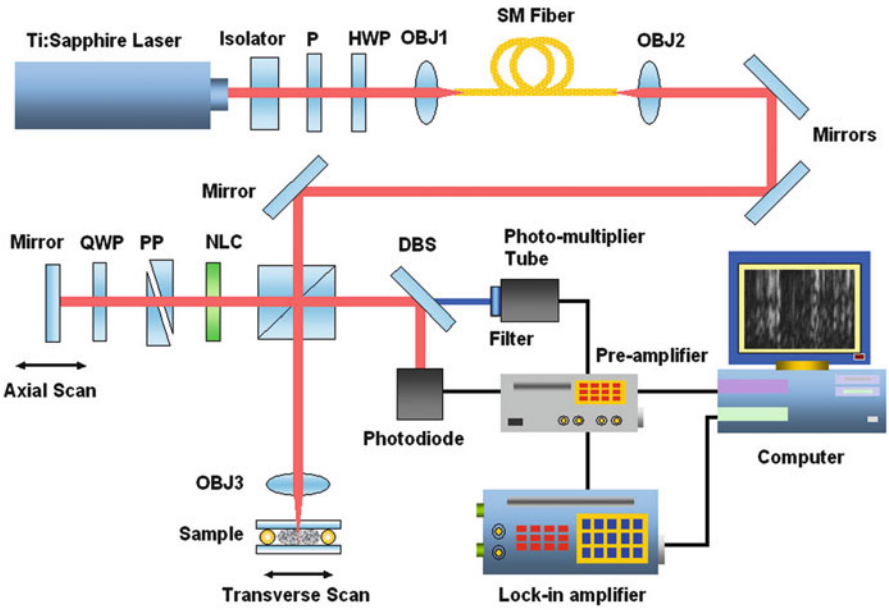

Fig. 49.14 High-resolution SH-OCT experimental setup: *P* polarizer, *HWP* half-wave plate, *QWP* quarter wave plate, *OBJ1-OBJ3* objectives, *NLC* nonlinear crystal, *PP* prism pair dispersion compensator, *DBS* dichroic beam splitter

signal can include a significant contribution from nearby non-focal regions. This degrades the imaging resolution and limits the imaging depth in conventional SH tomography experiments [13]. SH-OCT combines the sample structural sensitivity of SHG with the coherence gating of OCT and has the potential to allow deep-tissue imaging without the stringent requirement of high numeric aperture [14–17, 19]. In addition, regular OCT image can be obtained simultaneously with SH-OCT.

49.3.1 Time-Domain SH-OCT

The schematic of a time-domain SH-OCT system that combines the sample structural sensitivity of SHG with the coherence gating of OCT to produce high-contrast images of biological tissues is shown in Fig. 49.14 [15]. Femtosecond pulses from a Ti:sapphire laser are coupled into a section of nonlinear fiber. A continuum centered at 800 nm with a spectral width of 45 nm is generated from the fiber and used to illuminate a Michelson interferometer. In the sample arm, a microscope objective is used to deliver the excitation pulses to the sample and collect the backscattered fundamental and SH waves. In the reference arm, the SH wave is generated when the laser beam passes through a β-BaB_2O_4 nonlinear crystal. The beam reflects back from a mirror mounted on a piezoelectric actuator. In the detection arm, fundamental and SH interference fringes are detected by a photo

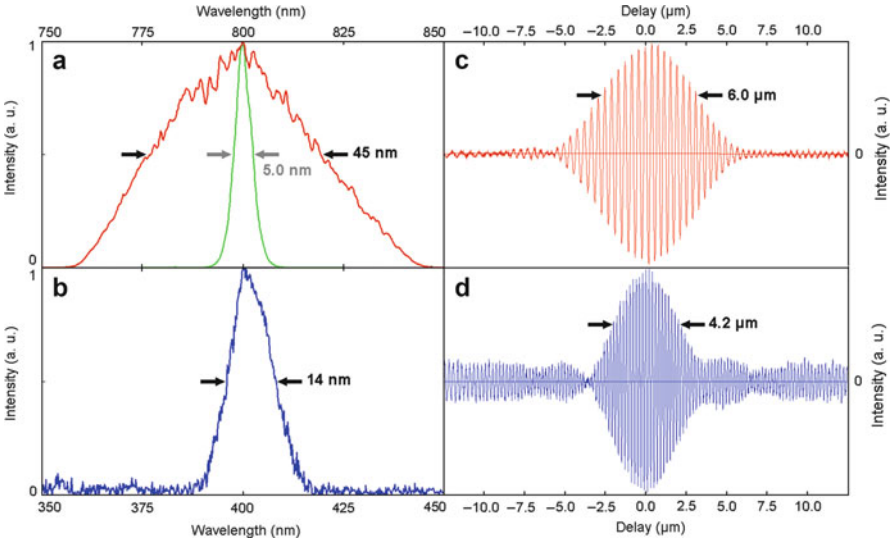

Fig. 49.15 (**a**) Spectrum of the fundamental wave. The *green curve* is the original spectrum of the laser, and the *red curve* is the spectrum of the continuum generated from the fiber. (**b**) Spectrum of the SH wave from the nonlinear crystal. (**c**) Coherence point spread function of the fundamental wave, showing a coherence length of 6.0 μm. (**d**) Coherence point spread function of the SH wave, showing a coherence length of 4.2 μm (From Ref. [15])

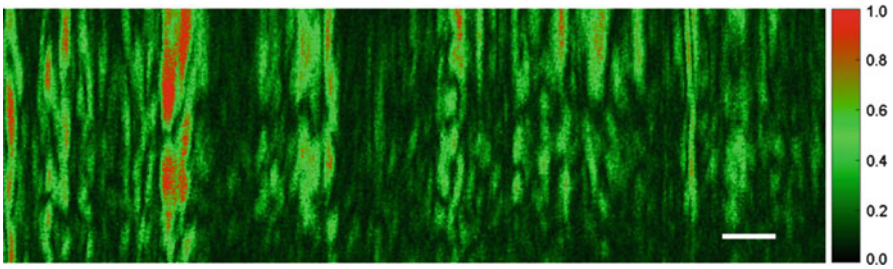

Fig. 49.16 A high-resolution SH-OCT image showing the collagen fiber bundles (fascicles) organization in the rat-tail tendon (Scale bar: 10 μm) (From Ref. [15])

diode and a photomultiplier, respectively, and the demodulated envelope signals are used for image construction. Measured in free space, OCT using a fundamental wave has an axial resolution of 6.0 μm, and SH-OCT has an axial resolution of 4.2 μm (Fig. 49.15), which corresponds to an axial resolution of 3 μm in biological tissue. The lateral resolution determined by the objective lens is 2 μm.

A high-resolution SH-OCT image of a rat-tail tendon is shown in Fig. 49.16. This image shows the collagen fibrils organization within an area of $160 \times 50\ \mu m^2$. As the tension-bearing element in the tendon, collagen appears in clearly defined, parallel, cable-like, and slightly wavy bundles. In this image, highly organized

collagen fiber bundles (fascicles) oriented in the same direction can be identified. Collagen is the predominant structural protein in most biological tissues, as well as an efficient source of SHG. Modifications of the collagen fibrillar matrix structure are associated with various physiologic processes, such as wound healing, aging, diabetes, and cancer. Therefore, SH-OCT is very promising as a sensitive probe in tissue morphology and physiology studies.

49.3.2 Fourier Domain SH-OCT

It has recently been shown that Fourier domain OCT (FD-OCT) has better sensitivity than time-domain OCT (TD-OCT) [51]. This sensitivity advantage of FD-OCT also applies to SH-OCT [18, 19]. Spectrometer-based FD SH-OCT techniques can significantly improve image sensitivity over TD SH-OCT. FD SH-OCT detects the echo time delays of light by measuring the interference spectrum of the light signal from the tissue. The detection system uses a spectrometer in conjunction with a high-speed, high-dynamic range CCD camera, photodiode array, or line-scan camera. The camera records the spectrum of the interference pattern, and the echo time delays of the light signal can be extracted with Fourier transform. FD-OCT does not require moving parts. In addition, since all of the reflected light is measured at once, there is a dramatic increase in detection sensitivity. This sensitivity improvement enables a 50–100 times increase in the imaging speed over standard TD SH-OCT systems.

The schematic of the FD SH-OCT system is shown in Fig. 49.17 [19]. The FD SH-OCT system consists of a Michelson interferometer illuminated by a femtosecond fiber light source. A self-starting, stretched-pulse Yb fiber laser generating femtosecond pulses centered at 1.03 μm wavelength with a 50 MHz repetition rate is used as the light source [19]. The mode-locked pulses from the fiber oscillator are temporally stretched in a 10 m single-mode fiber and amplified in yttrium-doped fibers pumped by two diode lasers. The output pulses are compressed by external grating pairs to 170 fs with an average power of 260 mW at 50 MHz repetition rate. The output spectra have an approximate Gaussian shape with a bandwidth of 13.5 nm (FWHM) that allows us to record FD SH-OCT images with 30 μm axial resolution. To increase the axial resolution, an 8.5 cm long high-index fiber is used to broaden the spectra. The broadened output spectral bandwidth is about 40 nm, and the pulse duration of the continuum spectra is less than 400 fs with an average power of 100 mW. A broadband, non-polarization beam splitter is used to support interference fringes at both the fundamental and SH wavelengths. In the sample arm, the beam is focused on the sample through a microscope objective.

Fundamental and SH waves backscattered from the sample are collected by the same excitation objective. In the reference arm, the SH wave is generated when the laser beam passes through a thin β-BaB_2O_4 (BBO) nonlinear crystal. The beam is then reflected back from a dichroic mirror mounted on a piezoelectric actuator. The dichroic mirror reflects 90 % of the SH wave and 5 % of the fundamental wave.

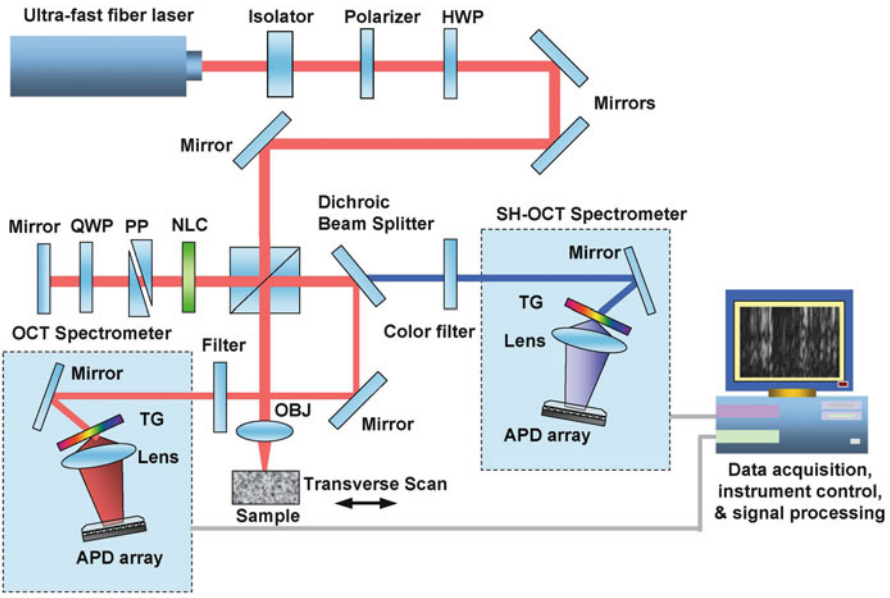

Fig. 49.17 Schematic diagram of the FD SH-OCT system set up: *HWP* half-wave plate, *QWP* quarter wave plate, *OBJ* objective, *NLC* nonlinear crystal, *PP* prism pair dispersion compensator, *TG* transmitting grating

A prism pair made from BK7 glass is inserted into the reference arm to compensate for the group velocity dispersion in the two arms. In the detection arm, a dichroic beam splitter is used to separate the beam according to the wavelength. Fundamental and SH interference fringes are detected with two high-resolution, high-sensitive spectrometers with 2,048 pixels, one centered at the fundamental wavelength and the other centered at the second harmonic wavelength. The SH-OCT spectrometer is designed to cover a spectral range of 100 nm with a spectral resolution of 0.15 nm. An appropriate band-pass filter is inserted before the entrance of the spectrometer to reject background noise.

After the SH spectral fringe signals are digitized and transferred to a computer, the average reference spectral is subtracted from the raw signal to remove the DC components. The signal is then divided by the average reference signal followed by the multiplication of a Gaussian profile to remove any artifact due to the variation of spectral response of the array detector. The fringe signal is then rescaled from wavelength space to frequency space by using spline interpolation and resampling. The linear resampled fringe data in the frequency space $I_j(k)$ is then Fourier transformed to obtain the complex fringe signal in spatial domain $S_j(z)$ where j denotes the jth A-line scan data obtained from jth spectral measurement. To increase the signal-to-noise ratio, multiple $S_j(z)$ at the same location are averaged. Assuming an optimal detector integration time of 10 ms and an average of 10 $S_j(z)$ for imaging construction, an FD SH-OCT image with 100 lateral pixel points can be obtained in 10 s.

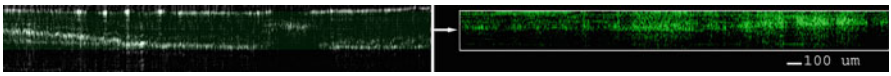

Fig. 49.18 OCT (*left*) and SH-OCT (*right*) images of fish scales. The dimension of each image is 3 mm × 0.46 mm (From Ref. [19])

We have used this prototype system to image fish skin from salmon (Fig. 49.18). Using continuum radiation generated in the fiber SH-OCT, images of fish scales from salmon were recorded. For these images, 50 mW of fundamental power was delivered on the sample. The CCD integration time of the second harmonic spectrometer was set at 20 ms and 50 A-scans were averaged. The CCD integration time of the fundamental spectrometer was set at 0.8 ms, and 50 A-scans were averaged. Figure 49.18 shows the image of the fish scales obtained simultaneously with both fundamental and second harmonic interferometers. The left-hand side shows an image of fish scales obtained by the fundamental OCT. Boundaries between different layers can be clearly identified. For clarity, the SH-OCT image is displayed on the right-hand side. The polarization of the SH is parallel to the fundamental beam polarization. The SH-OCT image on the right-hand side shows layer-like distribution of collagen fibrils. Highly ordered sections of the collagen bundles in the fish scales are clearly visible. The measured axial resolution of the SH-OCT image is 12 μm, and the measured axial resolution of the fundamental OCT image is 17 μm. Although SH-OCT resolution using this light source is not enough to resolve individual fiber bundles, the SH-OCT signal from collagen is clearly evident with an excitation wavelength of around 1.03 μm.

One of the concerns is the high peak power used for SH-OCT. We have performed an analysis on the damage threshold. Assume a beam waist diameter of 4 μm and an average power of incoming pulses incident on the sample as high as 50 mW with pulse duration of 50 fs and repetition rate of 40 MHz, the peak power density at the beam waist in the sample is estimated as

$$I_{\text{Peak}} = \frac{P_{\text{Peak}}}{\pi {w_0}^2} = \frac{\left(\dfrac{50 \times 10^{-3}}{50 \times 10^{-15} \times 40 \times 10^{6}}\right)}{\left(\pi \times \left(2 \times 10^{-4}\right)^2\right)} = 0.2\ \text{TW/cm}^2, \tag{49.5}$$

which is below the documented peak intensity threshold for loss in cell viability of several TW/cm^2 [6, 52]. The energy per pulse of the beam incident on the tissue is less than 1.3 nJ, corresponding to the energy density of 0.01 J/cm^2. This beam intensity is much less than the tissue damage threshold, which is in the range of 0.5–1.0 J/cm^2 [6, 53].

SH-OCT may offer several distinct advantages for imaging ordered, or partially ordered, biological tissues. First, the SHG signal from tissue is a very sensitive indicator of tissue structure and local symmetry changes and serves as a unique contrast mechanism in optical tomographic imaging. Second, coherence gating extends the capability of high-resolution detection of SHG signals since signals arising out of focal

volume can be further rejected. Third, decoupled axial and transverse scans enable two-dimensional tomographic imaging of a sample with only one-dimensional scanning of the probing beam, which is essential for in vivo endoscopic applications.

49.4 Summary

MPM/OCT and SH-OCT systems can acquire structural and functional imaging simultaneously on both tissue and cellular levels. The integration of nonlinear optical contrasts with OCT provides the biochemical specificity and the cellular level resolution to optical tomography. Given the rapid development of photonic crystal fibers that allow propagation of femtosecond laser and 2-D MEMS scanners, it is possible to integrate combined MPM/OCT and SH-OCT with a fiber-based endoscopic delivery system. Future research will improve the imaging speed and penetration depth of the integrated system and develop endoscopic MPM/OCT and SH-OCT systems for intraluminal in vivo imaging.

Acknowledgments We would like to thank many of our colleagues who have contributed to the MPM/OCT and SH-OCT projects at UCI and UBC. We want to acknowledge grant support from the National Institutes of Health (R01EB-00293, R01CA-91717, R01EB-10090, R01EY-021519, R01HL-105215, P41EB-015890), Air Force Office of Scientific Research (F49620-00-1-0371), the Beckman Laser Institute Endowment, Natural Sciences and Engineering Research Council of Canada, and the Canada Foundation for Innovation.

References

1. D. Huang, E.A. Swanson, C.P. Lin, J.S. Schuman, W.G. Stinson, W. Chang, M.R. Hee, T. Flotte, K. Gregory, C.A. Puliafito, J.G. Fujimoto, Optical coherence tomography. Science **254**(5035), 1178–1181 (1991)
2. M.R. Lee, J.A. Izatt, E.A. Swanson, D. Huang, J.S. Schumun, C.P. Lin, C.A. Puliafito, J.G. Fujimoto, Optical coherence tomography for ophthalmic imaging: new technique delivers micron-scale resolution. IEEE Eng. Med. Biol. Mag. **14**(1), 67–76 (1995)
3. W. Denk, J.H. Strickler, W.W. Webb, Two-photon laser scanning fluorescence microscopy. Science **248**, 73–79 (1990)
4. W.R. Zipfel, R.M. Williams, W.W. Webb, Nonlinear magic: multiphoton microscopy in the biosciences. Nat. Biotechnol. **21**, 1369–1377 (2003)
5. W.R. Zipfel, R.M. Williams, R.A. Christie, Y. Nikitin, B.T. Hyman, Live tissue intrinsic emission microscopy using multiphoton-excited native fluorescence and second harmonic generation. Proc. Natl. Acad. Sci. USA **100**, 7075 (2003)
6. C.K. Sun, C.C. Chen, S.W. Chu, T.H. Tsai, Y.C. Chen, B.L. Lin, Multiharmonic-generation biopsy of skin. Opt. Lett. **28**, 2488 (2003)
7. D. Kobat, N.G. Horton, C. Xu, In vivo two-photon microscopy to 1.6-mm depth in mouse cortex. J. Biomed. Opt. **16**(10), 106014 (2011)
8. E. Beaurepaire, L. Moreaux, F. Amblard, J. Mertz, Combined scanning optical coherence and two-photon-excited fluorescence microscopy. Opt. Lett. **24**, 969–971 (1999)
9. S. Tang, T.B. Krasieva, Z. Chen, B. Tromberg, Combined multiphoton microscopy and optical coherence tomography using a 12 femtosecond, broadband source. J. Biomed. Opt. **11**, 020502 (2006)

10. S. Tang, C.H. Sun, T.B. Krasieva, Z. Chen, B. Tromberg, Imaging sub-cellular scattering contrast using combined optical coherence and multiphoton microscopy. Opt. Lett. **32**, 503–505 (2007)
11. C. Vinegoni, T.S. Ralston, W. Tan, W. Luo, D.L. Marks, S.A. Boppart, Integrated structural and functional optical imaging combining spectral-domain optical coherence and multiphoton microscopy. Appl. Phys. Lett. **88**, 053901 (2006)
12. C. Joo, K.H. Kim, J.F. de Boer, Spectral-domain optical coherence phase and multiphoton microscopy. Opt. Lett. **32**, 623–625 (2007)
13. S. Yazdanfar, Y.Y. Chen, P.T.C. So, L.H. Laiho, Multifunctional imaging of endogenous contrast by simultaneous nonlinear and optical coherence microscopy of thick tissues. Micr. Res. Tech. **70**, 503–505 (2007)
14. Y. Jiang, I. Tomov, Y. Wang, Z. Chen, Second harmonic optical coherence tomography. Opt. Lett. **29**, 1090–1092 (2004)
15. Y. Jiang, I. Tomov, Y. Wang, Z. Chen, High-resolution second-harmonic optical coherence tomography of collagen in rat-tail tendon. Appl. Phys. Lett. **86**, 133901 (2005)
16. S. Yazdanfar, L.H. Laiho, P.T.C. So, Interferometric second harmonic generation microscopy. Opt. Express **12**, 2739 (2004)
17. B.E. Applegate, C. Yang, A.M. Rollins, J.A. Izatt, Polarization-resolved second-harmonic-generation optical coherence tomography in collagen. Opt. Lett. **29**, 2252–2254 (2004)
18. M.V. Sarunic, B.E. Applegate, J.A. Izatt, Spectral domain second harmonic optical coherence tomography. Opt. Lett. **30**, 2391–2393 (2005)
19. J. Su, I.V. Tomov, Y. Jiang, Z. Chen, High resolution frequency-domain second-harmonic optical coherence tomography. Appl. Opt. **46**, 1770–1775 (2007)
20. A. Zoumi, A. Yeh, B.J. Tromberg, Imaging cells and extracellular matrix in vivo by using second-harmonic generation and two-photon excited fluorescence. Proc. Natl. Acad. Sci. USA **99**, 11014 (2002)
21. P.J. Campagnola, M.D. Wei, A. Lewis, L.M. Loew, High-resolution nonlinear optical imaging of live cells by second harmonic generation. Biophys. J. **77**, 3341–3349 (1999)
22. P.J. Campagnola, L.M. Loew, Second-harmonic imaging microscopy for visualizing biomolecular arrays in cells, tissues and organisms. Nat. Biotechnol. **21**, 1356–1360 (2003)
23. Y.R. Shen, *The Principles of Nonlinear Optics* (Wiley, New York, 1984)
24. C. Xu, W.R. Zipfel, J.B. Shear, R.M. Williams, W.W. Webb, Multiphoton fluorescence excitation: new spectral windows for biological nonlinear microscopy. Proc. Natl. Acad. Sci. USA **93**, 10763–10768 (1996)
25. K. Konig, Multiphoton microscopy in life sciences. J. Microsc. **200**, 83–104 (2000)
26. G. Liu, Z. Chen, Fiber-based combined optical coherence and multiphoton endomicroscopy. J. Biomed. Opt. **16**(3), 036010 (2011)
27. B.W. Graf, S.A. Boppart, Multimodal in vivo skin imaging with integrated optical coherence and multiphoton microscopy. IEEE J. Sel. Top. Quantum Electron. **18**, 1280–1286 (2012)
28. M. Müller, J. Squier, G.J. Brakenhoff, Measurement of femtosecond pulses in the focal point of a high-numerical-aperture lens by two-photon absorption. Opt. Lett. **20**, 1038–1040 (1995)
29. M. Müller, J. Squier, R. Wolleschensky, U. Simon, G.J. Brakenhoff, Dispersion pre-compensation of 15 femtosecond optical pulses for high-numerical-aperture objectives. J. Microsc. **191**, 141–150 (1998)
30. A.F. Fercher, W. Drexler, C.K. Hizenberger, Optical coherence tomography–principles and applications. Rep. Prog. Phys. **66**, 239–303 (2003)
31. B. Jeong, B. Lee, M.S. Jang, H. Nam, S.J. Yoon, T. Wang, J. Doh, B.G. Yang, M.H. Jang, K.H. Kim, Combined two-photon microscopy and optical coherence tomography using individually optimized sources. Opt. Express **19**(14), 13089–13096 (2011)
32. S. Tang, Y. Zhou, K.K. Chan, T. Lai, Multiscale multimodal imaging with multiphoton microscopy and optical coherence tomography. Opt. Lett. **36**(24), 4800–4802 (2011)
33. S. Tang, Y. Zhou, M.J. Ju, Multimodal optical imaging with multiphoton microscopy and optical coherence tomography. J. Biophotonics **5**(5–6), 396–403 (2012)

34. M.T. Myaing, D.G. MacDonald, L. Xingde, Fiber-optic scanning two-photon fluorescence endoscope. Opt. Lett. **31**, 1076–1078 (2006)
35. L. Fu, A. Jain, H. Xie, C. Cranfield, M. Gu, Nonlinear optical endoscopy based on a double clad photonic crystal fiber and a MEMS mirror. Opt. Express **14**, 1027–1032 (2006)
36. W. Jung, S. Tang, D.T. McCormic, T. Xie, Y.C. Ahn, J. Su, I.V. Tomov, T.B. Krasieva, B.J. Tromberg, Z. Chen, Miniaturized probe based on a microelectromechanical system mirror for multiphoton microscopy. Opt. Lett. **33**(12), 1324–1326 (2008)
37. G. Liu, T. Xie, I.V. Tomov, J. Su, L. Yu, J. Zhang, B.J. Tromberg, Z. Chen, Rotational multiphoton endoscopy with a 1 micron fiber laser system. Opt. Lett. **34**(15), 2249–2251 (2009)
38. S. Tang, W. Jung, D. McCormick, T. Xie, J. Su, Y.C. Ahn, B.J. Tromberg, Z. Chen, Design and implementation of fiber-based multiphoton endoscopy with microelectromechanical systems scanning. J. Biomed. Opt. **14**(3), 034005 (2009)
39. G. Liu, K. Kieu, F.W. Wise, Z. Chen, Multiphoton microscopy system with a compact fiber-based femtosecond-pulse laser and handheld probe. J. Biophotonics **4**(1–2), 34–39 (2011)
40. I. Freund, M. Deutsch, Second-harmonic microscopy of biological tissue. Opt. Lett. **11**, 94–96 (1986)
41. J. Mertz, L. Moreausx, Second-harmonic generation by focused excitation of inhomogeneously distributed scatterers. Opt. Commun. **196**, 325–330 (2001)
42. L. Moreaux, O. Sandre, L. Mertz, Membrane imaging by second-harmonic generation microscopy. J. Opt. Soc. Am. B **17**, 1685 (2000)
43. P.J.A. Campagnola, C. Millard, M. Terasaki, P.E. Hoppe, C.J. Malone, W.A. Mohler, Three-dimensional high-resolution second-harmonic generation imaging of endogenous structural proteins in biological tissues. Biophys. J. **82**, 493 (2002)
44. D.A. Dombeck, K.A. Kasischke, H.D. Vishwasrao, M. Ingelsson, B.T. Hyman, W.W. Webb, Uniform polarity microtubule assemblies imaged in native brain tissue by second-harmonic generation microscopy. Proc. Natl. Acad. Sci. USA **100**, 7081–7086 (2003)
45. G. Cox, E. Kable, A. Jones, I.K. Fraser, F. Manconi, M.D. Gorrell, 3-dimensional imaging of collagen using second harmonic generation. J. Struct. Biol. **141**, 53 (2003)
46. Aghajan, H.K., Khalaj, B.H., Kailath, T.: Estimation of multiple 2D uniform motions by sensor array processing techniques. Presented at the image and video processing II, San Jose (1994) (unpublished)
47. Y.C. Guo, H.E. Savage, F. Liu, S.P. Schantz, P.P. Ho, R.R. Alfano, Subsurface tumor progression investigated by noninvasive optical second harmonic tomography. Proc. Natl. Acad. Sci. USA **96**, 10854 (1999)
48. E. Brown, T. McKee, E. diTomaso, A. Pluen, B. Seed, Y. Boucher, R.K. Jain, Dynamic imaging of collagen and its modulation in tumors in vivo using second-harmonic generation. Nat. Med. **9**, 796 (2003)
49. P. Wilder-Smith, K. Osann, N. Hanna, N. El Abbadi, M. Brenner, D.D.V. Messadi, T. Krasieva, In vivo multiphoton fluorescence imaging: a novel approach to oral malignancy. Lasers Surg. Med. **35**, 96–103 (2004)
50. D.A. Dombeck, M. Blanchard-Desce, W.W. Webb, Optical recording of action potentials with second-harmonic generation microscopy. J. Neurosci. **24**, 999 (2004)
51. R. Leitgeb, C.K. Hitzenberger, A.F. Fercher, M. Kulhavy, Performance of fourier domain vs. time domain optical coherence tomography. Opt. Express **11**, 889–894 (2003)
52. K. Konig, T.W. Becker, P. Fisher, I. Riemann, K.J. Halbhuber, Pulse-length dependence of cellular response to intense near-infrared laser pulses in multiphoton microscopes. Opt. Lett. **24**, 113–115 (1999)
53. B.M. Kim, J. Eichler, K.M. Reiser, A.M. Rubenchik, L.B. Dasilva, Collagen structure and nonlinear susceptibility: effects of heat, glycation, and enzymatic cleavage on second harmonic signal intensity. Lasers Surg. Med. **27**, 329–335 (2000)

Combined Endoscopic Optical Coherence Tomography and Laser Induced Fluorescence

50

Jennifer K. Barton, Alexandre R. Tumlinson, and Urs Utzinger

Keywords

Endoscopy • Dual-modality • Fluorescence imaging • Fluorescence spectroscopy • Optical coherence tomography

50.1 Introduction

Optical coherence tomography (OCT) and laser-induced fluorescence (LIF) are promising modalities for tissue characterization in human patients and animal models. OCT detects coherently backscattered light, whereas LIF detects fluorescence emission of endogenous biochemicals, such as reduced nicotinamide adenine dinucleotide (NADH), flavin adenine dinucleotide (FAD), collagen, and fluorescent proteins, or exogenous substances such as cyanine dyes. Given the complementary mechanisms of contrast for OCT and LIF, the combination of the two modalities could potentially provide more sensitive and specific detection of disease than either modality alone. Sample probes for both OCT and LIF can be implemented using small diameter optical fibers, suggesting a particular synergy for endoscopic applications. In this chapter, the mechanisms of contrast and diagnostic capability for both OCT and LIF are briefly examined. Evidence of complementary capability is described. Example published combined OCT–LIF systems are reviewed, one successful commercial instrument is discussed, and example applications are provided.

J.K. Barton (✉) • U. Utzinger
Biomedical Engineering, The University of Arizona, Tucson, AZ, USA

Optical Sciences, The University of Arizona, Tucson, AZ, USA
e-mail: barton@email.arizona.edu

A.R. Tumlinson
Carl Zeiss Meditec, Inc., Dublin, CA, USA

© Springer International Publishing Switzerland 2015

W. Drexler, J.G. Fujimoto (eds.), *Optical Coherence Tomography*,
DOI 10.1007/978-3-319-06419-2_51

50.2 Background on Optical Coherence Tomography

OCT provides high-resolution, depth-resolved images of scattering tissues. With micron-scale resolution and millimeter depth of imaging, OCT is ideal for examining superficial and optically accessible tissues. Most commonly, the amplitude of the backscattered signal is displayed to yield structural images. In this case, signal originates from index of refraction mismatches. Functional variants described elsewhere of this handbook include polarization-sensitive OCT, which is sensitive to tissue birefringence and optical axis orientation [1–4]; Doppler OCT, which measures the velocity of moving scatterers [5–7]; phase-contrast OCT, which is sensitive to small changes in optical path length [8, 9]; and molecular contrast OCT (MCOCT) [10–12], which includes measurement of changes in the source spectrum due to attenuation by endogenous or exogenous substances [13, 14] as well as detection of processes that yield coherent radiation, e.g., coherent anti-Stokes Raman scattering [15] and second harmonic generation [16, 17]. Several exogenous scattering agents have also been proposed to selectively enhance the OCT signal [18–23]. These additional mechanisms of contrast may augment the diagnostic capability of OCT. MCOCT, similar to LIF, has the potential to identify and quantify the presence of certain endogenous and targeted or untargeted exogenous molecules.

50.2.1 Diagnostic Accuracy of Optical Coherence Tomography

OCT has demonstrated promise for providing accurate diagnoses in a variety of organ sites. Several clinical applications are described in detail in this handbook. Diagnosis and management of retinal disorders, early cancer detection (especially in epithelial tissues), and detection of vulnerable plaque are perhaps the most widely studied applications.

The number of moderate- to large-scale clinical studies performed to assess diagnostic accuracy of OCT is currently modest. Example results from recent in vivo human cancer studies and ex vivo human artery studies, each using histology as the gold standard, as well as non-histologically confirmed in vivo ophthalmic studies, are summarized below. Sensitivity is the percentage of abnormal samples correctly classified, and specificity is the percentage of normal samples correctly classified.

1. *Esophagus*: The performance of endoscopic OCT for the diagnosis and exclusion of dysplasia in patients with Barrett's esophagus was evaluated in vivo in 33 patients. Results were the following: sensitivity, 68 %; specificity, 82 %; positive predictive value, 53 %; negative predictive value, 89 %; and diagnostic accuracy, 78 %. Diagnostic accuracy for the four endoscopists ranged from 56 % to 98 %. [24].

   In another study of 78 patients with Barrett's esophagus, the ability of OCT to detect high-grade dysplasia and carcinoma, differentiated from benign Barrett's esophagus, low-grade dysplasia, and metaplastic epithelium was evaluated. Sensitivity was 83 % with specificity of 68 %. Positive predictive value was 62 %,

negative predictive value was 87 %, and diagnostic accuracy was 74 %. No cases of invasive adenocarcinoma were missed [25].

2. *Urinary Bladder*: A study utilized the commercial Niris® (Imalux) system to examine 52 patients with suspicious lesions based on white-light cystoscopy. While the number of malignant lesions (carcinoma in situ or cancer) was small (14), OCT was able to identify all for 100 % sensitivity. Specificity was fairly low at 65 % [26].

   A two-center study examining 80 patients with OCT introduced through the working channel of a rigid cystoscope showed that OCT was able to differentiate benign conditions from urothelial dysplasia, carcinoma in situ, and invasive cancer with 82 % sensitivity and 85 % specificity. Positive predictive value was 51 %, but negative predictive value was 96 %, suggesting that OCT might be used to eliminate some unnecessary biopsies [25]. Further, members of this group performed another study utilizing polarization sensitive OCT. With the additional information available from polarization properties of the epithelium and connective tissue, they were able to increase sensitivity to 94 % and specificity to 84 % for flat malignant bladder lesions, a significantly better result than using conventional OCT [27].

3. *Colon*: Specific image features were found in OCT images of 35 patients with suspected inflammatory bowel disease. Segments affected by ulcerative colitis and Crohn's disease could be differentiated from normal segments with 100 % sensitivity and 78 % specificity [28].

   Another study showed that OCT could also differentiate adenoma ($n = 60$) from hyperplastic polyps ($n = 56$) with good sensitivity (92 %) and specificity (84 %) [25].

4. *Cervix*: OCT can be used to identify regions of cervical intraepithelial neoplasia (CIN) and squamous carcinoma in the cervix, although sensitivity and specificity vary depending upon the disease grade used as the threshold between "normal" and "abnormal." In one study of 120 women, utilizing CIN grade 2 as the threshold, a sensitivity and specificity of 85 % and 62 %, respectively, was obtained [29].

   In another study, 183 women who were human papillomavirus positive or had abnormal cytology received colposcopy, acetic acid visual inspection, and comprehensive biopsies. The addition of OCT to visual inspection increased sensitivity of detecting lesions greater than cervical intraepithelial neoplasia (CIN) grade 2 from 43 % to 62 %, while decreasing specificity from 96 % to 80 % [30]. A computer algorithm has been developed which can enable high specificity in differentiation of these high-grade lesion. Processing of 152 images in 74 patients yielded a sensitivity of 51 % with 92 % specificity [31].

5. Skin: OCT and polarization-sensitive OCT from 104 patients, mainly with basal cell carcinoma, actinic keratosis, and benign lesions, were obtained. While OCT could not reliably diagnose type of lesions, it was able to differentiate normal from lesion areas and identify lesion boundaries. Sensitivity of 79–94 % and specificity of 85–96 % were obtained in differentiating normal skin from lesions [32]. In another study of 112 patients, OCT image features could be

used to distinguish actinic keratosis from normal or sun-damaged skin with 86 % sensitivity and 83 % specificity [33].

6. *Artery*: A study of 323 regions in 8 cadaver hearts compared OCT and intravascular ultrasound (IVUS). The sensitivity/specificity of OCT to fibrous plaque, lipid-rich plaque, and calcified plaque was 91/88 %, 64/88 %, 77/94 %, and 67/97 %, respectively, superior to IVUS results. IVUS sensitivity/specificity was 55/79 %, 63/59 %, 10/96 %, and 76/98 %, respectively, for the same categories [34].

   Another study of 128 coronary arterial sites from 17 cadavers, using IVUS and OCT, also demonstrated the superiority of OCT. The sensitivity/specificity of OCT for calcification, fibrosis, and lipid pool was 100 %/100 %, 98 %/94 %, and 95 %/98 %, respectively, which was improved over the best ultrasound modality (integrated backscatter) with sensitivity/specificity of 100 %/99 %, 94 %/84 %, and 84 %/97 %, respectively [35].

7. *Eye:* Despite rarely having gold standard histological verification, OCT is clinically accepted as accurate for the detection and measurement of ocular parameters, such as retinal thickness, presence and width of vitreous adhesion, and presence and width of full thickness macular holes. Therefore, OCT has been used in several Phase III clinical drug trials. OCT has been used to screen for volunteer eligibility (criterion of minimum retinal thickness), to monitor drug effect on retinal thickness [36], and to determine drug-dosing timing based on retinal thickness measurement [37]. In one study of 652 study eyes in a drug trial, grading reproducibility with OCT was found to be high (kappa 0.87–0.91) [38].

While these studies have demonstrated that OCT can provide good to excellent diagnostic accuracy, these authors and others have pointed out limitations. First, most clinically practical (endoscopic) OCT systems have limited resolution. Lacking subcellular resolution, identification of cell types or visualization of markers of neoplasia such as abnormal nuclear size is not directly possible (although statistical image analysis may reveal certain cellular attributes). Even ultrahigh-resolution OCT systems cannot generally visualize subcellular structure at depth in highly scattering human tissue. This restriction can make differentiation between grades of dysplasia/neoplasia difficult with OCT. Given reliance on tissue architecture features for diagnosis, benign conditions such as scarring may be confused as pathology. OCT images also suffer from speckle, which can obscure features and boundaries.

50.3 Background on Laser-Induced Fluorescence

Fluorescence is radiative emission following stimulation of a molecule into an excited state [39]. Fluorescence is characterized by the absorption properties of the molecule, the lifetime of the excited state, the ratio of the radiative versus nonradiative decay rates (quantum yield), and the structure of the vibrational levels of the ground state (emission spectrum). The fluorescence emission spectrum

usually is independent of the excitation wavelength and is red shifted compared to the excitation. The emission spectrum is often a mirror image of the excitation spectrum, separated by the Stokes shift, because the structure of the vibrational levels is similar for the excited and the ground states. Fluorescence spectroscopy contains more information about the molecule's environment than does absorption spectroscopy. For example, upon polarized excitation, small fluorescence molecules exhibit more unpolarized emission compared to large molecules or molecules bound to rigid structures because the fluorescence lifetime limits the reorientation time of the molecule before emission. The fluorescence intensity can be quenched through static and dynamic pathways. Static pathways form new, less-fluorescent molecules through chemical reactions with the quencher and dynamic pathways increase nonradiative decay rates through collisions with the solvent. If two fluorescent molecules are in close proximity and their emission and absorption spectra overlap, energy transfer can occur from the donor molecule to the acceptor (Foerster Resonance Energy Transfer), making the emission characteristics dependent on the distance between the two molecules. The transfer efficiency between the donor and acceptor can also be measured through a decrease of the lifetime of the donor. Fluorescence emission is incoherent thus will not produce speckle.

50.3.1 Fluorophores

Fluorescence in the living tissue originates from endogenous fluorophores but can also be introduced by exogenous contrast agents or generated in genetically modified species expressing fluorescence proteins or enzymes capable of activating chemiluminescence. Endogenous fluorescence can be excited from intracellular constituents such as metabolites and proteins as well as interstitial components such as structural proteins. Several reviewers have discussed the application of endogenous fluorescence and surveyed the biologic fluorophores [40–45]. Endogenous fluorophores in the tissue are available at concentrations in the range of micromolar to hundreds of nanomolar. Their relatively low concentration and preferred excitation at short wavelengths suggest that they may not be amenable to interrogation by MCOCT. In general, endogenous tissue fluorescence with excitation below 300 nm is approximately an order of magnitude stronger than with UV-A (320–400 nm) excitation, and fluorescence emission with blue excitation is approximately another order of magnitude weaker than with UV-A excitation. Proteins are responsible for the high fluorescence efficiency of the tissue excited below 300 nm because many proteins contain the aromatic amino acids such as tyrosine, tryptophan, and phenylalanine [39].

Landmark studies have established a link between cellular metabolism and fluorescence emission [46–48]. Key fluorophores that correlate specifically with cellular activity include the electron carriers NAD and FAD. As a cell changes its metabolic activity, the balance between the reduced (NADH, $FADH_2$) and oxidized (NAD, FAD) form of the electron carrier shifts correspondingly as the

reduction–oxidation (redox) state of the cell fluctuates. Because only NADH and FAD exhibit significant fluorescence signals, the redox state can be estimated through a ratio of the peak emission values from these molecules assuming their concentrations are inversely linked to the nonfluorescing counterparts.

Type I collagen, one of the main components of the interstitial matrix, exhibits both optical scattering and autofluorescence, two properties that can potentially be exploited as a diagnostic marker of the interstitial matrix using both OCT and LIF. Significant fluorescence has also been noted from elastin fibers and keratin.

Fluorescence emission in the red was observed in animal sarcomas in the beginning of the twentieth century using a Wood's lamp [49] and later confirmed to originate from porphyrins [50]. There may be multiple sources of porphyrins in the tissue, such as incomplete heme-synthesis, microbes, or a by-product of some tumors [51, 52]. Additionally, the authors have shown that a chlorophyll-rich diet increases emission from the colon at 680 nm, which is consistent with the spectral profile of chlorophyll and its metabolites such as pheophorbide-*a* and pyropheophorbide-*a* [52–54], making chlorophyll in diet an important exogenous fluorophore in the colon.

Lipofuscin is ubiquitous as a by-product of frustrated metabolism in the lysosomal compartments of cells throughout the body. Increases in lipofuscin generally indicate a sustained insufficiency of a metabolic pathway and is usually associated with age or disease [55]. A complete lack of lipofuscin where it is usually noted in some degree may indicate a shutdown in metabolism or an extinction of a critical cell type [56].

Current contrast agent developments in molecular imaging can increase the visibility of molecular phenotypes, even though the target of interest might not exhibit itself a strong optical signature. Fluorescence-based reporters can be detected in very low quantities (picomolar, compared to tens of micromolar reporter concentration currently needed for MCOCT). Several exogenous compounds have been approved for in vivo clinical applications, e.g., visualization of the ocular vasculature with fluorescein or indocyanine green (ICG). Those compounds are intravenously injected and made available as systemic fluorescent substrate. Semiconductor nanocrystals compared to conventional fluorophores have relatively narrow and tunable emission spectra and are photochemically stable.

Protoporphyrin IX is an end product of metabolized delta-5-aminolevulinic acid (ALA), and ALA is thought to preferentially accumulate in tumors. Over the last 5 years, several studies have evaluated ALA-induced fluorescence for skin [57, 58], colon [59–61], larynx [62], and bladder cancer detection [63–65]. The measurement of ALA-induced fluorescence is compatible with combined OCT–LIF devices.

50.3.2 Diagnostic Accuracy of Laser Induced Fluorescence

Fluorescence spectroscopy has been proposed for the assessment of patients at increased risk for developing a disease, for demarcation and identification of lesions, and for prognostic follow-up after treatment. Early reports suggested that

quantitative endogenous fluorescence could discriminate between normal and malignant tissues [66]. In the 1980s, Alfano and coworkers reported endogenous fluorescence measurements in vitro [67], and, subsequently, through the advancement in fiber-optic light delivery and detection as well as the development of sensitive and portable spectral analyzers, a multitude of clinical and preclinical endogenous tissue spectroscopy studies have been conducted. Recent review articles summarize the chronological evolution and diagnostic performance of LIF up to the year 2000 [43] and summarize spectroscopic detection of neoplasia [44]. Clinical studies have been performed in the colon, cervix, bronchus, bladder, brain, oral cavity, larynx, skin, bile duct, breast, arteries, and stomach. Here we summarize recent results for several organ sites in Table 50.1. When available, performance of current clinical visual examination is also reported (* in Table 50.1). As with OCT, the diagnostic performance of LIF is highly variable but generally ranges from good to excellent. Recent significant studies in the two most published organ sites are described in additional detail below:

1. *Cervix*: Accurate optical diagnosis of cervical dysplasia could lead to a method where patients with an abnormal cytological screening result are triaged into those who do not need any further intervention and those who need a biopsy or potentially a treatment in the same visit. Several groups have reported recent results including a multicenter clinical trials by MediSpectra [68] with a single wavelength excitation source combined with diffuse reflectance measurements and a point-scanning device as well as SpectRx guided with similar approach [69]. The MediSpectra report indicated a 33 % increase in detection rate for high-grade disease while maintaining the specificity at the level of current clinical practice, while SpectRx also reported reduction in false-positive rate. In 2002 Chang and coworkers [70] as well as Georgakoudi and coworkers [71] published results of their studies on 147 and 44 patients, respectively. Chang reported that more than three to four excitation wavelengths do not improve performance and confirmed previous findings by Ramanujam [72]. He also reported low performance in detecting low-grade disease and distinguishing normal columnar tissue from high-grade disease. Georgakoudi reported results using an analytical model for extracting intrinsic fluorescence [73], reduced scattering and absorption [74], as well as estimates for average number and size of main scatterers [75]. Sensitivity was significantly improved when a combined trimodal approach was used while the specificity was maintained.
2. *Lung*: The LIFE systems from Xillix uses excitation between 380 and 460 nm emission and observes fluorescence in the green and red [76, 77]. The D-Light system® from Storz incorporates an additional white-light measurements [78], and the AFI system from Olympus utilizes two additional reflectance channels at 550 and 610 nm [79, 80]. The Pentax bronchoscope SAFE-1000 used blue excitation and observed green autofluorescence [81]. A European multicenter trial with the D-Light system® reported increased sensitivity [78] compared with the earlier multicenter trial by Lam et al. [76] with the Xillix system and corrected the sensitivity and specificity of white-light bronchoscopy reported

Table 50.1 Sensitivity and specificity obtained in select LIF clinical studies. Where available, sensitivity and specificity for a standard clinical method is given also in parentheses

Organ site	# Subjects/ samples	Sensitivity	Specificity	Source (year, reference, organization, ex wavelength/notes)
Cervix (colposcopy)	Meta-analysis	Many	Many	2007, [173] MDACC
	1,090	56 %	87 %	2007, [174] Medispectra, 337
	604/1,500	92 % (67 %)	50 % (54 %)	2004, [68] Medispectra, 337, mc, hg
	147/351	71 %	77 %	2002, [70] UT, multi ex, hg
	44/84	92 %	71 %	2002, [71] MIT, trim, SIL-Bx. nonSIL
	95/381	79 % (79 %)	78 % (76 %)	1996, [175] UT, 337, 380, 460, hg
Ovary	49/249	88 %	93 %	2012, [87] UA, 270–550
	30	100 %	69 %	2012, [176] UA, 365, imaging
	4	N.A.	N.A.	2011, [112] Groningen, Folate-FITC, intrao
	22/97	100 %	91 %	2009, [177] Manipal, 325
Fallopian tube	47	73 %	83 %	2011, [88] BCCA, imaging
Lung (wl bronchoscopy)	62	91 % (51 %)	26 % (50 %)	2006, [81] Hong Kong, 380–460
	1,173/1,978	82.3 % (57.9 %)	58.4 % (62 %)	2005, [78] Storz, mc, hg
	32/62	80 %	83 %	2004, [80] Olympus
	173/864	67 % (25 %)	66 % (90 %)	1998, [77] Xillix, mc, hg
Oral cavity (wl examination)	120	N.A.	N.A.	2009/10, [178, 179] Houston, 405, vis
	44/50	98 %	100 %	2009, [180] BCCA, 400–460, hg, vis
	4/4 (images)	91 % (75 %)	86 % (43 %)	2005, [181, 182] UT, visual
	15/91	96 %	96 %	2003, [98] MIT, trim
	76/343	100 % (100 %)	88 % (83 %)	2002, [183] UT, multi ex
	56/179	100 %	51 %	2002, [184] Munich, ALA,375–440
	50/137	88 %	57 %	AF
	7/199 (72)/(214)	100 % (99 %)	51 % (43 %)	ALA&AF (WL)
	15/45	94 % (76.5 %)	100 % (100 %)	1998, [185] UT,MDACC, 337, 365, 410
Breast	6	N.A.	N.A.	2009, [115] ICG, lymph node intrao
	N.A.	N.A.	N.A.	2009, [186] Manipal, 325
	17/104	100 %	96 %	2008, [187] MIT, multi ex
	3	N.A.	N.A.	2007, [99] Storz, Ductoscopy
	18/47	54 %	91 %	2005, [188] UW, multi ex
	32/56	70 %	92 %	2003, [101, 116] UW, multi ex
	63/911	99 %	99 %	1997, [189], Indore, 337

(*continued*)

Table 50.1 (continued)

Organ site	# Subjects/ samples	Sensitivity	Specificity	Source (year, reference, organization, ex wavelength/notes)
Colon (wl colonoscopy)	21	N.A.	N.A.	2013, [96] UA, 270–440
	88	Better than WL	N.A.	2012, [92] Asahikawa, AFI
	75	92 % (68 %)	N.A.	2001/10, [90, 190] PINPOINT, 400–450
	64	84 % (90 %)	60 % (64 %)	2007/8, [89, 191] AFI, 395–475
	NA/177	80 %	92 %	1992, [192] Wellman, 337
Barrett's esophagus	22	100 %	Increase	2012, [102], Amsterdam, AFI, NBI, HRE
	37/148	74 %	85 %	2003, [103] Wellman, 400
	16	100 %	97 %	2001, [104], MIT, 337, 397, 412, trim
	53/141	76 %	63 %	2003, [193] Lausanne, 505
Bladder	14/56	N.A.	N.A.	2013, [109] 308
	21	N.A.	N.A.	2012, [108], 650
	25/52	100 %	100 %	2003, [106] Singapore, 280, 330
	25/43	95/84 %	42/88 %	2001, [107] Munich, AFI alone, ALA & AFI
	75/130	95 %	73 %	1998, [105] Wellman, 337
Brain	3/13	N.A.	N.A.	2010, [110] UCDavis, 337 lifetime
	26/120	100 %	76 %	2001, [194] VU, primary tumor
		97 %	95 %	2004, [195] data from [194]

by Lam. The AFI system was tested on a small sample size, and only abnormal-appearing sites were included in the analysis [80]. A relatively high false-positive rate was reported which limits the positive predictive value [82], and difficulties in distinguishing preinvasive lesions and benign conditions were mentioned. However, a trial with the Pentax system also reported increased sensitivity but reduced specificity [81].

3. *Skin*: A skin autofluorescence reader has been developed to asses advanced glycation end products (AGEs) which show a fair correlation with collagen cross-link and AGE content of the skin (AGE Reader I, DiagnOptics BV Groningen, Netherlands) [83]. Such reading could be a predictor of health outcomes in diabetic patients [84] or could determine cardiovascular risk [85, 86].
4. *Ovary*: Tissue fluorescence was found to be statistically different in normal ovarian tissue between women at high risk for developing ovarian cancer versus women at normal risk especially in postmenopausal women; this result can potentially guide oophorectomy [87]. With the recent hypothesis that ovarian cancer might originate in the fallopian tube, it has been demonstrated that autofluorescence can be measured in the fallopian tubes in situ [88].
5. *Colon*: Xillix and Olympus developed autofluorescence (AF) colonoscopes that illuminate tissue in the violet–blue range. Several randomized trials comparing

AF endoscopy in the colon to standard video endoscopy, narrowband imaging (NBI), or high-resolution endoscopy have been published very recently. The outcomes of these studies have been mixed, with some indicating these AF endoscopes reduce polyp miss rate [89–92], especially for inexperienced colposcopists, and others showing no significant improvement of AF over other technologies [93–95]. Most recently UV imaging has been proposed to improve the detection rate of polyps [96, 97].

6. *Oral Cavity*: Two companies have created a visual autofluorescence system for the examination of the oral cavity. The VelScope™ (LED Medical) and Identafi™ (Remicalm) illuminate the tissue with specific excitation pattern, while the clinician observes the tissue fluorescence through filtered spectacles. The VelScope™ uses blue (400–460 nm) excitation light, while the Identafi™ uses light at 405 nm in combination with green reflectance. The devices have been identified as ideal for oral cancer screening but also for tumor margin delineation. Clinical performance is supported by previous studies using single point spectroscopy and multiple excitation wavelengths [98].
7. *Breast*: While there were limited reports of clinical translation of LIF for breast cancer imaging, there exists a commercial implementation of 1.3 mm diameter ductoscope with autofluorescence imaging capabilities using the DAFE system (Richard Wolf GmbH) [99]. Previously research with fiber-optic probes reported that diffuse reflectance spectroscopy did not improve sensitivity and specificity of fluorescence spectroscopy [100, 101].
8. *Esophagus*: Esophageal cancer detection was investigated with technologies similar to the one used for colonoscopy [102], and autofluorescence imaging combined with high-resolution endoscopy was found to have ideal sensitivity. In addition when combined with narrowband reflectance imaging, a reduced false-positive rate was demonstrated. Earlier work showed that single point spectroscopy at 400 nm excitation was most useful for clinical application [103], while others demonstrated excellent diagnostic performance using fluorescence at 337, 397, and 412 nm excitation [104].
9. *Bladder*: Initial results on bladder cancer diagnosis with autofluorescence [105, 106] as well as ALA-induced fluorescence were promising [107], and recently imaging systems have been developed to acquire NIR autofluorescence [108] or allow pulsed UV laser delivery [109].
10. *Brain*: Tumor demarcation was investigated in the brain using endoscopic fluorescence lifetime measurements [110] and also fluorescence and reflectance spectroscopy [111].
11. *Exogenous Contrast Agents*: Significant advances in intraoperative optical imaging of exogenous contrast agents have been reported recently. For example, folate-targeted fluorescein isothiocyanate (FITC) fluorescence was used to guide tumor debulking in ovarian cancer patients [112]; patency of bypass grafts were studied in patients using intravascular ICG [113]; and sentinel lymph node mapping was demonstrated in the esophagus in animals [114] and also applied in human studies for breast cancer lymph node mapping using open architecture equipment [115]. General lymphatic imaging was

demonstrated using ICG [116]. Aminolevulinic acid (ALA)-induced protoporphyrin IX fluorescence has been studied in several animal models. Its application was studied for peritoneal micrometastasis of ovarian cancer in a rodent animal model and showed that detection rate significantly increased, and fluorescence intensity in tumor versus surrounding tissue increases by 1.5 [117]. Such an approach could be combined with endoscopic devices such as the D-Light system® (Karl Storz, Germany); however, human clinical studies have not yet been reported.

50.4 Advantages of a Dual Modality System

The complementary nature of information provided by OCT and LIF (coherent backscatter versus incoherent fluorescence emission) creates the possibility that the combination of OCT and LIF may be more sensitive to tissue function and pathology than either modality alone. The two types of information may also facilitate signal interpretation and increase specificity. Viewing this potential advantage from two different perspectives, cross-sectional OCT images may help to correct and interpret LIF spectra, or LIF imaging/spectra may help to guide and interpret OCT images.

From the first perspective, LIF spectra may be difficult to interpret because they may be influenced by unknown subsurface structures. Spectra obtained at different lateral locations on an apparently smooth, homogeneous surface can vary in intensity and spectral shape. Without depth-resolved anatomical information, it may be difficult to determine if the variation is due to changes in tissue function, type, or thickness. For example, in a layered epithelial/stromal tissue, a relative decrease in the intensity of the fluorescence signal associated with collagen could be due to a true lessening of the fluorescence emission of the stroma or could be caused by a thickening of the overlying epithelium. Another example is given in Fig. 50.1. An OCT image/LIF spectra pair is shown, obtained from the luminal surface of an approximately 3 mm diameter bronchus of excised sheep lung. The spectral shape of the LIF signal is relatively constant, but the intensity is highly nonuniform. The OCT image shows clearly that strong LIF signal corresponds to locations with subsurface cartilage, indicating that the LIF intensity variation is due to normal anatomy.

Quantitative measures of tissue anatomy obtained with OCT can be used to correct LIF data. Several attempts have been made to separate tissue optical properties, such as scattering, absorption, and intrinsic fluorescence from extrinsic fluorescence, and to calibrate fluorescence measurements for illumination and detection conditions. The collected fluorescence depends on optical transport within the tissue [82, 118] and geometrical sensor sample relations [119–121]. LIF intensity is highly dependent upon the probe–sample separation, and OCT can provide this geometrical information with high accuracy. In fact, if only point LIF measurements are being obtained, only A-scan OCT capability is needed. A correction algorithm has been described by Warren et al. [119] using ultrasound A-mode data. A model of the fluorescence intensity was developed and verified with both Monte Carlo

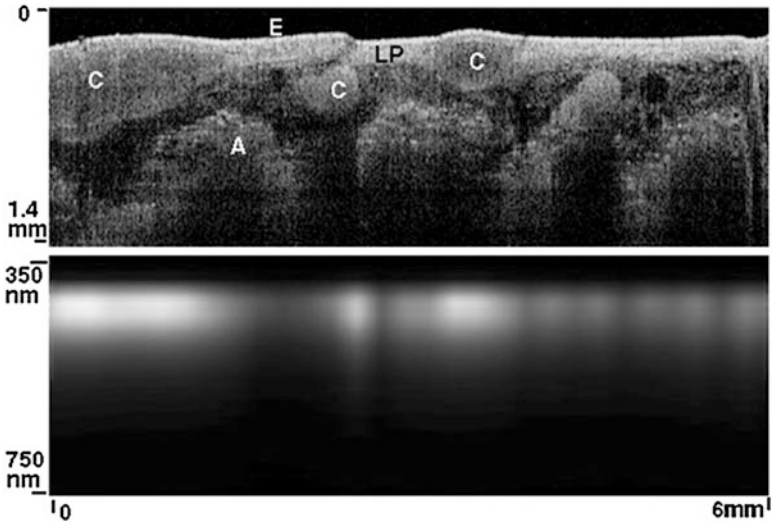

Fig. 50.1 OCT image (*top*) and LIF spectra (*bottom*) of excised sheep lung bronchus. Note the increase in emission intensity at lateral locations corresponding to subsurface cartilage (*C*). Other abbreviations: epithelium (*E*), lamina propria (*LP*), alveoli (*A*)

simulations and empirical data. A correction equation goes as $S_c = S_m/R^n$, where S_m is the measured fluorescence intensity, R is the probe–tissue separation, and $n = 1.1$ for aorta and 2 for theoretical, isotropic fluorescence emission.

Using mathematical models, the particular photon traveling paths can be predicted with a priori knowledge of the illumination and collection geometry, a diffuse reflection measurement, and assumptions about scattering and absorption properties. Zhang and coworkers developed a method that allows extraction of intrinsic fluorescence in semi-infinite media based on fluorescence and diffuse reflectance measurements under the same geometrical configuration [122], which subsequently has been used in several clinical studies as an analytical model. Sung et al. developed a similar analytical approach for two-layered tissue to predict intrinsic fluorescence from the stroma and epithelium separately [123]. This model depends on the epithelial thickness, a number that can be easily obtained with OCT. Fluorophore concentration can also be more accurately determined using tissue scattering and fluorophore depth measurements obtained from OCT. Yuan et al. corrected the measured concentration of a known fluorophore (Cy5.5 dye) in a phantom (tube of dye submerged in intralipid) [124]. This method could be employed to help quantity accumulation of, e.g., an exogenous dye in a discrete tumor. It would be less useful for correcting measurements of distributed endogenous fluorophores, although it could be modified to estimate true contributions from a buried layer (e.g., collagenous stroma) if optical properties and fluorophore concentration of tissue layers are assumed to be homogeneous.

From the second perspective, LIF imaging can guide OCT measurements and clarify inconclusive OCT scans. OCT provides a microscopic view, and thus in

many applications complete screening of the area of interest is impractical, necessitating a guidance technique. LIF imaging, which commonly has high sensitivity but low specificity, can be an ideal method to identify regions of interest for OCT imaging. A simple method of LIF-guided OCT can be implemented by using an OCT daughter probe in the surgical channel of a large endoscope. Additionally, LIF has the potential to clarify OCT scans containing little information due to homogeneous tissue with features below the resolution limit of OCT, such as might be found in a cellular tumor or scar tissue.

Several studies have shown the value of combining OCT and LIF. Kuranov et al. [125] used OCT and LIF to image neoplasms in the cervix and found that these two modalities combined produced fewer false-positive results than either modality alone: abnormally increased fluorescence due to inflammatory reactions was clearly differentiated from cancer by OCT; conversely, OCT-detected atypical structure could be clarified with LIF to simply be a mature scar. Another study [25] found that the PPV of fluorescence cystoscopy of flat bladder lesions was only 16 %, which could be increased to 43 % in addition of OCT. The data suggest that 78 % of biopsies based on fluorescent-positive findings could be avoided, if areas were classified as normal when OCT imaging revealed a regular layered structure.

50.5 Instrumentation Design Considerations

Combined OCT–LIF systems can be essentially two separate systems simply physically packaged together at the tissue location or can share optical and mechanical parts, light sources, and/or digital processing components. There are many possible variations; here we list some of the design considerations and some current/possible implementations. Design considerations for system combination include the type of OCT and LIF systems desired (e.g., full field or scanning OCT, point or imaging LIF), the spectral range of the light source(s) and LIF emission, the choice of endoscope materials, and safety. General optical design considerations are also discussed.

50.5.1 OCT and LIF Systems

Because various types of OCT systems are discussed in detail elsewhere in this handbook, they will not be discussed here. In general, LIF capability can be added to any type of OCT system, although the sharing of components is facilitated if the scan types are common (e.g., both one, two, or three dimensional scanning and full field). An appropriate method of signal separation (spectral, temporal, or spatial) is required.

Steady-state LIF measurements require a light source with a well-defined output spectrum, a conduit to transport the excitation light to the sample, illumination and collection optics, and a conduit to transport the emitted light back to a spectral analyzer for optical detection. Instrumentation for fluorescence measurements is well described by Lakowicz [39], and here we focus on spectral compatibility and common in vivo measurement limitations.

One of the major challenges in fluorescence detection is the signal to background ratio. Background signals are caused by instrument autofluorescence (see Sect. 50.5.4), ccc from the light source, and scattering within the spectral analyzer. Because endogenous signals can be weak, background signals need to be avoided. Out-of-band illumination suppression should reach 10^{-5} or 10^{-6} for endogenous tissue fluorophore measurements, especially in excitation ranges where the fluorescence efficiency is low (blue to green). Because the amount of collected instrument background is also dependent on the sample reflectivity, traditional subtraction of the sample signal by the instrument response to a negative standard (e.g., a measurement in water) has its limitations. As a rule of thumb, instrument background should be kept below 10–30 % of the sample signal. Traditionally, illumination and collection paths have been constructed separately [126] to reduce system autofluorescence. Irradiance levels on excitation optics are significantly higher than on collection optics making it necessary to incorporate autofluorescence reduction techniques in the illumination conduit and optical elements at the endoscope tip. In typical applications, the collection conduit will receive a significant amount of excitation light backscattered by the sample. If the stray light suppression capabilities of the detection system are exceeded (a spectrograph might have 10^{-4} suppression), the backscattered excitation light can also contribute to the signal background. This can be avoided by dampening excitation light in the detection path with long-pass filters before the emitted light is spectrally analyzed.

50.5.2 Spectral Range of LIF Sources and OCT Sources

For LIF, short-arc lamps have been used as a standard low-cost excitation source when coupled to an excitation monochromator or dielectric band-pass filters. Example radiance data for mercury–xenon and xenon lamps are shown in Fig. 50.2, top panel. Their broad emission range allows wavelength tunability, but a common disadvantage of short-arc lamps is the limited ability to focus light into small optical fibers. A large variety of laser modules has been developed for confocal microscopy, and most of these lasers are compact and sufficiently transportable for endoscopic fluorescence measurements. Example sources are shown in Fig. 50.2 and abbreviated as XeCl, xenon chloride (308 nm emission); HeCd, helium–cadmium (325 nm); N2, nitrogen (337 nm); Ar, argon (351, 364, 458, 488, and 514 nm); YAG, neodymium YAG (1,064, 532 nm); and HeNe, helium–neon (543, 633 nm). Because of the small Stoke's shift of most fluorophores, narrowband sources are preferred to enable efficient collection efficiency of emission light and rejection of excitation light. In contrast, OCT sources are by necessity broadband, with spectral widths of tens to hundreds of nanometers. Also, OCT sources are generally centered in the NIR, to enable greatest depth of imaging in highly scattering tissue. The light source emission spectra for some OCT sources (short-pulsed lasers, swept-wavelength lasers, and superluminescent diodes) are shown in Fig. 50.2. Also shown in Fig. 50.2 is the extinction spectrum of three tuned nanoshells (exogenous scattering agents) [127].

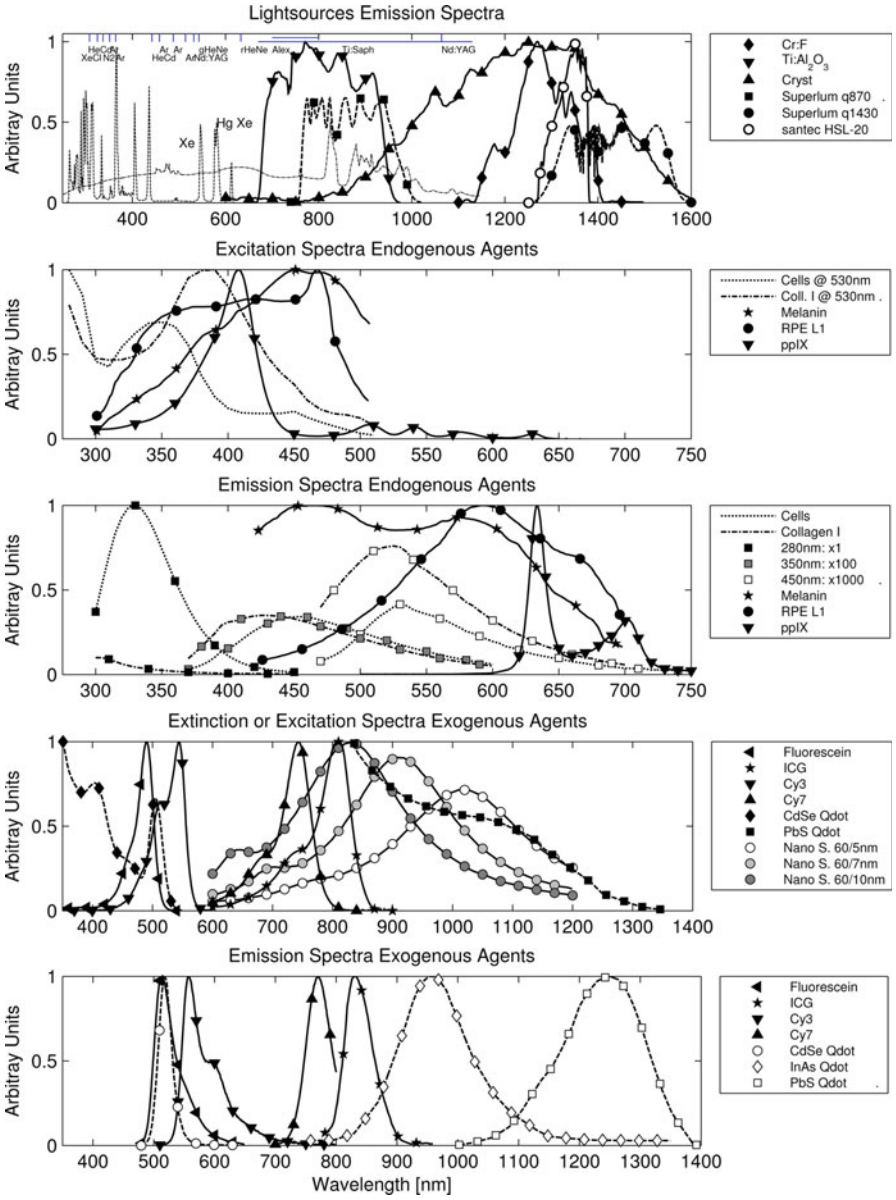

Fig. 50.2 Common light sources, absorbers, and emitters for combined OCT and LIF: *First panel*, illustration of common fluorescence excitation and OCT light sources. Xenon (*Xe*) and mercury–xenon (*Hg–Xe*) short-arc lamps are illustrated (Courtesy of Photon Technology International, Inc.). Published data from OCT sources using titanium sapphire ($Ti:Al_2O_3$) laser [196], chromium:forsterite (Cr:F) [197] and photonic crystal fibers (Cryst) [198], commercial superluminescent diodes (Superlum Broadlighters q870 and q1430), as well as spectrum of commercial swept source (santec, HSL-20) are shown. Excitation spectra of endogenous

50.5.3 Excitation and Emission and Range of Fluorophores

Epithelial tissues usually exhibit a strong fluorescence peak at 280 nm excitation and 350 nm emission, which is associated with tryptophan fluorescence (Fig. 50.2, bottom panel, cell emission at 280 nm excitation). Cells excited at UV-A wavelengths show strong fluorescence from NADH, which has a maximum at 350 nm excitation and 450 nm emission (Fig. 50.2, cell emission at 350 nm excitation), whereas the oxidized form NAD is not fluorescent [39]. Conversely, FAD fluoresces at a maximum at 450 nm excitation (blue) and 535 nm emission (Fig. 50.2, cell emission at 450 nm excitation), whereas the reduced form $FADH_2$ fluoresces minimally. Lipofuscin has a very broad excitation and emission spectra. The excitation spectrum is notable in particular because its peak at 470 nm is comfortably above the strong excitation bands of many other materials. Fluorescence from interstitial matrix is dominated by collagen; average fluorescence emission from polymerized collagen that was reconstituted from rat tail type I fragments is shown in Fig. 50.2 middle and bottom panel. Typical emission at 280 nm excitation/300 nm emission (consistent with tyrosine), 320 nm excitation/400 nm emission (consistent with the enzymatic cross-links lysyl hydroxypyridoxyline and hydroxylysyl hydroxypyridoxyline), and 370 nm excitation/450 nm emission (consistent with the nonenzymatic cross-links vesperlysine and crossline) can be observed. Unfortunately, at many excitation wavelengths, these collagen emission spectra overlap with the emission observed from cell suspensions. Porphyrins show an excitation maximum at 410 nm and two emission maxima at 630 and 690 nm, while the peak at 630 nm is substantially more intense (Fig. 50.2, protoporphyrin IX). Emission spectra from exogenous fluorophores fluorescein; cyanine dyes Cy3, Cy7, and ICG; and CdSe/InAs quantum dots are also shown in Fig. 50.2. Some of these agents have NIR excitation and/or emission.

Figure 50.2 illustrates that endogenous fluorescence, targeted fluorescence imaging, and optical coherence tomography can be spectrally incorporated because most endogenous components do not absorb or emit within the OCT illumination spectral range, and some exogenous agents are available outside that range. If spectral overlap occurs, LIF and OCT need to be time or spatially multiplexed. Spectral overlap has been used to advantage in one application [128], with simultaneous

Fig. 50.2 (continued) components are illustrated in the *second panel*: reconstituted collagen type I gel and epithelial cell suspension (OVCA 430) data is shown at 530 nm emission [199, 200]. Protoporphyrin IX [201] and melanin and lipofuscin granules extracted from RPE cells are illustrated [55]. Emission spectra corresponding to the compounds from the second panel are illustrated in the *third panel*: emission of collagen type I gel and an epithelial cell suspension is shown at 280, 350, and 450 nm excitation. The *fourth and fifth panels* illustrate excitation and emission spectra of exogenous agents: the absorption and emission of fluorescein (Molecular Probes/Invitrogen, ph9) is compared to a CdSe semiconductor nanocrystal [202, 203]. ICG, a clinically used NIR absorber, is illustrated [204]. Cyanine dyes are illustrated with examples of indocarbocyanine (Cy3) and indotricarbocyanine (Cy7) [201]. Extinction of gold nanoshells on a 60 nm silica core is illustrated as a potential OCT scattering contrast agent [127]. Selected quantum dot emission spectra from CdSe [202, 203], InAs [202], as well as PbS [205] are shown

OCT/ICG imaging in the eye's fundus. In this case, the same superluminescent diode (793 nm center wavelength, 22 nm spectral full width at half maximum) was used for OCT imaging and for excitation of ICG. The key in this implementation was proper selection of the dichroic filter separating backscattered source light (directed to the OCT detector) from fluorescence emission (directed to the LIF detector). This selection minimized distortion of the source correlation function and maximized collection efficiency of fluorescence emission. Excellent simultaneous OCT and ICG images were obtained. However, use of the same source for OCT and fluorescence excitation could become increasingly difficult as either the source bandwidth increases or fluorophore emission intensity decreases, unless very large Stoke's shift NIR-excitable agents become available.

A strategy to provide greater spectral separation has been described [129]. This custom system included a mode-locked Ti:sapphire laser and a 0.9 numerical aperture water immersion objective to generate simultaneous en face optical coherence and two-photon-excited fluorescence images. An image of a green fluorescent protein expressing drosophila embryo was presented; presumably endogenous fluorophore distribution could be imaged as well. Because fluorescence occurred at a much shorter wavelength range, no difficulties were encountered separating the fluorescence from the backscattered light. However, implementation of this method in an endoscopic fashion would be technically challenging because of high peak-power needs, three-dimensional scanning requirements, and the need to control probe–tissue separation.

50.5.4 Materials

As described above, many interesting endogenous fluorophores are best excited at ultraviolet wavelengths that also cause autofluorescence in most optical materials. Many glasses and polymers exhibit autofluorescence that is similar in spectral shape and range to the fluorescence of endogenous tissue fluorophores [130]. Because probe autofluorescence can easily become significant compared to the tissue signal, each component of the OCT–LIF system should be considered for autofluorescence, particularly if the excitation wavelength lies in the UV. The location of the element within the system is equally important as the absorption and emission characteristics of the material. Autofluorescence from an optically thick piece of fiber is generally more significant than from the same material used in a thin window. Additionally, isotropically emitted fluorescence is more easily collected from an element located near focus than from a lens or window located far from focus or in a low-numerical-aperture portion of the beam path. Lenses and windows made of fused silica and CaF_2 have low fluorescence under UV-A excitation and good NIR transmission and are recommended throughout the beam path. Thick windows near the tissue should be restricted to lowest fluorescence glasses, although very thin windows of other glasses and even some low-fluorescence plastic films may be acceptable [131]. Usually, some fluorescent materials must be used despite the best attempts to avoid them. For example,

the emission from even "low-fluorescence" ultraviolet transmitting optical epoxies is significant, and care should be taken to keep glue joints thin [132]. The jacketing materials available on many commercially available communications grade fibers ideal for OCT fluoresce strongly. Although fiber choice could be restricted only to low-fluorescence jacketed materials, it is often more practical to simply shield the fiber from UV-A excitation. This approach of hiding the fluorescent material behind absorbent material, a dichroic filter, or simply out of the beam path is the most flexible and commonly used. Care should be taken with items outside the device that may also autofluoresce, including tissue index matching gels, preservation media, culture plates, or wax mounting blocks.

50.5.5 Safety

The tip of a combined OCT–LIF endoscope is either in contact with or at a close distance to a tissue surface or body fluid and therefore should be analyzed for potential hazards. A thorough analysis of potential risks and protection against those risks are a requirement for human subject studies. Hazards include electrical shock hazards, clinical hazards, material toxicity hazards, and radiation hazards. Of unique importance to combined OCT–LIF systems is the fact that both systems may be operated concurrently, requiring cumulative radiation exposure analyses. Radiation exposure in the UV poses a different hazard than in the visible/NIR. UV exposure is a cumulative hazard due to the potentially ionizing energy of each photon (exposure limits can be calculated for repeated exposure over days), whereas visible and NIR light exposure is analyzed for potential thermal injuries. "Blue-light hazard" is unique to eye exposure, caused by free radical release due to interaction with visual photopigments [133]. Threshold limit values for radiation exposure are defined by several standardization organizations: The American National Standards Institute (ANSI) publishes maximal permissible exposure levels [134]; the American Conference of Governmental Industrial Hygienists (ACGIH) publishes similar threshold limit values (TLV) and biological exposure indices [135]. Applications which intentionally introduce light into the eye should verify that standards set for ophthalmic instruments ISO 15004-2 are met in addition to laser safety standards. In contrast to the above-listed standardization organizations, the International Commission on Non-Ionizing Radiation Protection (Oberschleissheim, Germany) makes their guidelines available online at no cost and publishes them in Health Physics. Usually the threshold limit values are expressed for laser beam [136, 137] and incoherent exposure [138, 139] of the eye and skin. For broadband UV exposure (<400 nm), the biologically effective radiation (device emission weighted by the biologic action spectrum, which is normalized at 270 nm) should not exceed the TLV for melano-compromised skin and eye (3 mJ/cm^2) [138]. The TLV for the skin and eye has also been recommended for the cervix in a guidance document developed by the US Food and Drug Administration's Center for Device and Radiological Health (CDRH) [140]. For the wavelength range of 0.38–1.4 μm, exposure limits are governed by

thermal injury to the skin and eye. Unfortunately, the authors are not aware of any studies evaluating combinational effects of NIR radiation and UV exposure.

50.5.6 Optical Design Considerations

The optical design of a combined system is a result of an attempt to optimally control the photon paths in the tissue for each modality, while meeting material constraints in the optical path and separating the signals (chromatically, spatially, or temporally) to the appropriate detector. The useful signal in OCT depends on photons that undergo a single scattering event in a nearly backscattering direction. The confocal design of typical OCT systems helps reject photons that take any other path. Lateral resolution is dependent upon the beam cross section at a given depth. Usually, a balance between lateral resolution and depth of focus is struck in order to avoid axially scanning the objective [141]. Conversely, LIF photons are typically allowed to take a circuitous path: the excitation light may be scattered multiple times before it is absorbed. If fluorescence conversion occurs, the emission spectrum of the intrinsic fluorescence will be modified as the emitted photons wander randomly through the tissue until they are absorbed by chromophores or released at the tissue surface. The path taken, and volume subsequently probed by the LIF system, depends on the tissue absorption and scattering properties as well as factors determined by the probe geometry: the insertion angles of excitation photons, the distance along the surface the collection to point (source-detector separation distance – SDSD), and the angles over which the photons are collected. Fiber-optic probes have been proposed for preferential depth-sensitive fluorescence sensing with the use of variable illumination and collection apertures [142, 143], illumination collection distances [143–146], and illumination collection angles [147–149].

Monte Carlo analysis of specific fiber-optic probe implementations on media with tissue-like optical properties and their associated experimental verifications show trends that are useful in designing an LIF probe. First, it is critical to control the distance between the illumination/collection fibers and the tissue for quantitative tissue analysis [145, 150]. When the illumination and collection areas are superimposed at the tissue surface (SDSD = 0), either by means of single illumination–collection fiber in contact with the tissue, or a spacer distal to a group of fibers that allows the illumination–collection areas to diverge over the same tissue area, the probe will be primarily sensitive to superficial layers less than 400 μm deep [142, 144, 145]. Similarly shallow tissue sampling can be achieved when source and collection fibers are separated at the tissue surface but are inclined towards each other to cause an overlap of the fiber numerical apertures in the superficial tissue [148, 149, 151]. The average probed depth can be increased from 700 to 1,200 μm by placing normally incident illumination and collection fibers that are directly in contact with the tissue at increased separation [142, 144, 145]. Evidence with diffuse reflectance modeling suggests that the probed depth can be increased yet further by inclining the fibers away from each other [152]. In general, greater overlap of the numerical apertures of the illumination and collection fibers improves collection efficiency while the

expected probing depth decreases. The lateral extent of a collected LIF photon's path has been relatively unexplored, although lateral resolution somewhat larger than the SDSD could be expected. Increasing the fiber core diameter and numerical aperture increases the light gathering capacity of the collection fiber but may have effects on the depth of collected fluorescence that depends upon the configuration. In cases with fibers in contact with the tissue, the size of the illumination and collection area introduces a superposition of many SDSDs, while the numerical aperture of the fiber introduces a superposition of many angles of insertion and collection. In addition to the depth selectivity provided by SDSD, some geometries appear to be optimally sensitive to fluorophore distribution rather than scattering properties of the tissue [153, 154]. Knowledge of tissue layer thicknesses from OCT images could help in the selection of optimal LIF illumination/detection fiber configurations.

In the case where the majority of information from LIF derives from direct emission from a fluorophore in a relatively superficial tissue layer, a confocal arrangement delivers significant advantages. Confocal arrangements are common in fluorescent microscopes because they have the potential to deliver high-resolution imaging with high contrast. High resolution derives from the tightly limited photon paths allowed by the confocal arrangement. Contrast is enhanced by spatial filtering of out-of-plane, unwanted fluorescence, including that from the optics of the instrument itself. In combination with point-scanning OCT, the two confocal modalities will share similar design needs and constraints.

Because OCT systems generally utilize single-mode fibers and LIF systems utilize multimode fiber (to optimize the collected fluorescence emission signal), the most straightforward OCT–LIF endoscope design utilizes separate fibers for each modality. Maintaining separate conduits for OCT and LIF minimizes the cross talk between the systems and helps maintain high signal-to-background ratio. The proximal coupling optics between the fibers and sources/detectors are also simplified. However, other fiber configurations are possible. Dual-clad fibers consist of a central core with two layers of cladding. The core can be made single mode, whereas the inner cladding has a large radius and high-numerical aperture (multimode). OCT light is channeled to the sample through the core. LIF excitation light can be carried by the core (if compatible) or the inner cladding. Remitted OCT, excitation, and emission light are coupled into the core and inner cladding. In addition to coupling light into the dual-clad fiber, the proximal optics must spatially separate returned OCT light which has propagated through the core from that which has taken unwanted paths through the inner cladding, and spectrally separate the OCT and fluorescence emission. Dual-clad fibers have successfully been used in OCT–LIF systems [155–158], and one system is described in more detail below.

Under certain conditions, multimode fiber bundles can also be used to carry both OCT and LIF signals, with the benefit of eliminating distal scanning. The use of a Fourier-domain OCT system incorporating a common-path interferometer mitigates the effect of wavefront distortions through the multimode fiber bundle, although cross talk between fibers can be an issue. A system was recently demonstrated that utilized a common fiber bundle and CCD detector for both OCT and fluorescence confocal imaging [159].

50.6 Combined OCT–LIF System Examples

Of many potential implementation, three designs are discussed below: a free-space ophthalmic, an endoscopic OCT–LIF point-scanning, and an OCT–LIF surface-imaging system. The free-space system is conceptually more simple, appropriate for ophthalmic imaging, and introduces several system design elements. Combined OCT–LIF endoscopes allow examination of a variety of mucosal tissues in situ. Clinically it is interesting to have tools that can monitor the disease noninvasively or to guide traditional biopsy techniques. Because tissue degrades structurally and biochemically with time after excision, in vivo endoscopic studies potentially have the most accurate and conclusive diagnostic capability. At the same time, the small packages and biocompatibility requirements of endoscopes present a challenge to the designer. The two very different combined OCT–LIF endoscopes presented here embody the design principles discussed in the previous section.

50.6.1 Scanning Laser Ophthalmoscope with OCT and Fluorescence

Fluorescence angiography with fundus photography or confocal scanning laser ophthalmoscopy (SLO) is an established technique to evaluate the circulation of the retina. Recently, fundus autofluorescence (FAF) imaging, primarily observing lipofuscin concentration, has been shown to be a valuable marker in multiple disease states [160]. Optical coherence tomography has revolutionized clinical retinal practice due to its ability to obtain high-resolution cross-sectional images in this highly stratified tissue that clearly differentiate disease states. The development of combined OCT–LIF systems for retinal imaging is a logical progression for streamlining the retina research and practice. Commercial devices (SPECTRALIS®, Heidelberg Engineering) [161] for comprehensive evaluation of retinal disorders provide similar functionality to a previously described combined research system [128, 162]. A system diagram of the research system from the Podoleanu group is illustrated in Fig. 50.3. This instrument is a good example of the use of a confocal architecture for both OCT and LIF, where confocality in the OCT channel is achieved by use of a single-mode fiber (small core size behaves as a pinhole) and the confocality of the SLO and indocyanine green (ICG) fluorescence channels reject out-of-focus light. The scanning confocal architecture of the SLO is highly compatible with time-domain, en face OCT. In this system, uniquely, a single light source is used for both OCT and fluorescence excitation, as the excitation spectrum of ICG (peak near 800 nm, see Fig. 50.2) overlaps with clinically useful OCT imaging wavelengths. Dichroic filters separate reflected light from fluorescence emission. Depth-resolved OCT can be collected simultaneously with en face SLO and ICG fluorescence. The resulting images from all modalities can be presented separately or superimposed. SPECTRALIS® OCT differs architecturally from the described research system by providing greater independence between the two systems. The system combines an independent, spectral-domain OCT system to an SLO system at a dichroic splitter. The two modalities are individually optimized for beam scanning speed, spectral band,

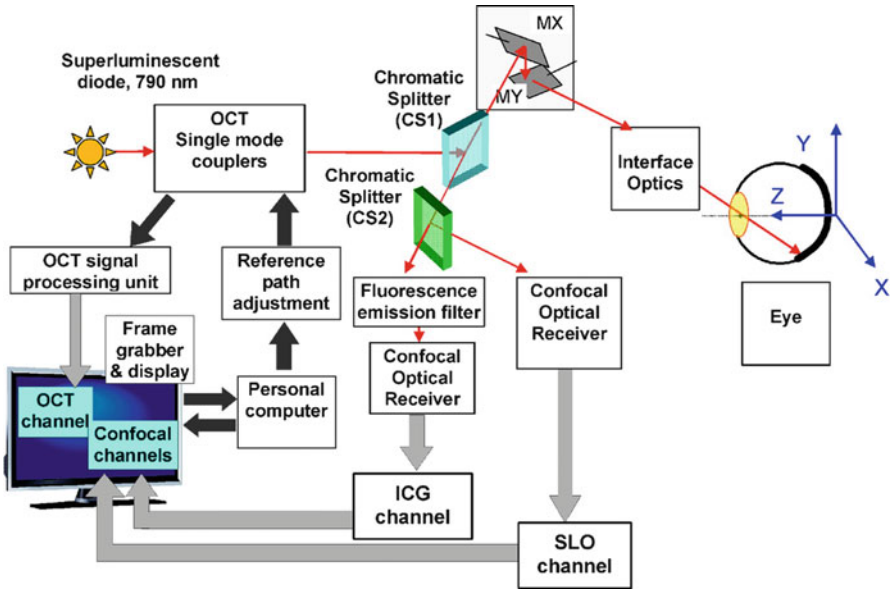

Fig. 50.3 System diagram of a free-space ophthalmic OCT/SLO/ICG imaging system. MX, MY: galvanometer mirrors of the x–y scanning pair (Reprinted from Ref. [162])

and beam geometry. The SLO provides a fast, registered fundus view, which the system uses as an aiming aid for the OCT beam, and maintains the ability to co-register SLO-based en face images and OCT B-scans.

50.6.2 Dual-Clad Fiber OCT–LIF Endoscope

An all-fiber OCT and point-scanning fluorescence endoscope was developed in the laboratory of Li [163]. The system, illustrated in Fig. 50.4, combines an OCT swept-source laser near 1,300 nm with blue laser light (488 nm) into the core of a dual-clad fiber. Reflected OCT and blue laser light, as well as fluorescence emission remitted from the tissue, are coupled into both the core and inner cladding of the dual-clad fiber. A custom dual-clad fiber coupler returns the core light back to the OCT subsystem. Weak fluorescence emission and strong reflected blue laser light are not detected by the OCT subsystem as they do not interfere with the OCT source and are outside the spectral bandwidth of the OCT optics and detector. The same fiber coupler directs light from the inner cladding to a multimode fiber. OCT and blue excitation light are eliminated with a band-pass filter prior to detection of fluorescence emission light by a photomultiplier tube. In the endoscope, optics consisted of a glass spacer and GRIN lens, which focus the light. A distal micromotor-mounted 45° reflector directs the light out the side of the endoscope and enables circumferential scanning. In an initial study, this endoscope was able to image ex vivo rabbit esophagus with approximately 14 μm OCT resolution to the

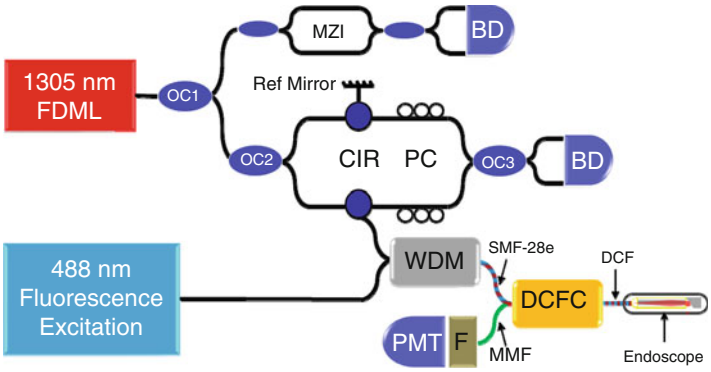

Fig. 50.4 Diagram of a combined OCT/point-scanning fluorescence system utilizing dual-clad fiber in the endoscope. *FDML* Fourier-domain mode-locking fiber laser, *OC* optical coupler, *MZI* Mach–Zehnder interferometer, *CIR* circulator, *PC* polarization controller, *BD* balanced detector, *WDM* wavelength division multiplexer, *DCFC* dual-clad fiber coupler, *PMT* photomultiplier tube, *F* band-pass filter; *green*, multimode fiber (*MMF*); *blue*/*red*, dual-clad fiber (*DCF*); *black*, single-mode fiber (*SMF-28e*) (Reprinted from Ref. [163])

depth of the muscularis mucosa. The fluorescence channel detected injected fluorescein sodium and possibly identified blood vessels.

50.6.3 Endoscopic OCT/Surface Fluorescence Imaging

Separate fiber conduits are used to carry OCT and LIF signals in the third example of a dual modality device [164]. A system and distal optics diagram is given in Fig. 50.5. In this instrument, spectral-domain OCT and surface-magnifying chromoendoscopy (SMC) are combined. SMC utilizes high magnification surface imaging with the FDA-approved vital dye methylene blue to visualize crypt patterns in the colon. Either the absorption or, as in this case, the fluorescence of methylene blue can be detected. The proximal subsystem construction was simplified by utilizing separate fibers. The OCT subsystem is a conventional spectral-domain system. The SMC subsystem consists of a red laser diode coupled via a microscope objective into a 30,000 element fiber bundle. To detect the fluorescence emission image, the fiber bundle face is imaged onto a low-noise CCD camera, through dichroic and emission filters. At the distal end of the endoscope, the fiber bundle is centered on a spacer/GRIN lens combination. Four OCT fibers (only one used) are arranged concentrically. A right-angle prism directs light out the side of the endoscope. An annulus limits the numerical aperture of the detected fluorescence emission light to prevent total internal reflection in the GRIN lens. Judicious use of aberrations including chromatic dispersion and astigmatism enables the SMC channel to focus to an image plane adjacent to the outer cylindrical surface of the covering glass envelope, while OCT light is focused to a diffraction-limited spot 190 μm inside the tissue. Linear movement of the optics within the glass envelope provides overlapping

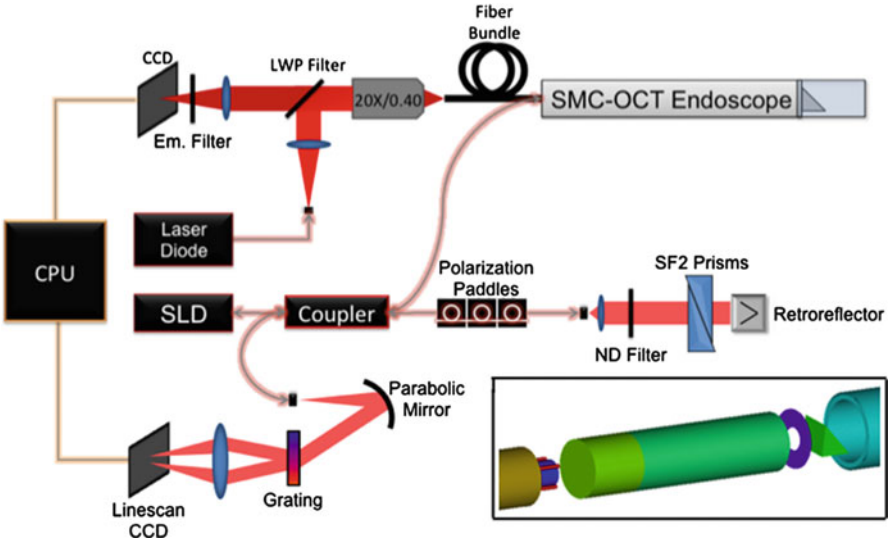

Fig. 50.5 Diagram of an endoscopic OCT/surface fluorescence imaging system. Fluorescence and OCT sources are fiber coupled into endoscope. A long-wave pass (*LWP*) filter is used to reflect excitation light and pass emission light in the SMC proximal setup, while neutral density (*ND*) filters attenuate OCT source power. Charge-coupled devices (*CCD*) are used to detect signal in each modality, and data is electronically transmitted to the central processing unit (*CPU*). Inset shows the distal tip optics. From *left* to *right*: *gold*, positioning ferrule; *navy*, 30,000 element fiber bundles; *red*, OCT single-mode fibers; *green*, spacer; *teal*, GRIN lens; *purple*, annulus; *green*, right-angle prism; *blue*, protective class envelope (Adapted from Ref. [164])

circular en face SMC images and a single cross-sectional OCT image. This system has been used to obtain time-serial images of cancer development in the mouse colon.

50.7 Example Applications

To conclude this chapter, we describe three example applications of combined OCT–LIF system: imaging of the human eye with an in-air OCT/autofluorescence system, ex vivo imaging of rat ovary with an endoscopic OCT/autofluorescence spectroscopy system, and in vivo imaging of mouse colon with an endoscopic OCT/surface fluorescence imaging system. Each of these examples provides evidence that the two modes of data obtained are complimentary.

50.7.1 Human Eye with Macular Degeneration

Automatic superposition of the multimodality images enable correlations to be made between en face autofluorescence measurements and cross-sectionally

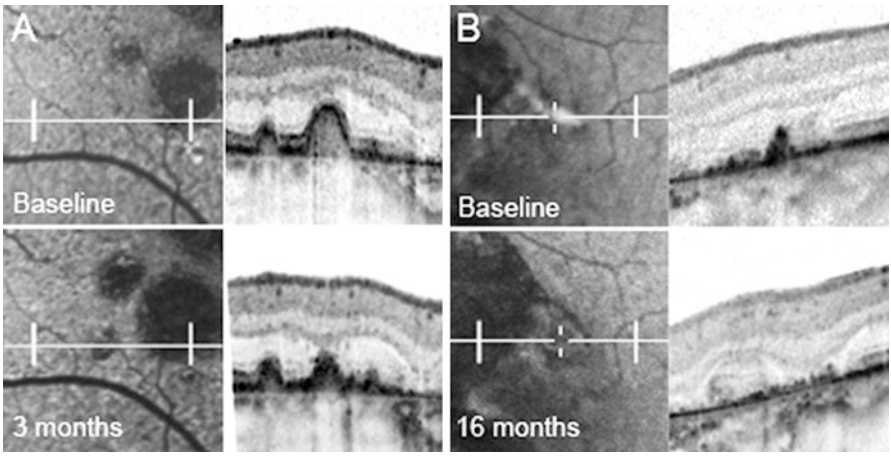

Fig. 50.6 Simultaneous autofluorescence and OCT imaging in the eyes with developing geographic atrophy (*GA*) due to age-related macular degeneration. (**a**) At baseline, a dome-shaped elevation OCT correlates with drusen material. There is irregular but still preserved fluorescence (*upper left*). After 3 months, a small lesion with decreased FAF has developed, and continuing structural changes are seen in OCT (*lower left*). (**b**) At baseline, there is an accumulation of hyperreflective material in the OCT scan that is spatially colocated with an intensely increased FAF signal (*upper right*). After 16 months, the hyperreflective material has disappeared, and retina structure is distorted on OCT (*lower right*) (Reprinted from Ref. [166])

visible structural changes in the retina. Autofluorescence signal arises primarily from lipofuscin concentration, normally located in the retinal pigment epithelium (RPE) [165]. OCT contrast originates primarily from the segregation of cellular structures in the neural retina, with cell bodies yielding low reflectance while their complex neural processes tend to scatter more light. The RPE contains a high concentration of melanin, which is strongly absorbed by OCT wavelengths. When the RPE is disrupted, the signal from the underlying choroidal tissue is hyperintense. For example, Fig. 50.6 shows two cases in which changes in both OCT and autofluorescence track the temporal progression of geographic atrophy in the perilesional zone, where macular degeneration-related vision loss is most likely to progress [166]. In the first case (A), structural thickening (drusen material) with normal fluorescence precedes an apparently decreasing thickness of drusen material but an abnormal development of decreased fluorescence. In a second case (B), an area of localized hyperreflectance in OCT is correlated with a region of hyperintense autofluorescence in a region that eventually shows structural changes in OCT that point clearly towards cell layer loss and development of geographic atrophy. Utilizing these two modalities in a combined instrument may be useful to track and predict retinal disease progression, elucidate mechanisms of disease, and evaluate the effects of therapeutic agents with greater accuracy and resolution.

50.7.2 Rat Ovary

A combined OCT–LIF was used to acquire images and spectra of 54 excised rat ovaries [167]. This system combines a time-domain OCT system with an autofluorescence point-spectroscopy system. Due to the integration time needed for autofluorescence spectroscopy, the relatively slow speed of a time-domain system was not the time-limiting factor. The endoscope combined a GRIN lens-based imaging system for the single-mode OCT fiber, with separate unlensed multimode excitation and emission collection fibers [168]. While this study was ex vivo, the endoscope was used in preparation for future minimally invasive in vivo studies. The goal of this study was to determine if OCT and/or LIF could distinguish between ovaries from normal cycling animals, postmenopausal ovaries (follicle depletion induced by i.p. injection of 4-vinylcyclohexene diepoxide or VCD), and ovaries with atypia or neoplasms induced by 7, 12-dimethylbenz-alpha-anthracene (DMBA). VCD was administered for 20 days at a dose of 160 mg/kg i.p. Three to five months later, some animals had a DMBA soaked suture (approximately 110 μg DMBA) placed through the right ovary. One to five months after suture insertion, the animals were sacrificed and the ovaries excised. Excess fat and connective tissue were trimmed prior to imaging; no superficial blood contamination was apparent.

Figure 50.7 shows a sequence of OCT images/LIF spectra and histology from a normal cycling ovary, VCD-treated follicle-deplete ovary, a VCD-/DMBA-treated ovary with atypia (follicular remnant degeneration), and a VCD-/DMBA-treated ovary with neoplastic cysts. In the cycling ovary, antral follicles and the bursa are seen. The VCD-treated ovary is much reduced in size, and only dense stroma with surface fat is seen, as would be expected in a follicle-deplete, postmenopausal ovary. Follicular remnant degeneration in the DMBA-treated ovary manifests as a multitude of small hypointense regions, whereas the cancerous cysts are large hypointense regions. The OCT images show excellent correspondence to histology at the tissue architecture level. While the DMBA-treated ovaries clearly appeared abnormal, a determination of neoplasia could not be made since the markers of cancer (e.g., abnormally large or irregular nuclei) were not identifiable at the resolution of this OCT system. Therefore, it appears that OCT may be of use in identifying abnormal-appearing ovaries but by itself cannot make a determination of atypical changes or neoplasia. Molecularly targeted contrast agents (absorption or scattering) could be of use to increase OCT's sensitivity and specificity to cancer.

With 325 nm excitation wavelength, the LIF spectra show peaks at approximately 390 and 450 nm and absorption at 420 nm, associated with collagen fluorescence, NADH fluorescence, and hemoglobin absorption, respectively. In the normal cycling ovary, the magnitude of the 450 nm peak is greater than the 390 nm peak, and the dip at 420 nm is well defined. This suggests that a relatively large amount of NADH and hemoglobin is present in the ovary. In contrast, LIF spectra from the follicle-deplete ovary is dominated by the 390 nm peak, indicative

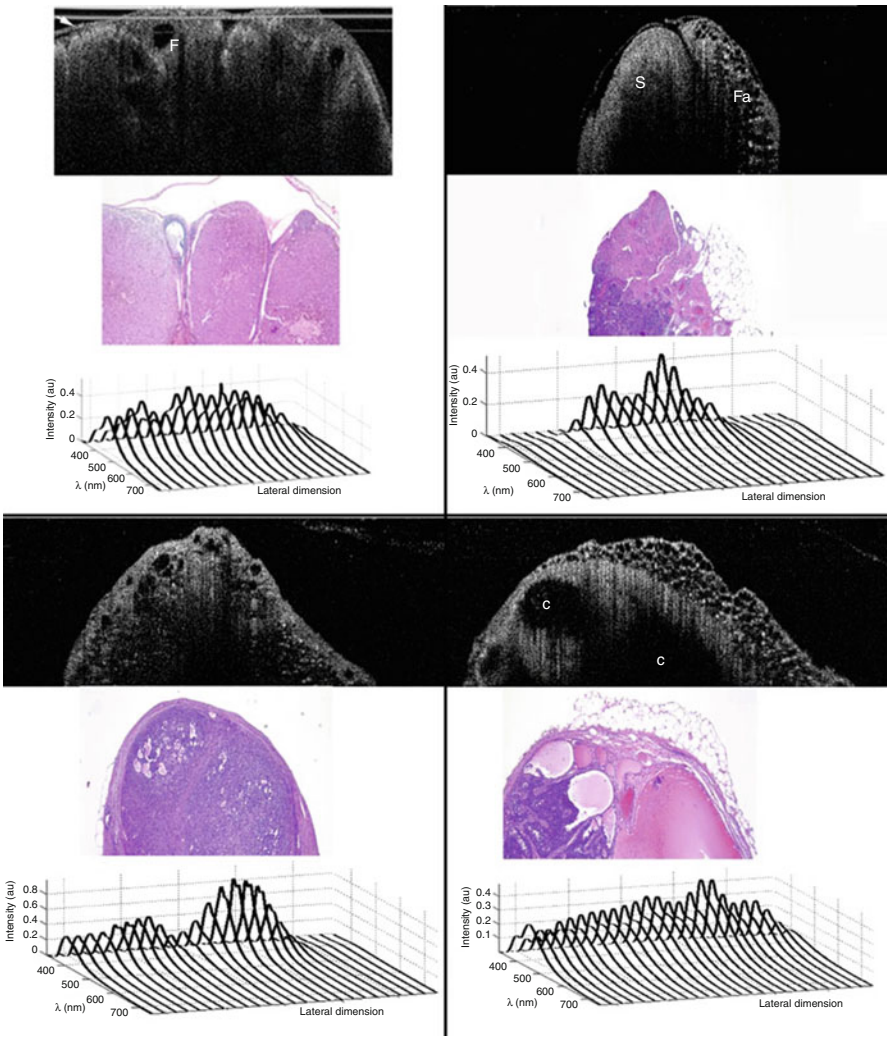

Fig. 50.7 A sequence of OCT images, LIF spectra, and histology from a normal cycling ovary (*top left*), VCD-treated follicle-deplete ovary (*top right*), a VCD-/DMBA-treated ovary with atypia–follicular remnant degeneration (*bottom left*), and a VCD-/DMBA-treated ovary with neoplastic cysts (*bottom right*). The normal cycling ovary shows follicular cysts (*F*), whereas the follicle-deplete ovary has only dense stroma (*S*) and fat (*Fa*). Many small abnormal cysts are seen in the atypical ovary, and large abnormal cysts (*C*) are seen in the neoplastic ovary. OCT images correlate well with histology. LIF shows a trend towards increased 450:390 nm fluorescence emission ratio in metabolically active ovaries (either normal cycling or atypical/neoplastic) compared to the follicle-deplete ovary. OCT images are 5 mm lateral × 1.4 mm deep, except normal cycling which is 4 mm lateral. Histology is to same scale as OCT. LIF data are presented over the same lateral range as the OCT images (Adapted from Ref. [167])

of high relative collagen content and less metabolic activity. There is also a relatively small amount of vasculature as seen from the LIF spectra (less pronounced dip at 420 nm), which was confirmed histologically. The DMBA-treated ovaries both show a relatively high 450 nm fluorescence peak and pronounced 420 nm absorption, similar to the cycling ovary. A comparison between groups shows statistically significant differences in the ratio of 390:450 nm fluorescence intensity of the cycling and cancerous groups, as compared to follicle-deplete group. A follow-on study investigating 162 freshly excised ovaries also saw changes in OCT structure and fluorescence emission spectra of normal versus cancerous ovaries [169].

In summary, the feasibility of using the combined OCT–LIF system to determine the presence of atypical and neoplastic changes in the ovary was shown. Different structures such as cysts, fatty regions, and follicular remnant degeneration were easily identified in the OCT images. There was preliminary evidence from this study that atypical cellular changes might be located in the regions identified by irregularly sized hypointense regions in the OCT images, but OCT could not directly distinguish atypical cells and areas of cancer. The LIF spectra provided information about hemoglobin content as well as the metabolic activity of the ovary and displayed significant changes between follicle-deplete emission ratios and both cycling and neoplastic emission ratios. Therefore, this study suggested that by utilizing combined OCT and LIF data, it may be possible to distinguish between cycling, follicle-depleted, non-atypical, atypical, and neoplastic ovaries.

50.7.3 Mouse Colon

The OCT–LIF endoscope provides access to the distal 3 cm of the mouse colon. In vivo monitoring in a mouse model may enable extrapolation about the capability of OCT–LIF to identify cancer in a human patient as well as aid in the development of chemotherapeutics. The normal mouse colon is approximately 300 μm thick with an average crypt measuring 100 by 20 μm. Epithelial cancers start as aberrant crypt foci (ACF) that are little larger than a collection of several crypts and may become large adenomas over 1 mm in diameter. In the digestive tract, chromophores common to other tissues (including collagen, NADH, and hemoglobin) are present in combination with those found in the digested food.

Several in vivo studies have been performed in mouse colon with dual modality OCT–LIF instruments. In some studies [170, 171], OCT images have been used to identify areas of the mouse colon that are abnormal and to use this data to isolate matching autofluorescence spectra associated with tumors. Statistically significant differences between normal and tumor tissues have been observed in LIF spectra, but the variation in fluorescence signal in normal tissue limits sensitivity and specificity. Details in the OCT image such as changes in mucosal layer thickness, or presence of adventitia surrounding the colon can be associated with fluctuations in the autofluorescence spectra. This highlights the complementary,

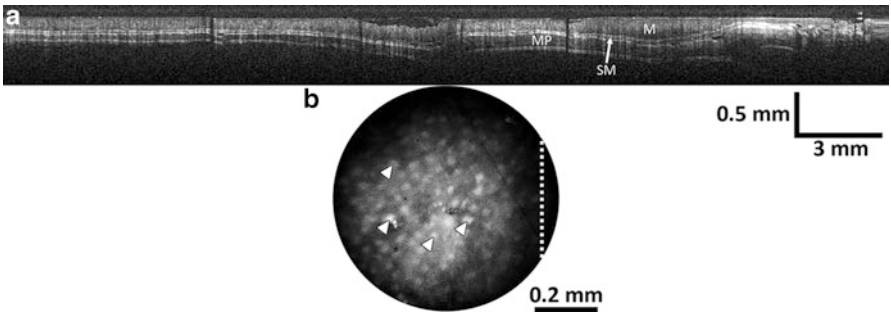

Fig. 50.8 Optical coherence tomography (*OCT*) image scanning the full 30 mm of the in vivo mouse colon (**a**) and surface magnifying chromoendoscopy (*SMC*) image taken at one location in the mouse colon (**b**). The layered structures of the colon, including the mucosa (*M*), submucosa (*SM*), and muscularis propria (*MP*), are easily identified in the OCT image, while *arrows* in the SMC image point to individual colonic crypts, and the *white dotted line* corresponds to the scan line of the specific OCT image (Reprinted from Ref. [164])

but nonorthogonal, nature of the datasets and the potential to improve fluorescence diagnostics with knowledge of the underlying tissue structure.

Rather than detecting autofluorescence, targeted fluorescent contrast agents can be used. In one study [172], the colon was lavaged with Cy5.5 dye conjugated to a vascular endothelial growth factor (VEGF) fragment, and a 633 nm HeNe laser was used for LIF excitation. The dye preferentially attached to VEGF receptor-2. Results showed significantly higher, but also highly variable, fluorescence emission intensity over adenoma. Also, a large variation in fluorescence emission was seen in regions of the colon which appeared normal on OCT images. A correlation was seen between fluorescence emission intensity of images of frozen sections and images of sections immunostained for VEGF receptor-2. These results suggest that expression of VEGF receptor-2 is not homogeneous in disease and that the LIF information provides information on molecular events not visible with OCT. Time-serial imaging might be performed to determine if adenoma with high levels of VEGF receptor-2 expression have more aggressive growth patterns.

An example image pair of mouse colon taken with the endoscopic OCT/surface fluorescence imaging system described above is given in Fig. 50.8. The top image shows a cross-sectional OCT image of the full 30 mm length of the mouse colon. The bottom image shows a 700 μm diameter field of view fluorescence surface-magnifying chromoendoscopy image at one location. In this case, the surface image with contrast agent enables high-contrast image of the crypt structure of the mouse colon. Due to the small size and low contrast of the crypts, this information cannot be seen in the OCT image. A targeted dye could be used to not only help visualize the structure of aberrant crypt foci (putative earliest stage of disease) but also overexpression of cell surface markers associated with early disease.

50.8 Conclusion

In this chapter, existing combined OCT–LIF endoscopic systems were described, and potential improvements in resolution and collection efficiency with alternative optical designs were presented. There is evidence that the combination of OCT and LIF is synergistic in several respects. First OCT can provide information about subsurface structures that can aid interpretation of LIF spectra. Second, quantitative measures of tissue layer thickness and probe–tissue separation can be used in models that seek to extract intrinsic fluorescence or correct for tissue distance. Third, LIF can provide information on tissue characteristics which are not visible to OCT. Finally, if criteria are properly developed for both modalities, the combination of the two may increase sensitivity and/or specificity to disease. Future work will help define the applications most enhanced by this dual modality approach.

References

1. G. Yao, L.V. Wang, Two-dimensional depth-resolved Mueller matrix characterization of biological tissue by optical coherence tomography. Opt. Lett. **24**(8), 537–539 (1999)
2. C.K. Hitzenberger, E. Gotzinger, M. Sticker, M. Pircher, A.F. Fercher, Measurement and imaging of birefringence and optic axis orientation by phase resolved polarization sensitive optical coherence tomography. Opt. Express **9**(13), 780–790 (2001)
3. J.F. de Boer, T.E. Milner, Review of polarization sensitive optical coherence tomography and Stokes vector determination. J. Biomed. Opt. **7**(3), 359–371 (2002)
4. J. Zang, S. Guo, W. Jung, J.S. Nelson, Z. Chen, Determination of birefringence and absolute optic axis orientation using polarization-sensitive optical coherence tomography with PM fibers. Opt. Express **11**(24), 3262–3270 (2003)
5. J.A. Izatt, M.D. Kulkarni, S. Yazdanfar, J.K. Barton, A.J. Welch, In vivo bidirectional color Doppler flow imaging of picoliter blood volumes using optical coherence tomography. Opt. Lett. **22**(18), 1439–1441 (1997)
6. V.X.D. Yang, M.L. Gordon, B. Qi, J. Pekar, S. Lo, E. Seng-Yue, A. Mok, B.C. Wilson, I.A. Vitkin, High speed, wide velocity dynamic range Doppler optical coherence tomography (Part I): system design, signal processing, and performance. Opt. Express **11**(7), 794–809 (2003)
7. G. Liu, W. Jia, V. Sun, B. Choi, Z. Chen, High-resolution imaging of microvasculature in human skin in-vivo with optical coherence tomography. Opt. Express **20**(7), 7694–7705 (2012)
8. M. Sticker, C.K. Hitzenberger, R. Leitgeb, A.F. Fercher, Quantitative differential phase measurement and imaging in transparent and turbid media by optical coherence tomography. Opt. Lett. **26**(8), 518–520 (2001)
9. C. Joo, T. Akkin, B. Cense, B.H. Park, J.F. de-Boer, Spectral-domain optical coherence phase microscopy for quantitative phase-contrast imaging. Opt. Lett. **30**(16), 2131–2133 (2005)
10. C. Yang, Molecular contrast optical coherence tomography: a review. Photochem. Photobiol. **81**(2), 215–237 (2005)
11. S.A. Boppart, A.L. Oldenburg, C. Xu, D.L. Marks, Optical probes and techniques for molecular contrast enhancement in coherence imaging. J. Biomed. Opt. **10**(4), 41208 (2005)
12. B.E. Applegate, C. Yang, J.A. Izatt, Theoretical comparison of the sensitivity of molecular contrast optical coherence tomography techniques. Opt. Express **13**(20), 8146–8163 (2005)
13. U. Morgner, W. Drexler, F.X. Kartner, X.D. Li, C. Pitris, E.P. Ippen, J.G. Fujimoto, Spectroscopic optical coherence tomography. Opt. Lett. **25**(2), 111–113 (2003)

14. K.D. Rao, M.A. Choma, S. Yazdanfar, A.M. Rollins, J.A. Izatt, Molecular contrast in optical coherence tomography by use of a pump-probe technique. Opt. Lett. **28**(5), 340–342 (2003)
15. W.A. Benalcazar, S.A. Boppart, Nonlinear interferometric vibrational imaging for fast label-free visualization of molecular domains in skin. Anal. Bioanal. Chem. **400**, 2817–2825 (2011)
16. Y. Jiang, I. Tomov, Y. Wang, Z. Chen, Second-harmonic optical coherence tomography. Opt. Lett. **29**(10), 1090–1092 (2004)
17. M.V. Sarunic, B.E. Applegate, J.A. Izatt, Spectral domain second-harmonic optical coherence tomography. Opt. Lett. **30**(18), 2391–2393 (2005)
18. C. Loo, A. Lin, M. Lee, J.K. Barton, N. Halas, J. West, R. Drezek, Nanoshell-enabled photonics-based imaging and therapy of cancer. Technol. Cancer Res. Treat. **3**, 33–40 (2004)
19. A.M. Winkler, P.F. Rice, R.A. Drezek, J.K. Barton, Quantitative tool for rapid disease mapping using optical coherence tomography images of azoxymethane treated mouse colon. J. Biomed. Opt. **15**(04), 041512 (2010)
20. M. Kirillin, M. Shirmanova, M. Sirotkina, M. Bugrova, B. Khlebtsov, E. Zagaynova, Contrasting properties of gold nanoshells and titanium dioxide nanoparticles for optical coherence tomography imaging of skin: Monte Carlo simulations and in vivo study. J. Biomed. Opt. **14**(2), 021017 (2009)
21. H. Cang, T. Sun, Z.Y. Li, J. Chen, B.J. Wiley, Y. Xia, X. Li, Gold nanocages as contrast agents for spectroscopic optical coherence tomography. OPt. Lett. **30**, 3048–3050 (2005)
22. T.M. Lee, A.L. Oldenburg, S. Sitafalwalla, D.L. Marks, W. Luo, F.J. Toublan, K.S. Suslick, S.A. Boppart, Engineered microsphere contrast agents for optical coherence tomography. Opt. Lett. **28**, 1546–1548 (2003)
23. Y. Changhuei, L.E.L. McGuckin, J.D. Simon, M.A. Choma, B.E. Applegate, J.A. Izatt, Spectral triangulation molecular contrast optical coherence tomography with indocyanine green as the contrast agent. Opt. Lett. **29**(17), 2016–2018 (2004)
24. G. Isenburg, M.V. Sivak, A. Chak, R.C. Wong, J.E. Willis, B. Wolf, D.Y. Rowland, A. Das, A. Rollins, Accuracy of endoscopic optical coherence tomography in the detection of dysplasia in Barrett's esophagus: a prospective, double-blinded study. Gastrointest. Endosc. **62**(6), 825–831 (2005)
25. E. Zagaynova, N. Gladkova, N. Shakhova, G. Gelikonov, V. Gelikonov, Endoscopic OCT with forward-looking probe: clinical studies in urology and gastroenterology. J. Biophotonics **1**(2), 114–128 (2008)
26. A. Karl, H. Stepp, E. Willmann, A. Buchner, Y. Hocaoglu, C. Stief, S. Tritschler, Optical coherence tomography for bladder cancer – ready as a surrogate for optical biopsy? Results of a prospective mono-centre study. Eur. J. Med. Res. **15**(3), 131–134 (2010)
27. N. Gladkova, O. Streltsova, E. Zagaynova, E. Kiseleva, V. Gelikonov, G. Gelikonov, M. Karabut, K. Yunusova, O. Evdokimova, Cross-polarization optical coherence tomography for early bladder-cancer detection: statistical study. J. Biophotonics **4**(7–8), 519–532 (2011)
28. P. Consolo, G. Strangio, C. Luigiano, G. Giacobbe, S. Pallio, L. Familiari, Optical coherence tomography in inflammatory bowel disease: prospective evaluation of 35 patients. Dis. Colon Rectum **51**(9), 1374–1380 (2008)
29. J.K. Gallwas, L. Turk, H. Stepp, S. Mueller, R. Ochsenkuehn, K. Friese, C. Dannecker, Optical coherence tomography for the diagnosis of cervical intraepithelial neoplasia. Lasers Surg. Med. **43**(3), 206–212 (2011)
30. N. Wulan, N. Rasool, S.E. Belinson, C. Wang, X. Rong, W. Zhang, Y. Zhu, B. Yang, N.J. Tresser, M. Mohr, R. Wu, J.L. Belinson, Study of the diagnostic efficacy of real-time optical coherence tomography as an adjunct to unaided visual inspection with acetic acid for the diagnosis of preinvasive and invasive neoplasia of the uterine cervix. Int. J. Gynecol. Cancer **20**(3), 422–427 (2010)
31. W. Kang, X. Qi, N.J. Tresser, M. Kareta, J.L. Belinson, A.M. Rollins, Diagnostic efficacy of computer extracted image features in optical coherence tomography of the precancerous cervix. Med. Phys. **38**(1), 107–113 (2011)

32. M. Mogensen, T.M. Joergensen, B.M. Nürnberg, H.A. Morsy, J.B. Thomsen, L. Thrane, G.B. Jemec, Assessment of optical coherence tomography imaging in the diagnosis of non-melanoma skin cancer and benign lesions versus normal skin: observer-blinded evaluation by dermatologists and pathologists. Dermatol. Surg. **35**(6), 965–972 (2009)
33. V. Korde, G. Bonnema, W. Xu, C. Krishnamurthy, J. Ranger-Moore, K. Saboda, L. Slayton, S. Salasche, J. Warneke, D. Alberts, J.K. Barton, Using optical coherence tomography to evaluate skin sun damage and precancer. Lasers Surg. Med. **39**, 687–695 (2007)
34. J. Rieber, O. Meissner, G. Babaryka, S. Reim, M. Oswald, A. Koenig, T.M. Schiele, M. Shapiro, K. Theisen, M.F. Reiser, V. Klauss, U. Hoffmann, Diagnostic accuracy of optical coherence tomography and intravascular ultrasound for the detection and characterization of atherosclerotic plaque composition in ex-vivo coronary specimens: a comparison with histology. Coron. Artery Dis. **17**(5), 425–430 (2006)
35. M. Kawasaki, B.E. Bouma, J. Bressner, S.L. Houser, S.K. Nadkarni, B.D. MacNeill, I.K. Jang, H. Fujiwara, G.J. Tearney, Diagnostic accuracy of optical coherence tomography and integrated backscatter intravascular ultrasound images for tissue characterization of human coronary plaques. J. Am. Coll. Cardiol. **48**(1), 81–88 (2006)
36. Diabetic Retinopathy Clinical Research Network, A randomized trial comparing intravitreal triamcinolone acetonide and focal/grid photocoagulation for diabetic macular edema. Ophthalmology **115**(9), 1447–1449 (2008)
37. F.G. Holz, W. Amoaku, J. Donate, R.H. Guymer, U. Kellner, R.O. Schlingemann, A. Weichselberger, G. Staurenghi, SUSTAIN Study Group, Safety and efficacy of a flexible dosing regimen of ranibizumab in neovascular age-related macular degeneration: the SUSTAIN study. Ophthalmology **118**(4), 663–671 (2011)
38. F.C. DeCroos, C.A. Toth, F.A. Folgar, S. Pakola, S.S. Stinnett, C.S. Heydary, R. Burns, G.J. Jaffe, Characterization of vitreoretinal interface disorders using OCT in the interventional phase 3 trials of ocriplasmin. Invest. Ophthalmol. Vis. Sci. **53**(10), 6504–6511 (2012)
39. J.R. Lakowicz, *Principles of Fluorescence Spectroscopy* (Kluwer Academic/Plenum, New York, 1999)
40. G.A. Wagnieres, W.M. Star, B.C. Wilson, In vivo fluorescence spectroscopy and imaging for oncological applications. Photochem. Photobiol. **68**, 603–632 (1998)
41. M.A. Mycek, B.W. Pogue, *Handbook of Biomedical Fluorescence* (Marcel Dekker, New York, 2003)
42. R. Richards-Kortum, E. Sevick-Muraca, Quantitative optical spectroscopy for tissue diagnosis. Annu. Rev. Phys. Chem. **47**, 555–606 (1996)
43. N. Ramanujam, Fluorescence spectroscopy of neoplastic and non-neoplastic tissues. Neoplasia **2**, 89–117 (2000)
44. K. Sokolov, M. Follen, R. Richards-Kortum, Optical spectroscopy for detection of neoplasia. Curr. Opin. Chem. Biol. **6**, 651–658 (2002)
45. T. Vo-Dinh, *Biomedical Photonics Handbook* (CRC Press, Boca Raton, 2003)
46. T. Galeotti, G.D.V. van Rossum, D.H. Mayer, B. Chance, On the fluorescence of NAD(P)H in whole-cell preparation of tumors and normal tissues. Eur. J. Biochem. **17**, 485–496 (1970)
47. B. Chance, Optical method. Annu. Rev. Biophys. Biophys. Chem. **20**, 1–28 (1991)
48. B. Thorell, B. Chance, Localization and kinetics of reduced pyridine nucleotide in living cells by microfluorometry. J. Biol. Chem. **234**, 3044–3050 (1959)
49. Policard, A study on the available aspects of experimental tumours examined by Wood's light. C. R. Seances Soc. Biol. Fil. **91**, 1423–1424 (1924)
50. F.N. Ghadially, W.J. Neish, Porphyrin fluorescence of experimentally produced squamous cell carcinoma. Nature **188**, 1124 (1960)
51. F.N. Ghadially, Red fluorescence of experimentally induced and human tumours. J. Pathol. Bacteriol. **80**, 345 (1960)

52. K.T. Schomacker, J.K. Frisoli, C. Compton, T.J. Flotte, J.M. Richter, N. Nishioka, T.F. Deutsch, Ultraviolet laser-induced fluorescence of colonic tissue: basic biology and diagnostic potential. Lasers Surg. Med. **12**, 63–78 (1992)
53. K.D. Ashby, J. Wen, P. Chowdhury, T.A. Casey, M.A. Rasmussen, J.W. Petrich, Fluorescence of dietary porphyrins as a basis for real-time detection of fecal contamination on meat. J. Agric. Food Chem. **51**, 3502–3507 (2003)
54. L.F. Ma, D. Dolphin, The metabolites of dietary chlorophylls. Phytochemistry **50**, 195–202 (1999)
55. M. Boulton, F. Docchio, P. Dayhaw-Barker, R. Ramponi, R. Cubeddu, Age-related changes in the morphology, absorption and fluorescence of melanosomes and lipofuscin granules of the retinal pigment epithelium. Vision Res. **30**, 1291–1303 (1990)
56. C.J. Kennedy, P.E. Rakoczy, I.J. Constable, Lipofuscin of the retinal pigment epithelium: a review. Eye (Lond.) **9**(Pt 6), 763–771 (1995)
57. M.B. Ericson, J. Uhre, C. Strandeberg, B. Stenquist, O. Larko, A.M. Wennberg, A. Rosen, Bispectral fluorescence imaging combined with texture analysis and linear discrimination for correlation with histopathologic extent of basal cell carcinoma. J. Biomed. Opt. **10**, 034009 (2005)
58. S. Andersson-Engels, G. Canti, R. Cubeddu, C. Eker, C. af Klinteberg, A. Pifferi, K. Svanberg, S. Svanberg, P. Taroni, G. Valentini, I. Wang, Preliminary evaluation of two fluorescence imaging methods for the detection and the delineation of basal cell carcinomas of the skin. Lasers Surg. Med. **26**, 76–82 (2000)
59. E. Endlicher, P. Rummele, F. Hausmann, H.C. Rath, R. Knuchel, R.C. Krieg, J. Scholmerich, H. Messmann, Detection of dysplastic lesions by fluorescence in a model of chronic colitis in rats after local application of 5-aminolevulinic acid and its esterified derivatives. Photochem. Photobiol. **79**, 189–192 (2004)
60. J. Gahlen, J. Stern, J. Pressmar, J. Bohm, R. Holle, C. Herfarth, Local 5-aminolevulinic acid application for laser light-induced fluorescence diagnosis of early staged colon cancer in rats. Lasers Surg. Med. **26**, 302–307 (2000)
61. C. Eker, S. Montan, E. Jaramillo, K. Koizumi, C. Rubio, S. Andersson-Engels, K. Svanberg, S. Svanberg, P. Slezak, Clinical spectral characterisation of colonic mucosal lesions using autofluorescence and delta aminolevulinic acid sensitisation. Gut **44**, 511–518 (1999)
62. M. Csanady, J.G. Kiss, L. Ivan, J. Jori, J. Czigner, ALA (5-aminolevulinic acid)-induced protoporphyrin IX fluorescence in the endoscopic diagnostic and control of pharyngolaryngeal cancer. Eur. Arch. Otorhinolaryngol. **261**, 262–266 (2004)
63. Y.T. Pan, T.Q. Xie, C.W. Du, S. Bastacky, S. Meyers, M.L. Zeidel, Enhancing early bladder cancer detection with fluorescence-guided endoscopic optical coherence tomography. Opt. Lett. **28**, 2485–2487 (2003)
64. M. Olivo, W. Lau, V. Manivasager, T.P. Hoon, C. Christopher, Fluorescence confocal microscopy and image analysis of bladder cancer using 5-aminolevulinic acid. Int. J. Oncol. **22**, 523–528 (2003)
65. V. Manivasager, P.W. Heng, J. Hao, W. Zheng, K.C. Soo, M. Olivo, A study of 5-aminolevulinic acid and its methyl ester used in in vitro and in vivo systems of human bladder cancer. Int. J. Oncol. **22**, 313–318 (2003)
66. R.M. Lycette, R.B. Leslie, Fluorescence of malignant tissue. Lancet **2**, 436 (1965)
67. R.R. Alfano, D.B. Tata, J.J. Cordero, P. Tomashefsky, F.W. Longo, M.A. Alfano, Laser induced fluorescence spectroscopy from native cancerous and normal tissue. IEEE J. Quantum Electron. **20**, 1507–1511 (1984)
68. W.K. Huh, R.M. Cestero, F.A. Garcia, M.A. Gold, R.S. Guido, K. McIntyre-Seltman, D.M. Harper, L. Burke, S.T. Sum, R.F. Flewelling, R.D. Alvarez, Optical detection of high-grade cervical intraepithelial neoplasia in vivo: results of a 604-patient study. Am. J. Obstet. Gynecol. **190**, 1249–1257 (2004)

69. T. DeSantis, N. Chakhtoura, L. Twiggs, D. Ferris, M. Lashgari, L. Flowers, M. Faupel, S. Bambot, S. Raab, E. Wilkinson, Spectroscopic imaging as a triage test for cervical disease: a prospective multicenter clinical trial. J. Low. Genit. Tract Dis. **11**, 18–24 (2007)
70. S.K. Chang, M.Y. Dawood, G. Staerkel, U. Utzinger, E.N. Atkinson, R.R. Richards-Kortum, M. Follen, Fluorescence spectroscopy for cervical precancer detection: is there variance across the menstrual cycle? J. Biomed. Opt. **7**, 595–602 (2002)
71. I. Georgakoudi, E.E. Sheets, M.G. Muller, V. Backman, C.P. Crum, K. Badizadegan, R.R. Dasari, M.S. Feld, Trimodal spectroscopy for the detection and characterization of cervical precancers in vivo. Am. J. Obstet. Gynecol. **186**, 374–382 (2002)
72. N. Ramanujam, M. Follen, A. Mahadevan, S. Thomsen, G. Staerkel, A. Malpica, R. Richards-Kortum, Cervical pre-cancer detection using a multivariate statistical algorithm based on laser induced fluorescence spectra at multiple excitation wavelengths. Photochem. Photobiol. **6**, 720–735 (1996)
73. J. Wu, M.S. Feld, R.P. Rava, Analytical model for extracting intrinsic fluorescence in turbid media. Appl. Opt. **32**, 3585–3595 (1993)
74. G. Zonios, L. Perelman, V. Backman, R. Manoharan, M. Fitzmaurice, J.V. Dam, M. Feld, Diffuse reflectance spectroscopy of human adenomatous colon polyps in vivo. Appl. Opt. **38**, 6628–6637 (1999)
75. L.T. Perelman, V. Backman, M. Wallace, G. Zonios, R. Manoharan, A. Nusrat, S. Shields, M. Seiler, C. Lima, T. Hamano, I. Itzkan, J. Van Dam, J.M. Crawford, M.S. Feld, Observation of periodic fine structure in reflectance from biological tissue: a new technique for measuring nuclear size distribution. Phys. Rev. Lett. **80**, 627–630 (1998)
76. S. Lam, T. Kennedy, M. Unger, Y.E. Miller, D. Gelmont, V. Rusch, B. Gipe, D. Howard, J.C. LeRiche, A. Coldman, A.F. Gazdar, Localization of bronchial intraepithelial neoplastic lesions by fluorescence bronchoscopy. Chest **113**, 696–702 (1998)
77. P. Pierard, J. Faber, J. Hutsebaut, B. Martin, G. Plat, J.P. Sculier, V. Ninane, Synchronous lesions detected by autofluorescence bronchoscopy in patients with high-grade preinvasive lesions and occult invasive squamous cell carcinoma of the proximal airways. Lung Cancer **46**, 341–347 (2004)
78. K. Haussinger, H. Becker, F. Stanzel, A. Kreuzer, B. Schmidt, J. Strausz, S. Cavaliere, F. Herth, M. Kohlhaufl, K.M. Muller, R.M. Huber, U. Pichlmeier, T. Bolliger, Autofluorescence bronchoscopy with white light bronchoscopy compared with white light bronchoscopy alone for the detection of precancerous lesions: a European randomised controlled multicentre trial. Thorax **60**, 496–503 (2005)
79. H. Hoshino, K. Shibuya, M. Chiyo, A. Iyoda, S. Yoshida, Y. Sekine, T. Iizasa, Y. Saitoh, M. Baba, K. Hiroshima, H. Ohwada, T. Fujisawa, Biological features of bronchial squamous dysplasia followed up by autofluorescence bronchoscopy. Lung Cancer **46**, 187–196 (2004)
80. M. Chiyo, K. Shibuya, H. Hoshino, K. Yasufuku, Y. Sekine, T. Iizasa, K. Hiroshima, T. Fujisawa, Effective detection of bronchial preinvasive lesions by a new autofluorescence imaging bronchovideoscope system. Lung Cancer **48**, 307–313 (2005)
81. B. Lam, M.P. Wong, S.L. Fung, D.C. Lam, P.C. Wong, T.Y. Mok, F.M. Lam, M.S. Ip, C.G. Ooi, W.K. Lam, The clinical value of autofluorescence bronchoscopy for the diagnosis of lung cancer. Eur. Respir. J. **28**, 915–919 (2006)
82. M. Keijzer, R.R. Richards-Kortum, S.L. Jacques, M.S. Feld, Fluorescence spectroscopy of turbid media: autofluorescence of the human aorta. Appl. Opt. **28**, 4286–4292 (1989)
83. R. Meerwaldt, R. Graaff, P.H. Oomen, T.P. Links, J.J. Jager, N.L. Alderson, S.R. Thorpe, J.W. Baynes, R.O. Gans, A.J. Smit, Simple non-invasive assessment of advanced glycation endproduct accumulation. Diabetologia **47**, 1324–1330 (2004)
84. M. Monami, C. Lamanna, F. Gori, F. Bartalucci, N. Marchionni, E. Mannucci, Skin autofluorescence in type 2 diabetes: beyond blood glucose. Diabetes Res. Clin. Pract. **79**, 56–60 (2008)

85. M.J. Noordzij, J.D. Lefrandt, E.A. Loeffen, B.R. Saleem, R. Meerwaldt, H.L. Lutgers, A.J. Smit, C.J. Zeebregts, Skin autofluorescence is increased in patients with carotid artery stenosis and peripheral artery disease. Int. J. Cardiovasc. Imaging **28**, 431–438 (2012)
86. R. Meerwaldt, H.L. Lutgers, T.P. Links, R. Graaff, J.W. Baynes, R.O. Gans, A.J. Smit, Skin autofluorescence is a strong predictor of cardiac mortality in diabetes. Diabetes Care **30**, 107–112 (2007)
87. R. George, M. Michaelides, M.A. Brewer, U. Utzinger, Parallel factor analysis of ovarian autofluorescence as a cancer diagnostic. Lasers Surg. Med. **44**, 282–295 (2012)
88. J.N. McAlpine, S. El Hallani, S.F. Lam, S.E. Kalloger, M. Luk, D.G. Huntsman, C. MacAulay, C.B. Gilks, D.M. Miller, P.M. Lane, Autofluorescence imaging can identify preinvasive or clinically occult lesions in fallopian tube epithelium: a promising step towards screening and early detection. Gynecol. Oncol. **120**, 385–392 (2011)
89. T. Matsuda, Y. Saito, K.I. Fu, T. Uraoka, N. Kobayashi, T. Nakajima, H. Ikehara, Y. Mashimo, T. Shimoda, Y. Murakami, A. Parra-Blanco, T. Fujimori, D. Saito, Does autofluorescence imaging videoendoscopy system improve the colonoscopic polyp detection rate?–a pilot study. Am. J. Gastroenterol. **103**, 1926–1932 (2008)
90. D. Ramsoekh, J. Haringsma, J.W. Poley, P. van Putten, H. van Dekken, E.W. Steyerberg, M.E. van Leerdam, E.J. Kuipers, A back-to-back comparison of white light video endoscopy with autofluorescence endoscopy for adenoma detection in high-risk subjects. Gut **59**, 785–793 (2010)
91. Y. Takeuchi, T. Inoue, N. Hanaoka, K. Higashino, H. Iishi, R. Chatani, M. Hanafusa, T. Kizu, R. Ishihara, M. Tatsuta, T. Shimokawa, N. Uedo, Autofluorescence imaging with a transparent hood for detection of colorectal neoplasms: a prospective, randomized trial. Gastrointest. Endosc. **72**, 1006–1013 (2010)
92. K. Moriichi, M. Fujiya, R. Sato, J. Watari, Y. Nomura, T. Nata, N. Ueno, S. Maeda, S. Kashima, K. Itabashi, C. Ishikawa, Y. Inaba, T. Ito, K. Okamoto, H. Tanabe, T. Mizukami, Y. Saitoh, Y. Kohgo, Back-to-back comparison of auto-fluorescence imaging (AFI) versus high resolution white light colonoscopy for adenoma detection. BMC Gastroenterol. **12**, 75 (2012)
93. G. Rotondano, M.A. Bianco, S. Sansone, A. Prisco, C. Meucci, M.L. Garofano, L. Cipolletta, Trimodal endoscopic imaging for the detection and differentiation of colorectal adenomas: a prospective single-centre clinical evaluation. Int. J. Colorectal Dis. **27**, 331–336 (2012)
94. T. Kuiper, F.J. van den Broek, A.H. Naber, E.J. van Soest, P. Scholten, R. Mallant-Hent, J. van den Brande, J.M. Jansen, A.H. van Oijen, W.A. Marsman, J.J. Bergman, P. Fockens, E. Dekker, Endoscopic trimodal imaging detects colonic neoplasia as well as standard video endoscopy. Gastroenterology **140**, 1887–1894 (2011)
95. F.J. van den Broek, P. Fockens, S. Van Eeden, M.A. Kara, J.C. Hardwick, J.B. Reitsma, E. Dekker, Clinical evaluation of endoscopic trimodal imaging for the detection and differentiation of colonic polyps. Clin. Gastroenterol. Hepatol. **7**, 288–295 (2009)
96. T.E. Renkoski, B. Banerjee, L.R. Graves, N.S. Rial, S.A. Reid, V.L. Tsikitis, V.N. Nfonsam, P. Tiwari, H. Gavini, U. Utzinger, Ratio images and ultraviolet C excitation in autofluorescence imaging of neoplasms of the human colon. J. Biomed. Opt. **18**, 16005 (2013)
97. K. Imaizumi, Y. Harada, N. Wakabayashi, Y. Yamaoka, H. Konishi, P. Dai, H. Tanaka, T. Takamatsu, Dual-wavelength excitation of mucosal autofluorescence for precise detection of diminutive colonic adenomas. Gastrointest. Endosc. **75**, 110–117 (2012)
98. M.G. Muller, T.A. Valdez, I. Georgakoudi, V. Backman, C. Fuentes, S. Kabani, N. Laver, Z. Wang, C.W. Boone, R.R. Dasari, S.M. Shapshay, M.S. Feld, Spectroscopic detection and evaluation of morphologic and biochemical changes in early human oral carcinoma. Cancer **97**, 1681–1692 (2003)
99. V.R. Jacobs, S. Paepke, H. Schaaf, B.C. Weber, M. Kiechle-Bahat, Autofluorescence ductoscopy: a new imaging technique for intraductal breast endoscopy. Clin. Breast Cancer **7**, 619–623 (2007)

100. G.M. Palmer, C. Zhu, T.M. Breslin, F. Xu, K.W. Gilchrist, N. Ramanujam, Comparison of multiexcitation fluorescence and diffuse reflectance spectroscopy for the diagnosis of breast cancer. IEEE Trans. Biomed. Eng. **50**, 1233–1242 (2003)
101. T.M. Breslin, F. Xu, G.M. Palmer, C. Zhu, K.W. Gilchrist, N. Ramanujam, Autofluorescence and diffuse reflectance properties of malignant and benign breast tissues. Ann. Surg. Oncol. **11**, 65–70 (2004)
102. M.A. Kara, J.J. Bergman, Autofluorescence imaging and narrow-band imaging for the detection of early neoplasia in patients with Barrett's esophagus. Endoscopy **38**, 627–631 (2006)
103. T.J. Pfefer, D.Y. Paithankar, J.M. Poneros, K.T. Schomacker, N.S. Nishioka, Temporally and spectrally resolved fluorescence spectroscopy for the detection of high grade dysplasia in Barrett's esophagus. Lasers Surg. Med. **32**, 10–16 (2003)
104. I. Georgakoudi, B.C. Jacobson, J. Van Dam, V. Backman, M.B. Wallace, M.G. Müller, Q. Zhang, K. Badizadegan, D. Sun, G.A. Thomas, L.T. Perelman, M.S. Feld, Fluorescence, reflectance, and light-scattering spectroscopy for evaluating dysplasia in patients with Barrett's esophagus. Gastroenterology **120**, 1620–1629 (2001)
105. F. Koenig, F.J. McGovern, H. Enquist, R. Larne, T.F. Deutsch, K.T. Schomacker, Autofluorescence guided biopsy for the early diagnosis of bladder carcinoma. J. Urol. **159**, 1871–1875 (1998)
106. W. Zheng, W. Lau, C. Cheng, K.C. Soo, M. Olivo, Optimal excitation-emission wavelengths for autofluorescence diagnosis of bladder tumors. Int. J. Cancer **104**, 477–481 (2003)
107. D. Frimberger, D. Zaak, H. Stepp, R. Knüchel, R. Baumgartner, P. Schneede, N. Schmeller, A. Hofstetter, Autofluorescence imaging to optimize 5-ALA-induced fluorescence endoscopy of bladder carcinoma. Urology **58**, 372–375 (2001)
108. M.C. Jacobson, R. deVere White, S.G. Demos, In vivo testing of a prototype system providing simultaneous white light and near infrared autofluorescence image acquisition for detection of bladder cancer. J. Biomed. Opt. **17**, 036011 (2012)
109. Ch. Schäfauer, D. Ettori, M. Rouprêt, V. Phé, J.M. Tualle, E. Tinet, S. Avrillier, Ch. Egrot, O. Traxer,O. Cussenot, Detection of bladder urothelial carcinomas using in vivo non-contact ultraviolet-excitedautofluorescence measurements converted into simple colour-coded images: a feasibility study. Urology (2013)
110. Y. Sun, N. Hatami, M. Yee, J. Phipps, D.S. Elson, F. Gorin, R.J. Schrot, L. Marcu, Fluorescence lifetime imaging microscopy for brain tumor image-guided surgery. J. Biomed. Opt. **15**, 056022 (2010)
111. S.K. Majumder, S. Gebhart, M.D. Johnson, R. Thompson, W.C. Lin, A. Mahadevan-Jansen, A probability-based spectroscopic diagnostic algorithm for simultaneous discrimination of brain tumor and tumor margins from normal brain tissue. Appl. Spectrosc. **61**, 548–557 (2007)
112. G.M. van Dam, G. Themelis, L.M. Crane, N.J. Harlaar, R.G. Pleijhuis, W. Kelder, A. Sarantopoulos, J.S. de Jong, H.J. Arts, A.G. van der Zee, J. Bart, P.S. Low, V. Ntziachristos, Intraoperative tumor-specific fluorescence imaging in ovarian cancer by folate receptor-alpha targeting: first in-human results. Nat. Med. **17**, 1315–1319 (2011)
113. D.P. Taggart, B. Choudhary, K. Anastasiadis, Y. Abu-Omar, L. Balacumaraswami, D.W. Pigott, Preliminary experience with a novel intraoperative fluorescence imaging technique to evaluate the patency of bypass grafts in total arterial revascularization. Ann. Thorac. Surg. **75**, 870–873 (2003)
114. C.P. Parungo, S. Ohnishi, S.W. Kim, S. Kim, R.G. Laurence, E.G. Soltesz, F.Y. Chen, Y.L. Colson, L.H. Cohn, M.G. Bawendi, J.V. Frangioni, Intraoperative identification of esophageal sentinel lymph nodes with near-infrared fluorescence imaging. J. Thorac. Cardiovasc. Surg. **129**, 844–850 (2005)
115. S.L. Troyan, V. Kianzad, S.L. Gibbs-Strauss, S. Gioux, A. Matsui, R. Oketokoun, L. Ngo, A. Khamene, F. Azar, J.V. Frangioni, The FLARE intraoperative near-infrared fluorescence imaging system: a first-in-human clinical trial in breast cancer sentinel lymph node mapping. Ann. Surg. Oncol. **16**, 2943–2952 (2009)

116. J.C. Rasmussen, I.C. Tan, M.V. Marshall, C.E. Fife, E.M. Sevick-Muraca, Lymphatic imaging in humans with near-infrared fluorescence. Curr. Opin. Biotechnol. **20**, 74–82 (2009)
117. C. Regis, P. Collinet, M.O. Farine, S. Mordon, Comparison of aminolevulinic acid- and hexylester aminolevulinate-induced protoporphyrin IX fluorescence for the detection of ovarian cancer in a rat model. Photomed. Laser Surg. **25**, 304–311 (2007)
118. S. Avrillier, E. Tinet, D. Ettori, J.M. Tualle, B. Gelebart, Influence of the emission-reception geometry in laser-induced fluorescence spectra from turbid media. Appl. Opt. **37**, 2781–2787 (1998)
119. S. Warren, K. Pope, Y. Yazdi, A.J. Welch, S. Thomsen, A.L. Johnston, M.J. Davis, R. Richards-Kortum, Combined ultrasound and fluorescence spectroscopy for physico-chemical imaging of atherosclerosis. IEEE Trans. Biomed. Eng. **42**, 121–132 (1995)
120. J. Qu, C. MacAulay, S. Lam, B. Palcic, Laser-induced fluorescence spectroscopy at endoscopy: tissue optics, Monte Carlo modeling, and in vivo measurements. Opt. Eng. **34**, 3334–3343 (1995)
121. J.Y. Qu, J.W. Hua, Calibrated fluorescence imaging of tissue in vivo. Appl. Phys. Lett. **78**, 4040–4042 (2001)
122. Q. Zhang, M.G. Muller, J. Wu, M.S. Feld, Turbidity-free fluorescence spectroscopy of biological tissue. Opt. Lett. **25**, 1451–1453 (2000)
123. S.K. Chang, D. Arifler, R. Drezek, M. Follen, R. Richards-Kortum, Analytical model to describe fluorescence spectra of normal and preneoplastic epithelial tissue: comparison with Monte Carlo simulations and clinical measurements. J. Biomed. Opt. **9**, 511–522 (2004)
124. S. Yuan, C.A. Roney, J. Wierwille, C. Chen, B. Xu, J. Jiang, H. Ma, A. Cable, R.M. Summers, Y. Chen, Combining optical coherence tomography with fluorescence molecular imaging: towards simultaneous morphology and molecular imaging. Phys. Med. Biol. **55**, 191–206 (2010)
125. R.V. Kuranov, V.V. Sapozhnikova, H.M. Shakhova, V.M. Gelikonov, E.V. Zagainova, S.A. Petrova, Combined application of optical methods to increase the information content of optical coherent tomography in diagnostics of neoplastic processes. Quantum Electron. **32**, 993–998 (2002)
126. U. Utzinger, R.R. Richards-Kortum, Fiber optic probes for biomedical optical spectroscopy. J. Biomed. Opt. **8**, 121–147 (2003)
127. S.J. Oldenburg, R.D. Averitt, S.L. Westcott, N.J. Halas, Nanoengineering of optical resonances. Chem. Phys. Lett. **288**, 243–247 (1998)
128. G.M. Dobre, A.G. Podoleanu, R.B. Rosen, Simultaneous optical coherence tomography – indocyanine green dye fluorescence imaging system for investigations of the eye's fundus. Opt. Lett. **30**(1), 58–60 (2005)
129. E. Beaurepaire, L. Moreaux, F. Amblard, J. Mertz, Combined scanning optical coherence and two-photon-excited fluorescence spectroscopy. Opt. Lett. **24**, 969–971 (1999)
130. S. Glass, TIE-36 fluorescence of optical glass, in *Technical Information, Optics for Devices*. (2004)
131. K.R. Hawkins, P. Yager, Nonlinear decrease of background fluorescence in polymer thin-films – a survey of materials and how they can complicate fluorescence detection in microTAS. Lab Chip **3**(4), 248–252 (2003)
132. M.J. Hodgin, Epoxies for optoelectronic packaging; applications and material properties. J. Microelectron. Electron. Packag. **1**(2), 108–116 (2004)
133. J. Wu, S. Seregard, P.V. Algvere, Photochemical damage of the retina. Surv. Ophthalmol. **51**, 461–481 (2006)
134. American National Standards Institute, *American National Standard for Safe Use of Lasers* (ANSI, New York, 2000)
135. American Conference of Governmental Industrial Hygienists, *2005 TLVs and BEIs* (ACGIH, Cincinnati, 2005)

136. International Commission on Non-Ionizing Radiation Protection, Guidelines on limits of exposure to laser radiation of wavelengths between 180 nm and 1,000 microm. Health Phys. **71**, 804–819 (1996)
137. International Commission on Non-ionizing Radiation Protection, Revision of guidelines on limits of exposure to laser radiation of wavelengths between 400 nm and 1.4 microm. Health Phys. **79**, 431–440 (2000)
138. International Commission on Non-Ionizing Radiation Protection, Guidelines on limits of exposure to ultraviolet radiation of wavelengths between 180 nm and 400 nm (incoherent optical radiation). Health Phys. **87**, 171–186 (2004)
139. International Commission on Non-Ionizing Radiation and Protection, Guidelines on limits of exposure to broad-band incoherent optical radiation (0.38 to 3 microm). Health Phys. **73**, 539–554 (1997)
140. Center for Devices and Radiological Health, *Guidance for Industry: Electro-Optical Sensors for the In Vivo Detection of Cervical Cancer and Its Precursors: Submission Guidance for an IDE/PMA* (US Department of Health and Human Services, New York, 1998)
141. A.F. Fercher, W. Drexler, C.K. Hitzenberger, Optical coherence tomography-principles and applications. Rep. Prog. Phys. **66**, 239–303 (2003)
142. C.F. Zhu, Q. Liu, N. Ramanujam, Effect of fiber optic probe geometry on depth-resolved fluorescence measurements from epithelial tissues: a Monte Carlo simulation. J. Biomed. Opt. **8**, 237–247 (2003)
143. Z. Changfang, L. Quan, N. Ramanujam, Effect of fiber optic probe geometry on depth-resolved fluorescence measurements from epithelial tissues: a Monte Carlo simulation. J. Biomed. Opt. **8**, 237–247 (2003)
144. T.J. Pfefer, K.T. Schomacker, M.N. Ediger, N.S. Nishioka, Multiple-fiber probe design for fluorescence spectroscopy in tissue. Appl. Opt. **41**, 4712–4721 (2002)
145. T.J. Pfefer, L.S. Matchette, A.M. Ross, M.N. Ediger, Selective detection of fluorophore layers in turbid media: the role of fiber-optic probe design. Opt. Lett. **28**, 120–122 (2003)
146. T.J. Pfefer, L.S. Matchette, R. Drezek, Influence of illumination-collection geometry on fluorescence spectroscopy in multilayer tissue. Med. Biol. Eng. Comput. **42**, 669–673 (2004)
147. J. Wang, P.T. Bender, U. Utzinger, R. Drezek, Depth sensitive reflectance measurements using oblique oriented fiber probes. J. Biomed. Opt. **20**, 44017 (2006)
148. M.C. Skala, G.M. Palmer, C.F. Zhu, Q. Liu, K.M. Vrotsos, C.L. Marshek-Stone, A. Gendron-Fitzpatrick, N. Ramanujam, Investigation of fiber-optic probe designs for optical spectroscopic diagnosis of epithelial pre-cancers. Lasers Surg. Med. **34**, 25–38 (2004)
149. Q. Liu, N. Ramanujam, Experimental proof of the feasibility of using an angled fiber-optic probe for depth-sensitive fluorescence spectroscopy of turbid media. Opt. Lett. **29**, 2034–2036 (2004)
150. T. Papaioannou, N.W. Preyer, Q.Y. Fang, A. Brightwell, M. Carnohan, G. Cottone, R. Ross, L.R. Jones, L. Marcu, Effects of fiber-optic probe design and probe-to-target distance on diffuse reflectance measurements of turbid media: an experimental and computational study at 337 nm. Appl. Opt. **43**, 2846–2860 (2004)
151. R.A. Schwarz, D. Arifler, S.K. Chang, I. Pavlova, I.A. Hussain, V. Mack, B. Knight, R. Richards-Kortum, A.M. Gillenwater, Ball lens coupled fiber-optic probe for depth-resolved spectroscopy of epithelial tissue. Opt. Lett. **30**, 1159–1161 (2005)
152. A.M.J. Wang, J.E. Bender, J. Pfefer, U. Utzinger, R.A. Drezek, Depth-sensitive reflectance measurements using obliquely oriented fiber probes. J. Biomed. Opt. **10**, 44017 (2005)
153. B.W. Pogue, G. Burke, Fiber-optic bundle design for quantitative fluorescence measurement from tissue. Appl. Opt. **37**, 7429–7436 (1998)
154. P.R. Bargo, S.A. Prahl, S.L. Jacques, Optical properties effects upon the collection efficiency of optical fibers in different probe configurations. IEEE J. Sel. Top. Quantum Electron. **9**, 314–321 (2003)

155. S.Y. Ryu, H.Y. Choi, J. Na, E.S. Choi, B.H. Lee, Combined system of optical coherence tomography and fluorescence spectroscopy based on double-cladding fiber. Opt. Lett. **33**, 2347–2349 (2008)
156. G. Liu, Z. Chen, Fiber-based combined optical coherence and multiphoton endomicroscopy. J. Biomed. Opt. **16**, 036010 (2011)
157. J. Xi, Y. Chen, Y. Zhang, K. Murari, M. Li, X. Li, Integrated multimodal endomicroscopy platform for simultaneous en face optical coherence and two-photon fluorescence imaging. Opt. Lett. **37**, 362–364 (2012)
158. J. Mavadia, J. Xi, Y. Chen, X. Li, An all-fiber-optic endoscopy platform for simultaneous OCT and fluorescence imaging. Biomed. Opt. Express **3**(11), 2851–2859 (2012)
159. H. Makhlouf, A.R. Rouse, A.F. Gmitro, Dual modality fluorescence confocal and spectral-domain optical coherence tomography microendoscope. Biomed. Opt. Express **2**(3), 634–644 (2011)
160. S. Schmitz-Valckenberg, F.G. Holz, A.C. Bird, R.F. Spaide, Fundus autofluorescence imaging: review and perspectives. Retina **28**(3), 385–409 (2008)
161. H.M. Helb, P. Charbel Issa, M. Fleckenstein, S. Schmitz-Valckenberg, H.P. Scholl, C.H. Meyer, N. Eter, F.G. Holz, Clinical evaluation of simultaneous confocal scanning laser ophthalmoscopy imaging combined with high-resolution, spectral-domain optical coherence tomography. Acta Ophthalmol. **88**(8), 842–849 (2010)
162. R.B. Rosen, M. Hathaway, J. Rogers, J. Pedro, P. Garcia, G.M. Dobre, A.G. Podoleanu, Simultaneous OCT/SLO/ICG imaging. Invest. Ophthalmol. Vis. Sci. **50**(2), 851–860 (2009)
163. J. Mavadia, X.J. Xi, Y. Chen, X. Li, An all-fiber-optic endoscopy platform for simultaneous OCT and fluorescence imaging. Biomed. Opt. Express **3**, 2851–2859 (2012)
164. R. Andrew Wall, J.K. Barton, Fluorescence-based surface magnifying chromoendoscopy and optical coherence tomography endoscope. J. Biomed. Opt. **17**(8), 086003 (2012)
165. C.J. Kennedy, P.E. Rakoczy, I.J. Constable, Lipofuscin of the retinal pigment epithelium: a review. Eye **9**(6), 763–771 (1995)
166. M. Fleckenstein, S. Schmitz-Valckenberg, C. Adrion, I. Krämer, N. Eter, H.M. Helb, C.K. Brinkmann, P. Charbel Issa, U. Mansmann, F.G. Holz, Tracking progression with spectral-domain optical coherence tomography in geographic atrophy caused by age-related macular degeneration. Invest. Ophthalmol. Vis. Sci. **51**(8), 3846–3852 (2010)
167. E.M. Kanter, R.M. Walker, S.L. Marion, M. Brewer, P.B. Hoyer, J.K. Barton, Dual modality imaging of a novel rat model of ovarian carcinogenesis. J. Biomed. Opt. **11**, 041123 (2006)
168. A.R. Tumlinson, L.P. Hariri, U. Utzinger, J.K. Barton, A miniature endoscope for simultaneous OCT-LIF measurement. Appl. Opt. **43**, 113–121 (2004)
169. L.P. Hariri, E.R. Liebmann, S.L. Marion, P.B. Hoyer, J.R. Davis, M.A. Brewer, J.K. Barton, Simultaneous optical coherence tomography and laser induced fluorescence imaging in rat model of ovarian carcinogenesis. Cancer Biol. Ther. **10**(5), 1–10 (2010)
170. L.P. Hariri, A.R. Tumlinson, N.H. Wade, D. Besselsen, U. Utzinger, E. Gerner, J.K. Barton, Endoscopic optical coherence tomography and laser induced fluorescence spectroscopy in a murine colon cancer model. Lasers Surg. Med. **38**, 305–313 (2006)
171. J. McNally, N. Kirkpatrick, L.P. Hariri, A.R. Tumlinson, D. Besselsen, E. Gerner, U. Utzinger, J.K. Barton, Task based imaging of colon cancer in a mouse model ($Apc^{Min/+}$). Appl. Opt. **45**, 3049–3062 (2006)
172. A.M. Winkler, P. Rice, J. Weichsel, J. Watson, M. Backer, J. Backer, J.K. Barton, In vivo, dual modality OCT/LIF imaging using a novel VEGF receptor targeted NIR fluorescent probe in the AOM-treated mouse model. Mol. Imaging Biol. **13**(6), 1173–1182 (2011)
173. J.A. Freeberg, J.L. Benedet, C. MacAulay, L.A. West, M. Follen, The performance of fluorescence and reflectance spectroscopy for the in vivo diagnosis of cervical neoplasia; point probe versus multispectral approaches. Gynecol. Oncol. **107**, S248–S255 (2007)

174. R.D. Alvarez, T.C. Wright, Effective cervical neoplasia detection with a novel optical detection system: a randomized trial. Gynecol. Oncol. **104**, 281–289 (2007)
175. N. Ramanujam, M.F. Mitchell, A. Mahadevan, S. Thomsen, A. Malpica, T. Wright, N. Atkinson, R. Richards-Kortum, Development of a multivariate statistical algorithm to analyze human cervical tissue fluorescence spectra acquired in vivo. Lasers Surg. Med. **19**, 46–62 (1996)
176. T.E. Renkoski, K.D. Hatch, U. Utzinger, Wide-field spectral imaging of human ovary autofluorescence and oncologic diagnosis via previously collected probe data. J. Biomed. Opt. **17**, 036003 (2012)
177. S.D. Kamath, R.A. Bhat, S. Ray, K.K. Mahato, Autofluorescence of normal, benign, and malignant ovarian tissues: a pilot study. Photomed. Laser Surg. **27**, 325–335 (2009)
178. T. Upile, W.K. Jerjes, H.J. Sterenborg, B.J. Wong, A.K. El-Naggar, J.F. Ilgner, A. Sandison, M.J. Witjes, M.A. Biel, R. van Veen, Z. Hamdoon, A. Gillenwater, C.A. Mosse, D.J. Robinson, C.S. Betz, H. Stepp, L. Bolotine, G. McKenzie, H. Barr, Z. Chen, K. Berg, A.K. D'Cruz, H. Sudhoff, N. Stone, C. Kendall, S. Fisher, A.J. MacRobert, A. Leunig, M. Olivo, R. Richards-Kortum, K.C. Soo, V. Bagnato, L.P. Choo-Smith, K. Svanberg, I.B. Tan, B.C. Wilson, H. Wolfsen, I. Bigio, A.G. Yodh, C. Hopper, At the frontiers of surgery: review. Head Neck Oncol. **3**(1), 7 (2011)
179. A.F. Zuluaga, N. Vigneswaran, R.K. Bradley, A.M. Gillenwater, C.M. Nichols, C. Poh, Identafi®3000 ultra a multispectral tool for improved oral lesion evaluation, in *Biomedical Optics, OSA Technical Digest (CD)* (Optical Society of America, paper BSuD105, 2010)
180. P.M. Lane, T. Gilhuly, P. Whitehead, H. Zeng, C.F. Poh, S. Ng, P.M. Williams, L. Zhang, M.P. Rosin, C.E. MacAulay, Simple device for the direct visualization of oral-cavity tissue fluorescence. J. Biomed. Opt. **11**, 024006 (2006)
181. E. Svistun, R. Alizadeh-Naderi, A. El-Naggar, R. Jacob, A. Gillenwater, R. Richards-Kortum, Vision enhancement system for detection of oral cavity neoplasia based on autofluorescence. Head Neck **26**, 205–215 (2004)
182. U. Utzinger, M. Bueeler, S. Oh, D.L. Heintzelman, E.S. Svistun, M. Abd-El-Barr, A. Gillenwater, R. Richards-Kortum, Optimal visual perception and detection of oral cavity neoplasia. IEEE Trans. Biomed. Eng. **50**, 396–399 (2003)
183. D.L. Heintzelman, U. Utzinger, H. Fuchs, A. Zuluaga, K. Gossage, A.M. Gillenwater, R. Jacob, B. Kemp, R.R. Richards-Kortum, Optimal excitation wavelengths for in vivo detection of oral neoplasia using fluorescence spectroscopy. Photochem. Photobiol. **72**, 103–113 (2000)
184. C.S. Betz, H. Stepp, P. Janda, S. Arbogast, G. Grevers, R. Baumgartner, A. Leunig, A comparative study of normal inspection, autofluorescence and 5-ALA-induced PPIX fluorescence for oral cancer diagnosis. Int. J. Cancer **97**(2), 245–252 (2002)
185. A. Gillenwater, R. Jacob, R. Ganeshappa, B. Kemp, A.K. El-Naggar, J.L. Palmer, G. Clayman, M.F. Mitchell, R. Richards-Kortum, Noninvasive diagnosis of oral neoplasia based on fluorescence spectroscopy and native tissue autofluorescence. Arch. Otolaryngol. Head Neck Surg. **124**, 1251–1258 (1998)
186. M.V. Chowdary, K.K. Mahato, K.K. Kumar, S. Mathew, L. Rao, C.M. Krishna, J. Kurien, Autofluorescence of breast tissues: evaluation of discriminating algorithms for diagnosis of normal, benign, and malignant conditions. Photomed. Laser Surg. **27**, 241–252 (2009)
187. Z. Volynskaya, A.S. Haka, K.L. Bechtel, M. Fitzmaurice, R. Shenk, N. Wang, J. Nazemi, R.R. Dasari, M.S. Feld, Diagnosing breast cancer using diffuse reflectance spectroscopy and intrinsic fluorescence spectroscopy. J. Biomed. Opt. **13**(2), 024012 (2008)
188. C. Zhu, G.M. Palmer, T.M. Breslin, F. Xu, N. Ramanujam, Use of a multiseparation fiber optic probe for the optical diagnosis of breast cancer. J. Biomed. Opt. **10**, 024032 (2005)
189. P.K. Gupta, S.K. Majumder, A. Uppal, Breast cancer diagnosis using N2 laser excited autofluorescence spectroscopy. Lasers Surg. Med. **21**(5), 417–422 (1997)

190. J. Haringsma, G.N. Tytgat, H. Yano, H. Iishi, M. Tatsuta, T. Ogihara, H. Watanabe, N. Sato, N. Marcon, B.C. Wilson, R.W. Cline, Autofluorescence endoscopy: feasibility of detection of GI neoplasms unapparent to white light endoscopy with an evolving technology. Gastrointest. Endosc. **53**, 642–650 (2001)
191. N. Uedo, K. Higashino, R. Ishihara, Y. Takeuchi, H. Iishi, Diagnosis of colonic adenomas by new autofluorescence imaging system: a pilot study. Digest. Endosc. **19**, S134–S138 (2007)
192. K.T. Schomacker, J.K. Frisoli, C.C. Compton, T.J. Flotte, J.M. Richter, N.S. Nishioka, T.F. Deutsch, Ultraviolet laser-induced fluorescence of colonic tissue: basic biology and diagnostic potential. Lasers Surg. Med. **12**, 63–78 (1992)
193. M.A. Ortner, B. Ebert, E. Hein, K. Zumbusch, D. Nolte, U. Sukowski, J. Weber-Eibel, B. Fleige, M. Dietel, M. Stolte, G. Oberhuber, R. Porschen, B. Klump, H. Hortnagl, H. Lochs, H. Rinneberg, Time gated fluorescence spectroscopy in Barrett's oesophagus. Gut **52**, 28–33 (2003)
194. W.C. Lin, S.A. Toms, M. Johnson, E.D. Jansen, A. Mahadevan-Jansen, In vivo brain tumor demarcation using optical spectroscopy. Photochem. Photobiol. **73**, 396–402 (2001)
195. A. Sivaramakrishnan, D. Graupe, Brain tumor demarcation by applying a LAMSTAR neural network to spectroscopy data. Neurol. Res. **26**, 613–621 (2004)
196. W. Drexler, U. Morgner, F.X. Kartner, C. Pitris, S.A. Boppart, X.D. Li, E.P. Ippen, J.G. Fujimoto, In vivo ultrahigh-resolution optical coherence tomography. Opt. Lett. **24**, 1221–1223 (1999)
197. B.E. Bouma, G.J. Tearney, I.P. Bilinsky, B. Golubovic, J.G. Fujimoto, Self-phase-modulated Kerr-lens mode-locked Cr:forsterite laser source for optical coherence tomography. Opt. Lett. **21**, 1839–1841 (1996)
198. I. Hartl, X.D. Li, C. Chudoba, R.K. Ghanta, T.H. Ko, J.G. Fujimoto, J.K. Ranka, R.S. Windeler, Ultrahigh-resolution optical coherence tomography using continuum generation in an air-silica microstructure optical fiber. Opt. Lett. **26**, 608–610 (2001)
199. N.D. Kirkpatrick, J.B. Hoying, S.K. Botting, J.A. Weiss, U. Utzinger, In vitro model for endogenous optical signatures of collagen. J. Biomed. Opt. **11**, 054021 (2006)
200. N.D. Kirkpatrick, C.P. Zou, M.A. Brewer, W.R. Brands, R.A. Drezek, U. Utzinger, Endogenous fluorescence spectroscopy of cell suspensions for chemopreventive drug monitoring. Photochem. Photobiol. **81**, 125–134 (2005)
201. J.M. Dixon, M. Taniguchi, J.S. Lindsey, PhotochemCAD 2: a refined program with accompanying spectral databases for photochemical calculations. Photochem. Photobiol. **81**, 212–213 (2005)
202. M. Bruchez, M. Moronne, P. Gin, S. Weiss, A.P. Alivisatos, Semiconductor nanocrystals as fluorescent biological labels. Science **281**, 2013–2016 (1998)
203. A.M. Smith, S. Nie, Chemical analysis and cellular imaging with quantum dots. Analyst **129**, 672–677 (2004)
204. R.C. Benson, H.A. Kues, Fluorescence properties of indocyanine green as related to angiography. Phys. Med. Biol. **23**, 159–163 (1978)
205. B.R. Hyun, H. Chen, D.A. Rey, F.W. Wise, C.A. Batt, Near-infrared fluorescence imaging with water-soluble lead salt quantum dots. J. Phys. Chem. B **111**, 5726–5730 (2007)

Integrated Optical Coherence Tomography (OCT) with Fluorescence Laminar Optical Tomography (FLOT)

51

Chao-Wei Chen and Yu Chen

51.1 Introduction

Multimodal optical imaging techniques offer more comprehensive understanding about the tissue under investigation. The trend of development has been focused on co-registered tomographic imaging and simultaneous anatomy and molecular imaging [1]. Ideally, one modality provides high-resolution structural images, and the other acquires the molecular, biochemical, or metabolic function. Being able to simultaneously acquire such complementary information is critical for clinical diagnosis and therapy. Multimodal imaging has been adopted in clinical settings, including combined PET/CT, SPECT/CT, and PET/MRI systems. Clinical research demonstrates the benefits of combined multimodal imaging technologies for diagnosing and staging of diseases, treatment planning, and monitoring response to therapy.

Furthermore, the synergy has evolved from offering complementary information to refining image reconstruction. For biomedical applications, by interpreting the structural and functional images simultaneously, one is able to improve the diagnostic accuracy which may be not achievable by each individual modality. Anatomically constrained magnetoencephalography (aMEG) combines the spatial resolution of a structural MRI scan with the temporal resolution of the

C.-W. Chen (✉)
Fischell Department of Bioengineering and Department of Electrical and Computer Engineering, University of Maryland, College Park, MD, USA
e-mail: willhyper@gmail.com

Y. Chen
Department of Electrical Engineering and Computer Science and Research Laboratory of Electronics, Massachusetts Institute of Technology, Cambridge, MA, USA

Biomedical Optics and Imaging Laboratory, Fischell Department of Bioengineering, University of Maryland, College Park, MD, USA

© Springer International Publishing Switzerland 2015

W. Drexler, J.G. Fujimoto (eds.), *Optical Coherence Tomography*,
DOI 10.1007/978-3-319-06419-2_52

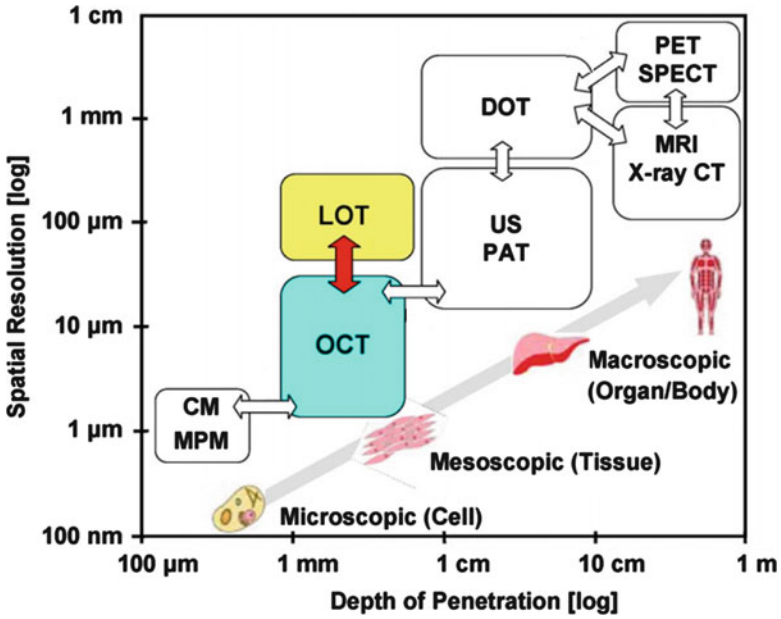

Fig. 51.1 Multi-scale biomedical imaging modalities and platforms for multimodal imaging (indicated by "⇔"). *PET* positron-emission tomography, *SPECT* single-photon emission computerized tomography, *MRI* magnetic resonance imaging, *X-ray CT* X-ray computerized tomography, *DOT* diffuse optical tomography, *US* ultrasound, *PAT* photoacoustic tomography, *OCT* optical coherence tomography, *LOT* laminar optical tomography, *CM* confocal microscopy, and *MPM* multiphoton microscopy (Reproduced from Ref. [20] with permission © 2010 IEEE)

MEG [2]. Similarly, X-ray-prior-guided diffuse optical tomography (DOT) improved optical contrast of malignancy of breast tumor [3].

Multimodal imaging has been pursued in mesoscopic (millimeter) scale. Pan et al. demonstrated that fluorescence-guided endoscopic optical coherence tomography (OCT) could enhance the efficiency and sensitivity of early bladder cancer diagnosis [4]. In animal model studies, they reported that the specificity of fluorescence detection of transitional cell carcinoma was significantly enhanced by fluorescence-guided OCT (53 % vs. 93 %), and the sensitivity of fluorescence detection also improved by combination with OCT (79 % vs. 100 %) [5]. Tumlinson et al. have developed a combined OCT and laser-induced fluorescence (LIF) spectroscopy imaging catheter for in vivo mouse colon imaging [6, 7]. Recently, combining OCT with reflectance-based fluorescence imaging has been reported by us and others [8, 9].

In this chapter, we focus on the combination of OCT and depth-resolved fluorescence tomography (based on laminar optical tomography, LOT) as a mesoscopically co-registered structural and molecular imaging platform (the red "⇔" in the Fig. 51.1). OCT is primarily based on contrasts from scattering, birefringence, and refractive index variations of the tissue, providing resolution of 1–10 μm and penetration depth of 1–2 mm of tissue microstructures.

Complementarily, LOT has been developed to perform functional imaging with 100 μm resolution and up to 2.5 mm depth [10–16]. LOT is an extension of confocal microscopy by using multiple-displaced-confocal-pinhole design to capture the photons traveling through different depths, and the image is obtained through transport-based reconstruction [10]. Fluorescence LOT (FLOT) additionally provides highly sensitive molecular information through fluorescence contrast agents [17, 18]. The comparable imaging scale and their complementary contrast mechanisms motivate the integration of OCT and FLOT as a multimodality imaging platform to provide tissue structural and molecular information in 3D in millimeter imaging scale. This chapter will describe the theoretical modeling, instrumentation, as well as biomedical applications of this new multimodal imaging modality.

51.2 Combined OCT and FLOT: Instrumentation

A co-registered OCT and line-scan FLOT system was developed in our lab [19, 20]. Figure 51.2 shows the schematic of the multimodal imaging system. The OCT subsystem utilized a wavelength-swept laser as the light source with a spectrum centered at 1,310 nm and bandwidth of 100 nm, thereby providing an axial resolution of 10 μm in the tissue. The laser operated at a sweeping rate of 16 K A-scan/s with an average output power of 12 mW. The output of the swept laser was split into two paths: 3 % was sent to a Mach–Zehnder interferometer (MZI); the remaining 97 % was equally distributed to the sample and reference arms of the OCT Michelson interferometer, which was composed of one circulator and one fiber-optic 50/50 splitter. The light in the sample arm passed through a collimator (C), a pair of galvanometer mirrors (X and Y), and an objective to the tissue. The power on the tissue was 4 mW with a spot size of 15 μm. The reference arm consisted of a dispersion compensation glass (DCG) and a polarization controller (PC). DCG matched the dispersion induced by the optics in the sample arm. The light returned from the sample and reference arms formed the interference signal, which was electronically detected by a balanced detector (BD). The output of BD was discretely sampled by a data acquisition board (DAQ, AlazarTech), which was triggered by the zero-crossings of the MZI fringes. The zero-crossings provided an equally spaced frequency clock, therefore eliminating the need to interpolate/resample the discrete interference signal and increase the speed of data processing. Lastly, discrete Fourier transform rendered the axial profile of the tissue (A-scan) with 2.5 mm imaging depth in 512 pixels. The sensitivity (the minimal detected signal) of the OCT subsystem was 95 dB.

The line-scan FLOT subsystem is shown in the right portion of Fig. 51.2. The excitation source was a continuous wave (CW) laser diode at 670 nm. A cylindrical lens was used to expand the illumination point to a line. Line illumination simplified the scanning mechanism by eliminating the scanning along the illumination dimension. The excitation line sequentially passed through a dichroic mirror (DM-2), galvanometer Y, and another dichroic mirror (DM-1) before illuminating on the tissue. The line illuminated on the tissue was 2.2 mm long in x-direction

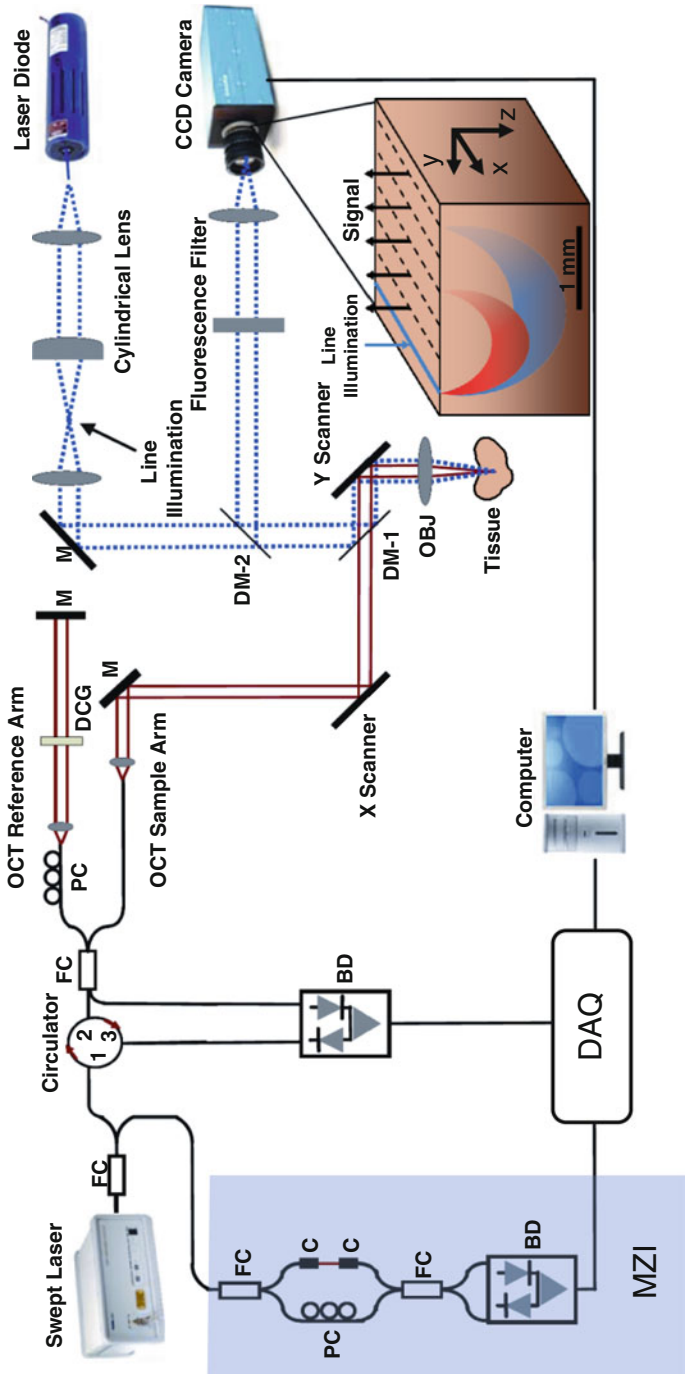

Fig. 51.2 Schematic of the combined OCT and line-scan FLOT system (Reproduced from Ref. [20] with permission © 2010 IEEE)

and 25 μm wide in y-direction. The illumination power was 8 mW. DM-1 integrated the FLOT optical axis and the OCT sample arm. Specifically, DM-1 transmitted the OCT light (at 1,300 nm) and reflected both the FLOT excitation and emission light (<850 nm). DM-2 further separated the excitation reflectance and the fluorescence emission light. The fluorescence light passed a band-pass filter (700 ± 10 nm) to the electron-multiplying CCD (EM-CCD, Cooke Corp.). EM-CCD served as a detector array with one-dimension (orthogonal to the line illumination) pixels collecting the lights with different separations from the illumination spot.

The total acquisition time of this OCT–FLOT co-registered system is 10 s for each 3D volume. For OCT, the beam was scanned in two axes. The fast scanning in x-direction was set at the speed of 25 Hz (x-scan was 2.5 mm wide in 624 pixels), and the slow scanning in y-direction was set at the speed of 0.1 Hz (y-scan was 2.5 mm wide in 256 pixels). For line-scanned FLOT, only scanning in y-direction was needed, therefore the scanning speed was the same as OCT y-scan. EM-CCD totally acquired 256 frames, each of which was exposed 30 ms. The resulting OCT 3D volume size is 624 (x) by 256 (y) by 512 (z) pixels (with voxel size of 4 μm × 10 μm × 4.4 μm, and FLOT image raw data is 501 (x) by 1,024 (y) (2.2 mm × 2.2 mm) by 256 frames. The rate-limiting factors were the FLOT CCD frame rate and the high number of OCT images acquired in the y-dimension. This 10 s acquisition time can be reduced by binning the EM-CCD detector arrays and/or reducing the camera field of view (FOV). If focusing on 2D (xz) cross-section imaging (B-scan) only, it shall be possible to perform real-time FLOT imaging by reading only partial regions of the EM-CCD.

51.3 FLOT Theory and Image Reconstruction

Depth-resolved FLOT image is obtained through image reconstruction process similar to that used in DOT [21]. The fluorescence signal $\mathrm{F}\left(\vec{r_d}, \hat{\Omega}_\mathrm{d}, \vec{r_s}, \hat{\Omega}_s\right)\left(\mathrm{Wm^{-2}sr^{-2}}\right)$ can be expressed as [17, 22]:

$$\mathrm{F}\left(\vec{r_d}, \hat{\Omega}_\mathrm{d}, \vec{r_s}, \hat{\Omega}_s\right) = \sigma_{\mathrm{ex}}\gamma \int \Phi_{ex}\left(\vec{r} - \vec{r_s}; \hat{\Omega}_s\right) C_f\left(\vec{r}\right) \widetilde{\Phi}_{em}\left(\vec{r} - \vec{r_d}; \hat{\Omega}_d\right) d^3\vec{r} \quad (51.1)$$

where $\sigma_{\mathrm{ex}}(\mathrm{m^2})$ is the absorption cross section of the fluorophores at the excitation wavelength, γ(unitless) is the spectral quantum yield of the fluorophore, $\Phi_{ex}\left(\vec{r} - \vec{r_s}; \hat{\Omega}_s\right)\left(\mathrm{Wm^{-2}sr^{-1}}\right)$ is the excitation fluence distribution calculated from the excitation photon radiance from a point source located at $\vec{r_s}$ and at the angle $\hat{\Omega}_s$, $\Phi_{em}\left(\vec{r} - \vec{r_d}; \hat{\Omega}_\mathrm{d}\right)\left(\mathrm{m^{-2}sr^{-1}}\right)$ is the probability density that a photon emitted by a source at position $\vec{r}$ will be detected by a detector located at $\vec{r_d}$ and at the angle $\hat{\Omega}_\mathrm{d}$, and $C_f\left(\vec{r}\right)\left(\mathrm{m^{-3}}\right)$ is the fluorophore concentration at position $\vec{r}$. Equation 51.1 can be discretized into voxels, which yields a matrix equation:

$$\mathrm{F} = JC \quad (51.2)$$

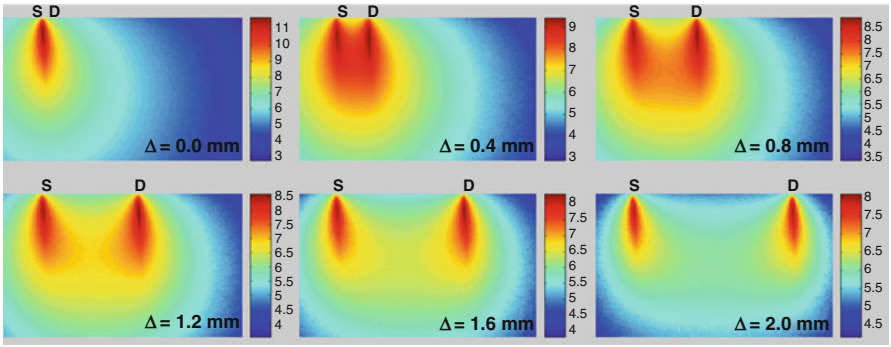

Fig. 51.3 Monte Carlo simulated measurement sensitivity distribution of FLOT measurements (log scale). Tissue geometry was 3 mm (lateral) by 2 mm (depth) with scattering coefficient $\mu_s = 8\ \text{mm}^{-1}$ for excitation and $7\ \text{mm}^{-1}$ for emission ($g = 0.9$) (Reproduced from Ref. [20] with permission © 2010 IEEE)

where F is the fluorescence measurements, C is the spatially distributed fluorophore concentration, and J is the sensitivity matrix that represents the spatial dependence of each measurement to the fluorophore concentration at each voxel. J is expressed as

$$J\left(\vec{r}_d,\vec{r}_s,\vec{r},\hat{\Omega}_s,\hat{\Omega}_\text{d}\right) = \sigma_\text{ex}\gamma\Phi_{ex}\left(\vec{r}-\vec{r}_s;\hat{\Omega}_s\right)\Phi_{em}\left(\vec{r}-\vec{r}_d;\hat{\Omega}_\text{d}\right) \tag{51.3}$$

The sensitivity distribution of FLOT can be calculated using Monte Carlo simulation (see Fig. 51.3). The sensitivity profile varies as the source–detector separation increases as well as the incidence/detection angle. Therefore, depth-dependent information is encoded in the multiple detector measurement and can be recovered through image reconstruction.

Image reconstruction was performed within individual plane (YZ) perpendicular to the illumination line (X). Two main approaches were implemented. First, simultaneous iterative reconstruction technique (SIRT) [23] was used in our phantom experiments and subsurface cancer imaging (Sect. 51.4). The nonnegativity of $C_f\left(\vec{r}\right)$ posts a hard constraint in the reconstruction; in other words, the negative elements will be replaced to zeros after each iteration. Iterations stopped until the change between iterations was <0.1 %. Second, the least square fitting with Tikhonov regularization [11] was used in the engineered tissue imaging (Sect. 51.6). The Tikhonov approach can be expressed as

$$C = \left[J^T J + \lambda^2 S_\text{Max}^2 I\right]^{-1} J^T \text{F} \tag{51.4}$$

where S_Max is the largest singular value in J, superscript $^\text{T}$ stands for transpose operation, and λ is the normalized regularization factor that leverages the signal level and noise level. The criteria of discrepancy principle were implemented to

determine λ, which was typically 3×10^{-4}. Because of explicit inversion, the time of the Tikhonov approach was faster than the SIRT approach. (0.06 s vs. 2 s).

51.4 Results: Phantom Experiments and Subsurface Cancer Imaging

The performance of the OCT–FLOT system was first demonstrated by imaging a tissue phantom, which consisted of a capillary tube with an inner diameter of 110 μm and an outer diameter of 130 μm, suspended in a scattering medium consisting of 2 % Intralipid mixed with Indian ink $\mu_a = 0.2\ \text{mm}^{-1}$, $\mu_s = 7.2\ \text{mm}^{-1}$ at 670 nm, and anisotropy factor $g = 0.9$, similar to those of biological tissues. The tube was filled with 10 μM fluorescent dye Cy5.5.

Figure 51.4 shows the comparison of OCT and FLOT images of a capillary tube phantom. OCT readily images the 3D structure of the tube as shown in Fig. 51.4a. Figure 51.4b shows the comparison of OCT cross-sectional image (YZ) and FLOT image at location "1" denoted in (A). Cross-sectional OCT revealed the capillary tube (indicated by the arrow) with approximately 0.6 mm beneath the surface. FLOT cross-sectional image showed a fluorescence object at the same location, with a slightly larger size due to the relatively larger FLOT resolution compared to OCT. Cross-sectional OCT and FLOT images at location "2" also showed good

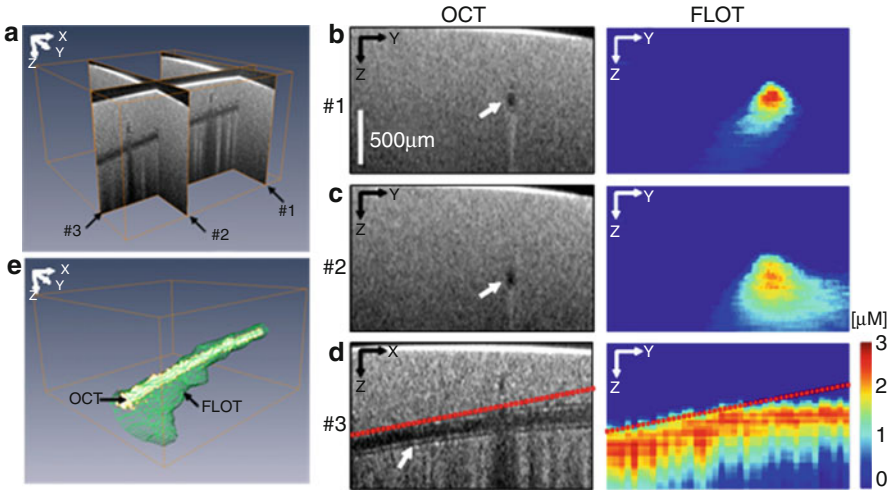

Fig. 51.4 Co-registration of OCT and line-scan FLOT of a capillary tube filled with fluorescence dye. (**a**) 3D OCT imaging showing three representative slices. (**b**) *Left*, OCT image (slice #1) of the capillary tube (*arrow*); *right*, FLOT image reconstruction of the fluorescence object. (**c**) OCT and FLOT images of different position (slice #2). (**d**) OCT and FLOT image (slice #3) reveal the curvature of the capillary tube (two identical *dotted lines* serve as the reference slopes). (**e**) 3D isosurface of FLOT image showed good co-localization with OCT (Reproduced from Ref. [19] with permission © 2009 OSA)

agreement with the tube depth of approximately 0.9 mm (Fig. 51.4c). Compared to (B), the FLOT image for deeper object showed slight enlargement in size. In addition, the peak values were slightly reduced when the object went deeper due to the enlargement of the reconstructed object size. Figure 51.4d shows the OCT cross-sectional image along the tube's longitudinal dimension (XZ). The tube was placed at an angle with respect to the horizontal axis, and slightly bending flat. The FLOT image (XZ) revealed similar contour of the capillary tube as shown by OCT. Also, this image was averaged over a range of 150 μm in y-dimension across the central axis of the tube; therefore, the results indicated nearly constant fluorophore concentration. Here OCT provided the structural information of the phantom, and the FLOT reconstructed image provides the fluorescence dye distribution information. In biomedical applications, FLOT would provide fluorescence-dye-targeted molecular information. Together, the hybrid OCT–FLOT system can be used for concurrent depth-resolved tissue structural and molecular imaging.

Using the same system, an animal model of breast cancer was imaged [20]. A triple negative human breast cancer cell line, MDA-MB-231, originally expanded from a pleural effusion, was obtained from the American Type Culture Collection (ATCC). Plasmid DNA encoding tdTomato (pRSETB-tdTomato) was cloned into the mammalian expression vector pEF-1α-myc/his (Invitrogen, Carlsbad, CA) generating pEF-1α-tdTomato. pEF-1α-tdTomato was stably transfected into MDA-MB-231 cells using the Amaxa Nucleofector II instrument (Amaxa Biosystems, Gaithersburg, MD), followed by fluorescence-activated cell sorting (FACS) of tdTomato-fluorescing cells, and further expansion without antibiotics. Prior to inoculation, MDA-MB-231-tdTomato cells displayed intense tdTomato fluorescence in cell culture as tested with live cell fluorescence microscopy [24].

One hundred thousand to two million MDA-MB-231-tdTomato cells were orthotopically inoculated in the mammary fat pad of anesthetized female athymic nude mice as previously described [25]. Tumor xenografts reached their final experimental size of about 5 mm^3 within 4 weeks. In vivo whole-body fluorescence imaging of MDA-MB-231-tdTomato tumor xenografts was confirmed using a commercially available optical imaging system, the Xenogen IVIS 200 Spectrum (Caliper Life Sciences, Hopkinton, MA) before in vivo OCT–FLOT imaging under anesthesia.

Figure 51.5 shows OCT–FLOT imaging of human breast cancer xenograft model in vivo. Figure 51.5a shows an OCT cross-sectional image of the breast tumor. The high scattering mouse skin layer limited the penetration depth. However, the boundary between the skin and the tumor remained visible (arrow). Figure 51.5b shows the co-registered FLOT image revealing the subcutaneous tumor (which was transfected with red fluorescence protein). Figure 51.5c is the fused OCT–FLOT image which shows the relative position and distribution of tumor regions underneath the skin. Figure 51.5d shows the corresponding histology confirming the presence of tumor. Figure 51.5e shows the OCT cross-sectional image of another region of the breast tumor. The boundary between skin and tumor

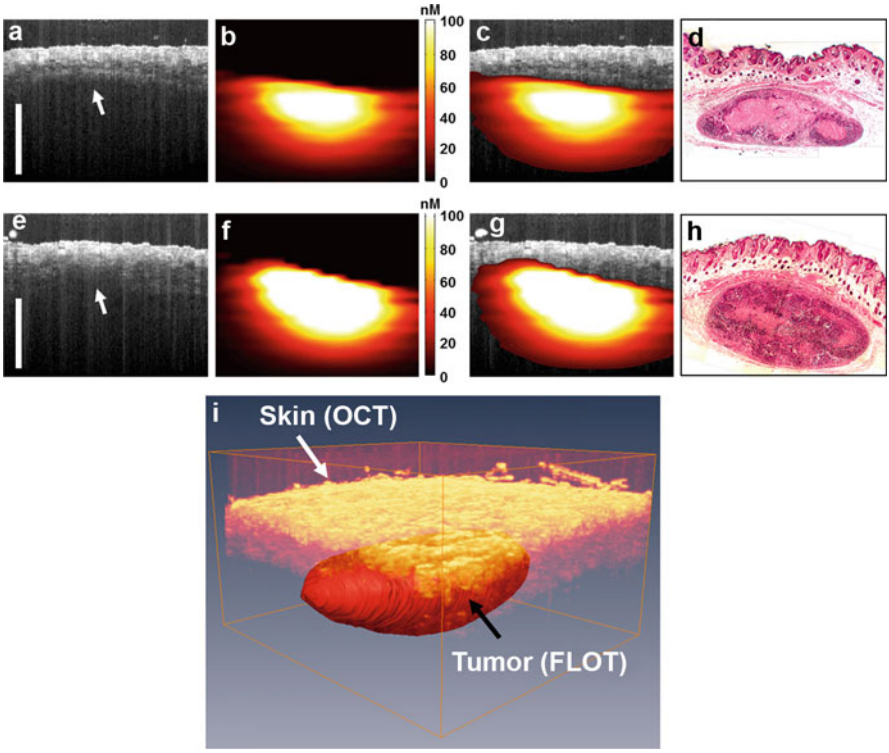

Fig. 51.5 OCT–FLOT of subcutaneous human breast tumor xenograft on mouse model in vivo. Breast cancer cells (MDA-MB-231) were constitutively labeled with tdTomato red fluorescence protein. (**a**) OCT cross-sectional image of breast tumor. Mouse skin layer shows high scattering, and the boundary between skin and tumor is clearly visible (*arrow*). (**b**) Co-registered FLOT image revealing subsurface tumor. (**c**) Fused OCT–FLOT image and (**d**) the corresponding histology. (**e**) OCT cross-sectional image of another region of the breast tumor. The boundary between skin and tumor was less well defined (*arrow*). (**f**) Co-registered FLOT image revealed a larger tumor volume than (**b**). (**g**) Fused OCT–FLOT image. The corresponding histology (**h**) confirmed the larger tumor size than (**d**). (**i**) Subcutaneous breast tumor xenograft in vivo was rendered in 3D. Tumor cells were transfected with red fluorescence protein (*RFP*) and displayed as isosurface of 30 nM of calibration dye Rhodamine 6G. Tumor size: $2.2 \times 2.3 \times 0.9$ mm^3. Bar: 1 mm (Reproduced from Ref. [20] with permission © 2010 IEEE)

was less well defined (arrow) indicating tumor invasion. Figure 51.5f shows the co-registered FLOT image revealing a larger tumor volume than that shown in (B). Figure 51.5g shows the fused OCT–FLOT image. The corresponding histology (h) confirms the larger tumor size than (d). Assuming oval-shaped tumor, FHWM of the long and short axes of the tumor were 2.17×0.92 mm^2 for the smaller tumor region (b) and 2.50×1.11 mm^2 for the larger tumor region (f). The histology findings indicated that the tumor sizes were 2.30×0.83 mm^2 and 2.33×1.25 mm^2, respectively (d, h). These results indicated that FLOT can visualize the difference in subsurface tumor sizes. Figure 51.5i shows the 3D view of mouse skin (from OCT)

and subsurface tumor (from FLOT). This result demonstrates the feasibility of simultaneous morphological and molecular imaging of subsurface tumor in mesoscopic scale using OCT–FLOT.

51.5 Improvement of FLOT Resolution Using Angled Configuration

One of the limitations for our current FLOT system is that the point spread function (PSF) enlarges when the object locates deeper [11, 20]. Our previous measurement (see Fig. 51.4e) indicated that the axial PSF was ~100 to 200 μm at ~0.6 mm depth and increased to ~300 to 400 μm at ~1 mm depth [20]. To overcome this limitation, we investigated the effects of source and detector angles on the imaging performance [26]. Previous work in optical spectroscopy suggests that using angled illumination–collection design (oblique illumination–collection) will enhance the depth selectivity of epithelium tissues [27–31]. The angular degree of freedom in the illumination and detector arms is investigated first using the theoretical analysis and simulation. Then we implemented this design and experimentally demonstrated that angled FLOT (aFLOT) increased the depth selectivity and resolution.

51.5.1 Theoretical Analysis and Simulation

Singular-value analysis (SVA) is a method to evaluate the richness of the content of the sensitivity matrix J by decomposing J into an eigenvalue spectrum and has been demonstrated in the optimization of DOT to achieve a favorable image resolution [32, 33]. SVD of J yields a triplet of matrices: $J = USV^T$. The magnitude of the singular values in S provides a measure of the relative effects of these image-space modes on the detected signal. These singular values are arranged in a magnitude-decreasing order with increasing image-space mode indices. In this study, we used SVA to investigate the optimization of resolution and sensitivity by varying the FLOT source incidence angle and detector detecting angle. For convenience, we studied cases where both angles were equal.

Figure 51.6 shows the sensitivity profiles of FLOT for a representative source–detector pair based on Monte Carlo simulation. Configurations with 0° (top row) and 30° (bottom row) incidence and detection angles showed distinct sensitivity patterns. For each configuration, different scattering coefficients (μ_s = 50, 100, and 150 cm^{-1}) were chosen as the background medium (left to right). The sensitivity map indicates the probability density of photons delivered to each location by the source and captured by the detector. Photon paths were more ballistic for low-scattering medium (μ_s = 50 cm^{-1}) but became more scattered in high-scattering medium (μ_s = 150 cm^{-1}). A set of singular values (SVs) of J are generated for each angle from 0 to 50° with 10° increment and plotted in Fig. 51.7. Figure 51.7a–c corresponds to different background scattering coefficients

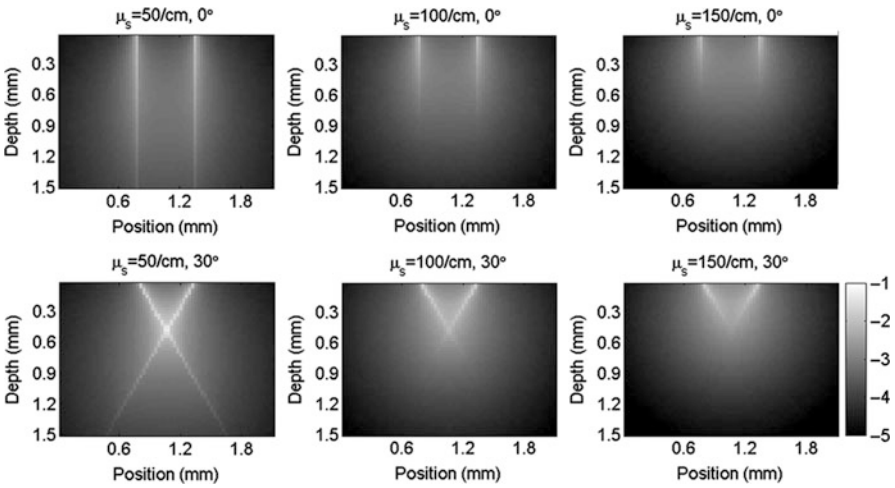

Fig. 51.6 Sensitivity maps (in log10 scale) for source–detector pair with 0° (*top row*) and 30° (*bottom row*) incidence/detection angles. For each configuration, a different scattering coefficient is specified for the medium (*left* to *right*). The sensitivity map indicates the probability density of photons delivered to the location by the source and captured at the location by the detector (Reproduced from Ref. [26] with permission © 2011 World Scientific Publishing Company)

(μ_s = 50, 100, 150 cm^{-1}, respectively). The threshold for the singular-value analysis was set to $10^{-3.6}$ (corresponding to the dynamic range of our EM-CCD detector). The number of SVs above the threshold represented a measure of the useful information contained in that data for image reconstruction. Figure 51.7d plots the number of useful SVs above the threshold for different scattering coefficients. From this figure, 30° configuration had the highest number of useful SVs, especially in low-scattering medium. It also showed that the angular advantage diminishes with increasing background scattering, because photons lose directionality in highly scattering medium, and as a result, both source and detector become more isotropic.

To validate the results from singular-value analysis, we performed image reconstruction of a point object (with unit intensity) under different configurations, using simulated measurement data (with 1.5 % Gaussian noise added). The point spread function along axial (z) direction through the position of a point object was quantified. As expected, axial point spread function (PSF_z) broadened, and its peak intensity decreased as the point object placed deeper. The details of PSF_z were further analyzed using two parameters: (1) the reconstructed peak intensity (or depth sensitivity) and (2) the interquartile range (IQR). IQR represents the range that bounds 50 % area centered around the maximum value under the PSF curve. IQR provides a more stable estimate of spread than FWHM in the presence of long-tail distribution [34]. Figure 51.8a–d shows the PSF_z peak intensity (or depth sensitivity) verses depth for different configurations. In general, at a given depth,

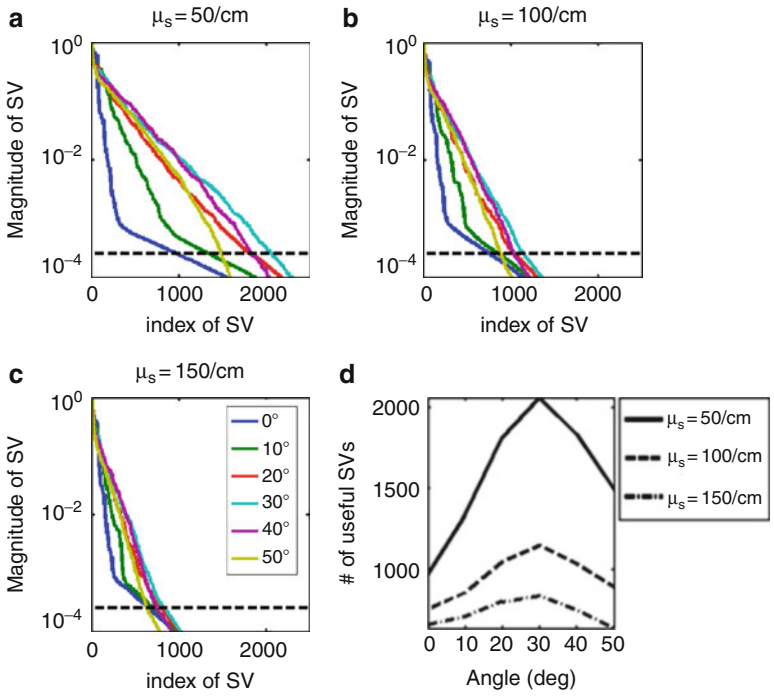

Fig. 51.7 Comparison of singular-value (*SV*) distributions among different incidence/detection angles. For convenience, same incidence and detection angels are specified. (**a**) SV distribution for $\mu_s = 50\,\mathrm{cm}^{-1}$, (**b**) SV distribution for $\mu_s = 100\,\mathrm{cm}^{-1}$, and (**c**) SV distribution for $\mu_s = 150\,\mathrm{cm}^{-1}$. Detection threshold was specified as $10^{-3.6}$ (*dotted horizontal lines* in **a**–**c**). Only SV above the threshold was considered carrying useful information for image reconstruction. (**d**) Plot of the number of SV above the threshold. FLOT arranged in 30° had more useful SVs than other configurations. It also showed the decrease of the angular advantage with increasing scattering (Reproduced from Ref. [26] with permission © 2011 World Scientific Publishing Company)

the 30° configuration had higher peak intensity (sensitivity) than 0° configuration, especially in the shallower depth region. The difference becomes less prominent for high-scattering medium. It is interesting to note that when normalizing these sensitivity curves to mean free path (MFP) ($1/\mu_s$) (i.e., replacing d with $\mu_s d$ in *x*-axis of the plot), only 30° configurations group together, as shown in Fig. 51.8d. The fact that normal configurations were not unified indicates that the underlying mechanisms between angled and normal configurations were different as photons significantly rely on backscattering to travel from source to detector in normal configurations, while the incidence and detection paths overlap in angled configurations. When normalized to MFP, the backscattering factor (as in 0° configuration) might not be linearly scaled.

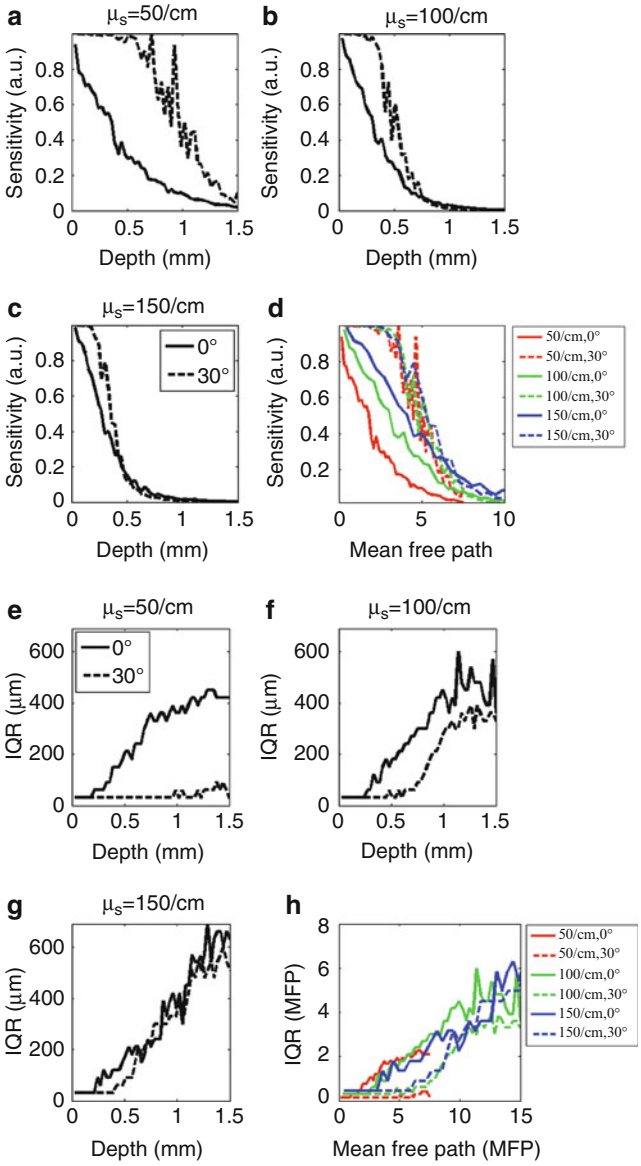

Fig. 51.8 (**a**–**d**) PSFz peak intensity verses depth for different source–detector angle configurations and background scattering. (**e**–**h**) PSFz interquartile range (*IQR*) verses depth for different source–detector angle configurations and background scattering coefficients (Reproduced from Ref. [26] with permission © 2011 World Scientific Publishing Company)

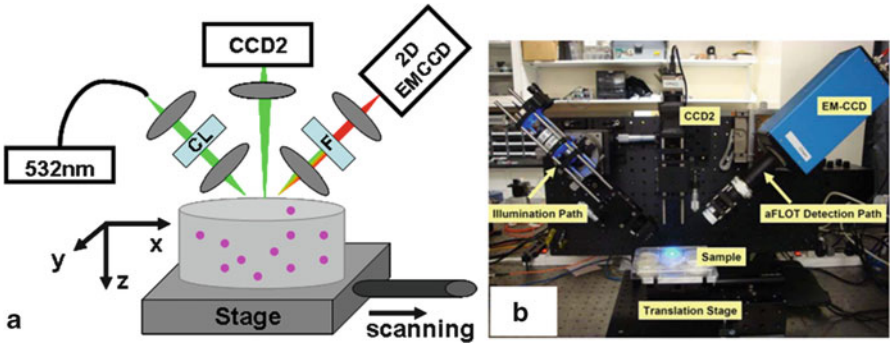

Fig. 51.9 (**a**) Schematic of the aFLOT system. *CL* cylindrical lens, *F* filter. (**b**) Photo of the 45–45° aFLOT system. The illumination–detection arms are arranged at 45° in air (or 30° inside the sample assuming an index of refraction of 1.4)

Figure 51.8e–h plot the IQR of PSF_z verses depth for different configurations. In general 30° configuration had smaller IQR (higher axial resolution) than 0° configuration. Especially, in low-scattering medium, IQR for 30° configuration remained ~30 μm up to 1 mm deep, and remains <100 μm up to 1.5 mm deep. In contrast, IQR for 0° configuration increased rapidly to ~400 μm at 1 mm deep. However, the difference between these two configurations becomes less prominent as background scattering coefficient increased, and as a result, the IQRs for both configurations were almost identical for high-scattering medium. Again, when normalized to MFP as shown in Fig. 51.8h, the grouping of the curves was observed. However, different from the sensitivity, the grouping (unifying) of IQR curves occurred at both normal and angled configurations. This result also indicated that IQR and sensitivity provide inherently different measures.

51.5.2 Experimental Validation

Figure 51.9 shows the schematic diagram and the photo of the angled FLOT system. Similar to our previous FLOT system, the excitation light source was expanded into line-field illumination using a cylindrical lens (CL). An emission filter (F) was placed in the detection axis to select only the fluorescence signal, which was recorded by the 12-bit EM-CCD. Another CCD (CCD2) was placed vertically to record the reflected light distribution to determine the reduced scattering coefficient of the sample using the technique of oblique-incidence reflectometry [35]. When acquiring aFLOT measurement, the translating stage was moved in y-direction (perpendicular to the line illumination along X) with a speed of 50 μm/s. EM-CCD recorded each XY frame with 0.4 s exposure time, and the total recording time was 170 s for one 3D dataset XYT.

Image reconstruction converted each YZ plane (2D) from YT measurements using Tikhonov regularization. In this study, 70 source–detector (SD) pairs with

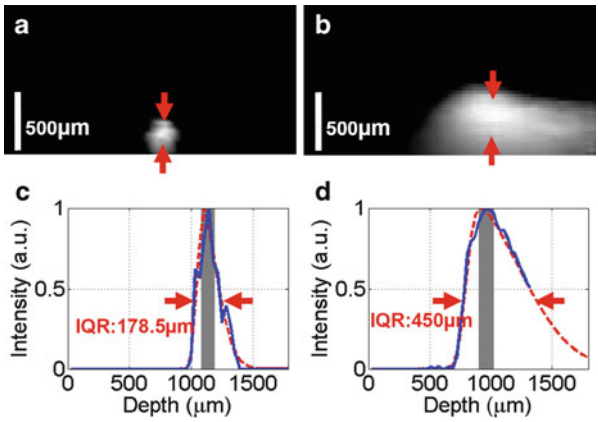

Fig. 51.10 Comparison of aFLOT (**a**, **c**) and conventional FLOT (**b**, **d**). (**a**, **b**) cross-sectional reconstruction; (**c**, **d**) axial profile through the center of the object. Gray area denotes the true dimension of the capillary tube. *IQR* Interquartile range

70 scanning positions were used to determine a single YZ FOV of 3 × 3 mm^2. Local YZ frames were then pieced together longitudinally to form a global FOV in YZ.

We then validated aFLOT imaging experimentally using the capillary tube phantom again. The capillary tube (110 μm in diameter) was filled with 1 μM fluorescent dye Rhodamine 6G and embedded at 1.2 mm deep inside 1 % Intralipid. The excitation wavelength was set to 532 nm and the filter was set to 605 ± 15 nm, based on the spectrum of Rhodamine 6G. Figure 51.10a shows the cross section of the reconstructed capillary tube phantom using aFLOT. The position of the capillary from the reconstructed image (∼1.14 mm) was close to the position independently measured using OCT (∼1.2 mm). As a comparison between angled and conventional FLOT systems, Fig. 51.10b shows the reconstruction using FLOT with normal incidence/detection. Figure 51.10c, d illustrates the central axial profiles of the reconstructed capillary tube shown in Fig. 51.10a, b, respectively. Quantitatively, interquartile range (IQR) was measured and compared. The measured IQR was 178.5 μm for the aFLOT system and was 450 μm for the conventional FLOT. This represents approximately 2.5-fold improvement in axial resolution when using aFLOT.

51.6 Results: Imaging Engineered Tissues

Regenerative medicine has emerged as an important discipline which aims at introducing living cells or functioning tissues to repair injury or replace damaged tissues or organs which lose functions. Optimization of regenerative medicine strategies includes the design of biomaterials, cell-seeding methods, cell-biomaterial interactions, and molecular signaling within the engineered tissue. One challenge is to nondestructively observe and quantify the distribution and migration of seeded cells throughout the bulk scaffold. The development of tissue

engineered products is limited by the lack of laboratory imaging techniques which are capable of nondestructive imaging of the three-dimensional morphology as well as the cell response of a tissue engineering scaffold. The current method for quantifying 3D cell distribution involves fluorescent confocal microscopy imaging of cryosectioned scaffolds followed by digital 3D image recompiling [36]. Although robust, this approach is destructive and time consuming, thereby may become a concern in longitudinal inspection of massive amount of samples.

FLOT (and aFLOT) overcomes the depth limitation of confocal microscopy by using multiple detectors to collect photon traveling through different depths. In this study, we experimentally demonstrated aFLOT imaging of two types of engineered tissues, respectively. Mesenchymal stem cells (MSCs) embedded in homogeneous EH-PEG hydrogels [37], which is low scattering ($\mu_s = 10$ cm^{-1}), was imaged through an incidence/detection angle of 45–45° aFLOT (as shown in Fig. 51.9). In the other experiment, a capillary (100 μm in diameter) containing 1 mM rhodamine 6G was embedded in a heterogeneous macroporous EH-PEG hydrogel [38, 39], which is high scattering ($\mu_s = 110$ cm^{-1}). This phantom was imaged through 45–0° aFLOT. The tomography of capillary was reconstructed and co-registered with that from OCT.

In the first experiment, we used the aFLOT system to image MSC distribution inside a low-scattering, homogeneous EH-PEG hydrogel [37], one common engineered tissue scaffold used for bone regeneration. To mimic cell migration, we controlled the cell-distribution thickness by preparing a bilayer phantom. The bottom layer was pure EH-PEG and was intentionally prepared thick (>6 mm). The top layer was EH-PEG mixed with MSCs (cell density = 10^4–10^5/mL) with thickness of 0.5, 1, 2, and 3 mm. Homogeneous EH-PEG had low scattering as shown in Fig. 51.11a, with typical reduced scattering coefficient of ~1 cm^{-1}, estimated by reflectometry [35]. For reconstruction, Monte Carlo simulation was performed to estimate photon distribution inside homogeneous EH-PEG. Optical properties of EH-PEG, including anisotropy $g = 0.9$, refractive index = 1.33, and absorption coefficient of 0.1 cm^{-1}, were assumed.

Figure 51.11b shows a YZ cross section from stacking of a homogenous EH-PEG phantom with top layer (2-mm thick) containing MSC, and Fig. 51.11c shows that from FLOT reconstruction. Stacking (as used in conventional 3D digital microscopy) provides a blurred yet quick 3D view of the sample due to the weak but nonzero scattering of the sample. FLOT image reconstruction using proper modeling improves the image quality as shown in Fig. 51.11c. Figure 51.11d is the composite 3D reconstruction of the same phantom. The FOV was 6.5 × 7.6 × 2.9 mm^3. Figure 51.11e renders together the phantoms with 0.5, 1, 2, and 3-mm thick MSC distributions on the top layer. Lastly, we show the histogram of stem-cell depth distribution of all four samples. The estimated cell-distribution depths were distinct and consistent with the nominal thickness of each sample during fabrication. One interesting point is that all the cell-distribution patterns peaked at the bottom surface, which may be attributed by

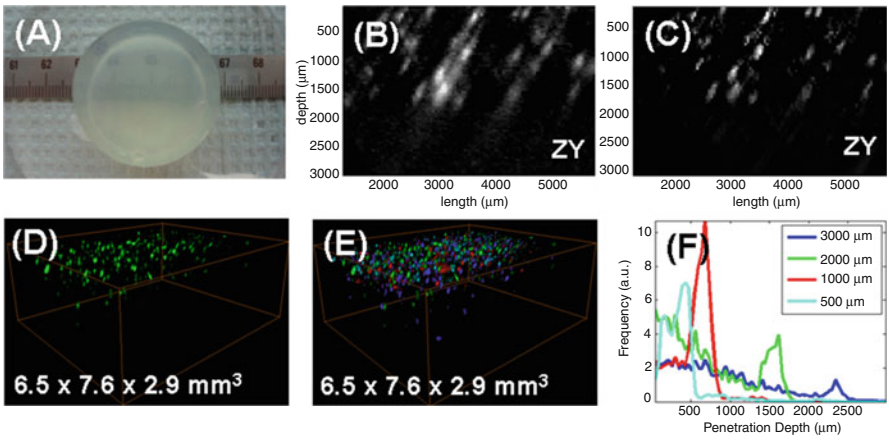

Fig. 51.11 3D aFLOT imaging of EH-PEG hydrogels with stem cells embedded at top layers. (**a**) Photo of a sample. Transparency indicates low scattering. (**b**) Stacking representation of a YZ cross section of the hydrogel with 2-mm thick top layer containing MSC. (**c**) Reconstruction of the same YZ cross section. Image reconstruction through Tikhonov regularization made MSC clearer. (**d**) 3D reconstruction of the same sample. (**e**) Combined view of four samples with different stem-cell-laden layer thickness: 0.5-mm (*cyan*), 1-mm (*red*), 2-mm (*green*), and 3-mm (*blue*). (**f**) Histogram of cell distribution

the condensation of cells or interface reflection. Further research is needed to confirm this finding. In addition, from Fig. 51.8, the detection sensitivity dropped toward deeper region so that the histogram also showed that the peaks declined toward deeper region. In summary, Fig. 51.11 demonstrates that aFLOT can resolve the depth-dependent distribution of cell clusters in the weakly scattering EH-PEG hydrogel.

In the second set of experiments where highly scattering macroporous EH-PEG was of interest, we changed the illumination–detection angles to 45–0° configuration for two reasons. First, we expected that the advantage of the 45–45° configuration diminished as the sample scattering coefficient was higher. Second, the camera could not maintain in focus over a few millimeter FOV if placed at 45°. We embedded a capillary tube (100 μm in diameter) containing 50 μM fluorescent dye indocyanine green (ICG) in a macroporous EH-PEG hydrogel, which was highly scattering at visible wavelength ($\mu_s = 110\ \text{cm}^{-1}$ at 530 nm). The scattering coefficient was reduced at near-infrared (NIR) wavelength ($\mu_s = 50\ \text{cm}^{-1}$ at 780 nm). This phantom was imaged through FLOT with 780 nm excitation. The FLOT tomography of the capillary was reconstructed and co-registered with that from OCT. Figure 51.12a shows the co-registered XZ and YZ cross sections. Figure 51.12b shows 3D FLOT image of the fluorescent capillary co-registered with macroporous EH-PEG hydrogel obtained by OCT. In this experiment, we demonstrated the capability of aFLOT imaging in heterogeneous macroporous scaffolds. These results indicate that OCT–FLOT represents a promising imaging

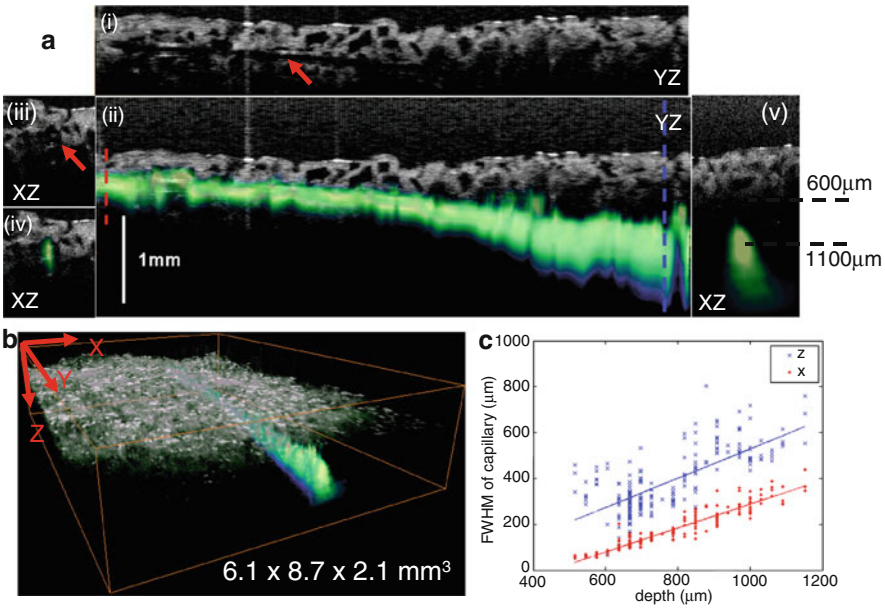

Fig. 51.12 (**a**) XZ and YZ cross sections of OCT/aFLOT tomogram. The *red arrow* indicates the position of the capillary. (**b**) 3D perspective view. (**c**) FWHM statistics of the capillary in each XZ cross sections verses depths. (*Blue* ×) is FWHM in z-direction. (*Red* •) is FWHM in x-direction. *Straight lines* are linear least square fits

technique to quantify the depth-resolved fluorophore distribution information in engineered tissue scaffold for investigating cell scaffold cellular and molecular interactions in situ.

51.7 Conclusion

In this chapter, we provided a summary of the instrument and algorithm for combined OCT–FLOT system for biomedical applications. Co-registered OCT morphological and FLOT molecular information can be resolved at millimeter imaging scale, which has strong potential to provide depth-resolved tissue structural and molecular imaging. This unique multimodality platform represents a new multimodal imaging regime that bridges the macroscopic and microscopic imaging regimes. By varying the source incidence and/or detector collection angles, angled FLOT promises to enhance the imaging resolution and depth sensitivity, especially for low-scattering medium. Examples of OCT–FLOT imaging of subsurface tumor and stem-cell-laden hydrogels are presented. OCT–FLOT could be a useful tool for investigating tissue structural and functional relationship in mesoscopic (mm) scales. Future work will focus on the utilization of OCT structural image as the a priori information to improve FLOT reconstruction.

Acknowledgment We acknowledge Dr. David Boas from Massachusetts General Hospital (MGH) for providing the Monte Carlo simulation code (tmcimg), and Drs. Heng Lian (NanYang Technological University, Singapore), Quan Zhang (MGH), and Qianqian Fang (MGH) for technical assistance in modifying the code. We also acknowledge the collaboration with Dr. James Jiang and Alex Cable (Thorlabs, Inc.) on OCT imaging, Drs. Kristine Glunde and Venu Raman (Johns Hopkins University) for breast cancer imaging, and Dr. John Fisher (University of Maryland) on tissue engineering and stem-cell imaging. This work is supported in part by the Nano-Biotechnology Award of the State of Maryland, the Minta Martin Foundation, the General Research Board (GRB) Award of the University of Maryland, the University of Maryland Baltimore (UMB) and College Park (UMCP) Seed Grant Program, the Prevent Cancer Foundation, the American Society for Laser Medicine and Surgery (ASLMS)'s A. Ward Ford Memorial Institute Research Grant, the National Institutes of Health grant (R21 AR059325-01A1, R21 EB012215-01A1, R21 DK088066-01A1), and the National Science Foundation grant (CBET-1135514).

References

1. R. Weissleder, M.J. Pittet, Imaging in the era of molecular oncology. Nature **452**(7187), 580–589 (2008)
2. A.M. Dale, A.K. Liu, B.R. Fischl, R.L. Buckner, J.W. Belliveau, J.D. Lewine, E. Halgren, Dynamic statistical parametric mapping: combining fMRI and MEG for high-resolution imaging of cortical activity. Neuron **26**(1), 55–67 (2000)
3. Q. Fang, J. Selb, S.A. Carp, G. Boverman, E.L. Miller, D.H. Brooks, R.H. Moore, D.B. Kopans, D.A. Boas, Combined optical and X-ray tomosynthesis breast imaging. Radiology **258**(1), 89–97 (2011)
4. Y.T. Pan, T.Q. Xie, C.W. Du, S. Bastacky, S. Meyers, M.L. Zeidel, Enhancing early bladder cancer detection with fluorescence-guided endoscopic optical coherence tomography. Opt. Lett. **28**(24), 2485–2487 (2003)
5. Z.G. Wang, D.B. Durand, M. Schoenberg, Y.T. Pan, Fluorescence guided optical coherence tomography for the diagnosis of early bladder cancer in a rat model. J. Urol. **174**(6), 2376–2381 (2005)
6. A.R. Tumlinson, L.P. Hariri, U. Utzinger, J.K. Barton, Miniature endoscope for simultaneous optical coherence tomography and laser-induced fluorescence measurement. Appl. Opt. **43**(1), 113–121 (2004)
7. J.B. McNally, N.D. Kirkpatrick, L.P. Hariri, A.R. Tumlinson, D.G. Besselsen, E.W. Gerner, U. Utzinger, J.K. Barton, Task-based imaging of colon cancer in the Apc(Min/+) mouse model. Appl. Opt. **45**(13), 3049–3062 (2006)
8. S. Yuan, C.A. Roney, J. Wierwille, C.W. Chen, B. Xu, G. Griffiths, J. Jiang, H. Ma, A. Cable, R.M. Summers, Y. Chen, Co-registered optical coherence tomography and fluorescence molecular imaging for simultaneous morphological and molecular imaging. Phys. Med. Biol. **55**(1), 191–206 (2010)
9. N. Iftimia, A.K. Iyer, D.X. Hammer, N. Lue, M. Mujat, M. Pitman, R.D. Ferguson, M. Amiji, Fluorescence-guided optical coherence tomography imaging for colon cancer screening: a preliminary mouse study. Biomed. Opt. Express **3**(1), 178–191 (2012)
10. A. Dunn, D. Boas, Transport-based image reconstruction in turbid media with small source-detector separations. Opt. Lett. **25**(24), 1777–1779 (2000)
11. E.M. Hillman, D.A. Boas, A.M. Dale, A.K. Dunn, Laminar optical tomography: demonstration of millimeter-scale depth-resolved imaging in turbid media. Opt. Lett. **29**(14), 1650–1652 (2004)
12. E.M.C. Hillman, S.A. Burgess, Sub-millimeter resolution 3D optical imaging of living tissue using laminar optical tomography. Laser Photonics Rev. **3**(1–2), 159–179 (2009)
13. E.M. Hillman, A. Devor, M.B. Bouchard, A.K. Dunn, G.W. Krauss, J. Skoch, B.J. Bacskai, A.M. Dale, D.A. Boas, Depth-resolved optical imaging and microscopy of vascular compartment dynamics during somatosensory stimulation. Neuroimage **35**(1), 89–104 (2007)

14. B.H. Yuan, Radiative transport in the delta-P1 approximation for laminar optical tomography. J. Innov. Opt. Health Sci. **2**, 149–163 (2009)
15. S.A. Burgess, M.B. Bouchard, B.H. Yuan, E.M.C. Hillman, Simultaneous multiwavelength laminar optical tomography. Opt. Lett. **33**(22), 2710–2712 (2008)
16. N. Ouakli, E. Guevara, S. Dubeau, E. Beaumont, F. Lesage, Laminar optical tomography of the hemodynamic response in the lumbar spinal cord of rats. Opt. Express **18**(10), 10068–10077 (2010)
17. E.M.C. Hillman, O. Bernus, E. Pease, M.B. Bouchard, A. Pertsov, Depth-resolved optical imaging of transmural electrical propagation in perfused heart. Opt. Express **15**, 17827–17841 (2007)
18. B.H. Yuan, S.A. Burgess, A. Iranmahboob, M.B. Bouchard, N. Lehrer, C. Bordier, E.M.C. Hillman, A system for high-resolution depth-resolved optical imaging of fluorescence and absorption contrast. Rev. Sci. Instrum. **80**(4), 043706 (2009)
19. S. Yuan, Q. Li, J. Jiang, A. Cable, Y. Chen, Three-dimensional coregistered optical coherence tomography and line-scanning fluorescence laminar optical tomography. Opt. Lett. **34**(11), 1615–1617 (2009)
20. Y. Chen, S. Yuan, J. Wierwille, R. Naphas, Q. Li, T.R. Blackwell, P.T. Winnard, V. Raman, K. Glunde, Integrated optical coherence tomography (OCT) and fluorescence laminar optical tomography (FLOT). IEEE J. Sel. Top. Quantum Electron. **16**, 755–766 (2010)
21. S.R. Arridge, Optical tomography in medical imaging. Inverse Probl. **15**(2), R41–R93 (1999)
22. R.J. Crilly, W.F. Cheong, B. Wilson, J.R. Spears, Forward-adjoint fluorescence model: Monte Carlo integration and experimental validation. Appl. Opt. **36**(25), 6513–6519 (1997)
23. A.C. Kak, M. Slaney, IEEE Engineering in Medicine and Biology Society, *Principles of Computerized Tomographic Imaging* (IEEE Press, New York, 1987). x, 329 p., [40] leaves of plates
24. P.T. Winnard Jr., J.B. Kluth, V. Raman, Noninvasive optical tracking of red fluorescent protein-expressing cancer cells in a model of metastatic breast cancer. Neoplasia **8**(10), 796–806 (2006)
25. K. Glunde, C.A. Foss, T. Takagi, F. Wildes, Z.M. Bhujwalla, Synthesis of 6′-O-lissamine-rhodamine B-glucosamine as a novel probe for fluorescence imaging of lysosomes in breast tumors. Bioconjug. Chem. **16**(4), 843–851 (2005)
26. C.W. Chen, Y. Chen, Optimization of design parameters for fluorescence laminar optical tomography. J. Innov. Opt. Health Sci. **4**, 309–323 (2011)
27. C.F. Zhu, Q. Liu, N. Ramanujam, Effect of fiber optic probe geometry on depth-resolved fluorescence measurements from epithelial tissues: a Monte Carlo simulation. J. Biomed. Opt. **8**(2), 237–247 (2003)
28. T.J. Pfefer, A. Agrawal, R.A. Drezek, Oblique-incidence illumination and collection for depth-selective fluorescence spectroscopy. J. Biomed. Opt. **10**(4), 044016 (2005)
29. L. Nieman, A. Myakov, J. Aaron, K. Sokolov, Optical sectioning using a fiber probe with an angled illumination-collection geometry: evaluation in engineered tissue phantoms. Appl. Opt. **43**(6), 1308–1319 (2004)
30. Q. Liu, N. Ramanujam, Experimental proof of the feasibility of using an angled fiber-optic probe for depth-sensitive fluorescence spectroscopy of turbid media. Opt. Lett. **29**, 2034–2036 (2004)
31. M.C. Skala, G.M. Palmer, C.F. Zhu, Q. Liu, K.M. Vrotsos, C.L. Marshek-Stone, A. Gendron-Fitzpatrick, N. Ramanujam, Investigation of fiber-optic probe designs for optical spectroscopic diagnosis of epithelial pre-cancers. Lasers Surg. Med. **34**(1), 25–38 (2004)
32. J.P. Culver, V. Ntziachristos, M.J. Holboke, A.G. Yodh, Optimization of optode arrangements for diffuse optical tomography: a singular-value analysis. Opt. Lett. **26**(10), 701–703 (2001)
33. E.E. Graves, J.P. Culver, J. Ripoll, R. Weissleder, V. Ntziachristos, Singular-value analysis and optimization of experimental parameters in fluorescence molecular tomography. J. Opt. Soc. Am. A Opt. Image Sci. Vis. **21**(2), 231–241 (2004)

34. A.A. Tanbakuchi, A.R. Rouse, A.F. Gmitro, Monte Carlo characterization of parallelized fluorescence confocal systems imaging in turbid media. J. Biomed. Opt. **14**(4), 044024 (2009)
35. L. Wang, S.L. Jacques, Use of a laser beam with an oblique angle of incidence to measure the reduced scattering coefficient of a turbid medium. Appl. Opt. **34**(13), 2362–2366 (1995)
36. P. Thevenot, A. Nair, J. Dey, J. Yang, L. Tang, Method to analyze three-dimensional cell distribution and infiltration in degradable scaffolds. Tissue Eng. C Methods **14**(4), 319–331 (2008)
37. M.W. Betz, P.C. Modi, J.F. Caccamese, D.P. Coletti, J.J. Sauk, J.P. Fisher, Cyclic acetal hydrogel system for bone marrow stromal cell encapsulation and osteodifferentiation. J. Biomed. Mater. Res. A **86A**(3), 662–670 (2008)
38. M.W. Betz, A.B. Yeatts, W.J. Richbourg, J.F. Caccamese, D.P. Coletti, E.E. Falco, J.P. Fisher, Macroporous hydrogels upregulate osteogenic signal expression and promote bone regeneration. Biomacromolecules **11**(5), 1160–1168 (2010)
39. C.W. Chen, M.W. Betz, J.P. Fisher, A. Paek, Y. Chen, Macroporous hydrogel scaffolds and their characterization by optical coherence tomography. Tissue Eng. C **17**, 101–112 (2011)

Photoacoustic / Optical Coherence Tomography

52

Michelle Gabriele Sandrian, Edward Zhang, Boris Považay, Jan Laufer, Aneesh Alex, Paul Beard, and Wolfgang Drexler

Keywords

Optical coherence tomography • Photoacoustic imaging • Photoacoustic tomography • Photoacoustic microscopy • Multimodal imaging

52.1 Introduction

Preliminary work describing the multimodal combination of optical coherence tomography (OCT) and photoacoustic (PA) imaging has demonstrated the potential for these two techniques to nicely complement each other, providing access to information about

M.G. Sandrian (✉)
Department of Ophthalmology, Department of Bioengineering Eye and Ear Institute, University of Pittsburgh, Pittsburgh, PA, USA
e-mail: mgabriele@gmail.com; sandrianmg@upmc.edu

E. Zhang
Department Medical Physics and Bioengineering, Malet Place Engineering Building, University College London, London, UK
e-mail: e.zhang@ucl.ac.uk

B. Považay
Center for Medical Physics and Biomedical Engineering, Medical University of Vienna, Vienna, Austria

OptoLab, HuCe - Bern University of Applied Sciences (BUAS), Postfach, Biel/Bienne, Switzerland
e-mail: boris.povazay@bfh.ch

J. Laufer
Institut für Optik und Atomare Physik, Sekretariat ER 1–1, Technische Universität Berlin, Berlin, Germany

Institut für Radiologie, Charité – Universitätsmedizin Berlin, Berlin, Germany
e-mail: jan.laufer@tu-berlin.de

© Springer International Publishing Switzerland 2015

W. Drexler, J.G. Fujimoto (eds.), *Optical Coherence Tomography*,
DOI 10.1007/978-3-319-06419-2_53

tissue scattering and absorption, respectively [1–10]. In practice, however, there exist limitations to combining OCT and PA using conventional methods for PA signal acquisition, and thus, there have been relatively few successful demonstrations of a combined approach. Of the multimodal systems that have been presented, one that may offer a solution for translation to clinical use employs an all-optical ultrasonic detection technique based on a Fabry-Perot interferometer (FPI)-based sensor. This chapter chronicles the efforts towards combining PA imaging and OCT, with a focus on a PA tomography (PAT)/OCT system that uses this FPI sensor for all-optical detection.

52.1.1 Photoacoustic Microscopy Versus Tomography

PA signals are generated using the photoacoustic effect: tissue is irradiated with short (typically nanosecond) pulses to create a localized thermal increase in endogenous absorbers such as hemoglobin and melanin or exogenous absorptive contrast agents. Absorption of these pulses leads to an initial pressure distribution, which results in broadband ultrasonic waves that propagate through tissue and any acoustic coupling medium and are detected via a transducer.

The majority of biological tissues are highly scattering, and most biological optical imaging techniques detect ballistically scattered photons and thus cannot penetrate further than one transport mean free path of isotropically scattered photons, or approximately 1 mm in depth [11]. Photon propagation transitions from ballistic to diffusive at one transport mean free path, and techniques that rely on the detection of multiple scattered photons in the diffusive regime, such as diffuse optical tomography (DOT), exhibit higher depth penetration with lower resolution. Photoacoustic techniques, however, allow for higher resolution than DOT because ultrasonic scattering is weaker than optical scattering. Hence, there are two main advantages offered by PA imaging over other optical approaches: the potential to reach higher depths and the possibility to access absorption properties of tissue.

In PA imaging, depth penetration and resolution are scalable. High axial resolution can be attained using an excitation laser with short (e.g., 1–10 ns) pulses and an acoustic detector with a high central frequency and broad bandwidth, and high

A. Alex
Department of Electrical and Computer Engineering, Lehigh University, Bethlehem, PA, USA
e-mail: aneeshalexp@gmail.com

P. Beard
Department of Medical Physics and Bioengineering, Malet Place Engineering Building, London, UK
e-mail: paul.beard@ucl.ac.uk

W. Drexler
Center for Medical Physics and Biomedical Engineering, Medical University of Vienna, General Hospital Vienna, Vienna, Austria
e-mail: wolfgang.drexler@meduniwien.ac.at

lateral resolution can be accomplished with a high numerical aperture lens to focus the excitation beam. An axial resolution of 7.6 μm has recently been demonstrated [12], and submicron lateral resolution has also been presented [13]. While penetration depth increases with lower frequency transducers, spatial resolution suffers with increased depth. Kruger et al. reported imaging of up to 40 mm using a 5 MHz transducer and 800 nm excitation source, but the axial resolution was only 250 μm [14].

Excitation of PA signals via illumination with either a focused or an unfocused light source and detection via focused or unfocused transducers has been accomplished. Though the naming convention varies in the literature, different modes of imaging exist which can generally be defined as follows:

- Optical resolution photoacoustic microscopy (OR-PAM): focused excitation beam. Lateral resolution is defined by the dimensions of the excitation beam and axial resolution is acoustically defined. OR-PAM relies on the detection of ballistic photons, so the maximum penetration depth is ~1mm. The detector can be focused or unfocused.
- Acoustic resolution photoacoustic microscopy (AR-PAM): focused detector. Lateral and axial resolution is acoustically defined. Excitation beam can be focused or unfocused but does not affect spatial resolution.
- Photoacoustic tomography (PAT): wide-field unfocused excitation beam, scanning planar transducer, or array of unfocused transducers that requires the use of reconstruction techniques to obtain an image.

52.1.2 Practical Limitations to Detecting PA Signals with Conventional Ultrasonic Transducers

One of the major constraints in the design of PA systems specifically for combination with OCT is that traditional approaches use scanned detectors or arrays with multiple detection elements so the physical size of the sensor obstructs the optical path required for OCT A-scan acquisition. Single element scanned transducers have been employed, where excitation of tissue occurs via a ring of illumination around the detector, allowing for backward (reflection)-mode detection of PA signals [15]. A problem with this approach, however, is that detector sensitivity scales with active element size, so while OCT acquisition might be possible using a small transducer that does not obstruct the beam, this would be at the expense of sensitive acoustic signal detection. In addition, measurement time using a single element detector is limited by mechanical scanning. While transparent transducer arrays may eventually offer a solution [16] with multiple detection channels allowing rapid acquisition of B-mode images and a transparent window for OCT measurement, further development of these arrays in PA systems is required.

52.1.3 Multimodal PA and OCT Systems

The combination of PA and OCT imaging systems has been presented by multiple groups [2, 3, 7–10, 17]. These systems allow access to both absorption and

scattering information from tissue and also have the potential to be used for functional information (e.g., spectroscopic PA imaging) with high-resolution structural context (from the detection of backscattered light with OCT) in one system [4]. Because published configurations, resolution, speed, and wavelength vary substantially, a summary of the **reported specifications from systems published to date is presented in Table** 52.1.

52.1.3.1 PAM/OCT

Li et al. demonstrated the use of OR-PAM/OCT for evaluating microcirculation in the mouse ear in 2009 [3]. The depth range was estimated to be 1.5 mm for OR-PAM, which was comparable to the 1.8 mm depth for OCT. While this was the first effort to show the feasibility of a multimodal combination with OCT, the transmission (forward) mode configuration required the sample to be very thin. In addition, a mechanically translated objective meant very slow acquisition time (2.5 frames/s), which further limits the application of this configuration. Despite these restrictions, the system was later used to look at neovascularization of a tissue scaffold in anesthetized animals, with the relatively thin mouse ear again used as a model [1].

An effort by Jiao et al. in 2009 looked at the microvasculature of the mouse ear using backward mode detection with an unfocused 15 MHz ultrasound transducer [2]. The authors presented synchronized simultaneous acquisition, though the measurement rate was limited by the excitation pulse repetition rate of the PAM system to 1,024 Hz, whereas a 24 kHz A-scan acquisition would have been possible given their OCT CCD integration time. Liu et al. applied this system for spectroscopic measurements (at 570 nm, 578 nm, 588 nm, and 590 nm) to measure oxygen saturation (sO_2) with a custom-built unfocused 35 MHz needle transducer [4]. They used these sO_2 levels together with Doppler OCT blood flow velocity and total hemoglobin concentration (from laboratory-based blood tests) to measure the metabolic rate in the mouse ear.

52.1.3.2 PAM/OCT for Ophthalmic Applications

Because one of the most common clinical applications of OCT imaging is in ophthalmology, a natural extension of multimodal PAM/OCT imaging is for in vivo retinal imaging. Access to absorption-based contrast could be used to evaluate the retinal pigment epithelium in diseases like age-related macular degeneration, and sO_2 measurements might be used to assess blood vessel status in diabetic retinopathy. Jiao et al. presented a combined PAM/OCT ophthalmoscope system that used an unfocused transducer placed directly on the sclera to acquire preliminary in vivo images of the rat retina at a 93 Hz frame rate (256 A-scans/frame; volumetric image in 2.7 s) [17]. The pulse energy of the excitation laser source was 10 μJ at the output of the laser and estimated to be less than 40 nJ/pulse at the sample. In a study published in 2012 by Song et al., this PAM/OCT system was further extended to include additional modalities like scanning laser ophthalmoscopy and fluorescein angiography and again demonstrated in the rat retina [5]. Despite these preliminary demonstrations in animals, it is unclear whether the pulse energy necessary to generate a PA signal is within the maximum permissible exposure limitation for the human retina.

Table 52.1 Comparison of published specifications for multimodal PA/OCT systems

		Li et al. 2009 [3]	Jiao et al. 2009 [2]	Jiao et al. 2010 [17]	Zhang et al. 2011 [8]	Yang et al. 2011 [6]	Zhang et al. 2012 [7]	Blatter et al. [18]	Lee et al. 2013 [9]	Xi et al. 2013 [10]
PA	**Excitation λ**	532 nm Nd:YAG (Elforlight SPOT)	532 nm Nd:YLF (Edge-Wave IS8II-E) pumped 580 nm dye (Sirah GmbH Cobra)	532 nm Nd:YAG (Elforlight SPOT-10-100-532)	355 nm Nd:YAG pumped OPO (Newport Spectra-Physics), output 410–2,100 nm (used 670 and 680 nm)	532 nm Nd:YAG pumped Ti:sapphire (Symphonics-TII, LS-2122)	532 nm Nd:YAG (Elforlight SPOT-10-100-532) pumped dye laser ($\lambda_o = 580$ nm, $\Delta\lambda = 20$ nm)	532 nm Nd:YAG (Coherent Corona)	1,064 nm Nd:YAG microchip (Teem Photonics SNP-20 F-100) coupled into PCF (output 600–1,700 nm)	532 nm Nd:YAG
	Excitation pulse	1.2 ns	6 ns	2 ns	8 ns	20 ns	2 ns	250 ns	0.7 ns	Not reported
	Excitation pulse repetition rate	Up to 20 kHz possible	1,024 Hz	Up to 30 kHz possible	50 Hz	15 Hz	Up to 30 kHz possible	5 kHz	21 kHz	10 Hz
	Detection configuration	Forward	Backward	Backward	Backward	Backward	Forward	Backward	Forward	Backward
	Transducer	75 MHz center frequency (−6 dB), focused (Olympus NDT V2022)	15 MHz, bandwidth 80 %, active element diameter 6 mm unfocused (Olympus NDT V313)	30 MHz bandwidth 50 %, active element diameter 1.0 mm unfocused needle (Custom)	39 MHz (−3 dB) FPI sensor with 1,550 nm interrogation laser (Custom)	35 MHz center frequency (−6 dB), unfocused (Olympus NDT Panametrics 5900PR)	30 MHz, bandwidth 50 %, active element diameter 0.4 mm unfocused needle (Custom)	Phase-sensitive OCT	30 MHz center frequency, acoustic bandwidth of ~ 18 MHz	10 MHz unfocused
	Axial resolution	14 μm	50 μm	23 μm	20 μm	~55 μm	23 μm	~375 μm	74.5 μm	Not reported

(*continued*)

Table 52.1 (continued)

		Li et al. 2009 [3]	Jiao et al. 2009 [2]	Jiao et al. 2010 [17]	Zhang et al. 2011 [8]	Yang et al. 2011 [6]	Zhang et al. 2012 [7]	Blatter et al. [18]	Lee et al. 2013 [9]	Xi et al. 2013 [10]
OCT	**Detection**	Spectrometer/ CCD	Spectrometer/ CCD	Spectrometer/ CCD	Spectrometer/ CCD	Swept-source/ DBD	Spectrometer/ CCD	Swept-source/ DBD	Spectrometer/ CCD	PD/RSOD line
	Light source	$\lambda_o = 829$ nm, $\Delta\lambda = 36.4$ nm SLD (InPhenix, IPSDD0803)	$\lambda_o = 840$ nm, $\Delta\lambda = 50$ nm SLD (Superlum)	$\lambda_o = 870$ nm, $\Delta\lambda = 100$ nm SLD (InPhenix)	$\lambda_o = 1{,}050$ nm, $\Delta\lambda = 70$ nm ASE (NP Photonics)	$\lambda_o = 1{,}310$ nm, $\Delta\lambda = 110$ nm (Santec HSL-2000)	Same as PA	$\lambda_o = 1{,}310$ nm FDML laser, 120 nm full bandwidth	Same as PA	$\lambda_o = 1{,}310$ nm, $\Delta\lambda = 75$ nm SLD (DenseLight, DL-BX9-CS3159A)
	Axial resolution	5.9 μm (tissue)	6 μm (tissue)	4 μm (tissue)	8 μm (tissue)	12 μm (air)	9.5 μm (air)	~12 μm (air)	14.5 μm	10 μm (air)
PA/ OCT	**Lateral resolution**	5 μm	20 μm (OCT) 7.8 μm (PA)	20 μm	18 μm (OCT) 50–100 μm (PA)	25 μm (OCT) ~450 μm (PA)	Not reported	Not reported	12 μm (OCT) 11.5 μm (PA)	15 μm
	Scanning	2D moving objective on translation stage	2D galvanometer scanning	2D galvanometer scanning	2D galvanometer scanning	Probe translated mechanically 1D	2D galvanometer scanning	Sample moving via 2D translation stage	Sample moving via 2D translation stage	Probe on 2D mechanical stage
	Scan rate	~1 kHz	1,024 Hz	24 kHz	47 kHz (OCT) 50 Hz (PA)	20 kHz(OCT) 15 Hz (PA)	5 kHz	5 kHz	Not reported	1 kHz (OCT) 10 Hz (PA)
	Simultaneous imaging?	No	Yes	Yes	No	No	Yes	Yes	No	No
	In vivo application	Mouse ear	Mouse ear	Rat retina	Mouse and human skin	N/A	Mouse ear	N/A	N/A	Mouse ear

ASE amplified spontaneous emission, *DBD* dual-balanced detector, *FPI* Fabry-Perot interferometer, *FDML* Fourier domain mode locked, *OPO* optical parametric oscillator, *PCF* photonic-crystal fiber, *PD* photodetector, *RSOD* rapid scanning optical delay, *SLD* superluminescent diode

52.1.3.3 PAM/OCT with a Single Light Source

Using a single light source for PAM excitation and OCT imaging would have several advantages including increased portability and simpler co-registration and synchronization. The first demonstration of a single pulsed light source for PAM/OCT by Zhang et al. (2012) is promising but has some important limitations [7]. Because the same light source and delivery system were used, the images were laterally co-registered. However, the source operates in the visible light range ($\lambda_o = 580$ nm, $\Delta\lambda = 20$ nm), where exposure limits are lower than at near-infrared (NIR) wavelengths and there is shallower penetration into tissue. In addition, the spectrum was very noisy and the quality of the OCT images suffered as a result. The source was also not operated at the maximum pulse repetition rate (30 kHz) but instead at 5 kHz. Considering these factors and the limited source bandwidth and axial resolution, this solution is suboptimal for most biological applications of OCT.

Lee et al. have presented PAM/OCT imaging of black and white human hair using a single nanosecond-pulsed supercontinuum NIR laser source [9]. The output range was 600–1,700 nm, though the spectrometer limited detection to between 650 and 900 nm, with the dominant wavelength band beyond 1,064 nm, making this wavelength range more appropriate for OCT imaging. However, many endogenous molecules that would provide spectroscopic contrast for PA imaging, such as hemoglobin, do not exhibit maximum absorb in this wavelength range. Furthermore, the forward mode configuration for PAM detection would limit any potential in vivo applications to thin samples, and the sample is translated mechanically, limiting the imaging speed.

52.1.3.4 Endoscopic Delivery

A step towards intraoperative PA and OCT imaging was made by Yang et al., who developed a miniaturized probe for endoscopic measurements of PAM/OCT signals along with conventional pulse-echo ultrasound [6]. The excitation pulse repetition rate was 15 Hz, which limited the speed of acquisition, but they presented sequential imaging of ex vivo of ovarian tissues at 740 nm with excitation energy of 1 mJ/pulse. The endoscope had a 5 mm diameter. Xi et al. also recently demonstrated PAM/OCT detection using a smaller endoscopic delivery probe with a diameter of 2.3 mm. Their system consisted of a low-frequency unfocused 10 Hz transducer with time-domain OCT detection at 1 kHz [10]. If scanning speed can be improved, these delivery systems may further extend the clinical utility of multimodal PA/OCT imaging.

52.1.3.5 All-Optical Detection

A major drawback to several of the multimodal approaches presented above – and the reason many of them have only been demonstrated in the mouse ear – is their forward mode detection configuration. Backward mode optical detection methods may eventually offer a more practical alternative with respect to clinical translation.

Noncontact photoacoustic sensing by optically probing tissue has recently been demonstrated [18–24]. These methods optically detect the displacement of tissue that occurs upon an acoustic wave reaching the surface. Especially promising for combination with OCT are approaches that use low-coherence interferometry (LCI) for

acoustic sensing. Wang et al. presented a method for PAM using homodyne LCI detection of surface displacement [24]. This approach, however, is very sensitive to ambient vibrations, which can change the optical path length more than the path length change that is expected from a PA disturbance. To account for this, the authors synchronized acquisition to the point at which the interferometer is most sensitive. One drawback to their approach is that their configuration only allows for combination with time-domain OCT detection, limiting their acquisition speed. The approach by Blatter et al. demonstrated simultaneous PA/OCT imaging using phase-sensitive swept-source OCT, which could potentially be much faster [18]. Currently, however, their implementation is limited to mechanically scanning the sample.

The next section (Sect. 52.2) describes the transduction of PA signals using an optical detection mechanism based on an FPI sensor and its combination with OCT as presented by Zhang et al. in 2011 [25]. To date, this is the only method to have been applied for in vivo human imaging.

52.2 Multimodal All-Optical PAT and OCT Imaging with Fabry-Perot Sensor

Beard and colleagues first described the fundamental principles of backward mode ultrasonic detection using a FPI sensor with an interrogation laser in 2004 [26]. There are multiple advantages associated with this optical approach over conventional sensing techniques for multimodal imaging. The sensor:

- Is interrogated using a laser in backward mode configuration, which means it is not necessary for the sample to be very thin
- Can be designed to have a transmission window that allows for combination with OCT at 1,050 nm

This section describes sensor transduction of ultrasonic signals in the context of one implementation of a PAT system combined with a spectral-domain OCT system at 1,050 nm [8].

52.2.1 Optical PAT Signal Detection Using Fabry-Perot Polymer Film Sensor and Interrogation Laser

The functional unit of the FPI ultrasonic transducer consists of two dielectric optical coatings that form the mirrors of an interferometer and are separated by a polymeric film spacer (Fig. 52.1) [25]. The dielectric coatings are designed to allow for reflection or transmission wavelength bands that are optimized according to application, and the polymeric spacer thickness governs the range of bandwidths to be detected. The FPI is produced on an acrylic substrate that is angled to avoid interference from the interface of the FPI and the substrate surface, and the entire sensor is coated with a layer of Parylene C to protect it from physical damage and prevent water from entering the space between the FPI mirrors.

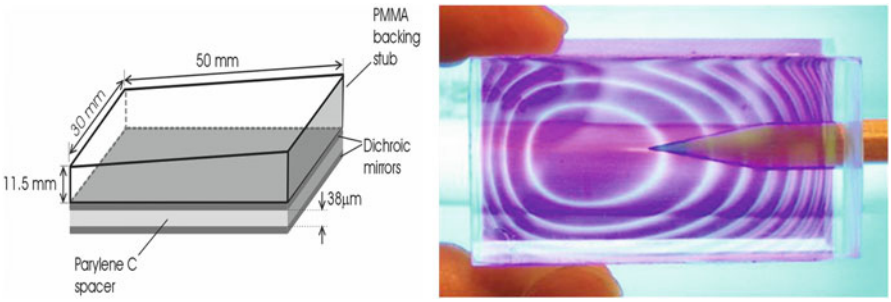

Fig. 52.1 (*Left*) Design of Fabry-Perot sensor; the active component of the sensor consists of a 38 μm polymer film spacer sandwiched between two dichroic mirrors forming an FPI. The sensor is on a wedged backing stub made of PMMA. (*Right*) Photograph of sensor under narrowband visible illumination demonstrating its transparent nature and FPI transmission fringes (Image reproduced with permission from Zhang E et al. [25])

The active side of the transducer is in contact with the sample, coupled with a small amount of water or transparent gel to ensure that acoustic waves propagating from tissue are incident upon it directly without passing through air. Stimulation of a photoacoustic wave is accomplished using nanosecond pulses from an excitation laser coupled into a multimode fiber that delivers unfocused illumination to the sample at a wavelength in which the dielectric coatings of the FPI are transmissive. Signal transduction occurs when an incident acoustic pressure wave changes the thickness of the polymer spacer, leading to a change in reflectivity of the sensor that is probed using a laser. This interrogation laser is a tunable continuous wave laser tuned to a wavelength in which the dielectric coatings are reflective; it is focused on the sensor surface. The laser is scanned in two dimensions across the FPI to allow for the acquisition of volumetric PA signals. Figure 52.2 provides a simplified illustration of the sensor, focused interrogation laser, and excitation light delivery via a multimode fiber.

52.2.1.1 Determining Optimal Bias Wavelength

The wavelength of interrogation that provides the most sensitivity for photoacoustic signal measurement – the optimal bias wavelength, λ_{opt} – varies from location to location on the sensor surface due to differences in thickness of the polymer film spacer that is vacuum-deposited onto the dielectric coatings during fabrication [25]. The main steps for determining λ_{opt} for each location of interest on the sensor can be summarized as follows:

1. Sweep the interrogation laser through a range greater than the free spectral wavelength range of the FPI while recording the reflected optical power with a photodiode; this provides the wavelength-dependent reflectivity interferometer transfer function (ITF), $R(\lambda)$.
2. Fit an Airy function to $R(\lambda)$.
3. Express $R(\lambda)$ as a function of phase and take derivative to obtain normalized phase sensitivity $S(\lambda)$.

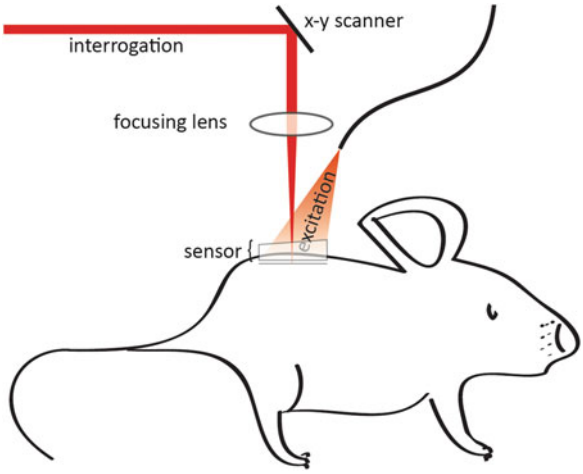

Fig. 52.2 Illustration of FPI sensing: excitation is accomplished via nanosecond-pulsed illumination using a multimode fiber, and the sensor is interrogated using a focused continuous wave laser beam. The sensor is placed in contact with the sample, coupled with a small amount of water or transparent gel so acoustic waves propagating from the sample are not attenuated in air

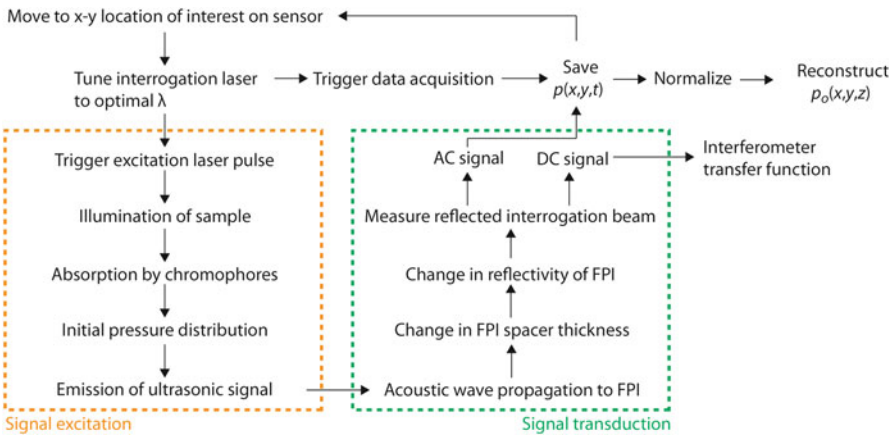

Fig. 52.3 Summary of steps for signal transduction using FPI

4. The maximum derivative of $S(\lambda)$ is considered the optimal bias wavelength (λ_{opt}).
5. Repeat steps 1–4 for every 2D point of interest on sensor.

52.2.1.2 Signal Transduction

The steps for signal excitation and transduction are summarized in Fig. 52.3. First, the interrogation laser is directed to the x-y location of interest on the sensor and tuned to the corresponding λ_{opt} for that location. This triggers both data acquisition and the firing of the excitation laser. Signal excitation results in the emission of broadband ultrasonic signals, which propagate to the FPI, modulating its thickness and, in turn, reflectivity. This change in reflected power is measured using a 50 MHz InGaAs photodiode-transimpedance amplifier that has AC- and DC-coupled output channels.

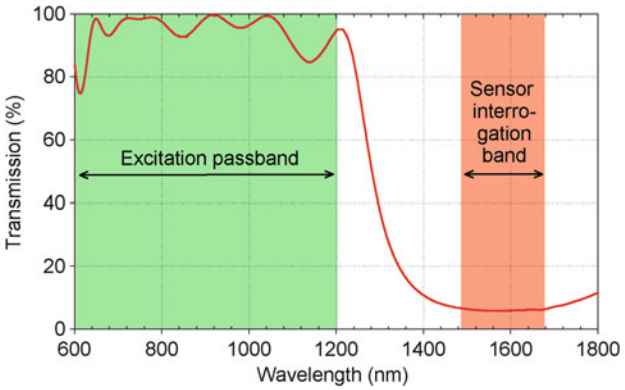

Fig. 52.4 Fabry-Perot sensor transmission characteristics; high transmission is observed between 600 and 1,200 nm for both excitation of photoacoustic signals and transmission of a 1,050 nm OCT source, and high reflectivity is achieved between 1,500 and 1,650 nm, for interrogation of the sensor by a 1,550 nm source (Image reproduced with permission from Zhang E et al. [25])

The DC output is digitized using an 8-bit analog-to-digital card (200 Ks/s); this channel is used to record the reflected optical power for the ITF acquisition as described in Sect. 52.2.1.1. The AC signal is digitized using an oscilloscope (300 MHz) and represents the time-varying optical power modulation that is caused directly by the photoacoustic pressure wave, $p(x,y,t)$. This signal is normalized to account for variations in interrogation laser power by dividing by the corresponding normalized phase sensitivity. Thus, when an acoustic signal modulates the thickness of the FPI, a phase shift is introduced and this is linearly converted to a modulation of optical power using the ITF. Time reversal and k-space reconstruction techniques are used to obtain the initial pressure distribution $p_o(x, y, z)$, which is directly proportional to energy absorbed [27].

52.2.1.3 PAT Sensor, Interrogation Laser, and Excitation Source

The sensor used herein consists of dielectric coatings used to form mirrors with greater than 95 % reflectivity between 1,500 and 1,650 nm and transmit light between 600 and 1,200 nm and a Parylene C spacer thickness of 20 μm to facilitate a frequency response on the order of tens of MHz (Fig. 52.4). The sensor has a -3 dB acoustic bandwidth of 39 MHz, and the free spectral range is 31.4 nm [25]. The reflectivity band was chosen such that a tunable 1,550 nm laser could be used for sensor interrogation. The interrogation laser is a tunable 1,550 nm continuous wave laser with an output range of 1,519–1,630 nm, wavelength resolution of 1 pm, output power of up to 10 mW, and settling time of ~50 ms (Thorlabs ECL5000DT).

The PAT signal excitation laser is a frequency-tripled 355 nm Nd:YAG (Newport Spectra-Physics) pumped optical parametric oscillator (OPO; GWU) with a tunable output range of 410–2,100 nm and wavelength-dependent output pulse energy of 12–36 mJ. The laser has ~8 ns pulses and a pulse repetition rate of 50 Hz. Light from the OPO is coupled into a 1.5-mm diameter multimode fiber and

delivered to tissue through the FPI sensor. Single pulses from the excitation laser are used at each location (no averaging takes place), so the 50 Hz repetition rate limits acquisition time to 20 ms per lateral scan location.

52.2.1.4 PAT Image Reconstruction

In tomographic photoacoustic imaging, signals are recorded as a function of lateral location on the sensor and time of arrival at the surface, $p(x,y,t)$. Thus, the initial pressure distribution, $p_o(x,y,z)$, must be reconstructed. This is accomplished using two different techniques: a fast *k*-space reconstruction algorithm and a slower time reversal approach. The former ignores frequency-dependent acoustic attenuation from soft tissue, while the latter is more computationally expensive but takes attenuation into account. The time reversal approach is thus better when looking at deeper structures, where acoustic waves have higher attenuation before reaching the FPI sensor. Additional details regarding specifics of reconstruction are available in references [27] and [28].

52.2.1.5 Combined PAT/OCT System

A schematic of the combined PAT/OCT system is shown in Fig. 52.5 [8]. As described above and demonstrated in Fig. 52.4, the Fabry-Perot sensor has a transmission band from 600 to 1,200 nm, making it amenable to OCT imaging using a 1,050 nm light source.

The light source used to obtain the OCT images presented in Sects. 52.2.2.1 and 52.2.2.2 is an amplified spontaneous emission (ASE) source (NP Photonics, Tucson, AZ) with a bandwidth of 70 nm and a center wavelength of 1,050 nm [29]. Light from the source is sent through an 80:20 fiber-based beam splitter to a free-space reference arm and to a sample arm that consists of a 2D galvanometer-driven scanner and focusing lens (Fig. 52.5). The OCT sample path is combined with the PAT interrogation path using a dichroic mirror. Backscattered light from the sample and reference arms is detected using a spectrometer in Czerny-Turner configuration and digital line InGaAs array (Goodrich SUI LDH1, Princeton, NJ) with 1,024 pixels at an A-scan sampling rate of 47 kHz. The raw spectral data is inverse Fourier transformed to obtain individual A-scan intensity profiles, and each B-scan consists of 512 A-scans separated by 12 μm. The axial and lateral resolutions of this OCT system are estimated to be 8 and 18 μm, respectively.

Light from the 1,550 nm PAT interrogation laser described in Sect. 52.2.1.3 is directed to the FPI from the source through a circulator and the common optical path (dichroic mirror, galvos, and focusing lens), and reflected light is sampled using the 50 MHz InGaAs photodiode-transimpedance amplifier and digitizing oscilloscope as detailed in Sect. 52.2.1.2. The lateral resolution of this PAT system was previously estimated to be ~66 μm at a depth of 5 mm, and it has an axial resolution of ~20 μm as determined primarily by the bandwidth of the sensor [25].

52.2.1.6 Alignment of PAT and OCT Images

To prevent a strong back reflection from the FPI sensor, which will saturate the InGaAs array, it is necessary to insert a glass wedge between the FPI sensor and

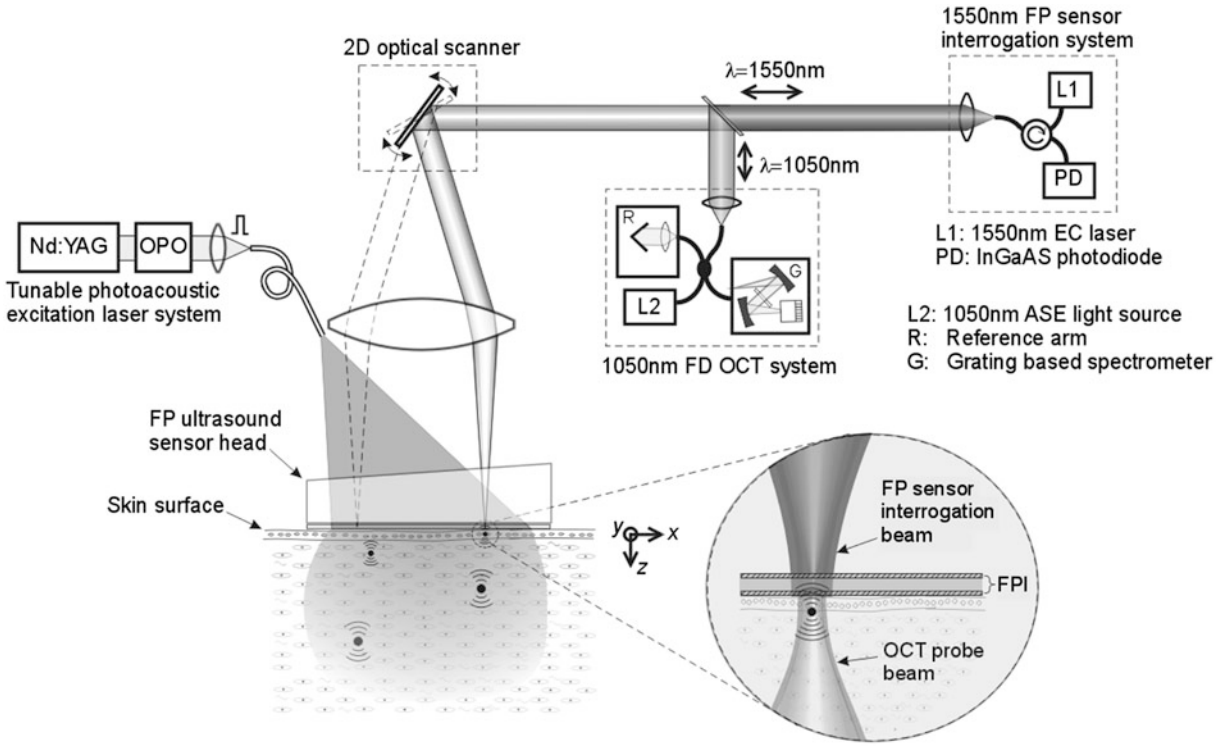

Fig. 52.5 Schematic of multimodal PAT/OCT imaging system. PAT excitation is achieved using a tunable Nd:YAG pumped OPO with nanosecond pulses, and the Fabry-Perot sensor is interrogated using a 1,550 nm laser focused on the interferometer surface. OCT images are acquired using a 1,050 nm source and spectrometer-based frequency domain detection. The beams of the 1,550 nm PAT interrogation laser and 1,050 nm OCT laser are combined using a dichroic mirror, and the same galvanometer-driven mirrors are used for 2D scanning of both systems (Image reproduced with permission from Zhang E et al. [8])

focusing lens while acquiring OCT images. This wedge is not in place when acquiring PAT images, so the PAT and OCT images are offset laterally from one another. A scattering and absorbing grid target is imaged by both modalities to calculate this offset; the offset is used to align images after acquisition. In addition to the lateral offset, there are substantial differences in lateral and axial step size between OCT and PAT images, with PAT images less densely sampled. Thus, PAT images are interpolated prior to registering the images.

52.2.2 Mouse Skin Imaging

One advantage to acquiring OCT and PAT signals from overlapping or identical regions of interest is that OCT gives PAT images context in the form of high-resolution structural information. Similarly, highly absorbing structures that appear as shadows in OCT images (e.g., blood vessels) can be observed with PA imaging.

A combination of PAT/OCT image acquired from the flank of a living anesthetized 5-week-old hairless female mouse placed on the FPI sensor, flank-side down, can be seen in Fig. 52.6. OCT and PAT images were acquired sequentially. Volumetric OCT images were acquired in 24 s and covered a 12.3 mm × 13 mm region with a lateral step size of 12.5 μm between A-scans, with a depth sampling interval equal to the axial resolution ($\Delta z = 6$ μm). PAT volumetric images were obtained in 7 min and covered the same region as OCT images but had a step size of 100 μm between A-scans; an excitation wavelength of 670 nm and a fluence of 14 mJ/cm^2 were used. The PAT axial sampling step size depended on the temporal sampling interval, which in this case was 20 ns. Assuming a speed of sound in tissue of 1,500 m/s, this corresponds to a depth spacing of $\Delta z = 30$ μm. The fast k-space reconstruction algorithm [28] was used to generate the PAT image.

Figure 52.6a shows corresponding single vertical OCT (gray scale) and PAT (red) cross sections. The OCT image provides detailed morphology of the skin including the dermis, panniculus carnosus, hypodermis, and skeletal muscle, while blood vessels are observed in the PAT images. Maximum intensity projections (MIP) from OCT, PAT, and OCT/PAT are presented in Fig. 52.6b–d and clearly show the differences in contrast mechanisms between the two modalities, with blood in vessels being highly absorbing and structures within the skin being highly scattering. Volumetric renderings (Fig. 52.6e–h) further illustrate the absorption-based contrast of PAT and scattering-based contrast of OCT.

52.2.3 Preclinical Imaging of Human Skin

The first demonstration of a combined PAT/OCT system in a human subject in vivo can be seen in Fig. 52.7. The hand of a healthy volunteer was placed on the sensor and held stationary for 4.6 min during the acquisition of a PAT image covering a 14 mm × 14 mm region of the palm with lateral distance of 120 μm between A-scans. As with the mouse imaging, depth sampling again took place in steps of

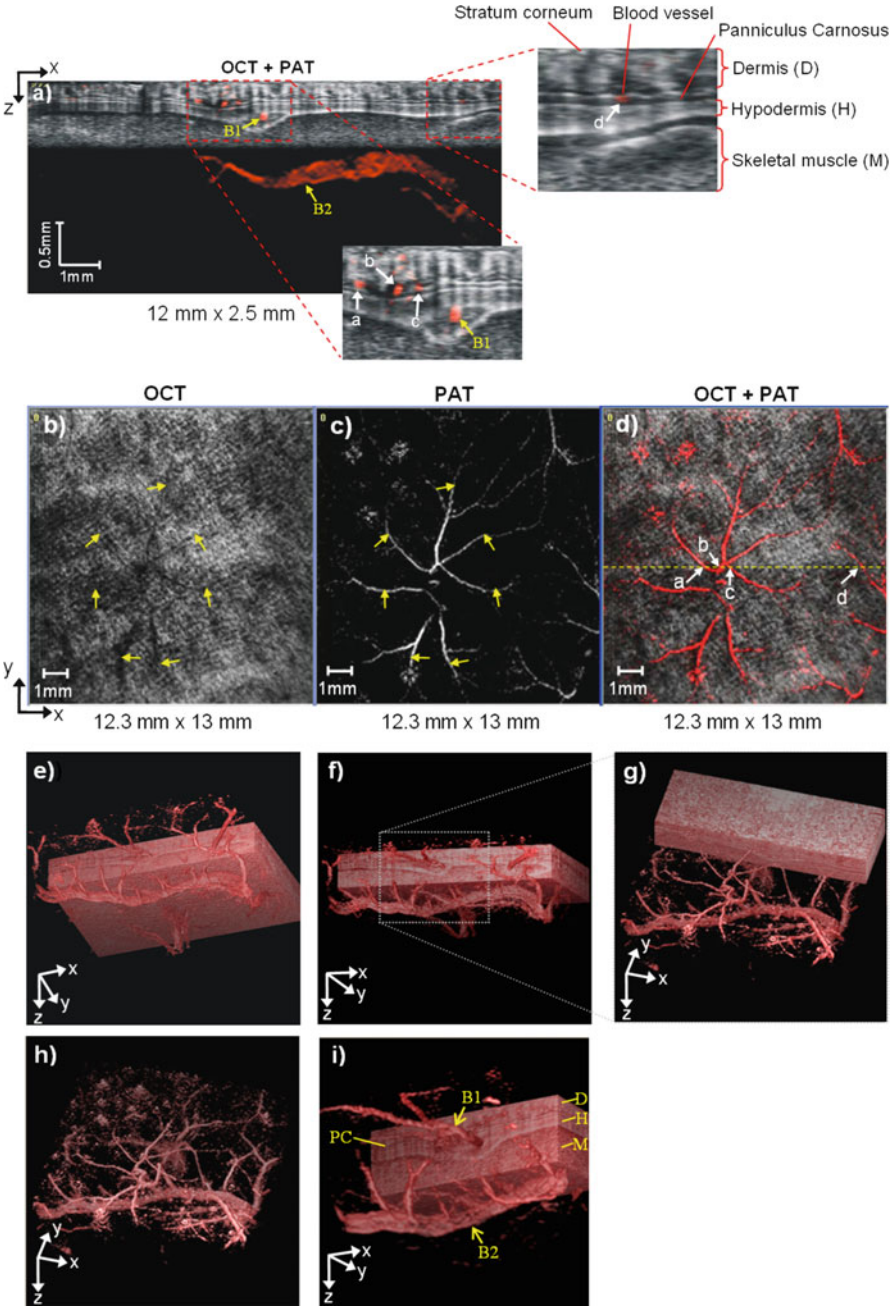

Fig. 52.6 In vivo PAT/OCT images of the mouse skin. (**a**) Fused PAT/OCT cross-sectional vertical (x–z) slice. The OCT image (*gray scale*) shows the layered skin morphology while the PAT image (*red*) shows several superficial blood vessels within the dermis, panniculus carnosus,

$\Delta z = 30$ μm (20 ns sampling interval). The excitation laser was tuned to 672 nm, and a beam diameter of 2 cm and fluence of 14 mJ/cm^2 were used. The PAT image was followed by an OCT image covering an area of 12.8 mm × 12.8 mm in steps of 12.5 μm between A-scans and took a total of 24 s.

A co-registered PAT and OCT cross section is shown in Fig. 52.7a. The stratum corneum, epidermal, and papillary dermal layers are evident in the OCT cross section, while subcutaneous blood vessels and dermal vessels are present in PAT images. Some absorption in the epidermis can be seen in PAT images as well; this is likely caused by melanin – a strong absorber – distributed throughout the layer. As with the mouse images, the OCT and PAT MIPs (Fig. 52.7b–d) demonstrate the difference in contrast mechanisms between the two modalities. Interestingly, many of the vessels that can be discerned using PAT are at a depth greater than the maximum penetration depth of OCT; this is especially clear in the volume renderings (Fig. 52.7e–g).

52.3 Limitations, Future Directions, and Potential Applications

52.3.1 Limitations and Future Directions for FPI PA Sensing

One major limitation to the current implementation of tomographic measurements with the FPI sensor is that imaging time depends on the excitation source. Unfortunately, sources that provide high enough pulse energy at multiple wavelengths for spectroscopic measurements, such as optical parametric oscillators, are expensive and impractical when it comes to large-scale clinical implementation where stable, easy-to-use lasers are necessary. While imaging times on the order of several minutes may be possible in some pathology with cooperative patients, scanning rates on par with OCT sources (e.g., several kHz to MHz) are desirable.

In addition to the prohibitively long PAT scan time, the slow excitation laser makes truly simultaneous imaging difficult. While one solution is to average multiple OCT A-scans in the time it takes to acquire one PAT A-scan, another is to intentionally slow down OCT acquisition to match that of PAT acquisition. Neither of these offers an ideal solution, though, since motion artifacts from the

Fig. 52.6 (continued) hypodermis (*B1*), and the skeletal muscle (*B2*). The lower inset shows an expanded view of the dermis and hypodermis and a cluster of three blood vessels (labeled *a*, *b*, and *c*), which form part of the vascular structure that can be seen in (**b–d**). The upper inset shows an expanded view of the skin layers and a blood vessel (labeled *d*), which can also be seen in (**d**). (**b**) OCT (x–y) MIP image. The *yellow arrows* indicate the location of blood vessels forming a star-shaped vascular structure. (**c**) PAT (x–y) MIP image. (**d**) Fused PAT/OCT (x–y) MIP image. The *horizontal dotted line* indicates the location of the x–z slice depicted in (**a**). The vessels labeled *a–d* correspond to those labeled in the two insets in (**a**). The (x–y) MIPs shown in (**b–d**) were computed over the depth range: $0.24 < z < 0.6$ mm. (**e–h**) Volume rendered representations of fused PAT/OCT image data at different viewing angles with the OCT image successively resected. The rendered image volume is 12 mm × 12 mm × 2 mm. (**i**) Expanded view of (**f**) over a 6 mm × 6 mm × 2 mm volume showing blood vessels *B1* and *B2*, dermis (*D*), panniculus carnosus (*PC*), hypodermis (*H*), and skeletal muscle (*M*) as identified in (**a**) (Image reproduced with permission from Zhang E et al. [8])

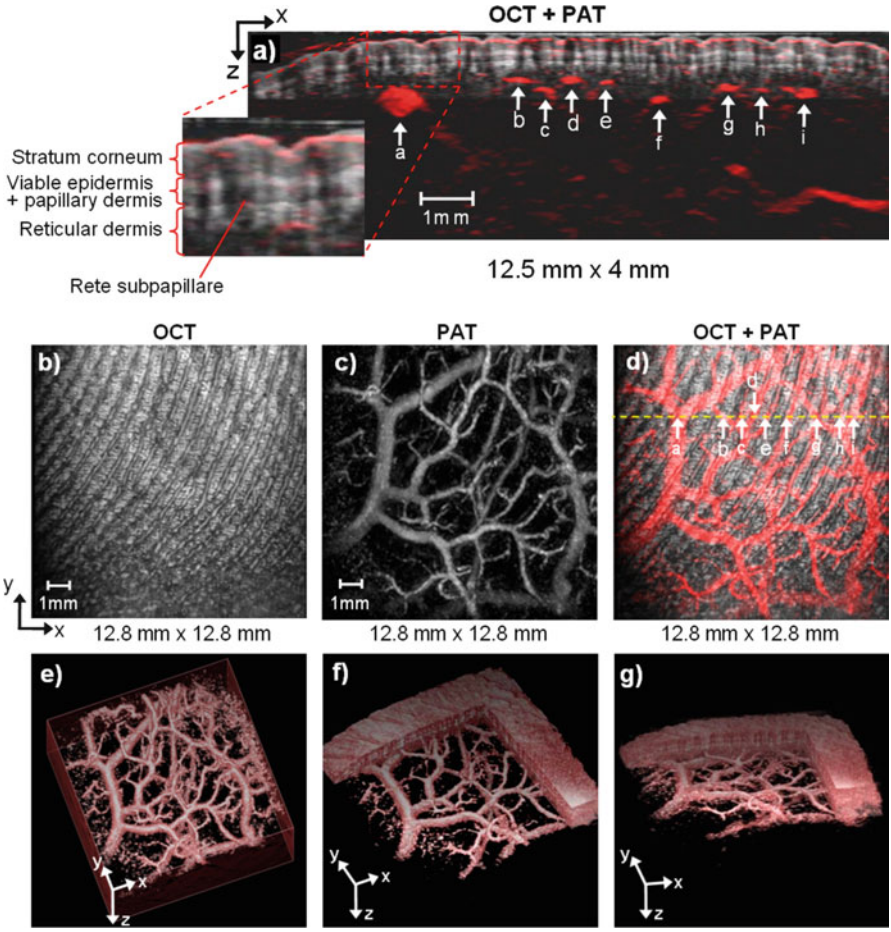

Fig. 52.7 In vivo OCT and PAT images of the human palm. (**a**) Fused PAT/OCT vertical (x–z) slice. (**b**) OCT (x–y) MIP image computed over the depth range $0 < z < 1.2$ mm. (**c**) PAT (x–y) MIP image computed over the depth range $0 < z < 5$ mm. (**d**) Fused PAT/OCT (x–y) MIP image. The *horizontal dotted line* indicates the location of the x–z slice shown in (**a**), with corresponding locations of blood vessels indicated by white arrows. (**e**–**g**) Volume rendered representations of fused PAT/OCT image data at different viewing angles. The rendered image volume is 14 mm × 14 mm × 5 mm (Image reproduced with permission from Zhang E et al. [8])

subject could easily result in a distorted/blurred OCT image. Until the speed of PAT excitation sources catches up with that of OCT, an interim solution would be to acquire from multiple points on the FPI surface in parallel using multiple interrogation beams. Another alternative would be to more seamlessly acquire the OCT and PAT images in sequence. This would mean eliminating the glass wedge that is placed on the sensor during OCT scanning, and would be possible if the incident angle of the OCT beam could be offset in the optical path.

Further development of the FPI sensor would also improve its utility in a clinical setting. For example, extending the transmission window below 600 nm would enable higher SNR of PA waves generated from hemoglobin and deoxyhemoglobin. Similarly, extending the transmission window past 1,200 nm would enable OCT imaging with 1,300 nm sources and hence deeper penetration into tissue. Finally, using the FPI sensor with a focused excitation source for microscopy mode imaging to provide comparable resolution and depth range to OCT is a logical next step, since significantly faster light sources are available.

52.3.2 Applications

Multimodal PA/OCT imaging has the potential to impact a broad range of clinical specialties by providing access to absorption-based contrast millimeters to centimeters in depth with 1–2 mm of scattering-based surface structural detail. As demonstrated above, in tomographic mode, deep absorbers can be visualized, while the imaging depths for microscopy mode PA imaging and OCT are comparable. Using endogenous absorbers such as deoxygenated and oxygenated hemoglobin for spectroscopic PA imaging will allow for even better visualization of blood vessels – a feature from which many fields could benefit.

Cancer imaging is an obvious application for this multimodal imaging platform, where hemoglobin would provide endogenous contrast for viewing tumor vasculature and OCT could provide corresponding superficial structural information. This would assist clinicians in planning and performing tumor resection, facilitate longitudinal evaluation of tumor growth, and help determine the effectiveness of treatment. Another endogenous absorber, melanin, could also be exploited for PA contrast in diagnosis and monitoring of melanoma when shorter excitation wavelengths are used.

In ophthalmology, where OCT imaging of the retina is already well established and part of routine clinical care, the addition of PA imaging could provide functional information in addition to structure. Assessment of the status of retinal vessels should improve the diagnosis of diseases such as glaucoma and wet age-related macular degeneration. One major challenge in building a system for retinal use, however, will be delivering enough energy to produce a photoacoustic signal while remaining within safety limitations for the eye.

After endoscopic delivery systems are further refined and tested in vivo, this would extend possible applications of PA/OCT imaging to include intraoperative use. In addition, the ability to access absorption and scattering properties of tissue using a multimodal combination of OCT and PA imaging may be valuable not only in the clinic but for studying preclinical models of disease and evaluating treatment success for novel therapeutic agents. The use of an FPI sensor to monitor tumor vascularization and treatment using PAT has already been demonstrated in animals [30], and the addition of OCT for structural information or even Doppler measurements might improve delineation of tumors for longitudinal monitoring.

Other animal models, such as transgenic zebrafish lines that express absorbing fluorochromes in specific tissue [31], should also be interesting to observe with a combined PA/OCT system.

While OCT has evolved to the point where it is regularly used in clinical practice, the widespread implementation of PA – and therefore multimodal PA/OCT – cannot occur until suitable light sources are developed. Sources for OCT are suitable for clinical application in terms of bandwidth, power, and price, but the same is not true for PA sources. As soon as stable nanosecond-pulsed lasers with high repetition rates and high output energy at multiple wavelengths are available, widespread testing and use of this multimodal platform in both a preclinical and clinical setting should be possible.

References

1. X. Cai, Y. Zhang, L. Li, S.-W. Choi, M.R. Macewan, J. Yao, C. Kim, Y. Xia, L.V. Wang, Investigation of neovascularization in three-dimensional porous scaffolds in vivo by a combination of multiscale photoacoustic microscopy and optical coherence tomography. Tissue Eng. Part C Methods **19**, 196–204 (2013)
2. S. Jiao, Z. Xie, H.F. Zhang, C.A. Puliafito, Simultaneous multimodal imaging with integrated photoacoustic microscopy and optical coherence tomography. Opt. Lett. **34**, 2961–2963 (2009)
3. L. Li, K. Maslov, G. Ku, L.V. Wang, Three-dimensional combined photoacoustic and optical coherence microscopy for in vivo microcirculation studies. Opt. Express **17**, 16450–16455 (2009)
4. T. Liu, Q. Wei, J. Wang, S. Jiao, H.F. Zhang, Combined photoacoustic microscopy and optical coherence tomography can measure metabolic rate of oxygen. Biomed. Opt. Express **2**, 1359–1365 (2011)
5. W. Song, Q. Wei, T. Liu, D. Kuai, J.M. Burke, S. Jiao, H.F. Zhang, Integrating photoacoustic ophthalmoscopy with scanning laser ophthalmoscopy, optical coherence tomography, and fluorescein angiography for a multimodal retinal imaging platform. J. Biomed. Opt. **17**, 061206 (2012)
6. Y. Yang, X. Li, T. Wang, P.D. Kumavor, A. Aguirre, K.K. Shung, Q. Zhou, M. Sanders, M. Brewer, Q. Zhu, Integrated optical coherence tomography, ultrasound and photoacoustic imaging for ovarian tissue characterization. Biomed. Opt. Express **2**, 2551–2561 (2011)
7. X. Zhang, H.F. Zhang, S. Jiao, Optical coherence photoacoustic microscopy: accomplishing optical coherence tomography and photoacoustic microscopy with a single light source. J. Biomed. Opt. **17**, 030502 (2012)
8. E.Z. Zhang, B. Povazay, J. Laufer, A. Alex, B. Hofer, B. Pedley, C. Glittenberg, B. Treeby, B. Cox, P. Beard, W. Drexler, Multimodal photoacoustic and optical coherence tomography scanner using an all optical detection scheme for 3D morphological skin imaging. Biomed. Opt. Express **2**, 2202–2215 (2011)
9. C. Lee, S. Han, S. Kim, M. Jeon, M.Y. Jeon, C. Kim, J. Kim, Combined photoacoustic and optical coherence tomography using a single near-infrared supercontinuum laser source. Appl. Opt **52**, 1824–1828 (2013)
10. L. Xi, C. Duan, H. Xie, H. Jiang, Miniature probe combining optical-resolution photoacoustic microscopy and optical coherence tomography for in vivo microcirculation study. Appl. Opt **52**, 1928–1931 (2013)
11. L.V. Wang, Tutorial on photoacoustic microscopy and computed tomography. IEEE J. Selected Top. Quantum Electron. **14**, 171–179 (2008)

12. C. Zhang, K. Maslov, J. Yao, L.V. Wang, In vivo photoacoustic microscopy with 7.6-μm axial resolution using a commercial 125-MHz ultrasonic transducer. J. Biomed. Opt. **17**, 116016 (2012)
13. C. Zhang, K. Maslov, S. Hu, R. Chen, Q. Zhou, K.K. Shung, L.V. Wang, Reflection-mode submicron-resolution in vivo photoacoustic microscopy. J. Biomed. Opt. **17**, 020501 (2012)
14. R.A. Kruger, R.B. Lam, D.R. Reinecke, S.P. Del Rio, R.P. Doyle, Photoacoustic angiography of the breast. Med. Phys. **37**, 6096–6100 (2010)
15. H.F. Zhang, K. Maslov, G. Stoica, L.V. Wang, Functional photoacoustic microscopy for high-resolution and noninvasive in vivo imaging. Nat. Biotechnol. **24**, 848–851 (2006)
16. J. Chen, M. Wang, J.-C. Cheng, Y.-H. Wang, P.-C. Li, X. Cheng, A photoacoustic imager with light illumination through an infrared-transparent silicon CMUT array. IEEE Trans. Ultrason. Ferroelectr. Freq. Control **59**, 766–775 (2012)
17. S. Jiao, M. Jiang, J. Hu, A. Fawzi, Q. Zhou, K.K. Shung, C.A. Puliafito, H.F. Zhang, Photoacoustic ophthalmoscopy for in vivo retinal imaging. Opt. Express **18**, 3967–72 (2010)
18. C. Blatter, B. Grajciar, P. Zou, W. Wieser, A.-J. Verhoef, R. Huber, R.A. Leitgeb, Intrasweep phase-sensitive optical coherence tomography for noncontact optical photoacoustic imaging. Opt. Lett. **37**, 4368–4370 (2012)
19. T. Berer, A. Hochreiner, S. Zamiri, P. Burgholzer, Remote photoacoustic imaging on solid material using a two-wave mixing interferometer. Opt. Lett. **35**, 4151–4153 (2010)
20. B.F. Pouet, R.K. Ing, S. Krishnaswamy, D. Royer, Heterodyne interferometer with two-wave mixing in photorefractive crystals for ultrasound detection on rough surfaces. Appl. Phys. Lett. **69**, 3782 (1996)
21. M. Paul, B. Betz, W. Arnold, Interferometric detection of ultrasound at rough surfaces using optical phase conjugation. Appl. Phys. Lett. **50**, 1569 (1987)
22. S.A. Carp, A. Guerra, S.Q. Duque, V. Venugopalan, Optoacoustic imaging using interferometric measurement of surface displacement. Appl. Phys. Lett. **85**, 5772 (2004)
23. G. Paltauf, R. Nuster, M. Haltmeier, P. Burgholzer, Photoacoustic tomography using a Mach-Zehnder interferometer as an acoustic line detector. Appl. Opt. **46**, 3352 (2007)
24. Y. Wang, C. Li, R.K. Wang, Noncontact photoacoustic imaging achieved by using a low-coherence interferometer as the acoustic detector. Opt. Lett. **36**, 3975–3977 (2011)
25. E. Zhang, J. Laufer, P. Beard, Backward-mode multiwavelength photoacoustic scanner using a planar Fabry-Perot polymer film ultrasound sensor for high-resolution three-dimensional imaging of biological tissues. Appl. Opt. **47**, 561–577 (2008)
26. P. Beard, E. Z. Zhang, B. Cox, Transparent Fabry Perot polymer film ultrasound array for backward-mode photoacoustic imaging. Proc. SPIE **5320**, 230–237 (n.d.)
27. B.E. Treeby, E.Z. Zhang, B.T. Cox, Photoacoustic tomography in absorbing acoustic media using time reversal. Inverse Probl. **26**, 115003 (2010)
28. K.P. Köstli, M. Frenz, H. Bebie, H.P. Weber, Temporal backward projection of optoacoustic pressure transients using fourier transform methods. Phys. Med. Biol. **46**, 1863–1872 (2001)
29. A. Alex, B. Povazay, B. Hofer, S. Popov, C. Glittenberg, S. Binder, W. Drexler, Multispectral in vivo three-dimensional optical coherence tomography of human skin. J. Biomed. Opt. **15**, 026025 (2010)
30. J. Laufer, P. Johnson, E. Zhang, B. Treeby, B. Cox, B. Pedley, P. Beard, In vivo preclinical photoacoustic imaging of tumor vasculature development and therapy. J. Biomed. Opt. **17**, 056016 (2012)
31. R. Ma, A. Taruttis, V. Ntziachristos, D. Razansky, Multispectral optoacoustic tomography (MSOT) scanner for whole-body small animal imaging. Opt. Express **17**, 21414–21426 (2009)

Multi-modal Endoscopy: OCT and Fluorescence

53

Jessica Mavadia-Shukla, Jiefeng F. Xi, and Xingde D. Li

Keywords.
Optical Coherence Tomography (OCT) • Fourier-domain OCT (FD-OCT) • Fluorescence • Two-photon Excitation • Endoscope • Dual-modal Endoscopy

53.1 Introduction

53.1.1 Optical Coherence Tomography

Optical coherence tomography (OCT) is a biomedical imaging modality based on the technique of low-coherence interferometry. Although it is usually analogous to ultrasound imaging, the millimeter range echo time delay is too small to be directly measured due to the celerity of light. One uses a broadband light source and the interference between two arms in a low-coherence interferometer, which provides a coherence gate and depth-resolved information. The depth (axial) resolution is inversely proportional to the spectral bandwidth of the light source and ranges from 1 to 15 μm in most OCT systems. The reference arm in an OCT system also provides heterodyne (or homodyne) gain to the weak backscattered light from biological sample, offering OCT the most significant detection sensitivity (i.e., 100–120 dB). The imaging penetration depth of OCT can often reach 2–3 mm in most highly scattering biological tissues when using a near-infrared (NIR) wavelength from 800 to 1,300 nm. In short, OCT fills a gap between the scales of high-frequency ultrasound and confocal microscopy, providing better resolution than the former as well as deeper penetration than the latter.

Recent development in Fourier-domain optical coherence tomography (FD-OCT) technology has significantly improved the imaging speed. It has been reported that an

J. Mavadia-Shukla • J.F. Xi • X.D. Li (✉)
Department of Biomedical Engineering, Johns Hopkins University, Baltimore, MD, USA
e-mail: xingde@jhu.edu

© Springer International Publishing Switzerland 2015

W. Drexler, J.G. Fujimoto (eds.), *Optical Coherence Tomography*,
DOI 10.1007/978-3-319-06419-2_54

A-scan rate from tens of kHz to over 1 MHz can be achieved [1–5]. Meanwhile, efforts have been devoted to developing OCT imaging probes to enable imaging of internal organs. Flexible fiber-optically based imaging probes have been integrated with high-speed FD-OCT in a wide range of medical instruments such as endoscopes, catheters, etc., to achieve real-time, even three-dimensional OCT imaging of internal organs [6–12].

53.1.2 Fluorescence

Fluorescence is the process by which light is emitted by a stimulated molecule or fluorophore when the excited electron returns to ground state. This phenomenon has been utilized for many years as a research tool and has evolved to become a standard imaging modality in a variety of fields such as biology, biochemistry, and medicine. Fluorescence can be quantified through various means such as fluorescence excitation and emission spectroscopy, fluorescence lifetime, fluorophore concentration, and quantum yield. These parameters can be sensitive to the local biochemical or physiological environment of the fluorophores and vary between pathologic and normal tissues, offering specific contrast for diagnosis. In addition to a variety of exogenous fluorophores, there are quite a few endogenous fluorophores in biological tissues including nicotinamide adenine dinucleotide (NADH) and flavin adenine dinucleotide (FAD) which are directly related to cellular metabolism, while others are directly related to tissue structures [13].

Fluorophores can be excited by one photon absorption or simultaneous absorption of multiple photons. In case of two-photon excited fluorescence (TPEF) [14], two photons team up within a small time window (attosecond) and excite a molecule. Practically, photons of the same energy are used, though theoretically any combination of photons that provide the necessary energy difference can be used. In order to provide the necessary conditions to enhance the probability of TPEF, photons are usually confined temporally, though the use of pulsed light sources, and spatially, with moderate to high numerical aperture (NA) optics [15]. The fluorescence signal is proportional to the square of the excitation intensity. Thus, TPF effectively occurs within the tight focal volume (corresponding to high excitation photon density), which intrinsically provides depth-resolved information compared to single-photon excited fluorescence.

53.1.3 Complementary Nature of OCT and Fluorescence Imaging

OCT is capable of visualizing micron-scale tissue structural morphologies with the imaging contrast predominantly sensitive to the scattering property of tissues. Fluorescence imaging techniques such as confocal or two-photon excitation fluorescence (TPEF) are able to provide depth-resolved submicron-scale images with the imaging contrast coming from exogenous or endogenous fluorophores, thus providing molecular information which cannot be obtained by OCT. The two complementary

imaging modalities provide important yet different optical information based on unique contrast mechanisms. There is, hence, a strong motivation for developing integrated platforms for performing both OCT and fluorescence imaging. Furthermore, this combination has proven effective in visualizing morphology and fluorophore distribution in several benchtop systems [16–21].

53.2 Instrumentation Design

53.2.1 Dual-Modality OCT and Single-Photon Fluorescence Endoscopy

The instrumentation design of such a dual-modality endoscope and system requires great consideration of several factors such as the method by which light will be combined, separated, and how scanning will be performed endoscopically to conduct real-time imaging. We will address these considerations in the following sections.

In order to simultaneously perform OCT and single-photon fluorescence imaging, we integrated both systems into a dual-modality imaging platform. The integrated imaging platform consists of two modules that are combined in the OCT sample arm through a dual-modal endoscope and several customized fiber-optic components. We will start with the endoscope design and the system-level integration will be discussed later in Sect. 53.2.1.2.

53.2.1.1 Endoscope Design

A few other groups have also designed multimodal imaging catheters [22, 23]; however, here, we will focus primarily on our design. We chose to implement an endoscope based upon a single fiber, since this design benefits from many advantages such as the ability to use the conventional scanning mechanisms (scanning with a proximally located fiber-optic rotary joint or with a distally located miniature motor), along with a pull-back mechanism, to provide 3D volumetric luminal imaging and is still able to maintain an overall compact size of the probe [24].

Some of the associated challenges with a single-fiber design, for example, are how to provide single-mode transmission for OCT wavelengths while providing high-efficiency multimode collection at fluorescence emission wavelengths and how to effectively separate OCT source light and fluorescence excitation light from OCT backscattered light and fluorescence emission light. These requirements were satisfied through the use of a custom dual-clad fiber (DCF) whose dimensions were a 9 μm core, 180 μm large inner cladding, and 200 μm outer cladding. The core of the DCF is able to provide single-mode transmission at OCT wavelengths while guiding fluorescence excitation in low-order mode. During recollection of the signal, the large inner cladding can be utilized to collect more fluorescence emission compared to the much smaller core, while the backscattered OCT light travels through both the core and the inner cladding of the DCF. In this way, we are able to satisfy the requirements of sending and receiving both OCT and fluorescence light to and from the sample.

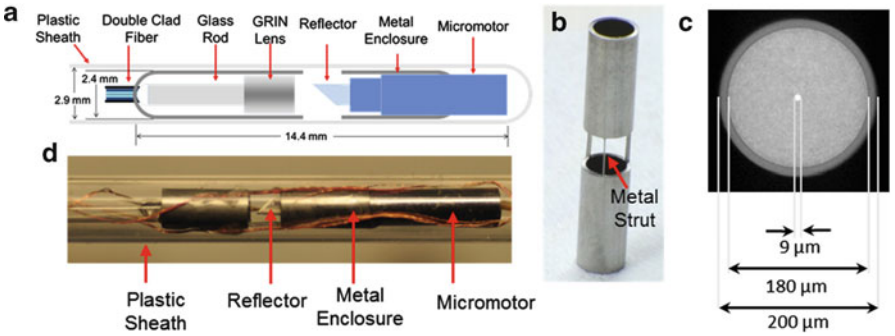

Fig. 53.1 (**a**) Schematic of distal end of the dual-modal endoscope design. (**b**) Photograph of a precision-cut metal enclosure (of an outer diameter 2.4 mm) with minimal beam blockage (i.e., less than 5 %). (**c**) A cross-sectional photograph of the custom dual-clad fiber, with dimensions labeled (9 µm core, 180 µm large inner cladding, and 200 µm outer cladding). (**d**) A photograph of the constructed endoscope of an overall diameter of 2.9 mm including the housing transparent sheath (Figure reprinted with permission from *Biomedical Optics Express*, Optical Society of America)

Though one of the advantages of a single-fiber approach is the ability to implement a traditional scanning mechanism, there are additional considerations for the choice of scanning mechanism due to the use of DCF in the endoscope. In principle, a proximal scanning mechanism such as a fiber-optic rotary joint can be used; however a custom rotary joint with a DCF needs to be fabricated. This approach is challenging because the rotary joint requires extremely precise alignment over a 360° rotation to prevent backscattered OCT light traveling in the inner cladding of the endoscope from being coupled into the single-mode fiber in the interferometer. Due to the different optical path length that OCT backscattered light in the inner cladding will experience from the backscattered light traveling through the core, the OCT image quality would be significantly compromised. Thus, we decided to implement a distally located miniature motor incorporated into the endoscope design with an off-the-shelf 1.9 mm diameter DC micromotor.

The overall endoscope optics design was similar to those published in earlier papers [11, 25, 26]. We used a glass rod after the DCF to expand the beam prior to focusing with a gradient index (GRIN) lens as shown in Fig. 53.1a. The key to this assembly was in the additional care taken to align, center, and stabilize the fiber and lens assembly with the micromotor and microreflector. In order to accomplish this, a custom metal enclosure was fabricated with three windows separated by ultrathin metal struts (~127 µm wide). This metal enclosure, as shown in Fig. 53.1b, provided sufficient mechanical stability while minimizing blockage to the imaging beam (only 5 % of the view blocked over 360°). In addition, the microreflector attached to the micromotor was positioned carefully in the center of the metal enclosure window so that the beam was able to be deflected 90° by the microreflector.

The overall working distance of this endoscope, as defined as the distance between the focal point and the outer surface of the metal enclosure, is governed

by the distance between the GRIN lens and the microreflector. The working distance was measured to be 1.9 mm and the lateral resolution was ~13.7 μm. The distal end of the endoscope has an overall diameter of 2.4 mm with a rigid length of 14.4 mm. Furthermore, for practical use, the entire endoscope was enclosed in an off-the-shelf transparent plastic sheath (outer diameter 2.9 mm) as shown in Fig. 53.1c. We were able to easily adjust the beam focus outside of the transparent sheath by tuning the distance between the microreflector and fiber-lens assembly, and the final beam focus was set at 1.6 mm outside of the sheath.

53.2.1.2 System Design

Thus far, we have discussed the endoscope design that enables the dual-modality OCT and fluorescence imaging; however, some of the challenges in the implementation of this imaging system are in how to combine and separate of light from two individual imaging modalities. The OCT module consists of a swept-source which is a home-built 40 kHz Fourier-domain mode-locking (FDML) fiber laser operating at a center wavelength of 1,305 nm with a 3 dB spectral bandwidth of ~140 nm. The OCT module also includes a Mach-Zehnder interferometer (MZI) to generate a calibration signal and a dual-balanced detector is utilized. The fluorescence imaging module consists of an argon ion laser at 488 nm for excitation and a photomultiplier tube (PMT) for detection.

There are a few methods by which to combine two light sources through free-space optics, a fiber-optic coupler or other fiber-optic devices. Using free-space optics is the most straightforward method, and this method has been widely used in benchtop systems. For endoscopy, this method proves to be bulky with a large footprint and is not portable enough to be used for clinical or animal imaging. For this reason, a fiber-optic approach is favored. In this case, since the OCT backscattered light will go through the coupling device, it is important to maintain a low roundtrip loss. We used a wavelength division multiplexer (WDM) which works at both the near infrared OCT source wavelengths and visible fluorescence excitation wavelengths, shown in Fig. 53.2.

The WDM allowed us to obtain a minimal insertion loss of 0.5 dB for OCT, and although the efficiency of transmitting fluorescence excitation was sub-optimal, we were able to obtain an ~60 % efficiency. This efficiency allowed us to have 3-mW fluorescence excitation light incident on the sample which was sufficient for fluorescence imaging.

The final challenge in the construction of this system lay in how to effectively separate the OCT backscattered light from the fluorescence emission light that are both collected by and transmitted through the endoscope. This posed a great challenge since we opted to implement an entirely fiber-optic platform. Our solution was to use a customized DCF coupler that consists of a single-mode fiber (SMF-28e) port, a multimode fiber port, and a DCF port.

On the forward path (from the source to the sample), the DCF coupler couples the OCT source and excitation source light traveling in the single-mode fiber to the single-mode core of the DCF (with a loss of 0.8 dB and 2.2 dB, respectively). On the return path (from the sample to the detector), the OCT backscattered light and

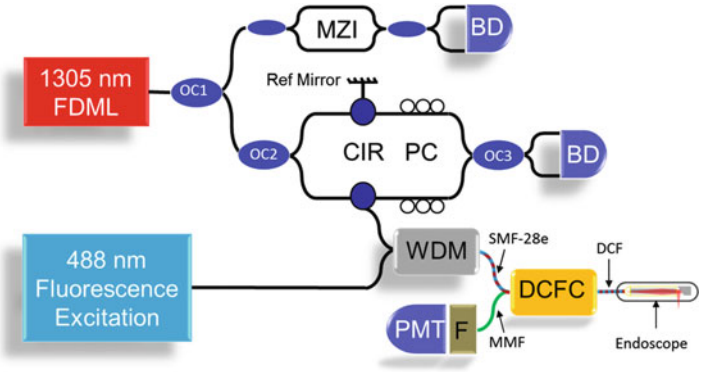

Fig. 53.2 Schematic of the dual-modality system capable of performing endoscopic OCT and fluorescence imaging simultaneously. *FDML* Fourier-domain mode-locking fiber laser, *OC* optical coupler (OC1 95/5, OC2 70/30, OC3 50/50), *MZI* Mach-Zehnder interferometer, *CIR* Circulator, *PC* polarization controller, *BD* balanced detector, *WDM* wavelength division multiplexer, *DCFC* double-clad fiber coupler, *PMT* photomultiplier tube, *F* band-pass filter; *Green*, multimode fiber (*MMF*); *blue*/*red*, double-clad fiber (*DCF*); *black*, single-mode fiber (*SMF*-28e) (Figure reprinted with permission from *Biomedical Optics Express*, Optical Society of America)

fluorescence emission travel through both the core and large inner cladding of the DCF in the endoscope. The DCF coupler allows the light traveling in the core of the DCF to be coupled back into the single-mode fiber port and the light traveling in the inner cladding of the DCF to be separated into the multimode fiber port. In this way, the OCT backscattered light seamlessly returns to the OCT system through fiber optics, where only light at the OCT source wavelengths are able to pass through the circulator and interfere with light from the OCT reference arm. Similarly the fluorescence emission, which travels mostly in the inner cladding of the DCF is coupled into the multimode fiber port and detected by a photomultiplier tube (PMT). Additionally, to avoid any potential leakage of fluorescence excitation light backscattered into the endoscope and transmitted through the inner cladding, band-pass filters were placed before the PMT. Both OCT and fluorescence signals are collected simultaneously during imaging and are digitized, displayed, and stored in a synchronized fashion.

53.2.2 Dual-Modality OCT and Two-Photon Fluorescence Endoscopy

Similar to the OCT and single-photon fluorescence imaging platform, the endoscope is a key component through which simultaneous high-resolution OCT and two-photon fluorescence imaging is performed. Here, an *en face* imaging system is considered for both OCT and two-photon fluorescence. We will start with the endoscope design, followed by the description of the system-level integration.

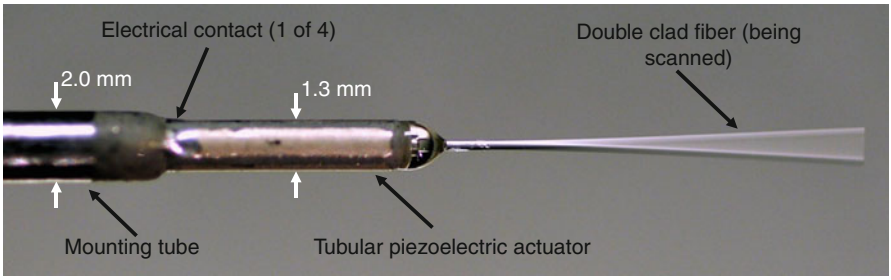

Fig. 53.3 Photograph of 1.3-mm-diameter four-quadrant, tubular piezoelectric actuator mounted on a 2.0-mm-diameter base. The double-clad fiber is threaded through the actuator and is being scanned

53.2.2.1 Endoscope Design

A lateral beam scanning mechanism is required in the endoscope for performing en face OCT and TPF imaging (which is conventionally realized by using galvanometric mirrors in a benchtop system). Here, we adopt our previously developed, piezoelectrically actuated, fiber-optic resonant scanner to achieve rapid lateral beam scanning [7, 27]. Although the movement of the piezoelectric (PZT) actuator is imperceptible, the attached fiber cantilever driven by the PZT actuator at or close to its resonant frequency could generate a large lateral deflection. According to a cantilever beam model, the zeroth-order resonant frequency of a fiber cantilever can be expressed as:

$$f = \frac{3.52}{4\pi}\sqrt{\frac{E}{\rho}}\left(\frac{R}{L^2}\right), \tag{53.1}$$

where E, ρ, R, and L are the Young's modulus, mass density, radius, and the length of the fiber cantilever, respectively. Figure 53.3 shows a photograph of a tubular, four-quadrant monolithic PZT beam scanner with a fiber threaded through the central hole. The overall diameter of the scanner including a housing unit can be as small as 2.0 mm. With an exposed fiber length of about 10 mm, the mechanical resonant frequency of the fiber cantilever of a 125 μm diameter is calculated as ~1 kHz based on Eq. 53.1 that is consistent with experimental results.

Depending on the driving frequency applied on the PZT actuator, either spiral or Lissajous scanning pattern can be achieved at the cantilever tip (as shown in Fig. 53.4). The spiral scan requires two orthogonal driving waveforms of the resonant frequency modulated by a slowly varied amplitude waveform leading to a circular field of view (Fig. 53.4a) [28]. Such a scanning pattern is easy to implement on tubular piezoelectric actuators, and image reconstruction is also quite simple. However, it suffers from nonuniform spatial sampling due to the fact that the tangential velocity of the scan trajectory increases as it moves from the center of the field of view. In practice, this leads to oversampling in the center

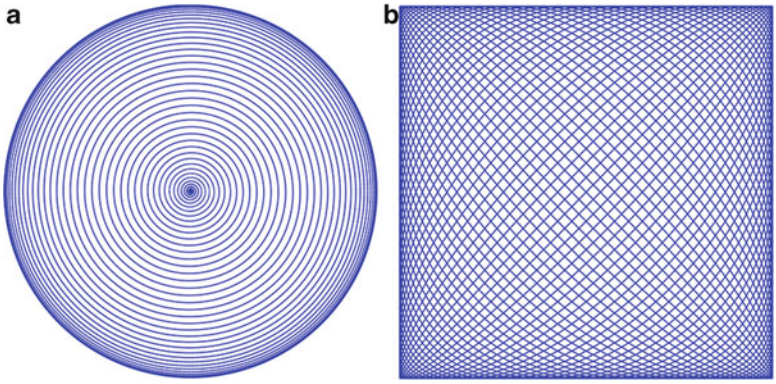

Fig. 53.4 Trajectories of fiber-optic cantilever tip. (**a**) Spiral pattern. (**b**) Lissajous pattern with a frequency ratio of 40:41

and undersampling at the periphery. On the other hand, Lissajous scan can be implemented with two driving waveforms with constant amplitudes but shifted frequencies that are close to the resonant one, leading to a rectangular field of view (Fig. 53.4b) [29]. In order to obtain a closed curve, the frequency ratio must be rational. In practice, the ratio of the two driving waveform frequencies is usually chosen to be close to 1. Although Lissajous scanning provides a better spatial sampling density, the complex trajectory makes reconstruction computationally intensive and sensitive to any perturbation.

Optical fiber is another critical component in the endoscope. Here, a customized double-clad fiber (DCF) was employed. The core diameter of the DCF is ~8 μm, similar to that of the standard single-mode fiber (i.e., SMF-28e®), ensuring both 1,550 nm (the excitation wavelength for TPF) and 1,310 nm (the center wavelength of the OCT light source), can be delivered in single mode through the core, hence achieving small focused spot size on the sample. The inner cladding of the DCF (ϕ175 μm) is able to effectively collect the two-photon fluorescence signal by utilizing its large area and NA. The NA of the DCF core and inner cladding were 0.14/0.12 (at 1,310 nm/1,550 nm) and 0.267 (at 1,550 nm), respectively.

The focusing lens represents a significant challenge in the integrated endoscopic system. The lens needs to have a high NA and low geometric aberrations for obtaining a near diffraction-limited focal spot size. Chromatic aberration should be taken into account due to wavelength difference between OCT, two-photon excitation, and emission wavelengths. In this system, the light from DCF cantilever tip was focused onto the sample by a miniature aspherical compound lens with a maximum NA of 0.8 and a magnification of ~0.22 (along the direction of fiber to sample). A minimal chromatic focal shift of the micro compound lens from the OCT wavelength (1,310 nm) to the two-photon excitation wavelength (1,550 nm) was measured to be ~11 μm.

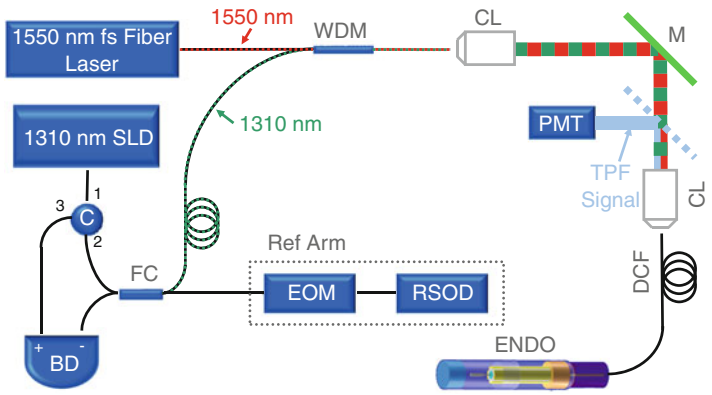

Fig. 53.5 Schematic of TPF/OCT multimodal endomicroscope system. *BD* balanced detector, *C* circulator, *CL* coupling lens, *DCF* double-clad fiber, *DM* dichroic mirror, *ENDO* miniature endoscope, *EOM* electro-optic modulator, *FC* fiber coupler, *LP* long pass filter, *M* mirror, *PMT* photomultiplier tube, *RSOD* rapid scanning optical delay line, *WDM* wavelength division multiplexer (Figure reprinted with permission from *Optics Letters*, Optical Society of America)

53.2.2.2 System Design

Figure 53.5 shows the dual-modal system schematic, which integrates the OCT and TPF imaging modalities, capable of performing endoscopic OCT and TPF imaging simultaneously [30]. In the OCT module, the light from a fiber-coupled superluminescent diode of a 13-mW output power with a central wavelength of 1,310 nm and a 3-dB bandwidth of 80 nm was delivered into a Michelson interferometer. In the TPF module, a 1,550 nm passive mode-locked amplified fiber laser was used as the excitation source. The laser generated ultrashort pulses (i.e., ~300 fs with a repetition rate of 42.5 MHz) with a maximum average power of ~155 mW. It operated in the soliton regime so that the laser pulses remain relatively unchanged inside the single-mode fiber (e.g., SMF-28e® or any fiber with the similar dispersion characteristics as SMF-28e®). Therefore, the TPF system does not require any specific dispersion compensation. A high-isolation wavelength division multiplexer (WDM) made of SMF-28e® was placed in the OCT sample arm to combine the 1,310 nm OCT light source with the 1,550 nm TPF excitation laser.

In order to separate the TPF emission and the OCT signal on the return path, a dichroic mirror (DM) was placed between a pair of coupling lenses. A photomultiplier tube (PMT) was used to collect the TPF emission signal reflected from the DM, while the OCT signal transmitted through the DM and was collected via the WDM placed in the OCT sample arm. Although some of the backscattered OCT light from the sample entered the inner cladding of the DCF in the endoscope, the single-mode fiber in the OCT sample arm can filter it out to avoid "ghost" OCT images. In order to perform optical heterodyne detection, an electro-optic modulator was inserted into the reference arm of the OCT module to introduce a beat frequency.

A rapid scanning optical delay line (RSOD) was used both to compensate the dispersion mismatch between the two OCT arms and to select the imaging depth of interest for the en face imaging [31]. A balanced detection scheme was employed in the OCT module to eliminate any DC components and increase the detection dynamic range.

53.3 Results

53.3.1 OCT and Single-Photon Fluorescence Endoscopy

Simultaneous intraluminal OCT and single-photon fluorescence imaging with the dual-modality endoscope was performed in *ex vivo* rabbit esophagus. The tissue was stained with three local injections of 1–2 mL 300 μM aqueous solution of fluorescein sodium from the submucosal side between the lamina propria and muscularis mucosa. The tissue was rinsed with buffered saline afterwards to get rid of excess dye. The endoscope, encased with a transparent plastic tube, was deployed in the esophagus, and volumetric imaging was performed by circumferentially scanning the imaging beam (by the micromotor), while the endoscope was pulled back within the stationary plastic tube.

Figure 53.6a shows a respective 2D circumferential frame depicting simultaneous OCT and fluorescence imaging. The 2D OCT image is shown in grayscale, while the fluorescence intensity is depicted as the overlaid colored annulus.

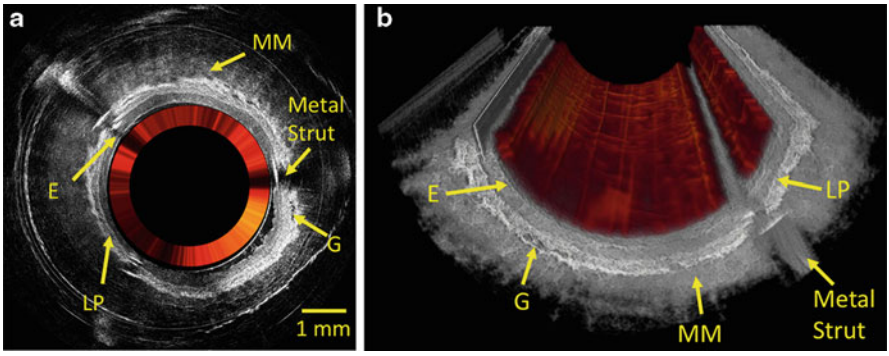

Fig. 53.6 Circumferential scanning and pull back were performed to obtain 3D volumetric OCT images and 2D fluorescence surface map of the esophagus with the dual-modal endoscope. (**a**) Representative 2D cross-sectional OCT image of *ex vivo* rabbit esophagus during one circumferential scan (*grayscale*) with the overlaid inner annulus (*red* hot colormap) of the fluorescence intensity. (**b**) The cut-away view of the 3D OCT volumetric image (*grayscale*) and the 2D fluorescence intensity map inlaid (*red* hot colormap) on top of the OCT image. In both the 2D OCT cross-sectional image and 3D volumetric OCT image the normal layered structures of the esophagus can be clearly visualized, including the epithelium (*E*), lamina propria (*LP*), muscularis mucosa (*MM*), and glands (*G*). The co-registered and simultaneously acquired fluorescence map shows striated structures which are believed to be vasculature. (Figure reprinted with permission from *Biomedical Optics Express*, Optical Society of America)

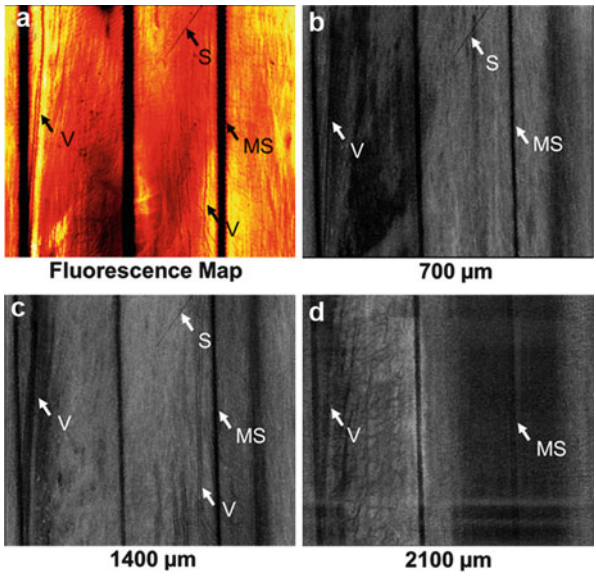

Fig. 53.7 (**a**) Unwrapped 2D Fluorescence image. (**b–d**) Unwrapped OCT images at 700 µm, 1,400 µm, and 2,100 µm depth. The *white arrows* on the OCT images (**b–d**) correspond to the *black arrows* in the fluorescence map (*A*) indicating correlating structures such as vasculature (*V*), suture (*S*), and metal strut (*MS*). The suture was used to provide a registration mark for both OCT and fluorescence intensity images (Figure reprinted with permission from *Biomedical Optics Express*, Optical Society of America)

Similarly Fig. 53.6b shows the cutaway view of the 3D volumetric image with the 3D OCT image shown in grayscale and the 2D fluorescence intensity map inlaid (red hot colormap). The 2D and 3D OCT images are able to visualize normal esophageal structures such as the epithelium, lamina propria, muscularis mucosa, and glands. The inlaid fluorescence images are complementary to the OCT images and display striated structures believed to be the vascular structures of the rabbit esophagus. Furthermore, co-registration and coincidence of the OCT images with the fluorescence intensity images can be seen at three signal poor points which correspond to the metal struts of the metal enclosure.

Imaging was performed with an OCT detection sensitivity of ~108 dB and a penetration depth of 1.7 mm. Both OCT and fluorescence intensity images were acquired simultaneously and were automatically co-registered. In order to demonstrate the correlation between the OCT and fluorescence intensity map, the intraluminal 3D OCT image was flattened into a 2D stack along the imaging depth 700 µm apart and compared with the 2D fluorescence map. Corresponding structures are indicated by the black arrows in the fluorescence map and white arrows in the OCT slices (Fig. 53.7b–d). We visualized a suture (used as a registration mark), striated structures believed to be vasculature and the three signal poor regions corresponding to the metal struts of the metal enclosure.

53.3.2 OCT and Two-Photon Fluorescence Endoscopy

Simultaneous OCT and TPF imaging was performed on both cell culture and *ex vivo* biological tissue. The resolutions were ~2.5 × 10.0 µm (lateral × axial) in air for

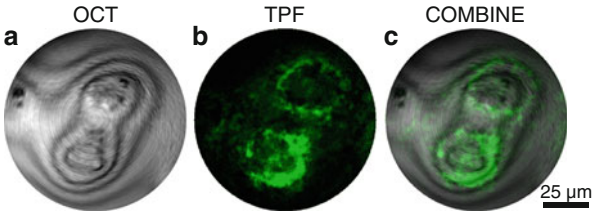

Fig. 53.8 (**a**) OCT and (**b**) TPF images of A431 cancer cells immunostained with anti-EGFR conjugated ICG micelles. (**c**) Superposition of the OCT and TPF images (Figure reprinted with permission from *Optics Letters*, Optical Society of America)

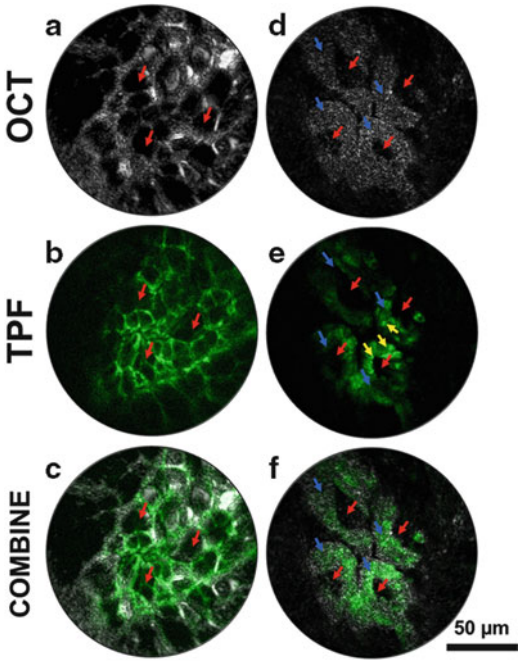

Fig. 53.9 (**a**) OCT, (**b**) TPF and (**c**) superposed images of mouse adipose tissue with local ICG administration. *Red arrow* shown in (**a**) and (**b**) indicates one of the adipocytes visualized under both imaging modalities. (**d**) OCT, (**e**) TPF, and (**f**) superposed images of mouse small intestine tissue with local ICG administration. *Blue arrows* shown in (**d**) and (**e**) indicate villus structures and *red arrows* indicate lacteals. The stronger fluorescence dots indicated by *yellow arrows* shown in (**e**) may be either enterocytes or lymphocytes. Both sets of images show great correlation between two imaging modalities (Figure reprinted with permission from *Optics Letters*, Optical Society of America)

OCT and ~1.2 × 5.7 μm (lateral × axial) for TPF imaging. Imaging was performed through a No. 1 cover glass placed on top of the sample and by a dry micro objective lens of a working distance 200 μm in air. The powers incident on the sample were ~30–50 mW (at 1,550 nm for TPF) and ~4.0 mW (at 1,310 nm for OCT).

Figure 53.8a, b show one set of representative OCT and TPF images of the A431 cancer cells incubated on a coverslip targeted with anti-EGFR conjugated ICG micelles. The superimposed OCT and TPF image is shown in Fig. 53.8c where the whole cell topology can be easily identified with OCT, while the cell membrane is enhanced under ICG TPF imaging. Figure 53.9a, b shows representative OCT and TPF images taken simultaneously from mouse adipose tissue. The overlaid image from the two modalities is shown in Fig. 53.9c, where the OCT and TPF images overlap well, particularly around the cell membranes. Simultaneous OCT and TPF imaging was also performed on mouse small intestine, and the representative OCT and TPF images are shown in Fig. 53.9d, e, respectively. The circular void structures in the OCT image may represent the intestinal villi (indicated by blue arrows) with the lacteals (indicated by red arrows) shown as the areas of lower backscattering on the OCT image. Similar structures were visualized on the TPF image as well. The brighter fluorescent spots (indicated by yellow arrows) on the villi may suggest either the enterocytes or lymphocytes actively absorbed the ICG molecules. The superposed image that is shown in Fig. 53.9f suggested that this endoscopic multimodal imaging platform is able to produce simultaneous imaging even with highly scattering tissues.

53.4 Conclusions

In this chapter, we have discussed the benefits and methodology of how to perform dual-modality OCT and fluorescence imaging endoscopically. The general design considerations were discussed, and key technological challenges and solutions were presented. Some representative images acquired by the dual-modal endoscopy platforms were also presented.

References

1. S.R. Chinn, E.A. Swanson, J.G. Fujimoto, Optical coherence tomography using a frequency-tunable optical source. Opt. Lett. **22**(5), 340–342 (1997)
2. A.F. Fercher, C.K. Hitzenberger, G. Kamp, S.Y. El-Zaiat, Measurement of intraocular distances by backscattering spectral interferometry. Opt. Commun. **117**(1–2), 43–48 (1995)
3. G. Häusler, M.W. Lindner, "Coherence Radar" and "Spectral Radar"—new tools for dermatological diagnosis. J. Biomed. Opt. **3**(1), 21–31 (1998)
4. R. Huber, M. Wojtkowski, J.G. Fujimoto, Fourier Domain Mode Locking (FDML): a new laser operating regime and applications for optical coherence tomography. Opt. Express **14**(8), 3225–3237 (2006)
5. W. Wieser, B.R. Biedermann, T. Klein, C.M. Eigenwillig, R. Huber, Multi-megahertz OCT: high quality 3D imaging at 20 million A-scans and 4.5 GVoxels per second. Opt. Express **18**(14), 14685–14704 (2010)
6. L. Huo, J.F. Xi, Y. Wu, X.D. Li, Forward-viewing resonant fiber-optic scanning endoscope of appropriate scanning speed for 3D OCT imaging. Opt. Express **18**(14), 14375–14384 (2010)
7. X. Liu, M.J. Cobb, Y. Chen, M.B. Kimmey, X.D. Li, Rapid-scanning forward-imaging miniature endoscope for real-time optical coherence tomography. Opt. Lett. **29**(15), 1763–1765 (2004)

8. Y. Pan, H. Xie, G.K. Fedder, Endoscopic optical coherence tomography based on a microelectromechanical mirror. Opt. Lett. **26**(24), 1966–1968 (2001)
9. G.J. Tearney, S.A. Boppart, B.E. Bouma, M.E. Brezinski, N.J. Weissman, J.F. Southern, J.G. Fujimoto, Scanning single-mode fiber optic catheter-endoscope for optical coherence tomography. Opt. Lett. **21**(7), 543–545 (1996)
10. P.H. Tran, D.S. Mukai, M. Brenner, Z. Chen, In vivo endoscopic optical coherence tomography by use of a rotational microelectromechanical system probe. Opt. Lett. **29**(11), 1236–1238 (2004)
11. J.F. Xi, L. Huo, Y. Wu, M.J. Cobb, J.H. Hwang, X.D. Li, High-resolution OCT balloon imaging catheter with astigmatism correction. Opt. Lett. **34**(13), 1943–1945 (2009)
12. J.M. Zara, S. Yazdanfar, K.D. Rao, J.A. Izatt, S.W. Smith, Electrostatic micromachine scanning mirror for optical coherence tomography. Opt. Lett. **28**(8), 628–630 (2003)
13. I. Georgakoudi, K.P. Quinn, Optical imaging using endogenous contrast to assess metabolic state. Annu. Rev. Biomed. Eng. **14**(14), 351–367 (2012)
14. W. Denk, J.H. Strickler, W.W. Webb, Two-photon laser scanning fluorescence microscopy. Science **248**(4951), 73–76 (1990)
15. M. Oheim, D.J. Michael, M. Geisbauer, D. Madsen, R.H. Chow, Principles of two-photon excitation fluorescence microscopy and other nonlinear imaging approaches. Adv. Drug Deliv. Rev. **58**(7), 788–808 (2006)
16. J.K. Barton, F. Guzman, A. Tumlinson, Dual modality instrument for simultaneous optical coherence tomography imaging and fluorescence spectroscopy. J. Biomed. Opt. **9**(3), 618–623 (2004)
17. E. Beaurepaire, L. Moreaux, F. Amblard, J. Mertz, Combined scanning optical coherence and two-photon-excited fluorescence microscopy. Opt. Lett. **24**(14), 969–971 (1999)
18. S.A. Boppart, Multimodality microscopy of cell dynamics in three-dimensional engineered and natural tissues. Complex Medical Engineering, 2009. IEEE Conference on Complex Medical Systems, Phoenix, AZ, April 9–11, (2009)
19. S. Tang, T.B. Krasieva, Z. Chen, B.J. Tromberg, Combined multiphoton microscopy and optical coherence tomography using a 12-fs broadband source. J. Biomed. Opt. **11**(2), 020502-020502 (2006)
20. S.A. Yuan, C.A. Roney, J. Wierwille, C.W. Chen, B.Y. Xu, G. Griffiths, J. Jiang, H.Z. Ma, A. Cable, R.M. Summers, Y. Chen, Co-registered optical coherence tomography and fluorescence molecular imaging for simultaneous morphological and molecular imaging. Phys. Med. Biol. **55**(1), 191–206 (2010)
21. Y.B. Zhao, B.W. Graf, E.J. Chaney, Z. Mahmassani, E. Antoniadou, R. DeVolder, H. Kong, M.D. Boppart, S.A. Boppart, Integrated multimodal optical microscopy for structural and functional imaging of engineered and natural skin. J. Biophotonics **5**(5–6), 437–448 (2012)
22. A.R. Tumlinson, L.P. Hariri, U. Utzinger, J.K. Barton, Miniature endoscope for simultaneous optical coherence tomography and laser-induced fluorescence measurement. Appl. Opt. **43**(1), 113–121 (2004)
23. H. Yoo, J.W. Kim, M. Shishkov, E. Namati, T. Morse, R. Shubochkin, J.R. McCarthy, V. Ntziachristos, B.E. Bouma, F.A. Jaffer, G.J. Tearney, Intra-arterial catheter for simultaneous microstructural and molecular imaging in vivo. Nat. Med. **17**(12), 1680-U1202 (2011)
24. J. Mavadia, J.F. Xi, Y. Chen, X.D. Li, An all-fiber-optic endoscopy platform for simultaneous OCT and fluorescence imaging. Biomed. Opt. Express **3**(11), 2851–2859 (2012)
25. H.L. Fu, Y.X. Leng, M.J. Cobb, K. Hsu, J.H. Hwang, X.D. Li, Flexible miniature compound lens design for high-resolution optical coherence tomography balloon imaging catheter. J. Biomed. Opt. **13**(6) (2008)
26. Y.C. Wu, J.F. Xi, L. Huo, J. Padvorac, E.J. Shin, S.A. Giday, A.M. Lennon, M.I.F. Canto, J.H. Hwang, X.D. Li, Robust high-resolution fine OCT needle for side-viewing interstitial tissue imaging. IEEE J. Sel. Top. Quant. Electron. **16**(4), 863–869 (2010)

27. Y. Zhang, M.L. Akins, K. Murari, J.F. Xi, M.J. Li, K. Luby-Phelps, M. Mahendroo, X.D. Li, A compact fiber-optic SHG scanning endomicroscope and its application to visualize cervical remodeling during pregnancy. Proc. Natl. Acad. Sci. **109**(32), 12878–12883 (2012)
28. M.T. Myaing, D.J. MacDonald, X.D. Li, Fiber-optic scanning two-photon fluorescence endoscope. Opt. Lett. **31**(8), 1076–1078 (2006)
29. W. Liang, K. Murari, Y. Zhang, Y. Chen, M.J. Li, X.D. Li, Increased illumination uniformity and reduced photodamage offered by the Lissajous scanning in fiber-optic two-photon endomicroscopy. J. Biomed. Opt. **17**(2), 021108–021101 (2012)
30. J.F. Xi, Y. Chen, Y. Zhang, K. Murari, M.J. Li, X.D. Li, Integrated multimodal endomicroscopy platform for simultaneous en face optical coherence and two-photon fluorescence imaging. Opt. Lett. **37**(3), 362–364 (2012)
31. Y. Chen, X.D. Li, Dispersion management up to the third order for real-time optical coherence tomography involving a phase or frequency modulator. Opt. Express **12**(24), 5968–5978 (2004)

Part V

OCT Applications

Application of Fourier Domain OCT Imaging Technology to the Anterior Segment of the Human Eye

54

Maciej Wojtkowski, Susana Marcos, Sergio Ortiz, and Ireneusz Grulkowski

Keywords

Anterior segment imaging • Corneal pachymetry • Corneal topography • Corneoscleral angle • Crystalline lens • Optical coherence tomography • Tonometry

54.1 Introduction

The anterior segment is the front part of the human eye, which forms the optical system and hence directly impacts vision (Fig. 54.1). It is also the part of the eye that is most exposed to the influences of the external environment. Traumatic or pathological changes in the anterior segment may lead to vision loss and, in some cases, even blindness. Since the eighteenth century, optical instrumentation for measuring and imaging the anterior segment of the human eye has been developing along with modern ophthalmology. Present-day ophthalmic clinics widely use devices such as slitlamp microscopes, gonioscopes, Javal keratometers, and Placido disk-based corneal topographers [1]. Additionally, imaging systems, like rotating Scheimpflug imaging, scanning slit topography, and ultrasound biomicroscopy, are commonly used to obtain quantitative information on the corneal thickness and topography, which may be especially useful for disease diagnosis, precise localization of lesions,

M. Wojtkowski (✉)
Faculty of Physics, Astronomy and Informatics, Institute of Physics, Nicolaus Copernicus University, Toruń, Poland
e-mail: Maciej.Wojtkowski@fizyka.umk.pl

S. Marcos • S. Ortiz
Instituto de Óptica "Daza de Valdés", Consejo Superior de Investigaciones Científicas, Madrid, Spain

I. Grulkowski
Department of Electrical Engineering and Computer Science and Research Laboratory of Electronics, Massachusetts Institute of Technology, Cambridge, MA, USA

© Springer International Publishing Switzerland 2015

W. Drexler, J.G. Fujimoto (eds.), *Optical Coherence Tomography*,
DOI 10.1007/978-3-319-06419-2_56

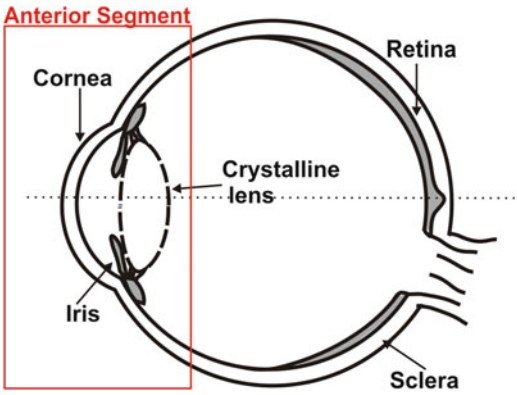

Fig. 54.1 Schematic horizontal section of the human eye

and planning of medical and surgical treatments (especially refractive surgery) [2]. Corneal thickness, contour, and shape of both surfaces can be measured using commercially available systems like Orbscan or Pentacam; however, all currently available technologies suffer from substantial speed limitations.

The optical system of the human eye comprises two optical elements: the cornea and the crystalline lens. The cornea is a quasi-transparent vault-shaped tissue at the front of the eye. It has no blood vessels and is composed of five main layers: epithelium, Bowman's membrane, stroma, Decemet membrane, and endothelium. The cornea provides 85 % of the power refraction, as the larger index of refraction change occurs in the air-cornea interface. The normal cornea is best fit by a prolate conicoid (steeper at the center than along the periphery). The average radius of the anterior corneal surface curvature is 7.87mm and that of the posterior corneal surface is 6.40 $\pm$ 0.28 mm [3]. The average reported corneal conic constants are 0.82 and 0.62 for anterior and posterior surfaces, respectively [3]. The average corneal central thickness is 550 nm [4]. The refractive index changes across layers, with an effective index of refraction of 1.3771 at 598.3 nm [5].

The crystalline lens is a biconvex transparent element that increasingly opacifies with age; it is composed of multiple layers of long fiber cells that originate from the equator and stretch toward the poles of the lens, forming suture patterns at the point where they meet. The lens is covered by an elastic membrane, known as the lens capsule. The anterior and posterior lens surfaces are typically described as having an aspheric prolate shape, with average radii of curvature and conic constants, respectively, of 11.76 mm and -4 for the anterior surface, and 5.96 and -3 for the posterior surface [6]. The typical lens thickness is calculated (in mm) as 2.93 + 0.0236 $\times$ age (in years) [7] in the unaccommodated state. The young crystalline lens can change its shape to focus on near and far objects. The lens capsule is attached via the zonular fibers (mostly around the lens equator) to the ciliary body and ciliary muscle. When the ciliary muscle contracts, the apex of the ciliary body moves toward the lens equator to release tension on the zonular fibers, and the capsule molds the lens into an accommodated form. With accommodation, the lens surfaces become steeper and lens thickness increases. Another interesting optical

feature of the crystalline lens is that the index of refraction is not constant but rather has a gradient distribution (both radially and axially) typically ranking from 1.36 in the nucleus to 1.44 at the surface [8]. The gradient refractive index (GRIN) results in a higher equivalent index (and therefore power) and typically in a more negative spherical aberration in the lens, which compensates for the positive spherical aberration of the cornea. The capability of the lens to shape upon an accommodative effort is lost with age (due to increased stiffness of the lens material). With age, the lens also undergoes shape changes due to its continuous growth throughout life and changes in the GRIN distribution.

In addition to the cornea and the lens, another important element in the anterior segment of the eye is the iris, a thin circular aperture responsible for controlling the diameter of the pupil, and therefore the amount of light entering the eye. Pupil diameter is controlled by ambient illumination, tends to contract upon accommodation of the crystalline lens, can be pharmaceutically controlled, and tends to decrease with aging.

Over the last two decades, there have been several developments in optical technology that have extended our ability to image and evaluate the anterior segment of the human eye. One of the most substantial developments in this field is the application of optical coherence tomography (OCT) to image and quantify morphologic structures of the human eye; this noncontact and noninvasive optical method is very well suited for biomedical applications [9–11]. OCT has found many applications in medicine and clinical practice, primarily because it offers noninvasive and noncontact imaging with relatively high sensitivity; this allows the detection of weakly diffusive, back-reflected light. In OCT applications, the measured thickness of the optically sectioned (coherence-gated) transverse layer is about an order of magnitude thinner than that achievable with scanning laser ophthalmoscopic (SLO) instruments. OCT also offers improved sensitivity due to additional filtering and amplification of the oscillatory interferometric signal. Optical coherence tomography has been most widely applied to retinal imaging [12–15]. This method was initially commercialized by Zeiss with three generations of retinal OCT devices (OCT1, OCT2, and Stratus OCT). Later, another time-domain OCT instrument was introduced to ophthalmology clinics – an en-face OCT/SLO device (OTI) that offers a unique combination of the two abovementioned imaging modalities [16–18]. At that time, it was rare to obtain in vivo three-dimensional images of the entire structure of the eye, primarily due to the physical and technical limitations of the TdOCT method that influenced measurements of time, sensitivity, and resolution.

Introduction of Fourier domain detection in OCT has opened new frontiers in OCT ophthalmic applications. Most importantly, the resultant substantial speed improvement enables rapid image acquisition, helping to reduce artifacts due to patient motion. Thus, it is currently possible to perform high-speed in vivo three-dimensional volumetric imaging over large scales within a reasonable time limit and without reducing system sensitivity [19–22]. Fourier domain OCT (FdOCT) had the additional advantage of making the system sensitivity independent of the axial resolution (i.e., the resolving power of the imaging system in the direction of the propagation of the probing light beam) [14, 21, 23–27]. There are currently

more than seven commercially available FdOCT instruments dedicated for retinal imaging; the functionality of most of them can be extended to cornea imaging, but only in the limited range of 2–3 mm.

The application of OCT to the anterior segment imaging is particularly of interest, since this could potentially provide substantial complementary information regarding the large-scale architecture of the cornea and the crystalline lens, or on small portions of tissue imaged with high spatial resolutions comparable to regular microscopy. The latter could be used for ophthalmic diagnoses, including detailed monitoring of the Bowman's membrane, corneal epithelium, stroma, capsule of the crystalline lens, intraocular lens surface, conjunctiva, or the corneoscleral junction. Meanwhile, large-scale imaging, covering a depth of 6 mm and 12 mm × 12 mm of the transverse range, can provide morphometric parameters, including the corneal thickness and topography, iridocorneal angle, and orientation of intraocular lens [28, 29]. Additionally, remarkable advances in the field of refractive surgery have created requirements for more accurate imaging and measurements of corneal curvature and topography [30]. Three commercially available instruments are exclusively dedicated to diagnoses of the anterior segment; each of them have an imaging light with a 1,300-nm central wavelength, which allows visualization of the whole anterior segment, from limbus to limbus and from the front corneal surface to the posterior surface of the crystalline lens [19]. This spectral bandwidth also ensures improved safety due to the high water absorption of 1,300-nm radiation compared to 800-nm light wavelengths. One of the commercial instruments is the Visante OCT (Carl Zeiss Meditec) and the second is the SlitLamp OCT (Heidelberg Engineering); both use TdOCT. These systems can only collect a couple of thousand A-scans per second; therefore, acquiring an image in a reasonable amount of time allows only a sparse sampling. Quantitative analysis of the cornea can be affected by motion artifacts and imperfections in patient adjustment (in asterisk scan patterns). Substantial improvement of the imaging speed would allow increased sampling density and reduce the influence of motion artifacts, which can be crucial for improved repeatability and accuracy of the corneal topography. The other commercially available OCT device for anterior segment imaging is the SS-1000 Casia (Tomey), the only commercial instrument that uses state-of-the-art technology with swept-source OCT. Unfortunately, this instrument does not exploit the full potential of swept-source OCT, because its imaging speed is 30,000 optical A-scans/s, similar to that of commercially available retinal SOCT devices.

54.2 Technical Advantages and Limitations of Anterior Segment FdOCT Instruments

Compared to retinal imaging, imaging the anterior segment of the human eye requires substantially different measurement conditions and instrumentation. The table in Fig. 54.2 presents the main parameters cited from literature [31–33] that are important for optical imaging of the anterior segment of the human eye; they determine the requirements and limitations in dynamic range, the sensitivity and

Dimensions			Sample	μ_a	μ_s	μ_t	n	D	T	Rd
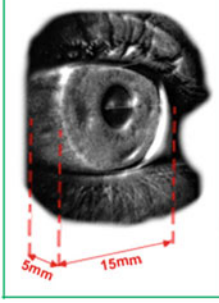	Wavelength [nm]	980	Sclera	0.90	27.0	27.9	1.41	1.00	0.32	0.400
			Aqueous Humor	0.75	0.59	1.34	1.33	0.10	0.84	0.004
			Vitreous Humor	0.47	0.03	0.50	1.34	0.20	0.83	0.001
			Cornea	0.33	1.58	1.91	1.37	0.25	0.77	0.039
			Lens	0.42	0.50	0.92	1.40	0.27	0.78	0.011
		1310								
			Sclera	1.40	19.0	20.4	1.40	1.00	0.30	0.230
			Aqueous Humor	1.63	0.65	2.28	1.34	0.10	0.77	0.004
			Vitreous Humor	1.53	0.21	1.74	1.34	0.20	0.67	0.002
			Cornea	0.71	2.24	2.96	1.37	0.25	0.66	0.037
			Lens	1.3	0.85	2.16	1.40	0.27	0.60	0.009

Fig. 54.2 Basic optical properties of ocular tissue for 980 nm and 1,310 nm: μ_a, absorption coefficient; μ_s, scattering coefficient; μ_t, extinction coefficient; n, refractive index; D, thickness in mm; T, transmittance; R, diffused reflectance; data collected from Refs. [31–33]

penetration depth of the optical imaging instrument. Careful analysis of these numbers will assist in choosing the optimal wavelength and imaging speed of the device. The most substantial restriction of OCT is the limited penetration depth of the probing light beam in biological tissues. Additionally, the multiple scattering of detected backscattered light substantially reduces the quality of reconstructed images. Therefore, OCT imaging is limited to applications in ocular anatomical structures that weakly scatter light with only a small amount of melanin or hemoglobin. In retinal imaging, the light has to travel through about 2.5 cm of ocular media (mostly through transparent tissues containing water, which strongly absorbs infrared radiation); thus, retinal OCT can only use wavelengths in the optical window of 400–1,100 nm. This limitation does not apply to anterior eye imaging. Typically, light in the near-infrared range ($\lambda = 0.8$–1.3 μm) penetrates well through optically transparent parts of the anterior segment, like the cornea, vitreous, and crystalline lens. However, penetration of the sclera (Fig. 54.2) and iris is still substantially limited. Typically, near-infrared light (700–1,300 nm) penetrates the sclera to a depth of approximately 1 mm. The iris has also low transmittance and high scattering, but it is difficult to determine their absolute values due to high individual variability of the melanin concentration.

The most important challenge in anterior segment imaging is that data must be collected from a much larger volume than for retinal OCT. To obtain all information about the entire corneal architecture, including the corneoscleral junction and the corneal apex, a volume of approximately 15 mm × 15 mm transversally and 5 mm in depth must be scanned. Thus, if a relatively high scanning density is maintained, along with high axial resolution, a substantially greater amount of data will be captured with the acquisition system and stored in the hard drives. For example, three-dimensional reconstruction of the anterior segment with a voxel size of 20 μm × 20 μm × 3 μm and 10-bit analog-to-digital conversion requires collection of 4.5 GB of data. In practice, this information must also be acquired during a short enough time to minimize the negative impact of sample motion; this

concern sets the fundamental speed requirements for the imaging devices to sample at the order of magnitude of gigasamples per second. Such requirements are highly demanding for the state-of-the-art technology, both regarding optical detection with the digitalization and transfer to PC. To meet the abovementioned specifications, an ideal OCT device should run with more than 500,000 A-scans/s to collect high-resolution volumetric data from the entire anterior segment within 1 s.

One feature that makes OCT attractive as a diagnostic tool is that it can perform imaging with resolutions comparable to that of histopathology. Longitudinal (axial) OCT resolution is determined by the central wavelength and spectral bandwidth of light. Another fundamental constraint is the limited lateral resolution, which is related to the finite numerical aperture (NA) of the optical system. This restriction has different effects on imaging, depending on whether OCT is used for imaging the fundus or the anterior segment of the eye. When imaging the retina, the natural optics of the eye limits the available NA and, for beams larger than 2–3 mm, introduces severe distortions of the wavefront, thus substantially degrading the lateral resolution of OCT devices. When imaging the anterior segment of the eye, the restricted optical performance obliges a trade-off between the lateral resolution and the measuring range [34]. Fourier domain OCT systems – those using parallel detection with a spectrometer (SOCT, SdOCT) or serial detection with swept source – have the broadest range of applications. Each type of FdOCT can be optimized for specific applications within the limits of the currently available detector technology and wideband light sources. It has been demonstrated that both types of high-speed FdOCT instruments can provide complementary information about the morphology and architecture of the anterior segment [34, 35].

54.2.1 Parallel Registration by FdOCT Using Spectrometer (SOCT, SdOCT)

Spectral OCT (SOCT) is especially well suited to imaging small portions of anterior segment tissue with high spatial resolutions, comparable to regular microscopy [36]. In fact small software and hardware modifications enable the conversion of a commercially available retinal system into an anterior segment imaging OCT instrument. However, in such case, the ergonomics of commercially available retinal OCT systems is not optimal. This configuration has already been optimized for ultrahigh-resolution retinal OCT imaging at 800 nm in laboratory setups or prototype instruments [19, 37, 38]. One of the examples of such ergonomic prototype device has been developed and introduced by Optopol Technology. Figure 54.3 shows examples of high-quality anterior segment imaging using SOCT Anterius instrument.

Despite limited imaging range of 800 nm high-resolution SOCT instruments, it has been demonstrated that this technology has a potential to become a powerful, noninvasive clinical corneal imaging modality that can enhance diagnosis and surgical treatments. Figure 54.4 shows examples of high-quality corneal imaging using laboratory SOCT instruments, which may be helpful in understanding clinical

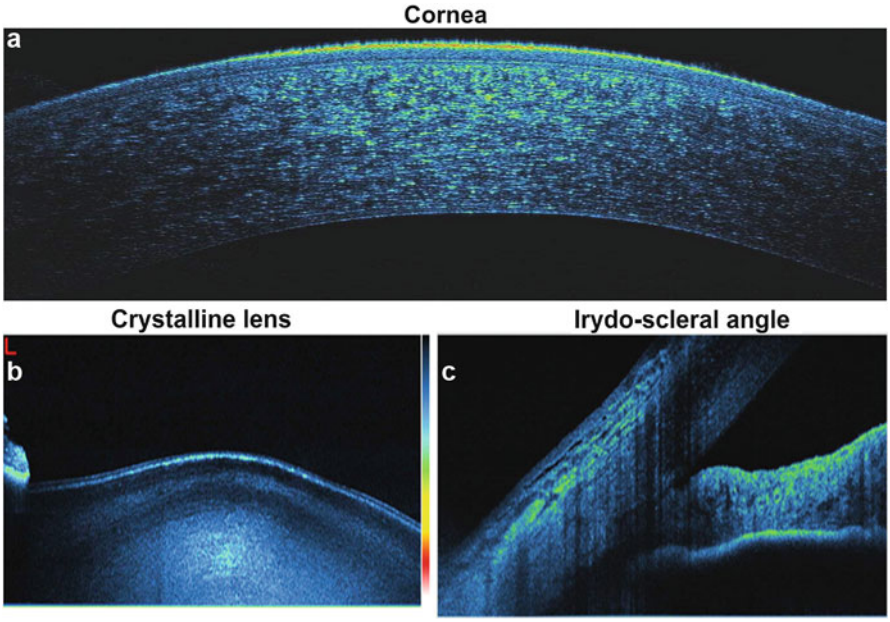

Fig. 54.3 High-quality cross-sectional imaging of the anterior segment of the human eye in vivo with 800-nm SOCT instrument (3 μm in tissue): (**a**) cornea, (**b**) corneoscleral angle, and (**c**) anterior part of the crystalline lens (Courtesy of Tomasz Bajraszewski, R&D Optopol Technology. Images obtained using the prototype SOCT Anterius instrument)

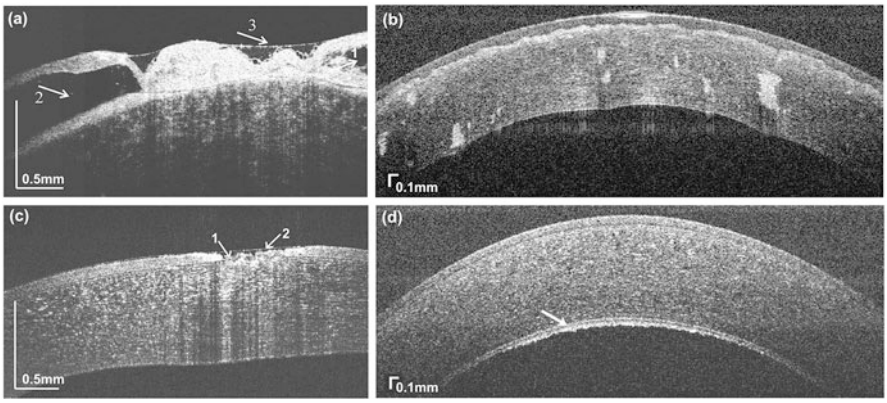

Fig. 54.4 High-quality corneal OCT imaging of pathologic cases. (**a**) End-stage bullous keratopathy; irregular thickness and reduplication of the epithelium, intraepithelial vesicles (*1*), bullae between the epithelium and Bowman layer (*2*), and tear film levels in the epithelial hollows (*3*). (**b**) granular corneal dystrophy with deposits in posterior anterior stroma. (**c**) corneal changes shortly after foreign body removal with epithelial defects (*1*) and tear fill levels in the hollows of the surface (*2*). (**d**) advanced Fuchs' endothelial dystrophy; *arrow* indicates thickened Descemet's membrane (Image reprinted from B. J. Kaluzny, et al. Cornea 25, 960–965, 2006 and Cornea 27, 830–832, 2008, copyright Lippincott Williams & Wilkins 2006 [36, 39])

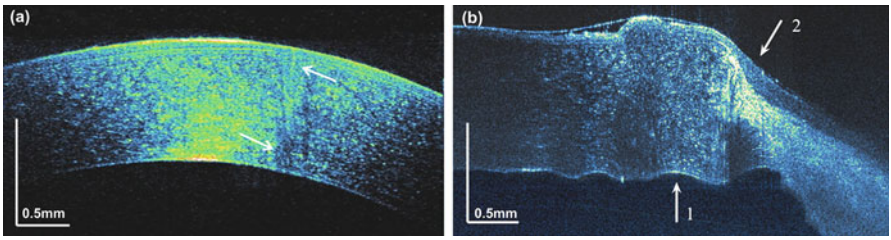

Fig. 54.5 OCT corneal imaging in incisional and refractive corneal procedures. (**a**) Scar after radial keratotomy 8 years after surgery; region of scar is indicated by *arrows*. (**b**) Eye surface 2 years after penetrating keratoplasty, (*1*) donor tissue and (*2*) host tissue (Image reprinted from B.J. Kaluzny et al., Cornea 25, 960–965, 2006, copyright Lippincott Williams & Wilkins 2006 [36])

pathologic features related to the various corneal diseases including corneal scars and keratitis, bullous keratopathy, epithelial defects, granular corneal dystrophy, and Fuchs endothelial dystrophy [36, 39, 40].

High-resolution SOCT also improves visualization of structures and their relationship to incisional and refractive corneal procedures like penetrating keratoplasty, phacoemulsification, Descemet membrane stripping, endokeratoplasty, corneal implantation for keratoconus, and laser in situ keratomileusis [36, 41]. Figure 54.5 shows examples of high-resolution imaging of cornea after radial keratotomy and penetrating keratoplasty visualizing various postoperative corneal changes like scars, change of the corneal architecture, or the morphology of donor-host corneal junction [36].

In the regular clinical practice, SOCT images of corneal abnormalities may enhance slitlamp biomicroscopic examination, and they can be especially useful in the preoperative and postoperative clinical treatment of patients undergoing cataract surgery. Figure 54.6 shows examples of high-quality and high-resolution imaging of anterior segment showing changes in Descement membrane morphology, corneal incision, intraepithelial vesicles, and posterior capsule opacification – all effects are secondary to the cataract surgery.

Large-scale architecture of the cornea and the crystalline lens can be also imaged using SOCT [34]. However, the SOCT instrument is much less flexible and more demanding than swept-source OCT device. This is mainly because SOCT technique has fundamental and technological limitations in imaging range and sensitivity, especially when the imaged sample has substantial curvature. In such cases, the combination of depth-dependent sensitivity drop-off [19] and fringe washout [42] effects will have a radical negative impact on image quality. Additionally, SOCT setup has limited options for adjusting the axial resolution and measurement range; these parameters depend on the design of the spectrometer and spectral range of the light source. Using a CMOS camera in the spectrometer improves the system's flexibility compared to CCD-based systems. In such a configuration, CMOS sensors usually enable programmable changes of the number of active pixels, which can improve the measurement speed. Unfortunately, reducing the number of active

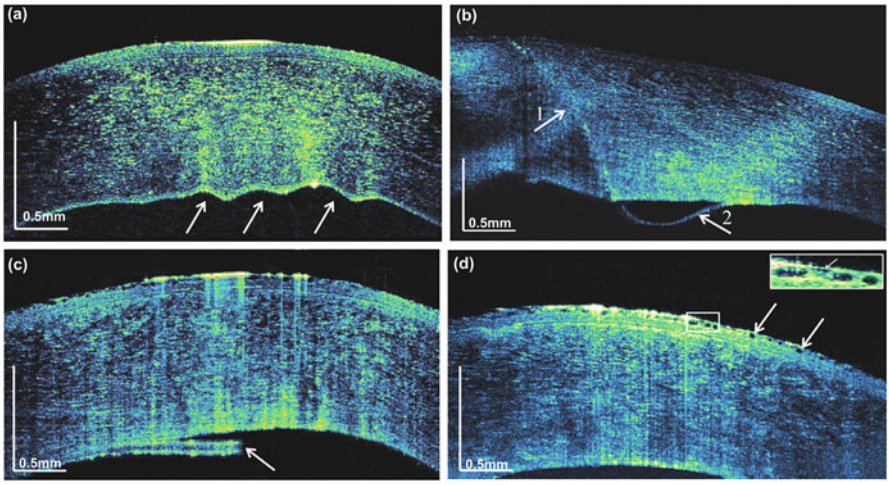

Fig. 54.6 OCT imaging of corneal changes after cataract surgery. (**a**) Folds of Descemet membrane (*arrows*), first day after surgery. (**b**) Corneal incision (*arrow 1*) and detachment of the thin posterior layer of the cornea (*arrow 2*), first day after surgery. (**c**) Partial removal of Descemet membrane (*arrow*), third day after surgery. (**d**) Intraepithelial vesicles caused by edema (*arrows*), third day after surgery; smallest resolved object (insert, *arrow*) is 25 mm wide and 5 mm deep (Image reprinted from B. J. Kaluzny et al., Cornea 25, 960–965, 2006, copyright Lippincott Williams & Wilkins 2006 [36])

CMOS camera pixels without changing the configuration of the optical elements in the spectrometer results in truncation of the spectrum (Fig. 54.7). Consequently, the axial resolution and sensitivity decrease together with the reduction of pixel number. The last column in the right panel of Fig. 54.7 shows the effective sensitivity values, considering both the shortening of the signal integration time and the truncation of the spectrum.

As presented in [34], even with all of these obstacles, it is possible to obtain high-quality cross-sectional OCT images of the entire cornea with an optimized OCT setup. In this case, high-speed imaging (118,000 A-scans/s) of the cornea and the crystalline lens simultaneously required very careful adjustment of the focal plane of the imaging lens and accurate positioning of the sample in respect to the zero optical path delay (OPD). This procedure helped to compensate the sensitivity roll-off of 20 dB over 5 mm. Figure 54.8 shows OCT images of the healthy eye of the same subject registered for different parameters, including sampling density, registration speed, and position in reference to zero OPD. According to the table in Fig. 54.7, the images were obtained with different sensitivities of 89 dB and 97 dB and axial resolutions 15 μm and 7 μm. Both systems had the same values of transverse resolution Δx (27 μm) and the confocal parameter ς (3.6 mm). Even with the relatively low axial resolution in Fig. 54.8 compared to that from Fig. 54.3, the architecture of the cornea, anterior surface of the lens, and irido-scleral angle are well reconstructed in Fig. 54.8b.

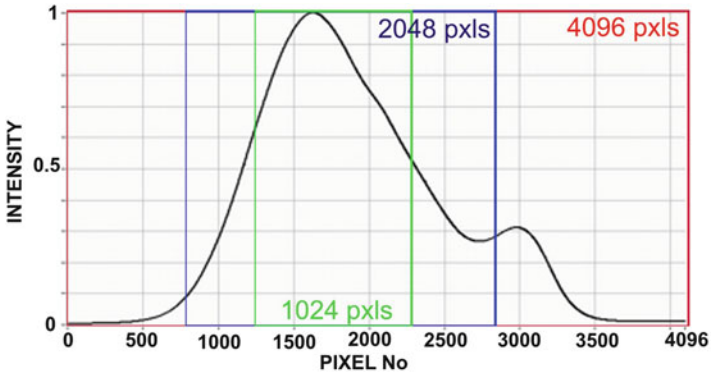

SOCT system parameters for different number of active pixels of the CMOS camera

Number of pixels	Axial resolution [μm]	Sensitivity at T_{exp}= 40us [dB]	Minimum repetition time $T_{rep}^{(min)}$ [μs]	Sensitivity at $T_{rep}^{(min)}$ [dB]
4096	6.9	102	14.2	97.5
2048	8.7	101	7.8	94
1024	15.4	98	4.7	89

Fig. 54.7 Spectrum of the light source used in the spectrometer-based FdOCT system. Areas of interest where the camera has captured 4,096, 2,048, and 1,024 pixels are indicated by *red*, *blue*, and *green rectangles*, respectively. The resolution decreases from 6.9 to 15.4 μm and the sensitivity drops by 4 dB if calculated for a given constant exposure time (T_{exp}) of 40 μs (Image reprinted with permission from OSA, I. Grulkowski, et al., Opt. Express 17, 4842–4858, 2009 [34])

54.2.2 Serial Registration by FdOCT Using Swept-Source Technology (SS-OCT, OFDI)

As mentioned above, an ideal OCT anterior segment imaging system should combine two functionalities: providing high-quality and high-resolution cross-sectional images and having a programmable mode for measuring larger volumes. One of the most important technological advantages of the swept-source OCT setup is more flexibility and robustness in the opto-mechanical design, which can make swept source more advantageous in commercialization. Another important advantage of swept-source OCT device is the substantially lower sensitivity roll-off, which enables more optimal use of the entire measurement range. Moreover, some

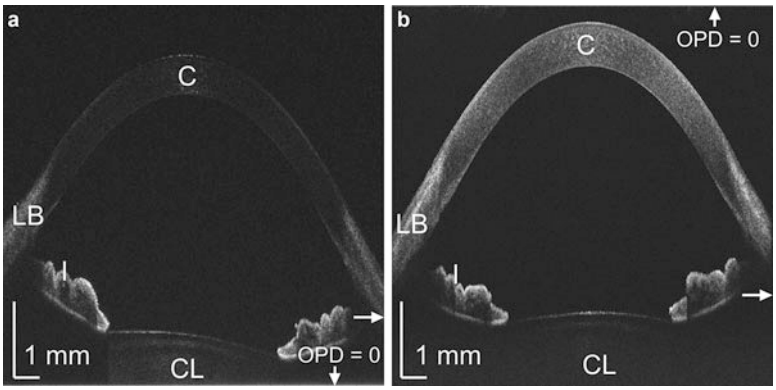

Fig. 54.8 2D OCT imaging of the cornea and anterior chamber using spectrometer-based Fourier detection: (**a**) single-line exposure time, 8.5 μs; repetition rate, ~117,000 A-scans/s; 10,000 × 1,024 pixels; 15 mm and (**b**) single-line exposure time, 53 μs; repetition rate, ~19,000 A-scans/s; 10,000 × 4,096 pixels; 15 mm. Structural elements are visible, including the cornea (*C*), limbus (*LB*), iris (*I*), and crystalline lens (*CL*). Position of zero optical path difference ($OPD = 0$) is indicated. *Horizontal arrows* show the position of the focal plane of the imaging lens (Image reprinted with permission from OSA, I. Grulkowski, et al., Opt. Express 17, 4842–4858, 2009 [34])

swept-source OCT devices are more flexible in the rapid adjustment of axial resolution and measurement range. Operating in different programmable regimes requires controlling the spectral span of light generated by the source; this can be done, for example, by flexible driving of the optical filter in the laser cavity. Unfortunately, not all designs of high-speed tunable light sources enable such control. The three major concepts behind achieving high-speed tuning differ in the method used for wavelength selection inside the laser cavity of the wavelength-swept source: one is based on a fast rotating polygonal mirror [43, 44], another based on a diffraction grating on a mechanically resonant galvo-scanner [45], and the third uses a Fabry-Perot tunable filter (FP-TF) [46, 47]. Only the third solution is able to switch between different modes by changing the amplitude of the FP-TF driving signal: the lower the amplitude of the driving signal, the narrower the wavelength scanning range. In principle, it is possible to choose any value for the axial resolution, limited only by the spectral bandwidth of SOA (highest resolution) or by the laser mode stability (lowest resolution). Gora et al. have demonstrated examples of bimodal operation of swept-source OCT [35]. The high speed of the swept-source OCT system enables high-definition imaging of large volumes, as well as high-accuracy reconstruction of certain portions of the anterior segment morphology, like the irido-scleral angle (Fig. 54.9).

The main limitation in the development of swept-source OCT technology is set by technological problems in developing swept sources for 800 nm and the visible range. Use of shorter optical wavelengths helps in optimization of the system performance in terms of image quality and the resolution. Also the speckle pattern can be reduced more effectively for shorter wavelengths. Finally in swept-source lasers, additional phase jitter can occur since the phase of registered interferometric

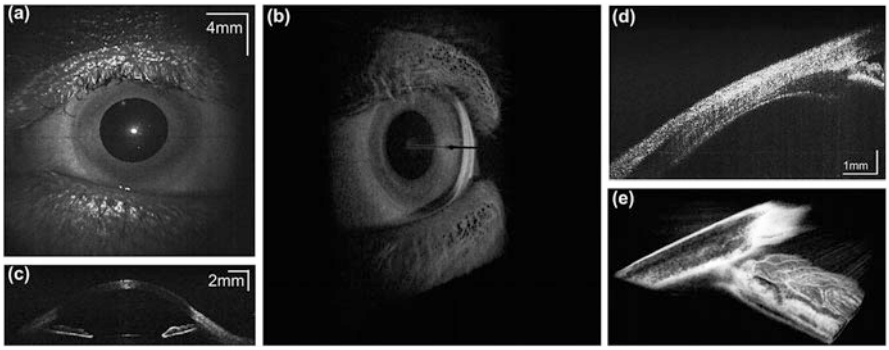

Fig. 54.9 Swept-source OCT imaging of the anterior segment of the human eye in vivo with single-line exposure time of 5 μs. (**a**) En-face view. (**b**) 3D rendering reconstructed from a 1,200 × 300 × 1,024 voxel dataset, with the size of the imaged volume 20 mm × 20 mm × 6 mm. (**c**) Representative cross-sectional image. (**d**) Cross-sectional image of the iridocorneal angle. (**e**) 3D rendering generated from the 3D data set (1,000 × 500 × 1,024 voxels) (Image reprinted with permission from OSA, M. Gora, et al., Opt Express 17, 14880–14894, 2009 [35])

signal is changed by mechanical filtering of optical frequency components in the laser cavity. One of the future challenges is in fast data processing and new algorithms for image processing, which can deliver more reliable and clinically significant information. Also high-speed systems provide huge amount of data which should be managed online.

54.2.3 Main Constrains of Anterior Segment FdOCT Method and Technology

One of the main objectives of high-quality and high-resolution in vivo anterior segment imaging is to achieve accuracy similar to that in microscopy. It is especially important for imaging of Bowman's layer, the epithelial and endothelial tissue layers in the cornea, endothelium, and the capsule of the crystalline lens. However, a careful look at any magnified OCT cross-sectional image reveals that high spatial frequency intensity modulations are superimposed on the reconstructed structure; this modulation is called speckle noise, or a speckle pattern [48]. This "speckle noise" deteriorates OCT image quality and resolution and it occurs always when scattering samples are imaged.

Speckles result from random phases of backscattered light reflected from a rough surface or tissue with scattering structures that are smaller than the focused beam. This stochastic intensity distribution will depend on two factors: irregularities in the imaged tissue and diversity in the phase of detected light. The latter is based on the spectral bandwidth of the light and the NA of the collecting optical system. One important parameter that defines the speckle field is the speckle size. The average speckle spot size will increase with decreases in NA and spectral bandwidth. Thus, the NA of the collecting optics determines the angular range of

scattered light that can be collected by the optical system: the greater the range, the smaller the average speckle size. Similarly, the NA of the device determines the lateral resolution of OCT; increasing NA leads to improved lateral resolution and reduced average speckle size. The electromagnetic field generates a different speckle pattern for each optical frequency component, resulting in additional modulation of the signal as a function of optical wavelength; moreover, after the Fourier transformation is applied, it also causes an intensity modulation in the axial direction. Therefore, two effects – transverse and axial – cause the speckle pattern in cross-sectional OCT images.

One of the main objectives of high-quality OCT imaging with micrometer resolution is to effectively reduce the contrast of speckles. Unfortunately, the presence of speckles is fundamentally related to the formation of the OCT image. In most cases, speckle noise reduction is achieved by averaging multiple images with variable, uncorrelated speckle patterns. Uncorrelated speckle patterns that originate from the same structure can be obtained by tracking speckles in space, over time, or by polarization diversity [49–51]. There are several ways to collect uncorrelated speckle patterns, such as compounding optical frequencies with two incoherent interferometer signals that use two light sources with different central wavelengths [52], applying light with orthogonal polarization states, using a partially spatially coherent light source [53, 54], angular compounding [55–59], inducing mechanical stress to the sample [60], or changing the position of the focusing objective [61]. The most common way of de-correlating the speckle pattern for in vivo imaging is the random spatial compounding method. In this method, a set of two- or three-dimensional images is acquired, with the expectation that the object's natural instability (bulk motion) will cause a small dither in the scanning beam on the object and that this will induce strong variability in the speckle pattern [62–65]. This method has been combined with an eye tracker system in the Spectralis OCT instrument that was brought to the market by Heidelberg Engineering [66]. However, this technique is not fully controlled and can depend on the stability of patient fixation. An eye tracker is used to minimize randomness [67, 68], but the accuracy of this type of device is less than 50 μm [69].

Szkulmowski et al. recently published a study that applied speckle averaging in anterior segment imaging with the spatial compounding technique; this technique is insensitive to sample bulk motion and allows precise control of lateral resolution [70]. The authors used a scanning protocol with a resonant scanner that applied fast beam deflection in the direction perpendicular to the tomogram lateral dimension. This scanning protocol reduced the time interval between the A-scans to be averaged to the repetition interval of the acquisition system. As a result, the averaging algorithm did not require sophisticated data processing to align tomographic images, it is nearly immune to bulk motion in the investigated sample, and it allows precise control of lateral shifts in the scanning beam on the object. The authors also demonstrated a method for optimizing the dithering amplitude using the contrast-to-noise value. Figure 54.10 shows examples of high-resolution and high-quality FdOCT imaging with reduced speckle contrast. Corneal imaging shows a slight change of the imaging contrast within the epithelial layer, forming two layers of

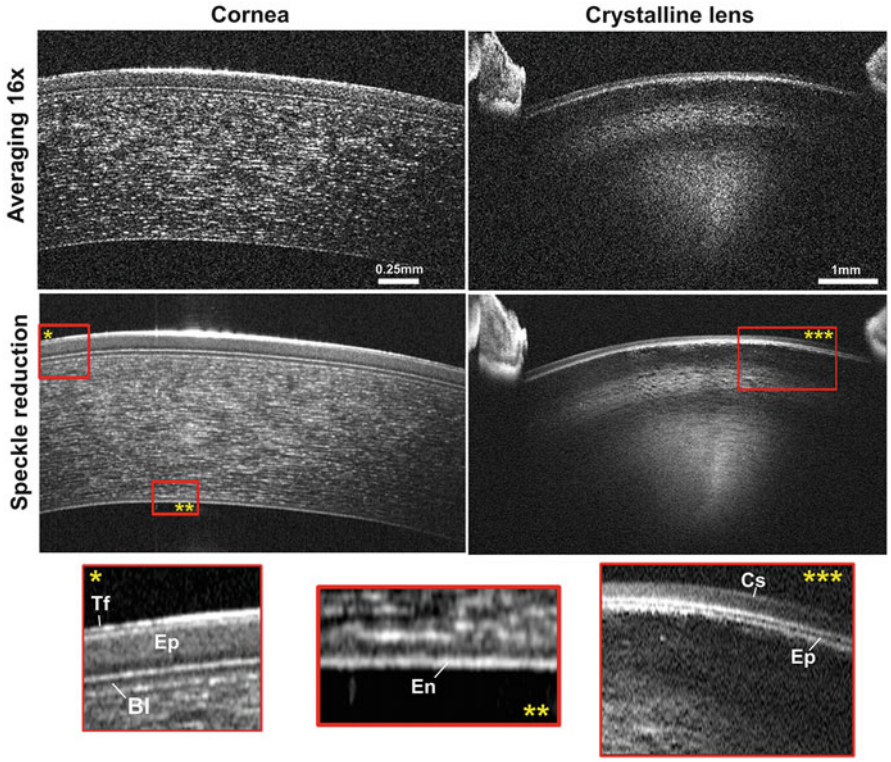

Fig. 54.10 Speckle reduction in OCT images. Axial resolution: 4.2 μm in tissue, imaging range 2.5 mm (cornea) and 7 mm (crystalline lens), imaging speed 200,000 lines/s. Speckle contrast was reduced by precise control of the orthogonal dither of the scanning beam set to 110 um (Image reprinted with permission from OSA, M. Szkulmowski, et al., Opt. Express 20, 1337–1359, 2012 [70])

different reflectivity; the Bowman layer is also visible with reasonable contrast, which is less clearly distinguishable in images without reduced speckle contrast. The reconstruction of the stroma in the posterior section of the cornea reveals a more homogeneous layer close to the endothelium, possibly indicating the presence of Descemet's membrane. It is also possible to distinguish the tear film, probably because the image was taken right after the eye blink, at the moment when the tear film was relatively thick. Speckle reduction also improves cross-sectional imaging of the crystalline lens, where the lens capsule and epithelium are clearly distinguishable. Furthermore, the internal structure of the lens is reconstructed, providing substantial new information about the refractive index distribution within the lens.

This method can only be used for objects with specific morphological symmetry, due to the trade-off between reduced speckle contrast in two dimensions (cross-sectional image) and resolution in the third coordinate (perpendicular to the plane of the cross section). Several technological considerations also limit the construction of highly efficient, high-resolution spectrometers and interferometers.

Ultimately, improved speckle reduction might require the introduction of novel techniques that remain to be discovered. However, there is a high probability that future state-of-the-art OCT technology will be free from speckle noise.

One of the main technological constraints of anterior segment FdOCT is limited axial imaging range. It is mostly caused by a combination of two fundamental technological limitations in Fourier detection scheme: sensitivity roll of due to the limited spectral resolution of the detection system (or instantaneous linewidth in swept source) [19] and additional presence of coherence noise and complex conjugate terms in the FdOCT signal [71]. As it was mentioned before, the sensitivity roll-off may be minimized by using swept-source OCT instruments [72]. However, the second effect is more fundamental and it cannot be solved by a development of better components or a careful design. For relatively thin objects like a retina, it is possible to design OCT instrument to set the total measurement range at least twice larger than the thickness of the measured sample. In such case, there is the possibility of separating the coherence noise components and complex conjugate images from the object's structure reconstruction via a proper selection of the optical path difference between the reference mirror and the first surface of the examined object [12]. However, this procedure may often fail in the case of the anterior segment imaging where measured object has usually significant curvature. In this case, in order to avoid complex conjugate terms and extend the imaging range, it is necessary to introduce a substantial modification to FdOCT technique, which enables to reconstruct complex representation of measured signal and differentiate between complex conjugate signal components. This modified technique is called complex FdOCT [71]. Complex FdOCT technique requires the optical path difference (OPD) between the arms of the OCT interferometer to be varied (either a constant rate or discreet steps synchronized with the detection system) during the acquisition of the interferometric signal. Constant OPD change introduces a carrier frequency for every wavenumber along the time axis. Then an application of two-dimensional Fourier transformation will translate the wavenumber-time space to the depth-velocity space. As a consequence, both complex conjugate images are separated and shifted in opposite directions along v axis. Filtering procedure of negative values of v is equivalent to application of Hilbert Transformation, which in turn provides the complex representation of the real signal. An example of application of a technique of complex conjugate image removal based on the FdOCT using spectrometer has been demonstrated by Grulkowski et al. [45]. Authors demonstrated imaging of the entire anterior segment of the human eye including the cornea, anterior chamber angle, iris, and the entire crystalline lens (Fig. 54.11).

54.3 Application of FDOCT to Ocular Morphometry

OCT allows acquisition of high-resolution images of the anterior segment of the eye. Several diagnostic applications only require visual inspection of the structures and are greatly benefited by the 3D view of the images. However, many cases

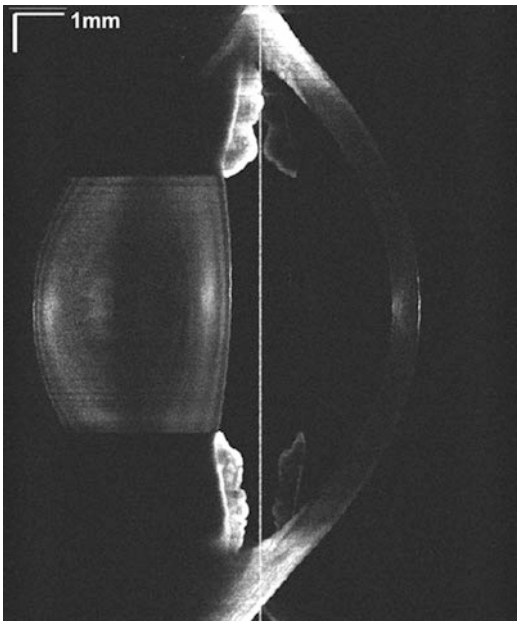

Fig. 54.11 Full-range complex FdOCT image of the entire anterior segment of eye (Image reprinted with permission from OSA, I. Grulkowski, et al., Opt. Express 17, 4842–4858, 2009 [34])

require full quantification of the images, particularly if the images are to be used to guide surgery (e.g., for selection of an intraocular lens to be implanted in cataract or phakic IOL surgery), for identification of candidates for refractive surgery, or for contact lens fitting.

Quantification of OCT images requires image processing algorithms for automatic retrieval of the surfaces and volumes of interest and to correct distortions present in the images. Generally, OCT images are affected by so-called fan distortion [73, 74], which arises from the scanning architecture of the OCT, typically consisting of two physically separated scanning mirrors and resulting in the image of a flat surface not appearing flat (typically with meridional differences in curvature). The amount of fan distortion can be theoretically predicted from the design parameters of the system (focal length of the collimating lens, distance between mirrors, etc.); it can be minimized by hardware, but must be fully corrected by calibrations of the system and software (relying on the computation of the cosine directors of each ray and the correspondence between the instrument coordinates and the local coordinates in space within the object volume) [75]. Correction of fan distortion improves the accuracy of the anterior surface shape reconstruction by 3 % [76]. Anterior segment OCT images are also subject to optical distortion, arising from the fact that objects (posterior cornea, iris, and anterior and posterior lens) are imaged through preceding refracting surfaces. In OCT, it is typically assumed that rays do not bend at the interface, as the optical distances are simply divided by the index of refraction to compute distances. Optical distortion correction is obtained from 3D ray tracing, considering refraction at every interface (subsequently for all surfaces) [77]. Correction of optical distortion improves accuracy of posterior corneal surface reconstruction by 6.2 % and by up to

30 % in reconstruction of the posterior lens shape [78]. Motion artifacts are another potential source of distortion. Decreasing acquisition times have attenuated the impact of subject motion, and motion correction algorithms have also been proposed to compensate for these errors by software [79].

High-resolution high-speed acquisition makes it possible to collect immense amounts of data in a short session. Quantification of these images requires automatic image processing, which allows identification of the structures of interest, correction, and parameterization. Image processing algorithms allow automatic characterization of anterior OCT images and include denoising algorithms, statistical thresholding, volume clustering, multilayer segmentation, axis reference estimates, 3D volume merging, geometrical distance calculation, and surface fitting (sphere, conics, and Zernike polynomials) [76]. Additionally, combining OCT images of the crystalline lens (acquired in vitro in two orientations: with the anterior surface up and the posterior surface up) with global search algorithms allows 3D reconstruction of the GRIN distribution of the crystalline lens [80]. Several studies have evaluated the potential impact of the presence of GRIN on the visualization of the posterior lens surface and its inclusion in optical distortion correction algorithms [81, 82].

Resolution of these challenges has enabled production of quantitative 3D anterior segment imaging (particularly anterior and posterior corneal surface elevation maps), anterior and posterior crystalline lens surface elevation maps, pachymetry, 3D biometry, crystalline lens or intraocular lens alignment in vivo, and crystalline lens GRIN distribution maps in vitro. Applications have been performed in normal eyes [76, 83], in eyes with corneal disease (keratoconus) [30, 83], and after corneal (intrastromal ring segments) [84] and intraocular (IOLs) implants [78].

The above-described methods allow full quantification of the anterior segment of the eye. Figure 54.12 shows a merged image of the cornea, iris, and lens in a normal eye (73 years old) in vivo and the corresponding reconstructed elevation maps for the corneal and lens surfaces. These images also allow estimation of pachymetry, anterior chamber depth, and intraocular lens tilt and decentration.

54.3.1 Corneal Topography

Quantitative analysis of corneal thickness and topography performed by FdOCT instruments has a significant potential in diagnosis of diseases, precise location of lesions, and planning of medical and surgical treatments. Additionally the remarkable advances in the field of refractive surgery have increased requirements for accurate measurements of corneal topography. Currently available systems, like rotating Scheimpflug (Orbscan, Pentacam), scanning slit topography, and ultrasound biomicroscopy are able to provide quantitative information about the corneal architecture [2]. Their main drawback is acquisition speed and limited dynamic range. Additionally the requirement of subjective fixation may always cause uncontrolled translation and rotation of measured cornea in respect to the instrument [85], which in turn may strongly influence the topographical analysis. Anterior segment OCT has significantly larger dynamic range when compared to other

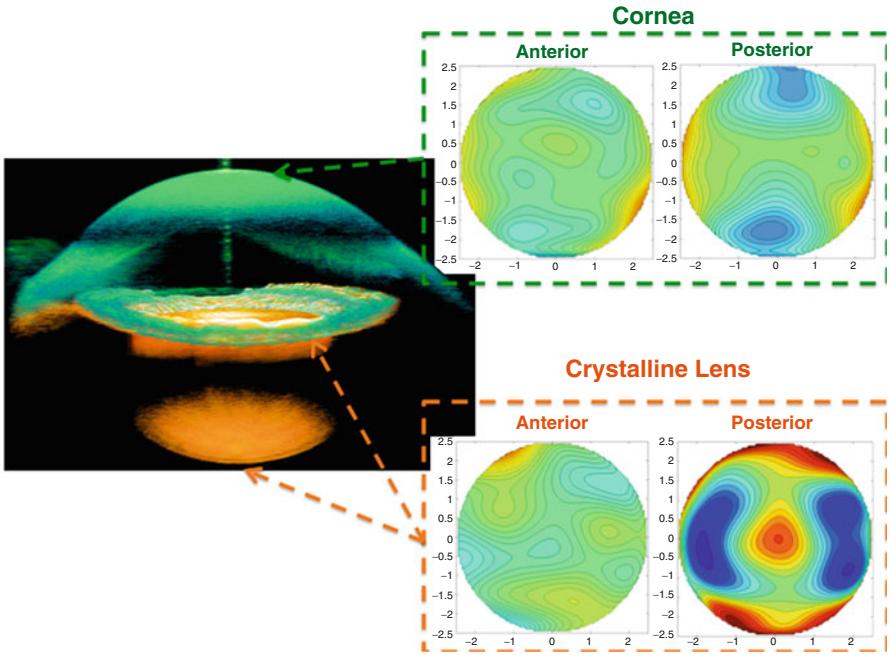

Fig. 54.12 3D full anterior segment in a normal eye, along with quantitative anterior and posterior corneal topographies, and anterior and posterior crystalline lens topography (Image reprinted with permission from OSA, Ortiz et al., Biomedical Optics Express 3, 814–825, 2012 [83])

corneal topographers. It has been already demonstrated that OCT-based anterior corneal topography in normal subjects is comparable (within 2 %) to that obtained using state-of-the-art clinical instruments (Placido disk videokeratoscopy and Scheimpflug images) [30, 76, 78, 83]. In addition, OCT-based corneal topographies show high repeatability (<1 %). Figure 54.13 shows a comparison of anterior corneal topography in a young patient obtained with different instruments and repeated measurements with OCT. The analysis is performed in the form of elevation maps (referred to the best-fitting sphere) as well as radii of curvature and asphericities obtained from biconic fittings.

High-speed OCT instrument with imaging speed of 200,000 A-scans/s. demonstrated by Gora et al. and Karnowski et al. [30, 35] enabled acquiring three-dimensional datasets within 250 ms with sampling density sufficient for quantitative analysis of the anterior segment of the eye [86, 87]. The analysis including reconstruction of corneal topography elevation BFS (best fit sphere) and thickness maps based on a dense raster scan OCT data with reduced number of motion artifacts was demonstrated for eye with a pathology (Fig. 54.14). One of the first demonstrations of high-speed OCT application to quantitative corneal analysis was published by Karnowski et al. [30]. Authors compared corneal topography for three pathologic corneas: keratoconus, a cornea with superficial postinfectious scar, and a cornea 5 months after penetrating keratoplasty. Measurements were performed by FdOCT,

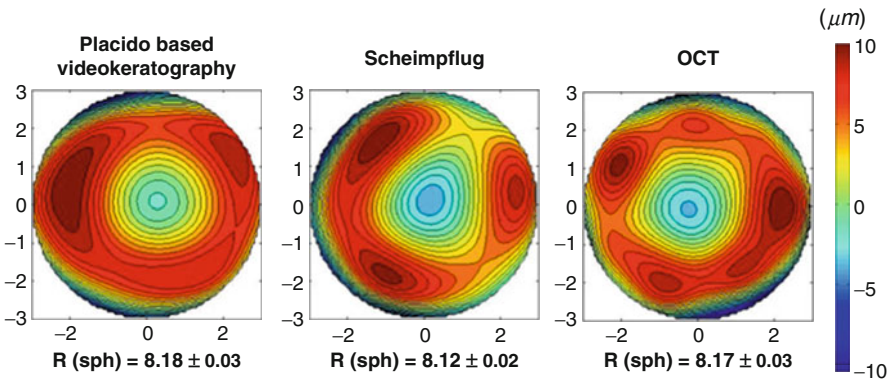

Fig. 54.13 Comparison of anterior corneal surface topography in one normal subject, obtained using commercial corneal topographers (Placido-based videokeratography and Scheimpflug), along with a custom OCT-based OCT (Image reprinted with permission from OSA, Ortiz et al., Biomedical Optics Express **2**, 3232–3247, 2011 [76])

conventional Placido-based topographer (PTC 110, Optopol Technology, Poland), and a rotating Scheimpflug camera (Pentacam HR, Oculus, Germany). Figure 54.14 shows the topographic analysis of a clinically significant keratoconic cornea. Anterior elevation topographies, central keratometry value K1, axis in a flat meridian, posterior corneal topography, and pachymetry were comparable for all instruments. More complicated case of the eye 5 months after penetrating keratoplasty are shown in right panel of Fig. 54.14. In this case, Placido reflections are very distorted. Although only a couple of rings in the center could be partially distinguished and analyzed by the computer, the Placido system provides a curvature map of the entire cornea, even the part that is hidden behind the upper lid. As it might be expected, the differences in central keratometry reading are very large in comparison to Pentacam and FdOCT. Anterior topographies from Pentacam and FdOCT show comparable patterns, but the elevated central island is located slightly higher on the OCT map, resulting in a significant difference in central keratometry readings.

Very practical advantage of morphometric analysis based on OCT data is that one instrument can provide information that was previously only possible to obtain with a few, independent, diagnostic devices. Additionally quantitative analysis of OCT data is usually associated with the reduction of the data dimension, which enables quick assessments of the condition of the ocular structure without requiring a one-by-one study of all cross-sectional images in 3D volumetric set of data.

54.3.2 Architecture of the Crystalline Lens

OCT imaging of the crystalline lens is challenging due to its considerable thickness ranging from 3.5 to 4.8 mm and its high transparency. In contrast to the imaging of the corneoscleral junction, higher diffuse reflectance and less absorption offered by

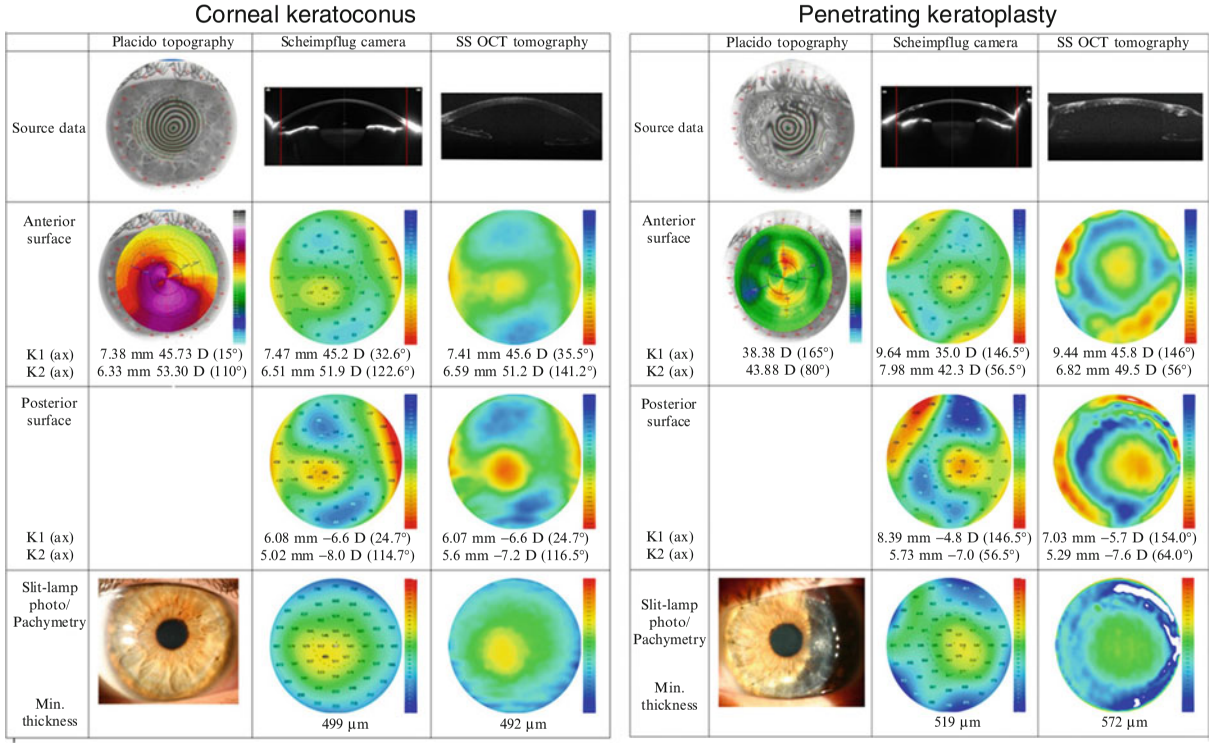

Fig. 54.14 Quantitative analysis of a keratoconic cornea (*left*) and a cornea 5 months after penetrating keratoplasty (*right*) with FdOCT, conventional Placido-based topographer (PTC 110, Optopol Technology, Poland), and a rotating Scheimpflug camera (Pentacam HR, Oculus, Germany). K1, K2 – central keratometry readings. The *red lines* on Scheimpflug images correspond to lateral size of cross-sectional images for FdOCT (Image reprinted with permission from OSA, K. Karnowski, et al., Biomedical Optics Express 9, 2709–2720, 2011 [30])

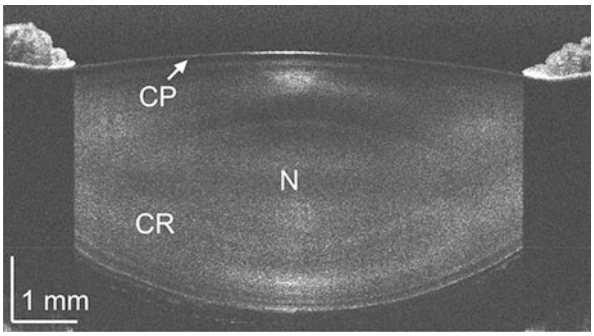

Fig. 54.15 OCT cross-sectional image of the crystalline lens: single-line exposure time 70 μs, transverse scanning density 15,000 A-scans per 9 mm, 4,096 pixels in each A-scan (*CP*, lens capsule; *N*, nucleus; and *CR*, cortex) (Image reprinted with permission from OSA, I. Grulkowski, et al., Opt. Express 17, 4842–4858, 2009 [34])

840 nm can help in visualization of healthy crystalline lenses. Figure 54.15 shows an image of a crystalline lens in a 30-year-old subject obtained with high transverse scanning density (15,000 A-scans in 9 mm). Under these imaging conditions, it is possible to easily distinguish characteristic structures of crystalline lens morphology such as capsule, cortex, and nucleus.

The quantitative OCT allows, for the first time, the obtainment of surface topographies of the crystalline lens (to date, most measurements in vivo have been limited to measurement of radii of curvature, in most cases in a single meridian). The OCT-based estimated lens radii of curvature for the anterior surface (10.27–14.14 mm) and posterior lens surface (6.12–7.54 mm) [84] are in good agreement with those obtained using Scheimpflug or Purkinke imaging – for the unaccommodated state and as a function of accommodation [88]. Besides phakometry, the quantification of full lens surface topography has allowed analyses of high-order terms and potential relationships between surface patterns in the anterior and posterior lens (such as a consistently found cross cylinder). Figure 54.16 shows anterior and posterior crystalline lens surface topographies in one subject (35 years old, unaccommodated state) and repeated measurements for one subject. The analysis is performed both as elevation maps (referred to the best-fitting sphere) and as radii of curvature and asphericities obtained from biconic fittings.

OCT has also enabled, for the first time, estimation of the 3D GRIN distribution in the crystalline lens in vitro. The GRIN is described using a four-variable model, with the index of refraction in the nucleus and in the surface, and meridional variations of the exponential decay. Figure 54.17 shows 2D maps of the GRIN distribution in isolated lenses of different ages (ranging from 6 to 72 years old) [80]. While there is no systematic variation in the values of the refractive index in the nucleus and surface, there is a strong variation in the exponential decay of the index variation, almost parabolic in the youngest eyes, and with a wide plateau in the older lenses.

Another interesting application of high-resolution FdOCT for lens imaging was presented by Kaluzny et al. in 2010 [89]. They demonstrated a unique ability of

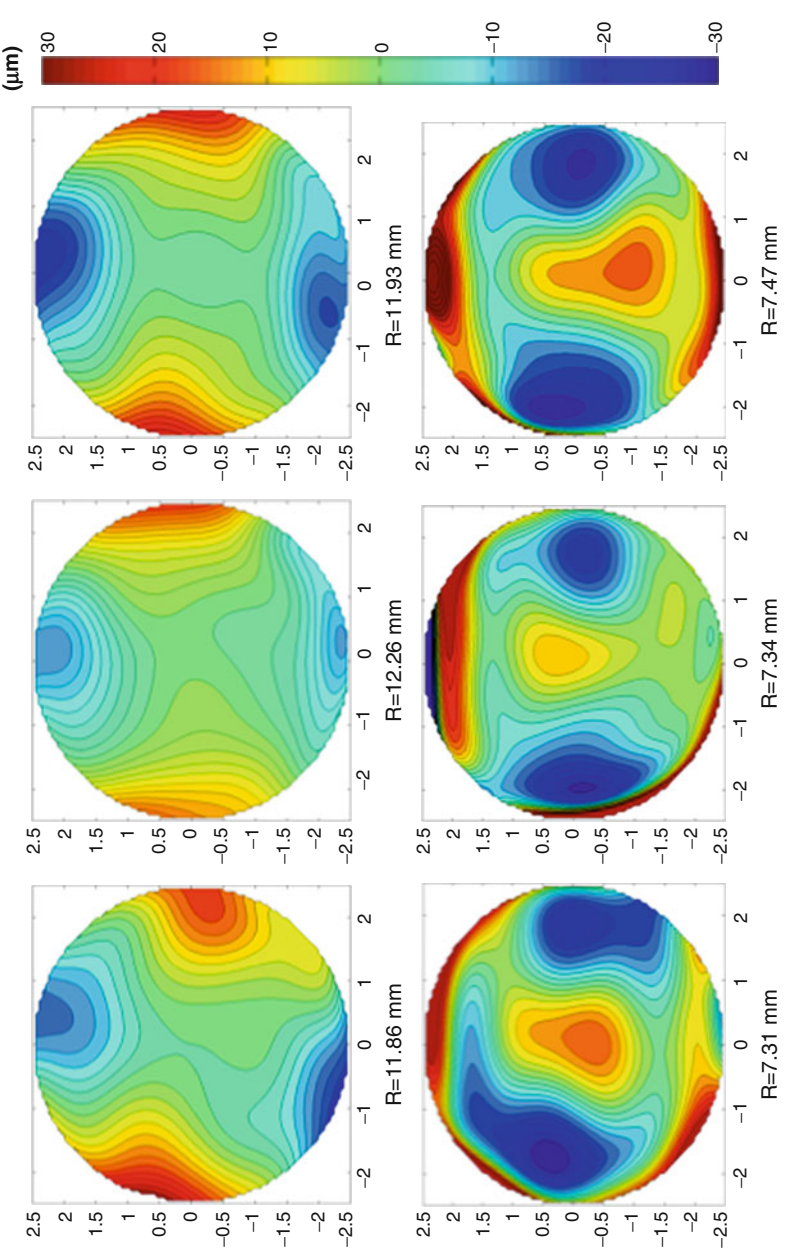

Fig. 54.16 Anterior and posterior crystalline lens topography in a young normal subject (unaccommodated state) (Image reprinted with permission from OSA, S. Ortiz, et al., Biomedical Optics Express 3, 2471–2488, 2012 [84])

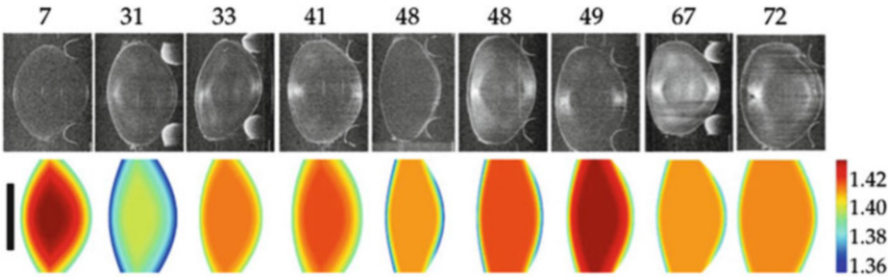

Fig. 54.17 OCT cross sections of human crystalline lenses of different ages (7–72 years old) and reconstructed gradient index of refraction (*GRIN*) distribution

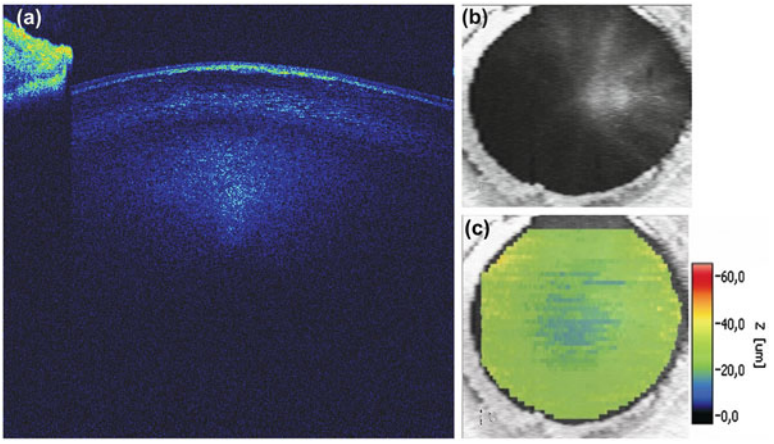

Fig. 54.18 Morphometry of the capsule of crystalline lens. (**a**) Ultrahigh-resolution OCT cross-sectional image of an anterior part of the lens and the pupillary margin of the iris. (**a**) En-face image of the iris and lens surface reconstructed from three-dimensional data. (**b**) Anterior lens capsule thickness map (mm). The area of examination is 7 mm by 7 mm (Image reprinted from B. J. Kaluzny et al., Br J Ophthalmol 94, 275–277 (2010), copyright BMJ group 2010 [89])

FdOCT system using femtosecond laser for precise cross-sectional evaluation of the capsular bag, estimation of its thickness, or visualization of the lens epithelium in vivo [89]. Figure 54.18 shows a high-accuracy thickness map of the anterior capsule of the crystalline lens.

54.4 Real-Time FDOCT Anterior Segment Imaging

The ultrahigh-speed performance offered by the FdOCT technology enables also video-rate monitoring of various dynamic processes in the anterior segment. An example of 3D (three-dimensions and time) imaging is shown in Fig. 54.19, where

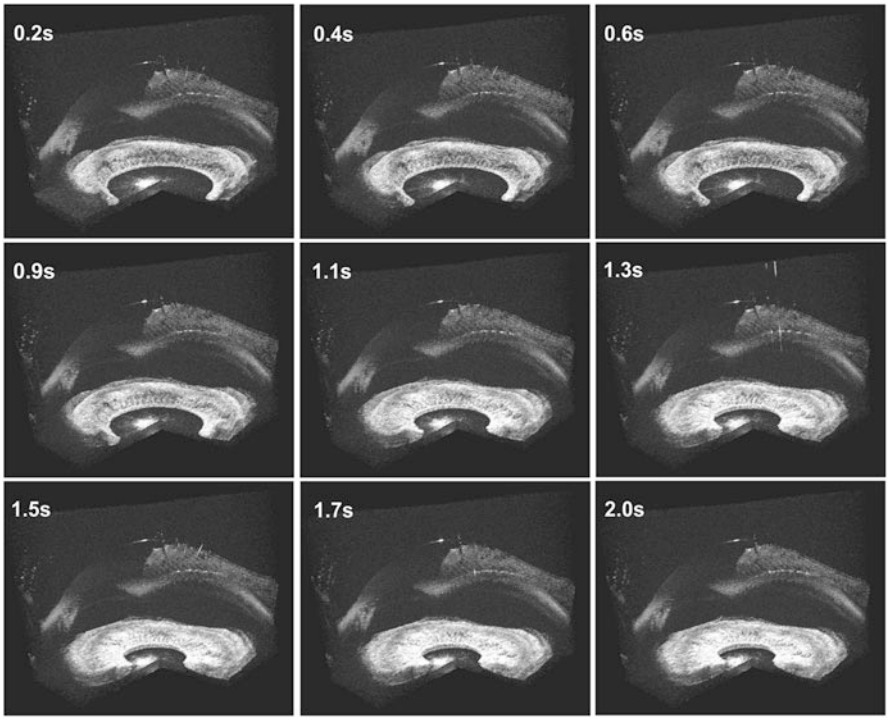

Fig. 54.19 4D OCT imaging using high-speed 800 nm, SOCT instrument: consecutive volume renderings of anterior segment of the human eye during pupillary contraction, volume size 300 × 100 × 1,024 pixels corresponding to 5 mm × 15 mm × 15 mm (Image reprinted with permission from OSA, M. Wojtkowski, Appl Opt 49, D30–61 (2010) [19])

the entire 3D scanning protocol was repeated in time giving real-time volumetric reconstruction of the blinking eye [34, 35]. Another interesting application for tracking dynamic changes in the anterior segment is to observe changes in a cross section of the human crystalline lens during the accommodation process. Grulkowski et al. demonstrated a sequence of nine frames chosen from 80 frames of an OCT movie [34]. The authors claimed that this movie was the first to demonstrate cross-sectional imaging of real-time dynamics of the lens during accommodation [34].

One example of a potential clinical application for high-speed, real-time OCT imaging is the assessment of dynamic processes that occur on the surface of the cornea. As it was demonstrated by Kaluzny et al., such monitoring may help in estimating of contact lens motion induced by blinking and tear film dynamics [90]. An example of a quantitative analysis of the movement of a rigid contact lens after a blink is shown in Fig. 54.20.

Another interesting application of real-time OCT is the assessment of corneal deformation after an air-puff – a concept similar to that used in noncontact tonometry [91].

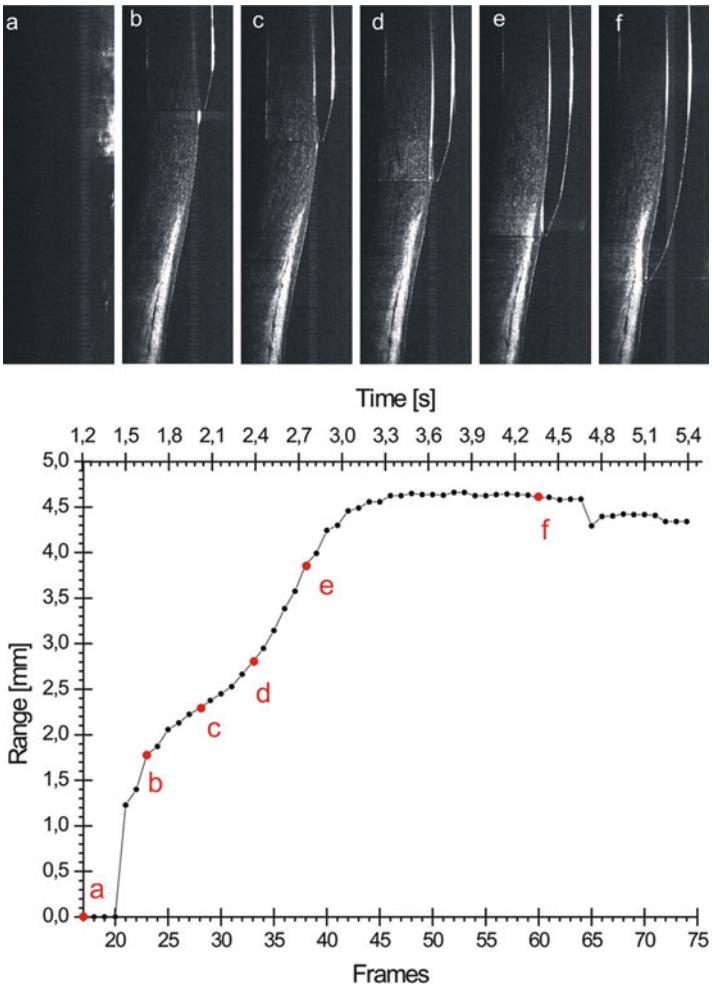

Fig. 54.20 Analysis of the blink-induced vertical movement of a rigid contact lens. *Left*: single frames from a 6-s movie of OCT cross-sectional images. *Right*: plot representing the relative blink-induced movement of the inferior lens edge as a function of frame number and/or time (Image reprinted from B. J. Kaluzny et al., Optom Vis Sci 84, 1104-1109 (2007) [90], copyright American Academy of Optometry 2007)

The geometric properties and integrity of the cornea rely on the mechanical properties of its constituent material. Several corneal diseases – such as keratoconus, which leads to corneal deformation and highly degraded optical quality – result from progressive corneal weakening and thinning. Emerging treatments for keratoconus (such as UV-riboflavin collagen cross-linking) attempt to increase corneal stiffness. Furthermore, several corneal treatments (incisional surgery, corneal laser surgery, and intrastromal implants) can be modulated by the biomechanical properties of the cornea. Our present knowledge of corneal biomechanical properties comes primarily

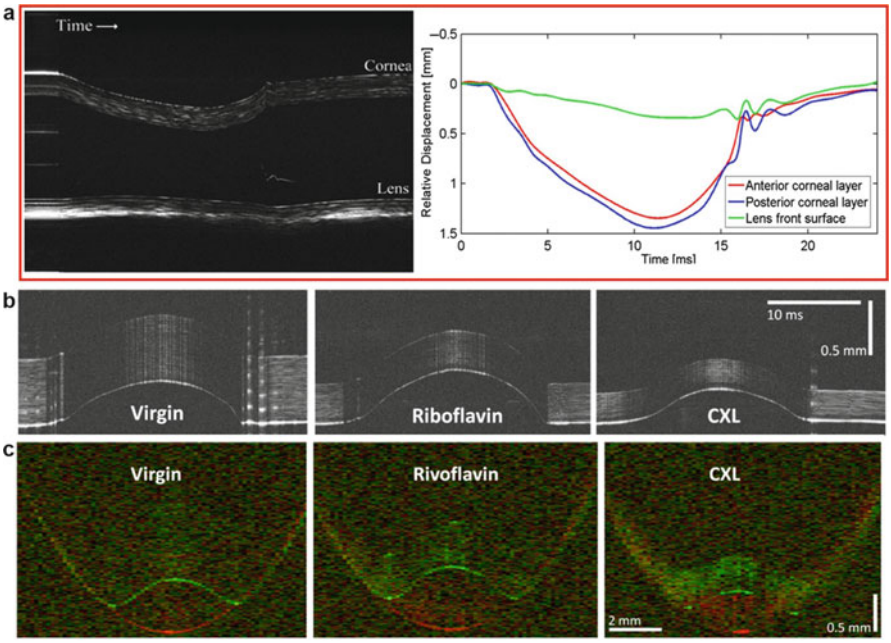

Fig. 54.21 Dynamic OCT imaging of the corneal deformation with an air puff. (**a**) M-scan (1,300 A-scans) showing the surface motion during the measurement along with a plot of a relative displacement of the cornea and lens (Reprinted with permission from OSA, D. Alonso-Caneiro et al. Opt Express 19, 14188–14199 (2011) [91]). (**b**) Deformation of the apex of the cornea as a function of time for the same cornea after application of riboflavin-dextran solution and after collagen cross-linking (CXL). (**c**) Cross-sectional images of a cornea that is undeformed (*red*) and at maximum deformation (*green*) from a corneal deformation sequence. A lower deformation is consistent with increased corneal stiffness. Measurements were performed with constant IOP power (Reprinted with permission from OSA, Dorronsoro et al., Biomedical Optics Express 3, 473–487, 2012 [96])

from lateral extensiometry techniques, corneal button or whole eye inflation, and 2D flap extensiometry performed on in vitro samples [92–94]. Patient diagnosis and predictions of corneal performance following a given corneal treatment require in vivo measurements of corneal biomechanical properties. Promising techniques for such measurements rely on the dynamic measurement of corneal deformation via anterior segment imaging upon air-puff applanation tonometry. A commercial instrument is available for this purpose, which combines Scheimpflug imaging with an air puff [95]. There are recent proposals for new methods based on OCT, which can measure geometrical distortions of cornea with high axial resolution and high speed. The advent of high-speed OCT systems (based on swept sources and spectral OCT systems with a CMOS camera) has enabled the high acquisition speeds required to image the deformation event within an air-pulse duration in the order of milliseconds.

Alonso-Caneiro et al. (2011) reported the acquisition of M-scans (A-scans of the anterior segment at central and peripheral locations as a function of time) during an air-puff event in normal subjects in vivo, using swept-source OCT [91].

The observed corneal deformation tended to increase with drug-induced decrease of intraocular pressure (IOP). Dorronsoro et al. (2012) [96] also reported acquisitions of M-scans, as well as sequences of B-scans during an air-puff event in virgin and treated porcine eyes in vitro, and in a human eye in vivo, using high-speed spectral-source OCT (Fig. 54.21). The porcine eyes were treated with riboflavin-dextran (a photosensitizer used in corneal cross-linking in a highly dehydrating solution) and with UV-riboflavin corneal cross-linking. Measurements were obtained while keeping IOP constant. Corneal deformation is affected by IOP as well as geometric properties of the cornea (particularly corneal thickness). However, substantial differences were found between riboflavin-only and full cross-linking treatments. As corneal geometry was the same before and after UV irradiation, these results indicate a substantial change in the biomechanical properties of the cornea. Corneal deformation is substantially less in the cross-linked corneas, revealing increased corneal stiffness.

Although analyses to date have been limited to the temporal and spatial parameters of corneal deformation (including deformation amplitude, deformation speed, and deformation duration), in the future, the full potential of air-puff OCT will be exploited via combination of the experimental data of corneal deformation with finite element modeling. The possibility of reconstructing corneal biomechanical parameters (such as the elasticity modulus, shear modulus, or viscoelastic time constants) at the individual level will open new avenues for the diagnosis of corneal diseases in which corneal stiffness is compromised, for evaluating the outcomes of procedures that modulate biomechanical corneal properties, and for guiding treatments that rely on corneal biomechanics.

Acknowledgments This work was supported by EuroHORCs, European Science Foundation and Foundation for Polish Science within the frames of EURYI Award EURYI-01/2008-PL (MW, IG) Spanish Government FIS2011-25637, CSIC Plan Equipa, and European Research Council Grant ERC-2011 AdG-294099 (SM, DO). Authors would like to acknowledge Bartłomiej Kałużny from Ophthalmic Clinic at Collegium Medicum NCU; Maciej Szkulmowski, Michalina Gora, Karol Karnowski, and Monika Fojt from Optical Biomedical Imaging Group at NCU; Tomasz Bajraszewski from Optopol Technology.

References

1. A. Konstantopoulos, P. Hossain, D.F. Anderson, Recent advances in ophthalmic anterior segment imaging: a new era for ophthalmic diagnosis? Br. J. Ophthalmol. **91**, 551–557 (2007)
2. A.C. Cheng, S.K. Rao, S. Lau, C.K. Leung, D.S. Lam, Central corneal thickness measurements by ultrasound, Orbscan II, and Visante OCT after LASIK for myopia. J. Refract. Surg. **24**, 361–365 (2008)
3. M. Dubbelman, H.A. Weeber, R.G.L. van der Heijde, H.J. Volker-Dieben, Radius and asphericity of the posterior corneal surface determined by corrected Scheimpflug photography. Acta Ophthalmol. Scand. **80**, 379–383 (2002)
4. B. Lackner, G. Schmidinger, S. Pieh, M.A. Funovics, C. Skorpik, Repeatability and reproducibility of central corneal thickness measurement with Pentacam, Orbscan, and ultrasound. Optom. Vis. Sci. **82**, 892–899 (2005)
5. J.G. Sivak, T. Mandelman, Chromatic dispersion of the ocular media. Vision Res. **22**, 997–1003 (1982)

6. M. Dubbelman, G.L. Van der Heijde, The shape of the aging human lens: curvature, equivalent refractive index and the lens paradox. Vision Res. **41**, 1867–1877 (2001)
7. M. Dubbelman, G.L. Van der Heijde, H.A. Weeber, The thickness of the aging human lens obtained from corrected Scheimpflug images. Optom. Vis. Sci. **78**, 411–416 (2001)
8. J.M. Pope, D.A. Atchison, B.A. Moffat, Age-related changes of the refractive index of the crystalline lens – response. Vision Res. **42**, 2809 (2002)
9. D. Huang, E.A. Swanson, C.P. Lin, J.S. Schuman, W.G. Stinson, W. Chang, M.R. Hee, T. Flotte, K. Gregory, C.A. Puliafito, J.G. Fujimoto, Optical coherence tomography. Science **254**, 1178–1181 (1991)
10. J.F. De Boer, T.E. Milner, M.J.C. van Gemert, J.S. Nelson, Two-dimensional birefringence imaging in biological tissue by polarization-sensitive optical coherence tomography. Opt. Lett. **22**, 934–936 (1997)
11. A.F. Fercher, W. Drexler, C.K. Hitzenberger, T. Lasser, Optical coherence tomography-principles and applications. Rep. Prog. Phys. **66**, 239–303 (2003)
12. M. Wojtkowski, R. Leitgeb, A. Kowalczyk, T. Bajraszewski, A.F. Fercher, In vivo human retinal imaging by Fourier domain optical coherence tomography. J. Biomed. Opt. **7**, 457–463 (2002)
13. N. Nassif, B. Cense, B.H. Park, S.H. Yun, T.C. Chen, B.E. Bouma, G.J. Tearney, J.F. de Boer, In vivo human retinal imaging by ultrahigh-speed spectral domain optical coherence tomography. Opt. Lett. **29**, 480–482 (2004)
14. M. Wojtkowski, V. Srinivasan, J.G. Fujimoto, T. Ko, J.S. Schuman, A. Kowalczyk, J.S. Duker, Three-dimensional retinal imaging with high-speed ultrahigh-resolution optical coherence tomography. Ophthalmology **112**, 1734–1746 (2005)
15. U. Schmidt-Erfurth, R.A. Leitgeb, S. Michels, B. Povazay, S. Sacu, B. Hermann, C. Ahlers, H. Sattmann, C. Scholda, A.F. Fercher, W. Drexler, Three-dimensional ultrahigh-resolution optical coherence tomography of macular diseases. Invest. Ophthalmol. Vis. Sci. **46**, 3393–3402 (2005)
16. A.G. Podoleanu, G.M. Dobre, R.G. Cucu, R. Rosen, P. Garcia, J. Nieto, D. Will, R. Gentile, T. Muldoon, J. Walsh, L.A. Yannuzzi, Y. Fisher, D. Orlock, R. Weitz, J.A. Rogers, S. Dunne, A. Boxer, Combined multiplanar optical coherence tomography and confocal scanning ophthalmoscopy. J. Biomed. Opt. **9**, 86–93 (2004)
17. R.B. Rosen, M. Hathaway, J. Rogers, J. Pedro, P. Garcia, G.M. Dobre, A.G. Podoleanu, Simultaneous OCT/SLO/ICG imaging. Invest. Ophthalmol. Vis. Sci. **50**, 851–860 (2009)
18. R.B. Rosen, M. Hathaway, J. Rogers, J. Pedro, P. Garcia, P. Laissue, G.M. Dobre, A.G. Podoleanu, Multidimensional en-face OCT imaging of the retina. Opt. Express **17**, 4112–4133 (2009)
19. M. Wojtkowski, High-speed optical coherence tomography: basics and applications. Appl. Opt. **49**, D30–D61 (2010)
20. M. Wojtkowski, V.J. Srinivasan, T.H. Ko, J.G. Fujimoto, A. Kowalczyk, J.S. Duker, Ultrahigh-resolution high-speed Fourier domain optical coherence tomography and methods for dispersion compensation. Opt. Express **12**, 2404–2422 (2004)
21. N.A. Nassif, B. Cense, B.H. Park, M.C. Pierce, S.H. Yun, B.E. Bouma, G.J. Tearney, T.C. Chen, J.F. de Boer, In vivo high-resolution video-rate spectral-domain optical coherence tomography of the human retina and optic nerve. Opt. Express **12**, 367–376 (2004)
22. R.A. Leitgeb, W. Drexler, A. Unterhuber, B. Hermann, T. Bajraszewski, T. Le, A. Stingl, A.F. Fercher, Ultrahigh resolution Fourier domain optical coherence tomography. Opt. Express **12**, 2156–2165 (2004)
23. M. Wojtkowski, T. Bajraszewski, P. Targowski, A. Kowalczyk, Real-time in vivo imaging by high-speed spectral optical coherence tomography. Opt. Lett. **28**, 1745–1747 (2003)
24. M. Wojtkowski, T. Bajraszewski, I. Gorczynska, P. Targowski, A. Kowalczyk, W. Wasilewski, C. Radzewicz, Ophthalmic imaging by spectral optical coherence tomography. Am J. Ophthalmol. **138**, 412–419 (2004)
25. S.H. Yun, G.J. Tearney, B.E. Bouma, B.H. Park, J.F. de Boer, High-speed spectral-domain optical coherence tomography at 1.3 mu m wavelength. Opt. Express **11**, 3598–3604 (2003)

26. S. Alam, R.J. Zawadzki, S. Choi, C. Gerth, S.S. Park, L. Morse, J.S. Werner, Clinical application of rapid serial fourier-domain optical coherence tomography for macular imaging. Ophthalmology **113**, 1425–1431 (2006)
27. B. Potsaid, I. Gorczynska, V.J. Srinivasan, Y. Chen, J. Jiang, A. Cable, J.G. Fujimoto, Ultrahigh speed spectral/Fourier domain OCT ophthalmic imaging at 70,000 to 312,500 axial scans per second. Opt. Express **16**, 15149–15169 (2008)
28. S. Radhakrishnan, J. Goldsmith, D. Huang, V. Westphal, D.K. Dueker, A.M. Rollins, J.A. Izatt, S.D. Smith, Comparison of optical coherence tomography and ultrasound biomicroscopy for detection of narrow anterior chamber angles. Arch. Ophthalmol. **123**, 1053–1059 (2005)
29. M. Miura, K. Kawana, T. Iwasaki, T. Kiuchi, T. Oshika, H. Mori, M. Yamanari, S. Makita, T. Yatagai, Y. Yasuno, Three-dimensional anterior segment optical coherence tomography of filtering blebs after trabeculectomy. J. Glaucoma **17**, 193–196 (2008)
30. K. Karnowski, B.J. Kaluzny, M. Szkulmowski, M. Gora, M. Wojtkowski, Corneal topography with high-speed swept source OCT in clinical examination. Biomed. Opt. Express **9**, 2709–2720 (2011)
31. D.K. Sardar, R.M. Yow, G.Y. Swanland, R.J. Thomas, A.T.C. Tsin, Optical properties of ocular tissues in the near infrared region – art. no. 613815. Ophthal. Technol. XVI **6138**, 13815 (2006)
32. M. Hammer, A. Roggan, D. Schweitzer, G. Muller, Optical-properties of ocular fundus tissues – an in-vitro study using the double-integrating-sphere technique and inverse Monte-Carlo simulation. Phys. Med. Biol. **40**, 963–978 (1995)
33. A.N. Bashkatov, E.A. Genina, V.I. Kochubey, V.V. Tuchin, Optical properties of human sclera in spectral range 370–2500 nm. Opt. Spectrosc. **109**, 197–204 (2010)
34. I. Grulkowski, M. Gora, M. Szkulmowski, I. Gorczynska, D. Szlag, S. Marcos, A. Kowalczyk, M. Wojtkowski, Anterior segment imaging with spectral OCT system using a high-speed CMOS camera. Opt. Express **17**, 4842–4858 (2009)
35. M. Gora, K. Karnowski, M. Szkulmowski, B.J. Kaluzny, R. Huber, A. Kowalczyk, M. Wojtkowski, Ultra high-speed swept source OCT imaging of the anterior segment of human eye at 200 kHz with adjustable imaging range. Opt. Express **17**, 14880–14894 (2009)
36. B.J. Kaluzny, J.J. Kaluzny, A. Szkulmowska, I. Gorczynska, M. Szkulmowski, T. Bajraszewski, M. Wojtkowski, P. Targowski, Spectral optical coherence tomography: a novel technique for cornea imaging. Cornea **25**, 960–965 (2006)
37. J.J. Kaluzny, M. Wojtkowski, A. Kowalczyk, Imaging of the anterior segment of the eye by spectral optical coherence tomography. Opt. Appl. **32**, 581–589 (2002)
38. M. Wojtkowski, B. Kaluzny, R.J. Zawadzki, New directions in ophthalmic optical coherence tomography. Optom. Vis. Sci. **89**, 524–542 (2012)
39. B.J. Kałużny, A. Szkulmowska, M. Szkulmowski, T. Bajraszewski, A. Wawrocka, M.R. Krawczynski, A. Kowalczyk, M. Wojtkowski, Granular corneal dystrophy in 830-nm spectral optical coherence tomography. Cornea **27**, 830–832 (2008)
40. B.J. Kaluzny, A. Szkulmowska, M. Szkulmowski, T. Bajraszewski, A. Kowalczyk, M. Wojtkowski, Fuchs' endothelial dystrophy in 830-nm spectral domain optical coherence tomography. Ophthalmic Surg. Lasers Imaging **40**, 198–200 (2009)
41. V. Christopoulos, L. Kagemann, G. Wollstein, H. Ishikawa, M.L. Gabriele, M. Wojtkowski, V. Srinivasan, J.G. Fujimoto, J.S. Duker, D.K. Dhaliwal, J.S. Schuman, In vivo corneal high-speed, ultra high-resolution optical coherence tomography. Arch. Ophthalmol. **125**, 1027–1035 (2007)
42. S.H. Yun, G.J. Tearney, J.F. de Boer, B.E. Bouma, Motion artifacts in optical coherence tomography with frequency-domain ranging. Opt. Express **12**, 2977–2998 (2004)
43. S.H. Yun, C. Boudoux, G.J. Tearney, B.E. Bouma, High-speed wavelength-swept semiconductor laser with a polygon-scanner-based wavelength filter. Opt. Lett. **28**, 1981–1983 (2003)
44. S. Yun, G. Tearney, J. de Boer, N. Iftimia, B. Bouma, High-speed optical frequency-domain imaging. Opt. Express **11**, 2953–2963 (2003)

45. R. Huber, M. Wojtkowski, J.G. Fujimoto, J.Y. Jiang, A.E. Cable, Three-dimensional and C-mode OCT imaging with a compact, frequency swept laser source at 1300 nm. Opt. Express **13**, 10523–10538 (2005)
46. M.A. Choma, K. Hsu, J.A. Izatt, Swept source optical coherence tomography using an all-fiber 1300-nm ring laser source. J. Biomed. Opt. **10**, 044009 (2005)
47. R. Huber, M. Wojtkowski, K. Taira, J. Fujimoto, K. Hsu, Amplified, frequency swept lasers for frequency domain reflectometry and OCT imaging: design and scaling principles. Opt. Express **13**, 3513–3528 (2005)
48. J.W. Goodman, *Statistical Optics* (Wiley, New York, 1985)
49. J.W. Goodman, Some fundamental properties of speckle. J. Opt. Soc. Am. **66**, 1145–1150 (1976)
50. J.M. Schmitt, Array detection for speckle reduction in optical coherence microscopy. Phys. Med. Biol. **42**, 1427–1439 (1997)
51. H. Ren, Z. Ding, Y. Zhao, J. Miao, J.S. Nelson, Z. Chen, Phase-resolved functional optical coherence tomography: simultaneous imaging of in situ tissue structure, blood flow velocity, standard deviation, birefringence, and Stokes vectors in human skin. Opt. Lett. **27**, 1702–1704 (2002)
52. M. Pircher, E. Gotzinger, R. Leitgeb, A.F. Fercher, C.K. Hitzenberger, Speckle reduction in optical coherence tomography by frequency compounding. J. Biomed. Opt. **8**, 565–569 (2003)
53. B. Karamata, P. Lambelet, M. Laubscher, R.P. Salathe, T. Lasser, Spatially incoherent illumination as a mechanism for cross-talk suppression in wide-field optical coherence tomography. Opt. Lett. **29**, 736–738 (2004)
54. J. Kim, D.T. Miller, E. Kim, S. Oh, J. Oh, T.E. Milner, Optical coherence tomography speckle reduction by a partially spatially coherent source. J. Biomed. Opt. **10**, 064034-064031–064034-064039 (2005)
55. N. Iftimia, B.E. Bouma, G.J. Tearney, Speckle reduction in optical coherence tomography by "path length encoded" angular compounding. J. Biomed. Opt. **8**, 260–263 (2003)
56. H. Wang, A.M. Rollins, Speckle reduction in optical coherence tomography using angular compounding by B-scan Doppler-shift encoding. J. Biomed. Opt. **14**, 030512 (2009)
57. M. Bashkansky, J. Reintjes, Statistics and reduction of speckle in optical coherence tomography. Opt. Lett. **25**, 545–547 (2000)
58. A.E. Desjardins, B.J. Vakoc, W.Y. Oh, S.M. Motaghiannezam, G.J. Tearney, B.E. Bouma, Angle-resolved optical coherence tomography with sequential angular selectivity for speckle reduction. Opt. Express **15**, 6200–6209 (2007)
59. M. Hughes, M. Spring, A. Podoleanu, Speckle noise reduction in optical coherence tomography of paint layers. Appl. Opt. **49**, 99–107 (2010)
60. B.F. Kennedy, T.R. Hillman, A. Curatolo, D.D. Sampson, Speckle reduction in optical coherence tomography by strain compounding. Opt. Lett. **35**, 2445–2447 (2010)
61. D.P. Popescu, M.D. Hewko, M.G. Sowa, Speckle noise attenuation in optical coherence tomography by compounding images acquired at different positions of the sample. Opt. Commun. **269**, 247–251 (2007)
62. T.M. Jorgensen, J. Thomadsen, U. Christensen, W. Soliman, B. Sander, Enhancing the signal-to-noise ratio in ophthalmic optical coherence tomography by image registration – method and clinical examples. J. Biomed. Opt. **12**, 041208 (2007)
63. Z.J. Yuan, B. Chen, H.G. Ren, Y.T. Pan, On the possibility of time-lapse ultrahigh-resolution optical coherence tomography for bladder cancer grading. J. Biomed. Opt. **14**, 050502 (2009)
64. R.J. Zawadzki, B. Cense, Y. Zhang, S.S. Choi, D.T. Miller, J.S. Werner, Ultrahigh-resolution optical coherence tomography with monochromatic and chromatic aberration correction. Opt. Express **16**, 8126–8143 (2008)
65. S. Marschall, T. Klein, W. Wieser, B.R. Biedermann, K. Hsu, K.P. Hansen, B. Sumpf, K.H. Hasler, G. Erbert, O.B. Jensen, C. Pedersen, R. Huber, P.E. Andersen, Fourier domain mode-locked swept source at 1050 nm based on a tapered amplifier. Opt. Express **18**, 15820–15831 (2010)

66. R.F. Spaide, H. Koizumi, M.C. Pozzoni, Enhanced depth imaging spectral-domain optical coherence tomography. Am J. Ophthalmol. **146**, 496–500 (2008)
67. D.X. Hammer, R.D. Ferguson, J.C. Magill, L.A. Paunescu, S. Beaton, H. Ishikawa, G. Wollstein, J.S. Schuman, Active retinal tracker for clinical optical coherence tomography systems. J. Biomed. Opt. **10**, 024038 (2005)
68. M. Hangai, M. Yamamoto, A. Sakamoto, N. Yoshimura, Ultrahigh-resolution versus speckle noise-reduction in spectral-domain optical coherence tomography. Opt. Express **17**, 4221–4235 (2009)
69. G. Gregori, P.J. Rosenfeld, Using OCT fundus images to evaluate the performance of the spectralis OCT eye tracking system, in *ARVO Annual Meeting 2011, Imaging of the Healthy and Diseased Retina I*. (Association for Research in Vision and Ophthalmology, Fort Lauderdale, 2011)
70. M. Szkulmowski, I. Gorczynska, D. Szlag, M. Sylwestrzak, A. Kowalczyk, M. Wojtkowski, Efficient reduction of speckle contrast in optical coherence tomography imaging. Opt. Express **20**, 1337–1359 (2012)
71. M. Wojtkowski, A. Kowalczyk, R. Leitgeb, A.F. Fercher, Full range complex spectral optical coherence tomography technique in eye imaging. Opt. Lett. **27**, 1415–1417 (2002)
72. R. Huber, M. Wojtkowski, J.G. Fujimoto, Fourier Domain Mode Locking (FDML): a new laser operating regime and applications for optical coherence tomography. Opt. Express **14**, 3225–3237 (2006)
73. V. Westphal, A.M. Rollins, S. Radhakrishnan, Correction of geometric and refractive image distortions in optical coherence tomography applying Fermat's principle. Opt. Express **10**, 397–404 (2002)
74. A. Podoleanu, I. Charalambous, L. Plesea, A. Dogariu, R. Rosen, Correction of distortions in optical coherence tomography imaging of the eye. Phys. Med. Biol. **49**, 1277–1294 (2004)
75. S. Ortiz, D. Siedlecki, L. Remon, S. Marcos, Optical coherence tomography for quantitative surface topography. Appl. Opt. **48**, 6708–6715 (2009)
76. S. Ortiz, D. Siedlecki, P. Perez-Merino, N. Chia, A. de Castro, M. Szkulmowski, M. Wojtkowski, S. Marcos, Corneal topography from spectral optical coherence tomography (sOCT). Biomed. Opt. Express **2**, 3232–3247 (2011)
77. S. Ortiz, D. Siedlecki, I. Grulkowski, L. Remon, D. Pascual, M. Wojtkowski, S. Marcos, Optical distortion correction in optical coherence tomography for quantitative ocular anterior segment by three-dimensional imaging. Opt. Express **18**, 2782–2796 (2010)
78. S. Ortiz, P. Perez-Merino, S. Duran, J. Birkenfeld, A. de Castro, S. Marcos, Full OCT anterior segment biometry: an application in cataract surgery. Biomed. Opt. Express **4**, 387–396 (2013)
79. M.F. Kraus, B. Potsaid, M.A. Mayer, R. Bock, B. Baumann, J.J. Liu, J. Hornegger, J.G. Fujimoto, Motion correction in optical coherence tomography volumes on a per A-scan basis using orthogonal scan patterns. Biomed. Opt. Express **3**, 1182–1199 (2012)
80. A. de Castro, S. Ortiz, E. Gambra, D. Siedlecki, S. Marcos, Three-dimensional reconstruction of the crystalline lens gradient index distribution from OCT imaging. Opt. Express **18**, 21905–21917 (2010)
81. D. Siedlecki, A. de Castro, E. Gambra, S. Ortiz, D. Borja, S. Uhlhorn, F. Manns, S. Marcos, J.M. Parel, Distortion correction of OCT images of the crystalline lens: gradient index approach. Optom. Vis. Sci. **89**, E709–E718 (2012)
82. D. Borja, D. Siedlecki, A. de Castro, S. Uhlhorn, S. Ortiz, E. Arrieta, J.M. Parel, S. Marcos, F. Manns, Distortions of the posterior surface in optical coherence tomography images of the isolated crystalline lens: effect of the lens index gradient. Biomed. Opt. Express **1**, 1331–1340 (2010)
83. S. Ortiz, P. Perez-Merino, N. Alejandre, E. Gambra, I. Jimenez-Alfaro, S. Marcos, Quantitative OCT-based corneal topography in keratoconus with intracorneal ring segments. Biomed. Opt. Express **3**, 814–825 (2012)
84. S. Ortiz, P. Perez-Merino, E. Gambra, A. de Castro, S. Marcos, In vivo human crystalline lens topography. Biomed. Opt. Express **3**, 2471–2488 (2012)

85. R. Navarro, L. Gonzalez, J.L. Hernandez, Optics of the average normal cornea from general and canonical representations of its surface topography. J. Opt. Soc. Am. A Opt. Image Sci. Vis. **23**, 219–232 (2006)
86. M.V. Sarunic, S. Asrani, J.A. Izatt, Imaging the ocular anterior segment with real-time, full-range Fourier-domain optical coherence tomography. Arch. Ophthalmol. **126**, 537–542 (2008)
87. L. Plesea, A.G. Podoleanu, Direct corneal elevation measurements using multiple delay en face optical coherence tomography. J. Biomed. Opt. **13**, 054054 (2008)
88. P. Rosales, M. Wendt, S. Marcos, A. Glasser, Changes in crystalline lens radii of curvature and lens tilt and decentration during dynamic accommodation in rhesus monkeys. J. Vis. **8**, 1811–1812 (2008)
89. B.J. Kaluzny, M. Gora, K. Karnowski, I. Grulkowski, A. Kowalczyk, M. Wojtkowski, Imaging of the lens capsule with an ultrahigh-resolution spectral optical coherence tomography prototype based on a femtosecond laser. Br. J. Ophthalmol. **94**, 275–277 (2010)
90. B.J. Kaluzny, W. Fojt, A. Szkulmowska, T. Bajraszewski, M. Wojtkowski, A. Kowalczyk, Spectral optical coherence tomography in video-rate and 3D imaging of contact lens wear. Optom. Vis. Sci. **84**, 1104–1109 (2007)
91. D. Alonso-Caneiro, K. Karnowski, B.J. Kaluzny, A. Kowalczyk, M. Wojtkowski, Assessment of corneal dynamics with high-speed swept source optical coherence tomography combined with an air puff system. Opt. Express **19**, 14188–14199 (2011)
92. G. Wollensak, Crosslinking treatment of progressive keratoconus: new hope. Curr. Opin. Ophthalmol. **17**, 356–360 (2006)
93. A. Elsheikh, D.F. Wang, M. Brown, P. Rama, M. Campanelli, D. Pye, Assessment of corneal biomechanical properties and their variation with age. Curr. Eye Res. **32**, 11–19 (2007)
94. S. Kling, H. Ginis, S. Marcos, Corneal biomechanical properties from two-dimensional corneal flap extensiometry: application to UV-riboflavin cross-linking. Invest. Ophthalmol. Vis. Sci. **53**, 5010–5015 (2012)
95. R. Ambrosio, D.G. Dawson, M. Salomao, F.P. Guerra, A.L.C. Caiado, M.W. Belin, Corneal ectasia after LASIK despite low preoperative risk: tomographic and biomechanical findings in the unoperated, stable, fellow eye. J. Refract. Surg. **26**, 906–911 (2010)
96. C. Dorronsoro, D. Pascual, P. Perez-Merino, S. Kling, S. Marcos, Dynamic OCT measurement of corneal deformation by an air puff in normal and cross-linked corneas. Biomed. Opt. Express **3**, 473–487 (2012)

Anterior Eye Imaging with Optical Coherence Tomography

55

David Huang, Yan Li, and Maolong Tang

Keywords

Anterior segment OCT • Corneal epithelial thickness map • Corneal refractive power • Fourier domain OCT • Intraocular lens power calculation • Keratoconus screening • LASIK planning and evaluation • Optical coherence tomography (OCT) • Pachymetry map • Scan geometry • Time-domain OCT

55.1 Background

55.1.1 The Development of Corneal and Anterior Segment OCT Technology

Optical coherence tomography [1] (OCT) was first used clinically for retinal imaging [2]. Most ophthalmologists are now familiar with the applications of OCT in clinical retinal imaging. Not surprisingly, the earliest clinical corneal OCT studies used commercially available retinal scanners such as OCT1, OCT2, or Stratus (Carl Zeiss Meditec, Inc., Dublin, CA) to image the cornea and measure central corneal and sublayer thicknesses [3–10]. However, the initial 840 nm retinal OCT scanners acquires up to 400 axial scans per second. While this is adequate for

Proprietary Interests: David Huang and Yan Li have significant financial interests in Optovue and Carl Zeiss Meditec, companies that may have a commercial interest in the results of this research and technology. Maolong Tang has a significant financial interest in Optovue. These potential conflicts of interest have been reviewed and managed by Oregon Health and Science University.

Financial Support: this study was supported by NIH grants R01 EY018184, a grant from Optovue Inc. and a grant from Research to Prevent Blindness, Inc.

D. Huang (✉) • Y. Li • M. Tang
Center for Ophthalmic Optics and Lasers, Casey Eye Institute and Department of Ophthalmology, Oregon Health and Science University, Portland, OR, USA
e-mail: davidhuang@alum.mit.edu

© Springer International Publishing Switzerland 2015

W. Drexler, J.G. Fujimoto (eds.), *Optical Coherence Tomography*,
DOI 10.1007/978-3-319-06419-2_57

obtaining a spot measurement on the cornea, it is far too slow for mapping the cornea or measuring the width of the anterior chamber.

The need for faster OCT systems and the popularization of corneal refractive surgery at the end of the twentieth century spurred the development of dedicated anterior segment OCT systems. In 2001, Radhakrishnan et al. first reported ocular imaging with a 1,310 nm wavelength OCT system developed in Professor Joseph Izatt's group [11]. The Izatt system featured a high-speed scanning delay line in the reference arm and took advantage of the higher power that can be safely used at the longer wavelength of 1,310 nm to achieve a high acquisition rate of 4,000 axial scans per second.

The scan geometry is one of the important choices to be made in designing anterior segment OCT systems. There are three possible scan geometries: sector, concentric, and rectangular (Fig. 55.1). A sector scan (Fig. 55.1a) sweeps the beam of light in a divergent fan. It is commonly used in ultrasound imaging. Retinal OCT systems employ the sector scan geometry, which matches well to the spherical geometry of the retina. Early anterior segment OCT prototypes also used this geometry, which allows wide scanning with a small objective lens [11]. Retinal scanners can also provide sector scans without additional adaptor lens (Fig. 55.1b). The primary drawback of using sector scans for corneal imaging is that the peripheral cornea reflection is nearly invisible because of the large off-perpendicular incidence angle. The second choice was the concentric scan geometry (Fig. 55.1c). This scan geometry maintains a perpendicular angle of incidence on the cornea. It produces very strong reflections from the boundaries of the cornea and from its internal lamellae (Fig. 55.1d); but unfortunately, these strong reflections obscure features of interest such as the LASIK flap interface or scar. Therefore, the concentric scan is not ideal for anterior eye imaging. Unlike the other two scan geometries, the rectangular scan geometry (Fig. 55.1e) offers the least image distortion. The strong specular reflection at the corneal vertex can offer a very precise central landmark in rectangular scans (Fig. 55.1f). The vertex provides a central reference point that is commonly used in corneal topography and corneal thickness mapping. Stromal details such as the LASIK flap interface can be well visualized in the pericentral and midperipheral cornea. The rectangular scan geometry provides the best contrast for corneal layers and pathologies and also allows wide-field scanning. Thus most anterior segment OCT systems now use this scanning geometry (Fig. 55.2).

Combining the rectangular scan geometry and the 1,310 nm wavelength Izatt anterior segment OCT engine, Professor David Huang collaborated with Professor Izatt's laboratory and developed a practical anterior segment OCT scanner. It can provide angle-to-angle wide-field full-range anterior eye scans (16-mm scan width and up to 8-mm scan depth in air) containing the cornea and the crystalline lens in the same image (Fig. 55.2a). The rectangular scan readily gave accurate biometric measurements such as the anterior chamber depth and width [12]. Later we used an anterior segment OCT prototype system (Carl Zeiss Meditec, Inc., Dublin, CA) with similar performance to map 10-mm diameter corneal thickness (pachymetry) with high repeatability [13].

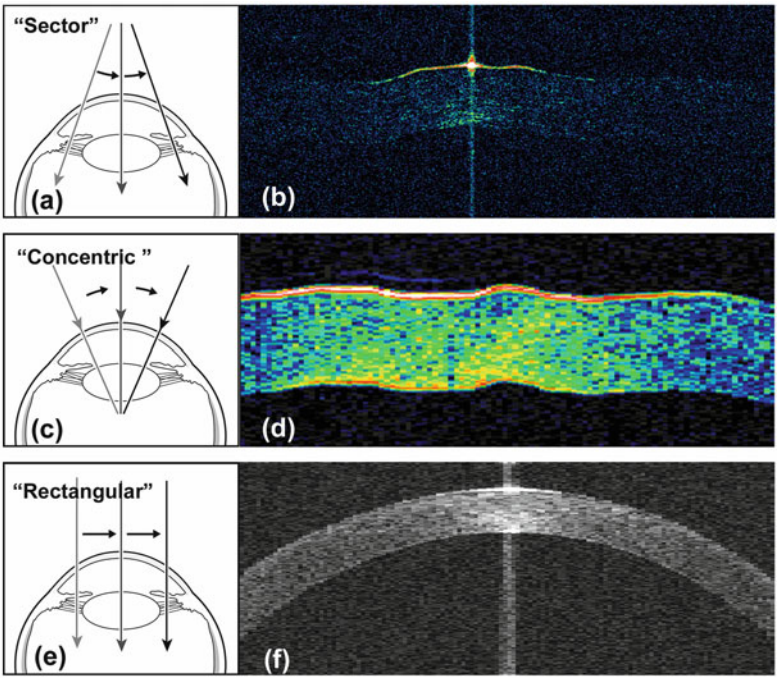

Fig. 55.1 Corneal OCT images obtained with three possible scan geometries. (**a**) Divergent "sector" scan geometry. (**b**) A corneal image taken with a retinal OCT scanner using the sector scan geometry. The scan width was 3 mm. Note weak reflections outside of the central 1 mm and obvious motion artifacts in the corneal contour. (**c**) Concentric or "arc" scan geometry. (**d**) An OCT image taken with an arc-scanning OCT prototype. The scan width was 4 mm. Note the obvious motion artifact. (**e**) "Rectangular" or "telecentric" scan geometry. (**f**) An OCT image taken with the wide-field anterior segment OCT prototype with rectangular scan geometry. The scan width was 10 mm

The original OCT technology is now classified as time-domain OCT, in which the reference mirror is moved through a range of delay, and the resulting inference patterns between the sample and reference beams are processed into an axial scan. The scanning speed in time-domain OCT is limited by having to physically cycle the reference mirror through the delay range. These systems can only collect a few thousands of axial scans per second. At this speed, quantitative corneal shape measurements such as the corneal topography are not possible due to the limited sampling rate and the influence of the eye movement. Luckily, new generation Fourier-domain OCT technology has been developed to speed up image acquisition. In Fourier-domain OCT, the reference mirror is stationary, and the axial scan is generated by Fourier transformation of spectral interference patterns between the sample and reference reflections. Advantages of Fourier-domain OCT include improvements in scanning speed and signal-to-noise ratio that are achieved through elimination of reference mirror movement and simultaneous detection

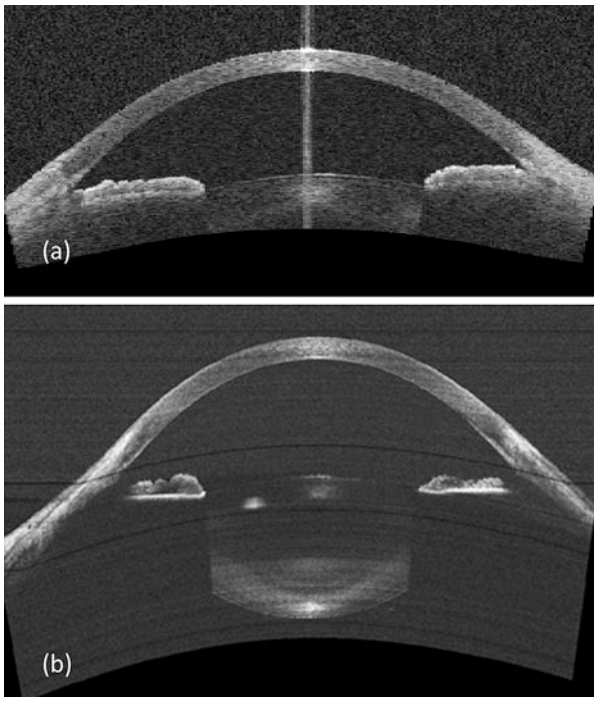

Fig. 55.2 Wide-field anterior eye scans obtained with a time-domain OCT (**a**) and a swept-source OCT (**b**)

of reflections from all layers of the target. There are two main ways of designing and constructing Fourier-domain OCT instruments. The first one is called spectrometer-based (or spectral-domain) OCT, in which the interferometric signal is detected by a spectrometer equipped with a high-speed line scan detector, such as a charge-coupled device (CCD) or complementary metal oxide semiconductor (CMOS) line camera. Spectrometer-based OCT systems capable of 6,700–310,000 axial scans per second were reported [14–16]. The second one is called swept-source OCT, which uses high-speed tunable lasers [17]. Swept-source OCT offers several advantages over spectrometer-based OCT, including reduced fringe washout, lower sensitivity roll-off with imaging depth, and longer imaging range, higher detection efficiencies [18]. The introduction of Fourier domain mode locking (FDML) enabled dramatic increases in sweep speeds by using a long fiber optic delay line in the laser cavity [19]. Anterior segment swept-source OCT instruments with imaging speed of 100,000–400,000 axial scans per second enabled 3D imaging of the entire cornea in 500–125 ms [18, 20, 21].

The increased sensitivity of both Fourier-domain OCT system designs comes at the price of limited usable imaging depth. The symmetric overlapping image artifact in Fourier-domain OCT images, referred to in the literature as the complex conjugate or mirror image artifact, occurs whenever the sample imaging depth spans both positive and negative distances compared with the length of the set

reference path in the Fourier-domain OCT interferometer [22]. Practical 840 nm hybrid retinal/corneal Fourier-domain OCT systems have sufficient speed and sensitivity for anterior segment imaging. However, their maximum imaging depth and width are usually limited to approximately 2 and 6 mm due to scanning optics optimized for retinal imaging. Dedicated Fourier-domain OCT corneal imaging systems allow both high speed and wide field of scan. Extended imaging depth can be achieved using full-depth (complex conjugate ambiguity resolution) or swept-source technology (Fig. 55.2b) [14, 15, 21].

55.1.2 Wavelength Affects Resolution and Penetration

Due to the technological limitations of detectors and accessibility of light sources, three optical frequency windows are commonly used in OCT imaging: centered at 840, 1,050, and 1,310 nm, respectively. An optimal choice of the OCT working wavelength depends on the application of interest. The axial resolution of an OCT system is proportional to the square of the central wavelength and inverse proportional to the bandwidth of the light source. Therefore, the shorter wavelength and broader bandwidth provide better resolution. To achieve maximum axial resolution (1–4 μm), for example, in retinal imaging, a spectral window centered at 840 nm is typically used. To get information from deeper layers with relatively high axial resolution of 6–15 μm, say, imaging of the anterior segment of the human eye, broadband light centered at 1,310 nm can be applied. OCT imaging with the central wavelength of 1,050 nm usually provides medium axial resolution of 4–10 μm [23].

On the other hand, OCT has a limited ability to image through opaque tissue due to signal attenuation by scattering. Scattering is wavelength dependent – the shorter the wavelength, the greater the scattering. In other words, longer wavelength gives deeper penetration. For scattering objects much smaller than infrared wavelength (i.e., collagen fibrils), scattering scales inversely with the fourth power of wavelength (the Raleigh approximation) [24]. Based on this approximate upper limit, the penetration of 1,310 nm light could be as much as six times deeper than that of 840 nm light. Indeed, we observe that 1,050 nm and 1,310 nm OCT is able to penetrate limbal tissue to visualize the scleral spur and angle recess (Fig. 55.3b, c), while 840 nm OCT cannot (Fig. 55.3a).

Moreover, light at the 1,310 nm wavelength is strongly absorbed by water – resulting in a retinal exposure that is less than 7 % of the power incident on the cornea (Fig. 55.4). In contrast, almost the entire 840 nm wavelength light that strikes the eye reaches the retina unabsorbed. Because most 1,310 nm light does not reach the sensitive retinal tissue, much higher power levels can be safely used on the eye. The eye exposure limit set by the American National Standards Institute (ANSI) [25] for extended eye exposure is 15 mW for 1,310 nm wavelength, compared to 0.7 mW for 840 nm wavelength. The ability to use 20 times more power for corneal and anterior segment OCT imaging means that scanning can be performed 20 times faster without sacrificing signal level.

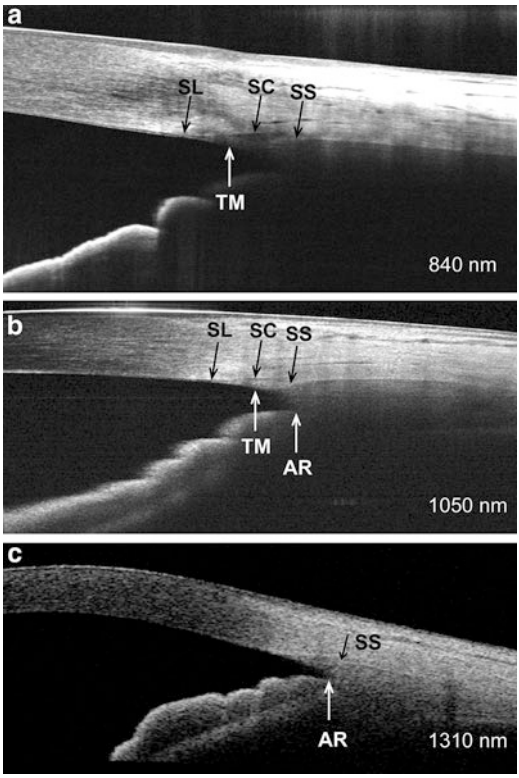

Fig. 55.3 A comparison of the anterior chamber angle imaged with 840 nm (**a**), 1,050 nm (**b**), and 1,310 nm (**c**) OCT systems. *AR* angle recess, *SC* Schlemm's canal, *SL* Schwalbe's line, *SS* scleral spur, and *TM* trabecular meshwork

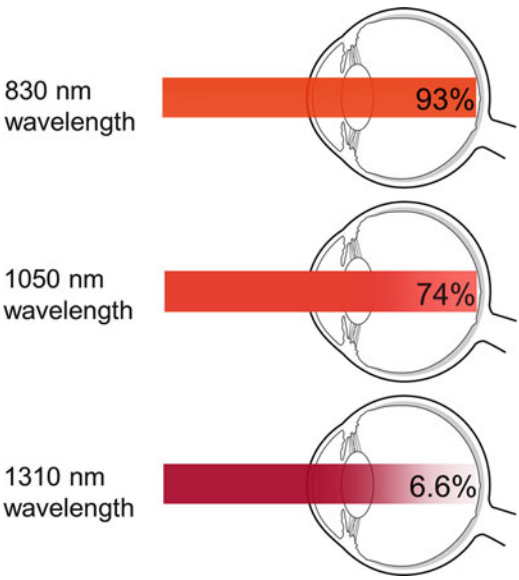

Fig. 55.4 Illustration showing the attenuation of light in the average eye in a single pass from the cornea to the retina. The calculations are based on 22 mm of water in front of the cornea

Table 55.1 Commercial OCT systems capable of anterior segment imaging

Manufacturer	Device	Axial resolution (μm)	Wavelength(nm)	Speed (A-scan/second)	Type
Bioptigen	Envisu	3	840	17,000	Fourier domain
Carl Zeiss Meditec	Visante	18	1,310	2,000	Time domain
Carl Zeiss Meditec	Cirrus	5	840	27,000	Fourier domain
Heidelberg	SL-OCT	18	1,310	200	Time domain
Heidelberg	Spectralis	3.9	870	40,000	Fourier domain
Optopol	Copernicus HR	3	850	52,000	Fourier domain
Optovue	RTVue-CAM	5	840	26,000	Fourier domain
Optovue	iVue	5	840	26,000	Fourier domain
Tomey	Casia	10	1,310	30,000	Fourier domain

55.1.3 Commercial Anterior Segment OCT Systems

The first commercial version of anterior segment OCT instruments (Visante and SL-OCT) introduced to the market in 2005/2006 was time-domain OCT systems. Later, Fourier-domain OCT systems (RTVue, Cirrus, Spectralis, Envisu, Casia, etc.) with speeds between 17,000 and 52,000 axial scans per second became available (Table 55.1). All current commercial anterior segment OCT systems operate in the near infrared, at either 840–870 or 1,310 nm. The longer wavelength of 1,310 nm penetrates more deeply through the sclera, limbus, angle, and iris. The shorter wavelength range of 840–850 nm cannot penetrate the sclera or iris, but can offer much higher resolution (Table 55.1). The 1,310 nm systems cannot perform retinal imaging due to water absorption in the vitreous medium. The 840–850 nm OCT systems are generally capable of both anterior segment and retinal imaging. However, the hybrid retina/cornea platforms have limited anterior segment imaging width. To image the entire width and depth of the anterior chamber, dedicated anterior segment scanning optics are necessary (Visante, SL-OCT, Casia, in Table 55.1).

55.2 Diagnostic and Surgical Applications

55.2.1 Mapping of Corneal Thickness

The measurement of corneal thickness (pachymetry) has important diagnostic and surgical applications. Central corneal thickness is routinely used to monitor corneal

edema and endothelial function [26–29], manage ocular hypertension [30, 31], and plan common keratorefractive surgeries such as laser in situ keratomileusis (LASIK) and photorefractive keratectomy (PRK).

Ultrasound pachymetry [32, 33] and several other techniques [34–37] provide only spot measurements, while scanning-slit optical pachymetry [38, 39], very high-frequency ultrasound imaging [40, 41], and optical coherence tomography allow mapping of a wide area of the cornea. Pachymetric mapping provides several advantages over spot measurements. Mapping can reveal abnormal patterns such as keratoconus and pellucid marginal degeneration. It also allows preoperative planning for surgeries that do not primarily concern just the center of the cornea, such as astigmatic keratotomy, intracorneal ring segment implantation, phototherapeutic keratectomy (PTK), and lamellar keratoplasty.

We used a time-domain anterior segment OCT prototype (Carl Zeiss Meditec Inc.) to study corneal thickness mapping [13]. The prototype is similar in performance to Zeiss Visante™ model which was approved by FDA in 2005. It operates at a wavelength of 1,310 nm with a scanning speed of 2000 axial scans per second. The cornea was scanned with 10-mm radial lines on 8 meridians centered on the vertex reflection. Each meridional line consisted of 128 A-scans. The entire scan pattern had 1,024 A-scans and was acquired in approximately 0.5 s. A cross-sectional OCT image is illustrated in Fig. 55.5a.

An automated computer algorithm was developed to locate the anterior and posterior corneal surfaces by identifying the signal peaks at the air–tear film and cornea–aqueous interfaces on each A-scan (Fig. 55.5b).

OCT uses light to probe the eye. The light changes its propagation direction at the interface between air and cornea due to refraction and causes significant distortion in OCT images. Image distortions due to refraction may also occur at other tissue index transition surfaces such as the cornea–aqueous interface. Moreover, OCT records the optical path length that the light travels rather than the physical dimensions. So a "dewarp" algorithm is needed to correct the beam refraction and to transform optical delay into actual physical dimensions (Eq. 55.1).

$$x = \text{Optical path length}/n \tag{55.1}$$

where x is the physical distance, and n is the group index of the medium.

Westphal et al. reported a backward transformation method using Fermat's principle by finding the minimum path to the corrected pixel [42]. They used backward transformation instead of forward transformation because the raw image in their study was distorted by the sector scan geometry, and in turn the incidence angle calculation was difficult. The anterior segment OCT prototype used in our study had a rectangular scan geometry (Fig. 55.1e, f). The normal of the interface and the incidence angle of the beam could be easily defined once the refraction interface is located. Therefore, a forward transformation using Snell's law was used for "dewarping" in our studies [22, 43]. The normal and the incidence angle (θ_1 in Fig. 55.5c) was calculated at each axial scan location (i.e., column of pixels). The beam propagating direction passing the interface was decided by θ_2.

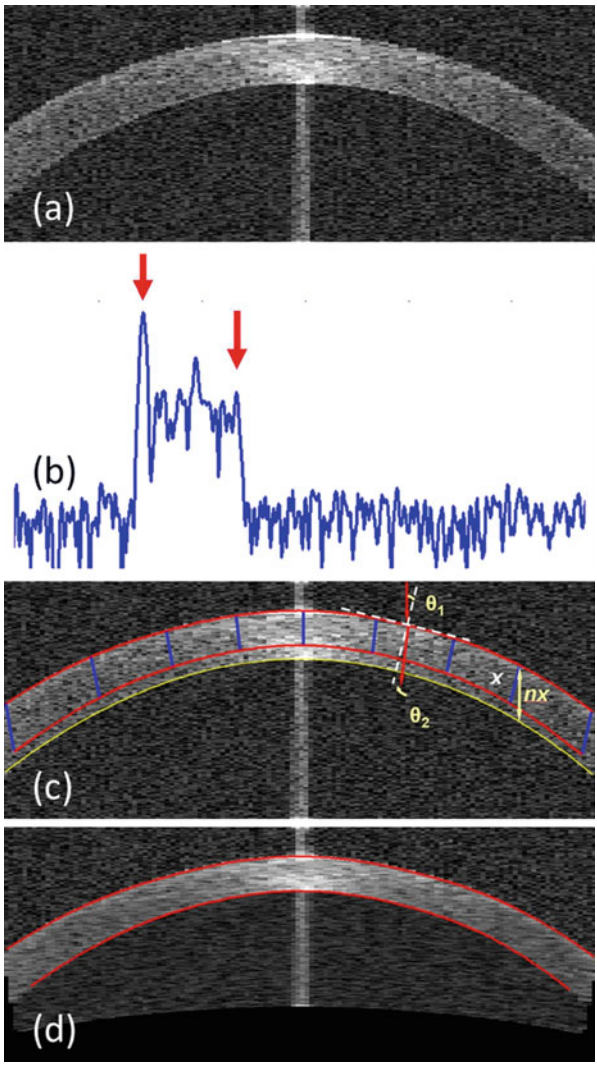

Fig. 55.5 OCT corneal thickness measurement. (**a**) Cross-sectional OCT image on a corneal meridian. (**b**) An OCT axial scan from pericentral cornea plotted on a logarithmic scale. The *arrows* mark the signal peaks at the anterior (*left*) and posterior (*right*) corneal boundaries located by the automated algorithm. (**c**) "Dewarp" to correct the image distortion due to refraction and transition of the corneal group index at the air–corneal interface. The OCT beam reached the cornea with incident angle θ_1 and refracted by angle θ_2. The *yellow double arrowhead line* represents the optical path length *nx* that OCT records. The blue lines indicated the physical distance *x* that the OCT beam travels in tissue. (**d**) Dewarped OCT cross section overlaid with detected corneal boundaries

According to Snell's Law: $n_1 \sin \theta_1 = n_2 \sin \theta_2$
We have

$$\theta_2 = \arcsin\left(\frac{n_1 \sin \theta_1}{n_2}\right) \tag{55.2}$$

where n_1 is the refractive index of the first medium, which equals 1.0 for air; n_2 is the group index of the second medium, which is 1.389 for human cornea (n_{cornea}) at 1.3-μm wavelength [44].

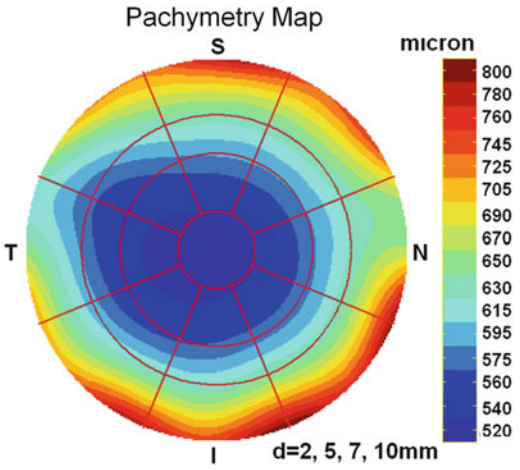

Fig. 55.6 OCT pachymetry (corneal thickness) map

The axial difference between the anterior (red line) and posterior (yellow) corneal surfaces represents the optical path length through cornea (*nx*, denoted by a yellow double-head arrow in Fig. 55.5c). The raw axial scans were then resampled along the refraction directions with a scaling factor of $1/n_{cornea}$. Figure 55.5d showed an example of corneal OCT image after "dewarping."

Corneal thickness was measured from the dewarped image (Fig. 55.5d) as the distance between the anterior and posterior surfaces along lines perpendicular to the anterior surface. A corneal thickness profile was generated from each meridional cross section. The computer algorithm registered the eight corneal cross sections and computed the corneal thickness (pachymetry) map by interpolation. The pachymetry map was presented on a banded color scale (Fig. 55.6). The map was divided into zones and sectors. The sector mean, maximum, and minimum pachymetry measurements within a diameter (D) less than 7 mm were computed. Reproducibility was assessed by the pooled standard deviations of the repeated measurements.

Forty-two eyes of 21 normal subjects were used in our clinical study [13]. The OCT pachymetry mapping and ultrasound central pachymetry (50 MHz CorneoGage 2, Sonogage, Cleveland, OH) were obtained three times on each eye. The average central ($D < 2$ mm) OCT corneal thickness (OCT_{Mean}) was compared with the ultrasound pachymetry. The OCT measurements correlated very well with ultrasound pachymetry (Pearson correlation $r = 0.97$). The Bland–Altman analysis showed that the OCT measurements were slightly thinner than those obtained with ultrasound pachymetry. The difference between the OCT_{Mean} and ultrasound was −6.4 μm (95 % limits of agreement: −23.2 to 10.4 μm). The difference was statistically (t-test, $P < 0.001$) but not clinically significant. Overall, the repeatability of the mean corneal thickness was roughly 2 μm for the three zones within the 7-mm diameter in OCT pachymetry maps.

Our results show that OCT is a reliable method of mapping corneal thickness. In our clinical practice, OCT is now routinely used to screen prospective patients seeking keratorefractive surgery. The thickness map is used to detect thin spots that may indicate keratoconus or pellucid marginal degeneration and to calculate the predicted residual stromal bed thickness after LASIK or PRK. We also track the disease progression in patients with corneal edema (swelling) with OCT. Because the measurement does not require contact, it is more easily tolerated than measurement with an ultrasound probe.

55.2.2 Epithelial Thickness Mapping

The corneal epithelium is the first cellular layer of the human cornea and protects the eye. Accurate and reproducible measurement of corneal epithelial thickness provides important information for assessing corneal remodeling after refractive surgeries such as photorefractive keratectomy and LASIK [45]. Moreover, deviations from normal epithelial thickness could be an early sign of keratoconus [46].

Fourier-domain OCT instruments can provide scan speeds 10–100 times faster than time-domain OCT instruments [47]. The enhanced speeds minimize the effect of eye movements during data acquisition and also allow higher definition imaging due to denser axial scans in the same transverse scan length. The higher scan speed also facilitates frame averaging that suppresses speckle noise. The epithelium–Bowman's layer boundary is a relatively weak interface presented in corneal OCT images.

We used a Fourier-domain OCT (RTVue-CAM, Optovue, Inc.) to investigate automatic epithelial thickness mapping. In this study, we enhanced the epithelial boundary by acquiring five repeated images and averaging them after the registration. The averaged image had higher signal-to-noise ratio than the single frame. Moreover, the Fourier-domain OCT system used in our study had an axial resolution of 5 μm, which is two to three times higher than that of time-domain instruments used in previous studies [48–51]. Not only does the higher resolution and higher speed of Fourier-domain OCT improve image quality, it also makes the automated corneal epithelial thickness mapping possible.

A "Pachymetry + Cpwr" scan pattern (6-mm scan diameter, 8 radials, 1,024 axial scans each, repeated five times) centered at the pupil center was used to map the cornea (Fig. 55.7a). Fourier-domain OCT image data were exported and processed with custom software. For each OCT scan, five repeated radial cross-sectional images on each meridian were registered and averaged (Fig. 55.7b). Next the air–tear interface and the epithelium–Bowman's layer boundary were automatically identified with a computer algorithm by increased signal intensity at corresponding boundaries (Fig. 55.7c, d) [52]. Corneal epithelial thickness was measured as the distance between the air–tear and the epithelium–Bowman's interfaces perpendicular to the anterior surface at the point of measurement. An epithelial thickness profile was generated from each meridional cross section. A 6-mm diameter epithelial thickness map was generated by interpolating epithelial thickness profiles calculated from each meridian.

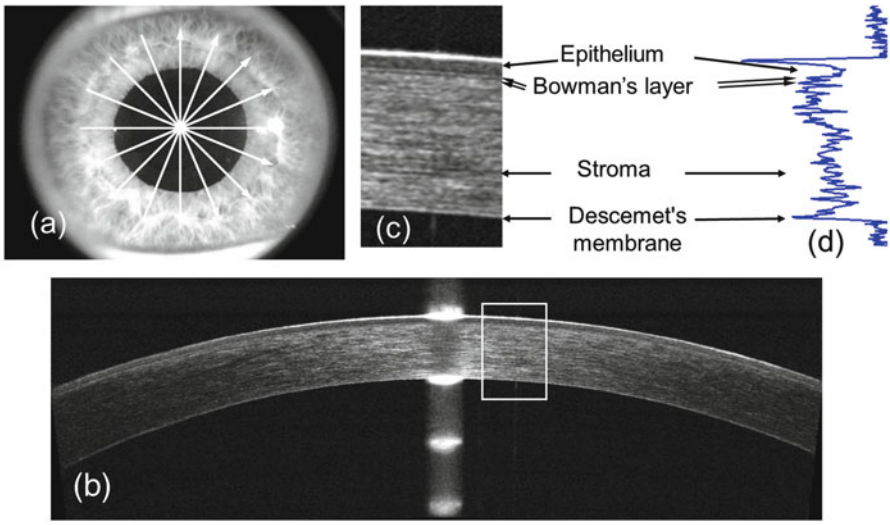

Fig. 55.7 (**a**) The "Pachymetry + Pwr" scan pattern consisted of 8 radial scans. (**b**) A cross-sectional corneal optical coherence tomography (*OCT*) image (average of five repeated frames). (**c**) A magnified section of OCT image shown in (**b**). (**d**) A corneal axial scan

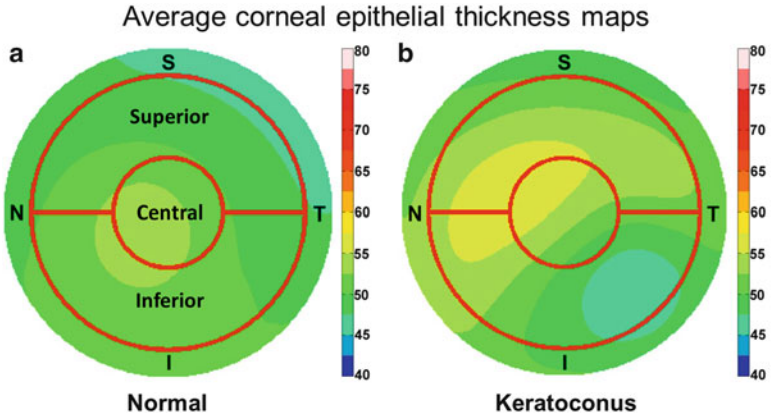

Fig. 55.8 Average epithelial thickness maps of the normal (**a**) and keratoconic (**b**) eyes

Only the central 5-mm diameter map was used for calculating epithelial thickness-based variables. The epithelial thickness map was divided into three zones by diameter and hemispheres: central 2 mm, superior 2–5 mm, and inferior 2–5 mm (Fig. 55.8a).

One hundred and three eyes of 54 normal subjects were involved in this study. Each eye was scanned three times within a single visit. Subjects were repositioned after each OCT scan. The average age of the normal subjects was 46.3 ± 13.4 years

Table 55.2 Cutoff values for optical coherence tomography pachymetric parameters. *I-S* inferior–superior octant difference, *IT-SN* inferotemporal–superonasal octant difference. The diagnostic cutoff threshold is 2.3 standard deviations below normal average (1st percentile of normal distribution). All measurements are made within central 5-mm diameter of the map

Pachymetric parameters	Minimum	Minimum–maximum	I-S	IT-SN
Cutoff (unit: μm)	472	−62	−52	−51

(range 19–65 years). The average steep K was 44.4 ± 1.4 diopter (D) (range 41.0–47.8 D) and the minimum corneal thickness was 529.1 ± 27.5 μm. The repeatability of central, superior, and inferior epithelial thickness measurement was less than 1.0 μm by pooled standard deviation. The average central, superior, and inferior epithelial thicknesses were 52.8 ± 3.9, 49.4 ± 3.8, and 51.2 ± 3.6 μm, respectively. The average epithelial thickness maps of all normal subjects were calculated (Fig. 55.8a). The left eye maps were mirrored to the right eye to calculate the average map of both eyes.

55.2.3 Keratoconus Screening

Keratoconus is the most important contraindication for laser refractive surgeries. Undetected corneal ectatic disorders can result in accelerated, progressive keratectasia and unpredictable visual outcome after LASIK and PRK. Current detection of early stage keratoconus (referred to as *forme fruste* keratoconus or FFK in medical literatures) relies primarily on Placido ring-based corneal topography [53–55]. However, topography does not screen out all eyes at risk [56]. Corneal thinning is a characteristic feature of keratoconus. Studies showed that the OCT pachymetric parameters listed in Table 55.2 are helpful in detecting the keratoconic eccentric focal thinning patterns [57]. If one parameter is abnormal (lower than the cutoff value), the cornea is likely to have keratoconus. If two or more parameters are abnormal, then the eye is very likely to have keratoconus or other ectatic conditions such as pellucid marginal degeneration [58].

The human corneal epithelium covers the surface of the cornea where it protects the eye and plays an important role in maintaining high optical quality. In diseases such as keratoconus, the thickness of the epithelium becomes altered to reduce corneal surface irregularity [46]. Therefore, the presence of an irregular stroma may be less measurable by frontal surface corneal topography. Analyzing the corneal epithelial and stromal thicknesses and shapes separately can facilitate the detection of the disease in its early stage [46, 59, 60]. We also used epithelial map information for keratoconus detection. We conducted a cross-sectional observational study involving 145 eyes from 76 normal subject and 35 keratoconic eyes from 22 patients. We calculated the average epithelial thickness map of keratoconic eyes (Fig. 55.8b) using the method described in Sect. 55.2.2 “epithelial thickness mapping.” Five diagnostic variables, including minimum, superior–inferior (S-I), minimum–maximum (MIN-MAX), map standard deviation (MSD), and pattern standard deviation (PSD), were calculated.

Several corneal epithelial thickness-based variables developed in this study showed good (minimum, AROC = 0.84; MIN-MAX, AROC = 0.88; RMSV, AROC = 0.89) to excellent (PSD, AROC = 1.00) diagnostic power in differentiating keratoconic from normal eyes. By far, PSD was the best variable. With a cutoff value of 0.057, PSD alone gave 100 % specificity and 100 % sensitivity. These variables could be applied to epithelial thickness maps from other imaging systems as well (e.g., very high-frequency ultrasound). Moreover, these variables may be useful for detecting *forme fruste* keratoconus (FFK or subclinical keratoconus). Further studies are needed to evaluate the performance of these variables in FFK detection.

55.2.4 Measuring Corneal Refractive Power

The refractive power of the cornea is determined by the anterior and posterior corneal surfaces. It is commonly measured by manual keratometer or simulated keratometry (Sim-K) from computerized corneal topography systems. Keratometry measures the anterior surface power and extrapolates total corneal power assuming the ratio of anterior and posterior radius is fixed. This assumption, however, leads to measurement error in the corneal power for eyes that have undergone refractive surgeries such as LASIK. Consequently, the calculated corneal power change deviates from the actual refractive change after LASIK.

The wide-field high-speed anterior segment OCT is capable of direct measurement of both anterior and posterior surfaces, thereby avoiding the erroneous assumption. In a study of 32 eyes from 17 LASIK patients, we evaluated the repeatability of OCT-based corneal power measurement by pooled standard deviation [61]. The repeatability is 0.79D for the anterior surface and 0.10D for the posterior surface. The former value is not as good as the conventional corneal topography systems, which usually have repeatability less than 0.25D. The main limitation is most likely the scanning speed. At 2,000 axial scan per second, eye movement during OCT scans still produces noticeable error in corneal power measurement. Nevertheless, if we combine the OCT-measured pachymetry map and anterior corneal topography, the resulting total corneal power can closely track the refractive change after LASIK [61].

55.2.5 LASIK Anatomy

An important use for OCT in LASIK surgery is in measuring the thickness of the flap and the residual stromal bed. In the LASIK procedure (Fig. 55.9), both the flap dissection and the laser treatment weaken the corneal structure. If the remaining stromal bed is less than 250 μm or if the eye has a preexisting condition that has weakened the cornea, there is a high risk of developing keratectasia or progressive focal thinning and bulging forward of the cornea [56]. To avoid this complication, a method is needed to measure the flap and stromal bed thickness [62].

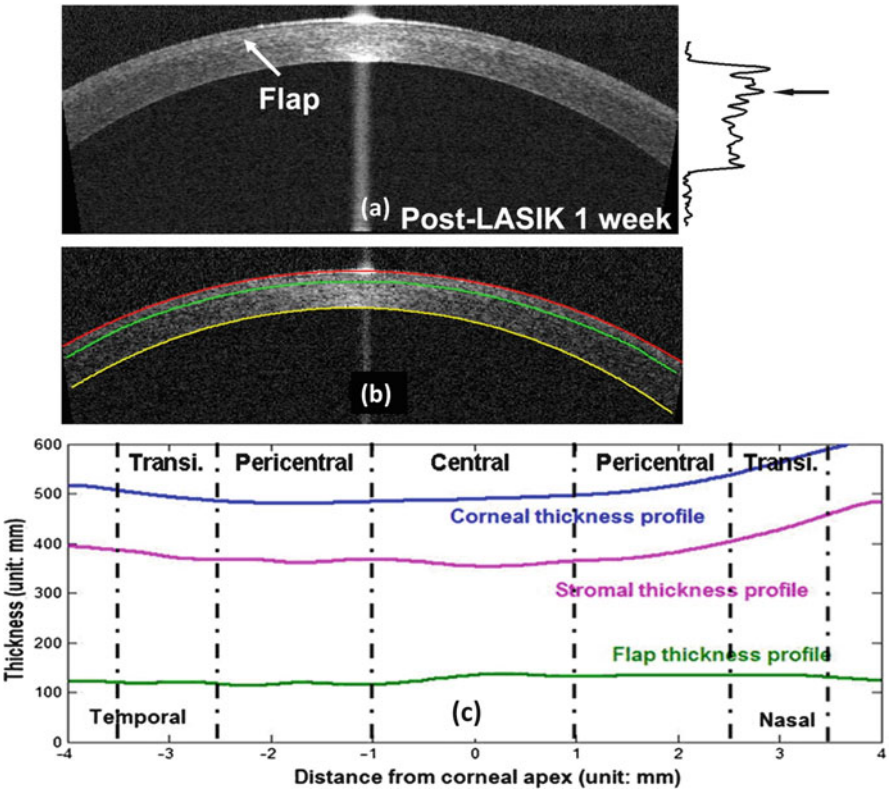

Fig. 55.9 (**a**) A post-LASIK 1 week OCT scan of 1,310 nm time-domain OCT. *Arrows* mark the location of the flap interface. (**b**) Corneal boundaries and flap interface overlaid on the OCT image. (**c**) Corneal, stromal bed, and flap thickness profiles

Currently, LASIK surgeons calculate the residual stromal bed by subtracting the expected flap thickness and ablation depth from the central corneal thickness measured by an ultrasound pachymeter. Some surgeons measure the stromal bed thickness with ultrasound pachymetry intraoperatively and calculate the flap thickness by subtracting the stromal bed thickness from the preoperative corneal thickness [63–71]. This approach has some drawbacks: risk of contamination and hydration change caused by contact of the ultrasound probe with the stromal bed and imprecision of two manually placed measurements. Furthermore, intraoperative ultrasound measurement is not universally practiced. Therefore, measurements of the flap and stromal bed thickness may not be available when needed at a later time for enhancement (repeat laser treatment) planning or complication management.

Optical coherence tomography provides a better solution – a noncontact method that produces high-resolution cross-sectional images from which flap and stromal thickness can be directly measured.

We conducted a longitudinal study to assess the corneal anatomic change after LASIK with the same high-speed anterior segment OCT prototype used in Sect. 55.2.1. Eighteen volunteers seeking refractive surgery participated in this prospective study. The preoperative manifest spherical equivalent (SE) refraction of the 36 eyes ranged from −1.25 to −9.25 diopters (D) (mean, −4.1 ± 2.3 D). The LASIK flap was created with an automated mechanical microkeratome (Hansatome, Bausch & Lomb, Inc., Rochester, NY). The head setting was either 160 μm or 180 μm. Ablations were performed with a scanning spot excimer laser (LADARVision 4000, Alcon Laboratories, Inc., Fort Worth, TX).

The OCT scans were performed preoperatively and at 1 day, 1 week, 3 months, and 6 months postoperatively. The patient cornea was scanned three times at each visit with an 8-mm long horizontal OCT pattern consisting of 512 axial scans. The LASIK flap can be distinguished by increased reflection at the flap interface and increased internal reflectivity (Fig. 55.9a). We developed automated computer algorithms to locate corneal boundaries and the flap interface (Fig. 55.9b). Flap and stromal thickness profiles (Fig. 55.9c) were then calculated. Ultrasound pachymetry was used to measure central corneal thickness before and 3 months after surgery. Residual stromal thickness was recorded during the surgery, both before and after laser ablation. Flap thickness was also calculated from the intraoperative ultrasound measurements.

Postoperative 1 week LASIK flap thickness correlated well with the ultrasound flap thickness (Pearson correlation coefficient $r = 0.81$). The OCT flap thickness was 143 ± 14 μm (mean ± SD, range 119–177) for the 180-μm Hansatome setting and 125 ± 12 (range 101–141) μm for the 160-μm setting. Bland–Altman analysis shows that the OCT measurements were greater than the ultrasound measurements (mean difference: 10.7 μm; 95 % limits of agreement, −8.8 to +30.2 μm). We believe the difference is due to an increase in postoperative flap hydration caused by the release of tensile stress. The repeatability of OCT flap measurement was 5 μm (pooled SD) within the central 5-mm diameter.

In our practice, we now routinely perform OCT imaging of post-LASIK cornea 1 week after the procedure (Fig. 55.10) with a 5-μm resolution Fourier-domain OCT (RTVue-CAM, Optovue, Inc.). The resulting flap thickness measurement is used to monitor the performance of the microkeratome and provide the flap thickness value used to calculate the predicted residual stromal bed thickness for subsequent LASIK patients. If the patient should need a second laser treatment (LASIK enhancement procedure), we also obtain an OCT scan to measure the stromal bed thickness available for laser ablation. We believe these measurements improve the safety of LASIK by preventing excessive laser treatment that could lead to an insufficient residual stromal bed of less than 250 μm.

55.2.6 Corneal Surgery

The ability of infrared light to penetrate through opaque cornea is used to its full advantage in the imaging of corneal scars, dystrophies, and other causes of corneal

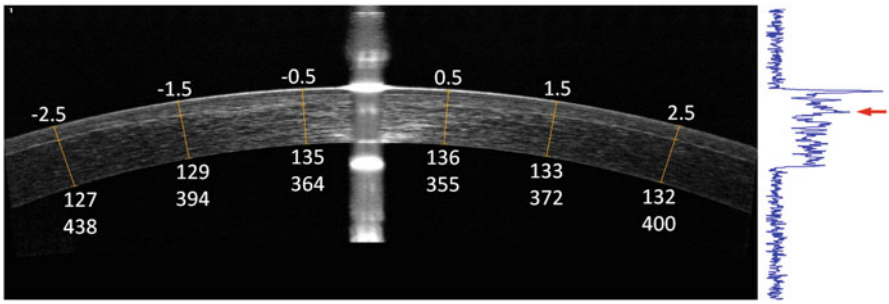

Fig. 55.10 A post-LASIK 1 week OCT scan of 840 nm Fourier-domain OCT. Eight consecutive frames were averaged

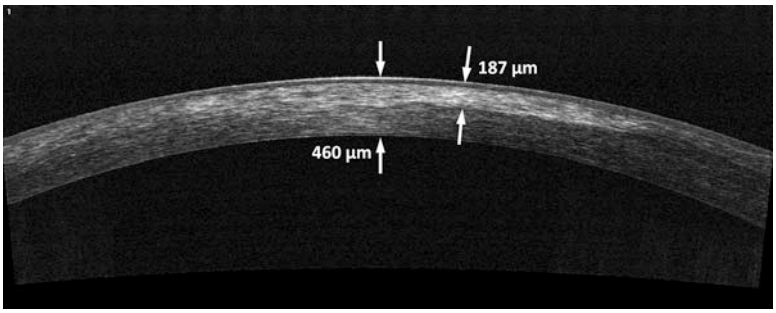

Fig. 55.11 A horizontal OCT of corneal scar with measurements of the corneal thickness and opacity depth

opacity (Fig. 55.11). In a series of 11 eyes with central corneal opacity, we have found that with OCT we were able to accurately measure the corneal thickness and opacity depth, providing useful information for the planning of excimer laser phototherapeutic keratectomy. It is interesting to note that in these cases, the Orbscan II (Bausch & Lomb), a slit-scanning corneal tomography system, significantly underestimated corneal thickness by an average of 157 µm. Thus, the much higher axial resolution of OCT was needed for the measurement of corneal thickness in the presence of corneal opacity.

Intracorneal ring (Intacs®) implantation is an alternative treatment for keratoconus that places two thin plastic ring segments into the stroma. These implants act as passive spacing elements in the midperiphery, shortening the arc length and thereby flattening the central cornea. The rate of complications caused by intracorneal ring is reported to be about 2 % [72]. Many of these complications were associated with shallow placement of the ring segments. Traditional evaluation of ring depth depends on slit-lamp examination by the surgeons. This measure is rough and highly objective. The wide-field anterior segment OCT is capable of imaging a wide area of the cornea and is helpful in better identifying those patients at greater risk of depth-related complications.

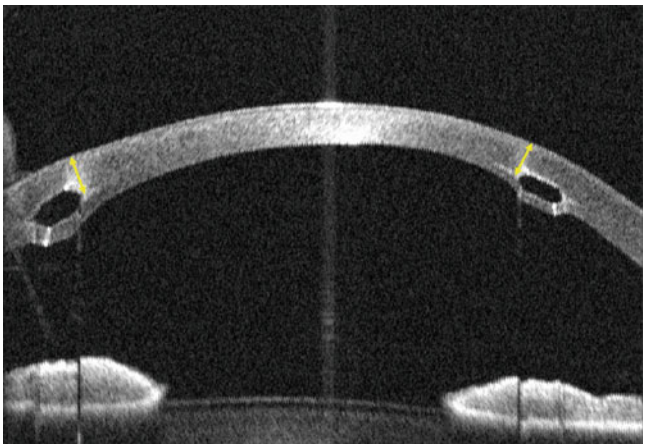

Fig. 55.12 A horizontal OCT scan of an eye after intracorneal ring implantation. The scan length is 12 mm. The segments are 350-μm thick on the left and 250 μm on the right. The depth of ring segment was measured from the inner tip of the ring segment to the anterior corneal surface (*arrows*). It has been recommended that the depth of ring segment is at about 70 % of total corneal thickness to decrease the chance of protrusion

Figure 55.12 is a cross-sectional OCT image of an intracorneal ring along one meridian. This scan can be repeated on different meridians to obtain a quick survey of ring segment depth over 360°. In a case study consisting of four patients who received intracorneal ring implantation, we found the average depth of ring segments was not closely correlated with the surgeons' slit-lamp impressions (r [2] = 0.68) [73]. Shallower segment depth was associated with greater corneal compression anterior to the segment ($p = 0.04$). Some ring segments show progressive shallowing further away from the incision where the segment was inserted. These findings are very useful for interpreting some depth-related complications that occur after intracorneal ring implantation.

Post-keratoplasty glaucoma is a frequent cause of irreversible corneal decompensation and subsequent graft failure [74, 75]. Diagnosis and management of these secondary types of glaucoma is frequently delayed since evaluating the type of glaucoma and measuring intraocular pressure after penetrating keratoplasty can be very challenging. Gonioscopic visualization of the anterior chamber angle is often obstructed by corneal scars, edema, and opacities at the host–recipient interface. Ultrasound biomicroscopy (UBM) is often used to visualize intraocular structures when slit-lamp biomicroscopy is blocked by opacities [76]. One drawback of UBM is the need for an immersion bath to couple the ultrasound from the transducer to the eye, introducing some inconvenience and discomfort. However, OCT imaging provides visualization of anterior segment structures behind an opaque cornea. Figure 55.13 is an OCT image that identified peripheral anterior synechiae as the cause of angle closure.

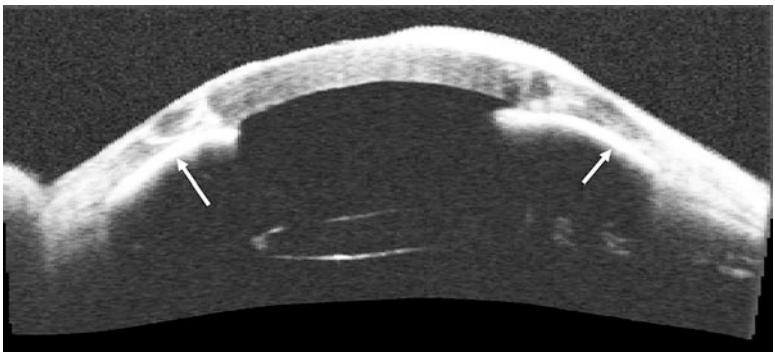

Fig. 55.13 Horizontal wide-field (16 mm) OCT of an eye with an opaque and edematous corneal transplant and elevated intraocular pressure. *Arrows* point to adhesions between the iris and cornea which block the outflow of aqueous fluid from the eye

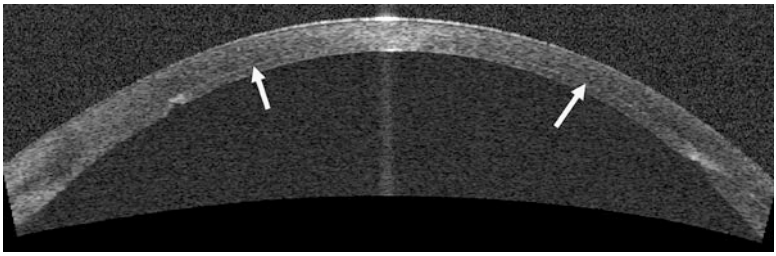

Fig. 55.14 OCT of a cornea after deep lamellar endothelial keratoplasty. The lamellar graft interface (*arrows*) is barely visible. Graft thickness uniformity and size match is excellent in this manually dissected case

Partial thickness corneal transplantation that replaces only the diseased endothelium (endothelial keratoplasty) while retaining the healthy anterior layers is gaining in popularity over full-thickness corneal transplantation (penetrating keratoplasty). It is used to treat corneal edema (swelling) caused by a diseased corneal endothelium. The advantages are fast visual recovery and little disturbance of the optical quality of the cornea (little induced astigmatism), compared to penetrating keratoplasty. Optical coherence tomography is a useful tool for management of post-endothelial keratoplasty patients because of its unique ability to visualize the surgically created layers. Figure 55.14 shows the successful result of one type of endothelial keratoplasty called deep laminar endothelial keratoplasty. The endothelial transplant is visualized as a thin posterior layer that fits well into the space created by the resected diseased endothelium. The edema has resolved, and the corneal thickness has been restored to its normal range. If the transplanted layer did not fully attach or if the edema remains, OCT would be the best modality to visualize the problem.

55.2.7 Assessment of Angle Closure Glaucoma

Angle closure glaucoma is a common cause of visual loss in Asian populations. It occurs in eyes with shallow anterior chambers where the peripheral iris could come forward to block the trabecular meshwork, the normal site of aqueous fluid outflow. Gonioscopy is the current standard for evaluating the anterior chamber angle. In gonioscopy, the physician uses a gonioprism that contacts the cornea to obtain an oblique reflected view of the anterior chamber angle and the trabecular meshwork. Gonioscopy, however, is highly subjective and requires specialized training. Cross-sectional imaging of the anterior chamber angle with either UBM or OCT is easier to interpret. Furthermore, objective quantification of the angle can be obtained from a cross section. Ultrasound biomicroscopy [77] and Scheimpflug photography [78] have been used for quantitative angle evaluation. However, OCT can provide the same detailed angle anatomy, with the further advantage of being noncontact and easy to perform.

Current OCT instruments commonly use 840, 1,050, or 1,310-nm wavelength light. The use of longer wavelength light to image the anterior chamber angle does have advantages: 1,310 and 1,050 nm lights show lower scattering and signal loss in turbid media [18, 79], permitting much better penetration through the limbus and sclera than is possible using shorter wavelengths.

This increased penetration allows 1,310-nm wavelength OCT to accurately measure gross angle morphology and visualize angle structures such as the iris root and scleral spur [11, 80, 81]. As a result, past studies used 1,310-nm OCT systems and developed quantitative angle parameters using scleral spur as the anatomical landmark [82–85]. The axial resolutions of the earlier OCT systems used in the abovementioned studies were limited to 15–20 μm and did not allow reliable identification of smaller angle structures such as the trabecular meshwork and Schwalbe's line. Newer OCT systems capable of producing axial resolutions of 1–5 μm are now available [86, 87]. This marked increase in resolution is due to the combination of broader bandwidth and shorter wavelength.

We used a 1,310-nm wavelength anterior segment OCT to assess the angle width. Images of an open angle and an occludable (narrow) angle are shown in Fig. 55.15. Corneal, scleral, and iris anatomy are visualized in detail. Features in the limbus and angle are clearly shown, including the scleral spur, ciliary body band, angle recess, and iris root. For angle measurements, it is particularly useful that the scleral spur is a highly reflective and easily identified on OCT. To take advantage of the highly contrasted scleral spur, we devised a diagnostic parameter called the trabeculo–iris space area (TISA-X) to quantify the angle opening. We define TISA-X as the aqueous space bounded by a roughly trapezoidal shape between the scleral spur, a point on the corneal endothelium X microns anteromedial from the scleral spur, and the intersections of the anterior iris surface with perpendicular lines drawn from the first two landmarks (Fig. 55.16a). We tested both TISA-500 and TISA-750. The 500-μm figure is anatomically meaningful because the average trabecular meshwork extends approximately 500 μm anteromedially from the scleral spur. The 750-μm figure used a greater portion of the images.

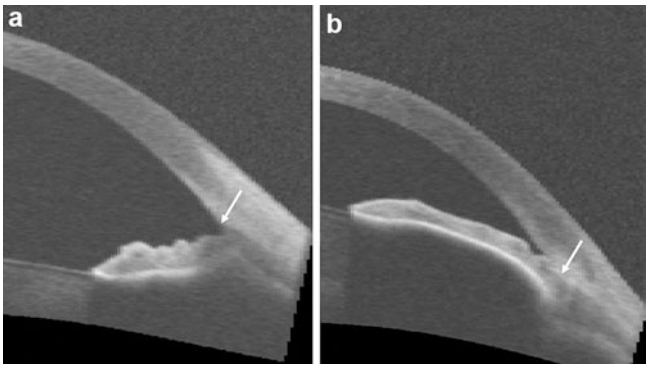

Fig. 55.15 OCT images of (**a**) an open anterior chamber angle and (**b**) an occludable (narrow) anterior chamber angle. *White arrows* indicate scleral spur locations

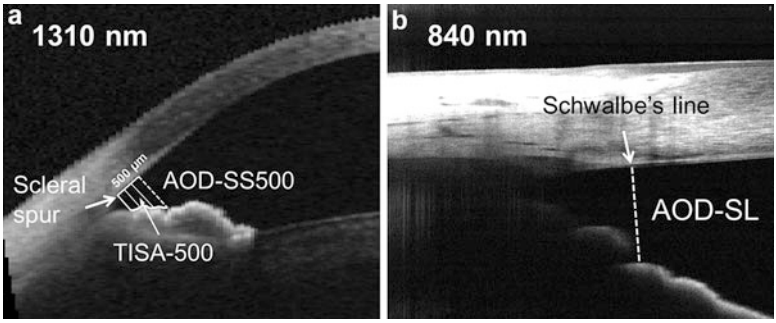

Fig. 55.16 Narrow angle diagnostic parameters of 1,310 nm (**a**) and 840 nm (**b**) OCT systems. AOD-SS500: angle opening distance measured 500 µm away from the scleral spur. TISA-500: trabeculo–iris space area 500 µm from the scleral spur. AOD-SL: angle opening distance at Schwalbe's line

We performed a clinical study to compare OCT and UBM parameters against gonioscopic grading by glaucoma specialists [82]. Thirty-one eyes of 28 subjects were examined. Eight eyes were judged to be occludable by gonioscopy. Subjects underwent OCT and UBM imaging of the nasal and temporal anterior chamber angles. Both OCT and UBM had excellent correlation with gonioscopy in terms of identifying occludable angles. We found that TISA-750 was better than TISA-500 for identifying gonioscopically occludable angles. A cutoff value of 0.12-mm [2] TISA-750 had 100 % sensitivity and 95.7 % specificity. This study showed that OCT is a reproducible method to assess the depth of the anterior chamber angle and validated it against both standard gonioscopy and UBM.

Fourier-domain OCT of 840-nm wavelength showed fine anatomical structures such as Schwalbe's line, trabecular meshwork, and scleral spur (Fig. 55.3a), but provided limited visualization of the angle recess. Schwalbe's line represents the

termination of Descemet's membrane and is approximately 500–750 μm anterior to the scleral spur. The distance between Schwalbe's line and the scleral spur represents the trabecular meshwork and the aqueous humor filtration distance. Schwalbe's line was proposed as an anatomical landmark because it could be consistently identified in 840-nm FD-OCT images. Several research groups recommended measuring angle opening distance at the Schwalbe's line (AOD-SL) for quantitative angle assessment (Fig. 55.16b) [88–90]. Further, AOD-SL has demonstrated good repeatability and strong correlation with gonioscopic grading. In a study reported by Qin et al. [90], 35 glaucoma patients were recruited. Each subject underwent darkroom gonioscopic examination, and a modified Shaffer grade was recorded for each of four quadrants. An occludable angle was defined as Grade 1 or lower in all quadrants. Angle scans were performed under standardized dim illumination conditions (6.6 foot candles) using a Fourier-domain OCT (RTVue-CAM, Optovue, Inc.). Schwalbe's line was visualized in 97.7 % of eyes scanned. Qin et al. also reported good repeatability for AOD-SL measurements with intra-observer coefficients of variation ranging from 9.8 % to 12.0 % and interobserver coefficients of variation ranging from 10.1 % to 13.3 %. Spearman's rho analysis showed strong correlation between AOD-SL measurements and gonioscopic grading with correlation coefficients of 0.80 for nasal angles and 0.81 for temporal angles. The occludable angle AOD-SL measurements ranged from 0 to 350 μm, and the non-occludable angle measurements ranged from 192 to 922 μm. Qin et al. determined a diagnostic cutoff value for occludable angle of 290 μm by performing receiver operating characteristic (ROC) analyses.

Optical coherence tomography is also useful for monitoring the results of treatment for narrow angle [91]. Narrow angle is often caused or exacerbated by a buildup of fluid behind the iris that pushes the peripheral iris forward. The fluid buildup is caused by blockage of fluid flow at the papillary margin due to tight apposition between the iris and the lens. A laser peripheral iridotomy can be performed to create a small hole in the iris as an alternate channel of fluid flow. This allows the iris to fall back and the angle to deepen. The use of OCT allows one to assess whether this procedure is effective.

We believe OCT will become an important tool for detecting narrow angle and monitoring the anatomic results of treatment. Further studies are needed to correlate the OCT measurements and the risk of acute glaucoma attacks due to pupil blockage and the risk of chronic intraocular pressure elevation and glaucoma. The availability of this precise tool for anatomic measurement may allow development of more objective and rational guidelines for treatment in this important class of disease.

55.2.8 Anterior Chamber Biometry and Intraocular Lens Implants

Phakic intraocular lens (IOL) implantation is performed to correct extreme myopia and hyperopia that are beyond the range of corneal procedures such as LASIK and

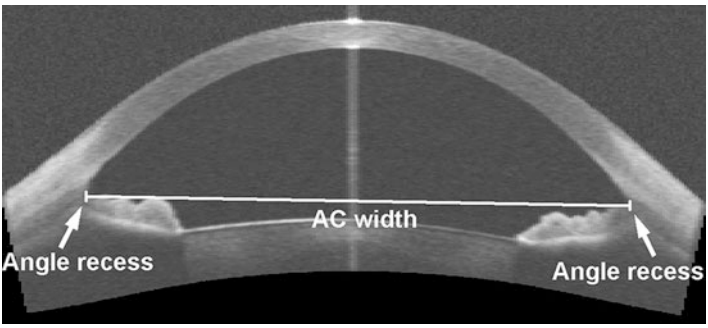

Fig. 55.17 A horizontal OCT scan showing the measurement of the anterior chamber width from angle recess to angle recess (*arrow*)

PRK. They are called "phakic" because the natural lens (phakos) is kept in place, as opposed to IOLs placed after cataract extraction, which are "aphakic" lenses. With the natural lens in place, there is very little room in the eye to add another lens. Thus, the design and fitting of phakic IOLs are more difficult. High-speed anterior segment OCT is able to make precise measurements that aid in the safe insertion of all three types of phakic IOLs now in use.

Anterior chamber width (ACW) measurement is clinically important for sizing angle-supported anterior chamber IOLs. An IOL that is too large can press on the iris root and produce pupil ovalization, while an IOL that is too small can lead to IOL movement, decentration, corneal endothelial damage, and iritis [92]. The traditional method for IOL sizing uses the external corneal diameter (CD), which was assumed to be correlated with the internal anterior chamber width. Typically, the IOL diameter is chosen to be the CD plus a constant such as 1 mm.

Increasing the speed of OCT to 2,000–4,000 axial scans per second allows accurate ACW measurement. For implantation of an angle-supported IOL, the relevant width is measured from angle recess to angle recess across the anterior chamber (Fig. 55.17). We used a wide-field anterior segment OCT system (4,000 axial scans per second) to measure the internal ACW and compared the result to external corneal diameter measurements in 20 normal subjects [12]. The ACW was 12.53 ± 0.47 mm (mean ± standard deviation) and the inter-image repeatability of measurement was 0.13 mm by pooled standard deviation. The difference between ACW and CD was 0.75 ± 0.44 (mean ± SD). Thus the use of OCT could potentially result in a threefold improvement in the precision of IOL fitting.

The iris-supported phakic IOL has been used to correct extreme myopia and hyperopia. Baikoff et al. has demonstrated that OCT is also useful for determining whether there is sufficient clearance between the IOL and the cornea and iris before surgery [93]. A well-fitted iris-supported phakic IOL is shown in Fig. 55.18.

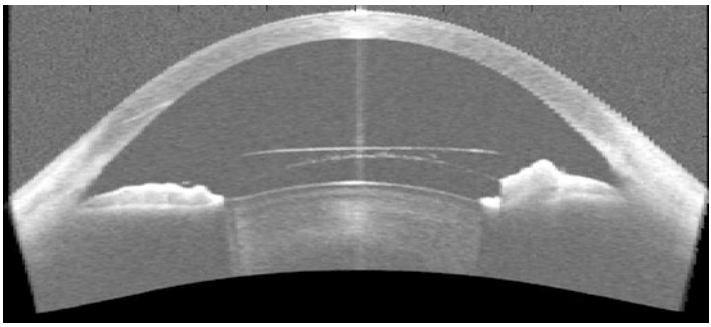

Fig. 55.18 A horizontal OCT scan of a phakic eye with an iris-fixed phakic intraocular lens (*IOL*) implant (Verisyse, AMO, Irvine, CA). There is good clearance of the IOL from the cornea, iris, and the natural lens

Yet a third type of phakic IOL is placed in the posterior chamber, between the iris and the natural lens. Although OCT cannot be used to measure the width of the ciliary sulcus space in the posterior chamber, it is useful to measure the consequence of poor sizing, such as contact with the natural lens (no vaulting) or excessive vaulting that cause chafing of the iris and pigment dispersion [94].

Phakic IOLs provide superior optical quality in the correction of extreme hyperopia and myopia, compared to LASIK. However, long-term safety is a major concern for these relatively new devices. By improving patient selection and IOL sizing, OCT may significantly improve the safety of phakic IOL implantation.

55.2.9 Intraocular Lens Power Calculation

Corneas after refractive surgeries require a method of directly measuring both anterior and posterior corneal power in order to obtain accurate corneal power measurement and intraocular lens (IOL) calculation. Slit-scanning tomography, rotating-slit Scheimpflug camera, and dual-Scheimpflug systems have all been used for this purpose [95–97]. However, the axial resolutions of these devices are between 50 and 100 μm, much lower than the resolution offered by current OCT technology. There have been a number of recent studies showing good repeatability and accuracy when using OCT to measure corneal power [98–100], and OCT is more accurate than other types of corneal tomography when taking measurements in the presence of corneal opacities [101].

The OCT-based IOL formula was published in a recent study [98]. In this study, Corneal power was measured with a Fourier-domain OCT system. Axial length, anterior chamber depth, and automated keratometry were measured with the IOLMaster. An OCT-based IOL formula was developed from these parameters. The formula used an eye model consisting of four optical surfaces: anterior corneal

surface, posterior corneal surface, IOL, and retina. The IOL was modeled as a thin lens. The formula traces the vergence of the light traveling through the eye, starting from the retinal plane to the anterior eye surface to predict refractive outcome after IOL implantation given the IOL model and power.

The OCT-based IOL formula used an eye model consisting of four optical surfaces: anterior corneal surface, posterior corneal surface, IOL, and retina. The IOL was modeled as a thin lens. Light traveled through the first three surfaces and focused on the retina. We traced the vergence of the light beam traveling through the eye, starting from the retinal plane to the anterior eye surface.

At the back of IOL, vergence

$$V_1 = n_2/l_1 \tag{55.3}$$

In front of IOL, vergence

$$V_1' = V_1 - P_1 \tag{55.4}$$

At the back of posterior corneal surface, vergence

$$V_2 = 1/\left(1/V_1' + l_2/n_2\right) \tag{55.5}$$

In front of posterior corneal surface, vergence

$$V_2' = V_2 - P_P \tag{55.6}$$

At the back of anterior corneal surface, vergence

$$V_3 = n_1/\left(n_1/V_2' + \mathrm{CCT}\right) \tag{55.7}$$

In front of anterior corneal surface, vergence

$$V_3' = V_3 - P_A \tag{55.8}$$

Where n_1 = refractive index of cornea, 1.376 is used
n_2 = refractive index of vitreous and aqueous humor, 1.336 is used
l_1 = vitreous length = AL – l_2
l_2 = IOL depth (also called effective lens position, see Eq. 55.10)
P_1 = IOL power

The vergence in front of anterior corneal surface V_3' is the refractive error at the corneal plane. The manifest refraction spherical equivalent (MRSE) at the spectacle plane is

$$\mathrm{MRSE} = 1/\left(1/V_3' + \text{vertex distance}\right) \tag{55.9}$$

A vertex distance of 12 mm was assumed in our calculations. Overall The IOL depth was predicted using a regression-derived formula:
If AL $< = 24.4$ mm:

$$\text{IOL depth} = 0.711 * \text{ACD} + 0.623 * \sqrt{\text{AL}} - 0.25 * P_P + (\text{pACD} - 8.11) \tag{55.10}$$

If AL > 24.4 mm:

$$\text{IOL depth} = 0.711 * \text{ACD} + 0.623 * \sqrt{[\text{AL} - 0.8 * (\text{AL} - 24.4)]} - 0.25 * P_P + (\text{pACD} - 8.11) \tag{55.11}$$

where P_P is posterior corneal power and pACD is the ACD constant, a constant given by the manufacturers to characterize a given lens.

The mean absolute error (MAE) of refractive prediction for OCT-based IOL formula was calculated. A total of 31 eyes of 24 subjects who had uncomplicated cataract surgery with monofocal IOL implantation were enrolled in the two sites. Twenty-two eyes of 16 subjects had previous myopic LVC ranged from −12.46 D to −0.88 D. Nine eyes of eight subjects had previous hyperopic LVC ranged from 0.66D to 5.52D.

For the myopic group, the MAE of OCT-based formula was 0.57 D, and the MAE of Haigis-L was 0.73 D ($p = 0.19$). We also reported a trend toward fewer large prediction errors using OCT, with 18 eyes (82 %) within 1 D of actual refractive outcome, compared with 16 eyes (73 %) within 1 D for Haigis-L. For the hyperopic group, the MAE of OCT-based IOL was 0.26 D, while Haigis-L had an MAE of 0.54 D ($p > 0.05$). There was a trend toward fewer large prediction errors using OCT, with nine eyes (100 %) within 1 D of actual refractive outcome, compared to seven eyes (78 %) within 1 D for Haigis-L. Given these results and the likelihood of future improvements to OCT systems, this technology has a promising future in cataract surgery.

55.2.10 Optical Coherence Tomography in Eye Banking

Eye banks currently employ a number of methods for assessing donor corneal tissue, including penlight exam, specular microscopy, slit-lamp biomicroscopy, medical record review, and family interview [102]. Although these evaluation techniques are largely successful in identifying the contraindications that bar corneas from use in procedures such as penetrating keratoplasty (PK), anterior lamellar keratoplasty (ALK), and endothelial keratoplasty (EK), some eye banks have recently begun adopting Fourier-domain OCT as a way of supplementing their standard procedures for tissue appraisal.

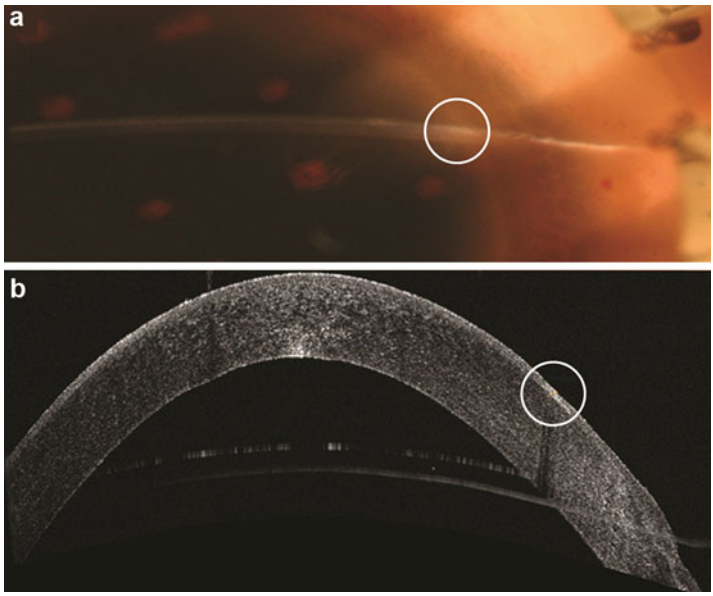

Fig. 55.19 (**a**) Slit-lamp microscopy shows corneal opacity, but its position cannot be determined precisely (*circle*). (**b**) OCT evaluation reveals scarring is actually limited to the corneal epithelium (*circle*)

OCT's unique ability to accurately map corneas over a wide area, and provide precise measurements of stromal opacities while avoiding tissue contamination [101, 103], makes it a potentially valuable instrument for screening donor corneas. This potential is bolstered by the Eye Bank Association of America's (EBAA) 2005 decision to expand the criteria for acceptable tissue: [102] corneas that had been deemed unsuitable for PK because of anterior scarring, central pterygia, or corneal refractive surgeries such as radial keratotomy (RK) are now being effectively used in EK procedures [104, 105]. It is therefore increasingly important that each donor cornea is evaluated both accurately and efficiently in order to make the best use of all available tissue. In an example shown in Fig. 55.19, the slit-lamp examination showed corneal opacity, but its precise position cannot be determined (Fig. 55.19a). However, upon OCT evaluation, it was shown that the cornea contained no stromal scarring, and, with a depth of 82 μm, the opacity was limited to the epithelium (Fig. 55.19b). The tissue was eventually used for EK.

The use of Fourier-domain OCT as an adjunct to standard tissue evaluation methods may provide eye banks with the information necessary to improve their decision-making processes and ensure that no donor cornea is wasted or misused.

55.3 Future Developments

Very high performance anterior segment OCT systems have already been demonstrated in research centers [18, 20, 22, 106–109]. The performance of commercial anterior segment OCT will also improve as the cost of implementation drops and clinical application grows.

With higher speed, three-dimensional visualization becomes possible. Figure 55.20a shows a rendering of a volumetric data set acquired with an ultrahigh speed swept-source OCT operating at 100 kHz for anterior segment imaging. The three-dimensional volume consists of 500 × 500 axial scans covering 16 × 16 mm [2] of the anterior eye. Extended depth imaging has been achieved swept-source technology. As an example, the cross-sectional image in Fig. 55.20b shows the cornea, iris, and entire crystalline lens and spans the entire transverse anterior chamber width, from limbus to limbus.

High-speed imaging also enables more reproducible measurement of the ocular structures. The short time frame of the high-speed measurement reduces the motion artifacts in the image and improves the accuracy of shape and dimension measurements. Several research groups demonstrated corneal topographic measurements with ultrahigh speed anterior segment OCT [20, 106, 107, 109–111]. Karnowski et al. presented corneal topographic maps obtained with a Fourier-domain OCT system operating at 108,000 axial scans per second [106]. They demonstrated good agreement between Fourier-domain OCT-based topographic maps and those obtained with a rotating Scheimpflug imaging and Placido topography (Fig. 55.21).

OCT competes with other imaging methods such as ultrasound imaging, slit-scanning tomography, Placido ring topography, and confocal scanning microscopy. It is unique in its versatility. And as the performance of OCT further improves, it can take over more of the applications currently performed with the other technologies.

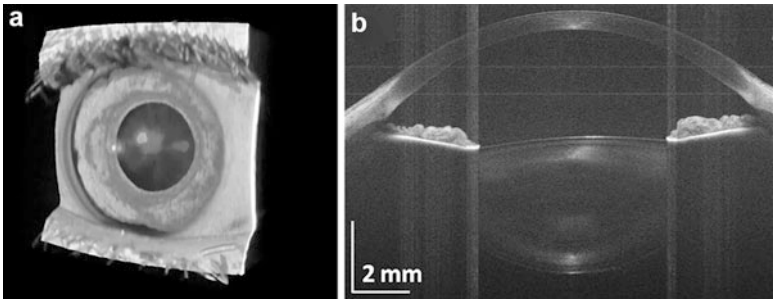

Fig. 55.20 Anterior segment imaging with VCSEL-OCT: (**a**) rendering of the volume, (**b**) central cross-sectional image was averaged by five consecutive B-scans (Reprinted from Grulkowski et al. [107])

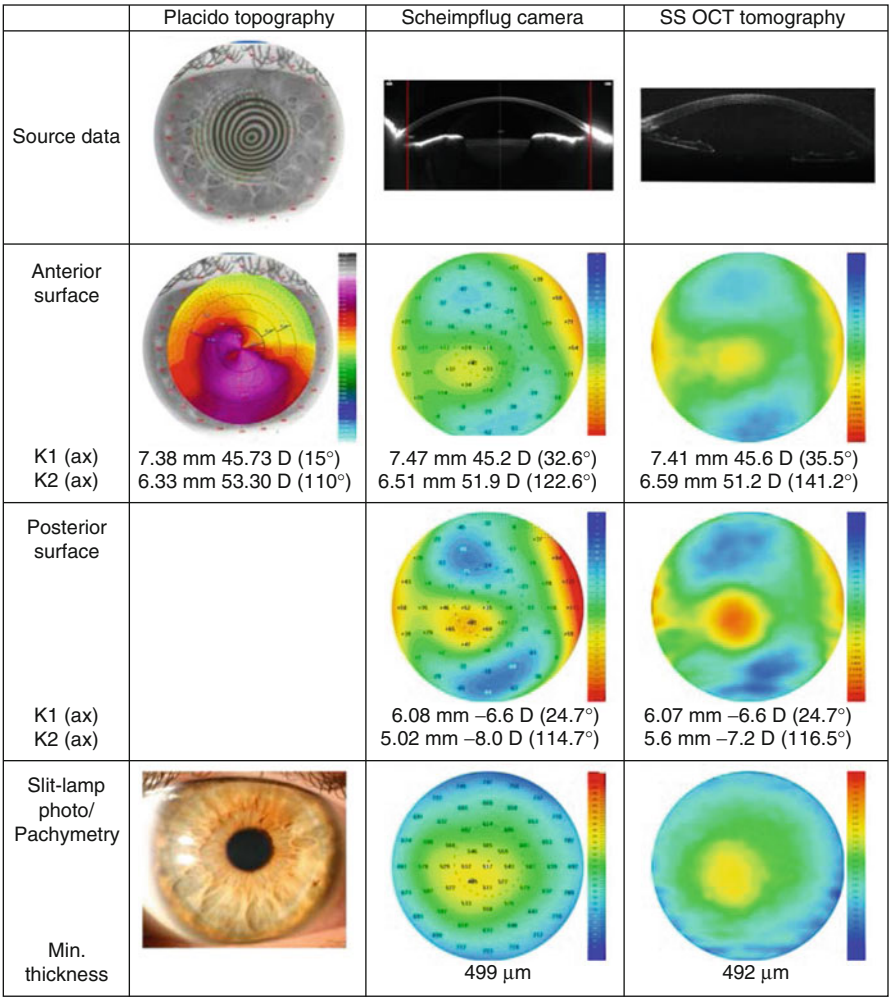

Fig. 55.21 Quantitative evaluation of a keratoconic cornea with high-speed swept-source OCT, rotating Scheimpflug imaging, and Placido topography. K1 and K2 indicate central keratometry readings (Reprinted from Karnowski et al. [106])

References

1. D. Huang, E.A. Swanson, C.P. Lin et al., Optical coherence tomography. Science **254**(5035), 1178–1181 (1991)
2. M.R. Hee, J.A. Izatt, E.A. Swanson et al., Optical coherence tomography of the human retina. Arch. Ophthalmol. **113**(3), 325–332 (1995)
3. M.J. Maldonado, L. Ruiz-Oblitas, J.M. Munuera et al., Optical coherence tomography evaluation of the corneal cap and stromal bed features after laser in situ keratomileusis for high myopia and astigmatism. Ophthalmology **107**(1), 81–87 (2000); discussion 8

4. C. Ustundag, H. Bahcecioglu, A. Ozdamar et al., Optical coherence tomography for evaluation of anatomical changes in the cornea after laser in situ keratomileusis. J. Cataract Refract. Surg. **26**(10), 1458–1462 (2000)
5. K. Hirano, Y. Ito, T. Suzuki et al., Optical coherence tomography for the noninvasive evaluation of the cornea. Cornea **20**(3), 281–289 (2001)
6. S. Muscat, N. McKay, S. Parks et al., Repeatability and reproducibility of corneal thickness measurements by optical coherence tomography. Invest. Ophthalmol. Vis. Sci. **43**(6), 1791–1795 (2002)
7. J. Wang, D. Fonn, T.L. Simpson, L. Jones, Relation between optical coherence tomography and optical pachymetry measurements of corneal swelling induced by hypoxia. Am. J. Ophthalmol. **134**(1), 93–98 (2002)
8. M. Bechmann, M.J. Thiel, A.S. Neubauer et al., Central corneal thickness measurement with a retinal optical coherence tomography device versus standard ultrasonic pachymetry. Cornea **20**(1), 50–54 (2001)
9. A.C. Wong, C.C. Wong, N.S. Yuen, S.P. Hui, Correlational study of central corneal thickness measurements on Hong Kong Chinese using optical coherence tomography, Orbscan and ultrasound pachymetry. Eye **16**(6), 715–721 (2002)
10. Y. Feng, J. Varikooty, T.L. Simpson, Diurnal variation of corneal and corneal epithelial thickness measured using optical coherence tomography. Cornea **20**(5), 480–483 (2001)
11. S. Radhakrishnan, A.M. Rollins, J.E. Roth et al., Real-time optical coherence tomography of the anterior segment at 1310 nm. Arch. Ophthalmol. **119**(8), 1179–1185 (2001)
12. J.A. Goldsmith, Y. Li, M.R. Chalita et al., Anterior chamber width measurement by high-speed optical coherence tomography. Ophthalmology **112**(2), 238–244 (2005)
13. Y. Li, R. Shekhar, D. Huang, Corneal pachymetry mapping with high-speed optical coherence tomography. Ophthalmology **113**(5), 792-9 e1-2 (2006)
14. N.M. Samy El Gendy, Li Y, Zhang X, Huang D. Repeatability of pachymetric mapping using Fourier domain optical coherence tomography in corneas with opacities. Cornea **31**(4), 418–423 (2012)
15. Y.L. Tan, L.S. Mohanram, S.E. Ti et al., Imaging late capsular bag distension syndrome: an anterior segment optical coherence tomography study. Clin. Ophthalmol. **6**, 1455–1458 (2012)
16. Y. Li, M. Tang, X. Zhang et al., Pachymetric mapping with Fourier-domain optical coherence tomography. J. Cataract Refract. Surg. **36**(5), 826–831 (2010)
17. S.R. Chinn, E.A. Swanson, J.G. Fujimoto, Optical coherence tomography using a frequency-tunable optical source. Opt. Lett. **22**(5), 340–342 (1997)
18. B. Potsaid, B. Baumann, D. Huang et al., Ultrahigh speed 1050nm swept source/Fourier domain OCT retinal and anterior segment imaging at 100,000 to 400,000 axial scans per second. Opt. Express **18**(19), 20029–20048 (2010)
19. R. Huber, M. Wojtkowski, J.G. Fujimoto, Fourier Domain Mode Locking (FDML): A new laser operating regime and applications for optical coherence tomography. Opt. Express **14**(8), 3225–3237 (2006)
20. M. Gora, K. Karnowski, M. Szkulmowski et al., Ultra high-speed swept source OCT imaging of the anterior segment of human eye at 200 kHz with adjustable imaging range. Opt. Express **17**(17), 14880–14894 (2009)
21. S.J. Lang, A. Cucera, G.K. Lang, Applications of optical coherence tomography in the anterior segment. Klin. Monbl. Augenheilkd. **228**(12), 1086–1091 (2011)
22. M.V. Sarunic, S. Asrani, J.A. Izatt, Imaging the ocular anterior segment with real-time, full-range Fourier-domain optical coherence tomography. Arch. Ophthalmol. **126**(4), 537–542 (2008)
23. M. Wojtkowski, High-speed optical coherence tomography: basics and applications. Appl. Opt. **49**(16), D30–D61 (2010)
24. H.C. van de Hulst, *Light Scattering by Small Particles* (Dover Publications, New York, 1981)

25. American National Standard for Safe Use of Lasers ANSI Z136.1-2000 (Laser Institute of America, American National Standards Institute, Inc., Orlando, 2000)
26. H. Cheng, A.K. Bates, L. Wood, K. McPherson, Positive correlation of corneal thickness and endothelial cell loss. Serial measurements after cataract surgery. Arch. Ophthalmol. **106**(7), 920–922 (1988)
27. B.A. Holden, G.W. Mertz, J.J. McNally, Corneal swelling response to contact lenses worn under extended wear conditions. Invest. Ophthalmol. Vis. Sci. **24**(2), 218–226 (1983)
28. M.R. O'Neal, K.A. Polse, In vivo assessment of mechanisms controlling corneal hydration. Invest. Ophthalmol. Vis. Sci. **26**(6), 849–856 (1985)
29. G.O. Waring 3rd, W.M. Bourne, H.F. Edelhauser, K.R. Kenyon, The corneal endothelium. Normal and pathologic structure and function. Ophthalmology **89**(6), 531–590 (1982)
30. J.D. Brandt, J.A. Beiser, M.O. Gordon et al., Central corneal thickness and measured IOP response to topical ocular hypotensive medication in the Ocular Hypertension Treatment Study. Am. J. Ophthalmol. **138**(5), 717–722 (2004)
31. R.P. Copt, R. Thomas, A. Mermoud, Corneal thickness in ocular hypertension, primary open-angle glaucoma, and normal tension glaucoma. Arch. Ophthalmol. **117**(1), 14–16 (1999)
32. I. Kozak, M. Hornak, T. Juhas et al., Changes in central corneal thickness after laser in situ keratomileusis and photorefractive keratectomy. J. Refract. Surg. **19**(2), 149–153 (2003)
33. Y.S. Rabinowitz, K. Rasheed, H. Yang, J. Elashoff, Accuracy of ultrasonic pachymetry and videokeratography in detecting keratoconus. J. Cataract Refract. Surg. **24**(2), 196–201 (1998)
34. M. Bohnke, B.R. Masters, R. Walti et al., Precision and reproducibility of measurements of human corneal thickness with rapid optical low-coherence reflectometry (OLCR). J. Biomed. Opt. **4**(1), 152–156 (1999)
35. D. Huang, J. Wang, C.P. Lin et al., Micron-resolution ranging of cornea anterior chamber by optical reflectometry. Lasers Surg. Med. **11**(5), 419–425 (1991)
36. J.W. McLaren, C.B. Nau, J.C. Erie, W.M. Bourne, Corneal thickness measurement by confocal microscopy, ultrasound, and scanning slit methods. Am. J. Ophthalmol. **137**(6), 1011–1020 (2004)
37. J. Nissen, J.O. Hjortdal, N. Ehlers et al., A clinical comparison of optical and ultrasonic pachometry. Acta Ophthalmol (Copenh) **69**(5), 659–663 (1991)
38. J.M. Gonzalez-Meijome, A. Cervino, E. Yebra-Pimentel, M.A. Parafita, Central and peripheral corneal thickness measurement with Orbscan II and topographical ultrasound pachymetry. J. Cataract Refract. Surg. **29**(1), 125–132 (2003)
39. V. Yaylali, S.C. Kaufman, H.W. Thompson, Corneal thickness measurements with the Orbscan Topography System and ultrasonic pachymetry. J. Cataract Refract. Surg. **23**(9), 1345–1350 (1997)
40. D.Z. Reinstein, R.H. Silverman, T. Raevsky et al., Arc-scanning very high-frequency digital ultrasound for 3D pachymetric mapping of the corneal epithelium and stroma in laser in situ keratomileusis. J. Refract. Surg. **16**(4), 414–430 (2000)
41. D.Z. Reinstein, R.H. Silverman, S.L. Trokel, D.J. Coleman, Corneal pachymetric topography. Ophthalmology **101**(3), 432–438 (1994)
42. V. Westphal, A.M. Rollins, S. Radhakrishnan, J.A. Izatt, Correction of geometric and refractive image distortions in optical coherence tomography applying Fermat's principle. Opt. Express **10**(9), 397–404 (2002)
43. R. Zawadzki, C. Leisser, R. Leitgeb, et al., Three-dimensional ophthalmic optical coherence tomography with a refraction correction algorithm. in *Optical Coherence Tomography and Coherence Techniques: SPIE*, ed. by W. Drexler, International Society for Optics and photonics, Munich, Germany, vol. 5140 (2003)

44. R.C. Lin, M.A. Shure, A.M. Rollins et al., Group index of the human cornea at 1.3-microm wavelength obtained in vitro by optical coherence domain reflectometry. Opt. Lett. **29**(1), 83–85 (2004)
45. D. Huang, M. Tang, R. Shekhar, Mathematical model of corneal surface smoothing after laser refractive surgery. Am. J. Ophthalmol. **135**(3), 267–278 (2003)
46. D.Z. Reinstein, M. Gobbe, T.J. Archer et al., Epithelial, stromal, and total corneal thickness in keratoconus: three-dimensional display with artemis very-high frequency digital ultrasound. J. Refract. Surg. **26**(4), 259–271 (2010)
47. J. Fujimoto, D. Huang, Introduction to optical coherence tomography, in *Imaging the Eye from Front to Back with RTVue Fourier-Domain Optical Coherence Tomography*, ed. by D. Huang, J. Duker, J. Fujimoto et al., 1st edn. (SLACK Incorporated, Thorofare, NJ, 2010)
48. J. Wang, J. Thomas, I. Cox, A. Rollins, Noncontact measurements of central corneal epithelial and flap thickness after laser in situ keratomileusis. Invest. Ophthalmol. Vis. Sci. **45**(6), 1812–1816 (2004)
49. S. Sin, T.L. Simpson, The repeatability of corneal and corneal epithelial thickness measurements using optical coherence tomography. Optom. Vis. Sci. **83**(6), 360–365 (2006)
50. S. Haque, T. Simpson, L. Jones, Corneal and epithelial thickness in keratoconus: a comparison of ultrasonic pachymetry, Orbscan II, and optical coherence tomography. J. Refract. Surg. **22**(5), 486–493 (2006)
51. Y. Feng, T.L. Simpson, Corneal, limbal, and conjunctival epithelial thickness from optical coherence tomography. Optom. Vis. Sci. **85**(9), E880–E883 (2008)
52. Y. Li, O. Tan, D. Huang, Normal and keratoconic corneal epithelial thickness mapping using Fourier-domain optical coherence tomography. in *Medical Imaging 2011: Biomedical Applications in Molecular, Structural, and Functional Imaging* (Lake Buena Vista, 2011), vol. Proc. SPIE 7965
53. X. Li, Y.S. Rabinowitz, K. Rasheed, H. Yang, Longitudinal study of the normal eyes in unilateral keratoconus patients. Ophthalmology **111**(3), 440–446 (2004)
54. J.C. Erie, S.V. Patel, J.W. McLaren et al., Effect of myopic laser in situ keratomileusis on epithelial and stromal thickness: a confocal microscopy study. Ophthalmology **109**(8), 1447–1452 (2002)
55. N. Maeda, S.D. Klyce, M.K. Smolek, H.W. Thompson, Automated keratoconus screening with corneal topography analysis. Invest. Ophthalmol. Vis. Sci. **35**(6), 2749–2757 (1994)
56. J.B. Randleman, B. Russell, M.A. Ward et al., Risk factors and prognosis for corneal ectasia after LASIK. Ophthalmology **110**(2), 267–275 (2003)
57. Y. Li, M. Tang, X. Zhang et al., Pachymetric mapping with Fourier-domain optical coherence tomography. J. Cataract Refract. Surg. **36**, 834–839 (2010)
58. Y. Li, D.M. Meisler, M. Tang et al., Keratoconus diagnosis with optical coherence tomography pachymetry mapping. Ophthalmology **115**(12), 2159–2166 (2008)
59. D.Z. Reinstein, T.J. Archer, M. Gobbe, Corneal epithelial thickness profile in the diagnosis of keratoconus. J. Refract. Surg. **25**(7), 604–610 (2009)
60. D.Z. Reinstein, T.J. Archer, M. Gobbe, Stability of LASIK in topographically suspect keratoconus confirmed non-keratoconic by Artemis VHF digital ultrasound epithelial thickness mapping: 1-year follow-up. J. Refract. Surg. **25**(7), 569–577 (2009)
61. M. Tang, Y. Li, M. Avila, D. Huang, Measurement of total corneal power before and after LASIK with high-speed optical coherence tomography. J. Cataract Refract. Surg. **32**, 1843–1850 (2006)
62. D. Huang, A reliable corneal tomography system is still needed. Ophthalmology **110**(3), 455–456 (2003)
63. S.A. Choudhri, S.K. Feigenbaum, J.S. Pepose, Factors predictive of LASIK flap thickness with the Hansatome zero compression microkeratome. J. Refract. Surg. **21**(3), 253–259 (2005)

64. V.D. Durairaj, J. Balentine, G. Kouyoumdjian et al., The predictability of corneal flap thickness and tissue laser ablation in laser in situ keratomileusis. Ophthalmology **107**(12), 2140–2143 (2000)
65. G.W. Flanagan, P.S. Binder, Precision of flap measurements for laser in situ keratomileusis in 4428 eyes. J. Refract. Surg. **19**(2), 113–123 (2003)
66. O. Giledi, M.G. Mulhern, M. Espinosa et al., Reproducibility of LASIK flap thickness using the Hansatome microkeratome. J. Cataract Refract. Surg. **30**(5), 1031–1037 (2004)
67. D. Miranda, S.D. Smith, R.R. Krueger, Comparison of flap thickness reproducibility using microkeratomes with a second motor for advancement. Ophthalmology **110**(10), 1931–1934 (2003)
68. M.S. Muallem, S.Y. Yoo, A.C. Romano et al., Corneal flap thickness in laser in situ keratomileusis using the Moria M2 microkeratome. J. Cataract Refract. Surg. **30**(9), 1902–1908 (2004)
69. Z.Z. Nagy, M. Resch, I. Suveges, Ultrasound evaluation of flap thickness, ablation depth, and corneal edema after laser in situ keratomileusis. J. Refract. Surg. **20**(3), 279–281 (2004)
70. G. Shemesh, I. Leibovitch, I. Lipshitz, Comparison of corneal flap thickness between primary and fellow eyes using three microkeratomes. J. Refract. Surg. **20**(5), 417–421 (2004)
71. R. Yildirim, C. Aras, A. Ozdamar et al., Reproducibility of corneal flap thickness in laser in situ keratomileusis using the Hansatome microkeratome. J. Cataract Refract. Surg. **26**(12), 1729–1732 (2000)
72. J. Ruckhofer, J. Stoiber, E. Alzner, G. Grabner, One year results of European Multicenter Study of intrastromal corneal ring segments. Part 2: complications, visual symptoms, and patient satisfaction. J. Cataract Refract. Surg. **27**(2), 287–296 (2001)
73. M. Lai, M. Tang, E. Andrade, et al., Assessing intrastromal corneal ring segment depth in keratoconic eyes using optical coherence tomography. J Cataract Refract Surg. **32**(11), 1860–5 (2006)
74. A.R. Irvine, H.E. Kaufman, Intraolar pressure following penetrating keratoplasty. Am. J. Ophthalmol. **68**(5), 835–844 (1969)
75. R.K. Lee, F. Fantes, Surgical management of patients with combined glaucoma and corneal transplant surgery. Curr. Opin. Ophthalmol. **14**(2), 95–99 (2003)
76. G. Marchini, A. Pagliarusco, A. Toscano et al., Ultrasound biomicroscopic and conventional ultrasonographic study of ocular dimensions in primary angle-closure glaucoma. Ophthalmology **105**(11), 2091–2098 (1998)
77. C.J. Pavlin, K. Harasiewicz, M.D. Sherar, F.S. Foster, Clinical use of ultrasound biomicroscopy. Ophthalmology **98**(3), 287–295 (1991)
78. H.B. Chen, K. Kashiwagi, S. Yamabayashi et al., Anterior chamber angle biometry: quadrant variation, age change and sex difference. Curr. Eye Res. **17**(2), 120–124 (1998)
79. A.M. Rollins, J.A. Izatt, Optimal interferometer designs for optical coherence tomography. Opt. Lett. **24**(21), 1484–1486 (1999)
80. D. Huang, Y. Li, S. Radhakrishnan, Optical coherence tomography of the anterior segment of the eye. Ophthalmol. Clin. North Am. **17**(1), 1–6 (2004)
81. S. Radhakrishnan, D. Huang, S.D. Smith, Optical coherence tomography imaging of the anterior chamber angle. Ophthalmol. Clin. North Am. **18**(3), 375–381 (2005), vi
82. S. Radhakrishnan, J. Goldsmith, D. Huang et al., Comparison of optical coherence tomography and ultrasound biomicroscopy for detection of narrow anterior chamber angles. Arch. Ophthalmol. **123**(8), 1053–1059 (2005)
83. S. Dorairaj, J.M. Liebmann, R. Ritch, Quantitative evaluation of anterior segment parameters in the era of imaging. Trans. Am. Ophthalmol. Soc. **105**, 99–108 (2007); discussion -10
84. W.P. Nolan, J.L. See, P.T. Chew et al., Detection of primary angle closure using anterior segment optical coherence tomography in Asian eyes. Ophthalmology **114**(1), 33–39 (2007)

85. L.M. Sakata, R. Lavanya, D.S. Friedman et al., Comparison of gonioscopy and anterior segment ocular coherence tomography in detecting angle closure in different quadrants of the anterior chamber angle. Ophthalmology **115**(5), 769–774 (2008)
86. R. Leitgeb, C. Hitzenberger, A. Fercher, Performance of Fourier domain vs. time domain optical coherence tomography. Opt. Express **11**(8), 889–894 (2003)
87. M. Choma, M. Sarunic, C. Yang, J. Izatt, Sensitivity advantage of swept source and Fourier domain optical coherence tomography. Opt. Express **11**(18), 2183–2189 (2003)
88. F. Memarzadeh, S. Mahdaviani, Y. Li, Interpretation of angle images, in *Imaging the eye from Front to Back with RTVue Fourier-Domain Optical Coherence Tomography*, ed. by D. Huang, J. Duker, B. Lumbroso et al., 1st edn. (SLACK Incorporated, Thorofare, NJ, 2010)
89. C.Y. Cheung, C. Zheng, C.L. Ho et al., Novel anterior-chamber angle measurements by high-definition optical coherence tomography using the Schwalbe line as the landmark. Br. J. Ophthalmol. **95**(7), 955–959 (2011)
90. B. Qin, B.A. Francis, Y. Li, et al., Anterior chamber angle measurements using Schwalbe's line with high resolution Fourier-domain optical coherence tomography. J Glaucoma. **22**(9), 84–8 (2013)
91. M.R. Chalita, Y. Li, S. Smith et al., High-speed optical coherence tomography of laser iridotomy. Am. J. Ophthalmol. **140**(6), 1133–1136 (2005)
92. J.J. Saragoussi, P. Othenin-Girard, Y.J. Pouliquen, Ocular damage after implantation of oversized minus power anterior chamber intraocular lenses in myopic phakic eyes: case reports. Refract. Corneal Surg. **9**(2), 105–109 (1993)
93. G. Baikoff, G. Bourgeon, H.J. Jodai et al., Pigment dispersion and Artisan phakic intraocular lenses: crystalline lens rise as a safety criterion. J. Cataract Refract. Surg. **31**(4), 674–680 (2005)
94. G. Baikoff, E. Lutun, J. Wei, C. Ferraz, Contact between 3 phakic intraocular lens models and the crystalline lens: an anterior chamber optical coherence tomography study. J. Cataract Refract. Surg. **30**(9), 2007–2012 (2004)
95. M.A. Qazi, I.Y. Cua, C.J. Roberts, J.S. Pepose, Determining corneal power using Orbscan II videokeratography for intraocular lens calculation after excimer laser surgery for myopia. J. Cataract Refract. Surg. **33**(1), 21–30 (2007)
96. E. Borasio, J. Stevens, G.T. Smith, Estimation of true corneal power after keratorefractive surgery in eyes requiring cataract surgery: BESSt formula. J. Cataract Refract. Surg. **32**(12), 2004–2014 (2006)
97. S. Sonego-Krone, G. Lopez-Moreno, O.V. Beaujon-Balbi et al., A direct method to measure the power of the central cornea after myopic laser in situ keratomileusis. Arch. Ophthalmol. **122**(2), 159–166 (2004)
98. M. Tang, Y. Li, D. Huang, An intraocular lens power calculation formula based on optical coherence tomography: a pilot study. J. Refract. Surg. **26**(6), 430–437 (2010)
99. M. Tang, A. Chen, Y. Li, D. Huang, Corneal power measurement with Fourier-domain optical coherence tomography. J. Cataract Refract. Surg. **36**(12), 2115–2122 (2010)
100. M. Tang, L. Wang, D.D. Koch et al., Intraocular lens power calculation after previous myopic laser vision correction based on corneal power measured by Fourier-domain optical coherence tomography. J. Cataract Refract. Surg. **38**(4), 589–594 (2012)
101. R.N. Khurana, Y. Li, M. Tang et al., High-speed optical coherence tomography of corneal opacities. Ophthalmology **114**(7), 1278–1285 (2007)
102. T.J. van den Berg, H. Spekreijse, Near infrared light absorption in the human eye media. Vision Res. **37**(2), 249–253 (1997)
103. A.S. Neubauer, S.G. Priglinger, M.J. Thiel et al., Sterile structural imaging of donor cornea by optical coherence tomography. Cornea **21**(5), 490–494 (2002)
104. R.L. Armour, P.J. Ousley, J. Wall et al., Endothelial keratoplasty using donor tissue not suitable for full-thickness penetrating keratoplasty. Cornea **26**(5), 515–519 (2007)

105. P.M. Phillips, M.A. Terry, N. Shamie et al., Descemet's stripping automated endothelial keratoplasty (DSAEK) using corneal donor tissue not acceptable for use in penetrating keratoplasty as a result of anterior stromal scars, pterygia, and previous corneal refractive surgical procedures. Cornea **28**(8), 871–876 (2009)
106. K. Karnowski, B.J. Kaluzny, M. Szkulmowski et al., Corneal topography with high-speed swept source OCT in clinical examination. Biomed. Opt. Express **2**(9), 2709–2720 (2011)
107. I. Grulkowski, J. Liu, B. Potsaid et al., Retinal, anterior segment and full eye imaging using ultrahigh speed swept source OCT with vertical-cavity surface emitting lasers. Biomed. Opt. Express **3**(11), 2733–2751 (2012)
108. W. Wieser, T. Klein, D.C. Adler et al., Extended coherence length megahertz FDML and its application for anterior segment imaging. Biomed. Opt. Express **3**(10), 2647–2657 (2012)
109. M. Zhao, A.N. Kuo, J.A. Izatt, 3D refraction correction and extraction of clinical parameters from spectral domain optical coherence tomography of the cornea. Opt. Express **18**(9), 8923–8936 (2010)
110. S. Ortiz, D. Siedlecki, P. Perez-Merino et al., Corneal topography from spectral optical coherence tomography (sOCT). Biomed. Opt. Express **2**(12), 3232–3247 (2011)
111. S. Ortiz, P. Perez-Merino, N. Alejandre et al., Quantitative OCT-based corneal topography in keratoconus with intracorneal ring segments. Biomed. Opt. Express **3**(5), 814–824 (2012)

Retinal Optical Coherence Tomography Imaging

56

Wolfgang Drexler and James G. Fujimoto

Keywords

2D and 3D retinal OCT • optophysiology • retinal OCT in animal models • retinal segmentation • Ultrahigh axial resolution

The eye is essentially transparent, transmitting light with only minimal optical attenuation and scattering providing easy optical access to the anterior segment as well as the retina. For this reason, ophthalmic and especially retinal imaging has been not only the first but also most successful clinical application for optical coherence tomography (OCT). This chapter focuses on the development of OCT technology for retinal imaging. OCT has significantly improved the potential for early diagnosis, understanding of retinal disease pathogenesis, as well as monitoring disease progression and response to therapy. Development of ultrabroad bandwidth light sources and high-speed detection techniques has enabled significant improvements in ophthalmic OCT imaging performance, demonstrating the potential of three-dimensional, ultrahigh-resolution OCT (UHR OCT) to perform noninvasive optical biopsy of the living human retina, i.e., the in vivo visualization of microstructural, intraretinal morphology in situ approaching the resolution of conventional histopathology. Significant improvements in axial resolution *and* speed not only enable three-dimensional rendering of retinal volumes but also high-definition, two-dimensional tomograms, topographic thickness maps of all major intraretinal layers, as well as volumetric quantification of pathologic intraretinal changes. These advances in OCT technology have also been successfully applied in several animal models of retinal

W. Drexler (✉)
Center for Medical Physics and Biomedical Engineering, Medical University of Vienna, General Hospital Vienna, Vienna, Austria
e-mail: Wolfgang.Drexler@meduniwien.ac.at

J.G. Fujimoto
Department of Electrical Engineering and Computer Science and Research Laboratory of Electronics, Massachusetts Institute of Technology, Cambridge, MA, USA

© Springer International Publishing Switzerland 2015

W. Drexler, J.G. Fujimoto (eds.), *Optical Coherence Tomography*,
DOI 10.1007/978-3-319-06419-2_58

pathologies. The development of light sources emitting at alternative wavelengths, e.g., around ~1,060 nm, not only enabled three-dimensional OCT imaging with enhanced choroidal visualization but also improved OCT performance in cataract patients due to reduced scattering losses in this wavelength region. Adaptive optics using deformable mirror technology, with unique high stroke to correct higher-order ocular aberrations, with specially designed optics to compensate chromatic aberration of the human eye, in combination with three-dimensional UHR OCT, recently enabled in vivo cellular resolution retinal imaging.

New medical imaging technologies can improve the diagnosis and clinical management disease. Furthermore, they can also contribute to a better understanding of disease pathogenesis and, therefore, to the development of novel therapies for disease. Thus, imaging technologies have a significant impact on medical research and clinical practice. For example, A-scan and B-scan ultrasonography are routinely used in ophthalmologic biometry and diagnosis to image and differentiate orbital disease and intraocular anatomy. These ultrasound measurements require physical contact with the eye and typically provide 150 μm longitudinal resolution by using a 10 MHz transducer [1, 2]. High-frequency (50 MHz) ultrasound can achieve axial resolution of 20–30 μm, but its penetration depth is limited to 4 mm because of acoustic attenuation in ocular media [3, 4]. Hence, only the anterior eye segment structures can be imaged with this high resolution. Scanning laser ophthalmoscopy or scanning laser tomography, invented in 1979, represented a major development in ophthalmic fundus imaging [5–7]. A focused laser spot is raster scanned on the retina, while the integrated backscattered light is measured to obtain high-quality, micron-scale, lateral resolution fundus images. Scanning laser ophthalmoscopy provides an *en face* view of the fundus with high transverse resolution and contrast. However, pupil aperture and ocular aberrations limit the axial resolution in the retina to several hundred microns (~300 μm). Axial image resolution has been a key parameter for ophthalmic imaging because of the stratified organization of the retina. In contrast to standard or confocal microscopy, axial and transverse resolution in OCT are decoupled, with the axial determined by the optical bandwidth of the light source and the transverse resolution determined by the focusing of the measurement beam onto the tissue. In this sense, OCT bridges the gap between the high resolution and limited penetration of confocal microscopy and the low resolution and high penetration of ultrasound. These properties make OCT a unique ophthalmic diagnostic modality in which high axial resolution, despite a long depth of focus (field) – a situation encountered with in vivo retinal imaging – can be accomplished. The earliest measurements of one-dimensional, axial information, analogous to ultrasound A-scans, were demonstrated in the mid 1980s [8–10]. OCT, the generation of cross-sectional or two-dimensional images, analogous to ultrasound B-scans, was first demonstrated in 1991 [11]. The first in vivo OCT imaging studies of the human retina were performed in 1993 (cf. Fig. 56.1a, b) [12, 13]. Since that time, OCT has rapidly developed as a noninvasive, medical diagnostic imaging modality that enables in vivo, cross-sectional visualization of the internal microstructure in biological systems (cf. Fig. 56.1c, d) [14–16]. OCT provides images of retinal

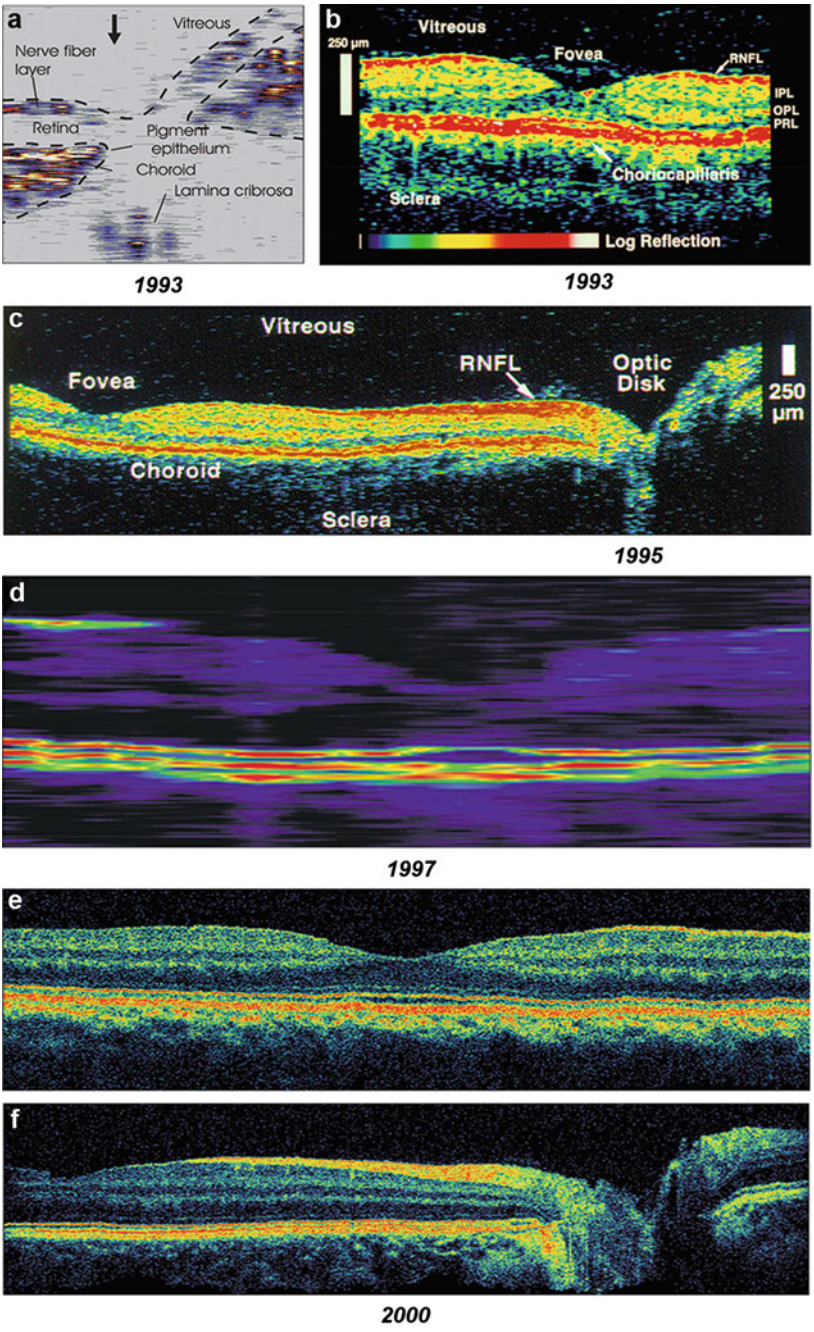

Fig. 56.1 (continued)

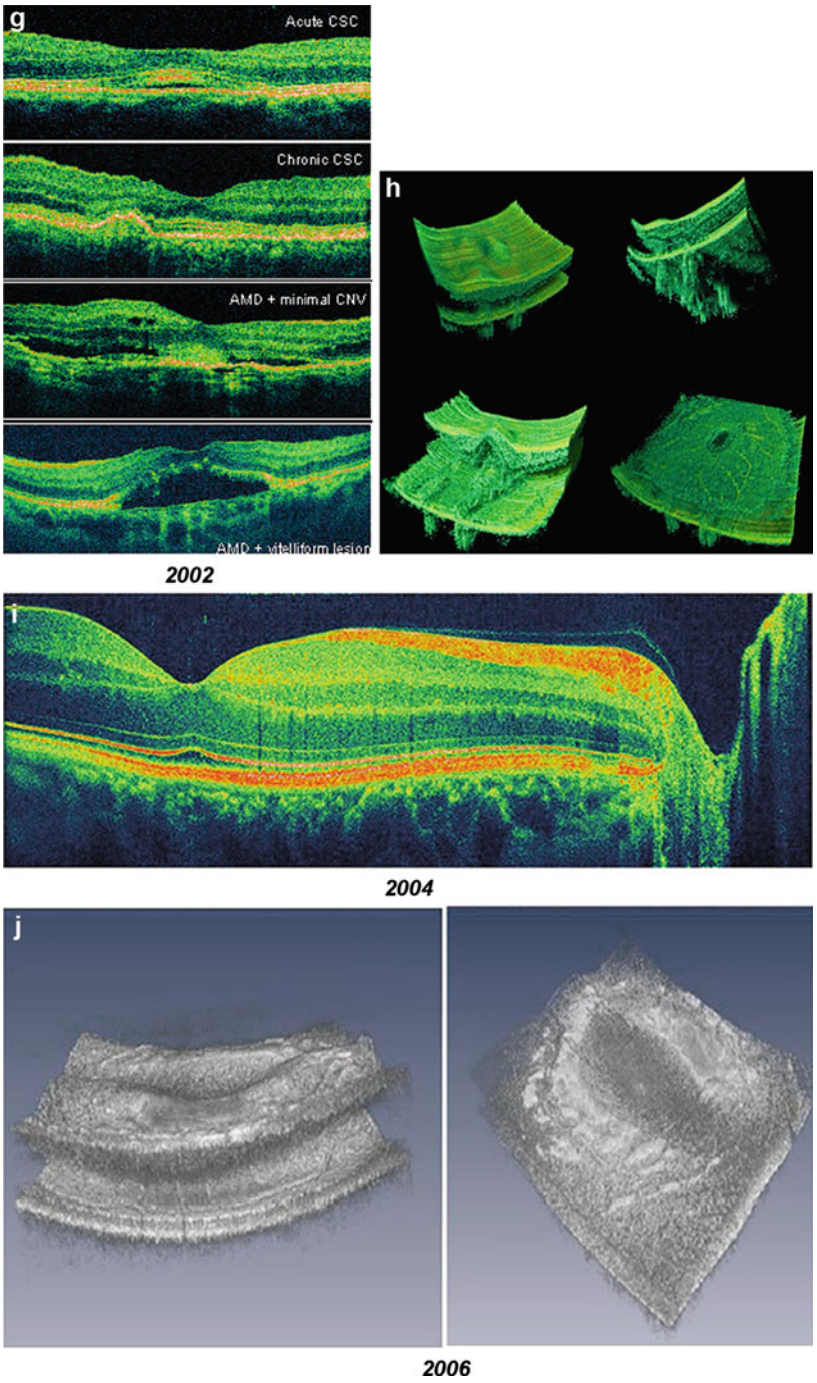

Fig. 56.1 (continued)

structure that cannot be obtained by any other noninvasive diagnostic technique. For these reasons, ophthalmic diagnosis is one of the most clinically developed OCT applications [17–37].

Since its invention, the original concept of OCT has been to enable noninvasive optical biopsy, i.e., the in situ imaging of tissue microstructure with a resolution approaching that of histology, but without the need for tissue excision and post-processing. A critical step towards this goal was the introduction of ultrahigh-resolution OCT (UHR OCT). Improving axial OCT resolution by one order of magnitude from the 10–15 μm to the sub-μm region enabled a noticeably superior visualization of tissue microstructure, e.g., all major intraretinal layers as well as cellular resolution OCT imaging in nontransparent tissue (cf. Fig. 56.1e, f) [38–41]. Since then, UHR OCT technology has been investigated in clinical settings to assess its clinical utility (cf. Fig. 56.1g). Cross-sectional studies in ~1,000 eyes with different pathologies demonstrated unprecedented visualization of all major intraretinal layers and provided important information about the photoreceptor layer [40, 42–50]. These studies demonstrated visualization of photoreceptor layer impairment in macular pathologies, such as macular holes, central serous chorioretinopathy, age-related macular degeneration, foveomacular dystrophies, Stargardt's dystrophy, and retinitis pigmentosa. For the first time, photoreceptor layer loss could be directly correlated with retinal function (visual acuity and microperimetry findings) in patients with Stargardt's dystrophy [43]. Studies also demonstrated the application of UHR OCT to monitor therapy as well as to contribute to a better understanding of disease pathogenesis [42, 44–46]. Advances in photonics technology, including the development of ultrabroad bandwidth and high-speed tunable light sources as well as high-speed detection techniques, have enabled a considerable improvement in the visualization capability of OCT in the last decade, thus establishing it as a state-of-the-art, noninvasive, complementary ophthalmic diagnostic methodology (cf. Fig. 56.1h–j). As a consequence, there have been numerous recent developments of OCT technology and considerable interest in this topic – especially in the field of ophthalmology. Objectively, this is evidenced by a tremendous increase in publications, patents, and companies involved in the field of OCT in recent years. It is noteworthy that about ~50 % of all OCT publications published to date have been in ophthalmic journals, demonstrating the major impact of OCT in this field. Another 25 % have been published in optical journals, reflecting the numerous technical advances that have been accomplished.

Fig. 56.1 Historic development of axial resolution and data acquisition speed in retinal OCT. In vivo retinal OCT imaging with 10–15 μm axial resolution with slow speed (2 Hz and low transverse sampling) (**a**, **b**) and high speed (100 Hz and improved transverse sampling) (**c**); 7–9 μm axial resolution with slow speed (2 Hz and low transverse sampling) (**d**); first in vivo ultrahigh-resolution (2–3 μm) imaging with high speed (160 Hz) of normal subjects (**e**, **f**) and patients (**g**); three-dimensional (**h**) and high-definition (**i**) ultrahigh-resolution (2–3 μm) imaging with 29,000 Hz; ultrahigh-speed (300,000 Hz) and high-resolution (10 μm) 3D retinal imaging at 1,050 nm with enhanced penetration into the choroid (**j**)

56.1 Two-Dimensional Ultrahigh-Resolution OCT Versus Histology: Improved Interpretation of Intraretinal Layers

The development of UHR OCT was a key step toward achieving noninvasive optical biopsy of the human retina, i.e., the visualization of intraretinal morphology in retinal pathologies approaching the level achieved with histopathology. Figure 56.2 depicts an example demonstrating that UHR OCT of a patient with a macular hole can provide similar information as histopathology, shown in a different postmortem eye at a comparable stage of disease.

In order to evaluate the potential of UHR OCT for enhanced visualization of intraretinal structures and to provide an improved basis for the correct interpretation of in vivo ophthalmic 2D UHR OCT tomograms of high clinical relevance, studies have been conducted to compare and correlate 2D UHR OCT cross-sectional images of ex vivo pig [51] and monkey (*Macaca fascicularis*) [52, 53] retinal specimens with histology. Figure 56.3a, b depict in vivo 2D UHR OCT of the foveal and optic disk regions in a nonhuman primate glaucoma model (*cynomolgus monkey*) compared with histology of the same retina at similar location. (This study was conducted in collaboration with Novartis Institutes for Biomedical Research by E. Polska and A. Doelemeyer.) Figure 56.2c, d show a comparison of in vitro ultrahigh-resolution OCT imaging (D) with histology (C) of a macular scan of a monkey retina, demonstrating excellent correlation of the OCT and tissue boundaries and the potential of 2D UHR OCT to visualize all major intraretinal layers. The results of these studies allow the extraction of clinically relevant structural retinal information with in vivo ultrahigh-resolution ophthalmic OCT tomograms and were an important step toward resolving the ambiguities that arose with 2D UHR OCT tomograms in trying to establish the correlation of OCT features with more than ten intraretinal layers.

Despite these studies comparing histology with 2D UHR OCT, it is noteworthy that a comprehensive, reliable delineation of *all* intraretinal layers has not yet been accomplished. The distal part of the retina including the retinal pigment epithelium (RPE), Bruch's membrane, choriocapillaris, and choroid complex remains a particular challenge. Currently, the "last," i.e., most strongest continuous distal signal in UHR OCT tomograms, has been interpreted as being the retinal pigment epithelium (RPE) layer. While literature describing the light-RPE interaction in the near-infrared region around 800 nm would confirm this, the relatively thick (up to 20–30 μm) appearance in UHR OCT tomograms is not consistent with the RPE as a monocellular layer.

Figure 56.4 shows a comparison of in vitro ultrahigh-resolution OCT imaging of a pig retina 2 h *postmortem* acquired with 1.4 μm axial and 3 μm transverse resolutions (B) with the corresponding frozen section imaged by differential interference contrast (DIC) microscopy (G). Fig. 56.4a shows a photograph of the fundus with the major retinal vessels indicating the OCT scan location with a bar. In a series of OCT scans, the initiation of a retinal detachment event was monitored within a time frame of 30 min (cf. Fig. 56.4c–f). Ultrahigh-resolution OCT visualized a focal elevation of the neural retina concomitant with an increase in subretinal

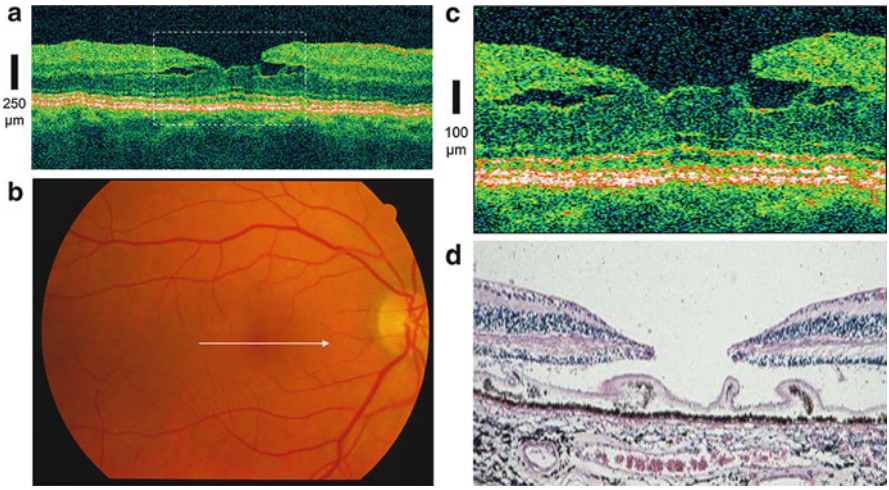

Fig. 56.2 In vivo optical biopsy using ultrahigh-resolution ophthalmic OCT (UHR OCT). UHR OCT of a patient with macular hole (**a**). Fundus photograph (**b**) indicates location of the OCT scan (*white arrow* in **b**). Twofold enlargement (**c**) of the central foveal region (indicated by *dashed white rectangle* in **a**) is compared with histology (**d**) of a different postmortem eye with comparable stage of macular hole (Histology (**d**) was kindly provided by R. Brancato, Italy)

space (cf. Fig. 56.4b, c). Fifteen minutes later, alterations were observed within the monolayered band of the pigment epithelium (PE) signal (cf. Fig. 56.4d). While still continuous, the PE signal appeared triple layered at the initial locus of detachment with a stripe of bright signal framed by two darker bands. After an additional 15 min, all retinal layers were found bent inward and the measurements of their relative thickness (not shown) indicated increased thickness of the proximal retinal layers (cf. Fig. 56.4e). In the PE signal, the bright inclusion increased while the innermost aspect of the signal appeared eroded (cf. Fig. 56.4f). Histological examination of the matching retinal position demonstrated a significantly extended region of detachment (Fig. 56.4g). The pigment epithelium was found to be lesioned at the initial locus of detachment, and fragments of tissue were dislocated into the subretinal lumen (Fig. 56.4g, asterisk).

In addition, the appearance of the RPE and distally adjacent layers, as visualized by in vivo UHR OCT, varies in eyes with different pathologies. Figure 56.5 depicts UHR OCT tomograms of a patient with central serous chorioretinopathy. Figure 56.5c, d show serous retinal detachments (indicated by asterisks), focal pigment epithelium detachments (cf. white arrow in Fig. 56.5d), and a "triple band appearance" (cf. Fig. 56.5c, white arrow) of the photoreceptor/RPE interface. Figure 56.5e–s show a selection of 15 B-scans from 60 that were raster scanned across a $3 \times 3 \times 1$ mm volume. The triple band appearance might be related to the outer tips of the photoreceptors or the anchorage of the outer segments between the RPE cells. Another important issue in the interpretation of UHR OCT tomograms is the ability to visualize Bruch's membrane. The focal feature in the pigment

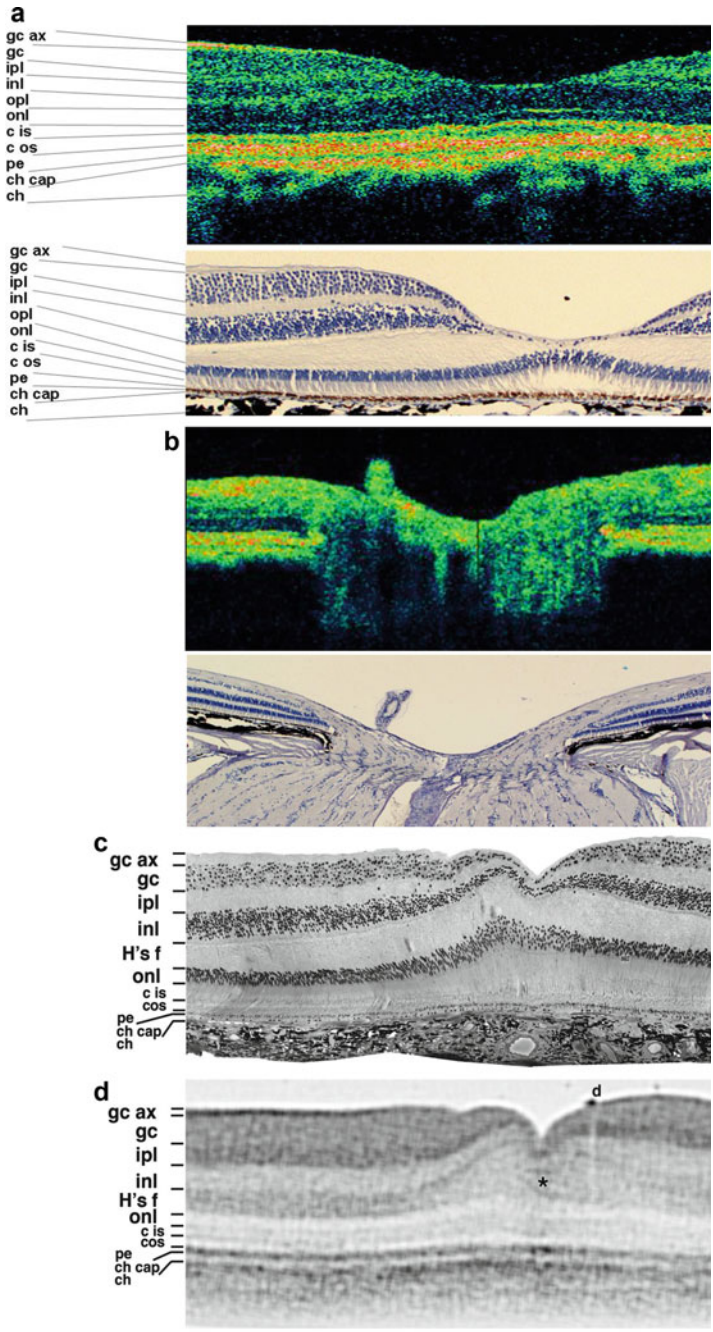

Fig. 56.3 (continued)

epithelium detachment depicted in Figs. 56.5d, f (cf. white arrows) might be interpreted as Bruch's membrane. However, this membrane is strongly attached to the RPE, and it is likely that this membrane is also detached along with the RPE. "Visualization" of Bruch's membrane by OCT is, therefore, problematic. Bruch's membrane thickens with age and is, at most, 5 μm thick in patients in the 75–90-year-old range, as measured histological in postmortem tissue [54, 55]. Since the in vivo UHR OCT axial resolution is at best 2–3 μm at 800 nm, it is not clear that UHR OCT is capable of resolving and visualizing Bruch's membrane. Figure 56.6 depicts representative UHR OCT tomograms of a patient with age-related macular degeneration (A, B) and pigment epithelium detachment (D) with corresponding fluorescent angiography (C) and a fundus photograph indicating the location of the OCT scans (C and E, white arrows). UHR OCT images (A, B, D) more clearly show a thin backscattering layer (yellow arrows) below the RPE layer that is suggestive of Bruch's membrane.

Although state-of-the-art ophthalmic OCT technology enables significantly improved visualization of intraretinal layers, caution is therefore imperative regarding proper interpretation of OCT tomograms, especially of the distal part of the retina, and more comprehensive studies are needed to clarify this issue. Figure 56.7 depicts a state-of-the-art OCT interpretation of intraretinal layers in a high-definition UHR OCT of the optic disk (A) and foveal (B) region of a normal subject. Labeling of intraretinal layers that could be confirmed by clinical investigations using UHR OCT and systematic studies comparing histology with UHR OCT in in vitro animal models are labeled white or black. From the proximal to the distal part of the retina, the nerve fiber layer (cf. Fig. 56.7a, NFL) as well as plexiform layers (cf. Fig. 56.7a, inner (IPL) and outer plexiform (OPL) layer) appear back-reflecting and therefore as a strong signal in the OCT tomogram. The ganglion cell layer (cf. Fig. 56.7a, GCL) and nuclear layer (cf. Fig. 56.7a, inner (INL) and outer nuclear ONL) layer appear less back-reflecting and therefore as a low signal in the OCT tomogram. The external limiting membrane (cf. Fig. 56.7b, ELM), the inner and outer photoreceptor segment (cf. Fig. 56.7b, IS PR, OS PR), as well as the choroid (cf. Fig. 56.7b) are also properly confirmed by literature. Red-labeled layers indicate that caution is imperative and the correct interpretation needs more conclusive studies to confirm correctness. This applies to the internal limiting membrane (cf. Fig. 56.7a, ILM) and the distal part of the retina involving probably the distal tips of the photoreceptors – sometimes also referred to Verhoeff's

Fig. 56.3 Ultrahigh-resolution OCT versus histology. In vivo ultrahigh-resolution OCT of the fovea (**a**, *top*) and optic disk region (**b**, *top*) of a nonhuman primate glaucoma model (*cynomolgus monkey*); this study has been conducted in collaboration with Novartis Institutes for Biomedical Research (by E. Polska and A. Doelemeyer) compared to hematoxylin and eosin stain (H&E) histology of the same retina at similar locations (**a** and **b**, *bottom*). Foveal portion of corresponding semithin histological section (**c**) and 2D UHR OCT image (**d**) of a perfusion fixed monkey retina (gc *ax* ganglion cell axon layer, *gc* ganglion cells, *ipl* inner plexiform layer, *inl* inner nuclear layer, *opl* outer plexiform layer, *Hf* fibers of Henle, *onl* Outer nuclear layer, *cis*/*cos* cone inner/outer segments, *pe* Pigment epithelial layer, *ch cap* choriocapillaris, *ch* choroid, *asterisk* darker faults in foveal floor indicative of foveal strain, *d* epiretinal debris)

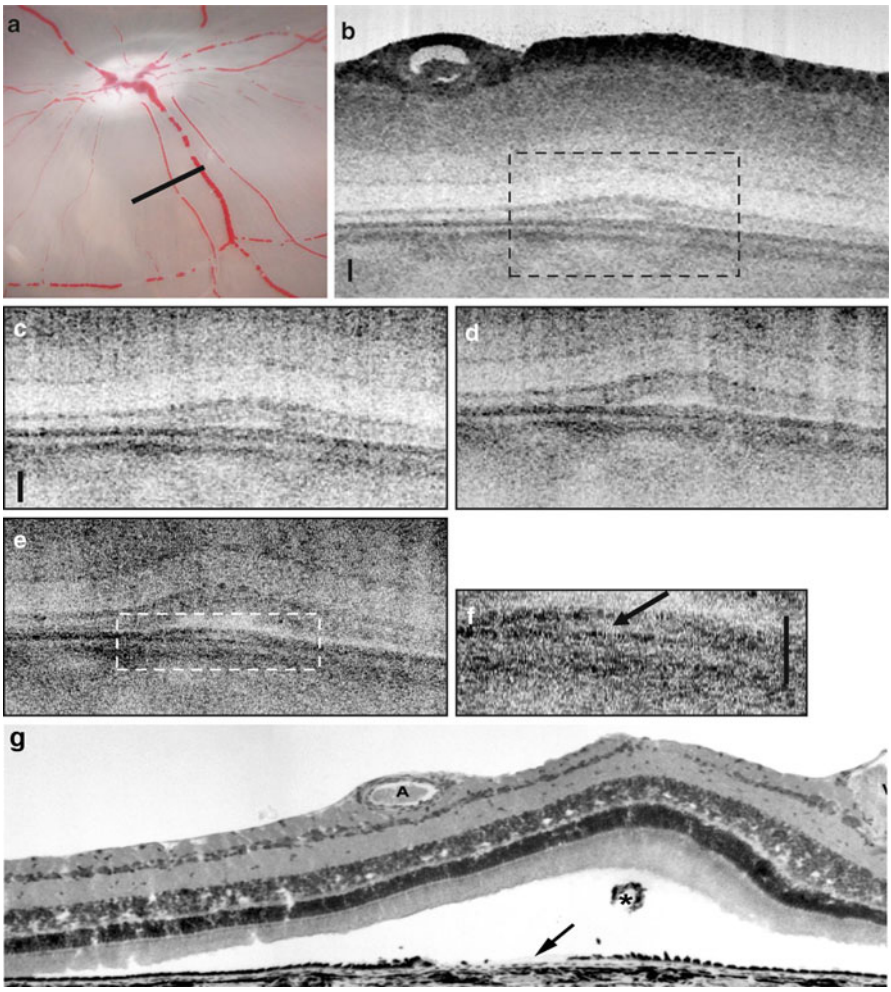

Fig. 56.4 Retinal pigment epithelium appearance in in vitro *UHR OCT*. Photograph of the in vitro fundus showing the papilla and major blood vessels. White bar indicates orientation of the OCT scan (**a**). Time lapse sequence of retinal detachment during in vitro ultrahigh-resolution OCT imaging with 1.4 μm axial ×3 μm transverse resolution. Full OCT image of an area of 0.7 × 2 mm consisting of 14,000 × 2,000 pixels (**d**). Enlarged image portions of the detachment zone covering an area of 0.5 × 0.5 mm consisting of 10,000 × 500 pixels, fast Fourier transform filtered for reduction of radial shadowing effects. Time intervals between these images are 15 min (**c**–**e**). In the aligned micrographs, progressive bending and swelling of tissue are evident. **a** All photoreceptor sublayers have begun to bend proximally resulting in a subretinal lumen. (**b**) The subretinal blebs have significantly increased. Underneath the detachment zone, the *dark* band of signal that corresponds to the pigment epithelium/Bruch's membrane complex is still continuous (*arrowheads*), but locally triple layered, as indicated by a *bright* inclusion. (**c**) The innermost aspect of the triple-banded signal appears interrupted. (**f**) Twofold enlargement of area indicated with *dashed line* in (**e**). Corresponding histological section (**g**). Tissue processing has led to more extended retinal detachment. Debris from the damaged pigment epithelium (*arrow*) is present in the subretinal space (*asterisk*). All scale bars: 50 μm

membrane (cf. Fig. 56.7b), the retinal pigment epithelium including Bruch's membrane (cf. Fig. 56.7b, RPE/BM), as well as choriocapillaris (cf. Fig. 56.7b).

56.2 Two-Dimensional, Clinical Ultrahigh-Resolution OCT

In several clinical feasibility studies [40, 42–50], 2D UHR OCT imaging has been performed using a laboratory prototype as well as a commercially available femtosecond titanium-sapphire laser light sources (INTEGRAL, Femtolasers Produktions GmbH, Austria) that generate bandwidths of 100–175 nm at 800 nm center wavelength [56]. These light sources can support 2–3 μm axial resolution in the retina. OCT imaging was performed with axial scan rates of up to 250 Hz using up to 800 μW incident power in the scanning OCT beam, which is well below the ANSI exposure limit. More than 1,000 eyes with a range of macular diseases, such as macular holes, macular edema, age-related macular degeneration, central serous chorioretinopathy, epiretinal membranes, and detachment of pigment epithelium and sensory retina, were studied. In addition, patients with glaucoma and different hereditary retinal diseases were also imaged. The purpose of these studies was to investigate the clinical feasibility of 2D UHR OCT to visualize and quantify intraretinal morphology changes, especially in the inner (IS PR) and outer segment (OS PR) of the photoreceptor layer in healthy subjects and patients with different macular pathologies.

Figure 56.8 shows a selection of 2D UHR OCT images of the central foveal region in a normal subject and in 11 patients with different retinal pathologies. A significantly better visualization of the extent of photoreceptor impairment in different retinal pathologies was possible, including the ability to distinguish between the inner and outer photoreceptor layers and correlate photoreceptor impairment with visual acuity (shown in Fig. 56.8). These studies demonstrated the potential of 2D UHR OCT to enhance early diagnosis by detecting subtle, early morphological intraretinal changes in a wide range of retinal diseases. Comparative studies using UHR and standard-resolution OCT imaging of different retinal pathologies showed that 2D UHR OCT could be used to guide the interpretation of images from commercial, standard-resolution OCT systems (cf. Figs. 56.9, 56.10, and 56.11). Studies have also demonstrated the application of UHR OCT to monitor therapy as well as to contribute to a better understanding of disease pathogenesis [42, 44–46].

56.3 High-Speed, Ultrahigh-Resolution OCT: Three-Dimensional and High-Definition OCT

UHR OCT imaging was initially based on time domain OCT and, therefore, had a fundamental time-bandwidth trade-off. As a result, operation with ultrahigh resolution required reduced imaging speeds in order to maintain sufficient detection sensitivity. Signal levels could not be increased by increasing light exposure because of the low power levels allowed for in vivo retinal imaging (~600–800 μW at 800 nm). As a consequence of the slow scanning/measurement

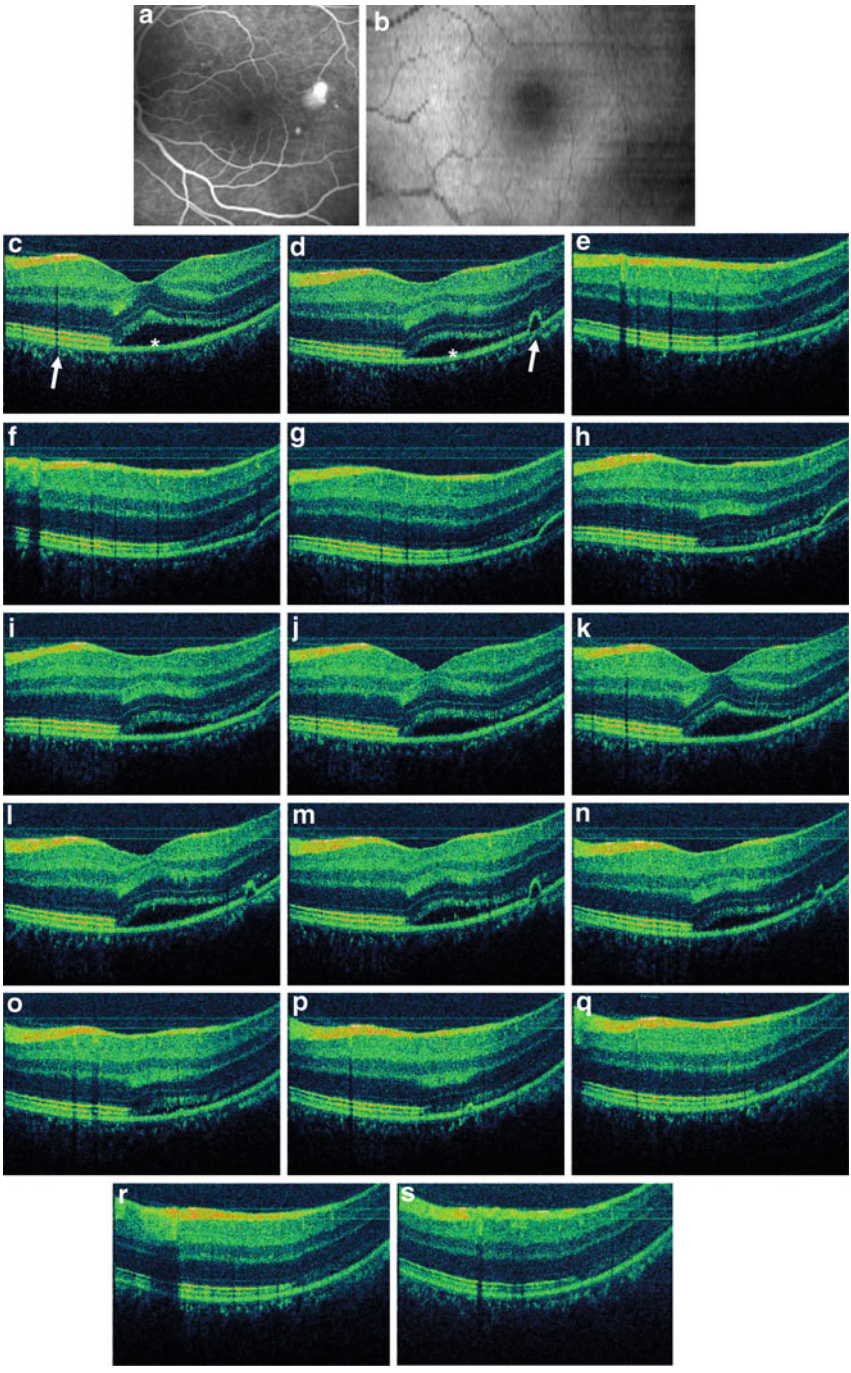

Fig. 56.5 (continued)

time, motion artifacts had to be corrected using post-processing algorithms, and only a limited number of A-scans per B-scan image can be obtained. State-of-the-art, time domain-based OCT systems have been developed to provide high scanning speeds of up to 8 kHz, i.e., 8,000 A -scans per second [57]; however the lower system sensitivity at the faster scanning speeds has prevented their use for retinal imaging. *En face* OCT [58–64] achieves very high imaging speeds by acquiring an *en face* retinal image at a specified depth. These *en face* imaging techniques are described in detail in other chapters.

A powerful alternative to time domain OCT for high-speed imaging is Fourier domain detection techniques where the entire depth-resolved tissue reflectance (A-scan) is obtained simultaneously, thereby removing the need for depth scanning [65–68]. This technique has been referred to in the literature as Fourier domain OCT (FD OCT), spectral domain OCT (SD OCT), swept source OCT (SS OCT), or optical frequency domain imaging (OFDI). This improvement is accomplished either by dispersing the interferometric information in space using a spectrometer setup ("spectral/Fourier domain OCT") or by encoding information in time by tuning a monochromatic light source in combination with a single photodetector ("swept source/Fourier domain OCT" or "optical frequency domain imaging").

The acquisition speed for both approaches – using a spectrometer as a detector or a tunable light source – is mainly limited by the readout rate of the camera which detects the spectrum or by the tuning speed of the light source, respectively. Since the scanning range and electronic detection bandwidth are decoupled, both approaches offer substantial improvements in sensitivity and a dramatic increase in the line rate (A-scan rate) without reducing the sensitivity performance compared with time domain OCT. Although the basic principle of spectral/Fourier domain OCT has been known since 1995 [65], lack of CCD technology and recognition of the sensitivity advantage delayed the experimental and clinical evaluation of this technique for almost a decade. Three groups working independently demonstrated the powerful advantage of this technique for improving data acquisition speed and sensitivity [69–71]. Spectral/Fourier domain OCT using a spectrometer for detection has been shown to enable high-speed [72–74], ultrahigh-resolution [75–77], as well as functional imaging [78, 79].

Despite the sensitivity and speed advantages, OCT using spectral/Fourier domain detection has limitations which are important to note. There is a significant loss of sensitivity and dynamic range as a function of depth, as shown in the tomograms of Fig. 56.12a–c. This effect occurs because of limitations

Fig. 56.5 Retinal pigment epithelium appearance in in vivo UHR OCT. Representative UHR OCT tomograms of a patient with central serous chorioretinopathy. Fluorescence angiogram (**a**) and OCT fundus view (**b**) generated from the UHR OCT A-scans are depicted. UHR OCT visualizes serous retinal detachment (cf. *asterisk* **c**, **d**), focal pigment epithelium detachments (cf. *white arrow* **d**), and "triple band appearance" (cf. *white arrow* **c**) of the photoreceptor/RPE/choriocapillaris/choroid interface. Selection of 15 B-scans from 60 that were raster scanned across a 3 × 3 × 1 mm volume (**e**–**s**)

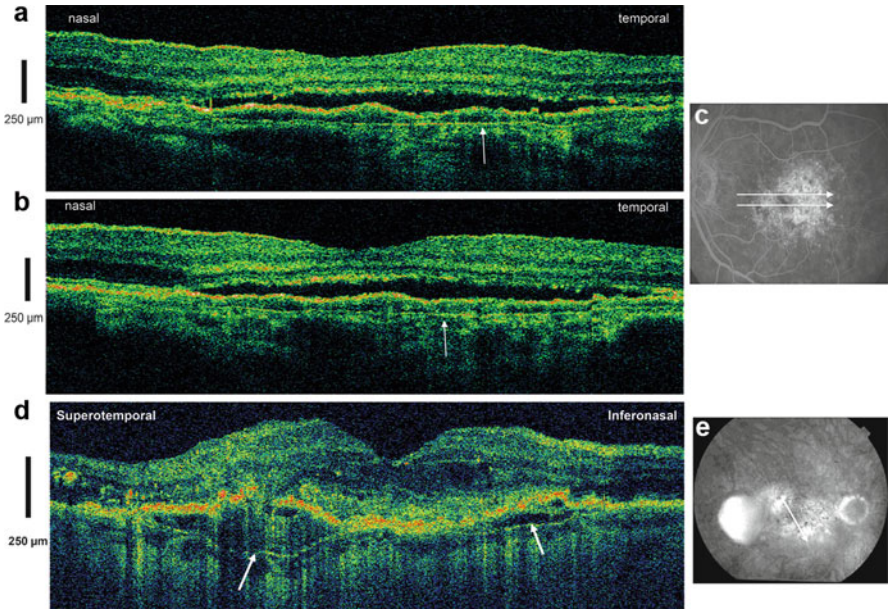

Fig. 56.6 Bruch's membrane appearance in in vivo UHR OCT. Representative UHR OCT tomograms of a patient with age-related macular degeneration (**a**, **b**) and pigment epithelium detachment (**d**) with corresponding fluorescent angiography (**c**) and fundus photo indicating the location of the OCT scans (**c** and **e**, *white arrows*). UHR OCT images (**a**, **b**, **d**) more clearly show a thin backscattering layer (*yellow arrows*) below the RPE layer that is suggestive of Bruch's membrane

in the spectrometer resolution and CCD pixel crosstalk as well as imperfect rescaling and post-processing of the interference signal. By employing new system calibration and signal post-processing techniques using a filter bank approach, this problem can be significantly reduced (cf. Fig. 56.12d–f). Finally, spectral/Fourier detection cannot distinguish echoes from positive and negative delays. This results in artifacts, such as those shown in Fig. 56.12g–k. Overlapping "mirror" images are produced if the tissue moves out of the measurement range. This problem can be solved by using more complex detection methods, which sacrifice scanning speed and/or sensitivity, but effectively double the depth measurement range [80–83].

The ability to achieve significantly higher scanning speeds while maintaining sensitivity is especially advantageous for ophthalmic OCT imaging, due to significant eye motions and the limited amount of power which is applicable according to laser safety standards. Figure 56.13 depicts a normal human optic disk measured by a third-generation, standard-resolution commercial OCT system (StratusOCT, ~10 µm axial resolution, 400 A-scans/s; cf. Fig. 56.13a), a UHR OCT laboratory

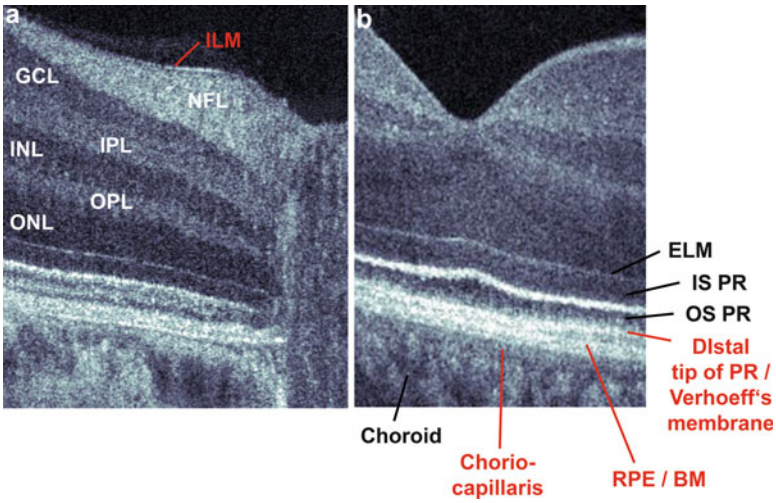

Fig. 56.7 Current state-of-the-art interpretation of intraretinal layers in OCT. High-definition UHR OCT of the optic disk (**a**) and foveal (**b**) region of a normal subject. Labeling of intraretinal layers that were confirmed by numerous previous studies is labeled *white* or *black*. *Red*-labeled layers indicate that interpretation needs additional studies to confirm. Nerve fiber layer (*NFL*), inner (*IPL*) and outer plexiform (*OPL*) layer, ganglion cell layer (*GCL*), inner (*INL*) and outer nuclear (*ONL*) layer, external limiting membrane (*ELM*), inner (*IS PR*) and outer photoreceptor segment (*OS PR*), choroid, internal limiting membrane (*ILM*), distal tips of the photoreceptors sometimes also referred to as Verhoeff's membrane, retinal pigment epithelium including Bruch's membrane (RPE/BM) and choriocapillaris

prototype using time domain detection (~3 μm axial resolution, ~150 A-scans/s; cf. Fig. 56.13b), and a high-speed UHR OCT laboratory prototype using spectral/Fourier domain detection (~3 μm axial resolution, ~25,000 A-scans/s; cf. Fig. 56.13c) [84]. Spectral/Fourier domain detection enables acquisition speeds equivalent to 25 million voxels (three-dimensional volume elements)/s, which is >50 times faster than standard-resolution OCT and >100 times faster than UHR OCT with time domain detection. The significantly higher acquisition speed not only reduces eye motion artifacts in B-scans (thereby preserving the "natural" contour of the posterior segment), but it also enables better delineation of the intraretinal layers because of the higher axial resolution, smaller speckle size, and increase in the number of transverse pixels (A-scans). Higher transverse sampling means that high-definition OCT images can be acquired. High-definition images have more transverse pixels (A-scans) across the same transverse B-scan range. This should not be confused with increased transverse resolution of the OCT image itself. Figures 56.14 and 56.15 depict examples of patients with macular holes comparing high-definition OCT images (cf. Figs. 56.14c and 56.15c) with a 10 mm length in the central foveal, sampled with 10,000 A-scans in 0.6 s [84] with

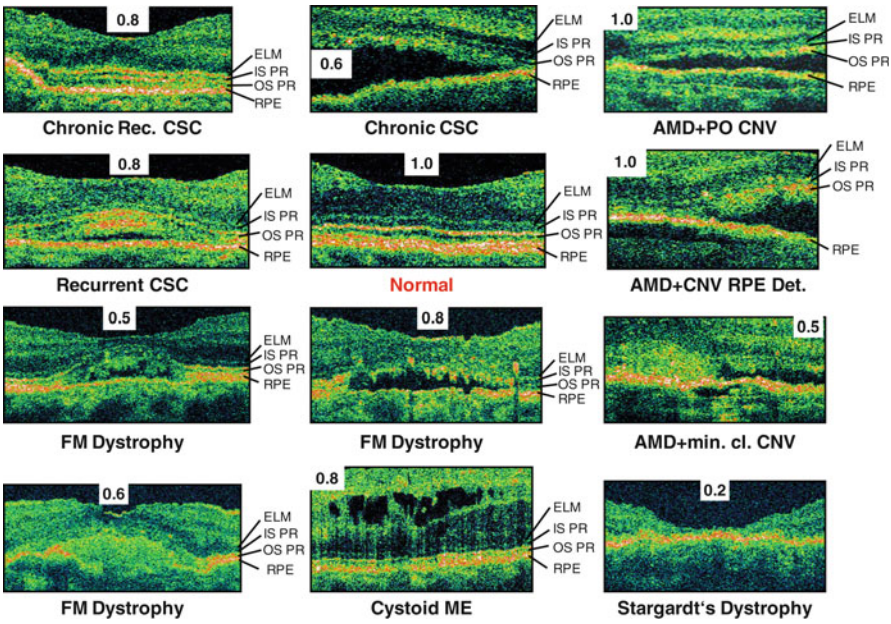

Fig. 56.8 Improved visualization of photoreceptor layer impairment in retinal pathologies using UHR OCT. UHR OCT of the central foveal region focusing on the external limiting membrane (*ELM*), inner (*IS PR*) and outer (*OS PR*) segment of the photoreceptor layer, and retinal pigment epithelium (*RPE*) region in a normal subject (labeled *red*) and 11 patients with different retinal pathologies. Visual acuity for each case is also indicated. *CSC* central serous chorioretinopathy, *FM* foveomacular, *ME* macular edema, *AMD* age-related macular degeneration, *CNV* choroidal neovascularisation, *min. cl*. minimal classic

a third-generation, standard-resolution commercial OCT system (StratusOCT, cf. Figs. 56.14b and 56.15b) sampled with 512 A-scans in 1.2 s. In Fig. 56.14c, cystic structures associated with the macular hole can be clearly visualized in the inner and outer nuclear layers. The intraretinal layers appear to be normal and external to the hole. By following the IS–OS junction from the parafoveal region to the macular hole, the image shows that the photoreceptor outer segment has lifted away from the normal anatomical position against the RPE, but stays intact and connected to the rest of the retina. Figure 56.15c depicts an example of epiretinal membrane pseudo-hole. Although this appears to be a cyst from the central scan, 3D UHR OCT data confirms that it is a pseudo-hole. The posterior hyaloid is visible and partially detached from the macula. The epiretinal membrane can be seen as well. In general, these membranes can be tracked and visualized in 3D UHR OCT data. Despite big changes of the inner layers, the photoreceptors have not changed much; hence the visual acuity is 20/25. Figure 56.16 shows a high-definition UHR OCT of a patient with macula hole, pre- (cf. Fig. 56.16a) and postoperatively (cf. Fig. 56.16b). Detailed intraretinal morphology can be visualized, especially in the photoreceptor area.

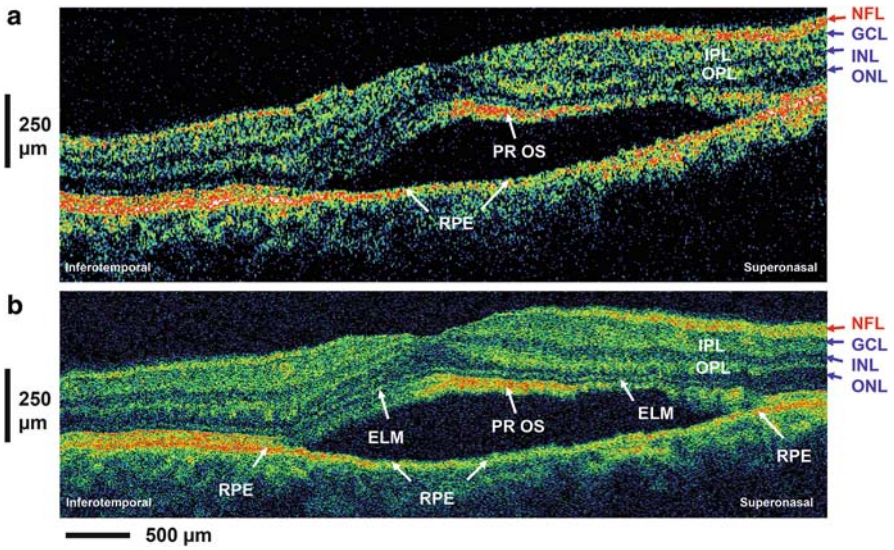

Fig. 56.9 Improved interpretation of commercial OCT using UHR OCT. Standard-resolution OCT (**a**) and ultrahigh-resolution OCT (**b**) image of a patient with central serous chorioretinopathy. Nerve fiber layer (*NFL*), inner (*IPL*) and outer plexiform (*OPL*) layer, ganglion cell layer (*GCL*), inner (*INL*) and outer nuclear (*ONL*) layer, external limiting membrane (*ELM*), outer photoreceptor segment (*PR OS*), retinal pigment epithelium (*RPE*)

Perhaps, the most striking advance associated with the high acquisition speed of OCT with Fourier domain detection is that it enables in vivo three-dimensional, ultrahigh-resolution OCT (3D-OCT). Fourier domain detection techniques enable 50–100 UHR OCT B-scans to be acquired during the time needed to acquire a single UHR OCT B-scan using time domain detection. Hence, a dense raster scan, consisting of multiple, closely spaced planes (B-scans), can be performed to cover a volume of the retina (cf. Fig. 56.17a, b). In analogy to scanning laser ophthalmoscopy measurements, 3D-OCT raster scans a retinal area, but it acquires full morphological information as a function of depth in the region of interest, without the need to scan the depth of focal plane. This measures a three-dimensional volumetric data set similar to that acquired with computed tomography (CT) or magnetic resonance (MR) imaging, but with microscopic resolution. It is possible to generate "fly-throughs" of the B-scans, i.e., a movie (time sequence) of adjacent B-scans using post-processing (cf. Fig. 56.17b). The 3D-OCT data set can also be used to generate tomograms with arbitrary position and orientation, according to the necessary diagnostic needs, such as in ultrahigh-resolution scanning laser ophthalmoscopy (SLO) in *en face* (C-mode) tomograms (cf. Fig. 56.16c). Another clinically important feature of 3D-OCT is that a virtual fundus image, i.e., an OCT fundus image similar to one obtained by standard fundus photography, can be directly generated from 3D-OCT data (cf. Fig. 56.17d). This OCT fundus image is generated by summing the 3D-OCT data set along the axial direction, thus

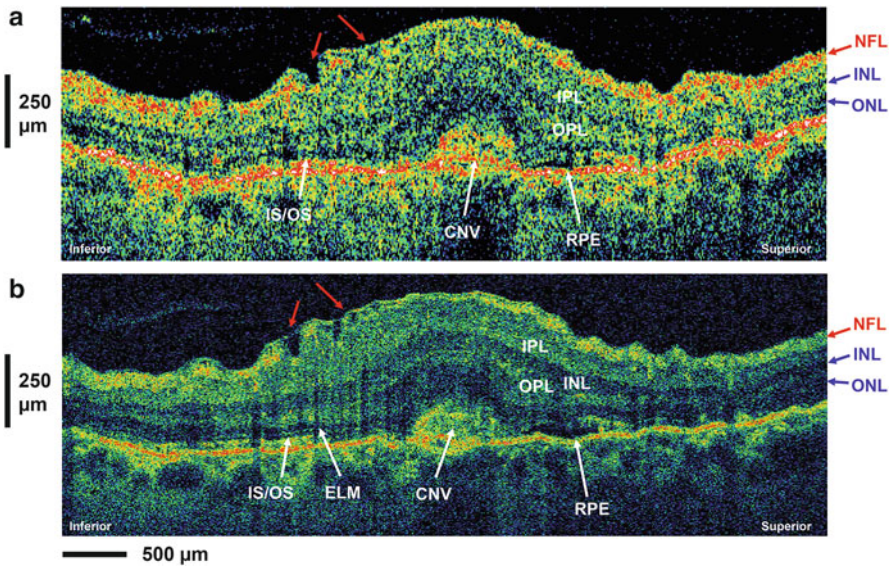

Fig. 56.10 Improved interpretation of standard-resolution commercial OCT using UHR OCT. Standard-resolution OCT (**a**) and ultrahigh-resolution OCT (**b**) image of a patient with choroidal neovascularization (*CNV*). Small irregularities in the NFL and ganglion cell layer with evidence of epiretinal membrane formation can be observed in both images (*red arrows*). Nerve fiber layer (*NFL*), inner (*IPL*) and outer plexiform (*OPL*) layer, inner (*INL*) and outer nuclear (*ONL*) layer, external limiting membrane (*ELM*), junction inner and outer photoreceptor segment (*IS–OS*), retinal pigment epithelium (*RPE*), choroidal neovascularization (*CNV*)

resulting in a pixel brightness value for each axial scan position. The OCT fundus image can be used to precisely and reproducibly register individual OCT tomograms with respect to fundus features.

56.4 Three-Dimensional, Clinical Ultrahigh-Resolution OCT

The first clinical investigations of ultrahigh-resolution 3D-OCT using spectral/Fourier domain detection for imaging retinal pathologies were conducted in several pilot studies [85, 86]. Figure 56.18 shows ultrahigh-resolution 3D-OCT in the foveal region of a normal subject. (Note that the axial dimension is enlarged by a factor of two when compared with the transverse dimensions in order to enable better visualization of the retina.) Figure 56.18a–h show three-dimensional (3D) renderings (software developed in collaboration with C. Glittenberg and S. Binder, Vienna, Austria) of the macular region from different virtual perspectives (cf. Fig. 56.18a–h) depicting the topography of the foveal depression. Three-dimensional rendering enables unprecedented flexibility in viewing, thereby allowing visualization of the retina from any direction, including from the posterior surface (cf. Fig. 56.18e). Figure 56.19 depicts high-definition (A, B) and

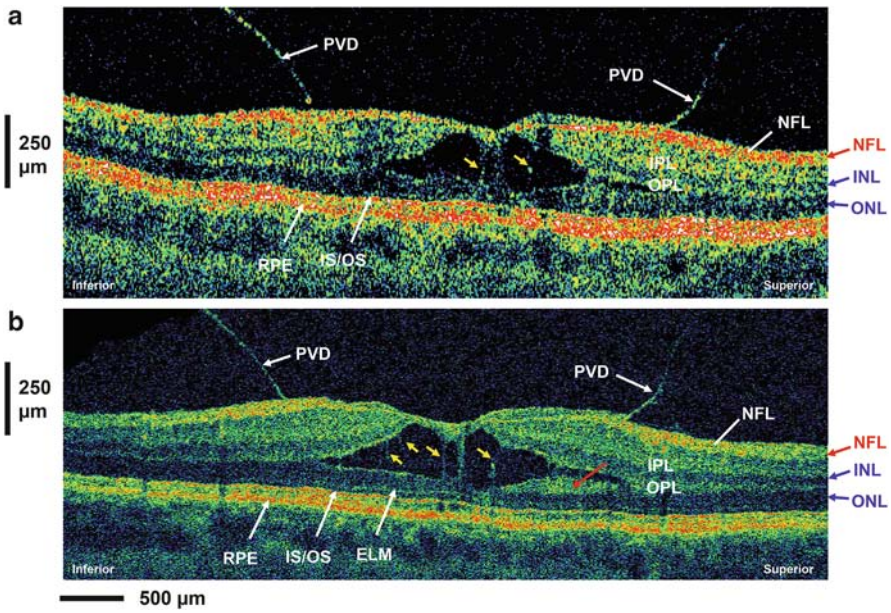

Fig. 56.11 Improved interpretation of standard-resolution commercial OCT using UHR OCT. Standard-resolution OCT (**a**) and ultrahigh-resolution OCT (**b**) image of a patient with vitreomacular traction. Posterior vitreous detachment (*PVD*) can be clearly visualized in both images. Distended structures (*yellow arrows*) spanning the separation in the sensory retina are suggestive of Müller cells. A highly backscattering layer (*red arrow*) adjacent to the ONL might be a portion of the OPL. Nerve fiber layer (*NFL*), inner (*IPL*) and outer plexiform (*OPL*) layer, ganglion cell layer (*GCL*), inner (*INL*) and outer (*ONL*) nuclear layer, external limiting membrane (*ELM*), junction inner and outer photoreceptor segment (*IS–OS*), retinal pigment epithelium (*RPE*)

three-dimensional rendering (C) of a patient with wet, age-related macular degeneration, which is indicated by RPE elevation and a choroidal neovascular membrane (CNV) underneath the RPE. There is fluid between the RPE and elevated photoreceptors. Note the jagged appearance of the photoreceptors where they are elevated. This may be due to photoreceptor disruption or lack of phagocytosis by the RPE, which can cause an elongation of the outer segments. The fluid in the retina looks more highly scattering than the vitreous. In addition, the fluid is more turbid than optically clear serous fluid. This may be due to proteinaceous material or deposits in this region. Figure 56.20 demonstrates 3D UHR OCT in the foveal region of a patient with RPE atrophy. (Note that the axial dimension is enlarged twofold, as compared to the other two dimensions, for better visualization.) The three-dimensional representation of the macular region is presented at different angled views (cf. Fig. 56.20a), thus depicting the pathologically change in the topography of the foveal depression and enabling unprecedented views in which the retina can be observed from any direction, including from below (cf. Fig. 56.20b). Figure 56.19e–h present virtual biopsy/"surgery" using 3D

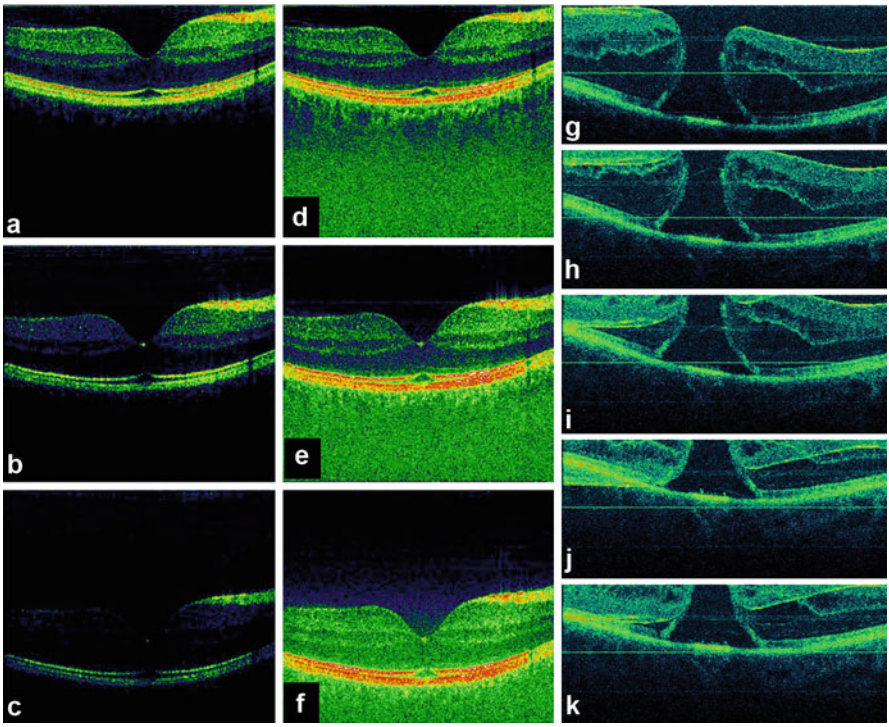

Fig. 56.12 Fundamental problems of three-dimensional UHR OCT (3D-OCT) based on spectral/Fourier domain detection. Depth-dependent sensitivity and dynamic range loss (**a**–**c**). System calibration and signal post-processing compensation for (**d**–**f**); artifacts caused by motion of the tissue/subject out of the measurement range (**g**–**k**). Fourier domain detection cannot distinguish between positive and negative echo delays, and as a consequence, "mirror" artifacts (**h**–**k**) are generated

UHR OCT in combination with 3D data rendering, which allows the user to excise and remove any given layer or part of the retinal volume in order to visualize intraretinal morphology. An important advantage of this method is that it is reversible, since the virtual retina can be reconstructed. Scanning a retinal volume with nearly isotropic (reasonably small equidistant) sampling intervals also avoids the need to decide on the orientation of any line scans that would be required with the time domain OCT. Figure 56.21 shows 3D UHR OCT of both eyes of a patient with a macular hole. The patient's right eye (cf. Fig. 56.21a) shows clear tomographic (cf. Fig. 56.21b) and topographic (cf. Fig. 56.21c) impairments due to the macular hole. The left eye (Fig. 56.21d) was diagnosed as normal with standard diagnostic techniques. By scanning the entire central foveal volume, 3D UHR OCT reduces the risk that retinal features indicating subtle tomographic (cf. Fig. 56.21e) and topographic (cf. Fig. 56.21f) photoreceptor impairment will be missed. Figure 56.22 depicts "virtual biopsy" or "virtual surgery" using ultrahigh-resolution 3D-OCT with 3D data rendering of a patient with macular hole. This virtual biopsy

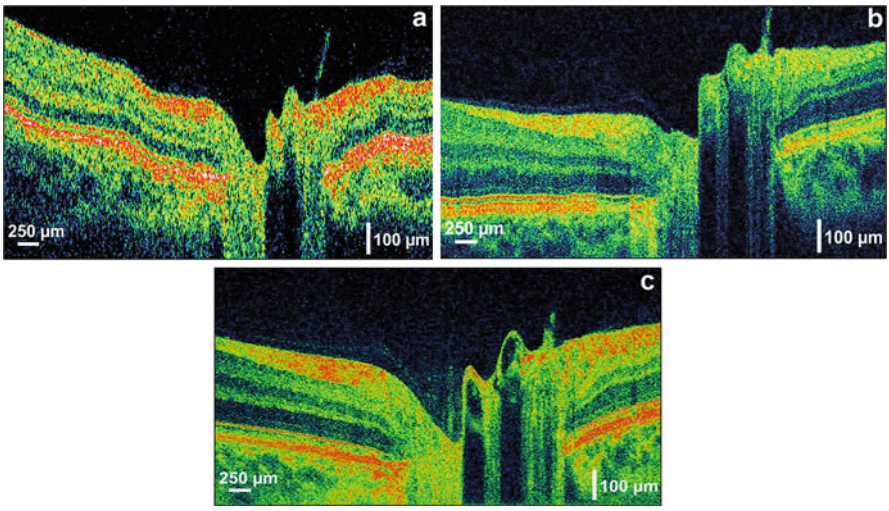

Fig. 56.13 Comparison of ophthalmic OCT technologies. The same human normal optic disk is measured by a third-generation standard-resolution commercial OCT system (**a**) (StratusOCT, ~10 µm axial resolution, 512 A-scans acquired in 1.3 s), UHR OCT performed with a time domain-based laboratory prototype (**b**) ~(3 µm axial resolution, 600 A-scans acquired in 4 s), and UHR OCT performed with spectral/Fourier domain detection (**c**) (~3 µm axial resolution, 2,048 A-scans acquired in 0.08 s). High speed enables motion artifact-free B-scans and significantly better delineation of the stratified appearance of the intraretinal layers

feature allows the investigator to virtually excise and remove any given layer or part of the retinal volume (cf. Fig. 56.22b–j) in order to visualize intraretinal morphology, with the advantage that it is a reversible (cf. Fig. 56.22k–o) procedure.

56.5 Ultrahigh-Resolution OCT in Animal Models

The improved visualization of intraretinal layers provided by ultrahigh-resolution OCT also promises to have significant impact in studies using animal models of retinal pathologies. Animal models, particularly the rodent and monkey, play an important role in studies of retinal diseases, such as age-related macular degeneration, diabetic retinopathy, glaucoma, and myopia [87, 88]. Because OCT is a noninvasive optical imaging modality, it enables longitudinal studies with repeated measurements on the same animal in order to track disease progression. In contrast with the standard techniques of euthanasia and histology, OCT imaging promises to significantly reduce the number of animals required for studies, while providing more complete information on the effects of biological variability between animals. This can enhance the efficiency and reduce the cost of drug discovery and preclinical development.

The earliest studies of ultrahigh-resolution OCT imaging in mouse retinas were performed with an UHR OCT system interfaced to an OCT microscope. Because the

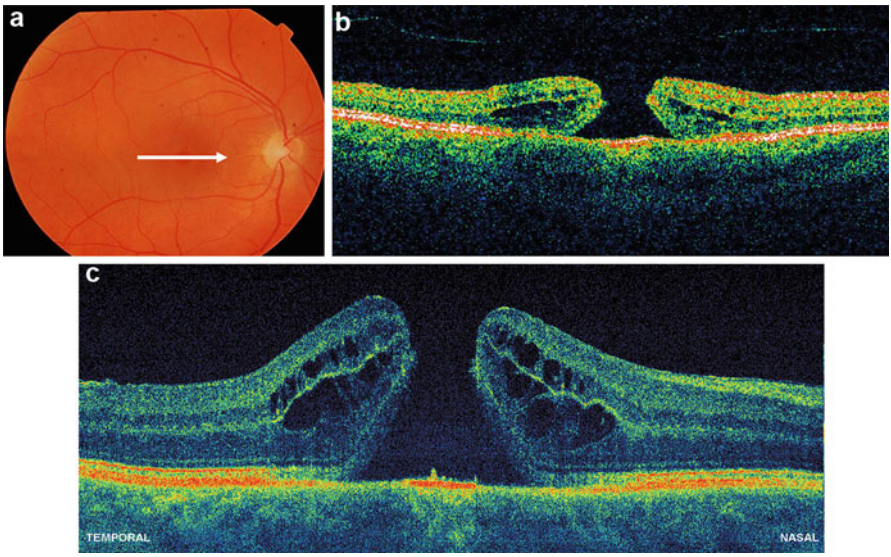

Fig. 56.14 High-definition UHR OCT using high-speed UHR OCT. Fundus photo indicating the location of the OCT scans (**a**). The same patient with macular hole is measured by a standard-resolution commercial OCT system (**b**) (StratusOCT, ~10 μm axial resolution, 512 A-scans acquired in 1.3 s) and high-definition UHR OCT performed with spectral/Fourier domain detection (**c**) (~3 μm axial resolution, 10,000 A-scans acquired in 0.6 s). Significantly improved visualization of intraretinal layers is accomplished due to increased axial OCT resolution and higher transverse sampling density, due to significantly improved data acquisition speed

mouse and rat retinas are thinner than the human retina, ultrahigh resolution is required to visualize intraretinal morphology. The UHR OCT images shown have ~1.5 μm axial image resolutions and were acquired using a broad bandwidth, femtosecond Ti: Sapphire laser light source and time domain detection. Despite the small size of the mouse retina, UHR OCT was able to delineate all major intraretinal layers. Figure 56.23a, b demonstrate UHR OCT imaging of the mouse retinal in comparison to histology. Despite the small dimensions of the mouse retinal, all major retinal layers can be visualized. Figure 56.23c, d depict UHR OCT in a mouse model of retinal degeneration, depicting a comparison of an Rd +/+wild-type mouse (cf. Fig. 56.23c) with an Rd −/− knockout mouse (5 months old; cf. Fig. 56.23d). (This study was performed in collaboration with Dr. Janice Lem from Tufts University School of Medicine and Joel Schuman from University of Pittsburgh Medical Center.) The UHR OCT image shows complete loss of the outer nuclear and outer plexiform layers in the retina of the Rd −/− knockout mouse, which is consistent with the expected pattern of structural degeneration. OCT has the powerful advantage that measurements can be performed over a period of time to longitudinally study disease progression. Figure 56.24 depicts the monitoring of glaucoma progression using in vivo UHR OCT imaging of the optic nerve head in a nonhuman primate glaucoma model (*cynomolgus monkey*). This study was conducted in collaboration with Novartis Institutes for

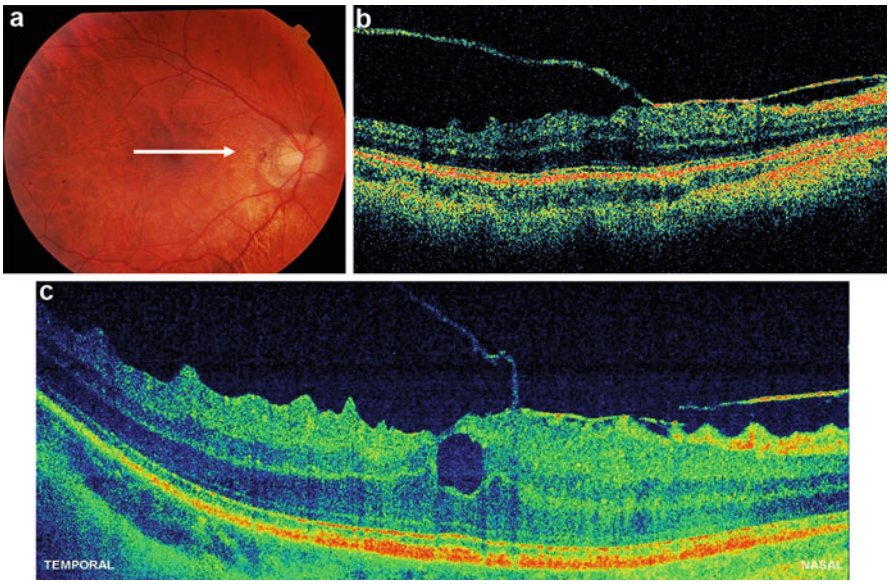

Fig. 56.15 High-definition UHR OCT using high-speed UHR OCT. Fundus photo indicating the location of the OCT scans (**a**). The same patient with a macular pseudo-hole is measured by a standard-resolution commercial OCT system (**b**) (StratusOCT, ~10 μm axial resolution, 512 A-scans acquired in 1.3 s) and high-definition UHR OCT performed with spectral/Fourier domain detection (**c**) (~3 μm axial resolution, 10.000 A-scans acquired in 0.6 s). Significantly improved visualization of intraretinal layers and the epiretinal membrane is accomplished by high-definition UHR OCT

Biomedical Research by E. Polska and A. Doelemeyer. Horizontal, cross-sectional images are depicted at baseline (cf. Fig. 56.24a), 20 days (cf. Fig. 56.24b), 34 days (cf. Fig. 56.24c), 48 days (cf. Fig. 56.24d), and 179 days (cf. Fig. 56.24e) after induction of unilateral ocular hypertension at approximately the same retinal location. The retinal nerve fiber layer in the circumpapillary region is clearly visualized, despite its atrophy due to increased ocular pressure. Furthermore, the cross section of the lamina cribrosa is clearly visualized at baseline (cf. Fig. 56.24a), which might also be used to detect early glaucomatous changes. In the advanced stages, the lamina cribrosa is severely thinned or even absent (cf. Fig. 56.24b–e), and vessels appear prominent, which is caused by significant cupping of the optic nerve head due to increased intraocular pressure (cf. Fig. 56.24f). UHR OCT can visualize the retinal nerve fiber layer (especially its posterior surface), quantify circumpapillary thickness distribution, and provide topographic information on the optical nerve head. Hence, UHR OCT promises to be a powerful technique to track the early stages of this disease in animal models.

With the introduction of spectral/Fourier domain detection, ultrahigh resolution with improved image quality and three-dimensional imaging became available for studies of retinal disease in animal models. Although the instrumentation

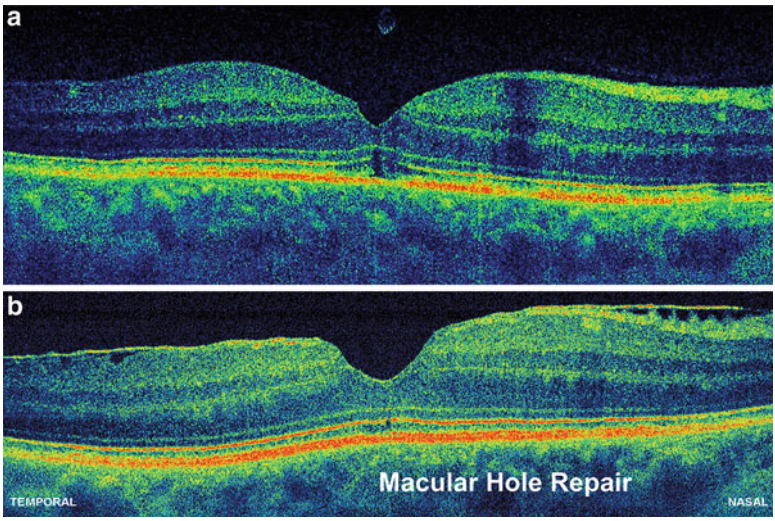

Fig. 56.16 High-definition UHR OCT using high-speed UHR OCT. High-definition UHR OCT performed with spectral/Fourier domain detection (**c**) (~3 μm axial resolution, 10.000 A-scans acquired in 0.6 s) in a patient with macular hole, pre- (**a**) and postoperatively (**b**). Detailed intraretinal morphology can be visualized, especially in the photoreceptor area

requirements are quite different from clinical instruments, many examination protocols and image display techniques that are applicable for clinical imaging in humans can also be applied for small animal imaging. Ultrahigh-resolution 3D-OCT imaging in a normal C57BL6 mouse (left A–E) and Long–Evans rat (right A–E) is depicted in Fig. 56.25. A high-speed (24,000 A-scans/s) OCT system with 2.8 μm axial resolution using a broad bandwidth, multiplexed superluminescent light diode (SLD) light source centered at 900 nm was used for this study [89]. A dense raster scan protocol acquiring 256 images of 512 axial scans each covering a 2.6 × 2.6 mm^2 region with a 10 × 5 μm^2 pixel spacing was used. An OCT fundus image can be generated from the 3D-OCT data (cf. Fig. 56.25a, left and right) and the UHR OCT B-scans precisely registered to fundus features (cf. Fig. 56.25b–d, left and right). All major intraretinal layers could be visualized (cf. Fig. 56.25e, left and right). Figure 56.26 shows a comparison of high-definition OCT images between a normal, young adult Sprague–Dawley (albino) rat and a normal, young adult Long–Evans (pigmented) rat. The inner retinal layers appear similar in both strains. In the Long–Evans rat, the photoreceptors comprise two highly reflective and well-defined bands proximal to the RPE. In the Sprague–Dawley rat, the photoreceptors comprise two highly reflective bands separated by a region of moderate reflectivity. There is increased penetration of the OCT signal to the sclera in the Sprague–Dawley rat, which is consistent with the lack of absorption from pigment in this albino strain.

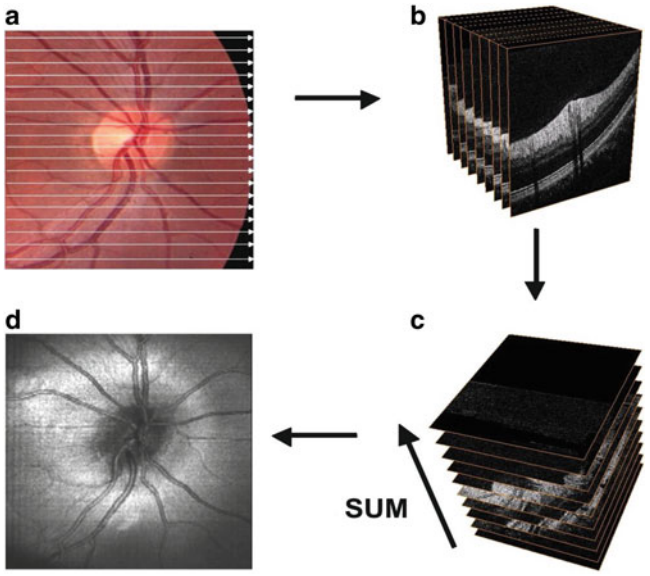

Fig. 56.17 Scanning and post-processing protocols in three-dimensional ultrahigh-resolution OCT. Several planes (B-scans) can be scanned of a whole retinal volume (**a**), resulting in a stack of adjacent B-scans (**b**). The 3D-OCT data set can be summed in the axial direction (**c**) to generate an en face image similar to scanning laser ophthalmoscope in *en face* (C-mode) tomograms (**d**). UHR OCT tomograms can be precisely and reproducibly registered to fundus features. The acquired data of the investigated volume can arbitrarily be cut according to the necessary diagnostic needs, e.g., an ultrahigh-resolution scanning laser ophthalmoscope in *en face* (C-mode) tomograms (**c**). OCT fundus image (**d**), i.e., an OCT view of the fundus similar to one obtained by standard fundus photography, which can be reproduced directly from 3D OCT data. This OCT fundus image is generated by summing the A-scan signal along the axial direction, thereby resulting in a brightness pixel value for each axial scan that can be used to register UHR OCT tomograms directly

56.6 Quantitative Analysis Using Three-Dimensional Ultrahigh-Resolution OCT

Another significant advantage of combining ultrahigh-resolution and high data acquisition speed is that it enables objective, quantitative measurements of intraretinal layers. Quantitative measurement, or morphometry, plays a central role in the early diagnosis of diseases such as glaucoma or diabetic retinopathy and enables objective assessment of progression or response to therapy. The improved axial resolution provided by UHR OCT enables clearer delineation of intraretinal layers. High-speed acquisition enables more sampling points (A-scans at different positions on the fundus), thus increasing coverage of the retina and reducing sampling errors. Data sets with higher numbers of transverse pixels also enable better differentiation of intraretinal layers.

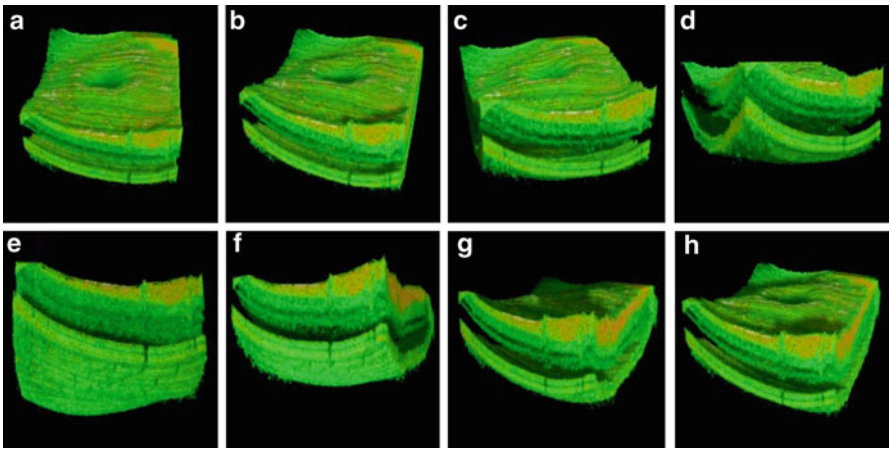

Fig. 56.18 Three-dimensional ultrahigh-resolution OCT of the normal human fovea. Three-dimensional representation (developed in collaboration with C. Glittenberg and S. Binder, Vienna, Austria) of the macular region at different angled views (note that the axial dimension is twofold enlarged compared to the other two dimensions), enabling unprecedented views that allow observation of the retina from any direction, including from below (**e**)

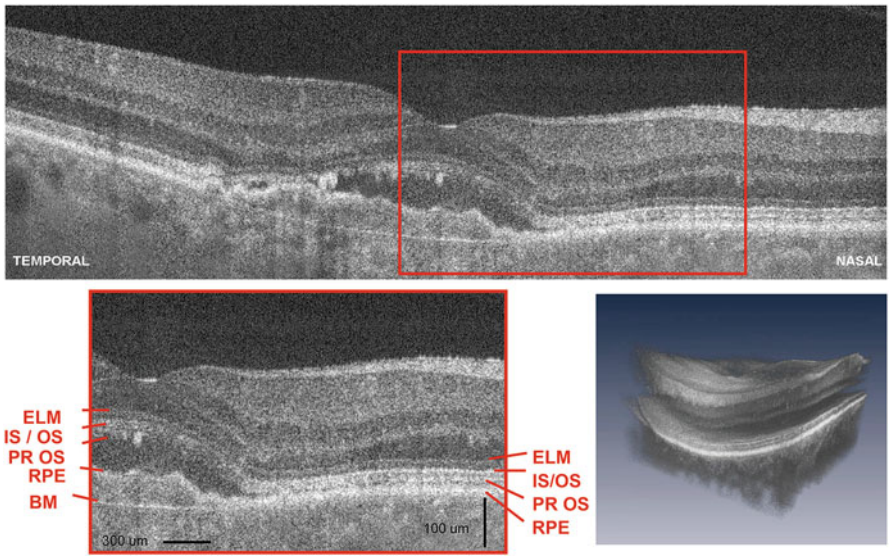

Fig. 56.19 Three-dimensional ultrahigh-resolution OCT of retinal pathologies. High-definition (**a**, **b**) and three-dimensional rendering (**c**) of a patient with wet age-related macular degeneration. (Rendering using commercial software) Enlargement (**b**) indicated as *red rectangle* in (**a**). *ELM* external limiting membrane, *IS–OS* junction between the inner and the outer photoreceptor segments, *PR OS* photoreceptor outer segment, *RPE* retinal pigment epithelium

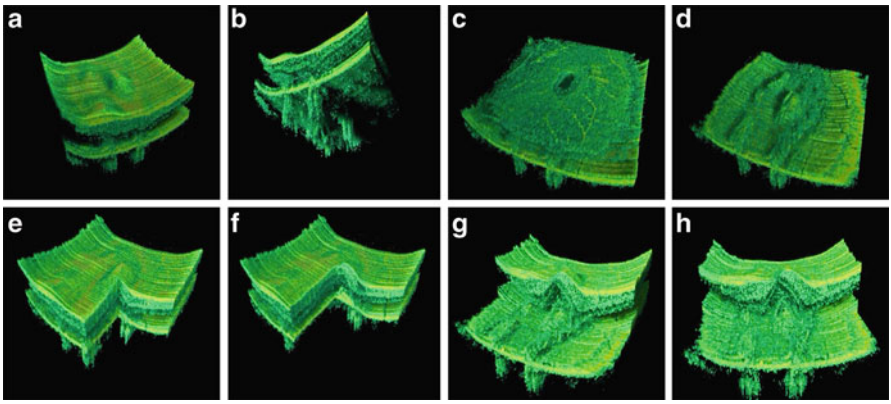

Fig. 56.20 Three-dimensional ultrahigh-resolution OCT of retinal pathologies. Three-dimensional UHR OCT enables unprecedented volumetric representation of the macular region of a patient with RPE atrophy at different angled views (**a**) including from below (**b**). Virtual biopsy/"surgery" using 3D UHR OCT (**e**–**h**) allows the user to excise and remove any given layer or part of the retinal volume in order to visualize intraretinal morphology

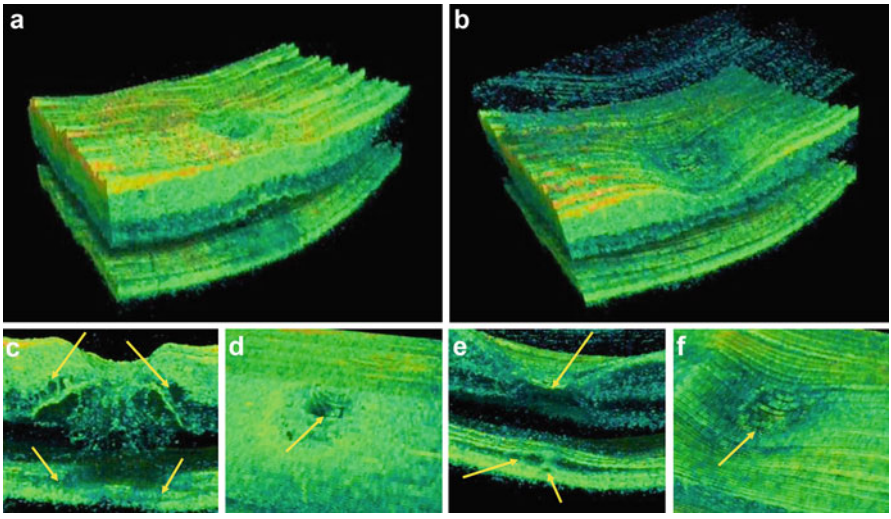

Fig. 56.21 Three-dimensional ultrahigh-resolution OCT of retinal pathologies. Three-dimensional UHR OCT of both eyes of a patient with a macular hole. The patient's right eye (**a**) shows clear tomographic (**b** *arrows* indicate intraretinal cysts (*top arrows*) and photoreceptor impairment (*bottom arrows*)) as well as topographic (**c** *arrow* indicates topographic change of foveal depression)) impairments due to the macular hole. The left eye (**d**) was diagnosed as normal. 3D UHR OCT clearly indicates early, subtle tomographic (**e** *arrows* indicate subtle morphological photoreceptor changes) and topographic (**f**) impairment

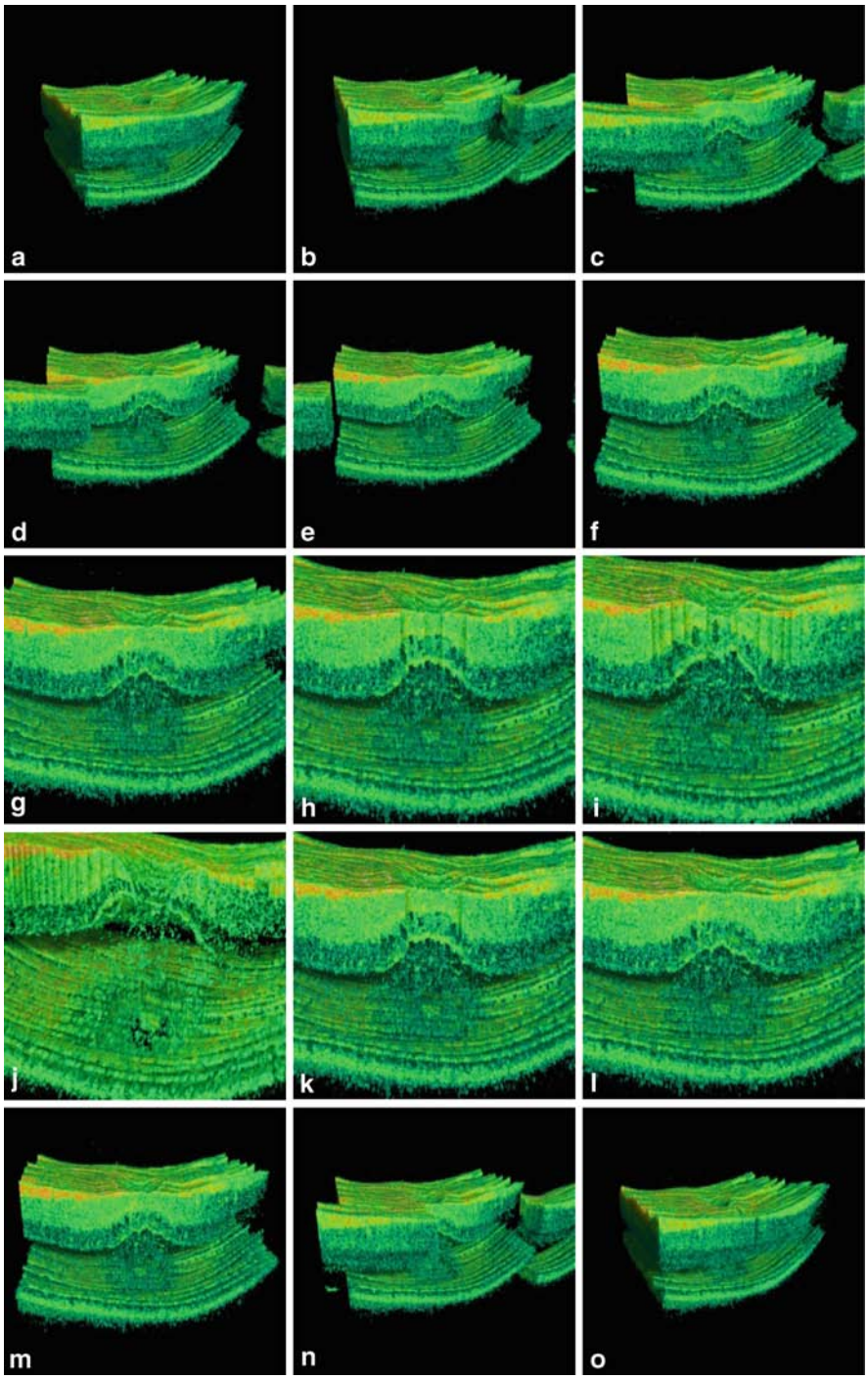

Fig. 56.22 (continued)

Figure 56.27 shows the use of 3D-OCT for the quantitative mapping of intraretinal layer thicknesses in the Long–Evans rat. Figure 56.27a shows an OCT fundus image with a white arrow showing the location of the enlarged cross-sectional image in Fig. 56.27b. Images are segmented, as shown in Fig. 56.27b. Figure 56.27c shows a map of retinal thickness, measured from the vitreoretinal interface to the photoreceptor inner and outer segment (IS–OS) junction, which is overlaid in color on the OCT fundus image. Figure 56.27d shows a map of NFL thickness. Thicknesses were computed by assuming a group refractive index of 1.4. Figure 56.28 shows a rendering of 3D-OCT data from the Long–Evans rat retina. The renderings enhance the NFL striations on the surface of the retina (Fig. 56.28a). Figure 56.28b shows that virtual slices can be created through the 3D data set, thus enabling visualization of 3D-OCT data along arbitrary planes. Figure 56.28c shows a cutaway rendering near the optic nerve head. Renderings can be manipulated in real time to visualize structure.

Three-dimensional UHR OCT can also be used for segmentation and two-dimensional thickness mapping of intraretinal layers from in vivo measurement in human retinas. Figure 56.29a depicts a representative UHR OCT B-scan consisting of 2,048 A-scans from a three-dimensional stack over a $5 \times 5 \times 1\ mm^3$ volume. Segmentation is used to quantify the distance from the junction between the inner and outer photoreceptors to the retinal pigment epithelium, representing the outer segment length of the photoreceptors (cf. Fig. 56.29b); the distance between the external limiting membrane and the retinal pigment epithelium, representing the total photoreceptor length (cf. Fig. 56.29c); and the thickness of the ganglion cell layer and the inner plexiform layer. These quantitative measurements may be important for early glaucoma diagnosis or the diagnosis of age-related macular degeneration (cf. Fig. 56.29d). Figure 56.30 depicts quantitative volumetric analysis of a normal optic disk using three-dimensional UHR OCT. Figure 56.30a illustrates a central, cross-sectional OCT image chosen from the three-dimensional set of 180 horizontal cross sections. Fig. 56.30b shows a three-dimensional (3D) rendering of the entire circumpapillary retinal nerve fiber layer across the entire set of 180 high-speed UHR-OCT images (yellow). Figure 56.30c shows the extracted and rendered nerve fiber layer with clearly visible contour of optic disk and surface profile. Figure 56.30d shows an example of processing the retinal nerve fiber layer, including thickness analysis in arbitrary chosen orthogonal planes. Quantitative volumetric analysis using three-dimensional UHR OCT can also be used to quantitatively monitor therapy. Figure 56.31 demonstrates volumetric analysis of the extent of epiretinal membrane (cf. Fig. 56.31b, d, e, h, j, k, respectively) and the volumetric extent of a macular hole (cf. Fig. 56.31a, c, f, g, i, l, respectively), pre- and postoperatively.

Fig. 56.22 Virtual biopsy or "surgery" of a patient with macular hole using 3D-OCT in combination with data rendering system. This virtual biopsy feature allows the user to excise and remove any given layer or part of the retinal volume (**b–j**) in order to visualize intraretinal morphology inside the tissue with the advantage that it is a reversible (**k–o**) procedure

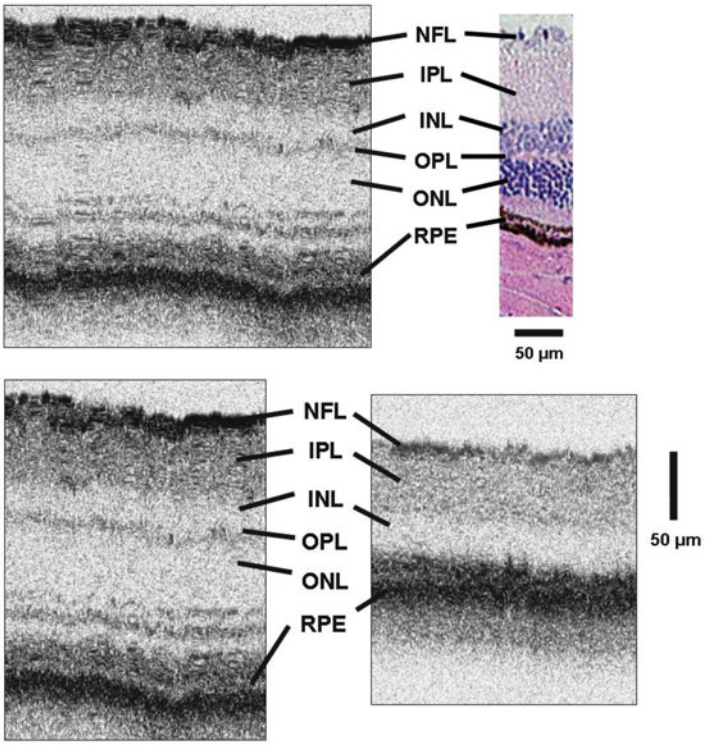

Fig. 56.23 Two-dimensional ultrahigh-resolution OCT in retinal animal models. Comparison of UHR OCT (**a**) with histology (**b**), all major retinal layers can be visualized; UHR OCT in mouse retinal degeneration, an Rd +/+ wild-type mouse (**c**) with an Rd −/− knockout mouse, 5 months old (**d**). UHR OCT is capable of visualizing the complete loss of the outer nuclear and outer plexiform layers in the retina of the Rd −/− knockout mouse (Study was performed in collaboration with S. Bursell, J. Lem, J. Schuman, Boston, USA)

Most attempts to segment OCT images usually build upon layer boundary detection and can yield spurious results, and many approaches have relied upon pre-registration of the tomograms or user input to obtain segmentation [90–92]. Recently automated segmentation algorithms for extracting the layers have been developed based on texture analysis (in collaboration with G. Powell, P. Rosin, D. Marshall, School of Computer Sciences, Cardiff University, UK). Texture analysis tries to identify the individual structure of the layers by their speckle pattern, rather than the boundaries, and might be only one building block of a comprehensive approach. Although speckle holds sub-resolution phase information that should help to identify similar structures, textures in different layers can be very similar, and moreover there are not always distinct boundaries in the speckle patterns between layers. Geometric techniques were also considered, but the nonuniformity of the boundaries between layers makes them difficult to model in a successful and consistent way. To perform effective classification, additional geometric information

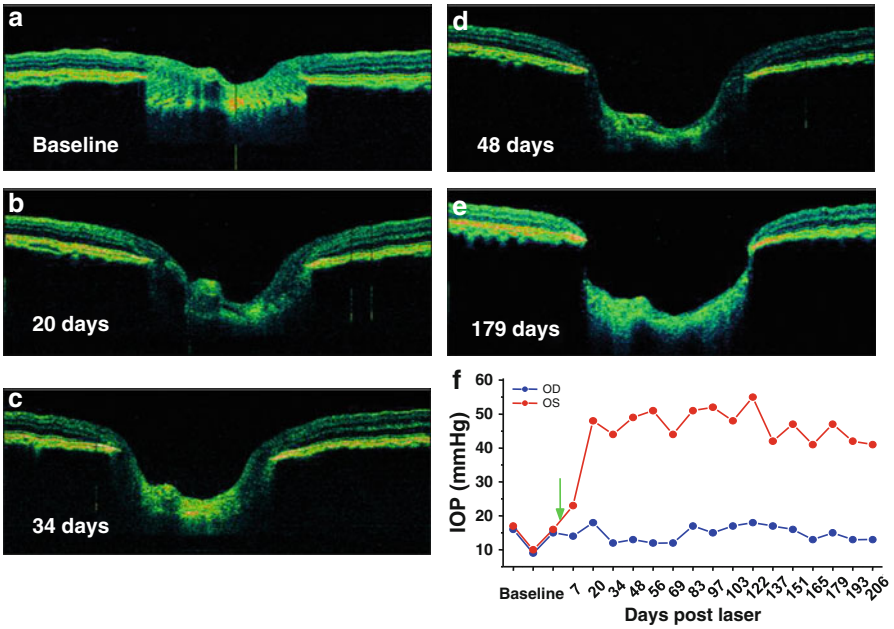

Fig. 56.24 Two-dimensional ultrahigh-resolution OCT in retinal animal models. Monitoring disease progression using in vivo UHR OCT of the optic nerve head in a nonhuman primate glaucoma model, the *cynomolgus monkey*. (This study was conducted in collaboration with Novartis Institutes for Biomedical Research by E. Polska and A. Doelemeyer.) Horizontal OCT images are depicted at baseline (**a**), 20 days (**b**), 34 days (**c**), 48 days (**d**), and 179 days (**e**) after induction of unilateral ocular hypertension. Measured intraocular pressure of test (*red*) and control eye (*blue*, **f**)

must be incorporated, although this is made difficult by the lack of precise and consistent shape of the layer boundaries. Instead, a set of simple local geometric features which have been found to substantially improve the results of using solely texture have been used. In preliminary results, various classifiers were tested and the most suitable classification, in terms of trade-off between accuracy, reliability, and computational efficiency, was to fit Gaussians to the features for each of the layers extracted from the training data. To classify a new (unseen) image, the incoming pixel to this feature space was compared, and through the use of the Mahalanobis distance, the most similar layer for its classification was used.

For the training, 480 images from only three different subjects were used, which were manually segmented by three independent, anatomically skilled operators. This data set was used to build a classifier, as described above. This classifier was then used to automatically segment a 3D volume that consisted of 60 OCT tomograms from a different subject in 2 min on a standard personal computer. Two example cross sections and their corresponding automatic segmentations are shown in Fig. 56.32. Figure 56.32a – (top) depicts a parafoveal cross section, and in Fig. 56.32c (top), a cross section of the fovea centralis is shown. All mayor layers

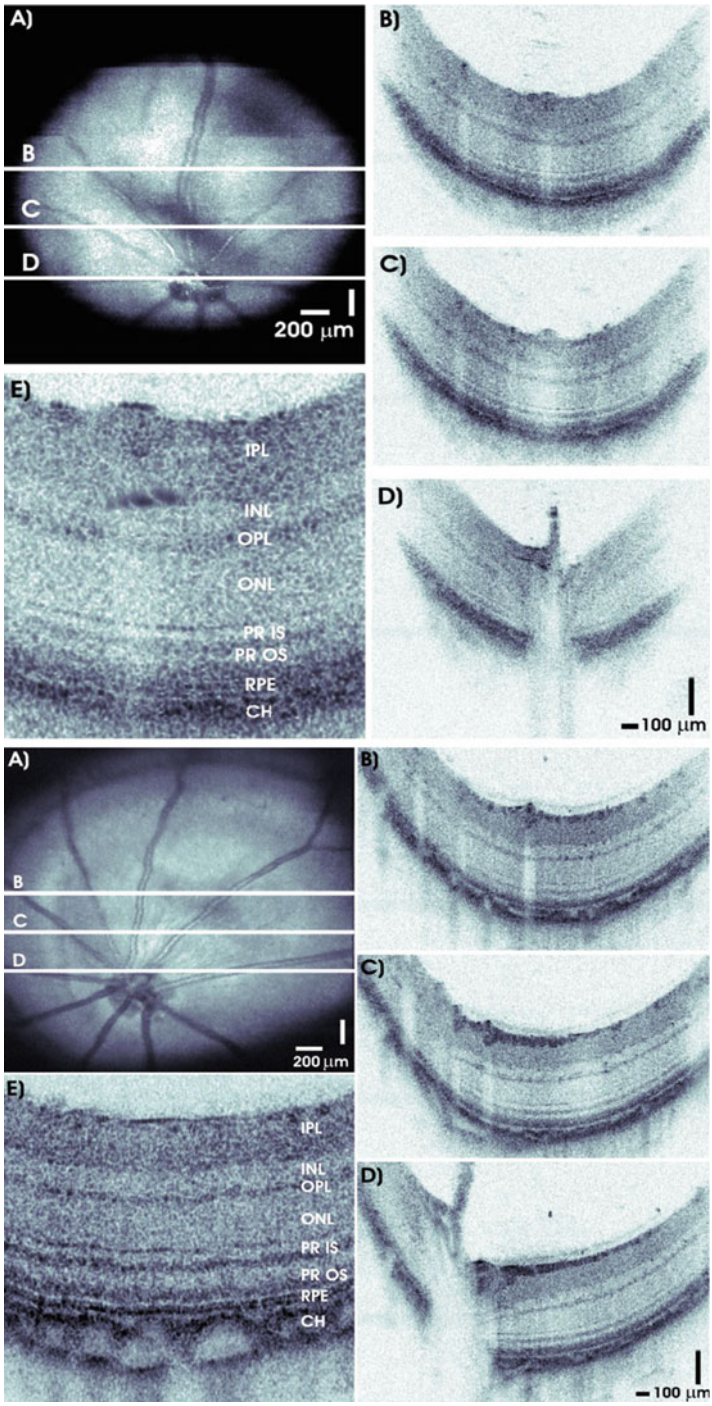

Fig. 56.25 (continued)

are visible and indicated. This includes the nerve fiber layer (NFL), ganglion cell layer and inner plexiform layer (GC/IPL), Henle fiber layer and outer plexiform layer (HF/OPL), outer nuclear layer (ONL), inner segment of photoreceptor layer (IS PR), outer segment of photoreceptor layer (OS PR), and the retinal pigment epithelium (RPE). The segmentation of these layers for the parafoveal tomogram (Fig. 56.32b (top)) and the central foveal tomogram (Fig. 56.32d – (top)) was achieved with reasonable accuracy, taking into account that no manual interaction was required. Thickness maps were then created for each of the eight layers, based on the segmentation results. These thickness maps are shown in Fig. 56.32 (bottom). As expected, GC/IPL (Fig. 56.32b (bottom)) appeared as the thickest layer, followed by NFL (Fig. 56.32c (bottom)) and ONL (Fig. 56.32e (bottom)). The preliminary results show the huge potential of this technique and are likely to improve with further training and fine tuning, as well as by combining standard boundary detection methods.

Assessment of the human retinal nerve fiber layer and retinal thickness at the optical nerve head for novel indicators of glaucoma staging from volumetric images, obtained by high-speed optical coherence tomography, has recently been presented. Three-dimensional UHR OCT at high axial resolution allows for extraction of the full retinal morphology. Analysis of this information helps to deduce pathognomonic parameters that allow for the easy and reliable quantification of disease and therapy progress by comparing true thicknesses in an individual subject. Quantification and localization of the NFL and optic nerve structures have become central to managing patients with glaucoma. There is an urgent need in diagnosis and staging for reliable, objective precursors and markers associated with pathological changes of the ganglion cell layer. Three-dimensional, ultrahigh-resolution optical coherence tomography holds particular promise in this respect, since it enables the volumetric assessment of intraretinal layers, including tomographic data for the retinal nerve fiber layer (RNFL) and optic nerve head (ONH) at the micrometer scale. The resolution advantage, in conjunction with full volumetric sampling, has enabled the development of more informative indices of axonal damage in glaucoma, when compared with the measurements of RNFL thickness and cup-to-disk ratio provided by other devices. In this work, the potential for UHR OCT to enable the combined analysis of tomographic and volumetric data on retinal structure is explored. A novel mapping method was developed, which used the three-dimensional minimal distance (3D-MDM) as the optical correlate of true RNFL thickness around the ONH region, thereby replacing the misleading, projected thickness with its 3D counterpart. Using this information, novel measures

Fig. 56.25 Three-dimensional ultrahigh-resolution OCT in retinal animal models. 3D OCT in a normal C57BL6 mouse (*left*) and a Long–Evans rat (*right*) using a dense raster scan protocol consisting of 256 images of 512 axial scans each, covering a 2.6 mm^2 region resulting in 10 × 5 μm pixel spacing. A fundus image generated from ultrahigh-resolution 3D OCT data (**a**, *left* and *right*) indicates the locations of three selected OCT B-scans (**b**–**d**, *left* and *right*). All major intraretinal layers can be visualized with ultrahigh-resolution OCT (**e**, *left* and *right*)

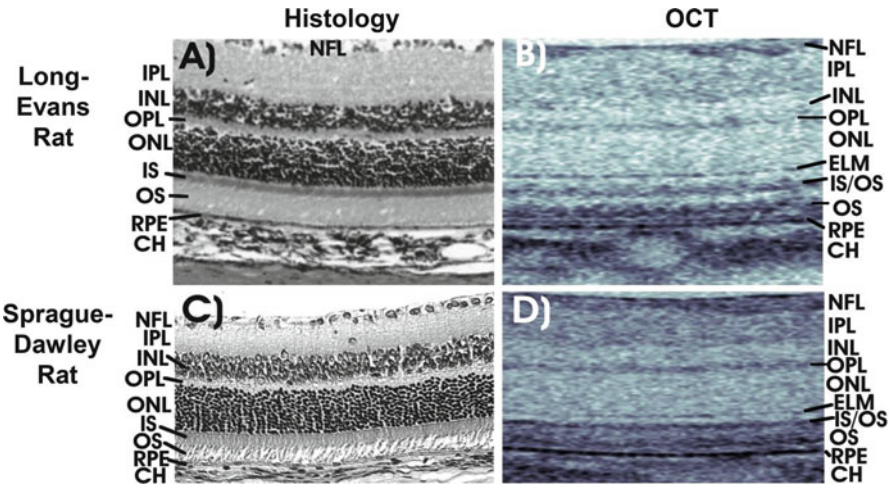

Fig. 56.26 Ultrahigh-resolution OCT in animal models versus histology. A comparison of cropped and enlarged OCT cross-sectional images (600 axial scans) between normal, young adult Sprague–Dawley (**a**) and Long–Evans (**b**) rats

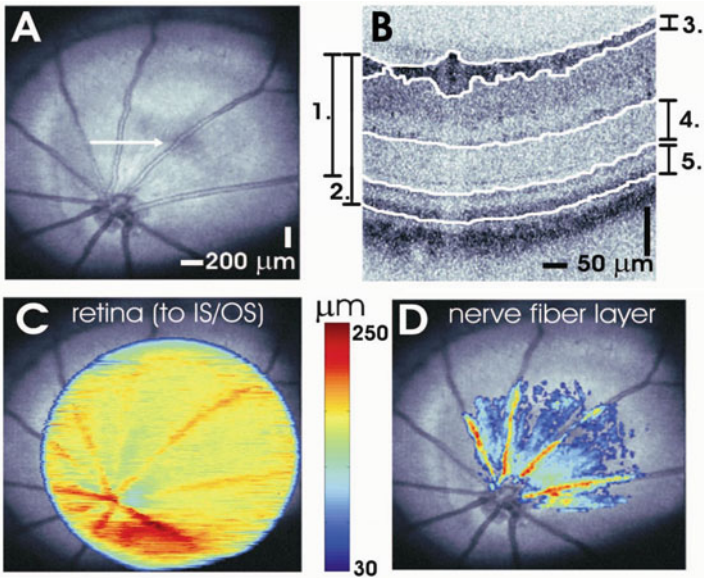

Fig. 56.27 Quantitative mapping of intraretinal layers using three-dimensional UHR OCT in animal models. A fundus image of the Long–Evans rat retina (**a**). Cross-sectional OCT images from the 3D-OCT data set are segmented to identify boundaries between retinal layers (**b**). Retinal thickness (**c**) and nerve fiber layer thickness (**d**) are overlaid as false color on the fundus image

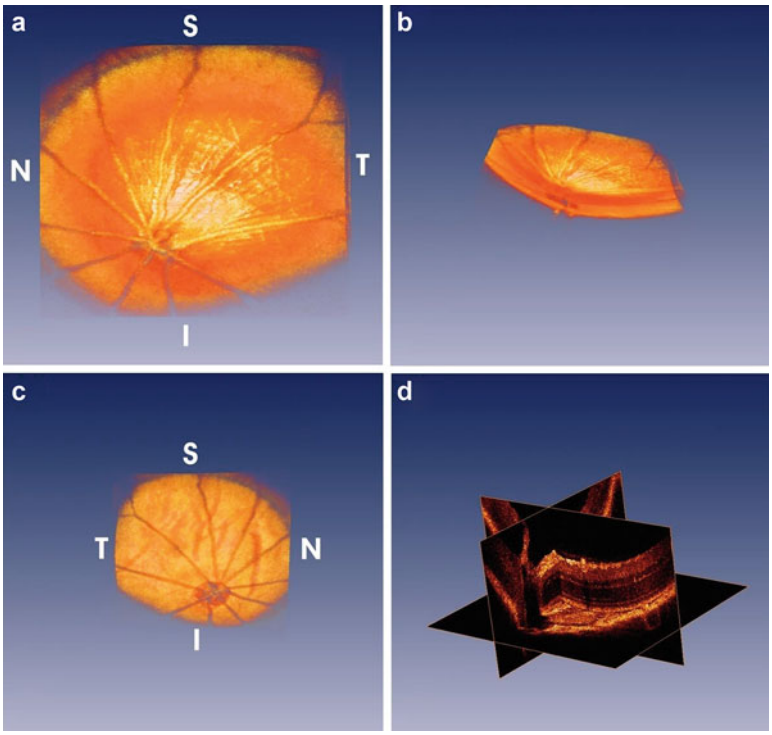

Fig. 56.28 Volumetric rendering using three-dimensional ultrahigh-resolution OCT in retinal animal models: (**a**) A rendering of a normal Long–Evans rat retina. (**b**) It is possible to create virtual slices through 3D-OCT data and view images along arbitrary planes. Cutaway renderings can simultaneously show intraretinal structure and retinal topography (**c**)

of retinal parameters resembling the complex geometrical distortions and features were found in many optic nerve heads. Quantification of three-dimensional surfaces leads to simple, automatically generated parameters to monitor disease progression that can be used to evaluate an individual situation. Preliminary studies found the relation between the cross-sectional areas of the RNFL and the optic nerve to be a useful and sensitive measure of axon loss. For the purposes of this pilot study, data was used from normal subjects and patients with characteristic optic nerve and RNFL changes secondary to glaucoma. Figure 56.33 depicts different mappings of a normal and two different glaucoma stages, based on a volumetric data set obtained by three-dimensional UHR OCT. Figure 56.33a shows fundus images obtained by averaging of the OCT volume across the depth. Figure 56.33b shows the projected and Fig. 56.33c the real thickness of the NFL. Figure 56.33d, e, respectively, depict the region above the optic nerve (black portion) for the full retinal thickness where the projected retinal thickness cannot be defined and give unreliable values that can be extracted. MDMs provide easily interpretable

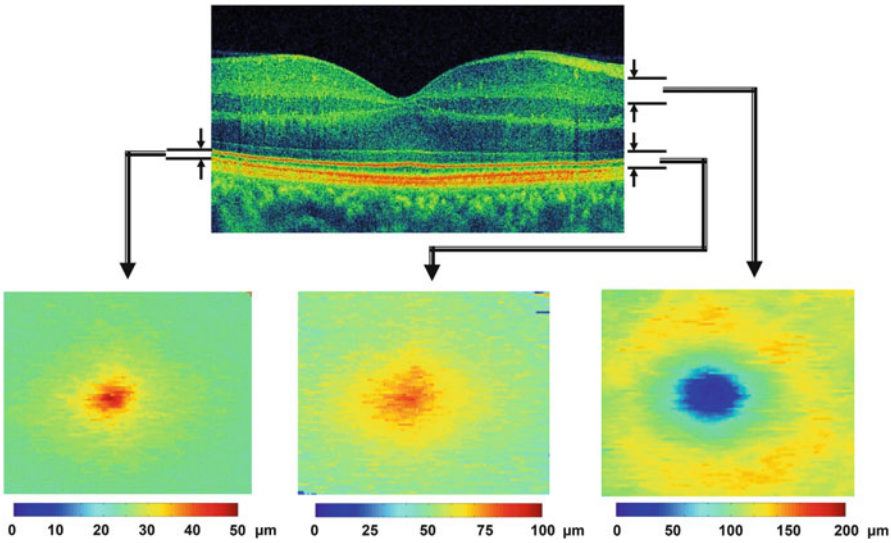

Fig. 56.29 Quantitative mapping of intraretinal layers using three-dimensional UHR OCT in humans: Representative UHR OCT B-scan consisting of 2,048 A-scans from a three-dimensional stack over a $4 \times 4 \times 1$ mm^3 volume (**a**); segmentation of the distance from the junction between the inner and outer photoreceptors to the retinal pigment epithelium, representing the outer segment length of the photoreceptors (**b**); the distance between the external limiting membrane and the retinal pigment epithelium, representing the total photoreceptor length (**c**); and the thickness of the ganglion cell layer and the inner plexiform layer (**d**)

visualization of local retinal thickness and surface roughness. We anticipate that increased imaging speed will allow higher-resolution and isotropic sampling of the ONH and improve the correct estimation of RNFL volumes and areas. The MDM technique appears to be robust and is less sensitive to the confounding effects of ONH tilt when compared to other imaging modalities, e.g., SLO.

56.7 Optophysiology: Depth-Resolved Retinal Physiology

The development of retinal diseases is often accompanied by changes, both in the retinal morphology and physiology. Various imaging modalities, such as fundus photography, ultrasound imaging, and optical coherence tomography (OCT), are commonly used for imaging retinal morphology. Electrophysiological tests, such as electroretinography [93] (ERG), multifocal ERG (mfERG), and electrooculography (EOG), are used for clinical assessment of retinal and pigment epithelial function. These electrophysiological methods allow clinicians to distinguish between diseases of the outer and inner retina and, in the case of multifocal ERG, to map retinal physiology with a modest transverse spatial resolution of $\sim 2^\circ$ ($\sim$600 µm). However, all ERG methods have limited depth selectivity, and currently, there is

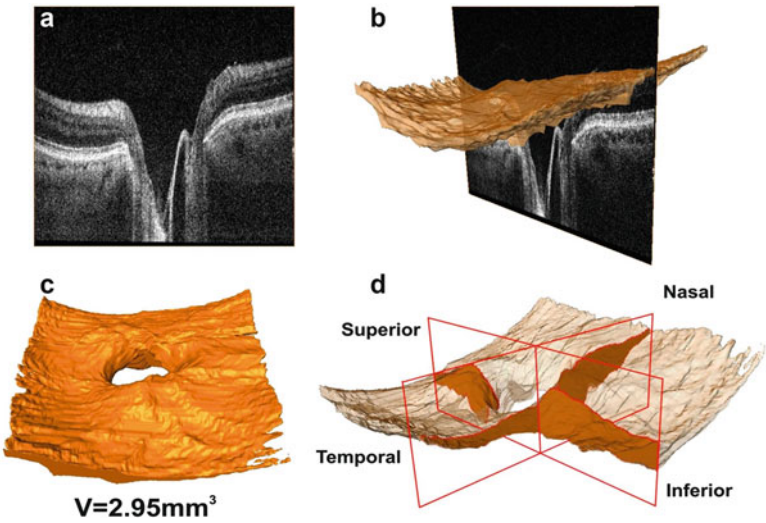

Fig. 56.30 Volumetric analysis of high-speed, ultrahigh-resolution OCT in a normal optic disk. Central, cross-sectional OCT image chosen from the three-dimensional set of 180 horizontal cross sections (**a**); three-dimensional (3D) rendering of the entire circumpapillary retinal nerve fiber layer across the entire set of 180 high-speed UHR OCT images (*yellow*, **b**); extracted and rendered nerve fiber layer with clearly visible contour of optic disk and surface profile (**c**); processing of extracted retinal nerve fiber layer, including thickness analysis in arbitrarily chosen orthogonal planes (**d**)

disagreement about the contributions of various cell populations to the components of mfERG signals. All electrophysiological methods require physical contact between the electrodes and biological tissue, which can result in patient discomfort. In addition, the ERG/EOG techniques are sensitive only to electrical potential changes in the retina and are, therefore, susceptible to any internal or external electrical noise sources.

OCT is sensitive to spatial variations in the optical reflectivity or scattering of tissue associated with local changes in refractive index or structure. Physiological processes that occur on the cellular level, such as membrane depolarization, cell swelling, and altered metabolism, can cause small, but detectable changes in the local optical properties of biological tissue. As an optical technique, OCT is sensitive to any processes that alter the optical reflectivity or scattering. Furthermore, the high sensitivity of OCT ($\sim$100 dB) enables detection of very weak optical signals. Therefore, OCT has great potential for noninvasive probing of tissue physiology.

This first demonstration that UHR OCT can be used for non-contact, high-resolution, spatially resolved probing of the physiological response to light stimulation in the retina was performed in 2006 [94]. To test if UHR OCT was capable of detecting changes in retina reflectivity or scattering triggered by light stimulation, a dark-adapted, living in vitro rabbit retina was exposed to

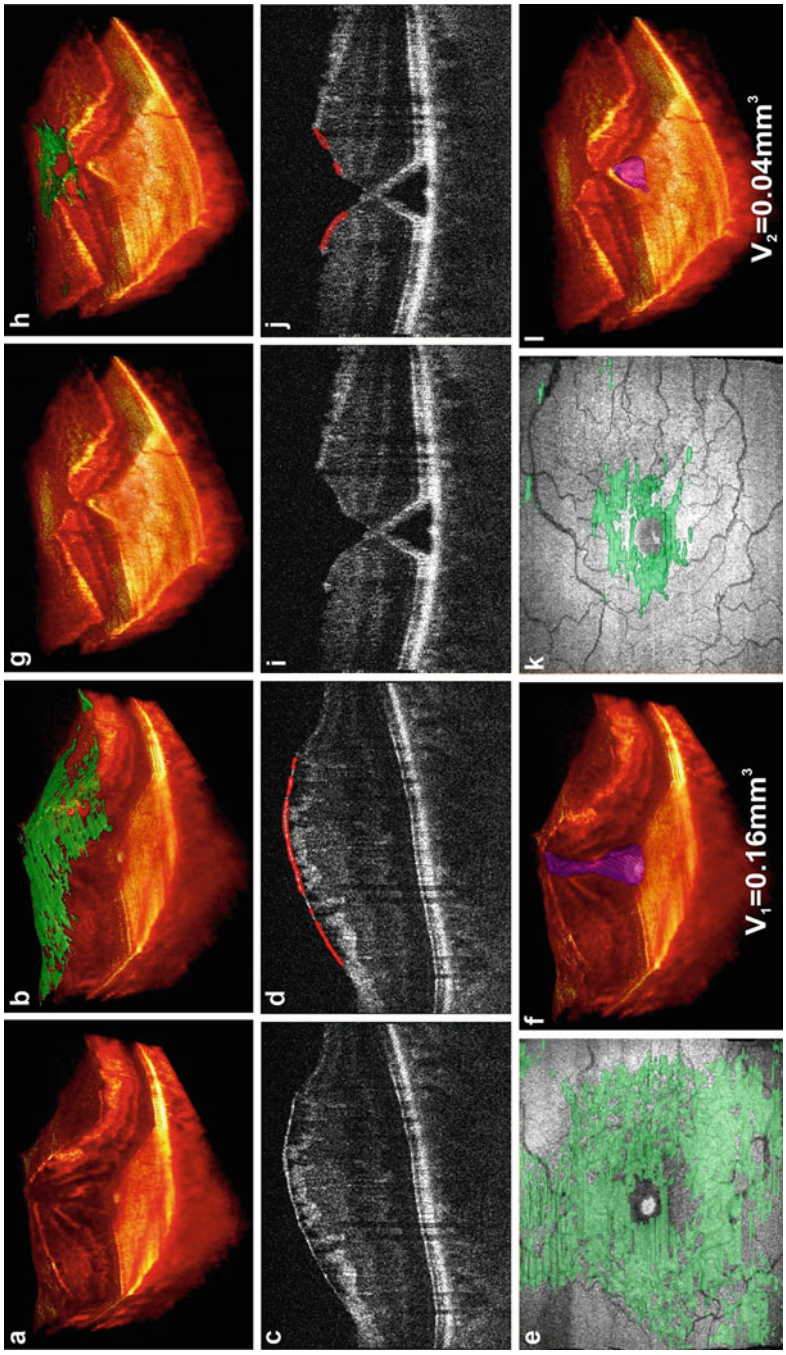

Fig. 56.31 Quantitative volumetric analysis using three-dimensional UHR OCT for quantitative therapy monitoring. Volumetric analysis of epiretinal membrane extent preoperatively (**b**, **d**, **e**) and postoperatively (**h**, **j**, **k**). Volumetric extent of a macular hole preoperatively (**a**, **c**, **f**) and postoperatively (**g**, **i**, **l**)

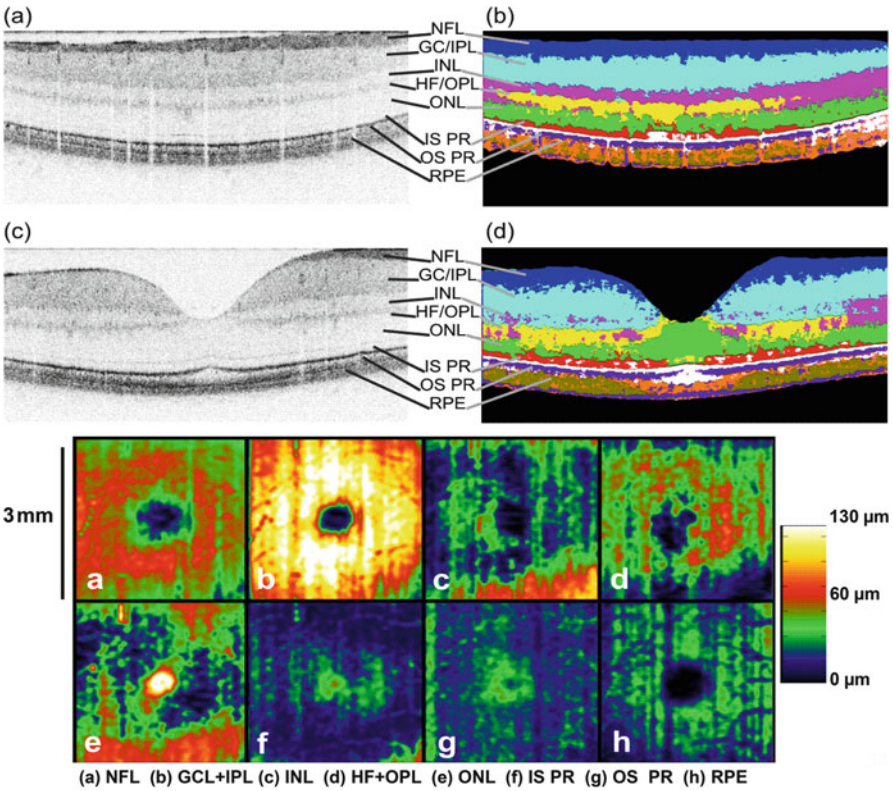

Fig. 56.32 Automatic texture-based segmentation algorithm. The original OCT images of a parafoveal tomogram (**a**, *top*) and a tomogram of the fovea centralis (**b** – *top*) show all the major retinal layers. The corresponding segmented images demonstrate applicability of the algorithm both for parafoveal (**c** – *top*) and central foveal (**d** – *top*) images. Thickness maps for the major retinal layers created from a 3D dataset of OCT images taken around the fovea centralis (developed in collaboration with G. Powell, P. Rosin, D. Marshall, School of Computer Sciences, Cardiff University, UK). (**a** – *bottom*) NFL (**b** – *bottom*) GCL/IPL (**c** – *bottom*) INL (**d** – *bottom*) HF/OPL (**e** – *bottom*) ONL (**f** – *bottom*) IS PR (**g** – *bottom*) OS PR (**h** – *bottom*) RPE

a single flash of white light, and UHR OCT data was acquired synchronously with ERG recordings. The OCT light source was a state-of-the-art broadband fiber laser operating at 1,250 nm with a 150 nm bandwidth, yielding a 4–5 µm axial image resolution in the retina. A long wavelength light source was chosen in order to avoid pre-stimulation of the dark-adapted retinas during the optical recordings. This light source is not suitable for in vivo human optophysiology measurements, because this wavelength is absorbed by water and the signal would be attenuated in ocular media.

During the functional experiments, the isolated retinas were stimulated with single, 200 ms long, white-light flashes (cf. Fig. 56.34). The time course of the light stimulus consisted of ∼2–3 s pre-stimulation and 4–6 s post-stimulation periods. Multiple UHR OCT depth reflectivity profiles (A-scans) were acquired at one

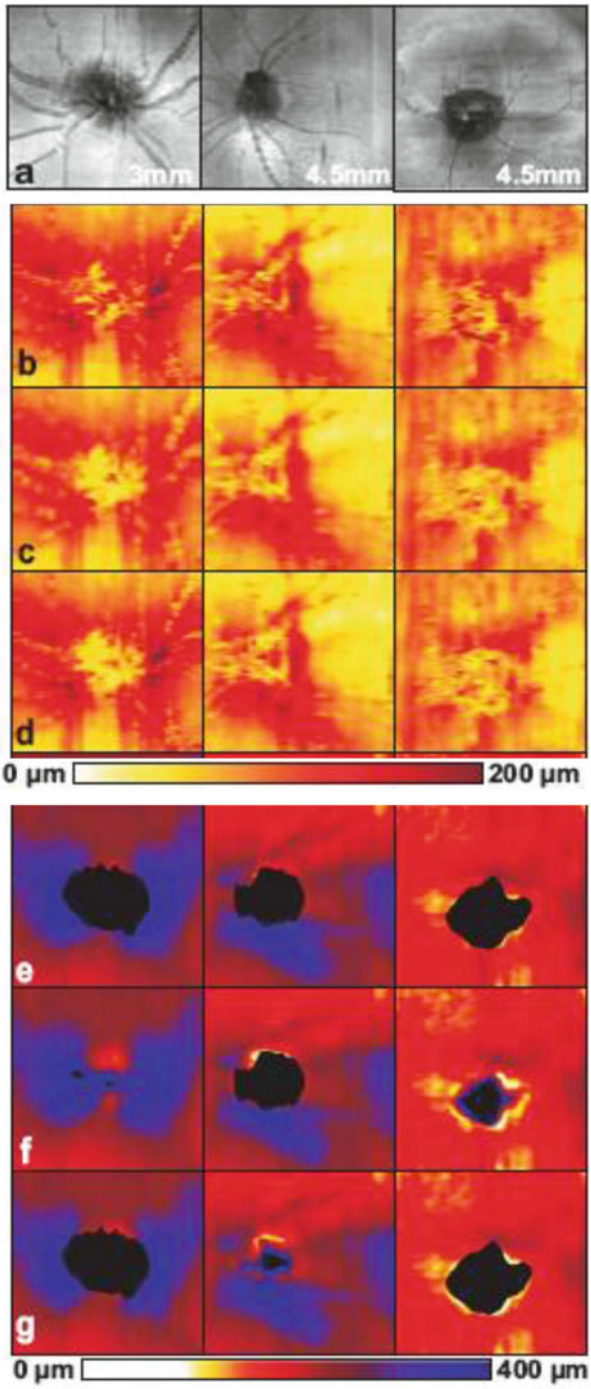

Fig. 56.33 Objective imaging parameters for glaucoma diagnosis using three-dimensional UHR OCT: two-dimensional views of retinal maps for normal (*left* in each row, transversal scanning range, 3 mm) intermediate glaucoma (*middle* in each row 4.5 mm transversal scanning range) and advanced glaucoma (*right* in each row 4.5 mm transverse scanning range). Nerve fiber layer and retinal thickness are color-coded. reconstructed fundus image at 800 nm (**a**), standard mapping of the nerve fiber layer NFL thickness (**b**), minimum distance map (*MDM*) of the NFL calculated for every point on the ILM (**c**), NFL-MDM at the *bottom* of the NFL (**d**), projected retinal thickness map (**e**), retinal thickness MDM measured from the ILM (**f**), and retinal thickness MDM at retinal pigment epithelium (RPE – **g**)

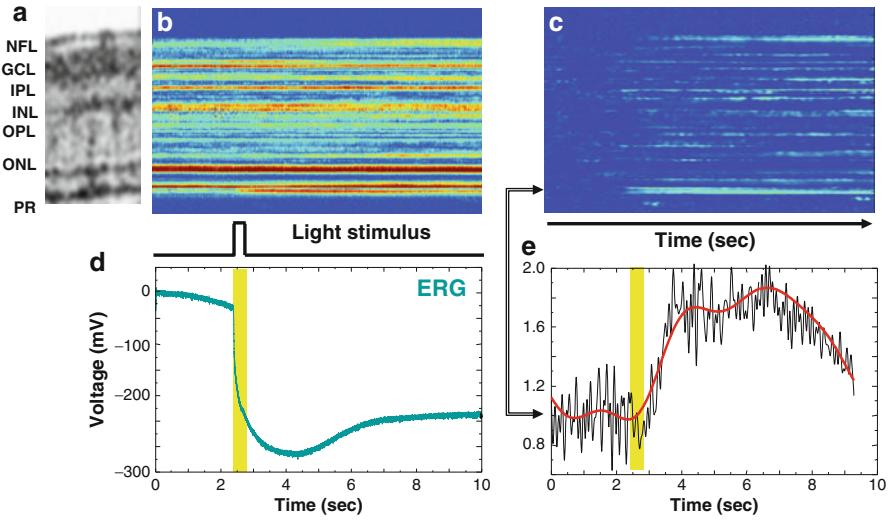

Fig. 56.34 Noninvasive, depth-resolved retinal physiology – in vitro optophysiology using functional OCT. In vitro UHR OCT of the rabbit retina (**a**). Raw (**b**) and differential (**c**, normalized by the background) optophysiological M-scans acquired during single flash stimulation (ERG and stimulus depicted in **d**). The change in the retinal optical backscattering (at a location corresponding to the outer segment of the photoreceptor layer) as a function of time is presented in (**e**), where the *yellow* boxes mark the time duration of the light stimulus

transverse location in the retina, synchronously with ERG recordings. The UHR OCT A-scans were combined to form a two-dimensional, raw data M-scan showing the retina reflectivity profile as a function of time (cf. Fig. 56.34b; procedure similar to M mode scanning in ultrasound imaging). The processing of the optical data involved application of a cross-correlation algorithm to account for any movement of the retina caused by the solution flow, calculation of the optical background (average over the pre-stimulation A-scans of each M-scan), and generation of differential M-scans (cf. Fig. 56.34 $\Delta I/I$, where I is the total optical signal and ΔI is the difference between the total signal and the average optical background determined from the pre-stimulation A-scans) of the raw data M-scans (cf. Fig. 56.34). The effect of fast variations in the optical speckle pattern detected by functional UHR OCT was minimized by applying a time-frequency filtering analysis.

Figure 56.34 shows an OCT retinal image of the rabbit retina (A), demonstrating that UHR OCT is capable of visualizing all major retinal layers. This morphological OCT image, acquired in the vicinity of the location where functional OCT data was recorded, is compared with a representative raw (B) and differential (C) M-scans acquired during single flash stimulation (ERG and stimulus depicted in Fig. 56.34). This comparison is essential to establish the morphological and possibly the physiological origins of any changes in the recorded optical signal, which was observed in the differential M-scan. Figure 56.34 shows a representative single

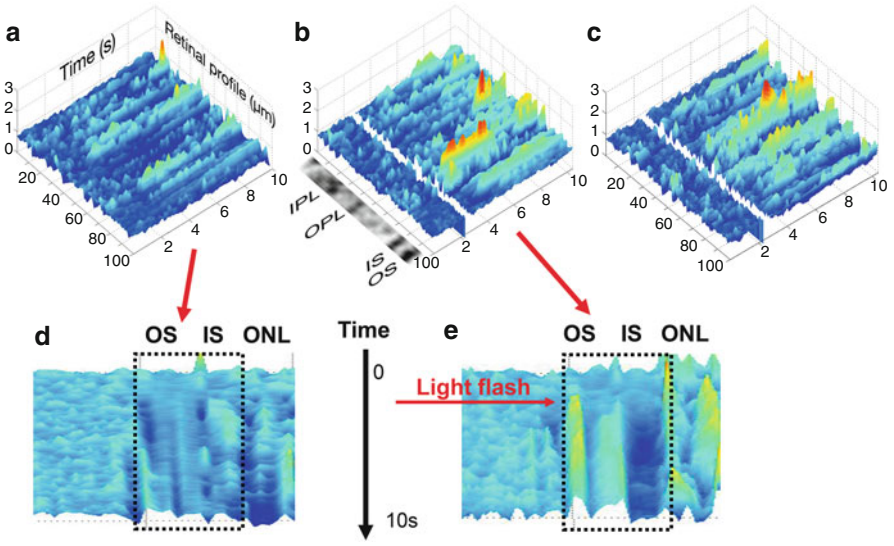

Fig. 56.35 Noninvasive, depth-resolved retinal physiology – in vitro optophysiology using functional OCT. Differential M-scans in 3D for better visualization of the time course and the magnitude of the observed positive and negative optical changes acquired during dark scan (**a**; *DS*), single flash stimulus (**b**; *SF*), and SF + photoreceptor inhibition (**c**). As expected, during DS (no light stimulus) the optical reflectivity of the PR layer did not change significantly with time. In the first and second type of experiments during SF recordings conducted in normal dark-adapted retinas, the reflectivity of the IS and OS of the PR layer exhibited significant negative and positive changes, respectively, after application of the light stimulus. In the case of KCl-inhibited PR function, the optical changes observed in the IS and OS of the PR layer appeared close to the optical background level and showed no correlation to the onset of the light stimulus. Comparison of optophysiological signals in 3D for DS and SF is depicted for more clarity in (**d**, **e**)

flash stimulus differential M-scan. The change in the retina optical backscattering (at a location corresponding to the outer segment of the photoreceptor layer (PR)) as a function of time is presented in Fig. 56.34, where yellow boxes mark the time duration of the light stimulus. The signal exhibits a rapid increase in optical backscattering, beginning simultaneously with the flash and then slowly returning to baseline. Similarly, though opposite in sign, changes are observed in the ERG recording (cf. Fig. 56.34d).

Figure 56.35a–c compare differential M-scans in 3D for better visualization of the time course and the magnitude of the observed positive and negative optical changes acquired during the dark scan (DS, no light stimulus), single flash stimulus (SF), and SF + photoreceptor inhibition. As expected during the dark scan, the optical reflectivity of the PR layer did not change significantly with time. In the first and second type of experiments during single flash stimulus recordings conducted

in normal dark-adapted retinas, the reflectivity of the IS and OS of the PR layer exhibited significant negative and positive changes, respectively, after application of the light stimulus. The onset of the optical signals correlated well with the onset of the light flash. Potassium chloride (KCl) was used to inhibit photoreceptor function, and the optical changes observed in the IS and OS of the PR layer appeared close to the optical background level and showed no correlation to the onset of the light stimulus. The comparison of optophysiological signals in 3D for dark scan and single flash stimulus is also depicted for more clarity in Fig. 56.35e. It is well known from physiology that action potentials induce depolarization in the cell membranes as well as cell size changes that might be detected not only by visualization of morphologic changes using UHR OCT but also by spatially resolved changes in backscattering over time. The exact origin of the optophysiologic signals is still not clear, but it might be related to the dipole reorientation (and, therefore, refractive index changes) at the photoreceptor membrane, light-induced isomerization of rhodopsin in the outer photoreceptor segment, or metabolic changes in the mitochondria of the inner photoreceptor segments.

Noninvasive in vivo functional optical imaging of the intact rat retina was recently demonstrated by using high-speed, UHR OCT with spectral/Fourier domain detection [95]. Imaging was performed with 2.8 μm axial image resolution at a rate of 24,000 A-scans/s in a Long–Evans rat. The advantage of using speed imaging is that it enables signal averaging which reduces the effects of noise from eye motion. A white-light stimulus (1.3 s) was applied to the dark-adapted rat retina, and the average reflectivities from different intraretinal layers were measured as a function of time (cf. Fig. 56.36). During each recording, a 160 × 160 mm^2 (64 × 64 pixels) area of the retina, corresponding to a volume data set, was measured within 162 ms, thus resulting in 6.2 volumes/s acquisition (cf. Fig. 56.36). Figure 56.36 shows an example of a single cross-sectional image. Figure 56.36d is obtained by averaging the photoreceptor outer segment reflectance from one volume. The physiologic noise from the baseline recording had a standard deviation of ∼1 %. A white-light stimulus induced an increase in backscattering of ∼12 %. The spatial distribution of the change in the OCT signal was consistent with an increase in backscatter from the photoreceptor outer segments. This demonstrates the ability to perform functional OCT imaging in the intact retina.

These results are preliminary, but they demonstrate the fundamental concepts of optophysiology. Further research and investigation is required; however, the ultimate goal is to develop an imaging technology that integrates structural and functional imaging at the level of retinal architectural morphology. Signal levels are very small and physiological noise as well as motion artifacts will be complicating factors. However, if these challenges can be overcome, then it will become possible to noninvasively visualize functional activation of the photoreceptors as well as neural transduction through individual retinal layers. Optophysiology remains an ambitious goal, but would have a profound impact on fundamental research as well as clinical diagnosis.

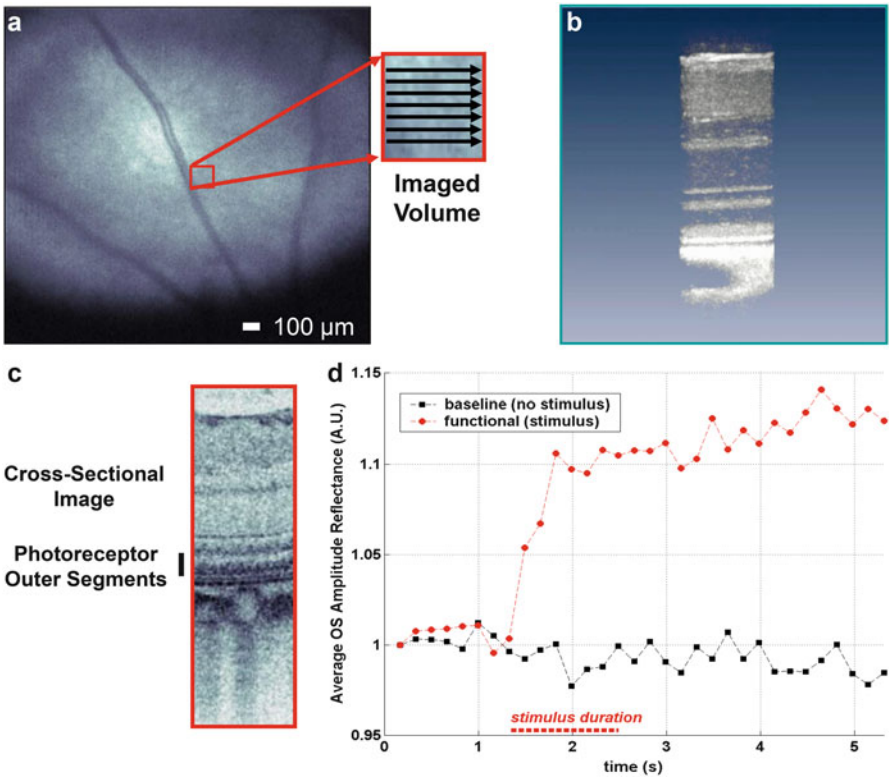

Fig. 56.36 Noninvasive, depth-resolved retinal physiology – in vivo optophysiology using functional OCT in the rat retina. A raster scan pattern is used to measure a volume of the retina as a function of time, each recording is a 160 × 160 µm area (64 × 64 pixels) transverse region, resulting in a 162 ms time resolution and 6.2 volumes/s (**a**). Functional measurements are performed by averaging the photoreceptor outer segment reflectance from one volume versus time (**b**, **c**). The physiologic noise from the baseline recording has a standard deviation of ∼1 %, while a *white*-light stimulus induces an increase in backscattering of ∼12 % (**d**)

56.8 Conclusion

The eye is an essentially transparent medium transmitting light with minimal optical attenuation and scattering and providing easy optical access to the anterior segment as well as the retina. Furthermore, ophthalmology, as a clinical specialty, has historically been open to new optical technologies. There is a wide spectrum of disease that can be diagnosed or monitored using retinal imaging. Therefore, ophthalmology was, and will continue to be, the dominant clinical specialty where new technological developments in OCT are applied.

Modern clinical practice requires the development of techniques to diagnose disease in its early stages, when treatment is most effective and irreversible damage can be prevented or postponed. OCT will play a powerful role in clinical ophthalmology because it enables structural imaging of the retina with resolutions higher than any other noninvasive imaging modality. The development of 3D-OCT imaging dramatically enhances the amount and quality of structural information available, promising to enable the development of a wide range of new markers for disease diagnoses and progression in the future. Diseases such as age-related macular degeneration are currently the subject of intense investigation, both to identify treatment criteria for anti-angiogenesis therapies as well as to identify structural markers that can predict disease progression from dry to wet phases.

High-speed 3D-OCT using spectral/Fourier domain detection methods promises to enable a wide range of new applications that could not have been foreseen in the past. One key issue that has emerged as a challenging, new area of research is how to effectively process and display 3D-OCT data for clinical applications. Modern OCT systems generate massive data sets that are equivalent to hundreds of individual OCT images. Although individual OCT images can be precisely registered to fundus features by using OCT fundus imaging, it is impractical to review all of these cross-sectional images one by one to identify pathology. Intelligent algorithms and image processing methods, therefore, play an increasing role in clinical diagnosis. Image processing for quantitative measurement, or morphometry, will be especially important for clinical applications. These techniques have the powerful advantage of condensing image information into a form that can be compared to populational norms for the diagnosis of disease or monitoring disease progression.

Current commercial OCT instruments have an improved axial image resolution of 5–7 μm, compared with earlier generations of OCT with 8–10 μm resolution. However, commercial instruments still have not reached the level of ultrahigh resolution (2–3 μm), which has been achieved in research prototype instruments. Although broadband superluminescent diode light source technology is improving and yielding better resolutions at lower cost, its price is still prohibitive for widespread clinical use. Furthermore, it is important to point out that spectral/Fourier domain detection has a trade-off between axial resolution and imaging depth. As noted previously, limitations in the size of available CCD line scan cameras mean that achieving 3 μm resolution results in a 1.5 mm imaging depth range. This makes an ultrahigh-resolution OCT instrument sensitive to alignment and difficult to use in general clinical practice. As improved CCD cameras become available and the cost of broadband light source technology continues to decrease, three-dimensional UHR OCT imaging will become increasingly available. Swept source/Fourier domain detection techniques promise to overcome many of the limitations inherent in spectral/Fourier domain detection techniques, but this area of investigation is still in its early stages.

Small animal imaging removes many of the constraints inherent in clinical imaging of human subjects. Therefore, ultrahigh-resolution OCT and AO techniques promise to play an increasingly important role in this area. As noted

previously, OCT enables repeated imaging on the same animal without the need for sacrifice. This capability will dramatically improve the efficiency of drug development and validation, since the role of biological variability is reduced and significantly fewer animals are needed for studies.

Perhaps one of the most promising areas of investigation is functional OCT imaging. Techniques such as Doppler flow, polarization-sensitive OCT (PS OCT), or depth-resolved functional imaging promise to integrate structural and functional information into a single measurement. Many advances in OCT technology, data analysis, and image processing techniques remain to be developed in this area. Functional imaging promises to take OCT to the next level. Doppler OCT enables identification of vasculature, and combined with high-speed 3D-OCT, quantitative mapping of the vascular network should ultimately be possible. Techniques such as PS OCT can provide information about architectural and cellular organization of retinal nerve fibers, whose changes in structure may be the earliest markers of atrophy, before thinning of the nerve fiber layer occurs. Finally, OCT optophysiology promises to enable imaging of neural activation on the level of individual retinal layers and, perhaps ultimately, by combining ultrahigh-resolution and AO OCT techniques, on the level of individual ganglion cells. Much more work must be done, but OCT holds the promise for continuing advances in fundamental research and improvements in clinical care for many years into the future.

Acknowledgements The authors would like to thank B. Herrmann, B. Hofer, and J.E. Morgan from the School of Optometry and Vision Science, Cardiff University; A.F. Fercher, R. Leitgeb, L. Schachinger, and H. Sattmann from the Center of Biomedical Engineering and Physics, Medical University Vienna, Austria; K. Bizheva from the University of Waterloo, Canada; and A. Stingl and T. Le from Femtolasers Produktions GmbH, Vienna, Austria.

The authors would also like to thank Desmond Adler, Iwona Gorczynska, Robert Huber, Tony Ko, Jonathan Liu, Vivek Srinivasan, and Maciej Wojtkowski from the Department of Electrical Engineering and Computer Science at the Massachusetts Institute of Technology; Jay S. Duker, Royce Chen, Caroline Baumal, Janice Lem, Brian Monson, Elias Reichel, Adam Rogers, and Andre J. Witkin from the New England Eye Center, Tufts–New England Medical Center, Tufts University; Joel S. Schuman, Michelle Gabriele Larry Kagemann, Gadi Wollstein, and Hiroshi Ishikawa from the UPMC Eye Center, Department of Ophthalmology, Eye and Ear Institute, University of Pittsburgh School of Medicine; Allen Clermont and Sven-Erik Bursell from the Beetham Eye Institute, Joslin Diabetes Center, Harvard Medical School, Boston; Andrzej Kowalczyk from the Institute of Physics, Nicolaus Copernicus University, Torun, Poland; and Vladimir Shidlovski and Sergei Yakubovich from Superlum Diodes, Ltd. We would also like to thank Dorothy Fleischer for her assistance in editing this chapter.

Financial support is acknowledged to Cardiff University, FP6-IST-NMP-2 STREPT (017128), the Christian Doppler Society, NP Photonics (Arizona, US), FEMTOLASERS GmbH (Vienna, Austria), Carl Zeiss Meditec Inc. (Dublin, CA, USA), Maxon Computer GmbH (Friedrichsdorf, Germany). FWF P14218-PSY, FWF Y 159, CRAF-1999-70549, Österreichische Nationalbank, Christian Doppler Gesellschaft, FEMTOLASERS Produktions GmbH, Carl Zeiss Meditec Inc.

This research was also supported at M.I.T. by the Air Force Office of Scientific Research and Medical Free Electron Laser Program FA9550-040-1-0046 and FA9550-040-1-0011, National Institutes of Health R01-EY011289-21 and R01-CA75289-10, and National Science Foundation ECS-0501478 and BES-0522845.

References

1. T. Olsen, The accuracy of ultrasonic determination of axial length in pseudophakic eyes. Acta Ophthalmol. Scand. **67**, 141–144 (1990)
2. J.C. Bamber, M. Trstam, Diagnostic ultrasound, in *The Physics of Medical Imaging*, ed. by S. Webb (Adam Hilger, Bristol, 1988), pp. 319–388
3. J.C. Pavlin, J.A. McWhae, H.D. McGowan, F.S. Foster, Ultrasound biomicroscopy of anterior segment tumors. Ophthalmology **99**, 1220–1228 (1992)
4. D.Z. Reinstein, R.H. Silverman, M.J. Rondeau, D.J. Coleman, Epithelial and corneal thickness measurements by high-frequency ultrasound digital signal processing. Ophthalmology **101**(1), 140–146 (1994)
5. R.H. Webb, G.W. Hughes, F.C. Delori, Confocal scanning laser ophthalmoscope. Appl. Opt. **26**, 1492–1499 (1987)
6. R.H. Webb, Flying spot TV ophthalmoscope. Appl. Opt. **19**, 2991–2997 (1979)
7. J. F. Bille, A. W. Dreher, G. Zinser, Scanning laser tomography of the living human eye. in *Noninvasive Diagnostic Techniques in Ophthalmology*, ed by B. R. Master (1990), Springer, New York, NY, pp. 528–547.
8. A.F. Fercher, E. Roth, Ophthalmic laser interferometer. Proc. SPIE **658**, 48–51 (1986)
9. J.G. Fujimoto, S. De Silvestri, E.P. Ippen, C.A. Puliafito, R. Marglois, A. Oseroff, Femtosecond optical ranging in biological systems. Opt. Lett. **11**, 150–152 (1986)
10. A.F. Fercher, K. Mengedoht, W. Werner, Eye length measurement by interferometer with partially coherent light. Opt. Lett. **13**, 186–188 (1988)
11. D. Huang, E.A. Swanson, C.P. Lin et al., Optical coherence tomography. Science **254**(5035), 1178–1181 (1991)
12. E.A. Swanson, J.A. Izatt, M.R. Hee et al., In-vivo retinal imaging by optical coherence tomography. Opt. Lett. **18**(21), 1864–1866 (1993)
13. A.F. Fercher, C.K. Hitzenberger, W. Drexler, G. Kamp, H. Sattmann, In-vivo optical coherence tomography. Am. J. Ophthalmol. **116**(1), 113–115 (1993)
14. J.G. Fujimoto, M.E. Brezinski, G.J. Tearney et al., Optical biopsy and imaging using optical coherence tomography. Nat. Med. **1**(9), 970–972 (1995)
15. A.F. Fercher, Optical coherence tomography. J. Biomed. Opt. **1**, 157–173 (1996)
16. J.G. Fujimoto, Optical coherence tomography for ultrahigh resolution in vivo imaging. Nat. Biotechnol. **21**(11), 1361–1367 (2003)
17. M.R. Hee, J.A. Izatt, E.A. Swanson et al., Optical coherence tomography of the human retina. Arch. Ophthalmol. **113**(3), 325–332 (1995)
18. C. A. Puliafito, M. R. Hee, J. S. Schuman, J. G. Fujimoto, Optical coherence tomography of ocular disease. (1995). Slack Inc, Thorofare, New Jersey
19. M.R. Hee, C.A. Puliafito, C. Wong et al., Cross-sectional imaging of macular holes and vitreomacular traction with Optical Coherence Tomography (Oct). Invest. Ophthalmol. Vis. Sci. **36**(4), S207–S (1995)
20. M.R. Hee, C.A. Puliafito, C. Wong et al., Quantitative assessment of macular edema with optical coherence tomography. Arch. Ophthalmol. **113**(8), 1019–1029 (1995)
21. M.R. Hee, C.A. Puliafito, C. Wong et al., Optical coherence tomography of central serous chorioretinopathy. Am. J. Ophthalmol. **120**(1), 65–74 (1995)
22. J.S. Schuman, M.R. Hee, C.A. Puliafito et al., Quantification of nerve-fiber layer thickness in normal and glaucomatous eyes using optical coherence tomography – a Pilot-Study. Arch. Ophthalmol. **113**(5), 586–596 (1995)
23. J.S. Schuman, T. PedutKloizman, E. Hertzmark et al., Reproducibility of nerve fiber layer thickness measurements using optical coherence tomography. Ophthalmology **103**(11), 1889–1898 (1996)
24. M.R. Hee, C.A. Puliafito, J.S. Duker et al., Topography of diabetic macular edema with optical coherence tomography. Ophthalmology **105**(2), 360–370 (1998)

25. R. Brancato, Optical coherence tomography (OCT) in macular edema. Doc. Ophthalmol. **97**(3–4), 337–339 (1999)
26. A. Gaudric, B. Haouchine, P. Massin, M. Paques, P. Blain, A. Erginay, Macular hole formation – New data provided by optical coherence tomography. Arch. Ophthalmol. **117**(6), 744–751 (1999)
27. M.E. Pons, R. Gurses-Ozden, H. Ishikawa, H.L. Dou, J.M. Liebmann, R. Ritch, Assessment of retinal nerve fiber layer (RNFL) internal reflectivity using optical coherence tomography (OCT). Invest. Ophthalmol. Vis. Sci. **40**(4), S839-S (1999)
28. D.S. Chauhan, R.J. Antcliff, P.A. Rai, T.H. Williamson, J. Marshall, Papillofoveal traction in macular hole formation – The role of optical coherence tomography. Arch. Ophthalmol. **118**(1), 32–38 (2000)
29. P. Massin, C. Allouch, B. Haouchine et al., Optical coherence tomography of idiopathic macular epiretinal membranes before and after surgery. Am. J. Ophthalmol. **130**(6), 732–739 (2000)
30. C. Bowd, L.M. Zangwill, C.C. Berry et al., Detecting early glaucoma by assessment of retinal nerve fiber layer thickness and visual function. Invest. Ophthalmol. Vis. Sci. **42**(9), 1993–2003 (2001)
31. C. Sanchez-Galeana, C. Bowd, E.Z. Blumenthal, P.A. Gokhale, L.M. Zangwill, R.N. Weinreb, Using optical imaging summary data to detect glaucoma. Ophthalmology **108**(10), 1812–1818 (2001)
32. H. Sanchez-Tocino, A. Alvarez-Vidal, M.J. Maldonado, J. Moreno-Montanes, A. Garcia-Layana, Retinal thickness study with optical coherence tomography in patients with diabetes. Invest. Ophthalmol. Vis. Sci. **43**(5), 1588–1594 (2002)
33. R.F. Spaide, Macular hole repair with minimal vitrectomy. Retin. J Retin. Vitreous Dis. **22**(2), 183–186 (2002)
34. S. Muscat, S. Parks, E. Kemp, D. Keating, Repeatability and reproducibility of macular thickness measurements with the Humphrey OCT system. Invest. Ophthalmol. Vis. Sci. **43**(2), 490–495 (2002)
35. R.F. Spaide, D. Wong, Y. Fisher, M. Goldbaum, Correlation of vitreous attachment and foveal deformation in early macular hole states. Am. J. Ophthalmol. **133**(2), 226–229 (2002)
36. C. Bowd, L.M. Zangwill, E.Z. Blumenthal et al., Imaging of the optic disc and retinal nerve fiber layer: the effects of age, optic disc area, refractive error, and gender. J. Opt. Soc. Am. a-Opt. Image Sci. Vis. **19**(1), 197–207 (2002)
37. J.S. Schuman, C.A. Puliafito, J.G. Fujimoto, *Optical Coherence Tomography of Ocular Disease* (Slack Inc, Thorofare, 2004)
38. W. Drexler, U. Morgner, F.X. Kartner et al., In vivo ultrahigh-resolution optical coherence tomography. Opt. Lett. **24**(17), 1221–1223 (1999)
39. W. Drexler, U. Morgner, R.K. Ghanta, F.X. Kartner, J.S. Schuman, J.G. Fujimoto, Ultrahigh-resolution ophthalmic optical coherence tomography. Nat. Med. **7**(4), 502–507 (2001)
40. W. Drexler, H. Sattmarin, B. Hermann et al., Enhanced visualization of macular pathology with the use of ultrahigh-resolution optical coherence tomography. Arch. Ophthalmol. **121**(5), 695–706 (2003)
41. W. Drexler, Ultrahigh-resolution optical coherence tomography. J. Biomed. Opt. **9**(1), 47–74 (2004)
42. T.H. Ko, J.G. Fujimoto, J.S. Duker et al., Comparison of ultrahigh- and standard-resolution optical coherence tomography for imaging macular hole pathology and repair. Ophthalmology **111**(11), 2033–2043 (2004)
43. E. Ergun, B. Hermann, M. Wirtitsch et al., Assessment of central visual function in Stargardt's disease/fundus flavimaculatus with ultrahigh-resolution optical coherence tomography. Invest. Ophthalmol. Vis. Sci. **46**(1), 310–316 (2005)
44. G. Wollstein, L.A. Paunescu, T.H. Ko et al., Ultrahigh-resolution optical coherence tomography in glaucoma. Ophthalmology **112**(2), 229–237 (2005)

45. T.H. Ko, J.G. Fujimoto, J.S. Schuman et al., Comparison of ultrahigh- and standard-resolution optical coherence tomography for imaging macular pathology. Ophthalmology **112**(11), 1922 (2005)
46. M.G. Wirtitsch, E. Ergun, B. Hermann et al., Ultrahigh resolution optical coherence tomography in macular dystrophy. Am. J. Ophthalmol. **140**(6), 976–983 (2005)
47. L.A. Paunescu, T.H. Ko, J.S. Duker et al., Idiopathic juxtafoveal retinal telangiectasis: new findings by ultrahigh-resolution optical coherence tomography. Ophthalmology **113**(1), 48–57 (2006)
48. T.H. Ko, A.J. Witkin, J.G. Fujimoto et al., Ultrahigh-resolution optical coherence tomography of surgically closed macular holes. Arch. Ophthalmol. **124**(6), 827–836 (2006)
49. C. Scholda, M. Wirtitsch, B. Hermann et al., Ultrahigh resolution optical coherence tomography of macular holes. Retina **26**(9), 1034–1041 (2006)
50. A.J. Witkin, T.H. Ko, J.G. Fujimoto et al., Ultra-high resolution optical coherence tomography assessment of photoreceptors in retinitis pigmentosa and related diseases. Am. J. Ophthalmol. **142**(6), 945–952 (2006)
51. M. Gloesmann, B. Hermann, C. Schubert, H. Sattmann, P.K. Ahnelt, W. Drexler, Histologic correlation of pig retina radial stratification with ultrahigh-resolution optical coherence tomography. Invest. Ophthalmol. Vis. Sci. **44**(4), 1696–1703 (2003)
52. E.M. Anger, A. Unterhuber, B. Hermann et al., Ultrahigh resolution optical coherence tomography of the monkey fovea. Identification of retinal sublayers by correlation with semithin histology sections. Exp. Eye Res. **78**(6), 1117–1125 (2004)
53. P.K. Ahnelt, W. Drexler, Comment on: ultrahigh resolution optical coherence tomography of the monkey fovea. Identification of retinal sublayers by correlation with semithin histology sections. Exp. Eye Res. **80**(3), 449–450 (2005). E.M. Anger et al. [Exp. Eye Res. 78 (2004) 1117–1125] by M.E.J. van velthoven and F.D. Verbraak
54. R.S. Ramrattan, T.L. van der Schaft, C.M. Mooy, W.C. de Bruijn, P.G. Mulder, P.T. de Jong, Morphometric analysis of Bruch's membrane, the choriocapillaris, and the choroid in aging. Invest. Ophthalmol. Vis. Sci. **35**(6), 2857–2864 (1994)
55. A. Okubo, R.H. Rosa Jr., C.V. Bunce et al., The relationships of age changes in retinal pigment epithelium and Bruch's membrane. Invest. Ophthalmol. Vis. Sci. **40**(2), 443–449 (1999)
56. A. Unterhuber, B. Povazay, B. Hermann et al., Compact, low-cost Ti: Al_2O_3 laser for in vivo ultrahigh-resolution optical coherence tomography. Opt. Lett. **28**(11), 905–907 (2003)
57. A.M. Rollins, M.D. Kulkarni, S. Yazdanfar, R. Ung-arunyawee, J.A. Izatt, In vivo video rate optical coherence tomography. Opt. Express **3**(6), 219–229 (1998)
58. A.G. Podoleanu, G.M. Dobre, D.A. Jackson, En-face coherence imaging using galvanometer scanner modulation. Opt. Lett. **23**(3), 147–149 (1998)
59. A.G. Podoleanu, M. Seeger, G.M. Dobre, D.J. Webb, D.A. Jackson, F. Fitzke, Transversal and longitudinal images from the retina of the living eye using low coherence reflectometry. J. Biomed. Opt. **3**, 12–20 (1998)
60. A.G. Podoleanu, J.A. Rogers, D.A. Jackson, Three dimensional OCT images from retina and skin. Opt. Express **7**(9), 292–298 (2000)
61. C.K. Hitzenberger, P. Trost, P.W. Lo, Q.Y. Zhou, Three-dimensional imaging of the human retina by high-speed optical coherence tomography. Opt. Express **11**(21), 2753–2761 (2003)
62. A.G. Podoleanu, G.M. Dobre, R.G. Cucu et al., Combined multiplanar optical coherence tomography and confocal scanning ophthalmoscopy. J. Biomed. Opt. **9**(1), 86–93 (2004)
63. G.M. Dobre, A.G. Podoleanu, R.B. Rosen, Simultaneous optical coherence tomography–Indocyanine Green dye fluorescence imaging system for investigations of the eye's fundus. Opt. Lett. **30**(1), 58–60 (2005)

64. R.G. Cucu, A.G. Podoleanu, J.A. Rogers, J. Pedro, R.B. Rosen, Combined confocal/en face T-scan-based ultrahigh-resolution optical coherence tomography in vivo retinal imaging. Opt. Lett. **31**(11), 1684–1686 (2006)
65. A.F. Fercher, C.K. Hitzenberger, G. Kamp, S.Y. El-Zaiat, Measurement of intraocular distances by backscattering spectral interferometry. Opt. Commun. **117**, 43–48 (1995)
66. B. Golubovic, B.E. Bouma, G.J. Tearney, J.G. Fujimoto, Optical frequency-domain reflectometry using rapid wavelength tuning of a Cr/sup 4+/: forsterite laser. Opt. Lett. **22**(22), 1704–1706 (1997)
67. F. Lexer, C.K. Hitzenberger, A.F. Fercher, M. Kulhavy, Wavelength-tuning interferometry of intraocular distances. Appl. Opt. **36**(25), 6548–6562 (1997)
68. G. Häusler, M.W. Lindner, Coherence Radar and Spectral Radar – new tools for dermatological diagnosis. J. Biomed. Opt. **3**, 21–31 (1998)
69. R. Leitgeb, C.K. Hitzenberger, A.F. Fercher, Performance of fourier domain vs. time domain optical coherence tomography. Opt. Express **11**(8), 889–894 (2003)
70. M.A. Choma, M.V. Sarunic, C.H. Yang, J.A. Izatt, Sensitivity advantage of swept source and Fourier domain optical coherence tomography. Opt. Express **11**(18), 2183–2189 (2003)
71. J.F. de Boer, B. Cense, B.H. Park, M.C. Pierce, G.J. Tearney, B.E. Bouma, Improved signal-to-noise ratio in spectral-domain compared with time-domain optical coherence tomography. Opt. Lett. **28**(21), 2067–2069 (2003)
72. M. Wojtkowski, R. Leitgeb, A. Kowalczyk, T. Bajraszewski, A.F. Fercher, In vivo human retinal imaging by Fourier domain optical coherence tomography. J. Biomed. Opt. **7**(3), 457–463 (2002)
73. S.H. Yun, G.J. Tearney, J.F. de Boer, N. Iftimia, B.E. Bouma, High-speed optical frequency-domain imaging. Opt. Express **11**(22), 2953–2963 (2003)
74. N. Nassif, B. Cense, B.H. Park et al., In vivo human retinal imaging by ultrahigh-speed spectral domain optical coherence tomography. Opt. Lett. **29**(5), 480–482 (2004)
75. R.A. Leitgeb, W. Drexler, A. Unterhuber et al., Ultrahigh resolution Fourier domain optical coherence tomography. Opt. Express **12**(10), 2156–2165 (2004)
76. M. Wojtkowski, V.J. Srinivasan, T.H. Ko, J.G. Fujimoto, A. Kowalczyk, J.S. Duker, Ultrahigh-resolution, high-speed, Fourier domain optical coherence tomography and methods for dispersion compensation. Opt. Express **12**(11), 2404–2422 (2004)
77. B. Cense, N.A. Nassif, T. Chen et al., Ultrahigh-resolution high-speed retinal imaging using spectral-domain optical coherence tomography. Opt. Express **12**(11), 2435–2447 (2004)
78. R.A. Leitgeb, L. Schmetterer, W. Drexler, A.F. Fercher, R.J. Zawadzki, T. Bajraszewski, Real-time assessment of retinal blood flow with ultrafast acquisition by color Doppler Fourier domain optical coherence tomography. Opt. Express **11**(23), 3116–3121 (2003)
79. B.R. White, M.C. Pierce, N. Nassif et al., In vivo dynamic human retinal blood flow imaging using ultra-high-speed spectral domain optical Doppler tomography. Opt. Express **11**(25), 3490–3497 (2003)
80. M. Wojtkowski, A. Kowalczyk, R. Leitgeb, A.F. Fercher, Full range complex spectral optical coherence tomography technique in eye imaging. Opt. Lett. **27**(16), 1415–1417 (2002)
81. R. Leitgeb, T. Bajraszewski, C.K. Hitzenberger, A.F. Fercher, Novel phase-shifting algorithm to achieve high-speed long-depth range probing by frequency domain optical coherence tomography. Proc. SPIE Int. Soc. Opt. Eng. **4956**, 101–108 (2003)
82. R.A. Leitgeb, C.K. Hitzenberger, A.F. Fercher, T. Bajraszewski, Phase-shifting algorithm to achieve high-speed long-depth-range probing by frequency-domain optical coherence tomography. Opt. Lett. **28**(22), 2201–2203 (2003)
83. M.A. Choma, C.H. Yang, J.A. Izatt, Instantaneous quadrature low-coherence interferometry with 3×3 fiber-optic couplers. Opt. Lett. **28**(22), 2162–2164 (2003)
84. V.J. Srinivasan, M. Wojtkowski, A.J. Witkin et al., High-definition and 3-dimensional imaging of macular pathologies with high-speed ultrahigh-resolution optical coherence tomography. Ophthalmology **113**(11), 2054 e1–14 (2006)

85. U. Schmidt-Erfurth, R.A. Leitgeb, S. Michels et al., Three-dimensional ultrahigh-resolution optical coherence tomography of macular diseases. Invest. Ophthalmol. Vis. Sci. **46**(9), 3393–3402 (2005)
86. B.K. Monson, P.B. Greenberg, E. Greenberg, J.G. Fujimoto, V.J. Srinivasan, J.S. Duker, High-speed, ultra-high-resolution optical coherence tomography of acute macular neuroretinopathy. Br. J. Ophthalmol. **91**(1), 119–120 (2007)
87. G. Karan, C. Lillo, Z. Yang et al., Lipofuscin accumulation, abnormal electrophysiology, and photoreceptor degeneration in mutant ELOVL4 transgenic mice: a model for macular degeneration. Proc. Natl. Acad. Sci. U. S. A. **102**(11), 4164–4169 (2005)
88. J. Ambati, A. Anand, S. Fernandez et al., An animal model of age-related macular degeneration in senescent Ccl-2- or Ccr-2-deficient mice. Nat. Med. **9**(11), 1390–1397 (2003)
89. V.J. Srinivasan, T.H. Ko, M. Wojtkowski et al., Noninvasive volumetric imaging and morphometry of the rodent retina with high-speed, ultrahigh-resolution optical coherence tomography. Invest. Ophthalmol. Vis. Sci. **47**(12), 5522–5528 (2006)
90. D.C. Fernandez, H.M. Salinas, C.A. Puliafito, Automated detection of retinal layer structures on optical coherence tomography images. Opt. Express **13**(25), 10200–10216 (2005)
91. M. Mujat, R.C. Chan, B. Cense et al., Retinal nerve fiber layer thickness map determined from optical coherence tomography images. Opt. Express **13**(23), 9480–9491 (2005)
92. D. Koozekanani, K. Boyer, C. Roberts, Retinal thickness measurements from optical coherence tomography using a Markov boundary model. IEEE Trans. Med. Imaging **20**(9), 900–916 (2001)
93. H.P. Scholl, E. Zrenner, Electrophysiology in the investigation of acquired retinal disorders. Surv. Ophthalmol. **45**(1), 29–47 (2000)
94. K. Bizheva, R. Pflug, B. Hermann et al., Optophysiology: depth-resolved probing of retinal physiology with functional ultrahigh-resolution optical coherence tomography. Proc. Natl. Acad. Sci. U. S. A. **103**(13), 5066–5071 (2006)
95. V.J. Srinivasan, M. Wojtkowski, J.G. Fujimoto, J.S. Duker, In vivo measurement of retinal physiology with high-speed ultrahigh-resolution optical coherence tomography. Opt. Lett. **31**(15), 2308–2310 (2006)

OCT Imaging in Glaucoma

57

Jessica E. Nevins, Gadi Wollstein, and Joel S. Schuman

Keywords
Ganglion cell layer • Glaucoma • Macula • Retinal nerve fiber layer (RNFL)

57.1 Glaucoma

Glaucoma is the second leading cause of irreversible blindness worldwide, and estimates put the total number of suspected cases of glaucoma at over 60 million worldwide [1]. The severity of the disease varies among ethnic groups with African-Americans 15 times more likely to be visually impaired and six to eight times more likely to be blinded by glaucoma compared to Caucasians [2, 3].

Glaucoma is characterized by optic neuropathy and progressive loss of retinal ganglion cells (RGCs) and their axons, which comprise the retinal nerve fiber layer (RNFL), with associated visual function loss [1, 4]. The structural loss of the optic nerve head is most easily seen in the superior and inferior poles [5]. Functional loss refers primarily to the presence of a characteristic visual field defect, particularly when locations are clustered and reproducibly present [5]. While the relationship between structure and function is a source of debate, it has been suggested that structural loss often precedes functional loss [6].

57.1.1 Glaucoma Risk Factors and Disease Spectrum

The cause of glaucoma is unknown; however, there are some risk factors associated with the disease. The main risk factor is elevated intraocular pressure (IOP).

J.E. Nevins (✉) • G. Wollstein • J.S. Schuman
UPMC Eye Center, Eye and Ear Institute, Ophthalmology and Visual Science Research Center, Department of Ophthalmology, University of Pittsburgh School of Medicine, Pittsburgh, PA, USA
e-mail: jenev37@gmail.com

© Springer International Publishing Switzerland 2015

W. Drexler, J.G. Fujimoto (eds.), *Optical Coherence Tomography*,
DOI 10.1007/978-3-319-06419-2_59

A normal range of IOP is between 10 and 21 mmHg. Other risk factors include, but are not limited to, family history of glaucoma, ethnic background, and older age [7].

Glaucoma is a family of eye diseases, and there are different classifications of the disease with different signs and symptoms. Primary closed-angle glaucoma is characterized by the contact of the iris and trabecular meshwork. This physical contact disrupts the trabecular meshwork from acting out its function, which is to drain the aqueous humor. When the drainage cannot keep up with the production, the pressure in the eye is increased. In some cases, this increase in pressure is rapid and is paired with pain, redness, and reduced vision. However, in other cases, the pressure elevation is gradual and milder, and the patients are asymptomatic. Primary open-angle glaucoma is characterized by an open angle between the iris and the trabecular meshwork with trabecular meshwork blockage at the microscopic level. There are also classifications of glaucoma that are linked to heredity, induced by steroid use, or related to trauma. Glaucoma disease severity is determined depending on how much vision loss has already occurred and the rate at which the vision loss is occurring (also referred to as progression of the disease).

57.2 OCT Background

Because RGC loss cannot be directly detected in a clinical examination, glaucoma diagnosis relies on identification of indirect cues, such as characteristic optic nerve and RNFL changes, along with visual field (VF) abnormalities. Optical coherence tomography (OCT) allows quantifiable observation of the optic nerve and RNFL structures.

57.2.1 OCT Advantages for Glaucoma

There are many advantages to using this technology in imaging the eye for glaucoma evaluation. First, imaging is done in vivo and there is no damage inflicted, allowing repeated scanning of the same area in the same eye, as well as imaging different locations in the same eye. With modern scanning techniques, volumetric scans can be acquired, rather than 2-dimensional cross-sectional data, providing the ophthalmologist with comprehensive information as to the eye morphology. The clinical ability to detect the disease at early stages or identify disease worsening is often challenging because glaucoma is a slowly progressing disease. By providing automated and reproducible quantification of ocular structures, OCT enhances clinical diagnostic performance. However, in the current commercially available devices, there is signal attenuation as the signal's penetration depth increases or when significant media opacities, such as cataracts, are present.

There are two main types of OCT devices currently commercially available – time domain (TD-) and spectral domain (SD-) OCT. Both TD- and SD-OCT devices apply the same basic scientific principles; however, SD-OCT technology has a faster scan rate and improved axial resolution.

Quantification of the peripapillary RNFL has become the most common indicator for clinical glaucoma evaluation [8, 9]. However, the introduction of SD-OCT, with its high resolution and fast scanning speed, has added the quantification of the macular ganglion cell layer as comparative a glaucoma indicator as the RNFL [10–15].

57.3 OCT Scanning Patterns

The fast scanning rate provided by SD-OCT allows flexibility in the types of scan patterns available to be employed. These patterns can vary as a single linear scan, a few parallel linear scans, densely packed parallel linear scans in a raster pattern, circular scans of a predetermined diameter, or a combination of scan patterns, such as linear and circular scans. The following scan protocol descriptions are those often used in glaucoma evaluation and are intended to be general and unspecific to any particular TD- or SD-OCT device.

57.3.1 Linear Scans

The linear scan is composed of sequential axial scans (A-scans) aligned together to create an optical cross section (B-scan) of the structure of interest. The length and density of the A-scans along the line vary among the various commercial devices. The linear scan protocol provides detailed visualization of structures sampled along the scan line, which is most relevant and beneficial for examination of localized damage or for comparison between superior and inferior retinal damage.

The raster scan consists of a series of parallel and equally spaced linear scans [16]. Spacing between the linear scans and length of the linear scans vary among the commercial devices and can be adjusted for some of them. This scanning protocol is mostly used for detailed visualization of the macula or the optic nerve head region.

The radial scan consists of a series of equally spaced linear scans centered through a common point, such as the fovea or optic nerve head center. The number and length of the linear scans vary among devices. This scan allows the acquisition of data from a relatively wide region. However, the sampling is dense closest to the centered point. More interpolation is necessary between lines as distance from the centered point increases. This could lead to a localized small abnormality occurring in the periphery of the scan to be undetected.

57.3.2 Circular Scans

A circular scan is conceptually identical to a linear scan that is bent into a circle. This scan pattern is the most important scan pattern with TD-OCT devices for glaucoma evaluation because its design samples from all retinal nerve fibers approaching the optic nerve head [17]. Three consecutive scans are

automatically acquired after positioning the scan at the desired location, and the average of the three scans is reported. Several SD-OCT devices offer the same scan pattern. Even though the sampling location of the retina is in similar locations for both technologies, TD- and SD-OCT measurements are not interchangeable.

57.3.3 Combination of Linear and Circular Scans

The combination of linear and circular scans is laid out as concentric circles centered on the intersection point of the radial scans. The radial and circular scans are registered along their crossed paths, which leads to dense sampling near the intersection of the radial scans. As the distance from the intersection increases and the spacing between radial scan lines is larger, the concentric circles provide most of the data. A disadvantage to this scan is the eye movement that can occur throughout the period of time between the beginning of the acquisition of the radial scans and the end of the acquisition of the circular scans. This movement degrades the scan registration accuracy. This scan pattern is used for imaging of the optic nerve head region.

57.3.4 Raster Scans

The 3D cube raster is a series of rapid succession captures of adjacent and parallel B-scans. All of the data from the scanning window is acquired, which allows later processing of any desired area or view within the scanning region. Presence of blood vessels and other structural landmarks enables the alignment of scans acquired from multiple visits.

The scanning window can be placed over the macula or the optic nerve head region with the size of the scanning window and the density of the scan lines varying among OCT devices. Some devices acquire isometric scans, in which the distance between sampling points is consistent and pixel size is the same in both x- and y-directions. Other devices acquire unisometric scans, in which the distance between sampling points is different in x- and y-directions, creating a rectangular scanning region. Unisometric scans are beneficial when one direction is more of interest than the other.

3D cube raster scans are the main scanning type used for glaucoma because of the large scanning areas possible in a single scan and the range of post-processing options.

57.3.5 Eye Motion Tracking

Even with increasing scan speeds, eye movement during image acquisition can cause image distortion and impair tissue quantification. Several SD-OCT devices

incorporate eye motion tracking systems that correct for eye movement during image acquisition. Scanning time with functioning eye motion tracking can be significantly extended for patients with much movement, due to the repetition of B-scans upon movement detection.

57.4 Image-Processing Protocols

In addition to advancing imaging protocols, SD-OCT also offers an array of advancing image processing. A few examples are sampling tissue in a desired location within a scanning window or more detailed layer segmentation.

Most devices present the images with a vertical stretch to more easily visualize cross-sectional details. Summing all values along each A-scan creates fundus images, which are also referred to as en face images. These images are 2-dimensional maps from the image window that resemble the appearance of a clinical biomicroscopic examination.

57.4.1 Repeated Scan (Image) Averaging

Repeated scan averaging reduces the noise level and improves the image quality. Averaging is most suitable for linear and radial scans because averaging only slightly increases the scan time duration. Averaging is less convenient for longer duration scan patterns, such as the 3D cube scans. Any further increase in scan duration leads to greater eye movement artifacts, along with other causes of scan quality deterioration. The number of repeats should also be considered because above a certain amount of image averaging, the image quality deteriorates due to small uncorrected movements that lead to smearing of the image.

57.4.2 Segmentation

Segmentation enables differentiation of certain structures in a region of interest. The RNFL in the peripapillary area and retinal layers in the macula are two examples of commonly segmented regions from images of the posterior aspect of the eye. Segmentation is automatically performed through identification of certain landmarks in the signal profile of each A-scan. Segmentation methods enable detection, quantification, and advanced post-processing of abnormalities in certain layers. However, in the presence of severely deformed structures, segmentation might fail because the typical landmarks required for the segmentation are not discernable. Therefore, it is recommended to routinely inspect segmentation performance to ensure validity.

57.4.3 Circumpapillary Retinal Thickness and Retinal Thickness Map

After applying the segmentation analysis on each of the A-scans, RNFL thickness is reported along a circle surrounding the optic nerve head. The thickness profile along the circle is provided in comparison to thickness profiles and measurements derived from a healthy population. This comparison enhances the ability to detect locations with apparent thinning or thickening of the RNFL. The typical circumpapillary RNFL thickness profile is described as a double hump pattern with thicker areas adjacent to the optic nerve head poles and thinner areas in the temporal and nasal aspects. It should be noted that RNFL measurements are not interchangeable among the SD-OCT devices. In addition to the visual representation of the RNFL profile, average thickness measurements are also provided for the entire circle, in quadrants and in smaller sectors. Many of the SD-OCT devices also provide RNFL thickness maps of the entire peripapillary region. This allows detection of abnormalities located outside the sampled circle of the circumpapillary scan used for the visual representation of the RNFL profile. Thickness measurements are compared to thickness values from a healthy population and are reported as a deviation map to highlight the locations of thickness abnormalities.

57.4.4 C-mode

C-mode produces an en face image of selected layers, or a slab, of an image by isolating the reflection to a thin layer of tissue within the B-scans. This method of image processing allows visualization of a selected plane, such as the retinal pigment epithelium, throughout the scanned region.

57.4.5 Progression Analysis

SD-OCT is a candidate to detect structural changes over time because the images provide accurate quantification of ocular structures. There are currently two types of progression analysis commercially used for detecting RNFL thickness loss. One analysis identifies progression at a location where the change is more than the expected variability at the same location in a normative database. The other analysis type is focused on rate of progression, where an eye is marked as progressing when the rate of change using linear regression is outside of the expected RNFL loss rate of a normative database.

57.5 Scanning Locations

Within the eye, there is more than one location that can be imaged to provide information related to glaucoma. At these different locations, certain scan patterns are more useful than others depending on tissue structure and location.

57.5.1 Optic Nerve Head

Various scan patterns are offered among the different SD-OCT devices for imaging the optic nerve head region. The most common patterns are raster scans, radial scans, and the combination of radial and circular scans. The disc margin is traditionally defined as Bruch's membrane opening and is automatically defined for some devices, while other devices require manual definition. The cup is defined by a plane parallel to the plane connecting the disc margin with a fixed offset that varies among the different devices. All devices provide quantification of optic nerve head structure areas, including the disc, rim and cup, as well as the cup to disc ratio.

SD-OCT scanning produces pairs of simultaneous images: one image that is focused more superficially and a mirror image with a deeper focus plane. In all conventional scanning, the first image with the superficial focus is used with the mirror image not being shown. However, in enhanced depth imaging (EDI) the mirror image is used. The deeper focus is useful for imaging structures deep within the optic nerve head, such as the lamina cribrosa. EDI is available with all scan patterns, but at the time of writing this section, it is used for qualitative analysis only.

57.5.2 Macula

Many of the scan patterns (linear, multiple parallel linear, radial, and raster scans) can be used in the macula region with different scan patterns reporting different information. While linear scans are valuable for detailed visualization along the scan line, other scan patterns provide structural information of the entire macula region. All devices are capable of reporting the macular retinal thickness spanning from the inner limiting layer to the photoreceptors or retinal pigment epithelium complex. However, a main reason behind the inability to compare thickness measurement values among devices is the precise layer at the outer retina varies among the SD-OCT devices. In addition to the total retinal thickness, some devices provide thickness measurements in defined sectors.

Advanced segmentation analysis is capable of separately identifying several of the retinal layers. Segmentation is based on identifying typical patterns in the signal profile of each individual A-scan. The utilization of this type of segmentation, as well as the number of individual layers provided, varies by SD-OCT device. There is a balance present between providing as many layers as possible and the robustness of the segmentation analysis. A benefit of this segmentation is the identification and quantification of specific retinal layers, improving the ability to detect structural changes in diseases where certain layers are specifically affected. Glaucoma is an example of such a disease because the ganglion cell layer is prone to the glaucomatous effect, and quantification of this layer individually can improve disease detection. While glaucoma specifically affects the inner retinal layers, a non-glaucoma disease affecting the outer retina can confound the

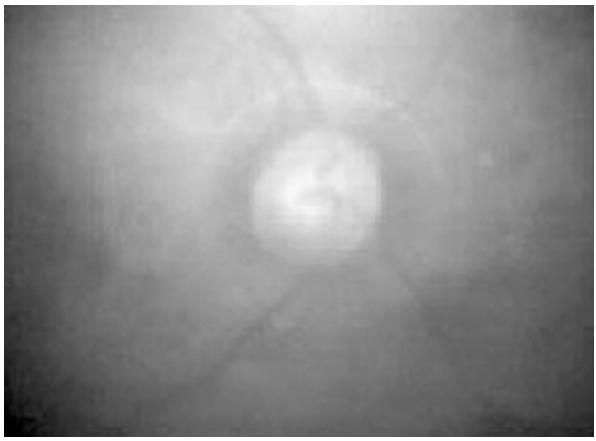

Fig. 57.1 Fast RNFL fundus image

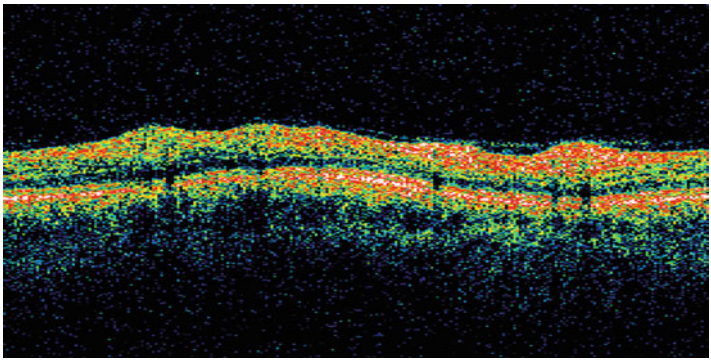

Fig. 57.2 RNFL cross-sectional image

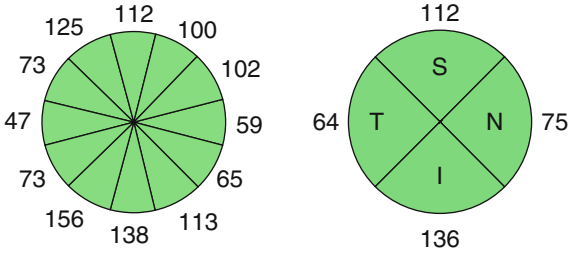

Fig. 57.3 RNFL sectoral thickness analysis

total retinal thickness measurements. In addition to providing quantitative summary parameters of the layers, some devices provide other representations of the data, such as thickness maps of individual layers and deviation maps from a population of healthy individuals.

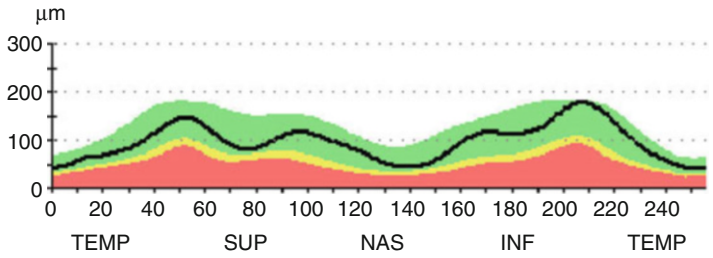

Fig. 57.4 RNFL thickness profile

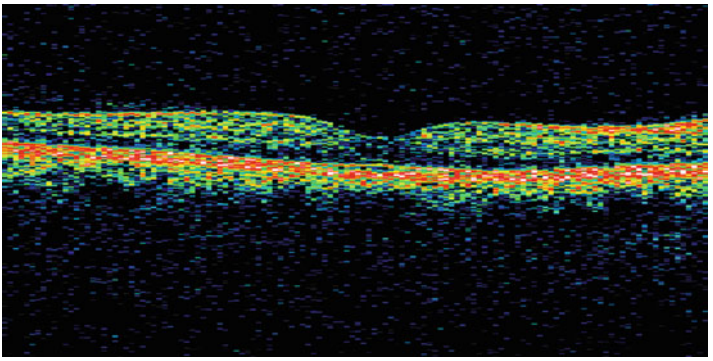

Fig. 57.5 Macula cross-sectional image

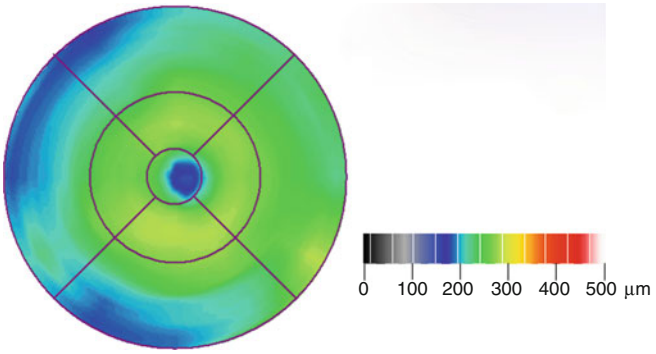

Fig. 57.6 Macula retinal thickness map

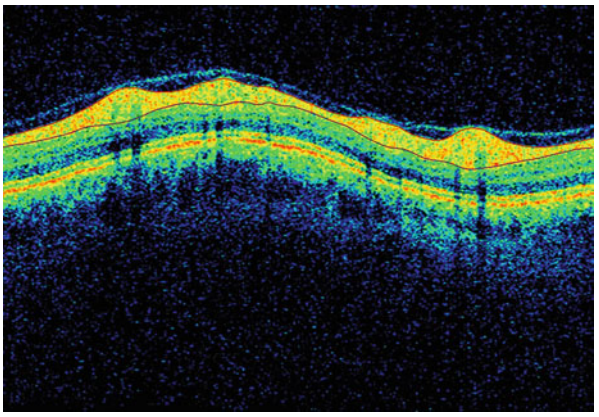

Fig. 57.7 Optic disc cube scan circumpapillary RNFL cross-sectional image

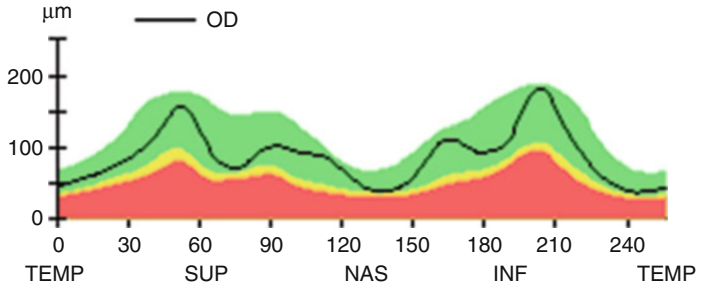

Fig. 57.8 RNFL thickness profile

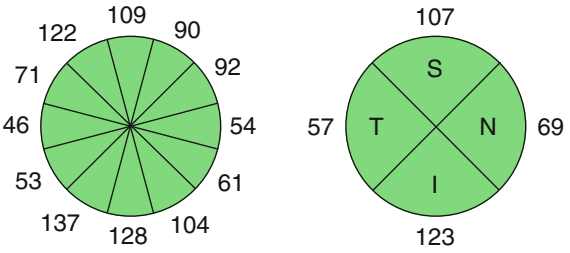

Fig. 57.9 RNFL quadrants and sectors

Another macula feature offered by some devices is C-mode sections. These sections focus on specific planes within the macula. One such example in the macula region is a C-mode section at the retinal pigment epithelium layer that highlights the presence of drusens as irregular "bumps" in the plane.

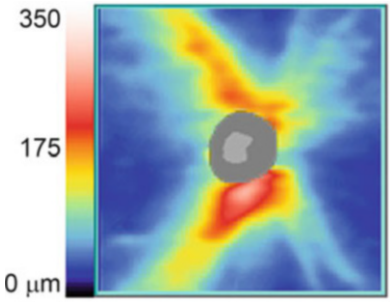

Fig. 57.10 RNFL thickness map

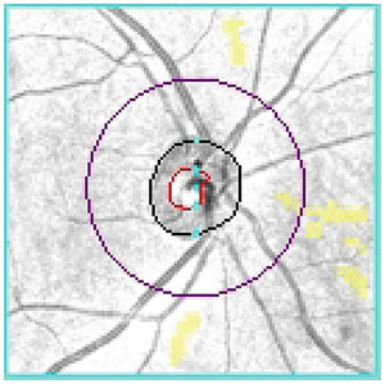

Fig. 57.11 RNFL deviation map on en face image with ONH disc and cup margins

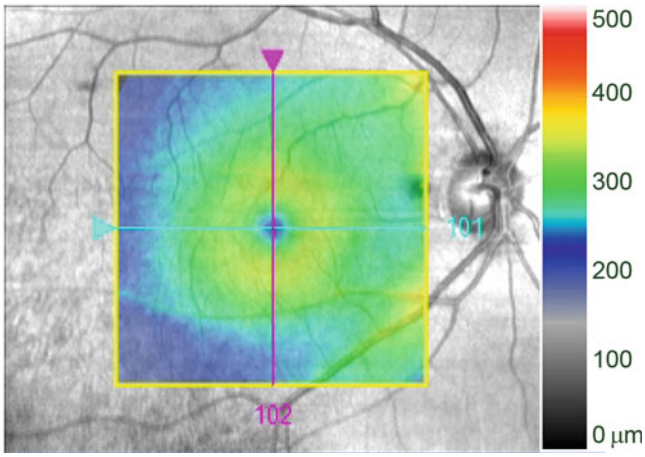

Fig. 57.12 Macula cube thickness analysis on LSO image

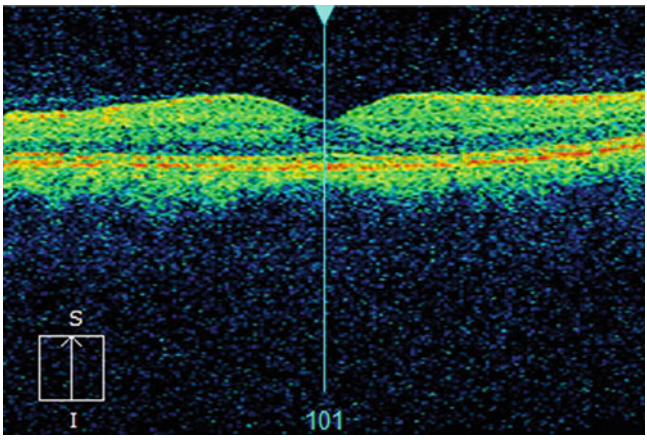

Fig. 57.13 Macula vertical cross-sectional image

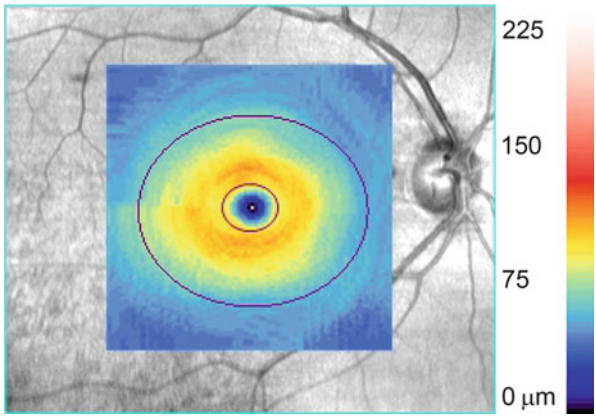

Fig. 57.14 Macula ganglion cell analysis thickness map

57.5.3 Anterior Segment

Anterior segment structures, such as the cornea, iris, and anterior lens, as well as the anterior chamber angle can be visualized with anterior segment OCT scanning. Devices with this scanning capability use a longer wavelength and higher power than typically used in OCT devices. Using a longer wavelength and higher power decreases acquisition time, which reduces the potential for motion artifacts in the scan.

In addition to devices solely for anterior segment imaging, several more conventional SD-OCT devices have the ability to provide anterior segment scanning by employing customized add-on apparatuses.

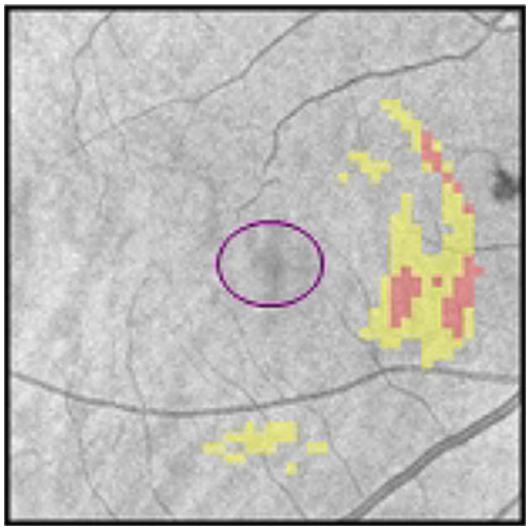

Fig. 57.15 Macula ganglion cell analysis deviation map

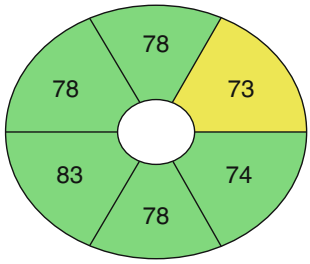

Fig. 57.16 Macula ganglion cell analysis sectors

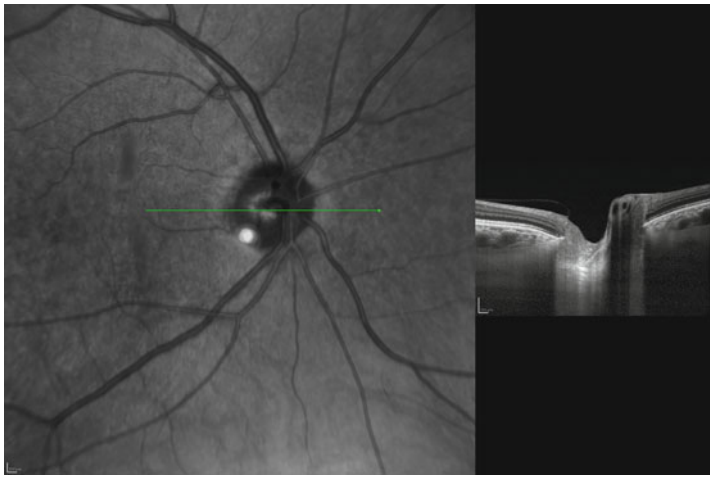

Fig. 57.17 Infrared CSLO image of ONH (*Left*) and SD-OCT line scan across ONH (*Right*)

Fig. 57.18 Infrared CSLO image of ONH (*Left*) and SD-OCT circle scan around ONH (*Right*)

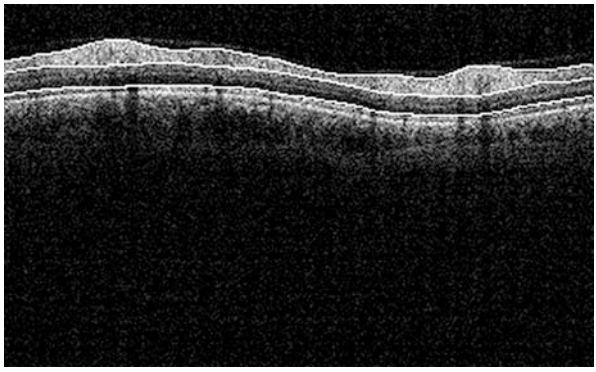

Fig. 57.19 Circumpapillary RNFL cross-sectional image

The quantitative information provided by the devices varies. For glaucoma purposes, the most useful information is the configuration of the anterior chamber angle and the corneal thickness, which has been indicated as a possible glaucoma risk factor. Many devices provide angle quantification, but no consistent parameters are used across the devices.

57.6 Cases

Three cases are provided to show OCT imaging of an eye with no glaucoma disease, an eye with early glaucoma, and an eye with severe glaucoma.

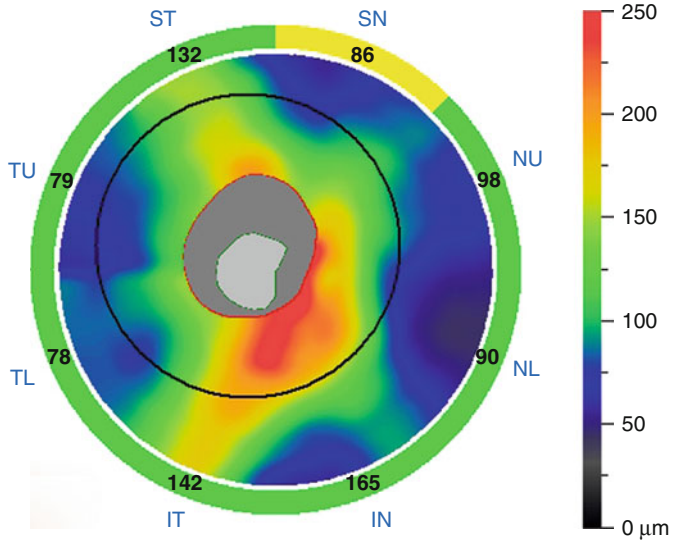

Fig. 57.20 ONH analysis

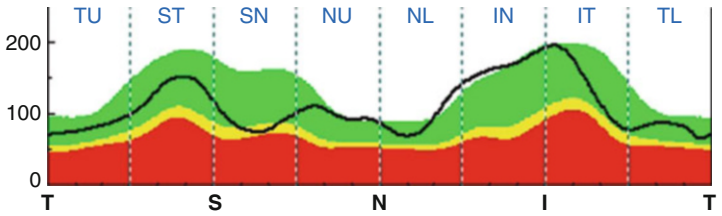

Fig. 57.21 Circumpapillary RNFL thickness analysis

57.6.1 Case 1: Healthy Eye

TD-OCT (Stratus; Carl Zeiss Meditec, Dublin, CA, USA) imaging of a healthy 48-year-old male reveals a normal RNFL thickness (Figs. 57.1, 57.2, 57.3, 57.4, 57.5, and 57.6). The fundus photo (Fig. 57.1) confirms the ONH was correctly centered during scanning. The circumpapillary RNFL cross section (Fig. 57.2), its quantification in sectors and quadrants (Fig. 57.3), and the RNFL thickness profile (Fig. 57.4) show all RNFL thickness measurements are within the normal limits (green background). Figure 57.5 displays the macula cross section with central thinning at the fovea. The macula retinal thickness map (Fig. 57.6) shows the normal retinal thickness with central foveal

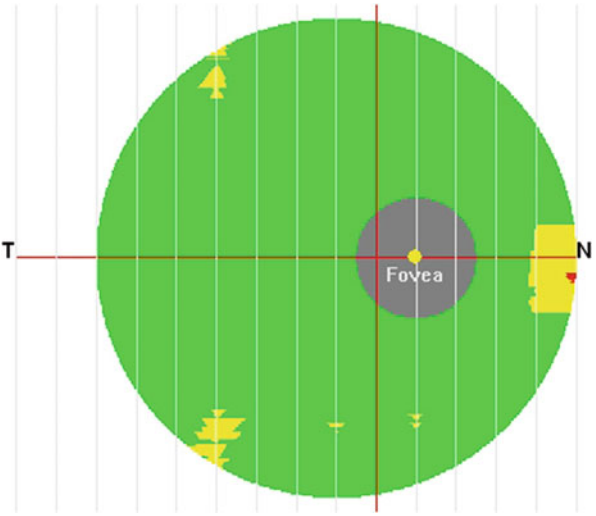

Fig. 57.22 Macula ganglion cell complex thickness significance map

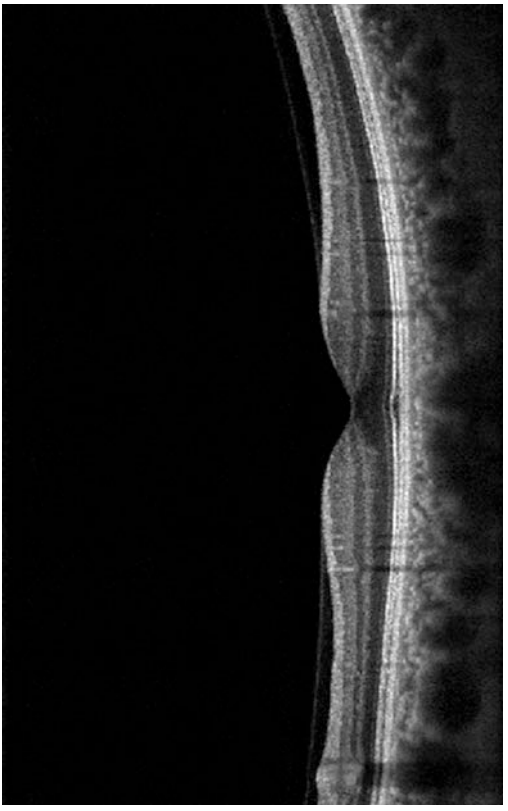

Fig. 57.23 Macula cross line image

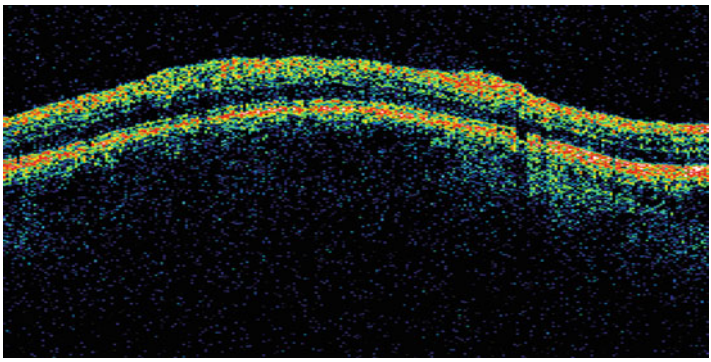

Fig. 57.24 RNFL cross-sectional image

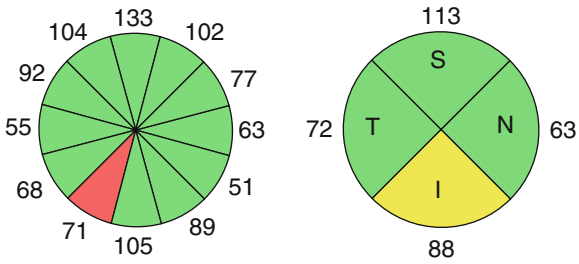

Fig. 57.25 RNFL sectoral thickness analysis

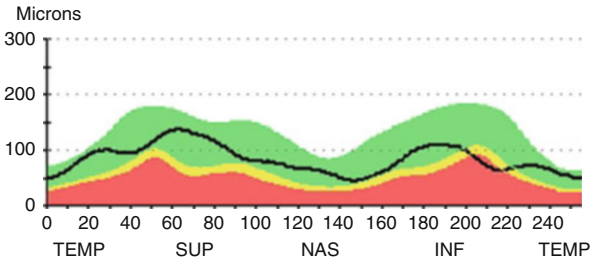

Fig. 57.26 RNFL thickness profile

thinning surrounded by the perifoveal thickening in a ring (or C) shape with gradual thinning of the retina toward the periphery of the scan.

SD-OCT (Cirrus HD-OCT; Carl Zeiss Meditec, Dublin, CA, USA) imaging of the same healthy eye (Figs. 57.7, 57.8, 57.9, 57.10, 57.11, 57.12, 57.13, 57.14, 57.15, and 57.16) includes this circumpapillary cross section reconstructed from the 3-dimensional scan (Fig. 57.7). The RNFL thickness profile and thickness values of

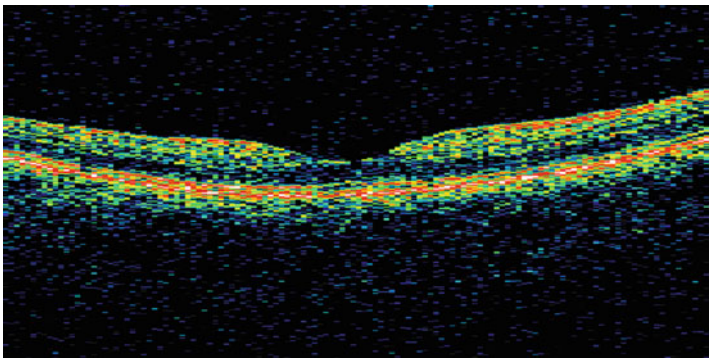

Fig. 57.27 Macula cross-sectional image

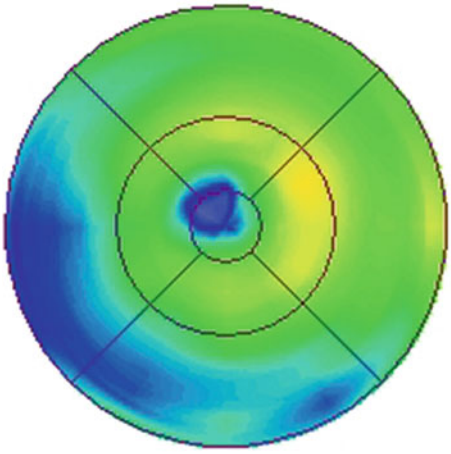

Fig. 57.28 Macula retinal thickness map

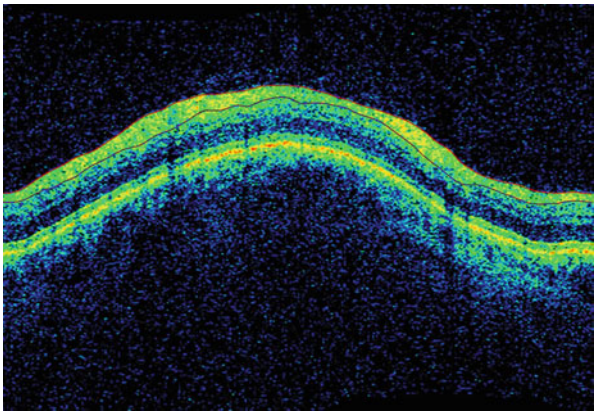

Fig. 57.29 Optic disc cube scan circumpapillary RNFL cross-sectional image

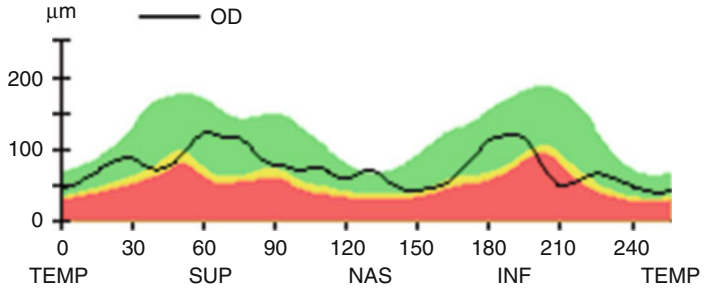

Fig. 57.30 RNFL thickness profile

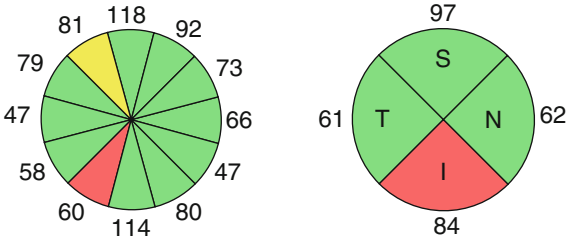

Fig. 57.31 RNFL quadrants and sectors

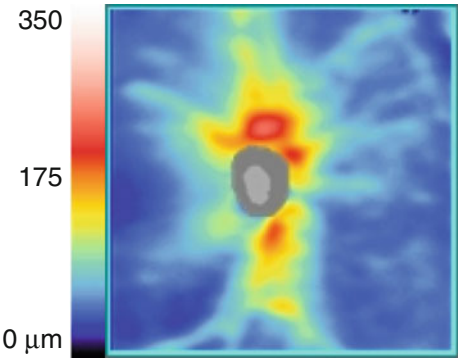

Fig. 57.32 RNFL thickness map

sectors and quadrants (Figs. 57.8 and 57.9) are all within the normal range. The peripapillary RNFL thickness map (Fig. 57.10) demonstrates the normal thickening adjacent to the superior and inferior poles of the optic nerve head with thinning of the RNFL at the nasal and temporal aspects. The en face image of the peripapillary region (Fig. 57.11) shows the sampling location of the circular scan with a diameter of 3.4 mm (purple) along with the automatically defined optic nerve head (black) and cup margins (red). RNFL thickness is compared with population-derived

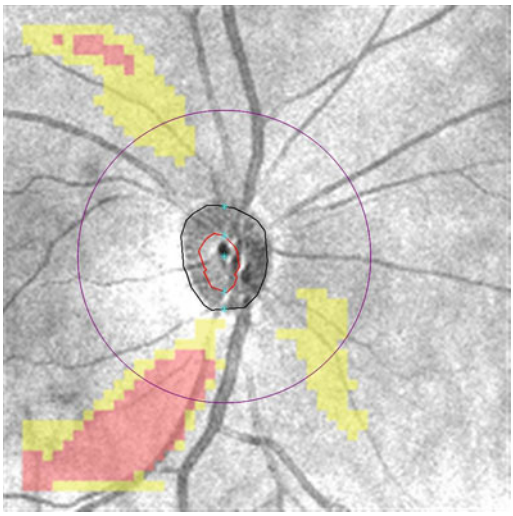

Fig. 57.33 RNFL deviation map on en face image with ONH disc and cup margins

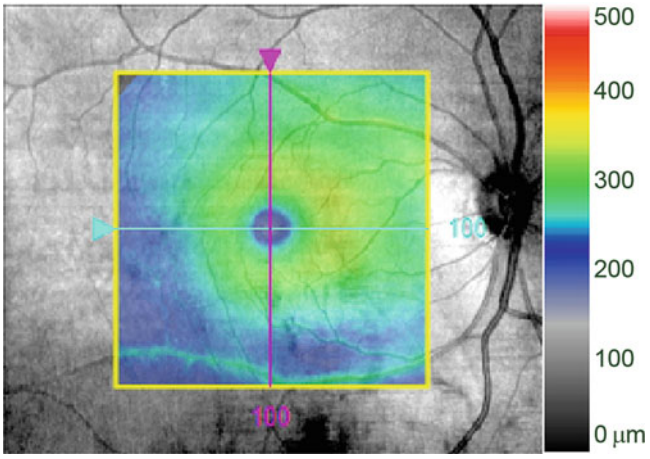

Fig. 57.34 Macula cube thickness analysis on LSO image

thickness measurements, and areas of borderline deviation are marked with yellow coloring. The rim thickness is normal and the yellow spots are minimal far from the disc margin. The thickness map of the macula (Fig. 57.12) and the vertical cross-sectional image (Fig. 57.13) display normal configuration of the macular region. The macular cube ganglion cell analysis (Figs. 57.14, 57.15, and 57.16) shows

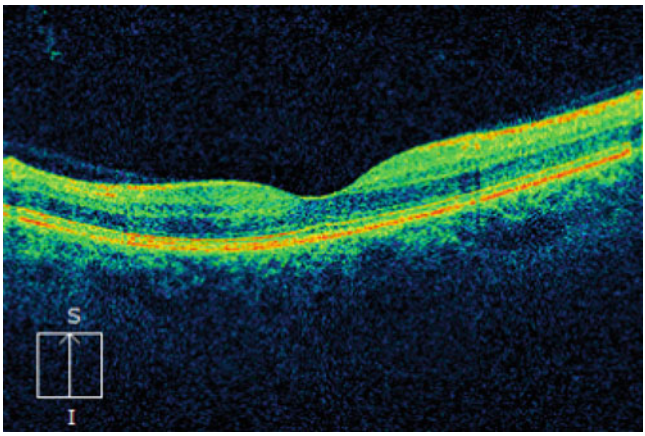

Fig. 57.35 Macula vertical cross-sectional image

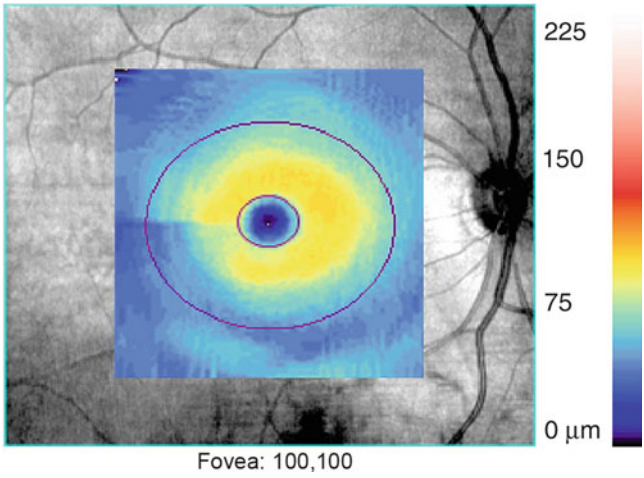

Fig. 57.36 Macula ganglion cell analysis thickness map

normal macula thickness with a localized borderline region at the nasal aspect of the macula by the thickness map (Fig. 57.14), deviation from normal map (Fig. 57.15), and sector measurements (Fig. 57.16). The one yellow sector in Fig. 57.16 corresponds to the few yellow/red spots in Fig. 57.15.

Another SD-OCT device (Spectralis; Heidelberg Engineering, Heidelberg, Germany), employing eye motion tracking and image averaging while scanning the same healthy eye, also shows a normal retinal thickness and ONH cupping with

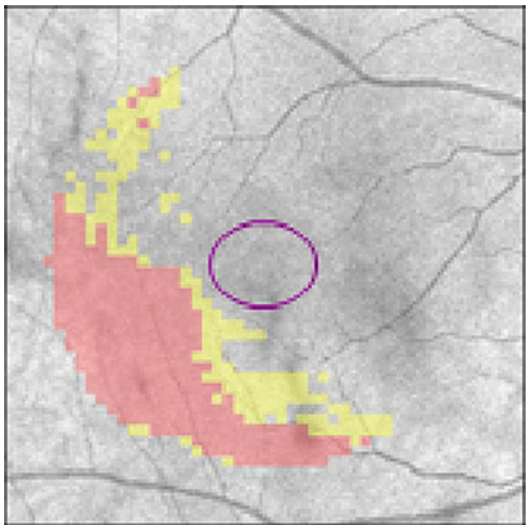

Fig. 57.37 Macula ganglion cell analysis deviation map

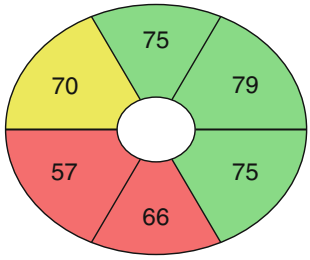

Fig. 57.38 Macula ganglion cell analysis sectors

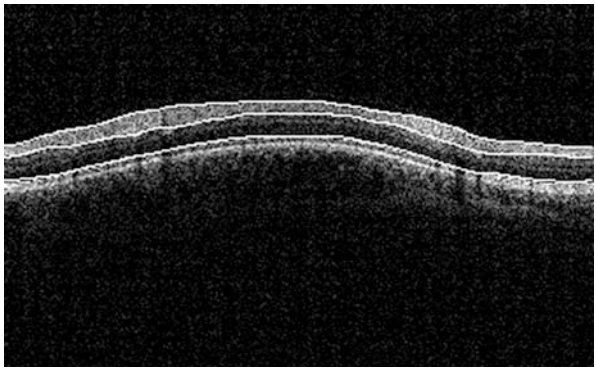

Fig. 57.39 Circumpapillary RNFL cross-sectional image

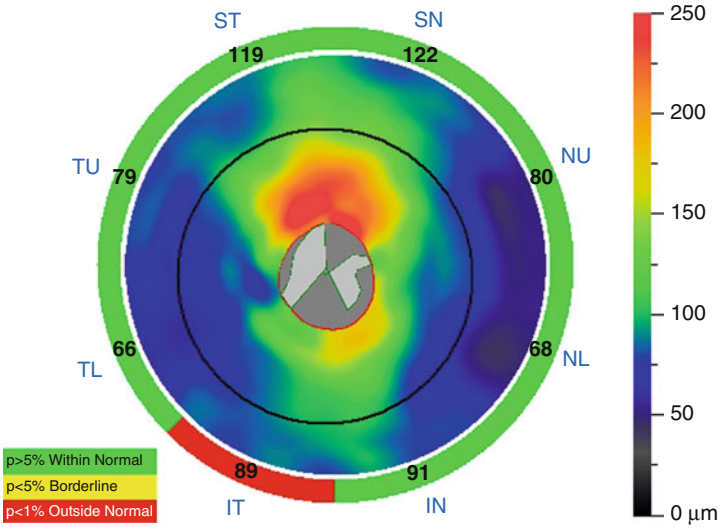

Fig. 57.40 ONH analysis

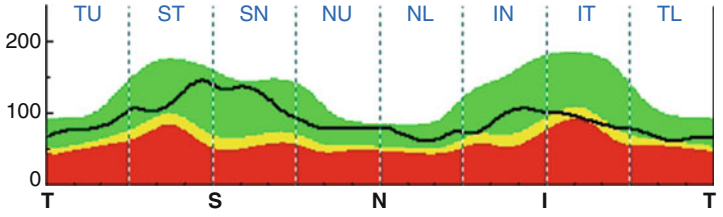

Fig. 57.41 Circumpapillary RNFL thickness analysis

the linear scan (Fig. 57.17) and circular scan (Fig. 57.18). For both scans, the left side of the figure is a scanning laser ophthalmoscopy image overlaid with the OCT scan location (green). Note the highly detailed cross-sectional images.

A third SD-OCT device (RTVue; Optovue, Fremont, CA, USA) also shows a normal RNFL thickness (Figs. 57.19, 57.20, 57.21, 57.22, and 57.23) when scanning the same healthy eye. Figure 57.19 displays the circumpapillary retinal cross section with delineation of the RNFL margins and the retinal pigment epithelium (all white lines). The ONH analysis (Fig. 57.20) provides the thickness map of the peripapillary region surrounded with the ring of sectoral measurements with the comparison with population-derived normal thickness. The RNFL thickness profile around the optic nerve head (Fig. 57.21) shows a normal profile with a small localized superonasal location with borderline RNFL thickness. The macula analysis (Fig. 57.22) indicates thickness values within the normal limits with a vertical cross section (Fig. 57.23) showing similar retinal thickness when comparing corresponding locations superior and inferior to the fovea.

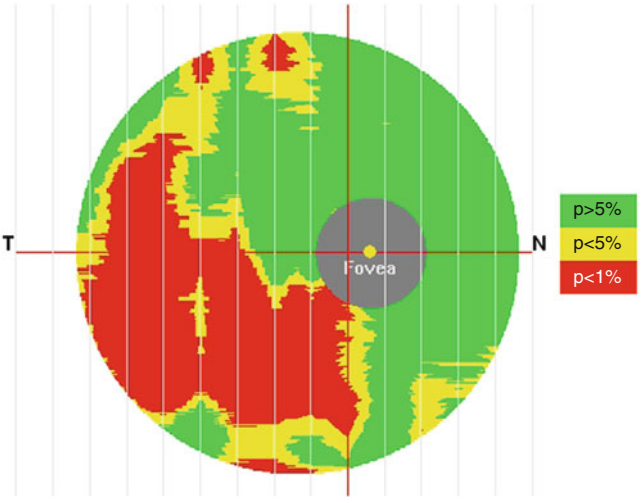

Fig. 57.42 Macula ganglion cell complex thickness significance map

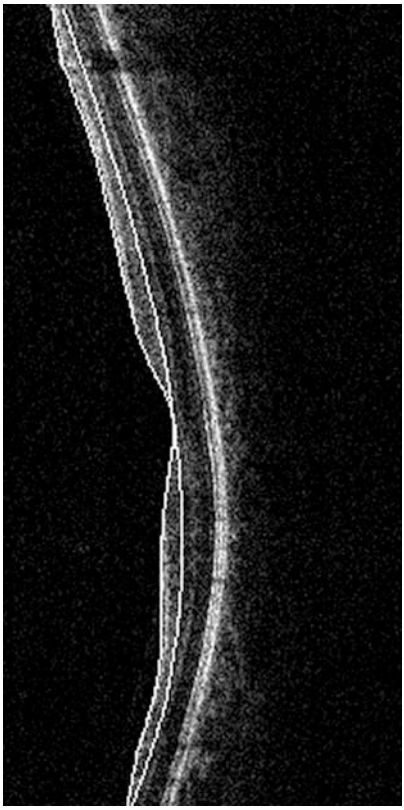

Fig. 57.43 Macula cross line image

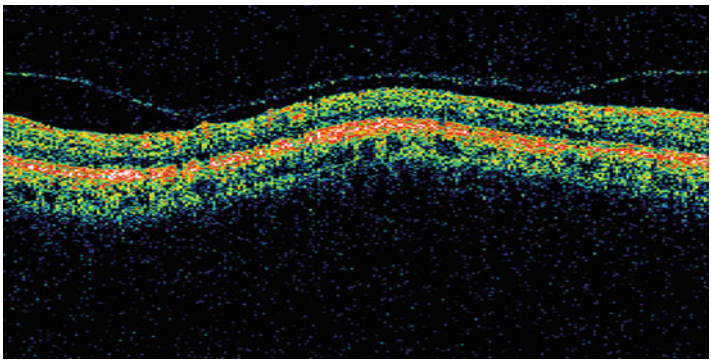

Fig. 57.44 RNFL cross-sectional image

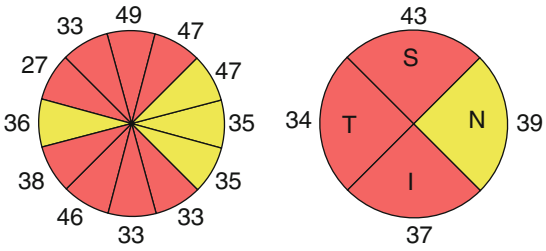

Fig. 57.45 RNFL sectoral thickness analysis

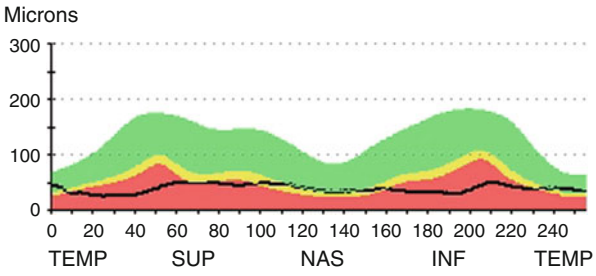

Fig. 57.46 RNFL thickness profile

57.6.2 Case 2: Early Glaucoma Eye

The left eye of a 52-year-old female demonstrated RNFL thinning as detected by TD-OCT (Stratus) imaging (Figs. 57.24, 57.25, 57.26, 57.27, and 57.28). Figure 57.24 displays the circumpapillary RNFL cross section. Analysis of the sectors, quadrants, and RNFL thickness profile (Figs. 57.25 and 57.26) shows mostly normal RNFL thickness measurements, except for thinning in the temporal inferior region. The vertical macula cross section shows thinning of the RNFL

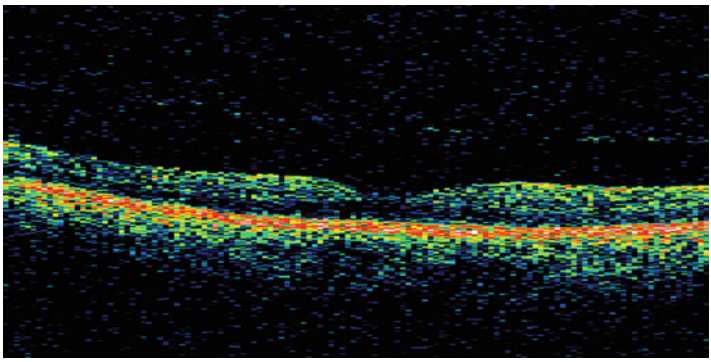

Fig. 57.47 Macula cross-sectional image

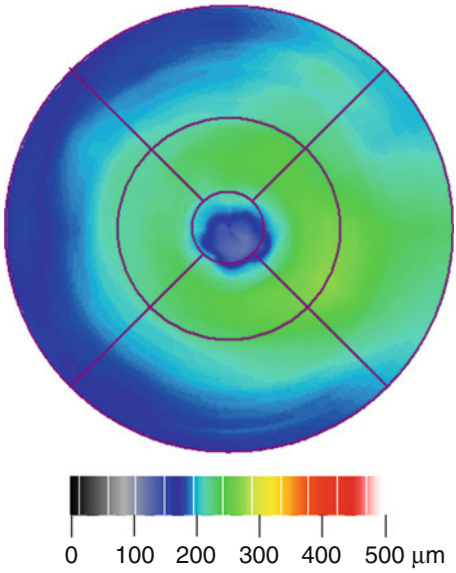

Fig. 57.48 Macula retinal thickness map

layer (upper red band) in the inferior macula (left side of the figure) (Fig. 57.27). The macula retinal thickness map (Fig. 57.28) shows thinning of the inferior macula marked by the blue color with attenuation of the perifoveal thickening in the same region.

SD-OCT (Cirrus, Carl Zeiss Meditec, Dublin, CA, USA) imaging (Figs. 57.29, 57.30, 57.31, 57.32, 57.33, 57.34, 57.35, 57.36, 57.37, and 57.38) of the same eye also reveals a thinning RNFL thickness. Figure 57.29 displays the optic disc cube

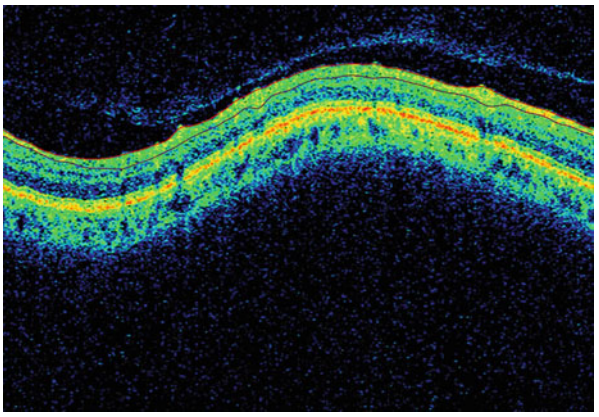

Fig. 57.49 Optic disc cube scan circumpapillary RNFL cross-sectional image

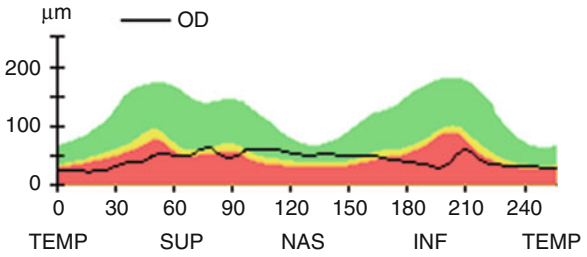

Fig. 57.50 RNFL thickness profile

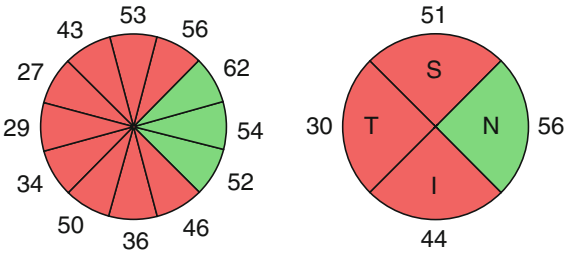

Fig. 57.51 RNFL quadrants and sectors

circumpapillary RNFL cross section. The coloring in the RNFL thickness profile, sectors, and quadrants (Figs. 57.30 and 57.31) indicates thinner RNFL thickness in the temporal inferior region. Thinning of the RNFL is noticeable inferiorly in the peripapillary thickness map (Fig. 57.32). The deviation map (Fig. 57.33) highlights thinning in the temporal inferior region (red and yellow marks). Another region of thinning appears in the temporal superior region that was difficult to identify by assessing the thickness map only. The thickness analysis of the macula (Fig. 57.34) and the vertical cross-sectional image (Fig. 57.35) display the inferior thinning.

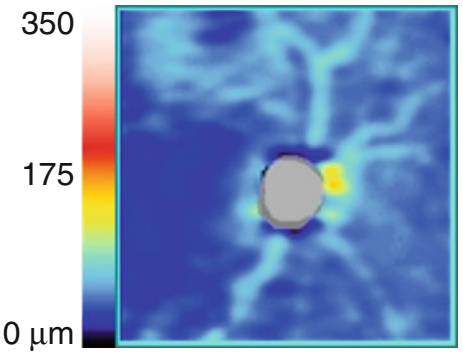

Fig. 57.52 RNFL thickness map

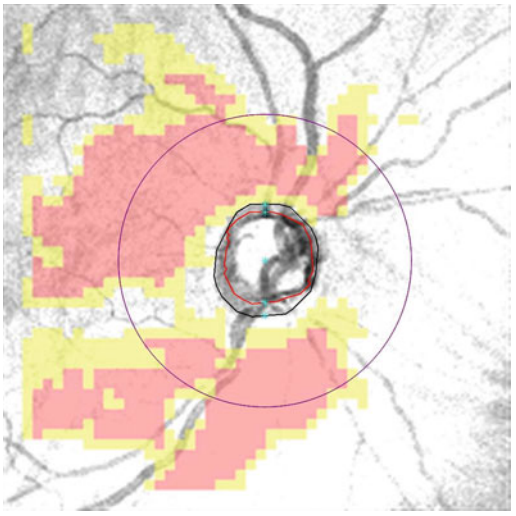

Fig. 57.53 RNFL deviation map on en face image with ONH disc and cup margins

The macular cube ganglion cell analysis (Figs. 57.36, 57.37, and 57.38) shows temporal and inferior thinning by the thickness map (Fig. 57.36), deviation map (Fig. 57.37), and sectors analysis (Figs. 57.38).

Another SD-OCT device (RTVue) also shows a thinner RNFL thickness (Figs. 57.39, 57.40, 57.41, 57.42, and 57.43) in the same eye. Figure 57.39 displays the circumpapillary RNFL cross section. The ONH analysis (Figs. 57.40 and 57.41) indicates thickness values within the normal limits, except for the thinning showed in the temporal inferior region. The macula ganglion cell complex analysis (Fig. 57.42) indicates thinning temporally and inferiorly. Figure 57.43 displays the macula cross line image with marked thinning in the inferior macula.

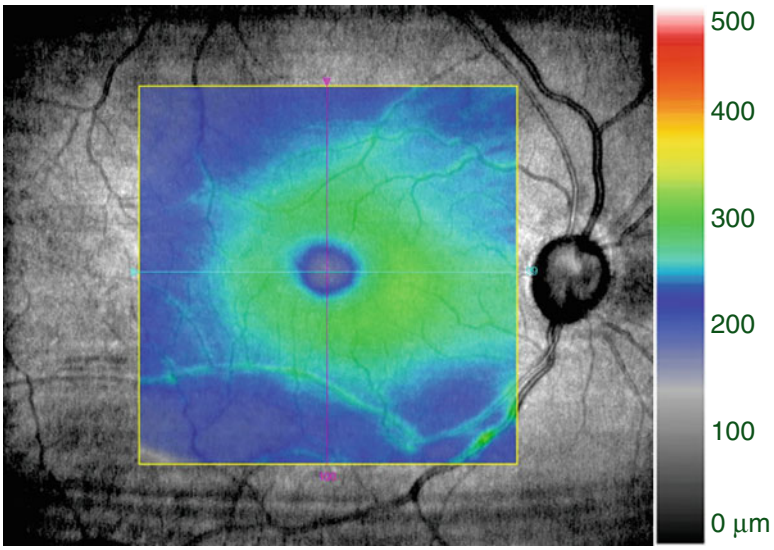

Fig. 57.54 Macula cube thickness analysis on LSO image

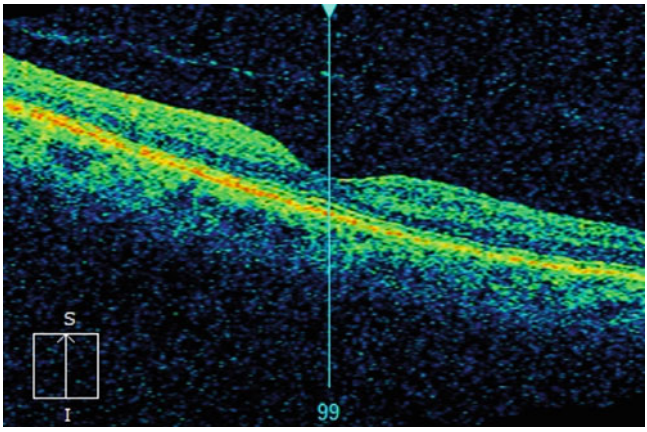

Fig. 57.55 Macula vertical cross-sectional image

57.6.3 Case 3: Severe Glaucoma Eye

The right eye of a 64-year-old female demonstrates severe glaucomatous damage. TD-OCT (Stratus) imaging (Figs. 57.44, 57.45, 57.46, 57.47, and 57.48) reveals thinning RNFL. Figure 57.44 displays the circumpapillary retinal cross section and segmentation of the RNFL with obliteration of both humps. Analysis of the sectors, quadrants, and RNFL thickness profile (Figs. 57.45 and 57.46)

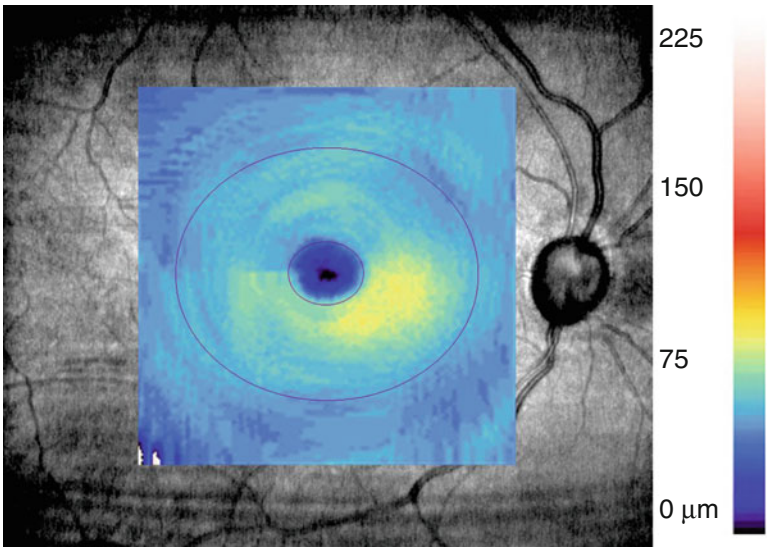

Fig. 57.56 Macula ganglion cell analysis thickness map

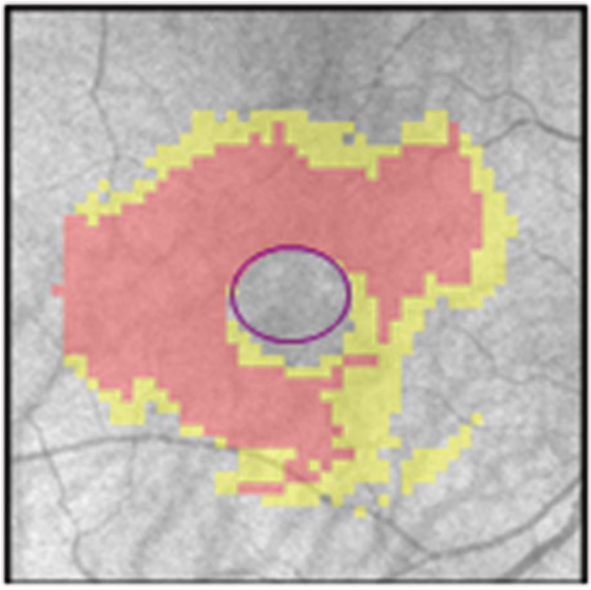

Fig. 57.57 Macula ganglion cell analysis deviation map

shows substantial inferior, superior, and temporal thinning and moderate nasal thinning. Vertical macula cross section demonstrates a total obliteration of the RNFL signal (upper red band) in both superior and inferior macula (Fig. 57.47). The macula retinal thickness map (Fig. 57.48) shows widespread thinning of retinal thickness.

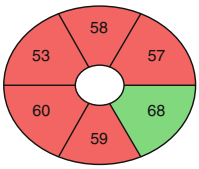

Fig. 57.58 Macula ganglion cell analysis sectors

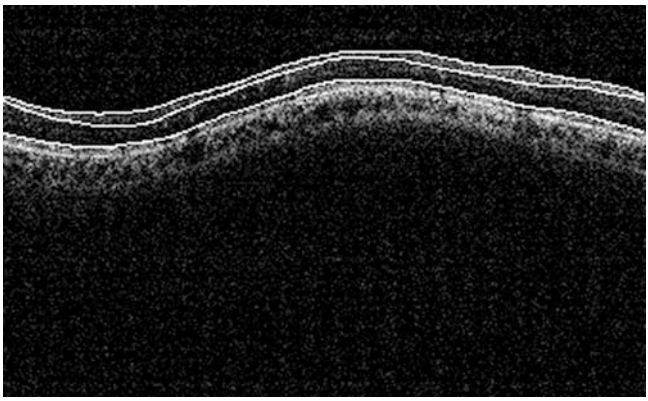

Fig. 57.59 Circumpapillary RNFL cross-sectional image

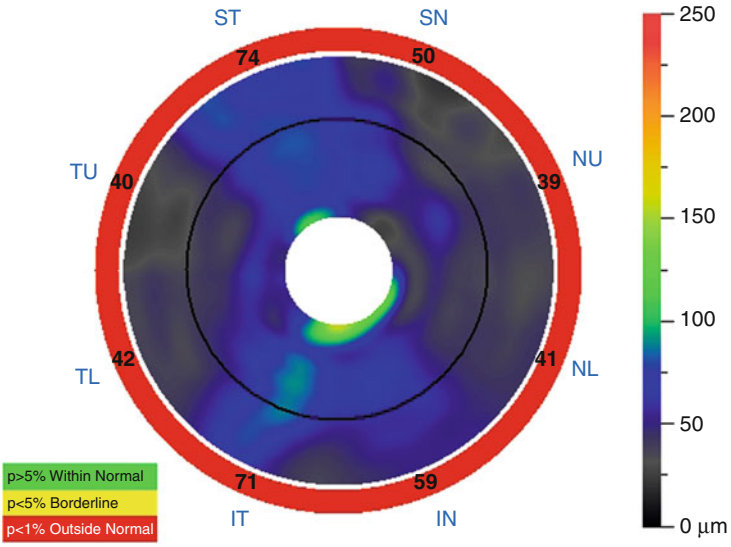

Fig. 57.60 ONH analysis

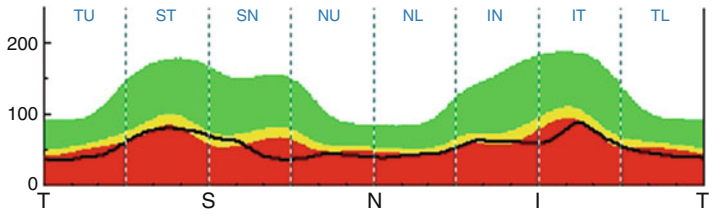

Fig. 57.61 Circumpapillary RNFL thickness analysis

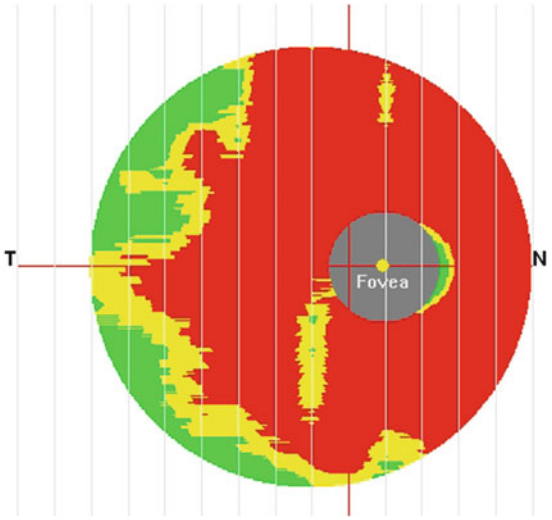

Fig. 57.62 Macula ganglion cell complex thickness significance map

SD-OCT (Cirrus HD-OCT) imaging (Figs. 57.49, 57.50, 57.51, 57.52, 57.53, 57.54, 57.55, 57.56, 57.57, and 57.58) of the same eye also reveals a thinning RNFL thickness. Figure 57.49 displays the optic disc cube derived circumpapillary cross section. The RNFL thickness profile, sectors, and quadrants (Figs. 57.50 and 57.51) indicate severely thinner RNFL thickness inferiorly, superiorly, and temporally. Severe abnormal loss is indicated in the peripapillary RNFL thickness map with total elimination of the typical configuration of thicker RNFL adjacent to the ONH poles (Fig. 57.52). The deviation map shows general enlargement of the ONH cup with neuroretinal thinning and a corresponding thinning of the RNFL (Fig. 57.53). The thickness analysis of the macula (Fig. 57.54) and the vertical cross-sectional image (Fig. 57.55) display marked thinning throughout. The macular cube ganglion cell analysis (Figs. 57.56, 57.57, and 57.58) shows more severe thinning in the superior region with some remaining thickness in the inferior region.

Another SD-OCT device (RTVue, Optovue, Fremont, CA, USA) also shows a thinner RNFL thickness (Figs. 57.59, 57.60, 57.61, 57.62, and 57.63) in the

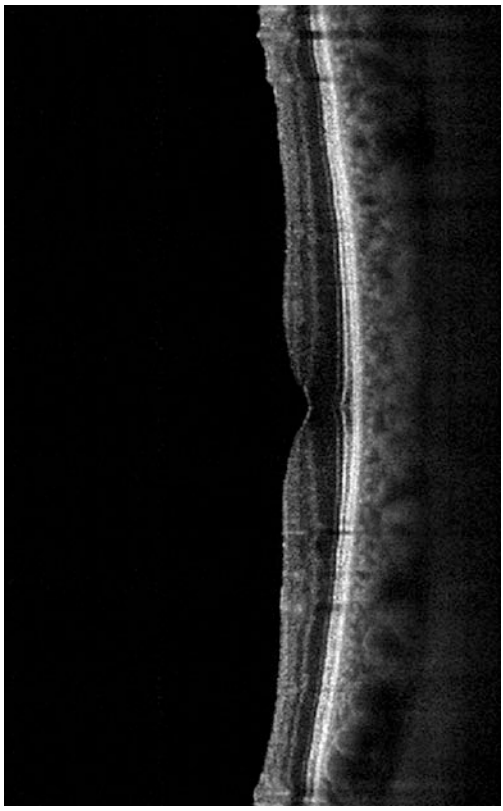

Fig. 57.63 Macula cross line image

same eye. Figure 57.59 displays the circumpapillary RNFL cross section. The ONH analysis (Figs. 57.60 and 57.61) indicates substantial thinning across all sectors. The macula ganglion cell complex analysis (Fig. 57.62) indicates very advanced thinning in the entire macula. Figure 57.63 displays the macular cross line image.

References

1. H.A. Quigley, A.T. Broman, The number of people with glaucoma worldwide in 2010 and 2020. Br. J. Ophthalmol. **90**, 262–267 (2006)
2. J.C. Javitt, A.M. McBean, G.A. Nicholson et al., Undertreatment of glaucoma among black Americans. N. Eng. J. Med. **325**, 1418–1422 (1991)
3. D.S. Friedman, H.D. Jampel, B. Munoz et al., The prevalence of open-angle glaucoma among blacks and whites 73 years and older: the salisbury eye evaluation glaucoma study. Arch. Ophthalmol. **124**, 1625–1630 (2006)
4. A. Sommer, N.R. Miller, I. Pollack et al., The nerve fiber layer in the diagnosis of glaucoma. Arch. Ophthalmol. **95**, 2149–2156 (1977)
5. P.J. Foster, R. Buhrmann, H.A. Quigley et al., The definition and classification of glaucoma in prevalence surveys. Br. J. Ophthalmol. **86**, 238–242 (2002)

6. A. Sommer, J. Katz, H.A. Quigley et al., Clinically detectable nerve fiber atrophy precedes the onset of glaucomatous field loss. Arch. Ophthalmol. **109**, 77–83 (1991)
7. A. Sommer, J.M. Tielsch, J. Katz et al., Relationship between intraocular pressure and primary open angle glaucoma among white and black Americans. Arch. Ophthalmol. **109**(8), 1090–1095 (1991)
8. F.A. Medeiros, L.M. Zangwill, C. Bowd et al., Evaluation of retinal nerve fiber layer, optic nerve head, and macular thickness measurements for glaucoma detection using optical coherence tomography. Am J. Ophthalmol. **139**, 44–55 (2005)
9. G. Wollstein, J.S. Schuman, L.L. Price et al., Optical coherence tomography longitudinal evaluation of retinal nerve fiber layer thickness in glaucoma. Arch. Ophthalmol. **123**, 464–470 (2005)
10. Z. Burgansky-Eliash, G. Wollstein, T. Chu et al., Optical coherence tomography machine learning classifiers for glaucoma detection: a preliminary study. Invest. Ophthalmol. Vis. Sci. **46**, 4147–4152 (2005)
11. K.R. Sung, D.Y. Kim, S.B. Park et al., Comparison of retinal nerve fiber layer thickness measured by Cirrus HD and Stratus optical coherence tomography. Ophthalmology **116**, 1264–1270 (2009)
12. M. Seong, K.R. Sung, E.H. Choi et al., Macular and peripapillary retinal nerve fiber layer measurements by spectral domain optical coherence tomography in normal tension glaucoma. Invest. Ophthalmol. Vis. Sci. **51**, 1446–1452 (2010)
13. H.L. Rao, L.M. Zangwill, R.N. Weinreb et al., Comparison of different spectral domain optical coherence tomography scanning areas for glaucoma diagnosis. Ophthalmology **117**, 1692–1699 (2010)
14. H. Ishikawa, D.M. Stein, G. Wollstein et al., Macular segmentation with optical coherence tomography. Invest. Ophthalmol. Vis. Sci. **46**, 2012–2017 (2005)
15. O. Tan, G. Li, A.T. Lu et al., Mapping of macular substrates with optical coherence tomography for glaucoma diagnosis. Ophthalmology **115**, 949–956 (2008)
16. M.R. Hee, J.A. Izatt, E.A. Scanson et al., Optical coherence tomography of the human retina. Arch. Ophthalmol. **113**, 325–332 (1995)
17. J.S. Schuman, M.R. Hee, C.A. Puliafito et al., Quantification of nerve fiber layer thickness in normal and glaucomatous eyes using optical coherence tomography. Arch. Ophthalmol. **113**, 586–596 (1995)

Intraoperative Retinal Optical Coherence Tomography

58

Justin Migacz, Oscar Carrasco-Zevallos, Paul Hahn, Anthony Kuo, Cynthia Toth, and Joseph A. Izatt

Keywords

Anterior segment surgery • Cataract surgery • Image guidance • Intraoperative imaging • Ophthalmic microsurgery • Optical coherence tomography • Vitreoretinal surgery

58.1 Introduction

Since its inception in 1991 [1], optical coherence tomography (OCT) imaging has revolutionized diagnostic ophthalmology and become the clinical standard of care for diagnosis of numerous retinal diseases. In this chapter, the emerging application of OCT for real-time, intraoperative diagnostic imaging and visualization of surgical maneuvers is reviewed. Intraoperative OCT provides surgeons with depth visualization in addition to the conventional en face surgical field of

J. Migacz (✉)
Department of Ophthalmology and Vision Science, University of California at Davis, Davis, CA, USA
e-mail: jvmigacz@ucdavis.edu

O. Carrasco-Zevallos
Fitzpatrick Institute for Photonics and Department of Biomedical Engineering, Duke University, Durham, NC, USA

P. Hahn • A. Kuo
Duke Eye Center and Department of Ophthalmology, Duke University Medical Center, Durham, NC, USA

C. Toth
Duke Eye Center and Departments of Ophthalmology and Biomedical Engineering, Duke University Medical Center, Durham, NC, USA

J.A. Izatt
Fitzpatrick Institute for Photonics and Departments of Biomedical Engineering and Ophthalmology, Duke University Medical Center, Durham, NC, USA

© Springer International Publishing Switzerland 2015

W. Drexler, J.G. Fujimoto (eds.), *Optical Coherence Tomography*,
DOI 10.1007/978-3-319-06419-2_60

view for both anterior segment eye surgery and vitreoretinal surgery and may facilitate evaluation of surgical procedures. Such advantages may enable OCT as a vital tool during surgical intervention in addition to its well-known diagnostic capabilities.

58.1.1 Benefits of OCT Imaging in Non-ophthalmic Microsurgeries

Microsurgeries are surgical procedures and techniques to manipulate and repair small (micron to millimeter scale) structures, such as small vessels, nerves, membranes, and other tissues. During microsurgery, surgical microscopes are commonly utilized to improve visualization of these small structures. Conventional surgical microscopes provide en face single or dual stereoscopic views of the surgical field, providing only limited perception of the third dimension. Thus, depth, or axial information, must largely be inferred by the surgeon. In addition to stereoscopy, the surgeon may rely on alternative cues such as instrument shadowing or tissue mechanical feedback to determine the depth of surgical tools within the surgical field. With its high-resolution tomographic imaging capabilities, OCT can offer direct visualization of the depth dimension, which may substantially facilitate surgical procedures as well as pre- and postoperative evaluation.

Recognizing such potential advantages, OCT has previously been investigated for use in a variety of non-ophthalmic surgeries [2, 3]. These include OCT guidance of laser ablation of tissue to enable real-time tracking of ablation dynamics and photodynamic therapy [4–6]. OCT has also been utilized to intraoperatively evaluate breast tumor margins. Micron-scale subsurface imaging allowed for more accurate assessment of surgical margins since tissue morphology not apparent in en face views was readily visible in tomographic images [7]. Brain tumors have also been evaluated with high-resolution OCT. A handheld OCT surgical probe was developed to image variations in optical backscatter representing margins between healthy and cancerous tissue. OCT was utilized to demarcate these tumor margins on cadaveric human cerebral cortex, demonstrating its potential for intraoperative use [8].

The feasibility of laparoscopic OCT imaging of endometriosis and ovarian carcinoma has been evaluated. OCT differentiation between pathological and normal tissue was investigated based on tissue morphological changes [9]. Moreover, OCT was utilized to determine if minimally invasive evaluation of gynecologic tissue in human cervical and uterine tissue was feasible [10]. Additionally, intraoperative OCT has been utilized to image human cartilage in normal and osteoarthritic knee joints during open knee surgery. Findings were compared to histology and landmarks identified in OCT correlated with histology. Changes in birefringence, which can serve as an indicator of collagen disorganization in early osteoarthritis, were evident in the OCT images [11]. Furthermore, OCT was utilized to evaluate microsurgical anastomoses of vessels and nerves. An OCT system incorporated into a surgical microscope enabled in vitro imaging of rabbit and human vessels and nerves. Arteries and nerves not visible in the conventional microscope's view were detected in OCT images [12].

58.1.2 Needs and Applications in Ophthalmology

In the modern ophthalmology clinic, OCT routinely enables rapid, noncontact, micrometer-scale visualization of retinal and anterior segment morphology. Translation of the clinical success of OCT into the operating room for better visualization of ophthalmic surgery is emerging as an exciting area of research. The following sections provide a brief review of aspects of anterior segment and vitreoretinal procedures which may particularly benefit from the potential ability of OCT to provide real-time, three-dimensionally resolved feedback to the surgeon.

58.1.2.1 Anterior Segment Surgical Procedures

OCT could potentially provide enhanced visualization of common anterior segment procedures intraoperatively, including keratoplasty (corneal transplantation) and cataract surgery.

In keratoplasty, either part of or the entire pathological cornea is replaced with a healthy, donor cornea. Multiple pathologies are addressed by keratoplasty. These include ectatic disorders resulting in thinned deformed corneas such as in keratoconus and keratoglobus and corneal endothelial decompensation from surgical trauma or genetic conditions resulting in visually disabling swelling of the cornea [13–15]. All of these pathologies result in degradation of visual acuity, necessitating keratoplasty to restore adequate patient vision.

In conventional penetrating keratoplasty, the entire cornea is removed and replaced with a donor cornea. The recovery time for a full corneal transplant can be up to a year, and such procedures are prone to complications such as irregular curvature due to manual suturing with resultant variable suture tension. To mitigate these complications, new surgical techniques have been developed for keratoplasty, including Descemet's stripping endothelial keratoplasty (DSEK) and deep anterior lamellar keratoplasty (DALK) for endothelial and anterior corneal diseases, respectively [16]. The goal of DSEK is to replace only the diseased endothelial layer, the innermost layer of the cornea, rather than the entire cornea. The majority of the cornea (about 95 %) remains untouched [17]. Likewise, in DALK, only the diseased anterior part of the cornea is replaced [18]. During this procedure, the diseased stromal tissue is separated anterior to Descemet's membrane. In contrast to DSEK, only the patient's Descemet's membrane and endothelium are retained; all anterior tissue is replaced by the healthy donor cornea.

For both DSEK and DALK keratoplasty procedures, precise knowledge and control of layer thicknesses throughout the procedure is required for surgical success. The entire cornea is only about 0.5 mm thick centrally, and tissue layers must be dissected and manipulated in both procedures with accuracy of tens of micrometers. Providing micrometer-scale delineation of corneal layers, intrasurgical OCT could dramatically enhance surgical control of these critical parameters which are vital to the success of these ambitious surgical procedures.

Cataract surgery is another commonly performed anterior segment procedure which could potentially benefit from intraoperative OCT guidance. Cataract

surgery is the most frequently performed surgical procedure in the USA; an estimated 20.5 million Americans over the age of 40 have cataract in either eye [19, 20]. Cataracts, defined as opacification or clouding of the lens, can eventually lead to blindness if untreated. The goal of cataract surgery is to replace the clouded lens with an artificial lens to improve visual acuity. Optimizing cataract surgery with image guidance, either by facilitating pre- and postoperative screening or by enabling micron-scale visualization of surgical maneuvers intraoperatively, would have a sizable public health benefit.

In modern small incision cataract surgery, there are important steps to the successful completion of the procedure. After a corneal limbal incision is created, a circular opening approximately 5.5 mm in diameter needs to be created in the anterior lens capsule. The cataractous lens then needs to be separated from the surrounding lens capsule, fragmented with phacoemulsification or femtosecond laser, and aspirated from the eye. The artificial intraocular lens can then be placed in the empty lens capsule. Finally, the corneal incision is verified to be watertight to complete the procedure.

OCT can potentially assist with visualization in each of these critical steps in cataract surgery when using standard phacoemulsification. Further, if the femtosecond laser is used, it could be argued that OCT guidance becomes critical as it provides guidance for the placement of the laser spots [21]. In either case, OCT may provide direct visualization of the corneal incision creation, enabling study of incision type and subsequent performance. OCT could monitor the creation of the anterior capsulotomy to provide guidance on its size. OCT's depth resolution importantly could allow the surgeon to monitor the depth of the phacoemulsification needle or laser spot placement during fragmentation to ensure that the posterior lens capsule is not violated. OCT could image the intraocular lens after insertion to determine its intraoperative orientation. And finally, OCT could be used to directly verify complete closure of the incision along its entire surface to prevent adverse events postoperatively from a leaking incision.

The ability of OCT to provide the axial third dimension to the conventional en face surgical microscope view provides additional and potentially critical information to improve the surgeon's technical precision and the patient's outcome in ocular anterior segment surgeries.

58.1.2.2 Vitreoretinal Surgeries

Vitreoretinal surgery involves critical microsurgical repair of pathologies of the retina and surrounding tissues. In contrast to anterior segment surgery, conventional operating room microscope visualization of retinal surgery requires additional optical accessories to image the retina through the patient's own cornea and lens, which are often of suboptimal quality in the elderly populations most at risk for vitreoretinal pathologies. These additional optical systems further reduce already limited stereopsis. Thus, additional three-dimensionally resolved anatomical information potentially provided by intraoperative OCT is especially promising for improving outcomes in vitreoretinal surgery.

Manipulation and removal of pathological membranes is a common feature of vitreoretinal surgeries which could benefit from intraoperative image guidance. Epiretinal membranes (ERMs) are thin layers of fibrous tissue which can develop on the surface of the retina. If these membranes cause traction, they induce mechanical disturbances leading to vision loss. ERMs can be associated with a variety of pathologies, including retinal detachment, retinal vein occlusions, and uveitis. However, ERMs most commonly develop in patients with no history of other related pathologies. When loss of vision affects the patient's ability to function, vitrectomy (removal of vitreous gel) with membrane peeling may be performed to surgically remove the ERM.

The vitreoretinal surgeon must similarly be equipped to address other pathological membranes. These include the native internal limiting membrane (ILM), in which abnormal tangential traction can prevent surgical closure of a full-thickness macular hole. Patients with proliferative diabetic retinopathy develop fibrovascular membranes in the vitreous cavity and on the retinal surface and may result in complex traction detachments. Retinal detachments due to retinal tears in eyes without diabetes may develop proliferative vitreoretinopathy, which manifests as development of membranes on or below the retinal surface and is a common cause of failure of surgical reattachment.

Microsurgical procedures to remove pathological membranes involve use of a variety of different tools utilized to peel these membranes from the retinal surface, including surgical forceps and membrane scrapers [22]. These membranes are on the order of tens of microns thick and nearly invisible without stains to improve visualization. The surgeon must be able to separate these delicate membranes from the retina with precision and without inducing trauma to the underlying retina. These maneuvers are currently performed under stereo zoom microscopy guidance without any axial information other than stereoscopy and indirect physical cues such as secondary folds of the retina. To provide precise, real-time feedback to surgeons, OCT has begun to be utilized during vitreoretinal surgery by several research groups and companies. In later sections of this chapter, the benefits of applying OCT to visualize different surgical procedures, including ERM and other membrane peeling, are discussed. Specifically, these groups have demonstrated that intraoperative OCT appears to help surgeons delineate pathological from healthy tissue and to help determine the anatomical success of these procedures.

58.2 Current Approaches to Intraoperative Ophthalmic OCT

In this section, we review the three distinct approaches for intraoperative ophthalmic OCT which have been reported to date: external handheld probe OCT (HHOCT), microscope-integrated OCT (MIOCT), and forward-imaging probe OCT. For each case, the relative advantages and disadvantages of the approach are discussed, and imaging examples from published reports on the techniques are provided.

58.2.1 External Handheld Probe Systems

Several research groups have reported on the use of handheld OCT (HHOCT) probes during pauses in ophthalmic surgery, mostly using a commercial HHOCT device from Bioptigen, Inc. (Durham, USA). This product was originally developed for use on animals and for patients such as infants who are unable to sit upright in front of a conventional tabletop OCT scanner [23] and was first suggested for intrasurgical use by Scott et al. [24] and then used in the operating room by Dayani et al. [25] as well as others [26–28]. Ray et al. employed the commercial handheld probe in a rigid holster mounted to the side of the surgical microscope for evaluation of retinal anatomy during macular surgery [29]. In this study, the mounted HHOCT probe was suspended over the eye and moved into position by the use of the microscope's foot pedal-controlled X-Y translation. Intraoperative imaging of the anterior segment using commercial and prototype cart-based systems has also been reported [30, 31]. These studies have demonstrated safe and effective imaging of corneal features at different stages of the procedure. A photograph illustrating the use of the Bioptigen HHOCT system during surgery in freehand mode is shown in Fig. 58.1.

The principal advantage of the intraoperative HHOCT systems used to date in freehand mode is alignment versatility. A well-trained operator, normally the surgeon or an assistant, tilts and translates the probe, wrapped in a clear, sterile, plastic bag, steadily over the patient's eye until good visibility of the retinal tissue is achieved. The freedom and range of tilting over the eye allows the surgeon to explore

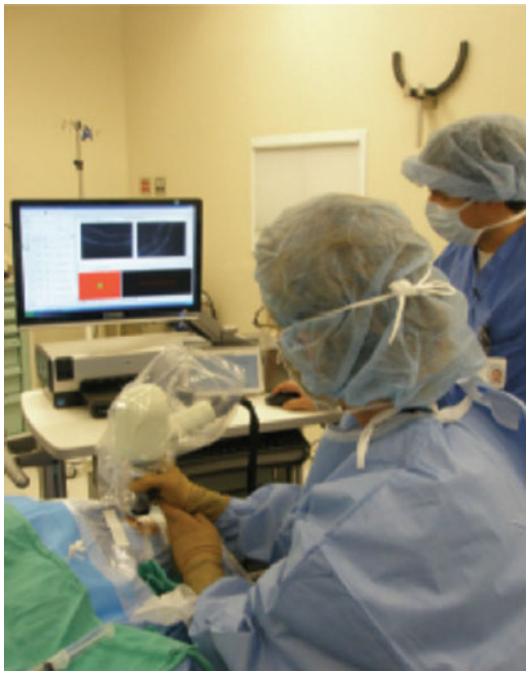

Fig. 58.1 A handheld OCT system in use at a pause in retinal surgery [25]

the retinal area and find the desired features quickly. The freedom of movement is particularly advantageous when the patient has reduced clarity through the pupil, such as with opacification of the lens capsule. The HHOCT used in microscope-mounted mode offers some stability advantage with foot pedal control over the freehand mode, however at the cost of alignment versatility.

The primary disadvantage of intraoperative HHOCT imaging is the unavoidable disruption to the procedure. The surgeon must remove any nonsecure surgical instruments from the eye and remove the operating microscope from the surgical field to bring the handheld probe into position.

Figure 58.2 illustrates HHOCT images taken in freehand mode immediately before and after surgical removal of the retinal ILM layer [25]. Postoperative morphology indicates reduced traction (tension), which is likely important for a favorable surgical outcome. The OCT images clearly demonstrate remnant ILM tissue. Under normal practices, membranes are stained to facilitate their visibility in the surgical microscope. OCT imaging can clearly delineate ILM and the underlying tissue when the ILM is peeled or elevated. Intraoperative HHOCT imaging also demonstrates small hemorrhages caused by instrument manipulation (Fig. 58.2(f)). This additional information may enable the surgeon to better assess whether the extent of peeling or other surgical maneuvers were adequate or whether additional maneuvers would be necessary.

Because intrasurgical HHOCT is based on use of a commercially available product, it has so far likely been used by more investigators and on more patients than the more advanced but still experimental systems described in the next sections. The handheld approach has been shown to be effective at quickly evaluating the morphological changes of the target tissue at various stages during operations and has thus served as a test bed for future development of OCT guidance of intrasurgical procedures.

58.2.2 Microscope-Integrated Systems

To take full advantage of the potential for real-time OCT imaging during surgery and to minimize disruptions required for HHOCT imaging, several groups have reported on OCT systems integrated directly into the optics of the surgical microscope [32–51]. This approach has been termed microscope-mounted (MMOCT) and microscope-integrated (MIOCT) optical coherence tomography. We shall use the latter throughout this review because it better emphasizes the simultaneous operation of both the microscope and OCT systems. The underlying objective for an MIOCT system is to achieve en face and OCT imaging simultaneously without compromising the surgical view.

Integrated OCT designs take advantage of the optical components of the surgical microscope, which are optimized to achieve high-resolution en face imaging under a long working distance objective. This is suitable for manipulations on the surface of the eye, such as for anterior segment procedures. Visualizing the retina is achieved by cancelling or compensating for the power of the patient's anterior optics, either by use of

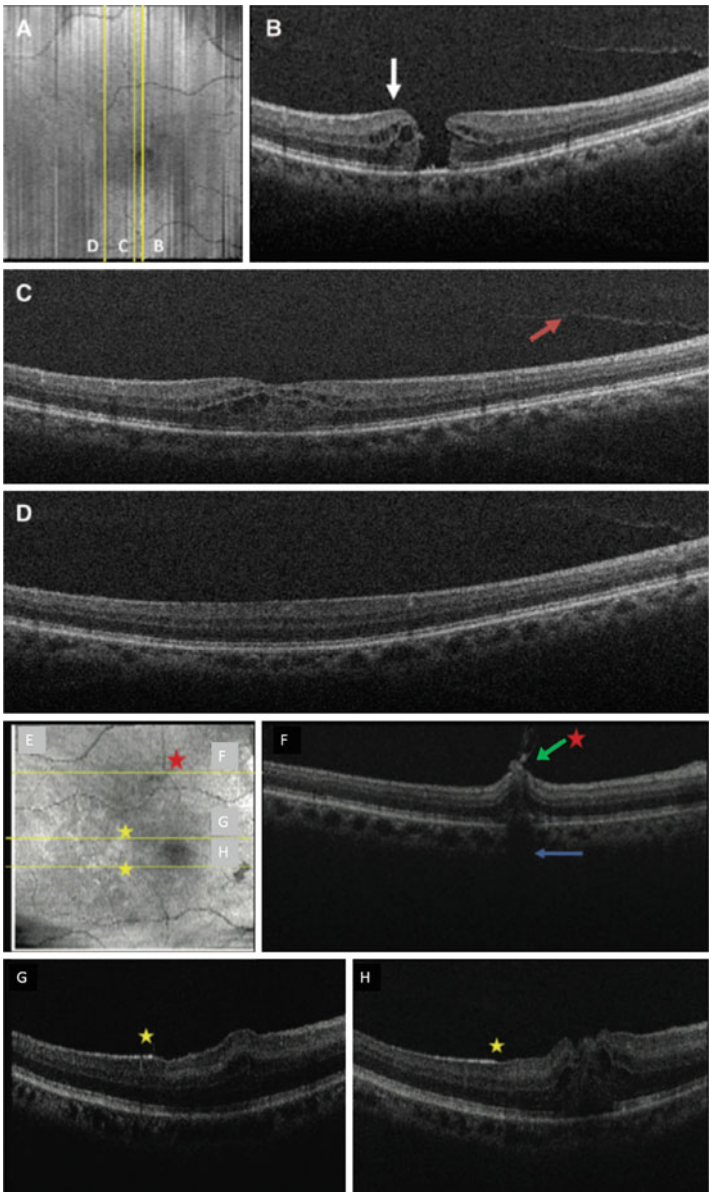

Fig. 58.2 HHOCT images of intraoperatively relevant features on a patient immediately before and after internal limiting membrane peeling [25]. In (**a**–**d**), images from an OCT volume dataset obtained pre-operatively are presented, while post-operative data obtained from the same location is shown in (**e**–**h**). (**a**, **e**) Surface volume projections of the volume datasets with yellow lines indicating positions of the individual B-scans shown following. In (**b**), cystic thickening adjacent to the macular hole is visible. In (**c**–**d**), partial vitreous separation is visible (*red arrow*). In (**f**), the green arrow indicates a pre-retinal hemorrhage corresponding to traumatic retinal hemorrhage caused by membrane peeling (*red star*). The yellow stars in (**g**–**h**) show remnant hyper-reflective ILM tissue

Fig. 58.3 The Duke prototype MIOCT system deployed in the ophthalmic operating room [42]. The surgeon's eyepieces face the camera and the assistant is at the microscope

a flat outer surface lens in contact with the cornea or by reimaging the fundus to an intermediate plane with a positive ophthalmic lens. The latter approach is akin to indirect ophthalmoscopy. Multiple vendors have produced a range of contact lenses and versatile modules that mount the appropriate reimaging optics to the underside of the microscope.

MIOCT systems may combine the OCT beam into the visual path of the microscope either by division of aperture, such as through use of the assistant optical path [44, 45], or by division of wavefront, such as by use of a dichroic beamsplitter [32, 34, 36–43, 46–51]. To take advantage of the above-mentioned methods of viewing the desired field (of either cornea or macula), the OCT beam must optimally match the microscope's normal vergence at the point of insertion, so that the OCT view matches and remains parfocal with the surgeon's view.

A disadvantage of MIOCT systems is that they potentially increase the size, weight, and complexity of the surgical microscope suspended above the patient during surgery. For example, the prototype MIOCT system in current testing by our group at Duke University adds bulk which increases the height of the microscope body (from working lens to surgeon eye pieces). This is primarily due to the fact that these systems are currently experimental prototypes built as add-ons to commercial surgical microscopes. If preliminary testing by research groups is successful, microscope manufacturers could mitigate ergonomic issues by more fully integrating OCT in the design of future microscopes.

A photograph of the Duke prototype MIOCT system in use during surgery is shown in Fig. 58.3. Further details of MIOCT optical design and published results to date are provided below in Sects. 58.3 and 58.4, respectively.

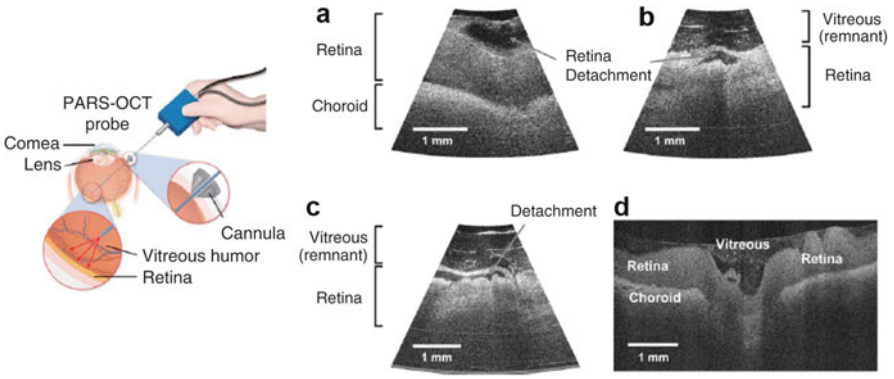

Fig. 58.4 Illustration of the forward-imaging endoscopic probe developed by Han et al. (*left*) and representative B-scans of porcine retinal tissue (*right*) [53]

58.2.3 Intraocular Forward-Imaging Endoscopic OCT Probes

The development of forward-imaging OCT probes was first reported by Boppart et al. early in the history of OCT [52], but they were not initially targeted toward ophthalmic applications. More than a decade later, Han et al. [53] published work on an OCT scanning endoscope integrated into a narrow 21 gauge (810 um diameter) needle for retinal imaging. This design achieved excellent retinal image quality in animal eyes (Fig. 58.4). An unusual feature was the central wavelength of 1,310 nm, which is conventionally used for anterior segment but not retinal imaging because of strong absorption in the vitreous [54]. This issue was circumvented by the fact that the tip of the intraocular endoscopic probe was placed in close proximity to the tissue to be scanned. The working distance of the endoscope was 0.78 mm, leaving little room for vitreal absorption or for much error in hand movement.

One disadvantage of handheld endoscopes for intraocular surgery is the additional need it places on the surgeon for probe manipulation. Typically, one of the surgeon's hands is used for holding an endoilluminator inside the ocular cavity to provide wide-angle illumination, while the second hand controls the tool that is actually manipulating the retinal tissue. Using endoscopic OCT imaging during tissue manipulations may therefore require the illumination to be fixed to a third insertion point in the sclera, such as in chandelier illumination.

Balicki et al. [55] reported an alternate intraocular probe design mounted inside a surgical needle. This effectively combined an OCT scanner with the manipulating surgical tool. However, the probe did not incorporate lateral scanning and thus only performed A-scans directly coaxial with the needle. Generating cross-sectional B-scans by sweeping the tool near the target tissue at a fixed distance by use of this probe was anticipated using robotic assistance, which may become prevalent in the future. This system also incorporated a fast ranging capability feedback to the motorized stage to compensate for patient motion by keeping the instrument tip at a fixed distance from the tissue.

To date, both of these forward-imaging ophthalmic probe systems have only been demonstrated on animal models.

58.3 Microscope-Integrated OCT System Design

In this section, we elaborate on the design and implementation details of MIOCT system hardware and control software, concentrating primarily on the system constructed and tested by our collaborative group at Duke University. We compare and contrast this design to those of other systems known to be under development, to the extent that details of these systems have been reported.

The Duke MIOCT system optical design and performance was first described by Tao et al. in 2010 [34] and the first human intrasurgical results (with the original custom-built OCT engine replaced by a commercial spectral-domain OCT console from Bioptigen, Inc.) were reported by Hahn et al. in 2012 [41, 42, 46]. An MIOCT system developed by Carl Zeiss Meditec (Jena, Germany) has been the subject of several reports by Binder et al. [32, 40]. A group at the University of Lubeck in Germany has developed and reported on a system which has been commercialized by OptoMedical Technologies GmBH (Lubeck, Germany) and Möller-Wedel (Wedel, Germany) [44, 45]. All three of these first-generation MIOCT systems share several similarities. All are based on spectrometer-based spectral-domain OCT engines operating near 850 nm wavelength, with coherence length (corresponding to axial resolution) of approximately 5 μm, and A-scan rates of 20–30 kHz. The principal distinction between first-generation systems appears to be in the sample arm scanner design and surgical microscope interface, which directly influences imaging performance. The Duke and Carl Zeiss systems are shared-objective designs utilizing the principle of division of wavefront, whereas the Möller-Wedel OCT design is based on division of aperture and occupies a separate collection path from the microscope visual optics.

The Duke MIOCT scanner optical design is illustrated in Fig. 58.5, along with a photograph of the scanner attached to a Leica M844 surgical microscope with an Oculus BIOM3 fundus viewing system. In this design, the OCT sample arm scanning beam is coupled into the infinity space directly above the microscope objective lens using a dichroic beamsplitter and aligned with the OCT optical axis midway between the stereo viewing path visual axes [34]. The OCT beam is shaped using a beam expander telescope prior to merging with the microscope visual path in order to achieve the standard lateral OCT resolution (~15 μm) expected by retinal specialists. Thus, the OCT beam aperture in the shared region is larger than either of the stereo view optical apertures, with an associated reduction in depth of field compared to the visual stereo view. Optical design and test performance of the MIOCT unit are also illustrated in Fig. 58.5.

Insertion of the OCT scanning beam in the infinity space of the microscope view provides minimum interference with the operation of microscope components and accessories such as the zoom module, laser filters, camera ports, and assistant eyepieces, all of which are optically upstream from this position. Stacking of

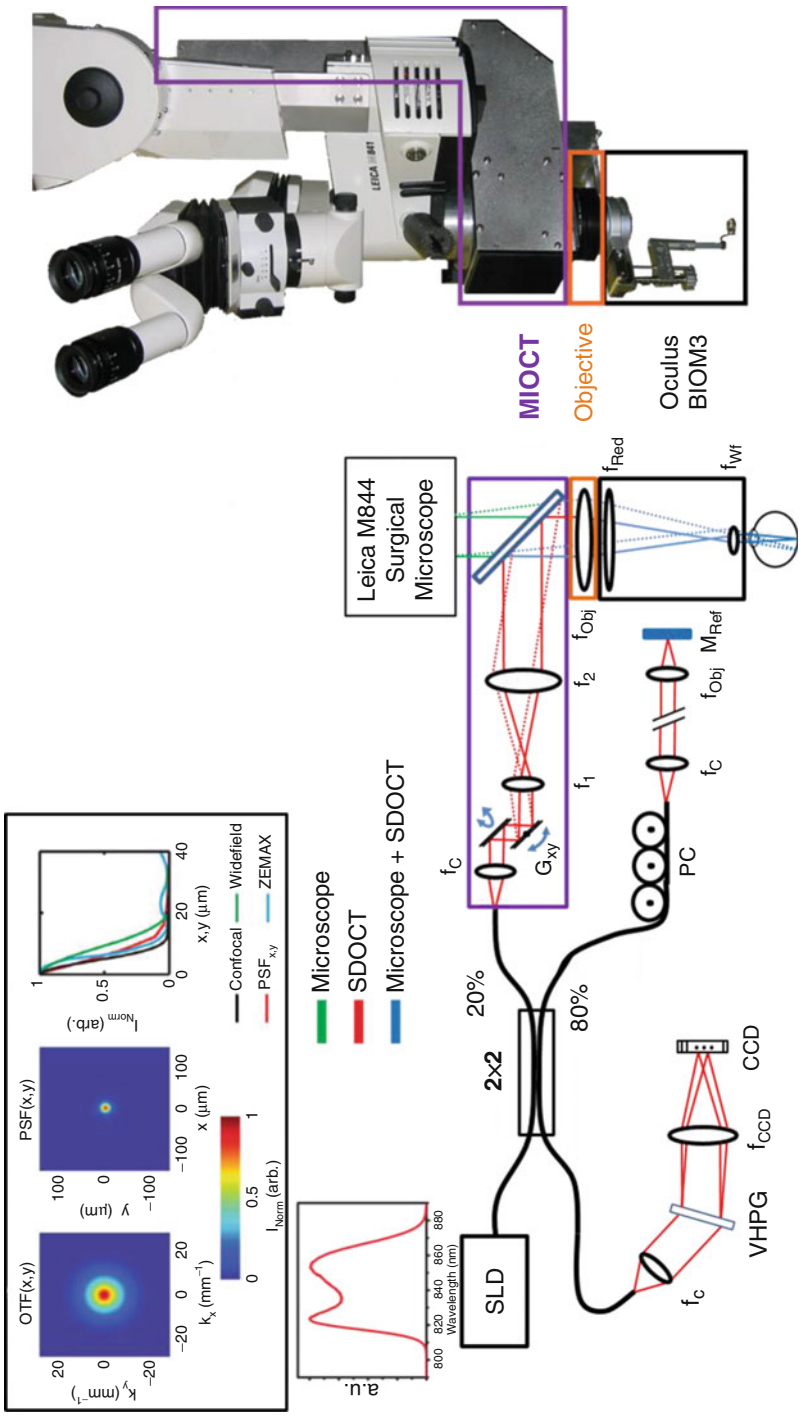

Fig. 58.5 The MIOCT system schematic (*left*) and microscope mounting (*right*) [43], as well as measured and simulated optical performance (inset) [34]

additional components in the infinity space does not alter the microscope resolution; however, care must be taken to avoid reducing the microscope field of view through vignetting, as well as to adjust the internal microscope illumination sources for extraocular and anterior segment work. The added height of the system (approximately 5 in. in the Duke system) can affect the posture of the surgeon and can be mitigated for shorter surgeons by using periscope oculars.

58.3.1 System Features for Managing the Challenging OR Environment

The Duke MIOCT scanner unit was designed as a surgical microscope accessory which is installed and aligned prior to surgery within approximately 10 min. The rest of the MIOCT system (the OCT "engine" and operating software) is a modified commercial spectral-domain OCT unit (from Bioptigen, Inc.) on a wheeled cart which is also brought into the operating room for MIOCT cases, similar to prior intraoperative OCT implementations [7]. All optical and electronic cabling between the OCT engine and the microscope-mounted scanner unit are suspended from the ceiling to avoid any tripping hazard.

Prior to use of the Duke MIOCT system in human surgical cases, extensive operating room evaluations were performed by having experienced anterior segment and retinal surgeons and surgical nurses interact with the MIOCT scanner unit in simulated surgeries. The participants were asked to evaluate how the scanner unit might interact with their normal surgical practices and maneuvers in a series of simulated tasks with defined evaluative assessments. The majority of responses identified no negative impact from having the device within their operating room environment. The overall impression was positive, and 100 % of surgeons and nurses reported that they would consider participating in human intraoperative MIOCT imaging trials [42]. Additional valuable feedback from these sessions, including recommendations on improved routing of the cables and rounding of the device edges, was also obtained to further improve the system.

58.3.2 Dynamic Navigation and Manual/Automated Tracking of Scanning Location

The principal advantage of microscope-integrated OCT scanning, in comparison to handheld systems described previously, is that microscope integration allows for the possibility of live image-based surgical guidance (as opposed to imaging during pauses in surgery). While current-generation clinical spectral-domain OCT systems routinely acquire B-scan images in real time, all available systems require at least several seconds for complete volume imaging of the macula. Even cutting-edge ultra-high speed swept-source OCT systems still cannot image the complete macula in real time in three dimensions with clinically acceptable optical power levels. A promising approach for matching the imaging rate capability of OCT with the

real-time needs of surgical guidance is to implement a feedback-controlled tracking system to align the position of the live OCT B-scan (or a limited set of B-scans which can be acquired quickly) with the position on the macula which is of most immediate interest to the surgeon, such as the tip of the surgical tool in use.

Intraoperative OCT tracking has been implemented on the Duke MIOCT system using both fully automated and semiautomated "manual" tracking approaches (Fig. 58.6) [47–50]. In both approaches, a copy of the video feed from the surgical camera was used as the source of feedback to locate the position of the surgical tool tip (or other feature of interest to the surgeon), in order to direct the OCT scan location to that vicinity. In the automated approach, custom image processing software was developed to automatically locate the tool position and orientation in the video stream. While successful in phantom studies, this software is not yet capable of handling the wide range of illumination conditions in live human surgery. As an interim step, a semiautomated "manual" version of tracking has been implemented which takes advantage of a human observer who can accommodate varying surgical conditions and can also react to instructions from the surgeon. In manual tracking with the Duke MIOCT system, the live surgical view is displayed on a separate tracking computer in custom software operated by a human operator who tracks the mouse cursor to the position of current surgical interest on the macula. The mouse position is translated to a pair-offset voltage signals that are summed with the fast voltage signals controlling the MIOCT lateral scan position. The manual tracking feature has been found to enhance ease of use of the Duke MIOCT system in live human surgery, by improving OCT image placement accuracy and speed of alignment. This capability has led to faster imaging sessions and visualization of instrument-tissue interaction, which was not possible in HHOCT implementations.

58.3.3 Scanning Orientation and Data Visualization

Since OCT volume datasets are acquired quickly in the B-scan direction, and then more slowly in the azimuthal direction, it can be important to choose the scanning direction based on prior knowledge of object motion in the scanning region. For intraoperative OCT imaging, there are many possibilities to orient scanning axes relative to tissue features and/or instrument position and trajectory. As an illustration, in Fig. 58.7, a series of OCT B-scans scans were taken both perpendicular and parallel to a common vitreoretinal surgical tool, the Tano Diamond Dusted Membrane Scraper™ [43]. These images were taken in cadaveric porcine eyes. The relative transmission and shadowing of the tool can be clearly seen, and the contact between the instrument and tissue can be examined easily. For tracking maneuvers, such an orthogonal scan pattern comprised of rapidly sequentially acquired orthogonal scans with their intersection locked to the tool position and their orientation matching the tool axis may be advantageous. Alternative patterns such as a fixed scan on morphologic features may also be desired.

In a busy operating room, the methodology used for displaying the MIOCT data to the surgeon may be nearly as important as the acquisition itself. With the

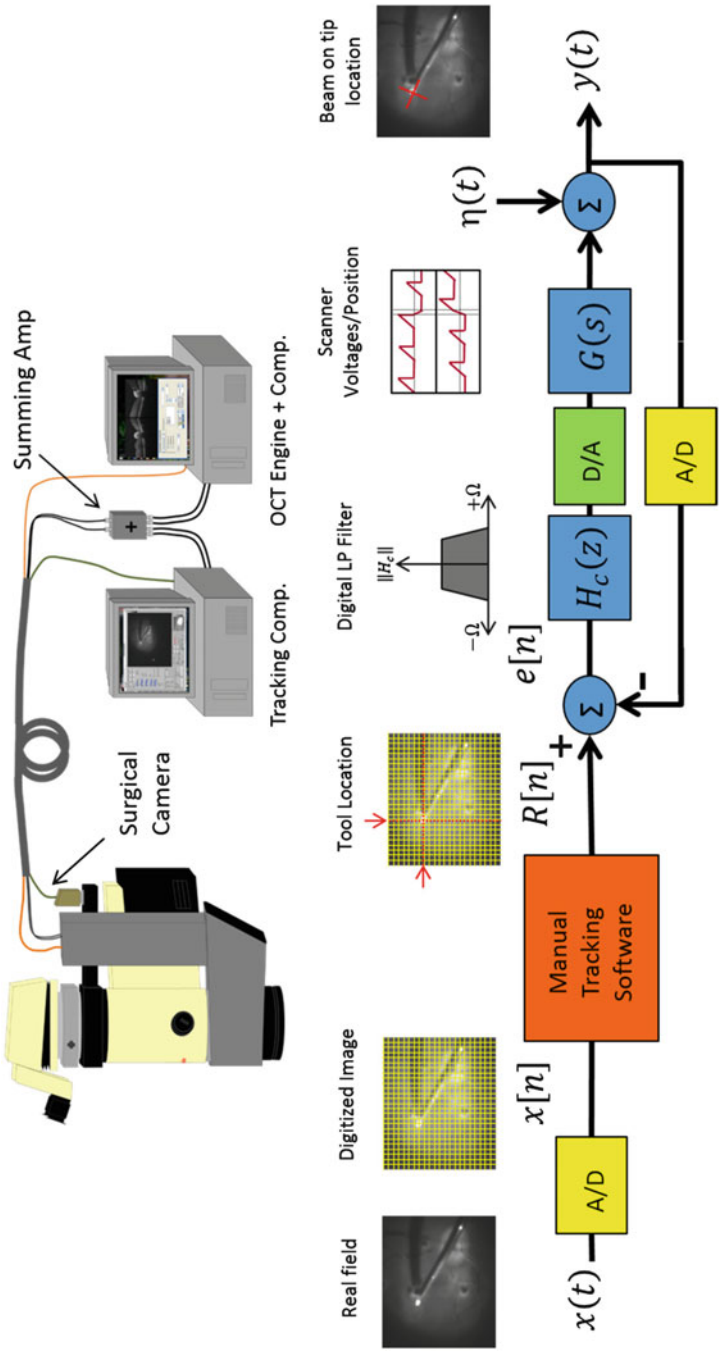

Fig. 58.6 The MIOCT tracking system being used in manual mode [50]. Hardware diagram of tracking and OCT computers (*above*), as well as the control system block diagram (*below*)

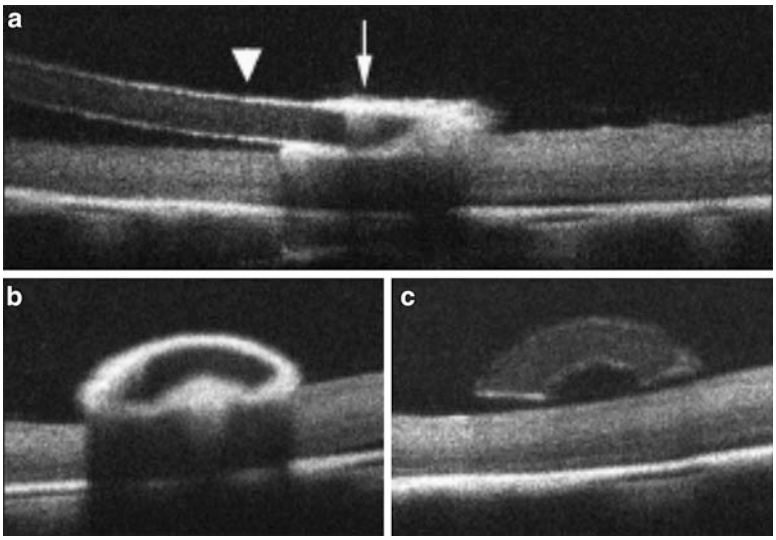

Fig. 58.7 Averaged B-scans of a surgical instrument in contact with a cadaveric porcine retina. (**a**) The view along the instrument axis. (**b**) and (**c**) are perpendicular views of the instrument from the locations at the diamond-dusted tool tip and along the instrument shaft, respectively. The highly scattering diamond-dusted section creates considerable shadowing over the retina, while the silicone shaft creates relatively little

emergence of GPU-based OCT data processing and image rendering [56], there are many options for displaying tomographic data designed to be intuitive to the user. In ultra-high-speed OCT systems (>100,000 A-scans per second) that can capture multiple volumes per second, displaying the entire dataset may be practical. For slower, current-generation systems, it may be better to display multiple registered B-scans in an isometric view. A conceptual example of this is shown in Fig. 58.8, reproduced from Hahn et al. [41], in which two orthogonal B-scans over a surgical tool are overlaid on top of an en face image and projected in a manner representing their relative directions. A likely future direction for MIOCT system development will be integration of such displays into potential "heads-up" displays which enable the surgeon to view live MIOCT image data without removing his or her eyes from the microscope.

58.4 Duke MIOCT Imaging Results

The Duke MIOCT system has been used extensively in human patient studies for both posterior segment (vitreoretinal) and anterior segment (corneal) procedures. In this section, we will review some of the findings that have been reported from studies involving the system at Duke University.

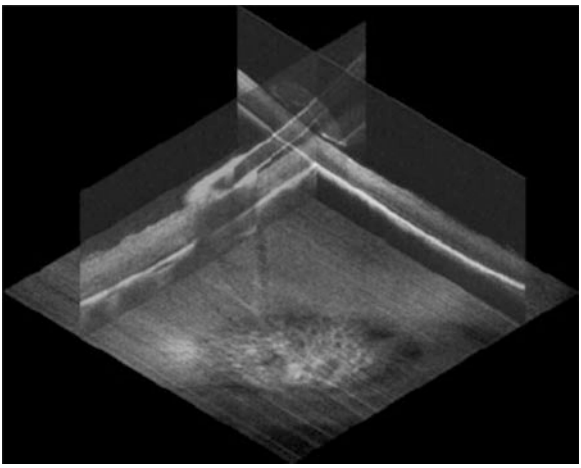

Fig. 58.8 A conceptual live orthogonal B-scan pattern visualization of a surgical instrument intersecting the macula suitable for a potential "heads-up" display [41]

58.4.1 Duke MIOCT Results in Vitreoretinal Procedures

Many vitreoretinal surgical procedures involve the removal of a membrane, such as an epiretinal membrane (ERM) or internal limiting membrane (ILM). These membranes are often difficult to visualize en face, and the surgeon typically uses stains for improved visualization. OCT imaging can often provide improved identification of these membranes, and an early goal for our studies was therefore to use OCT imaging to examine the retina immediately before and after membrane removal. In Fig. 58.9, OCT images taken shortly before and after membrane removal confirm the absence of the membrane following membrane peel.

Another example of verification of postoperative changes in retinal morphology is seen in Fig. 58.10 from Hahn et al. [42]. The patient received surgery to repair a full-thickness macular hole, which is caused by traction along the internal limiting membrane. The image following ILM peel suggests that the tissue near the hole is more relaxed than prior to peeling and therefore that removing the membrane has eased the traction. Remnants of the edge of the uplifted membrane (asterisks), small intraretinal cysts (arrowheads), as well as some subretinal fluid (arrow) are clearly visible. These features would likely not be visible in the en face surgical view and would likely not be present in follow-up imaging of the patient in the days following the procedure.

These data from human vitreoretinal cases demonstrate the ability of MIOCT to take evaluative images of the target tissue at pauses in the surgery and definitively identify changes that would not otherwise be detected. This is very similar to what has already been achieved using HHOCT probes in surgery. The acquisitions, however, were taken with the surgical microscope still in place over the patient creating little delay in the surgical procedure. Also, it allows for the visualization of tools undergoing surgical maneuvers, which will be discussed in Sect. 58.4.1.3.

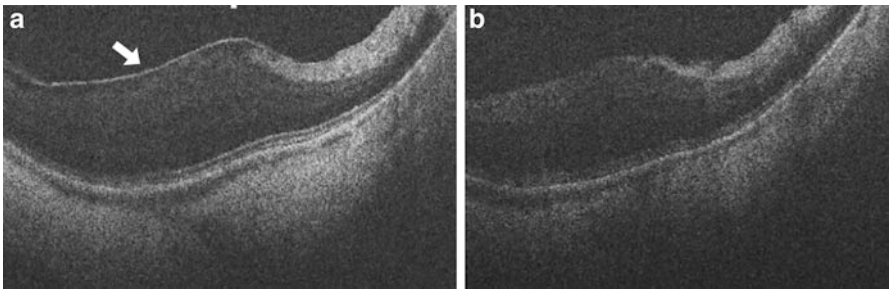

Fig. 58.9 Single B-scans showing a cross section of a diseased retinal directly prior to (**a**) and after (**b**) epiretinal membrane removal [50]. The membrane which is a *bright line* on the surface of the retina (*arrow*) in (**a**) is clearly absent in (**b**)

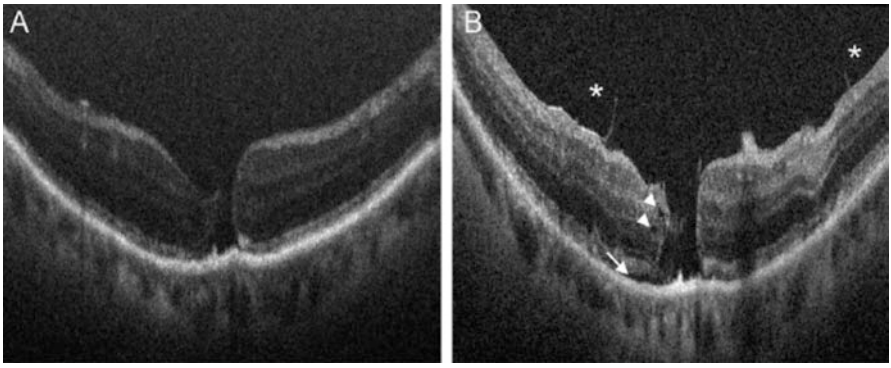

Fig. 58.10 A comparison of averaged B-scan images of the foveal region for a patient undergoing surgery to repair a full-thickness macular hole [42]. The internal limiting membrane was removed to reduce traction in the macula. As compared to the preoperative image in (**a**), the retinal tissue postoperatively in (**b**) appears more relaxed and corrugated, suggesting a reduction of traction. Remnants of uplifted ILM tissue (*asterisks*) as well as intraretinal cysts (*arrowheads*) and mild subretinal fluid (*arrow*) are clearly visible in (**b**) which was taken within minutes of the membrane peel

58.4.2 Duke MIOCT Results in Anterior Segment Procedures

The Duke MIOCT system has also been used to evaluate the state of the cornea in anterior segment procedures such as cataract extraction and DSEK [47]. In cataract surgery, the main incision near the corneal limbus is the entry point for tools to access the anterior chamber and to remove the natural, opacified crystalline lens. The incision does not normally require suturing at the conclusion of the surgery, but a hydration step does ensure the initial closure that then heals during the days following the surgery.

Intraoperative monitoring of the corneal incision at the conclusion of cataract extraction showed initial gaping of the incision which closes with stromal hydration, as illustrated in Fig. 58.11 [47]. Such direct confirmation of wound closure

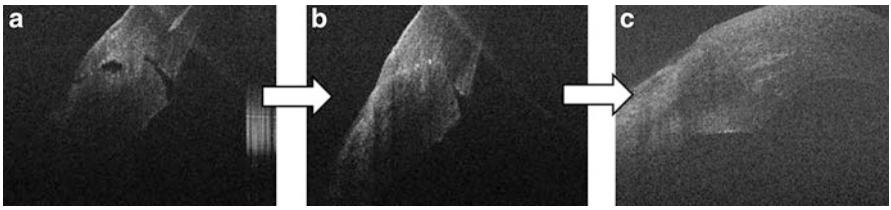

Fig. 58.11 Single B-scan views of the corneal incision wound at the end of cataract surgery before (**a**) and then after (**b**) the hydration closure step and 1 day following the surgery (**c**) [47]

could ensure wound security at the conclusion of the case. The first postoperative visit is typically a day later, and an inadvertently insecure wound could result in devastating introduction of pathological organisms into the eye. In successive cross-sectional B-scans shown in Fig. 58.11, wound opening was initially observed to be gaping (A), then closed by hydration (B), and then remaining closed in follow-up imaging one day after the procedure (C). The follow-up image was taken with a conventional tabletop SDOCT scanner in the clinic.

Dynamic MIOCT imaging of the keratome creating a corneal limbal incision was observed, as shown in Fig. 58.12. In the first frame during insertion (on the *left*), the tool has fully cut through the cornea and in subsequent frames is pushed farther into the anterior chamber. In frames depicting tool removal (on the *right*), the tool is shown backing out of the tissue. The last frame shows the status of the wound immediately after the blade is removed, with the wound mostly closed and some stromal disruption visible, appearing as lengthwise bright streaks that straddle the wound.

MIOCT has been used to monitor graft adherence in DSEK procedures, as illustrated in Fig. 58.13. Here, B-scan images were taken of the patient immediately following the implantation of the donor graft with a supporting air bubble in the anterior chamber. The donor graft was observed to be close to the host cornea, but residual interface fluid was clearly visible. Failure to address this gap intraoperatively would likely result in postoperative graft detachment and additional surgery. A few minutes after the injection of the full air tamponade and additional mechanical maneuvers, MIOCT revealed good apposition of the donor graft and host cornea across the entirety of the visible region.

58.4.3 Visualizing Surgical Tools Inside the Eye

The MIOCT system has clear advantages over intraoperative HHOCT in that it may be used to capture tomograms while surgical tools are maneuvering within the eye. Figure 58.14 shows an en face projection of OCT data captured while a pair of surgical forceps were inside the eye in the mid-vitreous cavity and out of axial range of the OCT B-scans [57]. The effect of the tool shadowing is clear in the representative B-scans which are also shown. This was the first published example of OCT imaging of tools in the eye during human vitreoretinal surgery.

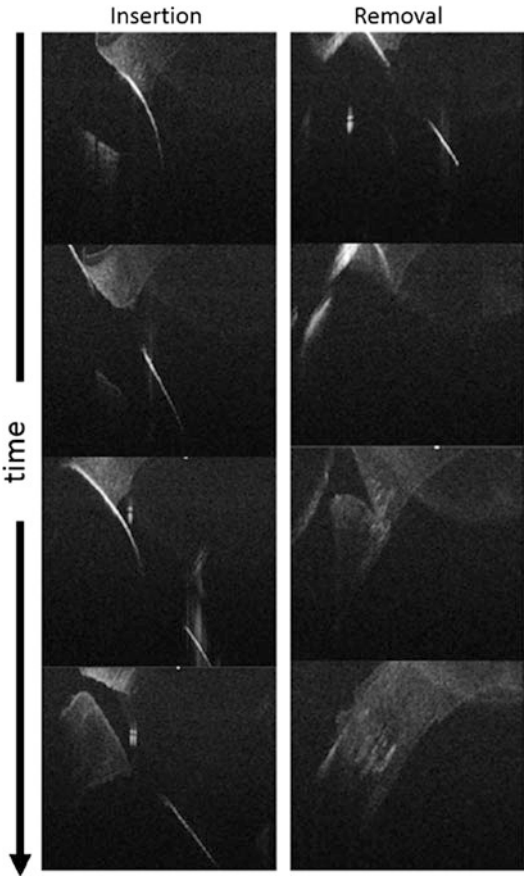

Fig. 58.12 B-scan sequence of corneal incision blade making a cut through the cornea

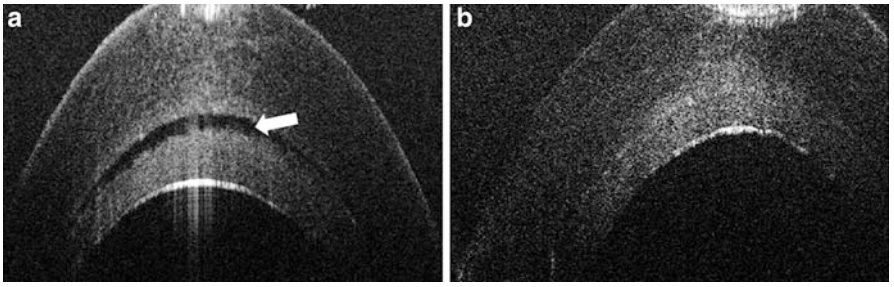

Fig. 58.13 Cross-sectional (single-frame) B-scan of the cornea, showing (**a**) interface fluid (*white arrow*) between the DSEK graft (inferior) and host cornea (superior) and (**b**) successful attachment of the graft to the host cornea [47]

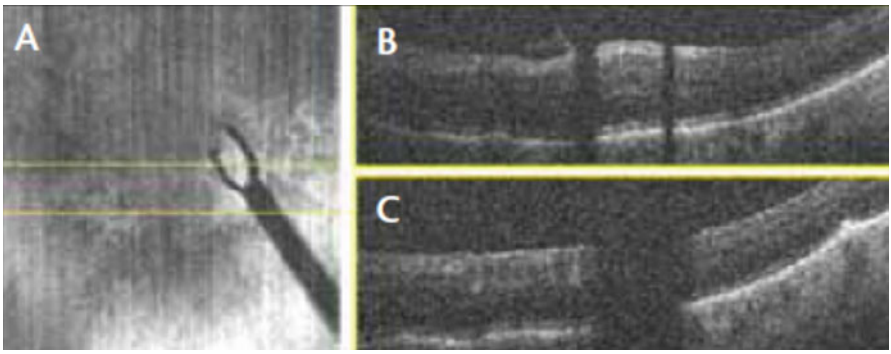

Fig. 58.14 OCT images taken while surgical instruments present in the vitreous cavity [57]. (**a**) A surface volume projection of forceps overlying a human retina and suspended safely in the mid-vitreous cavity. Complete shadowing under the metallic instrument is visible in the corresponding B-scans (**b–c**) at the positions indicated by the *green* and *orange lines* in (**a**)

OCT imaging of tool manipulation of cadaveric porcine model eyes has also been extensively documented by Hahn et al. [41], in which real-time MIOCT imaging of both forceps and membrane scraping tools were presented. The most dramatic of these are shown in Fig. 58.15, in which multiple frames of a linear B-scan sequence are shown. The porcine retina was being brushed by a Tano Diamond Dusted Membrane Scraper™ (Synergetics, O'Fallon, Missouri, USA) instrument from left to right. The sequence in the left column shows an aggressive scrape in which significant deflection of the retinal tissue is obvious. The right column shows a milder brushing motion in which little deflection can be noticed.

58.4.4 Visualizing Tools Despite Artifacts

Another significant advantage of MIOCT over HHOCT is the ability to visualize surgical tools manipulating target tissue. Ehlers et al. have extensively cataloged the appearance of various common vitreoretinal tools as imaged by the MIOCT in cadaveric porcine eyes [36]. OCT images that have tools visible in the frame show evidence of artifacts, either full shadowing (blockage), as can be seen in Figs. 58.14 and 58.15, or distortion of the tissue directly underneath the tool as in Fig. 58.15. Some imaging sessions revealed complex-conjugate reflections that, if misinterpreted, could mislead the surgeon as to the tool's actual location with respect to the tissue.

The distortion of tissue directly beneath a transparent tool or tool portion, such as the silicone shaft of the Tano Diamond Dusted Membrane Scraper™, is subtle but can also cause misinterpretation of the image. This is caused by the small difference in refractive index of the fluid in the ocular cavity and the tool body. Since the axial position of a surface in an OCT tomogram is dependent upon the total optical path

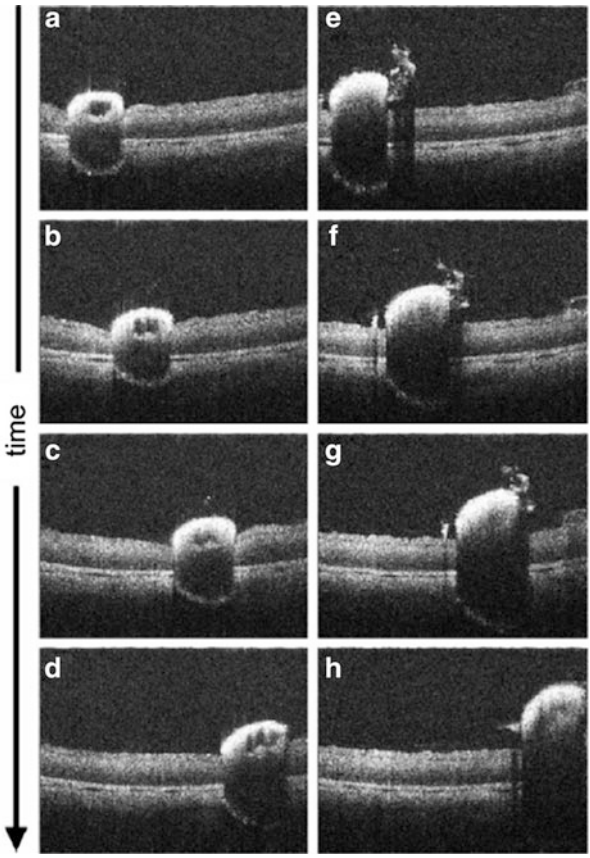

Fig. 58.15 B-scan sequence of the diamond-dusted scraper brushing along a cadaveric porcine retina [41]. (**a**–**d**) show the first example of an aggressive scrape. (**e**–**h**) show a second, milder scraping motion

length of material before it, the appearance of tissues underneath tools could potentially appear deeper than they actually are. As MIOCT becomes increasingly accepted, it is possible that new surgical tools may be specifically designed to minimize such imaging artifacts and to enhance the visibility of tools on OCT images which could also make them easier to track using automated methods.

58.5 Conclusions

Intraoperative ophthalmic OCT is still a relatively new field and several clinical trials are ongoing. Despite this early stage, very exciting results have emerged from research groups using OCT systems in human surgeries. In this chapter, we have reviewed the state of the art of handheld, microscope-integrated, and forward-imaging endoscopic OCT systems that have been used in ophthalmic procedures as well as the design considerations and relevant clinical results of the Duke MIOCT system.

Commercially available HHOCT systems have thus far been the most used in ophthalmic surgeries, while the forward-imaging probes have yet to be used in human subjects. Still, the HHOCT approach has only been adopted by a handful of researchers. It is likely that the other approaches, MIOCT and forward-imaging endoscopic probe OCT, will gain widespread adoption, as they can potentially be used with less interruption of normal surgical practice.

These intraoperative OCT techniques open new opportunities for surgeons to attain enhanced, depth-resolved, real-time visualization of surgery. Increased precision of instrument placement and immediate monitoring of anatomical changes to tissue may lead to better patient outcomes and enable new, more ambitious surgical interventions.

References

1. D. Huang, E. Swanson, C. Lin, J. Schuman, W. Stinson, W. Chang, M. Hee, T. Flotte, K. Gregory, C. Puliafito et al., Optical coherence tomography. Science **254**(5035), 1178–1181 (1991)
2. B.E. Bouma, G.J. Tearney, *Handbook of Optical Coherence Tomography* (Marcel Dekker, New York, 2002)
3. M.E. Brezinski, G.J. Tearney, S.A. Boppart, E.A. Swanson, J.F. Southern, J.G. Fujimoto, Optical biopsy with optical coherence tomography: feasibility for surgical diagnostics. J. Surg. Res. **71**(1), 32–40 (1997)
4. S.A. Boppart, J. Herrmann, C. Pitris, D.L. Stamper, M.E. Brezinski, J.G. Fujimoto, High-resolution optical coherence tomography-guided laser ablation of surgical tissue. J. Surg. Res. **82**(2), 275–284 (1999)
5. S.A. Boppart, J.M. Herrmann, C. Pitris, D.L. Stamper, M.E. Brezinski, J.G. Fujimoto, Real-time optical coherence tomography for minimally invasive imaging of prostate ablation. Comput. Aided Surg. **6**(2), 94–103 (2001)
6. H. Li, B.A. Standish, A. Mariampillai, N.R. Munce, Y. Mao, S. Chiu, N.E. Marcon, B.C. Wilson, A. Vitkin, V.X. Yang, Feasibility of interstitial Doppler optical coherence tomography for in vivo detection of microvascular changes during photodynamic therapy. Lasers Surg. Med. **38**(8), 754–761 (2006)
7. F.T. Nguyen, A.M. Zysk, E.J. Chaney, J.G. Kotynek, U.J. Oliphant, F.J. Bellafiore, K.M. Rowland, P.A. Johnson, S.A. Boppart, Intraoperative evaluation of breast tumor margins with optical coherence tomography. Cancer Res. **69**(22), 8790–8796 (2009)
8. S.A. Boppart, M.E. Brezinski, C. Pitris, J.G. Fujimoto, Optical coherence tomography for neurosurgical imaging of human intracortical melanoma. Neurosurgery **43**(4), 834–841 (1998)
9. S. Boppart, A. Goodman, J. Libus, C. Pitris, C. Jesser, M. Brezinski, J. Fujimoto, High resolution imaging of endometriosis and ovarian carcinoma with optical coherence tomography: feasibility for laparoscopic-based imaging. BJOG Int. J. Obstet. Gynaecol. **106**(10), 1071–1077 (1999)
10. C. Pitris, A. Goodman, S.A. Boppart, J.J. Libus, J.G. Fujimoto, M.E. Brezinski, High-resolution imaging of gynecologic neoplasms using optical coherence tomography. Obstet. Gynecol. **93**(1), 135–139 (1999)
11. X. Li, S. Martin, C. Pitris, R. Ghanta, D.L. Stamper, M. Harman, J.G. Fujimoto, M.E. Brezinski, High-resolution optical coherence tomographic imaging of osteoarthritic cartilage during open knee surgery. Arthritis Res. Ther. **7**(2), R318–R323 (2005)
12. S.A. Boppart, B.E. Bouma, C. Pitris, G.J. Tearney, J.F. Southern, M.E. Brezinski, J.G. Fujimoto, Intraoperative assessment of microsurgery with three-dimensional optical coherence tomography. Radiology **208**(1), 81–86 (1998)
13. J.A. Cameron, Keratoglobus. Cornea **12**(2), 124–130 (1993)

14. C.M. Kirkness, L.A. Ficker, A.D.M. Steele, N.S. Rice, The success of penetrating keratoplasty for keratoconus. Eye **4**(5), 673–688 (1990)
15. G.J. Melles, F. Lander, W.H. Beekhuis, L. Remeijer, P. Binder, Posterior lamellar keratoplasty for a case of pseudophakic bullous keratopathy. Am. J. Ophthalmol. **127**(3), 340–341 (1999)
16. I. Bahar, I. Kaiserman, P. McAllum, A. Slomovic, D. Rootman, Comparison of posterior lamellar keratoplasty techniques to penetrating keratoplasty. Ophthalmology **115**(9), 1525–1533 (2008)
17. F.W. Price, M.O. Price, Descemet's stripping with endothelial keratoplasty in 200 eyes. J. Cataract. Refract. Surg. **32**(3), 411–418 (2006)
18. M. Anwar, K.D. Teichmann, Deep lamellar keratoplasty: surgical techniques for anterior lamellar keratoplasty with and without baring of Descemet's membrane. Cornea **21**(4), 374–383 (2002)
19. N. Congdon, J. Vingerling, B. Klein, S. West, D. Friedman, J. Kempen, B. O'Colmain, S. Wu, H. Taylor, Prevalence of cataract and pseudophakia/aphakia among adults in the United States. Arch. Ophthalmol. **122**(4), 487 (2004)
20. J.C. Erie, K.H. Baratz, D.O. Hodge, C.D. Schleck, J.P. Burke, Incidence of cataract surgery from 1980 through 2004: 25-year population-based study. J. Cataract Refract. Surg. **33**(7), 1273–1277 (2007)
21. D.V. Palanker, M.S. Blumenkranz, D. Andersen, M. Wiltberger, G. Marcellino, P. Gooding, D. Angeley, G. Schuele, B. Woodley, M. Simoneau, Femtosecond laser-assisted cataract surgery with integrated optical coherence tomography. Sci. Transl. Med. **2**(58), 58–85 (2010)
22. T.H. Ko, A.J. Witkin, J.G. Fujimoto, A. Chan, A.H. Rogers, C.R. Baumal, J.S. Schuman, W. Drexler, E. Reichel, J.S. Duker, Ultrahigh-resolution optical coherence tomography of surgically closed macular holes. Arch. Ophthalmol. **124**(6), 827 (2006)
23. S. Radhakrishnan, A.M. Rollins, J.E. Roth, S. Yazdanfar, V. Westphal, D.S. Bardenstein, J.A. Izatt, Real-time optical coherence tomography of the anterior segment at 1310 nm. Arch. Ophthalmol. **119**(8), 1179 (2001)
24. A.W. Scott, S. Farsiu, L.B. Enyedi, D.K. Wallace, C.A. Toth, Imaging the infant retina with a hand-held spectral-domain optical coherence tomography device. Am. J. Ophthalmol. **147**(2), 364–373. e2 (2009)
25. P.N. Dayani, R. Maldonado, S. Farsiu, C.A. Toth, Intraoperative use of handheld spectral domain optical coherence tomography imaging in macular surgery. Retina (Philadelphia, Pa.) **29**(10), 1457–1468 (2009)
26. J.P. Ehlers, P.K. Gupta, S. Farsiu, R. Maldonado, T. Kim, C.A. Toth, P. Mruthyunjaya, Evaluation of contrast agents for enhanced visualization in optical coherence tomography. Invest. Ophthalmol. Vis. Sci. **51**(12), 6614–6619 (2010)
27. J.P. Ehlers, K. Kernstine, S. Farsiu, N. Sarin, R. Maldonado, C.A. Toth, Analysis of pars plana vitrectomy for optic pit-related maculopathy with intraoperative optical coherence tomography: a possible connection with the vitreous cavity. Arch. Ophthalmol. **129**(11), 1483 (2011)
28. L. Lee, S. Srivastava, Intraoperative spectral-domain optical coherence tomography during complex retinal detachment repair. Ophthalmic Surg. Lasers Imaging Off. J. Int. Soc Imaging Eye **42**, e71 (2011)
29. R. Ray, D.E. Baranano, J.A. Fortun, B.J. Schwent, B.E. Cribbs, C.S. Bergstrom, G.B. Hubbard 3rd, S.K. Srivastava, Intraoperative microscope-mounted spectral domain optical coherence tomography for evaluation of retinal anatomy during macular surgery. Ophthalmology **118**(11), 2212–2217 (2011)
30. T. Ide, J. Wang, A. Tao, T. Leng, G.D. Kymionis, T.P. O'Brien, S.H. Yoo, Intraoperative use of three-dimensional spectral-domain optical coherence tomography. Ophthalmic Surg. Lasers Imaging Off. J Int. Soc. Imaging Eye **41**(2), 250 (2010)
31. P.B. Knecht, C. Kaufmann, M.N. Menke, S.L. Watson, M.M. Bosch, Use of intraoperative Fourier-domain anterior segment optical coherence tomography during descemet stripping endothelial keratoplasty. Am J. Ophthalmol. **150**(3), 360–365.e2 (2010)

32. S. Binder, C.I. Falkner-Radler, C. Hauger, H. Matz, C. Glittenberg, Feasibility of intrasurgical spectral-domain optical coherence tomography. Retina **31**(7), 1332–1336 (2011)
33. G. Geerling, M. Muller, C. Winter, H. Hoerauf, S. Oelckers, H. Laqua, R. Birngruber, Intraoperative 2-dimensional optical coherence tomography as a new tool for anterior segment surgery. Arch. Ophthalmol. **123**(2), 253 (2005)
34. Y.K. Tao, J.P. Ehlers, C.A. Toth, J.A. Izatt, Intraoperative spectral domain optical coherence tomography for vitreoretinal surgery. Opt. Lett. **35**(20), 3315–3317 (2010)
35. G. Hüttmann, E. Lankenau, C. Schulz-Wackerbarth, M. Müller, P. Steven, R. Birngruber, Optical coherence tomography: from retina imaging to intraoperative use-a review. Klin. Monatsbl. Augenheilkd. **226**(12), 958 (2009)
36. J.P. Ehlers, Y.K. Tao, S. Farsiu, R. Maldonado, J.A. Izatt, C.A. Toth, Integration of a spectral domain optical coherence tomography system into a surgical microscope for intraoperative imaging. Invest. Ophthalmol. Vis. Sci. **52**(6), 3153–3159 (2011)
37. J.P. Ehlers, Y.K. Tao, S. Farsiu, R. Maldonado, J.A. Izatt, C.A. Toth, Visualization of real-time intraoperative maneuvers with a microscope-mounted spectral domain optical coherence tomography system. Retina **33**(1), 232–236 (2013)
38. Y. K. Tao, J. P. Ehlers, C. A. Toth, J. A. Izatt, Visualization of vitreoretinal surgical manipulations using intraoperative spectral domain optical coherence tomography. Proc. SPIE 7889, Optical Coherence Tomography and Coherence Domain Optical Methods in Biomedicine XV, **78890F** (2011). doi: 10.1117/12.875236.
39. Y. K. Tao, C. A. Toth, J. A. Izatt, Real-time intraoperative spectral domain optical coherence tomography for vitreoretinal surgery. in *BiOS*. International Society for Optics and Photonics. Proc. SPIE 7554, Optical Coherence Tomography and Coherence Domain Optical Methods in Biomedicine XIV, **75540F** (2010). doi: 10.1117/12.842594.
40. S. Binder, C. Falkner-Radler, C. Hauger, H. Matz, C. Glittenberg, Clinical applications of intrasurgical SD-optical coherence tomography. Invest Ophthalmol Vis Sci **51**, (2010). E-Abstract 268.
41. P. Hahn, J. Migacz, R. O'Connell, J.A. Izatt, C.A. Toth, Unprocessed real-time imaging of vitreoretinal surgical maneuvers using a microscope-integrated spectral-domain optical coherence tomography system. Graefes Arch. Clin. Exp. Ophthalmol. **251**(1), 213–220 (2013)
42. P. Hahn, J. Migacz, R. O'Connell, S. Day, A. Lee, P. Lin, R. Vann, A. Kuo, S. Fekrat, P. Mruthyunjaya, E.A. Postel, J.A. Izatt, C.A. Toth, Preclinical evaluation and intraoperative human retinal imaging with a high-resolution microscope-integrated spectral domain optical coherence tomography device. Retina **33**(7), 1328–1337 (2013). doi:10.1097/IAE.0b013e3182831293. Publish Ahead of Print
43. P. Hahn, J. Migacz, R. O'Connell, R.S. Maldonado, J.A. Izatt, C.A. Toth, The use of optical coherence tomography in intraoperative ophthalmic imaging. Ophthalmic Surg. Lasers Imaging **42**(Suppl), S85–S94 (2011)
44. C. Cursiefen, E. Lankenau, M. Krug, G. Huettmann, S. Oelckers, Intraoperative optical coherence tomography improves surgical performance in Descemet Membrane Endothelial Keratoplasty (DMEK). ARVO Meet. Abstr. **103**(20), (2012)
45. P. Steven, E. Lankenau, M. Krug, G. Huettmann, S. Oelckers, C. Cursiefen, Intraoperative optical coherence tomography improves surgical performance in Deep Anterior Lamellar Keratoplasty (DALK) and penetrating Keratoplasty (pKPL). Invest Ophthalmol Vis Sci **53**, (2012). E-Abstract 20
46. P. Hahn, J. Migacz, R. O'Connell, E. Yuan, T. Moreno, J. A. Izatt, C. A. Toth, Initial experience with human imaging of vitreoretinal surgical maneuvers using a custom microscope-mounted spectral domain optical coherence device. Invest Ophthalmol Vis Sci **53**, (2012). E-Abstract 3115
47. J. Migacz, A. Kuo, A. Dubis, O. Carrasco-Zevallos, C. A. Toth, J. A. Izatt, Real-time intraoperative assessment of the cornea with microscope integrated optical coherence tomography. Invest Ophthalmol Vis Sci **54**, (2013). E-Abstract 3586

48. J. Migacz, Z. Moustafa, S. J. Chiu, T. Moreno, P. Hahn, R. O'Connell, S. Farsiu, C. A. Toth, J. A. Izatt, Surgical instrument tracking image guidance for intraoperative OCT. Invest Ophthalmol Vis Sci **53**, (2012). E-Abstract 3125
49. J. V. Migacz, P. Hahn, R. V. O'Connell, C. Thomas, Z. Moustafa, C. Wang, S. J. Chiu, L. Dai, C. A. Toth, J. A. Izatt, Instrument tip-tracking ophthlamic intrasurgical SDOCT. SPIE Photon. West Conf. Present. **8213**(14), (2012)
50. J. V. Migacz, T. Moreno, F. Folgar, A. Dubis, P. Hahn, S. Farsiu, C. A. Toth, J. A. Izatt, Intraoperative SDOCT for vitreo-retinal surgery with an integrated fundus camera for closed-loop surgical instrument tracking. SPIE Photon. West Conf. Present. **8571**(41), (2013)
51. P. Hahn, J. Migacz, Y. K. Tao, J. P. Ehlers, J. A. Izatt, C. A. Toth, Real time cross-sectional intra-surgical imaging of retinal structures using a microscope-mounted OCT system. ARVO Meet. Invest Ophthalmol Vis Sci **52**, (2011). E-Abstract 1248
52. S.A. Boppart, B.E. Bouma, C. Pitris, G.J. Tearney, J.G. Fujimoto, M.E. Brezinski, Forward-imaging instruments for optical coherence tomography. Opt. Lett. **22**(21), 1618–1620 (1997)
53. S. Han, M.V. Sarunic, J. Wu, M. Humayun, C. Yang, Handheld forward-imaging needle endoscope for ophthalmic optical coherence tomography inspection. J. Biomed. Opt. **13**(2), 020505 (2008)
54. T.J. van den Berg, H. Spekreijse, Near infrared light absorption in the human eye media. Vis. Res. **37**(2), 249–253 (1997)
55. M. Balicki, J.-H. Han, I. Iordachita, P. Gehlbach, J. Handa, R. Taylor, J. Kang, Single fiber optical coherence tomography microsurgical instruments for computer and robot-assisted retinal surgery, in *Medical Image Computing and Computer-Assisted Intervention – MICCAI 2009*, ed. by G.-Z. Yang et al. (Springer, Berlin/Heidelberg, 2009), pp. 108–115
56. K. Zhang, J.U. Kang, Real-time intraoperative 4D full-range FD-OCT based on the dual graphics processing units architecture for microsurgery guidance. Biomed. Opt. Express **2**(4), 764 (2011)
57. P. Hahn, C.A. Toth, A microscope-integrated OCT system for true intrasurgical OCT acquisition. Retina Today, 61–63 (2012)

En-face Flying Spot OCT/Ophthalmoscope 59

Richard B. Rosen, Patricia Garcia, Adrian Gh. Podoleanu, Radu Cucu, George Dobre, Irina Trifanov, Mirjam E. J. van Velthoven, Marc D. de Smet, John A. Rogers, Mark Hathaway, Justin Pedro, and Rishard Weitz

59.1 Introduction

This is a review of a technique for high-resolution imaging of the eye that allows multiple sample sectioning perspectives with different axial resolutions. The technique involves the flying spot approach employed in confocal scanning laser ophthalmoscopy which is extended to OCT imaging via time domain en face fast lateral scanning. The ability of imaging with multiple axial resolutions stimulated the development of the dual en face OCT–confocal imaging technology. Dual imaging also allows various other imaging combinations, such as OCT with confocal microscopy for imaging the eye anterior segment and OCT with fluorescence angiography imaging.

59.2 Different Scanning Procedures

Flying spot imaging systems employ two devices that can scan the target in two mutually orthogonal directions, one axially, the other transversally. Different orientations of the image sectioning plane are possible, depending on the order which

R.B. Rosen (✉) • P. Garcia
New York Eye and Ear Infirmary Advanced Retinal Imaging Center, New York, NY, USA
e-mail: RRosen@NYEE.EDU

A.G. Podoleanu • R. Cucu • G. Dobre • I. Trifanov
Applied Optics Group, School of Physical Sciences, University of Kent, Canterbury, UK

M.E.J. van Velthoven • M.D. de Smet
Academic Medical Center, Amsterdam, The Netherlands

J.A. Rogers • M. Hathaway • J. Pedro • R. Weitz
Ophthalmic Technology Inc., Toronto, Canada

© Springer International Publishing Switzerland 2015

W. Drexler, J.G. Fujimoto (eds.), *Optical Coherence Tomography*,
DOI 10.1007/978-3-319-06419-2_61

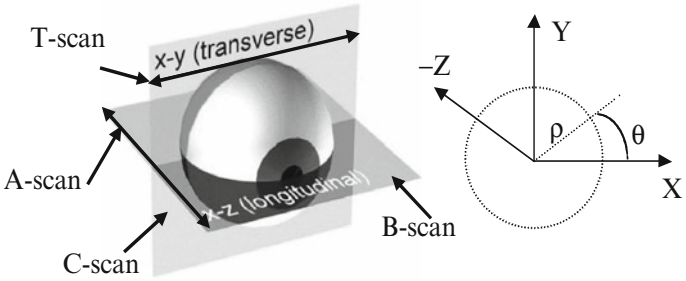

Fig. 59.1 Relative orientation of the axial scan (A-scan), en face scan (T-scan), longitudinal section (B-scan), and en face or transverse section (C-scan) (Reproduced with OSA's permission from [1] and copyright M. Seeger [2])

these devices are operated, scanning rates and the line scan orientation in the raster. The scanning terminology [1, 2] is illustrated in Fig. 59.1.

59.2.1 Flying Spot En Face (T-Scan) OCT

The differences between the longitudinal or axial priority scanning and en face or transverse priority scanning are presented below.

59.2.1.1 A-Scan-Based B-Scan

B-scan OCT images, as the first OCT image generated [3], are analogous to ultrasound B-scans and are obtained by collecting A-scans (Fig. 59.1) at adjacent transverse positions, as shown in Fig. 59.2 (top). The A-scans are one-dimensional sample reflectivity profiles acquired along the depth direction. The transverse scanning is performed in a transverse direction orthogonal to the axial direction (along the X or Y directions or can follow a circular pattern at constant radius ρ in polar coordinates in Fig. 59.1) at a slower pace than A-scanning as illustrated in Fig. 59.2 (top). The majority of reports on time domain OCT [4] in literature refer to this method of operation.

59.2.1.2 T-Scan-Based B-Scan

In this case, the transverse scanners sample the target at a fast rate [5, 6], and each line in the raster is a reflectivity profile in the lateral direction (T-scan) at a given depth in the sample as shown in Fig. 59.2 (middle). Transverse scanning can be performed either parallel to the X- or Y-axes, radially (at a given value of the polar angle θ) or circularly (at a given polar radius ρ). During acquisition of one T-scan, the position of the axial scanner is fixed. The example in Fig. 59.2 (middle) illustrates the generation of a B-scan from adjacent T-scans. In this particular example, the T-scans are parallel to the X-axis, while the axial scanner advances at a slower rate in depth, along the Z-axis.

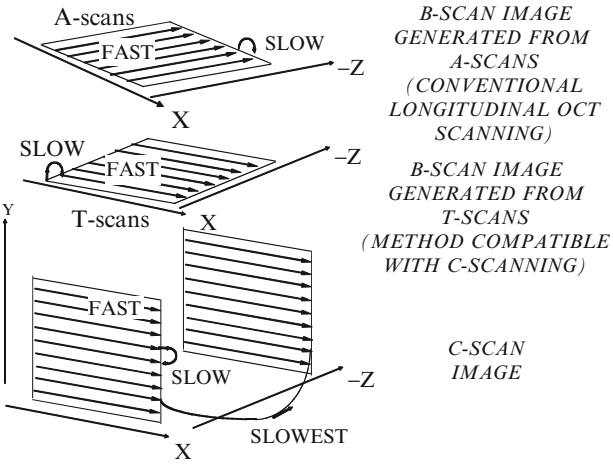

Fig. 59.2 Different modes of operation of the three scanners in a flying spot OCT system. (Reproduced with permission from OSA [19])

59.2.1.3 C-Scan

The OCT T-scanning procedure has a net advantage over OCT A-scanning as it also allows acquisition of C-scans, i.e., of transverse or en face OCT images at a given depth determined by the length of the reference path as illustrated in Fig. 59.2 (bottom). C-scans are transversal sections of the sample made from T-scans, usually performed along the X- or Y-axes, repeated at adjacent locations along the other orthogonal transverse direction (Y, X). The repetition of T-scans along the other transverse coordinate is performed at a slower rate (frame rate) as shown in Fig. 59.2 (bottom). C-scans can be acquired at successive axial positions, either by advancing the optical path difference in the OCT in steps after each complete transverse (XY) scan or continuously at a much slower speed than the frame rate. Such images can be created based on the path modulation introduced by the transversal scanners, as explained above, or by using a phase modulator or a frequency shifter. A fast en face OCT method (T-scan-based OCT method) was reported [7] using a stable high-frequency carrier (40 MHz) generated by use of an acousto-optic modulator and a resonant scanning mirror (4 kHz) for the priority scan (x-direction).

Using a spectral scanning delay line for depth scanning [8], capable of scanning in depth at the same rate as that of transversal scanning, a multimode OCT imaging system was demonstrated [9], capable of producing depth B(A) or en face B(T) cross-sectional images, as well as en face constant depth (C-scan) images. The time required to switch from one regime to the other is limited by the time required to operate the control software. Safety level calculations for maximum optical power allowed to the eye, in retinal imaging, showed that T-scan-based imaging, for lateral sizes larger than 100 pixels, allows at least 4 times more power to be delivered into the eye than in B(A) scan. Here the lateral pixel size is considered

as 10–15 μm. For larger image size, of 500 pixels, even more power could be used in T-scan regime than in the A-scan regime to generate B-scans. This has immediate consequences in terms of signal-to-noise ratio.

59.3 Simultaneous En Face OCT and Confocal Imaging

As T-scans are instrumental in generating both time domain en face OCT scans and confocal images, there are similarities and complementarities between the two imaging principles when applied to imaging the eye:

1. En face OCT images (Fig. 59.1) have the same orientation as standard fundus photographs [10] or confocal scanning laser ophthalmoscopy (SLO) images.
2. In both en face OCT and SLO, the depth scanning (optical path change in case of the OCT and focus change in case of the SLO) is much slower than the T-scan rate (performed at the frame rate).
3. The depth resolution in an SLO is limited by the eye aberrations, while the transversal resolution in OCT is affected by random interference effects from different scattering centers (speckle). Therefore there may be some compensating advantages to combining SLO with OCT technology for retinal imaging.
4. The higher depth resolution of OCT C-scan images tends to make structures in the retina appear more fragmented. In a single C-scan image, tissue features may also appear distorted by tilt making interpretation somehow difficult. However, ophthalmologists have extensive experience with the en face perspective of ocular disease as seen in the SLO images. In order to take advantage of their familiarity with the SLO imaging perspective in the interpretation of the OCT transversal images, it is useful to acquire and display pairs of OCT C-scans and SLO images simultaneously. High-quality SLO images can be used as reference for interpreting retinal C-scan OCT data. Additionally, the integration of confocal imaging in an OCT instrument facilitates the targeting of B-scan OCT acquisition which otherwise would require auxiliary imaging equipment to select the lateral location in the retina to be subsequently imaged with OCT.

59.3.1 OCT/SLO

The combination of confocal imaging and interferometry has already been discussed in microscopy [11], and a comparison between confocal and OCT imaging through scattering media has also been reported [12]. However, (i) the object here is the tissue, which imposes a safety power limit and requires special interface optics, and (ii) the same low coherence source is used for both confocal and interferometer channels with implications in terms of the obtainable signal-to-noise ratio.

A possible configuration combining OCT with confocal microscopy for the eye [13, 14] is shown in Fig. 59.3. Light from a pigtailed superluminescent diode, SLD, is injected into a single-mode directional coupler, DC1. Light in the object arm

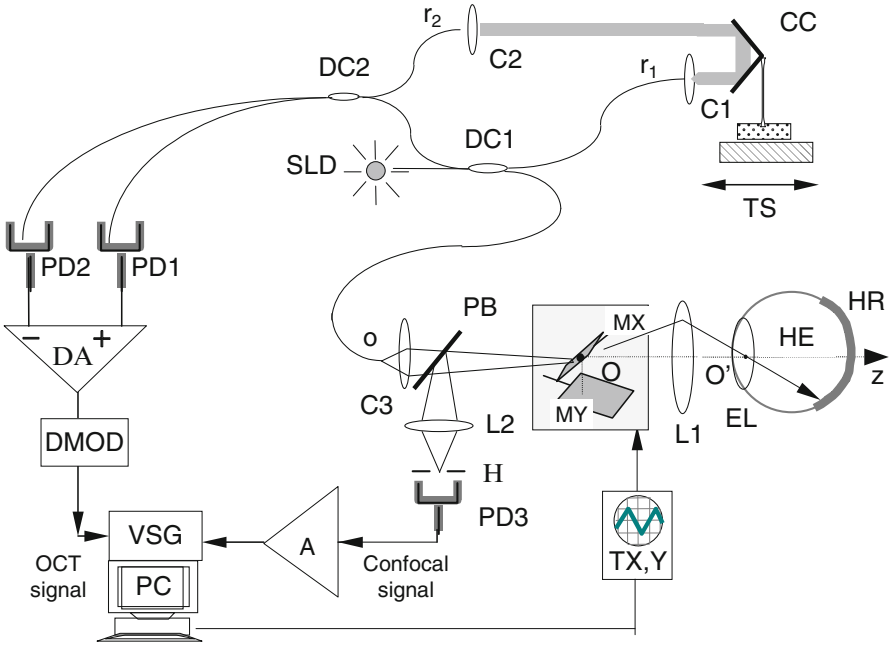

Fig. 59.3 Detailed schematic diagram of the time domain OCT/SLO apparatus using a plate beam splitter to divert light to a confocal receiver. *SLD* superluminescent diode; *C1, C2, C3* microscope objectives; *DC1, DC2* directional couplers; *TS* computer-controlled translation stage; *CC* corner cube; *M1, M2* mirrors; *MX, MY* orthogonal axes galvanometer mirrors; *TX(Y)* ramp generators; *DMOD* demodulation block; *L1* convergent lens; *PD1, PD2* photodetectors; *DA* differential amplifier; *PD3 and A* photodetector and amplifier, respectively, for the confocal receiver; *H* pinhole; *PB* plate beam splitter; *HE* patient's eye; *EL* eye lens; *HR* human retina; *PC* personal computer; *VSG* dual-input variable scan frame grabber (Reproduced by permission of the Institution of Engineering and Technology from [13])

propagates via the microscope objective C3 and plate beam splitter PB to a scanning mirror pair, MX, MY. A lens L1 images the galvanometer scanner aperture onto the eye pupil, EL. The reference beam is directed via microscope objectives C1 and C2 and a corner cube CC to a coupler DC2. The corner cube CC is mounted on a computer-controlled translation stage, TS, used to perform axial scanning. The light back reflected from the retina and transferred via couplers DC1 to DC2 interferes with the reference signal in the coupler DC2. Two silicon pin photodiodes, PD1 and PD2, in a balanced [15] configuration are used to detect the OCT signal, which is then demodulated by the demodulator block, DMOD, whose output is connected to the OCT channel input of the dual input variable scan frame grabber, VSG, controlled by a personal computer, PC.

A separate confocal receiver is built [16]. This consists of a plate beam splitter, PB, which reflects a fraction of the light backscattered by the retina via a focusing lens, L2, and a pinhole, H, to an avalanche photodiode, PD3, whose output is connected to the SLO channel input of VSG.

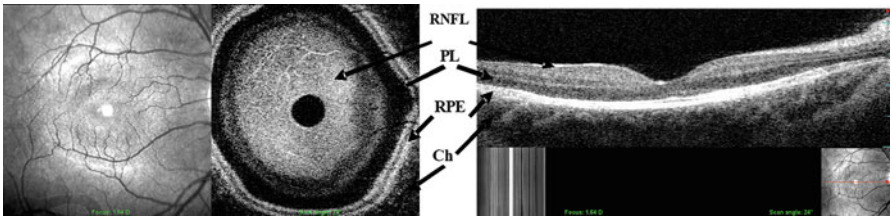

Fig. 59.4 Retinal images acquired with the OCT/confocal system. *Left*: C-scan regime with SLO image left and the OCT image right, collected at the level of the retinal nerve fiber layer, RNFL (which appears as a bright doughnut-shaped region in the center of the image); PL (*dark*): photoreceptor layer; RPE (*bright*): retinal pigment epithelium; Ch (*bright*): choroid. *Right*: B-scan regime with confocal images below, (*left*: simultaneous with the B-scanning and *right*: immediately preceding the B-scan acquisition). Lateral size in all images: 25°; in the B-scan regime image on the right, vertical size in the B-scan OCT image is 2 mm depth measured in air, while in the SLO image left bottom, it corresponds to the acquisition time of the B-scan OCT image, 0.5 s. The lateral variations of the shades in the SLO image indicate lateral movements of the eye during the acquisition. The retinal layers are clearly discernible in the OCT image and bears strong resemblance to histology [54]. (Republished with permission from Springer Science+Business Media, [55])

Ramp generators TX,Y drive the galvanometer scanner mirrors MX and MY and also trigger signal acquisition by the frame grabber.

Retinal images of a healthy eye, provided by the system described above, operating in the B- and C-scan regimes of operation, are shown in Fig. 59.4. In the left, images in the C-scan regime are shown, while in the right, images obtained in the B-scan regime.

59.3.2 En Face Scanning Allows High Transversal Resolution

Due to T-scanning, the B-scan time domain OCT images acquired with the en face method are continuous along the line in the raster, which improves their quality. This is not the case with standard OCT B-scan OCT images generated using fast axial scanning, where the lateral scanning is discrete. Since the scanning direction parallels the anatomic fabric of the retina, connected structures or associations between scattering points in the transverse section are better conserved by transverse scanning. This ultimately ensures the visualization of small lesions above, within, or beneath the retina which might otherwise be chopped up and lost in the reconstruction of the image based on depth priority scanning OCT.

59.3.3 Synergy Between the Channels

The confocal image with its pixel-to-pixel correspondence to the C-scan OCT holds additional value for data acquisition. For small movements, the confocal image can

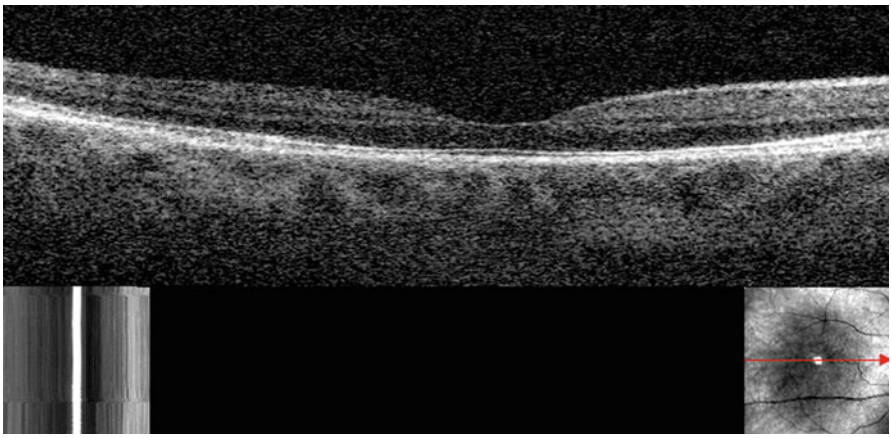

Fig. 59.5 B-scan section of the retina appears slightly elongated due to mild lateral eye movement during the scan. The SLO image in the *lower left* corner shows laterally displaced *vertical* trace pattern due to lateral eye movement during B-scan acquisition. The *lower right* image was collected in the C-scanning regime immediately before initiating the B-scan capture. (Republished with permission from Springer Science+Business Media, [55])

be used to track lateral eye movements between frames and for subsequent transversal alignment of OCT images in a stack of C-scans collected from different depths. In cases of large saccadic eye movements and blinks, the confocal image gives a clear indication of the OCT frames which need to be eliminated from a collected stack. The first artifact-free confocal image in the stack is used as a reference for the aligning procedure.

The SLO image acquired in the B-scanning regime has the appearance of a pattern of parallel vertical traces. Each horizontal line in this image corresponds to a depth position in the OCT B-scan. Lateral eye motion during B-scan acquisition causes lateral deviations of the vertical trace pattern in the SLO image. For example, in Fig. 59.4 right and Fig. 59.5, movements of the eye are indicated by lateral shifts of the traces in the SLO image (lower left box), while the system operates in the B-scan regime. The recorded deviations in the vertical trace pattern in the SLO image can easily be utilized to correct the lateral shift of the lines in the B-scan OCT image (above).

59.3.4 3D Imaging

3D imaging of the retina using SLO [17] is already common in clinical applications. En face sections collected from different depths [18] can be used to construct a 3D profile of the retina which can subsequently aid ophthalmologists in their clinical evaluations. In the same way, an OCT/confocal system can be used for 3D retinal imaging, however, with en face sections as thin as allowed by the source spectral

width. To collect the reflectivity distribution from a volume in the retina, the OCT/confocal system is operated in the C-scan regime collecting en face images at different depths. Ideally, the depth interval between successive frames should be much smaller than the system axial resolution, and the depth change applied only after the entire C-scan image was collected. However, in practice, to speed up the acquisition, the translation stage in Fig. 59.3 is moved continuously, and the depth interval is set slightly larger than the OCT depth resolution [19]. For instance, using 20 μm axial separation between successive OCT C-scans, 60 frames of image pairs from a volume corresponding to a total depth of 1.2 mm in air (sufficient to cover in the axial direction the optic nerve region in the retina) can be acquired in 30 s when operating at 2 Hz frame rate. After acquisition, the images can be aligned transversally using the first confocal image (or the first motion artifact-free confocal image), and the stack of OCT C-scans can be used to construct a 3D OCT volume of the retina [20]. 3D retinal OCT imaging is more convenient than aligning individual OCT C-scans acquired at different depths.

59.3.5 Topography

Topography of the fundus is difficult to perform using A-scan-based B-scans since it requires interpolation in the en face plan [21]. Topographic maps are normally presented from an en face perspective which suggests that stacks of C-scan OCT images could be a natural choice for topography. This procedure was demonstrated in a previous report [22]. Based on en face OCT, topography rendering should be similar to the method using a confocal SLO [23]. Topography of a normal macula is shown in Fig. 59.6 obtained using en face OCT.

59.3.6 New Challenges

New imaging technology brings new perspectives to the clinician, but also brings the requirement for new interpretations of imaging data. En face OCT is no exception to this rule. The higher depth resolution of OCT has the effect of fragmenting the C-scan OCT image [24] in comparison to a SLO image. As the imaging proceeds at a few frames a second, the inherent eye movements may result in significant changes in the size of fragments sampled from the tissue. The fragmentation is especially visible when imaging tissue tilted with respect to the system optical axis. The image on the right in Fig. 59.7 shows the challenges in interpreting and using en face OCT images. First, it is composed of structural features which are discontinuous and unfamiliar in shape.

Second, variations in tissue inclination with respect to the coherence wave surface alter the sampling of structures within the depth in the retina [25], producing novel section orientations with little resemblance to the ophthalmoscopic appearance of the fundus. The bright patches in the OCT image represent the intersection of the surface of optical path difference (OPD) = 0 with the tissue. Due to the

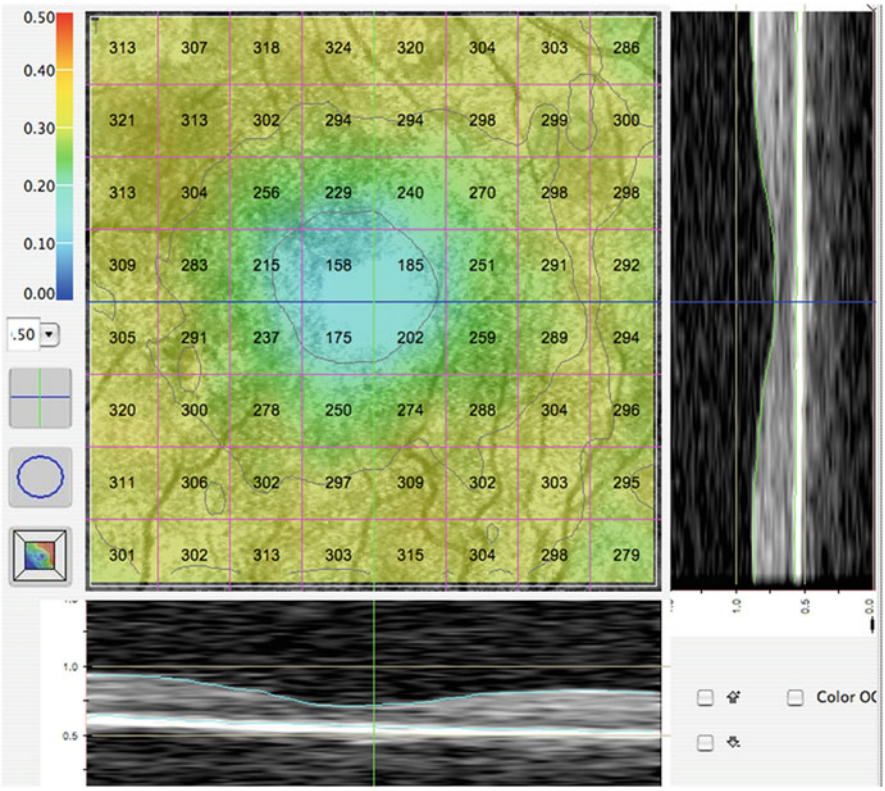

Fig. 59.6 Topographic map of a normal macula. 200 C-scans are aligned according to the vascular pattern with a grid showing the average thickness within each box superimposed on the SLO image. The B-scans below and on the *right side* of the map are reconstructed from the C-scan stack. Their lateral location is indicated by the *green* vertical and aqua horizontal cursors seen on the map. (Republished with permission from Springer Science+Business Media, [55])

specific way in which the retina is scanned, with the fan of rays converging onto the eye pupil, the surface of OPD = 0 is an arc circle with the center at the eye pupil. When we explore the depth, we practically change the radius of the arc. If the arc has a small radius, it may just only intersect the top of the optic nerve or the fovea with the rest of the arc in the aqueous/vitreous. The radius of the arc is increased by extending the length of the reference arm of the interferometer to explore the retina down to the level of the RPE and choroid. The orientation of the retinal tissue at the back of the eye is not perfectly circular, and this complicates the interpretation of the image even further.

Another confounding phenomenon noted is that despite the en face scanning orientation, tilting movements of the eye result in images which display several depths within a single section and may appear like a longitudinal OCT image. These two effects, (i) fragmentation and (ii) depth structures displayed in the C-scan images, are present in a confocal SLO with high depth resolution as well,

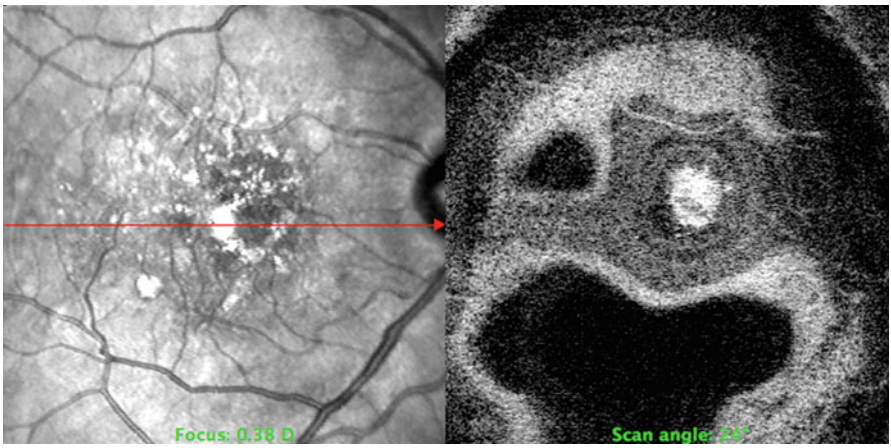

Fig. 59.7 Age-related macular degeneration with drusen and a choroidal neovascular membrane. The SLO image on the *left* demonstrates the superficial appearance lines of pigmentary change and scattered drusen. The OCT C-scan on the *right* demonstrates a tilting of the eye upward so that the image of the vitreous in the lower part of the image appears as a *black* chef's hat surrounded by the highly reflective nerve fiber layer which appears *white*. Beneath the macular drusen lies a serous detachment surrounding a highly reflective white choroidal membrane. (Republished with permission from Springer Science+Business Media, [55])

however, at a scale where they are regularly discarded. In a confocal SLO, the images do not look fragmented, and the depth structure is barely visible due to the coarse depth resolution, ~0.3 mm, comparable to the retinal thickness. Going in and out of focus results in a smooth transition from dark to bright areas in the image. Both problems mentioned above are brought about by the high depth resolution of OCT. We address the fragmentation problem by providing the confocal image, which guides the user, and by collecting many en face images at different depths and subsequently building the 3D profile. The other problem that the en face imaging may also display the depth structure requires further development of the interpretation process.

59.3.7 Clinical Use of the OCT/Ophthalmoscope: Pattern Recognition

Several prototypes of OCT/SLO systems were used to study a variety of clinic pathologies [26] including age-related macular degeneration, central serous retinopathy, macular hole, macular pucker, cystoid macular edema, diabetic maculopathy, and macular trauma. Specific recognizable patterns [27] in the en face OCT images were identified which correlate to a variety of anatomic disease entities. The dual display is particularly helpful to the clinician in correlating the deeper morphology to the surface appearance and facilitating interpretation of the often challenging new images. The subject interface is comprised of a standard chin

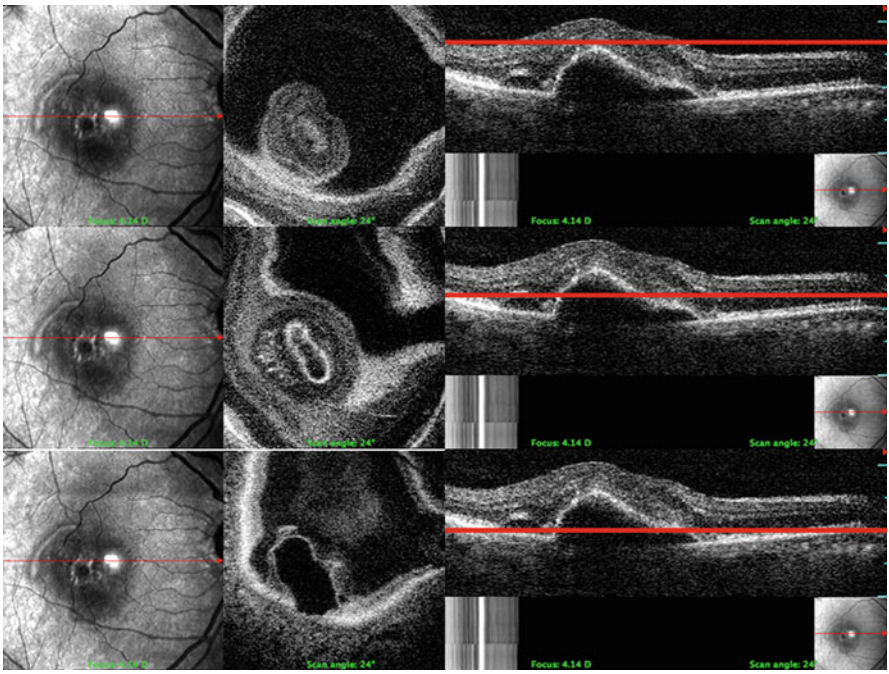

Fig. 59.8 Retinal angiomatous proliferation (RAP). The *top* image set demonstrates a C-scan slice superficial to the retinal pigment epithelial detachment. The small ovoid is the peak of the retinal elevation and is surrounded by a *black circular space* which is the vitreous. The *middle* slice cuts through the pigment epithelial detachment and the intraretinal neovascular complex. In the lowest series of images, the C-scan outlines the base of the pigment epithelial detachment and shows the choroid at the edges. (Republished with permission from Springer Science+Business Media, [55])

rest assembly which provides stability and comfort but allows some movement effects in the images to occur.

Figure 59.8 is a case of retinal angiomatous proliferation (RAP). Three pairs of C-scan OCT and confocal images are shown on the left. Each was taken at different depths as indicated by the lines in the B-scan OCT which was sampled along the line shown in the SLO image. By collecting a stack of OCT/SLO images, the volume of the retinal elevation could be evaluated.

Accurate volume assessment requires collection of a serial stack of C-scans at progressive depths. While the current instrument is equipped with such a feature, we had variable success using it in eyes with pathology due to their limited ability to maintain consistent fixation. We have found another feature of the system more useful, that which allows an easy switch between the two modes, B-scan and C-scan. Successive C-scan cuts viewed in conjunction with selected B-scan images allow the viewer to create a good mental picture of the three-dimensional aspects of the lesion despite the eye movements.

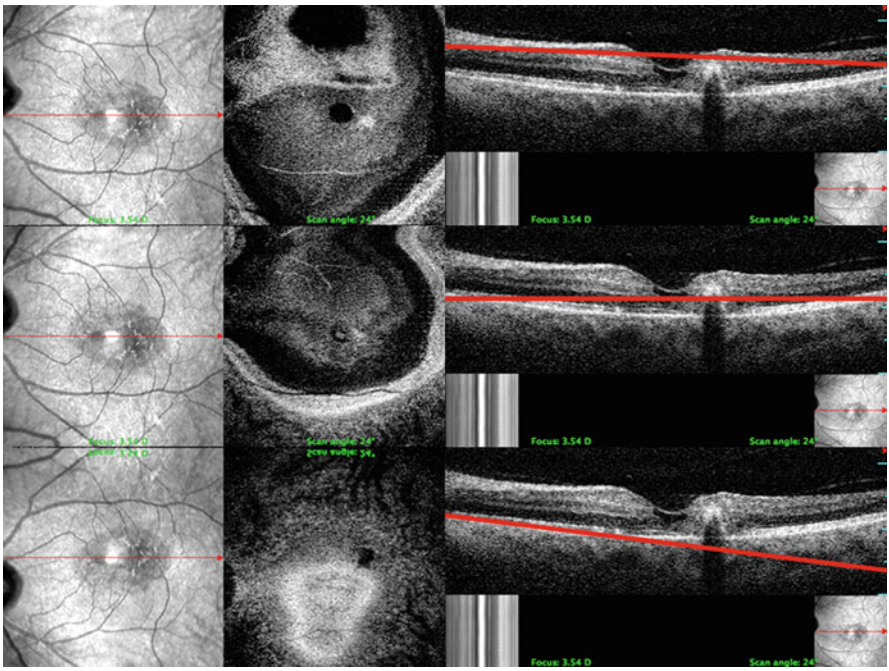

Fig. 59.9 Parafoveal telangiectasia. The lesion is temporal to the foveal depression. A series of confocal images and paired C-scan OCT images taken at different depths are shown. The B-scan OCT on the right of each pair shows the level and angle of the C-scan cut. Note the shadowing beneath the hyperreflective exudative lesion. (Republished with permission from Springer Science+Business Media, [55])

Interpretation of these images requires some careful thought. Due to the inclination of the walls of the thickened retina, the C-scan images often display structures from different depths, as visible in the B-scan OCT images on the right. As such, the C-scan OCT images alone may lead to a wrong interpretation. Comparing them with either of the B-scan image in Fig. 59.8 is helpful in establishing the orientation and the depths of features depicted in individual scans. The images in Fig. 59.8 show the two challenging features of the OCT C-scan imaging: patchy fragmented planes and display of structures from multiple depths for the tilted parts of the tissue. The elongated parts visible in the B-scan OCT images in Fig. 59.8 show up as circles of different intensities in the C-scan images, which indicate different structure in depth due to the discontinuity of optical parameters such as the index of refraction and backscattering coefficient. When we follow the cuts along the straight lines indicated, we can infer the intensity level in the corresponding part of the C-scan OCT image. Evaluating how the radius of the dark circles in Fig. 59.8 varies with depth, the volume of the lesion can be easily inferred.

Similar challenges are presented in the interpretation of the images in Fig. 59.9, a case of parafoveal telangiectasia. Three pairs of C-scan OCT/SLO images

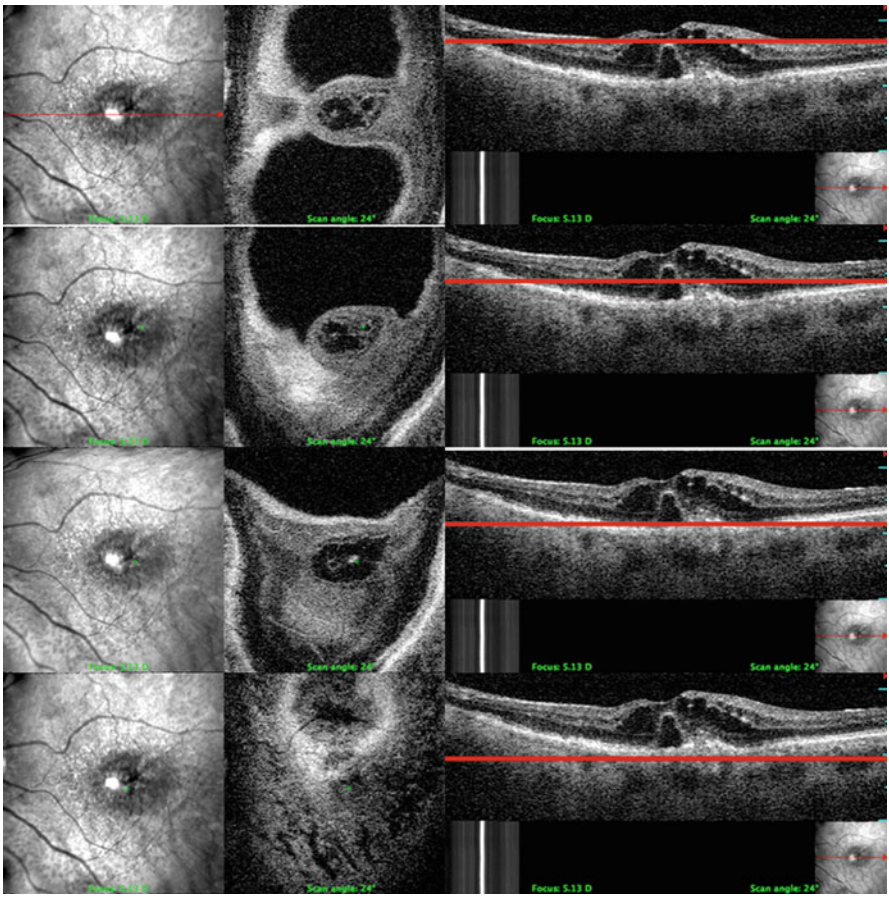

Fig. 59.10 Choroidal neovascular membrane with adjacent RPE detachment and overlying cystoid macular edema. The B-scan OCT images on the right feature *red lines* which indicate the level of the coronal slices. (Republished with permission from Springer Science+Business Media, [55])

acquired at increasing depth positions are shown. For ease in interpretation, the B-scan OCT is displayed on the right-hand side of each OCT/SLO pair. Here, the deepest C-scan OCT image (bottom pair) samples the choroid just touching the RPE. At this level only the shadow of the telangiectatic exudates can be seen. In the first raw, the dark circle in the C-scan is created by slicing through the foveal cone. The C-scan image in the middle raw cuts through the foveal floor which is the roof of an intrafoveal cyst. White edema residues are seen at the edge of the cone. The confocal image in each pair on the left displays the clinical appearance of the surface which reveals limited detail of the underlying pathological features.

Figure 59.10 demonstrates further how C-scan OCT images can enhance the understanding of anatomic relationships between different aspects of pathological

processes that effect complex retinal structure. The images presented are from a case of exudative age-related macular degeneration with a choroidal neovascular membrane [28] and overlying cystoid macular edema. While these two aspects of the lesion can be identified in the cross-sectional aspect of the B-scan OCT, separate C-scan sections reveal a more complete picture at the various interfaces of the components. The transverse direction of scanning is particularly effective at differentiating structures oriented horizontally.

The confocal view of the retina seen in each pair on the left demonstrates a diffusely increased reflex over a thickened central macula. From top to bottom, the image pairs demonstrate progressively deeper C-scan sections with paired B-scans marked with lines indicating the depth. The first section is taken though the inner retina and cuts through multiple perifoveal cysts. The section can be localized to the nerve fiber layer since it is at the same level of the retinal venule, which appears bright in the section. The second section cuts through the lower aspect of the cystic area which is seen surrounding the upper part of the neovascular complex. In this section the venule outline is dark since it is a shadow cast from the layer above. The third section cuts through the center of neovascular complex which appears highly reflective in the image. The bottom section shows the neovascular complex as a cystic area within the RPE bright ring surrounded by darker choroidal vessels.

Another important example of pathology, which demonstrates the clinical utility of the C-scan approach over the simple planar imaging of B-scan OCT, is seen in the case of a macular pucker [29] (Fig. 59.11). The confocal image shows the dragging of retinal blood vessels and loss of clarity characteristic of the epiretinal membranes that distort the macula. The B-scan OCT images have become standard clinical tools for displaying the bunching up of the vitreoretinal interface under the cellophane thin, but contracting blanketing membrane. The difficulty clinicians often encounter in approaching these membranes surgically is in defining their lateral extent in order to plan minimally damaging peeling. The C-scan sections in the pairs in the three raws highlight the tentacle-like extensions of the overlying tissue and help define the thickness and spread of irregularly shaped growth. The C-scan OCT image is patchy and displays fragments of depth structure for the tilted parts of the tissue.

59.3.8 Improved Resolution Using Ultrahigh-Resolution C-Scan Imaging (RR, MV, PG)

59.3.8.1 En Face Ultrahigh-Resolution OCT

Using a broadband light source in a system similar to the first generation of OCT/SLO systems allows for higher-resolution imaging and display of distinctive features. A SLO/en face ultrahigh-resolution (UHR) OCT prototype can acquire B- and C-scan OCT images with an axial resolution of about 3 μm and a lateral resolution around 15 μm. The system is based on a low-cost broadband lighter (Superlum, Russia) with a bandwidth (FWHM) of 150 nm at a central wavelength of 890 nm. Polarization controller paddles are added to input ports of the coupler to match the

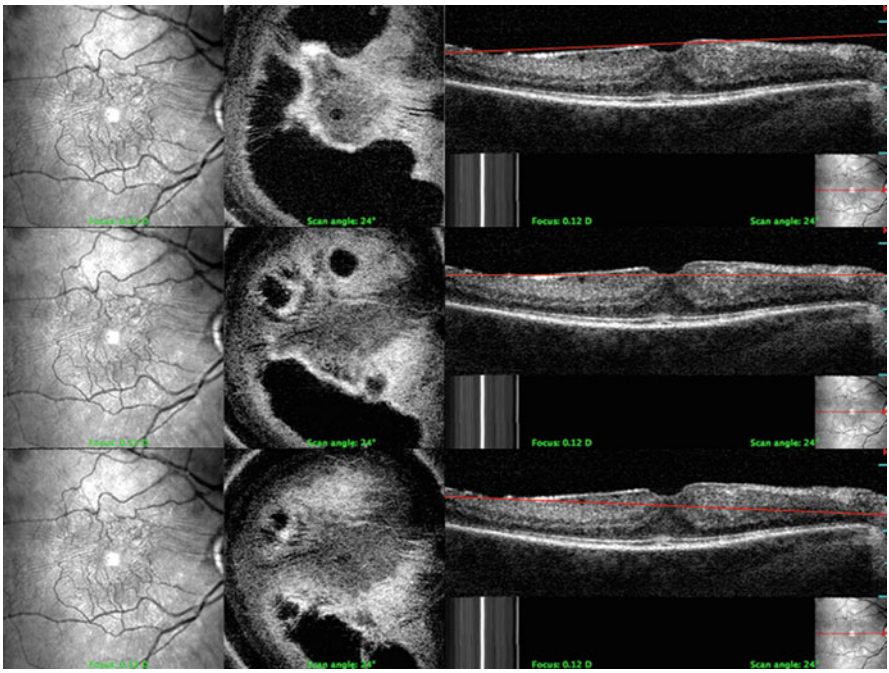

Fig. 59.11 Epiretinal membrane. The C-scan OCT images reveal the extent of the membrane and the presence of multiple cystic formations within the periphery of the membrane. Slight inferior tilting of the eye resulted in capture of irregular oval-shaped areas of vitreous within the three slice pairs shown. B-scan OCT images on the *right* show a *red line* which approximates the level and tilt of the scan angle. (Republished with permission from Springer Science+Business Media, [55])

states of polarization in the reference and sample arm. Dispersion imbalance, introduced by the interface optics and the eye refractive media, is also compensated [30].

UHR-OCT imaging [31, 32] demonstrates enhanced definition of the different retinal layers, the vitreoretinal interface, and the outer retina/RPE/choroid complex, as seen in Figs. 59.12 and 59.13. The latter has been subject to extensive discussion as to the exact interpretation. Averaging of multiple longitudinal scans [33] of the conventional Stratus OCT leads to the finding of three hyperreflective layers in this area, and it was suggested that the innermost layer correlates to the outer retinal segment, the middle layer to the outer retina–RPE interdigitations, and the most outer band to the actual retinal pigment epithelium. Closer examination of UHR-OCT images reported by W. Drexler et al. [32] also seems to show this triple layer. Both B- and C-scan OCT images from the system presented here definitely show this triple layer at the outer borders of the retina/RPE (Fig. 59.12) with a sharp cutoff above the choriocapillary layer.

UHR-OCT imaging substantially facilitates the understanding of the coronal (en face) C-scan OCT images. The improvement in the axial resolution leads to better delineation of the intraretinal layers. Figure 59.13 shows three consecutive

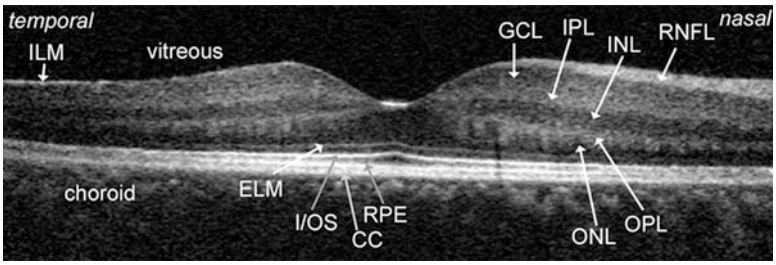

Fig. 59.12 Ultrahigh resolution B-scan OCT. The enhancement of axial resolution clarifies many of the internal retinal layers which are less defined at standard resolutions. This is especially evident in the outer retina where high reflectivity has tended to mask the subtle differences between thin layers. (Republished with permission from Springer Science+Business Media, [55])

C-scan OCT images of a healthy human eye fundus. The first section is taken at the vitreoretinal interface, showing the inner limiting membrane separate from the retinal nerve fiber layer and allowing for distinction of individual nerve fibers within this layer. The second C-scan shows the sharp delineation of the intraretinal layers, which allows for better appreciation and localization of subtle retinal changes within these layers. The third C-scan shows the triple hyperreflective band at the level of the outer retina–RPE junction and the thin external limiting membrane (ELM) layer. Even the external limiting membrane can be appreciated here.

With the improved quality of the B- and C-scan OCT images, it becomes easier to localize retinal pathologies which can be better appreciated. In cases of subtle retinal or subretinal changes, this will help in the diagnostic process. In cases of evident pathology, UHR imaging is not really necessary to make a diagnosis, but will help to better localize pathological change and to further understand the pathophysiology of retinal and choroidal diseases. The two clinical cases which follow demonstrate this further.

In Fig. 59.14, a C-scan OCT image acquired with a UHR-OCT/SLO is shown of a patient with an epiretinal membrane (macular pucker). The subtle folding of the retinal surface caused by this membrane can be clearly appreciated. The detailed pattern of this membrane, showing various points of traction, causes a very peculiar, wavy pattern of folds. This aspect could be compared with that in the B-scan OCT, which shows the epiretinal membrane (ERM) stretched out over the retinal surface and the folding of the retinal nerve fiber layer, but only in a one-dimensional way. The area that the epiretinal membrane covers exact location where it is pulling on the surface is best appreciated in the C-scan mode. Also, such an epiretinal membrane pattern as shown here would not be so evident in the regular OCT/SLO system.

In Fig. 59.15, UHR C-scan OCT images of a patient with a macular hole are shown, in comparison to a C-scan OCT image of the same patient made with the

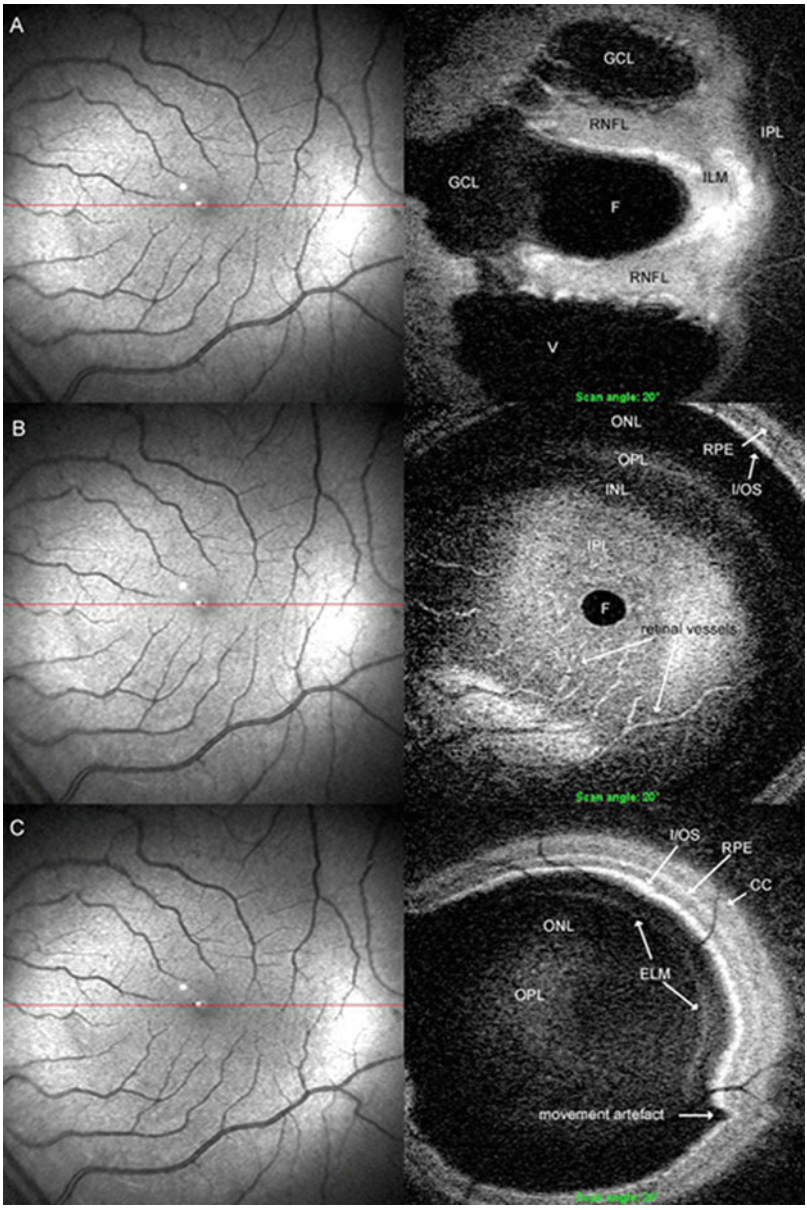

Fig. 59.13 SLO/UHR-C-scan pairs acquired from a healthy eye. (**a**) is the most superficial section demonstrating the patchy variability of depth recorded by transversal planar scanning. Adjacent patches demonstrate distinct features indicative of the layers captured. Pair (**b**) has been captured at a moment when the eye was well centered around fixation. The foveal depression is seen as a *circle* surrounded by concentric rings of successive layers. Pair (**c**) is the deepest image. The OCT reveals some movement with greater detail in the outer retina–RPE–choriocapillaris. (Republished with permission from Springer Science+Business Media, [55])

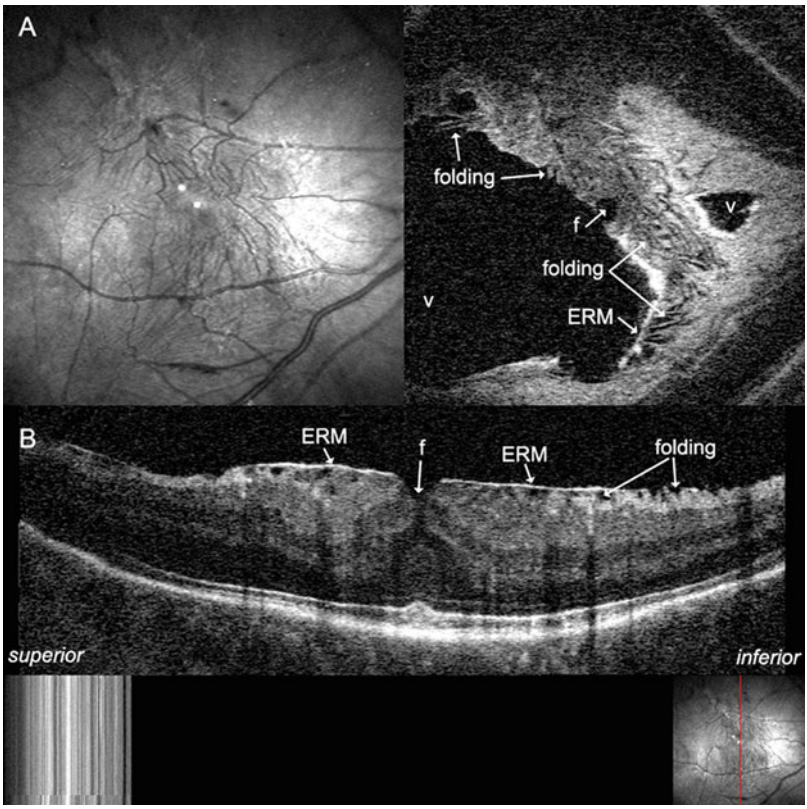

Fig. 59.14 Macular pucker. The SLO image (**a** *left*) displays fine swirling striations on the macular surface. The corresponding C-scan OCT image (**a**-*right*) shows the tilted orientation of the retina, revealing the edge of the macular surface in oblique cross section which highlights the infolding of the surface. The B-scan (**b**) shows the corrugated configuration of the retina due to the epiretinal membrane (ERM) and its effect on the middle layers as well as the surface. (Republished with permission from Springer Science+Business Media, [55])

regular system. The two frames are acquired by the two different systems but at the same level, to prove the more detailed information in the UHR image; the small septa between the cystic changes within the rim of the macular hole can be distinguished, and the lateral borders of these cystic changes are clearly demarcated. In the consecutive C-scan OCT images acquired at the level of the base of the macular hole, RPE irregularities are seen. However, these could also be remnants of the photoreceptor cell bodies that have been pulled out mechanically. These irregularities are also seen in the B-scan OCT image from the UHR system. These changes at the bottom of the hole could not be appreciated in the regular resolution system.

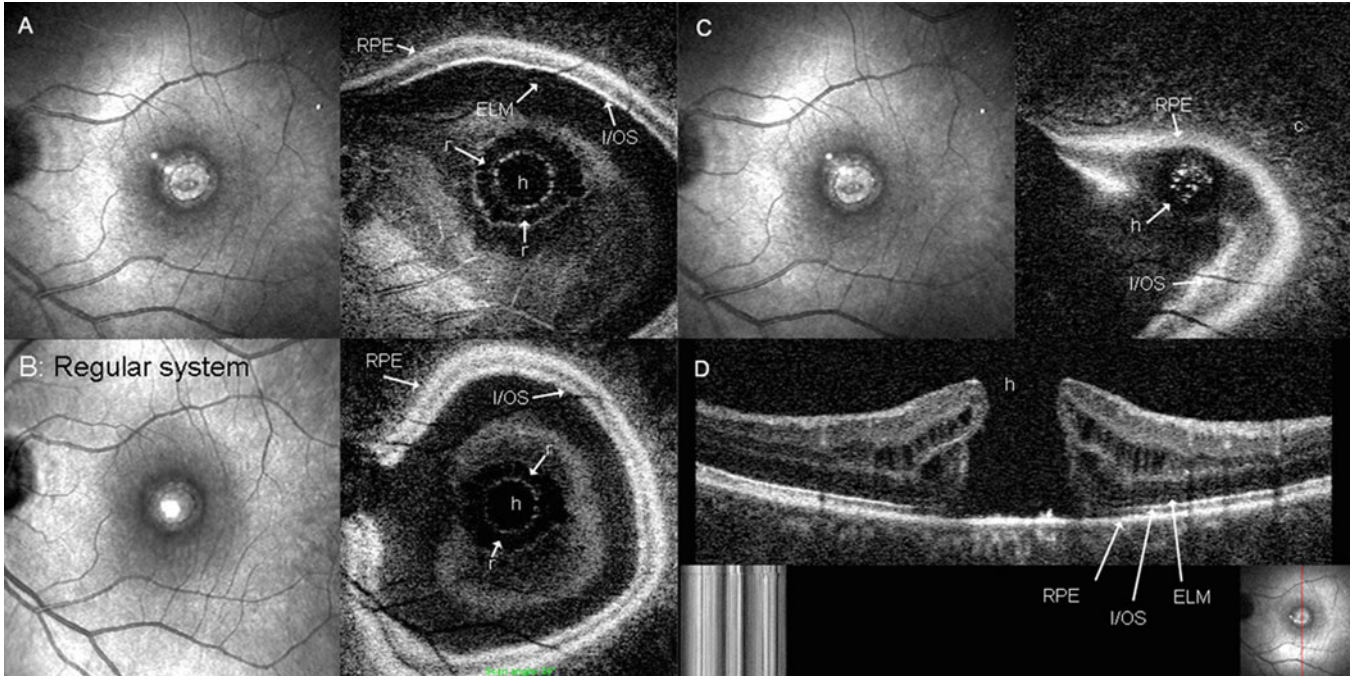

Fig. 59.15 Macular hole. UHR versus standard axial resolution OCT images comparison. Pair (**a**) demonstrates the added detail which is revealed by 3 μm axial resolution versus 10 μm axial resolution of pair (**b**). Pair (**c**) and image D are also UHR and provide details of the base of the hole and the internal retinal cysts more difficult to appreciate at 10 μm resolution. *RPE* retinal pigment epithelium, *ELM* external limiting membrane, *I/OS* inner/outer segment juncture, *h* macular hole. (Republished with permission from Springer Science+Business Media, [55])

59.4 Small Size Imaging

Cellular-level imaging has an increasing number of clinical applications as treatment options expand. Measurement of photoreceptor loss or rescue could be very useful in the evaluation of new pharmaceuticals, gene therapies, or stem cell implants. The ability to reliably detect microscopic progression of geographic atrophy could also significantly help shorten clinical trials, limiting prolonged studies of dead-end approaches, saving time, money, and effort. The optics of the eye has been a major limiting factor in achieving lateral resolution capable of detecting cellular boundaries. Cones range in size from 4.0 μm down to 0.5 μm in the foveal center, while rods are typically 2.5 μm in diameter. Adaptive optics [34] is now more used to overcome the eye aberrations, allowing the visualization of the cone mosaic in the living eye. Despite the exceptional resolution of the adaptive optics SLO, its complexity, size, and cost still pose significant barriers to its implementation as a workaday clinical tool. Lower-cost alternative solutions exist, by devising low aberration interface optics and using small angle scanners. At scanned fields reduced to 6.5° or less, it was possible to see clearly defined cone bodies at a location eccentric to the fovea [35, 36]. A clinical prototype, based on a modified commercial Opko-OTI SD-OCT/SLO, was developed by Hathaway and Weitz in 2009 which could exploit this enhanced resolution [37]. Utilizing the integrated OCT/SLO approach presented above, the current prototype allows consistent orientation at different levels of

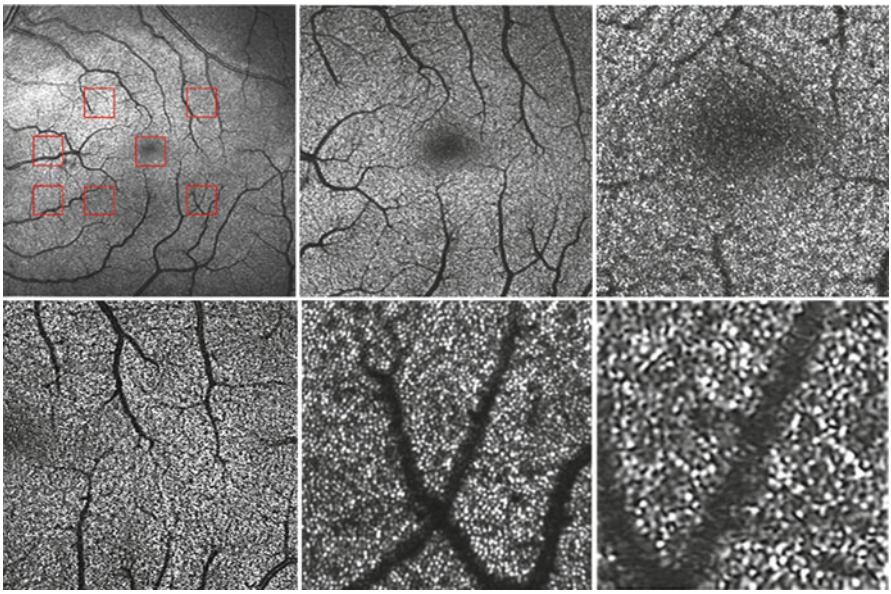

Fig. 59.16 Variable magnification achieved by alteration of scanning laser ophthalmoscope scanning angle. When the scanning resolution of the wide-field image is reduced, the perimacular cone mosaic becomes evident and accessible to post-processing counting algorithms, as shown in the last two images, lateral image size: 0.53 mm and 0.28 mm, respectively

zoom and correlation between OCT cross-sectional features, SLO en face landmarks, and flattened reformatted C-scan OCT slices. Figure 59.3 displays the real-time SLO small size images such obtained (Fig. 59.16).

59.5 Sequential En Face OCT/SLO Imaging

Switching off the reference beam in a configuration as that in Fig. 59.17 removes the high value of photodetected intensity and the noise associated with the high-power reference beam falling on the photodetectors. In this way, the photodetectors can reproduce a noise-free SLO signal. Elimination of the constant terms means that high gain photodetectors such as avalanche photodiodes (APD)s and photomultipliers can be employed, which however need to be swapped for low gain photodetectors such as

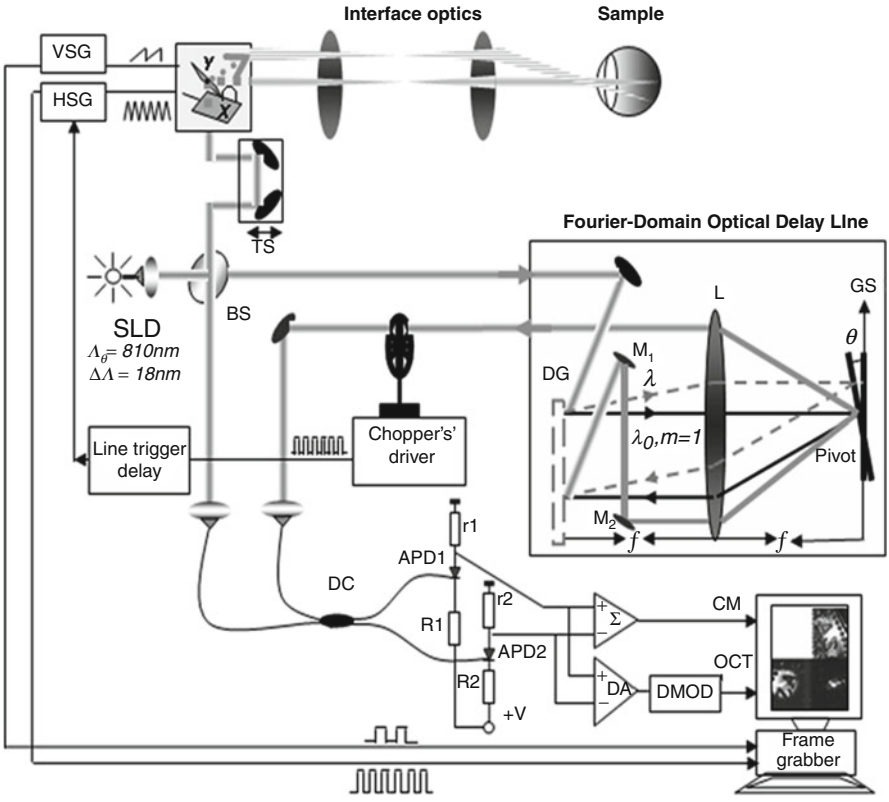

Fig. 59.17 Schematic diagram of the quasi-simultaneous en face OCT/SLO system [40]. *SLD* superluminescent diode (Superlum 361), *BS* beam splitter, *DC* broadband directional coupler, *DG* diffraction grating, M_1 M_2 mirrors, *GS* galvanometer scanner mirror, $APD_{1,2}$ avalanche photodetectors, *VSG* vertical signal generator, *HSG* horizontal signal generator, Σ summing amplifier, *DA* differential amplifier, *DMOD* demodulator block, $R_{1,2}$ ballast resistors, $r_{1,2}$ determine the sensitivity of the photodetection. (Reproduced with SPIE's permission from [39])

pin diode when the reference beam is reinstated on the photodetectors in the OCT regime. A technical solution is presented in [38] where APDs are used in both regimes, and a self-switching APD regime is employed based on the voltage drop on the resistors in series with the APDs. The advantage of such a configuration is its simplicity and also its efficiency in using the whole signal returned from the retina to produce either an OCT or an SLO image, i.e., no splitting of the signal is required.

59.5.1 Quasi-Simultaneous *En Face* OCT/SLO Imaging

Quasi-simultaneous imaging in the two regimes, OCT and CM, is achieved by using a chopper instead of the opaque screen, chopper which is controlled via a synchronization mechanism. This allows line-by-line operation, with a fast switching on the fly between the two regimes of operation, during the raster line of a dual frame image. The sensitivity of the OCT channel is not lowered, since no splitter is required. An additional difficulty was raised by the need to employ avalanche photodetectors (APD) in order to achieve sufficient signal-to-noise ratio in the CM channel. Low noise electronics and optimization of APD voltage combined with the optical power level in the reference beam lead to a signal-to-noise ratio in the OCT regime close to that achieved when using PIN photodetectors.

The system [39], as shown in Fig. 59.17, is based on a two-splitter low coherence hybrid interferometer optimized for broad bandwidth sources. Light from a superluminescent diode (SLD, Superlum, Moscow) centered at 810 nm with an 18 nm bandwidth is launched into the system through a single-mode optical fiber port and then is split by a plate beam splitter, BS, into an object and reference arm. The returned light from both arms is then routed into a second splitter, a broadband single mode directional coupler, DC. In the object arm of the interferometer, a pair of XY galvanometer scanners is employed to direct the beam via the interface optics to the object.

A Fourier-domain optical delay line scheme in the reference arm is employed for dispersion compensation and depth scanning. This works in transmission and exhibits low losses by traversing the diffraction grating only twice [40]. The delay line uses a diffraction grating DG, a lens L, and a tilting mirror GS in a *2f* configuration. The grating disperses a collimated beam, which is then imaged by an achromat lens L at a distance *f* away. A galvanometer scanner, GS, with its pivot located in the other focal plane of the lens, causes a linear phase ramp on the spectrum and redirects the rays back to the DG through L. Here the spectrum is recombined into a collimated beam. The outgoing beam exits the DG at a different point, O', parallel to the incoming beam. The amount of mirror tilt, θ, translates into a group delay for the output beam. This is based on the well-known property of the Fourier theorem that a linear phase in frequency domain corresponds to a group delay in time domain. To eliminate the walk-off, mirrors M_1 and M_2 are used to send the recombined beam back to GS, where the angular tilt is de-scanned.

A chopper (SR540, Stanford Research Systems) is used to square wave modulate the intensity of the reference beam. The chopper is powered by an adjustable voltage power supply, which is set to rotate the chopper at a repetition frequency of 500 Hz. The TTL pulses delivered by the chopper are then fed into a function synthesizer (8116A Pulse/Function Generator, 50 MHz, Hewlett Packard) that outputs a triangle waveform at 500 Hz to drive the line scanner. Mechanical and electric delays in the scanners require adjustment of the correct timing when the reference beam is toggled on and off. A delay is introduced by the block "line trigger delay" in the line delivering the TTL signal to the line frequency generator, and this is adjusted accordingly in order to synchronize the start of ray deflection over the object with the moment of toggling the reference beam power on and off. The chopper's frequency was sufficiently stable not to require any adjustments during the imaging. The frame scanner in the XY pair is driven by a vertical signal generator, VGS, with a sawtooth waveform at 1.5 Hz. The system operates differently during each ramp of the triangle sent to the line scanner. A similar approach was reported for generation of quasi-simultaneous OCT/OCT images with different depth resolutions [41], where a different coherence length source was used during each ramp. Here, the same source is employed, but the regime of operation is toggled from OCT to SLO synchronous with the X scanner.

The system can be used to generate cross-sectional images by using either transverse priority or depth priority scanning, and it is suitable for compensating the dispersion when scanning in depth [42]. However, for the present study we used only T-scans, where the carrier for the image bandwidth was created by the path modulation introduced by the galvanometer scanner determining the line in the final raster [6]. The detection unit employs two avalanche photodetectors, APD1 and APD2 (Mitsubishi PD1002). Essential for the operation regime here is their self-switching [43] depending on the optical power applied and the value of the ballast resistors, r_1 and r_2. Therefore, we have designed a special amplifier board which has allowed adjustment of the ballast resistor values and of the transimpedance in order to optimize the S/N ratio.

The CM signal is provided by the summing amplifier (Σ) where the two photodetected signals collected from resistors *r1* and *r2* are added up. The OCT signal is available at the output of the difference amplifier (DA) after demodulation in the demodulator block (DMOD). A dual-channel variable frame grabber (Bit flow, Raven) is used to display the two images.

Ideally, during the first half ramp applied to the line galvanometer scanner (X), of *1 ms* (ascending slope), the reference beam is on and the system provides the OCT signal (while the CM channel is saturated). During the second half ramp of *1 ms* (descending slope), the reference beam is blocked and the confocal signal is displayed (while the OCT channel provides a distorted CM image). For every line of *2 ms* in the raster, *1 ms* corresponds to the OCT regime and the next to the SLO (CM) regime of operation. Images of the optic nerve area obtained in these two regimes are shown in Fig. 59.18. The delay in producing SLO and OCT images is small, equal to the ramp duration; therefore, images can be considered as quasi-simultaneously obtained. They are however pixel-to-pixel correspondent.

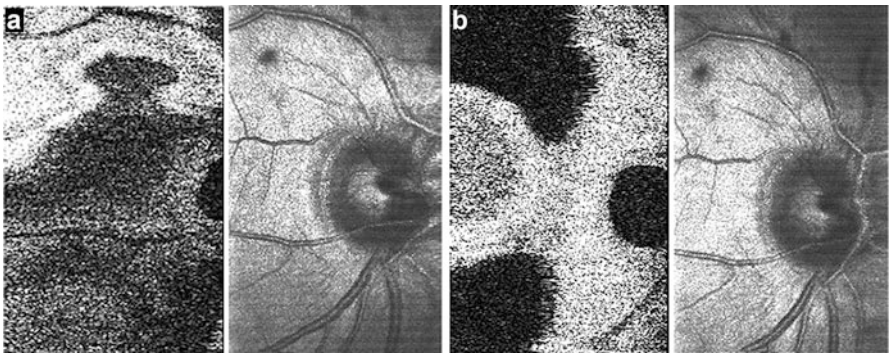

Fig. 59.18 Pairs of quasi-simultaneous C-scan OCT (*top*)/confocal (*bottom*) images of the optic nerve in vivo at different depths in the OCT channel. Image size: 4 mm (*horizontal*) × 7.5 mm (*vertical*). The images here have been cropped from the originals, and the OCT images were horizontally reverted to correspond to the SLO images. (Reproduced with SPIE's permission from [39])

In practice, there is a delay between the signal applied to the transversal scanner and the actual galvo mirror tilt, as well as other delays in the electronics circuitry, which requires correction via the "line trigger delay." The OCT and SLO images captured by the system are mirror-inverted with respect to the median of the frame grabber display window.

59.6 Simultaneous OCT and Fluorescence Angiography of the Retina

The addition of the confocal channel to the OCT channel provides the opportunity to implement all known applications of confocal microscopy with the added advantage of the complementary information provided simultaneously by the OCT channel. The first such application to be developed was infrared fluorescence angiography. A system which can simultaneously produce en face OCT and indocyanine green (ICG) angiographic fluorescence SLO images was designed [44]. The same optical source is used to produce the OCT image and excite the ICG. The system allows the clinician to examine the eye fundus with simultaneous corresponding *coronal* OCT sections and confocal ICG angiograms, displayed side by side. The system also facilitates capture of OCT B-scans by positioning a cursor line anywhere on the ICG image. This feature appears to be especially useful for studying lesions suspected of harboring choroidal neovascular membranes.

Fluorescence angiography using ICG dye [45, 46] is an established technique for studying blood circulation through the choroid of the eye. ICG is a well-tolerated contrast agent and is stimulated by infrared light which has greater penetration and is less phototoxic to the retina than shorter wavelength light [47].

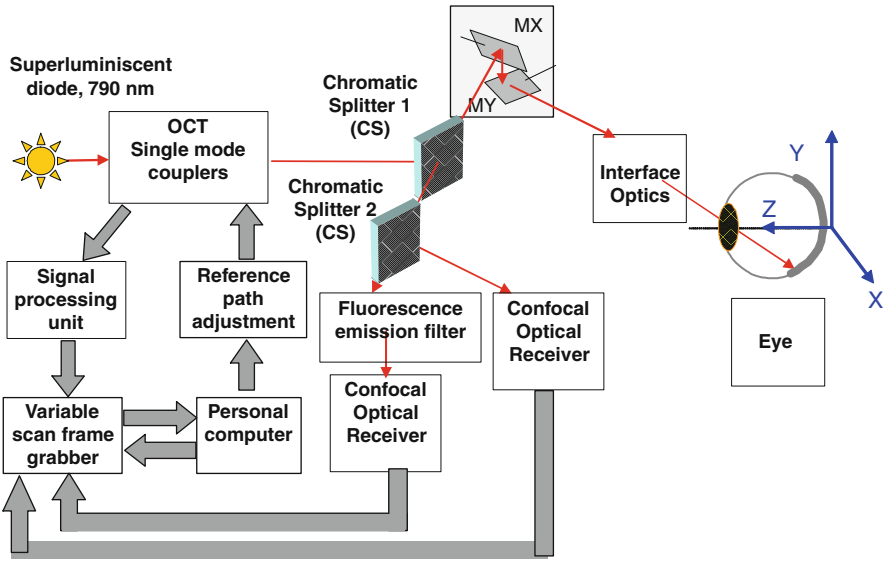

Fig. 59.19 General set-up of the combined OCT/SLO/ICG system. *MX, MY* galvanometer mirrors of the XY scanning pair. (Republished with permission from Springer Science+Business Media, [55])

The instrument, presented in a schematic diagram in Fig. 59.19, is a triple channel OCT/confocal ophthalmoscope/ICG angiographer with versatile scanning and image display capabilities allowing the acquisition of OCT and dual confocal images in B- or C-scan regime of operation. The splitter used in the OCT/SLO configuration [13] to divert some of the light to a separate confocal receiver was replaced by a chromatic splitter, CS [48]. This separates the retina-scattered light at the excitation wavelength, guided into the OCT channel, from the fluorescence signal, which is guided towards the fluorescence confocal receiver. The residual transmission of the chromatic splitter is sufficient to generate an image at the OCT wavelength.

To enhance the contrast of fluorescence in the confocal receiver, a supplementary filter is used in the fluorescence channel to attenuate any excitation band light that gets past CS.

To minimize the distortion of the OCT depth sampling profile (determined by the correlation function of the source), CS is used in transmission by the ICG channel and in reflection by the OCT channel. CS is a cold mirror with a transition wavelength, λ_{tr}, between the excitation band and fluorescence band. Superlum, Moscow, has devised a comparatively powerful SLD for this project, with a 5 mW optical power and $\Delta\lambda = 21$ nm spectral FWHM which gives a depth resolution in the retina of less than 9 μm (considering an index of refraction $n \sim 1.38$).

Following the injection of ICG dye into the patient's bloodstream (5 mg/ml), light from the SLD, guided through to the eye fundus by means of the interface optics, generates on one hand a reflected/backscattered return at the same wavelength (793 nm), which coherently combines with reference light to produce the OCT images, and on the other hand serves to excite fluorescence in any tissue structures containing the ICG dye, such as retinal and choroidal blood vessels. The acquisition of fluorescent images has to proceed rapidly, in less than a minute, due to the fast ICG disappearance rate from the bloodstream of between 18 % and 24 % per minute. Generating OCT, SLO, and ICG images at 2 Hz was found to provide a reasonably good trade-off between the acquisition speed requirement and the quality of the OCT images in terms of their signal-to-noise ratio.

The images in the three channels are displayed simultaneously in a four-up configuration with a fourth channel that overlays the OCT C-scan image on the ICG image. Figure 59.20 shows such images, the SLO (upper left), ICG fluorescence (lower left), OCT (upper right), and overlay channel featuring OCT on ICG (lower right) taken at two different times in the postinjection phase. In 30 s, 60 of such four-up sets of images are acquired, while the depth is explored over a range of typically 1.2 mm in retinal tissue. If the eye has moved considerably during the acquisition and essential parts from the retinal volume are missing, the acquisition can be repeated after the ICG bolus has passed. The pixel-to-pixel correspondence between the three images allows later association of morphologic features between the two images. Generally, just a few correct en face OCT images from the stack collected during the bolus passage are sufficient for subsequent transverse alignment of any other pairs of images. Figure 59.20 presents sets of images from an eye with an occult choroidal neovascular membrane beneath a serous retinal elevation. The confocal fluorescence image on the left in b reveals the location of active leakage within the lesion. Information on the depth-resolved morphology of the retina in these volumes is acquired by switching the system into the B-scan regime.

In these images, blood vessels are well defined in the ICG images while inconsistently revealed within the OCT images. At the same time, the depth resolution in the ICG channel is orders of magnitude lower than the OCT axial resolution, and morphology cannot be assessed accurately. Therefore we believe that such a system will have valuable applications by combining the complementary information supplied by the two channels. Regions of leakage, visible in the ICG image, can be selectively targeted by acquiring B-scan cross sections in the OCT channels as seen in the left hand side of c and in d.

Figure 59.21 further demonstrates this facility in evaluation of a retina of a patient with polypoidal choroidal vasculopathy, a peculiar variant of neovascular macular degeneration. In this case, the ICG angiography reveals a leash of abnormal vessels which originate near the nerve, extend inferotemporally, and terminate with bulbous endings. The accompanying OCT captures the sausage-shaped cuff of fluid surrounding the vessels which accounts

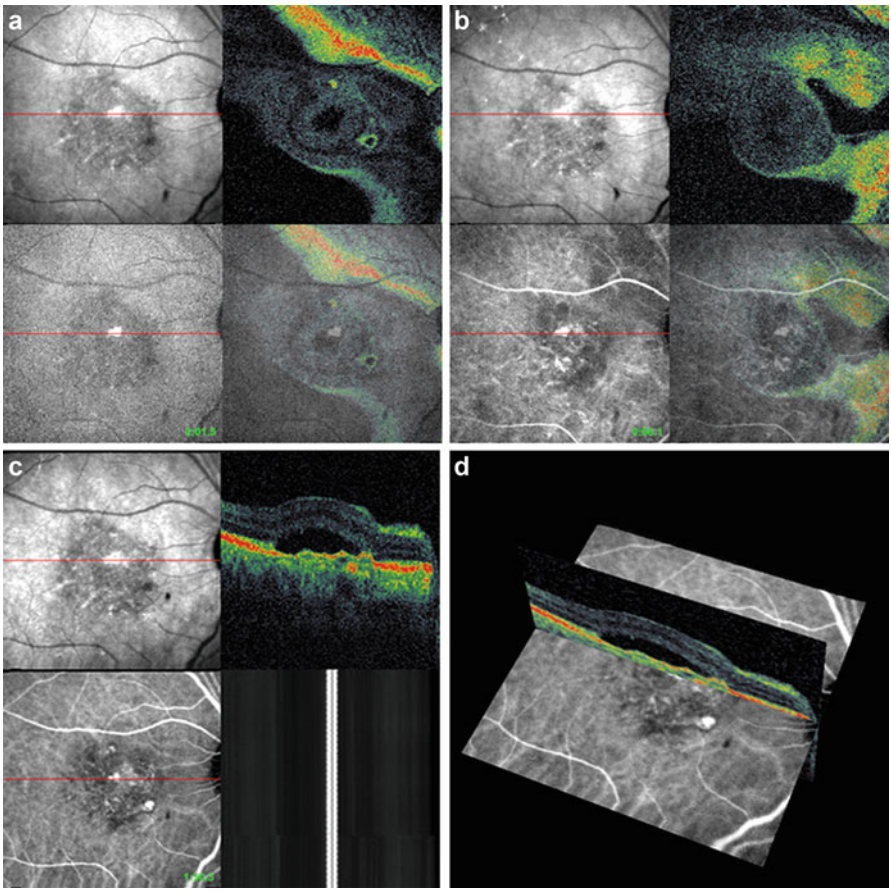

Fig. 59.20 SLO/OCT/ICG image sets acquired from a patient with occult choroidal neovascularization. (**a**) SLO (*upper left*), ICG fluorescence (*lower left*), en face OCT (*upper right*), and OCT/ICG overlay (*lower right*) images of the eye fundus of a patient in the preinjection phase at 1.5 s. (**b**) Same set of channels shown postinjection at 8.5 s. (**c**) SLO (*upper left*), ICG fluorescence (*lower left*), *B-scan* OCT (*upper right*), and confocal lines (*lower right*). The *red line* on the SLO image is the line where the B-scan OCT crossed the coronal slice. The confocal lines in the *lower right* show any movement artifacts during the acquisition of the OCT. D, 3D rendering of intersection of the ICG and the B-scan OCT planes. (Republished with permission from Springer Science+Business Media, [55])

for the lumpy "polypoidal" appearance in the confocal ophthalmoscopic images in the upper left quadrants of the display and in the cross sectional B-scan OCT in d. The overlay channel highlights the relationship between the vascular structures and the anatomic effect of the fluid leakage by displaying the vessels within the resulting cavitations.

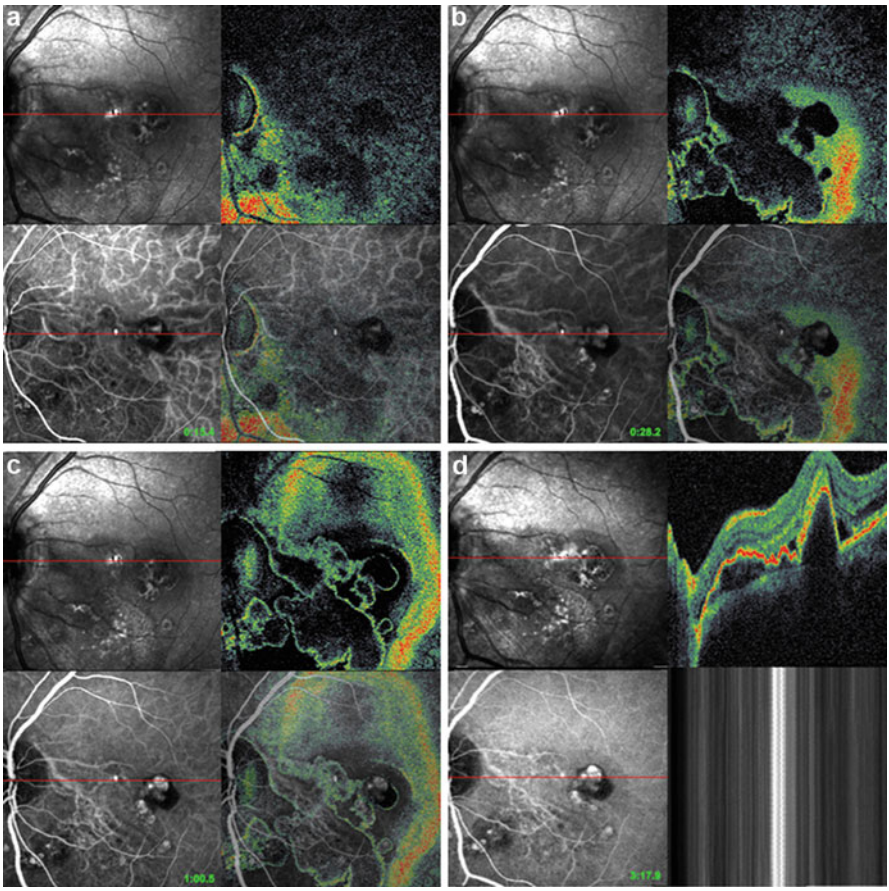

Fig. 59.21 ICG/OCT/SLO sets of patient with polypoidal choroidal neovascularization. (**a**) Early arterial phase of ICG sequence reveals lobular choroidal vessels. OCT depth is within the choroids and shows evidence of shadowing. (**b**) Mid arterial–venous phase demonstrates leash of abnormal vessels with hyperfluorescent bulbous ending. OCT image outlines the overlying serous elevation surrounding the vessels. (**c**) Full venous phase of the ICG angiogram shows increased leakage at vessel endings. The OCT reveals the outlines of the serous cuff around the vessels. (**d**) Late-phase ICG with B-scan OCT through area of leakage. The OCT reveals corrugated elevation of the RPE. The confocal image in the lower right confirms good alignment with minimal movement artifact. The Z-axis of the B-scan is expanded by the configuration of the multichannel display producing an exaggeration of the aspect ratio (© Copyright 2009 IOVS [45]). (Republished with permission from Springer Science+Business Media, [55])

59.7 Anterior Segment En Face OCT

Fast T-scanning followed by slower scanning along a transverse direction or slower depth scanning was also employed to acquire images from the anterior chamber. Continuous examination from the cornea to the lens is not possible using the same

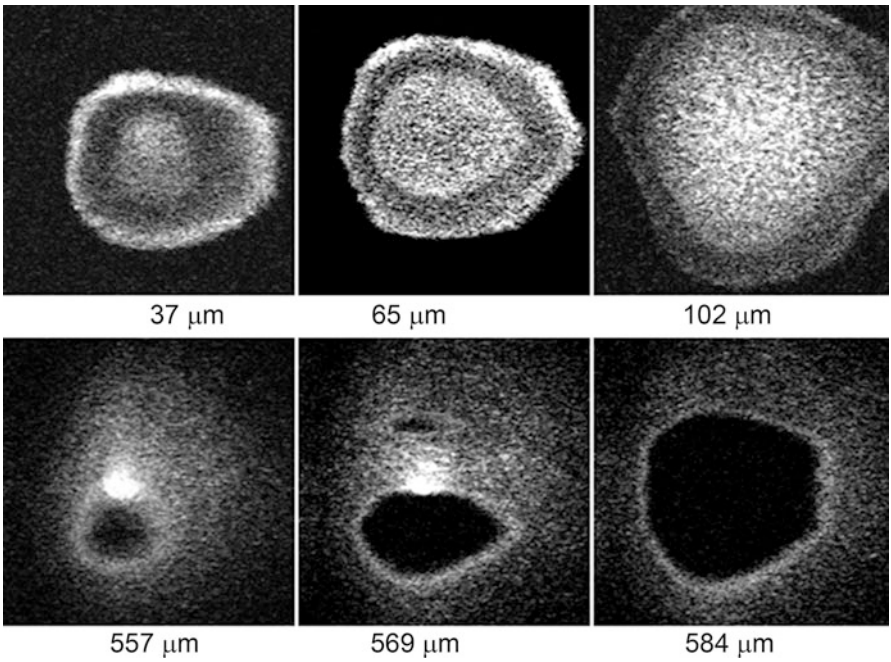

Fig. 59.22 En face OCT images of the cornea, 3 mm × 3 mm. All the depths are measured in air relative to the top of the cornea. (Reproduced with SPIE's permission from [51])

optical design confocal microscope [49]. The reflection from the tear film in front of the epithelium is 2 %. If a confocal instrument is set up to image the lens, then it can be used for imaging the cornea with limited success. The low numerical aperture of the interface optics precludes separation of the different layers in the cornea from the strong reflection at the air–tear film interface. Additionally, by changing the numerical aperture means that the depth resolution at the lens depth is less than that achievable at the cornea. Thirdly, due to the low reflectivity of the transparent tissue in the anterior eye structure, the confocal image exhibits low contrast. OCT addresses all these disadvantages and allows the same depth resolution from the cornea level up to very deep in the anterior chamber [50].

An OCT/confocal instrument was reported for collecting images from the cornea and the anterior chamber [51]. An SLD at 850 nm which delivered 300 μW to the eye was used, depth resolution in the cornea, slightly below 13 μm. To visualize the cornea only, a numerical aperture of the interface optics of 0.1 was used. This gave a transversal resolution of better than 20 μm and a depth of focus of 0.25 mm in both the OCT and confocal channel (the values are larger than those theoretically expected due to aberrations).

The C-scan images in Fig. 59.22 show the multilayer structure of the cornea. The top raw shows sections of the corneal epithelium. The Bowman layer is visible in transverse section, and its separation from the epithelium is transferred to the

distance between the two external and internal circles. The bottom raw displays C-scan images from the endothelium. In order to collect images in the anterior chamber as deep as from the lens, a lower numerical aperture interface optics was used, 0.02. This gives a long depth of focus with the disadvantage that the signal strength is just sufficient to allow visualization of the most important features in the anterior chamber. Figure 59.23 shows a couple of pairs of C-scan images, confocal and OCT, deep in the anterior chamber. The iris and the lens are visible. The images have been collected at a rate of one image pair per second. The images at the top are the confocal images. Scanning deep in the anterior chamber, the iris appears at

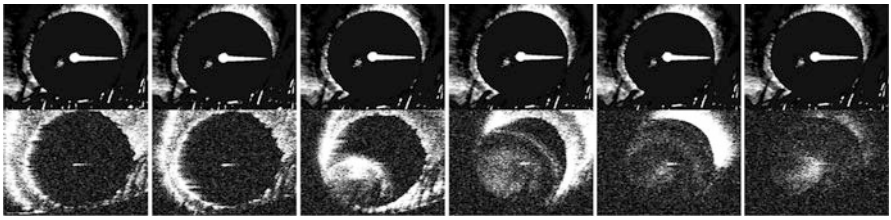

Fig. 59.23 Pairs of confocal (*top*) and OCT (*bottom*) images deep in the anterior chamber. Confocal images show the Purkinje reflections and the iris. Deeper, the lens is seen, offset from the optic axis, around the 3rd Purkinje image. 0.12 mm in air between the pairs. Image size is 6 mm × 6 mm. (Reproduced with SPIE's permission from [52])

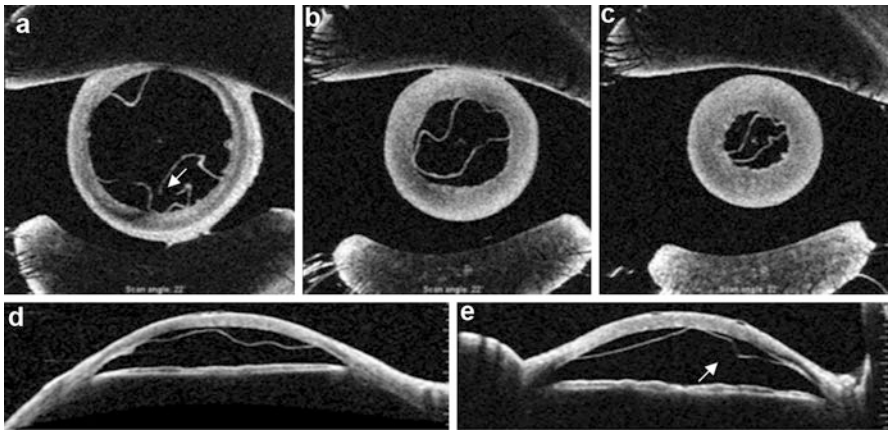

Fig. 59.24 Opaque cornea with bullous keratopathy and Descemet's detachment. (**a**) Coronal OCT section through the peripheral cornea reveals discontinuity in Descemet's membrane (*arrow*). (**b**) Coronal section through mid-peripheral cornea. (**c**) Coronal OCT through apical cornea. (**d**) Cross-sectional horizontal OCT through below corneal midline shows no defect. (**e**) Cross-sectional vertical OCT reveals same discontinuity (*arrow*) as (**a**). (Republished with permission from Springer Science+Business Media, [55])

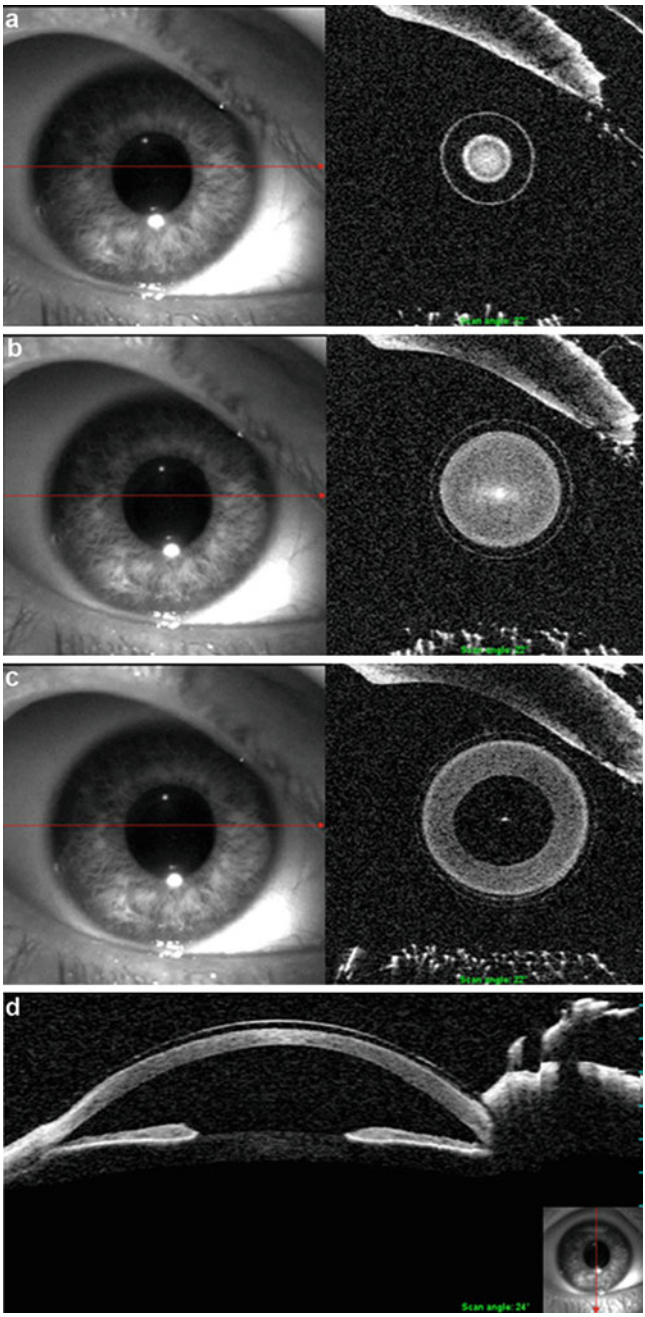

Fig. 59.25 Rigid contact on keratoconic cornea. (**a**) Apex of cornea surrounded by thin outline of contact lens. The distance to the outer ring reveals the fluid space between the *nipple* on the apex of the cornea and the lens. (**b**) The space between the contact lens and the cornea suggests close

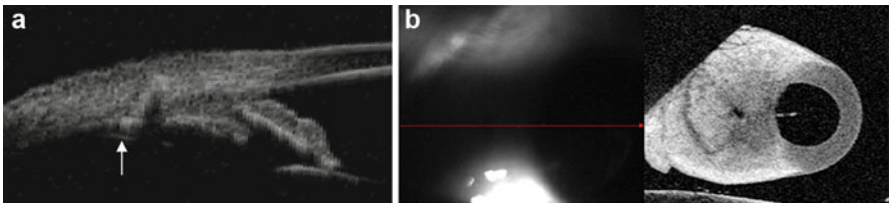

Fig. 59.26 Occult metallic foreign body. (**a**) The cross-sectional OCT demonstrates a small hyperreflective linear object in the sclera; (**b**) the coronal OCT reveals the scleral entry site and track along with linear extent of metallic fragment. (Republished with permission from Springer Science+Business Media, [55])

a depth of 3.5 mm. Clearly visible are the irregularities of the iris rim and the meshwork-like structure of the iris stroma. Then, at a depth of 4 mm, the lens becomes visible. The OCT images underneath show the en face sections around the first Purkinje reflected spot. The offset of the lens from the center of the image indicates how sensitive C-scan imaging is at off-axis orientation in comparison with the B-scan OCT imaging. The Purkinje reflections may be useful in aligning the eye axially, information difficult to handle when generating B-scan OCT images. The first two Purkinje images are visible in the confocal channel in Fig. 59.23.

The clinical value of en face OCT in the anterior segment can be demonstrated with a variety of examples where the pathology in question is so asymmetric that single cross-sectional OCT images are inadequate to image the anatomy. Figure 59.24 shows one such example in an eye with an edematous, opaque cornea and a detachment of Descemet's membrane. The images were taken with a system which incorporates a 1,310 nm source. While the cross-sectional images demonstrate the rumpled dehiscence of the corneal layer, the coronal images provide a much more complete picture of the phenomena.

The advantage of the en face perspective is further demonstrated in a series of images (Fig. 59.25) of a cornea with keratoconus fitted with a rigid gas-permeable contact lens. While the cross-sectional OCT shows the lens well fitted to the cornea, the coronal perspective actually reveals the fine disparity between the peak of the keratoconus *nipple* and the surrounding apex of the cornea.

Coronal imaging also extends to the sclera and may prove useful in detecting small defects such as occult rupture sites created by high-speed foreign bodies. Figure 59.26 shows an example of such a defect which had been covered by reactive swelling of the overlying tissue. While the cross-sectional OCT was able to find the small embedded missile, the en face OCT captured the internal tract and localized the object.

Fig. 59.25 (continued) approximation of curved surfaces in the mid cornea. (**c**) The distance between the lens and the peripheral cornea also suggests a good match between curves. (**d**) Cross-sectional OCT shows the contact lens on the cornea but does not reveal the fine profile of the *nipple*. (Republished with permission from Springer Science+Business Media, [55])

59.8 Conclusions

Simultaneously and quasi-simultaneously acquired real-time en face OCT images paired with confocal ophthalmic images provide unprecedented point-to-point correlation between surface and subsurface anatomy of the tissue. A variety of prototypes for different applications of this technology, including high depth resolution OCT and small size imaging have been reviewed demonstrating the clinical potential of the approach in the posterior segment. Similar technology was also demonstrated for the anterior segment. While the challenges to successful interpretation of these images appear substantial at first, once the clinician is familiarized with this perspective, its value in detecting and localizing occult pathology becomes obvious. The interest for the en face view has been revitalized by the progress in the acquisition speed and reduction in the processing time of spectral domain OCT. Significant volumes of the retinal tissue can now be acquired in a couple of seconds, which, after subsequent software cut, can lead to en face OCT images, however, collected during a time interval marginally longer than the time required by time domain OCT. Combination of spectral domain OCT with SLO is still possible [52] in pixel-to-pixel correspondence in transversal section, similar to the technology presented in this chapter. For large size images of the retina, spectral domain OCT is superior to time domain and determined the current widespread of OCT in imaging the eye. However, other time domain modalities are being developed, to reduce the acquisition time of volumes, based on parallel en face acquisition from several depths [53].

Acknowledgment Richard Rosen acknowledges the Lowenstein Foundation, the Leon Lane Foundation, the Gladys Brooks Foundation, the Lavoe Trust Foundation, the Audrey Monel Foundation, the Achelis-Bodman Foundation, the Peter Murphy Foundation, the Wise Family Foundation, and the JP Morgan Chase Foundation for their generous support of the Advance Retinal Imaging Center. Radu Cucu acknowledges the support of the New York Eye and Ear Infirmary Advanced Retina Imaging Laboratory Fund. Irina Trifanov and A. Podoleanu acknowledge the support of European Commission through the MC-EST project no 20353, HIRESOMI, awarded to the University of Kent. A. Podoleanu acknowledges the Leverhulme Trust, UK, for a research fellowship; several grants supported by Engineering Physical Sciences Research Council of the UK, such as EP/H004963/1; and the Advanced Grant from the European Research Council, 249889. A. Podoleanu is also supported by the NIHR Biomedical Research Centre at Moorfields Eye Hospital NHS Foundation Trust and UCL Institute of Ophthalmology.

References

1. J.A. Rogers, A.Gh. Podoleanu, G.M. Dobre, D.A. Jackson, F.W. Fitzke, Topography and volume measurements of the optic nerve using en-face optical coherence tomography, Opt. Express. **9**(10), 476–545 (2001). http://www.opticsexpress.org/abstract.cfm?URI=OPEX-9-10-533
2. M. Seeger, *3-D Imaging Using Optical Coherence Radar*, PhD thesis, University of Kent, 1997

3. D. Huang, E.A. Swanson, C.P. Lin, J.S. Schuman, W.G. Stinson, W. Chang, M.R. Hee, T. Flotte, K. Gregory, C.A. Puliafito, J.G. Fujimoto, Optical coherence tomography. Science **254**, 1178–1181 (1991)
4. B. Bouma, D.J. Tearney, S.A. Boppart, M.R. Hee, M.E. Brezinski, J.G. Fujimoto, High-resolution optical coherence tomographic imaging using a mode-locked Ti:Al2O3 laser source. Opt. Lett. **20**, 1486–1488 (1995)
5. A.G. Podoleanu, G.M. Dobre, D.J. Webb, D.A. Jackson, Coherence imaging by use of a Newton rings sampling function. Opt. Lett. **21**, 1789–1791 (1996)
6. A.G. Podoleanu, G.M. Dobre, D.A. Jackson, *En-face* coherence imaging using galvanometer scanner modulation. Opt. Lett. **23**, 147–149 (1998)
7. C.K. Hitzenberger, P. Trost, P.W. Lo, Q. Zhou, Three-dimensional imaging of the human retina by high-speed optical coherence tomography. Opt. Express **11**, 2753–2761 (2003)
8. C.C. Rosa, J. Rogers, A.Gh. Podoleanu, Fast scanning transmissive delay line optical coherence tomography. Opt. Lett. **30**, 3263–3265 (2005)
9. C.C. Rosa, J. Rogers, J. Pedro, A. Podoleanu, *Multiscan OCT System for A, T, B, C and 3-D Imaging, Biomedical Optics Conference, San Jose, 21–26 Jan. 2006, to be Published in the Proceedings of SPIE International Society for Optical Engineering*, (SPIE, Bellingham, 2006)
10. R. Rajadhyaksha, R. Anderson, R. Webb, Video-rate confocal scanning laser microscope for imaging human tissues in vivo. Appl. Opt. **38**, 2105–2115 (1999)
11. R. Juskaitis, T. Wilson, Scanning interference and confocal microscopy. J. Microsc. **176**, 188–194 (1994)
12. M. Kempe, W. Rudolph, E. Welsch, Comparative study of confocal and heterodyne microscopy for imaging through scattering media. J. Opt. Soc. Am. A **13**, 46–52 (1996)
13. A.G. Podoleanu, D.A. Jackson, Combined optical coherence tomograph and scanning laser ophthalmoscope. Electron. Lett. **34**, 1088–1090 (1998)
14. A.G. Podoleanu, R.B. Rosen, Combinations of techniques in imaging the retina with high resolution. Prog. Retin. Eye Res. **27**(4), 464–499 (2008)
15. A.G. Podoleanu, Unbalanced versus balanced operation in an OCT system. Appl. Opt. **39**, 173–182 (2000)
16. A.G. Podoleanu, D.A. Jackson, Noise Analysis of a combined optical coherence tomography and confocal scanning ophthalmoscope. Appl. Opt. **38**, 2116–2127 (1999)
17. D.U. Bartsch, M. Intaglietta, J.F. Bille, A.W. Dreher, M. Gharib, W.R. Freeman, Confocal laser tomographic analysis of the Retina in eyes with macular hole formation and other focal macular diseases. Am. J. Ophthalmol. **108**(3), 277–287 (1989)
18. F.E. Kruse, R.O.W. Burk, H.E. Volcker, G. Zinser, U. Harbarth, Reproducibility of topographic measurements of the optic nerve head with laser tomographic scanning. Ophthalmology **96**, 1320 (1989)
19. A.G. Podoleanu, J.A. Rogers, D.A. Jackson, S. Dunne, Three dimensional OCT images from retina and skin. Opt. Express **7**(9), 292–298 (2000)
20. Web page of group in Canterbury: http://www.kent.ac.uk/physical-sciences/research/aog/index.html
21. M.R. Hee, C.A. Puliafito, J.S. Duker, E. Reichel, J.G. Coker, J.R. Wilkins, J.S. Schuman, E.A. Swanson, J.G. Fujimoto, Topography of diabetic macular edema with optical coherence tomography. Ophthalmology **105**(2), 360–370 (1998)
22. R.B. Rosen, M.E.J. van Velthoven, P.M.T. Garcia, R.G. Cucu, M. de Smet, T.O. Muldoon, A.G. Podoleanu, Ultrahigh-Resolution combined coronal optical coherence tomography confocal scanning ophthalmoscope (OCT/SLO): a pilot study. Spektrum Augenheilkd **21**(1), 17–28 (2007)
23. A.W. Dreher, P.C. Tso, R.N. Weinreb, Reproducibility of topographic measurements of the normal and glaucomatous optic nerve head with the laser tomographic scanner. Am. J. Ophthalmol. **111**, 221–229 (1994)
24. A.G. Podoleanu, J.A. Rogers, D.A. Jackson, OCT *En-face* images from the Retina with adjustable depth resolution in real time. IEEE J. Sel. Top. Quant. Elect. **5**(4), 1176–1184 (1999)

25. M. Ohmi, K. Yoden, M. Haruna, Optical reflection tomography along the geometrical thickness. Proc. SPIE-Int. Soc. Opt. Eng. **4251**, 76–80 (2001)
26. M.E.J. Van Velthoven, F.D. Verbraak, L.A. Yannuzzi, R.B. Rosen, A.G. Podoleanu, M.D. De Smet, Imaging the Retina by *en-face* optical coherence tomography. Retina-J. Ret. Vit. Dis. **26**, 129–136 (2006)
27. R.B. Rosen, M. Hathaway, J. Rogers, J. Pedro, G. Patricia, P. Laissue, G.M. Dobre, A.G. Podoleanu, Multidimensional en-Face OCT imaging of the retina. Opt. Express **17**(5), 4112–4133 (2009)
28. T. Hashimoto, T. Harada, Confocal scanning laser microscopic findings of excised choroidal neovascular membranes of age-related macular degeneration and their comparison with the clinical features. Jap. J. Ophthalmol. **43**(5), 375–385 (1999)
29. E.M. Messmer, H.P. Heidenkummer, A. Kampik, Ultrastructure of epiretinal membranes associated with macular holes. Graefes Arch. Clin. Exp. Ophthalmol. **236**(4), 248–254 (1998)
30. R.G. Cucu, A.Gh. Podoleanu, J. Pedro, J.A. Rogers, R.B. Rosen, Combined confocal scanning ophthalmoscopy/*en face* T-scan based ultrahigh resolution OCT of the human retina in vivo, Opt. Lett. **31**(11), 1684–1687 (2006)
31. W. Drexler, H. Sattmann, B. Hermann, T.H. Ko, M. Stur, A. Unterhuber, C. Scholda, O. Findl, M. Wirtitsch, J.G. Fujimoto, A.F. Fercher, Enhanced visualization of macular pathology with the use of ultrahigh-resolution optical coherence tomography. Arch. Ophthalmol. **121**, 695–706 (2003)
32. T.H. Ko, J.G. Fujimoto, J.S. Schuman, L.A. Paunescu, A.M. Kowalevicz, I. Hartl, W. Drexler, G. Wollstein, H. Ishikawa, J.S. Duker, Comparison of ultrahigh- and standard-resolution optical coherence tomography for imaging macular pathology. Ophthalmology **112**, 1922 (2005)
33. B. Sander, M. Larsen, L. Thrane, J.L. Hougaard, T.M. Jorgensen, Enhanced optical coherence tomography imaging by multiple scan averaging. Br. J. Ophthalmol. **89**, 207–212 (2005)
34. J. Liang, D.R. Williams, D.T. Miller, Supernormal vision and high resolution retinal imaging through adaptive optics. J. Opt. Soc. Am. A Opt. Image Sci. Vis. **14**, 2884–2892 (1997)
35. A. Bradu, D. Merino, C. Dainty, R. Rosen, A. Podoleanu, *Small Size Imaging of the in-vivo Human Retina Using a Combined Confocal Scanning Ophthalmoscopy and T-scan Based En-Face OCT*, IOP, Imaging in the Eye III: Technologies and Clinical Applications, 22 Sept 2006
36. M. Pircher, B. Baumann, E. Götzinger, C.K. Hitzenberger, Retinal cone mosaic imaged with transverse scanning optical coherence tomography. Opt. Lett. **31**, 1821–1823 (2006)
37. R. Rosen, R. Weitz, M. Hathaway, *Near Adaptive Optics Quality Scanning Laser Ophthalmoscopy/Optical Coherence Tomography Imaging using Ultra High Resolution Confocal Microscopy and Ultra High Speed Spectral Domain Optical Coherence Tomography*, in Clinical EnFace OCT Atlas, (JayPee Brothers Medical Publishers, LTD, 2012)
38. A.G. Podoleanu, G.M. Dobre, R.G. Cucu, R.B. Rosen, Sequential OCT and confocal imaging. Opt. Lett. **29**(4), 364–366 (2004)
39. I. Trifanov, M. Hughes, A.G. Podoleanu, R.B. Rosen, Quasi-simultaneous optical coherence tomography and confocal imaging. J. Biomed. Opt. **13**(4), 044015 (2008)
40. C.C. Rosa, J. Rogers, A.G. Podoleanu, Fast scanning transmissive delay line for optical coherence tomography. Opt. Lett. **24**, 3263–3265 (2005)
41. A.G. Podoleanu, R.G. Cucu, R.B. Rosen, G.M. Dobre, J.A. Rogers, D.A. Jackson, Quasi-simultaneous OCT en-face imaging with two different depth resolutions. J. Phys. D Appl. Phys. **36**, 1696–1702 (2003)
42. C.C. Rosa, J. Rogers, J. Pedro, R. Rosen, A.G. Podoleanu, Multiscan time-domain optical coherence tomography for retina imaging. Appl. Opt. **46**(10), 1795–1808 (2007)
43. R. Cernat, A. Podoleanu, Avalanche photodiode based optical coherence tomography. Proc. SPIE-Int. Soc. Opt. Eng. **5459**, 185–191 (2004)
44. R.B. Rosen, M. Hathaway, J. Rogers, J. Pedro, P. Garcia, G. Dobre, A.G. Podoleanu, Simultaneous OCT/SLO/ICG imaging. Invest. Ophthalmol. Vis. Sci. **30**(2), 851–860 (2009)

45. L.A. Yanuzzi, R.W. Flower, J.S. Slatker (eds.), *Indocyanine Green Angiography* (Mosby/Elsevier, Philedelphia, PA, 1997). http://www.amazon.com/Indocyanine-Green-Angiography-Lawrence-Yannuzzi/dp/0815197748/ref=sr_1_7?s=books&ie=UTF8&qid=1420294767&sr=1-7&keywords=Indocyanine+Green+Angiography, http://www.us.elsevierhealth.com/article.jsp?pageid=379
46. A. Scheider, C. Schroedel, High resolution indocyanine green angiography with laser scanning ophthalmoscope. Am. J. Ophthalmol. **108**, 458–459 (1989)
47. W.J. Geeraets, E.R. Berry, Ocular spectral characteristics as related to hazards from lasers and other light sources. Am. J. Ophthalmol. **66**, 15–20 (1968)
48. G.M. Dobre, A.G. Podoleanu, R.B. Rosen, Simultaneous optical coherence tomography–Indocyanine green dye fluorescence imaging system for investigations of the eye's fundus. Opt. Lett. **30**, 58–60 (2005)
49. P. Furrer, J.M. Mayer, R. Gurny, Confocal microscopy as a tool for the investigation of the anterior part of the eye. J. Ocul. Pharmacol. Ther. **13**, 559–578 (1997)
50. S. Radhakrishnan, A.M. Rollins, J.E. Roth et al., Real-time optical coherence tomography of the anterior segment at 1310 nm. Arch. Ophthalmol-Chic **119**, 1179–1185 (2001)
51. A.G. Podoleanu, J.A. Rogers, G.M. Dobre, R.G. Cucu, D.A. Jackson, *En-face* OCT imaging of the anterior chamber. Proc. SPIE-Int. Soc. Opt. Eng. **4619**, 240–243 (2002)
52. A. Gh. Podoleanu, Principles of en face optical coherence tomography: real time and post processing en face imaging in ophthalmology in clinical enFace OCT Atlas, (JayPee Brothers Medical Publishers, LTD, New Delhi, India, 2013)
53. J.A. Rogers, A. Bradu, A.G. Podoleanu, Polarization maintaining multiple-depth en face optical coherence tomography system using active re-circulation loops in the non-stationary state. Opt. Express **20**, 29196–29209 (2012)
54. http://www.udel.edu/Biology/Wags/histopage/colorpage/cey/cey.htm
55. R.B. Rosen, P. Garcia, et al., En-face flying spot OCT/ophthalmoscope Optical Coherence Tomography, technology and applications. In: W. Drexler, J.G. Fujimoto (eds), Series: Biological and Medical Physics, Biomedical Engineering. XXVIII(1357), 448–474 (2008). Springer, Berlin, Heidelberg

Choroidal OCT

60

Marieh Esmaeelpour and Wolfgang Drexler

In the light of vast evidence, it is well accepted that there is choroidal involvement in the pathogenesis of many ocular diseases of the posterior pole. Histology of choroidal thickness (ChT) has revealed increased ChT correlated with a higher density of vessels in the superficial choroidal layers in open angle glaucoma [1], atrophy to choroidal capillary structure [2], and neovascularization in the choriocapillaris [3, 4] in aging and in age-related macular degeneration. Histological studies investigated biological structures in the eye with comparable high resolution to optical coherence tomography, but these were accompanied by preparation artifacts, shrinkages, and lack of blood supply to sustain vasculature volume [5]. Clinically the choroid is visualized by indocyanine green angiography, the insertion of a dye into the bloodstream that will stain blood vessels, even capillaries. This method shows alterations of choroidal vascular filling time and morphology already in elderly healthy subjects [6]. However, it lacks the third dimension and its use can be toxic and there is a risk of mortality.

Commercial OCTs at 800 nm are clinically used to image the retina and when used for choroidal imaging have a success rate of 74 % for reliably showing choroidal/scleral interface [7]. With the introduction of enhanced depth imaging (EDI) into commercial OCT systems, a new clinical investigation method for the choroid was presented [8]. Applying EDI, commercial OCT devices demonstrate choroidal penetration in scanned volumes only in thin choroids or by limiting imaging to few two-dimensional scans [8–10].

Recent interest in the choroid led a study with 3D-1,060 nm-OCT investigate choroidal thickness confined to central and four peripheral measurement locations in a healthy Japanese population [11]. However, analyzing the measurement at

M. Esmaeelpour (✉)
Center for Medical Physics and Biomedical Engineering, Medical University of Vienna, Vienna, Austria

W. Drexler
Center for Medical Physics and Biomedical Engineering, Medical University of Vienna, General Hospital Vienna, Vienna, Austria

© Springer International Publishing Switzerland 2015

W. Drexler, J.G. Fujimoto (eds.), *Optical Coherence Tomography*,
DOI 10.1007/978-3-319-06419-2_62

several image locations neglects the remaining data collected over the entire imaged field. Therefore, a method for mapping choroidal thickness needed to be developed that enabled statistical analysis of the entire imaged volume. The first study of choroidal visualization performance aimed to quantify the complete 3D-1,060 nm-OCT scan with ChT-maps in healthy subjects.

In a study with 34 healthy subjects, three-dimensional (3D) OCT volumes were acquired at 1,060 nm with 15–20 μm transverse resolution, about 7 μm axial resolution and 512 voxel per depth scan. For ChT-maps, a field of 36° × 36° scans with each degree corresponding to ~288 μm [12], centered on the fovea, was used. The OCT volume was averaged in both transversal directions within a field of ~1° to remove speckle and increase sensitivity. Axial ChT was defined as the distance between the center of the peaks originating from the RPE/Bruch's membrane/choriocapillaris (RBC) complex [13] and the choroidal-scleral interface (CSI). For the investigation of the ChT variation throughout the entire field of view, thickness maps were generated based on manual segmentation with segmentation in every 4th tomogram at the RBC complex and the CSI (Fig. 60.1). Two-dimensional ChT-maps, generated by local subtraction of the segmented height profiles were smoothed by transversal filtering, and splining between the slices, followed by a final two-dimensional median filter using a 15 × 15 kernel size. The resulting pixel distance was converted into optical distance using the depth sampling calibration for the 1,060 nm OCT system and further to physiological distance using a group refractive index of $n = 1.4$ (based on the refractive index of blood). This resulted in thickness maps for individual eyes.

For the statistical analysis of mean and variation of the ChT-maps of individual with similar ametropia, all the maps were aligned to each other in respect to the macula and optic nerve position with Matlab software (The MathWorks, Inc., Natick, USA). After correcting for differences in transversal area size with axial eye length (AL), an intensity overlay was introduced to exclude unreliable portions of the images with less than five measurements at one location. The images were evaluated along the depth-scan direction. ChT-maps were grouped by considering the eyes' refraction as myopic ($AL \geq 24.5$ mm, $n = 16$), emmetropic ($24.5 > AL \geq 23.4$ mm, $n = 20$), or hyperopic eyes ($AL < 23.4$ mm, $n = 28$) based on the normal AL variation with refraction and age [14–16]. Groups are described as characteristically myopic (long ALs), emmetropic (mid-length eyes), and hyperopic (short eyes). Mean and SD was obtained to create a compound map of average thickness for these three groups of eyes with color-coded thickness. For illustrating the location and extent of variation in the data sets, the coefficient of variation was found useful to allow comparison of widely different means. The coefficient of variation is expressed in percentage of the standard deviation from the mean.

Central ChT was measured beneath the fovea. Hyperopic eyes had a central ChT of 358 ± 96 μm (mean ± SD) and had the thickest choroid inferiorly but still within a 1,500 μm distance from the center. Emmetropic eyes had a ChT of 341 ± 95 μm, while myopic eyes had the thinnest choroid of the three groups with a central ChT of 213 ± 58 μm ($P < 0.001$, ANOVA, Bonferroni post-hoc testing) and an increase of thickness about 1,500 μm superior to the center (Fig. 60.2). The coefficient of

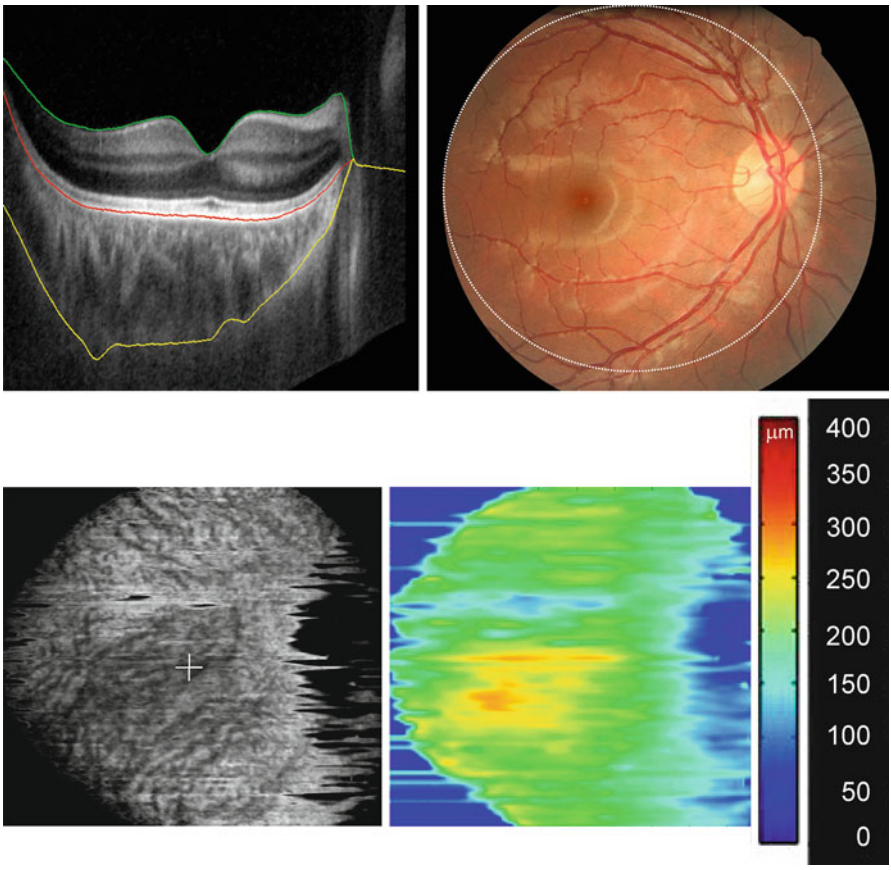

Fig. 60.1 1,060 nm OCT and choroidal thickness map generation in an example of automatic choroidal segmentation (*yellow line* border between sclera and choroid, *red line* RPE-Bruch's membrane/choriocapillaris complex, *green line* retina/vitreous interface). OCT image is taken within the area circled in fundus photograph. Choroid is segmented and averaged shown enface (*lower left image*) Choroidal thickness map generated for a healthy eye (*lower right image*)

variation was lowest in hyperopic eyes being less than 30 % over the majority of the ChT-map area. This study revealed also a decrease of ChT with age at the central and inferior location in eyes with longer ALs typically associated with myopia which is in agreement with the findings of other investigators [8, 11]. The mean of this study was much higher than found in studies with commercial systems (Table 60.1).

The healthy retina with macula and in its center, the fovea, has a structure that is accessible to localized averaged measurement: starting with the fovea centralis as an important measurement point and widening in concentric rings as suggested by the ETDRS study grid [17]. The ETDRS grid lends itself for measuring the choroid within the macula region, since the choroid is a major supplier of the macula and its

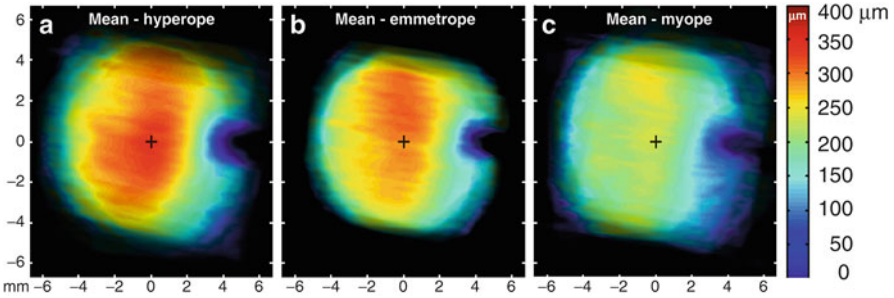

Fig. 60.2 Choroidal thickness maps grouped by axial eye length (*AL*) show a decrease in thickness mean with increasing AL (hyperope: AL<23.4 mm N = 28 eyes, emmetrope: 24.5> AL ≥23.4 mm N = 20 eyes, myope: AL ≥ 24.5 mm N = 16 eyes) [20]

Table 60.1 Choroidal thickness in healthy subjects measured with different OCTs

Investigators	Methods	Central choroidal thickness (mean ± SD)
Manjunath et al. [7]	Commercial OCT at 800 nm	272 ± 81 µm
Margolis and Spaide [8]	Commercial OCT with enhanced depth imaging at 800 nm	287 ± 76 µm
Zhang et al. [31]	Commercial OCT at 800 nm	172.1 (95 % CI 163.7–180.5) µm
Ikuno et al. [11]	Long wavelength OCT at 1 µm	354 ± 111 µm
Esmaeelpour et al. [20]	Long wavelength OCT at 1,060 nm	315 ± 106 µm

measurement is in this region of foremost interest [18]. However, the choroidal structure is unlike the retinal structure mainly a network of vessels with a characteristic segmental structure [19]. Choroidal thickness between the nasal, temporal, superior, and inferior fundus is distributed differently depending on age and AL [20]. Therefore, mapping in a region beyond the macula may allow a superior analysis. However, manual mapping is time consuming even if used only for research data.

60.1 Automatic Choroidal Thickness Segmentation

There are several challenges to automated choroidal segmentation. The first challenge is the low signal-to-noise ratio within the choroid and a washed out and irregular interface to the sclera. That is why previous OCT segmentation algorithms developed for the retina do not perform well with respect to choroidal segmentation requirements. Retinal segmentation algorithms vary depending on the number of layers to be segmented and on their robustness in the presence of speckle, shadows, morphologic irregularities (i.e., vessels, physiologic structural changes at the fovea and optic nerve head), and pathological changes in the tissue. In general most of the

existing approaches tend to be very sensitive to noise or missing data and often rely on well-contrasted boundaries or uniform layer structure. Intensity threshold-based algorithms utilize simple analysis along the depth scan's intensity profiles or find borders by investigating intensity gradients and are frequently confused by missing data, which leads to nonphysiologic results [21–26], thus, making them unsuitable for choroidal segmentation.

The second challenge is not being able to compare OCT images to the choroid itself in vivo for determining the true interface. One can only compare between different imaging modalities. Torzicky et al. segmented automatically in polarization-sensitive (PS) OCT images determining the anterior boundary of the choroid, the RPE, based on depolarization, and the posterior boundary, the CSI, based on the birefringence of the sclera [27]. The exact interface between choroid and sclera became subject to controversy because automatic segmentation of PS OCT images seems to overestimate choroidal thickness when compared to intensity based OCT imaging.

Kajic et al. achieved a robust automated choroid segmentation by using a statistical model that was built upon training data from manual segmentations by human operators [28]. Its advantage is that it can actively learn and determine the segmentation line in a low-signal, noisy environment such as in OCT tomograms in the region of the choroid without having to rely on boundary edge information. Statistical models can reproduce specific patterns of variability in shape and texture by analyzing the variations in shape across the training set. The key step of the statistical model training is the dimensionality reduction of the large set of features from the training data set. This is to enable the computational cost of the optimization method that is used to fit the model to the real data later on. The idea behind this concept is to find statistical dependencies between the produced features and reduce the dimensionality of the space by identifying only a certain number of the most prominent properties in the data set, represented by the most important eigenvectors.

To lower dimensions and to reduce multidimensional data sets for analysis, principal component analysis (PCA) is used. It is the standard vector space transform technique. It operates by calculating the eigenvalue decomposition of a data covariance matrix or singular value decomposition of a data matrix. Ideally, a relatively small number of eigenvectors with greatest eigenvalues can completely describe the original data.

The resulting pixel distance was converted into optical distance using the depth sampling calibration for the 1,060 nm OCT system and further to the anatomical distance. This resulted in thickness maps for individual eyes. Choroidal segmentation performed with a statistical model had as little as 13 % difference to manual segmentation, an error rate computed per tomogram, in a total of 871 tomograms, as a ratio of incorrectly classified pixels and the total layer surface. The reported difference between automated and manual retinal segmentation was comparable to the difference between manual and automated segmentation in the choroid [29]. Interobserver variability, measured by reimaging seven subjects (five healthy and two with dry AMD pathology) and comparing automatic segmentation of subfoveal ChT, ranged between 0 % and 10 % with a median of 1 % difference between the first and the second image [30]. Segmentation proved reliable even in

the presence of low signal (thick choroid), retinal pigment epithelium (RPE) detachments and atrophy, drusen, shadowing, and other artifacts.

Choroidal segmentation developed by other investigators [31] since uses vessel segmentation to identify the lower boundary of the choroid and envelope a surface to the lower vessels segmentation with a thin plate spline (TPS) approach [32]. While the segmentation is working, the main drawback responsible for a high rate of reported non-repeatability seems to be imaging OCT at 800 nm and not achieving the depth penetration needed for imaging the choroid.

60.2 Automatic Segmentation in Pathology

The generation of choroidal thickness maps was developed and applied first for normal healthy subjects to build a normative base. The choroid may be a novel biomarker for the major blinding eye diseases such as age-related macular degeneration and diabetes retinopathy. Statistical analysis using thickness maps in healthy proved practical to isolate areas of thinning or thickening and the extent of thickness alteration with axial eye length beside the classical measurement in the macula center. By illustrating how much a thinner choroid is related to an increasing AL, it becomes obvious that in studies of the choroid pathological eyes need to be matched not only by age but also by AL. Choroidal thickness mapping has also been established for swept source OCT, although segmented manually and investigators suggested applying the grid used by the Early Treatment Diabetic Retinopathy Study (ETDRS) [17] to facilitate reading of thickness values per area [33].

The use of choroidal thickness mapping was extended from healthy subjects to subjects with diabetes type 2 with a range of mild to clinically significant diabetic maculopathy [34]. A significantly lower choroidal thickness than healthy controls ($P < 0.05$) was found. Similarly in subjects with type 1 diabetes, choroidal thickness was reduced when compared to normal healthy subjects (Fig. 60.3) [30]. In type 1 diabetes choroidal thinning was not related to blood glycated hemoglobin or disease duration.

Capillary dropout in eyes with diabetes retinopathy is well documented [2, 35]. With current commercial OCTs, the choriocapillaris is not discernible as it is below the axial resolution of the present 800 and 1,060 nm instruments [36]. The magnitude of choroidal thickness alterations visualized in diabetes studies using thickness maps exceeds possible capillaries change [2, 37]. In both types of diabetes, choroidal thickness change is also present when clinical signs preceding retinopathy such as microaneurisms are not visible in the retina. This may suggest its role in hypoxia-induced injury and ischemia in the retina [38].

Vascular impairment in the choroid is also accounted for ischemia's role in AMD [39, 40]. A preliminary study on subjects with early AMD changes showed a decrease in choroidal thickness [41]. Drusen are deposits below the RPE and their presentation and area are suggested as biomarker for advancing into neovascular AMD [42] and have been associated with choroidal blood flow changes [43]. However, there are no studies with direct association with the choroid below the affected areas.

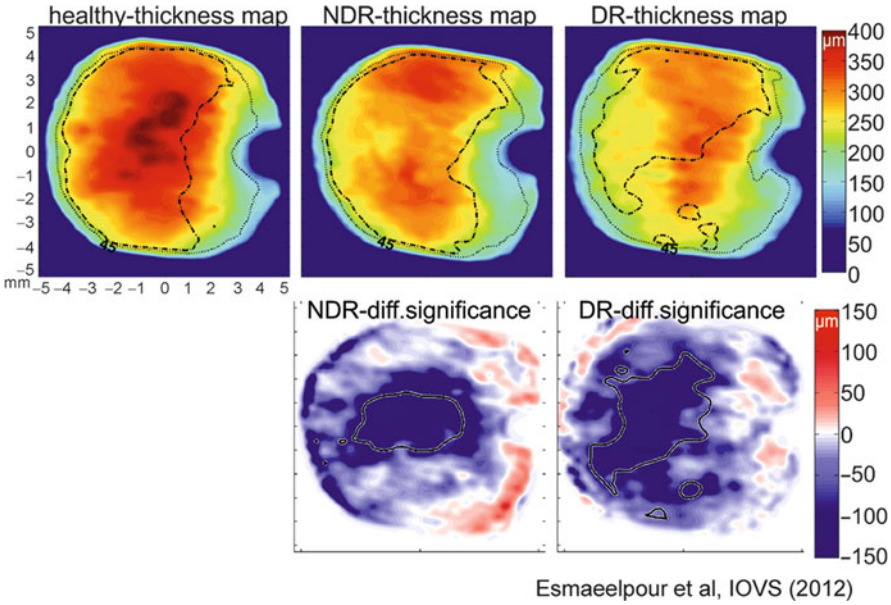

Fig. 60.3 Choroidal thickness and statistical difference contour maps in type 1 diabetes: choroidal thickness maps averaged for two disease stage groups compared with a healthy control group demonstrate that thickness is significantly decreased in NDR and DR group (*NDR* no diabetic retinopathy, *DR* diabetic retinopathy, first row averaged thickness maps with broken contour line representing 30 % variation), *lower row*; difference maps with central area of thinning, contour line represents $P < 0.05$

Another type of deposit associated with AMD are reticular pseudodrusen, which are granular hyper-reflective deposits in the subretinal space [44] suggested to be markers for inflammatory or atrophic vascular changes of the choroidal stroma [45, 46]. Using choroidal thickness mapping in 25 subjects with various types of AMD and pseudodrusen, we found a similarity between the shape of the affected area seen in autofluorescence images and areas with thicker choroid (Fig. 60.4). Thickness map observations show that choroidal areas coinciding with pseudodrusen area are thicker than other choroidal locations [47]. Using choroidal subfoveal thickness to relate to pseudorusen may be misleading as it is more likely to be associated with the severity of AMD rather than pseudodrusen.

Advanced AMD develops rapidly resulting in retinal exudates, with choroidal neovascularization in the choriocapillaris [3, 4], and is associated with functional changes of the choroid measured by laser Doppler [40]. Current treatment modality is intravitreal injection of vascular growth factor inhibitors (anti-VEGF) consisting of three initial injections in a four weekly routine and then treated "as needed" based on clinical findings, optical coherence tomography, and fluorescein angiography. In a current preliminary study, a group of 17 patients that underwent this treatment regime were imaged with 3D-1,060 nm OCT prior to treatment. After the three injections out of this cohort, seven patients were on clinically found

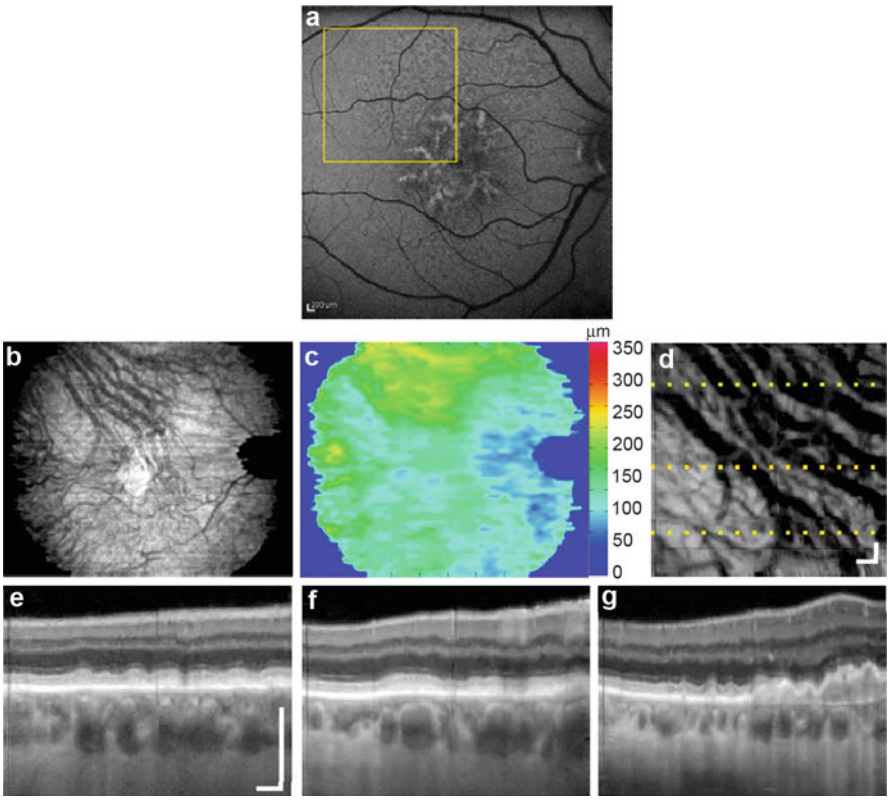

Fig. 60.4 The area where pseudodrusen are most prevalent coincides with the area of greater choroidal thickness. (**a**) Retinal autofluorescence image. (**b**) Enface 1,060 nm OCT image, averaged through the choroid. (**c**) Choroidal thickness map. (**d**) OCT image averaged from the superior temporal macula through the choroid (equal to the area shown in **a** with *lower right* corner ending at the fovea). (**e**–**g**) are tomograms taken at different distances from the fovea showing the distribution of different drusen and underlying choroid. While there is only a layer of large vessels underneath drusen (**g**), middle-size vessels belonging to Sattler's layer appear with an increasing number of pseudodrusen (**e**, **f**) [47]

successfully treated. These had initially a thinner choroid subfoveally than the patients that needed further injections. One eye became dry after five Anti-VEGF injections, while its fellow eye needed further treatment for the active neovascularization (Fig. 60.5). Although the successfully treated eye started with a larger fluid accumulation in the retina when compared to the fellow eye, it had a thinner choroid below the macula. This result may imply that the choroid in the ten non-successfully treated patients was more thickened and hence more affected than in the other patients. It has been postulated that inflammation is part of the pathogenesis of aging and AMD [48] and inflammation may be the reason for thickening in these patients. Another possibility may be fluid leakage not only into the retina but also into the choroid.

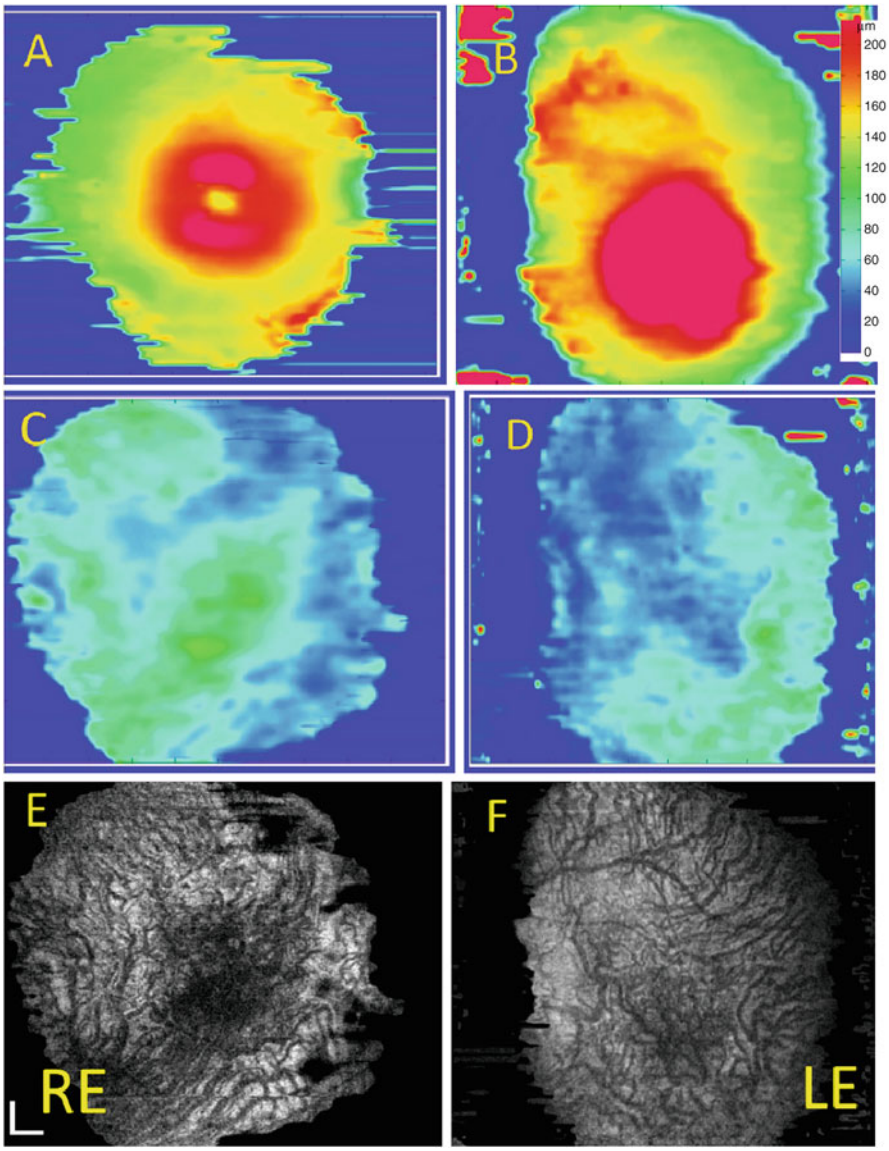

Fig. 60.5 Female subject (77 years old) with CNV type 1 in both eyes. Images were taken before treatment began. Although the right eye retinal thickness map shows a less edematous macular area than in the left retina, the right eye (*RE*) needs further injections, while the left eye (*LE*) was dry after the 5th injection. (**a**, **b**) Retinal thickness maps. (**c**, **d**) Choroidal thickness maps. (**e**, **f**) Enface of the choroidal vessel structure

60.3 Choroidal Vessel Segmentation

Vessel segmentation may provide a more in-depth analysis of choroidal change in ocular diseases. If choroidal vasculature changes with choroidal thickness, the type of change is still largely unknown. Choroidal vasculature has been modelled three dimensionally in vitro by using histology [49] and imagined two dimensionally in vivo by injecting intravitreal dye into the choroid [50]. The latter method is used clinically as it can pinpoint the exact location of activity such as of neovascularization in the choriocapillaries in AMD. It has the disadvantage of being highly invasive, possibly toxic with fatal risk. Alternatively vessels can be recognized noninvasively and in vivo by imaging their blood flow. The extension of OCT with Doppler signals enables in vivo volumetric vascular imaging by locating blood flow within the tissue. Although a good correlation exists between vessel diameter and blood flow velocity in the choroid [51], this type of vessel diameter calculation may underestimate the real diameter. A direct use of OCT choroidal images for vasculature segmentation is preferable as it improves specificity and accuracy of measurements.

Vessel segmentation algorithms used with other imaging modalities such as in MRI and CT rely on relatively high contrast, which allows achieving very high accuracy. Straightforward approaches for edge filtering such as Gabor filters [52] present difficulty when image vessel wall definition is low. Methods that use of seed points [53–55] are prone to segmentation leaks and if manual intervention is needed they are rendered impractical. Artificial intelligence and neural network-based methods require difficult to obtain training sets. Additionally, pixel-based classification algorithms [56] would have difficulty segmenting choroidal vessels based on texture features only. Because OCT background is hard to distinguish from the vessels, Rician distribution background modelling approach [57] encounters the same problem. OCT data intensities such as decreasing signal-to-noise ratio (SNR) with imaging depth, imposes a challenge to more than a hundred algorithms of vessel segmentation techniques, similar to the ones mentioned [58]. For 3D choroidal vessel quantification, a vessel segmentation algorithm is required that scales well with highly noisy data. All of the aforementioned methods require relatively high contrast and rely on various initializations and sequential tracking steps and/or require manual intervention of the operator which is extremely time costly and limited in the case of 3D data by human 2D vision (true 3D data can only be perceived as a 2D projection).

Vessel segmentation of choroidal stroma has been suggested by other investigators. Motaghiannezam et al. demonstrated an algorithm for automated vessel segmentation in three healthy eyes [59], whereas Zhang et al. investigated a cohort of 24 healthy eyes but could not successfully reproduce repeat segmentation in all eyes [31]. Their algorithm identified vessels in the choroidal stroma and assumed the remaining upper choroid to be equivalent to choriocapillaries. Another group of investigators analyzed choroidal vessels in eyes with AMD pathology and thin choroids [60] by pixel intensity without segmenting vessels.

Alternatively, a fully automated, robust vessel segmentation algorithm was developed for choroidal OCT, employing multiscale 3D edge filtering and

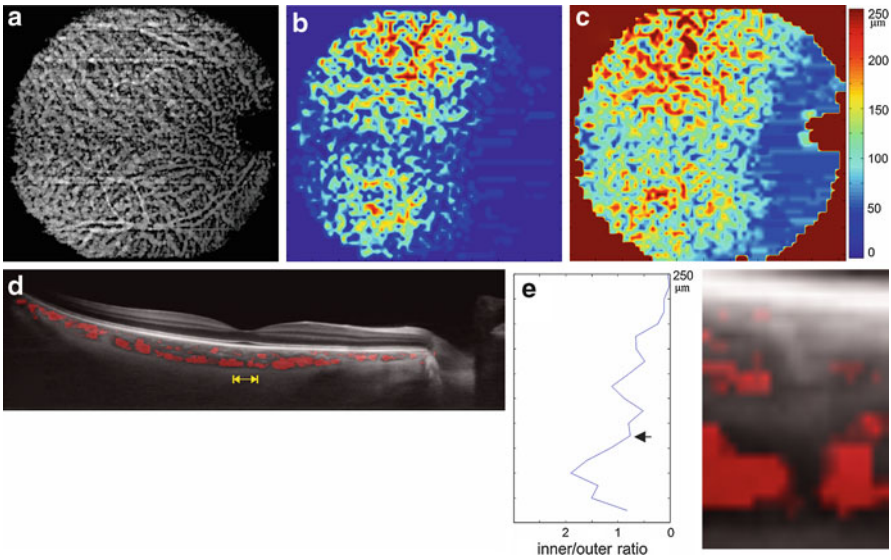

Fig. 60.6 Automatic segmentation of Haller's and Sattler's layer for thickness map generation. (**a**) An enface average of automatically segmented choroidal vessels. Based on diameter thresholding, thickness maps for Sattler's and Haller's layer are generated (**b**, **c**). (**d**) Central tomogram visualizes identified vessel voxels in red. Plot represents inner/outer voxel ratio of a 3D OCT data set with 1° diameter, taken from the location which is marked by *yellow arrows*. (**e**) The *black arrow* marks the border between Sattler's and Haller's layer that was detected based on the largest voxel ration and its local minimum

projection of "probability cones" to determine the vessel "core," even in the tomograms with low SNR. Based on the ideal vessel response after registration and multiscale filtering, with computed depth-related SNR, the vessel core estimate was dilated to quantify the full vessel diameter [61]. The novel algorithm extracts voxels belonging to vessels out of those voxels that belong to tissue (Fig. 60.6). The algorithm performs well when assessing qualitatively by viewing B-scan tomograms in data sets from healthy and patients with retinal pathologies, containing artifacts and extremely low signal due to shadows.

Further, the algorithm differentiates between the number of voxels that belong to outer vessel which have at least one neighboring voxel that is not a vessel voxel and inner voxels that are surrounded by other vessel voxels (Fig. 60.6). They yield themselves to useful statistics of morphological detail of the healthy and diseased choroid. These numbers are related to the distribution of the large and small choroidal vessels. Figure 60.6 shows that the ratio of inner to outer pixels, corresponding to the relative proportion of larger vessels, decreases from the sclera towards the RPE.

Vessel voxels segmented this way have been reproduced in a group of healthy eyes and eyes with dry AMD that were reimaged on a second study day [62]. Choroidal sublayers were segmented according to vessel voxel thresholding and

the coefficients of repeatability for Sattler's and Haller's layers were 35 % and 21 % in ten healthy eyes and 44 % and 31 % in ten AMD eyes, respectively. In representative cases of eyes with AMD and central serous chorioretinopathy, a comparison to vessel images taken with indocyanine green angiography (a dye for visualizing choroidal vessels in 2D field of view) confirmed that segmentation was no artifacts. In fact more vessels were visualized with OCT than with angiography with which vessels were obscured either by choroidal depth or by lesions.

By using inner to outer voxel plots to represent vessel diameter, it was possible to differentiate between Haller's and Sattler's layer. Haller's layer is characterized by large vessel diameter, whereas vessels in Sattler's layer are middle sized before they branch into capillary vessels in the inner choroid. While separating inner and outer choroid vessels within the OCT image allows for visualization of vessel incidence with depth, segmenting choroidal layers allows thickness mapping and may increase sensitivity to pathological changes. Mapping Sattler's and Haller's layer in a healthy normal data base of 40 subjects, it was possible to show that both layers' thicknesses correlate with each other, while paired t-test comparison showed a significant difference and that their thicknesses decrease with larger axial eye length.

References

1. Z.Q. Yin, Vaegan, T.J. Millar, P. Beaumont, S. Sarks, Widespread choroidal insufficiency in primary open-angle glaucoma. J. Glaucoma **6**(1), 23–32 (1997)
2. D.S. McLeod, G.A. Lutty, High-resolution histologic analysis of the human choroidal vasculature. Invest. Ophthalmol. Vis. Sci. **35**(11), 3799–3811 (1994)
3. S.H. Sarks, Ageing and degeneration in the macular region: a clinico-pathological study. Br. J. Ophthalmol. **60**(5), 324–341 (1976)
4. W.R. Green, S.N. Key, Senile macular degeneration: a histopathologic study. Trans. Am. Ophthalmol. Soc. **75**, 180–254 (1977)
5. M. Gloesmann, B. Hermann, C. Schubert et al., Histologic correlation of pig retina radial stratification with ultrahigh-resolution optical coherence tomography. Invest. Ophthalmol. Vis. Sci. **44**(4), 1696–1703 (2003)
6. Y.N. Ito, K. Mori, J. Young-Duvall, S. Yoneya, Aging changes of the choroidal dye filling pattern in indocyanine green angiography of normal subjects. Retina (Philadelphia, PA) **21**(3), 237–242 (2001)
7. V. Manjunath, M. Taha, J.G. Fujimoto, J.S. Duker, Choroidal thickness in normal eyes measured using Cirrus HD optical coherence tomography. Am J. Ophthalmol. **150**(3), 325–329.e1 (2010)
8. R. Margolis, R.F. Spaide, A pilot study of enhanced depth imaging optical coherence tomography of the choroid in normal eyes. Am J. Ophthalmol. **147**(5), 811–815 (2009)
9. Y. Ikuno, Y. Tano, Retinal and choroidal biometry in highly myopic eyes using spectral-domain optical coherence tomography. Invest. Ophthalmol. Vis. Sci. **50**(8), 3876–3880 (2009)
10. T. Fujiwara, Y. Imamura, R. Margolis, J.S. Slakter, R.F. Spaide, Enhanced depth imaging optical coherence tomography of the choroid in highly myopic eyes. Am J. Ophthalmol. **148**(3), 445–450 (2009)

11. Y. Ikuno, K. Kawaguchi, Y. Yasuno, T. Nouchi, Choroidal thickness in healthy Japanese subjects. Invest. Ophthalmol. Vis. Sci. **51**(4), 2173–2176 (2009)
12. N. Drasdo, C.W. Fowler, Non-linear projection of the retinal image in a wide-angle schematic eye. Br. J. Ophthalmol. **58**(8), 709–714 (1974)
13. E.M. Anger, A. Unterhuber, B. Hermann et al., Ultrahigh resolution optical coherence tomography of the monkey fovea. Identification of retinal sublayers by correlation with semithin histology sections. Exp. Eye Res. **78**(6), 1117–1125 (2004)
14. L. Llorente, S. Barbero, D. Cano, C. Dorronsoro, S. Marcos, Myopic versus hyperopic eyes: axial length, corneal shape and optical aberrations. J. Vis. **4**(4), 288–298 (2004)
15. K.E. Lee, B.E. Klein, R. Klein, Z. Quandt, T.Y. Wong, Association of age, stature, and education with ocular dimensions in an older white population. Arch. Ophthalmol. **127**(1), 88–93 (2009)
16. N.C. Strang, K.L. Schmid, L.G. Carney, Hyperopia is predominantly axial in nature. Curr. Eye Res. **17**(4), 380–383 (1998)
17. Anon, Photocoagulation for diabetic macular edema. Early Treatment Diabetic Retinopathy Study report number 1. Early Treatment Diabetic Retinopathy Study research group. Arch. Ophthalmol. **103**(12), 1796–1806 (1985)
18. G. Barteselli, J. Chhablani, S. El-Emam et al., Choroidal volume variations with age, axial length, and sex in healthy subjects: a three-dimensional analysis. Ophthalmology **119**(12), 2572–2578 (2012)
19. S.S. Hayreh, Submacular choroidal vascular pattern. Experimental fluorescein fundus angiographic studies. Albrecht. von Graefes. Arch. Klin. Exp. Ophthalmol. **192**(3), 181–196 (1974)
20. M. Esmaeelpour, B. Povazay, B. Hermann et al., Three-dimensional 1060 nm OCT: choroidal thickness maps in normals and improved posterior segment visualization in cataract patients. Invest. Ophthalmol. Vis. Sci. **51**(10), 5260–5266 (2010)
21. D. Cabrera Fernández, H.M. Salinas, C.A. Puliafito, Automated detection of retinal layer structures on optical coherence tomography images. Opt. Express **13**(25), 10200–10216 (2005)
22. M. Mujat, R. Chan, B. Cense et al., Retinal nerve fiber layer thickness map determined from optical coherence tomography images. Opt. Express **13**(23), 9480–9491 (2005)
23. K.A. Vermeer, J. Van der Schoot, H.G. Lemij, J.F. De Boer, Automated segmentation by pixel classification of retinal layers in ophthalmic OCT images. Biomed. Opt. Express **2**(6), 1743–1756 (2011)
24. M.V. Sarunic, A. Yazdanpanah, E. Gibson et al., Longitudinal study of retinal degeneration in a rat using spectral domain optical coherence tomography. Opt. Express **18**(22), 23435–23441 (2010)
25. A.K. Mishra, P.W. Fieguth, D.A. Clausi, Decoupled active contour (DAC) for boundary detection. IEEE Trans. Pattern Anal. Mach. Intell. **33**(2), 310–324 (2011)
26. J. Molnár, D. Chetverikov, D.C. DeBuc, W. Gao, G.M. Somfai, Layer extraction in rodent retinal images acquired by optical coherence tomography. Mach. Vis. Appl. **23**(6), 1129–1139 (2012)
27. T. Torzicky, M. Pircher, S. Zotter et al., Automated measurement of choroidal thickness in the human eye by polarization sensitive optical coherence tomography. Opt. Express **20**(7), 7564–7574 (2012)
28. V. Kajić, M. Esmaeelpour, B. Povazay, D. Marshall, P. L. Rosin, Automated choroidal segmentation of 1060 nm OCT in healthy and pathologic eyes using a statistical model. Biomed Opt Express. 1;**3**(1):86–103
29. V. Kajić, B. Povazay, B. Hermann et al., Robust segmentation of intraretinal layers in the normal human fovea using a novel statistical model based on texture and shape analysis. Opt. Express **18**(14), 14730–14744 (2010)
30. M. Esmaeelpour, S. Brunner, S. A. Shahrezaei et al., Choroidal thinning in diabetes type 1 detected by 3-dimensional 1060 nm optical coherence tomography. Invest. Ophthalmol. Vis. Sci. 3;53(11):6803-9 (2012)

31. L. Zhang, K. Lee, M. Niemeijer et al., Automated segmentation of the choroid from clinical SD-OCT. Invest. Ophthalmol. Vis. Sci. **53**(12):7510–9 (2012)
32. F.L. Bookstein, Principal warps: thin-plate splines and the decomposition of deformations. IEEE Trans. Pattern Anal. Mach. Intell. **11**(6), 567–585 (1989)
33. M. Hirata, A. Tsujikawa, A. Matsumoto et al., Macular choroidal thickness and volume in normal subjects measured by swept-source optical coherence tomography. Invest. Ophthalmol. Vis. Sci. **52**(8), 4971–4978 (2011)
34. M. Esmaeelpour, B. Povazay, B. Hermann et al., Mapping choroidal and retinal thickness variation in Type 2 diabetes using 3D-1060 nm-OCT. Invest. Ophthalmol. Vis. Sci. **52**(8):5311–6 (2011)
35. G.A. Lutty, J. Cao, D.S. McLeod, Relationship of polymorphonuclear leukocytes to capillary dropout in the human diabetic choroid. Am. J. Pathol. **151**(3), 707–714 (1997)
36. C. Torti, B. Povazay, B. Hofer et al., Adaptive optics optical coherence tomography at 120,000 depth scans/s for non-invasive cellular phenotyping of the living human retina. Opt. Express **17**, 19382–19400 (2009)
37. R.F. Mullins, M.N. Johnson, E.A. Faidley, J.M. Skeie, J. Huang, Choriocapillaris vascular dropout related to density of drusen in human eyes with early age-related macular degeneration. Invest. Ophthalmol. Vis. Sci. **52**(3), 1606–1612 (2011)
38. M. DeNiro, F.A. Al-Mohanna, Zinc transporter 8 (ZnT8) expression is reduced by ischemic insults: a potential therapeutic target to prevent ischemic retinopathy Deli MA, ed. PLoS ONE **7**(11), e50360 (2012)
39. J.E. Grunwald, T.I. Metelitsina, J.C. Dupont, G.-S. Ying, M.G. Maguire, Reduced foveolar choroidal blood flow in eyes with increasing AMD severity. Invest. Ophthalmol. Vis. Sci. **46**(3), 1033–1038 (2005)
40. A. Boltz, A. Luksch, B. Wimpissinger et al., Choroidal blood flow and progression of age-related macular degeneration in the fellow eye in patients with unilateral choroidal neovascularization. Invest. Ophthalmol. Vis. Sci. **51**(8), 4220–4225 (2010)
41. A. Wood, A. Binns, T. Margrain et al., Retinal and choroidal thickness in early age-related macular degeneration. Am J. Ophthalmol. **152**(6), 1030–1038.e2 (2011)
42. Anon, A randomized, placebo-controlled, clinical trial of high-dose supplementation with vitamins C and E, beta carotene, and zinc for age-related macular degeneration and vision loss: AREDS report no. 8. Arch. Ophthalmol. **119**(10), 1417–1436 (2001)
43. T.L. Berenberg, T.I. Metelitsina, B. Madow et al., The association between drusen extent and foveolar choroidal blood flow in age-related macular degeneration. Retina (Philadelphia, PA) **32**(1), 25–31 (2012)
44. S. Schmitz-Valckenberg, J.S. Steinberg, M. Fleckenstein et al., Combined confocal scanning laser ophthalmoscopy and spectral-domain optical coherence tomography imaging of reticular drusen associated with age-related macular degeneration. Ophthalmology **117**(6), 1169–1176 (2010)
45. J.D. Gass, R.G. Weleber, D.R. Johnson, Non-Hodgkin's lymphoma causing fundus picture simulating fundus flavimaculatus. Retina (Philadelphia, PA) **7**(4), 209–214 (1987)
46. M.A. Sohrab, R.T. Smith, H. Salehi-Had, S.R. Sadda, A.A. Fawzi, Image registration and multimodal imaging of reticular pseudodrusen. Invest. Ophthalmol. Vis. Sci. **52**(8), 5743–5748 (2011)
47. P. Haas, M. Esmaeelpour, S. Ansari-Shahrezaei, W. Drexler, S. Binde, Choroidal thickness in patients with reticular pseudodrusen using 3D 1060-nm OCT maps. Invest Ophthalmol Vis Sci. **55**(4):2674–2681 (2014)
48 F. Parmeggiani, M.R. Romano, C. Costagliola et al., Mechanism of inflammation in age-related macular degeneration. Mediat. Inflamm. **2012**, 546786 (2012)
49. J.M. Olver, Functional anatomy of the choroidal circulation: methyl methacrylate casting of human choroid. Eye (Lond) **4**(Pt 2), 262–272 (1990)
50. J.S. Slakter, L.A. Yannuzzi, D.R. Guyer, J.A. Sorenson, D.A. Orlock, Indocyanine-green angiography. Curr. Opin. Ophthalmol. **6**(3), 25–32 (1995)

51. M. Miura, S. Makita, T. Iwasaki, Y. Yasuno, An approach to measure blood flow in single choroidal vessel using Doppler optical coherence tomography. Invest. Ophthalmol. Vis. Sci. **53**(11), 7137–7141 (2012)
52. R.M. Rangayyan, F.J. Ayres, F. Oloumi, F. Oloumi, P. Eshghzadeh-Zanjani, Detection of blood vessels in the retina with multiscale Gabor filters. J. Electron. Imaging **17**(2), 023018–023018 (2008)
53. P.J. Yim, P.L. Choyke, R.M. Summers, Gray-scale skeletonization of small vessels in magnetic resonance angiography. IEEE Trans. Med. Imaging **19**(6), 568–576 (2000)
54. S. Aylward, E. Bullitt, S. Pizer, D. Eberly, Intensity ridge and widths for tubular object segmentation and description, in *Proceedings of the Workshop on Mathematical Methods in Biomedical Image Analysis, 1996*, San Francisco. (1996) pp. 131–138
55. N.-Y. Lee, Automatic generation of 3D vessels model using vessels image matching based on adaptive control points, in *Advanced Language Processing and Web Information Technology, International Conference on* (IEEE Computer Society, Los Alamitos, 2007), pp. 265–270
56. R. Nekovei, Y. Sun, Back-propagation network and its configuration for blood vessel detection in angiograms. IEEE Trans. Neural. Netw. **6**(1), 64–72 (1995)
57. A.C.S. Chung, J.A. Noble, Statistical 3D vessel segmentation using a rician distribution, in *Medical Image Computing and Computer-Assisted Intervention – MICCAI'99*, ed. by C. Taylor, A. Colchester. Lecture Notes in Computer Science (Springer, Berlin/Heidelberg, 1999), pp. 82–89. Available at: http://link.springer.com/chapter/10.1007/10704282_9. Accessed 25 Jan 2013
58. C. Kirbas, F. Quek, A review of vessel extraction techniques and algorithms. ACM Comput. Surv. **36**(2), 81–121 (2004)
59. R. Motaghiannezam, D.M. Schwartz, S.E. Fraser, In vivo human choroidal vascular pattern visualization using high-speed swept-source optical coherence tomography at 1060 nm. Invest. Ophthalmol. Vis. Sci. **53**(4), 2337–2348 (2012)
60. M. Sohrab, K. Wu, A.A. Fawzi, A pilot study of morphometric analysis of choroidal vasculature in vivo, using en face optical coherence tomography. PLoS ONE **7**(11), e48631 (2012)
61. V. Kajić, M. Esmaeelpour, C. Glittenberg et al., Automated three-dimensional choroidal vessel segmentation of 3D 1060 nm OCT retinal data. Biomed. Opt. Express **4**(1), 134–150 (2013)
62. M. Esmaeelpour, V. Kajic, B. Zabihian, R. Othara, S. Ansari-Shahrezaei, L. Kellner, I. Krebs, S. Nemetz, M.F. Kraus, J. Hornegger, J.G. Fujimoto, W. Drexler, S. Binder, Choroidal Haller's and Sattler's layer thickness measurement using 3-dimensional 1060-nm optical coherence tomography. PLoS One. **9**(6):e99690 (2014)

Retinal AO OCT

61

Robert J. Zawadzki and Donald T. Miller

Keywords

Adaptive optics • Age-related macular degeneration • Choroidal vasculature • Color blindness phenotyping • Eye • Glaucoma • Image quality of the eye • Image registration • Macular Telangiectasia • Medical optics instrumentation • Microscopy • Monochromatic and chromatic aberrations • Motion artifact correction • Non-invasive assessment of the visual system • Ocular aberrations • Ophthalmic optics • Ophthalmology • Optic nerve head • Optic neuropathies • Optical biopsy • Optical coherence tomography • Phase-sensitive AO-OCT • Photoreceptors • Polarization-sensitive AO-OCT • Retina • Retinal nerve fiber layer • Retinal pigment epithelium • Retinal vasculature • Retinitis pigmentosa • Retinopathy of prematurity • Wavefront corrector • Wavefront sensor

61.1 Introduction

The last 20 years have experienced extraordinary advances in optical technology to image noninvasively and at high resolution the posterior segment of the eye. Two of the most impactful technological advancements over this period have arguably been optical coherence tomography (OCT) and adaptive optics (AO). OCT provides unprecedented, micron-scale axial resolution (<3 μm) and sensitivity to detect reflections from essentially any retinal layer, including those that are highly

R.J. Zawadzki (✉)
Vision Science and Advanced Retinal Imaging Laboratory (VSRI) Department of Ophthalmology and Vision Science, University of California Davis, Sacramento, CA, USA

UC Davis RISE Eye–Pod Laboratory, Department of Cell Biology and Human Anatomy, University of California Davis, Davis, CA, USA

D.T. Miller
School of Optometry, Indiana University, Bloomington, IN, USA

© Springer International Publishing Switzerland 2015

W. Drexler, J.G. Fujimoto (eds.), *Optical Coherence Tomography*,
DOI 10.1007/978-3-319-06419-2_63

transparent [1, 2]. OCT has become a standard diagnostic tool for evaluating health of the posterior segment, for example, for macular holes, central serous chorioretinopathy, age-related macular degeneration, macular edema, diabetic retinopathy, and glaucoma.

Unlike OCT, AO is not an imaging modality, but rather a technology that can be used in combination with imaging modalities to improve their performance. AO works by measuring and correcting ocular aberrations at real time. Its benefit is greatest when the pupil is large (>6 mm), which has the added benefit of minimizing the blurring effects caused by diffraction. Correction of ocular imperfections across a large pupil results in unprecedented lateral resolution (2–3 μm), sufficient for resolving individual cells *en face* [3–5]. AO was originally developed for ground-based telescopes to remove atmospheric blur and later incorporated into retinal imaging in the mid-1990s. Since then, AO for the eye has experienced exponential growth resulting in the first textbook devoted to the topic in 2006 [4]. Essentially all facets of AO have undergone substantive development for use with the eye, including its wavefront sensor, wavefront corrector, and control algorithm. In addition, AO has been integrated into a wide range of retina camera architectures to increase their resolution and sensitivity including the three principle types: flood-illuminated ophthalmoscope [3, 6–9], scanning laser ophthalmoscope (SLO) [10–15], and OCT [16–28]. Collectively these have become a valuable suite of imaging tools for vision and clinical research. Individually, each has distinct technical strengths that define the types of fundus imaging applications they are best suited for.

The aim of this chapter is to focus on the latter combination: adaptive optics – optical coherence tomography (AO-OCT). Success of the individual technologies, AO and OCT, has led to considerable effort by several research groups over the last decade to combine them for high-resolution, three-dimensional imaging of the retina. The resulting 3D resolution holds considerable promise to improve the research and clinical utility of OCT: for probing structure and function of the microscopic retina and for earlier detection, more precise diagnosis, and improved treatment monitoring of posterior segment disease.

Several excellent chapters in this book already cover the theoretical and experimental underpinnings of OCT. Thus this chapter focuses on the other key aspects of AO-OCT, especially those important for the design and implementation of AO in OCT systems. With that overriding principle, the chapter is divided into three main parts. First is a summary of our current understanding of the key optical properties of the eye. These properties underlie the motivation for AO-OCT and define the design requirements of AO-OCT systems. This is followed by a discussion of AO technologies and the technical benefits of adding AO to OCT. The second part surveys AO-OCT designs reported in the literature. Unlike flood illumination and SLO modalities that have effectively one principle design configuration, OCT embodies several fundamentally different ones, resulting in a wide variety of AO-OCT systems that have been attempted. The last part reviews some of the latest scientific and clinical uses of this powerful technology and a look to future developments in this rapidly growing field.

61.2 Imaging Properties of the Eye

The eye is unique, unlike any other organ in the body, it represents a complete imaging system including refracting optics (cornea and crystalline lens), aperture (iris), and photosensitive detector (retina/fundus). All of these are of course necessary for the eye to perform its critical function, vision, which it does amazingly well. However, when we purposely reverse the direction of light to view the retina and fundus, for example, examination with OCT, the completeness of the system – in particular the ocular media and iris – is less than ideal. The ocular system imposes severe constraints on how well we can image the back of the eye and the finest microscopic detail we can resolve.

Improved understanding of the optical properties of the eye has enabled AO-OCT to surpass the natural lateral resolution limits imposed by our eyes. This required overcoming the eye's intrinsic monochromatic and chromatic aberrations and minimizing its diffraction effects. Here we summarize the pertinent aspects of each for AO-OCT imaging. Our discussion is limited to the human eye, but it is worth noting that there is growing activity in experimental imaging in animal models using the same technology [29, 30].

61.2.1 Monochromatic Aberrations of the Eye

Monochromatic aberrations of the eye vary spatially across the eye's pupil, vary over time, and vary with field location at the retina. These fundamental properties (spatial, temporal, and field dependence) dictate the performance requirements of AO for effective correction of ocular aberrations and are discussed in order below.

The spatial distribution of ocular aberrations varies considerably among subjects and often does not correspond to the classical aberrations of manufactured optical systems, for example, Seidel aberrations. Instead, Zernike polynomials – orthonormal over circular pupils – are the most popular for representing ocular aberrations [31, 32]. Zernikes are not the most efficient polynomial representation of the eye's aberrations, but are only slightly less compact than the principal modes that derive from a principal components analysis [33, 34]. Zernikes are also mathematically simpler and have well-established properties. The now ubiquitous use of Zernike polynomials is perhaps best reflected by the vision community's establishment and universal acceptance of a single naming convention for the Zernike coefficients and polynomials as described by the OSA/VSIA Standards Taskforce [35].

Today monochromatic aberrations of the eye are well characterized. Detailed measurements of the spatial distribution of wave aberrations for central vision have been made in large populations of normal, healthy adult eyes with large pupils [33, 34, 36], including the pooling of data collected at ten laboratories (2,560 eyes) [37]. More recent studies have also been reported, including a retrospective analysis of 24,000 patients [38], expansion to peripheral aberrations [39, 40], and the effects of age, accommodation, refractive state, refractive surgery, and disease [41–49].

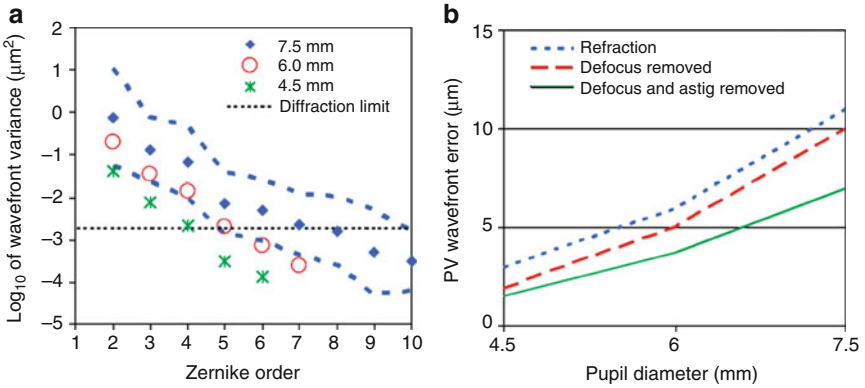

Fig. 61.1 Spatial properties of ocular aberrations in a large population of 100 normal eyes. (**a**) Log_{10} of the wavefront variance after a conventional refraction using trial lenses is plotted as a function of Zernike order and pupil size (4.5, 6.0, and 7.5 mm). *Diamonds* and corresponding *dashed curves* represent the mean and mean ± two times the standard deviation of the log_{10}(wavefront variance), respectively, for a 7.5 mm pupil. *Star* and *open circle* correspond to 4.5 and 6.0 mm pupils. *Thin, horizontal dashed line* corresponds to λ/14 RMS for λ = 0.6 μm. (**b**) PV wavefront error that encompasses 95 % of the population is plotted as a function of pupil diameter. Three second-order states are shown: (i) residual aberrations after a conventional refraction using trial lenses (*short dashed lines*), (ii) all aberrations present with zeroed Zernike defocus (*long dashed lines*), and (iii) all aberrations present with zeroed defocus and astigmatism (*solid lines*) (Reproduced with permission from OSA, Ref. [5])

The spatial characteristics of the ocular aberrations most important for AO are spatial fidelity (frequency composition) and magnitude (peak-to-valley (PV) wavefront error). Both are captured by the Zernike representation – spatial fidelity by the Zernike order and magnitude by the Zernike coefficient – and both are strongly influenced by pupil size. As an example, Fig. 61.1 (left) shows the wavefront variance decomposed by Zernike order for a population of about 100 normal subjects, most in their early twenties [34]. Data points are shown for three pupil sizes, 4.5, 6.0, and 7.5 mm, which span the range over which AO is typically applied to the human eye. For comparison, the maximum physiological pupil size for young subjects is nominally 8 mm. In Fig. 61.1 (left), the power decreases monotonically (approximately linear on a logarithmic scale) with second-order aberrations dominating the total wavefront error. Power also decreases monotonically with decreasing pupil size. The 7.5 mm pupil represents the most demanding condition for AO and requires correction of Zernike polynomials up through at least tenth order to reach diffraction-limited imaging.

Figure 61.1 (right) shows the corresponding PV wavefront error that encompasses 95 % of the population as a function of pupil size (4.5–7.5 mm). Three curves are shown that correspond to three different second-order states (defined in the figure caption). As expected, the PV error increases monotonically with pupil size and is strongly dependent on the second-order state. The PV error for the 7.5 mm pupil ranges from 7 to 11 μm depending on the second-order state.

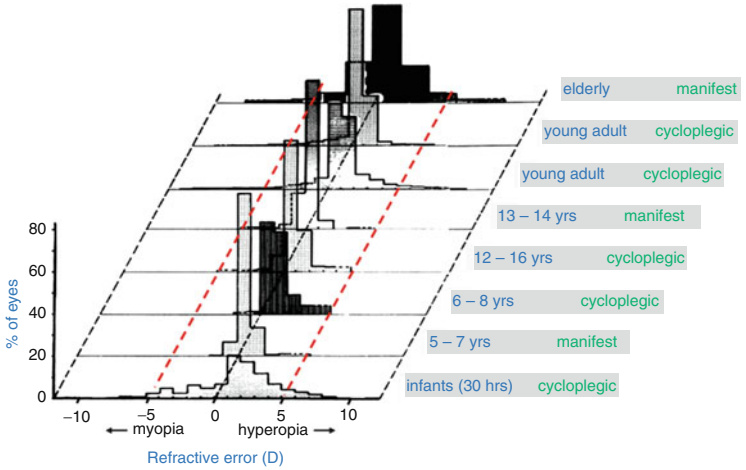

Fig. 61.2 Refractive error distributions sorted by age group and refraction (manifest or cycloplegic) (Graph reproduced and modified with permission from Elsevier, Ref. [50])

The largest error of 11 μm represents the most demanding condition for AO correction. Note that for this study, each subject was meticulously refracted with trial lenses. Typically, AO systems operate under less ideal conditions in which the second-order aberrations are only coarsely corrected or not at all. Under these non-ideal conditions, second-order aberrations can readily surpass the PV error shown in the figure by several times. As such, careful design of an AO system must take into account the anticipated refractive state of the population and the expected manner in which corrective trial and translating lenses and other means are applied in conjunction with AO.

Figure 61.2 provides a sense of the refractive state across eyes, showing cross-sectional refractive error distributions from several studies [50]. The distribution is not simple. It depends on many factors including population, age, education, and refractive state. Based on the figure distributions, a reasonable design goal for AO might be to correct errors up to +/−5 diopters as that covers a large percentage of eyes regardless of the factors shown.

The population measurements in Fig. 61.1 represent essentially static wave aberrations and therefore do not capture the temporal behavior of the ocular media. Two early pivotal studies elucidated the temporal dynamics using a power spectral method and investigated their impact on AO performance [51, 52]. Figure 61.3 (left) shows results from one of these studies, specifically temporal traces of the wavefront error for one subject and a model eye and (right) the corresponding temporal power spectra. As suggested in the figure, temporal fluctuations are found in all of the eye's aberrations, not just defocus, even when the eye's accommodation is paralyzed. In both studies, the reported temporal fluctuations decreased at $f^{-4/3}$, where f is the temporal frequency. This decrease is evident in the temporal power spectrum shown in Fig. 61.3 (right).

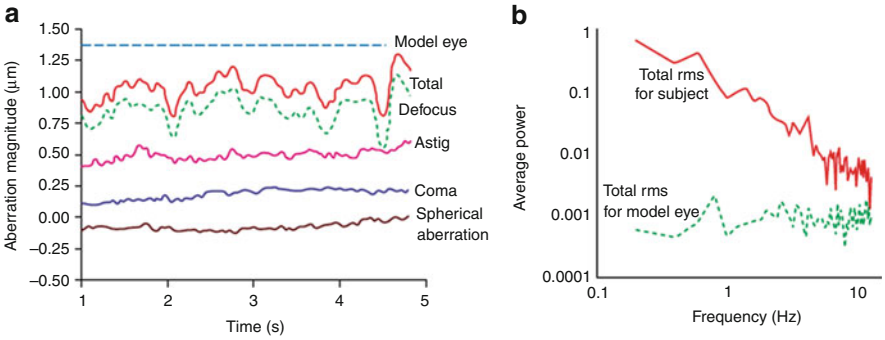

Fig. 61.3 Temporal properties of ocular aberrations [51]. (**a**) Temporal traces of the total RMS wavefront error and Zernike terms: defocus, astigmatism, coma, and spherical aberration for one subject. A trace of the total RMS wavefront error for an artificial eye is also shown and reflects the sensitivity of the instrument. (**b**) Average temporal power spectra are shown for the fluctuations in the total RMS wavefront error for a model eye and one subject whose accommodation was paralyzed. Aberrations were computed for a 4.7 mm pupil size (Reproduced with permission from OSA, Ref. [51])

The vast majority of the aberration power lies below 1–2 Hz, suggesting effective AO correction needs only a temporal bandwidth of a couple Hertz and an AO loop rate roughly 20 times faster.

Finally monochromatic aberrations of the eye also vary with field location at the retina. That is, image quality (or more precisely the point spread function or optical transfer function) at one point on the retina differs from that at another point when sufficiently separated. This difference in image quality stems from the fact that the ocular aberrations originate at the cornea and crystalline lens rather than at the pupil of the eye. Rays originating from different field locations on the retina will therefore take slightly different paths through the ocular media, accumulating different phase delays or equivalently different aberrations. In general there is a local region about any point on the retina in which the path differences are sufficiently small that the ocular aberrations are effectively constant. This region is termed the isoplanatic patch [53]. The diameter of the patch depends on the properties of the eye, but also on the definition of image quality, for example, use of the stringent Maréchal criterion, $\lambda/14$ μm RMS (Strehl ratio = 0.8) yields a narrower isoplanatic diameter than the more relaxed criterion of 1 rad^2 (Strehl ratio = 0.37).

Anecdotal evidence in the AO literature indicates the isoplanatic patch diameter for the human eye is a couple of degrees. Experiments to directly measure the patch size have only recently been conducted. A detailed survey of efforts in this area coupled with a more thorough analysis was published by Bedggood et al. [54]. Figure 61.4 shows a representative result from this study, plotting isoplanatic patch diameter as a function of the residual wavefront RMS at the patch edge. As expected, the patch size increases as the criterion relaxes, i.e., larger residual RMS. As an example, diffraction-limited AO-OCT imaging at 850 nm wavelength requires a wavefront RMS correction of 61 nm or better. Using this as

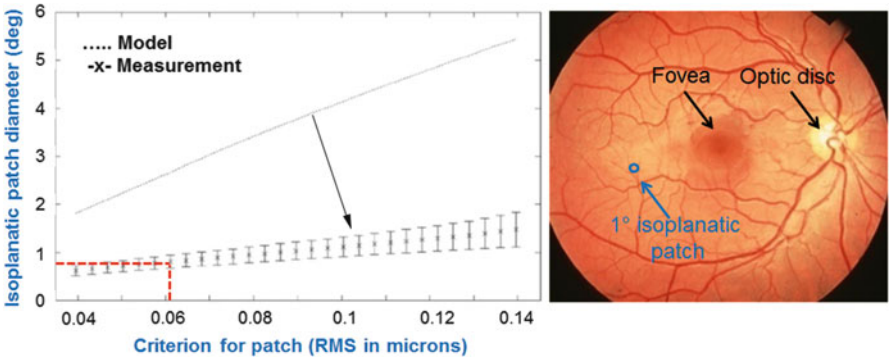

Fig. 61.4 (*left*) Isoplanatic properties of ocular aberrations. Isoplanatic patch diameter is plotted versus residual wavefront RMS at the patch edge after perfect correction of ocular aberrations at the patch center. Data points are average measurements across seven healthy subjects with error bars at ±1 standard deviation. Predicted patch diameter is also shown using the Liou Brennan schematic eye that clearly overestimates the measured diameter by several times [55]. Pupil size for both is 6 mm (Reproduced with permission from SPIE, Ref. [54]). (*right*) A 1° isoplanatic patch is superimposed on a conventional 45° fundus image, illustrating the vast difference in size

a criterion for the residual RMS at the patch edge in Fig. 61.4, the corresponding isoplanatic diameter is predicted to be somewhat less than one degree consistent with anecdotal evidence and other measurements reported in the literature. The narrowness of the isoplanatic patch has severe clinical consequences for AO-OCT as images at the isoplanatic size are substantially smaller than those collected with standard clinical instruments, a point illustrated by Fig. 61.3 (right). Shown is a fundus photograph with a standard 45° field of view and a 1° isoplanatic patch superimposed. While the fundus photograph can be captured in a single flash, AO-OCT performing at the diffraction limit requires tiling of 2,000 1° images – each with its unique AO correction – to cover the same field!

61.2.2 Chromatic Aberrations of the Eye

In addition to monochromatic aberrations, the human eye also suffers from significant chromatic ones (see Fig. 61.5), due primarily to its watery composition whose refractive index varies with wavelength. The longitudinal (LCA) and transverse (TCA) components of the ocular chromatic aberrations have been extensively studied at visible [56] and more recently near-infrared wavelengths up to 1,070 nm [57–59]. LCA and TCA refer to the variation in focus and image size with wavelength, respectively, both effectively blurring the patient's vision or conversely the retinal image. Historically, interest in chromatic aberrations of the eye was driven by their impact on visual performance. This led to the design of numerous achromatizing lenses [60–65], many of which were shown effective at correcting the eye's LCA, which is largely uniform across eyes and insensitive to field angle.

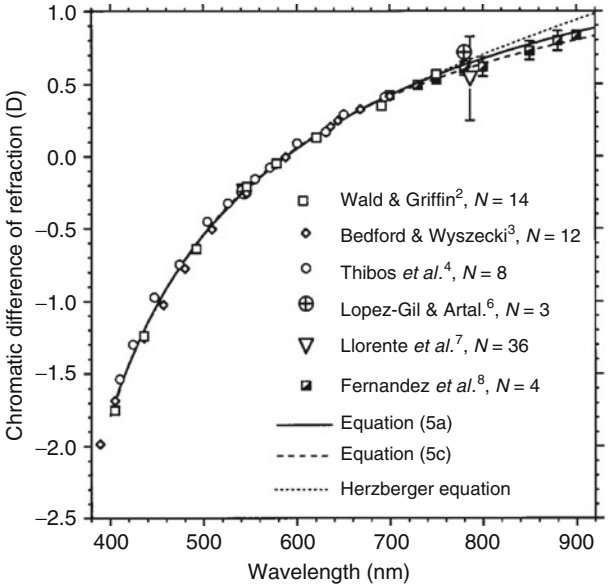

Fig. 61.5 Chromatic difference of refraction from several experimental studies and theoretical models that collective cover the visible spectrum and extend into the near infrared. All data were set to be zero at 590 nm. Close agreement between studies occurs largely because of the relatively small intersubject variation in chromatic aberrations [58]. (Reproduced with permission from OSA, Ref. [58])

In contrast, correcting the eye's TCA has proven significantly more difficult, partly as TCA varies across eyes and is highly sensitive to field angle. In some cases, slight misalignment of the achromatizing lens to the eye was found to substantially increase the TCA, well above that which is intrinsic to the eye. Despite the mixed success of using achromatizing lenses to improve visual performance, its recent use in high-resolution retinal imaging, in particular AO-OCT, has proven beneficial. AO-OCT instruments have several key attributes that reduce the demand on the achromatizing lens. These include a comparatively small field of view, imaging at near-infrared wavelengths, a limiting pupil that is specified by the retina camera rather than the eye, better stabilization of the subject's head, and raster scanning of the retina using galvanometer scanning mirrors.

61.2.3 Image Quality of the Eye

Retinal image quality is degraded not only by aberrations, but also diffraction, which for pupil diameters of less than about 3 mm is actually the largest source of image blur. A pupil about 3 mm in diameter – which is a typical pupil size under bright viewing conditions – generally provides the best optical performance in the

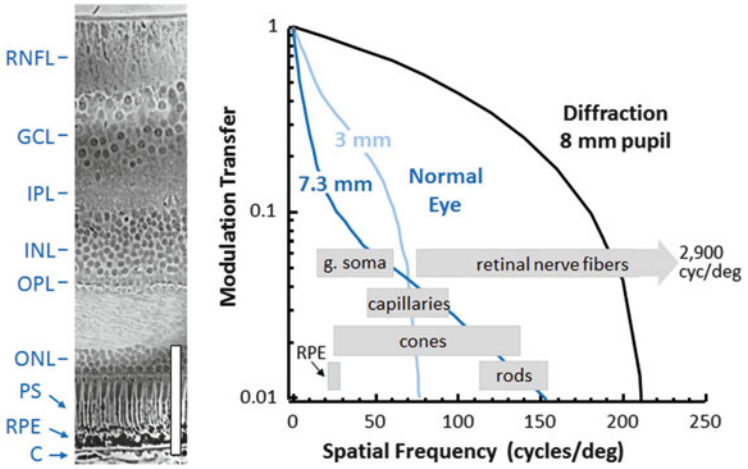

Fig. 61.6 (*left*) Histological cross section of primate retina with labels and scale bar (100 μm) added. (Cross section is reproduced with permission from the Royal Society of London [66].) (*right*) MTF of the eye under normal viewing is shown with pupils that are 3 and 7.3 mm in diameters and with the best refraction achievable using trial lenses averaged across 14 eyes. Also shown is the diffraction-limited MTF for the 8 mm pupil. The area between the normal and diffraction curves represents the range of contrast and spatial frequencies inaccessible with a normal eye, but reachable with AO. Also indicated is the range of fundamental frequencies defining several clinically important cell-sized structures. The ganglion soma (g. soma) range corresponds to sizes in the foveal margin and superior periphery with mean diameters of 11.7 μm (25.6 cyc/deg) and 15.8 μm (19 cyc/deg), respectively [67]. Individual retinal nerve fibers can get as large as 3.9 μm (75 cyc/deg), but the most probable axon diameter is about 0.45 μm (660 cyc/deg) [68]. Retinal capillary diameters are shown for central retina with mean size of 4.9 μm (61.2 cyc/deg) [69]. Cone row-to-row spacing (derived from cone density) is shown for the central +/−15°, averaged over the four meridians [70]. Rod row-to-row spacing is shown for 4.5 and 17° retinal eccentricity, again from histology [70, 71]. RPE spacing is shown for 5–20° in the superior retina [72]. Key: *RNFL* retinal nerve fiber layer, *GCL* ganglion cell layer, *IPL* inner plexiform layer, *INL* inner nuclear layer, *OPL* outer plexiform layer, *ONL* outer nuclear layer, *PS* photoreceptor segments, *RPE* retinal pigment epithelium, *C* choroid

range of spatial frequencies that are important for normal vision. Increasing the pupil size does increase the high-spatial-frequency cutoff, allowing finer details to be discerned, but at the high cost of increasing the deleterious effects of aberrations. Clearly, the very best optical performance would come from correcting all the eye's aberrations across the dilated pupil.

Quantitatively, the effects of diffraction and aberrations on corrected and uncorrected pupils of various diameters are best illustrated by the modulation transfer function (MTF). Figure 61.6 shows the MTF for normal pupils 3 and 7.3 mm in diameter and for a large corrected 8 mm pupil. The large corrected pupil has a higher optical cutoff frequency and an increase in contrast across all spatial frequencies. Peering inward through normal-sized pupils, only large cell bodies (ganglion and retinal pigment epithelium) and the largest cone

photoreceptors and capillaries should be resolved without substantial penalty in contrast due to poor MTF. But with the corrected 8-mm pupil, essentially all cells can be discerned if the cells possess sufficient intrinsic contrast with surrounding tissue. Even some single retinal nerve fibers (ganglion cell axons) should be resolved, although such large caliper fibers are scarce and the most probable diameter is more than three times beyond the 8 mm diffraction limit. Nevertheless at the cellular level, a large corrected pupil is critical for making use of the spatial frequencies that define single cells in the retina.

61.3 Adaptive Optics

An ophthalmic AO system consists of the same principle components as those employed in ground-based telescopes: wavefront sensor, wavefront corrector, and control system. These components are highlighted in the simplified AO schematic of Fig. 61.7 (see figure caption for details). The wavefront sensor and corrector operate in closed loop, and the correction imparted on the wavefront is based on the wavefront sensor measurement. The effectiveness of these components depends fundamentally on their ability to measure, correct, and track ocular monochromatic aberrations, the extent to which depends strongly on the spatial and temporal properties of the aberrations as described in the previous section. General ophthalmic requirements for these (measure, correct, and track) are presented here.

61.3.1 Wavefront Sensor

There is an abundance of optical sensors for wavefront measuring with many representing highly mature devices. These include the Shack-Hartman wavefront sensor (SHWS), shearing interferometer, pyramid sensor, curvature sensor, phase diversity, laser ray tracing, phase-shifting interferometer, and common-path interferometer. While several of these have been applied to the eye and others continue to attract interest, to date almost all operational AO systems for the eye have been constructed using the SHWS. As such, we confine our attention to this sensor type, though much of which will be applicable to the other sensors.

A first-order design of the SHWS entails evaluation of four key properties: (1) spatial sampling, (2) dynamic range, (3) accuracy, and (4) signal to noise. These are set primarily by the characteristics of the lenslet and CCD/CMOS arrays of the sensor, and therefore, selection of these two components is critical. Spatial sampling of the sensor is specified by the number of lenslets that fills the pupil of the eye. The necessary number of lenslets for reliable representation of the ocular aberrations depends on the composition of the ocular aberrations, pupil size of the eye, and to a lesser extent the SH wavelength. A general rule of thumb is that one lenslet is required for every Zernike mode that is to be measured. Based on this, reliable representation up through tenth Zernike order requires at least 63 lenslets that uniformly cover the pupil. In practice, SHWSs routinely sample the pupil with

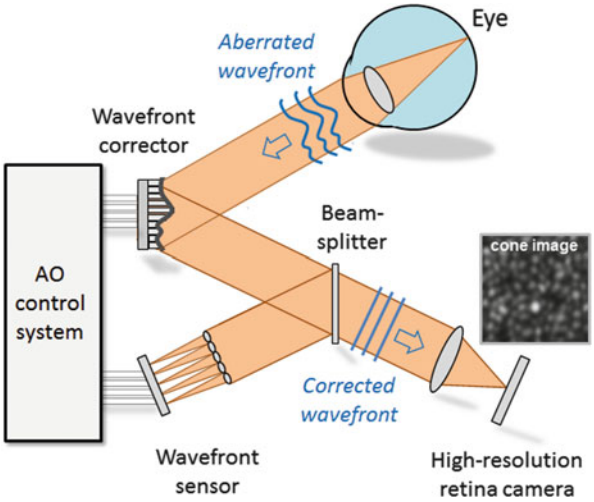

Fig. 61.7 Concept schematic of AO applied to the eye. The wavefront sensor (shown here as a Shack Hartmann implementation) works by measuring the reflection of a light beam that is focused onto the subject's retina. The reflection is distorted as it passes back through the refracting media of the eye. A two-dimensional lenslet array, placed conjugate with the eye's pupil, samples the exiting wavefront forming an array of images of the retinal spot. A CCD or CMOS sensor records the displacement of the spots, from which first local wavefront slopes and then global wavefront shape are determined. Wavefront compensation is realized with a deformable mirror. The mirror lies in a plane conjugate with the subject's pupil and the lenslet array of the SHWS. For retinal imaging, a light source (not shown) illuminates the retina, some of which is reflected out of the eye, reflects from the wavefront corrector, and forms an aerial image at the retina camera

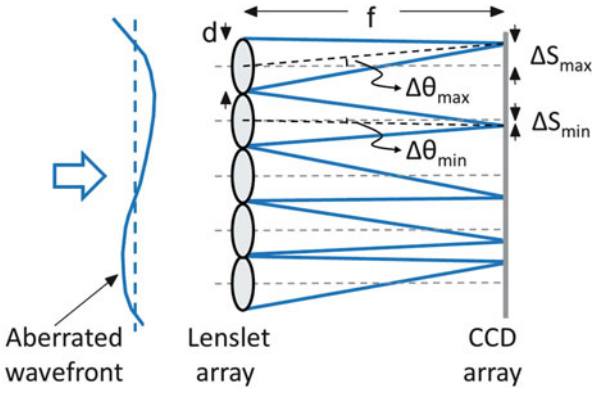

Fig. 61.8 Schematic illustrates the principle operation of the Shack-Hartmann wavefront sensor

much higher density. There is little cost to do so since there is an abundance of light for the sensor. Oversampling makes the measurements more robust (to pupil edge effects, eye motion, drying of the precorneal tear film, and system noise) and applicable to eyes with a wider range of aberrations. Schematic of the SHWS is shown in Fig. 61.8.

Dynamic range refers to the maximum wavefront slope, $\Delta\theta_{max}$, that can be measured by the SHWS. $\Delta\theta_{max}$ is typically expressed as $\Delta S_{max}/f$, where ΔS_{max} is the maximum displacement of the lenslet spot (=lenslet radius) and f the lenslet focal length. Since spherical and cylindrical refractive errors typically consume much of the dynamic range of the sensor, it is often more useful to convert ΔS_{max} to a maximum measurable defocus (diopters), expressed by $D = \Delta\theta_{max}/$ (pupil radius). For example, a lenslet diameter of 0.4 mm and a lenslet focal length of 24 mm give a $\Delta\theta_{max}$ and D of 8.3 mrad and 2.44 diopters, respectively, for a 6.8 mm eye pupil. In general, the dynamic range can be increased by increasing the lenslet diameter, decreasing the lenslet focal length, or decreasing the pupil diameter.

Accuracy refers to the minimum wavefront slope, $\Delta\theta_{min}$, that can be measured by the SHWS. $\Delta\theta_{min}$ is expressed as $\Delta S_{min}/f$, where ΔS_{min} is the minimum detectable displacement of the lenslet spot. ΔS_{min} depends on the pixel size of the SHWS detector, diameter of lenslet spot at the detector (which is a function of the lenslet diameter and focal length), accuracy of the centroiding and thresholding algorithms, and signal to noise of the captured SHWS spot image. In general, sub-pixel accuracy is routinely achieved [73]. While the SHWS parameters can be manipulated to increase accuracy, dynamic range of the sensor also depends on the lenslet diameter and focal length, but inverse of that for accuracy thereby creating a clear trade-off between these two SHWS properties. This trade-off can be partly avoided with smarter centroiding algorithms. For example, cross-correlation techniques have been used to locate centroids of spots outside the conventional search box area. This approach – which is employed in some commercial wavefront sensor systems – substantially increases the dynamic range of the system without loss in accuracy.

Signal to noise of the captured SHWS spot images is limited by the amount of light that can be safely directed into the eye, number of pixels per lenslet focal spot, quantum efficiency of the SHWS detector, and throughput efficiency of the SHWS. Fortunately, ophthalmic AO systems operate under relaxed light requirements, certainly well above the ~100 photons/lenslet needed to close astronomical AO loops. A typical ophthalmic AO system, running at tens of milliseconds exposure time, has at least ~500,000 detected photons/lenslet, this with hundreds of lenslets that sample the pupil. Such high light levels permit use of relatively low quantum efficient CCD and CMOS detectors and tens of pixels that sample the core.

61.3.2 Wavefront Corrector

The effectiveness of AO to correct ocular aberrations has historically been limited by the performance of the wavefront corrector, the most expensive AO component. This device dynamically imparts an ideally conjugate aberration profile onto the incident wavefront, thus canceling the original aberrations.

Wavefront correctors first applied to the eye were developed primarily for compensation of atmospheric turbulence, a common example being macroscopic discrete actuator deformable mirrors (DMs), such as those manufactured by

Xinetics, Inc. [74]. Specifically, their actuator number, stroke, influence function, and speed were tailored to the spatial and temporal properties of the atmosphere [75] rather than that of the eye [33, 34, 51, 52]. Stroke refers to the dynamic range of the corrector and limits the largest wavefront error that can be corrected. Larger stroke provides better correction of large-magnitude aberrations. Actuator number across the eye's pupil and actuator influence function (localized deflection of the mirror surface that results when a single actuator is pushed or pulled) determine the fidelity of the correction. More actuators and a more localized influence provide better correction of high-spatial-frequency aberrations, i.e., aberrations of high order. The dynamic range of these first devices did not match that needed for the eye and provided incomplete compensation of ocular aberrations. Also, their kilohertz response was overkill for the 1–2 Hz fluctuations of the ocular aberrations, and the devices themselves were generally bulky, with large mirror surfaces (∼several centimeters or more) that required long focal length relay optics to magnify the pupil of the eye.

Since then, there have been several extensive theoretical studies that have evaluated the performance of general wavefront corrector classes [76, 77] as well as specific commercial devices [78, 79]. These studies along with empirical evaluations have helped define corrector parameters for eye use, in particular the required actuator stroke, number, and influence function. Other important corrector parameters include temporal response, surface reflectivity for broadband use, corrector diameter, and of course cost.

In recent years, an expanding array of alternative wavefront corrector technologies has flooded the market, replacing the previous small market driven by atmospheric turbulence applications. These new technologies have been a welcome relief, generating a range of commercial devices that span all four major corrector classes: segmented, discrete actuator, bimorph, and membrane wavefront correctors. Figure 61.9 shows representative devices from the four classes that have been applied to the eye. These new devices provide substantially improved corrector performance specifically in the areas needed for ocular applications. Additionally, their small mirror footprint and lower cost are enabling AO technology to jump from the vision research laboratory to the clinic and into turnkey commercial AO ophthalmic cameras.

61.3.3 Control System

The control system performs the critical step of rapidly and repeatedly converting the raw output of the wavefront sensor into voltage commands that shape the corrector surface, i.e., the deformation created by the sum response of the corrector actuators. The control loop takes into account the number, arrangement, and interaction of lenslets and actuators; the influence function and stroke of actuators; temporal response of the AO components; and a desired performance criteria, e.g., minimize the RMS wavefront error. The control loop can be characterized in terms of its spatial and temporal properties.

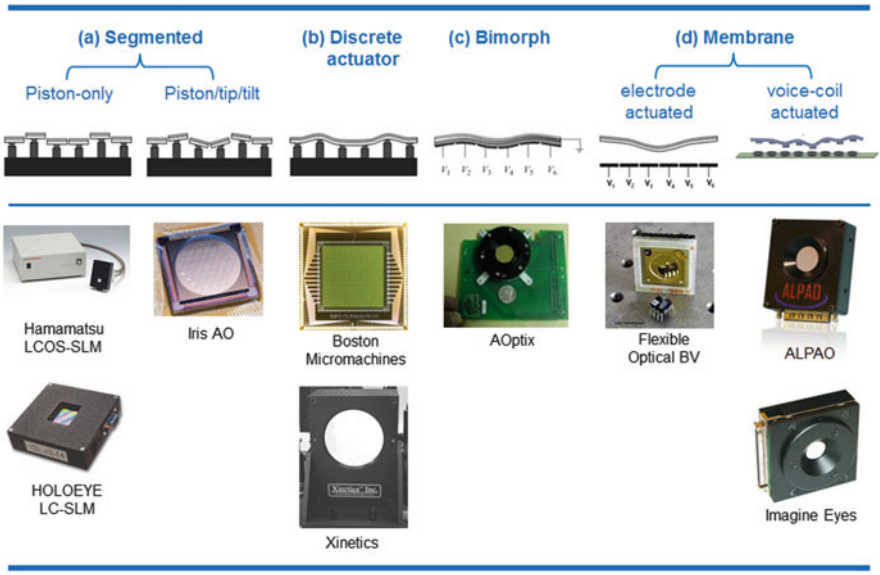

Fig. 61.9 Four main classes of wavefront correctors with specific devices that have been applied to the eye. (**a**) Piston-only segmented correctors consist of an array of small planar mirrors whose axial motion (piston) is independently controlled. Liquid-crystal spatial light modulators control the wavefront in a similar fashion, but use changes in refractive index rather than physical displacement of a mirror surface. Piston/tip/tilt segmented correctors add independent tip and tilt motion to the piston-only correctors. (**b**) Discrete actuator deformable mirrors consist of a continuous, reflective surface and an array of actuators, each capable of producing a local deformation in the surface. (**c**) Bimorph mirrors consist of a layer of piezoelectric material sandwiched between a continuous top electrode and a bottom, patterned electrode array. A top mirrored layer is added to the top continuous electrode. An applied voltage causes a deformation of the top mirrored surface. (**d**) Electrode-actuated membrane mirrors consist of a grounded, flexible, reflective membrane sandwiched between a transparent top electrode and an underlying array of patterned electrodes, each of which is capable of producing a global deformation in the surface. Voice-coil actuated membrane mirrors provide similar global deformation, but realized with miniaturized voice-coil actuators that make no contact with the membrane. Note that photographs of the devices are not shown to scale

Spatial (static) control starts with the layout of lenslets and actuators. Typical AO systems for the eye sample each actuator with two to ten lenslets. This oversampling increases the tolerance to alignment errors and permits detection of all corrector modes. Spatial control of the wavefront corrector using the wavefront sensor is normally realized (based on a linear systems approach) by a multiplication of two matrices, one representing the wavefront sensor output, S, (slope measurements) and the other a reconstructor matrix, A^+, representing the interaction of each actuator with each lenslet (control matrix). This single matrix multiplication,

$$V = A^+ \; S, \tag{61.1}$$

provides the voltages, V, that are applied to the corrector actuators. This approach – commonly referred to as the direct slop method – is fast and efficient. Another common approach is based on modal reconstruction in which wavefront slope measurements are converted to Zernike aberration modes (or other modal set) that in turn are converted to applied voltages. This approach allows explicit control of individual modes, including which ones are sent to the corrector.

Because of the high demand on corrector performance, a recent control strategy has been to distribute the demand across two wavefront correctors using a woofer-tweeter concept. In this arrangement, a large-stroke wavefront corrector (woofer) corrects large-amplitude, low-order aberrations and a high-spatial fidelity wavefront corrector (tweeter) corrects low-magnitude high-fidelity aberrations [25, 80–84]. However, mirror technology is catching up. New voice-coil-actuated membrane deformable mirrors offer both large stroke and relatively high number of actuators and have demonstrated comparable performance to that of woofer-tweeter systems [85].

Spatial properties, however, do not fully characterize the control system as they do not capture the closed-loop performance of AO. Specifically, they neglect the temporal dynamics of the ocular aberrations and the time delays associated with measuring the wavefront slopes and computing and applying the control voltages. Taking into account these temporal effects is critical for optimizing system performance and is accomplished by modeling temporal control as a cascade of transfer functions, each representing an independent component of the system. Details of this process are illustrated in Fig. 61.10 (top) using a block diagram representation of the AO control loop. As an example of the utility of the transfer function approach, Fig. 61.10 (bottom) shows predicted and measured traces of the power rejection magnitude (derived from the transfer functions) for representative AO configurations, one being five times faster than the other. The power rejection magnitude permits determining the cutoff frequency of the AO system, being defined as the frequency at which the power rejection magnitude first reaches 1. For the two configurations in Fig. 61.10, cutoff frequencies occur at 0.5 and 2.0 Hz, with the former consistent with the experimental measurements shown. Note that a cutoff of 0.5 Hz indicates that temporal frequencies below 0.5 Hz are (at least partially) corrected by the system, while those above 0.5 Hz are (at least partially) amplified. Because the vast majority of the aberration power in the eye lies below 1–2 Hz (see Fig. 61.3b), the 2.0 Hz bandwidth AO configuration should be adequately fast and provide improved performance over the 0.5 Hz system.

Finally, it is worth mentioning that there is growing interest in wavefront sensorless control of AO systems for imaging biological structures for which AO cannot establish a reliable wavefront that can be corrected by a wavefront corrector. Bonora et al. have recently published a short review of wavefront sensorless techniques including demonstration of a wavefront sensorless AO-OCT system [86]. Future refinements of this technique, beyond the simple implementation presented in their chapter, should allow its extension to in vivo applications. Interestingly an example of sensorless adaptive optics scanning laser ophthalmoscopy (AO-SLO) for imaging in vivo human retina has been recently presented [87].

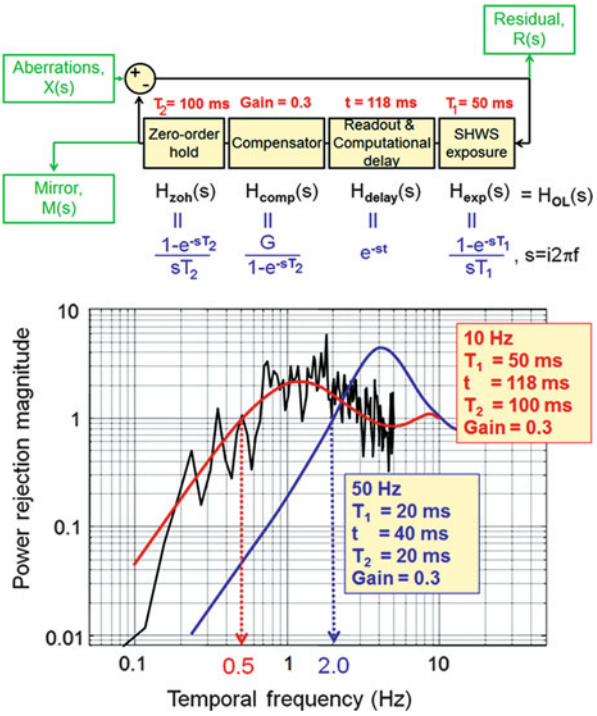

Fig. 61.10 (*top*) Block diagram of the AO system for modeling temporal performance. Input/output parameters $M(s)$, $X(s)$, and $R(s)$ depict the time-varying aberrations of the eye, residual aberrations after correction, and wavefront corrector voltages. For temporal analysis, the AO system is decomposed as a linear cascade of independent transfer functions, in this case the four AO stages that most often limit temporal performance in ophthalmic AO systems: SHWS exposure, sensor readout and computation of V, integral compensator, and finally holding mirror position for one AO loop period. T_1 is the exposure duration of the SHWS detector, T_2 is the sampling period of the AO loop, and t is the total delay to readout the sensor and compute V. (*bottom*) Experimental and theoretical curves for the power rejection magnitude of an ophthalmic AO system. Experimental curve (*jagged, black line*) was obtained on one eye using a gain of 0.3 for a 6.8 mm pupil. The corresponding theoretical curve (*solid, red*) was based on the actual system parameters given in the *leftmost box* on the plot. The second theoretical curve (*blue*) predicts the performance of an AO system that is five times faster. System parameters are given in the *rightmost box*

61.4 Adding AO to OCT

61.4.1 AO Benefits

AO permits access to the full retinal reflection that exits a large pupil of the eye (>6 mm). This translates into three technical benefits for OCT that improve the visualization and detection of microscopic structures in the retina: (1) higher lateral resolution, (2) a smaller lateral speckle size, and (3) higher collection efficiency for

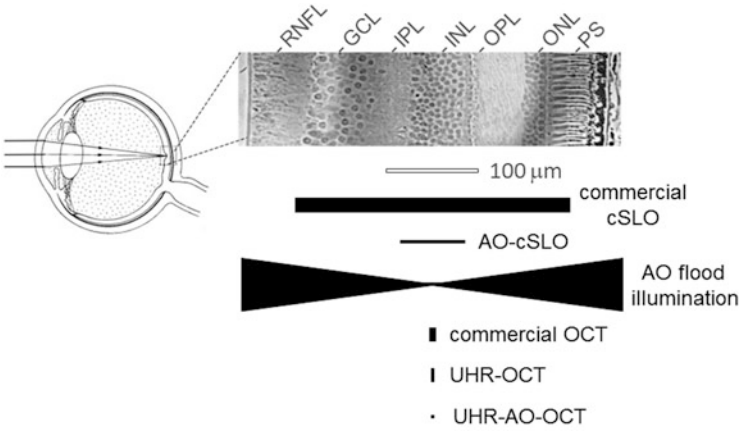

Fig. 61.11 Comparison of (*top*) cell size in a histological cross section of the human retina to (*bottom*) the resolving capability of the major types of retinal imaging modalities with and without AO. The vertical and horizontal dimensions of the *solid black symbols* denote, respectively, the lateral and axial resolution of the instruments. Examples shown include the commercial confocal scanning laser ophthalmoscope (*cSLO*), adaptive optics with confocal scanning laser ophthalmoscope (*AO-cSLO*), adaptive optics flood illumination, commercial OCT, ultrahigh-resolution OCT (*UHR-OCT*), and adaptive optics with ultrahigh-resolution OCT (*AO-UHR-OCT*). See key in Fig. 61.6 for retina labels (Reproduced with permission from The Royal College of Ophthalmologists, Ref. [27])

light backscattered from the retina. Of these three, lateral resolution has received considerably the most attention, but the other two add significant performance value. The benefit of each is discussed below.

The addition of AO typically increases the lateral resolution by approximately six times over commercial OCT. Of course to take advantage of this resolution requires increased A-scan sampling so that the closeness of the individual A-scans does not compromise the improved optical resolution. Current state-of-the-art adaptive optics, ultrahigh-resolution OCT (AO-UHR-OCT) has an isotropic 3D resolution of $2.5 \times 2.5 \times 3\ \mu m^3$ (width × length × depth) in retinal tissue. Two of these three dimensions are governed by conventional optics (diffraction and aberrations), and therefore, the resolution volume is highly sensitive (goes as the square) to AO performance and actually more so than OCT that acts only on a single dimension, depth. Figure 61.11 compares the size of this 3D resolution element of AO-UHR-OCT (smallest black symbol) to that of OCT without AO and to that of two other major imaging modalities – confocal scanning laser ophthalmoscope and flood illumination – with and without AO. As shown, the addition of AO to UHR-OCT or commercial OCT improves the resolution volume by 36 times. Furthermore, AO-UHR-OCT has a resolution volume that is 72 times better than that of commercial OCT, taking into account AO and the two times improvement in axial resolution afforded by the wider source spectrum. In general, AO-UHR-OCT provides the best resolving capability of any of the imaging modalities and the only instrument able to resolve cells in all three dimensions.

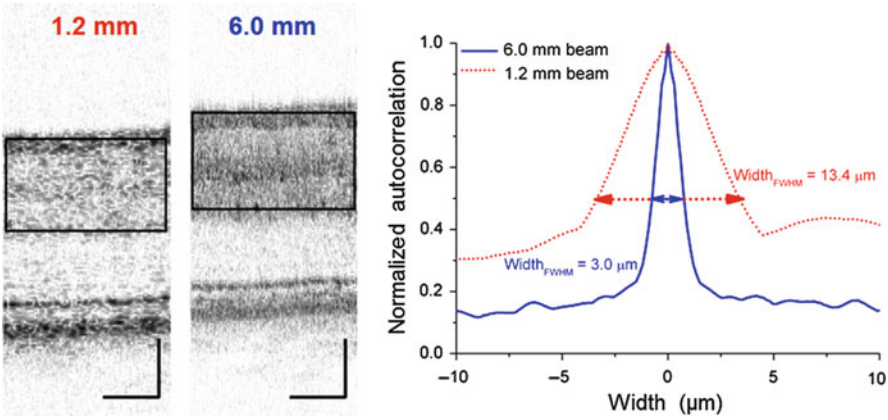

Fig. 61.12 (*left*) B-scans of the same retinal patch taken with the same AO-OCT system, but with 1.2 mm and 6.0 beams. Focus of the AO was near the outer plexiform layer; wavelength was 840 nm. (*right*) The FWHM lateral width of speckle was determined from the width dimension of the two-dimensional autocorrelation of the demarcated area in the B-scans. Only the upper retinal layers were included in the analysis because the autocorrelation algorithm was sensitive to abrupt changes in intensity (Reproduced with permission from OSA, Ref. [88])

The second benefit of AO is reduced lateral speckle size. The interferometric nature of OCT generates high-contrast speckle that permeate the entire OCT image and masks structural details, especially those at the resolution limit of the system. Since lateral speckle size is inversely related to pupil (beam) diameter, the larger pupil size afforded with AO (>6 mm) reduces theoretically the lateral dimension of speckle. For current state-of-the-art UHR-AO-OCT, this corresponds to a reduction of roughly six times and a corresponding speckle volume of 36 times compared to that of standard commercial OCT. Cense et al. [88] confirmed this improvement by a speckle analysis of B-scans acquired 3° from the foveal center. In Fig. 61.12, two examples are given, without (1.2 mm beam) and with (6.0 mm beam) AO. Analyzed over many B-scans, the FWHM lateral speckle diameter was equal to 14 ± 1 μm (1.2 mm beam) and 3.1 ± 0.1 μm (6.0 mm beam), consistent with the calculated FWHM diffraction-limited airy disk sizes of 14 and 3 μm, respectively.

This reduction in speckle size noticeably improves the appearance of the OCT image when magnified as illustrated by the commercial OCT and UHR-AO-OCT examples of Fig. 61.13. At the magnification shown, the B-scan in Fig. 61.13b has a photographic-like quality that shows clear delineation of the various neuronal layers. Speckle appears largely absent and certainly inconsequential for examining the retinal features visible in the image. Magnification necessary to view the microscopic features (see Fig. 61.13c), however, presents a very different view. Speckle and image blur are now obvious artifacts and mask retinal features that would otherwise be present in the image. This is particularly evident by comparing B-scan acquired with commercial system Spectralis (Heidelberg Engineering, Heidelberg Germany) (Fig. 61.13c) to the AO-UHR-OCT B-scan (Fig. 61.13d),

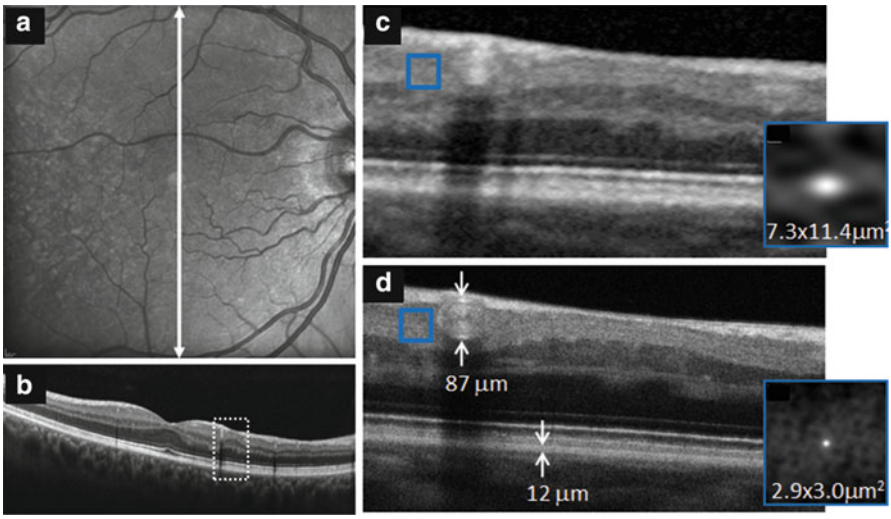

Fig. 61.13 Comparison of fast B-scans acquired of the same patch of retina of a 62-year-old subject with Heidelberg Spectralis and AO-UHR-OCT systems [89]. Spectralis images are shown for (**a**) 20° fundus view and (**b**) vertical B-scan that traverses the fovea. Region highlighted by the *white*, *dashed box* (3° wide) is magnified and displayed in (**c**). The highlighted region crosses an arcuate RNFL defect. AO-UHR-OCT B-scan is shown in (**d**). Both Spectralis and AO-UHR-OCT images are an average of 7 fast B-scans, the UHR-AO-OCT with 0.9 µm spacing. The averaging is consistent with the default averaging mode of the Spectralis system, for a fairer comparison. Insets show the autocorrelation (*gray* scale map) for the region inside the superimposed box in (**c**, **d**), respectively (Reproduced with permission from Elsevier, Ref. [89])

which is of essentially the same patch of retina. Although maximum lateral resolution and structural detail are confined to the depth of focus (~60 µm) that straddles the focal plane (which is at the retinal nerve fiber layer in the figure), speckle is noticeably smaller throughout the entire image. Thus most of the visual difference between the commercial OCT and UHR-AO-OCT B-scans is due to differences in speckle size. Based on the autocorrelation insets, the lateral dimension of speckle is 5× smaller (because of AO) and the axial dimension of speckle roughly 2× smaller (because of UHR-OCT).

A larger pupil and wider spectral light source decrease the lateral and axial dimensions of speckle, but further improvement in AO-OCT image clarity can be gained by reducing contrast of the speckle. Figure 61.14 shows one such example [25]. Because retinal nerve fiber bundles (RNFB) on the local level share the same orientation, averaging of adjacent B-scans (which are orthogonal to the bundle direction) is used to reduce speckle contrast without sacrificing spatial information of the RNFB cross section (width and thickness). Thus bundle clarity is improved as shown in the figure.

The third benefit of adding AO to OCT is the higher collection efficiency for light backscattered from the retina, which translates into higher SNR. In theory a gain of approximately 8–12 dB is expected, based on the difference in pupil

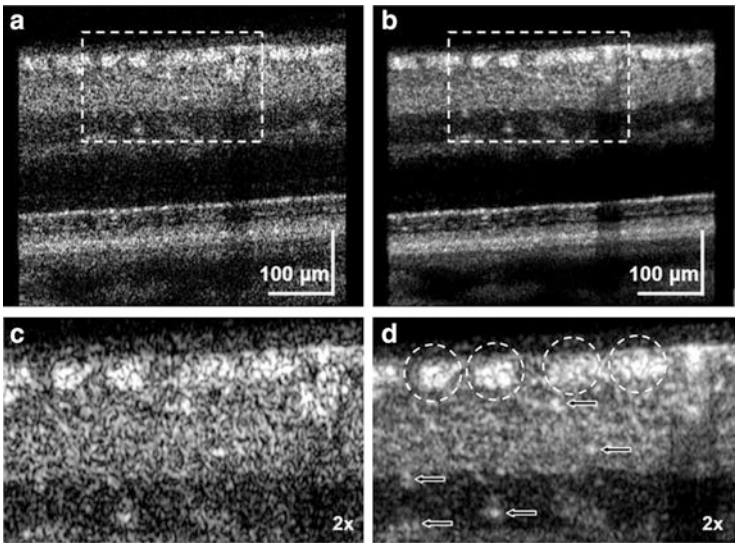

Fig. 61.14 Comparison of (**a**) single and (**b**) averaged B-scans obtained with AO-UHR-OCT system. AO focus was set at inner retina layers at 9° S 4.5° NR eccentricity of healthy 55-year-old volunteer. *Dashed rectangles* in **a** and **b** correspond to the magnified regions shown in **c** and **d**, respectively. Averaging was over ten AO-UHR-OCT frames. *Dashed circles* indicate location of the nerve fiber bundles. *Arrows* indicate location of micro capillaries in the inner retina. Note improved visibility of retinal nerve fiber bundles with averaging (Reproduced with permission from OSA, Ref. [25])

size between conventional OCT and AO-OCT systems and the angular distribution of reflected light expected due to the Stiles-Crawford effect. This effect originates in photoreceptors, typically the brightest layer in the retina and therefore influences SNR [90]. Our measurements approach this theoretical estimate. Specifically, the comparison between measurements taken with the 1.2 mm beam without AO and the 6.0 mm beam with AO (based on Fig. 61.12 setup) demonstrated an increase in dynamic range of at least 4 dB. This number can be further increased by an estimated 4 dB when the AO system is focused at a highly reflective layer, such as the photoreceptor or RPE, as opposed to the inner plexiform layer that was used in the experiment. Adding these numbers, the total gain was 8 dB [88].

61.4.2 AO Disadvantages

AO in OCT is attractive because of the improved resolution, reduced speckle, and increased sensitivity, but these come at a cost. Pragmatic ones include increased system complexity, physical size, and expense. Along with these though are fundamental performance disadvantages, two principle ones being reduced depth of focus, and increased sensitivity to chromatic aberrations, both caused by the larger pupil size.

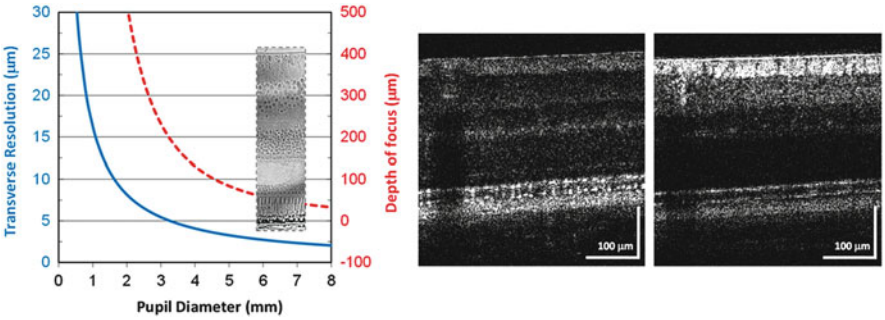

Fig. 61.15 (*left*) Transverse resolution (*solid, blue*) and depth of focus (*dashed, red*) as a function of pupil diameter for an unaberrated eye. Resolution at the focal plane is defined by $1.22\,\lambda f_e/d$, where λ is the wavelength of light (800 nm), f_e is the focal length of the eye (16.7 mm), and d is the pupil diameter. Assuming a Gaussian beam intensity profile, depth of focus is specified as two times the Rayleigh range. (*right*) Example of narrow depth of focus of an AO-UHR-OCT system [89]. B-scans were acquired of the same retinal location with AO focus at the photoreceptor segments (*left*) and retinal nerve fiber bundles (*right*). Shift in focus was 0.4 Diopters, which was generated by the AO wavefront corrector (Reproduced with permission from Elsevier, Ref. [89])

Depth of focus is inversely related to pupil size and trades-off with lateral resolution. Figure 61.15 shows this fundamental trade-off for an unaberrated eye, in this example at a wavelength of 800 nm. Using the pupil sizes in the AO-OCT example of Fig. 61.12, a 1.2 mm pupil provides a transverse resolution of 13.6 μm and a depth of focus of 1.45 mm. The depth of focus exceeds the retinal thickness by several times, making all retinal layers equally in focus, but at inadequate resolution to resolve cells. Increasing the pupil diameter to 6 mm increases the transverse resolution sufficiently for single-cell imaging (2.7 μm), but at the expense of a much narrower depth of focus, just 58 μm. This depth of focus barely covers a single neural layer in the retina (see Fig. 61.15) and thus precludes imaging the full retina thickness simultaneously and necessitates careful focusing of a single layer of interest, for example, photoreceptor segments. Such axial restriction clearly undermines the power of most OCT modalities that rapidly acquire information in depth (A-scans), either simultaneously as in SD-OCT or nearly so as in swept source OCT.

While high lateral resolution and large depth of focus cannot be realized simultaneously with conventional optics, methods to optimize this trade-off are well established in the optics literature albeit showing limited success. These methods are just beginning to be applied to AO-OCT systems [91]. Non-conventional approaches that take advantage of the phase information intrinsic in the OCT image offer considerably more promise. These approaches have been demonstrated to remove focus blur and other aberrations in post-detection, though under well-controlled conditions and specialized samples [92]. While promising, major questions remain as to their robustness to work in living tissue such as the eye.

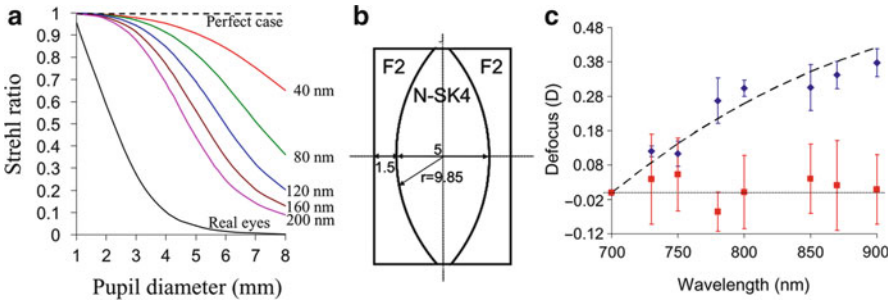

Fig. 61.16 (**a**) Polychromatic Strehl ratio of the human eye computed as a function of pupil diameter at the eye and spectral bandwidth of the imaging light source. *Colored, solid lines* depict perfect correction of ocular monochromatic aberrations, thus image quality is limited by diffraction and chromatic effects. *Black, dashed line* depicts perfect correction of both monochromatic and chromatic aberrations of the eye. *Black, solid line* depicts average of four real eyes with all aberrations present (Reproduced with permission from OSA, Ref. [93]). (**b**) Customized achromatizing lens for correction of ocular chromatic aberrations in the near infrared. (**c**) Chromatic difference of refraction (defocus) in the near infrared with and without the achromatizing lens (*red* and *blue color*, respectively) shown in (**b**). Error bars depict the standard deviation of measurements on five subjects. The *black, dashed line* is the predicted curve for the human eye, the near-infrared portion of that shown in Fig. 61.5. The *dotted line* denotes perfect chromatic correction (Reproduced with permission from OSA, Ref. [96])

Another fundamental performance disadvantage of AO is that it increases the sensitivity of OCT to chromatic aberrations. As discussed in Sect. 61.2.2 and shown in Fig. 61.5, the human eye has significant chromatic aberrations. Recent work by Fernández and Drexler [93] has shown that ocular chromatic aberrations can significantly decrease the detected signal and degrade the lateral resolution of AO-OCT, the extent to which depends strongly on the spectral bandwidth of the OCT source and pupil size. Figure 61.16 illustrates this dependence, plotting Strehl ratio of the eye as a function of pupil diameter (1–8 mm) and spectral bandwidth (40–200 nm). The plot shows image quality monotonically decreases with pupil size and bandwidth. At small pupil sizes typical of conventional OCT (<2 mm), Strehl ratio is negligibly impacted by chromatic aberrations regardless of the bandwidth, even 200 nm. However, at pupil sizes useful for AO (>6 mm), lateral resolution noticeably drops for bandwidths that exceed that of standard OCT (>40 nm). For bandwidths used in UHR-AO-OCT (>100 nm), image quality is predicted to fall below a Strehl of 0.5, this all with perfect AO correction of monochromatic aberrations. Thus given the typical bandwidths of OCT sources, and especially those for UHR-OCT, the benefit of AO correction of monochromatic aberrations is only useful if the chromatic aberrations are corrected too. The present solution is to insert a customized achromatizing lens into the AO-OCT sample arm to provide a fixed correction of the expected average chromatic aberrations in the human eye. Numerous labs have reported such lenses and have demonstrated improvement in image quality [83, 94, 95]. The design of one such lens is shown in Fig. 61.16b; its effectiveness to compensate chromatic aberrations in five subjects is validated in Fig. 61.16c [96].

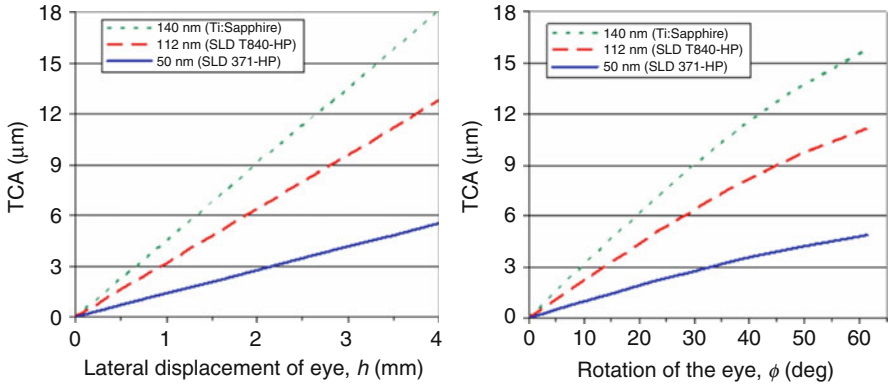

Fig. 61.17 Modeling of TCA as a function of (*left*) lateral misalignment of the eye, *h*, and (*right*) off-axis imaging, φ. (*Left*) TCA is plotted as a function of lateral displacement of the eye's nodal point relative to the optical axis of the retina camera. (*Right*) TCA is plotted as a function of eye rotation (defined as the angle between the camera's optical axis and the eye's achromatic axis). The eye's entrance pupil remains centered on the camera's optical axis, which is a common experimental alignment protocol. Three near-infrared bands were chosen that correspond to specific OCT light sources (Reproduced with permission from OSA, Ref. [25])

Achromatizing lenses are critical for correction of LCA in the eye, but provide no benefit for TCA, which can be substantial and can dilute the benefit of the LCA and AO correction. Zawadzki et al. [25] recently investigated theoretically and experimentally the impact of the eye's LCA and TCA on the performance of high-resolution retina cameras and strategies to minimize them. They determined the extent to which TCA impacts retinal imaging and the conditions under which it can be held at acceptable levels. As discussed in their paper, the two primary contributors of TCA for retinal imaging are (1) errors in the lateral positioning of the eye, *h*, relative to the optical axis of the retina camera and (2) off-axis imaging, φ, i.e., imaging away from the achromatic axis of the eye. Two of their key results are shown in Fig. 61.17. The left plot shows the predicted TCA as a function of lateral displacement of the eye's nodal point from the camera's optical axis. Larger displacements as well as wider source spectra are predicted to generate larger TCA. Use of a pupil camera and bite-bar stage permits accurate positioning of the subject's pupil, likely within about ±0.5 mm. This precision of pupil alignment should be sufficient to keep TCA at acceptable levels. However, clinical use of AO-OCT ultimately means replacing the bite-bar stage with a chin and forehead rest. For these instruments, larger positioning errors are expected.

Figure 61.17 (right) shows the predicted TCA for off-axis imaging when the eye's entrance pupil remains centered on the camera's exit pupil. The figure shows that larger rotations as well as wider source spectra lead to larger TCA. As an example for the SLD T840-HP source (UHR-AO-OCT), the TCA remains below 3.5 µm up to ±16° of rotation. This suggests that the central portion of the retina – from the fovea out to about the optic disk – can be imaged with this source

with relatively small TCA. This interpretation assumes the achromatic axis intersects the retina near the fovea. The 50 nm source will allow even larger rotation ($\pm 39°$), while the 140 nm less ($\pm 11°$). Perhaps of most importance, these predictions represent fundamental limits on the accessibility of the microscopic retina with AO-OCT. The exact numbers will change depending on source spectrum, eye alignment, pupil size, and chromatic aberrations, but hard limits exist and impose serious consequences on imaging performance.

61.5 Examples of AO-OCT Systems

Not surprisingly, development of AO-OCT systems has closely followed advances of the underlying AO and OCT technologies. For AO, these advances have largely been in improved componentry (wavefront sensors and correctors), optical designs (aberration free), and control algorithms that better account for the unique properties of the eye. While considerable AO advances have occurred in these areas, the basic configuration of ophthalmic AO has remained unchanged, being based on the same three components: wavefront sensor, wavefront corrector, and control algorithm.

In contrast, OCT has progressed rapidly along several different design configurations, each taking advantage of different key technologies, especially those for light generation and detection. Major development of these configurations occurred more or less sequentially, and thus AO-OCT development has mirrored these transitions. Over the last nine years, all major OCT design configurations have been demonstrated with AO. AO-OCT combinations include time-domain *en face* (xy) flood-illumination OCT using an areal CCD, time-domain tomographic scanning (xz) ultrahigh-resolution OCT, time-domain *en face* scanning (xy) OCT, high-resolution spectral-domain OCT, ultrahigh-resolution spectral-domain OCT, and more recently swept source OCT.

Regardless of design configuration, AO-OCT performance has been commonly assessed using standard AO and OCT metrics, but ultimately judged by the quality of the retinal image and retinal microstructure that is revealed. Consistent with the rest of the ophthalmic AO field, the retinal cell of choice to assess retinal image quality has been the cone photoreceptor. This is due in part to the cone's high contrast in reflection, regular arrangement that varies predictively with retinal eccentricity and stratified 3D reflectance profile.

Here we present the major AO-OCT design configurations that have been developed, categorized broadly by time-domain and Fourier-domain types. Emphasis is on the first systems reported.

61.5.1 AO with TD-OCT

The first implementations of AO-OCT were based on TD-OCT, the method ubiquitous of OCT up to about 2004. This included a flood-illuminated version based on

an areal CCD [16] and a conventional version based on tomographic scanning (xz) [17]. These first instruments demonstrated the potential of the combined technologies, but fundamental technical limits, primarily in speed, precluded their scientific and clinical use. Nevertheless they represented first steps toward more practical designs that became possible with new OCT methods. The one notable new time-domain method that has been combined with AO and continues to be developed is high-speed transverse scanning TD-OCT (TS-OCT) [22, 24].

Here we briefly describe these first AO-TD-OCT designs based on flood-illumination TD-OCT, tomographic TD-OCT, and transverse-scanning TD-OCT.

61.5.1.1 Flood-Illuminated TD-OCT

The first demonstration of AO-OCT was reported in a conference proceeding a decade ago by Don Miller's laboratory [16] using an *en face* coherence-gated OCT camera. AO consisted of a 37-actuator Xinetics mirror and a SHWS that executed up to 22 measurements and corrections per second across a 6.8 mm pupil. Coherence gating was realized with a free-space Michelson interferometer that employed an areal CCD camera for recording 2D retinal interferograms, with sets of four acquired in less than 7 ms. Axial position of the retina was dynamically tracked using an independent TD-OCT that controlled a voice coil stage. The figure above shows schematic of first AO with flood-illuminated TD-OCT (Fig. 61.18).

Characterization of system performance illustrated the key advantages of parallel detection: no beam scanning and straightforward integration into flood-illuminated AO architecture. The parallel detection scheme demonstrated sufficient sensitivity and resolution for imaging retinal tissue in postmortem [97]. But intrinsic axial motion of the living eye proved challenging for the system's auxiliary TD-OCT tracker and slow readout of the CCD.

61.5.1.2 TD-OCT

The second AO-TD-OCT system was reported by Hermann et al. [17], this one using conventional TD-OCT similar to that in the Zeiss Stratus OCT, but of ultrahigh axial resolution. The system represented collaboration between Wolfgang Drexler's and Pablo Artal's laboratories. The AO system consisted of a 37-actuator OKO DM and a SHWS with separate laser beacon. The design demonstrated clear performance advantages of AO in the living eye and did not suffer from the gating problem of the earlier AO-TD-OCT system. A schematic of their system is shown in the figure above (Fig. 61.19).

Along with clear performance advantages, however, were also clear performance disadvantages. These included the relatively slow OCT acquisition speed and modest performance of the AO system (no active correction during image acquisition and a small pupil size, 3.7 mm). Collectively, these resulted in limited improvement in image quality and considerable degradation from the influence of transverse eye motion [98] that becomes pronounced at high magnification of the retina.

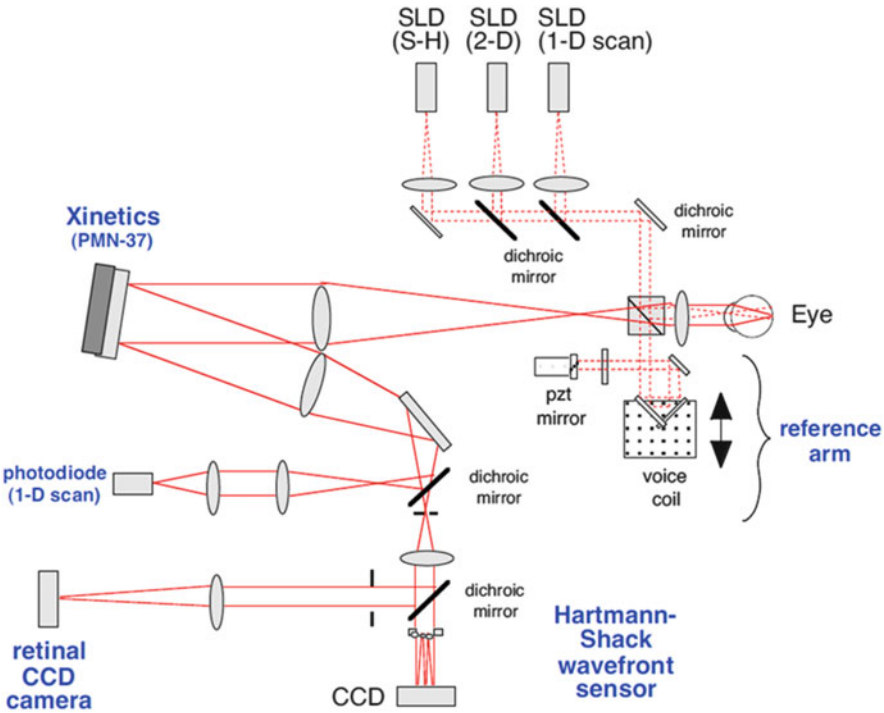

Fig. 61.18 Schematic of the first AO TD-OCT system. It consisted of a flood-illuminated *en face* OCT system (CCD-based) for optical sectioning the retina at 10 μm axial resolution, a 1-D OCT axial scanner for tracking the axial position of the subject's retina, and an AO system (consisting of a Shack Hartmann wavefront sensor and a 37 actuator Xinetics mirror) for measuring and compensating the aberrations of the eye. Separate SLD light sources were employed for each of the three subsystems. A separate incoherent light source for flood illuminating the retina was added to the camera (but is not shown) (Reproduced with permission from SPIE, Ref. [16])

61.5.1.3 Transverse Scanning TD-OCT (TS-OCT)

The more recent combination of AO with transverse scanning OCT (TS-OCT) has resulted in the most effective implementation to date of TD-OCT with AO. In TS-OCT, the "thin" coherence-gated C-scans are recorded at relatively fast speeds (2–27 Hz frame rate), with the higher rates significantly reducing transverse motion artifacts. Other advantages of TS-OCT include direct integration with SLO imaging architectures [99] and implementation of dynamic focus [100]. Adrian Podoleanu's and Chris Dainty's laboratories developed the first TS-OCT system with AO [22]. In their AO-TS-OCT system, the same light source was used for imaging and wavefront sensing. A 37-actuator OKO DM with Badal optometer provided wavefront correction. The acquisition speed of this instrument was 2 Hz/C-scan, which exposed the C-scan images to substantial motion artifacts. The figure above shows schematic of their AO with transverse scanning TD-OCT [22] (Fig. 61.20).

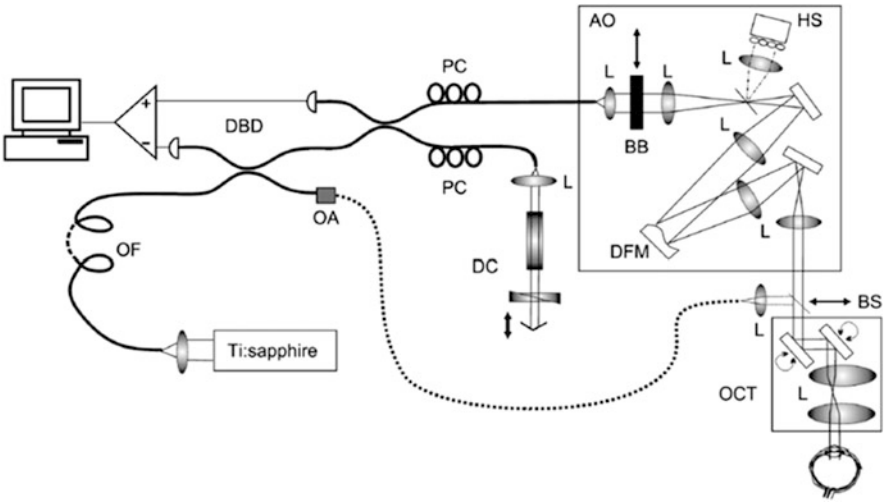

Fig. 61.19 AO UHR OCT system: *DBD* dual balanced detection, *PCs* polarization controllers, *OA* optical attenuator, *OF* 100 m of optical fiber, *DC* dispersion compensation, *L's* achromatic doublet lenses, *BB* removable beam blocker, *DFM* deformable mirror, *BS* removable beam splitter (Reproduced with permission from OSA, Ref. [17])

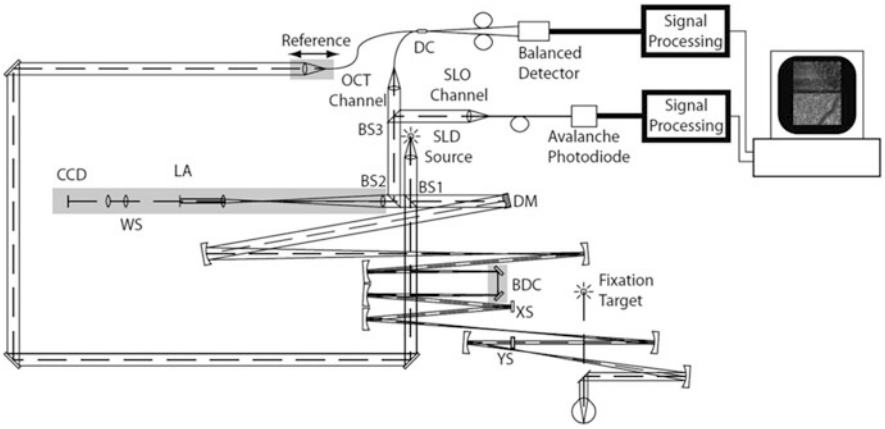

Fig. 61.20 AO-OCT/SLO system; *SLD* Superluminescent diode, *BS* beam splitter, *DM* deformable mirror, *BDC* Badal defocus corrector, *XS* X scanner, *YS* Y scanner, *WS* wavefront sensor, *LA* lenslet array, *DC* directional coupler (Reproduced with permission from OSA, Ref. [22])

Much higher C-scan rates were realized with an AO-TS-OCT system developed by Christoph Hitzenberger's and John Werner's laboratories [24]. This system permitted direct comparison of cone photoreceptor images obtained simultaneously with SLO and OCT. The AO system in this AO-TS-OCT system consisted of

a 37-actuator AOptix DM and a SHWS using the same light source as for imaging. Michael Pircher's laboratory from Vienna Medical University has continued working on improved design and data acquisition schemes for transverse scanning TD-OCT systems [101, 102]. These include application of auxiliary spectral domain partial coherence interferometer that tracked and compensated at ~200 Hz for the axial position of the cornea and lens-based AO-SLO system that is compatible with his TD-OCT data acquisition. Today AO-TS-OCT continues to be developed and represents a viable alternative to Fourier-domain-based AO-OCT systems, which are discussed next.

61.5.2 AO with Fourier-Domain OCT

The first reports of AO Fourier-domain OCT (AO-FD-OCT) occurred shortly after major developments in FD-OCT, most notably theoretical and experimental investigations into the substantial sensitivity advantage of FD-OCT over TD-OCT [103–105]. This led to a rapid transition of AO-OCT systems from TD-OCT to FD-OCT. Today, FD-OCT is employed in almost all AO-OCT systems, with spectral-domain OCT (SD-OCT), the principle design configuration, and swept source OCT (SS-OCT) gaining increased interest. Here we present the first examples of AO-FD-OCT based on line-illuminated SD-OCT, scanning spot SD-OCT, and scanning spot SS-OCT.

61.5.2.1 Line-Illuminated Spectral-Domain OCT

First implementation of AO-OCT with FD-OCT was reported by Zhang et al. [18]. A line field (or parallel) SD-OCT system was developed and integrated with an AO system similar to that reported by the same laboratory in their earlier AO-TD-OCT system [16]. The retina was illuminated with a line using a cylindrical lens and the reflectance detected in the Fourier domain using a grating to disperse the line across an areal camera [106, 107]. In this way, the illuminated line resulted in a B-scan image composed of simultaneously recorded A-scans, which greatly reduced the system's sensitivity to eye motion. Figure 61.21 shows a schematic of their system.

Comparison of retinal images captured with and without AO showed clear improvement in image clarity and resolution afforded by the AO. The images also showed for the first time distinguishing features of cone photoreceptors at two depths: the regular spacing of bright spots at the cone inner-segment/outer-segment (IS/OS) junction and the posterior tip of the outer segment (PTOS), also called cone outer-segments tips (COST). Disadvantages of line field SD-OCT were its relatively low (B-scan) duty cycle and lack of a vertical scanner to reposition the B-scan on the retina, both of which prevented volume imaging.

61.5.2.2 Spectral-Domain OCT

Shortly after line-illuminated AO-SD-OCT, two additional AO-SD-OCT systems were reported, both based on conventional xy raster scanning. Raster scanning

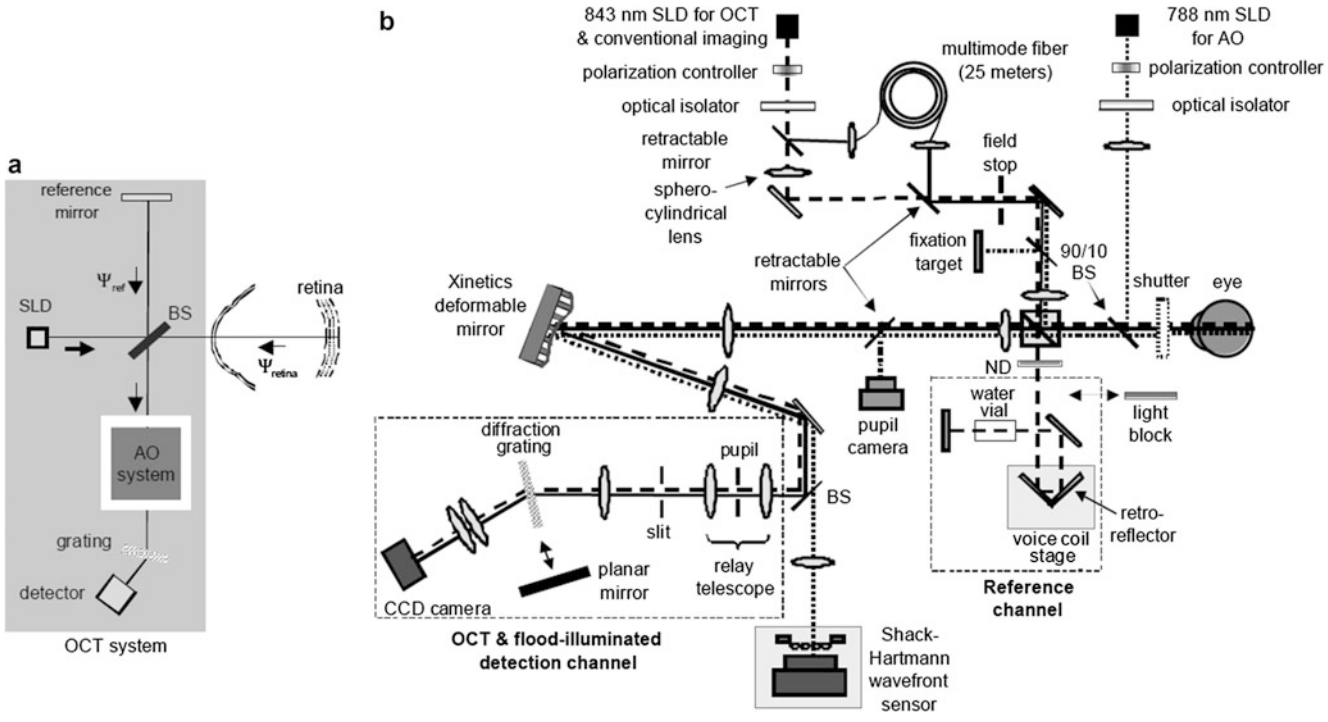

Fig. 61.21 (**a**) Concept layout shows the AO system as part of the SD-OCT detection channel. (**b**) Detailed layout of the AO parallel SD-OCT retina camera. The camera consists of four subsystems. (1) AO system corrects the ocular aberrations using a 788 nm SLD, Shack-Hartmann wavefront sensor, and Xinetics deformable mirror (*short dashed line*). (2) Pupil retro-illumination and fixation channels permit alignment of the subject's eye to the retina camera. (3) Conventional flood illumination is used to validate focusing in the retina and the physical size of microstructures in the retina (*solid line*). (4) Parallel SD-OCT acquires single shot B-scan images of the retina (*long dashed line*) (Reproduced with permission from OSA, Ref. [18])

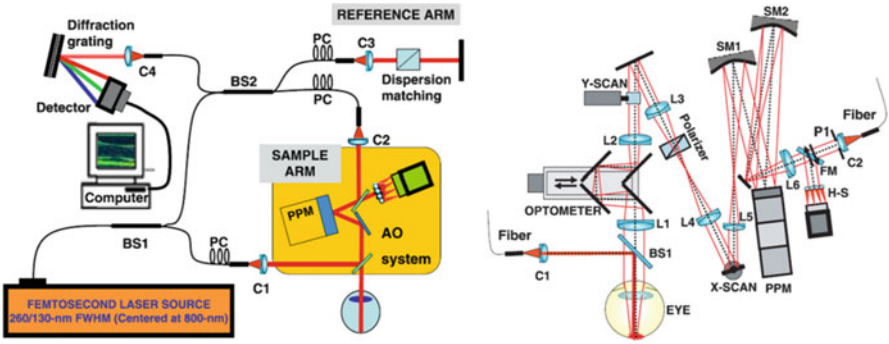

Fig. 61.22 Experimental apparatus. (*Left*): The frequency-domain interferometer incorporates the AO system in the sample arm, performing the aberration correction before the acquisition of the retinal images. An ultra-broad bandwidth laser source is used for retinal illumination. (*Right*): Detailed schematic of the sample arm. The eye's exit pupil is optically conjugate to the two scanning mirrors, the PPM, the H-S wavefront sensor, and the collimator that connects the system to the interferometer, C2. The system incorporates a motorized optometer for correcting defocus independently of the PPM (Reproduced with permission from Elsevier, Ref. [20])

offered considerable flexibility in the scan pattern, including that for volume imaging [19, 20]. The second of the two systems extended the earlier AO-TD-OCT collaborative work of Drexler's and Artal's laboratories [20]. Ocular correction was realized with a high-density liquid-crystal spatial light modulator (LCSLM) in conjunction with a Badal optometer. A separate fiber was used to deliver light for wavefront sensing in "single path" configuration. Figure 61.22 shows schematic of first LCSLM-based AO with raster scanning SD-OCT.

Despite excellent performance of the AO correction as measured by the wavefront sensor (Strehl Ratio ~ 0.95), the AO-OCT images did not demonstrate the same high image quality nor provided the resolution to resolve cone photoreceptors. This led to a detailed analysis and discovery by the authors that the wide spectral bandwidth (130 nm) of their light source exposed the system to significant ocular chromatic blur. This initiated considerable effort in the field to develop customized achromatizing lenses to correct for this effect as described in Sects. 61.4.2 and 5.3 of this review.

The second scanning spot AO-SD-OCT system was developed in Werner's laboratory in collaboration with Joseph Izatt's and Scot Olivier's groups [19]. Their system used the same light source for imaging and wavefront sensing. A large-stroke 37-actuator AOptix DM provided correction. The figure below shows schematic of first DM-based raster scanning AO-SD-OCT system (Fig. 61.23).

As demonstration of AO system performance, authors showed reduced depth of focus in the AO-OCT B-scans compared to that for conventional OCT, the difference is due to the larger numerical aperture of AO-OCT compared to conventional OCT. B-scan images of photoreceptor structure was consistent to that previously reported by Zhang et al. [18]. In addition, the authors reported first AO-OCT images of the 3D

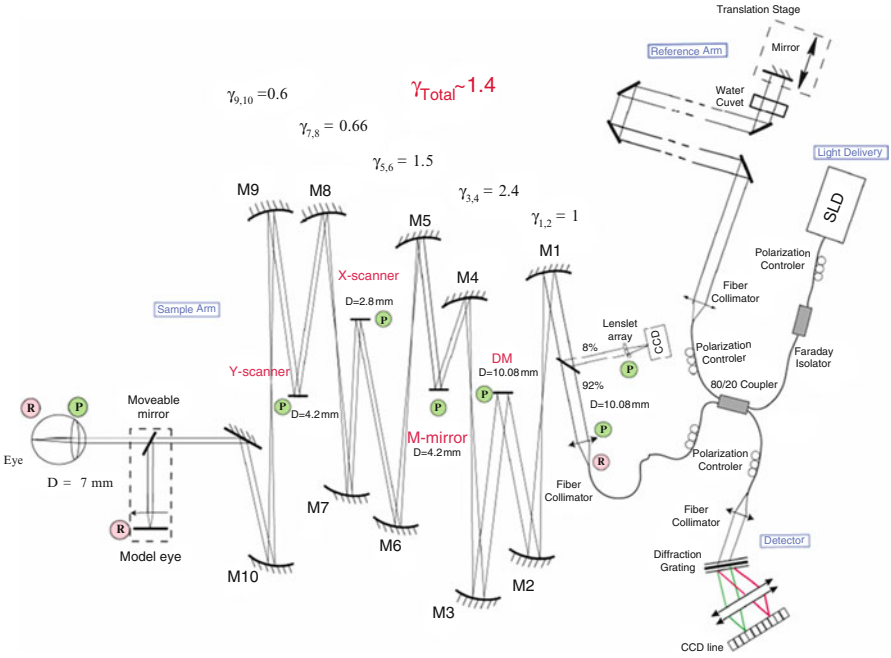

Fig. 61.23 Schematic of UC Davis AO-OCT experimental setup constructed on a standard laboratory optical table occupying 1 × 1 m. The reference arm length is the same as that of the sample arm, but is shown truncated for simplification. Key: γ magnification, *D* diameter, *DM* deformable mirror, *M1–M10* spherical mirrors, *P* pupil plane, *R* retinal plane (Reproduced with permission from OSA, Ref. [19])

architecture of in vivo cone photoreceptors and retinal capillaries. Because of the slow image acquisition (several seconds per volume), however, motion artifacts in transverse direction blurred the visibility of cone photoreceptors in extracted C-scans. Zhang et al. subsequently reported an AO-OCT system that integrated a higher-speed line-scan camera, acquiring A-scans three times faster (75,000 A-scans/s) [21]. The AO system was similar to that described in Zawadzki et al. [19], but a key difference was placement of the AOptix DM on the same side of the scanners as the subject's eye, which provided improved correction of refractive error. The figure below shows schematic of first implementation of AO-SD-OCT with the DM placed on the same side of the xy scanners as the eye (Fig. 61.24).

Imaging at higher speeds and smaller patches of cones increased the volume acquisition rate to 6.7 Hz (150 ms/vol). The high volume rate greatly minimized eye motion artifacts and enabled clear visualization of cone photoreceptor mosaic in *en face*.

These first AO-SD-OCT reports were followed by a large number of developments that targeted improvements in AO-SD-OCT system design and performance and included an expanded list of laboratories pursuing AO-OCT. Improvements continue to be made in essentially all aspects of AO and SD-OCT subsystems, including key components such as system design, OCT light source, OCT detectors,

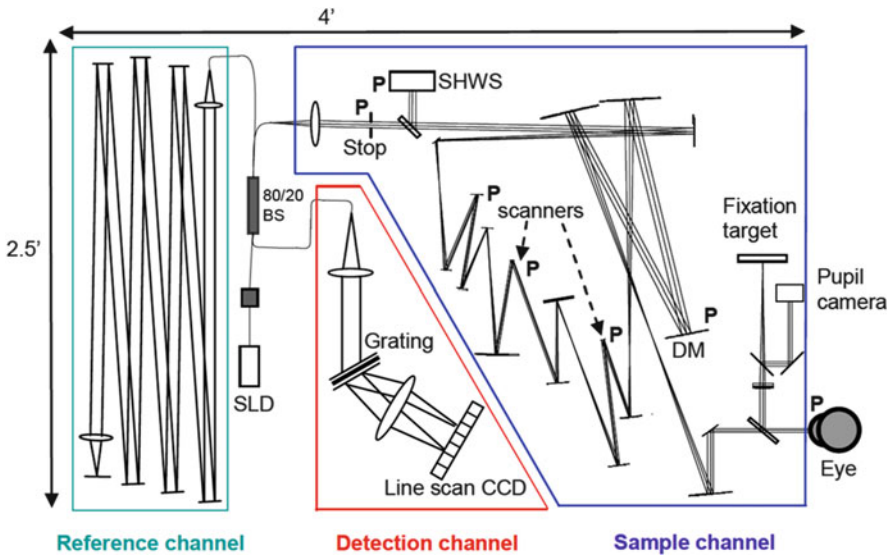

Fig. 61.24 Layout of the AO SD-OCT retina camera. The AO system is integrated into the sample channel. BS, DM, and P refer to the fiber beam splitter, AOptix deformable mirror, and planes that are conjugate to the pupil of the eye, respectively (Reproduced with permission from OSA, Ref. [21])

AO system components, and AO performance evaluation [108] as well as applications of different data acquisition, processing, analysis, and visualization.

A recent AO-OCT system from Yoshiaki Yasuno's laboratory at University of Tsukuba has been used to explore new directions in AO-FD-OCT design (see Fig. 61.25) [109]. In particular, the authors focused on the application of 1 μm imaging window for better visualization of choriocapillaris and choroid. Additional design features included an "off-plain" configuration for reduced system aberrations and a lens-based Badal optometer in "double pass" realized with linear polarizers to block back reflections.

The "off-plain" design follows that employed in AO-SLO systems [110–112], where system lateral resolution was found to significantly improve. More recent AO-OCT systems have extended the "off-plain" concept in ways that provide even further performance improvement and design flexibility [113, 114]. It should be noted that while these recent system developments have occurred largely with SD-OCT systems, the developments are in many cases equally applicable to the other OCT configurations. SD-OCT remains the configuration of choice, but that may change rapidly as the field matures and new technologies develop.

61.5.2.3 Swept Source: OCT

SS-OCT has undergone substantial development in recent years and today represents an attractive alternative to SD-OCT, owing in large part to SS-OCT's higher

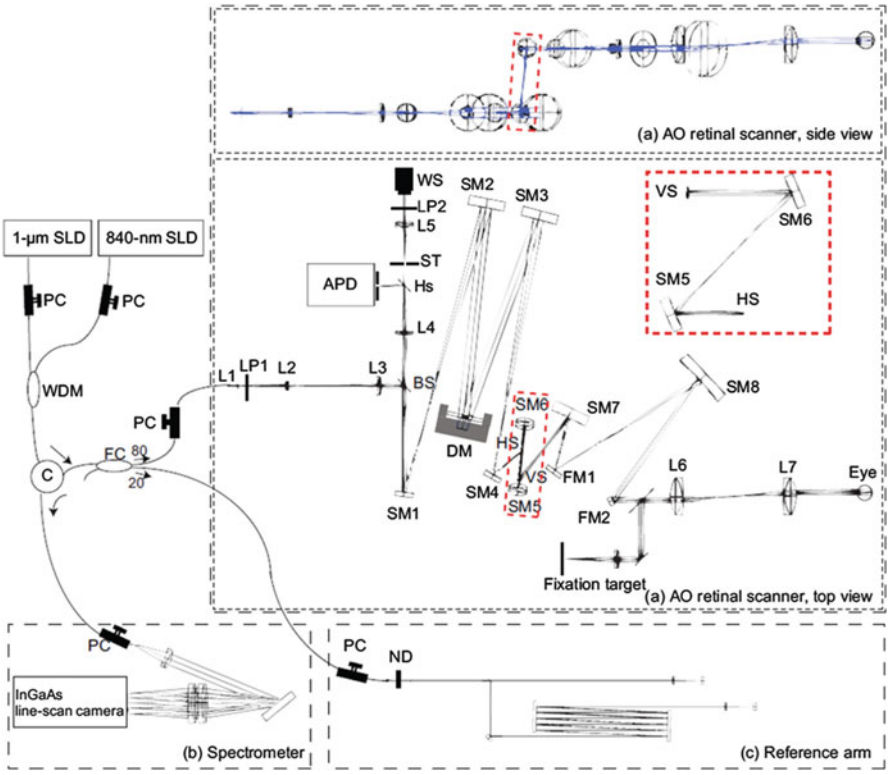

Fig. 61.25 Schematic of the AO-OCT. *WDM* Wavelength division multiplexing coupler, *C* Circulator, *PC* Polarization controller, *FC* Fiber coupler. (**a**) The side and top views of the optical setup of the AO retinal scanner. *L#* Lenses, *LP#* Linear polarizers, *BS* Beam splitter, *Hs* Harmonic separator, *ST* Stop, *SM#* Spherical mirrors, *FM#* Flat mirrors, *WS* Wavefront sensor, *DM* Deformable mirror, *VS* Vertical galvanometric scanner, *HS* Horizontal resonant scanner mounted galvanometric scanner, *APD* Avalanche photodiode. (**b**) Reference arm. *ND* ND filter. (**c**) Spectrometer (Reproduced with permission from OSA, Ref. [109])

imaging speeds and flatter sensitivity roll off with depth. Despite these advantages, however, only a couple of peer-reviewed publications have demonstrated AO-SS-OCT systems. Figure 61.26 shows schematic of first implementation of AO SS-OCT system from Physical Science Inc. [115].

Slow progress in development of AO SS-OCT systems has been due to the restricted spectral range (>1 μm) and bandwidth (modest axial resolution), even among state-of-the-art swept sources. However, swept source technology continues to develop, and sources at shorter wavelengths (~800 nm) and with broader spectral bandwidths will eventually be available. With these advances, SS-OCT may overtake SD-OCT as the configuration of choice for future AO-OCT systems.

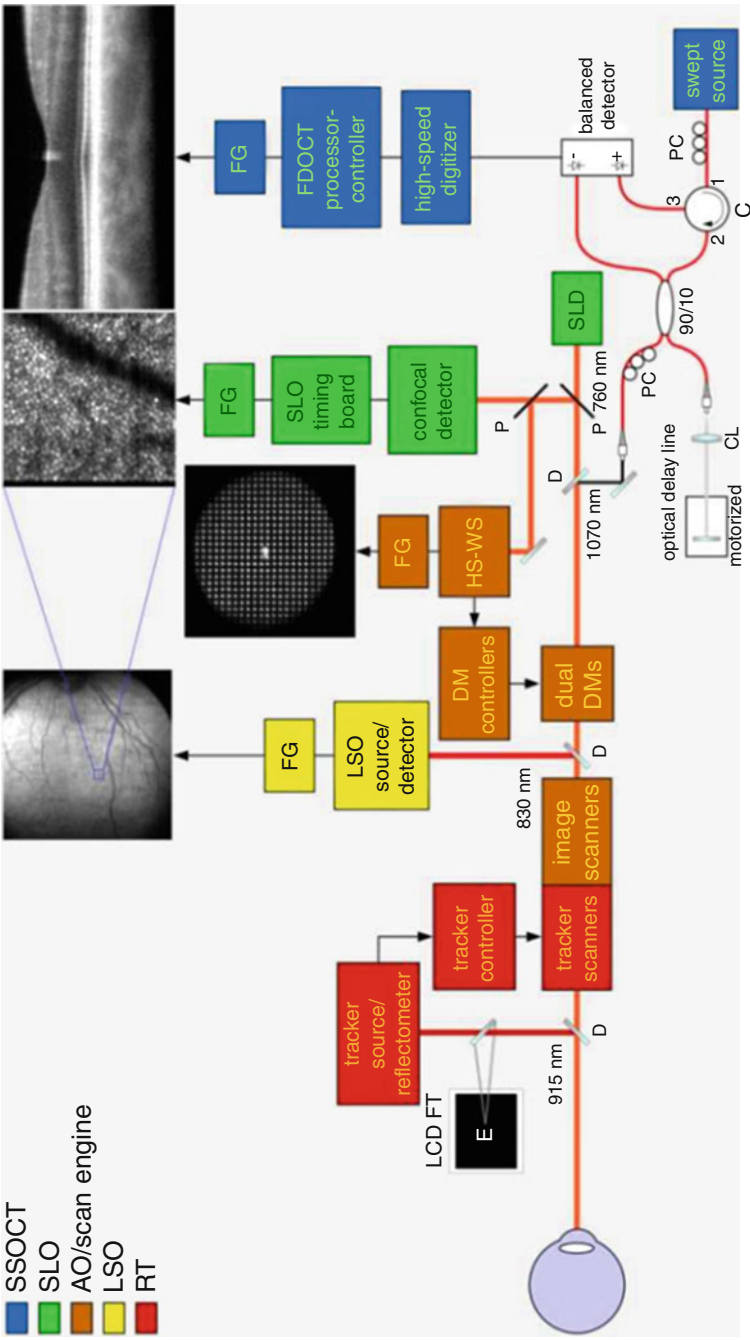

Fig. 61.26 Block diagram of multimodal AO retinal imager. *D* dichroic beamsplitter, *P* pellicle beamsplitter, *FC* fiber coupler, *FG* framegrabber, *C* cilculator, *PC* polarization controllers, *DM* deformable mirror (Reproduced with permission from OSA, Ref. [115])

61.5.3 Ultrahigh-Resolution AO-OCT (Chromatic Aberration Correction)

As discussed in Sect. 61.4.2, the use of spectrally broad bandwidth light sources for ultrahigh-resolution OCT can substantially degrade lateral resolution owing to the intrinsic chromatic aberrations of the eye. To correct this effect, custom achromatizing lenses are added to the AO-OCT to provide equal but opposite LCA to that of the eye. To this end, the achromatizing lens has been evaluated at two different positions in the AO-OCT sample arm, the corresponding systems of which are presented in Fig. 61.27 [25, 26].

Both achromatizing lens' positions are optically conjugate to the eye pupil plane. In the configuration proposed by Fernández et al., the customized lens occupies a separate pupil plane downstream of the SHWS sensor. In contrast to the configuration proposed by Zawadzki et al., the lens is placed adjacent to the collimating lens of the fiber input thereby taking advantage of an already existing pupil plane and being upstream of the SHWS. Thus main disadvantages of the first configuration are possible back reflections from the achromatizing lens that can create artifacts in the SHWS and need for an additional pupil plane. The main disadvantage of the second configuration is that it corrects the ocular LCA as seen by the WFS only in single pass. Therefore, broadband light sources may require spectral filtering immediately in front of the SHWS or additional post-processing of the SHWS spots in order to avoid wavefront errors caused by chromatic blur of the WFS spots. Given the push to extend AO-UHR-OCT to even higher axial resolution (<2 μm), the impact of chromatic aberrations and how best to correct for it will continue to garner attention.

61.5.4 Multimodal AO-OCT Systems

Combination of OCT with other imaging modalities provides additional, complimentary retinal information, which has proven useful in commercial ophthalmic OCT instruments. Often OCT images are acquired simultaneously with SLO images, the latter used for image registration and navigational purposes. Such multimodal use is also applicable to AO-based imaging systems. One particularly attractive combination is AO-OCT with AO-SLO fluorescent imaging as the two probe fundamentally different cellular mechanisms. Recently, Physical Sciences Inc. (PSI) proposed a multimodal AO-OCT system that included SLO and fluorescent SLO channels as well as a large field of view imager and retinal tracking [29] (Figs. 61.28 and 61.29).

Another example of a multimodal AO-OCT system that includes intensity-based SLO has been recently published by Zawadzki et al. [116]. The authors demonstrated that simultaneously acquired AO-SLO images can be used to extract retinal motion present during AO-OCT imaging and then correct for that motion in post-processing of the AO-OCT data [117]. More examples of retina tracking and motion correction of AO-OCT images can be found in Sect. 61.6.4.

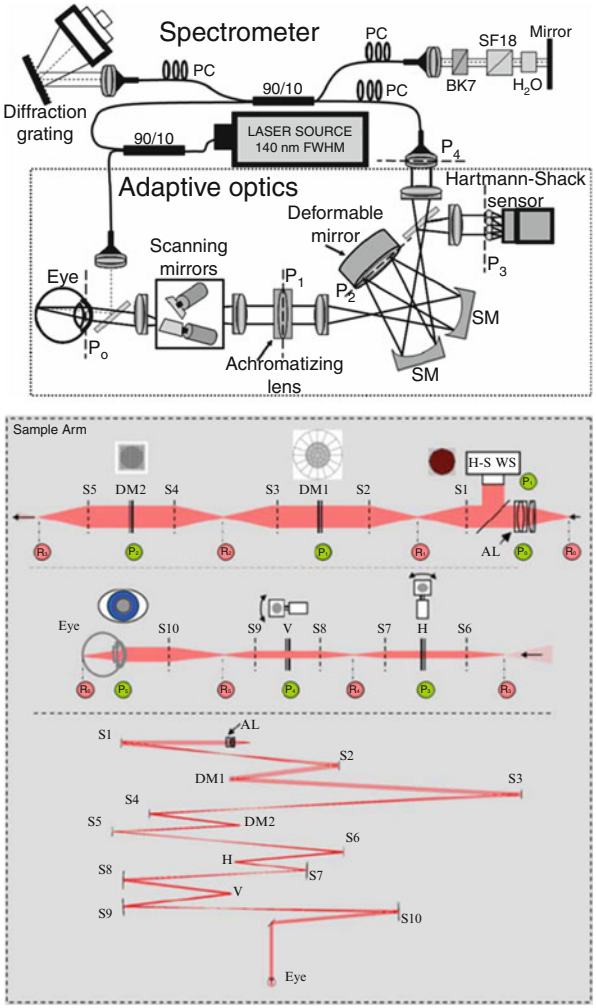

Fig. 61.27 Chromatic aberrations of the eye have been corrected by placement of a customized achromatizing lens at two different positions in the AO-OCT sample arm. These positions are (*top*) between SHWS and the eye and (*bottom*) between fiber collimator and SHWS. (*top*) Experimental system consists of two parts: an AO system (in *dashed lines*) responsible for pancorrection of ocular optical aberrations and a UHROCT system for high-speed retinal imaging. Charged coupled device (*CCD*), polarization controller (*PC*), borosilicate-crown glass (*BK7*), silicate fluoride (*SF18*), H2O (*water*), conjugate planes of the AO system (*Px*), fiber optical beam splitter with 90–10 % splitting ratio (90/10). (*bottom*): *Upper panel* shows unfolded schematic of the AO-UHR-OCT sample arm. The light travels from left to right in the upper panel. P and R refer to pupil and retinal conjugate planes, respectively; *AL* achromatizing lens, *S* spherical mirror, *V* vertical, *H* horizontal scanner. *Lower panel* shows Zemax screenshot of the sample arm layout. Note the location of the achromatizing lens, which is positioned adjacent to the collimating lens in the pupil conjugate plane, P0 (Reproduced with permission from OSA, Ref. [25, 26])

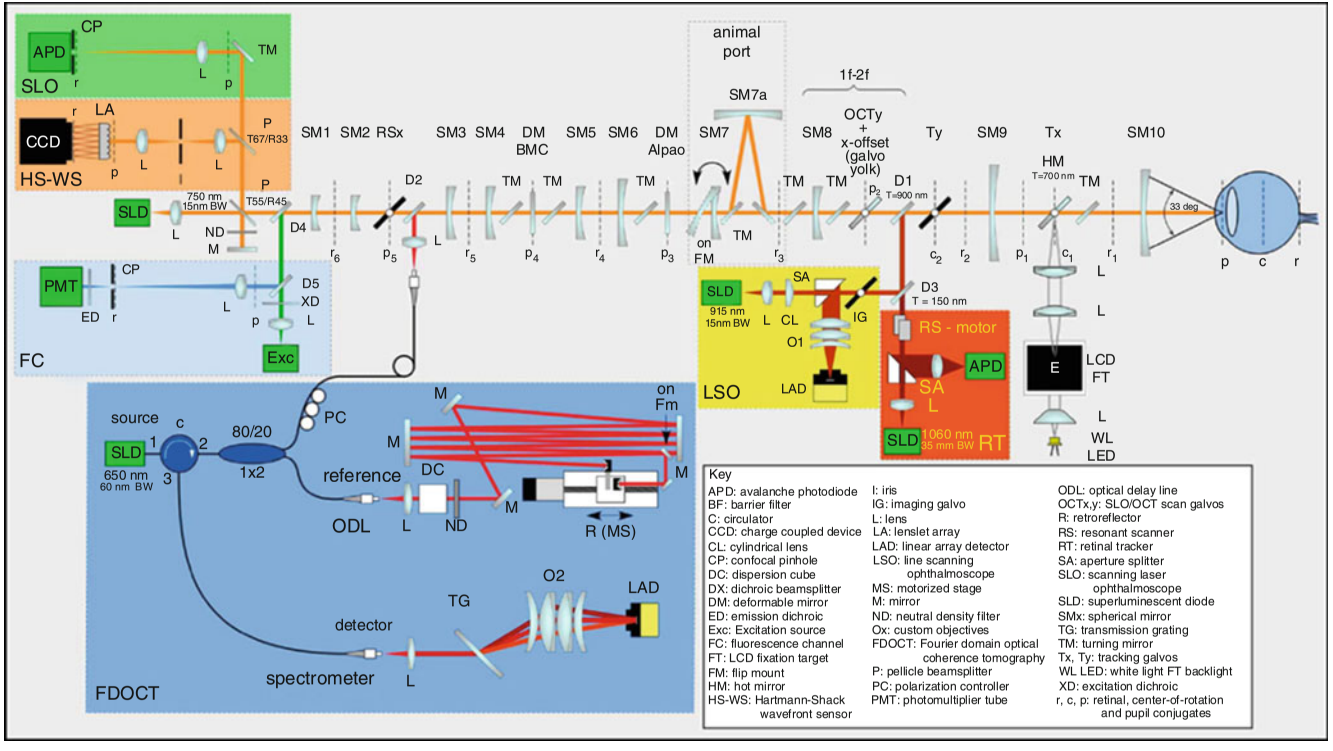

Fig. 61.28 Unfolded optical schematic of the multimodal adaptive optics system (*MAOS*) imager. Subcomponents of the system are the LSO wide-field imager, *SLO* scanning laser opthalmoscopy, *FC* Fluorescent Channel; FD-OCT optical coherence tomography, and the AO subsystem (wavefront compensation and correction). *RT* retinal tracker, Each subsystem is highlighted by a *colored box* (Reproduced with permission from OSA, Ref. [29])

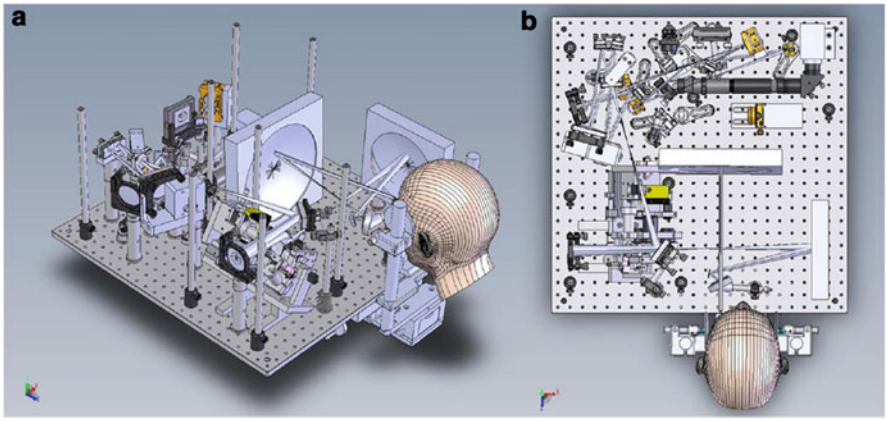

Fig. 61.29 Integrated SolidWorks-Zemax opto-mechanical model of MAOS. (**a**) Isometric view. (**b**) *Top view*. Small platforms mounted above the main optical table for the OCT optical delay line and spectrometer are not shown. Fluorescence detection channel is not included in this version (Reproduced with permission from OSA, Ref. [29])

61.6 Selected Topics on AO-OCT Development

Parallel to the development of AO-OCT along different OCT design configurations, AO-OCT has also progressed rapidly along other engineering fronts. These additions have enabled it to probe more powerfully and accurately structure and function of the cellular retina. Many of these developments mirrored that ongoing in the OCT field, for example, the many methods that take advantage of the complex signal detected by OCT. A few representative developments are described in this section: polarization-sensitive imaging of retinal birefringence, contrast enhancement and quantification of retinal and choroidal blood flow, and phase imaging of photoreceptor growth.

The section ends with a discussion of eye motion artifacts and their correction. This topic represents a fourth engineering front that has been heavily investigated in recent years. Correction of eye motion is applicable to almost any AO-OCT in vivo use because it is almost always present, even in a fixating eye, and leads to distortion and mis-registration in the image. Eye motion is a serious obstacle to effective use of AO-OCT and more problematic than for standard OCT owing to the higher magnification and denser sampling of A-scans. A diverse range of solutions to minimize eye motion artifacts in AO-OCT are currently under investigation and will be summarized here.

61.6.1 Polarization-Sensitive AO-OCT

The polarization state of light carries additional information about the retinal tissue, in particular its birefringence, which is a meridional variation in refractive index

that differentially retards transmitted light polarized along the fast and slow axes of the tissue. Various layers of the retina are well known to alter the polarization state, primary ones being the retinal nerve fiber layer, Henle's fiber layer, and RPE. Change in birefringence has been suggested a sensitive indicator of disease onset, leading to increased clinical attention and the development of ophthalmoscopes with polarization-sensitive detection. In the last decade, polarization-sensitive OCT (PS-OCT) has garnered considerable interest as it enables simultaneous intensity and depth-resolved measurements of the polarization state in the retina [118–121]. PS-OCT, however, is not without limitations, most notably poor lateral resolution owing to the small beam size at the eye (<2 mm) and ocular aberrations as well as large speckle. Collectively, these limit PS-OCT from probing highly localized changes of birefringence that occur on a microscopic level in the retina, for example, variations in birefringence of adjacent retinal nerve fiber bundles. The integration of AO into PS-OCT provides a solution to this problem, allowing access to the full polarization information that exits a large pupil of the eye (>6 mm).

Cense et al. [88] investigated the benefit of AO for PS-OCT measurements. With AO-PS-OCT, they measured the double pass phase retardation per unit depth with values ranging from 0.25°/μm to 0.65°/μm in the birefringent nerve fiber layer 6° from the fovea, with the highest values being noticeably higher than previously reported with PS-OCT. This wide range may reflect local differences in birefringence that are expected to occur between and among RNF bundles and are too fine to be resolved without AO.

Figure 61.30 shows another example that highlights the capability of AO-PS-OCT to detect localized variations in phase retardation. In this case tissue immediately above a 70 μm diameter arterial was found to be extremely birefringent, up to three times more than the adjacent RNFL tissue. The B-scans in the figure show intensity and false color cumulative phase retardation images that were reconstructed from the same AO-PS-OCT data. Location of high (red arrow) and low (blue arrow) birefringent RNFL tissue is indicated in the phase retardation image.

61.6.2 Flow-Contrast Methods in AO-OCT

Flow-contrast methods enhance the visibility of retinal vessels by detecting temporal dynamics in the OCT phase signal that are generated by blood flow. Application of this method to capillary mapping is challenging owing to the small size of the capillaries (5–10 μm) and the little light they reflect. Thus the increased resolution and sensitivity afforded by AO may critically improve detection. One caveate, however, is that the smaller spot size formed at the retina (due to AO) must be properly accounted for in the flow-contrast method. If not, it will exacerbate phase noise and motion distortions and ultimately compromise contrast performance. First use of flow-contrast methods in AO-OCT systems compared intensity and power Doppler-based imaging of capillary beds (see Fig. 61.31) [122]. Results demonstrate enhanced visibility of individual vessels as evident in the figure example.

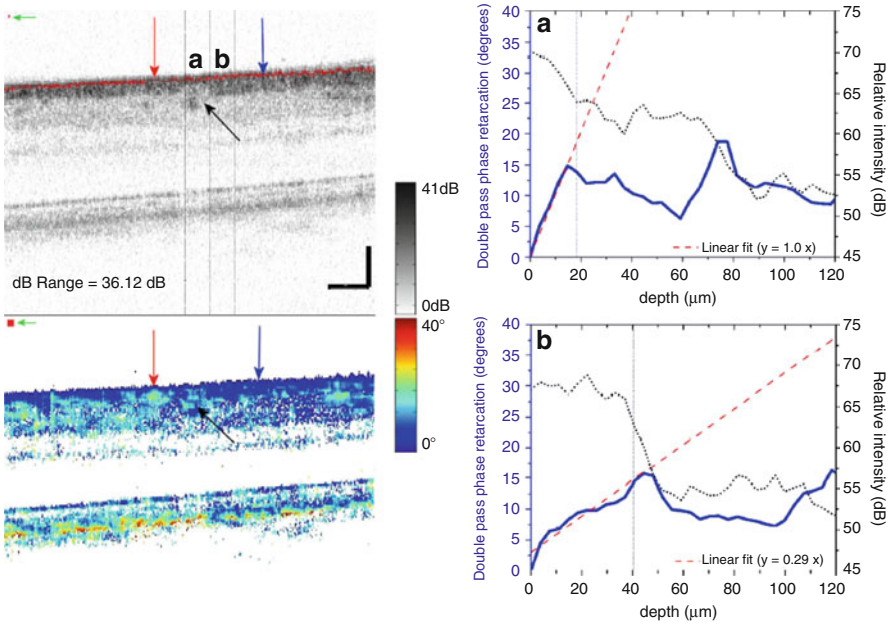

Fig. 61.30 Intensity (*top left*) and cumulative double pass phase retardation (*bottom left*) obtained with AO-PS-OCT. 3° B-scan bisects the nasal/temporal retina with the left and right edges at 4.5° and 7.5° superior of the foveal center, respectively. RNFL birefringence causes the cumulative double pass phase retardation to increase from 0° (*dark blue*) to approximately 30° (*light blue/green*) over a depth of less than 50 μm. The *red* and *blue arrows* point to RNFL regions that exhibit high and low birefringence, respectively. Distance between these regions of extreme RNFL birefringence is just 200 μm. The *black arrow* points to a 70 μm wide small blood vessel that was identified as arterial. Large changes in phase retardation spanning more than 50° is evident in the RPE and is suggestive of rapid changes in fast axis orientation associated with polarization scrambling. In the intensity image, the size of the red block (follow *green arrow*) represents the footprint (width × depth) of the AO-OCT point spread function at the plane of focus as well as the mean speckle size throughout the entire retina. In the DPPR image, the *red block* represents the 14 μm × 14 μm averaging kernel. Data was scaled in the vertical direction assuming an index of refraction of 1.38 and scale bars indicate a length of 100 μm. The two plots on the right show data that encompasses the blood vessel (**a**) and data that was taken next to the vessel (**b**) (Reproduced with permission from OSA, Ref. [88])

61.6.3 Phase-Sensitive AO-OCT for Photoreceptor Imaging

The cone photoreceptor's outer-segment (OS) experiences minute changes in optical path length, both in response to visible stimuli and as a matter of its daily course of renewal and shedding. These changes are of interest to quantify function in healthy cells and assess dysfunction in diseased ones. While intensity-based AO-OCT provides sufficient resolution to distinguish cone photoreceptors in three dimensions, it has not been able to measure cone OS dynamics, whose scale is smaller than UHR OCT's axial resolution of a few microns.

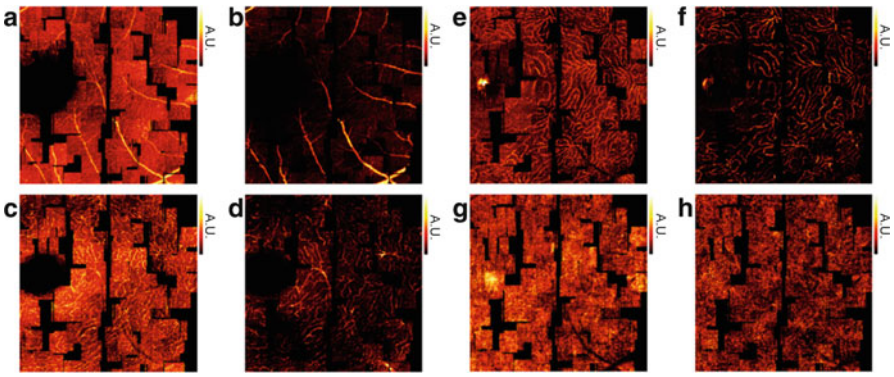

Fig. 61.31 Wide-field *en face* projections of intensity (**a**, **c**, **e**, **g**) and Doppler power (**b**, **d**, **f**, **h**) images at different depths in the retina: GCL and IPL (**a**, **b**), IPL/INL boundary (**c**, **d**), INL/OPL boundary (**e**, **f**), and choriocapillaris (**g**, **h**) (Reproduced with permission from OSA, Ref. [122])

A solution to this problem was presented by Jonnal et al. [123] who took advantage of phase information encoded in the AO-OCT signal. Specifically, they extracted phase differences between the bright reflections that straddle individual cone OSs, thereby effectively converting the OS into a single-cell interferometer. The beauty of this arrangement is that it is immune to axial eye motion (analogous to a common-path interferometer), yet exquisitely sensitive to sub-wavelength changes that occur inside the OS, for example, disk renewal and shedding. As reported, this approach improved the sensitivity of their AO-OCT system to OS length changes by more than an order of magnitude, down to 45 nm, which is slightly thicker than a single OS disk. The figure above shows an example of tracking phase differences between IS/OS and PTOS reflections over time (Fig. 61.32).

61.6.4 Motion Artifact Correction in AO-OCT

Like all in vivo retinal imaging techniques, AO-OCT suffers the effects of involuntary eye movements that occur in all three dimensions and under normal fixation. The resulting image blur and distortion diminish the visibility of retinal structures, especially those at the cellular level, and create real challenges for both laboratory and clinic use. Several approaches to mitigate these effects have been investigated for AO-OCT, in many cases parallel to their development with standard OCT. Principal ones are briefly summarized.

The simplest approach to reduce eye motion artifacts in AO-OCT is to acquire images fast, as with high-speed line-scan cameras in the detection channel of SD-OCT or high-speed swept sources in SS-OCT. Limiting the number of necessary data samples per volume is also beneficial. But neither higher speeds nor smaller volumes eliminate them. In addition, higher speeds require more light to achieve the same SNR and a hard limit exists to the amount of light that can safely

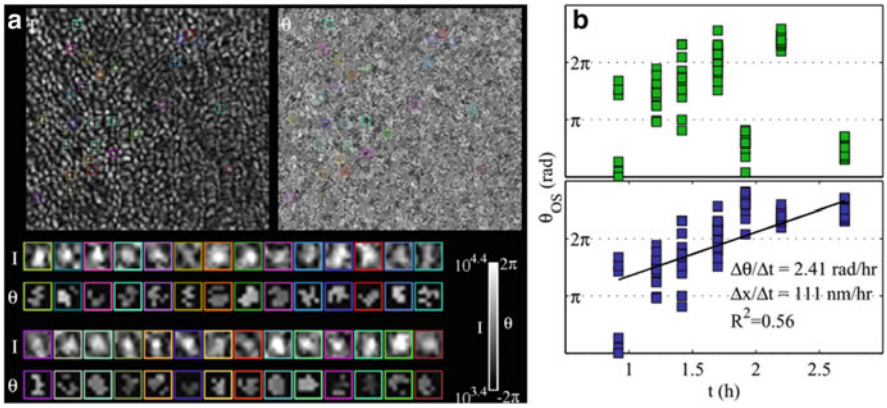

Fig. 61.32 (**a**) Tracking intensity and phase of individual cones over time. (*Upper left*) An *en face* projection of the cone mosaic of a normal subject is shown, constructed by co-adding intensities of IS/OS and PTOS pixels for each A-scan in the volume. *Colored boxes* designate locations of example cones, as they are tracked through the time series. (*Upper right*) An *en face* projection of θ_{OS}, phase difference between IS/OS and PTOS reflections. *Colored boxes* designate locations of the same example cones shown in the intensity projection. Roughly circular patches of correlated phase are visible in the phase projection. (*Bottom*) Views of the example cones shown in the *en face* intensity and phase projections. In each row of box pairs, the top box shows an enlarged view of the intensity projection and the bottom box shows an enlarged view of the phase projection, as indicated by the I and θ symbols at the *left*. In the phase projections, excluded pixels are not shown; correlation among included pixels is visually apparent. In the enlarged phase projections, many cones do not appear circular. The reasons for this are, presumably, eye motion, which often warps the image of the cone, and segmentation errors, which may cause spurious exclusion of A-scans, leading to shape irregularities and discontinuities (**b**) Representative phase changes in a single cone. The temporally wrapped data are shown in the top plot (*green markers*) and temporally unwrapped data shown in the bottom plot (*blue markers*). Linear fit of the unwrapped data reveals an OS elongation of this cone to be 111 nm/h (Reproduced with permission from OSA, Ref. [123])

enter the eye. Thus highly reflecting retinal structures like photoreceptors, RPE, and retinal nerve fiber bundles are the most suitable targets for fast image acquisition systems. Given these constraints, further improvement in motion correction must be found elsewhere.

One area is post-processing. Early attempts (see example in Fig. 61.33) treated each fast B-scan as a rigid body that could be translated in depth and laterally along adjacent B-scans [21, 26]. Due to lack of information along the slow scanning axis, motion artifacts in that dimension could not be corrected. Zawadzki et al. [80] described strategies to optimize this rigid body method for AO-OCT retina volumes.

To remove motion artifacts in both lateral dimensions – a necessity for tracking individual cells over time, for example, cones – required more sophisticated algorithms. Kocaoglu et al. [124] reported a feature-based registration algorithm that split the *en face* projection into strips and then scaled and sheared each strip based on the location of landmark cones. Using this algorithm on acquired movies of cone photoreceptors, motion artifacts were reduced by more than an order of

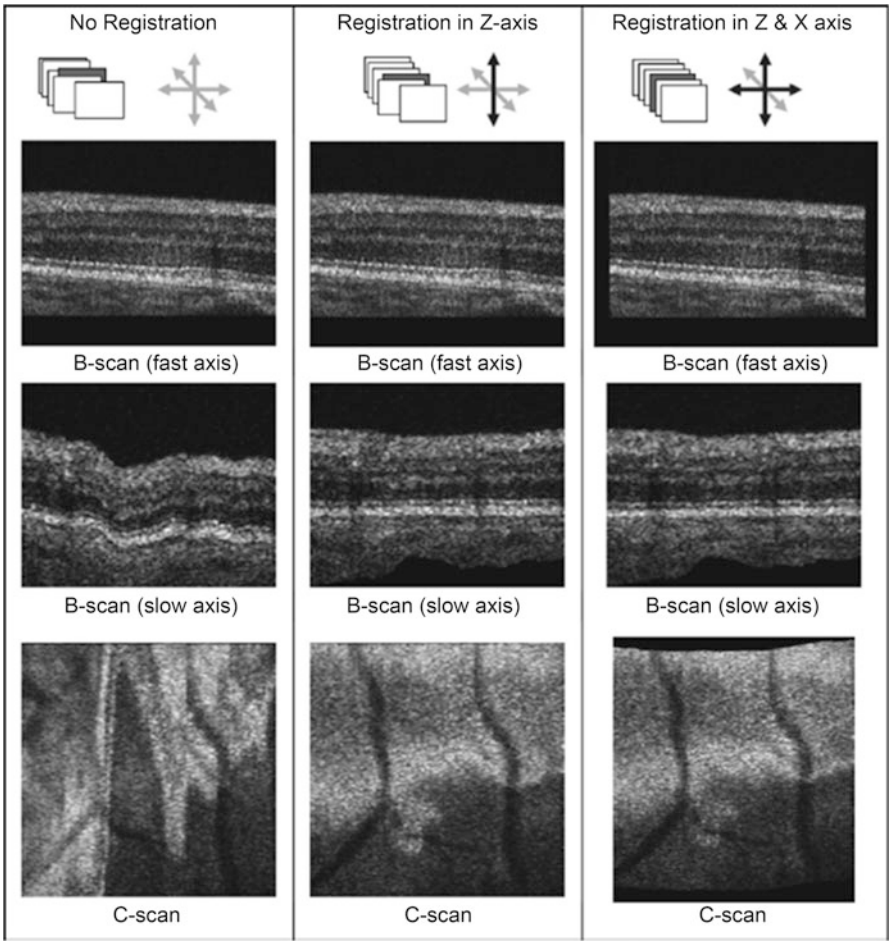

Fig. 61.33 AO-OCT B-scans before and after motion correction with a rigid-body, self-registration algorithm. Different degrees of registration (none, Z-axis, Z and X axis) are shown, their impact illustrated for a representative fast-axis B-scan (*top*), slow-axis B-scan (*middle*), and C-scan (*bottom*). Registered and unregistered axes are denoted by *black* and *gray arrows*, respectively (Reproduced with permission from OSA, Ref. [80])

magnitude, from 15 to 1.3 μm root mean square, the latter sufficient for identifying and tracking cones. More recently, Jonnal et al. [123] developed an algorithm that cross-correlated narrow strips (approximately the width of a single cone) with a reference image to determine local shifts. By combining with axial registration of A-scans, they were able to track individual cone OSs in all three dimensions.

Improvements in motion correction can also be gained with additional hardware, for example, the addition of a separate imaging system dedicated to retina tracking. Multimodal AO-SLO/AO-OCT systems have been developed where fast AO-SLO

frames are acquired simultaneously with OCT B-scans. Tracking algorithms applied to the AO-SLO frames extract retina positions that are used to register AO-OCT B-scans in the volume. First reports of applying this combined AO-SLO/AO-OCT approach have been recently demonstrated [117]. An alternative hardware approach is active tracking [125]. While more hardware intensive, it is attractive as it can compensate for eye motion larger than the imaging field of view and permit repeated imaging of the same patch of retina, both generally not correctable by post-processing.

61.7 Applications of AO-OCT

AO-OCT has been applied to a broad range of scientific and clinical studies of the ocular fundus. Much of the motivation behind these studies has been to determine exactly what can be visualized and what new information can be obtained with AO-OCT, whether in a normal or diseased eye. While much of this work is in the early stages, results to date are encouraging, demonstrating the potential of AO-OCT to study noninvasively retinal structure and function in ways previously not possible. Below we present a brief survey of these main application areas as reported in the literature, categorized by scientific and clinical directions. It should be noted that widespread use of AO-OCT remains a work in progress, largely limited by the complexity and customization of current systems and the need for skilled system operators. As these obstacles fall, AO-OCT will become a more integral, and perhaps indispensable, imaging tool for the scientific and clinical communities.

61.7.1 AO-OCT in Vision Science

Vision is a complex process. While the retina is only one of many components involved, its role is critical, capturing and transducing photons into an electrical signal and providing the first steps of signal processing. Normal vision requires normal function of the retina, and thus the retina has significant scientific interest. Imaging methods that use light to probe, noninvasively, structure and function of the retina have proven highly effective, but proper interpretation of the detected return requires understanding of how light interacts with retinal tissue, that is, the optical properties of the retina. It is in this context that AO-OCT may make its most important contributions to vision science, improving our understanding of cellular-level light-tissue interactions that occur at each layer in the retina and their correlate with cell anatomy and physiology.

61.7.1.1 Optical Biopsy: (Living Histology)

AO-OCT systems have been used to capture volume images of retinal structures that were previously only visible with histology. Of course the lateral resolution of

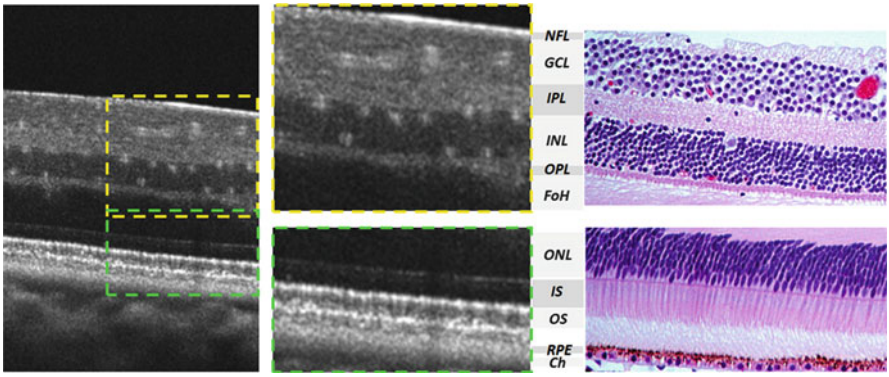

Fig. 61.34 AO-OCT B-scan of the retina compared to histology from light microscopy at a similar retinal location

AO-OCT is ultimately limited by the numerical aperture of the eye, which is notably less than that of light microscopy. But a more important distinction between the two methods is the source of image contrast. Contrast in AO-OCT is the differences in the intensity of backscattered light, which originate from differences in the intrinsic refractive indices of the tissue. For histology, contrast has no refractive index origin. Instead, it is created artificially by impregnating the tissue sample with pigments and fluorescent molecules that are designed to highlight specific organelles and molecules. Thus the two methods produce highly different images of the same tissue (see, for example, Fig. 61.34), and this makes comparison of the two exceedingly difficult.

Figure 61.35 provides an example of the types of retinal microstructures that can be visualized within a given volume of retinal tissue imaged with AO-OCT. The AO-OCT volume is a composite made by re-imaging the same retinal patch, with focus systematically shifted to different depths, in this way preserving the high image quality provided by AO for the retinal layer of interest. Extracted *en face* slices (from top to bottom) are shown of individual RNFBs, microstructures in the ganglion cell layer, retinal capillaries, and outer segments of cone photoreceptors.

The next sections present several scientific examples that have been reported in the literature and make use of AO-OCT for studying targeted layers in the retina. Examples include the photoreceptor mosaic, retinal and choroidal microvasculature, retinal nerve fiber bundles, RPE, Bruchs membrane, and the optic nerve head.

61.7.1.2 Photoreceptor Morphology and Function

Cone photoreceptors have been imaged with a variety of AO-OCT [21, 80] and UHR-AO-OCT configurations [25, 26, 94, 124]. Early studies revealed the reflectance bands observed at the IS/OS junction, and the posterior tips of the OS in standard OCT were actually composed of a regular distribution of punctated

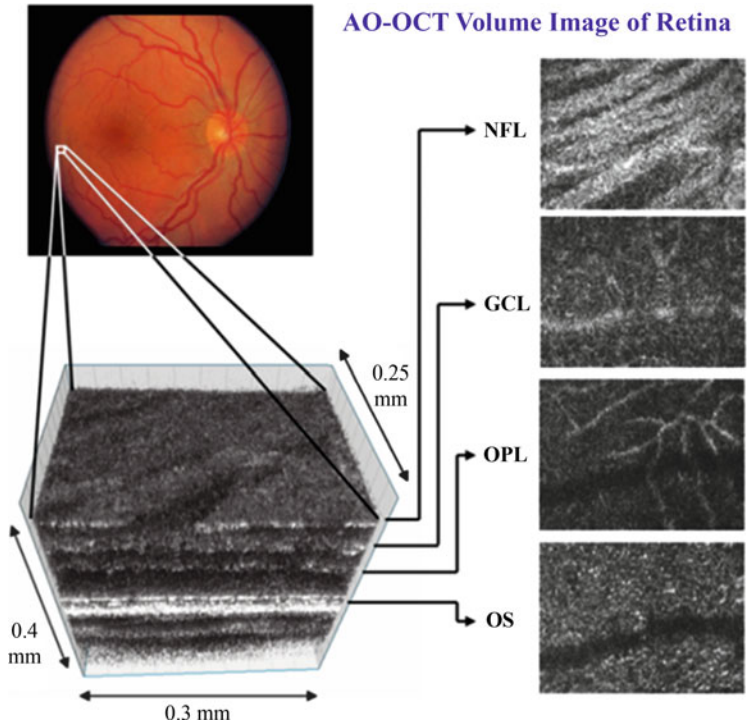

Fig. 61.35 AO-OCT volume of retinal structures acquired over 0.25 × 0.3 mm^2 area at 10° TR eccentricity on a healthy, 32-year-old volunteer. Numerous microscopic structures can be seen in C-scans sectioned at different depths in the volume (*right*). Key: *GCL* ganglion cell layer, *NFL* retinal nerve fiber layer, *OPL* outer plexiform layer, *OS* cone photoreceptor outer segments (Reprinted with permission from SPIE, Ref. [126])

reflections, each originating from a single cone cell. AO-OCT studies further revealed that these punctated reflections were highly correlated between the IS/OS and posterior tip layers, and their spacing was consistent with expected cone spacing. Collectively, these observations give substantive evidence that these reflectance bands occur inside cones and on opposite ends of the cones' outer segments.

More detailed and exhaustive studies of the 3D structure of cones, however, have been slowed by eye motion artifacts that prevent tracking of individual cones across frames of AO-OCT videos. This bottleneck was recently addressed using high-speed image acquisition (up to 200 KHz) to reduce the deleterious effects of eye motion on volumetric images and a novel post-processing registration/dewarping method to further reduce eye motion effects [124]. The combination of the two reduced eye motion to less than a fraction of a cone width. With this level of motion compensation, individual cones were tracked over periods as long

as 10 days. This time duration is more than adequate for studying the physiological processes of disk renewal and phagocytosis at the individual cone level, processes that are known to be disrupted by retinal disease such as age-related macular degeneration (ARMD) and retinitis pigmentosa (RP).

Indeed using post-processing registration and high-speed imaging in conjunction with phase-sensitive AO-OCT (Sect. 61.6.3), sub-resolution changes in the cone outer segment were measured in hundreds of cones over matters of hours. Across all cones, the OS was found to elongate at rates of about 150 nm/h, which is consistent with earlier reports in which renewal was inferred from histology [127, 128] as well as in previous in vivo findings by the same authors using an AO flood-illumination system [129].

In a separate cone length analysis using only intensity of the backscatter, AO-UHR-OCT was shown to be sufficiently sensitive to measure real length differences between individual cones in the same retinal patch and required no more than five measurements of OS length to achieve 95 % confidence. We know of no other imaging modality that can monitor foveal or parafoveal cones over time with comparable resolution in all three dimensions.

With AO-OCT, cones have been resolved as close as 0.25° from the fovea (the most critical area of patient vision), which is the densest packing of cones observed to date with OCT methods. Figure 61.36 shows representative *en face* and cross-sectional views of individual cones acquired with two different high-speed UHR-AO-OCT systems. Note the level of cone detail at the different retinal eccentricities and in both views, for example, the decrease in cone outer-segment length with retinal eccentricity.

61.7.1.3 Retinal and Choroidal Vasculature

AO-OCT systems have proven highly effective at sectioning the various capillary beds of the retina and distinguishing individual capillaries, all based on direct intensity imaging. Numerous reports of such imaging can be found in the AO-OCT literature. Sectioning of the AO-OCT volume at the IPL/INL and OPL/INL layers (with system focus at the same layer) generally provides well-defined networks of capillaries. Figures 61.37 and 61.38 show examples of capillary imaging in two different AO-OCT studies [95, 131]. The first illustrates the extent of the capillary beds by montaging many AO-OCT volumes. The second study investigated the capability of AO-OCT to image the tiny capillaries proximal to the foveal avascular zone. Capillary diameter measurements were found consistent with histology reported in the literature (average, 4.7 μm compared to 5.1 μm) and furthermore supported the view that the vast majority of capillaries in the retina are likely detectable with UHR-AO-OCT, based solely on direct intensity imaging.

To date AO-OCT vascular imaging has been mainly directed at direct intensity imaging of the tiniest of vessels in the retina, for good reason as the benefit of AO is most pronounced for the smallest vessels. However, OCT itself has undergone major development to enhance vessel contrast and quantify flow, the former with flow-contrasting OCT methods and the latter with Doppler OCT [132]; both

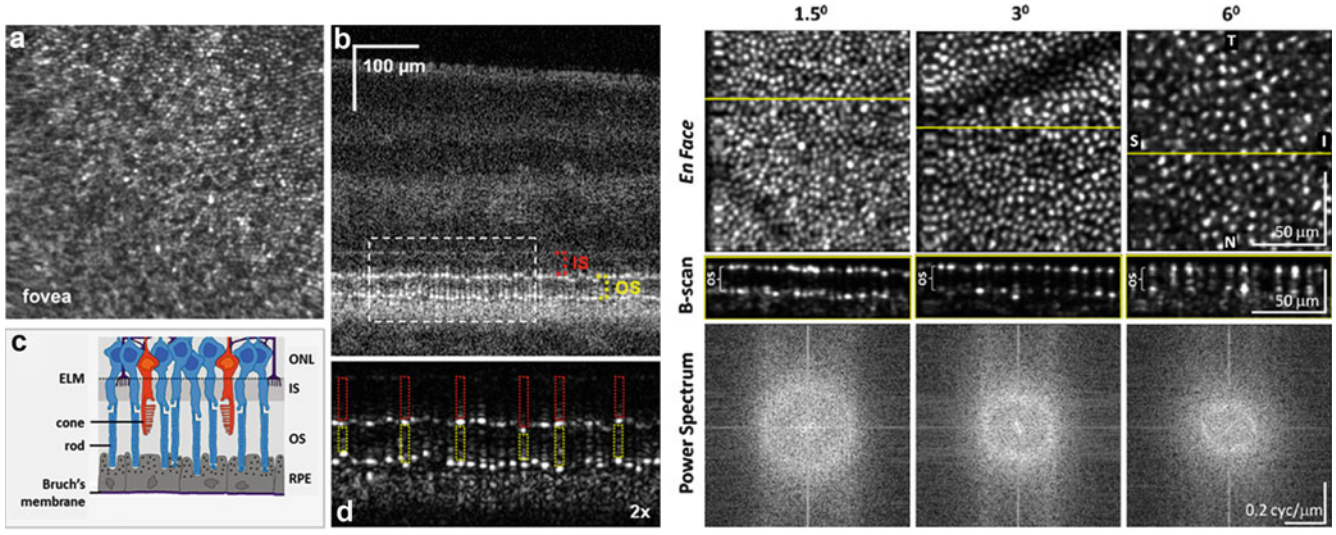

Fig. 61.36 *Left*: Comparison of photoreceptor mosaic imaged with different modalities. (**a**) AO-SLO imaging (linear intensity scale) [130]; (**b**) AO-OCT imaging (logarithmic intensity scale); (**c**) simplified schematic of the cellular structures in outer retina layers; and (**d**) twofold enlargement of the photoreceptor layers (linear intensity scale) from the AO-OCT image (*panel b*). *Dashed red rectangles* show examples of cone photoreceptors ISs. *Dashed yellow rectangles* show examples of cone photoreceptors OSs (Results reproduced with permission from OSA, Ref. [25]). *Right*: (*top row*) AO-OCT cone photoreceptor images of one subject at 1.5°, 3°, and 6° temporal to the fovea. (*middle row*) Cross-sectional images (fast B-scans) of the PL-RPE complex are shown for the same three retinal eccentricities with location indicated by the *yellow lines* on the *en face* images. (*bottom row*) Power spectra were computed from the corresponding *en face* images. Rings of concentrated power and centered on zero spatial frequency are visible and denote the fundamental cone spacing (Results reproduced with permission from OSA, Ref. [124]). Key: *ELM* external limiting membrane, *IS* photoreceptor inner segment, *ONL* outer nuclear layer, *OS* photoreceptor outer segment, *PL* photoreceptor layer, *RPE* retinal pigment epithelium. *N*, *T*, *S*, and *I* denote nasal, temporal, superior, and inferior directions at the retina

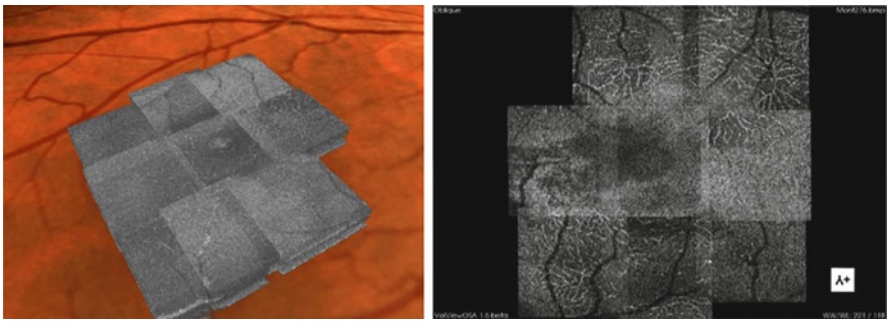

Fig. 61.37 Visualization of the large FOV AO-OCT volume *Left*, view of the volume with co-registered fundus photo *Right*, screenshot from OSA ISP with the slicing plane view of the large FOV AO-OCT volume Note the clear visualization of microcapillaries and foveal avascular zone when altering the location of the slicing plane (Results reproduced with permission from OSA. Ref. [95])

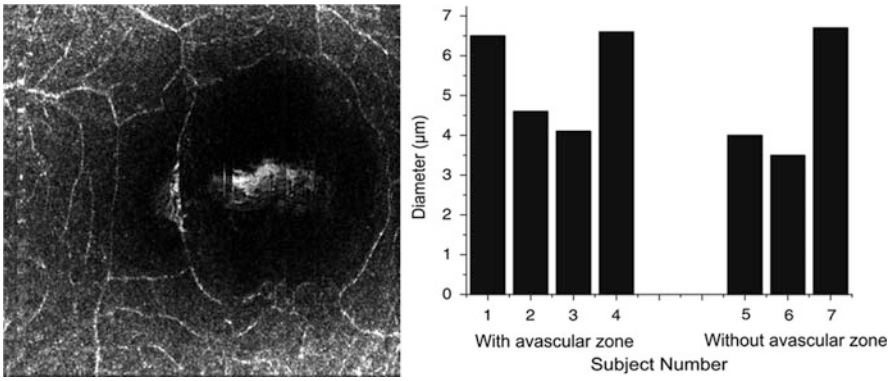

Fig. 61.38 UHR-AO-OCT imaging of the retinal capillaries proximal to the foveal avascular zone. (*left*) *En face* projection (3° × 3°) through the multi-laminar networks of capillaries that define the foveal avascular zone is shown in a normal subject. A well-defined foveal avascular zone is evident. System focus was optimized for vessel clarity. Central bright spot is a residual of the fovea reflex that was not completely removed in post-processing when the capillary subregion was extracted (Results reproduced with permission from *Eye (London, England)*. Ref. [27]). (*right*) Average diameter of retinal capillaries in subjects with and without a foveal avascular zone (*FAZ*). Measurements were taken at the FAZ edge (with) and across fovea (without). The average and SD across all seven subjects is 5.1 ± 1.4 μm, which is consistent with histology (average, ~4.7 μm) (Results reproduced with permission from ARVO. Ref. [131])

methods are described in detail in other chapters. These methods rely on sensing phase or intensity variations created by blood flow and have proven effective for monitoring total retinal blood flow [133] as well as mapping the extensive retinal and choroidal vasculature [134–139]. Both are likely to take on significant roles in

clinical diagnosis. While the integration of AO in either remains largely unexplored, the increased lateral resolution and sensitivity of AO are fundamental and may ultimately improve performance of these methods beyond that of their current form.

61.7.1.4 Retinal Nerve Fiber Layer

AO-OCT imaging represents a potential means to measure cross-sectional RNFB dimensions owing to its micron-level 3D resolution. There have been several observational reports showing the 3D profile of RNFBs in subjects using AO-OCT [25, 83, 94]. Although these early observations are highly encouraging, they were limited to single images acquired on single subjects with no measurements of the RNFB cross section.

More recently, AO-OCT was used to measure the dimensions of RNFBs in five subjects (29–62 years of age; four clinically normal) at the same retinal eccentricities using the same system. Details of the study can be found in Kocaoglu et al. [89]. Taken from this study, Fig. 61.39 (left) plots the average width and thickness of the RNFBs, revealing bundles at the more central location are flatter in cross section, but of similar width. Bundle clarity (individuation) in both cross section and *en face* views was found to vary with subject and retinal location. Interestingly, the overriding determination of bundle clarity was size of the gap between adjacent bundles rather than the size of the bundles themselves. Spacing between adjacent bundles was on the order of a few microns compared to the size of bundles that was on the order of tens of microns. Bundle contrast was also critical for identifying bundles. The reflectance of RNFB tissue was found to be two times brighter (3 dB) than that of the Müller cells that surround the bundles (gaps). This difference provided sufficient contrast to distinguish bundle from gap when resolution allowed.

Repeated imaging of the same bundles over months and years is critical in longitudinal studies, and for detecting and monitoring, for example, slow RNFB changes that occur with progression of disease such as glaucoma. Kocaoglu et al. demonstrated the efficacy of imaging the same bundles 7 months apart, finding width and thickness RNFB measurements at the two time points to be strongly correlated, $p < 0.0005$ (see Fig. 61.39 (right)). In general, results of this study and that of earlier ones suggest that UHR-AO-OCT is capable of measuring the cross-sectional profile of individual bundles even at locations where bundles are increasingly thin (<15 μm) and the same bundles at multiple time points.

61.7.1.5 Retinal Pigment Epitelium, Bruchs Membrane, Choriocapillaris

The RPE is the pigmented cell layer just outside the neurosensory retina that nourishes retinal photoreceptors and is firmly attached to the underlying Bruchs membrane that overlies the choriocapillaris. The RPE is composed of a monolayer of hexagonal cells (RPE cells). The retinal pigment epithelium transports metabolic waste from the photoreceptors across Bruch's membrane to the choroid. Choriocapillaris is a thin layer of the choroid adjacent to Bruch's membrane and consisting

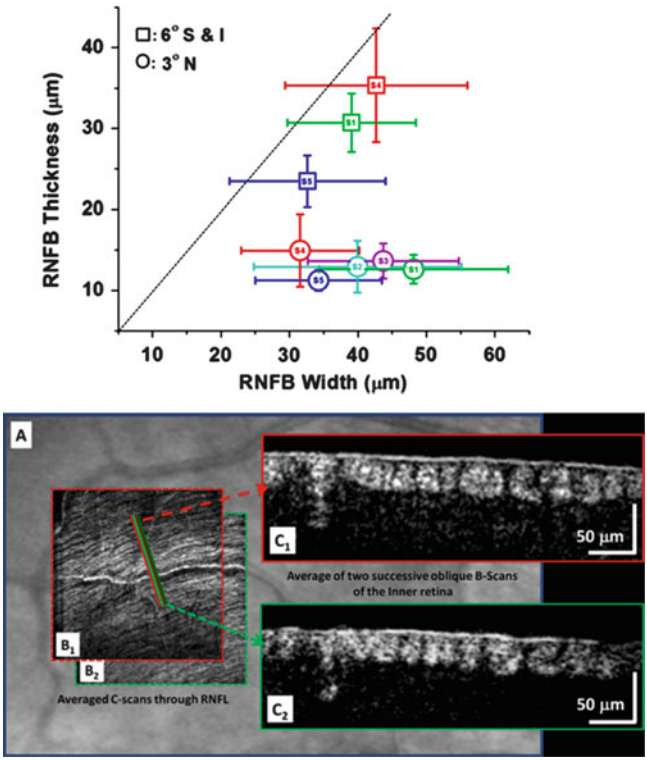

Fig. 61.39 (*left*): Average width and thickness of RNFBs measured at 3° nasal (*N*) and 6° superior (*S*) and inferior (*I*) retinal eccentricities for five subjects. Error bars represent the distribution of RNFB sizes measured at each retinal eccentricity. For reference, the *dashed line* denotes a perfectly circular bundle (width = thickness). (*right*): UHR-AO-OCT images acquired 7 months apart on the same subject. (**a**) Wide-field SLO image facilitated registration of the projected C-scans. (*B1* and *B2*) C-scans averaged through the RNFL reveal the diagonal striation pattern of RNFBs and the presence of retinal vasculature. *Solid lines* denote the first imaging session, *dashed lines* the second. (*C1* and *C2*) Averaged (2), oblique B-scans of the same retinal location (Reproduced with permission from Elsevier, Ref. [89])

of a network of capillaries which supplies nutrients to the retina. These three structures play pivotal role in health of the photoreceptors and the retina placing it in the center of aging and retinal degenerations studies. Therefore, detailed visualization of this complex is very important both in clinical and research settings. Figure 61.40 shows example AO-OCT volumetric visualization of photoreceptor-RPE-choriocapillaris complex [94].

Beside visualization of volumetric cellular morphology of photoreceptor/RPE/choriocapillaris complex, simple averaged AO-OCT B-scans also proved to be helpful in studying these key retinal structures offering details surpassing those available by UHR OCT. Figure 61.41 shows an example of two averaged B-scans

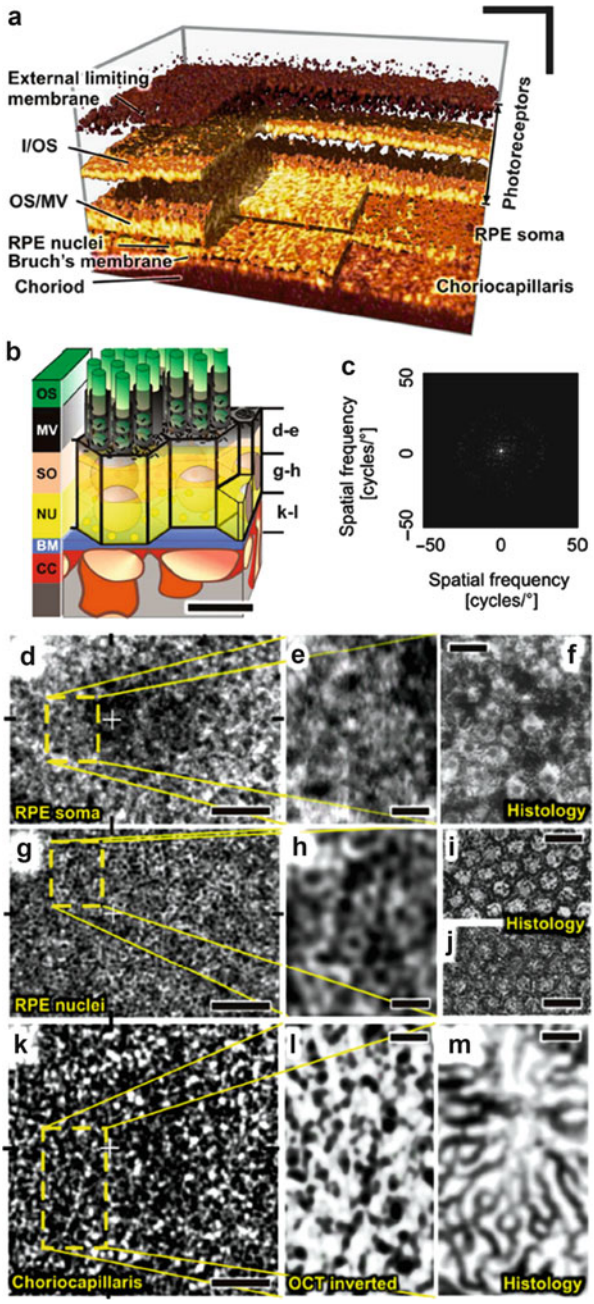

Fig. 61.40 Visualization of foveal retinal pigment epithelium (*RPE*) cells and choriocapillaris. (**a**) 3D rendered OCT volume of a 28-year-old normal male Caucasian retina at the fovea after filtering with ATF. (**b**) Schematic of RPE cell. *OS* outer segments, *MV* microvilli, *SO* inner portion

of outer retina acquired at two retinal eccentricities: fovea and 6° temporal retina (TR) [140]. Such a detailed view of the photoreceptor and RPE bands should allow new studies of these structures.

61.7.1.6 Optic Nerve Head

The optic nerve head (ONH) is part of the fundus where ganglion cell axons exit the eye to form the optic nerve. The optic nerve head is also the entry point for the major blood vessels that supply the retina. Given the importance of the ONH for vision and its susceptibility to disease, most notably glaucoma, the ability to visualize and detect minute changes at the microscopic level in the ONH carry considerable scientific and clinical interest. Figure 61.42 shows examples by two different groups in which AO-OCT was used to image microscopic structures in the ONH [94, 95]. Both studies revealed minute details in the pores formed by the collagenous fibers of the lamina cribrosa, a mesh-like structure which allows nerve fibers and vessels of the optic nerve to pass through the sclera.

However, it is important to mention that AO-enhanced imaging of the ONH is not trivial due to highly scattering and axially extended ONH structures making it difficult to extract reliable wavefront sensor data. Therefore, special attention has to be paid during imaging to AO control to ensure its correct operation. Previously mentioned wavefront sensorless approaches [86] might become a viable alternative in ONH imaging. Additionally, DaeYu et al. have published recently work on extending axial depth range of AO-OCT system by removing complex conjugate artifact in AO-FD-OCT and applying it to ONH imaging [142]. This method allows positioning of the imaged ONH structure near the zero path length difference, where sensitivity of the system is the highest, without possibility of generating mirror complex conjugate artifacts by eye motion or ONH structures extending axially. This feature might be important in future more-automated clinical screening of ONH by AO-OCT.

Fig. 61.40 (continued) of RPE soma, *NU* nuclear (basal) portion of RPE soma, *BM* Bruch's membrane, *CC* choriocapillaris. Also indicated are the levels corresponding to panels (**c–d**, **f–g,** and **j–k**). (**c**) 2D power spectrum of the RPE cell mosaic obtained by averaging of 15 *en face* slices followed by filtering of the resulting power spectrum with BPF4–500. (**d**) Sectioned image at the level of the RPE soma (average of 15 *en face* sections filtered with ATF). At this depth, signal-producing elements are mainly melanin granules inferior to the inner portion of the RPE cell, also magnified in (**e**). (**f**) Histological section from a normal human fovea for comparison. (**g**) Basal RPE exposing structure of the RPE cell mosaic at the level of the cell nuclei (average of 14 *en face* sections the filtered with BPF4–500). (**h**) Enlarged portion of **g** with *yellow circles* enclosing seven hexagonally arranged clusters of RPE cells. (**i–j**) Light micrographs of tangentially sectioned tissue showing an *en face* view of human RPE cells from an 18- and 42-year-old Caucasian male, respectively. (**k**) Sectioned image at the level of the choriocapillaris (averaging of five *en face* sections filtered with ATF). The emerging, structure possibly corresponds to microvessels. (**l**) Inverted and enlarged selected portion of **k**. (**m**) Histology of a human choriocapillaris in alkaline phosphatase preparation. Scale bars: 100 μm for **a**, **d**, **g**, **k**; 20 μm for **e–f**, **h–j**, **l–m** 10 μm for **b**. *White* cross hairs in **d**, **g,** and **k** denote the foveal center (Reproduced with permission from OSA, Ref. [94])

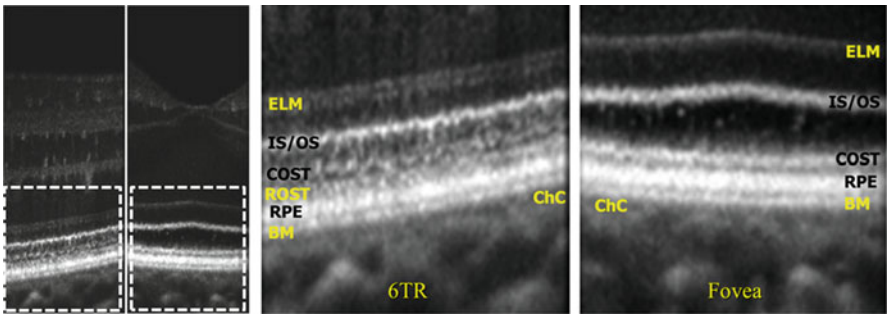

Fig. 61.41 Visualization of outer retina by AO-OCT system. Four outer retinal bands seen on commercial OCT systems can be attributed to the external limiting membrane (*ELM*), the boundary between the inner and outer segments (*IS*/*OS*), end tips of cone photoreceptor outer segments (*COST*), and the retinal pigment epithelium (*RPE*). Additional layers including possible doubling of external limiting membrane (*ELM*), end tips of rod photoreceptor outer segments (*ROST*), Bruch's membrane (*BM*), and choriocapillaris (*CC*) are not visible with current commercial OCT instruments (Reproduced with permission from ISIE/ARVO, Ref. [140])

61.7.2 Clinical Imaging with AO-OCT

This section summarizes key studies that employed AO-OCT to image retinal disease. The clinical potential of AO-OCT lies in its ability to not only diagnose disease early in the process but also improve the monitoring of disease progression and the treatment of disease. It is commonly accepted that minute structural and physiological changes in the disease process precede changes in visual function (visual acuity; contrast sensitivity), often the clinical standard for assessing patient vision. The strategy with AO-OCT then is to capitalize on its micron-scale 3D resolution and high sensitivity to detect these subtle changes. While this direction for AO-OCT is in its infancy, the examples presented here illustrate the potential clinical utility of this imaging technology. Examples include age-related macular degeneration, glaucoma, RNFL defect, retinopathy of prematurity as well as imaging of patients with clinically unexplained vision loss, and color blindness phenotyping.

61.7.2.1 Age-Related Macular Degeneration

ARMD is a leading cause of vision loss among people 50 years of age and older. In its most common form, it gradually destroys the outer retina (photoreceptors, RPE, Bruch's membrane) of the macula, the part that provides sharp vision. Much of the research to date with AO-OCT has focused on this same area, in particular photoreceptors, but in normal healthy eyes. This makes for a natural extension to diseased eyes whose outer retina is affected, for example, with ARMD. Figure 61.43 shows one example, a clinical evaluation of a patient with late-state

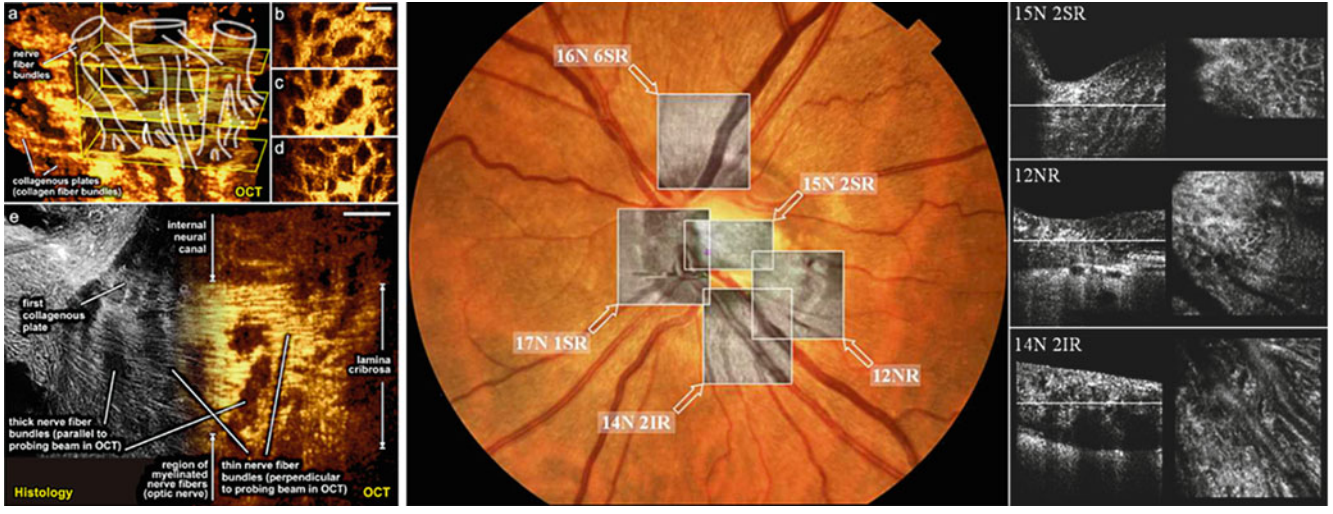

Fig. 61.42 (*left*): Pores and collagenous fibers of the lamina cribrosa (*LC*). **a** 3D rendered volume of the LC (filtered with ATF). **b–d** Single *en face* sections (filtered with ATF) denoted by *yellow rectangles* in **a. e** Lateral section of the LC (*left*) as seen by histology of a human LC (selected portion of Fig. 1 from Kotecha et al. [141]) for comparison with OCT (*right*), obtained after averaging five fast-scan-axis tomograms filtered with ATF. Collagen fiber bundles oriented orthogonal to the probing beam appear bright (Reproduced with permission from OSA, Ref: [94]). (*right*): Visualization of the ONH microscopic structures imaged with AO-OCT. *Left*: screenshot from volume renderer after co-registration of five 3D AO-OCT datasets with fundus photo. *Right*, three AO-OCT volumes shown on the *left*: 15N 2SR (), 12NR, and 14N 2IR *White lines* on the B-scans correspond to the depth of the C-scans reconstructed from the same volume. Multiple microscopic structures including lamina cribrosa and blood vessels are easily recognizable (Reproduced with permission from OSA, Ref. [95])

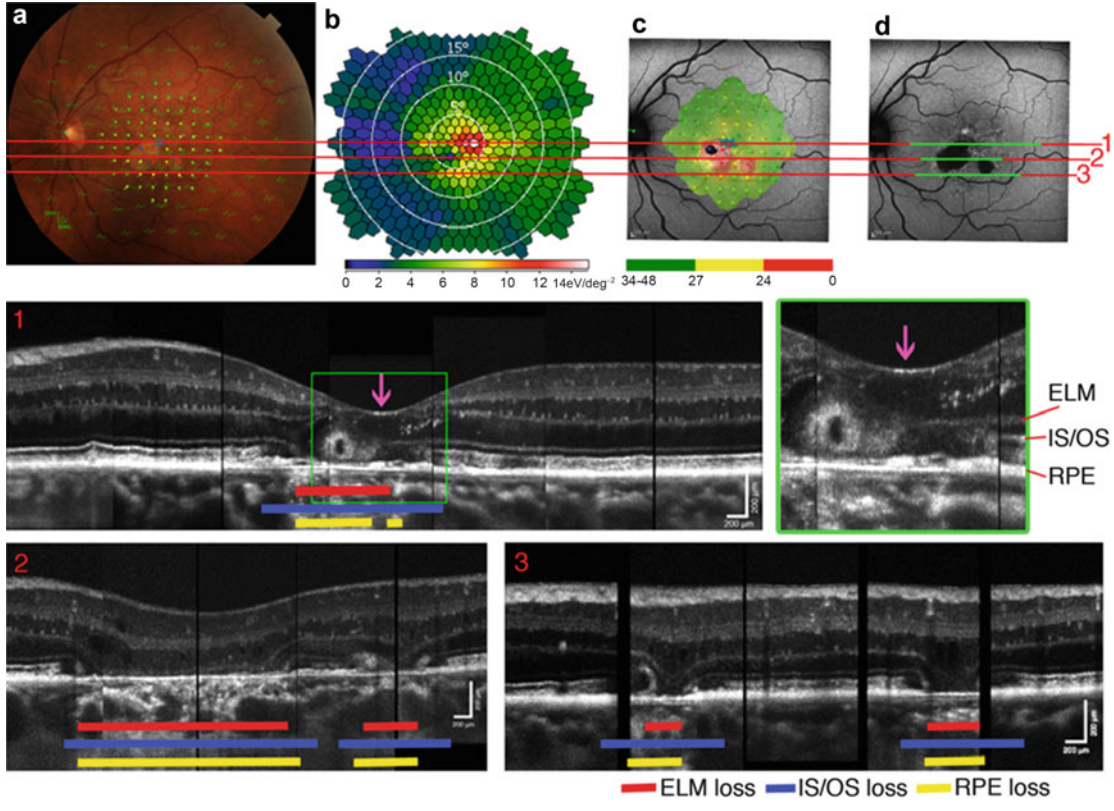

Fig. 61.43 Diagnostic and AO-OCT results from patient with ARMD Geographic Atrophy. *Panel a* is the color fundus photograph (*CF*) with the multifocal electroretinogram (*mfERG*) traces and micro perimetry (*mP*) sensitivity superimposed. *Panel b* shows the mfERG response density map; panel **c** shows the mP

ARMD geographic atrophy (GA) [143]. To help interpret the AO-OCT images, several standard clinical tests (see figure caption) were also collected on the same eye and are shown in the figure.

61.7.2.2 Retinitis Pigmentosa

Retinitis pigmentosa (RP) is an inherited, degenerative eye disease that causes severe vision impairment and often blindness. RP is caused by abnormalities of the photoreceptors (rods and cones) that result in photoreceptor loss accompanied by changes in the RPE. Recent AO-OCT study of RP patient by Považay et al. [144] revealed atrophy in the photoreceptor layer with "drusen-like" appearances especially in the foveal center and significant reduction of cone densities. Results from that study are shown in Fig. 61.44.

61.7.2.3 Glaucomatous and Non-glaucomatous Optic Neuropathies

Optic neuropathy refers to a host of eye diseases that damage the optic nerve. Glaucoma, the most common form of optic neuropathy, can cause excavation of the optic disk along with characteristic loss of visual field due to ganglion cell death. Despite glaucoma being characterized as a disease of the optic disk and inner retina, a detailed look at the outer retina with AO-OCT in a recent study of glaucomatous and non-glaucomatous optical neuropathy patients suggested otherwise [145, 146]. Specifically, AO-based systems including AO-OCT revealed changes in the photoreceptor layer that accompanied the optic neuropathy [147]. Results from that study are shown in Fig. 61.45.

61.7.2.4 RNFL Defect

Early detection of axonal tissue loss is critical for managing diseases that destroy the RNFL such as glaucoma. Axonal tissue loss in the RNFL has been reported to be one of the earliest detectable glaucomatous changes, preceding morphologic changes in optic nerve head and visual field loss [148, 149]. Fundus photography, scanning laser polarimetry, scanning laser ophthalmoscopy, and optical coherence tomography have been used to analyze RNFL loss in glaucomatous eyes [150–153]. Regardless of method, however, none have the necessary lateral and axial resolution to image the cross-sectional profile of individual RNFBs as they traverse the retinal surface. In contrast, AO-OCT has been demonstrated to measure both thickness and width variations of individual RNFBs (see Sect. 61.7.1.4) and to differentiate RNFBs from the radial fibers of Müller

Fig. 61.43 (continued) sensitivity map superimposed on the Fundus Auto Fluorescence (*FAF*), and *panel d* is the FAF. The *three numbered green lines* in *panel d* correspond to the three B-scan montages shown below. The *magenta arrow* in B-scan 1 shows the PRL. The *red*, *blue*, and *yellow bars* on the B-scans correspond to ELM, IS/OS, and RPE loss, respectively. The magnified B-scan section shows remaining RPE that corresponds to the location of the PRL (Reproduced with permission from ARVO, Ref. [143])

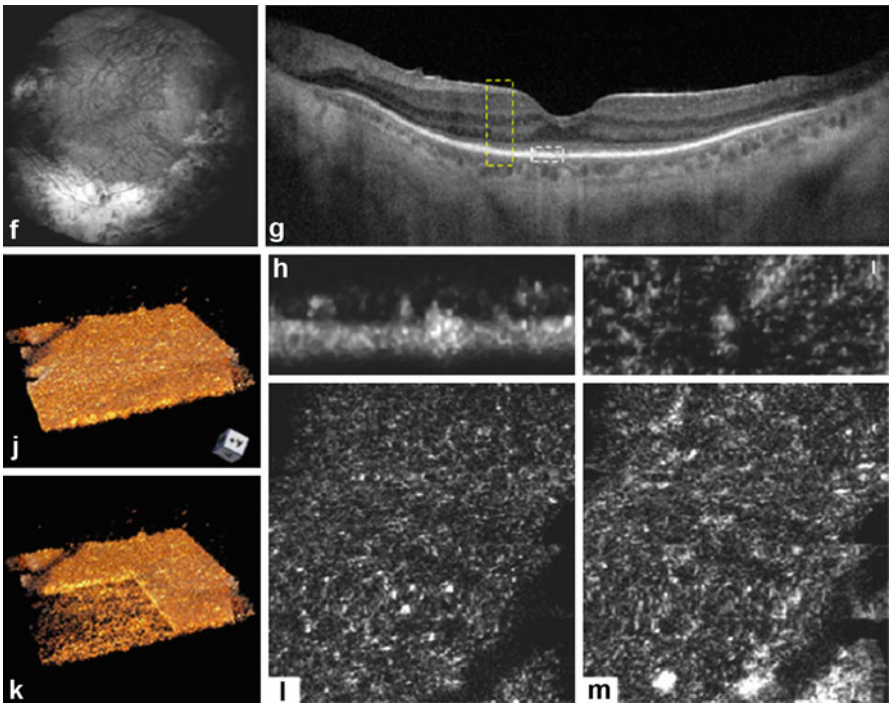

Fig. 61.44 (**f**) *En face* wide field (∼35° × 35°) fundus image of the choroid using 1,060 nm 3D-OCT; (**g**) high definition (2,048 pixel) 1,060 nm 3D-OCT scan over 35°; cellular-resolution retinal imaging using AO OCT: (**h**) cross section and *en face* image (**i**) of s volume at the level of the retinal pigment epithelium; retinal location indicated by *white dashed line* in (**g**); (**j**) volumetric AO OCT at 4° isotropic parafoveal; retinal location indicated by *yellow dashed line* in (**g**); (**k**) volumetric rendering at 4°; (**l**) *en face* images at the level of the inner/outer photoreceptor junction at 6°; (**m**) at the level of the tips of the outer photoreceptors at 6° (**m**) (Reproduced with permission from OSA, Ref. [144])

cells that separate the bundles. This opens the possibility to extend known morphological differences in RNFL thickness between normal, aging, and diseased retinal axonal tissue to morphological differences in RNFB area and volume. While this remains future work, Fig. 61.46 illustrates a rather extreme example, the use of an AO-UHR-OCT system to map an arcuate defect in the RNFL. At the affected location, the area and volume of the individual bundles are clearly reduced almost to the point where the bundles no longer exist [89].

61.7.2.5 Retinopathy of Prematurity

Retinopathy of prematurity (ROP) is a potentially blinding disorder that alters development of the central retina and primarily affects prematurely born babies such as those receiving intensive neonatal care that is thought to be caused by disorganized growth of the retinal vasculature and can lead to complications

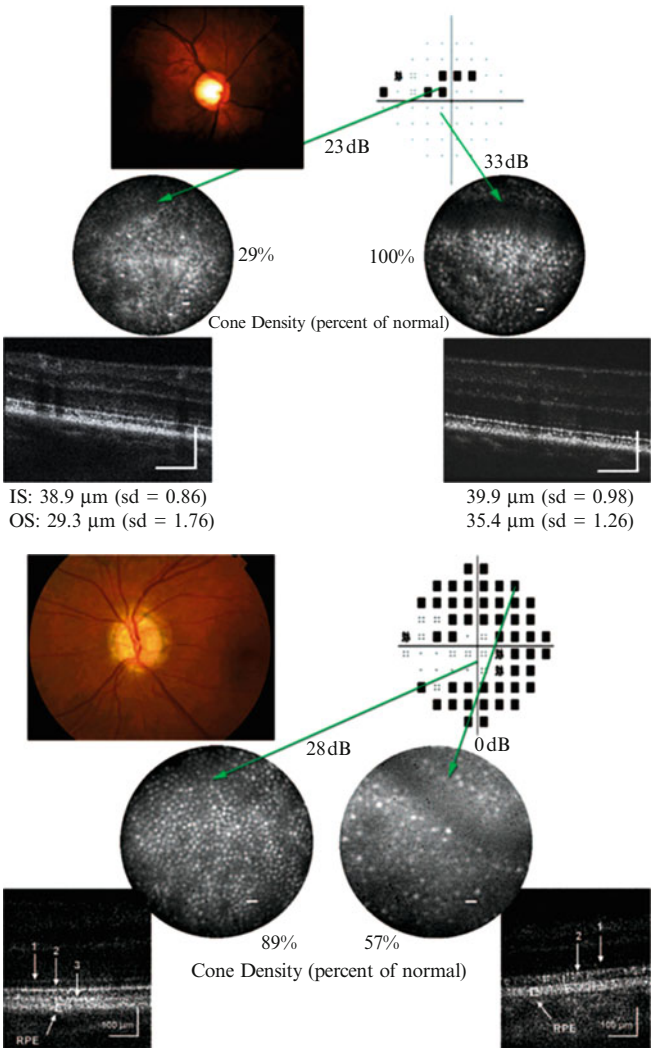

Fig. 61.45 Examination of the (*left*) right and (*right*) left eyes of a 63-year-old patient with primary open-angle glaucoma. For each eye, standard diagnostics included optic disk photography and visual fields (Humphrey Visual Field). Images at select retinal locations were also acquired with AO flood illumination and AO-OCT systems. *Green arrows* show the high-resolution retinal images from areas of higher (*white*/*gray squares*) and lower (*black squares*) visual sensitivity. Below each AO flood image is a corresponding AO-OCT B-scan with focus on the outer retina. Mean length and standard deviation of inner (*IS*) and outer segments (*OS*) are shown below the B-scans. Labels *1*, *2*, and *3* in the AO-OCT images refer to outer limiting membrane, IS/OS junction, and cone photoreceptor outer-segment tips, respectively. Note that the left B-scan (*right eye*) is normal with three visible outer retinal layers and the right (*left eye*) is abnormal with only two visible outer retinal layers. Scale bars for the AO flood illumination and AO-OCT images are 10 and 100 µm, respectively (Reproduced with permission from Nature Publishing Group, Ref. [147])

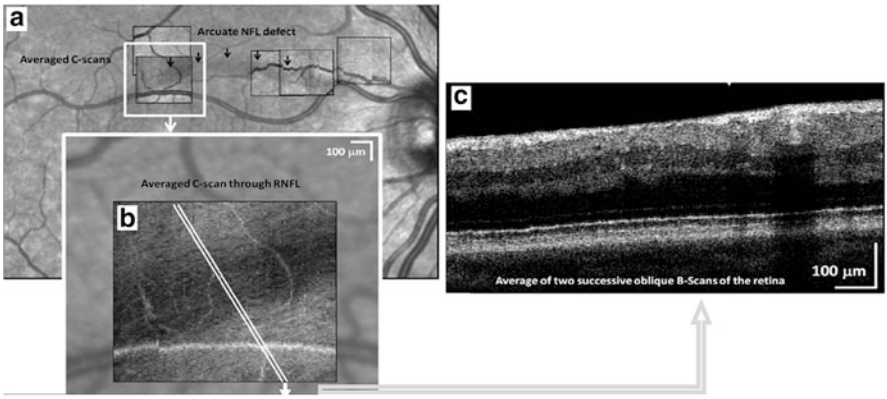

Fig. 61.46 AO-UHR-OCT images of the arcuate RNFL defect in a 62-year-old patient. (**a**) AO-UHR-OCT volumes are laterally registered to the wide-field SLO image using projection C-scans. (**b**) Enlarged view of a C-scan averaged through the RNFL and revealing faint RNFBs traversing diagonally upward from left to right. *Darkened strip* corresponds to the defect area. (**c**) B-scan obtained by averaging two successive oblique B-scans that are approximately perpendicular to the RNFB direction (Reproduced with permission from Elsevier, Ref. [89])

including scarring, retinal detachment, myopia, and amblyopia. While standard clinical methods provide coarse assessment of central retina developments in ROP, the use of AO-OCT in a recent study by Hammer et al. [154] revealed significant differences at the fine structural level, in particular that of the foveal microvasculature. Examples from this study are given in Fig. 61.47, which shows AO-OCT *en face* and cross-sectional views of the fovea of normal and ROP subjects. Absence of a foveal avascular zone is evident in Fig. 61.24 (right: e, g), a hallmark feature of ROP.

61.7.2.6 Unexplained Vision Loss

Unexplained vision loss refers to an apparent visual dysfunction whose cause cannot be determined by standard clinical examination, for example, diagnosis of an abnormality or lesion in the visual pathway. The high sensitivity of AO-OCT to detect subtle changes at the cellular level in retinal tissue offers not only the possibility to localize the source of these changes but also to do so earlier in the process. Figure 61.48 shows two cases where AO-OCT revealed subclinical changes in the foveal morphology [25]. These changes were highly localized to where vision was reduced suggesting the two originate from the same retinal abnormality.

61.7.2.7 Macular Telangiectasia

Idiopathic Juxtafoveal Macular Telangiectasia (MacTel) is a blinding condition of the retina caused by pathologically dilated blood vessels (telangiectasia) near the fovea. Disease progression involves scarring of the retina and accumulation

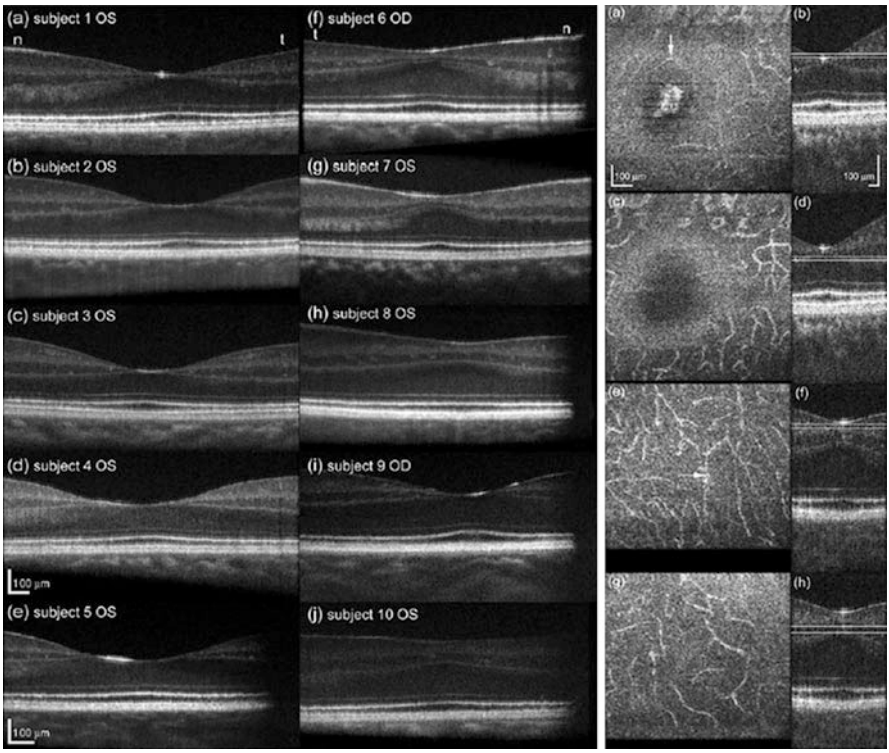

Fig. 61.47 Comparison of fine structures in the fovea of ROP and normal subjects. (*Left*): Composite AO-OCT B-scans from ten eyes: (**a**–**e**) control and (**f**–**j**) ROP subjects. (**d**) Scale bar for (**a**–**d**, **f**–**i**). (**e**) Scale bar for (**e**, **f**). (*Right*): Retinal vasculature in (**a**–**d**) control and (**e**–**h**) ROP subjects. *En face* views (**a**, **c**, **e**, **g**) were created by averaging the axial slices shown between the horizontal lines in the corresponding B-scans (**b**, **d**, **f**, **h**). (**a**, **e**) Vessels in the IPL; (**c**, **h**) vessels in the OPL. Raster scan size is 873 × 873 μm (Reproduced with permission from ARVO, Ref. [154])

of liquid-filled cysts that in turn compromise photoreceptors and can lead to permanent vision loss. In an already mentioned report describing AO-OCT imaging of retinal pathologies, Považay et al. [144] imaged structural changes associated with MacTel. A representative result from their study is shown in Fig. 61.49.

61.7.2.8 In Vivo Phenotyping of Red/Green Color Blindness in 3D

Normal human color vision is trichromatic, being based on three spectrally distinct cone classes. Color vision deficiency is usually manifested by the absence of one of the classes and is usually inherited. Depending on the type of underlying gene mutation, the color deficiency can also be accompanied with retinal disease and dysfunction of photoreceptors. Figure 61.50 shows an example of applying

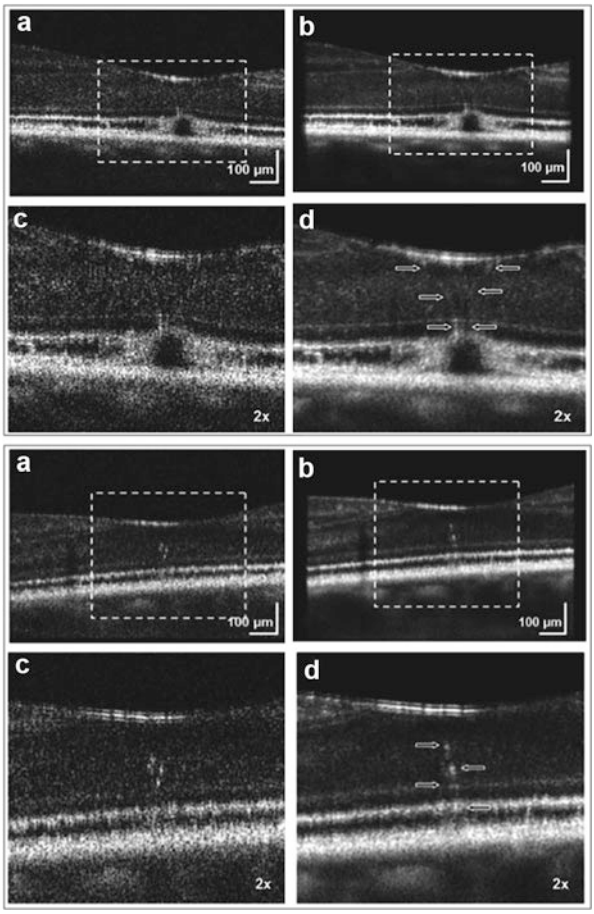

Fig. 61.48 AO-UHR-OCT imaging of two patients, (*left*) one with micro-traction and (*right*) the other with a micro scotoma. (*left*): AO-UHR-OCT images of 65-year-old subject reveal vitreal micro traction in the central fovea. Due to its small size, the traction was misdiagnosed using standard clinical imaging modalities including commercial OCT and fundus photography. *Arrows* indicate probable stress lines. (*right*): AO-UHR-OCT images of 55-year-old subject reveals hyper-reflections (denoted by *arrows*) in the outer nuclear layer near the foveal center and could not be explained using standard clinical imaging modalities (commercial OCT and fundus photography). The location of the hyper-reflections coincided with the micro scotoma, thus suggesting the two are related. For both cases, a single AO-OCT B-scan is shown in (**a**) and an average of ten B-scans in (**b**). Magnified views of the dashed rectangles in (**a**) and (**b**) are shown in (**c**) and (**d**), respectively (Reproduced with permission from OSA, Ref. [25])

AO-OCT to phenotype cone photoreceptors in patients with red/green color deficiency due to a Cys203Arg genetic mutation [94]. Phenotyping in this study involved measuring cone photoreceptor density and segment lengths in both normal and red/green deficient patients.

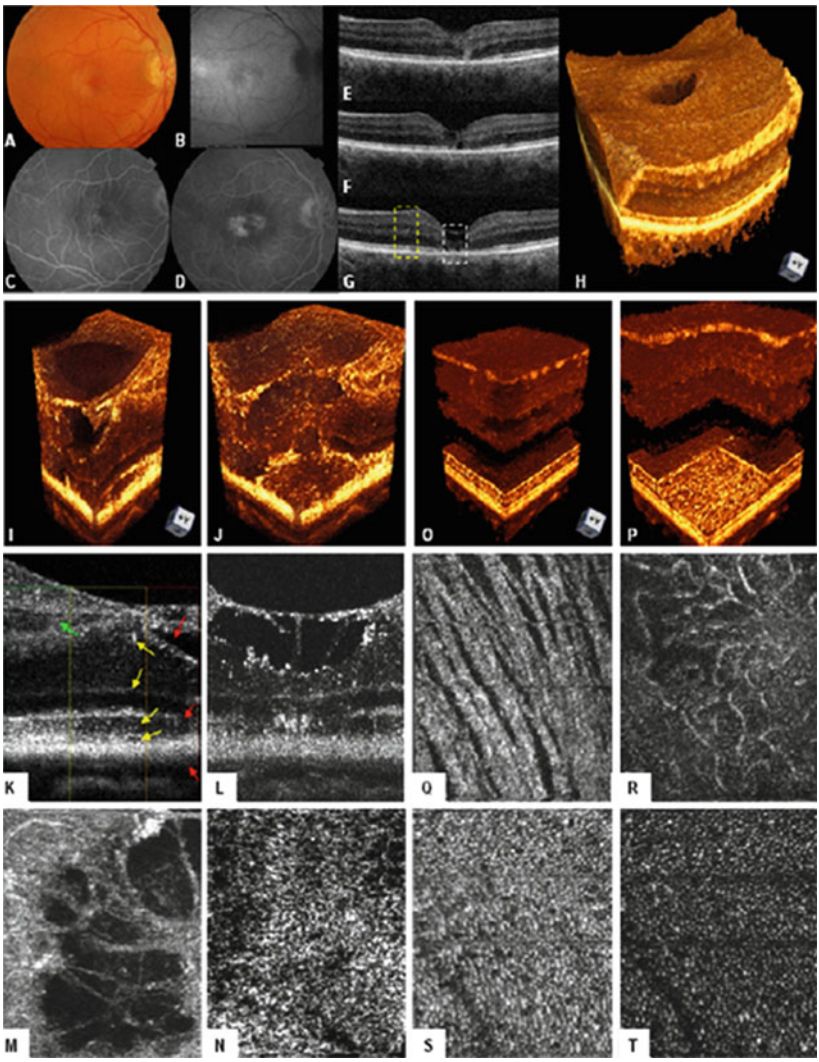

Fig. 61.49 3D-OCT (**e–h**) and AO OCT (**i–t**) at 800 nm of a patient with Type 2 Macular Telangiectasia: (**a**) fundus photo; (**b**) autofluorescence fundus image; **c** fluorescein angiography (early phase); (**d**) fluorescein angiography (late phase); (**e–g**) representative cross section from 3D-OCT, taken from (**h**); (**h**) 3D-OCT at 800 nm over 20° × 20°; cellular-resolution retinal imaging using AO OCT: (**i**) isotropic, volumetric AO OCT at 0°, retinal location indicated by *white dashed line* in (**g**); (**j**) volumetric rendering at 0°; cross sections (**k**, **l**) and *en face* images at the level of the outer nuclear layer (**m**) and retinal pigment epithelium (**n**) at 0°; *arrows* in (**k**) indicate areas of little (*green*), medium (*yellow*) and significant (*red*) impairment; (**o**) isotropic volumetric AO OCT at 6° parafoveal location, retinal location indicated by *yellow dashed line* in (**g**); *en face* images at the level of the nerve fiber bundles at 6° (**q**); capillaries in the inner nuclear layer at 6° (**r**); inner/outer photoreceptor junction at 6° (**s**) and at the level of the tips of the outer photoreceptors at 6° (**t**) (Reproduced with permission from OSA, Ref. [144])

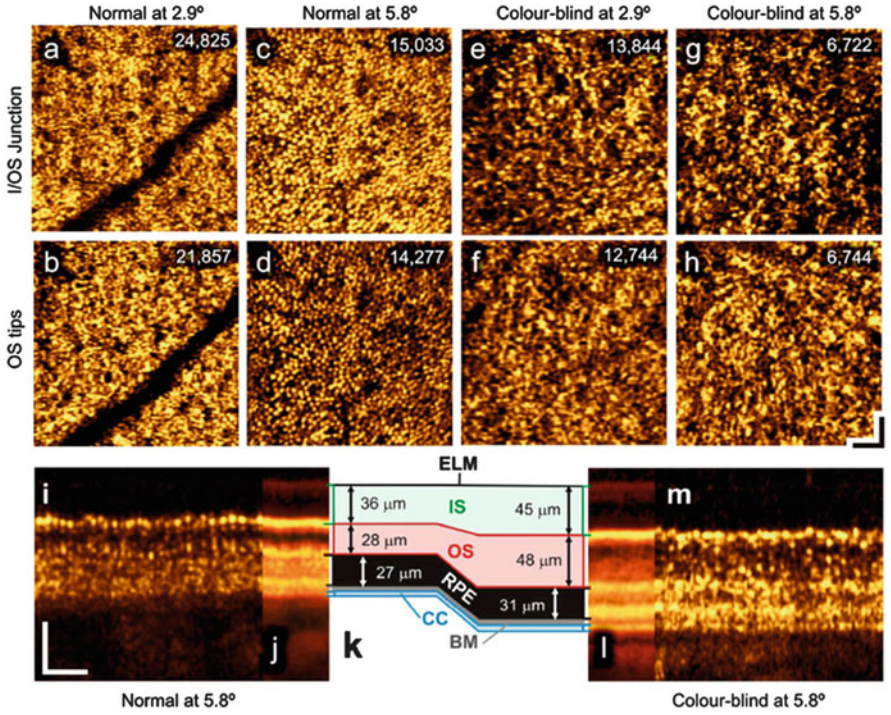

Fig. 61.50 Cellular phenotyping in a normal and *red/green* color-blind patient at 2.9° and 5.8° temporal. (**a**–**h**) *En face* images at the IS/OS and PTOS tips after averaging of 15–22 slices and bandpassed filtered. Photoreceptor densities per mm^2 are indicated at the *top-right corner* of each panel. (**i**–**m**) Comparison of photoreceptor distributions in a normal (**i**–**j**) and color-blind (**l**–**m**) subject at 5.8° temporal. Tomograms obtained by averaging five cross sections filtered with ATF are shown in **i** and **m**, while in **j** and **l**, portions of integrations obtained from 200 fast-scan-axis tomograms filtered with AFT are shown to emphasize transversal cell densities. Layer thicknesses for the IS, OS and RPE are depicted in **k**. Scale bars: 50 μm (Reproduced with permission from ARVO, Ref. [94])

61.8 Conclusions

The last decade has witnessed the creation of powerful high-resolution systems based on AO and OCT to achieve an ambitious goal of cellular-resolution imaging in all three dimensions in the living human eye. Here we presented key aspects of designing and implementing such AO-OCT systems. Particular attention was devoted to the relevant optical properties of the eye that ultimately define these systems, AO componentry and operation tailored for ophthalmic use, and of course use of the latest technologies and methods in OCT for ocular imaging. In less than a decade, AO has been integrated into every major OCT design configuration, many of which we described and compared. Early scientific and clinical studies show exciting potential of AO-OCT to image the microscopic retina and fundus in ways not previously possible with other noninvasive methods. While the

last decade has experienced tremendous advances in AO-OCT, one can only imagine that the next decade will witness even more. Perhaps in the not too distant future, AO-OCT will be ubiquitous in ocular imaging, both in the scientific and clinical communities.

References

1. D. Huang, E.A. Swanson, C.P. Lin et al., Optical coherence tomography. Science **254**, 1178–1181 (1991)
2. W. Drexler, J.G. Fujimoto (eds.), *Optical Coherence Tomography Technology and Applications* (Springer, New York, 2008)
3. J. Liang, D.R. Williams, D.T. Miller, Supernormal vision and high resolution retinal imaging through adaptive optics. J. Opt. Soc. Am. A **14**, 2884–2892 (1997)
4. J. Porter, H. Queener, J. Lin, K. Thorn, A. Awwal (eds.), *Adaptive Optics for Vision Science: Principles, Practices, Design and Applications* (Wiley, New York, 2006)
5. D.T. Miller, A. Roorda, Adaptive optics in retinal microscopy and vision, in *Handbook of Optics Volume III*, ed. by M. Bass, J.M. Enoch, V. Lakshminarayanan (McGraw Hill, New York, 2009), pp. 15.1–15.30
6. V. Larichev, P.V. Ivanov, N.G. Iroshnikov, V.I. Shmalhauzen, L.J. Otten, Adaptive system for eye-fundus imaging. Quantum Electron. **32**, 902–908 (2002)
7. N. Ling, Y. Zhang, X. Rao, X. Li, C. Wang, Y. Hu, W. Jiang, Small table-top adaptive optical systems for human retinal imaging, in *High-Resolution Wavefront Control: Methods, Devices, and Applications IV*, ed. by J.D. Gonglewski, M.A. Vorontsov, M.T. Gruneisen, S.R. Restaino, R.K. Tyson. Proc. SPIE, 4825 (2002), pp. 99–108
8. M. Glanc, E. Gendron, F. Lacombe, D. Lafaille, J.F. Le Gargasson, P. Lena, Towards wide-field imaging with AO. Opt. Commun. **230**, 225–238 (2004)
9. J. Rha, R.S. Jonnal, K.E. Thorn, J. Qu, Y. Zhang, D.T. Miller, AO flood-illumination camera for high speed retinal imaging. Opt. Express **14**, 4552–4569 (2006)
10. A. Roorda, F. Romero-Borja, W.J. Donnelly, H. Queener, T.J. Hebert, M.C.W. Campbell, AO scanning laser ophthalmoscopy. Opt. Express **10**, 405–412 (2002)
11. Y. Zhang, S. Poonja, A. Roorda, MEMS-based AO scanning laser ophthalmoscopy. Opt. Lett. **31**, 1268–1270 (2006)
12. D.C. Gray, W. Merigan, J.I. Wolfing, B.P. Gee, J. Porter, A. Dubra, T.H. Twietmeyer, K. Ahamd, R. Tumbar, F. Reinholz, D.R. Williams, In vivo fluorescence imaging of primate retinal ganglion cells and retinal pigment epithelial cells. Opt. Express **14**, 7144–7158 (2006)
13. D.X. Hammer, R.D. Ferguson, C.E. Bigelow, N.V. Iftimia, T.E. Ustun, S.A. Burns, AO scanning laser ophthalmoscope for stabilized retinal imaging. Opt. Express **14**, 3354–3367 (2006)
14. K. Grieve, P. Tiruveedhula, Y. Zhang, A. Roorda, Multi-wavelength imaging with the adaptive optics scanning laser ophthalmoscope. Opt. Express **14**, 12230–12242 (2006)
15. S.A. Burns, R. Tumbar, A.E. Elsner, D. Ferguson, D.X. Hammer, Large-field-of-view, modular, stabilized, adaptive-optics-based scanning laser ophthalmoscope. J. Opt. Soc. Am. A **24**, 1313–1326 (2007)
16. D.T. Miller, J. Qu, R.S. Jonnal, K. Thorn, Coherence gating and AO in the eye, in *Coherence Domain Optical Methods and Optical Coherence Tomography in Biomedicine VII*, ed. by V. Valery, V. Tuchin, J.A. Izatt, J.G. Fujimoto. Proc. SPIE, 4956 (2003), pp. 65–72
17. B. Hermann, E.J. Fernández, A. Unterhuber, H. Sattmann, A.F. Fercher, W. Drexler, P.M. Prieto, P. Artal, Adaptive-optics ultrahigh-resolution optical coherence tomography. Opt. Lett. **29**, 2142–2144 (2004)
18. Y. Zhang, J. Rha, R.S. Jonnal, D.T. Miller, AO parallel spectral domain optical coherence tomography for imaging the living retina. Opt. Express **13**, 4792–4811 (2005)

19. R.J. Zawadzki, S. Jones, S.S. Olivier, M. Zhao, B.A. Bower, J.A. Izatt, S.S. Choi, S. Laut, J.S. Werner, Adaptive-optics optical coherence tomography for high-resolution and high-speed 3D retinal in vivo imaging. Opt. Express **13**, 8532–8546 (2005)
20. E.J. Fernández, B. Považay, B. Hermann, A. Unterhuber, H. Sattmann, P.M. Prieto, R. Leitgeb, P. Ahnelt, P. Artal, W. Drexler, Three-dimensional AO ultrahigh-resolution optical coherence tomography using a liquid crystal spatial light modulator. Vision Res. **45**, 3432–3444 (2005)
21. Y. Zhang, B. Cense, J. Rha, R.S. Jonnal, W. Gao, R.J. Zawadzki, J.S. Werner, S. Jones, S. Olivier, D.T. Miller, High-speed volumetric imaging of cone photoreceptors with AO spectral-domain optical coherence tomography. Opt. Express **14**, 4380–4394 (2006)
22. D. Merino, C. Dainty, A. Bradu, A.G. Podoleanu, Adaptive optics enhanced simultaneous en-face optical coherence tomography and scanning laser ophthalmoscopy. Opt. Express **14**, 3345–3353 (2006)
23. C.E. Bigelow, N.V. Iftimia, R.D. Ferguson, T.E. Ustun, B. Bloom, D.X. Hammer, Compact multimodal adaptive-optics spectral-domain optical coherence tomography instrument for retinal imaging. J. Opt. Soc. Am. A **24**, 1327–1336 (2007)
24. M. Pircher, R.J. Zawadzki, J.W. Evans, J.S. Werner, C.K. Hitzenberger, Simultaneous imaging of human cone mosaic with adaptive optics enhanced scanning laser ophthalmoscopy and high-speed transversal scanning optical coherence tomography. Opt. Lett. **33**, 22–24 (2008)
25. R.J. Zawadzki, B. Cense, Y. Zhang, S.S. Choi, D.T. Miller, J.S. Werner, Ultrahigh-resolution optical coherence tomography with monochromatic and chromatic aberration correction. Opt. Express **16**, 8126–8143 (2008)
26. E.J. Fernández, B. Hermann, B. Považay, A. Unterhuber, H. Sattmann, B. Hofer, P.K. Ahnelt, W. Drexler, Ultrahigh resolution optical coherence tomography and pancorrection for cellular imaging of the living human retina. Opt. Express **16**, 11083–11094 (2008)
27. D.T. Miller, O.P. Kocaoglu, Q. Wang, S. Lee, Adaptive optics and the eye (super resolution OCT). Eye (London, England) **25**(3), 321–330 (2011)
28. M. Pircher, R.J. Zawadzki, Combining adaptive optics with optical coherence tomography: unveiling the cellular structure of the human retina in vivo. Expert Rev. Ophthalmol. **2**(6), 1–25 (2007)
29. D.X. Hammer, R.D. Ferguson, M. Mujat, A. Patel, E. Plumb, N. Iftimia, T.Y.P. Chui, J.D. Akula, A.B. Fulton, Multimodal adaptive optics retinal imager: design and performance. J. Opt. Soc. Am. A **29**(12), 2598–2607 (2012)
30. J. Yifan R.J. Zawadzki, M.V. Sarunic, Adaptive optics optical coherence tomography for in vivo mouse retinal imaging. J. Biomed. Opt. **18**(5), 056007-056007 (2013)
31. C.E. Campbell, A new method for describing the aberrations of the eye using Zernike polynomials. Opt. Vis. Sci. **80**(1), 79–83 (2003)
32. G. Dai, *Wavefront Optics for Vision Correction* (SPIE Press, Bellingham, 2008)
33. J. Porter, A. Guirao, I.G. Cox, D.R. Williams, Monochromatic aberrations of the human eye in a large population. J. Opt. Soc. Am. A **18**, 1793–1803 (2001)
34. L.N. Thibos, X. Hong, A. Bradley, X. Cheng, Statistical variation of aberration structure and image quality in a normal population of healthy eyes. J. Opt. Soc. Am. A **19**, 2329–2348 (2002)
35. L.N. Thibos, R.A. Applegate, J.T. Schwiegerling, R. Webb, VISA Standards Taskforce Members, Standards for reporting the optical aberrations of eyes. J. Refract. Surg. **18**, S652–S660 (2002)
36. L. Wang, D.D. Koch, Ocular higher-order aberrations in individuals screened for refractive surgery. J. Cataract Refract. Surg. **29**, 1896–1903 (2003)
37. T.O. Salmon, C. van de Pol, Normal-eye Zernike coefficients and root-mean-square wavefront errors. J. Cataract Refract. Surg. **32**, 2064–2074 (2006)

38. A. Hartwig, D.A. Atchison, IOVS papers in press. Published on October 2, 2012 as Manuscript iovs.12-10610. Analysis of higher order aberrations in a large clinical population. Invest. Ophthalmol. Vis. Sci., 1–19 (2012)
39. M.T. Sheehan, A.V. Goncharov, V.M. O'Dwyer, V. Toal, C. Dainty, Population study of the variation in monochromatic aberrations of the normal human eye over the central visual field. Opt. Express **15**(12), 7367–7380 (2007)
40. J. Shen, L.N. Thibos, Peripheral aberrations and image quality for contact lens correction. Opt. Vis. Sci. **88**(10), 1196–1205 (2011)
41. M.J. Collins, C.F. Wildsoet, D.A. Atchison, Monochromatic aberrations and myopia. Vision Res. **35**, 1157–1163 (1995)
42. X. Hong, L. Thibos, Longitudinal evaluation of optical aberrations following laser in situ keratomileusis surgery. J. Refract. Surg. **16**, S647–S650 (2001)
43. X. Cheng, A. Bradley, X. Hong, L. Thibos, Relationship between refractive error and monochromatic aberrations of the eye. Optom. Vis. Sci. **80**, 43–49 (2003)
44. S. Amano, Y. Amano, S. Yamagami, T. Miyai, K. Miyata, T. Samejima, T. Oshika, Age-related changes in corneal and ocular higher-order wavefront aberrations. Am J. Ophthalmol. **137**, 988–992 (2004)
45. H. Cheng, J.K. Barnett, A.S. Vilupuru, J.D. Marsack, S. Kasthurirangan, R.A. Applegate, A. Roorda, A population study on changes in wave aberrations with accommodation. J. Vis. **4**, 272–280 (2004)
46. J. Porter, G. Yoon, S. MacRae, I. Cox, D.R. Williams, Aberrations induced in customized laser refractive surgery due to shifts between natural and dilated pupil center locations. J. Cataract Refract. Surg. **32**, 21–32 (2006)
47. H. Radhakrishnan, W.N. Charman, Age-related changes in ocular aberrations with accommodation. J. Vis. **7**, 11–21 (2007)
48. S. Pantanelli, S. MacRae, T.M. Jeong, G. Yoon, Characterizing the wave aberration in eyes with keratoconus or penetrating keratoplasty using a high dynamic range wavefront sensor. Ophthalmology **114**, 2013–2021 (2007)
49. A. Denoyer, G. Rabut, C. Baudouin, Tear film aberration dynamics and vision-related quality of life in patients with dry eye disease. Ophthalmology **119**, 1811–1818 (2012)
50. R.W. Everson, Age variation in refractive error distributions. Optom. Weekly **64**(9), 31–34 (1973)
51. H. Hofer, P. Artal, B. Singer, J.L. Aragón, D.R. Williams, Dynamics of the eye's wave aberration. J. Opt. Soc. Am. A **18**, 497–506 (2001)
52. L. Diaz-Santana, C. Torti, I. Munro, P. Gasson, C. Dainty, Benefit of higher closed–loop bandwidths in ocular AO. Opt. Express **11**, 2597–2605 (2003)
53. D.L. Fried, Anisoplanatism in AO. J. Opt. Soc. Am. **72**, 52–61 (1982)
54. P. Bedggood, M. Daaboul, R. Ashman, G. Smith, A. Metha, Characteristics of the human isoplanatic patch and implications for AO retinal imaging. J. Biomed. Opt. **13**, 024008 (2008)
55. H.-L. Liou, N.A. Brennan, Anatomically accurate, finite model eye for optical modeling. J. Opt. Soc. Am. A **14**, 1684–1694 (1997)
56. D.A. Atchison, G. Smith, *Optics of the Human Eye* (Butterworth-Heinemann, Oxford, 2000)
57. E.J. Fernández, A. Unterhuber, P.M. Prieto, B. Hermann, W. Drexler, P. Artal, Ocular aberrations as a function of wavelength in the near infrared measured with a femtosecond laser. Opt. Express **13**, 400–409 (2005)
58. D.A. Atchison, G. Smith, Chromatic dispersions of the ocular media of human eyes. J. Opt. Soc. Am. A **22**, 29–37 (2005)
59. E.J. Fernández, P. Artal, Ocular aberrations up to the infrared range: from 632.8 to 1070 nm. Opt. Express **16**(26), 21199–21208 (2008)
60. A.C. van Heel, Correcting the spherical and chromatic aberrations of the eye. J. Opt. Soc. Am. **36**, 237–239 (1947)

61. R.E. Bedford, G. Wyszecki, Axial chromatic aberration of the human eye. J. Opt. Soc. Am. **47**, 564–565 (1957)
62. A.L. Lewis, M. Katz, C. Oehrlein, A modified achromatizing lens. Am. J. Optom. Physiol. Opt. **59**, 909–911 (1982)
63. R. Navarro, J. Santamaria, J. Bescos, Accommodation-dependent model of the human eye with aspherics. J. Opt. Soc. Am. A **2**, 1273–1281 (1985)
64. I. Powell, Lenses for correcting chromatic aberration of the eye. Appl. Opt. **20**, 4152–4155 (1981)
65. Y. Benny, S. Manzanera, P.M. Prieto, E.N. Ribak, P. Artal, Wide-angle chromatic aberration corrector for the human eye. J. Opt. Soc. Am. A **24**, 1538–1544 (2007)
66. B.B. Boycott, J.E. Dowling, Organization of the primate retina: light microscopy. Philos. Trans. R. Soc. Lond. B **255**, 109–184 (1969)
67. J. Stone, E. Johnston, The topography of primate retina: a study of the human, bushbaby, and new- and old-world monkeys. J. Comp. Neurol. **196**(2), 205–223 (1981)
68. T.E. Ogden, Nerve fiber layer of the primate retina: morphometric analysis. Invest. Ophthalmol. Vis. Sci. **25**(1), 19–29 (1984)
69. D.M. Snodderly, R.S. Weinhaus, J.C. Choi, Neural-vascular relationships in central retina of macaque monkeys (Macaca fascicularis). J. Neurosci. **12**(4), 1169–1193 (1992)
70. C.A. Curcio, K.R. Sloan, R.E. Kalina, A.E. Hendrickson, Human photoreceptor topography. J. Comp. Neurol. **292**(4), 497–523 (1990)
71. N. Doble, S.S. Choi, J.L. Codona, J. Christou, J.M. Enoch, D.R. Williams, In vivo imaging of the human rod photoreceptor mosaic. Opt. Lett. **36**(1), 31–33 (2011)
72. J.I.W. Morgan, A. Dubra, R. Wolfe, W.H. Merigan, D.R. Williams, In vivo autofluorescence imaging of the human and macaque retinal pigment epithelial cell mosaic. Invest. Ophthalmol. Vis. Sci. **50**(3), 1350–1359 (2009)
73. D.R. Neal, J. Copland, D. Neal, Shack-Hartmann wavefront sensor precision and accuracy, in *Advanced Characterization Techniques for Optical, Semiconductor, and Data Storage Components*, ed. by A. Duparré, B. Singh. Proc. SPIE, 4779 (2002), pp. 148–160
74. B.R. Oppenheimer, D.L. Palmer, R.G. Dekany, A. Sivaramakrishnan, M.A. Ealey, T.R. Price, Investigating a Xinetics Inc. deformable mirror. Proc. SPIE **3126**, 569–579 (1997)
75. R.K. Tyson, *Principles of Adaptive Optics*, 2nd edn. (Academic, Boston, 1998)
76. D.T. Miller, L.N. Thibos, X. Hong, Requirements for segmented correctors for diffraction-limited performance in the human eye. Opt. Express **13**, 275–289 (2005)
77. N. Doble, D.T. Miller, G. Yoon, D.R. Williams, Requirements for discrete actuator and segmented wavefront correctors for aberration compensation in two large populations of human eyes. Appl. Opt. **46**, 4501–4514 (2007)
78. G.T. Kennedy, C. Paterson, Correcting the ocular aberrations of a healthy adult population using microelectromechanical (MEMS) deformable mirrors. Opt. Commun. **271**, 278–284 (2007)
79. T. Farrell, E. Daly, E. Dalimier, C. Dainty, Task-based assessment of deformable mirrors. Proc. SPIE **6467**, 64670F (2007)
80. R.J. Zawadzki, S.S. Choi, S.M. Jones, S.S. Oliver, J.S. Werner, Adaptive optics-optical coherence tomography: optimizing visualization of microscopic retinal structures in three dimensions. J. Opt. Soc. Am. A **24**, 1373–1383 (2007)
81. D.C. Chen, S.M. Jones, D.A. Silva, S.S. Olivier, High-resolution adaptive optics scanning laser ophthalmoscope with dual deformable mirrors. J. Opt. Soc. Am. A **24**, 1305–1312 (2007)
82. W. Zou, X. Qi, S.A. Burns, Wavefront-aberration sorting and correction for a dual-deformable-mirror adaptive-optics system. Opt. Lett. **33**(22), 2602 (2008)
83. B. Cense, E. Koperda, J.M. Brown, O.P. Kocaoglu, W. Gao, R.S. Jonnal, D.T. Miller, Volumetric retinal imaging with ultrahigh-resolution spectral-domain optical coherence tomography and adaptive optics using two broadband light sources. Opt. Express **17**(5), 4095–4111 (2009)

84. C. Li, N. Sredar, K.M. Ivers, H. Queener, J. Porter, A correction algorithm to simultaneously control dual deformable mirrors in a woofer-tweeter adaptive optics system. Opt. Express **18**(16), 16671–16684 (2010)
85. A. Dubra, Y. Sulai, J.L. Norris, R.F. Cooper, A.M. Dubis, D.R. Williams, J. Carroll, Noninvasive imaging of the human rod photoreceptor mosaic using a confocal adaptive optics scanning ophthalmoscope. Biomed. Opt. Express **2**(7), 1864–1876 (2011)
86. S. Bonora, R.J. Zawadzki, G. Naletto, U. Bortolozzo, S. Residori, in *Devices and Techniques for Sensorless Adaptive Optics, Adaptive Optics Progress*, ed. by R. Tyson (2012), ISBN:978-953-51-0894-8, InTech
87. H. Hofer, N. Sredar, H. Queener, C. Li, J. Porter, Wavefront sensorless adaptive optics ophthalmoscopy in the human eye. Opt. Express **19**(14160–14171), 14160–14171 (2011)
88. B. Cense, W. Gao, J.M. Brown, S.M. Jones, R.S. Jonnal, M. Mujat, B.H. Park, J.F. de Boer, D.T. Miller, Retinal imaging with polarization-sensitive optical coherence tomography and adaptive optics. Opt. Express **17**(24), 21634–21651 (2009)
89. O.P. Kocaoglu, B. Cense, R.S. Jonnal, Q. Wang, S. Lee, W. Gao, D.T. Miller, Imaging retinal nerve fiber bundles using optical coherence tomography with adaptive optics. Vis. Res. **51**(16), 1835–1844 (2011)
90. W. Gao, B. Cense, Y. Zhang, R.S. Jonnal, D.T. Miller, Measuring retinal contributions to the optical Stiles-Crawford effect with optical coherence tomography. Opt. Express **16**(9), 6486–6501 (2008)
91. K. Sasaki, K. Kurokawa, S. Makita, Y. Yasuno, Extended depth of focus adaptive optics spectral domain optical coherence tomography. Biomed. Opt. Express **3**(10), 2353–2370 (2012)
92. S.G. Adie, B.W. Graf, A. Ahmad, P.S. Carney, S.A. Boppart, Computational adaptive optics for broadband optical interferometric tomography of biological tissue. Proc. Natl. Acad. Sci. U. S. A. **109**(19), 7175–7180 (2012)
93. E.J. Fernández, W. Drexler, Influence of ocular chromatic aberration and pupil size on transverse resolution in ophthalmic adaptive optics optical coherence tomography. Opt. Express **13**(20), 8184–8197 (2005)
94. C. Torti, B. Považay, B. Hofer, A. Unterhuber, J. Carroll, P.K. Ahnelt, W. Drexler, Adaptive optics optical coherence tomography at 120,000 depth scans/s for non-invasive cellular phenotyping of the living human retina. Opt. Express **17**(22), 19382–19400 (2009)
95. R.J. Zawadzki, S.S. Choi, A.R. Fuller, J.W. Evans, B. Hamann, J.S. Werner, Cellular resolution volumetric in vivo retinal imaging with adaptive optics–optical coherence tomography. Opt. Express **17**(5), 4084–4094 (2009)
96. E.J. Fernández, A. Unterhuber, B. Povazay, B. Hermann, P. Artal, W. Drexler, Chromatic aberration correction of the human eye for retinal imaging in the near infrared. Opt. Express **14**(13), 6213–6225 (2006)
97. J. Qu, R.S. Jonnal, D.T. Miller, Parallel optical coherence tomography using a CCD camera. Chin. Opt. Lett. **2**(8), 475–476 (2004)
98. L.A. Riggs, J.C. Armington, F. Ratliff, Motions of the retinal image during fixation. J. Opt. Soc. Am. **44**(4), 315–321 (1954)
99. A.G. Podoleanu, D.A. Jackson, Combined optical coherence tomograph and scanning laser ophthalmoscope. Electron. Lett. **34**(11), 1088–1090 (1998)
100. M. Pircher, E. Gotzinger, C.K. Hitzenberger, Dynamic focus in optical coherence tomography for retinal imaging. J. Biomed. Opt. **11**(5), 054013 (2006)
101. M. Pircher, B. Baumann, E. Götzinger, H. Sattmann, C.K. Hitzenberger, Simultaneous SLO/OCT imaging of the human retina with axial eye motion correction. Opt. Express **15**(25), 16922–16932 (2007)
102. M. Pircher, E. Götzinger, H. Sattmann, R.A. Leitgeb, C.K. Hitzenberger, In vivo investigation of human cone photoreceptors with SLO/OCT in combination with 3D motion correction on a cellular level. Opt. Express **18**(13), 13935–13944 (2010)
103. R. Leitgeb, C.K. Hitzenberger, A.F. Fercher, Performance of Fourier domain vs. time domain optical coherence tomography. Opt. Express **11**(8), 889–894 (2003)

104. J.F. De Boer, B. Cense, B.H. Park, M.C. Pierce, G.J. Tearney, B.E. Bouma, Improved signal-to-noise ratio in spectral-domain compared with time-domain optical coherence tomography. Opt. Lett. **28**(21), 2067–2069 (2003)
105. M.A. Choma, M.V. Sarunic, C. Yang, J.A. Izatt, Sensitivity advantage of swept source and Fourier domain optical coherence tomography. Opt. Express **11**(18), 2183–2189 (2003)
106. A.F. Zuluaga, R. Richards-Kortum, Spatially resolved spectral interferometry for determination of subsurface structure. Opt. Lett. **24**(8), 519–521 (1999)
107. B. Grajciar, M. Pircher, A.F. Fercher, R.A. Leitgeb, Parallel Fourier domain optical coherence tomography for in vivo measurement of the human eye. Opt. Express **13**(4), 1131–1137 (2005)
108. J.W. Evans, R.J. Zawadzki, S.M. Jones, S.S. Olivier, J.S. Werner, Error budget analysis for an adaptive optics optical coherence tomography system. Opt. Express **17**(16), 13768 (2009)
109. K. Kurokawa, K. Sasaki, S. Makita, M. Yamanari, B. Cense, Y. Yasuno, Simultaneous high-resolution retinal imaging and high-penetration choroidal imaging by one-micrometer adaptive optics optical coherence tomography. Opt. Express **18**(8), 8515–8527 (2010)
110. S.A. Burns, R. Tumbar, A.E. Elsner, D. Ferguson, D.X. Hammer, Large-field-of-view, modular, stabilized, adaptive-optics-based scanning laser ophthalmoscope. J. Opt. Soc. Am. A Opt. Image Sci. Vis. **24**(5), 1313–1326 (2007)
111. A. Dubra, Y. Sulai, Reflective afocal broadband adaptive optics scanning ophthalmoscope. Biomed. Opt. Express **2**(6), 1757–1768 (2011)
112. D. Merino, J.L. Duncan, P. Tiruveedhula, A. Roorda, Observation of cone and rod photoreceptors in normal subjects and patients using a new generation adaptive optics scanning laser ophthalmoscope. Biomed. Opt. Express **2**, 2189–2201 (2011)
113. Z. Liu, O.P. Kocaoglu, R.S. Jonnal, Q. Wang, D.T. Miller, Performance of an off-axis ophthalmic adaptive optics system with toroidal mirror, in *Adaptive Optics: Methods, Analysis and Applications, OSA Technical Digest (CD)* (Optical Society of America, 2011), paper AMA4
114. S.H. Lee, J.S. Werner, R.J. Zawadzki, Reflective afocal adaptive optics: optical coherence tomography retinal imaging system. *Proc. SPIE*, 8567, Ophthalmic Technologies XXIII, 856722 (2013)
115. M. Mujat, R.D. Ferguson, A.H. Patel, N. Iftimia, N. Lue, D.X. Hammer, High resolution multimodal clinical ophthalmic imaging system. Opt. Express **18**, 11607–11621 (2010)
116. R.J. Zawadzki, S.M. Jones, S. Pilli, S. Balderas-Mata, D.Y. Kim, S.S. Olivier, J.S. Werner, Integrated adaptive optics optical coherence tomography and adaptive optics scanning laser ophthalmoscope system for simultaneous cellular resolution in vivo retinal imaging. Biomed. Opt. Express **2**(6), 1674 (2011)
117. A.G. Capps, R.J. Zawadzki, Q. Yang, D.W. Arathorn, C.R. Vogel, B. Hamann, J.S. Werner, Correction of eye-motion artifacts in AO-OCT data sets, in *SPIE BiOS* (2011), pp. 78850D–78850D
118. J.F. de Boer, T.E. Milner, M.J.C. van Gemert, J.S. Nelson, Two-dimensional birefringence imaging in biological tissue by polarization-sensitive optical coherence tomography. Opt. Lett. **22**(12), 934–936 (1997)
119. J.F. de Boer, T.E. Milner, J.S. Nelson, Determination of the depth-resolved Stokes parameters of light backscattered from turbid media by use of polarization-sensitive optical coherence tomography. Opt. Lett. **24**(5), 300–302 (1999)
120. C.K. Hitzenberger, E. Goetzinger, M. Sticker, M. Pircher, A.F. Fercher, Measurement and imaging of birefringence and optic axis orientation by phase resolved polarization sensitive optical coherence tomography. Opt. Express **9**(13), 780–790 (2001)
121. Y. Yasuno, S. Makita, Y. Sutoh, M. Itoh, T. Yatagai, Birefringence imaging of human skin by polarization-sensitive spectral interferometric optical coherence tomography. Opt. Lett. **27**(20), 1803–1805 (2002)
122. K. Kurokawa, K. Sasaki, S. Makita, Y.-J. Hong, Y. Yasuno, Three-dimensional retinal and choroidal capillary imaging by power Doppler optical coherence angiography with adaptive optics. Opt. Express **20**, 22796–22812 (2012)

123. R.S. Jonnal, O.P. Kocaoglu, Q. Wang, S. Lee, D.T. Miller, Phase-sensitive imaging of the outer retina using optical coherence tomography and adaptive optics. Biomed. Opt. Express **3**, 104–124 (2012)
124. O.P. Kocaoglu, S. Lee, R.S. Jonnal, Q. Wang, A.E. Herde, J.C. Derby, W. Gao, D.T. Miller, Imaging cone photoreceptors in three dimensions and in time using ultrahigh resolution optical coherence tomography with adaptive optics. Biomed. Opt. Express **2**(4), 748–763 (2011)
125. O.P. Kocaoglu, R.D. Ferguson, R.S. Jonnal, Z. Liu, Q. Wang, D.X. Hammer, D.T. Miller, Adaptive optics optical coherence tomography with dynamic retinal tracking, *Society of Photo-Optical Instrumentation Engineers' International Symposium on Ophthalmic Technologies XXIII*, San Francisco, 2–3 Feb 2013
126. R.J. Zawadzki, Y. Zhang II, S.M. Jones, S.S. Choi, B. Cense, D. Chen, A.R. Fuller, D.T. Miller, S.S. Olivier, J.S. Werner, Application of adaptive optics: optical coherence tomography for in vivo imaging of microscopic structures in the retina and optic nerve head. *Proc. SPIE*, 6426, Ophthalmic Technologies XVII, 64261O (2007)
127. R.H. Steinberg, I. Wood, R.H. Steinberg, Phagocytosis by pigment epithelium of human retinal cones. Nature **252**(5481), 305–307 (1974)
128. D.H. Anderson, S.K. Fisher, Disc shedding in rodlike and conelike photoreceptors of tree squirrels. Science **187**(4180), 953–955 (1975)
129. R.S. Jonnal, J.R. Besecker, J.C. Derby, O.P. Kocaoglu, B. Cense, W. Gao, Q. Wang, D.T. Miller, Imaging outer segment renewal in living human cone photoreceptors. Opt. Express **18**(5), 5257–5270 (2010)
130. M. Wojtkowski, B. Kaluzny, R.J. Zawadzki, New directions in ophthalmic optical coherence tomography. Optom. Vis. Sci. **89**(5), 524 (2012)
131. Q. Wang, O.P. Kocaoglu, B. Cense, J. Bruestle, R.S. Jonnal, W. Gao, D.T. Miller, Imaging retinal capillaries using ultrahigh-resolution optical coherence tomography and adaptive optics. Invest. Ophthalmol. Vis. Sci. **52**(9), 6292–6299 (2011)
132. Z. Chen, G. Liu, *Doppler Optical Coherence Tomography. Handbook of Coherent-Domain Optical Methods* (Springer, New York, 2013), p. 889, 1, 889. ISBN 978-1-4614-5175-4
133. B. Baumann, B. Potsaid, M.F. Kraus, J.J. Liu, D. Huang, J. Hornegger, . . ., J.G. Fujimoto, Total retinal blood flow measurement with ultrahigh speed swept source/Fourier domain OCT. Biomed. Opt. Express **2**(6), 1539–1552 (2011)
134. D.Y. Kim, J. Fingler, J.S. Werner, D.M. Schwartz, S.E. Fraser, R.J. Zawadzki, In vivo volumetric imaging of human retinal circulation with phase-variance optical coherence tomography. Biomed. Opt. Express **2**(6), 1504 (2011)
135. L. An, P. Li, T.T. Shen, R. Wang, High speed spectral domain optical coherence tomography for retinal imaging at 500,000 A-lines per second. Biomed. Opt. Express **2**(10), 2770 (2011)
136. Y.J. Hong, S. Makita, F. Jaillon, M.J. Ju, E.J. Min, B.H. Lee, . . ., Y. Yasuno, High-penetration swept source Doppler optical coherence angiography by fully numerical phase stabilization. Opt. Express **20**(3), 2740–2760 (2012)
137. Y. Jia, O. Tan, J. Tokayer, B. Potsaid, Y. Wang, J.J. Liu, . . . D. Huang, Split-spectrum amplitude-decorrelation angiography with optical coherence tomography. Opt. Express **20**(4), 4710–4725 (2012)
138. B. Braaf, K.A. Vermeer, K.V. Vienola, J.F. de Boer, Angiography of the retina and the choroid with phase-resolved OCT using interval-optimized backstitched B-scans. Opt. Express **20**(18), 20516–20534 (2012)
139. C. Blatter, T. Klein, B. Grajciar, T. Schmoll, W. Wieser, R. Andre, . . . R.A. Leitgeb, Ultrahigh-speed non-invasive widefield angiography. J. Biomed. Opt. **17**(7), 0705051–0705053 (2012)
140. R.J. Zawadzki, A.T. Ishida, J.S. Werner, Interpretation of the outer retina bands seen on OCT and AO-OCT B-scans, in *ISIE/ARVO Annual Conference, Paper: 200*. Retinal Imaging I (2012)
141. A. Kotecha, S. Izadi, G. Jeffery, Age-related changes in the thickness of the human lamina cribrosa. Br. J. Ophthalmol. **90**(12), 1531–1534 (2006)

142. D.Y. Kim, J.S. Werner, R.J. Zawadzki, Complex conjugate artifact-free adaptive optics optical coherence tomography of in vivo human optic nerve head. J. Biomed. Opt. **17**(12), 126005–126005 (2012)
143. A. Panorgias, R.J. Zawadzki, A.G. Capps, A.A. Hunter, L.S. Morse, J.S. Werner, Multimodal assessment of microscopic retinal morphology and retinal function in patients with geographic atrophy. Investigative Ophthalmology and Visual Science, **54**(6), 4372–4384 (2013)
144. B. Považay, B. Hofer, C. Torti, B. Hermann, A.R. Tumlinson, M. Esmaeelpour, . . ., W. Drexler, Impact of enhanced resolution, speed and penetration on three-dimensional retinal optical coherence tomography. Opt. Express **17**(5), 4134–4150 (2009)
145. S.S. Choi, R.J. Zawadzki, J.L. Keltner, J.S. Werner, Changes in cellular structures revealed by ultra-high resolution retinal imaging in optic neuropathies. Invest. Ophthalmol. Vis. Sci. **49**(5), 2103–2119 (2008)
146. S.S. Choi, R.J. Zawadzki, M.C. Lim, J.D. Brandt, J.L. Keltner, N. Doble, J.S. Werner, Evidence of outer retinal changes in glaucoma patients as revealed by ultrahigh-resolution in vivo retinal imaging. Br. J. Ophthalmol. **95**(1), 131–141 (2011)
147. J.S. Werner, J.L. Keltner, R.J. Zawadzki, S.S. Choi, Outer retinal abnormalities associated with inner retinal pathology in nonglaucomatous and glaucomatous optic neuropathies. Eye **25**(3), 279–289 (2011)
148. A. Sommer, N.R. Miller, I. Pollack, A.E. Maumenee, T. George, The nerve fiber layer in the diagnosis of glaucoma. Arch. Ophthalmol. **95**, 2149–2156 (1977)
149. A. Sommer, J. Katz, H.A. Quigley, N.R. Miller, A.L. Robin, R.C. Richter et al., Clinically detectable nerve fiber atrophy precedes the onset of glaucomatous field loss. Arch. Ophthalmol. **109**, 77–83 (1991)
150. W.F. Hoyt, L. Frisen, N.M. Newman, Fundoscopy of nerve fiber layer defects in glaucoma. Invest. Ophthalmol. Vis. Sci. **12**, 814–829 (1973)
151. F.A. Medeiros, L.M. Alencar, L.M. Zangwill, C. Bowd, G. Vizzeri, P.A. Sample et al., Detection of progressive retinal nerve fiber layer loss in glaucoma using scanning laser polarimetry with variable corneal compensation. Invest. Ophthalmol. Vis. Sci. **50**, 1675–1681 (2009)
152. J. Caprioli, H.J. Park, S. Ugurlu, D. Hoffman, Slope of the peripapillary nerve fiber layer surface in glaucoma. Invest. Ophthalmol. Vis. Sci. **39**, 2321–2328 (1998)
153. M. Seong, K.R. Sung, E.H. Choi, S.Y. Kang, J.W. Cho, T.W. Um et al., Macular and peripapillary retinal nerve fiber layer measurements by spectral domain optical coherence tomography in normal-tension glaucoma. Invest. Ophthalmol. Vis. Sci. **51**, 1446–1452 (2010)
154. D.X. Hammer, N.V. Iftimia, R.D. Ferguson, C.E. Bigelow, T.E. Ustun, A.M. Barnaby, A.B.. Fulton, Foveal fine structure in retinopathy of prematurity: an adaptive optics Fourier domain optical coherence tomography study. Invest. Ophthalmol. Vis. Sci. **49**(5), 2061–2070 (2008)

Acousto Optic Modulation Based En face AO SLO OCT

62

Michael Pircher and Christoph K. Hitzenberger

Keywords

Adaptive optics • Cellular imaging • Cone photoreceptors • En face OCT • Ophthalmology • Photoreceptor imaging • Scanning Laser Ophthalmoscope • SLO • SLO/OCT

62.1 Introduction

The classical scanning scheme of optical coherence tomography (OCT) [1] is based on A-scans, i.e., the fast scanning direction is the axial direction, perpendicular to the sample surface. This approach can be very sensitive using Fourier-domain OCT because the whole imaging depth can be recorded simultaneously [2]. Most applications target layered structures and require only low or moderate transverse resolution, and therefore, this approach represents the best available choice. However, in some applications, it also has considerable disadvantages: with increasing transverse resolution, the depth of focus (DOF, i.e., the zone of best sharpness) will be limited. Approaching microscopic resolution which lies in the order of a few micrometer results in a decrease of DOF down to a few tens of micrometer. This limits the benefit of FD-OCT in these applications because in order to sharply image the entire volume with a depth of $\sim$1 mm, the recording and stitching of several volumes (with different focal positions) are required. This can be quite time-consuming and the stitching might become problematic. An additional problem in the case of in vivo applications (e.g., retinal imaging) arises from artifacts caused by sample motion which are more pronounced in systems using

M. Pircher (✉) • C.K. Hitzenberger
Center for Medical Physics and Biomedical Engineering, Medical University of Vienna, Vienna, Austria
e-mail: michael.pircher@meduniwien.ac.at

© Springer International Publishing Switzerland 2015

W. Drexler, J.G. Fujimoto (eds.), *Optical Coherence Tomography*,
DOI 10.1007/978-3-319-06419-2_64

high magnifications. Especially microscopic structures that are only visible in the en face, the imaging plane (e.g., cone photoreceptor mosaic) can be heavily distorted even in the case of fast FD-OCT systems.

For these niche applications, transversal scanning (TS) or en face OCT can be an alternative. Here the fast scanning direction is set along the transversal extensions of the sample similar to a confocal scanning microscope. This scanning protocol requires the much less sensitive time domain OCT technique. However, sensitivity can be partly regained in the case of a scattering sample by the increase of the collection efficiency when using higher numerical aperture. Time domain OCT requires the generation of a suitable carrier frequency which deserves some additional consideration in TS-OCT. The first TS-OCT scheme reported generated the carrier frequency by the path length modulation induced by the transversal galvanometer scanners [3], which, however, has the drawback of a varying carrier frequency. We developed an alternate method of carrier frequency generation based on acousto-optic modulators (AOMs) that generate a very stable and adjustable carrier frequency [4]. Originally, this technique has been developed as an alternative for high-speed imaging, and we demonstrated the capability of the method in a variety of applications [5–9]. However, with the discovery of the sensitivity advantage of FD-OCT [2, 10], the original intention became obsolete. Nevertheless, in the case of high transverse resolution imaging, AOM-based TS-OCT has advantageous properties that allow it to compete with FD-OCT in certain applications. Since the transversal priority scanning scheme requires only a slow progression of the coherence gate in axial direction, a dynamic matching of the focal plane with the coherence gate is easily possible, thus allowing high transversal resolution throughout the entire sample depth [11]. This is a clear advantage as compared to classical A-scan-based OCT including FD-OCT where a low depth of focus limits the usable imaging depth. One application requiring high transverse resolution is cellular imaging of the human retina. Because of the permanent eye motion, imaging artifacts are in general a limiting factor when using high magnification. The scanning scheme of TS-OCT minimizes the sensitivity to transverse motion artifacts and allows the recording of basically motion artifact-free OCT images of the retinal photoreceptors in the human eyes in vivo. In this chapter, we present the underlying principle of the AOM-based TS-OCT technology and focus on the application of TS-OCT for retinal high-resolution imaging with and without adaptive optics (AO).

62.2 Carrier Frequency Generation by Acousto-Optic Frequency Shifting

An acoustic wave propagating through an optically transparent medium generates a periodic modulation of the refractive index via the elasto-optic effect. This provides a moving phase grating which can diffract an incident light beam into one or more directions. This phenomenon is known as the acousto-optic diffraction and can be used to modulate the light beam in various ways [12]. To achieve high

diffraction efficiency for a single diffraction order, acousto-optic cells are usually operated in the Bragg regime. In this case, the orientation of the incident light beam with respect to the acoustic wave in the cell is such that the wave vectors fulfill the condition:

$$\mathbf{k}_{\mathrm{d}} = \mathbf{k}_{\mathrm{i}} + \mathbf{k}_{\mathrm{a}}. \tag{62.1}$$

where $\mathbf{k}_{\mathrm{d}}$, $\mathbf{k}_{\mathrm{i}}$, and $\mathbf{k}_{\mathrm{a}}$ are the wave vectors of the diffracted light beam, incident light beam, and acoustic wave, respectively. The frequency of the diffracted light beam ν_{d} is shifted from the frequency of the incident beam ν_{i} by an amount equal to the frequency of the acoustic wave ν_{a}. Depending on the relative orientation of incident light beam and acoustic wave, this frequency shift is upward or downward:

$$\nu_{\mathrm{d}} = \nu_{\mathrm{i}} \pm \nu_{\mathrm{a}}. \tag{62.2}$$

To enable heterodyne detection in an OCT instrument, the frequencies of reference and sample beams have to differ. The amount of this frequency difference is the carrier frequency. This is the frequency that is detected by a photodetector in the detection arm of the low-coherence interferometer in case of path length matching of the two arms.

In the original time domain A-scan-based systems, the frequency of the reference beam is automatically shifted as a result of the Doppler shift caused by the moving reference mirror. In our TS-OCT system, the frequency shift is generated by one or two AOMs placed in the reference arm (placement of the AOMs in the sample arm would also work in principle). If only one AOM is used, the carrier frequency is equal to the acoustic frequency ν_{a} (or $2\nu_{\mathrm{a}}$ if the AOM is passed twice). Since ν_{a} is usually several tens of MHz, the carrier frequency is rather high in this case. On the one hand, this enables very high scanning speeds; however, it requires high-speed detectors and amplifiers which usually have a poorer signal-to-noise ratio (SNR) than slower detectors/amplifiers. For this reason, frequently two AOMs are used. They are operated at slightly different frequencies $\nu_{1\mathrm{a}}$ and $\nu_{\mathrm{a}2}$. One AOM is oriented to upshift the light frequency and the other to downshift the frequency, so that the net frequency shift (and the net carrier frequency) is much lower, on the order of a few 100 kHz to a few MHz, thus enabling the use of slower low-noise detectors/amplifiers.

62.3 Interferometer Setups of SLO/OCT and Dynamic Focusing

In principle different interferometer configurations can be used for AOM-based en face OCT: Michelson and Mach–Zehnder interferometers. However, we discuss the operating principle of such an instrument with reference to a Mach–Zehnder interferometer scheme. This design [13] (c.f. Fig. 62.1) enables balanced detection and incorporates the simultaneous recording of a scanning laser ophthalmoscope (SLO) channel.

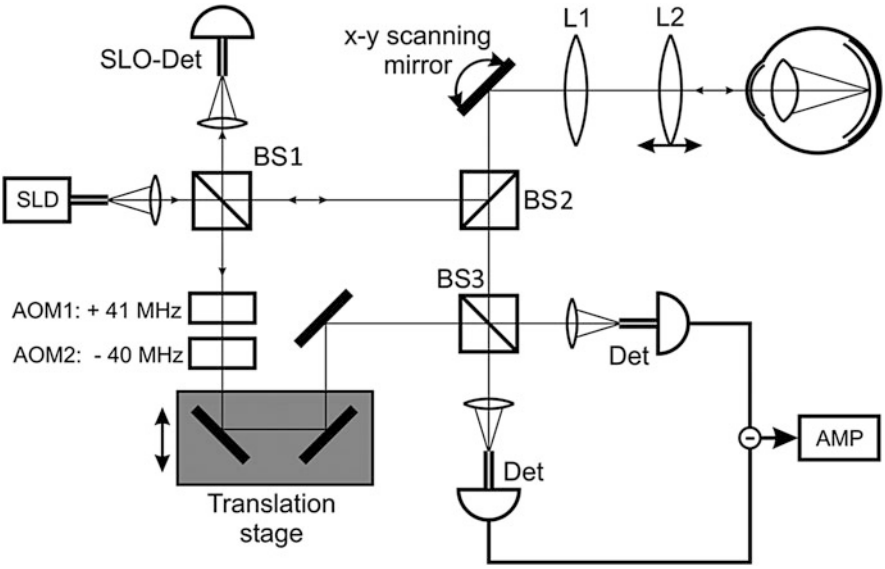

Fig. 62.1 Sketch of AOM-based Mach–Zehnder interferometer for retinal imaging. *AMP* amplifier, *AOM* acousto-optic modulator, *BS* beam splitter, *Det* single-mode fiber pigtailed detector, *L1* and *L2* lenses, *SLD* superluminescent diode, *SLO-Det* scanning laser ophthalmoscope detector (single-mode fiber pigtailed) (Reproduced from Pircher et al. [13] by permission of the Optical Society of America)

A low coherent light source emits a beam of short coherence length, centered at optical frequency ν_0. This beam illuminates the interferometer where it is split by BS1 into two components: a reference beam and a sample beam. The reference beam traverses two AOMs with different frequency shifts (ν_1 and ν_2, resulting in a net light frequency shift of $\Delta\nu$). The angular spreads of the frequency-shifted beams caused by the two oppositely oriented AOMs cancel each other largely. This allows the use of very broadband light sources, thus enabling ultrahigh-resolution TS-OCT [9, 14]. After traversing the AOMs, the beam is reflected at two reference mirrors that are mounted on a translation stage. These act as a variable path delay unit (PDU) that is used to vary the length of the reference path between successive en face scans, thus changing the position of the coherence gate within the sample (in this case the retina). The beam is recombined with the sample beam at the beam splitter that is located at the interferometer exit (BS3). The sample beam traverses another beam splitter (BS2) and is directed to an x–y scanning unit. The telescope located after the scanning unit images the pivot point of the scanners onto the pupil plane of the eye. The last lens of the telescope is mounted on a translation stage that can be simultaneously moved with the change of the coherence gate, thus enabling a simultaneous shift of the focal position with the coherence gate [11]. The light is backscattered from the retina and split into

two parts at the beam splitter BS2. One part is directed to the interferometer entrance where it is partly reflected by BS1 and is coupled into a single-mode fiber. This light is detected by an avalanche photodiode. Although it records part of the light backscattered from the sample, this light is not brought to interference with the reference beam. Therefore, this detector records a simple intensity image from the retina without coherence gating similar to a commonly used SLO [15, 16] detector. As will be discussed later on, this additional signal is essential for alignment, focusing, and post-processing purposes.

The other light part exiting BS2 is directed to the beam splitter at the interferometer exit (BS3) where it is recombined with the reference arm. Light from both exits is coupled into single-mode fibers and is detected by a dual balanced detector. The light-induced electrical signals from both interferometer exits are phase shifted by 180° between each other which enable the dual balanced detection by simply subtracting the two recorded signals before amplification. This procedure reduces source noise and excess noise [17]. In order to allow a pixel to pixel correspondence between SLO and OCT channels, the two OCT detectors have to be confocal to the SLO detector, and the signals are recorded simultaneously using the same data acquisition board.

Subject aligning and data recording are done in the following way. First, the focus is adjusted by moving the last lens and using the information of the SLO channel. Then the PDU is set to place the coherence gate to the location of the cone photoreceptors (junction between inner and outer segments of cones), a location that provides high backscattering signal. Shortly before starting the 3D data recording, the coherence gate and the focus are set deeper into the tissue (within the choroid). The x–y scanner scans the complete x–y plane corresponding to the depth position of the coherence gate (the layer thus scanned is the so-called coherence layer; its thickness is equal to the coherence length). If the sample beam hits a backreflecting or backscattering site within the coherence layer, the backscattered light will interfere with the reference beam. Since sample and reference beams differ in frequency by an amount $\Delta\nu$, the resulting interference signal will oscillate at $\Delta\nu$ (the beat frequency). $\Delta\nu$ constitutes a very stable carrier frequency that can easily be extracted by filtering with a band pass filter centered at $\Delta\nu$. The magnitude of the signal thus extracted is a measure of reflectivity of the sample as a function of the transversal position at the depth defined by the PDU. The signal magnitude is encoded on a grayscale. The signal from the SLO channel is recorded in parallel. However, the depth resolution of this channel is determined by the numerical aperture and the resulting depth of focus. After one en face scan, the PDU and focus settings are changed to move the coherence layer closer to the surface of the sample, and another en face scan is recorded. Step by step, the coherence layer is shifted through the sample. In this way, a 3D data set of a selected region of the sample is recorded. Figure 62.2 illustrates the transversal scanning scheme, as compared to the conventional, A-scan-based scheme, for the case of retinal imaging.

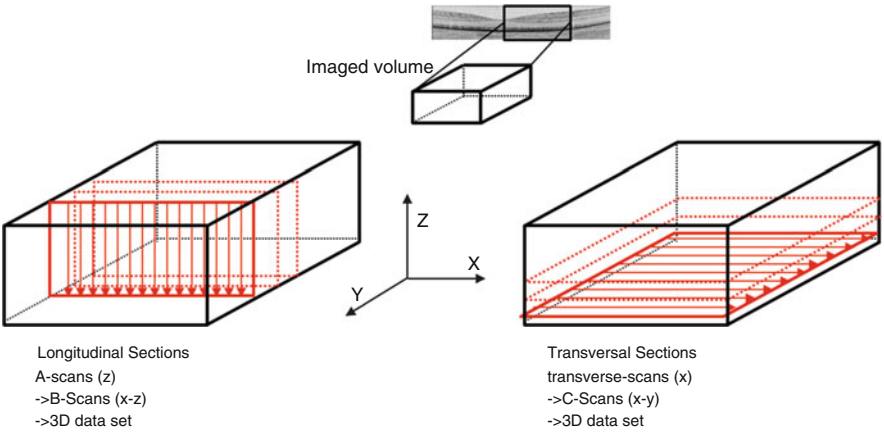

Fig. 62.2 Comparison of conventional longitudinal scan pattern (*left*) and transversal scan pattern (*right*)

62.4 Axial Eye Tracking and Transverse Motion Correction

Imaging the retina in vivo at high magnifications is challenging because of permanent eye motion. This motion will be present in all three dimensions. In FD-OCT axial eye motion is regarded as a minor problem because of the high axial imaging speed. Although axial motion is present in B-scans and in 3D volumes, these artifacts can largely be corrected in post-processing by, e.g., using correlation techniques between different B-scans. On the other hand, transverse motion artifacts can be a limiting factor. To overcome this, either hardware-based transverse eye tracking (2D) [18] has to be implemented or the transverse extension of the imaged volume has to be significantly reduced [19]. The scanning priority in TS-OCT is different; therefore, transverse eye motion can be corrected similar to high-resolution SLO systems in post-processing [20]. Axial eye motion, however, is a limiting factor for 3D measurements and has therefore to be corrected.

Our group introduced a concept for axial eye tracking that is based on an accurate measurement of the corneal apex position. The depth position of the cornea is then used to adapt accordingly the length of the reference arm of the TS-OCT instrument [21]. A sketch of an improved instrument is shown in Fig. 62.3 [22]. The system consists of several parts: the TS-OCT part, a separate FD low-coherence interferometer (LCI) for measuring the corneal apex position, and a part for changing very rapidly the length of the reference arm. The TS-OCT setup is similar to the scheme presented in Fig. 62.1. However, in order to improve the light efficiency within the instrument, additional polarization-sensitive components have been implemented. For details, refer to reference [22]. The LCI is based on a 90:10 fiber splitter and is operated at 1,300 nm with a bandwidth of 55 nm resulting in a depth resolution of ~14 μm. Only 10 % of the light is directed to the sample arm. Via a dichroic mirror, the sample beam is coupled into the sample

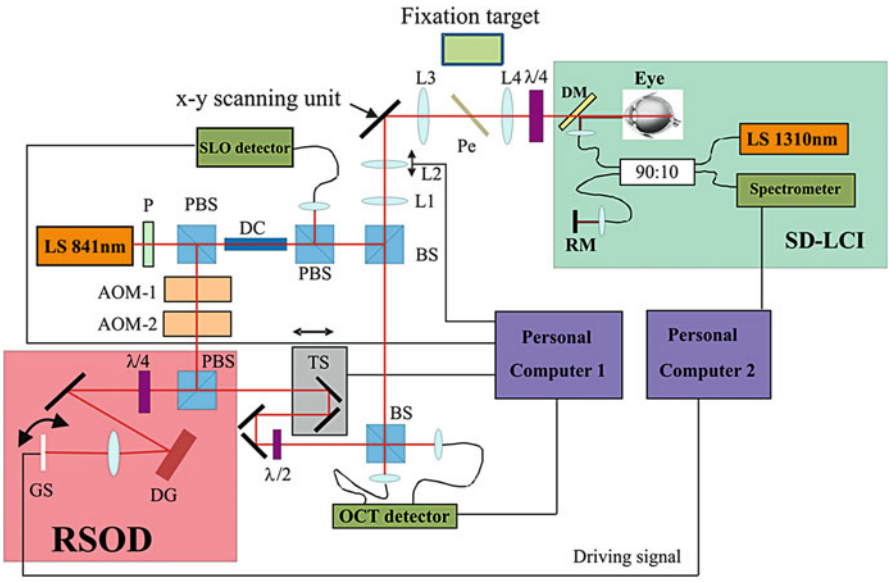

Fig. 62.3 Scheme of a TS-OCT instrument with implemented high-speed axial eye motion correction. *RSOD* rapid scanning optical delay line, *SD-LCI* spectral domain low coherence interferometer, *LS* light source, *P* polarizer, *DC* dispersion compensation glass rods, *BS* beam splitter, *L1–L4* lenses (L1 $f = 50$ mm, L2 $f = 20$ mm, L3 $f = 40$ mm, L4 $f = 80$ mm), *AOM* acousto-optic modulator, *TS* translation stage, *PBS* polarizing beam splitter, *DM* dichroic mirror, *RM* reference mirror, *DG* diffraction grating, *Pe* Pellicle, *GS* galvo scanner, x–y scanning unit consists of a resonant scanner and a galvo scanner (Imaging optics between the two scanning mirrors are omitted for clarity) (Reproduced from Pircher et al. [22] by permission of the Optical Society of America)

beam of the TS instrument and is directed to the eye. A collimated beam incident on the cornea is used which is essential in order to minimize influences of transverse motion on the measured apex position [23]. Moreover, only the corneal reflex is detected (no internal structure), resulting in a single OCT signal. Even though the depth resolution of the LCI is moderate, the peak position of the OCT signal can be determined very accurately. Light that is backscattered from the cornea is brought to interference with the light from the reference arm and is detected with a spectrometer. The spectrometer consists of a reflective diffraction grating and an InGaAs line scan camera that can be operated with up to 7 kHz.

While the measurement of the corneal position can be done very fast, the corresponding adaption of the reference arm length can be a limiting factor because of the inertia of the optical components. Even if a high-speed translation stage is used, residual axial eye motion remains [21]. In order to improve the adaption speed, we implemented a technology that is well known from the pre-FD-OCT area: the rapid scanning optical delay line (RSOD) [24]. The RSOD which is placed into the reference arm of the TS-OCT interferometer (c.f. Fig. 62.3) consists of a diffraction grating, a lens, and a galvanometer scanner. The pivot point of the

scanner is adjusted in order to change the group delay only (no additional phase delay is introduced). The improved axial eye motion correction speed ensures that residual correction errors are well below the depth resolution of the system. The tracking system is based on measurement of the corneal position. Hence, it cannot distinguish between axial eye motion and axial eye length changes caused by, e.g., fundus pulsation. However, these length changes are in the order of a few microns [25] and can therefore be neglected.

Using the information from the SLO channel, transverse motion correction can be done in post-processing similar to SLO instruments. For this purpose the cross correlation between each recorded SLO frame with a reference frame (chosen by the user) is calculated, and the frame is shifted according to the displacement from the position of the reference frame. All frames are averaged to produce a new reference frame that should be free of in-frame distortions (provided that the number of averaged frames is sufficiently large). The previous step is repeated using this new reference frame and applying the transformation matrix to the OCT images. Together with axial eye tracking, this procedure allows the recording of 3D volumes of the retina with negligible eye motion artifacts [22]. While the abovementioned procedure is sufficient for imaging without AO assistance, the implementation of AO requires an additional step. In a final step, each frame is divided into several subframes consisting of a certain number of transverse lines. The cross correlation is then performed between each subframe and a reference frame resulting in an improved transverse motion correction, because this procedure partly compensates for in-frame distortions [20].

62.5 High-Resolution Imaging of the Human Retina

It is known from histology that the photoreceptors in the human eye (rods and cones) are arranged in a very regular way resulting in a mosaic pattern [26]. In the fovea, the spot of best vision (in the healthy eye), the cone density and the regularity are highest. The density decreases exponentially with increasing eccentricity from the fovea. While there are no rods present in the fovea, the rod density reaches a maximum at around 12–20° eccentricity from the fovea.

One of the major challenges in retinal imaging using OCT in the past decade was the visualization of the cone mosaic. Using other imaging technologies, it was demonstrated quite early that in healthy eyes with good optics, the correction of low-order aberrations (e.g., defocus and astigmatism) can be sufficient in order to resolve cones in the periphery of the fovea [27]. Unfortunately, the field of view of these initial instruments was limited to a very small patch on the retina. An augmentation of cone visualization capabilities and extending the field of view were achieved with the introduction of adaptive optics (AO) [28–35]. AO corrects a variety of aberrations even of higher orders. Hence, the cone mosaic could be successfully imaged using AO-equipped imaging technologies as flood illumination fundus cameras [36] and SLO [37]. However, the depth resolution of these imaging techniques is rather limited and prevents the visualization of different

interfaces of cone photoreceptors. OCT provides the necessary depth resolution, but its transversal resolution in the retina is commonly restricted by low NA to ~20 μm which is not sufficient to resolve individual cones. The low NA is a compromise between transverse resolution and depth of focus, thus maintaining the transverse resolution over the entire imaging depth (i.e., the retinal thickness).

The first attempt to improve the transverse resolution by combining adaptive optics with OCT has been made in 2003 by the group of D. T. Miller at Indiana University [38]. The approach used full field OCT but faced sensitivity issues when applied in vivo. Later work used AO in an A-scan-based OCT system; however, visualization of individual cones could not be demonstrated with these initial setups [39, 40]. It took another year until transversal structures of a spacing similar to that of photoreceptors could be shown in OCT B-scans using AO-OCT by two different groups [41, 42]. However, both instruments had rather slow 3D imaging capabilities, preventing motion artifact-free 2D imaging of the cone mosaic in the en face imaging plane.

Our group picked up the initial abovementioned idea of cone imaging without using AO assistance. Because TS-OCT has the same scanning protocol as SLO, this technique is ideally suited for recording (nearly) motion artifact-free en face images of the retinal structure. We used the setup shown in Fig. 62.1 for this purpose and demonstrated cone mosaic imaging (in the en face plane) with OCT for the first time [13].

The system employed a moderately wide sampling beam of ~4 mm diameter, enabling transverse resolutions sufficient to resolve the somewhat wider cone spacing at the periphery of the fovea but small enough to avoid excessive ocular aberrations and therefore (in the healthy eye) the necessity of adaptive optics. In addition the standard detection configuration in OCT is already confocal because it is based on using single-mode fibers [43]. The additional confocal SLO detector (also single-mode fiber coupled) operates in parallel to the OCT channel and provides an essential tool for correct subject and focus alignment. After the implementation of faster camera technology or fast swept source OCT technology, the simple concept of moderate sample beam diameter (and confocal arrangement) for cone photoreceptor imaging has been successfully translated to FD-OCT instruments [44–46].

Axial motion artifacts, however, limited the performance of our initial instrument to 2-dimensional imaging (B-scans or C-scans). Full 3D imaging capability was achieved by the implementation of an axial eye tracker [21, 22]. Figure 62.4 shows example images recorded in a healthy subject with a TS-OCT instrument that is equipped with an axial tracker. Figure 62.4a shows a B-scan retrieved from 3D data which demonstrates the capabilities of the axial tracker and the dynamic focus. The images were recorded at ~4° eccentricity from the fovea and cover a volume of 1° (x) × 1° (y) × 500 μm (z). Note that despite the high transverse resolution, the entire depth is imaged sharply which could up to now not be achieved in the retina using FD-OCT. Similar to standard OCT, four distinct posterior layers can be observed. However, there is still some controversy on the labeling of these layers. We strongly favor the following association and provide different evidences for this labeling later on: (1) external limiting membrane (ELM), (2) boundary between inner

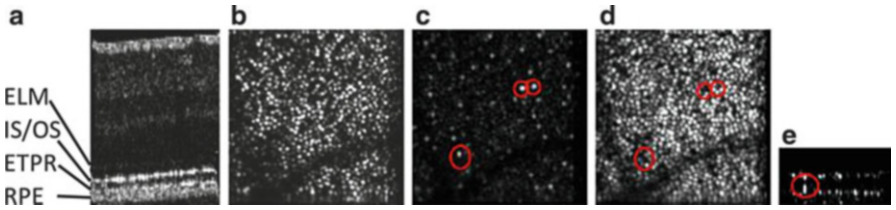

Fig. 62.4 TS-OCT images retrieved from a 3D volume. (**a**) Exemplary overview B-scan, (**b**) junction between inner and outer segments of photoreceptors, (**c**) within cone outer segments (locations of BRS that show no signal within the ETPR are marked with a *red circle*), (**d**) ETPR layer, (**e**) exemplary B-scan located at the position of the *lower left red circle* in (**c**) and (**d**) (Reproduced from Pircher et al. [22] by permission of the Optical Society of America)

and outer segments of photoreceptors (IS/OS), (3) end tips of photoreceptors (ETPR), and (4) retinal pigment epithelium (RPE). As can be observed in Fig. 62.4b, d, two layers, the IS/OS and ETPR, show a similar cone mosaic pattern as is known from SLO imaging. The appearance in both layers can be explained by the wave guiding properties of the cones [47]. The outermost layer does not show the cone mosaic and appears in general more diffuse than the previous two layers. Using polarization-sensitive OCT, a polarization scrambling was observed from this layer [8, 48, 49]. Data from patients and in vitro measurements showed that melanin is one cause for the polarization scrambling and that the layer can hence be associated with the RPE [50–52].

Interestingly, as is shown in Fig. 62.4c, e, bright reflecting spots (BRSs) within the outer segments of the cones can be observed at some transverse locations. Defects within the cone outer segments could be one possible explanation for these signals. Using a Fourier analysis of the cone mosaic yields Yellott's rings [53], and the radius of each ring is a direct measure of the row to row spacing of the cones. This spacing can be translated into cone density. Figure 62.5a shows the cone density measured at different eccentricities from the fovea for five subjects. The measured densities are in good agreement with values known from histology and show that for four out of five healthy subjects, the cone mosaic could be resolved down to $\sim 2^\circ$ eccentricity from the fovea without the use of adaptive optics. In addition we measured the density of the BRS which shows some kind of maximum at 3–4° eccentricity from the fovea (c.f. Fig. 62.5b).

62.6 Temporal Changes of Human Cone Photoreceptors

The outer segments of cone photoreceptors contain the photopigment and are built up by a stack of densely packed membrane discs. In order to prevent photochemical damage, these outer segment discs are renewed with time [54, 55]. New discs are generated at the IS/OS junction, while at the location of the ETPR, the outermost of these discs is shed followed by phagocytosis of this tissue by the retinal pigment epithelium [56]. The growth rate of the outer segments is known

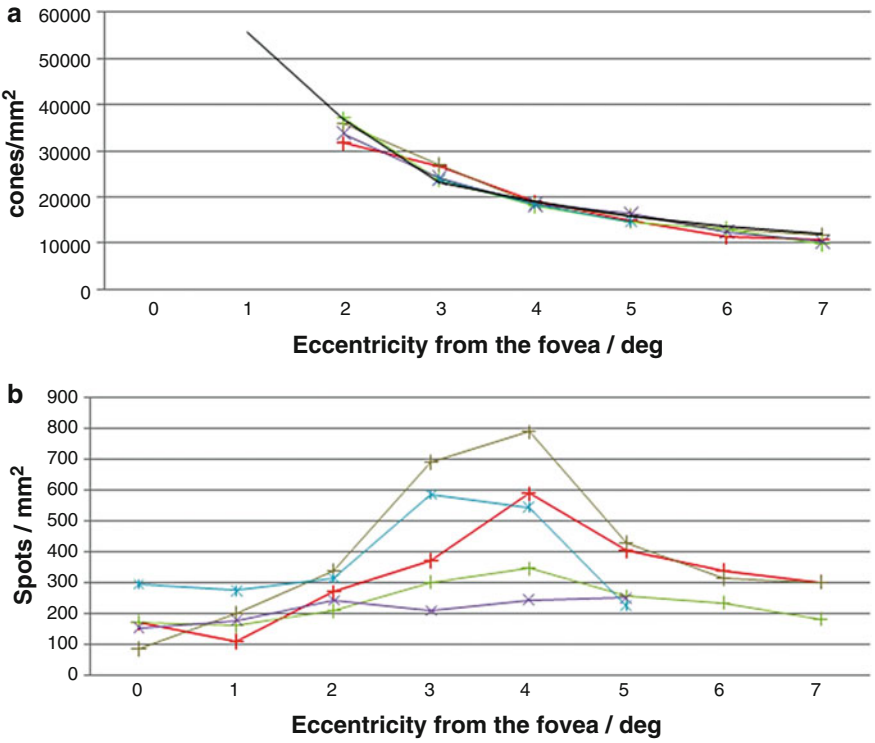

Fig. 62.5 (**a**) Measured cone density of five volunteers at different eccentricities from the fovea (*black line*: data from Ref [26]). (**b**) Measured bright reflections (*BR*) within the cone outer segments at different eccentricities (each color corresponds to a different subject) (Reproduced from Pircher et al. [22] by permission of the Optical Society of America)

from animal experiments and lies in the order of ~100 nm per hour [57, 58]. An investigation of these changes in vivo in humans is quite challenging. Recently, a first approach used a fundus camera equipped with adaptive optics to measure indirectly changes caused by cone renewal [59]. The retina was illuminated with a temporally coherent light source. This leads to interference effects between the signals arising from different depths (e.g., IS/OS and ETPR). Depending on the axial distance between the interfaces, constructive or destructive interference will occur, leading to intensity changes in the observed backscattered light from each cone if the distance between the reflection sites varies with time. With the generation of new discs, the length of the outer segment is changing leading to sinusoidal intensity fluctuations with time (several hours). Note that these length changes are much smaller than 1 μm and can therefore not be observed with standard OCT within a few hours.

TS-OCT has the capability to record high-resolution 3D volumes without noticeable motion artifacts. Hence, the observation of exactly the same location on the retina over time becomes possible. In order to investigate temporal changes

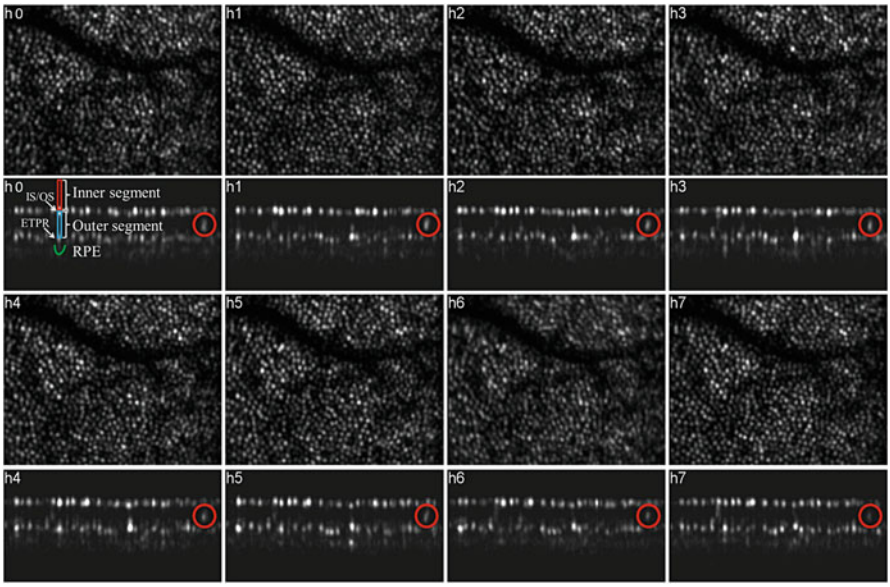

Fig. 62.6 Depth-integrated OCT images (∼0.94° × 0.7°) and representative B-scan images (0.94° × 120 μm) of the cone mosaic recorded over a period of 7 h at the same position. The number in the *upper left* corner indicates the measurement time. *Red circles* mark a bright reflection spot (*BRS*) within the outer segments of the cones. The images demonstrate exact relocation and stability over extended times

caused by the renewal process, we performed measurements over different periods of time [60]. The first period lasted 7 h with ten 3D measurements every hour, while the second period lasted 96 h performing ten 3D measurements every 24 h. Out of the ten measurements at each time point, a minimum of five measurements were averaged in order to minimize influences of subject alignment. Figure 62.6 shows en face images of the cone mosaic recorded within the first measurement period at ∼4° eccentricity as well as an exemplary B-scan at the same location [60]. As can be observed from the images, the residual registration error between the 3D data sets is smaller than the extension of a single cone. In the en face images, intensity fluctuations of individual cones can be observed. The B-scans reveal that both interfaces, the IS/OS junction and the ETPR, show these fluctuations. The depth position of the two layers remains rather constant (i.e., smaller than the detection limit of the system) for each individual cone within 7 h. In addition, the depth position of a BRS (marked with a red circle in Fig. 62.6) stays at the same location. The expected length change by new disc generation for this time period is smaller than 1 μm and hence not detectable with our system. These small changes can only be detected using the phase information of an OCT signal as was recently demonstrated by R. S. Jonnal et al. [61]. The origin of the observed intensity fluctuations is unclear. These cannot be explained by an

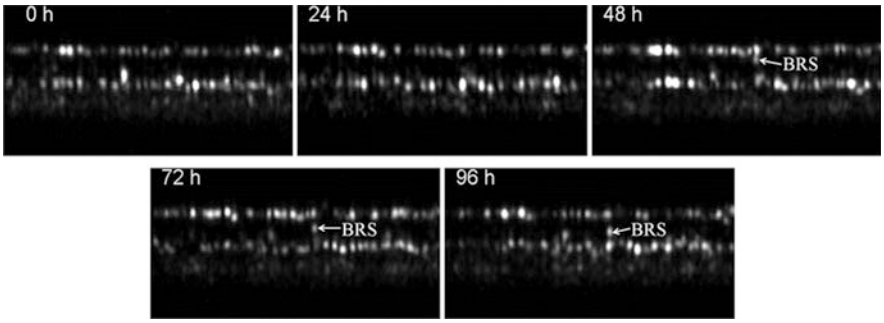

Fig. 62.7 Representative B-scan recorded at the same location over the entire measurement period of 96 h (the number in the *upper left* corner indicates the measurement time) containing a BRS that appears at hour 48. Image extension, ~0.88° × 120 μm^2; retinal eccentricity, ~4° nasal from the fovea) (Reproduced from Pircher et al. [60] by permission of the Optical Society of America)

interference phenomenon as mentioned above observed by the flood illumination system because the TS-OCT instrument uses a low-coherence light source with a coherence length of only ~4 μm in tissue, much smaller than the outer segment length. However, we do believe that the changes may be caused by the generation of new discs at the IS/OS interface.

In order to detect potential length changes with our system, the observation period has to be extended. Figure 62.7 shows exemplary B-scans recorded at the same location within the second measurement period (i.e., 96 h). The intensity fluctuations at the IS/OS and ETPR are more pronounced than in the previous measurement period. In addition changes of the depth position of the ETPR can be observed while the depth position of the IS/OS junction stays constant. These changes are likely caused by the disc shedding process. Depending on the phase within the shedding process, the outer segment length will be shorter (after disc shedding) or longer (right before disc shedding) which is one possible explanation for our observation. Most interestingly, at hour 48, one of the abovementioned BRSs appears shortly below the IS/OS junction and apparently moves in the successive frames toward the ETPR layer. We measured for two healthy volunteers the motion speed of all BRSs and found an average speed of ~110 nm per hour which quite matches the cone renewal speed that is expected from animal experiments and which was measured with other methods [59, 61]. One hypothesis to explain our observation is the following: Cracks or defects in the packing arrangement of the cone outer segment discs give rise to a change in the refractive index and therefore to a strong OCT signal that we observe as BRS. With the generation of new discs at the IS/OS junction, the defect moves together with the surrounding discs slowly toward the ETPR until the discs are finally shed by the RPE. However, in order to support this hypothesis, more measurements are needed.

62.7 Adaptive Optics TS-OCT

Although cone photoreceptors could be resolved with the abovementioned instrument, the visualization is limited to subjects with good eye optics and to eccentricities from the fovea that are larger than ~2°. In order to visualize foveal cones or even rod photoreceptors as was demonstrated recently with AO-SLO instruments [62–64], a further increase of transverse resolution is necessary. This, however, can only be achieved with the implementation of adaptive optics. First, AO-equipped TS-OCT instruments have been presented several years ago [65, 66]. However, both instruments did not incorporate an axial eye tracker which greatly limited their performance. Nevertheless, the cone density from both layers (IS/OS and ETPR) could be measured at different eccentricities from the fovea starting with an eccentricity as close as 0.7° [66].

Based on our experiences with AO-SLO and TS-OCT, we very recently presented the first results obtained with the combination of these two techniques [67]. The sample arm is based on an AO-SLO instrument that uses lenses instead of mirrors for imaging [64]. Figure 62.8 shows en face images of the fovea recorded with the new instrument. Individual foveal cones can be resolved with both imaging modalities which have, up to now, not been demonstrated using OCT. The representative B-scan (Fig. 62.8c) is located at the fovea centralis and shows the elevation of the IS/OS junction due to the longer outer segments' length at this location. Note that the transverse extension is greatly enlarged in comparison to standard OCT images which results in a less pronounced appearance of the elevation. Both layers (IS/OS and ETPR) show the cone mosaic (images not shown here) and therefore the typical discrete spacing of the photoreceptors within the B-scan (as has previously been shown at some eccentricity from the fovea). As is known from standard OCT imaging, the depth separation between ETPR and RPE is less pronounced in this area than at larger eccentricities. Nevertheless, the discrete spacing that appears only within the ETPR and not the RPE allows a differentiation between the two layers in Fig. 62.8c. Although the ELM is visible in Fig. 62.8c, the signal intensity is too weak in order to determine if a similar cone mosaic can be observed from this layer.

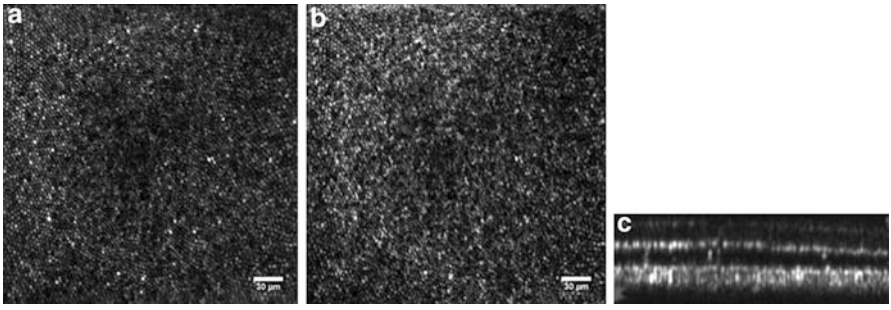

Fig. 62.8 AO-TS-OCT images of foveal cones. (**a**) SLO channel, (**b**) depth-integrated OCT channel (**c**) representative B-scan through the central fovea

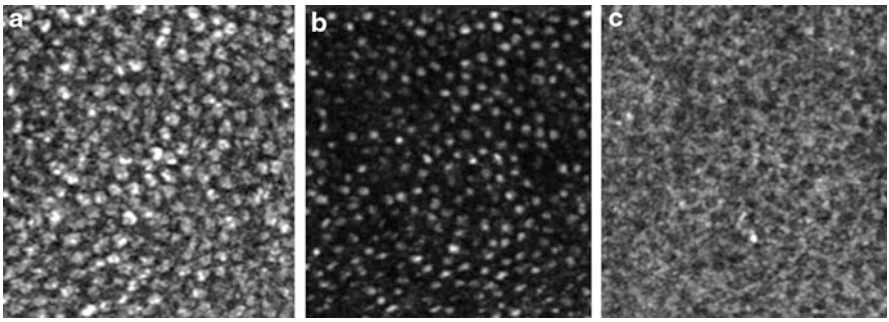

Fig. 62.9 AO-TS-OCT en face images of the cone and rod mosaic. (**a**) IS/OS junction, (**b**) ETPR, (**c**) end tips of rod photoreceptors

At larger eccentricities from the fovea, we expect to observe cones and rods. It is known from histology that the outer segments of rods are slightly longer than that of cones. Although individual rods could be visualized using AO-SLO, the depth resolution of these instruments is insufficient to separate the different interfaces of the outer segments. On the other hand, high-resolution OCT showed the appearance of an additional layer at larger eccentricities from the fovea that was associated with the posterior tips of rods (even though the transverse resolution did not allow for the visualization of individual rods) [68]. We used our AO-TS-OCT instrument to investigate this area with high resolution in all three dimensions. Figure 62.9 shows en face images retrieved at different imaging depths recorded at $\sim 7^{\circ}$ eccentricity from the fovea. Figure 62.9a corresponds to the IS/OS junction. At this layer a signal from both photoreceptor types (cones and rods) is expected. Therefore, we can observe high reflective spots of larger width corresponding to the cones that are surrounded by very small spots corresponding to individual rods. However, the large spots appear somehow speckled, i.e., appear to consist of smaller structures. A similar appearance has been observed with AO-SLO [63]. If we go deeper into the tissue to the location of the ETPR layer (c.f. Fig. 62.9b), we observe only the cone mosaic. Note that within this layer, the individual cones do not show the abovementioned speckled appearance. The measured spacing of the cones corresponds to the expected cone density at this eccentricity. When setting the coherence gate further into the tissue (at the location of the end tips of the rods), a completely different pattern is observed (c.f. Fig. 62.9c). At the locations of the cones, dark patches can be observed that are surrounded by smaller structures which correspond to individual rods.

62.8 Conclusion and Outlook

Although FD-OCT is well suited for a huge variety of different applications, TS-OCT can be beneficial for some niche applications as high-resolution retinal imaging. With the development of even faster FD-OCT setups operating at A-scan

rates in the MHz range, the benefit of greatly reduced transverse motion artifacts could be alleviated (at least for a large field of view [69]). However, these systems provide less sensitivity than standard OCT systems, and for an entirely sharp 3D data set, several recorded volumes have to be stitched together. Moreover, current systems are operated in the 1,050-nm regime which reduces the achievable transverse resolution and probably makes the implementation of AO more complex.

The combination of TS-OCT with AO requires some experimental effort (especially with the implementation of the axial eye tracker), but initial results are quite promising. The implementation of AO correction alleviates the limitation of the previous instrument (only healthy volunteers with good eye optics could be imaged) and enlarges the number of measurable subjects. Nevertheless, the next step must be to investigate the applicability of this technology for patient imaging.

Acknowledgements We thank F. Felberer, Center for Medical Physics and Biomedical Engineering, Medical University of Vienna, for contributing to this work and B. Baumann, T. Torzicky, and S. Zotter, Center for Medical Physics and Biomedical Engineering, Medical University of Vienna; J. S. Kroisamer and U. Schmidt-Erfurth, Department of Ophthalmology, Medical University of Vienna; and R.J. Zawadzki and J.S. Werner, Department of Ophthalmology and Vision Science, UC-Davis, for cooperation.

Financial support from the Austrian Science Fund (FWF grants P19624-B02 and P22329-N20) is acknowledged.

References

1. D. Huang, E.A. Swanson, C.P. Lin, J.S. Schuman, W.G. Stinson, W. Chang, M.R. Hee, T. Flotte, K. Gregory, C.A. Puliafito, J.G. Fujimoto, Optical coherence tomography. Science **254**, 1178–1181 (1991)
2. R. Leitgeb, C.K. Hitzenberger, A.F. Fercher, Performance of Fourier domain vs. time domain optical coherence tomography. Opt. Express **11**, 889–894 (2003)
3. A.G. Podoleanu, G.M. Dobre, D.A. Jackson, En-face coherence imaging using galvanometer scanner modulation. Opt. Lett. **23**, 147–149 (1998)
4. C.K. Hitzenberger, P. Trost, P.W. Lo, Q.Y. Zhou, Three-dimensional imaging of the human retina by high-speed optical coherence tomography. Opt. Express **11**, 2753–2761 (2003)
5. M. Pircher, E. Goetzinger, R. Leitgeb, C.K. Hitzenberger, Three dimensional polarization sensitive OCT of human skin in vivo. Opt. Express **12**, 3236–3244 (2004)
6. M. Pircher, E. Goetzinger, R. Leitgeb, C.K. Hitzenberger, Transversal phase resolved polarization sensitive optical coherence tomography. Phys. Med. Biol. **49**, 1257–1263 (2004)
7. M. Pircher, E. Götzinger, R. Leitgeb, H. Sattmann, O. Findl, C.K. Hitzenberger, Imaging of polarization properties of human retina in vivo with phase resolved transversal PS-OCT. Opt. Express **12**, 5940–5951 (2004)
8. M. Pircher, E. Götzinger, O. Findl, S. Michels, W. Geitzenauer, C. Leydolt, U. Schmidt-Erfurth, C.K. Hitzenberger, Human macula investigated in vivo with polarization-sensitive optical coherence tomography. Invest. Ophthalmol. Vis. Sci. **47**, 5487–5494 (2006)
9. K. Wiesauer, M. Pircher, E. Götzinger, S. Bauer, R. Engelke, G. Ahrens, G. Grutzner, C.K. Hitzenberger, D. Stifter, En-face scanning optical coherence tomography with ultra-high resolution for material investigation. Opt. Express **13**, 1015–1024 (2005)

10. J.F. de Boer, B. Cense, B.H. Park, M.C. Pierce, G.J. Tearney, B.E. Bouma, Improved signal-to-noise ratio in spectral-domain compared with time-domain optical coherence tomography. Opt. Lett. **28**, 2067–2069 (2003)
11. M. Pircher, E. Götzinger, C.K. Hitzenberger, Dynamic focus in optical coherence tomography for retinal imaging. J. Biomed. Opt. **11**, 054013 (2006)
12. I.C. Chang, Acousto-optic devices and applications, in *Handbook of Optics*, ed. by M. Bass 2nd edn., vol II, (McGraw-Hill, Inc., NewYork, Optical Society of America, 1995)
13. M. Pircher, B. Baumann, E. Götzinger, C.K. Hitzenberger, Retinal cone mosaic imaged with transverse scanning optical coherence tomography. Opt. Lett. **31**, 1821–1823 (2006)
14. M. Pircher, E. Goetzinger, R.A. Leitgeb, H. Sattmann, C.K. Hitzenberger, Ultrahigh resolution polarization sensitive optical coherence tomography. *Coherence Domain Opt. Methods Opt. Coherence Tomogr. Biomed.* IX **5690** 257–262 (2005)
15. R.H. Webb, G.W. Hughes, Scanning laser ophthalmoscope – design and applications. J. Opt. Soc. Am. **72**, 1808–1808 (1982)
16. R.H. Webb, G.W. Hughes, Scanning laser ophthalmoscope. IEEE Trans. Biomed. Eng. **28**, 488–492 (1981)
17. A.M. Rollins, J.A. Izatt, Optimal interferometer designs for optical coherence tomography. Opt. Lett. **24**, 1484–1486 (1999)
18. R.D. Ferguson, D.X. Hammer, L.A. Paunescu, S. Beaton, J.S. Schuman, Tracking optical coherence tomography. Opt. Lett. **29**, 2139–2141 (2004)
19. O.P. Kocaoglu, S. Lee, R.S. Jonnal, Q. Wang, A.E. Herde, J.C. Derby, W.H. Gao, D.T. Miller, Imaging cone photoreceptors in three dimensions and in time using ultrahigh resolution optical coherence tomography with adaptive optics. Biomed. Opt. Express **2**, 748–763 (2011)
20. S.B. Stevenson, A. Roorda, Correcting for miniature eye movements in high resolution scanning laser ophthalmoscopy, Proc. SPIE 5688, Ophthalmic Technologies XV, **145** (2005)
21. M. Pircher, B. Baumann, E. Goetzinger, H. Sattmann, C.K. Hitzenberger, Simultaneous SLO/OCT imaging of the human retina with axial eye motion correction. Opt. Express **15**, 16922–16932 (2007)
22. M. Pircher, E. Götzinger, H. Sattmann, R.A. Leitgeb, C.K. Hitzenberger, In vivo investigation of human cone photoreceptors with SLO/OCT in combination with 3D motion correction on a cellular level. Opt. Express **18**, 13935–13944 (2010)
23. C.K. Hitzenberger, Measurement of corneal thickness by low-coherence interferometry. Appl. Optics **31**, 6637–6642 (1992)
24. G.J. Tearney, B.E. Bouma, J.G. Fujimoto, High-speed phase- and group-delay scanning with a grating-based phase control delay line. Opt. Lett. **22**, 1811–1813 (1997)
25. L. Schmetterer, S. Dallinger, O. Findl, K. Strenn, U. Graselli, H.G. Eichler, M. Wolzt, Noninvasive investigations of the normal ocular circulation in humans. Invest. Ophthalmol. Vis. Sci. **39**, 1210–1220 (1998)
26. C.A. Curcio, K.R. Sloan, R.E. Kalina, A.E. Hendrickson, Human photoreceptor topography. J. Comp. Neurol. **292**, 497–523 (1990)
27. D.T. Miller, D.R. Williams, G.M. Morris, J.Z. Liang, Images of cone photoreceptors in the living human eye. Vision Res. **36**, 1067–1079 (1996)
28. N. Doble, High-resolution, in vivo retinal imaging using adaptive optics and its future role in ophthalmology. Expert Rev. Med. Devices **2**, 205–216 (2005)
29. P. Godara, A.M. Dubis, A. Roorda, J.L. Duncan, J. Carroll, Adaptive optics retinal imaging: emerging clinical applications. Optom. Vis. Sci. **87**, 930–941 (2010)
30. K.M. Hampson, Adaptive optics and vision. J. Mod. Opt. **55**, 3425–3467 (2008)
31. D.T. Miller, O.P. Kocaoglu, Q. Wang, S. Lee, Adaptive optics and the eye (super resolution OCT). Eye **25**, 321–330 (2011)
32. A. Pallikaris, Adaptive optics ophthalmoscopy: results and applications. J. Refract. Surg. **21**, S570–S574 (2005)
33. A. Roorda, Applications of adaptive optics scanning laser ophthalmoscopy. Optom. Vis. Sci. **87**, 260–268 (2010)

34. D.R. Williams, Imaging single cells in the living retina. Vision Res. **51**, 1379–1396 (2011)
35. M. Pircher, R. Zawadzki, Combining adaptive optics with optical coherence tomography: unveiling the cellular structure of the human retina in vivo. Expert Rev. Ophthalmol. **2**, 16 (2007)
36. J.Z. Liang, D.R. Williams, D.T. Miller, Supernormal vision and high-resolution retinal imaging through adaptive optics. J. Opt. Soc. Am. A Opt. Image Sci. Vis. **14**, 2884–2892 (1997)
37. A. Roorda, F. Romero-Borja, W.J. Donnelly, H. Queener, T.J. Hebert, M.C.W. Campbell, Adaptive optics scanning laser ophthalmoscopy. Opt. Express **10**, 405–412 (2002)
38. R.S. Jonnal, J. Qu, K. Thorn, D.T. Miller, En-face coherence gating of the retina with adaptive optics. Invest. Ophthalmol. Vis. Sci. **44**, U275–U275 (2003)
39. E.J. Fernandez, B. Povazay, B. Hermann, A. Unterhuber, H. Sattmann, P.M. Prieto, R. Leitgeb, P. Ahnelt, P. Artal, W. Drexler, Three-dimensional adaptive optics ultrahigh-resolution optical coherence tomography using a liquid crystal spatial light modulator. Vision Res. **45**, 3432–3444 (2005)
40. B. Hermann, E.J. Fernandez, A. Unterhuber, H. Sattmann, A.F. Fercher, W. Drexler, P.M. Prieto, P. Artal, Adaptive-optics ultrahigh-resolution optical coherence tomography. Opt. Lett. **29**, 2142–2144 (2004)
41. R.J. Zawadzki, S.M. Jones, S.S. Olivier, M.T. Zhao, B.A. Bower, J.A. Izatt, S. Choi, S. Laut, J.S. Werner, Adaptive-optics optical coherence tomography for high-resolution and high-speed 3D retinal in vivo imaging. Opt. Express **13**, 8532–8546 (2005)
42. Y. Zhang, J.T. Rha, R.S. Jonnal, D.T. Miller, Adaptive optics parallel spectral domain optical coherence tomography for imaging the living retina. Opt. Express **13**, 4792–4811 (2005)
43. T. Dabbs, M. Glass, Single-mode fibers used as confocal microscope pinholes. Appl. Optics **31**, 705–706 (1992)
44. B. Potsaid, B. Baumann, D. Huang, S. Barry, A.E. Cable, J.S. Schuman, J.S. Duker, J.G. Fujimoto, Ultrahigh speed 1050nm swept source/Fourier domain OCT retinal and anterior segment imaging at 100,000 to 400,000 axial scans per second. Opt. Express **18**, 20029–20048 (2010)
45. B. Potsaid, I. Gorczynska, V.J. Srinivasan, Y.L. Chen, J. Jiang, A. Cable, J.G. Fujimoto, Ultrahigh speed spectral/Fourier domain OCT ophthalmic imaging at 70,000 to 312,500 axial scans per second. Opt. Express **16**, 15149–15169 (2008)
46. T. Schmoll, A.S.G. Singh, C. Blatter, S. Schriefl, C. Ahlers, U. Schmidt-Erfurth, R.A. Leitgeb, Imaging of the parafoveal capillary network and its integrity analysis using fractal dimension. Biomed. Opt. Express **2**, 1159–1168 (2011)
47. J.M. Enoch, Wave-guide modes in retinal receptors. Science **133**, 1353 (1961)
48. E. Götzinger, B. Baumann, M. Pircher, C.K. Hitzenberger, Polarization maintaining fiber based ultra-high resolution spectral domain polarization sensitive optical coherence tomography. Opt. Express **17**, 22704–22717 (2009)
49. E. Götzinger, M. Pircher, W. Geitzenauer, C. Ahlers, B. Baumann, S. Michels, U. Schmidt-Erfurth, C.K. Hitzenberger, Retinal pigment epithelium segmentation by polarization sensitive optical coherence tomography. Opt. Express **16**, 16410–16422 (2008)
50. S. Zotter, M. Pircher, T. Torzicky, B. Baumann, H. Yoshida, F. Hirose, P. Roberts, M. Ritter, C. Schutze, E. Gotzinger, W. Trasischker, C. Vass, U. Schmidt-Erfurth, C.K. Hitzenberger, Large-field high-speed polarization sensitive spectral domain OCT and its applications in ophthalmology. Biomed. Opt. Express **3**, 2720–2732 (2012)
51. B. Baumann, S.O. Baumann, T. Konegger, M. Pircher, E. Gotzinger, F. Schlanitz, C. Schutze, H. Sattmann, M. Litschauer, U. Schmidt-Erfurth, C.K. Hitzenberger, Polarization sensitive optical coherence tomography of melanin provides intrinsic contrast based on depolarization. Biomed. Opt. Express **3**, 1670–1683 (2012)
52. B. Baumann, E. Götzinger, M. Pircher, C.K. Hitzenberger, Measurements of depolarization distribution in the healthy human macula by polarization sensitive OCT. J. Biophotonics **2**, 426–434 (2009)

53. J.I. Yellott, Spectral-analysis of spatial sampling by photoreceptors – topological disorder prevents aliasing. Vision Res. **22**, 1205–1210 (1982)
54. R.W. Young, Renewal of photoreceptor cell outer segments. J. Cell Biol. **33**, 61 (1967)
55. R.W. Young, D. Bok, Participation of retinal pigment epithelium in rod outer segment renewal process. J. Cell Biol. **42**, 392 (1969)
56. D.H. Anderson, S.K. Fisher, R.H. Steinberg, Mammalian cones – disk shedding, phagocytosis, and renewal. Invest. Ophthalmol. Vis. Sci. **17**, 117–133 (1978)
57. C.J. Guerin, G.P. Lewis, S.K. Fisher, D.H. Anderson, Recovery of photoreceptor outer segment length and analysis of membrane assembly rates in regenerating primate photoreceptor outer segments. Invest. Ophthalmol. Vis. Sci. **34**, 175–183 (1993)
58. D.H. Anderson, S.K. Fisher, P.A. Erickson, G.A. Tabor, Rod and cone disk shedding in the Rhesus-monkey retina – a quantitative study. Exp. Eye Res. **30**, 559–574 (1980)
59. R.S. Jonnal, J.R. Besecker, J.C. Derby, O.P. Kocaoglu, B. Cense, W.H. Gao, Q. Wang, D.T. Miller, Imaging outer segment renewal in living human cone photoreceptors. Opt. Express **18**, 5257–5270 (2010)
60. M. Pircher, J.S. Kroisamer, F. Felberer, H. Sattman, E. Götzinger, C.K. Hitzenberger, Temporal changes of human cone photoreceptors observed in vivo with SLO/OCT. Biomed. Opt. Express **2**, 100–112 (2011)
61. R.S. Jonnal, O.P. Kocaoglu, Q. Wang, S. Lee, D.T. Miller, Phase-sensitive imaging of the outer retina using optical coherence tomography and adaptive optics. Biomed. Opt. Express **3**, 104–124 (2012)
62. A. Dubra, Y. Sulai, Reflective afocal broadband adaptive optics scanning ophthalmoscope. Biomed. Opt. Express **2**, 1757–1768 (2011)
63. A. Dubra, Y. Sulai, J.L. Norris, R.F. Cooper, A.M. Dubis, D.R. Williams, J. Carroll, Noninvasive imaging of the human rod photoreceptor mosaic using a confocal adaptive optics scanning ophthalmoscope. Biomed. Opt. Express **2**, 1864–1876 (2011)
64. F. Felberer, J.S. Kroisamer, C.K. Hitzenberger, M. Pircher, Lens based adaptive optics scanning laser ophthalmoscope. Opt. Express **20**, 17297–17310 (2012)
65. D. Merino, C. Dainty, A. Bradu, A.G. Podoleanu, Adaptive optics enhanced simultaneous en-face optical coherence tomography and scanning laser ophthalmoscopy. Opt. Express **14**, 3345–3353 (2006)
66. M. Pircher, R.J. Zawadzki, J.W. Evans, J.S. Werner, C.K. Hitzenberger, Simultaneous imaging of human cone mosaic with adaptive optics enhanced scanning laser ophthalmoscopy and high-speed transversal scanning optical coherence tomography. Opt. Lett. **33**, 22–24 (2008)
67. F. Felberer, J.S. Kroisamer, B. Baumann, S. Zotter, U. Schmidt-Erfurth, C.K. Hitzenberger, and M. Pircher, Adaptive optics SLO/OCT for 3D imaging of human photoreceptors in vivo, Biomedical Optics Express **5**, 439–456 (2014)
68. V.J. Srinivasan, B.K. Monson, M. Wojtkowski, R.A. Bilonick, I. Gorczynska, R. Chen, J.S. Duker, J.S. Schuman, J.G. Fujimoto, Characterization of outer retinal morphology with high-speed, ultrahigh-resolution optical coherence tomography. Invest. Ophthalmol. Vis. Sci. **49**, 1571–1579 (2008)
69. W. Wieser, B.R. Biedermann, T. Klein, C.M. Eigenwillig, R. Huber, Multi-megahertz OCT: high quality 3D imaging at 20 million A-scans and 4.5 GVoxels per second. Opt. Express **18**, 14685–14704 (2010)

Small Animal Retinal Imaging

63

WooJhon Choi, Wolfgang Drexler, and James G. Fujimoto

Keywords
Functional imaging • Mouse • Optophysiology • Rat • Small animal

63.1 Introduction

Developing and validating new techniques and methods for small animal imaging is an important research area because there are many small animal models of retinal diseases such as diabetic retinopathy, age-related macular degeneration, and glaucoma [1–6]. Because the retina is a multilayered structure with distinct abnormalities occurring in different intraretinal layers at different stages of disease progression, there is a need for imaging techniques that enable visualization of these layers individually at different time points. Although postmortem histology and ultrastructural analysis can be performed for investigating microscopic changes in the retina in small animal models, this requires sacrificing animals, which makes repeated assessment of the same animal at different time points impossible and increases the number of animals required. Furthermore, some retinal processes such as neurovascular coupling cannot be fully characterized postmortem.

Optical coherence tomography (OCT) for small animal ophthalmic imaging is highly attractive for multiple reasons. OCT has the key advantage that it is noninvasive, so that imaging can be performed repeatedly in the same animals

W. Choi • J.G. Fujimoto (✉)
Department of Electrical Engineering and Computer Science and Research Laboratory of Electronics, Massachusetts Institute of Technology, Cambridge, MA, USA
e-mail: jgfuji@mit.edu

W. Drexler
Center for Medical Physics and Biomedical Engineering, Medical University of Vienna, General Hospital Vienna, Vienna, Austria
e-mail: wolfgang.drexler@meduniwien.ac.at

© Springer International Publishing Switzerland 2015

W. Drexler, J.G. Fujimoto (eds.), *Optical Coherence Tomography*,
DOI 10.1007/978-3-319-06419-2_65

over time. This can facilitate accurate assessment of longitudinal changes by reducing the effects of biological variability and promises to improve the efficiency of fundamental studies of disease mechanisms or pharmaceutical development. Furthermore, recent advances in OCT technology and new OCT techniques will enable integrated ultrahigh-resolution structural and functional imaging of the retina. In addition, small animal OCT studies can also be an important translational step for developing and validating new technology and methods prior to clinical implementation.

The initial development of ophthalmic OCT imaging techniques in animal models was largely driven by investigation of laser-induced retinal injury in the rabbit and rhesus monkey models in the late 1990s [7–9]. Although there are many other animal models including the ones used for the above experiments, this chapter focuses on murine retinal imaging since it is one of the more widely used species, due to the ease of handling, low cost for maintenance, and availability of transgenic strains. OCT imaging of the murine retina was first demonstrated in mice using time domain OCT in 2001 [10]. Since then, multiple studies investigating rat and mouse models of retinal diseases have been reported using commercial as well as prototype spectral domain OCT systems [11–15]. Readers are advised to search the literature independently for applications of OCT on small animal models of retinal diseases, since there are a large number of studies and this is outside of the scope of this chapter. This chapter focuses on in vivo murine ophthalmic imaging using advanced OCT technology and new OCT techniques. Small animal imaging interface designs will be also discussed, since the human and murine eye sizes are considerably different, which necessitates a different optical scanning design. An overview of structural and functional ophthalmic OCT imaging techniques in small animal models will also be provided.

63.2 Small Animal Imaging Interface

Small animal ophthalmic imaging was historically considered challenging due to the small eye size. However, with a proper imaging interface, imaging can still be performed reliably. Two different types of imaging interfaces have been widely used for small animal imaging.

One approach is to use a telecentric scanning configuration with a thin glass cover slip gently put on the cornea to suppress corneal refraction [16]. Compared to human eyes, in small animals the dilated pupil diameter relative to the size of the eye globe is large. Therefore, a relatively large area on the retina can be scanned using this approach. Eye drops such as hydroxypropyl methylcellulose can be used for corneal hydration as well as maintaining good contact between the cover slip and cornea.

The main advantage of this approach is that the optical design for the imaging interface can be relatively simple since it does not require detailed knowledge about the optics of the murine eye. Commercial microscope objectives can be used to obtain a high transverse resolution <10 μm in air. This scanning configuration can

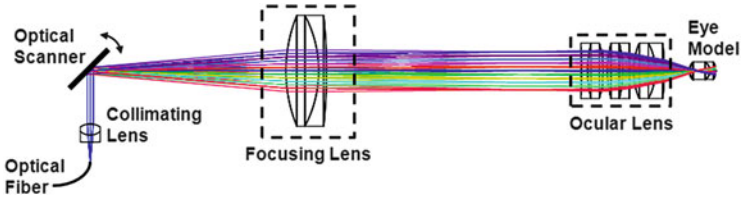

Fig. 63.1 A noncontact, small animal OCT imaging interface with the scan pivot located at the pupil of the murine eye. The imaging interface uses multiple achromatic lenses and a rat eye model based on reference [19]. The collimated beam after the ocular lens is focused on the retina by the optics in the rat eye. For a $1/e^2$ beam diameter of 1.4 mm at the cornea, a spot size of ~15 μm on the retina can be obtained, ignoring aberration from the rat eye. The optical layout was originally generated in the ray-tracing software Zemax and modified

be used for anterior eye as well as whole eye imaging, in which case the cover slip is no longer necessary. However, this approach has several drawbacks for retinal imaging. First, intraocular pressure can be increased due to the extra pressure applied by the cover slip. This can potentially affect ocular hemodynamics as well as the retinal contour for structural imaging. Second, the field of view is limited by the pupil diameter due to the telecentric scanning. The fully dilated pupil diameter is typically ~3 mm in the rat and ~2 mm in the mouse [17, 18]. Residual refraction from the small animal lens and cornea makes the field of view even smaller than the pupil diameter. Although it is possible to move the field of view to a different region on the retina, this typically requires multiple iterations of alignment including readjusting the cover slip, which could be relatively time-consuming.

Another approach is to use a scanning configuration with the scan pivot position located at the pupil as shown in Fig. 63.1, similar to a human retinal imaging interface. In this configuration, the optical beam remains collimated after the ocular lens and is focused on the retina by the optics of the murine eye. Therefore, it is critical to use a correct eye model to achieve optimal performance. Multiple paraxial eye models with radii of curvature, thicknesses, and indices of refraction of different components in the murine eye are available in the literature [17–19], which can be used in a ray-tracing software to simulate and design a small animal imaging interface. Figure 63.1 shows an example of a pivoted scanning imaging interface, using a rat eye model based on reference [19]. According to this eye model, a spot size of ~15 μm on the retina can be obtained for a $1/e^2$ beam diameter of 1.4 mm at the cornea, ignoring aberration from the rat eye. A similar performance can also be expected in the mouse eye.

This pivoted scanning configuration has several advantages. First, there is little to no risk of increasing intraocular pressure since there is no cover slip contact to the cornea required. Second, the scanned area on the retina can be more accurately calibrated using an ideal eye model, which is challenging with telecentric scanning due to the unknown pressure applied by the cover slip on the eye. Third, the field of view is limited by the ocular lens diameter as opposed to the pupil in this case, and it

is possible to move the field of view to the region of interest simply by adjusting the orientation of the murine eye with respect to the optical axis of the imaging interface. However, these optical designs can be more demanding, and different imaging interfaces are required for imaging different animal species due to the structural differences in the eyes.

63.3 Structural Imaging

Although the murine retina is thinner than the human retina, all major retinal layers observed in the human retina can also be found in the murine retina. For small animal imaging, the optic nerve head can be used as a landmark for alignment and imaging since the murine retina does not have a macula.

63.3.1 Ultrahigh-Resolution Retinal Imaging

Ultrahigh-resolution retinal OCT imaging in animals was first demonstrated in pig and monkey eyes ex vivo in 2003 and 2004 using time domain detection techniques in order to establish a comparison of OCT image features with histological findings [20, 21]. In vivo spectral domain ultrahigh-resolution OCT imaging in the murine retina was demonstrated in 2006 [16, 22]. Ultrahigh-resolution OCT imaging in vivo is challenging because any dispersion mismatch between the sample and reference arms results in a broadening of the axial point spread function. Spectral domain OCT has an advantage that the dispersion mismatch can be numerically compensated by using readily accessible phase information in the spectral OCT signal [23, 24], thereby facilitating ultrahigh-resolution retinal imaging.

Figure 63.2 shows a comparison of a representative histology and ultrahigh-resolution OCT image in a Long-Evans rat [16]. The ultrahigh-resolution system had a bandwidth of 145 nm centered at 890 nm, resulting in an axial resolution of ~2.8 μm in tissue. The transverse resolution was ~10 μm in air. The imaging speed was 24,000 A-scans per second. Histology was performed in a sex- and age-matched animal to obtain 7-μm-thick paraffin sections registered to the optic disc. All major retinal layers visible in the human retina can also be observed in the ultrahigh-resolution OCT image of the rat retina with an excellent correspondence to histology. However, a quantitative thickness comparison between histology and OCT images may result in errors since histology tends to generate processing artifacts [20]. The OCT image is displayed in grayscale with brighter pixels corresponding to higher backscattered intensity. Relative backscattered intensities of different intraretinal layers are similar to those observed in the human retina, with the highly backscattering retinal pigment epithelium and relatively less backscattering inner and outer nuclear layers as shown in Fig. 63.2b. It should be noted that the ganglion cell layer cannot be clearly visualized in the OCT image due to speckle and the extremely thin ganglion cell layer thickness in the rat retina.

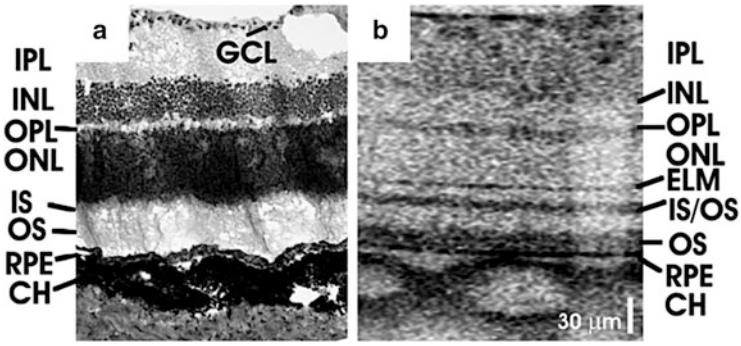

Fig. 63.2 A comparison of a (**a**) representative histology and (**b**) ultrahigh-resolution OCT image in a Long-Evans rat retina near the optic nerve head. *GCL* ganglion cell layer, *IPL* inner plexiform layer, *INL* inner nuclear layer, *OPL* outer plexiform layer, *ONL* outer nuclear layer, *IS* photoreceptor inner segment, *OS* photoreceptor outer segment, *RPE* retinal pigment epithelium, *CH* choroid, *ELM* external limiting membrane, *IS*/*OS* photoreceptor inner and outer segment junction. Scale bar: 30 μm (Image reproduced from Srinivasan et al. [16])

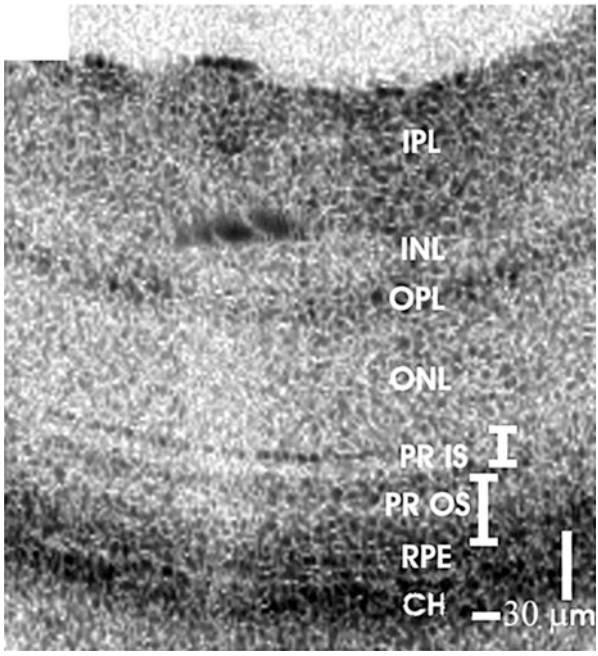

Fig. 63.3 A representative ultrahigh-resolution OCT image from a normal C57BL6 mouse. *IPL* inner plexiform layer, *INL* inner nuclear layer, *OPL* outer plexiform layer, *ONL* outer nuclear layer, *PR IS* photoreceptor inner segment, *PR OS* photoreceptor outer segment, *RPE* retinal pigment epithelium, *CH* choroid (Image reproduced from Srinivasan et al. [16])

Figure 63.3 shows a representative ultrahigh-resolution OCT image from a normal C57BL6 mouse acquired with the same ultrahigh-resolution OCT system [16]. All major intraretinal layers except the ganglion cell layer can be clearly visualized in the mouse retina with ultrahigh-resolution OCT.

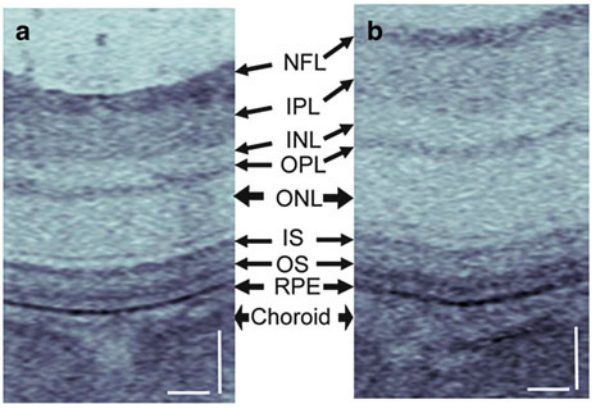

Fig. 63.4 Ultrahigh-resolution OCT can visualize changes in intraretinal layer thickness produced by intravitreal injection of (**a**) saline vehicle control versus (**b**) carbonic anhydrase-I in streptozotocin-induced diabetic rats. Scale bar: 50 μm (Image reproduced from Gao et al. [11])

Figure 63.4 shows an example application of ultrahigh-resolution OCT technology in a rat model of retinal disease using the same OCT system as in Figs. 63.2 and 63.3 [11]. Using ultrahigh-resolution OCT, it was possible to observe retinal edema produced by intravitreal injection of carbonic anhydrase-I, an intracellular enzyme identified in the proliferative diabetic retinopathy vitreous proteome, in a streptozotocin-induced diabetic rat model. The identification of structural changes in early disease or processes such as vascular permeability changes is important because these can serve as surrogate markers for investigating the molecular pathways of disease for the development of new pharmaceuticals.

In addition to increasing the axial resolution using ultrahigh-resolution OCT, it is also possible to increase the transverse resolution in small animal retinal imaging using adaptive optics. Since the numerical aperture available in the murine eye is larger than that in the human eye, the maximum theoretically achievable transverse resolution on the retina with adaptive optics is higher in small animals than in humans [25, 26]. Therefore, combining ultrahigh-resolution OCT and adaptive optics would enable ultrahigh-resolution imaging of the small animal retina in all three dimensions. However, visualization of tissue at the cellular level not only requires ultrahigh axial and transverse resolutions but also high enough contrast between different subcellular organelles, which in histology is provided by difference in staining properties. Although current ultrahigh-resolution OCT technology does not yet enable cellular level visualization, it is still possible to detect morphologic alternations in the intraretinal structure due to retinal diseases, which is a powerful advantage over histology.

63.3.2 Ultrahigh-Speed Retinal Imaging

Ultrahigh-resolution spectral domain OCT system design is more challenging than standard resolution system design because of the broader bandwidth required for

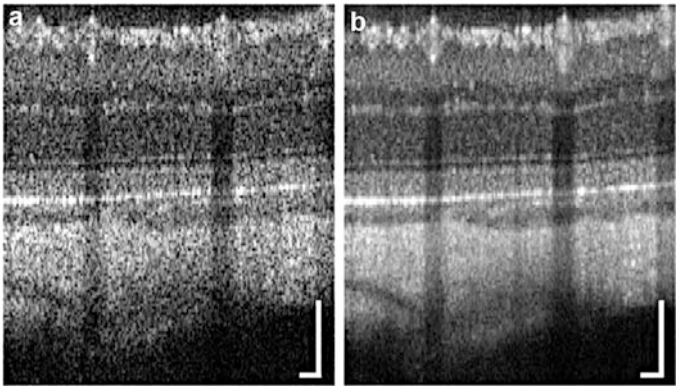

Fig. 63.5 Ultrahigh-speed OCT images extracted from a volumetric data set (**a**) before averaging and (**b**) after averaging six neighboring OCT B-scans. The volumetric data set consisting of 700 × 700 A-scans was acquired from a 1.5 × 1.5-mm^2 area centered at the optic nerve head in a Sprague Dawley rat. The effect of averaging can be clearly seen in terms of speckle reduction and increase in signal-to-noise ratio, which greatly enhances visualization of intraretinal layers. Scale bar: 100 μm

ultrahigh axial resolution. Therefore, many commercial OCT systems currently offer axial resolutions of 5–7 μm in tissue. Recent advances in CCD and CMOS camera technology enabled ultrahigh-speed spectral domain OCT with an imaging speed >200 kHz A-scan rate with a system complexity comparable to commercial spectral OCT systems at slower imaging speeds [27]. While ultrahigh-resolution OCT provides a higher axial resolution and inherently smaller speckle size, ultrahigh-speed imaging enables spatial compounding and image averaging methods to enhance visualization of intraretinal layers in small animals by reducing the effects of speckle.

Figure 63.5 shows OCT images from a normal Sprague Dawley rat. The ultrahigh-speed spectral domain OCT system had an imaging speed of 244,000 A scans per second. The bandwidth of the light source was ∼55 nm centered at 840 nm, yielding an axial resolution of 5.7 μm in tissue. The theoretical spot size on the retina using a standard rat eye model was ∼15 μm. While Fig. 63.5a shows a single OCT B-scan consisting of 700 A-scans, Fig. 63.5b shows an average of six neighboring B-scans uniformly distributed in a thin strip ∼13-μm thick. Note that speckle is dramatically suppressed by averaging multiple neighboring B-scans due to spatial compounding. This comes at the cost of slight reduction in the effective transverse resolution, but enhancement in image quality due to speckle suppression and increased signal-to-noise ratio outweighs the trade-off for most applications. Because Sprague Dawley rats have significantly less pigment in the retinal pigment epithelium and choroid than in Long-Evans rats, OCT images of the Sprague Dawley retina can visualize down to the sclera, which can be useful for applications where choroidal or scleral abnormalities are expected.

It should be noted that ultrahigh resolution and ultrahigh speed are not fundamentally incompatible in spectral domain and swept source OCT. With advances in OCT technology, it will be possible to achieve ultrahigh imaging speeds and ultrahigh axial resolutions simultaneously, thereby combining the advantages of the two techniques in a single OCT system.

63.3.3 Long Wavelength Imaging

In human retinal imaging, absorption of light by water in the anterior eye and vitreous limits the usable wavelength range. Therefore, human retinal OCT imaging typically uses near-infrared (NIR) wavelengths shorter than 900 nm or around 1,060 nm, where absorption of light is negligible or within a transmission window [28]. Unlike wavelengths shorter than 900 nm where ultrahigh-resolution retinal imaging with a broadband NIR light source is feasible, wavelengths around 1,060 nm are at a local minimum in water absorption which has a relatively narrow bandwidth [29], which makes achieving an axial resolution <5 μm in the human retina challenging regardless of the light source bandwidth. In addition human retinal OCT imaging at wavelengths $>1{,}150$ nm is impossible since almost all light is absorbed by the anterior eye and vitreous.

The axial eye length is $\sim$6.1 mm in the rat and $\sim$3.3 mm in the mouse [17, 18], considerably shorter than the axial eye length of $\sim$24 mm in humans. According to the Beer-Lambert law, due to the shorter axial eye lengths, water absorption will be considerably less severe in the murine eye than in the human eye as shown in Fig. 63.6. This implies that retinal OCT imaging using longer wavelengths can be achieved in murine eyes. In both rat and mouse eyes, the water absorption window at $\sim$1,060 nm does not have the same bandwidth limiting effects as in the human eye, making ultrahigh-resolution retinal imaging feasible at these wavelengths in the murine eye. Furthermore, there is a significant transmission through the ocular media even at $\sim$1,300 nm wavelength. Multiple studies have investigated long wavelengths for retinal OCT imaging in the murine eye. The first demonstration of retinal imaging in the mouse eye using time domain OCT utilized wavelengths centered at $\sim$1,280 nm [10]. Spectral domain ultrahigh-resolution retinal imaging at $\sim$1,060 nm wavelengths with an axial resolution <3 μm was demonstrated in the rat eye [30]. Retinal imaging at $\sim$1,310 nm was demonstrated in the rat eye using spectral domain OCT [31].

Using longer wavelengths for small animal OCT imaging may have advantages in small animal models of ocular diseases that develop cataracts and/or other forms of ocular opacity such as vitreous hemorrhage or choroidal neovascularization. Longer wavelengths have reduced scattering, and better visualization of the retina and choroid has been demonstrated in human subjects and patients with cataracts [32, 33]. Ocular opacities caused by blood are also expected to affect the OCT image quality less at longer wavelengths [34].

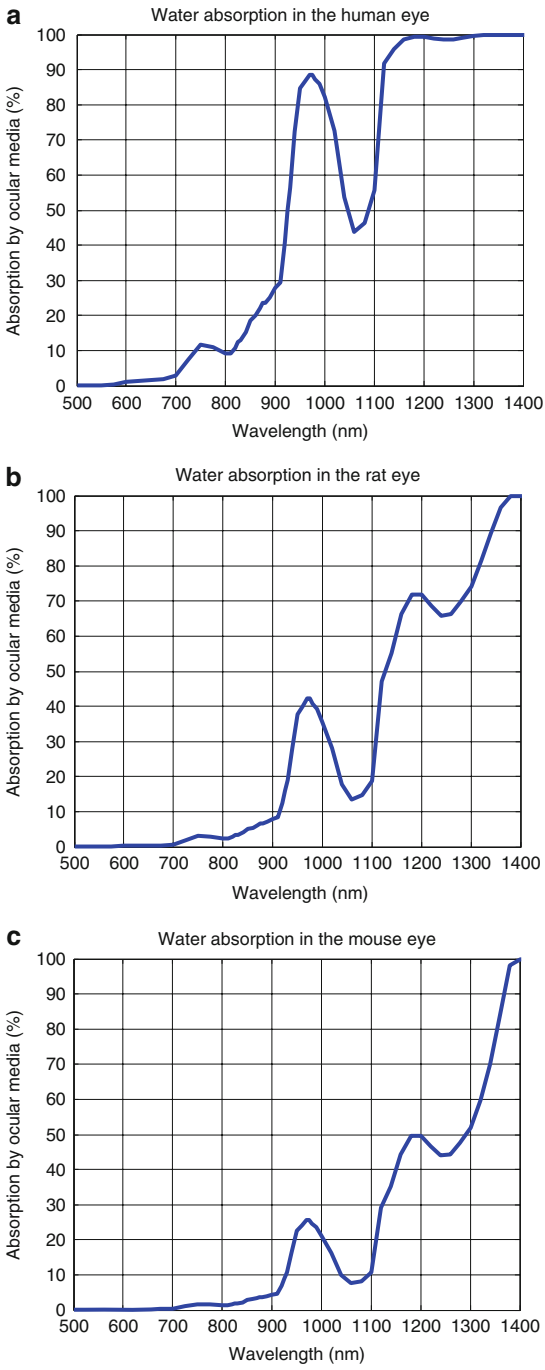

Fig. 63.6 Absorption of light by water as a function of wavelength in (**a**) the human eye, (**b**) the rat eye, and (**c**) the mouse eye. Axial eye lengths of 24, 6.1, and 3.3 mm were assumed for the human, rat, and mouse eyes, respectively. Water absorption coefficients were obtained from Ref. [28]

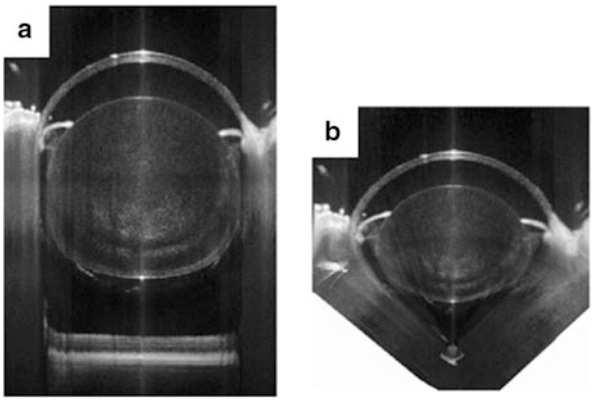

Fig. 63.7 An OCT image of a whole eye of a MF1 mouse (**a**) before refraction correction and (**b**) after refraction correction (Image reproduced from Wang et al. [37])

63.3.4 Whole Eye Imaging

Whole eye imaging using Fourier domain OCT is significantly easier in murine eyes than in human eyes due to the relatively short axial eye lengths in small animals. Although time domain OCT can also be used for whole eye imaging in small animals [35], Fourier domain OCT such as spectral domain or swept source OCT has the advantage that imaging can be performed orders of magnitude faster due to its inherently higher sensitivity. Faster imaging speeds at a given signal-to-noise ratio are advantageous since image averaging can be performed in order to reduce the effects of speckle and increase image quality. Because the numerical aperture of the imaging interface is limited for small animal whole eye imaging due to the relatively long depth of focus required, the signal-to-noise ratio tends to be relatively low for whole eye imaging. Therefore, higher quality images provided by image averaging is essential for better layer visualization and more accurate biometry. Multiple studies have demonstrated whole eye imaging in the mouse and rat eyes using swept source OCT [36–38].

An example of long wavelength ophthalmic OCT imaging in small animals is shown in Fig. 63.7 [37]. The images were acquired with a swept source OCT system using 1,060-nm wavelengths with an imaging speed of 28,000 A-scans per second. The imaging interface was using the telecentric scanning configuration. In order to achieve a sufficient imaging range, a full range OCT imaging algorithm was used, resulting in a total imaging range of 6 mm [39]. High-quality OCT images of mouse eyes were acquired by averaging 50 OCT B-scans with 512 A-scans each. It should be noted that with telecentric scanning, the effective transverse scan range on the retina is essentially limited to a single spot due to optical refraction from the anterior eye. This effect is clearly seen after refractive correction during post-processing as shown in Fig. 63.7b. Regardless, biometric parameters such as axial lengths and radii of curvature of the cornea, anterior chamber, lens, and vitreous can be extracted using whole eye OCT imaging.

63.4 Functional Imaging

In addition to structural imaging, OCT can also be used for functional imaging in the murine retina. In this section, functional imaging techniques such as measurements of intraretinal layer reflectivity in response to light stimuli, retinal blood flow measurements using Doppler OCT, OCT angiography imaging of the retinal capillary network, and spectroscopic OCT imaging will be discussed. Functional imaging can be more demanding than simple structural imaging because it typically requires differential measurements. Ultrahigh-resolution physiology measurements need to detect differential changes in intraretinal layer reflectivities. Doppler OCT requires time differential measurements in the OCT phase. OCT angiography of the retinal capillary network requires mapping of intensity and/or phase changes in time. Spectroscopic OCT measures differential absorption at different wavelengths.

63.4.1 Ultrahigh-Resolution Physiology Measurement

Intrinsic signals from biological tissue detected with optical imaging techniques can be used for measuring neural activity. In the brain, cortical activity can be mapped by imaging intrinsic signals using optical techniques [40]. In the retina, changes in intrinsic optical signals in response to light stimuli have been detected using fundus reflectometry [41, 42]. Although different imaging techniques may measure different types of intrinsic signals, OCT has the advantage that it can detect depth-resolved changes in optical properties of intraretinal layers in response to visual light stimulus. Using time domain OCT, measurement of changes in optical scattering properties activated by visible light was demonstrated ex vivo in the isolated retinae of the frog and rabbit [43, 44]. Figure 63.8 shows an example of ex vivo measurements of backscattered reflectance in the rabbit retina using time domain OCT [44]. As shown in Fig. 63.8d, e, it can be seen that the backscattered reflectance changes in different intraretinal layers due to the visual stimulus.

However, because OCT is a noninvasive imaging technique, it can also be used for in vivo functional measurement of changes in scattering properties of intraretinal layers. In vivo OCT measurement of intrinsic optical signals is challenging because of the small layer thicknesses, speckle, and eye motion. Speckle produces a random spatial fluctuation in backscattered light intensity, which makes quantitation of backscattered reflectivity challenging. Eye motion makes imaging the same location on the retina as a function of time difficult and also introduces noise due to changes in speckle with parasitic eye motion. Ultrahigh-resolution OCT imaging has an advantage that the multilayered retinal structure can be resolved with a $<$3-μm axial resolution. Although the transverse resolution is not as fine as the axial resolution for OCT without adaptive optics, the spatial variation in the retina in the transverse direction is typically significantly less than that in the axial direction. High-speed imaging with spectral domain OCT (as opposed to time domain OCT) enables novel scanning and signal averaging schemes which can reduce the effects of speckle and eye motion.

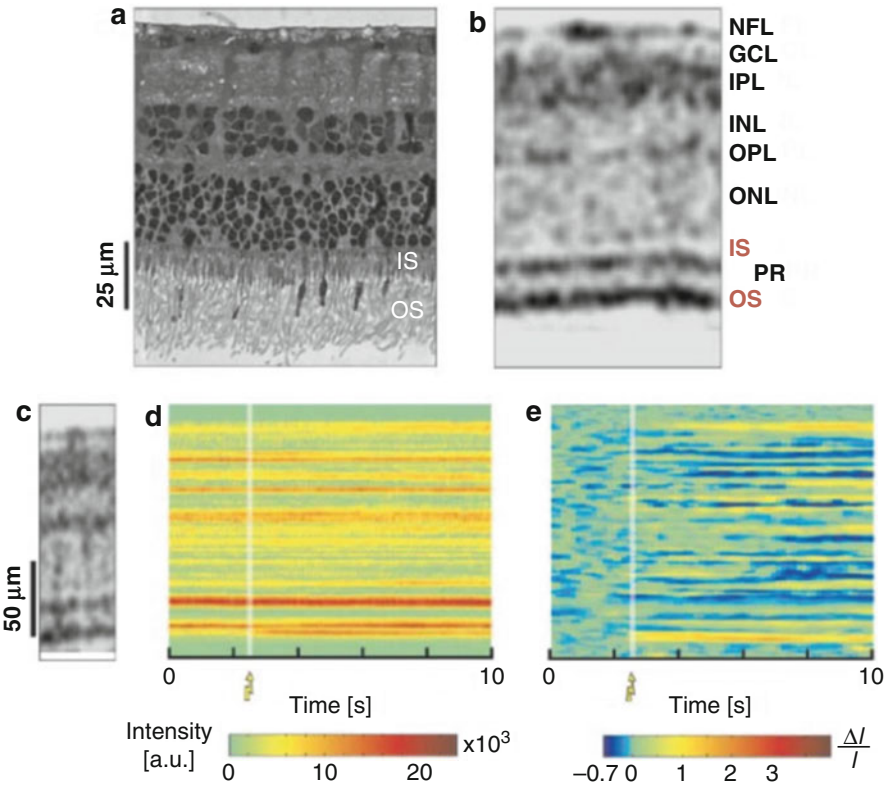

Fig. 63.8 (**a**) A histologic cross section of the rabbit retina compared with (**b**) an ultrahigh-resolution time domain OCT image. (**c**) An example of OCT A-scans repeatedly acquired from the same position on the retina. (**d**) OCT A-scans acquired from the same position before and after visual stimulus. (**e**) Differential OCT A-scans calculated from (**d**) by taking the ratio of the changes in signal intensity relative to baseline and the signal intensity at baseline. The white bar shows the onset and duration of the visual stimulus (Image reproduced from Bizheva et al. [44])

In vivo measurements of functional changes in intrinsic optical signal were first demonstrated in the rat retina using ultrahigh-resolution spectral domain OCT [22]. Measurements were performed in Long-Evans rats, using a high-speed ultrahigh-resolution spectral domain OCT system at 24,000 axial scans per second with a 2.8-µm axial image resolution. Animals were dark adapted before measurements were taken. Because the OCT light source was in the NIR wavelength range, the OCT beam was not visible to the animals. In order to compensate eye motion and reduce speckle, a small area of $160 \times 160\ \mu m^2$ was repeatedly scanned on the retina at a 6.2-Hz volume acquisition rate. Eye motion in the transverse direction was corrected by cross-correlating sequential volumes, and A-scans were aligned in the axial direction with respect to the photoreceptor inner and outer segment junction.

Figure 63.9 shows the results of ultrahigh-resolution functional physiology measurements. Figure 63.9a shows the percent change in amplitude reflectance as

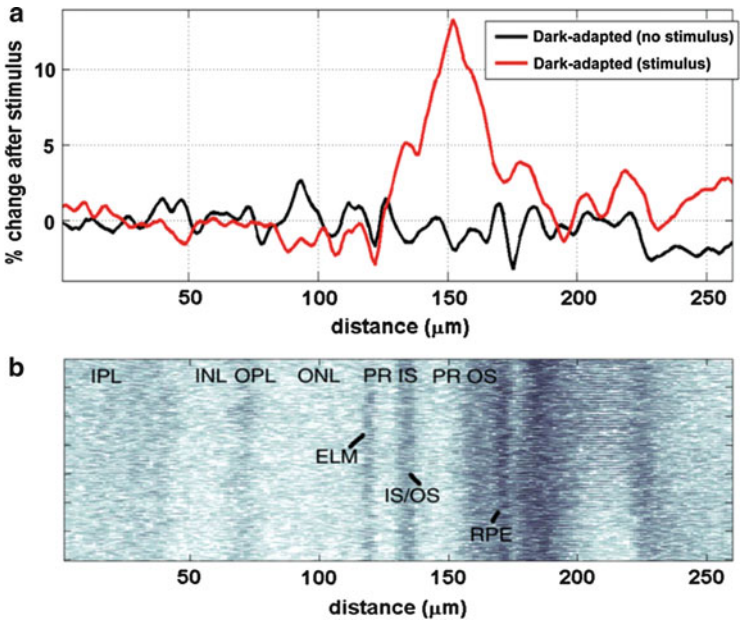

Fig. 63.9 (**a**) Functional OCT measurement showing changes in the backscattered intensity at different depths in the retina before and after visual light stimulus. (**b**) An example showing A-scans from a single volume after aligning with respect to the IS/OS junction, displayed in logarithmic scale for comparison with (**a**). The light stimulus produced an increase in backscattered intensity primarily at the photoreceptor outer segment (Image reproduced from Srinivasan et al. [22])

a function of imaging depth before and after applying a light stimulus on the rat retina with respect to a baseline measurement. Note that the amplitude reflectance was calculated by averaging all A-scans from a single volume after correcting for transverse and axial eye motions in order to reduce speckle. The stimulus resulted in a maximum increase of ~12 % in backscattered amplitude reflectance. Figure 63.9b, which shows all A-scans from a single OCT volume for comparison, indicates that the increase in reflectance was primarily localized to the photoreceptor outer segment.

The volume acquisition rate of 6.2 Hz is rapid enough for visualizing the time course of changes in backscattered amplitude reflectance at the photoreceptor outer segment. Figure 63.10 shows a plot of percent reflectance changes at the photoreceptor outer segment versus time. The standard deviation of reflectance changes in reference to the baseline at the stimulus onset was <1 %, which is significantly smaller than the maximum functionally induced increase in reflectance of ~12 %.

It has to be emphasized that although the increase of ~12 % in amplitude reflectance measured with ultrahigh-resolution OCT is significant, the effect was localized to the photoreceptor outer segment. As can be seen in the OCT image, the photoreceptor outer segment is only a small fraction of the entire retina with

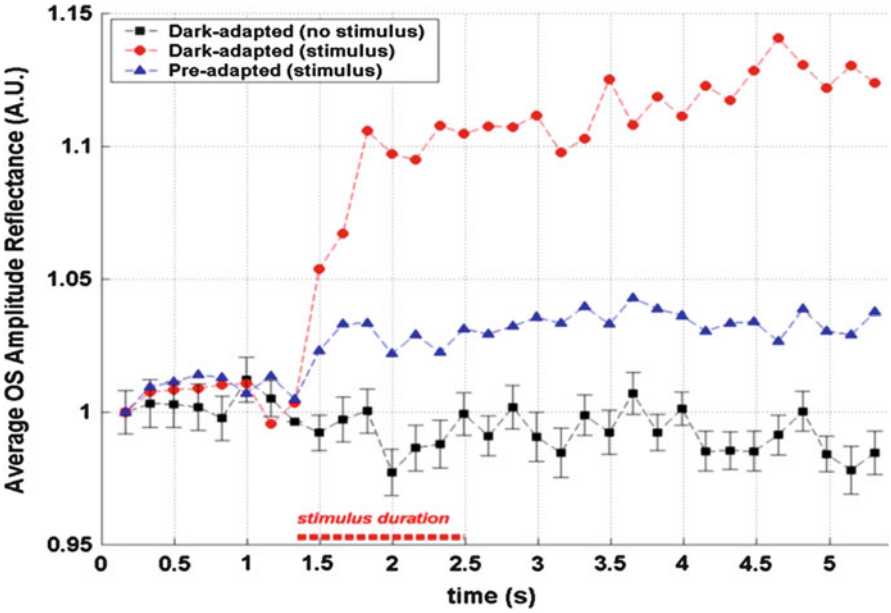

Fig. 63.10 The percent changes in amplitude reflectance at the photoreceptor outer segment at different time points. Each data point is calculated from a single OCT volume. The error bar shows noise (standard deviation of amplitude reflectance values at different time points) of the measurement technique in reference to the amplitude reflectance at the stimulus onset. Stimulus duration is indicated with the *dotted line* at the bottom of the plot (Image reproduced from Srinivasan et al. [22])

relatively weak backscattering when compared to the RPE and RNFL. The photoreceptor outer segment reflectance accounts for only a small fraction of the total reflectance as measured with fundus reflectometry. Therefore, ultrahigh-resolution spectral domain OCT can enable more sensitive measurements compared to other fundus imaging techniques which do not have depth resolution. One disadvantage is relatively slow imaging speeds of current commercial OCT systems for wide field imaging, but advances in OCT imaging techniques are expected to overcome this problem. In vivo optophysiology measurements using optical coherence tomography have also been performed in the chicken retina [45, 46].

63.4.2 Doppler OCT and OCT Angiography

Doppler OCT and OCT angiography are functional extensions of OCT that use repeated scanning protocols to measure flow-induced changes in the OCT signal in time. Spectral domain OCT is especially powerful for Doppler retinal blood flow measurement because spectral domain OCT provides direct access to phase

information required for detecting Doppler shifts [47, 48]. Due to the relatively fast erythrocyte speeds in larger retinal arteries and veins, Doppler OCT of large vessels typically requires sequential A-scans acquired from the same location within a short time interval. This can be achieved by densely oversampling in the transverse direction relative to the OCT beam spot size. In contrast, due to the relatively slow erythrocyte speeds in retinal capillaries, OCT angiography of capillaries typically requires multiple B-scans repeatedly acquired from the same location. The longer time interval between B-scans is used to detect slower flows by mapping time fluctuations in intensity and/or phase on a pixel by pixel basis [49–56]. In this section, applications of these techniques on small animal imaging will be discussed. For small animal imaging, Doppler OCT can be used for measuring pulsatile total retinal blood flow and OCT angiography for visualizing the retinal capillary network in three dimensions. Readers interested in further technical and historical details of these techniques are referred to other relevant chapters in this book for more information.

Doppler OCT for measuring blood flow in individual retinal arteries and veins has been demonstrated in the rat retina [31]. However, these methods require measuring the Doppler angle between the OCT probe beam and blood vessel in individual arteries and veins to calculate blood flow, because Doppler OCT measures the velocity components parallel to the OCT probe beam. With the development of high-speed Fourier domain OCT, en face Doppler OCT measurements became possible [57, 58]. The en face technique measures total blood flow by raster scanning an area that intercepts the blood vessel and summing the axial blood flow velocity components in an en face plane over the blood vessel cross-sectional area. This technique dramatically simplifies the measurement of blood flow because the Doppler angle is not needed. However, high OCT imaging speeds are required because a volumetric OCT data set must be acquired.

Recent advances in OCT technology enabled ultrahigh OCT imaging speeds of $>$100 kHz making en face Doppler OCT measurement of total retinal blood flow possible in the small animal retina. Measuring pulsatile total retinal blood flow in small animals is challenging because of the rapid heart rate. In the normal anesthetized animal, the heart rate is typically 300–400 beats per minute in rats and $>$400 beats per minute in mice, which is $>5\times$ faster than in humans.

Pulsatile total retinal arterial blood flow measurements in rats were demonstrated using an ultrahigh-speed spectral domain OCT system at 244,000 A-scans per second [59]. As shown in Fig. 63.11, major retinal blood vessels emerge out from the central retinal artery located at the optic nerve head. By repeatedly scanning a 200 $\times$ 200-μm area centered at the central retinal artery with 150 $\times$ 25 A-scans, a volume acquisition rate of $\sim$55 Hz can be achieved, fast enough to resolve pulsatile blood flow. For a spot size of $\sim$15 μm, the scan pattern corresponds to an oversampling of $\sim 11\times$ in the fast scan direction, which is sufficient for Doppler imaging.

Figure 63.12 was obtained by calculating total retinal arterial blood flow values for all acquired volumes individually and plotting them as a function of time. Pulsatile total retinal arterial blood flow can be clearly visualized. For comparison,

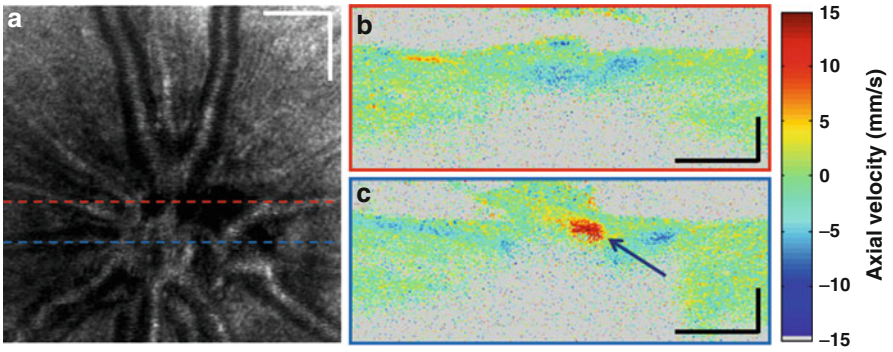

Fig. 63.11 (**a**) An OCT fundus projection image centered at the optic nerve head of a normal rat. (**b**, **c**) Doppler B-scan images acquired from the *red* and *blue dotted lines*. The Doppler images clearly show the location of the central retinal artery (indicated with an *arrow* in (**c**)) relative to the fundus projection image. All scale bars: 100 μm (Images reproduced from Choi et al. [59])

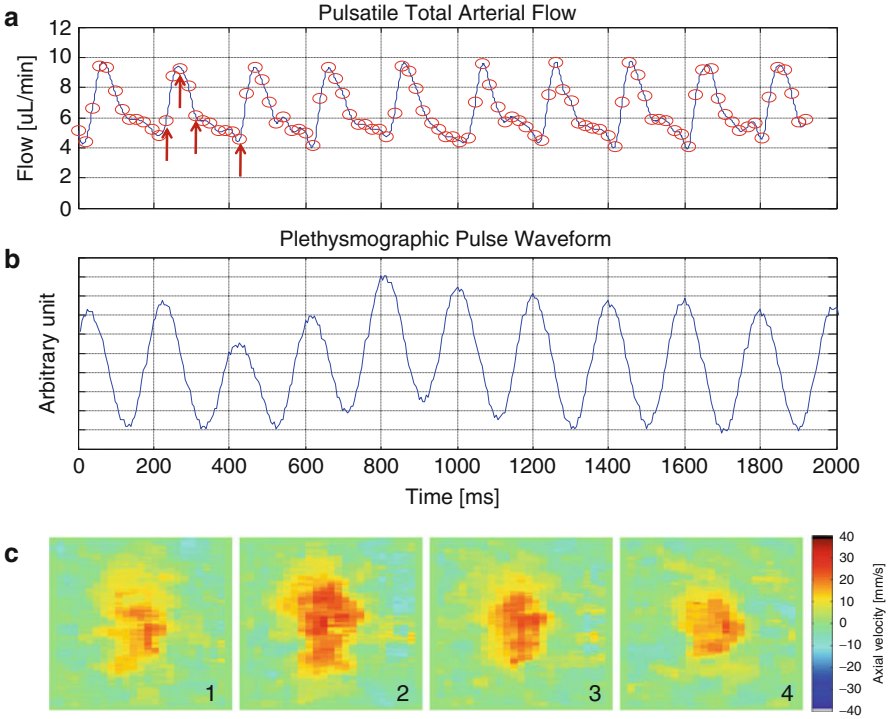

Fig. 63.12 (**a**) Pulsatile total retinal arterial blood flow measured from a normal Sprague Dawley rat. (**b**) Simultaneously acquired plethysmographic waveform. (**c**) En face Doppler images extracted from time points indicated by arrows in (**a**) 200 × 200 μm^2. Time variation in the axial velocity profile corresponding to pulsatility can be clearly visualized (Images reproduced from Choi et al. [59])

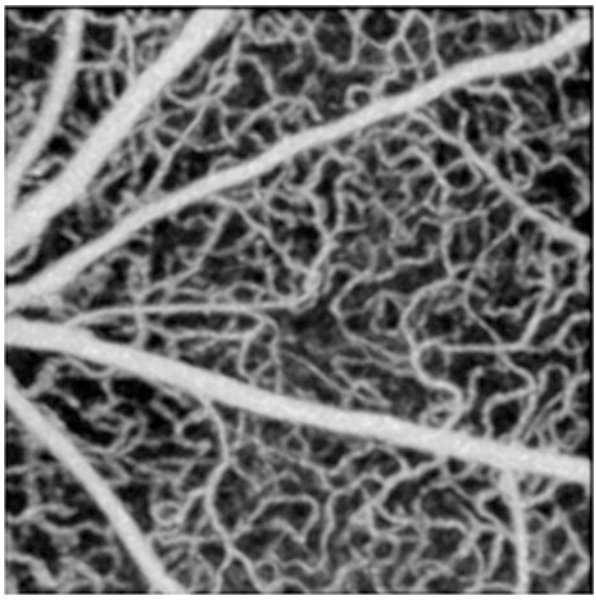

Fig. 63.13 An OCT angiogram acquired from a normal Sprague Dawley rat using speckle variance OCT angiography. 1 × 1 mm^2 field of view

a plethysmographic waveform was simultaneously acquired with a pulse oximeter from a probe attached to the hindlimb footpad of the rat and is shown in Fig. 63.12b. The same instantaneous heart rate can be seen in the blood flow waveform. The en face Doppler images in Fig. 63.12c show blood flow velocity profiles in an en face plane at different time points indicated by arrows in Fig. 63.12a. Pulsatility in the velocity profiles can be clearly visualized.

It is also possible to perform OCT angiography in the murine retina using ultrahigh-speed spectral domain OCT. Because the area of the small animal retina is much smaller than the human retina and the total image acquisition time in anesthetized animals can be significantly longer than in human subjects, data acquisition with high A-scan oversampling is possible and high-quality OCT angiograms can be generated. As an example, Fig. 63.13 shows an en face maximum projection OCT angiogram of a rat retina over a 1 × 1-mm^2 area with 300 × 300 pixels. 300 A-scans were acquired per B-scan at 300 B-scan locations. From each B-scan location, 17 repeated B-scans were acquired, requiring a total of 300 × 300 × 17 A-scans. The example shown performs OCT angiography using speckle variance from the OCT intensity signal, without phase information. Similar techniques using OCT intensity and/ or phase information have been demonstrated by different research groups [49–56], and many other techniques can be applied to visualize the small animal retinal capillary network [31]. OCT angiography has the advantage that it generates a three-dimensional image of the vasculature and because it does not require injected contrast agents, repeated measurements can be easily performed. However, it should be noted that OCT angiography cannot detect vessel leakage which is possible using fluorescein or indocyanine green angiography.

Doppler OCT and OCT angiography can be useful for investigating small animal models of ocular disease where vascular abnormalities are expected during disease progression as well as understanding basic physiology. These techniques have the advantage that they are noninvasive and repeated measurements can be performed on the same animals over time to track disease progression.

63.4.3 Spectroscopic Imaging

Spectroscopic imaging in the murine retina is perhaps one of the more underinvestigated research areas in small animal OCT. Historically, one of the major applications of interest for spectroscopic OCT imaging was noninvasive blood oxygen saturation measurement in the retina [60, 61]. Conventional spectroscopic imaging using fundus cameras has been challenging due to difficulties in calibration from factors such as unknown optical path lengths and effects from chromophores other than oxy- and deoxyhemoglobin in the retina. Spectroscopic OCT, however, can be a promising alternative to spectroscopic fundus imaging because it enables depth-resolved imaging, thereby offering calibrated optical path lengths and isolating parasitic light absorption and scattering from chromophores other than hemoglobin. Despite these advantages, using near-infrared (NIR) wavelengths for measuring blood oxygen saturation with spectroscopic OCT has been difficult since in this wavelength range, hemoglobin absorption is small and scattering dominates absorption [61]. Therefore, OCT using visible light could be advantageous for this application.

Development of supercontinuum light sources provided access to spatially single-mode light, which is necessary for optical fiber-based OCT, in the visible wavelength range with output power sufficient for high signal-to-noise OCT imaging. Recently, visible light OCT utilizing a supercontinuum light source has been demonstrated for retinal blood oxygen saturation measurements in Long-Evans rats [62]. The study demonstrated measurement of oxygen saturation by analyzing the spectrum of backscattered light from the posterior vessel wall. The results were promising in that different blood oxygen saturation levels were observed in retinal arteries and veins as expected, although there were still challenges that needed to be overcome.

One of the advantages of using small animals for developing spectroscopic OCT techniques for blood oxygen saturation measurement is that oxygen saturation can be modulated using an inhaled gas mixture beyond limits that are feasible in human subjects due to safety issues. This can greatly facilitate calibration and validation of new techniques. As with other structural and functional OCT imaging techniques, spectroscopic OCT for retinal blood oximetry can be useful for investigating small animal models of retinal diseases.

Spectroscopic OCT imaging in small animals can also be useful for quantitating the concentration of exogenous dyes or molecular probes introduced by intravitreal or intravenous injection. For example, alterations in retinal vascular permeability, which cannot be directly visualized by structural imaging or OCT angiography, might be visualized with spectroscopic OCT using exogenous dyes. Unlike other

fundus imaging techniques, spectroscopic OCT may provide a more sensitive way to quantify dye concentrations in vivo since it measures depth-resolved backscattered intensity in all three dimensions. Since OCT is an in vivo optical imaging technique, the procedure time can be significantly shorter than performing spectrophotometric analysis on excised retinal tissue, which is a significant advantage for high-throughput small animal studies. Therefore, although it remains largely an underexplored area, spectroscopic OCT imaging may be a powerful technique for quantitative imaging of the small animal retina, especially given developments in exogenous contrast agents and molecular probes.

63.5 Summary

This chapter reviewed key OCT structural and functional imaging techniques that can be applied for small animal retinal imaging. Although this chapter focused on imaging the murine retina, most imaging techniques would also be applicable in other animal models. Designing an optimized small animal imaging interface was reviewed. Structural imaging with ultrahigh-resolution and ultrahigh-speed OCT was discussed. Ultrahigh-resolution imaging may be useful for detecting small focal pathologies, while ultrahigh-speed imaging provides a complimentary way of enhancing image quality. Future advances in OCT technology are expected to combine the advantages of both ultrahigh-resolution and ultrahigh-speed OCT. Several functional OCT imaging techniques such as optophysiology measurement, Doppler OCT blood flow measurement, OCT angiography, and spectroscopic OCT were also briefly reviewed. These functional extensions of OCT promise to provide powerful new approaches for understanding physiology and enable more complete and sensitive characterization of small animal models of retinal diseases. The ability to perform repeated measurements in the same animals is especially important for studies of disease progression or treatment response. The ability to rapidly and quantitatively image surrogate markers of disease should have an impact on both fundamental science and pharmaceutical discovery and development.

Acknowledgements We would like to acknowledge scientific contributions from Dr. Bernhard Baumann and Jonathan Liu. The authors of this chapter were sponsored in part by the National Institute of Health (NIH R01-EY011289-27, R01-EY013178-12, R44-EY022864-01, R01-CA075289-16), Air Force Office of Scientific Research (AFOSR FA9550-10-1-0551 and FA9550-12-1-0499), and a Samsung Scholarship.

References

1. A. Junod, A.E. Lambert, W. Stauffac, A.E. Renold, Diabetogenic action of streptozotocin – relationship of dose to metabolic response. J. Clin. Investig. **48**, 2129 (1969)
2. A.F. Nakhooda, A.A. Like, C.I. Chappel, F.T. Murray, E.B. Marliss, Spontaneously diabetic wistar rat metabolic and morphologic studies. Diabetes **26**, 100–112 (1977)

3. W.J. Heriot, P. Henkind, R.W. Bellhorn, M.S. Burns, Choroidal neovascularization can digest Bruch membrane – a prior break is not essential. Ophthalmology **91**, 1603–1608 (1984)
4. E.T. Dobi, C.A. Puliafito, M. Destro, A new model of experimental choroidal neovascularization in the rat. Arch. Ophthalmol. **107**, 264–269 (1989)
5. R.N. Frank, A. Das, M.L. Weber, A model of subretinal neovascularization in the pigmented rat. Curr. Eye Res. **8**, 239–247 (1989)
6. J.C. Morrison, C.G. Moore, L.M.H. Deppmeier, B.G. Gold, C.K. Meshul, E.C. Johnson, A rat model of chronic pressure-induced optic nerve damage. Exp. Eye Res. **64**, 85–96 (1997)
7. C.A. Toth, R. Birngruber, S.A. Boppart, M.R. Hee, J.G. Fujimoto, C.D. DiCarlo, E.A. Swanson, C.P. Cain, D.G. Narayan, G.D. Noojin, W.P. Roach, Argon laser retinal lesions evaluated in vivo by optical coherence tomography. Am. J. Ophthalmol. **123**, 188–198 (1997)
8. J.A. Zuclich, S.T. Schuschereba, H. Zwick, S.A. Boppart, J.G. Fujimoto, F.E. Cheney, B.E. Stuck, A comparison of laser-induced retinal damage from infrared wavelengths to that from visible wavelengths. Lasers Light Ophthalmol. **8**, 15–30 (1997)
9. W.P. Roach, C.P. Cain, D.G. Narayan, G.D. Noojin, S.A. Boppart, R. Birngruber, J.G. Fujimoto, C.A. Toth, Retinal response of Macaca mulatta to picosecond laser pulses of varying energy and spot size. J. Biomed. Opt. **9**, 1288–1296 (2004)
10. Q. Li, A.M. Timmers, K. Hunter, C. Gonzalez-Pola, A.S. Lewin, D.H. Reitze, W.W. Hauswirth, Noninvasive imaging by optical coherence tomography to monitor retinal degeneration in the mouse. Invest. Ophthalmol. Vis. Sci. **42**, 2981–2989 (2001)
11. B.B. Gao, A. Clermont, S. Rook, S.J. Fonda, V.J. Srinivasan, M. Wojtkowski, J.G. Fujimoto, R.L. Avery, P.G. Arrigg, S.E. Bursell, L.P. Aiello, E.P. Feener, Extracellular carbonic anhydrase mediates hemorrhagic retinal and cerebral vascular permeability through prekallikrein activation. Nat. Med. **13**, 181–188 (2007)
12. M. Ruggeri, H. Webbe, S.L. Jiao, G. Gregori, M.E. Jockovich, A. Hackam, Y.L. Duan, C.A. Puliafito, In vivo three-dimensional high-resolution imaging of rodent retina with spectral-domain optical coherence tomography. Invest. Ophthalmol. Vis. Sci. **48**, 1808–1814 (2007)
13. K.H. Kim, M. Puoris'haag, G.N. Maguluri, Y. Umino, K. Cusato, R.B. Barlow, J.F. de Boer, Monitoring mouse retinal degeneration with high-resolution spectral-domain optical coherence tomography. J. Vis. **8**, 17.1–11 (2008)
14. M.D. Fischer, G. Huber, S.C. Beck, N. Tanimoto, R. Muehlfriedel, E. Fahl, C. Grimm, A. Wenzel, C.E. Reme, S.A. van de Pavert, J. Wijnholds, M. Pacal, R. Bremner, M.W. Seeliger, Noninvasive, in vivo assessment of mouse retinal structure using optical coherence tomography. Plos One **4**(10), e7507 (2009)
15. A. Clermont, T.J. Chilcote, T. Kita, J. Liu, P. Riva, S. Sinha, E.P. Feener, Plasma kallikrein mediates retinal vascular dysfunction and induces retinal thickening in diabetic rats. Diabetes **60**, 1590–1598 (2011)
16. V.J. Srinivasan, T.H. Ko, M. Wojtkowski, M. Carvalho, A. Clermont, S.E. Bursell, Q.H. Song, J. Lem, J.S. Duker, J.S. Schuman, J.G. Fujimoto, Noninvasive volumetric imaging and morphometry of the rodent retina with high-speed, ultrahigh-resolution optical coherence tomography. Invest. Ophthalmol. Vis. Sci. **47**, 5522–5528 (2006)
17. A. Hughes, A schematic eye for the rat. Vision Res. **19**, 569–588 (1979)
18. C. Schmucker, F. Schaeffel, A paraxial schematic eye model for the growing C57BL/6 mouse. Vision Res. **44**, 1857–1867 (2004)
19. A. Chaudhuri, P.E. Hallett, J.A. Parker, Aspheric curvatures, refractive-indexes and chromatic aberration for the rat eye. Vision Res. **23**, 1351–1363 (1983)
20. M. Gloesmann, B. Hermann, C. Schubert, H. Sattmann, P.K. Ahnelt, W. Drexler, Histologic correlation of pig retina radial stratification with ultrahigh-resolution optical coherence tomography. Invest. Ophthalmol. Vis. Sci. **44**, 1696–1703 (2003)
21. E.M. Anger, A. Unterhuber, B. Hermann, H. Sattmann, C. Schubert, J.E. Morgan, A. Cowey, P.K. Ahnelt, W. Drexler, Ultrahigh resolution optical coherence tomography of the monkey fovea. Identification of retinal sublayers by correlation with semithin histology sections. Exp. Eye Res. **78**, 1117–1125 (2004)

22. V.J. Srinivasan, M. Wojtkowski, J.G. Fujimoto, J.S. Duker, In vivo measurement of retinal physiology with high-speed ultrahigh-resolution optical coherence tomography. Opt. Lett. **31**, 2308–2310 (2006)
23. M. Wojtkowski, V.J. Srinivasan, T.H. Ko, J.G. Fujimoto, A. Kowalczyk, J.S. Duker, Ultrahigh-resolution, high-speed, Fourier domain optical coherence tomography and methods for dispersion compensation. Opt. Express **12**, 2404–2422 (2004)
24. B. Cense, N. Nassif, T.C. Chen, M.C. Pierce, S. Yun, B.H. Park, B. Bouma, G. Tearney, J.F. de Boer, Ultrahigh-resolution high-speed retinal imaging using spectral-domain optical coherence tomography. Opt. Express **12**, 2435–2447 (2004)
25. Y. Geng, K.P. Greenberg, R. Wolfe, D.C. Gray, J.J. Hunter, A. Dubra, J.G. Flannery, D.R. Williams, J. Porter, In vivo imaging of microscopic structures in the rat retina. Invest. Ophthalmol. Vis. Sci. **50**, 5872–5879 (2009)
26. Y. Geng, L.A. Schery, R. Sharma, A. Dubra, K. Ahmad, R.T. Libby, D.R. Williams, Optical properties of the mouse eye. Biomed. Opt. Express **2**, 717–738 (2011)
27. B. Potsaid, I. Gorczynska, V.J. Srinivasan, Y.L. Chen, J. Jiang, A. Cable, J.G. Fujimoto, Ultrahigh speed Spectral/Fourier domain OCT ophthalmic imaging at 70,000 to 312,500 axial scans per second. Opt. Express **16**, 15149–15169 (2008)
28. G.M. Hale, M.R. Querry, Optical constants of water in the 200-nm to 200-μm wavelength region. Appl. Opt. **12**, 555–563 (1973)
29. A. Unterhuber, B. Povazay, B. Hermann, H. Sattmann, A. Chavez-Pirson, W. Drexler, In vivo retinal optical coherence tomography at 1040 nm-enhanced penetration into the choroid. Opt. Express **13**, 3252–3258 (2005)
30. S. Hariri, A.A. Moayed, A. Dracopolos, C. Hyun, S. Boyd, K. Bizheva, Limiting factors to the OCT axial resolution for in-vivo imaging of human and rodent retina in the 1060nm wavelength range. Opt. Express **17**, 24304–24316 (2009)
31. Z. Zhi, W. Cepurna, E. Johnson, T. Shen, J. Morrison, R.K. Wang, Volumetric and quantitative imaging of retinal blood flow in rats with optical microangiography. Biomed. Opt. Express **2**, 12 (2011)
32. B. Povazay, B. Hermann, A. Unterhuber, B. Hofer, H. Sattmann, F. Zeiler, J.E. Morgan, C. Falkner-Radler, C. Glittenberg, S. Blinder, W. Drexler, Three-dimensional optical coherence tomography at 1050 nm versus 800 nm in retinal pathologies: enhanced performance and choroidal penetration in cataract patients. J. Biomed. Opt. **12**, 041211 (2007)
33. M. Esmaeelpour, B. Povazay, B. Hermann, B. Hofer, V. Kajic, K. Kapoor, N.J.L. Sheen, R.V. North, W. Drexler, Three-dimensional 1060-nm OCT: choroidal thickness maps in normal subjects and improved posterior segment visualization in cataract patients. Invest. Ophthalmol. Vis. Sci. **51**, 5260–5266 (2010)
34. A. Roggan, M. Friebel, K. Dorschel, A. Hahn, G. Muller, Optical properties of circulating human blood in the wavelength range 400–2500 NM. J. Biomed. Opt. **4**, 36–46 (1999)
35. X. Zhou, J. Xie, M. Shen, J. Wang, L. Jiang, J. Qu, F. Lu, Biometric measurement of the mouse eye using optical coherence tomography with focal plane advancement. Vision Res. **48**, 1137–1143 (2008)
36. L. Wang, B. Hofer, Y.P. Chen, J.A. Guggenheim, W. Drexler, B. Povazay, Highly reproducible swept-source, dispersion-encoded full-range biometry and imaging of the mouse eye. J. Biomed. Opt. **15**(4), 046004 (2010) http://dx.doi.org/10.1117/1.3463480
37. L. Wang, B. Považay, Y.P. Chen, B. Hofer, W. Drexler, J.A. Guggenheim, Heritability of ocular component dimensions in mice phenotyped using depth-enhanced swept source optical coherence tomography. Exp. Eye Res. **93**, 482–490 (2011)
38. J.J. Liu, I. Grulkowski, M.F. Kraus, B. Potsaid, C.D. Lu, B. Baumann, J.S. Duker, J. Hornegger, J.G. Fujimoto, In vivo imaging of the rodent eye with swept source/Fourier domain OCT. Biomed. Opt. Express **4**, 351–363 (2013)
39. B. Hofer, B. Povazay, A. Unterhuber, L. Wang, B. Hermann, S. Rey, G. Matz, W. Drexler, Fast dispersion encoded full range optical coherence tomography for retinal imaging at 800 nm and 1060 nm. Opt. Express **18**, 4898–4919 (2010)

40. A. Grinvald, E. Lieke, R.D. Frostig, C.D. Gilbert, T.N. Wiesel, Functional architecture of cortex revealed by optical imaging of intrinsic signals. Nature **324**, 361–364 (1986)
41. K. Tsunoda, Y. Oguchi, G. Hanazono, M. Tanifuji, Mapping cone- and rod-induced retinal responsiveness in macaque retina by optical imaging. Invest. Ophthalmol. Vis. Sci. **45**, 3820–3826 (2004)
42. M.D. Abramoff, Y.H. Kwon, D. Ts'o, P. Soliz, B. Zimmerman, J. Pokorny, R. Kardon, Visual stimulus-induced changes in human near-infrared fundus reflectance. Invest. Ophth. Vis. Sci. **47**, 715–721 (2006)
43. X.-C. Yao, A. Yamauchi, B. Perry, J.S. George, Rapid optical coherence tomography and recording functional scattering changes from activated frog retina. Appl. Optics **44**, 2019–2023 (2005)
44. K. Bizheva, R. Pflug, B. Hermann, B. Povazay, H. Sattmann, P. Qiu, E. Anger, H. Reitsamer, S. Popov, J.R. Taylor, A. Unterhuber, P. Ahnelt, W. Drexler, Optophysiology: depth-resolved probing of retinal physiology with functional ultrahigh-resolution optical coherence tomography. Proc. Natl. Acad. Sci. U. S. A. **103**, 5066–5071 (2006)
45. A.A. Moayed, S. Hariri, V. Choh, K. Bizheva, In vivo imaging of intrinsic optical signals in chicken retina with functional optical coherence tomography. Opt. Lett. **36**, 4575–4577 (2011)
46. A. Akhlagh Moayed, S. Hariri, V. Choh, K. Bizheva, Correlation of visually evoked intrinsic optical signals and electroretinograms recorded from chicken retina with a combined functional optical coherence tomography and electroretinography system. J. Biomed. Opt. **17**, 0160111–0160115 (2012)
47. R.A. Leitgeb, L. Schmetterer, W. Drexler, A.F. Fercher, R.J. Zawadzki, T. Bajraszewski, Real-time assessment of retinal blood flow with ultrafast acquisition by color Doppler Fourier domain optical coherence tomography. Opt. Express **11**, 3116–3121 (2003)
48. B.R. White, M.C. Pierce, N. Nassif, B. Cense, B.H. Park, G.J. Tearney, B.E. Bouma, T.C. Chen, J.F. de Boer, In vivo dynamic human retinal blood flow imaging using ultra-high-speed spectral domain optical Doppler tomography. Opt. Express **11**, 3490–3497 (2003)
49. S. Makita, Y. Hong, M. Yamanari, T. Yatagai, Y. Yasuno, Optical coherence angiography. Opt. Express **14**, 7821–7840 (2006)
50. J. Fingler, D. Schwartz, C.H. Yang, S.E. Fraser, Mobility and transverse flow visualization using phase variance contrast with spectral domain optical coherence tomography. Opt. Express **15**, 12636–12653 (2007)
51. Y.K. Tao, A.M. Davis, J.A. Izatt, Single-pass volumetric bidirectional blood flow imaging spectral domain optical coherence tomography using a modified Hilbert transform. Opt. Express **16**, 12350–12361 (2008)
52. L. An, R.K.K. Wang, In vivo volumetric imaging of vascular perfusion within human retina and choroids with optical micro-angiography. Opt. Express **16**, 11438–11452 (2008)
53. A. Mariampillai, B.A. Standish, E.H. Moriyama, M. Khurana, N.R. Munce, M.K.K. Leung, J. Jiang, A. Cable, B.C. Wilson, I.A. Vitkin, V.X.D. Yang, Speckle variance detection of microvasculature using swept-source optical coherence tomography. Opt. Lett. **33**, 1530–1532 (2008)
54. B.J. Vakoc, R.M. Lanning, J.A. Tyrrell, T.P. Padera, L.A. Bartlett, T. Stylianopoulos, L.L. Munn, G.J. Tearney, D. Fukumura, R.K. Jain, B.E. Bouma, Three-dimensional microscopy of the tumor microenvironment in vivo using optical frequency domain imaging. Nat. Med. **15**, 1219–U151 (2009)
55. L.F. Yu, Z.P. Chen, Doppler variance imaging for three-dimensional retina and choroid angiography. J. Biomed. Opt. **15**(1), 016029 (2010)
56. C. Blatter, T. Klein, B. Grajciar, T. Schmoll, W. Wieser, R. Andre, R. Huber, R.A. Leitgeb, Ultrahigh-speed non-invasive widefield angiography. J. Biomed. Opt. **17**(7), 070505 (2012)
57. V.J. Srinivasan, S. Sakadzic, I. Gorczynska, S. Ruvinskaya, W.C. Wu, J.G. Fujimoto, D.A. Boas, Quantitative cerebral blood flow with optical coherence tomography. Opt. Express **18**, 2477–2494 (2010)
58. B. Baumann, B. Potsaid, M.F. Kraus, J.J. Liu, D. Huang, J. Hornegger, A.E. Cable, J.S. Duker, J.G. Fujimoto, Total retinal blood flow measurement with ultrahigh speed swept source/Fourier domain OCT. Biomed. Opt. Express **2**, 1539–1552 (2011)

59. W. Choi, B. Baumann, J.J. Liu, A.C. Clermont, E.P. Feener, J.S. Duker, J.G. Fujimoto, Measurement of pulsatile total blood flow in the human and rat retina with ultrahigh speed spectral/Fourier domain OCT. Biomed. Opt. Express **3**, 1047–1061 (2012)
60. D.L. Faber, E.G. Mik, M.C.G. Aalders, T.G. van Leeuwen, Light absorption of (oxy-) hemoglobin assessed by spectroscopic optical coherence tomography. Opt. Lett. **28**, 1436–1438 (2003)
61. D.J. Faber, E.G. Mik, M.C.G. Aalders, T.G. van Leeuwen, Toward assessment of blood oxygen saturation by spectroscopic optical coherence tomography. Opt. Lett. **30**, 1015–1017 (2005)
62. J. Yi, Q. Wei, W. Liu, V. Backman, H.F. Zhang, Visible-light optical coherence tomography for retinal oximetry. Opt. Lett. **38**, 1796–1798 (2013)

Optical Coherence Tomography in Tissue Engineering

64

Youbo Zhao, Ying Yang, Ruikang K. Wang, and Stephen A. Boppart

Keywords

Cellular imaging • Optical coherence tomography • Optical imaging • Regenerative medicine • Scaffolds • Tissue engineering

64.1 Introduction to Tissue Engineering

As life expectancy increases and mortality rates decrease in the developed world, tissue replacement is frequently required to treat biological wear and tear associated with ageing and accidental damage [1, 2]. Despite the rapid development of modern clinical technologies, the field of medicine faces major challenges in finding solutions for such ageing-linked degeneration, disease, or trauma. Autogenic grafting still remains the gold standard for repair and replacement of tissues and organs.

Y. Zhao
Biophotonics Imaging Laboratory, Beckman Institute for Advanced Science and Technology, University of Illinois at Urbana-Champaign, Urbana, IL, USA

Y. Yang
Institute for Science and Technology in Medicine, School of Medicine, Keele University, Stoke-on-Trent, UK

R.K. Wang
Department of Bioengineering, University of Washington, Seattle, WA, USA

Department of Automation Engineering, Northeastern University at Qinhuangdao, Hebei, Peoples' Republic of China

S.A. Boppart (✉)
Biophotonics Imaging Laboratory, Beckman Institute for Advanced Science and Technology, University of Illinois at Urbana-Champaign, Urbana, IL, USA

Departments of Bioengineering, Electrical and Computer Engineering, and Medicine, University of Illinois at Urbana-Champaign, Urbana, IL, USA
e-mail: boppart@illinois.edu

© Springer International Publishing Switzerland 2015

W. Drexler, J.G. Fujimoto (eds.), *Optical Coherence Tomography*,
DOI 10.1007/978-3-319-06419-2_66

Viability, immunocompetence, and high incorporation rate are the main advantages of autologous grafting. However, donor site morbidity and the risk of infection and limited availability are the common drawbacks of this procedure. The use of allogeneic tissue or organs offers another option, but the graft immunogenicity and the risk of infection and disease transmission lead to high rates of failure. A third option for repair and replacement of the tissue and organs is the use of a prosthesis made from synthetic materials, which has gained wide acceptance in certain situations, such as orthopedic surgery, where total hip replacement is now a standard practice. The main problem of this technique, however, is premature failure due to lack of biocompatibility. This often leads to a short service time and malfunction of the prosthesis.

Seeking new therapy options has led to the utilization of isolated cells, including stem cells transplantation, instead of tissue or intact organ transplantation. It is reported that transplantation of fetal stem cells and a cell line which can release human ciliary neurotrophic factor (CNTF) have been tested in animal models and human trials to treat Huntington's disease [3]. Delivery of islets from the pancreas has been investigated over a few decades to restore normal blood glucose levels for diabetes patients. It is recognized that enhanced efficiency of cell therapies may be achieved by localization and differentiation of the cells into the correct phenotype in vitro or the generation of matrix with the required quantity and organization in artificial scaffolds before injection or implantation into patients. These investigations have given rise to a new therapy or methodology: tissue engineering.

Over the past decade, tissue engineering has emerged as a promising therapeutic solution in regenerative medicine in the realization of biologically functional implants [4]. Distinct from the aforementioned treatments, tissue engineering conjures up visions of organs built from cellular components in the laboratory until the constructs have reached "maturity," ready to be transplanted into desperately ill patients [5]. In principle, tissue engineering applies engineering approaches to induce specific cells or stem cells to grow into the required tissues in vitro. Synthetic or natural macromolecules are manipulated into a temporary scaffold where cells can be converted into functional tissues. The great advantage of tissue engineering is twofold. First, it has less risk of donor site morbidity because it commonly only involves a small biopsy to obtain a patient's own cell source. Second, the generated tissue is biologically fully functioning and there is no immunogenicity, making the technique equivalent to autologous grafting. Regardless of its short history, tissue engineering promises a bright future when compared with current treatments for the repair and replacement of damaged or diseased tissues.

Developing and repairing tissues and organs in the human body is a highly controlled and well-programmed process consisting of a series of events and steps. Replication and realization of this process in vitro are major challenges for biologists and engineers. To form functional tissues through tissue engineering, three basic elements are required: patient cells or engineered stem cells in a specific quality and quantity, scaffolds with the appropriate biological geometry of the original organ or tissue in which cells can grow and differentiate, and a suitable biochemical and biophysical environment which maintains the physiological conditions for the cells and guides them to deposit the required matrix during development.

64.1.1 Bioreactor (Culture Environment)

A suitable bioreactor is one of the three key elements in tissue engineering. It allows for creation and control of a culture environment that facilitates cell growth and differentiation for successful development of physiologically relevant organs or tissues [6]. Requirements for desired bioreactors are not limited to mimicking this dynamic environment but also include methods for enhancing the microenvironment, which may accelerate cell proliferation and differentiation. Static culture is simple in design and operation, but several studies have revealed that the supply of oxygen and soluble nutrients into the center of three-dimensional (3-D) constructs in in vitro culture is a critical limitation [7]. Also, traditional cell seeding by means of pipettes and relying on gravity as a principle force for cell settlement and subsequent adhesion to the scaffold pores has been questioned because of low efficiency and resulting nonuniformity of cell distribution in the scaffold [8]. To reduce the problems of mass transfer of nutrient and gas exchange, and low efficiency in cell seeding, several types of bioreactors have been designed, such as spinner flasks, rotating wall vessels, and perfusion systems. In fact, a bioreactor is a system optimally designed to simulate the physiological environment for the creation, physical conditioning, and testing of cells, tissues, support structures, and organs in vitro [9].

All bioreactors include methods for the mixing of oxygen and nutrients through the medium and thereby reduce concentration gradients through the thickness of the constructs [10]. Shear forces are usually produced in bioreactors due to the movement of culture media. In addition to shear forces, extra load features can be added to bioreactors for load-bearing tissues. An axial compression force and tensile force have been achieved in some bioreactors [11, 12]. The application of mechanical forces in bioreactors directs cellular activity and maintains cell phenotype in some engineered tissues, for instance, bone and cartilage [13, 14].

64.1.2 Scaffold

The scaffold as a template for seeding cells is a key component in tissue engineering. The three-dimensional scaffold provides the necessary support for cells to proliferate and maintain their differentiation function, and its architecture defines the ultimate shape of the new tissue. The primary task of the scaffold is to act as a temporary matrix for anchoring cells. The requirements of supporting cell growth into functional tissue make it essential for the scaffold to have several unique features. High porosity is a prerequisite, to provide space for the cells to occupy and generate extracellular matrix. The porous structure also facilitates angiogenesis; thus, blood vessels can grow if there is also an adequate supply of oxygen and nutrients to the center of the construct. The ability of the scaffold to degrade in the biological environment via either enzymatic or hydrolytic reactions is another key feature. The elimination rate of the temporary scaffold template should correspond with the rate of tissue turnover, with the goal of having the construct be eventually replaced by a new tissue.

The materials used to fabricate the scaffold are derived either from natural materials, e.g., collagen, chitosan, or from synthetic polymers, mainly from the polyester family. The mechanical parameters and processing properties of these materials can be tailored by molecular weight, crystallinity, and the ratio of comonomers in the copolymers. One unique feature of synthetic polymers is that they can be processed by various methods. In addition, it is possible to combine drug release techniques to fabricate scaffolds which can release modulating molecules such as growth factors, hormones, and ion channel agonists via control release strategies.

64.1.3 Cells

Cells both comprise and generate the building materials for all types of tissues. Not only do they produce signals to control the production of proteins which comprise the matrix, but they also direct the location and organization where the protein synthesis and deposition must occur. There are several considerations in the selection of cells for tissue engineering. In the original definition, a specific mature cell type is used to grow the specific target tissue; for instance, isolated bone cells for bone tissue. The advance in stem cell biology creates another potential cell source: stem cells, either from embryos or from adults. When using stem cells, the major issues are how to culture stem cells while they remain in an undifferentiated state until expansion to the targeted cell number is achieved and how to differentiate the stem cells into a pure and specific cell type. Cell seeding density influences tissue turnover in engineered constructs. Seeding cells into a scaffold at high density has been associated with enhanced tissue formation in 3-D constructs [15]. Too low a seeding density prevents cell-cell interaction. However, the cell number usually is limited by the biopsy size and/or the extent of cell expansion. Therefore, it is often required to seed cells with the highest possible efficiency.

64.2 Current Imaging and Monitoring Techniques

The growth of cells in 3-D scaffolds and the conversion of cells into functional tissues is a long and highly dynamic process. To mimic the body environment, various stimulation conditions have been applied. Monitoring and evaluating cell activities in response to these stimulations and treatments are vital to improve the success rate of tissue formation. However, monitoring and evaluating engineered tissue constructs are much more difficult and complex than for natural tissues due to the presence of scaffold materials and the immature features of the constructs. The full utilization of existing imaging methods and the exploitation of new modalities for monitoring and evaluating engineered constructs are essential to maximize and optimize the functions of the three basic elements in tissue engineering.

There are several key questions to be addressed for the successful development of engineered constructs:

- How do culture conditions (parameters of the bioreactors) affect the activity of the cells within the 3-D scaffold and the final organization of the developed tissue?
- What are the optimal parameters for the scaffold and substrate, and how are they most effectively characterized and evaluated?
- How are the seeded cells distributed spatially within the 3-D scaffolds, and how do they migrate, proliferate, and differentiate within the 3-D scaffold during the lengthy culture period?
- Is it possible to quantify the cell viability and the tissue turnover in the 3-D scaffold in response to various mechanical and biological stimulations?
- How does the implanted tissue evolve and interact with the host environments following transplantation, and how can the efficacy of the treatment be evaluated?

In the tissue engineering field, the existing imaging techniques – light microscopy, confocal microscopy, and micro-CT – are the most widely used tools. In addition, electron microscopy is frequently used on fixed samples to visualize the localization and attachment of single cells with the scaffold.

64.2.1 Light Microscopy and Histology

Light microscopy is a traditional but very powerful tool in the biological field. Various stains and fluorescent dyes can be selected to enhance contrast and to differentiate individual components within a complex biological system. The high resolution, selectable contrast, simple application, and inexpensive use of light microscopy make it an essential technique in every biological laboratory. However, the penetration depth of visible and fluorescent light is very limited. Only thin and transparent samples can be visualized. Inevitably, all tissue or organ samples must be cut into thin sections approximately 3–10 μm thick via conventional paraffin embedding and microtome sectioning or through cryosectioning processing before viewing by light or fluorescent microscopy. These sample preparation methods and histological analysis are not only time-consuming but may also introduce structural artifacts or the loss of some biological or material components because all specimens must be subjected to a dehydration and rehydration cycle. Most importantly, observation by light microscopy is the end-point evaluation and a destructive analysis technique. The same issues arise for transmission and scanning electron microscopy, which is used to further resolve cellular features at the submicron scale. Electron microscopy, too, requires destruction of the sample or specimen for analysis.

64.2.2 Confocal and Two-Photon Microscopy

The emergence of confocal microscopy was a revolution in the microscopy field. By labeling with fluorophores, optically nontransparent specimens with a 3-D

structure could be visualized at high resolution. Up to approximately 100 μm thickness, confocal microscopy can acquire sample images with a focused beam of light and collection of the fluorescent signal via a pinhole aperture that spatially rejects light from out of focus areas of the specimens. Optical sectioning eliminates the requirements of physical sectioning as in histological analysis, enabling the observation of viable cells in the scaffold, and the online measurement of cell activities and tissue turnover.

The drawback of confocal microscopy, however, is the limited penetration depth and the often necessary use of fluorophores. Except for a few engineered tissues, for instance, skin and cornea, the engineered constructs are relatively thick, ranging from a few millimeters to centimeters. The penetration depth in confocal microscopy limits the observation to the surface of the constructs. In addition, to achieve thin optical sectioning, high numerical aperture (NA) optics are frequently required, potentially limiting the working distance between the objective and the tissue surface. The fluorescent labeling may also affect the long-term viability of cells in the constructs.

Fluorescent molecules may absorb two photons simultaneously before emitting light. The use of two-photon excitation has enabled two-photon microscopy. This microscopy technique has advantages over one-photon techniques including efficient background rejection, low photo damage, and enhanced depth discrimination. Using two-photon excitation, where a fluorescent chromophore simultaneously absorbs two incident long-wavelength photons before it fluoresces, can greatly reduce photobleaching [16]. However, the sample penetration depth under this modality is still limited to several hundreds of microns in highly scattering tissue.

64.2.3 Microcomputed Tomography

Microcomputed tomography (μ-CT) is the micron-scale version of X-ray computed tomography used extensively in medical fields. However, instead of keeping the samples or specimens (patients) immobile, the samples in μ-CT are rotated and resolutions as high as 2–10 μm can be realized. Its popularity can be attributed to its ability to provide precise quantitative and qualitative information on the 3-D morphology of specimens. Micro-CT is a nondestructive modality and essentially no additional steps are needed to prepare samples for scanning. However, ionizing X-ray radiation is used, which can affect the viability and health of living specimens. The absorption and contrast ability of X-rays to high-density materials in the biological field are preferential to bone tissue due to the calcium and phosphorus elements. Thus, the best application of μ-CT in tissue engineering is the evaluation of bone cell growth within the scaffold. The degree of mineralization within the 3-D scaffolds can be very clearly delineated [17, 18]. A scaffold made from polymeric materials has low X-ray attenuation, but the contrast of air and polymer is sufficiently high to differentiate them. Therefore, μ-CT has additional applications for the assessment of scaffold architecture, such as pore size, porosity, and pore interconnectivity. Recently, the correlation of strain level around a porous scaffold has been investigated and correlated with the degree of

mineralization of engineered bone within the constructs [19]. The application of micro-CT in tissue engineering is more or less limited to bone tissue generation since other types of tissues lack strong contrast among the components under an X-ray source.

64.3 OCT as an Investigative Tool for Tissue Engineering

The fabrication of thick 3-D tissue constructs has been limited by our ability to visualize the complex cellular dynamics and morphological organizational events occurring deep within these constructs. Therefore, an alternative approach, free from the limitations described above, is highly desirable for successful tissue engineering.

Optical coherence tomography (OCT) [20] has recently emerged as a promising imaging technique, mainly for medical applications. The original development of OCT was for transparent tissues, such as corneal and retinal tissues [21]. Current OCT technology enables nontransparent, soft and hard tissues to be examined in vivo, including the skin [22], gastrointestinal tract [23], nervous systems [24], cartilage [25], and respiratory tract [26], to name only a few. Clearly, the capabilities of OCT provide enormous potential to overcome a number of limitations currently experienced in tissue engineering for monitoring cell growth and morphology within porous scaffolds. In the past decade, the instrumentation of OCT has been continuously investigated and developed. The resolution, the penetration depth, and the functionality of OCT have improved dramatically. Several features in OCT are unique and highly attractive for tissue engineering. Measurements by OCT can be realized online and in a nondestructive manner. The resolution is up to the cellular dimension (0.9–10 μm), and the penetration depth for a nontransparent object can be up to 2 mm, well within the size scale of most complex 3-D engineered tissues.

In this chapter, we discuss the application of OCT to tissue engineering. Imaging examples with OCT and its enabling functions and variants, such as Doppler OCT (DOCT), polarization sensitive OCT, optical coherence microscopy (OCM), etc., are overviewed. For clarity, we arbitrarily divide these imaging examples into separate sections where specific investigations of one of the three main elements in tissue engineering, i.e., bioreactors, scaffolds, and cells, are discussed. Imaging with multimodal microscopes that combine OCT/OCM with other imaging modalities is also introduced, which enables new specific applications in tissue engineering with extended functions and new contrast abilities. The potential of using OCT and multimodal imaging technology for in vivo monitoring of postimplantation dynamics and evaluation of the treatment efficacy is discussed in the last section.

64.3.1 Overview of OCT and Its Functional Variants

Although OCT has a relatively short history since inception, a number of different modes of operation have evolved over the past decade which enable the

visualization and quantification of many different parameters of biological tissue. In addition to standard OCT imaging of cellular and tissue microstructure, functional OCT modes include methods sensitive to flow or tissue movement, birefringence, metabolic states, and biomechanical properties, among others. Operating as both a structural and functional imaging modality, OCT may tackle many different monitoring tasks in tissue engineering.

Time-domain OCT (TD-OCT) was the first version of OCT used widely in the early 1990s [20]. Improvements in the light source, the interferometer design, and the beam delivery system have led to time-domain OCT being widely used to image the microstructures of tissue in clinical trials and the research laboratories. Its simple construction and low cost add merit for its wide application. In the mid-1990s, it was realized that OCT imaging could be performed in the spectral domain (frequency domain OCT, FD-OCT) without the requirement of scanning the optical delays in TD-OCT. Because FD-OCT is achieved without movement of the reference arm, imaging speed is dramatically improved. More importantly, there is a gain in the detection sensitivity and phase stability compared to its counterpart. Such features are very useful for investigating fast dynamic biological systems where speed of data acquisition is vital. Another recent advance in OCT is the development of swept-source OCT (SS-OCT), which is also referred to as time-encoded frequency domain OCT or optical frequency domain imaging (OFDI). In SS-OCT [27], the spectrally resolved interference is recorded based on fast detection of a temporally swept narrow linewidth laser through a broad bandwidth. In addition to improved sensitivity [28], SS-OCT offers much higher imaging speed (up to million A-scans per second [29]), which is enabled by the availability of the stable fast wavelength tuning swept sources, such as the Fourier domain mode-locked laser [30]. Other chapters (► Chaps. 1 "Introduction to OCT," ► 6, "Complex and Coherence-Noise Free Fourier Domain Optical Coherence Tomography," and ► 8, "Complex Conjugate Removal in SS Optical Coherence Tomography") in this book provide specific details on these types of OCT systems.

Combining the Doppler effect with OCT enables the detection of Doppler frequency shifts due to tissue movement or fluid flow, thereby mapping these physiological or functional changes, such as blood flow, to the structural OCT image of the tissue. Thus, Doppler OCT opens another window to detect functional changes, such as abnormal blood flow in the skin or retina, and to track the velocity of moving scatterers within the tissue. In the field of tissue engineering, this has been preliminarily exploited to monitor fluid flow within a construct in a bioreactor [31] or within microfluidic precursors to vascular constructs [32].

The development of high-resolution polarization-sensitive OCT (PS-OCT) has attracted considerable interest since a number of biological tissues have a well-organized matrix, mainly consisting of collagen fibers. The change of the fiber organization, reflected in the spatial distribution of detected birefringence, may indicate disease or abnormality. Thus, PS-OCT can detect structural change in tendon, muscle, or cartilage, depending on the change of birefringence. This technique can also be used to monitor the architecture of newly formed matrix in engineered cartilage and tendon [33, 34].

In addition to providing structural information, or the functional information described above, OCT techniques can be used for extracting spectroscopic information [35–38]. Spectroscopic OCT has been investigated by using appropriate time-frequency analysis. In general, spectroscopic OCT has at least two imaging targets: imaging spectral absorption and spectral scattering. Separation of the two signals can retrieve molecular information either about endogenous molecules or about exogenous contrast agents that provide a more dramatic difference in detected spectral absorption or scattering.

Viewing tissue at the cellular level is a significant challenge for OCT. The highest longitudinal resolution achieved for OCT to date has been obtained by using a state-of-the-art femtosecond Ti:sapphire laser. Using this source, in vivo subcellular imaging with longitudinal resolution of less than 1 μm was demonstrated [39]. Alternatively, the development of full-field optical coherence microscopy (ffOCM) has achieved sub-micrometer resolution using a broadband white-light source [40]. Laser-scanning OCM, which uses high NA objectives to obtain high transverse resolution, has also been demonstrated to be promising for investigation of engineered tissue [41–43].

While OCT has emerged as a promising imaging tool in tissue engineering, it has specific limitations that still need to be considered and addressed. The most predominant one is the low contrast of OCT images, which are normally formed based on the spatial variance of localized refractive index. To improve the contrast of OCT, a few types of exogenous contrast agents, such as microbubbles [44], inert metal nanoparticles [45], microspheres [46], and magnetic nanoparticles [47], among others, have been proposed and demonstrated. Considering the potential side effects of these agents, and the fact that there is normally no organized clearance system in engineered tissue, the use of contrast agents is not preferred. Because of this, the combination of OCT with other imaging modalities, such as fluorescence-based microscopy techniques and nonlinear microscopy, may offer a good option to develop with OCT in tissue engineering. In particular, because OCT can use ultrafast short-pulse laser sources that offer broad spectral bandwidth, such as the common Ti:sapphire laser, integrated microscope systems can be constructed to also perform two-photon excited fluorescence (TPEF) simultaneously [48]. The combination of OCT with multiphoton microscopy (MPM, including TPEF and second harmonic generation (SHG) [49] microscopy) has been exploited for high-resolution imaging of engineered tissue [43, 50]. Moreover, the multimodal imaging system has demonstrated the ability to track cellular dynamics in vivo, showing the potential for investigation and monitoring of the dynamics of cells and engineered tissues following transplantation [51].

64.3.2 OCT Imaging of Bioreactors

Given the complexity of the bioreactor systems for tissue engineering, which involve sophisticated architecture, different types of materials, and dynamic perfusion flow, the observation of developing tissue in bioreactors is nontrivial. Moreover, the growth of an engineered tissue in a bioreactor has specific requirements. For example,

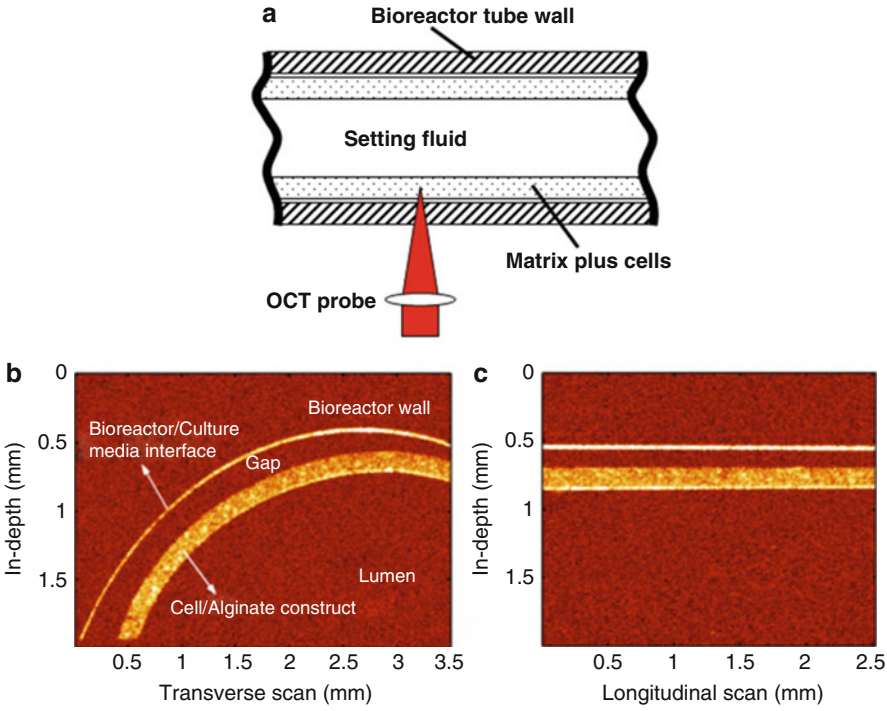

Fig. 64.1 OCT imaging of a bioreactor with its engineered tissue construct. (**a**) Schematic of the bioreactor. (**b**) Transverse and (**c**) longitudinal OCT scan. The *bright pixels* within the construct represent the cells. The outer interface of the bioreactor in OCT image is not shown (Reprinted with permission from [31])

the developing tissue must be bathed in a solution of nutrients at all times, and imaging of tissue should be performed repeatedly without interrupting the development of the tissue. A typical tissue engineering bioreactor, in which the tissue-engineered construct is produced and grown, needs to remain absolutely sterile throughout the weeks to months of operation prior to the harvesting of the living construct for surgical implantation into the patient [52]. During this time, the evolving architecture of the tissue requires constant monitoring in a noninvasive, nondestructive manner and at an acceptable cost.

The nutrients in bioreactors are supplied in the cell or tissue culture medium, which surrounds and perfuses the tissue. This medium typically has a refractive index in the order of 1.34 [53]. Biomedical grade (Food and Drug Administration-approved) plastics have precisely known refractive indices, e.g., Delrin, an acetyl copolymer (Dupont, Wilmington, DE, USA) with a refractive index of 1.48. Given this heterogeneous group of discrete refractive indices in a typical bioreactor, and in the tissue and growth medium, it is possible to obtain OCT images of the bioreactor and the engineered tissue in these culture conditions.

As an example, Fig. 64.1 shows OCT images of a bioreactor within which a hydrogel tube (approx. 4 mm outside diameter by 20 cm in length) with encapsulated mesenchymal stem cells was formed by extruding the cell/alginate solution using a solution of 1 % $CaCl_2$ in 0.9 % saline using a combined fabrication device/bioreactor [31]. From the OCT images, it is evident that the bioreactor contains an inner lining that is composed of living cells within an alginate hydrogel and a distinct inner lumen containing culture medium. The engineered construct is separated from the bioreactor wall by a thin layer of culture medium. In addition, the distribution of the cells within the hydrogel can be visualized, with the cells appearing as bright spots in the OCT images. This appearance is because the cells have relatively high refractive indices compared to that of the hydrogel scaffold, providing the imaging contrast.

64.3.3 OCT Imaging of Scaffold and Substrate

Scaffolds used in tissue engineering act as templates and provide mechanical, chemical, and biological support for tissue regeneration. They are commonly 3-D structures with porous or fibrous degradable structures. The parameters of the scaffold, such as material, pore size, porosity, and pore interconnection, affect the cell activity and cell distribution within the scaffolds. OCT can evaluate and monitor the architecture of the scaffolds and the cellular distribution without sample preparation, which provides instant feedback on the growth and development of the engineered tissue.

Recently, OCT along with appropriate imaging processing algorithms was used to investigate parameters of the porous scaffold, including volume porosity, pore interconnectivity, and pore size [54]. Accurate characterization of these parameters provides valuable feedback for better control of the fabrication conditions. Figure 64.2 shows OCT images of porous hydrogel scaffolds fabricated using the porogen-leaching technique [55] with different formulations. The images are obtained using a swept-source Fourier-domain OCT system (Thorlabs Inc.) with a laser source at 1,300 nm and a broadband spectrum of 100 nm, which provided an axial resolution of 8 μm. The micropores and hydrogels are well resolved in both the cross-sectional and en face images, which also reveal the pore size and density. The color-coded 3-D-labeling images show the interconnectivity of different groups of pores. Based on this information, and assisted with appropriate algorithms, quantitative pore density and interconnectivity can be determined [54].

In order to provide a better nutrient supply to the porous and thick 3-D constructs, the integration of a perfusion method becomes essential in various bioreactors. In addition to a better exchange of nutrients and waste, perfusion generally exerts mechanical stimulation on the engineered tissue, which accelerates the maturation of the constructs. It is essential to attain the information about the relationship between perfusion rate and fluid shear stress in 3-D porous scaffolds and their dependence on the main parameters of the scaffolds such as pore density, pore size, and shape. Potentially, this can be done with DOCT (Doppler optical

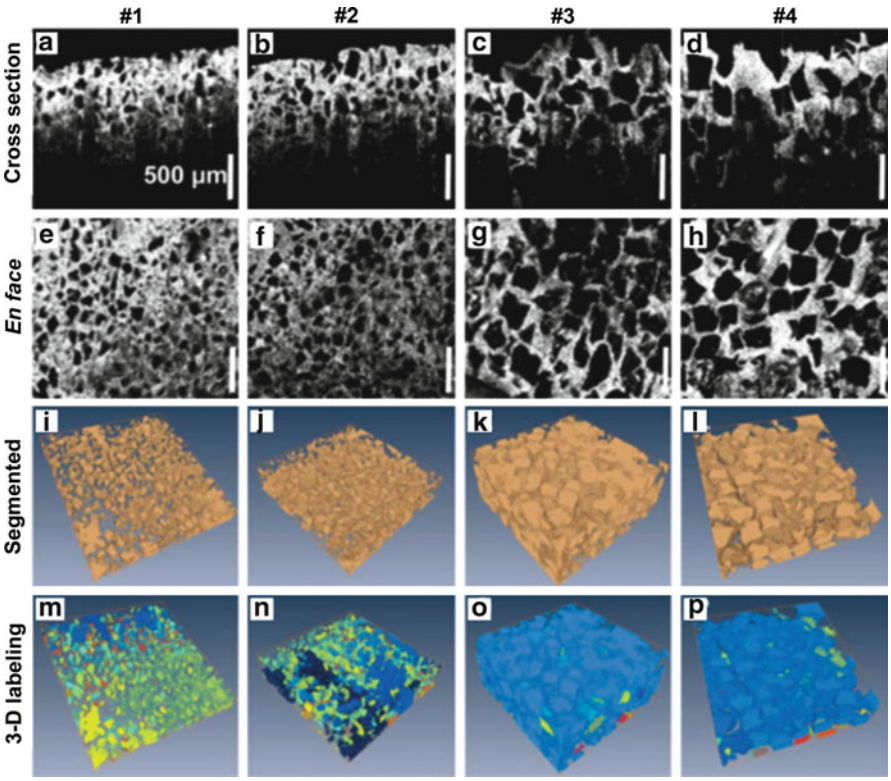

Fig. 64.2 (**a**–**d**) Cross-sectional and (**e**–**h**) en face OCT of scaffolds with different volume porosities. For scaffolds #1–4, the calculated volume porosities are 24.4 % ± 7.5 %, 18.1 % ± 10.3 %, 41.4 % ± 6.0 %, and 39.7 % ± 7.7 %, respectively. En face images are taken at a depth of 100 μm. (**i**–**l**) 3-D observation of the pores segmented from OCT images. (**m**–**p**) 3-D observation of isolated and connected pore groups through the 3-D labeling process. *Different colors* indicate different groups. 3-D images are analyzed using a depth range of 0–300 μm (Reprinted with permission from [54])

coherence tomography), a functional variant of traditional OCT. DOCT uses additional phase information from the complex OCT signals, which can be used to monitor the directions and velocities of moving particles in the backscattered spectrum. It is therefore possible to provide information regarding both the scaffold architecture and local fluid flow through 3-D scaffold, simultaneously.

The shear stress from fluid flow can be directly related to the fluid velocity measured by DOCT:

$$\tau = \mu \frac{\partial v}{\partial n} = \mu \frac{\partial v_z}{\partial z} \cdot \frac{2}{\sin 2\alpha} \left(\mathrm{dyn \cdot cm^{-2}}\right) \tag{64.1}$$

where V is the flow velocity vector and V_z is the component of the velocity in the z direction (probe beam direction) measured by DOCT. This calculation and

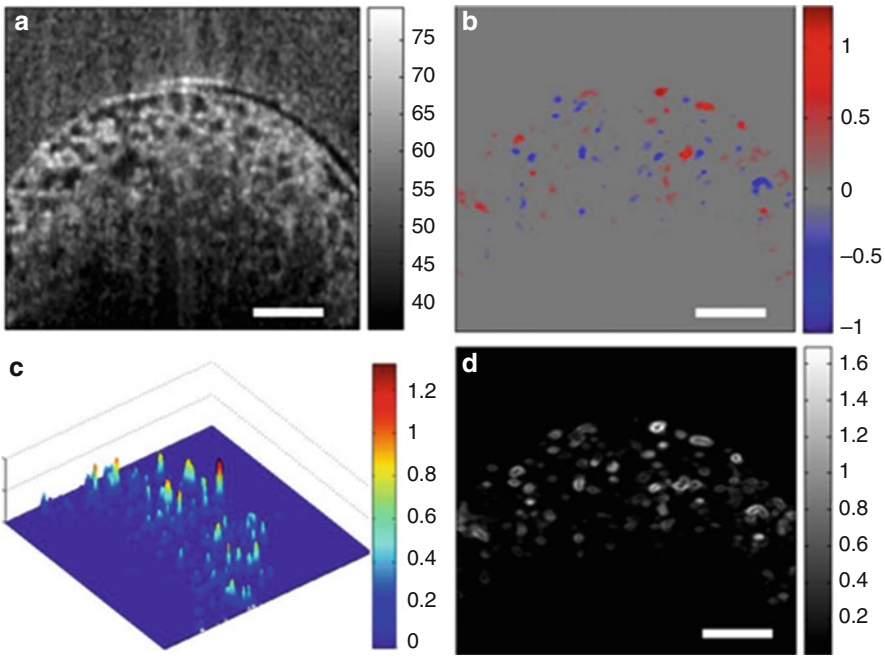

Fig. 64.3 DOCT monitored the fluid flow in a low-porosity chitosan scaffold in situ. Shown are, respectively, (**a**) the microstructural image, (**b**) the bidirectional local fluid flow map, (**c**) the 3-D plot of magnitudes of the flow velocities, and (**d**) the corresponding local shear stress distribution in a typical X-Z section. The units for color bars shown are (**a**) dB, (**b**) mm/s, (**c**) mm/s, and (**d**) dyn/cm^2 respectively. The *white scale bars* indicate 200 μm (Reprinted with permission from [57])

other technical details regarding DOCT can be found in ref. [56] and ▶ Chaps. 42, "Doppler Fourier Domain Optical Coherence Tomography for Label-Free Tissue Angiography" and ▶ 45, "Optical Coherence Tomography in Cancer Imaging" in this book. In addition, since DOCT can provide both the 3-D microstructural morphology and 3-D flow map for each pores in a scaffold, the combination of the structural and flow images permits the direct measurement of porosity and interconnectivity for the porous scaffolds. The porosity is defined as the ratio of total pore volume to total scaffold volume as determined by the OCT structural images, which is typically determined by block image processing.

A typical cross-sectional OCT image of a low-porosity chitosan scaffold (LPCS) with a pore size ranging from 30 to 100 μm is presented in Fig. 64.3a. The chitosan scaffold is fabricated by a freeze-drying technique using a 2 % chitosan solution in acetic acid. The scaffolds, with different porosity and pore size, were obtained by adjusting the freezing rate [58]. A spectral-domain DOCT system, which used a superluminescent diode with a central wavelength of 842 nm and a measured axial resolution of ~7 μm in air, was used to acquire these images. The bidirectional flow velocity map obtained by DOCT is presented in Fig. 64.3b. Both the distributions and the magnitudes of the flow can be seen. The magnitudes of bidirectional

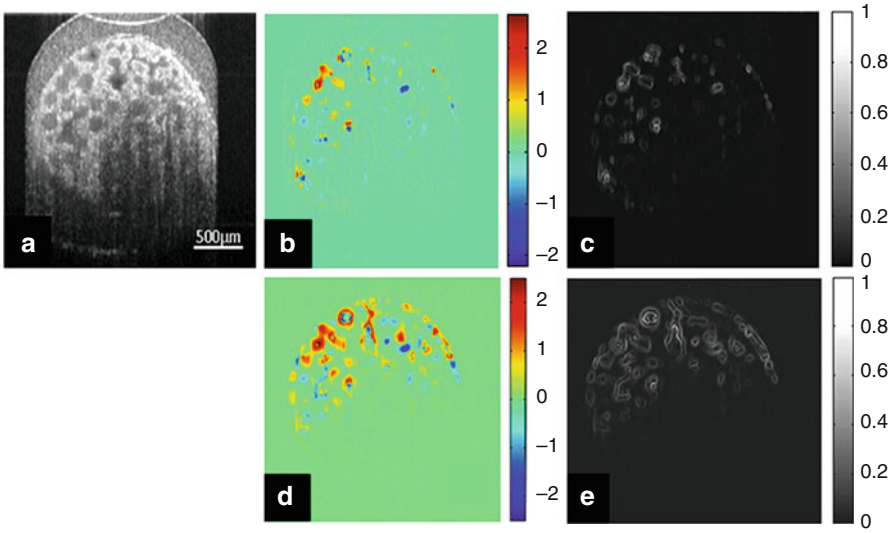

Fig. 64.4 (**a**–**c**) DOCT images for chitosan scaffolds with round-shaped pore structures: (**a**) structural image, (**b**) flow rate, and (**c**) shear stress. (**d**–**e**) DOMAG images of the same scaffolds in (**a**), showing the better resolution of the flow rate (**d**) and shear stress (**e**)

flow velocities were calculated and plotted in Fig. 64.3c. It is seen that there are variations of velocities within pores, indicating a heterogeneous distribution of flow velocity in the porous structures. Although the input flow rate was constant, the local fluid flow in this complex construct varied greatly in both magnitude and direction. Furthermore, the flow in the micropores did not show parabolic distributions. Consequently, the fluid shear stress, as shown in Fig. 64.3d, differed from pore to pore, with values ranging from 0 to 1.65 dyn cm^{-2}. Nevertheless, the maximum fluid shear stress was generally located at the pore walls. Based on the quantitative comparison between the distributions of shear stresses at the pore walls of scaffolds with different porosity, dependence of shear stress on porosity, pore interconnectivity, and shape can also be characterized.

The real flow rate can be further investigated with the technology called as Doppler optical microangiography (DOMAG) [59]. DOMAG combines the phase-resolved technique in DOCT and flow signals from optical microangiography (OMAG), which generates low-noise flow images, reflecting the real flow rate more precisely. Comparison between OMAG and DOCT on the fluid flow measurement in chitosan scaffolds (with round-shaped pore structure) is shown in Fig. 64.4. Figure 64.4a is the structural image of the scaffold. Figure 64.4b, c are from DOCT and Fig. 64.4d, e are from DOMAG for flow rate (d) and shear stress (e), respectively. There are two improvements for these images. First is the higher penetration depth of the image and second is the much clearer flow pattern in each pore using the DOMAG technique, which resulted in more accurate shear stress images (Fig. 64.4e). It is reported that the background noise from a non-flow region

of the scaffold and random noise were imposed onto DOCT flow images, resulting in a difficulty to precisely measure small flow velocity [57, 59]. DOMAG is able to tackle this issue and separate the background flow signals from the background signals, which leads to low-noise images.

In addition, the mechanical properties are important parameters of a scaffold, which affect the development and regeneration of the tissue [60, 61]. The relationship between cell dynamics and the mechanical properties of a scaffold is complex. Cell activities are affected by the mechanical parameters of the environment, but these mechanical properties also have considerable impact on the growth and the behavior of cells. A good understanding and control of this interaction will help us improve regeneration of the desired tissue. Normally, the biomechanical properties of tissues are characterized by elastography. Traditionally, this has been performed with ultrasound or MRI, but recently elastography has been demonstrated in OCT in a technique called optical coherence elastography (OCE). One initial application has been for investigating the biomechanical properties of myocardial tissues [62]. The high resolution and sensitivity of OCE makes it suitable for detecting changes at the cellular level in engineered tissues [62]. As cells seeded in scaffolds proliferate and the engineered tissue develops, the cells increase in number and secrete extracellular matrix. During this process, the biomechanical properties of the engineered tissue will be altered, and these subtle changes can be detected with OCE in a spatially and temporally resolved manner.

Figure 64.5 shows a representative array of structural and OCE images acquired from a 3-D scaffold, with half of the scaffold seeded with cells and the other half serving as a cell-free control. The samples were imaged over a culture time of 10 days, and at each time point, the OCE images were analyzed to generate both displacement and strain maps, which are color coded to indicate regions of higher stiffness. The cell-seeded regions increased significantly in stiffness over the culture period, demonstrating that OCE could be used to measure the stiffness and biomechanical parameters from the engineered tissue in a spatially resolved, nondestructive manner. Related to engineered tissues, OCE was used to image the changing biomechanical properties in the developing *Xenopus laevis* tadpole, which exhibited a more markedly different range of tissue stiffness attributed to organo- and morphogenesis [63]. Much of our understanding of the complex processes in the field of developmental biology (▶ Chap. 67, "Optical Coherence Tomography for Gastrointestinal Endoscopy") can be applied to the field of tissue engineering, where we wish to control the growth and organization of engineered tissues in 3-D and under an array of pharmacological and mechanical stimuli.

64.3.4 OCT Imaging of Cell Dynamics

64.3.4.1 Cell Growth Profiles

In addition to bioreactors and scaffolds, activities of cells in these environments eventually determine the regeneration of the tissue. Because the environmental parameters have a critical influence on cell growth and the deposition of matrix,

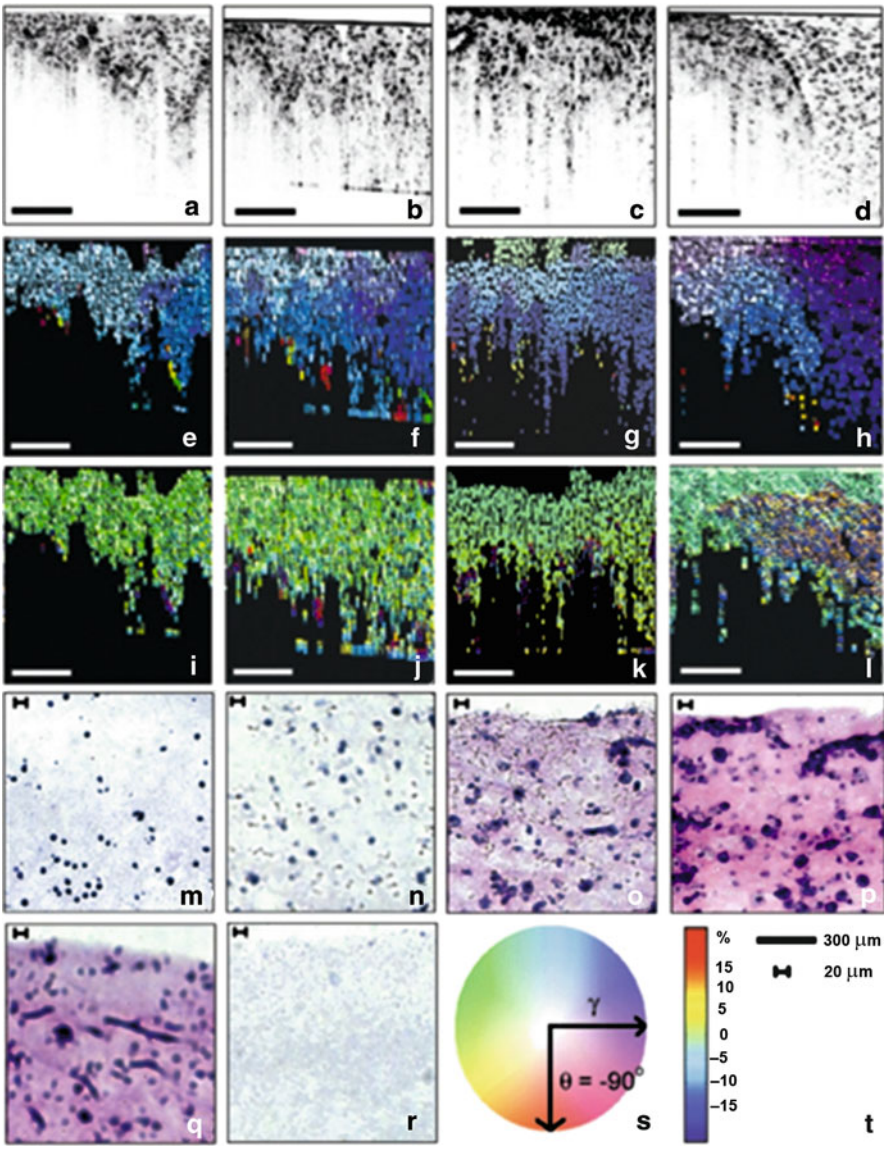

Fig. 64.5 Optical coherence elastography of engineered tissues. (**a**–**d**) Structural OCT images on day 0, 3, 7, and 10, respectively, of the boundary between the cell-seeded region (*left*) and the cell-free region (*right*). (**e**–**h**) Displacement maps on day 0, 3, 7, and 10, respectively, color coded using the scale in (s). (**i**–**l**) Strain maps on day 0, 3, 7, and 10, respectively, using the color scale in (**t**). (**m**–**p**) Corresponding histology from the cell-seeded tissue regions. (**q**) Histological image of cells after 10 days of incubation without embedded microspheres. (**r**) Histological image of a cell-free scaffold and microspheres. The size *scale bar* represents 300 μm in (**a**–**l**) and 20 μm in (**m**–**r**) (Reprinted with permission from [63])

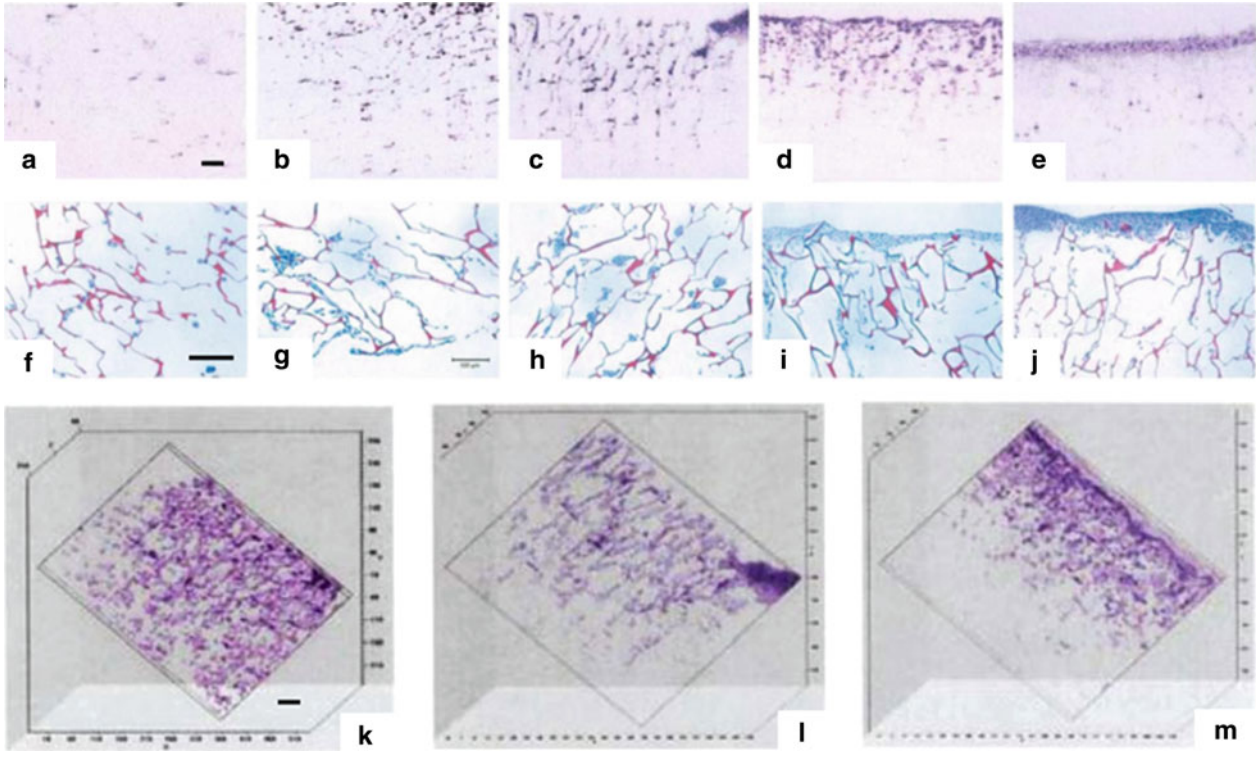

Fig. 64.6 Two- and three-dimensional OCT of a cell-seeded porous scaffold. Fibroblast cells were seeded in a chitosan scaffold and imaged at days 1, 3, 5, 7, and 9 (**a**–**e**, respectively) to show cell distribution changes. Initial cell seeding distribution is relatively uniform, but at later days, cells migrated toward surface to form a dense cell layer. Corresponding validating histology (**f**–**j**) is shown, along with 3-D OCT images at days 3, 5, and 7 (**k**–**m**, respectively). *Scale bar* represents 100 μm (Modified figure reprinted with permission from [64])

revealing the cell growth profiles within scaffolds will greatly increase our understanding of how to control culture conditions and optimize growth patterns. OCT has been utilized in this regard [54, 64–68]. Because of the difference in refractive index between cells and scaffolds, which results in the variation of backscattering of light from the different regions, OCT has the appropriate capability to investigate cell dynamics in engineered tissue.

Figure 64.6 shows OCT images, corresponding histology, and 3-D visualization of a fibroblast cell population seeded in a chitosan scaffold and imaged over several days, revealing the cell growth profiles and dynamics. Cells were cultured and imaged at days 1, 3, 5, 7, and 9. Initially, the chitosan scaffold provided very little scattering for OCT, as the index of refraction was similar to the surrounding media. As the seeded fibroblasts populated the scaffold, attached, and deposited extracellular matrix, the more highly backscattering extracellular matrix provided clear OCT signals, and OCT images revealed the porous structures of the scaffold. Interestingly, over time, the initial population of cells that were evenly distributed began to migrate toward the surface of the scaffold, likely in response to limited nutrients and waste exchange at the deeper regions. After 9 days, a high-density cell layer is observed at the surface and confirmed both with 3-D OCT and histological observations [64].

A quantitative measurement of cell growth is shown in Fig. 64.7. An OCT image from a blank poly (lactide) (PLA) scaffold immersed in water is shown in Fig. 64.7a. The scaffold has a 90 % porosity and 250–350 μm pore size. It can be seen that the pore structure is clearly delineated. An imaging depth of around 1.2 mm is achieved, despite the highly scattering nature of the scaffold. The imaging contrast is primarily provided by the difference in refractive indices between the polymer and water. The polymer wall reflects the light to a greater extent, thus appears brighter, while the pore appears as a darker area in the OCT image. Such contrast provides an opportunity to estimate the porosity from the OCT images. Figure 64.7b illustrates the OCT image acquired from a PLA scaffold seeded with MG63 bone cells and cultured for 4 weeks under static conditions. Structural changes are noted as compared to the blank scaffold. The pore size and porosity have decreased significantly, i.e., the darker areas in the images are reduced. From the cell seeding procedure and the expected cell growth profile, the increased brighter areas in the scaffolds are attributed to the cells and the extracellular matrix generated by the cells, increasing the optical scattering properties of the constructs and leading to an increased backscattering of the OCT signals.

The pores within the scaffolds were initially filled with seeded cells. Occupation of pores continued as cells proliferated and differentiated, producing extracellular matrix. Thus, pore size and porosity of scaffolds become dynamic parameters in the culture period, which are closely correlated to cell growth profiles and tissue turnover. It is hypothesized that the quantification of porosity change with culture time and conditions can reveal information about the cell growth profile. A local porosity analysis of scaffolds has been proposed to quantify the porosity change, in which large and continuous defects in scaffolds (i.e., pore size >500 μm) are

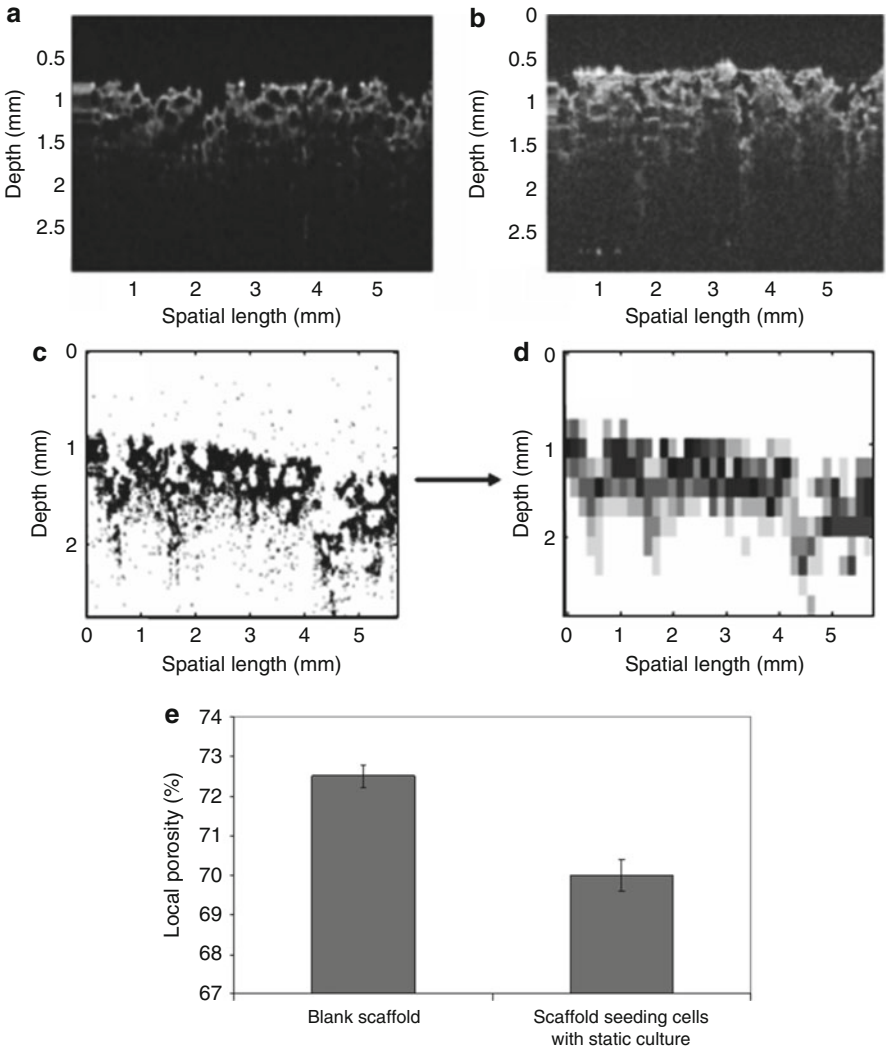

Fig. 64.7 OCT images porous scaffold seeded with cells. (**a**) A blank PLA scaffold and (**b**) a PLA scaffold seeded with MG63 bone cells following static culture for 4 weeks. (**c**, **d**) Accompanying diagrams illustrate an algorithm for calculating local porosity. (**e**) Resulting bar-chart comparison between a blank and seeded scaffold. *The error bars* represent standard deviation (Modified figures reprinted with permission from [56])

excluded. For each OCT scan, a threshold is set to discriminate between true empty pores and the pore walls. After binarization, the local porosity is calculated by a block processing method [56] demonstrated in Fig. 64.7c, d. The difference of porosity with statistical significance between a blank scaffold and cell-seeded scaffold is presented by this calculation method (Fig. 64.7e).

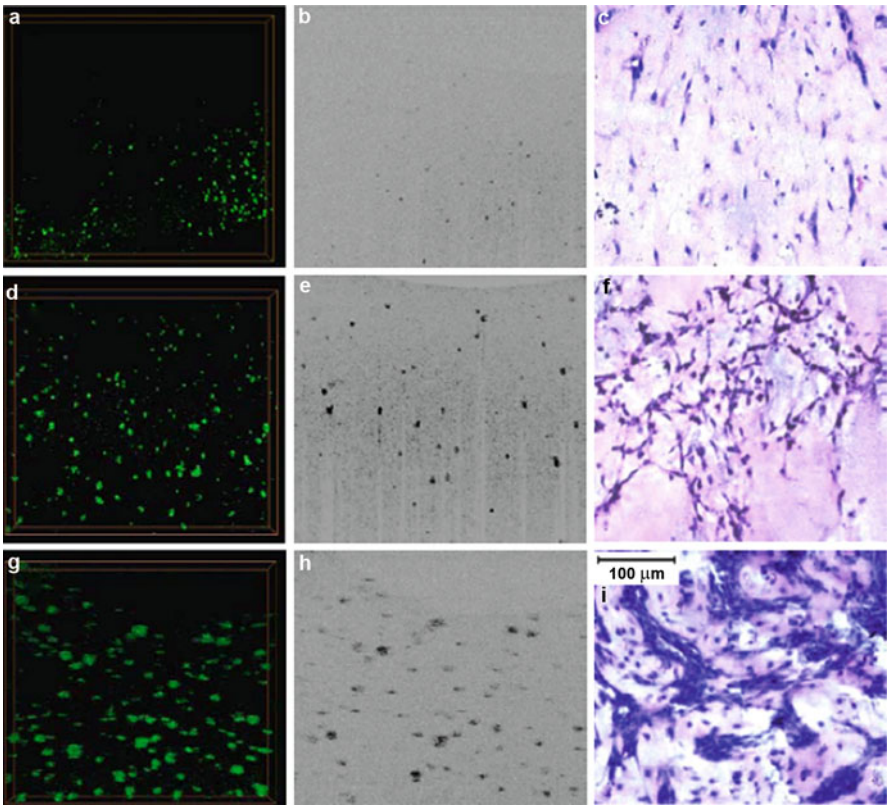

Fig. 64.8 OCT of cell proliferation in 3-D scaffolds. Images were acquired with low (5×10^4 cells) initial cell density. 3-D OCT images (**a**, **d**, **g**) and 2-D (x–z) OCT images (**b**, **e**, **h**) of engineered tissues were acquired on day 0 (**a**–**c**), day 4 (**d**–**f**), and day 8 (**g**–**i**). Histological images stained with H&E (**c**, **f**, **i**) are shown to confirm cell proliferation over time. Scale bar in (**i**) is applicable for all images (Figures reprinted with permission from [69])

64.3.4.2 3-D Cellular Dynamics (Proliferation and Migration)

Our understanding of cell dynamics in 3-D engineered tissues has been limited by our ability to visualize these processes. The use of OCT may play a significant role in tracking these dynamic cellular processes in not only engineered tissues but also for a more basic understanding of fundamental cell behavior. The proliferation patterns of cells within the engineered tissue scaffolds can be monitored, as shown in Fig. 64.8. Three-dimensional OCT imaging shows expanding scattering regions of cells after several days in culture. The increase in scattering is likely the result of both increasing cell numbers in these focal regions but also from the deposition of extracellular matrix secreted by the viable cells.

In addition to cell proliferation, cell migration plays an important role in tissue growth and development. Using repeated OCT imaging over several hours, the

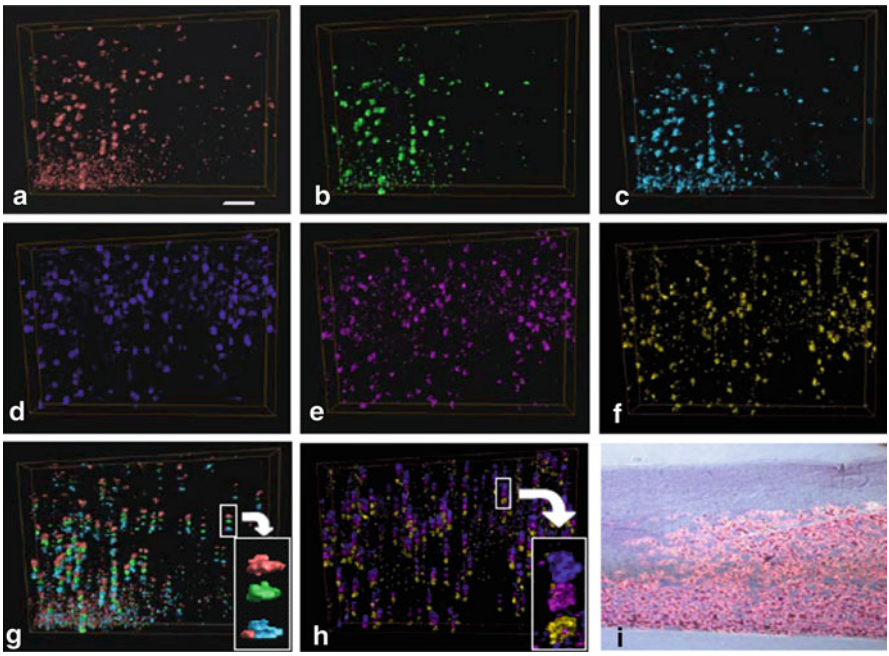

Fig. 64.9 OCT of cell migration. 3-D OCT images demonstrate the migration of macrophages (**a**–**f**). Cells at different points in time are labeled with different colors. The interval time is 40 min between (**a/b**, **b/c**, **d/e**, and **e/f**) and 120 min between (**c/d**). Individual OCT images are merged to form composite images of individual cell migration in 3-D space (**g**, **h**). Composite (**g**) is composed of (**a**–**c**) and composite (**h**) is a composed of (**d**–**f**). Insets in (**g**, **h**) show color-coded single-cell migration. Corresponding histology after the study is shown in (**i**), with macrophages collecting at the bottom. Scale bar is 200 μm (Reprinted image with permission from [69])

migration of macrophage cells was tracked as they moved through a 3-D agarose scaffold in response to a chemoattractant gradient. Images in Fig. 64.9 show the color-coded 3-D spatial position changes over time, with the downward cell migration toward the chemoattractant noted.

A second example of cell migration involves cell invasion through tissues, which is an essential step for tumor cells to metastasize. The invasive behavior of tumor cells in part depends on the cellular factors such as enzymes that enable cells to degrade their matrix components as well as on the characteristics of the extracellular matrix surrounding the cell. Therefore, a good knowledge of the cell-matrix interaction is useful when seeking treatment strategies aimed not only at cell killing but also at inhibition of tumor cell invasion and metastases. OCT offers a potential tool to observe and evaluate this process (Fig. 64.10). A model system with lung tumor cells grown on a collagen gel has been reported as a means to evaluate the tumor cell invasion ability [70]. The lung tumor cells grown on the gel with varying combinations of cell seeding number and collagen gel concentration have been scanned in OCT. It was found that OCT can differentiate cells and the gel.

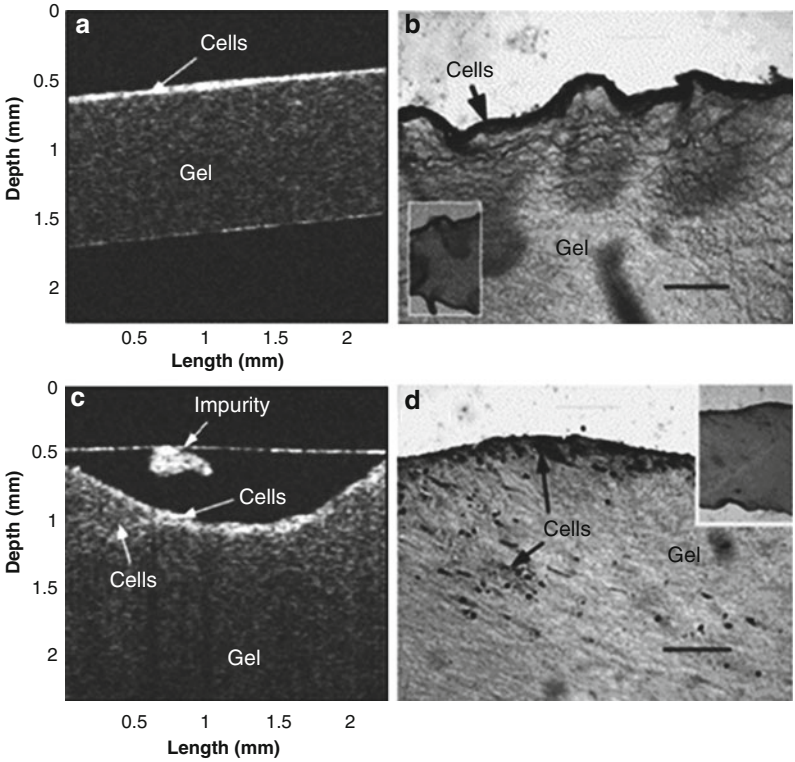

Fig. 64.10 OCT of tumor cell migration. (**a**) OCT image of lung cancer cells seeded on a collagen gel with (**b**) corresponding histological section of the specimen. (**c**) OCT image and (**d**) corresponding histology showing tumor cell invasion into the gel. *Scale bar* represents 100 μm (Reprinted with permission from [70])

With 1×10^6 lung cancer cells seeding on a collagen gel of 2.5 mg/ml concentration, a well-defined two-layer OCT image was obtained: a thin, brighter layer on top of a homogeneous, thick, and darker layer (Fig. 64.10a). The boundary between the layers is sharply delineated. By the nature of the cell seeding procedure, the brighter top layer is ascribed to the cells, while the underlying layer corresponds to the gel. The well-defined two-layer image indicates that there is no cell migration into the gel. However, OCT of the tumor cells seeded on a collagen gel of 1.5 mg/ml concentration invading into the collagen gel can also be visualized and confirmed by histological section images. The OCT images of the tumor cells on the gel reveal invasion, as shown in the image as a brighter diffuse top cellular layer plus additional similarly bright cellular foci infiltrating within the gel layer (Fig. 64.10c). Validation by histological sectioning of the cell and gel complex has drawn the same conclusion, which demonstrates that OCT can become a convenient optical imaging tool to study the dynamic process of tumor cell invasion nondestructively and in real time.

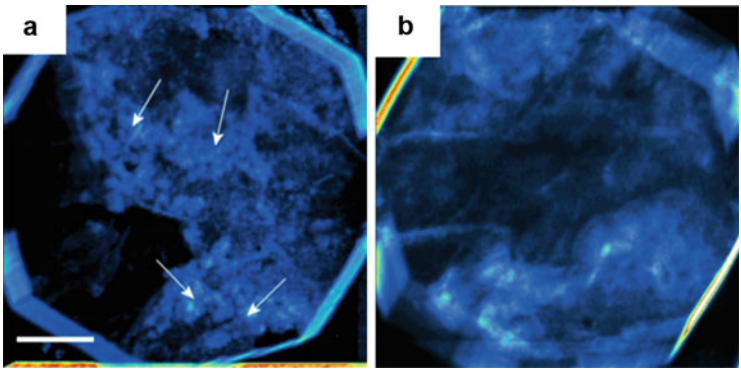

Fig. 64.11 Full-field OCT images of a PLLA scaffold. (**a**) Scaffold seeded with 1×10^6 bone cells and cultured for 1 week, compared with (**b**) that of a blank scaffold. Representative examples of cells are indicated by *arrows*. *Scale bar* represents 50 μm (Modified figures reprinted with permission from [67])

64.3.4.3 Single Cell Identification and Differentiation

We have shown that OCT has the capability to image and monitor cell dynamics in engineered tissue, but only populations or clusters of aggregated cells are resolved. Higher imaging resolutions are needed to visualize single cells and subcellular organelles with OCT. The high-resolution variant of OCT is called optical coherence microscopy (OCM) which uses high NA optics and ultrabroad bandwidth light sources, such as a tungsten lamp, to realize high resolution in 3-D [40], where the axial resolution is governed by the bandwidth of light source, as in conventional OCT, and the transverse resolution is determined by the high NA optics. In contrast to the cross-sectional images of traditional OCT, OCM usually generates images of en face planes, as in confocal or multiphoton microscopy. OCM operates in two modes, i.e., full-field OCM (ffOCM) and scanning OCM. ffOCM has been used to visualize individual pores and cell populations in tissue-engineered constructs. Figure 64.11 provides an example of images acquired with ffOCM where bone cells (1×10^6) were seeded in a PLLA scaffold for 1 week, together with an image from a blank scaffold for comparison [67]. Here several clusters of cells with roughly spherical cell morphology are seen attached to the PLLA scaffold wall in the 3-D microenvironment. Although still in a developmental stage, it is likely that ffOCT could not only offer the ability to visualize small cell populations in 3-D microenvironment as well as their attachment to and interaction with the scaffold wall but also provide informative sensory feedback to optimize scaffold manufacturing.

In scanning OCM, the transverse resolution is improved at the expense of the confocal parameter, and images are acquired in the en face plane by raster scanning the tight focus across the en face plane. Like ffOCM, scanning OCM can image deeper into highly scattering specimens, compared to confocal of multiphoton microscopy, because of the coherence-gated detection that rejects multiply scattered photons.

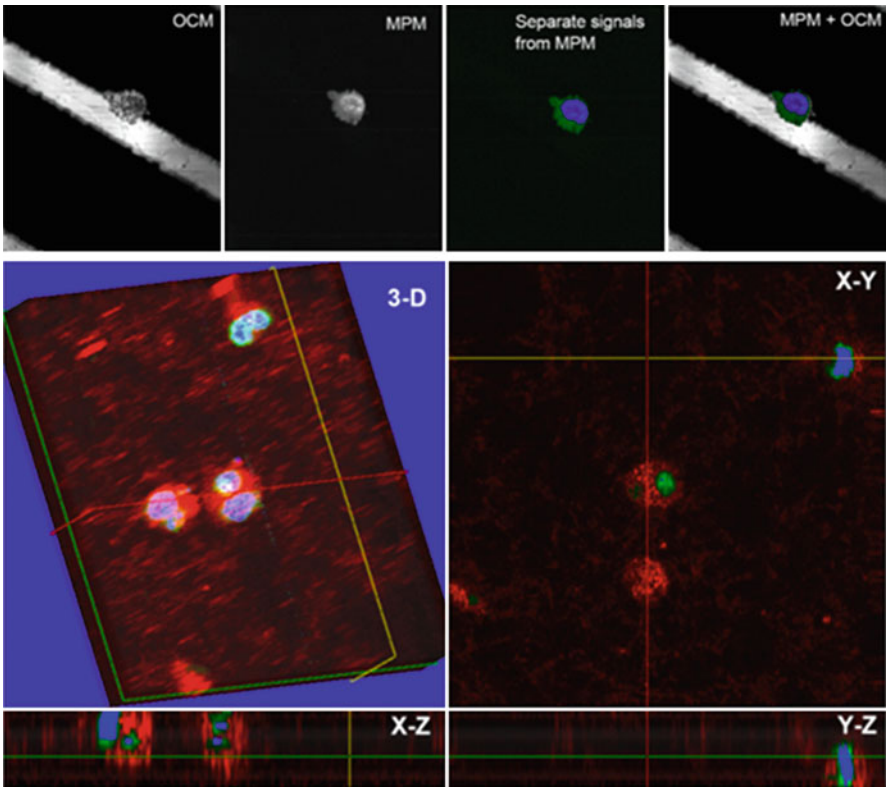

Fig. 64.12 Fibroblasts cultured on a microtextured (grooved) substrate and in a 3-D Matrigel matrix. (*Top row*) Multiple channels of OCM and MPM imaging data reveal information of the cell labeled with GFP and a DNA dye, as well as the unlabeled substrate ridges. (*Bottom images*) Overlaid OCM and MPM images of fibroblast cells in a 3-D scaffold show both structural and functional information (Modified figure used with permission from [42])

An example of cellular imaging with scanning OCM is shown in Fig. 64.12. These images were acquired with a multimodality microscope that combined spectral-domain OCM and multiphoton microscopy, as well as enable other spectroscopic OCM analysis [42, 71]. Two sets of images are shown in Fig. 64.12 that are relevant to tissue engineering. In addition to structural imaging, it is frequently advantageous to collect functional information pertaining to the behavior of the cells or tissue. The multimodality approach can achieve this, as OCM can provide the overall background scattering of not only cells but also the scaffold, while multiphoton microscopy can be used to detect specific labeled proteins or cellular structures and provide functional imaging as these proteins are expressed. A single fibroblast is shown in Fig. 64.12 (top row), attached to the top edge of a microgrooved polymer substrate. This fibroblast has been transfected with green fluorescent protein linked to the expression of vinculin, a cell-adhesion protein. Additionally, this fibroblast was co-labeled with a DNA dye to identify

the nucleus. The OCM image reveals both the cell and the grooved substrate, which provides more spatially relevant information than just the multiphoton image of the cell alone. This multimodality approach enables tracking of singly labeled cells of subcellular features against the background microenvironment. This is most relevant when observing single cells, or small populations of cells in 3-D engineered tissues, as is also shown in Fig. 64.12. Here, several fibroblasts are visualized in 3-D and, because of their 3-D microenvironment, take on a more spherical morphology, as opposed to the elongated spindle-shaped morphology when cultured in 2-D or subjected to external mechanical stimuli. OCM enables tracking of single cells, or small populations of cells in 3-D microenvironments, which will likely extend our basic understanding of cell dynamics in the developing engineered tissues, under different growth conditions and following external mechanical stimuli and under different pharmacological modulators.

In addition, recent efforts have been directed at identifying various cell populations within engineered tissues. While the use of fluorescent or OCT-sensitive contrast agents have been one means of identifying molecules or cells [37, 72, 73], analysis of the spectroscopic OCT signal can possibly provide insight into the spectral-scattering properties of individual cells, possible eliminating the need to add exogenous contrast agents that may either alter the function of the cells or reduce their viability in long-term cultures. Light-scattering spectroscopy has been shown to be sensitive to the size of dominant scatterers such as nuclei [74]. While much of this work has been in the use of wide-field techniques, efforts to use a tightly focused beam for spatially and depth-resolved imaging have been successful [75–77]. The high-numerical aperture optics used in OCM can address the inherent trade-off between high spectral and spatial resolution. By spatially confining the volume from which a spectrally scattered signal is generated, it may be possible to extract more information about the complex types, sizes, and numbers of scatterers [77]. The use of OCM enables this to be done not only in 2-D but also in depth.

Examples of the use of spectroscopic OCT/OCM to utilize the spectral-scattering information from a 2-D culture of cells and from a 3-D agarose scaffold seeded with cells are shown in Fig. 64.13. Wavelength-dependent spectral-scattering plots are shown for locations near the cell center and in the periphery, using a multimodality microscope that combines OCM with multiphoton microscopy [42]. By examining the autocorrelation of the signal from each of these locations, and measuring the full width at 80 % of the magnitude, it may be possible to identify scatterers or enhance contrast within spectroscopic OCT/OCM images [71, 78]. Using structural and spectroscopic OCT, images from 3-D cultures of macrophages or fibroblasts show interesting features. While the structural OCT images appear similar, with cells appearing more as amorphous scattering regions, the spectroscopic OCT images, using the autocorrelation width of the spectrally scattered signal, clear differences are noted between the cell populations. The macrophages exhibit a narrow autocorrelation peak compared to the fibroblasts, likely because the macrophages are more spherical in morphology, compared to the more spindle-shaped morphology of the fibroblasts. It still remains to be determined, however, what cellular components are most significantly affecting the SOCT signal.

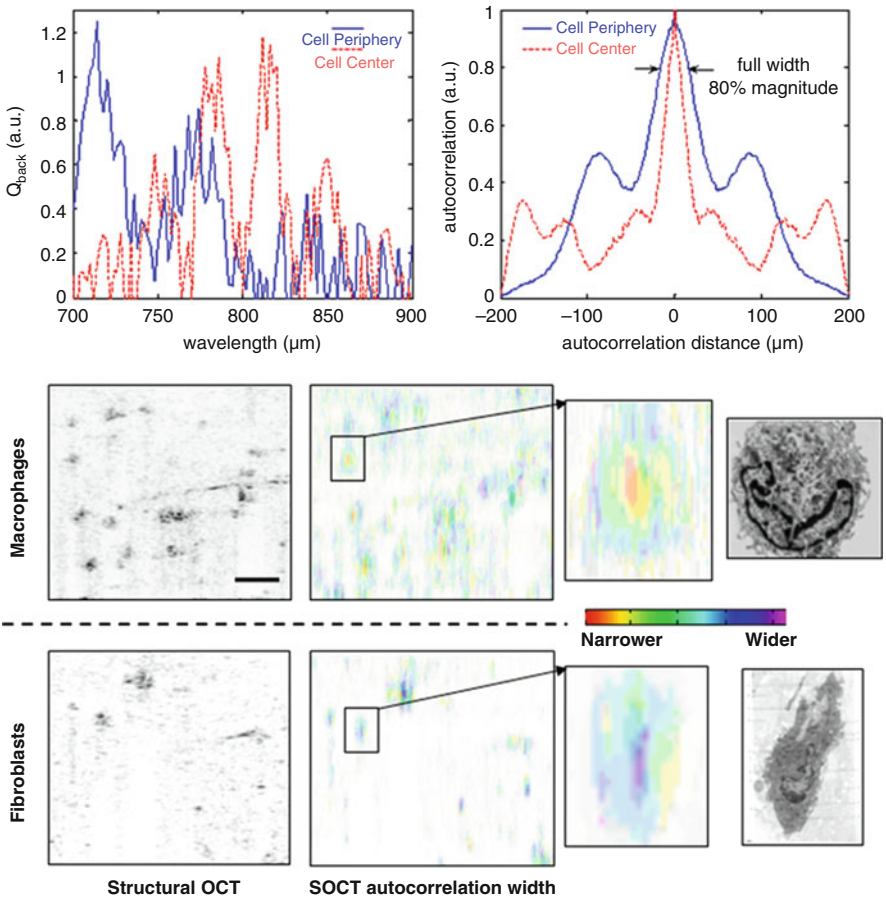

Fig. 64.13 Spectral-scattering data from single cells. (*Top row*) Spectral-scattering data and autocorrelation data from a single cell using spectroscopic spectral-domain OCM. Data was acquired from the cell center (over the nucleus) and from the cell periphery (from the cytoplasm). (*Middle, bottom rows*) Structural and spectroscopic OCT images of macrophages and fibroblasts in a 3-D scaffold. The spectroscopic OCT autocorrelation width may be used to distinguish cell types. *Scale bar* represents 100 μm (Modified figure used with permission from [77])

64.3.4.4 Imaging Cell Behaviors Under Static and Dynamic Growth Conditions

Static culture of constructs has been a simple, traditional, and widely used method. Recently, the use of mechanical stimulation applied during the growth of constructs in culture and in bioreactors has shown to improve cell distribution and enhance the biological and physiological activity of the cells. The remaining challenge is to nondestructively characterize cell activity and cell growth dynamics in response to these stimuli, both quantitatively and qualitatively. On the cellular level, structural OCM data, coupled with more functionally relevant multiphoton imaging of

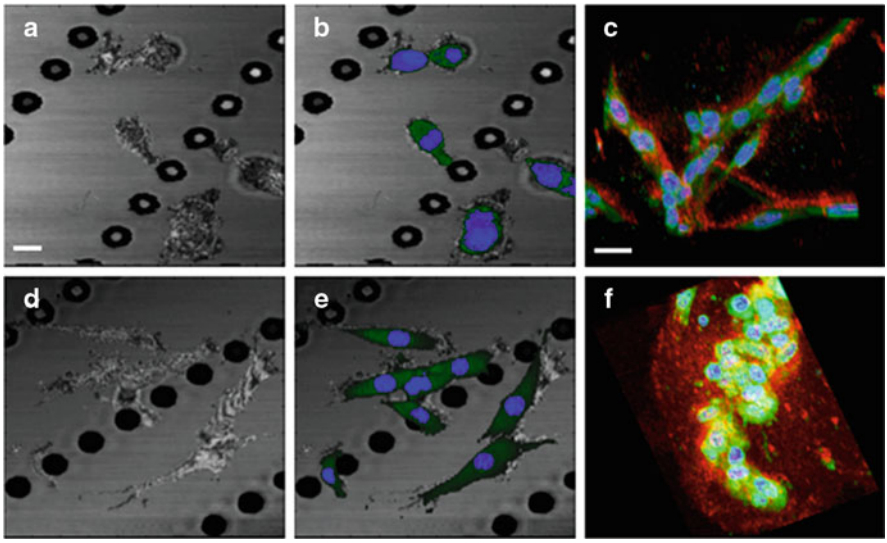

Fig. 64.14 Multimodality imaging of cells under static and dynamic culture conditions. (**a**, **b**, **d**, **e**) Images were acquired with a combined OCM-MPM microscope and represent GFP-vinculin and DNA-labeled fibroblasts on a flexible micro-pegged substrate and, (**c**, **f**) in a flexible 3-D agarose gel. Images were taken under static (**a**–**c**) and dynamic (**d**–**f**) culture conditions and show distinctly different cell morphology and GFP-vinculin expression patterns. *Scale bars* represent 100 μm (Reprinted with permission from [50])

GFP-vinculin expression has been demonstrated [42]. Examples of both micro-topography and 3-D scaffolds are shown in Fig. 64.14. Fibroblasts transfected to expressed GFP with vinculin were seeded on a 2-D topographic poly(dimethyl-siloxane) (PDMS) polymer scaffold comprised of rows of micro-pegs, and in a 3-D agarose scaffold [50]. OCM enabled the visualization of all scattering structures, from both the cells and from the scaffolds. Multiphoton microscopy detected the two-photon fluorescence from GFP-vinculin, which revealed more of the functional behavior of the cells interacting with the scaffold or with other cells. The flexible PDMS scaffold was subsequently amenable to mechanical stimuli by 18-h 5 % cyclic equibiaxial stretching. Similarly, the 3-D agarose gel was subjected to uniaxial mechanical stretching. Following mechanical stimulation, cells in both scaffolds exhibited reorientation along the direction of stretch, as well as a marked increase in GFP-vinculin expression. Further OCM/OCT imaging is possible for extended periods of time, and ongoing efforts are characterizing both the qualitative and quantitative parameters associated with mechanical stimuli.

The effect of static and dynamic growth conditions on cellular behaviors can be semi-quantified based on the OCT image data using the same technique described in section 64.3.4.1, Figure 64.7c–d. A systematical study has been undertaken [56] in which a bone cell-PLA construct was subjected to perfusion culture conditions in a bioreactor in comparison to static culture. The full osteogenesis culture media was flowed continuously through the construct at 0.1 ml/min flow rate for 1 week after

3 weeks of static culture. Compared to the construct which used the same type of scaffold and cell seeding conditions but grown under static cultured for 4 weeks, perfusion culture generates dramatic changes in cell growth profile as manifested by the increased number of closed pores and interconnected structures in the OCT image. By calculating the local porosity based on the OCT images, a statistically significant lower porosity in the perfused construct is demonstrated compared to the construct cultured under static conditions, implying that culture in perfusion conditions improves cell proliferation and tissue turnover. This evaluation derived from the OCT images is consistent with the protein analysis of the constructs in a parallel work [79]. These results demonstrate that OCT is capable of monitoring cell growth profiles under different culture conditions based on its ability to quantify the change of pore architecture in the constructs.

64.3.5 Integrated Imaging Methods

While OCT, OCM, and its many variants such as spectroscopic, polarization, and Doppler analysis provide a wide range of diagnostic information on engineered tissues, further insight can be gained by integrating OCT with other imaging methods. In particular, fluorescence-based and nonlinear imaging modalities can assist OCT with investigation of engineered tissue by providing new contrasts and functional extensions.

The implementation of high numerical-aperture optics in OCM confers many advantages including higher transverse imaging resolution, en face sectioning deep into highly scattering specimens, and potentially higher image contrast due to both the confocal and coherence rejection of out-of-plane photons. OCM has been combined with confocal fluorescent microscopy in a colinear geometry to visualize fluorescently stained osteoblasts and the structure of a microporous polymeric scaffold [80]. The use of multiphoton microscopy confers many advantages for biological imaging including improved resolution, deeper imaging penetration, and less absorption or risk of thermal injury to cells with the use of longer wavelengths of light. It has been recognized that both multiphoton microscopy (MPM) and OCM can utilize the same laser source, such as the commonly used mode-locked titanium:sapphire laser [42, 81]. An example application of multimodal microscope for tissue engineering is shown in Fig. 64.15, where representative images OCM, MPM, and spectroscopic OCM are presented. The images in Fig. 64.15 demonstrate the multimodality approach, where in addition to OCM, spectroscopic OCM analysis methods can reveal the location of strong spectral scatterers (nuclei) in the OCM data (Fig. 64.15b). These findings are validated using multiphoton microscopy of nuclei stained with a fluorescent DNA dye (red) that identifies the spatial position of the nuclei within the cells in this culture.

As another example, a multimodal microscope combining OCM, MPM, and fluorescence lifetime imaging microscopy (FLIM) [82] has also been demonstrated for imaging of engineered tissue [43]. Incorporation of FLIM adds new contrast capabilities, as evident by images of a microporous fibroblast-seeded hydrogel scaffold that were obtained with different modalities (Fig. 64.16). As shown in Fig. 64.16,

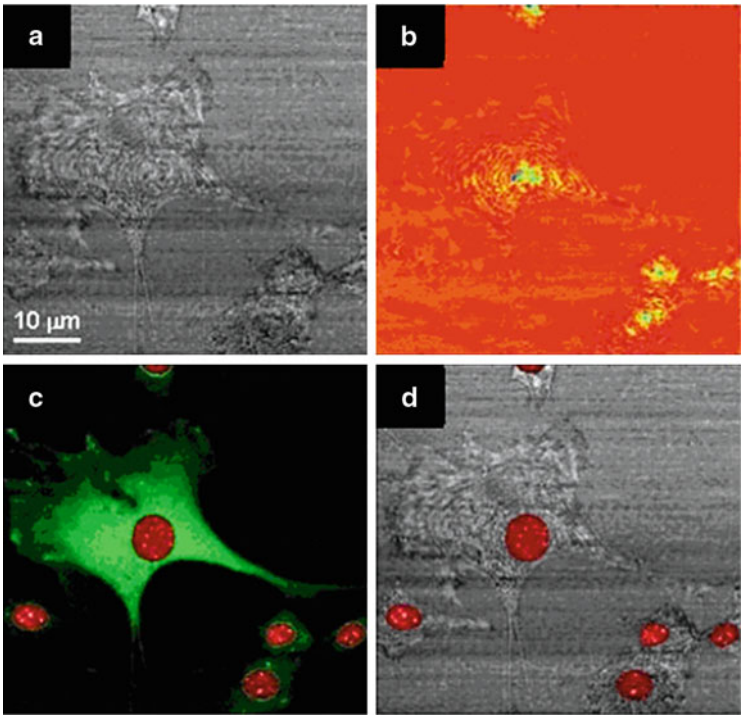

Fig. 64.15 Multimodality microscopy. Images acquired simultaneously from GFP-vinculin and DNA-labeled fibroblasts. (**a**) Spectral-domain OCM. (**b**) Spectroscopic OCM showing regions of strong spectral scattering corresponding to the location of the nuclei. (**c**) MPM with *green* representing the GFP-vinculin and *red* representing the DNA dye. (**d**) Overlay of OCM and the MPM DNA dye signals validating the locations of the nuclei in the cells as detected by spectroscopic OCM (Reprinted with permission from [71])

while the cell morphology and the microporous structure of the hydrogel are clearly differentiated and well observed with both OCM and MPM, they are not well separated in the MPM image, because of the spectral overlap between the autofluorescence from the hydrogel and the autofluorescence from cells. In some cases of fluorescence imaging of engineered tissue, in fact, autofluorescence from the scaffold material may interfere with visualizing the details of the cellular structures, and other contrast mechanisms must be used for better signal separation. FLIM clearly distinguishes the hydrogel from the cells based on the different lifetimes of the two fluorescence emissions, shown as different colors in Fig. 64.16. Additionally, FLIM has been demonstrated for monitoring cellular metabolism based on the lifetime change of autofluorescence from reduced nicotinamide adenine dinucleotide (NADH) and flavin adenine dinucleotide (FAD) [83]. This functional molecular imaging has also been demonstrated with the integrated system, showing its capability to evaluate the health and viability of the developing or mature engineered tissue [43].

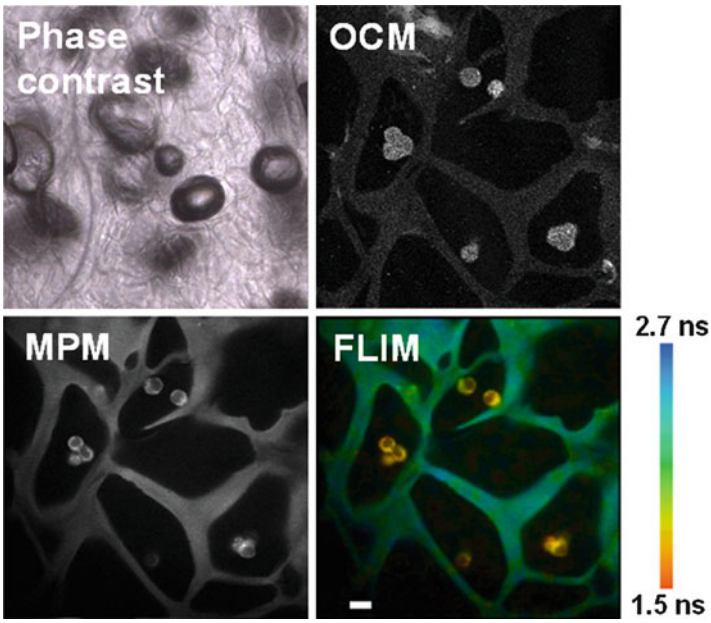

Fig. 64.16 Multimodal images of a microporous 3-D hydrogel scaffold seeded with 3T3 fibroblasts. Representative images are based on phase contrast, OCM, MPM, and FLIM. *Scale bar* represents 20 μm (Reprinted with permission from [43])

64.4 In Vivo Investigation of Post-Implant Cell Dynamics Using OCT

Functional replacement of natural tissues by engineered tissues is the ultimate goal of tissue engineering and regenerative medicine. Posttransplant dynamics and restorative processes have to be investigated and monitored to obtain the necessary information to evaluate the efficacy of treatment. This information will also be used for guiding the control of the culturing conditions to produce physiologically relevant tissues or organs. In this context, a high-resolution, noninvasive imaging tool is highly desired to longitudinally monitor the integration of implanted tissue and the response from the natural tissue at the transplant site. OCT holds promise in this regard. For example, OCT has recently been used to monitor the wound-healing process after implantation of a hydrogel scaffold [84]. As shown in Fig. 64.17, OCT images reveal the structures of wound beds in normal and diabetic mice 7 days after engraftment of hydrogel scaffolds composed of N-carboxyethyl chitosan, oxidized dextran, and hyaluronan. Comparisons between OCT images and their corresponding histological sections demonstrated the unique utility of OCT to unequivocally track the presence of the hydrogel in the wound bed and additionally to discern the morphophysiological transformation of the healing wound covered by the hydrogel scaffold. Generation of granulation tissue and degradation of the

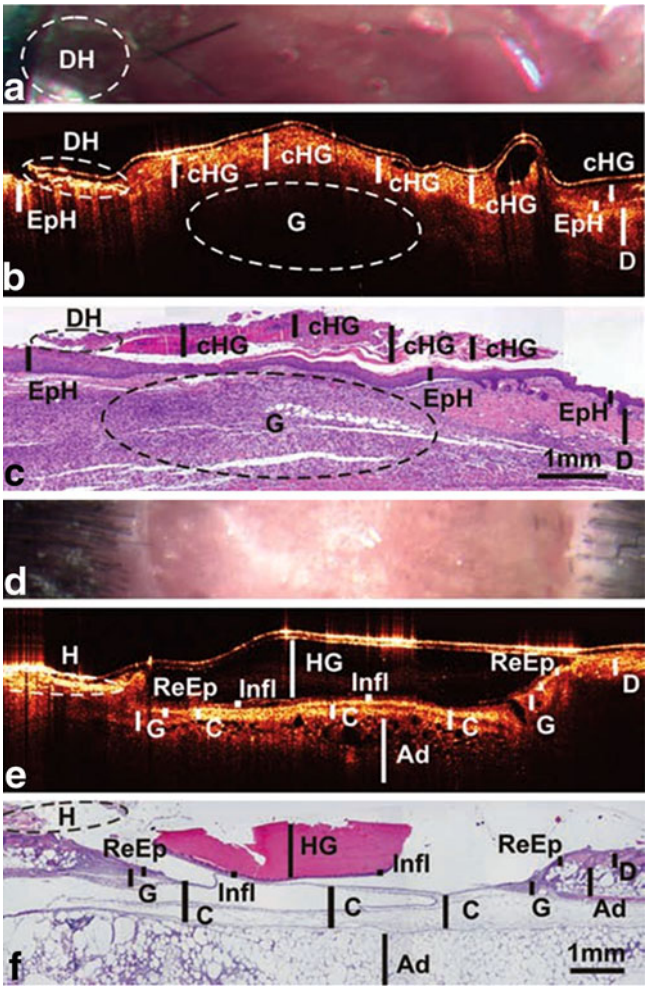

Fig. 64.17 Surface, cross-sectional OCT images, and histological sections of hydrogel implant-assisted wound healing in normal (**a–c**) and diabetic (**d–f**) mice. *D* dermis, *G* granulation tissue, *C* connective tissue, *Infl* inflammatory reaction, *EpH* epidermal hyperplasia, *HG* hydrogel implant, *cHG* cell-infiltrated HG that underwent partial degradation (showing increased scattering), *DH* dehydrated hydrogel implant (ultrahigh scattering), and *H* hair (high scattering). Because of high scattering in cHG, the underlying structures, for example, EpH and granulation tissue, were not detectable in OCT image (**b**) (Reprinted with permission from [84])

hydrogel scaffold is observed in the normal mouse. The formation of granulation and connective tissue and the presence of a non-degraded scaffold in the diabetic mouse are clearly resolved by the OCT images and confirmed with histological images in parallel, showing the capability of using OCT to monitor the morphological changes associated with the wound-healing process.

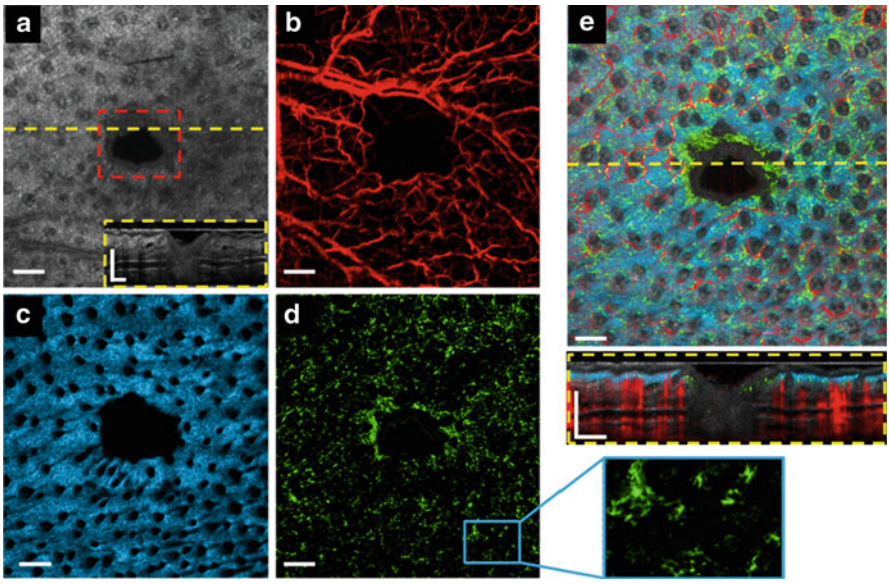

Fig. 64.18 Multimodal imaging of ear skin in a GFP BM-transplanted mouse 10 days following an excisional wound. (**a**) En face structural OCT section showing individual hair follicles and the wound site (*red box*). Cross-sectional image in the inset shows various layers of the skin at the position of the *yellow dashed line*. (**b**) Projection of the OCT phase variance volume along the axial dimension showing the microvascular network. (**c**) Wide-area SHG mosaic of collagen. The central dark region represents the wound, while the hair follicles appear as smaller dark regions. (**d**) Wide-area TPEF mosaic of the GFP expressing BM-derived cells in the skin and a magnified view of individual GFP cells. (**e**) En face image of the four modalities overlaid and cross-sectional view (*bottom*) at the position of the *yellow dashed line*. Scale bars are 250 μm (Reprinted with permission from [51])

As a further advance, the wound-healing process may be better characterized by OCT combined with other intravital imaging modalities. Complementary imaging techniques that have cellular resolution will facilitate the observation of cellular dynamics in detail. One example is shown in Fig. 64.18, which shows multimodal images of a wound bed in bone-marrow (BM)-transplanted GFP-mouse skin obtained with an integrated microscope combining OCT and MPM.

An OCT image is presented in Fig. 64.18a, which visualizes structural features based on the optical scattering properties and, in particular, resolves the different skin layers including the epidermis, dermis, and subcutaneous fat. OCT phase variance [85], which is another functional variant of OCT, provides a view of the microvasculature based on the dynamic motion of blood flow retrieved from the phase variance in OCT data. SHG imaging visualizes the collagen matrix in the dermis of the skin and provides a view of the individual hair follicles, in addition to the collagen reorganization within the wound (Fig. 64.18c). TPEF imaging allows individual BM-derived GFP-expressing cells to be detected in the skin (Fig. 64.18d). The combination of these modalities allows a wide range of complementary

information about living skin to be obtained noninvasively. Overlaying these modalities allows the microenvironments of individual GFP cells to be visualized in three dimensions (Fig. 64.18e). Most importantly, this multimodal imaging combination is noninvasive and does not require the use of exogenous contrast agents, making it suitable for repeated imaging to observe dynamics that occur during skin regeneration. This technology holds the promise for studying the post-engraftment dynamics of cells and tissues, such as in the case of skin wounds and grafts, skin contraction, scarring, vascular network regeneration, collagen deposition, etc., which are important processes associated with wound healing and tissue regeneration.

64.5 Summary

This chapter has explored and reviewed the use of OCT in the field of tissue engineering. Many of the extensions of the OCT technology, including OCM, spectroscopic OCT/OCM, polarization-sensitive OCT, Doppler OCT, and OCE have only further expanded our ability to interrogate engineered tissues. As the field of tissue-engineering transitions from 2-D to 3-D cultures, from static to dynamic growth conditions, and from in vitro to in vivo constructs, it is clear that OCT will offer new investigative methods that will expand our understanding of complex cellular processes and how these contribute to the organization of cells into a functional and physiologically meaningful engineered tissue that would have medical application.

Acknowledgements We wish to thank our many colleagues and collaborators conducting research in this area, and apologize that due to length requirements, we are unable to highlight more results. Some of the recent studies reported in this chapter were supported in part by a grant from the U.S. National Science Foundation (CBET 10-33906, S.A.B.).

References

1. T.B.L. Kirkwood, Human senescence. Bioessays **18**, 1009–1016 (1996)
2. S. Tuljapurkar, N. Li, C. Boe, A universal pattern of mortality decline in the G7 countries. Nature **405**, 789–792 (2000)
3. C.G. Thanos, W.J. Bell, P. O'Rourke, K. Kauper, S. Sherman, P. Stabila, W. Tao, Sustained secretion of ciliary neurotrophic factor to the vitreous, using the encapsulated cell therapy-based NT-501 intraocular device. Tissue Eng. **10**, 1617–1622 (2004)
4. Y. Yang, A.J. El Haj, Bone tissue engineering. Scope **13**, 33–35 (2004)
5. L.G. Griffith, G. Naughton, Tissue engineering – current challenges and expanding opportunities. Science **295**, 1009–1014 (2002)
6. D. Wendt, S.A. Riboldi, M. Cioffi, I. Martin, Bioreactors in tissue engineering: scientific challenges and clinical perspectives. Adv. Biochem. Eng. Biotechnol. **112**, 1–27 (2009)
7. I. Martin, D. Wendt, M. Heberer, The role of bioreactors in tissue engineering. Trends Biotechnol. **22**, 80–86 (2004)
8. D. Wendt, A. Marsano, M. Jakob, M. Heberer, I. Martin, Oscillating perfusion of cell suspensions through three-dimensional scaffolds enhances cell seeding efficiency and uniformity. Biotechnol. Bioeng. **84**, 205–214 (2003)

9. V. Barron, E. Lyons, C. Stenson-Cox, P.E. McHugh, A. Pandit, Bioreactors for cardiovascular cell and tissue growth: a review. Ann. Biomed. Eng. **31**, 1017–1030 (2003)
10. K.J. Gooch, J.H. Kwon, T. Blunk, R. Langer, L.E. Freed, G. Vunjak-Novakovic, Effects of mixing intensity on tissue-engineered cartilage. Biotechnol. Bioeng. **72**, 402–407 (2001)
11. P. Akhyari, P.W.M. Fedak, R.D. Weisel, T.Y.J. Lee, S. Verma, D.A.G. Mickle, R.K. Li, Mechanical stretch regimen enhances the formation of bioengineered autologous cardiac muscle grafts. Circulation **106**, 1137–1142 (2002)
12. T. Davisson, S. Kunig, A. Chen, R. Sah, A. Ratcliffe, Static and dynamic compression modulate matrix metabolism in tissue engineered cartilage. J. Orthop. Res. **20**, 842–848 (2002)
13. A.M. Freyria, Y. Yang, H. Chajra, C.F. Rousseau, M.C. Ronziere, D. Herbage, A.J. El Haj, Optimization of dynamic culture conditions: effects on biosynthetic activities of chondrocytes grown in collagen sponges. Tissue Eng. **11**, 674–684 (2005)
14. J.R. Mauney, S. Sjostorm, J. Blumberg, R. Horan, J.P. O'Leary, G. Vunjak-Novakovic, V. Volloch, D.L. Kaplan, Mechanical stimulation promotes osteogenic differentiation of human bone marrow stromal cells on 3-D partially demineralized bone scaffolds in vitro. Calcif. Tissue Int. **74**, 458–468 (2004)
15. L.E. Freed, R. Langer, I. Martin, N.R. Pellis, G. Vunjak-Novakovic, Tissue engineering of cartilage in space. Proc. Natl. Acad. Sci. U. S. A. **94**, 13885–13890 (1997)
16. L.H. Laiho, S. Pelet, T.M. Hancewicz, P.D. Kaplan, P.T.C. So, Two-photon 3-D mapping of ex vivo human skin endogenous fluorescence species based on fluorescence emission spectra. J. Biomed. Opt. **10**, 024016 (2005)
17. A.C. Jones, B. Milthorpe, H. Averdunk, A. Limaye, T.J. Senden, A. Sakellariou, A.P. Sheppard, R.M. Sok, M.A. Knackstedt, A. Brandwood, D. Rohner, D.W. Hutmacher, Analysis of 3D bone ingrowth into polymer scaffolds via micro-computed tomography imaging. Biomaterials **25**, 4947–4954 (2004)
18. S. Cartmell, K. Huynh, A. Lin, S. Nagaraja, R. Guldberg, Quantitative microcomputed tomography analysis of mineralization within three-dimensional scaffolds in vitro. J. Biomed. Mater. Res. A **69A**, 97–104 (2004)
19. E. Baas, J.H. Kuiper, Y. Yang, M.A. Wood, A.J. El Haj, In vitro bone growth responds to local mechanical strain in three-dimensional polymer scaffolds. J. Biomech. **43**, 733–739 (2010)
20. D. Huang, E.A. Swanson, C.P. Lin, J.S. Schuman, W.G. Stinson, W. Chang, M.R. Hee, T. Flotte, K. Gregory, C.A. Puliafito, J.G. Fujimoto, Optical coherence tomography. Science **254**, 1178–1181 (1991)
21. M.R. Hee, J.A. Izatt, E.A. Swanson, D. Huang, J.S. Schuman, C.P. Lin, C.A. Puliafito, J.G. Fujimoto, Optical coherence tomography of the human retina. Arch. Ophthalmol. **113**, 325–332 (1995)
22. N.D. Gladkova, G.A. Petrova, N.K. Nikulin, S.G. Radenska-Lopovok, L.B. Snopova, Y.P. Chumakov, V.A. Nasonova, V.M. Gelikonov, G.V. Gelikonov, R.V. Kuranov, A.M. Sergeev, F.I. Feldchtein, In vivo optical coherence tomography imaging of human skin: norm and pathology. Skin Res. Technol. **6**, 6–16 (2000)
23. J.G. Fujimoto, M.E. Brezinski, G.J. Tearney, S.A. Boppart, B.E. Bouma, M.R. Hee, J.F. Southern, E.A. Swanson, Optical biopsy and imaging using optical coherence tomography. Nat. Med. **1**, 970–972 (1995)
24. S.A. Boppart, B.E. Bouma, C. Pitris, J.F. Southern, M.E. Brezinski, J.G. Fujimoto, In vivo cellular optical coherence tomography imaging. Nat. Med. **4**, 861–865 (1998)
25. W. Drexler, D. Stamper, C. Jesser, X.D. Li, C. Pitris, K. Saunders, S. Martin, M.B. Lodge, J.G. Fujimoto, M.E. Brezinski, Correlation of collagen organization with polarization sensitive imaging of in vitro cartilage: implications for osteoarthritis. J. Rheumatol. **28**, 1311–1318 (2001)
26. Y. Yang, S. Whiteman, D.G. van Pittius, Y.H. He, R.K.K. Wang, M.A. Spiteri, Use of optical coherence tomography in delineating airways microstructure: comparison of OCT images to histopathological sections. Phys. Med. Biol. **49**, 1247–1255 (2004)

27. S.R. Chinn, E.A. Swanson, J.G. Fujimoto, Optical coherence tomography using a frequency-tunable optical source. Opt. Lett. **22**, 340–342 (1997)
28. M.A. Choma, M.V. Sarunic, C.H. Yang, J.A. Izatt, Sensitivity advantage of swept source and Fourier domain optical coherence tomography. Opt. Express **11**, 2183–2189 (2003)
29. R. Huber, D.C. Adler, V.J. Srinivasan, J.G. Fujimoto, Fourier domain mode locking at 1050 nm for ultra-high-speed optical coherence tomography of the human retina at 236,000 axial scans per second. Opt. Lett. **32**, 2049–2051 (2007)
30. R. Huber, M. Wojtkowski, J.G. Fujimoto, Fourier Domain Mode Locking (FDML): a new laser operating regime and applications for optical coherence tomography. Opt. Express **14**, 3225–3237 (2006)
31. C. Mason, J.F. Markusen, M.A. Town, P. Dunnill, R.K. Wang, Doppler optical coherence tomography for measuring flow in engineered tissue. Biosens. Bioelectron. **20**, 414–423 (2004)
32. C.W. Xi, D.L. Marks, D.S. Parikh, L. Raskin, S.A. Boppart, Structural and functional imaging of 3D microfluidic mixers using optical coherence tomography. Proc. Natl. Acad. Sci. U. S. A. **101**, 7516–7521 (2004)
33. S.G. Guo, J. Zhang, L. Wang, J.S. Nelson, Z.P. Chen, Depth-resolved birefringence and differential optical axis orientation measurements with fiber-based polarization-sensitive optical coherence tomography. Opt. Lett. **29**, 2025–2027 (2004)
34. S.J. Matcher, C.P. Winlove, S.V. Gangnus, The collagen structure of bovine intervertebral disc studied using polarization-sensitive optical coherence tomography. Phys. Med. Biol. **49**, 1295–1306 (2004)
35. U. Morgner, W. Drexler, F.X. Kartner, X.D. Li, C. Pitris, E.P. Ippen, J.G. Fujimoto, Spectroscopic optical coherence tomography. Opt. Lett. **25**, 111–113 (2000)
36. C. Xu, D.L. Marks, M. Do, S.A. Boppart, Separation of absorption and scattering profiles in spectroscopic optical coherence tomography using a least-squares algorithm. Opt. Express **12**, 4790–4803 (2004)
37. C. Xu, J. Ye, D.L. Marks, S.A. Boppart, Near-infrared dyes as contrast-enhancing agents for spectroscopic optical coherence tomography. Opt. Lett. **29**, 1647–1649 (2004)
38. C. Xu, P.S. Carney, S.A. Boppart, Wavelength-dependent scattering in spectroscopic optical coherence tomography. Opt. Express **13**, 5450–5462 (2005)
39. J.G. Fujimoto, Optical coherence tomography for ultrahigh resolution in vivo imaging. Nat. Biotechnol. **21**, 1361–1367 (2003)
40. L. Vabre, A. Dubois, A.C. Boccara, Thermal-light full-field optical coherence tomography. Opt. Lett. **27**, 530–532 (2002)
41. J.A. Izatt, M.R. Hee, G.M. Owen, E.A. Swanson, J.G. Fujimoto, Optical coherence microscopy in scattering media. Opt. Lett. **19**, 590–592 (1994)
42. C. Vinegoni, T.S. Ralston, W. Tan, W. Luo, D.L. Marks, S.A. Boppart, Integrated structural and functional optical imaging combining spectral-domain optical coherence and multiphoton microscopy. Appl. Phys. Lett. **88**, 053901 (2006)
43. Y.B. Zhao, B.W. Graf, E.J. Chaney, Z. Mahmassani, E. Antoniadou, R. DeVolder, H. Kong, M.D. Boppart, S.A. Boppart, Integrated multimodal optical microscopy for structural and functional imaging of engineered and natural skin. J. Biophotonics **5**, 437–448 (2012)
44. J.K. Barton, J.B. Hoying, C.J. Sullivan, Use of microbubbles as an optical coherence tomography contrast agent. Acad. Radiol. **9**, S52–S55 (2002)
45. L. Tong, Q.S. Wei, A. Wei, J.X. Cheng, Gold nanorods as contrast agents for biological imaging: optical properties, surface conjugation and photothermal effects. Photochem. Photobiol. **85**, 21–32 (2009)
46. T.M. Lee, A.L. Oldenburg, S. Sitafalwalla, D.L. Marks, W. Luo, F.J.J. Toublan, K.S. Suslick, S.A. Boppart, Engineered microsphere contrast agents for optical coherence tomography. Opt. Lett. **28**, 1546–1548 (2003)
47. R. John, R. Rezaeipoor, S.G. Adie, E.J. Chaney, A.L. Oldenburg, M. Marjanovic, J.P. Haldar, B.P. Sutton, S.A. Boppart, In vivo magnetomotive optical molecular imaging using targeted magnetic nanoprobes. Proc. Natl. Acad. Sci. U. S. A. **107**, 8085–8090 (2010)

48. W. Denk, J.H. Strickler, W.W. Webb, 2-Photon laser scanning fluorescence microscopy. Science **248**, 73–76 (1990)
49. P.J. Campagnola, L.M. Loew, Second-harmonic imaging microscopy for visualizing biomolecular arrays in cells, tissues and organisms. Nat. Biotechnol. **21**, 1356–1360 (2003)
50. W. Tan, C. Vinegoni, J.J. Norman, T.A. Desai, S.A. Boppart, Imaging cellular responses to mechanical stimuli within three-dimensional tissue constructs. Microsc. Res. Tech. **70**, 361–371 (2007)
51. B.W. Graf, E.J. Chaney, M. Marjanovic, S.G. Adie, M.D. Lisio, M. Valero, C.M.D. Boppart, S.A. Boppart, Long-term time-lapse multimodal intravital imaging of regeneration and bone-marrow-derived cell dynamics in skin. Technology **1**, 8–19 (2013)
52. A. Ratcliffe, L.E. Niklason, Bioreactors and bioprocessing for tissue engineering. Ann. NY Acad. Sci. **961**, 210–215 (2002)
53. J.R. Mourant, J.P. Freyer, A.H. Hielscher, A.A. Eick, D. Shen, T.M. Johnson, Mechanisms of light scattering from biological cells relevant to noninvasive optical-tissue diagnostics. Appl. Optics **37**, 3586–3593 (1998)
54. C.W. Chen, M.W. Betz, J.P. Fisher, A. Paek, Y. Chen, Macroporous hydrogel scaffolds and their characterization by optical coherence tomography. Tissue Eng. C **17**, 101–112 (2011)
55. Y.S. Nam, J.J. Yoon, T.G. Park, A novel fabrication method of macroporous biodegradable polymer scaffolds using gas foaming salt as a porogen additive. J. Biomed. Mater. Res. **53**, 1–7 (2000)
56. Y. Yang, P. Bagnaninchi, M. Wood, A.J. El Haj, E. Guyot, A. Dubois, R.K. Wang, Monitoring cell profile in tissue engineered constructs by OCT. Proc. SPIE **5695**, 51–57 (2005)
57. Y.L. Jia, P.O. Bagnaninchi, Y. Yang, A. El Haj, M.T. Hinds, S.J. Kirkpatrick, R.K.K. Wang, Doppler optical coherence tomography imaging of local fluid flow and shear stress within microporous scaffolds. J. Biomed. Opt. **14**, 034014 (2009)
58. P.O. Bagnaninchi, Y. Yang, N. Zghoul, N. Maffulli, R.K. Wang, A.J. El Haj, Chitosan microchannel scaffolds for tendon tissue engineering characterized using optical coherence tomography. Tissue Eng. **13**, 323–331 (2007)
59. R.K. Wang, L. An, Doppler optical micro-angiography for volumetric imaging of vascular perfusion in vivo. Opt. Express **17**, 8926–8940 (2009)
60. C.M. Yang, C.S. Chien, C.C. Yao, L.D. Hsiao, Y.C. Huang, C.B. Wu, Mechanical strain induces collagenase-3 (MMP-13) expression in MC3T3-E1 osteoblastic cells. J. Biol. Chem. **279**, 22158–22165 (2004)
61. C.J. Hunter, S.M. Imler, P. Malaviya, R.M. Nerem, M.E. Levenston, Mechanical compression alters gene expression and extracellular matrix synthesis by chondrocytes cultured in collagen I gels. Biomaterials **23**, 1249–1259 (2002)
62. J.M. Schmitt, OCT elastography: imaging microscopic deformation and strain of tissue. Opt. Express **3**, 199–211 (1998)
63. H.J. Ko, W. Tan, R. Stack, S.A. Boppart, Optical coherence elastography of engineered and developing tissue. Tissue Eng. **12**, 63–73 (2006)
64. W. Tan, A. Sendemir-Urkmez, L.J. Fahrner, R. Jamison, D. Leckband, S.A. Boppart, Structural and functional optical imaging of three-dimensional engineered tissue development. Tissue Eng. **10**, 1747–1756 (2004)
65. X. Liang, B.W. Graf, S.A. Boppart, Imaging engineered tissues using structural and functional optical coherence tomography. J. Biophotonics **2**, 643–655 (2009)
66. D. Levitz, M.T. Hinds, N. Choudhury, N.T. Tran, S.R. Hanson, S.L. Jacques, Quantitative characterization of developing collagen gels using optical coherence tomography. J. Biomed. Opt. **15**, 026019 (2010)
67. Y. Yang, A. Dubois, X.P. Qin, J. Li, A.J. El Haj, R.K. Wang, Investigation of optical coherence tomography as an imaging modality in tissue engineering. Phys. Med. Biol. **51**, 1649–1659 (2006)
68. P. Bagnaninchi, Y. Yang, N. Maffuli, R.K. Wang, A.J. El Haj, Monitoring the tissue formation and organization of engineered tendon by optical coherence tomography. Proc. SPIE **6084**, 608419 (2006)

69. W. Tan, A.L. Oldenburg, J.J. Norman, T.A. Desai, S.A. Boppart, Optical coherence tomography of cell dynamics in three-dimensional tissue models. Opt. Express **14**, 7159–7171 (2006)
70. Y. Yang, J. Sule-Suso, A.J. El Haj, P.R. Hoban, R.K. Wang, Monitoring of lung tumour cell growth in artificial membranes. Biosens. Bioelectron. **20**, 442–447 (2004)
71. C. Xu, C. Vinegoni, T.S. Ralston, W. Luo, W. Tan, S.A. Boppart, Spectroscopic spectral-domain optical coherence microscopy. Opt. Lett. **31**, 1079–1081 (2006)
72. A.L. Oldenburg, F.J.J. Toublan, K.S. Suslick, A. Wei, S.A. Boppart, Magnetomotive contrast for in vivo optical coherence tomography. Opt. Express **13**, 6597–6614 (2005)
73. C.H. Yang, M.A. Choma, L.E. Lamb, J.D. Simon, J.A. Izatt, Protein-based molecular contrast optical coherence tomography with phytochrome as the contrast agent. Opt. Lett. **29**, 1396–1398 (2004)
74. V. Backman, M.B. Wallace, L.T. Perelman, J.T. Arendt, R. Gurjar, M.G. Muller, Q. Zhang, G. Zonios, E. Kline, T. McGillican, S. Shapshay, T. Valdez, K. Badizadegan, J.M. Crawford, M. Fitzmaurice, S. Kabani, H.S. Levin, M. Seiler, R.R. Dasari, I. Itzkan, J. Van Dam, M.S. Feld, Detection of preinvasive cancer cells. Nature **406**, 35–36 (2000)
75. R.N. Graf, A. Wax, Nuclear morphology measurements using Fourier domain low coherence interferometry. Opt. Express **13**, 4693–4698 (2005)
76. Y.L. Kim, Y. Liu, V.M. Turzhitsky, R.K. Wali, H.K. Roy, V. Backman, Depth-resolved low-coherence enhanced backscattering. Opt. Lett. **30**, 741–743 (2005)
77. C. Xu, P.S. Carney, W. Tan, S.A. Boppart, Light-scattering spectroscopic optical coherence tomography for differentiating cells in 3-D cell culture. Proc. SPIE **6088**, 608804 (2006)
78. D.C. Adler, T.H. Ko, P.R. Herz, J.G. Fujimoto, Optical coherence tomography contrast enhancement using spectroscopic analysis with spectral autocorrelation. Opt. Express **12**, 5487–5501 (2004)
79. M.A. Wood, Y. Yang, P.B.M. Thomas, A.J. El Haj, Using dihydropyridine-release strategies to enhance load effects in engineered human bone constructs. Tissue Eng. **12**, 2489–2497 (2006)
80. J.P. Dunkers, M.T. Cicerone, N.R. Washburn, Collinear optical coherence and confocal fluorescence microscopies for tissue engineering. Opt. Express **11**, 3074–3079 (2003)
81. E. Beaurepaire, L. Moreaux, F. Amblard, J. Mertz, Combined scanning optical coherence and two-photon-excited fluorescence microscopy. Opt. Lett. **24**, 969–971 (1999)
82. E.B. van Munster, T.W.J. Gadella, Fluorescence lifetime imaging microscopy (FLIM). Microsc. Tech. **95**, 143–175 (2005)
83. D.G. Buschke, J.M. Squirrell, J.J. Fong, K.W. Eliceiri, B.M. Ogle, Cell death, non-invasively assessed by intrinsic fluorescence intensity of NADH, is a predictive indicator of functional differentiation of embryonic stem cells. Biol. Cell **104**, 352–364 (2012)
84. Z.J. Yuan, J. Zakhaleva, H.G. Ren, J.X. Liu, W.L. Chen, Y.T. Pan, Noninvasive and high-resolution optical monitoring of healing of diabetic dermal excisional wounds implanted with biodegradable in situ gelable hydrogels. Tissue Eng. C **16**, 237–247 (2010)
85. S. Makita, Y. Hong, M. Yamanari, T. Yatagai, Y. Yasuno, Optical coherence angiography. Opt. Express **14**, 7821–7840 (2006)

4-D OCT in Developmental Cardiology

65

Michael W. Jenkins and Andrew M. Rollins

Keywords

4-D imaging • Biomechanical forces • Heart development • Congenital heart defects • Gated imaging • Heart development • Optical coherence tomography • Prospective gating • Retrospective gating

65.1 Introduction

The heart of a human fetus begins beating approximately 3 weeks after conception. At this point, the heart is a linear tube. Next, the heart will form first a simple c-shaped loop and then an s-shaped loop before forming the four chambers of the adult heart. This critical process is a complex coordination of many events where small deviations can lead to abnormal development and congenital heart defects (CHDs). Mechanisms of CHDs remain largely unclear despite being the focus of many investigations. Contributing factors of CHDs include single-gene mutations, complex chromosomal rearrangements [1], and environmental agents (e.g., alcohol [2], viral infections [1, 3], hypoxia [4, 5], etc.). Although strong evidence exists to suggest that altered cardiac function can lead to CHDs [6–15], few studies have investigated the influential role of cardiac function and biophysical forces on the development of the cardiovascular system due to a lack of proper in vivo imaging tools. The lack of in vivo imaging instrumentation for early embryos becomes even more dire when one considers the fact that causes of CHDs are most likely multifactorial. For example, if a gene mutation alters molecular signaling and

M.W. Jenkins (✉)
Department of Pediatrics, Case Western Reserve University, Cleveland, OH, USA
e-mail: mwj5@case.edu

A.M. Rollins
Department of Biomedical Engineering, Case Western Reserve University, Cleveland, OH, USA

© Springer International Publishing Switzerland 2015

W. Drexler, J.G. Fujimoto (eds.), *Optical Coherence Tomography*,
DOI 10.1007/978-3-319-06419-2_67

cardiac function, it is currently not possible to discern if the resultant defects are produced by the altered mechanical function or molecular signaling or a combination. Imaging tools for investigating the live embryonic cardiovascular system early in development would have three major benefits. First, quantifying cardiac function and forces can be a sensitive assay to determine critical time points in the sequence of events leading to CHDs giving clues to the underlying mechanisms. Second, quantifying forces impinging on the cardiovascular system during both normal and abnormal development would enable one to determine the causal relationship between biophysical forces and molecular signaling. Lastly, imaging can be implemented to monitor interventions for improved accuracy and precision.

A suitable in vivo imaging modality for investigating early stage embryonic hearts must have high spatial resolution to resolve the pertinent structures (e.g., endocardium, myocardium, etc.) in the minute heart tube, sufficient depth penetration and field of view to visualize the heart in vivo, and high temporal resolution for real-time imaging. Common animal models utilized for heart development research include avian (e.g., chicken and quail), murine, zebrafish (*Danio rerio*), fruit fly (*Drosophila melanogaster*), and frog (*Xenopus laevis*). Microscopy (e.g., confocal) has the spatial resolution, penetration depth, and temporal resolution for in vivo investigations involving the zebrafish, frog, and fruit fly. Unfortunately, these models do not develop a four-chambered heart and have significant limitations, although they are excellent models for genetic screening. Optical coherence tomography (OCT) has become increasingly popular as a tool for investigating development of the four-chambered heart (avian and murine) [16–18]. Avian and murine hearts develop in a very similar manner to humans. OCT has greater penetration depth (1–2 mm) than microscopy which allows in vivo imaging of the avian and murine heart early in development when the heart is a looping tube. OCT also maintains high enough resolution (2–20 μm) to discern features of the developing heart tube which can be less than a millimeter in length and can achieve high temporal resolution.

Figure 65.1 orients the reader to the anatomical structures of the developing embryo and typical OCT images [19]. Panel A shows a bright-field microscopy image of an early stage quail embryo (stage 14). Arrows designate the inflow and outflow (outflow tract) portion of the heart tube. The green dotted line reveals the location of the OCT cross-sectional image in panel B. From panel B, one can see the three main structures in the developing heart tube. The myocardium forms the exterior of the heart and is only two cell layers thick at the time point shown. The epicardium does not develop until later. The endocardium forms the lumen of the heart tube and is in direct contact with the blood. Finally, the cardiac jelly is a gelatinous material between the endocardium and myocardium and is essential for proper development of the valves and septa. Panels C and D demonstrate the capability of Doppler OCT to perform flow imaging in the outflow tract. The top panel shows forward flow (red), while the bottom panel displays retrograde flow (blue). Doppler OCT offers the ability to measure hemodynamic function and forces in the early embryo heart. The images in Fig. 65.1 demonstrate the potential of OCT to be useful in developmental cardiology studies.

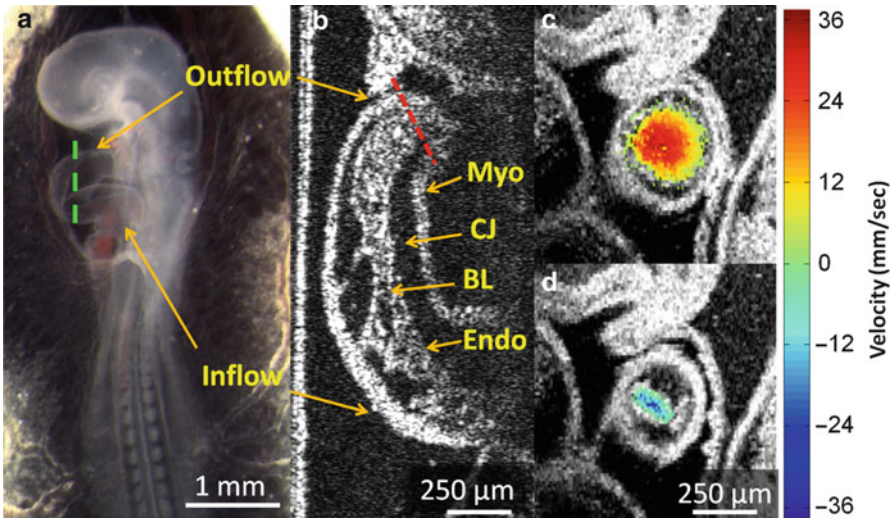

Fig. 65.1 Anatomical structure of the developing embryo. (**a**) displays a quail embryo imaged at 12× magnification. (**b**) shows a B-scan image of the quail embryo heart imaged by OCT. The *green dotted line* approximates the location of the B-scan. OCT allows visualization of all layers in the heart tube (myocardium, cardiac jelly, and endocardium) in both the inflow and outflow regions. (**c**, **d**) Doppler OCT data are overlaid on a structural B-scan of the outflow tract during diastole and systole. The *red dotted line* in B gives the approximate location. The color map is shown to the *right of* the image. *Myo* myocardium, *CJ* cardiac jelly, *BL* blood, *Endo* endocardium

Early demonstrations of imaging the developing heart using OCT demonstrated its ability to visualize cardiac dynamics in one and two spatial dimensions versus time [20–23]. 1-D and 2-D imaging over time opens up the possibility of many exciting experiments. However, biomechanical forces acting upon the heart are often spatially heterogeneous and varying in time. For example, not only does shear stress on the endocardium vary greatly along the length of the heart tube, but certain regions experience oscillatory shear due to regurgitant flow [10]. In order to fully assess complex patterns of biophysical forces, it is necessary to image the beating heart with high spatiotemporal resolution in four dimensions (x, y, z, and time). This is what we refer to as 4-D imaging. Cardiac function and the resultant forces are constantly evolving throughout development. Biomechanical cues are vital for proper growth and maturation. Shear stress on and stretch of the endocardium, strain in the myocardium, and electrical signals have all been implicated as necessary for normal development [6–15]. Also, small deviations in biomechanics can signify that the embryo is developing a CHD. Deciphering the complex spatial and temporal patterns of biomechanical forces acting upon the heart is necessary to fully understand the role of function in the developing embryo.

Numerous solutions over the past several years have demonstrated 4-D OCT imaging of the developing cardiovascular system. This chapter will focus on these solutions and explain their context in the evolution of 4-D OCT imaging. The first sections describe the relevant techniques (prospective gating, direct 4-D imaging,

retrospective gating), while later sections focus on 4-D Doppler imaging and measurements of force implementing 4-D OCT Doppler. Finally, the techniques are summarized, and some possible future directions are discussed.

65.2 Prospective Gating

Cardiac-gated imaging enables the capture of 4-D image data sets by mitigating motion artifacts when the temporal resolution of the system is inadequate for direct 4-D imaging (real-time volumetric imaging). Because cardiac motion is highly repetitive, one can build up a 4-D image set of the beating heart over multiple beats. For prospective gating, a physiological signal is used to trigger data acquisition at specific phases of the cardiac cycle. After several heartbeats, one collects data of the beating volumetric heart by acquiring more data at each cardiac phase with each subsequent heartbeat. Prospective gating has been implemented in several medical imaging modalities found in the clinic including MRI and CT [24, 25].

In 2006 Jenkins et al. used a prospective gating technique to capture 4-D OCT images of beating avian and murine hearts [26]. Because of the difficulties of obtaining a steady physiological trigger signal, the heart was excised and paced as a first step to prove the principle. Specifically, hearts were excised in a Tyrode solution and placed between two platinum plates. A 50 ms electrical pulse both paced the heart and triggered data acquisition. The Tyrode bath was kept at room temperature which lowered the heart rate and enabled pacing at 1 Hz. A time domain OCT system with a bandwidth centered around 1,300 nm acquired data at 4,000 A-scans/s with an axial resolution of 14 μm and a lateral resolution of 10 μm. Sixteen cardiac volumes were captured per heartbeat with imaging of one heart lasting less than 5 min. Chicken embryos were imaged at stage 13, 15, and 20, corresponding to 2–3 days of development, while mouse embryos were imaged on day 13.5. Images were averaged and filtered to reduce noise before correcting the aspect ratio and creating surface renderings of the 4-D structures. Measurements of cardiac volume, ejection fraction, and wall thickness were demonstrated, although some of the measured values probably differ from in vivo measurements made under physiological conditions. This work demonstrated the feasibility of 4-D OCT imaging of a paced, excised heart, but not of the beating heart in an intact, living embryo.

Obtaining ECG signals from patients in the clinic is a simple procedure and can easily be utilized to gate image acquisition. Unfortunately, obtaining a proper ECG signal from an early stage embryo is both difficult and invasive. To overcome this challenge and enable in vivo 4-D imaging, Jenkins et al. designed a prospective gating technique by triggering data acquisition with a laser Doppler velocimetry (LDV) signal [27]. Briefly, a commercial LDV needle probe (Moor Instruments Incorporated, Wilmington, Delaware) was positioned adjacent to a vitelline vessel of a stage 14 quail embryo cultured on the yolk in a Petri dish on a temperature-controlled heating pad (37 °C). The choice of vitelline vessel was not important as long as a strong signal was obtained. The signal was conditioned and then directed

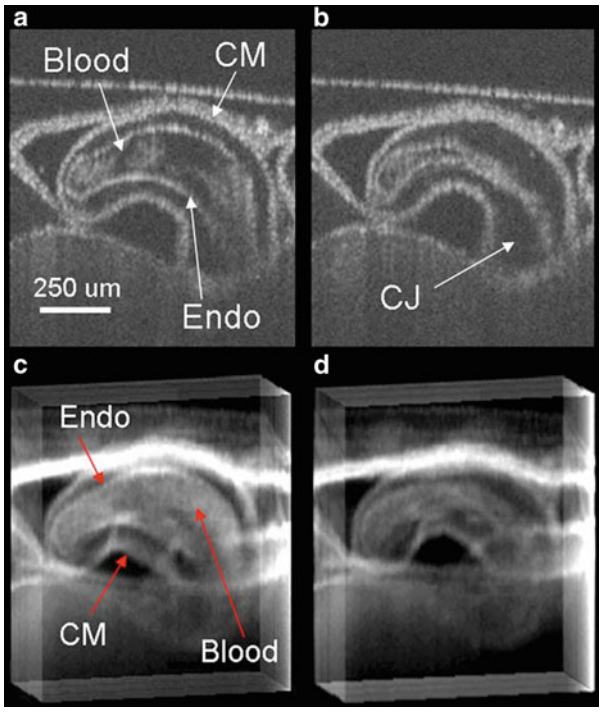

Fig. 65.2 Prospective gating employing a laser Doppler velocimetry (LDV) probe. (**a**) OCT B-scan acquired during diastole cut coronal to the body of the embryo. (**b**) OCT B-scan acquired during systole cut coronal to the body of the embryo. (**c**) Digitally reconstructed radiograph image acquired during diastole. (**d**) Digitally reconstructed radiograph acquired during systole. Digitally reconstructed radiographs project signal intensity along the sagittal orientation. *CM* is the compact myocardium, *endo* is the endocardium, and *CJ* is the cardiac jelly

to a commercial R-wave detector (AccuSync Medical Research Corporation), which produced two triggers: one at the peak of the LDV signal and one at the bottom of the downward slope. Finally, a field programmable gate array (FPGA) received inputs from the R-wave detector and a line-sync from the OCT delay line to produce a frame sync and to control the scanning. The OCT system was identical to the one used in the previous study. Eight heart volumes were collected. Figure 65.2 displays 2-D cross-sections and 3-D volumes (digitally reconstructed radiographs) of a stage 14 quail embryo heart in vivo during systole and diastole. Excellent initial results were demonstrated with prospective OCT gating using LDV, but the requirement of an external signal is a disadvantage relative to direct 4-D imaging and signal-free retrospective gating (which have become feasible using current, high-speed OCT systems) due to decreased set up time. However, prospective gating does require less computation time than retrospective gating which can be advantageous for certain applications.

65.3 Direct 4-D Imaging

Direct 4-D imaging is defined as real-time volumetric imaging without the aid of gating techniques. Until recently, OCT systems were not capable of 4-D imaging of embryo hearts without gating due to insufficient imaging speed, but as speeds have

dramatically increased, 4-D imaging has become feasible with limited spatiotemporal resolution. This step forward is attributed to the paradigm shift to frequency-domain OCT systems and the development of high-speed swept laser sources [28–33]. Details of these developments are presented in other chapters of this book.

Jenkins et al. demonstrated direct 4-D imaging of embryonic quail hearts using a Fourier domain mode-locked (FDML) laser [34]. The high-speed swept source allowed imaging speeds of 100,000 A-scans/s. The axial resolution in tissue was 7 μm, while the lateral resolution was 15 μm. 4-D imaging of stage 14 quail embryos was collected at ten volumes/s (70 × 150 A-lines/volume). Embryos were cultured on a yolk in a Petri dish and imaged on a temperature-controlled plate (37 °C). Because the embryos were not imaged in an incubator, the heart rates were slightly depressed (∼2 Hz), resulting in 4–6 volumes per heartbeat. Several visualization techniques were also demonstrated, including digital reconstructed radiographs, Sobel filtering, and multiplanar reformatting. Figure 65.3 displays the top view of a stage 14 quail embryo heart where a 3-D Sobel mask was applied to the data to bring out the edges of the structures. In 2008, Gargesha et al., using a similar system, demonstrated that volume visualizations applying a 2-D opacity transfer function and image denoising could improve 3-D visualizations and automated segmentation of 4-D data sets [35]. Considering that the maximum wall velocity can reach almost 2 mm/s, a volume must be imaged in 5 ms in order to reduce motion artifact below 10 μm [34]. The authors noted that in order to accurately capture the 3-D motion of the heart tube without gating, faster imaging systems were needed.

Yelin et al. demonstrated 4-D OCT imaging of stage 49 *Xenopus laevis* hearts using a wavelength-swept laser with a polygon scanner-based spectral filter [36]. 54,000 A-scans/s were captured allowing for 20 volumes/s with each volume consisting of 60 × 45 × 256 pixels. The axial resolution was 10 μm in tissue. Embryos were covered by an anesthesia solution and positioned ventral side up on an agar plate. Displacement maps were constructed to show myocardial motion at different phases in the cardiac cycle. Again, although 4-D imaging was demonstrated, meaningful measurements were not possible because of the limited speed of the system.

Direct 4-D OCT imaging is attractive for several reasons which include decreased procedure time, reduced post processing, no increased noise due to abnormal beats, and the ability to capture nonperiodic events like arrhythmias. Over the last several years, FDML lasers have increased OCT imaging speed dramatically including a demonstration of 20 MHz A-line rates [37]. This extraordinary increase can enable direct 4-D imaging with sufficient spatiotemporal sampling (e.g., volumes 2 mm × 1.25 mm transversely in 5 ms) and obviate the need for gating.

Unfortunately, an OCT system this fast is very complex and expensive. Data acquisition and handling are extremely challenging, and adequate commercial DAQ products are not presently available. Real-time data visualization at these rates is also a challenge. Several demonstrations have been reported of real-time 4-D OCT display of tissue structures utilizing graphics processing units (GPU) [38–40].

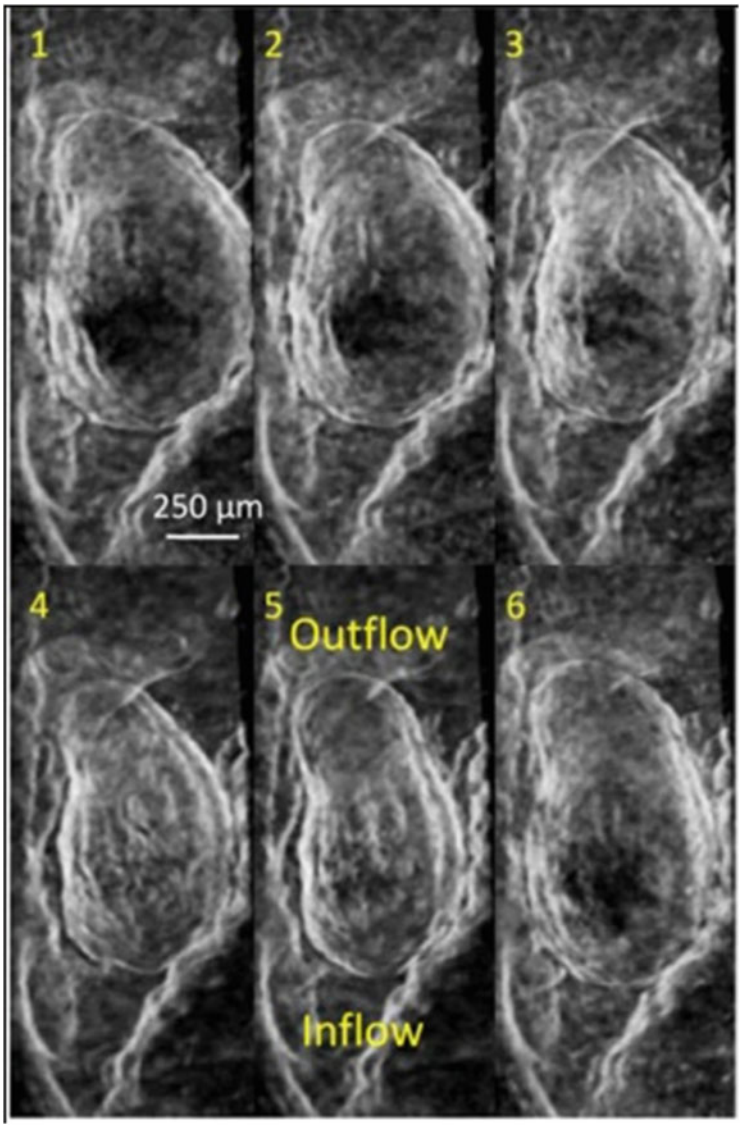

Fig. 65.3 Top view (*ventral*) of a beating stage 14 quail heart (six phases in the cardiac cycle). Data are visualized as an edge-enhanced volume rendering (Data was collected through 4-D direct imaging)

Although these systems need to improve data throughput to visualize the developing embryo heart in a meaningful way, it is likely that new developments in OCT technology and GPUs will enable this in the future.

4-D Doppler OCT imaging will remain difficult without gating. Doppler OCT requires denser spatial sampling than is needed for structural OCT, slowing

imaging speed. Also, because scanning speed dictates the detectable velocity range, capturing 4-D Doppler datasets would be require innovative scanning patterns.

65.4 Retrospective Gating

65.4.1 Signal-Based Retrospective Gating

A signal-based retrospective gating scheme records a physiological signal simultaneously with the image data. Unlike prospective gating where the physiological signal gates data acquisition, here the signal is utilized in a post processing algorithm to parse the data into the appropriate phases of the cardiac cycle creating a 4-D data set. Yazdanfar et al. first demonstrated retrospective gating of a *Xenopus laevis heart* on an OCT system with a scanning rate of 8 A-scans/s [41]. By utilizing the structural OCT signal to determine the number A-scans per heartbeat, the authors obtained five Doppler and structural frames per heartbeat. Building on this first demonstration, Mariampillai et al. implemented a signal-based retrospective gating technique to capture both 4-D structure and Doppler images of stage 51 *Xenopus laevis* hearts [42]. The system comprised two OCT systems; one an adapted commercial swept source OCT system (Thorlabs, SL1325-P16) for imaging and the second a time domain OCT system to capture a Doppler optical cardiogram used as the gating signal. The swept source system had an A-line rate of 16 kHz and was capable of real-time imaging at 25 fps (structural) and 12 fps (Doppler). Briefly, stage 51 *Xenopus laevis* embryos were anesthetized with lidocaine and placed in a shallow V-groove with solution. The time domain OCT system with a rapid scanning optical delay (RSOD) line had an A-line rate of 12.95 kHz. The system recorded from one of the two vessels exiting the heart and operated in M-mode (no scanning). The M-mode Doppler signal was processed, and the mean and standard deviation of the heart rate were calculated from the optical cardiogram, and cardiac cycles with variations below 1.75 standard deviations were kept. Next, the cardiac cycle was separated into equally spaced temporal bins. B-scans acquired from the swept source OCT system were placed into the correct bin by time stamp and reassembled. Finally, 4-D surface reconstructions of both the structure and Doppler images were presented. Signal-based retrospective gating has some promise, but like prospective gating it requires a more complex technical setup and additional setup time between embryos and has lost favor among research groups investigating embryonic cardiac dynamics in favor of signal-free gating.

65.4.2 Image-Based Retrospective Gating

Image-based retrospective gating (or signal-free, i.e., not requiring an external signal) has become the current standard for 4-D OCT imaging in developmental cardiology studies [43–45]. This technique records images continuously, without gating, over

several heart cycles, then rearranges out-of-order data based upon image similarity and obviates the need for extra signals to synchronize data. Although the system complexity is greatly reduced, the gating algorithm requires extra processing time. Gargesha et al. demonstrated 4-D reconstructed imaging of embryonic hearts using an image-based retrospective OCT gating technique by adapting an algorithm originally applied to confocal microscopy images of living zebrafish embryos [44]. The technique consisted of capturing B-scans (500 A-lines) longitudinal to the heart tube at a single location for at least 1.5 heartbeats before translating to a parallel slice 9 μm away. This process was continued until the entire heart was imaged (∼80 slices). The embryos were imaged under physiological conditions by controlling temperature and humidity in an environmental imaging chamber. The scanning orientation was chosen to minimize motion artifacts. The B-scan interval for the system was 4.27 ms. It was previously determined that the maximum error in displacement due to a 5 ms time step was 10 μm [34]. If the first A-scans in the B-scan were captured 5 ms before the last A-scans of the B-scan, there would be a 10 μm displacement error if the velocity of the heart wall was 2 mm/s. Since the maximum wall velocity for stage 14 quail embryo is 2 mm/s, the B-scan interval was fast enough to assume that the motion was frozen during each B-scan.

The gating algorithm consisted of four main steps:

1. Ascertain the period of the heart cycle.
2. Determine relative time shifts between adjacent image slice locations.
3. Establish absolute shifts to align slices with user-selected starting time.
4. Reorder image data.

These steps are similar for all works discussed in this section unless stated otherwise. Before step 1, the data can be decimated to reduce processing time or alternatively can be synchronized based upon a subset of wavelet coefficients from the image [43, 44]. (1) To calculate period of the heart cycle, a string-length minimization method was applied [46, 47]. Image data at each slice location was wrapped into a single cardiac cycle for each guess of the period. An objective function computed the sum of squared differences between temporally adjacent reordered slices and the sum of squared differences between frame times. The period that minimizes the objective function was chosen, and the data were reassembled into one correctly ordered cardiac cycle. The data were then interpolated to create B-scans evenly spaced in time. (2) The sequence of B-scans at each transverse position has a different starting point in the cardiac cycle so the temporal shift between the transverse positions must be determined. The relative shift in time between adjacent transverse positions was determined by maximizing the cross-correlation coefficient between the images as the relative shift was varied. (3) The absolute shift of each slice location was set corresponding to a user-defined reference slice at the middle of the heart tube. The reference shifts were progressively applied to each consecutive slice moving outward from the middle giving an array of correct starting offsets for each slice position. (4) The determined period and absolute shifts were employed to reorder the data. Figure 65.4 shows an example of data obtained with this image-based retrospectively gated OCT imaging method.

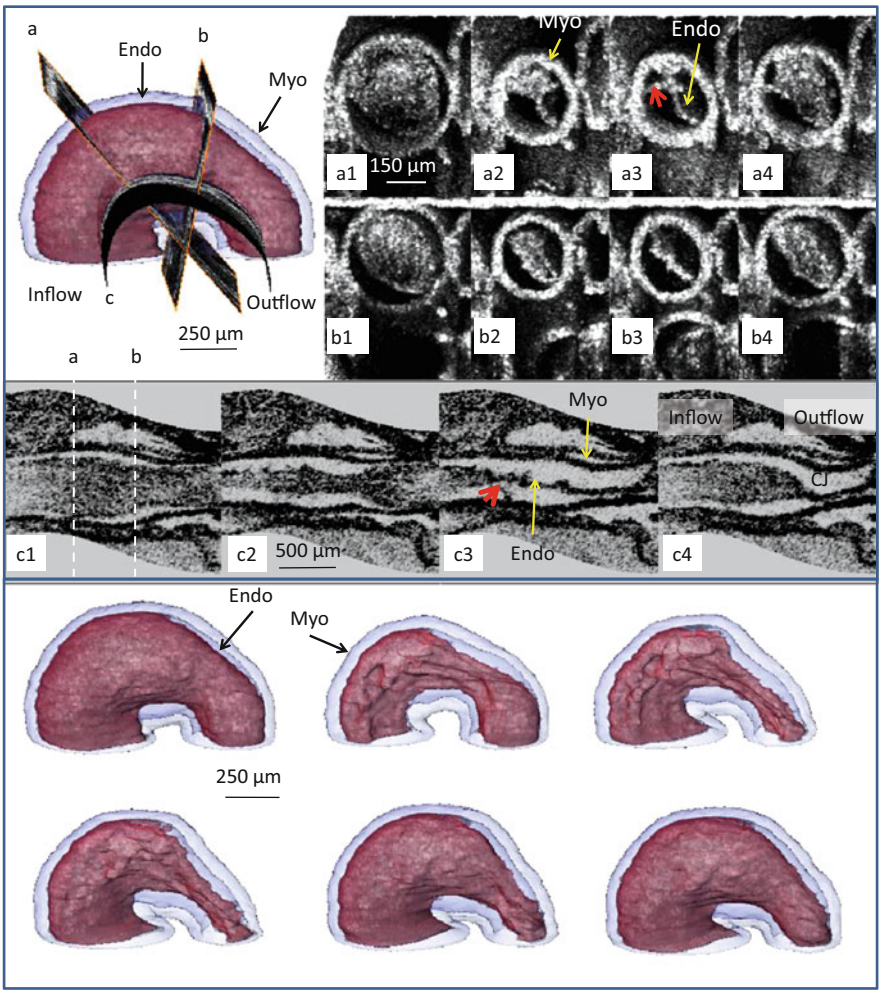

Fig. 65.4 Image-based retrospective gating. Upper *left panel* displays the location of the three slices (**a**, **b**, and **c**) on the 3-D heart. *A1–4* and *B1–4* slices at locations (**a**, **b**) oriented orthogonal to the heart tube at several different time points during the cardiac cycle. *C1–4* illustrates the ability to visualize a curved surface through the center of the length of the heart tube. The locations of slices (**a, b**) are indicated with the *white dashed lines*. The *bottom panel* displays surface renderings as the heart progresses through a cardiac cycle. The endocardium is in *red* and the myocardium in transparent *blue*. *Myo* myocardium, *Endo* endocardium

Gargesha et al. validated the gating algorithm by comparing the retrospectively gated results to directly recorded volumetric imaging of the same samples [44]. Knowing the time delay between slices in the directly imaged volume, the accuracy of the gating algorithm was determined by finding the slices in the directly imaged volume that correlated best with volumes in the gated image set. The maximum

error was 18.7 ms, and the standard deviation of the error was 4.7 ms indicating that the gating algorithm would be capable of producing 200 volumes/s with minimal displacement error (<10 μm). It is likely that this displacement error would increase for OCT systems with slower A-scan rates, and further enhancements in the algorithm would be needed.

Liu et al. demonstrated a similar retrospective gating algorithm to image the outflow tract of stage 18 chicken embryos [45]. A spectral domain OCT system acquired 40 B-scans/s consisting of 250 A-lines. The resolution of the system was 10 μm axial and 16 μm lateral. The eggshell was opened to enable imaging, while temperature and humidity were not controlled and the heart rate was depressed. The Liu algorithm differed from the algorithm described above in several ways. First, instead of maximizing the similarity between adjacent B-scan sequences by varying the relative shift, similarity was maximized between adjacent M-mode images extracted along the same line perpendicular to the B-scans (essentially using one line per image), which increased computational efficiency. To improve accuracy, images were recorded over five cardiac cycles instead of 1.5–2. Furthermore, B-scan slice sequences were transverse to the heart tube. Finally, an extra perpendicular B-scan sequence longitudinal to the outflow tract was utilized to correct the phase lag between adjacent image sequences. Briefly, the phase lag was computed by extracting two M-scans from the sequence of B-scans longitudinal to the outflow tract. By computing the distance between the M-scans and the phase between maximal contractions, the phase lag could be computed. For this measurement, the velocity of the contraction wave was assumed constant in the outflow tract. Reconstructions consisted of 180 volumes per cardiac cycle.

Recently, Happel et al. designed a gating algorithm implementing rotational image acquisition, where each set of B-scan sequences is rotated from one another providing a central A-scan common to all B-scan sequences [48]. The common A-scan was utilized to determine the relative shift between each B-scan sequence. Images were collected with a Thorlabs swept source OCT system (OCS1300SS). Fifty B-scans (>9 images/heartbeat) were acquired in 2.4 s (>5 heartbeats) at every angle (every 2°) at a frame rate of 21 B-scans/s (each B-Scan consisted of 512 A-lines). The axial resolution was 9 μm in tissue, while the lateral resolution was 25 μm. Twenty volumes per cardiac cycle were assembled. Validation was done by acquiring B-scan sequences collected at positions differing from those taken in the 4-D data set and correlating them with the reconstructed data. From Fig. 65.5, one can see that the reconstructed data compares favorably to the validation B-scan sequences.

Larina et al. demonstrated a similar rotational method called sequential turning acquisition and reconstruction (STAR) [49]. The main difference with the STAR method is that it preserves the order of the frames in a single B-scan sequence by applying a nonuniform, elastic registration instead of interleaving the frames from multiple heart cycles. This allows reconstructions even with variations in the heartbeat over a single B-scan sequence and enables the analysis of features with aperiodic motion within each B-scan sequence. One of the advantages of rotational image acquisition includes having a common A-scan in each B-scan sequence

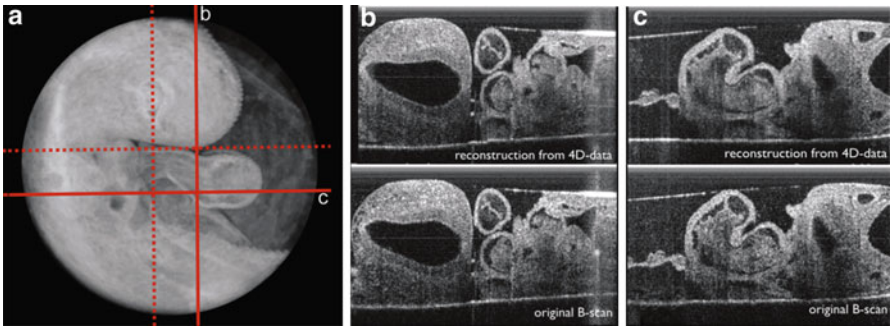

Fig. 65.5 Retrospective gating implementing rotational image acquisition. (**a**) displays a 4-D image set collected with rotational image acquisition. The *red lines* indicate the position of *b* and *c*. (**b**) B-scan from the reconstructed 4-D data looks comparable to a standard B-scan at position *b* taken after the 4-D scan was completed. (**c**) respective images from position *c*

which mitigates the accumulation of registration errors when computing relative shifts across parallel slices. This can be extremely useful when imaging with a slower OCT system. Another advantage is that monitoring the common A-scan during image acquisition can provide feedback on whether the embryo has moved, which would increase image artifacts. A disadvantage of the technique is an increasing voxel size at greater distances from the center.

More recently, Bhat et al. employed two orthogonal sets of parallel OCT slice sequences to produce 4-D images of live cultured mouse and rat embryos [50]. Each orthogonal set was recorded similarly to previous techniques [44]. By acquiring two datasets in perpendicular orientations instead of one, the authors could produce more accurate and self-validating reconstructions by employing similarity between datasets to improve spatiotemporal registration. This technique can eliminate errors that accumulate between adjacent B-scans as one progresses across the field of view. This can be especially useful for slower OCT systems that have greater accumulation errors. Figure 65.6a, c shows the two reconstructed datasets in magenta and green processed independently and together. Figure 65.6b, d illustrates the absolute differences between the two datasets. Clearly, inter-volume synchronization has improved the alignment of the data.

Similar image-based retrospective gating techniques can also be implemented with 2-D + time image data. Applications include reducing noise [51] and increasing the field of view [52].

65.5 4-D Doppler OCT and Shear Stress

Hemodynamics are a crucial regulator of the cardiovascular system during development. As with 4-D structural OCT imaging, 4-D Doppler can allow one to visualize the heterogeneous patterns of biophysical forces impinging on the embryonic heart. As mentioned above, Mariampillai produced the first 4-D Doppler

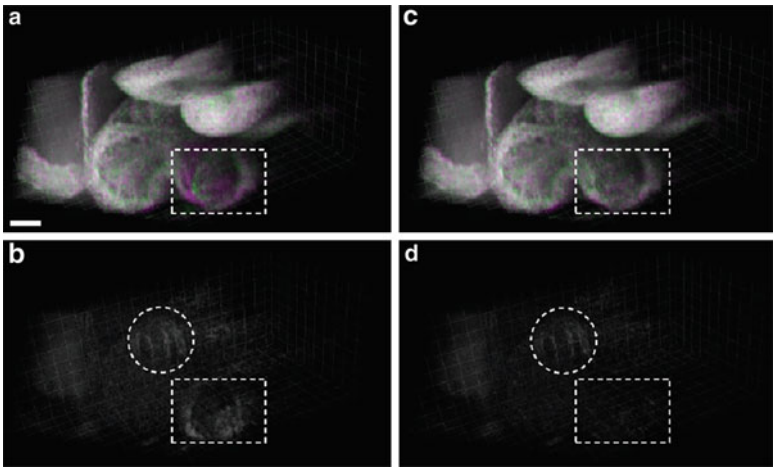

Fig. 65.6 4-D OCT gating employing two orthogonal sets of parallel OCT slice sequences. (**a**) Both orthogonal image sets processed independently. The Y-dataset is false-colored magenta, while the X-dataset is false-colored *green*. When the data from both datasets are in-sync, their colors add up to produce *gray*. (**b**) The absolute difference between the two datasets when processed separately. (**c**) X and Y datasets are synchronized using information from the other dataset. (**d**) The absolute difference between the datasets when both volumes contribute to the synchronization. The *dotted boxes* represent regions that exhibit improved alignment using both volumes for the synchronization. The *dotted circles* show a region in the outflow tract that is mismatched between the X and Y datasets due to sample movement between acquisitions. Scale bar is 100 μm

images of an embryonic *Xenopus laevis* heart [42]. Unfortunately, several issues needed solving before quantitative measurements of blood flow and hemodynamic forces could be extracted from these 4-D data sets. First, blood velocities in the heart cover a large dynamic range. Systems with low A-line rates will have excessive phase wrapping, while imaging fast enough to avoid phase wrapping may lead to lower signal-to-noise ratios especially for slower velocities. Phase wrapping occurs when the phase difference between adjacent A-scans exceeds π. For example, a 2π phase shift would be identical to no shift and cannot be distinguished without additional information. In order to accurately calculate velocities, Doppler data must be unwrapped. Second, Doppler OCT measures relative velocity because it is only sensitive to blood flow in the direction parallel with the OCT beam. Absolute velocities in blood vessels can be quickly determined by scanning the 3-D geometry of the vessel and finding the velocity vector in the direction of the vessel. In a 3-D structure that loops around and is constantly moving (e.g., embryonic heart), determining absolute velocity can be quite challenging.

Ma et al. calculated absolute flow velocity in the outflow tract of a stage 18 chicken embryo [53]. A spectral domain system with an A-line rate of 47 kHz, an axial resolution of 14 μm in air, and a lateral resolution of 16 μm was employed. 4-D data sets were first acquired and then synchronized using the previously

described image-based retrospective gating algorithm [45]. Adjacent A-scans overlapped by 75 % enabling Doppler measurements. To avoid phase wrapping, the phase difference range was shifted from [-π, π] to either [0, 2π] or [−2π, 0] allowing the projection velocity range to be [−24 mm/s, 24 mm/s]. Next the centerline of the outflow tract was determined to find the absolute velocity (velocity vector parallel to the heart tube). First, the volume corresponding to the maximum expansion in the outflow tract was selected. Next, a snake algorithm [54] segmented the myocardial layer at each slice location. The centroids of each segmentation are connected to make up the centerline. The angle between the centerline vector and the vector of the beam propagation enables the calculation of absolute velocity. It is assumed that blood flow is parallel to the centerline and that the direction of blood flow remained parallel to the centerline for the entire cardiac cycle. The errors induced from these assumptions were not determined and may be significant. However, increased accuracy could be achieved by calculating a centerline for multiple phases in the cardiac cycle. Figure 65.7 shows reconstructions of an outflow tract and the computed centerline. The maximum blood flow velocity at the inlet of the outflow tract was 35 mm/s, while at the outlet it was 50 mm/s, the difference owing to tapering of the tube.

In 2010, Jenkins et al. collected 4-D Doppler data to demonstrate several new hemodynamic measurements [55]. An FDML laser-based OCT system with an A-line rate of 117 kHz and an axial and lateral resolution of ∼10 μm was employed. All imaging was performed in an environmental chamber to insure the embryos developed under physiological conditions. 4-D data sets were first acquired and then synchronized using the previously described image-based retrospective gating algorithm [44]. To enable Doppler imaging, the A-scan spacing was 1.3 μm. Doppler data was unwrapped using a Goldstein algorithm [56]. By having access to the entire 4-D Doppler dataset, one could make several new measurements including cardiac output, stroke volume, and shear rate/stress on the endocardium. Also, pulsed Doppler traces could be accurately extracted at the inflow and outflow of the heart tube. Stroke volume and cardiac output were computed utilizing the en face plane obviating the need to determine absolute velocity. One could integrate the Doppler signal spatially in the en face plane across the lumen to yield flow and integrate over time to yield flow per second or per heartbeat. To measure shear rate/stress, an image plane orthogonal to the blood flow was identified, and the velocity gradient near the endocardium was determined. Several assumptions were made to make the shear measurements. First, the blood was assumed to be a Newtonian fluid with a dynamic viscosity of 5 mPa s. Next, it was assumed that the blood flow was laminar and dominated by viscous forces, and finally the blood was assumed to travel parallel to the direction of the heart tube. Hemodynamic measurements were presented for two stage 14 quail embryos. Stroke volumes of 0.04 and 0.038 μL were recorded, while cardiac output was 0.123 and 0.124 μL/s for the two embryos. Maximum shear rate and stress were found in the outflow tract. Maximum shear rate was 1,521 and 1,834 1/s, while maximum shear stress was 7.6 and 9.2 Pa. These measurements are not feasible without 4-D imaging and can hopefully serve as powerful metrics to discern abnormal development.

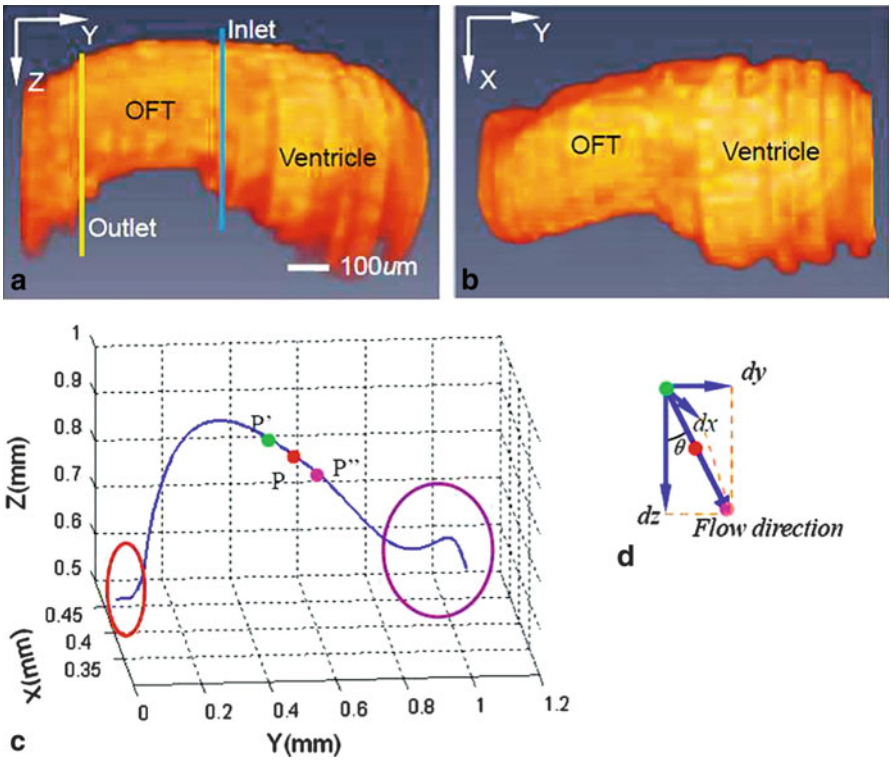

Fig. 65.7 Determining absolute flow in the outflow tract of the chicken embryo. (**a**) Segmentation of the embryonic chick outflow tract walls (*side view*). The *blue line* indicates the inlet, while the *yellow line* indicates the outlet of the outflow tract. (**b**) Top view of segmentation in (**a**). (**c**) Centerline through the heart tube. (**d**) Flow direction is calculated by determining the tangent to the centerline

Recently, Peterson et al. measured shear stress on extended regions of the endocardial surface of an embryonic quail heart over time producing 4-D shear maps [19]. The imaging system employed was described previously [55]. Again, a Goldstein algorithm was employed to unwrap the phase of the Doppler data [56], and the same assumptions for shear stress calculations were made as in [55]. To determine absolute velocity and the velocity gradient normal to the endocardial wall, the endocardium was segmented, and centerlines were calculated for each volume using a TEASAR (tree-structure extraction algorithm for accurate and robust skeletons) algorithm [57]. It was assumed that blood flowed in the direction of the centerline. Tangent lines at each point along the centerline were calculated to determine the velocity direction and estimate absolute blood flow. A surface mesh of the endocardial wall was used to determine the normal vector to the endocardial surface at each location and thereby determine the velocity gradient near the wall. Figure 65.8 shows results from the shear stress algorithm. The pattern of shear stress is heterogeneous and displays the largest stresses on the inner curvature of the

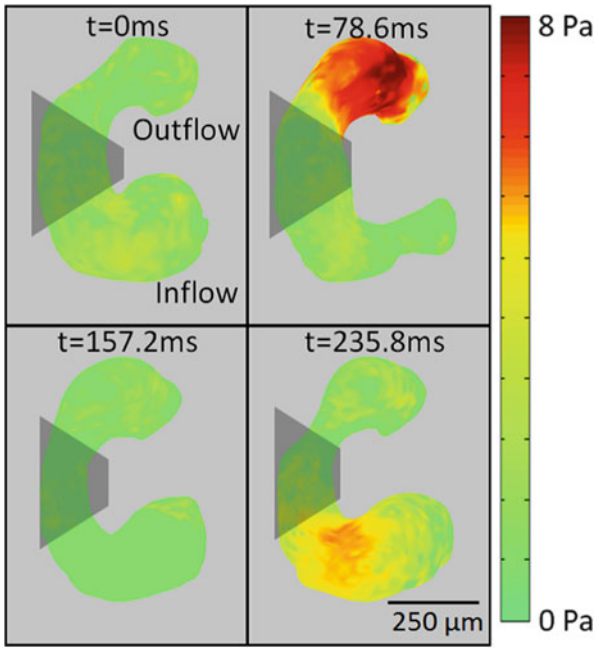

Fig. 65.8 Endocardial shear stress in a quail embryo at four evenly spaced time points during the cardiac cycle, which lasted 367 ms. The shear stress values are color mapped onto the endocardial surface. The shear stress could not be calculated in the *gray* region because flow was nearly perpendicular to the OCT beam

outflow tract. Another prominent region is displayed near the inflow region of the tube. Both regions of higher shear stresses are thought to be where future valves and septa will develop [58]. Recent evidence has shown that shear stress may be important for the development of valves in the zebrafish heart [10]. Future experiments correlating shear stress patterns with molecular expression and subsequent heart development will enable us to understand how altered shear patterns can lead to congenital heart defects.

Liu et al. approximated shear on the endocardium of the outflow tract of a stage 18 chick embryo using a finite element (FE) model of the heart tube (see Fig. 65.9 [17]). 4-D OCT data were utilized to determine the dynamic geometry of the heart tube and the outflow tract (OFT) centerline [59]. Briefly, the OFT centerline was determined from the volume representing the time point when the OFT was most constricted. Five equally spaced cross-sections perpendicular to the OFT centerline were chosen to characterize the geometry and wall dynamics in the model. Pressure measurements at the ventricle and aortic sac using a servo-null micro-pressure system were used for boundary conditions. Unfortunately, it was not possible to record pressure measurements and 4-D OCT images from the same embryo. Ultrasound helped correlate the phase of the pressure waves and OCT data. The model showed that the highest shear levels were located at the inner curvature of the OFT in close proximity to the cardiac cushions. A second study by Liu et al. enhanced the method by improving segmentation of the outflow tract and adding measurements of myocardial wall

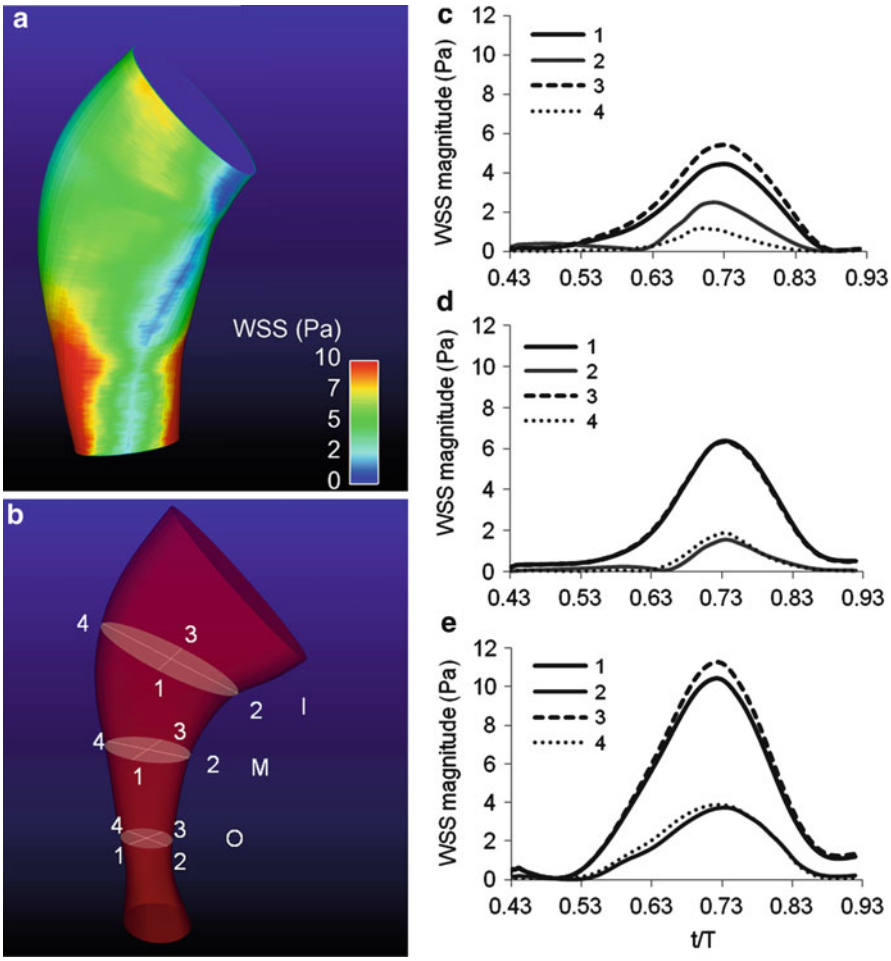

Fig. 65.9 Computing wall shear stress at the outflow tract using computational fluid dynamics. (**a**) Wall shear stress on the outflow tract during the greatest expansion of the tube. (**b**) Outflow tract model displaying cross-sectional planes (*I*, *M*, and *O*) and four points on each plane used for analysis in **c**–**e**. (**c**–**e**) Wall shear stress at the four points on plane *l* (**c**), plane *M* (**d**), and plane *O* (**e**)

stresses and circumferential strain of the endocardium and myocardium [17]. Myocardial wall stress was estimated using the Laplace law where pressure, radius, and wall thickness are utilized to determine stress. Circumferential strain was estimated by measuring the change in circumference in comparison to the maximum circumference divided by the maximum circumference for the five orthogonal slices. Also, the model was validated by comparing blood velocity obtained from the OCT data along the centerline with blood velocity predicted in the model. It was found that circumferential strain in the myocardium and endocardium decreased distally, and myocardial wall stresses increased distally.

Also, the surface of the cardiac cushions experienced maximal wall shear stresses. Although modeling only approximates the measurements, it can be a useful tool when technology is incapable of obtaining the results.

65.6 Conclusion

Several robust techniques have been developed for 4-D OCT imaging. The first wave of technology development saw the implementation of a varied set of gating techniques. Image-based retrospective gating has now become the standard technique, and research groups are starting to focus on measurements that can be made exclusively with 4-D OCT datasets (e.g., mapping shear stress patterns [19]). Stresses and strains on the myocardium and endocardium are beginning to be measured from OCT images [59–61], and eventually 4-D imaging may allow maps of stress and strain across the entire heart. Also, one can now use these new metrics to differentiate abnormal from normal function. For example, 4-D OCT confirmed slower blood filling in hearts exposed to acute hypoxia [62]. 4-D OCT could become a powerful screening tool early in embryonic development as heart function can be a sensitive gauge of normalcy of cardiogenesis. Ultimately, one would like to utilize 4-D OCT to determine how biophysical forces modulate molecular expression and lead to congenital heart defects. Garita et al. began to correlate the location of mechanotransducing molecules (e.g., fibronectin, tenascin C, α-tubulin, and nonmuscle myosin II) with specific cardiac structures in OCT and optical coherence microscopy (OCM) images [58]. Future work must focus on applying 4-D OCT imaging to help identify signaling pathways that are activated by biophysical forces and which pathways present the biggest threat to developing CHDs.

Acknowledgments The authors wish to thank Lindsy Peterson, Shi Gu, Ganga Karanamuni, Madhusudhana Gargesha, David L. Wilson, and Michiko Watanabe for their contributions. Some research presented here was supported in part by the National Institutes of Health (RO1HL083048, R01HL095717, R21HL115373), the Interdisciplinary Biomedical Imaging Training Program NIH T32EB007509, and the American Recovery and Reinvestment Act (ARRA) funds through NHLBI, NIH grant number R01HL091171.

References

1. M.E. Mitchell et al., The molecular basis of congenital heart disease. Semin. Thorac. Cardiovasc. Surg. **19**(3), 228–237 (2007)
2. C.N. Steeg, P. Woolf, Cardiovascular malformations in the fetal alcohol syndrome. Am. Heart J. **98**(5), 635–637 (1979)
3. C.A. Neill, Etiology of congenital heart disease. Cardiovasc. Clin. **4**(3), 137–147 (1972)
4. A. Tintu et al., Hypoxia induces dilated cardiomyopathy in the chick embryo: mechanism, intervention, and long-term consequences. PLoS One **4**(4), e5155 (2009)
5. J. Wikenheiser et al., Altered hypoxia-inducible factor-1 alpha expression levels correlate with coronary vessel anomalies. Dev. Dyn. **238**(10), 2688–2700 (2009)

6. B. Hogers et al., Extraembryonic venous obstructions lead to cardiovascular malformations and can be embryolethal. Cardiovasc. Res. **41**(1), 87–99 (1999)
7. B. Hogers et al., Unilateral vitelline vein ligation alters intracardiac blood flow patterns and morphogenesis in the chick embryo. Circ. Res. **80**(4), 473–481 (1997)
8. J.R. Hove et al., Intracardiac fluid forces are an essential epigenetic factor for embryonic cardiogenesis. Nature **421**(6919), 172–177 (2003)
9. M. Reckova et al., Hemodynamics is a key epigenetic factor in development of the cardiac conduction system. Circ. Res. **93**(1), 77–85 (2003)
10. J. Vermot et al., Reversing blood flows act through klf2a to ensure normal valvulogenesis in the developing heart. PLoS Biol. **7**(11), e1000246 (2009)
11. K. Yashiro, H. Shiratori, H. Hamada, Haemodynamics determined by a genetic programme govern asymmetric development of the aortic arch. Nature **450**(7167), 285–288 (2007)
12. D. Panakova, A.A. Werdich, C.A. Macrae, Wnt11 patterns a myocardial electrical gradient through regulation of the L-type Ca(2+) channel. Nature **466**(7308), 874–878 (2010)
13. N.C. Chi et al., Cardiac conduction is required to preserve cardiac chamber morphology. Proc. Natl. Acad. Sci. U. S. A. **107**(33), 14662–14667 (2010)
14. R.E. Godt, R.T. Fogaca, T.M. Nosek, Alterations of myocardial contraction associated with a structural heart defect in embryonic chicks. Adv. Exp. Med. Biol. **453**, 453–458 (1998). discussion 459
15. B. Sankova, J. Machalek, D. Sedmera, Effects of mechanical loading on early conduction system differentiation in the chick. Am. J. Physiol. Heart Circ. Physiol. **298**(5), H1571–H1576 (2010)
16. M.W. Jenkins, M. Watanabe, A.M. Rollins, Longitudinal imaging of heart development with optical coherence tomography. Sel. Top. Quantum Electron. IEEE J **18**(3), 1166–1175 (2012)
17. A. Liu et al., Biomechanics of the chick embryonic heart outflow tract at HH18 using 4D optical coherence tomography imaging and computational modeling. PLoS Biol. **7**(7), e40869 (2012)
18. I.V. Larina et al., Imaging mouse embryonic cardiovascular development. Cold Spring Harb. Protoc. **2012**(10), 1035 (2012). p. pdb.top071498
19. L.M. Peterson et al., 4D shear stress maps of the developing heart using Doppler optical coherence tomography. Biomed. Opt. Express **3**(11), 3022–3032 (2012)
20. S.A. Boppart et al., Noninvasive assessment of the developing Xenopus cardiovascular system using optical coherence tomography. Proc. Natl. Acad. Sci. U. S. A. **94**(9), 4256–4261 (1997)
21. T.M. Yelbuz et al., Optical coherence tomography: a new high-resolution imaging technology to study cardiac development in chick embryos. Circulation **106**(22), 2771–2774 (2002)
22. V.X. Yang et al., High speed, wide velocity dynamic range Doppler optical coherence tomography (Part II): Imaging in vivo cardiac dynamics of *Xenopus laevis*. Opt. Express **11**(14), 1650–1658 (2003)
23. M.A. Choma et al., Images in cardiovascular medicine: in vivo imaging of the adult *Drosophila melanogaster* heart with real-time optical coherence tomography. Circulation **114**(2), e35–e36 (2006)
24. U.J. Schoepf et al., Electrocardiographically gated thin-section CT of the lung. Radiology **212**(3), 649–654 (1999)
25. Y.P. Du et al., A comparison of prospective and retrospective respiratory navigator gating in 3D MR coronary angiography. Int. J. Cardiovasc. Imaging **17**(4), 287–294 (2001). discussion 295-6
26. M.W. Jenkins et al., 4D embryonic cardiography using gated optical coherence tomography. Opt. Express **14**(2), 736–748 (2006)
27. M.W. Jenkins et al., In vivo gated 4D imaging of the embryonic heart using optical coherence tomography. J. Biomed. Opt. **12**(3), 030505 (2007)
28. S. Yun et al., High-speed optical frequency-domain imaging. Opt. Express **11**(22), 2953–2963 (2003)
29. A.F. Fercher et al., Measurement of Intraocular distances by backscattering spectral interferometry. Opt. Commun. **117**(1–2), 43–48 (1995)

30. J.F. de Boer et al., Improved signal-to-noise ratio in spectral-domain compared with time-domain optical coherence tomography. Opt. Lett. **28**(21), 2067–2069 (2003)
31. R. Leitgeb, C. Hitzenberger, A. Fercher, Performance of Fourier domain vs. time domain optical coherence tomography. Opt. Express **11**(8), 889–894 (2003)
32. M. Choma et al., Sensitivity advantage of swept source and Fourier domain optical coherence tomography. Opt. Express **11**(18), 2183–2189 (2003)
33. R. Huber, M. Wojtkowski, J.G. Fujimoto, Fourier Domain Mode Locking (FDML): a new laser operating regime and applications for optical coherence tomography. Opt. Express **14**(8), 3225–3237 (2006)
34. M.W. Jenkins et al., Ultrahigh-speed optical coherence tomography imaging and visualization of the embryonic avian heart using a buffered Fourier Domain Mode Locked laser. Opt. Express **15**(10), 6251–6267 (2007)
35. M. Gargesha et al., Denoising and 4D visualization of OCT images. Opt. Express **16**(16), 12313–12333 (2008)
36. R. Yelin et al., Multimodality optical imaging of embryonic heart microstructure. J. Biomed. Opt. **12**(6), 064021 (2007)
37. W. Wieser et al., Multi-megahertz OCT: high quality 3D imaging at 20 million A-scans and 4.5 GVoxels per second. Opt. Express **18**(14), 14685–14704 (2010)
38. Y.F. Jian, K. Wong, M.V. Sarunic, Graphics processing unit accelerated optical coherence tomography processing at megahertz axial scan rate and high resolution video rate volumetric rendering. J. Biomed. Opt. **18**(2), 26002 (2013)
39. K. Zhang, J.U. Kang, Graphics processing unit-based ultrahigh speed real-time Fourier domain optical coherence tomography. IEEE J. Sel. Top. Quantum Electron. **18**(4), 1270–1279 (2012)
40. D.H. Choi et al., Spectral domain optical coherence tomography of multi-MHz A-scan rates at 1310 nm range and real-time 4D-display up to 41 volumes/second. Biomed. Opt. Express **3**(12), 3067 (2012)
41. S. Yazdanfar, M. Kulkarni, J. Izatt, High resolution imaging of in vivo cardiac dynamics using color Doppler optical coherence tomography. Opt. Express **1**(13), 424–431 (1997)
42. A. Mariampillai et al., Doppler optical cardiogram gated 2D color flow imaging at 1000 fps and 4D in vivo visualization of embryonic heart at 45 fps on a swept source OCT system. Opt. Express **15**(4), 1627–1638 (2007)
43. M. Liebling et al., Four-dimensional cardiac imaging in living embryos via postacquisition synchronization of nongated slice sequences. J. Biomed. Opt. **10**(5), 054001-054001 (2005)
44. M. Gargesha et al., High temporal resolution OCT using image-based retrospective gating. Opt. Express **17**(13), 10786–10799 (2009)
45. A. Liu et al., Efficient postacquisition synchronization of 4-D nongated cardiac images obtained from optical coherence tomography: application to 4-D reconstruction of the chick embryonic heart. J. Biomed. Opt. **14**(4), 044020–044020 (2009)
46. M.M. Dworetsky, A period-finding method for sparse randomly spaced observations of 'How long is a piece of string?'. Mon. Not. R. Astron. Soc. **203**, 917–924 (1983)
47. R.F. Stellingwerf, Period determination using phase dispersion minimization. Astrophys. J. **224**, 953–960 (1978)
48. C.M. Happel et al., Rotationally acquired four-dimensional optical coherence tomography of embryonic chick hearts using retrospective gating on the common central A-scan. J. Biomed. Opt. **16**(9), 096007–096007 (2011)
49. I.V. Larina et al., Sequential turning acquisition and reconstruction (STAR) method for four-dimensional imaging of cyclically moving structures. Biomed. Opt. Express **3**(3), 650–660 (2012)
50. S. Bhat et al., 4D reconstruction of the beating embryonic heart from two orthogonal sets of parallel optical coherence tomography slice-sequences. Med. Imaging IEEE Trans. on **32**(3), 578–588 (2013)
51. S. Bhat et al., Multiple-cardiac-cycle noise reduction in dynamic optical coherence tomography of the embryonic heart and vasculature. Opt. Lett. **34**(23), 3704–3706 (2009)

52. J. Yoo et al., Increasing the field-of-view of dynamic cardiac OCT via post-acquisition mosaicing without affecting frame-rate or spatial resolution. Biomed. Opt. Express **2**(9), 2614–2622 (2011)
53. Z. Ma et al., Measurement of absolute blood flow velocity in outflow tract of HH18 chicken embryo based on 4D reconstruction using spectral domain optical coherence tomography. Biomed. Opt. Express **1**(3), 798–811 (2010)
54. M. Kass, A. Witkin, D. Terzopoulos, Snakes – active contour models. Int. J. Comp. Vision **1**(4), 321–331 (1988)
55. M.W. Jenkins et al., Measuring hemodynamics in the developing heart tube with four-dimensional gated Doppler optical coherence tomography. J. Biomed. Opt. **15**(6), 066022 (2010)
56. R.M. Goldstein, H.A. Zebker, C.L. Werner, Satellite radar interferometry – two-dimensional phase unwrapping. Radio Sci. **23**(4), 713–720 (1988)
57. M. Sato et al. TEASAR: Tree-structure extraction algorithm for accurate and robust skeletons, in *Proceedings of the Eighth Pacific Conference on Computer Graphics and Applications*, 2000, pp. 281–287, 449.
58. B. Garita et al., Blood flow dynamics of one cardiac cycle and relationship to mechanotransduction and trabeculation during heart looping. Am. J. Physiol. Heart Circ. Physiol. **300**(3), H879–H891 (2011)
59. A. Liu et al., Quantifying blood flow and wall shear stresses in the outflow tract of chick embryonic hearts. Comp. Struct. **89**(11–12), 855–867 (2011)
60. P. Li et al., In vivo functional imaging of blood flow and wall strain rate in outflow tract of embryonic chick heart using ultrafast spectral domain optical coherence tomography. J. Biomed. Opt. **17**(9), 096006 (2012)
61. P. Li, R.K.K. Wang, Optical coherence tomography provides an ability to assess mechanical property of cardiac wall of developing outflow tract in embryonic heart in vivo. J. Biomed. Opt. **17**(12), 120502 (2012)
62. S. Gu et al., Optical coherence tomography captures rapid hemodynamic responses to acute hypoxia in the cardiovascular system of early embryos. Dev. Dyn. **241**(3), 534–544 (2012)

OCT and Coherence Imaging for the Neurosciences

66

Jonghwan Lee and David A. Boas

66.1 Introduction

The brain plays a central role in most of our life's activity, including consciousness, perception, limb control, emotion, communication, and logical thinking. While the brain has been an intense subject of human interest since the beginning of human history, it is only relatively recently that science and technology has started to unveil the mystery of how the brain works.

The most fundamental building block of the brain is the neuron. Neurons are small cells consisting of a body ($\sim$10 μm in diameter) and projections (typically $>$100 μm). It has two types of projections: axons and dendrites. A neuron accepts electrochemical signal inputs from other neurons through its dendrites, integrates these inputs at its body to determine whether to fire an output signal, and then sends the output through its axon to other neurons. The connections between neurons are called synapses, where an axon meets with a dendrite and electrical signals are transmitted in a chemical way mediated by neurotransmitters. The human brain is an immensely complex system, consisting of about one hundred billion ($\sim 10^{11}$) neurons and one hundred trillion ($\sim 10^{14}$) synapses. These neurons and synapses form a huge neuronal network, and information processing within our brain is accomplished by the complex communications occurring in the network. Therefore, measuring and imaging neuronal activity in the living brain are critical prerequisites for studying how the brain works.

Neuronal activity is based on a difference in the electrical potential across the neuron's membrane due to an imbalance of ionic concentrations (sodium and potassium are more abundant in extracellular and intracellular spaces, respectively).

J. Lee (✉) • D.A. Boas
Martinos Center for Biomedical Imaging, Massachusetts General Hospital, Harvard Medical School, Charlestown, MA, USA
e-mail: jonghwan@nmr.mgh.harvard.edu; dboas@nmr.mgh.harvard.edu

© Springer International Publishing Switzerland 2015

W. Drexler, J.G. Fujimoto (eds.), *Optical Coherence Tomography*,
DOI 10.1007/978-3-319-06419-2_68

When a neuron is excited (i.e., depolarized), sodium ions flow into and potassium ions flow out of the neuron across its membrane, weakening the initial ionic unbalance. Since the initial imbalance is important for normal functioning of neurons, neurons have active (ATP-consuming) pumps to draw potassium into and pump sodium out of them, restoring the ionic unbalance. Oxygen and glucose are supplied to meet these metabolic needs for the neuron's active pumping of ions, location by location, moment to moment. The regulated supply of oxygen and glucose is particularly important since the brain has a very limited reserve of these energy substrates. Oxygen and glucose are mainly supplied by cerebral blood flow (CBF). The current paradigm for understanding this brain's energy supply regulation is neurovascular coupling, a range of mechanisms underlying how local neuronal activity adjusts arteriolar tone (and thus local CBF) to meet the spatiotemporally varying metabolic needs. As the brain's blood flow regulation is critical for its normal functioning and thus relates with various brain diseases, neurovascular coupling and the associated hemodynamic responses are important subjects in the neurosciences.

This chapter describes how optical coherence tomography (OCT)-based technologies have advanced in vivo imaging of neuronal and vascular dynamics occurring within the brain cortex. OCT enables μm-resolution and high-speed imaging of tissue structure [1], facilitating a number of basic and clinical studies in ophthalmology [2], cancer biology [3], and neuroscience [4]. In this chapter, we describe OCT-based technologies for μm-resolution imaging of tissue dynamics, especially in the brain cortex of a living animal. First, as CBF plays an important role in normal brain function, we review OCT imaging techniques for quantitative measurement of CBF in the resting-state brain. Traditional Doppler OCT has been used for this purpose, and recently integration of OCT with dynamic light scattering analysis has been suggested. Next, as CBF transiently varies in response to brain activation, this chapter also describes how OCT technologies have advanced imaging of neurovascular coupling and led to novel findings. Dynamic OCT imaging of the brain cortex suggests that the OCT signal spatiotemporally varies in response to brain activation, providing a laminar profile of the response. Furthermore, the high imaging speed and spatial resolution of OCT enables monitoring of blood flow responses not only in arteries and veins but also within the network of capillaries. While these hemodynamic responses occur on the timescale of several seconds, excitation of neurons occurs much faster, on the timescale of milliseconds. Therefore, this chapter will finish by discussing the feasibility of imaging fast neuronal activity with OCT. OCT-based technologies introduced in this chapter, for in vivo imaging of cerebral cortex dynamics ranging from milliseconds to hours, have enabled a range of important new studies of the healthy and diseased brain.

66.2 OCT Imaging of Cerebral Blood Flow Velocity: Steady-State Dynamics

CBF is a physiological quantity that is closely related with healthy brain functions and thereby is important for the study of brain pathophysiology. It has thus far been

measured with various optical methods. Laser Doppler flowmetry is used to measure blood flow at a fixed point [5, 6], and its imaging corollary provides a 2-D map of blood flow [7]. Doppler OCT enables depth-resolved measurement of axial flow velocity with microscopic resolution, resulting in a 3-D map of blood flow [8]. This section describes this application of Doppler OCT to quantitative imaging of CBF. Then, we review a recently proposed method that integrates OCT with dynamic light scattering analysis to measure both the axial and transverse components of CBF velocity.

66.2.1 Doppler OCT Imaging of CBF

Doppler OCT generally repeats A-scans at a fixed position to measure temporal variations in the phase of the OCT signal. The phase variation is approximately linearly dependent on the axial motion of scatterers in the given voxel and thus can be used for quantification of the velocity of scatterer flow [9, 10]. This Doppler OCT measurement of the axial flow velocity can be used to perform absolute measurements of CBF either by estimating vessel angles [11] or by processing volumetric data [12]. In detail, using three-dimensional Doppler OCT and cranial window preparations, Srinivasan et al. introduced a method of absolute flow calculation that does not require explicit knowledge of vessel angles. They showed that OCT estimates of absolute CBF values in rats agree with prior measures by hydrogen clearance, a gold-standard measurement of CBF (Fig. 66.1).

Doppler OCT imaging of CBF displays features characteristic of general blood flow, including conservation along non-branching vascular segments and at branch points [13]. For example, Fig. 66.2 shows how Doppler OCT-measured CBF confirms the conservation of flow at branching vessels. In addition, this study demonstrated that Doppler OCT flow values correlate with hydrogen clearance flow values when both are measured simultaneously. These data validated Doppler OCT as a noninvasive quantitative method to measure tissue perfusion.

66.2.2 Dynamic Light Scattering Optical Coherence Tomography (DLS-OCT)

While Doppler OCT generally measures the axial component of CBF velocity, a recently proposed method integrating OCT with dynamic light scattering (DLS) analysis enables measurement of the transverse component of flow velocity independently of and simultaneously with the axial velocity. This section provides a technical description of the integration, DLS-OCT, and the next section discusses its application to brain cortex imaging. DLS is widely used to quantify the dynamics of scattering particles by analyzing the autocorrelation function of light scattered from the particles, enabling an analysis of the particles' diffusion and/or flow velocity [14–16]. Integration of DLS with OCT will provide μm-resolution 3-D imaging of heterogeneous diffusion and flow but requires a suitable

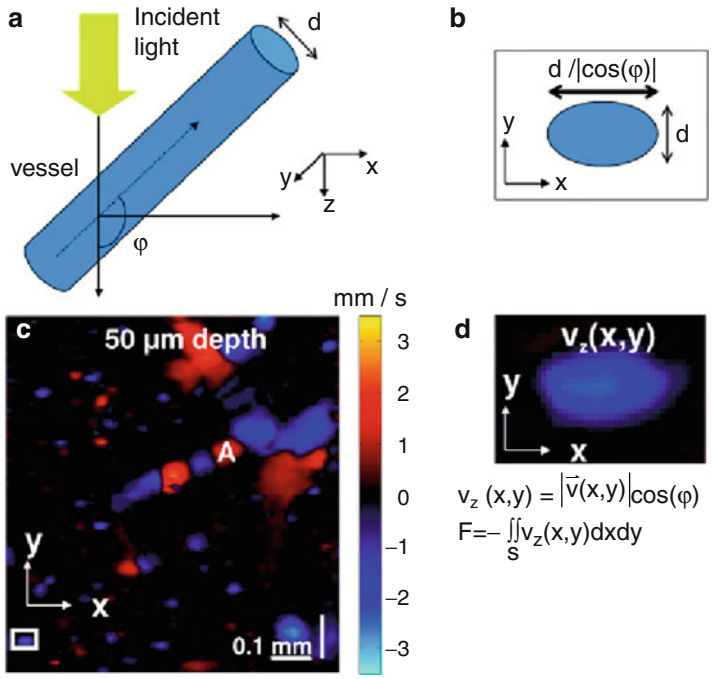

Fig. 66.1 Calculation of CBF from Doppler OCT measurement of the flow velocity. (**a**) Blood vessels can be oriented at any angle φ relative to the incident light. (**b**) The area of the vessel in the en face (*xy*) plane is inversely proportional to cos(φ). (**c**) En face cut at a depth of 50 μm through a 3-D map of the axial velocity (averaged over ten volumes). (**d**) Zoom of a venule showing the axial component of flow velocity over the vessel cross section (upsampled to reduce pixellation). While the area of the vessel in the xy plane is inversely proportional to cos(φ), the axial component of the velocity is proportional to cos(φ). Therefore, the flow F can be obtained from the en face map of the axial velocity, $v_z(x,y)$ (Reprinted from [12] with permission)

DLS theory [17–22] for accurate implementation. Recently, Lee et al. proposed such a DLS theory by deriving the field autocorrelation function directly from the complex-valued OCT signal and validated DLS-OCT measurement of diffusion and flow through phantom experiments [23].

Dynamic OCT imaging of a sample produces four-dimensional (space and time) data of the complex-valued reflectivity, $R(\mathbf{r}, t)$. The field autocorrelation function is obtained as

$$g(\mathbf{r},\tau) = E\left[\frac{\langle R^*(\mathbf{r},t)R(\mathbf{r},t+\tau)\rangle_t}{\langle R^*(\mathbf{r},t)R(\mathbf{r},t)\rangle_t}\right] \tag{66.1}$$

where * denotes the complex conjugate, $< >_t$ indicates an average over time, and $E[\ ]$ means the average over initial positions of the scatterers. When static

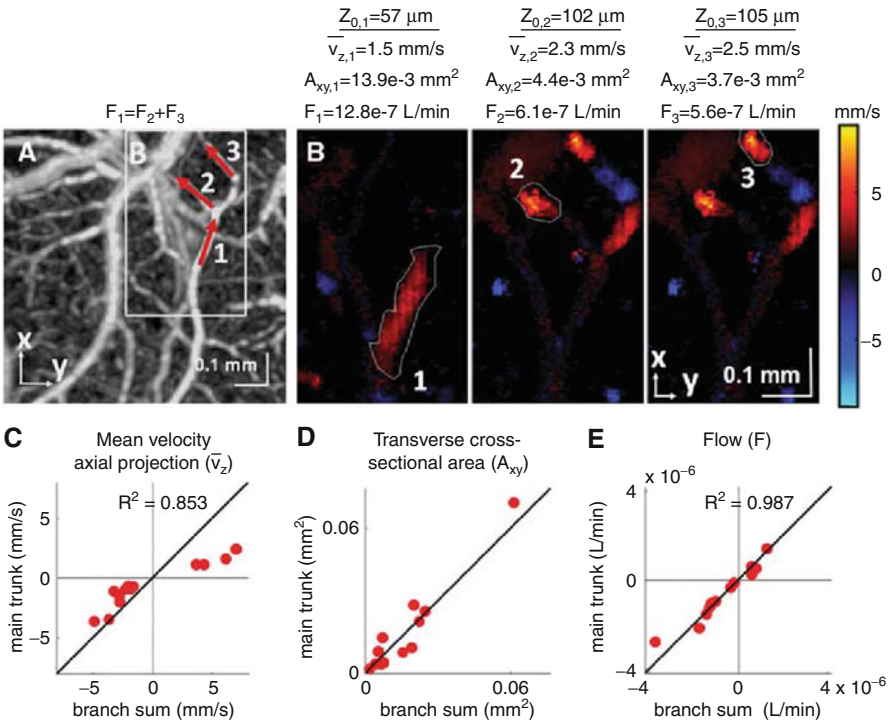

Fig. 66.2 Conservation of Doppler OCT-measured CBF at branch points in a thinned rat skull preparation. (**a**) OCT angiogram showing three locations in a branching vessel. (**b**) En face Doppler OCT images, presenting the axial flow velocity, at two depths corresponding to the main trunk location (*1*) and two branch locations (*2*, *3*) shown in panel A. Plots of mean axial velocity (**c**), transverse cross-sectional area (**d**), and flow (**e**) in the main trunk and summed over branches in 13 branching vessels are shown (Reprinted from [13] with permission)

and moving particles are mixed in the OCT probing volume and the moving particles can exhibit either translational or diffusive motion (Fig. 66.3a), the OCT signal can be expressed by

$$R(t) = \sum_{j=1}^{N_S} e^{-2h^2 r_{Sj}^2} e^{iqz_{Sj}} + \sum_{j=1}^{N_F} e^{-2h^2 r_{Fj}^2(t)} e^{iqz_{Fj}(t)} + \sum_{j=1}^{N_E} e^{-2h^2 r_{Ej}^2(t)} e^{iqz_{Ej}(t)} \qquad (66.2)$$

where q is the representative scattering vector and h is the inverse of voxel size. The scattering cross sections of the particles are considered to be similar. Detailed descriptions of the other quantities and assumptions are given in [23]. The movement of a particle can be expressed by the self-interaction term of the Van Hove space-time correlation function [24], that is, the probability that the particle which was initially at position $\mathbf{r_i}$ at time t_i is found at position $\mathbf{r_f}$ at time t_f, $P_1(\mathbf{r_f}, t_f|\mathbf{r_i}, t_i)$.

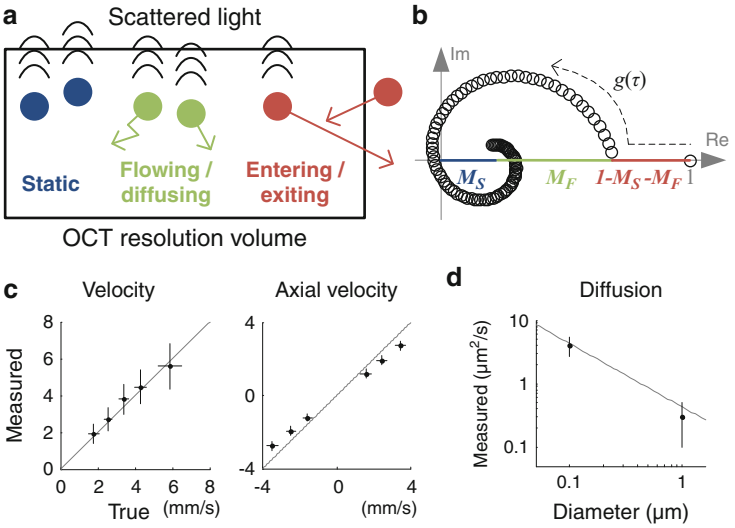

Fig. 66.3 Theory and validation of DLS-OCT. (**a**) Particles within the OCT resolution volume can be categorized into three groups: static, flowing or diffusing, and entering or exiting particles. For clarification, entering/exiting particles enter into or exit out of the voxel during a single measurement time step, resulting in stochastic fluctuations of the OCT signal. (**b**) The general behavior of the field autocorrelation function in the complex plane predicted by DLS-OCT theory. M_S and M_F are approximately proportional to the fractions of static and flowing/diffusing particles, respectively, weighted by their scattering cross sections. It adequately explained the measured ones. (**c**) Phantom validation of DLS-OCT measurement of the flow velocity using a piezoelectrical sample with controlled velocity. The velocity (*left*) means the absolute velocity, $(v_t^2 + v_z^2)^{1/2}$. (**d**) Phantom validation of DLS-OCT measurement of the diffusion coefficient using microsphere samples with different diameters. The *gray line* shows the Einstein-Stroke equation (Reprinted from [23] with permission)

The probability of a particle exhibiting both translational and diffusive motions with the velocity v and the diffusion coefficient D can be formulated by

$$P_1\left(\mathbf{r_f}, t_f | \mathbf{r_i}, t_i\right) = \frac{1}{2\sqrt{\pi D\left(t_f - t_i\right)}} e^{-\frac{\left|\mathbf{r_f} - \mathbf{r_i} - v\left(t_f - t_i\right)\right|^2}{4D\left(t_f - t_i\right)}}. \tag{66.3}$$

Then, the field autocorrelation function of the OCT signal (Eq. 66.2) whose $r_F(t)$ and $z_F(t)$ satisfy Eq. 66.3 was obtained as

$$\begin{aligned} g(\mathbf{r}, \tau) = {} & M_S(\mathbf{r}) + M_F(\mathbf{r})\, e^{-h_t^2 v_t^2(\mathbf{r})\tau^2 - h^2 v_z^2(\mathbf{r})\tau^2} e^{-q^2 D(\mathbf{r})\tau} e^{iq v_z(\mathbf{r})\tau} \\ & + \left[1 - M_S(\mathbf{r}) - M_F(\mathbf{r})\right]\delta(\tau) \end{aligned} \tag{66.4}$$

where $M_S(\mathbf{r})$, $M_F(\mathbf{r})$, $v_t(\mathbf{r})$, $v_z(\mathbf{r})$, and $D(\mathbf{r})$ are the parameters of particle dynamics to be estimated for each position while the others are the parameters given by the

measurement system. M_S is the fraction of the static particles, M_F is the fraction of the moving particles, v_t is the transverse component of the flow velocity, v_z is the axial component, and D is the effective diffusion coefficient quantifying the diffusive motion of particles as in Eq. 66.3. This autocorrelation function adequately explained the general behavior of the experimental measurements (Fig. 66.3b).

Phantom experiments validated DLS-OCT measurement of the flow velocity and diffusion (Fig. 66.3c). For the velocity measurement, a piezoelectrically actuated static sample was used to simulate axial movements of particles while transverse movements were implemented by galvanometric lateral scanning of the OCT beam. The absolute and axial velocities were reliably measured across various true values of the flow velocity and angle. Microsphere samples of 0.1 and 1 μm in diameter were used for validating the diffusion measurement. The measured diffusion coefficient agreed with the theoretical values given by the Einstein-Stokes equation. The diffusion coefficient was estimated to be sufficiently small in the velocity phantom experiment, while the diffusion phantom experiment resulted in negligible velocities. These results confirmed that DLS-OCT can effectively distinguish whether the motion is translational or diffusive and accurately measure either the flow velocity or the diffusion coefficient.

66.2.3 DLS-OCT Imaging of CBF Velocity

Based on the validated DLS-OCT measurement of the flow velocity and diffusion coefficient, DLS-OCT imaging of the living rodent cortex was performed. A-scans were repeated 100 times over ~2 ms at a fixed position, and the position was moved in a raster manner to scan the volume of interest of the cortex. The 4D (space and time) complex-valued field reflectivity of the sample was obtained and then was used to produce the 4D (space and time lag) autocorrelation function data. Analysis of the 4D autocorrelation function data led to 3-D maps of the transverse and axial velocities, the diffusion coefficient, and the coefficient of determination (R^2).

As shown in Fig. 66.4a, the absolute velocity map clearly revealed the structure of the vascular anatomy and cerebral blood flow. The axial velocity map showed the axial component of the flow velocity, which looked very similar to conventional Doppler OCT images (e.g., Fig. 66.1c). The flow direction determined by the axial and transverse velocities agreed with the structural direction of vessels (Fig. 66.4a, right).

When the diffusion map is overlaid with the absolute velocity map (Fig. 66.4b), high-diffusion and low-velocity voxels were observed at the boundary of vessels. Interestingly, the vessel boundaries also exhibited a characteristic low coefficient of determination (Fig. 66.4c). Single-plane images without projection clearly showed the result that the vessel boundaries exhibit high diffusion, low velocity, and low R^2. At the circular cross-sections of the vessels (Fig. 66.4c, blue arrows), high-velocity and high-R^2 blood flow are surrounded by the high-diffusion, low-velocity, and low-R^2 dynamics of the vessel boundaries. In particular, the low R^2 means that

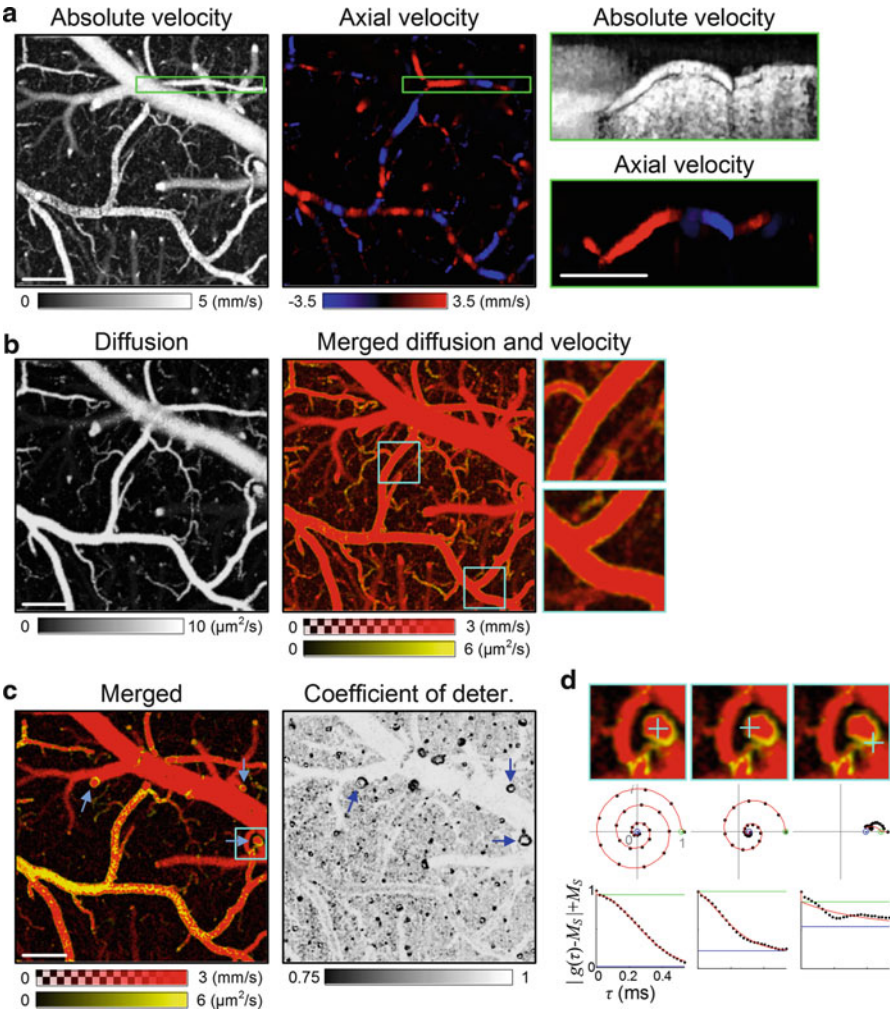

Fig. 66.4 DLS-OCT imaging of the brain cortex in a rat thinned skull preparation. (**a**) The first image presents the maximum projection (MP) of the 3-D map of the absolute velocity along the depth (i.e., en face), and the second image presents the en face signed maximum projection (SMP) of the 3-D map of the axial velocity. The images with the *green* boundary show the MP of absolute velocity and the SMP of the axial velocity along the transverse direction (i.e., cross-sectional) over the volume indicated as the *green box* in the en face images. The SMPs of the axial velocity are presented over the range from $-5/\sqrt{2}$ to $5/\sqrt{2}$ mm/s, where a negative velocity (*blue color*) means that blood flows toward the surface of the cortex. (**b**) The first image presents the en face MP of the 3-D map of the diffusion coefficient. In the second image, the diffusion image (*yellow*) is overlaid with the absolute velocity image (*red*). The 3× magnified images of the *cyan* boxes are presented to clearly show the characteristic dynamics of the vessel boundaries. This merged image is presented with smaller ranges of the velocity and diffusion coefficient for higher contrast. (**c**) Single planes of the merged map and the coefficient of determination map at a depth of 120 μm are presented. (**d**) Examples of the autocorrelation function are presented for three voxels (*cyan crosses*) that are located in the plane indicated as the *cyan box* in (*C*). The *middle*

the motion was neither translational nor diffusive; it might be oscillatory due to the interaction between blood flow and the tension of the vessel walls.

In addition to CBF imaging, DLS-OCT maps revealed another interesting dynamic occurring in the brain cortex. Along with high-NA OCT structural imaging, which identifies neuronal cell bodies in its minimum intensity projection (Fig. 66.5, MinIP; [25]), high-NA DLS-OCT imaging was performed on the cortex. The diffusion map revealed high-diffusion spots in the nonvascular area. They are different from vessel boundaries in that they showed high R^2 whereas the vessel walls exhibited the characteristic low R^2 values. Therefore, another map was introduced to represent diffusion masked with high R^2 ($R^2 > 0.998$, green color in Fig. 66.5). These high-diffusion high-R^2 green spots were morphologically confined when viewed in 3-D, whereas the high diffusion observed at vessel walls extended over a vascular segment. The positions of the green spots were highly correlated with those of neuronal cell bodies. Meanwhile, the green spots generally did not fill the whole area of cell bodies (e.g., Fig. 66.5b). Some of their morphology (e.g., the first three in Fig. 66.5b, where green spots surround a smaller dark sphere), was quite similar to those of intracellular motility in the cytoplasm observed in a high-resolution in vitro imaging study [26]. The mean diffusion as a function of the distance from the nucleic center also showed that the peak diffusion did not locate at the center of cell bodies (Fig. 66.5c). These results on morphology suggest that the green spots are distributed over the space surrounding nuclei, likely in the cytoplasm. Finally, the diffusion coefficient of the spots agrees with those of the motion of intracellular organelles measured in vitro [27–29]. Therefore, the green spots likely represent the diffusion-like movements of intracellular organelles.

66.3 OCT Imaging of Hemodynamic Responses: Second-Timescale Transient Dynamics

As described in the Introduction, when the brain is activated, additional oxygen and glucose should be supplied via increased blood flow in association with spatiotemporally varying metabolic needs. Neurovascular coupling represents the current paradigm for understanding this energy supply regulation of the brain. This current paradigm focuses on how local neuronal activity adjusts arteriolar tone (and thus local CBF) in association with metabolic needs ([30] for review). A number of studies have discovered a range of mechanisms underlying this coupling. Neurotransmitter-mediated signaling from neurons and astrocytes to vascular smooth muscles that dilate and constrict arterioles plays a major role in regulating CBF [31, 32]. When this energy supply regulation does not work, neurons and glia

Fig. 66.4 (continued) row shows the autocorrelation function data (*black dots*) and their fits (*red lines*) in the complex plane, where the estimated M_S and $M_S + M_F$ are presented as the *blue* and *green circles*, respectively. The *bottom row* shows decay of the M_F-terms. The coefficients of determination of these three voxels are $R^2 = 0.999$, 0.988, and 0.647. All scale bars, 100 μm (Reprinted from [23] with permission)

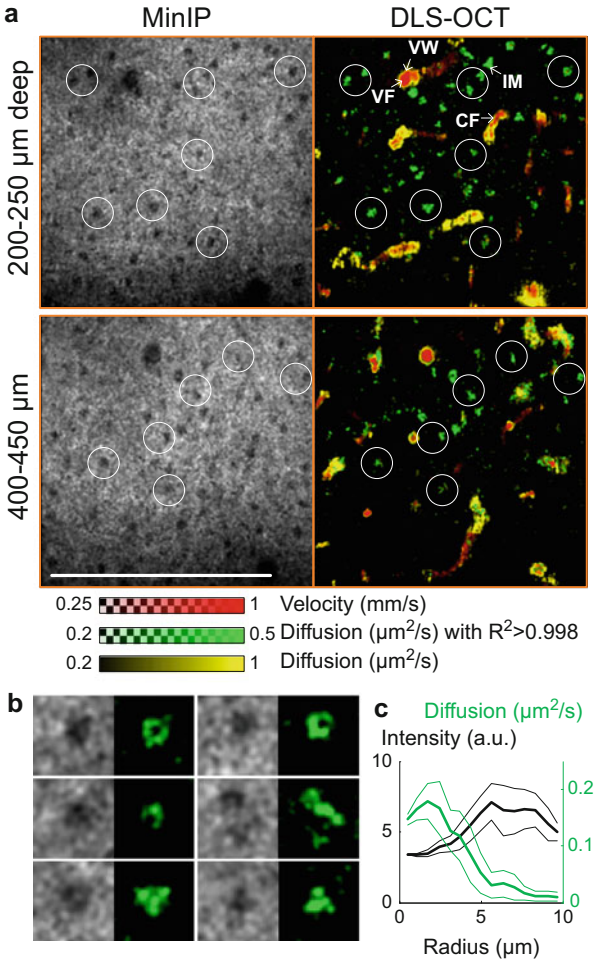

Fig. 66.5 DLS-OCT imaging of neuronal intracellular motility. (**a**) High-NA DLS-OCT imaging of the brain cortex. The velocity and diffusion images (*red* and *yellow*) are superimposed with the map of diffusion with high R^2 (*green*). *White circles* are collocated to visually guide the spatial correlation between the positions of neuronal cell bodies (*dark spots* in MinIP) and neuronal IM (*green spots*). Not all cell bodies are marked. *VF* vessel flow, *CF* capillary flow, and *VW* vessel wall. The small range of the diffusion coefficient is used to increase the image contrast. Scale bar, 200 μm. (**b**) Several examples of neuronal nuclei observed in MinIP and neuronal IM observed in the high-R^2 diffusion map. Image size, 25 × 25 μm, for each. (**c**) The mean intensity (*black*) and diffusion (*green*) as the function of the distance from the nucleic centers ($n = 10$) (Data are presented in mean ± SD) (Reprinted from [94] with permission)

become injured or die. Since such an inadequate supply occurs in various disorders of the brain, understanding the mechanisms is a prerequisite for developing therapies to correct defects in blood flow control occurring in stroke [33], hypertension [34], and Alzheimer's disease [33]. This section describes how OCT can

advance in vivo imaging of neurovascular coupling. This section introduces studies that used OCT for imaging of such neurovascular coupling.

The current paradigm has recently been challenged by the concept that capillaries also contribute to blood flow regulation in response to neuronal activity, so-called neuro-capillary coupling. This concept is supported by recent studies showing that contractile cells called pericytes can control the diameter of capillaries [35], and substances altering the arteriole diameter can contract and relax pericytes as well [36], likely due to alteration of the intracellular Ca^{2+} concentration of pericytes [37]. For example, pericytes (and thus capillaries) constrict in response to noradrenaline and dilate in response to glutamate in brain slices [35]. Extending our knowledge of blood flow dynamics down to the capillary level will be helpful as the capillary bed works as a direct interface through which oxygen and glucose are supplied to the tissue. Regulation of blood flow at the capillary level, however, has been only demonstrated either in vitro or in pathological conditions [38, 39]. Capillary flow regulation in response to neural activation has yet to be demonstrated in vivo under physiological conditions [40], but this is advancing rapidly. Furthermore, there are controversial reports on the in vivo capillary flow responses. Being different from arterioles, capillaries have been reported to exhibit highly heterogeneous responses to neural activation [41, 42] and even nearly stochastic distributions during baseline [43], potentially masking neural activity-induced responses of single capillaries [44].

Due to the nature of capillary flow responses, demonstrating neuro-capillary coupling in vivo requires systematic measurement of blood flow over a reasonably large number of capillaries at the same time. To date, capillary flow responses have been measured by tracking fluorescence-labeled single RBCs with either video microscopy (VM) [43] or two-photon microscopy (TPM) [41, 45]. Those techniques, however, are generally not suitable for the systematic measurement of large numbers of capillaries since they measure the responses over only several capillaries within a single focal plane (VM) or capillary by capillary (TPM). Meanwhile, OCT generally enables a larger imaging volume per time, but the existing OCT-based technologies, including Doppler OCT and DLS-OCT described in the previous section, are still far from achieving the target number of capillaries (>100) with sufficient temporal resolution (~ 1 s) as they require many consecutive scans per position to estimate the flow speed [23, 46, 47]. This section introduces another OCT-based technology for measurement of flow speed and its application to high-speed volumetric imaging of blood flow speed over hundreds of capillaries at the same time.

66.3.1 Slow Changes in the OCT Signal Associated with Neural Activation

Intrinsic optical signal (IOS) generally images oxygenated and deoxygenated hemoglobin concentration at the surface of cortex. Therefore, it can image hemodynamic responses to neural activation while providing two-dimensional,

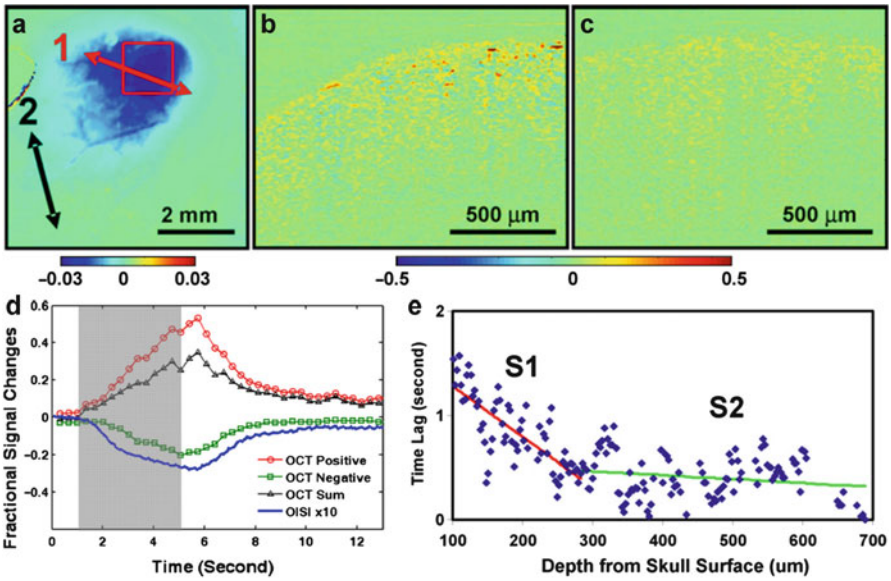

Fig. 66.6 IOS and OCT imaging of brain activation. (**a**) Localization of activation area in IOS imaging. Two OCT scans are denoted by *arrows 1* (*red*) and *2* (*black*). (**b**) Cross-sectional map of fractional changes in the OCT intensity at time window 4–6 s over the activation region denoted by the *arrow 1* during the stimulation of the contralateral forepaw. (**c**) Functional OCT image at time window 4–6 s over the scan denoted by *arrow 2*. (D) Plots of positive, negative, and summation OCT signals at regions with significance level $\alpha < 0.001$. The time course of IOS signal ($\times 10$) is also included to show the temporal correspondence. (**e**) Plot of the averaged time lags at the same depth (from the skull surface) versus the depth. Two distinct regions are indicated by different slopes (*S1* and *S2*) (Reprinted from [48] with permission)

depth-integrated activation maps of brain activity. Whereas general IOS imaging does not provide depth-dependent information of the hemodynamic response, OCT can measure the depth profile of neurovascular coupling. Chen et al. [48] performed IOS imaging to identify an activated region of rat somatosensory cortex during forepaw electrical stimulation and repeated OCT B-scans on the activated and control regions (Fig. 66.6a), resulting in 3-D (x,z,t) OCT data. At every voxel, a temporal fractional change in the OCT intensity signal was obtained with respect to its baseline. This functional OCT signal was significantly larger in the activated region (Figs. 66.6b, c). The mean of the functional OCT signals exhibits time courses similar to that of IOS, with a net positive change that occurs during the activation period (Fig. 66.6d). When the OCT signal is integrated over depth, its lateral profile was highly correlated with that of IOS, supporting that the OCT signals represent hemodynamic responses to neural activation. These OCT signals revealed a laminar profile of hemodynamic responses that a deeper area responds earlier than a superficial area (Fig. 66.6e). This is consistent with the fact that the neuronal activity initiates in the deeper layers of the cortex and then propagates to the superficial cortex. While the neural propagation occurs over only 10's of

milliseconds, the delay in the vascular response is 100's of milliseconds. The greater delay in the vascular response indicates intriguing laminar differences in neurovascular coupling that requires further study. These laminar OCT results were recently elucidated further in [49].

66.3.2 Quantitative OCT Imaging of Hemodynamic Responses

The above study showed OCT signal changes in response to neuronal activity that were similar to the hemodynamic responses measured by IOS imaging, but it remains unclear what mechanisms are driving those OCT signal changes. Srinivasan et al. measured brain activation-evoked changes in blood flow and total hemoglobin in the rat somatosensory cortex [50]. They performed IOS imaging to identify the activated region and chose an OCT scanning line (Fig. 66.7a). Then, Doppler OCT imaging was performed during somatosensory activation for measuring fractional changes in blood flow (Fig. 66.7b for baseline, Fig. 66.7d for flow in the draining vein). In addition, activation-induced changes in the extinction coefficient were measured to estimate dynamics of the total hemoglobin concentration (Fig. 66.7c). Assuming single scattering, the OCT signal profile $R(z,t)$ is determined by the extinction coefficient $\mu_t(t)$ and the backscattering $A(t)$, which are time-varying variables due to brain activation. Using this relation, a least-squares fit was performed to determine $\Delta\mu_t(t)$ as shown in Fig. 66.7d (blue). As a result, the time course of $\Delta\mu_t$ was nearly identical to that of ΔHbT measured by IOS, supporting that the OCT extinction coefficient changes over time were closely related to changes in the total hemoglobin concentration. In contrast, the Doppler OCT-measured flow response showed a faster relaxation than both the ΔHbT and $\Delta\mu_t$ responses, which is consistent with the well-known delayed recovery in cerebral blood volume [51].

66.3.3 Statistical Intensity Variation (SIV) Imaging of Capillary Network Flux

The above study showed that OCT is useful for the measurement of blood flow responses in arteries and veins, but it did not observe responses in individual capillaries. Since cerebral capillaries are known to respond to neural activation in a highly heterogeneous manner, a high-statistical-significance study of capillary responses will require an imaging method that simultaneously monitors changes in blood flow over a sufficient number of capillaries. Existing methods, including video microscopy, two-photon microscopy, Doppler OCT, and DLS-OCT, are not sufficient for this purpose; hence, another OCT-based method is proposed.

The intensity of the OCT signal at a voxel basically represents the amplitude of light backscattered from the voxel. According to the Mie scattering theory, 1-μm wavelength light is supposed to be largely scattered by particles of 0.1–10 μm in diameter. Therefore, we can expect that within capillaries, RBCs (~6.5 μm in

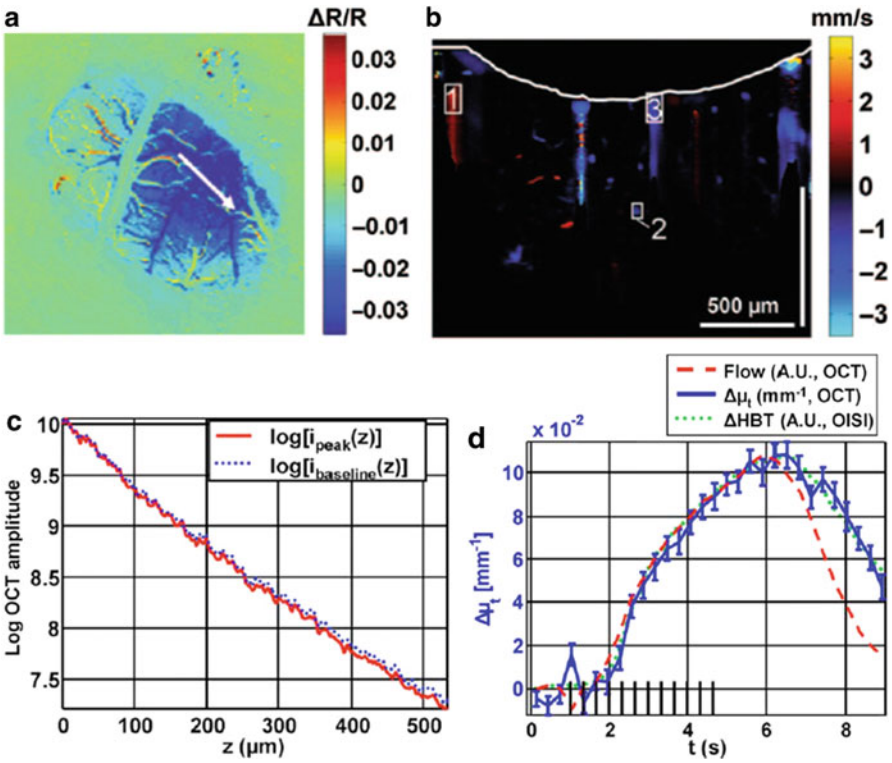

Fig. 66.7 Quantitative OCT imaging of cortical hemodynamic responses. (**a**) Fractional IOS image at peak activation. The OCT scan is shown as the *white arrow*. (**b**) Doppler OCT image at baseline with cortical surface indicated by the *white line*. (**c**) Profile of the natural logarithm of OCT amplitude versus depth, during the baseline (0–1 s, *dotted line*) and peak activation (5–7 s, *solid line*). (**d**) Time courses of $\Delta\mu_t$ measured by OCT (*solid blue*), flow in the draining vein measured by Doppler OCT (*dashed red*), and ΔHbT measured by IOS imaging (*dotted green*) (Reprinted from [50] with permission)

diameter) will result in large OCT signals compared to blood plasma. If this is true, the OCT signal at a given voxel located in a capillary should go up and come back down when an RBC passes. This idea has been validated in that individual RBC passage through a capillary appeared as a peak in the time course of the OCT intensity signal of the voxel located at the capillary center (Fig. 66.8a). This OCT identification of individual RBC passage can be used for quantifying the flow properties of RBCs such as the flux [RBC/s], speed [mm/s], and linear density [RBC/mm]. Although this technique enables us to obtain 3D maps of capillary network flow but is still not fast enough to trace hemodynamic responses, the finding that RBC passage results in OCT intensity variation leads to the possibility of rapid volumetric imaging of capillary network flow via statistical analysis of the intensity variation.

We first defined a metric quantifying the intensity variation between the two consecutive B-scans,

$$SIV(z,x,y) \equiv \frac{E\left[\{I(z,x,t_2;y) - I(z,x,t_1;y)\}^2\right]}{E\left[\frac{1}{2}\{I^2(z,x,t_2;y) + I^2(z,x,t_1;y)\}\right]}$$

where $I(z,x,t_1;y)$ and $I(z,x,t_2;y)$ are the first and second B-scans at a given Y-position, respectively, and $E[]$ denotes ensemble averaging. The ensemble averaging can be implemented by averaging over neighboring voxels and/or repeated volumes. This ensemble averaging will minimize the stochastic speckle effect in the OCT intensity. A single SIV value would not quantify RBC flow properties because the value will depend on the space and time of its acquisition. Instead, if one gathers SIVs in a random manner from a given capillary segment, which is conceptually identical to a random sampling of SIVs from the time course embedding the RBC peaks (Fig. 66.8a, for example), then the mean SIV will increase as the speed increases (i.e., sharper peaks), but it will also increase as the density increases (i.e., more peaks for unit time). Here, numerical simulation and experimental measurements in Fig. 66.8b demonstrated that the mean SIV is linearly dependent of the RBC flux, where (Flux) = (Density) × (Speed).

An example of SIV imaging of the rodent cerebral cortex in the cranial window preparation is shown in Fig. 66.8d. In order to gather SIV values along capillary segment paths, one needs to know the position vectors of each capillary. While there are several methods to do this, Hessian matrix analysis can be used and then the mean SIV for each capillary segment can be converted into the RBC flux. In this way, a 3D flux map over a vectorized capillary network can be obtained (Fig. 66.8e).

As SIV imaging only requires two B-scans per Y position, it enables us to measure the RBC flux over hundreds of capillaries nearly at the same time. Therefore, the technique is suitable for quantifying how the RBC flux varies with functional activation across hundreds of capillaries, overcoming the limitations in the previous measurements owing to the diversity of capillary flow responses. For example, properly splitting the ROI achieved the desired temporal resolution enough to trace fast hemodynamic responses, consequently leading to a temporal series of 20 consecutive SIV volumes with a temporal sampling frequency of 1.3 s ($\Delta T = T_{n+1} - T_n$). This dynamic SIV imaging was performed over an ROI near the center of functional activation in the somatosensory cortex corresponding to forepaw stimulation that was identified with intrinsic optical signal (IOS) imaging (Fig. 66.9b). One of the temporal series of 20 SIV volumes is presented in Fig. 66.9c. About 200 capillary segments were identified, and following data analysis led to a temporal series of 20 capillary network flux maps, one of which is shown in Fig. 66.9d. This means that SIV imaging technique enabled us to trace how the RBC flux varies with activation over hundreds of capillaries (Fig. 66.8e). Some capillaries exhibited early flux increases while some exhibited late increases or even decreases.

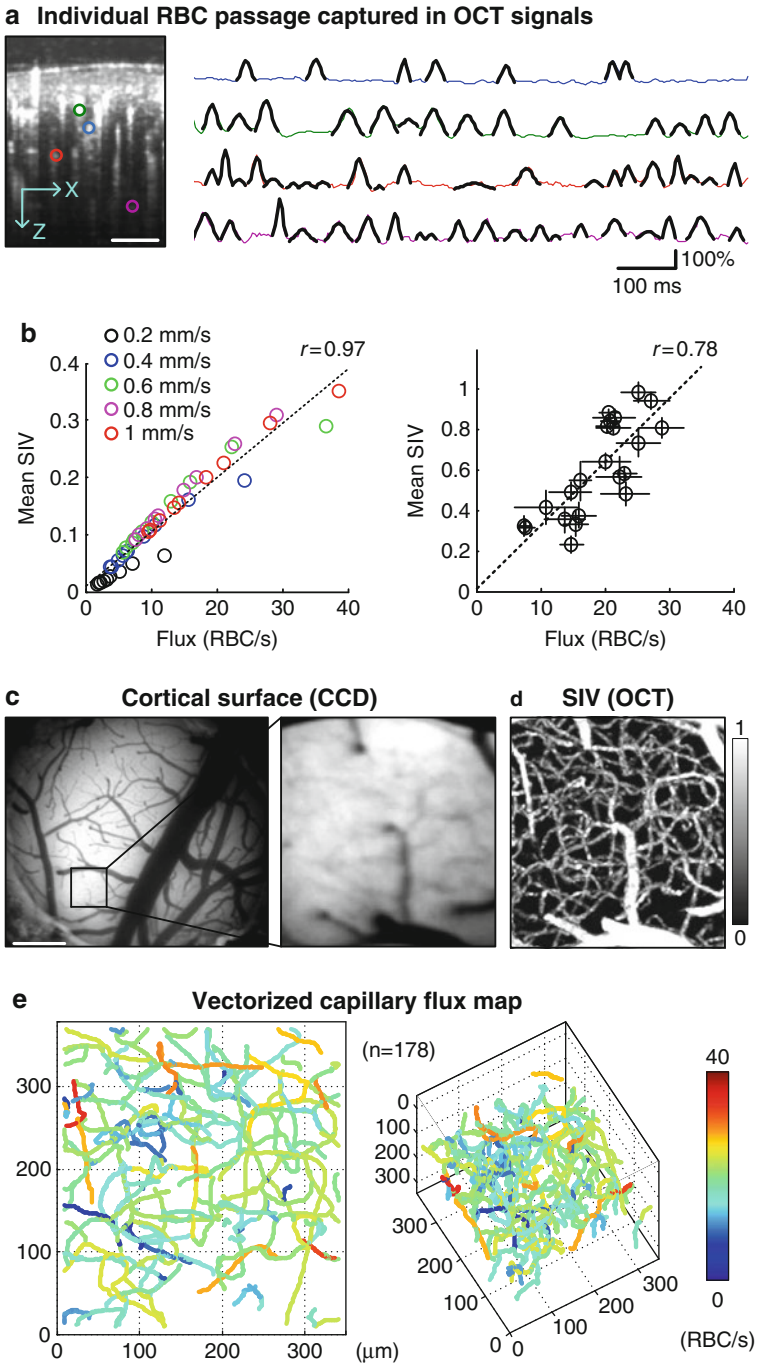

Fig. 66.8 (continued)

66.4 OCT Imaging of Neuronal Activity: Millisecond-Timescale Transient Dynamics

As traditional microelectrode recordings of neural signals can damage brain tissue, noncontact and label-free optical recording of the neural signal (a.k.a., fast optical signal; FOS) has been studied for a long time. Since the original study in 1949 [56], many scientists have demonstrated FOS measurements of neuronal activity in isolated nerves [57–63], cultured neurons [64, 65], retinal tissue [66, 67], live brain slices [68], exposed cortices [69], and the human brain [70–75]. This section describes OCT-based studies extending the FOS measurements into depth-resolved single-cell-resolution in vivo imaging. Despite its potential impact, in vivo imaging of FOS has often been considered controversial and elusive [76]. Our group also reported a failure in detecting FOS in the monkey brain [77]. These difficulties are likely due to the living animal's motion artifacts and the partial volume effect of the lower-resolution imaging methods presently used in vivo. In order to break through these current barriers, we need to further improve motion correction algorithms [78–85] for suppressing cardiac and respiratory motion artifacts from phase-resolved dynamic OCT imaging data; and we need to reduce the partial volume effect. OCT's μm resolution (smaller than single neurons) will clearly minimize the partial volume effect and could be utilized to demonstrate single-cell-resolution imaging of FOS in vivo. This section introduces current progress to overcome these barriers.

66.4.1 Motion Correction for FOS Imaging In Vivo

To improve the sensitivity of in vivo OCT signal to neuronal activity, Lee et al. have proposed motion correction algorithms to suppress cardiac and respiratory motion artifacts from millisecond-scale, phase-resolved dynamic OCT imaging data [86]. They found that, in the regime of their OCT resolution and animal preparation protocol, the animal's cardiac motions cause global phase fluctuations (GPFs, filled triangle in Fig. 66.10a) while the respiratory motions cause bulk image shifts (BISs, empty triangle in Fig. 66.10a). The algorithms were shown to enhance the metric of image stability (e.g., the cross-correlation in Fig. 66.10b), the noise map (Fig. 66.10c), and reduction of phase signal noise (Fig. 66.10d).

Fig. 66.8 SIV imaging of capillary network RBC flux. (**a**) Cross-sectional OCT angiogram of the rodent cerebral cortex (*left*) and RBC passage captured in OCT intensity time courses (*right*). Each *line* presents the time course of relative changes in the OCT intensity at the center of each capillary indicted by the color *circles*. Each peak (*overlaid black* pieces) represents single RBC passage. Scale bar, 100 μm. (**b**) Numerical simulation (*left*) and experimental validation (*right*) of the SIV relation to the RBC flux. Twenty-two capillaries were analyzed in the experimental validation. Data are presented as mean±SD. (**c**) CCD image of the brain cortex through the cranial window. (**d**) *En face* maximum intensity projection (MIP) of the SIV volume data. Ten volumes were averaged. (**e**) 3D flux map of the capillary network (Reprinted from Lee et al. [95] with permission)

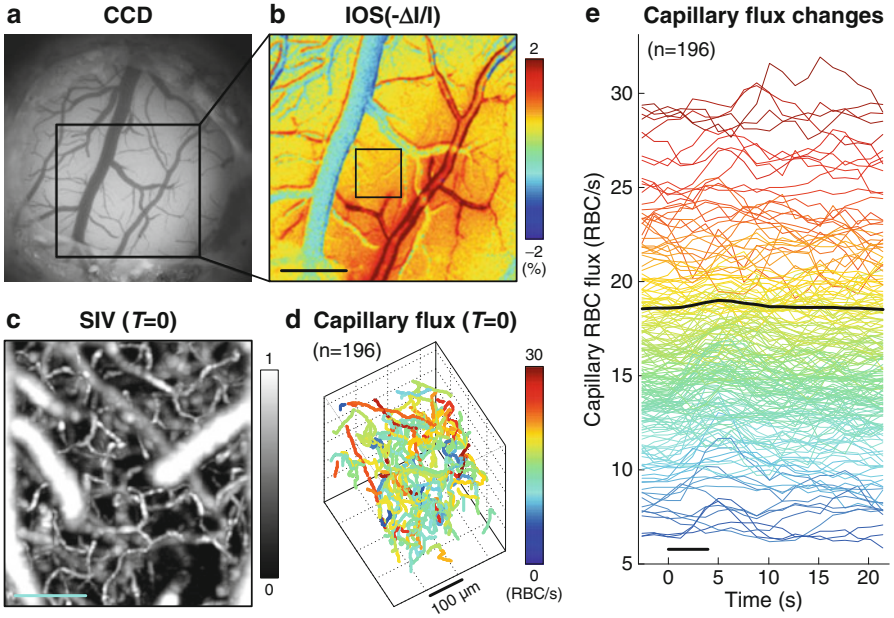

Fig. 66.9 SIV imaging of capillary network flux responses to neural activation. (**a**) A CCD image of the rodent somatosensory cortex. (**b**) IOS imaging of the hemodynamic response of the cortical surface. As we used 570-nm illumination, a decrease in the CCD intensity (*red color*) represents an increase in the blood volume. Scale bar, 500 μm. (**c**) *En face* MIP of SIV at $T=0$ s. A temporal series of 20 SIV volumes like this were obtained. We located the OCT focus at a slightly deeper area to include the capillaries near the neurons of the somatosensory cortex. Scale bar, 100 μm. (**d**) Capillary network flux map at $T=0$ s. A temporal series of 20 flux maps like this were obtained. (**e**) Time courses of RBC flux changes of the 196 capillaries during functional activation. A change in the mean flux averaged across capillaries is presented by the thick black curve. The peak change was 2.2 % and highly significant ($p<10^{-8}$). The black bar in the bottom indicates the duration of forepaw stimulation (3 Hz for $T=0$–4 s) (Reprinted from Lee et al. [95] with permission)

66.4.2 Preliminary Results of In Vivo FOS Imaging of Neuronal Activity

The somatosensory cortical region activated by forepaw stimulation was identified with CCD IOS imaging (Fig. 66.11a). We chose a line (the cross-sectional plane in 3-D) for ms-scale dynamic OCT imaging. From this 3-D (x,z,t) intensity data, we excluded the voxels of vessels and their multiple-scattering shadows by employing a threshold on the baseline noise level. The intensity signals of the surviving voxels were averaged over ten runs of stimulation (3 Hz for 10 s followed by 20 s rest, for each run) and fit with the canonical response function (see caption of Fig. 66.11b for details and example results)

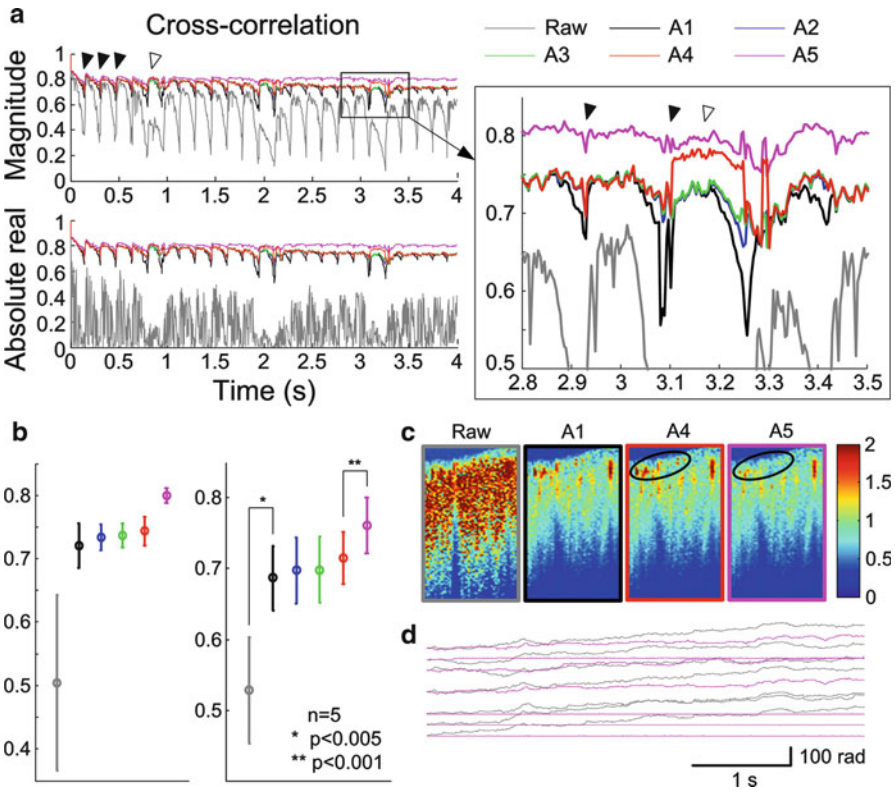

Fig. 66.10 Motion correction for OCT imaging of FOS. (**a**) The cross-correlation of each frame to the first frame is presented as the metric of image stability. The absolute real of the complex-valued cross-correlation (*bottom*) represents the stability of phase signals. The image stability was significantly reduced by either GPFs or BISs. Each color shows the result of different combinations of algorithms (legend). A5 was computationally most expensive but most effective. (**b**) The mean cross-correlation of the later 2 s (*left*). The superior performance of A5 was statistically confirmed across five animals (*right*). (**c**) Noise maps resulted from different combinations of algorithms. A5 was particularly effective in reducing noise at the surface (*black circles*). (**d**) A5 also significantly reduced noise of the OCT phase signals, by more than the two orders of magnitude at many voxels (Reprinted from [86] with permission)

$$f(t) = a(t - t_0)^2 e^{-b(t-t0)} s(t - t_0) \tag{66.7}$$

where a, b, and t_0 are fitting coefficients and $s(t)$ is the step function, which in turn estimated the peak response, $a(2/b)^2 e^{-2}$, peak time, $t_0 + 2/b$, and relaxation time, $1/b$. This fitting estimated each surviving voxel's peak response, peak time, and relaxation time (Fig. 66.11c), which enabled grouping of the various responses by their temporal characteristics (Fig. 66.11d) and revealed a depth profile of the FOSs (Fig. 66.11e).

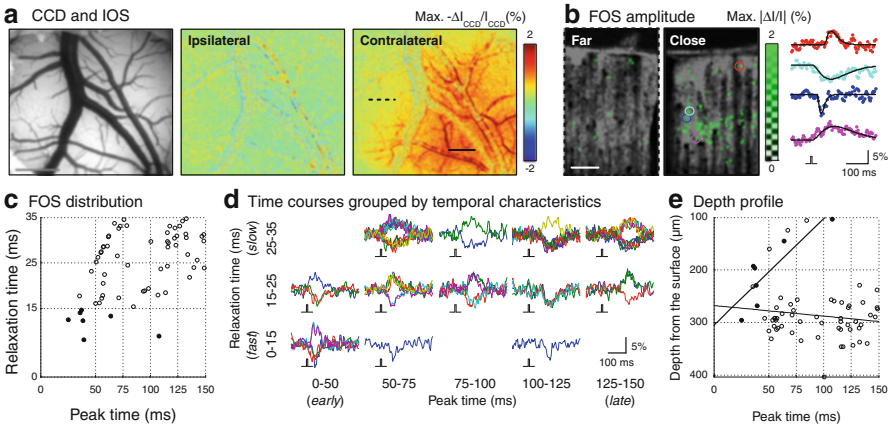

Fig. 66.11 Preliminary results of OCT imaging of FOS. (**a**) CCD imaging of IOS. The signed maximum of the inverted relative change in the CCD intensity ($-\Delta I_{CCD}/I_{CCD}$) is presented (*color images*). The solid and *dotted black lines* indicate the OCT scanning positions close to and far from the AC, respectively. Scale bar, 500 μm. (**b**) Voxels with the baseline std/mean >2 % were excluded. Each surviving voxel's time course was fit with a canonical response function (e.g., right). Only voxels with good fitting ($R^2 > 0.6$) were chosen, and their maximum absolute changes ($|\Delta I/I|$) are presented as *green* on the map of tissue stability (baseline mean/std). Scale bar, 100 μm. (**c**) Distribution of FOS in the peak and relaxation time. (**d**) When grouped by the peak and relaxation time, FOS exhibited highly diverse time courses, from *early fast* to *late slow*. The time courses of *fast* FOS were similar to those of in vitro FOS of action potential. Not all the FOS here would represent neuronal activity; further validation is needed as outlined in the text. Color is random. (**e**) Distribution of FOS in depth and peak time. *Fast* FOS (relaxation time <15 ms) exhibited upward propagation (*filled circles*, $p = 0.015$) while *slow* FOS stayed at depth with varying peak times (*empty circles*). The significance of *fast* versus *slow* FOSs needs further consideration but may relate to action potentials versus synaptic activity

OCT imaging of in vivo FOS of neuronal activity should be validated by showing that (i) the FOS is significantly larger in the ROI close to the activated center (AC) (e.g., Fig. 66.11b) and smaller with ipsilateral stimulation, (ii) its time courses agree with those of in vitro and ex vivo FOSs found in the literature [57, 59, 61, 68, 87], (iii) its laminar and/or temporal structure agrees with well-known characteristics [88], and (iv) it satisfies the five criteria established in [74].

66.5 Summary and Future Direction

This chapter described how OCT-based technologies enable μm-resolution imaging of vascular and neuronal dynamics occurring in the brain cortex of a living animal, leading to novel findings in the neurosciences. First, Doppler OCT is used for quantitative measurement of baseline CBF, an important endpoint in studies of cerebral pathophysiology. We also reviewed the recent integration of OCT with DLS for in vivo imaging of both flow and diffusion of intracellular organelles. Next, we described how CBF responses to brain activation with the time constant of a few

seconds can be measured with OCT. Compared to conventional IOS imaging, OCT provides depth-resolved information of the hemodynamic responses to brain activation. SIV imaging was shown to have potential to enable a systemic study of how the capillary network flow responds to brain activation. Finally, we presented preliminary results supporting the potential of OCT to measure fast optical signals in vivo with millisecond temporal resolution.

DLS-OCT has been shown to measure both the axial and transverse components of CBF velocity (Fig. 66.4), but its applicability to quantitative imaging of capillary flow velocity has yet to be demonstrated. When validated, DLS-OCT imaging could be simultaneously performed with SIV imaging for cross validation. In addition to the CBF imaging, DLS-OCT is likely able to image the diffusion-like motion of intracellular organelles (i.e., intracellular motility, IM). This energy-consuming IM is directly related to and thus can represent cellular metabolism and viability but has been measured only in vitro by existing methods based on fluorescence [89, 90] or DLS [26, 28, 29, 91, 92]. Further validation that the high-diffusion spots revealed in DLS-OCT imaging (Fig. 66.5) really represent IM is needed. Once validated, DLS-OCT will, for instance, be useful for the study of stroke pathology, characterizing the spatio-temporal correlation between reduction in arterial blood flow, associated changes in capillary flow and neuronal viability (IM), and final tissue infarction.

SIV imaging enabled us to monitor RBC flux changes over hundreds of capillaries during activation with ~1 s temporal resolution. This functional study will help reveal how capillary flow responds to neural activation at the network level and with high statistical significance and thus enable us to test the hypothesis that cerebral capillaries may regulate blood flow during brain activation.

OCT-based in vivo FOS imaging of neuronal activity seems promising but still far from robust demonstration. Whereas voxels of vessels were excluded in Fig. 66.11, one may directly identify voxels of neurons using high-NA OCT imaging (e.g., Fig. 66.5a) prior to functional OCT imaging. Also, one can use the phase of the OCT signal which is very sensitive to displacement of scatterers. FOS has been shown to originate from morphological changes in neurons during excitation [93]. When the SNR of the phase signal is not sufficiently high for robust imaging of FOS despite the motion correction (Fig. 66.10d), one may have to employ additional signal processing techniques including wavelet decomposition (WD) and independent component analysis (ICA). WD will help filter out fluctuations with scales other than the known FOS's characteristic time constant. ICA will be performed across, for instance, the 8×8 voxels surrounding a neuron (30×30 μm, 64 channels), filtering out common phase fluctuations due to either residual motion artifact or tissue compression oriented by and propagated from RBC passage in neighboring capillaries.

When demonstrated, FOS imaging technology will be useful for visualizing the microscopic 3-D pattern of neuronal activity propagation in the brain cortex and for pursuing minimally invasive human brain signal recording technology with miniaturized optical systems in the future (potentially enabling ultra-multichannel micro-optode arrays with reconfigurable recording sites in 3-D).

These μm-scale live connection and brain signal recording studies, along with the feasible applications of other OCT-based technologies introduced in this chapter, will enable a range of studies of how the brain works and how it fails in pathological conditions.

References

1. D. Huang, E. Swanson, C. Lin, J. Schuman, W. Stinson, W. Chang, M. Hee, T. Flotte, K. Gregory, C. Puliafito, J. Fujimoto, Optical coherence tomography. Science **254**, 1178–1181 (1991)
2. W. Drexler, U. Morgner, R.K. Ghanta, F.X. Kärtner, J.S. Schuman, J.G. Fujimoto, Ultrahigh-resolution ophthalmic optical coherence tomography. Nat. Med. **7**, 502 (2001)
3. G.J. Tearney, M.E. Brezinski, B.E. Bouma, S.A. Boppart, C. Pitris, J.F. Southern, J.G. Fujimoto, In vivo endoscopic optical biopsy with optical coherence tomography. Science **276**, 2037–2039 (1997)
4. S.A. Boppart, B.E. Bouma, M.E. Brezinski, G.J. Tearney, J.G. Fujimoto, Imaging developing neural morphology using optical coherence tomography. J. Neurosci. Methods **70**, 65–72 (1996)
5. M.D. Stern, In vivo evaluation of microcirculation by coherent light scattering. Nature **254**, 56–58 (1975)
6. U. Dirnagl, B. Kaplan, M. Jacewicz, W. Pulsinelli, Continuous measurement of cerebral cortical blood flow by laser-Doppler flowmetry in a rat stroke model. J. Cereb. Blood Flow Metab. **9**, 589–596 (1989)
7. B.M. Ances, J.H. Greenberg, J.A. Detre, Laser Doppler imaging of activation-flow coupling in the rat somatosensory cortex. Neuroimage **10**, 716–723 (1999)
8. J.A. Izatt, M.D. Kulkarni, S. Yazdanfar, J.K. Barton, A.J. Welch, In vivo bidirectional color Doppler flow imaging of picoliter blood volumes using optical coherence tomography. Opt. Lett. **22**, 1439–1441 (1997)
9. Z. Chen, T.E. Milner, D. Dave, J.S. Nelson, Optical Doppler tomographic imaging of fluid flow velocity in highly scattering media. Opt. Lett. **22**, 64–66 (1997)
10. R. Leitgeb, L. Schmetterer, W. Drexler, A. Fercher, R. Zawadzki, T. Bajraszewski, Real-time assessment of retinal blood flow with ultrafast acquisition by color Doppler Fourier domain optical coherence tomography. Opt. Express **11**, 3116–3121 (2003)
11. Y. Wang, B.A. Bower, J.A. Izatt, O. Tan, D. Huang, In vivo total retinal blood flow measurement by Fourier domain Doppler optical coherence tomography. J. Biomed. Opt. **12**, 041215–041215 (2007)
12. V.J. Srinivasan, S. Sakadzic, I. Gorczynska, S. Ruvinskaya, W. Wu, J.G. Fujimoto, D.A. Boas, Quantitative cerebral blood flow with optical coherence tomography. Opt. Express **18**, 2477–2494 (2010)
13. V.J. Srinivasan, D.N. Atochin, H. Radhakrishnan, J.Y. Jiang, S. Ruvinskaya, W. Wu, S. Barry, A.E. Cable, C. Ayata, P.L. Huang, D.A. Boas, Optical coherence tomography for the quantitative study of cerebrovascular physiology. J. Cereb. Blood Flow Metab. **31**, 1339–1345 (2011)
14. N.A. Clark, J.H. Lunacek, G.B. Benedek, A study of Brownian motion using light scattering. Am. J. Phys. **38**, 575–585 (1970)
15. D.J. Durian, D.A. Weitz, D.J. Pine, Multiple light-scattering probes of foam structure and dynamics. Science **252**, 686–688 (1991)
16. D.A. Boas, A.G. Yodh, Spatially varying dynamical properties of turbid media probed with diffusing temporal light correlation. J. Opt. Soc. Am. A **14**, 192–215 (1997)
17. R.V. Edwards, J.C. Angus, M.J. French, J. John, W. Dunning, Spectral analysis of the signal from the laser Doppler flowmeter: time-independent systems. J. Appl. Phys. **42**, 837–850 (1971)

18. D.P. Chowdhury, C.M. Sorensen, T.W. Taylor, J.F. Merklin, T.W. Lester, Application of photon correlation spectroscopy to flowing Brownian motion systems. Appl. Opt. **23**, 4149–4154 (1984)
19. T.W. Taylor, C.M. Sorensen, Gaussian beam effects on the photon correlation spectrum from a flowing Brownian motion system. Appl. Opt. **25**, 2421–2426 (1986)
20. P.N. Pusey, W. Van Megen, Dynamic light scattering by non-ergodic media. Phys. A **157**, 705–741 (1989)
21. J.G.H. Joosten, E.T.F. Geladé, P.N. Pusey, Dynamic light scattering by nonergodic media: Brownian particles trapped in polyacrylamide gels. Phys. Rev. A **42**, 2161–2175 (1990)
22. A.B.. Leung, K.I. Suh, R.R. Ansari, Particle-size and velocity measurements in flowing conditions using dynamic light scattering. Appl. Opt. **45**, 2186–2190 (2006)
23. J. Lee, W. Wu, J.Y. Jiang, B. Zhu, D.A. Boas, Dynamic light scattering optical coherence tomography. Opt. Express **20**, 22262–22277 (2012)
24. L. Van Hove, Correlations in space and time and Born approximation scattering in systems of interacting particles. Phys. Rev. **95**, 249–262 (1954)
25. V.J. Srinivasan, H. Radhakrishnan, J.Y. Jiang, S. Barry, A.E. Cable, Optical coherence microscopy for deep tissue imaging of the cerebral cortex with intrinsic contrast. Opt. Express **20**, 2220–2239 (2012)
26. T. Yamauchi, H. Iwai, Y. Yamashita, Label-free imaging of intracellular motility by low-coherent quantitative phase microscopy. Opt. Express **19**, 5536–5550 (2011)
27. K. Jacobson, J. Wojcieszyn, The translational mobility of substances within the cytoplasmic matrix. Proc. Natl. Acad. Sci. U. S. A. **81**, 6747–6751 (1984)
28. R. Dzakpasu, D. Axelrod, Dynamic light scattering microscopy. A novel optical technique to image submicroscopic motions. II: experimental applications. Biophys. J. **87**, 1288–1297 (2004)
29. D.D. Nolte, R. An, J. Turek, K. Jeong, Holographic tissue dynamics spectroscopy. J. Biomed. Opt. **16**, 087004 (2011)
30. D. Attwell, A.M. Buchan, S. Charpak, M. Lauritzen, B.A. MacVicar, E.A. Newman, Glial and neuronal control of brain blood flow. Nature **468**, 232–243 (2010)
31. K.R. Ko, A.C. Ngai, H.R. Winn, Role of adenosine in regulation of regional cerebral blood flow in sensory cortex. Am. J. Physiol. **259**, H1703–H1708 (1990)
32. Y. Ido, K. Chang, T.A. Woolsey, J.R. Williamson, NADH: sensor of blood flow need in brain, muscle, and other tissues. FASEB J. **15**, 1419–1421 (2001)
33. C.W. Leffler, D.W. Busija, R. Mirro, W.M. Armstead, D.G. Beasley, Effects of ischemia on brain blood flow and oxygen consumption of newborn pigs. Am. J. Physiol. Heart Circ. Physiol. **257**, H1917–H1926 (1989)
34. H. Girouard, C. Iadecola, Neurovascular coupling in the normal brain and in hypertension, stroke, and Alzheimer disease. J. Appl. Physiol. **100**, 328–335 (2006)
35. C.M. Peppiatt, C. Howarth, P. Mobbs, D. Attwell, Bidirectional control of CNS capillary diameter by pericytes. Nature **443**, 700–704 (2006)
36. D. Shepro, N. Morel, Pericyte physiology. FASEB J. **7**, 1031–1038 (1993)
37. D.G. Puro, Physiology and pathobiology of the pericyte-containing retinal microvasculature: new developments. Microcirculation **14**, 1–10 (2010)
38. M. Yemisci, Y. Gursoy-Ozdemir, A. Vural, A. Can, K. Topalkara, T. Dalkara, Pericyte contraction induced by oxidative-nitrative stress impairs capillary reflow despite successful opening of an occluded cerebral artery. Nat. Med. **15**, 1031–1037 (2009)
39. F. Fernández-Klett, N. Offenhauser, U. Dirnagl, J. Priller, U. Lindauer, Pericytes in capillaries are contractile in vivo, but arterioles mediate functional hyperemia in the mouse brain. Proc. Natl. Acad. Sci. **107**, 22290–22295 (2010)
40. N. B. Hamilton, D. Attwell, C. N. Hall, Pericyte-mediated regulation of capillary diameter: a component of neurovascular coupling in health and disease. Front. Neuroenerg. **2**, 1–14 (2010)

41. B. Stefanovic, E. Hutchinson, V. Yakovleva, V. Schram, J.T. Russell, L. Belluscio, A.P. Koretsky, A.C. Silva, Functional reactivity of cerebral capillaries. J. Cereb. Blood Flow Metab. **28**, 961–972 (2007)
42. M.L. Schulte, J.D. Wood, A.G. Hudetz, Cortical electrical stimulation alters erythrocyte perfusion pattern in the cerebral capillary network of the rat. Brain Res. **963**, 81–92 (2003)
43. M. Tomita, Y. Tomita, M. Unekawa, H. Toriumi, N. Suzuki, Oscillating neuro-capillary coupling during cortical spreading depression as observed by tracking of FITC-labeled RBCs in single capillaries. Neuroimage **56**, 1001–1010 (2011)
44. D. Kleinfeld, Cortical blood flow through individual capillaries in rat vibrissa S1 cortex: stimulus-induced changes in flow are comparable to the underlying fluctuations in flow, in *International Congress Series* (Elsevier, Amsterdam, 2002), pp. 115–122
45. D. Kleinfeld, P.P. Mitra, F. Helmchen, W. Denk, Fluctuations and stimulus-induced changes in blood flow observed in individual capillaries in layers 2 through 4 of rat neocortex. Proc. Natl. Acad. Sci. **95**, 15741–15746 (1998)
46. H. Ren, C. Du, Z. Yuan, K. Park, N.D. Volkow, Y. Pan, Cocaine-induced cortical microischemia in the rodent brain: clinical implications. Mol. Psychiatry **17**, 1017–1025 (2011)
47. V.J. Srinivasan, H. Radhakrishnan, E.H. Lo, E.T. Mandeville, J.Y. Jiang, S. Barry, A.E. Cable, OCT methods for capillary velocimetry. Biomed. Opt. Express **3**, 612–629 (2012)
48. Y. Chen, A.D. Aguirre, L. Ruvinskaya, A. Devor, D.A. Boas, J.G. Fujimoto, Optical coherence tomography (OCT) reveals depth-resolved dynamics during functional brain activation. J. Neurosci. Methods **178**, 162–173 (2009)
49. P. Tian, I.C. Teng, L.D. May, R. Kurz, K. Lu, M. Scadeng, E.M. Hillman, A.J. De Crespigny, H.E. D'Arceuil, J.B. Mandeville, J.J. Marota, B.R. Rosen, T.T. Liu, D.A. Boas, R.B. Buxton, A.M. Dale, A. Devor, Cortical depth-specific microvascular dilation underlies laminar differences in blood oxygenation level-dependent functional MRI signal. Proc. Natl. Acad. Sci. U. S. A. **107**, 15246–15251 (2010)
50. V.J. Srinivasan, S. Sakas, I. Gorczynska, S. Ruvinskaya, W. Wu, J.G. Fujimoto, D.A. Boas, Depth-resolved microscopy of cortical hemodynamics with optical coherence tomography. Opt. Lett. **34**, 3086–3088 (2009)
51. J.B. Mandeville, J.J. Marota, C. Ayata, G. Zaharchuk, M.A. Moskowitz, B.R. Rosen, R.M. Weisskoff, Evidence of a cerebrovascular postarteriole windkessel with delayed compliance. J. Cereb. Blood Flow Metab. **19**, 679–689 (1999)
52. Y. Wang, R. Wang, Autocorrelation optical coherence tomography for mapping transverse particle-flow velocity. Opt. Lett. **35**, 3538–3540 (2010)
53. A.K. Dunn, H. Bolay, M.A. Moskowitz, D.A. Boas, Dynamic imaging of cerebral blood flow using laser speckle. J. Cereb. Blood Flow Metab. **21**, 195–201 (2001)
54. Y. Sato, S. Nakajima, N. Shiraga, H. Atsumi, S. Yoshida, T. Koller, G. Gerig, R. Kikinis, Three-dimensional multi-scale line filter for segmentation and visualization of curvilinear structures in medical images. Med. Image Anal. **2**, 143–168 (1998)
55. S.N. Jespersen, L. Ostergaard, The roles of cerebral blood flow, capillary transit time heterogeneity, and oxygen tension in brain oxygenation and metabolism. J. Cereb. Blood Flow Metab. **32**, 264–277 (2012)
56. D.K. Hill, R.D. Keynes, Opacity changes in stimulated nerve. J. Physiol. **108**, 278–281 (1949)
57. L.B. Cohen, R.D. Keynes, B. Hille, Light scattering and birefringence changes during nerve activity. Nature **218**, 438–441 (1968)
58. I. Tasaki, A. Watanabe, R. Sandlin, L. Carnay, Changes in fluorescence, turbidity, and birefringence associated with nerve excitation. Proc. Natl. Acad. Sci. U. S. A. **61**, 883–888 (1968)
59. L.B. Cohen, Changes in neuron structure during action potential propagation and synaptic transmission. Physiol. Rev. **53**, 373–418 (1973)
60. A. Watanabe, S. Terakawa, Alteration of birefringence signals from squid giant axons by intracellular perfusion with protease solution. Biochim. Biophys. Acta **436**, 833–842 (1976)

61. K.M. Carter, J.S. George, D.M. Rector, Simultaneous birefringence and scattered light measurements reveal anatomical features in isolated crustacean nerve. J. Neurosci. Methods **135**, 9–16 (2004)
62. X.C. Yao, A. Foust, D.M. Rector, B. Barrowes, J.S. George, Cross-polarized reflected light measurement of fast optical responses associated with neural activation. Biophys. J. **88**, 4170–4177 (2005)
63. T. Akkin, C. Joo, J.F. de Boer, Depth-resolved measurement of transient structural changes during action potential propagation. Biophys. J. **93**, 1347–1353 (2007)
64. R.A. Stepnoski, A. LaPorta, F. Raccuia-Behling, G.E. Blonder, R.E. Slusher, D. Kleinfeld, Noninvasive detection of changes in membrane potential in cultured neurons by light scattering. Proc. Natl. Acad. Sci. U. S. A. **88**, 9382–9386 (1991)
65. S. Oh, C. Fang-Yen, W. Choi, Z. Yaqoob, D. Fu, Y.K. Park, R.R. Dassari, M.S. Feld, Label-free imaging of membrane potential using membrane electromotility. Biophys. J. **103**, 11–18 (2012)
66. X.-C. Yao, J.S. George, Dynamic neuroimaging of retinal light responses using fast intrinsic optical signals. Neuroimage **33**, 898–906 (2006)
67. K. Bizheva, R. Pflug, B. Hermann, B. Považay, H. Sattmann, P. Qiu, E. Anger, H. Reitsamer, S. Popov, J. Taylor, Optophysiology: depth-resolved probing of retinal physiology with functional ultrahigh-resolution optical coherence tomography. Proc. Natl. Acad. Sci. U. S. A. **103**, 5066–5071 (2006)
68. J. Lee, S.J. Kim, Spectrum measurement of fast optical signal of neural activity in brain tissue and its theoretical origin. Neuroimage **51**, 713–722 (2010)
69. D.M. Rector, K.M. Carter, P.L. Volegov, J.S. George, Spatio-temporal mapping of rat whisker barrels with fast scattered light signals. Neuroimage **26**, 619–627 (2005)
70. G. Gratton, P.M. Corballis, E. Cho, M. Fabiani, D.C. Hood, Shades of gray matter: noninvasive optical images of human brain responses during visual stimulation. Psychophysiology **32**, 505–509 (1995)
71. J. Steinbrink, M. Kohl, H. Obrig, G. Curio, F. Syre, F. Thomas, H. Wabnitz, H. Rinneberg, A. Villringer, Somatosensory evoked fast optical intensity changes detected non-invasively in the adult human head. Neurosci. Lett. **291**, 105–108 (2000)
72. F. Syre, H. Obrig, J. Steinbrink, M. Kohl, R. Wenzel, A. Villringer, Are VEP correlated fast optical signals detectable in the human adult by non-invasive nearinfrared spectroscopy (NIRS)? Adv. Exp. Med. Biol. **530**, 421 (2003)
73. G. Gratton, M. Fabiani, Shedding light on brain function: the event-related optical signal. Trends Cogn. Sci. **5**, 357–363 (2001)
74. M.A. Franceschini, D.A. Boas, Noninvasive measurement of neuronal activity with near-infrared optical imaging. Neuroimage **21**, 372–386 (2004)
75. G. Gratton, C.R. Brumback, B.A. Gordon, M.A. Pearson, K.A. Low, M. Fabiani, Effects of measurement method, wavelength, and source-detector distance on the fast optical signal. Neuroimage **32**, 1576–1590 (2006)
76. J. Steinbrink, F.C.D. Kempf, A. Villringer, H. Obrig, The fast optical signal–Robust or elusive when non-invasively measured in the human adult? Neuroimage **26**, 996–1008 (2005)
77. H. Radhakrishnan, W. Vanduffel, H.P. Deng, L. Ekstrom, D.A. Boas, M.A. Franceschini, Fast optical signal not detected in awake behaving monkeys. Neuroimage **45**, 410–419 (2009)
78. M. Zaitsev, C. Dold, G. Sakas, J. Hennig, O. Speck, Magnetic resonance imaging of freely moving objects: prospective real-time motion correction using an external optical motion tracking system. Neuroimage **31**, 1038–1050 (2006)
79. O. Speck, J. Hennig, M. Zaitsev, Prospective real-time slice-by-slice motion correction for fMRI in freely moving subjects. Magn. Reson. Mater. Phys. Biol. Med. **19**, 55–61 (2006)
80. A.Z. Kyme et al., Real-time 3D motion tracking for small animal brain PET. Phys. Med. Biol. **53**, 2651 (2008)
81. V. Zhou, A. Kyme, S. Meikle, R. Fulton, An event-driven motion correction method for neurological PET studies of awake laboratory animals. Mol. Imaging Biol. **10**, 315–324 (2008)

82. S.R. Goldstein, M.E. Daube-Witherspoon, M.V. Green, A. Eidsath, A head motion measurement system suitable for emission computed tomography. IEEE Trans. Med. Imaging **16**, 17–27 (1997)
83. M. Pircher, E. Götzinger, H. Sattmann, R.A. Leitgeb, C.K. Hitzenberger, In vivo investigation of human cone photoreceptors with SLO/OCT in combination with 3D motion correction on a cellular level. Opt. Express **18**, 13935–13944 (2010)
84. J.Y. Ha, M. Shishkov, M. Colice, W.Y. Oh, H. Yoo, L. Liu, G.J. Tearney, B.E. Bouma, Compensation of motion artifacts in catheter-based optical frequency domain imaging. Opt. Express **18**, 11418–11427 (2010)
85. S. Gioux, Y. Ashitate, M. Hutteman, J.V. Frangioni, Motion-gated acquisition for in vivo optical imaging. J. Biomed. Opt. **14**, 064038–064038 (2009)
86. J. Lee, V. Srinivasan, H. Radhakrishnan, D.A. Boas, Motion correction for phase-resolved dynamic optical coherence tomography imaging of rodent cerebral cortex. Opt. Express **19**, 21258–21270 (2011)
87. A.J. Foust, D.M. Rector, Optically teasing apart neural swelling and depolarization. Neuroscience **145**, 887–899 (2007)
88. R. Miller, Neural assemblies and laminar interactions in the cerebral cortex. Biol. Cybern. **75**, 253–261 (1996)
89. B. Herman, D.F. Albertini, A time-lapse video image intensification analysis of cytoplasmic organelle movements during endosome translocation. J. Cell Biol. **98**, 565–576 (1984)
90. C.P. Brangwynne, G.H. Koenderink, F.C. MacKintosh, D.A. Weitz, Cytoplasmic diffusion: molecular motors mix it up. J. Cell Biol. **183**, 583–587 (2008)
91. D.B. Sattelle, D.J. Green, K.H. Langley, Subcellular motions in nitella flexilis studied by photon correlation spectroscopy. Phys. Scr. **19**, 471 (1979)
92. C. Joo, C.L. Evans, T. Stepinac, T. Hasan, J.F. de Boer, Diffusive and directional intracellular dynamics measured by field-based dynamic light scattering. Opt. Express **18**, 2858–2871 (2010)
93. J. Lee, D.A. Boas, S. Kim, Multiphysics neuron model for cellular volume dynamics. IEEE Trans. Biomed. Eng. **58**, 3000–3003 (2011)
94. J. Lee, H. Radhakrishnan, W. Wu, A. Daneshmand, M. Climov, C. Ayata, D.A. Boas, Quantitative imaging of cerebral blood flow velocity and intracellular motility using dynamic light scattering-optical coherence tomography. J. Cereb. Blood Flow Metab. **33**, 819–825 (2013)
95. J. Lee, J. Y. Jiang, W. Wu, D.A. Boas, Statistical intensity variation analysis for rapid volumetric imaging of capillary network flux. Biomed. Opt. Express **5**, 1160–1172 (2014)

Optical Coherence Tomography for Gastrointestinal Endoscopy

67

Wei Kang, Xin Qi, Hui Wang, and Andrew M. Rollins

Keywords

Barrett's esophagus • Dysplasia diagnosis • Endoscopic imaging • Image analysis • Optical coherence tomography

67.1 Gastrointestinal Endoscopy Review

Gastroenterology, the study of the human digestive system and the treatment of associated disorders, has promoted and benefitted from the development of endoscopy. Many disorders of the gastrointestinal (GI) tract, cancer in particular, arise within the innermost layer, i.e., the mucosa. Gastroenterologists rely substantially on visual examination of the inner surface with an optical device (i.e., endoscope) and the microscopic interpretation of biopsy samples. However, the conclusive proof of benefit is lacking for some prototypical disorders, such as Barrett's esophagus (BE).

Gastrointestinal mucosae (e.g., of the esophagus, colon, pancreatic duct, bile duct, etc.) consist of three distinct sub-layers: an innermost layer or layers of cells (epithelium), a middle layer of connective tissue (lamina propria), and a layer of muscle cells (muscularis mucosa). The focus of this chapter is cancer that involves or arises in the epithelium. As a gross simplification, the initial step of cancerous

W. Kang (✉)
St. Jude Medical, Westford, MA, USA
e-mail: wxk29@case.edu

X. Qi
Rutgers University, Piscataway, NJ, USA

H. Wang
American Medical Systems, San Jose, CA, USA

A.M. Rollins
Department of Biomedical Engineering, Case Western Reserve University, Cleveland, OH, USA

© Springer International Publishing Switzerland 2015

W. Drexler, J.G. Fujimoto (eds.), *Optical Coherence Tomography*,
DOI 10.1007/978-3-319-06419-2_69

transformation may be genetic mutation(s), followed by the appearance of abnormalities within the epithelial cells and evidence of deviant behavior of these cells, the latter attributes being readily evident by standard histopathology. There is frequently a precancerous stage in which cells are clearly abnormal, but not yet cancerous. In such cases, the descriptive term dysplasia is applied. In general, dysplasia indicates risk that frank cancer will develop if the dysplastic tissue is not treated or removed. Dysplasia is usually subclassified as low grade (LGD) or high grade (HGD); if especially severe but noninvasive, it may be labeled carcinoma in situ. Eventually, the dysplastic cells transform to cancer and may escape the confines of the epithelium, in which case the lesion is termed invasive and is conclusively cancerous. Epithelial cancers may progressively invade the deeper layers of gut wall to adjacent and then distant lymph nodes and to more distant organs. With increasing degree of invasion, the prognosis for the patient worsens. Conversely, the prognosis is usually good if the malignancy is discovered when least invasive, or, optimally, when the process is in a precancerous stage.

Since 1886, the endoscopic diagnosis of pathologic disorders has been based essentially on visual inspection [1]. However, dysplastic epithelium may or may not be recognizable at endoscopy. The most common form of identifiable GI dysplasia is the precancerous (adenomatous) colon polyp. Although polyps can be small, and subtle in appearance, nevertheless the majority can be visualized (and removed) using standard endoscopes. A precursor of the precancerous polyp may be the so-called aberrant crypt focus (ACF) [2–4]. Normally, the epithelial cells lining the colonic crypts have a monotonous, regular appearance. When neoplastic changes occur in the cells comprising the crypts (e.g., enlargement), the crypt takes on an aberrant appearance; groups or patches of such aberrant crypts are termed foci. There is an association between an increase in the density of ACF in the colon and malignancy. Special techniques, such as chromoendoscopy with magnifying endoscopes or OCT (Sect. 67.4), may visualize ACF.

Disorders in which early epithelial dysplastic changes are usually not clearly visible at endoscopy, such as BE, are more challenging. Of the various disorders that increase the risk of cancer, BE is prototypical. In recent decades, the incidence of esophageal adenocarcinoma has increased more rapidly than that of any other malignant neoplasm in the United States [5] and Western Europe [6]. The reason (s) for this are not fully identified, but the increase appears to be related in large part to a corresponding increase in the incidence of BE, an acquired condition which increases the risk of adenocarcinoma at least 30-fold [7–13]. Most patients in whom BE is diagnosed undergo surveillance, which involves the performance of endoscopy at regular intervals. The objective of surveillance is to detect dysplasia or early stage cancer. Subtle morphologic changes in the dysplastic mucosa are sometimes detectable endoscopically, but in the majority of precancerous cases are not discernible within the overall disease process. Thus, the usual surveillance program with these conditions includes obtaining large numbers of biopsies in the hope that extensive tissue sampling will detect the presence of dysplasia and thereby afford the opportunity for treatment prior to the appearance of frank cancer. Because these diseases are chronic, adherence to this surveillance approach dictates that

endoscopic biopsies be obtained at scheduled intervals throughout the life of the patient or until the organ at risk is removed surgically. There is considerable debate regarding the efficacy of surveillance endoscopy because of the lack of randomized trials to support its value. Several studies do suggest the survival advantage of endoscopic surveillance [14–20]. However, in addition to cost and a small risk of complications, the most serious shortcoming is sampling error. Even though large numbers of biopsies are obtained according to standard protocols, the fraction of the mucosal surface sampled is tiny in relation to the overall surface area at risk for cancer, which is often a large segment of the esophagus. Thus, long-term commitment to a costly surveillance technique of uncertain benefit is a difficult clinical decision.

An ability to interrogate the status of the mucosa at endoscopy would be highly desirable for dysplastic changes usually not visible. Endoscopic biopsy interpretation is based on visual assessment of a small sample of mucosa using a microscope. Potentially, the realization of this capability in "real time" at endoscopy could greatly enhance diagnosis. It might reduce the frequency of unnecessary biopsies; perhaps even eventually eliminate the need for biopsies in some cases. The capability of comprehensively examining long segments of GI tubular organ is also attractive to eliminate the sampling error inherent in the current procedure.

The many efforts to improve endoscopic diagnosis, to move beyond reliance on visual inspection alone, have taken numerous directions. These include endoscopic ultrasound (EUS), chromoendoscopy, narrowband imaging (NBI), fluorescence endoscopy, Raman spectroscopy, and confocal endoscopy. Of these, only EUS has become established as a clinical modality. EUS provides an image representation of the tissue layers of the esophageal wall. Thus, EUS can be used to determine the invasiveness (stage) of a tumor. For example, EUS is the most accurate test available for preoperative staging of esophageal cancer [21]. Unfortunately, efforts to utilize EUS to detect high-grade dysplasia (HGD) in Barrett's esophagus have been disappointing [22, 23]. Rather than displaying a white-balanced endoscopic image, NBI adjusts the ratio of red, green, and blue channels to enhance the contrast in mucosal morphology and microvasculature. The morphology and vascular pattern are altered in the transition from intestinal metaplasia to dysplasia [24]. NBI has very high sensitivity and specificity in detecting HGD, but cannot differentiate low-grade dysplasia from non-dysplasia [25, 26]. However, it is believed that the morphologic/microvascular changes are not universally present in all cases [26]. Laser-induced fluorescence (LIF) has been studied most extensively. Fluorescence has been investigated for both endoscopic imaging and point spectroscopy [27–29]. The major obstacle facing LIF for dysplasia diagnosis is a high rate of false-positive diagnosis.

An optical technology that provides an in situ image with a resolution comparable to microscopy would be potentially ideal for endoscopic surveillance of disorders of the gut that confer an increased risk for malignancy. The potential for optical coherence tomography (OCT) in GI tract imaging is apparent. Cross-sectional, or better yet, 3D images in high resolution with detailed microstructure may provide "optical biopsy". It could significantly improve accuracy of biopsies by

demonstrating regions of mucosa with a high probability of harboring dysplasia or occult cancer. In theory, such technology might even obviate the need for biopsies.

67.2 Review of Endoscopic OCT in Esophagus and Colon

Endoscopic OCT (EOCT) has numerous potential applications in the gastrointestinal (GI) tract. The detection of dysplasia and occult malignancy has been a primary goal since early EOCT research efforts. Esophagus and colon have been most extensively studied, which may be attributed to the ease of OCT imaging catheter deployment. Most imaging catheters, especially those used in early studies, are inserted into the accessory channel of the endoscopes. The catheters are semirigid with a fix focal distance and therefore require some inner space for positioning. Esophagus and colon are readily accessible at endoscopy. Positioning the catheter was easily guided to the areas of interest by the video camera. Although imaging of the bile and pancreatic ducts is a logical extension of EOCT, the catheter probe must be smaller and deflected at a considerable angle, sometimes exceeding 90°. Therefore, there are fewer bile and pancreatic duct studies. The following sections will mainly focus on the state-of-the-art EOCT researches in esophagus and colon.

67.2.1 Esophagus

BE studies can be considered prototypical because the current endoscopic methods for the management of this condition are suboptimal. EOCT research has focused substantially on this disorder. The hypothesis has been that dysplastic transformation changes the tissue architecture and optical properties, especially scattering, of the normal mucosa, which can be detected by EOCT. If it can be demonstrated that EOCT accurately diagnoses dysplasia and occult malignancy in BE, its value in clinical gastroenterology is effectively established.

In order to demonstrate the potential for BE diagnosis by EOCT, studies were first conducted to show that EOCT can obtain interpretable images in normal, premalignant, and malignant esophagus [30–40]. The success is attributed to both the high resolution, and the distinct backscattering property of different tissues in the esophageal mucosa. The penetration depth was sufficient compared to the thickness of the mucosa. The potential of "optical biopsy" was investigated by researchers to study whether diagnosis could be made by examining the microstructure in situ. Several clinical trials were then carried out to investigate the feasibility of EOCT to detect specialized intestinal metaplasia for the purpose of BE screening [41, 42], diagnose dysplasia for Barrett's surveillance [43–46], and identify subsquamous Barrett's glands [47]. The diagnostic criteria for detecting abnormality in the epithelium were mainly based on the glandular or layered architecture, surface topology, reflectivity of epithelium, and image penetration depth. Table 67.1 summarizes the performance of a first-generation time-domain EOCT to identify specialized intestinal metaplasia, differentiate non-dysplastic from dysplastic tissue, and differentiate high-grade

Table 67.1 Diagnostic performance of EOCT for esophageal disorder

Disorder	Sensitivity (%)	Specificity (%)
Specialized intestinal metaplasia [42]	81	57–66
Dysplasia [43]	68	82
HGD/carcinoma [44]	83	75

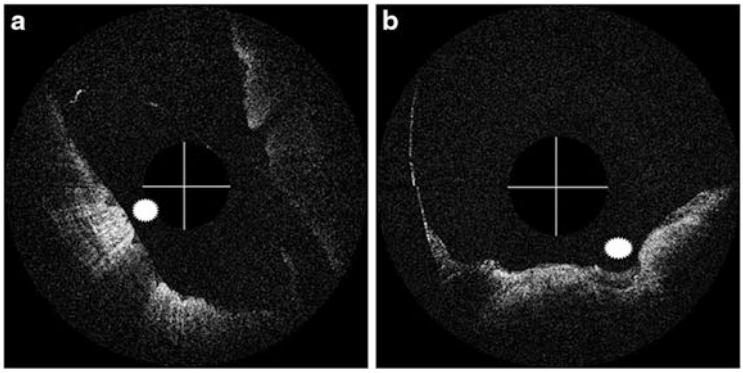

Fig. 67.1 Endoscopic TD-OCT images from a study in dysplasia diagnosis [43]. (**a**) LGD (area marked by *sunburst*). (**b**) HGD (area marked by *sunburst*). Two criteria for diagnosing dysplasia were selected: reduced light scattering and loss of tissue architecture. *Solid lines* are each 2 mm in length

dysplasia (HGD)/carcinoma from low-grade dysplasia (LGD) (Fig. 67.1). Due to significant interobserver variability when diagnosing dysplasia in BE [43], computer-aided diagnosis algorithms were developed to provide a quantitative measurement [45, 46] of dysplasia in BE compared to non-dysplasia in BE. The demonstrated sensitivity of 78–82 % and specificity of 74–90 % could potentially reduce diagnostic variability in classifying dysplasia in BE.

The early EOCT studies above utilized the first-generation EOCT system built in a time-domain configuration. Those early EOCT imaging systems had two major disadvantages: slow imaging speed and small field of view. Therefore, the surface area of mucosa interrogated in any given image was exceedingly small (typically about 6 mm image width by 25 μm slice thickness), making such systems unsuitable for interrogation of large mucosal regions.

One of the latest advances in OCT technology was ultrafast imaging speed, which led to the advent of the second-generation EOCT system. These new EOCT systems benefit from ultrahigh A-scan acquisition rate of Fourier-domain OCT. Miniature catheter probes with centering balloons and more than 10 mm working distance are another key technology which allows for scanning a lumen with a large diameter. New technologies make comprehensive esophageal screening and surveillance possible [48–53]. It was recognized that EOCT imaging could be extended to cover a much larger area of mucosa than that sampled by the conventional biopsy forceps. The aim of eliminating sampling error in current BE

diagnosis procedures has motivated the development the second-generation of EOCT for volumetric esophageal imaging.

The feasibility of this second-generation EOCT was first demonstrated in swine esophagus in vivo [49, 51, 52]. More than three centimeters of esophagus was visualized up to the muscularis externa (smooth muscle) with unparalleled resolution in minutes. 3D reconstruction allows the longitudinal and en face views, in addition to the conventional cross-sectional views. The entire circumference can be scanned with rotary catheter probes when the tissue is expanded with cylindrical balloons. The vasculature in the muscularis mucosa was clearly visualized by extracting the Doppler shift from OCT signal. The impact of the balloon compressing the tissue was questioned [54]. A double-balloon catheter was proposed as an alternative design so that the mucosa to be imaged was not in contact with balloons [52]. A catheter probe without the centering balloon was also demonstrated [55]. This probe achieved higher lateral resolution due to short working distance, with the tradeoff of imaging only a portion of the circumference. Also demonstrated was the feasibility of producing laser ablation marks in live swine using the OCT catheter probe [56]. The ablation site was visualized both in EOCT images and biopsy slides. This technology may be potentially utilized in a clinical setting to precisely correlate EOCT with pathology.

Pilot clinical trials have also been reported [50, 55, 57]. The image acquisition required only minutes to accomplish. No complications have been reported resulting from the imaging procedure. A variety of microscopic features were observed that were consistent with histopathologic findings, including squamous mucosa, intestinal metaplasia with and without dysplasia, Barrett's glands, and esophageal erosion. 3D EOCT has also been investigated as a comprehensive imaging tool to detect residual Barrett's glands after ablation treatments [55, 58]. It may benefit the ablation procedure by reducing the recurrence of Barrett's esophagus and the need for secondary ablation and potentially further increase the complete eradication rate of intestinal metaplasia.

67.2.2 Colon

The early clinical EOCT studies in colonoscopy, similar to early esophageal studies, were limited by the imaging speed and field of view of the first-generation EOCT systems. These studies investigated the backscattering profile of single cross-sectional images. Shen et al. discovered that EOCT demonstrated disruption of the wall structure in the majority (90 %) of patients with Crohn's disease, whereas the disrupted structure was present in significantly fewer cases (16.7 %) of ulcerative colitis [59]. Consolo et al. demonstrated that mucosal backscattering alteration was an effective feature to detect inflammatory bowel disease in colon with sensitivity of 100 % and specificity of 78 % [60]. 3D endomicroscopy of a large area in the colonic wall with high resolution has recently been demonstrated with the advent of the Fourier-domain EOCT technology, enabling the visualization of single crypts [61].

One of the potential clinical applications was to identify ACF, a possible precursor of precancerous polyps. Qi et al. developed an automated algorithm for colonic crypt segmentation and morphologic feature characterization [62]. The algorithm was applied to 3D OCT images obtained from excised human colonic tissues, which demonstrated the potential to differentiate ACF from normal crypts.

67.3 EOCT Key Technologies

State-of-the-art EOCT research focuses substantially on cancer precursor detection in large areas within the GI tract in a clinical setting. Visualizing the tubular organs requires several key technologies. Most of these technologies are developed in the sample arm, making the common OCT configuration usable in the GI tract. The image acquisition has to be fast because the EOCT procedure is expected to be accomplished within minutes. The imaging probe has to be reasonably small and flexible which allows for easy deployment in the lumen of tubular organs. The optical and mechanical design of the catheter directs the probing beam so that the large mucosal area of the tubular organ can be scanned. On the software side, motion artifact correction is required because physiological motion causes artifacts with similar characteristics as nonuniform rotary distortion (NURD). This causes significant misalignment along the longitudinal direction, and the distorted images may diminish the utility of 3D EOCT. Computer-aided diagnosis (CAD) algorithms are also potentially important to assist the challenging tasks of discerning dysplasia and other abnormalities, by providing objective and quantitative interpretation, reducing inter- and intra-observer variability, and speeding image interpretation. 3D EOCT procedures may yield thousands of images per patient. Analysis of these data by the unaided human reader will not be practical.

67.3.1 EOCT System

Currently, swept-source OCT is more often implemented for endoscopic applications than spectral-domain OCT. Currently, commercially available swept laser sources have higher line-scan rates than that of line-scan cameras used for spectrometers for the wavelength of 1,310 nm, which is commonly used in dense tissue imaging. The sensitivity falloff range in a swept-source system is usually more than 6 mm, compared to less than 2 mm in spectral-domain OCT. The complex conjugate artifact can be more easily resolved, e.g., with frequency shifting [63] or other technologies. Swept-source OCT can also be built with all fiber-optic components, without the need to design and maintain a high-speed spectrometer. While SDOCT may potentially have advantages over SSOCT in terms of axial resolution and phase stability, and high-quality EOCT has been implemented in both SSOCT and SDOCT configurations [31, 64, 65], in the foreseeable future, swept-source OCT will likely remain the preferred configuration for gastroenterologic applications.

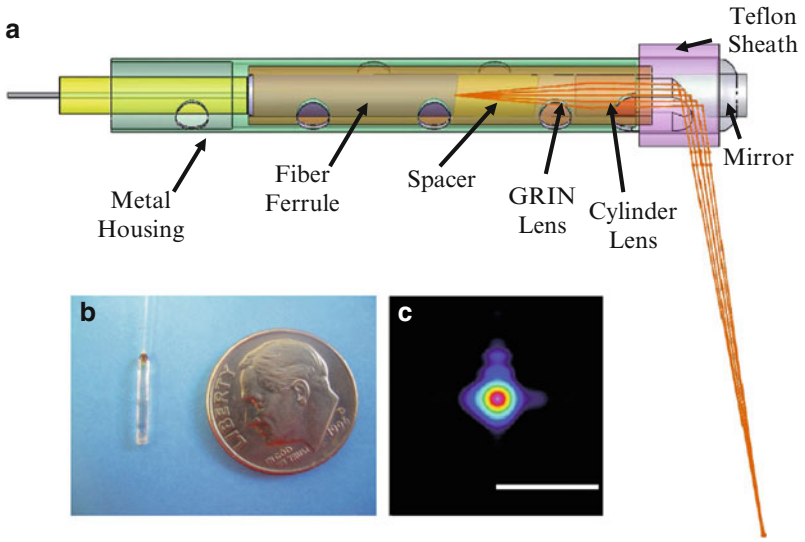

Fig. 67.2 (**a**) The mechanical model of the probe design. (**b**) An assembled fiber-optic probe without metal housing. (**c**) Beam profile measured by a beam analyzer. (Bars: 100 μm)

67.3.2 Miniature Probe

The fiber-optic probe guides the light from the EOCT system to the internal organ, focuses the beam onto the mucosa of the luminal wall, and collects the image-bearing backscattered light. A small outer diameter and short rigid parts are preferred for ease of use, especially when the probe in intended to be introduced through the accessory channel of an endoscope. The side-viewing design is most commonly used. When driven in a helical scanning pattern, the probing beam can scan the inner wall of the tubular organs. The probe may be used with or without a centering balloon, depending on the application and the needed optical performance. Balloon-based probes have long working distances, corresponding to the diameter of the balloon. The probe beam passes through the balloon and is maintained in focus on the entire circumference. They are mostly used for large, straight tubular organs, e.g., esophagus. For a typical (Gaussian) beam, the consequence of a long working distance is a larger beam waist, in other words, lower lateral resolution. Probes without balloons typically have a working distance barely longer than the outer protecting catheter sheath and may therefore be focused to a sharper spot. They are placed directly adjacent to the tissue when imaging, and if the organ has a large diameter, only a portion of the circumference is scanned. Short working distance probes are the better choice for imaging pancreatic/bile duct, which have small lumens, and colon if it is to be imaged in a targeted, rather than comprehensive way.

Figure 67.2a shows an example of a probe design for a balloon catheter [52]. A single-mode fiber was fixed in a ferrule followed by a glass spacer to expand the beam before entering a GRIN lens. A separate cylinder rod lens was attached after

the GRIN lens to correct the astigmatism induced by the protecting sheath. All optical components have polished surfaces angled at 8° to prevent back reflection. The length of the spacer may be selected to result in the desired working distance of the lens group. The lens group and ferrule were assembled in a metal housing. A gold mirror was glued at the tip of the metal housing to deflect the beam by 80° relative the optical axis. The overall numerical aperture of the probe is 0.024. The total outer diameter of the fiber probe, including the metal housing, is 1.7 mm. The rigid tip (medal housing) is about 2 cm long. Figure 67.2b shows the size of an assembled probe without the metal housing. Figure 67.2c shows the lateral beam profile at a 9 mm working distance, as measured by a beam analyzer. The spot had a minimal ellipticity of 0.98 with a FWHM diameter of 33 μm.

In order to perform the helical pattern scanning, a rotary motor and a translational motor were utilized to drive the proximal end of a flexible shaft. The metal housing of the probe was attached to the distal end of the flexible shaft. The flexible shaft can mostly prevent nonuniform rotary distortion (NURD). To further suppress NURD, The position encoder in the rotary motor was used to trigger the OCT A-scan acquisition at equal angular increments.

67.3.3 Balloon Catheter

BA balloon centers a long working distance probe to maintain focus and to stabilize the probe to suppress motion artifacts. The conventional balloon design uses a single balloon, with its two necks attached to the outer sheath using biocompatible epoxy. The imaging probe is placed within the balloon, and the probe beam passes through the balloon and is focused into the adjacent mucosa. It has been shown that catheter pressure on colonic mucosa significantly alters the tissue appearance [66]. This raises the question of whether balloon pressure or contact compresses the mucosa and affects OCT image features that are diagnostic of dysplasia within BE.

Double balloons were proposed as an alternative design [52]. Figure 67.3a illustrates the double-balloon design that allows two imaging schemes to be employed (with and without balloon-tissue contact) to investigate the influence of pressure. For imaging with no balloon-tissue contact, the images were obtained in the gap between the two balloons (labeled beam position (1)). The fiber probe could also be placed within the distal balloon (labeled beam position (2)) to acquire images through the balloon in the conventional way. The length of the gap was well controlled in order to limit the extent of lumen contraction between the balloons and keep the tissue within the axial imaging range. Holes were made in the outer sheath within the balloons so that they were inflated and deflated from the proximal end of the catheter. The outer sheath had an outer diameter of 2.4 mm. The small diameter allowed the catheter to be inserted through the accessory channel of the endoscope (Fig. 67.3b). The deployment and operation of the catheter probe were observed from the camera of the endoscope, so that images were acquired from the esophageal segments of interest (Fig. 67.3c). Figure 67.3d represents a swine esophageal image in anatomic (cross-sectional) view. The diameters of

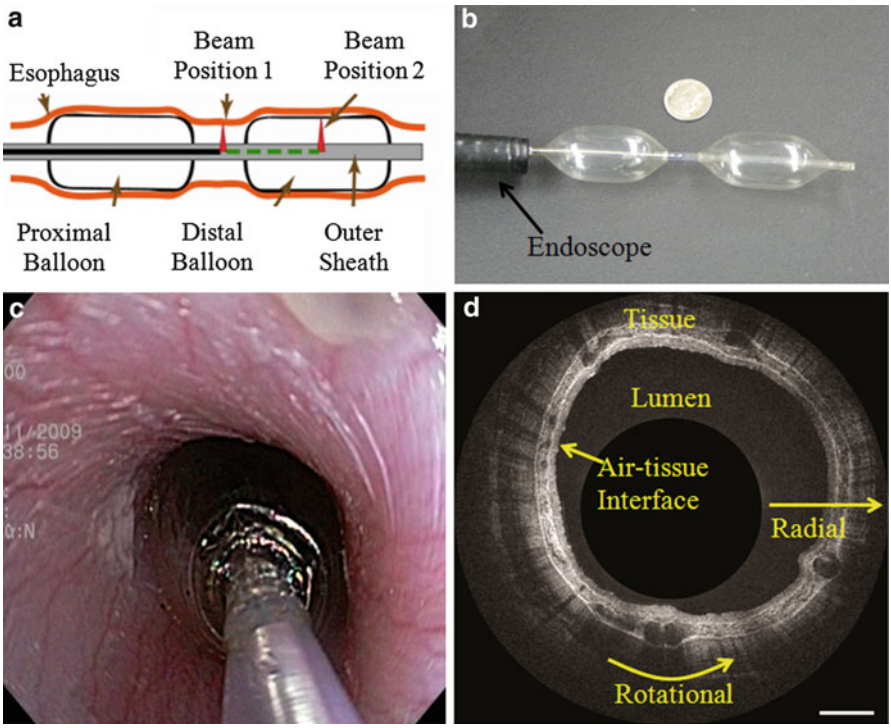

Fig. 67.3 (**a**) Schematic of the double balloon design. The beam can be located between two balloons for imaging without balloon-tissue contact (*solid black line*) or in a balloon for imaging with contact (*dashed green line*). (**b**) The double-balloon catheter (compared with a dime) inserted through the GI endoscope and inflated. (**c**) The deployment of the balloon catheter in swine esophageal observed from the camera of the endoscope. (**d**) A cross-sectional image of swine esophagus in anatomic view (Bar: 1 mm)

the imaged esophagi were around 18 mm, but in order to visualize the tissue structure, the images are displayed with a diameter of about 3 mm.

67.3.4 Motion Artifact Correction

In previous sections, several methods have been introduced for the purpose of motion artifact suppression, i.e., triggering with the encoder in the rotary motor, rotating the probe with a flexible shaft, and stabilizing it with the balloon. However, when imaging living subjects, motion artifact may not be completely suppressed. A study has shown that the motion artifact can be caused by physiological motion, e.g., respiration and heart beating [57]. Figure 67.4a demonstrates an example of motion artifact in the swine esophagus in vivo. Cross-sectional images were acquired for one minute without pulling the probe and stacked in the order of time (time axis). All of the above motion suppression methods were applied.

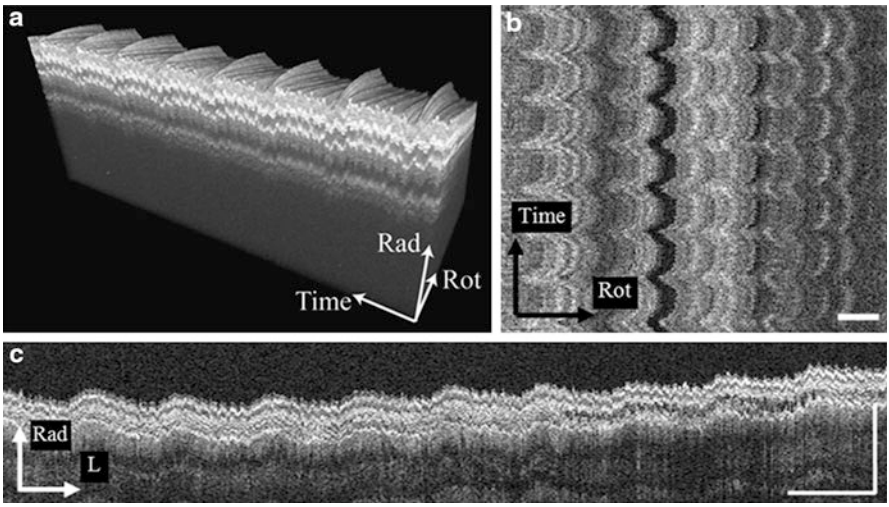

Fig. 67.4 (**a**) 3D reconstruction of swine esophageal images obtained without pulling the probe. The radial-rotational plane should not change over time if there was no motion artifact. (**b**) The en face view of the plane 300 μm deep in (**a**) shows rotational motion. (**c**) The radial-longitudinal view from the 3D reconstruction shows the radial motion (*Rad* radial, *Rot* rotational, *L* longitudinal. Bar: 1 mm)

Ideally without motion, these images should be identical. However, the time-radial plane (Fig. 67.4c) illustrates how the reconstruction is substantially distorted radially. Figure 67.4b is an en face plane extracted from the same volume within the layer of the muscularis mucosa (approximately 300 μm from the mucosal surface). In this view, rotational distortion is clearly observed. Motion artifact along the longitudinal direction (perpendicular to the cross-section) is also prominent. However it cannot be clearly visualized without additional imaging mechanism (i.e., Doppler shift detection [67]). Here, motion artifacts refer to the radial and rotational components if not otherwise specified.

Kang et al. proposed an automatic image registration method to suppress motion artifact during esophageal imaging [57]. Registration started with the detection of esophageal lumen, assuming the air-tissue interface had the highest radial gradient. The detection was formulated as a global optimization problem, which sought a contiguous curve with only one pixel from each A-scan. The summation of the radial gradient value on the curve was a global maximum among all the possible curves. To correct for radial motion, the detected lumen surface was aligned to a circle by translating each A-scan in the radial direction. Local box matching (LBM) was then applied to estimate the rotational motion. LBM matched large regions of interest (ROI) in each image to the previous image by cross-correlation and therefore estimated the bulk rotational motion artifact of the ROIs. Each ROI consisted of a few hundred of A-scans. The rotational position of each individual A-scan was then finely adjusted by considering the bulk motion of the adjacent ROIs in the same cross-sectional image. This method can be categorized as a template

update method in the field of computer vision [68]. In this case, the previous cross-sectional image was the template. Accumulated registration error occurred because LBM did not distinguish tissue motion from the actual variation in the anatomical structure. To visualize the natural tissue structure, the slowly varying components in the motion trace were preserved during the final image reconstruction.

67.3.5 CAD

CAD algorithms have been proposed to analyze colonic crypt morphological patterns [69] and to classify dysplasia in BE [45, 46]. CAD algorithms usually consist of steps including region of interest (ROI) segmentation, feature extraction and selection, and finally classification. It is critical to first identify appropriate and quantifiable target features for computer processing before CAD algorithm development. The straightforward approach is to adopt and quantify the diagnostic criteria established by human expert readers.

EOCT visualizes the 3D structure of the colonic mucosa, which is one of the advantages over other competing colonoscopic imaging technologies, such as high magnification chromoendoscopy. The crypts within aberrant crypt foci (ACF) have larger lumens and are oriented less parallel to each other in three dimension than normal crypts are [70]. Qi et al. proposed to characterize the crypt morphology using 3D image processing to quantify these 3D morphological features [69]. The process was demonstrated using freshly resected segments of colon from patients undergoing surgery to remove cancer. Crypts were first segmented on each en face section of the 3D dataset. Features, such as area of the lumen and density of crypts (counts per square millimeter), were calculated. The centroids of each segmented crypt were then connected to represent the crypt morphological skeleton. Straightness (i.e., a skeletons' spatial linearity) and parallelism (i.e., the similarity of the skeletons' spatial orientation) were computed. All the features were quantified for ACF, normal tissue, and normal-appearing tissue adjacent to cancer (NA). Different feature values were observed between ACF and normal/NA tissue, which may potentially be useful for differentiating abnormal crypts from data acquired in vivo.

CAD algorithms have also been developed to potentially assist in diagnosis of dysplasia in BE [45, 46]. The transformation from normal to dysplastic mucosa in BE includes the size, shape, and density of epithelial nuclei, which affects the tissue attention and backscattering properties. Loss of structure associated with normal histological organization (i.e., homogeneity, layering) has been observed in dysplastic tissue [37, 43, 71]. Some of these previous observations were quantified, such as backscattering coefficient and intensity-based texture parameters, for CAD algorithms. New features, such as the stripe pattern associated with surface topology, were also proposed for CAD algorithms [72, 73]. A stripe pattern was often observed in non-dysplastic tissue and seldom observed in dysplastic tissue. This pattern was quantified by the stripe density and orientation. This method was demonstrated using clinical EOCT images from patients undergoing regularly scheduled BE surveillance, where diagnoses were confirmed by biopsy.

The receiver operating characteristic (ROC) curve of each feature was calculated to select those with best classification accuracy. Principle component analysis was applied to reduce feature redundancy and increase algorithm robustness. Only a few principle components that accounted for the most variance in the feature space were selected as input for the multivariate classification algorithms. Multiple classification methods were compared. In this case, decision tree combined with bootstrapping yielded best classification accuracy. Bootstrapping consisted of construction of multiple classification training sets, each using a randomly selected subset of the EOCT training images. Each training set generated a decision tree, and then each test image was classified by majority voting of those decision trees [45, 46].

67.4 Recent EOCT Imaging Studies

It has been shown that endoscopic OCT (EOCT) can obtain interpretable images of gastrointestinal (GI) mucosal microstructure, differentiate GI mucosal types, and detect abnormality ever since the first-generation time-domain systems [30–40, 59, 74–76]. State-of-the-art EOCT studies in GI tract utilize the second-generation Fourier-domain systems. The aims have been extended to investigate the clinical impact of ultrafast image acquisition, eliminate sampling error, and visualize new diagnostic features, such as buried glands in BE and crypt patterns in colon in vivo.

67.4.1 Animal Studies

Swine esophagus is a commonly used animal model for in vivo studies to demonstrate feasibility of new technology. Kang et al. reported a spectral-domain EOCT system together with double-balloon catheter probe [52]. The fiber probe was rotated at 10 rev/s and pulled back at 2 cm per minute. One centimeter to three centimeter segments of esophagus were imaged. Each cross-sectional frame consisted of 4,700 A-scans. The image resolution was 9 μm, 33 μm, and 33 μm in radial, rotational, and longitudinal directions, respectively. The image voxel size was 4 μm, 11 μm, and 33 μm in the three directions. Swine were sedated, intubated, ventilated, and maintained under anesthesia for the duration of the procedure. During the imaging study, video endoscopy was used to guide the probe deployment and through the endoscope accessory channel and balloon inflation.

Both double-balloon and single-balloon images were obtained from the same esophageal segment (Fig. 67.5) in order to evaluate relative image quality and the effects of the pressure of the balloon on the OCT appearance of the mucosa. Figure 67.5a is a representative cross-sectional image of the swine esophagus without balloon-tissue contact. The same radially compressed visualization method used in Fig. 67.3d is applied here. Tissue layers and structures can be clearly observed, including the squamous epithelium, lamina propria, muscularis mucosa, submucosa, muscularis propria, and blood vessels in the muscularis mucosa.

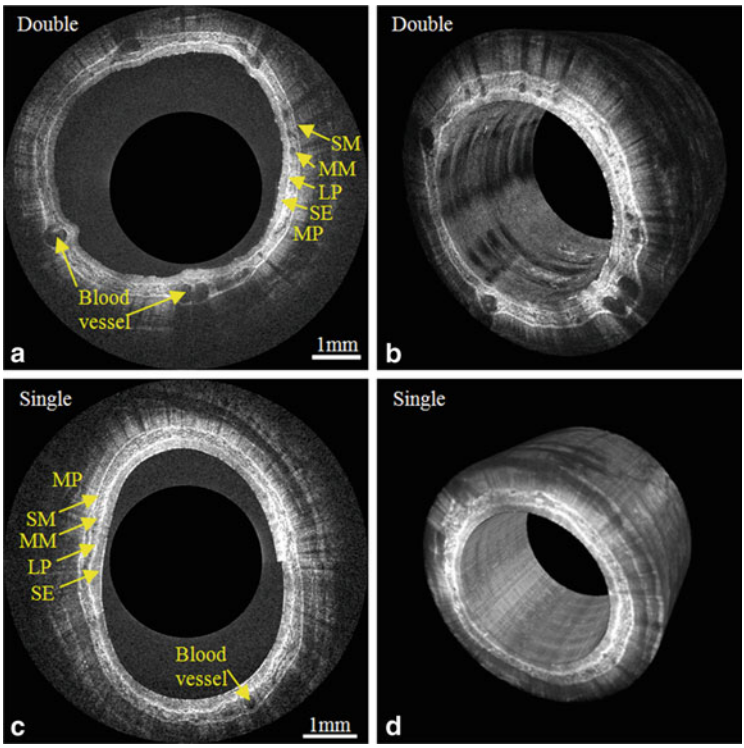

Fig. 67.5 (**a**) A representative cross-sectional image of a swine esophagus with the double-balloon imaging scheme. The layered structure that can be observed includes the squamous epithelium (*SE*), lamina propria (*LP*), muscularis mucosa (*MM*), submucosa (*SM*), and muscularis propria (*MP*). (**b**) 3D reconstruction of a 17 mm long section of swine esophagus obtained with the double-balloon imaging scheme. (**c**) A representative cross-sectional image of the single-balloon imaging scheme. (**d**) 3D reconstruction of 10 mm long segment with single-balloon imaging scheme

The imaging depth exceeds 1 mm. Figure 67.5b shows a 3D reconstruction visualizing a 17 mm long segment obtained within 50 s, using the double-balloon scheme. Figure 67.5c, d show a representative cross-sectional image and the corresponding 3D reconstruction obtained with the single-balloon scheme (10 mm segment obtained within 30 s). The typical layers of the esophagus can also be clearly recognized. The imaging depth in the single-balloon images is greater than that of the double balloon, with multiple layers of muscularis propria visible. However, detailed structure in the muscularis mucosa, especially blood vessels, is more clearly observed in the double-balloon images. The glandular structure and the blood vessels are barely recognized in the single-balloon image. The natural mucosal surface topology is apparent in the double-balloon image, whereas the mucosal surface was compressed and smoothed by the balloon in the single-balloon image. The balloon-flattened surface resulted in more stable illumination and therefore more uniform image brightness. Also, the tissue motion artifact was less

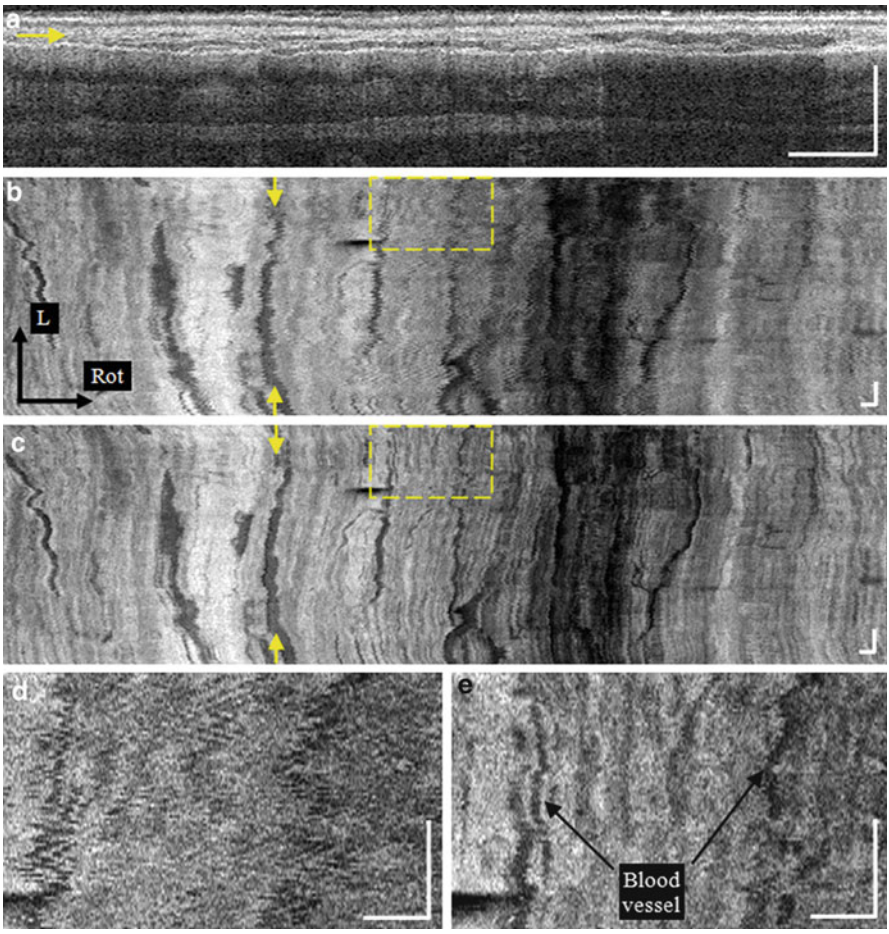

Fig. 67.6 (**a**) The registered radial-longitudinal view of Fig. 67.4c. The *arrow* indicates the position of (**c**). (**b**) The en face view from the original 3D sequence. *Arrows* indicate the position of Fig. 67.4c. (**c**) The registered en face view of (**b**). *Arrows* indicate the position of (**a**). (**d**) The enlarged view of the *dash square* in (**b**). (**e**) The enlarged view of the *dash square* in (**c**). Note the reduced motion artifact and improved contrast in (**c**) and (**e**) compared to (**b**) and (**d**) (*Rad* radial, *L* longitudinal, *Rot* rotational. Bars: 1 mm)

significant with single-balloon imaging due to the balloon support. These observations suggest the need to further investigate the advantages and disadvantages of balloon-tissue contact and pressure, how tissue features of diagnostic significance in BE are altered, and how the changes affect detection of dysplasia in BE.

Figure 67.6 demonstrates the results of correcting the motion artifact caused by physiological movement. Figure 67.6a shows the corrected radial-longitudinal cross sections of Fig. 67.4c. Figure 67.6b, c is the corresponding en face views within the muscularis mucosa layer, uncorrected and corrected, respectively. The yellow arrows indicate the positions of Figs. 67.4c and 67.6a, respectively.

The saw-tooth artifacts in both the radial and rotational directions are corrected and the tissue layers are aligned. The muscularis mucosa has a rich vascular network, which can be visualized more clearly in the corrected en face view. Figure 67.6d, e is enlarged views of the regions indicated in the dashed yellow rectangles in Fig. 67.6b, c, respectively. The motion artifact correction algorithm is able to recover detailed features in Fig. 67.6e which is otherwise obscure in Fig. 67.6d. The corrected images effectively reveal the otherwise distorted microstructure in the esophageal mucosa. Further investigation into the motion trajectories revealed that the frequency components associated with the motion were the fundamental frequencies or higher-order harmonics of respiration and heart beating. Notably, such motion artifacts were not suppressed by increasing the pressure of the balloon to improve stability or other real-time mechanisms [57]. Post-acquisition correction of motion artifact effectively improves the EOCT image quality. Such a correction algorithm is a key component of an EOCT system and may enhance the potential clinical utility.

67.4.2 Clinical Studies

A clinical pilot study was conducted at the University Hospitals Case Medical Center (UHCMC), Cleveland, Ohio, under a protocol approved by the Institutional Review Board of UHCMC. Patients undergoing endoscopic surveillance for BE were eligible for inclusion in the study. Patients with a diagnosis of adenocarcinoma or esophageal stricture were excluded. Informed consent was obtained from each patient.

An initial endoscopic inspection was performed before acquiring OCT images. When a segment of BE (>2 cm in length) was identified, the balloon was inserted through the accessory channel. The balloon was deployed and inflated within the BE segment under endoscopic guidance. 3D volumetric images were obtained by pulling the probe for 1 cm. The balloon pressure was maintained at 100 mmHg. The OCT catheter was extracted after OCT imaging. Biopsies were obtained from four quadrants of the imaged segment for histopathology. The surveillance procedure then continued according to the standard protocol.

67.4.2.1 Normal and Non-Dysplastic Esophagus

Figure 67.7 shows the images of normal esophageal mucosa and non-dysplastic BE from a patient undergoing BE surveillance. The diagnosis was later confirmed by histopathologic examination of a biopsy of the same tissue segment. The EOCT system utilized for the clinical study has a similar configuration as Ref. [52]. Figure 67.7a is a rectangular view of the proximal normal esophagus. The rectangular view displays an unwrapped cross-sectional image before it is transformed into anatomic view (i.e., Fig. 67.4a). The normal esophagus has a stratified squamous epithelium which typically appears in EOCT as a thick layer with consistent thickness and homogeneous intensity. The layered architecture can be clearly visualized, especially the boundary between epithelium and lamina propria. Fibrous, glandular, and vascular structures are apparent beneath the epithelium in

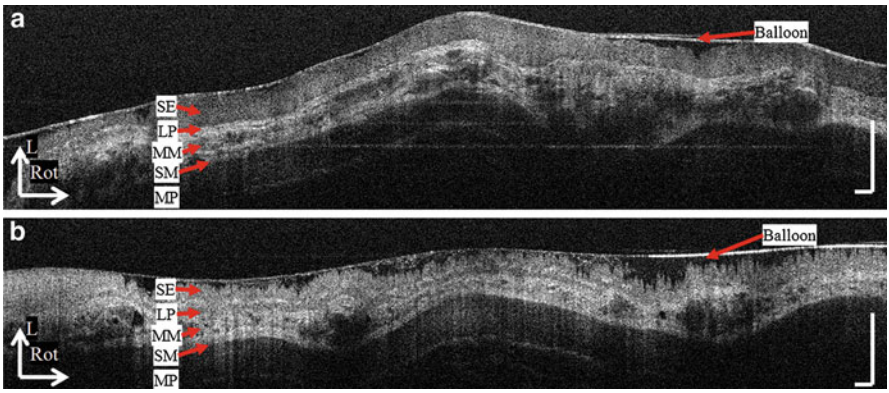

Fig. 67.7 (**a**) Normal esophageal image from a patient undergoing BE surveillance showing distinct layered architecture and homogeneous epithelium. (**b**) Non-dysplastic Barrett's esophageal image. The layers become less distinct with a thinner and irregular epithelium (*SE* squamous epithelium, *LP* lamina propria, *MM* muscularis mucosa, *SM* submucosa, *MP* muscularis propria. Bars: 1 mm in two directions. *Rad* radial, *Rot* rotational)

the lamina propria, muscularis mucosa, and submucosa. The imaging depth is typically more than 1 mm, which allows the visualization of muscularis propria. In non-dysplastic Barrett's esophagus (Fig. 67.7b), the epithelium has higher backscattering and appears less homogeneous, probably due to the transformation from a stratified squamous epithelium to a columnar epithelium associated with specialized intestinal metaplasia. The layered structure is still visible. However, the epithelium is thinner, and the boundary between the epithelium and the lamina propria becomes less distinct.

67.4.2.2 Dysplastic BE

The lack of layered architecture is usually observed in EOCT images of dysplastic esophagus. Figure 67.8 shows images obtained from an esophageal segment where both HGD and normal esophagus existed. Figure 67.8a was obtained from the segment where HGD was later diagnosed. The boundary between epithelium and lamina propria is no longer visible within the entire image. On the other hand, the lamina propria in normal epithelium is clearly identified in Fig. 67.8b, which was obtained from the normal segment. Figure 67.8c, d are the enlarged views of the dashed squares in Fig. 67.8a, b, respectively. Unlike the homogeneous intensity typical in the normal epithelium, the backscattering varies significantly along the dysplastic tissue.

Surface morphology may be a characteristic feature for BE. Figure 67.9 shows the mucosal surface from a patient when both normal and HGD esophagus were imaged. The balloon was not fully expanded in the esophagus, leaving a gap where the tissue surface was visualized. Figure 67.9a obtained from a normal segment has the normal layered structure and homogeneous epithelium. The surface is smooth compared to the fingerlike morphology in the HGD segment (Fig. 67.9b). A 3D reconstruction in the vicinity of Fig. 67.9b is shown in Fig. 67.9c. The raw data was

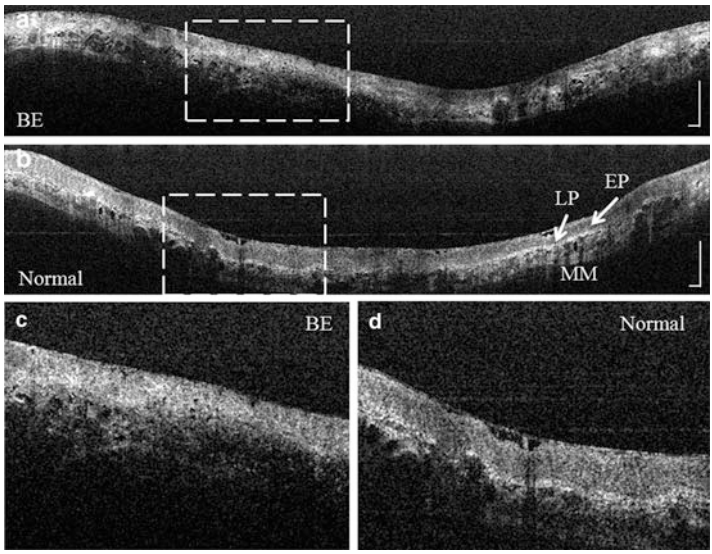

Fig. 67.8 (**a**) Image from an esophageal segment with HGD, where the layered structure can not be identified. (**b**) A cross-sectional image of normal esophagus, where the epithelium (*EP*), lamina propria (*LP*), and muscularis mucosa (*MM*) are clearly identified. (**c**) An enlarged view of the *dashed square* in (**a**). (**d**) An enlarged view of the *dashed square* in (**b**) (Bars: 1 mm in two directions)

first corrected for motion artifact, so that the microstructure in the mucosa was well aligned. The image of the balloon was removed to expose the tissue surface. The irregular pattern in Fig. 67.9b seems to be caused by the elongated folding of the epithelium along the longitudinal direction (indicated by arrows in Fig. 67.9c). Such folding is not observed in normal esophageal mucosa. However, the reason to form the folding is not understood.

Small glandular structures are observed in dysplastic tissue near the tissue surface. Figure 67.10a is an en face view of the 3D reconstruction of Fig. 67.9c showing the mucosa at a depth of 300 μm from the balloon surface. The signal void zone at the top middle of the image is a gap between the tissue surface and the balloon. Yellow arrows indicate representative BE glands. Figure 67.10b is a cross-sectional view from the 3D reconstruction. Its position in Fig. 67.10a is indicated by the red arrows. The corresponding glands are also indicated by yellow arrows. Compared to normal esophageal glands in the muscularis mucosa, these glands are shallower (only a few hundred microns from the tissue surface) and smaller (approximately 100 μm in diameter). These buried Barrett's glands have been observed prior to and post BE ablation treatment [77]. The latter situation suggests that such treatment sometimes fails to eradicate BE completely. The detection of buried Barrett's glands after radio-frequency ablation and cryospray ablation has been demonstrated [58, 78]. The ability to rapidly obtain highly resolved, in-depth images makes EOCT a unique and promising technology for real-time surgery planning and BE eradication assessment. The motion artifact correction algorithm

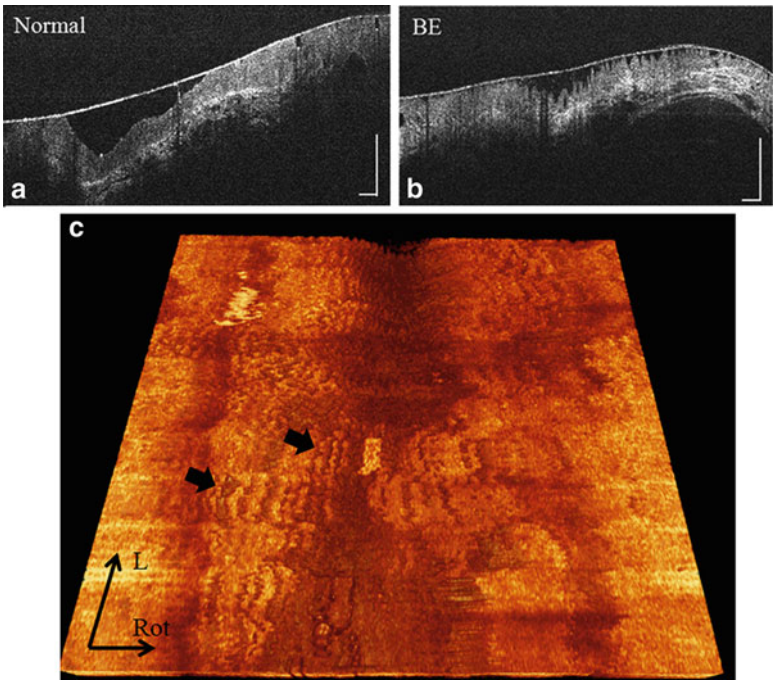

Fig. 67.9 (**a**) A cross-sectional image of the normal esophagus, the balloon was not fully in contact with the tissue. (**b**) A cross-sectional image of dysplastic BE with fingerlike pattern on the surface. (**c**) 3D reconstruction of (**b**) suggests that the fingerlike pattern may be a cross-sectional view of the longitudinal folding (indicated by *arrows*) (Bars: 1 mm in two directions. *L* longitudinal, *Rot* rotational)

described in Sect. 67.3 accurately registered the otherwise mis-aligned small glands in 3D, which may potentially facilitate automated gland counting and analysis.

CAD for Dysplasia Diagnosis

Previously, Qi et al. reported a computer-aided diagnosis (CAD) method for detecting dysplasia and classifying EOCT images of BE in clinical trials [45]. Initial work was further improved to include the use of multiple image frames per examination site [46]. Site-based CAD is possible when 3D esophageal OCT images are available and can potentially be incorporated into future 3D EOCT surveillance. The efficacy of these CAD methods was tested by classifying the examination sites in three ways. First, sites were classified into two categories as non-dysplastic or dysplastic (low grade and high grade). The best classification performance was achieved by using ten frames per site and requiring at least four frames to be positive to classify the site as positive. It yielded sensitivity of 0.78 (95 % CI: 0.54–0.92), specificity of 0.90 (95 % CI: 0.67–0.98), and accuracy was 0.84 (95 % CI: 0.68–0.93). Second, sites were classified into two categories as non-high-grade dysplastic or high-grade dysplastic. The best classification result

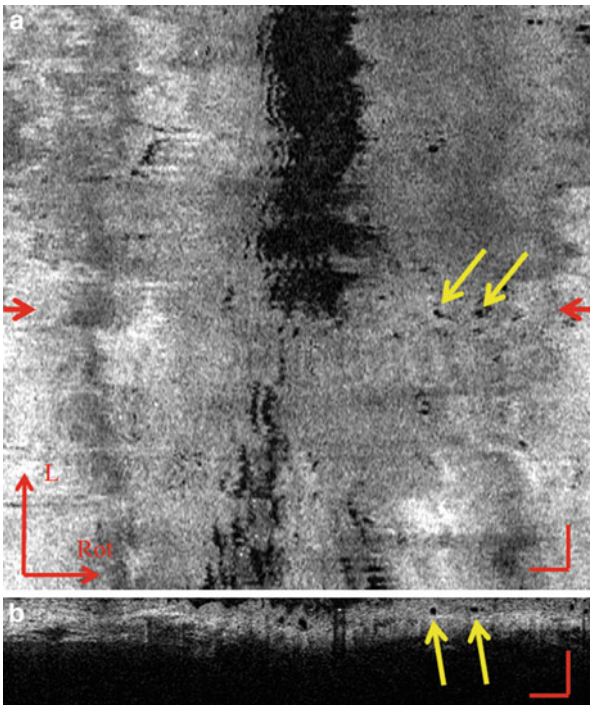

Fig. 67.10 (**a**) An en face view of Fig. 67.9c showing the buried Barrett's glands. (**b**) The corresponding cross-sectional view. The position in (**a**) is indicated by *red arrow*. *Yellow arrows* indicate the buried Barret's glands found in the two views (Bars: 1 mm to two directions. *L* longitudinal, *Rot* rotational)

was obtained by using nine frames per site and requiring two frames to be positive, which yielded sensitivity of 0.67 (95 % CI: 0.46–0.85) and specificity of 1.00 (95 % CI: 0.83–1.00). Third, sites were classified into three categories as non-dysplastic, low-grade dysplastic, or high-grade dysplastic. Using the conservative criteria for multi-image classification, no high-grade dysplastic biopsy sites were misclassified as low-grade or non-dysplastic. Furthermore, no low-grade dysplastic biopsy sites were misclassified as non-dysplastic. However, several non-dysplastic sites and low-grade sites were misclassified as high-grade dysplastic. The use of multiple EOCT images at a single examination location improves classification accuracy over the previous use of a single image. The image analysis presented here should be translatable to 3D comprehensive imaging. Based on these results, it is apparent that CAD has the potential to aid detecting the presence or absence of dysplasia in surveillance of large surface areas of Barrett's mucosa when using EOCT.

67.5 Future Directions

The current status of EOCT can be summarized as feasible, safe, and comprehensive. EOCT has some extremely desirable attributes, namely, rapid imaging speed, large field of view, and a depth of penetration sufficient for detailed imaging of all regions of the GI tract that approaches the degree of resolution offered by

microscopy of ex vivo tissues. Because EOCT systems are portable, compact, relatively inexpensive, and easy to deliver imaging probes, there is no impediment to the widespread implementation of EOCT in clinical practice. Unfortunately, despite these remarkable characteristics, no study to date has conclusively established a clinical application for comprehensive EOCT that is without question superior to existing methods. Moreover, there are a number of competing technologies, with almost no comparative studies of any of these modalities. Given the problems and vagaries of health care, the only thing that insures success is incontrovertible evidence of clinical utility, evidence that is sufficient to justify costs.

Of the numerous potential clinical applications of EOCT, one that may meet the greatest clinical need is the detection of dysplasia. The clinical studies of diagnostic efficacy require histopathology as the gold standard. One remaining technical challenge is to provide biopsy concordance for EOCT images, especially for the commonly used the balloon catheter. EOCT and video endoscopy cannot visualize simultaneously the same esophageal segment when the inflated balloon occludes and compresses the tissue. Ideally, the biopsy should be obtained after EOCT imaging to avoid blood obscuring the image. Suter et al. have proposed to use laser-induced marking of the esophagus, which can be identified during EOCT and later in video endoscopy [56].

Malpositioning of a single rigid balloon near the gastroesophageal junction has also been reported in a clinical setting [50]. Alternative balloon-based and non-balloon-based catheters are a topic of ongoing studies [52, 55, 58].

Assessment of mucosal radio-frequency ablation (RFA) treatment using EOCT has recently drawn attention [58, 79]. Among multiple available BE ablation technologies, RFA results in few serious complications and significantly decreases the rate of progression from HGD to cancer in BE [80]. However, Zhou et al. have showed that most patients have buried Barrett's glands after RFA treatment [58]. These buried glands contain metaplastic cells, from which the risk of cancer development is not known. The abroad acceptance of RFA may bring opportunities for new clinical applications for EOCT, one of which is to identify submucosal glands as an indicator of BE eradication. EOCT is by far the most promising tool to study buried glands.

Because an EOCT system suitable for surveillance of large mucosal areas would generate incredible amounts of data, it is highly improbable that the findings could be interpreted by an endoscopist in real time. Even the interpretation of archived data would be difficult and no doubt prone to error. Thus, it seems certain that computer-assisted image analysis will be needed for applications such as dysplasia diagnosis or buried glands detection.

In summary, endoscopic OCT has shown to have strong potential to become a useful tool in the GI endoscopy clinic. However, for EOCT to become an established routine endoscopic practice in the clinic, further improvements in technology are needed and clinical studies that demonstrate unique and efficacious applications must be carried out.

Acknowledgements The authors thank Michael W. Jenkins, Zhao Wang, Yinsheng Pan, Zhilin Hu, Gerard A. Isenberg, Amitabh Chak, and Michael Sivak. Some research presented here was supported in part by the National Institutes of Health (R01CA114276).

References

1. W.S. Haubrich, J.M. Edmonson, History of endoscopy, in *Gastroenterologic Endoscopy*, ed. by M.V. Sival (Saunders, Philadelphia, 2000), pp. 2–15
2. T.P. Pretlow et al., Aberrant crypts: putative preneoplastic foci in human colonic mucosa. Cancer Res. **51**, 1564–1567 (1991)
3. L. Roncucci et al., Aberrant crypt foci in patients with colorectal cancer. Br. J. Cancer **77**, 2343–2348 (1998)
4. T. Takayama et al., Aberrant crypt foci of the colon as precursors of adenoma and cancer. N. Engl. J. Med. **339**, 1277–1284 (1998)
5. W.J. Blot et al., Rising incidence of adenocarcinoma of the esophagus and gastric cardia. JAMA **265**, 1287–1289 (1991)
6. J. Powell, C.C. McConkey, The rising trend in esophageal adenocarcinoma and gastric cardia. Eur. J. Cancer Prev. **1**, 265–269 (1992)
7. J. Lagergren et al., Symptomatic gastroesophageal reflux as a risk factor for esophageal adenocarcinoma. N. Engl. J. Med. **340**, 825–831 (1999)
8. H. Pohl, H.G. Welch, The role of overdiagnosis and reclassification in the marked increase of esophageal adenocarcinoma incidence. J. Natl. Cancer Inst. **97**, 142–146 (2005)
9. K.K. Wang, R.E. Sampliner, Updated guidelines 2008 for the diagnosis, surveillance and therapy of Barrett's esophagus. Am. J. Gastroenterol. **103**, 788–797 (2008)
10. K.R. DeVault, Epidemiology and significance of Barrett's esophagus. Dig. Dis. **18**, 195–202 (2000)
11. E. Montgomery et al., Dysplasia as a predictive marker for invasive carcinoma in Barrett esophagus: a follow-up study based on 138 cases from a diagnostic variability study. Hum. Pathol. **32**, 379–388 (2001)
12. T.R. DeMeester, Surgical therapy for Barrett's esophagus: prevention, protection and excision. Dis. Esophagus **15**, 109–116 (2002)
13. D. Hurschler et al., Increased detection rates for Barrett's oesophagus without rise in incidence of oesophageal adenocarcinoma – a ten-year survey in Eastern Switzerland. Swiss Med. Wkly. **133**, 507–514 (2003)
14. J.M. Streitz Jr. et al., Endoscopic surveillance of Barrett's esophagus. Does it help? J. Thorac. Cardiovasc. Surg. **105**, 383–387 (1993). discussion 387 – 8, Mar 1993
15. J.H. Peters et al., Outcome of adenocarcinoma arising in Barrett's esophagus in endoscopically surveyed and nonsurveyed patients. J. Thorac. Cardiovasc. Surg. **108**, 813–821 (1994). discussion 821 – 2, Nov 1994
16. J.W. van Sandick et al., Impact of endoscopic biopsy surveillance of Barrett's oesophagus on pathological stage and clinical outcome of Barrett's carcinoma. Gut **43**, 216–222 (1998)
17. R. Incarbone et al., Outcome of esophageal adenocarcinoma detected during endoscopic biopsy surveillance for Barrett's esophagus. Surg. Endosc. **16**, 263–266 (2002)
18. M.K. Ferguson, A. Durkin, Long-term survival after esophagectomy for Barrett's adenocarcinoma in endoscopically surveyed and nonsurveyed patients. J. Gastrointest. Surg. **6**, 29–35 (2002). discussion 36, Jan-Feb 2002
19. D.A. Corley et al., Surveillance and survival in Barrett's adenocarcinomas: a population-based study. Gastroenterology **122**, 633–640 (2002)
20. A. Fountoulakis et al., Effect of surveillance of Barrett's oesophagus on the clinical outcome of oesophageal cancer. Br. J. Surg. **91**, 997–1003 (2004)
21. V.D. Jacques, Endosonographic evaluation of the patient with esophageal cancer. Chest **112**, 184S–190S (1997)
22. G.W. Falk, M.F. Catalano, M.V. Sivak Jr., Endosonography in the evaluation of with Barrett's esophagus and high-grade dysplasia. Gastrointest. Endosc. **40**, 207–212 (1994)
23. I.A. Scotiniotis, M.L. Kochman, J.D. Lewis, E.E. Furth, E.F. Rosato, G.G. Ginsberg, Accuracy of EUS in the evaluation of Barrett's esophagus and high-grade dysplasia or intramucosal carcinoma. Gastrointest. Endosc. **54**, 689–696 (2001)

24. B.C. Wilson, Detection and treatment of dysplasia in Barrett's esophagus: a pivotal challenge in translating biophotonics from bench to bedside. J. Biomed. Opt. **12**, 051401 (2007)
25. P. Sharma et al., The utility of a novel narrow band imaging endoscopy system in patients with Barrett's esophagus. Gastrointest. Endosc. **64**, 167–175 (2006)
26. M.A. Kara et al., Detection and classification of the mucosal and vascular patterns (mucosal morphology) in Barrett's esophagus by using narrow band imaging. Gastrointest. Endosc. **64**, 155–166 (2006)
27. M. Panjehpour, B.F. Overholt, T. Vo-Dinh, R.C. Haggit, D.H. Edwards, F.P. Buckley, Endoscopic fluorescence detection of high-grade dysplasia in Barrett's esophagus. Gastroenterology **111**, 93–101 (1996)
28. M.A. Kara, M.E. Smits, W.D. Rosmolen, A.C. Bultje, F.J. Kate, P. Fockens, G.N. Tytgat, J.J. Bergman, A randomized crossover study comparing light-induced fluorescence endoscopy with standard videoendoscopy for the detection of early neoplasia in Barrett's esophagus. Gastrointest. Endosc. **61**, 671–678 (2005)
29. E. Endlicher, R. Knuechel, T. Hauser, R.-M. Szeimies, J. Scholmerich, H. Messmann, Endoscopic fluorescence detection of low and high grade dysplasia in Barrett's oesophagus using systemic or local 5-aminolaevulinic acid sensitisation. Gut **48**, 314–319 (2001)
30. J.G. Fujimoto et al., Optical biopsy and imaging using optical coherence tomography. Nat. Med. **1**, 970–972 (1995)
31. G.J. Tearney et al., In vivo endoscopic optical biopsy with optical coherence tomography. Science **276**, 2037–2039 (1997)
32. A. Sergeev et al., In vivo endoscopic OCT imaging of precancer and cancer states of human mucosa. Opt. Express **1**, 432–440 (1997)
33. K. Kobayashi et al., High-resolution cross-sectional imaging of the gastrointestinal tract using optical coherence tomography: preliminary results. Gastrointest. Endosc. **47**, 515–523 (1998)
34. B.E. Bouma, G.J. Tearney, Power-efficient nonreciprocal interferometer and linear-scanning fiber-optic catheter for optical coherence tomography. Opt. Lett. **24**, 531–533 (1999)
35. A.M. Rollins et al., Real-time in vivo imaging of human gastrointestinal ultrastructure by use of endoscopic optical coherence tomography with a novel efficient interferometer design. Opt. Lett. **24**, 1358–1360 (1999)
36. M.V. Sivak Jr. et al., High-resolution endoscopic imaging of the GI tract using optical coherence tomography. Gastrointest. Endosc. **51**, 474–479 (2000)
37. B.E. Bouma et al., High-resolution imaging of the human esophagus and stomach in vivo using optical coherence tomography. Gastrointest. Endosc. **51**, 467–474 (2000)
38. X.D. Li et al., Optical coherence tomography: advanced technology for the endoscopic imaging of Barrett's esophagus. Endoscopy **32**, 921–930 (2000)
39. S. Jackle et al., In vivo endoscopic optical coherence tomography of esophagitis, Barrett's esophagus, and adenocarcinoma of the esophagus. Endoscopy **32**, 750–755 (2000)
40. G. Zuccaro et al., Optical coherence tomography of the esophagus and proximal stomach in health and disease. Am. J. Gastroenterol. **96**, 2633–2639 (2001)
41. J.M. Poneros et al., Diagnosis of specialized intestinal metaplasia by optical coherence tomography. Gastroenterology **120**, 7–12 (2001)
42. J.A. Evans et al., Identifying intestinal metaplasia at the squamocolumnar junction by using optical coherence tomography. Gastrointest. Endosc. **65**, 50–56 (2007)
43. G. Isenberg et al., Accuracy of endoscopic optical coherence tomography in the detection of dysplasia in Barrett's esophagus: a prospective, double-blinded study. Gastrointest. Endosc. **62**, 825–831 (2005)
44. J.A. Evans et al., Optical coherence tomography to identify intramucosal carcinoma and high-grade dysplasia in Barrett's esophagus. Clin. Gastroenterol. Hepatol. **4**, 38–43 (2006)
45. X. Qi et al., Computer-aided diagnosis of dysplasia in Barrett's esophagus using endoscopic optical coherence tomography. J. Biomed. Opt. **11**, 044010 (2006)
46. X. Qi et al., Image analysis for classification of dysplasia in Barrett's esophagus using endoscopic optical coherence tomography. Biomed. Opt. Express **1**, 825–847 (2010)

47. M.J. Cobb et al., Imaging of subsquamous Barrett's epithelium with ultrahigh-resolution optical coherence tomography: a histologic correlation study. Gastrointest. Endosc. **71**, 223–230 (2009)
48. S.H. Yun et al., Comprehensive volumetric optical microscopy in vivo. Nat. Med. **12**, 1429–1433 (2006)
49. B.J. Vakoc et al., Comprehensive esophageal microscopy by using optical frequency-domain imaging (with video). Gastrointest. Endosc. **65**, 898–905 (2007)
50. M.J. Suter et al., Comprehensive microscopy of the esophagus in human patients with optical frequency domain imaging. Gastrointest. Endosc. **68**, 745–753 (2008)
51. H.L. Fu et al., Flexible miniature compound lens design for high-resolution optical coherence tomography balloon imaging catheter. J. Biomed. Opt. **13**, 060502 (2008)
52. W. Kang et al., Endoscopically guided spectral-domain OCT with double-balloon catheters. Opt. Express **18**, 17364–17372 (2010)
53. J. Xi et al., High-resolution OCT balloon imaging catheter with astigmatism correction. Opt. Lett. **34**, 1943–1945 (2009)
54. A.F. Peery, N.J. Shaheen, Optical coherence tomography in Barrett's esophagus: the road to clinical utility. Gastrointest. Endosc. **71**, 231–234 (2010)
55. D.C. Adler et al., Three-dimensional optical coherence tomography of Barrett's esophagus and buried glands beneath neosquamous epithelium following radiofrequency ablation. Endoscopy **41**, 773–776 (2009)
56. M.J. Suter et al., Image-guided biopsy in the esophagus through comprehensive optical frequency domain imaging and laser marking: a study in living swine. Gastrointest. Endosc. **71**, 346–353 (2010)
57. W. Kang et al., Motion artifacts associated with in vivo endoscopic OCT images of the esophagus. Opt. Express **19**, 20722–20735 (2011)
58. C. Zhou et al., Characterization of buried glands before and after radiofrequency ablation by using 3-dimensional optical coherence tomography (with videos). Gastrointest. Endosc. **76**, 32–40 (2012)
59. B. Shen, G. Zuccaro Jr., T.L. Gramlich, N. Gladkova, P. Trolli, M. Kareta, C.P. Delaney, J.T. Connor, B.A. Lashner, C.L. Bevins, F. Feldchtein, F.H. Remzi, M.L. Bambrick, V.W. Fazio, In vivo colonoscopic optical coherence tomography for transmural inflammation in inflammatory bowel disease. Clin. Gastroenterol. Hepatol. **2**, 1080–1087 (2004)
60. P. Consolo et al., Optical coherence tomography in inflammatory bowel disease: prospective evaluation of 35 patients. Dis. Colon Rectum **51**, 1374–1380 (2008)
61. D.C. Adler et al., Three-dimensional endomicroscopy of the human colon using optical coherence tomography. Opt. Express **17**, 784–796 (2009)
62. X. Qi et al., Automated quantification of colonic crypt morphology using integrated microscopy and optical coherence tomography. J. Biomed. Opt. **13**, 054055 (2008)
63. A.M. Davis et al., Heterodyne swept-source optical coherence tomography for complete complex conjugate ambiguity removal. J. Biomed. Opt. **10**, 064005 (2005)
64. D.C. Adler et al., Three-dimensional endomicroscopy using optical coherence tomography. Nat. Photonics **1**, 709–716 (2007)
65. W. Kang et al., Endoscopically guided spectral-domain OCT with double-balloon catheters. Opt. Express **18**, 17364–17372 (2010)
66. V. Westphal et al., Correlation of endoscopic optical coherence tomography with histology in the lower-GI tract. Gastrointest. Endosc. **61**, 537–546 (2005)
67. J.Y. Ha et al., Compensation of motion artifacts in catheter-based optical frequency domain imaging. Opt. Express **18**, 11418–11427 (2010)
68. I. Matthews et al., The template update problem. IEEE Trans. Pattern Anal. Mach. Intell. **26**, 810–815 (2004)
69. X. Qi et al., Automated quantification of colonic crypt morphology using integrated microscopy and optical coherence tomography. J. Biomed. Opt. **13**, 054055 (2008)
70. S. Tamura et al., Pit pattern and three-dimensional configuration of isolated crypts from the patients with colorectal neoplasm. J. Gastroenterol. **37**, 798–806 (2002)

71. P.R. Pfau et al., Criteria for the diagnosis of dysplasia by endoscopic optical coherence tomography. Gastrointest. Endosc. **58**, 196–202 (2003)
72. A.S.T. Barritt, N.J. Shaheen, Should patients with Barrett's oesophagus be kept under surveillance? The case against. Best Pract. Res. Clin. Gastroenterol. **22**, 741–750 (2008)
73. Y. Chen et al., Ultrahigh resolution optical coherence tomography of Barrett's esophagus: preliminary descriptive clinical study correlating images with histology. Endoscopy **39**, 599–605 (2007)
74. G.J. Tearney et al., Optical biopsy in human pancreatobiliary tissue using optical coherence tomography. Dig. Dis. Sci. **43**, 1193–1199 (1998)
75. J.M. Poneros et al., Optical coherence tomography of the biliary tree during ERCP. Gastrointest. Endosc. **55**, 84–88 (2002)
76. P. Singh et al., In vivo optical coherence tomography imaging of the pancreatic and biliary ductal system. Gastrointest. Endosc. **62**, 970–974 (2005)
77. S. Ban et al., Histopathologic aspects of photodynamic therapy for dysplasia and early adenocarcinoma arising in Barrett's esophagus. Am. J. Surg. Pathol. **28**, 1466–1473 (2004)
78. T.H. Tsai et al., Comparison of tissue architectural changes between radiofrequency ablation and cryospray ablation in Barrett's esophagus using endoscopic three-dimensional optical coherence tomography. Gastroenterol. Res. Pract. **2012**, 684832 (2012)
79. T.H. Tsai et al., Structural markers observed with endoscopic 3-dimensional optical coherence tomography correlating with Barrett's esophagus radiofrequency ablation treatment response (with videos). Gastrointest. Endosc. **76**, 1104–1112 (2012)
80. N.J. Shaheen et al., Radiofrequency ablation in Barrett's esophagus with dysplasia. N. Engl. J. Med. **360**, 2277–2288 (2009)

Endoscopic Optical Coherence Tomography

68

Chao Zhou, James G. Fujimoto, Tsung-Han Tsai, and Hiroshi Mashimo

Keywords

Endoscopic OCT • Imaging probe • Gastrointestinal cancers • Barrett's esophagus • Optical biopsy • Radiofrequency ablation

68.1 Introduction

New gastrointestinal (GI) cancers are expected to affect more than 290,200 new patients and will cause more than 144,570 deaths in the United States in 2013 [1]. When detected and treated early, the 5-year survival rate for colorectal cancer increases by a factor of 1.4 [1]. For esophageal cancer, the rate increases by a factor of 2 [1]. The majority of GI cancers begin as small lesions that are difficult to identify with conventional endoscopy. With resolutions approaching that of histopathology, optical coherence tomography (OCT) is well suited for detecting the changes in tissue microstructure associated with early GI cancers. Since the lesions are not endoscopically apparent, however, it is necessary to survey a relatively large area of the GI tract. Tissue motion is another limiting factor in the GI tract; therefore, in vivo imaging must be performed at extremely high speeds. OCT imaging can be performed using fiber optics and miniaturized lens systems,

C. Zhou (✉)
Department of Electrical Engineering and Computer Science and Research Laboratory of Electronics, Massachusetts Institute of Technology, Cambridge, MA, USA

Department of Electrical and Computer Engineering, Lehigh University, Bethlehem, PA, USA
e-mail: chaozhou@lehigh.edu

J.G. Fujimoto • T.-H. Tsai
Department of Electrical Engineering and Computer Science and Research Laboratory of Electronics, Massachusetts Institute of Technology, Cambridge, MA, USA

H. Mashimo
Veteran Affairs Boston Healthcare System, Harvard Medical School, Boston, MA, USA

© Springer International Publishing Switzerland 2015

W. Drexler, J.G. Fujimoto (eds.), *Optical Coherence Tomography*,
DOI 10.1007/978-3-319-06419-2_70

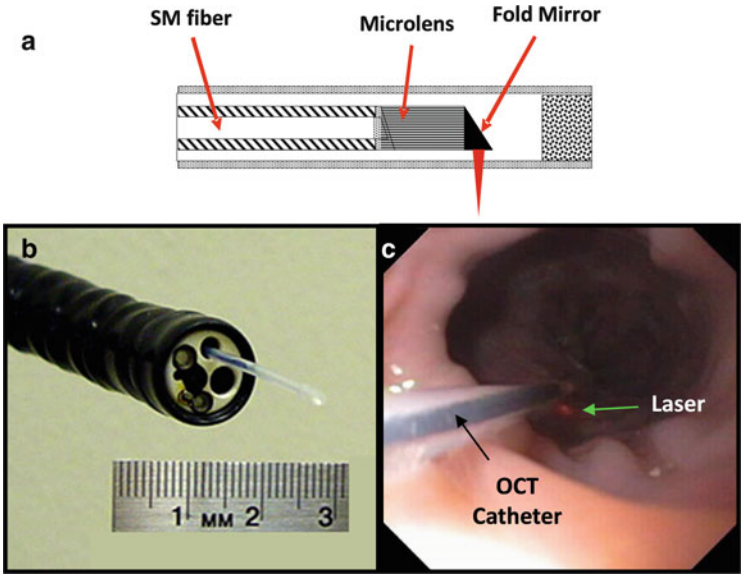

Fig. 68.1 (**a**) Schematic of endoscopic OCT probe with 1.8 mm diameter. (**b**) Photo of the OCT probe in the working channel of the endoscope. **c** Endoscopic view of OCT probe in human esophagus

enabling endoscopic OCT inside the human body in conjunction with conventional video endoscopy. An OCT probe can be inserted through the working channel of a standard endoscope, thus enabling depth-resolved imaging of tissue microstructure in the GI tract with micron-scale resolution simultaneously with the endoscopic view (Fig. 68.1).

The first demonstration of in vivo endoscopic OCT was performed in 1997 [2]. This study demonstrated OCT imaging of the gastrointestinal and pulmonary tracts in the rabbit using a 1 mm diameter fiber optic catheter and suggested the potential for internal body OCT imaging using noninvasive or minimally invasive devices. Early endoscopic OCT imaging studies of the human gastrointestinal (GI) tract were performed by several groups. Studies were performed in the esophagus and stomach [3–9], small and large intestine [5, 7, 10–12], and bile duct [13, 14]. Barrett's esophagus was clearly differentiated from normal esophageal mucosa, and esophageal adenocarcinoma could also be distinguished from nonneoplastic tissues. Endoscopic OCT was also shown to provide complementary information to endoscopic ultrasound for staging and tumor resection [10, 15]. OCT was demonstrated to detect specialized intestinal metaplasia in Barrett's esophagus patients [16, 17] and transmural inflammation in inflammatory bowel disease patients [12]. OCT was also investigated for differentiating hyperplastic from adenomatous polyps in the colon [11]. Endoscopic OCT studies have shown promise for detection of high-grade dysplasia in Barrett's esophagus. Evans et al. reported a sensitivity of 83 % and specificity of 75 % for detecting high-grade dysplasia and intramucosal carcinoma with blinded scoring of OCT images

from 55 patients [18]. Isenberg et al. reported a sensitivity of 68 % and a specificity of 82 %, with an accuracy of 78 % for the detection of dysplasia from 33 patients with Barrett's esophagus [19]. Using computer-aided tissue classification techniques applied to OCT images, Qi et al. reported a sensitivity of 82 % and specificity of 74 % for identifying dysplasia in 13 patients [20].

With advances in laser light sources, OCT image resolutions approaching a few microns have been achieved [21–27]. Ultrahigh-resolution OCT imaging has reduced speckle size and overall improved image quality [28, 29]. The earliest ultrahigh-resolution endoscopic OCT imaging study in 2004 achieved 4 μm axial image resolution using a femtosecond Cr:Forsterite laser at 1,300 nm and demonstrated endoscopic imaging in vivo in the rabbit gastrointestinal tract [30]. Endoscopic OCT in small animals with even higher, 3.2 μm axial resolution, was demonstrated in the mouse using Ti:Sapphire laser at 800 nm [31, 32]. The first clinical ultrahigh-resolution endoscopic OCT study was performed using a prototype instrument with a Cr:Forsterite laser, surveying a cross section of pathologies including Barrett's esophagus, high-grade dysplasia, and adenocarcinoma [29].

3D-OCT endoscopic imaging became possible using high-speed OCT with Fourier domain detection. Ultrahigh-resolution spectral/Fourier domain endoscopic OCT at 20 kHz axial scan rates with 2.4 μm axial resolution using a Ti:Sapphire laser was demonstrated in the mouse colon [31, 32]. Using swept-source/Fourier domain technologies at 1,300 nm wavelengths, in vivo 3D-OCT volumetric imaging of the porcine esophagus and artery was demonstrated at 10 kHz and 54 kHz axial scan rates in 2006 and 2007, respectively [33, 34]. Using Fourier domain mode locking (FDML) laser technology, record axial scan rates of 100 kHz were achieved and demonstrated for in vivo endoscopic 3D-OCT imaging in the rabbit [35] and human [36–42] gastrointestinal tract with an axial resolution of 7 um. These endoscopic studies demonstrate the impact of advances in OCT imaging technology on endoscopic OCT applications.

Gastroenterology is an especially relevant application for OCT because of the high incidence rates of GI pathologies, the clinical benefits of early detection, and the need for pre- and post-treatment assessment of therapies. In this chapter, we summarize recent advances in endoscopic OCT ranging from technology development, including ultrahigh-resolution OCT, ultrahigh-speed OCT, and endoscopic probe development, as well as clinical applications such as imaging GI pathology and assessment of endoscopic therapies.

68.2 Ultrahigh-Resolution Endoscopic OCT

Image resolution is one of the most critical parameters governing the performance of OCT systems, and therefore achieving ultrahigh image resolutions has been a key objective for endoscopic OCT. The axial image resolution of OCT is inversely proportional to the bandwidth of the light source and in order to achieve ultrahigh resolution, broad bandwidth light sources are required. The majority of previous clinical OCT studies were performed using superluminescent diode (SLD)

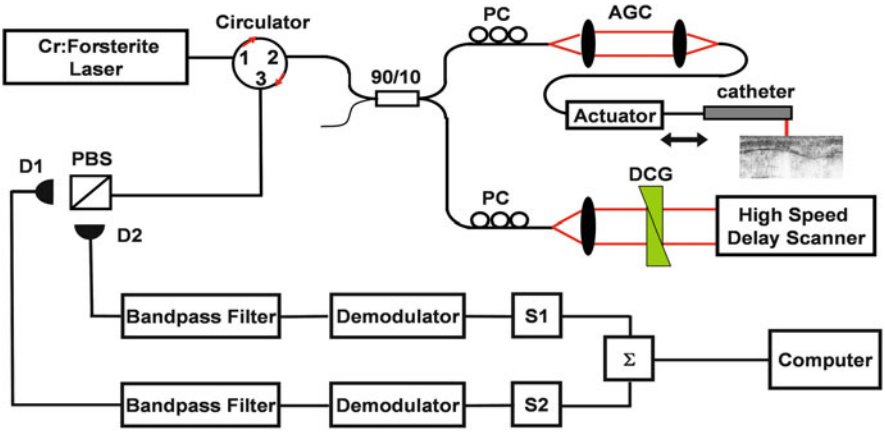

Fig. 68.2 Schematic of an early ultrahigh-resolution (*UHR*) endoscopic OCT system. A broadband Cr:Forsterite laser light source is used to achieve <5 μm axial image resolution. The system used time domain detection and operated at imaging speeds of 3,000 axial scans per second. The system uses a dual circulator interferometer with dual-balanced detection

light sources with axial resolutions of ~10–15 μm. With recent advances in broadband femtosecond lasers, OCT image resolutions in the 2–5 μm range were demonstrated by our group and others [21–27].

Working in collaboration with LightLab Imaging, our group and collaborators developed an ultrahigh resolution endoscopic OCT system by adapting a commercial imaging engine to use an advanced femtosecond Cr4+:Forsterite laser light source (see Fig. 68.2). Although the complexity and cost of femtosecond light sources limits their potential for widespread clinical use, they can provide powerful performance advantages for small-scale validation studies. The system included several innovative features in OCT design to support very broad optical bandwidths necessary to achieve ultrahigh resolutions [30]. The axial resolution was ~3.6 μm in tissue, corresponding to a 3–4× improvement over previous OCT technology. A fiber-optic probe was also developed for endoscopic OCT imaging. The probe was 1.8 mm in diameter and used an optical fiber, micro lens, and microprism which were distally actuated in either a push-pull or rotary motion to generate longitudinal or transverse OCT images at 4 Hz frame rate.

Prior to clinical imaging studies, this technology was validated by performing in vivo imaging of the gastrointestinal and pulmonary tracts of the New Zealand White rabbit, correlating images with histology [30]. Figure 68.3a shows an example in vivo OCT image of the rabbit esophagus and trachea. The tracheal hyaline cartilage (hc) is visible through the esophageal wall, demonstrating the ability to achieve deep image penetration at these long wavelengths. In addition, the structural details of the tracheal mucosa and trachealis muscle are visible. The vacuous region below the tracheal wall at the bottom of the image is the tracheal airway. The corresponding histological section in Fig. 68.3b shows good correlation with the architecture seen in the OCT image. Trichrome staining was used in the histology to enhance delineation of cartilage rings in the trachea.

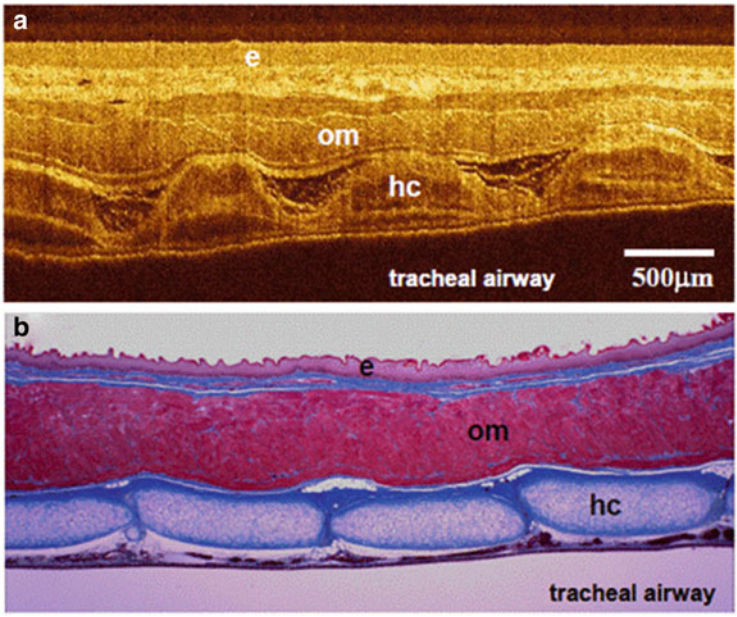

Fig. 68.3 (**a**) In vivo OCT image of the rabbit esophagus and trachea viewed intraluminally from the esophagus and (**b**) corresponding histology with trichrome staining. Tracheal hyaline cartilage (*hc*) between the tracheal mucosa and trachealis muscle is visualized. Note the excellent image quality which can be achieved using a broadband light source and ultrahigh-resolution OCT (From Hertz et al. [30])

Clinical ultrahigh-resolution endoscopic OCT studies were performed at the VA Boston Healthcare System [29]. Patients with previously diagnosed Barrett's esophagus or undergoing elective colonoscopy were recruited from the endoscopy clinic at the VA Medical Center. A total of 112 patients (95 in Barrett's esophagus group and 17 in colonoscopy group) were imaged. Imaging was performed by introducing the OCT probe into the endoscope working channel, providing simultaneous endoscopic and OCT views. Figure 68.4 shows representative ultrahigh-resolution endoscopic OCT images of the human esophagus. Figure 68.4a shows normal squamous epithelium with a characteristic layered architecture, and Fig. 68.4b shows a representative image of Barrett's esophagus. OCT images of Barrett's esophagus show clear differences in architectural morphology compared to normal esophageal squamous mucosa. The layered architecture is replaced by glandular structures, and low-backscattering Barrett's glands are observed in the mucosa with interlaced regions of high-backscattering connective tissue corresponding to the lamina propria. Figure 68.4c shows a representative OCT image of high-grade dysplasia. High-grade dysplasia is characterized by irregular, distorted, and cribriform or villiform glandular architecture and is more heterogeneous than non-dysplastic Barrett's epithelium. Figure 68.4d shows an OCT image of esophageal adenocarcinoma with epithelial disruption and stromal infiltration

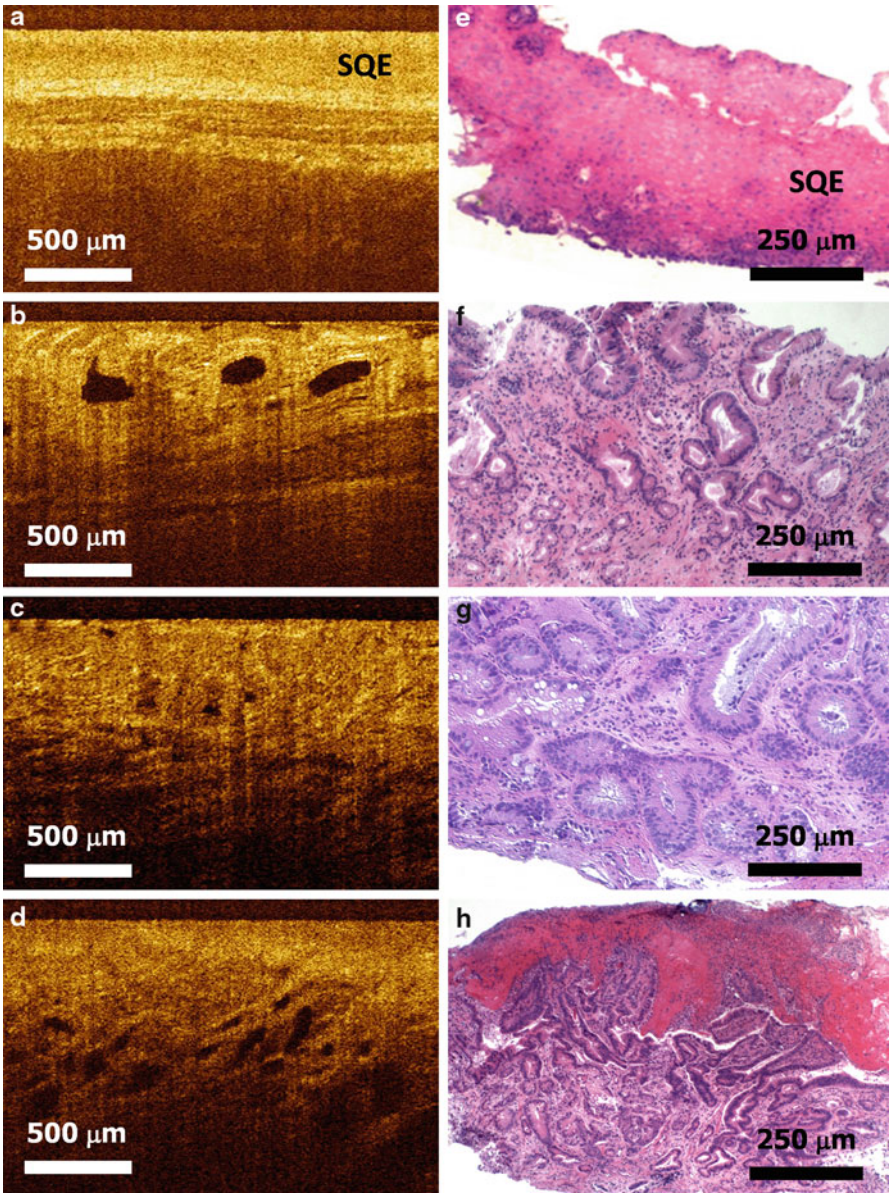

Fig. 68.4 Ultrahigh-resolution endoscopic OCT of esophageal pathology in human subjects. (**a**) Squamous mucosa of normal esophagus. (**b**) Barrett's esophagus. (**c**) High-grade dysplasia. (**d**) Adenocarcinoma. (**e**–**h**) Corresponding pinch biopsy histology to OCT images (From Chen et al. [29])

extending from the superficially ulcerated carcinoma. OCT images show progressive increase in architectural irregularity from Barrett's mucosa to high-grade dysplasia and eventually to adenocarcinoma. Overall, ultrahigh-resolution OCT images showed good correlation with architectural morphology in histology (see Fig. 68.4e–h) [29]. The enhanced image resolution and reduced speckle size enabled ultrahigh-resolution OCT to visualize changes in tissue architectural heterogeneity more clearly than standard resolution OCT; however, imaging speeds were still limited compared with current technologies. In addition, although this study was the first to demonstrate ultrahigh-resolution endoscopic OCT in patients, the limited enrollment and small numbers of dysplasia cases made it difficult to identify OCT image features which could be correlated with histology and used to detect dysplasia.

68.3 Ultrahigh-Speed Endoscopic OCT

Recent advances in Fourier domain detection techniques enable dramatic increases in imaging speed [43–45]. These advances have had a powerful impact across multiple OCT applications ranging from ophthalmology to endoscopy. Ultrahigh speeds are important for enabling broader coverage, which is necessary for the large surface areas in the gastrointestinal tract. Ultrahigh speeds are also critical for 3D endoscopic OCT which requires the acquisition of large volumetric data sets in vivo. Swept-source/Fourier domain detection has achieved the highest imaging speeds to date and is a central focus of current research. Frequency-swept laser sources are a key technology for swept-source/Fourier domain OCT. The repetition rate of the laser sweep and the sweep range determine the OCT imaging axial scan repetition rate and axial resolution, respectively. Early swept lasers used a tunable filter with a diffraction grating and rotating polygon mirror to achieve sweep rates of 15.7–115 kHz with ~10–15 μm axial resolutions [46, 47]. These advances in technology enabled in vivo endoscopic OCT imaging in the porcine esophagus and coronary artery at axial scan rates of 10 kHz and 54 kHz, respectively with ~7 μm image resolution [33, 34].

68.3.1 Ultrahigh-Speed Endoscopic OCT Using FDML Lasers

The development of Fourier domain mode locking (FDML) in 2006 provided a new technique to overcame fundamental limitations in sweep rate of conventional swept lasers, enabling record OCT imaging speeds in multiple applications [35, 48–51]. FDML lasers use a long optical fiber in the laser cavity to store and regenerate the entire frequency sweep, avoiding the need to build up lasing from amplified spontaneous emission as the laser frequency is swept. This enables FDML lasers to achieve sweep rates not attainable using conventional swept lasers and to perform 3D-OCT imaging at unprecedented speeds. Higher acquisition

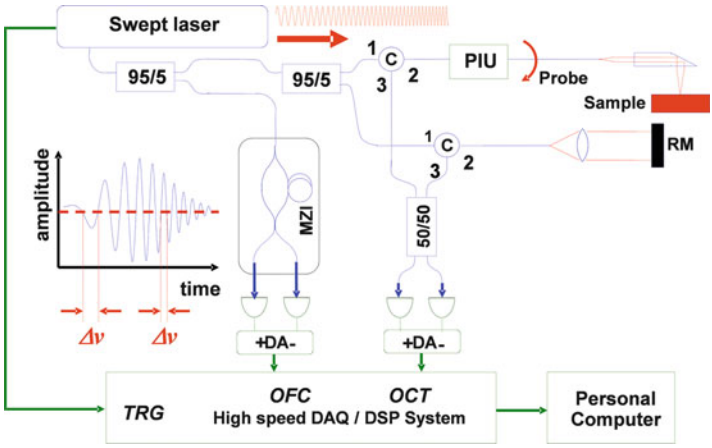

Fig. 68.5 OCT system for ultrahigh-speed endoscopic 3D-OCT imaging. The system uses swept-source/Fourier domain OCT with a high-speed Fourier domain modelocked (FDML) laser. The system uses a dual circulator interferometer with dual-balanced detection. A Mach Zhender interferometer is used to measure the frequency sweep to recalibrate the OCT signal so that it is linear in frequency or wavenumber

speed enables increased field of view, high volumetric sampling densities, and reduced motion artifacts for in vivo 3D-OCT imaging. FDML lasers were used to demonstrate 3D-OCT imaging with record speeds of 370 kHz axial scan rates in 2006 [52]. In addition, FDML lasers have extremely broad tuning ranges of 160 nm at ~1,300 nm wavelengths, supporting axial resolutions of ~5–7 μm in tissue. Swept-source OCT using FDML laser technology enables up to a ~50–100× improvement in speed and up to a ~2–3× improvement in resolution compared with previous time domain OCT technology.

Working in collaboration with LightLab Imaging, our group and collaborators developed a prototype endoscopic OCT instrument using an FDML laser at ~1,310 nm. Figure 68.5 shows a schematic of this system. The system used a dual circulator interferometer geometry for maximum signal collection efficiency combined with a dual-balanced detector. A Mach Zhender interferometer and dual-balanced detector was used to measure the frequency sweep produced by the FDML laser. The Mach Zhender calibration signal is used to recalibrate the OCT signal so that it is linear in the frequency space (k-space) before it is Fourier transformed. The prototype instrument achieved axial scan rates of 100 kHz and 5–7 μm axial resolution in tissue with real-time display and capture capabilities at 50 frames per second. To validate the prototype 3D-OCT system prior to clinical studies in humans, we performed in vivo 3D-OCT endoscopic imaging studies of the rabbit gastrointestinal tract, demonstrating record endoscopic imaging speeds in 2007 [35].

The increased imaging speed enabled a 9 mm segment of colon to be imaged with a high axial scan density in <18 s. Figure 68.6a shows a representative single radial OCT image of the rabbit colon with an inset showing an enlarged view of the

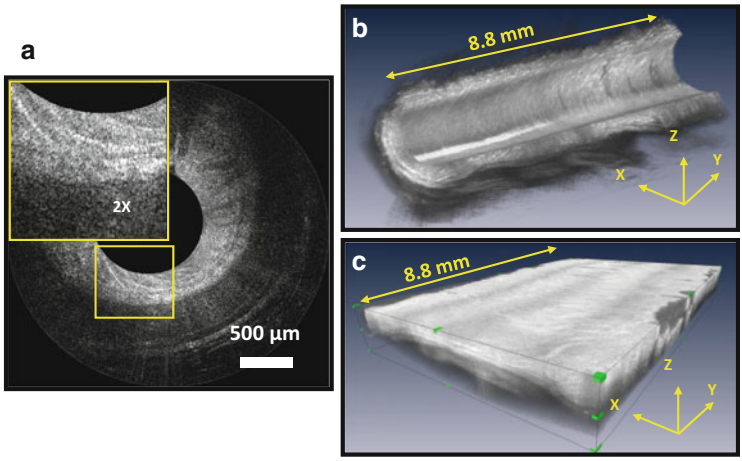

Fig. 68.6 3D-OCT endoscopic imaging at record 100 kHz axial scan rates is enabled by swept-source OCT with FDML laser technology. (**a–c**) 3D-OCT images of rabbit colon in vivo. (**a**) Single radial frame. (**b**) 3D cutaway rendering. (**c**) Unfolded volume shows tissue as rectangular slab (From Adler et al. [35])

epithelium. Colonic crypts are clearly distinguishable as dark regions surrounded by bright, filament-like bands of lamina propria. The complete volumetric data set is composed of 885 radial frames, which can be processed and displayed in three dimensions. Figure 68.6b shows a cutaway view of the rendered data set. 3D-OCT data allows virtual manipulation of tissue to facilitate visualization. Figure 68.6c shows a rectangular volume rendering, created by performing a "virtual incision" along the colon and unfolding. In addition, cross-sectional images with arbitrary orientations can be synthesized from the 3D-OCT data set. Figure 68.7a shows a longitudinal (YZ) cross section taken from near the center of the unfolded colon volume. Figure 68.7b shows an average of seven consecutive YZ slices to reduce speckle noise. Figure 68.7c shows an enlarged view of a region of Fig. 68.7b. The cross-sectional OCT correlates well with histology as shown in Fig. 68.7d although the thicknesses of the tissue layers are different in OCT compared to histology due to compression of the in vivo tissue by the imaging probe and changes in tissue from histological processing.

In order to evaluate the performance of ultrahigh-speed endoscopic OCT in clinical settings, we performed studies at the VA Boston Healthcare System [36–42, 53]. Figure 68.8 shows representative images obtained in vivo from the colon of a human subject [36]. Figure 68.8a is an en face image of normal columnar epithelial tissue formed by axial summation of the entire 3D logarithmic data set. Summation over the full axial range reduces speckle noise, while preserving only those image features that persist over significant depths. Macroscale tissue folds are visible in the mucosal surface. A mottled texture is observed due to the presence of a regular, uniform crypt pattern. Crypts are the main glandular structures in the human colon, and changes in crypt size and appearance are associated with the earliest forms of

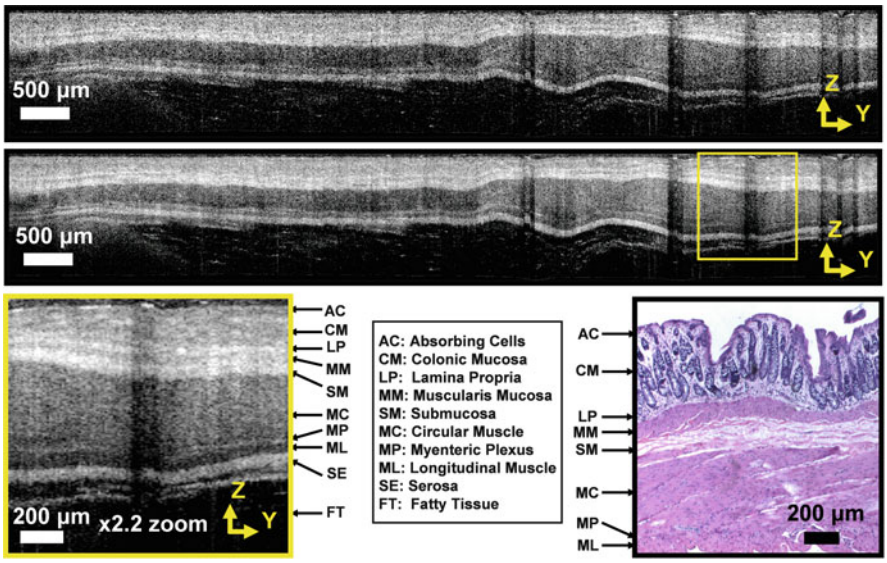

Fig. 68.7 Volumetric 3D-OCT enables the generation of arbitrary cross sections and the use of averaging to improve image quality. (**a**) Single cross-sectional image of rabbit colon in vivo from 3D-OCT data set. (**b**) Average of seven consecutive frames reduces speckle noise. (**c**) Enlarged view shows layered structure of colon. (**d**) Representative histology correlates with OCT images (From Adler et al. [35])

colorectal cancer [54]. The ability to assess the 3D structure of crypts is of potential value for future applications in cancer detection and treatment. Figure 68.8b shows a cross section oriented along the XZ axis, which is the fast rotational axis during data acquisition. Consistent with previous results in ex vivo human tissue [28], optical transmission is increased through the crypt lumens. Figure 68.8c shows a cross-sectional YZ plane, which is the slow pullback axis during data acquisition. Uniform crypt structures are also visible in this plane. Both cross sections were formed by averaging consecutive slices over a 20 µm thickness to reduce speckle noise. Figure 68.8d shows an enlarged region of Fig. 68.8a. The microstructural en face crypt pattern is clearly visualized and is consistent with the representative en face histology image shown in Fig. 68.8e. Figure 68.8f shows a white light video endoscopy image near the OCT imaging site. The mucosa appears regular, and the crypt pattern is difficult to distinguish by conventional endoscopy.

68.3.2 Ultrahigh-Speed Endoscopic OCT Based on VCSEL Wavelength-Swept Light Sources

One of the most significant recent advances in OCT technology has been the development of vertical cavity surface emitting lasers (VCSEL) for swept-source OCT [55, 56]. The VCSEL operates with a single longitudinal mode instead of

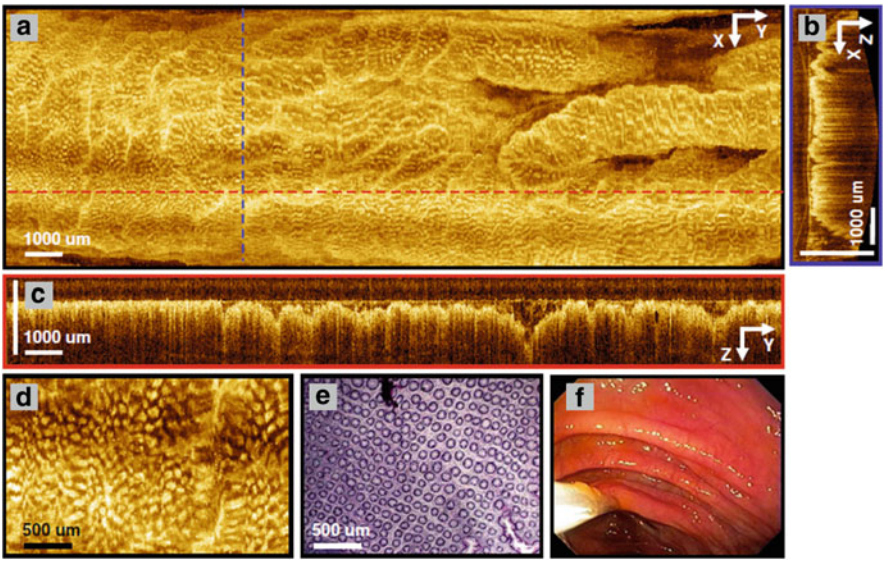

Fig. 68.8 3D-OCT images of columnar epithelial tissue in the human colon. (**a**) En face image constructed by axial summation of the entire data set. *Dashed lines* show locations of cross sections. (**b**) XZ cross section showing typical columnar structure. (**c**) YZ cross section. (**d**) Enlarged view of (**a**), showing en face crypt pattern. (**e**) Representative en face histology of human colon. (**f**) White light video endoscopy image of region analyzed with 3D-OCT (From Adler et al. [36])

multiple modes and therefore has an extremely narrow instantaneous linewidth which enables a long imaging range. The micron-scale cavity length of VCSELs and the rapid MEMS response also enable extremely high imaging speeds. The VCSEL also has the advantage that both the sweep frequency and wavelength tuning range can be adjusted to support multiple operating modes with different speed, resolution, and imaging ranges. These are powerful features which make the VCSEL a promising technology for high-speed and long-range OCT imaging [57]. We developed a micromotor-based catheter with an outer diameter of 3.2 mm for ultrahigh-speed endoscopic OCT using a VCSEL swept source at a 1 MHz axial scan rate [58]. Since this study involves imaging probe technology, further details are described in the next section.

68.4 Endoscopic OCT Probe Technologies

Endoscopic probes are another critical technology for endoscopic OCT. In vivo endoscopic OCT imaging is challenging because fast optical scanning must be implemented inside a miniaturized imaging probe. Many scanning mechanisms have been investigated in catheter-based endoscopic OCT systems, such as proximally actuating a torque cable with a rotating fiber and microprism module at the

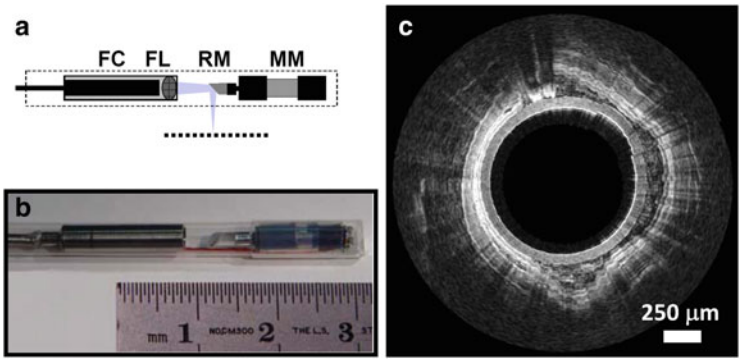

Fig. 68.9 Micromotor probes avoid the need for proximal actuation. (**a**, **b**) Schematic and photo of micromotor probe. (**c**) In vivo OCT image of rabbit esophagus showing normal squamous epithelial structure (From Herz et al. [30])

distal end [2, 34, 35, 59, 60], distally actuating a fiber with a galvanometer [3], distally actuating a fiber with piezoelectric transducer [61–63], and distal beam scanning using microelectromechanical systems (MEMS) [64–67]. Imaging using proximal rotary actuation can cover a large area with a simple probe design and has been used in most endoscopic OCT applications to date. In upper GI imaging, proximal rotary scanning has been combined with inflatable balloons which serve to dilate the esophagus and stabilize the OCT probe at a controlled distance from the lumen. These methods enable dramatic improvements in imaging coverages. However proximal scanning can be unstable because the rotation is translated from the proximal end using a long torque cable to the distal imaging optics. Nonuniform rotation from torsional flexibility and friction over the torque cable length creates artifacts that limit the image quality even if the transverse optical resolution is high. The scanning speed is also limited because the torque cable becomes unstable at rotation speeds higher than a few hundred Hz. By contrast, distal scanning methods using PZT or MEMS-based actuators can provide micron-scale precision scanning because the mechanical motion is not transmitted over a long distance. However distal scanning methods are difficult to implement because the scanner must fit within the catheter.

68.4.1 Endoscopic OCT Probes Based on Micromotor Technologies

Advances in micromotor technology enable distal rotary scanning within small catheter diameters and provide large image areas while maintaining high speed and uniform rotary scanning. OCT micromotor catheters were demonstrated as early as 2004 for ultrahigh-resolution in vivo imaging of the rabbit GI tract [30, 68]. Figure 68.9 shows the schematic and photo of the imaging probe developed by our group [30]. The OCT beam was rotationally scanned by a tilted mirror actuated by a micromotor. The fiber collimator and focusing lens were attached to a cable

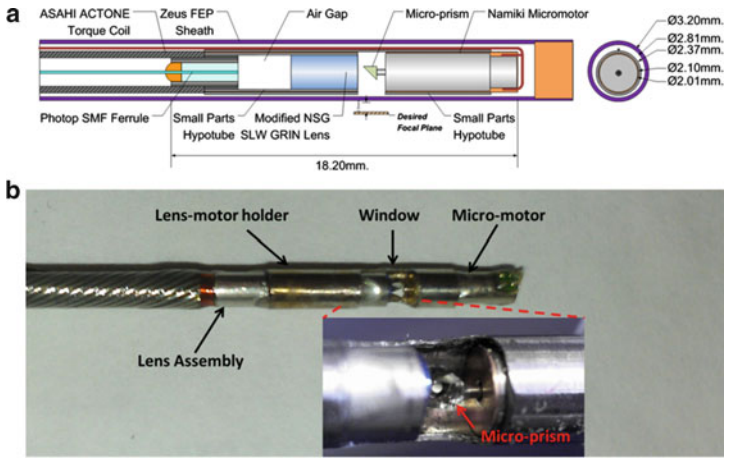

Fig. 68.10 (**a**, **b**) Schematic diagram and photograph of the micromotor probe. The probe sheath has a 3.2 mm outer diameter, and the motor and optics can be pulled back inside the sheath to generate a 3D-OCT spiral scan pattern (From Tsai et al. [58])

that enables the distal focus depth to be adjusted by longitudinally translating the fiber and lens assembly. This enables the probe to be focused on structures at different depths. The assembly fits in a 4.8 mm outer diameter stainless steel housing that is enclosed within a 5 mm outer diameter transparent plastic sheath. In vivo imaging of rabbit esophagus was demonstrated at 2 frames/s with ~3.7 μm axial and ~8 μm transverse resolutions. Esophageal epithelium, lamina propria, and muscular mucosa can be delineated in the OCT image. Other groups have used micromotor-based OCT catheters for endoscopic upper airway imaging, studying smoke-induced injury in animal models with imaging frame rates of 20 fps [69].

Although micromotor can achieve very high rotary scan speeds, early imaging studies were limited to 50 fps acquisition speeds because of the limited axial scan rates which were supported by the OCT imaging system. Using VCSEL swept-source technology described in the previous section, it is possible to achieve ultrahigh-speed endoscopic OCT using a micromotor [58]. Figure 68.10a shows a schematic diagram of a newer version micromotor-based catheter. A microprism was mounted on a 2 mm diameter, 6 mm long micromotor (Namiki Precision, Inc.). The OCT beam was focused by a fiber-GRIN lens assembly, reflected by the rotating microprism and focused outside of the catheter sheath to a spot size of 8 μm in tissue. The motor and GRIN lens were mounted inside a hypotube with a cutaway window that enables imaging over ~70 % of the microprism rotation. A transparent plastic sheath with 2.8 mm inner diameter and 3.2 mm outer diameter was used to house the motor and optics. By pulling back the optical and motor assembly during the rotary image acquisition, a volumetric spiral scanning pattern can be generated. The micromotor drive voltage was less than 5 V and could operate at speeds from 1,200 to 72,000 rpm, corresponding to frame rates from

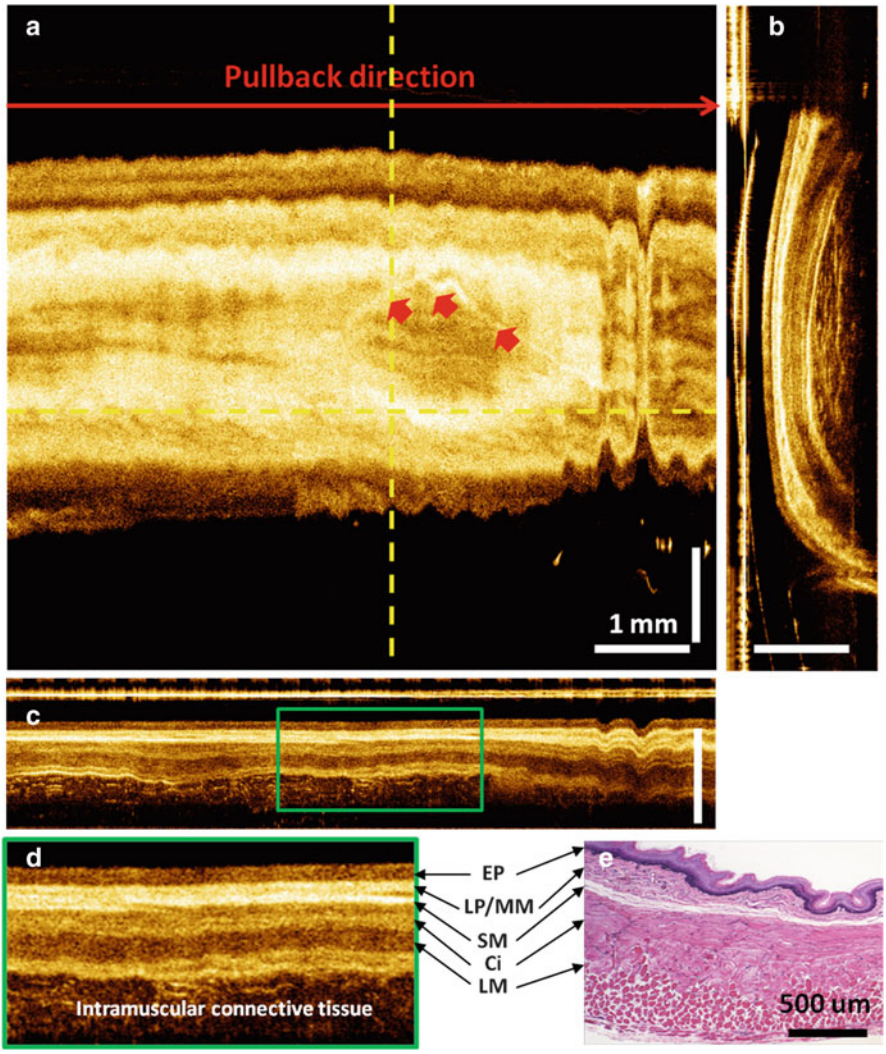

Fig. 68.11 3D-OCT volumetric images from rabbit esophagus in vivo using a micromotor probe and high-speed VCSEL swept-source OCT system. (**a**) En face image of the 3D data set averaged over 15 um at a depth of 150 um. (**b**, **c**) Cross-sectional images in the rotary and pullback directions. (**d**) Zoomed region showing detailed structure. (**e**) Representative histology (From Tsai et al. [58])

20 to 1,200 fps. Figure 68.10b shows a photograph of the micromotor probe. The VCEL light source operated at high 1 MHz axial scan rates and enabled high frame rates with dense sampling.

Figure 68.11 shows a 3D-OCT data set from the rabbit esophagus in vivo. The high-speed micromotor probe combined with the high axial scan rate of the VCSEL

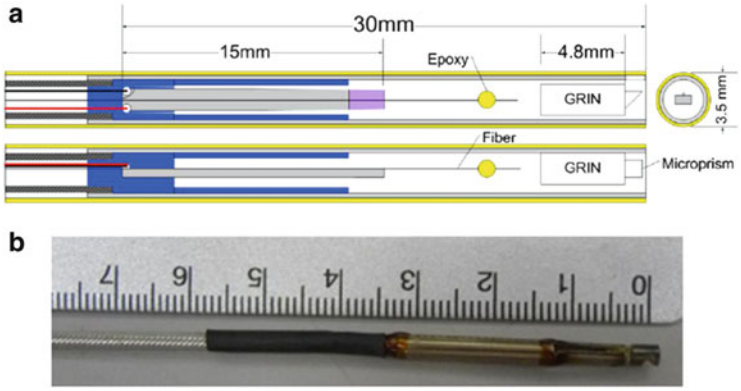

Fig. 68.12 (**a**, **b**) Schematic and photo of the PZT scanning probe. The PZT bender can produce large deflections with a low actuation voltage. 3D-OCT data is obtained by pulling back the actuator and optics from the proximal end of the probe, scanning a raster-like pattern (From Tsai et al. [63])

swept-source OCT enabled 3,000 frames of 2,500 axial scans each to be acquired in 7.5 s (i.e. 400fps), covering a volume size of 7.5 × 7.5 × 1.3 mm (x-y-z). The high axial scan rate enabled dense sampling corresponding to a pixel spacing of 4 × 2.5 × 5.2 um in the x-y-z directions, respectively. The cross-sectional OCT images (Fig. 68.11b–d) show normal esophageal layers including the epithelium (EP), lamina propria/muscularis mucosa (LP/MM), submucosa (SM), circular muscle (Ci), and longitudinal muscle (LM). The OCT images correlate well with representative histology (Fig. 68.11e). The volumetric data set could be processed and displayed in three dimensions. The images shown were generated by averaging three consecutive images perpendicular to the viewing direction in order to reduce speckle. Figure 68.11a, c shows the en face view and cross-sectional view along the pullback direction. The en face view (Fig. 68.11a) is averaged over a depth of 15 um and demonstrates the large field of view that can be achieved. Motion artifacts from cardiac motion are visible in the image. En face images are useful to differentiating features such as vasculature versus glands which can appear similar in isolated cross-sectional images.

68.4.2 Endoscopic OCT Probes Based on PZT Technologies

High-speed endoscopic OCT probes can also be developed using other types of distal actuators such as cantilever PZT scanners [63]. Figure 68.12 shows the schematic diagram of a PZT-based probe design. A tapered 15 mm PZT bender (Piezo Systems, Inc.) was used to scan an optical fiber at its resonance frequency. A drop of epoxy (~40 mg) was placed on the fiber tip to increase the mass and reduce the resonant frequency to ~500 Hz. The fiber tip was angle cleaved at 8° to reduce backreflection. The scanning beam was focused with a GRIN lens objective

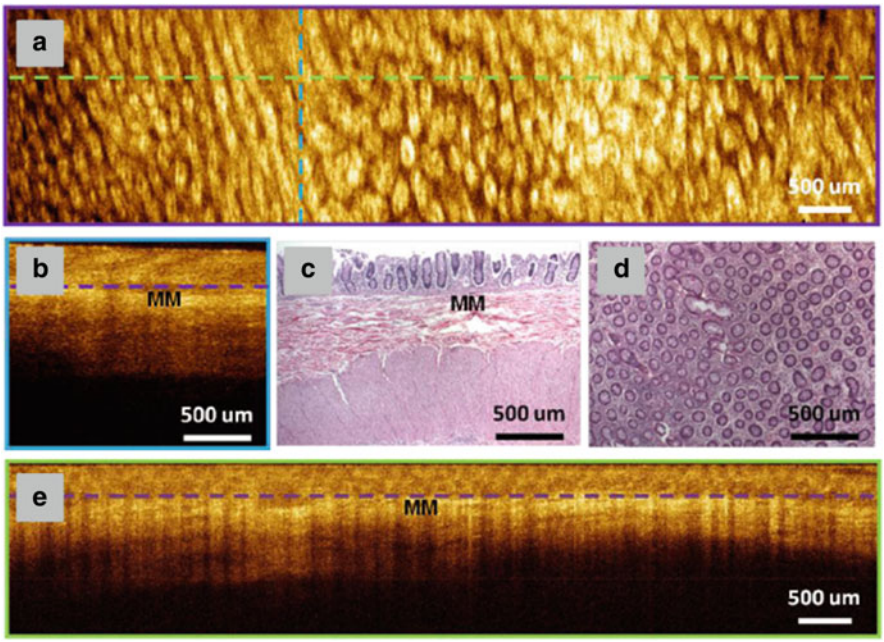

Fig. 68.13 Volumetric 3D-OCT images of a human colon specimen ex vivo. (**a**) En face image at a depth of 350 μm. (**b**) Cross-sectional image along the fast-scan direction. (**c**) Representative cross-sectional histology of the human colon with hematoxylin and eosin stain. (**d**) Representative en face histology of the human colon. (**e**) Cross-sectional image along the pullback direction. *MM* muscularis mucosa (From Tsai et al. [63])

with a microprism glued on distal end to reflect the laser beam. The spot size and scan range could be adjusted by changing the magnification. In this prototype probe, the working distance was set to be 500 μm in tissue, and the focused spot size was 20 μm, corresponding to ~23 μm in tissue. The lateral scanning range was ~2 mm with the PZT bender driven at 10 V (peak to peak) and a frequency of 480 Hz. The PZT bender has the advantage that the actuation voltage is very low. A thin holder mounts the PZT bender on a 2 mm outer diameter torque coil which can be pulled back from the proximal end of the probe. This produces a rater-like scan pattern for acquiring 3D-OCT data. Figure 68.12b shows the photo of the probe. The outer diameter was 3.5 mm with a rigid length of the catheter of ~30 mm.

Imaging was performed in the rabbit GI tract in vivo as well as in human colon specimens ex vivo using an ultrahigh-speed swept-source OCT system with an FDML light source at 480 kHz axial rate with 8 um axial image resolution [63]. Figure 68.13 shows an ex vivo 3D-OCT data set from a freshly excised human colon specimen. Figure 68.13a shows an en face OCT image at a depth of 350 μm averaged over 15 μm depth. Individual crypts in the colon specimen are clearly visualized in the en face plane. Figures 68.13b and e show representative cross-sectional images along the fast-scan and pullback directions, respectively.

Both en face and cross-sectional images show columnar epithelial structure and correlate well with representative histology of human colon in Fig. 68.13c, d.

68.5 Clinical Applications of High-Speed Endoscopic OCT

Endoscopic OCT has been extensively investigated for GI applications by many groups, as described previously. In this section we summarize a representative series of clinical studies performed by our group using endoscopic OCT to visualize GI pathologies [29, 36, 37, 41, 42], as well as to evaluate tissue morphological changes associated with endoscopic therapies [38–40, 53]. These clinical studies were performed at the VA Boston Healthcare System with study protocols approved by the institutional review boards at Massachusetts Institute of Technology, Harvard Medical School, and VA Boston Healthcare System.

68.5.1 Visualizing GI Pathology Using Endoscopic OCT

Barrett's Esophagus: Barrett's esophagus (BE) is a common condition associated with gastroesophageal reflux disease (GERD) where the normal squamous epithelium of the esophagus is replaced by metaplastic columnar epithelium [70, 71]. In the United States, about 5.6 % of the population is affected by BE [72]. Patients with BE have an increased risk of developing esophageal adenocarcinoma, [73] which is a lethal disease with less than 20 % 5-year survival rate. In the past 30 years, the incidence of esophageal adenocarcinoma in white males has increased 300–500 % [74, 75]. Conventional endoscopic imaging lacks sensitivity for detecting high-grade dysplasia, the immediate precursor to esophageal cancer. Therefore, there is considerable interest in developing new imaging techniques which can detect and guide the treatment of dysplasia associated with BE and esophageal cancer.

Using an ultrahigh-speed endoscopic OCT system described in Sect. 68.3, we performed 3D endoscopic OCT imaging in patients with Barrett's esophagus (Fig. 68.14) [37]. Volumetric data sets allow the generation of en face images, thereby enabling precise registration of cross-sectional data with en face features. Projection techniques can be used to selectively display specific depths within the tissue, enhancing image contrast for specific architectural features. Cross-sectional images with arbitrary orientation can also be generated from the 3D data. The en face view (Fig. 68.14a) and cross-sectional views (Fig. 68.14b, c) illustrate the characteristic glandular structures associated with Barrett's esophagus, which can be easily distinguished from the layered structure of the normal esophagus. The enlarged view of glandular structures (Fig. 68.14d) correlates well with the histology of Barrett's esophagus shown in Fig. 68.14e. 3D-OCT endomicroscopy is capable of differentiating glandular and squamous epithelium in vivo. This ability could be important for applications such as the assessment of endoscopic therapies at multiple time points, since it provides an inherent positional registration that is difficult to obtain with isolated cross-sectional OCT images.

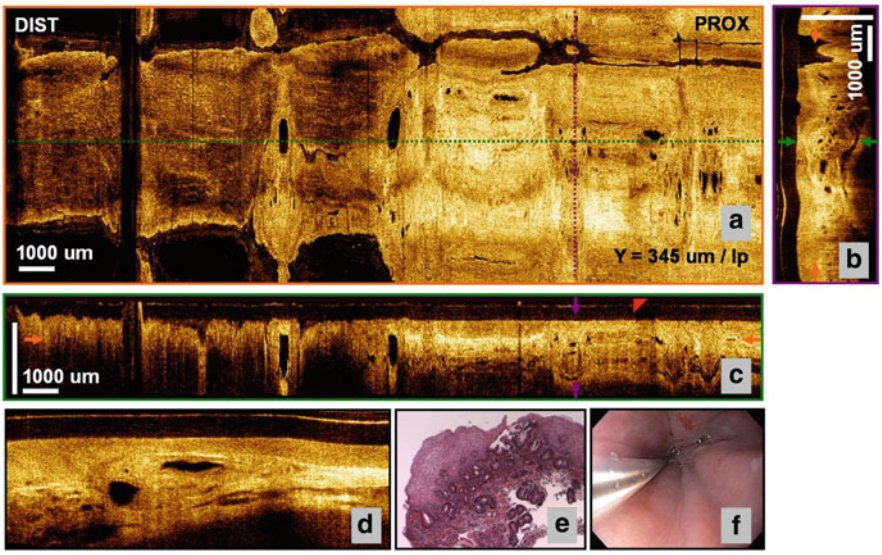

Fig. 68.14 3D-OCT images in Barrett's esophagus. (**a**) En face image constructed by axial summation of a thin slice (~20 um) in the 3D data. (**b**) A cross section in the probe rotary scan direction shows the characteristic glandular structures associated with Barrett's esophagus. (**c**) A cross section along pullback direction also shows glandular structures. (**d**) Zoomed view of cross section. (**e**) Representative histology of Barrett's esophagus. (**f**) White light video endoscopy image of region imaged with 3D-OCT (From Adler et al. [37])

Cervical Inlet Patch: Cervical inlet patch (CIP) is characterized by the presence of heterotopic columnar gastric mucosa in the upper esophagus, most commonly located just below the upper esophageal sphincter (UES). Other sites for heterotopic gastric mucosa have been reported in the duodenum, jejunum, cystic duct, ampulla of Vater, gallbladder, rectum, and the anus, but their etiology and pathologic significance remain unclear [76–80]. The incidence of CIP has been reported to be as low as 1 % and as much as 10 % of endoscopic cases in adult studies [81, 82]. A large autopsy series of 1,000 children demonstrated a CIP prevalence of 4.5 % [83]. During esophagogastroduodenoscopy, the region just below the UES is often quickly traversed after overcoming initial resistance. CIP is usually best seen at the end of an exam when withdrawing the endoscope back through the esophagus and specifically looking for the condition. One study found almost a six- to eightfold increase in the incidence, from 0.3 % to 2.3 %, depending upon the endoscopist's awareness of this entity and thoroughness of examination [84]. Although generally asymptomatic, CIP can present with dysphagia [85], stricture [86], ulcers [87], bleeding [88], or fistula [89].

We have used endoscopic OCT to evaluate epithelial changes in CIP patients compared to normal esophagus, Barrett's esophagus, normal stomach, and duodenum [41, 42]. Figure 68.15 shows white light endoscopy and endoscopic OCT images obtained from a 30-year-old Caucasian patient. As shown in Fig. 68.15a,

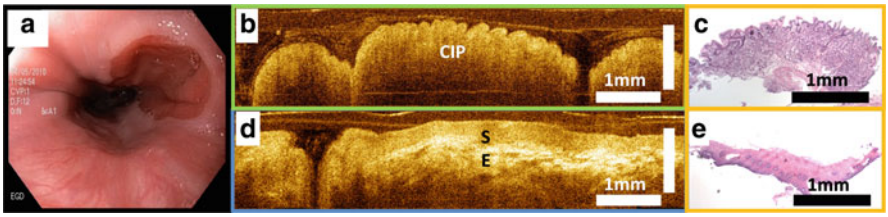

Fig. 68.15 3D-OCT images of cervical inlet patch (*CIP*). (**a**) Endoscopic view of CIP. (**b**) Cross-sectional OCT shows columnar epithelium in CIP. (**c**) Corresponding histology of (**b**). (**d**) Cross-sectional OCT image of normal squamous epithelium of the esophagus. (**e**) Corresponding histology of (**d**) (From Zhou et al. [42])

a pink circular lesion was observed under white light endoscopy in the upper esophagus (spanning 20–22 cm from the incisors) during retraction of the endoscope. Three-dimensional endoscopic OCT images were obtained of the region under direct visualization with white light endoscope by passing the probe through the standard accessory channel. Cross-sectional OCT images along the probe pullback direction clearly demonstrated columnar epithelium in the CIP region (Fig. 68.15b) and the surrounding normal squamous epithelium (Fig. 68.15d), respectively. Biopsies taken from the imaged lesion confirmed the finding of CIP. The OCT features matched representative H&E histology shown in Fig. 68.15c, e.

Ulcerative Colitis: We also performed clinical studies using endoscopic 3D-OCT in the lower gastrointestinal tract [36]. Ulcerative colitis (UC) is a chronic inflammatory condition of the GI tract that produces abscesses, ulcerations, and bleeding. UC affects up to 780,000 individuals in the United States and Canada and is newly diagnosed in 7,000–46,000 individuals per year [1]. UC is associated with a $\sim 5\times$ increase in risk of developing colorectal cancer compared to the general population, with colorectal cancer accounting for one sixth of all deaths in UC patients [90]. Unfortunately, early-stage dysplastic lesions are often flat, diffuse, and multifocal in these individuals [91]. As a result dysplastic lesions are easily obscured by the gross inflammatory background of UC, making early detection extremely challenging. UC represents a disease that can potentially benefit from 3D-OCT endomicroscopy examination for detection of lower GI abnormalities.

Figure 68.16 shows 3D-OCT endomicroscopy images acquired in the rectum near the anal verge of a UC patient. The imaged volume was $8 \times 20 \times 1.6$ mm and was acquired in 20 s. Figure 68.16a shows an en face image formed by axial summation over 20 um at a depth of 350 um below the luminal surface. When compared to normal squamous and columnar mucosa, UC tissue appears highly irregular. Large subsurface voids and bands of hyperscattering, possibly fibrotic tissue, are apparent. A wedge of comparatively normal tissue is visible at the right of the image. Figure 68.16b shows a cross section in the probe rotary scan direction through the region that reveals a regular, layered architecture consistent with anal

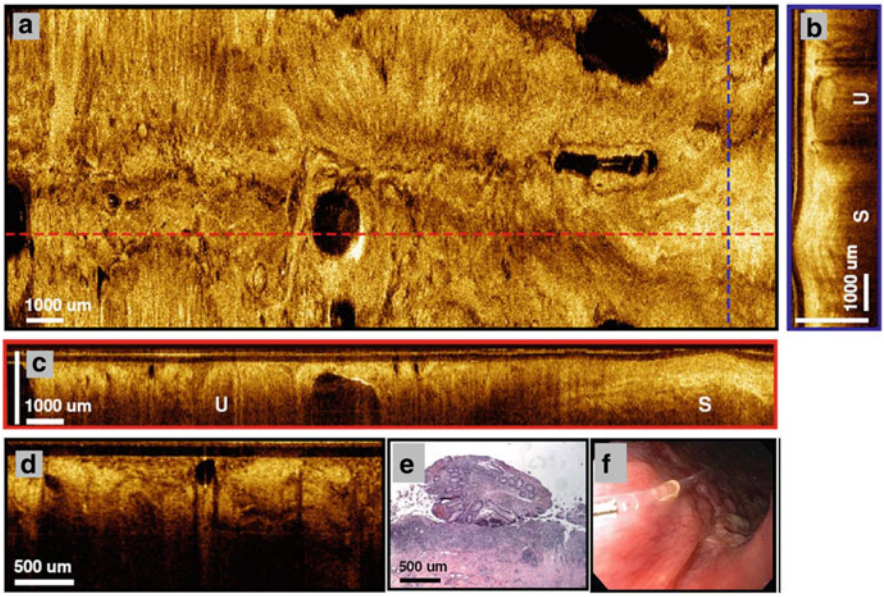

Fig. 68.16 3D-OCT images of ulcerative colitis. (**a**) En face image constructed by summing a 20 um axial section. Large, subsurface voids and ulcerations are present, while the regular crypt pattern is absent. *Dashed lines* show the locations of cross-sectional images. (**b**) A cross section in the probe rotary scan direction contains normal squamous epithelium S and ulcerative colitis U. (**c**) A cross section along the pullback direction shows similar structure. (**d**) Close-up view of the left portion of (**c**) shows disorganized structure and superficial voids. (**e**) Representative histology of UC shows an ulcerative pseudopolyp. (**f**) White light video endoscopy image of UC shows the 3D-OCT probe. The tissue surface is inflamed and ulcerations are visible (From Adler et al. [36])

squamous mucosa. The epithelium is thicker when compared to healthy subjects, possibly resulting from healing in response to prior treatment with anti-inflammatory medications. The ulcerated region exhibits a loss of layered or columnar architecture, superficial edema, and a large subsurface abnormality consistent with submucosal fibrosis. Figure 68.16c shows a longitudinal cross section with UC and normal squamous tissue visible on the left and right sides of the image, respectively. Figure 68.16d shows enlarged regions of Fig. 68.16c. Representative histology of UC in glandular mucosa is shown in Fig. 68.16e. Lymphocytic mucosal infiltration is present along with submucosal fibrosis. Ulceration results in the formation of a pseudopolyp as the epithelium is stripped away to expose the submucosa. Figure 68.16f shows a white light video endoscopy image of a patient with active UC. The mucosa appears red, inflamed, and ulcerative. The 3D-OCT catheter is also shown in position prior to imaging.

These results demonstrate that 3D-OCT can visualize subsurface features associated with inflammation. However the larger challenge is to assess if OCT can detect dysplastic changes associated with UC. However even with advances in imaging speed, OCT still has a small field of view compared with the area of the

lower GI tract. Since dysplastic changes occur focally, and it is impractical to image the lower GI tract at high resolution, OCT must be used in conjunction with a wide field imaging or detection technique which could identify regions of interest for focal high-resolution imaging. Furthermore, it would be necessary to demonstrate in a blinded study that reading OCT images has sufficient sensitivity and specificity to detect dysplasia compared with pinch biopsy and histology. This would require a larger scale clinical study. These types of issues represent some of the ongoing challenges in the development of endoscopic OCT.

68.5.2 Evaluating Therapeutic Response Using Endoscopic OCT

Endoscopic therapies are emerging as preferred treatments for a range of GI diseases due to their shorter recovery time compared with surgery. 3D-OCT endomicroscopy can potentially enhance endoscopic therapies by providing image guidance for optimal treatment planning. 3D-OCT could also be used to monitor therapy and assess healing and recurrence. Finally, 3D-OCT imaging can provide depth-resolved information when excisional biopsy is contraindicated, such as in radiation proctitis, where the risk of bleeding is high.

Radiofrequency Ablation of Barrett's Esophagus: Radiofrequency ablation (RFA) is an emerging endoscopic therapy for treating dysplastic BE [92–96]. Utilizing electrode arrays, RFA catheters deliver radiofrequency energy to the surface of esophageal tissues to ablate dysplastic BE with a low stricture rate [97, 98]. Recent studies have shown that at 1-year follow-up from the initial RFA treatment, complete eradication of dysplasia (CE-D) was achieved in 90.5 % of patients with low-grade dysplasia (LGD) and in 81 % of patients with high-grade dysplasia (HGD) [96]. At 2-year follow-up, CE-D was achieved in 98 % and 93 % of patients with LGD and HGD, respectively [99]. Complete eradication of intestinal metaplasia (CE-IM) was achieved in 93 % of patients with dysplasia after 2 years [99] and in 92 % of patients with non-dysplastic BE (NDBE) at 5-year follow-up [100]. In spite of these promising results, it should also be noted that patients typically require multiple treatment sessions in order to achieve complete eradication of dysplasia or intestinal metaplasia.

After RFA, new squamous epithelium generally replaces previous BE epithelium. However, residual BE glands can become "buried" by the neosquamous epithelium. The subsquamous intestinal metaplasia (SSIM) is not visible by conventional endoscopy, even when supplemented by chromogen or narrow band imaging (NBI). The malignant potential of SSIM is unknown [101–103]; however, SSIM was found in 25 % patients before and in 5 % patients after successful RFA treatment when detected by random biopsies [96]. However, SSIM is likely underappreciated with the current surveillance protocol of four-quadrant random biopsies every 1–2 cm along the area of apparent BE, since the area of neosquamous epithelium is not routinely biopsied in clinical practice. Furthermore, the sampling area ($\sim$1–2 mm^2) and depth [94, 100, 104] of biopsy is limited, even when using large-capacity biopsy forceps.

OCT imaging depth is 1–2 mm in human esophagus, enabling evaluation of tissue morphology underneath the squamous epithelium. The advent of high-speed endoscopic OCT systems [34–36, 60] enables 3D and comprehensive imaging. Since the location of SSIM is unpredictable, the ability of 3D-OCT to perform high-resolution, depth-resolved imaging of large areas holds great potential for identifying and characterizing SSIM before and after ablative therapies. We recently reported a clinical study demonstrating that SSIM can be effectively detected using 3D-OCT in a cohort of 27 patients undergoing RFA treatment [40].

In this section, we summarize clinical OCT studies of RFA treatment response. During the standard endoscopic procedure, the lower one third of the patient's esophagus was first surveyed with high definition white light endoscopy. Then, multiple 3D-OCT data sets were acquired over different quadrants at the gastro-esophageal junction (GEJ). After 3D-OCT imaging, BE regions identified endoscopically were ablated using an RFA catheter (BARRX Halo 90) per standard protocol [96]. Patients received a follow-up endoscopy 6–8 weeks after RFA treatment. If no BE was identified endoscopically, random 4-quadrant pinch biopsies were taken around the GEJ. The patient received additional RFA treatment if intestinal metaplasia (IM) was found based on histology or was followed 1 year later if complete eradication of IM (CE-IM) was achieved.

Figure 68.17a shows representative en face projection OCT images from a patient in the Pre-CE-IM group. Here, columnar epithelium (left) and squamous epithelium (right), as well as the SCJ, can be clearly identified. The location of SSIM is marked as red dots. Cross-sectional OCT images corresponding to the dashed brown and blue lines in Fig. 68.17a is shown in Fig. 68.17b, c, respectively. SSIM, indicated by red arrows, is clustered under the squamous epithelium. Figure 68.17d, e is 3× zoomed views of the SSIM regions shown in Fig. 68.17b, c, respectively. A double-band feature, as also described by other groups [105], can be observed from some SSIM. From the entire patient cohort, SSIM was identified in 72 % (13/18) patients in the Pre-CE-IM group and 63 % (10/16) patients in the Post-CE-IM group using OCT. Furthermore, as shown in Fig. 68.18, the number of SSIM per patient observed in the Post-CE-IM group [7.1 (9.3), mean (standard deviation), median = 5] is significantly lower compared to the number of SSIM per patient observed in the Pre-CE-IM group [34.4(44.6), median = 26.5; $p = 0.02$].

In a related study involving 33 BE patients, we found that the BE thickness measured with OCT prior to RFA is a predictor of RFA treatment response [38]. As shown in Fig. 68.19a, the average BE thickness prior to RFA was significantly thinner for the CE-IM group compared to the Non-CE-IM group (average BE thickness, 257 ± 60 um versus 403 ± 86 um, $p < 0.0001$). Figure 68.19b shows ROC curves using average and maximum BE thickness to predict RFA treatment response. The area under the curve (AUC) was 0.942 ($p < 0.001$) and 0.934 ($p < 0.001$) using the average and maximum BE thickness, respectively. An average BE thickness of 333 um was determined from the ROC curve to achieve the best prediction accuracy. Using this decision threshold, a sensitivity of 92.3 % (12/13), specificity of 85 % (17/20), PPV of 80 %, NPV of 94.4 %, and an accuracy of 87.9 % (29/33) were obtained for predicting RFA treatment response using the

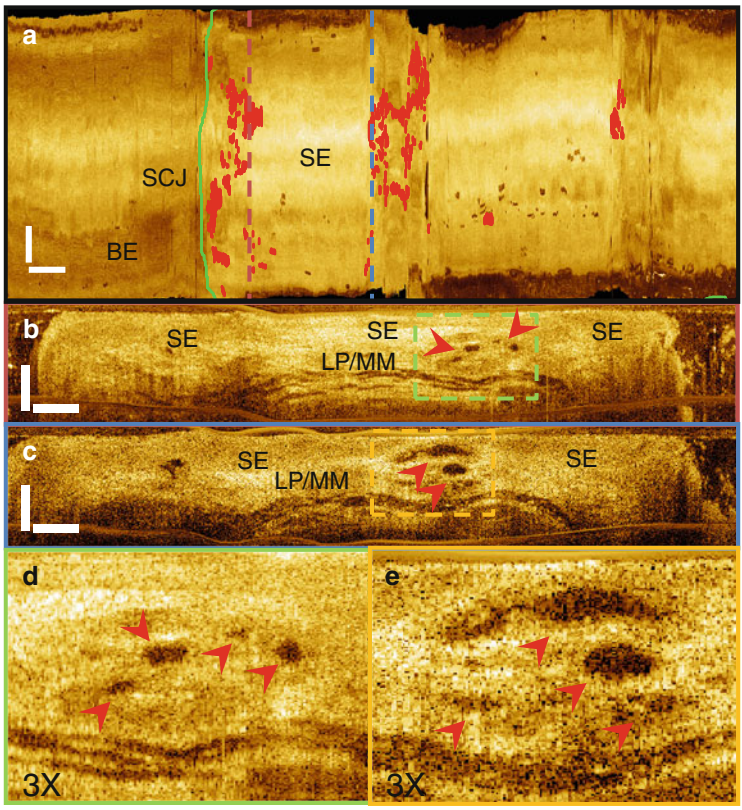

Fig. 68.17 OCT images from a patient in the Pre-CE-IM group. (**a**) En face projection over the full imaging depth of the 3D-OCT data (log OCT signal). The SCJ is marked as a *green line* with columnar epithelium on the left and squamous epithelium on the *right*. Buried glands are marked as *red dots*. (**b**, **c**) Cross-sectional OCT images corresponding to the *dashed brown* and *blue lines* in (**a**). The *red arrows* indicate buried glands. (**d**, **e**) 3× zoomed views of the buried glands regions shown in (**b**, **c**). *SCJ* squamous columnar junction, *BE* Barrett's esophagus, *LP/MM* lamina propria/muscularis mucosa. Scale bars: 1 mm in (**a**), 500 μm in (**b**), and (**c**) (From Zhou et al. [40])

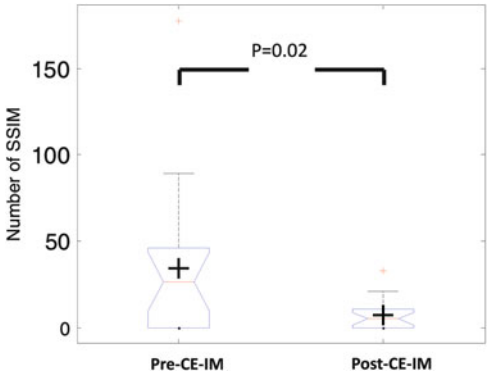

Fig. 68.18 Comparison of the number of buried glands observed per patient in the Pre-CE-IM and Post-CE-IM groups. The number of buried glands per patient was significantly lower in the Post-CE-IM group [7.1(9.3), median = 5] compared to the Pre-CE-IM group [34.4(44.6), median = 26.5; $p = 0.02$] (From Zhou et al. [40])

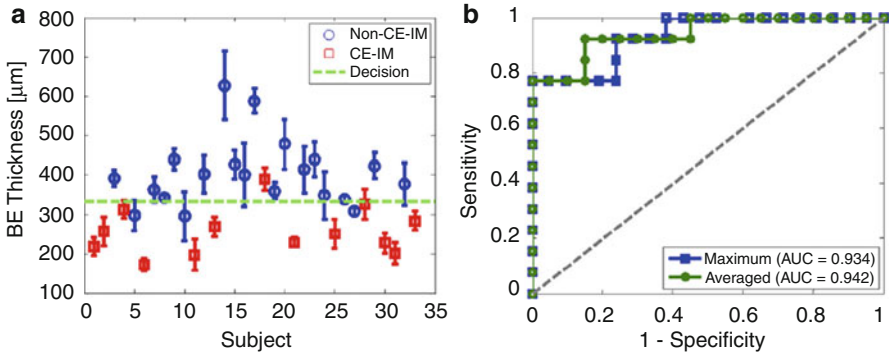

Fig. 68.19 (**a**) Scatter plot of the average Barrett's esophagus (*BE*) epithelium thickness measured by optical coherence tomography. *Blue circles*: non-complete eradication of intestinal metaplasia group. *Red crosses*: complete eradication of intestinal metaplasia group. *Green dotted line*: discrimination threshold at 333 m as determined from the average BE thickness receiver operating characteristic (*ROC*) curve in (**b**). (**b**) ROC curves of treatment response prediction by using average (*green*) and maximum (*blue*) BE thickness. The area under the curve values was 0.942 ($P < .001$) and 0.934 ($P < .001$) by using the average and maximum BE thicknesses, respectively. *BE* Barrett's esophagus, *CE-IM* complete eradication of intestinal metaplasia, *AUC* area under the curve (From Tsai et al. [38])

average BE thickness measured with OCT prior to the RFA treatment. The BE thickness measured with OCT was not correlated with the length of BE ($p = 0.88$) or the number of prior RFA treatments ($p = 0.24$).

The relationship between thickness of BE and RFA treatment response is not surprising because the standard RFA treatment parameters may not be sufficient to ablate the full BE thickness if there are thickness variations. Current RFA treatment protocols do not permit large variations in the treatment parameters, since overtreatment would increase stricture rate. If OCT measurements of BE thickness could be used for treatment planning and dose determination, this may improve the efficacy of RFA. Conversely, OCT might also be used to guide RFA treatment in real time. These approaches are complicated by the fact BE regions in the esophagus are nonuniform and BE thickness may also exhibit inhomogeneity. These inhomogeneities, combined with concerns about strictures which would result from overtreatment, make the development and validation of OCT image planned or image-guided treatment complex and challenging. However, if this problem could be addressed, it would have the potential to significantly reduce the procedural complexity of RFA.

Radiofrequency Ablation of Radiation Proctitis: Radiation proctitis (RP) is a chronic inflammatory condition that causes bleeding, diarrhea, mucous discharge, rectal pain, and fecal incontinence. RP is a common side effect of pelvic radiation therapy, which is often used to treat prostate and cervical cancers. RP affects 5.0–7.5 % of patients who undergo pelvic radiation therapy [106] and therefore is a significant cause of GI morbidity. 3D-OCT imaging was used to assess endoscopic therapy for RP, imaging three RP patients at different time points following

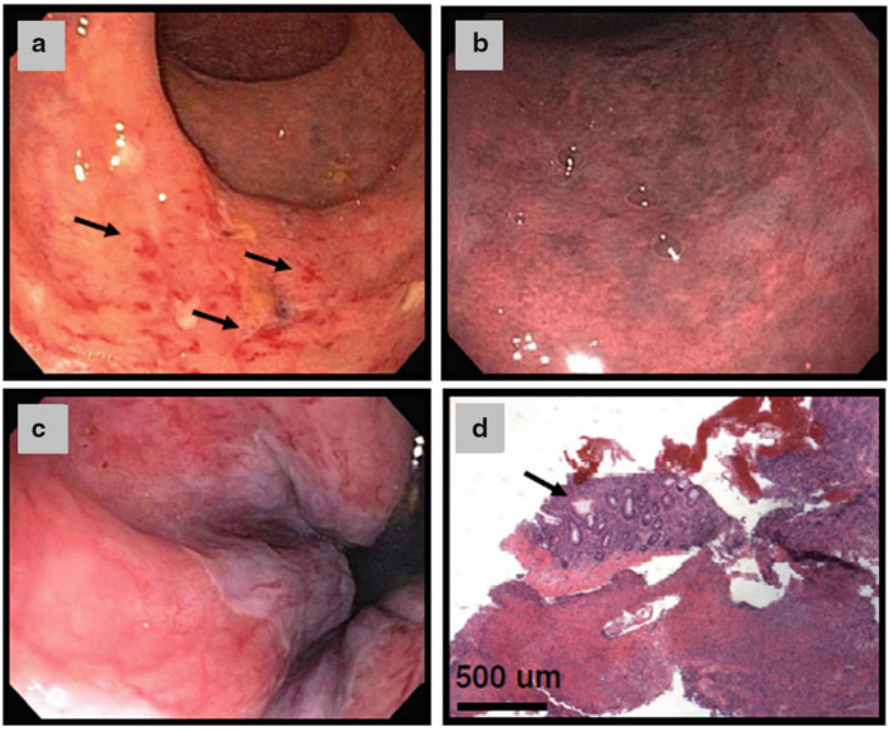

Fig. 68.20 Conventional examination of radiation proctitis. (**a**) White light video endoscopy image of radiation proctitis prior to treatment with radiofrequency ablation. *Arrows* indicate regions of bleeding and ulceration. (**b**) Image 12 months after treatment. (**c**) Image 14 months after treatment. (**d**) Representative cross-sectional histology image of radiation proctitis. *Arrow* indicates a large superficial vessel (From Adler et al. [36])

endoscopic treatment with RFA [36, 53]. Figure 68.20a–c shows white light video endoscopy images from an RP patient prior to treatment and at 12 and 14 months post treatment. Prior to treatment, bleeding vessels and ulcerations are clearly apparent. At 12 months post treatment, the rectal mucosa shows some residual inflammation, but bleeding has markedly decreased. At 14 months post treatment, the rectum appears largely normal. Figure 68.20d shows representative histology of RP, with inflammatory infiltrates and large superficial vessels present. Pinch biopsy was not obtained because it is contraindicated in subjects with RP due to the risk of bleeding. Figure 68.21 shows 3D-OCT images of the same RP volunteer 14 months after the RFA therapy. Figure 68.21a shows an en face image formed by axial summation of a 20 um thick section centered at a depth of 460 sum beneath the luminal surface. This 3D-OCT data was acquired over the dentate line, which is clearly visible as the dividing region between crypt-laden columnar epithelium on the left side of the image and smooth squamous epithelium on the right. There are no large edematous regions, and the subsurface cyst-like structures exhibit less hypointensity with a thicker layer of epithelial tissue on top. Figure 68.21b, c shows

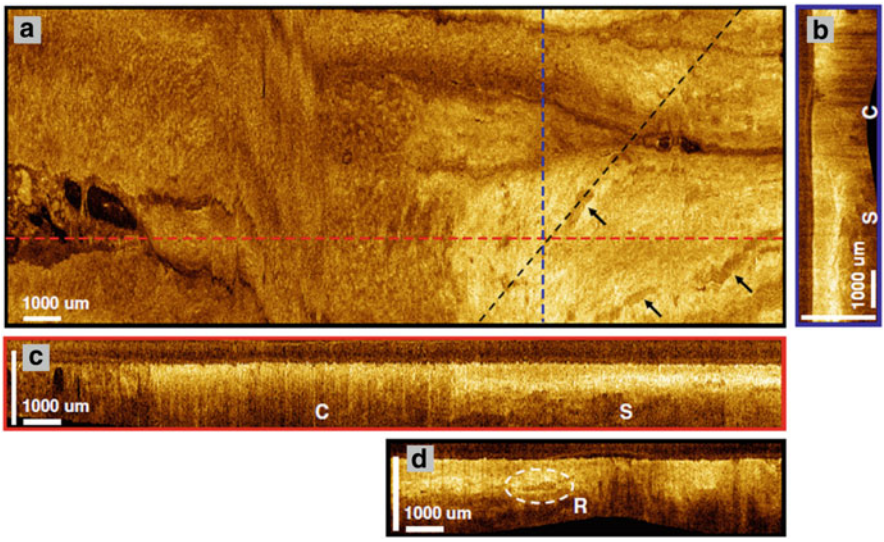

Fig. 68.21 3D-OCT images of radiation proctitis 14 months after treatment. (**a**) 20 um en face summation. Columnar epithelium proximal of the dentate line appears normal. Squamous epithelium is largely normal, with likely former ectatic vessels shown by *arrows*. *Dashed lines* show locations of cross-sectional images. (**b**) A cross section in the probe rotary direction showing regular squamous *S* and columnar *C* epithelium. (**c**) Cross sections in the longitudinal pullback direction showing similar features. (**d**) Arbitrary cross section through the long axis of an ectatic vessel remnant *R* (From Adler et al. [36])

cross-sectional images in the probe rotary scan direction and along the longitudinal direction, respectively, illustrating the transition from normal squamous to normal columnar epithelium. Figure 68.21d shows a virtual image plane oriented parallel to the long axis of one subsurface cyst-like structure. The structure can be easily located by comparing the cross section to the en face view in Fig. 68.21a. These structures may be remnants of the RP inflammation, which are covered in normal squamous epithelium following radiofrequency ablation treatment. 3D-OCT can enable measurement of pathologic structures, suggesting the possibility of quantitative assessment of disease progression, treatment, healing, and recurrence.

68.6 Conclusions

This chapter provided an overview of endoscopic OCT, which emphasizes on ultrahigh resolution and ultrahigh speed imaging technologies, probe technologies, and recent clinical studies which were performed using endoscopic OCT. These OCT technologies and advanced endoscopic imaging probes make it possible to obtain 3D volumetric images of human GI tract with unprecedented imaging resolution and speed. Endoscopic 3D-OCT enables visualization of subsurface

and/or small abnormal GI structures which cannot be seen with standard white light endoscopy. Compared to pinch biopsy, endoscopic OCT provides a 100× or more area of coverage and deeper sampling depth, which could be used to reduce sampling errors associated with pinch biopsy. In addition, real-time in vivo imaging of the GI morphology can be obtained noninvasively using endoscopic OCT, providing instantaneous feedback to the endoscopist. With further development, endoscopic 3D-OCT promises to be a powerful tool for screening GI pathologies and evaluating endoscopic therapies in clinical practices.

Acknowledgment The authors gratefully acknowledge the contributions of Dr. Desmond Adler, Dr. Yu Chen, Dr. Qing Huang, Dr. Joseph Schmitt, Dr. Yuankai Tao, Osman Ahsen, Hsiang-Chieh Lee, and Kaicheng Liang. The authors also acknowledge the facility support from VA Boston Healthcare System. This work was supported by the NIH grants R01-CA75289, R44CA101067, and R00-EB010071 (CZ); Air Force Office of Scientific Research FA9550-10-1-0063; and Medical Free Electron Laser Program FA9550-10-1-0551.

References

1. Cancer facts and figures, American Cancer Society2010 (2013)
2. G.J. Tearney, M.E. Brezinski, B.E. Bouma, S.A. Boppart, C. Pitvis, J.F. Southern et al., In vivo endoscopic optical biopsy with optical coherence tomography. Science **276**, 2037–2039 (1997)
3. A. Sergeev, V. Gelikonov, G. Gelikonov, F. Feldchtein, R. Kuranov, N. Gladkova et al., In vivo endoscopic OCT imaging of precancer and cancer states of human mucosa. Opt. Express **1**, 432–440 (1997)
4. B.E. Bouma, G.J. Tearney, C.C. Compton, N.S. Nishioka, High-resolution imaging of the human esophagus and stomach in vivo using optical coherence tomography. Gastrointest. Endosc. **51**((4) Pt 1), 467–474 (2000)
5. M.V. Sivak Jr., K. Kobayashi, J.A. Izatt, A.M. Rollins, R. Ung-Runyawee, A. Chak et al., High-resolution endoscopic imaging of the GI tract using optical coherence tomography. Gastrointest. Endosc. **51**((4) Pt 1), 474–479 (2000)
6. S. Jäckle, N. Gladkova, F. Feldchtein, A. Terentieva, B. Brand, G. Gelikonov et al., In vivo endoscopic optical coherence tomography of esophagitis, Barrett's esophagus, and adenocarcinoma of the esophagus. Endoscopy **32**, 750–755 (2000)
7. S. Jäckle, N. Gladkova, F. Feldchtein, A. Terentieva, B. Brand, G. Gelikonov et al., In vivo endoscopic optical coherence tomography of the human gastrointestinal tract–toward optical biopsy. Endoscopy **32**, 743–749 (2000)
8. X.D. Li, S.A. Boppart, J. Van Dam, H. Mashimo, M. Mutinga, W. Drexler et al., Optical coherence tomography: advanced technology for the endoscopic imaging of Barrett's esophagus. Endoscopy **32**, 921–930 (2000)
9. G. Zuccaro, N. Gladkova, J. Vargo, F. Feldchtein, E. Zagaynova, D. Conwell et al., Optical coherence tomography of the esophagus and proximal stomach in health and disease. Am. J. Gastroenterol. **96**, 2633–2639 (2001)
10. A. Das, M.V. Sivak Jr., A. Chak, R.C. Wong, V. Westphal, A.M. Rollins et al., High-resolution endoscopic imaging of the GI tract: a comparative study of optical coherence tomography versus high-frequency catheter probe EUS. Gastrointest. Endosc. **54**, 219–224 (2001)
11. P.R. Pfau, M.V. Sivak Jr., A. Chak, M. Kinnard, R.C. Wong, G.A. Isenberg et al., Criteria for the diagnosis of dysplasia by endoscopic optical coherence tomography. Gastrointest. Endosc. **58**, 196–202 (2003)

12. B. Shen, G. Zuccaro Jr., T.L. Gramlich, N. Gladkova, P. Trolli, M. Kareta et al., In vivo colonoscopic optical coherence tomography for transmural inflammation in inflammatory bowel disease. Clin. Gastroenterol. Hepatol. **2**, 1080–1087 (2004)
13. U. Seitz, J. Freund, S. Jaeckle, F. Feldchtein, S. Bohnacker, F. Thonke et al., First in vivo optical coherence tomography in the human bile duct. Endoscopy **33**, 1018–1021 (2001)
14. J.M. Poneros, G.J. Tearney, M. Shiskov, P.B. Kelsey, G.Y. Lauwers, N.S. Nishioka et al., Optical coherence tomography of the biliary tree during ERCP. Gastrointest. Endosc. **55**, 84–88 (2002)
15. I. Cilesiz, P. Fockens, R. Kerindongo, D. Faber, G. Tytgat, F. Ten Kate et al., Comparative optical coherence tomography imaging of human esophagus: how accurate is localization of the muscularis mucosae? Gastrointest. Endosc. **56**, 852–857 (2002)
16. J.M. Poneros, S. Brand, B.E. Bouma, G.J. Tearney, C.C. Compton, N.S. Nishioka, Diagnosis of specialized intestinal metaplasia by optical coherence tomography. Gastroenterology **120**, 7–12 (2001)
17. J.A. Evans, B.E. Bouma, J. Bressner, M. Shishkov, G.Y. Lauwers, M. Mino-Kenudson et al., Identifying intestinal metaplasia at the squamocolumnar junction by using optical coherence tomography. Gastrointest. Endosc. **65**, 50–56 (2007)
18. J.A. Evans, J.M. Poneros, B.E. Bouma, J. Bressner, E.F. Halpern, M. Shishkov et al., Optical coherence tomography to identify intramucosal carcinoma and high-grade dysplasia in Barrett's esophagus. Clin. Gastroenterol. Hepatol. **4**, 38–43 (2006)
19. G. Isenberg, M.V. Sivak, A. Chak, R.C.K. Wong, J.E. Willis, B. Wolf et al., Accuracy of endoscopic optical coherence tomography in the detection of dysplasia in Barrett's esophagus: a prospective, double-blinded study. Gastrointest. Endosc. **62**, 825–831 (2005)
20. X. Qi, M.V. Sivak, G. Isenberg, J.E. Willis, A.M. Rollins, Computer-aided diagnosis of dysplasia in Barrett's esophagus using endoscopic optical coherence tomography. J. Biomed. Opt. **11**, 10 (2006)
21. W. Drexler, U. Morgner, F.X. Kartner, C. Pitris, S.A. Boppart, X.D. Li et al., In vivo ultrahigh-resolution optical coherence tomography. Opt. Lett. **24**, 1221–1223 (1999)
22. W. Drexler, U. Morgner, R.K. Ghanta, F.X. Kärtner, J.S. Schuman, J.G. Fujimoto, Ultrahigh-resolution ophthalmic optical coherence tomography. Nat. Med. **7**, 502–507 (2001)
23. I. Hartl, X.D. Li, C. Chudoba, R.K. Hganta, T.H. Ko, J.G. Fujimoto et al., Ultrahigh-resolution optical coherence tomography using continuum generation in an air-silica microstructure optical fiber. Opt. Lett. **26**, 608–610 (2001)
24. S. Bourquin, A.D. Aguirre, I. Hartl, P. Hsiung, T.H. Ko, J.G. Fujimoto et al., Ultrahigh resolution real time OCT imaging using a compact femtosecond Nd:Glass laser and nonlinear fiber. Opt. Express **11**, 3290–3297 (2003)
25. Y. Wang, Y. Zhao, J.S. Nelson, Z. Chen, R.S. Windeler, Ultrahigh-resolution optical coherence tomography by broadband continuum generation from a photonic crystal fiber. Opt. Lett. **28**, 182–184 (2003)
26. K. Bizheva, B. Povazay, B. Hermann, H. Sattmann, W. Drexler, M. Mei et al., Compact, broad-bandwidth fiber laser for sub-2-microm axial resolution optical coherence tomography in the 1300-nm wavelength region. Opt. Lett. **28**, 707–709 (2003)
27. W. Drexler, Ultrahigh-resolution optical coherence tomography. J. Biomed. Opt. **9**, 47–74 (2004)
28. P.L. Hsiung, L. Pantanowitz, A.D. Aguirre, Y. Chen, D. Phatak, T.H. Ko et al., Ultrahigh-resolution and 3-dimensional optical coherence tomography ex vivo imaging of the large and small intestines. Gastrointest. Endosc. **62**, 561–574 (2005)
29. Y. Chen, A.D. Aguirre, P.L. Hsiung, S. Desai, P.R. Herz, M. Pedrosa et al., Ultrahigh resolution optical coherence tomography of Barrett's esophagus: preliminary descriptive clinical study correlating images with histology. Endoscopy **39**, 599–605 (2007)
30. P.R. Herz, Y. Chen, A.D. Aguirre, J.G. Fujimoto, H. Mashimo, J. Schmitt et al., Ultrahigh resolution optical biopsy with endoscopic optical coherence tomography. Opt. Express **12**, 3532–3542 (2004)

31. A.R. Tumlinson, B. Povazay, L.P. Hariri, J. McNally, A. Unterhuber, B. Hermann et al., In vivo ultrahigh-resolution optical coherence tomography of mouse colon with an achromatized endoscope. J. Biomed. Opt. **11**, 8 (2006)
32. A.R. Tumlinson, J.K. Barton, B. Povazay, H. Sattman, A. Unterhuber, R.A. Leitgeb et al., Endoscope-tip interferometer for ultrahigh resolution frequency domain optical coherence tomography in mouse colon. Opt. Express **14**, 1878–1887 (2006)
33. S.H. Yun, G.J. Tearney, B.J. Vakoc, M. Shishkov, W.Y. Oh, A.E. Desjardins et al., Comprehensive volumetric optical microscopy in vivo. Nat. Med. **12**, 1429–1433 (2006)
34. B.J. Vakoc, M. Shishko, S.H. Yun, W.Y. Oh, M.J. Suter, A.E. Desjardins et al., Comprehensive esophageal microscopy by using optical frequency-domain imaging (with video). Gastrointest. Endosc. **65**, 898–905 (2007)
35. D.C. Adler, Y. Chen, R. Huber, J. Schmitt, J. Connolly, J.G. Fujimoto, Three-dimensional endomicroscopy using optical coherence tomography. Nat. Photonics **1**, 709–716 (2007)
36. D.C. Adler, C. Zhou, T.H. Tsai, J. Schmitt, Q. Huang, H. Mashimo et al., Three-dimensional endomicroscopy of the human colon using optical coherence tomography. Opt. Express **17**, 784–796 (2009)
37. D.C. Adler, C. Zhou, T.H. Tsai, H.C. Lee, L. Becker, J.M. Schmitt et al., Three-dimensional optical coherence tomography of Barrett's esophagus and buried glands beneath neosquamous epithelium following radiofrequency ablation. Endoscopy **41**, 773–776 (2009)
38. T.H. Tsai, C. Zhou, Y.K. Tao, H.C. Lee, O.O. Ahsen, M. Figueiredo et al., Structural markers observed with endoscopic 3-dimensional optical coherence tomography correlating with Barrett's esophagus radiofrequency ablation treatment response. Gastrointest. Endosc. **76**, 1104–1112 (2012)
39. T.H. Tsai, C. Zhou, H.C. Lee, Y.K. Tao, O.O. Ahsen, M. Figueiredo et al., Comparison of tissue architectural changes between radiofrequency ablation and cryospray ablation in Barrett's esophagus using endoscopic three-dimensional optical coherence tomography. Gastroenterol. Res. Pract. **2012**, 684832 (2012)
40. C. Zhou, T.H. Tsai, H.C. Lee, T. Kirtane, M. Figueiredo, Y.K.K. Tao et al., Characterization of buried glands before and after radiofrequency ablation by using 3-dimensional optical coherence tomography (with videos). Gastrointest. Endosc. **76**, 32–40 (2012)
41. C. Zhou, T. Kirtane, T.H. Tsai, H.C. Lee, D.C. Adler, J.M. Schmitt et al., Cervical inlet patch-optical coherence tomography imaging and clinical significance. World J. Gastroenterol. **18**, 2502–2510 (2012)
42. C. Zhou, T. Kirtane, T.H. Tsai, H.C. Lee, D.C. Adler, J. Schmitt et al., Three-dimensional endoscopic optical coherence tomography imaging of cervical inlet patch. Gastrointest. Endosc. **75**, 675–677 (2012)
43. M.A. Choma, M.V. Sarunic, C.H. Yang, J.A. Izatt, Sensitivity advantage of swept source and Fourier domain optical coherence tomography. Opt. Express **11**, 2183–2189 (2003)
44. J.F. de Boer, B. Cense, B.H. Park, M.C. Pierce, G.J. Tearney, B.E. Bouma, Improved signal-to-noise ratio in spectral-domain compared with time-domain optical coherence tomography. Opt. Lett. **28**, 2067–2069 (2003)
45. R. Leitgeb, C.K. Hitzenberger, A.F. Fercher, Performance of Fourier domain vs. time domain optical coherence tomography. Opt. Express **11**, 889–894 (2003)
46. S.H. Yun, G.J. Tearney, J.F. de Boer, N. Iftimia, B.E. Bouma, High-speed optical frequency-domain imaging. Opt. Express **11**, 2953–2963 (2003)
47. W.Y. Oh, S.H. Yun, B.J. Vakoc, G.J. Tearney, B.E. Bouma, Ultrahigh-speed optical frequency domain imaging and application to laser ablation monitoring. Appl. Phys. Lett. **88**, 103902 (2006)
48. R. Huber, M. Wojtkowski, J.G. Fujimoto, Fourier Domain Mode Locking (FDML): a new laser operating regime and applications for optical coherence tomography. Opt. Express **14**, 3225–3237 (2006)

49. R. Huber, D.C. Adler, J.G. Fujimoto, Buffered Fourier domain mode locking: unidirectional swept laser sources for optical coherence tomography imaging at 370,000 lines/s. Opt. Lett. **31**, 2975–2977 (2006)
50. M.W. Jenkins, D.C. Adler, M. Gargesha, R. Huber, F. Rothenberg, J. Belding et al., Ultrahigh-speed optical coherence tomography imaging and visualization of the embryonic avian heart using a buffered Fourier domain mode locked laser. Opt. Express **15**, 6251–6267 (2007)
51. R. Huber, D.C. Adler, V.J. Srinivasan, J.G. Fujimoto, Fourier domain mode locking at 1050 nm for ultra-high-speed optical coherence tomography of the human retina at 236,000 axial scans per second. Opt. Lett. **32**, 2049–2051 (2007)
52. D.C. Adler, R. Huber, J.G. Fujimoto, Phase-sensitive optical coherence tomography at up to 370,000 lines per second using buffered Fourier domain mode-locked lasers. Opt. Lett. **32**, 626–628 (2007)
53. C. Zhou, D.C. Adler, L. Becker, Y. Chen, T.-H. Tsai, M. Figueiredo et al., Effective treatment of chronic radiation proctitis using radiofrequency ablation. Ther. Adv. Gastroenterol. **2**, 149–156 (2009)
54. T. Takayama, S. Katsuki, Y. Takahashi, M. Ohi, S. Nojiri, S. Sakamaki et al., Aberrant crypt foci of the colon as precursors of adenoma and cancer. N. Eng. J. Med. **339**, 1277–1284 (1998)
55. I. Grulkowski, J.J. Liu, B. Potsaid, V. Jayaraman, C.D. Lu, J. Jiang et al., Retinal, anterior segment and full eye imaging using ultrahigh speed swept source OCT with vertical-cavity surface emitting lasers. Biomed. Opt. Express **3**, 2733–2751 (2012)
56. V. Jayaraman, G.D. Cole, M. Robertson, A. Uddin, A. Cable, High-sweep-rate 1310 nm MEMS-VCSEL with 150 nm continuous tuning range. Electron. Lett. **48**, 867–868 (2012)
57. I. Grulkowski, J.J. Liu, B. Potsaid, V. Jayaraman, J. Jiang, J.G. Fujimoto et al., High-precision, high-accuracy ultralong-range swept-source optical coherence tomography using vertical cavity surface emitting laser light source. Opt. Lett. **38**, 673–675 (2013)
58. T.H. Tsai, B. Potsaid, Y.K. Tao, V. Jayaraman, J. Jiang, P.J.S. Heim et al., Ultrahigh speed endoscopic optical coherence tomography using micromotor imaging catheter and VCSEL technology. Biomed. Opt. Express **4**, 1119–1132 (2013)
59. G.J. Tearney, S.A. Boppart, B.E. Bouma, M.E. Brezinski, N.J. Weissman, J.F. Southern et al., Scanning single-mode fiber optic catheter-endoscope for optical coherence tomography. Opt. Lett. **21**, 543–545 (1996)
60. M.J. Suter, B.J. Vakoc, P.S. Yachimski, M. Shishkov, G.Y. Lauwers, M. Mino-Kenudson et al., Comprehensive microscopy of the esophagus in human patients with optical frequency domain imaging. Gastrointest. Endosc. **68**, 745–753 (2008)
61. X.M. Liu, M.J. Cobb, Y.C. Chen, M.B. Kimmey, X.D. Li, Rapid-scanning forward-imaging miniature endoscope for real-time optical coherence tomography. Opt. Lett. **29**, 1763–1765 (2004)
62. A.D. Aguirre, J. Sawinski, S.W. Huang, C. Zhou, W. Denk, J.G. Fujimoto, High speed optical coherence microscopy with autofocus adjustment and a miniaturized endoscopic imaging probe. Opt. Express **18**, 4222–4239 (2010)
63. T.H. Tsai, B. Potsaid, M.F. Kraus, C. Zhou, Y.K. Tao, J. Hornegger et al., Piezoelectric-transducer-based miniature catheter for ultrahigh-speed endoscopic optical coherence tomography. Biomed. Opt. Express **2**, 2438–2448 (2011)
64. Y.T. Pan, H.K. Xie, G.K. Fedder, Endoscopic optical coherence tomography based on a microelectromechanical mirror. Opt. Lett. **26**, 1966–1968 (2001)
65. W. Jung, D.T. McCormick, J. Zhang, L. Wang, N.C. Tien, Z.P. Chen, Three-dimensional endoscopic optical coherence tomography by use of a two-axis microelectromechanical scanning mirror. Appl. Phys. Lett. **88**, 3 (2006)
66. K.H. Kim, B.H. Park, G.N. Maguluri, T.W. Lee, F.J. Rogomentich, M.G. Bancu et al., Two-axis magnetically-driven MEMS scanning catheter for endoscopic high-speed optical coherence tomography. Opt. Express **15**, 18130–18140 (2007)

67. J.J. Sun, S.G. Guo, L. Wu, L. Liu, S.W. Choe, B.S. Sorg et al., 3D in vivo optical coherence tomography based on a low-voltage, large-scan-range 2D MEMS mirror. Opt. Express **18**, 12065–12075 (2010)
68. P.H. Tran, D.S. Mukai, M. Brenner, Z.P. Chen, In vivo endoscopic optical coherence tomography by use of a rotational microelectromechanical system probe. Opt. Lett. **29**, 1236–1238 (2004)
69. S.-W. Lee, A.E. Heidary, D. Yoon, D. Mukai, T. Ramalingam, S. Mahon et al., Quantification of airway thickness changes in smoke-inhalation injury using in-vivo 3-D endoscopic frequency-domain optical coherence tomography. Biomed. Opt. Express **2**, 243–254 (2011)
70. P.R. Allison, A.S. Johnstone, The oesophagus lined with gastric mucous membrane. Thorax **8**, 87–101 (1953)
71. B.J. Reid, X.H. Li, P.C. Galipeau, T.L. Vaughan, Barrett's oesophagus and oesophageal adenocarcinoma: time for a new synthesis. Nat. Rev. Cancer **10**, 87–101 (2010)
72. T.J. Hayeck, C.Y. Kong, S.J. Spechler, G.S. Gazelle, C. Hur, The prevalence of Barrett's esophagus in the US: estimates from a simulation model confirmed by SEER data. Dis. Esophagus **23**, 451–457 (2010)
73. A.P. Naef, M. Savary, L. Ozzello, Columnar-lined lower esophagus – acquired Lesion with malignant predisposition – Report on 140 cases of Barretts esophagus with 12 adenocarcinomas. J. Thorac. Cardiovasc. Surg. **70**, 826–835 (1975)
74. S.S. Devesa, W.J. Blot, J.F. Fraumeni Jr., Changing patterns in the incidence of esophageal and gastric carcinoma in the United States. Cancer **83**, 2049–2053 (1998)
75. N. Shaheen, D.F. Ransohoff, Gastroesophageal reflux, Barrett esophagus, and esophageal cancer: clinical applications. JAMA **287**, 1982–1986 (2002)
76. H.T. Debas, H. Chaun, F.B. Thomson, P. Soon-Shiong, Functioning heterotopic oxyntic mucosa in the rectum. Gastroenterology **79**, 1300–1302 (1980)
77. N.S. Mann, S.K. Mann, E. Rachut, Heterotopic gastric tissue in the duodenal bulb. J. Clin. Gastroenterol. **30**, 303–306 (2000)
78. N. Xeropotamos, A.S. Skopelitou, C. Batsis, A.M. Kappas, Heterotopic gastric mucosa together with intestinal metaplasia and moderate dysplasia in the gall bladder: report of two clinically unusual cases with literature review. Gut **48**, 719–723 (2001)
79. O. Boybeyi, I. Karnak, S. Gucer, D. Orhan, M.E. Senocak, Common characteristics of jejunal heterotopic gastric tissue in children: a case report with review of the literature. J. Pediatr. Surg. **43**, e19–e22 (2008)
80. P. Orizio, V. Villanacci, G. Bassotti, D. Falchetti, F. Torri, G. Ekema, Heterotopic gastric mucosa in the cystic duct. Int. J. Surg. Pathol. **19**, 364 (2009)
81. F. Borhan-Manesh, J.B. Farnum, Incidence of heterotopic gastric mucosa in the upper oesophagus. Gut **32**, 968–972 (1991)
82. P. Tang, M.J. McKinley, M. Sporrer, E. Kahn, Inlet patch: prevalence, histologic type, and association with esophagitis, Barrett esophagus, and antritis. Arch. Pathol. Lab. Med. **128**, 444–447 (2004)
83. L.E. Rector, M.L. Connerly, Aberrant mucosa in the esophagus in infants and children. Arch. Pathol. **31**, 285–294 (1941)
84. C. Azar, F. Jamali, H. Tamim, H. Abdul-Baki, A. Soweid, Prevalence of endoscopically identified heterotopic gastric mucosa in the proximal esophagus: endoscopist dependent? J. Clin. Gastroenterol. **41**, 468–471 (2007)
85. N. Akbayir, C. Alkim, L. Erdem, H.M. Sokmen, A. Sungun, T. Basak et al., Heterotopic gastric mucosa in the cervical esophagus (inlet patch): endoscopic prevalence, histological and clinical characteristics. J. Gastroenterol. Hepatol. **19**, 891–896 (2004)
86. C.S. Yarborough, R.C. McLane, Stricture related to an inlet patch of the esophagus. Am. J. Gastroenterol. **88**, 275–276 (1993)
87. M. Byrne, K. Sheehan, E. Kay, S. Patchett, Symptomatic ulceration of an acid-producing oesophageal inlet patch colonized by helicobacter pylori. Endoscopy **34**, 514 (2002)

88. R. Bataller, J.M. Bordas, J. Ordi, J. Llach, J.I. Elizalde, F. Mondelo, Upper gastrointestinal bleeding: a complication of "inlet patch mucosa" in the upper esophagus. Endoscopy **27**, 282 (1995)
89. B. Kohler, G. Kohler, J.F. Riemann, Spontaneous esophagotracheal fistula resulting from ulcer in heterotopic gastric mucosa. Gastroenterology **95**, 828–830 (1988)
90. J.A. Eaden, K.R. Abrams, J.F. Mayberry, The risk of colorectal cancer in ulcerative colitis: a meta-analysis. Gut **48**, 526–535 (2001)
91. S.H. Itzkowitz, N. Harpaz, Diagnosis and management of dysplasia in patients with inflammatory bowel diseases. Gastroenterology **126**, 1634–1648 (2004)
92. R.D. Odze, G.Y. Lauwers, Histopathology of Barrett's esophagus after ablation and endoscopic mucosal resection therapy. Endoscopy **40**, 1008–1015 (2008)
93. R. Pouw, J. Gondrie, C. Sondermeijer, F. ten Kate, T. van Gulik, K. Krishnadath et al., Eradication of Barrett esophagus with early neoplasia by radiofrequency ablation, with or without endoscopic resection. J. Gastrointest. Surg. **12**, 1627–1637 (2008)
94. J.G. Jacques, H.M. Bergman, Radiofrequency ablation – great for some or justified for many? N. Engl. J. Med. **360**, 2353–2355 (2009)
95. C. Ell, O. Pech, A. May, Radiofrequency ablation in Barrett's esophagus. N. Engl. J. Med. **361**, 1021–1021 (2009)
96. N.J. Shaheen, P. Sharma, B.F. Overholt, H.C. Wolfsen, R.E. Sampliner, K.K. Wang et al., Radiofrequency ablation in Barrett's esophagus with dysplasia. N. Engl. J. Med. **360**, 2277–2288 (2009)
97. B. Dunkin, J. Martinez, P. Bejarano, C. Smith, K. Chang, A. Livingstone et al., Thin-layer ablation of human esophageal epithelium using a bipolar radiofrequency balloon device. Surg. Endosc. **20**, 125–130 (2006)
98. V.K. Sharma, K.K. Wang, B.F. Overholt, C.J. Lightdale, M.B. Fennerty, P.J. Dean et al., Balloon-based, circumferential, endoscopic radiofrequency ablation of Barrett's esophagus: 1-year follow-up of 100 patients (with video). Gastrointest. Endosc. **65**, 185–195 (2007)
99. N.J. Shaheen, B.F. Overholt, R.E. Sampliner, H.C. Wolfsen, K.K. Wang, D.E. Fleischer et al., Durability of radiofrequency ablation in Barrett's esophagus with dysplasia. Gastroenterology **141**, 460–468 (2011)
100. D.E. Fleischer, B.F. Overholt, V.K. Sharma, A. Reymunde, M.B. Kimmey, R. Chuttani et al., Endoscopic radiofrequency ablation for Barrett's esophagus: 5-year outcomes from a prospective multicenter trial. Endoscopy **42**, 781–789 (2010)
101. J. Chennat, A.S. Ross, V.J. Konda, S. Lin, A. Noffsinger, J. Hart et al., Advanced pathology under squamous epithelium on initial EMR specimens in patients with Barrett's esophagus and high-grade dysplasia or intramucosal carcinoma: implications for surveillance and endotherapy management. Gastrointest. Endosc. **70**, 417–421 (2009)
102. N.A. Gray, R.D. Odze, S.J. Spechler, Buried metaplasia after endoscopic ablation of Barrett's esophagus: a systematic review. Am. J. Gastroenterol. (2011). doi:10.1038/ajg.2011.255
103. P. Yachimski, G.W. Falk, Subsquamous intestinal metaplasia: implications for endoscopic management of Barrett's esophagus. Clin. Gastroenterol. Hepatol. (2011). doi:10.1016/j.cgh.2011.10.009
104. N.J. Shaheen, A.F. Peery, B.F. Overholt, C.J. Lightdale, A. Chak, K.K. Wang et al., Biopsy depth after radiofrequency ablation of dysplastic Barrett's esophagus. Gastrointest. Endosc. **72**, 490–496 (2010)
105. M.J. Cobb, J.H. Hwang, M.P. Upton, Y.C. Chen, B.K. Oelschlager, D.E. Wood et al., Imaging of subsquamous Barrett's epithelium with ultrahigh-resolution optical coherence tomography: a histologic correlation study. Gastrointest. Endosc. **71**, 223–230 (2010)
106. S.S. Donaldson, Radiation proctitis after prostate carcinoma-therapy. JAMA **271**, 819–820 (1994)

Imaging Coronary Atherosclerosis and Vulnerable Plaques with Optical Coherence Tomography

69

Guillermo J. Tearney, Ik-Kyung Jang, Manubu Kashiwagi, and Brett E. Bouma

Keywords
Intravascular OCT • Atherosclerosis • Plaques • Fibroatheroma • Thin-capped fiberoatheroma • TCFA • Vunerable plaque • Macrophages • Stent deployment

69.1 Introduction

Acute myocardial infarction (AMI) is the leading cause of death in the United States and industrialized countries [1, 2]. Research conducted over the past 15 years has demonstrated that several types of minimally or modestly stenotic atherosclerotic plaques, termed vulnerable plaques, are precursors to coronary thrombosis, myocardial ischemia, and sudden cardiac death. Postmortem studies have identified one type of vulnerable plaque, the thin-capped fibroatheroma (TCFA), as the culprit lesion in approximately 80 % of sudden cardiac deaths [3–7]. Over 90 % of TCFAs are found within the most proximal 5.0 cm segment of each of the main coronary arteries (left anterior descending, LAD; left circumflex, LCx; and right coronary artery, RCA) [3, 5].

G.J. Tearney (✉)
Wellman Center for Photomedicine, Massachusetts General Hospital, Harvard Medical School, Boston, MA, USA

Department of Pathology, Massachusetts General Hospital, Boston, MA, USA
e-mail: gtearney@partners.org

I.-K. Jang
Division of Cardiology, Massachusetts General Hospital and Harvard Medical School, Massachusetts, Boston, MA, USA

M. Kashiwagi
Wellman Center for Photomedicine, Massachusetts General Hospital, Boston, MA, USA

B.E. Bouma
Wellman Center for Photomedicine, Massachusetts General Hospital, Harvard Medical School, Boston, MA, USA

© Springer International Publishing Switzerland 2015

W. Drexler, J.G. Fujimoto (eds.), *Optical Coherence Tomography*,
DOI 10.1007/978-3-319-06419-2_71

The TCFA is typically a minimally occlusive plaque characterized histologically by the following features: (1) thin fibrous cap (<65 μm), (2) large lipid pool, and (3) activated macrophages near or within the fibrous cap [3, 5, 7–9]. It is hypothesized that these features predispose TCFAs to rupture in response to biomechanical stresses [10, 11]. Following rupture and the release of procoagulant proteins, such as tissue factor, a substrate for thrombus formation is created, leading to an acute coronary event [12, 13]. While TCFAs are associated with the majority of AMIs, recent autopsy studies have shown that coronary plaques with erosions or superficial calcified nodules may also precipitate thrombosis and sudden occlusion of a coronary artery [3, 5, 14, 15].

Although autopsy studies have been valuable in determining features of culprit plaques, the retrospective nature of these studies limits their ability to quantify the risk of an individual plaque for causing acute coronary thrombosis. For instance, TCFAs are a frequent autopsy finding in asymptomatic or stable patients and are found with equal frequency in culprit and non-culprit arteries in acute coronary syndromes [16]. Moreover, disrupted TCFAs have been found in 10 % of noncardiac deaths [16]. Recent findings of multiple ruptured plaques [17] and increased systemic inflammation in acute patients [18–20] have challenged the notion of a single vulnerable plaque as the precursor for AMI [19, 21, 22]. An improved understanding of the natural history and clinical significance of these lesions would accelerate progress in diagnosis, treatment, and prevention of coronary artery disease (CAD).

An attractive approach to studying the evolution of vulnerable plaques is noninvasive or intracoronary imaging of individual lesions at multiple time points. Unfortunately, the microscopic features that characterize vulnerable plaque are not reliably identified by conventional imaging technologies such as intravascular ultrasound (IVUS) [23–28], computed tomography (CT) [29–32], and magnetic resonance imaging (MRI) [32–35]. While experimental intracoronary imaging modalities, such as integrated backscatter IVUS [36, 37], virtual histology IVUS [38, 39], elastography [32, 40], angioscopy [41–45], near-infrared spectroscopy [46], fluorescence spectroscopy [47–49], Raman spectroscopy [50, 51], and thermography [52, 53], have been investigated for the detection of vulnerable plaque, no method to date has been shown to reliably identify all of the characteristic features of these lesions.

69.2 Optical Coherence Tomography

Intracoronary optical coherence tomography (OCT) is an invasive microscopic imaging technology that has been developed for the identification of vulnerable plaque [54–57]. OCT acquires cross-sectional images of tissue reflectance and, since it may be implemented through an optical fiber probe, it is readily adaptable to coronary catheters [58] for insertion into coronary arteries and circumferential imaging of arterial pathology. The first investigation of vascular optical coherence tomography ex vivo demonstrated the potential of this technique to identify arterial microstructure [59]. Subsequent development of OCT technology enabled image acquisition at rates sufficient for intracoronary imaging in human patients [60–62]. In this chapter, we review studies conducted with this technology at the Massachusetts

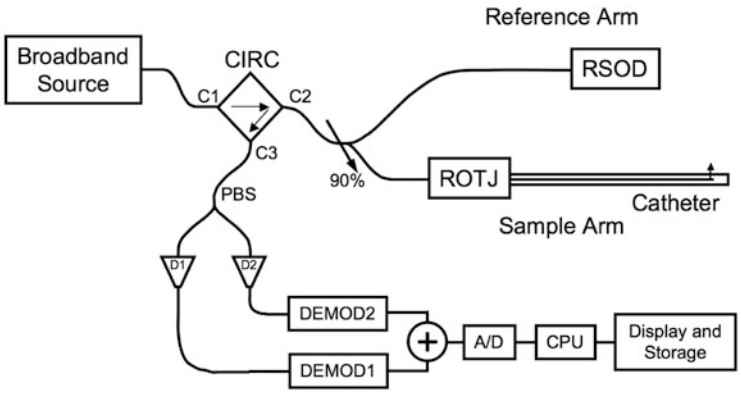

Fig. 69.1 Schematic of the time-domain intracoronary optical coherence tomography system. Polarized, broad bandwidth light passes through a circulator (CIRC, port C1 to port C2) and is split into reference and sample arms via a 10/90 fiber-optic beam splitter. The optical path length (group delay) of the reference arm is scanned by translating the galvanometer of the rapidly scanning optical delay (*RSOD*) line. Sample arm light is coupled into the catheter by a rotating optical junction (*ROTJ*). Light returned from the reference and sample arms is combined at the splitter and transmitted back to the circulator at port C2. The circulator then passes this light through port C3 to a polarizing beam splitter (*PBS*). The two orthogonal polarization states are detected separately by photodiodes D1 and D2. The two signals are demodulated and summed to create the final output signal, which is digitized (A/D) and transferred to the CPU. Detection of the fringe patterns created by sample and reference arm interference allows one radial scan (A-line) to be constructed that maps tissue reflectivity to a given axial or depth location. A cross-sectional image is generated by repeating this process at successive transverse locations on the sample while the ROTJ rotates the internal components of the catheter

General Hospital (MGH). Results from these studies show that a wide variety of microscopic features, including those associated with TCFAs, can be identified by OCT imaging both ex vivo and in living human patients. These findings suggest that this technology will play an important role in improving our understanding of coronary artery disease, guiding local therapy, and decreasing the mortality of AMI.

69.3 Optical Coherence Tomography System

A schematic of the OCT system is shown in Fig. 69.1 [61]. Briefly, the system consisted of a polarization-diverse fiber-optic nonreciprocal interferometer, which operated in the time domain. The light source was centered at 1,300 nm and had a Gaussian spectral full-width-at-half-maximum of 70 nm, providing an axial resolution of approximately 8 μm in tissue. The transverse resolution, determined by the focal spot size produced by the probe, was 25 μm. Group delay scanning at a rate of 2 kHz was conducted by utilizing a phase-control rapidly scanning optical delay (RSOD) in the reference arm [63]. Images (500 pixels transverse $\times$250 pixels axial) were obtained at four frames per second and stored digitally. A custom-built fiber-optic rotary junction was utilized for catheter-based circumferential imaging,

and a galvanometer mirror was used for the free-space experiments [64]. Catheters were constructed by modifying a commercially available 3.0F (950 μm diameter), rapid-exchange IVUS catheter to incorporate a central fiber, a distal gradient index (GRIN) lens, and a deflecting prism, which were rotated to construct a circumferential image [64].

69.4 Ex Vivo Studies

Plaque characterization The first steps in validating this imaging modality were to establish and test the accuracy of objective image criteria for discrimination of atherosclerotic plaque types ex vivo. A total of 357 specimens (162 aortas, 105 carotid bulbs, and 90 coronary arteries) were obtained from 90 cadavers (48 male, 42 female, mean age 74.5 ± 13.25). The specimens were examined fresh, less than 72 h postmortem. Imaging was conducted at physiologic temperature (37 °C). For the training set, 50 cadaver plaques were imaged by OCT and correlated with histology obtained at the imaging site [57]. Registration was accomplished by placing ink marks on the tissue prior to imaging so that both OCT images and histopathology slides contained visibly recognizable reference points. Fibrous plaques were characterized by homogeneous, signal-rich regions, fibrocalcific plaques by signal-poor regions with sharp borders, and lipid-rich plaques by signal-poor regions with diffuse borders (Fig. 69.2). Two blinded readers prospectively applied these criteria to images of the remaining 307 plaques (validation set). Using histopathologic diagnosis as the gold standard, the accuracy of OCT for characterizing plaque type was then determined. These criteria yielded a sensitivity and specificity ranging from 71 % to 79 % and 97 % to 98 % for fibrous plaques, 95–96 % and 97 % for fibrocalcific plaques, and 90 %–94 % and 90–92 % for lipid-rich plaques, respectively (overall agreement, $\kappa = 0.84$). These results demonstrated that objective OCT criteria are highly sensitive and specific for differentiating lipid-rich plaques from other plaque types [57].

Quantification of macrophage content Macrophages are central to the etiology of coronary artery disease [12, 65–67]. Due to the high quantity of intracellular phagolysosomes containing lipid and other cellular debris, we hypothesized that the refractive index contrast provided by the cytoplasm of macrophages would result in a strong optical signal from these cells (Fig. 69.3). Furthermore, since macrophages are typically heterogeneously distributed in atherosclerotic tissue, the spatial variance of OCT signal in plaques with high macrophage content should also be elevated. In order to test this hypothesis, cap macrophage and smooth muscle densities of 27 necrotic core fibroatheromas were quantified by analyzing indirect horseradish immunoperoxidase staining of paraffin-embedded tissue sections incubated with CD68 and smooth muscle actin monoclonal antibodies, respectively [68]. Hematoxylin was the counterstain. Morphometric measurements (single 10×, cross-sectional field) of cell density (% area stained) within a 500 μm (lateral) ×125 μm (axial) region of interest were then compared to the normalized standard deviation (NSD) of the OCT signal intensity at corresponding locations [68].

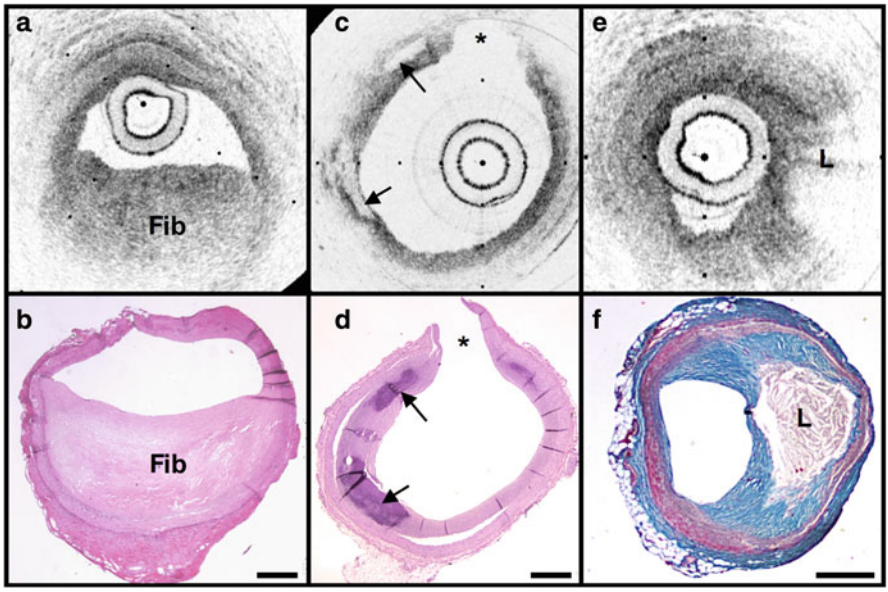

Fig. 69.2 OCT images and corresponding histology for fibrous (**a**, **b**), calcific (**c**, **d**), and lipid-rich (**e**, **f**) plaque types (obtained ex vivo). In fibrous plaques, the OCT signal (*Fib*) is observed to be strong and homogenous. In comparison, both calcific (*arrows*) and lipid-rich regions (*L*) appear as signal-poor regions within the vessel wall. Lipid-rich plaques have diffuse or poorly demarcated borders while the borders of calcific nodules are sharply delineated. (**b**, **d**) Hematoxylin and eosin; (**f**) Masson's trichome; original magnification 40×. Scale bars, tick marks, 500 μm

We found a high degree of positive correlation between OCT and histologic measurements of fibrous cap macrophage density ($r = 0.84$, $p < 0.0001$) and a negative correlation between OCT and histologic measurements of smooth muscle actin density ($r = -0.56$, $p < 0.005$). A range of NSD thresholds (6.15–6.35 %) yielded greater than 90 % sensitivity and specificity for identifying caps containing >10 % CD68 staining. This study demonstrated that the high contrast and resolution of OCT enables the quantification of macrophages within fibrous caps of atherosclerotic plaques. The impact of this finding was significant, as prior to this work there was no established tool that could permit the investigation of these crucial inflammatory cells in patients.

Other plaque features While the previously described studies demonstrated accurate characterization of features associated with TCFAs, OCT is capable of identifying additional plaque components that may be associated with acute coronary events. These features are described below:

Calcific nodules Calcific nodules have been associated with plaque thrombosis in a minority of cases [3, 5]. Calcium by OCT appears as a signal-poor region with a sharp delineation between the nodule and the surrounding tissue (Fig. 69.2c). In our histopathologic study of plaque characterization, we were able to use this criterion to diagnose calcific nodules with 96 % sensitivity and 97 % specificity [57].

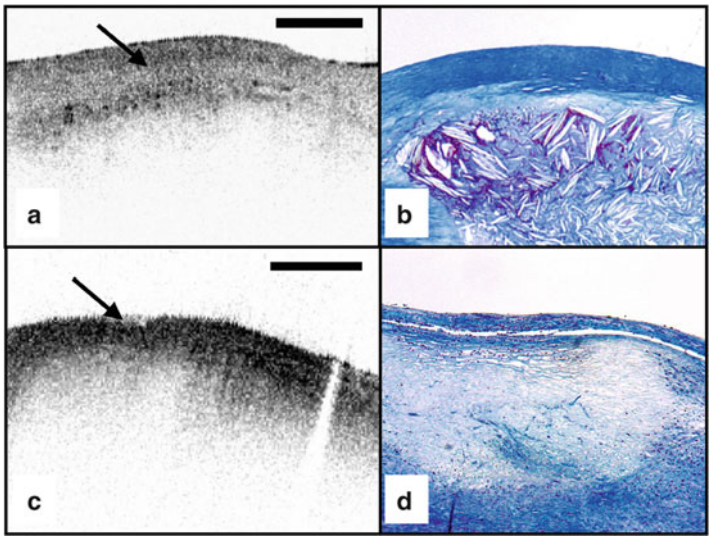

Fig. 69.3 (**a**) OCT image of a fibroatheroma with a low density of macrophages within the fibrous cap (*arrow*) (obtained ex vivo). (**c**) OCT image of a fibroatheroma with a high density of macrophages within the fibrous cap (*arrow*). (**b**, **d**) Histology corresponding to (**a**) and (**c**), respectively; Masson's trichome; original magnification 40×. Scale bars (both OCT and histology), 500 μm

Thrombus Differentiation of thrombus from plaque is critical for accurate plaque characterization. In addition, there is evidence to suggest that thrombus type, platelet-rich versus red blood cell-rich, is an indicator of the flow conditions associated with the thrombus formation and could be an important predictor of the efficacy of thrombolytic therapy [69]. We have conducted a study to correlate histopathologic sections of thrombus with OCT. Our preliminary results suggest that a "red" thrombus (red blood cell-rich) rapidly attenuates the signal in a manner similar to whole blood (Fig. 69.4a). In contrast, a "white" thrombus (platelet-rich) appears to exhibit a homogeneous moderate-strong signal with significantly less attenuation (Fig. 69.4b) [62]. In our experience, both forms of thrombus are usually easily distinguished from the arterial wall proper [70].

Macrophages at the cap-lipid pool border High-resolution cross-sectional optical imaging affords the unique opportunity to study the location of macrophage accumulations within a given plaque cross section. Using our macrophage dataset [68], we found that 84 % of OCT images demonstrated a high signal at the junction between the cap and the lipid pool (Fig. 69.5a, b) when CD68 staining at this interface was greater than 50 %.

Cholesterol crystals Research investigating the biomechanical properties of atherosclerotic plaques has shown that the presence of cholesterol crystals increases the stiffness of lipid pools and, as a result, may decrease the likelihood of plaque rupture [71]. Images of cholesterol crystals demonstrate oriented, linear, highly reflecting structures within the plaques (Fig. 69.5e, f) [72].

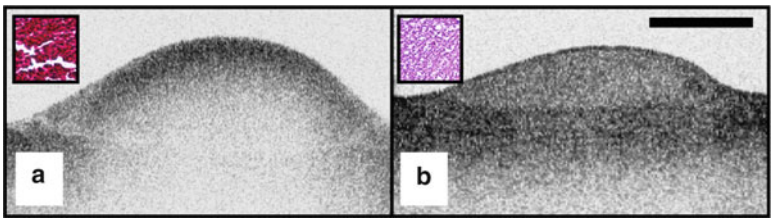

Fig. 69.4 OCT images of red blood cell-rich (**a**) and platelet-rich (**b**) thrombi (obtained ex vivo). The red blood cell-rich thrombus demonstrates high OCT signal attenuation, whereas the platelet-rich thrombus shows a homogeneous scattering signal with relatively little attenuation. Insets depict corresponding histology sections from each thrombus; hematoxylin and eosin; original magnification 40×. Scale bar, 500 μm

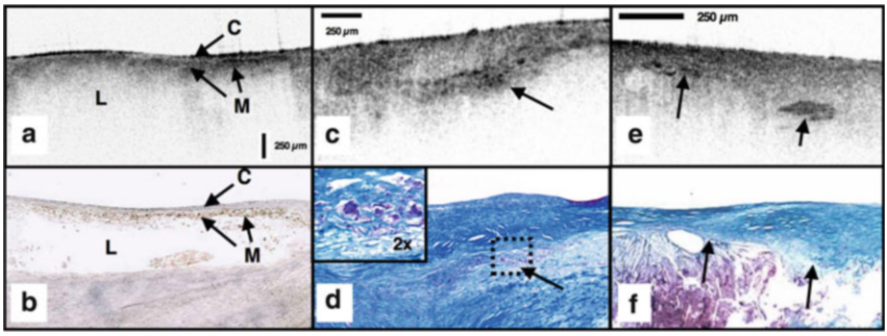

Fig. 69.5 (**a**) OCT image of a fibroatheroma with macrophages (**M**) present at the cap (**C**) lipidpool (**L**) interface (obtained ex vivo). (**c**) Cholesterol crystals (arrows) appear as signal-rich linear structures. (**b**, **d**) Histology corresponding to (**a**) and (**c**); (**b**) CD68; (**d**) Masson's trichome; (**e**) cholesterol crystals with corresponding Masson's trichrome histology (**f**) ; original magnification 40x. Scale bars (both OCT and histology), 250 μm

Neovascularization. Neovascularization in coronary plaque is also considered to relate with plaque vulnerability [73]. Although there is little histopathologic validation of IVOCT for neovascularization, an international community of IVOCT experts believes that the OCT images of neovascularization are identified as small, continuous regions with little or no IVOCT backscattering (presumably due to the removal of blood via flushing), frequently observed over several frames [74].

69.5 Clinical Studies

Histopathologic validation of qualitative and quantitative image criteria ex vivo provided a foundation for interpreting data obtained from living human patients. Between January 2000 and September 2003, a total of 83 patients undergoing routine percutaneous coronary intervention (PCI) were enrolled in a study at

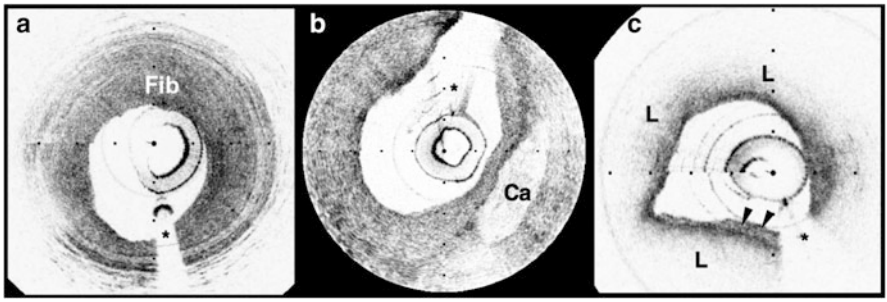

Fig. 69.6 OCT images of coronary plaques acquired from living human patients (obtained in vivo). (**a**) Fibrous plaque (*Fib*); (**b**) calcific nodule (*Ca*); (**c**) TCFA with circumferential lipid pool (*L*) and a region consistent with a platelet-rich thrombus (*arrowheads*). *Guidewire artifacts. Tick marks, 500 μm

the Massachusetts General Hospital (Boston, MA) to investigate the feasibility of intracoronary OCT. Informed consent was obtained for all patients. Imaging was performed in culprit lesions and remote sites with IVUS and OCT pre- and postcoronary intervention [62, 75]. Clear visualization of the arterial wall was accomplished by use of intermittent saline flushes (8–10 cm^3) through the guide catheter. All patients tolerated the procedure well without short- or long-term complications. Images demonstrating detailed arterial microstructure were successfully obtained in all patients studied and in all three major coronary arteries [62, 75]. To compare IVUS and OCT, images were registered by angiographic visualization of the catheter tip, anatomical landmarks, and guide catheter tip location. Summaries of the results from our clinical study are described below:

OCT images obtained in living patients contained the same image features as those obtained ex vivo. All of the characteristics of macrophage-rich TCFAs as well as the additional plaque features described in the previous section were observed in vivo; there were no image features in the clinical data that had not been observed ex vivo (Fig. 69.6) [62]. These observations suggest that image interpretation criteria and algorithms validated ex vivo can also be applied to images obtained from patients.

OCT observations were consistent with IVUS, the current gold standard for intracoronary imaging [62]. Although IVUS is unable to resolve microstructural features associated with vulnerable plaque, it can identify non-atherosclerotic (normal) vessels, large thrombi, calcific deposits, and pronounced arterial disruptions. While unconfirmed, indirect evidence suggests that IVUS may detect large lipid deposits [24]. A study was conducted, comparing 17 OCT-IVUS image pairs obtained from ten patients [62]. In all cases where IVUS identified these characteristics, blinded OCT observations were consistent (Table 69.1). OCT detected additional cases of intimal hyperplasia, thrombus, intimal disruption, and lipid pool not identified by IVUS [62].

Table 69.1 IVUS and OCT findings for corresponding image pairs ($n = 17$)

Feature	A. Identified by *both* OCT and IVUS	B. Identified by OCT *alone*
Intimal hyperplasia	3 (3 patients)	8 (7 patients)
Internal elastic lamina	NE	11 (8 patients)
External elastic lamina	NE	10 (7 patients)
Plaque	17 (10 patients)	0
Fibrous plaque	13 (10 patients)	0
Calcific plaque	4 (4 patients)	0
Echolucent region	2 (2 patients)	2 (2 patients)

Taken from Jang et al. [62]
All features of the vessel wall structure identified by the IVUS reader were seen in the corresponding OCT image (column A). Additional findings by OCT that were not identified by the IVUS reader are enumerated in column B
IVUS intravascular ultrasound, *NE* not evaluated, *OCT* optical coherence tomography

Imaging of culprit lesions demonstrated a higher prevalence of TCFA in patients with acute coronary disease than patients with stable coronary disease [76]. In this analysis, TCFA was defined as a plaque with lipid area $\geq$2 quadrants and cap thickness <65 μm. From a total of 57 patients, 20 presented with AMI, 20 with an acute coronary syndrome (ACS), and 17 with stable angina pectoris (SAP) [77]. TCFAs identified by OCT were found in 13 AMI patients (65 %), 9 with ACS (45 %), and 3 with SAP (18 %) [76]. TCFAs were more prevalent in acute presentations (AMI and ACS) of CAD (55 % versus 18 %, $p = 0.012$) [76]. Plaque disruption was found more frequently in acute CAD (20 % versus 12 %, $p = 0.053$) and calcifications were more frequent in stable disease (41 % versus 12 %, $p = 0.049$) [76]. These findings represent the first observation of presentation-dependent plaque morphology in living human patients and confirm our current knowledge of the relationship between morphology and patient outcome that has been obtained in previous autopsy studies [3–7].

Macrophage content was significantly higher in fibroatheroma caps in patients with acute presentations of CAD versus *caps in patients with SAP* [78, 79]. For this study, we created NSD (macrophage density) images (Fig. 69.7) and analyzed the macrophage distributions in both culprit and remote plaques ($n = 225$) of 49 patients with different clinical syndromes. Macrophage density was found to be significantly higher in the AMI (5.54 ± 1.48 %) and ACS (5.86 ± 2.01 %) groups compared to the SAP group (4.14 ± 1.81 %) ($p < 0.003$) [78, 79].

Both focal and multifocal elevations of macrophage density were associated with severity of clinical presentation [79]. There is great interest in understanding the role of focal versus multifocal plaque features in the pathogenesis of acute coronary thrombosis. The unique ability of OCT to quantify macrophage content and observe the spatial distribution of plaque macrophages provides a valuable tool for investigating this critical question. Supporting the concept of focal risk, sites of plaque rupture demonstrated a greater macrophage density than non-rupture sites (6.95 ± 0.48 %, 5.71 ± 0.37 %; $p = 0.01$) [79]. In addition, macrophage density was significantly higher at the surface (first 50 μm) of culprit plaques in comparison

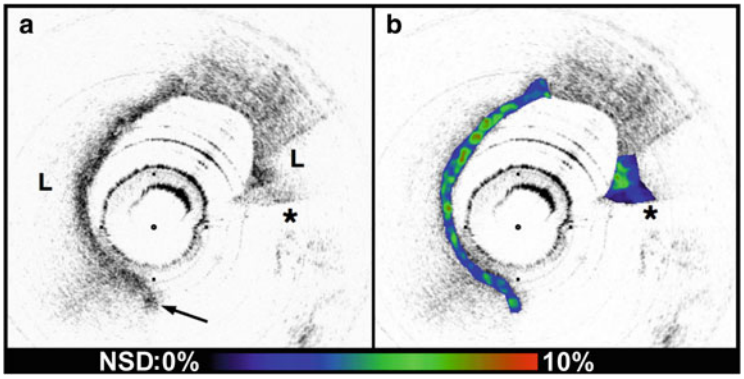

Fig. 69.7 (**a**) Conventional OCT image of a ruptured TCFA obtained from a patient with AMI (obtained in vivo). (**b**) In this image, macrophage density data (*NSD*) from the fibrous cap is displayed using a color look up table. *L* lipid pool, *arrow* intimal disruption, *guidewire artifact. Tick marks, 500 μm

to remote lesions, indicating that superficial macrophages confer a higher risk for developing an acute thrombus [79]. This finding represents a new understanding of the role of macrophages in the pathogenesis of acute coronary disease and may provide an additional parameter to assess individual plaque risk.

We also found evidence in support of the multifocal hypothesis. Macrophage densities at remote sites were correlated with measurements at culprit sites within the same patient ($r = 0.66$; $p = 0.01$) [79]. Fibrous plaques, which are not considered to be high-risk lesions, had a higher macrophage content in patients with acute disease, compared with stable patients ($p = 0.025$) [79]. Taken together, these results suggest that both focal and generalized macrophage distributions play important roles governing the severity of CAD (Table 69.2).

Neointimal hyperplasia and neoatherosclerosis. After these initial demonstrations, OCT has been widely applied for investigating many aspects of coronary artery disease in clinical trials, including evaluation of coronary artery plaque, stent placement, stent strut coverage by neointimal hyperplasia, and stent neoatherosclerosis [80–82]. In general, these studies have shown that IVOCT is capable of detecting plaque rupture, fibrous cap erosion, and intraluminal thrombus, all of which are considered to be vulnerable features of coronary artery disease [80]. Regarding stent-related lesions, OCT could clearly visualize thin neointima and uncovered struts after drug-eluting stent (DES) implantation [81, 82]. IVOCT has also been used to provide information regarding the prognosis of coronary artery disease. One observational IVOCT trial demonstrated that TCFA and neovascularization are independent predictors of luminal progression [83]. Although this result seems to support that the TCFA has the potential to precipitate plaque progression in vivo, whether or not OCT-derived TCFA leads to ACS still remains an open question. A recent pathological study showed that neoatherosclerosis and

Table 69.2 OCT findings from MGH clinical study ($n = 57$). TCFA indicates thin-cap fibroatheroma (lipid ≥2 quadrants + fibrous cap thickness ≤65 μm)

Finding	AMI ($n = 20$)	ACS ($n = 20$)	SAP ($n = 17$)	*P*
Lipid plaque, no. of quadrants	18	18	15	
1	0	3	5	
2	7	8	5	
3	5	5	3	
4	6	2	2	
Lipid-rich plaque (≥2 quadrants)	18	15	10	0.09
Fibrous cap thickness (μm)[a]	47.0 ($n = 18$)	53.8 ($n = 18$)	102.6 ($n = 15$)	0.034
TCFA	13 ($n = 18$)	9 ($n = 18$)	3 ($n = 15$)	0.012
Plaque disruption	5	3	2	0.053
Calcification	2	3	7	0.049
Thrombus	4	5	6	

Taken from Jang et al. [70]
[a]Median

consequent plaque vulnerability can occur even in previously stented lesions after long incubation period [84]. An in vivo OCT observational study revealed that late-phase BMS (>5 years) showed higher incidence of vulnerable atherosclerotic changes, including lipid-laden intima, intimal disruption, and thrombus, than early-phase BMS (<6 months) [85]. Neoatherosclerosis in the stented lesion is currently thought to be an emerging, yet important mechanism of very late stent failure, including thrombosis and restenosis [86, 87].

Limitations of TD-OCT technology for intravascular use. With IVOCT, blood interposed in between the catheter and the arterial wall attenuates the OCT light and signal to the point where only a few hundred microns can be seen through without total degradation of the OCT image quality. Saline purging adequately removes blood from the field, but at the slow frame rates (4–8 fps), intracoronary TD-OCT with saline flushing reduces to a single or few frame cross-sectional measurement. As a result, large area screening of vessel pathology over the entire artery is difficult with this methodology. Proximal balloon occlusion of the coronary artery followed by saline perfusion has been used with good effect [88, 89]. Proximal balloon occlusion is undesirable, however, because of its potential to injure the vessel wall and cause temporary myocardial ischemia.

69.6 Optical Frequency-Domain Imaging

A second-generation form of OCT, termed optical frequency-domain imaging (OFDI) or frequency-domain OCT (FD-OCT), has been developed for clinical use.

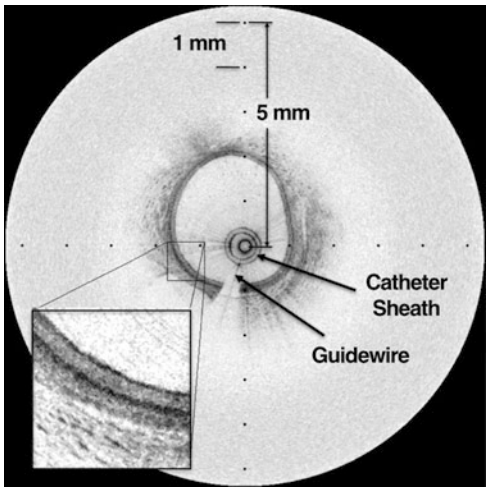

Fig. 69.8 Cross-sectional OFDI image of swine coronary artery, obtained in vivo. Inset shows an expanded view (×3) of coronary wall, demonstrating intima, media, and adventitia. Tick marks, 1 mm

These technologies have now essentially solved intraluminal blood difficulty by imaging and significantly faster than that possible with TD-OCT [90]. The system provides imaging at rates exceeding 100/s and imaging depth ranges greater than 5 mm. In 2006, swine studies were performed to provide a preliminary test of the utility of intracoronary OFDI in vivo and to assess the use of an injector pump (MedRad; Mark IV) for delivering saline through the guide catheter. Multivessel imaging was performed in four swine with several pullbacks per vessel and saline delivery rates ranging from 1 to 4 cm^3/s. In each case, the guide catheter was a seven Fr Cordis BrightTip. For each pullback, the longitudinal length of the vessel over which diagnostic-quality images were obtained was quantified. For all data, the pullback speed was set to 16.2 mm/s corresponding to a longitudinal pitch of 150 μm. A total of 56 pullbacks were performed in four swine: 22 in the RCA, ten in the LAD, and 24 in the circumflex arteries. Clear visualization of the vessels was terminated by either (1) the retraction of the imaging core within the guide catheter (33 of 56 pullbacks), (2) the end of acquisition (11 of 56 pullbacks), or (3) blood reentering the field of view (12 of 56 pullbacks). Including pullbacks in all three arteries, for a saline delivery rate of 4 cm^3/s, the average pullback length was 73 mm (average time = 4.5 s); for 3 cm^3/s, the average length was 52 mm (avg time = 3.2 s); for 2 cm^3/s, the average length was 47 mm (avg time 2.9 s); and for 1 cm^3/s, the average length was 37 mm (2.3 s).

Figure 69.8 shows a cross-sectional image obtained from the OFDI data set, obtained from a swine in vivo. Image quality is at least as good as that obtained from prior-generation OCT systems and the increased ranging depth is evident. Volumetric data from a 4.0-cm coronary artery segment, obtained from a living swine, pre- and post-stenting is shown in Fig. 69.9. Each volumetric dataset was acquired in approximately 3 s [90]. The data was rendered using Osirix 2.2 and viewed

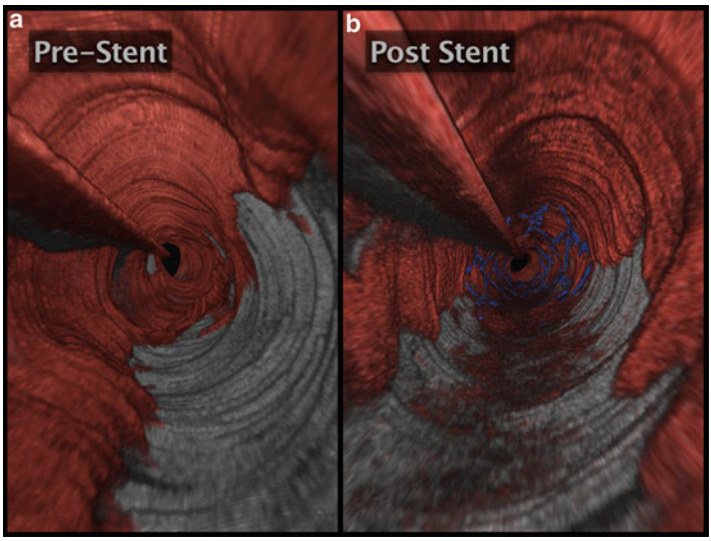

Fig. 69.9 Fly-through views of three-dimensional coronary OFDI images, obtained in vivo following a 3 s nonocclusive saline purge. Intima and media are rendered with a *red color* look up table. Adventitia is *gray* and stent is rendered in *blue*. (**a**) Pre-stent, post balloon angioplasty rendering demonstrates details of the intimal and medial disruption following balloon overinflation. (**b**) Post-stent rendering of same area shows microthrombi adherent to the struts and the exposed adventitia

in flythrough mode. These results demonstrate that blood obscuration during intracoronary imaging can be overcome by a rapid nonocclusive saline purge.

After initial imaging in swine in vivo, a first clinical experience with intracoronary OFDI was reported in 2008, demonstrating first in human application of this technology in three patients undergoing PCI for coronary artery disease [91]. Following catheter placement over the wire, an automated contrast injection was used to inject a nonocclusive lactated Ringers/radiocontrast flush through the guide catheter. Flush rates ranged between 2 and 4 ml/s and automated pullback at 5, 10, and 20 mm/s occurred over a duration that ranged from 3 to 6 s. Figure 69.10 shows three-dimensional images of a right coronary artery (RCA) obtained from a patient who had a history of BMS placement in the proximal RCA 9 s prior and underwent DES placement at another more distal RCA site immediately before OFDI imaging. In this patient, IVOCT enabled the clear visualization of key features within the coronary artery wall, including lipid pool, macrophages, calcifications, and both covered and uncovered stent struts. The high-speed image acquisition of these technologies allowed three-dimensional comprehensive volumetric microscopy to be conducted over very long segments of the coronary artery with less than 20 ml saline flush and rapid helical scanning of the catheter's optics [91]. This methodology of saline/radiocontrast flushing and rapid pullback for image acquisition has now been widely adopted by the IVOCT field.

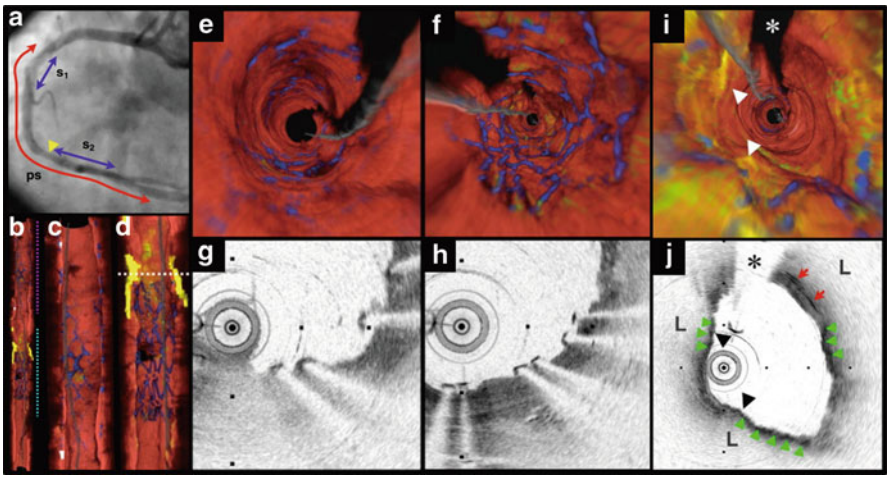

Fig. 69.10 OFDI images of right coronary artery. (**a**) Left anterior oblique angiogram after stent deployment, showing previous (s1, BMS) and current (s2, DES) stents and 7.0-cm optical frequency-domain imaging (OFDI) pullback segment (ps). (**b**) Cutaway view of entire 3-dimensional volume rendered OFDI data set (*top* = proximal; *bottom* = distal). (**c**) Expanded view of segment denoted by magenta *dotted line* in (**b**), showing the BMS. (**d**) Expanded view of segment denoted by cyan *dotted line* in (**b**), showing the DES. *White dotted line* in (**d**) is through a lipid-rich lesion, proximal to the DES. (**e**) Fly-through view (distal-proximal) of the BMS shows covered struts underneath the surface of the artery wall, as well as some struts that appear near the luminal surface. (**f**) Fly-through view (distal-proximal) of the DES demonstrates uncovered struts. (**d** and **h**) OFDI cross-sectional images of the BMS and DES, respectively. The OFDI appearance of the struts is different for the two stents. (**i**) Fly-through view (distal-proximal) demonstrates a circumferential lipid-rich lesion with abundant macrophages, partially covered by the stent. (**j**) An OFDI cross-sectional image obtained at location of *white arrowheads* in (**i**) and *dotted line* in (**d**) shows a circumferential lipid pool (*L*). Thin cap sites (*black arrowheads*) can be identified at multiple locations within the cross-sectional image. Macrophages (*green arrowheads*) and cholesterol crystals (*red arrows*) can also be seen. *Guide wire artifact (Figure and legend taken from Ref [91])

69.7 OFDI in Clinical Use

Now that this imaging technique has been made practical via the advent of second-generation technologies and high-speed imaging, IVOCT is expected to help cardiologists make more informed decisions by providing detailed information about the pathology of the artery wall in vivo, which should improve patient outcome. OCT-guided intervention is currently under investigation to demonstrate such improvement [92–94]. For example, results from a single center registry to evaluate the safety and feasibility of OCT-guided PCI were reported in 2010 [92], concluding that FD-OCT has potential to become a safety guidance tool for PCI. In another retrospective trial, IVOCT disclosed adverse features requiring further intervention in 34.7 % patients and OCT-guided intervention provided a significantly lower risk of cardiac death or myocardial infarction event

compared to angiography-guided intervention [93]. However, because evidence about OCT-guided intervention has not been fully investigated in randomized, controlled trials, further outcome-based studies should be conducted to validate the improvement in patient outcome afforded by IVOCT guidance of interventional procedures.

69.8 Current Challenges and Developments

A recent trend in IVOCT is the combination of IVOCT with other imaging technologies in the same catheter. Recently an integrated OCT ultrasound (US) probing system for intravascular imaging applications has been developed [95]. One of the major limitations of IVOCT is its relatively shallow imaging penetration depth. It is difficult, and sometimes impossible, to evaluate lesions behind lipid and/or macrophages, where OCT signal is highly attenuated at depth [96]. Although the resolution of IVUS is lower than OCT, ultrasound usually can see through the entire coronary artery wall, even for thick atheroma. Therefore, the multimodality application of IVUS and IVOCT could provide both the deep structural information via IVUS as well as the superficial detail of OCT. A miniature integrated OCT and IVUS catheter system already has been tested in in vivo animal model [97]. If commercialized and translated for clinical use, IVOCT-IVUS may become an important tool for coronary artery imaging and interventions. Another multimodality approach is a catheter-based combination of IVOCT and near-infrared fluorescence (NIRF) imaging, a technique that has now been demonstrated in rabbits in vivo [98]. This multimodality technology simultaneously provides images of colocalized molecular and microstructural information. This NIRF-IVOCT device may prove to be a powerful investigational imaging modality and may also have practical clinical implications when molecular fluorescence agents are available for human use.

69.9 Conclusion

To date, optical coherence tomography has had a tangible impact on the quest to understand and identify the vulnerable plaque. It is the only method demonstrated to be capable of measuring all of the microscopic features associated with TCFAs. Our knowledge of the morphology of plaques associated with AMI, previously predicated on retrospective autopsy studies, has now been confirmed in living human patients with this technology. Clinical studies suggest that IVOCT will become important in vivo imaging device for investigating coronary artery disease. Specifically IVOCT should provide better understanding of the vascular response to coronary intervention and eventually be used to guide and improve clinical outcomes. The promise of intracoronary OCT is great, yet these potential benefits must be demonstrated in well-designed, large-scale clinical trials. While there is still much to be done, we anticipate that the unique capabilities of OCT as an

intracoronary imaging device will serve the cardiology community well as it advances to understand, identify, and ultimately treat coronary artery disease and vulnerable plaque.

69.10 Credits

This chapter was taken in part from Tearney GJ, Jang IK, and Bouma BE. Optical coherence tomography for imaging the vulnerable plaque. Journal of Biomedical Optics 2006;11:2010021–7.

Studies by the authors described in this chapter were funded in part by the Center for Integration of Medicine and Innovative Technology (development of the imaging platform), Guidant Corporation, and the National Institutes of Health (grants R01-HL70039 and R01-HL76398).

Massachusetts General Hospital has a licensing arrangement with Terumo Corporation. Drs. Tearney and Bouma have the rights to receive royalties as part of this licensing arrangement. Dr. Bouma receives sponsored research from Terumo Corporation.

References

1. American Heart Association: Heart and Stroke Facts: 1996, Statistical Supplement
2. American Heart Association: Heart Disease and Stroke Statistics – 2013 Update
3. F.D. Kolodgie, A.P. Burke, A. Farb, H.K. Gold, J. Yuan, J. Narula, A.V. Finn, R. Virmani, The thin-cap fibroatheroma: a type of vulnerable plaque: the major precursor lesion to acute coronary syndromes. Curr. Opin. Cardiol. **16**, 285–292 (2001)
4. R. Virmani, F.D. Kolodgie, A.P. Burke, A. Farb, S.M. Schwartz, Lesions from sudden coronary death: a comprehensive morphological classification scheme for atherosclerotic lesions. Arterioscler. Thromb. Vasc. Biol. **20**, 1262–1275 (2000)
5. R. Virmani, A.P. Burke, A. Farb, F.D. Kolodgie, Pathology of the unstable plaque. Prog. Cardiovasc. Dis. **44**, 349–356 (2002)
6. M.J. Davies, Stability and instability: two faces of coronary atherosclerosis. The Paul Dudley white lecture 1995. Circulation **94**, 2013–2020 (1996)
7. E. Falk, Why do plaques rupture? Circulation **86**, III30–III42 (1992)
8. M.J. Davies, Detecting vulnerable coronary plaques. Lancet **347**, 1422–1423 (1996)
9. G.K. Sukhova, U. Schonbeck, E. Rabkin, F.J. Schoen, A.R. Poole, R.C. Billinghurst, P. Libby, Evidence for increased collagenolysis by interstitial collagenases-1 and -3 in vulnerable human atheromatous plaques. Circulation **99**, 2503–2509 (1999)
10. G.C. Cheng, H.M. Loree, R.D. Kamm, M.C. Fishbein, R.T. Lee, Distribution of circumferential stress in ruptured and stable atherosclerotic lesions. A structural analysis with histopathological correlation. Circulation **87**, 1179–1187 (1993)
11. R.T. Lee, A.J. Grodzinsky, E.H. Frank, R.D. Kamm, F.J. Schoen, Structure-dependent dynamic mechanical behavior of fibrous caps from human atherosclerotic plaques. Circulation **83**, 1764–1770 (1991)
12. P.R. Moreno, V.H. Bernardi, J. Lopez-Cuellar, A.M. Murcia, I.F. Palacios, H.K. Gold, R. Mehran, S.K. Sharma, Y. Nemerson, V. Fuster, J.T. Fallon, Macrophages, smooth muscle cells, and tissue factor in unstable angina. Implications for cell-mediated thrombogenicity in acute coronary syndromes. Circulation **94**, 3090–3097 (1996)

13. A.G. Zaman, G. Helft, S.G. Worthley, J.J. Badimon, The role of plaque rupture and thrombosis in coronary artery disease. Atherosclerosis **149**, 251–266 (2000)
14. A.C. van der Wal, A.E. Becker, C.M. van der Loos, P.K. Das, Site of intimal rupture or erosion of thrombosed coronary atherosclerotic plaques is characterized by an inflammatory process irrespective of the dominant plaque morphology. Circulation **89**, 36–44 (1994)
15. A. Farb, A.P. Burke, A.L. Tang, T.Y. Liang, P. Mannan, J. Smialek, R. Virmani, Coronary plaque erosion without rupture into a lipid core. A frequent cause of coronary thrombosis in sudden coronary death. Circulation **93**, 1354–1363 (1996)
16. E. Arbustini, M. Grasso, M. Diegoli, A. Pucci, M. Bramerio, D. Ardissino, L. Angoli, S. de Servi, E. Bramucci, A. Mussini et al., Coronary atherosclerotic plaques with and without thrombus in ischemic heart syndromes: a morphologic, immunohistochemical, and biochemical study. Am. J. Cardiol. **68**, 36B–50B (1991)
17. G. Rioufol, G. Finet, I. Ginon, X. Andre-Fouet, R. Rossi, E. Vialle, E. Desjoyaux, G. Convert, J.F. Huret, A. Tabib, Multiple atherosclerotic plaque rupture in acute coronary syndrome: a three-vessel intravascular ultrasound study. Circulation **106**, 804–808 (2002)
18. L.M. Biasucci, G. Liuzzo, C. Colizzi, A. Maseri, The role of cytokines in unstable angina. Expert Opin. Investig. Drugs **7**, 1667–1672 (1998)
19. W. Cascells, M. Naghavi, J.T. Willerson, Vulnerable atherosclerotic plaque: a multifocal disease. Circulation **107**, 2072–2075 (2003)
20. R. Krams, D. Segers, B.M. Gourabi, W. Maat, C. Cheng, C. van Pelt, L.C. van Damme, P. de Feyter, T. van der Steen, C.L. de Korte, P.W. Serruys, Inflammation and atherosclerosis: mechanisms underlying vulnerable plaque. J. Interv. Cardiol. **16**, 107–113 (2003)
21. A. Maseri, V. Fuster, Is there a vulnerable plaque? Circulation **107**, 2068–2071 (2003)
22. D.J. Kereiakes, The emperor's clothes: in search of the vulnerable plaque. Circulation **107**, 2076–2077 (2003)
23. P.G. Yock, P.J. Fitzgerald, Intravascular ultrasound: state of the art and future directions. Am. J. Cardiol. **81**, 27E–32E (1998)
24. M. Yamaguchi, M. Terashima, K. Awano, M. Kijima, S. Nakatani, S. Daikoku, K. Ito, Y. Yasamura, K. Miyatake, Morphology of vulnerable coronary plaques: insights from follow-up of patients examined by intravascular ultrasound before an acute coronary event. J. Am. Coll. Cardiol. **35**, 106–111 (2000)
25. A.J. Martin, L.K. Ryan, A.I. Gotlieb, R.M. Henkelman, F.S. Foster, Arterial imaging: comparison of high-resolution US and MR imaging with histologic correlation. Radiographics **17**, 189–202 (1997)
26. P. Schoenhagen, S.E. Nissen, Understanding coronary artery disease: tomographic imaging with intravascular ultrasound. Heart **88**, 91–96 (2002)
27. J.M. Tobis, J. Mallery, D. Mahon, K. Lehmann, P. Zalesky, J. Griffith, J. Gessert, M. Moriuchi, M. McRae, M.-L. Dwyer, N. Greep, W.L. Henry, Intravascular ultrasound imaging of human coronary arteries in vivo: analysis of tissue characterizations with comparison to in vitro histological specimens. Circulation **83**, 913–926 (1991)
28. F. Prati, E. Arbustini, A. Labellarte, B. Dal Bello, L. Sommariva, M.T. Mallus, A. Pagano, A. Boccanelli, Correlation between high frequency intravascular ultrasound and histomorphology in human coronary arteries. Heart **85**, 567–570 (2001)
29. J.A. Rumberger, T. Behrenbeck, J.F. Breen, P.F. Sheedy 2nd, Coronary calcification by electron beam computed tomography and obstructive coronary artery disease: a model for costs and effectiveness of diagnosis as compared with conventional cardiac testing methods. J. Am. Coll. Cardiol. **33**, 453–462 (1999)
30. N.D. Wong, A. Vo, D. Abrahamson, J.M. Tobis, H. Eisenberg, R.C. Detrano, Detection of coronary artery calcium by ultrafast computed tomography and its relation to clinical evidence or coronary artery disease. Am. J. Cardiol. **73**, 223–227 (1994)
31. M.J. Budoff, B.H. Brundage, Electron beam computed tomography: screening for coronary artery disease. Clin. Cardiol. **22**, 554–558 (1999)

32. M. Naghavi, M. Madjid, M.R. Khan, R.M. Mohammadi, J.T. Willerson, S.W. Casscells, New developments in the detection of vulnerable plaque. Curr. Atheroscler. Rep. **3**, 125–135 (2001)
33. F.M. Baer, P. Theissen, J. Crnac, M. Schmidt, M. Jochims, H. Schicha, MRI assessment of coronary artery disease. Rays **24**, 46–59 (1999)
34. J.F. Toussaint, G.M. LaMuraglia, J.F. Southern, V. Fuster, H.L. Kantor, Magnetic resonance images lipid, fibrous, calcified, hemorrhagic, and thrombotic components of human atherosclerosis in vivo. Circulation **94**, 932–938 (1996)
35. G. Helft, S.G. Worthley, V. Fuster, Z.A. Fayad, A.G. Zaman, R. Corti, J.T. Fallon, J.J. Badimon, Progression and regression of atherosclerotic lesions: monitoring with serial noninvasive magnetic resonance imaging. Circulation **105**, 993–998 (2002)
36. J.C. Machado, F.S. Foster, Ultrasonic integrated backscatter coefficient profiling of human coronary arteries in vitro. IEEE Trans. Ultrason. Ferroelectr. Freq. Control **48**, 17–27 (2001)
37. M.P. Urbani, E. Picano, G. Parenti, A. Mazzarisi, L. Fiori, M. Paterni, G. Pelosi, L. Landini, In vivo radiofrequency-based ultrasonic tissue characterization of the atherosclerotic plaque. Stroke **24**, 1507–1512 (1993)
38. A. König, M.P. Margolis, R. Virmani, D. Holmes, V. Klauss, Technology insight: in vivo coronary plaque classification by intravascular ultrasonography radiofrequency analysis. Nat. Clin. Pract. Cardiovasc. Med. **5**, 219–229 (2008)
39. G.A. Rodriguez-Granillo, H.M. García-García, E.P. Mc Fadden, M. Valgimigli, J. Aoki, P. de Feyter, P.W. Serruys, In vivo intravascular ultrasound-derived thin-cap fibroatheroma detection using ultrasound radiofrequency data analysis. J. Am. Coll. Cardiol. **46**, 2038–2042 (2005)
40. C.L. de Korte, A.F.W. van der Steen, E.I. Cespedes, G. Pasterkamp, S.G. Carlier, F. Mastik, A.H. Schoneveld, P.W. Serruys, N. Bom, Characterization of plaque components and vulnerability with intravascular ultrasound elastography. Phys. Med. Biol. **45**, 1465–1475 (2000)
41. Y. Ueda, M. Asakura, O. Yamaguchi, A. Hirayama, M. Hori, K. Kodama, The healing process of infarct-related plaques. J. Am. Coll. Cardiol. **38**, 1916–1922 (2001)
42. M. Asakura, Y. Ueda, O. Yamaguchi, T. Adachi, A. Hirayama, M. Hori, K. Kodama, Extensive development of vulnerable plaques as a pan-coronary process in patients with myocardial infarction: an angioscopic study. J. Am. Coll. Cardiol. **37**, 1284–1288 (2001)
43. K. Kodama, A. Hirayama, Y. Ueda, Usefulness of coronary angioscopy for the evaluation of hyperlipidemia. Nippon Rinsho Jpn. J. Clin. Med. **60**, 927–932 (2002)
44. K. Mizuno, H. Nakamura, Percutaneous coronary angioscopy: present role and future direction. Ann. Med. **25**, 1–2 (1993)
45. S. Waxman, Characterization of the unstable lesion by angiography, angioscopy, and intravascular ultrasound. Cardiol. Clin. **17**, 295–305 (1999). viii
46. P.R. Moreno, R.A. Lodder, K.R. Purushothaman, W.E. Charash, W.N. O'Connor, J.E. Muller, Detection of lipid pool, thin fibrous cap, and inflammatory cells in human aortic atherosclerotic plaques by near-infrared spectroscopy. Circulation **105**, 923–927 (2002)
47. A. Christov, R.M. Korol, E. Dai, L. Liu, H. Guan, M.A. Bernards, P.B. Cavers, D. Susko, A. Lucas, In vivo optical analysis of quantitative changes in collagen and elastin during arterial remodeling. Photochem. Photobiol. **81**, 457–466 (2005)
48. L. Marcu, Q. Fang, J.A. Jo, T. Papaioannou, A. Dorafshar, T. Reil, J.H. Qiao, J.D. Baker, J.A. Freischlag, M.C. Fishbein, In vivo detection of macrophages in a rabbit atherosclerotic model by time-resolved laser-induced fluorescence spectroscopy. Atherosclerosis **181**, 295–303 (2005)
49. L. Marcu, M.C. Fishbein, J.M. Maarek, W.S. Grundfest, Discrimination of human coronary artery atherosclerotic lipid-rich lesions by time-resolved laser-induced fluorescence spectroscopy. Arterioscler. Thromb. Vasc. Biol. **21**, 1244–1250 (2001)
50. T.J. Romer, J.F. Brennan 3rd, M. Fitzmaurice, M.L. Feldstein, G. Deinum, J.L. Myles, J.R. Kramer, R.S. Lees, M.S. Feld, Histopathology of human coronary atherosclerosis by quantifying its chemical composition with Raman spectroscopy. Circulation **97**, 878–885 (1998)

51. H.P. Buschman, G. Deinum, J.T. Motz, M. Fitzmaurice, J.R. Kramer, A. van der Laarse, A.V. Bruschke, M.S. Feld, Raman microspectroscopy of human coronary atherosclerosis: biochemical assessment of cellular and extracellular morphologic structures in situ. Cardiovasc. Pathol. **10**, 69–82 (2001)
52. W. Casscells, B. Hathorn, M. David, T. Krabach, W.K. Vaughn, H.A. McAllister, G. Bearman, J.T. Willerson, Thermal detection of cellular infiltrates in living atherosclerotic plaques: possible implications for plaque rupture and thrombosis. Lancet **347**, 1447–1451 (1996)
53. C. Stefanadis, K. Toutouzas, E. Tsiamis, C. Stratos, M. Vavuranakis, I. Kallikazaros, D. Panagiotakos, P. Toutouzas, Increased local temperature in human coronary atherosclerotic plaques: an independent predictor of clinical outcome in patients undergoing a percutaneous coronary intervention. J. Am. Coll. Cardiol. **37**, 1277–1283 (2001)
54. F.J. van der Meer, D.J. Faber, D.M. Baraznji Sassoon, M.C. Aalders, G. Pasterkamp, T.G. van Leeuwen, Localized measurement of optical attenuation coefficients of atherosclerotic plaque constituents by quantitative optical coherence tomography. IEEE Trans. Med. Imaging **24**, 1369–1376 (2005)
55. N.A. Patel, D.L. Stamper, M.E. Brezinski, Review of the ability of optical coherence tomography to characterize plaque, including a comparison with intravascular ultrasound. Cardiovasc. Intervent. Radiol. **28**, 1–9 (2005)
56. E. Regar, J.A. Schaar, E. Mont, R. Virmani, P.W. Serruys, Optical coherence tomography. Cardiovasc. Radiat. Med. **4**, 198–204 (2003)
57. H. Yabushita, B.E. Bouma, S.L. Houser, H.T. Aretz, I.K. Jang, K. Schlendorf, C.R. Kauffman, M. Shishkov, D.H. Kang, E.F. Halpern, G.J. Tearney, Characterization of human atherosclerosis by optical coherence tomography. Circulation **106**, 1640–1645 (2002)
58. G.J. Tearney, S.A. Boppart, B.E. Bouma, M.E. Brezinski, N.J. Weissman, J.F. Southern, J.G. Fujimoto, Scanning single-mode fiber optic catheter-endoscope for optical coherence tomography. Opt. Lett. **21**, 543–545 (1996)
59. M.E. Brezinski, G.J. Tearney, B.E. Bouma, J.A. Izatt, M.R. Hee, E.A. Swanson, J.F. Southern, J.G. Fujimoto, Optical coherence tomography for optical biopsy: properties and demonstration of vascular pathology. Circulation **93**, 1206–1213 (1996)
60. G.J. Tearney, M.E. Brezinski, B.E. Bouma, S.A. Boppart, C. Pitris, J.F. Southern, J.G. Fujimoto, In vivo endoscopic optical biopsy with optical coherence tomography. Science **276**, 2037–2039 (1997)
61. B.E. Bouma, G.J. Tearney, Power-efficient nonreciprocal interferometer and linear-scanning fiber-optic catheter for optical coherence tomography. Opt. Lett. **24**, 531–533 (1999)
62. I.K. Jang, B.E. Bouma, D.H. Kang, S.J. Park, S.W. Park, K.B. Seung, K.B. Choi, M. Shishkov, K. Schlendorf, E. Pomerantsev, S.L. Houser, H.T. Aretz, G.J. Tearney, Visualization of coronary atherosclerotic plaques in patients using optical coherence tomography. J. Am. Coll. Cardiol. **39**, 604–609 (2002)
63. G.J. Tearney, B.E. Bouma, J.G. Fujimoto, Phase and group delay relationships for the phase control rapid-scanning optical delay line. Opt. Lett. **22**, 1811–1813 (1997)
64. M. Shishkov, B.E. Bouma, I.K. Jang, H.T. Aretz, S.L. Houser, T.J. Brady, K. Schlendorf, G.J. Tearney, presented at the *Optical Society of America Biomedical Topical Meetings 2000*, Miami, 2000
65. P.R. Moreno, E. Falk, I.F. Palacios, J.B. Newell, V. Fuster, J.T. Fallon, Macrophage infiltration in acute coronary syndromes: implications for plaque rupture. Circulation **90**, 775–778 (1994)
66. C.L. Lendon, M.J. Davies, G.V. Born, P.D. Richardson, Atherosclerotic plaque caps are locally weakened when macrophage density is increased. Atherosclerosis **87**, 87–90 (1991)
67. M.J. Davies, P.D. Richardson, N. Woolf, D.R. Katz, J. Mann, Risk of thrombosis in human atherosclerotic plaques: role of extracellular lipid, macrophage, and smooth muscle cell content. Br. Heart J. **69**, 377–381 (1993)
68. G.J. Tearney, H. Yabushita, S.L. Houser, H.T. Aretz, I.K. Jang, K. Schlendorf, C.R. Kauffman, M. Shishkov, E.F. Halpern, B.E. Bouma, Quantification of macrophage content in atherosclerotic plaques by optical coherence tomography. Circulation **107**, 113–119 (2003)

69. S. Goto, S. Handa, Coronary thrombosis. Effects of blood flow on the mechanism of thrombus formation. Jpn. Heart J. **39**, 579–596 (1998)
70. I.K. Jang, M.J. Hursting, When heparins promote thrombosis: review of heparin-induced thrombocytopenia. Circulation **111**, 2671–2683 (2005)
71. H.M. Loree, A.J. Grodzinsky, S.Y. Park, L.J. Gibson, R.T. Lee, Static circumferential tangential modulus of human atherosclerotic tissue. J. Biomech. **27**, 195–204 (1994)
72. G.J. Tearney, I.K. Jang, B.E. Bouma, Evidence of cholesterol crystals in atherosclerotic plaque by optical coherence tomographic (OCT) imaging. Eur. Heart J. **24**, 1462 (2003)
73. P.R. Moreno, K.R. Purushothaman, V. Fuster, D. Echeverri, H. Truszczynska, S.K. Sharma, J.J. Badimon, W.N. O'Connor, Plaque neovascularization is increased in ruptured atherosclerotic lesions of human aorta: implications for plaque vulnerability. Circulation **110**, 2032–2038 (2004)
74. M. Vorpahl, M. Nakano, R. Virmani, Small black holes in optical frequency domain imaging matches intravascular neoangiogenesis formation in histology. Eur. Heart J. **31**, 1889 (2010)
75. I.K. Jang, G. Tearney, B. Bouma, Visualization of tissue prolapse between coronary stent struts by optical coherence tomography: comparison with intravascular ultrasound. Circulation **104**, 2754 (2001)
76. I.K. Jang, G.J. Tearney, B. MacNeill, M. Takano, F. Moselewski, N. Iftima, M. Shishkov, S. Houser, H.T. Aretz, E.F. Halpern, B.E. Bouma, In vivo characterization of coronary atherosclerotic plaque by use of optical coherence tomography. Circulation **111**, 1551–1555 (2005)
77. C.P. Cannon, A. Battler, R.G. Brindis, J.L. Cox, S.G. Ellis, N.R. Every, J.T. Flaherty, R.A. Harrington, H.M. Krumholz, M.L. Simoons, F.J. Van De Werf, W.S. Weintraub, K.R. Mitchell, S.L. Morrisson, R.G. Brindis, H.V. Anderson, D.S. Cannom, W.R. Chitwood, J.E. Cigarroa, R.L. Collins-Nakai, S.G. Ellis, R.J. Gibbons, F.L. Grover, P.A. Heidenreich, B.K. Khandheria, S.B. Knoebel, H.L. Krumholz, D.J. Malenka, D.B. Mark, C.R. McKay, E.R. Passamani, M.J. Radford, R.N. Riner, J.B. Schwartz, R.E. Shaw, R.J. Shemin, D.B. Van Fossen, E.D. Verrier, M.W. Watkins, D.R. Phoubandith, T. Furnelli, American College of Cardiology key data elements and definitions for measuring the clinical management and outcomes of patients with acute coronary syndromes. A report of the American College of Cardiology Task Force on Clinical Data Standards (Acute Coronary Syndromes Writing Committee). J. Am. Coll. Cardiol. **38**, 2114–2130 (2001)
78. B.D. MacNeill, B.E. Bouma, H. Yabushita, I.K. Jang, G.J. Tearney, Intravascular optical coherence tomography: cellular imaging. J. Nucl. Cardiol. **12**, 460–465 (2005)
79. B.D. MacNeill, I.K. Jang, B.E. Bouma, N. Iftimia, M. Takano, H. Yabushita, M. Shishkov, C.R. Kauffman, S.L. Houser, H.T. Aretz, D. DeJoseph, E.F. Halpern, G.J. Tearney, Focal and multi-focal plaque macrophage distributions in patients with acute and stable presentations of coronary artery disease. J. Am. Coll. Cardiol. **44**, 972–979 (2004)
80. T. Kubo, T. Imanishi, S. Takarada, A. Kuroi, S. Ueno, T. Yamano, T. Tanimoto, Y. Matsuo, T. Masho, H. Kitabata, K. Tsuda, Y. Tomobuchi, T. Akasaka, Assessment of culprit lesion morphology in acute myocardial infarction: ability of optical coherence tomography compared with intravascular ultrasound and coronary angioscopy. J. Am. Coll. Cardiol. **50**, 933–939 (2007)
81. D. Matsumoto, J. Shite, T. Shinke, H. Otake, Y. Tanino, D. Ogasawara, T. Sawada, O.L. Paredes, K. Hirata, M. Yokoyama, Neointimal coverage of sirolimus-eluting stents at 6-month follow-up: evaluated by optical coherence tomography. Eur. Heart J. **28**, 961–967 (2007)
82. T. Sawada, J. Shite, T. Shinke, S. Watanabe, H. Otake, D. Matsumoto, Y. Imuro, D. Ogasawara, O.L. Paredes, M. Yokoyama, Persistent malapposition after implantation of sirolimus-eluting stent into intramural coronary hematoma: optical coherence tomography observations. Circ. J. **70**, 1515–1519 (2006)
83. S. Uemura, K. Ishigami, T. Soeda, S. Okayama, J.H. Sung, H. Nakagawa, S. Somekawa, Y. Takeda, H. Kawata, M. Horii, Y. Saito, Thin-cap fibroatheroma and microchannel findings

in optical coherence tomography correlate with subsequent progression of coronary atheromatous plaques. Eur. Heart J. **33**, 78–85 (2012)
84. K. Inoue, K. Abe, K. Ando, S. Shirai, K. Nishiyama, M. Nakanishi, T. Yamada, K. Sakai, Y. Nakagawa, N. Hamasaki, T. Kimura, M. Nobuyoshi, T.A. Miyamoto, Pathological analyses of long-term intracoronary Palmaz-Schatz stenting; is its efficacy permanent? Cardiovasc. Pathol. **13**, 109–115 (2004)
85. M. Takano, M. Yamamoto, S. Inami, D. Murakami, T. Ohba, Y. Seino, K. Mizuno, Appearance of lipid-laden intima and neovascularization after implantation of bare-metal stents extended late-phase observation by intracoronary optical coherence tomography. J. Am. Coll. Cardiol. **55**, 26–32 (2009)
86. M. Kashiwagi, H. Kitabata, A. Tanaka, K. Okochi, K. Ishibashi, K. Komukai, T. Tanimoto, Y. Ino, S. Takarada, T. Kubo, K. Hirata, M. Mizukoshi, T. Imanishi, T. Akasaka, Very late clinical cardiac event after BMS implantation: in vivo optical coherence tomography examination. JACC Cardiovasc. Imaging **3**, 525–527 (2010)
87. G. Guagliumi, V. Sirbu, G. Musumeci, R. Gerber, G. Biondi-Zoccai, H. Ikejima, E. Ladich, N. Lortkipanidze, A. Matiashvili, O. Valsecchi, R. Virmani, G.W. Stone, Examination of the in vivo mechanisms of late drug-eluting stent thrombosis: findings from optical coherence tomography and intravascular ultrasound imaging. JACC Cardiovasc. Interv. **5**, 12–20 (2012)
88. F. Prati, E. Regar, G.S. Mintz, E. Arbustini, C. Di Mario, I.K. Jang, T. Akasaka, M. Costa, G. Guaqliumi, E. Grube, Y. Ozaki, F. Pinto, P.W. Serruys, Expert's OCT Review Document, Expert review document on methodology, terminology, and clinical applications of optical coherence tomography: physical principles, methodology of image acquisition, and clinical application for assessment of coronary arteries and atherosclerosis. Eur. Heart J. **31**, 401–415 (2010)
89. H. Kataiwa, A. Tanaka, H. Kitabata, H. Matsumoto, M. Kashiwagi, A. Kuroi, H. Ikejima, H. Tsujioka, K. Okochi, T. Tanimoto, T. Yamano, S. Takarada, N. Nakamura, T. Kubo, M. Mizukoshi, K. Hirata, T. Imanishi, T. Akasaka, Head to head comparison between the conventional balloon occlusion method and the non-occlusion method for optical coherence tomography. Int. J. Cardiol. **21**, 186–190 (2011)
90. S.H. Yun, G.J. Tearney, B.J. Vakoc, M. Shishkov, W.Y. Oh, A.E. Desjardins, M.J. Suter, R.C. Chan, J.A. Evans, J.K. Jang, N.S. Nishioka, J.F. de Boer, B.E. Bouma, Comprehensive volumetric optical microscopy in vivo. Nat. Med. **12**, 1429–1433 (2006)
91. G.J. Tearney, S. Waxman, M. Shishkov, B.J. Vakoc, M.J. Suter, M.I. Freilich, A.E. Desjardins, W.Y. Oh, L.A. Bartlett, M. Rosenberg, B.E. Bouma, Three-dimensional coronary artery microscopy by intracoronary optical frequency domain imaging. JACC Cardiovasc. Imaging **1**, 752–761 (2008)
92. F. Imola, M.T. Mallus, V. Ramazzotti, A. Manzoli, A. Pappalardo, A. Di Giorgio, M. Albertucci, F. Prati, Safety and feasibility of frequency domain optical coherence tomography to guide decision making in percutaneous coronary intervention. EuroIntervention **6**, 575–581 (2010)
93. F. Prati, L. Di Vito, G. Biondi-Zoccai, M. Occhipinti, A. La Manna, C. Tamburino, F. Burzotta, C. Trani, I. Porto, V. Ramazzotti, F. Imola, A. Manzoli, L. Materia, A. Cremonesi, M. Albertucci, Angiography alone versus angiography plus optical coherence tomography to guide decision-making during percutaneous coronary intervention: the Centro per la Lotta contro l'Infarto-Optimisation of Percutaneous Coronary Intervention (CLI-OPCI) study. EuroIntervention **8**, 823–829 (2012)
94. N. Viceconte, P.H. Chan, E.A. Barrero, L. Ghilencea, A. Lindsay, N. Foin, C. Di Mario, Frequency domain optical coherence tomography for guidance of coronary stenting. Int. J. Cardiol. **166**, 722–728 (2013)
95. J. Yin, H.C. Yang, X. Li, J. Zhang, Q. Zhou, C. Hu, K.K. Shung, Z. Chen, Integrated intravascular optical coherence tomography ultrasound imaging system. J. Biomed. Opt. **15**, 010512 (2010)

96. G.J. Tearney, E. Regar, T. Akasaka, T. Adriaenssens, P. Barlis, H.G. Bezerra, B. Bouma, N. Bruining, J.M. Cho, S. Chowdhary, M.A. Costa, R. de Silva, J. Dijkstra, C. Di Mario, D. Dudek, E. Falk, M.D. Feldman, P. Fitzgerald, H.M. Garcia-Garcia, N. Gonzalo, J.F. Granada, G. Guagliumi, N.R. Holm, Y. Honda, F. Ikeno, M. Kawasaki, J. Kochman, L. Koltowski, T. Kubo, T. Kume, H. Kyono, C.C. Lam, G. Lamouche, D.P. Lee, M.B. Leon, A. Maehara, O. Manfrini, G.S. Mintz, K. Mizuno, M.A. Morel, S. Nadkarni, H. Okura, H. Otake, A. Pietrasik, F. Prati, L. Räber, M.D. Radu, J. Rieber, M. Riga, A. Rollins, M. Rosenberg, V. Sirbu, P.W. Serruys, K. Shimada, T. Shinke, J. Shite, E. Siegel, S. Sonoda, M. Suter, S. Takarada, A. Tanaka, M. Terashima, T. Thim, S. Uemura, G.J. Ughi, H.M. van Beusekom, A.F. van der Steen, G.A. van Es, G. van Soest, R. Virmani, S. Waxman, N.J. Weissman, G. Weisz, International Working Group for Intravascular Optical Coherence Tomography (IWG-IVOCT), Consensus standards for acquisition, measurement, and reporting of intravascular optical coherence tomography studies: a report from the International Working Group for Intravascular Optical Coherence Tomography Standardization and Validation. J. Am. Coll. Cardiol. **59**, 1058–1072 (2012)
97. J. Yin, X. Li, J. Jing, J. Li, D. Mukai, S. Mahon, A. Edris, K. Hoang, K.K. Shung, M. Brenner, J. Narula, Q. Zhou, Z. Chen, Novel combined miniature optical coherence tomography ultrasound probe for in vivo intravascular imaging. J. Biomed. Opt. **16**, 060505 (2011)
98. H. Yoo, J.W. Kim, M. Shishkov, E. Namati, T. Morse, R. Shubochkin, J.R. McCarthy, V. Ntziachristos, B.E. Bouma, F.A. Jaffer, G.J. Tearney, Intra-arterial catheter for simultaneous microstructural and molecular imaging in vivo. Nat. Med. **17**, 1680–1684 (2011)

Cardiovascular Optical Coherence Tomography

70

Taishi Yonetsu, Martin Villiger, Brett E. Bouma, and Ik-Kyung Jang

Keywords

Cardiovascular OCT • Intravascular OCT • Coronary atherosclerosis • Plaques • Vulnerable plaque • Thrombus • Stent implantation

70.1 Introduction

The potential of optical coherence tomography (OCT) for intravascular imaging and assessing the microstructure of atherosclerosis was suggested already by Huang et al. at the very beginning of OCT [1]. For ophthalmology, the eye provides a natural window for OCT to image the retinal microstructure, and OCT has rapidly become the standard imaging modality to diagnose retinal disease and assess disease progression and response to therapy [1, 2]. Intravascular imaging is more invasive by nature and requires imaging through a catheter probe. This has triggered the development of advanced fiber-optic OCT systems with compact, rotating fiber probes, to image the vessel by circumferentially scanning the luminal wall [3, 4]. In 1998, we established the first cardiac OCT research group at the Massachusetts General Hospital to explore the clinical applications of OCT.

T. Yonetsu (✉)
Department of Cardiology, Tsuchiura Kyodo Hospital, Tsuchiura, Ibaraki, Japan
e-mail: yonetsu@gmail.com

M. Villiger • B.E. Bouma
Wellman Center for Photomedicine, Massachusetts General Hospital, Harvard Medical School, Boston, MA, USA
e-mail: mvilliger@partners.org; bouma@mgh.harvard.edu

I.-K. Jang
Division of Cardiology, Massachusetts General Hospital and Harvard Medical School, Massachusetts, Boston, MA, USA
e-mail: ijang@partners.org

© Springer International Publishing Switzerland 2015

W. Drexler, J.G. Fujimoto (eds.), *Optical Coherence Tomography*,
DOI 10.1007/978-3-319-06419-2_72

The first imaging of rabbit aorta was reported by Fujimoto et al. [5], followed by the first swine measurements in vivo by Tearney et al. [6], and finally the first assessment of coronary arteries in patients by Jang et al. [7].

Because of its invasiveness, intravascular imaging is exclusively used in the catheterization laboratory on patients undergoing percutaneous coronary intervention (PCI). Further, because the optical properties of blood are disadvantageous for imaging with OCT, a clearing agent has to be administered to the coronary artery to displace the blood and provide a clear view on the vessel wall. The speed advantage provided by the faster Fourier or spectral domain OCT systems has proved indispensible as it enabled the imaging of longer vessel segments with only a small amount of clearing agent.

These developments have allowed intravascular OCT to be rapidly adopted in clinical research and recently also in clinical practice. With its unprecedented spatial resolution, OCT is a powerful tool to visualize plaque characteristics and help to guide and evaluate vascular response to PCI. OCT is becoming one of the standard modalities to evaluate plaque vulnerability by identifying the presence of lipid content, thin fibrous cap, or macrophage accumulation. Further, after stent implantation, OCT can assess strut apposition and coverage, neointimal hyperplasia, and neoatherosclerosis. In order to provide uniform terminology and standards on the cardiovascular use of OCT and interpretation of the images, a consensus document has been published through an international standardization initiative [8]. Recently, new applications for OCT in intravascular imaging are being explored, such as transplant vasculopathy, monitoring of renal sympathetic ablation, or guiding the crossing of chronic total occlusions.

The scope of this chapter is to highlight the steps taken to bring intravascular OCT from bench to bedside over the last 15 years. We will give a general description of atherosclerosis and its pathophysiology and the specific technical implementation of OCT for intravascular imaging through a fiber-optic probe. The motivation is to provide sufficient medical details to provide a basic introduction to the terminology, principles, and challenges of intracoronary imaging.

70.2 Coronary Artery Disease

Acute cardiac events such as myocardial infarction (MI) and sudden cardiac death (SCD) remain the leading causes of death in the Western world. The underlying cause of these events is atherosclerosis, which consists in the continuous buildup of atherosclerotic plaques in the coronary arteries. The coronary arteries are divided into the right and left branches, which supply the myocardium with blood. The main branch on the right side is the right coronary artery (RCA); the left side has the left main trunk, which divides into two branches, the left anterior descending (LAD) and the left circumflex (LCX). The coronary vessel wall is composed of three layers, respectively, from the *lumen*: *intima*, *media*, and *adventitia*. The *intima* is built of a single layer of endothelial cells, which are in direct contact with the circulating blood. Its subendothelial layer composed of extracellular matrix contains loosely scattered smooth muscle cells. The *intima* is separated from the *media* by the inner elastic *lamina*. The *media* is made of smooth muscle cells densely

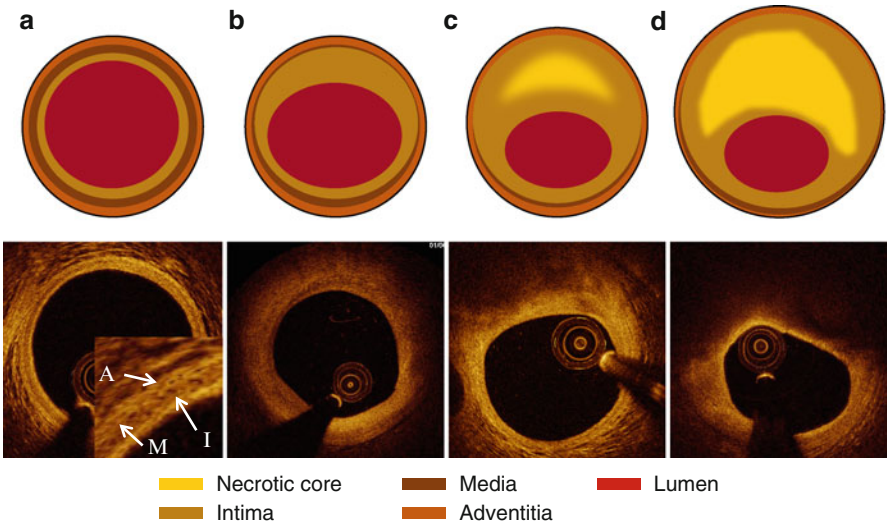

Fig. 70.1 Appearance of atherosclerotic plaque (**a**) The normal coronary artery is structured into intima (*I*), media (*M*), and adventitia (*A*), which are clearly visualized by OCT. (**b**) Pathologic intimal thickening is characterized by the thickening of the intimal layer in the absence of a necrotic core. With the progression of atherosclerosis, the border between intima and media becomes diffuse. (**c**) A fibrous cap atheroma with its typical necrotic core covered by a fibrous cap. **(d)** A thin-cap fibroatheroma is recognized as a rupture-prone plaque and is characterized by a thin fibrous cap overlying a large necrotic core, usually accompanied by inflammation in the fibrous cap and expansive arterial remodeling

packed within a matrix of elastin and collagen. The outer elastic *lamina* separates the *media* from the *adventitia*, which is a layer of connective tissue. Figure 70.1a depicts a schematic representation of the normal vessel and gradual progression of atherosclerosis, together with a corresponding OCT image.

Atherosclerosis is caused by the accumulation of fatty material in the intimal layer of the arteries, accompanied by chronic inflammation. According to the currently accepted view, once monocytes penetrate into the vessel wall, they are taken up by macrophages and become foam cells, which owe their name to their histological appearance. The subsequent signaling cascade eventually results in an advanced lesion with a lipid or necrotic core. The intimal layer that separates the necrotic core from the vessel lumen is usually reinforced by additional collagen and is referred to as the fibrous cap. "Plaque vulnerability"is a term employed to describe the risk of this cap to rupture. Many factors contribute to the mechanical integrity of the fibrous cap, but its thickness is traditionally used as the most obvious indicator of vulnerability, defining lesions with a thin fibrous cap covering a fibroatheroma (TCFA) as most prone to rupture. Figure 70.1b–d displays different presentations of typical atherosclerotic plaques.

A plaque rupture would expose thrombogenic substrates such as von Willebrand factor attracting platelets and fibrin, which results in formation of thrombus. The fate of plaque rupture is determined by three factors: degree of occlusion, duration of occlusion, and the level of preexisting collaterals. When thrombus is

nonocclusive, it may become organized leading to rapid progression of atherosclerosis which is clinically silent. When the lumen is partially occluded, the patient develops unstable angina or myocardial infarction without elevation of the ST segment in the electrocardiogram depending on the duration of occlusion and the level of preexisting collaterals. These events are frequently classified as non-ST elevation acute coronary syndromes (NSTE-ACS). When occlusive thrombus persists for more than 20 min, damage to the myocardium becomes irreversible, manifesting in an ST-elevation (STEMI). Another important underlying mechanism for MI or SCD is plaque erosion, particularly in young women and in smokers. It may be responsible for MI or SCD in up to 30–40 % of cases.

Patients with an acute coronary event are usually treated with antithrombotic medications and frequently by percutaneous coronary intervention (PCI). During PCI, a catheter is introduced through the femoral or radial artery to gain access to the coronary arteries. The goal of the procedure is to reopen the flow-limiting lesion, commonly by balloon angioplasty followed by the placement of stents. Balloon angioplasty is performed by inflating a carefully sized balloon inside the identified artery segment to widen the lumen and reestablish sufficient blood flow. The subsequent placement of a coronary stent, a mesh-like structure placed in the artery with a similar inflating balloon, helps to maintain the gained lumen diameter. The initial use of bare-metal stents (BMS) has frequently caused complications due to neointimal growth within the stent, ultimately resulting in restenosis of the vessel. Drug-eluting stents (DES) reduce this restenosis by releasing drugs that block cell proliferation. Hopes are high that bioabsorbable scaffolds currently under development help to further reduce complications. These scaffolds are eventually fully absorbed and provide a more natural compliant structure that is better accepted by the vessel than the previous metallic stents.

The catheterization laboratory is equipped with a fluoroscope to perform angiography by administration of a radiopaque agent. The contrast agent absorbs the X-Ray irradiation and produces a negative contrast on the angiogram and allows the real-time visualization of the vasculature. Angiography is also the primary diagnostic tool to identify the severity of the lesion in the coronary vasculature. The various catheters have radiopaque markers for visualization on the angiogram. A thin (0.0014″) guide wire is first used to gain access to the coronary arteries. A wide guiding catheter is placed at the ostium. The balloon catheters for angioplasty and stenting, and diagnostic imaging modalities such as OCT or intravascular ultra sound (IVUS), are then advanced over the guide wire into the coronary artery.

70.3 State-of-the-Art Intravascular OCT

Several chapters of this book are dedicated to the thorough discussion of the theory and instrumentation of OCT. In view of this, we only give a short description of the basic principles of OCT but highlight some aspects specific to intracoronary imaging.

Optical coherence tomography (OCT) is a high-resolution imaging modality that generates cross-sectional images of tissue microstructure [1]. It utilizes coherence

gating to select scattering signals from a defined depth within the tissue by interfering the sample light with a known reference signal. The first-generation OCT technology was based on "time domain" detection (TD-OCT). Near-infrared light with a large spectral bandwidth, and corresponding short coherence length, was focused onto the tissue. Combined with the reference signal, only light from the sample depth corresponding to the reference arm length created an interference signal at the detector. Mechanically scanning the reference arm length sequentially retrieved the axial sample reflectivity profile. Dramatic improvements in sensitivity and imaging speed could be achieved by detection in the Fourier domain. This detection scheme is also known as spectral domain OCT, swept source OCT, or optical frequency domain imaging (OFDI). Optical frequency domain imaging operates with a frequency-swept laser source, changing the wavelength as a function of time over the available spectral range [9, 10]. The reference arm is kept at a stationary position, and the interference between the sample and the reference light now creates a signal whose frequency is proportional to the offset of the signal from the reference arm length. Fourier transformation of this recorded fringe signal recovers the axial sample profile with a single wavelength sweep. Because the signal of a single reflecting element in the sample is reconstructed by combining the detected signal of all wavelengths, a large sensitivity advantage results, which was pointed out independently by three different research groups in 2003 [11–13]. This understanding spurred the development of wavelength-swept laser sources and resulted in an impressive decrease in sweep times, resulting in a dramatic improvement of imaging speeds for OCT. This was vital for intracoronary imaging, as the slow imaging time of previous TD-OCT systems required proximal occlusion or continuous flushing with saline or contrast agent (the same agent used for angiography) to displace the blood. The resulting ischemia and limitation on the injected flushing volume restrained the field of view that could be imaged. The increase in imaging speed was essential to achieve imaging of significant segments of the coronary arteries with injection of only a small volume of clearing agent and make intravascular imaging practical.

Figure 70.2 depicts a schematic of a typical intravascular OFDI system. The wavelength-swept laser source operates with repetition rates of 50–200 kHz centered around 1,300 nm and spanning 120–140 nm, resulting in axial resolution in tissue of 6–8 um [14]. The fiber-based interferometer employs fiber circulators for an efficient signal transduction [15] and shifts the reference signal with an acousto-optic modulator to remove depth degeneracy [16]. The sample arm consists of several meters of single-mode fiber, connecting through the rotary junction to the catheter and providing sufficient manipulation range for its operation in a clinical setting. As a result, the polarization state of the light propagating along the fiber is not preserved, and polarization diverse dual-balanced detection is advantageous. The structural OCT signal is obtained by taking the sum of the squared norm of the reconstructed A-line of each channel. This renders the signal independent of the actual polarization state of the light at the detector and makes the tomogram insensitive to catheter motion.

The rotary junction consists of a static collimator on the system side. On the catheter side, a second collimator, which is part of the spinning catheter, couples the

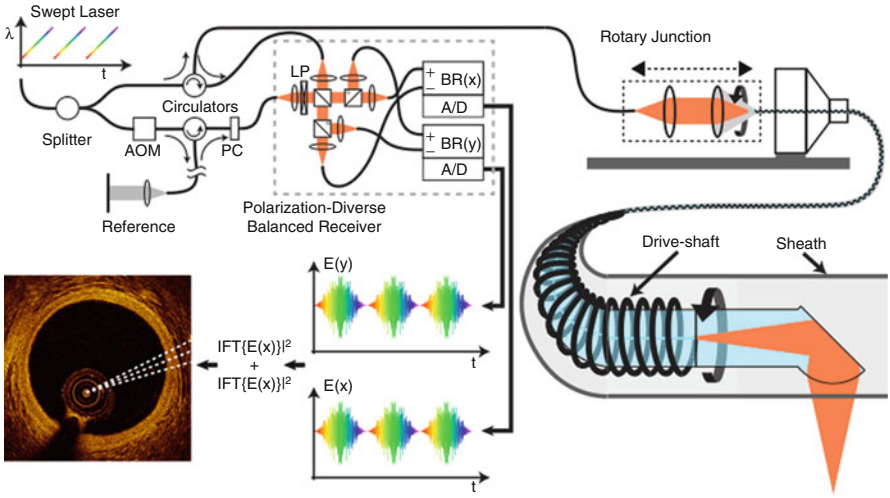

Fig. 70.2 Principle of intravascular optical frequency domain imaging. The fiber-based interferometer is composed of a fiber coupler, splitting the sample and reference light and employs circulators, and acousto-optic modulator (*AOM*) and polarization controller (*PC*) to align the reference light with the linear polarizer (*LP*) at the receiver. *BR* balanced receiver, *A/D* analog to digital conversion. The rotary junction couples light to the rotating fiber probe and can pull back the probe within the static sheath. The tomogram is built up by the sequential depth scans, computed from both polarization channels of the receiver

light into a single-mode fiber, as shown in Fig. 70.2. The fiber-optic probe is at the distal end of this fiber. The probe is composed either of a graded index fiber, followed by a reflecting prism, or an angle-polished ball lens. The ball lens can be fabricated in an integrative way directly at the fiber tip, by heating a carefully sized coreless fiber that was previously spliced to the guiding single-mode fiber, with a fiber-optic splicer, followed by angle polishing. The fiber connecting the collimator and the fiber probe is protected by a coiled driveshaft which transmits the torque for spinning of the catheter and protects the fiber. The assembly of the fiber probe and the driveshaft containing the sample fiber is contained within a sheath, similar to the ones used in IVUS, with a diameter of 2.6 Fr (0.87 mm). The sheath is fabricated from transparent polyethylene at the distal end to enable the sample light to focus through the sheath material onto the vessel wall. The static sheath protects the vasculature from the rotating probe and also enables the pulling back of the fiber probe within this sheath to perform a helical scan pattern on the lumen surface. The focal length of the probe is adjusted to generate a focus of 25–30 μm intensity full width at half maximum at an offset of ∼2 mm from the sheath surface.

The first report of a system similar to this description was given in 2006 by Yun et al. [17]. Current commercial systems operate in a very similar fashion and allow frame rates, containing 512 A-lines per rotation, of up to 158 frames per second, and pullback speeds as high as 40 mm/s.

70.4 Technology Translation and Commercial Development

The success of intravascular OCT as a research tool and its current adoption to clinical practice was largely facilitated by early commercial translation of this technology. The availability of commercial instruments is important for the widespread access of the clinical community to new technology and has helped to gather many of the insights discussed in the following sections.

LightLab Imaging, Inc. introduced the M2 imaging system in Europe already in 2002. This first-generation TD-OCT instrument operated with 15 frames per second (200 axial scans per frame) using saline flushing and occlusion balloons. The later M3 system was introduced in Japan in 2007 and improved imaging speed to 20 frames per second (240 axial scans per frame). The first commercial frequency domain system, the C7XR TM, was introduced in 2010 and achieved imaging speeds of 100 frames per second (500 axial scans per frame). This represented a more than tenfold increase in imaging speed, enabling higher frame rates and an increased axial scan density, improving significantly the image quality. The higher frame rate also resulted in faster pullback speeds, which enabled occlusion-free imaging using injection of contrast to displace the blood. (C8 OPTIS system became available in the United States. We will have a new system within a couple of weeks. Do you want to add it?)

Recently, Terumo Inc. (Tokyo, Japan) has entered the market for intravascular OCT imaging by introducing the Lunawave OFDI system, first in Europe in 2012, and then followed by Japan in 2013. It provides imaging at 158 frames per second and pullback speeds of up to 40 mm/s over a length of 150 mm. These improvements in imaging speeds and system performances facilitate the clinical adoption of intravascular OCT and promise to enable a wide range of clinical studies.

Besides the application for intracoronary imaging, Avinger (Redwood City, CA) has launched an intravascular crossing device with OCT image guidance to corkscrew through chronic total occlusions (CTO) in the peripheral vasculature. From the OCT signal, the clinician can identify the vessel wall and guide the crossing catheter through the lesion without cutting through the vessel wall.

70.5 Ex Vivo Validation Studies

Besides attempting the challenge of in vivo measurements, early studies thoroughly investigated the architectural features that can be visualized with OCT and validated these observations with histology. From a correlation study of 357 atherosclerotic arterial segments from 90 human cadavers, we established the OCT definition of fibrous, fibrocalcific, and lipid-rich plaques (Fig. 70.3). A high sensitivity and specificity (90–98 %) of these criteria and high reproducibility between two observers was demonstrated [18]. Besides plaque characterization, different types of intraluminal thrombus (red thrombus and white thrombus) were reported [19]. Figure 70.4a, b displays an example of a red and a white thrombus.

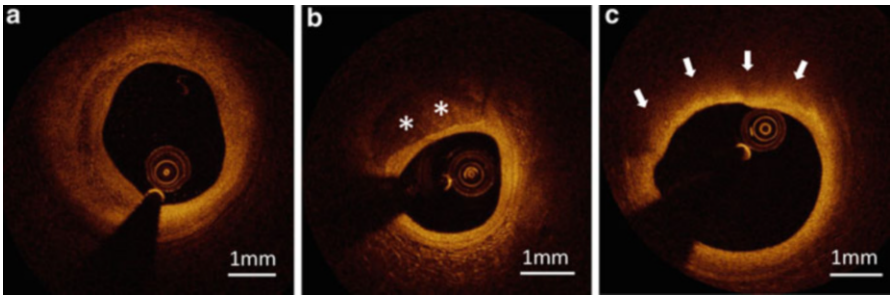

Fig. 70.3 (**a**) Fibrous plaque is characterized by homogeneous, signal-rich regions. (**b**) Fibrocalcific plaques are identified by well-delineated, signal-poor regions with sharp borders (*asterisks*). **(c)** Lipid is characterized by signal-poor regions with diffuse borders (*arrows*)

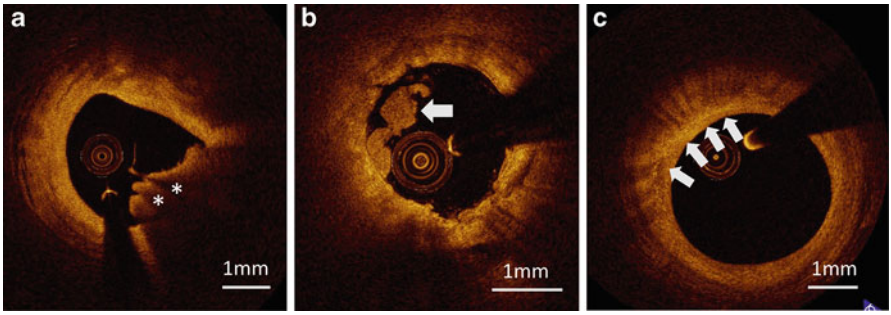

Fig. 70.4 (**a**) Red thrombus is defined as a mass protruding to the lumen, showing high signal intensity on the surface with rapid signal attenuation along depth (*asterisks*). (**b**) White thrombus is a protruding mass showing a lower backscattering signal with low signal attenuation (*arrow*). (**c**) Macrophage accumulation is characterized by increased signal intensity within the plaque, accompanied by heterogeneous backward shadows (*arrows*)

Further, we demonstrated the capability of OCT to visualize macrophage accumulation [20]. The infiltration and accumulation of macrophages is an essential component of vulnerable plaques. The resolution of OCT is insufficient to accurately resolve these macrophages. However, due to their significant uptake of lipids, they approach a size similar to the axial resolution of OCT and comprise a structure with a relatively heterogeneous index of refraction. Normal or fibrous intimal tissue consists of many scattering agents spaced on a sub-resolution scale and results in a homogenously scattering layer with fully developed speckle. The signal from the macrophages, however, is composed of more discrete scattering centers of the macrophage wall and the extracellular matrix but with only little contribution from the intracellular structures. The resulting intensity pattern features a contrast that is sufficiently different from the normal intimal tissue to enable clear identification of regions with macrophages. Frequently, the macrophages also cast a shadow on the underlying tissue. Figure 70.4c shows an

example of macrophage accumulation. Using an adequately normalized standard deviation to quantify macrophage accumulation from the OCT intensity signal within regions of interest in the fibrous cap, a close correlation with the percent area of CD68 positive cells determined by histology was demonstrated [20]. Although the potential of quantifying macrophages by OCT has attracted a significant amount of attention, it is still awaiting more widespread application and should be validated in subsequent studies and with more recent imaging devices.

The superior spatial resolution of OCT is crucial for the measurement of fibrous cap thickness and identification of TCFA. In pathology, TCFA is defined as an advanced atherosclerotic plaque showing a large necrotic core with infiltration of inflammatory cells and a thin overlaying fibrous cap. In an ex vivo histology study, an excellent correlation between OCT and histology-measured fibrous cap thickness ($r = 0.90$) was demonstrated, based on 35 lipid-rich plaques from 102 coronary segments in 38 human cadavers [21]. This makes OCT the only in vivo imaging modality that has been validated with histology to be able to accurately measure fibrous cap thickness.

70.6 First Intravascular Imaging

After promising results from such ex vivo studies and first in vivo animal studies [5, 6], our group at MGH performed the first in-patient study in 2002 [7]. The OCT instrument was a prototype developed at MGH, and the OCT catheter used in this study was constructed using modified 3.2 Fr IVUS catheters (Fig. 70.5). The fiber probe had a miniature gradient index lens and a microprism to focus the optical beam onto the lumen. The bulk system rotary junction allowed a catheter rotation speed of up to 8 rotations per second. The limited image acquisition rate of this TD-OCT system required 8–10 cc of saline to be intermittently flushed through the guiding catheter to displace the blood and clear the view. Both IVUS and intravascular OCT were performed on 17 lesions from ten patients. The comparison demonstrated the potentially superior diagnostic ability of OCT over IVUS for the detection of various plaque components [7].

In a subsequent study, we analyzed the culprit lesions for a broader range of clinical presentations, including patients with STEMI, NSTE-ACS, and stable angina pectoris (SAP) [22]. Out of 69 patients enrolled in the study, sufficient image quality was obtained in 57 patients (20 STEMI, 20 NSTE-ACS, and 17 SAP). TCFA, defined as a plaque with less than 65 μm of fibrous cap thickness and more than 90° of lipid, was more frequently observed in STEMI and NSTE-ACS patients as compared to SAP patients (72 %, 50 %, and 20 %, respectively, $p = 0.012$). Further, the measured fibrous cap thickness was thinner in STEMI and NSTE-ACS patients than in SAP (47.0 μm, 53.8 μm, and 102.6 μm, respectively, $p = 0.034$). This was the first study that demonstrated significant differences in plaque characteristics in vivo depending on the clinical presentation. Moreover, these first in-man studies confirmed the safety and feasibility of intracoronary OCT.

Whereas TD-OCT has been widely used as a research tool for the study of atherosclerosis, its slow imaging speed either required the use of occlusion

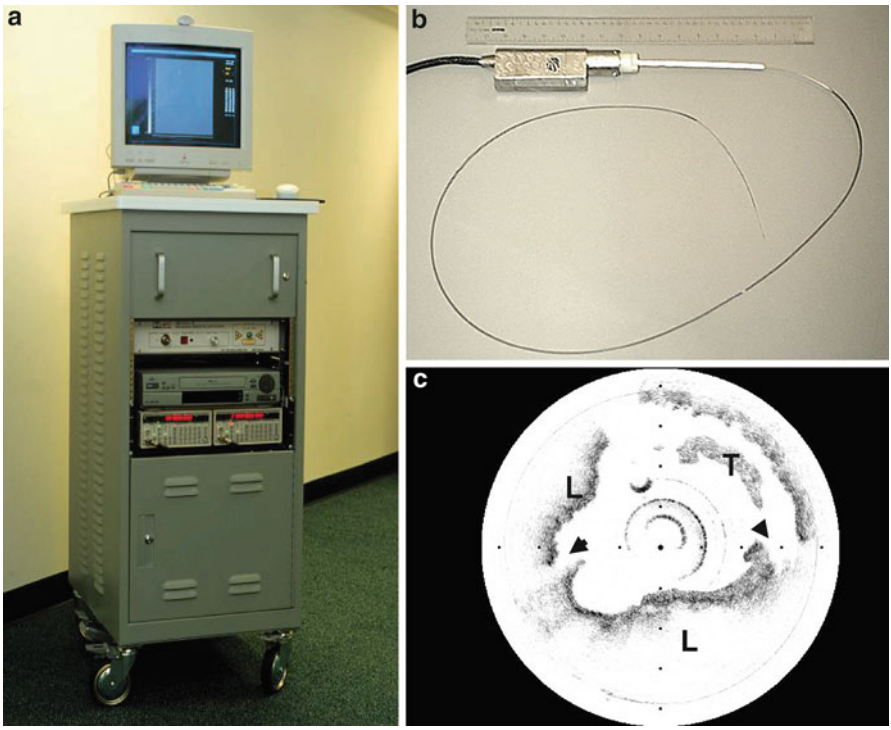

Fig. 70.5 (**a**) Prototype OCT imaging system and (**b**) OCT catheter, used for the first human study. (**c**) OCT visualization of ruptured plaque (*arrowheads*: site of rupture; *T* thrombus, *L* lipid)

balloons, which made the imaging procedure more cumbersome and uncomfortable for the patient, or only permitted the imaging of relatively small sections of the arteries. The advent of the faster spectral domain systems has largely overcome these limitations. We reported the first human in vivo imaging with a spectral domain system in 2008 [23]. The commercial availability of spectral domain systems since 2010 made these advantages also accessible to the wider clinical community and has aided in the ongoing clinical adoption of intravascular OCT.

70.7 Assessment of Coronary Atherosclerosis

In this section we are describing important insights regarding plaque morphology and the pathogenesis of ACS gained by the use of OCT in patients. Previously, clinical imaging modalities such as IVUS, angiography, or computed tomography (CT) lacked sufficient resolution to assess crucial parameters of plaque characteristics. The unprecedented spatial resolution by OCT provided access to decisive plaque features that were correlated extensively with clinical presentation and contributed to clarifying the pathophysiology of coronary atherosclerosis.

Estimating macrophage density by computing the normalized standard deviation in the OCT signal of fibrous and lipid-rich plaques was found to be significantly higher in ACS patients compared to SAP patients [24]. This matches well with the understanding that macrophage accumulation weakens the fibrous cap and hence makes it more prone to rupture [25].

Patients presenting with ACS are known to have lesions with expansive arterial remodeling. The remodeling index is expressed quantitatively by the ratio of the cross-sectional area of the external elastic lamina at the lesion site, with a reference point presenting a more normal vessel appearance. Positive remodeling corresponds to an increased external elastic lamina cross section at the lesion with respect to the reference. Negative remodeling, although less frequent, represents a smaller vessel diameter at the lesion site than at the proximal reference. The remodeling index is a parameter established from IVUS and requires imaging through the entire thickness of the lesion. As such, it is beyond the reach of OCT. In a study where we sequentially imaged with IVUS and OCT [26], we found that TCFA was more frequently observed in lesions with positive remodeling than in those with intermediate or negative remodeling (80 %, 38.5 %, and 5.6 %, respectively, $p < 0.001$). Likewise, the number of lipid quadrants of the lesions correlated positively with the remodeling index [26].

Another factor that is considered to contribute to plaque stability is intra-plaque neovascularization. These blood vessels are shown in OCT images as vesicular structures, or micro-channels, within the plaque. Neovascularization visualized with OCT has been associated with a thin fibrous cap [27], poor responsiveness to statin therapy [28], and plaque progression [29].

The spatial resolution of OCT also enables to study the detailed morphology of fibrous cap disruptions. Tanaka et al. [30] analyzed plaque disruption in 43 patients and compared the features with the exertion level of the patients at the onset of ACS. They found that shoulder-type rupture was more frequent in patients on exertion than those at rest. In another study investigating plaque rupture, STEMI patients were found to suffer more ruptures than patients presenting with NSTE-ACS (70 % vs. 47 %, $p = 0.033$), and cap disruption tended to be directed against the flow in STEMI patients [31].

Cap thickness is generally considered one of the most important predictors of plaque rupture. In a pathological study the minimal fibrous cap thickness was measured in the histological sections of 41 ruptured plaques that had caused sudden cardiac death [32]. The 95th percentile value was found at 65 μm and is the widely accepted threshold for a rupture-prone plaque. Yonetsu et al. [33] performed an assessment of the minimal fibrous cap thickness in an OCT study comparing ruptured with non-ruptured lipid-rich plaques in vivo. A fibrous cap thickness <80 μm was found as the 95th percentile value, which is consistent with expected tissue shrinkage of 10–20 % during histopathologic processing.

Besides the culprit lesion, non-culprit or remote lesions were also studied by OCT. Non-culprit lesions of patients with ACS presented more vulnerable features than remote lesions of patients with SAP: greater lipid amount, thinner fibrous cap thickness, and more neovascularization close to the lumen [34]. These results

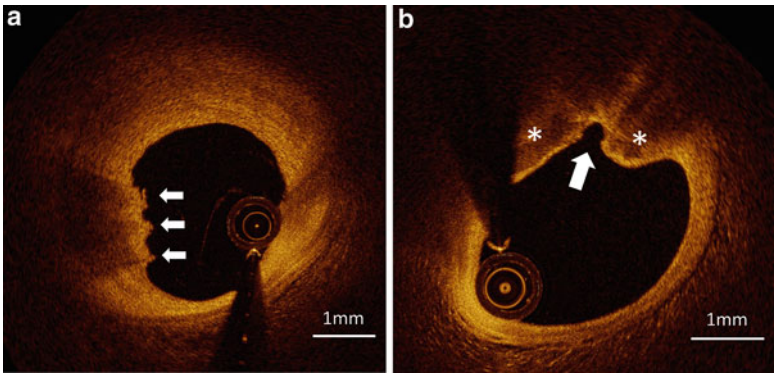

Fig. 70.6 (**a**) Definite erosion is defined as a lesion with thrombus (*arrows*) allowing visualization of the entire underlying intact plaque. (**b**) Calcified nodule is visualized as a lesion with a disrupted fibrous cap (*arrow*) overlying protruding nodular calcium (*asterisks*)

suggested that ACS is a systemic, pan-vascular disease rather than a focal phenomenon of the coronary arteries.

With its ability to precisely assess relevant plaque characteristics, OCT could prove to be ideally suited to evaluate the pathophysiology of ACS [35]. Ruptured plaque is recognized as the primary cause of ACS. However, pathological studies showed that plaque erosion and calcified nodules account for approximately 20 % of sudden cardiac deaths and 25–40 % of acute coronary thrombosis [36–38]. Plaque erosion is defined in pathology as the formation of a thrombus on the surface of a non-ruptured plaque with denudation of the endothelial layer [36]. And a calcified nodule is defined as a calcified plaque with dysfunctional or entirely lacking endothelial layer, resulting in a protruding calcium nodule without fibrous cap [36]. The resolution of OCT is insufficient to detect the presence or absence of the endothelial layer, and the limited image penetration makes it difficult to detect a fibrous plaque behind a massive thrombus [39]. This makes it difficult to apply the pathological definitions directly to OCT. Instead, we proposed an alternative OCT definition of plaque erosion and calcified nodules in collaboration with pathologists. Our definition classifies the culprit lesions of ACS into plaque rupture, calcified nodules, definite erosion, probable erosion, and an unclassified (other) group [40]. Figure 70.6 displays an example of definite erosion and calcified nodules. Using this definition, we analyzed a total of 126 ACS culprit lesions with OCT and found that 55 (44 %) showed plaque rupture, 39 (23 %) OCT-identified erosion (23 definite erosions and 16 probable erosions), and 10 (8 %) OCT-derived calcified nodules. Erosion was found more frequently in younger patients and NSTE-ACS rather than STEMI. This corresponded well with data from pathology, suggesting that the OCT-derived definition of erosion matches well the pathological definition. Taking into account the different mechanisms and patient backgrounds leading to ACS, it would be important to consider different therapeutic strategies for these patients. The current treatment strategy for ACS

patients, and especially STEMI, presumes that coronary thrombosis occurs as an effect of plaque rupture. However, cases caused by erosion or calcified nodules could be treated with antithrombotic agents instead of stenting, because these lesions theoretically have less occlusive plaque underneath the thrombus and thus could be dissolved with antithrombotic therapy.

70.8 Complications with and Response to Stent Implantation

For the assessment of atherosclerosis, OCT has been used primarily as a research tool to improve the understanding of the pathophysiology of ACS. However, OCT offers the possibility to assess a large spectrum of lesion features directly in the catheterization laboratory and could in the future enable a personalization of the therapy and pharmacologic treatment. Still, a substantial amount of clinical evidence to this end is needed. As a tool for assisting in the placement of stents and identifying complications, however, there may exist a more direct path to clinical utility for intravascular OCT [41]. OCT can help in the selection of the appropriate stent length, diameter, and tapering with a pre-procedural pullback. A repeat pullback can then verify the correct placement of the stent and recognize complications that require further intervention.

A wealth of information has been gathered using OCT as a research tool on the vessel response to stent implantation and possible complications. OCT has proven much more sensitive to mechanical complications caused by stent placement onto the vessel wall than IVUS [42, 43]. Tissue protrusion, which includes prolapsed tissue components and intra-stent thrombus, is detectable by OCT in the majority of implanted stents [42, 44, 45]. Stent edge dissection has been found to vary depending on the plaque type at the stent edge, gender, and clinical presentation [46, 47]. Moreover, the presence of lipid pool at the proximal stent edge has been associated with increased risk of postprocedural myocardial infarction [48]. Incomplete apposition is also common immediately after stenting, with an incidence varying from 10 % to 60 % according to underlying plaque characteristics [42, 45]. The stent struts are optically opaque, but their apposition to the vessel wall can be indirectly assessed by taking into account metal and polymer thickness relative to the lumen [49]. Figure 70.7a shows an example of a malapposed stent. Initial studies using repeated OCT examinations reported that most edge dissections and intramural protrusions were resolved at 6–8 months follow-up [43, 50]. Resolution of incomplete stent apposition was found to be dependent on the distance between the strut and lumen [50].

Restenosis within the stent due to excessive neointimal growth was largely resolved with the advent of DES. The initial enthusiasm was tempered with the low but persistent occurrence of late stent thrombosis (LST). OCT was used in a number of studies to examine the coverage and apposition of stents at various time points after implantation to study the vascular response to stent implantation [51–54]. Guagliumi et al. revealed a correlation between the presence of uncovered struts and malapposition with the occurrence of LST [55]. Ideally, the stent

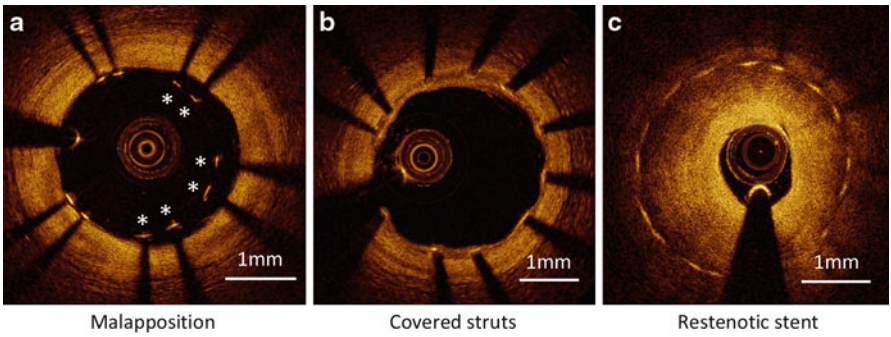

Fig. 70.7 (**a**) Malapposed stent struts are not attached to the lumen wall. (**b**) A covered strut is present if the endothelial layer is visible over the reflection of stent strut. (**c**) In stents with restenosis, various patterns of thick neointimal tissue are visible inside the stent

should be integrated by the host vessel into the intima to obtain a vessel with a re-endothelialized lumen, as visualized in the example in Fig. 70.7b. Whereas a moderate neointimal coverage is desirable, excessive neointimal regrowth would lead to restenosis. Although drastically reduced with the use of DES, this phenomenon still occurs in a small number of patients. OCT has been utilized to evaluate the tissue characteristics of such neointimal hyperplasia and develop a classification into homogenous, heterogeneous, and layered architecture according to the visualization with OCT [56]. Figure 70.7c depicts a stent with significant neointimal regrowth reducing significantly the available lumen cross section.

Atherosclerosis within the neointimal tissue inside the stent presents an alternative potential mechanism for LST. This development of lipid pools and vulnerable atherosclerotic lesions within the stent was termed neoatherosclerosis. It has been investigated by OCT [57] and pathology [58]. Neoatherosclerosis was also observed in DES, especially in patients who presented with ACS caused by in-stent restenosis [59]. We investigated 138 stents with >100 μm neointimal coverage, categorized into early (<9 months), intermediate (9–48 months), and delayed phases (>48 months), to compare the incidence of neoatherosclerosis between BMS and DES. Neoatherosclerosis was more frequent in DES compared to BMS in both the early and intermediate phases, whereas no difference was observed in the delayed phase [60].

Implantation of metallic stents, including BMS and DES, has been the primary mode of PCI for more than two decades. Despite the many remaining challenges, contemporary PCI has a very low incidence of adverse complications. The advent of absorbable scaffolds might help to further alleviate the problems remaining with the vascular response to the "foreign" materials. Such bioabsorbable scaffolds are currently being developed and investigated in clinical trials and become available in some parts of the world [61–64]. OCT is the best available in vivo imaging modality to evaluate the vascular responses to stent implantation and stent resorption and should help us improve clinical practice.

70.9 Future Developments and Other Cardiovascular Applications

In addition to the described applications, intracoronary OCT has also been reported to identify spontaneous coronary dissection [65]. This is a rare but challenging clinical situation, and OCT was shown to improve outcome and patient management. Similarly, OCT was used to investigate cardiac allograft vasculopathy [66], which is one of the major causes of graft failure in heart transplant recipients. This condition is difficult to detect because of the lack of symptoms other than sudden cardiac death. OCT might be able to assist an early diagnosis of this allograft vasculopathy.

Ongoing developments of OCT technology hold promise for further improvements in imaging contrast that could provide additional insight into plaque morphology. Increased spatial resolution generated tomograms with spectacular detail, resolving cellular and subcellular structures, but is challenging to achieve through an imaging catheter [67]. Polarization-sensitive (PS) OCT is an extension of classical OCT and determines the polarization state of the light scattered from the sample [68]. It enables the measure of birefringence, an optical property that is increased in tissue with fibrillar architecture such as collagen. In an early study we demonstrated the potential of PS-OCT to quantify collagen and smooth muscle cell content in aortic plaques [69]. Collagen is the primary extracellular matrix macromolecule that imparts mechanical stability to a plaque and could provide an essential parameter to assess plaque vulnerability in vivo. Translation of PS-OCT to the catheter setting suitable for intracoronary imaging has proved difficult [70], but recent results for managing these challenges are encouraging [71, 72].

Although OCT provides detailed structural imaging with unprecedented spatial resolution, the limited imaging depth is insufficient to quantify plaque burden (cross-sectional vessel area to the outer elastic lamina) and lacks molecular specificity. Combination of OCT with other imaging modalities to combine the strong points of different techniques is currently explored [73]. Combination of near-infrared fluorescence and OCT in a single multimodal catheter has recently been reported [74].

In addition to imaging the coronary arteries, the instrumentation developed for intracoronary imaging is perfectly suitable to assess a wide range of peripheral vessels. Intravascular OCT imaging of the carotid [75], the radial [76], and the infrainguinal artery [77] have been reported.

For the management of resistant hypertension, transcatheter renal sympathetic ablation has been recently proposed as an efficient way to suppress the increased nerve activity associated with hypertension. OCT has been used to investigate and assess the ablation process and may be able to provide new insights on the acute effects of this therapy [78].

OCT may also improve our understanding and management of pulmonary hypertension [79]. We reported the visualization of intimal thickening in patients with pulmonary artery hypertension using OCT [80]. OCT findings could serve as a surrogate of pathological severity and may help improve patient management of pulmonary hypertension.

OCT also attracted interest to guide the crossing of chronic total occlusions [81]. Avinger Inc. (Redwood, CA) has commercialized an OCT system integrating a CTO crossing device and OCT into a single and obtained FDA clearance in 2012.

70.10 Conclusion

OCT has been used for intracoronary imaging for the past 15 years. It served both as a research tool and increasingly also as a clinical instrument. With its high spatial resolution, OCT has enabled to study the microstructure of atherosclerotic plaques and stent implants in human patients with unprecedented detail. OCT has contributed to our understanding of the in vivo pathophysiology of coronary artery disease and has aided in evaluating outcomes after stent implantation. The utility of OCT as a clinical tool to assist PCI has continuously increased thanks to technological innovation and increased imaging speed. Although some studies demonstrated the usefulness of OCT for the guidance of PCI [41] and the prediction of short-term outcomes after PCI [82–84], there is currently no convincing data demonstrating that the use of OCT would improve clinical outcomes. Given the invasiveness of intravascular OCT, it is difficult to conduct a large-scale, long-term, randomized controlled trial to demonstrate evidence-based clinical efficacy of OCT. To address this challenge, the Massachusetts General Hospital (MGH) OCT Registry was created in 2009. This is a multicenter registry of patients undergoing intracoronary OCT imaging for any clinical presentation. Twenty sites across six countries (United States 5, Japan 4, Korea 5, Australia 3, China 2, and Singapore) participate in this registry, which targets 3,000 cases with clinical follow-up of 5 years. We believe that the data accumulated in this registry may be able to answer many of the unsolved questions including the ultimate utility of OCT in the clinical setting. Whereas the merits of OCT as a powerful research tool are unquestioned, the demonstration of improved patient outcome is the goal of any clinical diagnostic tool. This is also a necessity to obtain a reimbursement code for the routine use of intravascular OCT, which then would trigger its widespread application and make it a commercially viable market.

References

1. D. Huang, E.A. Swanson, C.P. Lin, J.S. Schuman, W.G. Stinson, W. Chang, M.R. Hee, T. Flotte, K. Gregory, C.A. Puliafito, Optical coherence tomography. Science **254**(5035), 1178–1181 (1991)
2. W. Drexler, J.G. Fujimoto, State-of-the-art retinal optical coherence tomography. Prog. Retin. Eye Res. **27**(1), 45–88 (2008)
3. G.J. Tearney, M.E. Brezinski, S.A. Boppart, B.E. Bouma, N. Weissman, J.F. Southern, E.A. Swanson, J.G. Fujimoto, Catheter-based optical imaging of a human coronary artery. Circulation **94**, 3013 (1996)
4. G.J. Tearney, M.E. Brezinski, B.E. Bouma, S.A. Boppart, C. Pitvis, J.F. Southern, J.G. Fujimoto, In vivo endoscopic optical biopsy with optical coherence tomography. Science **276**(5321), 2037–2039 (1997)

5. J.G. Fujimoto, S.A. Boppart, G.J. Tearney, B.E. Bouma, C. Pitris, M.E. Brezinski, High resolution in vivo intra-arterial imaging with optical coherence tomography. Heart **82**, 128 (1999)
6. G.J. Tearney, I.-K. Jang, D.-H. Kang, H.T. Aretz, S.L. Houser, T.J. Brady, K. Schlendorf, M. Shishkov, B.E. Bouma, Porcine coronary imaging in vivo by optical coherence tomography. Acta Cardiol. **55**(4), 233–237 (2000)
7. I.K. Jang, B.E. Bouma, D.H. Kang, S.J. Park, S.W. Park, K.B. Seung, K.B. Choi, M. Shishkov, K. Schlendorf, E. Pomerantsev, S.L. Houser, H.T. Aretz, G.J. Tearney, Visualization of coronary atherosclerotic plaques in patients using optical coherence tomography: comparison with intravascular ultrasound. J. Am. Chem. Soc. **39**(4), 604–609 (2002)
8. F. Pratti, E. Regar, G.S. Mintz, E. Arbustini, C. Di Mario, I.-K. Jang, T. Akasaka, M. Costa, G. Guagliumi, E. Grube, Y. Ozaki, F. Pinto, P.W. Serruys, Expert review document on methodology, terminology, and clinical applications of optical coherence tomography: physical principles, methodology of image acquisition, and clinical application for assessment of coronary arteries and atherosclerosis. Eur. Heart J. **31**, 401–415 (2010)
9. B. Golubovic, B.E. Bouma, G.J. Tearney, J.G. Fujimoto, Optical frequency-domain reflectometry using rapid wavelength tuning of a Cr4+: forsterite laser. Opt. Lett. **22**(22), 1704–1706 (1997)
10. S.R. Chinn, E.A. Swanson, J.G. Fujimoto, Optical coherence tomography using a frequency-tunable optical source. Opt. Lett. **22**(5), 340–342 (1997)
11. R. Leitgeb, C.K. Hitzenberger, A.F. Fercher, Performance of Fourier domain vs. time domain optical coherence tomography. Opt. Express **11**(8), 889–894 (2003)
12. M.A. Choma, M.V. Sarunic, C.H. Yang, J.A. Izatt, Sensitivity advantage of swept source and Fourier domain optical coherence tomography. Opt. Express **11**(18), 2183–2189 (2003)
13. J.F. de Boer, B. Cense, B.H. Park, M.C. Pierce, G.J. Tearney, B.E. Bouma, Improved signal-to-noise ratio in spectral-domain compared with time-domain optical coherence tomography. Opt. Lett. **28**(21), 2067–2069 (2003)
14. S. Yun, G. Tearney, J. de Boer, N. Iftimia, B. Bouma, High-speed optical frequency-domain imaging. Opt. Express **11**(22), 2953–2963 (2003)
15. B.E. Bouma, G.J. Tearney, Power-efficient nonreciprocal interferometer and linear-scanning fiber-optic catheter for optical coherence tomography. Opt. Lett. **24**(8), 531–533 (1999)
16. S. Yun, G. Tearney, J. de Boer, B. Bouma, Removing the depth-degeneracy in optical frequency domain imaging with frequency shifting. Opt. Express **12**(20), 4822–4828 (2004)
17. S.H. Yun, G.J. Tearney, B.J. Vakoc, M. Shishkov, W.Y. Oh, A.E. Desjardins, M.J. Suter, R.C. Chan, J.A. Evans, I.K. Jang, N.S. Nishioka, J.F. de Boer, B.E. Bouma, Comprehensive volumetric optical microscopy in vivo. Nat. Med. **12**(12), 1429–1433 (2006)
18. H. Yabushita, B.E. Bouma, S.L. Houser, H.T. Aretz, I.K. Jang, K.H. Schlendorf, C.R. Kauffman, M. Shishkov, D.H. Kang, E.F. Halpern, G.J. Tearney, Characterization of human atherosclerosis by optical coherence tomography. Circulation **106**(13), 1640–1645 (2002)
19. T. Kume, T. Akasaka, T. Kawamoto, Y. Ogasawara, N. Watanabe, E. Toyota, Y. Neishi, R. Sukmawan, Y. Sadahira, K. Yoshida, Assessment of coronary arterial thrombus by optical coherence tomography. Am. J. Cardiol. **97**(12), 1713–1717 (2006)
20. G.J. Tearney, H. Yabushita, S.L. Houser, H.T. Aretz, I.K. Jang, K.H. Schlendorf, C.R. Kauffman, M. Shishkov, E.F. Halpern, B.E. Bouma, Quantification of macrophage content in atherosclerotic plaques by optical coherence tomography. Circulation **107**(1), 113–119 (2003)
21. T. Kume, T. Akasaka, T. Kawamoto, H. Okura, N. Watanabe, E. Toyota, Y. Neishi, R. Sukmawan, Y. Sadahira, K. Yoshida, Measurement of the thickness of the fibrous cap by optical coherence tomography. Am. Heart J. **152**(4), 755 e1–755 e4 (2006)
22. I.K. Jang, G.J. Tearney, B. MacNeill, M. Takano, F. Moselewski, N. Iftima, M. Shishkov, S. Houser, H.T. Aretz, E.F. Halpern, B.E. Bouma, In vivo characterization of coronary atherosclerotic plaque by use of optical coherence tomography. Circulation **111**(12), 1551–1555 (2005)

23. G.J. Tearney, S. Waxman, M. Shishkov, B.J. Vakoc, M.J. Suter, M.I. Freilich, A.E. Desjardins, W.Y. Oh, L.A. Bartlett, M. Rosenberg, B.E. Bouma, Three-dimensional coronary artery microscopy by intracoronary optical frequency domain imaging. JACC Cardiovasc. Imaging **1**(6), 752–761 (2008)
24. B.D. MacNeill, I.-K. Jang, B.E. Bouma, N. Iftimia, M. Takano, H. Yabushita, M. Shishkov, C.R. Kauffman, S.L. Houser, H.T. Aretz, D. DeJoseph, E.F. Halpern, G.J. Tearney, Focal and multi-focal plaque macrophage distributions in patients with acute and stable presentations of coronary artery disease. J. Am. Coll. Cardiol. **44**(5), 972–979 (2004)
25. C.L. Lendon, M.J. Davies, G.V. Born, P.D. Richardson, Atherosclerotic plaque caps are locally weakened when macrophages density is increased. Atherosclerosis **87**(1), 87–90 (1991)
26. O.C. Raffel, F.M. Merchant, G.J. Tearney, S. Chia, D.D. Gauthier, E. Pomerantsev, K. Mizuno, B.E. Bouma, I.K. Jang, In vivo association between positive coronary artery remodelling and coronary plaque characteristics assessed by intravascular optical coherence tomography. Eur. Heart J. **29**(14), 1721–1728 (2008)
27. J. Tian, J. Hou, L. Xing, S.-J. Kim, T. Yonetsu, K. Kato, H. Lee, S. Zhang, B. Yu, I.-K. Jang, Significance of intraplaque neovascularisation for vulnerability: optical coherence tomography study. Heart **98**(20), 1504–1509 (2012)
28. J. Tian, J. Hou, L. Xing, S.-J. Kim, T. Yonetsu, K. Kato, H. Lee, S. Zhang, B. Yu, I.-K. Jang, Does neovascularization predict response to statin therapy? Optical coherence tomography study. Int. J. Cardiol. **158**(3), 469–470 (2012)
29. S. Uemura, K.-I. Ishigami, T. Soeda, S. Okayama, J.H. Sung, H. Nakagawa, S. Somekawa, Y. Takeda, H. Kawata, M. Horii, Y. Saito, Thin-cap fibroatheroma and microchannel findings in optical coherence tomography correlate with subsequent progression of coronary atheromatous plaques. Eur. Heart J. **33**(1), 78–85 (2012)
30. A. Tanaka, T. Imanishi, H. Kitabata, T. Kubo, S. Takarada, T. Tanimoto, A. Kuroi, H. Tsujioka, H. Ikejima, S. Ueno, H. Kataiwa, K. Okouchi, M. Kashiwaghi, H. Matsumoto, K. Takemoto, N. Nakamura, K. Hirata, M. Mizukoshi, T. Akasaka, Morphology of exertion-triggered plaque rupture in patients with acute coronary syndrome: an optical coherence tomography study. Circulation **118**(23), 2368–2373 (2008)
31. Y. Ino, T. Kubo, A. Tanaka, A. Kuroi, H. Tsujioka, H. Ikejima, K. Okouchi, M. Kashiwagi, S. Takarada, H. Kitabata, T. Tanimoto, K. Komukai, K. Ishibashi, K. Kimura, K. Hirata, M. Mizukoshi, T. Imanishi, T. Akasaka, Difference of culprit lesion morphologies between ST-segment elevation myocardial infarction and non-ST-segment elevation acute coronary syndrome: an optical coherence tomography study. JACC Cardiovasc. Interv. **4**(1), 76–82 (2011)
32. A.P. Burke, A. Farb, G.T. Malcom, Y.H. Liang, J. Smialek, R. Virmani, Coronary risk factors and plaque morphology in men with coronary disease who died suddenly. N. Engl. J. Med. **336**(18), 1276–1282 (1997)
33. T. Yonetsu, T. Kakuta, T. Lee, K. Takahashi, N. Kawaguchi, G. Yamamoto, K. Koura, K. Hishikari, Y. Iesaka, H. Fujiwara, M. Isobe, In vivo critical fibrous cap thickness for rupture-prone coronary plaques assessed by optical coherence tomography. Eur. Heart J. **32**(10), 1251–1259 (2011)
34. K. Kato, T. Yonetsu, S.-J. Kim, L. Xing, H. Lee, I. McNulty, R.W. Yeh, R. Sakhuja, S. Zhang, S. Uemura, B. Yu, K. Mizuno, I.-K. Jang, Nonculprit plaques in patients with acute coronary syndromes have more vulnerable features compared with those with non-acute coronary syndromes: a 3-vessel optical coherence tomography study. Circ. Cardiovasc. Imaging **5**(4), 433–440 (2012)
35. P. Maurovich-Horvat, C.L. Schlett, H. Alkadhi, M. Nakano, P. Stolzmann, M. Vorpahl, H. Scheffel, A. Tanaka, W.C. Warger, A. Maehara, S. Ma, M.F. Kriegel, R.K. Kaple, H. Seifarth, F. Bamberg, G.S. Mintz, G.J. Tearney, R. Virmani, U. Hoffmann, Differentiation of early from advanced coronary atherosclerotic lesions: systematic comparison of CT, intravascular US, and optical frequency domain imaging with histopathologic examination in ex vivo human hearts. Radiology **265**(2), 393–401 (2012)

36. R. Virmani, F.D. Kolodgie, A.P. Burke, A. Farb, S.M. Schwartz, Lessons from sudden coronary death: a comprehensive morphological classification scheme for atherosclerotic lesions. Arterioscler. Thromb. Vasc. Biol. **20**(5), 1262–1275 (2000)
37. A. Farb, A.P. Burke, A.L. Tang, T.Y. Liang, P. Mannan, J. Smialek, R. Virmani, Coronary plaque erosion without rupture into a lipid core. A frequent cause of coronary thrombosis in sudden coronary death. Circulation **93**(7), 1354–1363 (1996)
38. E. Arbustini, B. Dal Bello, P. Morbini, A.P. Burke, M. Bocciarelli, G. Specchia, R. Virmani, Plaque erosion is a major substrate for coronary thrombosis in acute myocardial infarction. Heart **82**(3), 269–272 (1999)
39. R. Vergallo, T. Yonetsu, K. Kato, H. Jia, F. Abtahian, J. Tian, S. Hu, I. McNulty, B. Yu, L.M. Biasucci, F. Crea, I.-K. Jang, Evaluation of culprit lesions by optical coherence tomography in patients with ST-elevation myocardial infarction. Int. J. Cardiol. **168**, 1592 (2013)
40. H. Jia, F. Abtahian, A.D. Aguirre, S. Lee, S. Chia, H. Lowe, K. Kato, T. Yonetsu, R. Vergallo, S. Hu, J. Tian, H. Lee, S.J. Park, Y.S. Jang, O.C. Raffel, K. Mizuno, S. Uemura, T. Itoh, T. Kakuta, S.Y. Choi, H.L. Dauerman, A. Prasad, C. Toma, I. McNulty, S. Zhang, B. Yu, V. Fuster, J. Narula, R. Virmani, I.K. Jang, In vivo diagnosis of plaque erosion and calcified nodule in patients with acute coronary syndrome by intravascular optical coherence tomography. J. Am. Coll. Cardiol. **62**, 1748 (2013)
41. F. Prati, L. Di Vito, G. Biondi-Zoccai, M. Occhipinti, A. La Manna, C. Tamburino, F. Burzotta, C. Trani, I. Porto, V. Ramazzotti, Angiography alone versus angiography plus optical coherence tomography to guide decision-making during percutaneous coronary intervention: the Centro per la Lotta contro l'Infarto-Optimisation of Percutaneous Coronary Intervention (CLI-OPCI) study. EuroIntervention **8**(7), 823–829 (2012)
42. B.E. Bouma, G.J. Tearney, H. Yabushita, M. Shishkov, C.R. Kauffman, D. DeJoseph Gauthier, B.D. MacNeill, S.L. Houser, H.T. Aretz, E.F. Halpern, I.K. Jang, Evaluation of intracoronary stenting by intravascular optical coherence tomography. Heart **89**(3), 317–320 (2003)
43. T. Kume, H. Okura, Y. Miyamoto, R. Yamada, K. Saito, T. Tamada, T. Koyama, Y. Neishi, A. Hayashida, T. Kawamoto, K. Yoshida, Natural history of stent edge dissection, tissue protrusion and incomplete stent apposition detectable only on optical coherence tomography after stent implantation – preliminary observation. Circ. J. **76**(3), 698–703 (2012)
44. N. Gonzalo, P.W. Serruys, T. Okamura, Z.J. Shen, Y. Onuma, H.M. Garcia-Garcia, G. Sarno, C. Schultz, R.J. van Geuns, J. Ligthart, E. Regar, Optical coherence tomography assessment of the acute effects of stent implantation on the vessel wall: a systematic quantitative approach. Heart **95**(23), 1913–1919 (2009)
45. T. Kubo, T. Imanishi, H. Kitabata, A. Kuroi, S. Ueno, T. Yamano, T. Tanimoto, Y. Matsuo, T. Masho, S. Takarada, A. Tanaka, N. Nakamura, M. Mizukoshi, Y. Tomobuchi, T. Akasaka, Comparison of vascular response after sirolimus-eluting stent implantation between patients with unstable and stable angina pectoris: a serial optical coherence tomography study. JACC Cardiovasc. Imaging **1**(4), 475–484 (2008)
46. N. Gonzalo, P.W. Serruys, T. Okamura, Z.J. Shen, H.M. Garcia-Garcia, Y. Onuma, R.J. van Geuns, J. Ligthart, E. Regar, Relation between plaque type and dissections at the edges after stent implantation: an optical coherence tomography study. Int. J. Cardiol. **150**(2), 151–155 (2011)
47. M. Zeglin-Sawczuk, I.-K. Jang, K. Kato, T. Yonetsu, S. Kim, S.-Y. Choi, C. Kratlian, H. Lee, H.L. Dauerman, Lipid rich plaque, female gender and proximal coronary stent edge dissections. J. Thromb. Thrombolysis **36**, 507 (2013)
48. F. Imola, M. Occhipinti, G. Biondi-Zoccai, L. Di Vito, V. Ramazzotti, A. Manzoli, A. Pappalardo, A. Cremonesi, M. Albertucci, F. Prati, Association between proximal stent edge positioning on atherosclerotic plaques containing lipid pools and postprocedural myocardial infarction (from the CLI-POOL study). Am. J. Cardiol. **111**(4), 526–531 (2013)
49. J. Tanigawa, P. Barlis, C. Di Mario, Intravascular optical coherence tomography: optimisation of image acquisition and quantitative assessment of stent strut apposition. EuroIntervention **3**(1), 128–136 (2007)

50. H. Kawamori, J. Shite, T. Shinke, H. Otake, D. Matsumoto, M. Nakagawa, R. Nagoshi, A. Kozuki, H. Hariki, T. Inoue, T. Osue, Y. Taniguchi, R. Nishio, N. Hiranuma, K.-I. Hirata, Natural consequence of post-intervention stent malapposition, thrombus, tissue prolapse, and dissection assessed by optical coherence tomography at mid-term follow-up. Eur. Heart J. Cardiovasc. Imaging **14**, 865 (2013)
51. J.S. Kim, I.K. Jang, C. Fan, T.H. Kim, S.M. Park, E.Y. Choi, S.H. Lee, Y.G. Ko, D. Choi, M.K. Hong, Y. Jang, Evaluation in 3 months duration of neointimal coverage after zotarolimus-eluting stent implantation by optical coherence tomography: the ENDEAVOR OCT trial. JACC Cardiovasc. Interv. **2**(12), 1240–1247 (2009)
52. J.-S. Kim, C. Fan, D. Choi, I.-K. Jang, J.M. Lee, T.H. Kim, S.M. Park, S.I. Paik, Y.-G. Ko, M.-K. Hong, Y. Jang, N. Chung, Different patterns of neointimal coverage between acute coronary syndrome and stable angina after various types of drug-eluting stents implantation; 9-month follow-up optical coherence tomography study. Int. J. Cardiol. **146**(3), 341–346 (2011)
53. J.-S. Kim, B.-K. Kim, I.-K. Jang, D.-H. Shin, Y.-G. Ko, D. Choi, M.-K. Hong, Y.-K. Cho, C.-W. Nam, S.-H. Hur, J.-H. Choi, Y.B. Song, J.Y. Hahn, S.H. Choi, H.C. Gwon, Y. Jang, ComparisOn of neointimal coVerage betwEen zotaRolimus-eluting stent and everolimus-eluting stent using Optical Coherence Tomography (COVER OCT). Am. Heart J. **163**(4), 601–607 (2012)
54. J. Hou, H. Jia, H. Liu, Z. Han, S. Yang, C. Xu, J. Schmitt, S. Zhang, B. Yu, I.-K. Jang, Neointimal tissue characteristics following sirolimus-eluting stent implantation: OCT quantitative tissue property analysis. Int. J. Cardiovasc. Imaging **28**(8), 1879–1886 (2012)
55. G. Guagliumi, V. Sirbu, G. Musumeci, R. Gerber, G. Biondi-Zoccai, H. Ikejima, E. Ladich, N. Lortkipanidze, A. Matiashvili, O. Valsecchi, R. Virmani, G.W. Stone, Examination of the in vivo mechanisms of late drug-eluting stent thrombosis: findings from optical coherence tomography and intravascular ultrasound imaging. JACC Cardiovasc. Interv. **5**(1), 12–20 (2012)
56. N. Gonzalo, P.W. Serruys, T. Okamura, H.M. van Beusekom, H.M. Garcia-Garcia, G. van Soest, W. van der Giessen, E. Regar, Optical coherence tomography patterns of stent restenosis. Am. Heart J. **158**(2), 284–293 (2009)
57. M. Takano, M. Yamamoto, S. Inami, D. Murakami, T. Ohba, Y. Seino, K. Mizuno, Appearance of lipid-laden intima and neovascularization after implantation of bare-metal stents extended late-phase observation by intracoronary optical coherence tomography. J. Am. Coll. Cardiol. **55**(1), 26–32 (2009)
58. G. Nakazawa, F. Otsuka, M. Nakano, M. Vorpahl, S.K. Yazdani, E. Ladich, F.D. Kolodgie, A.V. Finn, R. Virmani, The pathology of neoatherosclerosis in human coronary implants bare-metal and drug-eluting stents. J. Am. Coll. Cardiol. **57**(11), 1314–1322 (2011)
59. S.J. Kang, G.S. Mintz, T. Akasaka, D.W. Park, J.Y. Lee, W.J. Kim, S.W. Lee, Y.H. Kim, C. Whan Lee, S.W. Park, S.J. Park, Optical coherence tomographic analysis of in-stent neoatherosclerosis after drug-eluting stent implantation. Circulation **123**(25), 2954–2963 (2011)
60. T. Yonetsu, J.S. Kim, K. Kato, S.J. Kim, L. Xing, R.W. Yeh, R. Sakhuja, I. McNulty, H. Lee, S. Zhang, S. Uemura, B. Yu, T. Kakuta, I.K. Jang, Comparison of incidence and time course of neoatherosclerosis between bare metal stents and drug-eluting stents using optical coherence tomography. Am. J. Cardiol. **110**(7), 933–939 (2012)
61. H. Tamai, K. Igaki, E. Kyo, K. Kosuga, A. Kawashima, S. Matsui, H. Komori, T. Tsuji, S. Motohara, H. Uehata, Initial and 6-month results of biodegradable poly-l-lactic acid coronary stents in humans. Circulation **102**(4), 399–404 (2000)
62. P.W. Serruys, Y. Onuma, J.A. Ormiston, B. de Bruyne, E. Regar, D. Dudek, L. Thuesen, P.C. Smits, B. Chevalier, D. McClean, J. Koolen, S. Windecker, R. Whitbourn, I. Meredith, C. Dorange, S. Veldhof, K. Miquel-Hebert, R. Rapoza, H.M. Garcia-Garcia, Evaluation of the second generation of a bioresorbable everolimus drug-eluting vascular scaffold for treatment of de novo coronary artery stenosis: six-month clinical and imaging outcomes. Circulation **122**(22), 2301–2312 (2010)

63. R. Erbel, C. Di Mario, J. Bartunek, J. Bonnier, B. de Bruyne, F.R. Eberli, P. Erne, M. Haude, B. Heublein, M. Horrigan, C. Ilsley, D. Böse, J. Koolen, T.F. Lüscher, N. Weissman, R. Waksman, Temporary scaffolding of coronary arteries with bioabsorbable magnesium stents: a prospective, non-randomised multicentre trial. Lancet **369**(9576), 1869–1875 (2007)
64. M. Haude, R. Erbel, P. Erne, S. Verheye, H. Degen, D. Böse, P. Vermeersch, I. Wijnbergen, N. Weissman, F. Prati, R. Waksman, J. Koolen, Safety and performance of the drug-eluting absorbable metal scaffold (DREAMS) in patients with de-novo coronary lesions: 12 month results of the prospective, multicentre, first-in-man BIOSOLVE-I trial. Lancet **381**(9869), 836–844 (2013)
65. F. Alfonso, M. Paulo, N. Gonzalo, J. Dutary, P. Jimenez-Quevedo, V. Lennie, J. Escaned, C. Banuelos, R. Hernandez, C. Macaya, Diagnosis of spontaneous coronary artery dissection by optical coherence tomography. J. Am. Coll. Cardiol. **59**(12), 1073–1079 (2012)
66. J. Hou, H. Lv, H. Jia, S. Zhang, L. Xing, H. Liu, J. Kong, S. Zhang, B. Yu, I.-K. Jang, OCT assessment of allograft vasculopathy in heart transplant recipients. JACC Cardiovasc. Imaging **5**(6), 662–663 (2012)
67. L. Liu, J.A. Gardecki, S.K. Nadkarni, J.D. Toussaint, Y. Yagi, B.E. Bouma, G.J. Tearney, Imaging the subcellular structure of human coronary atherosclerosis using micro-optical coherence tomography. Nat. Med. **17**(8), 1010–1014 (2011)
68. J.F. de Boer, T.E. Milner, Review of polarization sensitive optical coherence tomography and stokes vector determination. J. Biomed. Opt. **7**(3), 359–371 (2002)
69. S.K. Nadkarni, M.C. Pierce, B.H. Park, J.F. de Boer, P. Whittaker, B.E. Bouma, J.E. Bressner, E. Halpern, S.L. Houser, G.J. Tearney, Measurement of collagen and smooth muscle cell content in atherosclerotic plaques using polarization-sensitive optical coherence tomography. J. Am. Coll. Cardiol. **49**(13), 1474–1481 (2007)
70. M. Villiger, E.Z. Zhang, S. Nadkarni, W.-Y. Oh, B.E. Bouma, B.J. Vakoc, Artifacts in polarization-sensitive optical coherence tomography caused by polarization mode dispersion. Opt. Lett. **38**(6), 923–925 (2013)
71. E.Z. Zhang, W.-Y. Oh, M.L. Villiger, L. Chen, B.E. Bouma, B.J. Vakoc, Numerical compensation of system polarization mode dispersion in polarization-sensitive optical coherence tomography. Opt. Express **21**(1), 1163–1180 (2013)
72. M. Villiger, E. Z. Zhang, S. K. Nadkarni, W.-Y. Oh, B. J. Vakoc, and B. E. Bouma, Spectral binning for mitigation of polarization mode dispersion artifacts in catheter-based optical frequency domain imaging, Opt. Express **21**(14), 16353–16369 (2013)
73. C.V. Bourantas, H.M. Garcia-Garcia, K.K. Naka, A. Sakellarios, L. Athanasiou, D.I. Fotiadis, L.K. Michalis, P.W. Serruys, Hybrid intravascular imaging. J. Am. Chem. Soc. **61**(13), 1369–1378 (2013)
74. H. Yoo, J.W. Kim, M. Shishkov, E. Namati, T. Morse, R. Shubochkin, J.R. McCarthy, V. Ntziachristos, B.E. Bouma, F.A. Jaffer, G.J. Tearney, Intra-arterial catheter for simultaneous microstructural and molecular imaging in vivo. Nat. Med. **17**(12), 1680–1684 (2011)
75. S. Yoshimura, M. Kawasaki, K. Yamada, Y. Enomoto, Y. Egashira, A. Hattori, K. Nishigaki, S. Minatoguchi, T. Iwama, Visualization of internal carotid artery atherosclerotic plaques in symptomatic and asymptomatic patients: a comparison of optical coherence tomography and intravascular ultrasound. AJNR Am. J. Neuroradiol. **33**(2), 308–313 (2012)
76. T. Yonetsu, T. Kakuta, T. Lee, K. Takayama, K. Kakita, T. Iwamoto, N. Kawaguchi, K. Takahashi, G. Yamamoto, Y. Iesaka, H. Fujiwara, M. Isobe, Assessment of acute injuries and chronic intimal thickening of the radial artery after transradial coronary intervention by optical coherence tomography. Eur. Heart J. **31**(13), 1608–1615 (2010)
77. D. Karnabatidis, K. Katsanos, I. Paraskevopoulos, A. Diamantopoulos, S. Spiliopoulos, D. Siablis, Frequency-domain intravascular optical coherence tomography of the femoropopliteal artery. Cardiovasc. Intervent. Radiol. **34**(6), 1172–1181 (2011)
78. S. Ierna, G. Biondi-Zoccai, C. Bachis, M. Occhipinti, L. Di Vito, A. Ricciardi, C. Pappone, F. Prati, Transcatheter renal sympathetic ablation for resistant hypertension: in vivo insights in humans from optical coherence tomography. Int. J. Cardiol. **165**, 1–3 (2012)

79. Y. Fukumoto, H. Shimokawa, Recent progress in the management of pulmonary hypertension. Circ. J. **75**(8), 1801–1810 (2011)
80. J. Hou, H. Qi, M. Zhang, L. Meng, Z. Han, B. Yu, I.-K. Jang, Pulmonary vascular changes in pulmonary hypertension: optical coherence tomography findings. Circ. Cardiovasc. Imaging **3**(3), 344–345 (2010)
81. P. Tyczynski, N. Kukreja, E. Pieri, C. Di Mario, Optical frequency domain imaging guided crossing of a stumpless chronic total occlusion. Int. J. Cardiol. **148**(2), 231–233 (2011)
82. T. Lee, T. Yonetsu, K. Koura, K. Hishikari, T. Murai, T. Iwai, T. Takagi, Y. Iesaka, H. Fujiwara, M. Isobe, T. Kakuta, Impact of coronary plaque morphology assessed by optical coherence tomography on cardiac troponin elevation in patients with elective stent implantation. Circ. Cardiovasc. Interv. **4**(4), 378–386 (2011)
83. T. Yonetsu, T. Kakuta, T. Lee, K. Takahashi, G. Yamamoto, Y. Iesaka, H. Fujiwara, M. Isobe, Impact of plaque morphology on creatine kinase-MB elevation in patients with elective stent implantation. Int. J. Cardiol. **146**(1), 80–85 (2011)
84. I. Porto, L. Di Vito, F. Burzotta, G. Niccoli, C. Trani, A.M. Leone, L.M. Biasucci, R. Vergallo, U. Limbruno, F. Crea, Predictors of periprocedural (type IVa) myocardial infarction, as assessed by frequency-domain optical coherence tomography. Circ. Cardiovasc. Interv. **5**(1), 89–96 (2012). S1–6

Intravascular OCT

71

Joseph M. Schmitt, Desmond Adler, and Chenyang Xu

Keywords
Blood vessel • Cardiac • Coronary • FDOCT • Imaging • Intravascular • IVUS • OCT • Stent

71.1 Why Intravascular Imaging?

The limitations of angiography provide the main motivation for the development of intravascular imaging technologies. To acquire a coronary angiogram, a bolus of radiopaque contrast medium is injected into the target arterial branch via a guide catheter placed in the aortic ostium of the main trunk of the right or left coronary artery. During the injection, a sequence of fluoroscopic X-ray images is recorded. Each image represents an instantaneous two-dimensional projection ('shadowgram') of the beating heart, in which the opacified lumens of the coronary arteries appear as dark structures in a background of weakly attenuating soft tissue. The narrowing of an artery, referred to as a 'stenosis' or 'lesion', can be detected as a sudden reduction in its diameter.

As illustrated in Fig. 71.1, the dimensions of eccentric lesions are susceptible to distortion in single-projection angiograms. Visualization of an artery from inside its lumen overcomes these projection distortions and improves sensitivity to thrombus and other radiolucent structures. A cross-sectional OCT image, like the image shown in Fig. 71.1b, shows the actual shape of the lumen cross section and enables visualization of structures inside the wall of the artery. Although multi-plane coronary angiography systems and multi-detector computed tomography systems are available that can synthesize more accurate cross-sectional views of arterial lumens from multiple projections, these imaging systems are too complicated and time consuming to use routinely for guidance of PCI in real time.

J.M. Schmitt (✉) • D. Adler • C. Xu
St. Jude Medical, Westford, MA, USA
e-mail: jschmitt@sjm.com

© Springer International Publishing Switzerland 2015

W. Drexler, J.G. Fujimoto (eds.), *Optical Coherence Tomography*,
DOI 10.1007/978-3-319-06419-2_74

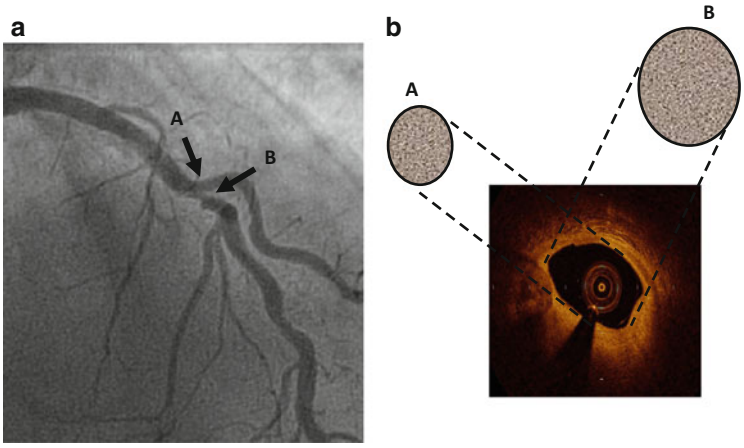

Fig. 71.1 Illustration of the effects of projection angle on angiographic visualization of an eccentric lesion. (**a**) Coronary angiogram of a lesion in the left-anterior descending artery. (**b**) Apparent diameters of the lumen of a cross section of the lesion, viewed from the two projection directions *A* and *B*. The OCT image of the artery shown here shows the actual cross section of the lumen

Length distortion ('foreshortening') is another important limitation of angiography that results from viewing arteries from a single projection angle. Foreshortening occurs when arteries bend sharply in the direction of the X-ray source or detector. To avoid selecting a stent that is too short to cover an entire lesion, the cardiologist must choose the appropriate projection angle for measurement of lesion length. Intravascular OCT and IVUS imaging systems incorporate constant-speed pullback mechanisms to acquire spiral image sequences from which length of lesions can be measured with minimal foreshortening.

Over the years since the first intravascular ultrasound studies were performed in the late 1980s, the importance of assessing the composition and thickness of the plaque prior to treatment of coronary lesions has become increasingly recognized [25]. For the most part, angiography is limited to detecting blood flow alterations caused be narrowing of the vessel lumen. Except for subtle clues that signal the presence of ruptured plaque and thrombus, angiography is blind to structures inside the arterial wall. Therefore, lesions that contain soft, diffusely thickened fibro-fatty tissue or hard calcified tissue are difficult to distinguish by angiography alone. Even arteries with walls distended by thick plaques that are composed of highly thrombotic lipid and cholesterol deposits can remain undetected in routine diagnostic angiograms. Since heavily calcified lesions are often difficult to expand with a balloon and increase the risk of vessel perforations, intravascular imaging technologies that visualize the distribution of superficial calcium in lesions can be valuable for guiding stent implantation. Although composition-specific treatment guidelines have not yet been established, the development of such guidelines continues to be an active area clinical research that has been enabled by advances in intravascular imaging [37].

Better visualization of stented arteries has been another driving force behind the development of intravascular imaging technologies. Stents are not seen clearly enough in standard angiograms to determine reliably whether the struts of an expanded stent contact the wall of the artery over its entire circumference. When a drug-eluting stent is poorly expanded, its effectiveness can be diminished if a portion of the drug elutes into the bloodstream rather than the arterial wall. On the other hand, over-expansion of a stent can cause tears ('dissections') in the arterial wall. Intravascular imaging is used frequently as an adjunct to angiography for optimizing stent expansion and for guiding repair of flow-limiting dissections. In follow-up procedures, intravascular imaging is also employed as a clinical research tool for observing neointimal proliferation, thrombus formation and other biological responses of the arterial wall to different types of stents in different patient populations. These and other applications of OCT are described in greater detail in Sect. 71.4.

71.2 Intravascular OCT Technology

Imaging coronary arteries in the beating heart is a challenging application that places stringent demands on the design and manufacture of intravascular OCT systems. Although these systems have many components in common with other endoscopic OCT systems, a number of application-specific technical features merit closer examination.

71.2.1 Brief History

Since the first in vivo OCT images of coronary arteries were acquired in animal studies in 1999 [9], intravascular OCT has evolved via parallel advances in technology and clinical application (Fig. 71.2). Early work focused on correlating OCT images of different plaque types with histology and IVUS images. An important early milestone was the publication of the results of the first patient study, performed with an OCT system built by researchers at the Massachusetts General Hospital (MGH, Boston, MA, USA) ([17]). At the same time as these patient studies were being carried out, LightLab Imaging, Inc. (Westford, MA, USA) was evaluating the first commercial prototypes of intracoronary OCT systems [10, 13]. Based on time-domain OCT with mechanical path-length scanning mechanisms, this first generation of OCT systems captured cross-sectional images at a line rates of 1,000–2,400 lines/s at frame rates of 5–10 frames/s. Because of their limited image acquisition speeds, early instruments could capture only snapshot images while the blood was cleared from the artery during injection of a bolus of saline or angiographic contrast medium through the guide catheter. During the period 2000–2003, other prototype coronary catheters were developed that incorporated custom flush injection ports for blood clearance and allowed imaging through percutaneous transluminal coronary angioplasty (PTCA) balloons.

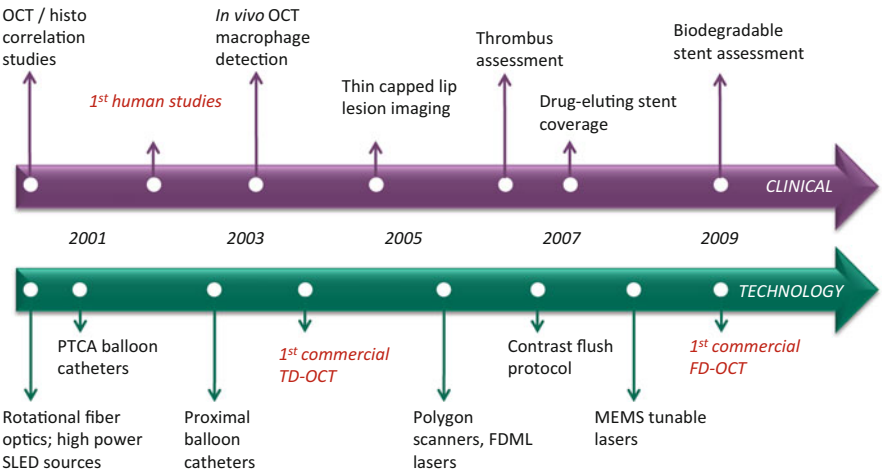

Fig. 71.2 Milestones in intravascular OCT which evolved via parallel advances in technology and clinical application

Nonetheless, the application of coronary OCT was limited to a few clinical research studies until the M2 OCT Imaging System (LightLab Imaging, Inc, Westford, MA; Goodman, Ltd., Nagoya, Japan) was released for sale in Japan and the European Union in 2004. The M2 system utilized an OCT imaging wire (ImageWire^{TM}) inserted through the central lumen of a low-profile occlusion balloon catheter (Helios^{TM}). This catheter delivery system enabled pullback imaging over arterial segments several centimeters long. Approximately 30 s were required to obtain a pullback image over a 3-cm length of artery (Fig. 71.2).

After the commercial release of the LightLab M2 system and its faster (4,800 lines/s; 20 frames/s) successor, the M3 system, the application of OCT expanded rapidly. In particular, the ability of OCT to characterize the various manifestations of atherosclerosis and thrombosis was demonstrated [18, 20, 21]. Results of early OCT studies provided insight into the mechanisms of plaque formation, distribution, and growth, especially in patients suffering from acute coronary syndromes [19, 24]. The high resolution of OCT and its ability to distinguish different plaque types were recognized as potential advantages of OCT in PCI guidance and optimization. OCT also played an important role in understanding the vascular response of arteries to implantation of the first generation of drug-eluting stents, as well as several other novel therapeutic devices introduced in the years between 2002 and 2009 [14, 26].

Although imaging speed had long been seen as the key to achieving more detailed scans of longer vessel segments without inducing ischemia [31], the speed of the M3 OCT system was close to the limit imposed by mechanically scanned time-domain OCT technology. With the development of frequency-domain OCT, a new chapter in intravascular imaging was opened [2]. The first published in vivo study of intracoronary frequency-domain OCT imaging was

performed using a prototype system developed at the Massachusetts General Hospital [49]. Based on a swept-source laser, this system acquired images at 100 frames/s, without loss of resolution, imaging range, or signal-to-noise ratio in comparison with its time-domain predecessors. The first commercially available frequency-domain OCT system (C7XR™, LightLab Imaging/St. Jude Medical, Westford, MA), was introduced in the European Union in 2009 and in the United States in 2010. Based on a swept-source laser, the C7XR™ OCT Imaging System images a 5.4 cm segment of a coronary artery in less than 3 s during the injection of a bolus of angiographic contrast medium. Scheduled to be released in Japan in 2012, but not yet cleared for sale by the US Food and Drug Administration, St. Jude Medical's latest commercial OCT system (ILUMIEN OPTIS™, LightLab Imaging/St. Jude Medical, Westford, MA) captures images of 7.5 cm arterial segments at 180 frames/s. Both of these systems are enabled by the development of rapid contrast injection protocols with software triggering that automatically detects blood clearance. The ILUMIEN OPTIS™ also incorporates wireless pressure-sensing technology for measurement of fractional flow reserve (FFR).

71.2.2 Clinical FD-OCT System

Intravascular FD-OCT systems, such as the C7XR™ and ILUMIEN™, consist of five main modules: an electro-optical engine; a catheter interface device (consisting of a drive motor and optical coupler or 'DOC'); an imaging catheter; a data acquisition and processing system; and a software package for displaying and interacting with the resultant image data. In this section the ILUMIEN is used to illustrate a state-of-the-art clinical system architecture. Although the ILUMIEN system is also capable of performing intravascular pressure measurements using fractional flow reserve (FFR) technology, this section focuses on the OCT sub-system of the ILUMIEN.

A schematic diagram of an electro-optical engine is shown in Fig. 71.3. The engine contains the swept laser, OCT interferometer, and ancillary optics and electronics needed for generating the appropriate data acquisition events. To maximize the delivery of light onto the sample and minimize losses as backscattered light returns from the sample, a dual-circulator design with an asymmetric input split ratio is used for the OCT interferometer. The majority of the light from the swept laser is directed to the OCT interferometer via a fiber-optic splitter S1. A second splitter S2 directs a portion of the light to the sample arm via a first circulator C1 and DOC, and a portion of the light to the reference arm via a second circulator C2 and path-adjustable reference mirror. As the interface between the catheter and the imaging system, the DOC contains a fiber optic rotary coupler mounted to a translation stage. Light from the sample and reference arms is combined in a third splitter S3 and the resulting interference signal is detected by a dual-balanced receiver D1. This interference signal is routed to the analog input of a data acquisition (DAQ) card in a personal computer (PC).

OCT image lines are generated from the digitized interference signal via a fast Fourier transform (FFT). Prior to the FFT operation, the interference signals must be

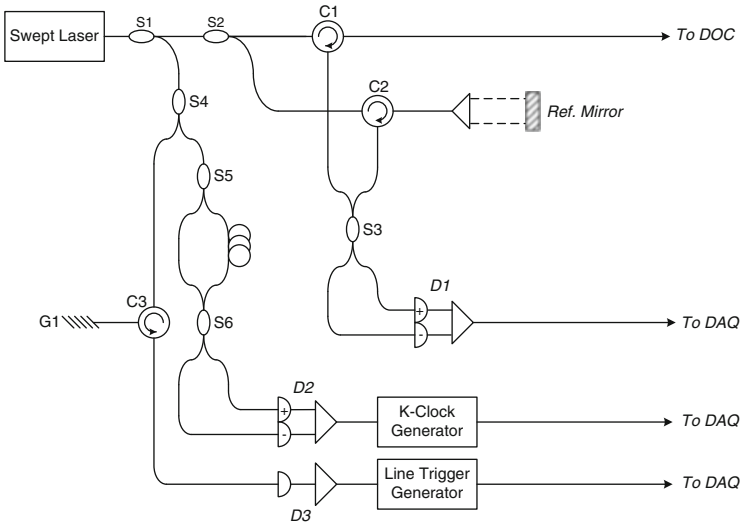

Fig. 71.3 Schematic diagram of the electro-optical engine inside the ILUMIEN OCT imaging system

made linear in optical frequency k with respect to time and must also be parsed into segments corresponding to complete laser sweep cycles. An electronic line trigger, which pulses once per laser sweep, is generated via a fiber Bragg grating G1 attached to a circulator C3 and photodetector D3. The fiber Bragg grating is a narrow-band reflective filter with a reflection peak selected to match the center wavelength of the laser sweep. The resulting line trigger is routed to the trigger input of the DAQ card.

To ensure that the interference signal is sampled at uniformly-spaced optical frequency points, an electronic k-clock is generated from a Mach-Zehnder interferometer (MZI) with a fixed path offset [32]. The MZI consists of two 50/50 optical couplers S5 and S6 with a small relative path offset between the two fibers linking the couplers. The fixed interference pattern generated by the MZI is detected by a dual-balanced receiver D2. Zero crossings of the interference pattern are electronically determined by the k-clock circuit and converted into a digital pulse train, which is subsequently routed to the external clock input of the DAQ card.

A schematic of the distal tip of the DragonFly^{TM} imaging catheter is shown in Fig. 71.4a. The catheter has a 2.7 F (0.9 mm) distal outer diameter and is compatible with 6F (2 mm) guide catheters. A rapid-exchange (Rx) tip design allows delivery of the catheter over conventional 0.014″ intracoronary guidewires. Radiopaque bands demarcate the distal tip of the catheter as well as the approximate position of the imaging lens. A detail of the lens is shown in Fig. 71.4b. The lens is constructed from three segments of optical fiber with tightly controlled lengths are fusion-spliced to one another. A first coreless fiber section acts as a beam expander, allowing the light to fully fill the aperture of a multimode fiber section. The multimode fiber focuses the beam into a second angle-polished coreless section. The fiber-air interface acts as a total internal reflector, directing the beam out the side of the catheter.

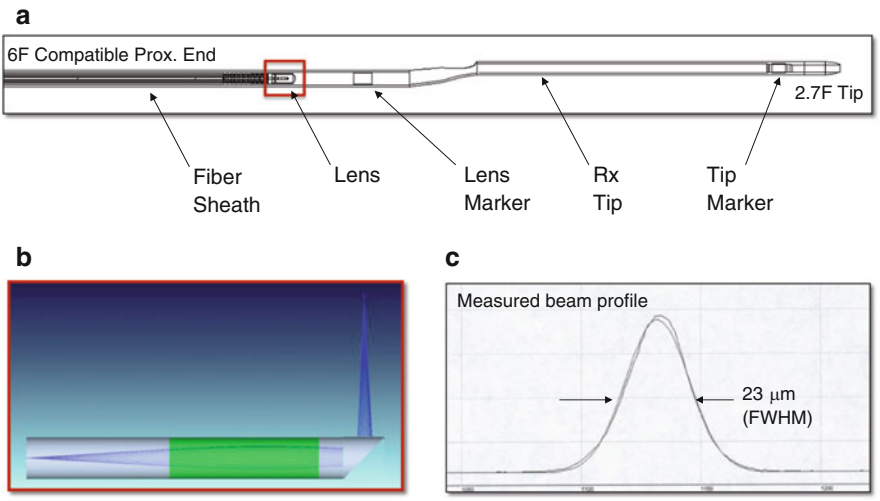

Fig. 71.4 (**a**) Schematic diagram of the distal section of the Dragonfly imaging catheter. (**b**) Detailed schematic of the fused fiber lens. (**c**) Beam profile of a typical fiber lens

Figure 71.4c shows the lateral intensity profile of the beam at the focal plane. A focal spot of 23 um FWHM is obtained at a working distance of approximately 1–2 mm. The catheter is designed to rotate at 100 Hz and pull back at up to 25 mm/s, allowing a 54 mm vessel segment to be imaged in under 3 s. Highly-scattering red blood cells are temporarily cleared from the vessel during the pullback via an intracoronary injection of a viscous fluid, such as iodinated contrast dye used for fluoroscopy, through the guide catheter.

After the OCT data have been acquired, the ILUMIEN software converts the individual image lines into polar frames and displays the data to the user. Figure 71.5 shows a typical screen shot from the ILUMIEN software. The cross-sectional B-mode image representing one rotational frame is displayed in the center of the screen. The longitudinal L-mode image showing a cut through one plane of the pullback is displayed in the bottom of the screen. The axis of the L-mode cut plane is shown as a yellow and blue bar through the middle of the B-mode image. A variety of measurement tools, including length, area, and percent stenosis, can be accessed using the right-hand toolbar. Quantitative measurement values appear in the left-hand information box. Additional visualization modes, such as a 3D rendering and a longitudinal plot of the mean vessel diameter, can also be accessed using a series of checkboxes on the left-hand side of the screen.

71.3 Plaque Characterization

The detailed natural history of atherosclerosis is still an active area of research. Plaques are typically classified by their composition (fibrous, lipid-rich, calcific,

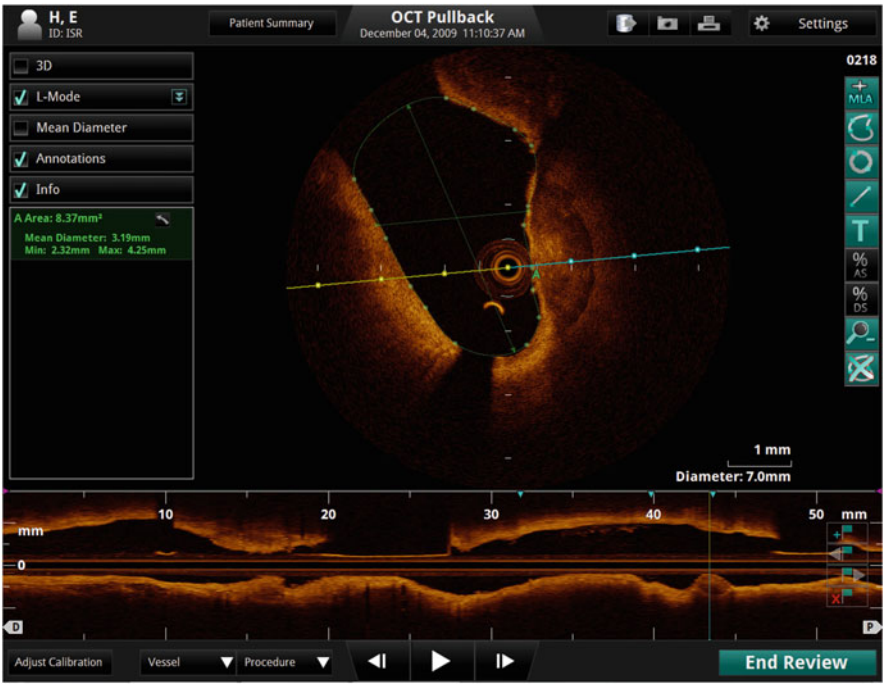

Fig. 71.5 Screen shot of a representative intravascular OCT pullback visualized on the ILUMIEN system software

etc.), as determined by histology. According to the guidelines published by American Heart Association and later revised by Virmani [36, 45], the evolution of plaque can be depicted as a series of complex branching steps, staged roughly according to the age and severity of the plaque (Fig. 71.6). Certain plaques reach a stable size and remain asymptomatic; others grow large enough to encroach on the lumen of the vessel and cause chest pain and other symptoms of myocardial ischemia; still others have thrombogenic properties that cause components of the blood to adhere and form clots. Plaques that thrombose and cause the rapid formation of intravascular blood clots are responsible heart attacks that can be fatal if not treated promptly.

Plaque visualization is important for treatment planning. The first experimental OCT studies were performed on post-mortem samples of excised aortas in mid-90s. In these studies, the salient features of fibroatheroma and fibrocalcific plaques seen in OCT images were first described [5]. In 2002, Yabushita et al. published a qualitative image classification scheme based on correlation of OCT images with histology [48]. Fibrous tissue was identified in OCT images as homogeneously signal-rich regions, calcified tissue as heterogeneous signal-poor regions with sharp borders, and lipid tissue as homogeneously signal-poor regions with diffuse borders. Later, by comparing the OCT images to IVUS images, Jang et al. confirmed that the same criteria were applicable to in vivo OCT images [17]. As intracoronary OCT imaging has become more widespread, additional tissue components have

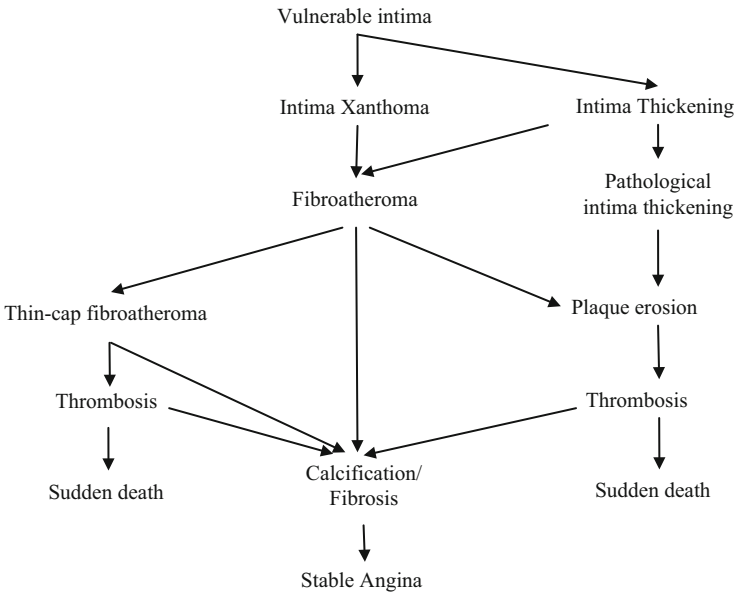

Fig. 71.6 Alternative pathways for progression of atherosclerosis (Adapted from Ref. [45])

been identified. Tearney et al. reported that macrophage foam cells can be detected and quantified with high sensitivity and selectivity by calculating the normalized standard deviation in user-selected regions of interest [40]. Kume et al. reported that red and white thrombus can be distinguished based on their signal-attenuation properties [21], an observation that has been confirmed by subsequent studies [29]. Figure 71.7 shows a few examples of OCT images of different plaque types and their corresponding histology images. The qualitative OCT image features and corresponding bulk optical properties of main coronary artery tissue types are summarized in Table 71.1. An international consensus document (referred to as the Consensus Standard from here on) was recently published to serve as a reference for the interpretation of intravascular OCT images [41].

Although the level of diagnostic accuracy with which coronary lesions and tissue components can be classified based on qualitative criteria alone is quite high, there is still a need for improving tissue-typing accuracy to facilitate real-time decision-making by interventional cardiologists who are less skilled in intravascular image interpretation. In addition, there were some drawbacks to the application of qualitative criteria in the evaluation of certain plaque types, especially lipid-rich plaques. For example, fibrous cap thickness and lipid plaque burden are important variables involved in plaque vulnerability that would benefit from more stringent quantitative measurement criteria. According to the pathology studies, most vulnerable plaques are composed of thin microphage-infiltrated fibrous caps (<65 μm) overlying a large necrotic lipid core [46]. However, although there is a well-delineated border between fibrous cap and the lipid pool in histology, the edge of a diffuse border cannot be

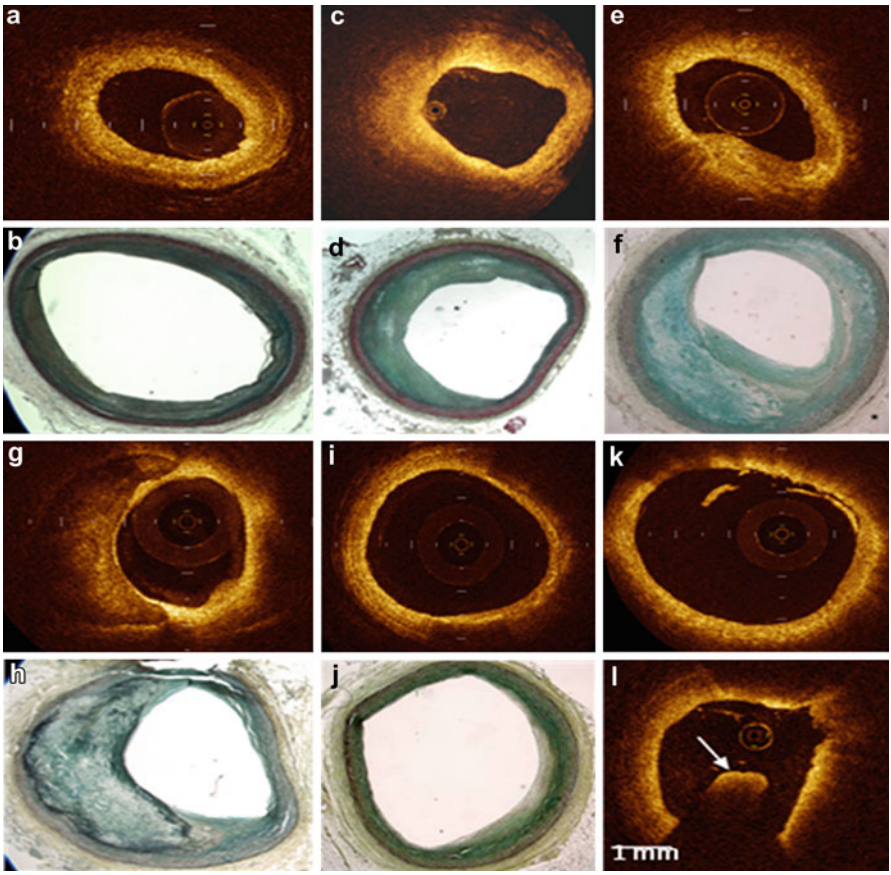

Fig. 71.7 (**a–j**) OCT and corresponding histology for different plaque types: (**a–b**) mostly healthy artery, (**c–d**) fibrotic plaque, (**e–f**) fibroatheroma, (**g–h**) fibrocalcific plaque, (**i–j**) foam cells. (**k**, **l**) OCT image of a *red* and *white* thrombus, respectively

Table 71.1 OCT image features of main coronary artery tissue types

Tissue	Qualitative OCT features
Fibrous tissue	Homogeneous, signal-rich, birefringent
Calcification tissue	Heterogeneous, sharply bordered, signal-poor, low birefringence
Lipid-rich tissue	Signal-rich at the top, high attenuation regions; low birefringence
Red thrombus	Signal-rich at the top, high attenuation region
White thrombus	Signal rich, low attenuation
Macrophage foam cells	Heterogeneous, lumpy, signal rich; very high attenuation, shadowing often evident; low birefringence
Intima	Signal-rich layer near lumen
Media	Signal-poor middle layer
Adventitia	Signal-rich, heterogeneously textured outer layer

defined precisely in OCT by visual inspection. At present, cardiologists must rely on extensive experience and a good physical understanding of OCT images to identify thin-capped fibroatheromas (TCFAs) that are prone to rupture [19, 30].

Both hardware and software approaches have been taken to improve the accuracy and speed of intravascular tissue characterization. Because the collagen fiber bundles and smooth muscle cells tend to be highly organized and anisotropic, these plaque components are more birefringent than lipid and other disorganized plaque components. Consequently, polarization-sensitive OCT has been proposed to increase the image contrast between the fibrous cap and the lipid tissue [11]. Unfortunately, since poorly organized tissue typically is not very birefringent, current methods cannot measure polarization rotation precisely over the short optical paths within the thickness of a thin fibrous cap (<65 μm).

As is the case for any new imaging method, qualitative OCT observations usually have greater utility if they are based on fundamental physical explanations. According to the single-scattering theory, the intensity of OCT signal $I(z)$ of a homogeneous tissue decreases exponentially with depth z, according to

$$I(z) = A(z)\mu_b \exp(-2\mu_t z/n)$$

where $A(z)$ represents the optical capture efficiency of OCT system, μ_b is the backscattering coefficient, μ_t is the total attenuation coefficient, and n is the refractive index. Several investigators have attempted to measure backscattering and attenuation coefficients by imaging post-mortem arteries from the lumen side [23, 43]. Good quantitative correspondence between cross-sectional OCT and histological image data has been difficult to achieve in these studies for several reasons: (1) the imaging depth of OCT in thick plaques is limited; (2) plaques are heterogenous and multi-layered, (3) histological processing distorts or destroys certain tissue components, and (4) precise registration of tissue slices and OCT cross-sections is difficult to maintain in long vessel segments. Xu et al. demonstrated that the optical coefficients could be measured more accurately on transversely sectioned arteries, where each plaque component can be exposed and more easily registered with histology [47]. Figure 71.8 shows the transversely scanned OCT images sectioned at two different depths, the corresponding rotary OCT scanning images, and histology images of representative fibroatheroma and fibrocalcific plaques. While the rotary OCT images were consistent with the previously published qualitative criteria, the transversely scanned OCT images showed that the lipid regions were signal-rich at the top layer, and only became signal-poor at deeper layers as the result of high signal attenuation. The backscattering and attenuation coefficients were determined for calcified tissue ($\mu_b = 4.9 \pm 1.5\ mm^{-1}$, $\mu_t = 5.7 \pm 1.4\ mm^{-1}$), fibrous tissue ($\mu_b = 18.4 \pm 6.4\ mm^{-1}$, $\mu_t = 6.4 \pm 1.2\ mm^{-1}$), and lipid tissue ($\mu_b = 28.1 \pm 8.9\ mm^{-1}$, $\mu_t = 13.7 \pm 4.5\ mm^{-1}$). In later studies similar results were obtained for attenuation coefficients measured from rotary OCT images (healthy vessel wall and intimal thickening: 2–5 mm^{-1}, necrotic core: >10 mm^{-1}, macrophage infiltration: >12 mm^{-1}) [44].

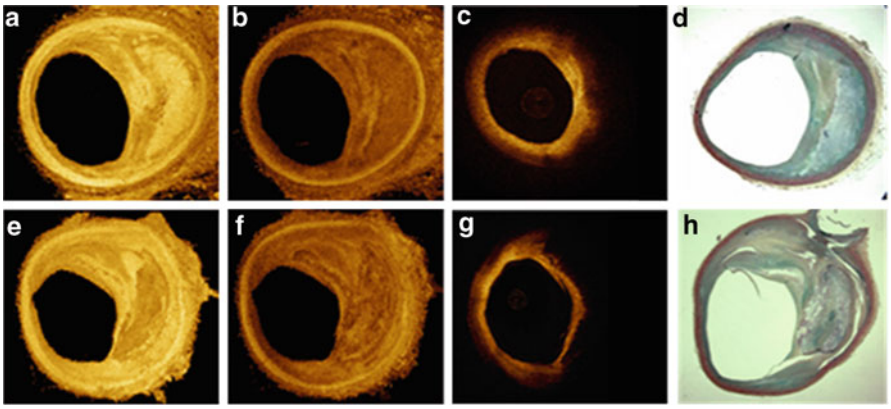

Fig. 71.8 Comparison of transverse OCT images at 50 μm (**a**, **e**) and 500 μm (**b**, **f**) below the surface, with corresponding rotary OCT images (**c**, **g**) and histological sections (**d**, **h**) for a representative fibrolipid plaque (*top row*) and a fibrocalcific plaque (*bottom row*). A consistent intensity mapping was used for **a–c** and **e–g**

Although quantification of intensity-based parameters (attenuation, backscattering, and texture) offers new insights into the interpretation of OCT images, this approach suffers from its own limitations. Similar to birefringence, attenuation is measured by averaging differential measurements over a distance. The minimum distance over which accurate measurements of attenuation can be obtained is typically 10–20 times the axial resolution of the OCT system. Current measurements also require averaging of neighboring scan lines to reduce the effects of speckle noise.

With the advances provided by three-dimensional frequency-domain OCT systems and improved resolution, the potential for rapid and automatic identification of plaque types may be realized in the near future. To achieve this goal, researchers must develop more effective signal acquisition and processing methods that take advantage of both qualitative and quantitative features of different plaque types.

71.4 Clinical Applications

The current clinical applications of intravascular OCT are directly primarily toward improving the safety and efficacy of PCI in patients with complex coronary anatomy or ambiguous lesion morphology. OCT also continues to play an important role in clinical trials of new pharmacological therapies, stents, and other interventional devices. In this section, examples of specific applications are discussed under separate headings.

71.4.1 Stent Planning and Deployment

Since stents are the foremost therapeutic tools of modern interventional cardiology, it is not surprising that guidance and evaluation of coronary stenting

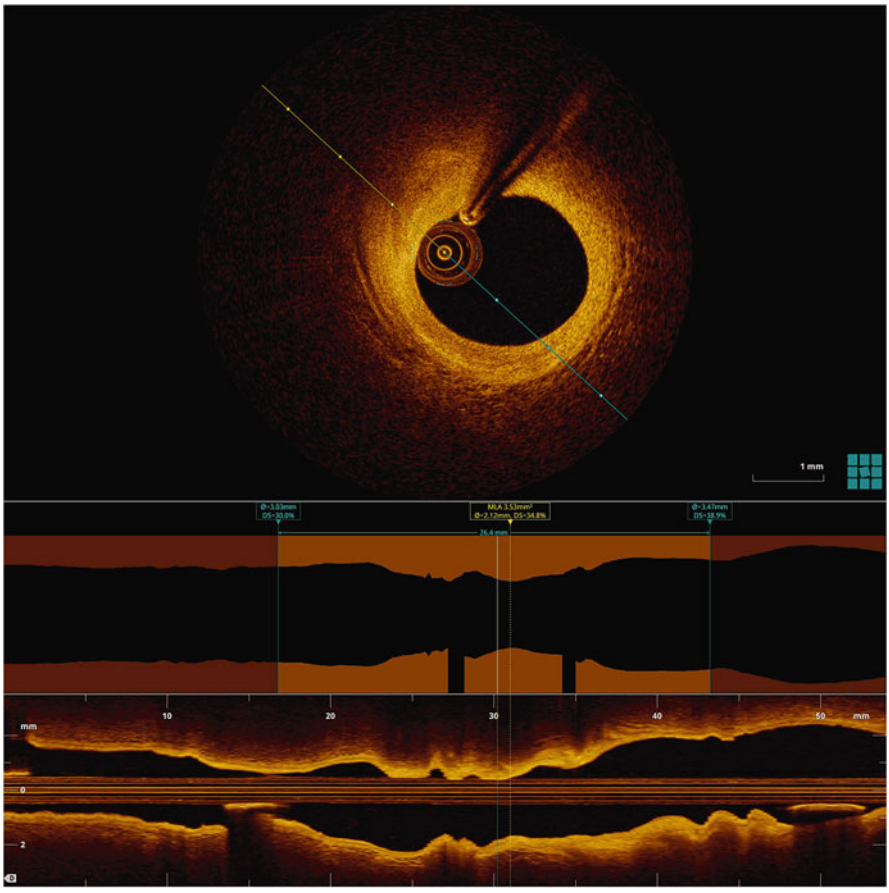

Fig. 71.9 A graphical display panel from the ILUMIEN OPTIS™ OCT imaging system (St. Jude Medical, Westford, MA). The upper panel shows a cross section of an artery at a user-selected frame and the bottom panel shows the longitudinal-mode (L-mode) view of the same artery along a user-selected plane. In the center panel, a computer-generated lumen profile shows the variations in the mean diameter of the artery along its length. The narrowed region of the artery lies within the highlighted region of the lumen profile. The measured values of the areas and diameters of the minimum lumen area and diameter are provided along with measurements at user-selected reference cross sections

procedures have become one of the most important applications of OCT [28, 15]. For optimization of the type and size of a stent before deployment, OCT enables the cardiologist to assess the composition and dimensions of a coronary lesion in three dimensions along its entire length. OCT provides superior contrast and resolution of arterial pathology compared to IVUS [4] and the ability of OCT to measure lumen area with high accuracy facilitates the assessment of lesion severity, especially in arteries with small cross sections [34, 16].

Recently developed software tools for PCI optimization take advantage of the clear delineation of the lumen boundary provided by FD-OCT. Figure 71.9 is an

example of a graphical display panel from an ILUMIEN OPTIS™ intravascular imaging system (St. Jude Medical, Westford, MA) that shows a cross-sectional OCT image of a coronary artery and its corresponding volumetric lumen profile before stenting. Derived from a computer-generated three-dimensional contour of the vessel, the lumen profile shows the mean diameter or area of the vessel lumen along the entire length of the imaged segment of the artery (5.4 cm in this example). In this example the stenosed region of the vessel is highlighted between the blue frame markers. The mean diameter profile facilitates identification of the narrowed vessel cross sections that warrant closer examination. It also provides information about the lengths, diameters, and areas at user-selected cross sections within the stenosed region. This information enables the cardiologist to choose the appropriate stent and to plan strategies for expanding the stent to achieve an optimal vessel profile. Note that, at the time of this writing, the ILUMIEN OPTIS™ system has been cleared for market in Japan only and has not yet been cleared by the US Food and Drug Administration for sale in the United States.

71.4.2 Immediate Post-Stent Assessment

The struts of a properly deployed stent contact the blood vessel along its entire length and expand the narrowed segment in a way that restores its normal tapered contour. Early IVUS studies of bare metal stents found that application of inadequate balloon pressure during stent deployment can lead to incomplete stent expansion and greater rates of target vessel revascularization and restenosis [8]. Incomplete stent apposition of drug-eluting stents has been implicated as one of the factors that contribute to the development of late stent thrombosis, a potentially fatal complication of coronary intervention [6]. Because of its ability to visualize individual stent struts, OCT is a powerful tool for detection and quantification of malapposition [15]. Stent expansion can also be assessed readily with OCT by comparing the stented diameter of the vessel with the diameters of reference segments in which minimal disease is evident.

Figure 71.10 shows examples of OCT images of stented arteries with well-apposed and malapposed struts. Stent measurements with OCT are highly reproducible [12] and separations smaller than 20 μm between the vessel wall and the outer edge of the stent can be discerned [42]. The clinical significance of the mean distance and spatial distribution of malapposition at the time of stent implantation has not yet been defined and is an active area of research.

OCT imaging has been instrumental in the development of optimum deployment techniques for new types of stents, particularly bioabsorbable vascular scaffolds (BVS) and stents designed for treatment of complex bifurcation lesions [1, 27, 33, 39]. Unlike metal stents, polymer BVS are not radiopaque; therefore, their degree of expansion and dissolution over time cannot be seen directly by x-ray fluoroscopy. OCT images the polymer struts clearly and their optical transparency facilitates visualization of the vessel wall through the stent.

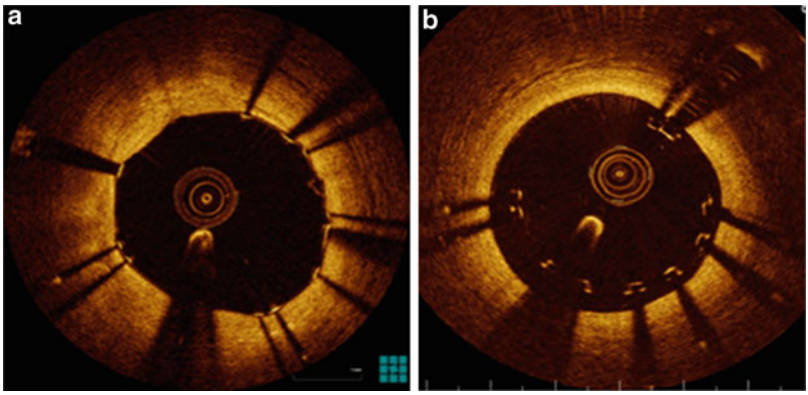

Fig. 71.10 Examples of OCT images of stented coronary arteries. (**a**) Stent with well-apposed struts (**b**) Stent with malapposed struts (5–9 o'clock)

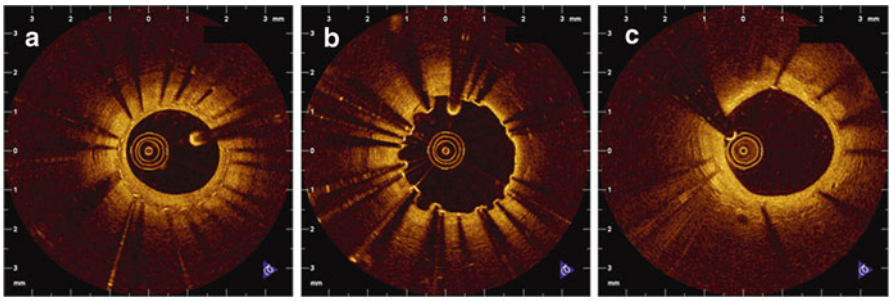

Fig. 71.11 Examples of OCT images of stented coronary arteries at follow-up. Images (**a**, **b**) were acquired from the same stent at two different locations. Image (**c**) was obtained from a stent in a different patient. Note that the variations in the thickness and uniformity of the neointimal growth inside the stent

71.4.3 Follow-Up Stent Assessment

How the artery responds to the implantation of a stent depends not only on the physical construction of the stent and how it is deployed, but also on characteristics of the arterial tissue in which is implanted and the biochemical composition of the circulating blood. The OCT images in Fig. 71.11 give an impression of the wide variety of vascular responses to stent implantation that have been observed during follow-up exams in different patients–and even at different locations in the same artery of an individual patient. Bare metal stents, which were the only type of stent available before the approval of the first drug-eluting stent in Europe in 2002, have relatively high restenosis rates (20–30 %). Because of their lower restenosis rates, drug-eluting stents have become the preferred type of stent for treatment of patients with stable coronary artery disease. The large majority of patients treated with the latest generation of stents do not

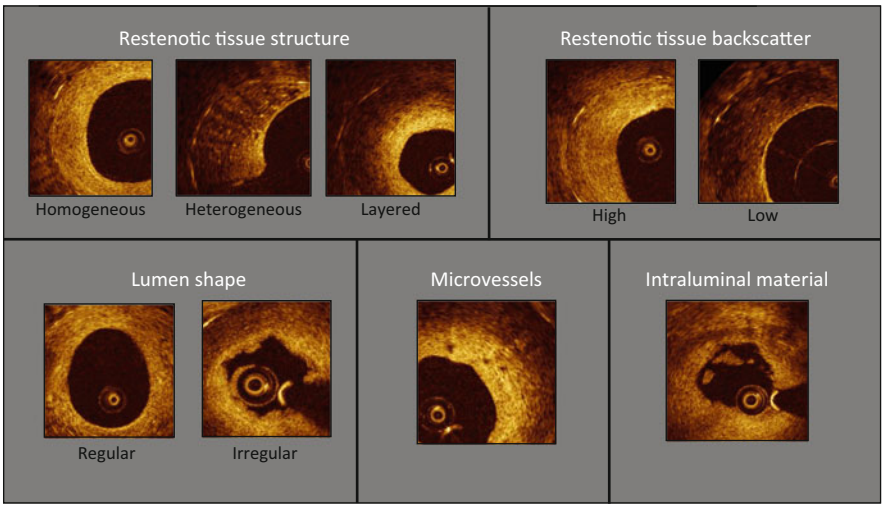

Fig. 71.12 Forms of restenotic tissue coverage on stents, as seen by OCT (Adapted from Ref. [12], with publisher's permission)

experience complications related to the stent that are clinically significant, but a substantial fraction of patients (typically 5–10 %) still undergo revascularization procedures to treat myocardial ischemia or infarction caused by stent restenosis or thrombosis. Although rare (0.5–2 %), stent thrombosis has a particularly high mortality rate (greater than 50 %) [7]. Consequently, identifying the variables that influence stent thrombosis has been a focus of numerous OCT studies.

The tissue that covers drug-eluting stents in asymptomatic patients, which normally remains thin (<200 μm) within 1 year of implantation, is difficult to visualize unambiguously with imaging modalities other than OCT. Stent restenosis is characterized by abnormally thick growth of the tissue inside a stent at angiographic follow-up, for which treatment is warranted if blood flow is compromised. Figure 71.12 illustrates a few of the forms of restenotic tissue coverage that have been documented in OCT studies [12]. Long-term follow-up studies have documented features in OCT images that are associated with late (>12 months) and very late (>36 months) stent thrombosis [36]. Among the goals of these studies is to identify patients at high risk for stent thrombosis so that the cardiologist can select the appropriate type and course of anticoagulant therapy.

71.4.4 Acute Coronary Disease

Intravascular OCT imaging has a number of unique diagnostic capabilities for assessment of culprit lesions in patients suffering from acute coronary syndromes (ACS). The defining symptom of ACS is sudden chest pain, often at rest or with minimal exertion. ACS is usually associated with the intermittent formation of

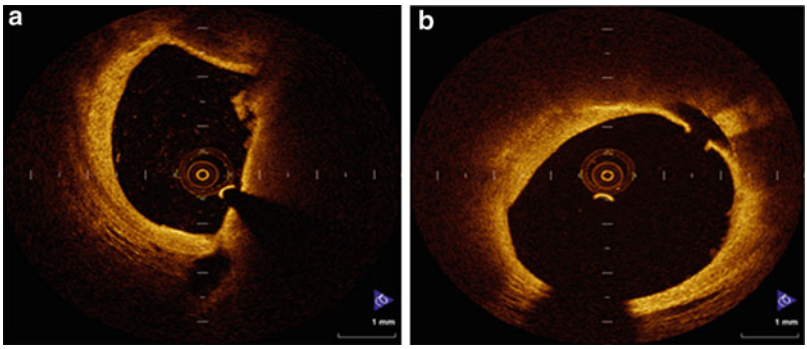

Fig. 71.13 Examples of OCT images of suspected ruptured plaques observed during percutaneous coronary intervention

thrombus that blocks blood flow to the heart muscle. If the blockage is severe, the patient can experience a debilitating – or fatal – myocardial infarction. In the majority of cases, the thrombus-initiating event is the rupture of a vulnerable plaque, which is defined histologically as plaque containing a large lipid core with a thin (<65 um) fibrous cap and an accumulation of macrophages localized within the cap [46]. Numerous studies have been performed to validate OCT's ability to detect thin fibrous caps, macrophages, thrombus, and other features of vulnerable and ruptured plaque [19, 21, 22, 38, 40]. Among the available imaging modalities, OCT may be best modality for detection of these features in vivo [19, 38]. Figure 71.13 show examples of OCT images of suspected ruptured plaques that were acquired from two patients undergoing PCI. Figure 71.13a shows a small mass of thrombus attached to a fissure in a thin fibrous cap (arrow) overlying a highly attenuating eccentric plaque (2–6 o'clock). Figure 71.13b shows a small ruptured plaque in which a void has formed in the intima that exposes the underlying plaque material. The very bright, highly attenuating strips of tissue above the rupture appear to be the remnants of a macrophage-rich cap. Since no in vivo reference standard now exists for direct comparison, the verification of OCT observations relies on correlation with histological findings in autopsy specimens.

The desire to predict which lesions – stented or unstented – will lead to sudden, unexpected cardiac events continues to motivate investigations of the role of OCT in guiding treatment of ACS patients. Demonstration of the diagnostic capabilities of OCT in well-controlled multi-center trials may encourage more effort toward the development of therapies to prevent plaque rupture and thrombosis.

71.5 Future of Intravascular OCT

Although the future of technical progress in any field is difficult to predict, certain trends in medical practice in general and cardiovascular imaging specifically are likely to influence the course of development of intravascular OCT.

1. First, demographics and health care economics will continue to drive demand for lower-cost imaging systems and catheters. Technological improvements that result in higher system performance at correspondingly higher cost that can only be procured by the best-financed research institutions will be eschewed in favor of technologies or manufacturing processes that remove complexity, reduce cost, and thereby extend the reach of OCT into mainstream clinical settings.
2. Second, the increasing workload of interventional cardiologists will require that intravascular imaging systems become increasingly multimodal, automated, and better integrated into the clinical workflow. The demand to combine physiological, morphological, and chemical sensing tools such as FFR, OCT, intravascular ultrasound, and optical spectroscopy on the same hardware platform, or even on the same catheter, is likely to increase. When merged with workhorse angiography X-ray systems, these ancillary technologies can provide the cardiologist with a single set of system controls and displays. To support this integration and ease the burden of interpreting multimodal data, advanced software will need to be developed to provide automated measurements and feature segmentation.
3. Third, an increased focus on evidence-based best clinical practices with links to physician reimbursement will increase the need for large-scale clinical trials to demonstrate the patient outcome benefits of technologies such as OCT. Although this trend is already being observed throughout the medical device industry, OCT and other advanced diagnostic modalities will be particularly challenged given their lack of direct therapeutic effect and increased cost over the default scenario of performing PCI procedures under angiographic guidance only.

References

1. P. Barlis, J. Tanigawa, C. Di Mario, Eur. Heart J. **28**, 2319 (2007)
2. P. Barlis, J.M. Schmitt, EuroIntervention **4**, 529 (2009)
3. H.G. Bezerra, M.A. Costa, G. Guagliumi, A.M. Rollins, D.I. Simons, JACC Cardiovasc. Interv. **2**, 1035 (2009)
4. B.E. Bouma, G.J. Tearney, H. Yabushita, M. Shishkov, C.R. Kauffman, D. DeJoseph, B.D. MacNeill, S.L. Hausler, H.T. Aretz, E.F. Halpern, I.K. Jang, Heart **89**, 317 (2003)
5. M.E. Brezinski, G.J. Tearney, B.E. Bouma, J.A. Izatt, M.R. Hee, E.A. Swanson, J.F. Southern, J.G. Fujimoto, Circulation **93**, 1206 (1996)
6. S. Cook, P. Wenaweser, M. Togni, M. Billinger, C. Morger, C. Seiler, R. Vogel, O. Hess, B. Meier, S. Windecker, Circulation **115**, 2426 (2007)
7. D.E. Cutlip, D.S. Baim, K.K.L. Ho, J.J. Popma, A.J. Lansky, D.J. Cohen, J.P. Carrozza, M.S. Chauhan, O. Rodriguez, R.E. Kuntz, Circulation **102**, 1967 (2001)
8. P. de Jaegere, H. Mudra, H. Figulla, Y. Almagor, S. Doucet, I. Penn, A. Columbo, C. Hamm, A. Bartorelli, M. Rothman, M. Nobuyoshi, T. Yamaguchi, V. Voudris, C. diMario, S. Makovski, D. Hausmann, S. Rowe, S. Rabinovich, M. Sunamura, G.A. van Es, Eur. Heart J. **19**(1214) (1998)
9. J.G. Fujimoto, S.A. Boppart, G.J. Tearney, B.E. Bouma, C. Pitris, M.E. Brezinski, Heart **82**, 128 (1999)

10. U. Gerckens, L. Buellesfeld, E. MacNamara, E. Grube, Herz **28**, 496 (2003)
11. S.D. Giattina, B.K. Courtney, P.R. Herz, M. Harman, S. Shortkroff, D.L. Stamper, B. Liu, J.G. Fujimoto, M.E. Brezinski, Int. J. Cardiol. **107**, 400 (2006)
12. N. Gonzalo, H.M. Garcia-Garcia, P.W. Serruys, K.H. Commissaris, H. Bezerra, P. Gobbens, M. Costa, E. Regar, EuroIntervention **5**, 224 (2009)
13. E. Grube, U. Gerckens, L. Buellesfeld, P.J. Fitzgerald, Circulation **106**, 2409 (2002)
14. G. Guagliumi, G. Musumeci, V. Sirbu, H.G. Bezerra, N. Suzuki, L. Fiocca, A. Matiashvili, N. Lortkipanidze, A. Trivisonno, O. Valsecchi, G. Biondi-Zoccai, M.A. Costa, JACC Cardiovasc. Interv. **3**, 531 (2010)
15. G. Guagliumi, T. Akasaka, V. Sirbu, T. Kubo, Optical coherence tomography, Chapter 60, in *Textbook of Interventional Cardiology*, ed. by E.J. Topol, P.S. Teirstein (Elsevier, Philadelphia, 2012)
16. G. Guagliumi, V. Sirbu, C. Petroff, D. Capodanno, G. Musumeci, H. Yamamoto, A. Elbasiony, C. Brushett, A. Matiashvili, N. Lortkipanidze, O. Valsecchi, H.G. Bezerra, J.M. Schmitt, Volumetric assessment of lesion severity with optical coherence tomography: relationship with fractional flow reserve. EuroIntervention **8**, 1172–1181 (2013)
17. I.K. Jang, B.E. Bouma, D.H. Kang, S.J. Park, S.W. Park, K.B. Seung, K.B. Choi, M. Shishkov, K. Schlendorf, E. Pomerantsev, S.L. Houser, H.T. Aretz, G.J. Tearney, S.A. Boppart, G.J. Tearney, J. Am. Coll. Cardiol. **39**, 604 (2002)
18. I.K. Jang, G.J. Tearney, B. MacNeill, M. Takano, F. Moselewski, N. Iftima, M. Shishkov, S.L. Houser, H.T. Aretz, E.F. Halpern, B.E. Bouma, Circulation **111**, 1551 (2005)
19. T. Kubo, T. Imanishi, S. Takarada, A. Kuroi, S. Ueno, T. Yamano, T. Tanimoto, Y. Matsuo, T. Masho, K. Tsuda, Y. Tomobuchi, T. Akasaka, J. Am. Coll. Cardiol. **50**, 933 (2007)
20. T. Kume, T. Akasaka, T. Kawamoto, N. Watanabe, E. Toyota, Y. Neishi, R. Sukmawan, Y. Sadahira, K. Yoshida, Circ. J. **29**, 903 (2005)
21. T. Kume, T. Akasaka, T. Kawamoto, Y. Ogasawara, N. Watanabe, E. Toyota, Y. Neishi, R. Sukmawan, Y. Sadahira, K. Yoshida, Am. J. Cardiol. **97**, 1713 (2006)
22. T. Kume, T. Akasaka, T. Kawamoto, H. Okura, N. Watanabe, E. Toyota, Y. Neishi, R. Sukmawan, Y. Sadahira, K. Yoshida, Am. Heart J. **152**, e1 (2006)
23. D. Levitz, L. Thrane, M. Frosz, P. Andersen, C. Andersen, S. Andersson-Engels, J. Valanciunaite, J. Swartling, P. Hansen, Opt. Express **12**(249) (2004)
24. B.D. MacNeill, I.K. Jang, B.E. Bouma, N. Iftimia, M. Takano, H. Yabushita, M. Shiskov, C.R. Kauffman, S.L. Houser, H.T. Aretz, D. DeJoseph, E.F. Halpern, G.J. Tearney, J. Am. Coll. Cardiol. **44**, 972 (2004)
25. G.S. Mintz, S.E. Nissen, W.D. Anderson, S.R. Bailey, R. Erbel, P.J. Fitzgerald, F.J. Pinto, K. Rosenfield, R.J. Siegel, E.M. Tuzcu, P.G. Yock, R.A. O'Rourk, J. Abrams, E.R. Bates, B.R. Brodie, P.S. Douglas, G. Gregoratos, M.A. Hlatky, J.S. Hochman, S. Kaul, C.M. Tracy, D.D. Waters, W.L. Winters, J. Am. Coll. Cardiol. **37**, 1478 (2001)
26. A. Murata, D. Wallace-Bradley, A. Tellez, C. Alviar, M. Aboodi, A. Sheehy, L. Coleman, L. Perkins, G. Nakazawa, G. Mintz, G.L. Kaluza, R. Virmani, J. Am. Coll. Cardiol. Img. **3**, 76 (2010)
27. J.A. Ormiston, P.W. Serruys, E. Regar, D. Dudek, L. Thuesen, M.W. Webster, Y. Onuma, H.M. Garcia-Garcia, R. McGreevy, S. Veldhof, Lancet **371**, 899 (2008)
28. F. Prati, G. Guagliumi, G.S. Mintz, M. Costa, E. Regar, T. Akasaka, P. Barlis, G.J. Tearney, I.K. Jang, E. Arbustini, H.G. Bezerra, Y. Osaki, N. Bruining, D. Dudek, M. Radu, A. Erglis, P. Motreff, F. Alfonso, K. Toutouzas, N. Gonzalo, P.W.J. Serruys, C. Di Mario et al., Eur. Heart J. **10**, 1093 (2012)
29. J. Rieber, O. Meissner, G. Babaryka, S. Reim, M. Oswald, A. Koenig, T.M. Schiele, M. Shapiro, K. Theisen, M.F. Reiser, V. Klauss, U. Hoffmann, Coron. Artery Dis. **17**, 425 (2006)
30. T. Sawada, J. Shite, H.M. Garcia-Garcia, T. Shinke, S. Watanabe, H. Otake, D. Matsumoto, Y. Tanino, D. Ogasawara, H. Kawamori, H. Kato, N. Miyoshi, M. Yokoyama, P.W. Serruys, K. Hirata, Eur. Heart J. **29**, 1136 (2008)

31. J.M. Schmitt, R. Huber, J.G. Fujimoto, Chapter 28: Limiting ischemia with fast fourier-domain imaging, in *Optical Coherence Tomography in Cardiovascular Research*, ed. by E. Regar, P.W. Serruys, (Taylor and Francis, London, 2006), pp. 256–266
32. J.M. Schmitt, U.S. Patent 7,916,387, issued 29 March 2011
33. P.W. Serruys, J.A. Ormiston, Y. Onumo, E. Regar, N. Gonzalo, H.M. Garcia-Garcia, K. Nieman, N. Bruining, C. Dorange, K. Miguel-Hebert, S. Veldhof, M. Webster, L. Thuesen, D. Dudek, Lancet **373**, 897 (2009)
34. Y. Shiono, H. Kitabata, T. Kubo, T. Masuno, S. Ohta, Y. Ozaki, H. Sougawa, M. Orii, K. Shimamura, K. Ishibashi, K. Komukai, T. Tanimoto, T. Yamaguchi, K. Hirata, M. Mizukoshi, T. Imanishi, T. Akasaka, Circ. J. **76**, 2218 (2012)
35. V. Sirbu, G. Guagliumi, G. Musumeci, Eur. Heart J. **29**(suppl), 127 (2008)
36. H.C. Stary, A.B.. Chandler, R.E. Dinsmore, V. Fuster, S. Glagov, W. Insull, M.E. Rosenfeld, C.J. Schwartz, W.D. Wagner, R.W. Wissler, Arterioscler. Thromb. Vasc. Biol. **15**, 1512 (1995)
37. G.W. Stone, A. Maehara, A.J. Lansky, B. de Bruyne, E. Cristea, G.S. Mintz, R. Mehran, J. McPherson, N. Farhat, S.P. Marso, H. Parise, B. Templin, R. White, Z. Zhang, P.W. Serruys, N. Engl. J. Med. **364**, 226 (2011)
38. A. Tanaka, T. Imanishi, H. Kitabata, T. Kubo, S. Takarada, T. Tanimoto, A. Kuroi, H. Tsujioka, H. Ikejima, S. Ueno, H. Kataiwa, K. Okouchi, M. Kashiwaghi, H. Matsumoto, K. Takemoto, N. Nakamura, K. Hirata, M. Mizukoshi, T. Akasaka, Circulation **107**, 118 (2008)
39. S. Tanimoto, P.W. Serruys, L. Thuesen, D. Dudek, B. deBruyne, B. Chevalier, J.A. Ormiston, Catheter. Cardiovasc. Interv. **70**, 515 (2007)
40. G.J. Tearney, H. Yabushita, S.L. Houser, H.T. Aretz, I.K. Jang, K.H. Schlendorf, C.R. Kauffman, M. Shishkov, E.F. Halpern, B.E. Bouma, Circulation **107**, 113 (2003)
41. G.J. Tearney, E. Regar, T. Akasaka, T. Adriaenssens et al., J. Am. Coll. Cardiol. **59**, 1058 (2012)
42. M. Terashima, S. Rathore, Y. Suzuki, Y. Nakayama, H. Kaneda, K. Nasu, M. Habara, O. Katoh, T. Suzuki, J. Invasive Cardiol. **21**, 602 (2009)
43. F.J. van der Meer, D.J. Faber, D.M. Baraznji Sassoon, M.C. Aalders, G. Pasterkamp, T.G. van Leeuwen, IEEE Trans. Med. Imaging **24**, 1369 (2005)
44. G. van Soest, T. Goderie, E. Regar, S. Koljenovic, G.L. van Leenders, N. Gonzalo, S. van Noorden, T. Okamura, B.E. Bouma, G.J. Tearney, J.W. Oosterhuis, P.W. Serruys, A.F. van der Steen, J. Biomed. Opt. **15**, 011105 (2010)
45. R. Virmani, F.D. Kolodgie, A.P. Burke, A. Farb, S.M. Schwartz, Arterioscler. Thromb. Vasc. Biol. **20**, 1262 (2000)
46. R. Virmani, A.P. Burke, A. Farb, F.D. Kolodgie, J. Am. Coll. Cardiol. **47**, C13 (2006)
47. C. Xu, J.M. Schmitt, S.G. Carlier, R. Virmani, J. Biomed. Opt. **13**, 034003 (2008)
48. H. Yabushita, B.E. Bouma, S.L. Houser, H.T. Aretz, I.K. Jang, K.H. Schlendorf, C.R. Kauffmman, M. Shishkov, D.H. Kang, E.F. Halpern, G.J. Tearney, Circulation **106**, 1640 (2002)
49. S.H. Yun, G.J. Tearney, B.J. Vakoc, M. Shiskov, Y.O. Wang, A.E. Desjardins, M.J. Suter, R.D. Chan, J.A. Evans, I.K. Jang, N.S. Nishioka, J.F. deBoer, B.E. Bouma, Nat. Med. **12**, 1429 (2006)

Development of Integrated Multimodality Intravascular Imaging System for Assessing and Characterizing Atherosclerosis

72

Zhongping Chen

Keywords
Intravascular OCT • Intravascular ultrasound • IVUS • Atherosclerosis • Vunerable plaque • Fluorescence • Elastography • Multimodal imaging

72.1 Introduction

Atherosclerosis is one of the major causes of morbidity and mortality in developed countries. The major cause (86 %) of cardiovascular deaths is from heart attacks and the major cause (45 %) of deaths from brain aneurysms is due to less obtrusive plaques known as vulnerable plaques that rupture suddenly and trigger a blood clot or thrombus that blocks blood flow [1–4]. Atherosclerosis is a progressive disease that is characterized by the accumulation of lipids, cholesterol, fibrous constituents, monocytes, and various other inflammatory cells in the arterial wall. These deposits form vascular lesions known as atheromatous plaques, which contain necrotic cores and are separated from the arterial intima by a fibrous cap composed of collagen and smooth muscle cells [4, 5]. Upon plaque maturation, the fibrous caps become thin and increasingly susceptible to tearing, which increases vulnerability to plaque rupture. Rupture of these vulnerable plaques releases inflammatory elements of the necrotic core into the artery, causing thrombosis. This leakage may lead to obstruction of arterial blood flow and angina and/or myocardial infarction, which can be lethal [6]. Atherosclerosis is the single most important contributor to cardiovascular disease-related deaths.

Z. Chen
The Edwards Life Sciences Center for Advanced Cardiovascular Technology, Beckman Laser Institute, Irvine, CA, USA

Department of Biomedical Engineering, Beckman Laser Institute, University of California Irvine, Irvine, CA, USA
e-mail: z2chen@uci.edu

© Springer International Publishing Switzerland 2015

W. Drexler, J.G. Fujimoto (eds.), *Optical Coherence Tomography*,
DOI 10.1007/978-3-319-06419-2_73

Early detection of plaque lesions is the first and most necessary step towards preventing the lethal consequences of atherosclerosis. Currently, many biomedical imaging techniques aimed at imaging and assessing vulnerable plaques have been reported in literature, including angiography, magnetic resonance imaging (MRI), intravascular ultrasound (IVUS), optical coherence tomography (OCT), intravascular near infrared spectral imaging, intravascular fluorescence imaging, and intravascular photoacoustic tomography (IVPAT) [7–16].

Unfortunately, atherosclerosis exhibits an asymptomatic nature, as vulnerable plaques grow without causing any detrimental side effects until rupturing [4]. Due to this complication, the information provided by a single clinical arterial imaging technique is often insufficient to diagnose vulnerable plaque formation at an early stage. Although the understanding of vulnerable plaques is still at an early stage, previous research based on pathological studies has demonstrated that a plaque's stability is strongly affected by the plaque's morphology and tissue chemical composition [3, 4, 7, 17, 18]. Structurally, the thickness of the fibrous cap is a reliable indicator of plaque vulnerability [7, 19]. Chemically, the intralesion lipid density and the cholesterol content are important parameters that correlate with the vulnerability of the lesion [7, 20, 21]. Therefore, an optimal imaging modality for diagnosis and characterization of plaques should combine high spatial resolution capable of resolving fibrous cap thickness, deep imaging depth capable of assessing plaque burden and vessel remodeling, and molecular sensitivity capable of determining tissue composition and tissue mechanical properties [7].

IVUS and OCT are currently the two most commonly used modalities in the clinic for diagnosing cardiovascular diseases, which allow direct tomographic visualization of cross-sectional images from inside the vessel lumen [7, 22–25]. However, the spatial resolution of IVUS is inadequate to distinguish the microstructure of plaques, especially an accurate thickness of the thin fibrous cap. On the other hand, OCT is a recently developed optical-based technology that can provide real-time, high-resolution, 3-dimensional images with micrometer resolution which is one to two orders better than that of IVUS [24–28]. However, the drawback of OCT is its limited penetration depth, which makes it difficult for OCT to image the complete depth of a large lipid pool. Over the past few years, we have developed an integrated OCT/US imaging probe that enables simultaneous intravascular OCT and intravascular US (IVUS) imaging [29–31]. Integration of intravascular OCT/US is significant because it combines the advantages of the high spatial resolution of OCT and the broad imaging depth of US, which enables quantification of the thickness of both the fibrous cap and plaques. Although each optical probing technique provides access to relevant diagnostic parameters, integration of several modalities is necessary to gather the information required to establish a robust method for early detection of plaque vulnerability.

While the combined IVUS/OCT system can achieve depth penetration and superior resolution, the combined IVUS/OCT system lacks the capability to accurately assess plaque composition and mechanical properties. Several intravascular imaging modalities with molecular sensitivity have been reported.

These include intravascular near infrared spectroscopy (NIRS), Raman, CARS, and fluorescence imaging [9, 17, 21, 32–39]. These imaging modalities use contrast that involve specific molecular electronic and vibrational energy state transitions and therefore can be used to identify tissue composition. Integration of OCT with fluorescence has recently been reported [21, 40].

In addition to structural and chemical composition, tissue mechanical properties provide critical information to assess the vulnerability of plaques [41–45]. The stress in the cap increases with decreasing thickness and increasing macrophage infiltration. High strain locations in the vessel wall indicate the presence of vulnerable plaques [41–44]. We have developed phase-resolved acoustic radiation force optical coherence elastography (PR-ARF-OCE) to image and quantify mechanical properties of vascular tissues [46].

In this chapter, we will review several multimodality intravascular imaging systems including intravascular OCT/US, OCT/fluorescence, and OCT/PR-ARF-OCE.

72.2 Integrated Intravascular OCT/US Imaging

Although the understanding of vulnerable plaques is at an early stage, previous research has demonstrated that thin-cap fibroatheroma (TCFA) accounts for approximately 80 % of all sudden cardiac deaths [18]. TCFAs have been histologically identified with the following pathological features: thin fibrous cap (<65 μm), large lipid pool, and macrophages near or within the fibrous cap [18, 47].

Intravascular ultrasound (IVUS) has been used in the clinic for the diagnosis of atherosclerosis since it permits direct tomographic visualization of cross-sectional images of the vessel wall [22, 48, 49]. IVUS can image more than 5 mm deep inside tissues to cover the full thickness of plaques [50]. However, IVUS resolution is on the order of 50–200 μm, which is not enough to resolve the fibrous cap thickness. OCT is a recently developed optical-based technology that can provide real-time, high-resolution, 3-dimensional images with micrometer resolution which is one to two orders of magnitude better than that of IVUS [24]. OCT images provide details at a higher resolution on the order of 5–20 μm, which can be used to accurately assess the thickness of a plaque fibrous cap. However, OCT has limited imaging depth and cannot quantify the full thickness of the plaque. Therefore, IVUS and OCT provide complementary information that are critical for characterizing TCFA [19, 51]. Recently, Sawada et al. studied the feasibility of the combined use of IVUS and OCT data (images acquired separately) for detecting thin-cap fibroatheroma (TCFA) from 56 patients. The results clearly showed that neither modality alone was sufficient for detecting TCFAs and that the combined use of OCT and IVUS would significantly increase the sensitivity and specificity for detection of TCFAs [19, 52, 53].

Currently, multimodal intracoronary imaging requires introducing separate imaging probes [19]. This practice not only requires a laborious matching procedure for image co-registration and fusion, but it is also time consuming and costly [52, 53].

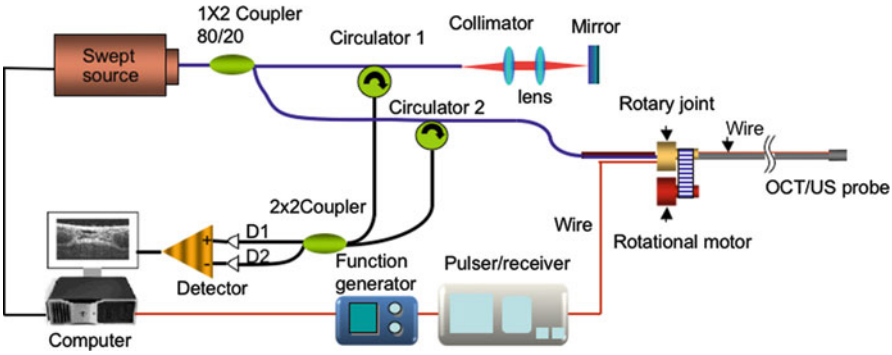

Fig. 72.1 Schematic of US/OCT imaging system with an integrated probe [30]

Therefore, it is significantly advantageous to integrate IVUS/OCT imaging into a single system. Over the past few years, recognizing the complementary nature of OCT and US imaging, we have developed a miniature integrated OCT/US system for intravascular imaging applications [29–31]. Figure 72.1 shows the schematic of the integrated intravascular OCT/US system [29–31]. For the US system, a single sinusoidal wave centered at 50 MHz is generated by a pulser to excite the transducer. The echo signal is received by a broadband receiver. For the OCT system, light from a swept source (1310 nm) is split by an 80/20 1 × 2 coupler. A circulator is used in each arm to redirect backscattered and back-reflected light to the two input ports of a 50/50 2 × 2 coupler for balanced detection. Both US and OCT signals are digitized by a 12-bit data acquisition board. A function generator provides synchronization signals to both the pulser and the data acquisition board [30].

We have designed and developed several different integrated OCT/US probes for intravascular imaging [29–31]. Figure 72.2 shows an integrated probe with a focused ring ultrasound transducer [31]. The homemade 50 MHz focused ring transducer has an effective aperture of 2-mm with a 0.8-mm hole at the center to make room for the OCT probe. The coaxial US and light beams have a common focal length of 4 mm, and both are steered into tissue by a 45° mirror along their pathway. Co-registered rabbit aorta images from the integrated intravascular OCT/US system is shown in Fig. 72.3 [31]. Figure 72.4 shows another design of an integrated OCT/US probe that has an outer diameter of less than 0.7 mm [29]. In vitro OCT and US images of human coronary artery with pathology, as well as in vivo images of vascular tissue in rabbit and porcine animal models, were obtained using this integrated OCT/US probe. Figure 72.5 shows an intravascular OCT/US image from a human coronary artery specimen with a calcified plaque [29]. The plaque can be identified in both OCT and US images. From the OCT image, the plaque cap, as highlighted by the arrow, can be clearly identified due to the high axial resolution and high contrast of OCT. However, the OCT system could not visualize the entire depth features of the vessel wall. On the other

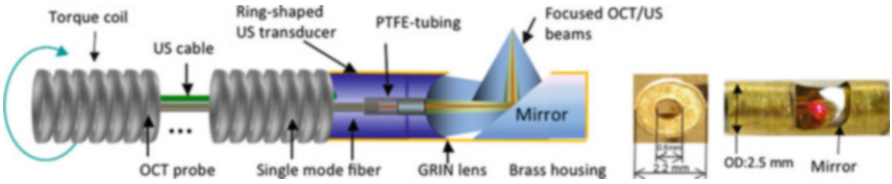

Fig. 72.2 An integrated probe with a focused ring ultrasound transducer [31]

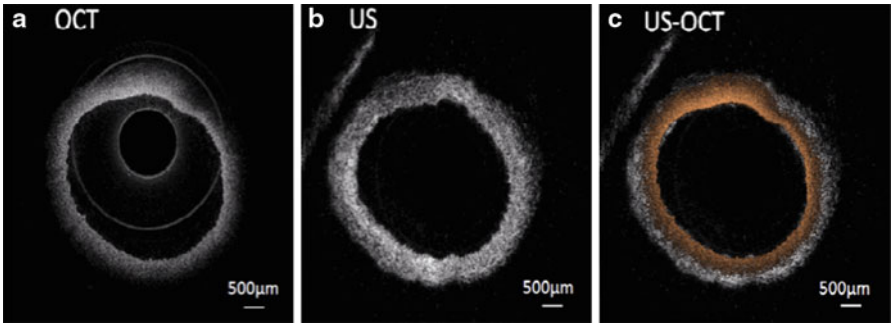

Fig. 72.3 Co-registered rabbit aorta images from an integrated intravascular OCT/US system [31]

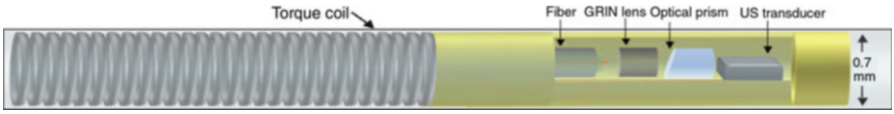

Fig. 72.4 Integrated miniature intravascular OCT-US probe with linear aligned US transducer [29]

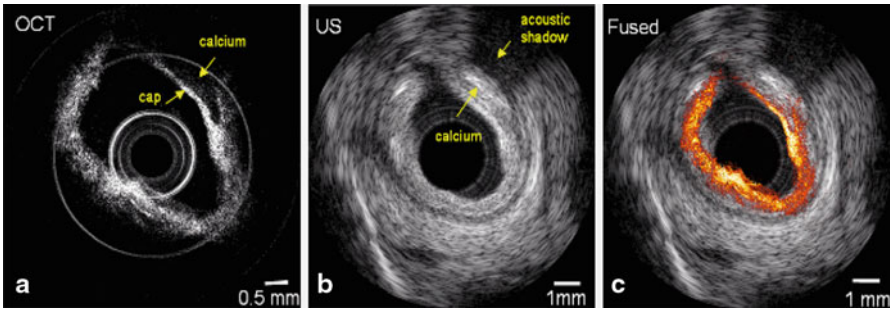

Fig. 72.5 OCT/US images of human coronary artery specimen from an integrated OCT/US system. (**a**) OCT image, (**b**) ultrasound image, (**c**) overlaid OCT/US image [29]

hand, in the US image, the acoustic shadow as pointed by the arrow indicates the location of the plaque and US provides much deeper penetration depth than OCT. However, from the US image, one can hardly distinguish the border between calcium and the surrounding tissue due to inferior resolution of US. We have obtained, to the best of our knowledge, the first in vivo images of vascular tissue in rabbit and porcine animal models using this integrated OCT/US probe [29]. Although further research and development is required to translate this technology to clinical practice, these results clearly demonstrated the potential of the integrated IVUS/OCT system.

72.3 Integrated Intravascular OCT and Fluorescence Imaging

Diagnosis of the latent vulnerability of a plaque lesion relies on both structural and tissue chemical compositions. Although OCT has been used for vulnerable plaque evaluation due to its high resolution, it lacks molecular specificity for identification of tissue composition in plaques. Intravascular fluorescence molecular imaging provides biomolecular information of atherosclerosis inside the blood vessel [21, 54]. It is known that macrophage infiltration affects plaque stability [55]. A fluorescent tagged antibody, such as Annexin V, that targets apoptotic macrophages can provide critical information to determine vulnerability of plaques [56]. In addition, fluorescent lifetime measurement has also been used for the detection of macrophage/foam cell infiltration and discrimination of lipid-rich lesions in atherosclerotic artery [6]. Therefore, an integrated OCT/fluorescence imaging system combining the high spatial resolution of OCT with the molecular sensitivity of fluorescence imaging is capable of resolving both microstructure and biomolecular information at the same time [21, 40].

Integration of intravascular OCT and fluorescence imaging has been reported by a number of groups [21, 40]. The schematic of an integrated swept source OCT-fluorescence system based on a micro motor is shown in Fig. 72.6 [40]. For the OCT system, a swept laser with a center wavelength of 1310 nm, FWHM bandwidth of 100 nm, and output power of 8 mW is used as the light source. The laser beam is split in an 80/20 ratio by a 1 $\times$ 2 coupler, with 80 % of the power directed to the WDM input port then to the combined OCT and fluorescence probe, and 20 % to the reference arm. Two circulators are used in the reference and sample arms, respectively, to redirect backscattered and back-reflected light to the two input ports of a 50/50 2 $\times$ 2 coupler for balanced detection. For the fluorescence imaging system, a continuous-wave (CW) laser diode with a center wavelength of 635 nm and output power of 5 mw is used as the excitation source for fluorescence imaging. A photomultiplier tube (PMT) is used to detect fluorescence emission light. The excitation light and the OCT beam are combined together with a wavelength division multiplexer (WDM coupler 635/1,310). A double-clad fiber (DCF) combiner with one single-mode fiber port, one multimode fiber port, and one DCF port is used to deliver the OCT and fluorescence excitation light beams to the sample and collect the OCT fluorescence signals. The OCT and

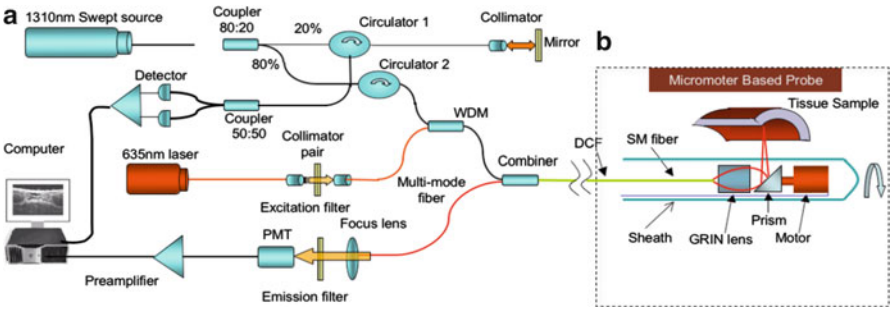

Fig. 72.6 Schematic of the OCT/fluorescence system. *Black line* denotes single-mode fiber (*SMF28*), *red line* denotes multimode fiber, and *blue line* denotes double-clad fiber (*DCF*). (**b**) Intravascular probe based on a DCF combiner. OCT and fluorescence excitation light are transported through the single-mode core of the DCF; the back-reflected fluorescence emission light is collected through the inner cladding of the DCF [40]

fluorescence excitation light are transported through the 8 μm core of the DCF, and the back-reflected fluorescence emission light is collected through the 105 μm inner cladding of the DCF. Subsequently, the backscattered OCT signal from the sample is coupled back through the single-mode fiber port of the combiner and the WDM coupler to the OCT system. Fluorescence emission light backscattered from the sample is coupled back through the multimode fiber port of the combiner and detected by the PMT. The use of a single-mode DCF core to deliver the fluorescence excitation light improves the lateral resolution of the fluorescence image. The schematic diagram of the dual-modality intravascular probe is shown in Fig. 72.6b. A micro motor is used for circumferential scanning of the inner blood vessel wall. This distal scanning design eliminates the disadvantage of unstable vibration and uneven rotational speed in a proximal scanning design and can be applied to more flexible materials without the need of rotational torque transfer [57]. A linear motor outside the endoscope is used to pull back the entire probe to create 3-D helical OCT scanning and to achieve a 2-D superficial fluorescence intensity image. OCT and fluorescence emission signals are digitized by a two-channel, 250 M samples/s 12 bit data acquisition card and transferred to a computer for processing.

We have used integrated OCT/fluorescence to image the aorta of a New Zealand white rabbit. Annexin V conjugated Cy 5.5 was used as the fluorescent contrast to target the plaques and stain the tissue. Annexin V is an antibody that targets apoptotic macrophages which accumulate in the necrotic core, a key characteristic of vulnerable plaques [56]. OCT/fluorescence images from phantom plaques are shown in Fig. 72.7. Figure 72.7a shows the schematic of the two phantom plaques inside the blood vessel wall. Figure 72.7b illustrates the fused fluorescence-OCT image of the model plaques. Figure 72.7c shows the 3-D OCT image and Fig. 72.7d shows that the OCT image of the mimic plaque matches well with the 2-D fluorescence intensity image. This experiment demonstrates that our system is capable of obtaining both OCT and fluorescence intensity signals simultaneously. We can choose different agents to target various molecular factors in vulnerable plaques.

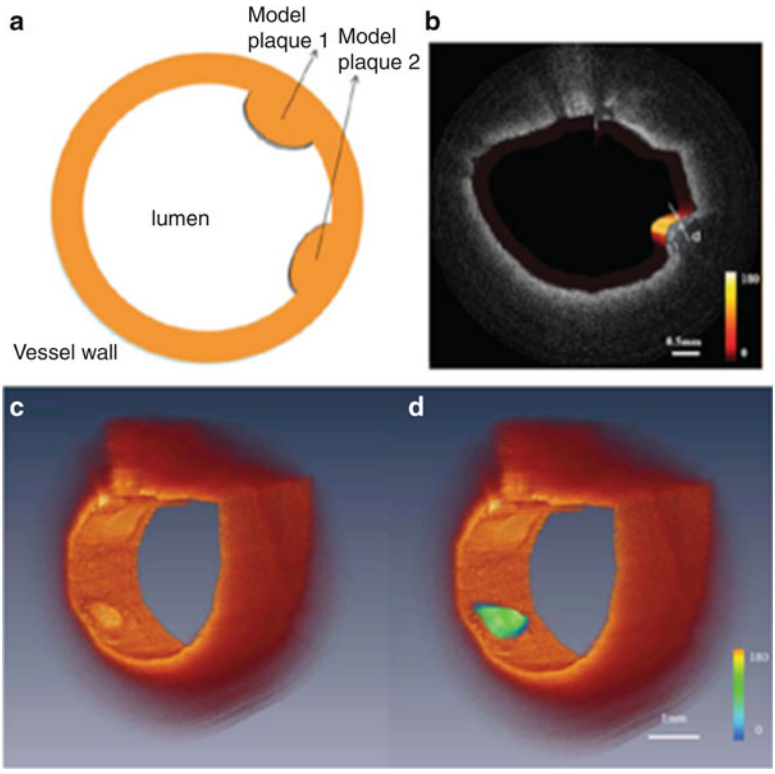

Fig. 72.7 (**a**) Schematic of model plaques, (**b**) fused OCT/fluorescence image of normal rabbit aorta with phantom plaques. The thickness of the plaque cap is around 128 μm as indicated in label (**d**). The color scale in (**b**) shows the relative intensity of the fluorescence signal. (**c**) 3D OCT image and (**d**) combined 3-D OCT/fluorescence image [40]

72.4 Phase-Resolved Acoustic Radiation Force Optical Coherence Elastography (ARF-OCE)

Tissue mechanical properties provide critical information to assess the vulnerability of plaques [41–45]. The stress in the cap increases with decreased thickness and increased macrophage infiltration. High strain locations in the vessel wall indicate the presence of vulnerable plaques [41–44]. Elastography is an imaging technique [58], which measures the local deformation of tissue induced by stress to estimate the strain and stiffness which are directly related to the biomechanical properties. Elastography has become a powerful technique to distinguish healthy and diseased tissues, particularly in cardiovascular research.

Significant progress has been made in developing intravascular ultrasound (IVUS) elastography [42, 59–62]. However, since the dimensions of the structural components of the vulnerable atherosclerotic plaques, such as fibrous caps and

carotid arteries, are on the order of 50–200 μm, the resolution of the IVUS imaging system, which lies in the range of 150–300 μm [63], is not sufficient to resolve the entire structural details of plaques.

Optical coherence elastography (OCE) has a superior micrometer scale resolution and is therefore suitable for imaging subtle mechanical changes in the early stages of disease [64]. Excitation and detection are generally the two prominent characteristics of an OCE system. There are two main categories of OCE with respect to the excitation method: static/quasi-static excitation OCE and dynamic excitation OCE [65, 66]. The former applies compression to the subject statically/quasi-statically and measures the relaxation dynamics, which has limited imaging speed for in vivo imaging. The latter dynamically excites the subject using various waveforms and detects the induced displacement in a gated time window, which enables a much higher imaging speed and makes it possible for in vivo imaging. For the detection system, a phase-resolved OCT system can detect displacements with up to nanometer sensitivity [67]; this is especially important for intravascular imaging as better sensitivity in displacement measurements means reduced force needs to be applied to a vessel wall to quantify tissue mechanical properties. Phase-resolved dynamic OCE has been investigated previously for shear wave propagation detection [68, 69], but this method requires separation of excitation and detection points which limits the speed and spatial resolution. Adaptation of this method is difficult for in vivo real-time 2D and 3D vascular elastography.

We recently developed a phase-resolved ARF-OCE system that uses an acoustic wave to apply pressure to the tissue and uses phase-resolved OCT to evaluate the elastic properties of vascular tissue [46]. The ARF-OCE combines the high-speed excitation of ARF with sub-micrometer/nm detection sensitivity of phase-resolved OCT. This elastography technique allows high-speed and high-resolution point-by-point mapping of local strains in atherosclerotic coronary tissue. Since the mechanical properties of fibrous and fatty plaques are different, PR-ARF-OCE has the potential to differentiate between various plaque components.

Phase-resolved ARF-OCE utilizes chirped acoustic radiation forces to produce excitation along the sample's axial direction and phase-resolved Doppler OCT to measure the vibration of the sample. Figure 72.8 shows imaging of a section of atherosclerotic human coronary artery with phase-resolved ARF-OCE. An OCT intensity image, shown in Fig. 72.8a, provides a general morphological view of the tissue with no obvious evidence of the presence of atherosclerosis. By applying a 500 Hz chirped acoustic radiation force onto the tissue, a strong vibration phase contrast can be clearly imaged using ARF-OCE (Fig. 72.8b). The region indicated by the white arrow in ARF-OCE image is characterized by less vibration and therefore represents less elastic, stiffer tissue such as plaques. The strong vibration representing softer tissue is indicated by yellow arrows. In this ARF-OCE image the stiffer tissue, in this case atherosclerotic plaque, is clearly distinguished from the softer (usually normal) tissue area highlighted by brighter colors. The transition between the plaque and normal region appears blue (indicated by blue arrows) and

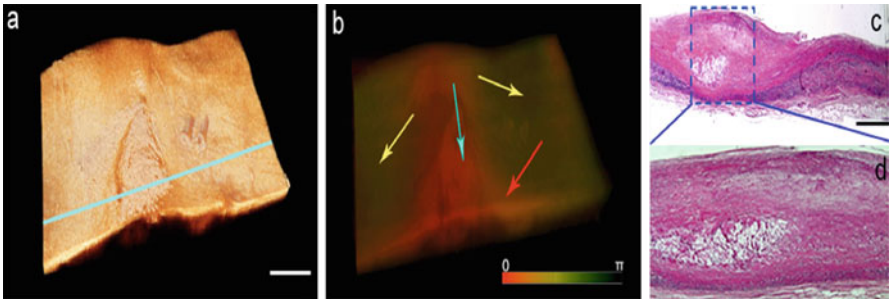

Fig. 72.8 (**a**) OCT structural, (**b**) ARF-OCE phase images of a human cadaver coronary artery under 500-Hz, 350-mV AM modulated excitation; an atherosclerotic lesion was identified as the *red* region corresponding to the *blue box* in (**c**). (**c**) Histological image and (**d**) close-up view of the atherosclerotic lesion. Scale bars: 1 mm [46]

is characterized by intermediate elasticity. This result clearly shows that our ARF-OCE method has great potential to quantitatively characterize mechanical properties of vascular plaques, which may provide critical information towards determining plaque vulnerability.

72.5 Summary

Recent landmark intravascular imaging studies have highlighted the morphological characteristics of high-risk plaques and have generated substantial interest in this area [2, 21, 70–76]. These studies have led to substantial developments in basic science and clinical understanding of plaque stability and progression [77]. They have emphasized the areas requiring further investigation and the urgent need for more intravascular studies [78]. It is particularly important to address functional and compositional aspects of high-risk plaques. Our current knowledge of inflammatory pathways and mechanisms is solely provided by either postmortem specimens of coronary vasculature or circulatory biomarkers. However, the first are not representative of the sequence of events during plaque development, while the later are not representative of the local microenvironment [79]. In vivo imaging, therefore, is of utmost importance despite the fact that it is not currently used for day-to-day clinical practice [80]. It will enable the further understanding of plaque disruption mechanisms and development of strategies for the prevention of acute coronary events, including sudden death.

The clinical need and value for an imaging system that can identify patients with vulnerable plaques at high risk of rupture has been discussed extensively in the literature [7, 81–83] and also highlighted in this year's NIH/NHLBI Working Group Report on Detection of High-risk Atherosclerotic Plaque [80]. Currently there is no imaging system that can reliably determine plaque risk or predict late occlusion after drug-eluting stent placement [7, 82, 84]. Several interventional procedures to treat vulnerable plaques at high risk of rupturing are under clinical

trials [85–87]. The widespread clinical application of these measures requires the improved risk stratification of vulnerable plaques with better predictive power [80, 88]. The ability to detect these vulnerable plaques noninvasively is likely to serve as a powerful stimulus for an increased effort in the development of such therapies [85–87]. This chapter describes integration of intravascular OCT with ultrasound, fluorescence, and elastography. A number of other label-free optical techniques, such as second harmonic generation (SHG) imaging of collagen, two-photon excited fluorescence (TPEF) imaging of elastin, CARS imaging of lipids, and photoacoustic imaging of absorption contrast, have not yet reached the stage of clinical studies but have shown great potential for atherosclerotic research [8–16]. An integrated intravascular imaging modality that can measure structure, chemical composition, and tissue mechanical properties and detect and characterize vulnerable plaques will provide a critically important tool for monitoring the progression of disease and evaluating the efficacy of intervention. The surveillance and early diagnosis of vulnerable lesions will prove to be of the utmost importance in further efforts to tailor therapeutic interventions in patients at risk [89].

Acknowledgments I would like to thank many of our colleagues who have contributed to the intravascular imaging project at UCI Beckman Laser Institute, Department of Medicine Cardiology Division, and Department of Biomedical Engineering, particularly the students and postdoctoral fellows. In addition, I would like to thank my collaborators, Drs. Qifa Zhou and K. Kirk Shung, as well as their students at USC NIH Ultrasonic Transducer Resource Center and Department of Biomedical Engineering, for joint development of miniature ultrasound transducers for the intravascular imaging project. Finally, I also want to acknowledge grants support from the National Institutes of Health (R01EB-10090, R01EY-021529, R01HL-105215, R01HL-125084, and P41EB-015890), Air Force Office of Scientific Research (FA9550-04-0101), and the Beckman Laser Institute Endowment.

References

1. J. Narula, W.H. Strauss, The popcorn plaques. Nat. Med. **13**, 532–534 (2007)
2. C. Weber, H. Noels, Atherosclerosis: current pathogenesis and therapeutic options. Nat. Med. **17**(11), 1410–1422 (2011)
3. R. Virmani, F.D. Kolodgie, A.P. Burke, A.V. Finn, H.K. Gold, T.N. Tulenko, S.P. Wrenn, J. Narula, Atherosclerotic plaque progression and vulnerability to rupture: angiogenesis as a source of intraplaque hemorrhage. Arterioscler. Thromb. Vasc. Biol. **25**(10), 2054–2061 (2005)
4. J. Narula, H.W. Strauss, Imaging of unstable atherosclerotic lesions. Eur. J. Nucl. Med. Mol. Imaging **32**(1), 1–5 (2005)
5. R. Virmani, F.F. Kolodgie, A.P. Burke, A.V. Finn, H.K. Gold, T.N. Tulenko, S.P. Wrenn, J. Narula, Atherosclerotic plaque progression and vulnerability to rupture: angiogenesis as a source of intraplaque hemorrhage. Arterioscler. Thromb. Vasc. Biol. **25**(10), 2054–2061 (2005)
6. L. Marcu, Q. Fang, J. Jo, T. Papaioannou, A. Dorafshar, T. Reil, J. Qiao, J. Baker, J. Freischlag, M. Fishbein, In vivo detection of macrophages in a rabbit atherosclerotic model by time-resolved laser-induced fluorescence spectroscopy. Atherosclerosis **181**(2), 295–303 (2005)
7. R. Puri, M.I. Worthley, S.J. Nicholls, Intravascular imaging of vulnerable coronary plaque: current and future concepts. Nat. Rev. Cardiol. **8**(3), 131–139 (2011)

8. P.J. Campagnola, A.C. Millard, M. Terasaki, P.E. Hoppe, C.J. Malone, W.A. Mohler, Three-dimensional high-resolution second-harmonic generation imaging of endogenous structural proteins in biological tissues. Biophys. J. **82**(1), 493–508 (2002)
9. M.B. Lilledahl, O.A. Haugen, C.D. Lange-Davies, L.O. Svaasand, Characterization of vulnerable plaques by multiphoton microscopy. J. Biomed. Opt. **12**(4), 044005 (2007)
10. H.W. Wang, I.M. Langohr, M. Sturek, J.X. Cheng, Imaging and quantitative analysis of atherosclerotic lesions by CARS-based multimoddal nonlinear optical microscopy. Arterioscler. Thromb. Vasc. Biol. **29**, 1342 (2009)
11. H.W. Wang, T.T. Le, J.X. Cheng, Label-free imaging of arterial cells and extracellular matrix using a multimodal CARS microscope. Opt. Commun. **281**, 1813–1822 (2008)
12. A. Zoumi, X. Lu, S. Ghassan, B.J. Tromberg, Imaging coronary artery microstructure using second-harmonic and two-photon fluorescence microscopy. Biophys. J. **87**, 2778–2786 (2004)
13. W. Wei, X. Li, Q. Zhou, K.K. Shung, Z. Chen, Integrated ultrasound and photoacoustic probe for co-registered intravascular imaging. J. Biomed. Opt. **16**(10), 106001 (2011)
14. P. Wang, H.W. Wang, M. Sturek, J.X. Cheng, Bond-selective imaging of deep tissue through the optical window between 1600 and 1850 nm. J. Biophotonics **5**(1), 25–32 (2012)
15. K. Jansen, A.F. van der Steen, H.M. van Beusekom, J.W. Oosterhuis, G. van Soest, Intravascular photoacoustic imaging of human coronary atherosclerosis. Opt. Lett. **36**(5), 597–599 (2011)
16. B. Wang, J.L. Su, J. Amirian, S.H. Litovsky, R. Smalling, S. Emelianov, Detection of lipid in atherosclerotic vessels using ultrasound-guided spectroscopic intravascular photoacoustic imaging. Opt. Express **18**(5), 4889–4897 (2010)
17. P.R. Moreno, R.A. Lodder, K.R. Purushothaman, W.E. Charash, W.N. O'Connor, J.E. Muller, Detection of lipid pool, thin fibrous cap, and inflammatory cells in human aortic atherosclerotic plaques by near-infrared spectroscopy. Circulation **105**(8), 923–927 (2002)
18. F.D. Kolodgie, A.P. Burke, A. Farb, H.K. Gold, J. Yuan, J. Narula, A.V. Finn, R. Virmani, The thin-cap fibroatheroma: a type of vulnerable plaque: the major precursor lesion to acute coronary syndromes. Curr. Opin. Cardiol. **16**(5), 285–292 (2001)
19. T. Sawada, J. Shite, H.M. Garcia-Garcia, T. Shinke, S. Watanabe, H. Otake, D. Matsumoto, Y.D. Tanino, H. Ogasawara, H. Kawamori, N. Kato, M. Miyoshi, P.W. Yokoyama, P.W. Serruys, K.I. Hirata, Feasibility of combined use of intravascular ultrasound radiofrequency data analysis and optical coherence tomography for detecting thin-cap fibroatheroma. Eur. Heart J. **29**, 1136–1146 (2008)
20. S. Waxman, F. Ishibashi, J.E. Muller, Detection and treatment of vulnerable plaques and vulnerable patients: novel approaches to prevention of coronary events. Circulation **114**(22), 2390–2411 (2006)
21. H. Yoo, J.W. Kim, M. Shishkov, E. Namati, T. Morse, R. Shubochkin, J.R. McCarthy, V. Ntziachristos, B.E. Bouma, F.A. Jaffer, G.J. Tearney, Intra-arterial catheter for simultaneous microstructural and molecular imaging in vivo. Nat. Med. **17**(12), 1680–1684 (2011)
22. B.N. Potkin, A.L. Bartorelli, J.M. Gessert, R.F. Neville, Y. Almagor, W.C. Roberts, M.B. Leon, Coronary artery imaging with intravascular high-frequency ultrasound. Circulation **81**(5), 1575–1585 (1990)
23. L. Landini, L. Verrazzani, Spectral characterization of tissues microstructure by ultrasounds: a stochastic approach. IEEE Trans. Ultrason. Ferroelectr. Freq. Control **37**(5), 448–456 (1990)
24. D. Huang, E.A. Swanson, C.P. Lin, J.S. Schuman, W.G. Stinson, W. Chang, M.R. Hee, T. Flotte, K. Gregory, C.A. Puliafito et al., Optical coherence tomography. Science **254**(5035), 1178–1181 (1991)
25. G.J. Tearney, I.K. Jang, B.E. Bouma, Optical coherence tomography for imaging the vulnerable plaque. J. Biomed. Opt. **11**(2), 021002 (2006)
26. M.U. Farooq, A. Khasnis, A. Majid, M.Y. Kassab, The role of optical coherence tomography in vascular medicine. Vasc. Med. **14**(1), 63–71 (2009)

27. G. Pasterkamp, E. Falk, H. Woutman, C. Borst, Techniques characterizing the coronary atherosclerotic plaque: influence on clinical decision making. J. Am. Coll. Cardiol. **36**(1), 13–21 (2000)
28. M.E. Brezinski, G.J. Tearney, B.E. Bouma, J.A. Izatt, M.R. Hee, E.A. Swanson, J.F. Southern, J.G. Fujimoto, Optical coherence tomography for optical biopsy – properties and demonstration of vascular pathology. Circulation **93**(6), 1206–1213 (1996)
29. J. Yin, X. Li, J. Jing, J. Li, D. Mukai, S. Mahon, A. Edris, K. Hoang, K.K. Shung, M. Brenner, J. Narula, Q. Zhou, Z. Chen, Novel combined miniature optical coherence tomography ultrasound probe for in vivo intravascular imaging. J. Biomed. Opt. **16**(6), 060505 (2011)
30. J. Yin, H.C. Yang, X. Li, J. Zhang, Q. Zhou, C. Hu, K.K. Shung, Z. Chen, Integrated intravascular optical coherence tomography ultrasound imaging system. J. Biomed. Opt. **15**(1), 010512 (2010)
31. X. Li, J. Yin, C. Hu, Q. Zhou, K.K. Shung, Z. Chen, High-resolution coregistered intravascular imaging with integrated ultrasound and optical coherence tomography probe. Appl. Phys. Lett. **97**(13), 133702 (2010)
32. S. Waxman, S.R. Dixon, P. L'Allier, J.W. Moses, J.L. Petersen, D. Cutlip, J.C. Tardif, R.W. Nesto, J.E. Muller, M.J. Hendricks, S.T. Sum, C.M. Gardner, J.A. Goldstein, G.W. Stone, M.W. Krucoff, In vivo validation of a catheter-based near-infrared spectroscopy system for detection of lipid core coronary plaques: initial results of the SPECTACL study. JACC Cardiovasc. Imaging **2**(7), 858–868 (2009)
33. H.P. Buschman, E.T. Marple, M.L. Wach, B. Bennett, T.C. Schut, H.A. Bruining, A.V. Bruschke, A. van der Laarse, G.J. Puppels, In vivo determination of the molecular composition of artery wall by intravascular Raman spectroscopy. Anal. Chem. **72**(16), 3771–3775 (2000)
34. T.J. Romer, J.F. Brennan 3, G.J. Puppels, A.H. Zwinderman, S.G. van Duinen, A. van der Laarse, A.F. van der Steen, N.A. Bom, A.V. Bruschke, Intravascular ultrasound combined with Raman spectroscopy to localize and quantify cholesterol and calcium salts in atherosclerotic coronary arteries. Arterioscler. Thromb. Vasc. Biol. **20**(2), 478–483 (2000)
35. F.A. Jaffer, C. Vinegoni, M.C. John, E. Aikawa, H.K. Gold, A.V. Finn, V. Ntziachristos, P. Libby, R. Weissleder, Real-time catheter molecular sensing of inflammation in proteolytically active atherosclerosis. Circulation **118**(18), 1802–1809 (2008)
36. L. Marcu, J.A. Jo, Q. Fang, T. Papaioannou, T. Reil, J.H. Qiao, J.D. Baker, J.A. Freischlag, M.C. Fishbein, Detection of rupture-prone atherosclerotic plaques by time-resolved laser-induced fluorescence spectroscopy. Atherosclerosis **204**(1), 156–164 (2009)
37. L. Marcu, Fluorescence lifetime in cardiovascular diagnostics. J. Biomed. Opt. **15**(1), 011106 (2010)
38. H.W. Wang, I.M. Langohr, M. Sturek, J.X. Cheng, Imaging and quantitative analysis of atherosclerotic lesions by CARS-based multimodal nonlinear optical microscopy. Arterioscler. Thromb. Vasc. Biol. **29**(9), 1342–1348 (2009)
39. R.S. Lim, A. Kratzer, N.P. Barry, S. Miyazaki-Anzai, M. Miyazaki, W.W. Mantulin, M. Levi, E.O. Potma, B.J. Tromberg, Multimodal CARS microscopy determination of the impact of diet on macrophage infiltration and lipid accumulation on plaque formation in ApoE-deficient mice. J. Lipid Res. **51**(7), 1729–1737 (2010)
40. S. Liang, A. Saidi, J. Jing, G. Liu, J. Li, J. Zhang, C. Sun, J. Narula, Z. Chen, Intravascular atherosclerotic imaging with combined fluorescence and optical coherence tomography probe based on a double-clad fiber combiner. J. Biomed. Opt. **17**(7), 070501 (2012)
41. R.A. Baldewsing, J.A. Schaar, C.L. de Korte, F. Mastik, P.W. Serruys, A.F. van der Steen, Intravascular ultrasound elastography: a clinician's tool for assessing vulnerability and material composition of plaques. Stud. Health Technol. Inform. **113**, 75–96 (2005)
42. C.L. de Korte, A.F. van der Steen, Intravascular ultrasound elastography: an overview. Ultrasonics **40**(1–8), 859–865 (2002)
43. C.L. de Korte, M.J. Sierevogel, F. Mastik, C. Strijder, J.A. Schaar, E. Velema, G. Pasterkamp, P.W. Serruys, A.F. van der Steen, Identification of atherosclerotic plaque components with

intravascular ultrasound elastography in vivo: a Yucatan pig study. Circulation **105**(14), 1627–1630 (2002)
44. J.D. Allen, K.L. Ham, D.M. Dumont, B. Sileshi, G.E. Trahey, J.J. Dahl, The development and potential of acoustic radiation force impulse (ARFI) imaging for carotid artery plaque characterization. Vasc. Med. **16**(4), 302–311 (2011)
45. J. Rogowska, N.A. Patel, J.G. Fujimoto, M.E. Brezinski, Optical coherence tomographic elastography technique for measuring deformation and strain of atherosclerotic tissues. Heart **90**(5), 556–562 (2004)
46. W. Qi, R. Chen, L. Chou, G. Liu, J. Zhang, Q. Zhou, Z. Chen, Phase-resolved acoustic radiation force optical coherence elastography, J. Biomed. Opt. **17**, 110505 (2012)
47. R. Virmani, A.P. Burke, A. Farb, F.D. Kolodgie, Pathology of the unstable plaque. Prog. Cardiovasc. Dis. **44**(5), 349–356 (2002)
48. L. Landini, L. Verrazzani, Spectral characterization of tissues microstructure by ultrasounds – a stochastic approach. IEEE Trans. Ultrason. Ferroelectr. Freq. Control. **37**(5), 448–456 (1990)
49. S.W.E. van de Poll, C.L. de Korte, A.F.W. van der Steen, G.J. Puppels, A. van der Laarse, Coronary atherosclerotic plaque characterization using IVUS elastography and Raman spectroscopy, in 2000 I.E. Ultrasonics Symposium. Proceedings. An International Symposium (Cat. No.00CH37121)|2000 I.E. Ultrasonics Symposium. Proceedings. An International Symposium (Cat. No.00CH37121), 10.1109/ULTSYM.2000.921666 (2000)
50. A.F. Low, G.J. Tearney, B.E. Bouma, I.K. Jang, Technology insight: optical coherence tomography – current status and future development. Nat. Clin. Pract. Cardiovasc. Med. **3**, 154–162 (2005)
51. A. Sukiennik, M. Radomski, M. Rychter, J. Kubica, Usefulness of optical coherence tomography in the assessment of atherosclerotic culprit lesions in acute coronary syndromes. Comparison with intravascular ultrasound and virtual histology. Cardiol. J. **15**, 561–566 (2008)
52. P.M. Patel, Z. Chen, When the doctor needs an engineer to be the matchmaker. EuroIntervention **8**(1), 19–23 (2012)
53. L. Raber, J.H. Heo, M.D. Radu, H.M. Garcia-Garcia, G.G. Stefanini, A. Moschovitis, J. Dijkstra, H. Kelbaek, S. Windecker, P.W. Serruys, Offline fusion of co-registered intravascular ultrasound and frequency domain optical coherence tomography images for the analysis of human atherosclerotic plaques. EuroIntervention **8**(1), 98–108 (2012)
54. M.A. Calfon, C. Vinegoni, V. Ntziachristos, F.A. Jaffer, Intravascular near-infrared fluorescence molecular imaging of atherosclerosis: toward coronary arterial visualization of biologically high-risk plaques. J. Biomed. Opt. **15**(1), 011107 (2010)
55. P. Libby, Inflammation in atherosclerosis. Nature **420**(6917), 868–874 (2002)
56. B.L. Kietselaer, C.P. Reutelingsperger, G.A. Heidendal, M.J. Daemen, W.H. Mess, L. Hofstra, J. Narula, Noninvasive detection of plaque instability with use of radiolabeled annexin A5 in patients with carotid-artery atherosclerosis. N. Engl. J. Med. **350**(14), 1472–1473 (2004)
57. J. Su, J. Zhang, L. Yu, Z. Chen, in vivo three-dimensional microelectromechanical endoscopic swept source optical coherence tomography. Opt. Express **15**, 10390–10396 (2007)
58. J. Ophir, I. Cespedes, H. Ponnekanti, Y. Yazdi, X. Li, Elastography: a quantitative method for imaging the elasticity in biological tissues. Ultrason. Imaging **13**, 111–134 (1991)
59. K.J. Glaser, A. Manduca, R.L. Ehman, Review of MR elastography applications and recent developments. J. Magn. Reson. Imaging **36**(4), 757–774 (2012)
60. J.A. Schaar, C.L. de Korte, F. Mastik, C. Strijder, G. Pasterkamp, E. Boersma, P.W. Serruys, A.F.W. van der Steen, Characterizing vulnerable plaque features with intravascular elastography. Circulation **108**(21), 2636–2641 (2003)
61. P.-F. Zhang, H.-J. Su, M. Zhang, J.-F. Li, C.-X. Liu, S.-F. Ding, Y. Miao, L. Chen, X.-N. Li, X. Yi, Y. Zhang, Atherosclerotic plaque components characterization and macrophage infiltration identification by intravascular ultrasound elastography based on b-mode analysis: validation in vivo. Int. J. Cardiovasc. Imaging **27**(1), 39–49 (2011)

62. R.A. Baldewsing, J.A. Schaar, C.L. d. Korte, F. Mastik, P.W. Serruys, A.F.W. v.d. Steen, Intravascular ultrasound elastography: a clinician's tool for assessing vulnerability and material composition of plaques, in *Plaque Imaging: Pixel to Molecular Level*, ed. by J.S. Suri, C. Yuan, D.L. Wilson, and S. Laxminarayan (IOS Press, Washington DC, 2005), pp. 75–96
63. F. Prati, E. Arbustini, A. Labellarte, B. Dal Bello, L. Sommariva, M.T. Mallus, A. Pagano, A. Boccanelli, Correlation between high frequency intravascular ultrasound and histomorphology in human coronary arteries. Heart **85**(5), 567–570 (2001)
64. J.M. Schmitt, OCT elastography: imaging microscopic deformation and strain of tissue. Opt. Express **3**(6), 199 (1998)
65. J.F. Greenleaf, M. Fatemi, M. Insana, Selected methods for imaging elastic properties of biological tissues. Annu. Rev. Biomed. Eng. **5**, 57–78 (2003)
66. M. Fatemi, J.F. Greenleaf, Ultrasound-stimulated vibro-acoustic spectrography. Science **280**(5360), 82–85 (1998)
67. J. Zhang, B. Rao, L. Yu, Z. Chen, High-dynamic-range quantitative phase imaging with spectral domain phase microscopy. Opt. Lett. **34**(21), 3442–3444 (2009)
68. M. Razani, A. Mariampillai, C. Sun, T.W. Luk, V.X. Yang, M.C. Kolios, Feasibility of optical coherence elastography measurements of shear wave propagation in homogeneous tissue equivalent phantoms. Biomed. Opt.Express **3**(5), 972–980 (2012)
69. C. Li, G. Guan, X. Cheng, Z. Huang, R.K. Wang, Quantitative elastography provided by surface acoustic waves measured by phase-sensitive optical coherence tomography. Opt. Lett. **37**(4), 722–724 (2012)
70. G.W. Stone, A. Maehara, A.J. Lansky, B. de Bruyne, E. Cristea, G.S. Mintz, R. Mehran, J. McPherson, N. Farhat, S.P. Marso, H. Parise, B. Templin, R. White, Z. Zhang, P.W. Serruys, A prospective natural-history study of coronary atherosclerosis. N. Engl. J. Med. **364**(3), 226–235 (2011)
71. J.J. Wykrzykowska, G.S. Mintz, H.M. Garcia-Garcia, A. Maehara, M. Fahy, K. Xu, A. Inguez, J. Fajadet, A. Lansky, B. Templin, Z. Zhang, B. de Bruyne, G. Weisz, P.W. Serruys, G.W. Stone, Longitudinal distribution of plaque burden and necrotic core-rich plaques in nonculprit lesions of patients presenting with acute coronary syndromes. JACC Cardiovasc. Imaging **5**(3 Suppl), S10–S18 (2012)
72. J.A. McPherson, A. Maehara, G. Weisz, G.S. Mintz, E. Cristea, R. Mehran, M. Foster, S. Verheye, L. Rabbani, K. Xu, M. Fahy, B. Templin, Z. Zhang, A.J. Lansky, B. de Bruyne, P.W. Serruys, G.W. Stone, Residual plaque burden in patients with acute coronary syndromes after successful percutaneous coronary intervention. JACC Cardiovasc. Imaging **5**(3 Suppl), S76–S85 (2012)
73. S.J. Brener, G.S. Mintz, E. Cristea, G. Weisz, A. Maehara, J.A. McPherson, S.P. Marso, N. Farhat, H.E. Botker, O. Dressler, K. Xu, B. Templin, Z. Zhang, A.J. Lansky, B. de Bruyne, P.W. Serruys, G.W. Stone, Characteristics and clinical significance of angiographically mild lesions in acute coronary syndromes. JACC Cardiovasc. Imaging **5**(3 Suppl), S86–S94 (2012)
74. E.A. Sanidas, A. Maehara, G.S. Mintz, T. Kashiyama, J. Guo, J. Pu, Y. Shang, B. Claessen, G.D. Dangas, M.B. Leon, J.W. Moses, G.W. Stone, Y. Ueda, Angioscopic and virtual histology intravascular ultrasound characteristics of culprit lesion morphology underlying coronary artery thrombosis. Am. J. Cardiol. **107**(9), 1285–1290 (2012)
75. A.J. Lansky, V.G. Ng, A. Maehara, G. Weisz, A. Lerman, G.S. Mintz, B. De Bruyne, N. Farhat, G. Niess, I. Jankovic, D. Lazar, K. Xu, M. Fahy, P.W. Serruys, G.W. Stone, Gender and the extent of coronary atherosclerosis, plaque composition, and clinical outcomes in acute coronary syndromes. JACC Cardiovasc. Imaging **5**(3 Suppl), S62–S72 (2012)
76. P.A. Calvert, D.R. Obaid, M. O'Sullivan, L.M. Shapiro, D. McNab, C.G. Densem, P.M. Schofield, D. Braganza, S.C. Clarke, K.K. Ray, N.E. West, M.R. Bennett, Association between IVUS findings and adverse outcomes in patients with coronary artery disease: the VIVA (VH-IVUS in Vulnerable Atherosclerosis) Study. JACC Cardiovasc. Imaging **4**(8), 894–901 (2012)

77. A.V. Finn, Y. Chandrashekhar, J. Narula, Vulnerable plaques: from PROSPECT to prospects. . .. J. Am. Coll. Cardiovasc. Imaging **5**, 334–336 (2012)
78. G.W. Stone, A. Maehara, G.S. Mintz, The reality of vulnerable plaque detection. JACC Cardiovasc. Imaging **4**(8), 902–904 (2011)
79. J.L. Fleg, G.W. Stone, Z.A. Fayad, J.F. Granada, T.S. Hatsukami, F.D. Kolodgie, J. Ohayon, R. Pettigrew, M.S. Sabatine, G.J. Tearney, S. Waxman, M.J. Domanski, P.R. Srinivas, J. Narula, Detection of high-risk atherosclerotic plaque: report of the NHLBI Working Group on current status and future directions. JACC Cardiovasc. Imaging **5**(9), 941–955 (2012)
80. J. Narula, V. Dilsizian, From better understood pathogenesis to superior molecular imaging, and back. JACC Cardiovasc. Imaging **1**(3), 406–409 (2008)
81. E. Braunwald, Epilogue: what do clinicians expect from imagers? J. Am. Coll. Cardiol. **47**(8 Suppl), C101–C103 (2006)
82. D.H. Kusters, J. Tegtmeier, L.J. Schurgers, C.P. Reutelingsperger, Molecular imaging to identify the vulnerable plaque–from basic research to clinical practice. Mol. Imaging Biol. **14**(5), 523–533 (2012)
83. J.S. Suri, C. Kathuria, F. Molinari, *Atherosclerosis disease management* (Springer, London, 2011)
84. M.E. Brezinski, Current capabilities and challenges for optical coherence tomography as a high-impact cardiovascular imaging modality. Circulation **123**(25), 2913–2915 (2012)
85. B. Meier, Plaque sealing by coronary angioplasty. Heart **90**(12), 1395–1398 (2004)
86. J.J. Wykrzykowska, R. Diletti, J.L. Gutierrez-Chico, R.J. van Geuns, W.J. van der Giessen, S. Ramcharitar, H.E. Duckers, C. Schultz, P. de Feyter, M. van der Ent, E. Regar, P. de Jaegere, H.M. Garcia-Garcia, R. Pawar, N. Gonzalo, J. Ligthart, J. de Schepper, N. van den Berg, K. Milewski, J.F. Granada, P.W. Serruys, Plaque sealing and passivation with a mechanical self-expanding low outward force nitinol vShield device for the treatment of IVUS and OCT-derived thin cap fibroatheromas (TCFAs) in native coronary arteries: report of the pilot study vShield Evaluated at Cardiac hospital in Rotterdam for Investigation and Treatment of TCFA (SECRITT). EuroIntervention **8**, 945–954 (2012)
87. D.J. Kereiakes, A.M. Szyniszewski, D. Wahr, H.C. Herrmann, D.I. Simon, C. Rogers, P. Kramer, W. Shear, A.C. Yeung, K.A. Shunk, T.M. Chou, J. Popma, P. Fitzgerald, T.E. Carroll, D. Forer, D.C. Adelman, Phase I drug and light dose-escalation trial of motexafin lutetium and far red light activation (phototherapy) in subjects with coronary artery disease undergoing percutaneous coronary intervention and stent deployment: procedural and long-term results. Circulation **108**(11), 1310–1315 (2003)
88. M. Oberhoff, K.R. Karsch, Who wants his plaque sealed? Eur. Heart J. **24**(6), 494–495 (2003)
89. N. Carter-Monroe, S.K. Yazdani, E. Ladich, F.D. Kolodgie, R. Virmani, Introduction to the pathology of carotid atherosclerosis: histologic classification and imaging correlation, in *Atherosclerosis disease management*, ed. by J.S. Suri, C. Kathuria, F. Molinari (Springer, New York, 2011), p. 3

OCT in Dermatology

73

John Holmes and Julia Welzel

Keywords
Optical coherence tomography • Skin • Dermatology • Skin cancer • Basal cell carcinoma • Non-invasive diagnosis • Optical biopsy

73.1 Introduction

When the first OCT devices were developed in the 1990s, one of the first targets for the researchers was skin [1], simply because it is so easy to access. Even the first primitive devices produced images in which features such as the dermal/epidermal junction (DEJ) and sweat ducts could be easily discerned [2]. However, this early promise imaging skin has taken a long while to bear fruit, while ophthalmic OCT has become mainstream and adopted into the standard of clinical care. Why is this? For OCT to find commercial clinical application in dermatology, it must provide clear benefits to the clinician over and above current clinical practice.

In current practice, the clinician typically diagnoses skin conditions such as cancer in a two-step process: first, "clinical diagnosis" by trained eye, palpitation of the lesion, and use of a handheld liquid-contact magnifier ("dermatoscope") and then if the lesion is considered suspicious, a biopsy is taken: a sample of skin removed, preserved, sliced, and examined by a highly skilled histopathologist. Pathology is a highly developed science, and very detailed information regarding

Disclosures: The author Jon Holmes is an employee of Michelson Diagnostics Ltd., a commercial manufacturer of dermatological OCT instruments for scientific and clinical applications.

J. Holmes (✉)
Michelson Diagnostics Ltd, Orpington, UK
e-mail: jon.holmes@vivosight.com

J. Welzel
Klinikum Augsburg, Augsburg, Germany

© Springer International Publishing Switzerland 2015

W. Drexler, J.G. Fujimoto (eds.), *Optical Coherence Tomography*,
DOI 10.1007/978-3-319-06419-2_75

the disease can be extracted from study of the tissue structure and cells. The question for the clinician is: why should I use OCT? In ophthalmology, biopsy is not generally a possibility, so OCT provides a clear immediate benefit. For the dermatologist, OCT must provide enough new, accurate information beyond clinical diagnosis, which enables clinically important decisions to be made **without resorting to biopsy**. As it is easy to biopsy skin, and the pathology provides a lot of detail, this is a tough criterion to meet! On the other hand, a biopsy is invasive, needs a topical anesthesia, does not show dynamic changes, leads to scarring, and cannot be repeated at the same site again. It seems that the resolution available with OCT is unlikely to match what is available to the pathologist, but in practice, many clinical decisions do not require this degree of detail. The challenge for the OCT system developer is to provide just enough information for key clinical decisions to be quickly, reliably, and usefully made, in applications where avoiding biopsy is desirable.

Where might avoiding biopsy be useful? A biopsy involves cutting the skin and can therefore leave a scar, which is undesirable to patients for cosmetic reasons, or there may be clinical reasons connected with the patient's age and infirmity, the difficulty of the lesion site, or the patient's clinical history. Some skin conditions are "field" conditions in which a large area of skin is affected with multiple lesions; it is usually impractical to biopsy every one. Biopsy is not ideal for use in conjunction with noninvasive therapies such as topical creams or photodynamic therapy, because the whole point of using these therapies is to avoid cutting the skin and leaving scars. Finally, biopsy is by its nature a "sample" process in which the diagnosis is made of the tissue that is actually removed, and so there is significant risk that the biopsy could actually miss the diseased tissue or even entirely remove it leaving only healthy tissue behind which is nevertheless unnecessarily treated. Biopsy cannot map the edges of a tumor (except by a very time-consuming and laborious procedure called "Mohs micrographic surgery" [3]), so that when the tumor is treated, there is a danger that not all of it is removed, leading to a subsequent recurrence.

In all these cases, OCT imaging has the potential to provide clinical benefits above current practice of clinical diagnosis and biopsy. Efforts to develop suitable technology and validate it are discussed in the sections that follow below. There is a reason to be optimistic, as significant progress has been made in the last 2–3 years on technology and OCT image interpretation, resulting in use of OCT on a routine clinical basis at a few "early adopter" clinics [4].

73.2 Technology

The theory of OCT is described in detail in the first part of this book and to avoid repetition is not repeated here. However, it is instructive to consider certain design decisions that have direct impact on the clinical utility of OCT in dermatology.

73.2.1 Wavelength

Most OCT research in dermatology has been using the 1,300 nm band, which is convenient because of a good compromise between image resolution and depth penetration. At this wavelength, water absorption is restricted, and the scattering coefficient of tissue is such that imaging depths of 1 mm or more can be routinely achieved. In 2007, Carrion and coworkers compared images of excised tissue from animal models at 810 nm, 1,330 nm, and 1,570 nm [4]. They concluded that depth penetration increased with wavelength, but image detail and contrast was greater at shorter wavelengths, and 1,330 nm was a good compromise. In 2010 Drexler and coworkers compared in vivo images of skin, obtained at three wavelengths 800 nm, 1,000 nm, and 1,300 nm [5], and also concluded that 1,300 nm provides greater depth penetration with acceptable image detail and contrast. For most dermatology applications, depth penetration of at least 1 mm is desirable, and most dermatological researchers and OCT equipment manufacturers have preferred 1,300 nm.

73.2.2 Probe Design

There are several factors that are of key consideration in the design of OCT probes for dermatology. These relate both to imaging performance and, crucially, to ease of use in the hands of the dermatologist. Dermatology is a "high-throughput" clinical profession: a typical dermatologist will see literally thousands of patients per year and will meet the patient, examine the lesion, and make a clinical decision (or take a biopsy) in a matter of minutes. Also, nearly all patients come in an outpatient setting and are in the clinic only for a short time. This means that the scan itself must be very quick, otherwise the clinician and the patient will be inconvenienced and will refuse to take the time and trouble. It should also be remembered that patients will also have more than one lesion, and the lesions themselves can be sizeable – several cm diameter is not uncommon – and may require multiple scans to characterize.

Another requirement is that the probe should be easy to handle and lesions can be scanned in any desired location on the patient. Skin cancers are common on sites such as the earlobe, the cleft at the side of the nose, around the ocular depression, and on the eyelid itself. If these sites are not easily scanned, the utility of the scanner will be compromised for the clinician.

This then leads to the following basic requirements for the probe:

- Light, compact, easy to point at awkward locations.
- Scanning process must be quick and straightforward and cover a good portion of the lesion.
- Easy to clean, for hygiene reasons.
- Image resolution quality sufficient to show clinical features of diagnostic interest and with sufficient depth penetration.

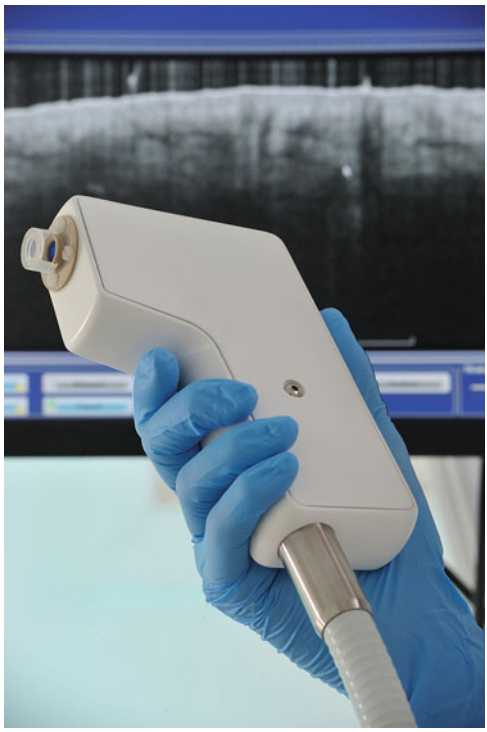

Fig. 73.1 Michelson Diagnostics VivoSight OCT probe

These requirements are to some extent in conflict. For example, high image resolution can be achieved by using a high-NA objective lens, but this reduces the field of view to 1–2 mm, which is often too small in comparison to the lesion diameter for efficient scanning. Also the high-NA lens may also be rather bulky, preventing access to crevices. In addition, the focal depth is reduced, so that it is only possible to scan to 1 mm + by mechanically adjusting the focus during the scan, increasing the time for the scan.

Commercial products have tackled these requirements with varying success. The first OCT product aimed specifically at skin applications was the time-domain OCT scanner "SkinDex" made by ISIS Optronics GmbH [6]. This is no longer available but features in many of the earlier clinical studies. Thorlabs has developed OCT scanners for scientific use based on Fourier-domain OCT [7], and these have been used by many research teams for feasibility studies, although they do not have regulatory clearance for medical use. In 2009 Michelson Diagnostics launched the VivoSight scanner [8] for dermatological applications (Fig. 73.1). This product has CE mark and FDA clearance for medical use and is gaining acceptance for routine clinical use as well as research applications. It has a relatively large field of view (6 mm scan width) and provides real-time images with a resolution of $<$7.5 μm to a depth of over 1 mm, in a compact probe package (Fig. 73.1, 73.2). This enables morphological features to be clearly discerned, but is not sufficient to show cells.

Also available are the Agfa SKINTELL [9], which has CE mark, and LLTech Light-CT [10], which is aimed at scanning excised biopsy samples. They both feature high-NA objective lenses, potentially enabling visualization of more clinical detail, but at the expense of being quite bulky.

The rapid growth of installed commercial scanners will surely lead to growth in the number of research publications supporting a wide variety of clinical applications.

73.2.3 Polarization-Sensitive OCT

An important constituent of skin tissue is collagen, which is highly birefringent. The collagen fibers themselves are very small and difficult to resolve optically unless very high-NA optics is used. Polarization-sensitive OCT has been studied for possible use in managing burns [21], because heat denatures the collagen, and studying dermal response to cosmetic treatments [22]. A difficulty is that the images are quite hard to interpret visually.

73.2.4 Doppler OCT and Speckle Variance OCT

The use of phase-sensitive OCT for detection and quantification of fluid flow, especially blood flow, has been widely studied. The theory of Doppler OCT is discussed in detail elsewhere in this book. For dermatologists, imaging blood flow has many advantages and potential applications. There are many clinical conditions, and treatments for them, in which inflammation occurs resulting in increased blood supply to the affected region. OCT could be of use to monitor the effects of the treatment by showing the reduction in blood flow.

In addition, some conditions result in abnormal blood vessel growth, such as port-wine stains, rosacea, and, perhaps most importantly, tumors. Thus, there is a clear clinical need to image blood vessels. Although these are visible in "ordinary" OCT images as dark streaks and have some diagnostic value, techniques that can highlight areas of flow and even quantify it would have more clinical value.

Doppler OCT is exquisitely sensitive, and some remarkably detailed images of blood vessel structures in skin have been obtained [11]. However, it suffers from two problems. The first of these is that it is almost too sensitive: even the tiniest motion of the subject with respect to the probe produces a huge background signal. The excellent images produced to date have been obtained by "clamping" the probe to the subject, which is not a clinically useful technique. While some work has been done on motion compensation, oversensitivity has so far prevented use of Doppler OCT in practical clinical instruments. A second problem is that by its nature Doppler OCT measures flow parallel to the interrogating beam, which is normally perpendicular to the skin surface, but most blood flow is at 90° to that. In the worst case, only vertically oriented blood vessels can be seen in the image.

More recently, a technique known as speckle variance OCT has been studied [12]. Here, the intensity variance between consecutive images of the same tissue is calculated, the idea being that stationary tissue produces a stationary invariant speckle pattern, whereas blood produces rapid changes. Very impressive images of the "arboreal" blood vessel structures produced by a basal cell carcinoma have recently been produced [13]. However, this approach also suffers from sensitivity to background subject motion, and more work is required. There is also a problem that unlike Doppler OCT, the rate of flow cannot be easily quantified from the speckle variance signal. This may or may not limit its clinical value.

Despite these limitations, it seems inevitable that with further development, blood-flow imaging with OCT will eventually reach the clinic in practical instruments for routine use, and the clinical benefits are potentially huge.

73.2.5 Elastography OCT

Elastographic OCT has also been studied [14, 15]. Here, a mechanical stimulus is applied to the skin and the response in the OCT image observed, for example, by detecting the change or movement in the laser speckle pattern in the image. Researchers claim that it is thereby possible to distinguish regions of the skin that have different Young's modulus, and this may have clinical applications.

73.2.6 Gels and Optical Clearing

Due to differences in the refraction between air and skin, the skin surface reflects at 1,300 nm and so there is typically a large "entrance signal" at the skin/air boundary. This is undesirable, because the bright reflection can wash out surface detail such as the thin stratum corneum, can saturate the detection electronics leading to artifacts, and reduces the "light budget" available for probing deeper into the tissue. There are various approaches to addressing this problem. One approach is to use a contact probe, i.e., the probe has a transparent surface that directly contacts the skin, so that there is no air/skin interface. For this to work well, a fluid such as water or ultrasound gel is typically used to ensure an airtight interface and for refraction index matching, because skin has a similar refraction index of about 1.33 compared to water.

Simply coating the skin with gel also has some benefit in reducing the entrance signal. On the other hand, a gel could modify the skin or confuse the viewer into thinking it is a feature of the skin itself. It remains to be seen whether clinical users feel that use of gel is worth the effort.

Vargas et al. reported that glycerol or other chemicals can have a beneficial effect in improving the depth penetration [16]. This is attributed to hydration of the tissue resulting in index matching. However, the effect takes time to have a useful effect and is unlikely to be adopted in busy dermatology clinics.

73.3 Image Interpretation

Although some features of the skin can be readily discerned such as sweat ducts, dermal/epidermal junction, etc., understanding of the presentation in OCT images of many common clinically important features is still developing and being studied. This is critical in order for the images to be used in the clinic on a routine basis. For example, it must be clearly understood not only how common pathologies such as basal cell carcinoma (BCC) nests present in the images but also similar but benign growths and variations of the most common types such as sclerodermiform BCCs. More generally, the principles behind how and why given tissue types appear as they do must be researched and understood. This is a topic of very active current study.

In general, OCT images reveal tissue morphology, but not details of individual cells (Fig. 73.2). In skin, we observe the following, based on detailed correlation with histology:

Intensity: Some tissue types appear brighter, others darker. Brighter tissue is more strongly scattering. Darker tissue is more weakly scattering and/or absorbing. Collagen-rich scar tissue is often brighter in appearance. In addition, some features like keratosis or calcification can cast shadows on the tissue below them. Blood and lymphatic vessels are usually dark due to the absorption by water.

Layers: Skin is a layered structure and these layers can often be discerned, especially the dermal/epidermal junction. Distortion of layers or damage to or absence of layer junctions can be strongly indicative of disease.

Shapes: Dermatological appendages such as hair follicles and sebaceous glands can be identified by their shape, coupled with intensity. This also applies to diseased tissue. For example, basal cell carcinomas typically present as dark ovoid features with a slightly darker rim, whereas cysts are typically circular with a bright wall. Vessels appear as dark streaks.

Texture: Different tissue types exhibit characteristic textures. Cancerous tissue is usually devoid of texture; healthy tissue is often mottled in appearance. Scar tissue has a swirly appearance.

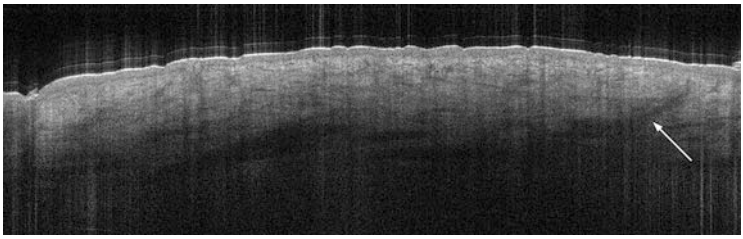

Fig. 73.2 OCT image of healthy skin at the forearm. The first superficial layer is the epidermis. The dermis shows signal poor longish or round structures corresponding to lymphatic and blood vessels. Hair follicles cross the dermis in an oblique way (*arrow*). Image size 6 × 1.9 mm (This and all other images in this chapter were obtained using a VivoSight OCT scanner)

Location: The location of features can also have diagnostic value. Dark streaks suggestive of blood vessels located unusually near the surface and close to an ovoid structure may well indicate a tumor.

These and other indicative features have been documented in an "OCT Manual" published by Michelson Diagnostics with contributions from leading dermatologists and freely available on the Internet [17].

73.4 Applications of OCT in Dermatology

73.4.1 Publications

The availability of practical commercial products with CE and FDA clearance for clinical use is rapidly driving up the publication of research papers in dermatology. Figure 73.3 shows the number of papers referencing "optical coherence tomography" and "skin" indexed by PubMed [18] in a search on 30th December 2013 and categorized by the authors based on choice of publication journal, paper title, and abstract. Papers were categorized as follows:

1. "Technology" papers – the primary subject of the paper is OCT technology itself: engineering, theory, and analysis of the OCT images. These papers are mostly published in technical journals. Only papers that specifically reference skin as the target end user application have been included in the analysis, and papers that merely used skin as a convenient test subject for a new OCT development were excluded.

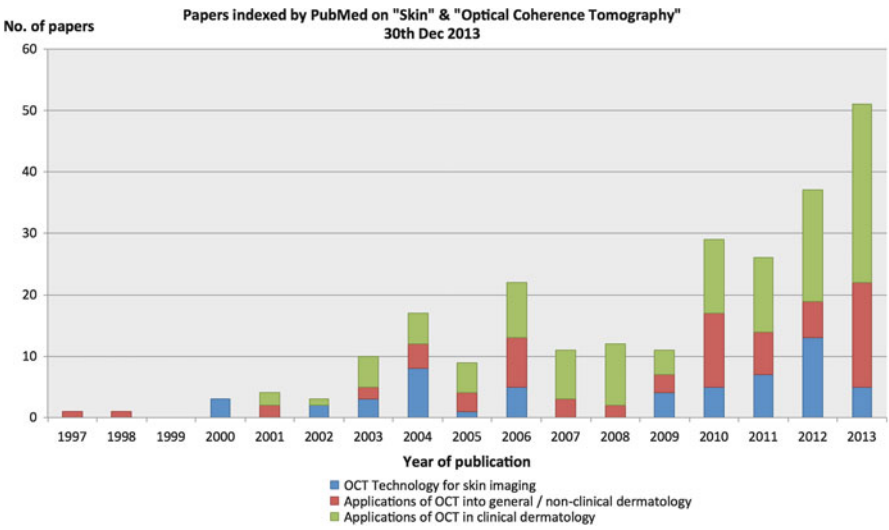

Fig. 73.3 OCT publications in dermatology by year of publication and type

2. General/nonclinical dermatology papers – the primary subject of the paper is the research into skin and skin properties using OCT as a tool. This includes papers studying the structure and properties of normal skin and also nonclinical applications such as cosmetics research and research into drug delivery.
3. Clinical dermatology papers – the primary subject of the paper is research into skin pathology and/or the application of OCT to diagnosis, mapping, or monitoring of treatments of skin pathologies. These papers are all published in clinical journals.

73.4.2 Analysis

In total, 247 papers were indexed since 1997, and the number is continuing to grow at an encouraging rate. This is a larger number than in most other clinical specialties except ophthalmology and cardiovascular (see also ▶ Chap. 84, "OCT Technology Transfer and the OCT Market" by Eric Swanson in this book) and is an indication that OCT is gaining acceptance as a practical and useful imaging modality by dermatologists.

The first papers, published in 1997 and 1998 by Welzel and coworkers, describe the appearance of healthy skin in OCT and show some exemplary images of diseased skin [1, 2]. This was followed by papers in 2000 [19] in which Knuttel and coworkers described the use of OCT to measure skin parameters such as the thickness of the stratum corneum and scattering coefficient of tissue layers. In 2001 enough data had been collected to enable J. Welzel to publish a review paper mentioning potential clinical applications including diagnosis of skin diseases and monitoring of treatment effects [20].

Publications increased gradually in the following years but have increased more sharply since 2010 as dermatologists started applying OCT in more systematic fashion to both clinical and nonclinical applications. These are discussed in more detail below.

73.4.3 Tissue Engineering

Tissue engineering is concerned with the development of artificially grown sections of tissue for use in the repair of damaged human tissue, for example, bone cartilage. In dermatology, one of the main potential applications is repair of wounds, especially diabetic ulcers, which are a huge burden on the world's health resources. OCT has potential use both for noninvasively monitoring the growth of the artificial tissue in the biofactories [21–23] and also, potentially, for monitoring the implanted tissue to assess its viability.

73.4.4 Transdermal Drug Delivery

Pharmaceutical companies are very interested in drug delivery mechanisms as alternatives to hypodermic syringes, for example, patches equipped with hollow microneedles

filled with a drug. The biomechanical interaction of the microneedles with skin tissue is critical to the correct operation of these devices and is an area where OCT can potentially help, by direct real-time imaging needle implantation process. For example, Donnelly and coworkers at University of Belfast have imaged soluble microneedles [24, 25].

73.4.5 Hair and Alopecia

OCT may have application on studying hair abnormalities and causes of alopecia. Bartels and coworkers showed that OCT can be used to noninvasively measure hair shafts on normal and hair affected by alopecia areata with discrimination [26]. Lademann and coworkers also studied the same technique as a method of screening for doping substances [27]. It is possible to image hair follicles, and OCT may prove to be of interest to companies studying hair shaving and hair removal products.

73.4.6 Tattoos

Tattoos are commonly treated with high-power laser pulses. There is potential for OCT to be used to image the tattooed skin pretreatment, in order to assess the depth of the pigment, so that the laser can be adjusted for maximum effect. This has been studied and considered feasible by Morsy and coworkers [28].

73.4.7 Planning and Monitoring Treatment of Vascular Complaints

Skin vascular conditions such as port-wine stains and rosacea are, like tattoos, commonly treated with pulsed laser. There is interest in using OCT to image the blood vessels pretreatment in order to determine their diameter and depth and then to image posttreatment to validate the effects of the laser therapy [29, 30]. As noted above, it is unlikely that these applications will develop into routine clinical procedures before blood-flow imaging based on Doppler or speckle variance OCT is developed in a commercially available product.

73.4.8 Cosmetic Treatments, Skin Ageing and Wrinkles

OCT has attracted some interest from companies developing cosmetic treatments for "rejuvenating" or temporarily ameliorating the apparent effects of skin ageing. 3D OCT can be used to obtain topographic maps of the skin surface with resolution of 10 μm or better. This is higher than is easily available from commercially available alternatives; however, these are much cheaper to buy and also have much larger field of view than is typically available from an OCT instrument. Of more interest is

measurement of epidermal thickness. The epidermis swells when hydrated, reducing wrinkle depth. OCT can be used to accurately measure epidermal thickness over time, thereby offering the researcher a means of quantitatively evaluating both the magnitude of the effect of a cosmetic treatment and how long it lasts.

73.4.9 Actinic Keratosis and Nonmelanoma Skin Cancer

OCT imaging of nonmelanoma skin cancer (NMSC) like squamous-cell carcinoma (SCC) with its precursors actinic keratosis (AK) and Bowen's disease as well as the most common type of NMSC, basal cell carcinoma (BCC), has been intensively studied. NMSC is a very common disease, mainly affecting elderly patients with pale skin complexion and a history of sun exposure. The lifetime risk for NMSC in this group of persons is about 30 %. The diagnosis by the naked eye is not always easy, because there are no marked changes in skin color or appearance. The skin shows in many cases of NMSC only a slight keratosis and induration. Using dermoscopy, more specific signs like "arboreal" vessels in BCC may lead to a correct diagnosis, but for confirmation or distinguishing from inflammatory skin reactions, it is frequently necessary to take a biopsy. Because sun damage is the main risk factor, the lesions start as solitary plaques but evolving within years into a so-called field cancerization where the whole epidermis within a region like the bald head exhibits malignant cells.

There are several alternatives to surgical treatment of NMSC. In AK, topical treatments for single lesions like laser therapy, cryotherapy, and curettage as well as application of diclofenac gel, imiquimod as an immune modulating agent, or photodynamic therapy for field cancerization are efficient. SCC and BCC can be treated as well with imiquimod or photodynamic therapy, but these noninvasive treatments are restricted to superficial lesions because of the limited penetration depth of the drugs. To choose the most suitable therapeutic regime and for control of clearance, it is imperative to determine the diagnosis, the tumor thickness, and the lateral borders of the lesion.

In OCT of AK, the stratum corneum is severely thickened, often with bright parallel lines corresponding to parakeratosis. The dermoepidermal junction can still be defined in in situ lesions with no infiltrative growth (Fig. 73.4). In contrast, SCC exhibits tumor conglomerates, which expand from the epidermis to upper parts of the dermis. The imaging of SCC is often disturbed by signal shadowing caused by hyperkeratosis.

BCC shows very typical findings in OCT (Fig. 73.5): There are sharply demarcated tumor nests with homogenous, epidermis-like signal distribution, deriving from the epidermis and surrounded by a small signal poor rim. This line is caused by scattering differences between palisading keratinocytes at the border of the tumor and the surrounding mucinous stroma. Superficial, nodular, cystic, or fibrotic subtypes of BCC can be distinguished using OCT. The lower border as well as lateral margins can be defined, because the homogenous signal intensity of the tumor differs from the healthy dermis with its irregular distribution of collagen, adnexal structures, and vessels [31–36].

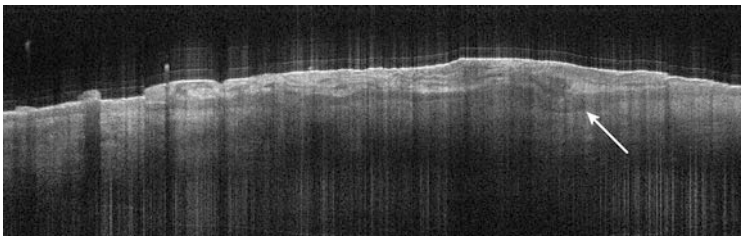

Fig. 73.4 Actinic keratosis at the cheek. The stratum corneum is severely thickened and composed of parallel bright lines. The dermoepidermal border is still detectable (*arrow*), leading to the conclusion that there is no invasive growth. Image size 6 × 1.9 mm

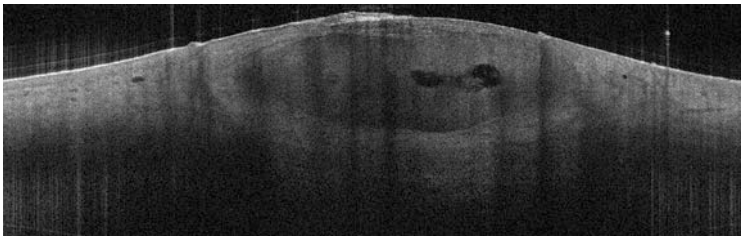

Fig. 73.5 Small nodular basal cell carcinoma at the back with a central cystic degeneration. Image size 6 × 1.9 mm

The capability of OCT to quickly and noninvasively aid the determination of the lesion thickness, lateral extent, and character is of particular value in the management of AK and NMSC. Potential applications of OCT to AK and NMSC include:

- Confirming the clinical diagnosis of BCC without needing to take a biopsy
- Deciding whether an AK lesion has developed into invasive SCC requiring more radical treatment than cryotherapy
- Determining whether a BCC is superficial and therefore will respond to noninvasive therapy or must be treated surgically
- Monitoring the progress and checking the final cure of NMSCs and AKs undergoing noninvasive treatments
- Targeting biopsies to the focal area of tumor
- Assessing the lateral extent of NMSCs prior to surgery

OCT is currently being routinely applied to these applications at a small but growing number of public clinics and commercial practises. In Germany, training courses in OCT image interpretation for professional dermatologists are available. More than 3,000 patients have been scanned by the end of 2013, and the number is set to rise rapidly in 2014 and beyond as the clinical experience, evidence, and the number of users build.

73.4.10 Melanoma Screening and Diagnosis

In principle, melanoma diagnosis is an attractive application for noninvasive optical diagnostic tools such as OCT. It is a fairly common potentially lethal disease and is very difficult to diagnose early, yet early diagnosis is critical for patient survival. Current practice involves visual assessment of pigmented lesions followed by dermoscopy and biopsy of suspicious lesions. The ratio of biopsies to actual diagnosed melanoma is quite high – typically 10:1 or 20:1 – so the burden of "unnecessary" biopsies on the national medical system is severe. Ideally, a noninvasive scan would detect suspicious lesions more effectively than visual techniques.

Unfortunately, this is a challenging task and not necessarily ideally suited to OCT. At the most commonly used imaging wavelength (1,300 nm), melanin is not a strong scatterer, and so it is difficult to pick out melanocytes in the OCT images, let alone identify malignancy. Additionally, the resolution is not high enough to distinguish single cells. Confocal laser microscopy has a higher resolution and is already well established for noninvasive imaging of nevi and malignant melanomas. Initial feasibility studies using OCT for diagnosis of pigmented lesions have not been altogether encouraging. From the point of view of the clinician, the diagnostic capability of OCT depends on whether its capability to image tissue morphology alone (as opposed to cells) has sufficient discriminatory power. In 2007, Gambichler and coworkers studied images from 75 patients with 51 benign nevi (BN) and 40 malignant melanomas (MM) [37]. They identified morphological features of MM not present in BN including marked architectural disarray, diffuse patchy reflectivity of the reticular dermis, and "icicle-shaped" structures. However, for OCT to be adopted into clinical use, these and other features would have to be shown to have high sensitivity and specificity in a large patient cohort.

However, OCT may have a role, for example, to accurately measure the thickness of suspicious lesions (melanomas with invasion below 1 mm depth have much worse prognosis and are treated differently from superficial or "in situ" lesions) as a guide to treatment (Fig. 73.6).

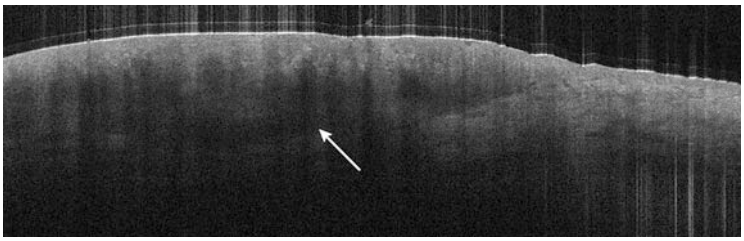

Fig. 73.6 Malignant melanoma at the abdomen. The tumor shows an irregular signal distribution with bright signals. The lower border of the tumor is detectable (*arrow*). Image size 6 × 1.9 mm

73.4.11 Wound Assessment and Monitoring of Healing, Including Trauma and Burns

As mentioned above, polarization-sensitive OCT (PS-OCT) has potential application in assessment of burns. Burn thickness is difficult to assess and is clinically important for the prognosis of the healing process and the decision to treat. If a burn is too deep, the skin will not regrow. In 2008, Todorovic and coworkers developed a PS-OCT probe and tested it by measuring burn thickness on a porcine model and reported excellent agreement with histology [38]. More recently, Kim and coworkers studied PS-OCT scans of two pediatric patients [39]. They reported that superficial burns exhibited the same layered structure as healthy tissue but with more visible vasculature and reduced birefringence and deep burns showed loss of layered structure, absent vasculature, and further reduced birefringence. They concluded that these parameters could be used for noninvasive assessment of burns.

These results are encouraging, although there are some practical issues to consider. Ideally, the OCT probe should not contact the wound, to minimize infection and collateral damage to the healing process. However, imaging without contact to maintain steadiness and adjust the focus distance is not easy. Secondly, serious burns are often large-area effects, and an OCT scan cannot usually capture the whole area of damage, risking an incorrect diagnosis. It therefore remains uncertain whether OCT will compete with other emerging optical techniques [40].

There is also potential for use of OCT to monitor wound healing, by imaging inflammation, by regrowth of the epidermis and the vasculature [41], and with tissue-engineered implants. Wang and coworkers reported use of OCT on a murine model in which OCT was able to delineate the epidermis, the implant, inflammation and reepithelialization, and finally resorption of the implant [42]. The above limitations for burns also apply to this application.

73.4.12 Psoriasis

One of the main symptoms of psoriasis is the development of skin "plaques" with thickened epidermis. In principle, OCT could be used to study the severity of the disease by imaging and measurement of the epidermis (Fig. 73.7). This was studied by Welzel et al. and Morsi et al. [43, 44]. Similar results were reported by Phillips et al. [45]. However, it is not clear whether there is a strong clinical need for this, except perhaps to assist development of the effects of therapies [46].

A potentially exciting application of OCT is in the early assessment and detection of psoriatic arthritis (PsA). PsA is a debilitating disease of the joints that can develop in psoriasis sufferers, and there is currently no test except for the symptoms of joint pain. It is treatable with drugs, but it is highly desirable to detect early to prevent its development and loss of quality of life for the sufferer. A paper by Castillo-Gallego et al. [47] studied the potential for OCT to detect PsA by imaging fingernails of psoriasis sufferers. In their study, 290 fingernails from 17 patients (4 with Ps, 13 with PsA) and 12 healthy controls were imaged and

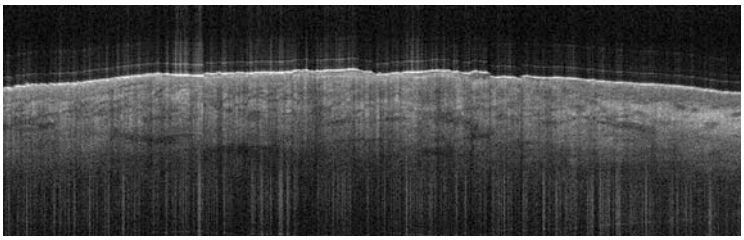

Fig. 73.7 A psoriatic plaque at the chest. The stratum corneum is slightly thickened. The epidermis shows an acanthosis with an irregular border to the dermis, corresponding to papillomatosis. Image size 6 × 1.9 mm

the images assessed in a blinded analysis. They reported good correlation between the blinded assessment of OCT images and clinical assessment. Further work is required to determine if there is predictive value for PsA.

73.4.13 Onychomycosis

Onychomycosis is a very common fungal disease of the nails. It is mainly treated topically and more recently with pulsed thermal laser. It is difficult to distinguish from other conditions such as psoriasis or lichen planus. OCT may have a role in diagnosis and monitoring efficacy of treatment. Abuzahra and coworkers imaged 18 patients of which 10 had fungal nail disease, 2 psoriasis, 1 lichen planus, and 5 controls and reported that OCT detected fungal elements in all 10 afflicted patients via the appearance of highly scattering elongated structures inside the nail plate [48]. This finding was recently confirmed by Nandanan and coworkers [49]. Sattler et al. compared different diagnostic methods for onychomycosis and found OCT to be inferior to confocal microscopy regarding specificity [50].

73.4.14 Scleroderma

Scleroderma is a debilitating autoimmune disease, producing changes in the skin, blood vessels, muscles, and internal organs. Symptoms include changes to the skin. Abignano et al. reported that the OCT images of 66 skin regions in 22 patients showed loss of the hyporeflective epidermal layer and the loss of clear visualization of the epidermal junction and have potential application as a surrogate outcome measure in intervention studies or as predictive of skin involvement in systemic sclerosis [51].

73.4.15 Blood Glucose Monitoring

OCT is just one of many optical techniques that have been studied in relation to blood glucose measurement for the potential application to diabetes patients.

As early as 2002, Larin et al. reported a pilot study, which showed promise [52]. This and subsequent studies attempted to determine changes in blood glucose from the attenuation coefficient of light in skin. The idea is that blood glucose strongly affects this parameter – seen as the "slope" of the OCT signal with depth. These findings were repeated by other groups [53]. Despite these findings, OCT has yet to emerge as a viable technique for blood glucose monitoring, perhaps because of the size of the equipment compared to many other approaches that are being developed.

73.5 Conclusions

The sheer number of different applications of OCT explored by researchers is indicative of the power of the technique. Over the past decade, studies have developed from preliminary exploratory images to systematic and repeatable evaluations of OCT with clearly defined protocols for the diagnosis of diseases and monitoring of treatments. Coupled with this, great advances have been made in the understanding of OCT images. Practical commercial OCT instrument have been launched and obtained regulatory approval.

In a few areas, notably nonmelanoma skin cancer, this has resulted in actual use in dermatology clinics on a routine basis for the benefit of patients and a steady growth in the installed base. We can also expect further developments in the technology of commercial instruments: lighter, smaller probes, blood-flow visualization, and ever higher image resolution. However, it is clear that large-scale systematic multicenter trials will be required to establish OCT more firmly as a standard tool for the practicing dermatologist, and these have yet to be reported in the literature. To the author's knowledge, some of these are already in the pipeline, and we can therefore expect that OCT will be increasingly adopted by dermatologists in the coming years as an essential tool in their armory against skin disease.

There are some other noninvasive imaging methods like confocal laser microscopy and multiphoton tomography, which are competitors to OCT. Both have a higher resolution and are more valuable for diagnosis of pigmented lesions but at the expense of detection depth and field of view. Deeper parts of skin tumors or dermal skin diseases cannot be imaged, which is especially problematic for basal cell carcinomas. Therefore, OCT may be the best technology for diagnosis of nonmelanoma skin cancer and other nonpigmented lesions. Additionally, it may be interesting to combine the methods, i.e. OCT with multiphoton tomography [54] to get both overview and high resolution.

References

1. J. Welzel, E. Lankenau, R. Birngurber, R. Engelhardt, Optical coherence tomography of the human skin. J. Am. Acad. Dermatol. **37**(6), 958–963 (1997)
2. J. Welzel, E. Lankenau, R. Birngruber, R. Engelhardt, Optical coherence tomography of the human skin. Curr. Probl. Dermatol. **26**, 27–37 (1998)

3. F. Mohs, Chemosurgical treatment of cancer of the ear; a microscopically controlled method of excision. Surgery **21**(5), 605–622 (1947)
4. Michelson Diagnostics Ltd, Press release OCT dermatology training centre to be set up in Bonn, (June 2012), www.michelsondiagnostics.com
5. L. Carrion, M. Lestrade, Z. Xu, G. Touma, R. Maciedjko, M. Bertrand, Comparative study of optical sources in the near infrared for optical coherence tomography applications. J. Biomed. Opt. **12**(1), 014017 (2007)
6. A. Knüttel, S. Bonev, W. Knaak, New method for evaluation of in vivo scattering and refractive index properties obtained with optical coherence tomography. J. Biomed. Opt. **9**(2), 265–273 (2004)
7. Thorlabs GmbH. www.thorlabs.com/navigation.cfm?guide_id=2039. Accessed 16 Nov 2012
8. Michelson Diagnostics Ltd. www.michelsondignostics.com. Accessed 16 Nov 2012
9. Agfa Healthcare. www.agfahealthcare.com/global/en/main/products_services/dermatology/oct/skintell.jsp. Accessed 16 Nov 2012
10. LL Tech SAS. www.lltechimaging.com. Accessed 16 Nov 2012
11. B. Vakoc et al., Three-dimensional microscopy of the tumor microenvironment in vivo using optical frequency domain imaging. Nat. Med. **15**, 1219–1223 (2009)
12. M. A et al., Speckle variance detection of microvasculature using swept-source optical coherence tomography. Opt. Lett. **33**(13), 1530–1532 (2008)
13. C. Blatter et al., In situ structural and microangiographic assessment of human skin lesions with high-speed OCT. Biomed. Opt. Exp **3**(10), 2636–2646 (2012)
14. J. Schmitt, OCT elastography: imaging microscopic deformation and strain of tissue. Opt. Express **3**(6), 1990–211 (1998)
15. A. Grimwood, Elastographic contrast generation in optical coherence tomography from a localized shear stress. Phys. Med. Biol **55**(18), 5515 (2010)
16. G. Vargas, E.K. Chan, J.K. Barton, H.G. Rylander 3rd, A.J. Welch, User of an agent to reduce scattering in skin. Laser Surg. Med. **24**(2), 133–141 (1999)
17. Michelson Diagnostics Ltd. www.michelsondiagnostics.co/octmanualtopmenu.html. Accessed 16 Nov 2012
18. US National Library of Medicine/National Institutes of Health. www.ncbu.nlm.nih.gov/pubmed. Accessed 16 Nov 2012
19. A. Knüttel, Spatially confined and temporally resolved refractive index and scattering evaluation in human skin performed with optical coherence tomography. J. Biomed. Opt. **5**(1), 83–92 (2000)
20. J. Welzel, Optical coherence tomography in dermatology: a review. Skin Res. Technol. **7**(1), 1–9 (2001)
21. R. Schmitt, U. Marx, H. Walles, L. Schober, Structural analysis of artificial skin equivalents. Proc. SPIE OSA Biomed. Opt. **8091**, 80911Q (2011)
22. J.T. LaCroix, J. Xia, M.A. Heidekker, A fully automated approach to quantitatively determine thickness of tissue-engineered cell sheets. Ann. Biomed. Eng. **37**(7), 1348–1357 (2009)
23. L.W. Smith, M. Bonesi, R. Smallwood, S.J. Matcher, S. MacNeil, Using swept source optical coherence tomography to monitor the formation of neo-epidermis in tissue-engineered skin. J. Tissue Eng. Regen. Med. **4**(8), 652–685 (2010)
24. R.F. Donnelly et al., Optical coherence tomography is a valuable tool n the study of the effects of microneedle geometry on skin penetration characteristics and in-skin dissolution. J. Control. Release **147**(3), 333–341 (2010)
25. M. Garland, E. Caffarel-Salvador, K. Migalski, D. Wooflsomn, R. Donnelly, Dissolving polymeric microneedle arrays for electrically assisted drug delivery. J. Control. Release **159**(1), 52–59 (2012)
26. N.G. Bartels, I. Jahnke, A. Patelzt, H. Richter, J. Lademann, U. Blume-Peytavi, Hair shaft abnormalities in alopecia areata evaluated by optical coherence tomography. Skin Res. Technol. **17**(2), 201–205 (2011)

27. J. Lademann et al., Optical coherent tomography for in vivo determination of changes in hair cross section and diameter during treatment with glucocorticosteroids – a simple method to screen for doping substances? Skin Pharmacol. Physiol. **21**, 312–317 (2008)
28. H. Morsy, M. Mogensen, L. Thrane, G. Jemec, Imaging of intradermal tattoos by optical coherence tomography. Skin Res. Technol. **13**(4), 444–448 (2007)
29. F. Bazant-hegemark, I. Meglinkski, N. Kandamany, B. Monk, N. Stone, Optical coherence tomography: a potential tool for unsupervised prediction of treatment response for port-wine stains. Photodiagn. Photodyn. Ther. **5**(3), 191–197 (2008)
30. S. Zhao et al., Imaging port wine stains by fiber optical coherence tomography. J. Biomed. Opt. **15**(3), 036020 (2010)
31. T. Maier, M. Braun-Falco, R.P. Laubender, T. Ruzicka, C. Berking, Actinic keratosis in the en-face and slice imaging mode of high definition optical coherence tomography and comparison with histology. Br. J. Dermatol. **168**(1), 120–128 (2013)
32. T. Maier, M. Braun-Falco, T. Hinz, M.H.Schmid-Wendtner, T. Ruzicka, C. Berking, Morphology of basal cell carcinoma in high definition optical coherence tomography: en-face and slice imaging mode, and comparison with histology. J. Eur. Acad. Dermatol. Venereol. **27**(1), e97–104 (2013)
33. M. Mogensen, B.M. Nürnberg, L. Thrane, T.M. Jørgensen, P.E. Andersen, G.B. Jemec, How histological features of basal cell carcinomas influence image quality in optical coherence tomography. J. Biophotonics **4**(7–8), 544–551 (2011)
34. M. Mogensen, T.M. Joergensen, B.M. Nürnberg, H.A. Morsy, J.B. Thomsen, L. Thrane, G.B. Jemec, Assessment of optical coherence tomography imaging in the diagnosis of non-melanoma skin cancer and benign lesions versus normal skin: observer-blinded evaluation by dermatologists and pathologists. Dermatol. Surg. **35**(6), 965–972 (2009)
35. M. Mogensen, B.M. Nürnberg, J.L. Forman, J.B. Thomsen, L. Thrane, G.B. Jemec, In vivo thickness measurement of basal cell carcinoma and actinic keratosis with optical coherence tomography and 20-MHz ultrasound. Br. J. Dermatol. **160**(5), 1026–1033 (2009)
36. M. Mogensen, G.B. Jemec, Diagnosis of nonmelanoma skin cancer/keratinocyte carcinoma: a review of diagnostic accuracy of nonmelanoma skin cancer diagnostic tests and technologies. Dermatol. Surg. **33**(10), 1158–1174 (2007)
37. Gambichler et al., Characterization of benign and malignant melanocytic skin lesions using optical coherence tomography in vivo. J. Am. Acad. Dermatol. **57**(4), 629–637 (2007)
38. Todorovic et al., In vivo burn imaging using Mueller optical coherence tomography. Opt. Express **16**(14), 10279–10284 (2008)
39. Kim et al., In vivo imaging of human burn injuries with polarization-sensitive optical coherence tomography. J. Biomed. Opt. **17**(6), 066012 (2012)
40. M. Kaiser, A. Yafi, M. Cinat, B. Choi, A.J. Durkin, Noninvasive assessment of burn wound severity using optical technology: a review of current and future modalities. Burns **37**(3m), 377–386 (2011)
41. Y. Ferraq, D. Black, J. Theunis, S. Mordon, Superficial wounding model for epidermal barrier repair studies: comparison of erbium:YAG laser and the suction blister method. Lasers Surg. Med. **44**(7), 525–532 (2012)
42. Z. Wang, H. Pan, J. Liu, W. Chen, Y. Pan, Assessment of dermal would repair after collagen implantation with optical coherence tomography. Tissue Eng. C Meth. **14**(1), 35–45 (2008)
43. J. Welzel, M. Bruhns, H.H. Wolff, Optical coherence tomography in contact dermatitis and psoriasis. Arch. Dermatol. Res. **295**(2), 50–55 (2003)
44. Morsy et al., Optical coherence tomography imaging of psoriasis vulgaris: correlation with histology and disease severity. Arch. Dermatol. Res. **302**, 105–111 (2010)
45. Phillips et al., Dermal reflectivity determined by optical coherence tomography is an indicator of epidermal hyperplasia and dermal edema within inflamed skin. JBO Lett. **16**(4), 040503 (2011)
46. M.H. Zulfakar et al., In vivo response of GsdmA3Dfl/+mice to topically applied anti-psoriatic agents: effects on epidermal thickness, as determined by optical coherence tomography and H&E staining. Exp. Dermatol. **20**(3), 269–272 (2011)

47. Castillo-Gallego et al., A comparison of optical coherence tomography and clinical assessment of nail disease in psoriasis and Psoriatic Arthritis. Arthritis Rheum. **vol 63** (Suppl 10), 200 (2011)
48. F. Abuzahra et al., Pilot study: optical coherence tomography as a non-invasive diagnostic perspective for real time visualization of onychomycosis. Mycoses **53**(4), 334–339 (2009)
49. N. Nandanan, J. Fisher, D. Siegel, O. Markowitz, Optical coherence tomography imaging of onychomycosis, Poster presented at EADV (2012)
50. G. Rothmund, E.C. Sattler, R. Kaestle, C. Fischer C.J. Haas, H. Starz, J. Welzel, Confocal laser scanning microscopy as a new valuable tool in the diagnosis of onychomycosis – comparison of six diagnostic methods. Mycoses **56**(1), 47–55 (2013)
51. Abignano et al., Optical coherence tomography: a new imaging technique that allows detailed visualization of affected scleroderma skin [abstract]. Arthritis Rheum. **63**(Suppl 10), 705 (2011)
52. K. Larin, M. Motamedi, M.S. Eledrisi, R.O. Esenaliev, Noninvasive blood glucose monitoring with optical coherence tomography. Diabetes Care **25**(12), 2263–2267 (2002)
53. R. Kuranov et al., In vivo study of glucose-induced changes in skin properties assessed with optical coherence tomography. Phys. Med. Biol. **51**(16), 3885 (2006)
54. K. König, M. Speicher, R. Bückle, J. Reckfort, G. McKenzie, J. Welzel, M.J. Koehler, P. Elsner, M. Kaatz, Clinical optical coherence tomography combined with multiphoton tomography of patients with skin diseases. J. Biophotonics **2**(6–7), 389–397 (2009)

Dental OCT

74

Petra Wilder-Smith, Linda Otis, Jun Zhang, and Zhongping Chen

Keywords
Dental OCT • Oral • Dentistry • Dentin • Enamel • Pulp • Gingival tissue • Tooth decay • Caries • Erosion • Oral mucosa

The oral cavity is a diverse environment that includes oral mucosa, gingival tissues, teeth, and their supporting structures. Oral health is currently evaluated through three main avenues: visual/tactile examination, periodontal probing, and radiographic imaging. After the surfaces are dried with a gentle stream of air, visual examination of the teeth and surrounding soft tissue is completed. Clinicians tactically explore the surface hardness of teeth to detect dental caries while demineralization of the enamel and soft tissue inflammation are characterized by changes in visual characteristics. Probes are also placed between the soft tissue and tooth to assess periodontal health. Radiographs are used to determine the internal structural integrity of the teeth and alveolar bone. Although radiographs are highly sensitive for detecting regions of carious

P. Wilder-Smith
Beckman Laser Institute, University of California Irvine, Irvine, CA, USA
e-mail: pwsmith@uci.edu

L. Otis
Oncology and Diagnostic Sciences, University of Maryland School of Dentistry, Baltimore, MD, USA

J. Zhang
Department of Biomedical Engineering, The Beckman Laser Institute, University of California Irvine, Irvine, CA, USA

Z. Chen (✉)
The Edwards Life Sciences Center for Advanced Cardiovascular Technology, Beckman Laser Institute, Irvine, CA, USA

Department of Biomedical Engineering, The Beckman Laser Institute, University of California Irvine, Irvine, CA, USA
e-mail: z2chen@uci.edu

© Springer International Publishing Switzerland 2015

W. Drexler, J.G. Fujimoto (eds.), *Optical Coherence Tomography*,
DOI 10.1007/978-3-319-06419-2_76

demineralization and alveolar bone loss, they have several limitations. Since radiographs are two dimensional, precisely locating the position of a carious lesion or osseous defect is impossible. Radiographs cannot distinguish active from inactive disease and cannot identify periodontal disease until after bone loss has occurred. Finally, radiography uses harmful ionizing radiation and provides no information on soft tissue status.

Optical coherence tomography (OCT), a well-known technique for creating noninvasive, high-resolution (<20 μm) images of biological microstructure, has been used in dentistry. In vitro images of porcine dental tissues were first reported in 1998 [1]; subsequently in vivo imaging of human dental tissue proved that OCT could be used as a valuable diagnostic aid for several applications within dental medicine [2, 3]. The goal of dental OCT is to produce in vivo images of oral microstructure that can be used to make qualitative and quantitative assessments of oral tissues. In particular, OCT images depict at high resolution clinically important anatomical features such as the location of the soft tissue attachment, morphological changes in gingival tissue, tooth decay, enamel thickness and decay as well as structural integrity of dental restorations. Because OCT images both the hard and soft tissue structures of the oral cavity at high resolution, it offers the unique capacity to identify dental disease before destructive changes have progressed allowing for earlier intervention than is possible with current diagnostic modalities.

The oral cavity begins at the lips and ends posteriorly at the area of the palatine tonsils. This chapter will focus on the following structures within the oral cavity:

1. The hard dental tissues, i.e., the teeth.
2. The periodontal tissues, i.e., the supporting tissues for the teeth. These include soft tissues, as well as cementum, periodontal ligament, and bone.
3. The oral mucosa, i.e., the lining of the oral cavity.

This section will address all the anatomical structures within the oral cavity that are listed above. A brief review of normal oral structures will be followed by a summary of the pathologies affecting each structure, a discussion of existing diagnostic tools, and an overview of diagnostic usage of OCT in each structure to date. In the final section, the authors present their views on the potential use of OCT in dentistry in the future.

74.1 Hard Dental Tissues

74.1.1 Definition of Dental Hard Tissues

The tooth consists of enamel, dentin, and pulp (Fig. 74.1). The close relationship that exists during the formation of these three tissues is maintained in the structure of the tooth.

74.1.1.1 Enamel

Consisting of 95 % mineral, 1 % water, and 4 % organic material by weight [4], enamel is the hardest structure of the body. The inorganic content of enamel consists of a crystalline calcium phosphate known as hydroxyapatite, which is also found in bone, calcified cartilage, dentin, and cementum. Although the vast

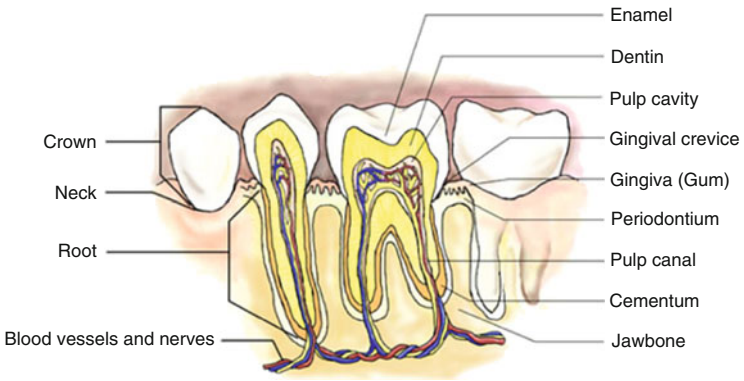

Fig. 74.1 Structure of tooth and periodontium (DeEtte M. DeVille, M.D. AMA atlas of the body: the teeth © Copyright 1999 American Medical Association)

majority of the enamel is occupied by densely packed hydroxyapatite crystals, a fine lacy network of organic material appears between the crystals. The bulk of this organic material is made up of the TRAP (tyrosine-rich amelogenin protein) peptide sequence tightly bound to the hydroxyapatite crystal as well as nonamelogenin proteins [4].

Because of its high mineral content, enamel is extremely hard and brittle. Ground sections of enamel reveal roughly rodlike cylindrical structures 4–6 um in diameter within the enamel, which owe their existence to a highly organized pattern of hydroxyapatite crystal orientation. For the most part, the long axes of the crystals run parallel to the longitudinal axis of the rod. This is particularly true for crystals along the central axis of the rod. Crystals more distant from the central axis, however, flare laterally to an increasing degree as they approach the rod periphery. The interrod region is an area surrounding each rod in which crystals are oriented in a different direction from those constituting the rod [4]. The capacity of OCT to image the orientation of the enamel rods and interrod region is illustrated in Fig. 74.2.

The enamel surface varies with age. In unerupted teeth, it consists of a structureless cuticle 0.5–1.5-um thick [4] overlying a 5-nm thick layer of small loosely packed crystallites interspersed with a few large platelike crystals and cuticular material [4]. This layer merges into the subsurface enamel, where 50-nm crystals are loosely packed. The subsurface layer forms the enamel surface due to rapid loss of the primary cuticle and the surface layer of small crystallites soon after eruption. An organic deposit called the salivary pellicle is present on the tooth surface, usually covered by a layer of dental plaque [4]. The important role of dental plaque in fostering dental decay will be discussed below.

74.1.1.2 Dentin-Pulp Complex

The dentin supports the enamel. The junction between the two tissues is a series of scallops where crystals of enamel and dentin intermix. Dentin and pulp are embryologically, histologically, and functionally the same tissue and are therefore

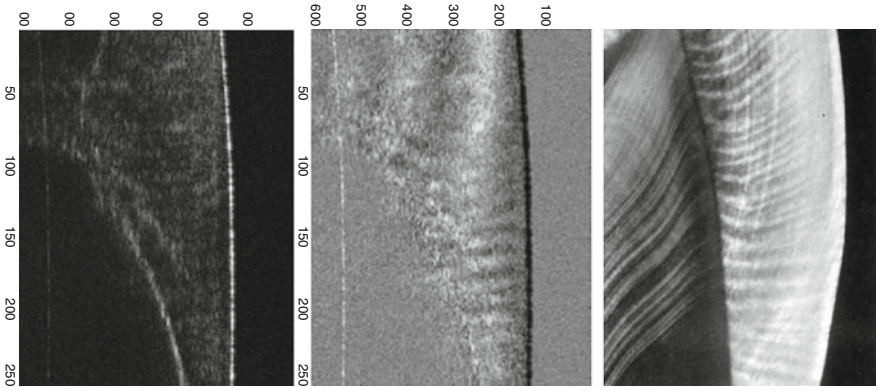

Fig. 74.2 Conventional and polarization-sensitive OCT images and a ground section of a human tooth reveal the superior capacity of polarization-sensitive OCT to image the orientation of the enamel rods and the interrod region. The junction between the enamel and dentin is characterized by a series of scallops where dentin and enamel intermix [6]

considered together here [5]. Mature dentin is, chemically, by weight, approximately 70 % inorganic material, 20 % organic material, and 10 % water (adsorbed onto the surface of the mineral or in interstices between crystals). The main inorganic component is hydroxyapatite; the main organic phase is type 1 collagen with fractional inclusions of glycoproteins, proteoglycans, phosphoproteins, and some plasma proteins. Approximately 56 % of the mineral phase is within the collagen. Due to its inorganic phase, dentin is slightly harder than bone and softer than enamel [5]. Physically, dentin has an elastic quality; it is bound to the enamel at the dentinoenamel junction and covered by cementum in the root of the tooth [5].

Forming the bulk of the tooth, dentin consists of multiple closely packed dentinal tubules traversing its entire thickness and containing the cytoplasmic extensions of odontoblasts that once formed the dentin and now maintain it. The cell bodies of these odontoblasts lie along the inner aspect of the dentin, where they also form the peripheral boundary of the dental pulp [5]. The dental pulp is the soft connective tissue occupying the pulp space in the central area of the tooth, which is divided into the coronal (upper) portion, the pulp chamber, and the lower portion, the root canal. The root canals end at the apical foramen, where the main blood vessels and nerves to the pulp enter and leave the tooth. Through the apical foramen, pathologies can migrate between the pulp and the periodontium [5].

Three types of dentin are recognized in human teeth [5]. The bulk of the tooth consists of primary dentin. The structurally somewhat less regular secondary dentin develops after root formation is complete. Tertiary dentin is produced in reaction to noxious stimuli such as decay or dental procedures and is very heterogeneous in its structure. Viewed microscopically, dentin consists of several structural features. Dentinal tubules are tapered structures approximately 2.5 um in diameter near the pulp, narrowing down to approximately 900 um near the dentinoenamel junction [5]. They extend through the entire thickness of the dentin from the

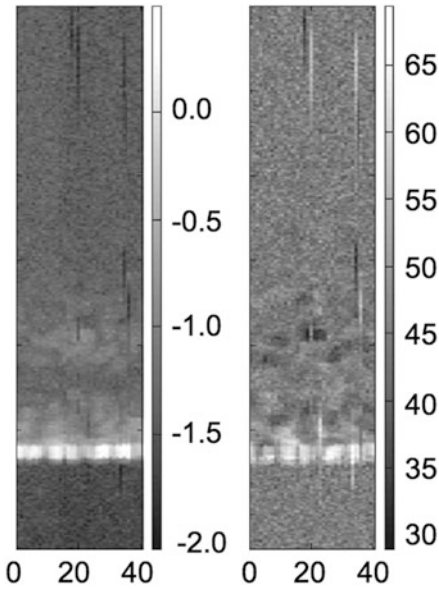

Fig. 74.3 OCT images of a human tooth near the DEJ reveal irregular masses of decreased signal intensity that were 10–20 μm in diameter and consistent with the morphology of interglobular dentin that can be seen in conventional and PS-OCT [6]

dentinoenamel junction to the pulp, following an S-shaped path. At their pulpal end, the tubules are generally thought to contain the process of an odontoblast bathed in dentinal fluid, although there is some uncertainty regarding the exact nature of tubule content [5]. The tubular structure of dentin permits the rapid progression of pathologies and accentuates the pulpal response to dentinal events [5]. It also allows for excellent light propagation into the pulp.

Within the dentinal tubule exits a hypermineralized (40 % more than regular dentin) ring of intratubular dentin causing a progressive reduction and the potential for eventual obliteration of the lumen of the tubule [5]. Exact mechanisms and causes are still uncertain. Intertubular dentin is located between the dentinal tubules and consists of a tightly woven network of type 1 collagen fibrils arranged roughly at right angles to the dentinal tubules, with apatite crystals deposited between and parallel to the fibrils. The ground substance consists of phosphoproteins, proteoglycans, and γ-carboxyglutamate [5]. Interglobular dentin consists of areas of unmineralized or hypomineralized dentin where zones of mineralization have failed to fuse. Here the normal architectural pattern of the tubules remains unchanged, except for the lack of intratubular dentin. The intraglobular dentin can be visualized in PS-OCT images of dentin (Fig. 74.3).

The dental pulp is the soft connective tissue that supports the dentin. Principal cells within the pulp include odontoblasts, undifferentiated mesenchymal cells, fibroblasts, macrophages, and other immunocompetent cells [5]. The major vessels and nerves lie in the central portion of the pulp. The principal collagen fibers of the pulp are type l and type lll collagen [5] in a glycosaminoglycan-, glycoprotein-, and water-containing ground substance.

74.1.2 OCT Imaging of the Hard Dental Tissues

Marked light scattering limits the transmission of visible light at 400–700-nm wavelengths through tooth substance. The relationship between light scattering in enamel and wavelength (λ) is defined as $1/\lambda^3$. At longer wavelengths exceeding 1,500 nm, light absorption by water becomes a limiting factor for the absorption of infrared (IR) light [6–8] Therefore, OCT imaging of the tooth is best performed at wavelengths between 700 and 1,500 nm, with excellent penetration to a depth of 1.5–3 mm. In 2000, Otis et al. demonstrated the superior imaging and penetration of OCT systems using a 1,310-nm vs. 850-nm light source [9].

In 1998, Colston et al. presented the first in vivo optical coherence tomography (OCT) images of dental tissue [1]. The authors presented a dental optical coherence tomography system with a very promising feature – the incorporation of the interferometer sample arm and transverse scanning optics into a handpiece suitable for intraoral use. Examples of use of this imaging system for dentistry illustrated its potential for diagnosis of periodontal disease, detection of caries, and evaluation of dental restorations. The average imaging depth of this system varied from 3 mm in hard tissues to 1.5 mm in soft tissues. Axial resolution was 15 μm (free space). The system had a lateral resolution of 50 μm and an average total lateral scan distance of 12 mm. The total scan time for each image was approximately 45 s. Further studies by this and other groups have clearly demonstrated the effectiveness of OCT for rapid, high-resolution imaging of dental tissues using OCT (please see the appropriate sections below).

Active work in the area of OCT probe development has greatly enhanced the applicability of OCT imaging for dental applications [10–20]. Figure 74.4 shows the schematic diagram and picture of a miniature probe based on a dual axis microelectromechanical system (MEMS) mirror [11]. The MEMS mirror provides high-speed, 2-axis scanning while occupying a very small volume with extremely low power consumption. The dimensions of the MEMS mirror in Fig. 74.4b are 800-mm diameter, and both axes are capable of scanning up to 30° angles at frequencies greater than 3 kHz with good linearity. The packaged probe with an outer diameter 5.0 mm or smaller can be assembled, which is sufficiently compact for dental applications (Fig. 74.4c).

The 2D MEMS probe shown in Fig. 74.4c has been used for in vivo imaging of animal models and human subjects. The representative in vivo 3D images from rabbit and human tissues are shown in Fig. 74.5. These images were acquired employing the FD-OCT system, which provides adequate imaging speed for 3D imaging.

In addition to side-viewing probes based on MEMS, forward-viewing probes based on cantilever-type scanning have been demonstrated by several groups [19–24]. The scanning probes are driven by either PZT, electrostatic, or magnetic force [19–24]. Recently, a forward-view OCT scanning probe based on a fiber-cantilever piezotube scanner was developed by using a semi-resonant scan strategy for a better scan performance (Fig. 74.6a) [20]. A cantilever weight was attached to the fiber cantilever to reduce the resonance frequency down to 63 Hz, well in the desirable range for FD-OCT. By driving the two axes at slightly different

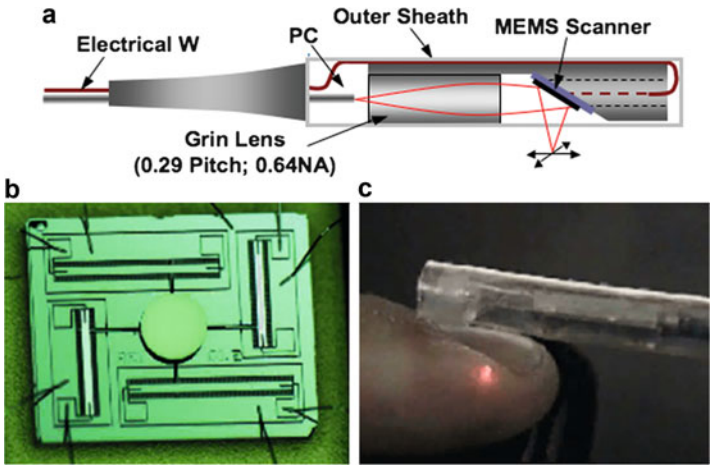

Fig. 74.4 (**a**) Schematic diagram of endoscopic probe; (**b**) photo of a vertical 2-D scanning MEMS based on comb-drive actuator. (**c**) photo of assembled 2-D miniature probe [11]

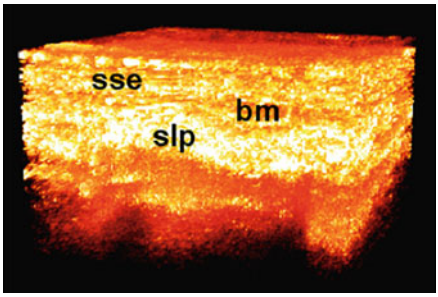

Fig. 74.5 In vivo 3D imaging of true human vocal cord obtained by a FD-OCT system using the 2D MEMS probe. Image size is 1 × 1 × 1.4 mm. Important structures, such as the stratified squamous epithelium (*sse*), basement membrane (*bm*), and superficial lamina propria (*slp*), are clearly visible

frequencies, a low-order Lissajous pattern was obtained for a 2D area scan (Fig. 74.6b). 3D OCT images were successfully acquired in an acquisition time of 1.56 s for a tomogram volume of 2.2 × 2.2 × 2.1 mm^3 (Fig. 74.6c).

These studies demonstrate the capabilities of a miniature probe for 3D OCT imaging. A 3D OCT system employing a high-speed, compact scanner may have the potential to expand the applications of OCT for dental and oral imaging and may revolutionize areas of clinical medicine as well as medical research.

74.1.3 Pathologies of Hard Dental Tissues

74.1.3.1 Decay

The most common pathological condition of the tooth is decay or caries. Cause is a confluence of cariogenic diet and inadequate oral hygiene on a susceptible tooth

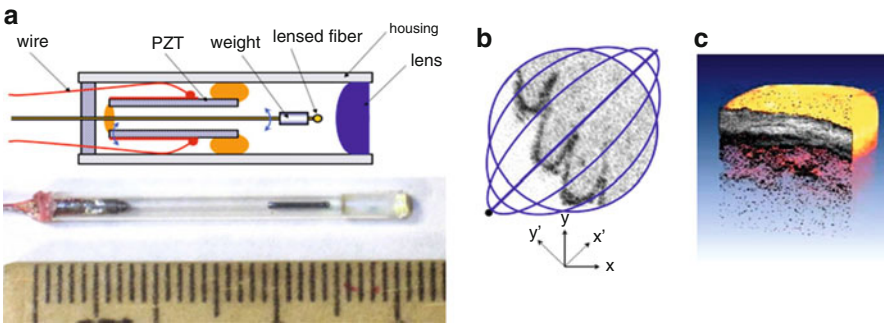

Fig. 74.6 (**a**) Schematic design and picture of the fabricated OCT scanning catheter. The dimensions are given in millimeters; (**b**) schematic Lissajous scan pattern (*blue lines*) in the XY plane laid over an OCT *en face* image; (**c**) the 3D-rendered tomogram [20]

surface. Microorganisms multiply at the tooth surface, forming a layer of plaque. These microorganisms produce lactic and acetic acid, reducing the pH to levels as low as 3.5. At lower pHs, hydroxyapatite becomes increasingly soluble, leading to rapid demineralization and increased porosity and permeability as the calcium bound to the hydroxyapatite is ionized and washed out by the saliva. Decayed or carious lesions usually are associated with a darkening in color. However, some carious enamel lesions appear bright at the surface, especially in their early stages and are thus difficult to detect [25]. An important characteristic of the early carious lesion is that most of the demineralization occurs at the subsurface level, so that a well-mineralized surface zone remains in place for some time. This has an important implication for the early detection of carious lesions, namely, the inability to detect early lesions by clinical visual inspection of the tooth surface alone.

Diagnostic confidence also has significant impact on whether the clinician chooses to initiate further preventive therapy or restorative intervention. When caries reach the dentin, the response is sequential. Frequently at this stage, the enamel is physically still grossly intact, and bacterial invasion has not occurred. However, the lesion has increased the permeability of enamel to acid and other chemical stimuli, which now evoke a response from the dentin-pulp complex such as the deposition of tertiary dentin. Once the enamel cavitates, bacteria reach the dentin surface, and destruction of dentin begins [26].

Current Methods for Diagnosis of Caries

The technologies currently available to dental clinicians for the detection of dental caries have limited sensitivity, and there is controversy surrounding the "gold standard" for caries diagnosis. Detection of pit and fissure caries by all current methods is low. While radiographs reveal approximal lesions with moderate sensitivity and high specificity, occlusal caries are grossly underestimated in radiographic examinations [27–29]. Moreover, the widespread use of fluorides has increased the diagnostic difficulty of pit and fissure caries because enamel remineralization conceals dentinal lesions that continue to progress [29, 30].

Recently, tactile examination with a sharp explorer has been discouraged, since this may produce breakdown of the enamel surface or transfer cariogenic organisms to unaffected sites. Moreover, probing does not increase diagnostic accuracy as compared with visual examination alone [31]. Thus, visual diagnosis has been suggested as the diagnostic method of choice for pit and fissure caries [32, 33]. Trained observers detect small pit and fissure lesions by visual examination with a sensitivity of 0.6 and a specificity of 0.8. This means that 40 % of true dentinal lesions are classified as sound and that 15 % of sound surfaces are classified as diseased. In populations with a low prevalence of caries, the disease usually progresses slowly. Thus, in low prevalence caries populations, traditional diagnostic techniques worked because it is better to err toward false-negative diagnoses than to restore a sound tooth. Limited sensitivity worked in classical operative approaches, because teeth were not restored until caries involvement was significant and then the restoration was extended to include all tooth structure in the vicinity that would be considered "susceptible to caries." Current therapies first employ preventive strategies when lesions are small and the caries risk is low. When the tooth surface is cavitated, caries significantly involve the dentin, or when caries risk is high, the diseased dentin is removed with minimal surrounding tooth structure. For today's dentistry, the sensitivity of traditional diagnostic methods is unacceptable. The materials and operative technology permit placement of small restorations with removal of only the diseased dentin and a minimal amount of sound tooth structure. The success of these minimally invasive operative approaches depends on locating the precise region of active caries and determining with certainty that the remaining tooth structure is caries free [33]. A more precise caries diagnostic method would greatly improve the current standard of dental preventive and restorative care, with a major impact on dental health care delivery [34].

Dentists continue to rely primarily on visual and tactile examination, supported by radiographic data. However, early detection of demineralization and quantification of tooth substance loss using these techniques is extremely difficult, so that dental erosions are usually diagnosed at a relatively advanced stage when substantial irreversible enamel loss has occurred.

OCT Diagnosis of Caries

Studies indicate that OCT is a powerful technique for detecting subsurface changes in the material properties of dental tissues. OCT reliably identifies changes in dentin under sealants and adjacent to the margins of composite restorations. Comparing OCT profiles over time should allow clinicians to quickly detect potential sites of disease progression or monitor the results of remineralization therapy. Most groups have taken one of two approaches to use OCT for the detection and assessment of dental caries, using either conventional time-domain OCT or polarization-sensitive OCT.

Conventional Time-Domain OCT

Amaechi et al. [35] described the quantitative assessment of dental caries using A-scans (depth versus reflectivity curve), B-scans (longitudinal images), and C-scans (transverse images at constant depth). While the B- and C-scans

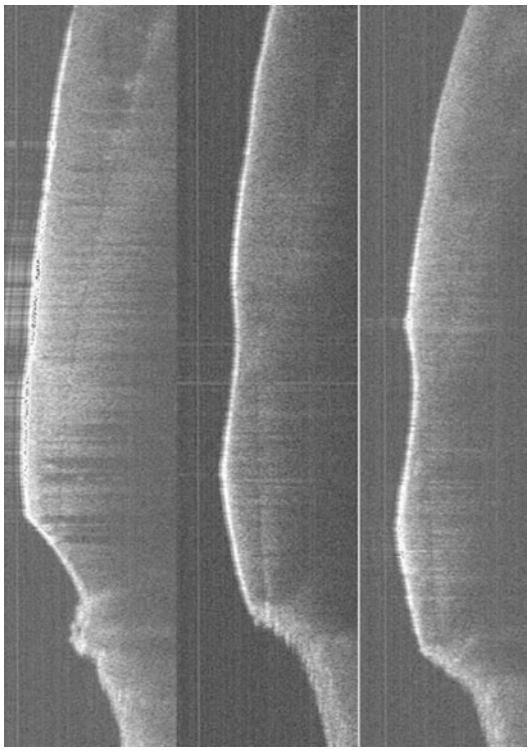

Fig. 74.7 The three OCT images show baseline enamel thickness following two five-minute exposures to a cola beverage (Otis unpublished data)

qualitatively described the lesion detected, the A-scan which showed the depth-resolved reflectivity (dB) of the tooth tissue was used for the quantitative analysis. The percentage reflectivity loss ($R_{\%}$) in demineralized tissue, which related to the amount of mineral loss, increased with greater demineralization time. It was concluded that, using this approach, OCT could quantitatively monitor the mineral changes in a caries lesion on a longitudinal basis. In a later paper, the same group confirmed this correlation using QLF (quantitative light-induced fluorescence) [36].

A novel approach by Ko et al. combined optical coherence tomography (OCT) and Raman spectroscopy to provide morphological information and biochemical specificity for detecting and characterizing incipient carious lesions found in extracted human teeth [37]. OCT imaging of tooth samples demonstrated increased light backscattering intensity at sites of carious lesions as compared to the sound enamel (Fig. 74.7). Using Raman microspectroscopy and fiber-optic-based Raman spectroscopy to characterize the caries further, they demonstrated excellent potential for a new fiber-optic diagnostic tool enabling dentists to identify early caries lesions with greater sensitivity and specificity. In a follow-up study, Sowa et al. compared the caries diagnostic capabilities of the A-scan intensity, the OCT attenuation coefficient as well as the mean and standard deviation of the lognormal fit to the histogram of the A-scan ensemble. The OCT attenuation coefficient showed the highest discriminatory capacity. However, direct analysis of the

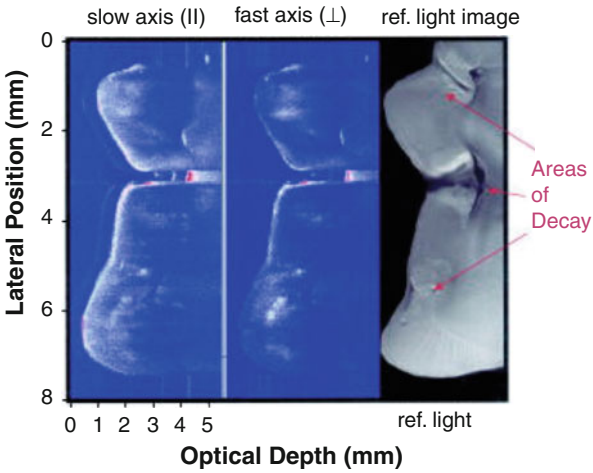

Fig. 74.8 Slow and fast axis OCT scans across the top of a third molar with occlusal decay. The reflected light image of the tooth section is shown on the right for comparison. All three carious areas are resolved in the OCT images with very strong scattering (*red*) in the base of the fissure shown in the *center*. The intensity varies from –40 to 10 dB with intensities of less than –39 dB demarcated in *blue* and those of intensity greater than 5 dB in *red* [43]

A-scans or the histogram of A-scan intensities also showed good diagnostic discrimination [38].

The capability of OCT for early detection and evaluation of root caries was described by Amaechi et al. [39]; its potential for detecting and mapping deficient restorations was also demonstrated by de Mello et al. [40].

Polarization-Sensitive OCT

Birefringence of dentin and enamel provides PS-OCT with a contrast agent useful in indicating pre-carious or carious lesions [31]. PS-OCT can provide additional information related to the mineralization status and/or the scattering properties of the dental materials (Fig. 74.8). Several authors have described the use of PS-OCT for detection and diagnosis of demineralization and dental caries [41–46].

74.1.3.2 Dental Erosion, Attrition, Abrasion, and Cracking

Erosion is defined as the progressive loss of hard dental tissue by chemical processes not involving bacterial action. Repeated or prolonged exposure of teeth to acid leads to selective dissolution of specific components of the tooth surface, with eventual loss of tooth substance, hypersensitivity, caries, functional impairment, and even tooth fracture. The critical pH for enamel dissolution is 5.5. It is estimated up to 80 % of children and over 40 % of adults demonstrate substantial loss of tooth substance, an increasing proportion of which may be related to dental exposure to gastroesophageal reflux disease [47–51]. If enamel demineralization is detected sufficiently early, the enamel can be remineralized before damage becomes irreversible.

Loss by wear of tooth or restoration surface caused by tooth-to-tooth contact during mastication or parafunction is defined as attrition, whereas loss of dental tissue by wear from exogenous substances such as toothbrushes is termed abrasion. Enamel tissue loss is permanent, potentially disfiguring and can be costly and sometimes challenging to repair or mask.

Hairline cracks and fractures in the tooth tend to occur after trauma or excessive loading, especially in older patients. If these remain undetected, they can lead to pain, flawed diagnosis, and inappropriate or failed therapy.

Current Methods for Diagnosis of Dental Erosion, Attrition, Abrasion, and Fracture

The technologies currently available to dentists for the diagnosis of tooth loss include visual inspection and radiography. Diagnosis usually occurs at a relatively advanced stage (1) when substantial enamel loss has occurred, (2) damage is irreversible, and (3) differential etiological diagnosis is very tenuous. Monitoring the effectiveness of remineralizing therapies is not possible with conventional clinical tools. Diagnostic tools for cracks and fractures are limited to visual inspection and probing, neither of which is reliable. Radiographs are seldom useful.

OCT Diagnosis of Dental Erosion, Attrition, Abrasion, and Fracture

Optical coherence tomography (OCT) techniques are well suited to the quantification and imaging of enamel loss [40]. A recent publication described the use of in vivo OCT imaging to determine the effectiveness of a proton pump inhibitor to treat gastroesophageal reflux (GERD) by measuring enamel loss through erosion from OCT images [51]. The study was significant in that researchers were able to identify an association between the medication and a reduced enamel erosion vs. the control (placebo) group after a period of only 4 weeks based on the imaging data (Fig. 74.9). Several studies report on the effectiveness of OCT imaging for detecting tooth fractures and cracks, including hairline cracks in the root surface (Fig. 74.10). OCT imaging gave results compatible to far more expensive micro-CT that uses ionizing radiation. Visual observation was relatively ineffective [52, 53].

74.1.4 Caries Prevention: Fluorides and Sealants

The most common methods of caries prevention include systemic fluoride ingestion during tooth development, topical fluoride application, especially during and directly after tooth eruption, and the use of dental sealants. Typically, sealants are placed over vulnerable areas of the teeth, especially the fissures of erupting permanent teeth, to protect them from demineralization and decay during their first few years in the oral cavity, when they are most vulnerable to demineralization and decay. Early detection of decay under sealants is important to avoid major spread of decay underneath the protective covering.

74.1.5 Diagnosing Sealant and Restoration Integrity

Radiographic evaluation and clinical examinations such as visualization and tactile probing of restoration margins are the less than adequate modalities currently available to clinicians. The capacity of OCT to image dental composite restorations

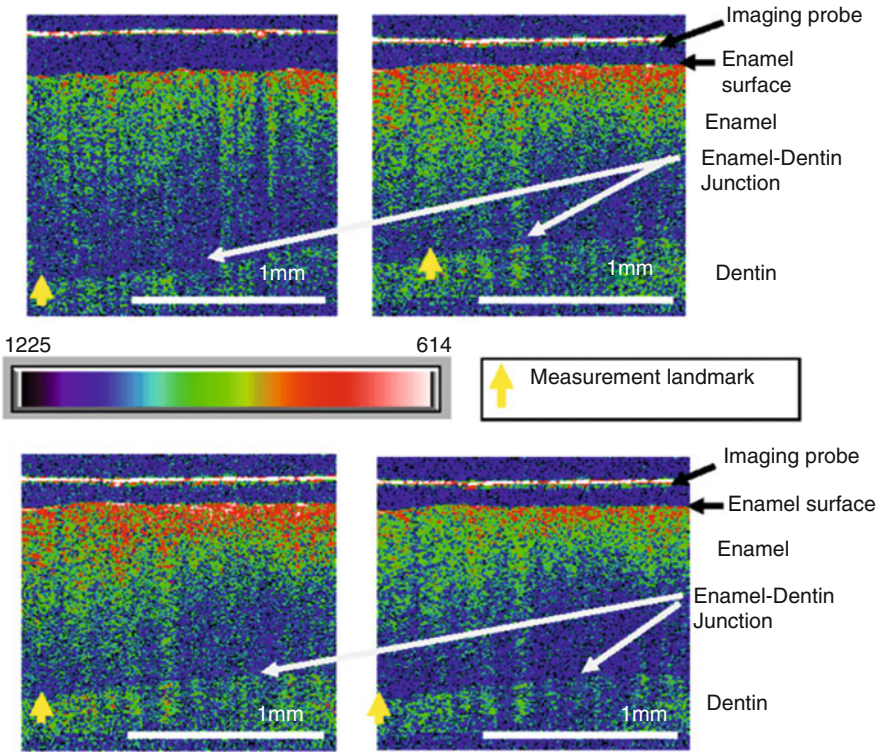

Fig. 74.9 *Above*: In vivo OCT images with pseudo-color superimposition of the same tooth before and after 3-week treatment with placebo. The optical signal near the tooth surface has increased as shown by the greater preponderance of *green* versus *blue*. *Below*: In vivo OCT images with pseudo-color superimposition of the same tooth before and after 3-week treatment with esomeprazole 20 mg bid. The optical signal near the tooth surface has decreased as shown by the reduced preponderance of *red* versus *green* [51]

offers a superior assessment as compared to radiographic imaging [54, 55]. In one study the internal characteristics of facial composite restoration were distinguished, and variations in cavosurface margins accurately identified teeth in restorations with axial cavity depths of 1, 2, and 3 mm. When the teeth were subsequently sectioned, photomicrographs revealed that OCT images depicted with fidelity the composite restorations, dentin-enamel junction (DEJ), and external tooth contours. Minimal spatial distortion of the axial wall was noted in the restorations with axial depths of 1 and 2 mm [56].

OCT has also been shown to identify accurately occlusal sealants and composite restorations [57]. In one study, 21 dentists were asked to interpret OCT images of 9 premolars that were either not restored, contained an occlusal sealant, or were restored with a composite restoration. Following a brief training period, 21 dentists evaluated the OCT images following a randomized blind protocol. The sensitivity

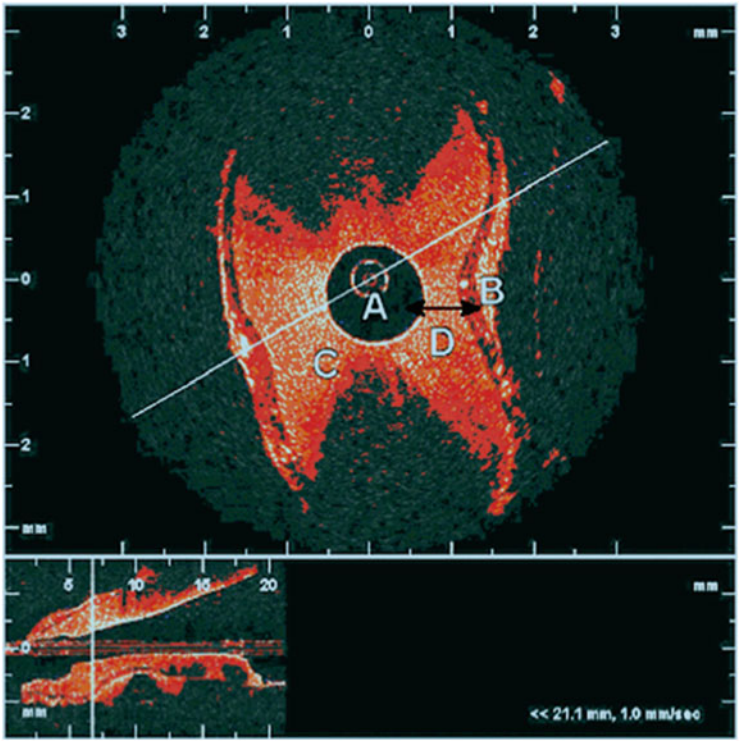

Fig. 74.10 The OCT output at 7 mm from the apex shows a cross-section of a prepared canal. (***A***) The root canal, (***B***) cementum, and (***C***) dentinal tubules. (***D***) "Risk zone" (canal wall 1-mm thick) [52]

of OCT to discriminate composite and sealants was greater than 0.92, while the specificity of discrimination was greater than 0.94. The capacity of OCT to discriminate sealants from non-restored occlusal surfaces was slightly less (sensitivity 0.88; specificity 0.86) but still within a clinically acceptable level. Inter- and intra-rater reliabilities as measured by the kappa statistic also revealed excellent performance by dentists using OCT ($k = 0.82$–1.0). This study also demonstrated that dentists who were previously unfamiliar with OCT images could be trained to interpret the images with a high degree of accuracy.

Not only does OCT detect sealants, it also effectively diagnoses decay underneath sealants. A study by Holtzman et al. evaluating the ability of dentists to detect decay beneath commonly used dental sealants using OCT found that, after 90 min training, dentists were able to detect tooth decay in enamel and under sealants more accurately using OCT than with visual or radiographic examination (Fig. 74.11). Detection using OCT was somewhat better prior to sealant placement than afterward. This effect varied in size depending on the type of sealant used. Radiographic diagnosis was also less accurate after sealant placement. Of the four dental sealants,

Delton provided excellent positive predictive value and the best post-sealant negative predictive values [58].

A paper by Jones et al. described the effective use of polarization-sensitive optical coherence tomography (PS-OCT) to image lesions underneath composite sealants [59]. The polarization-sensitive system, recording images in both the parallel and perpendicular axes, was useful for enhancing the image contrast of the artificial caries and minimizing the interference of the strong reflections at surface interfaces. The artificial lesions could be detected under 750 μm of visibly opaque sealant. Tooth-colored sealants allow deeper imaging depth. The artificial lesions could be detected under 1,000 μm of sealant.

Finally, OCT can be used to assess the internal structure and marginal adaptation of cemented crowns. Cross-sectional images were made in duplicate on the midfacial surface of cemented functional crowns with well-adapted margins and no clinical evidence of recurrent caries. The internal structure and marginal adaptation of porcelain fused to metal crowns were clearly visualized in teeth imaged in vivo. Characteristic image layers that corresponded to incisal and body porcelain were visualized [60].

Using three-dimensional OCT imaging, it is possible to evaluate the structural integrity and wear of composite resin restorations. An OCT contour map of restoration surfaces can be used to quantify volumetric loss or surface changes in a restorative material over time. Wear estimates correlate well with the value as determined by the traditional method of measuring composite wear, the ML scale ($r = 0.86$; $p < 0.05$). OCT images can record changes in the restoration surface that occurred with occlusal function. It was also shown that a region of catastrophic failure not visible clinically or radiographically was detected by OCT [61].

74.2 Periodontal Tissues

Periodontal diseases are a major cause of tooth loss. They are plaque-induced inflammatory disorders that result in the loss of tooth support through the apical migration of connective tissue attachment which results in the resorption of alveolar bone. To establish the diagnosis of periodontitis, it is necessary to detect the loss of connective tissue attachment and alveolar bone [62]. Traditionally, the location of the periodontal attachment has been estimated by mechanically measuring the distance a probe penetrates the soft tissues surrounding the tooth. Attachment level is defined clinically as the distance from a fixed reference point on the tooth (the cementoenamel junction) to the most apical extent of probe penetration. Probing depth is the distance from the gingival margin to the most apical extent of probe penetration. Accurate assessment of probing depth and changes in soft tissue attachment level are critically important in periodontics.

Current methods of periodontal probing use conventional, mechanical, or pressure-sensitive probes. Unfortunately, as a measurement technique, periodontal

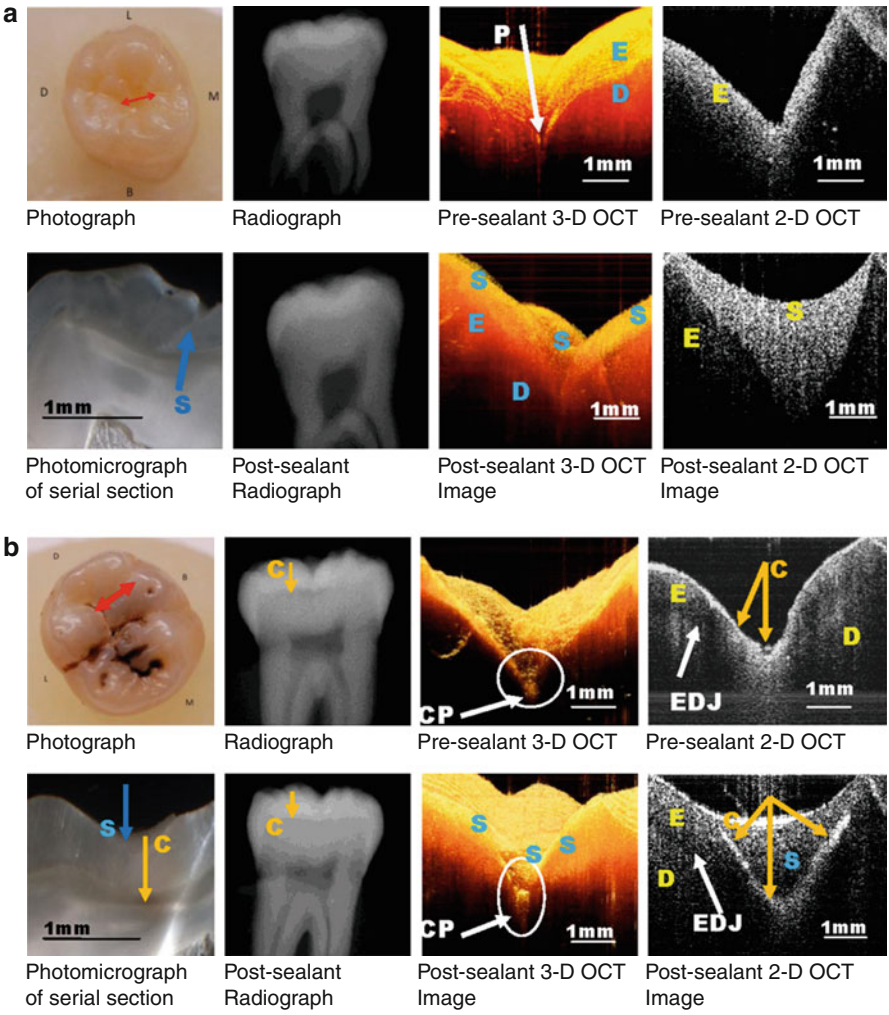

Fig. 74.11 Typical pre- and post-sealant photographic, radiographic, and OCT images as well as photomicrograph of histological section of healthy tooth (**a**) and carious tooth (**b**). (**a**) Images of healthy tooth sample pre- and post-sealant (Fuji TRIAGE sealant) *Above*: LHS: photograph with *red arrow* indicating OCT scan line; *Center left*: pre-sealant radiograph; *Center right*: pre-sealant 3D OCT image; RHS: pre-sealant 2D OCT image. *Below*: LHS: photomicrograph of histological section of tooth, *blue arrow* indicates sealant; *Center left*: post-sealant radiograph; *Center right*: post-sealant 3D OCT image; RHS: post-sealant 2D OCT image. P-occlusal pit; *E* enamel, *D* dentin, *S* sealant. (**b**) Images of decayed tooth sample pre- and post-sealant (Delton sealant) *Above*: LHS: photograph with *red arrow* indicating OCT scan line; *Center left*: pre-sealant radiograph with *yellow arrow* indicating caries (*C*); *Center right*: pre-sealant 3D OCT image with carious occlusal pit (*CP*) indicated by *white arrow*; RHS: pre-sealant 2D OCT image with occlusal caries (*C*) indicated by *yellow arrow* and EDJ indicated by *white arrow*. *Below*: LHS: photomicrograph of histological section of tooth, *blue arrow* indicates sealant (*S*), and *yellow arrow* indicates caries; *Center left*: post-sealant radiograph with *yellow arrow* indicating caries

probing has several sources of error that make it somewhat imprecise [63]. For example, the extent of probe penetration varies with insertion force [64], inflammatory status of the tissues [65], and diameter of the probe tip [66, 67]. Therefore, under routine clinical conditions, periodontal probes have an average measurement error of approximately ± 1 mm [68]. Examiner variation is a major source of error for conventional probes. Training and calibrating examiners decrease but do not eliminate examiner error. Probing errors also result from patient characteristics, such as anatomical differences in tooth contour, particularly in furcation areas. Probing error varies for different sites within the mouth [69]. Patient discomfort can also result in erroneous measurements [69]. Measurement error limits the ability to identify subtle differences in clinical values, which may be important in early disease detection and intervention. These errors diminish the likelihood of accurately identifying etiological factors correlated with disease progression. Finally, a fundamental limitation is that probing cannot identify disease activity status – which is important, given the cyclical and intermittent nature of periodontal disease activity.

OCT is particularly well suited for periodontal diagnosis, generating ultrahigh resolution cross-sectional images of dental tissues. It has been shown that OCT reliably depicts soft and hard tissue boundaries of the periodontium [70]. Moreover, OCT offers a precision of measurement that is not possible with traditional diagnostic methods. All current periodontal probing methods rely on physical measurements at single points along the tooth surface. To characterize a tooth using current probing methods, points are usually assessed. Thus, all current methods are not only tedious but also assume a direct relationship between these linear point measurements and the area of root surface attachment. OCT, on the other hand, provides rapid, consistent, and reproducible images of the surface topography, pocket morphology, and attachment level that is digitally recorded. These images pinpoint with greater accuracy sites of disease progression. OCT also provides quantitative information regarding the thickness and character of the gingiva, root surface irregularities, and the distribution of subgingival calculus. OCT may delineate changes in the optical properties or structural integrity of the gingival fiber. Comparing OCT images over time should allow clinicians to quickly detect potential sites of disease progression, perhaps even before attachment is lost. OCT images should prove to be extremely valuable in maintaining sites during supportive periodontal therapy. Electronic and visual recording of clinical data avoids subjectivity and transcription error that is associated with current metric techniques [65]. OCT has the capacity to detect disease in the soft tissue early, before bone resorption occurs. When Doppler algorithms are combined with OCT, blood flow can be localized and qualified (Fig. 74.12) offering the exciting potential to distinguish active from non-active periodontitis. Blood flow measurements may

Fig. 74.11 (continued) (*C*); *Center right*: post-sealant 3D OCT image with carious occlusal pit (*CP*) indicated by *white arrow*; RHS: post-sealant 2D OCT image where *white arrow* indicates EDJ and *yellow arrow* indicates caries. P-occlusal pit; *E* enamel, *D* dentin; *S* sealant, *C* caries, *CP* carious pit, *EDJ* enamel-dentin junction [58]

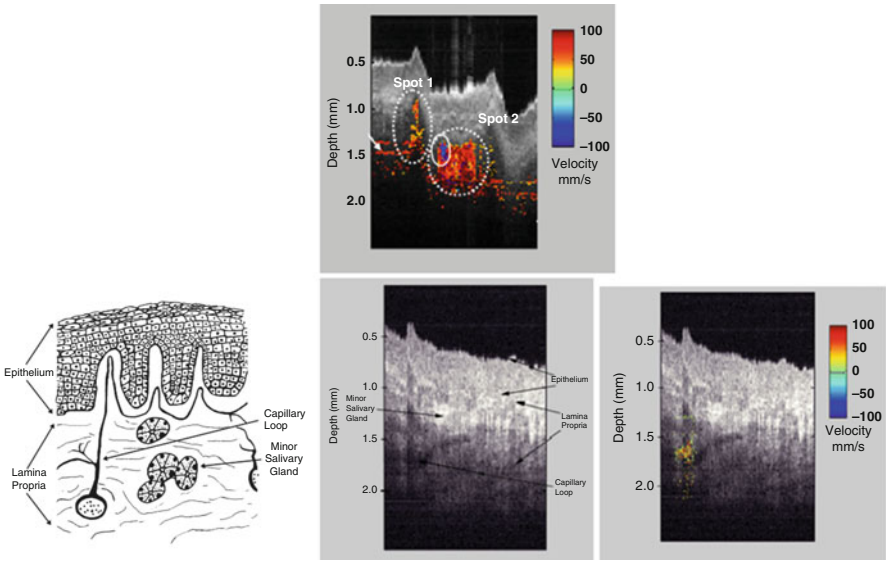

Fig. 74.12 Doppler OCT illustrating blood flow in a human lip [72]

also help elucidate the pathogenesis of periodontitis associated with diabetes and smoking [71, 72].

In a study by Baek et al., the successful use of OCT for monitoring periodontal ligament changes during orthodontic tooth movements was reported in rats [73] (Fig. 74.13). Clinical periodontal probing depth has been shown to correlate well with that measured in OCT images. The midfacial surface of 14 non-restored teeth (1 mandibular and 3 maxillary incisors, 4 maxillary and 6 mandibular premolars) was imaged using a prototype OCT system (1,310-nm wavelength light source, 14 mW, 95 dB dynamic range, 0.46 numerical aperture). Following OCT imaging, probing depths were measured in duplicate using a Michigan 0 probe. Important anatomic features including soft tissue surface contour, gingival crest, periodontal sulcus, and DEJ were identified in OCT images of all of the teeth examined. The cementoenamel junction was identified in 18 of the 28 images; the alveolar bone was presumptively identified in 20 of the 28 images. Probing depth as measured in OCT images was strongly correlated to probing depth as measured by conventional probing measurement ($r = 0.83$; $p < 0.05$). The midfacial surfaces of two restored teeth were imaged (1 maxillary molar, 1 maxillary premolar). Restoration margins and internal restoration contours were visualized and did not interfere with interpretation of OCT images of soft tissue landmarks.

Similarly, an all fiber-optic clinical OCT system was used to obtain 12-mm occlusal-apical OCT images of eight premolars in four healthy volunteers. Images were made in duplicate at the mesial facial line angle. This system employed a 6 mW, 1,310-nm light source and produced images that had an axial resolution of 21 μm. The images of periodontal tissues were similar to those obtained in

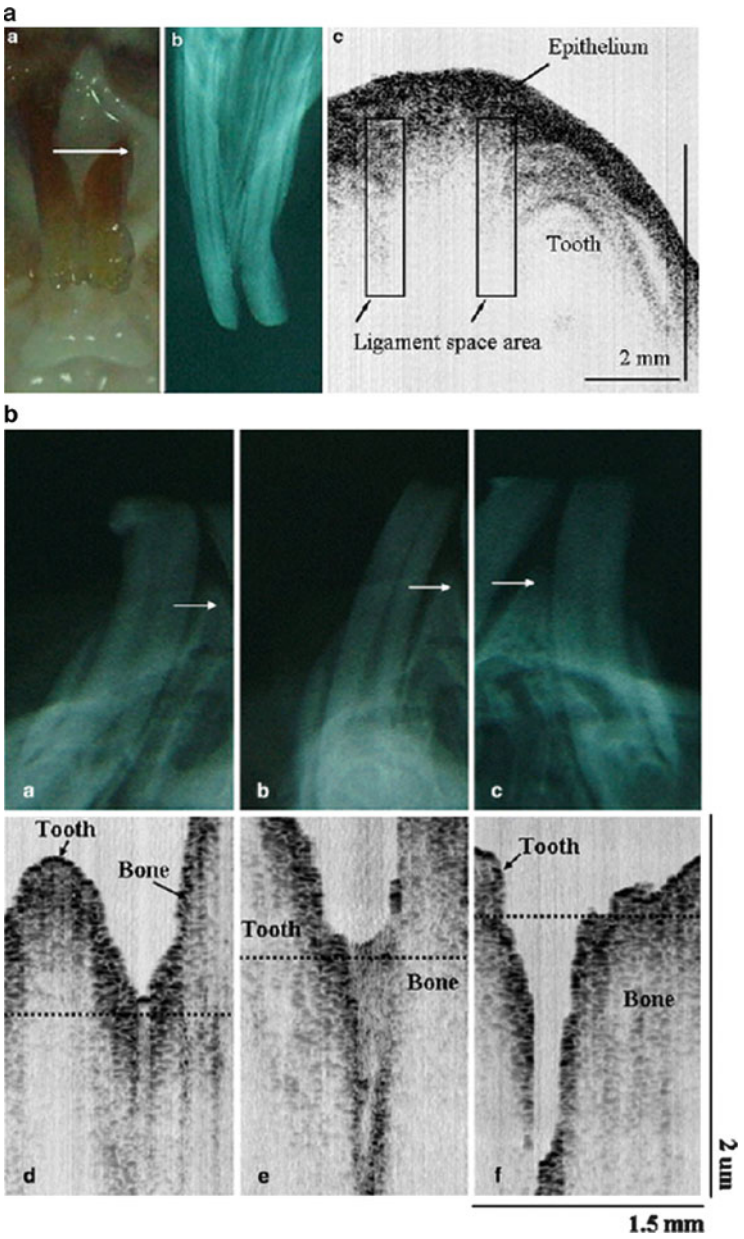

Fig. 74.13 Maxillary anterior tooth of a white rat. (**a**) shows data from the control group to which no orthodontic force was applied: (*a*) optical photograph; (*b*) radiographic image; (*c*) OCT image [73]. (**b**) shows radiographic (*top*) and OCT images (*bottom*) of the maxillary anterior teeth under several orthodontic forces: (*a*, *d*) 5 gf; (*b*, *e*) 10 gf; (*c*, *f*) 30 gf forces, respectively. The two-dimensional OCT image in the *bottom* was taken along the *arrow* direction in each of the *top* (radiographic) figures [73]

previous studies. Characteristic signals representing the sulcus and attached tissues were identified in all images. Premolar sulcular depth as determined from the OCT images ranged from 1.1 to 2.5 and was strongly correlated with probing depth ($r = 0.88$; $p < 0.05$). We defined attached tissues in the OCT images by a uniform signal intensity with no discernable tissue interfaces that extended from the base of the sulcus to the alveolar crest. Measurement of attached tissues in the OCT images ranged from 1.1 to 3.8 mm. The lowest values for attached tissues were found in three teeth with coronal restorations. Signals presumptively identified as the alveolar crest were identified in 60 of the 64 images. The thickness of the gingiva covering the alveolar crest ranged from 0.4 to 1.4 mm. Two teeth had characteristic signals representative of the root surface covered by a thin mucosal tissue; these sites were presumptively identified as fenestration defects. While the OCT images of the root surface are unmistakable, definitive proof of OCT to image fenestration defects requires further investigation. The results of this study, however, convincingly demonstrate capacity of OCT to determine gingival thickness and the shape and contour of the alveolar crest. Visualizing these anatomical features represents a significant contribution to periodontal surgical treatment planning.

74.3 Dental Implants

Endosseous dental implants have been established as a predictable treatment modality for the replacement of missing teeth. While only 2 % of implants fail within the first year, the failure rate rises to 10 % at 5 years and nearly 15 % at 10 years [74, 75]. A successful implant is defined as one that is not mobile and has no peri-implant radiolucencies, no clinical signs of infection, and no discomfort or pain [76–89]. Favorable vertical soft tissue relationships have been demonstrated to be important in the success of dental implants, particularly in maintaining crestal bone height [83]. Peri-implantitis is defined as an inflammatory process affecting the tissues around an osseointegrated implant in function, resulting in progressive loss of supporting bone around the implant [82–84]. The prevalence of peri-implantitis is unknown, although researchers estimate that it ranges from 8 % to as high as 44 % [82–84]. The diagnosis of peri-implantitis is complicated because adequate diagnostic methods to evaluate soft tissues are unavailable and because it is difficult to monitor crestal bone loss around implants. Ideally, implants should lose minimal bone. The implant is at significant risk when more than one-half of the implant height has lost crestal contact [74, 88].

Studies have shown that once peri-implant inflammation is established, it is difficult to eradicate. Unequivocally, any sign of peri-implantitis threatens the longevity of implant restorations and represents a significant health care cost. For these reasons, after implant placement, patients should be examined at regular intervals to evaluate clinical signs and symptoms of peri-implant disease and to receive maintenance therapy [78, 82, 89].

Current implant diagnostic procedures rely on visual estimates of clinical signs of inflammation or single-point physical measurements, such as probing depth.

These techniques lack sufficient sensitivity to detect peri-implantitis at an early stage. Current methods are also subject to high levels of measurement error, and extensive clinical calibration of examiners is required to achieve inter-examiner reliability. The inability to detect problems early jeopardizes effective care. More sensitive tests are needed to understand the causes of late implant failure, to reliably evaluate differences in clinical outcomes between various implant systems, or to evaluate the success of therapeutic interventions for the treatment of peri-implantitis [82, 90].

74.3.1 Expected Improvement of Implant Diagnoses Using OCT

OCT can be used clinically to detect early peri-implantitis with greater sensitivity than current diagnostic methods (Figs. 74.13a, b), with images providing rapid, consistent, and reproducible documentation of peri-implant soft tissue morphology and attachment level. Quantitative information regarding microstructural architecture including the character of the gingiva as well as implant soft tissue relationships is generated. More importantly, OCT identifies the earliest signs of inflammation, so minimal that clinical examination is unlikely to distinguish them. Comparing OCT images over time should prove to be extremely valuable in monitoring health in implant sites during maintenance therapy. Moreover, OCT imaging offers the exciting potential to detect peri-implantitis before significant osseous destruction occurs.

Histological studies in animals have shown that gingival connective tissue forms a scar-like fibrous connective tissue adjacent to titanium implant surfaces, while peri-implantitis is characterized by a disorganized connective tissue containing more vascular elements. Our preliminary data demonstrate that in OCT images of healthy implant sites, collagen appears well organized, and, because of its birefringent nature, it produces a characteristic high OCT signal intensity. OCT images of soft tissue surrounding failing implants are markedly different from images of healthy implant sites and are characterized by linear signal deficits, low-intensity collagen signals, and pronounced increases in vascular elements. To evaluate the feasibility of OCT imaging for implant diagnoses, we conducted preliminary studies in three patients with failing implants. Figure 74.14a demonstrates a 6-mm OCT image made from the midfacial surface of a healthy dental implant site. The peri-implant tissues show no clinical signs of inflammation, and the probing depth measured 1 mm. Figure 74.14b is an OCT image of a plasma-coated IMZ implant. This image illustrates the characteristic findings associated with failing implants, low collagen signal, and increased vascular elements.

OCT will improve clinical evaluation of peri-implant soft tissues and will provide significant advantages over existing diagnostic procedures. Two- or three-dimensional OCT images can depict the topography of the implant sulcus and the relationship of implant soft tissue interfaces. These images can be stored in the patient record and be used to monitor implant health over time. The imaging process is painless, and patient acceptance is far greater than for other dental procedures. Because OCT is noninvasive, it can be performed repeatedly without any risk to the patient.

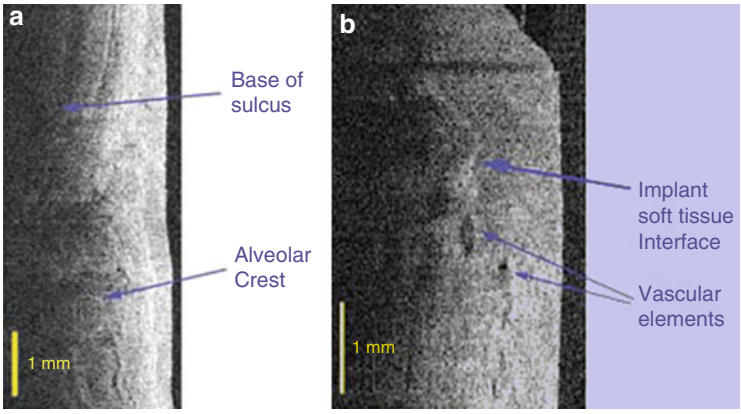

Fig. 74.14 (**a**) OCT image of a healthy dental implant. (**b**) OCT image of failing dental implant

74.4 Oral Dysplasia and Malignancy

According to the American Cancer Society, 1,220,100 patients were diagnosed with cancer in the year 2000. In the same year, 552,200 persons were expected to succumb to cancer [91]. Despite significant advances in cancer treatment, early detection of oral cancer and its curable precursors remains the best way to ensure patient survival and quality of life. Oral cancer will claim approximately 10,000 lives in the USA this year [92, 93]. Accounting for 96 % of all oral cancers, squamous cell carcinoma is usually preceded by dysplasia presenting as white epithelial lesions on the oral mucosa (leukoplakia). Leukoplakias develop in 1–4 % of the population [94]. Malignant transformation, which is quite unpredictable, occurs in 1–40 % of leukoplakias over 5 years. Dysplastic lesions in the form of erythroplakias carry a risk for malignant conversion of 90 %. Tumor detection is complicated by a tendency toward field cancerization, leading to multicentric lesions [94]. Current techniques require surgical biopsy of lesions, which are often benign, yet they detect malignant change too late. Of all oral cancer cases documented by the National Cancer Institute Surveillance, Epidemiology, and End Results Program, advanced lesions outnumbered localized lesions more than 2:1. Five-year survival rate is 75 % for those with localized disease at diagnosis but only 16 % for those with cancer metastasis [92, 93].

Two basic facts indicate that early detection of oral malignancy should be possible to a far greater extent than is currently seen:

1. ***Oral cancer is predominantly preceded by white or red lesions which are visible to the naked eye and which are often present for a considerable period of time prior to transformation.*** A noninvasive diagnostic modality would permit monitoring of these lesions at regular intervals and detection of transformation and any treatment needs at a very early, relatively harmless stage.

2. ***High-risk populations are clearly defined.*** Tobacco use, alcohol abuse, urban environment, African-American background, poor diet, and frequent exposure to sunlight are primary predisposing factors for oral malignancy [95, 96]. A fast, mobile, relatively inexpensive noninvasive diagnostic modality would permit regular screening for oral lesions and subsequent transformation at an early, relatively harmless stage.

74.4.1 Existing and Emerging Techniques for Oral Diagnosis

1. **Visual examination and biopsy** Oral cancer can be detected by dentists and physicians, but physicians do not routinely inspect their patients for suspicious oral lesions, and dentists are also remiss in the early diagnosis and referral for oral cancer. Since 11 % of dentists and 45 % of physicians do not feel adequately trained to complete an effective oral cancer examination, this results in their failure to examine for oral cancer [96]. The current approach to detecting the transformation of leukoplakia/erythroplakia to squamous cell carcinoma is regular surveillance combined with biopsy or surgical excision. However, visual examination provides very poor diagnostic accuracy, and biopsy techniques are invasive and unsuitable for regular screening of high-risk sectors of the population. Adequate visual identification and biopsy of all such lesions to ensure that they are all recognized and diagnosed are difficult, given the often multifocal nature of oral malignancy [93].
2. **Vital staining** Several studies have investigated the use of vital staining with agents such as Lugol iodine, toluidine blue, and tolonium chloride for detection of oral malignancy. Although the sensitivity of these agents in the hands of experts generally approximates 90 %, specificity of these agents is poor; sensitivity rapidly decreases when this modality is used by nonexperts such as screeners in field units. Extensive clinical experience is necessary to perform these examinations adequately [97–103].
3. **Oral brush cytology** Using cytological examination of "brush biopsy" samples as a noninvasive method of oral diagnosis has been shown to provide moderate sensitivity levels of detection of oral epithelial dysplasia or squamous cell carcinoma (70–90 %) but poor specificity (3–44 %). Thus, this approach is of limited diagnostic value without augmentation by traditional biopsy [103–105].
4. **Photosensitizers** Topical or systemic application of photosensitizers can render pathologic tissues fluorescent when exposed to specific wavelengths of light [106]. While several studies have demonstrated the use of porphyrins as photosensitizers, their accumulation in skin after systemic administration can cause phototoxic reactions upon exposure to sunlight [107, 108]. An alternative approach is to stimulate synthesis of photosensitizing agents in situ with a photoinactive precursor. The photosensitizer protoporphyrin IX (PpIX) is an immediate precursor of heme in the biosynthetic pathway for heme. In certain types of cells and tissues, the rate of PpIX synthesis is determined by the rate of

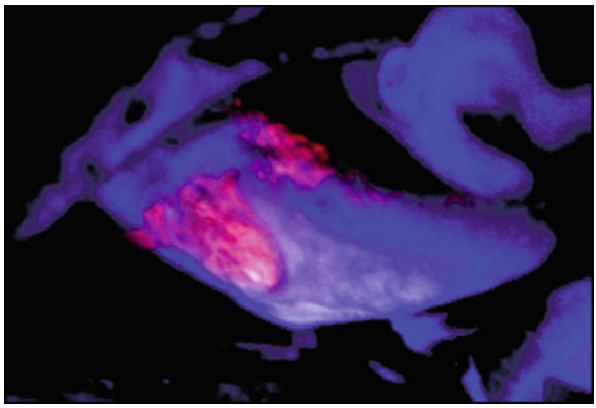

Fig. 74.15 Fluorescence imaging of squamous cell carcinoma of the tongue (*reddish color*) 3 h after topical application of Photofrin® [109]

synthesis of 5-aminolevulinic acid (ALA), which in turn is regulated via a feedback control mechanism governed by the concentration of free heme. The presence of exogenous ALA bypasses the feedback control of this process, inducing the intracellular accumulation of photosensitizing concentrations of PpIX. A selective accumulation of PpIX occurs in areas of increased metabolism such as tumor cells [106]. The resulting tissue-specific photosensitization provides the basis for using ALA-induced PpIX for photodynamic diagnosis and therapy, whereby far lower light doses are used for photodynamic diagnosis. This technique has shown great promise in animal and human studies for head and neck cancers including oral lesions [108–111] (Fig. 74.15). Limitations include the localization of induced fluorescence to the surface layers of the epithelium and the fluorescence caused by common coexisting clinical pathologies such as candidal superinfection, hyperplasia, atrophy, and ulceration.

5. **Spectroscopy** Various types of optical spectroscopy have been investigated to effect a noninvasive, real-time in situ assessment of tissue pathology. All of these methods have one basic principle in common: the optical spectrum of a tissue contains information about the biochemical composition and/or the structure of the tissue which conveys diagnostic information. Malignancy-related biochemical and morphologic changes perturb tissue absorption, fluorescence, and scattering properties. The biochemical information can be obtained by measuring absorption/reflectance, fluorescence, or Raman scattering signals. Structural and morphological information may be obtained by techniques that assess the elastic-scattering properties of tissue [112, 113].

   Reflectance spectroscopy can probe changes in epithelial nuclei that are important in precancer detection, such as mean nuclear diameter, nuclear size distribution, and nuclear refractive index [114]. Applications under investigation include the cervix [115], skin [116], colon [117], oral cavity [114], and esophagus [118].

   Fluorescence spectroscopy can probe changes in epithelial cell metabolism, by assessing mitochondrial fluorophores, and epithelial-stromal

interactions, by assessing the decrease in collagen cross-link fluorescence that occurs with precancer. Areas of application include the cervix, skin, bladder, oral cavity, and esophagus [113, 118–132].

Raman spectroscopy uses laser excitation and the scattering effect is observed in the target tissues. Inelastic scattering results in a frequency shift in the reflected Raman spectra, which are functions of the type of molecules in the sample. Thus, the Raman spectra hold useful information on the different chemical compounds. Raman spectroscopy has been investigated for medical diagnosis applications in general and for the investigation of sites such as the skin, cervix, larynx, esophagus, and colon [115, 119, 133–144].

Significant challenges to the use of diagnostic spectroscopy include the often low signal-to-noise ratio, difficulty in identifying the precise source of signals, data quantification issues, and establishing definitive diagnostic milestones and endpoints. Limited tissue penetration and concerns about mutagenicity when using UV light present further clinical challenges. The abundance of data/information generated in association with our incomplete understanding of the carcinogenesis process render data analysis and interpretation very complex. Many studies have been performed on small numbers of small biopsy samples which do not necessarily translate directly or accurately to the clinical situation.

6. **Optical coherence microscopy** This modality combines the subcellular resolution of confocal microscopy with the increased sensitivity and penetration depth of optical coherence tomography (OCT) to noninvasively acquire details similar to that available in histologic tissue evaluation. Typically, a resolution of 2 μm and a 200- to 500-μm field of view at a penetration depth of up to 600 μm are reported in the literature [145–150]. This suggests that OCM has the potential to image epithelial tissues with the subcellular resolution needed to assess their pathologic state. Challenges include the small field of view, limited penetration depth (although better than confocal reflectance microscopy), and the need for an intraoral probe.
7. **Confocal reflectance microscopy** In vivo confocal imaging resembles histological tissue evaluation, except that three-dimensional subcellular resolution is achieved noninvasively and without stains. In epithelial structure, resolution of 1 μm has been achieved with a 200–400-μm field of view. In skin, where cytoplasmic melanin provides a strong source of backscattering, confocal microscopes have captured morphologic changes in cytologic structure and visualized microvasculature in both basal cell carcinomas and melanomas [151–158]. In amelanotic epithelial tissues, where cell nuclei provide the primary source of reflected light, recent work showed that reflectance confocal imaging of normal and precancerous cervical tissue can characterize nuclear size, nuclear density, and nuclear-to-cytoplasmic ratio without the need for tissue sectioning or staining. In these ex vivo studies, confocal images were used to discriminate high-grade cervical precancers with a sensitivity of 100 % and a specificity of 91 % in a study of 25 samples [159, 160]. Similarly, nuclear-to-cytoplasmic

differences from images of normal and esophageal cancer cells were used to identify cancer with a diagnostic accuracy of 90 % [161]. Confocal imaging of oral mucosa has resolved subcellular detail in the lip and tongue [162] and oral squamous cell carcinoma from multiple sites [163]. While this technology can provide detailed images of tissue architecture and cellular morphology, a very small field of view and limited penetration depth of 250–500 μm considerably reduce the clinical usefulness of this approach.

74.4.2 OCT Diagnosis

Performing studies in the hamster cheek pouch model and in humans, the macroscopic and vascular status of healthy, dysplastic, and malignant oral mucosa has been imaged using in vivo OCT/ODT. Multiple epithelial and subepithelial layers as well as the presence or absence of basement membrane can be visualized. Epithelial invasion during malignant transformation was clearly identified. Blood vessel presence, size, and localization relative to tumor tissue were visible, and blood flow could be quantified [164, 165]. In oral malignancy, small blood vessels were often seen in close proximity to tumor tissue, and using IHC a progressively increased blood vessel count with decreasing level of tumor differentiation was demonstrated [166, 167].

Movement artifacts during OCT registration in human subjects do not appear to be a problem when using the newer, faster imaging systems. As long as patients are seated comfortably in a clinical chair with headrest and neck support, this was not an issue at all, as evidenced by Fig. 74.16. Epithelium, lamina propria, and basement membrane are clearly visible. Structural appearance in the OCT image parallels histological appearance, showing epithelial thickening, loss of stratification in lower epithelial strata, epithelial downgrowth, and presence of basement membrane in dysplastic tissue (Fig. 74.16).

In a clinical study involving 50 patients with leukoplakia or erythroplakia, oral lesions, pre-standardized clinicians were able to diagnose oral lesions from noninvasive in vivo OCT images with approx. 85 % accuracy vs. the gold standard, surgical biopsy, and histopathology [164]. Another study in 73 patients with 78 suspicious oral lesions identified similar levels of diagnostic accuracy [165]. These data demonstrate the excellent capability of in vivo OCT for detecting and diagnosing oral soft tissue pathologies in patients.

74.5 Future Potential

The potential for OCT-based diagnostics in the oral cavity is excellent. The penetration depth of this modality in oral hard and soft tissues is adequate for most dental applications. Ongoing innovations, such as the development of Fourier-domain OCT, which enable up to 100× faster acquisition of 3D OCT images, and of spectral OCT, which provide enhanced imaging contrast, will permit spatially

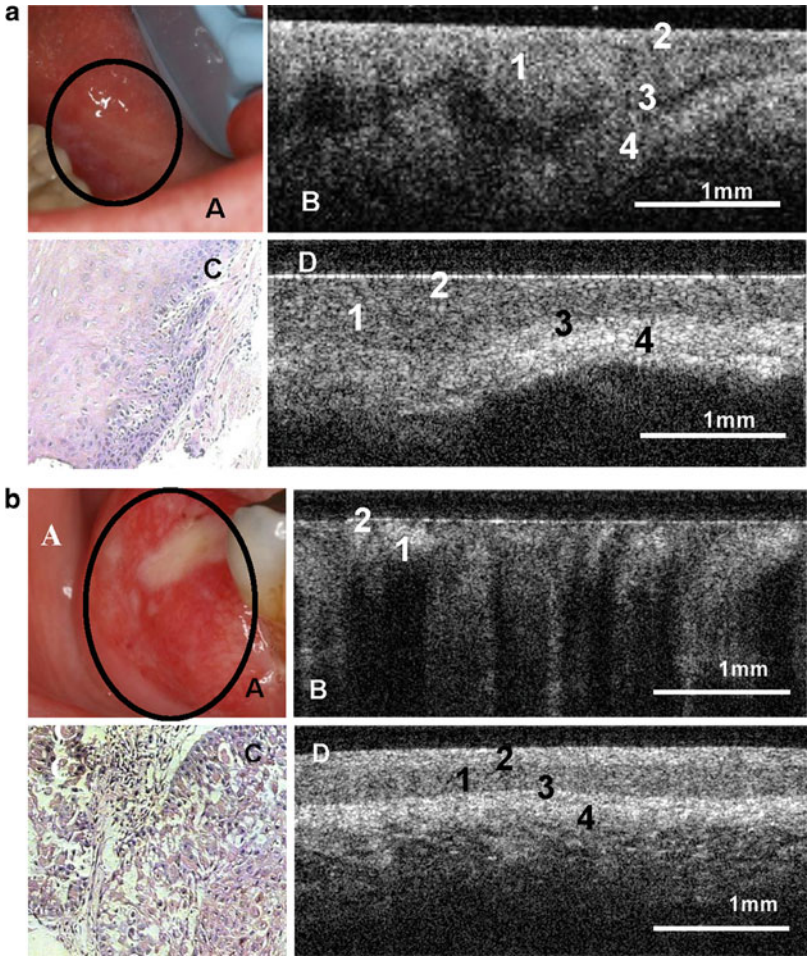

Fig. 74.16 (**a**) Photograph (A), in vivo OCT image (B), and H&E (C) of dysplastic buccal mucosa. In vivo OCT image of normal buccal Mucosa is shown in (D). (**b**) Photograph (A), in vivo OCT image (B), and H&E (C) of alveolar ridge with squamous cell carcinoma. In vivo OCT image of normal alveolar Mucosa is shown in (D). 1-stratified squamous epithelium, 2-keratinized epithelial surface layer, 3-basement membrane, 4-subucosa

resolved detection and quantification of changes within the tissues such as demineralization through their spectroscopic properties. Emerging MEMS-based and 3D techniques are significant factors permitting enhanced speed and effectiveness of the images obtained. Based on the data available to date, direct clinical in vivo imaging shows great potential for improving diagnostic capabilities in the oral cavity for applications ranging from decay, through periodontal disease, to oral malignancy.

References

1. B.W. Colston, M.J. Everett, L.B. DaSilva, L.L. Otis, P. Stroeve, H. Nathel, Imaging of hard and soft tissue in the oral cavity by optical coherence tomography. Appl. Optics **37**(16), 3582–3585 (1998)
2. B.W. Colston Jr., S. Sathyam, L.B. DaSilva, M.J. Everett, P. Stroeve, L.L. Otis, Dental OCT. Opt. Express **3**, 230–238 (1998)
3. L.L. Otis, M.J. Everett, U.S. Sathyam, B.W. Colston Jr., Optical coherence tomography: a new imaging technology for dentistry. J. Am. Dent. Assoc. **131**(4), 511–514 (2000)
4. A. Nanci, A.R. Ten Cate, Ten Cate's oral histology: development, structure, and function (Elsevier Mosby, St. Louis, MO, 2013), pp. 239–256
5. A. Nanci, A. R. Ten Cate, Ten Cate's oral histology: development, structure, and function (Elsevier Mosby, St. Louis, MO, 2013), pp. 169–217
6. L. Otis, Y. Chen, Q. Zhu, Characterization of dentin by optical coherence tomography. J. Dent. Res. **82**, A 3979 (2004)
7. J.A. Izatt, K. Kobayashi, M.V. Sivak, J.K. Barton, A.J. Welch, Optical coherence tomography for biodiagnostics. Opt. Photon. News **8**, 41–47 (1997)
8. Z. Ding, High-resolution optical coherence tomography over a large depth range with an axicon lens. Opt. Lett. **27**, 4 (2002)
9. L.L. Otis, B.W. Colston Jr., M.J. Everett, H. Nathel, Dental optical coherence tomography: a comparison of two in vitro systems using a light source at 1310 nm. Dentomaxillofac. Radiol. **29**(2), 85–89 (2000)
10. Y. Pan, Z. Li, T. Xie, C.R. Chu, Hand-held arthroscopic optical coherence tomography for in vivo high-resolution imaging of articular cartilage. J. Biomed. Opt. **8**(4), 648–654 (2003)
11. W.G. Jung, J. Zhang, L. Wang, P. Wilder-Smith, Z. Chen, D. McCormick, N.C. Tien, Three-dimensional optical coherence tomography employing A 2-axis microelectromechanical scanning mirror. IEEE Journal of Selected Topics in Quantum Electronics 11, 806–810 (2005)
12. J.M. Zara, S. Yazdanfar, K.D. Rao, J.A. Izatt, S.M. Smith, Electrostatic micromachine scanning mirror for optical coherence tomography. Opt. Lett. **28**, 828–830 (2003)
13. P. Tran, D.S. Mukai, M. Brenner, Z. Chen, In vivo endoscopic optical coherence tomography using rotational MEMS probe. Opt. Lett. **29**, 1236–1239 (2004)
14. Y. Wang, M. Bachman, G.P. Li, S. Guo, B. Wong, Z. Chen, Low-voltage polymer-based scanning cantilever for in vivo optical coherence tomography. Opt. Lett. **30**, 53–55 (2005)
15. W.G. Jung, J. Zhang, L. Wang, Z. Chen, D.T. McCormick, N.C. Tien, Three-dimensional endoscopic optical coherence tomography by use of a two-axis microelectromechanical scanning mirror. Appl. Phys. Lett. **88**, 163901–163903 (2006)
16. W.G. Jung, L. Zhang, J. Wang, Z. Chen, D.T. McCormick, N.C. Tien, Three-dimensional optical coherence tomography employing a 2-axis microelectromechanical scanning mirror. IEEE J. Sel. Top. Quantum Electron. **11**, 806–810 (2005)
17. A.D. Aguirre, P.R. Hertz, Y. Chen, J.G. Fujimoto, W. Piyawattanametha, L. Fan, M.C. Wu, Two-axis MEMS scanning catheter for ultrahigh resolution three-dimensional and en face imaging. Opt. Express **15**, 2445–2453 (2007)
18. J.T.W. Yeow, V.X.D. Yang, A. Chahwan, M.L. Gordon, B. Qi, I.A. Vitkin, B.C. Wilson, A.A. Goldenberg, Micromachined 2-D scanner for 3-D optical coherence tomography. Sensors Actuators A **117**, 331–340 (2005)
19. X. Liu, M.J. Cobb, Y. Chen, M.B. Kimmey, X. Li, Rapid-scanning forward-imaging miniature endoscope for real-time optical coherence tomography. Opt. Lett. **29**(15), 1763–1765 (2004)
20. S. Moon, S.W. Lee, M. Rubinstein, B.J. Wong, Z. Chen, Semi-resonant operation of a fiber-cantilever piezotube scanner for stable optical coherence tomography endoscope imaging. Opt. Express **18**(20), 21183–21197 (2010)
21. S.A. Boppart, B.E. Bouma, C. Pitris, J.G. Tearney, J.G. Fujimoto, M.E. Brezinski, Forward-imaging instruments for optical coherence tomography. Opt. Lett. **22**(21), 1618–1620 (1997)

22. N.R. Munce, A. Mariampillai, B.A. Standish, M. Pop, K.J. Anderson, G.Y. Liu, T. Luk, B.K. Courtney, G.A. Wright, I.A. Vitkin, V.X. Yang, Electrostatic forward-viewing scanning probe for Doppler optical coherence tomography using a dissipative polymer catheter. Opt. Lett. **33**(7), 657–659 (2008)
23. E.J. Min, J. Na, S.Y. Ryu, B.H. Lee, Single-body lensed-fiber scanning probe actuated by magnetic force for optical imaging. Opt. Lett. **34**(12), 1897–1899 (2009)
24. L. Huo, J. Xi, Y. Wu, X. Li, Forward-viewing resonant fiber-optic scanning endoscope of appropriate scanning speed for 3D OCT imaging. Opt. Express **18**(14), 14375–14384 (2010)
25. M.H. Niemz, *Laser-tissue interactions* (Springer, Berlin, 1996), pp. 178–195
26. A. Nanci, A.R. Ten Cate, Ten Cate's oral histology: development, structure, and function (Elsevier Mosby, St. Louis, MO, 2013), pp. 462–465.
27. A. Lussi, Validity of diagnostic and treatment decisions of fissure canes. Caries Res. **25**, 296–303 (1991)
28. A. Wenzel, N. Pitts, E.H. Verdonschott, H. Kalsbeek, Developments in radiographic caries diagnosis. Dent **21**, 131–140 (1993)
29. R.B. Nytun, M. Raadal, I. Espelid, Diagnosis of dentin involvement in occlusal caries based on visual and radiographic examination of the teeth. Scand. J. Dent. Res. **100**, 144–148 (1992)
30. K.L. Weerheijm, H.J. Groen, A.J.J. Bast, J.A. Kieft, M.A.J. Eijkman, W.E. van Amerongen, Clinically Undetected occlusal dentine caries: a radiographic comparison. Caries Res. **26**, 305–309 (1992)
31. K.R. Ekstrand, D.N. Ricketts, C. Longbottom, N.B. Pitts, Visual and tactile assessment of arrested initial enamel lesions. Caries Res. **39**(3), 173–177 (2005)
32. K.R. Ekstrand, I. Kuzmina, L. Bjomdal, A. Thyistrup, Relationship between external and histologic features of progressive stages of caries in the occlusal fossa. Caries Res. **29**, 243–250 (1995)
33. K.R. Ekstrand, D.N. Ricketts, E.A. Kidd, Do occlusal carious lesions spread laterally at the enamel-dentin junction? A histolopathological study. Clin. Oral Investig. **2**(1), 15–20 (1998)
34. A. Wenzel, E.H. Verdonschot, G.J. Truin, K.G. Konig, Accuracy of visual inspection, fiber-optic transillumination, and various radiographic image modalities for the detection of occlusal caries in extracted non-cavitated teeth. J. Dent. Res. **71**(12), 1934–1937 (1992)
35. B.T. Amaechi, S.M. Higham, A.G.H. Podoleanu, J.A. Rogers, D.A. Jackson, Use of optical coherence tomography for assessment of dental caries: quantitative procedure. J. Oral Rehabil. **28**(12), (2001)
36. B.T. Amaechi, A. Podoleanu, S.M. Higham, D.A. Jackson, Correlation of quantitative light-induced fluorescence and optical coherence tomography applied for detection and quantification of early dental caries. J. Biomed. Opt. **8**(4), 642–647 (2003)
37. A.C. Ko, L.P. Choo-Smith, M. Hewko, L. Leonardi, M.G. Sowa, C.C. Dong, P. Williams, B. Cleghorn, Ex vivo detection and characterization of early dental caries by optical coherence tomography and Raman spectroscopy. J. Biomed. Opt. **10**(3), 031118 (2005)
38. M.G. Sowa, D.P. Popescu, J.R. Friesen, M.D. Hewko, L.P. Choo-Smith, A comparison of methods using optical coherence tomography to detect demineralized regions in teeth. J. Biophotonics **4**(11–12), 814–823 (2011)
39. B.T. Amaechi, A.G. Podoleanu, G. Komarov, S.M. Higham, D.A. Jackson, Quantification of root caries using optical coherence tomography and microradiography: a correlational study. Oral Health Prev. Dent. **2**(4), 377–382 (2004)
40. L.S. de Melo, R.E. de Araujo, A.Z. Freitas, D. Zezell, N.D. Vieira, J. Girkin, A. Hall, M.T. Carvalho, A.S. Gomes, Evaluation of enamel dental restoration interface by optical coherence tomography. J. Biomed. Opt. **10**(6), 64027 (2005)
41. P. Ngaotheppitak, C.L. Darling, D. Fried, Measurement of the severity of natural smooth surface (interproximal) caries lesions with polarization sensitive optical coherence tomography. Lasers Surg. Med. **37**(1), 78–88 (2005)

42. Y. Chen, L.L. Otis, D.Q. Piao, Q. Zhu, Characterization of dentin enamel and carious lesion by a polarization-sensitive optical coherence tomography system. Appl. Optics **44**(11), 2041–2048 (2005)
43. D. Fried, J. Xie, S. Shafi, J.D. Featherstone, T.M. Breunig, C. Le, Imaging caries lesions and lesion progression with polarization sensitive optical coherence tomography. J. Biomed. Opt. **7**(4), 618–627 (2002)
44. A. Baumgartner, S. Dichtl, C.K. Hitzenberger, H. Sattmann, B. Robl, A. Moritz, A.F. Fercher, W. Sperr, Polarization-sensitive optical coherence tomography of dental structures. Caries Res. **34**(1), 59–69 (2000)
45. H. Kang, C.L. Darling, D. Fried, Nondestructive monitoring of the repair of enamel artificial lesions by an acidic remineralization model using polarization-sensitive optical coherence tomography. Dent. Mater. **28**(5), 488–494 (2012)
46. T. Louie, C. Lee, D. Hsu, K. Hirasuna, S. Manesh, M. Staninec, C.L. Darling, D. Fried, Clinical assessment of early tooth demineralization using polarization sensitive optical coherence tomography. Lasers Surg. Med. **42**(10), 738–745 (2010)
47. A. Milosevic, Toothwear: aetiology and presentation. Dent. Update **25**, 6–11 (1998)
48. J. Meurmann, J. Toskala, P. Nuutinien, E. Klemetti, Oral and dental manifestations in gastroesophageal reflux disease. Oral Surg. Oral Med. Oral Pathol. **78**, 583–589 (1994)
49. B. Gregory-Head, D.A. Curtis, Erosion caused by gastroesophageal reflux: diagnostic considerations. J. Prosthodont. **6**, 278–285 (1997)
50. D.W. Bartlett, D.F. Evans, B.G. Smith, The relationship between gastro-oesophageal reflux disease and dental erosion. J. Oral Rehabil. **23**, 289–297 (1996)
51. C.H. Wilder-Smith, P. Wilder-Smith, H. Kawakami-Wong, J. Voronets, K. Osann, A. Lussi, Quantification of dental erosions in patients with GERD using optical coherence tomography before and after double-blind, randomized treatment with esomeprazole or placebo. Am. J. Gastroenterol. **104**(11), 2788–2795 (2009). doi:10.1038/ajg.2009.441
52. H. Shemesh, G. van Soest, M.K. Wu, P.R. Wesselink, Detection of root surface fractures with swept-source optical coherence tomography (SS-OCT). Photomed. Laser Surg. **31**(1), 23–27 (2013). doi:10.1089/pho.2012.3383
53. T. Yoshioka, H. Sakaue, H. Ishimura, A. Ebihara, H. Suda, Y. Sumi, Diagnosis of vertical root fractures with optical coherence tomography. J. Endod. **34**(6), 739–742 (2008)
54. G.Q. Monteiro, M.A. Montes, A.S. Gomes, C.C. Mota, S.L. Campello, A.Z. Freitas, Marginal analysis of resin composite restorative systems using optical coherence tomography. Dent. Mater. **27**(12), e213–e223 (2011)
55. T.A. Bakhsh, A. Sadr, Y. Shimada, J. Tagami, Y. Sumi, Non-invasive quantification of resin-dentin interfacial gaps using optical coherence tomography: validation against confocal microscopy. Dent. Mater. **27**(9), 915–925 (2011)
56. L.L. Otis, J.C. Meiers, Refraction artifacts cause spatial distortion in OCT images. J. Dent. Res. **79**(SI), 456 (2000)
57. L.L. Otis, R.I. al-Sadhan, J. Meiers, D. Redford-Badwal, Identification of occlusal sealants using optical coherence tomography. J. Clin. Dent. **14**(1), 7–10 (2003)
58. J.S. Holtzman, K. Osann, J. Pharar, K. Lee, Y.C. Ahn, T. Tucker, S. Sabet, Z. Chen, R. Gukasyan, P. Wilder-Smith, Ability of optical coherence tomography to detect caries beneath commonly used dental sealants. Lasers Surg. Med. **42**(8), 752–759 (2010)
59. R.S. Jones, M. Staninec, D. Fried, Imaging artificial caries under composite sealants and restorations. J. Biomed. Opt. **9**(6), 1297–1304 (2004)
60. L.L. Otis, B.W. Colston, M.J. Everett, Optical coherence tomography: a novel assessment of coronal restorations. J. Dent. Res. **77**, 824 (1998)
61. L.L. Otis, B.W. Colston, M.J. Everett, Optical coherence topography: a novel assessment of composite wear. J. Dent. Res. **77**, 276 (1998)
62. A. Badersten, R. Nilveus, J. Egelberg, Reproducibility of probing attachment level measurements. J. Clin. Periodontol. **11**, 475–485 (1984)

63. G.C. Armitage, G.K. Svanbern, H. Loe, Microscopic evaluation of clinical measurements of connective tissue attachment levels. J. Clin. Periodontol. **4**(3), 173–190 (1977)
64. U. van der Velden, Errors in the assessment of pocket depth in vitro. J. Clin. Periodontol. **5**, 182–187 (1978)
65. H. Kingman, H. Loe, A. Anerun, Boysen, Errors in measuring parameters associated with periodontal health and disease. J. Periodontol. **62**, 77–486 (1991)
66. M.K. Jeffcoat, M.S. Reddy, A comparison of probing and radiographic methods for detection of periodontal disease progression. Curr. Opin. Dent. **1**, 45–51 (1991)
67. M.C.K. Yang, Y.Y. Namgung, R.G. Marks, I. Magnusson, W.B. Clark, Change detection on longitudinal data in periodontal research. J Periodont Res **28**, 152–160 (1993)
68. M.A. Espeland, U.E. Zappa, P.E. Hogan, C. Simona, H. Graf, Cross-sectional and longitudinal reliability for clinical measurement of attachment loss. J. Clin. Periodontol. **18**, 126–133 (1991)
69. M.J. Novak, Diagnosis of periodontal diseases: reaction paper. Adv. Dent. Res. **5**, 37–40 (1991)
70. L.L. Otis, D. Piao, Q. Zhu, Optical coherence tomography of oral soft tissues. J Acad Laser Dent **12**(4), 16 (2004)
71. D.Q. Piao, Q. Zhu, L.L. Otis, Doppler angle and flow velocity mapping by combined Doppler shift and Doppler bandwidth measurements in Optical Doppler tomography. Opt. Lett. **28**(13), 1120–1122 (2003)
72. L.L. Otis, D. Piao, C.W. Gibson, Q. Zhu, Quantifying labial blood flow using optical Doppler tomography. Oral Surg. Oral Med. Oral Pathol. Oral Radiol. Endod. **98**, 189–194 (2004)
73. J. Na, B.H. Lee, J.H. Baek, E.S. Choi, Optical approach for monitoring the periodontal ligament changes induced by orthodontic forces around maxillary anterior teeth of white rats. Med. Biol. Eng. Comput. **46**(6), 597–603 (2008)
74. C.E. Misch, *Dental implant prosthetics* (Elsevier Mosby, St. Louis, Mo, 2005)
75. T. Berglundh, L. Persson, B. Klinge, A systematic review of the incidence of biological and technical complications in implant dentistry reported in prospective longitudinal studies of at least 5 years. J. Clin. Periodontol. **29**(Suppl 3), 197–212 (2002)
76. T. Albrektsson, L. Sennerby, Direct bone anchorage of oral implants: clinical and experimental considerations of the concept of osseointegration. Int. J. Prosthodont. **3**(1), 30–41 (1990)
77. D. Buser, H.P. Weber, N.P. Lang, Tissue integration of non-submerged implants. 1-year results of a prospective study with 100 ITI hollow-cylinder and hollow-screw implants. Clin. Oral Implants Res. **1**(1), 33–40 (1990)
78. M. Esposito, J. Hirsch, U. Lekholm, P. Thomsen, Differential diagnosis and treatment strategies for biologic complications and failing oral implants: a review of the literature. Int. J. Oral Maxillofac. Implants **14**(4), 473–490 (1999)
79. C.E. Misch, The implant quality scale: a clinical assessment of the health – disease continuum. Oral Health **88**(7), 15 (1998)
80. R.T. Kao, D.A. Curtis, P.A. Murray, Diagnosis and management of peri-implant disease. J. Calif. Dent. Assoc. **25**(12), 872–880 (1997)
81. M.S. Block, J.N. Kent, Prospective review of integral implants. Dent. Clin. North Am. **36**(1), 27–37 (1992)
82. G.E. Salvi, N.P. Lang, Diagnostic parameters for monitoring peri-implant conditions. Int. J. Oral Maxillofac. Implants **19**(Suppl), 116–127 (2004)
83. A. Mombelli, N.P. Lang, The diagnosis and treatment of peri-implantitis. Periodontol. 2000 **17**, 63–76 (1998)
84. A. Mombelli, Etiology, diagnosis, and treatment considerations in peri-mplantitis. Curr. Opin. Periodontol. **4**, 127–136 (1997)
85. L.J. Heitz-Mayfield, N.P. Lang, Antimicrobial treatment of peri-implant diseases. Int. J. Oral Maxillofac. Implants **19**(Suppl), 128–139 (2004)

86. B. Klinge, A. Gustafsson, T. Berglundh, A systematic review of the effect of anti-infective therapy in the treatment of peri-implantitis. J. Clin. Periodontol. **29**(Suppl 3), 213–225 (2002)
87. A.M. Roos-Jansaker, S. Renvert, J. Egelberg, Treatment of peri-implant infections: a literature review. J. Clin. Periodontol. **30**(6), 467–485 (2003)
88. M.C. Manz, Factors associated with radiographic vertical bone loss around implants placed in a clinical study. Ann. Periodontol. **5**(1), 137–151 (2000)
89. M. Esposito, P. Thomsen, L.E. Ericson, U. Lekholm, Histopathologic observations on early oral implant failures. Int. J. Oral Maxillofac. Implants **14**(6), 798–810 (1999)
90. J.W. Verhoeven, M.S. Cune, C. de Putter, Reliability of some clinical parameters of evaluation in implant dentistry. J. Oral Rehabil. **27**(3), 211–216 (2000)
91. American Cancer Society, *Cancer Facts and Figures* (American Cancer Society, Atlanta, 2000), p. 4
92. J. Regezi, J. Sciubba (eds.), *Oral Pathology* (W.B.Saunders, Philadelphia, 1993), pp. 77–90
93. California Department of Health Services. *Cancer Surveillance Section Annual Report*, March 1999
94. D.P. Slaughter, H.W. Southwick, W. Smejkal, Field cancerization in oral stratified squamous epithelium. Cancer **6**, 963–968 (1953)
95. U.S. Department of Health and Human Services. A National Call to Action to Promote Oral Health http://www.nidr.nih.gov/sgr/nationalcalltoaction.htm. Rockville: Department of Health and Human Services, Public Health Service, Centers for Disease Control and Prevention, National Institutes of Health, National Institute of Dental and Craniofacial Research, May 2003. Report No.: 03-5303
96. P.E. Petersen, T. Yamamoto, Community Improving the oral health of older people: the approach of the WHO Global Oral Health Programme. Dent. Oral Epidemiol. **33**(2), 81–92 (2005)
97. J.B. Epstein, R. Feldman, R.J. Dolor, S.R. Porter, The utility of tolonium chloride rinse in the diagnosis of recurrent or second primary cancers in patients with prior upper aerodigestive tract cancer. Head Neck **25**(11), 911–921 (2003)
98. J.B. Epstein, L. Zhang, M. Rosin, Advances in the diagnosis of oral premalignant and malignant lesions. J. Can. Dent. Assoc. **68**(10), 617–621 (2002)
99. S. Silverman, C. Migliorati, J. Barbosa, Toluidine blue staining in the detection of oral precancerous and malignant lesions. Oral Surg. Oral Med. Oral Pathol. **57**, 379–382 (1984)
100. J. Epstein, C. Scully, U. Spinelli, Toluidine blue and Lugol's iodine solution for the assessment of oral malignant disease and lesions at risk of malignancy. J. Oral Pathol. Med. **21**, 160–163 (1992)
101. Patton LL, The effectiveness of community-based visual screening and utility of adjunctive diagnostic aids in the early detection of oral cancer. Oral Oncol. **41**, 708–723 (2003)
102. M.A. Onofre, M.R. Sposto, C.M. Navarro, Reliability of toluidine blue application in the detection of oral epithelial dysplasia and in situ and invasive squamous cell carcinomas. Oral Surg. Oral Med. Oral Pathol. Oral Radiol. Endod. **91**(5), 535–540 (2001)
103. T.W. Poate, J.A. Buchanan, T.A. Hodgson, P.M. Speight, A.W. Barrett, D.R. Moles, C. Scully, S.R. Porter, An audit of the efficacy of the oral brush biopsy technique in a specialist Oral Medicine unit. Oral Oncol. **40**(8), 829–834 (2004)
104. G.R. Ogden, J.G. Cowpe, M.W. Green, Detection of field change in oral cancer using oral exfoliative cytologic study. Cancer **68**, 1611–1615 (1991)
105. M.P. Rosin, J.B. Epstein, K. Berean, S. Durham, J. Hay, X. Cheng et al., The use of exfoliative cell samples to map clonal genetic alterations in the oral epithelium of high-risk patients. Cancer Res. **57**, 5258–5260 (1997)
106. J.C. Kennedy, R.H. Pottier, Endogenous protoporphyrin IX, a clinically useful photosensitizer for photodynamic therapy. J. Photochem. Photobiol. **14**, 275–292 (1992)
107. R.C.J. Benson, Treatment of diffuse transitional cell carcinoma in situ by whole bladder hematoporphyrin derivative photodynamic therapy. J. Urol. **134**, 675–678 (1985)

108. K. Svanberg, I. Wang, R. Rydell, A. Elner, J. Wennerberg, L. Pais Clemente, E. Cardosa, R. Pratas, M. Pais Clemente, S. Andersson-Engels, S. Svanberg, Fluorescence diagnostics of head and neck cancer utilizing oral administration of δ-Amino Levulinic acid. SPIE **2371**, 129–141 (1995)
109. C.J. Chang, P. Wilder-Smith, Topical application of photofrin for photodynamic diagnosis of oral neoplasms. Plast. Reconstr. Surg. **115**, 1877–1886 (2005)
110. A. Leunig, K. Rick, H. Stepp, R. Gutmann, G. Alwin, R. Baumgartner, J. Feyh, Fluorescence imaging and spectroscopy of 5-aminolevulinic acid-induced protoporphyrin IX for the detection of neoplastic lesions in the oral cavity. Am. J. Surg. **172**(6), 674–677 (1996)
111. C.S. Betz, H. Stepp, S. Arbogast, G. Grevers, R. Baumgartner, A. Leunig, A comparative study of normal inspection, autofluorescence and 5-ALA-induced PPIX fluorescence for oral cancer diagnosis. Int. J. Cancer **97**, 245–252 (2002)
112. I.J. Bigio, S.G. Bown, Spectroscopic sensing of cancer and cancer therapy: current status of translational research. Cancer Biol. Ther. **3**(3), 259–267 (2004)
113. K. Sokolov, M. Follen, R. Richards-Kortum, Optical spectroscopy for detection of neoplasia. Curr. Opin. Chem. Biol. **6**(5), 651–658 (2002)
114. K. Sokolov, R. Drezek, K. Gossage, R. Richards-Kortum, Reflectance spectroscopy with polarized light: is it sensitive to cellular and nuclear morphology. Opt. Expr. **5**, 302–317 (1999)
115. I. Georgakoudi, E. Sheets, M.G. Muller, V. Backman, C.P. Crum, K. Badizadegan, R.R. Dasari, M.S. Feld, G.R. Harrison, Trimodal spectroscopy for the detection and characterization of cervical precancers in vivo. Am. J. Obstet. Gynecol. **186**, 374–382 (2002)
116. I. Georgakoudi, B.C. Jacobson, J. Van Dam, V. Backman, M.B. Wallace, M.G. Muller, Q. Zhang, K. Badizadegan, D. Sun, G.A. Thomas et al., Fluorescence, reflectance, and light-scattering spectroscopy for evaluating dysplasia in patients with Barretts esophagus. Gastroenterology **120**, 1620–1629 (2001)
117. R.J. Nordstrom, L. Burke, J.M. Niloff, J.F. Myrtle, Identification of cervical intraepithelial neoplasia (CIN) using UV-excited fluorescence and diffuse-reflectance tissue spectroscopy. Lasers Surg. Med. **29**, 118–127 (2001)
118. R.A. Weersink, J.E. Hayward, K.R. Diamond, M.S. Patterson, Accuracy of noninvasive in vivo measurements of photosensitizer uptake based on a diffusion model of reflectance spectroscopy. Photochem. Photobiol. **66**, 326–335 (1997)
119. G. Zonios, L. Perelman, V. Backman, R. Manoharan, M. Fitzmaurice, J. Van Dam, M.S. Feld, Diffuse reflectance spectroscopy of human adenomatous colon polyps in vivo. Appl. Opt. **38**, 6628–6637 (1999)
120. R.R. Alfano, D.B. Tata, J. Cordero, P. Tomashefsky, F.W. Longo, M.A. Alfano, Laser induced fluorescence spectroscopy from native cancerous and normal tissue. IEEE J. Quant. Electron. **20**, 1507–1511 (1984)
121. G.A. Wagnieres, W.M. Star, B.C. Wilson, In vivo fluorescence spectroscopy and imaging for oncological applications. Photochem. Photobiol. **68**, 603–632 (1998)
122. N. Ramanujam, Fluorescence spectroscopy of neoplastic and non neoplastic tissues. Neoplasia **2**, 89–117 (2000)
123. R. Drezek, C. Brookner, I. Pavlova, I. Boiko, A. Malpica, R. Lotan, M. Follen, R. Richards-Kortum, Autofluorescence microscopy of fresh cervical-tissue sections reveals alterations in tissue biochemistry with dysplasia. Photochem. Photobiol. **73**, 636–641 (2001)
124. I. Georgakoudi, B.C. Jacobson, M.G. Muller, E.E. Sheets, K. Badizadegan, D.L. Carr-Locke, C.P. Crum, C.W. Boone, R.R. Dasari, J. Van Dam et al., NAD(P)H and collagen as in vivo quantitative fluorescent biomarkers of epithelial precancerous changes. Cancer Res. **62**, 682–687 (2002)
125. R. Drezek, K. Sokolov, U. Utzinger, I. Boiko, A. Malpica, M. Follen, R. Richards-Kortum, Understanding the contributions of NADH and collagen to cervical tissue fluorescence spectra: modeling, measurements, and implications. J. Biomed. Opt. **6**, 385–396 (2001)
126. A. Zuluaga, U. Utzinger, A. Durkin, H. Fuchs, A. Gillenwater, R. Jacob, B. Kemp, J. Fan, R. Richards-Kortum, Fluorescence excitation emission matrices of human tissue: a system for in vivo measurement and data analysis. Appl. Spectr. **53**, 302–311 (1998)

127. R.A. Zangaro, L. Silveira, R. Manoharan, G. Zonios, I. Itzkan, R. Dasari, J. Van Dam, M.S. Feld, Rapid multiexcitation fluorescence spectroscopy system for in vivo tissue diagnosis. Appl. Opt. **35**, 5211–5219 (1997)
128. N. Ramanujam, M. Follen Mitchell, A. Mahadevan-Jansen, S.L. Thomsen, G. Staerkel, A. Malpica, T. Wright, N. Atkinson, R. Richards-Kortum, Cervical pre-cancer detection using a multivariate statistical algorithm based on laser induced fluorescence spectra at multiple excitation wavelengths. Photochem. Photobiol. **6**, 720–735 (1996)
129. H. Zeng, C. MacAulay, D.I. McLean, B. Palcic, Reconstruction of in vivo skin autofluorescence spectrum from microscopic properties by Monte Carlo simulation. J. Photochem. Photobiol. **38**, 234–240 (1997)
130. D.E. Hyde, T.J. Farrel, M.S. Patterons, B.C. Wilson, A diffusion theory model of spatially resolved fluorescence from depth dependent fluorophore concentrations. Phys. Med. Biol. **46**, 369–383 (2001)
131. Q. Zhang, M. Muller, J. Wu, M.S. Feld, Turbidity free fluorescence spectroscopy of biological tissue. Opt. Lett. **25**, 1451–1453 (2000)
132. F. Koenig, F.J. McGovern, H. Enquist, R. Larne, T.F. Deutsch, K.T. Schomacker, Autofluorescence guided biopsy for the early diagnosis of bladder carcinoma. J. Urol. **159**, 1871–1875 (1998)
133. S. Andersson-Engels, C. Klinteberg, K. Svanberg, S. Svanberg, In vivo fluorescence imaging for tissue diagnostics. Phys. Med. Biol. **42**, 815–824 (1997)
134. N. Stone, C. Kendall, J. Smith, P. Crow, H. Barr, Raman spectroscopy for identification of epithelial cancers. Faraday Discuss. **126**, 141–157 (2004)
135. M. Culha, D. Stokes, T. Vo-Dinh, Surface-enhanced Raman scattering for cancer diagnostics: detection of the BCL2 gene. Expert Rev. Mol. Diagn. **3**(5), 669–675 (2003)
136. T.C. Bakker Schut, M.J. Witjes, H.J. Sterenborg, O.C. Speelman, J.L. Roodenburg, E.T. Marple, H.A. Bruining, G.J. Puppels, In vivo detection of dysplastic tissue by Raman spectroscopy. Anal. Chem. **72**(24), 6010–6018 (2000)
137. N. Stone, P. Stavroulaki, C. Kendall, M. Birchall, H. Barr, Raman spectroscopy for early detection of laryngeal malignancy: preliminary results. Laryngoscope **110**(10 Pt 1), 1756–1763 (2000)
138. A. Mahadevan-Jansen, M.F. Mitchell, N. Ramanujam, A. Malpica, S. Thomsen, U. Utzinger, R. Richards-Kortum, Abstract near-infrared Raman spectroscopy for in vitro detection of cervical precancers. Photochem. Photobiol. **68**(1), 123–132 (1998)
139. L.-P. Choo-Smith, H.G.M. Edwards, H.P. Endtz, J.M. Kros, F. Heule, H. Barr, J.S. Robinson Jr., H.A. Bruining, G.J. Puppels, Medical applications of Raman spectroscopy: from proof of principle to clinical implementation. Biopolymers **67**, 1–9 (2002)
140. M.G. Shim, L.M. Song, N.E. Marcon, B.C. Wilson, In vivo near-infrared Raman spectroscopy: demonstration of feasibility during clinical gastrointestinal endoscopy. Photochem. Photobiol. **72**(1), 146–150 (2000)
141. I.J. Bigio, J.R. Mourant, Ultraviolet and visible spectroscopies for tissue diagnostics: fluorescence spectroscopy and elastic scattering spectroscopy. Phys. Med. Biol. **42**, 803–814 (1997)
142. M.B. Wallace, L.T. Perelman, V. Backman, J.M. Crawford, M. Fitzmaurice, M. Seiler, K. Badizadegan, S.J. Shields, I. Itzkan, R.R. Dasari et al., Endoscopic detection of dysplasia in patients with Barrett's esophagus using light-scattering spectroscopy. Gastroenterology **119**, 677–682 (2000)
143. V. Backman, R. Gurjar, K. Badizadegan, I. Itzkan, R.R. Dasari, L.T. Perelman, M.S. Feld, Polarized light scattering spectroscopy for quantitative measurement of epithelial cellular structures in situ. IEEE J. Sel. Top. Quant. Electron. **5**, 1019–1026 (1999)
144. J.R. Mourant, M. Canpolat, C. Brocker, O. Esponda-Ramos, T.M. Johnson, A. Matanock, K. Stetter, J.P. Freyer, Light scattering from cells: the contribution of the nucleus and the effects of proliferative status. J. Biomed. Opt. **5**, 131–137 (2000)

145. A.L. Clark, A. Gillenwater, R. Alizadeh-Naderi, A.K. El-Naggar, R. Richards-Kortum, Detection and diagnosis of oral neoplasia with an optical coherence microscope. J. Biomed. Opt. **9**(6), 1271–1280 (2004)
146. J.W. Hettinger, M.M. de la Pena, W.R. Myers, M.E. Williams, A. Reeves, R.L. Parsons, R.C. Haskell, R. Wang, J.I. Medford, Optical coherence microscopy. A technology for rapid, in vivo, non-destructive visualization of plants and plant cells. Plant Physiol. **123**, 3–15 (2000)
147. A. Reeves, R.L. Parsons, J.W. Hettinger, J.I. Medford, In vivo three-dimensional imaging of plants with optical coherence microscopy. J. Microsc. **208**, 177–189 (2002)
148. J.A. Izatt, M.D. Kulkarni, H.W. Wang, K. Kobayashi, M.V. Sivak, Optical coherence tomography and microscopy in gastrointestinal tissues and human skin. IEEE J. Sel. Top. Quantum Electron. **2**, 1017–1028 (1996)
149. A.D. Aguirre, P. Hsiung, T.H. Ko, I. Hartl, J.G. Fujimoto, High-resolution optical coherence microscopy for high-speed, in vivo cellular imaging. Opt. Lett. **28**, 2064–2066 (2003)
150. J.A. Izatt, M.R. Hee, G.M. Owen, Optical coherence microscopy in scattering media. Opt. Lett. **19**, 590 (1994)
151. C. Bertrand, P. Corcuff, In vivo spatio-temporal visualization of the human skin by real-time confocal microscopy. Scanning **16**, 150–154 (1993)
152. P. Corcuff, G. Gonnord, G.E. Piérard, J.L. Lévéque, In vivo confocal microscopy of human skin: a new design for cosmetology and dermatology. Scanning **18**, 351–355 (1996)
153. B.R. Masters, D.J. Aziz, A.F. Gmitro, J.H. Kerr, T.C. O'Grady, L. Goldman, Rapid observation of unfixed, unstained human skin biopsy specimens with confocal microscopy and visualization. J. Biomed. Optics **2**, 437–445 (1997)
154. S. González, M. Rajadhyaksha, G. Rubinstein, R.R. Anderson, Characterization of psoriasis in vivo by reflectance confocal microscopy. J. Med. (Westbury) **30**, 337–356 (1999)
155. S. Gonzalez, M. Rajadhyaksha, A. Gonzalez-Serva, W.M. White, R.R. Anderson, Confocal reflectance imaging of folliculitis in vivo: correlation with routine histology. J. Cutaneous Pathol. **26**, 201–205 (1999)
156. K.J. Busam, K. Hester, C. Charles, D.L. Sachs, C.R. Antonescu, S. Gonzalez, A.C. Halpern, Detection of clinically amelanotic malignant melanoma and assessment of its margins by in vivo confocal scanning laser microscopy. Archiv. Dermatol. **137**, 923–929 (2001)
157. R.G. Langley, M. Rajadhyaksha, P.J. Dwyer, A.J. Sober, T.J. Flotte, R.R. Anderson, Confocal scanning laser microscopy of benign and malignant melanocytic skin lesions in vivo. J. Am. Acad. Dermatol. **45**, 365–376 (2001)
158. S. Gonzalez, Z. Tannous, Real-time in vivo confocal reflectance microscopy of basal cell carcinoma. J. Am. Acad. Dermatol. **47**, 869–874 (2002)
159. T. Collier, A. Lacy, R. Richards-Kortum, A. Malpica, M. Follen, Near real-time confocal microscopy of amelanotic tissue: detection of dysplasia in ex vivo cervical tissue. Acad. Radiol. **9**(5), 504–512 (2002)
160. R.A. Drezek, T. Collier, C.K. Brookner, A. Malpica, R. Lotan, R.R. Richards-Kortum, M. Follen, Laser scanning confocal microscopy of cervical tissue before and after application of acetic acid. Am. J. Obstet. Gynecol. **182**, 1135–1139 (2000)
161. H. Inoue, T. Igari, T. Nishikage, K. Ami, T. Yoshida, T. Iwai, A novel method of virtual histopathology using laser-scanning confocal microscopy in-vitro with untreated fresh specimens from the gastrointestinal mucosa. Endoscopy **32**, 439–443 (2000)
162. W.M. White, M. Rajadhyaksha, S. Gonzalez, R.L. Fabian, R.R. Anderson, Noninvasive imaging of human oral mucosa in vivo by confocal reflectance microscopy. Laryngoscope **109**, 1709–1717 (1999)
163. A.M. Clark, A.M. Gillenwater, T.G. Collier, R. Alizadeh-Naderi, A.K. El-Naggar, R. Richards-Kortum, Confocal microscopy for real-time detection of oral cavity neoplasia. Clin. Cancer Res. **9**, 4714–4721 (2003)

164. P. Wilder-Smith, T. Krasieva, W.G. Jung, J. Zhang, Z.P. Chen, K. Osann, B. Tromberg, Non-invasive imaging of oral premalignancy and malignancy. Invited contribution to special edition. J. Biomed. Optics **10**(5), 050601-1-8 (2005)
165. P. Wilder-Smith, W.G. Jung, M. Brenner, K. Osann, H. Beydoun, D. Messadi, Z. Chen, Optical coherence tomography for the diagnosis of oral malignancy. Lasers Surg. Med. **35**, 269–275 (2004)
166. P. Wilder-Smith, K. Lee, S. Guo, J. Zhang, K. Osann, Z. Chen, D. Messadi, In vivo diagnosis of oral dysplasia and malignancy using optical coherence tomography: preliminary studies in 50 patients. Lasers Surg. Med. **41**(5), 353–357 (2009)
167. Z. Hamdoon, W. Jerjes, R. Al-Delayme, G. McKenzie, A. Jay, C. Hopper, Structural validation of oral mucosal tissue using optical coherence tomography. Head Neck Oncol. **4**, 29 (2012). doi:10.1186/1758-3284-4-29

Anatomic Optical Coherence Tomography of Upper Airways

75

Anthony Chin Loy, Joseph Jing, Jun Zhang, Yong Wang, Said Elghobashi, Zhongping Chen, and Brian J. F. Wong

75.1 Introduction

The upper airway is a complex and intricate system responsible for respiration, phonation, and deglutition. Obstruction of the upper airways, as in obstructive sleep apnea (OSA), afflicts 12–18 million Americans. Pharyngeal size and shape are important factors in the pathogenesis of OSA. Nocturnal loss in pharyngeal muscular tone combined with high pharyngeal resistance leads to collapse of the airway and periodic partial or complete upper airway obstruction. These episodes, though brief, can lead to significant adverse health outcomes, including cardiac,

A. Chin Loy
Department of Otolaryngology Head and Neck Surgery, The Beckman Laser Institute, University of California Irvine, Irvine, CA, USA

J. Jing • J. Zhang
Department of Biomedical Engineering, The Beckman Laser Institute, University of California Irvine, Irvine, CA, USA

Y. Wang • S. Elghobashi
Department of Mechanical and Aerospace Engineering, University of California Irvine, Irvine, CA, USA

Z. Chen (✉)
The Edwards Life Sciences Center for Advanced Cardiovascular Technology, Beckman Laser Institute, Irvine, CA, USA

Department of Biomedical Engineering, Beckman Laser Institute, University of California Irvine, Irvine, CA, USA
e-mail: z2chen@uci.edu

B.J.F. Wong (✉)
Department of Otolaryngology Head and Neck Surgery, Department of Biomedical Engineering, Department of Surgery, The Beckman Laser Institute, University of California Irvine, Irvine, CA, USA
e-mail: bjwong@uci.edu

© Springer International Publishing Switzerland 2015

W. Drexler, J.G. Fujimoto (eds.), *Optical Coherence Tomography*,
DOI 10.1007/978-3-319-06419-2_77

neurologic, and metabolic sequelae. Though prevalent in the population, the pathogenesis of OSA is poorly understood. The most common explanation in the literature assumes that OSA is a function of decreased pharyngeal size with concomitant increased pharyngeal resistance. These factors combined with the relaxation of the pharyngeal dilator muscles predispose the pharynx to collapse during sleep.

The three major areas of obstruction are the nose, the palate, and the hypopharynx though it is more likely the combination of two or more of these areas that contribute to OSA. In the Fujita classification, the patterns of obstruction were classified by anatomic location:

1. Type 1: collapse in the retropalatal region only
2. Type 2: collapse in both the retropalatal and retrolingual regions
3. Type 3: collapse in the retrolingual region only

The identification of the area of collapse is needed to direct surgical treatment though this is not often accomplished, and clinical judgment largely dictates the selection of operative approach. Operations and procedures are directed at the most common areas of obstruction. Nasal surgery includes septoplasty, turbinate reduction, and correction of internal and external valve deformities. Nasal surgery rarely corrects OSA by itself, but does allow greater nasal patency for use of Continuous Positive Airway Pressure (CPAP). The most common operation used to treat OSA is the uvulopalatopharyngoplasty (UPPP), which is performed by resecting redundant palatal and pharyngeal tissue. Though it is the most common operation for OSA, the procedure has a widely cited success rate of less than 50 % depending on the severity of disease [1]. Other OSA operations escalate in complexity and address other organs and tissue, but lack of detailed anatomic information on the site or level of obstruction leads to modest improvement in a majority of patients. More aggressive procedures include base of tongue reduction, advancement of the maxilla and mandible to anteriorly displace the base of tongue, suspension of the larynx to the chin, and even tracheostomy.

The failure rate in the surgical treatment OSA stems from a lack of diagnostic information on the site and mechanism of airway collapse. Current diagnostic techniques include magnetic resonance imaging (MRI) and computed tomography (CT), though these studies are not routinely ordered, as MRI and CT are expensive, inconvenient for the patient, generally performed during wakefulness, and in the case of CT necessitate exposure to ionizing radiation. MRI provides great detail of the soft tissue structures of the upper airways while avoiding exposure to ionizing radiation. However, the study is expensive, while the length and noise of the exam may prevent collection of sleep data without sedation. Use of sedatives alters normal physiological control of the pharyngeal musculature and hence limits the utility of this approach in mimicking natural sleep. In regard to young children, sedation is necessary to perform MRI. Computed tomography provides detailed images of bone and soft tissue and is a considerably shorter exam than MRI. However, the exposure to ionizing radiation limits serial examinations over the respiratory cycle, limits the use of multiple exams to document postoperative

changes, and again is applied conservatively in children. Both MRI and CT provide information at a single point in time; they fail to provide volumetric data over the course of the breathing cycle.

More frequently, in-office fiber-optic endoscopy is used to estimate the loci for pharyngeal collapse in the OSA patient. Use of the Mueller maneuver, inhalation against a closed nose and mouth, to identify areas of obstruction is commonly used to better identify surgical treatment targets. The image of the airway through an endoscope is subject to significant distortion due to the wide-angle optics of these instruments. Measurements of airway diameter are thus largely subjective and are dependent on the relative location of the endoscope within the airway [2].

Polysomnography remains the gold standard in the diagnosis of OSA. Polysomnography (e.g., sleep study) is a multiparametric test used in the study of sleep and as a diagnostic tool in sleep medicine. It is an overnight diagnostic test performed during natural sleep that includes electroencephalography; electrooculography; measurement of nasal and oral airflow; electromyography, body, chest, and abdomen position monitors; electrocardiography; and pulse oximetry. Though extensive, it provides only physiological data for diagnosis; it does not provide structural data for treatment [1]. In face of the limitations of current clinically available methods to diagnose OSA, multiple alternative technologies have been proposed as a means to identify the locus of airway obstruction. Sampson's group in Perth developed a long-range optical coherence tomography (LR-OCT) system as a minimally invasive and cost-effective means of acquiring detailed structural data of the upper airway [3, 4]. It is safe for use in patients requiring multiple scans as no ionizing radiation is involved. It allows the physician to acquire serial data sets for the analysis of pre- and postoperative states. The lack of ionizing radiation also makes it safe for extended exposure, and the use of contemporary Fourier-domain technology facilitates rapid data collection with the entire length of an airway scanned in less than 1 min. In LR-OCT, a very small diameter catheter (smaller than conventional endoscopes) is inserted through the nose and into the pharynx. The placement of this imaging probe is similar to the placement of a feeding tube, pH monitor, or fiber-optic endoscope – all of which are routinely placed by physicians in multiple specialties. The probe tip rotates thus acquiring axial images of the pharynx, which can be reconstructed to evolve a structural image of the airway. In this implementation, the technology functions as an optical range finder, and high-resolution anatomic information of the subsurface tissues is not required. LR-OCT provides detailed structural and quantitative data of the upper airway that is not provided by current diagnostic imaging [5]. This information is crucial to the advancement of understanding the pathophysiology of OSA and the application of treatment to specific problem areas of the airway.

Conventional OCT provides detailed three-dimensional tomographic images of tissues with high axial and lateral resolution and beyond ophthalmology has found several uses in the imaging of hollow organs such as the urinary [6], GI [7], and pulmonary systems [8–12] However, the conventional use of OCT in the upper airways for structural imaging is limited due to a scanning range of only a few

millimeters or less. Long-range optical coherence tomography (LR-OCT) works as an optical range finder in circumstances where detailed microanatomic information on the surface is not required. Rather than focusing on microscopic substructure, LR-OCT increases the axial scanning range to image macroscopic anatomy [13]. This application is well suited for imaging the upper airway, where gross images can be used to examine the contours of the airway.

Long-range OCT systems were first described by Leitgeb, who used a phase shifting algorithm in order to double the effective imaging range of conventional OCT. With the increased imaging distance, the system used by Leitgeb also utilized frequency-domain optical coherence tomography to achieve high-speed probing [14]. In Sampson's group the use of LR-OCT in the upper airway is first mentioned in 2003 to measure the area of the human pharynx in patients with sleep apnea. The LR-OCT used at that time had a radial scanning range of 26 mm and a rotation rate of 5 Hz [15]. When first demonstrated by Huang in 1991, OCT was primarily used in ophthalmic imaging. Compared to the systems being used today, OCT was dominated by time-domain imaging. Time-domain imaging is limited by the need to scan through various path lengths in the reference arm in order for the sample arm to be interpreted. In the dynamic upper airway, slow scanning speeds produce motion artifact during the respiratory cycle [16]. In 1995, Fercher described Fourier-domain OCT (FD-OCT), which allowed for high-speed image acquisition (up to 100 times) and a decreased signal-to-noise ratio when compared with time-domain OCT [17]. FD-OCT measures all the optical echoes at once rather than sequentially as in time-domain OCT. This significantly increases sensitivity. Mechanical scanning of the reference path is unnecessary in FD-OCT, increasing the axial scan rate and imaging speed [18]. In recent studies utilizing a time-domain system, a lengthwise scan of the upper airway (12–18 cm) is completed in 12 min [19]. In the following, we describe an LR-OCT system using Fourier domain that is capable of completing a scan of comparable distance of the human airway in under a minute. The increased speed of acquisition decreases motion artifact experienced in previous experiments and negates the need to use respiratory gating to account for changes in the diameter of the airway that would be experienced in slower systems. There has been an increased level of interest in FD-OCT since then with developments improving the quality and speed of the systems. Recent systems employing Fourier-domain locked lasers have shown imaging speeds up to 370,000 axial scans/s, 100 times faster than standard OCT [20].

75.2 Current System

The current system is a catheter-based Fourier-domain optical coherence tomography (Fig. 75.1). Output light from a 1,310-nm swept source laser (26-mW average power, 50-kHz A-scan rate, 102-nm FWHM bandwidth, 5-mm coherence length in air) is split by a 90–10 couple into sample and reference arms, respectively. The reference arm utilizes an acousto-optic modulator (AOM) to generate a carrier

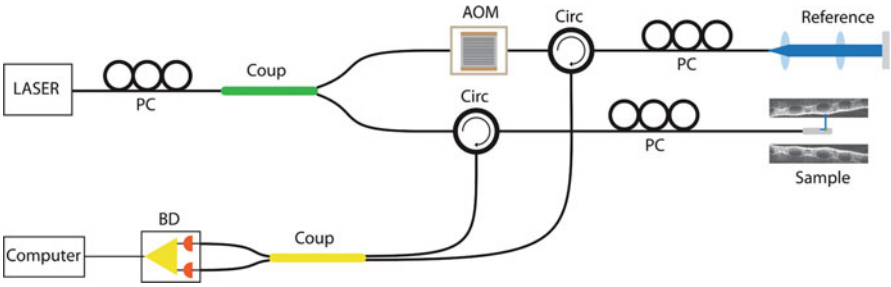

Fig. 75.1 Current long-range OCT system

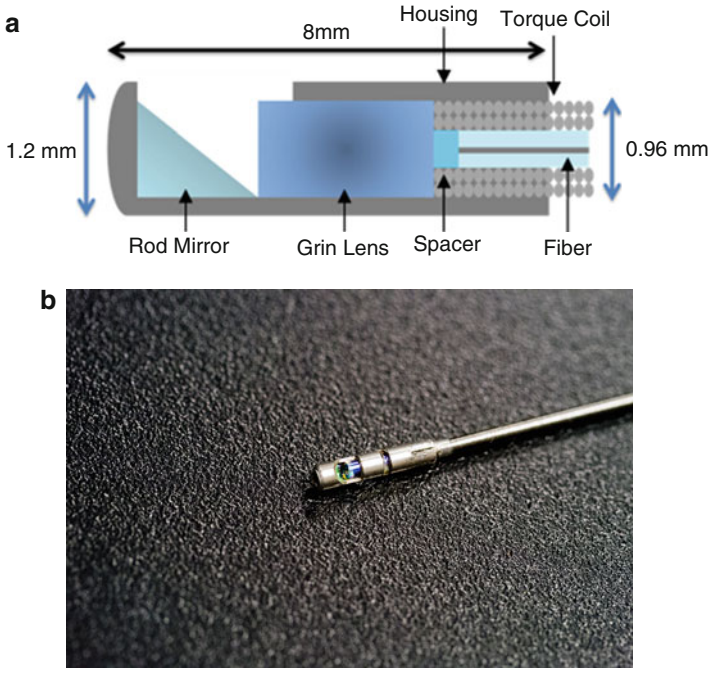

Fig. 75.2 Schematic (**a**) and picture (**b**) of LR-OCT probe

frequency of 150 MHz. No modulator is used in the sample arm to maximize signal and prevent insertion loss typically seen in AOMs. The resulting signal is converted in a voltage signal by a balanced detector and sampled by a 12-bit data acquisition card. Digitizing is performed at a sampling rate of 1 GHz allowing complete coverage of the wavelength sweep in 8192 points to optimize subsequent fast Fourier transform (FFT) calculations. The endoscopic OCT probe (Fig. 75.2) has an outer diameter (OD) of 1.2 mm, smaller than conventional endoscopes currently used in clinics. Rotational scanning is accomplished by using a fiber-optic rotary

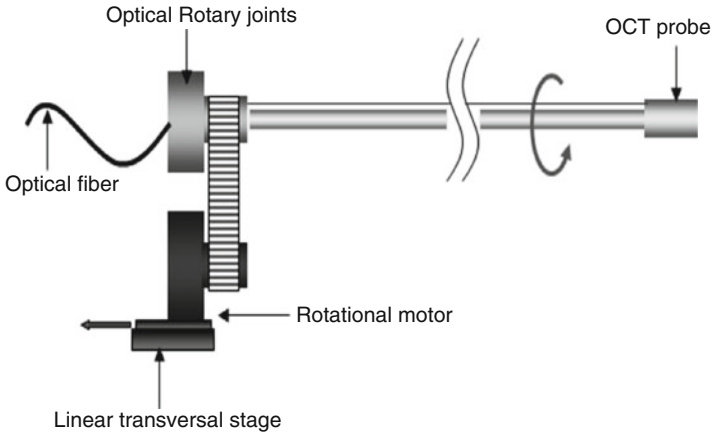

Fig. 75.3 Schematic of external rotational motor and probe

joint coupled with an externally mounted rotational motor. Torque from the motor is translated from the proximal to the distal end of the probe by a triple wound commercially available torque coil (outer diameter, 0.965 mm) (Fig. 75.3). The probe was designed to have an extended working distance of 20 mm. A Gradient Index Rod (GRIN) lens (0.23 pitch, 1-mm OD) combined with a measured spacer made of no-core fiber focuses the light from the probe. The no-core fiber was first spliced and then cleaved to leave a 150-um portion at the end of a standard single mode fiber. UV glue was used to attach fiber and GRIN lens and placed within a custom-designed metal housing. The probe is able to achieve a frame rate of 25 frames per second with each frame having 2,000 A-scans. During imaging, the probe is protected using a fluorinated ethylene propylene (FEP) sheath (OD 1.8 mm) that is first introduced into the airway. A dual motor linear stage was used for linear translation at 0.5 cm/s allowing for helical scanning over 20 cm in the span of 40 s. The axial resolution of the system was 10 μm in tissue and the lateral resolution was 112 μm, which is mainly a trade-off with extending the working distance of the probe.

Acquired OCT data is processed using a modified algorithm [21]. An FFT is first performed to convert the signal into the frequency domain. Multiplication by the Heaviside function isolates the positive frequencies, and an inverse FFT is performed to obtain a complex time-domain signal. A demodulation step removes the carrier frequency from this term and compensates the dispersion cause by the acousto-optic modulator (AOM) by multiplying the negative phase values of a single A-scan obtained when the optical path length difference (OPD) of the reference arm with the AOM and sample arm is zero. The resulting remapped data is linearized in the K-domain via a recalibration step followed by a final FFT to recover the spatial information. Our OCT software package is written entirely

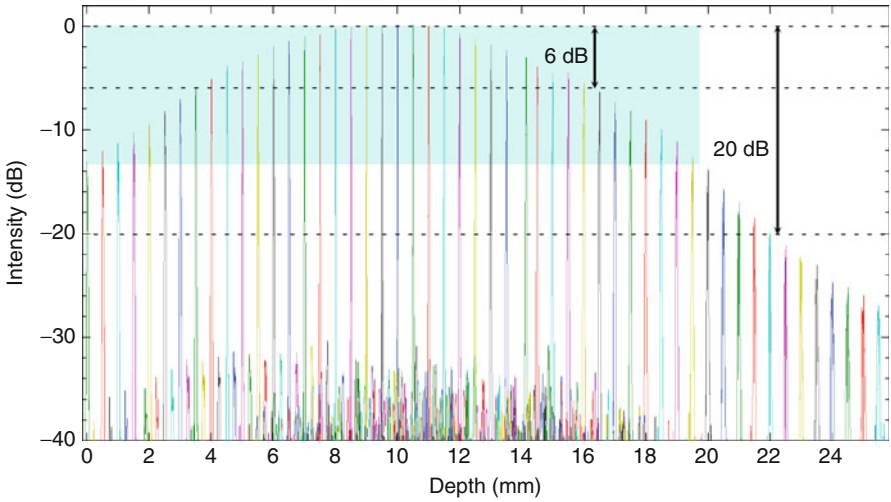

Fig. 75.4 Sensitivity of the current LR-OCT system as a function of depth

in C++ and features a multithreaded design for data acquisition, image processing, and display that allows for maximizing computational throughput. The entire OCT algorithm is processed on a commercial graphical processing unit (GPU) using Nvidia's CUDA package. This allows for frame-by-frame processing with a maximal frame rate of 25 frames per second for a given frame size of 2,000 A-lines.

75.3 Validation

The point spread function (PSF) versus imaging range graph (Fig. 75.4) was acquired by using a partial reflector at various distances and normalizing by the measured power. The system features a 6 dB sensitivity roll off at 12 mm total offset, which is in line with the expected imaging range give the removal of the mirror image.

In order to test the imaging capabilities of our system, a silicone airway was constructed. The airway was selected from a collection of adult CT scans devoid of pathology in the upper airway. The CT scan was loaded into commercial 3D rendering software, Amira, and a Standard Tessellation Language (stl) file was created for use as a model. Using rapid prototyping hardware, a phantom airway was molded in a green silicone matrix to ensure reflective properties compatible with the anatomical optical coherence tomography (aOCT) hardware (Fig. 75.4). The endoscopic LR-OCT probe and FEP sheath was introduced into the model airway in similar fashion to that of an actual research subject.

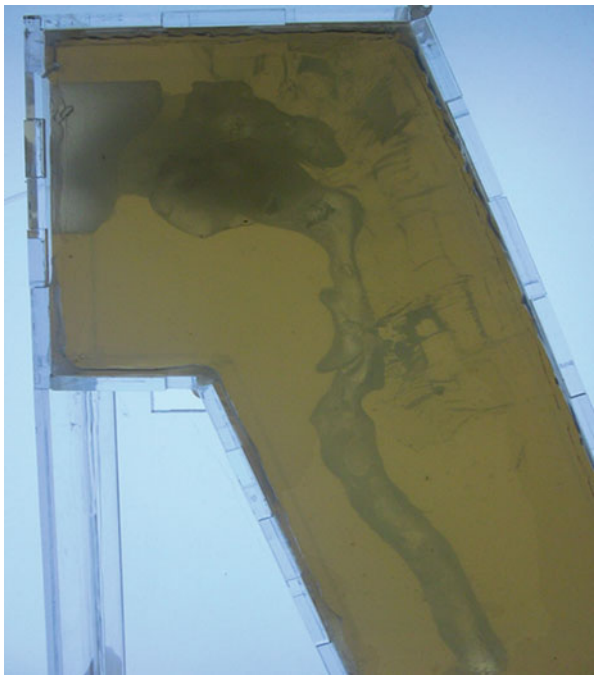

Fig. 75.5 Translucent model of normal phantom airway

A translucent model airway (Fig. 75.5), an exact copy of the green silicone phantom, was constructed to observe the pathway of probe and FEP sheath in the upper airway. A pullback scan of the phantom airway was performed. The resulting OCT data was compared against the original CT scan. As expected, the acquired OCT images are highly correlated with the original CT scan slices (Fig. 75.6).

75.4 In Vivo Human Studies

In vivo human adult imaging has been performed on adult and pediatric subjects. Patients' upper airway was anesthetized using 4 % topical lidocaine administered bilaterally through the nostril; likewise the pharynx was anesthetized with an aerosolized benzocaine. Ten minutes was allowed to elapse in order for the anesthesia to take full effect. The subject was placed into the classical position for in-office fiber-optic endoscopy exam. The FEP sheath was inserted into the anesthetized nostril along the length of the upper airway to the level of the esophagus. FEP tubing was marked as it exited the nostril for repositioning in case movement of the pharynx shifted the probe out of position. The tubing was secured using paper tape attached to the bridge of the nose. The LR-OCT probe was

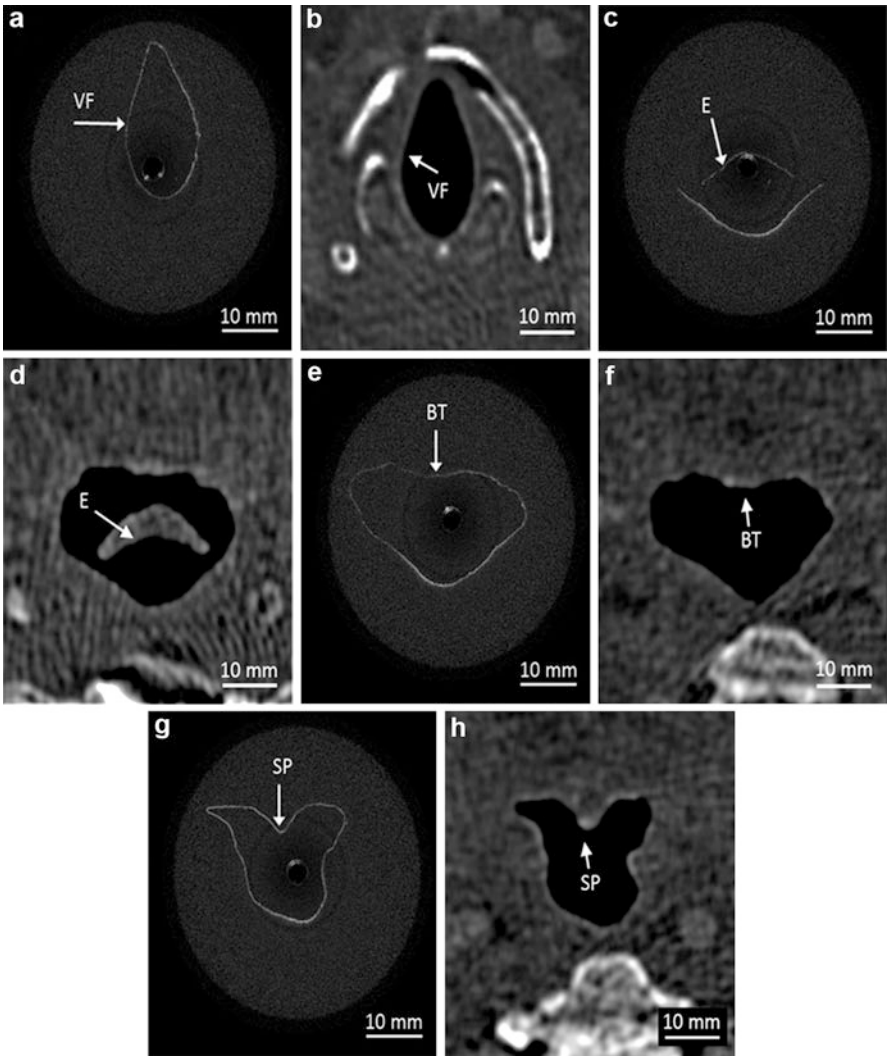

Fig. 75.6 Comparison of OCT images (**a**, **c**, **e**, **g**) in model with normal CT scan (**b**, **d**, **f**, **h**). Vocal folds (*VF*), epiglottis (*E*), base of tongue (*BT*), and soft palate (*SP*)

then advanced down the FEP tubing until resistance was appreciated (signifying the probe has reached the end of the FEP tubing). Placement of the FEP tubing and probe was confirmed using a flexible laryngoscope introduced through the second nostril, after which the laryngoscope was removed. The LR-OCT probe was retracted through the airway at a rate of 0.5 cm per second over a distance ranging from 18 to 23 cm. Multiple sets of images were taken from each subject.

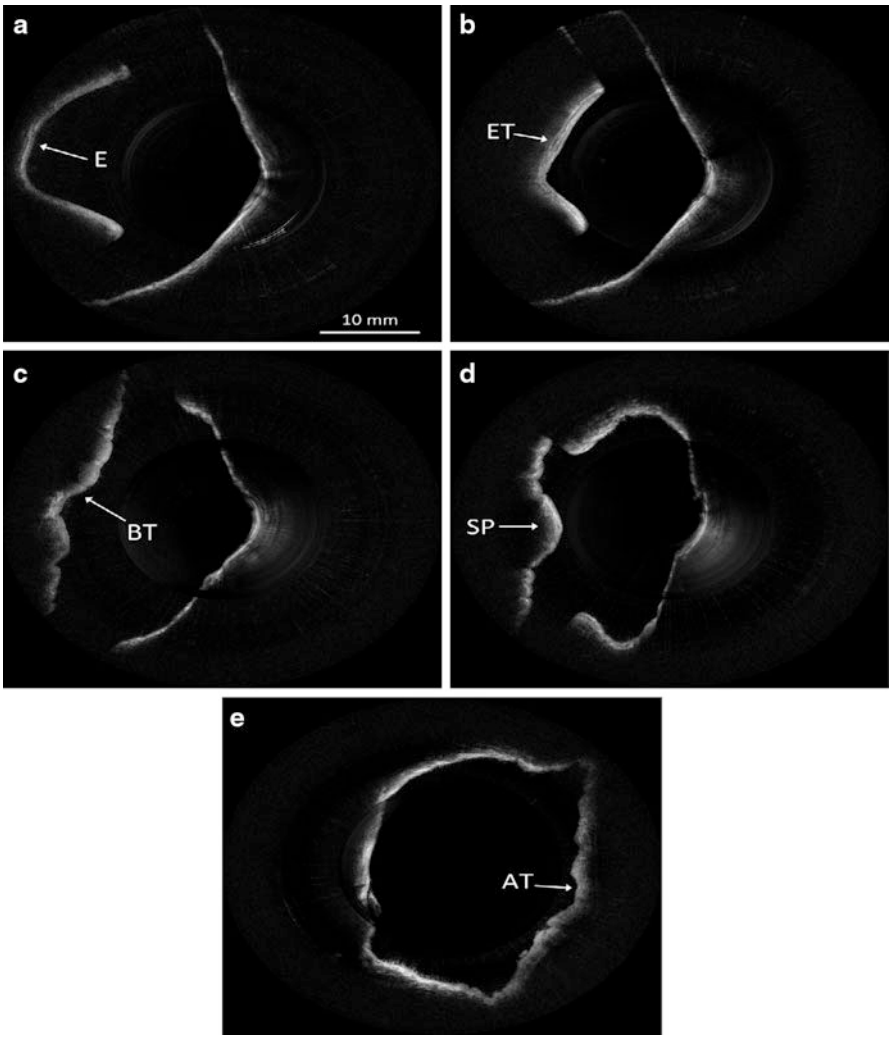

Fig. 75.7 Examples of in vivo LR-OCT images

Examples of acquired OCT data are shown in Fig. 75.7. Each cross-sectional image is 43 × 43 mm. Anatomical structures such as the epiglottis (Fig. 75.7a), base of tongue (Fig. 75.7b) with associated tonsillar tissue, the soft palate and uvula (Fig. 75.7c), and adenoidal tissue (Fig. 75.7d) can be identified by their distinct tissue characteristics. Unlike OCT data acquired in phantom testing, up to 1.5 mm of tissue penetration was achieved and tissue substructure such as the elastic cartilage in the epiglottis can be seen.

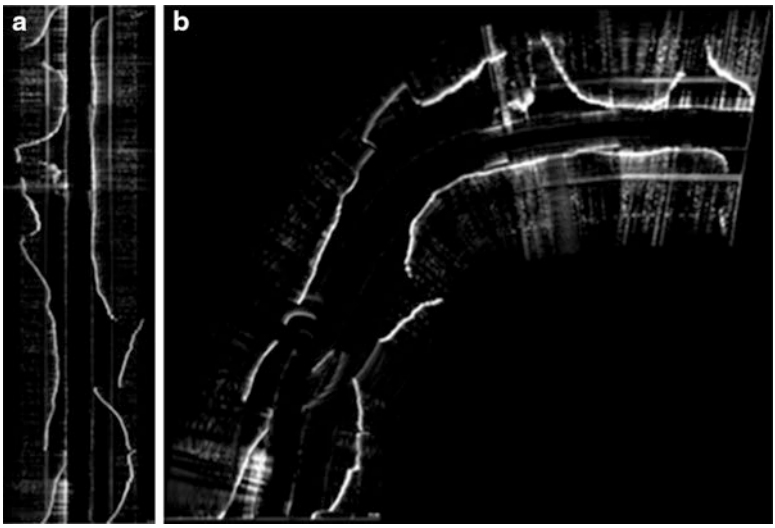

Fig 75.8 (**a**) Stacked LR-OCT data (*sagittal view*) as unprocessed linear data. (**b**) Stacked LR-OCT data (*sagittal view*) after applied bending algorithm

75.5 Image Reconstruction/Rendering

OCT images are loaded into Mimics, a commercially available 3D rendering software. Anatomically, the airway contains many bends, the most exaggerated of which occurs around the area of the soft palate and continues onto the nasal passageways. However, OCT assumes the images are acquired in a linear fashion. Unlike CT or MRI, OCT axial slices deviate from one another in an absolute coordinate system in both X-Y-Z linear displacement and at least 1 angular degree of rotations freedom. Serial OCT images must be transformed to fit along a curved airway and aligned along the "common axis." In order to fashion the linear LR-OCT data to represent the anatomical curve, a custom algorithm is used (Fig. 75.8). Using Cartesian coordinates from a series of CT scans acquired from normal patients. The database contains a variety of subjects, classified by age and sex. The acquired OCT data is matched to a CT scan that most closely correlates patient age and gender. The software creates a bend in sagittal slices of the OCT data creating an image that closely resembles the anatomic curvature. Figure 75.9 displays an example of data collection from a standard CT scan.

The literature has described an OCT probe with integrated magnetic tracking which accurately locates the tip of the OCT probe within the lumen of the airway in 3D space (X, Y, Z coordinates). This configuration can provide patient-specific airway curvatures without the need for third-party software [22]. Commercial magnetic tracking systems are now available in a small form factor (0.56 mm).

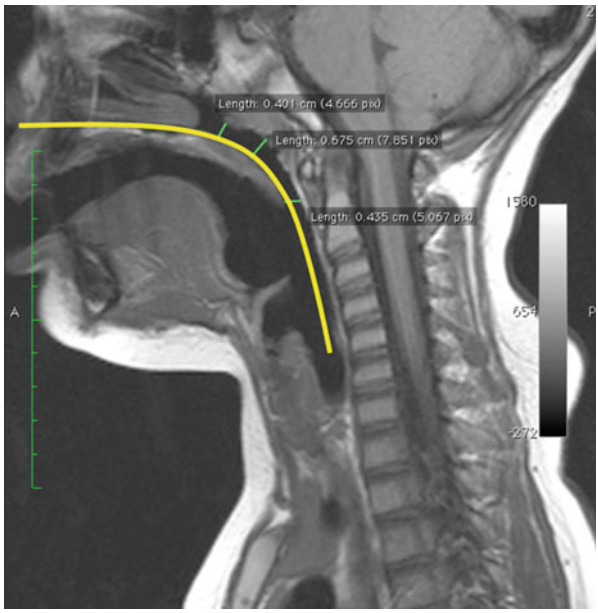

Fig. 75.9 Collection of Cartesian coordinates from normal CT scans for use in custom algorithm

Integration with the existing LR-OCT probe has the limitation of increasing the OD of the probe, necessitating larger outer FEP sheaths, which may lead to increased patient discomfort. However, improvements in the technology may produce smaller tracking beacons that will add negligible bulk to the LR-OCT probe.

After creating the bent upper airway, LR-OCT data is loaded into Mimics 3D rendering software for construction of a volumetric model (Fig. 75.10). Using Mimics, we are able to create accurate 3D renderings of the upper airway that will be used in simulations to visualize flow in normal and obstructed (as in those with OSA) airways. In Mimics, the OCT data is visualized in three planes (axial, sagittal, and coronal). As seen in Fig. 75.7, primarily at the area of the epiglottis, the anterior pharyngeal wall is missing. This is caused by structures (such as the epiglottis) that cannot be penetrated by the infrared light of the LR-OCT probe. This causes a gap in the OCT data, primarily at the level of the vallecula and the anterior pharyngeal wall. During the creation of the volumetric rendering, an individual equipped with endoscopic video data collected at the time of OCT imaging must use intra-frame interpolation and knowledge of anatomy to fill in missing data from the volume. As mentioned before, the epiglottis blocks the area of the anterior pharyngeal wall, which manifests as a gap in the OCT data. In order to compensate for this lack of information, the vallecula (the area between the posterior wall of the epiglottis and the anterior pharyngeal wall) is excluded from the reconstruction. Instead, it is assumed that the epiglottis forms the anterior pharyngeal wall. In simulations of flow based on CT data, the area of the vallecula does not significantly alter the flow within the airway (Fig. 75.11).

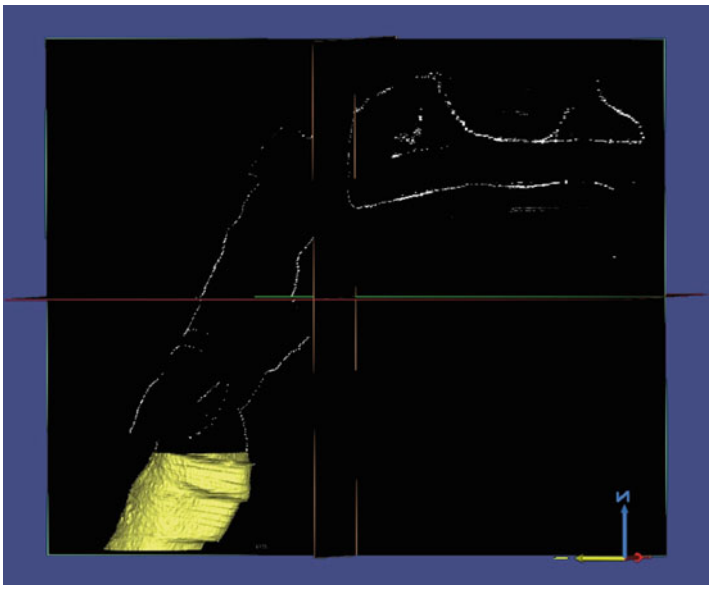

Fig. 75.10 3D reconstruction (partial) of LR-OCT stack in Mimics™

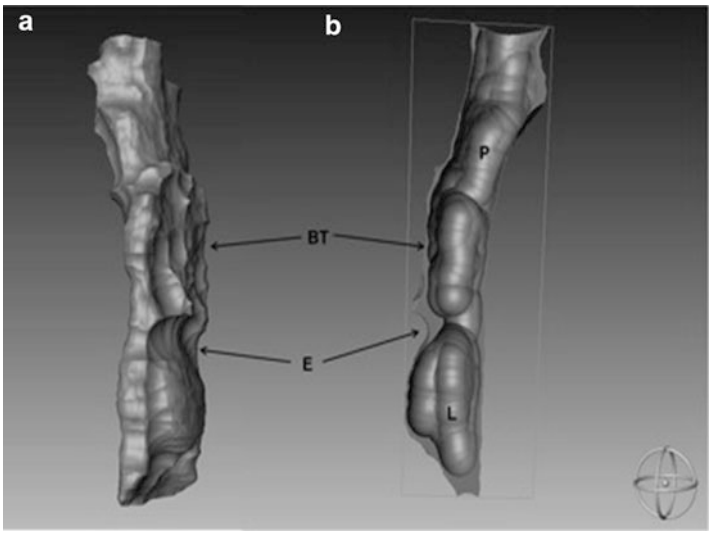

Fig. 75.11 Completed linear 3D reconstruction of LR-OCT data. Pharynx (*P*), base of tongue (*BT*), epiglottis (*E*), and larynx (*L*)

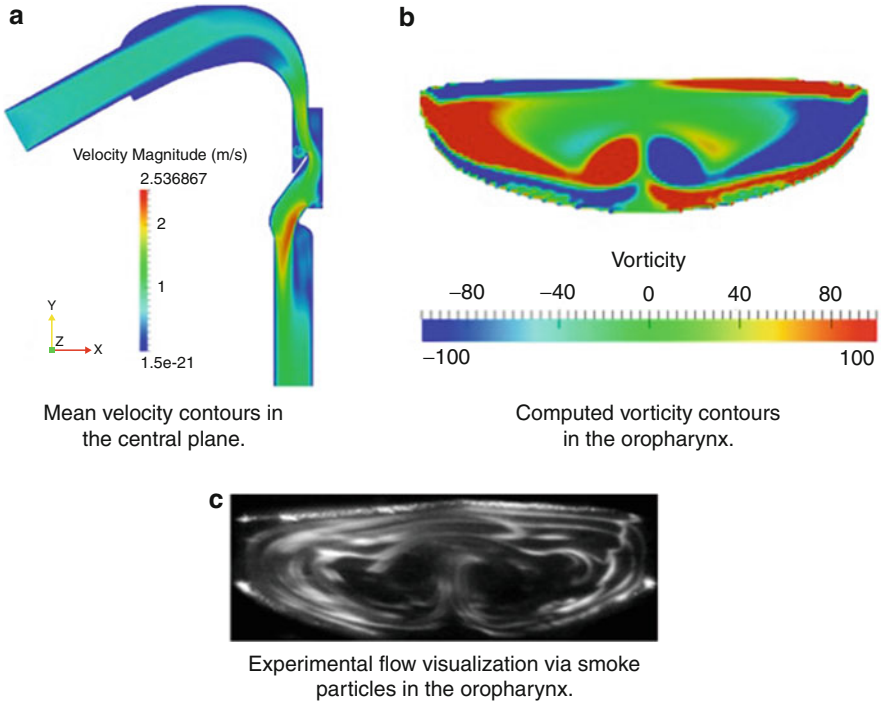

Fig. 75.12 Results of flow simulation in the idealized ETA model

75.6 Numerical Simulations and Modeling

Upper airway reconstructions created from Mimics are used to model flow using direct numerical simulation (DNS) via the lattice Boltzmann method (LBM). These flow models can be used to locate areas of possible obstruction. The simulations based on the DNS-LBM have been compared to other DNS methods for several canonical flows with similar results. Simulation of flow in an idealized ETA model geometry is presented in Fig. 75.12. Results of this simulation agree with the experimental images from the smoke array visualization.

Similar to the idealized ETA model, flow through a full upper airway reconstruction of OCT data with the bending algorithm applied (Fig. 75.13) can be visualized. Application of inlet and outlet parameters creates flow, both pressure and velocity, through the model and can be seen at various points within the upper airway (Fig. 75.14a, b).

Fig. 75.13 Full 3D reconstruction of upper airway OCT data with bending algorithm applied nasopharynx (*NP*), soft palate (*SP*), base of tongue (*BT*), and epiglottis (*E*)

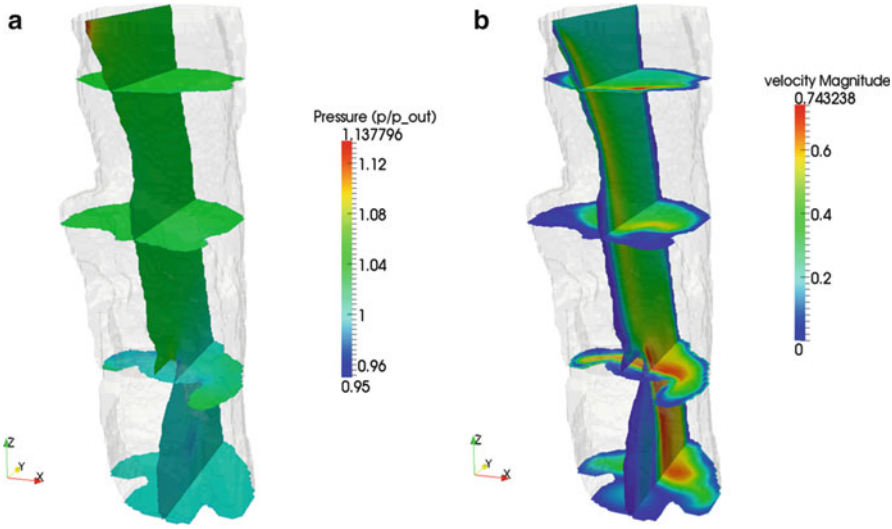

Fig. 75.14 (**a**) Pressure measurement at various levels of bent OCT data. (**b**) Air velocity measurement at various levels of bent OCT data

75.7 Conclusion

The pathophysiology of OSA is not clearly understood although it has been recognized as pathology for greater than 30 years. While polysomnography remains the standard for diagnosis, it only provides insight as to the diagnosis and does not provide anatomical detail for use in corrective surgery. Adjunct studies such as CT and MRI are not routinely used in diagnosis and management of this condition due to high cost, inconvenience, and exposure to potentially harmful radiation [23]. aOCT represents a technology that is ideally suited for use in imaging of the upper airway by being minimally invasive, easily portable, safe during extended imaging sessions, and well tolerated in awake or asleep patients [24]. The ability to simulate flow in accurate three-dimensional reconstructions can provide insight to physicians of individualized areas of obstruction. As it stands, surgical procedures for OSA are given, at best, a 50 % success rate. Localization of problem areas could lead to directed surgery and increased success rates.

aOCT is not without limitation. At certain locations within the upper airway, particularly in the hypopharynx where the epiglottis is located, more anterior tissues obstruct the imaging beam of the aOCT probe from focusing on tissues posterior to the proximal tissue. This creates gaps in axial data slices that must be manually created by correlating endoscopic images and anatomical knowledge to those particular aOCT data slices. An acquired aOCT stack is also assumed to be linear since the acquisition is recorded relative to the catheter and not in three-dimensional space. Though standardized curves extracted from age- and gender-adjusted CT scans can be applied to stacked axial OCT scans, further development of miniature magnetic tracking devices, which do not add additional bulk to aOCT probes, would allow for anatomically accurate curves to be applied to individual patient data.

aOCT has been shown to be comparative with CT for both cross-sectional area and airway structure. It can rapidly image a dynamic airway without exposure to ionizing radiation and can be used as an adjunct to polysomnography or in-office endoscopy with minimal discomfort for the patient. Time-domain systems were limited by slow scanning speeds, lower signal-to-noise ratio, and short imaging distance. Fourier-domain aOCT shows a significant scanning speed boost that is compatible with acute changes in airway structure over the breathing cycle and minimized motion artifact. An increased signal-to-noise ratio maximizes data acquisition and allows for more accurate 3D reconstructions for flow analysis.

In conclusion, imaging of upper airways with diameter of up to 3 cm was achieved in fully cognizant test subjects with minimal discomfort. Compared to an anatomical TD-OCT system, the long-range FD-OCT system not only increases the imaging speed significantly but also enhances the imaging sensitivity to enable visualization of the fine anatomical tissue structure in the airway. Combining this structural information with DNS flow simulations, we can better estimate the site and causes of airway obstruction and better select and design surgery for patients with upper airway resistance.

References

1. C. Cummings, B. Haughey, J. Thomas, *Cummings Otolaryngology: Head and Neck Surgery*, 5th edn. (Mosby, Philadelphia, 2010)
2. M. Leigh, J. Armstrong, A. Paduch, J. Walsh, D. Hillman, P. Eastwood, D. Sampson, Anatomical optical coherence tomography for long-term portable quantitative endoscopy". IEEE Trans. Biomed. Eng. **55**(4), 1438–1446 (2008)
3. Z. Abramson, S. Susarla, M. Troulis, L. Kaban, Age-related changes of the upper airway assessed by 3-dimensional computed tomography. J. Craniofac. Surg. **20**, 657–663 (2009)
4. J. Walsh, M. Leigh, A. Paduch, K. Maddison, J. Armstrong, D. Sampson, D. Hillman, P. Eastwood, Effect of body posture on pharyngeal shape and size in adults with and without obstructive sleep apnea". Sleep **31**(11), 1543–1549 (2008)
5. J. Armstrong, M. Leigh, I. Walton, A. Zvyagin, S. Alexandrov, S. Schwer, D. Sampson, In vivo size and shape measurement of the human upper airway using endoscopic long- range optical coherence tomography. Opt. Express **11**(15), 1817–1826 (2003)
6. G. Tearney, M. Brezinski, J. Southern, B. Bouma, S. Boppart, J. Fujimoto, Optical biopsy in human urologic tissue using optical coherence tomography. J. Urol. **157**, 1915–1919 (1997)
7. J. Izzat, M. Kulkarni, H. Wang, K. Kobayashi, M. Sivak, Optical coherence tomography and microscopy in gastrointestinal tissues. IEEE J. Sel. Top. Quant. Electron. **2**(4), 1017–1028 (1996)
8. J. Williamson, R. McLauglin, W. Noffsinger, A. James, V. Baker, A. Curatolo, J. Armstrong, A. Regli, K. Shepard, G. Marks, D. Sampson, D. Hillman, P. Eastwood, Elastic properties of the central airways in obstructive lung diseases measured using anatomical optical coherence tomography. Am. J. Respir. Crit. Care Med. **183**, 612–619 (2011)
9. R. McLaughlin, J. Armstrong, S. Becker, J. Walsh, A. Jain, D. Hillman, P. Eastwood, D. Sampson, Respiratory gating of anatomical optical coherence tomography images of the human airway. Opt. Express **17**(8), 6568–6577 (2009)
10. J. Williamson, R. McLaughlin, M. Phillips, J. Armstrong, S. Becker, J. Walsh, D. Sampson, D. Hillman, P. Eastwood, Using optical coherence tomography to improve diagnostic and therapeutic bronchoscopy. Chest **136**(1), 272–276 (2009)
11. P. Williamson, A. James, M. Phillips, D. Sampson, D. Hillman, P. Eastwood, Quantifying dimensions of the tracheobronchial tree: methods, limitations and emerging techniques. Eur. Respir. J. **34**(1), 42–55 (2009)
12. J. Williamson, J. Armstrong, R. McLaughlin, P. Noble, A. West, S. Becker, A. Curatolo, W. Noffsinger, H. Mitchell, M. Phillips, D. Sampson, D. Hillman, P. Eastwood, Measuring airway dimensions during bronchoscopy using anatomical optical coherence tomography. Eur. Respir. J. **35**(1), 34–41 (2010)
13. J. Walsh, M. Leigh, A. Paduch, K. Maddison, D. Philippe, J. Armstrong, D. Sampson, D. Hillman, P. Eastwood, Evaluation of pharyngeal shape and size using anatomical optical coherence tomography in individuals with and without obstructive sleep apnea. J. Sleep Res. **17**, 230–238 (2008)
14. R. Leitgeb, C. Hitzenberger, A. Fercher, Phase-shifting algorithm to achieve high-speed long-depth-range probing by frequency-domain optical coherence tomography. Opt. Lett. **28**(22), 2201–2203 (2003)
15. J. Armstrong, M. Leigh, D. Sampson, J. Walsh, D. Hillman, P. Eastwood, Quantitative upper airway imaging with anatomic optical coherence tomography. Am. J. Respir. Crit. Care Med. **173**, 226–233 (2006)
16. S. Huang, A. Aguirre, R. Huber, D. Adler, J. Fujimoto, Swept source optical coherence microscopy using a Fourier domain mode-locked laser. Opt. Express **15**(10), 6210–6217 (2007)
17. A. Fercher, W. Drexler, C. Hitzenberger, T. Laser, Optical coherence tomography- principles and applications. Rep. Prog. Phys. **66**, 239–303 (2003)

18. A. Fercher, C. Hitzenberger, G. Kamp, S. El-Zaiat, Measurement of intraocular distances by backscattering spectral interferometry. Opt. Commun. **117**, 43–48 (1995)
19. A. Lucey, A. King, G. Tetlow, J. Wang, J. Armstrong, M. Leigh, A. Paduch, J. Walsh, D. Sampson, P. Eastwood, D. Hillman, Measurement, reconstruction, and flow-field computation of the human pharynx with application to sleep apnea. Trans. Biomed. Eng. **57**(10), 2535–2548 (2010)
20. R. Huber, M. Wojtkowski, J. Fujimoto, Fourier Domain Mode Locking (FDML): a new laser operating regime and applications for optical coherence tomography. Opt. Express **14**(8), 3225–3237 (2006)
21. J. Zhang, J. Nelson, Z. Chen, Removal of a mirror image and enhancement of the signal-to-noise ration in Fourier-domain optical coherence tomography by use of an electro-optical phase modulator. Opt. Lett. **30**(2), 147–149 (2005)
22. B. Lau, R. McLaughlin, A. Curatolo, R. Kirk, D. Gerstmann, D. Sampson, Imaging true 3D endoscopic anatomy by incorporating magnetic tracking with optical coherence tomography: proof-of-principle for airways. Opt. Express **18**(26), 27173–27180 (2010)
23. S.P. Patil, H. Schneider, A.R. Schwartz, P.L. Smith, Adult obstructive sleep apnea: pathophysiology and diagnosis. Chest **132**(1), 325–337 (2007)
24. J. Armstrong, M. Leigh, J. Walsh, D. Hillman, P. Eastwood, D. Sampson, Anatomical optical coherence tomography for imaging the human upper airway. In: W. Drexler, J.G. Fujimoto (eds), *Optical Coherence Tomography. Biological and Medical Physics, Biomedical Engineering* (2008), Springer Berlin Heidelberg, pp. 1269–1292

Optical Coherence Tomography in Pulmonary Medicine

76

Septimiu Dan Murgu, Matthew Brenner, Zhongping Chen, and Melissa J. Suter

Keywords
Bronchoscopy • Endomicroscopy • Lung • Optical coherence tomography • Pulmonary

76.1 Introduction

Advances in pulmonary diagnostics and therapeutics offer a major potential for optical imaging applications both in clinical practice and research settings. Complexities of pulmonary structures and function have restricted widespread OCT investigations and clinical applications, but these will likely be overcome by developments in OCT technology [1]. Some factors that have limited adaptation of OCT into the pulmonary setting in the past have been the shallow depth of penetration, resolution limitations,

S.D. Murgu (✉)
The University of Chicago, Chicago, IL, USA
e-mail: smurgu@medicine.bsd.uchicago.edu

M. Brenner
Pulmonary and Critical Care Medicine, UC Irvine Medical Center, Orange, CA, USA
e-mail: mbrenner@uci.edu

Z. Chen
The Edwards Life Sciences Center for Advanced Cardiovascular Technology, Beckman Laser Institute, Irvine, CA, USA

Department of Biomedical Engineering, Beckman Laser Institute, University of California Irvine, Irvine, CA, USA
e-mail: z2chen@uci.edu

M.J. Suter
Pulmonary and Critical Care Unit, Harvard Medical School and Massachusetts General Hospital, Boston, MA, USA
e-mail: msuter@partners.org

© Springer International Publishing Switzerland 2015

W. Drexler, J.G. Fujimoto (eds.), *Optical Coherence Tomography*,
DOI 10.1007/978-3-319-06419-2_78

relatively slow access times, need to examine large surface areas with numerous branching airways, motion artifacts, as well as a need for development of practical imaging probes to reach the relevant locations in a minimally invasive way. Considerable recent engineering and analytical advances in OCT technology [2–8] have already overcome several of these obstacles and will enable much more extensive investigations into the role for structural and functional pulmonary OCT imaging [1].

There is a wide range of significant clinical pulmonary needs that may be fulfilled by the real-time, high-resolution imaging capabilities of OCT. In a number of these potential pulmonary clinical application areas, the shallow depth of penetration of OCT is adequate enough for the required purposes. For other applications, however, such as defining the depth of penetration of airway tumors or determining airway structural changes in tracheal strictures or malacia, a combination of OCT and high-frequency endobronchial ultrasonography may be more appropriate to visualize the entire central airway wall in cross section [9]. As with any diagnostic or therapeutic clinical tool, the evolution of OCT in pulmonary medicine will be based on knowledge of potential uses, understanding of where the capabilities and limitations meet the clinical needs, and cognizance of areas where OCT is unlikely to be helpful. Many of the initially reported pulmonary OCT studies have focused on areas of highest likelihood for demonstration of success [10–17]. This approach very reasonably demonstrates feasibility and proof of concept, but it must be emphasized that the areas of initial focus and current investigations may not ultimately be the areas of highest beneficial yield in the long-term application of OCT in pulmonary medicine. Evidence suggests, however, that OCT is a promising tool for detection of early airway cancer, facilitating biopsy of peripheral pulmonary nodules, assessing airway remodeling in asthma and chronic obstructive pulmonary disease (COPD), and potentially guiding therapeutic bronchoscopic interventions [1, 18].

76.2 Overview of Pulmonary Anatomy and Physiology: Unique Aspects Relevant to OCT and F-OCT

There are a number of very unique structural and functional components to the pulmonary system relevant to issues of OCT imaging. The major function of the lungs involves gas exchange between the circulatory system and the environment [19]. Anatomically, this requires a very large surface area containing both fine capillaries and alveolar surfaces in close contact for gas exchange. The average adult lung volume is roughly 2–4 l in the resting state (functional residual capacity) [20], with extremely large alveolar surface areas exposed directly to the external environment, providing a potential portal for infection and inhalation injuries. The total alveolar surface area where gas exchange takes place is approximately the size of a tennis court (140 M^2) in an adult [21] (p. 12). The air is conducted into the lungs through the airway system which consists of the upper airway, larynx, trachea, and proximal bronchi. The bronchi rapidly branch in multiple generations like branches on a tree to reach all regions within the lungs [19] (Fig. 76.1). Up to 23 generations of branching occur (Fig. 76.2) [22] to reach the >3 million respiratory bronchioles

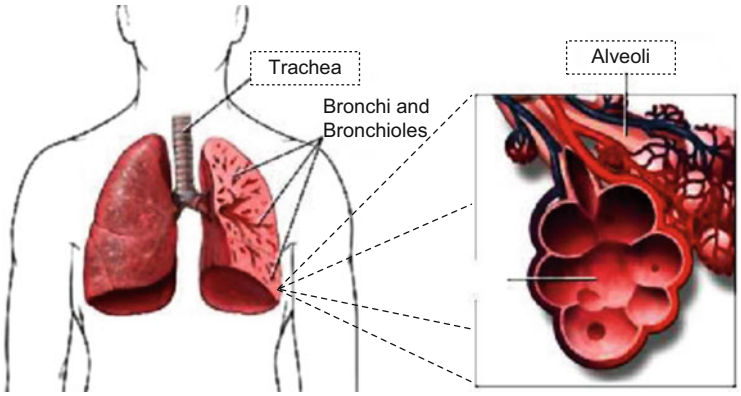

Fig. 76.1 Lungs, airways (including trachea and branching bronchi and bronchioles), and distal alveoli where gas exchange takes place (Modified from http://images.google.com/imgres?imgurl = http://images.webmd.com/images/hw/media65/medical/hw/h5551557.jpg&imgrefurl = http://my.webmd.com/hw/health_guide_atoz/hw141715.asp&h=300&w=460&sz=26&tbnid=jBlE6ZHtW7QJ:&tbnh=81&tbnw=125&hl=en&start=3&prev=/images%3Fq%3Dlungs%2Bairways%26svnum%3D10%26hl%3Den%26lr%3D)

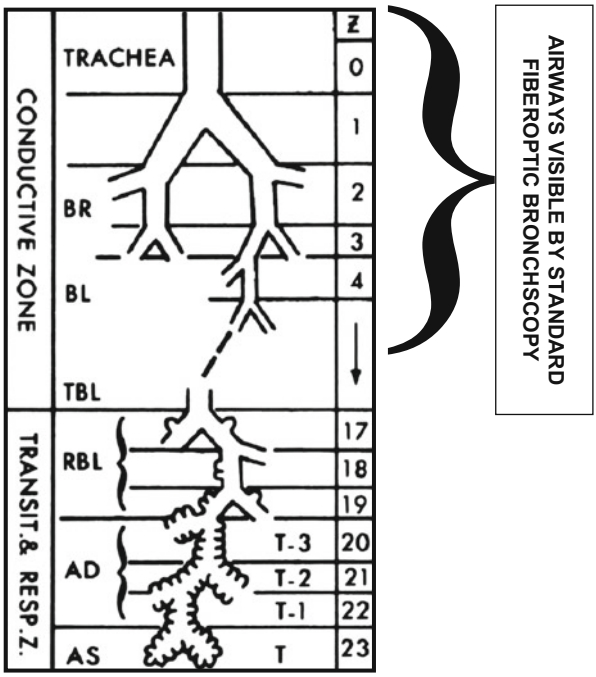

Fig. 76.2 Schematic of airway generations and airway regions accessible for visual examination by flexible fiber-optic bronchoscopy (Modified from Weibel et al. [22])

and alveolar air sacs (generation branches 17–23) [20] (page 6). As the number of branching airway generations increases, their individual luminal diameters decrease in size [19]. Therefore, it is not possible to examine most of the conducting airways within a patient (in contrast, e.g., to the single lumen found in the gastrointestinal tract). Only a few generations of branching can be routinely examined by standard airway endoscopic diagnostic techniques (Fig. 76.2). For more distal airway anatomic examinations, new technologies are needed, along with the ability to guide diagnostic tools to the exact place of interest. This is now possible given the advances in navigational bronchoscopy, a technique that provides a three-dimensional virtual road map and enables a physician to maneuver through multiple branches of the bronchial tree and reach predefined target areas in the lung parenchyma. A significant amount of relevant pathology, however, occurs in the proximal airways, at levels reachable by current bronchoscopic methods, and within areas that can be readily visualized by existing OCT methods. Specifically, OCT can be used for detecting and defining the exact extent of laryngeal and large airway tumors in many cases [23, 24], detecting airway remodeling in asthma and COPD [25], and facilitating understanding of the upper and central airway mechanics in obstructive sleep apnea (OSA), asthma, and COPD [26, 27].

As with any new technology, the exact clinical role for OCT in pulmonary diagnostics and therapeutics will be defined and evolve over time. Anatomic regions of the pulmonary organ system where OCT may be of clinical or research value include the larynx, vocal cords, proximal airways (including trachea with an average of 1.5 cm^2 area and decreasing sized bronchi and bronchioles), smaller gas-exchanging lung structures (including respiratory bronchioles and alveoli of roughly 200–300 μm diameter and 8 μm wall thickness) [20] (Fig. 76.3), and pleural space between the chest wall and lungs (including parenchymal pleura and visceral pleura covering the lung surface) (Fig. 76.4) [15]. In addition, in the pulmonary vascular system including pulmonary arteries, arterioles, more than 300 million alveolar capillary segments (where gas exchange takes place with the blood) [20] (page 13), pulmonary veins, as well as bronchial arteries, capillaries, and veins, OCT may have future applications.

76.3 Standard External Imaging Techniques for Lung and Airway Examination

76.3.1 Chest X-Ray

Chest radiographs are relatively inexpensive, with excellent depth of penetration (the entire thorax can be imaged). Standard chest radiographs are two-dimensional composite shadows of tissue structures, with maximal resolution on the order of millimeters. Digital imaging and subtraction techniques may further improve diagnostic capabilities for chest radiographs and other imaging techniques [28]. Chest radiographs, however, are insensitive for detecting early airway or parenchymal malignancies or structural changes in the airways that can be detected by higher-resolution optical technologies.

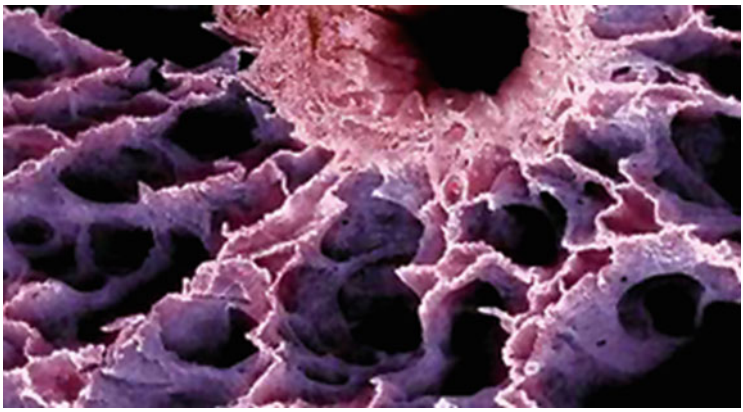

Fig. 76.3 Scanning electron micrograph of bronchiole and distal alveolar structures. Alveoli are approximately 200–300 um in diameter. Fine pulmonary capillary networks perfuse the capillary walls (From http://images.google.com/imgres?imgurl = http://www.visualsunlimited.com/images/watermarked/310/310003.jpg&imgrefurl = http://www.visualsunlimited.com/browse/vu310/vu310003.html&h=251&w=350&sz=28&tbnid=hXOAXFGrrlwJ:&tbnh=83&tbnw=116&hl=en&start=8&prev=/images%3Fq%3Dalveoli%2BSEM%26svnum%3D)

76.3.2 Computed Tomography

High-resolution CT scanning is three-dimensional and also has excellent penetration with resolution on the order of hundreds of microns to millimeters [28–30]. Various reconstruction algorithms can be applied including airway surface renderings for "virtual" "bronchoscopy" [29, 31–33]. However, virtual bronchoscopy is limited in ability to evaluate the mucosal surface of the respiratory tract reliably. Although the overall surface form can be detected, mucosal color, irregularity, or friability cannot be assessed [33]. Studies show that CT imaging detects changes in airway wall thickness in obstructive airway disorders, and these correlate with disease severity and bronchial biopsy measurements of airway wall thickness [34]. However, beyond the fifth airway generation, CT's resolution is inadequate, and in addition, CT cannot detect or measure morphological changes in the airway structured microlayers. These limitations are potentially overcome by optical technologies.

76.3.3 Positron Emission Tomography

Positron emission scanning is relatively low resolution but provides functional information that may be useful in differentiating benign from malignant pathology, particularly in conjunction with CT scanning [35, 36]. PET scanning may be particularly useful for detection of unsuspected metastatic malignant disease in lung cancer patients [35]. As a functional imaging modality, integrated chest PET CT scanning is currently used in diagnostic algorithms for indeterminate pulmonary nodules and staging of cancers.

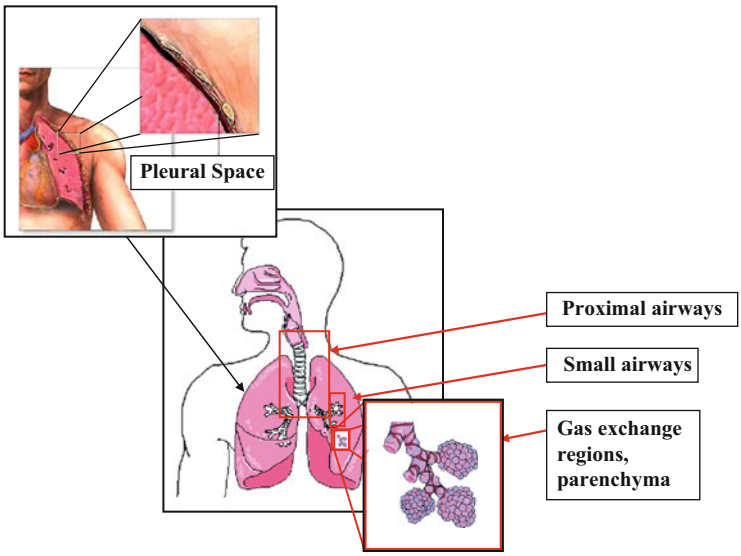

Fig. 76.4 Potential areas for pulmonary OCT clinical and research applications including proximal airways larynx and trachea, bronchi, smaller airways and bronchioles, gas exchanging regions and lung parenchyma, and pleural space (Modified from http://www.smartdraw.com/resources/examples/medical/images/respiratory_full.gif and http://images.google.com/imgres?imgurl = http://www.uscuh.com/CWS/ADAM/Surgery/graphics/Chesttubeinsertion_1.jpg&imgrefurl = http://www.uscuh.com/CWS/ADAM/Surgery/Chesttubeinsertion_1.html&h=320&w=400&sz=13&tbnid=1kw9f2O5YMIJ:&tbnh=96&tbnw=120&hl=en&start=12&prev=/images%3Fq%3Dpleural%2Bspace%26svnum%3D10%26hl%3Den%26lr%3D)

76.3.4 Magnetic Resonance Imaging

MRI imaging is rapidly advancing for thoracic imaging with improvements in acquisition times but is used primarily for mediastinal and proximal vascular structure evaluation in the thorax at this time [28, 30]. MRI is used occasionally in tracheobronchomalacia and for detecting involvement of the chest wall structures by tumor [30, 37]. The depth of penetration is throughout the thorax, and imaging resolution is on the order of millimeters [29].

76.4 Direct Examination Techniques for Airways, Lung Parenchyma, and Pleura

76.4.1 Flexible Bronchoscopy

Flexible bronchoscopy is performed either trans-orally or trans-nasally using flexible endoscopes that are usually at least 100 cm in length and have outer diameters ranging from 3 to 6.5 mm. The bronchoscopes are now commonly

videoendoscopes. The bronchoscopes most commonly have a light source, imaging modality (CCD chip or fiber bundle), and a hollow "working channel" usually ranging from 1.2 to 2.8 mm. Specimens can be obtained including suctioning, saline lavage, brushing, and needle and forceps biopsies (generally of maximal diameter on the order of 1–2.5 mm). The working channels allow the passage of therapeutic instruments (laser, electrocautery, cryotherapy probes) or novel diagnostic tools such as OCT, radial EBUS, or CFM probes. Generally, 3–4 orders of bronchial branching can be directly visualized with standard flexible bronchoscopy, but ultrathin flexible bronchoscopy using flexible scopes of 2–3 mm and working channels of 1 mm allow access to more distal airways and pulmonary abnormalities peripherally situated within the lung parenchyma. The major advantage of flexible bronchoscopy is its versatility. Flexible bronchoscopy can be performed in awake patients with or without moderate sedation. Its use is easily learned, and it enables the operator to reach the distal aspects of branching airways with minimal trauma or patient discomfort. Diagnostic procedures, including those with biopsies, can usually be performed in less than 10 min. Procedures can be performed using topical anesthesia, and bronchoscopy can be done at the patient's bedside or in an outpatient setting. White light bronchoscopy, however, can only image mucosal surfaces. For cancer, for instance, even for visible endobronchial lesions, combined bronchoscopic modalities (brushings, washings, biopsy) result in a diagnostic rate that is less than 100 %, mainly because of sampling errors (biopsies are performed from areas of tumor necrosis, inflammation, or fibrosis). High-magnification bronchoscopy (HMB) provides information of the bronchial mucosa with a maximum magnification of 110 times, thus revealing subepithelial microvessels in the large airways, potentially useful to abnormal vascular networks in the large airway in asthma and lung cancer [38, 39]. HMB, however, is still a surface imaging modality with a resolution of approximately 20 μm. Many pathologic subepithelial vessels have a diameter less than that; in addition, HMB cannot distinguish neovascularization from vasodilation [40].

76.4.2 Rigid Bronchoscopy

Rigid bronchoscopy is usually performed in conjunction with interventional therapeutic procedures. These include laser resection, tumor debulking, silicone and metal stent insertion, or dilatation of benign tracheal or bronchial strictures. Rigid bronchoscopes generally range in size from 5 to 12 mm diameter and 12 to 45 cm in length. Working channels can be as large as 7 mm in addition to the visualization optics. Rigid bronchoscopes can visualize up to four orders of bronchial branching and are primarily focused on proximal airways. Visualization is direct, and resolution is governed by the quality of Hopkins lens rigid telescopes. Airway surface anatomy is visualized with rigid bronchoscopy usually using straight lens telescopes with a digital or other high-grade video camera easily attached to the telescope head. Lateral viewing telescopes of 30, 45, and even 90° can be used, but are infrequently employed today because of the ready availability of the flexible

Fig. 76.5 (*Left*) 12 mm diameter rigid bronchoscope (Bryan Corp, Woburn MA, USA). Note 5 mm rigid telescope, attached digital camera, 3 mm suction catheter placed through sideport and black flexible Racine connector allowing mechanical ventilation and oxygenation. (*Center*) Flexible videobronchoscope (Olympus, Tokyo JP) (From The Essential Bronchoscopist© bronchoscopy.com.uci.edu). (*Right*): Flexible fiber-optic bronchoscope seen on end. Note 2.8 hollow working channel)

bronchoscope. It is noteworthy that probes or catheters placed through the rigid tube need to be sufficiently firm so that they can be manipulated inside the open tube (Fig. 76.5). This is the case, for example, for existing silicone suction catheters, quartz laser delivery fibers, OCT probes, or radial EBUS (Fig. 76.6). In addition to limitation of white light bronchoscopy, rigid bronchoscopy may restrict the wide application of novel optical technologies in pulmonary medicine because of its limited applications and availability among pulmonologists. Furthermore, the systems can be cumbersome to use in conjunction with dedicated OCT probes, since through a hollow tube, the operator has to accommodate the telescope and the OCT probe and sometimes forceps and laser fibers (Fig. 76.7). This limitation, however, can be potentially overcome by development of integrated WLB-OCT laser systems.

76.4.3 Autofluorescence Bronchoscopy (AFB)

The main rationale for the development of AFB is the fact that WLB is not sensitive enough for detecting abnormalities that are only a few cells thick or below the tissue surface. AFB is based on the hypothesis that differences in epithelial thickness, blood flow, and tissue fluorophore concentration cause abnormal tissues to have diminished red and substantially diminished green fluorescence as compared to normal tissues when exposed to 440–480 nm wavelength blue light excitation (Fig. 76.8); thus, autofluorescence (AF) cannot be seen during conventional WLB as the intensity of fluorescence is very low and is overwhelmed by the reflected and backscattered light. Successful localization of a dysplastic lesion is possible using AFB, whereas WLB is normal. The intensity of green fluorescence is measured, and an abnormally low "green" fluorescent area is identified as a cold spot on a normal green background. The published evidence shows that AFB has a better sensitivity than WLB for detecting intraepithelial lesions [41]. The specificity, however, is low (~60 % vs ~90 % for WLB) due to false-positive

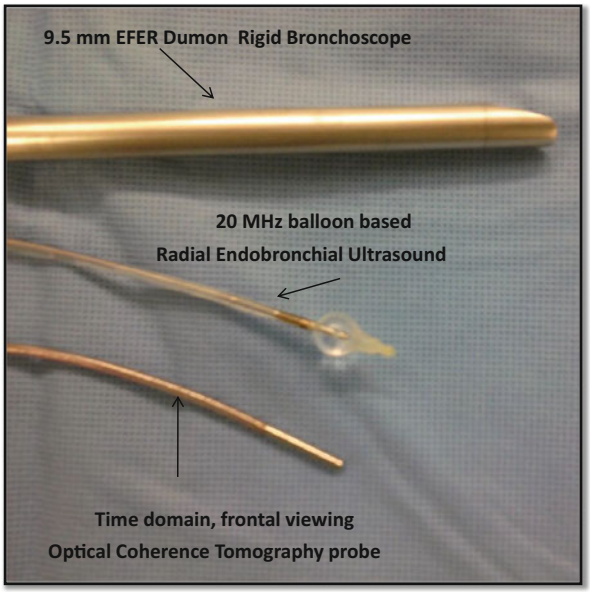

Fig. 76.6 The rigid bronchoscope accommodates a variety of instruments including the telescopes, forceps, suction catheters, laser fibers, as well as optical and ultrasound imaging probes. This is a close view of the 9.5 mm EFER-Dumon rigid bronchoscope, the radial ultrasound probe with its water-filled balloon and the optical coherence tomography probe

fluorescence with inflammation, mucosal gland hyperplasia, and interobserver error. To increase specificity, one may need to obtain information about tissue structure (via OCT or CFM) [24].

76.4.4 Narrow Band Imaging (NBI)

The rationale for development of NBI relies on the fact that malignant and dysplastic lesions are characterized by abnormal angiogenesis which can be detected visually as vessel entanglement and abnormal proliferation within the bronchial mucosa [42]. NBI uses blue light centered at 415 nm and green light centered at 540 nm corresponding to the maximal hemoglobin absorption peaks. The blue light highlights the superficial capillaries, whereas the green light can penetrate deeper and highlight the larger blood vessels in the submucosa (Fig. 76.9). Preliminary studies suggest that NBI can improve detection of dysplasia and CIS compared with WLB [43, 44]. The routine clinical utility of NBI, however, remains unknown as the natural history of the above premalignant lesions is not completely well understood, the indications for NBI have not been well established, and inter- and intra-observer reliability recognizing normal and abnormal NBI images needs to be further defined.

76.4.5 Confocal Endomicroscopy (CEM)

Confocal endomicroscopy (CEM) provides an image of a thin section within a biological sample, where the microscope's objective is replaced by a flexible

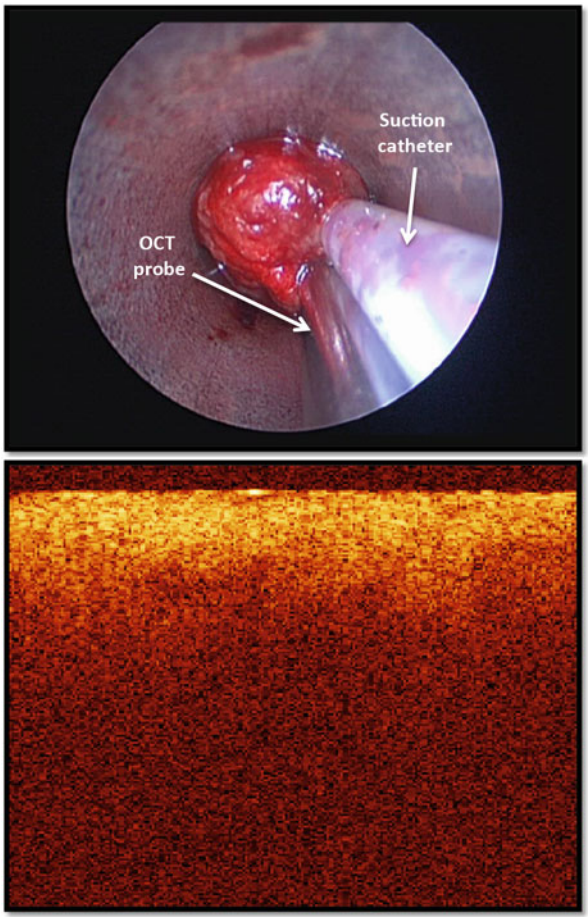

Fig. 76.7 The suction catheter and a time domain forward viewing OCT probe are placed over an endobronchial tumor just before its removal from the airway (*top panel*). The OCT tomogram revealed a pattern of homogeneous light backscattering layer and absence of normal layered microstructures which characterize the normal airway wall (*bottom panel*)

fiber-optic miniprobe [45]. CEM offers spatial resolution down to the submicron range and depth of penetration of approximately 0.5 mm, which should provide sufficient optical information to distinguish benign from early malignant lesions since cellular changes in CIS and dysplasia occur in less than 1 mm in depth, if optical contrast is sufficient. The basement membrane and upper submucosa can be imaged with good quality. Disorganization of the fiber network was seen indicating basement membrane disruption that was observed in the majority of metaplastic and dysplastic samples and all CIS and invasive cancers [45]. CEM has been also investigated in vivo for studying airway remodeling in asthma [46]. While there was no difference in CEM patterns between asthma patients and healthy controls, there was an association between post-bronchodilator FEV_1 % predicted and both histologic and CEM elastic fiber patterns. These findings suggest there may be a structure-function relationship between extracellular matrix in the airway wall

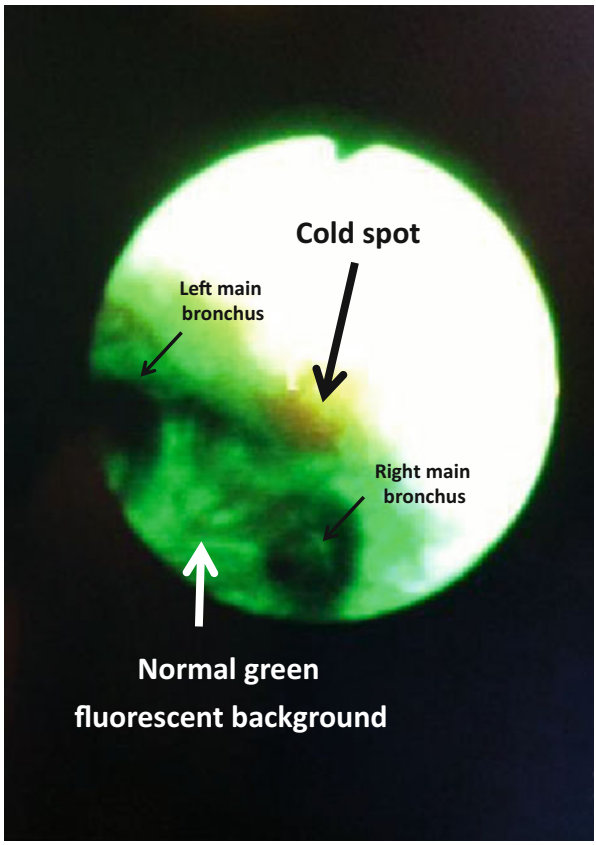

Fig. 76.8 Abnormal tissues have diminished green fluorescence as compared to normal tissues when exposed to 440–480 nm wavelength blue light excitation. The intensity of green fluorescence is measured, and an abnormally low "*green*" fluorescent area is identified as a "*cold spot*" on a normal green background (*arrow*)

and lung function. Because cells do not emit strong autofluorescence with the current commercially available technology, the epithelial cells are not visible. In addition, the fragile epithelium can be scrapped off during the imaging procedure. Studies are needed to evaluate if CEM can distinguish normal from specific abnormalities (dysplasia, inflammation, fibrosis, malignancy), not just normal from abnormal tissues [47]. Furthermore, since the depth of penetration is limited, this technique will likely be appropriate in a multimodality bronchoscopic imaging platform, combining it with technologies able to visualize the cartilage and its potential invasion (i.e., EBUS) and reveal alterations in the airway wall microstructure (i.e., OCT).

76.4.6 Pleuroscopy

Pleuroscopy is a procedure that allows physicians to access to the pleural space. It is also known in the literature as thoracoscopy, medical thoracoscopy,

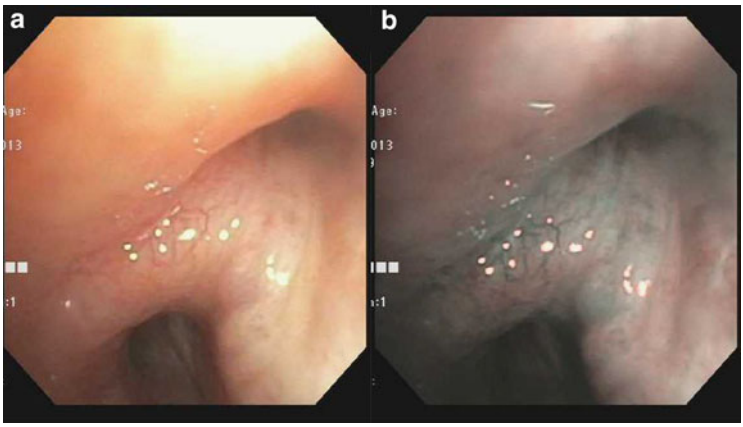

Fig. 76.9 (**a**) White light bronchoscopy at the level of primary right carina (RC1) shows submucosal tumor infiltration. (**b**) Narrow band imaging at the same anatomic site: the blue light highlights the superficial capillaries, whereas the green light can penetrate deeper and highlight the larger blood vessels in the submucosa

or video-assisted thoracic surgery (VATS). In general, however, VATS refers to thoracoscopy performed in the operating room using single-lung ventilation. During medical thoracoscopy, the operator (surgeon or interventional pulmonologist) can perform parietal pleural biopsies, drainage of pleural effusions, and pleurodesis either in an endoscopy suite or operating room. In addition to these procedures, during VATS, thoracic surgeons can also perform lung biopsy, resection of pulmonary nodules or blebs, lobectomy, pneumonectomy, or esophagectomy [48]. Either rigid or flexible instruments can be used for these interventions, but surgeons use mostly rigid instrumentation. Disposable plastic or reusable stainless steel trocars come in different sizes (5–13 mm) and allow the passage of telescopes with different angles of vision (0° for direct viewing and 30–50°) for oblique panoramic viewing of the pleural cavity. In addition, other instruments such as forceps or optical probes can be passed through the trocar inside the thoracic cavity and potentially assist with selection of a biopsy site (Fig. 76.10). The flex-rigid pleuroscope (model LTF 160 or 240; Olympus, Tokyo, Japan) is designed like a bronchoscope with a handle and a shaft of 7 mm outer diameter. The 2.8 mm working channel accommodates forceps, electrosurgical and laser probes, and other accessories (Fig. 76.10). The yield of thoracoscopic parietal pleural biopsy for malignant pleural effusions is 90–100 % [49]. It is possible that the addition of optical technologies will maximize this yield, especially for early-stage mesothelioma, which could resemble pleural inflammation. Overall, however, the limited published clinical evidence available to date does not support the use of autofluorescence or NBI in addition to white light thoracoscopy for the diagnosis of malignant pleural effusion [50, 51].

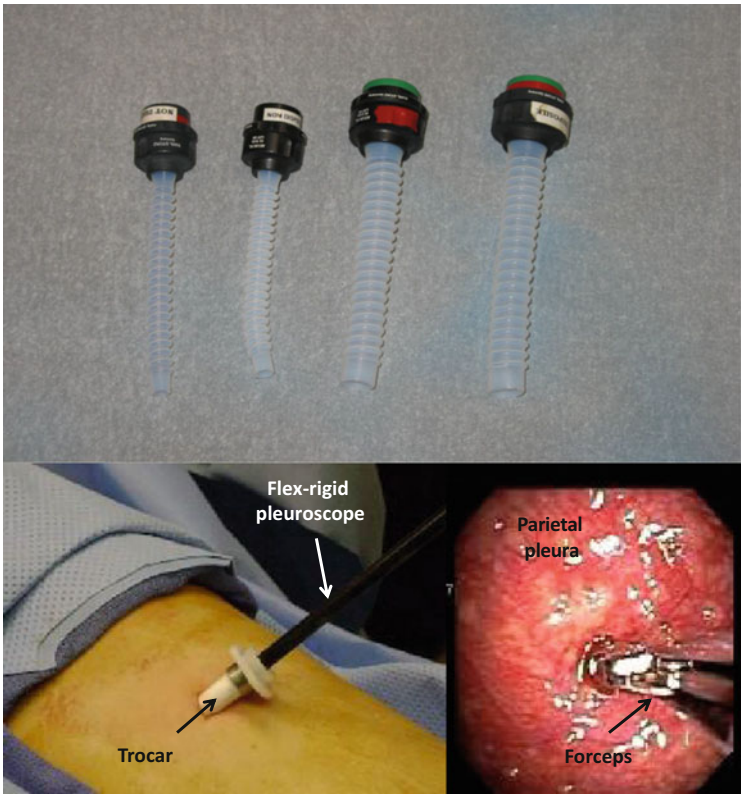

Fig. 76.10 Trocars allow insertion of various instruments (*top panel*). The 2.8 mm working channel of the flex-rigid pleuroscope accommodates forceps, electrosurgical and laser probes, and other accessories (*bottom panel*)

76.5 Anatomic Regions of the Pulmonary System Amenable to Potential Clinical OCT Applications

76.5.1 Pulmonary Airway Tree

OCT has been demonstrated in a number of studies to acquire images with sufficient contrast and resolution to reliably identify many of the normal architectural features of the airway, parenchyma, and pleura. Deviations from this normal structure such as the loss of the layering of the airway wall, or the visibility of alveoli in the parenchyma, may be indicative of the presence of a pathologic abnormality. The initial reports of OCT in pulmonary medicine involved studies of normal and abnormal tracheal, bronchial, and bronchiolar anatomy in excised tissue specimens [10, 12–14, 52]. The ability of OCT to differentiate epithelial, subepithelial, glandular, cartilaginous, and muscular structures within the trachea of humans and animal models was demonstrated. However, the development and

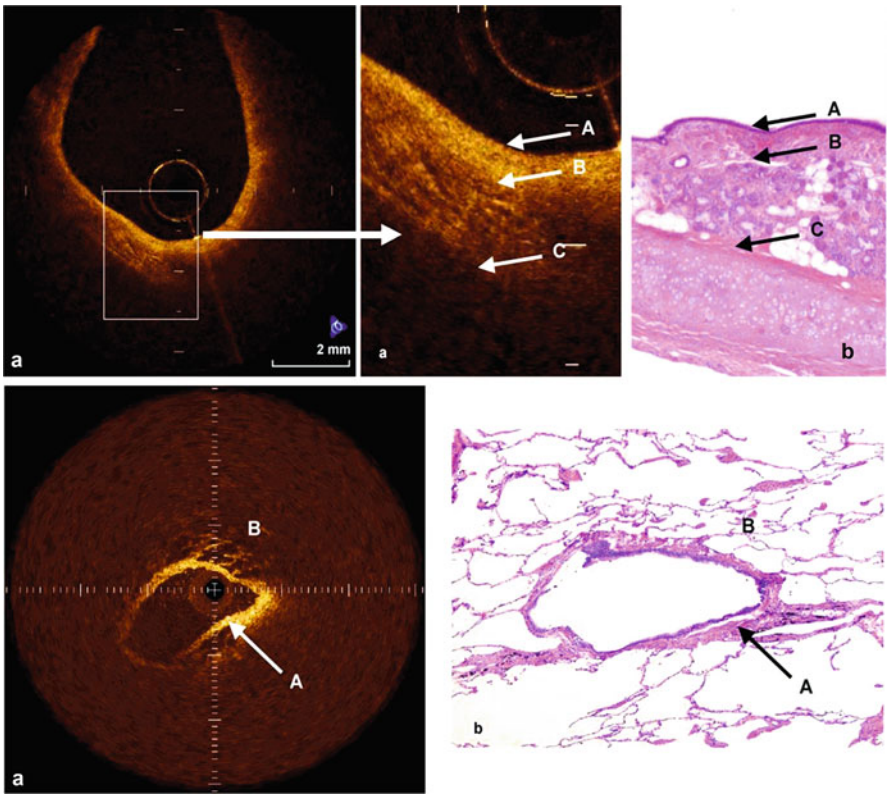

Fig. 76.11 Rotational probe images from human lung specimens compared to corresponding histology from Tsuboi [10]. Images obtained from a SLD laser system (1,300 nm center λ, 70 nm bandwidth). *Top image* shows the OCT image (**a**), and histological finding (**b**), of normal bronchus. The bronchial mucosal and submucosal layer (*A*) appear homogenous in OCT image. The submucosal layer is relatively reflective due to the presence of extracellular matrix. A gap can be seen between the submucosa (*A*) and smooth muscle layer (*B*), and cartilage layer shows much scattering (*C*). Epithelium, mucosa, and cartilage are clearly differentiated, as well as a number of glandular tissues and microvessels by both OCT and histology. (**a**) OCT images, (**b**) histological finding, (*A*) mucosal and submucosal layer, (*B*) smooth muscle layer, (*C*) cartilage. *Bottom* figures show the OCT image (**a**), and histological findings (**b**), of normal peripheral bronchus and alveoli. The uniform bronchial wall (*A*), and the structure of alveoli (*B*), containing air can be observed. (**a**) OCT images, (**b**) histological finding, (*A*) peripheral bronchus, (*B*) alveoli (From [10])

validation of accurate image interpretation criteria to reliably assess OCT images of pulmonary tissues obtained in vivo is a necessary step if OCT is to be adopted in the clinical setting. A number of groups are assessing the close similarity between OCT imaging and standard histologically stained excised specimens (Figs. 76.11, 76.12 and 76.13) [10, 12, 15, 16, 24, 53] and are now beginning to use this information for develop interpretation guidelines (Table 76.1) [53].

These OCT features can be applied to a multitude of benign and malignant processes in the large and small airways. In addition to airway cancer, OCT can be

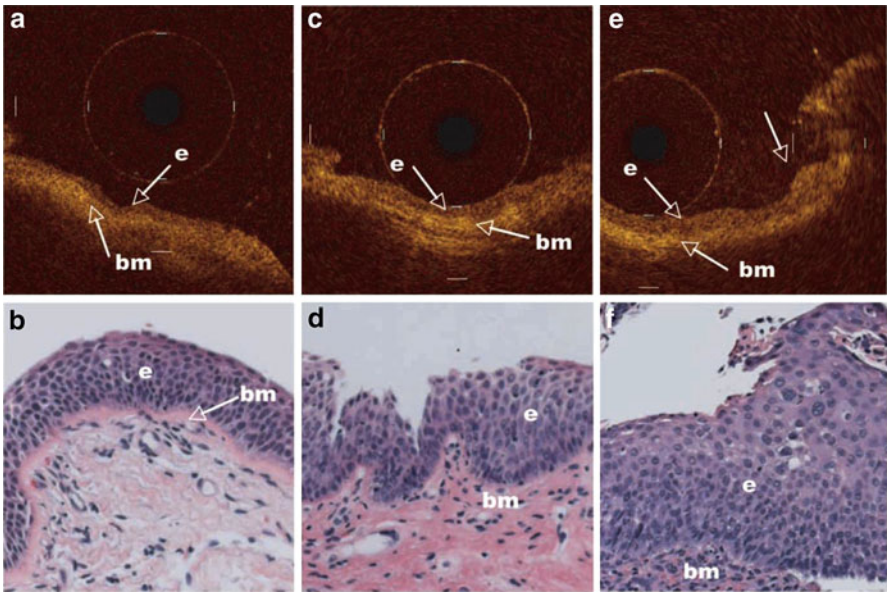

Fig. 76.12 Representative OCT images of an area with mild dysplasia (**a**), moderate dysplasia (**c**), and severe dysplasia (**e**) and corresponding H&E-stained histologic sections (**b**, **d**, and **f**; original magnification, ×20). The nuclei in the epithelium become recognizable as *darker dots* with moderate dysplasia or worse. The *arrow* in the OCT image of the area with severe dysplasia points to the corresponding elevated area in the H&E section (Reprinted with permission from [24])

used to study airway wall thickness and remodeling in asthma, COPD, and bronchiectasis [25, 26]. Long-range OCT applications allow the study of airway compliance and potentially facilitate the identification of flow limiting segments in asthma, COPD, tracheomalacia, and obstructive sleep apnea [54–58]. This is clinically relevant for several reasons: (1) it facilitates airway selection for novel bronchoscopic asthma treatments (bronchial thermoplasty); (2) leads to better understanding of central airway mechanics (elastic properties, dynamic compression) in asthma and COPD; (3) allows measurement of the central airway lumen at normal and stenotic sites, potentially guiding bronchoscopic interventions; and (4) facilitates quantitative evaluation of the upper airway dynamics and localization of the sites of obstruction during polysomnography or continuous positive airway pressure thus potentially guiding surgical interventions for OSA.

76.5.2 Lung Parenchyma

OCT can potentially be used to study focal or diffuse lung parenchymal processes. Current research is limited to ex vivo studies aiming to understand normal and

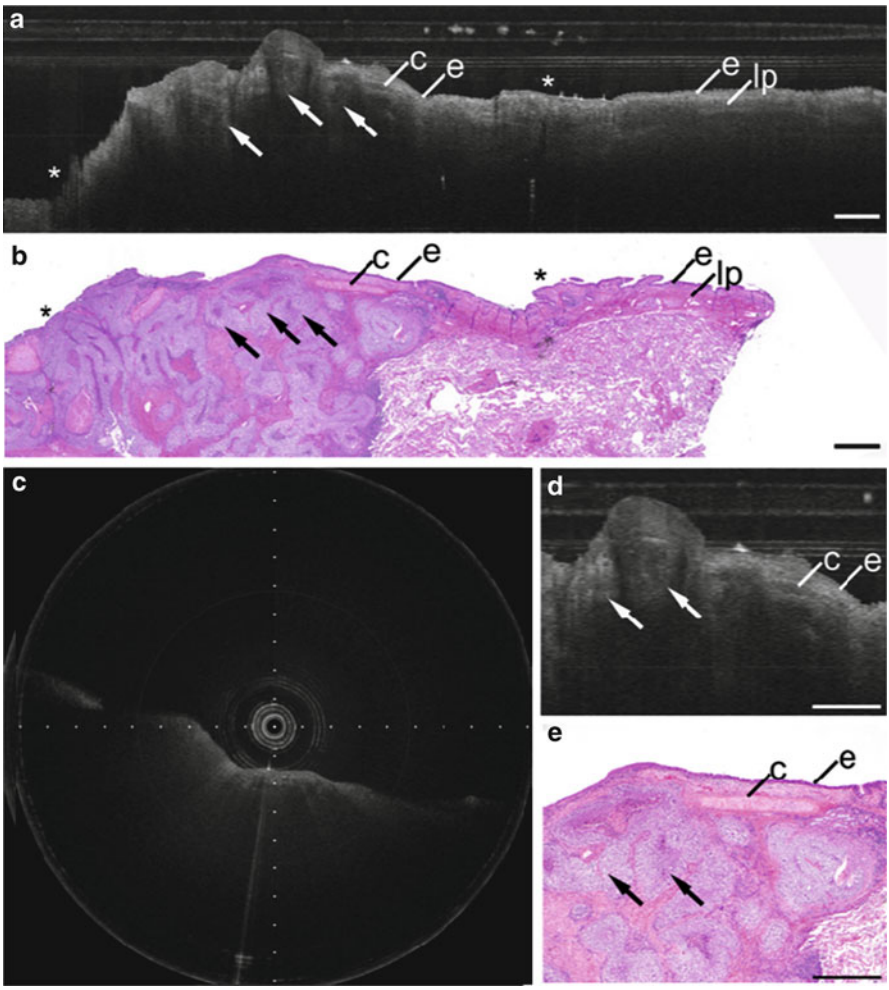

Fig. 76.13 Bronchoscopic catheter-based OCT of squamous cell carcinoma, baseloid type. (**a**) OCT longitudinal section and (**b**) corresponding histology. (**c**) OCT cross section. (**d**, **e**) Higher magnification OCT longitudinal section and corresponding histology. *e* epithelium, *lp* lamina propria, *c* cartilage, *Arrows* nests of hyperintense squamous cell carcinoma with signal-poor central necrosis, *Asterisks* ink marks for registration. *Scale bars* 1.0 mm. (Reprinted with permission from [53])

pathologic alveolar structure and dynamics [1, 59]. Current limitations in clinical applications include technical challenges due to the invasive access to the alveolar space (may require pleuroscopy) and OCT imaging itself of the alveoli due to changes in the refractive index of air, tissue, and mucus (may require liquid filling index matching). Potential clinical applications would likely require a bronchoscopic approach in which the OCT probe is guided to a target previously identified on computed tomography. This is now possible using electromagnetic

Table 76.1 OCT image interpretation features for benign and malignant pulmonary pathology (reprinted with permission [53])

Pathology	Imaging features
Normal	
Airway	Layered architecture, including
	Respiratory epithelium and underlying basement membrane
	Lamina propria
	Cartilaginous rings
Parenchyma	Thin, lattice-like alveolar architecture with signal void spaces
Neoplastic	
Adenocarcinoma	Loss of layered architecture
	Mass with signal heterogeneity with rapid attenuation
	Atypical gland formation
Mucinous adenocarcinoma	Signal intense alveolar wall thickening
	Preserved lattice-like architecture
	Signal poor intra-alveolar mucin
	Homogeneous signal intense tumor-associated scar may be seen
Squamous cell carcinoma, basaloid type	Loss of layered architecture
	Mass with signal heterogeneity with rapid attenuation
	Irregular tumor nests with:
	Signal-intense periphery corresponding to malignant cells
	Signal-poor center corresponding to central necrosis
Salivary gland adenocarcinoma, adenoid cystic carcinoma	Luminal mass protrusion
	Uniform distribution of signal-intense trabeculae
	Small pseudocystic spaces filled with mucin can be seen
	Intact overlying respiratory epithelium may be present
Benign	
Cartilaginous hamartoma	Lobulated mass with well-delineated borders and
	Evenly dispersed, fine-scale regions of high signal intensity
	Background of uniform, moderate signal intensity
Fibrosis	
Usual interstitial fibrosis	Diffuse, signal dense subpleural fibrosis
	Irregularly shaped, signal poor subpleural cysts
Focal mild subpleural fibrosis, idiopathic	Focal, signal dense pleural fibrosis
	Interspersed lattice-like alveoli with mildly thickened alveolar walls

navigation bronchoscopy, which provides a three-dimensional virtual road map that enables a physician to maneuver through multiple branches of the bronchial tree. Once the desired location is achieved, the insertion of a needle probe could allow OCT imaging and biopsy of the desired region (i.e., focal lung mass or alveolar space) [60–62]. In addition, one could gain more information about the basic alveolar dynamics during normal breathing and artificial ventilation [63]. This information could potentially be used to prevent alveolar damage and guide protective lung ventilation strategies in patients with acute respiratory distress syndrome (ARDS), though this is speculative at this time [64].

76.5.3 Pleura

The pleural space is a virtual space between the lungs and their surrounding thoracic structures including the chest wall, mediastinum, and diaphragmatic surface (Fig. 76.4). The pleural space is a site of important thoracic pathology including primary malignancies, metastatic malignancy, fluid collections (benign and malignant), infection, and traumatic and inflammatory conditions. Accurate diagnosis of pleural disease may require open thoracotomy or thoracoscopic examination. Detecting malignancy in the pleural space is essential for proper staging and management of lung cancers. Diagnostic yield from thoracentesis (pleural fluid drainage) is often low. Yield from thoracoscopy is substantially higher. It is uncertain at this time whether OCT will have a role in pleural diagnostics, though it is reasonable to speculate that the ability to obtain high-resolution functional and structural characteristics of pleural spaces and surfaces prior to biopsy would be of potential benefit. This may particularly apply to mesothelioma for which the pleural findings on white light imaging may be nonspecific and deeper pleural biopsies are usually necessary for diagnosis. It is likely that if OCT will have a role in pleural investigations, it will be in a multimodal approach in conjunction with white light thoracoscopy and potentially NBI or AF. OCT may be particularly useful in guiding the site of thoracoscopic biopsy, if studies will confirm that tumor can be distinguished from adjacent nonmalignant findings. Current research in OCT imaging of the pleura is limited to animal studies which demonstrate that fine structures such as the visceral pleura and alveoli were able to be visualized with OCT at high resolution, but it remains to be determined whether OCT is capable of differentiating between benign and malignant pathologies [15, 65].

76.5.4 Pulmonary Vascular Tree

Pulmonary vessels can be accessed for OCT imaging at the time of right heart catheterization. The pulmonary vascular wall changes due to hypertrophy of the intima and media (such as in pulmonary arterial hypertension) or detection of flaps inside the lumen (due to thrombus) can be detected by OCT. This could have diagnostic and consequent therapeutic implications since OCT can potentially

distinguish chronic thromboembolic hypertension from other etiologies [66]. Technically, however, application techniques for OCT imaging of the pulmonary vasculature are not obvious since it may require proximal balloon occlusion and injection of saline or lactated Ringer solution to facilitate penetration of light. These limitations have already been addressed in intracoronary OCT imaging where increases in image acquisition times have negated the need for proximal balloon occlusion and require only a very short saline, lactated Ringers solution, or radiocontrast flush (<10 mL total). Therefore, it is feasible that with further investigation and refinement of imaging techniques, these issues may additionally be overcome in the pulmonary vasculature.

76.6 Pulmonary OCT Imaging Systems and Approaches

76.6.1 Endobronchial

The use of OCT to study the lung in the clinical setting has been predominantly restricted to assessment of airways within the tracheobronchial tree that are accessible with a standard bronchoscope. Endobronchial OCT imaging is typically performed by inserting the OCT catheter through the accessory port of a standard bronchoscope (Fig. 76.14) [10, 24, 53, 67]. Alternative placement of catheters into the more distal airways may be achieved using CT, or fluoroscopic guidance, or by using a guide sheath in conjunction with electromagnetic guidance techniques.

Endobronchial OCT imaging may be performed using a variety of catheter designs. Prior studies have included both circumferential [10, 24, 41, 54] and linear scanning [15, 16] mechanisms, which may be actuated either proximally outside the patient or at the distal tip of the catheter using miniature motors [68] or galvanometric scanners. The designs of both linear and circumferential catheters that are actuated proximally typically consist of an optical inner core encased inside an optically transparent sheath. The primary purpose of the sheath, which is typically single use, is to protect the patient from contact with the reusable inner optical core and to prevent contamination of the optical core with bodily fluids. A common design of the inner optical core consists of a fiber to transmit the OCT signal, coupled to a focusing element which may consist of a gradient index lens [15], ball lens, or other focusing element and a reflecting surface such as a prism to redirect the light to the tissue surface at an angle of approximately 90° to the catheter. The entire optical assembly is encased inside a metal drive shaft to provide added protection to the optical components against breakage and to convey the necessary translational actuation from the proximal end during tissue scanning. The primary difference between linear and circumferential scanning catheters is that the proximal end of circumferential scanning catheters is attached to an optical rotary junction. Together both actuation methods can be used to achieve spiral cross-sectional imaging to capture volumetric images of entire bronchial segments. While many scanning mechanisms may be used to collect OCT images of the airways,

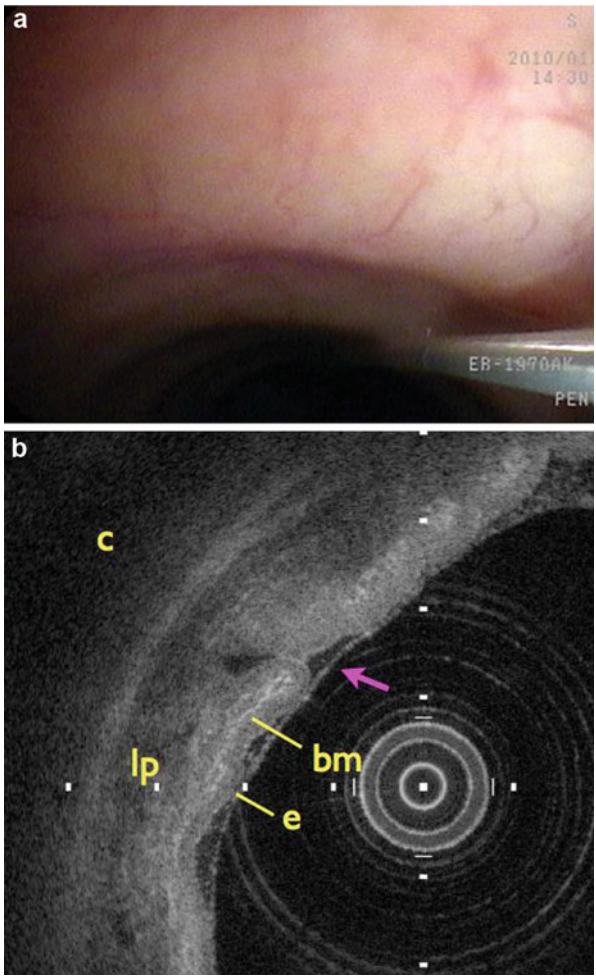

Fig. 76.14 Clinical endobronchial OCT imaging. (**a**) Spiral cross-sectional OCT catheter extending through the accessory port of a standard bronchoscope into the airway lumen. (**b**) Cross-sectional OCT image highlighting the normal layered architecture of the airway wall. *e* epithelium, *bm* basement membrane, *lp* lamina propria, *c* cartilage

circumferential and spiral cross-sectional scanning catheters have been used predominantly for clinical studies in order to acquire complete cross-sectional imaging of the entire airway lumen.

76.6.2 Transbronchial and Transthoracic

In order for OCT to play a future role the evaluation of lung pathology and the guidance of biopsy acquisition, access to regions of the lung that extend beyond the central airways is necessary. This may be through transbronchial approaches where a needle or catheter is passed through the airway wall in order to reach the surrounding parenchyma or through transthoracic approaches where a needle or catheter is passed through the chest wall into the lung. Although no transbronchial

or transthoracic OCT catheters are currently available for clinical use, a number of groups are actively working on the development of these much needed imaging tools.

A number of small diameter rigid OCT needle probes have been developed by research laboratories that may be adapted for transthoracic use [69–73]. In these designs the imaging optics are traditionally housed within the stainless steel hypodermic needles to ensure that the needle probe maintains a small diameter profile to minimize possible tissue damage. To conduct imaging the entire needle is rotated or translated. In many potential clinical applications of transthoracic OCT imaging, it may be useful to obtain biopsy specimens for histopathological analysis prior to imaging. Therefore, one limitation to these OCT needle probes is that it is not possible to obtain tissue specimens for diagnosis through the same imaging needle. Recently, Kuo et al. demonstrated an OCT-guided core-needle biopsy system incorporating a vacuum-assisted rigid breast needle biopsy console, which was modified to accommodate the OCT imaging probe [61]. This work highlights the potential of OCT image guidance for biopsy site selection with rigid needle designs.

Transbronchial OCT imaging requires the development of flexible OCT needle probes that can be passed through the auxiliary channel of the bronchoscope in a similar fashion to standard transbronchial fine-needle aspiration techniques. Tan et al. have developed a narrow diameter flexible OCT catheter that is not only compatible with standard transbronchial needles but additionally facilitates OCT imaging and subsequent tissue sampling through the same needle (Fig. 76.15) [62].

76.6.3 Pleural

Imaging of the lung pleura has been conducted by a number of groups; however, its use has been limited to early preclinical studies. These studies have utilized noncontact benchtop galvanometric scanners [74] and handheld tunable galvanometric probes for use during thoracoscopic surgery [65] to conduct imaging of the pleura and the underlying alveoli. Due to the penetration limitation of OCT, removal of the overlying muscle is necessary to create a thoracic window when using the noncontact galvanometric scanners. These studies have been conducted to both look at the normal pleural and alveolar structure and dynamics and to assess malignancy [65, 74].

76.7 Lung Cancer: Potential Role for OCT

Lung cancer remains the leading cause of cancer death in men and women in the United States. In 2009, for instance, 205,974 people in the United States were diagnosed with lung cancer, and 158,081 people died from it (US Cancer Statistics Working Group. United States Cancer Statistics: 1999–2009 Incidence and Mortality Web-based Report. Atlanta (GA): Department of Health and Human Services,

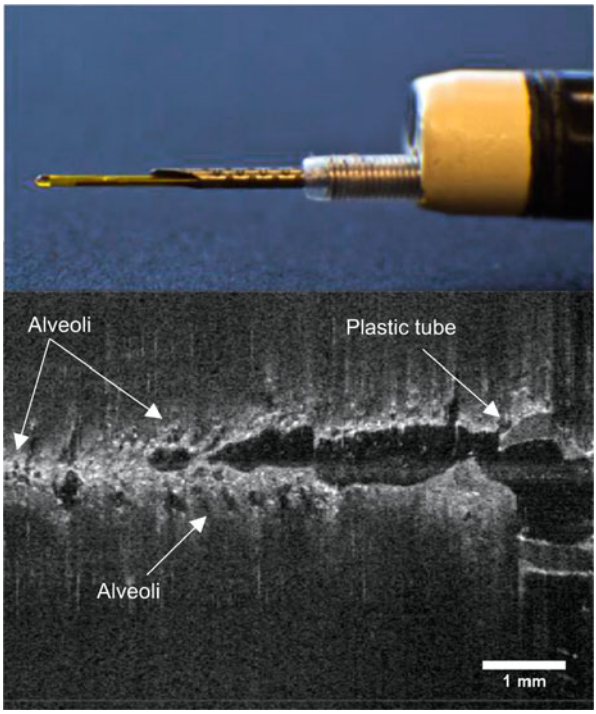

Fig. 76.15 Flexible transbronchial OCT imaging catheter housed within a 21 gauge transbronchial needle that is advanced through the accessory port of a standard flexible bronchoscope. (**b**) Longitudinal reconstruction of an OCT dataset obtained using the transbronchial OCT catheter in (**a**) from an inflated swine lung ex vivo (Modified with permission from [62])

Centers for Disease Control and Prevention, and National Cancer Institute; 2013. Available at: http://www.cdc.gov/uscs). Metastasis from lung cancer is present in over 50–60% of patients at the time of diagnosis [75], and only 40–50 % of patients currently survive for >5 years after curative-intent surgical resection of presumptively local disease. A significant proportion of patients develop local or distant recurrence following attempted curative resection [76, 77].

In addition, only 15 % of lung cancer cases are found at the localized early stage. When lung cancer is detected and diagnosed in an early stage and surgery is possible, the 5-year survival rates can reach 85 % [78] compared to <15 % 5-year survival for later stages (http://ukprc.udy.edu/policynewsletter1-1.pdf). For the vast majority of patients with limited stage non-small cell lung cancer, accurate and complete surgical resection is currently the only potentially curative approach. Accurate staging and assessment of operative margins is important both for cure and to avoid either excessive or inadequate surgical resection. Local recurrence occurs in 5–20 % of patients, depending on the pathologic staging of the tumor. Fifty percent of all recurrences are diagnosed in the first 24 months after presumed curative treatment, demonstrating another shortfall of current diagnostic capabilities. In addition to early detection, better identification of tumor boundaries and subsequent improved resection procedures should potentially lead to reduction in recurrence rates, improved survival, and reduction in inadvertent non-curative surgical procedures. Furthermore, increasingly, lung cancer care is personalized

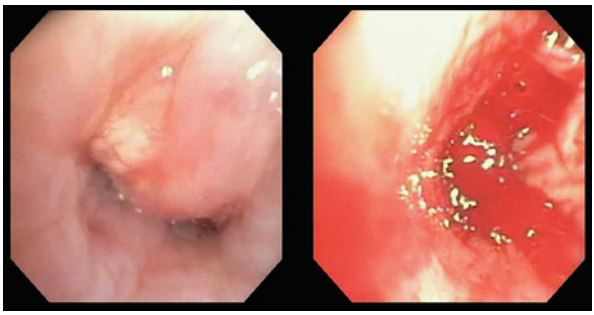

Fig. 76.16 Endobronchial tumor in the bronchus intermedius before (*left panel*) and after biopsy (*right panel*). Before biopsy, the tumor surface is heterogeneous showing areas of prominent vascularity resulting in immediate post biopsy bleeding

based on predictive and prognostic molecular markers. Targeted therapy is the new paradigm in lung cancer management, but this strategy requires sufficient tissue for these molecular analyses to be performed. Thus, it is important to develop improved methods for (1) early detection of endobronchial lung cancer; (2) accurate diagnosis and improved tumor specimen quality and quantity; (3) determination of location, borders, extent, and stage of disease; and (4) diagnostic guidance for peripheral lung nodules. High-resolution OCT imaging may have potential to fulfill some of these needs.

76.7.1 OCT-Guided Biopsy

In a number of endobronchial, peripheral parenchymal lung nodules and pleural malignancies, in which pathophysiologic abnormalities may present at or near airway or pleural surfaces, advances in real-time, high-resolution endoscopy with OCT offer potential to develop the near histologic level endoscopic evaluation capabilities needed for pulmonary and thoracic surgical cancer detection diagnostics. While the majority of lung cancers originate in the periphery, a substantial proportion of tumors (particularly squamous cell cancer) arise in or metastasize to proximal airways, where they may be visualized by current level OCT techniques [10, 15]. In airway diagnosis and treatment, selection of bronchoscopic biopsy sites is prone to sampling errors, and the biopsy procedure may be associated with airway bleeding possibly leading to hypoxemia and hemodynamic instability. This limits the number of biopsies and potential sampling sites, as well as diagnostic accuracy, while it increases risks and expense. Biopsy yield rates vary based on the underlying disease, the patient's ability to tolerate the procedure, and for malignant disease – on the location, depth, appearance, size, extent, cell type, and degrees of vascularity and necrosis. Endobronchial tumors often have regions of fibrosis, vascularity, necrosis, or areas where the tumor is located below the visible airway surface, leading to non-diagnostic endobronchial biopsies, misinterpretation of malignancy borders, or bleeding (Fig. 76.16). Using current white light flexible techniques, the bronchoscopic yield, in terms of diagnostic sensitivity and specificity for endobronchial malignancy, is variable. Rates for diagnosing visible

lesions in patients with endobronchial tumors have been reported between 75 % and 98 %, while non-visualized endobronchial tumors have been diagnosed at rates of 25–65 %. Overall specificity has been reported at 64–96 %, and pathologic diagnostic error rates of 1.5–3 % have been reported [79–92]. For central tumors the maximal diagnostic yield was not achieved until the 4th forceps biopsy, and for peripheral lesions accuracy continued to increase through the 6th forceps biopsy in another study [83]. Thus, improved guidance for airway biopsy would increase yield and decrease risks associated with the large number of biopsies currently necessary for diagnosis. The excellent sensitivity of AF has potential airway cancer screening value, and the usefulness of AF would be dramatically enhanced if methods for more specific optical evaluation of suspicious regions can be added to the sensitive but nonspecific AF screening [15]. In the future, we speculate that multimodality imaging may combine autofluorescence imaging, OCT, endobronchial ultrasound, and confocal endoscopy in various combinations based on clinical application needs, location, and resolution requirements [15, 93]. In this way, OCT may be ideal for early proximal airway malignancy detection when combined with field narrowing AFB modalities discussed previously [24]. In addition, OCT may be of assistance in guiding endobronchial biopsy sites, improving biopsy yield for endobronchial lesions, obtaining more representative specimen for molecular analysis, and reducing complications. Airway tumors are frequently friable, prone to bleeding, with substantial vascularity, as well as containing areas of necrosis and epithelial or fibrotic layers covering the tumor. OCT may be useful in identifying areas of high yield within large mucosal and submucosal tumors of the proximal airways. Submucosal vessels prone to bleeding could potentially be identified by OCT prior to biopsy as well.

In patients with airway cancer, a study of OCT demonstrated tissue structural changes in proximal airways of patients with documented, biopsy-confirmed bronchogenic carcinomas [10]. Whether these findings are specific for malignancy, or whether similar changes may be seen in patients with benign endobronchial pathology, remains to be determined by clinical investigations. This study involved use of a commercial OCT system and flexible fiber-optic rotational probe passed through the working channel of a bronchoscope. Resolution was reported to be 16 μm in axial and lateral directions [10] (Fig. 76.7). The authors examined normal and cancerous proximal airways in vivo and in freshly excised surgical specimens. The findings in the cancerous lesions in five patients are summarized in Table 76.2 (from Tusboi et al. [10]).

The majority of lung cancers, however, are peripheral (i.e., beyond the fourth to fifth generation). This leads investigators to systematically study chest computed tomography (CT) as a screening tool for lung cancer detection. Three randomized controlled studies evaluated the role of low-dose CT scan screening on the rate of death from lung cancer [94, 95]. Only the NLST study had a large number of patients (53,454 vs 4,104 vs 2,811) [94] and found a dramatic 20 % reduction in lung cancer mortality compared to those screened with CXR (RR 0.80, 95 % CI 0.73–0.93, $p = 0.004$). No difference in lung cancer mortality was reported in the DANTE trial ($RR = 0.97$, 95 % CI 0.71–1.32, $p = 0.83$) [19] or the DLSCT study

Table 76.2 OCT findings of central type lung cancer patients

					Normal bronchus			Tumor
No.	Age	Sex	Pathologic type	Location	Layer structure	Alveoli	Uneven distribution	Loss of layer structure
1	60	Male	Squamous	Right B4+5	+	N	+	+
2	56	Male	Squamous	Left B6a	+	+	+	+
3	65	Male	Squamous	Trachea	+	N	+	+
4	68	Male	Squamous	Right B1a	+	N	+	+
5	77	Male	Small	Left upper bronchus	+	+	+	+

+ Detected, *N* not performed

($RR = 1.15$, 95 % CI 0.83–1.61, $p = 0.06$) [23]. The NLST, however, is not only the largest study but also involved longer follow-up (6.5 vs 2.8 and 4.8 years median) and participants at slightly higher risk (30 vs 20 and 20 pack years of smoking for NLST vs DANTE and DLCST, respectively). The current data support a significant reduction in deaths from lung cancer resulting from several rounds of low-dose CT screening of individuals at risk (smokers and former smokers who are aged 55–74 and who have smoked for 30 pack years or more and either continue to smoke or have quit within the past 15 years). However, it is recommended that screening should be done in the settings that can deliver the comprehensive care provided to NLST study participants, which involves among other factors a multidisciplinary program and with a defined intervention algorithm. This is especially relevant for lung cancer screening since the average nodule detection rate is around 20 % but varied from 3–30 % in the randomized controlled studies. Since most studies reported that >90 % of nodules were benign, concerns exist about the potential negative impact on patient safety and health-care costs (i.e., the need for invasive procedures performed for benign disease). It is therefore desirable to obtain a diagnosis in a minimally invasive fashion without compromising a patient's safety. While CT-guided transthoracic needle biopsy and aspiration have an accuracy of 80 % and 95 %, respectively, for confirming lung cancer in peripheral lesions, the complication rates are not insignificant (pneumothorax ~13 %, hemoptysis ~6 %). Therefore, obtaining tissue bronchoscopically could be more cost-effective, especially if lung cancer screening will become standard of care. For peripheral parenchymal lesions, a systematic review showed that the overall sensitivity of conventional bronchoscopy with transbronchial biopsy, brushings, and lavage is 69 %. The sensitivity of all modalities for peripheral lesions less than 2 cm or greater than 2 cm were 0.33 and 0.62, respectively [81].

Electromagnetic navigation bronchoscopy (ENB) allows physicians to navigate through the airways and reach a target lesion in the periphery of the lung. While navigation is successful in 90 % of patients, the diagnostic yield is ~70 % with a pneumothorax rate of 1.5–3 %. The discrepancy between the ability to navigate and obtain a diagnosis is partly related to the fact that ENB guides the bronchoscopist to the lesion, but is not an endoscopic tool. The use of forceps, needles,

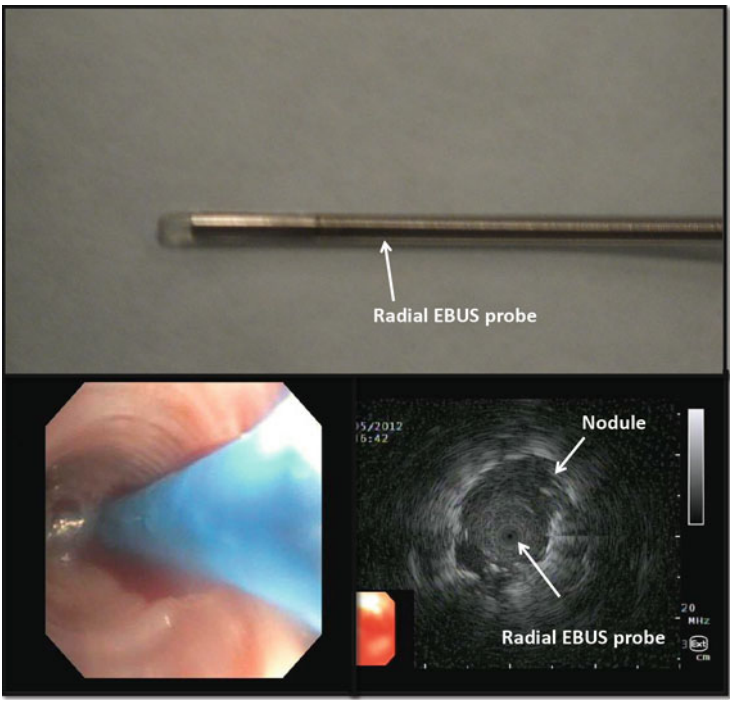

Fig. 76.17 To increase the probability that the biopsy instruments are inside the lesion, the 20 MHz high-frequency radial ultrasound probe (*top panel*) can be inserted through the guide catheter (*bottom left*) and confirm its location within the peripheral lung nodule (*bottom right*)

or brushes to obtain samples usually under fluoroscopy guidance is still necessary. To increase the probability that the instruments are inside the lesion, high-frequency radial probe ultrasound (R-EBUS) can be inserted through the guide catheter and visualize the nodule (Fig. 76.17). Results of studies show that the diagnostic yield of combined R-EBUS with ENB was ~90 %, better than either R-EBUS or ENB alone [96]. With R-EBUS, however, the probe still has to be removed before the sampling instruments are inserted. This could lead to guiding sheath displacement potentially reducing the yield. The development of integrated OCT core-needle biopsy systems can potentially solve this problem [61, 62]. This catheter-based 3-D OCT imaging can be used for real-time image guidance for target tissue localization and imaging of tissue immediately prior to biopsy. In a recent study six readers trained in simple image interpretation criteria were able to successfully differentiate between OCT images of solitary pulmonary nodules and lung parenchyma with a sensitivity and specificity >95 % providing support for the use of OCT-guided biopsy of these lesions [97]. OCT has additionally been demonstrated to differentiate tumor from non-tumor tissues including necrosis, fibrosis, and calcification [98]. Since such OCT images of biopsied ex vivo tumor specimens acquired during core-needle placement correlate with corresponding

histology, these systems can potentially not only localize the lesion but avoid the actual aspiration, specimen retrieval, and processing, if the OCT probe is in the undesirable areas (normal lung tissue, highly vascular or necrotic nodule regions).

76.7.2 OCT Tumor Margin Assessment

During lung cancer resections, despite apparently clean margins based on preoperative and intraoperative evaluations, local airway recurrence rates of 17–26 % after what was thought to be complete resections were reported [99–101]. OCT may have a role in identification of tumor boundaries in the mucosa and submucosa of airways and thus potentially facilitate intraoperative decisions in regard to tumor-free bronchial margins. Determining the proximal and distal boundaries of airway involvement is an important step in staging lung cancer, as well as in determining resectability, operability, extent of resection, and resection margins. Since recurrence at the site of resection must be avoided, preoperative and intraoperative methods for determining the tumor boundaries would be very useful. Accurate clinical diagnosis of endobronchial cancer, and its peripheral margins, is crucial to choosing the correct surgical or medical therapeutic regimen. This is particularly significant when a thoracic resection procedure (tracheal resection, thoracotomy or thoracoscopy with lobectomy, sleeve resection, or pneumonectomy) is being considered with curative intent, and ensuring adequacy of staging and surgical margins around a suspected primary malignant lesion is essential for proper therapy. Identification of unsuspected microinvasion, submucosal spread not visible on the surface, or of small satellite lesions by OCT and AFB could theoretically improve accuracy of biopsy tumor margin assessment, leading to more effective treatment. The role of OCT in such evaluations remains to be determined. However, although OCT may theoretically be very helpful if benign from malignant airway tissue can be readily distinguished, utility may still be limited for detecting tumor margins by the shallow depth of penetration, since deeper level tumor invasion cannot be assessed with current OCT technology. Indeed, the cartilage in the large airway is not entirely visualized in cross section, but this can be done by applying high-frequency endobronchial ultrasonography, method shown to impact treatment decisions in patients with airway cancer [102]. For airway tumors in particular, it is likely that OCT will be used in combination with other modalities. For instance, results of studies show that combination of NBI and AF shows higher sensitivity (93.7 %) and specificity (86.9 %) in the assessment of lung cancer extension when compared to WLB alone [103]. OCT could further improve the specificity for this application of optical technologies.

76.7.3 Optical Biopsy

Some innovators in the development OCT have proposed the concept of “optical biopsy” in which OCT high-resolution imaging may replace current traditional

tissue biopsy methods [104, 105]. While this is a valuable long-term research target, even ultrahigh-resolution OCT imaging is unlikely to replace tissue biopsy for pulmonary diagnostics in the near future. While biopsy specimen examination for histologic appearance may soon be rivaled by ultrahigh-resolution techniques (if endogenous or exogenous contrast is adequate), a range of other information obtained from tissue biopsy may still be unobtainable until considerable scientific advances have been made. For example, special immunologic staining for cellular antigens to characterize tissue origin and define histologic subtypes or infectious agents currently requires excised tissue for staining and/or culture. While it is conceivable that in vivo fluorescent probes with analogous capabilities may someday become available, the broad range of antigen-specific probes necessary will undoubtedly take many years to develop. In addition, malignant cells and many infectious agents are cultured in the laboratory for DNA analysis, metabolites, subtyping, and chemosensitivity or antibiotic sensitivity testing. This is especially relevant now in the treatment of lung cancer, where decisions about prognosis and predictions about response to specific agents are based on molecular markers for which tissue analysis remains necessary.

Thus, the major role for OCT in pulmonary diagnostics will likely include guiding biopsy sites and assessing response to therapeutic interventions in the near term.

76.8 Inhalational Injury

The lung is a unique organ in which internal tissue is exposed to large volumes of external air (greater than 10,000 l/day inhaled and exhaled, with more than 5,700 l/day of blood flowing through the lungs) [21] (page 7), allowing potential exposure to environmental toxins, particulate matter, infectious agents, as well as thermal stresses and smoke. Depending on the nature of the exposure, the predominant injuries may occur in the proximal airways, distal airways, alveoli, or even the pleural space. Some initial investigations have focused on OCT proximal airway exposures. In studies involving pulmonary inhalation-related pathology, OCT was capable of detecting submucosal edema and glandular crowding in a septic inhalation injury airway animal model [16, 106, 107]. In victims of smoke and thermal inhalation, swelling, edema, sloughing, and obstruction of airways are a major cause of morbidity and mortality (Fig. 76.18). It is difficult to determine the extent of airway injury early after smoke and thermal inhalation exposures. Therefore, many patients must be prophylactically intubated in order to assure a patent airway if swelling occurs. OCT has the potential to detect early airway inflammation and progress of airway swelling in a minimally invasive way. In addition, long-range FD OCT may allow not only monitoring of the airway wall thickness but also measurement of the lumen cross-sectional area [57]. Future clinical studies will be needed to determine the value of OCT monitoring in this setting. In addition,

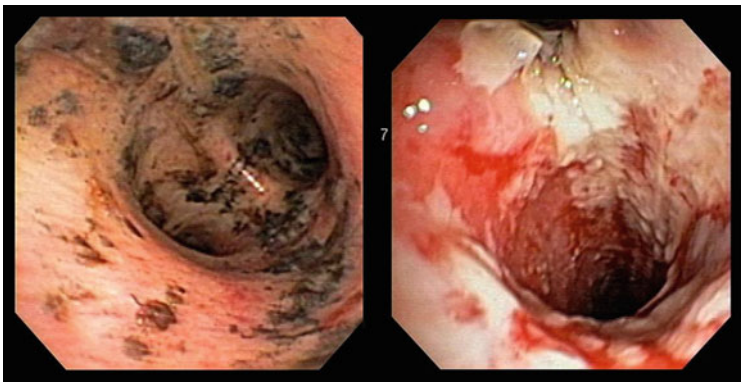

Fig. 76.18 Examples of airway mucosal findings on bronchoscopy in patients with smoke and thermal inhalation injury. Erythema and carbonaceous particulate material can be visualized at earlier stages (*left panel*) followed by edema, mucosal necrosis, sloughing, and obstruction of the airways (*right panel*)

we speculate that OCT may potentially be useful for evaluating submucosal blood flow changes or structural matrix changes using Doppler and polarization-sensitive OCT.

76.9 Asthma

Asthma currently affects over 300 million individuals worldwide, and the prevalence is continually increasing [108]. Approximately 10 % of asthmatics have uncontrolled or poorly controlled symptoms [109], and it is this population that urgently needs improved targeted therapies and management strategies in order to reduce the high morbidity and socioeconomic burden, estimated to be 14.7 billion dollars annually in the United States alone [108]. Asthma refers to individuals with reversible airway obstruction and bronchial hyperresponsiveness. Though classically thought to be a chronic inflammatory disease, studies have recognized groups of individuals with severe asthma in the absence of eosinophils [110, 111]. It is now understood that asthma is not a single disease but is rather a collection of multiple asthma phenotypes [112, 113]. The exact mechanisms behind the pathophysiology of asthma remain uncertain which may be due in part to a lack of available imaging tools with sufficient spatial and temporal resolution to dynamically assess airway structure and function in vivo. OCT has been used to assess airway wall thickness [25] and biomechanical properties [26, 58]. It remains to be seen, however, if OCT will enable the evaluation of all of the hallmark features of asthma including inflammation, remodeling, and hyperresponsiveness. With continued improvements in image resolution to the micron scale, increases in acquisition speed for dynamic imaging, and increases in contrast through Doppler or polarization-sensitive OCT, OCT may become an invaluable tool in assessing asthma.

OCT may be beneficial in improving our understanding of asthma, phenotyping asthma to better match individuals to appropriate therapeutics, guide and monitor response to therapies, and may be useful in guiding critical decision making in the drug development pipeline.

76.10 Commercial Pulmonary Clinical OCT systems

In recent years a number of clinical endoscopic OCT systems have become, or will likely soon become, commercially available including systems by Imalux Corporation [114], St. Jude Medical (Lightlab Imaging) [115], Terumo Corporation [116], Tomophase Corporation [117], Volcano Corporation [118], and NinePoint Medical [119]. At present only Tomophase is focused on the development of systems dedicated for pulmonary use; however, due to the synergy of system and catheter requirements across organ systems, many of the seminal OCT work conducted in the pulmonary space has been performed using commercial and research system designed for intracoronary or gastrointestinal imaging.

76.11 Technological Challenges and Recent Advancements

76.11.1 Multimodality OCT Systems

In many cases a single imaging modality is insufficient to comprehensively investigate pulmonary tissues. Ultimately, multimodality imaging with a variety of methods that may include combinations of endobronchial ultrasound, white light optical imaging, OCT imaging, fluorescence imaging, and fluorescence and non-fluorescence confocal endoscopy may someday be used to optimize the characterization, structure, and function of tissues and to augment or to provide complementary diagnostic information. The fusion of optical imaging technologies, while still in the early stages of development, is currently the focus of many leading research laboratories with investigators conducting preliminary feasibility and proof-of-principle studies evaluating complementary co-registered imaging technologies and developing hybrid systems and catheters. One example includes the recent development of a dual-modality needle probe by Lorenser et al. that enables both fluorescence imaging and simultaneous OCT [120]. The investigators used this multimodality imaging catheter to acquire images of an excised sheep lung following the administration of fluorescein. This dual-modality imaging catheter may be useful in conducting fluorescein angiography of pulmonary vasculature to assess microvascular leakage [121] or for molecular imaging techniques similar to those recently developed for intracoronary imaging [122]. Additional examples of multimodality OCT imaging systems initially developed for cardiovascular applications but with the potential to be adapted to the lung include OCT and fluorescence spectroscopy [123], combined reflectance, fluorescence, Raman spectroscopy [124], OCT and positron detection [125], and OCT and ultrasound [126–128].

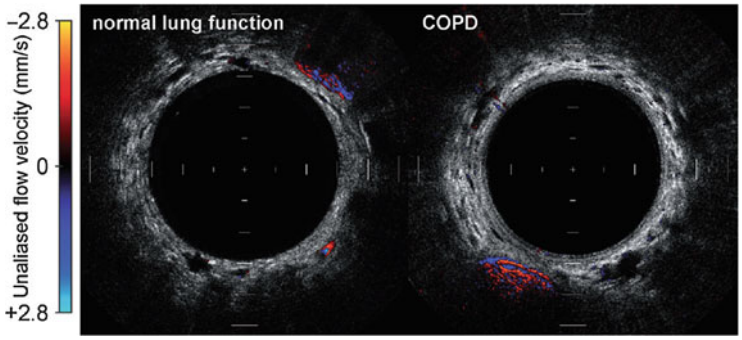

Fig. 76.19 Color Doppler optical coherence tomography images from the airways of (*left*) a subject with normal lung function and (*right*) a subject with moderate COPD, $FEV_1/FVC = 61\ \%$ and $FEV_1 = 60\ \%$ predicted. The detected vasculature using color Doppler OCT imaging (colored) has been overlaid onto the structural OCT images (*gray scale*). Velocity aliasing is apparent from the presence of adjacent positive and negative velocity pixels. Note that the airway remodeling indicated by the airway wall thickening is the COPD subject. Fiducial markers are spaced 0.25 mm apart, assuming air as the imaging medium (Reprinted with permission from [34])

76.11.2 Doppler OCT

In addition to the microstructural information provided by OCT, functional information can be obtained using Doppler OCT [129–131]. Doppler OCT provides a measure of the flow of blood in the microvasculature and in larger vessels. Preliminary studies have demonstrated the use of Doppler OCT to evaluate the pulmonary vasculature in the airways of smokers and healthy volunteers with the goal of identifying changes or remodeling of the vasculature associated with the development of COPD (Fig. 76.19) [34]. With the increase in imaging speed and sensitivity, Doppler OCT has the potential to be a clinically useful imaging tool to assess changes to the pulmonary vasculature in response to various disease processes including tumor angiogenesis and COPD-associated vascular remodeling.

76.11.3 Polarization-Sensitive OCT

Polarization-sensitive OCT is another embodiment of OCT that provides a measure of tissue birefringence by detecting polarization changes in the light returning from the tissue sample being imaged [132]. When light travels through tissues that exhibit form birefringence, orthogonal polarization components of the light will undergo a phase retardation with respect to one another. The degree of phase retardation is dependent on the orientation of the polarization state with respect to the organized linear structures within the tissue, such as collaged fibers and smooth muscle cells [133, 134]. The detected birefringence increases in tissues containing highly organized linear structures. PS-OCT provides complementary image

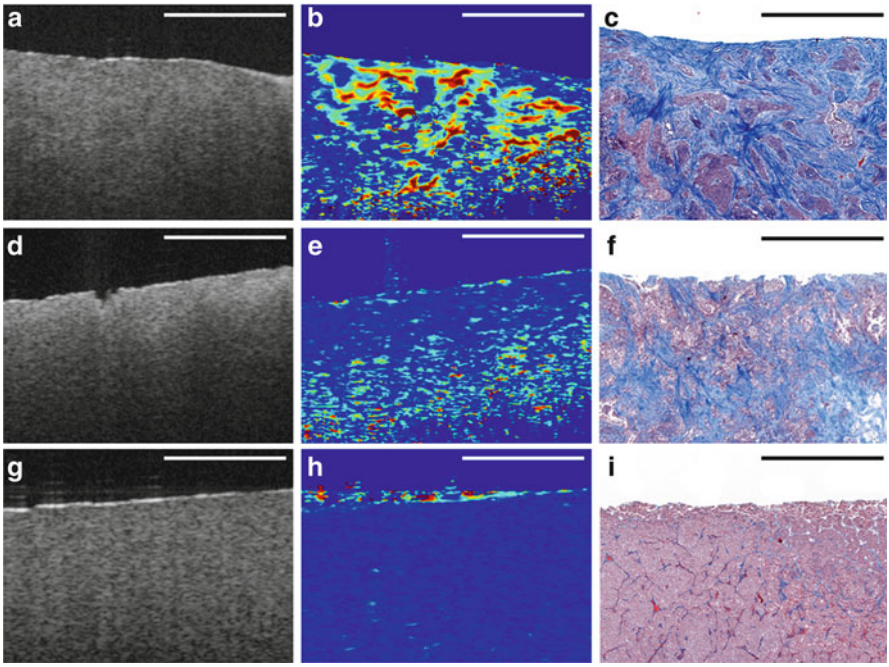

Fig. 76.20 Polarization-sensitive OCT (PS-OCT) of tumor and tumor-associated desmoplasia in ex vivo lung. (**a**) Structural OCT of squamous cell carcinoma with dense desmoplastic fibrosis. (**b**) PS-OCT of squamous cell carcinoma with dense desmoplastic fibrosis, with high birefringence in the fibrotic component. (**c**) Trichrome stain of squamous cell carcinoma with dense desmoplastic fibrosis, displaying deep *blue* staining in areas of dense fibrosis. (**d**) Structural OCT of adenocarcinoma with early desmoplasia. (**e**) PS-OCT of adenocarcinoma with early desmoplasia showing moderate birefringence in the lower half where more organized collagen is present and less birefringence in the upper half where tumor is admixed with young, poorly organized collagen and elastic fibers. (**f**) Trichrome stain confirming more organized desmoplasia in the lower half staining deeper *blue* and less organized desmoplasia in the upper half staining lighter *blue gray*. (**g**) Structural OCT of carcinoid tumor and (**h**). PS-OCT of carcinoid tumor showing little to no birefringence. In both the structural and PS-OCT images, there is a high signal intensity artifact across the surface of the tissue sample. (**i**) Trichrome stain confirming lack of significant collagen with the carcinoid. Scalebars: 1 mm (Reprinted with permission from [98])

information to structural OCT images that may assist in the identification of lung tissues such as the presence of fibrosis or airway smooth muscle.

Recently, Hariri et al. demonstrated in ex vivo lung resections of pulmonary nodules the potential of PS-OCT for guiding biopsy site selection to ensure that diagnostic quality tissue is obtained [98]. Structural OCT can be used to identify normal airway and parenchyma, necrosis, and calcification, but it does not have the necessary contrast to differentiate tumor from non-diagnostic desmoplastic fibrosis. The authors demonstrated that PS-OCT provides additional contrast to the OCT images by detecting a strong birefringence signature in regions of dense desmoplastic fibrosis (Fig. 76.20).

76.11.4 Increased Imaging Speeds

With the current speeds of catheter-based OCT systems, typically in excess of 100 frames per second, motion artifacts in cross-sectional 2D images do not appear to be an issue in the pulmonary imaging. However, when volumetric OCT imaging is required, for example, when imaging bronchial segments spanning multiple airway generations, respiratory and cardiac motion causes longitudinal dithering of the OCT catheter with respect to the bronchial wall. Although still in the early developmental phases, investigators are currently exploring respiratory gating techniques [67], novel scanning and reconstruction patterns [135], and catheter stabilization devices such as wire cage designs to mitigate the longitudinal blurring.

76.11.5 Increased Imaging Resolution

Practical methods for obtaining 1–2 μm resolution are needed for endobronchial diagnostics. The resolution of OCT systems has been steadily increasing over the years, and it is now possible to conduct benchtop imaging on the 1–2 μm scale. Such systems have been used to study mucociliary transport in the normal airway and alterations to this behavior in response to cystic fibrosis or COPD where mucus flow is compromised [136]. However, maintaining this high resolution in catheter-based systems, which are necessary for many in vivo pulmonary imaging applications, remains a technical challenge that needs to be overcome if these systems are to make a real impact in the clinical setting.

76.12 Potential Pulmonary OCT Applications for Future Investigation

As ongoing advances are made in OCT technology and site delivery probe capabilities, many potential areas for pulmonary OCT application can be envisioned. Examples of such applications may include (but would certainly not be limited to) areas listed here in Table 76.3.

76.13 Conclusion

Recent advances in OCT open broad areas of potential applicability for clinical and research applications in pulmonary medicine. Undoubtedly, other applications for OCT in the pulmonary and thoracic clinical arena will be described as OCT technology becomes more advanced and more widely available to researchers and clinicians in the future.

Table 76.3 Potential areas for future clinical and research OCT applications in pulmonary medicine

Providing in situ three-dimensional tomographic images and velocity profiles of blood perfusion in human tracheo-bronchi at discrete spatial locations in either the epithelial or mucosal layers, potentially useful for determining tumor margins as well as for determining remodeling/therapy effects in asthma
Confirm intralesional location of the biopsy and aspiration instruments for peripheral nodules
Guide needles and forceps towards the areas void of necrosis/fibrosis during sampling procedures of the pulmonary nodules
Determining burn/tracheal injury depth and airway lumen cross-sectional area with fast image acquisition systems (long-range FD OCT). This may provide guidance regarding the optimal depth for airway management assessment
Monitoring tracheobronchial tissue perfusion and viability in lung transplants
Monitoring bronchoconstriction and determining smooth muscle mass in asthma before and after therapeutic interventions such as bronchial thermoplasty
Monitoring laser-tissue effects and potentially avoiding normal airway injury during laser treatments of airway lesions
Monitoring the effects of pharmacological intervention on bronchial microcirculation (e.g., effects of vasoactive compounds or inflammatory mediators)
Optimizing oncologic treatment dosimetry by assessing and quantifying alterations in tissue microvascular and matrix structure from external beam irradiation, brachytherapy, or photodynamic therapy (PDT)
Assessing inflammation and hyperemia in chronic bronchitis/bronchiectasis/cystic fibrosis
Pleural space investigations of malignant and inflammatory processes
Examining dynamic structural and functional changes in airways during respiratory cycling

References

1. M.J. Suter, S. Lam, M. Brenner, Optical techniques in pulmonary medicine. Expert Rev. Respir. Med. **6**(2), 143–145 (2012)
2. J.F. de Boer, B. Cense, B.H. Park, M.C. Pierce, G.J. Tearney, B.E. Bouma, Improved signal-to-noise ratio in spectral-domain compared with time-domain optical coherence tomography. Opt. Lett. **28**(21), 2067–2069 (2003)
3. M.A. Choma, K. Hsu, J.A. Izatt, Swept source optical coherence tomography using an all-fiber 1300-nm ring laser source. J. Biomed. Opt. **10**(4), 44009 (2005)
4. M.V. Sarunic, B.E. Applegate, J.A. Izatt, Spectral domain second-harmonic optical coherence tomography. Opt. Lett. **30**(18), 2391–2393 (2005)
5. J. Zhang, J.S. Nelson, Z. Chen, Removal of a mirror image and enhancement of the signal-to-noise ratio in Fourier-domain optical coherence tomography using an electro-optic phase modulator. Opt. Lett. **30**(2), 147–149 (2005)
6. S.H. Yun, G.J. Tearney, B.E. Bouma, B.H. Park, J.F. de Boer, High-speed spectral-domain optical coherence tomography at 1.3 mu m wavelength. Opt. Express **11**(26), 3598–3604 (2003)
7. B. Cense, N.A. Nassif, T.C. Chen, M.C. Pierce, Y. Seok-Hyun, B.H. Park et al., Ultrahigh-resolution high-speed retinal imaging using spectral-domain optical coherence tomography. Opt. Express **12**(11), 2435–2447 (2004)
8. S.H. Yun, G.J. Tearney, J.F. de Boer, B.E. Bouma, Pulsed-source and swept-source spectral-domain optical coherence tomography with reduced motion artifacts. Opt. Express **12**(23), 5614–5624 (2004)

9. S.D. Murgu, H.G. Colt, D. Mukai, M. Brenner, Multimodal imaging guidance for laser ablation in tracheal stenosis. Laryngoscope **120**(9), 1840–1846 (2010). Epub 2010/07/02
10. M. Tsuboi, A. Hayashi, N. Ikeda, H. Honda, Y. Kato, S. Ichinose et al., Optical coherence tomography in the diagnosis of bronchial lesions. Lung Cancer **49**(3), 387–394 (2005)
11. C. Pitris, M.E. Brezinski, B.E. Bouma, G.J. Tearney, J.F. Southern, J.G. Fujimoto, High resolution imaging of the upper respiratory tract with optical coherence tomography: a feasibility study. Am. J. Respir. Crit. Care Med. **157**(5 Pt 1), 1640–1644 (1998)
12. Y. Yang, S. Whiteman, D.G. van Pittius, Y. He, R.K. Wang, M.A. Spiteri, Use of optical coherence tomography in delineating airways microstructure: comparison of OCT images to histopathological sections. Phys. Med. Biol. **49**(7), 1247–1255 (2004)
13. K.W. Gossage, T.S. Tkaczyk, J.J. Rodriguez, J.K. Barton, Texture analysis of optical coherence tomography images: feasibility for tissue classification. J. Biomed. Opt. **8**(3), 570–575 (2003)
14. J. Woonggyu, Z. Jun, P.B.B. Wilder-Smith, M. Reza, M. Brenner, S. YongJin et al. ed. Optical coherence tomography in pulmonary imaging: feasibility study. SPIE-Int. Soc. Opt. Eng. **5316**, 48–55 (2004)
15. N. Hanna, D. Saltzman, D. Mukai, Z. Chen, S. Sasse, J. Milliken et al., Two-dimensional and 3-dimensional optical coherence tomographic imaging of the airway, lung, and pleura. J. Thorac. Cardiovasc. Surg. **129**(3), 615–622 (2005)
16. W. Jung, J. Zhang, R. Mina-Araghi, N. Hanna, M. Brenner, J.S. Nelson et al., Feasibility study of normal and septic tracheal imaging using optical coherence tomography. Lasers Surg. Med. **35**(2), 121–127 (2004)
17. S. Han, N.H. El-Abbadi, N. Hanna, U. Mahmood, R. Mina-Araghi, W.G. Jung et al., Evaluation of tracheal imaging by optical coherence tomography. Respiration **72**(5), 537–541 (2005)
18. R. Hou, T. Le, S.D. Murgu, Z. Chen, M. Brenner, Recent advances in optical coherence tomography for the diagnoses of lung disorders. Expert Rev. Respir. Med. **5**(5), 711–724 (2011). Epub 2011/10/01
19. J.B. West, *Respiratory Physiology – the Essentials*, 3rd edn. (Williams & Wilkins, Baltimore, 1985). x, 183pp
20. A. Wanner, *Pulmonary Diseases : Mechanisms of Altered Structure and Function*, 1st edn. (Little, Brown, Boston, 1983). viii, 280pp
21. A. Taylor, H. Kai, R. Hyatt, J. Parker, *Clinical Respiratory Physiology* (Saunders, Philadelphia, 1989). x, 300pp
22. E.R. Weibel, *Morphometry of the Human Lung* (Springer, Berlin, 1963). xi, 151 p. illus., diagrs. 26 cm p
23. O.R. Hughes, N. Stone, M. Kraft, C. Arens, M.A. Birchall, Optical and molecular techniques to identify tumor margins within the larynx. Head Neck **32**(11), 1544–1553 (2010). Epub 2010/01/22
24. S. Lam, B. Standish, C. Baldwin, A. McWilliams, J. le Riche, A. Gazdar et al., In vivo optical coherence tomography imaging of preinvasive bronchial lesions. Clin. Cancer Res. **14**(7), 2006–2011 (2008). Epub 2008/04/03
25. H.O. Coxson, B. Quiney, D.D. Sin, L. Xing, A.M. McWilliams, J.R. Mayo et al., Airway wall thickness assessed using computed tomography and optical coherence tomography. Am. J. Respir. Crit. Care Med. **177**(11), 1201–1206 (2008). Epub 2008/03/04
26. J.P. Williamson, R.A. McLaughlin, W.J. Noffsinger, A.L. James, V.A. Baker, A. Curatolo et al., Elastic properties of the central airways in obstructive lung diseases measured using anatomical optical coherence tomography. Am. J. Respir. Crit. Care Med. **183**(5), 612–619 (2011). Epub 2010/09/21
27. J.P. Williamson, J.J. Armstrong, R.A. McLaughlin, P.B. Noble, A.R. West, S. Becker et al., Measuring airway dimensions during bronchoscopy using anatomical optical coherence tomography. Eur. Respir. J. **35**(1), 34–41 (2010). Epub 2009/06/23

28. K. Doi, Current status and future potential of computer-aided diagnosis in medical imaging. Br. J. Radiol. **78**(1), S3–S19 (2005)
29. C. Schaefer-Prokop, M. Prokop, New imaging techniques in the treatment guidelines for lung cancer. Eur. Respir. J. Suppl. **35**, 71s–83s (2002)
30. N.L. Muller, Computed tomography and magnetic resonance imaging: past, present and future. Eur. Respir. J. Suppl. **35**, 3s–12s (2002). Epub 2002/06/18
31. E.F. Haponik, S.L. Aquino, D.J. Vining, Virtual bronchoscopy. Clin. Chest Med. **20**(1), 201–217 (1999)
32. C.M. Jones, T. Athanasiou, Is virtual bronchoscopy an efficient diagnostic tool for the thoracic surgeon? Ann. Thorac. Surg. **79**(1), 365–374 (2005)
33. S.E. Finkelstein, R.M. Summers, D.M. Nguyen, D.S. Schrump, Virtual bronchoscopy for evaluation of airway disease. Thorac. Surg. Clin. **14**(1), 79–86 (2004)
34. K. Ohtani, A.M. Lee, S. Lam, Frontiers in bronchoscopic imaging. Respirology **17**(2), 261–269 (2012). Epub 2011/12/01
35. M.P. Mac Manus, R.J. Hicks, PET scanning in lung cancer: current status and future directions. Semin. Surg. Oncol. **21**(3), 149–155 (2003)
36. S.S. Shim, K.S. Lee, B.T. Kim, M.J. Chung, E.J. Lee, J. Han et al., Non-small cell lung cancer: prospective comparison of integrated FDG PET/CT and CT alone for preoperative staging. Radiology **236**(3), 1011–1019 (2005)
37. S.D. Murgu, H.G. Colt, Tracheobronchomalacia and excessive dynamic airway collapse. Respirology **11**(4), 388–406 (2006). Epub 2006/06/15
38. K. Shibuya, H. Hoshino, M. Chiyo, K. Yasufuku, T. Iizasa, Y. Saitoh et al., Subepithelial vascular patterns in bronchial dysplasias using a high magnification bronchovideoscope. Thorax **57**(10), 902–907 (2002)
39. G. Yamada, H. Takahashi, N. Shijubo, T. Itoh, S. Abe, Subepithelial microvasculature in large airways observed by high-magnification bronchovideoscope. Chest **128**(2), 876–880 (2005). Epub 2005/08/16
40. H. Tanaka, G. Yamada, T. Saikai, M. Hashimoto, S. Tanaka, K. Suzuki et al., Increased airway vascularity in newly diagnosed asthma using a high-magnification bronchovideoscope. Am. J. Respir. Crit. Care Med. **168**(12), 1495–1499 (2003)
41. N. Ikeda, A. Hayashi, K. Iwasaki, H. Honda, M. Tsuboi, J. Usuda et al., Comprehensive diagnostic bronchoscopy of central type early stage lung cancer. Lung Cancer **56**(3), 295–302 (2007). Epub 2007/02/13
42. R.L. Keith, Y.E. Miller, R.M. Gemmill, H.A. Drabkin, E.C. Dempsey, T.C. Kennedy et al., Angiogenic squamous dysplasia in bronchi of individuals at high risk for lung cancer. Clin. Cancer Res. **6**(5), 1616–1625 (2000)
43. F.J. Herth, R. Eberhardt, D. Anantham, D. Gompelmann, M.W. Zakaria, A. Ernst, Narrow-band imaging bronchoscopy increases the specificity of bronchoscopic early lung cancer detection. J. Thorac. Oncol. **4**(9), 1060–1065 (2009). Epub 2009/08/26
44. B.D. Vincent, M. Fraig, G.A. Silvestri, A pilot study of narrow-band imaging compared to white light bronchoscopy for evaluation of normal airways and premalignant and malignant airways disease. Chest **131**(6), 1794–1799 (2007). Epub 2007/05/17
45. L. Thiberville, S. Moreno-Swirc, T. Vercauteren, E. Peltier, C. Cavé, G. Bourg Heckly, In vivo imaging of the bronchial wall microstructure using fibered confocal fluorescence microscopy. Am. J. Respir. Crit. Care Med. **175**(1), 22–31 (2007)
46. C.Y. Yick, J. von der Thusen, E. Bel, P. Sterk, P. Kunst, In vivo imaging of the airway wall in asthma: fibered confocal fluorescence microscopy in relation to histology and lung function. Respir. Res. **12**(1), 85 (2011)
47. J.J. Filner, E.J. Bonura, S.T. Lau, K.K. Abounasr, D. Naidich, R.C. Morice et al., Bronchoscopic fibered confocal fluorescence microscopy image characteristics and pathologic correlations. J. Bronchology Interv. Pulmonol. **18**(1), 23–30 (2011). Epub 2011/01/01
48. P. Lee, P.N. Mathur, H.G. Colt, Advances in thoracoscopy: 100 years since Jacobaeus. Respiration **79**(3), 177–186 (2010). Epub 2010/01/23

49. F. Rodriguez-Panadero, J.P. Janssen, P. Astoul, Thoracoscopy: general overview and place in the diagnosis and management of pleural effusion. Eur. Respir. J. **28**(2), 409–422 (2006)
50. M.G. Chrysanthidis, J.P. Janssen, Autofluorescence videothoracoscopy in exudative pleural effusions: preliminary results. Eur. Respir. J. **26**(6), 989–992 (2005). Epub 2005/12/02
51. N. Schonfeld, C. Schwarz, J. Kollmeier, T. Blum, T.T. Bauer, S. Ott, Narrow band imaging (NBI) during medical thoracoscopy: first impressions. J. Occup. Med. Toxicol. **4**, 24 (2009). Epub 2009/08/28
52. C. Pitris, S.A. Boppart, B.E. Bouma, J.G. Fujimoto, Cellular and neoplastic tissue imaging with optical coherence tomography. Conference on Lasers and Electro-Optics CLEO'98, San Francisco, CA, May 3–8, paper CtuL5 (1998)
53. L.P. Hariri, M.B. Applegate, M. Mino-Kenudson, E.J. Mark, B.D. Medoff, A.D. Luster et al., Volumetric optical frequency domain imaging of pulmonary pathology with precise correlation to histopathology. Chest **143**(1), 64–74 (2013). Epub 2012/03/31
54. J.P. Williamson, R.A. McLaughlin, M.J. Phillips, J.J. Armstrong, S. Becker, J.H. Walsh et al., Using optical coherence tomography to improve diagnostic and therapeutic bronchoscopy. Chest **136**(1), 272–276 (2009)
55. J. Armstrong, M. Leigh, I. Walton, A. Zvyagin, S. Alexandrov, S. Schwer et al., In vivo size and shape measurement of the human upper airway using endoscopic long range optical coherence tomography. Opt. Express **11**(15), 1817–1826 (2003)
56. J.H. Walsh, M.S. Leigh, A. Paduch, K.J. Maddison, D.L. Philippe, J.J. Armstrong et al., Evaluation of pharyngeal shape and size using anatomical optical coherence tomography in individuals with and without obstructive sleep apnoea. J. Sleep Res. **17**(2), 230–238 (2008)
57. J. Jing, J. Zhang, A.C. Loy, B.J. Wong, Z. Chen, High-speed upper-airway imaging using full-range optical coherence tomography. J. Biomed. Opt. **17**(11), 110507 (2012). Epub 2012/12/12
58. C. Robertson, S.W. Lee, Y.C. Ahn, S. Mahon, Z. Chen, M. Brenner et al., Investigating in vivo airway wall mechanics during tidal breathing with optical coherence tomography. J. Biomed. Opt. **16**(10), 106011 (2011). Epub 2011/10/28
59. C.I. Unglert, W.C. Warger, J. Hostens, E. Namati, R. Birngruber, B.E. Bouma et al., Validation of two-dimensional and three-dimensional measurements of subpleural alveolar size parameters by optical coherence tomography. J. Biomed. Opt. **17**(12), 126015 (2012). Epub 2012/12/14
60. R.A. McLaughlin, X. Yang, B.C. Quirk, D. Lorenser, R.W. Kirk, P.B. Noble et al., Static and dynamic imaging of alveoli using optical coherence tomography needle probes. J. Appl. Physiol. **113**(6), 967–974 (2012). Epub 2012/07/10
61. W.C. Kuo, J. Kim, N.D. Shemonski, E.J. Chaney, D.R. Spillman Jr., S.A. Boppart, Real-time three-dimensional optical coherence tomography image-guided core-needle biopsy system. Biomed. Opt. Express **3**(6), 1149–1161 (2012). Epub 2012/06/29
62. K.M. Tan, M. Shishkov, A. Chee, M.B. Applegate, B.E. Bouma, M.J. Suter, Flexible transbronchial optical frequency domain imaging smart needle for biopsy guidance. Biomed. Opt. Express **3**(8), 1947–1954 (2012). Epub 2012/08/10
63. M. Gaertner, P. Cimalla, S. Meissner, W.M. Kuebler, E. Koch, Three-dimensional simultaneous optical coherence tomography and confocal fluorescence microscopy for investigation of lung tissue. J. Biomed. Opt. **17**(7), 071310 (2012). Epub 2012/08/17
64. L. Kirsten, M. Gaertner, C. Schnabel, S. Meissner, E. Koch, Four-dimensional imaging of murine subpleural alveoli using high-speed optical coherence tomography. J. Biophotonics **6**(2), 148–152 (2013). Epub 2012/04/14
65. T. Xie, G. Liu, K. Kreuter, S. Mahon, H. Colt, D. Mukai et al., In vivo three-dimensional imaging of normal tissue and tumors in the rabbit pleural cavity using endoscopic swept source optical coherence tomography with thoracoscopic guidance. J. Biomed. Opt. **14**(6), 064045 (2009)
66. S. Tatebe, Y. Fukumoto, K. Sugimura, M. Nakano, S. Miyamichi, K. Satoh et al., Optical coherence tomography as a novel diagnostic tool for distal type chronic thromboembolic pulmonary hypertension. Circ. J. **74**(8), 1742–1744 (2010). Epub 2010/05/27

67. R.A. McLaughlin, J.J. Armstrong, S. Becker, J.H. Walsh, A. Jain, D.R. Hillman et al., Respiratory gating of anatomical optical coherence tomography images of the human airway. Opt. Express **17**(8), 6568–6577 (2009)
68. J. Li, M. de Groot, F. Helderman, J. Mo, J.M. Daniels, K. Grunberg et al., High speed miniature motorized endoscopic probe for optical frequency domain imaging. Opt. Express **20**(22), 24132–24138 (2012). Epub 2012/11/29
69. X. Li, C. Chudoba, T. Ko, C. Pitris, J.G. Fujimoto, Imaging needle for optical coherence tomography. Opt. Lett. **25**(20), 1520–1522 (2000). Epub 2007/12/11
70. D. Lorenser, X. Yang, R.W. Kirk, B.C. Quirk, R.A. McLaughlin, D.D. Sampson, Ultrathin side-viewing needle probe for optical coherence tomography. Opt. Lett. **36**(19), 3894–3896 (2011). Epub 2011/10/04
71. J. Wu, M. Conry, C. Gu, F. Wang, Z. Yaqoob, C. Yang, Paired-angle-rotation scanning optical coherence tomography forward-imaging probe. Opt. Lett. **31**(9), 1265–1267 (2006). Epub 2006/04/28
72. V.X. Yang, Y.X. Mao, N. Munce, B. Standish, W. Kucharczyk, N.E. Marcon et al., Interstitial Doppler optical coherence tomography. Opt. Lett. **30**(14), 1791–1793 (2005)
73. A.M. Zysk, S.G. Adie, J.J. Armstrong, M.S. Leigh, A. Paduch, D.D. Sampson et al., Needle-based refractive index measurement using low-coherence interferometry. Opt. Lett. **32**(4), 385–387 (2007). Epub 2007/03/16
74. S. Meissner, L. Knels, C. Schnabel, T. Koch, E. Koch, Three-dimensional Fourier domain optical coherence tomography in vivo imaging of alveolar tissue in the intact thorax using the parietal pleura as a window. J. Biomed. Opt. **15**(1), 016030 (2010). Epub 2010/03/10
75. http://www.medicinenet.com
76. S. Bota, J.B. Auliac, C. Paris, J. Metayer, R. Sesboue, G. Nouvet et al., Follow-up of bronchial precancerous lesions and carcinoma in situ using fluorescence endoscopy. Am. J. Respir. Crit. Care Med. **164**(9), 1688–1693 (2001)
77. R.S. Fontana, D.R. Sanderson, L.B. Woolner, W.F. Taylor, W.E. Miller, J.R. Muhm, Lung cancer screening: the Mayo program. J. Occup. Med. **28**(8), 746–750 (1986)
78. http://www.lungcancer.org
79. P.A. Kvale, F.R. Bode, S. Kini, Diagnostic accuracy in lung cancer; comparison of techniques used in association with flexible fiberoptic bronchoscopy. Chest **69**(6), 752–757 (1976)
80. D.C. Zavala, Diagnostic fiberoptic bronchoscopy: techniques and results of biopsy in 600 patients. Chest **68**(1), 12–19 (1975)
81. G. Schreiber, D.C. McCrory, Performance characteristics of different modalities for diagnosis of suspected lung cancer: summary of published evidence. Chest **123**(1 Suppl), 115S–128S (2003)
82. J.T. Stringfield, D.J. Markowitz, R.R. Bentz, M.H. Welch, J.G. Weg, The effect of tumor size and location on diagnosis by fiberoptic bronchoscopy. Chest **72**(4), 474–476 (1977)
83. J. Popovich Jr., P.A. Kvale, M.S. Eichenhorn, J.R. Radke, J.M. Ohorodnik, G. Fine, Diagnostic accuracy of multiple biopsies from flexible fiberoptic bronchoscopy. A comparison of central versus peripheral carcinoma. Am. Rev. Respir. Dis. **125**(5), 521–523 (1982)
84. A.R. Gellert, R.M. Rudd, G. Sinha, D.M. Geddes, Fibreoptic bronchoscopy: effect of experience of operator on diagnostic yield of bronchial biopsy in bronchial carcinoma. Br. J. Dis. Chest **76**(4), 397–399 (1982)
85. A.R. Gellert, R.M. Rudd, G. Sinha, D.M. Geddes, Fibreoptic bronchoscopy: effect of multiple bronchial biopsies on diagnostic yield in bronchial carcinoma. Thorax **37**(9), 684–687 (1982)
86. R.M. Rudd, A.R. Gellert, D.A. Boldy, P.R. Studdy, M.C. Pearson, D.M. Geddes et al., Bronchoscopic and percutaneous aspiration biopsy in the diagnosis of bronchial carcinoma cell type. Thorax **37**(6), 462–465 (1982)
87. M.T. Chuang, A. Marchevsky, A.S. Teirstein, P.A. Kirschner, J. Kleinerman, Diagnosis of lung cancer by fibreoptic bronchoscopy: problems in the histological classification of non-small cell carcinomas. Thorax **39**(3), 175–178 (1984)

88. A. Dasgupta, P. Jain, O.A. Minai, S. Sandur, Y. Meli, A.C. Arroliga et al., Utility of transbronchial needle aspiration in the diagnosis of endobronchial lesions. Chest **115**(5), 1237–1241 (1999)
89. British Thoracic Society Bronchoscopy Guidelines Committee, a Subcommittee of the Standards of Care Committee of the British Thoracic Society. British thoracic society guidelines on diagnostic flexible bronchoscopy. Thorax. **56**(Suppl 1), i1–21 (2001)
90. A. Ernst, G.A. Silvestri, D. Johnstone, Interventional pulmonary procedures: guidelines from the American College of Chest Physicians. Chest **123**(5), 1693–1717 (2003)
91. U.B. Prakash, Advances in bronchoscopic procedures. Chest **116**(5), 1403–1408 (1999)
92. S. Lam, H. Shibuya, Early diagnosis of lung cancer. Clin. Chest Med. **20**(1), 53–61 (1999). x
93. R.S. DaCosta, B.C. Wilson, N.E. Marcon, Optical techniques for the endoscopic detection of dysplastic colonic lesions. Curr. Opin. Gastroenterol. **21**(1), 70–79 (2005)
94. The National Lung Screening Trial Research Team. Reduced lung-cancer mortality with low-dose computed tomographic screening. N. Engl. J. Med. **365**(5), 395–409 (2011)
95. M. Infante, S. Cavuto, F. Lutman, G. Brambilla, G. Chiesa, G. Ceresoli et al., A randomized study of lung cancer screening with spiral computed tomography: three-year results from the DANTE trial. Am. J. Respir. Crit. Care Med. **180**(5), 445–453 (2009)
96. R. Eberhardt, D. Anantham, A. Ernst, D. Feller-Kopman, F. Herth, Multimodality bronchoscopic diagnosis of peripheral lung lesions: a randomized controlled trial. Am. J. Respir. Crit. Care Med. **176**(1), 36–41 (2007). Epub 2007/03/24
97. L.P. Hariri, M. Mino-Kenudson, M.B. Applegate, E.J. Mark, G.J. Tearney, M. Lanuti et al., Towards the guidance of transbronchial biopsy: identifying pulmonary nodules with optical coherence tomography. Chest **144**(4), 1261–1268 (2013)
98. L.P. Hariri, M. Villiger, M.B. Applegate, M. Mino-Kenudson, E.J. Mark, B.E. Bouma et al., Seeing beyond the bronchoscope to increase the diagnostic yield of bronchoscopic biopsy. Am. J. Respir. Crit. Care Med. **187**(2), 125–129 (2013). Epub 2013/01/17
99. G. Okawara, Y.C. Ung, B.R. Markman, J.A. Mackay, W.K. Evans, Postoperative radiotherapy in stage II or IIIA completely resected non-small cell lung cancer: a systematic review and practice guideline. Lung Cancer **44**(1), 1–11 (2004)
100. H.C. Fernando, R.S. Santos, J.R. Benfield, F.W. Grannis, R.J. Keenan, J.D. Luketich et al., Lobar and sublobar resection with and without brachytherapy for small stage IA non-small cell lung cancer. J. Thorac. Cardiovasc. Surg. **129**(2), 261–267 (2005)
101. P. De Leyn, W. Rots, G. Deneffe, P. Nafteux, W. Coosemans, D. Van Raemdonck et al., Sleeve lobectomy for non-small cell lung cancer. Acta Chir. Belg. **103**(6), 570–576 (2003)
102. Y. Miyazu, T. Miyazawa, N. Kurimoto, Y. Iwamoto, K. Kanoh, N. Kohno, Endobronchial ultrasonography in the assessment of centrally located early-stage lung cancer before photodynamic therapy. Am. J. Respir. Crit. Care Med. **165**(6), 832–837 (2002). Epub 2002/03/19
103. B. Zaric, B. Perin, H.D. Becker, F.F. Herth, R. Eberhardt, S. Jovanovic et al., Combination of narrow band imaging (NBI) and autofluorescence imaging (AFI) videobronchoscopy in endoscopic assessment of lung cancer extension. Med. Oncol. **29**(3), 1638–1642 (2012). Epub 2011/08/10
104. J.G. Fujimoto, M.E. Brezinski, G.J. Tearney, S.A. Boppart, B. Bouma, M.R. Hee et al., Optical biopsy and imaging using optical coherence tomography. Nat. Med. **1**(9), 970–972 (1995)
105. G.J. Tearney, M.E. Brezinski, B.E. Bouma, S.A. Boppart, C. Pitris, J.F. Southern et al., In vivo endoscopic optical biopsy with optical coherence tomography. Science **276**(5321), 2037–2039 (1997)
106. J. Yin, G. Liu, J. Zhang, L. Yu, S. Mahon, D. Mukai et al., In vivo early detection of smoke-induced airway injury using three-dimensional swept-source optical coherence tomography. J. Biomed. Opt. **14**, 060503 (2009)
107. S.W. Lee, A.E. Heidary, D. Yoon, D. Mukai, T. Ramalingam, S. Mahon et al., Quantification of airway thickness changes in smoke-inhalation injury using in-vivo 3-D endoscopic frequency-domain optical coherence tomography. Biomed. Opt. Express **2**(2), 243–254 (2011)

108. R. Pawankar, G.W. Canonica, S.T. Holgate, R.F. Lockey, Allergic diseases and asthma: a major global health concern. Curr. Opin. Allergy Clin. Immunol. **12**(1), 39–41 (2012). Epub 2011/12/14
109. National Asthma Education and Prevention Program. Expert Panel Report 3 (EPR-3): guidelines for the diagnosis and management of Asthma-Summary Report 2007. J. Allergy Clin. Immunol. **120**(5 Suppl), S94–S138 (2007), Epub 2007/12/06
110. L. Jayaram, M.M. Pizzichini, R.J. Cook, L.P. Boulet, C. Lemiere, E. Pizzichini et al., Determining asthma treatment by monitoring sputum cell counts: effect on exacerbations. Eur. Respir. J. **27**(3), 483–494 (2006). Epub 2006/03/02
111. S.E. Wenzel, L.B. Schwartz, E.L. Langmack, J.L. Halliday, J.B. Trudeau, R.L. Gibbs et al., Evidence that severe asthma can be divided pathologically into two inflammatory subtypes with distinct physiologic and clinical characteristics. Am. J. Respir. Crit. Care Med. **160**(3), 1001–1008 (1999). Epub 1999/09/03
112. A. Sittka, J. Vera, X. Lai, B. Schmeck, Asthma phenotyping, therapy, and prevention: what can we learn from systems biology? Pediatr. Res. **73**(4–2), 543–552 (2013). Epub 2013/01/15
113. S.E. Wenzel, Asthma phenotypes: the evolution from clinical to molecular approaches. Nat. Med. **18**(5), 716–725 (2012). Epub 2012/05/09
114. http://www.imalux.com
115. http://www.sjm.com
116. http://www.terumo.com
117. http://www.tomophase.com
118. http://www.volcanocorp.com
119. http://www.ninepointmedical.com
120. D. Lorenser, B.C. Quirk, M. Auger, W.J. Madore, R.W. Kirk, N. Godbout et al., Dual-modality needle probe for combined fluorescence imaging and three-dimensional optical coherence tomography. Opt. Lett. **38**(3), 266–268 (2013). Epub 2013/02/06
121. M. Suter, J. Reinhardt, P. Montague, P. Taft, J. Lee, J. Zabner et al., Bronchoscopic imaging of pulmonary mucosal vasculature responses to inflammatory mediators. J. Biomed. Opt. **10**(3), 034013 (2005). Epub 2005/10/19
122. H. Yoo, J.W. Kim, M. Shishkov, E. Namati, T. Morse, R. Shubochkin et al., Intra-arterial catheter for simultaneous microstructural and molecular imaging in vivo. Nat. Med. **17**(12), 1680–1684 (2011)
123. J.K. Barton, F. Guzman, A. Tumlinson, Dual modality instrument for simultaneous optical coherence tomography imaging and fluorescence spectroscopy. J. Biomed. Opt. **9**(3), 618–623 (2004). Epub 2004/06/11
124. O.R. Scepanovic, Z. Volynskaya, C.R. Kong, L.H. Galindo, R.R. Dasari, M.S. Feld, A multimodal spectroscopy system for real-time disease diagnosis. Rev. Sci. Instrum. **80**(4), 043103 (2009). Epub 2009/05/02
125. D. Piao, M.M. Sadeghi, J. Zhang, Y. Chen, A.J. Sinusas, Q. Zhu, Hybrid positron detection and optical coherence tomography system: design, calibration, and experimental validation with rabbit atherosclerotic models. J. Biomed. Opt. **10**(4), 44010 (2005). Epub 2005/09/24
126. X. Li, J. Yin, C. Hu, Q. Zhou, K.K. Shung, Z. Chen, High-resolution coregistered intravascular imaging with integrated ultrasound and optical coherence tomography probe. Appl. Phys. Lett. **97**(13), 133702 (2010)
127. J. Yin, H.C. Yang, X. Li, J. Zhang, Q. Zhou, C. Hu et al., Integrated intravascular optical coherence tomography ultrasound imaging system. J. Biomed. Opt. **15**(1), 010512 (2010)
128. J. Yin, X. Li, J. Jing, J. Li, D. Mukai, S. Mahon et al., Novel combined miniature optical coherence tomography ultrasound probe for in vivo intravascular imaging. J. Biomed. Opt. **16**(6), 060505 (2011)
129. Z. Chen, T.E. Milner, D. Dave, J.S. Nelson, Optical Doppler tomographic imaging of fluid flow velocity in highly scattering media. Opt. Lett. **22**, 64–66 (1997)

130. Z. Chen, T.E. Milner, S. Srinivas, X.J. Wang, A. Malekafzali, M.J.C. van Gemert et al., Noninvasive Imaging of in vivo blood flow velocity using optical Doppler tomography. Opt. Lett. **22**, 1119–1121 (1997)
131. Y. Zhao, Z. Chen, C. Saxer, S. Xiang, J.F. de Boer, J.S. Nelson, Phase-resolved optical coherence tomography and optical Doppler tomography for imaging blood flow in human skin with fast scanning speed and high velocity sensitivity. Opt. Lett. **25**, 114–116 (2000)
132. J.F. de Boer, T.E. Milner, M.J. van Gemert, J.S. Nelson, Two-dimensional birefringence imaging in biological tissue by polarization-sensitive optical coherence tomography. Opt. Lett. **22**(12), 934–936 (1997). Epub 1997/06/15
133. S.K. Nadkarni, M.C. Pierce, B.H. Park, J.F. de Boer, P. Whittaker, B.E. Bouma et al., Measurement of collagen and smooth muscle cell content in atherosclerotic plaques using polarization-sensitive optical coherence tomography. J. Am. Coll. Cardiol. **49**(13), 1474–1481 (2007). Epub 2007/04/03
134. T. Xie, S. Guo, J. Zhang, Z. Chen, G.M. Peavy, Determination of characteristics of degenerative joint disease using optical coherence tomography and polarization sensitive optical coherence tomography. Laser Surg. Med. **38**, 852–865 (2006)
135. M.J. Suter, M. Applegate, A. Braune, C. Chee, V.J. Kelly, K.M. Tan et al., Volumetric microscopy of airway dynamics using optical frequency domain imaging. Am. J. Respir. Crit. Care Med. **185**, A4348 (2012)
136. L. Liu, K.K. Chu, G.H. Houser, B.J. Diephuis, Y. Li, E.J. Wilsterman et al., Method for quantitative study of airway functional microanatomy using micro-optical coherence tomography. PLoS One **8**(1), e54473 (2013). Epub 2013/02/02

OCT in Gynecology

77

Irina A. Kuznetsova, Natalia D. Gladkova, Valentin M. Gelikonov, Jerome L. Belinson, Natalia M. Shakhova, and Felix I. Feldchtein

Keywords

Gynecologic OCT • OCT colposcopy • endometrial OCT imaging • Cervical leukoplakia • Cervical metaplasia • OCT laparoscopy

77.1 Introduction: Motivation for OCT Application in Gynecology

Timely and efficient diagnosis of diseases of the female reproductive system is very important from the social viewpoint [1, 2]. Diagnostic efficacy of the existing techniques still needs improvement since malignant neoplasms of the female reproductive system organs are stable leaders among causes of death (over 35.9 %) [3]. Each year, 851.9 thousand genital cancer cases are recorded worldwide [1, 2].

Cervical cancer is among the most common malignant neoplasm in women and the most common cause of death from cancer in young women worldwide. It commonly occurs at the height of women's productive lives often when they

I.A. Kuznetsova (✉)
Nizhny Novgorod Regional Hospital, Nizhny Novgorod, Russia

N.D. Gladkova
Medical Academy, Nizhny Novgorod, Russia

V.M. Gelikonov • N.M. Shakhova
Institute of Applied Physics Russian Academy of Sciences, Nizhny Novgorod, Russia

J.L. Belinson
Cleveland Clinic Foundation, Cleveland, OH, USA

F.I. Feldchtein
Imalux Corporation, Cleveland, OH, USA

Institute of Applied Physics Russian Academy of Sciences, Nizhny Novgorod, Russia

© Springer International Publishing Switzerland 2015

W. Drexler, J.G. Fujimoto (eds.), *Optical Coherence Tomography*,
DOI 10.1007/978-3-319-06419-2_79

still have young children at home. Yearly, 510,000 new cervical cancer cases are registered worldwide, and of these cases, 288,000 women die, and over 5–6 billion dollars is spent on patient treatment [2].

A decrease in the cervical cancer incidence has occurred in the senior age group, while a significant increase is observed for women in the early reproductive age group (by 2 % yearly, on the average) [4–6]. In the USA, according to the data of the American Oncological Society as of 2002, 47 % of the cervical cancer patients are women up to 35 years old [7]. Cervical cancer in young women has a less favorable prognosis, because it progresses faster, late stage is observed more frequently than in the senior age group, and consequently 5-year survival is lower [7].

Initial risk stratification for cervical neoplasia is performed using screening techniques including Pap smear and HPV (human papilloma virus) testing. The next step for diagnosis is a visual examination of the cervix. The potentially neoplastic lesions can be better visualized using application of acetic acid. The unmagnified examination of the cervix is known as VIA (visual examination with acetic acid), and the magnified examination using low-magnification, long working distance microscope, is known as colposcopy. Both VIA and colposcopy are frequently combined with biopsies. Histopathology evaluation of the biopsies serves as a "gold standard" for diagnosis.

However, the diagnostic efficacy of the visual examination with biopsy is limited. Similar visual abnormalities can be observed for a variety of cervical conditions, benign and malignant, which reduces specificity and positive predictive value. Correct interpretation of colposcopic features requires high skills and long-term clinical experience, which makes colposcopy very subjective and limits interobserver agreement [8–10].

In addition, histological processing of biopsy requires several days or even weeks, which creates several problems. In most cases, treatment decisions cannot be made until histology results are received and reviewed, which requires more visits and increases healthcare cost and patient anxiety. In underdeveloped countries (which account for 80 % of the world's cervical cancer cases), additional visits can be difficult or impractical. Therefore, in many cases a real-time decision should be made without biopsy results, representing a difficult tradeoff between potentially unnecessary treatment because of oversensitive but not specific diagnostics and, alternatively, potentially leaving early and curable cervical cancer untreated which could then grow into a life-threatening condition.

OCT is known to visualize in vivo and noninvasively tissue microstructure with spatial resolution approaching the histologic level and therefore can be expected to guide biopsies and to provide real-time tissue structure information when biopsies are contraindicated or impractical. Although thorough clinical studies are required to determine if OCT can be suitable for this purpose in gynecology in general and for cervical cancer in particular, the early results look encouraging.

The first in vivo OCT images of the uterine cervix were obtained by a Nizhny Novgorod team in 1997 [11]. Later, the clinical feasibility of OCT in gynecology was discussed in a number of papers [12–22]. The papers published by the MIT group in 1999 [23, 24] described the OCT features typical for a normal exocervix

(a sharp, high-contrast interface between stratified squamous epithelium and connective tissue stroma), endocervix (visualization of cervical glands), and endometrium (contrast of glands). It was shown that the possibility to detect neoplastic changes in stratified squamous epithelium by the OCT is associated with the disappearance of the interface between the epithelium and connective tissue. These findings were later confirmed in the studies performed by the CCF group [25, 26] and the University of Texas at Austin [27].

The OCT potential for pelvic organ visualization during laparoscopy was explored in several papers [12, 15, 23, 28, 29]. The Nizhny Novgorod group [15] and the MIT group [29] explored the use of OCT to assess the functional condition of the fallopian tubes in reproductive gynecology. A University of Arizona group, considering four categories of the ovarian conditions (norm, endometriosis, high neoplasia risk, and neoplasia), formulates the OCT features to differentiate between benign and malignant processes [28].

In this chapter, we present a wide spectrum of the OCT studies of different parts of the female reproductive system and demonstrate the potential of the clinical use of a new visualization method in gynecological practice.

77.2 OCT-Colposcopy

77.2.1 Methodology and Patient Selection

During the OCT study of the female reproductive system, 235 patients were enrolled at the Nizhny Novgorod Regional Hospital and Regional Oncology Clinic.

All patients signed the voluntary informed consent. The study was approved by the Ethical Committee for scientific studies with human subjects.

The majority of work was performed on the uterine cervix. Two hundred five patients were enrolled in the cervical OCT study, average age 36.5 years.

The cervical OCT was performed for the patients with:

(i) History of abnormal colposcopic findings
(ii) Abnormal results of Pap smear (ASCUS, LSIL, HSIL)
(iii) Positive HPV test for oncogenic viral type

Exclusion criterion was age under 18.

The breakdown of exocervical conditions is shown in Table 77.1 for the studied group of patients.

77.2.1.1 Uterine Cervix OCT Protocol

The cervical study OCT involved several stages:

- Review of patient history including cytology results
- Visual examination/colposcopy and identification of regions of interest (ROI)
- OCT of identified ROI
- Biopsy of ROI, when clinically appropriate
- Histopathology evaluation of biopsy and comparison with OCT and colposcopic findings

Table 77.1 In vivo OCT study of the female reproductive system

Total studied, $n = 205$				
Normal, $n = 30$ (14.6 %)	Benign pathological conditions, $n = 113$ (55.1 %)	Malignant pathological conditions, $n = 52$ (25.4 %)		Pregnant $n = 10$ (4.9 %)
	Ectopy, $n = 47$	CIN III, $n = 28$	Uterine cervix cancer, $n = 24$	
	Exocervicitis, $n = 28$			
	Endometriosis, $n = 7$			
	Cervical erosion, $n = 10$			
	Leukoplakia, $n = 12$			
	CIN I–II, $n = 19$			

OCT does not require additional preparation of the patient and anesthesia.

During the OCT studies, we used a compact portable OCT system developed and constructed at the Institute of Applied Physics of the Russian Academy of Sciences (Nizhniy Novgorod, Russia). The device received Russian regulatory authority certification for clinical use in August 2005.

The unit has the following technical characteristics:

- Central wavelength 1,300 nm
- Radiation power: not exceeding 6.0 mW
- Spatial resolution: 10–20 μm
- In-depth scanning range – up to 2 mm
- Lateral scanning range 1–2 mm
- Acquisition time for two-dimensional 200 × 200 pixel image: 1.5–2 s

The device is compact and has the following dimensions: 250 × 400 × 450 mm. The weight is 10 kg. All optical and electronic parts of the OCT unit are located inside a console.

The cervical OCT was performed using a detachable, reusable forward-looking OCT probe with an outer diameter 2.7 mm (Fig. 77.1a, b). The probe can be cold disinfected or sterilized. Alternatively, a disposable sterile sheath with an optically transparent membrane (Fig. 77.1b) was used to hold the probe and prevent contamination; in this case the probe was not in direct contact with the patient tissues.

To perform OCT, the probe was applied to the cervical area of interest under the colposcope control. To reduce artifacts related to unintentional movements of the probe and the study object, the distal end of the probe or the sheath membrane was in contact with the tissue.

The obtained images were interpreted directly at the time of the patient examination.

Later, we conducted a comparative analysis of the OCT and histological data. The material obtained by the biopsy, loop electro excision procedure (LEEP), and hysterectomy was subject to histological assessment. The guided biopsy was performed under the colposcopic control immediately after the OCT imaging only when clinically indicated. Cervical histopathology was obtained for 138 out of 205 (67.3 %) patients. The specimen volume and depth were sufficient for identifying the structures in the OCT image with size usually equal to 1.7 × 1.5 mm.

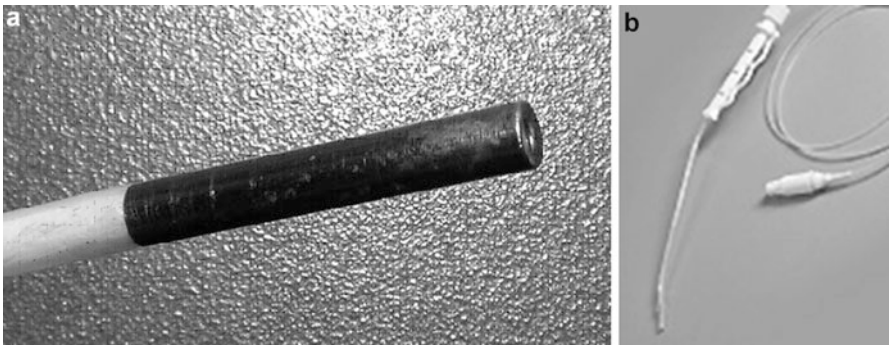

Fig. 77.1 OCT probe distal tip (**a**) and a disposable sheath (*Imalux Corporation*) (**b**)

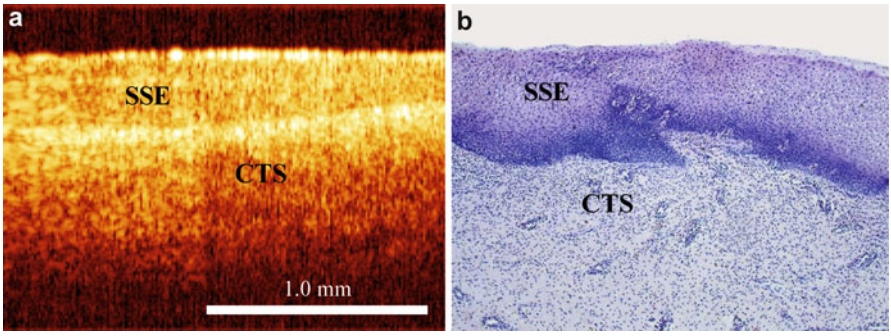

Fig. 77.2 OCT image (**a**) and parallel histology (**b**) of the cervical mucosa. *SSE* is the stratified squamous epithelium and *CTS* is the connective tissue stroma. OCT vertical scale is normalized to 1.4 refraction index

77.2.2 OCT Images of Normal Cervix: Impact of Age and Hormonal Status on the OCT Image

Thirty patients with an unchanged uterine cervix were enrolled in the study. Some of these patients had colposcopy as a stage of preparation for radical hysterectomy. The cervical OCT was performed in vivo during colposcopy 1 day before the surgery. The cervical area to image was chosen at 12 o'clock of a conventional dial, 1 cm from the cervical channel, and the ex vivo imaging was performed of the same area of the fresh surgical specimen, followed by histopathological evaluation.

Figure 77.2 shows typical OCT image (a) and the parallel histology (b) of the unchanged normal cervix. The upper homogeneous layer with moderate signal level corresponds to a stratified squamous epithelium in the histological specimen. The lower, brighter layer in the OCT images corresponds to the connective tissue stroma of the cervical mucosa.

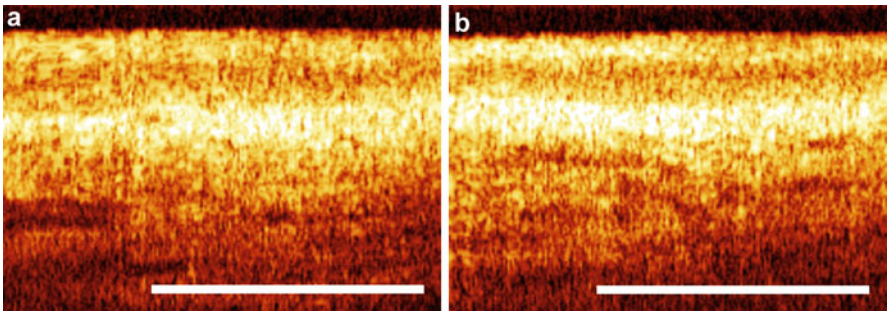

Fig. 77.3 OCT images of the normal cervical mucosa. (**a**) Before application of 5 % acetic acid, (**b**) after application of 5 % acetic acid

The interlayer interface corresponds to the basal membrane location; however, the basal membrane itself is extremely thin (several nanometers) and cannot be directly visualized using light.

After the application of 5 % acetic acid, optical backscattering increases, which is consistent with visual appearance (especially for the acetowhite epithelium) (Fig. 77.3).

We consistently observed a two-layered image with an even, sharp, and continuous interface between the layers as the main sign of the normal exocervical OCT appearance for any age group.

77.2.2.1 OCT Study of the Epithelial Thickness of the Cervical Mucosa

Since the stratified squamous epithelium is well delineated in the normal cervical OCT images, the thickness can be easily measured. This thickness changes significantly depending on the menstrual cycle phase since it is known to be hormonal status dependent. The colpocytological study was performed for ten patients in the group with normal uterine cervix. We used karyopyknotic index (KI) and maturation index (MI) as commonly accepted means to assess hormonal status [30]. Figure 77.4 shows OCT cervical images for two patients in the same age group but with different estrogenic saturation level. For the first patient, 24 years old, the KI on the 24th day of the menstrual cycle was 28 and the MI was 0/44/56, the epithelial thickness was measured 250 μm (Fig. 77.4a) in the OCT image. The second patient, 30 years old, on the 17th day of the menstrual cycle, had KI equal to 0 and MI 0/89/11. Accordingly, the epithelial thickness was 160 μm.

More pronounced differences can be observed between different age groups (Fig. 77.5). Pronounced proliferation with $KI = 32$ and $MI = 0/26/51$ was detected for a 29-year-old patient on the 12th day of the menstrual cycle. In the OCT image (Fig. 77.5a), the epithelial thickness was 275 μm. Epithelial atrophy with $KI = 0$ and $MI = 12/88/0$ was visualized for a 65-year-old patient (Fig. 77.5b) with the epithelial thickness reduced to 100 μm.

Therefore, OCT visualizes and allows objective in vivo measurement of the epithelial thickness variation in the cervical mucosa, including changes related to the hormonal status.

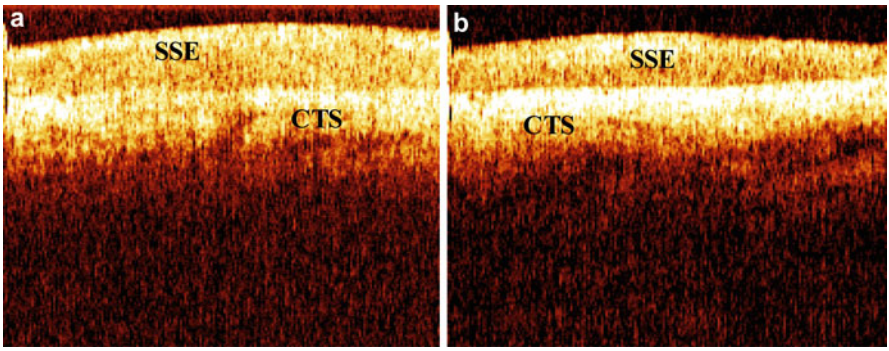

Fig. 77.4 OCT images of the cervical mucosa for two patients in the same age group: (**a**) a 24-year-old patient on the 24th day of the menstrual cycle, KI is 28, MI is 0/44/56, the SSE thickness is 250 μm; (**b**) a 30-year-old patient on the 17th day of the menstrual cycle, KI is 0, MI is 0/89/11, the SSE thickness is 160 μm. *SSE* is a stratified squamous epithelium and *CTS* is the connective tissue stroma

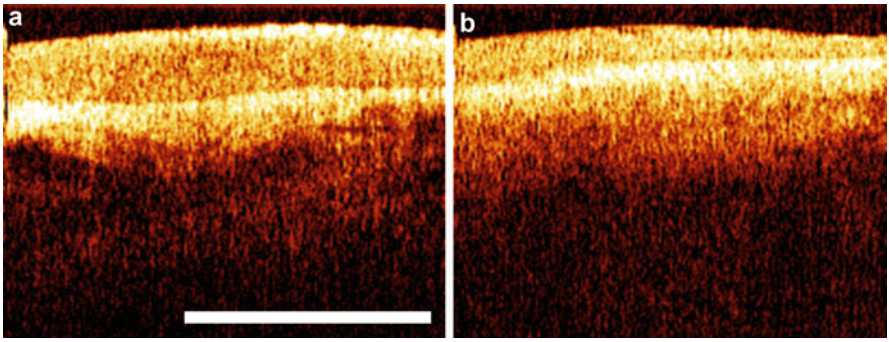

Fig. 77.5 OCT images of the cervical mucosa for two patients in different age groups: (**a**) 29-year-old patient on the 12th day of the menstrual cycle with $KI = 32$ and $MI = 0/26/51$, the SSE thickness is 275 μm, (**b**) 65-year-old, 20 years postmenopausal, $KI = 0$ and $MI = 12/88/0$, the SSE thickness is 100 μm

77.2.3 OCT Images of Benign Processes

77.2.3.1 Ectopy and Metaplasia

The normal cervical OCT appearance serves as a good baseline, and changes of this pattern can be associated with different benign and malignant pathological conditions.

Cervical ectopy (or ectropion) is a very common benign cervical condition. According to the histological data, the stromal base of ectopy is loose, infiltrated by inflammatory cells, and has a papillary shape with formation of crypts. The stromal papillae are covered by a single-row cuboidal epithelium. In the majority

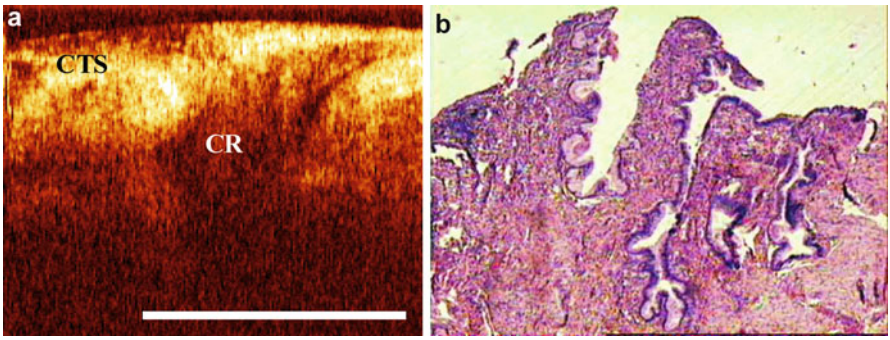

Fig. 77.6 OCT images (**a**) and parallel histology (**b**) of the cervical ectropion. *CTS* is the connective tissue stroma and *CR* is the mucus-filled crypts

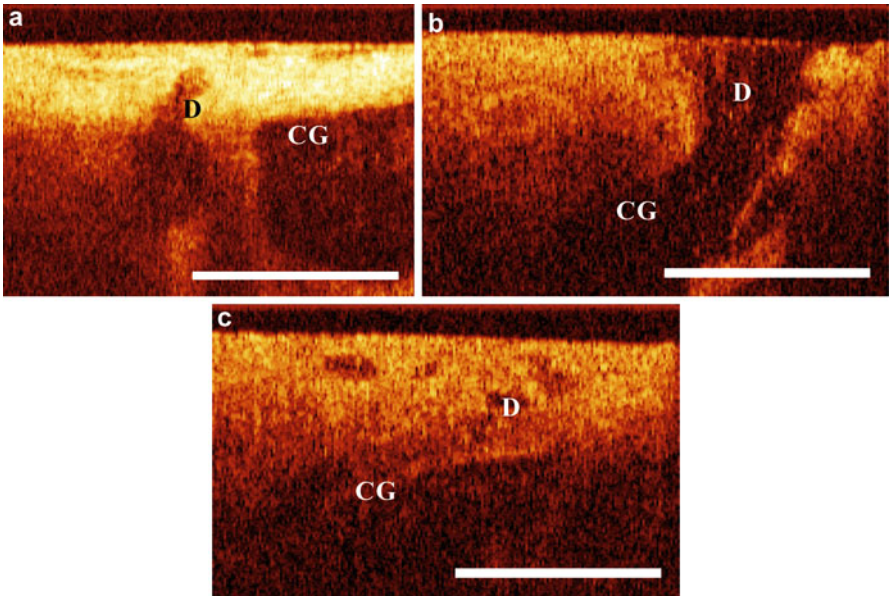

Fig. 77.7 (**a**–**c**) OCT images of structural regeneration elements. *CG* are cervical glands and *D* are the ducts of the cervical glands

of cases, ectropion is visualized in the form of a non-layered structural image (Fig. 77.6a) in which chaotically located various shaped and brightness regions are observed. Comparing OCT images and histology slides, we found that bright (strongly scattering) parts correspond to the CTS, while dark (weakly scattering) parts correspond to the mucus-filled space between the stromal papillas.

The squamous regeneration process is accompanied by formation of structural elements (open ducts and cervical glands). The OCT is capable of visualizing these structures in vivo (Fig. 77.7).

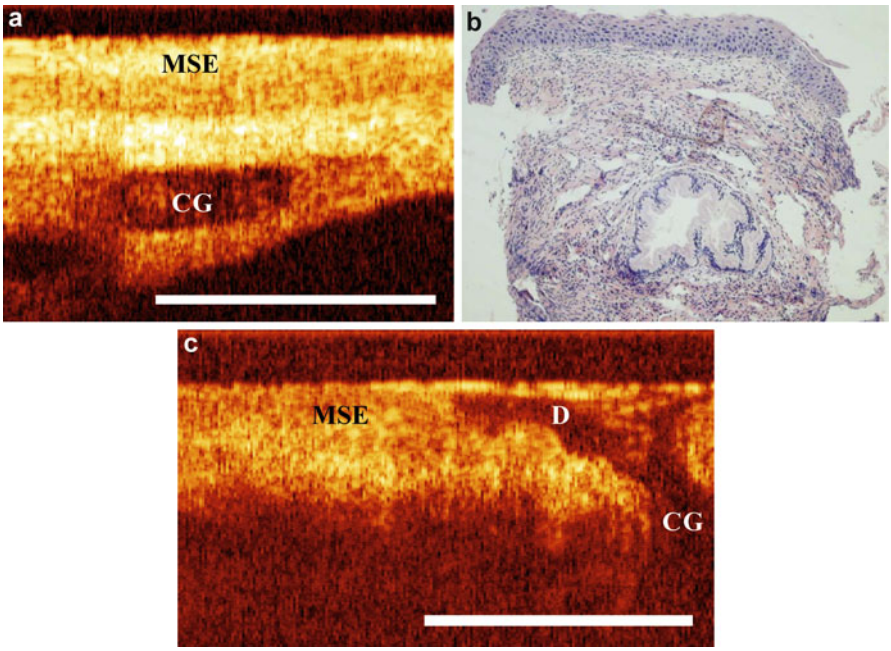

Fig. 77.8 OCT image of mature metaplastic epithelium (**a**, **c**) and parallel histology (**b**). *CG* are the closed cervical glands. *MSE* is the mature squamous epithelium. (**c**) *D* are the ducts of the cervical glands

Once the formation of a mature metaplastic epithelium is completed, the cervical mucosa is visualized as a sharp double-layered image with an even interlayer interface, resembling original squamous epithelium. However, closed cervical glands are seen under that new squamous epithelium (Fig. 77.8), which makes it different from the normal (original) squamous cervical mucosa.

77.2.3.2 Cervicitis

OCT images of inflammatory cervical changes may look different. OCT images still may have a sharp double-layered appearance. However, the contrast between SSE and stroma can be substantially reduced or completely lost. We associate it with the cellular infiltration changing stromal optical properties. In some OCT images, multiple sharp round and/or linear cavities with a low signal level (Fig. 77.9) can be observed. These cavities can be associated with edema and/or cervical glands.

As in normal cervical mucosa, application of acetic acid reduces the stratification contrast and increase brightness of the upper layer (Fig. 77.10).

In some cases, severe inflammation can completely erase the contrast of the epithelium-stromal interface, creating structureless OCT images (Fig. 77.11).

The inflammatory process can be accompanied by epithelial hyperplasia, acanthosis, and papillomatosis, which are visualized as an increase in the upper moderately scattering layer thickness and discontinuous nature of the interlayer interface (Fig. 77.12).

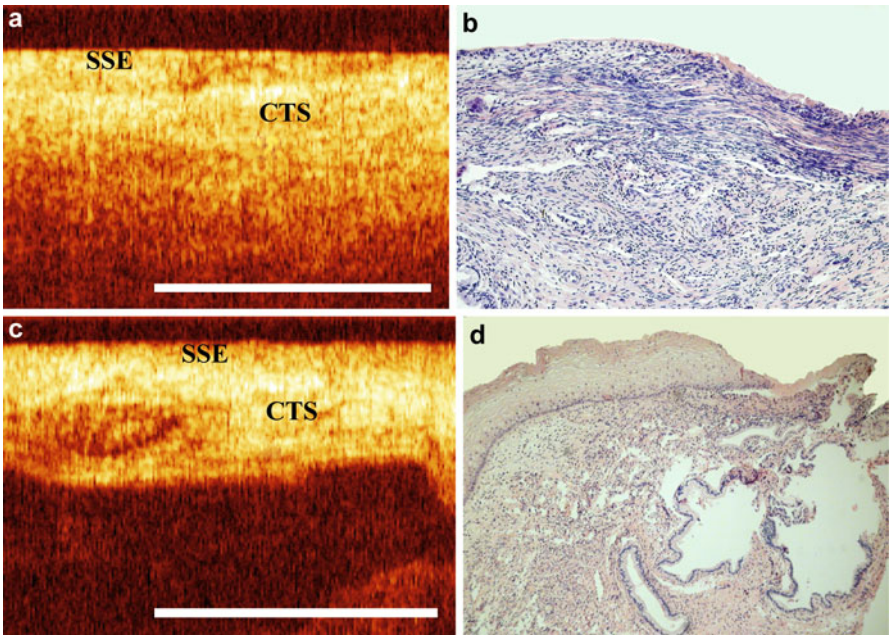

Fig. 77.9 OCT images (**a**, **c**) and histology (**b**, **d**) of the cervical mucosa with cervicitis. *SSE* is the thinned stratified squamous epithelium. *CTS* is the connective tissue stroma

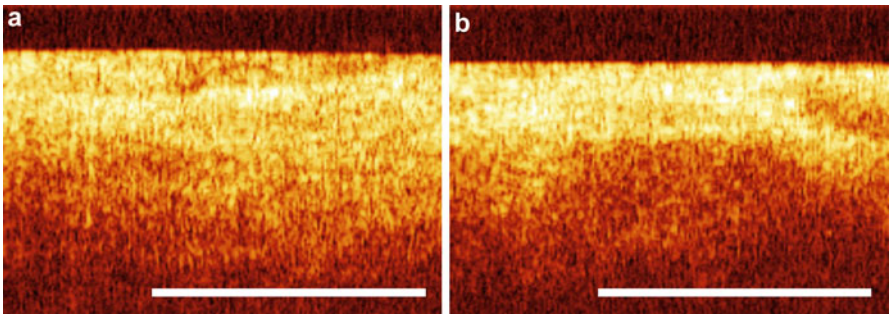

Fig. 77.10 OCT images of the cervicitis. (**a**) Before acetic acid application; (**b**) after the acetic acid application

77.2.3.3 Cervical Leukoplakia

Hyperkeratosis

In the presence of mild hyperkeratosis, the cervical mucosa is still visualized in OCT as a structural layered image (Fig. 77.13). The keratinization is responsible for an increase in the superficial brightness of the image. The interface between the layers could be discontinuous with reduced contrast, because of papillomatosis, which frequently accompanies hyperkeratosis.

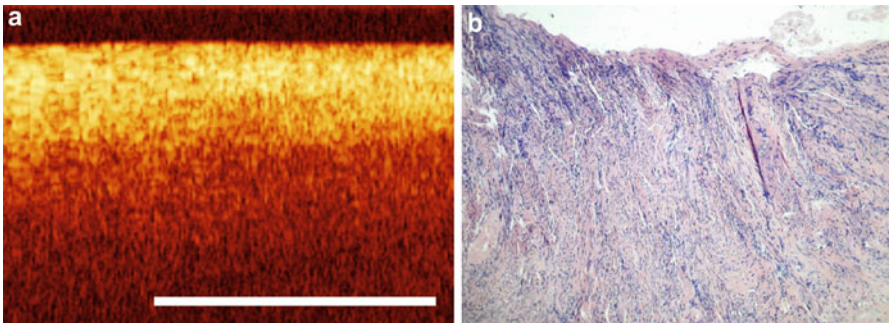

Fig. 77.11 OCT image (**a**) and histology (**b**) of the inflamed cervical mucosa

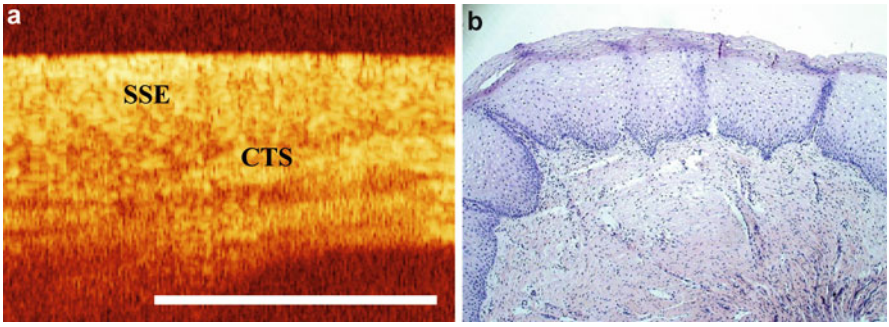

Fig. 77.12 OCT image (**a**) and histology (**b**) of cervical mucosa with inflammatory process of the viral etiology (*HPV*). *SSE* is the hyperplastic stratified squamous epithelium, *CTS* is the connective tissue stroma

77.2.3.4 Cervical Intraepithelial Neoplasia Grade I (CIN I)

CIN I (minimal degree of CIN) tends to regress spontaneously in 70 % of cases. Even if it progresses to CIN II and III and ultimately to the cervical cancer, it is a slow process and can be identified and successfully treated if regular examinations are performed. Therefore, according to the modern guidelines [31, 32], CIN I is considered a benign condition and no immediate treatment is required. CIN I is frequently accompanied by inflammation and appears by OCT to be very similar to inflammation, ranging from normal appearance to homogeneous image (Fig. 77.14a–e).

77.2.3.5 Cervical Intraepithelial Neoplasia Stages II and III (CIN II and III)

With CIN II and III (also known as moderate dysplasia and severe dysplasia/carcinoma in situ), atypical cellular changes involve a larger part of the epithelium. As a result, loss of contrast between epithelium and stroma is observed in the majority of cases (Fig. 77.15a).

In the minority of cases, the stratification can be still seen in the OCT, which could be considered false negative OCT reading for CIN II–III (Fig. 77.15e).

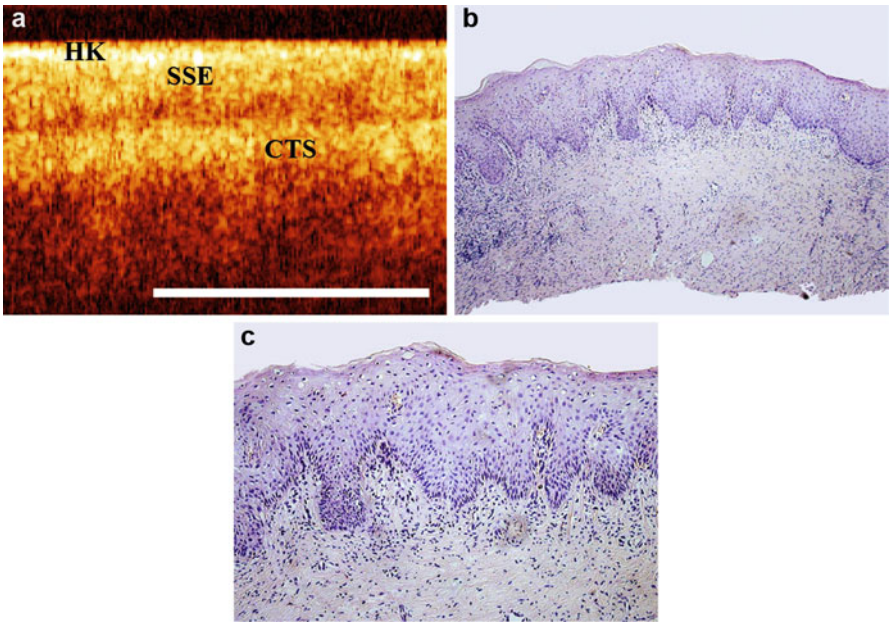

Fig. 77.13 OCT image (**a**) and histology (**b**, **c**) of the cervical mucosa with the mild hyperkeratosis. *HK* is the hyperkeratosis, *SSE* is the stratified squamous epithelium, and *CTS* is the connective tissue stroma

77.2.3.6 Invasive Cervical Cancer

It is natural to expect that invasive cervical cancer completely erases the interface between epithelium and stroma, and in fact, it does happen in the majority of cases (Fig. 77.17). However, in rare cases (Fig. 77.16c) high-contrast stratified OCT image can be observed, even though no appropriate thickness level is seen in the parallel histology. One of the explanations can be the focal nature of the process and difficulties to match precisely the biopsy with OCT imaging location. As stated in [33], "the presence of intact BM surrounding a tumor is not proof that a lesion is not invasive" since cancer can produce its own basement membrane.

We can summarize that a normal exocervical OCT image always has a two-layer image with high contrast between the stratified squamous epithelium and stroma. Benign processes typically preserve this two-layer appearance; however, severe inflammation can substantially reduce the contrast. Neoplastic processes, as a rule, erase the two-layer appearance.

77.2.4 OCT as a Tool to Increase the Efficacy of Visual Cervical Examination

Early feasibility data about cervical OCT obtained by several groups [25, 27, 34] suggests that OCT may be useful to improve the efficacy of visual cervical

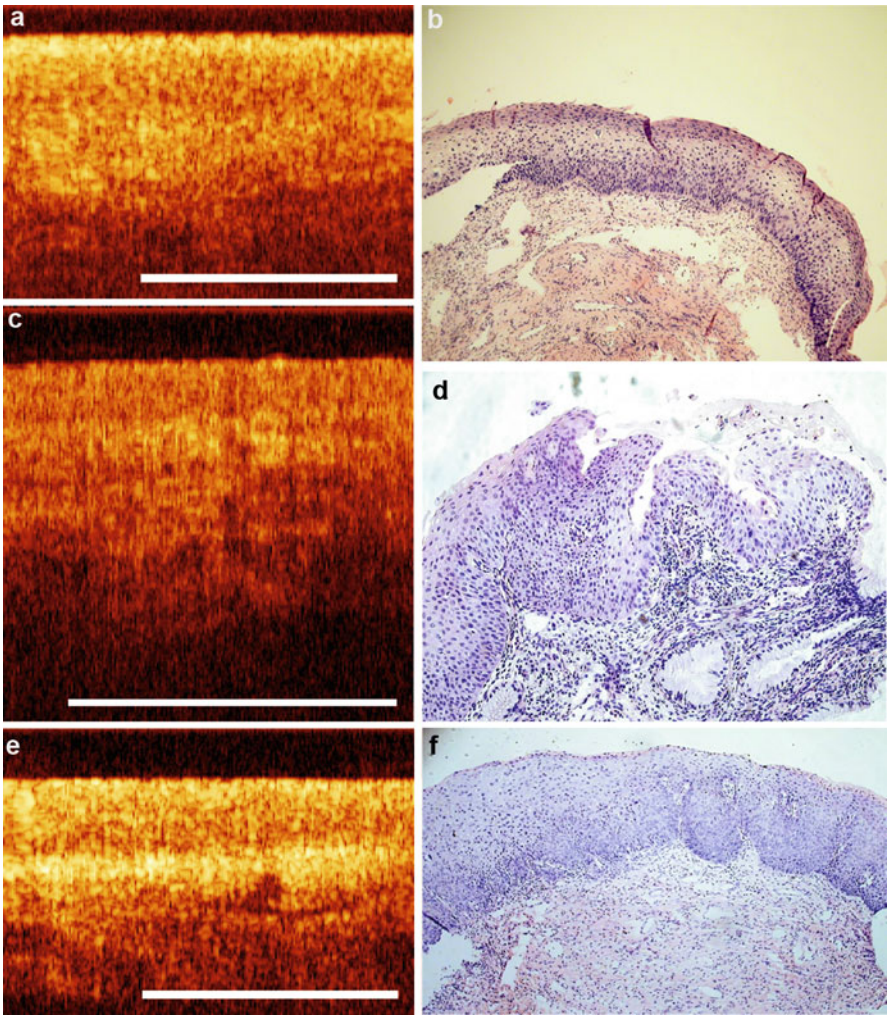

Fig. 77.14 OCT images (**a**, **c**, **e**) and parallel histology (**b**, **d**, **f**) of CIN I

examination – either unmagnified or colposcopic. A clinical trial was done to test this application [35]. The study was designed at the Cleveland Clinic Foundation (CCF) and conducted partially at the CCF and partially at Hospital Maternidad Nuestra Senora de la Altagracia, Santo Domingo, Dominican Republic. The protocol was designed to assess OCT use in two different clinical settings. First, as an aid to cervical cancer screening using unmagnified visual inspection with acetic acid (VIA) in low-resource settings. By increasing the specificity of the examination, this could allow "point of service" diagnosis and treatment without biopsy confirmation. The second setting would be applying OCT to traditional cervical cancer diagnostic programs along with colposcopy and biopsy to increase specificity by directing the biopsies.

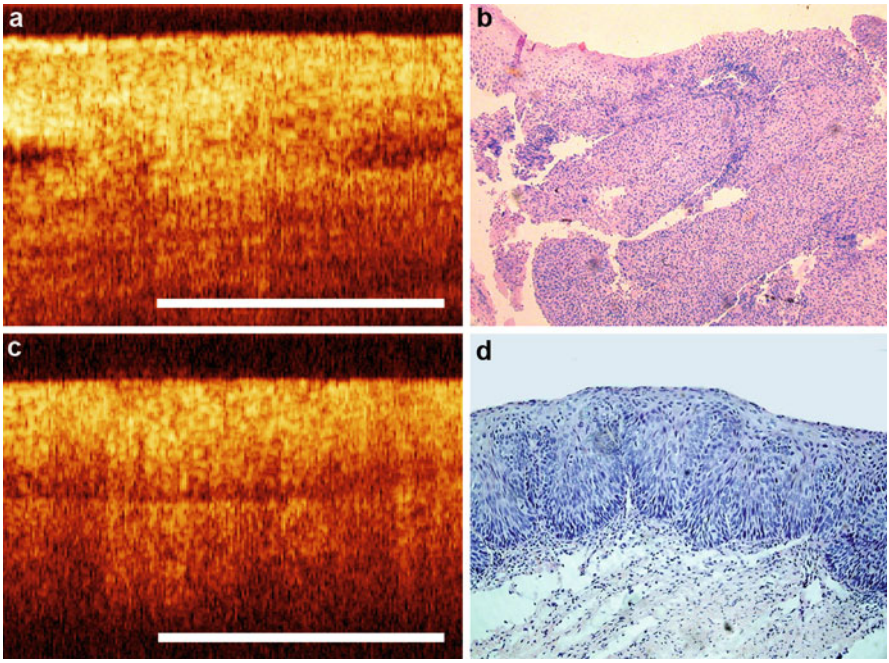

Fig. 77.15 OCT images (**a**, **c**) and parallel histology (**b**, **d**) of the cervical mucosa in the presence of CIN III

77.2.4.1 Materials and Methods

Two hundred twenty patients were enrolled in the study. The inclusion criteria were (a) 18 years of age and older; (b) patients had to sign an informed consent document stating that they understood the investigational nature of the proposed study. Exclusion criteria were: (a) subject was a prisoner; (b) was pregnant, (c) had a prior hysterectomy, (d) or had prior treatment for preinvasive or invasive cervical cancer.

The OCT system used in the study was made by Imalux Corporation (Cleveland OH, USA) and operated at 980 center wavelength, with 45 nm bandwidth and 10 mW source power. It had 25 μm lateral resolution and 11 μm axial resolution (in tissue) and acquired 200 × 200 pixel images in 1 s. A detachable probe with 2.7 mm outer diameter and disposable sheath (Fig. 77.1) was used.

The protocol included five steps:

Step 1 – Unmagnified Visual Inspection using Acetic Acid (VIA). Acetic acid (5 %) was applied to the cervix, and after 1 min VIA was performed. The visual inspection diagnosis was recorded by quadrant.

Step 2 – A digital photograph was taken of the cervix following visual inspection.

Step 3 – Colposcopy. Acetic acid (5 %) was reapplied to the cervix, colposcopy was performed, and observations were recorded by quadrant.

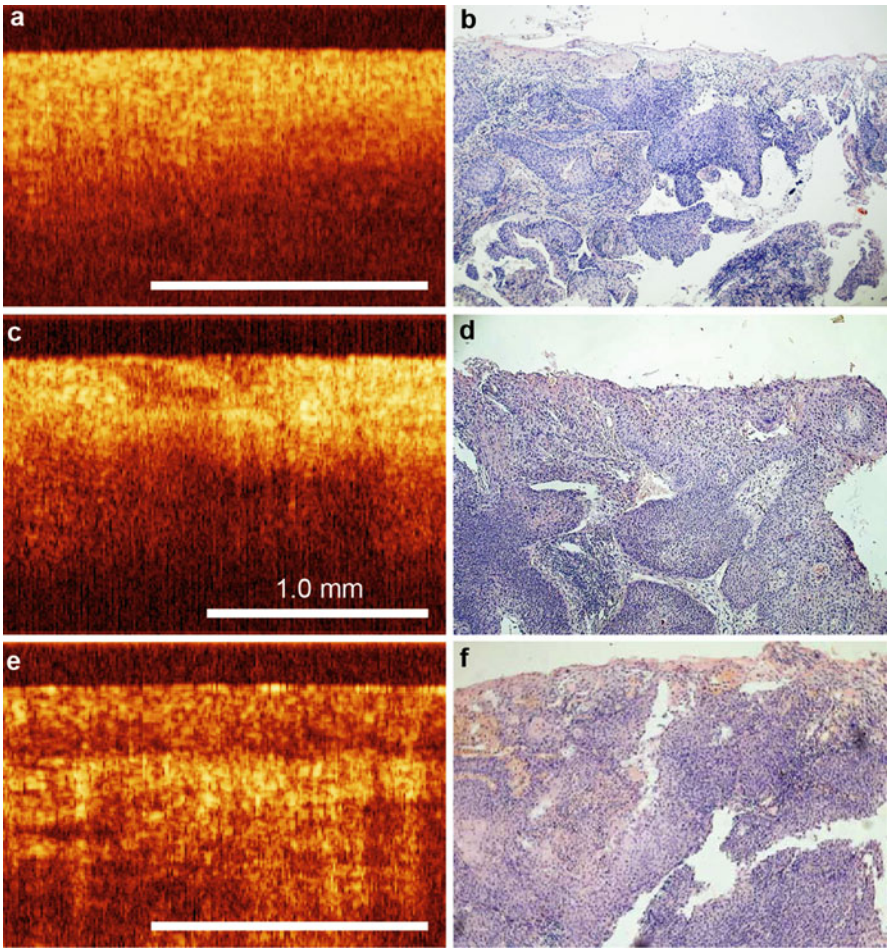

Fig. 77.16 OCT images (**a**, **c**, **e**) and parallel histology (**b**, **d**, **f**) of the cervical mucosa in the presence of invasive cervical carcinoma. Image e represents a rare exception of false negative OCT for invasive carcinoma

Step 4 – Optical coherence tomography. OCT imaging was performed from 2, 4, 8, to 10 o'clock at the squamocolumnar junction (SCJ) as well as any additional abnormal areas found by VIA, Colposcopy, or both VIA and Colposcopy.

Step 5 – Biopsies. Biopsies were taken in each quadrant and appropriately labeled from all VIA, Colposcopic, and VIA and Colposcopic positive areas. In addition, a biopsy was taken from each quadrant at 2, 4, 8, or 10 o'clock at the SJC, matching OCT imaging sites.

After completion of the study protocol, all patients found to have high-grade precancer or true invasive cancer received regular treatment according to standard protocols.

The biopsy material was evaluated by a single histopathologist at the CCF, however a team of gynecologic pathologists at the CCF served as consultants for difficult cases.

Patient information, histopathology and OCT images were then de-identified and coded. Three investigators at CCF interpreted the coded OCT images after all patient examinations had been completed. They each diagnosed the images independently using the following scale: OCT images were graded as *normal* if a well-organized, simple two-layer structure was seen with a sharp interface between the squamous epithelium and the underlying connective tissue, *abnormal* if the tissue was unstructured with, no apparent interface present, and *indeterminate* if irregularities on the images suggested artifacts or physiologic alterations (swelling of the epithelium, edema of the stromal layer or inflammation) and did not meet diagnostic criteria for normal or abnormal.

In order to provide information as to the application of OCT for limited and varying clinical circumstances (i.e. screening, added to VIA, or added to colposcopy), the images were read three separate times for each patient. First, the images were read knowing only the patient's age. Second, they were read with knowledge of the VIA impression by quadrant, and with access to a non-magnified digital image of the cervix. Finally, the OCT images were interpreted with full knowledge of the referral Pap results, the colposcopic diagnosis by quadrant, and viewing a magnified digital photograph of the cervix.

Subsequently, the results of the OCT readings were compared with parallel histopathology. 1,215 OCT images were matched to the final histopathology diagnosis. All statistical processing and data management was performed at the University of North Carolina at Chapel Hill. Histologically, CIN II or greater was considered as positive for neoplasia diagnosis.

Due to the difficulty with patient compliance and patient follow-up, this clinic in the Dominican Republic used very liberal criteria for a colposcopic and/or VIA abnormal area. The per patient sensitivity and specificity of VIA alone was 76 % and 34 % respectively. For VIA with OCT the sensitivity decreased to 53 %, but specificity was nearly doubled to 61 %. If we separate the results for lesions at the SJC, into abnormal areas identified by VIA and those areas interpreted as normal, we will see that on per site basis, OCT had 52 % sensitivity and 64 % specificity in the SJC areas where VIA did not detect any lesions. Therefore we think that OCT has the potential to improve sensitivity of random biopsies in the SCJ area and should be studied prospectively.

For the colposcopy alone, per patient sensitivity/specificity was 39 %/71 % if CIN II colposcopic impression was considered as a positive reading and 93 %/11 % if CIN I colposcopic impression was considered as a positive. The last case is typical in the standard of care because a colposcopic reading of CIN I is associated with a high enough risk of actually having CIN II so a biopsy is recommended. The OCT with colposcopy had sensitivity 46 % and specificity 65 %.

The interobserver agreement was 0.4, which is considered moderate to fair.

Receiver Operating Characteristic (ROC) curves were also generated to access the quality of OCT as a diagnostic test for lesions at the SCJ and lesions distant from

the SCJ. OCT demonstrated to be a fair diagnostic tool (ROC 0.73) adjunctive to VIA and colposcopy in accurately identifying lesions distant from the SCJ.

We envision that in a low-resource setting OCT, directed by VIA, could improve the specificity of the screening examination in detecting CIN II allowing for a single episode of care that includes both diagnosis and treatment without histological confirmation. This "point of care" model for diagnosis and treatment of preinvasive disease would be ideal in areas with a limited health care infrastructure, limited human and financial resources, and with limited ability to have a patient recall system for follow-up care.

In the developed world (moderate to high-resource setting) OCT could be considered in the future perform an "optical biopsy". The optical biopsy would be taken at areas determined to be suspicious by colposcopy allowing for the selection of key areas for biopsy. This could reduce the number of unnecessary biopsies taken, while increasing the number of histologically significant biopsies (true positives). A typical application would be areas of extensive squamous metaplasia (both mature and immature) or determining the margins for a loop electro excision procedure (LEEP) in a young patient with a wide transformation zone.

In this study, the physician acquiring OCT images was unable to see them during the session. We believe that OCT will perform better in a "real-time" setting. In other words, that in order to truly measure the efficacy of OCT combined with visual examination, future clinical studies should include "real-time readings" with OCT. This would reduce the false positives caused by improper positioning at the SCJ, as normal endocervical mucosa looks unstructured in OCT. Furthermore, by reviewing the OCT images during the gynecological examination the clinician will be able to fully integrate the patient history (including Pap smear results), the visual examination before and after acetic acid and the colposcopy impression.

The OCT "optical biopsy" impression could then be compared to the results of histological biopsies taken at the precise area that corresponds to the OCT image. A study with OCT impressions completed in real-time is currently being conducted therefore modeling the use of the OCT as a single episode of care imaging modality.

We believe that OCT could potentially show greatest utility in the management of cervical dysplasia in low-resource settings where a single episode of care is most desirable. The algorithm would be primary screening with VIA and then OCT as the secondary screen for VIA positives. Appropriate treatment or referral would then be based on the OCT and VIA findings.

77.2.4.2 Cross-Polarization OCT: Principles, Device, Results

OCT is an optical interference-based technique and therefore is intrinsically sensitive to the polarization of the backscattered radiation. Nevertheless, for traditional structural OCT polarization sensitivity is often considered as a disturbing factor creating image artifacts. However, light polarization changes in the biotissues can create additional contrast and make OCT more specific. That is why polarization-sensitive OCT (PS-OCT) is one of the known enhancements in the OCT development and subject of intensive studies [36–53].

In particular, PS-OCT can visualize tissue birefringence associated with optical anisotropy in the biotissues, via measurement of phase retardation between polarization components [37, 43, 45, 46, 49, 50] and/or the Stokes parameters [41, 42, 51]. Another phenomenon, the cross-polarization scattering, i.e., the scattering to the orthogonal polarization, can be observed in biotissues independently on birefringence. We call the version of PS-OCT, focusing on comparison between images resulted from cross-polarization and co-polarization scattering of the same biotissue, as cross-polarization OCT (CP-OCT) [47, 52].

In this section, we present some preliminary results obtained using a two-channel portable device for CP-OCT, based on polarization-maintaining (PM) fiber and having an endoscopic OCT probe with 2.7 outer diameter.

77.3 PS-OCT System Design and Performance

The functional diagram of the all-fiber PS-OCT system is shown in Fig. 77.17.

Partially polarized radiation from a superluminescent source with central wavelength $\lambda = 980$ nm is transmitted through Faraday isolator 3 and then through polarizer 4 to increase the polarization degree. Polarization controller 16a is used to optimize power at polarizer output, while the polarization controller 16b is used for selective excitation of one of the polarization modes of PM fiber. For explanation purposes, we assume that a slow polarization mode is excited. Therefore, the radiation in the sample and reference arms in the forward direction of the device has linear polarization state. Radiation backscattered from the biological object has an orthogonal component in addition to the initial polarization, which excites the second polarization mode of the PM fiber in the sample arm. Radiation coming back from the reference arm contains an equal mix of two polarization modes, because of quarter-wave plate located at 22.5° to the initial linear polarization.

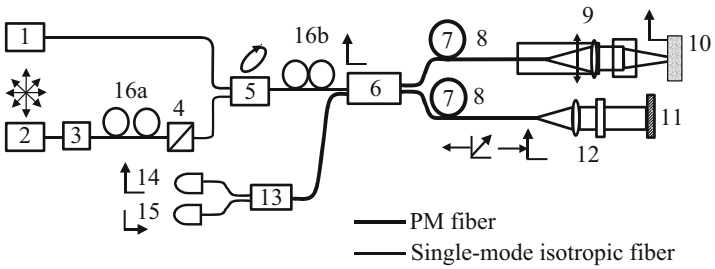

Fig. 77.17 Schematic diagram of the all-fiber PS-OCT system: *1* $\lambda = 630$ nm red aiming laser, *2* $\lambda = 980$ nm superluminescent diode (*SLD*), *3* Faraday isolator, *4* SM fiber polarizer, *5* wave division multiplexer, 6–3 dB PM fiber coupler, *7* piezofiber optical path modulators, *8* PM fiber fixed delay line, *9* endoscopic probe with lateral scanning, *10* sample, *11* reference mirror, *12* quarter-wave plate at 22.5° to PM fiber axes, *13* all-fiber polarization beam splitter, *14*, *15* photoreceivers, *16*a, *16b* polarization controllers

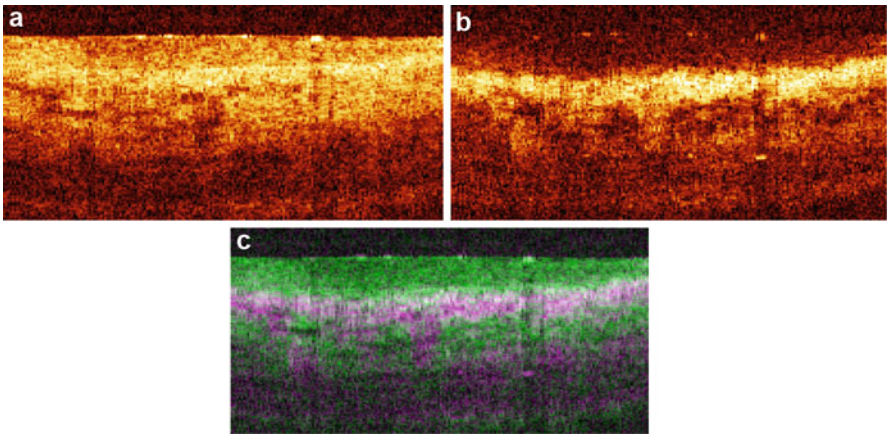

Fig. 77.18 Normal uterine cervix. Patient X. 49 years old. OCT image in parallel (**a**), orthogonal (**b**) polarizations, and simultaneously in two polarizations (**c**)

Waves returned from the signal and reference arms are recombined in the polarization-independent 3 dB coupler [42]. Despite the substantial (several mm) walk-off between slow and fast polarization, the optical path difference between interfering components remains the same, because slow sample polarization interferes only with slow polarization in the reference arm, whereas fast sample polarization interferes only with fast reference polarization. Therefore, the signal in orthogonal polarizations originates simultaneously from the same place of the sample. Then, recombined optical signals in fast and slow polarizations are separated into two detecting channels by a polarization-dependent splitter [50] and then are independently processed by an identical analogue circuitry, digitized, stored, and visualized on a PC display.

Note that Faraday isolator is essential to prevent a strong cross talk between fast and slow channels, associated with the light source reaction to the interference-modulated back-reflected light. With Faraday isolator, this cross talk was suppressed to at least −30 dB level. The use of the all-fiber design allowed us to develop a small-size ($40 \times 40 \times 16$ cm) portable device suitable for clinical studies.

Figures 77.18, 77.19, and 77.20 show three types of the OCT images: in co-polarized (parallel) component, cross-polarized (orthogonal) components, and their mix in complementary colors (green and magenta). Figure 77.18 shows the OCT images of the normal uterine cervix. OCT images of the normal exocervix demonstrate a stratified structure. Parallel OCT component (Fig. 77.18a) is just a regular "structural" image. In orthogonal polarization, the contrast between epithelium and connective tissue stroma is greatly enhanced (Fig. 77.18b) because of different spatial compositions of epithelium and stroma. The main stromal components are the horizontally oriented fibers ensuring substantial depolarization, which creates strong orthogonal OCT signal.

The additional contrast created by PS-OCT can be used to differentiate between OCT images and associated conditions, which look very similar in regular

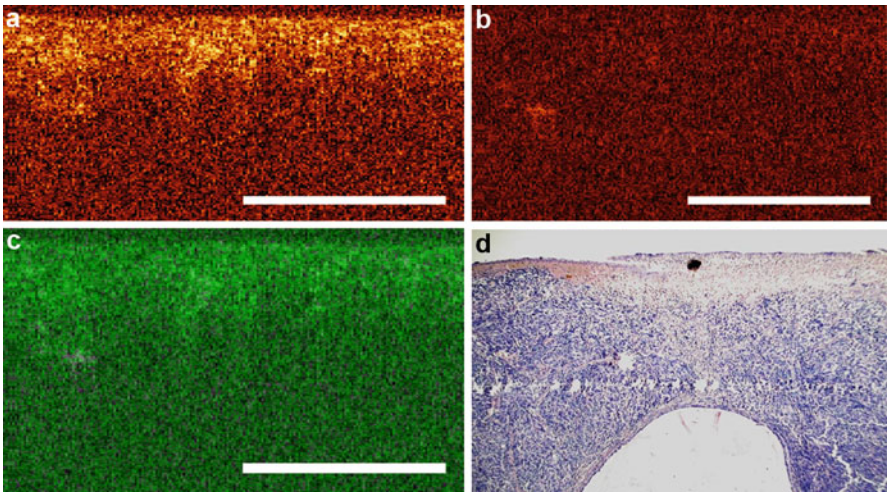

Fig. 77.19 Squamous cell cervical carcinoma. The OCT image in parallel (**a**), orthogonal (**b**) polarizations, and simultaneously in two polarizations (**c**); corresponding histology (**d**)

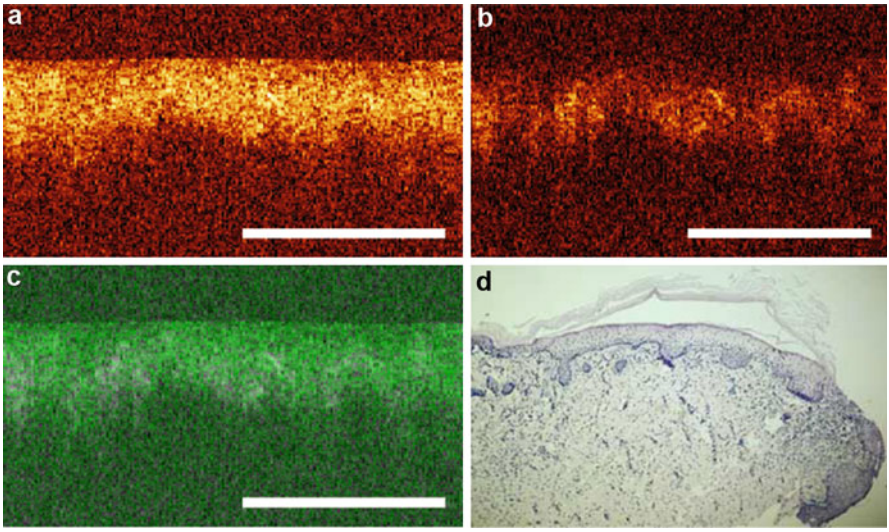

Fig. 77.20 Acetowhite epithelium. OCT image in parallel (**a**), orthogonal (**b**) polarizations, and simultaneously in two polarizations (**c**); histology: leukoplakia

structural OCT. Several illustrating examples are shown in Figs. 77.19 and 77.20. Figure 77.19a demonstrating invasive cervical cancer and Fig. 77.20a, with cervical leukoplakia, show a very similar loss of the layered horizontal structure in parallel polarization in both cases. Therefore, in regular structural OCT the image 43.20a will be interpreted as a malignant condition and will be a false positive.

Table 77.2 Ex vivo OCT endometrial imaging with parallel histopathology

Totally examined, $n = 25$				
Normal endometrium in proliferation phase, $n = 5$	Normal endometrium in secretory phase, $n = 6$	Endometrial atrophy, $n = 4$	Simple endometrial hyperplasia, $n = 6$	Endometrial cancer, $n = 4$

However, in orthogonal polarization leukoplakia looks very different (Fig. 77.20b), because fiber orientation is preserved for the leukoplakia and lost for the cancer.

Therefore, we can expect that additional contrast associated with CP-OCT can potentially increase specificity of OCT, especially for conditions having poor contrast images in parallel polarization.

77.4 OCT-Hysteroscopy

77.4.1 OCT Images of Normal Endometrium, Impact of Age and Hormonal Status

In this section, we show the results of the OCT endometrial ex vivo imaging with parallel histopathology. For this purpose, we conducted a post-hysterectomy OCT study of the surgical material. The uterine wall fragment 1×1 cm^2 was excised from the entire specimen 15–20 min after the hysterectomy. For orientation, two needles were introduced into the specimen around the OCT probe. The scanning line coincided with the direction defined by the needles. Three to five OCT images were acquired from each position of the probe. Then, the specimen with needles was fixed to a cardboard with orientation marks. In histopathology processing, specimen was sliced parallel to the OCT scanning line outlined by the needles.

Twenty-five specimens were included in the OCT study of endometrium, average patient aged 46.8 years. We tried to represent the entire spectrum of the endometrial conditions and all age groups in the sample.

The breakdown of the endometrial conditions is shown in Table 77.2.

77.4.1.1 Results

The endometrium of a woman in the reproductive age in the proliferation phase is visualized in the form of a structureless OCT image (Fig. 77.21).

Histological comparisons show that only the functional endometrial layer is visualized in the OCT images. We believe that in the low-contrast pattern in Fig. 77.21c, areas with brighter signal correspond to the stromal papillas, while the areas with a lower brightness correspond to the glands. In the secretion phase, the OCT image of endometrium is changed (Fig. 77.22): OCT images become stratified.

Comparison with the histology shows that the stratified structure in OCT corresponds to the stromal papilla bent by the OCT probe.

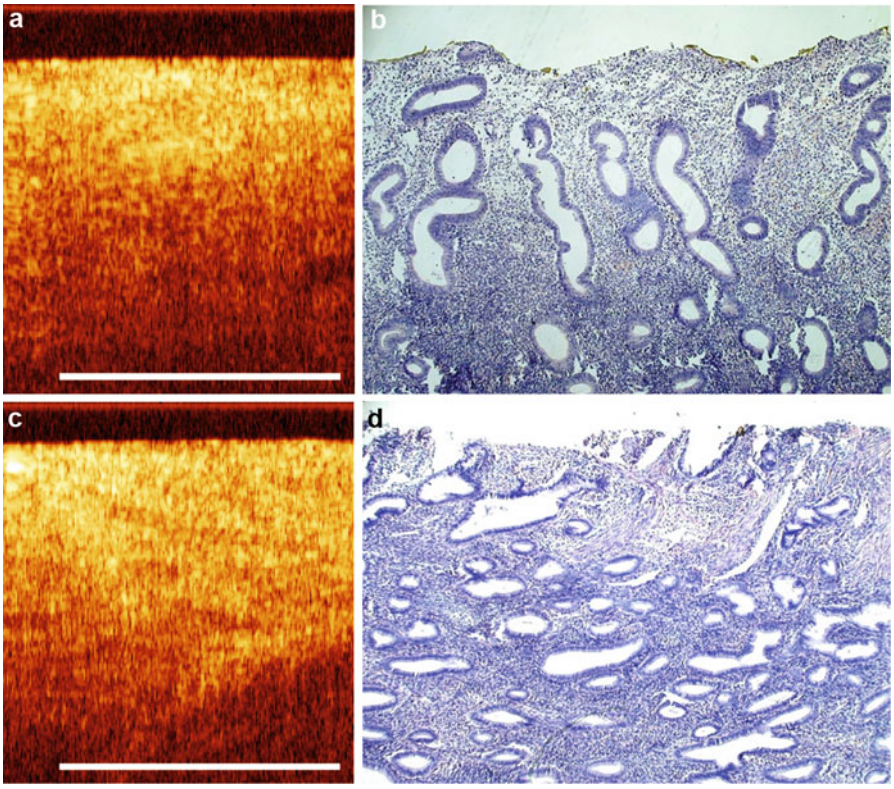

Fig. 77.21 OCT image of normal endometrium (**a**, **c**) in the proliferation phase and parallel histologies (**b**, **d**)

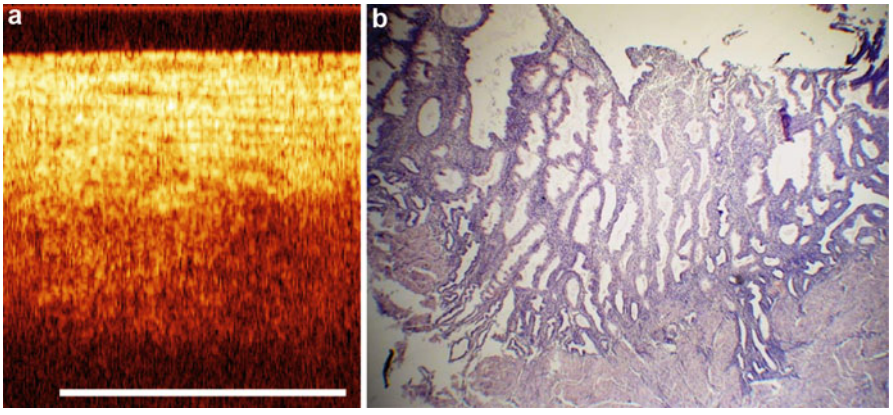

Fig. 77.22 OCT image of normal endometrium in the secretion phase (**a**) and parallel histology (**b**)

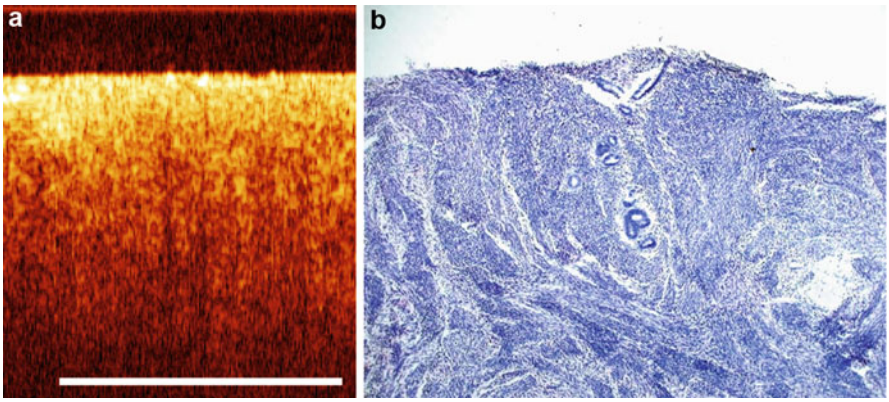

Fig. 77.23 OCT image (**a**) of atrophic endometrium and parallel histology (**b**)

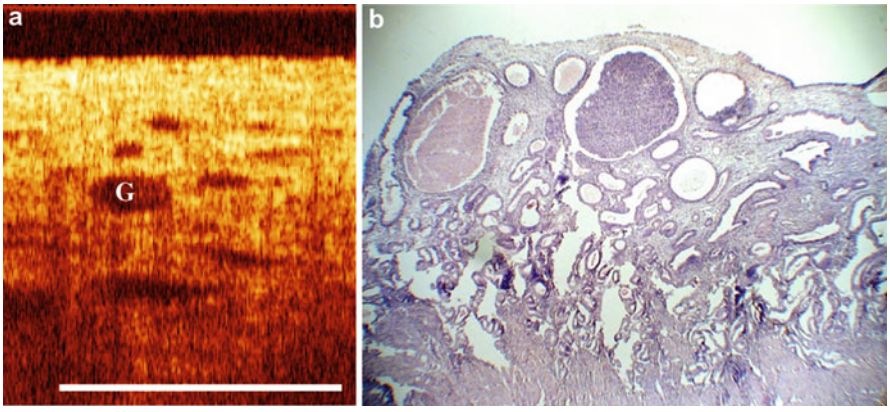

Fig. 77.24 OCT images of the endometrial polyp (**a**) and parallel histology (**b**). *G* glands

In the presence of atrophic changes, endometrium OCT image is structureless (Fig. 77.23).

In an endometrial polyp, OCT can visualize dilated glands, which are represented by round and elongated dark spots (Fig. 77.24).

Endometrial neoplasia looks completely homogeneous in OCT (Fig. 77.25).

In conclusion, endometrial structure makes it challenging for OCT application, because normal endometrium is too thick (up to 1 cm) and image frequently appears homogeneous and unstructured. However, OCT can see some differences, associated with menstrual cycle and with some pathologic conditions. Therefore, future studies could be worthwhile.

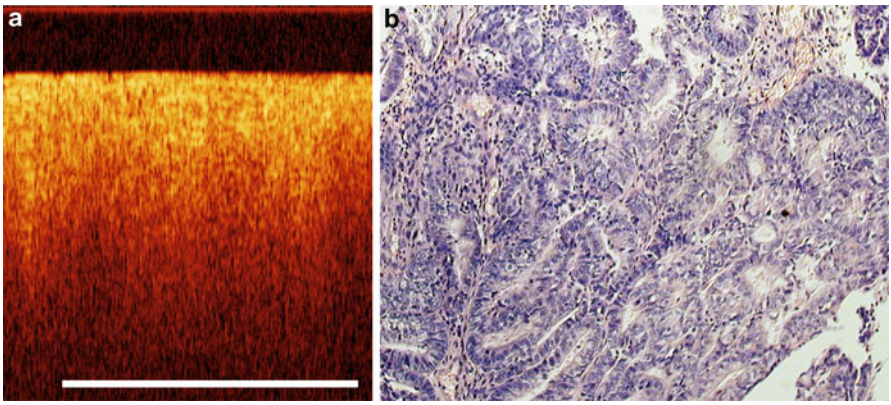

Fig. 77.25 OCT image (**a**) of well-differentiated endometrial adenocarcinoma and parallel histology (**b**)

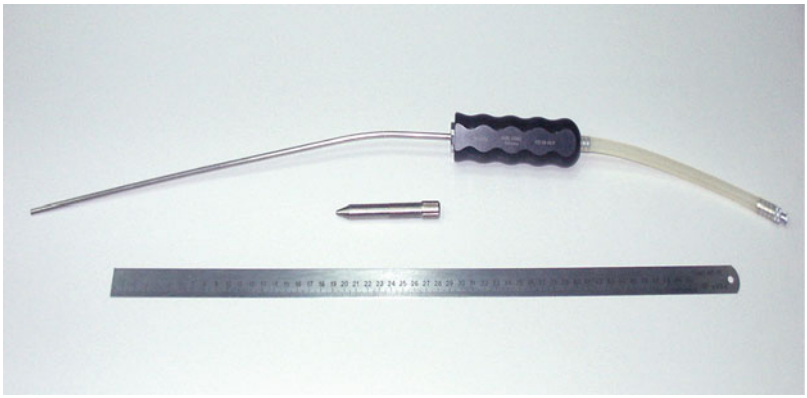

Fig. 77.26 OCT probe laparoscopic holder (*Karl Storz*)

77.5 OCT-Laparoscopy

To study the potential applications for OCT to assess the pelvis organs, we conducted several OCT laparoscopies and obtained OCT images of the uterine body, fallopian tubes, ovaries, and peritoneum of the pelvis. The OCT probe was introduced into the pelvic cavity through an additional trocar using a special rigid holder (Fig. 77.26). The study was performed with five female patients with different gynecological pathologies, when laparoscopy was clinically indicated. Since biopsies were not indicated in these cases, the OCT images were not compared with parallel histological data.

The outer uterine body OCT images have poor contrast (Fig. 77.27).

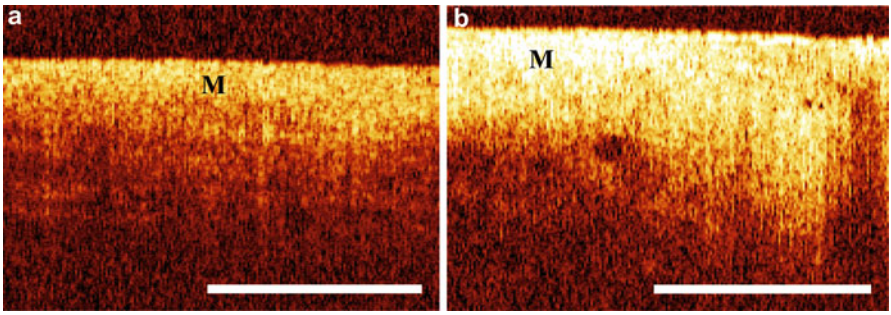

Fig. 77.27 OCT images of the uterine body surface (**a**, **b**). M myometrium

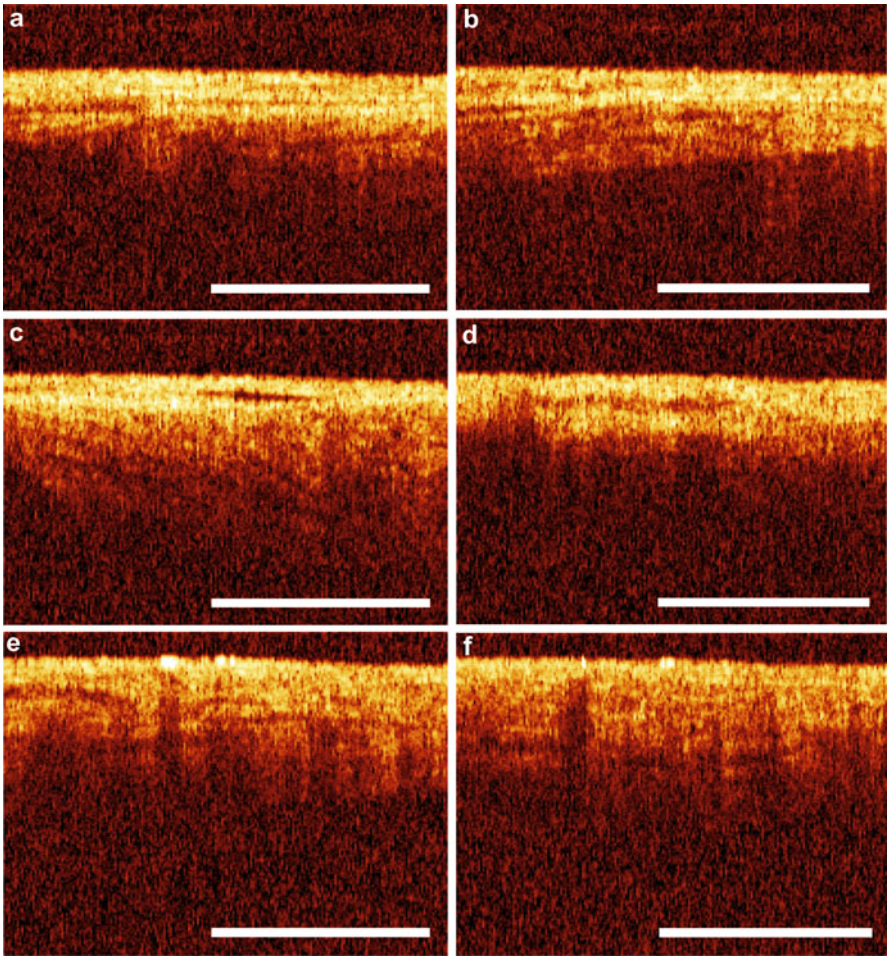

Fig. 77.28 OCT images of a normal fallopian tube wall (**a**–**d**). An OCT image of the fallopian tube with ectopic (fallopian) pregnancy changes (**e**, **f**)

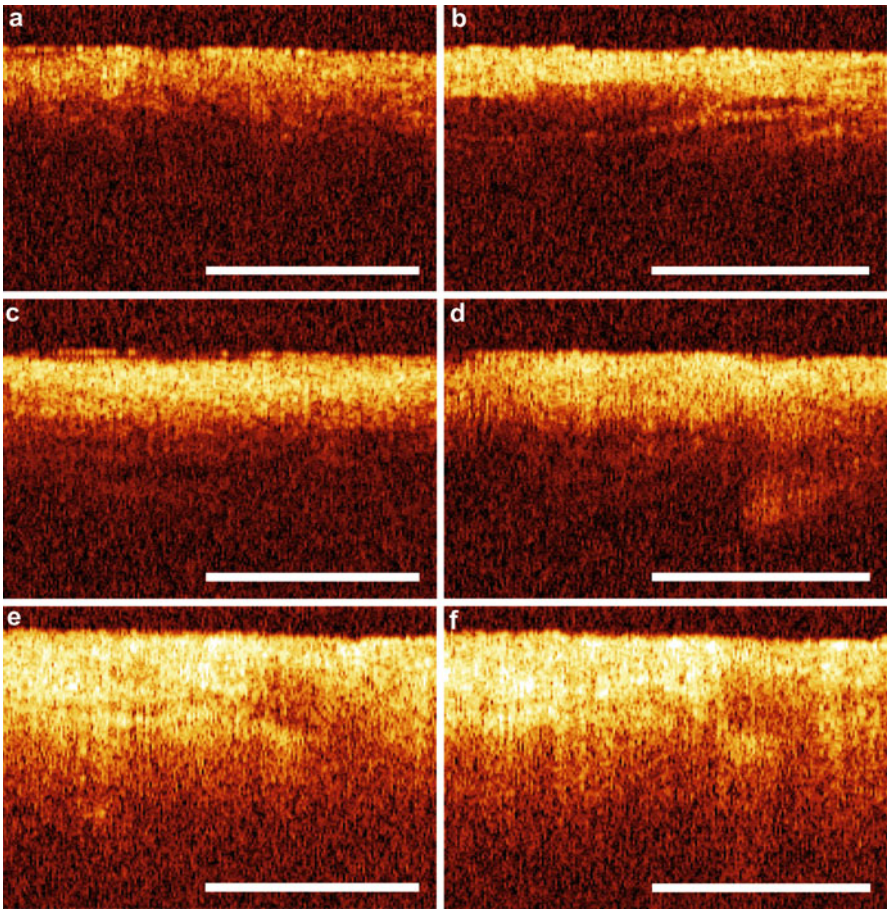

Fig. 77.29 OCT images of the ovaries

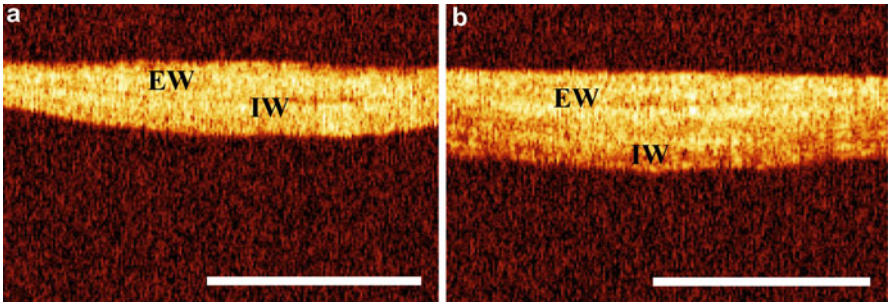

Fig. 77.30 OCT images of the capsule wall of serous cystic adenoma (**a**, **b**). *EW* is the external wall of the ovarian cyst capsule, *IW* is the internal wall of the capsule

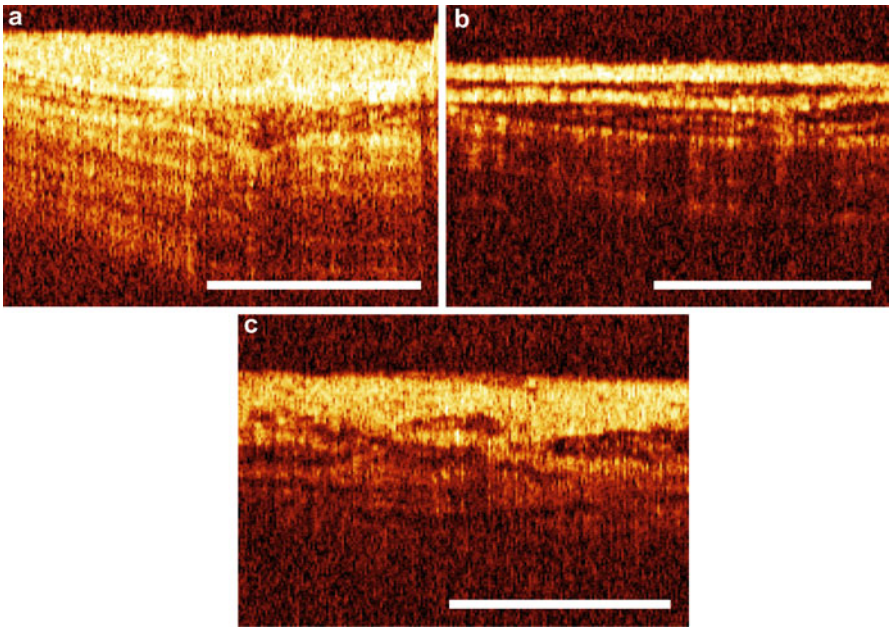

Fig. 77.31 OCT images of the pelvic peritoneum. (**a**) Normal; (**b**) inflammation; (**c**) endometriosis

A normal fallopian tube wall is visualized as a stratified image with sharp intermittent layer interfaces (Fig. 77.28a).

The OCT images of the ovaries (Fig. 77.29) do not show any stratified structure; however, penetration depth may differ significantly. We believe that it is mostly associated with thickness of tunica albuginea. Tunica albuginea is a very strongly scattering connective tissue, so if it is thick enough (0.2 mm or more), then non-scattered light cannot penetrate beyond it. If it is thinner, or more transparent, then follicles and/or a corpus luteum can be seen under the tunica (Fig. 77.29e, f).

Figure 77.30 shows an OCT image of serosal ovarian cystoma. We can see the wall structure and thickness. The image of the wall allowed ruling out noninvasively the papillary growth inside the tumor.

The normal pelvic peritoneum has stratified high-contrast OCT image (Fig. 77.31a).

During an inflammatory process, the OCT image of the peritoneum is changed (Fig. 77.31b), and typical edematous pattern with transparent liquid accumulation can be seen. The endometriosis creates significant changes in the OCT image (Fig. 77.31c): stratification is no longer seen, and irregular dark structures, which we believe correspond to the endometriosis foci, are visualized.

The presented exploratory results show that in vivo OCT images of the pelvic organs have some recognizable patterns, which creates some promise for their clinical use. However, substantial research work has to be further performed to show feasibility of OCT applications in this area.

References

1. A. Jemal, T. Murray, E. Ward, A. Samuels, R.C. Tiwari, A. Ghafoor et al., Cancer statistics, 2005. CA Cancer J. Clin. **55**(1), 10–30 (2005)
2. D.M. Parkin, F. Bray, J. Ferlay, P. Pisani, Global cancer statistics, 2002. CA Cancer J. Clin. **55**(2), 74–108 (2005)
3. World Health Report. (Geneva, WHO, 1997)
4. Cancer Strategies for the New Millenium. WHO conference. (2001)
5. S.A. Mangan, L.A. Legano, C.M. Rosen, Increased prevalence of abnormal Papanicolaou smears in urban adolescents. Arch. Pediatr. Adolesc. Med. **151**, 481–484 (1997)
6. P.S. Anderson, C.D. Runowicz, Beyond the pap test. New techniques for cervical cancer screening minimizing false-negative results. Women's Health Prim. Care (2001), pp. 753–758
7. D.S. Chi, R.M. Lanciano, A.P. Kudelka, Cervical cancer, in *Cancer Management: A Multidisciplinary Approach, Medical, Surgical & Radiation Oncology*, ed. by R. Pazdur, L.R. Coia, W.J. Hoskins, L.D. Wagman (PRR, Melville, 2002)
8. C. Balas, A novel optical imaging method for the early detection, quantitative grading, and mapping of cancerous and precancerous lesions of cervix. IEEE Trans. Biomed. Eng. **48**(1), 96–104 (2001)
9. E. Burghardt, H. Pickel, F. Girardi, *Colposcopy, Cervical Pathology: Textbook and Atlas*, 3rd rev. and enl. edn. (Thieme, Stuttgart, 1998).
10. R.J. Nordstrom, L. Burke, J.M. Niloff, J.F. Myrtle, Identification of cervical intraepithelial neoplasia (CIN) using UV-excited fluorescence and diffuse-reflectance tissue spectroscopy. Lasers Surg. Med. **29**(2), 118–127 (2001)
11. A.M. Sergeev, V.M. Gelikonov, G.V. Gelikonov, F.I. Feldchtein, R.V. Kuranov, N.D. Gladkova et al., In vivo endoscopic OCT imaging of precancer and cancer states of human mucosa. Opt. Express **1**(13), 432–440 (1997)
12. F.I. Feldchtein, G.V. Gelikonov, V.M. Gelikonov, R.V. Kuranov, A.M. Sergeev, N.D. Gladkova et al., Endoscopic applications of optical coherence tomography. Opt. Express **3**(6), 257–269 (1998)
13. F.I. Feldchtein, V.M. Gelikonov, G.V. Gelikonov, A.M. Sergeev, N.M. Shakhova, A.V. Shakhov et al., *OCT Applications in Intraoperative Monitoring and Treatment Control. Conference on Lasers and Electro-Optics* (OSA, Baltimore, 1999), pp. 335–336
14. F.I. Feldchtein, N.D. Gladkova, L.B. Snopova, E.V. Zagaynova, O.S. Streltzova, A.V. Shakhov et al., Blinded recognition of optical coherence tomography images of human mucosa precancer, in *Coherence Domain Optical Methods in Biomedical Science and Clinical Applications VII Proc of SPIE*, ed. by V.V. Tuchin, J.G. Fujimoto, J.A. Izatt (2003), p. 89–94
15. N.M. Shakhova, F.I. Feldchtein, A.M. Sergeev, Applications of optical coherence tomography in gynecology, in *Handbook of Optical Coherence Tomography*, ed. by B.E. Bouma, G.J. Tearney (Marcel Dekker, New York, 2002), pp. 649–672
16. N.M. Shakhova, G.V. Gelikonov, V.A. Kamensky, R.V. Kuranov, V.V. Sapozhnikova, I.V. Turchin et al., New advances in optical coherence tomography for diagnostics of cervical neoplasia, in *Optical coherence tomography and Coherence Techniques Pros of SPIE*, ed. by W. Drexler (2003), p. 138–143
17. N.M. Shakhova, V.M. Gelikonov, V.A. Kamensky, R.V. Kuranov, I.V. Turchin, Clinical aspects of the endoscopic optical coherence tomography and the ways for improving its diagnostic value. Laser Phys. **12**(4), 617–626 (2002)

18. N.M. Shakhova, T.S. Kachalina, N.D. Gladkova, I.A. Kuznetzova, Y.P. Chumakov, F.I. Feldchtein et al., Capabilities of optical coherence tomography in diagnosing of precancer and cancer of uterine cervix. in *17th International Cancer Congress*, 1998 (Mozzilli editore, Rio de Janeiro, 1998), pp. 1191–1195.
19. N.M. Shakhova, T.S. Kachalina, I.A. Kuznetzova, Y.P. Chumakov, F.I. Feldchtein, V.M. Gelikonov et al., Capabilities of OCT in diagnosing pathological processes, functional states, and treatment adequacy in gynecology, in *Optical Biopsies and Microscopic Techniques III Proc of SPIE*, ed. by I.J. Bigio, H. Schneckenburger, J. Slavik, K. Svanberg, P.M. Viallet (1999), p. 72–79
20. N.M. Shakhova, I.A. Kuznetzova, N.D. Gladkova, L.B. Snopova, V.V. Pochinko, Y.P. Chumakov et al., Endoscopic OCT for imaging of uterine body and cervix pathologies, in *Coherence Domain Optical Methods in Biomedical Science and Clinical Applications II Proc of SPIE,* ed. by V.V. Tuchin, J.A. Izatt (SPIE, 1998), pp. 59–66
21. N.M. Shakhova, I.A. Kuznetzova, T.S. Kachalina, N.D. Gladkova, V.M. Gelikonov, V.A. Kamensky et al., Optical coherence tomography in diagnosis of cervical neoplasia, in *5th International Multidisciplinary Congress "Eurogin 2003"*, ed. by J. Monsonego (Monduzzi Editore S.p.A. – Medimond, Paris, 2003), pp. 225–229
22. N.M. Shakhova, V.V. Sapozhnikova, V.A. Kamensky, R.V. Kuranov, V.B. Loshenov, S.A. Petrova et al., Optical methods for diagnosis of neoplastic processes in the uterine cervix and vulva. J. Appl. Res. **3**(2), 144–155 (2003)
23. S.A. Boppart, A. Goodman, J.J. Libus, C. Pitris, C.A. Jesser, M.E. Brezinski et al., High resolution imaging of endometriosis and ovarian carcinoma with optical coherence tomography: feasibility for laparoscopic-based imaging. Br. J. Obstet. Gynaecol. **106**(10), 1071–1077 (1999)
24. C. Pitris, A. Goodman, S.A. Boppart, J.J. Libus, J.G. Fujimoto, M.E. Brezinski, High-resolution imaging of gynecologic neoplasms using optical coherence tomography. Obstet. Gynecol. **93**(1), 135–139 (1999)
25. P.F. Escobar, J.L. Belinson, A. White, N.M. Shakhova, F.I. Feldchtein, M.V. Kareta et al., Diagnostic efficacy of optical coherence tomography in the management of preinvasive and invasive cancer of uterine cervix and vulva. Int. J. Gynecol. Cancer **14**(3), 470–474 (2004)
26. P.F. Escobar, L. Rojas-Espaillat, J.L. Belinson, Optical diagnosis of cervical dysplasia. Int. J. Gynaecol. Obstet. **89**(1), 63–64 (2005)
27. A.F. Zuluaga, M. Follen, I. Boiko, A. Malpica, R. Richards-Kortum, Optical coherence tomography: a pilot study of a new imaging technique for noninvasive examination of cervical tissue. Am. J. Obstet. Gynecol. **193**(1), 83–88 (2005)
28. M.A. Brewer, U. Utzinger, J.K. Barton, J.B. Hoying, N.D. Kirkpatrick, W.R. Brands et al., Imaging of the ovary. Technol. Cancer. Res. Treat. **3**(6), 617–627 (2004)
29. J.M. Herrmann, M.E. Brezinski, B.E. Bouma, S.A. Boppart, C. Pitris, J.F. Southern et al., Two- and three-dimensional high-resolution imaging of the human oviduct with optical coherence tomography. Fertil. Steril. **70**(1), 155–158 (1998)
30. J.S. Berek, E.Y. Adashi, P.A. Hillard, H.W. Jones, *Novak's Gynecology*, 12th edn. (Williams & Wilkins, Baltimore, 1996)
31. T.C. Wright, J.T. Cox, L.S. Massad, L.B. Twiggs, E.J. Wilkinson, 2001 consensus guidelines for the management of women with cervical cytological abnormalities. JAMA-J. Am. Med. Assoc. **287**(16), 2120–2129 (2002)
32. T.C. Wright, J.T. Cox, L.S. Massad, J. Carlson, L.B. Twiggs, E.J. Wilkinson, 2001 consensus guidelines for the management of women with cervical intraepithelial neoplasia. Am. J. Obstet. Gynecol. **189**(1), 295–304 (2003)
33. D. Rush, E. Hyjek, R.N. Baergen, L.H. Ellenson, E.C. Pirog, Detection of microinvasion in vulvar and cervical intraepithelial neoplasia using double immunostaining for cytokeratin and basement membrane components. Arch. Pathol. Lab. Med. **129**(6), 747–753 (2005)
34. I.A. Kuznetzova, N.M. Shakhova, T.S. Kachalina, N.D. Gladkova, A.V. Myakov, R.R. Iksanov et al., Optical coherence tomography in diagnosing of cervical cancer. *Coherence Domain Optical Methods in Biomedical Science and Clinical Applications III Proc of SPIE* (2000), p. 440–447

35. P.F. Escobar, L. Rojas-Espaillat, S. Tisci, C. Enerson, J. Brainard, V. De La Rosa et al., Optical coherence tomography as a diagnostic aid to visual inspection and colposcopy for pre-invasive and invasive cancer of the uterine cervix. Int. J. Gynecol. Cancer **16**(5), 1815–1822 (2006)
36. B. Cense, H.C. Chen, B.H. Park, M.C. Pierce, J.F. de Boer, In vivo birefringence and thickness measurements of the human retinal nerve fiber layer using polarization-sensitive optical coherence tomography. J. Biomed. Opt. **9**(1), 121–125 (2004)
37. B. Cense, T.C. Chen, B.H. Park, M.C. Pierce, J.F. de Boer, In vivo depth-resolved birefringence measurements of the human retinal nerve fiber layer by polarization-sensitive optical coherence tomography. Opt. Lett. **27**(18), 1610–1612 (2002)
38. Y. Chen, L. Otis, D. Piao, Q. Zhu, Characterization of dentin, enamel, and carious lesions by a polarization-sensitive optical coherence tomography system. Appl. Opt. **44**(11), 2041–2048 (2005)
39. M.A. Choma, M.V. Sarunic, C.H. Yang, J.A. Izatt, Sensitivity advantage of swept source and Fourier domain optical coherence tomography. Opt. Express **11**(18), 2183–2189 (2003)
40. D.P. Dave, T.E. Milner, Optical low-coherence reflectometer for differential phase measurement. Opt. Lett. **25**(4), 227–229 (2000)
41. J.F. de Boer, T.E. Milner, Review of polarization sensitive optical coherence tomography and Stokes vector determination. J. Biomed. Opt. **7**(3), 359–371 (2002)
42. J.F. De Boer, T.E. Milner, J.S. Nelson, Determination of the depth-resolved stokes parameters of light backscattered from turbid media by use of polarization- sensitive optical coherence tomography. Opt. Lett. **24**(5), 300–302 (1999)
43. J.F. de Boer, T.E. Milner, M.J.C. van Gemert, J.S. Nelson, Two-dimensional birefringence imaging in biological tissue by polarization-sensitive optical coherence tomography. Opt. Lett. **22**(12), 934–936 (1997)
44. J.F. de Boer, S.M. Srinivas, A. Malekafzali, Z.P. Chen, J.S. Nelson, Imaging thermally damaged tissue by polarization sensitive optical coherence tomography. Opt. Express **3**(6), 212–218 (1998)
45. J.F. de Boer, S.M. Srinivas, B.H. Park, T.H. Pham, Z.P. Chen, T.E. Milner et al., Polarization effects in optical coherence tomography of various biological tissues. IEEE J. Sel. Top. Quantum Electron. **5**(4), 1200–1204 (1999)
46. M.J. Everett, K. Schoenenberger, B.W.J. Colston, L.B. Da Silva, Birefringence characterization of biological tissue by use of optical coherence tomography. Opt. Lett. **23**(3), 228–230 (1998)
47. F.I. Feldchtein, G.V. Gelikonov, V.M. Gelikonov, R.R. Iksanov, R.V. Kuranov, A.M. Sergeev et al., In vivo OCT imaging of hard and soft tissue of the oral cavity. Opt. Express **3**(6), 239–250 (1998)
48. D. Fried, J. Xie, S. Shafi, J.D. Featherstone, T.M. Breunig, C. Le, Imaging caries lesions and lesion progression with polarization sensitive optical coherence tomography. J. Biomed. Opt. **7**(4), 618–627 (2002)
49. M.R. Hee, D. Huang, E.A. Swanson, J.G. Fujimoto, Polarization-sensitive low-coherence reflectometer for birefringence characterization and ranging. J. Opt. Soc. Am. **9**, 903–908 (1992)
50. M.C. Pierce, B.H. Park, B. Cense, J.F. de Boer, Simultaneous intensity, birefringence, and flow measurements with high-speed fiber-based optical coherence tomography. Opt. Lett. **27**(17), 1534–1536 (2002)
51. C.E. Saxer, J.F. de Boer, B.H. Park, Y.H. Zhao, Z.P. Chen, J.S. Nelson, High-speed fiber-based polarization-sensitive optical coherence tomography of in vivo human skin. Opt. Lett. **25**(18), 1355–1357 (2000)
52. J.M. Schmitt, S.H. Xiang, Cross-polarized backscatter in optical coherence tomography of biological tissue. Opt. Lett. **23**(13), 1060–1062 (1998)
53. I.M. Stockford, S.P. Morgan, P.C.Y. Chang, J.G. Walker, Analysis of the spatial distribution of polarized light backscattered from layered scattering media. J. Biomed. Opt. **7**(3), 313–320 (2002)

Endoscopic Optical Coherence Tomography in Urology

78

Yingtian Pan, Wayne Waltzer, and Zhangqun Ye

78.1 Introduction

Clinical statistics has shown a stable prevalence of bladder cancer in recent years, which by far remains among the most common types of malignancy in the USA. With smoking as the most well-established risk factor, bladder cancer is the fourth most common cancer occurrences in male population [1]. In the year of 2014, an estimated 74,690 new cases are expected to occur with estimated 15,880 deaths. Bladder cancer often refers to transitional cell carcinoma (TCC) as it originates primarily from the epithelial cell layer (i.e., urothelium) of the bladder. Unlike prostate-specific antigen (PSA) for prostate cancer screening, there is currently no effective screening technique approved or recommended for the population at average risk [2–5]. As a result, hematuria (i.e., blood in the urine) is often the first clinical symptom of bladder cancer. Fortunately, urinary bladder is more accessible than prostate glands endoscopically; thus cytology following white-light cystoscopy has been the gold standard for current clinical detection of bladder cancer. This is important because bladder cancer if diagnosed prior to muscle invasion (e.g., superficial or at <pT2 stages) is curable by transurethral resection (TUR) following intravesical therapy [6]. Therefore, noninvasive early detection is crucial for the management of bladder cancer patients.

Early diagnosis of TCC, in particular, carcinoma in situ (CIS) of the bladder remains a clinical challenge [7, 8]. Although advanced molecular test such as urine cytology [5, 6], fluorescence in situ hybridization (FISH) [9], and bladder tumor antigen (BTA) [10] may provide high sensitivity and specificity in detecting high-grade TCC, it is insensitive to low-grade TCC, resulting in an overall 28–50 % of

Y. Pan (✉) • W. Waltzer
Stony Brook University, Stony Brook, USA

Z. Ye
Tonji Medical College and Affiliated Hospital, Wuhan, Peoples' Republic of China

© Springer International Publishing Switzerland 2015

W. Drexler, J.G. Fujimoto (eds.), *Optical Coherence Tomography*,
DOI 10.1007/978-3-319-06419-2_80

sensitivity. Additionally, as the cancer cells detected in the urine specimen can be from anywhere in the urinary tract, this technique is not capable of locating the cancerous lesions. On the other hand, due to their resolution limitation or other technical imperfection [11], current medical imaging techniques such as intravenous pyelogram (IVP), CAT, MRI, and ultrasound fail to provide useful diagnosis except for large, high-stage invasive bladder tumors. White-light imaging or cystoscopy (i.e., WLI) via direct visual inspection of bladder epithelium (urothelium) is often performed to locate TCC with subsequent TUR of suspicious lesions of the bladder and/or biopsies to verify malignancy. WLI has proven highly efficient for detecting papillary TCC, but it is common clinical scenarios that the bladder of a patient with positive cytology appears unremarkable under cystoscopy and 80–90 % of all preclinical malignancies of bladder CIS (i.e., a type of flat but high-grade aggressive TCC) demonstrate no significant outgrowth [6]. Since current cystoscopy provides no depth resolution, conclusive diagnosis and staging of malignancy relies on random biopsy which may miss nonpapillary TCC (e.g., ~50 % of CIS [6, 7, 12]) and lead to high false-positive rates due to difficulties in differentiating them from benign inflammatory lesions. For the same reason, in the separation of recurrent TCC from benign lesions such as necrosis, scar induced by previous TUR treatments often frustrates the urologists performing surveillance cystoscopy. Clinical surveys reveal [12, 13] that possibly because of inadequate detection by urine cytology and WLI (gold standard), bladder cancer has remained the highest recurrence rate (e.g., ~50 %) among all cancer types and is the most expensive cancer to treat. For instance, ~1.2 million cystoscopies are performed in the USA annually, yet ~40 % of patients with initial superficial TCC ($<$pT2) eventually develop muscle invasive (i.e., $\geq$pT2), life-threatening TCC. Therefore, a more effective imaging technique that can see below the bladder surface at a high resolution to enable early diagnosis is highly desirable for optimizing the management of bladder cancer that may lead to a significant decrease in mortality from this disease.

With the advent of technological advances, a number of emerging optical imaging methods have shown the potential to enhance current cystoscopic procedures for the diagnosis of bladder tumor. For instance, fluorescence cystoscopy using 5-aminolevulinic acid (5ALA) and hypericin has been shown to improve the detection of bladder cancer and CIS in particular [8, 14–16]. Compared with 5ALA, hexaminolevulinate (HAL, e.g., Hexvix® in Europe and Cysview® in the USA) reduces the drug induction time from 4–5 h to 1 h before fluorescence cystoscopy. A recent multicenter clinical study in the EU and USA concluded [15, 17] a considerably improved diagnostic accuracy by comparison to WLI, e.g., up to 30 % more identification of CIS and potentially reduced recurrence rate. Despite some debates regarding its phototoxicity and relatively low diagnostic specificity (e.g., high false-positive rates due to inclusion of benign lesions that are mainly associated with inflammations of the bladder mucosa), the US Food and Drug Administration (FDA) approved Cysview as an adjunct to WLI for the detection of non-muscle-invasive papillary TCC in patients with known or suspected bladder cancer in mid-2010. Narrowband imaging (NBI) as an alternative approach has

been reported [18, 19] to improve the sensitivity for TCC diagnosis by enhancing the contrast of bladder epithelium and subsurface vasculature at different depths (e.g., 415 nm blue light for shallow and 514 nm green light for deep blood vessel visualization). Although NBI also suffers low diagnostic specificity, it circumvents the need for contrast agent (e.g., Hexvix) and thus reduces the associated cost and patient discomfort. Confocal endoscopy and Raman spectroscopy have also been reported to detect bladder cancers by providing subcellular morphology [20, 21] and molecular contrast of cancer cells, respectively. Interestingly, the latter may improve the specificity by discriminating inflammatory tissue and TCC, which remains a common problem of fluorescence and NBI cystoscopy for bladder cancer diagnosis. Noteworthily, in vivo Raman spectroscopy although potentially more objective may have to be combined with or guided by other cystoscopic imaging techniques to provide both high sensitivity and specificity for bladder cancer diagnosis [21, 22].

In contrast to 5ALA fluorescence, NBI and Raman techniques that detect biochemical and molecular features of bladder cancer, optical coherence tomography (OCT) has been applied to imaging the morphological alternations of bladder caused by tumorigenesis [23, 24]. As an emerging optical technique, OCT offers the unique capabilities that enable 2-D and even 3-D cross-sectional imaging of biological tissue such as bladder wall at superb resolution (e.g., 1–10 μm axial resolution) and up to 2 mm of depths, making it a promising imaging technology for detecting various superficial tumors like bladder cancer. Since its first introduction in the early 1990 [25], OCT has been fully developed to the clinical arena (e.g., for routine ophthalmological diagnosis) [26]. In addition to its successful clinical adoption in ophthalmology, there have been active research, development, and clinical studies to explore its applications in diagnosing disorders in many other non-translucent tissues such as dental cavities, vulnerable plaques in coronary vessels, as well as cancers in the skin, oral cavity, bronchus, esophagus, lung, colon, cervix, and urinary bladder [27]. For the majorities of these applications, various miniature OCT probes (e.g., OCT endoscopes) are needed to access internal organs noninvasively or minimally invasively. Recent technological advances that may have significant impacts on in vivo OCT diagnoses of epithelial cancers include the development of laser-scanning probes for endoscopic OCT [27–29], Doppler OCT (DOCT) to permit subsurface vasculatural imaging (e.g., tumor microenvironment) [30–32], and polarization-sensitive OCT [33, 34] and contrast-enhanced OCT [35] to provide more specific diagnosis. Importantly, compared to initial time-domain OCT, spectral-domain OCT and more recent swept-source OCT render in vivo 2-D and even 3-D volumetric OCT imaging of biological tissue in real time and at higher detection sensitivity (i.e., SNR) [36, 37]. On the other hand, ultrahigh-resolution OCT (μOCT) by utilizing ultra-broadband laser (e.g., ultrashort-pulse laser) has been reported to enable in vivo subcellular imaging of biological tissue [38, 39], which may shed some light on its capability for subcellular identification of cancerous cells (e.g., cancer grading). Here, we summarize the technological development and the results from our lab and others on preclinical and clinical studies of OCT for bladder cancer diagnosis.

78.2 Methods

78.2.1 OCT Engines

Like many other OCT groups, the study of our lab on OCT diagnosis of bladder cancer has spanned the transition from early time-domain OCT (TDOCT) to recent spectral-domain OCT (SDOCT). The results presented below include those acquired from both TDOCT and SDOCT engines accordingly. Figure 78.1 depicts the schematic diagram of TDOCT (a) and SDOCT (b) setups.

For TDOCT (a), a pigtailed broadband light source whose power, central wavelength, and FWHM spectral bandwidth are $I_0 = 18$ mw, $\lambda_0 = 1{,}310$ nm, and

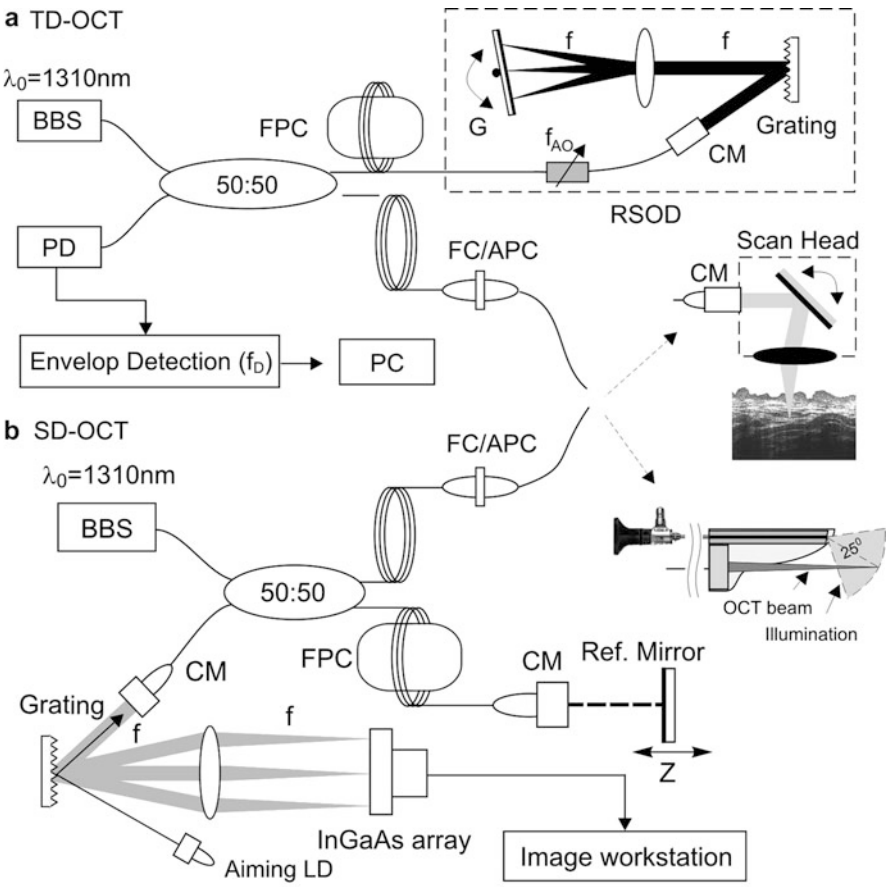

Fig. 78.1 Schematic diagrams of TDOCT and SDOCT setups. (**a**) TD-OCT, (**b**) SD-OCT. BBS: broad band source, *CM* collimator, *FPC* fiber polarization controller, *G* galvanometer scanner, *PD* photo diode, *RSOD* rapid-scanning optical delay line, *AO* differential acousto-optic modulator (e.g., $f_{AO} = 2$ MHz), *LD* aiming *red* or *green* laser diode

$\Delta\lambda = 78$ nm, respectively, is employed to illuminate a fiber-optic Michelson interferometer (e.g., 2×2 fiber-optic coupler) which splits the light equally into the reference and sample arms and recombines the interference in the detection arm. A rapid-scanning grating-lens-based optical delay (RSOD) is used to provide axial scan (A-scan), i.e., to vary optical pathlength delay in the reference arm. As RSOD separates phase and group delays permitting independent control of Doppler frequency shift f_D and bandwidth Δf of the OCT signal, a custom AO modulator is used to provide ultra-stable f_D at 2 MHz (to eliminate f_D drift due to scanning instability) and thus effectively enhance system SNR [40]. The sample arm is connected to either a benchtop scanning probe for ex vivo bladder characterization or a laser-scanning endoscope for in vivo bladder imaging through an FC/APC connector [29]. Typical system specifications are lateral resolution $\Lambda = 12$ μm for benchtop OCT probe and $\Lambda = 16$ μm for OCT endoscope, axial resolution $L_c = 10$ μm (coherence length), SNR ≈ 100 dB, and 2D image rate up to 2–4 fps (limited by the scanning rate $f_G \leq 1$ kHz of RSOD).

For SDOCT (b), the system is illuminated by a broader-band pigtailed source (e.g., $I_0 = 8$ mw, $\lambda_0 = 1{,}300$ nm, $\Delta\lambda = 90$ nm), providing an axial resolution of $L_c \approx 8$ μm. Compared to TDOCT, it employs spectral radar to implement axial scanning, which circumvents the need for mechanical scanning (e.g., RSOD) and thus drastically enhances the A-scan rate to 7.7–92 kHz (limited by the line-scan cameras employed) [41]. In addition, the parallel detection scheme of SDOCT enables it to dramatically improve the system SNR (i.e., by a factor of $N^{1/2}$ enhancement, where N is the pixel number of the spectral graph) [36]. It also allows us to easily couple a red or green aiming laser back into the fiber retrospectively through a diffraction peak (e.g., $m = -1$ order) of the spectral camera to instantaneously trace the region of interest under 2D/3D OCT scans. Typical system specifications are lateral resolution $\Lambda = 10$ μm for benchtop OCT probe and $\Lambda = 12$ μm for OCT endoscope, axial resolution $L_c = 8$ μm, SNR ≈ 112 dB, and 2D image rate up to 8–100 fps (limited by the line-scan camera, $f_{InGaAs} \leq 92$ kHz).

78.2.2 OCT Endoscopes

The combined high resolution and intermediate image depth of OCT have attributed it uniquely attractive for optically guided biopsy to permit noninvasive delineation of epithelium and the underlying morphology to detect epithelial cancers and stage their invasion. However, the development of high-fidelity laser-scanning catheters for EOCT remains a challenge. Endoscopic laser-scanning approaches that have been reported include rotary fiber with 90° microprism [27], coherent fiber bundles or rod lens endoscope [42], PZT-actuated swinging fiber [24], etc. The major engineering challenge lies in the compromise of light coupling efficiency (SNR) and beam quality (focusing capability), light scanning linearity/rate and range (FOV), and catheter size and flexibility. Typically, OCT endoscopes can be categorized to either size-view or front-view EOCT probes. 2-D and even 3-D

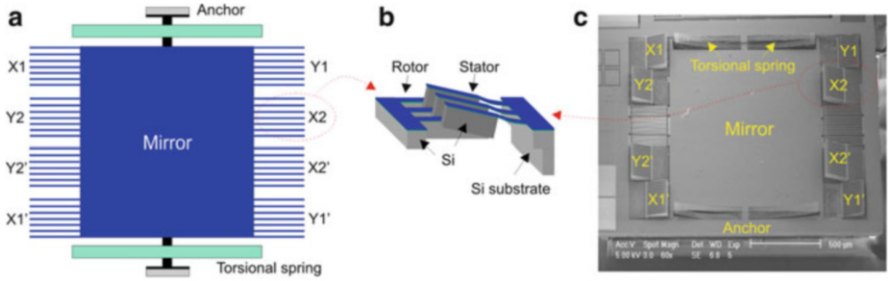

Fig. 78.2 E-ST mirror with curled comb drive. (**a**) Topology of the micromirror; (**b**) sketch of curved comb-drive finger structure, (**c**) scanning electron micrograph (*SEM*). X/Y denotes the comb drives with anchors on the curled/level sides, respectively [46, 54]

side-view EOCT [43] suitable for imaging tubular tissue (e.g., coronary artery, esophagus, colon) has been well developed using a motorized rotary fiber joint or a micro motor together with a push-pull actuator. Front-view EOCT suitable for imaging flat tissue (e.g., oral cavity, cervix, bladder) remains a technical hurdle because it needs to be inserted into the instrument channel (e.g., 16–22Fr) of a conventional endoscope for white-light image guidance [24]. In other words, the challenge is to provide a large FOV with high lateral resolution in a slender catheter. To tackle the challenge, we have developed microelectromechanical systems (MEMS)-based cystoscopic OCT (MEMS COCT) that provides a viable solution to front-view EOCT [29]. MEMS COCT takes advantage of deep reactive-ion-etch (DRIE) CMOS-MEMS mirror technology such as small size, high speed/precision, excellent laser steering capability, and potentially low cost, all of which are crucial for high-performance endoscopic laser scanning [44, 45]. The technique has been dramatically improved to optimize the performances of EOCT (e.g., SNR, resolution, packaging, reliability) [46] and validated in ex vivo and in vivo preclinical studies as well as in vivo clinical study to examine its utility and potential limitations for bladder cancer diagnosis.

Unlike those used for optical switch, MEMS mirrors used for endoscopic applications require large actuation, large size, high linearity, and fast speed. Both electrostatic (E-ST) and electrothermal (E-TH) MEMS mirrors have been developed and tested for endoscopic laser steering. Figure 78.2 exemplifies a sketch and scanning electron micrograph of an E-ST MEMS mirror, illustrating its operating principle. The chip comprises pairs of integrated MEMS z-axis curled comb-drive micro actuators (A, B) fabricated by CMOS micromachining process, allowing for a large angular actuation (C) driven under a bidirectional sweeping voltage on two sides of the mirror. Typical angular actuation (θ) for a 1×1 mm^2 mirror is $\leq 10^\circ$ at $18V_{p\text{-}p}$. The primary advantage of E-ST mirror is of high scanning speed ($\leq$10 kHz) and precision [44].

Figure 78.3 shows an E-TH mirror driven by a bimorph hinge consisting of a stack of Al and SiO_2 thin films embedded with an integrated poly-Si resistor (i.e., an E-TH actuator). Due to residual stress and difference in the thermal expansion

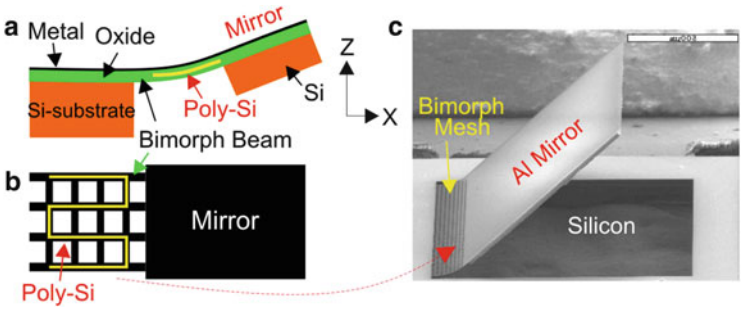

Fig. 78.3 An E-TH mirror with embedded curled poly-Si drive. (**a**) Schematic of an embedded poly-Si beam structure; (**b**) top view with x-axis-oriented poly-Si resistor; (**c**) SEM of a 32° T-TH MEMS mirror (1×1 mm^2 Al-coated mirror) [50, 51, 54]

properties between these two thin layers, the hinge curls up to an initial bending angle (θ_0) above the chip plane and θ varies with the temperature (T) within the bimorph. Thus, the embedded poly-Si resistor acts as the heat source to angularly actuate the mirror, and the actuation range θ can be adjusted by parameters such as the length of the stacked hinge and the differential thermal expansion coefficient between Al and SiO_2. The typical actuation angle attained is $\theta = 17°$, providing a lateral optical scanning over 35° – surpassing the need for endoscopic OCT [29]. The resonant frequency of a 1.2×1.1 mm^2 E-TH mirror is roughly 160–250 Hz, exceeding the speed requirement for 2D COCT. Technical issues encountered in E-TH mirrors, e.g., hysteresis, buckling, and nonlinearity, have been either eliminated or minimized to ensure high-fidelity COCT imaging [45, 47]. The lateral resolution of COCT reaches $\Lambda = 12$–16 μm, which is determined by focal length f (f = 8–10 mm) of the scan lens and beam size ϕ (eventually limited by MEMS mirror size, e.g., 1.2×1.1 mm^2).

Figure 78.4 illustrates the packaging of MEMS-based COCT and the integration to a commercial 22Fr rigid cystoscope via its instrument channel to enable white-light image-guided OCT imaging diagnosis. Despite compromised SNR due to light loss, the first in vivo image result demonstrated the capability of MEMS COCT for delineating the morphology of porcine bladder (a close homologue to human bladder) [22].

78.3 Preclinical Studies

78.3.1 Bladder Morphology Imaged by OCT and Histology

Despite the contrast difference between OCT (backscattering) and histology (H&E stain), Fig. 78.5 shows the morphology of normal human bladder imaged by ex vivo OCT and the corresponding histology, indicating a close correlation for the identifications. For instance, the urothelium (U) is a thin (~110 μm), uniform,

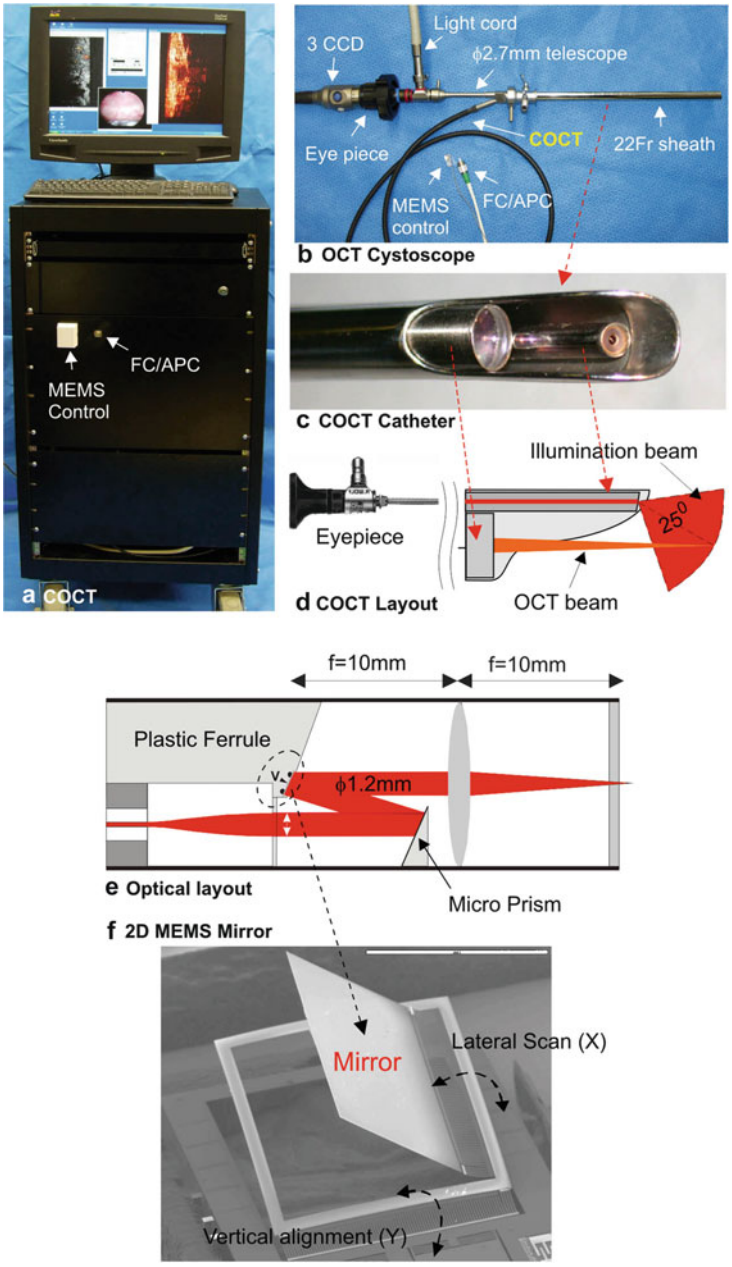

Fig. 78.4 MEMS-based COCT system. (**a**) A picture of the main COCT image station; (**b**) OCT cystoscope that fits in a 22Fr rigid sheath and connects to the main system via fiber/electric cables; (**c**) A picture of an COCT catheter using a ϕ2.7 mm telescope for visual guidance; (**d**) coordination between surface/EOCT scopes; (**e**) optical layout of the COCT catheter; (**f**) an SEM of an MEMS mirror (1.2×1.3 mm^2) [50, 54]

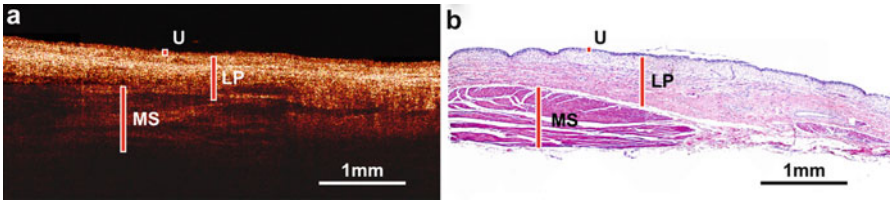

Fig. 78.5 Human bladder under proper stretch imaged by ex vivo OCT and histology, showing close correlations. Three layers in the human bladder wall critical for the diagnosis of bladder cancer prognosis, e.g., urothelium (*U*), lamina propria (*LP*), and the upper muscularis (*MS*), are delineated based on their backscattering differences [57]

and relatively low-scattering superficial layer; lamina propria (LP) is ~550 μm thick and highly scattering and heterogeneous because of compositions of mostly random collagens; the upper muscularis (MS) appears largely bifurcated, likely representing the interfaces between the smooth muscle collagen bundles. This result demonstrates the resolution of OCT to delineate morphological details of human bladder and thus the potential to track their changes (e.g. tumors) so as to determine the level of invasion of early bladder cancers (e.g., to stage TA, T1, flat, or not deeply invasive) toward the bladder wall, while conventional cystoscopy often fails. It is noteworthy that although an issue for in vivo scenario, the ex vivo OCT image contrast of bladder, particularly urothelium, strongly depends on sample preparation (e.g., stretch). As the specimen was refrigerated, most of the hardened muscularis in Fig. 78.5 had to be dissected in order to stretch the bladder for OCT examination.

78.3.2 Animal Bladder Carcinogenesis Imaging

OCT as a new diagnostic imaging modality must undergo throughout a validation process by a clinically proven method (i.e., histology – gold standard for cancer diagnosis) before it can be applied for human studies. In our lab, various animal TCC models have been used to systemically characterize OCT for identifications of the morphological alternations induced by carcinogenesis, which includes (1) female Fischer rats exposed to N-methyl nitrosourea (MNU) – an alkylating agent – to reproducibly induce cystitis, hyperplasia, and neoplasia (i.e., TCC) [23], (2) AY-27 cell instillation to generate multifocal TCCs in rat bladder [48], and (3) SV-40 T transgenic model to develop dysplasia, carcinoma in situ (CIS), and frank TCC in mouse bladder [49]. These protocols allowed us to define the structural and even physiological events that occurred as TCC developed in the urothelium and invaded into the underlying layers to characterize the changes in OCT images.

Figure 78.6 shows the result of ex vivo 3D OCT of rat bladder cancer (by MNU model), in which the 3-D image dataset captured in ~6 s was reconstructed by 32 sequential 2D OCT sections with 80 μm interval. Three hyperplastic lesions and

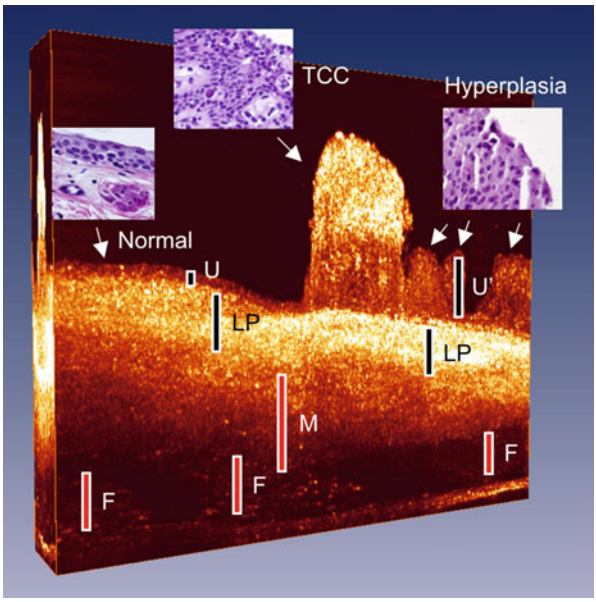

Fig. 78.6 3D OCT of rat bladder ex vivo. Image size: L6 mm × D2.1 mm × 2.5 mm, image acquisition: 6 s. *White/blue dashed circles*: 1 TCC and 3 hyperplastic lesions, respectively [46]

1 TCC (stage Ta) were identified based on their backscattering differences – $V_{U'}/V_U \approx 1.07$ for hyperplasia and $V_{U''}/V_U \approx 1.87$ for TCC – where V_U, $V_{U'}$, and $V_{U''}$ are the averaged backscattering values of normal urothelium, hyperplasia, and neoplasia measured by OCT, respectively. This suggests the potential role of backscattering as a natural biomarker for OCT diagnosis of early urothelial cancer primarily determined by enhanced nuclear-to-cytoplasmic ratio (NC ratio). To further study this effect, optical modeling of nuclear morphology, i.e., NC ratio changes by nuclear size, polarity, and density induced by carcinogenesis, is shown in Fig. 78.7, which collaborates with result in Fig. 78.6. In the modeling, urothelial backscattering coefficient μ_b was calculated using the corresponding histomorphometric data [50].

In addition to diagnosis of TCC, OCT may be further used to detect bladder cancer margins. Figure 78.8 shows that 3D OCT can accurately locate the margins of a large papillary TCC. Panel 1–1′ shows that the bladder wall (e.g., U) was normal except thickened LP with excessive angiogenesis (large blood vessels, BVs). Panel 2–2′ shows the edge to TCC (stage TA) where the interface between slightly thickened urothelium U′ (210 μm) with enhanced backscattering $(V_{U'}/V_U \approx 1.47)$ and the inflammatory LP was clear. Panel 3–3′ shows thick urothelium U″ (~540 μm) with high backscattering $(V_{U''}/V_U \approx 1.78)$. OCT shows the TCC invaded into LP, but the abrupt attenuation induced by high urothelial scattering and absorption of large BVs prevents OCT to separate it from stage T1 or T2. Histology (3–3′) confirms it a T1 TCC and the lateral tumor margin (dashed red circle).

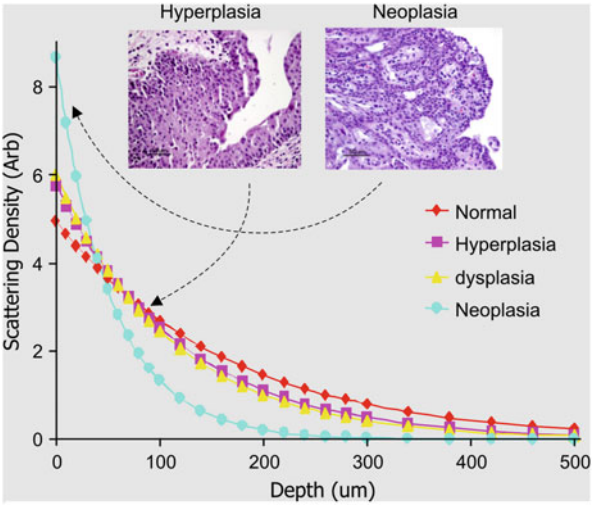

Fig. 78.7 Simulated OCT signals of urothelial backscattering versus depth during carcinogenesis by statistical evaluation of urothelial nuclear density from histological images. Normal, hyperplastic, and early dysplastic epithelia show low backscattering whereas neoplastic epithelium exhibits a ~60 % increase in backscattering [50, 57]

78.3.3 MEMS-Based OCT

In parallel to animal carcinogenesis study, preclinical study on COCT was performed to test its feasibility for clinical human examinations and to provide feedbacks for improving COCT probe design and fabrication. Figure 78.9 compares in vivo 2-D COCT image of porcine bladder (acquired at ~6 fps) and 2-D ex vivo OCT image of almost identical bladder cross section by the benchtop setup. Except a smaller lateral size (2.9 mm vs. 6 mm) and slight decrease (~8 dB) in image SNR due to light coupling loss in the OCT endoscope, COCT enables delineation of the morphology of pig bladder such as U, LP, and MS (identified by the interfaces between large collagen fiber bundles). Figure 78.9 demonstrates technological advances in MEMS-based COCT that allows providing comparable sensitivity and resolution to benchtop OCT; therefore, the results of ex vivo studies including animal TCC studies are potentially transferable to in vivo COCT studies [46].

Additional challenge for in vivo COCT diagnosis of early bladder cancer may include effective image guidance because of large surface areas to be randomly scanned across human bladder. In addition to white light, 5ALA and NBI were tested to assist OCT scans. For instance, Fig. 78.10 compares the results of rat bladder lesions ((a) inflammation, (b) hyperplasia, (c) TCC) with 5ALA fluorescence and 2D COCT, which shows that these two methods compliment each other. Both detected TCC, but the benign lesions false-positively identified by 5ALA fluorescence were corrected by COCT as LP inflammation and hyperplasia (reversible and thus no clinical significance) [48]. This suggests that 5ALA-guided COCT can effectively guide COCT for detecting bladder cancers while reducing the high false-positive rates of 5ALA by OCT to exclude benign lesions [51].

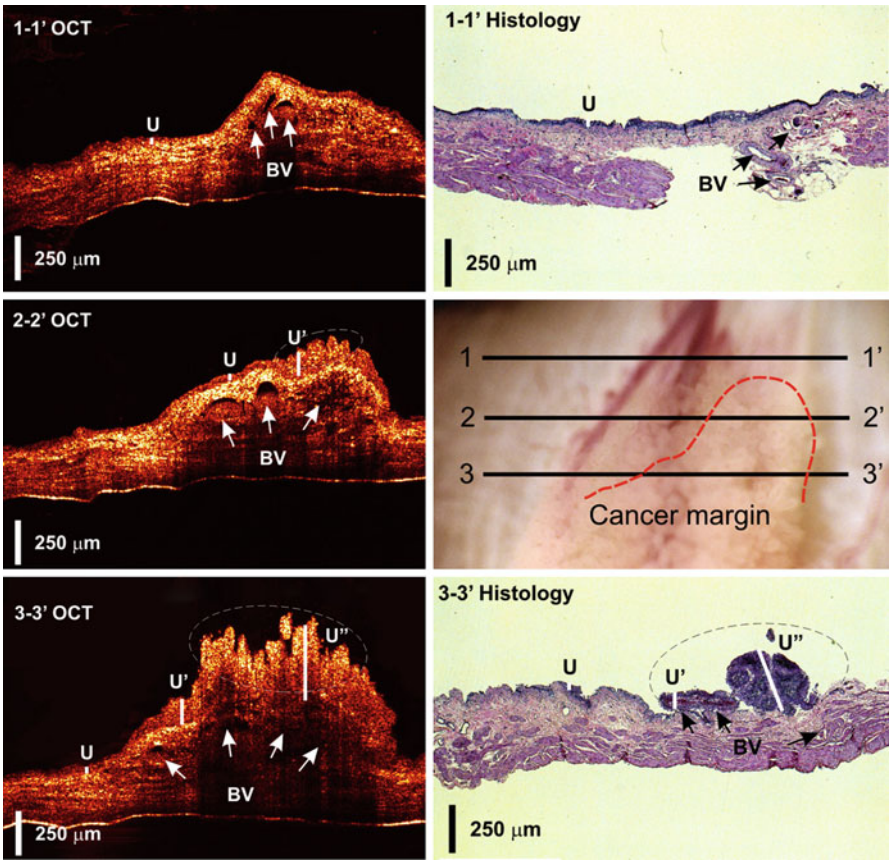

Fig. 78.8 A papillary TCC imaged by OCT and histology. Panels (1–1′) to (3–3′) were OCT sections indicated in the surface image, which covered the transition of morphological changes from "normal" to cancerous bladder areas. Corresponding histological evaluations are presented for 1–1′ and 3–3′ sections. BV: blood vessels (indicated by *arrows*); U, U′: normal and cancerous urothelia, respectively. *White dash-circled* areas: TCCs with drastically increased backscattering. *Red-dashed line*: precise TCC margin. The results demonstrate the potential of OCT for providing accurate precise bladder cancer margins

78.4 In Vivo Clinical Diagnosis

After successful ex vivo validation and in vivo feasibility studies, human studies were initiated in 2005 to examine the utility and potential limitations of COCT on patients suspected of TCC and scheduled to undergo operating-room (OR) cystoscopy. Patient enrollment criteria were those scheduled for transurethral biopsy or resection of bladder tumors. Figure 78.4 shows how MEMS COCT was integrated with conventional WLI for OR diagnosis of bladder tumor (clinical validation). For example, Fig. 78.11 compares the results of WLI,

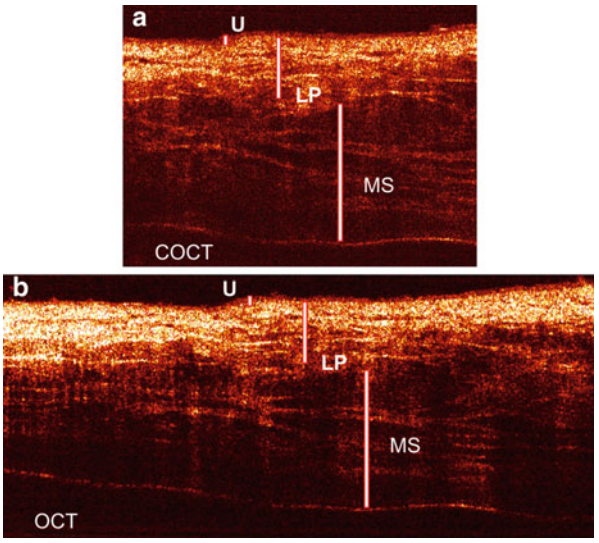

Fig. 78.9 Fresh porcine bladder imaged by COCT (**a**) and benchtop OCT (**b**). Except a slight decrease in SNR in COCT, both clearly delineate bladder morphology from urothelium *U* to muscularis *MS* [46]

COCT, and histology of three OR cases [52]. Panel a is a typical normal human bladder in vivo, which resembles porcine bladder in Fig. 78.9 in that bladder layers such as U, LP, and M were well delineated by COCT and correlated with histology. Panel b and panel c are two typical nonpapillary TCCs, in which lesion b exhibited low urothelial μ_b whereas lesion c exhibited high urothelial μ_b. Interestingly, our clinical data (based on 150 cases) indicated that unlike rat TCC model in Figs. 78.8 and 78.10, most human TCC cases (76 %) exhibited no significant μ_b enhancement; thus COCT diagnosis of TCC solely based on enhanced μ_b is not suitable for human uses. Histomorphometric analyses revealed that TCC c was composed of small but denser nuclei (similar to rat MNU model) which increased μ_b, whereas TCC b was composed of enlarged nuclei (similar to SV40-T CIS model in Fig. 78.15) resulting in minor or no μ_b increase.

On the other hand, it was found that human TCC exhibited increased μ_b heterogeneity which likely resulted from increased architectural variation, e.g., random excessive growth or loss of polarity caused by carcinogenesis. For instance, the COCT signals (black curves) from yellow lines in normal U (a) and in TCC (b) were plotted collaterally with the results (red curves) after speckle reduction, showing that the μ_b heterogeneity as presented by standard deviation were $\sigma = 0.303$ in TCC vs. $\sigma = 0.173$ in normal urothelium, namely, increased 75 %. As a result, the diagnostic criteria of TCC were modified from evaluating enhanced urothelial μ_b to its heterogeneity σ. This approach has been proven effective in the later clinical validation studies. In addition, it has been found that a large FOV is crucial to in vivo image evaluation of urothelial heterogeneity; in this respect, MEMS-based COCT offers unique advantages owing to its large FOV (4.8×2.4 mm^2) and high image fidelity (e.g., SNR) (Fig. 78.12).

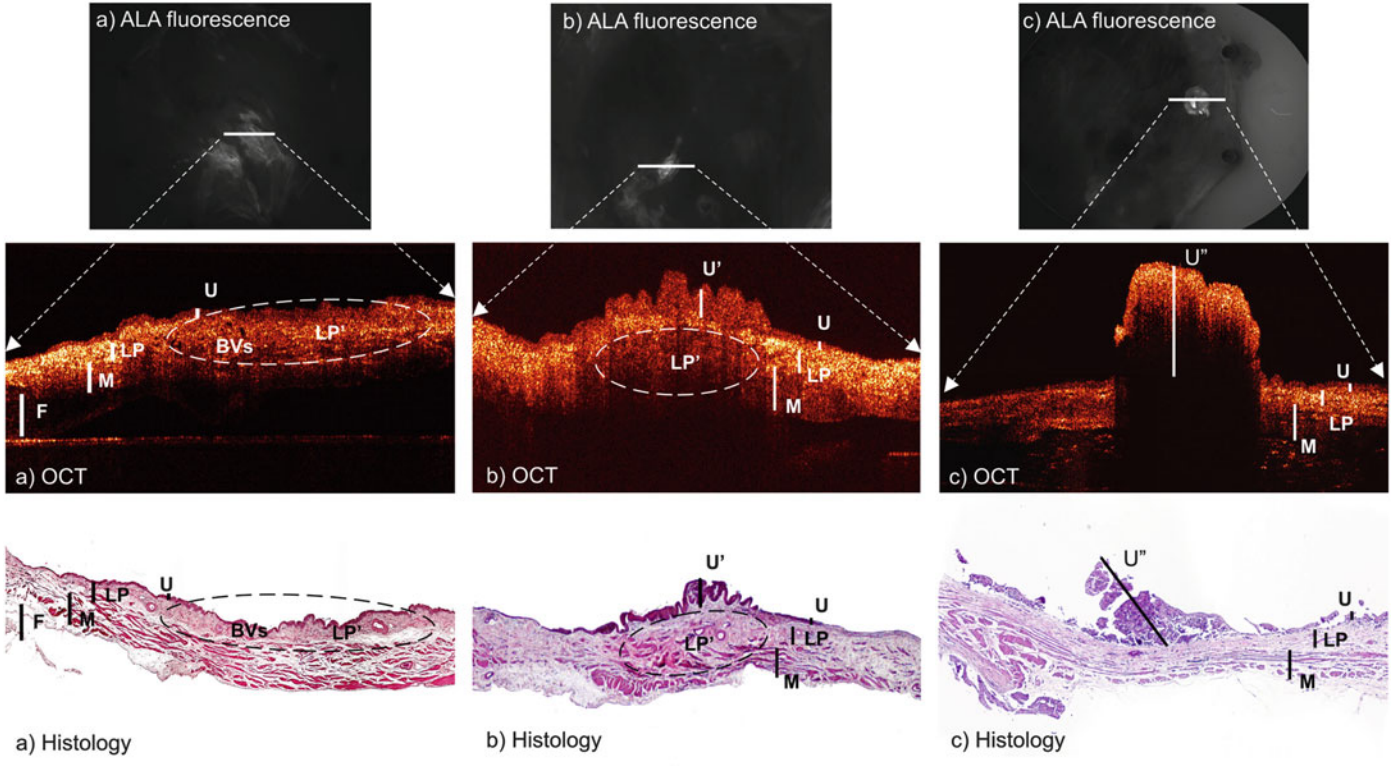

Fig. 78.10 5ALA fluorescence (ϕ30 mm), COCT (4.9 × 2.4 mm^2), and histology of three rat bladders. *U, U′, U″* normal, hyperplastic, neoplastic urothelia, *LP* lamina propria, *M* muscularis, *LP'* inflammatory lesion, *BVs* vasodilatation. Fluorescence detected all three lesions "+" (either benign or malignant), but COCT could differentiate them as (**a**) "−" minor edema (*LP'*), (**b**) "−" hyperplasia (*U′*) with edema (*LP'*), and (**c**) "+" TCC (*U″, pTa*) [48]

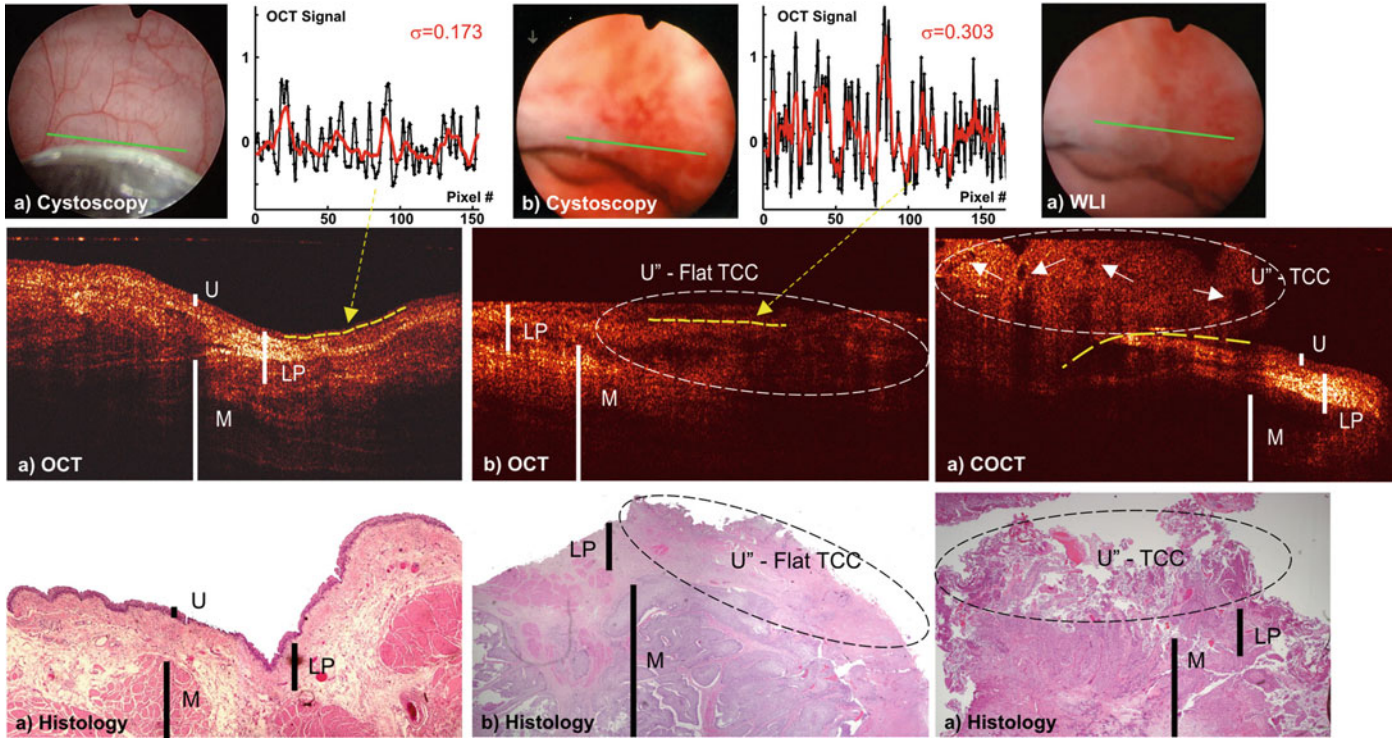

Fig. 78.11 In vivo human bladders imaged by WLI, COCT (4.5 × 2.2 mm^2), and histology. *U*, *U″* normal, nonpapillary TTCs, *N* necrosis. (**a**) normal bladder; (**b**, **c**) nonpapillary TCCs (pT2, LG) with μ_b low in (**b**) and high in (**c**). *Dashed yellow lines*: selected to analyze the original OCT signals (*black curves*) and the urothelial heterogeneity after speckle reduction (*red curves*). Apparently, the μ_b heterogeneity shown as the standard deviation ($\sigma = 0.303$) of *red curves* in TCC (**b**) is 75 % higher than that ($\sigma = 0.173$) in normal urothelium (a), i.e., $\sigma_{TCC}/\sigma_{NR} = 1.752$ [52]

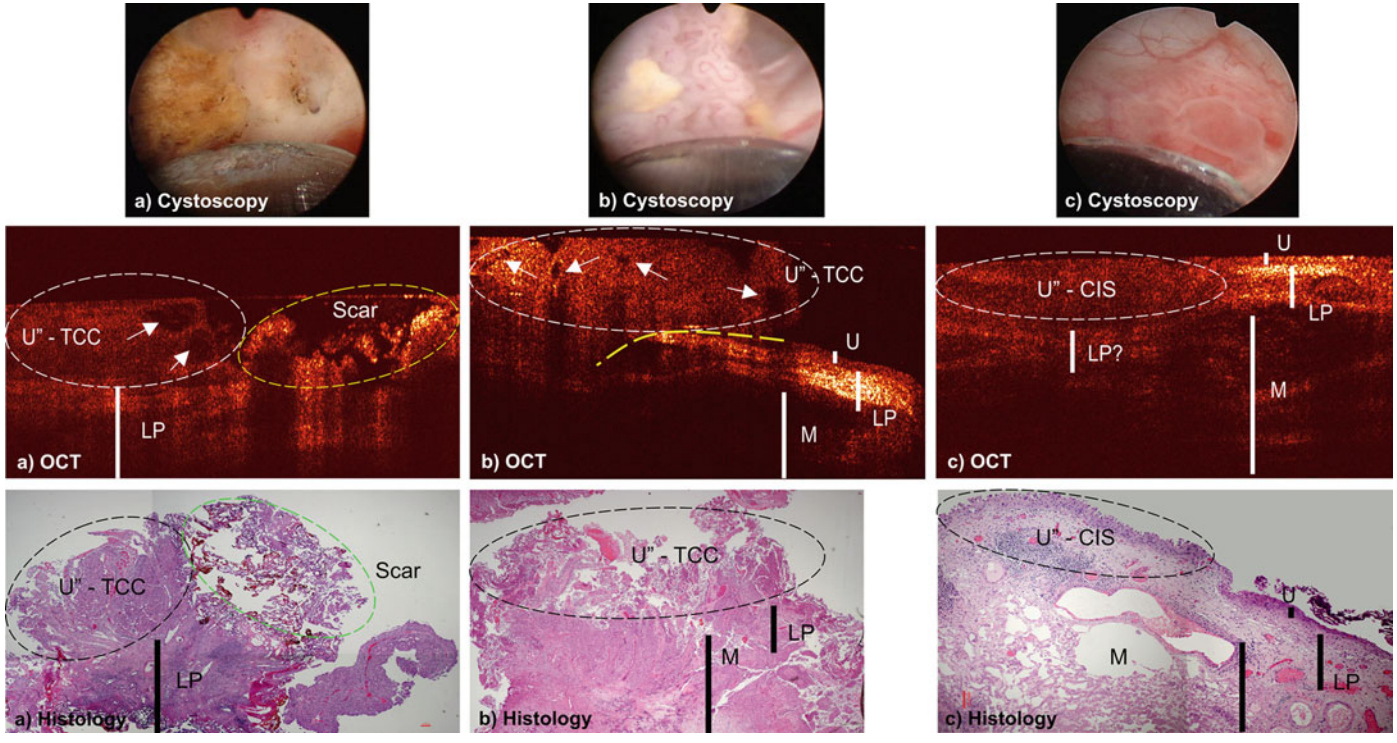

Fig. 78.12 In vivo human bladders imaged by surface image (ϕ30 mm), COCT (4.5 × 2.2 mm^2), and histology. U, U″: normal and papillary TTC or CIS. (**a**) Residual TCC post TURBT (LG), (**b**) papillary TCC (LG), (**c**) CIS. The *yellow line* marks the uncovered tumor margin. Scar, induced by previous TURBT, was differentiated from residual TCC as ultrahigh μ_b with rugged surface. Papillary TCC was identified by enhanced heterogeneity (e.g., honey nests) as pointed by *arrows*. COCT failed to grade CIS, thus unable to differentiate it from low-grade TCC

As TCCs are often associated with other bladder diseases such as inflammation, cystitis, and wounds induced by previous resections, COCT diagnosis of TCC based on morphological changes can be complicated. Figure 78.12 shows a group of three more OR cases to highlight the complexities of clinical diagnoses. For example, prior resections might dramatically alter the architectural "templates" of normal bladder (e.g., U, LP, and M), and detection of residual or recurrent tumor from scar or necrosis remains a major challenge in surveillance cystoscopy, which COCT may play an active role. As shown in panel a, WLI hardly detected any specific difference due to the changes by resections, whereas COCT diagnosed the left lesion as residual TCC based on its papillary features and the right lesion as scar based on its ultrahigh backscattering with very rugged surface topography of scar or necrotic lesions, which was later confirmed by histology. Panel b shows that WLI was able to roughly identify the boundary of papillary TCC, whereas COCT owing to its depth resolution could see through large papillary TCC to precisely locate the lateral cancer margin (dashed yellow line). It is noteworthy that due to reduced image depth within cancerous lesions, staging of TCC by COCT was generally limited to T0, Ta, and T1 without substantive outgrowth. Panel c exemplifies the diagnosis of CIS, i.e., a high-grade, aggressive, and lethal TCC. As the lesion was flat and nonspecific except slightly reddish like an inflammatory lesion under WLI, random biopsies were taken for a conclusive diagnosis. COCT was able to diagnose the lesion as a flat TCC based on enhanced urothelial μ_b heterogeneity with missing U-LP junction. Here, the large FOV was crucial, because it allowed COCT to scan across the transition to adjacent normal bladder to assure that the dashed area was cancerous urothelium. The diagnosis of CIS was confirmed by histology, but COCT was unable to stage the tumor (e.g., low-grade LG or high-grade HG). In his respect, subcellular imaging could provide more accurate diagnosis/grading.

Clinical studies suggest that incomplete transurethral resection (TUR) of bladder tumor may lead to high recurrence rates in current bladder cancer management [12, 13]. Because of large FOV (4.8×2.4 mm^2) of MEMS COCT, multiple COCT scans (e.g., center plus eight edges) on each lesion could be performed to accurately landmark the tumor margin and then overlapped on the surface image to guide TUR. In vivo results in Fig. 78.13 demonstrate the efficacy of COCT for providing accurate tumor margin. Depending on the tumor size, 4–12 scans could provide sufficient coverage of the tumor contour as highlighted by the dark dashed line. Critical importance of this function is to accurately highlight the boundary of a flat TCC or an invasive TCC with coexisting CIS.

Results of clinical statistics based on 176 OR cases (148 patients) are summarized in Table 78.1. Compared with the patient population of office cystoscopy, the OR cases presented here tend to contain more advanced cancers and fall short of control cases, thus resulting in underestimated diagnostic specificity. Meanwhile, the OR cases may likely include more patients with complicated symptoms, e.g., referred due to inconclusive office cystoscopy or surveillance cystoscopy.

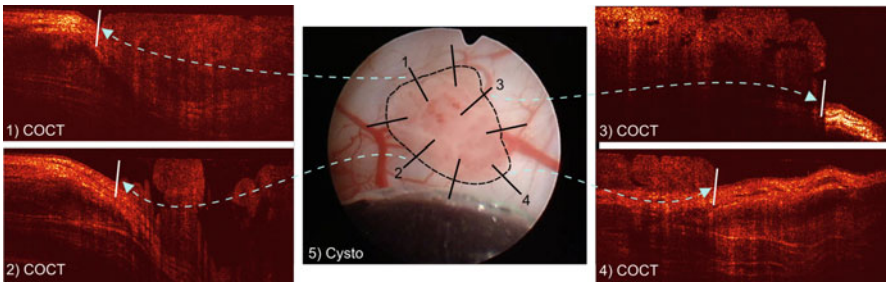

Fig. 78.13 In vivo COCT to landmark the boundary of human TCC (pT1) for accurate image guidance of TUR. A total of eight more COCT scans were performed to locate TCC boundary (*dash line*) of a ϕ13 mm TCC where the *solid dark lines* marked the position of each COCT scan and the *white lines* in each scan were the tumor margins. All eight COCT scans were completed in approximately 98 s by using spectral-domain COCT and then overlapped on the surface image

Table 78.1 Diagnostic sensitivities and specificities of TCC calculated on a per case basis

Methods		OCT		Cyst		Cyto		p-values		
Tumors		n/N	%	n/N	%	n/N	%	OCT : Cyst	OCT : Cyto	Cyst : Cyto
CIS (pTis)		4/5	80	0/5	0	2/5	40	**0.048**	0.524	0.444
pTa-pT1	LG	31/38	81.2	31/38	81.2	5/29	17.2	1.000	0.0001	0.0001
	HG	16/16	100	11/16	68.8	4/9	44.4	0.043	0.002	0.397
Superficial (<pT2)		51/59[a]	86.4	42/59	71.2	11/43	25.6	**0.043**	0.00001	0.00001
≥pT2		23/23	100	20/23	87.0	13/17	76.5	0.233	0.026	0.432
Sensitivity (SN)		74/82	**90.3**	62/82	75.6	24/60	40.0	**0.013**	0.0001	0.0001
Specificity (SP)		78/94	**83.0**	66/94	70.2	67/71	94.4	**0.039**	0.026	0.0001

Cyst: cystoscopy, *Cyto*: cytology, *N*: total number, *LG*: low grade, *Superficial*: all pTis, and pTa-pT1 tumors. Cytology data for 12 cases were unavailable

[a]Among eight false-negative cases, three were in the retro area (e.g., bladder neck) inaccessible by rigid COCT

The results in Table 1 demonstrate the efficacy of COCT to significantly enhance current clinical methods (e.g., cystoscopy, cytology) for bladder cancer diagnosis ($p < 0.05$). Compared with WLI, the diagnostic sensitivity (SN) and specificity (SP) were increased from $SN_{Cyst} = 75.6$ % and $SP_{Cyst} = 70.2$ % to $SN_{OCT} = 90.3$ % and $SP_{OCT} = 83$ %. If the three cases inaccessible by rigid COCT were excluded, the sensitivity could move up to $SN_{OCT} = 93.7$ %. The related positive and negative predicted values were improved from $PPV_{Cyst} = 68.8$ % and $NPV_{Cyst} = 76.6$ % to $PPV_{OCT} = 82.2$ % and $NPV_{OCT} = 90.7$ %. More detailed data analyses reveal that the major clinical impacts of COCT were on superficial TCC cases (<pT2),

Table 78.2 Diagnostic sensitivities and specificities of CIS calculated on a per lesion basis

Methods	OCT		Cyst		Cyto		p-values		
Tumors	n/N	%	n/N	%	n/N	%	OCT : Cyst	OCT : Cyto	Cyst : Cyto
CIS (pTis)	11/12	**91.7**	5/12	41.7	6/10	60.0	**0.027**	0.135	0.392

in particular, on the CIS cases [52]. Because of limited CIS enrollments and CIS often coexists with TCC, Table 78.1 is replotted on a per lesion basis in Table 78.2. The comparative data indicate that COCT as an optical biopsy tool allowed for significantly enhancing the diagnosis of CIS from $SN_{Cyst} = 41.7\ \%$ to $SN_{OCT} = 91.7\ \%$ ($p = 0.027$).

78.5 Discussion and Future Work

The outcome of our pilot clinical studies demonstrates the potential of MEMS COCT to significantly ($p < 0.05$) enhance current endoscopic procedures for the diagnosis of early superficial bladder cancers, especially CIS, and for detecting residual or recurrent tumors in surveillance cystoscopy following prior TUR and/or intravesical therapy. Based on the results of these OR cases, WLI was able to efficaciously guide COCT for locating suspicious lesions across bladder wall within 10 min; in other words, 5ALA fluorescence-guided COCT, although potentially more effective, may not be absolutely necessary for OR diagnosis of TCC with MEMS COCT. Nevertheless, a number of other limitations and technical issues have been noted, some of which are addressable but some of which are determined by the physical limitations of OCT technology and may need to combine other imaging approaches for viable solutions.

78.5.1 Quantitative Diagnosis of CIS by Subcellular OCT

Although it has been found that the majority of bladder cancers encountered in our clinical studies could be instantaneously diagnosed by direct visual identification of COCT images/movies, image identifications of some lesions (e.g., CIS or residual TCC) were not so straightforward, especially for physicians without OCT training; therefore, approaches to enable more quantitative diagnosis may be desirable for future clinical adoption of COCT.

Apparently, direct measures of nuclear size increase (i.e., NC ratio increase) of urothelial cells will be important for diagnosis of bladder CIS. In this respect, subcellular imaging capability is required, for instance, by subcellular OCT. Although ultrahigh-resolution OCT (μOCT) has been reported to provide subcellular images of relatively larger thus less scattering cells such as mesenchymal cells in African frog tadpole and animal adipocytes [38, 39], μOCT (not optical coherence

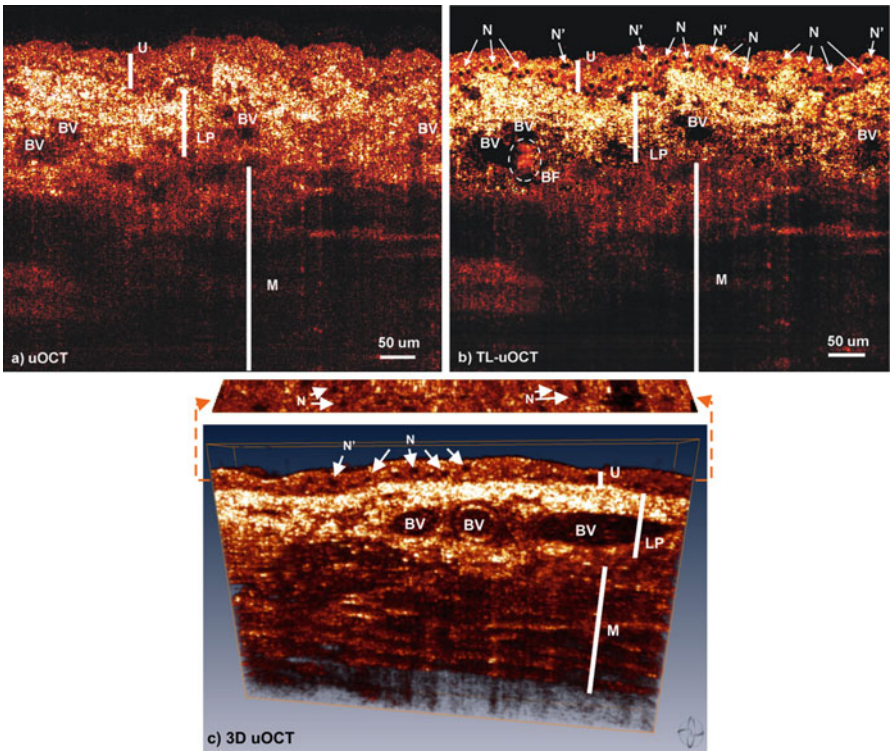

Fig. 78.14 TL-μOCT images of a fresh living normal mouse bladder. (**a**) μOCT (snap shoot) without subcellular details; (**b**) TL-μOCT that uncovers subcellular details; (**c**) 3D TL-μOCT to enable 3D subcellular imaging. A compact Ti:Al_2O_3 laser was used to provide axial resolution of $\Delta z \leq 1.8$ μm and a commercial low-NA achromat (f10 mm/0.25 NA) was used to provide $\Lambda \approx 2.8$ μm lateral resolution [54]

microscopy or OCM primarily by confocal gating rather than coherence gating) of highly scattering mammalian cells such as epithelial cells is hindered by the overwhelming speckle noise and multiple scattering. To solve the problem, we developed time-lapse μOCT (TL-μOCT) which successfully uncovered subcellular details of urothelial cells [53]. TL-μOCT is based on time-lapse averaging to scramble the phase noise of local multiple scattering from intracellular micro-organelles (contributing more to backscattering than nucleus that favors forward scattering) by taking advantage of their micro motion. This method only works for live urothelial cells (because of insufficient micro motion in dead cells or tissue) and the optimal time lapse was 0.7-0.1 s depending on the physiological condition of bladder. Figure 78.14 shows that TL-μOCT was able to uncover subcellular details (e.g., nuclei) of urothelium in living mouse bladder. Importantly, as TL-μOCT only uses a low-NA commercial achromat (f10 mm/NA0.25) to enable subcellular

imaging of urothelium (on focal plane) and architectural imaging of the underlying bladder wall (e.g., LP, M) at up to 700 μm of depths without focal tracking, this technique may be uniquely suitable for endoscopic in vivo optical biopsy to diagnose and grade flat TCC (e.g., CIS) [54].

To validate the utility of TL-μOCT for bladder cancer diagnosis and grading, animal carcinogenesis study was performed and the results are presented in Fig. 78.15. Surprisingly, panel a) shows that the nuclear size ($N \approx 6.7 \pm 1.1\mu m$, $m = 6$) of normal mouse bladder measured by TL-μOCT closely matched the histological counterpart ($N \approx 6.0 \pm 0.8\mu m$, $m = 6$). More interestingly, panel b and panel c further demonstrated the resolution of TL-μOCT to track nuclear enlargement in bladder cancer cells. Apparently, urothelial heterogeneity increases in both lesions reflecting the excessive random growing nature of carcinogenesis, which is consistent with clinical COCT imaging findings. For RAS model b, the measured nuclear size $N' \approx 12.3 \pm 1.6\mu m$ ($m = 10$) measured by TL-μOCT matched $N' \approx 11.4 \pm 1.5\mu m$ ($m = 10$) by histology (LG). For SV-40T model c, $N'' \approx 13.4 \pm 1.3\mu m$ ($m = 10$) measured by TL-μOCT well correlated with $N'' \approx 12.9 \pm 0.9\mu m$($m = 10$) by histology (HG). These results clearly show the potential of TL-μOCT for subcellular image diagnosis and grading of TCC, which is crucial to clinical diagnosis of CIS (high-grade flat TCC). Because of low-NA optics needed for TL-μOCT, this method can be translated into an endoscopic OCT catheter for in vivo diagnosis, and it allows for extended depth of field (e.g., >100 μm for subcellular resolution and >700 μm for OCT imaging) without the need for focal tracking.

78.5.2 Quantitative Diagnosis of CIS by 3D OCT

Although the results presented in Figs. 78.14 and 78.15 demonstrate the capability of TL-μOCT for subcellular image diagnosis and grading of CIS, this technique employs high-cost ultrafast laser which may limit its clinical adoption unless high-power ultra-broadband LED sources will be available in the future. An alternative method for quantitative CIS diagnosis has been developed in our lab by employing 3D OCT.

It is shown in Fig. 78.11 that urothelial heterogeneity (e.g., standard deviation σ of urothelial backscattering μ_b) is increased in TCC and thus used for TCC diagnosis. Mathematically, spatial averaging of μ_b is needed to effectively minimize speckle noise to evaluate the embedded architectural heterogeneity σ. This usually does not pose a problem for 2D OCT by averaging μ_b along the cross section (z-x plane) except for some CIS lesions whose urothelia are too thin (e.g., ~100 μm or even less) to implement effective μ_b averaging for separation between random speckle artifacts and structural heterogeneity (σ). To tackle the challenge, 3D OCT was proposed to enable effective μ_b averaging and thus speckle noise reduction, and transgenic mouse CIS model (SV-40 T) was employed for validation studies. Figure 78.16 shows the results that the subtle textural changes of urothelial

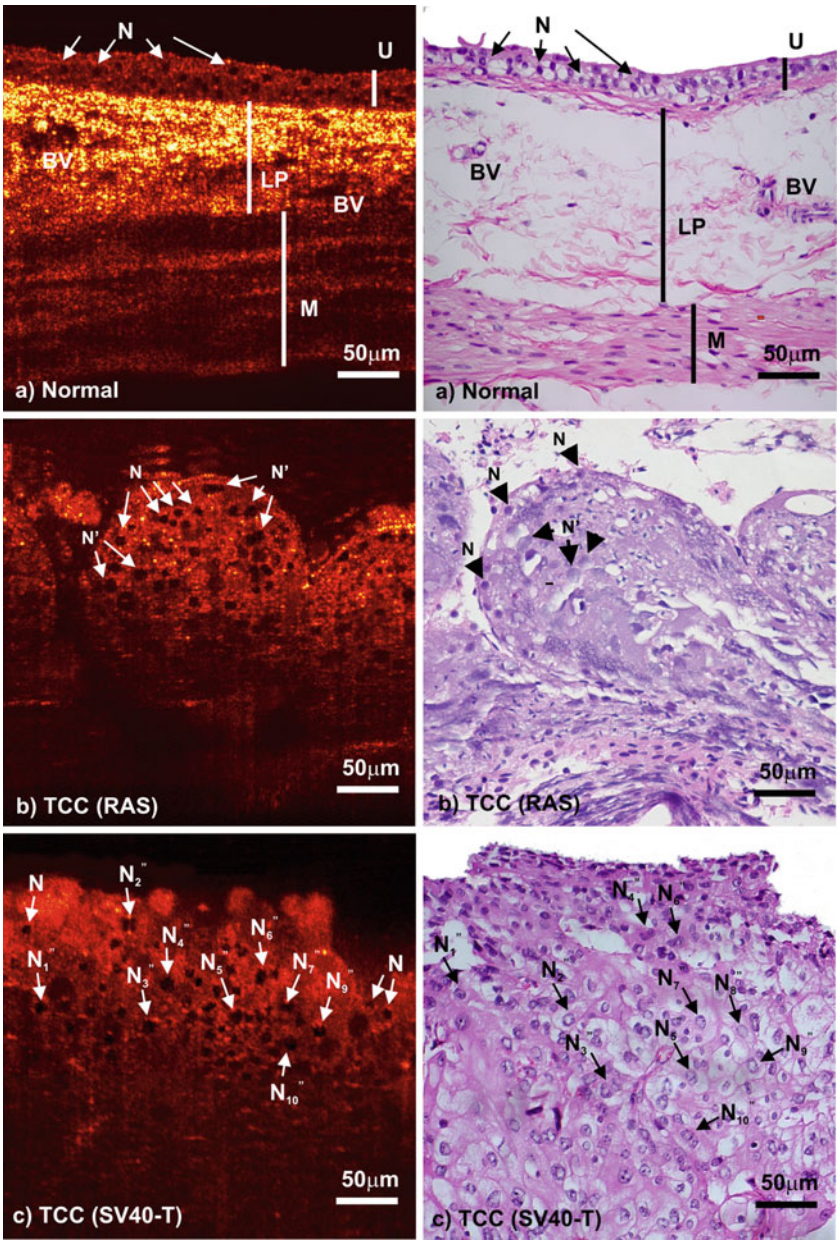

Fig. 78.15 Subcellular images of fresh living mouse bladder with TL-μOCT (time lapse: $\tau \approx 0.7$ s with four-frame average). (**a**) Normal bladder with nuclear size measured by μOCT/histology, N = 6.7 ± 1.1μm/N = 6.0 ± 0.8μm; (**b**) TCC (RAS, LG), N″ = 13.4 ± 1.3μm/N″ = 12.9 ± 0.9μm; (**c**) TCC (SV40-T, HG), N″ = 13.4 ± 1.3μm/N″ = 12.9 ± 0.9μm (based on $N''_i = 1-10$). *U* urothelium, *LP* lamina propria, *M* muscularis, *BV* blood vessel, *N, N', N''* nuclear sizes of normal urothelium, low-grade and high-grade TCCs [53]

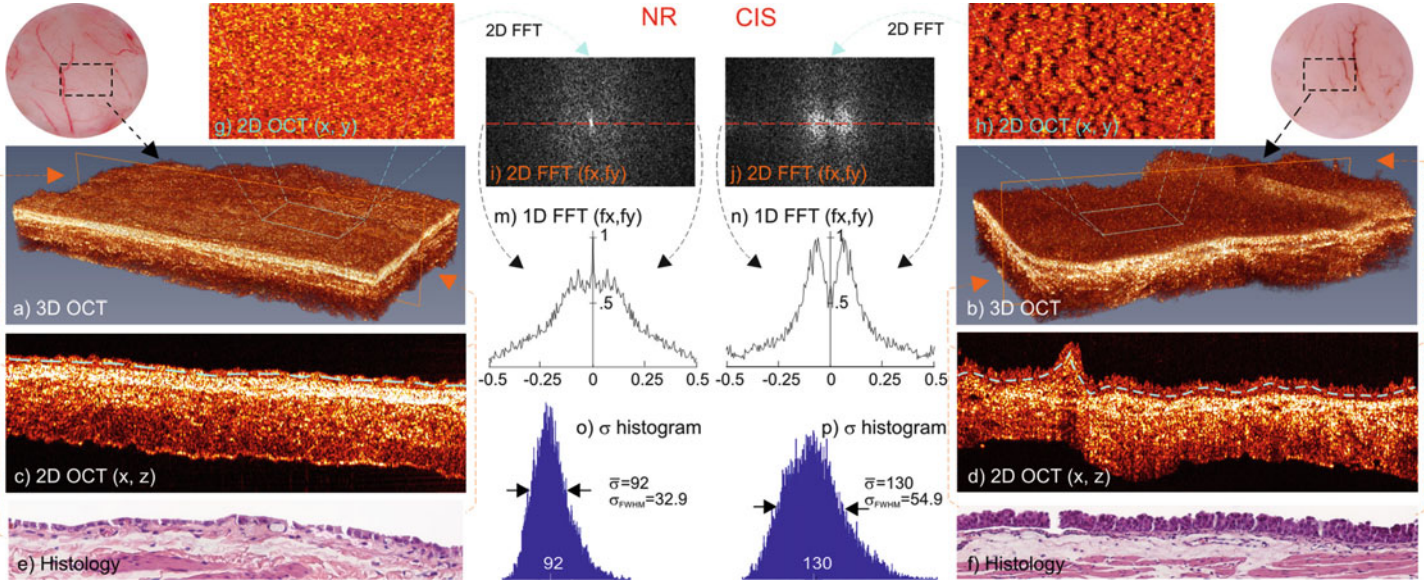

Fig. 78.16 En face standard deviation σ(x,y) of 3D COCT images of mouse bladders. Image size (**g**, **h**): 100 × 200 pixels. σ(x, y) was acquired by first segmenting the bladder surface, averaging first 5 pixels axially, and calculating standard deviation. (*Left*) normal urothelium (*NR*); (*Right*) early CIS (SV-40T) invisible by surface image and not differentiable by 2D OCT. CIS can be separated from NR by their texture difference. Increase in σ and broadening of Δσ-histogram (*o*, *p*) as well as those of 2D/1D FFT (*i*, *j*; *m*, *n*) in CIS reflect urothelial heterogeneity, i.e., 130/92 = 47 % increase in CIS. Without quantitative analysis (FFT or histogram), visual difference of enface OCT (**g**, **h**) btw NR and CIS can be observed [55]

heterogeneity induced by CIS can be readily differentiated by our new 3D OCT algorithm [55]. At such early "stage" of CIS, even pathological diagnosis to differentiate it from dysplasia was difficult. WLI completely failed to identify the lesions; 2D OCT was unable to predict or affirm the diagnosis except identifying a minor urothelial thickening; however, 3D OCT with image processing (e.g., 2D FFT and σ histogram) clearly differentiated it as CIS as a result of more effective 3D speckle reduction to dramatically improve pattern recognition and allow for accurate quantitative analysis. Both 2D FFT and σ histogram showed urothelial heterogeneity (e.g., 47 % increase) in CIS induced by carcinogenesis [56]. As the area needed for en face urothelial averaging is small (e.g., 100 pixels or 200 μm along y-axis), endoscopic adoption can be easily implemented by employing a 2D MEMS mirror for rigid 3D COCT or a rotary fiber probe with a push-pull actuator for flexible 3D COCT developments.

78.5.3 Improving TCC Staging by Combining High-Frequency Ultrasound

In addition to noninvasive early diagnosis (preferably grading) of bladder cancer, staging its invasion into the underlying bladder layers especially into the muscularis (i.e., pT2) is crucial to the management of bladder cancer patients. It is known that the effective penetration depth of OCT imaging (e.g., at $\lambda = 1.3$ μm) is ultimately limited by multiple scattering of biological tissue, which can range from 0.5 to 3 mm depending on tissue type. For urinary bladder, the image depth of OCT is around 1.5–2 mm, which usually allows for imaging the bladder architecture down to the upper part of the muscularis layer (i.e., upper MS). However, large papillary TCCs that outgrow >2 mm over the bladder surface are common clinical cases. Additionally, because of denser tumor vasculature and increased structural heterogeneity, excessive light attenuation in TCC has been common findings, which in turn reduces the effective image depth of OCT in tumor areas. It has been found in our clinical studies that COCT is not suitable for staging large papillary TCC (≥pT1).

To overcome this physical limitation, other medical imaging modalities have been explored, among which high-frequency ultrasound (HFUS) has been found to compliment to OCT to improve TCC staging capability. Interestingly, based on the results of our recent rat TCC validation studies (using AY27 model), that a dual-modality imaging modality combining OCT and HFUS can complement each other: COCT was able to diagnose TCC that HFUS failed due to its limited resolution, whereas HFUS was able to stage TCC to pT2b (muscle invasion) that COCT failed due to its limited imaging depth. Figure 78.17 exemplifies that HFUS mistakenly diagnosed two inflammatory lesions (upper panels) as TCCs which were corrected by OCT as benign lesions, whereas HFUS staged a large TCC (lower panels) as pT2b/T3 that OCT failed to stage due to insufficient imaging depth for solid large cancers like this. This result suggests that a dual-imaging cystoscopic approach that combines COCT and transurethral HFUS will substantially enhance

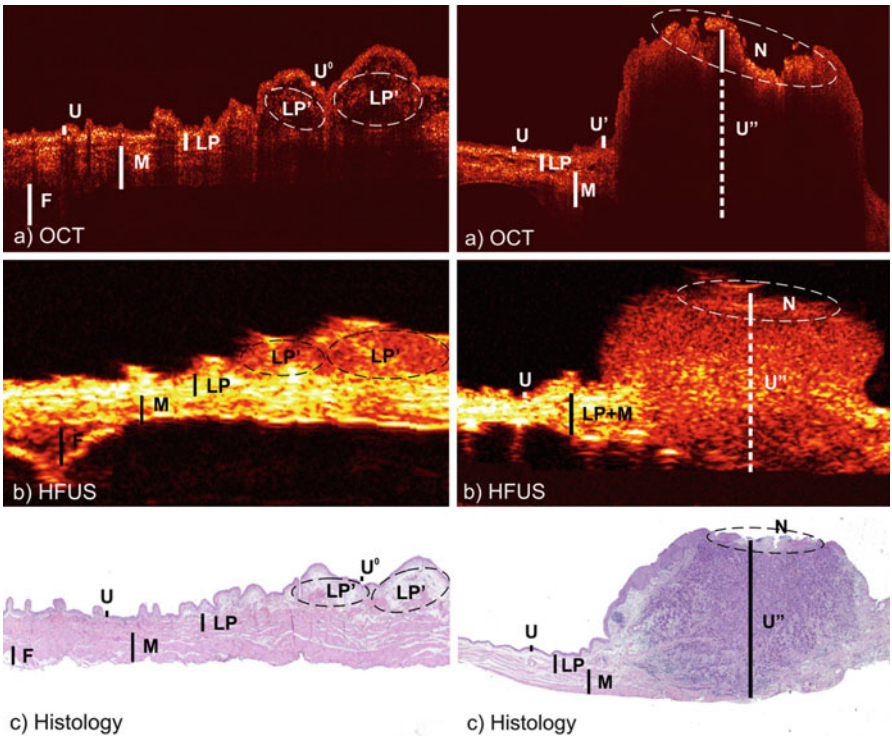

Fig. 78.17 Rat bladders imaged ex vivo by COCT, HFUS, and histology. Image size: 6×2.8 mm^2 (image fusion applied to COCT). (*Upper panels*) Two benign inflammatory lesions misdiagnosed as TCC by HFUS was corrected by COCT; (*Lower panel*) papillary TCC failed to be staged by COCT was determined by HFUS as T2b or T3 tumor. *U, U′, U″* normal urothelium, hyperplasia, TTC, *F* fatty layer, *LP'* inflammatory lesion, *N* necrosis [57]

the diagnosis and staging of bladder cancers. In this respect, studies have been reported that develop combined endoscopic OCT and ultrasound [58].

Acknowledgments Special thanks to the following collaborators who have made important contributions to the presented work: M. Zeidel, MD, and J. Lavelle, MD, in the University of Pittsburgh Medical Center participated in MNU-based rat TCC study; G. Fedder, PhD, in the ECE Department of Carnegie Mellon University and H. K. Xie, PhD, in the ECE Department of University of Florida participated in the MEM mirror development; X. R. Wu, MD, in the New York University Medical Center provided SV-40 T transgenic mouse model; and W. Waltzer, MD, R. Bhalla, MD, F. Darras, MD, Z. Frischer, J. Kim, MD, J. X. Liu, MD, K. Schroyer, MD, and C. W. Du, PhD, in the Stony Brook University Medical Center participated in the clinical studies. T. Q. Xie, PhD, Z. G. Wang, Z. J. Yuan, Z. Wu, PhD, B. Chen, PhD, and H. G., Ren PhD in the Department of Biomedical Engineering of Stony Brook University participated in the technological development and preclinical validation studies. This work was supported in part by the Whitaker Foundation, the National Institutes of Health (R01DK059265, RC1DA028534, 1R21DA032228, 1R01DA029718), and institutional funds (e.g., Fusion Award).

References

1. American Cancer Society, Cancer Facts and Figures (2014), pp. 4–6
2. American Cancer Society, Cancer Facts and Figures (2014), p. 22
3. G.D. Steinberg, B.F. Schwartz (ed.), *Bladder Cancer Workup* (2002), http://emedicine.medscape.com/article/1953022-overview
4. C.M. Sturgeon, M.J. Duffy, B.R. Hofmann, R. Lamerz, H.A. Fritsche, K. Gaarenstroom, J. Bonfrer, T.H. Ecke, H.B. Grossman, P. Hayes, R.-T. Hoffmann, S.P. Lerner, F. Löhe, J. Louhimo, I. Sawczuk, K. Taketa, E.P. Diamandis, NACB Laboratory Medicine Practice Guidelines for Use of Tumor Markers in Liver, Bladder, Cervical, and Gastric Cancers, Clinical Chemistry **56**(6), e1–e48 (2010)
5. S.F. Shariat, J.A. Karam, Y. Lotan, P.I. Karakiewizc, Critical evaluation of urinary markers for bladder cancer detection and monitoring. Rev. Urol. **10**(2), 120–135 (2008)
6. E.M. Messing, W. Catalona, Urothelial tumors of the urinary tract, in *Campbell's Urology*, ed. by P.C. Walsh, A. Retik, E.D. Vaughan, A.J. Wein, 7th edn. (W. B. Saunders Company, Philadelphia, 1998), pp. 2327–2389
7. J. Flamm, S. Dona, The significance of bladder quadrant biopsies in patients with primary superficial bladder carcinoma. Eur. Urol. **16**, 81–85 (1989)
8. M. Kriegmair, D. Zaak, K.-H. Rothenberger, J. Rassweiler, D. Jocham, F. Eisenberger, R. Tauber, A. Stenzl, A. Hofstetter, Transurethral resection for bladder cancer using 5-aminolevulinic acid induced fluorescence endoscopy versus white light endoscopy. Urology **168**, 475–478 (2002)
9. M.F. Sarosdy, P. Schellhammer, G. Bokinsky, P. Kahn, R. Chao, L. Yore, J. Zadra, D. Burzon, G. Osher, J.A. Bridge, S. Anderson, S.L. Johansson, M.L. Lieber, M. Soloway, Clinical evaluation of a multi-target fluorescent in situ hybridization assay for detection of bladder cancer. J. Urol. **168**, 1950 (2002)
10. H. Leyh, M. Marberger, P. Conort, C. Sternberg, V. Pansadoro, F. Pagano, P. Bassi, L. Boccon-Gibod, V. Ravery, U. Treiber, L. Ishak, Comparison of the BTA stat test with voided urine cytology and bladder wash cytology in the diagnosis and monitoring of bladder cancer. Eur. Urol. **35**, 52–56 (1999)
11. D. Pode, D. Golijanin, Y. Sherman, P. Lebensart, A. Shapiro, Immunostaining of Lewis X in cells from voided urine, cytopathology and ultrasound for noninvasive detection of bladder tumors. J. Urol. **159**, 389–393 (1998)
12. J. Desgrippes, D. Izadifar, D. Beurton et al., Diagnosis and prediction of recurrence and progression in superficial bladder cancers with DNA image cytometry and urinary cytology. BJU Int. **85**, 434–436 (2002)
13. P. Mariappan, G. Smith, A.D. Lamb et al., Pattern of recurrence changes in noninvasive bladder tumors observed during 2 decades. J. Urol. **177**, 867 (2007)
14. C.D. Dominicis, M. Liberti, G. Perugia, C.D. Nunzio, F. Sciobica, A. Zuccalà, A. Sarkozy, F. Lori, Role of 5-aminolevulinic acid in the diagnosis and treatment of superficial bladder cancer: improvement in diagnostic sensitivity. Urology **59**, 1059–1062 (2001)
15. H.B. Grossman, L. Gomella, Y. Fradet, A. Morales, J. Presti, C. Ritenour, U. Nseyo, M.J. Droller, A phase III, multicenter comparison of hexaminolevulinate fluorescence cystoscopy and white light cystoscopy for the detection of superficial papillary lesions in patients with bladder cancer. J. Urol. **178**, 62–67 (2007)
16. A.A. Kamuhabwa, T. Roskams, L. Baert, P.A. De Witte, Microscopic quantification of hypercin fluorescence in an orthotopic rat bladder tumor model after intravesical instillation. Int. J. Oncol. **22**, 933–937 (2004)
17. T. O'Brien, K. Thomas, Bladder cancer: photodynamic diagnosis can improve surgical outcome. Nat. Rev. Urol. **7**, 598–599 (2010)
18. R.T. Bryan, L.J. Billingham, D.M. Wallace, Narrow-band imaging flexible cystoscopy in the detection of recurrent urothelial cancer of the bladder. BJU Int. **101**, 702–706 (2007)

19. H.W. Herr, S.M. Donat, A comparison of white-light cystoscopy and narrow-band imaging cystoscopy to detect bladder tumour recurrences. BJU Int. **102**, 1111–1114 (2008)
20. M.-A. D'Hallewin, S.E. Khatib, A. Leroux, L. Bezdetnaya, F. Guillemin, Endoscopic confocal fluorescence microscopy of normal and tumor bearing rat bladder. J. Urol. **174**, 105–109 (2005)
21. R.O. Draga, M.C. Grimbergen, P.L. Vijverberg, C.F. van Swol, T.G. Jonges, J.A. Kummer, J.L. Bosch, In vivo bladder cancer diagnosis by high-volume Raman spectroscopy. Anal. Chem. **82**, 5993–5999 (2010)
22. E.C. Cauberg, D.M. de Bruin, D.J. Faber, T.G. van Leeuwen, J.J. de la Rosette, T.M. de Reijke, A new generation of optical diagnostics for bladder cancer: technology, diagnostic accuracy, and future applications. Eur. Urol. **56**, 287–297 (2009)
23. Y. Pan, J.P. Lavelle, S. Meyers, G. Pirtskhalaishvili, M.L. Zeidel, D.L. Frakas, Detection of tumorigenesis in rat bladders with OCT. Med. Phys. **28**, 2432–2440 (2001)
24. E.V. Zagaynova, O. Streltsova, N.D. Gladkova, L.B. Snopova, G.V. Gelikonov, F.I. Feldchtein, A.N. Morozov, In vivo optical coherence tomography feasibility for bladder disease. J. Urol. **167**, 1492–1496 (2002)
25. D. Huang, E.A. Swanson, C.P. Lin, J.S. Schuman, W.G. Stinson, W. Chang, M.R. Hee, T. Flotte, K. Gregory, C.A. Puliafito, J.G. Fujimoto, Optical coherence tomography. Science **254**, 1178–1181 (1991)
26. B.E. Bouma, G.J. Tearney (eds.), *Handbook of Optical Coherence Tomography* (Marcel Dekker, New York, 2002)
27. G.J. Tearney, M.E. Brezinski, B.E. Bouma, S.A. Boppart, C. Pitris, J.F. Southern, J.G. Fujimoto, In vivo endoscopic optical biopsy with optical coherence tomography. Science **276**, 2037–2039 (1997)
28. A.M. Sergeev, V.M. Gelikonov, G.V. Gelikonov, F.I. Feldchtein et al., In vivo endoscopic OCT imaging of precancer and cancer states of human mucosa. Opt. Express **1**, 432–440 (1997)
29. Y.T. Pan, H.K. Xie, G.K. Fedder, Endoscopic optical coherence tomography based on a microelectromechanical mirror. Opt. Lett. **26**, 1966–1968 (2001)
30. R.K. Wang, S.L. Jacques, Z. Ma, S. Hurst, S.R. Hanson, A. Gruber, Three dimensional optical angiography. Opt. Express **15**, 4083–4097 (2007)
31. B.J. Vakoc, R.M. Lanning, J.A. Tyrrell, T.P. Padera, L.A. Bartlett, T. Stylianopoulos et al., Three-dimensional microscopy of the tumor microenvironment in vivo using optical frequency domain imaging. Nat. Med. **15**, 1219–1223 (2009)
32. H. Ren, C. Du, Z. Yuan, K. Park, N.D. Volkow, Y. Pan, Cocaine-induced cortical microischemia in the rodent brain: clinical implications. Nat. MP **17**, 1017–1025 (2012)
33. J.F. de Boer, S. Srinivas, A. Malekafzali, Z.P. Chen, J.S. Nelson, Imaging thermally damaged tissue by polarization sensitive optical coherence tomography. Opt. Express **3**, 212–218 (1998)
34. E. Götzinger, M. Pircher, B. Baumann, C. Ahlers, W. Geitzenauer, U. Schmidt-Erfurth, C.K. Hitzenberger, Three-dimensional polarization sensitive OCT imaging and interactive display of the human retina. Opt. Express **17**, 4151–4165 (2009)
35. C. Xu, J. Ye, D.L. Marks, S.A. Boppart, Near-infrared dyes as contrast-enhancing agents for spectroscopic optical coherence tomography. Opt. Lett. **29**, 1647–1649 (2004)
36. J.F. de Boer, B. Cense, B. Park, M.C. Pierce, G.J. Tearney, B.E. Bouma, Improved signal-to-noise ratio in spectral-domain compared with time-domain optical coherence tomography. Opt. Lett. **28**, 2067–2069 (2003)
37. T. Klein, W. Wieser, C.M. Eigenwillig, B.R. Biedermann, R. Huber, Megahertz OCT for ultrawide-field retinal imaging with a 1050 nm Fourier domain mode-locked laser. Opt. Express **19**, 3044–3062 (2011)
38. S.A. Boppart, B.E. Bouma, C. Pitris, J.F. Southern, M.E. Brezinski, J.G. Fujimoto, In vivo cellular optical coherence tomography imaging. Nat. Med. **4**, 861–865 (1998)
39. W. Drexler, Ultrahigh-resolution optical coherence tomography. JBO **9**, 47–74 (2004)

40. T.Q. Xie, Z.G. Wang, Y.T. Pan, High-speed optical coherence tomography using fiber optic acousto-optic phase modulation. Opt. Express **11**, 3210–3219 (2003)
41. Z.G. Wang, Z.J. Yuan, H.Y. Wang, Y.T. Pan, Increasing the imaging depth of spectral-domain OCT by using interpixel shift technique. Opt. Express **14**, 7014–7023 (2006)
42. D. Daniltchenko, M. Sachs, E. Lankenau, F. Koenig, G. Huettmann, D. Schnorr, S. Al-Shukri, S. Loening, Optical coherence tomography of the urinary bladder: the potential of a high-resolution visual investigation technique for endoscopic diagnostics. Opt. Spectrosc. **10**, 40–45 (2006)
43. J. Tearney, S. Waxman, M. Shishkov, B.J. Vakoc, M.J. Suter, M.I. Freilich, A.E. Desjardins, W.Y. Oh, L.A. Bartlett, M. Rosenberg, B.E. Bouma, Three-dimensional coronary artery microscopy by intracoronary optical frequency domain imaging. JACC Cardiovasc. Imaging **1**, 752–761 (2008)
44. H.K. Xie, Y.T. Pan, G. Fedder, Endoscopic optical coherence tomographic imaging with a CMOS-MEMS micromirror. Phys. A **103**, 237–241 (2003)
45. T.Q. Xie, H.K. Xie, G.K. Fedder, Y.T. Pan, Endoscopic optical coherence tomography with a modified MEMS mirror. Elect. Lett. **39**, 1535–1536 (2003)
46. Z.G. Wang, C.S. Lee, W.C. Waltzer, J.X. Liu, H.K. Xie, Z.J. Yuan, Y.T. Pan, In vivo bladder imaging with MEMS-based endoscopic spectral domain optical coherence tomography. J. Biomed. Opt. **12**, 033703 1-9 (2007)
47. H.K. Xie, Y.T. Pan, G. Fedder, A CMOS-MEMS micromirror with large out-of-plane actuation. J. MEMS **12**(4), 450–457 (2003)
48. Z.G. Wang, D. Durand, M. Schoenberg, Y.T. Pan, Combined fluorescence imaging and optical coherence tomography for diagnosis of early bladder cancer in an animal model: a comparative study. J. Urol. **174**, 2376–2381 (2005)
49. T.T. Sun, X.R. Wu, Transgenic mouse models for human bladder cancer, US Patent 6323390
50. T. Xie, M.L. Zeidel, Y.T. Pan, Detection of tumorigenesis in urinary bladder with optical coherence tomography: optical characterization of morphological changes. Opt. Express **10**, 1431–1443 (2002)
51. Y.T. Pan, T.Q. Xie, C.W. Du, S. Bastacky, M.L. Zeidel, Enhancing early bladder cancer detection with fluorescence-guided endoscopic optical coherence tomography. Opt. Lett. **28**, 2485–2487 (2003)
52. H.G. Ren, W.C. Waltzer, J.L. Liu, F. Darras, D. Schulsinger, H. Adler, R. Bhalla, Z.J. Yuan, Y.T. Pan, Diagnosis of bladder cancer with MEMS-based cystoscopic optical coherence tomography. (Gold J.) Urology. **74**, 1351–1357 (2009)
53. Y.T. Pan, Z.L. Wu, Z.J. Yuan, Z.G. Wang, C.W. Du, Subcellular imaging of epithelium with time-lapse optical coherence tomography. JBO Lett. **12**(5), 1–3 (2007). 050504
54. Z.J. Yuan, B. Chen, H.G. Ren, Y.T. Pan, On the possibility of time-lapse ultrahigh-resolution optical coherence tomography for bladder cancer grading. JBO Lett. **15**(4), 1–3 (2009)
55. H.G. Ren, W.C. Waltzer, J.L. Liu, Y.T. Pan, Enhancing the detection of carcinoma in situ of the urinary bladder by three-dimensional optical coherence tomography. J. Urol. **184**, 1459–1506 (2010)
56. H.G. Ren, K. Park, R. Pan, W. Waltzer, K. Shroyer, Y.T. Pan, Early detection of carcinoma in situ of the bladder: a comparative study of white light cystoscopy, narrow band imaging, 5-ALA fluorescence cystoscopy and 3D optical coherence tomography. J. Urol. **187**, 1063–1070 (2012)
57. Z.J. Yuan, Z.G. Wang, Y.T. Pan, High-resolution imaging diagnosis and staging of bladder cancer: a comparison between optical coherence tomography and high-frequency ultrasound. JBO **13**, 1–10 (2008). 054007
58. J. Yin, X. Li, J. Jing, J. Li, D. Mukai, S. Mahon, A. Edris, K. Hoang, K. Shung, M. Brenner, J. Narula, Q. Zhou, Z.P. Chen, Novel combined miniature optical coherence tomography ultrasound probe for in vivo intravascular imaging. JBO Lett. **16**, 1–3 (2011). 060505

Optical Coherence Tomography in Kidney Transplantation

79

Peter M. Andrews, Jeremiah Wierwille, and Yu Chen

Keywords

Acute tubular necrosis • Doppler optical coherence tomography • Glomerulus • Kidney transplantation • Optical coherence tomography (OCT) • Renal blood flow • Renal blood flow

End-stage renal disease (ESRD) is associated with both high mortality rates and an enormous economic burden [1]. The preferred treatment option for ESRD that can extend patients' lives and improve their quality of life is kidney transplantation. However, organ shortages continue to pose a major problem in kidney transplantation. Most kidneys for transplantation come from heart-beating cadavers. Although non-heart-beating cadavers represent a potentially large pool of donor kidneys, these kidneys are not often used due to the unknown extent of damage to the renal tubules (i.e., acute tubular necrosis or "ATN") induced by ischemia (i.e., lack of blood flow). Also, ischemic insult suffered by kidneys awaiting transplantation frequently causes ATN that leads to varying degrees of delayed graft function (DGF) after transplantation. Finally, ATN represents a significant risk for eventual graft and patient survival [2, 3] and can be difficult to discern from rejection. In present clinical practice, there is no reliable real-time test to determine

P.M. Andrews (✉)
Department of Biochemistry, Molecular and Cellular Biology, Georgetown University Medical Center, Washington, DC, USA
e-mail: andrewsp@georgetown.edu

J. Wierwille
Fischell Department of Bioengineering, University of Maryland, College Park, MD, USA

Y. Chen
Department of Electrical Engineering and Computer Science and Research Laboratory of Electronics, Massachusetts Institute of Technology, Cambridge, MA, USA

Biomedical Optics and Imaging Laboratory, Fischell Department of Bioengineering, University of Maryland, College Park, MD, USA

© Springer International Publishing Switzerland 2015

W. Drexler, J.G. Fujimoto (eds.), *Optical Coherence Tomography*,
DOI 10.1007/978-3-319-06419-2_81

the viability of donor kidneys and whether or not donor kidneys might exhibit ATN. Therefore, there is a critical need for an objective and reliable real-time test to predict ATN to use these organs safely and utilize the donor pool optimally. In this review, we provided preliminary data indicating that OCT can be used to predict the post-transplant function of kidneys used in transplantation.

Previous studies by one of us (Andrews et al.) have shown that the noninvasive microscopic imaging of donor kidneys can be used to determine posttransplant renal function by analyzing the ATN suffered by superficial nephrons [4]. In the past, we have demonstrated that optical coherence tomography (OCT) can be used to image the status of superficial nephrons in a noninvasive fashion and in real time in normal living and insulted rodent kidneys [5, 6]. More recently, clinical trial studies have demonstrated the ability of OCT to image human donor kidneys both prior to and following their transplantation. This imaging was accomplished in a sterile, noninvasive fashion, providing real-time images of superficial renal tubules and glomeruli through the intact connective tissue renal capsule. In addition to evaluating the status of superficial nephrons, we demonstrated the ability of Doppler OCT (DOCT) to evaluate glomerular blood flow [7]. This chapter describes the rationale for imaging donor kidneys with OCT and the studies that have provided the background to support this rationale.

79.1 The Need for a Better Test to Predict Posttransplant Renal Outcome

More than half a million US residents have end-stage renal disease (ESRD), which is associated with high mortality rates (157.3 deaths per 1,000 patient years) and a huge economic burden (more than $30 billion per year) [1]. The treatment options for ESRD include dialysis and kidney transplantation. Transplantation is the preferred option because it promises to extend the patients' lives and also improve their quality of life. Currently, with over 77,500 patients annually waiting for kidney transplants, organ shortages pose a major problem in kidney transplantation. While the vast majority of kidneys used for transplantation are obtained from heart-beating cadavers, many kidneys available for transplant are not utilized because of their unknown status (i.e., from non-heart-beating cadavers, long storage times, etc.). Also, ischemic insult suffered by cadaver kidneys awaiting transplantation frequently causes acute tubular necrosis (ATN) leading to varying degrees of delayed graft function (DGF) after transplantation, which represents a significant risk for eventual graft and patient survival [3], and can be difficult to discern from rejection. The incidence of DGF is estimated to be 15–70 % [8]. Unfortunately, in present clinical practice, there is no reliable test to determine the viability of donor kidneys and whether or not donor kidneys might exhibit DGF. A timely biochemical analysis of kidneys has proven disappointing with no biochemical criteria proving accurate [9]. Therefore, there is a critical need for objective and reliable tests to predict posttransplant outcome to use organs safely and utilize the donor pool optimally.

79.2 Noninvasive Imaging to Predict Posttransplant Renal Outcome

Conventional light microscopy of excision kidney biopsies are not as useful to evaluate kidney pathology as noninvasive imaging procedures because of dramatic destructive artifacts to the kidney tubules associated with such biopsies [10]. In addition, unlike noninvasive imaging procedures, excision biopsies are destructive to kidneys, take time to analyze, and image only small segments of the kidney (i.e., cannot provide global imaging of numerous regions across the kidney surface). Previous studies by one of us (Andrews et al.) have shown that a noninvasive imaging technique termed tandem scanning confocal microscopy (TSCM) could be used to determine the degree of ATN by analyzing the superficial nephrons of living rabbit donor kidneys [4]. Using TSCM, Andrews et al. observed that the histopathological changes (e.g., ATN) of superficial proximal tubules of rabbit kidneys for transplant correlated closely with subsequent posttransplant renal function [11] (see Fig. 79.1). This is not surprising in that the status of superficial proximal convoluted tubules is indicative of the status of proximal convoluted tubules throughout the entire kidney cortex. Other investigators have also used near-infrared confocal microscopy [12] and multiphoton microscopy [13–15] to demonstrate the ability to perform noninvasive imaging of kidney structure and function in animal models. However, the maximum penetration depth associated with these microscopy procedures is limited (about 100 μm for TSCM), which makes it difficult to impossible to nondestructively image the human kidney using the foregoing noninvasive imaging microscopic techniques, especially if it is surrounded by an intact human renal capsule. Indeed, in a previous clinical trial, we found that the limited penetrating ability of TSCM precluded us from imaging human donor kidneys even when an attempt was made to remove the renal capsule [unpublished observations]. Also, conventional bulky systems TSCM are awkward in orientating the kidney specimens and especially difficult when attempting to image the kidney in situ.

79.3 Advantages of Optical Coherence Tomography (OCT) as a Noninvasive Imaging Procedure to Evaluate the Transplant Kidneys

OCT is a rapidly emerging imaging modality that can function as a type of "optical biopsy," providing cross-sectional images of tissue morphology in situ and in real time [16, 17]. OCT is similar to ultrasound imaging, except that it uses the echo delay of light instead of sound to generate images. OCT is safer than X-ray technologies, is much less expensive than MRI devices, and provides higher resolution images than ultrasound. By employing broadband optical light sources, OCT can achieve axial resolutions of 1–10 μm, more than an order of magnitude above that obtainable for high-frequency ultrasound. As a result, OCT can provide very high-resolution images of organs and tissues in a noninvasive manner. This potential

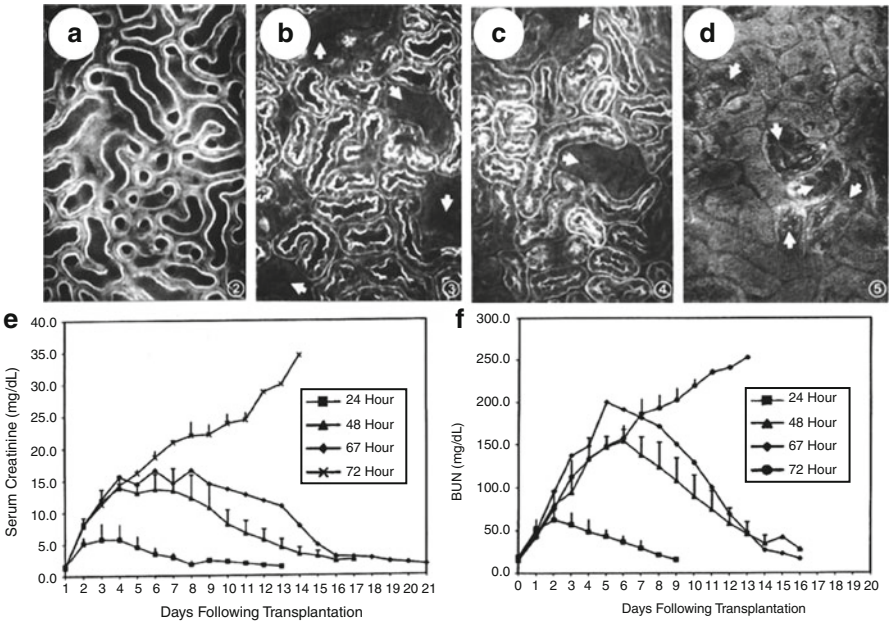

Fig. 79.1 TSCM images of subcapsular proximal convoluted tubules of a rabbit kidney: 1 h (hr) (**a**), 24 h (**b**), 48 h (**c**) and 72 h (**d**) following harvesting. With increasing storage time, TSCM images depict the degeneration of the superficial proximal tubules. Summary of the serum creatinine (*SCr*) (**e**) and blood urea nitrogen (*BUN*) values (**f**) measured at various days posttransplantation. As the storage time increased, the posttransplant SCr and BUN values increased. All the rabbits in the 24-, 48-, and 67-h groups exhibited various degrees of DGF but eventually survived. SCr and BUN returned to normal values. All rabbits in the 72-h group eventually died of uremia (Reproduced from Ref. [11] with permission © 2002 S. Karger AG, Basel)

has been demonstrated in a number of biomedical applications including ophthalmology [18–20], cardiology [21, 22], gastroenterology [23–26], dermatology [27], dentistry [28], urology [29], and gynecology [30], among others. In contrast to other forms of noninvasive light microscopy, OCT can image with longer working distances, with improved penetration depth, and without the need for tissue contact. Not only can it image up to depths of ~1–2 mm in most light-scattering tissues, OCT can also provide three-dimensional images in arbitrary planes. Finally, OCT can be performed using a thin flexible sterile endoscope or catheter [31, 32] or even with a needle [33], enabling ease of use and the possibility of imaging deep within a solid tissue or organ. To make OCT more applicable to the clinical situation, we developed a handheld OCT unit that has proven highly effective in our preliminary clinical trials. OCT has proven especially valuable in studying the living kidney because excisional biopsies are not only invasive, damaging, and can only sample a very small region of the kidney but also produce severe artifacts that are difficult to distinguish from ischemia and other injuries. In preliminary clinical investigations, we have provided evidence demonstrating OCT's capability for imaging intact living human kidney microstructures both ex vivo and in vivo (i.e., following

transplant into patient). Since the morphology of superficial proximal tubules correlates very well with posttransplantation renal function [11], the information obtained by OCT could be useful to evaluate the donor kidney status.

79.4 OCT Studies of the Kidney Using a Rat Model

Initially, we investigated the ability of OCT to provide clinically relevant information using a rat kidney model [5]. Figure 79.2a shows the cross-sectional OCT image of rat renal cortex ex vivo. OCT clearly visualizes the uriniferous tubule lumens that appear as low backscattering (dark regions), while the parenchyma appears as high backscattering (bright regions). Figure 79.2b shows the 3D OCT image that reveals the shape and contour of winding proximal convoluted tubules. Similar patterns are presented in the en face OCT image (planes parallel to the kidney surface) shown in Fig. 79.2c. Renal glomeruli can be visualized (Fig. 79.2d), with a narrow circular space corresponding to Bowman's space. This study demonstrated that OCT has high resolution and sufficient penetration depth to visualize the microstructures in the outer cortex of the rat kidney.

We subsequently studied the capability of using OCT to monitor kidney structural changes in response to ischemic insult in the living rat (i.e., in vivo) [6]. A laparotomy was performed on the anesthetized animal and the living kidneys exposed for in situ observation. We observed the kidneys prior to, during, and following exposure to renal ischemia induced by clamping the renal artery. Again, OCT enabled visualization of the morphology of both uriniferous tubules and renal glomeruli. When renal ischemia was induced, OCT revealed dramatic shrinkage of

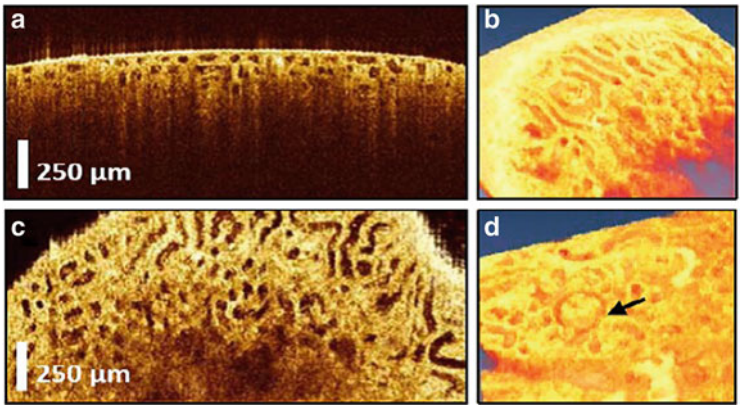

Fig. 79.2 (**a**) OCT imaging of rat kidney microanatomy ex vivo. (**a**) Cross-sectional image of renal cortex revealing the proximal tubules. (**b**) 3D view. (**c**) En face image of the proximal convoluted tubules. (**d**) 3D view revealing the glomerulus (*arrow*) (Reproduced from Ref. [5] with permission © 2007 Society of Photo-Optical Instrumentation Engineers)

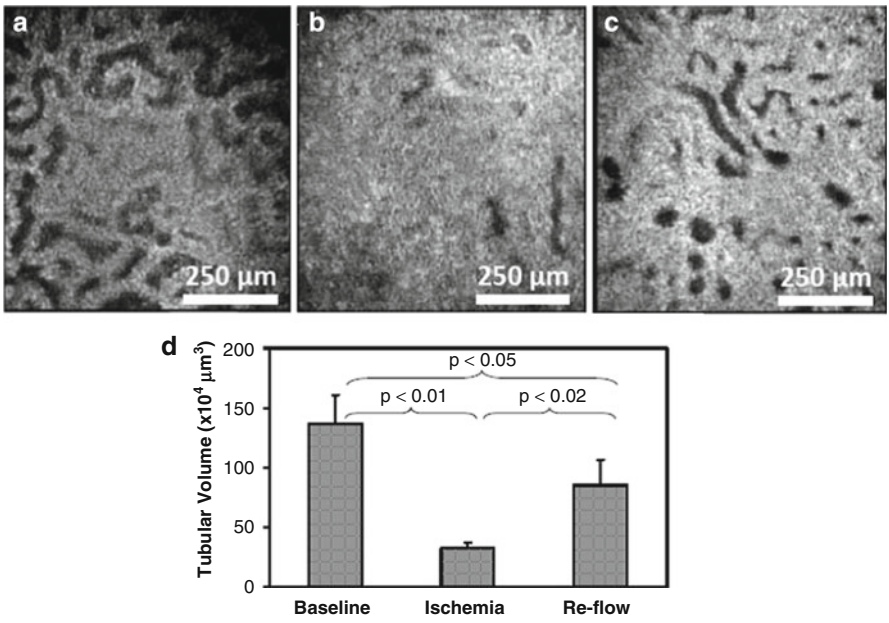

Fig. 79.3 (**a**) En face OCT image of a rat kidney in vivo prior to an ischemic insult. The lumens are relatively uniform. (**b**) OCT image of the tubules taken following 15 min of normothermic renal ischemia. After ischemia, the majority of the tubules have shrunk. (**c**) OCT image of the tubules taken 30 min after reperfusion; the tubular lumens have reopened. (**d**) Total tubule volume before, during, and following renal ischemia showing statistically significant changes (Reproduced from Ref. [6] with permission © 2008 USCAP, Inc)

tubular lumens due to the swelling of the proximal tubule cells (Fig. 79.3a–c). Total occlusion of the tubule lumens occurred within a minute following onset of ischemia. 3D segmentation provided an estimation of changes in the total tubular volumes in response to ischemia (Fig. 79.3d). Pretreatment with intravenous mannitol (1.0 ml of 25 % mannitol solution) protected the tubules from ischemic-induced swelling. These observations demonstrated that OCT represents an exciting new approach to visualize renal histopathological changes in vivo.

79.5 Noninvasive Imaging of Renal Microcirculation Using Doppler OCT

We have demonstrated that OCT can be used in a Doppler mode (DOCT) to image microvascular blood flow in the kidney [7]. This is an additional parameter to measure following kidney transplantation, in view of studies indicating that blood perfusion may be correlated with both intermediate and long-term graft function [34, 35]. Also, intrarenal hemodynamic abnormalities are thought to be a primary factor associated with the onset and progression of acute injury [36], as well as

diabetic nephropathy [37, 38], and focal segmental glomerulosclerosis (FSGS) [39]. Real-time assessment of renal morphological and hemodynamic changes could therefore help to evaluate the kidney condition and offer valuable information to predict the prognosis of injury or disease, lending to the development of patient-specific management strategies. Currently, there is no sensitive and objective tool for clinical monitoring of renal microcirculatory changes. In the past, renal blood flow (RBF) has been monitored using a number of different imaging modalities including positron emission tomography (PET) [40–45], magnetic resonance angiography (MRA) [46–49], Doppler ultrasound (US) [50–53], and contrast-enhanced ultrasound (CE) [54, 55]. While these techniques allow for noninvasive, wide field-of-view (FOV) imaging, they do not have sufficient resolution to detect changes in renal microcirculation. Optical imaging techniques that have higher resolutions and greater sensitivities could be a more feasible method for monitoring and evaluating microcirculatory changes, especially in an intraoperative setting. Studies using confocal [11, 12, 56] and multiphoton microscopy [13–15] have demonstrated the ability to image kidney microstructure and function (blood flow and filtration rate) in animal glomerular capillaries. However, again the penetration depth has been limited to several hundred microns, and they require the need to administer contrast agents to determine flow. Therefore, using these imaging modalities for human studies pose certain challenges due to the capsule surrounding the human kidney, which can be several hundred microns thick, and the need to inject contrast agents into the patient. OCT and its functional extension DOCT are emerging imaging technologies that have the capacity to provide real-time imaging of tissue in a noninvasive fashion with high resolution near that of conventional histopathology. DOCT can be used to visualize blood flow noninvasively by measuring the Doppler frequency shifts in the OCT interference signal caused by moving scatterers that are label-free, such as red blood cells [57]. DOCT has been used to image and quantify blood flow in vivo for multiple clinical applications including retina [58–61], skin [62–64], and gastrointestinal tract [65], among others.

In a recent study, we investigated the feasibility of DOCT to image kidney microcirculation, specifically, glomerular blood flow. DOCT is able to capture 3D data sets consisting of a series of cross-sectional images in real time, which enables label-free and noninvasive quantification of glomerular blood flow. The kidneys of adult, male Munich-Wistar rats were exposed through laparotomy procedure after being anesthetized. Following exposure of the rat kidney beneath the OCT/DOCT microscope, glomerular blood flow was observed as shown in Fig. 79.4. Figure 79.4a, d, g show en face OCT intensity images revealing the kidney microstructure. Uriniferous tubules are readily identified surrounding the glomerulus, which is the circular structure in the middle of the image surrounded by the crescent-shaped capsular space of Bowman. Figure 79.4b, e, h show corresponding DOCT image from the same plane depicting red blood cell (RBC) velocity in numerous glomerular capillaries. As indicated by the color map, red to yellow represents increasing velocity of blood flow in one direction, while blue to cyan represents increasing velocity of blood flow in the opposite direction. Therefore, the mixture of these colors seen in the DOCT images demonstrates the varying

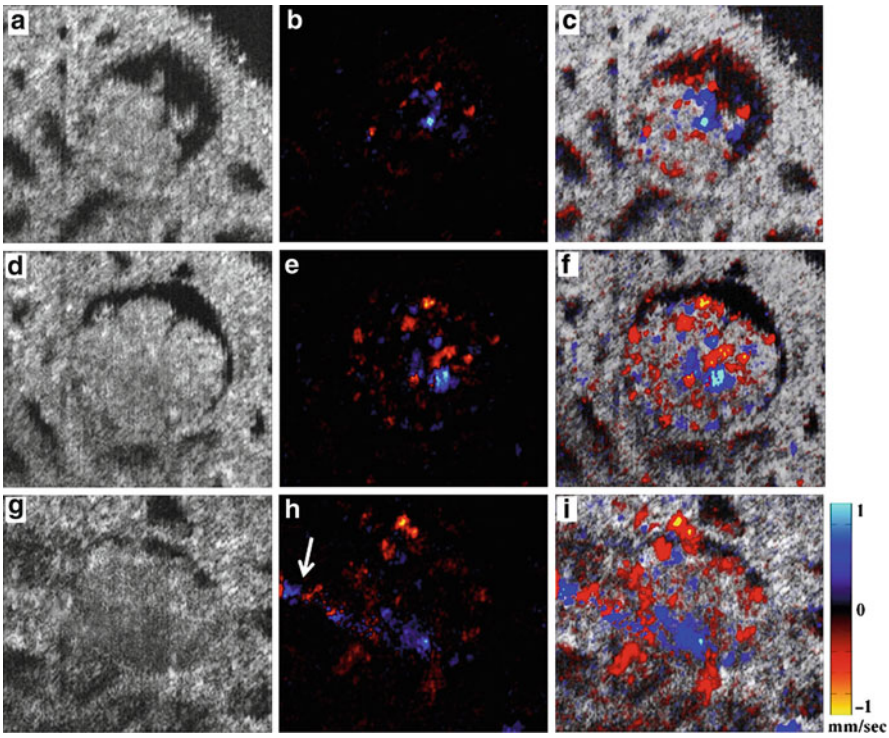

Fig. 79.4 OCT/DOCT imaging of a rat glomerulus. (**a**, **d**, **g**) Represent OCT en face views of single glomerulus. (**b**, **e**, **h**) Represent DOCT en face view of the same imaging plane. (**c**, **f**, **i**) Represent fused OCT/DOCT image showing spatial agreement between the OCT image and the corresponding DOCT image. The three images in each row correspond to the same imaging plane. Depth (**a**–**c**) = 440 μm; (**b**–**f**) = 470 μm; (**g**–**i**) = 545 μm. OCT/DOCT provides virtual sectioning of the glomerulus. The *arrow* in **h** represents the vascular pole (i.e., afferent/efferent arterioles). Image size: 325 × 278 μm (Reproduced from Ref. [7] with permission © 2011 USCAP, Inc)

velocities as well as the convoluted nature of blood flow through the glomerular capillaries. Figure 79.4c, f, i are the fused OCT/DOCT images demonstrating the spatial location of the DOCT signal within the glomerulus.

The effects of acute mannitol and angiotensin II infusion were also observed. DOCT imaging enables real-time monitoring of blood flow changes in three separate physiological states: baseline, following injection of 0.1–0.2 ml mannitol (250 mg/ml), which increases renal blood flow [66–68], and 200 ng/kg body weight angiotensin II [69], which decreases renal blood flow [70–73]. Glomerular blood flow was quantified for the induced physiological states and compared with baseline measurements. Figure 79.5 shows representative glomeruli imaged under each condition. Baseline DOCT is depicted in Fig. 79.5b with mannitol and angiotensin II in Fig. 79.5d, f respectively. After infusion of mannitol, a significant increase in blood flow was observed, and following infusion of angiotensin II,

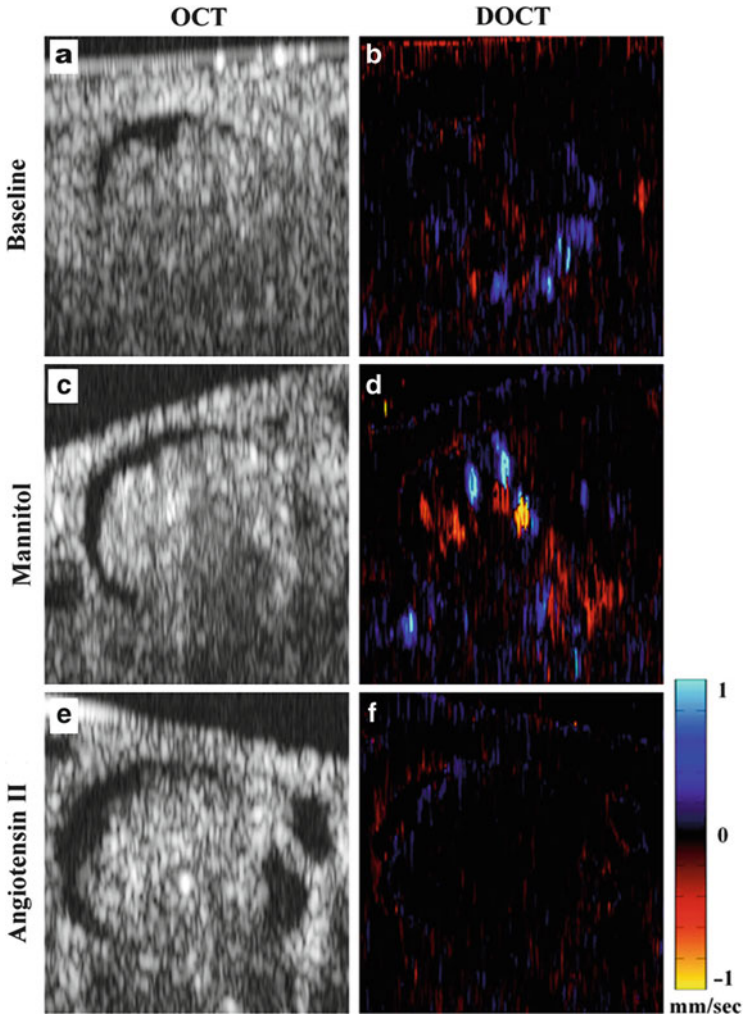

Fig. 79.5 Representative OCT and DOCT images (XZ) from three different physiological states. (**a**–**b**) Baseline, (**c**–**d**) after mannitol, and (**e**–**f**) after angiotensin II. Comparison among the images shows differences in the observed DOCT signal in different glomeruli under altered blood flow conditions. Image size: 294 × 278 μm (Reproduced from Ref. [7] with permission © 2011 USCAP, Inc)

a significant decrease in blood flow was observed. Corresponding OCT images are presented in Fig. 79.5a, c, e for identification of glomerular region in the DOCT images.

3D DOCT data were subsequently analyzed by computing two parameters: cumulative Doppler volume (CDV) and Doppler flow range (DFR). CDV was calculated by summing together the volume of segmented voxels within the glomerular volume containing DOCT signals that were above the background

threshold: CDV $= \sum_{xyz} V(x, y, z)$, where V(x, y, z) is individual voxel volume and the threshold velocity is set to ±0.05 mm/s. Doppler flow was calculated by integrating the DOCT velocity signal over the lateral cross-sectional (en face) area of the segmented DOCT signal at each depth position. Integration over the en face plane eliminates the angle-dependent uncertainty of the Doppler velocity, therefore providing an accurate quantitation of flow as defined by [74] Flow $= \iint_{xy} v_z(x, y, z)dxdy$, where $v_z(x, y, z)$ is the DOCT velocity over the xy segmented DOCT area. DFR was then defined as the flow rate at 99 % area under the curve (AUC) of the 3D flow histogram. Figure 79.6 shows the blood flow histograms of three glomeruli to illustrate differences in blood flow rate and blood volume between the induced physiological states. The aforementioned dynamic changes in blood flow detected under altered physiological conditions demonstrate the real-time imaging capability of DOCT to quantitatively image the kidney microvasculature for transplant graft evaluation.

Figure 79.7a, b shows the DFR and CDV values from seven different physiological states in the same rat. For each state, an average number of $n \approx 4$ glomeruli were analyzed. Both DFR and CDV increase dramatically after injection of mannitol. It is interesting to note that after both the first and second mannitol injection, the DFR and CDV values returned to near-baseline levels during the "recovery" period indicating that the effects of the mannitol were wearing off (∼15–20 min elapsed since injection). Shortly after administering the third mannitol injection to increase blood flow (∼10 min), angiotensin II was injected. This injection of angiotensin II reduced both DFR and CDV dramatically, well below the baseline level. This result demonstrates that DOCT can quantitatively image renal blood flow in vivo, thereby providing valuable diagnostic information for vascular function in addition to structural information from OCT.

These preliminary results using animal models demonstrate that OCT/DOCT can provide valuable information that would be valuable for determining the status of renal transplants.

79.6 OCT Imaging of Human Kidney Microstructure

Figure 79.8 shows the schematic of the high-speed, high-resolution, Fourier-domain OCT system that was used to obtain the first 3D OCT imaging of human kidneys [75]. A wavelength-swept laser light source generating 100-nm bandwidth at 1,310-nm central wavelength was employed, yielding approximately 10-μm axial image resolution in the tissue. The laser used to acquire the preliminary data operates at a sweep rate of 16 kHz, and the real-time imaging was performed at 30 frames per second (video rate). A Michelson interferometer composed of a circulator and a fiber-optic 50/50 splitter was used to generate the OCT interference signal. The reference arm consists of a stationary mirror (M) and a polarization

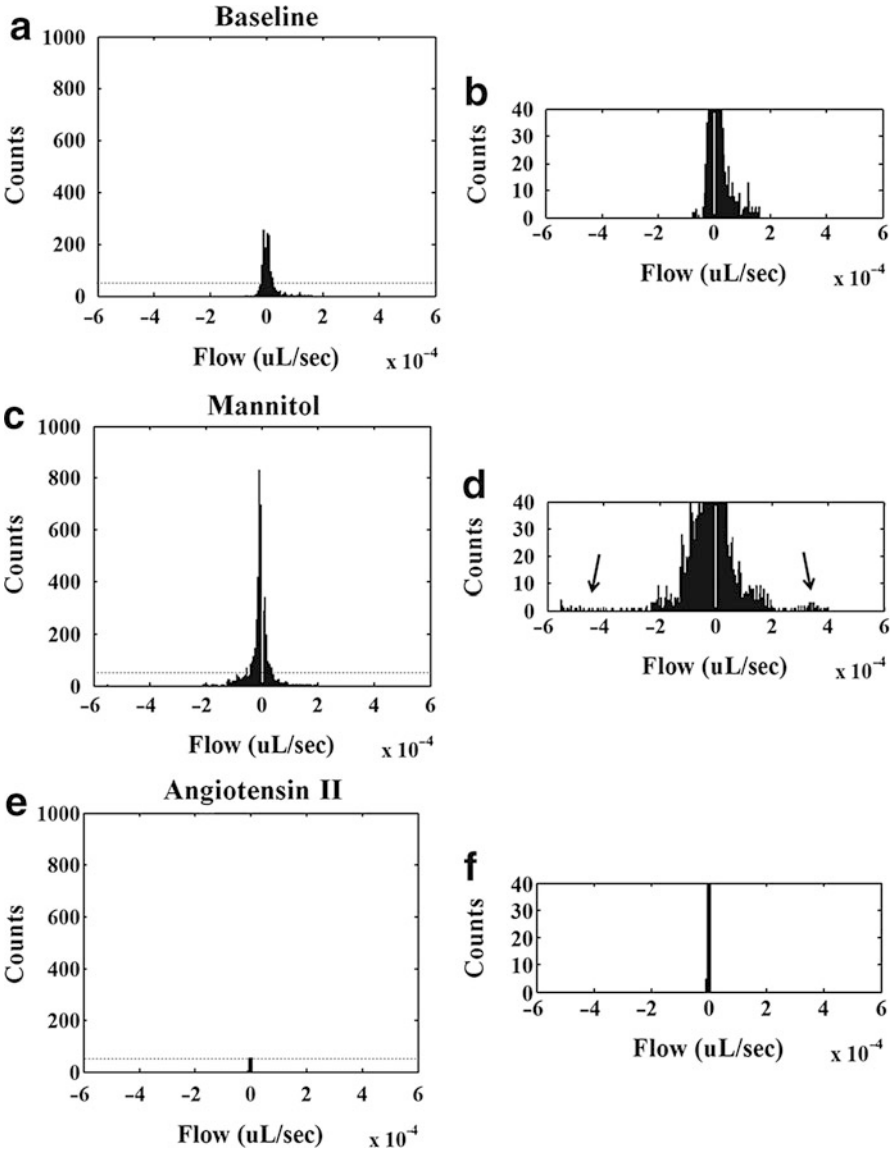

Fig. 79.6 Blood flow histogram comparison. (**a**–**b**) Baseline blood flow histogram. (**c**–**d**) Blood flow histogram following injection of mannitol. (**e**–**f**) Blood flow histogram following injection of angiotensin II. Each histogram represents a compilation of the segmented DOCT signal at every en face plane through the depth of a single glomerulus. Plots on the *lower row* are close-up versions at the base of the histograms (below the *dashed line*) in the *upper row* (Reproduced from Ref. [7] with permission © 2011 USCAP, Inc)

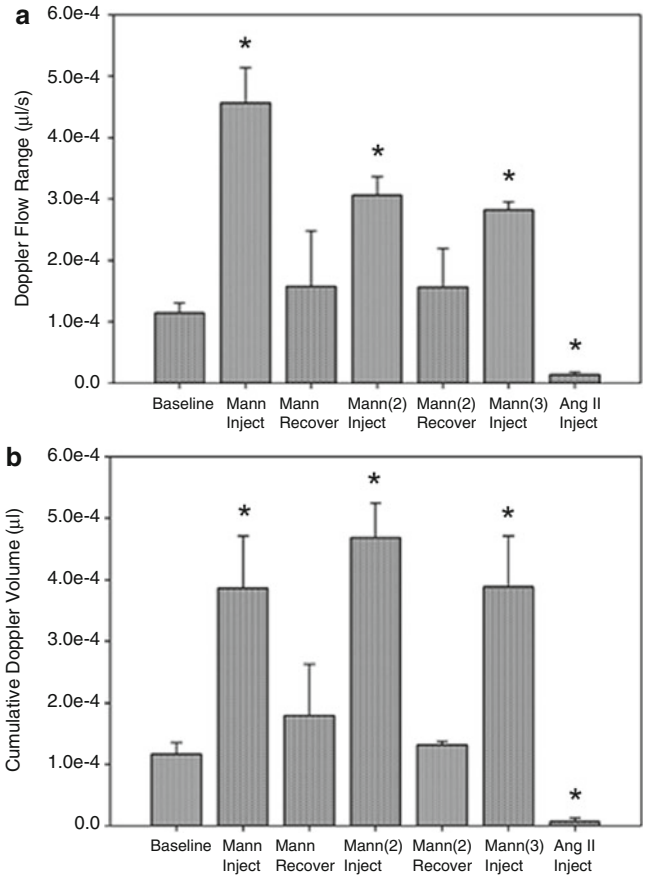

Fig. 79.7 In vivo quantification of DOCT imaging parameters of rat glomeruli. (**a**) Doppler flow range; (**b**) cumulative Doppler volume. Each of these parameters was measured in multiple glomeruli under seven separate conditions. *Asterisk* (*) indicates $p < 0.05$ compared to "baseline." Labels: *Mann*, mannitol; *Ang II*, angiotensin II (Reproduced from Ref. [7] with permission © 2011 USCAP, Inc)

controller (PC). The light from the sample arm was steered by a pair of galvanometer mirrors (X and Y), then focused by an objective lens onto the sample. The power on the sample was 4 mW with a spot size of 15 µm. The system's sensitivity was 95 dB.

3D OCT volumes ($2.5 \times 2.5 \times 2.5$ mm^3, with $512 \times 512 \times 512$ pixels) were obtained noninvasively from various locations on human kidneys obtained through the Washington Regional Transplant Consortium (WRTC) and preserved (i.e., fixed) with 2 % glutaraldehyde. Figure 79.9 shows a representative cross-sectional OCT image of the human kidney and the corresponding conventional light microscopic histology. Because under normal circumstances the kidney will be surrounded by the renal capsule (i.e., thick layer of dense connective tissue), it is

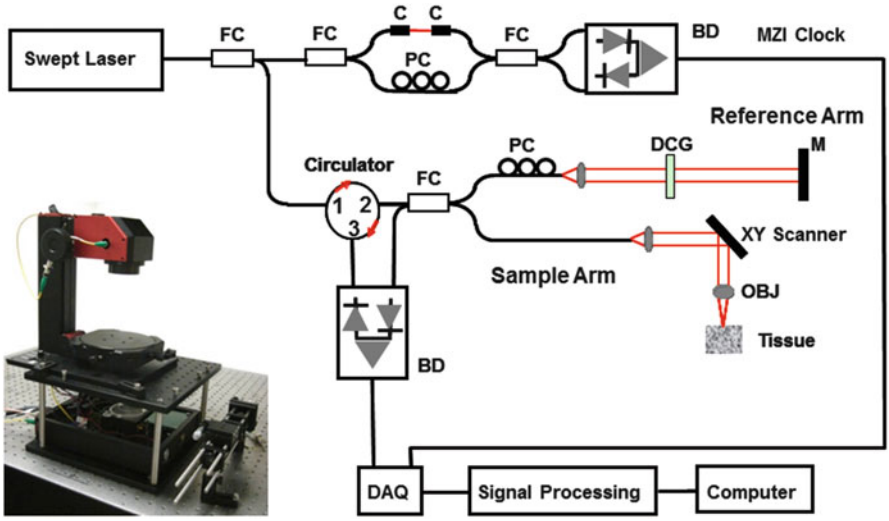

Fig. 79.8 Schematics of the Fourier-domain OCT system used in kidney imaging studies. *Inset* shows the photo of OCT microscope (Reproduced from Ref. [75] with permission © 2009 Optical Society of America)

important to evaluate OCT's capability to image the tissue structures through the renal capsule. Unlike in the previously described TSCM studies (see above), the presence of the renal capsule did not prevent imaging of subcapsular kidney tubules and glomeruli. A corresponding histological image (Fig. 79.9b) shows correlation of the anatomic features observed by OCT with traditional light microscopic histological sections. Renal glomeruli could also be visualized in the upper cortex as light-dense, round-oval capillary tufts and the Bowman's space as a light-lucent area surrounding the tufts (Fig. 79.9c) [76]. These results demonstrated OCT's capability to reveal the histological features in the intact human kidney and underscored its promise for clinical kidney imaging in vivo.

79.7 Clinical Trials of Renal Transplants

In collaboration with Drs. Joseph Melancon and Mathew Cooper, Directors of Kidney and Pancreatic Transplantation at Georgetown University Medical Center (GUMC), we performed clinical imaging of human donor kidneys using OCT prior to transplant (i.e., ex vivo) and OCT/DOCT following transplant (i.e., in vivo) [77]. The study was approved by the IRB and all patients signed consent forms. The IRB approved the OCT as a "nonsignificant" risk to the patients. Figure 79.10 shows the portable OCT unit used in the clinical trial, which consists of a portable cart (holding the computer, laser, optical, and electronic components), a handheld probe containing the objective lens, and a real-time user interface for image display and quantification. A cage

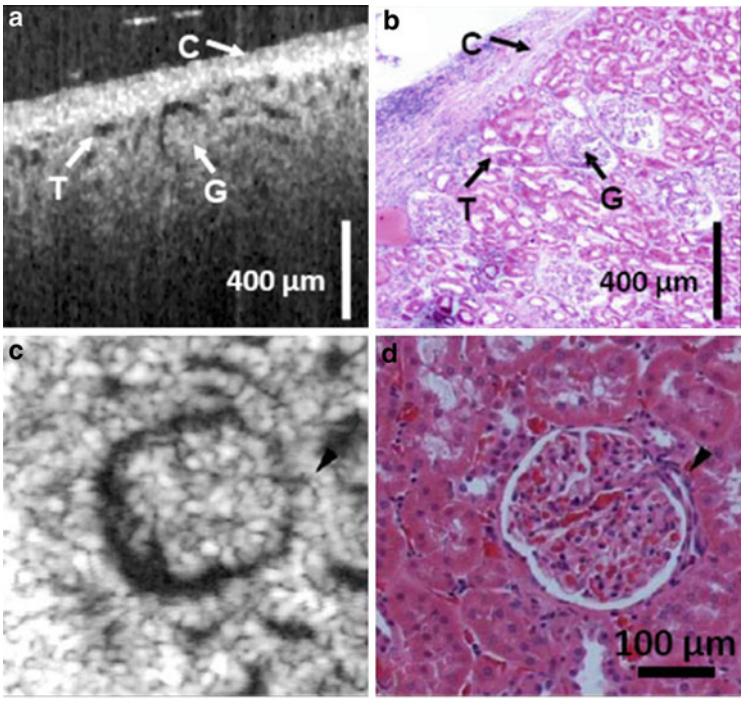

Fig. 79.9 (**a**) Cross-sectional OCT image of human kidney ex vivo. Uriniferous tubules (*T*), glomeruli (*G*), and the kidney capsule (*C*) are distinguishable. (**b**) Representative histology of the corresponding area in the human kidney (Reproduced from Ref. [75] with permission © 2009 Optical Society of America) (**c**) En face OCT image of human kidney ex vivo. Glomerulus shows light-dense capillary loops surrounded by a space corresponding to the capsular space of Bowman (**d**) Histology (Reproduced from Ref. [76] with permission 2010 American Urological Association Education and Research, Inc)

consisting of metallic bars attached to a metallic ring endpiece surrounds the imaging objective lens that makes up the handheld probe. The length of the bars of the cage is adjusted to a proper working distance (i.e., approximately 3 cm.), so that any object place near the ring at the end of the cage is within the correct working distance for imaging (i.e., the cage serves as a spacer for correct working distance). Two issues that were initially encountered in these studies were (1) sterility and (2) keeping the laser beam from being impeded by a buildup of moisture on the glass objective lens. Since the handheld OCT probe is connected to the imaging system by a 6-ft length of cords, the cords were covered with a sterile sleeve, similar to that used for ultrasound imaging with the sterilized handheld probe exposed at the end of the sleeve. This setup worked well for imaging the kidney ex vivo while the donor kidney is being stored in sterile bowl filled with sterile ice (i.e., an ice bath) prior to its transplantation. However, when the sterilized handheld unit is used to image the donor kidneys following their transplant into the patients, temperature differences between the transplanted kidneys warmed by reperfusion of blood and the colder objective lens within the handheld

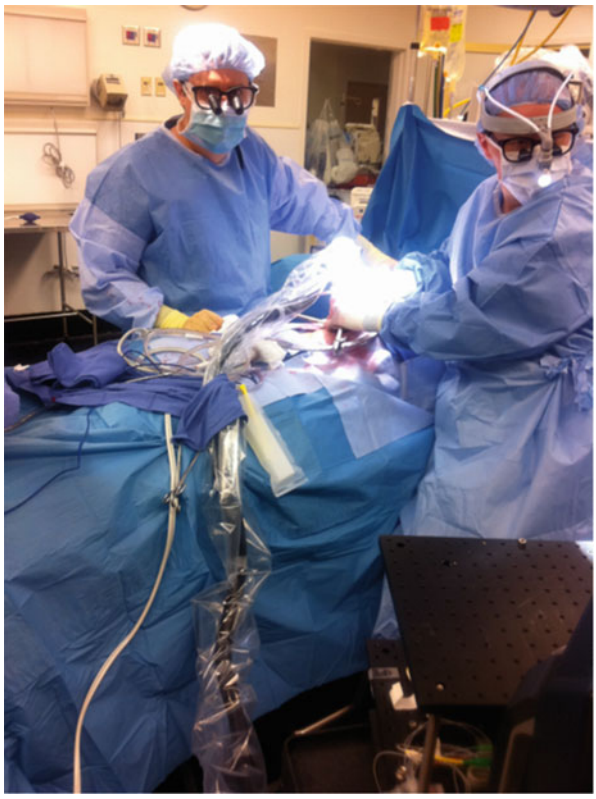

Fig. 79.10 A transplant surgeon holding the sterilized handheld imaging probe over an implanted human donor kidney

probe resulted in a rapid buildup of condensation on the objective lens surface, resulting in a diminished signal. This condensation issue was effectively addressed by covering the entire handheld probe (containing the objective lens) as well as the 6 ft of cords with the sterile camera sleeve. A 1-cm circular hole cut in the end of the sleeve permitted unimpeded passage of the laser signal. The circular hole cut in the sterile sleeve was then covered with sterile, adhesive, transparent "Tegaderm" film (3M Health Care, St. Paul MN). The ultrathin Tegaderm film did not significantly impede the OCT beam and provided a barrier to moisture as well as a sterile interface between the OCT imaging probe and the kidney being imaged. Using this setup, we imaged the harvested donor kidney with the handheld OCT imaging probe (covered by a sterile sleeve and Tegaderm) both while the kidney was being stored in the sterile ice bath prior to its transplantation and in situ, following its reimplantation into the recipient. Imaging the entire surface of the harvested donor kidney ex vivo (i.e., both sides and all poles) took less than several minutes and provided a holistic evaluation of the pretransplant organ. After transplantation and following revascularization of this same donor kidney within the transplant recipient, OCT/DOCT imaging was performed again to detect Doppler flow as well as morphological features of the transplanted kidney. Once transplanted into the patient, only the upper exposed

surface of the kidney was available for imaging. Again, imaging took less than several minutes. This kind of global, noninvasive, real-time histopathological perspective is, of course, not possible when using the invasive, potentially damaging, and artifact-prone procedure of excising renal biopsies. At the Georgetown University Medical Center, kidneys from living donors are protected from ischemia by pretreating the patients with intravenous mannitol (up to 50 g intravenously), flushing the excised kidneys with Viaspan (i.e., also known as the University of Wisconsin solution, or UW solution), and then storage on ice for variable periods of time prior to their transplant. However, Georgetown University Medical Center, as part of the Washington Regional Transplant Consortium/Community, also accepts cadaver kidneys preserved using other procedures including cold storage in Euro-Collins solution and hypothermic pulsatile perfusion preservation.

In our initial studies, we evaluated ten kidneys from living donors and one that was harvested from a heart-beating cadaver. We correlated our data with posttransplant renal function, by analyzing posttransplant serum creatinine levels. Serum creatinine levels are the most universal biological marker for estimating the glomerular filtration with a good prognostic value. In all cases but one, the transplants resulted in a rapid return to normal renal function as reflected by serum creatinine levels (i.e., serum creatinine levels below 1.5 mg/dL). In the one case, however, the serum creatinine remained elevated has not yet (i.e., 6 months later) returned to normal. This kidney had suffered additional normothermic ischemia due to revascularization problems encountered during the implantation procedure. This also was the only donor kidney that revealed no open renal tubules when examined using OCT following its implantation into the recipient. The elevated serum creatinine levels resulted in a biopsy to determine if the elevated serum creatinine levels represented rejection. Histopathological analysis verified that the elevated serum creatinine levels were a result of ischemia rather than rejection. This observation supports our premise that the openness of the uriniferous tubules is a direct reflection of posttransplant renal function. Figure 79.11 shows representative images of in vivo imaging of subsurface kidney structure and function obtained after transplantation. Renal capsule, parenchyma, and uriniferous tubules are clearly visualized. Three to five layers of tubule lumens are visible and open, denoting active renal filtration and a functioning kidney. Also, blood flow within small and large vessels was captured indicating cortical perfusion within the transplant kidney. These results demonstrate the feasibility of OCT/DOCT imaging of the transplant kidney in the OR room during transplantation procedures. Specifically, the OCT/DOCT following grafting shows both the morphological and functional response of the transplant kidney.

Previous studies of donor kidneys from cadavers indicated that the proximal tubules in these kidneys are initially open and then undergo a progressive closing over time during their cold storage (unpublished observations). The openness of these tubules reflects the fact that these cadaver kidneys are flushed with preservative with little or no intervening ischemic time. Intravenous infusion of mannitol will similarly maintain the proximal convoluted tubules of living donor kidneys open and protect them from swelling by acting as an impermeant osmotic agent.

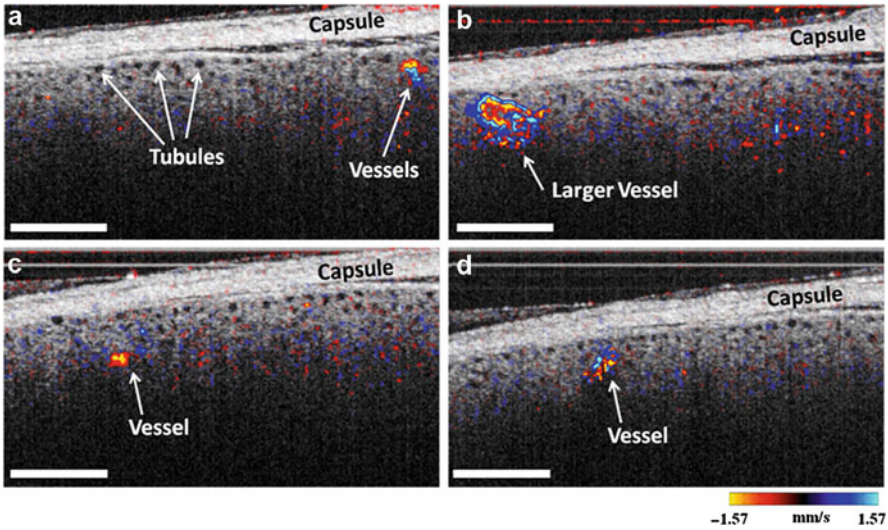

Fig. 79.11 In vivo human kidney showing open tubules and cortical blood flow. Open tubules appear round and relatively uniform across all images. Also, a larger blood vessel is seen in (**b**) against some smaller vessels observed in (**a**, **c**, and **d**). Scale bar = 500 μm, DOCT color map unit = mm/s (Reproduced from Ref. [77] with permission)

In our studies of living human kidney transplants, we found that when the mannitol was infused 30 min prior to harvesting, the proximal convoluted tubules were swollen and the tubule lumens occluded. However, in two donor kidneys that were harvested within 15–10 min following intravenous infusion of mannitol, the proximal tubules remained more open and protected. These two kidneys also demonstrated the fastest return to normal renal function following transplantation as indicated by normal serum creatinine levels within several days instead of a week or more which was seen for the other living donor kidneys. These observations supported our earlier DOCT studies of rat kidneys wherein the effects of the mannitol injection were wearing off ∼15–20 min following injection. While mannitol is believed to have a half-life of 1–2 h, the foregoing observations indicate a need to harvest living donor kidneys within minutes following mannitol infusion. More recently, we expanded these studies to include 14 living donors that received mannitol 15 minutes or less prior to clamping the renal artery (Group A), and 13 living donors that received intravenous mannitol 30 minutes or more before clamping the renal artery (Group B) Again, OCT revealed that this change in timing of manniitol administration (i.e., reducing the timing to 15 minutes or less prior to clamping) protected the human donor proximal tubules from normothermic induced cell swelling. An evaluation of post-transplant recovery of renal function showed that this protection resulted in significantly faster return to normal renal function [78]. This important protocol change is an example of how OCT has provided valuable new clinical insights that improves patient outcomes.

79.8 Image-Processing Algorithms to Quantitatively Assess the Morphometric Parameters of Renal Transplants

Our animal and human studies undertaken thus far have indicated that there are a number of likely morphological parameters that are candidates for algorithm-based image processing to determine posttransplant renal function. One is the mean tubule lumen diameter. Our studies have shown that more open tubules reflect better posttransplant function. Second is the variability in average tubule luminal diameter. The latter may reflect the fact that S1 segments of the proximal convoluted tubules appear to be more sensitive to ischemia than S2 segments as was seen by us in a previous study of ischemic rodent kidneys [79]. However, S2 proximal tubule segments make up the majority of cortical proximal convoluted tubules and the relative role of ATN associated with S1 versus S2 in human kidneys is not yet known. Third is the irregularity in the profiles of the tubule lumens. Irregular profiles in the tubule lumens can result from cellular debris within the lumens (mainly from a disrupted microvillous brush border) lining the tubule lumens as well as from cell swelling. Fourth is the number of open tubules per unit area of cortex (tubular density), and fifth the total tubule luminal space per unit area of cortex. The latter parameter may be the most important because it reflects the overall available filtering surface area in the donor kidney. Together, these foregoing parameters reflect the tubule cell damage resulting from acute tubular necrosis (ATN), which is the main insult resulting in posttransplant renal failure in transplanted donor kidneys. As previously noted, we found that this kind of parameters can predict the extent of ATN in a renal transplant animal model [11]. It should be noted, however, that the data collected in this earlier study were derived from the most superficial proximal convoluted tubules (i.e., one layer deep in the kidney cortex) using TSCM. Using OCT, we are able to see four to five layers or more deep in the human kidney even with an intact renal capsule. Therefore, we are able to image significantly more proximal convoluted tubules than those can be imaged using the aforementioned TSCM imaging. Nevertheless, as previously mentioned, it is important to note that the status of superficial proximal tubule reflects the status of proximal tubules throughout the renal cortex (i.e., including those deeper in the cortex).

The degree of ATN suffered by individual kidneys depends also on a variety of factors including preservation methods and donor background (i.e., age, health, race, weight, etc.). We have previously reported that even the amount of protein in the diet can significantly affect postischemic ATN [80]. Therefore, it is very difficult to predict the degree of ATN suffered by a kidney prior to its transplant without some objective measure. By using OCT, the transplant surgeon can make the most efficient use of available donor kidneys (including the use of kidney from non-heart-beating cadavers), eliminate the possible use of bad donor kidneys, provide a measure of expected posttransplant renal function, and allow better distinction between posttransplant immunological rejection and ischemic-induced acute renal failure. The latter was confirmed in our recent clinical trial data, wherein OCT imaging indicated that there was renal insult to the transplanted kidney (i.e., the tubular lumens were closed following transplant), with this being subsequently verified by

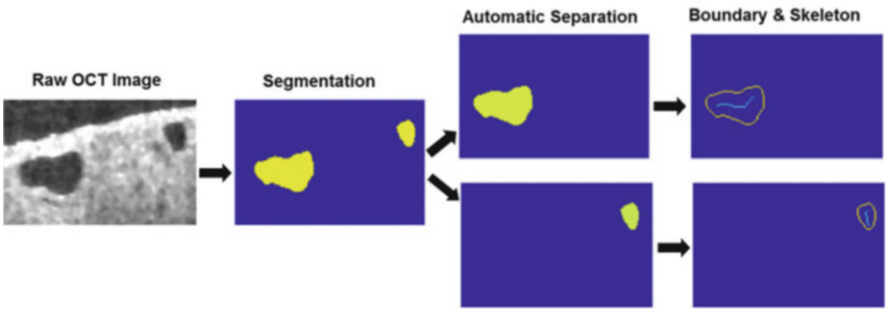

Fig. 79.12 Flowchart of the automatic image-processing algorithm developed by Dr. Chen's Lab, which includes four major steps: (*1*) image segmentation from the raw OCT image; (*2*) automatic region separation and selection; (*3*) finding the boundary and skeleton for each isolated regions to calculate the mean tubular diameter, and (*4*) sum all segmented regions to estimate the tubular volume. Computer-estimated results have been validated with manual measurements (Reproduced from Ref. [75] with permission © 2009 Optical Society of America)

traditional histopathological data showing that post-transplant elevated serum creatinine levels were a result of ischemia rather than rejection.

To provide diagnostic information obtained by 3D OCT, there is a need to develop automatic image-processing methods to quantitatively evaluate kidney morphology. Computer-aided analysis promises to automatically analyze a large volume of data quickly and therefore will be very helpful for providing the clinicians with quantitative diagnostic information in a timely manner and minimizing the inter- and intra-observer errors. With this in mind, we have developed an automatic image-processing algorithm to quantitatively evaluate the imaging parameters of kidney microstructures, such as tubular diameters and density. The algorithm for tubular diameter quantification includes three major steps (see Fig. 79.12): (1) Automatically segment the kidney structures (such as tubules) from the kidney parenchyma using their distinct backscattering intensities; (2) Automatically separate each isolated (not connected) tubular segment by an intelligent image-processing algorithm, which automatically fills each region to its boundary and assigns an index value to every segmented region of interest (ROI). This approach allows different regions be individually selected for further analysis; (3) Quantify the average diameter of each region as follows: the boundary (B) and skeleton (S) of each segmented region are automatically generated using morphological thinning, and the local radius for every pixel (b) on the boundary (B) is calculated by using the shortest distance between the pixel (b) to the skeleton (S), i.e., $Radius(b) = \min\left(\underset{\forall s \in S}{dist.}(b, s)\right)$. The averaged dimension of each region is then calculated by averaging all boundary pixels. In addition, tubular density can be quantified by dividing the sum of the segmented tubular regions by the total renal region (tubules plus parenchyma). Furthermore, DOCT parameters (DFR and CDV) can be quantified using the algorithm described previously.

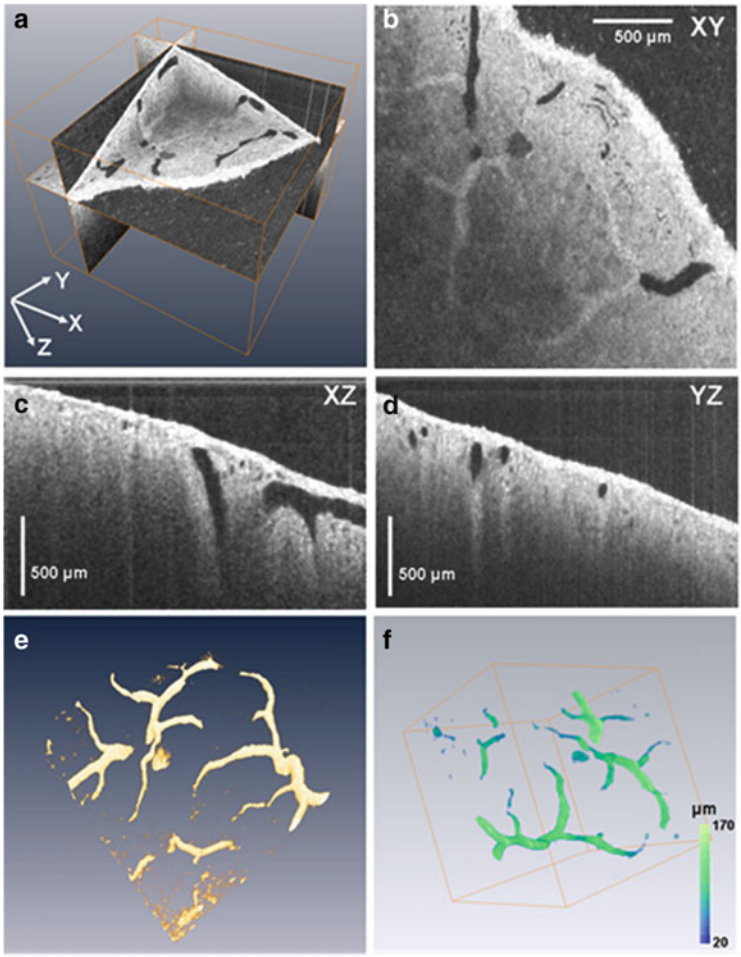

Fig. 79.13 (**a**) 3D cut-through view of the human kidney (case 1). The renal blood vessels as well as the kidney parenchyma are visualized. (**b–d**) Representative OCT images. (**e**) 3D volumetric image of the segmented renal vasculature. (**f**) Automatic quantification of the vessel diameter and color coded on the structural image (Reproduced from Ref. [75] with permission © 2009 Optical Society of America)

Figure 79.13a is the 3D view of one representative ROI (region of interest) in a human kidney ex vivo (case 1). Figure 79.13b–d shows the representative images along the three orthogonal planes (XY, YZ, XZ). Detailed kidney vascular structures can be visualized in all these image planes. Figure 79.13e shows the segmented 3D vascular tree. Figure 79.13f shows the automatic quantification of vascular diameters for different regions, which ranges from 30 to 150 µm. Figure 79.14a is the 3D view of another ROI from a different human kidney ex vivo (case 2). Figure 79.14b–d shows the representative images. Detailed kidney

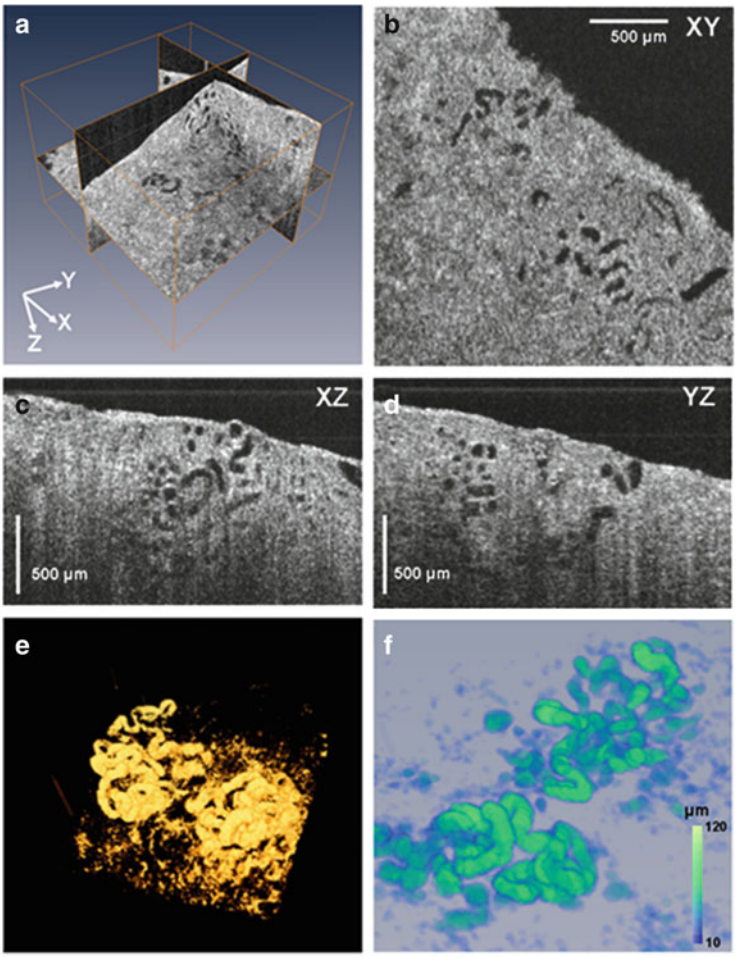

Fig. 79.14 (**a**) 3D cut-through view of the human kidney (case 2). The distended convoluted tubules as well as the kidney parenchyma are visualized. (**b–d**) Representative OCT images. (**e**) 3D image of the segmented distended convoluted tubules. (**f**) Automatic quantification of the tubular diameter (Reproduced from Ref. [75] with permission © 2009 Optical Society of America)

tubular structures can be visualized in all these image planes. OCT shows distended convoluted tubular structure, which is clearly visualized in the segmented 3D view, as shown in Fig. 79.14e, where comprehensive examination of morphological features, such as the tubular curvature and interconnectivity, is possible. Figure 79.14f shows the automatic quantification of tubular diameters for different regions. The distended tubular lumen shows approximately 70–90 µm in diameter. Figure 79.15a is the 3D view of the third example of human kidney ex vivo (case 3). Figure 79.15b–d shows the representative images. Detailed kidney microstructures

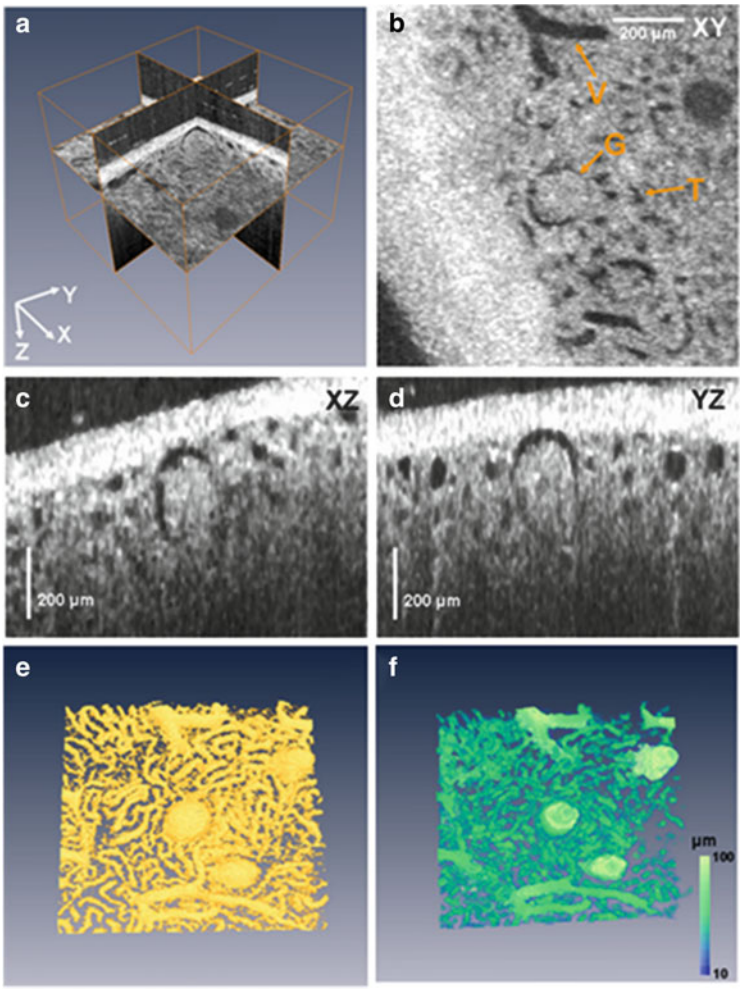

Fig. 79.15 (**a**) 3D cut-through view of the human kidney (case 3). Various renal microstructures including the blood vessels (*V*), uriniferous tubules (*T*), and glomeruli (*G*) are visualized. **b–d** Representative OCT images. **e** 3D view of the segmented renal microstructures. **f** Automatic quantification of the lumen diameter (Reproduced from Ref. [75] with permission © 2009 Optical Society of America)

can be visualized in all these image planes. Figure 79.15e shows the segmented 3D structures. Figure 79.15f shows the automatic quantification of lumen diameters for different regions. The glomeruli are surrounded by an expanded network of uriniferous tubules and blood vessels. The diameters of the glomeruli are measured to be approximately 200 µm. These results show the capability of OCT to visualize and quantify renal microstructures. The quantification accuracy of this procedure has been validated by conventional histological analysis.

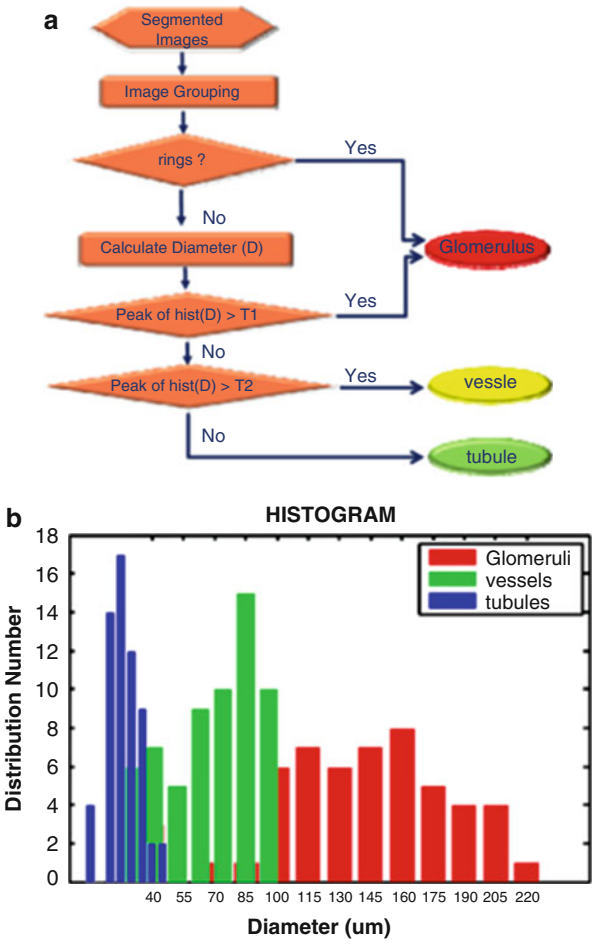

Fig. 79.16 (**a**) Flowchart of the human kidney image classification algorithm. Hist (D) means the histogram of diameter; T1 and T2 are empirical thresholds. (**b**) Histogram depicting the size distribution of kidney structures (glomeruli, blood vessels, and tubules

Additional 3D automated algorithms need to be developed in order to further develop or (1) classify different renal structures such as tubules, glomeruli, and vessels and (2) determine tubular diameters and densities in 3D. Our preliminary image classification algorithm operates on the isolated ROIs of each 3D set of kidney images obtained from OCT segmentation. A flowchart describing the classification algorithm is shown in Fig. 79.16a. Classification of kidney structures is based on each set of spatially interconnected image voxels (groups). We developed a 3D labeling algorithm to automatically identify regions that are spatially connected in 3D [81]. After labeling, label indices can be used to select and extract stereo-isolated groups from the kidney. Each region is a group representing interconnected renal structures.

Figure 79.17a shows the results of the image classification scheme for one representative data set. The three groups of human kidney microstructures are distinguished by different colors. All three classifications are clearly visible

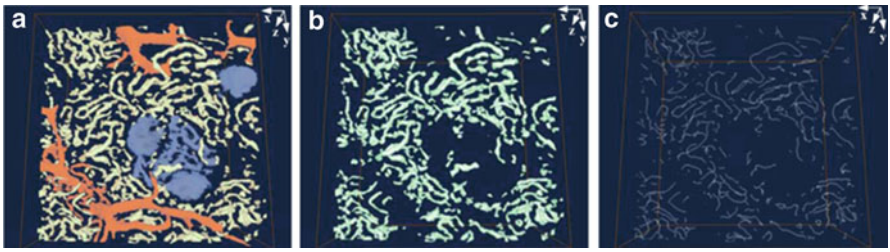

Fig. 79.17 Human kidney image classification and automated tubule analysis. Classification of kidney features is color coded: *green*, glomeruli; *red*, blood vessels; *beige*, tubules. All three classes of microstructures are present within this data set. (**b**) Segmented OCT showing tubular structures only. (**c**) 3D skeletonization of segmented tubules

in Fig. 79.17a, but it is evident that some structures are mislabeled (such as the adjacent uriniferous tubules near the glomeruli). Since the proximal convoluted tubule is physically attached to the glomerulus, this error in group classification is not unexpected. It might be possible to correct this error by using image opening and structure thinning strategies (erosion and dilation) to further separate segmented features in the data set. But, even with the minor misclassification of the juxtaposed tubules, the tubule diameters and density values will not be affected because the glomerulus and the mislabeled tubule will be removed as shown in Fig. 79.17b and will not contribute to the calculations (density = tubular voxels/(tubular voxels + parenchymal voxels), where parenchymal voxels are not including glomeruli and vessel groups. Nonetheless, optimizing the OCT segmentation process will improve image grouping and, thus, the overall classification algorithm. Other more advanced techniques for OCT segmentation, such as marker-controlled watershed segmentation [82], are being studied. Also, it would be useful to employ more advanced image-processing methods to improve classification of groups. Increasing the number of parameters to include the boundary curvature for each group (tubules have high surface curvature radially compared to glomeruli) and the degree of skeleton branching (glomeruli skeleton is more highly branched whereas tubule skeleton branching is minimal) that can be used for criterion will allow better group analysis. Ultimately, the best classification criteria will be based empirically upon which parameters provide the best results and improve the accuracy of the algorithm.

After classification, tubular regions will be selected for further analysis (Fig. 79.17b). Then, 3D skeletonization will be performed on the segmented tubular volume to obtain an interconnected skeleton of the entire tubular network (Fig. 79.17c). The minimum distance between every skeleton element to the 3D boundary of the tubule surface can be computed automatically for the complete volume to yield a distribution of tubule diameters for the entire 3D tubular network. This approach promises to be more accurate than the 2D boundary computation method from the initial algorithm described above. 3D computation does not restrict the boundary of the group to lie only within the current XZ frame where the primary segmented ROI appears but enables the determination of the diameter

along the central axis of the tubule. Furthermore, as automatic image processing for 3D data sets could be time-consuming, graphic processing units (GPUs) can be used to perform parallel computing to accelerate the computational process [83–85].

79.9 Discussions and Conclusions

OCT is a powerful medical imaging technology that can reveal microstructure and blood flow in biological tissue in a noninvasive fashion and in real time. Our preliminary results demonstrate the feasibility of using OCT to assess donor kidney status prior to and immediately following reperfusion by examining tubular morphology and renal blood flow. With ~12-μm axial and ~15-μm transverse resolution and 16-kHz axial scan rate, our OCT system revealed renal tubules and cortical blood vessels in real time during transplantation procedures. 3D imaging is critical to kidney imaging as it not only provides comprehensive volumetric information but also enables integration of DOCT signals over en face plane to quantify flow information correctly [74]. Due to significant motion from the handheld scanner, 3D OCT imaging was not able to be performed in clinical settings with our current image acquisition speed. Higher speed imaging systems (i.e., 55-kHz SS-OCT), however, are now commercially available from Thorlabs, which employ a novel tunable filter technology with a highly efficient laser cavity designed to achieve a broad wavelength tuning range (>120 nm) at high sweep rates. Excellent coherence length (6 mm) is maintained during the high-speed tuning of the swept-source laser, which supports greater OCT imaging depths and higher imaging rates in samples compared to our currently 16-kHz SS-OCT imaging system. 3D OCT volumes with 256 × 256 × 512 pixels can be acquired in ~1 s, thereby reducing the motion artifacts significantly. In addition, Thorlabs recently developed a VCSEL-based swept-source laser running at 760-kHz axial scan rate at 1.3 μm with 100-nm tuning range [86]. Alternatively, Fourier-domain mode-locked (FDML) lasers [87] enable ultrahigh-speed OCT imaging up to MHz A-scan rates [88, 89] and therefore would be an ideal candidate for wide-field kidney imaging. These novel light sources will bring new clinical tools capable of in vivo, volumetric imaging of tissue pathology with an unprecedented axial scan rate.

Motion artifacts might be present during imaging acquisition especially during in vivo imaging. One can stabilize the kidney against the abdominal wall using standard instruments to reduce motion artifacts while imaging. The OCT handheld probe (using the "cage" as a spacer) can also be gently placed on the kidney surface to further minimize motion. Also, the OCT probe can be attached to an articulating arm to reduce the tremor of the surgeons' hand. In addition, cross-correlation algorithms can be applied to correct the motion artifacts [90].

This study demonstrates the feasibility of OCT/DOCT imaging of the human kidney during kidney transplantation. OCT/DOCT imaging results were compared with standard biomarker (serum creatinine) measurements that reflect post-graft

renal function. However, this study is only an initial pilot study. However, the preliminary results of this study suggest that OCT/DOCT is a useful tool in intraoperative monitoring and evaluation of the transplant kidney for predicting post-graft function after ischemia-reperfusion injury. Furthermore, by comparing quantitative imaging parameters with post-graft function, the diagnostic potential of OCT will be investigated. However, this requires additional patient numbers to definitively identify any correlation with graft outcome. In addition, improved diagnostic parameters with 3D imaging will better assist in determining the capacity of OCT to predict post-graft renal function.

Acknowledgments We would like to thank Dr. James Jiang and Alex Cable from Thorlabs Inc. for technical support and Chao-Wei Chen, Dr. Wei Gong, and Dr. Hsing-Wen Wang from University of Maryland for assistance. This work is supported in part by NIH R21-EB012215, R21-DK088066, R01-DK094877, and R21-AG042700.

References

1. United States renal data system annual data report. (2013)
2. N. Perico, D. Cattaneo, M.H. Sayegh, G. Remuzzi, Delayed graft function in kidney transplantation. Lancet **364**(9447), 1814–1827 (2004)
3. F. Sanfilippo, W.K. Vaughn, E.K. Spees, B.A. Lucas, The detrimental effects of delayed graft function in cadaver donor renal transplantation. Transplantation **38**(6), 643–648 (1984)
4. P.M. Andrews, Noninvasive vital microscopy to monitor tubular necrosis of cold-stored kidneys. Transplantation **57**(8), 1143–1148 (1994)
5. Y. Chen, P.M. Andrews, A.D. Aguirre, J.M. Schmitt, J.G. Fujimoto, High-resolution three-dimensional optical coherence tomography imaging of kidney microanatomy ex vivo. J. Biomed. Opt. **12**(3), 034008 (2007)
6. P.M. Andrews, Y. Chen, M.L. Onozato, S.W. Huang, D.C. Adler, R.A. Huber, J. Jiang, S.E. Barry, A.E. Cable, J.G. Fujimoto, High-resolution optical coherence tomography imaging of the living kidney. Lab. Invest. **88**(4), 441–449 (2008)
7. J. Wierwille, P.M. Andrews, M.L. Onozato, J. Jiang, A. Cable, Y. Chen, In vivo, label-free, three-dimensional quantitative imaging of kidney microcirculation using Doppler optical coherence tomography. Lab. Invest. **91**(11), 1596–1604 (2011)
8. M. Szostek, R. Danielewicz, B. Lagiewska, M. Pacholczyk, Z. Rybicki, G. Michalak, L. Adadynski, J. Walaszewski, W. Rowinski, Successful transplantation of kidneys harvested from cadaver donors at 71 to 259 minutes following cardiac arrest. Transplant. Proc. **27**(5), 2901–2902 (1995)
9. J. Light, Viability testing in the non-heart-beating donor. Transplant. Proc. **32**(1), 179–181 (2000)
10. A.B. Maunsbach, The influence of different fixatives and fixation methods on the ultrastructure of rat kidney proximal tubule cells. I. Comparison of different perfusion fixation methods and of glutaraldehyde, formaldehyde and osmium tetroxide fixatives. J. Ultrastruct. Res. **15**(3), 242–282 (1966)
11. P.M. Andrews, B.S. Khirabadi, B.C. Bengs, Using tandem scanning confocal microscopy to predict the status of donor kidneys. Nephron **91**(1), 148–155 (2002)
12. V. Campo-Ruiz, G.Y. Lauwers, R.R. Anderson, E. Delgado-Baeza, S. Gonzalez, Novel virtual biopsy of the kidney with near infrared, reflectance confocal microscopy: a pilot study in vivo and ex vivo. J. Urol. **175**(1), 327–336 (2006)

13. J.J. Kang, I. Toma, A. Sipos, F. McCulloch, J. Peti-Peterdi, Quantitative imaging of basic functions in renal (patho)physiology. Am. J. Physiol. Renal Physiol. **291**(2), F495–F502 (2006)
14. K. Dunn, R. Sandoval, K. Kelly, P.C. Dagher, G.A. Tanner, S.J. Atkinson, R.L. Bacallao, B.A. Molitoris, Functional studies of the kidney of living animals using multicolor two-photon microscopy. Am. J. Physiol. Cell Physiol. **283**(3), C905–C916 (2002)
15. W. Yu, R.M. Sandoval, B.A. Molitoris, Rapid determination of renal filtration function using an optical ratiometric imaging approach. Am. J. Physiol. Renal Physiol. **292**(6), F1873–F1880 (2007)
16. D. Huang, E.A. Swanson, C.P. Lin, J.S. Schuman, W.G. Stinson, W. Chang, M.R. Hee, T. Flotte, K. Gregory, C.A. Puliafito, J.G. Fujimoto, Optical coherence tomography. Science **254**(5035), 1178–1181 (1991)
17. J.G. Fujimoto, Optical coherence tomography for ultrahigh resolution in vivo imaging. Nat. Biotechnol. **21**(11), 1361–1367 (2003)
18. M.R. Hee, J.A. Izatt, E.A. Swanson, D. Huang, J.S. Schuman, C.P. Lin, C.A. Puliafito, J.G. Fujimoto, Optical coherence tomography of the human retina. Arch. Ophthalmol. **113**(3), 325–332 (1995)
19. C.A. Puliafito, M.R. Hee, J.S. Schuman, J.G. Fujimoto, *Optical Coherence Tomography of Ocular Diseases Thorofare* (Slack, Thorofare, 1996)
20. G. Wollstein, L.A. Paunescu, T.H. Ko, J.G. Fujimoto, A. Kowalevicz, I. Hartl, S. Beaton, H. Ishikawa, C. Mattox, O. Singh, J. Duker, W. Drexler, J.S. Schuman, Ultrahigh-resolution optical coherence tomography in glaucoma. Ophthalmology **112**(2), 229–237 (2005)
21. M. Brezinski, Characterizing arterial plaque with optical coherence tomography. Curr. Opin. Cardiol. **17**(6), 648–655 (2002)
22. I.K. Jang, B. Bouma, B. MacNeill, M. Takano, M. Shishkov, N. Iftima, G.J. Tearney, In-vivo coronary plaque characteristics in patients with various clinical presentations using optical coherence tomography. Circulation **108**(17), 373–373 (2003)
23. B.E. Bouma, G.J. Tearney, C.C. Compton, N.S. Nishioka, High-resolution imaging of the human esophagus and stomach in vivo using optical coherence tomography. Gastrointest. Endosc. **51**, 467–474 (2000)
24. M.V. Sivak Jr., K. Kobayashi, J.A. Izatt, A.M. Rollins, R. Ung-Runyawee, A. Chak, R.C. Wong, G.A. Isenberg, J. Willis, High-resolution endoscopic imaging of the GI tract using optical coherence tomography. Gastrointest. Endosc. **51**, 474–479 (2000)
25. X.D. Li, S.A. Boppart, J. Van Dam, H. Mashimo, M. Mutinga, W. Drexler, M. Klein, C. Pitris, M.L. Krinsky, M.E. Brezinski, J.G. Fujimoto, Optical coherence tomography: advanced technology for the endoscopic imaging of Barrett's esophagus. Endoscopy **32**(12), 921–930 (2000)
26. Y. Chen, A.D. Aguirre, P.L. Hsiung, S. Desai, P.R. Herz, M. Pedrosa, Q. Huang, M. Figueiredo, S.W. Huang, A. Koski, J.M. Schmitt, J.G. Fujimoto, H. Mashimo, Ultrahigh resolution optical coherence tomography of Barrett's esophagus: preliminary descriptive clinical study correlating images with histology. Endoscopy **39**(7), 599–605 (2007)
27. J. Welzel, E. Lankenau, R. Birngruber, R. Engelhardt, Optical coherence tomography of the human skin. J. Am. Acad. Dermatol. **37**(6), 958–963 (1997)
28. L.L. Otis, M.J. Everett, U.S. Sathyam, B.W. Colston Jr., Optical coherence tomography: a new imaging technology for dentistry. J. Am. Dent. Assoc. **131**(4), 511–514 (2000)
29. A.V. D'Amico, M. Weinstein, X. Li, J.P. Richie, J. Fujimoto, Optical coherence tomography as a method for identifying benign and malignant microscopic structures in the prostate gland. Urology **55**(5), 783–787 (2000)
30. C. Pitris, A. Goodman, S.A. Boppart, J.J. Libus, J.G. Fujimoto, M.E. Brezinski, High-resolution imaging of gynecologic neoplasms using optical coherence tomography. Obstet. Gynecol. **93**(1), 135–139 (1999)
31. G.J. Tearney, S.A. Boppart, B.E. Bouma, M.E. Brezinski, N.J. Weissman, J.F. Southern, J.G. Fujimoto, Scanning single-mode fiber optic catheter-endoscope for optical coherence tomography. Opt. Lett. **21**(7), 543–545 (1996)

32. P.R. Herz, Y. Chen, A.D. Aguirre, J.G. Fujimoto, H. Mashimo, J. Schmitt, A. Koski, J. Goodnow, C. Petersen, Ultrahigh resolution optical biopsy with endoscopic optical coherence tomography. Opt. Express **12**(15), 3532–3542 (2004)
33. X. Li, C. Chudoba, T. Ko, C. Pitris, J.G. Fujimoto, Imaging needle for optical coherence tomography. Opt. Lett. **25**(20), 1520–1522 (2000)
34. T. Yamamoto, T. Tada, S.V. Brodsky, H. Tanaka, E. Noiri, F. Kajiya, M.S. Goligorsky, Intravital videomicroscopy of peritubular capillaries in renal ischemia. Am. J. Physiol. Renal Physiol. **282**(6), F1150–F1155 (2002)
35. M. Angelescu, T. Kraus, M. Wiesel, O. Hergesell, U. Haberkorn, E. Klar, Assessment of renal graft function by perioperative monitoring of cortical microcirculation in kidney transplantation. Transplantation **75**(8), 1190–1196 (2003)
36. Y. Ogasawara, K. Takehara, T. Yamamoto, R. Hashimoto, H. Nakamoto, F. Kajiya, Quantitative blood velocity mapping in glomerular capillaries by in vivo observation with an intravital videomicroscope. Methods Inf. Med. **39**(2), 175–178 (2000)
37. H.N. Ibrahim, T.H. Hostetter, Diabetic nephropathy. J. Am. Soc. Nephrol. **8**(3), 487–493 (1997)
38. G.T. O'Bryan, T.H. Hostetter, The renal hemodynamic basis of diabetic nephropathy. Semin. Nephrol. **17**(2), 93–100 (1997)
39. I. Ichikawa, A. Fogo, Focal segmental glomerulosclerosis. Pediatr. Nephrol. **10**(3), 374–391 (1996)
40. Z. Szabo, J. Xia, W.B. Mathews, P.R. Brown, Future direction of renal positron emission tomography. Semin. Nucl. Med. **36**(1), 36–50 (2006)
41. L. Juillard, M.F. Janier, D. Fouque, L. Cinotti, N. Maakel, D. Le Bars, P.Y. Barthez, N. Pozet, M. Laville, Dynamic renal blood flow measurement by positron emission tomography in patients with CRF. Am. J. Kidney Dis. **40**(5), 947–954 (2002)
42. N. Kudomi, N. Koivuviita, K.E. Liukko, V.J. Oikonen, T. Tolvanen, H. Iida, R. Tertti, K. Metsarinne, P. Iozzo, P. Nuutila, Parametric renal blood flow imaging using [15O]H_2O and PET. Eur. J. Nucl. Med. Mol. Imaging **36**(4), 683–691 (2009)
43. E.U. Nitzsche, Y. Choi, D. Killion, C.K. Hoh, R.A. Hawkins, J.T. Rosenthal, D.B. Buxton, S.C. Huang, M.E. Phelps, H.R. Schelbert, Quantification and parametric imaging of renal cortical blood flow in vivo based on Patlak graphical analysis. Kidney Int. **44**(5), 985–996 (1993)
44. H.R. Middlekauff, E.U. Nitzsche, A.H. Nguyen, C.K. Hoh, G.G. Gibbs, Modulation of renal cortical blood flow during static exercise in humans. Circ. Res. **80**(1), 62–68 (1997)
45. N.M. Alpert, C.A. Rabito, D.J. Correia, J.W. Babich, B.H. Littman, R.G. Tompkins, N.T. Rubin, R.H. Rubin, A.J. Fischman, Mapping of local renal blood flow with PET and H (2)(15)O. J. Nucl. Med. **43**(4), 470–475 (2002)
46. N. Michoux, X. Montet, A. Pechere, M.K. Ivancevic, P.Y. Martin, A. Keller, D. Didier, F. Terrier, J.P. Vallee, Parametric and quantitative analysis of MR renographic curves for assessing the functional behaviour of the kidney. Eur. J. Radiol. **54**(1), 124–135 (2005)
47. J.P. Vallee, F. Lazeyras, H.G. Khan, F. Terrier, Absolute renal blood flow quantification by dynamic MRI and Gd-DTPA. Eur. Radiol. **10**(8), 1245–1252 (2000)
48. L. Bokacheva, H. Rusinek, J.L. Zhang, V.S. Lee, Assessment of renal function with dynamic contrast-enhanced MR imaging. Magn. Reson. Imaging Clin. N. Am. **16**(4), 597–611 (2008), viii
49. C. De Bazelaire, N.M. Rofsky, G. Duhamel, M.D. Michaelson, D. George, D.C. Alsop, Arterial spin labeling blood flow magnetic resonance imaging for the characterization of metastatic renal cell carcinoma(1). Acad. Radiol. **12**(3), 347–357 (2005)
50. H. Akinbi, S. Abbasi, P.L. Hilpert, V.K. Bhutani, Gastrointestinal and renal blood flow velocity profile in neonates with birth asphyxia. J. Pediatr. **125**(4), 625–627 (1994)
51. F. van Bel, G.L. Guit, J. Schipper, M. van de Bor, J. Baan, Indomethacin-induced changes in renal blood flow velocity waveform in premature infants investigated with color Doppler imaging. J. Pediatr. **118**(4 Pt 1), 621–626 (1991)
52. S.N. Wong, R.N. Lo, E.C. Yu, Renal blood flow pattern by noninvasive Doppler ultrasound in normal children and acute renal failure patients. J. Ultrasound Med. **8**(3), 135–141 (1989)

53. T. Yura, S. Yuasa, M. Fukunaga, K.F. Badr, H. Matsuo, Role for Doppler ultrasound in the assessment of renal circulation: effects of dopamine and dobutamine on renal hemodynamics in humans. Nephron **71**(2), 168–175 (1995)
54. K. Kalantarinia, J.T. Belcik, J.T. Patrie, K. Wei, Real-time measurement of renal blood flow in healthy subjects using contrast-enhanced ultrasound. Am. J. Physiol. Ren. Physiol. **297**(4), F1129–F1134 (2009)
55. D.H. Kay, M. Mazonakis, C. Geddes, G. Baxter, Ultrasonic microbubble contrast agents and the transplant kidney. Clin. Radiol. **64**(11), 1081–1087 (2009)
56. P.M. Andrews, W.M. Petroll, H.D. Cavanagh, J.V. Jester, Tandem scanning confocal microscopy (TSCM) of normal and ischemic living kidneys. Am. J. Anat. **191**(1), 95–102 (1991)
57. V. Yang, M. Gordon, B. Qi, J. Pekar, S. Lo, E. Seng-Yue, A. Mok, B. Wilson, I. Vitkin, High speed, wide velocity dynamic range Doppler optical coherence tomography (Part I): system design, signal processing, and performance. Opt. Express **11**(7), 794–809 (2003)
58. S. Yazdanfar, A.M. Rollins, J.A. Izatt, Imaging and velocimetry of the human retinal circulation with color Doppler optical coherence tomography. Opt. Lett. **25**(19), 1448–1450 (2000)
59. L. Yu, Z. Chen, Doppler variance imaging for three-dimensional retina and choroid angiography. J. Biomed. Opt. **15**(1), 016029 (2010)
60. Y. Wang, B.A. Bower, J.A. Izatt, O. Tan, D. Huang, Retinal blood flow measurement by circumpapillary Fourier domain Doppler optical coherence tomography. J. Biomed. Opt. **13**(6), 064003 (2008)
61. R.M. Werkmeister, N. Dragostinoff, M. Pircher, E. Gotzinger, C.K. Hitzenberger, R.A. Leitgeb, L. Schmetterer, Bidirectional Doppler Fourier-domain optical coherence tomography for measurement of absolute flow velocities in human retinal vessels. Opt. Lett. **33**(24), 2967–2969 (2008)
62. J. Barton, J.A. Izatt, M.D. Kulkarni, S. Yazdanfar, A.J. Welch, Three-dimensional reconstruction of blood vessels from in vivo color Doppler optical coherence tomography images. Dermatology **198**(4), 355–361 (1999)
63. Y. Zhao, Z. Chen, C. Saxer, Q. Shen, S. Xiang, J.F. de Boer, J.S. Nelson, Doppler standard deviation imaging for clinical monitoring of in vivo human skin blood flow. Opt. Lett. **25**(18), 1358–1360 (2000)
64. H. Li, B.A. Standish, A. Mariampillai, N.R. Munce, Y. Mao, S. Chiu, N.E. Marcon, B.C. Wilson, A. Vitkin, V.X.D. Yang, Feasibility of interstitial Doppler optical coherence tomography for in vivo detection of microvascular changes during photodynamic therapy. Lasers Surg. Med. **38**(8), 754–761 (2006)
65. V.X.D. Yang, S.J. Tang, M.L. Gordon, B. Qi, G. Gardiner, M. Cirocco, P. Kortan, G.B. Haber, G. Kandel, I.A. Vitkin, B.C. Wilson, N.E. Marcon, Endoscopic Doppler optical coherence tomography in the human GI tract: initial experience. Gastrointest. Endosc. **61**(7), 879–890 (2005)
66. W.M. Stahl, Effect of mannitol on the kidney: changes in intrarenal hemodynamics. N. Engl. J. Med. **272**, 382–386 (1965)
67. K.E. Lindstrom, L. Ronnstedt, G. Jaremko, B. Haraldsson, Physiological and morphological effects of perfusing isolated rat kidneys with hyperosmolal mannitol solutions. Acta Physiol. Scand. **166**(3), 231–238 (1999)
68. R. Behnia, E. Koushanpour, E.A. Brunner, Effects of hyperosmotic mannitol infusion on hemodynamics of dog kidney. Anesth. Analg. **82**(5), 902–908 (1996)
69. X. Deng, W.J. Welch, C.S. Wilcox, Role of nitric oxide in short-term and prolonged effects of angiotensin II on renal hemodynamics. Hypertension **27**(5), 1173–1179 (1996)
70. L. Ekelund, J. Gothlin, Effect of angiotensin on normal renal circulation determined by angiography and a dye dilution technique. Acta. Radiol. Diagn. (Stockh) **18**(1), 39–48 (1977)
71. J.H. Gothlin, J. Krakenes, S. Tvete, The effects of angiotensin on the diagnostics and haemodynamics in renal angiography. Eur. J. Radiol. **3**(4), 328–330 (1983)
72. J.E. Hall, J.P. Granger, Renal hemodynamic actions of angiotensin II: interaction with tubuloglomerular feedback. Am. J. Physiol. **245**(2), R166–R173 (1983)

73. K.M. Denton, W.P. Anderson, R. Sinniah, Effects of angiotensin II on regional afferent and efferent arteriole dimensions and the glomerular pole. Am. J. Physiol. Regul. Integr. Comp. Physiol. **279**(2), R629–R638 (2000)
74. V.J. Srinivasan, S. Sakadzic, I. Gorczynska, S. Ruvinskaya, W. Wu, J.G. Fujimoto, D.A. Boas, Quantitative cerebral blood flow with optical coherence tomography. Opt. Express **18**(3), 2477–2494 (2010)
75. Q. Li, M.L. Onozato, P.M. Andrews, C.W. Chen, A. Paek, R. Naphas, S. Yuan, J. Jiang, A. Cable, Y. Chen, Automated quantification of microstructural dimensions of the human kidney using optical coherence tomography (OCT). Opt. Express **17**(18), 16000–16016 (2009)
76. M.L. Onozato, P.M. Andrews, Q. Li, J. Jiang, A. Cable, Y. Chen, Optical coherence tomography of human kidney. J. Urol. **183**(5), 2090–2094 (2010)
77. P.M. Andrews, H.W. Wang, J. Wierwille, W. Gong, J. Verbesey, M. Cooper, Y. Chen, Optical Coherence Tomography of the Living Human Kidney. Journal of Innovative Optical Health Sciences **7**, 1350064 (2014)
78. P.M. Andrews, M. Cooper, J. Verbesey, S. Ghasemian, D. Rogalsky, P. Moody, A. Chen, P. Alexandrov, H.W. Wang, Y. Chen, Mannitol Infusion within 15 min of Cross-Clamp Improves Living Donor Kidney Preservation. Transplantation in press (2014)
79. P.M. Andrews, S.B. Bates, Improving Euro-Collins flushing solution's ability to protect kidneys from normothermic ischemia. Miner. Electrolyte Metab. **11**(5), 309–313 (1985)
80. P.M. Andrews, S.B. Bates, Dietary protein prior to renal ischemia dramatically affects postischemic kidney function. Kidney Int. **30**(3), 299–303 (1986)
81. C.W. Chen, M.W. Betz, J.P. Fisher, A. Paek, Y. Chen, Macroporous hydrogel scaffolds and their characterization by optical coherence tomography. Tissue Eng. C **17**, 101–112 (2011)
82. X. Qi, Y.S. Pan, Z.L. Hu, W. Kang, J.E. Willis, K. Olowe, M.V. Sivak, A.M. Rollins, Automated quantification of colonic crypt morphology using integrated microscopy and optical coherence tomography. J. Biomed. Opt. **13**(5), 054055 (2008)
83. K. Zhang, J.U. Kang, Real-time intraoperative 4D full-range FD-OCT based on the dual graphics processing units architecture for microsurgery guidance. Biomed. Opt. Express **2**(4), 764–770 (2011)
84. K. Zhang, J.U. Kang, Graphics processing unit accelerated non-uniform fast Fourier transform for ultrahigh-speed, real-time Fourier-domain OCT. Opt. Express **18**(22), 23472–23487 (2011)
85. K. Zhang, J.U. Kang, Real-time 4D signal processing and visualization using graphics processing unit on a regular nonlinear-k Fourier-domain OCT system. Opt. Express **18**(11), 11772–11784 (2011)
86. V. Jayaraman, J. Jiang, H. Li, P.J.S. Heim, G.D. Cole, B. Potsaid, J.G. Fujimoto, A. Cable, OCT imaging up to 760 kHz axial scan rate using single-mode 1310 nm MEMS-Tunable VCSELs with >100 nm tuning range, in *Conference on Lasers and Electro-Optics: Applications and Technology*, (Optical Society of America, Baltimore, 2011), p. PDPB2
87. R. Huber, M. Wojtkowski, J.G. Fujimoto, Fourier Domain Mode Locking (FDML): a new laser operating regime and applications for optical coherence tomography. Opt. Express **14**(8), 3225–3237 (2006)
88. T.H. Tsai, B. Potsaid, M.F. Kraus, C. Zhou, Y.K. Tao, J. Hornegger, J.G. Fujimoto, Piezoelectric-transducer-based miniature catheter for ultrahigh-speed endoscopic optical coherence tomography. Biomed. Opt. Express **2**(8), 2438–2448 (2011)
89. W. Wieser, B.R. Biedermann, T. Klein, C.M. Eigenwillig, R. Huber, Multi-megahertz OCT: high quality 3D imaging at 20 million A-scans and 4.5 GVoxels per second. Opt. Express **18**(14), 14685–14704 (2010)
90. A. Ahmad, S.G. Adie, E.J. Chaney, U. Sharma, S.A. Boppart, Cross-correlation-based image acquisition technique for manually-scanned optical coherence tomography. Opt. Express **17**(10), 8125–8136 (2009)

Intraoperative OCT in Surgical Oncology

80

Fredrick A. South, Marina Marjanovic, and Stephen A. Boppart

Keywords
Optical coherence tomography • Intraoperative • Surgical • Breast • Lymph node • Brain • Cancer • Imaging

80.1 Introduction

80.1.1 Intraoperative Imaging of Cancer Using Optical Techniques

The global incidence of cancer is rising, putting an increasingly heavy burden upon health care. It is estimated that 12.7 million cancer cases and 7.6 million cancer deaths occurred worldwide in 2008 [1]. In 2012, an estimated 1.6 million new cancer cases and 0.5 million cancer deaths will occur in the United States alone [2]. With one out of every four deaths in the United States caused by cancer, the need to effectively detect and treat cancer is one of the most significant

F.A. South
Beckman Institute for Advanced Science and Technology, University of Illinois at Urbana–Champaign, Urbana, IL, USA

Department of Electrical and Computer Engineering, University of Illinois at Urbana–Champaign, Urbana, IL, USA

M. Marjanovic
Beckman Institute for Advanced Science and Technology, University of Illinois at Urbana–Champaign, Urbana, IL, USA

S.A. Boppart (✉)
Biophotonics Imaging Laboratory, Beckman Institute for Advanced Science and Technology, University of Illinois at Urbana-Champaign, Urbana, IL, USA

Departments of Bioengineering, Electrical and Computer Engineering, and Medicine, University of Illinois at Urbana-Champaign, Urbana, IL, USA
e-mail: boppart@illinois.edu

© Springer International Publishing Switzerland 2015

W. Drexler, J.G. Fujimoto (eds.), *Optical Coherence Tomography*,
DOI 10.1007/978-3-319-06419-2_82

problems faced in health care today. Effective cancer treatment typically depends upon early detection and, for most solid tumors, successful removal of the cancerous tumor tissue via surgical procedures. Difficulties arise when attempting to differentiate between normal and tumor tissue during surgery. Unaided visual examination of the tissue provides only superficial, low-resolution information and often with little visual contrast. Imaging modalities such as ultrasound and positron emission tomography have been developed for intraoperative cancer imaging [3, 4]. Though these modalities are widely used for cancer screening and diagnostics, their use in the operating room is limited by low spatial resolution. Optical imaging provides cellular resolution and numerous forms of contrast mechanisms, allowing for more precise localization of the tumor tissue. It is also relatively inexpensive and highly portable, making it well suited for intraoperative applications.

Many optical imaging modalities have potential for guiding surgical oncology procedures [5, 6]. The majority of these modalities are fluorescence based and require the use of fluorescent-labeled dyes, cells, nanoparticles, or molecular probes [7]. Unfortunately, the use of fluorescent labels introduces issues with bioavailability, specificity, toxicity, and regulatory approval. Therefore, a label-free imaging method would be preferred for surgical imaging. Raman spectroscopy and autofluorescence imaging do not require application of labels or contrast agents and have been proposed for surgical use. Weak signal, high background fluorescence, and complicated probe design have slowed progress toward surgical applications of Raman spectroscopy [8]. Autofluorescence imaging is confounded by uncertain tumor specificity due to the complex biological mechanisms that influence the autofluorescence process [9]. Other label-free methods include wide-field optical spectroscopy which probes the molecular heterogeneity of the tumor environment [10, 11]. The large field-of-view and molecular contrast are advantageous, but the method is dependent upon patient demographics and has markedly lower resolution than many other optical imaging methods.

While each of the above methods may play an important role in cancer imaging, optical coherence tomography (OCT) is currently the most promising solution for real-time, cellular-resolution, label-free structural imaging in biological tissue [12, 13]. Full-field OCT is an alternative to standard scanning OCT and is being explored for in situ use [14]. Further details on full-field OCT can be found in ► Chaps. 25, "Time Domain Full Field Optical Coherence Tomography Microscopy" and ► 26, "Assessment of Breast, Brain and Skin Pathological Tissue Using Full Field OCM".

80.1.2 OCT in Cancer Screening, Guided Biopsy, and Surgical Resection

Cancer screening and detection is typically performed using imaging modalities such as ultrasound, x-ray computed tomography, magnetic resonance imaging, single-photon emission tomography, and positron emission tomography [15]. These modalities have large fields-of-view and high depth penetration making

them well suited for screening applications. However, if a large field-of-view is not necessary, OCT could be used for screening at higher resolutions not possible with other modalities. OCT has already been used to detect cancer in many different applications such as dermatology, endoscopy, colonoscopy, gynecology, and urology, discussed elsewhere in this book.

Despite advances in cancer detection by medical imaging, biopsy followed by histology remains the gold standard for cancer diagnosis. After detection by imaging, tumors are typically sampled using needle biopsy. However, the rate of misdiagnosis for core needle biopsy is disturbingly high [16]. This points to a need for high-resolution guided biopsy, and the recent work on OCT-guided needle biopsy is quite promising [17, 18]. Further information on needle probe imaging can be found in ► Chap. 81, "Optical Coherence Tomography in a Needle Format".

Following detection and diagnosis of cancer, standard treatment involves surgical removal of the tumor. Even when the tumor location has been determined by presurgical imaging, movement of soft tissues over time can make locating and removing the tumor difficult. Using OCT it is possible to image immediately prior to and during resection, providing real-time feedback to the surgeon. One example of this is the imaging of nonmelanoma skin cancer in situ [19, 20]. In one study in particular, OCT was used to demarcate the boundary of a tumor immediately before removal via Mohs surgery [20]. The surgery was then performed in a standard way. Because the tumor extended beyond the area visible on the surface, two stages of resection were required. This suggests that superficial information was insufficient for predicting the extent of the tumor and guiding the resection. In contrast, the OCT images accurately predicted the extent of the tumor due to the ability to identify subsurface margins.

Identification of some tumor margins is even more challenging. Resection of malignant glioma of the brain, for example, does not exhibit a clear brain-tumor interface. Current intraoperative imaging methods such as ultrasound and MRI lack the resolution necessary to detect the ambiguous tumor boundary. As a result, there is only about 30 % correlation between the surgeon's estimate of "complete removal of visible tumor" and "clearance of enhancement on MRI" [21]. This indicates that high-resolution image-guided surgery is necessary. In one study, OCT was used to image ex vivo brain tumors from both a mouse model and human patients [22]. In the mouse model, OCT clearly distinguished between normal tissue, the diffuse tumor edge, and the heterogeneous solid tumor. The results were verified by histology. Glioma tumors typically infiltrate the surrounding brain tissue by migrating along myelinated fiber tracts. Patient survival rate is directly related to the removal of highly invaded tissue. On the other hand, it may be desirable to leave areas of low invasion undisturbed. The ability of OCT to distinguish these areas is a key advantage over existing methods. Imaging was also performed on ex vivo human tissue immediately following excision with similar results to the mouse model.

The first in vivo intraoperative brain study was performed in 2009 [23]. The OCT sample arm was mounted in a flexible arm that enabled noncontact imaging inside the surgical cavity. Both ex vivo and in vivo studies were performed for comparison.

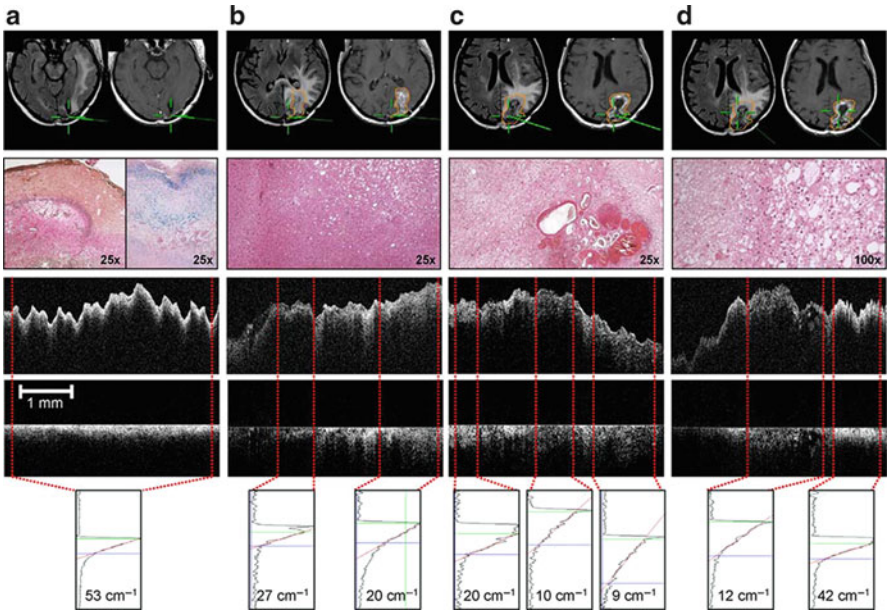

Fig. 80.1 Intraoperative OCT imaging during resection of glioblastoma (WHO grade IV), which recurred after initial surgery and radiation. A pilot laser was used to focus the OCT probe on the target volume. The center of the scan line was registered by the acquisition of marker points using a neuronavigation system. (**a**) Collagen-rich cortical scar: H&E stained (*left*) and with deposition of iron pigmented macrophages (*right*; Berlin blue reaction). (**b**) Microcystic changes within the tumor infiltration zone. (**c**) Highly cellular tumor with vascular proliferations and pleomorphic tumor cells. (**d**) Pleomorphic tumor cells (*right*) and tumor necrosis (*left*) within the center of the tumor (**b**–**d** H&E staining) (From Ref. [23], published by Springer Science+Business Media)

The ex vivo imaging distinguished between normal tissue, tumor infiltrate, solid tumor, and necrosis, verifying results from the previous study. Additionally, the attenuation coefficients were calculated and found to vary according to tissue condition. In vivo imaging was performed on nine patients with a total of 42 imaging sites using a time-domain OCT system. Images were taken from several areas during each surgery. Due to motion during imaging, an automated algorithm was used to detect the surface and realign the OCT A-scans. Figure 80.1 depicts representative results from scarred tissue, tumor infiltrate, solid tumor, and necrotic tissue, respectively. The imaging location, histology, OCT data, realigned OCT data, and attenuation profile are shown for each tissue type. Data from all nine patients was examined by a "blinded" investigator, and each image was evaluated as "normal light attenuation," "loss of normal light attenuation," or "loss of normal light attenuation with a pathological tissue microstructure." Histology slides were evaluated as "no tumor," "diffuse tumor infiltration," and "solid tumor." There was a clear correlation between the OCT and histology results. A total of 12 histological samples were found to have no tumor present. Nine of these were correctly identified as normal by OCT. The remaining 3 were incorrectly identified as

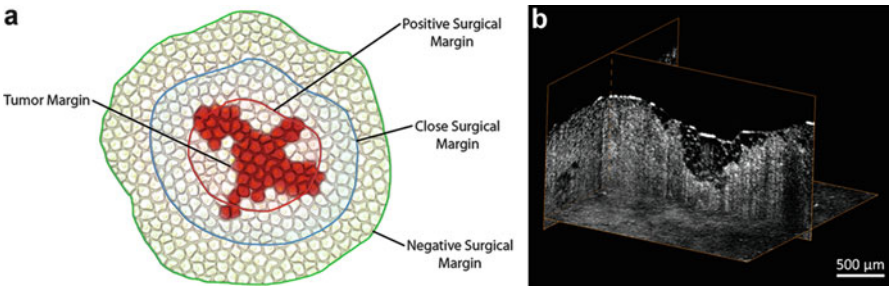

Fig. 80.2 Surgical margins and tumor margins in breast cancer surgery. (**a**) Surgical classification of the tumor margin status depends on the distance of cancer cells from the surface of the resected tissue. If the surgical margin is located along the tumor margin or the tumor cells are found beyond the surgical margin, the surgical margin is considered "positive" (*red line*). A "close" surgical margin (*blue line*) does not have tumor cells within 1 mm or 2 mm from the surgical margin. Otherwise, a surgical margin is considered "negative" (*green line*). The tumor margin follows the edge of the solid tumor itself, and it does not include any metastatic cells that may have migrated away from the primary solid tumor mass (Own work published in SPIE Proceedings, doi:10.1117/12.2040315) [70]. (**b**) Three-dimensional OCT image of a positive margin from an excised human breast tumor mass (Own work unpublished)

loss of normal light attenuation due to micro-hemorrhage of the tissue. Out of 15 diffuse tumor infiltrations, all showed loss of attenuation and 9 showed pathological microstructure. Histological results indicated 15 solid tumors, all of which showed loss of attenuation and pathological microstructure in OCT. Overall, the results indicate that OCT can be used to successfully identify in vivo glioma and the surrounding infiltration, possibly improving the success rate of current surgical procedures.

80.2 Applications in Breast Cancer

80.2.1 Intraoperative Assessment of Tumor Margins: Background

Early cancer detection with x-ray mammography, ultrasound, and MRI allows surgeons in most cases to remove smaller tumors while preserving as much of the normal breast tissue as possible (during lumpectomy procedures). After the surgery, histopathology is performed on the excised tissue to assess the margin status. If the margin contains cancer cells ("positive" margin) or the cancer is present within a certain depth of the resected surface ("close" margin), then the patient is advised to undergo re-excision surgery until a "negative" margin is achieved (Fig. 80.2a). In a survey, 31 % of radiation oncologists defined a close margin as having no cells within 1 mm and an additional 38 % defined it to be no cells within 2 mm of the surface [24]. Since then more studies correlated the width of uninvolved margins to local recurrence of cancer, which has allowed surgeons to use 1 mm to define a "negative" margin and encourage breast conservation surgeries [25, 26].

In a large number of studies, it was found that the margin status was the key predictor of local recurrence of cancer, and positive margins have contributed significantly to a high rate of repeated surgeries [27–38]. A positive margin, with cancer cells on the surface of the resected tissue, occurs in at least 30–35 % of cases, and an additional 10–15 % are classified as close margins [37].

Currently, no real-time intraoperative method exists to rapidly assess the status of lumpectomy margins to determine if additional tissue needs to be removed [39, 40]. None of the investigated techniques, including frozen section analysis, touch prep cytology, specimen radiography, and radiofrequency spectroscopy, satisfy the necessary requirements. Frozen section analysis has a sensitivity of 73 % and a specificity of 98 % compared to paraffin section analysis for breast cancer, but is not widely accepted due to difficulties in performing frozen sections on adipose tissue and increased operating room time (∼20–30 min) [39]. Overall, current histological methods cannot rapidly determine the surgical margin status due to time, cost, and technology limitations. Touch prep cytology with reported sensitivities of 75 % and specificities of 83 % can rapidly assess the entire margin area [41]. However, this technique requires that the tumor cells are present at the surface and that they detach and adhere to the slide for microscopic examination. Touch prep cytology does not provide information about the presence of cancer cells beneath the surface and thus is unable to determine close and negative margins. Surgeons can visualize tumor margins using intraoperative specimen radiography by displaying two-dimensional x-ray projections. Unfortunately, this technique has a rather low sensitivity (49 %) and specificity (73 %) which is primarily due to its inability to identify diffuse microscopic processes, especially where the tumor boundary is poorly defined [42, 43]. Radiofrequency spectroscopy with low sensitivity (71 %) and specificity (68 %), shallow penetration depth (100 μm), and low resolution offers very limited detection within 1–2 mm for margin classification [44].

Among all optical techniques, OCT has the greatest potential for in situ label-free intraoperative margin assessment in breast-conserving surgeries, since it acquires high-resolution images in the same physical range as that used in histological analysis to classify surgical margins as positive, close, or negative (Fig. 80.2b). Figure 80.3 shows some representative OCT images of negative and positive surgical margins obtained ex vivo from resected breast tumors. The observations made by OCT were confirmed by histopathology.

80.2.2 Intraoperative Assessment of Tumor Margins: Results

The first study to demonstrate breast cancer imaging using OCT was conducted using a preclinical rat model [45]. Virgin female rats were injected with carcinogen N-methyl-N-nitrosourea (MNU), leading to the development of invasive mammary tumors. Three-dimensional imaging of the palpable tumors was performed with a time-domain OCT system centered at 800 nm with 2 μm axial and 10 μm transverse resolutions. Healthy mammary tissue was found to have a heterogeneous

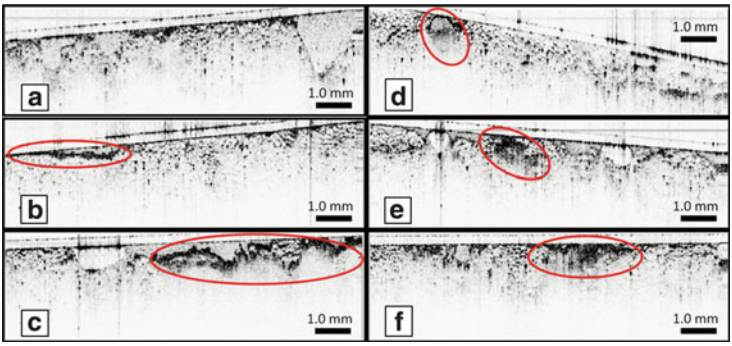

Fig. 80.3 Intraoperative OCT images of resected breast tissue specimens a human patient diagnosed with ductal carcinoma in situ (DCIS). (**a**) OCT of normal tissue was identified by the homogenous pattern of large adipose cells. (**b–d**) Readily identified surgical artifacts are also shown. (**b**) Surface blood appeared as a thin film of scatterers. (**c**) Cauterized tissue exhibited a distinct patch-like appearance. (**d**) Potential duct with a mixed distribution of low- and high-scattering areas. (**e**, **f**) Positive margins contained tumor cells and tissue represented by a highly scattering area that was more heterogeneous and disruptive compared to the surrounding tissue architecture (Adapted from [48])

structure composed of mixed adipose and stroma. In the OCT data, individual adipocytes appeared as segmented oval-shaped objects, while stroma appeared dense and highly scattering. OCT imaging of early-stage tumors revealed thickening and stronger scattering in the ductal morphology, suggesting precancerous changes prior to full tumor invasion. Late-stage solid tumor was identified as dense and highly scattering, similar to the scattering intensity from stroma. Despite this similarity, the morphology of the tumor caused it to appear distinct from the surrounding tissue. While the tumor margin boundary was visible in the 2D representation, 3D visualization facilitated detection of the tumor boundary. Results from this study suggest that while single tumor cells may be challenging to locate, precancerous changes and significant tumor invasion can be detected using OCT.

For OCT to guide surgical procedures, it is necessary to understand how specific histological features appear in OCT images of human breast tissue. To accomplish this goal, a comparison study was conducted between OCT and the corresponding histology sections of human breast tissue [46]. Two-dimensional and three-dimensional spectral-domain OCT imaging was performed at a center wavelength of 1090 nm with 3.5 μm axial and 6 μm transverse resolutions. A total of 119 specimens were imaged from 35 patients covering several pathologies including ductal carcinoma in situ (DCIS), infiltrating tumor, and microcalcifications. Specimen radiography was performed on freshly excised tissue in the pathology lab to guide OCT imaging to suspicious sites. A non-blinded comparison was made between OCT and histology findings. Analysis of healthy tissue revealed clear visualization of adipose, stroma, ducts, and glands. Benign changes including cysts, fibroadenoma, and ductal hyperplasia were also visible. Comparison results for lobular DCIS are shown in Fig. 80.4a. Normal adipose tissue and

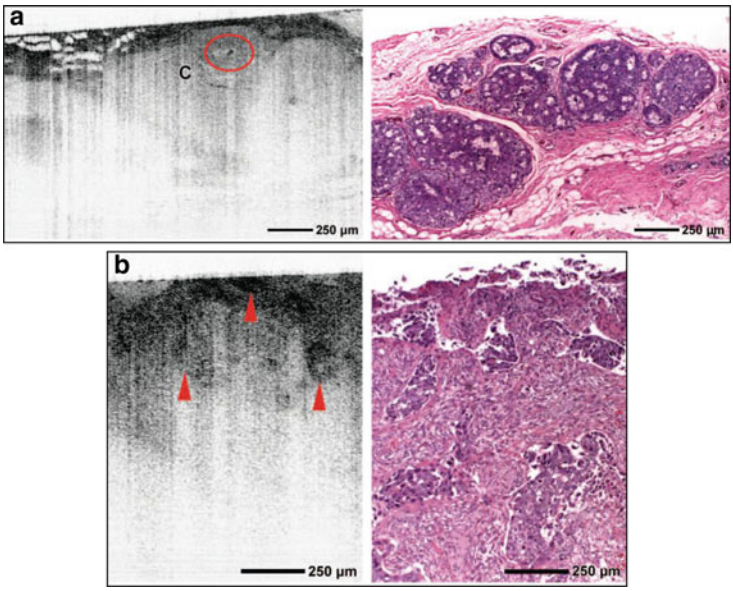

Fig. 80.4 Comparison of tumor features in OCT and histology. (**a**) OCT image and corresponding histology of DCIS lesions in lobules. Tumor cells within lobules appear uniformly low scattering. Dilatation and architectural distortion of the lobules are visible. A microcalcification (*C*, circled area) within the lobules appears highly scattering with pronounced shadowing. (**b**) OCT image and corresponding histology of infiltrating ductal carcinoma. Highly scattering regions (*arrowheads*), which correspond to tongues of invasive cancer, are visible (Adapted from [46], reprinted with permission from Radiological Society of North America)

stroma are visible along the surface of the sample. Enlarged, low-scattering DCIS lobules visibly distort the surrounding structure, and a microcalcification is visible as a small high-scattering area. OCT and histology comparison of invasive ductal carcinoma is shown in Fig. 80.4b. Tumor appears as highly scattering irregular "tongues" which protrude into the desmoplastic stroma. Separate calcifications are also visible. Solid infiltrative ductal carcinoma was also imaged, yet it was difficult to distinguish from stroma due to the highly scattering uniform structure. Results from the comparison study demonstrate that OCT is capable of detecting normal, benign, and malignant tissue structures in the human breast.

A study comparing OCT, optical coherence microscopy (OCM), and histology of breast tissue has shown similar results [47]. An integrated OCT-OCM system was used with 4 μm axial resolution and 14 μm or 2 μm transverse resolution for OCT and OCM, respectively. A total of 34 benign and 10 malignant ex vivo specimens were imaged 2–6 h post resection. A non-blinded comparison of OCT with histology located adipose, stroma, benign lobules and ducts, cysts, and in situ and invasive carcinoma. These results were consistent with previous studies, with the addition of higher-resolution optical scattering data provided by OCM.

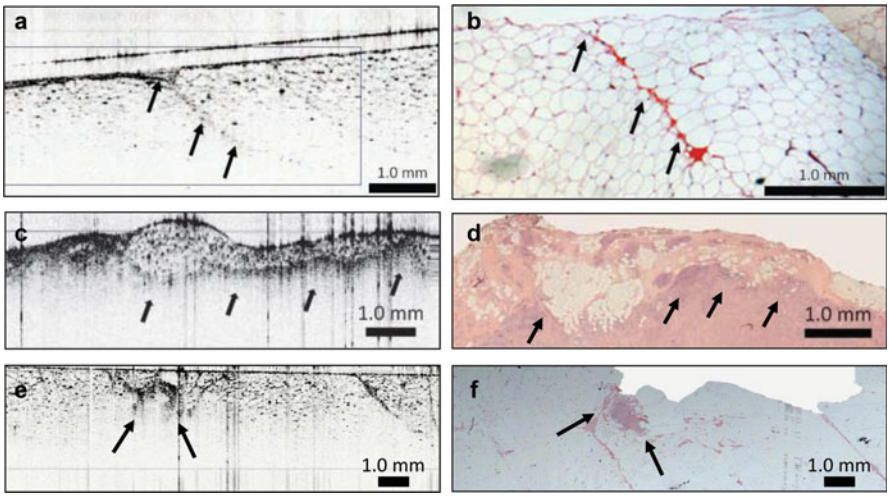

Fig. 80.5 Surgical margins imaged using OCT. (**a**) OCT and (**b**) histology of a negative tumor margin. Adipose cells and microvasculature (*arrows*) are present. (**c**) OCT and (**d**) histology of positive tumor margin. OCT shows a distinct heterogeneously scattering region (*arrows*) with small, highly scattering foci indicative of collections of tumor cells. (**e**) OCT and (**f**) histology of positive tumor margin with an isolated tumor focus (*arrows*) (Adapted from [48])

The first intraoperative OCT breast margin assessment study was published by Nguyen et al. [48]. A portable spectral-domain OCT system was constructed for imaging in the operating room. The system performed 3D imaging at a center wavelength of 1,310 nm with 5.9 μm axial and 35 μm transverse resolutions. A total of 37 patient specimens were imaged immediately following resection. Suspicious areas were located for OCT imaging by visual inspection and palpation. The imaged areas were then marked with surgical ink for correlation with histology. Seventeen of the patient specimens were used as a training set. The training set data included both negative (no tumor present) and positive (tumor present) margins and revealed confounding factors such as pooled blood and cauterized tissue which both appeared highly scattering, mimicking the scattering signature of tumor tissue. When classifying negative and positive margins, these confounding factors must be carefully considered (Fig. 80.3). Highly scattering blood on the tissue surface was easily removed by flushing the tissue with saline. Cauterized tissue was identified as a highly irregular, intensely scattering, and highly attenuating surface that blocked all signals from beneath the cauterized and charred surface. The remaining 20 patient specimens were used to determine the feasibility of tumor margin assessment using OCT. Out of the 20 margins, 11 were diagnosed histologically positive and 9 were diagnosed histologically negative. A blinded analysis of OCT data was performed and compared with histology results. OCT data sets containing tumor cells or tumor tissue were classified as positive, while data sets void of tumor were classified as negative. Representative tumor margins are shown in Fig. 80.5. As expected, tumor cells are identified by high scattering and

heterogeneous structure, in contrast with normal fibroadipose tissue. Comparison of OCT analysis and histology resulted in 100 % specificity and 82 % sensitivity for using OCT to identify positive margins intraoperatively in real time, compared to postoperative assessment of histological tissue sections. This demonstrates that intraoperative breast margin assessment with OCT is feasible and warrants further study.

80.2.3 Intraoperative Assessment of Sentinel Lymph Nodes: Background

Lymph nodes are anatomically distributed along locoregional drainage patterns in the body and function as filters to capture and retain potentially harmful macromolecules and microorganisms and provide a tissue microenvironment to facilitate immunological surveillance of various antigens. Lymph nodes have a well-defined structure with an outer capsule, subcapsular sinus, cortex containing follicles, medullary sinuses, medullary cords, and hilus [49]. The organization of the lymph node is well suited for its filtering role. The lymph enters through the afferent lymphatic vessels into the marginal sinuses, under the capsule, and moves into the medullary sinuses (Fig. 80.6a). The system of sinuses retains the particles, facilitating immune cells in their monitoring functions.

Inactivated (normal) lymph nodes contain a relatively small number of active immune cells. Upon interaction with antigens, lymph nodes became enlarged mainly due to the recruitment and activation of lymphocytes and macrophages involved in the primary immune response. In the case of a metastatic node, in addition to the inflammatory response, there is also the presence of infiltrating and dividing cancer cells. It is well known that cancer cells from the primary metastatic tumor often travel via the lymphatic system and accumulate in the lymph nodes. Most of the lymph from the breasts (80–100 %) drains into the axillary lymph nodes, making them important in the staging of breast cancer. In the past, it was common to remove 10–30 axillary lymph nodes in order to stage disease progression using postoperative histopathological analysis and determine the most appropriate therapeutic treatment. However, removal of lymph nodes can cause disruption of the lymphatic drainage network and obstruction of lymphatic flow, leading to long-term complications such as numbness, sensitivity, and accumulation of lymph fluid or lymphedema. To decrease these postoperative morbidities and complications, most surgeons are now removing only the sentinel lymph nodes (the first nodes collecting the lymph from the tumor site, Fig. 80.6) for biopsy [50]. It was shown in clinical studies that sentinel lymph nodes are sufficient for staging breast cancer and assessment of metastasis [51].

There are several techniques that are currently used to identify and localize lymph nodes before their resection. A radioactive tracer (technetium-99) and a dye (methylene blue) are injected preoperatively near the site of the tumor [50, 52]. They are allowed to circulate, and the sentinel nodes are identified by

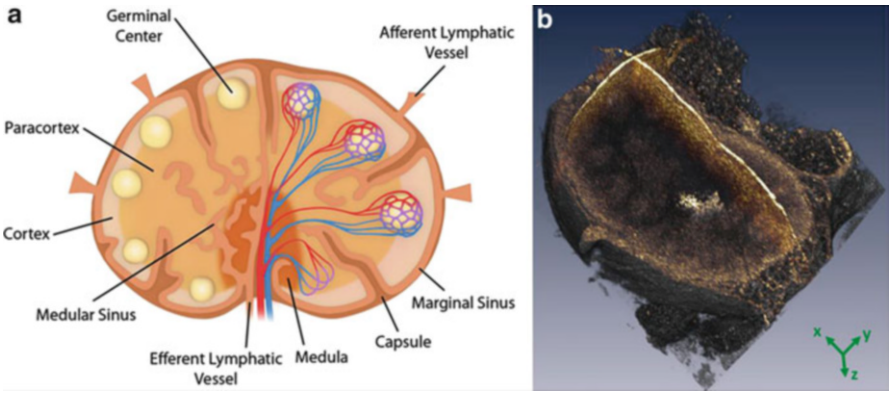

Fig. 80.6 Lymph node anatomy. (**a**) Diagram of a lymph node indicating basic structural components (Own work unpublished). (**b**) Three-dimensional transcapsular OCT of a normal rat lymph node featuring an intact capsule and follicular structures that were distinguishable from the background cortex based on their spheroidal pattern of optical scattering (Adapted from [64], reprinted with kind permission from Springer Science and Business Media)

the color or the level of radioactivity. After resection, lymph nodes are processed and analyzed using standard histological techniques. Fluorescence techniques using near-infrared dye [53, 54] that could provide better localization of the lymph node are also being investigated, but none of the mentioned techniques can provide the assessment of the lymph node status.

Intraoperative techniques currently used for the staging of cancer by assessing lymph nodes require lymph node resection and dissection to expose the internal structure for high-resolution imaging [55, 56] or prolong the surgery. Surgeons often send suspicious nodes for a quick assessment via frozen sections, which could take 20–30 min to perform, increasing the time that the patient is under general anesthesia [57, 40]. Most of the other noninvasive imaging modalities currently used in the clinical setting (x-ray, MRI, CT) can provide information only about the size and general morphology of the lymph nodes [58] and cannot provide any information about the presence of cancer cells in the early stages of metastasis [59, 60]. With a 1–2 mm imaging penetration depth, OCT has a potential for intraoperative in situ imaging of intact lymph node structure and assessment of status, primarily by imaging the capsule and the outer cortex containing the follicles and germinal centers (Fig. 80.6b) [45, 61, 48]. During metastatic progression, cancer cells first infiltrate sentinel lymph nodes in the subcapsular region, and the architectural changes in lymph node morphology all primarily occur in the outer cortex and capsular regions, which are within the imaging depth of OCT [61–65]. In addition, the proliferation of adipocytes in and around the lymph nodes has also been correlated with metastatic involvement, which can be identified and imaged with OCT [71].

80.2.4 Intraoperative Assessment of Sentinel Lymph Nodes: Results

Initial OCT research in lymph node imaging was published in 2005 where three-dimensional time-domain OCT imaging was performed on both rat and human lymph nodes [61]. Many important structures were detected such as the capsule, cortex, sinuses, and follicles. Two freshly excised metastatic human lymph nodes were also imaged and exhibited highly scattering tumorous and necrotic areas. This study demonstrated that although the entire depth of the node cannot be imaged, transcapsular OCT imaging of intact lymph node is still capable of detecting many diagnostically significant features.

To better understand the image characteristics of metastatic node progression, a longitudinal animal study was conducted with imaging performed at several stages of tumor invasion [64]. Rats were injected with mammary tumor cells in the left footpad, forming tumors that metastasized to the popliteal lymph nodes. Injected rats were sacrificed for imaging on days 3, 5, 7, and 9 postinjection. Imaging was performed using a three-dimensional spectral-domain system centered at 800 nm with 2 μm axial and 12 μm transverse resolution, and results were compared to histology. A healthy node from a control animal was imaged on day 0 to serve as a reference point for the following days. The node appeared normal as expected with an intact capsule, low-scattering subcapsular layer, and distinct circular follicle structures. Nodes from injected rats imaged on days 3, 5, 7, and 9 showed increasing levels of inflammation, macrophage invasion, disruption of normal structure, and tumor invasion. En face and cross-sectional OCT images of the day 3, day 7, and day 9 nodes are shown in Fig. 80.7. Nodes resected and imaged on day 3 exhibited mild inflammation which appeared as a loss of distinction between the capsule to subcapsular boundary and an area of low-scattering fluid in the subcapsular area. OCT images from day 5 show increased inflammation in the subcapsular space. Invading macrophages and tumor cells were discovered in the inflammation site by histology. In the day 7 node, low-scattering areas of subcapsular inflammation continued to grow, and the cortex became more homogeneous. Severe inflammation and invasion of macrophages into the node appeared as a large, irregular, low-scattering area. The day 9 node was completely metastatic with little to no original lymph tissue remaining. The OCT image appeared mildly scattering and uniform with few distinguishing features. The knowledge gained in this preclinical longitudinal OCT study can be used as a guide when attempting to stage human lymph node metastases.

More recent studies have imaged normal, reactive, and metastatic human lymph nodes using OCT following surgical resection. In one study, 18 samples were imaged in 3D using time-domain OCT at a central wavelength of 1,320 nm and an isometric resolution of 11 μm [62]. An additional 12 samples were imaged with similar quality using swept-source OCT at 1,325 nm with 12 μm axial and 15 μm transverse resolution. OCT of normal human nodes showed expected nodal structures with adipose tissue surrounding the node. A benign reactive node exhibited normal structure with enlarged germinal centers possibly due to

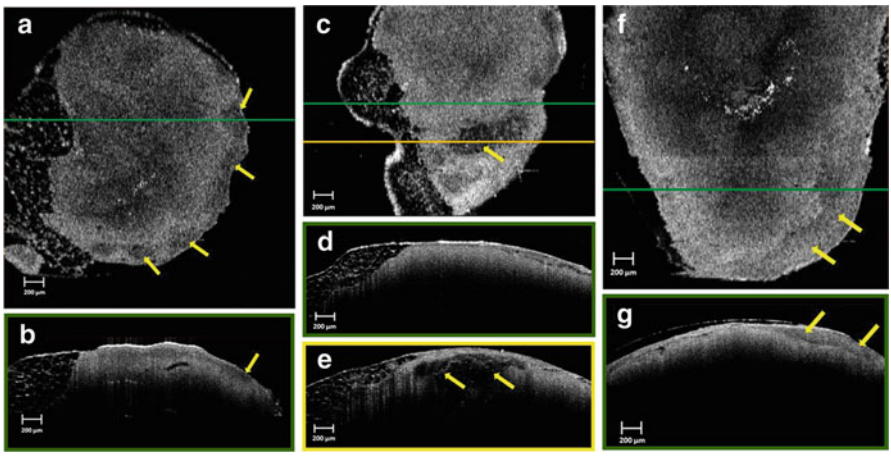

Fig. 80.7 Metastatic progression in lymph nodes. En face (**a**, **c**, **f**) and cross-sectional OCT (**b**, **d**, **e**, **g**) are shown. (**a**, **b**) Rat lymph node imaged on day 3 after injection of cancer cells into the hindlimb footpad. Mild inflammation is observed in the subcapsular region (*arrows*). (**c**–**e**) Rat lymph node imaged on day 7. OCT shows inflammation resulting from invasion of macrophages (*arrows*) and a more homogeneous high-scattering cortex is evident, where follicle structures are no longer visible. (**f**, **g**) Rat lymph node imaged on day 9. OCT shows effacement of node structure and a small area of remaining lymphocytes (*arrows*). In all cases, the *green* and *yellow* frames around the cross-sectional OCT images correspond to the horizontal lines of the same color in the corresponding en face images (Adapted from [64], reprinted with kind permission from Springer Science and Business Media)

an inflammatory response. En face OCT and corresponding histology of two metastatic nodes are shown in Fig. 80.8. Both nodes have been invaded by ductal carcinoma resulting in irregular areas of high optical scattering in the OCT data. In another study, human nodes were imaged using the same system described by Nguyen and colleagues [48]. A total of 17 ex vivo nodes were imaged intraoperatively immediately following resection [63]. Results were similar to those reported above, with inflammation and tumor invasion deteriorating the normal node structure. Representative results are shown in Fig. 80.9. Importantly, of the 30 sentinel nodes resected during this study, 84 % were diagnosed as normal, emphasizing the significant need for in vivo node assessment.

In each of the OCT lymph node studies, normal nodes were clearly distinguished from reactive and highly metastatic nodes. However, differentiating between reactive nodes and newly established metastases remains difficult due to similarities in structure and scattering properties. One possible solution is parametric imaging using the optical attenuation coefficient to provide contrast between various node structures [65, 66]. Future studies are needed to address this issue, as many lymph nodes are reactive due to inflammation from treatment or surgery and may not necessarily contain metastatic infiltrates.

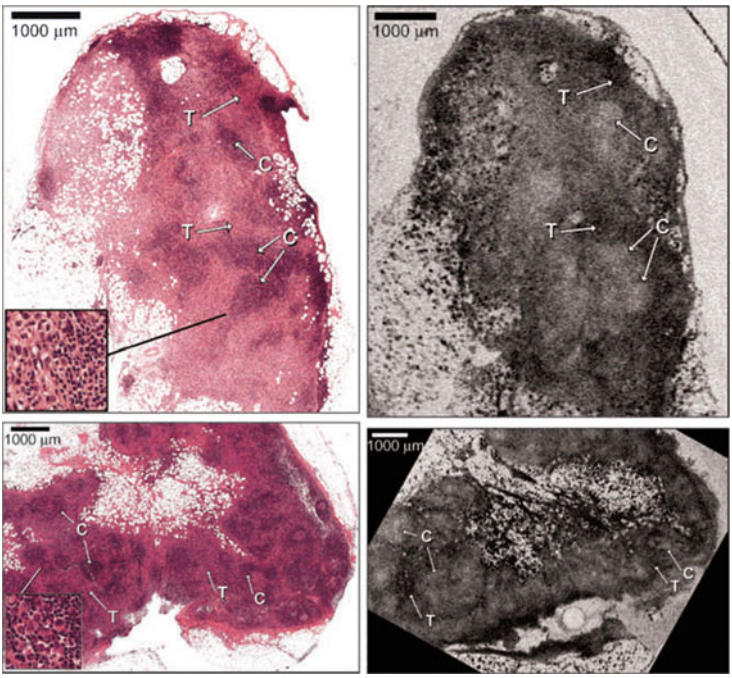

Fig. 80.8 Histology and corresponding OCT images of metastatic human nodes from ductal breast carcinoma. Two different nodes are shown (*top*, *bottom*). Insets in H&E images show the morphology of the metastatic carcinoma at higher magnification. Areas effaced by diffuse sheets of metastatic tumor cells are shown (*T*), as well as areas of uninvolved cortex (*C*) [48, 62]

80.3 Future Outlook

The studies discussed in this chapter have demonstrated that OCT is capable of imaging several tissues of interest in surgical oncology. These results should encourage the development of improved OCT imaging systems and larger clinical studies to demonstrate effectiveness and ease of use suitable for the operating room. While many of the studies presented here imaged tissue ex vivo immediately following resection, in vivo imaging is highly preferred. Imaging in vivo makes it possible to leave healthy tissue intact and also eliminates the confounding artifacts in OCT images associated with surgical removal such as loss of blood and lymphatic circulation and change of shape. To avoid motion artifacts, high-speed scanning is necessary for imaging in vivo. Additionally, processing and visualization of data must be done in near real time for guided surgery to be most effective. Three-dimensional imaging is also preferred over two-dimensional imaging as it provides a more comprehensive view of the tissue. Imaging in 3D can also identify small features such as microcalcifications which may be easily missed in 2D imaging.

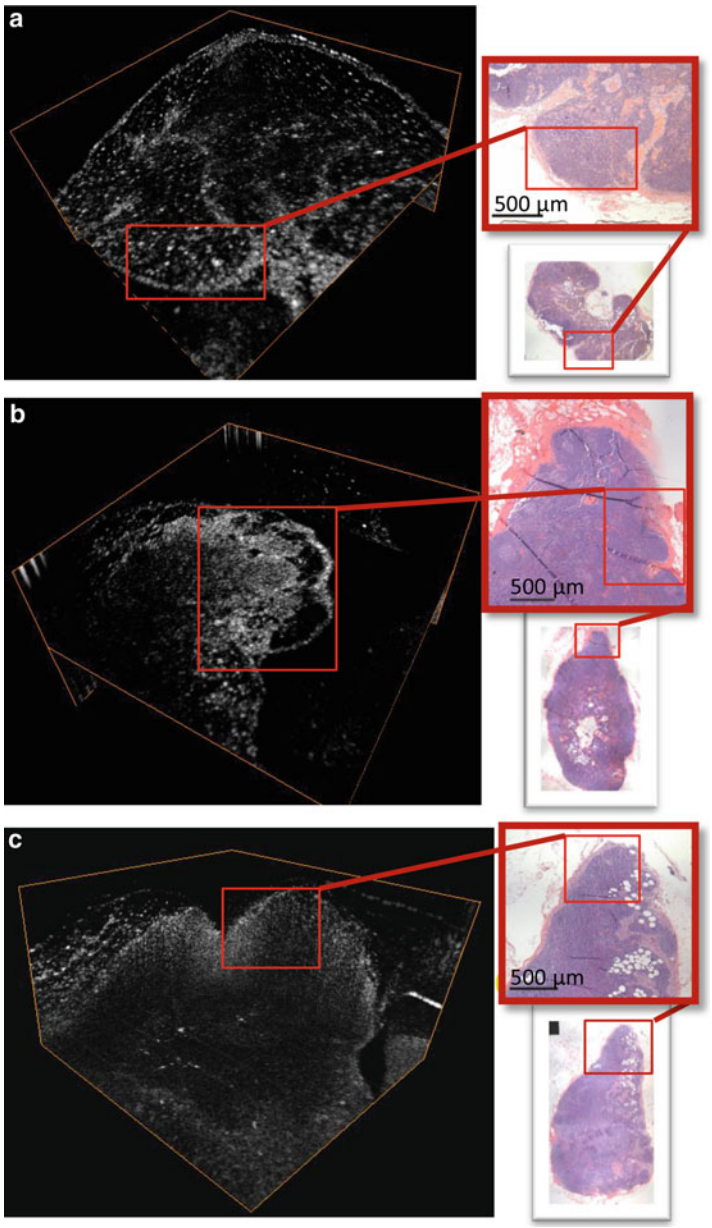

Fig. 80.9 3D OCT and corresponding histology of human lymph nodes. (**a**) Normal human lymph node with distinct capsule and cortex. (**b**) Reactive human lymph node showing inflammatory disturbance of nodal structure. (**c**) Metastatic node exhibiting a loss of distinct nodal structures (Adapted from [63])

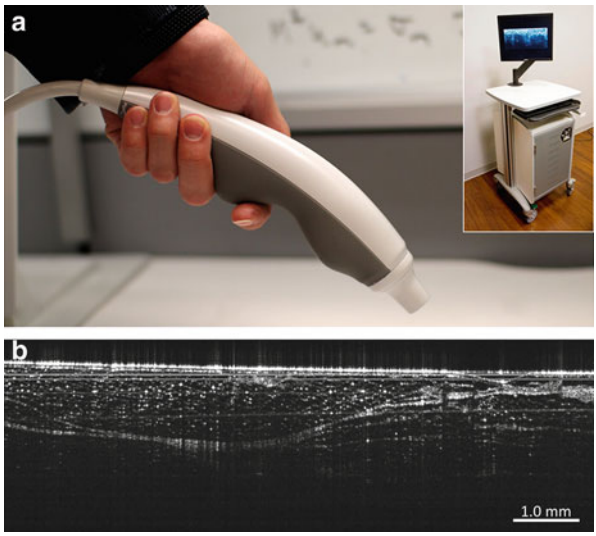

Fig. 80.10 Commercial intraoperative imaging system. (**a**) Handheld probe and portable cart designed for in vivo surgical imaging of breast cancer using interferometric synthetic aperture microscopy (ISAM). (**b**) Real-time ISAM image of normal adipose and parenchymal tissue acquired in vivo within the surgical tumor cavity in a patient undergoing a lumpectomy procedure for breast cancer (Images courtesy of Diagnostic Photonics, Inc.)

The high resolution of OCM provided improved image quality over OCT, demonstrating that increased resolution is a key factor in identifying tissue structures [47]. However, OCM is limited by lower penetration depth and slower acquisition speed than OCT. An alternative may be found in computed imaging methods, such as interferometric synthetic aperture microscopy (ISAM) and computational adaptive optics [67, 68] (see ▶ Chap. 31, "Interferometric Synthetic Aperture Microscopy (ISAM)"). While the resolution may not reach the level of OCM, it is possible to improve resolution throughout the entire imaging range while still acquiring and processing data at high speed. Recently, a handheld ISAM imaging system and probe have been developed as a commercial devices for in vivo breast imaging during surgical procedures. The system and preliminary in vivo data depicting a negative tumor margin are shown in Fig. 80.10. A high-speed OCT/ISAM system can be operated much like a real-time ultrasound imaging system where the probe generating fast 2D cross-sectional images is rapidly moved across tissue surfaces. Or in another configuration, OCT can be integrated into a surgical microscope for intraoperative tumor imaging [69]. Using position information from the surgical microscope and high-speed image processing of the OCT data, the automated system can perform composite 3D imaging over several square centimeters. These new in vivo imaging systems demonstrate that OCT is a highly flexible technology and may be deployed in configurations most well suited for the application.

Preclinical animal studies, human feasibility studies, and the development of suitable OCT hardware have set the stage for OCT to impact the field of surgical oncology. As this technology and target application is commercialized and larger human studies are performed, it is likely that OCT will be found useful in guiding intraoperative procedures.

Acknowledgments We would like to thank our colleagues for their work which contributed to this chapter. We regret that we were unable to include more results from others due to space limitations. A portion of the research presented here was supported in part by grants from the US National Institutes of Health (R01 EB012479 and R01 CA166309, S.A.B.).

References

1. A. Jemal, F. Bray, M.M. Center, J. Ferlay, E. Ward, D. Forman, Global cancer statistics. CA Cancer J. Clin. **61**, 69–90 (2011)
2. R. Siegel, D. Naishadham, A. Jemal, Cancer statistics, 2012. CA Cancer J. Clin. **62**, 10–29 (2012)
3. J.K. Karwowski, R.B. Jeffrey, I.R. McDougall, R.J. Weigel, Intraoperative ultrasonography improves identification of recurrent thyroid cancer. Surgery **132**, 924–928 (2002)
4. V.E. Strong, J. Humm, P. Russo, A. Jungbluth, W.D. Wong, F. Daghighian, L. Old, Y. Fong, S.M. Larson, A novel method to localize antibody-targeted cancer deposits intraoperatively using handheld PET beta and gamma probes. Surg. Endosc. **22**, 386–391 (2008)
5. V. Ntziachristos, J.S. Yoo, G.M. van Dam, Current concepts and future perspectives on surgical optical imaging in cancer. J. Biomed. Opt. **15**, 066024 (2010)
6. S. Keereweer, J.D. Kerrebijn, P.B. van Driel, B. Xie, E.L. Kaijzel, T.J. Snoeks, I. Que, M. Hutteman, J.R. van der Vorst, J.S. Mieog, A.L. Vahrmeijer, C.J. van de Velde, R.J. Baatenburg de Jong, C.W. Löwik, Optical image-guided surgery-where do we stand? Mol. Imaging Biol. **13**, 199–207 (2011)
7. H. Kobayashi, M. Ogawa, R. Alford, P.L. Choyke, Y. Urano, New strategies for fluorescent probe design in medical diagnostic imaging. Chem. Rev. **110**, 2620–2640 (2010)
8. A. Nijsssen, S. Koljenovic, T.C. Bakker Schut, P.J. Caspers, G.J. Puppels, Towards oncological application of Raman spectroscopy. J. Biophotonics **2**, 29–36 (2009)
9. D.C.G. De Veld, M.J. Witjes, H.J. Sterenborg, J.L. Roodenburg, The status of in vivo autofluorescence spectroscopy and imaging for oral oncology. Oral Oncol. **41**, 117–131 (2005)
10. S. Kennedy, J. Geradts, T. Bydlon, J.Q. Brown, J. Gallagher, M. Junker, W. Barry, N. Ramanujam, L. Wilke, Optical breast cancer margin assessment: an observational study of the effects of tissue heterogeneity on optical contrast. Breast Cancer Res. **12**, R91 (2010)
11. J.Q. Brown, T.M. Bydlon, L.M. Richards, B. Yu, S.A. Kennedy, J. Geradts, L.G. Wilke, M.K. Junker, J. Gallagher, W.T. Barry, N. Ramanujam, Optical assessment of tumor resection margins in the breast. IEEE J. Sel. Topics Quant. Electron. **16**, 530–544 (2010)
12. A.M. Zysk, F.T. Nguyen, A.L. Oldenburg, D.L. Marks, S.A. Boppart, Optical coherence tomography: a review of clinical development from bench to bedside. J. Biomed. Opt. **12**, 051403 (2007)
13. B.J. Vakoc, D. Fukumura, R.K. Jain, B.E. Bouma, Cancer imaging by optical coherence tomography: preclinical progress and clinical potential. Nat. Rev. Cancer **12**, 363–368 (2012)
14. A. Latrive, A.C. Boccara, In vivo and in situ cellular imaging full-field optical coherence tomography with a rigid endoscopic probe. Biomed. Opt. Express **2**, 2897–2904 (2011)
15. J.V. Frangioni, New technologies for human cancer imaging. J. Clin. Oncol. **26**, 4012–4021 (2008)
16. R.M. Pijnappel, M. van den Donk, R. Holland, W.P. Mali, J.L. Peterse, J.H. Hendriks, P.H. Peeters, Diagnostic accuracy for different strategies of image-guided breast intervention in cases of nonpalpable breast lesions. Br. J. Cancer **90**, 595–600 (2004)
17. W.C. Kuo, J. Kim, N.D. Shemonski, E.J. Chaney, D.R. Spillman, S.A. Boppart, Real-time three-dimensional optical coherence tomography image-guided core-needle biopsy system. Biomed. Opt. Express **3**, 1149–1161 (2012)
18. R.A. McLaughlin, B.C. Quirk, A. Curatolo, R.W. Kirk, L. Scolaro, D. Lorenser, P.D. Robbins, B.A. Wood, C.M. Saunders, D.D. Sampson, Imaging of breast cancer with optical coherence

tomography needle probes: feasibility and initial results. IEEE J. Sel. Topics Quant. Electron. **18**, 1184–1191 (2012)
19. M. Mogensen, G.B.E. Jemec, Diagnosis of nonmelanoma skin cancer/keratinocyte carcinoma: A review of diagnostic accuracy of nonmelanoma skin cancer diagnostic tests and technologies. Dermatol. Surg. **33**, 1158–1174 (2007)
20. R. Pomerantz, D. Zell, G. McKenzie, D.M. Siegel, Optical coherence tomography used as a modality to delineate basal cell carcinoma prior to Mohs micrographic surgery. Case Rep. Dermatol. **3**, 212–218 (2011)
21. F.K. Albert, M. Forsting, K. Sartor, H.P. Adams, S. Kunze, Early postoperative magnetic-resonance-imaging after resection of malignant glioma - objective evaluation of residual tumor and its influence on regrowth and prognosis. Neurosurgery **34**, 45–61 (1994)
22. H.J. Bohringer, D. Boller, J. Leppert, U. Knopp, E. Lankenau, E. Reusche, G. Huttmann, A. Giese, Time-domain and spectral-domain optical coherence tomography in the analysis of brain tumor tissue. Lasers Surg. Med. **38**, 588–597 (2006)
23. H. Bohringer, E. Lankenau, F. Stellmacher, E. Rausche, G. Huttmann, A. Giese, Imaging of human brain tumor tissue by near-infrared laser coherence tomography. Acta Neurochir. **151**, 507–517 (2009)
24. A. Taghian, M. Mohiuddin, R. Jagsi, S. Goldberg, E. Ceilley, S. Powell, Current perceptions regarding surgical margin status after breast-conserving therapy: results of a survey. Ann. Surg. **24**, 629–639 (2005)
25. M.F. Dillon, A.D. Hill, C.M. Quinn, E.W. McDermott, N. O'Higgins, A pathologic assessment of adequate margin status in breast-conserving therapy. Ann. Surg. Oncol. **13**, 333–339 (2006)
26. A. Luini, J. Rososchansky, G. Gatti, S. Zurrida, P. Caldarella, G. Viale, G. Rosali Dos Santos, A. Frasson, The surgical margin status after breast-conserving surgery: discussion of an open issue. Breast Cancer Res. Treat. **113**, 397–402 (2009)
27. D. Aziz, E. Rawlinson, S.A. Narod, P. Sun, H.L. Lickley, D.R. McCready, C.M. Holloway, The role of reexcision for positive margins in optimizing local disease control after breast-conserving surgery for cancer. Breast J. **12**, 331–337 (2006)
28. G.A. Cefaro, D. Genovesi, R. Marchese, L.A. Ursini, E. Cianchetti, E. Ballone, M. Di Nicola, Predictors of local recurrence after conservative surgery and whole-breast irradiation. Breast Cancer Res. Treat. **98**(3), 329–335 (2006)
29. C. Cellini, S.T. Hollenbeck, P. Christos, D. Martins, J. Carson, S. Kemper, E. Lavigne, E. Chan, R. Simmons, Factors associated with residual breast cancer after re-excision for close or positive margins. Ann. Surg. Oncol. **11**, 915–920 (2004)
30. J.L. Connolly, J. Boyages, A.J. Nixon, G. Peiro, I. Gage, B. Silver, A. Recht, J.R. Harris, S.J. Schnitt, Predictors of breast recurrence after conservative surgery and radiation therapy for invasive breast cancer. Mod. Pathol. **11**, 134–139 (1998)
31. M.F. Dillon, E.W. Mc Dermott, A. O'Doherty, C.M. Quinn, A.D. Hill, N. O'Higgins, Factors affecting successful breast conservation for ductal carcinoma in situ. Ann. Surg. Oncol. **14**, 1618–1628 (2007)
32. T.L. Huston, R. Pigalarga, M.P. Osborne, E. Tousimis, The influence of additional surgical margins on the total specimen volume excised and the reoperative rate after breast-conserving surgery. Am. J. Surg. **192**, 509–512 (2006)
33. A. McIntosh, G. Freedman, D. Eisenberg, P. Anderson, Recurrence rates and analysis of close or positive margins in patients treated without re-excision before radiation for breast cancer. Am. J. Clin. Oncol. **30**, 146–151 (2007)
34. A.P. Schouten van der Velden, S.L. Van de Vrande, C. Boetes, P. Bult, T. Wobbes, Residual disease after re-excision for tumour-positive surgical margins in both ductal carcinoma in situ and invasive carcinoma of the breast: the effect of time. J. Surg. Oncol. **96**, 569–574 (2007)
35. C.D. Scopa, P. Aroukatos, A.C. Tsamandas, C. Aletra, Evaluation of margin status in lumpectomy specimens and residual breast carcinoma. Breast J. **12**, 150–153 (2006)

36. M.C. Smitt, K.W. Nowels, M.J. Zdeblick, S. Jeffrey, R.W. Carlson, F.E. Stockdale, D.R. Goffinet, The importance of the lumpectomy surgical margin status in long-term results of breast conservation. Cancer **76**, 259–267 (1995)
37. G.P. Swanson, K. Rynearson, R. Symmonds, Significance of margins of excision on breast cancer recurrence. Am. J. Clin. Oncol. **25**, 438–441 (2002)
38. G. Zavagno, E. Goldin, R. Mencarelli, G. Capitanio, P. Del Bianco, R. Marconato, S. Mocellin, G. Marconato, V. Belardinelli, F. Marcon, D. Nitti, Role of resection margins in patients treated with breast conservation surgery. Cancer **112**, 1923–1931 (2008)
39. T.P. Olson, J. Harter, A. Munoz, D.M. Mahvi, T. Breslin, Frozen section analysis for intraoperative margin assessment during breast-conserving surgery results in low rates of re-excision and local recurrence. Ann. Surg. Oncol. **14**, 2953–2960 (2007)
40. S.A. McLaughlin, L.M. Ochoa-Frongia, S.M. Patil, H.S. Cody, L.M. Sclafani, Influence of frozen-section analysis of sentinel lymph node and lumpectomy margin status on reoperation rates in patients undergoing breast-conservation therapy. J. Am. Coll. Surg. **206**, 76–82 (2008)
41. E.K. Valdes, S.K. Boolbol, J.M. Cohen, S.M. Feldman, Intra-operative touch preparation cytology; does it have a role in re-excision lumpectomy? Ann. Surg. Oncol. **14**, 1045–1050 (2007)
42. S. Goldfeder, D. Davis, J. Cullinan, Breast specimen radiography: can it predict margin status of excised breast carcinoma? Acad. Radiol. **13**, 1453–1459 (2006)
43. B. Erguvan-Dogan, G.J. Whitman, V.A. Nguyen, M.J. Dryden, R.J. Stafford, J. Hazle, K.R. McAlee, M.J. Phelps, M.F. Ice, H.M. Kuerer, L.P. Middleton, Specimen radiography in confirmation of MRI-guided needle localization and surgical excision of breast lesions. AJR Am. J. Roentgenol. **187**, 339–344 (2006)
44. T. Karni, I. Pappo, J. Sandbank, O. Lavon, V. Kent, R. Spector, S. Morgenstern, S. Lelcuk, A device for real-time, intraoperative margin assessment in breast-conservation surgery. Am. J. Surg. **194**, 467–473 (2007)
45. S.A. Boppart, W. Luo, D.L. Marks, K.W. Singletary, Optical coherence tomography: feasibility for basic research and image-guided surgery of breast cancer. Breast Cancer Res. Treat. **84**, 85–97 (2004)
46. P.L. Hsiung, D.R. Phatak, Y. Chen, A.D. Aquirre, J.G. Fujimoto, J.L. Connoly, Benign and malignant lesion in the human breast depicted with ultrahigh resolution and dimensional optical coherence tomography. Radiology **244**, 865–874 (2007)
47. C. Zhou, D.W. Cohen, Y. Wang, H.-C. Lee, A.E. Mondelblatt, T.-H. Tsai, A.D. Aguirre, J.G. Fujimoto, J.L. Connolly, Integrated optical coherence tomography and microscopy for ex vivo multiscale evaluation of human breast tissues. Cancer Res. **70**, 10071–10079 (2010)
48. F.T. Nguyen, A.M. Zysk, E.J. Chaney, J.G. Kotynek, U.J. Oliphant, F.J. Bellafiore, K.M. Rowland, P.A. Johnson, S.A. Boppart, Intraoperative evaluation of breast tumor margins with optical coherence tomography. Cancer Res. **69**, 8790–8796 (2009)
49. C.L. Willard-Mack, Normal structure, function, and histology of lymph nodes. Toxicol. Pathol. **34**, 409–424 (2006)
50. D. Krag, T. Ashikaga, S.P. Harlow, D.L. Weaver, Development of sentinel node targeting technique in breast cancer patients. Breast J. **4**, 67–74 (1998)
51. U. Veronesi, G. Paganelli, G. Viale, A. Luini, S. Zurrida, V. Galimberti, M. Intra, P. Veronesi, C. Robertson, P. Maisonneuve, G. Renne, C. De Cicco, F. De Lucia, R. Gennari, A randomized comparison of sentinel node biopsy with routine axillary dissection in breast cancer. N. Eng. J. Med. **349**, 546–553 (2003)
52. W.D. Blessing, A.J. Stolier, S.C. Teng, J.S. Bolton, G.M. Fuhrman, A comparison of methylene blue and lymphazurin in breast cancer sentinel node mapping. Am. J. Surg. **184**, 341–345 (2002)
53. B.E. Schaafsma, J.S. Mieog, M. Hutteman, J. van der Vorst, P. Kuppen, C. Löwik, J.V. Frangioni, C. van de Velde, A.L. Vahrmeijer, The clinical use of indocyanine green as a near-infrared fluorescent contrast agent for image-guided oncologic surgery. J. Surg. Oncol. **104**, 323–332 (2011)

54. L. Sampath, W. Wang, E.M. Sevick-Muraca, Near-infrared fluorescent optical imaging for nodal staging. J. Biomed. Opt. **13**, 041312 (2008)
55. K.J. Rosbach, D. Shin, T.J. Muldoon, M.A. Quraishi, L.P. Middleton, K.K. Hunt, F. Meric-Bernstam, T.-K. Yu, R. Richards-Kortum, W. Yang, High-resolution fiber optic microscopy with fluorescent contrast enhancement for the identification of axillary lymph node metastases in breast cancer: a pilot study. Biomed. Opt. Express **1**, 911–922 (2010)
56. N.Q. Nguyen, A.V. Biankin, R.W. Leong, D.K. Chang, P.H. Cosman, P. Delaney, J.G. Kench, N.D. Merrett, Real time intraoperative confocal laser microscopy-guided surgery. Ann. Surg. **249**, 735–737 (2009)
57. R. Ali, A.M. Hanly, P. Naughton, C.F. Castineira, R. Landers, R.A. Cahill, R.G. Watson, Intraoperative frozen section assessment of sentinel lymph nodes in the operative management of women with symptomatic breast cancer. World J. Surg. Oncol. **6**, 69 (2008)
58. M. Torabi, S.L. Aquino, M.G. Harisinghani, Current concepts in lymph node imaging. J. Nucl. Med. **45**, 1509–1518 (2004)
59. M. Gadd, Sentinel lymph node biopsy for staging early breast cancer: minimizing the trade-off by maximizing the accuracy. Ann. Oncol. **20**, 973–975 (2009)
60. M.L. Quan, D. McCready, The evolution of lymph node assessment in breast cancer. J. Surg. Oncol. **99**, 194–198 (2009)
61. W. Luo, F.T. Nguyen, A.M. Zysk, T.S. Ralston, J. Brockenbrough, D.L. Marks, A.L. Oldenburg, S.A. Boppart, Optical biopsy of lymph node morphology using optical coherence tomography. Technol. Cancer Res. Treat. **4**, 539–547 (2005)
62. R.A. McLaughlin, L. Scolaro, P. Robbins, S. Hamza, C. Saunders, D.D. Sampson, Imaging of human lymph nodes using optical coherence tomography: potential for staging cancer. Cancer Res. **70**, 2579–2584 (2010)
63. F.T. Nguyen, A.M. Zysk, E.J. Chaney, S.G. Adie, J.G. Kotynek, U.J. Oliphant, F.J. Bellafiore, K.M. Rowland, P.A. Johnson, S.A. Boppart, Optical Coherence Tomography: the intraoperative assessment of lymph nodes in breast cancer. IEEE Eng. Med. Biol. Mag. **29**, 63–70 (2010)
64. R. John, S.G. Adie, E.J. Chaney, M. Marjanovic, K.V. Tangella, S.A. Boppart, Three-dimensional optical coherence tomography for optical biopsy of lymph nodes and assessment of metastatic disease. Ann. Surg. Oncol. **20**, 3685–3693 (2012)
65. R.A. McLaughlin, L. Scolaro, P. Robbins, C. Saunders, S.L. Jacques, D.D. Sampson, Parametric imaging of cancer with optical coherence tomography. J. Biomed. Opt. **15**, 046029 (2010)
66. L. Scolaro, R.A. McLaughlin, B.R. Klyen, B.A. Wood, P.D. Robbins, C.M. Saunders, S.L. Jacques, D.D. Sampson, Parametric imaging of the local attenuation coefficient in human axillary lymph nodes assessed using optical coherence tomography. Biomed. Opt. Express **3**, 366–379 (2012)
67. T.S. Ralston, D.L. Marks, P.S. Carney, S.A. Boppart, Interferometric synthetic aperture microscopy. Nat. Phys. **3**, 129–134 (2007)
68. S.G. Adie, B.W. Graf, A. Ahmad, P.S. Carney, S.A. Boppart, Computational adaptive optics for broadband optical interferometric tomography of biological tissue. Proc. Natl. Acad. Sci. U. S. A. **109**, 7175–7180 (2012)
69. M. Finke, S. Kantelhardt, R. Bruder, E. Lankenau, A. Giese, A. Schweikard, Automatic scanning of large tissue areas in neurosurgery using optical coherence tomography. Int. J. Med. Robot. Comput. Assist. Surg: MRCAS **8**, 327–336 (2012)
70. S. J. Erickson-Bhatt, R. Nolan, N. D. Shemonski, S. G. Adie, J. Putney, D. Darga, D. T. McCormick, A. Cittadine, M. Marjanovic, E. J. Chaney, G. L. Monroy, F. A. South, P. S. Carney, K. A. Cradock, Z. G. Liu, P. S. Ray, S. A. Boppart, In vivo intra-operative breast tumor margin detection using a portable OCT system with a handheld surgical imaging probe. Proc. SPIE **8935**, 89351C (2014)
71. J. Yamaguchi, H. Ohtani, K. Nakamura, I. Shimokawa, T. Kanematsu, Prognostic impact of marginal adipose tissue invasion in ductal carcinoma of the breast. Am. J. Clin. Pathol. **130**, 382–388 (2008)

Optical Coherence Tomography in a Needle Format

81

Dirk Lorenser, Robert A. McLaughlin, and David D. Sampson

Keywords

Breast cancer • Deep-tissue imaging • Fiber-optic probes • Imaging needle • Interstitial imaging • Lung imaging • Microscope-in-a-needle

81.1 Introduction

OCT has the potential to be used in vivo and in real time, avoiding the need to excise tissue and allowing minimally invasive imaging of disease in situ. The promise of such high-resolution optical imaging has been referred to as an "optical biopsy" [1]. Despite its great potential, OCT imaging has been restricted in clinical applications by its extremely limited imaging depth, typically only 2–3 mm in tissue.

Miniaturized fiber-optic probes for OCT offer the potential to image deep within the body. It is possible to miniaturize the distal scan head and encase it within a medical needle – an OCT needle probe [2], as shown in Fig. 81.1a. The extreme miniaturization of such probes, down to outer diameters of ≈0.3 mm, is made possible by all-fiber distal focusing optics as shown in Fig. 81.1b, where a coreless silica spacer made of no-core fiber (NCF) and a graded-index (GRIN) fiber

D. Lorenser (✉) • R.A. McLaughlin
Optical+Biomedical Engineering Laboratory, School of Electrical, Electronic and Computer Engineering, The University of Western Australia, Crawley, WA, Australia
e-mail: dirk.lorenser@uwa.edu.au

D.D. Sampson
Optical+Biomedical Engineering Laboratory, School of Electrical, Electronic and Computer Engineering, The University of Western Australia, Crawley, WA, Australia

Centre for Microscopy, Characterisation and Analysis, The University of Western Australia, Crawley, WA, Australia

© Springer International Publishing Switzerland 2015

W. Drexler, J.G. Fujimoto (eds.), *Optical Coherence Tomography*,
DOI 10.1007/978-3-319-06419-2_83

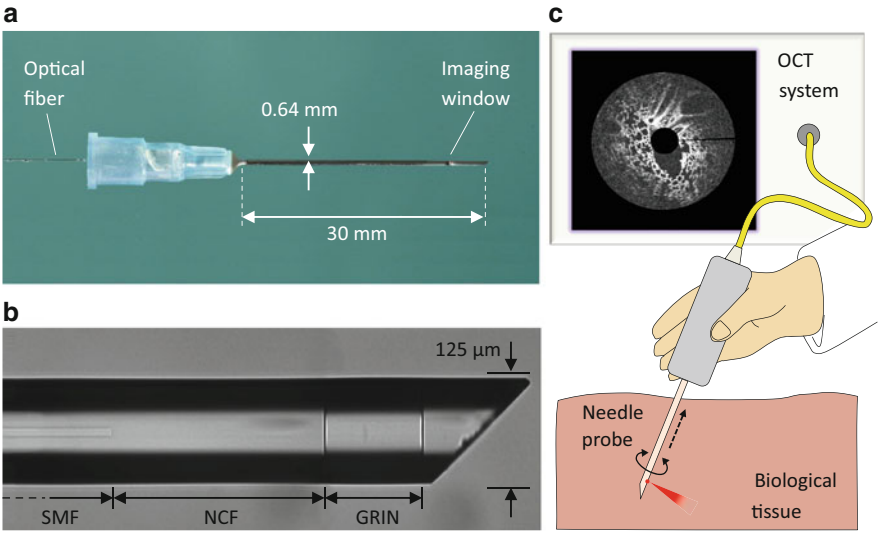

Fig. 81.1 (**a**) An OCT needle probe, consisting of a miniaturized side-viewing fiber-optic probe mounted inside a hypodermic needle with an imaging window near the tip. (**b**) Microscope image of a side-viewing fiber-optic probe designed for integration into a needle. *SMF* single-mode fiber, *NCF* no-core fiber, *GRIN* graded-index fiber. (**c**) Illustration of an envisaged OCT needle imaging system with a compact hand-held needle scanner

microlens have been fusion-spliced directly to the end of the delivery fiber, and a side-deflecting mirror has been realized by angle polishing the fiber tip. A number of promising applications are emerging, including cancer diagnosis [3, 4], pulmonary imaging [5, 6], imaging of the eye [7, 8], and imaging of the brain [9, 10]. The long-term vision of this rapidly evolving field is to create high-speed, handheld OCT needle scanners that allow clinicians to perform real-time in vivo imaging, as illustrated in Fig. 81.1c.

In this chapter, we will review the development and deployment of OCT needle probe technology and examine its use in preclinical and clinical applications.

81.2 Technology

Needle probes replace the sample-arm optics of a conventional OCT scanner. The tasks of the sample-arm optics are to scan and focus the incident light and to collect the weak backscattered light from the sample with high efficiency. Therefore, they define or significantly influence a number of key performance parameters of the OCT system, such as:

- Transverse resolution
- Depth of focus (DOF)
- Sensitivity
- Imaging speed

Losses or backreflections in the sample-arm optics will reduce the system sensitivity, whereas aberrations and alignment errors will negatively impact the transverse resolution and DOF. In a well-designed conventional free-space sample-arm setup consisting of a collimator, galvanometer mirrors, and a compound scan lens, minimal losses and diffraction-limited probe beam quality over the entire field of view can easily be simultaneously achieved using high-quality antireflection-coated optics. In the case of miniaturized sample-arm optics, such as those found in endoscopic or needle probes, the small dimensions and the available fabrication methods often force the probe designer to make trade-offs that negatively impact the performance of the OCT system. Recent advances in probe design and fabrication, however, have shown that needle probes can attain sensitivities and resolution comparable to bulk-optic sample arms [11].

81.2.1 Probe Optics

81.2.1.1 Probe Optics and Output Beam Parameters

The probe optics collimate or focus the diverging beam which is emitted from the single-mode fiber (SMF) of the OCT system and direct it into the sample, as illustrated in Fig. 81.2a. The focusing elements in the probe optics are typically realized using either GRIN optics or refractive optics. GRIN optics can be used either in the form of discrete GRIN rod lenses [12, 2] or in the form of short sections of multimode GRIN fiber that are directly fusion-spliced to the SMF [13–17, 11] in combination with coreless silica spacers made of no-core fiber (NCF). Due to its great importance for fiber probes, the use of GRIN multimode fiber as microlenses will be treated in more detail in Sect. 81.2.1.3. Examples of refractive optics are discrete ball lenses [8] or ball lenses that are directly formed on the end of fiber tips using fusion splicers [18, 12, 6]. Lensed fibers per se are not capable of imaging unless they are combined with some form of scanning mechanism, as will be discussed in Sect. 81.2.2. The most common scanning concept is rotation/pullback scanning in a side-facing configuration using a side-deflecting microreflector, as illustrated in Fig. 81.2a.

This technique has its origins in catheter-based OCT systems [19, 20]. In side-facing configurations, complications due to astigmatism and beam distortion can arise if the beam must exit the needle through a nonplanar output interface (e.g., when an enclosing catheter or transparent casing is used). These issues will be addressed in the discussion of specific probe designs in Sects. 81.2.3 and 81.2.4. While the majority of OCT needle probes have Gaussian or Gaussian-like output beams (practical probes often exhibit beam distortion due to aperture diffraction and aberrations, as will be explained in Sect. 81.2.1.3), it has recently been shown that it is feasible to extend the depth of focus (DOF) of miniaturized fiber-based probes using phase masks [21, 22]. Such advanced probe designs utilizing probe optics with additional wavefront-shaping elements have non-Gaussian output beams that maintain an approximately constant central lobe diameter over a large axial distance in the focal region, as illustrated in Fig. 81.2b.

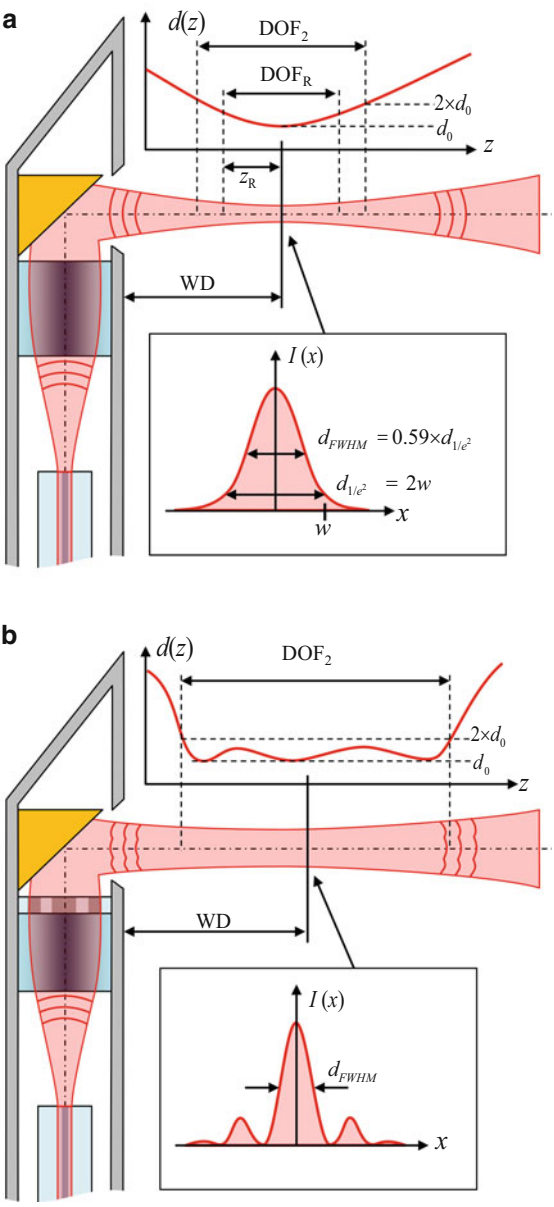

Fig. 81.2 Probe beam parameters. (**a**) Needle probe with a Gaussian output beam, using a GRIN lens which refocuses the beam emitted from the SMF into the sample volume. *WD* working distance, DOF_R depth of focus using the Rayleigh range criterion, DOF_2 depth of focus using the factor-of-two criterion. (**b**) Needle probe with a wavefront-shaped output beam which is generated by a phase mask after the focusing optics. The beam features an extended DOF compared to a Gaussian but its transverse profile has sidelobes

The axial and transverse resolutions of an OCT system are defined as the respective full-width at half-maximum (FWHM) of its three-dimensional (3D) point-spread function (PSF) [23, 24]. While the axial extent of the PSF is largely determined by the coherence length of the light source, the transverse extent of the PSF is determined by the intensity profile of the probe beam. For Gaussian probe

beams, the $1/e^2$ diameter of the beam waist is sometimes quoted as the transverse resolution of the system even though this is not consistent with the widespread use of the FWHM in the axial direction. We prefer to adhere to the FWHM definition of the transverse resolution, which has the additional benefit of yielding more meaningful values for the central lobe diameters of aberrated or non-Gaussian output beams which may have sidelobes or pedestals that exceed relative levels of $1/e^2$. This is very important for the characterization of probe designs that use wavefront-shaping elements, such as phase masks, in order to generate focal regions with an extended DOF, as illustrated in Fig. 81.2b. For an ideal Gaussian profile, the FWHM transverse resolution is given by

$$d_{FWHM} = \sqrt{\frac{\ln(2)}{2}} d_{1/e^2} \approx 0.59 \cdot d_{1/e^2} \approx 0.37 \cdot \frac{\lambda_0}{NA}, \tag{81.1}$$

where λ_0 is the wavelength in vacuum and NA is the numerical aperture. To define the DOF of the OCT imaging system, the double Rayleigh range is often used in the case of ideal Gaussian beams (see, e.g., [25]). The Rayleigh range criterion typically underestimates the perceived useful imaging depth range in OCT because a 40 % (factor of $\sqrt{2}$) change in transverse resolution is hardly visible due to the effects of logarithmic compression of the images and speckle. Similar to the reasoning for choosing the FWHM beam diameters to define the transverse resolution, we prefer to define the DOF as the range over which the FWHM beam diameter stays smaller than twice its minimum value in the focal region. This definition is more robust for numerically evaluating the DOF of probes that have wavefront-shaped output beams, which can have beam diameter variations within the useful imaging depth range that exceed a factor of $\sqrt{2}$, as illustrated in Fig. 81.2b. For an ideal Gaussian beam, the DOF according to the factor-of-two definition is simply a factor of $\sqrt{3}$ larger than the DOF according to the Rayleigh range criterion:

$$\mathrm{DOF}_2 = \sqrt{3} \cdot \mathrm{DOF}_\mathrm{R} = \sqrt{3} \cdot 2 \cdot z_R = \sqrt{3} \cdot 2 \cdot \frac{n\pi w_0^2}{\lambda_0}, \tag{81.2}$$

where n is the sample refractive index and w_0 is the waist radius. We use the subscripts "2" and "R" to denote the DOF according to the factor-of-two or Rayleigh range criteria, respectively.

Another useful parameter for characterizing the output beam quality in the case of aberrated or wavefront-shaped output beams is the Strehl ratio S. The Strehl ratio of an aberrated system is defined as the ratio of its focal spot peak intensity to that of an equivalent diffraction-limited system [26]. Here, it allows the estimation of the penalty in the detected signal level (from a point scatterer) incurred by non-Gaussian output beams that are used to trade off a reduced focal spot intensity for an increased DOF. The Strehl ratio is difficult to obtain from measurements, but it can often be calculated by optical design software (e.g., it can easily be computed for simulated output beams obtained using the beam propagation method [22] which is described in Sect. 81.2.1.3), and therefore, it is mainly used as a figure of merit for optimization and

comparison of probe designs. In the case of a simulated beam with a focal spot peak intensity $\hat{I}$ and total integrated beam power P, the Strehl ratio can be defined as [22]

$$S = \frac{\hat{I}}{\hat{I}_{Gauss}} = \frac{\hat{I}\pi w_{Gauss}^2}{2P}, \tag{81.3}$$

where w_{Gauss} is the $1/e^2$ waist radius of a suitably defined reference Gaussian beam (e.g., an ideal Gaussian beam with the same FWHM focal spot diameter as the simulated beam).

81.2.1.2 ABCD Matrix Modeling

The optical design of micro-optic systems, such as miniaturized fiber-based probes for OCT, cannot generally be performed using the ray-tracing methods used in classical lens design because the approximations of geometrical optics are not satisfied (the size of the wavelength is no longer negligible compared to the dimensions of the optical elements, which means that diffraction effects will have a strong influence). Scalar wave theory is, therefore, required to properly simulate the propagation of the optical field through the optical elements of the probe. While several optical engineering software packages offer such functionality, they tend to be costly and complex to use. A simple but very effective alternative to a numerical scalar wave simulation is paraxial ABCD matrix transformations of Gaussian beams [27, 28]. Since the beam emitted by a SMF can be well approximated by a fundamental Gaussian mode [29], ABCD matrices can be used to calculate its transformation by the optical elements of the probe if these can be described sufficiently well by their paraxial, or first-order, optical properties (i.e., aberrations can be neglected). If no limiting apertures are present in the optics, this formalism fully accounts for diffraction and yields exact results within the regime of validity of the paraxial approximation, as the Gaussian beam is an exact solution of the paraxial wave equation [27]. Most optical beams used for OCT imaging lie well within the paraxial regime, which is a good approximation for beam divergence angles up to $\sim 30°$, corresponding to a numerical aperture of ~ 0.5 [27].

A very convenient feature of the ABCD matrix approach is that the Gaussian beam solution of the paraxial wave equation is separable in x and y, which means that independent complex beam parameters can be assumed in two orthogonal directions and that these can be transformed independently [27].

The ABCD matrix formalism lends itself to implementation in technical computing tools such as Matlab, making it ideal for fast and flexible design calculations. For this reason, ABCD matrix modeling has proven to be a useful framework for basic probe design and analysis [30, 15, 13, 16, 11] and as a simple tool for calculating approximate values for an optical design, which can then be experimentally optimized to yield the desired output beam characteristics. Furthermore, the possibility of working with astigmatic beams allows the study of the effects of astigmatism introduced by curved interfaces and to develop methods for its

compensation [31, 16, 11, 32, 17]. As an example of the usefulness of the ABCD method, we will show in Sect. 81.2.4.1 how it can be used to derive a simple method for astigmatism compensation in needle probes [11] which exploits the "focal shift" effect that occurs when focusing at low Fresnel numbers.

While the ABCD matrix simulation method is a very useful tool for probe design, one must be aware of its limitations. Firstly, the inability to model the effects of aberrations and aperture diffraction can cause it to yield incorrect or inaccurate results in many probe designs using GRIN fiber lenses because of beam distortion resulting from the finite core diameter and nonideal refractive index profiles [22]. Secondly, the ABCD matrix method is limited to probe designs that generate ideal Gaussian output beams, and therefore, it cannot be used to study advanced probe designs incorporating wavefront-shaping elements, such as phase masks or axicons, to generate non-Gaussian or Bessel-like focal regions with an extended DOF [21, 22]. In such cases, a more general wave-optic-based modeling technique such as the beam propagation method is required, as will be explained in the following subsection.

81.2.1.3 Advanced Numerical Modeling Using the Beam Propagation Method

The beam propagation method (BPM) [33] is a numerical technique for simulating wave propagation through inhomogeneous media. It has found widespread application in the simulation of beam propagation through atmospheric turbulence [34] and laser resonators [35], as well as in the analysis of waveguides, including GRIN fibers [36]. We have recently demonstrated its application to the accurate modeling and design of fiber-optic probes using GRIN fiber lenses [22], showing that the BPM can overcome the shortcomings of the ABCD matrix method. The BPM simulation results presented in [22] revealed a number of interesting insights about the aberrations introduced by the deviation of the refractive index profile of the GRIN fiber from the ideal parabolic shape, as well as highlighting the power of this technique for the simulation of advanced probe designs using GRIN phase masks to extend the DOF (see also Sect. 81.2.4.4). The BPM provides the probe designer with a very versatile toolbox covering a broad variety of optical elements. It allows the modeling of free-space propagation, arbitrary GRIN media, arbitrary phase or amplitude masks, and refractive surfaces [37, 21].

Our implementation of the BPM closely follows the one described in [36]. The starting point is the scalar Helmholtz equation in a weakly inhomogeneous medium with a spatially dependent refractive index $n\left(\vec{r}\right)$:

$$\left[\nabla^2 + k\left(\vec{r}\right)^2\right] E = 0, \tag{81.4}$$

where $k\left(\vec{r}\right) = n\left(\vec{r}\right) k_0$ and k_0 denotes the propagation constant in vacuum. In optical fibers, the refractive index variation is on the order of a few percent,

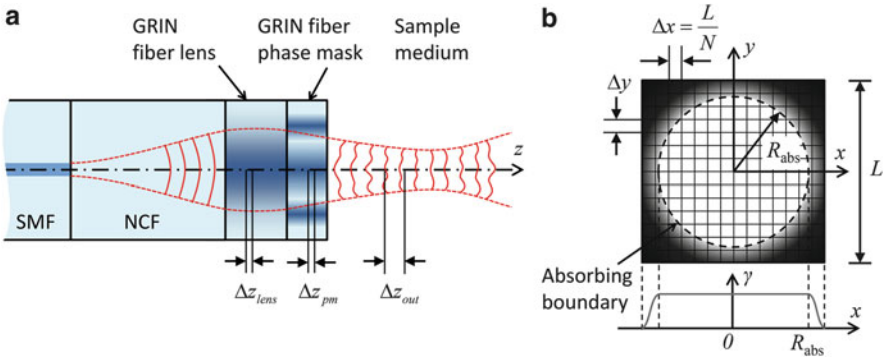

Fig. 81.3 (**a**) Schematic of the BPM simulation geometry for a fiber-optic probe. *SMF* single-mode fiber, *NCF* no-core fiber. (**b**) The $N \times N$ simulation grid with size L and with an absorbing boundary of radius R_{abs} (Figure adapted from [22])

and therefore, the refractive index can be expressed as $n\left(\vec{r}\right) = \overline{n} + \delta n(x, y)$, where $\overline{n}$ is a constant background refractive index (e.g., the index of the silica cladding) and $\delta n(x, y)$ is a small transverse index variation. The scalar field amplitude can be written as $E(x, y, z) = \tilde{u}(x, y, z)\exp\left(-i\overline{k}z\right)$, where $\overline{k} = \overline{n}k_0$ is the propagation constant in the background medium and $\tilde{u}(x, y, z)$ is a complex wave amplitude. For small axial step sizes Δz, an approximate solution to Eq. 81.4 can be written in operator notation:

$$\tilde{u}(x, y, z + \Delta z) \cong \exp\left(\hat{D}\Delta z\right)\exp\left(\tilde{N}\Delta z\right)\tilde{u}(x, y, z), \tag{81.5}$$

where $\hat{D}$ is the diffraction operator in a homogeneous medium with the background refractive index $\overline{n}$ and $\tilde{N}$ is an operator which accounts for the inhomogeneity of the refractive index. We can therefore approximate the propagation in the inhomogeneous medium as a repeated cycle of free-space propagation in a thin slice of homogeneous material of thickness Δz and multiplication of the wavefront with a phase screen $\exp\left(\hat{N}\Delta z\right) = \exp[-ik_0\delta n(x, y)\Delta z]$. For computational efficiency, the diffraction operator is applied in the spatial frequency domain. The simulation geometry is illustrated in Fig. 81.3a. The complex amplitude of the approximately Gaussian beam emitted by the SMF [29] is used as the input field to the BPM simulation, which begins at the NCF/GRIN interface. The field is then numerically propagated through the GRIN fiber lens, through the optional GRIN fiber phase mask, and into the sample medium with BPM step sizes Δz_{lens}, Δz_{pm}, and Δz_{out}, respectively. In the transverse dimensions, the field is sampled on a $N \times N$ Cartesian grid of size L. The criteria that govern the appropriate choice of step size Δz and transverse sampling intervals Δx, Δy are discussed in [22]. In order to prevent large-angle diffracted light from reaching the edges of the grid and causing artifacts in the FFT, we apply an "absorbing boundary" (a two-dimensional (2D) window function) to the field amplitude in the spatial domain at every BPM step as illustrated in Fig. 81.3b.

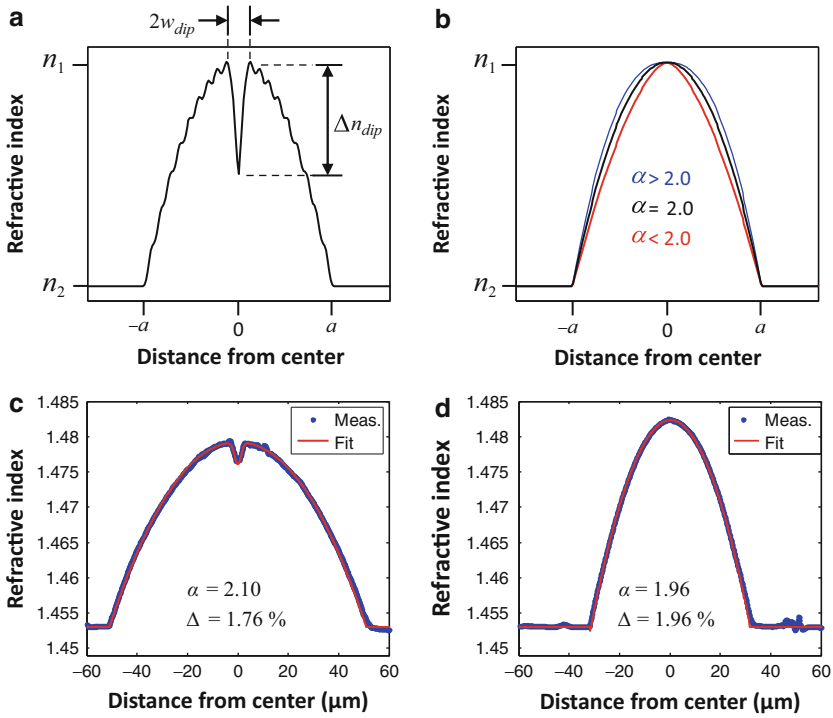

Fig. 81.4 (**a**) Power-law refractive index profile with central dip and ripple. (**b**) Effect of the power-law exponent α on the profile shape. (**c**, **d**) Measured index profiles and power-law fits of commercial GRIN multimode fibers (the cladding index n_2 is set to the refractive index $n = 1.453$ of pure silica at 800 nm). (**c**) 100-μm core-diameter GRIN MMF (100/140 MMF, POFC, Taiwan). (**d**) 62.5-μm core-diameter GRIN MMF (GIF625, Thorlabs, USA) (Figure adapted from [22])

One of the main motivations for using the BPM to simulate fiber-optic probes is that it allows the modeling of realistic GRIN fiber lenses [22]. While the ABCD matrix of a GRIN lens is a highly idealized model representing a perfect square-law medium of infinite transverse extent, the refractive index profiles of real GRIN fibers differ from this ideal in a number of ways, as illustrated in Fig. 81.4a. Firstly, the profile is never a perfect parabola, but it is described by a power-law profile that is truncated at the core radius a of the multimode fiber (MMF):

$$n(r) = \begin{cases} n_1\left[1 - 2\Delta\left(\frac{r}{a}\right)^{\alpha}\right]^{1/2} & r < a \\ n_2 = n_1(1 - 2\Delta)^{1/2} & r \geq a \end{cases} \tag{81.6}$$

where $\Delta = (n_1^2 - n_2^2)/2n_1^2$ is the relative index difference between the core and cladding refractive indices n_1 and n_2 (for small index differences, $\Delta \cong \Delta n/n_1$, where $\Delta n = n_1 - n_2$). The influence of the power-law exponent α on the profile shape is indicated in Fig. 81.4b. Secondly, the profiles of GRIN fibers fabricated using the

modified chemical vapor deposition (MCVD) method exhibit a characteristic central index dip as well as ripples, where the dip results from "burn-off" of dopant during the high-temperature collapse of the preform, and the ripples result from the deposition of a finite number of layers of changing composition in order to approximate the desired power-law shape [38]. Improved preform fabrication methods [14, 39] have led to a new generation of high-bandwidth GRIN MMFs with smooth refractive index profiles which are free of the central index dip that plagues legacy GRIN MMFs. However, these modern high-bandwidth GRIN MMFs are only available with small core diameters of 50 and 62.5 μm, limiting their use to probe designs with relatively low numerical aperture (NA) and short working distance (WD). Furthermore, their index profiles tend to exhibit a more or less pronounced deviation from the ideal parabolic shape that is purposely introduced by the manufacturer in order to minimize pulse broadening in the targeted operating wavelength band [40–42]. Thus, large core-diameter fibers drawn from preforms of such high-bandwidth GRIN MMFs [14] will not necessarily behave as ideal GRIN lenses.

Two example index profiles of commercial GRIN fibers together with their best-fit power-law profiles are shown in Fig. 81.4c and d. Figure 81.4c shows a 100-μm-core-diameter GRIN MMF (100/140 MMF, POFC, Taiwan) which was profiled on an EXFO NR-9200 fiber analyzer at a wavelength of 655 nm. The fiber has an α parameter of 2.1 and a central index dip. We have observed that fiber probes made using this GRIN fiber exhibit significant beam distortions that can be reproduced in BPM simulations [22]. Figure 81.4d shows a 62.5-μm-core-diameter GRIN MMF (GIF625, Thorlabs, USA) which we have used extensively in recent work [16, 11, 43, 32] because probes fabricated using this fiber have exhibited very good Gaussian-like beam quality and shown fairly good agreement with ABCD matrix calculations. This observation is not surprising when one considers the index profile (data provided by Thorlabs), which has a near-parabolic shape with an α parameter of 1.96 and no measurable dip in the center.

A deviation of the refractive index profile from the ideal parabolic shape in a GRIN lens is equivalent to spherical aberration (SA) in a refractive lens, with $\alpha > 2$ producing positive SA and $\alpha < 2$ producing negative SA [22]. This can be seen in Figs. 81.5a and b, which show BPM simulation results of lensed fibers with power-law GRIN profiles that have α parameters of 2.15 and 1.85, respectively (these values are representative of the maximum deviations from the ideal which one may encounter in real GRIN MMFs). The simulated probes consist of SMF with a mode-field diameter of 5 μm at an operating wavelength of 800 nm, with a 275-μm-long section of NCF and a 280-μm-long section of GRIN MMF with a core diameter of 100 μm, $\Delta = 2$ %, and cladding index $n_2 = 1.453$. For an aberration-free GRIN fiber with $\alpha = 2.0$ (or a gradient parameter $g \cong \sqrt{2\Delta/a} = 4\text{mm}^{-1}$), an ABCD matrix simulation yields an ideal Gaussian output beam with a working distance of 390 μm and a $1/e^2$ focal spot diameter of 8.5 μm (FWHM diameter of 5 μm), which is shown for comparison by the dotted curves in the plots of Figs. 81.5a and b (bottom). When the α-parameter of the index profile is "de-tuned" to a value of 2.15 (causing a deformation of the profile shape which is just barely noticeable compared to the ideal

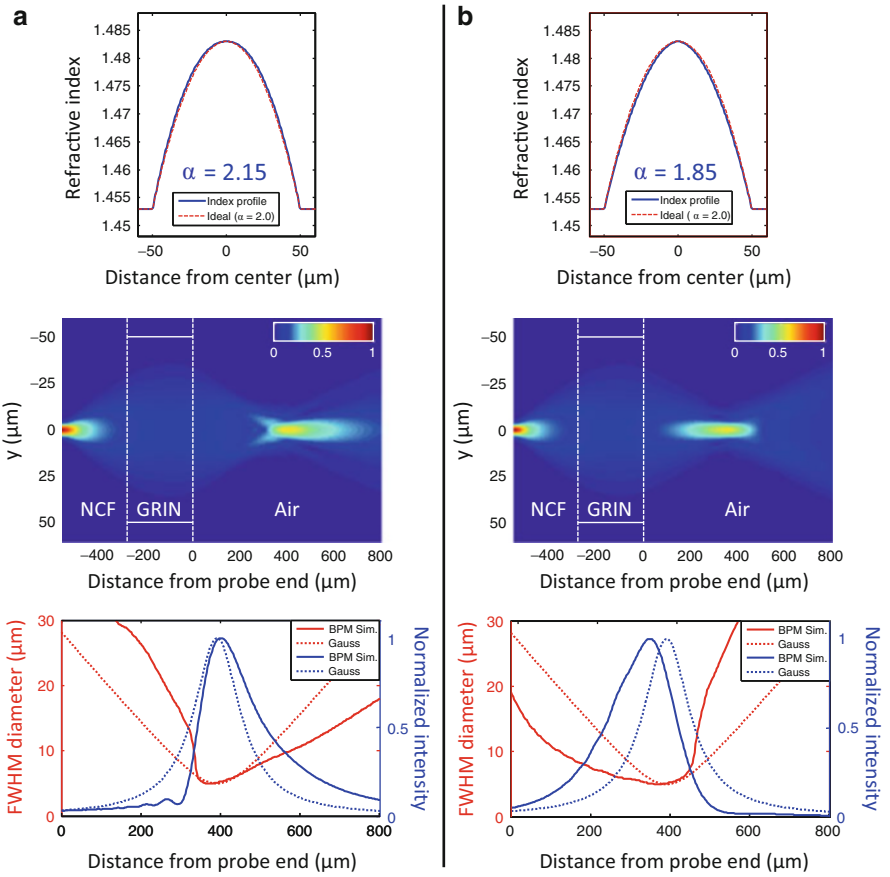

Fig. 81.5 BPM simulation results of lensed fiber probes using GRIN fiber lenses that have nonparabolic refractive index profiles with α parameters of 2.15 (**a**) and 1.85 (**b**). *Top*: refractive index profile of the GRIN fiber compared to an ideal parabolic profile with $\alpha = 2.0$. *Middle*: simulated E-field amplitude in the entire simulated region. *Bottom*: FWHM beam diameter and on-axis intensity of the simulated output beam (*solid lines*) compared to the ideal Gaussian beam that would result in the case of a parabolic profile (*dotted lines*) (Figure adapted from Ref. [22])

parabolic curve in Fig. 81.5a (top)), the focal region takes on an asymmetric shape characteristic of spherical aberration. The focal spot intensity is reduced with a Strehl ratio of $S = 0.77$, while the DOF remains approximately the same as in the aberration-free case. When the α parameter is de-tuned to 1.85, however, the output beam DOF is increased by a factor 1.44 at the cost of only a very slightly reduced Strehl ratio of $S = 0.96$, showing that GRIN profiles with $\alpha < 2.0$ can potentially be used to enhance the DOF of fiber probes.

Using the BPM, we have also investigated the effects of the central index dip and index ripple on the output beam [22]. The results indicate that the detrimental

effects of such anomalies in the index profile are not as serious as one might expect. This can be understood when one recognizes that the dip and the index ripple are aberrations with high spatial frequencies that generate large-angle diffracted waves which, for parameters that are representative of realistic index profiles, carry only a small percentage of the incident beam power and rapidly lose intensity as they propagate away from the probe end due to their strong divergence. By contrast, the majority of the incident beam power remains in an essentially unperturbed component of the wavefront which converges normally to form an almost unaltered focal region with only a minor reduction in Strehl ratio and no significant change in DOF. This is in stark contrast to index profile aberrations with low spatial frequencies, such as nonideal α parameters or systematic deviations from the power-law model, which will have a strong influence on the intensity distribution in the focal region even for very small index profile errors on the order of a few percent [22]. This finding is important for specifying the fabrication tolerances of customized preforms for high-quality GRIN fiber lenses.

Our results show that the BPM enables accurate simulation of fiber probes using a realistic model of the refractive index profile of the GRIN fiber, which is important in the design of high-performance miniaturized fiber-optic probes for OCT. Furthermore, in Sect. 81.2.4.4, we will demonstrate the use of the BPM for studying schemes for extending the DOF of miniaturized fiber probes using GRIN fiber phase masks.

81.2.2 Scan Mechanisms

OCT *imaging*, in the sense that 2D or 3D structural information is obtained, is only possible if the probe beam can be scanned within the sample. In the following, we will give a categorization of scanning probes, based on mechanical and optical principles, which is independent of the technical details of the scan mechanism implementation. This categorization will allow us to gain some insight into the advantages and disadvantages of different classes of currently employed scan mechanisms, and it is general enough to accommodate future developments.

Firstly, probes can be categorized into forward-facing and side-facing types (see Fig. 81.6). Generally, the requirements of the application dictate which of these two is preferable.

Furthermore, probes can be categorized according to their scan mechanisms. There are two main categories of scan mechanisms: beam scanning and probe scanning. The two categories and some of their variations are illustrated in Fig. 81.7. Beam scanning involves a movement of the beam path inside the probe housing, allowing the probe to remain stationary during the scan. Probe scanning, on the other hand, mechanically actuates the entire probe (or a mechanical subcomponent thereof which defines the emitting beam aperture), while the beam path inside the probe is unchanged. Beam scanning probes are more challenging to miniaturize, as they usually require moving parts inside the probe housing. For this reason, probes with submillimeter dimensions generally utilize probe scanning.

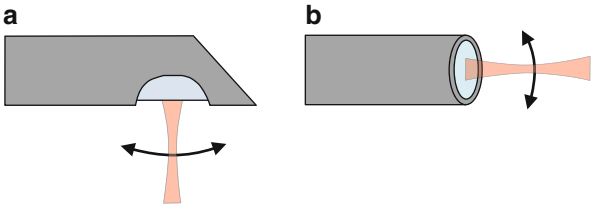

Fig. 81.6 Side-facing (**a**) and forward-facing (**b**) probes. The indicated beam scanning motions in (**a**) and (**b**) are just examples, and a variety of other possibilities exist in both cases

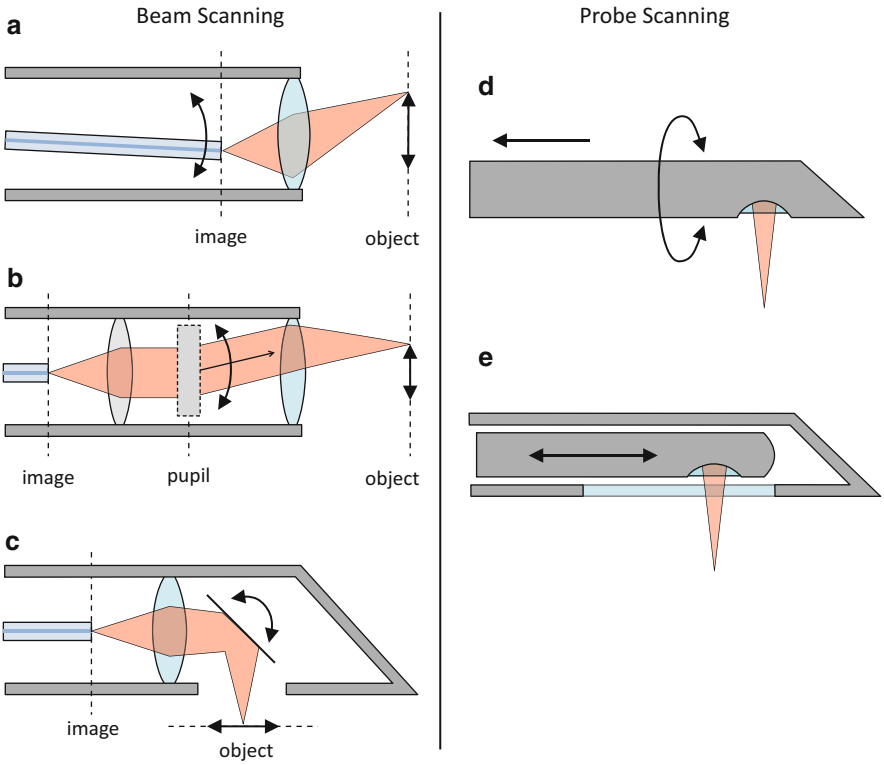

Fig. 81.7 Overview of some basic scan mechanisms, categorized into "beam scanning" and "probe scanning". (**a**) Image-space scanning (using an oscillating fiber tip in this example). (**b**) Pupil scanning. The *dashed grey rectangle* represents a beam deflection mechanism, which can be implemented using various technologies – see text for practical examples. (**c**) Object-space scanning. (**d**) Rotation/pullback scanning. (**e**) Linear-scanning probe inside an outer housing

In beam scanning, the moving beam is projected out of the probe housing into the sample by the probe optics. The probe optics form an imaging system which images scattered light from the sample (the object) onto the sample-arm fiber tip (the image). Using terminology from imaging optics, we can further subdivide beam scanning techniques as "image-space scanning" (Fig. 81.7a), "pupil scanning" (Fig. 81.7b), or "object-space scanning" (Fig. 81.7c). Although Fig. 81.7a, b

shows forward-facing configurations for pupil and image-space scanning, they can in principle also be realized as side-facing types by adding mirrors or prisms to deflect the beam outward at a chosen angle.

Image-space scanning (Fig. 81.7a) can be performed by actuating the tip of the sample-arm fiber. The probe beam focal spot is thereby scanned in the sample over a range, which is determined by the magnification of the probe optics. The concept of image-space scanning has been implemented in endoscopic probe designs using oscillating fiber tips [44], but the miniaturization of these designs to submillimeter diameters has proven to be challenging. Small-diameter forward-facing OCT probes of this type have been reported with outer diameters (ODs) of 2.4 and 2.2 mm using tubular four-quadrant piezoelectric actuators [45] and electrostatic actuators [46], respectively.

Pupil scanning (Fig. 81.7b) involves an angular deflection of the collimated beam in the pupil plane of the imaging optics. This is the principle of conventional beam scanning solutions based on galvanometer mirrors, which are positioned in the back focal plane of the scan lens. Beam deflection mechanisms for pupil-scanning probes have been realized with MEMS mirrors [47] and with counterrotating wedged GRIN lens pairs (paired-angle-rotation scanning, PARS [48]). In pupil-scanning arrangements, MEMS mirror solutions require a folded beam path geometry, resulting in relatively large probe diameters of several millimeters. However, PARS probes have been miniaturized to needle dimensions as small as 21 gauge (21G, OD 0.82 mm) in a forward-facing configuration [7].

Object-space scanning (Fig. 81.7c) sacrifices some of the working distance of the probe optics, but is often used in side-facing miniaturized MEMS mirror probes [49, 50] because the MEMS mirror can conveniently serve as the output beam deflector, which directs the beam sideways out of the probe. Although probes of this type with diameters down to 2.6 mm have been demonstrated [50], MEMS technology does not yet seem to allow miniaturization to submillimeter dimensions at the time of writing and is, therefore, mainly targeted toward endoscopic OCT applications.

An elegant variation of beam scanning involves the use of long and thin GRIN relay rods, which can be inserted into hypodermic needles. By scanning the incident light at the proximal end face of the GRIN relay rod, the relayed and focused beam is scanned in object space at the distal end of the relay. The key advantage of this approach is that the scan mechanism does not need to be miniaturized to the diameter of the needle and can be relocated into a larger-diameter housing to which the needle is attached. Submillimeter diameter needle probes of this kind have been demonstrated for multiphoton and confocal endomicroscopy [51, 52] and OCT [53]. In these needle probes, the GRIN relay rod is an integral part of the distal focusing optics. Depending on the scanning mechanism at the proximal end face of the relay (e.g., by scanning the sample-arm fiber tip [52] or scanning an image of it using a galvanometer mirror and objective lens [53]), they can be classified as either image-space or pupil-scanning types, respectively.

In order to achieve the highest possible degree of miniaturization, probe-scanning techniques (Fig. 81.7d, e) must be used, with the smallest reported probe of this kind

being encased in a 30G needle (0.31 mm OD) [16]. Probe-scanning designs must be side facing in order to enable at least 2D scanning capability. The most widespread approach is the rotation/pullback method of Fig. 81.7d, where B-scans are acquired over one probe rotation and then stacked along the translation direction to generate a 3D image in a similar fashion to endoscopy [20]. An alternative is to perform a fast translation along the probe axis to acquire a 2D image, as illustrated in Fig. 81.7e, and needle probes of this design have been employed in applications that require a fast 2D scan in a plane parallel to the needle axis, such as dynamic imaging of alveoli [5] and Doppler imaging [12, 54].

An interesting new development in the area of probe scanning is to use freehand motion to scan over a region of interest [55, 8, 56]. This approach can be combined with methods to correct for the resulting nonuniformity of the scan motion as well as the misalignment of adjacent A-lines in the OCT image data, either by using feedback control to actively compensate the probe position during the scan [55] or by post-processing of the OCT image data in combination with location data from a position sensor [56].

81.2.3 A Review of Published Needle Probe Designs

In the following subsections, we will give an overview of the technical evolution of OCT needle probes that are capable of acquiring 2D or 3D images via some form of scanning, as described in Sect. 81.2.2. The term "imaging needle," which was coined in [2], is useful because it differentiates such scanning needle designs from "point-sensing" fiber probes that are integrated into needles, typically in a forward-facing configuration. Point-sensing needles measure 1D structural information from A-scans acquired at a stationary position or during needle advancement, and a number of examples have been reported. Sequences of A-scans (M-mode) acquired during needle advancement can be displayed as 2D arrays of depth versus time that allow the successive penetration of tissue layers to be visualized [57] (see also Sect. 81.3.1.2). Alternatively, the relative displacement of scatterers in consecutive A-scans can be analyzed in order to determine the mechanical properties of soft tissue that lies ahead of the needle [58]. Processing of single A-scans acquired with point-sensing needles has been used to obtain localized tissue parameters such as the refractive index [59, 60] or attenuation coefficient [4]. An exhaustive discussion of the technology and applications of point-sensing needles lies outside the scope of this section, and we will, therefore, focus our attention on imaging needles.

81.2.3.1 Side-Facing Rotation/Pullback Imaging Needles

The first demonstrated OCT imaging needle probe [2] was a side-facing design for 2D rotation scanning (see Fig. 81.8a). Even though the distal focusing optics used discrete micro-optical components (a 250-μm diameter GRIN lens and a micro-mirror), it already achieved very compact dimensions with an OD of only 0.41 mm (27G). The use of discrete micro-optics introduces challenges related to precision alignment of components inside the needle shaft, and it requires angled or

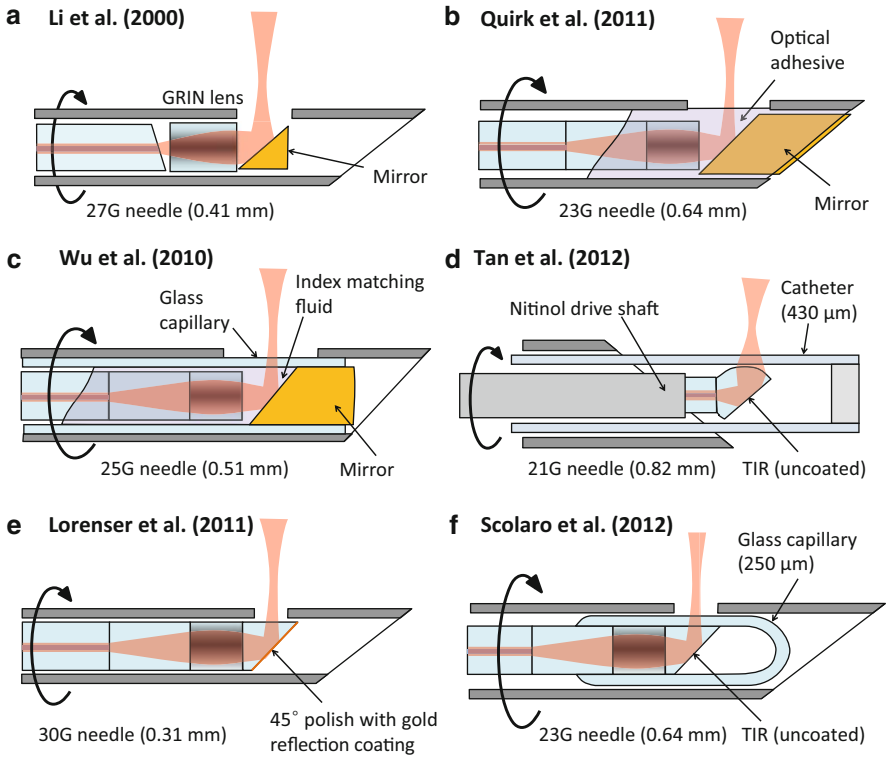

Fig. 81.8 Side-facing needle designs for rotation/pullback scanning. (**a**) The first demonstrated OCT imaging needle probe [2]. (**b**) The first needle probe to generate full 3D OCT data sets using rotation/pullback scanning [61]. (**c**) A capillary-encased design with a robust optical-quality output window that can be flat polished for elimination of astigmatism [17]. (**d**) A catheter-based needle probe for biopsy guidance in lungs [6]. (**e**) The smallest demonstrated OCT imaging needle probe [16]. (**f**) A fully fused capillary-encased needle design capillary-encased needle design with an astigmatism-free output beam and with the highest reported sensitivity [11]

antireflection-coated interfaces in order to avoid backreflections which can introduce image artifacts and reduce the sensitivity. For this reason, many subsequent probe designs were based on "monolithic" all-fiber distal focusing optics using fusion-spliced GRIN fiber lenses or fused ball lenses. The great advantage of such all-fiber probe designs is that they can be fabricated using established fusion splicing technology, which is reproducible and self-aligning. Furthermore, the fusion-spliced optics assembly practically eliminates backreflections from optical interfaces.

Figure 81.8b shows an example of such a design, which was the first OCT needle probe to demonstrate full 3D imaging using combined rotation and pullback [61]. A 23G (0.64 mm OD) side-facing probe was made using a GRIN-lensed fiber which

was embedded together with a side-deflecting mirror in UV-curing optical adhesive. Due to the relatively high refractive index contrast between the GRIN fiber end face and the optical adhesive, this interface can be conveniently employed as the reference reflector in a common-path OCT configuration, as was done in Refs. [61, 3, 43]. A drawback of this design is the lack of mechanical robustness of the optical adhesive surface that forms the interface with the sample medium. Mechanical and chemical wear can degrade the optical quality of this interface, leading to deterioration in the sensitivity and beam quality after prolonged use. Furthermore, the shape of the optical adhesive surface cannot be exactly controlled, leading to some distortion and astigmatism in the output beam [43]. An improved needle probe design with an OD of 0.51 mm (25G) using a flat-polished capillary output window has been demonstrated to address this problem [17] (see Fig. 81.8c). By using index-matching fluid inside the capillary, it was shown that the astigmatism could be almost completely eliminated in this design, and the glass capillary provides a robust optical-quality output window interface, at the cost of a more complex fabrication and assembly process.

An example of an all-fiber probe using a fused ball lens is shown in Fig. 81.8d [6]. This 21G (0.82-mm OD) design uses a polyimide catheter to encase the fiber probe, in order to maintain the refractive power of the ball lens in air and to serve as a protective sheath that allows rotation/pullback scanning of the probe while keeping the needle and catheter stationary. The astigmatism which is introduced by the catheter was partially compensated by the shape of the ball lens, which has different radii of curvature in the sagittal and tangential planes.

Ultrathin needle probes with a diameter of only 0.31 mm (30G) were presented in [16] and [32]. These probes use an all-fiber distal optics design that was initially proposed in a patent covering a variety of ultrathin fiber probes for endoscopy [62], where an angle-polished NCF section that is added after the GRIN lens section is used as the side-deflecting mirror as shown in Fig. 81.8e. The angle-polished probe tip is coated with gold in order to maintain its reflectivity under immersion in fluids. A drawback of this probe design is the astigmatism which the beam acquires as it exits from the side of the fiber cladding, which behaves as a cylindrical lens. However, it was shown in [16] and [32] that the astigmatism is reduced to a tolerable level under the near-index-matched conditions existing when the probe is inserted into tissue. This probe design and some of its recent improvements will be presented in more detail in Sect. 81.2.4.2. A needle-like catheter probe incorporating a similar angle-polished GRIN-lensed fiber was presented in [9] for imaging of brain tissue. The 360-μm OD catheter was delivered via a 24G (0.57-mm OD) needle, and the astigmatism of the probe was compensated using index-matching fluid inside the catheter.

An advanced 23G (0.64-mm OD) needle probe design which uses an angle-polished fiber under total internal reflection (TIR) is shown in Fig. 81.8f [11]. The TIR is maintained under fluid immersion by encasing the angle-polished fiber probe inside a microcapillary which is collapsed and fused onto the fiber. The capillary acts as a robust, well-defined optical window, and its astigmatism is compensated

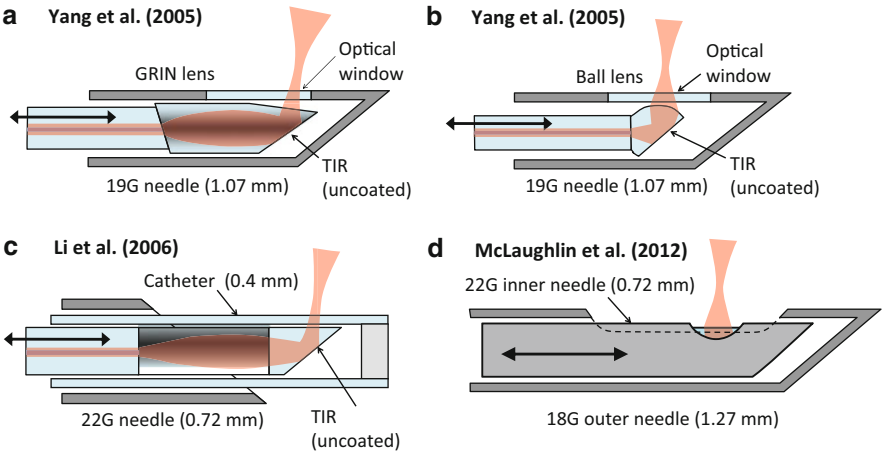

Fig. 81.9 Side-facing linear-scanning needle designs. (**a**, **b**) Early designs employed in the first demonstration of needle-based Doppler imaging [12]. (**c**) Advanced catheter-based design for needle-based Doppler imaging [54]. (**d**) Linear-scanning needle for dynamic lung imaging [5]

using a novel optical design that exploits the focal shift effect [11]. This design achieved the highest reported sensitivity for an OCT needle probe (112 dB) and will be discussed in more detail in Sect. 81.2.4.1.

81.2.3.2 Side-Facing Linear-Scanning Imaging Needles

In contrast to rotation/pullback scanning which combines a fast rotation with a slow linear motion in order to acquire a 3D cylindrical volume, linear-scanning needle probes perform a rapid linear motion along the needle axis in order to generate fast 2D image frames. This can be advantageous for applications where a fast update rate of a large rectangular 2D field of view (FOV) is desirable.

The first linear-scanning OCT needle probes were developed for Doppler imaging and are shown in Fig. 81.9a, b [12]. Two versions were demonstrated, one with an angle-polished GRIN lens and one with an angle-polished ball lens. In both cases, TIR at the angle-polished interface was ensured by sealing the side opening in the 19G (1.1-mm OD) needle with a flat plastic window. These probes allowed imaging at a rate of 1–2 Hz over a linear scan range of ~2.5 mm. In a later version [54], the dimensions of the probe were reduced by using all-fiber probe optics consisting of GRIN fiber and an angle-polished NCF tip section that were enclosed in a protective catheter that was delivered via a 22G (0.72-mm OD) needle as illustrated in Fig. 81.9c.

Another application which requires a fast 2D frame rate over a large FOV is dynamic imaging of lungs, where a 1.27-mm OD (18-G) linear-scanning needle probe was demonstrated [5] (see Fig. 81.9d and also Sect. 81.4.2.3). An inner side-facing needle probe with a similar design to the one shown in Fig. 81.8b was actuated inside the outer 18G needle at a rate of 3 Hz over a linear scan range of ~12 mm.

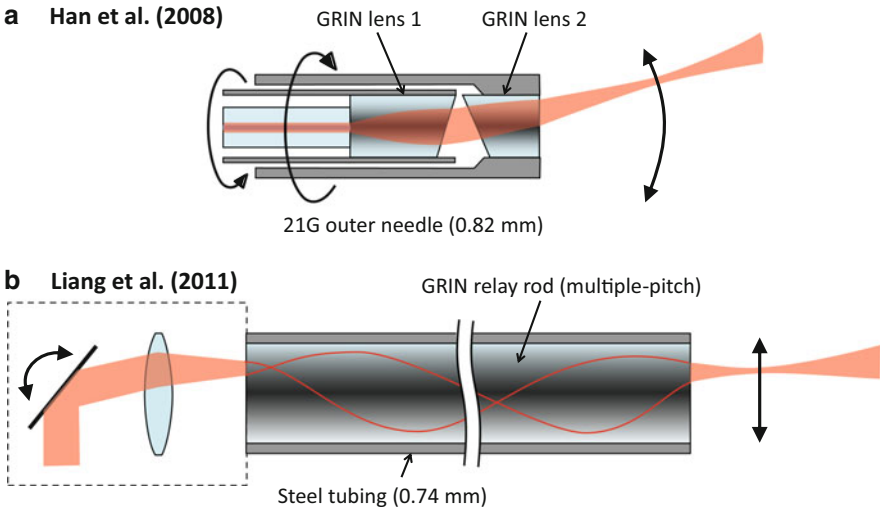

Fig. 81.10 Forward-facing needle probe designs. (**a**) Paired-angle-rotation scanning (*PARS*) needle [7]. (**b**) A design based on a GRIN relay rod, employing proximal scanning via galvanometer mirrors housed in a handpiece (*dashed rectangle*) [53]

81.2.3.3 Forward-Facing Imaging Needles

The mechanical requirements of a sharp needle tip for easy tissue penetration are not straightforward to combine with the optical requirements of a forward-facing imaging system. For this reason, forward-facing imaging needle probes are typically only used for special applications where a blunt front end is acceptable or even desirable.

A forward-facing OCT needle probe concept called paired-angle-rotation scanning (PARS) [48, 7] has been developed for aiding specialized surgical procedures in the eye. As illustrated in Fig. 81.10a, two angled GRIN lenses are mounted in an inner and an outer needle that rotate in opposite directions, causing the output beam to perform a fanlike sweep back and forth on a line trajectory ahead of the needle. The smallest demonstrated probe of this type had an OD of 0.82 mm (21G) [7].

Another application which requires needlelike forward-facing OCT probes is interventional guidance in neurosurgery. Figure 81.10b shows a 0.74-mm OD (slightly larger than 22G) forward-facing needle incorporating a 0.5-mm-diameter, 12-cm-long GRIN relay rod that was proposed for this application [53]. The input beam to the GRIN relay rod was scanned using galvanometer mirrors that were incorporated into a prototype handpiece attached to the needle. The FOV of this probe was a circular region of 0.44-mm diameter, limited by the diameter of the GRIN relay rod. As an alternative to this approach, somewhat larger, forward-facing needle-like probes with outer diameters of ~2 mm have been developed that employ an electrostatically actuated oscillating fiber tip inside the needle shaft [46, 10].

81.2.4 Advanced Needle Probe Designs

81.2.4.1 High-Sensitivity Anastigmatic Imaging Needles

OCT needle imaging systems must achieve optical performance comparable to high-end benchtop systems in order to deliver the image quality that is required for clinical applications. The main source of degraded performance in current side-facing OCT needle probes lies in the optics required for deflecting the beam perpendicular to the needle axis, as they tend to introduce losses and beam distortion. We have recently presented a high-optical-quality OCT needle probe that achieves sensitivity and resolution comparable to conventional free-space OCT sample arms [11]. The probe achieves very low optical losses by utilizing total internal reflection (TIR) from an angle-polished fiber tip, encased in a glass microcapillary, as shown in Figs. 81.11a and b. Fusion of the capillary to the fiber provides a robust, optical-quality output window that minimizes beam distortion. Furthermore, the probe features a novel anastigmatic design, which exploits the "focal shift" phenomenon for focused Gaussian beams to achieve equal working distances (WDs) for both axes.

The anastigmatic design concept can be conveniently analyzed using ABCD matrices [27]. As was outlined in Sect. 81.2.1.2, the Gaussian beams transformed using this formalism are exact wave-optic solutions in the paraxial regime and, therefore, intrinsically exhibit the focal shift which is observed when focusing at low Fresnel numbers [63, 27]. Consider a side-facing probe with a cylindrical output window with radius R as shown in Fig. 81.12a. The refractive indices of the cylindrical output window and the sample are n_1 and n_2, respectively. When the initially circularly symmetric beam is deflected sideways out of the probe, its symmetry is broken by the cylindrical interface with refractive power $\Phi = (n_2 - n_1)/R$ that acts only in the x-axis (we use a sign convention where the radius R is negative for a concave surface, yielding a positive refractive power for $n_2 < n_1$). The output beam therefore becomes astigmatic, with WDs and focal spot diameters that will generally be different in the x- and y-axes, as illustrated in Fig. 81.12a. Directly after the cylindrical interface, the complex output beam parameter [27] in the y-direction is equal to

$$\tilde{q}_{2y} = -WD_y + iz_{Ry}, \tag{81.7}$$

where the minus sign is included to account for the fact that the working distance is a positive number. Inside the probe, directly at the input to the cylindrical interface, the complex beam parameter of the circularly symmetric beam is $\tilde{q}_1 = (n_1/n_2)\tilde{q}_{2y}$. The beam parameter of the output beam in the x-direction is obtained by transforming this beam with the ABCD matrix of the curved interface:

$$\tilde{q}_{2x} = \frac{\tilde{q}_1}{-\frac{\Phi}{n_2}\tilde{q}_1 + \frac{n_1}{n_2}} = \frac{\tilde{q}_{2y}}{-\frac{\Phi}{n_2}\tilde{q}_{2y} + 1}. \tag{81.8}$$

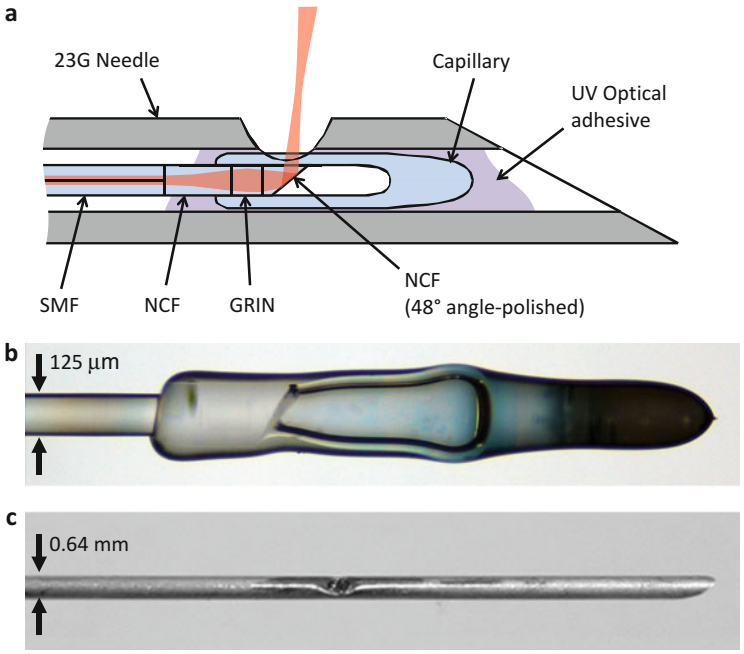

Fig. 81.11 (**a**) Schematic of the anastigmatic TIR imaging needle design. (**b**) Bright-field image of the angle-polished fiber probe encased in a fused glass microcapillary. (**c**) Photo of the fully assembled side-viewing 23G needle (Figure adapted from Ref. [11])

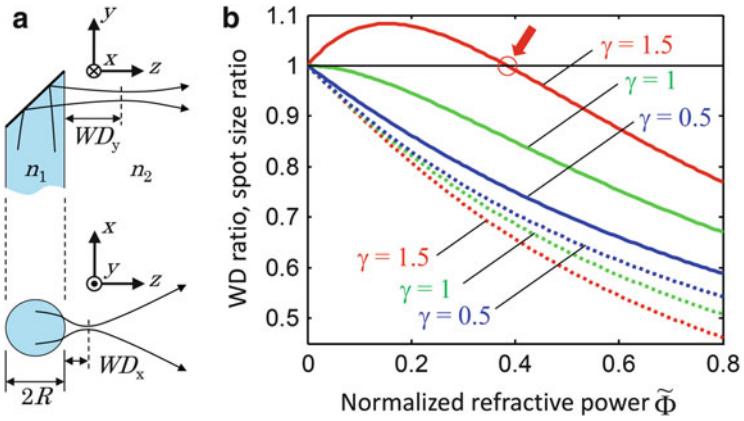

Fig. 81.12 (**a**) Schematic of a side-viewing probe with astigmatism resulting from the curved output window interface. n_1, n_2, refractive indices of output window and sample, respectively; WD_x, WD_y: WD in x and y, respectively; and R, radius of curvature of the output interface. (**b**) Curves illustrating the WD ratio and spot size ratio as a function of the normalized refractive power, obtained by evaluating Eqs. 81.10 and 81.11 for different values of γ. *Solid curves*, WD ratio; *dotted curves*, spot size ratio. The *arrow* indicates the anastigmatic point (Figure adapted from Ref. [11])

If we introduce the dimensionless variables $\widetilde{\Phi} = WD_y\Phi/n_2$ and $\gamma = z_{Ry}/WD_y$, we can write the right-hand side of Eq. 81.8 as

$$\tilde{q}_{2x} = \frac{-WD_y}{\left(1+\widetilde{\Phi}\right)^2 + \gamma^2\widetilde{\Phi}^2}\left[\widetilde{\Phi}\left(1+\gamma^2\right) + 1 - i\gamma\right]. \tag{81.9}$$

After comparing the real and imaginary parts with $\tilde{q}_{2x} = -WD_x + iz_{Rx}$, one obtains the following two dimensionless expressions for the ratios of the WDs and spot sizes in the x- and y-directions [11]:

$$\frac{WD_x}{WD_y} = \frac{1 + (1+\gamma^2)\widetilde{\Phi}}{\left(1+\widetilde{\Phi}\right)^2 + \gamma^2\widetilde{\Phi}^2} \tag{81.10}$$

$$\frac{w_{0x}}{w_{0y}} = \frac{1}{\sqrt{\left(1+\widetilde{\Phi}\right)^2 + \gamma^2\widetilde{\Phi}^2}}. \tag{81.11}$$

The two ratios given by Eqs. 81.10 and 81.11 are plotted in Fig. 81.12b as a function of the normalized refractive power $\widetilde{\Phi}$ for different values of the parameter γ. The curves in Fig. 81.12b can be interpreted as the result of a thought experiment in which a Gaussian beam is transmitted through an initially planar interface between media with the refractive indices n_1 and n_2, coming to a focus with Rayleigh range z_{Ry} at a working distance WD_y (thereby determining the parameter γ). One can then imagine increasing the normalized refractive power $\widetilde{\Phi}$ by "bending" the interface in the x-direction. While the y-direction is unaffected, the WD and focal spot radius of the x-direction begin to deviate from WD_y and w_{0y} with increasing refractive power. For beams with $\gamma > 1$, the WD of the x-direction initially increases and then decreases again, going through an anastigmatic point where the WDs of the two axes are equal (red arrow in Fig. 81.12b).

This seemingly counterintuitive focusing behavior of Gaussian beams within the Rayleigh range is a manifestation of the focal shift effect (the shift between the wave-optic and geometric-optic foci) that occurs at low Fresnel numbers [63]. For a given normalized refractive power $\widetilde{\Phi}$, the optimum γ can be found by setting $WD_x/WD_y = 1$ in Eq. 81.10, yielding

$$\gamma_{opt} = \sqrt{\frac{1+\widetilde{\Phi}}{1-\widetilde{\Phi}}}. \tag{81.12}$$

One can see from Eq. 81.12 that anastigmatic solutions are only possible for $\widetilde{\Phi} < 1$. We can therefore summarize that, for a cylindrical interface with a fixed refractive power Φ, anastigmatic solutions exist under two conditions:

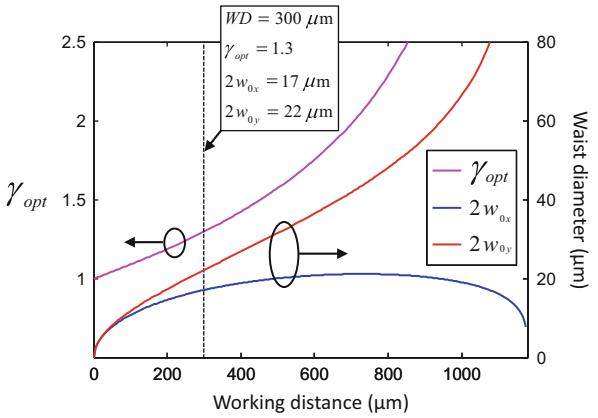

Fig. 81.13 Accessible output beam parameters within the constraints of the anastigmatic solution for a curved interface between a 250-μm-diameter borosilicate glass capillary and water at a wavelength of 1300 nm. The optimum γ parameter that corresponds to the anastigmatic solution is shown by the *magenta curve* (*left axis*). The *red* and *blue curves* show the $1/e^2$ waist diameters of the elliptical focal spot (*right axis*). The *dashed vertical line* indicates the design goal for the anastigmatic TIR needle discussed in the text

- The working distance WD_y of the axis that is unaffected by the cylindrical interface must be smaller than its Rayleigh range z_{Ry}. (This is the condition $\gamma > 1$.)
- The working distance WD_y must be smaller than $WD_{y,\max} = n_2/\Phi$. (This is the condition $\widetilde{\Phi} < 1$.)

We will illustrate the anastigmatic design concept with a numerical example that will lead us to our chosen design for the anastigmatic TIR needle. The starting point was the requirement that the $1/e^2$ focal spot diameter of the probe should be close to 20 μm, which corresponds to an FWHM transverse resolution of 12 μm that is commensurate with the axial resolution of our 1300-nm swept-source (SS) OCT system. Our capillary-encased TIR needle uses a 250-μm-diameter borosilicate microcapillary with a refractive index of $n_1 = 1.46$, and our sample medium is water with $n_2 = 1.32$ at the operating wavelength of 1300 nm. The refractive power Φ is, therefore, 1,120 m^{-1}. The Rayleigh range in water for a 20-μm focal spot diameter is 320 μm. In order to fulfill the requirement $\gamma > 1$ for our desired focal spot diameter, we will aim for a WD of 300 μm, which translates to a normalized refractive power $\widetilde{\Phi}$ of 0.25. From Eq. 81.12, we calculate $\gamma_{opt} = 1.3$, which means that our focal spot diameter in the *y*-direction must be adjusted to 22 μm in order to obtain the anastigmatic solution for the given refractive power and desired working distance of 300 μm. The focal spot is slightly elliptical, with a diameter of 17 μm in the *x*-axis (obtained via Eq. 81.11). Anastigmatic solutions with longer working distances can be obtained at the cost of a stronger ellipticity of the focal spot, as illustrated in Fig. 81.13, which shows the accessible beam parameters as a function of the WD. The dashed vertical line indicates our design goal with a WD of 300 μm.

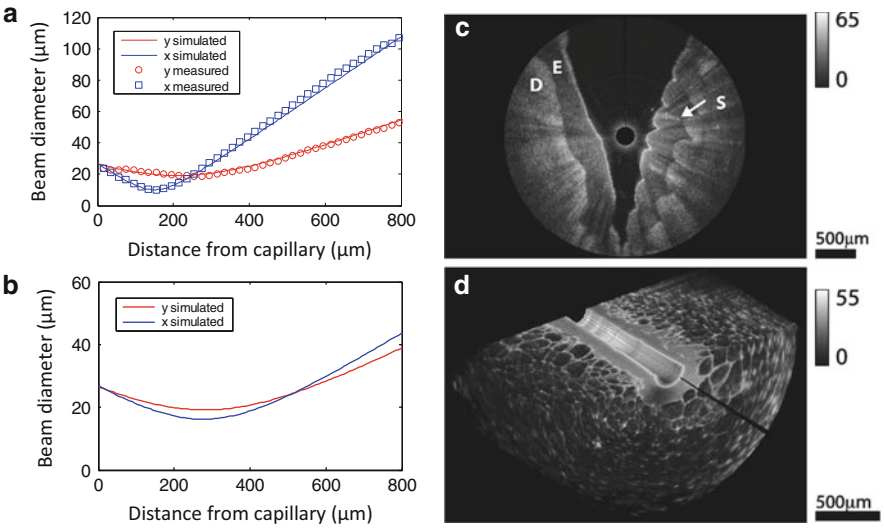

Fig. 81.14 Beam profile characterization and OCT images obtained with the anastigmatic TIR needle probe. (**a**) Measured and simulated beam profiles in air. (**b**) Simulated beam profile in water. (**c**) Radial OCT needle image of the surface of a finger and thumb. *E* epidermis, *D* dermis, *S* sweat duct. (**d**) Cutaway view of a rendered 3D OCT needle image of a cucumber. The needle tract is visible at the center of the volume with its rotation origin marked by the wedge at *lower right*. Colormaps in (**c**) and (**d**) are in dB (Figure adapted from Ref. [11])

Our fabricated anastigmatic TIR needle probe used the above calculation as a guide, and the desired output beam parameters were obtained by iterative optimization of the lengths of the NCF and GRIN fiber sections. As explained in [11], the precise calculation of the anastigmatic solution in our TIR needle is slightly more complex as the refractive index mismatch between the silica fiber claddings ($n = 1.447$), and the borosilicate capillary creates a second (but much weaker) cylindrical interface which must be included in the ABCD matrix calculation. The effect is small, however, and the results of the above calculation are sufficient as a starting value for the experimental optimization of the beam parameters. The measured and simulated output beam parameters in air are shown in Fig. 81.14a. The simulated beam parameters in water are quite close to our desired anastigmatic solution, with almost equal working distances of $WD_x = 270$ µm and $WD_y = 280$ µm and $1/e^2$ focal spot diameters of 16 µm and 19 µm in the x- and y-directions, respectively.

Due to the very low losses introduced by the TIR side-deflecting optics, our fabricated needle probe achieved a record high sensitivity of 112 dB when used in conjunction with the 1300-nm SS-OCT system described in Sect. 81.2.5.3. The good beam quality and high sensitivity of this needle probe yield image quality that is comparable to that obtained with bulk-optic scanning sample arms, as can be seen in the example images in Figs. 81.14c and d.

81.2.4.2 Ultrathin Imaging Needles

To minimize trauma resulting from needle insertion in applications such as imaging of small animals or delicate organs, it is desirable to use very thin needles. The smallest side-facing probe diameters can be achieved with all-fiber distal optics employing an angle-polished fiber tip as a beam deflector. This conceptually simple design poses two substantial challenges. Firstly, the output beam acquires significant astigmatism as it exits the fiber cladding, which acts as a strong cylindrical lens. Secondly, the application of a metallic or dielectric reflective coating to the polished end face is problematic, as the simultaneous coating of the beam output window must be avoided. In [16], we showed that these challenges can be overcome, and we demonstrated an ultrathin all-fiber probe that was encased in a 30G needle (0.31-mm OD), which is the smallest-diameter side-facing needle probe reported in the literature.

The probe was used in conjunction with an 840-nm spectral-domain (SD) OCT system (see Sect. 81.2.5.3) to generate 3D images of lung tissue [16, 5]. An improved, second-generation ultrathin needle was presented in [32], with a range of enhancements in the optical and mechanical properties. The second-generation ultrathin needle was used in conjunction with a 1300-nm SS-OCT system (see Sect. 81.2.5.3) to generate the first 3D needle OCT images of skeletal mouse muscle tissue [32].

The schematic of the ultrathin needle design is shown in Fig. 81.15a. The "monolithic" all-fiber distal focusing optics consist of the usual combination of a NCF spacer and a GRIN fiber lens, but with an additional section of NCF spliced to the end, which is subsequently polished at a 45° angle. A high-reflecting metal coating consisting of a thin chrome adhesion layer and a gold reflection layer is applied to the angle-polished NCF using a thermal vacuum deposition process. In our initial ultrathin needle probe which operated at 840 nm, this metal coating introduced significant absorption losses which represented a large part of the relatively high measured round-trip attenuation γ_P of 10 dB for light returning from a unity reflector placed at the working distance (see Sect. 81.2.5.2). In the second-generation ultrathin needle probe at 1300 nm, the absorption of the metal coating was much lower, leading to a measured round-trip attenuation γ_P of only 2.5 dB.

A fusion-spliced and angle-polished fiber probe, before application of the metal coating, is shown in Fig. 81.15b, and a fully assembled ultrathin 30-G needle probe is shown in Fig. 81.15c. The side opening in the second-generation ultrathin needle depicted in Fig. 81.15c has a diameter of only 140 μm and was drilled by nonthermal ablation with a femtosecond laser in order not to compromise the structural integrity and surface quality of the very thin hypodermic tubing [32].

When the ultrathin needles are inserted into tissue, the immersion in tissue fluids reduces the strong astigmatism introduced by the fiber cladding to a tolerable level, allowing imaging over a range of ~550 μm with FWHM resolution <18 μm in the case of the 840-nm needles [16] and over a range of ~700 μm with FWHM resolution <20 μm in the case of the second-generation 1300-nm needles [32]. The 840-nm needles had a measured sensitivity of 84 dB at 2 μs exposure time. (However, imaging of biological tissue was performed with a longer exposure

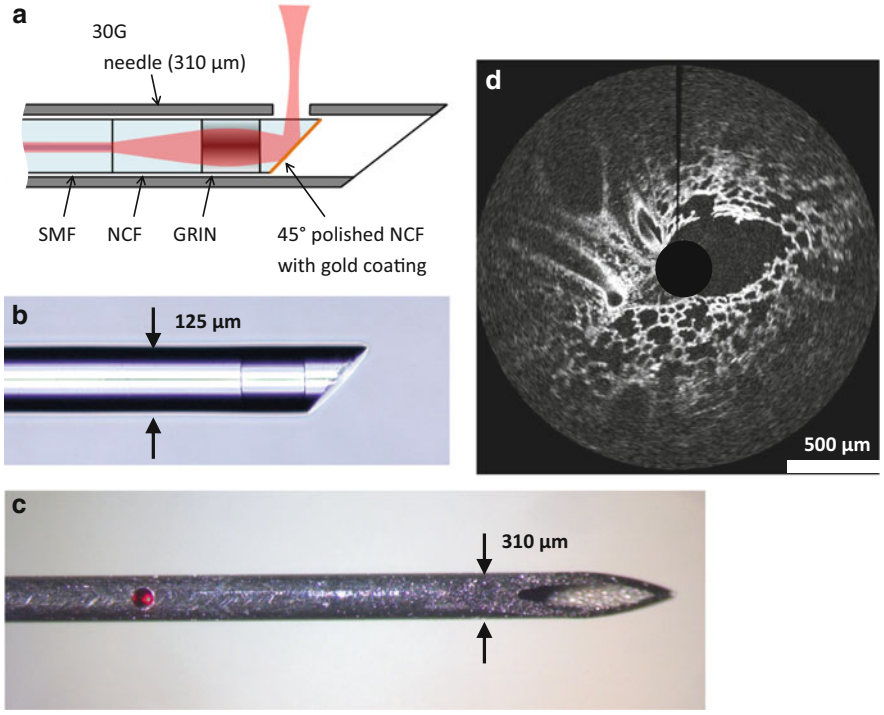

Fig. 81.15 (**a**) Schematic of the ultrathin OCT needle probe design. (**b**) Phase contrast microscope image of the all-fiber distal focusing optics with the angle-polished fiber tip reflector before application of the metal reflection coating. (**c**) A fully assembled 30G ultrathin OCT needle, showing the precision-drilled side opening fabricated by nonthermal ablation with a femtosecond laser. (**d**) Radial OCT image of a saline-inflated rat lung, obtained with the 840-nm ultrathin needle, showing alveoli and several bronchioles (Figure parts adapted from Ref. [32])

time of 13 µs, leading to an expected sensitivity of ~92 dB.) This was sufficient to generate 3D OCT images of lung tissue with good contrast, clearly resolving alveolar structure and bronchioles, as shown in Fig. 81.15d and in Sect. 81.4.2.2. However, attempts at imaging skeletal muscle tissue were unsuccessful using the 840-nm needles, presumably because the sensitivity was not sufficient to detect the relatively weak contrast of myofibers in solid tissue. The 1300-nm needles had a substantially higher measured sensitivity of 108 dB, due to the reduced optical losses of the metal reflection coating and the higher underlying sensitivity of the 1300-nm SS-OCT system compared to the 840-nm SD-OCT system. This enabled us to perform 3D needle OCT imaging of skeletal mouse muscle tissue, showing myofiber structure, tendon, and connective tissue [32].

81.2.4.3 Multimodality Imaging Needles

The diagnostic utility of OCT needle probes can be further enhanced if their capability of generating 3D images of tissue microstructure is combined with

a complementary functional modality such as fluorescence, which provides information about the biochemical composition of the tissue. OCT and fluorescence imaging can be conveniently combined in fiber-based probes using double-clad fiber (DCF) [64], where the core of the DCF guides the single-moded incident and returning long-wavelength OCT signals, as well as the few-moded, short-wavelength fluorescence excitation light. The returning fluorescence signal is efficiently collected by the inner cladding of the DCF due to its high NA and large diameter. This DCF-based combination of OCT and fluorescence imaging was initially demonstrated with bare fiber probes [65, 66]. It was subsequently implemented in endoscopic probes [67, 68] and needle probes [43].

A dual-modality DCF needle probe is shown in Fig. 81.16a [43]. The probe design is very similar to the one shown in Fig. 81.8b, except that DCF is used instead of SMF in a GRIN-lensed fiber that is embedded in UV curing optical adhesive together with a 0.3-mm-diameter mirror inside a 23G (0.64-mm OD) needle. The DCF (SM-9/105/125-20A, Nufern, USA) has a 9-μm core that is single moded over the 1300-nm OCT wavelength band and few moded at the 488-nm fluorescence excitation wavelength (estimated number of modes ~20). The inner and outer cladding diameters are 105 and 125 μm, respectively, with a NA of 0.20. The probe is designed for common-path OCT operation. For this reason, the NCF and GRIN fiber sections that are spliced to the end of the DCF are dimensioned to produce a slightly expanded, collimated output beam that has its beam waist located at the GRIN fiber end face in order to obtain a well-defined backreflection which serves as the OCT reference signal. The calculated −32 dB Fresnel reflection produced by the refractive index contrast between the optical adhesive and the GRIN fiber core has a power level that lies close to the optimum reference arm power for the employed SS-OCT system. The measured backreflection of −34 dB was in good agreement with this expected value. The FWHM output beam diameter in water at 1300 nm stays in the range 12–35 μm over a distance of ~1 mm from the needle. The fluorescence excitation beam at 488 nm has a similar diameter to the OCT beam over the same distance.

The DCF needle probe was connected to a 1300-nm SS-OCT system as shown in Fig. 81.16a. The SS-OCT system (see Sect. 81.2.5.3 and Fig. 81.22 for details) was modified to enable simultaneous fluorescence imaging with 488-nm excitation and detection at >500 nm (e.g., for detecting fluorescein with a peak emission wavelength of ~520 nm). The 488-nm excitation light is injected into the core of the sample-arm SMF via the aiming laser input of the SS-OCT system (see Fig. 81.22). The sample-arm SMF is spliced to a DCF coupler [69, 66] that couples out the returning fluorescence signal from the inner cladding while leaving light in the core unperturbed. The fluorescence signal is detected with a PMT and co-registered with the OCT signal, whereby every OCT A-scan has an associated fluorescence intensity measurement representing the integrated fluorescence collected from that radial direction. The rotation/pullback needle scan, therefore, generates a cylindrical 3D OCT image and a corresponding 2D fluorescence map.

The three frames in Fig. 81.16b–d show a dual-modality image of a sheep lung obtained with the DCF needle probe. Figure 81.16b is a 2D section from the 3D OCT data set, showing the characteristic honeycomb structure of the alveolar

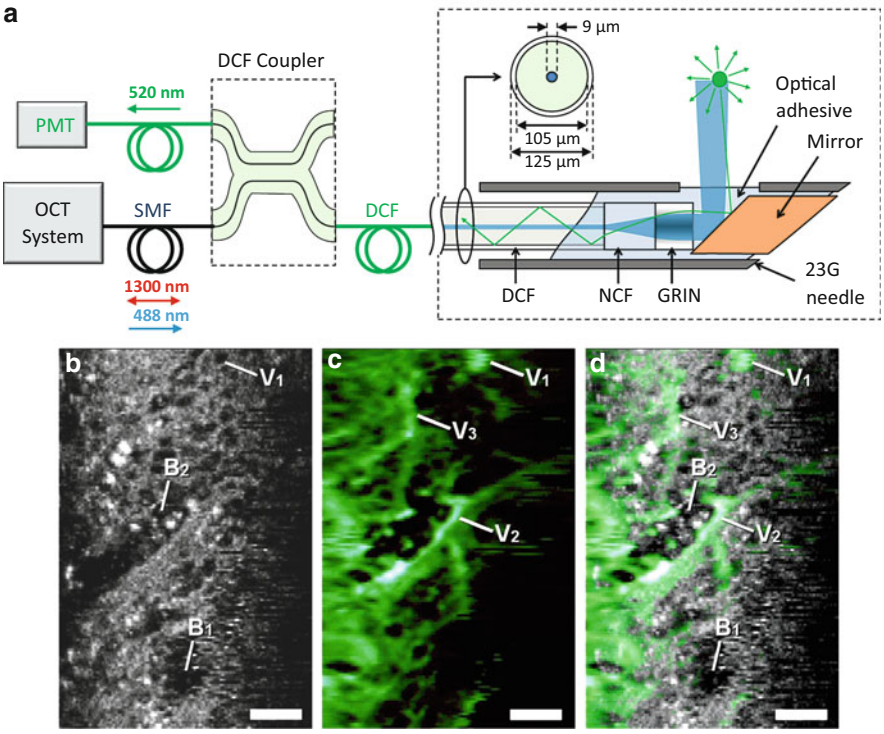

Fig. 81.16 (**a**) Schematic of the dual-modality needle system for combined OCT and fluorescence imaging. *PMT* photomultiplier tube, *DCF* double-clad fiber. (**b**, **c**, **d**) Imaging results of a dual-modality needle scan of a saline-inflated sheep lung with fluorescein solution infused through the vasculature. OCT (**b**), fluorescence (**c**), and combined OCT+fluorescence image (**d**). *B* bronchiole and *V* blood vessel. Scale bars, 200 µm (Figure adapted from Ref. [43])

network, as well as two bronchioles (labeled B_1 and B_2) and a vessel (V1). Figure 81.16c shows the corresponding fluorescence image, obtained via a radial projection of the fluorescence map onto the observed plane, with several vessels (labeled V_1, V_2 and V_3) visible as areas of high signal. Figure 81.16d displays the fused data sets. Anatomically, bronchioles are typically accompanied by a parallel vessel, as demonstrated by the bronchiole/vessel pair, B_2 and V_2. Note that V1 presents as a local region of low backscatter in the OCT image, indistinguishable from the bronchioles, whereas the fluorescence information indicates that V1 is most likely a vessel, not a bronchiole.

These early results demonstrate that combined OCT plus fluorescence needle images provide improved tissue differentiation over OCT alone. With the potential to image both autofluorescence and exogenous fluorescence contrast agents, we believe that the further development of dual-modality probe technology will enable clinical applications of OCT in tissues where structural contrast alone is not sufficiently specific.

81.2.4.4 Extending the Depth of Focus

Using state-of-the-art broadband light sources, it is possible to perform OCT imaging with a high axial resolution of a few micrometers. However, it is not straightforward to increase the transverse OCT resolution to similar values without severely compromising the useful depth of focus (DOF) due to the strong divergence of the tightly focused beam. This problem has been addressed in bulk-optic OCT scanners, amongst other means, by generating focal regions with an extended DOF using axicons [71, 25] or pupil phase masks [115]. However, these solutions cannot be directly applied to miniaturized fiber-optic probes because the focal regions of such probes are typically formed in a diffraction regime of low Fresnel number [63] where the optical design methods and approximations used in bulk-optic systems and classical microscopy are no longer valid. (The Fresnel number of an optical system is defined as $N = a^2/(\lambda L)$, where a is the radius of the limiting aperture, λ is the wavelength, and L is the distance from the aperture [26].) As an example, the Fresnel number of a fiber-optic probe with aperture diameter of 100 μm and a WD of 1 mm is ~2 at a wavelength of 1300 nm, whereas the Fresnel numbers of beams focused with bulk-optic lenses or microscope objectives are on the order of 100–1,000. Modeling of low-Fresnel-number systems such as fiber-optic probes requires rigorous wave-optic simulation tools that can calculate the true 3D diffracted field in the focal region. The beam propagation method (BPM) which was presented in Sect. 81.2.1.3 is ideally suited for this task, as it is valid for arbitrary Fresnel numbers [22]. Using the BPM, we have shown that focal regions with extended DOF can still be generated in the low-Fresnel-number regime using GRIN axicons [22] or GRIN phase masks [21]. The concept behind the generation of extended-DOF beams using an axicon is illustrated in Fig. 81.17.

Regardless of its technical realization, the optical functionality of an axicon can be approximated by a phase mask of the form $\exp(ik\,\beta r)$ that transforms an incident plane wavefront into a converging conical wavefront with a characteristic convergence angle β and radial coordinate r. This converging wave field has an effective numerical aperture $NA = n_{out} \sin \beta$, with n_{out} denoting the refractive index of the medium on the output side of the axicon. It forms a diffraction pattern in the region immediately adjacent to the axicon which has a Bessel-like transverse intensity distribution and extends over an axial distance $L \approx a/\tan\beta$ determined by the boundary of the geometrical shadow that results from the finite aperture radius a. Two practical realizations of axicons are shown in Fig. 81.17. The first is the well-known refractive axicon that takes on the form of a conical lens (Fig. 81.17b) [70], and the second realization is a GRIN element with a linear refractive index profile (Fig. 81.17c) [22].

The GRIN axicon has three useful characteristics that make it particularly attractive for fiber-optic probes. Firstly, if it is fabricated in the form of a GRIN fiber, it can simply be added to the end of the fiber probe in the usual manner via fusion splicing without requiring additional manufacturing processes (such as etching, micromachining, or polishing in the case of refractive axicons). Secondly, its NA (which is given by $(n_1 - n_2)t/a$) can be simply tailored by adjusting the length t of the spliced section. Thirdly, its NA is independent of the output medium

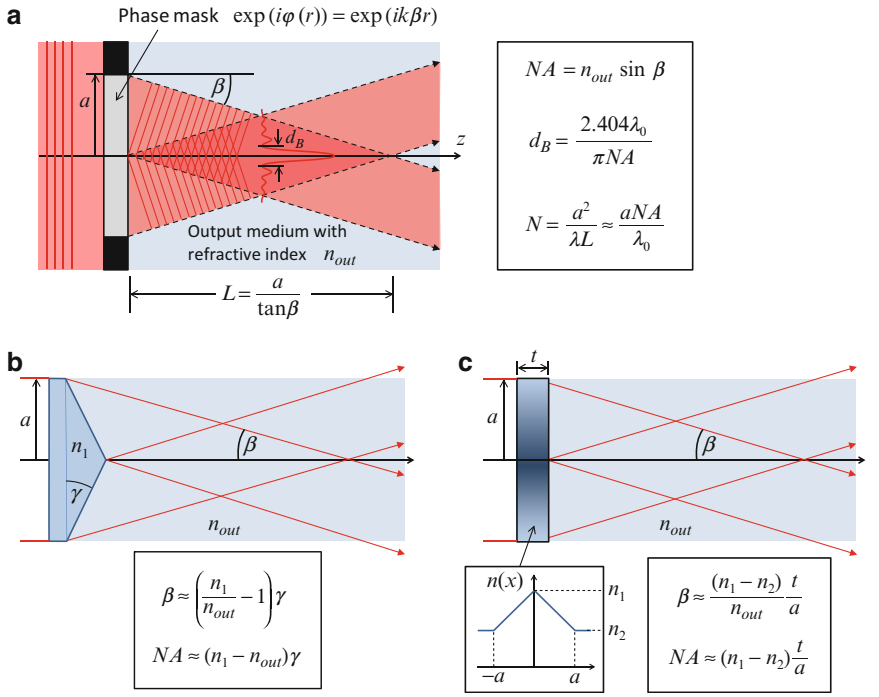

Fig. 81.17 (**a**) Geometry of a generalized axicon and relations for the numerical aperture *NA*, the Bessel beam central lobe diameter d_B, and the Fresnel number *N*. (**b**) Geometry and approximate equations for a refractive axicon. (**c**) Geometry and approximate equations for a GRIN axicon. The equations in (**b**) and (**c**) are valid in the paraxial regime where $\sin\beta \approx \tan\beta \approx \beta$

refractive index, which means that the transverse resolution of the probe remains invariant under immersion in tissue fluids, as opposed to refractive axicons that will suffer a strong reduction of their refractive power.

Figure 81.18 shows the BPM simulation results for a fiber-optic probe using a GRIN fiber axicon at a wavelength of 800 nm [22]. The probe design shown in Fig. 81.18a is based on a standard lensed fiber consisting of NCF and GRIN fiber spliced to SMF, in order to create an expanded and collimated beam with a $1/e^2$ diameter of 66 µm which is used as the input to the 95-µm-long GRIN axicon section with the refractive index profile shown in Fig. 81.18b. Using the analytical equations for a GRIN axicon phase mask from Fig. 81.17c, we calculate the following expected values for the Bessel-like output beam: NA of 0.057, central lobe diameter of 10.7 µm, and an axial range of L = 880 µm (using values of $n_1 = 1.483$, $n_2 = 1.453$, $a = 50$ µm, and $t = 95$ µm). The Fresnel number of this system is 3.6. The output beam E-field amplitude simulated with the BPM is shown in Fig. 81.18c together with the geometrical shadow boundary lines. The simulated beam is in good overall agreement with the approximate analytical values, with a central lobe that has a diameter of ~12 µm and which extends over an axial range

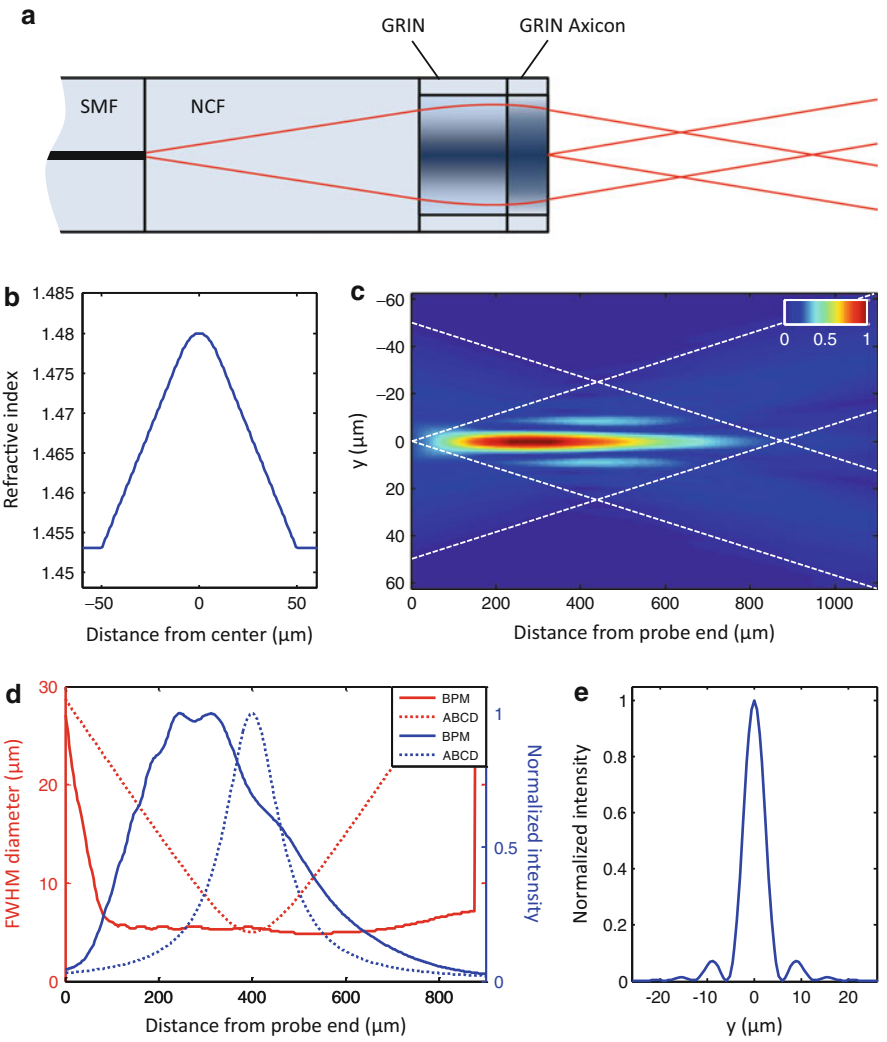

Fig. 81.18 BPM simulation of a fiber probe with extended DOF using an axicon-like GRIN fiber phase mask. (**a**) Schematic of the probe. (**b**) Index profile of the axicon-like GRIN fiber. (**c**) E-field amplitude in the entire simulated region. The *dashed white lines* indicate the boundaries of the geometrical shadow. (**d**) FWHM beam diameter and on-axis intensity of the simulated output beam (*solid lines*) and an ideal Gaussian beam with the same focal spot diameter (*dotted lines*). (**e**) Transverse intensity profile of the Bessel-like beam at ~300 μm from the probe end (Figure adapted from Ref. [22])

of ~800 μm. Figure 81.18d shows the FWHM beam diameter and on-axis intensity as a function of distance from the probe, together with the corresponding curves of a reference Gaussian beam with the same FWHM waist diameter of 5 μm. The transverse intensity profile of the peak at ~300 μm from the probe is shown

in Fig. 81.18e. The useful DOF of this beam will be determined by the acceptable relative intensity of the sidelobes, which gradually increases to 50% of the central lobe intensity at the far end of the DOF. If the full range of ~800 μm is used, we get a DOF gain of 3.3 compared to the reference Gaussian beam, obtained at the cost of a reduced Strehl ratio of 0.56. This example shows that the DOF gain which can be obtained with low-Fresnel-number axicons is significant, but much smaller than in the case of bulk-optic axicons with large Fresnel numbers. The reduced DOF gain comes with the advantage of a much higher central lobe intensity than in the bulk-optic case, because the number of sidelobes in the Bessel-like output field is strongly reduced. Hence, the problem of strong sensitivity penalties that are incurred with bulk-optic axicons [71, 25] is not an issue in the low-Fresnel-number regime [116]. Unfortunately, GRIN fiber axicons are not commercially available at the time of writing, but their fabrication is feasible using existing preform fabrication techniques.

Alternatively, micro-axicons using aspheric refractive surfaces could be used to obtain similar results, but their practical realization will require advanced fabrication techniques. A refractive micro-axicon with <1-mm diameter was demonstrated in [72], showing comparable performance to bulk-optic axicons. Early proof-of-concept work has shown that SMF tips with etched micro-axicons of the type used for near-field microscopy provide some DOF gain compared to a flat-cleaved SMF [73], but the tiny aperture diameter of the SMF core results in extremely short working distances which are much smaller than the fiber radius, making them unsuitable for side-facing scanning probes.

As an alternative approach to custom-made axicon-like structures, we have shown that it is also possible to obtain quite substantial DOF gains of ~2 in miniaturized fiber-optic probes by using very simple phase masks consisting of overfilled sections of conventional (parabolic) GRIN fiber [21]. This extended-DOF (EDOF) concept is shown in Fig. 81.19a. The probe design is again based on a normal lensed fiber using an NCF spacer and GRIN fiber lens section. The phase mask section which is appended after the GRIN lens section consists of GRIN fiber with a core diameter that is smaller than the transverse extent of the beam, as illustrated in Fig. 81.19b. The rays traced in Fig. 81.19a show that the effect of this arrangement can be intuitively understood as a "double-focus" lens, with the small core of the phase mask affecting only the central portion of the beam (see Fig. 81.19b). Using the BPM, the output beam from such an EDOF probe was simulated at a wavelength of 820 nm (see Figs. 81.19c and d). The probe uses GRIN fibers with 100- and 32-μm core diameter for the lens and phase mask sections, respectively. The simulated output beam intensity in water (refractive index $n = 1.33$) is shown in Fig. 81.19c. The FWHM beam diameter and the normalized on-axis intensity are shown in Fig. 81.19d. The minimum FWHM beam diameter is 6 μm, and the DOF is 874 μm. Compared with a reference Gaussian beam of the same minimum FWHM diameter (dotted curves in Fig. 81.19d), a DOF gain of 1.9 is obtained at the cost of a moderate reduction in Strehl ratio ($S = 0.57$).

The practical realization of the EDOF probe design shown in Fig. 81.19a is currently still difficult due to aberrations and imperfections in the refractive index profiles of commercially available GRIN fibers, especially in the case of large core

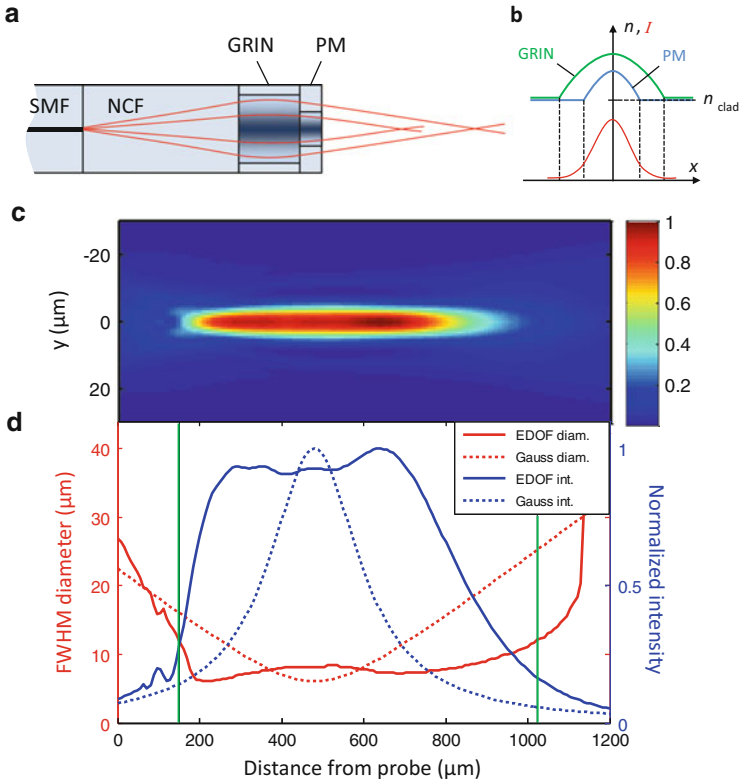

Fig. 81.19 BPM simulation of a fiber probe with extended DOF using a simple phase mask consisting of an overfilled GRIN fiber. (**a**) Schematic of the probe. *PM* phase mask, *SMF* single-mode fiber, *NCF* no-core fiber, *GRIN* graded-index fiber. (**b**) Illustration of the refractive index profiles of the GRIN lens (*green*, *upper line*) and the phase mask (*blue*, *middle line*) relative to the Gaussian beam intensity profile (*red*, *bottom line*): n_{clad}, cladding refractive index. (**c**) Simulated output beam intensity distribution in water. (**d**) Simulated FWHM diameter and normalized on-axis intensity of the output beam in water. The *dotted lines* show the values for an ideal Gaussian beam. The *vertical green lines* indicate the boundaries of the extended DOF (Figure adapted from Ref. [21])

diameters (see Sect. 81.2.1.2). An experimental validation of this concept was, therefore, performed using a slightly modified version of the EDOF probe which used a refractive hemispherical lens in combination with a 50-µm-core-diameter GRIN fiber phase mask. A DOF gain of 1.55 was experimentally demonstrated using this probe, not far from the expected value of ~1.7 that was predicted by the BPM simulation [21]. In order to evaluate the perceived improvement in imaging performance that results from this DOF gain, OCT scans of a lemon sample were acquired with the EDOF probe and also with a conventional lensed fiber probe that had the same transverse resolution. The comparison of the results showed that the increased DOF leads to a visible improvement in the OCT images [21].

In summary, current work on extended-DOF beams for OCT needle imaging is still in the proof-of-concept stage, showing promising early results and highlighting a wide range of interesting opportunities for innovation in the areas of microfabrication and custom GRIN materials.

81.2.5 OCT Needle Imaging Systems

In this section, we will discuss two important points that need to be considered when building an OCT needle imaging system:

- Should the needle probe be operated in a common-path configuration or with a reference arm?
- How will the needle probe affect the sensitivity of the OCT system?

We will also present two examples of spectral-domain (SD) OCT needle imaging systems that were built specifically for clinical use and which have been used extensively in our recent work. While some early work with needle probes was performed with time-domain (TD) OCT systems, practically all current systems employ swept-source or spectrometer-based SD-OCT due to the inherent sensitivity advantage [74]. Hence, we limit our discussion to SD-OCT in this section.

81.2.5.1 Common-Path Versus Separate Reference Arm

In a common-path interferometer configuration, the reference signal is obtained from a well-defined reflection within the probe. In most cases, this will be a strong Fresnel reflection from an interface within the probe optics [75, 43], but alternative designs have been proposed that incorporate a miniaturized beam splitter at the probe tip [76]. Common-path and dual-arm (i.e., with a separate reference arm) interferometer configurations both have advantages and drawbacks that need to be assessed in view of the envisaged application. Figures 81.20a and b shows a SD-OCT system with a needle probe sample arm in a Michelson interferometer configuration (a) and in a common-path (Fizeau) interferometer configuration (b).

The great advantage of the common-path configuration is that it eliminates "down-lead sensitivity" by avoiding issues of polarization or dispersion mismatch between the reference and sample arms, as well as polarization fading due to fiber perturbation during scanning [75]. These characteristics convey a high level of robustness and a quick and easy interchange of probes, which are highly desirable for clinical systems. The main drawback of the common-path configuration is that the reference reflectivity cannot be adjusted during operation and must, therefore, be optimally chosen beforehand. The choice of reference reflectivity, thus, becomes an integral part of the probe design and fabrication process [75, 76, 43]. For this reason, a dual-arm configuration is preferable in research systems, as it allows the user to choose the optimum reference arm power for maximum system sensitivity independently of the zero delay position. However, in this case, numerical dispersion compensation is typically required when using all-fiber needle probes [16], as an air gap and bulk optics in the reference arm cannot be avoided if a certain amount of delay adjustment is desired.

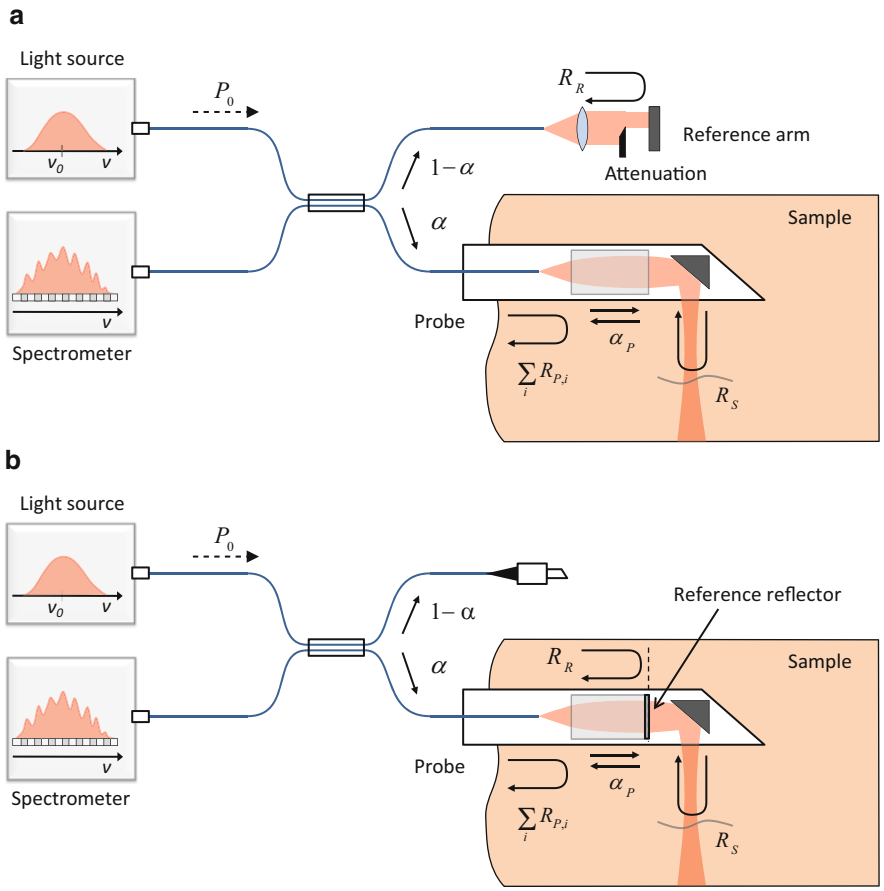

Fig. 81.20 Schematic of fiber-based SD-OCT systems with a needle probe sample arm in (**a**) Michelson and (**b**) common-path (Fizeau) configuration

81.2.5.2 Sensitivity

Needle probes can have a strong impact on the sensitivity of the OCT system due to losses and parasitic backreflections in the distal optics. This is illustrated in Fig. 81.20a, b, where the probe optics introduces a loss α_P as well as backreflections with reflectivities $R_{P,i}$. The loss α_P acts in double pass and is, therefore, better quantified via the round-trip attenuation of the probe $\gamma_P = \alpha_P^2$, which can be measured with a unity reflector placed at the working distance. The signals returning from $R_{P,i}$ are detrimental in two ways. Firstly, they can appear as unwanted structure in the OCT image or generate parasitic "ghost images" of the sample if they are within the imaging depth range (as they are typically situated at negative distances from the zero delay, they also often appear as broadened bands in the image after numerical dispersion compensation). Secondly, even if they are outside the imaging depth range, they will add shot noise and beat noise which

reduce the system sensitivity [77–79]. Fortunately, such backreflections can be kept very low in fusion-spliced all-fiber probes so that needle OCT systems can operate close to the shot-noise limit if the round-trip loss γ_P of the probe is minimized. For SD-OCT (both spectrometer-based or swept-source), the shot-noise-limited sensitivity is given by [74, 80]

$$\sum_{SNL} = \frac{\eta P \gamma_S \tau}{h\nu_0} \tag{81.13}$$

where η is the overall efficiency of the detector (the quantum efficiency of the photodetector in the case of swept-source systems, or the combination of the spectrometer losses and the quantum efficiency of the detector array in spectrometer-based systems), P is the average optical power of the source (in the case of swept-source systems, the mean power during the sweep must be used by applying a correction factor to the average source power which takes into account the sweep duty cycle), γ_S is the fraction of the source power that reaches the detector for the case of a unity reflector in the sample arm (following the notation in [80]), τ is the integration time or sweep duration (for spectrometer-based or swept-source systems, respectively), h is Planck's constant, and ν_0 is the center frequency of the broadband light source. From Eq. 81.13, it is evident that the sensitivity is directly proportional to the round-trip attenuation γ_P of the probe, which is included in γ_S (in the example of Fig. 81.20a, $\gamma_S = \alpha(1-\alpha)\gamma_P$, where α is the power-splitting ratio of the coupler). If parasitic backreflections can be neglected, the parameter γ_P is indicative of the sensitivity loss caused by the needle probe, and it is, therefore, a very useful figure of merit for assessing its optical quality [16, 32].

81.2.5.3 Examples of OCT Needle Imaging Systems

In this section, we give two examples of SD-OCT needle imaging systems that have been used successfully in our recent work.

Figure 81.21 shows a 840-nm spectrometer-based SD-OCT system which we have used extensively for OCT needle imaging, both in common-path [61, 3, 58, 56, 5] and in dual-arm [16, 5] configuration. The source is a superluminescent diode (S-840-B-I-20, Superlum, Ireland) with a center wavelength of 836 nm, an average power of 20 mW, and a bandwidth of 50 nm, yielding an axial resolution in air of 7.6 µm (or 9.3 µm after spectral reshaping [81] of the double-peaked spectrum to a Hann-window profile in order to reduce sidelobes in the axial point-spread function). The spectrometer is a commercial *k*-linear (linear in wavenumber) unit (Hyperion 830 1500, Thorlabs HL AG, Germany) incorporating a high-speed CMOS line scan camera (spL4096-140 km, Basler Vision Techn., Germany). The *k*-linear spectral data eliminates the need for computationally intensive resampling before performing the Fourier transform, allowing a real-time display of the OCT needle scan. The system employs a simple Michelson interferometer using a broadband 50/50 fiber coupler. The reference arm can simply be blocked or disconnected when using common-path needle probes. If the reference arm is

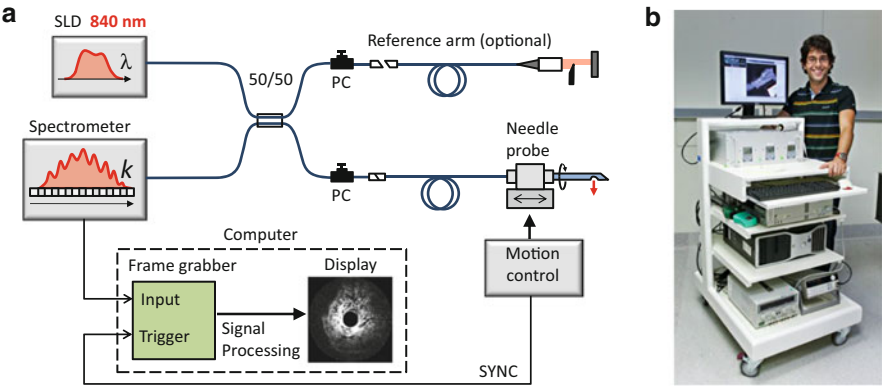

Fig. 81.21 A portable 840-nm SD-OCT needle imaging system. (**a**) System schematic. *SLD* superluminescent diode, *SYNC* synchronization signal from motion control unit, *PC* polarization controller. (**b**) The system shown in (**a**), packaged on a trolley for clinical use

used with needle probes, any air gap in the adjustable delay section must be numerically dispersion compensated in post-processing due to the relatively high material dispersion of silica fiber at 840 nm.

With a bulk-optic galvanometer-scanning sample arm, the measured sensitivity of the system is 100 dB at an exposure time of 36 μs, which is quite close to the theoretical shot-noise limit (104 dB). Using low-loss needle probes, imaging with sensitivities approaching 100 dB is, therefore, feasible with this system.

The synchronization of the OCT data acquisition with the needle scan motion is performed via the trigger input of the frame grabber card, which receives synchronization pulses from the custom-built motion control unit that drives the stepper motors of the rotation/pullback scanning setup.

Figure 81.22 shows a 1300-nm swept-source (SS) OCT system which is being used by our group for OCT needle imaging, both in common-path [43] and in dual-arm [11, 32] configuration. The source is a wavelength-swept laser (Axsun, USA) with an average power of 40 mW, a sweep rate of 50 kHz, and a total sweep range of 100 nm, giving an axial resolution in air of 13 μm (or 21 μm if a Hann window is applied to the spectral data to reduce sidelobes in the axial point-spread function). The source provides a *k*-linear clock output that is generated using a Mach-Zehnder interferometer (MZI) and which is connected to the external clock input of the digitizer card (500 MS/s, 12-bit, model no. ATS9350, Alazar Technologies, Canada). In analogy to the use of *k*-linear spectrometers in SD-OCT systems, this eliminates the need for resampling of the spectral data that is acquired during the wavelength sweep of the laser, allowing real-time display of the OCT scan.

The interferometer configuration of this system was designed to enable the use of balanced detection with common-path needle probes, as well as for allowing easy conversion between dual-arm and common-path operation. When using

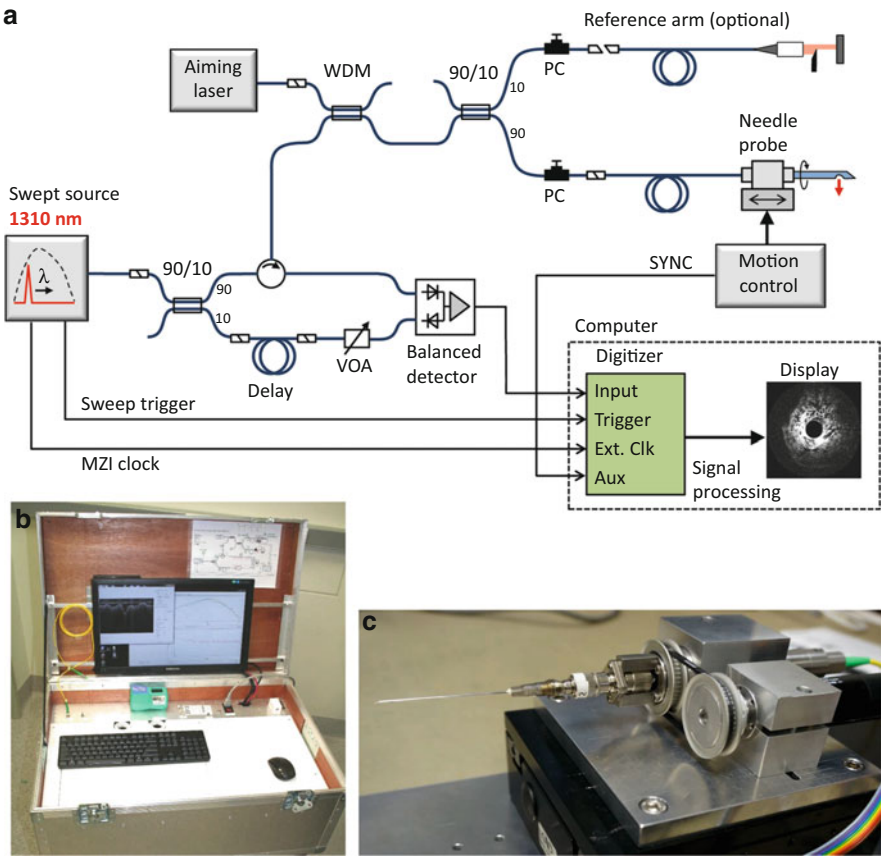

Fig. 81.22 A portable 1300-nm SS-OCT needle imaging system. (**a**) System schematic. *MZI* Mach-Zehnder interferometer, *WDM* wavelength-division multiplexer, *VOA* variable optical attenuator, *SYNC* synchronization signal, *PC* polarization controller (Figure adapted from Ref. [32]). (**b**) The system shown in (**a**), integrated into a rugged carry case for easy portability. (**c**) A prototype motorized rotation/pullback assembly for 3D needle scanning

high-speed wavelength-swept lasers, balanced detection is essential for suppressing the comparatively high relative intensity noise (RIN) of these sources [82]. However, the commonly employed interferometer configurations for balanced detection use a 50/50 coupler before the balanced detector to mix the reference and sample-arm signals [82, 83]. While the 50/50 coupler provides robust "auto-alancing" of the power levels incident on the two inputs of the balanced receiver, it becomes ineffective in common-path operation where the returning sample and reference signals travel in the same fiber.

The interferometer layout in Fig. 81.22a implements a very simple but effective "manual-balancing" variant of balanced detection, which operates as follows. The wavelength-swept laser output signal is split using a 90/10 coupler, with 90%

directed into the interferometer via a circulator and 10% directed to the balanced detector, where it is subtracted from the returning signal from the interferometer after applying a delay which equalizes the optical path lengths from the source to the two balanced detector inputs. The only drawbacks of this arrangement are that it requires a manual adjustment of a variable optical attenuator (VOA) before every measurement in order to balance the incident power levels at the balanced detector, and it does not suppress self-interference signals from parasitic reflections within the interferometer arms (otherwise the common-path signal would also be suppressed). However, the two main benefits of balanced detection are achieved: suppression of RIN and the cancellation of the DC component of the signal (thereby preventing the saturation of the photoreceiver and making optimum use of the dynamic range of the digitizer input). Using this balanced detection method, our system achieves measured sensitivities up to 114 dB with bulk-optic sample arms (the theoretical shot-noise limit is ~117 dB), and this system was used in [11] to demonstrate the highest reported sensitivity from an OCT needle probe (112 dB).

The synchronization of the data acquisition with the needle scan in an SS-OCT system is not as straightforward as in the case of spectrometer-based SD-OCT systems, because the periodic wavelength sweep of the source determines the fundamental timing behavior of the system. In the system shown in Fig. 81.22a, this problem has been solved by using the auxiliary input of the digitizer card for "gating" the sweep trigger signal, whereby the leading edge of a synchronization pulse from the needle motion control unit "arms" the digitizer card so that it acquires an A-scan at the occurrence of the next sweep trigger pulse from the source. All subsequent sweep trigger pulses are ignored until the digitizer is armed again by the next synchronization pulse. This concept is practical if the scan data acquisition rate stays well below the sweep rate of the source, as it obviously results in an unpredictable timing error which has a maximum value equal to the period of the sweep rate (20 μs in the case of our 50-kHz source). This error is negligible for our current prototype needle scanning systems which have data acquisition rates that are one order of magnitude lower than the sweep rate of the source. However, we believe that the demand for short acquisition times in clinical applications will soon lead to high-speed scanning needles that will utilize the full speed potential of modern wavelength-swept lasers.

81.3 Applications of OCT Needle Probes

OCT images recorded with needle probes for the most part represent validations of technical designs rather than forays into specific applications per se. This situation reflects the relative immaturity of needle probe technical development and the relatively small number of groups seeking to advance this field, although both these factors have changed a great deal over the last 2 years. Below, in Sect. 81.3.1, we firstly consider needle probe imaging in animal tissues – from the perspective of simply demonstrating imaging in particular

tissues, as well as of systematic application specifically intended for animals and animal models. In Sect. 81.3.2, we consider such imaging in human tissues and finally discuss limitations and prospects for future applications. In the next section, Sect. 81.4, we present two case studies highlighting the state of the art, one in animals and one in humans.

81.3.1 Needle Probes Demonstrated in Animal Models and Tissues

Needle probes for in vivo applications in animals must typically satisfy more stringent demands on needle size than in human applications, because of the small size of many animal models (e.g., mice, rats). These demands can be met, depending on the application, by not using an outer protective sheath, which also simplifies their fabrication. Below, we consider needle probes applied to animal tissues by tissue constituent and type.

81.3.1.1 Vasculature, Blood, and Blood Flow

In 2005, the first OCT needle probe capable of Doppler measurements was reported. Although rather large, employing a 19G (1.06-mm OD) "echogenic" needle (as employed in interventional radiology: the surface finish provides enhanced visibility under ultrasound), side-viewing linear B-scan imaging was demonstrated in a live rat [12]. The B-scan images featured superimposed Doppler signals and were reported for several anatomical locations. In 2006, an improved 22G version was used to demonstrate the feasibility of monitoring the effects of photodynamic therapy in a rat model of prostate cancer [54]. Microvascular changes in response to the therapy, occurring deep within a tumor mass, were successfully visualized and quantified.

Over the next several years, this research progressed to more extensive studies [84, 85], eventually incorporating high-frequency (40 MHz) ultrasound to guide the needle to the site of the tumor [85], as shown in Fig. 81.23. Although the Doppler flow maps reported in these works displayed only a small portion of the full vascular architecture, they were still very effective in monitoring the reductions in flow over time that resulted from the therapy (see Fig. 81.24). As a result, a relationship was established between the percentage of tumor necrosis post-treatment and the rate of vascular flow reduction [85]. The authors raised the very interesting prospect, yet to be realized, of a clinical role for real-time microvascular monitoring in optimizing photodynamic therapy treatment in individual patients.

More recently, a similar imaging probe with Doppler flow capability based on a forward-looking GRIN rod design in a steel needle of 0.74-mm OD (slightly larger than standard 22G) has been demonstrated [53]. The overall motivation of the research in this case is in the development of surgical guidance tools, primarily for guidance during stereotactic procedures in the brain. Demonstration of in vivo OCT and superimposed Doppler flow imaging (0.44-mm lateral field of view) was reported for insertion in sheep brain and for surface access of rat femoral vessels [53].

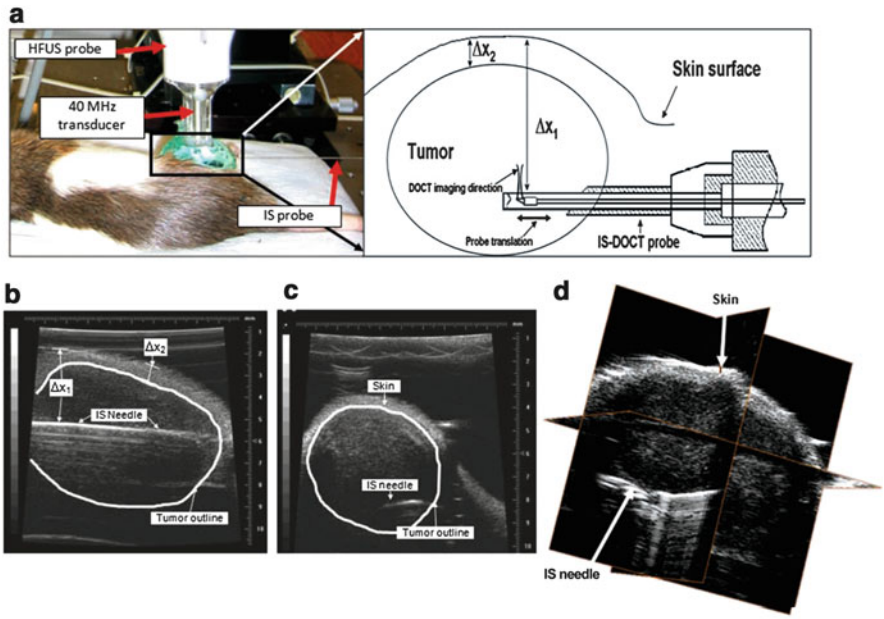

Fig. 81.23 (**a**) The experimental setup showing the external high-frequency ultrasound (*HFUS*) probe and interstitial Doppler OCT probe inserted into the tumor. (**b**) HFUS side view of the interstitial probe in the tumor mass. (**c**) Corresponding end-on view. (**d**) 3D visualization. The major ticks in the vertical and horizontal scales are 1-mm increments. *White* outlines represent tumor borders (**b**, **c**) (Reproduced with permission from Ref. [85])

81.3.1.2 Brain

The most prominent optical modalities for microscopic imaging in the brain have been one- and two-photon fluorescence microscopy [86], in which GRIN rod lenses have been used to construct bare-glass, high-NA imaging probes for high-resolution microscopy in live rat and mouse brains. Such lenses, with diameters in the range 0.350–1.0 mm and a few tens of millimeters in length, are not sufficiently robust to be used for clinically approved applications in humans without protective sheaths. The main motivation for such probes has been the study of neurological processes and diseases such as cancer and Alzheimer's disease in animal models of the brain [87].

Although OCT does not enjoy the resolution or specific targeting capability of these methods, it has been demonstrated to be capable of motion detection in one dimension [14], detection of blood vessels [53] and anatomical landmarks [88, 57], and surgical guidance and treatment monitoring in the live rat brain [88]. Building on their earlier catheter-based studies of ex vivo human brains [9], the authors of Ref. [88] developed a needle with multifunctional capability, including OCT imaging, wire cutting, and fluid delivery [88]. Simultaneous delivery of a therapeutic agent, monitoring of its delivery and effect on live rat brains, as well as creation and imaging of a focal lesion were very effectively demonstrated (see Fig. 81.25).

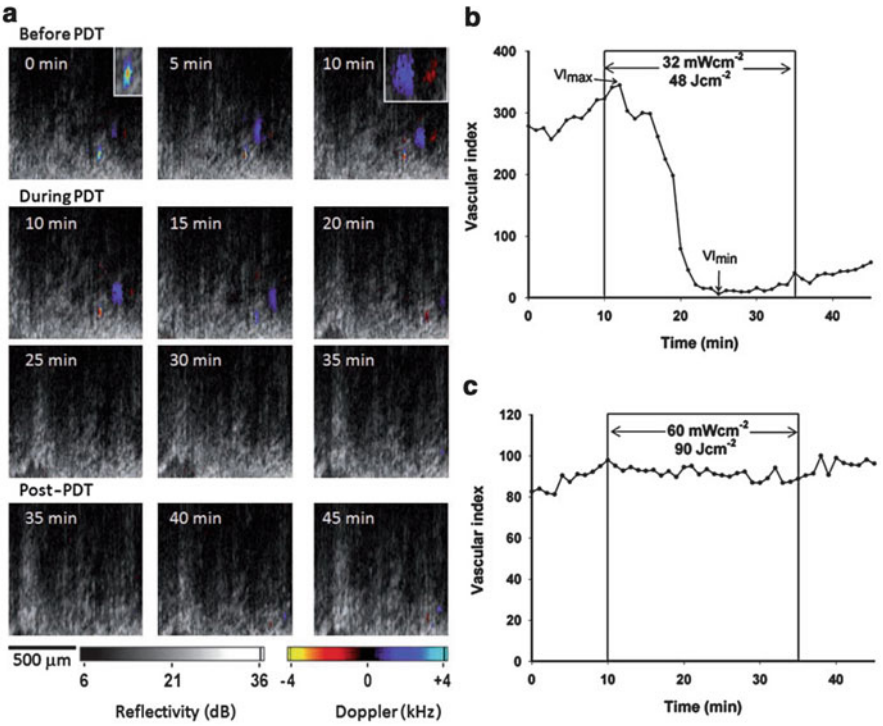

Fig. 81.24 (**a**) Interstitial Doppler OCT imaging sequence of color-Doppler blood flow detection overlaid onto structural OCT images before, during, and post-PDT treatment. The *inserts* show aliasing (0 min) and counter-propagating flow (10 min). (**b**) Vascular index as a function of time in a single animal showing the flow shutdown during PDT light exposure. (**c**) Control animal (light, no photosensitizer) (Reproduced with permission from Ref. [85])

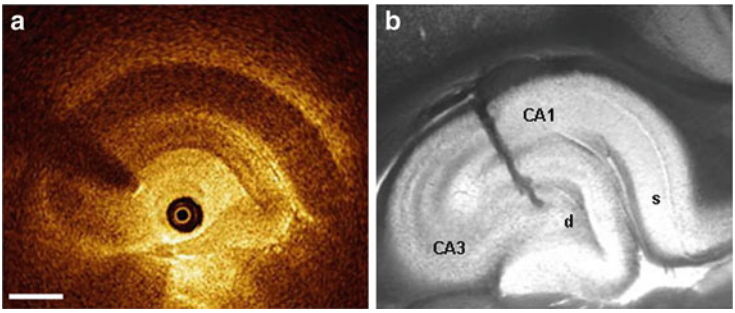

Fig. 81.25 Focal lesioning in vivo using OCT. (**a**) OCT image of a rat hippocampus showing lesion of Schaffer collaterals without lesioning overlying structures. (**b**) Postmortem section of rat brain verifying accuracy of lesion. Hippocampal CA1, CA3, dentate (*d*), and subiculum (*s*) are indicated. Scale bar, 0.5 mm (Reproduced with permission from Ref. [88])

As discussed above, a forward-looking probe developed to explore guidance in brain surgery has shown the feasibility of detection of blood vessels in the sheep brain, although the accompanying OCT images did not show appreciable structure [53]. More recently, with similar motivation, a very small profile 125-μm-diameter bare-glass probe has been used to probe the in vivo rat brain [57]. Two novel elements were the use of a high-precision surgical navigation system to control the probe and, in the absence of B-mode scanning, the presentation of successive A-scans aligned in depth (M-mode). The authors presented evidence capacity to observe the main brain structures, such as the corpus callosum and hippocampus, axon bundles, and the differentiation of gray and white matter [57].

81.3.1.3 Airways and Lungs

The first paper to show full three-dimensional OCT imaging in a needle probe was published by our group [61] using a 23G side-viewing, counterrotated, and translated needle probe to image saline-filled ex vivo sheep lung tissue. This was closely followed by several other works in lung tissues of preterm lambs, rats, and pigs [16, 5]. This work is presented as a case study in Sect. 81.4. Such proof-of-principle imaging of alveoli and associated airway morphology is motivated by the potential to study preclinical models of airway physiology and a range of diseases, with important implications for human disease diagnosis and treatment.

Recently, the use of an OCT needle probe to guide transbronchial needle aspiration, which is the sampling of small amounts of human airway tissue, was proposed. A side-viewing rotating OCT probe of 0.43-mm OD compatible with a 21G transbronchial biopsy needle was demonstrated capable of imaging alveoli in air-filled ex vivo pig lungs (see Fig. 81.26) [6]. The motivation for this research is to confirm the placement of the transbronchial biopsy needle within a peripheral pulmonary lesion prior to biopsy in order to improve the diagnostic yield [89].

81.3.1.4 Eye

The first proposal to use OCT needle probes in the eye was published in 2008 [7]. The motivation was in aiding vitrectomy, the surgical removal of the vitreous humor, which is a required precursor to other surgeries for the treatment of severe eye diseases such as retinal detachment. The success of vitrectomy depends upon the complete local removal of the vitreous humor, which may be difficult to visualize through a fiber-bundle endoscope inserted through an incision into the patient's eye. OCT may provide better visualization because of its inherent sensitivity to scattering and because the probe is able to be placed very close to the retinal surface, thereby maximizing the sensitivity. The novel forward-looking design combining two rotating GRIN rod lenses (see also Sect. 81.2.3.3), first described in 2006 by the same group [48], was improved and incorporated into a 21G needle (0.82-mm OD). Forward-looking radial B-scan segment images (approx. 30°) of the retina of an enucleated porcine eye, with cornea, lens, and vitreous removed, were reported.

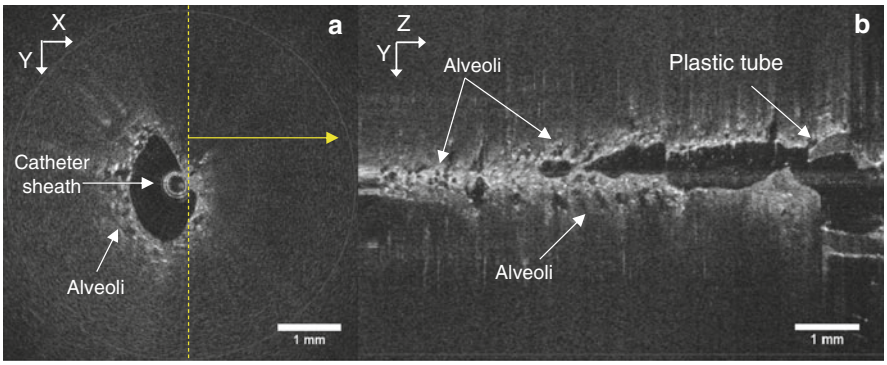

Fig. 81.26 Cross-sectional (**a**) and longitudinal (**b**) OCT images of the inflated pig lung obtained with the imaging needle. (**a**) 5.6-mm circumferential cross-sectional OCT image of lung parenchyma with clear visualization of alveoli. (**b**) An 8.2-mm × 5.6-mm YZ longitudinal reconstruction obtained from the location identified in "a" *(dashed yellow line)* (Reproduced with permission from Ref. [6])

In other work, a handheld OCT system was developed for image-guided intervention during microsurgery. The system is designed not for insertion but for hand scanning of a forward-looking 20G needle probe over a surface. It was demonstrated on ex vivo bovine retina [55].

81.3.1.5 Other Animal Tissues

The first demonstration of an OCT needle probe, reported in 2000 [2], showed an image of muscle tissue acquired in the leg of a live hamster. The 90° segment of a radial B-scan image was taken with a rotating, side-facing 27G needle and showed muscle fascicles (bundles of muscle fibers) and evidence of signal fading induced by birefringence. Still higher resolutions than OCT, capable of revealing sarcomeres at 15-mm depth in bovine muscle tissue, have been demonstrated in fluorescence-based confocal microscopy needle probes, generating en face images at depth in tissue by scanning the proximal end face of a GRIN rod lens [52].

Radial and linear B-scans from needles inserted into various excised animal tissues, including pig spleen and pancreas, and mouse esophagus were presented in [17]. Example B-scan images are shown in Fig. 81.27, reproduced from Ref. [17]. More recently, motivated by core biopsy guidance, images of cat lymphoma wrapped in chicken tissue were reported in [90].

81.3.2 Needle Probes Demonstrated in Human Tissues

Most of the research reported to date on OCT needle probes is motivated by their application in humans for eventual clinical use. Although many catheter-based OCT studies in humans have been reported, no human in vivo OCT imaging needle studies have been reported. Such first-in-human studies are an exciting prospect for

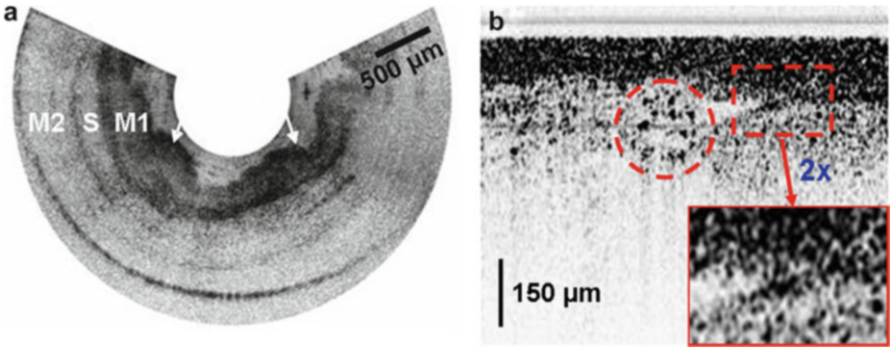

Fig. 81.27 (**a**) Ex vivo OCT radial B-scan segment of fresh mouse esophageal tissue. *M1* mucosa, *S* submucosa, *M2* muscularis. *Arrows* indicate epithelium. (**b**) Ex vivo OCT linear B-scan of fresh pig pancreatic tail. The structure indicated by the *circle* may be related to islets of Langerhans (Reproduced with permission from Ref. [17])

the future. Optical microscopy in humans has been reported, however, in a proof-of-principle image of muscle tissue in vivo by needle-based multiphoton microscopy [91]. Below, we survey reports of needle probe measurements on human tissues.

81.3.2.1 Breast and Lymph Nodes

The first measurements using an OCT needle probe on human tissue (excised breast cancer specimens) were reported in 2005 [4]. The objective was to develop a guide for fine-needle aspiration biopsy, in which smaller quantities of human breast tissue are extracted for diagnosis than for core biopsy. Better guidance is expected to lead to fewer sampling errors, an important consideration in cost and patient convenience when samples are sent off site for histopathological analysis. The 23G probe comprised a bare single-mode fiber, and forward-looking A-scans were recorded from adipose, fibro-glandular, and invasive ductal carcinoma tissues. Subsequently, in 2009, the same group used an improved system on 89 excised tissue samples. The resulting classifier achieved 80% sensitivity and 84% specificity in the correct differentiation of adipose, fibrous, and tumor tissue types [92].

More recently, our group has demonstrated OCT needle probe imaging of breast cancer and associated axillary lymph nodes [3, 93], to be described in detail in the first case study in Sect. 81.4.

81.3.2.2 Brain

In a 2005 study, a LightLab commercial OCT system (St. Jude Medical, MN, USA) was used to image thawed fresh-frozen coronal brain sections. The catheter was inserted into the brain via a 24G hypodermic needle, and pullback scans from the side-viewing, rotating probe were performed. Radial B-scan images showing a range of brain structures were presented, including one from a subject with Creutzfeldt-Jakob disease, as well as a three-dimensional partial reconstruction of a blood vessel in the human putamen. The authors observed that the gray matter–white matter junction

is one structure that OCT can detect with high contrast. This junction can serve as a landmark for guiding deep brain stimulation procedures, such as those developed to treat Parkinson's disease. The authors also pointed to evidence of the detection of vacuoles in Creutzfeldt-Jakob disease and suggested the method may prove useful in other spongiform encephalopathies as a rapid in vivo or ex vivo screening test [9]. The contrast between gray and white matter was subsequently confirmed in research on ex vivo brain slices reported (by substantially the same group) in 2011, in research directed toward the guidance of stereotactic neurosurgery employing a 12-cm-long forward-looking imaging needle with 0.44-mm field of view [53].

81.3.2.3 Skin

No needle probes have been developed for the specific purpose of imaging skin, but a number of incidental examples of images of skin have been reported [17, 55, 11]. Generally, they show inferior quality, in some attribute, to images recorded with non-needle OCT systems. Recently, improved needle systems have begun to evolve (as discussed in Sect. 81.2.4), and thus, Fig. 81.14c above shows a superior recent example of skin imaging with a 23G side-looking counterrotating needle probe in a 3D OCT system with a measured sensitivity of 112 dB [11].

81.3.3 Issues and Perspective on Applications

Most studies reported to date are proof-of-principle, with imaging conducted predominantly in animal tissues. The more advanced applications of OCT needle probes in preclinical imaging are in neuroscience [88], lung morphology [5], and tumor treatment [85] and, in humans, in surgical guidance [53], biopsy guidance [6], and intraoperative tumor margin identification [3].

Key challenges have restricted the advancement of OCT needle probes to date – the difficulty of maintaining high-sensitivity and high-resolution OCT imaging while miniaturizing the probe, the difficulty inherent in many applications of not having available full three-dimensional information, and the difficulty of navigating based only on the needle's inherently limited field of view.

The first challenge has been periodically met in two-dimensional imaging systems [85, 88] and, lately, in three-dimensional systems [11]. It is apparent that this challenge is largely one of good engineering design and realization.

The challenge of the need for three-dimensional imaging in order to address the application need is faced by OCT imaging in general and has seen the wide emergence of three-dimensional imaging systems. Such three-dimensional imaging is in general necessary to create closely corresponding OCT images and histopathology, which is a prerequisite for effective engagement with the pathologists who are essential in interpreting OCT images [94]. Such engagement remains in its infancy.

An important aspect of needle probes is guidance to the correct site for imaging. The use of ultrasound guidance with good effect has been reported by several groups in studies on animal [85] and on human tissues [93]. Magnetic tracking, which provides absolute coordinates, has also been recently used to guide freehand

scanning [56], and surface tracking has been used for noncontact surface imaging needle probes [55]. Most recently, an OCT needle probe has been connected to a stereotactic surgical navigation frame, which provides five-degree-of-freedom stepper motor movement with 1-μm resolution and 30-μm overall accuracy [57].

Many needle scanning systems incorporate precision rotation and translation setups that are cumbersome and do not scan with sufficient speed to make in vivo imaging in humans feasible. However, some systems have already evolved to be well suited for clinical applications [6], and it is very likely that more will soon follow.

The most substantial studies reported to date have been in the assessment of photodynamic therapy in the rat prostate cancer model [85], employing Doppler OCT – a major technical achievement in itself – and the A-scan studies on human breast cancer samples [92]. These latter studies highlight the general difficulty in extracting sufficient information from A-scans to make definitive assessments. The range and promise of these early needle-based studies augurs well for OCT needle probes to make significant clinical impact in the future. Further evidence of this promise is contained in the next section.

81.4 Case Studies

In this section, we explore the potential use of OCT needle probes through two specific case studies: tumor margin assessment in breast cancer and preclinical assessment of lung alveoli.

81.4.1 Breast Cancer

81.4.1.1 Background

Breast cancer is the most commonly diagnosed cancer in women [95], with 235,000 new cases diagnosed each year in the USA alone [96]. The primary treatment for breast cancer is surgery to remove the cancerous tissue. If the tumor is well contained within a small region of tissue, then the patient will often choose to undergo breast-conserving surgery (lumpectomy). Approximately 43% of patients will choose a lumpectomy as their initial surgical treatment [97]. In this procedure, only the tumor is excised, and the remainder of the breast is left intact. If not all malignant tissue is removed, then the patient is likely to suffer a recurrence of the cancer. To reduce this risk, the surgeon removes both the tumor and a margin of additional healthy tissue (tumor margin), typically ∼2–5 mm. Successful surgery relies critically on accurate identification of the edge of the tumor [98].

After surgery, the excised tissue is assessed by a pathologist. Because of the complexities of tissue preparation and the logistics of its examination, it typically takes several days before the pathology results are available to the surgeon. If malignant tissue is found to be too close to the edge of the excised tissue (typically <2 mm), then it is likely that some cancer was left in the patient, and the patient may need to undergo additional surgery. A study of 612 patients found that

approximately one third had poor margins (<5 mm) and one quarter were required to undergo a second surgery [99]. Repeat surgery due to poor margins is both traumatic for the patient and a significant cost to health-care providers.

81.4.1.2 OCT Needle Probes for Margin Assessment

OCT offers the potential for the assessment of tumor margins in fresh tissue, prior to histological evaluation. Scans acquired from the surface of fresh, excised human breast cancer samples have demonstrated visualization of both normal and malignant tissue structures [100–102], and techniques have been proposed to allow automatic differentiation of tissue types [103, 92]. However, intraoperative surgical guidance requires assessment of the tissue prior to excision, where such tissue is significantly beyond the 2–3-mm image penetration depth of OCT.

OCT needle probes offer the potential to image deep below the tissue surface. Figure 81.28 demonstrates an OCT needle probe image of a human breast tumor margin, acquired on a fresh, ex vivo tissue sample. This sample was obtained from a 70-year-old female with a 21-mm, grade 3 invasive ductal carcinoma.

The side-facing probe used here was of the type shown in Fig. 81.8b, encased in a 23G (0.64-mm OD) needle and with a length of 30 mm. The focusing optics yielded a spot with an FWHM transverse resolution of ∼12 μm at a distance of 300 μm from the side window of the needle. The probe was mounted on a motorized rotation/pullback assembly for 3D scanning. It was counterrotated at 2 Hz to acquire 2D radial B-scans consisting of 800 A-scans per 360° rotation, and the pullback step size was 7 μm per rotation. Only clockwise rotations were used to form the 3D OCT data set to minimize artifacts from tissue drag.

The needle probe was interfaced with the 840-nm SD-OCT needle scanning system described in Sect. 81.2.5.3 and operated in a common-path configuration, thereby eliminating "down-lead sensitivity" of the sample arm during scanning (see Sect. 81.2.5.1).

The OCT needle probe was inserted into the tumor and withdrawn while performing rotation/pullback scanning. The reconstruction of the 3D OCT data yielded a dense cylindrical image volume (length 2.36 mm, diameter 1.60 mm, assuming a group refractive index for tissue of $n = 1.4$), with 900 pixels per A-scan and using linear interpolation to compute values for pixels not positioned directly along an A-scan. After imaging, the tissue specimen was fixed in formalin, processed in accordance with standard laboratory procedures, and hematoxylin and eosin (H&E)-stained sections were prepared.

Figure 81.28a shows an image extracted from the 3D OCT data volume. Using in-house visualization software developed in C++, the optimal oblique image slice was extracted to match the H&E-stained histology section, shown in Fig. 81.28b. For this sample, the oblique OCT slice was positioned parallel and adjacent to the needle probe, with the horizontal axis of the image orientated along the direction of needle retraction. Note that each vertical column of the image intersects a different radial B-scan, with the horizontal section through the center of the image being closest to the probe. The reduced signal at the top and bottom of the image corresponds to tissue that is more distant from the needle probe.

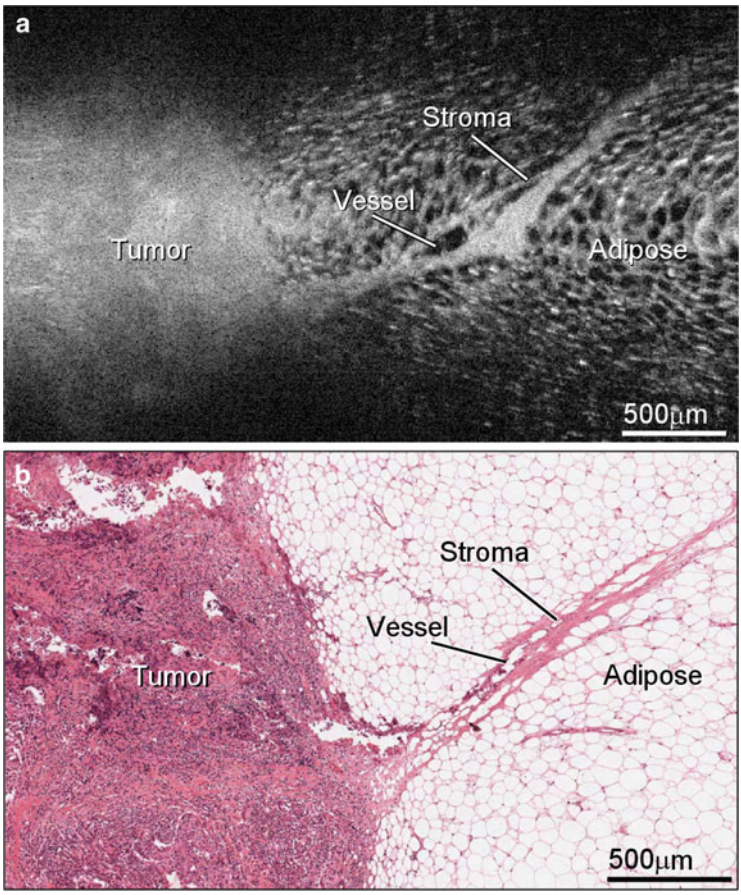

Fig. 81.28 (**a**) Longitudinal reconstructed OCT image of a tumor margin, acquired with a 23G OCT needle probe. The horizontal axis of the image is aligned with the direction of needle retraction during scanning. The imaging plane is positioned adjacent and parallel to the needle (hence the needle is not visible in the image). (**b**) Colocated hematoxylin and eosin (*H&E*)-stained histology (Images adapted from Ref. [3])

Malignant tissue appears as a homogeneous region of high backscatter (light gray), corresponding to invasive carcinoma. A strand of normal fibrous stroma can be seen extending from the area of malignancy, containing a vascular space labeled in both images (vessel). We observe a clear delineation between the dense tumor and the honeycomb structure evident in the surrounding adipose tissue.

Figure 81.29 demonstrates an OCT needle probe inserted under ultrasound guidance into a fresh ex vivo breast tumor specimen. OCT and histology images were acquired on a sample obtained from a 71-year-old female with a 15-mm grade 1 invasive ductal carcinoma. In this case, the 23G (0.64-mm OD) OCT needle probe was inserted through an 18G (1.27-mm OD) guide needle and positioned at the edge of the tumor. The purpose of the guide needle was to indicate the exact location

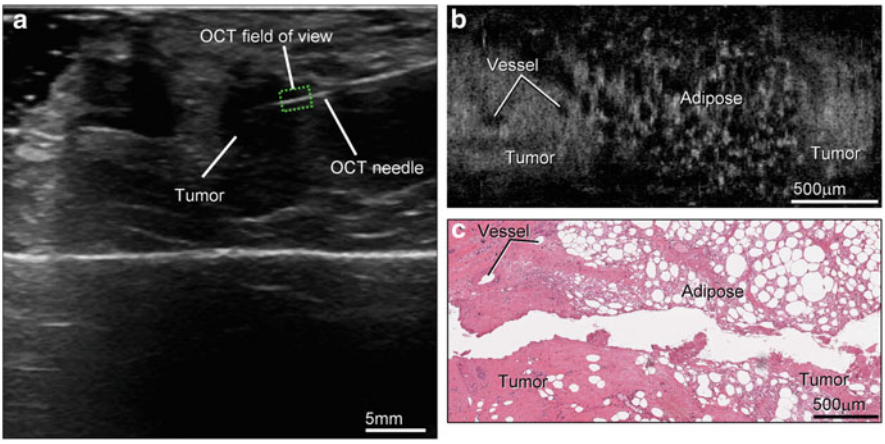

Fig. 81.29 (**a**) Ultrasound guidance of an OCT needle probe during insertion into a breast cancer tumor, showing OCT field of view. (**b**) Longitudinal reconstructed OCT image acquired at boundary of tumor. Horizontal axis of the image is aligned with the direction of needle retraction during scanning. (**C**) Colocated H&E-stained histology (Images adapted from Ref. [93])

scanned for later histological validation; thus, it was left in situ after imaging and the entire sample was fixed in formalin. A slice was obtained along the length of the guide needle, and an H&E-stained section was prepared, as shown in Fig. 81.29c. The optimal matching OCT scan was extracted from the 3D data volume, shown in Fig. 81.29b: a longitudinal image extracted along the direction of needle retraction. Regions of desmoplastic tumor stroma and intervening adipose tissue are visible in both OCT and the histology section. A honeycomb pattern corresponding to the cytoplasmic membranes of individual adipocytes is evident in the OCT. Two vascular structures are also apparent in both OCT and histology images.

We note that the limited field of view of an OCT needle probe scan (typically only 1–2 mm from the needle tip) is insufficient to image an entire tumor margin in a single scan. However, in a clinical scenario, the probe may be inserted multiple times along the planned tumor margin, allowing the clinician to inspect the tissue immediately prior to excision. Such a tool is not intended as a replacement for postoperative histology, but as an intraoperative aid to reduce the incidence of involved tumor margins. Given the large number of lumpectomies performed and the high re-excision rate from involved tumor margins, even a modest improvement in surgical guidance would save thousands of patients each year from an unnecessary second surgery.

81.4.2 Lung Imaging

81.4.2.1 Background

The lungs comprise a network of branching airways, beginning from the larger bronchi extending to the smaller bronchioles, and terminating in a large number of

alveolar sacs. Elastin and collagen fibers within the alveoli walls allow them to expand and contract during respiration, and their walls are interlaced with small capillaries which facilitate gas exchange with the blood. There are a range of diseases which alter the structure and function of the alveoli. Chronic obstructive pulmonary disease [104] is characterized by the destruction of the alveolar walls and the permanent enlargement of these airspaces. In contrast, pulmonary fibrosis [105] presents as a thickening of the alveolar walls caused by fibrotic (scar) tissue with greatly reduced elasticity. These two conditions account for over three quarters of all lung transplants [106].

Imaging of lung tissue has the potential to reveal structural, functional, and anatomical abnormalities that occur during these disease processes. Characterizing the progression of these changes presents new possibilities in the assessment of response to treatment. The heterogeneous nature of these lung diseases makes this problematic in human subjects. However, in the more controlled scenarios of animal disease models, imaging techniques offer the attractive possibility of longitudinal assessment, where the animal may act as its own control subject. In this case study, we show proof-of-principle measurements demonstrating the ability of OCT needle probes to image lung parenchyma in an ex vivo setting.

81.4.2.2 3D OCT Needle Probes to Visualize Alveoli

Ex vivo studies have shown that OCT may be used to image individual alveoli [107, 108] and in vivo OCT imaging using a thoracic window has been demonstrated in both mouse and rabbit models [109–111]. However, such techniques are limited to peripheral lung tissue due to the limited penetration of OCT.

OCT needle probes extend this imaging capability deep into the lung, without the need for excision of tissue. The delicate nature of lung tissue puts additional restrictions on needle diameter to minimize trauma during imaging. In this section, we demonstrate the application of a side-viewing OCT needle probe with an OD of 310 μm. The probe design is described in detail in Sect. 81.2.4.2 and illustrated in Fig. 81.15.

For this case study, imaging was performed on fresh, isolated ex vivo lungs, extracted from a rat model. Adult rats were euthanized by CO_2 inhalation and exsanguinated prior to removal of lung lobes. Following tracheal cannulation, lungs were inflated by a syringe filled with isotonic saline.

Figure 81.30 shows representative OCT images extracted from a 3D needle probe scan. The radial image of Fig. 81.30a was constructed from one full rotation of the probe. The needle hole (labeled n) can be seen at the center of the image, surrounded by alveoli and a small blood vessel (labeled v1) to the left of the image. The alveoli present as small regions of low backscatter (dark gray), delineated by the more highly backscattering alveoli walls (light gray). Figure 81.30b highlights the value of acquiring a 3D pullback scan, showing the relative position of multiple vessels and bronchioles not visible in a single radial image. As with the earlier breast tumor scans, the longitudinal OCT image was extracted from the data volume in a plane parallel and adjacent to the imaging needle. Its location relative

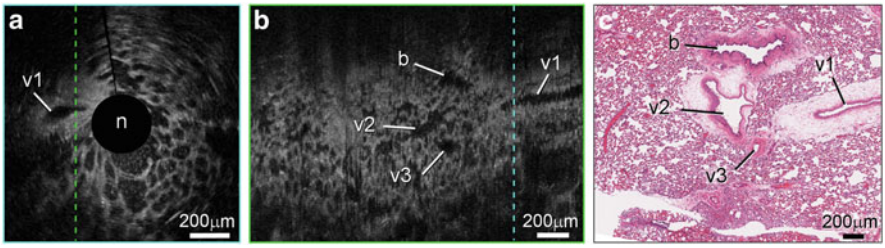

Fig. 81.30 Rat lung images acquired with an OCT needle probe. (**a**) Radial OCT image acquired from one rotation of the probe. *Dashed green vertical line* shows location of the longitudinal image shown in (**b**). (**b**) Longitudinal reconstructed OCT image showing a bronchiole and multiple vessels, with the horizontal axis aligned with the direction of needle retraction. The *dashed cyan vertical line* shows location of the radial B-scan shown in (**a**). (**c**) Corresponding H&E section. *n* needle hole, *b* bronchiole, v1, v2, v3 blood vessels (Images adapted from Ref. [5])

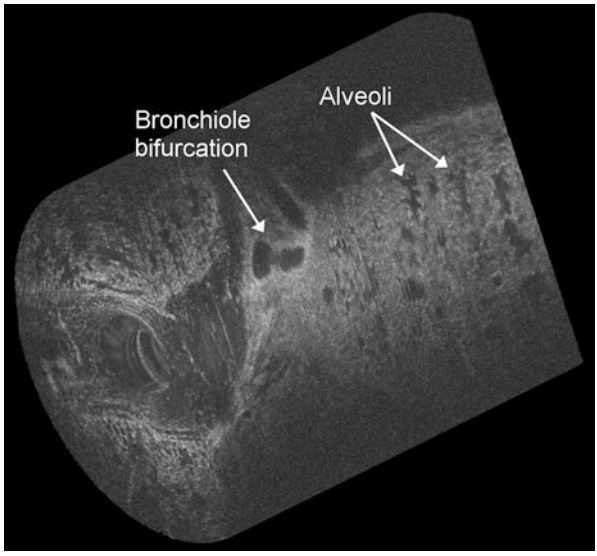

Fig. 81.31 3D visualization of fetal lamb lung. The cylindrical image volume has been sliced along a plane parallel to the needle tract, revealing alveoli and bifurcation of bronchioles. The length of the cylindrical volume is 2 mm and the diameter is 1.66 mm (Image adapted from Ref. [5])

to the radial scan is indicated by the dashed green line in Fig. 81.30a. A bronchiole (labeled b) and three vessels (labeled v1, v2, v3) are visible, showing the correspondence with the colocated H&E-stained histology section in Fig. 81.30c. Orthogonal views of vessel v1 are visible in both radial and longitudinal OCT images (Figs. 81.30a and b).

Using the same experimental setup, images were also acquired from an intact preterm lamb lung containing amniotic fluid. The OCT needle probe was inserted into the freshly dissected lungs and counterrotated over a 2-mm pullback range. Figure 81.31 shows a 3D volume rendering generated from the OCT data set. By manipulating the rendered volume, it is possible to explore the complex

3D structures present in the image data. In this image, a section of the cylindrical data volume has been cropped to reveal the bifurcation of a pair of bronchioles. A video animation of this volume rendering is available as supplementary data in Ref. [5].

Extending from this excised lung model to an in vivo scenario is possible by the insertion of the needle probe through the chest wall. As with transthoracic lung biopsies and fine-needle aspiration biopsies, the use of OCT needle probes carries a risk of pneumothorax, and some tissue trauma will occur. In our measurements, the introduction of the OCT needle probe was found to cause some local trauma to pulmonary structures. The development of small caliber (0.31-mm OD) OCT needle probes, which are significantly smaller than the needles currently used for lung biopsies, is an important step forward in reducing these complications and making in vivo measurements feasible. An alternative approach using a flexible transbronchial OCT needle probe has recently been proposed [6]. This allows insertion of the needle from inside an airway, penetrating out into the surrounding parenchymal tissue, avoiding insertion through the chest wall.

81.4.2.3 Dynamic OCT Needle Probes

OCT needle probes may also be used to acquire dynamic scans of lung tissue. The dynamic probe used in this study was described in Sect. 81.2.3.2 and is illustrated schematically in Fig. 81.9d. In brief, a side-facing, inner imaging needle (0.72-mm OD) was translated back and forth within an enclosing outer needle (1.27-mm OD). This linear motion had a stroke of 12 mm and a rate of 3 Hz. The light beam was emitted through a slit window (length 20 mm) in the outer needle, allowing acquisition of a time sequence of 2D images.

The needle was inserted into a fresh, ex vivo isolated pig lung infused with saline. During imaging, the pressure was cycled between 0- and 20-cm H_20 to simulate cyclical lung inflation and deflation.

Figure 81.32 shows two images acquired during simulated (a) maximum deflation and (b) maximum inflation. The OCT needle probe is positioned along the top of the image, with the light beam orientated downward. The void at the top of the image shows a narrow saline-filled region immediately adjacent to the needle. Figure 81.32c shows the images in (a) and (b) superimposed: maximum deflation (green) and inflation (red), with evidence of both expansion and recruitment of alveoli. A video showing multiple “breath cycles” is available as supplementary data in Ref. [5].

Dynamic OCT acquisitions such as these have the potential to assess viscoelastic properties of lung tissue, by tracking the displacement of parenchymal tissue in response to pressure fluctuations. Comparable measurements have been performed in vivo in an endoscopic setting for human airway compliance [112], and initial measurements have been demonstrated with a needle probe [58], using analysis techniques from optical coherence elastography [113, 114]. Dynamic OCT needle probes present the opportunity to perform such measurements in situ at different locations and depths within the lung, which may be useful in the scenario of lung disease which is inherently heterogeneous.

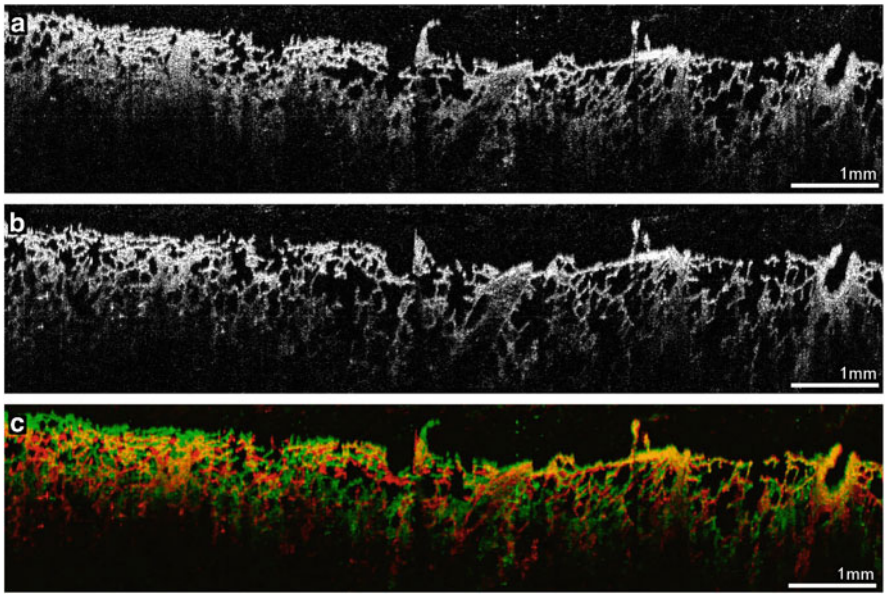

Fig. 81.32 A dynamic sequence of images of a pig lung, showing simulated (**a**) deflation and (**b**) inflation. (**c**) Superimposed images of deflation (*green*) and inflation (*red*) (Image adapted from Ref. [5])

OCT needle probes open new possibilities for the assessment of lung physiology in both health and disease. This case study demonstrates the high level of structural detail visible with an OCT needle probe, allowing visualization of alveoli, bronchioles, and vessels deep within the lung, both statically and dynamically.

81.5 Conclusion

OCT needle probe technology has reached a level of maturity that enables 2D and 3D scanning with image quality comparable to state-of-the-art benchtop systems. Some technical challenges remain, such as increasing the scanning speed or enhancing the depth of focus, but it is very likely that these will be gradually resolved in the medium term with continued engineering advances. We have shown that OCT needle probe technology has opened up a variety of possible application areas where minimally invasive deep-tissue access is required, and the current literature reflects the very promising but still exploratory nature of these investigations. Unlike endoscopic OCT, which has found a commercial foothold in cardiology and gastroenterology, OCT needle probes are still searching for their commercial niche, although some compelling clinical applications such as intraoperative assessment of breast cancer tumor margins or biopsy guidance have already been identified.

References

1. J.G. Fujimoto, Optical coherence tomography for ultrahigh resolution in vivo imaging. Nat. Biotechnol. **21**(11), 1361–1367 (2003)
2. X. Li, C. Chudoba, T. Ko, C. Pitris, J.G. Fujimoto, Imaging needle for optical coherence tomography. Opt. Lett. **25**(20), 1520–1522 (2000)
3. R.A. McLaughlin, B.C. Quirk, A. Curatolo, R.W. Kirk, L. Scolaro, D. Lorenser, P.D. Robbins, B.A. Wood, C.M. Saunders, D.D. Sampson, Imaging of breast cancer with optical coherence tomography needle probes: feasibility and initial results. IEEE J. Sel. Top. Quantum Electron. **18**(3), 1184–1191 (2012)
4. N.V. Iftimia, B.E. Bouma, M.B. Pitman, B. Goldberg, J. Bressner, G.J. Tearney, A portable, low coherence interferometry based instrument for fine needle aspiration biopsy guidance. Rev. Sci. Instrum. **76**(6), 064301–064306 (2005)
5. R.A. McLaughlin, X. Yang, B.C. Quirk, D. Lorenser, R.W. Kirk, P.B. Noble, D.D. Sampson, Static and dynamic imaging of alveoli using optical coherence tomography needle probes. J. Appl. Physiol. **113**(6), 967–974 (2012)
6. K. Tan, M. Shishkov, A. Chee, M. Applegate, B. Bouma, M. Suter, Flexible transbronchial optical frequency domain imaging smart needle for biopsy guidance. Biomed. Opt. Express **3**(8), 1947–1954 (2012)
7. S. Han, M.V. Sarunic, J. Wu, M. Humayun, C. Yang, Handheld forward-imaging needle endoscope for ophthalmic optical coherence tomography inspection. J. Biomed. Opt. **13**(2), 020505 (2008)
8. M. Zhao, Y. Huang, J.U. Kang, Sapphire ball lens-based fiber probe for common-path optical coherence tomography and its applications in corneal and retinal imaging. Opt. Lett. **37**(23), 4835–4837 (2012)
9. M.S. Jafri, S. Farhang, R.S. Tang, N. Desai, P.S. Fishman, R.G. Rohwer, C.M. Tang, J.M. Schmitt, Optical coherence tomography in the diagnosis and treatment of neurological disorders. J. Biomed. Opt. **10**(5), 051603 (2005)
10. C. Sun, K.K. Lee, B. Vuong, M.D. Cusimano, A. Brukson, A. Mauro, N. Munce, B.K. Courtney, B.A. Standish, V.X. Yang, Intraoperative handheld optical coherence tomography forward-viewing probe: physical performance and preliminary animal imaging. Biomed. Opt. Express **3**(6), 1404 (2012)
11. L. Scolaro, D. Lorenser, R.A. McLaughlin, B.C. Quirk, R.W. Kirk, D.D. Sampson, High-sensitivity anastigmatic imaging needle for optical coherence tomography. Opt. Lett. **37**(24), 5247–5249 (2012)
12. V.X.D. Yang, Y.X. Mao, N. Munce, B. Standish, W. Kucharczyk, N.E. Marcon, B.C. Wilson, I.A. Vitkin, Interstitial Doppler optical coherence tomography. Opt. Lett. **30**(14), 1791–1793 (2005)
13. W. Emkey, C. Jack, Analysis and evaluation of graded-index fiber lenses. J. Lightwave Technol. **5**(9), 1156–1164 (1987)
14. W.A. Reed, M.F. Yan, M.J. Schnitzer, Gradient-index fiber-optic microprobes for minimally invasive in vivo low-coherence interferometry. Opt. Lett. **27**(20), 1794–1796 (2002)
15. Y. Mao, S. Chang, S. Sherif, C. Flueraru, Graded-index fiber lens proposed for ultrasmall probes used in biomedical imaging. Appl. Opt. **46**(23), 5887–5894 (2007)
16. D. Lorenser, X. Yang, R.W. Kirk, B.C. Quirk, R.A. McLaughlin, D.D. Sampson, Ultrathin side-viewing needle probe for optical coherence tomography. Opt. Lett. **36**(19), 3894–3896 (2011)
17. Y. Wu, J. Xi, L. Huo, J. Padvorac, E. Shin, S.A. Giday, A.A. Lennon, M.F. Canto, J.F. Hwang, X.F. Li, Robust high-resolution fine OCT needle for side-viewing interstitial tissue imaging. IEEE J. Sel. Top. Quantum Electron. **16**(4), 863–869 (2010)
18. H.Y. Choi, S.Y. Ryu, J. Na, B.H. Lee, I.-B. Sohn, Y.-C. Noh, J. Lee, Single-body lensed photonic crystal fibers as side-viewing probes for optical imaging systems. Opt. Lett. **33**(1), 34–36 (2008)

19. G.J. Tearney, S.A. Boppart, B.E. Bouma, M.E. Brezinski, N.J. Weissman, J.F. Southern, J.G. Fujimoto, Scanning single-mode fiber optic catheter-endoscope for optical coherence tomography. Opt. Lett. **21**(7), 543–545 (1996)
20. D.C. Adler, Y. Chen, R. Huber, J. Schmitt, J. Connolly, J.G. Fujimoto, Three-dimensional endomicroscopy using optical coherence tomography. Nat. Photonics **1**(12), 709–716 (2007)
21. D. Lorenser, X. Yang, D.D. Sampson, Ultrathin fiber probes with extended depth of focus for optical coherence tomography. Opt. Lett. **37**(10), 1616–1618 (2012)
22. D. Lorenser, X. Yang, D.D. Sampson, Accurate modeling and design of graded-index fiber probes for optical coherence tomography using the beam propagation method. IEEE Photonics J. **5**(2), 3900015 (2013)
23. P.D. Woolliams, R.A. Ferguson, C. Hart, A. Grimwood, P.H. Tomlins, Spatially deconvolved optical coherence tomography. Appl. Opt. **49**(11), 2014–2021 (2010)
24. D. Huang, E.A. Swanson, C.P. Lin, J.S. Schuman, W.G. Stinsin, W. Chang, M.R. Hee, T. Flotte, K. Gregory, C.A. Puliafito, J.G. Fujimoto, Optical coherence tomography. Science **254**, 1178–1181 (1991)
25. R.A. Leitgeb, M. Villiger, A.H. Bachmann, L. Steinmann, T. Lasser, Extended focus depth for Fourier domain optical coherence microscopy. Opt. Lett. **31**(16), 2450–2452 (2006)
26. M. Born, E. Wolf, *Principles of Optics* (Cambridge University Press, Cambridge, UK, 1999)
27. A.E. Siegman, *Lasers* (University Science, Mill Valley, 1986)
28. H. Kogelnik, T. Li, Laser beams and resonators. Proc. IEEE **54**(10), 1312–1329 (1966)
29. D. Marcuse, Gaussian approximation of the fundamental modes of graded-index fibers. J. Opt. Soc. Am. **68**(1), 103–109 (1978)
30. W. Jung, W.A. Benalcazar, A. Ahmad, U. Sharma, H. Tu, S.A. Boppart, Numerical analysis of gradient index lens based optical coherence tomography imaging probes. J. Biomed. Opt. **15**(6), 066027 (2010)
31. W.A. Benalcazar, W. Jung, S.A. Boppart, Aberration characterization for the optimal design of high-resolution endoscopic optical coherence tomography catheters. Opt. Lett. **37**(6), 1100–1102 (2012)
32. X. Yang, D. Lorenser, R. A. McLaughlin, R. W. Kirk, M. Edmond, M. C. Simpson, M. D. Grounds, D. D. Sampson, Imaging deep skeletal muscle structure using a high-sensitivity ultrathin side-viewing optical coherence tomography needle probe. Biomed. Opt. Express **5**(1), 136–148 (2014)
33. J. Van Roey, J. Van der Donk, P.E. Lagasse, Beam-propagation method: analysis and assessment. J. Opt. Soc. Am. **71**(7), 803–810 (1981)
34. J.A. Fleck, J.R. Morris, M.D. Feit, Time-dependent propagation of high energy laser beams through the atmosphere. Appl. Phys. A Mater. Sci. Process. **10**(2), 129–160 (1976)
35. E.A. Sziklas, A.E. Siegman, Mode calculations in unstable resonators with flowing saturable gain. 2: fast Fourier transform method. Appl. Opt. **14**(8), 1874–1889 (1975)
36. M.D. Feit, J.A. Fleck Jr., Light propagation in graded-index optical fibers. Appl. Opt. **17**(24), 3990–3998 (1978)
37. A. Ishikawa, M. Izutsu, T. Sueta, Beam propagation method analysis of optical waveguide lenses. Appl. Opt. **29**(34), 5064–5068 (1990)
38. A. Carnevale, U.C. Paek, Empirical evaluation of profile variations in an MCVD optical waveguide fiber using modal structure analysis. Bell Syst. Tech. J. **62**(7), 1937–1954 (1983)
39. D. Mazzarese, G.E. Oulundsen III, F.T. McMahon II, M.T. Owsiany, Method of collapsing a tube for an optical fiber preform. U.S. Patent No. 6,718,800
40. R. Olshansky, D.B. Keck, Pulse broadening in graded-index optical fibers. Appl. Opt. **15**(2), 483–491 (1976)
41. D. Marcuse, Calculation of bandwidth from index profiles of optical fibers. 1: theory. Appl. Opt. **18**(12), 2073–2080 (1979)
42. G.E. Peterson, A. Carnevale, U.C. Paek, J.W. Fleming, Numerical calculation of optimum alpha for a germania-doped silica lightguide. Bell Syst. Tech. J. **60**(4), 455–470 (1981)

43. D. Lorenser, B.C. Quirk, M. Auger, W.-J. Madore, R.W. Kirk, N. Godbout, D.D. Sampson, C. Boudoux, R.A. McLaughlin, Dual-modality needle probe for combined fluorescence imaging and three-dimensional optical coherence tomography. Opt. Lett. **38**(3), 266–268 (2013)
44. E.J. Seibel, Q.Y.J. Smithwick, Unique features of optical scanning, single fiber endoscopy. Lasers Surg. Med. **30**(3), 177–183 (2002)
45. X. Liu, M.J. Cobb, Y. Chen, M.B. Kimmey, X. Li, Rapid-scanning forward-imaging miniature endoscope for real-time optical coherence tomography. Opt. Lett. **29**(15), 1763–1765 (2004)
46. N.R. Munce, A. Mariampillai, B.A. Standish, M. Pop, K.J. Anderson, G.Y. Liu, T. Luk, B.K. Courtney, G.A. Wright, I.A. Vitkin, Electrostatic forward-viewing scanning probe for Doppler optical coherence tomography using a dissipative polymer catheter. Opt. Lett. **33**(7), 657–659 (2008)
47. Y. Pan, H. Xie, G.K. Fedder, Endoscopic optical coherence tomography based on a microelectromechanical mirror. Opt. Lett. **26**(24), 1966–1968 (2001)
48. J. Wu, M. Conry, C. Gu, F. Wang, Z. Yaqoob, C. Yang, Paired-angle-rotation scanning optical coherence tomography forward-imaging probe. Opt. Lett. **31**(9), 1265–1267 (2006)
49. J. Sun, S. Guo, L. Wu, L. Liu, S.W. Choe, B.S. Sorg, H. Xie, 3D in vivo optical coherence tomography based on a low-voltage, large-scan-range 2D MEMS mirror. Opt. Express **18**(12), 12065–12075 (2010)
50. L. Liu, L. Wu, J. Sun, E. Lin, H. Xie, Miniature endoscopic optical coherence tomography probe employing a two-axis microelectromechanical scanning mirror with through-silicon vias. J. Biomed. Opt. **16**(2), 026006 (2011)
51. J.C. Jung, M.J. Schnitzer, Multiphoton endoscopy. Opt. Lett. **28**(11), 902–904 (2003)
52. R.S. Pillai, D. Lorenser, D.D. Sampson, Deep-tissue access with confocal fluorescence microendoscopy through hypodermic needles. Opt. Express **19**(8), 7213–7221 (2011)
53. C.P. Liang, J. Wierwille, T. Moreira, G. Schwartzbauer, M.S. Jafri, C.M. Tang, Y. Chen, A forward-imaging needle-type OCT probe for image guided stereotactic procedures. Opt. Express **19**(27), 26283–26294 (2011)
54. H. Li, B.A. Standish, A. Mariampillai, N.R. Munce, Y. Mao, S. Chiu, N.E. Marcon, B.C. Wilson, A. Vitkin, V.X.D. Yang, Feasibility of interstitial Doppler optical coherence tomography for in vivo detection of microvascular changes during photodynamic therapy. Lasers Surg. Med. **38**(8), 754–761 (2006)
55. Y. Huang, X. Liu, C. Song, J.U. Kang, Motion-compensated hand-held common-path Fourier-domain optical coherence tomography probe for image-guided intervention. Biomed. Opt. Express **3**(12), 3105–3118 (2012)
56. B.Y. Yeo, R.A. McLaughlin, R.W. Kirk, D.D. Sampson, Enabling freehand lateral scanning of optical coherence tomography needle probes with a magnetic tracking system. Biomed. Opt. Express **3**(7), 1565–1578 (2012)
57. Y.J. Xie, T. Bonin, S. Loffler, G. Huttmann, V. Tronnier, U.G. Hofmann, Coronal in vivo forward-imaging of rat brain morphology with an ultra-small optical coherence tomography fiber probe. Phys. Med. Biol. **58**(3), 555–568 (2013)
58. K.M. Kennedy, B.F. Kennedy, R.A. McLaughlin, D.D. Sampson, Needle optical coherence elastography for tissue boundary detection. Opt. Lett. **37**(12), 2310–2312 (2012)
59. A.M. Zysk, S.G. Adie, J.J. Armstrong, M.S. Leigh, A. Paduch, D.D. Sampson, F.T. Nguyen, S.A. Boppart, Needle-based refractive index measurement using low-coherence interferometry. Opt. Lett. **32**(4), 385–387 (2007)
60. A.M. Zysk, D.L. Marks, D.Y. Liu, S.A. Boppart, Needle-based reflection refractometry of scattering samples using coherence-gated detection. Opt. Express **15**(8), 4787–4794 (2007)
61. B.C. Quirk, R.A. McLaughlin, A. Curatolo, R.W. Kirk, P.B. Noble, D.D. Sampson, In situ imaging of lung alveoli with an optical coherence tomography needle probe. J. Biomed. Opt. **16**(3), 036009 (2011)

62. E. Swanson, C.L. Petersen, E. McNamara, R.B. Lamport, D.L Kelly, Ultra-small optical probes, imaging optics, and methods for using same. United States Patent U.S. Patent No. 6,445,939
63. Y. Li, E. Wolf, Three-dimensional intensity distribution near the focus in systems of different Fresnel numbers. J. Opt. Soc. Am. A **1**(8), 801–808 (1984)
64. D. Yelin, B.E. Bouma, S.H. Yun, G.J. Tearney, Double-clad fiber for endoscopy. Opt. Lett. **29**(20), 2408–2410 (2004)
65. S.Y. Ryu, H.Y. Choi, J. Na, E.S. Choi, B.H. Lee, Combined system of optical coherence tomography and fluorescence spectroscopy based on double-cladding fiber. Opt. Lett. **33**(20), 2347–2349 (2008)
66. L. Wang, H.Y. Choi, Y. Jung, B.H. Lee, K.T. Kim, Optical probe based on double-clad optical fiber for fluorescence spectroscopy. Opt. Express **15**(26), 17681–17689 (2007)
67. H. Yoo, J.W. Kim, M. Shishkov, E. Namati, T. Morse, R. Shubochkin, J.R. McCarthy, V. Ntziachristos, B.E. Bouma, F.A. Jaffer, Intra-arterial catheter for simultaneous microstructural and molecular imaging in vivo. Nat. Med. **17**(12), 1680–1685 (2011)
68. J. Mavadia, J. Xi, Y. Chen, X. Li, An all-fiber-optic endoscopy platform for simultaneous OCT and fluorescence imaging. Biomed. Opt. Express **3**(11), 2851–2859 (2012)
69. S. Lemire-Renaud, M. Rivard, M. Strupler, D. Morneau, F. Verpillat, X. Daxhelet, N. Godbout, C. Boudoux, Double-clad fiber coupler for endoscopy. Opt. Express **18**(10), 9755–9764 (2010)
70. J.H. McLeod, The axicon: a new type of optical element. J. Opt. Soc. Am. **44**(8), 592 (1954)
71. Z. Ding, H. Ren, Y. Zhao, J.S. Nelson, Z. Chen, High-resolution optical coherence tomography over a large depth range with an axicon lens. Opt. Lett. **27**(4), 243–245 (2002)
72. K.S. Lee, J.P. Rolland, Bessel beam spectral-domain high-resolution optical coherence tomography with micro-optic axicon providing extended focusing range. Opt. Lett. **33**(15), 1696–1698 (2008)
73. K.M. Tan, M. Mazilu, T.H. Chow, W.M. Lee, K. Taguchi, B.K. Ng, W. Sibbett, C.S. Herrington, C.T.A. Brown, K. Dholakia, In-fiber common-path optical coherence tomography using a conical-tip fiber. Opt. Express **17**(4), 2375–2384 (2009)
74. M. Choma, M. Sarunic, C. Yang, J. Izatt, Sensitivity advantage of swept source and Fourier domain optical coherence tomography. Opt. Express **11**(18), 2183–2189 (2003)
75. U. Sharma, N.M. Fried, J.U. Kang, All-fiber common-path optical coherence tomography: sensitivity optimization and system analysis. IEEE Sel. Top. Quantum Electron. **11**(4), 799–805 (2005)
76. A.R. Tumlinson, J.K. Barton, B. Považay, H. Sattman, A. Unterhuber, R.A. Leitgeb, W. Drexler, Endoscope-tip interferometer for ultrahigh resolution frequency domain optical coherence tomography in mouse colon. Opt. Express **14**(5), 1878–1887 (2006)
77. D.D. Sampson, T.R. Hillman, Optical coherence tomography, in *Lasers and Current Optical Techniques in Biology, vol. 4. Comprehensive Series in Photochemical and Photobiological Sciences*, ed. by G. Palumbo, R. Pratesi (The Royal Society of Chemistry, Cambridge, UK, 2004), pp. 481–571
78. R.A. McLaughlin, D. Lorenser, D.D. Sampson, Needle Probes in Optical Coherence Tomography, in *Handbook of Coherent-Domain Optical Methods: Biomedical Diagnostics, Environmental Monitoring, and Material Science*, ed. By V.V. Tuchin (Springer, New York, 2013)
79. R.C. Haskell, D. Liao, A.E. Pivonka, T.L. Bell, B.R. Haberle, B.M. Hoeling, D.C. Petersen, Role of beat noise in limiting the sensitivity of optical coherence tomography. J. Opt. Soc. Am. A **23**(11), 2747–2755 (2006)
80. R. Leitgeb, C. Hitzenberger, A. Fercher, Performance of fourier domain vs. time domain optical coherence tomography. Opt. Express **11**(8), 889–894 (2003)
81. R. Tripathi, N. Nassif, J.S. Nelson, B.H. Park, J.F. de Boer, Spectral shaping for non-Gaussian source spectra in optical coherence tomography. Opt. Lett. **27**(6), 406–408 (2002)

82. S. Yun, G. Tearney, J. de Boer, N. Iftimia, B. Bouma, High-speed optical frequency-domain imaging. Opt. Express **11**(22), 2953–2963 (2003)
83. A.M. Rollins, J.A. Izatt, Optimal interferometer designs for optical coherence tomography. Opt. Lett. **24**(21), 1484–1486 (1999)
84. B.A. Standish, X. Jin, J. Smolen, A. Mariampillai, N.R. Munce, B.C. Wilson, I.A. Vitkin, V.X.D. Yang, Interstitial Doppler optical coherence tomography monitors microvascular changes during photodynamic therapy in a Dunning prostate model under varying treatment conditions. J. Biomed. Opt. **12**(3), 034022 (2007)
85. B.A. Standish, K.K.C. Lee, X. Jin, A. Mariampillai, N.R. Munce, M.F.G. Wood, B.C. Wilson, I.A. Vitkin, V.X.D. Yang, Interstitial Doppler optical coherence tomography as a local tumor necrosis predictor in photodynamic therapy of prostatic carcinoma: an in vivo study. Cancer Res. **68**(23), 9987–9995 (2008)
86. J.C. Jung, A.D. Mehta, E. Aksay, R. Stepnoski, M.J. Schnitzer, In vivo mammalian brain imaging using one-and two-photon fluorescence microendoscopy. J. Neurophysiol. **92**(5), 3121–3133 (2004)
87. Y. Kienast, L. von Baumgarten, M. Fuhrmann, W.E.F. Klinkert, R. Goldbrunner, J. Herms, F. Winkler, Real-time imaging reveals the single steps of brain metastasis formation. Nat. Med. **16**(1), 116–122 (2010)
88. M.S. Jafri, R. Tang, C.M. Tang, Optical coherence tomography guided neurosurgical procedures in small rodents. J. Neurosci. Methods **176**(2), 85–95 (2009)
89. L.P. Hariri, M. Villiger, M.B. Applegate, M. Mino-Kenudson, E.J. Mark, B.E. Bouma, M.J. Suter, Seeing beyond the bronchoscope to increase the diagnostic yield of bronchoscopic biopsy. Am. J. Respir. Crit. Care Med. **187**(2), 125–129 (2013)
90. W.C. Kuo, J. Kim, N.D. Shemonski, E.J. Chaney, D.R. Spillman, S.A. Boppart, Real-time three-dimensional optical coherence tomography image-guided core-needle biopsy system. Biomed. Opt. Express **3**(6), 1149–1161 (2012)
91. M.E. Llewellyn, R.P.J. Barretto, S.L. Delp, M.J. Schnitzer, Minimally invasive high-speed imaging of sarcomere contractile dynamics in mice and humans. Nature **454**(7205), 784–788 (2008)
92. M. Mujat, R.D. Ferguson, D.X. Hammer, C. Gittins, N. Iftimia, Automated algorithm for breast tissue differentiation in optical coherence tomography. J. Biomed. Opt. **14**(3), 034040 (2009)
93. A. Curatolo, R.A. McLaughlin, B.C. Quirk, R.W. Kirk, A.G. Bourke, B.A. Wood, P.D. Robbins, C.M. Saunders, D.D. Sampson, Ultrasound-guided optical coherence tomography needle probe for the assessment of breast cancer tumor margins. Am. J. Roentgenol. **199**(4), W520–W522 (2012)
94. R.A. McLaughlin, L. Scolaro, P. Robbins, S. Hamza, C. Saunders, D.D. Sampson, Imaging of human lymph nodes using optical coherence tomography: potential for staging cancer. Cancer Res. **70**(7), 2579–2584 (2010)
95. American Cancer Society, *Global cancer facts & figures*, vol. 861811 (American Cancer Society, Atlanta, 2011)
96. R. Siegel, D. Naishadham, A. Jemal, Cancer statistics, 2013. CA Cancer J. Clin. **63**(1), 11–30 (2013)
97. X. Du, D.H. Freeman Jr., D.A. Syblik, What drove changes in the use of breast conserving surgery since the early 1980s? The role of the clinical trial, celebrity action and an NIH consensus statement. Breast Cancer Res. Treat. **62**(1), 71–79 (2000)
98. A.C. Neuschatz, T. DiPetrillo, M. Steinhoff, H. Safaii, M. Yunes, M. Landa, M. Chung, B. Cady, D.E. Wazer, The value of breast lumpectomy margin assessment as a predictor of residual tumor burden in ductal carcinoma in situ of the breast. Cancer **94**(7), 1917–1924 (2002)
99. M.F. Dillon, A.D.K. Hill, C.M. Quinn, E.W. McDermott, N. O'Higgins, A pathologic assessment of adequate margin status in breast-conserving therapy. Ann. Surg. Oncol. **13**(3), 333–339 (2006)

100. P.-L. Hsiung, D.R. Phatak, Y. Chen, A.D. Aguirre, J.G. Fujimoto, J.L. Connolly, Benign and malignant lesions in the human breast depicted with ultrahigh resolution and three-dimensional optical coherence tomography. Radiology **244**(3), 865–874 (2007)
101. F.T. Nguyen, A.M. Zysk, E.J. Chaney, J.G. Kotynek, U.J. Oliphant, F.J. Bellafiore, K.M. Rowland, P.A. Johnson, S.A. Boppart, Intraoperative evaluation of breast tumor margins with optical coherence tomography. Cancer Res. **69**(22), 8790–8796 (2009)
102. C. Zhou, D.W. Cohen, Y. Wang, H.-C. Lee, A.E. Mondelblatt, T.-H. Tsai, A.D. Aguirre, J.G. Fujimoto, J.L. Connolly, Integrated optical coherence tomography and microscopy for ex vivo multiscale evaluation of human breast tissues. Cancer Res. **70**(24), 10071–10079 (2010)
103. A.M. Zysk, S.A. Boppart, Computational methods for analysis of human breast tumor tissue in optical coherence tomography images. J. Biomed. Opt. **11**(5), 054015 (2006)
104. P.J. Barnes, Chronic obstructive pulmonary disease. N. Engl. J. Med. **343**(4), 269–280 (2000)
105. N. Khalil, R. O'Connor, Idiopathic pulmonary fibrosis: current understanding of the pathogenesis and the status of treatment. Can. Med. Assoc. J. **171**(2), 153–160 (2004)
106. E.P. Trulock, L.B. Edwards, D.O. Taylor, M.M. Boucek, B.M. Keck, M.I. Hertz, Registry of the International Society for Heart and Lung Transplantation: twenty-second official adult lung and heart-lung transplant report–2005. J. Heart Lung Transplant. **24**(8), 956–967 (2005)
107. S.A. Boppart, B.E. Bouma, C. Pitris, G.J. Tearney, J.G. Fujimoto, Forward-imaging instruments for optical coherence tomography. Opt. Lett. **22**(21), 1618–1620 (1997)
108. N. Hanna, D. Saltzman, D. Mukai, Z. Chen, S. Sasse, J. Milliken, S. Guo, W. Jung, H. Colt, M. Brenner, Two-dimensional and 3-dimensional optical coherence tomographic imaging of the airway, lung, and pleura. J. Thorac. Cardiovasc. Surg. **129**(3), 615–622 (2005)
109. J. Bickenbach, R. Dembinski, M. Czaplik, S. Meissner, A. Tabuchi, M. Mertens, L. Knels, W. Schroeder, P. Pelosi, E. Koch, W.M. Kuebler, R. Rossaint, R. Kuhlen, Comparison of two in vivo microscopy techniques to visualize alveolar mechanics. J. Clin. Monit. Comput. **23**(5), 323–332 (2009)
110. M. Mertens, A. Tabuchi, S. Meissner, A. Krueger, K. Schirrmann, U. Kertzscher, A.R. Pries, A.S. Slutsky, E. Koch, W.M. Kuebler, Alveolar dynamics in acute lung injury: heterogeneous distension rather than cyclic opening and collapse. Crit. Care Med. **37**(9), 2604–2611 (2009)
111. S. Meissner, L. Knels, C. Schnabel, T. Koch, E. Koch, Three-dimensional Fourier domain optical coherence tomography in vivo imaging of alveolar tissue in the intact thorax using the parietal pleura as a window. J. Biomed. Opt. **15**(1), 016030 (2010)
112. J.P. Williamson, R.A. McLaughlin, W.J. Noffsinger, A.L. James, V.A. Baker, A. Curatolo, J.J. Armstrong, A. Regli, K.L. Shepherd, G.B. Marks, D.D. Sampson, D.R. Hillman, P.R. Eastwood, Elastic properties of the central airways in obstructive lung diseases measured using anatomical optical coherence tomography. Am. J. Respir. Crit. Care Med. **183**(5), 612–619 (2011)
113. C. Sun, B. Standish, V.X.D. Yang, Optical coherence elastography: current status and future applications. J. Biomed. Opt. **16**(4), 043001 (2011)
114. B.F. Kennedy, T.R. Hillman, R.A. McLaughlin, B.C. Quirk, D.D. Sampson, In vivo dynamic optical coherence elastography using a ring actuator. Opt. Express **17**(24), 21762–21772 (2009)
115. Liu, Linbo, Cheng Liu, Wong Chee Howe, C. J. R. Sheppard, Nanguang Chen. Binary-phase spatial filter for real-time swept-source optical coherence microscopy. Optics Letters **32**(16), 2375–2377 (2007)
116. Lorenser, Dirk, C. Christian Singe, Andrea Curatolo, David D. Sampson, Energy-efficient low-Fresnel-number Bessel beams and their application in optical coherence tomography. Opt. Lett. **39**(3), 548–551 (2014)

OCT for Examination of Artwork

82

Piotr Targowski, Magdalena Iwanicka, Bogumiła J. Rouba, and Cecilia Frosinini

Keywords

Examination of easel paintings • Laser ablation • Leonardo da Vinci • LIBS • Noninvasive examination of artworks • Structural examination

82.1 Introduction

There are certain specific demands of any examination technique that is used for the investigation of artworks. At present, it is usually expected to be noninvasive, which means that it should not interfere with the substance of a historic monument in any way. There are no systematic studies on this matter regarding OCT. However, it is usually assumed that the intensity of the probing infrared beam proclaimed safe for the human retina is also safe for any kind of historic object. Additionally, OCT data collection is fast, and neither object preparation nor use of a sample chamber is necessary. The OCT examination may, therefore, be repeated as many times and in as many places as desired. The alternative to such noninvasive examination is collection of a sample of the structure being examined. The sampled material is then usually embedded in a synthetic resin and the cross section revealed by careful polishing. A specimen prepared in this way is then inspected visually under a microscope, usually with white light illumination or by examination of

P. Targowski (✉)
Institute of Physics, Department of Physics, Astronomy and Informatics, Nicolaus Copernicus University, Toruń, Poland
e-mail: ptarg@fizyka.umk.pl

M. Iwanicka • B.J. Rouba
Institute for the Study, Restoration and Conservation of Cultural Heritage, Nicolaus Copernicus University, Toruń, Poland

C. Frosinini
Opificio delle Pietre Dure e Laboratori di Restauro, Firenze, Italy

© Springer International Publishing Switzerland 2015

W. Drexler, J.G. Fujimoto (eds.), *Optical Coherence Tomography*,
DOI 10.1007/978-3-319-06419-2_84

UV-excited fluorescence, and cross-sectional photomicrographs are taken. Other methods of examination of samples comprise chemical spot and staining tests [1] or the use of spectroscopic techniques, e.g., micro-Raman [2]. The identification of strata is usually unequivocal, but collecting samples for analysis is always limited by conservation ethics to just a few places, usually where some losses or cracks have occurred. Nevertheless, the samples should be as small as possible. The cross sections obtained are usually of the size of 0.5–1 mm (however, the damage area is prone to be larger than the diameter of the cross section and visible to the naked eye). All these limitations result in the poor representativeness of the sampling technique as compared with noninvasive ones such as OCT.

In contrast with medical applications, where OCT apparatuses are highly specialized and usually designed for specific organs or tissues, in the case of the imaging of artworks, an instrument capable of an inspection of a wide diversity of objects is required. Artworks are composed of various materials and have a broad range of sizes (some paintings have dimensions of a few meters) and different accessibility – for example, restricted access when displayed, either vertically or horizontally; specific storage or display conditions (close humidity and temperature control); and availability for transport. These require a transportable apparatus capable of working on the object without removing it from its permanent installation site. There is no doubt that these requirements can easily be fulfilled by portable OCT systems utilizing fiber optics and compact light sources.

In the context of the diversity of objects, a major limitation of what may be examined with OCT lies in the transparency of their subsurface structures. Sometimes this drawback eliminates whole groups of artworks. In the case of paintings, however, deep examination of usually at least some particular areas may be carried out, thanks to the IR transparency of the pigments used, whereas in other areas, examination is limited just to the transparent varnish layers (if present). Nevertheless, with the increasing sensitivity of modern Fourier Domain instruments, the number of accessible objects is systematically increasing. A good example of this kind is the use of OCT for examination of some, in principle, visible-light-impermeable materials such as sandstone [3]. Apart from the desired high sensitivity, the wavelength used is an important factor to be considered in the choice of OCT instrument for examination of works of art. This subject has been addressed in an early paper by Szkulmowska et al. [4] and later by Liang et al. [5]. The latter report has been expanded lately into a more comprehensive study [6]. The general conclusion from all these contributions is that longer wavelengths offer greater depth of examination. Consequently, in [6], the authors point to 2.2 μm as the most suitable wavelength from the point of view of the transparency of pigments. On the other hand, when compared to those utilizing near-infrared light (750–950 nm), portable OCT instruments working at significantly longer wavelengths ($>$1.3 μm) offer considerably lower axial resolutions. The trade-off between this and depth of examination must always be carefully considered in the context of the desired application. Nevertheless, the present authors generally prefer resolution-priority instruments over transparency-priority systems because, in our opinion, insufficient

resolution eliminates many of the potential applications completely, whereas the lack of transparency may often be compensated by appropriate choice of the areas of examination. Most of the OCT images presented herein were obtained with a portable spectral-domain instrument equipped with a superluminescent source (870 nm central wavelength, 200 nm bandwidth, 0.8 mW at the object) with 3.1 μm axial resolution (in air) and 13 μm lateral resolution.

The convenient feature of many objects of art from the point of view of the applicability of OCT for their examination is their thin-layered subsurface structure. Most of the varnished paintings executed with the traditional technique, as well as polished furniture, stained glass, and many other artifacts, fall into this category. The fact that the axial resolution is commonly two-to-threefold higher than the lateral resolution in typical OCT systems makes this technique especially well suited for differentiation of thin layers in multiply stratified objects.

However, the ultimate feasibility of employing OCT for the examination of a particular piece of artwork can be evaluated only after reviewing the conclusions provided here for the end user (a conservator–restorer, curator, or art historian) to consider. Some examples of this kind of analysis are given in the following sections.

82.2 Overview of Application of the OCT Technique to Examination of Objects of Art

Reports of the application of OCT for examination of artworks [7] have been present in the literature only since 2004 [8–11]. Three major directions were recognized from the very beginning. Most attention has been focused on the examination of subsurface structures of easel paintings, including properties of varnish and glaze layers. A second area of interest is the examination of glass objects: from ancient glass artifacts through stained glass to glaze layers on ceramics. The third group encompasses artworks made of semitransparent mineral gemstones like jades and similar materials. A more detailed review of all of these applications has just recently been published [12].

82.2.1 Application of OCT to Examination of Easel Paintings

Paintings are multilayer structures of varied composition. The straightforward application of OCT is aimed at the examination of the transparent, subsurface layers, decisive for visual appreciation. These typically consist of a transparent varnish layer with semitransparent glazes underneath.

The varnish plays a protective role against the environment and is fundamental for final appreciation [13]. It does not usually scatter light within its structure. Glazes are composed of dyes or pigments embedded in a binder (oil, tempera, or other) at rather low concentration, thus ensuring their partial permeability to visible light. They therefore scatter IR radiation only very moderately. Below the glazes (if present), one or a few layers of opaque paint are present. The bulk of these layers

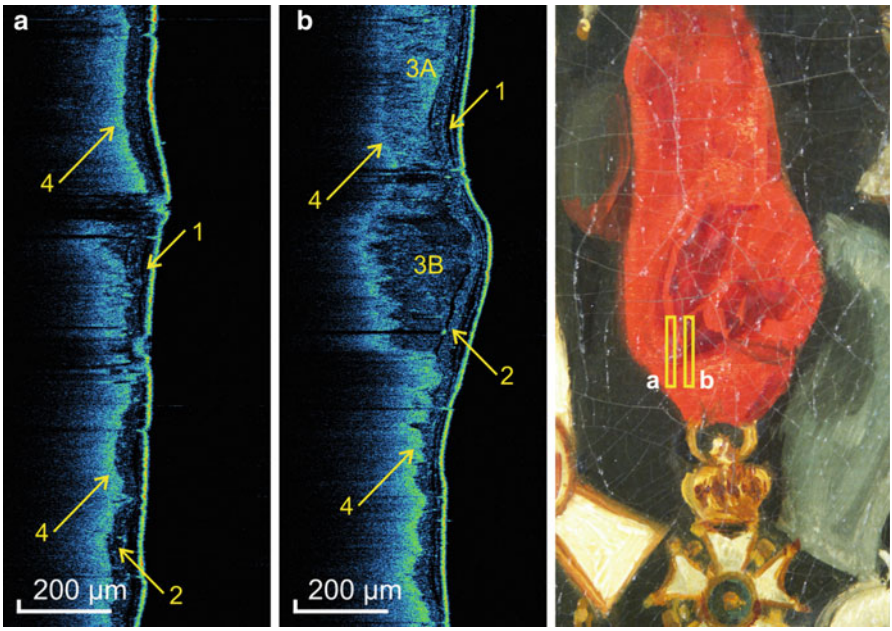

Fig. 82.1 Exemplary results of examination of a painting on canvas (*Portrait of Sir John Wylie* by P. Franck, N., Copernicus University, Toruń); (**a**, **b**) OCT tomograms: from the top, at least three layers of varnish (*1*) and then the glaze layer (*2*) are visible. Below, another thick glaze layer (*3A*, *B*, **b**) on top of the opaque paint layer (*4*) is seen. The depth scale bar is drawn for a medium of $n_R = 1.5$

is usually not accessible to OCT examination because of either high scattering or high absorption. Underneath the paint layers, there is a ground layer acting as an intermediate stratum between the paint and the support – usually a canvas or wood panel.

Easel paintings, especially those executed according to traditional techniques, bearing many layers of semitransparent glazes and of varnish, are usually very rewarding objects for OCT examination. Organic dyes used in glaze layers often have a significant permeability to the probing light. As an example, the results of OCT examinations (Fig. 82.1a, b) of a nineteenth century oil painting on canvas in two areas of the red-order ribbon are given. In this case, up to three layers of varnish (1) are seen on top of a continuous glaze layer (2). In the right-hand-side tomogram (Fig. 82.1b), three different paint layers are seen below it. The bottom one (4) scatters the probing light (770–970 nm) extensively, which thus limits the range of examination. Comparison with the photograph of the area examined allows identification of this layer as a bright red paint responsible for the main tint of the ribbon. Onto this background, subtle shades are added with a darker semitransparent paint (3A, B Fig. 82.1b). This layer reveals a continuous structure. In the upper region (3A) of the tomogram, it has a thickness of 120–150 µm and scatters light moderately. In the center (3B), this layer becomes thicker (up to 200 µm) and more

transparent. This difference in the scattering properties is directly linked with the multilayer painting technique: the intensity of color was obtained by varying the concentration of dye/pigment in the binder. It is worthwhile noting that these semitransparent layers are not present in the left-hand-side tomogram (1a), collected in the close proximity to the former. This demonstrates a common feature of the use of OCT for artwork analysis: to reveal comprehensive information, examination needs to be made in many places, since the structure of the object may vary rapidly and unpredictable over a short distance. Despite the significant amount of information provided by the representative tomogram shown in Fig. 82.1, this figure also illustrates a major drawback of using OCT for examination of artworks: the applicability of the technique is often constrained by the limited permeability of the structure investigated. In the case of paintings, it is very unlikely that support and ground layers will be accessible using this technique.

The OCT examination of varnish and glaze layers of paintings was, from the very beginning, considered an advantageous alternative to sampling. Despite the aforementioned limitations, OCT examination, due to its noninvasiveness and thus the possibility of being performed in as many places as desired, must be regarded as exhibiting improved representativeness [11]. It was early shown [14] that images obtained with OCT are congruent with cross-sectional photomicrographs of the sample taken in the same place after the OCT examination. Latour et al. used full-field OCT microscopy to analyze the structure of pigmented paint layer with superb resolution [15]. The morphology of varnish and glaze layers has been studied to attain a better understanding of the author's technique, as well as of the present state of preservation and of previous alterations and restoration attempts. For instance, the ability of OCT to localize a certain paint layer in relation to the other strata was used to analyze the chronology of historical inscriptions in an eighteenth-century painting, some of which inscriptions were identified as secondary, added during past renovations [16]. By OCT examination, it was possible to link these inscriptions to events from the history of the person portrayed and consequently make properly informed decisions regarding the program for restoration of the painting. In the same account, it was shown that the signature in another painting examined is located between two layers of varnish, so that its execution probably does not coincide with the final stage of the artwork, suggesting forgery.

The ability of OCT to image the top layers of a painting has also been used as a direct aid to the restoration. Preliminary studies by Fontana et al. [16] and Liang et al. [17] revealed the possibility of using OCT to monitor the solvent cleaning of varnish. It has been shown that, with OCT, it is possible to monitor the thickness of the remaining layer of varnish [17] as well as the preservation of the surface of the paint layer underneath [18]. This subject has been further investigated by Iwanicka et al. [19, 20] reporting examples of selective overpaint and varnish removal from historic paintings.

In spite of the fact that the upper layers of paintings are the most popular subject of examinations, in some cases, it has also proved possible to use OCT for examination of underdrawing [11, 18, 21–23] – a preparatory layer often present under the paint layers, used by the artist for the preliminary design of the

composition, sometimes not completely followed in the final result. These are very important features for art historians in studying the evolution of creation of the image. Underdrawings are usually examined with IR cameras, but in that case, the image is blurred by scattering of the illuminating light in the paint layers covering them. When OCT is employed instead, the signal is depth separated by the coherent detection and unwanted signal easily eliminated. The same mechanism can be used to sharpen the image of gold punch marks covered by a thick layer of lacquer [22].

In addition to analysis of the structure, OCT can be used for the tracking of certain destruction processes and thus aid in resolving the state of preservation of the artwork. Delamination of paint layers may be caused by poor adhesion between the layers and/or a mechanical impact. One of the possible causes of poor adhesion, common in the nineteenth century, is the use of canvas with commercial oil primer layers. If this support was used a long time after fabrication, it would have been extremely dry, and if covered with an oil paint layer, the final structure would have become very sensitive to delamination. A second factor – mechanical impact, apart from inflicting surface abrasion – may cause delamination penetrating beyond the perimeter of the area of visible destruction, under the layers in seemingly good condition, and thus be very difficult to detect. This was the case of the oil painting on canvas analyzed by the present authors a few years ago (Fig. 4 in [24]): the delamination was clearly seen to be extending out from the damaged area (varnish loss) and localized between the thick pigmented varnish layer and the glaze.

Similar damage is quite common for a particular painting technique called *Hinterglasmalerei* (reverse painting on glass) [25]. This modality, popular in the folk art of Central Europe (especially in the present south Germany, Poland, Slovakia, and Romania) until the mid-twentieth century, is characterized by employing a sheet of glass as both support and protection for the painting. Since it was designed to be viewed through glass, the details (contour and lights) were painted first, directly onto the glass, followed by glazes and opaque paints. The background layers were added at the end – in this way, the painting process was reversed as compared to classic painting technique. The obvious disadvantage of this method of painting is poor adhesion of the paint to the glass. Thus, extensive delamination is a common destructive phenomenon in these objects. Moreover, the detachments are difficult to examine and evaluated physically, because they are isolated from both sides by being sandwiched between the glass and the paint layer. OCT is here an obvious method of choice because it penetrates well through glass and, due to the high refractive index gradient in such places, is very sensitive to delaminations and blisters [26, 27].

In Fig. 82.2, an exemplary tomogram from a reverse painting on glass is presented, together with a graphic model of the structure. The whole volume of the glass support (6) is visible here, with the probing beam penetrating from the right-hand side (through the glass). Paint layers of different absorbing properties (1, 2, 3) are discernible behind the glass sheet. The adhesion of these layers to the support may be established instantly: in the upper part of the tomogram, the high intensity of light scattered at the inner surface of the glass indicates the existence

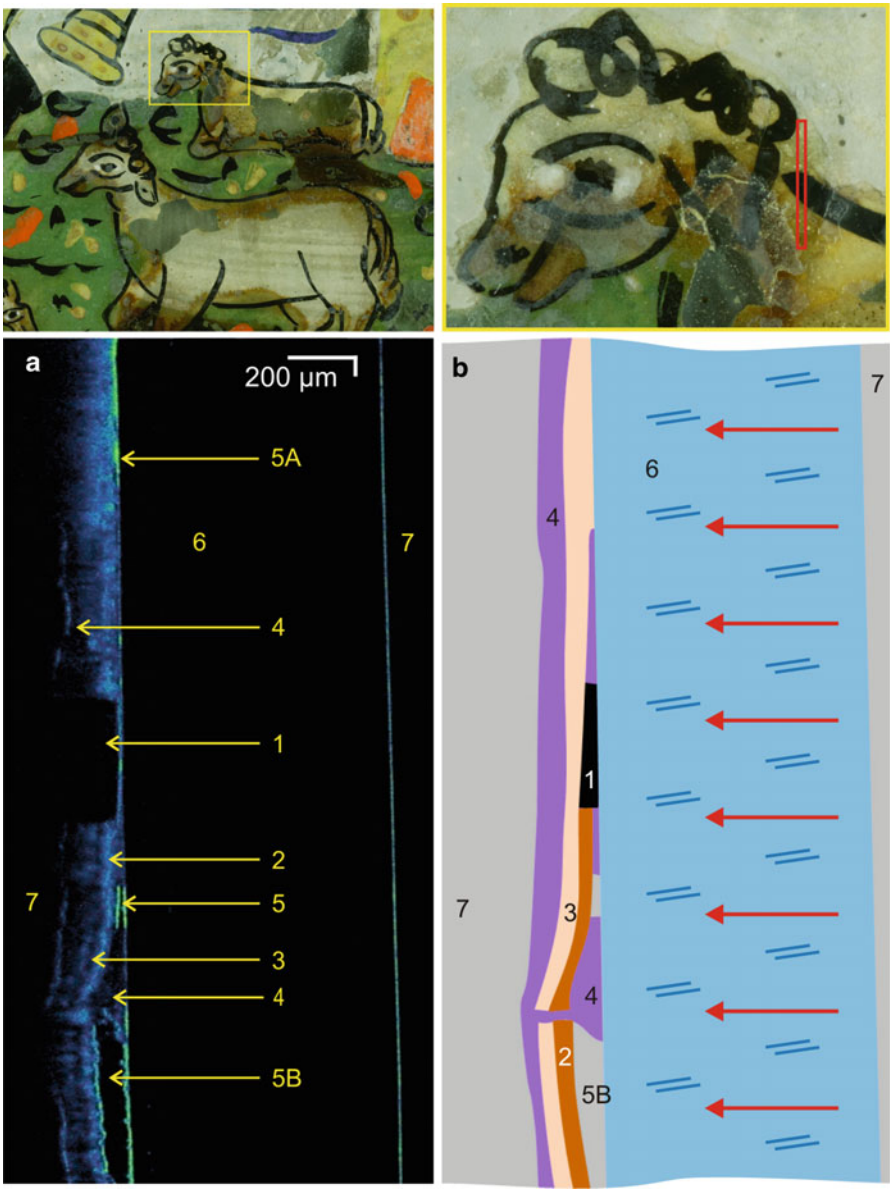

Fig. 82.2 Results of the OCT examination of the reverse painting on glass *St. Wendelin*, nineteenth century, Ethnographic Museum in Toruń, Poland, oil on glass (fragment); (**a**) tomogram obtained in the region indicated by the *red-outlined bar* in the macrophotograph above. The depth scale bar is drawn for a medium of $n_R = 1.5$; (**b**) graphic model of the structure of the painting derived from the OCT data; (*1*) contour (nontransparent paint layer), (*2*) glaze, (*3*) semitransparent paint layer, (*4*) consolidation adhesive, (*5A*) early detachment of paint layer, (*5B*) developed detachment of paint layer, (*6*) glass, and (*7*) air (Photography: W. Grzesik)

merely of a delamination, whereas in the lower part, there is a fully developed blister (5B), partially filled with a consolidation adhesive (4). In the past, there had been some attempts to repair the damage with use of consolidant applied from the back, which was supposed to penetrate through all of the paint layers to eventually fill the voids between glass and paint. As could be detected by OCT, this treatment was not always successful. Moreover, as discovered at other locations in the same object, the consolidant itself had deteriorated with time, losing adhesion to the glass and developing tent-shaped deformations (Fig. 4D in [27]).

In addition to examining the state of preservation, OCT was also used to monitor the consolidation process [19, 28]. In particular, the wetting of glass by consolidant can conveniently be monitored by OCT in real time.

Besides the practical applications of OCT in the examination of paintings, more fundamental studies – on the drying processes of varnishes – were conducted by Liang et al. [21] and continued by Lawman and Liang with combined use of NMR [29] and multi-interface OCT profilometry [30]. In this specific case of a transparent layer of varnish on a glass substrate at both interfaces, the refractive index change is significant and is described by a step function. The OCT A-scan can be approximated by a point-spread function (PSF) in this place. By locally fitting a Gaussian function, the authors were able to localize the interface to a precision ($rms = 55$ nm) two orders of magnitude better than the axial resolution of their instrument (6.5 μm), but only when both interfaces were far enough from each other. In these, and similar studies by Targowski et al. [31], it was confirmed that the ability of varnish to follow the roughness of the paint surface depends mostly on its molecular weight, in accordance with earlier results by de la Rie [13].

82.2.2 Application of OCT to Examination of Historic Glass

There is no doubt that OCT is well suited to the examination of glass objects, since this material is generally transparent. Thus, its internal structure can usually be examined within the whole depth of imaging of the OCT system employed. If the glass object contains structures of different scattering properties, they can be precisely traced with OCT [5, 18, 32, 33].

Apart from examination of structure for inventory purposes, some destructive processes in historic glass may be analyzed with OCT. In the case of stained glass, the advance of atmospheric corrosion [34] is the most important evaluation to carry out in the determination of its state of preservation. This process, caused by the moisture from precipitation at the outer side and condensation at the inner side of the glass sheet, essentially comprises two steps. During the first (called leaching), alkali and alkaline-earth ions are rinsed from the glass and replaced by H^+ or H_3O^+ ions. As a result, a gel layer rich in silica is formed on the surface of the glass. During the second step, water penetrates into this layer, and the glass may be destroyed both chemically and mechanically by freezing if subjected to low enough temperatures. This silica-rich layer may have one of several different optical properties, depending on the glass composition. Usually it has a porous structure

and thus a high-scattering coefficient, although sometimes it is perfectly transparent, but of different refractive index. In both cases, it can be detected with OCT [18, 33, 35]. By contrast with the standard examination technique, SEM–BSE (Scanning Electron Microscopy–Backscattered Electrons), using polished cross sections, no prior preparation of the glass is necessary. In principle, with a portable instrument, it should be possible to examine stained glass without dismounting it from the windows. It is worthwhile noting that the detection of the depth range of the gel layer is usually obstructed by multiple scattering of the OCT probing light within this structure, which is seen as fading tails in the A-scan signal. This disadvantage may be overcome if the other side of the glass is accessible and has not deteriorated: examination through the transparent glass then reveals sharp boundaries to the gel layer [27].

Another kind of historic glass destruction is called crizzling. This is caused by imbalance in the ingredients during their preparation and demonstrates itself as a network of fine cracks at one or both surfaces of the glass piece. When the object is stored under inappropriate environmental conditions, these lesions may develop with time and can eventually lead to the total destruction of the object. The OCT examination of such an artifact [27] revealed that the depth of the cracks on a given side of the glass sheet is uniform but different from that on the other side.

82.2.3 Application of OCT to Examination of Craftsmanship (Musical Instruments, Gemstones, Ceramics)

Lacquer coating on musical instruments is a layer of similar properties to those of varnish on paintings. In both cases, high axial resolution is a decisive factor for successful OCT imaging. Since these coatings are always transparent to visible light, the necessary resolution may well be achieved using OCT with probing light in the visible rather than the infrared range of wavelengths. Latour et al. [36] used red light ($\lambda_{center} = 650$ nm, $\Delta\lambda = 150$ nm) in a full-field time-domain OCT system equipped with a Mirau objective. They presented results of examination of lacquer coating an eighteenth-century Italian violin, preceded by laboratory tests on model samples of flame maple and lacquered wood. They showed, for the first time, evidence of the ability of OCT to reveal the internal structure of the wood (up to 50 μm of optical depth), but some of the conclusions concerning the structure of the coatings on the violin were ambiguous. Another application, encompassing the examination of both painting and craftsmanship, is seen in the imaging of painted enamel on a ceramic tile [18].

Jade art objects of art have been a focus of OCT examination from the very beginning right through to the present. In 2004, Yang et al. [8], using objects from the National Museum of Taiwan, proved that OCT may be used to detect forged archaeological jades, since this semitransparent stone scatters the probing light differently when it has been aged artificially. Natural ageing is a very slow process as compared with the artificial one which is induced by extensive heating. As a result of the latter, counterfeit objects have a more heterogeneous structure

which is possible to differentiate from the more homogeneous, naturally aged one by OCT examination. Similar examples have been reported by Liang et al. [18]. This qualitative conclusion was developed quantitatively by Chang et al. [37], who defined a statistical measure of texture of the OCT image as being a vector in a 6D space composed of three parameters derived from the histogram of the image and three calculated directly from the pixel values of the B-scan. The length of this vector, together with the second parameter representing the translucency of the object, may be used for characterization of various jades, including the detection of fraud. In parallel with this holistic study, details of the structure of jades, in particular the morphology of cracks, have been studied by Yang [38].

Another sort of object for which the use of OCT for examination was noticed early on [9] is the glaze layer on ceramics. Those studies have been continued by other authors [18, 33], focusing on analysis of different phases (and phase boundaries) within the glaze layer [39, 40], the presence and size of air bubbles [40], and the morphology of cracks [38]. The aim of these efforts was to provide a tool useful for identification of the origin, method of production, and thus, in some cases again, recognition of fraud. In the specific case of Egyptian faience, it is possible to distinguish between three ancient production methods by analyzing their cross sections with SEM. In their recent paper, Liang et al. [41] showed that this is also possible noninvasively with OCT operating at 930 nm.

Some attention has also been given to examination of parchment with OCT in the context of its degradation caused by the presence of iron-gall ink. After application, this kind of ink undergoes chemical processes resulting in its change from almost colorless through blue to a final dark brown tint. Simultaneously, acidic components of the ink cause degradation of the support which, in some cases, may eventually lead to the total destruction of the document. Conveniently, radiation of 830 nm is practically not absorbed by this ink. OCT examination is therefore possible also for areas of support covered by the ink and thus most exposed to this degradation factor. Such a study was performed by Góra et al. [42] with utilization of standard as well as polarization-sensitive (PSOCT) techniques. It was shown that OCT of this wavelength is able to image the subsurface structure of parchment with the iron-gall ink thereon, and some evidence of degradation of the parchment was found.

82.2.4 Laser Ablation Control by OCT

Laser ablation of solids is a well-established technique and may be precisely controlled by pulse duration and energy. Therefore, it is used as a fine tool also for the examination and restoration of art objects. In this section, two applications of OCT as a monitoring device of the laser ablation process will be presented. There is no doubt that in both cases, these specific utilizations can be considered only as examples from much wider field of application.

82.2.4.1 Absolute Depth Profiling with LIBS and OCT

Laser-induced breakdown spectroscopy (LIBS, or sometimes LIPS) is a technique of elemental composition analysis by spectral examination of emission from a small plume of plasma generated by the laser pulse. It is mostly used for determination of the composition of metal alloys. The diameter of the crater is usually less than 200 μm, and thus, this technique may be considered as micro-destructive. It is therefore usually regarded as an acceptable method for examination of art objects [43]. Its modality, called LIBS stratigraphy, is especially useful: a tray of pulses is delivered to the same spot on the object, and the ablation crater is created gradually. After each pulse, the plasma spectrum is registered and the intensity of chosen spectral lines determined (Fig. 82.3a). In this way, a depth profile of concentration of a given element may be revealed and eventually associated with a particular layer of the structure examined. A significant drawback of this approach lies in the lack of information about the exact depth of the crater after each pulse. Moreover, for multilayer objects, the ablation rate usually varies from stratum to stratum, and the dependence of depth on the pulse number is not linear. Therefore, for true depth calibration of the concentration profiles, the depth of the crater should be determined noninvasively after each laser pulse. The idea of using OCT for this purpose comes from the group of Sabsabi but, since the US patent [44] and a paper by Dufour et al. [45], has not been further pursued. A similar experiment was previously described by Papazoglou et al. [46] who employed a white light interferometer, similar in principle to a full-field TdOCT system. Amaral et al. [47] have analyzed some historic Brazilian coins using a commercial TdOCT instrument to determine the final depth of the crater after applying the whole train of pulses. To estimate the depth of the crater after each pulse, they assumed a constant ablation rate throughout the whole experiment. Although for metal alloys this seems acceptable, the present authors have shown that this is definitely not the case for paint layers (Fig. 82.3b). In these experiments, performed both on model samples [48] and a historic painting [49], we used spectral-domain OCT instrument after each laser pulse as a fast profilometer. In this way, the combined LIBS/OCT experiment could be performed in a reasonable time and the true depth profile recovered (Fig. 82.3c). Moreover, from changes in ablation rates, the locations of interfaces between strata were determined and confirmed by the analysis of OCT B-scans obtained in the same place. Obviously, such confirmation was possible only within semitransparent strata, whereas the crater depth and ablation rate determinations from the surface profile were feasible throughout. In Fig. 82.3, the first boundary (I/II) can be determined from the OCT B-scan and identified as lying between two layers of varnish, whereas the second boundary (II/III) is clearly visible as a change of the ablation rate (slope of the data in Fig. 82.3b) and is identified from the OCT B-scan as the varnish/opaque paint interface. The third boundary is not visible in OCT imaging as lying within the opaque structure, but can be identified clearly by the increase in strontium concentration. It is worthwhile noting that information about elemental concentration is important for both curators and conservators, as it helps in understanding the painter's technique, in distinguishing between original and non-original areas in the painting, and sometimes in the dating of the artwork.

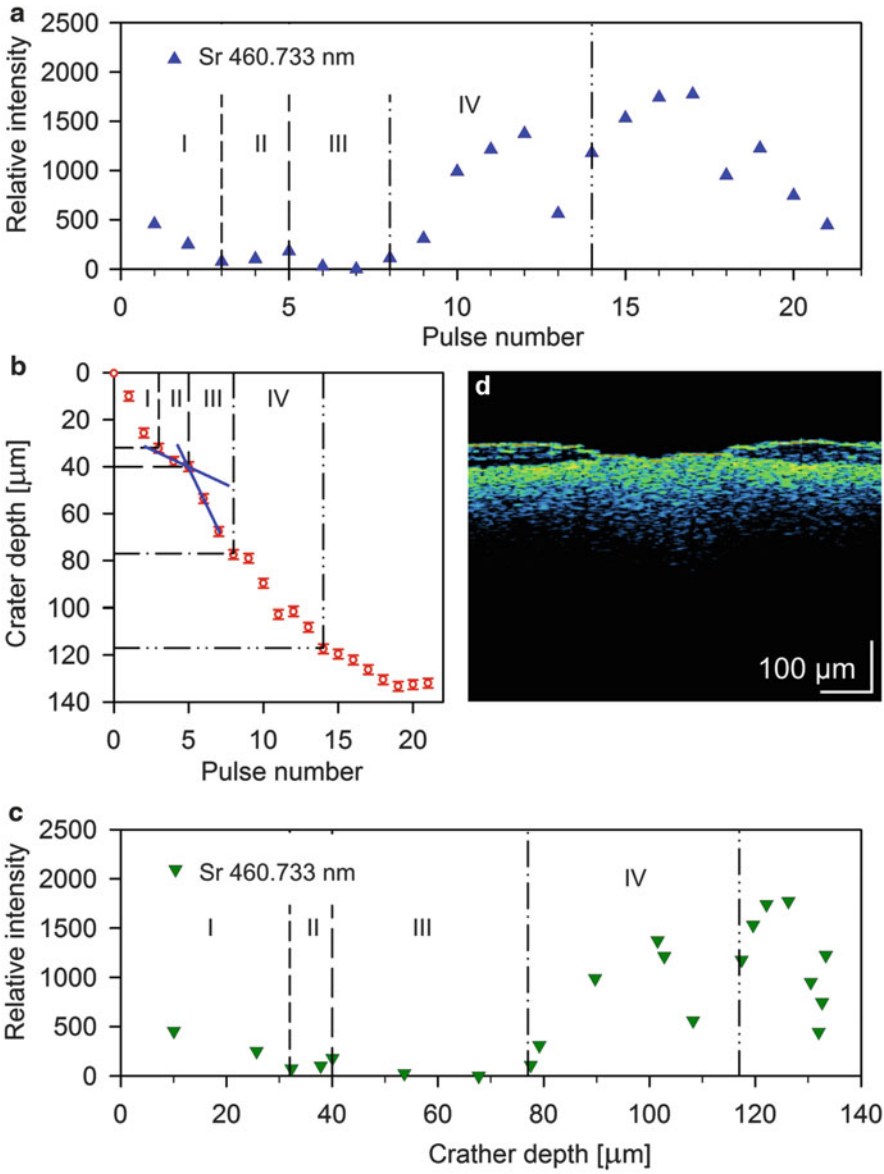

Fig. 82.3 Exemplary result obtained with an LIBS/OCT instrument (Data from [49]); (**a**) depth profile of strontium obtained by LIBS stratigraphy at line 460.733 nm; (**b**) crater depth determined from OCT data – evidence for strata boundary at 40 µm from the change of ablation rate is marked (see text for description of strata I to IV); (**c**) true depth profile determined from LIBC/OCT data; (**d**) OCT cross section after the 4th pulse; the vertical scale bar is drawn for a medium of $n_R = 1.5$

82.2.4.2 Monitoring Varnish Removal with the Use of OCT

Laser ablation paint removal is an interesting and effective alternative to chemical and/or mechanical treatment. It is used, for instance, by the US Navy to remove old paint from aircraft carriers and submarines [50], as well as in aircraft maintenance. In the case of art conservation, it is also a well-established technique for the cleaning of stone and metal sculptures: the operator uses a freehand laser head, and the process is monitored visually. The situation is much more complicated in the case of laser removal of varnish or paint layers from paintings and similar objects [51]. Here, the underlying strata are usually as vulnerable to laser ablation as are the layers to be removed, and very often, in contrast with the abovementioned industrial applications and stone/metal cleaning, it is desirable to leave a thin layer of the stratum, most of which is removed, in order to protect the underlying structure from possible damage. Laser ablation of varnish is thus still in the experimental stages of implementation and is recommended only if the varnish is very difficult to dissolve and remove chemically or if the underlying paint layer is very sensitive to the solvents to be used. In a series of papers [32, 52, 53], the present authors have demonstrated the feasibility of using OCT to monitor the thickness of the remaining layer of varnish. However, the key to real-world application is the ability to monitor this process in real time with OCT. Proof of concept was demonstrated with an SDOCT system capable of the imaging in real time of two frames per second (FPS) comprising two B-scans each made up of 200 A-scans [54, 55]. However, this imaging speed (limited mostly by data-processing capability) is substantially too slow for monitoring ablation performed under realistic conditions. This deficiency can be overcome by very fast data processing with massive parallel calculations on Graphic Processor Units (GPU) [56–58]. That principle, when employed for the setup designed for the laser monitoring of ablation [59], was operating with 6 FPS each comprising four B-scans each made up of 1,000 A-scans, at a speed limited by the acquisition time (40 μs/A-scan). In our opinion, this technology opens the gate to successful practical application of real-time monitoring, but much more work is still needed to ensure an acceptable level of safety for working with unique art objects.

82.3 Exemplary Results of the Examination of Paintings

The following examples come from the mutual research performed by physicists responsible for the instrumentation and art conservators interested in solving real problems emerging from their everyday practice. In the cases presented, OCT aided in the resolution of sequence and of deterioration processes within the secondary layers of paintings. These studies fall into two categories: (1) type, origin, and range of deterioration of historical/contemporary varnishes and (2) sequence, thickness, and continuity of both primary and secondary layers in the areas altered during past renovations.

82.3.1 Resolving Deterioration Processes Within the Varnish Layers

Leonardo da Vinci's monumental unfinished panel painting, *Adoration of the Magi*, was commissioned in 1481 for the main altar in the monastery church of San Donato a Scopeto near Florence. It was abandoned by the painter in 1482 when he went to Milan to work for Ludovico Sforza [60]. This big panel (246 × 243 cm) has been a part of the collection of the Uffizi Gallery in Florence since 1670. Over the last 500 years, it has undergone several treatments, mostly retouching and re-varnishing. OCT examination of the painting was performed in the Opificio delle Pietre Dure (OPD) in Florence, as a part of an extensive multi-instrumental examination.

Among the issues articulated by the conservators was the origin of some discolored vertical areas, not related to the depicted scene, obscuring a full appreciation of the painting. The OCT examination (Fig. 82.4) revealed differences in the structure of the thick upper varnish layer (1) within and outwith the optically altered vertical stripes. The discolored area corresponds to the presence of strong scattering in this varnish layer. The scattering centers are distributed homogeneously in the bulk of the varnish and indicate alteration of its structure. The microcracks which are responsible for this create the effect of blooming of the varnish on a macroscopic scale and are usually caused by exposure to excessive moisture. The vertical orientation of these areas suggests streaks of water running down the surface of the painting at some unidentified past time. OCT examination disclosed the presence, under this bloomed varnish, of a thin and transparent layer of earlier varnish (2), not affected by blooming.

Another task investigated at the suggestion of the conservators was to establish the nature and the cause of some specific local discoloration which had occurred in the eighteenth-century painting *Lady with a bouquet of flowers*. Fifteen years after the last conservation–restoration, white structures started to appear on the surface. The damage was either repeating the craquelure pattern or due to some accidental man-caused abrasion, as suggested by its shape. Microscopic examination (Fig. 82.5c) of the affected regions revealed that the questioned deterioration was limited to the varnish layer alone.

Since it was known that during the previous restoration two layers of dammar varnish of the same kind had been applied, the aim of the OCT examination was to resolve which of them was tending to peel off. This information was crucial to the design of a new conservation program, which was intended to be as minimalistic as possible. If both varnishes were to be removed, the vast amount of inpainting (retouching), carried out in previous conservation efforts to reconstruct lost or deteriorated parts of the work under the varnishes, would probably be destroyed.

As a result of the OCT scanning, it was confirmed that the whitish deterioration was caused by delamination of the varnish (3A in Fig. 82.5a, b), together with some local tenting (3B) and losses (3C). As can clearly be seen from the figure (Fig. 82.5b), the delamination has occurred at the boundary (yellow arrow in Fig. 82.5b) between the thick upper layer of dammar varnish (1) and the thin lower layer. The reason for this phenomenon might be the difference in thickness

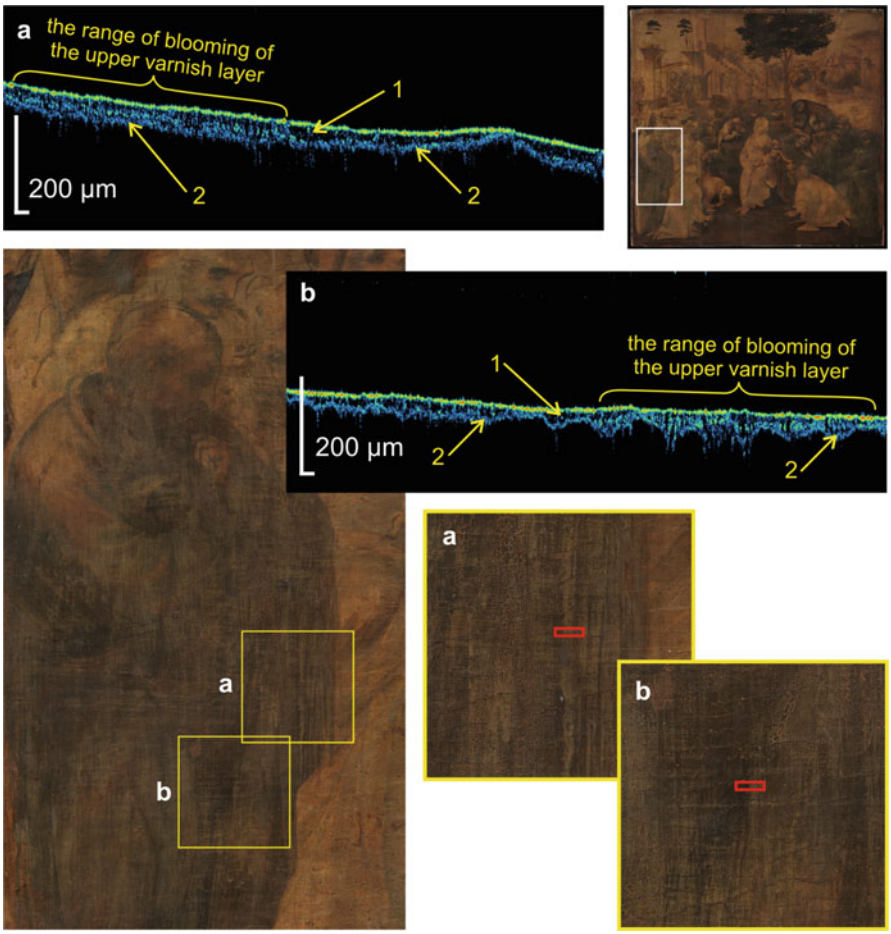

Fig. 82.4 Results of the OCT examination of Leonardo da Vinci's *Adoration of the Magi*, late fifteenth century, oil on wood, Uffizi Gallery, Florence; (**a**, **b**) tomograms obtained in places indicated by *red bars*: (*1*) upper varnish layer, locally bloomed and (*2*) lower varnish layer, transparent. The vertical scale bar is drawn for a medium of $n_R = 1.5$ (Photos: OPD, Florence)

between the two dammar layers. The information obtained provided the basis for deciding on the conservation treatment – in the end, only the upper layer of varnish was removed, with the lower layer left intact to protect the inpainting.

82.3.2 OCT Imaging of Overpainting on Varnish

Overpainting is the addition of secondary paint layers altering and hiding the original composition of a painting. During their lifetime, paintings were treated in this way because of an urge for renovation. However, until the beginning of the

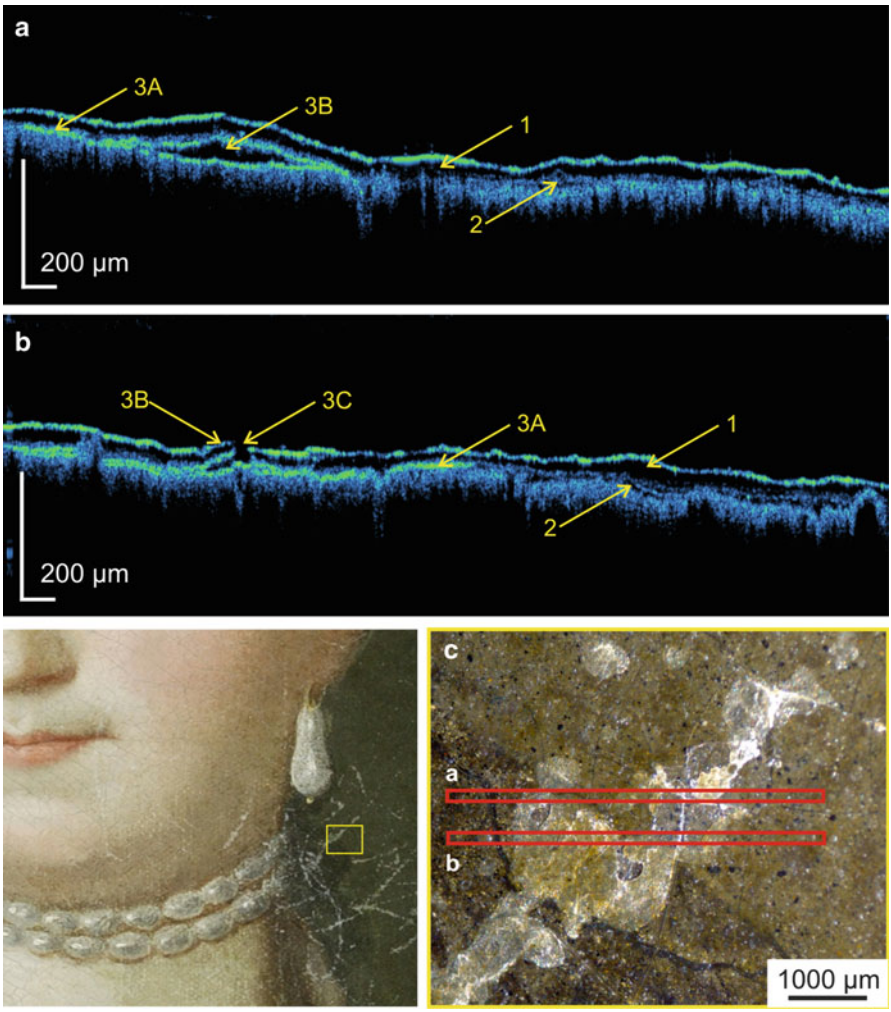

Fig. 82.5 Results of the OCT examination of the painting *Lady with a bouquet of flowers*, eighteenth century, oil on canvas (fragment), District Museum in Chojnice, Poland; (**a**, **b**) tomograms obtained in the places indicated by *red bars* in the microphotography (**c**) of the area examined; (*1*) upper layer of dammar varnish, (*2*) lower layer of dammar varnish, (*3A*) early stage of delamination, (*3B*) local tenting of the scale of the varnish, and (*3C*) loss in varnish caused by the delamination process. The vertical scale bar is drawn for a medium of $n_R = 1.5$ (Photos: E. Ryś, M. Iwanicka)

twentieth century, according to the past doctrines of the aesthetics and renovation of paintings, the original substance of artworks was considered less important than their general visual appreciation. Hence, whole composition areas damaged due to time, environmental factors, mishandling, or improper treatment (e.g., overcleaning) were given new modelling by overpainting. In theory

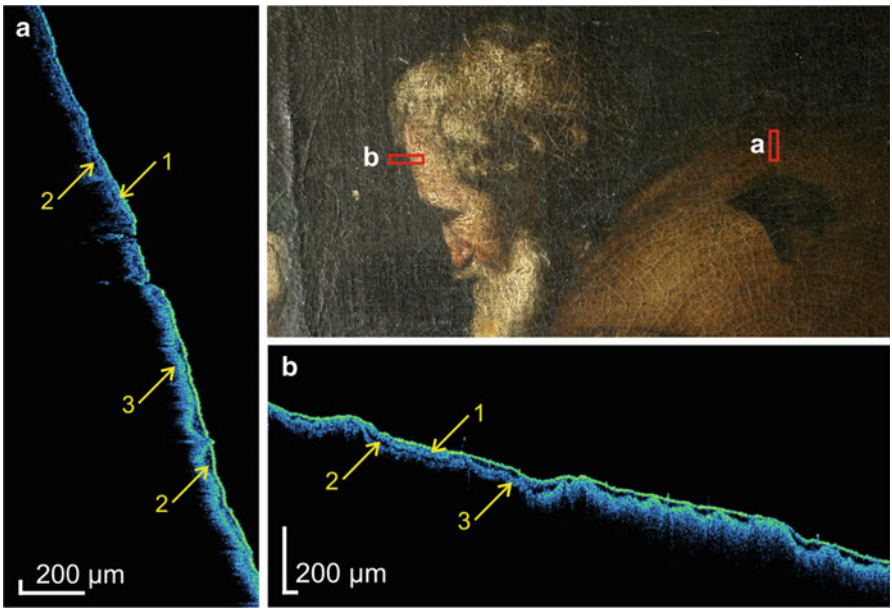

Fig. 82.6 Results of the OCT examination of the painting *Adoration of the shepherds*, after Jusepe de Ribera**,** seventeenth century, oil on canvas (fragment), Franciscan monastery in Pakość, Poland; (**a**, **b**) tomograms obtained in places indicated by red bars in the photograph; (*1*) layer of overpaint, (*2*) varnish, and (*3*) primary paint layer. The in-depth scale bar is drawn for a medium of $n_R = 1.5$ (Photo: M. Dyniec)

overpainting can easily be distinguished and mapped out by means of observation of UV-induced fluorescence of the painting. The secondary layers tend to have fluorescence weaker than the original, more ancient ones. This rule can, however, be misleading in some cases, due to the special properties of certain pigments and the strong fluorescence of some secondary varnishes [61]. For this reason, sampling is usually employed in order to corroborate surmise about the sequence of primary and secondary layers. From the perspective of the conservator, the important issues are not only resolution of the range and thickness of the overpaint but also knowing if there is a layer of varnish in between the primary and secondary paint layers. The existence of such a layer, increasing the safety of the treatment for removal of overpaint, can be naturally established by means of classic sample cross-section analysis. However, only noninvasive examination in many spots can confirm that this varnish layer, if present, is constant in thickness across the area in question.

In the painting *Adoration of the shepherds*, the aforementioned configuration of layers was suspected. OCT scanning at the boundary between the overpainted background area and the figure of St. Joseph revealed the existence of an overpaint, about 40 µm thick (1 in Fig. 82.6), lying on a very thin (about 5 µm) varnish layer (2). The upper surface of the primary paint layer is easily visible in the tomograms presented.

82.3.3 OCT Imaging of Retouching Between Varnishes

Retouching (inpainting) is usually the final stage of the restoration process of a damaged paint layer, performed by the conservators in order to integrate the painting both visually and aesthetically. According to the contemporary theory of conservation, inpainting should be applied only within the actual perimeter of paint loss and should not be laid down directly onto the primary paint layer, so that it can eventually be easily removed if later required. Similar to overpainting, retouching is usually mapped by means of UV-induced fluorescence imaging. However, the practice shows that such identification may be hindered if the retouching lies underneath a layer of varnish of strong UV fluorescence and/or significant thickness.

In the case of *Madonna of the Yarnwinder (Madonna dei Fusi)*, an oil painting attributed to Leonardo da Vinci, some issues regarding the positioning and evaluation of the retouching were clarified on examination by OCT.

Owing to the en face OCT imaging (depth separated by coherent detection), it was possible to establish the sequence of layers in the restored areas, as well as to recover the outline of the retouching and compare it to the contour of actual paint losses. Exemplary slices of such a multilayer structure are shown in Fig. 82.7. In the background area near the Madonna's face, retouching exhibiting strong UV fluorescence is localized (Fig. 82.5d). In the OCT B-scan obtained in that area (Fig. 82.7a), it is mainly retouching between varnish layers (1A, 1B) that are visible (2B). Comparison of the tomogram with the coherence-gate images (Fig. 82.7d, e, f) revealed the existence of two layers of retouching of totally different shape, positioned at different depths within the structure of the painting.

Retouching easily discernible in UV-induced fluorescence lies on the surface of the painting (Fig. 82.7d, coherence-gate depth: 6 μm) and is visible in the OCT tomogram as a thin layer, strongly scattering the probing light (2A in Fig. 82.7a). The layer clearly localized between the varnishes (2B) is the same as that seen in the coherence-gate imaging obtained at a depth of 18 μm (Fig. 82.7e). It is worth noticing the difference in size and shape of this retouching when compared to the superficial one. However, analysis of the range of paint loss (visible in Fig. 82.7f, gate depth: 35 μm) leads to the conclusion that in the region examined, retouching at both depths exceeds the area of the actual loss underneath. At the same level as the paint losses, the texture of the canvas is detectable, imprinted in the paint layer (Fig. 82.7f). This is the result of a former restoration treatment, i.e., transfer of the painting from its support. Since the structure of the contemporary canvas now present in the painting is not consistent with the imprint (as discovered by Fontana et al. by means of 3D conoscopic measurements [62]), it should be assumed that the imprint is the result of a previous transfer.

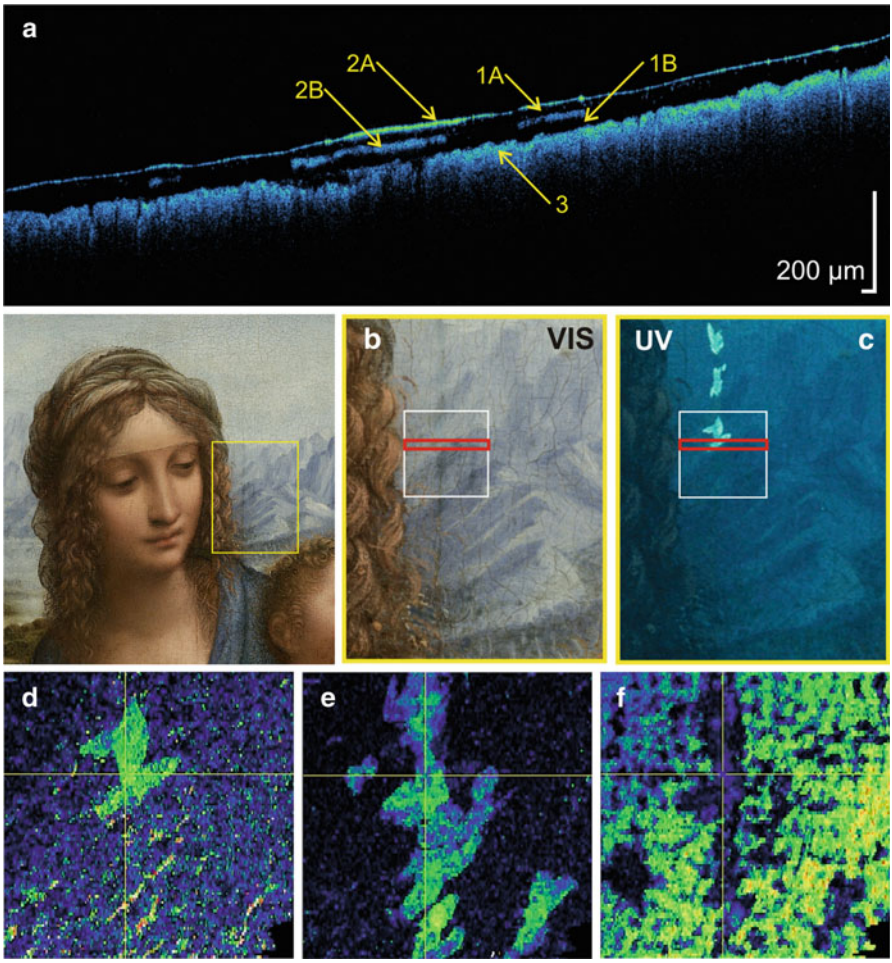

Fig. 82.7 Results of the OCT examination of the painting *Madonna of the Yarnwinder (Madonna dei Fusi)*, attributed to Leonardo da Vinci, early sixteenth century, oil on wood (fragment); (**a**) OCT tomogram obtained in the region indicated by red bars in the photographs (**b**, **c**); (**d**, **e**, **f**) OCT en face images obtained from different depths under the surface (0, 18, 35 µm, respectively). (*1A*, *1B*) varnishes, (*2A*, *2B*) two stages of retouching, and (*3*) primary paint layer. The vertical scale bar is drawn for a medium of $n_R = 1.5$ (photo: OPD, Florence)

Another example of noninvasive evaluation of retouching in the *Madonna of the Yarnwinder* (Fig. 82.8) concerns the area of the background. The OCT B-scan reveals the multilayer structure of the painting in this region, including well-preserved glazes (3) over the paint layers (4, 5). This observation was then confirmed by coherence-gate images, clearly showing that the paint layer is intact (Fig. 82.8c) under the retouching (bright patch in Fig. 82.8b).

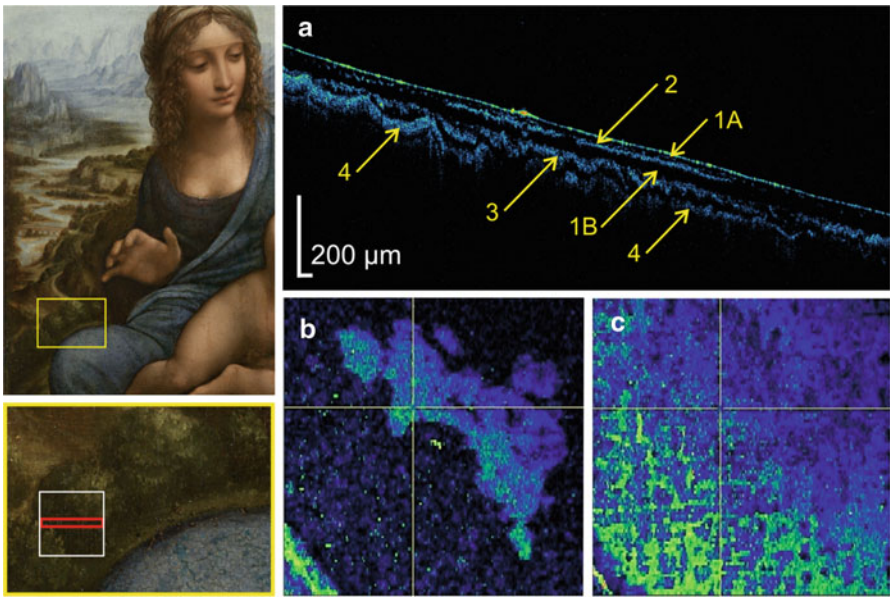

Fig. 82.8 Results of the OCT examination of the painting *Madonna of the Yarnwinder (Madonna dei Fusi)*, attributed to Leonardo da Vinci, early sixteenth century, oil on wood (fragment); (**a**) OCT tomogram obtained in the region indicated by red bars in the photograph; (**b**, **c**) en face images obtained from different depths under the surface (19, 44 μm, respectively). (*1A*, *1B*) varnishes, (*2*) retouching, and (*3*) primary glaze over the paint layer (*4*). The vertical scale bar is drawn for a medium of $n_R = 1.5$ (photo: OPD, Florence)

82.4 Conclusions

In the case of easel paintings executed in the traditional technique, OCT examination aids in resolving the structure of the primary layers (varnishes, glazes, and some semitransparent paint layers) as long as they are transparent enough to near-IR radiation. In our opinion, however, the most useful applications of this noninvasive technique for the practice of conservation are those aimed at the examination of the state of preservation and stage of deterioration, as well as of the range and nature of alterations of the upper layers of the painting, e.g., deteriorated varnishes, glazes, overpainting, and retouching. This advantage of OCT over classic invasive sample analysis arises from the possibility of examining areas large enough to cover boundaries between regions of the painting which differ in color, saturation, glossiness, etc., and therefore are suspected to exhibit some alteration. In such cases, analysis of the continuity of layers over areas of several millimeters helps to resolve complicated issues related to the history of the painting.

As for the examination of other types of artworks, the most promising would again seem to be studies aimed at resolving the structure of the object and its state of preservation.

The examples exhibited in this contribution prove that in the case of some art objects, it is possible to solve conservation issues exclusively by means of noninvasive examination. Optical coherence tomography fully deserves to be considered a fast, and practical, albeit nonuniversal, tool in assisting the conservator both in decisions as to the optimal course to take in the conservation process and in evaluation of its course and the results obtained.

Acknowledgments The results shown in Figs. 82.1 and 82.4, 82.5, 82.6, 82.7, and 82.8 were obtained with an instrument built within the EU Community FP7 Research Infrastructures Programme under the CHARISMA Project (Grant Agreement 228230) and co-funded by the Polish Government. The participation of Anna Szkulmowska, Marcin Sylwestrzak, Ewa A. Kaszewska, Łukasz Ćwikliński, and Maciej Szkulmowski of the Nicolaus Copernicus University in Toruń, Poland, and Jan Marczak, Wojciech Skrzeczanowski, Antoni Rycyk, and Roman Ostrowski of the Military University of Technology in Warsaw, Poland, as well as of Roberto Bellucci of the Opificio delle Pietre Dure, Florence, Italy, is gratefully acknowledged. Authors thank Robert Dale for critical reading of the manuscript.

References

1. R. Mazzeo, in *Scientific Examination for the Investigation of Paintings. A Handbook for Conservator-Restorers*, ed. by D. Pinna, M. Galeotti, R. Mazzeo (Centro Di, Firenze, 2009), pp. 193–196
2. J.-C. Dran, S. Pages-Camagna, in *Scientific Examination for the Investigation of Paintings. A Handbook for Conservator-Restorers*, ed. by D. Pinna, M. Galeotti, R. Mazzeo (Centro Di, Firenze, 2009), pp. 188–190
3. E. Bemand, M. Bencsik, H. Liang, Proc. SPIE **8084**, 80840H (2011)
4. A. Szkulmowska, M. Góra, M. Targowska, B. Rouba, D. Stifter, E. Breuer, P. Targowski, in *Lasers in the Conservation of Artworks. LACONA VI Proceedings, Vienna, Austria, September 21–25, 2005*, ed. by J. Nimmrichter, W. Kautek, M. Schreiner (Springer, Berlin/Heidelberg/New York, 2007), pp. 487–492
5. H. Liang, B. Peric, M. Hughes, A. Podoleanu, M. Spring, D. Saunders, Proc. SPIE **6618**, 661805 (2007)
6. H. Liang, R. Lange, B. Peric, M. Spring, Appl Phys B **111**, 5378 (2013)
7. For a complete list of papers on the application of OCT to the examination of artwork, see: http://www.oct4art.eu
8. M.L. Yang, C.W. Lu, I.J. Hsu, C.C. Yang, Archaeometry **46**, 171 (2004)
9. P. Targowski, B. Rouba, M. Wojtkowski, A. Kowalczyk, Stud. Conserv. **49**, 107 (2004)
10. H. Liang, R. Cucu, G. Dobre, D.A. Jackson, J. Pedro, C. Pannell, D. Saunders, A.G. Podoleanu, Proc. SPIE **5502**, 378 (2004)
11. H. Liang, M. Gomez Cid, R. Cucu, G. Dobre, A. Podoleanu, J. Pedro, D. Saunders, Opt. Express **13**, 6133 (2005)
12. P. Targowski, M. Iwanicka, Appl. Phys. A **106**, 265 (2012)
13. E.R. de la Rie, Stud. Conserv. **32**, 1 (1987)
14. T. Arecchi, M. Bellini, C. Corsi, R. Fontana, M. Materazzi, L. Pezzati, A. Tortora, Opt. Spectrosc. **101**, 23 (2006)
15. G. Latour, J. Moreau, M. Elias, J.-M. Frigerio, Proc. SPIE **6618**, 661806 (2007)
16. P. Targowski, M. Iwanicka, L. Tymińska-Widmer, M. Sylwestrzak, E.A. Kwiatkowska, Acc. Chem. Res. **46**, 826 (2010)
17. R. Fontana, M. Bellini, C. Corsi, M. Mastroianni, M. Materazzi, L. Pezzati, A. Tortora, Proc. SPIE **6618**, 661808 (2007)

18. H. Liang, B. Peric, M. Hughes, A.G. Podoleanu, M. Spring, S. Roehrs, Proc. SPIE **7139**, 713915 (2008)
19. M. Iwanicka, P. Targowski, E.A. Kwiatkowska, M. Sylwestrzak, in *Lasers in the Conservation of Artworks IX. Proceedings of the International Conference on Lasers in the Conservation of Artworks (Lacona IX), 7–10 September 2011, London, UK*, ed. by D. Saunders, M. Strlič, C. Korenberg, N. Luxford, K. Birkhölzer (Archetype Publications, London, 2013), pp. 11–25
20. M. Iwanicka, D. Kończalska, P. Targowski, B.J. Rouba, in *New Insights into the Cleaning of Paintings: Proceedings from the Cleaning 2010 International Conference*, ed. by M.F. Mecklenburg, A.E. Charola, R.J. Koestler, 2010, pp. 27–29
21. H. Liang, M. Cid, R. Cucu, G. Dobre, B. Kudimov, J. Pedro, D. Saunders, J. Cupitt, A. Podoleanu, Proc. SPIE **5857**, 261 (2005)
22. D.C. Adler, J. Stenger, I. Gorczynska, H. Lie, T. Hensick, R. Spronk, S. Wolohojian, N. Khandekar, J.Y. Jiang, S. Barry, Opt. Express **15**, 15972 (2007)
23. M. Spring, H. Liang, B. Peric, D. Saunders, A. Podoleanu, in *Proceedings of ICOM-CC Triennial Conference*, ed. by J. Bridgland, vol. II (Allied Publishers, New Delhi, 2008), pp. 633–639
24. B. Rouba, P. Karaszkiewicz, L. Tymińska-Widmer, M. Iwanicka, M. Góra, E. Kwiatkowska, P. Targowski, e-Journal of NDT (2008), http://www.ndt.net/article/art2008/papers/143Targowski.pdf
25. M. Dupont, K. Hinrichs, in *Proceedings of ICOM-CC 8thTriennial Meeting*, ed. by K. Grimstad, vol. 3 (Getty Conservation Institute, Sydney, 1987), pp. 957–967
26. M. Iwanicka, L. Tymińska-Widmer, B. Rouba, E.A. Kwiatkowska, M. Sylwestrzak, P. Targowski, in *Lasers in the Conservation of Artworks VIII. Proceedings of the International Conference on Lasers in the Conservation of Artworks (Lacona VIII), 21–25 September 2009, Sibiu, Romania*, ed. by R. Radvan, J.F. Asmus, M. Castillejo, P. Pouli, A. Nevin (CRC Press/Taylor & Francis, London, 2011), pp. 209–214
27. P. Targowski, P. Karaszkiewicz, B.J. Rouba, D. Markowski, L. Tymińska-Widmer, M. Iwanicka, E.A. Kwiatkowska, M. Sylwestrzak, in *The Art of Collaboration: Stained-Glass Conservation in the Twenty-First Century*, ed. by M.B. Shepard, L. Pilosi, S. Strobl (Brepols, Turnhout, 2010), pp. 127–134, Vol. Corpus Vitrearum USA, Occasional Papers II
28. M. Iwanicka, E.A. Kwiatkowska, M. Sylwestrzak, P. Targowski, Proc. SPIE **8084**, 80840G (2011)
29. S. J. Lawman, Ph.D. Thesis, Nottingham Trent University, 2011
30. S. Lawman, H. Liang, Appl. Opt. **50**, 6039 (2011)
31. P. Targowski, M. Góra, M. Wojtkowski, Las. Chem. (2006). doi:10.1155/2006/35373
32. P. Targowski, B. Rouba, M. Góra, L. Tymińska-Widmer, J. Marczak, A. Kowalczyk, Appl. Phys. A **92**, 1 (2008)
33. M. Hughes, Ph.D. Thesis, University of Kent, 2010
34. C.G. Pantano, J.P. Hamilton, Rivista della Stazione Sperimentale dell Vetro **30**, 81 (2000)
35. J. Kunicki-Goldfinger, P. Targowski, M. Góra, P. Karaszkiewicz, P. Dzierżanowski, Stud. Conserv. **54**, 117 (2009)
36. G. Latour, J.P. Echard, B. Soulier, I. Emond, S. Vaiedelich, M. Elias, Appl. Opt. **48**, 6485 (2009)
37. S. Chang, Y. Mao, C. Flueraru, G. Chang, Opt. Eng. **49**, 063602 (2010)
38. M.-L. Yang, A. M. Winkler, J. Klein, A. Wall, J. K. Barton, In: G. Liu (ed.), *Selected Topics in Optical Coherence Tomography* (InTech, 2012), doi:10.5772/31213. Available from: http://www.intechopen.com/books/selected-topics-in-optical-coherence-tomography/using-optical-coherence-tomography-to-characterize-the-crack-morphology-of-ceramic-glaze-and-jade
39. M.-L. Yang, A.M. Winkler, J.K. Barton, P.B. Vandiver, Archaeometry **51**, 808 (2009)
40. M.-L. Yang, A.M. Winkler, J. Klein, J.K. Barton, Stud. Conserv. **57**, 67 (2012)
41. H. Liang, M. Sax, D. Saunders, M. Tite, J. Archaeol. Sci. **39**, 3683 (2012)
42. M. Góra, M. Pircher, E. Götzinger, T. Bajraszewski, M. Strlic, J. Kolar, C.K. Hitzenberger, P. Targowski, Las. Chem. (2006). doi:10.1155/2006/68679

43. C. Fotakis, D. Anglos, V. Zafiropulos, S. Georgiu, V. Tornari, in *Lasers in the Preservation of Cultural Heritage: Principles and Applications* (CRC Press/Taylor & Francis, Boca Raton, 2007), pp. 53–93
44. V. Detalle, M. Dufour, J.-P. Monchalin, M. Sabsabi, L. St-Onge, U.S. Patent No. 6,873,419 (2005)
45. M.L. Dufour, G. Lamouche, V. Detalle, B. Gauthier, P. Sammut, Insight **47**, 216 (2005)
46. D.G. Papazoglou, V. Papadakis, D. Anglos, J. Anal. Atom. Spectrom. **19**, 483 (2004)
47. M.M. Amaral, M.P. Raele, A.Z. de Freitas, G.S. Zahn, R.E. Samad, N.D. Vieira, L.V.G. Tarelho, Proc. SPIE **7391**, 73910I (2009)
48. E.A. Kwiatkowska, J. Marczak, R. Ostrowski, W. Skrzeczanowski, M. Sylwestrzak, M. Iwanicka, P. Targowski, Proc. SPIE **7391**, 73910J (2009)
49. P. Targowski, E.A. Kwiatkowska, M. Sylwestrzak, J. Marczak, W. Skrzeczanowski, R. Ostrowski, E. Szmit-Naud, M. Iwanicka, in *Lasers in the Conservation of Artworks VIII. Proceedings of the International Conference on Lasers in the Conservation of Artworks (Lacona VIII), 21–25 September 2009, Sibiu, Romania*, ed. by R. Radvan, J.F. Asmus, M. Castillejo, P. Pouli, A. Nevin (CRC Press, Taylor & Francis Group, London, 2011), pp. 143–147
50. J.P. Nemeth, Naval application of laser ablation paint removal technology (Navy Metalworking Center, 2010). Available from: http://db.materialoptions.com/ASETSDefense/SEDB/Related/Qual_Eng_Data/CTC-%20Naval%20Application%20of%20Laser%20Ablation%20Paint%20Removal%20Technology%20-%20Final%20Project%20Report_Final.pdf
51. P. Pouli, A. Selimis, S. Georgiou, C. Fotakis, Acc. Chem. Res. **43**, 771 (2010)
52. M. Góra, A. Rycyk, J. Marczak, P. Targowski, A. Kowalczyk, Proc. SPIE **6429**, 64292V (2007)
53. P. Targowski, R. Ostrowski, J. Marczak, M. Sylwestrzak, E.A. Kwiatkowska, Proc. SPIE **7391**, 739115 (2009)
54. M. Góra, P. Targowski, A. Kowalczyk, J. Marczak, A. Rycyk, in *Lasers in the Conservation of Artworks. Proceedings of the International Conference Lacona VII, Madrid, Spain, 17–21 September 2007*, ed. by M. Castilleo, P. Moreno, M. Oujja, R. Radvan, J. Ruiz (CRC Press/Taylor & Francis, London, 2008), pp. 23–27
55. P. Targowski, M. Góra, J. Marczak, A. Rycyk, B. J. Rouba, SPIE Newsroom, http://spie.org/x34801.xml?ArticleID=x34801. doi:10.1117/2.1200904.1589 (2009)
56. M. Sylwestrzak, M. Szkulmowski, D. Szlag, P. Targowski, Photon. Lett. Poland **2**, 137 (2010)
57. M. Sylwestrzak, D. Szlag, M. Szkulmowski, I. Gorczyńska, D. Bukowska, M. Wojtkowski, P. Targowski, J. Biomed. Opt. **17**, 100502 (2012)
58. K. Zhang, J.U. Kang, Opt. Express **18**, 11772 (2010)
59. P. Targowski, J. Marczak, E.A. Kwiatkowska, M. Sylwestrzak, A. Sarzyński, in *Lasers in the Conservation of Artworks IX. Proceedings of the International Conference on Lasers in the Conservation of Artworks (Lacona IX), 7–10 September 2011, London*, ed. by D. Saunders, M. Strlič, C. Korenberg, N. Luxford, K. Birkhölzer (Archetype Publications, London, 2013), pp. 26–31
60. F. Zöllner, J. Nathan, *Leonardo da Vinci, 1452–1519: The Complete Paintings and Drawings* (Taschen, Köln, 2003)
61. E.R. de la Rie, Stud. Conserv. **17**, 102 (1982)
62. R. Fontana, M.C. Gambino, M. Greco, L. Marras, M. Materazzi, E. Pampaloni, A. Pelagotti, L. Pezzati, P. Poggi, C. Sanapo, Proc. SPIE **5857**, 58570L (2005)

Nondestructive Material Testing Using OCT

83

D. Stifter

Keywords

Optical coherence tomography • Nondestructive testing • Nondestructive evaluation • Technical materials • Non-biomedical applications

83.1 Introduction

The fact that optical coherence tomography (OCT) provides information on internal structures of scattering tissue in a noninvasive way [1] has led to a broad acceptance of OCT for dedicated biomedical imaging and diagnostics applications. Outside the biomedical field, an irreversible alteration of an object under investigation by the characterization method itself is likewise undesirable, especially in the case that such an object has to be further used with its original state maintained. For this purpose, a variety of so-called nondestructive testing methods is nowadays at hand and to a large extent – depending on the required information which has to be extracted from the sample – successfully applied.

In analogy to the *noninvasiveness* of OCT for biomedical applications, there is obviously a huge potential of OCT to add valuable contributions to *nondestructive testing* and *evaluation* (NDT/NDE) of semitransparent, scattering materials with structural features in the micron scale [2]. Especially the following facts render OCT favorable, usually giving fast and immediate results: (i) no preparatory steps are generally needed for the sample prior the investigation; (ii) no coupling media are required as it is the case, e.g., ultrasound testing; (iii) no special safety precautions have to be taken; and (iv) the achievable resolution is not determined by the sample size, e.g., as in X-ray computed tomography (X-CT).

D. Stifter
Center for Surface and Nanoanalytics (ZONA), Johannes Kepler University (JKU) Linz, Linz, Austria
e-mail: david.stifter@jku.at

© Springer International Publishing Switzerland 2015

W. Drexler, J.G. Fujimoto (eds.), *Optical Coherence Tomography*,
DOI 10.1007/978-3-319-06419-2_85

Within this chapter, the promising potential of OCT for applications in NDT outside the biomedical field is highlighted, focusing on the – to date – investigated material systems, the extracted information of structural or functional character, and presenting dedicated application examples of OCT for NDT.

83.2 Materials Suitable for OCT Investigations

Shortly after the introduction of the OCT method itself [1], the potential of OCT for tasks in NDT was already recognized and demonstrated for bulk polymer and fiber-epoxy composite samples [3] as well as for ceramic structures [4]. However, according to the optical nature and working principle of OCT, usually relying on the detection of back-reflected light in the near-infrared spectral region between 800 and 1,550 nm, there are some restrictions imposed by the materials under test, especially for successful subsurface imaging. In contrast to biomedical applications where the number of types of tissues exhibiting distinctively different optical properties is to a certain extent limited, a quite diverse situation can be found for man-made materials and structures, with wide ranges of different refractive indices (e.g., from ~1.4 to 1.55 for most common polymers to higher than 2 for certain ceramics [5] or even above 3.5 or 4 for selected semiconductors like silicon or germanium) and with strongly varying scattering and absorption properties. In addition, technical structures often exhibit smooth surfaces, interfaces, abrupt phase and material boundaries, as, e.g., in multilayer and composite materials, which can give at first rise to distinctive imaging artifacts caused by strong multiple reflections. Furthermore, distortions of the internal sample geometry in dimensional metrology due to variations in the refractive indices (i.e., optical path lengths versus geometrical path lengths) can likewise be experienced. Consequently, it is often beforehand not clear how OCT will perform for a specific imaging and evaluation task, even if similar materials have already been successfully tested. An instructive example is given in Fig. 83.1 where wedges made from different turbid polymer materials that are commonly used in polymer injection molding were imaged by OCT, once at a center wavelength of 840 nm and once at 1,550 nm [2].

All polymer samples of this study exhibited a similar visual appearance (e.g., level of turbidity), and complementary absorbance measurements in reflection geometry in the visible and near-infrared wavelength region between 500 and 2,500 nm also showed no significant differences between the specimens. Nevertheless, they all performed differently when imaged by OCT. In order to determine the overall penetration depth for the two selected wavelength regions, the polymer wedges were imaged by OCTs which were adjusted to the same sensitivity level. The arrows in Fig. 83.1 represent the level of depth where the backside of the sample is still visible, i.e., simulating a void structure in the polymer bulk. The additional arrows in the 1,550 nm images on the left side are marking for comparison the penetration depth measured at 840 nm. Since light absorption by water is usually of no concern for polymer imaging – a fact which holds true for most technical materials – longer wavelengths are in general more favorable for larger

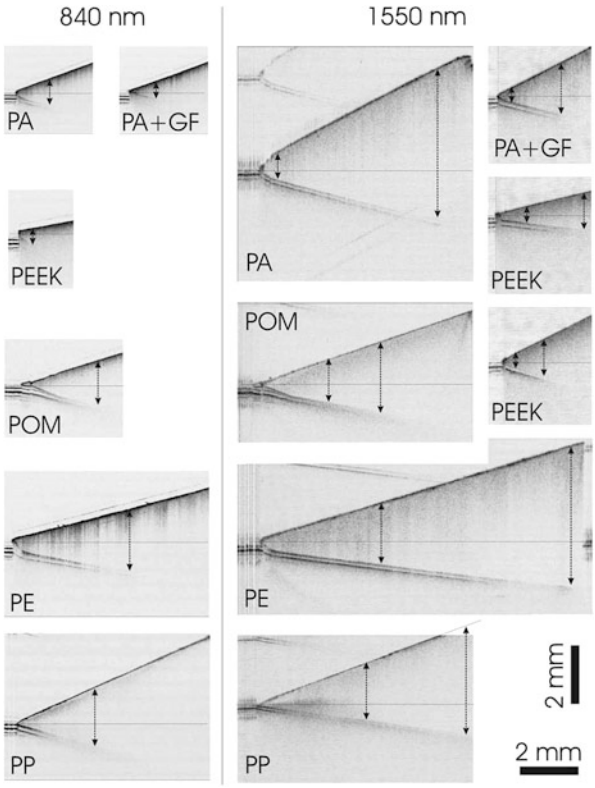

Fig. 83.1 Penetration depth study for various polymer materials, imaged at 840 and 1,550 nm: polyamide (*PA*), polyamide filled with glass fibers (*PA + GF*), polyether ether ketone (*PEEK*), polyoxymethylene (*POM*), polyethylene (*PE*), polypropylene (*PP*) (Reprinted with kind permission from Springer Science + Business Media: Fig. 6 from: D. Stifter, "Beyond biomedicine: a review of alternative applications and developments for optical coherence tomography," Appl. Phys. B, vol. 88, p. 337, © Springer 2007)

imaging depths due to decreased attenuation by scattering [6]. In the example of Fig. 83.1, the scattering behavior is influenced by the different internal morphologies of the polymer samples with crystallites and granular structures of varying length scales. Since the solidification and crystallization behavior of polymer melts is largely dependent on the processing conditions (e.g., temperature, pressure, flow velocity, and shear field gradients in polymer extrusion and injection molding [7]), the situation further complicates, as does the addition of various kinds of fillers (e.g., short glass fibers, talcum, silica, carbon particles, etc.) and pigments to the polymer material, exemplified in Fig. 83.1 for the polyamide (PA) sample filled by 30 wt.% with short glass fibers (GF).

An analogous situation as for the above-presented bulk polymer samples holds true for other material systems. Consequently, for a new envisaged NDT task, a thorough feasibility study for the material or structure of interest will mostly be necessary, although all types of (semi-)transparent media are in principle eligible for OCT imaging. To date, OCT studies have been carried out and reported for a variety of (partly natural) materials, among which can be found:

– Polymers, in the form of bulk material as well as thin films, including paints, organic coatings, layers of adhesives, and bonding agents

– Paper, papyrus, wood, leaves, fruits, and seeds
– Semiconductors
– Metal oxides and corrosion products
– Glass, ceramics, and ceramic glazes
– (Semi-)precious stones and pearls
– ...

The potential applications for OCT multiply when considering composite structures made from the above-listed materials, like glass fiber-reinforced polymer materials with enhanced mechanical properties, micro (opto-)electro-mechanical systems (MEMS, MOEMS) or encapsulated multilayer organic solar cells. A detailed description of already identified applications and results from feasibility studies performed on the above-listed materials and combinations thereof – as reported in literature – is now given in the following.

83.3 Applications of OCT for NDT

In contrast to biomedical OCT imaging, with the diagnostics of retinal diseases being the main driving force for commercial scanners, it has to be stated that no analogous *killer application* could yet be identified for OCT in NDT. However, several material imaging and evaluation studies have been carried out, which already led in some cases even to routine tasks in NDT/NDE with corresponding commercialized OCT scanners and measurement devices.

In this context it is useful to reconsider at first the different types of application areas which take benefit from NDT: the preservation of the original status of a sample is of utmost importance not only in industry, e.g., for the investigation and quality control of final products, but also of products being in an intermediate manufacturing status prior further costly or time-consuming processing steps, most preferably carried out in situ and without introducing additional delay. Likewise, precious or unique objects should also not be altered by the applied investigation method, a task experienced, e.g., in the evaluation of gems and pieces of jewelry, but mostly now emerging in the field of art and cultural heritage conservation [8]. Finally, also for research and development, the nondestructive character of an investigation method is needed, especially if the *same* sample has to be characterized by additional methods in order to learn about complementary properties or if the same sample has to be repeatedly measured in case of time-dependent investigations, like ageing and degradation studies. On shorter time scales, investigations which also can be of destructive nature, as, e.g., mechanical tests, take benefit from continuous nondestructive monitoring in order to study the performance of a single specimen. Summarizing, in the following general situations, NDT methods are indispensable, namely, for:

- (Industrial) quality control of final products (also online)
- Guidance of the production process itself (preferably in situ or online after crucial processing/manufacturing steps), including:

  - Full, 100 % quality control
  - Investigation of small representative areas from each sample
  - Batch inspection by taking samples (off line, on site)
- Evaluation of precious or unique samples like:
  - Precious stones, gems, and pearls (for classification purposes)
  - Art objects for archaeometry, conservation, and detection of forgery
  - Documents, banknotes, etc., for applications concerning security
- Research and development
  - Nondestructive material characterization before or during complementary investigations (e.g., fracture tests), leading also to
  - Repeated measurements on the same sample over time, and including
  - Studies of physical phenomena which are not directly accessible or easily influenced (e.g., flow behavior of liquids)

For the above-listed points, several instructive examples of OCT being successfully applied have been reported and are laid out in the next sections. They are listed according to the category of information obtained from the individual measurements, starting with the evaluation of the pure surface structure, proceeding to thickness measurements of layered systems, to imaging of internal 3D structures and finally leading to the determination of functional information.

83.3.1 Surface Metrology

The principle of white light or low-coherence interferometry (WLI, LCI) was already used in the 1980s for remote sensing of distances in an unambiguous way, e.g., in a point-wise sensing style like standard OCT with fiber optics [9] or by using area sensors for parallel detection [10]. The latter technique, being called coherence probe (CP) imaging, uses a Linnik interferometer in a basically similar setup as full-field (FF) OCT [11] and was immediately introduced for the measurement of surface topographies, with fully automated metrology systems for the inspection of line widths and defects of ***resist structures*** on ***Si wafers*** [12]. Further developments focusing on the profilometry capabilities of this technique soon followed, including a coherence scanning microscope in Michelson configuration [13] or a Mirau correlation microscope [14] with increased stability against vibrations and providing amplitude and phase information for accurate surface measurements as demonstrated on photoresist trenches for ***integrated circuits***. Interestingly, the sectioning capabilities for such CP or correlation microscopes when using medium-to-high numerical aperture (NA) objectives do not solely rely on the temporal coherence properties of the light source (which is mostly also spatially incoherent) but also on the fact that interference can only occur for regions on the sample where the curvature of the wave front matches (correlates with) the one of the reference field [15]. Only, when using such full-field detectors for thicker object structures, the noninterference background image is – compared to conventional OCT – not sufficiently suppressed, which can lead to detector saturation and decreased sensitivity. However, these techniques were most successfully further

developed for the investigation of surfaces, leading to, e.g., scanning white light interferometers (SWLI) which are nowadays routinely used for topography measurements, providing even subnanometer precision on smooth homogenous surfaces by an evaluation of the phase or phase slope information [16]. Equally, dedicated profilometers for rough surfaces have early been reported [17] and applied, e.g., as so-called coherence radar on high aspect ratio features (up to 2 cm deep bore holes with 5 mm in diameter) of ***machined industrial parts*** [18].

Simultaneously to the full-field approaches described above, the point-wise detection scheme of conventional OCT, generally using fiber optics together with spatially coherent sources and exhibiting shot-noise-limited performance, emerged [1]. Here, the detection of weak backscattering features, in contrast to the evaluation of the strongly reflecting air/surface interface, was of prime interest, inspired by the optical low-coherence and coherence-domain reflectometry (OLCR, OCDR) techniques which were originally introduced for the characterization of ***optical waveguide components*** [19, 20] and already used for depth measurements of trench structures in ***memory chips*** [21]. Since both approaches, i.e., full-field CPM vs. conventional point-wise scanning OCT, have their same origin in LCI, OCT is repeatedly subject of surface evaluation studies including ***surface shape*** [22] and ***roughness*** measurements [23]. In this context also efforts in, e.g., providing validated procedures for reliable surface characterization with OCT, which are conform and linked to recognized standards, are essential [24]. However, one has to mention that OCT might not always be the first choice for such surface metrology tasks: especially for easy accessible surfaces with moderately inclined slopes and features, OCT has to compete with other dedicated commercialized surface metrology devices based on techniques like confocal microscopy [25], the above-introduced SWLI, wavelength scanning interferometry (a swept-source (SS) variant of WLI in the Fourier domain (FD)) [26], digital holography [27], or chromatic confocal microscopy (CCM) [28], a principle which relies on chromatic length aberration of specialized lenses to measure distances and results in simple, robust, and cost-effective sensors. These techniques were even further enhanced: e.g., CCM can be combined with the principle of spectral interferometry (SI) – similar to spectral-domain (SD) OCT – to form a hybrid chromatic confocal spectral interferometry (CCSI) sensor for surface metrology of uncooperative surfaces, taking profit from the interferometric gain (like OCT) and from the evaluation of the phase [28]. Nevertheless, OCT systems and dedicated OCT-like sensors were commercialized and are increasingly offered for surface metrology (although such commercial devices are sometimes even not referring to OCT but are just simply called interferometric or topography sensors), with advantageous performance especially for the evaluation of ***high aspect ratio structures***, ***specularly*** or very ***weak reflecting slopes***, and – by using fiber-optic sensor tips or thin needles – for areas which are hard to reach, like the ***interior of bore holes***, ***tubes***, ***and cylinders***.

An example for the topography evaluation of high aspect ratio features is given in Fig. 83.2, with laser-drilled holes, exhibiting an average depth of 1 mm and an average width at mid-depth of 100 μm, in a carbon fiber-reinforced carbon (CFC) composite structure. Such structures are used in the so-called divertor of nuclear

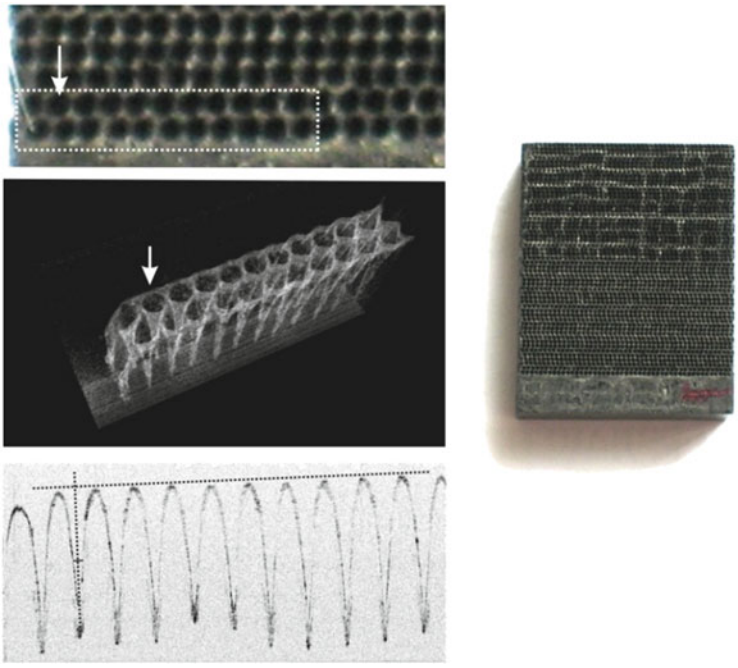

Fig. 83.2 Laser-drilled holes with high aspect ratio in a CFC structure evaluated by OCT. *Top* and *right*: photograph of sample and enlarged surface area indicating the reconstructed volume measured by OCT (*middle*). *Bottom*: cross-section through one row of holes, with an average depth of 1 mm and an average width of 100 µm at mid-depth. (OCT software by M. Wurm, UAR GmbH, Austria), (Sample courtesy of Plansee SE, Austria)

fusion reactors and need efficient cooling, realized by interlocking these structures to a layer of copper. Due to the rough nature of the surface in the inside of the holes (partly caused by exposed fiber ends during machining), the strong inclination, and increased light absorption by carbon, conventional surface metrology tools (like SWLI and confocal microscopy) failed. In contrast, the high sensitivity of OCT ensures that the topography can successfully be traced down to the bottom of the holes. Comparative dimensional measurements on polished sections as well as by X-CT have proven the accuracy of OCT and were leading to a dedicated OCT-based inspection system with automated image evaluation [29].

Further reported examples for surface profilometry with OCT include the shape determination for grinding ***optical lenses*** [30, 31] or surface roughness measurements on ***paper*** [32] and pharmaceutical ***tablets*** [33]. OCT was also used to evaluate the response of surface cracks on an artistic ***painting*** as well as deformations of the canvas during humidity changes [34]. In addition to the examination of ***silicon V-grooves*** [35], ***MEMS*** structures [36] and the determination of shape and deformation of ***semiconductor wafers*** [37], real-time reflectivity and topography measurements of ***integrated circuit*** (IC) structures with FF-OCT [38] and topography measurements of MEMS and ICs from phase maps with SS-FF-OCT [39] were reported.

Modified OCT techniques were used, e.g., to determine the topography of metallic surfaces, like ***ball grid arrays*** or ***electrodes*** with a so-called parallel OCT system [40, 41] where each pixel of the 2D detector array has an own demodulation circuit, or to quantitatively reconstruct surface profiles (like those of ***microlens arrays***) by differential phase-contrast OCT [42].

Finally, it shall be mentioned that the high sensitivity, robustness, and rather long-working distance of such OCT-based sensors and systems render them very suitable for online monitoring during machining/processing as well as for the quality control of moving parts. In the context to the above-presented example of Fig. 83.2, in situ monitoring of ***laser drilling***, ***structuring***, and ***machining*** of materials like ***steel, ceramics***, ***glass***, or ***polymers*** [43–46] even with automatic real-time guidance [47] was reported or – in the field of art diagnostics – the in situ monitoring of laser ablation for removing aged ***varnish layers*** from paintings [48]. Further applications also include OCT/LCI measurements simultaneously performed with laser-induced breakdown spectroscopy (LIBS) for complementary elemental analysis [49, 50]. With respect to surfaces, which are not easily accessible, metering the level of ***liquids*** (e.g., of molten glass in glass melting ovens [51]) or gauging in-line hot float glass [52] shall be mentioned, as well as a study for the in situ determination of the roughness of chemical mechanical ***polishing pads*** for semiconductor wafers which are covered by a wet and slurry containing layer [53]. The last example leads to the application of OCT to provide a profile of a buried/coated surface, as demonstrated for the dynamic monitoring of the drying process of varnish on paint in order to study the formation of surface roughness [54], for analyzing (varnish-covered) imprints of tools which were used for ***gold punch decorations*** as found, e.g., on Renaissance panel paintings [55], as well as for buried topographies of ***printed electronics*** (e.g., radio-frequency antenna) in a comparative study with topography measurements by WLI and contact profilometry [56].

83.3.2 Thickness Evaluation of Layers and Thin Films

The acquisition of profiles from buried surfaces immediately leads to the determination of layer and film thicknesses, a task where OCT has equally to compete with a variety of other optical techniques like with the above-introduced chromatic confocal principle or with (spectroscopic) reflectometry or ellipsometry [57], which are routinely used, e.g., in the semiconductor industry for layers ranging from several hundreds of micron down to (sub-)monolayers. As to the original LCI techniques, one of the first motivation was to use a Michelson interferometer as a remote gauge for distance measurements between two reflecting surfaces [58]. Thickness measurements of ***dielectric layers*** on metal surface by coherence scanning microscopy followed [13], which naturally lead to the extension of WLI for the characterization of layered structures [59], as nowadays routinely used and exemplified, e.g., with SWLI for the evaluation of transparent thin films in ***MEMS*** and ***MOEMS devices*** [60]. In this context, it has to be also noted that an abundance of

variations and modification of the abovementioned LCI and OCT-like methods for surface profilometry and thickness metrology exists. One example is spectrally resolved line-field interferometry, for which a 2D detector as in CPM or FF-OCT is used, but the light is spectrally dispersed in one direction on the detector chip (like in spectral-domain OCT (SD-OCT) using 1D cameras) and a line from the sample is imaged along the other axis. In such a way 1D thickness profiles of transparent thin films on patterned surfaces can be acquired in one shot [61], as it was demonstrated before for pure surface metrology [62, 63].

From these examples, it follows that conventional OCT can also be used as a distance gauge for plane-parallel surfaces/interfaces delimiting transparent and non-scattering materials. In such cases one has to cope with artifacts arising from, e.g., multiple interference [64]; however, the determination of the thickness of single ***semiconductor wafers*** or ***multilayer semiconductor structures***, as demonstrated in [65] for wide band gap materials as GaAsP/GaP heterostructures, is quite straightforward. Also wafers of silicon (with a band gap of ∼1.1 eV) are equally transparent [66] and suitable for thickness measurements when using the 1,300 nm and 1,500 nm wavelength range. Such evaluations are especially important in the context of wafer back grinding and etching to ensure the required uniformity in thickness together with a characterization in terms of flatness and bow/warp, parameters which have to be optimized for a successful 3D integration of (opto-) electronic devices by wafer stacking.

In order to obtain the true geometrical thickness of layers, the refractive index has to be known, as it is usually the case for standard semiconductor materials. If an unknown overlayer is situated on top of a nominally flat substrate (e.g., on a polished wafer surface) and exhibits thickness variations or lateral structuring, the determination of the refractive index is also easily accomplished by evaluating the deviation of the imaged substrate profile from a straight line [67, 68]. In general, however, focus tracking can be used to determine simultaneously with the thickness also the (group) refractive index [69, 70] or phase and group indices, and thickness [71]. The hardening process of UV-cured epoxy was monitored in such a way by detecting variations of the refractive index [72]. Finally, refractive index profiles of graded refractive index rod lens could be determined by iterative fitting of the optical path length calculated by ray tracing [73].

In addition to the examples involving thickness measurements given above, the full potential of OCT is exploited for samples where the type and strength of the reflectivity of the individual surface and interfaces strongly differ, e.g., for a smooth layer on a rough surface or a weakly reflecting coating on top of a mirror-like metallic surface, as well as for complex multilayer structures, and – most important – for layers with embedded scattering features which can obscure the underlying interfaces. In these cases, the conventional measurement approach using SWLI, CCM, confocal microscopy, and related techniques mostly fails and calls for the high sensitivity and depth discrimination capability of OCT. The evaluation of complex and not fully transparent ***multilayer polymer foils*** is consequently one example, where OCT can efficiently contribute, as shown in the example of Fig. 83.3 by using an ultrahigh resolution (UHR) OCT

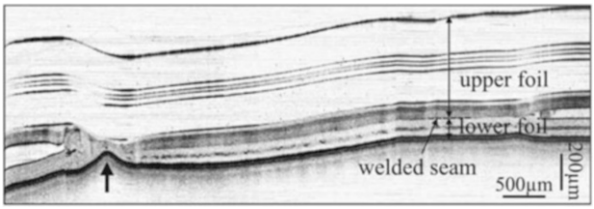

Fig. 83.3 Cross-section of a welded structure from two polymer multilayer foils for thickness evaluation, with a thermally damaged region (indicated by *arrow*) (Reprinted from: K. Wiesauer, M. Pircher, E. Götzinger, S. Bauer, R. Engelke, G. Ahrens, G. Grützner, C. Hitzenberger, and D. Stifter, "En-face scanning optical coherence tomography with ultra-high resolution for material investigation," Opt. Express, vol. 13, p. 1015, 2005, with permission from the Optical Society of America © 2005)

for imaging in the 800 nm wavelength range [67]. The multilayer structure itself consists of two welded foils with a total of 12 individual, partly scattering layers. These individual layers define the mechanical properties and partly represent different gas diffusion barriers, as required for modified atmosphere packaging in the food industry.

With the advent of high speed acquisition by FD-OCT, on-line thickness measurements of such multilayer foils during the production, e.g., by blow film extrusion, can successfully be performed to control the correct dimensions of each layer, by simply using a static point sensor and monitoring a 1D profile of the foil, which is normally moving at a velocity of several tens of meters per minute. Even solutions to cope with the adverse conditions during production, like fluttering of the foils, have been developed: ambiguous mirror terms when the sample crosses the zero optical path delay can be suppressed by, e.g., tailoring the sensitivity profile in SD-OCT with a hardware-based approach and without the need of additional data post-processing [74].

As to the characterization of other layered 2D material systems, the thickness measurement of ***coatings*** on high-quality glossy photo-paper has been shown as well as that – in some cases – imaging through the entire thickness range of some kinds of ***paper sheets*** is possible [75]. However, typically the imaging depth is limited to tens of micrometers for ordinary paper, and a clearing agent (like benzyl alcohol) is needed to detect the backside due to the high scattering properties of the fiber network and the embedded fillers [76].

A similar role of the glossy top coating on paper (beside influencing the printability) plays the ***varnish*** layer on artistic paintings by enhancing the visual appearance and color saturation due to reduced diffuse scattering from the rough paint surface and increased specular reflections (away from the observer's eye) from the smoother varnish surface. A dedicated task in art conservation is the removal of aged varnish, as already pointed out in the above section. Thus, precise knowledge of the thickness as well as information on multiple layers of varnish being potentially present is crucial for a gentle restoration procedure. Similarly to the evaluation of thicknesses and structure of varnish layers [77–80], also ***paint*** layers themselves are

of interest. However, they usually show quite high absorption and decreased penetration caused by scattering, especially in the visible wavelength range. Imaging at longer wavelengths seems preferable, as proven, e.g., in a comparative study using a 820 nm and 1,550 nm OCT system for a variety of different commercially available artist oil paints [81]. In this context, it shall be noted that also the thickness determination of industrial paint layers and multilayer paint systems is a challenging task for OCT [82] (even when confocally enhancing the OCT technique [83]), since such paint structures are usually designed to achieve a high level of opaqueness to efficiently hide the underlying substrate. The addition of diverse, highly scattering filler materials (like, e.g., SiO_2 particles acting as matting agent or wax particles as forming aids) beside the standard pigments render the situation worse, even for thin paint layer thicknesses of around 10–20 μm. Therefore, usually only topmost and rather transparent clear coatings can be monitored, although approaches, e.g., speckle noise reduction by angular compounding, were introduced in order to improve the detection of interfaces of paint layers [84].

Further public reports on thickness measurements include the evaluation of thin (∼1–3 μm) encapsulation/protection layers for ***printed organic electronics***, which are needed to avoid degradation of the devices by exposure to the ambient (oxygen, humidity) [56, 85], the evaluation of roll-to-roll coated polymer ***solar cell*** structures [86]), or of paint layers on ***stained glass*** [79]. Thickness measurements were also performed on glass substrates covered by indium tin oxide (ITO) ***conducting*** **glass** (together with the distribution of refractive index and transmission coefficient) [87] as well as quantitative phase imaging to determine the thickness of structured 300 nm ITO films [88]. Evaluation of thicknesses and defects of ***liquid crystal display*** (LCD) multilayer structures were equally reported [89], as well as the determination of inner gap distances of individual red-green-blue (RGB) LCD pixels, together with an evaluation of spectral information (absorbance of R,G,B pixels), defects, and the cover glass thickness [90].

Other examples of industrially relevant applications for OCT or OCT-like sensors in thickness evaluation encompass the characterization of loudspeaker ***membranes***, of ***skins*** for dry-aged sausages, or of ***adhesive layers*** between stacked sensor structures deposited on glass substrates as well as of thin polymer layers deposited on ***drug-eluting stents***.

On-axis thickness evaluations of multiple ***optical elements*** and whole optical systems were reported [91], as well as a fully developed application for automated ***contact lens*** metrology: the thickness and prism, which is the maximum difference in thickness over the full azimuth at a fixed distance from the edge of the lens, is automatically measured and evaluated using refraction correction and image processing/segmentation [92].

Besides rather planar structures, the evaluation of coating thicknesses and diameter of ***optical fibers*** with FD-OCT was demonstrated [93]. Coating thickness measurements of ***pharmaceutical tablets*** (deposited, e.g., by drum spray coating) prove to be a further promising application [94–96] for OCT and to be more accurate than indirect methods, like measuring the gain in weight or diameter of the tablets. A similar geometry is experienced when determining the thickness of

the so-called nacre layer of ***pearls*** produced by oysters around an artificially inserted nucleus, as demonstrated in [97, 98], leading to automated thickness evaluation [99] and dedicated commercial systems for this task.

83.3.3 Imaging of Inner Structures

Besides focusing solely on the surface and on the thickness of covering layers, imaging of the interior of scattering materials is more in-line with the original motivation of OCT and used in NDT to evaluate and verify inner structures and geometries, which can be introduced in an intended way or represent flaws and defects. Naturally, when measuring the thickness of overlaying (multi-)layers, the simultaneous detection of such embedded features is at hand (and also mentioned in nearly all references from the above section), including defects in ***ITO glass*** [87], structures and defects in ***LCD devices*** [89, 90], bad contact areas between protective coatings and ***printed electronics*** substrates [85], or delaminated and misfolded regions of ***multilayer foil*** structures [100]. Real-time imaging of chip-type ***light-emitting devices*** (LEDs) shall also be mentioned, featuring inspection tasks with respect to correct wire interconnections as well as with respect to the volume and status of the included fluorophore material [101].

In context to the example of ***pearl*** investigations of the above section, hierarchical structures built during the nacre formation [98] and a variety of additional aspects could be determined by means of depth-resolved OCT imaging in order to classify pearls, namely, the distinction between bead-nucleated and non-bead-nucleated ones as well as the identification of the type of nucleus used in the pearl production (e.g., freshwater shell or giant clam nuclei) [102]. These studies were further driven and used to distinguish between different types of pearls and pearl treatments (like bleaching, buffing, coating, filling (with epoxy) or dyeing), also by combining OCT with simultaneously performed laser-induced fluorescence (LIF) measurements [103] as exemplified in Fig. 83.4: besides the nacre thickness, the fine structure of the layer as well as the inner features of the nucleus can be determined and used together with the characteristic spectral fingerprint from LIF for nondestructive pearl evaluation.

Staying with the examples of precious or unique specimens by OCT, the evaluation of ***jade*** objects shall be treated: originally introduced to study the subsurface structure in order to distinguish between naturally whitened and artificially treated ones (i.e., by burning) to detect forgery of ancient jade objects [104], further studies followed, especially in hindsight for the classification of diverse types of jade by evaluating the texture and – due to the high penetration depth of several millimeters – to give a guide for artistic carving (i.e., to avoid internal cracks and non-jade inclusions) [105]. Crack structures (linear ones which are open to the air versus cloudy clusters and networks sealed off from the surface) were further investigated for jade materials and classified in detail (inclination, depth, crack initiation sites, etc.) [106]. In the same study, the investigations were also extended towards the characterization of crack morphologies in (ancient) ***ceramic***

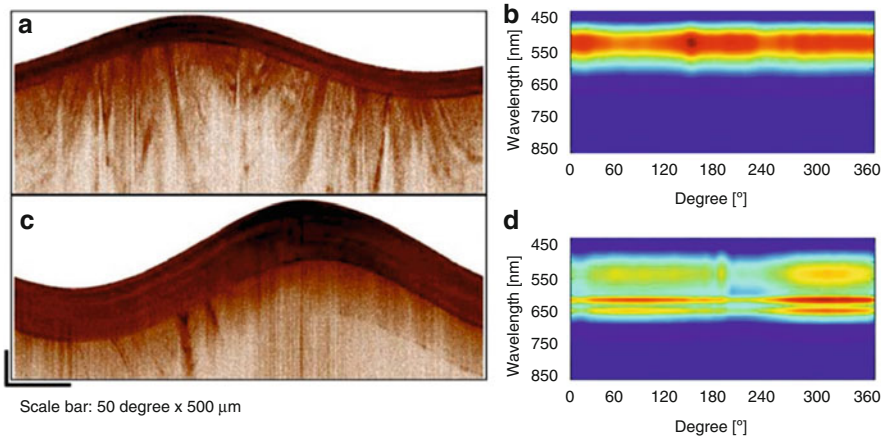

Fig. 83.4 OCT cross-sections (azimuthal scans) of an Akoya (**a**) and Tahitian (**c**) pearl. Corresponding LIF spectra (**b**, **d**) of the pearls simultaneously measured during OCT acquisition (Reprinted after: M. J. Ju, S. J. Lee, Y. Kim, J. G. Shin, H. Y. Kim, Y. Lim, Y. Yasuno, and B. H. Lee, "Multimodal analysis of pearls and pearl treatments by using optical coherence tomography and fluorescence spectroscopy," Opt. Express, vol. 19, p. 6420, 2011, with permission from the Optical Society of America © 2011)

glaze layers. In general, investigations of glaze layers were among the first applications for art diagnosis [34], and especially by studying the subsurface structure, as performed, e.g., in detail on ancient Egyptian faience [107] or Chinese glazes [108], OCT can help to identify the type of ceramics and provide valuable insight to the production techniques formerly used. Similarly, art conservation studies of ***historic glass***, especially for the imaging of corrosion layers on stained glass or the diagnosis for crizzling (i.e., a network of fine cracking caused by an imbalance of the ingredients and reducing the transparency), have been performed [109]. But not only for ancient glasses has OCT proved to be a promising NDT tool: the investigation of laser-induced damage sites in costly large-aperture ***optical components*** has been suggested [110] which could be used in the future to monitor post-processing procedures for damage mitigation [111]. Besides imaging unwanted subsurface features (like cracks and voids induced by laser damage), the verification of intently introduced structures is of interest, as shown for femtosecond laser structuring of ***fused silica*** [112] and ***glass*** with, e.g., an embedded laser-written waveguide coupler [113]. In case that data is written inside a material, OCT can be used for reliable ***data retrieval***, as, e.g., demonstrated with FF-OCT on 3D laser-structured sol-gels [114] or for multilayer optical discs with OCDR [115].

Bulk ***ceramic*** parts and ceramic layers are widely used, e.g., for high-strength hybrid bearings or as thermal barrier coatings protecting blades in gas turbine engines. However, the performance of these materials is crucially dependent on surface and subsurface defects, like cracks in the material itself or delaminations between ceramic layer and substrate, with an early study for subsurface detection of cracks in such scattering ceramic materials, like ***silicon nitride*** given in [4].

The evaluation of layered structures in piezoelectric transducer (***PZT***) composite ceramics and defects in ***silicon carbide*** followed [5, 116] with a detailed study of the geometry of so-called Hertzian cracks in silicon nitride balls as used for bearings [117]. In this context, also a comparative study for optical NDT methods (with confocal microscopy and laser backscatter measurements) on subsurface flaws in silicon nitride ceramics was performed [118]. However, one has to state that due to the high scattering nature of such ceramic materials, the imaging depth is significantly restricted: as an example ***thermal barrier coatings*** (e.g., yttria-stabilized zirconia (YSZ) coatings for gas turbine engines) were evaluated with OCT to find a new inspection method for monitoring their condition and predicting failure (i.e., spallation). Imaging with wavelengths below 1 μm resulted in penetration depths of less than 300 μm but only for electron beam physical vapor deposition (EB-PVD) coatings. In case of air plasma-sprayed coatings [119], which exhibit a far more scattering structure than the columnar one of EB-PVD, the imaging depth is further reduced [120]. Similarly, a limited penetration depth around 260 μm was found even for the 1.3 μm spectral range when imaging ***alumina***-based ceramics which are used, e.g., as inert container material for microfluidic structures: the geometry of embedded channels, cavities, the position of metal stripes (electrodes) and again the detection of defects as well as the thickness determination of covering layers and roughness were the origin of interest in these studies [121, 122]. Additionally, Monte Carlo simulations were performed to predict the performance of OCT for depth-resolved imaging depending upon the optical/scattering parameters of these materials. Finally, in the context of ceramic materials, the evaluation of domain boundaries in ***periodically poled ferroelectrics*** shall be mentioned: the (unwanted) refractive index changes near the anti-parallel domain walls, which are in the order of 10^{-4}, could successfully be traced [123].

Regarding pronounced scattering, the multiple interfaces between fibers and air or between fibers and embedded fillers play a similar role as the grainy and porous structure of most ceramic materials presented above. Consequently, structural imaging of fibrous networks like ***paper*** is also for OCT a challenging task, as already seen for the thickness measurements presented in the prior section. Nevertheless, useful information can be extracted by, e.g., studying larger-scale paper simulation networks; insight on the filler content can be obtained by evaluating the slope of the backscattered depth profile signal [76]; or the degree of paper porosity can be deduced from OCT measurements when compared with Monte Carlo simulations [124]. Similar challenges in coping with scattering have to be met for the characterization of, e.g., electro-spun ***polymer fiber web*** structures [125]. However, when transparent fiber structures are embedded in a homogenous medium, OCT imaging with penetration depths of even several millimeters is easily accomplished (especially at wavelengths around 1,550 nm [126]), with ***glass fiber-reinforced polymer*** (GFRP) composites as prominent examples shown in Fig. 83.5: novel, knitted glass fiber fabrics embedded in an epoxy matrix and exhibiting improved mechanical properties were investigated by ultrahigh resolution (UHR) OCT [127]. In contrast, for ***carbon fiber composites*** (CFCs), usually

Fig. 83.5 3D data sets of knitted GFRP structures (scan areas: (**a**, **b**) 5 × 5 mm^2, (**c**) 3 × 3 mm^2; thickness of displayed stacks: 300 μm) (Reprinted from Comp. Sci. Technol. vol. 67, p. 3051, 2007, K. Wiesauer, M. Pircher, E. Götzinger, C. K. Hitzenberger, R. Oster, and D. Stifter, "Investigation of glass–fibre reinforced polymers by polarisation-sensitive, ultra-high resolution optical coherence tomography: Internal structures, defects and stress", with permission from Elsevier © 2007)

only the surface structure can be evaluated due to the strong absorption of the fibers [100], which is also valid, e.g., for ***carbon nanotubes*** (CNTs) as filler materials in epoxy resin, as shown in a recent study to clarify the effect of plasma treatment on the dispersion of the CNTs in the matrix [128].

Depth-resolved imaging tasks in material research for OCT in the context of the evaluation of GFRPs can be found for the prediction of mechanical properties by acquiring the internal structure but are also concerned with the detection and classification of defects like cracks, kink bands, fiber matrix de-bonding, voids, dry spots, and large-scale delaminated areas [129], as also shown in comparison with other NDT methods like X-CT and confocal microscopy [130]. Equally, the permeability of the fiber structure for infiltration with the liquid epoxy matrix material was predicted by image-processed OCT cross-sections [131]. Concerning the visibility of the glass fiber structure, it has to be noted that there is improved contrast when rather low-refractive-index matrix materials are used [132] and that high resolution or even better UHR-imaging is of advantage when not only whole fiber bundles but individual fibers should be resolved [127]. In the case of short ***fiber-filled polymer composites***, resolving the individual fiber pieces is essential for the determination of the fiber orientation which influences the isotropy of mechanical properties: by advanced image processing algorithms, the fiber orientation was automatically deduced from UHR-FF-OCT images and verified with micro X-CT [133]. Other types of polymer composites are equally promising for OCT imaging due to their translucent nature, with one example of OCT being used to study thermal degradation effects in ***microsphere filled polymers*** [134]. Another task in the development of novel polymer materials, which have to meet increasing performance requirements, e.g., for future automotive applications, is the evaluation of the distribution of different polymer phases in ***polymer blends***, as shown for polypropylene-rubber blends with UHR-OCT, which gave even superior contrast than synchrotron phase-contrast CT [100]. Naturally, when pure ***bulk polymers*** without any additional inclusions are present (see also Fig. 83.1), OCT is very promising for the imaging of the structure of whole injection-molded parts [126], of co-extruded polymer panels [100], or of polymer foams [67].

As example for natural composites, ***wooden specimens*** are worth to be mentioned, with an instructive study given in [135] where the structure of the wood fibers was successfully imaged with a FF-OCT for an eighteenth-century violin below (transparent) ground paint and varnish layers. This application leads us further to the evaluation of other natural materials like the detection of subsurface features in melon ***seeds*** hinting at a virus disease [136], imaging of major structures within tomato seeds [137], or hull thickness determination of lupin seeds by OCT as a novel screening method to classify different genotypes with respect to the de-hulling abilities or nutritional aspects [138]. To study selected aspects of ***food*** can be helpful for quality control (screening of internal defects and rots in onion bulbs [139]) as well as for food engineering and storage, with the evaluation of the microstructure of ***cereals*** (swelling and rehydration behavior when exposed to liquids) and the investigation of lenticels (i.e., pores for gas exchange) and wax layer of ***apples*** as recently introduced examples [140]. Finally, ***protein crystals*** were imaged and the structure compared to those of salt crystals in order to facilitate automated sorting in the future [141].

The successful detection of embedded and hidden structures is also of prime interest with respect to ***security applications***. In order to verify the authenticity of paper representing a certain value (e.g., money, checks, tickets), the reliable identification of characteristic features is essential, as it was done for identifying counterfeit bank notes by retrieving the internal structure of security cash holograms [142]. Likewise, the imaging of security threads embedded in paper has been proven [143] and was developed further towards fast and automatic detection for a transportation speed of the documents up to 1 m/s [144]. In this context, a simple, handheld, and manually operated device was also presented, which enables the detection of visually hidden 2D security features (e.g., a digital image/emblem placed behind a light-scattering medium) [145]. This application is very close to the one involving the evaluation of ***artistic underdrawings*** in paintings (i.e., preliminary sketches of the painting by the artist). This task can be successfully accomplished using OCT with higher contrast and better detail visibility than conventional imaging with an IR camera [78]. An example for this application is given in Fig. 83.6 in which summed voxel projections of the region below the paint layers clearly unveil the underdrawing below the paint [55].

At the end of this section, OCT imaging of structures within ***liquid*** and ***gaseous phases*** are given: applications in this area include the evaluation of vapor bubble formation during laser ablation with ultrahigh speed OCT [146] or the microscopic investigation of the nucleation process of vapor bubbles on heated surfaces (with respect to contact angle, bubble diameter, base diameter) within boiling liquids [147]. Furthermore, the crystallization process of polymer melts in a slit die of an extruder was monitored in situ [148], as well as flow patterns within single microdroplets (seeded with scattering particles) in electrowetting-based microfluidic devices [149], or the flow behavior of fluids within 3D microfluidic mixing structures [150].

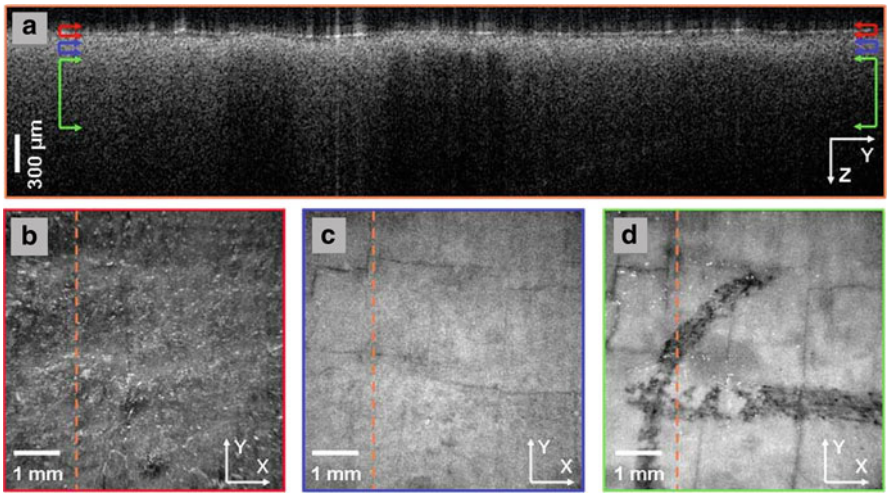

Fig. 83.6 OCT images of underdrawing features in an artistic painting. (**a**) single cross-section with indicated depth regions for the summed voxel projections in (**b**, **c**, and **d**). (**b**): summed voxel projection en face image of varnish layer. **c**: summed voxel projection en face image of paint layer. (**d**): summed voxel projection en face image of underdrawing layer (Reprinted from: D. C. Adler, J. Stenger, I. Gorczynska, H. Lie, T. Hensick, R. Spronk, S. Wolohojian, N. Khandekar, J. Y. Jiang, S. Barry, A. E. Cable, R. Huber, and J. G. Fujimoto, "Comparison of three-dimensional optical coherence tomography and high resolution photography for art conservation studies," Opt. Express, vol. 15, p. 15972, 2007, with permission of the Havard Art Museum and the Optical Society of America © 2007)

83.3.4 Modified Contrast and Functional Material Imaging

All information obtained by OCT in the application examples from the above section is in principle of structural nature and originating from relative intensity variations of light back-reflected from spatially separated features. However, already in conventional 2D microscopy different imaging modes have been developed, which allow highlighting specific aspects and extracting additional information from the imaged structures by, e.g., ***modifying the contrast***. In this context, differential phase-contrast microscopy shall be mentioned which gives enhanced contrast in conventional microscopy for transparent, weakly scattering samples and which has been used in combination with OCT to reconstruct profiles and path length distributions within, e.g., microlens arrays [42]. Another example for enhancing contrast of nearly transparent samples in microscopy is dark-field (DF) imaging, which could also be realized for point scanning optical coherence microscopy (OCM) [151]. Likewise, point defects were detected in dielectric multilayer coatings with a FF-OCM variant by measuring at an increased oblique angle to avoid the direct specular back-reflection of the layers (i.e., DF imaging) [152]. Especially when regarding FF-OCM, the whole concept of optical image filtering in the Fourier plane (FP) can even be transferred to the interferometric detection approach

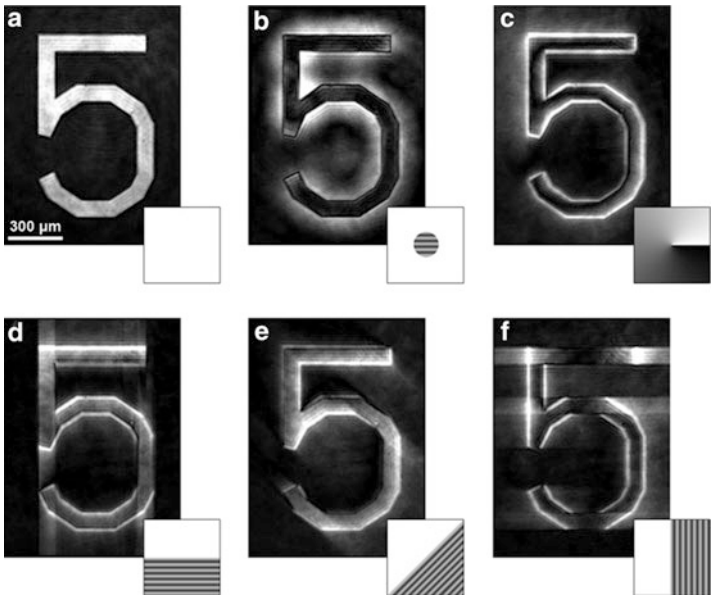

Fig. 83.7 FF-OCM en face images of a test figure taken (**a**) in the bright-field mode, (**b**) dark-field mode, (**c**) with spiral phase contrast, (**d**–**f**) with Schlieren contrast in different directions. The small images in the *lower right* corners represent the (gray-scale encoded) phase delay introduced by the SLM in the FP (Reprinted from: S. E. Schausberger, B. Heise, C. Maurer, S. Bernet, M. Ritsch-Marte, and D. Stifter, "Flexible contrast for low-coherence interference microscopy by Fourier-plane filtering with a spatial light modulator.," Opt. Lett., vol. 35, p. 4154, 2010, with permission from the Optical Society of America © 2010)

of LCI: by using a so-called spatial light modulator (an addressable pixel array for selectively shifting the phase) in the FP, contrast modes like DF, spiral phase contrast (an effective edge filter realized by performing the Hilbert transform in the FP), or Schlieren contrast (enhancing edges in certain orientations) can be realized on the fly, as shown in Fig. 83.7 and proven on layered samples in [153].

The contrast in the above examples is arising from spatial frequencies in the lateral direction. However, it is quite useful to link additional material properties to contrast and – as a final step – to quantitatively determine these properties within the scattering materials. One example is OCT elastography [154] for the evaluation of ***mechanical properties*** by tracking the ***displacement*** of features within the sample, which is subjected to stress, in a spatially resolved way. The displacement can be obtained by cross-correlations of speckle patterns, analogous to conventional digital image correlation (DIC) performed to monitor ***deformations*** on surfaces for full-field strain analysis (FFSA). In case of large deformations, which can lead to uncorrelated speckle patterns between subsequent image frames, the evaluating of the temporal statistical behavior and maps of local dissimilarities of the speckle pattern of OCT cross-sections was shown to mark regions of enhanced plastic

deformation during tensile tests on polymer samples [155], thereby providing complementary information to FFSA data, which was simultaneously taken from the surface [156].

Besides DIC, an established technique to monitor displacement and deformation of surfaces can be found in electronic speckle pattern interferometry (ESPI). In combination with a broadband light source, the principle of ESPI and LCI can also be combined to monitor the deformation of subsurface interfaces within scattering materials, as shown for adhesive-bonded joints [157] or for the layered coating on the famous Chinese terracotta warriors of the First Qin Emperor [158]. Instead of using a broadband source, a wavelength scanning ESPI variant was used in [159] and extended towards the determination of all orthogonal displacement components (3D displacement sensitivity) [160]. In this context, in-plane and out-of-plane displacement measurements was accomplished by, e.g., phase-contrast SD-OCT, as exemplified on a polymer phantom [161].

Besides speckle tracking for small-scale deformations, the evaluation of the Doppler shift is suitable for the evaluation of larger speckle motions as used for OCT elastography [162]. In the same way, ***velocity profiles*** in scattering fluids can effectively be measured by Doppler OCT, as, e.g., demonstrated for the microfluidic mixing devices presented in the above section [150] or for the study on the bubble nucleation process on heated surfaces [147]. Two-phase flow (gas bubbles within liquid) was equally investigated, revealing the velocity profile of toroidal vortices close to the gas-liquid interfaces [163]. Furthermore, imaging of electroosmotic ***flow dynamics*** in microfluidic channels [164] and secondary flow phenomena in curved serpentine mixers [165] were successfully obtained with phase-resolved optical Doppler tomography. Velocity profiles could recently also be directly measured in a rheometer for obtaining a dynamic phase diagram of a polymer solution, indicating so-called linear, shear-banding, and wall-slip regimes as a function of the molecular weight and concentration [166].

Additional contrast and information can also be obtained by evaluating the ***polarization state*** of the back-reflected light, as it was demonstrated for material characterization: parchment degradation by iron gall ink, i.e., the standard writing and drawing ink from the twelfth to the nineteenth century exhibiting corrosive behavior), was studied in this way using polarization-sensitive (PS)-OCT [167]. PS-OCT was also successfully applied to visualize solidified flow patterns and regions under internal stress within injection-molded polymer parts [126]. Especially ***birefringent layers*** in such polymer parts, e.g., caused by a highly oriented polymer morphology which forms close to surface during injection molding due to increased shear forces, can effectively be identified [2, 68] and even monitored in situ during solidification [148]. Furthermore, the ***stress distribution*** within photoresist molds for miniature gear wheels [168] was successfully mapped by transversal UHR-PS-OCT [169]: besides the detection of defects at the substrate-resist interface [67], the PS data could be used to quantitatively determine the amount of residual stress [170], as it was also demonstrated before on bulk polymer samples under mechanical loading [171]. Quantification of stress by PS-OCT was also accomplished for GFRPs under static load with a time-domain PS-OCT [172],

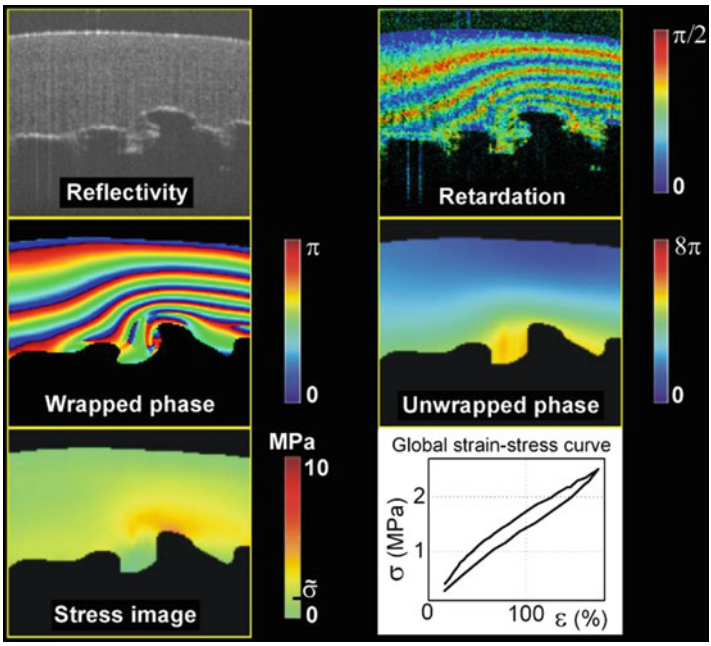

Fig. 83.8 Single-frame excerpt from dynamic SD-PS-OCT recordings of an elastomer test sample (average thickness: 1 mm) under cyclic loading, showing the original reflectivity and retardation images (*top* images, retardation image: *color* encoded), the calculated wrapped and unwrapped phase images (*middle row*), the obtained stress image with indicated average stress obtained from the cross-sectional image (*bottom left*), and the simultaneously measured global strain-stress curve (*bottom right*) (Reprinted from: D. Stifter, E. Leiss-Holzinger, Z. Major, B. Baumann, M. Pircher, E. Götzinger, C. K. Hitzenberger, and B. Heise, "Dynamic optical studies in materials testing with spectral-domain polarization-sensitive optical coherence tomography.," Opt. Express, vol. 18, p. 25712, 2010, with permission from the Optical Society of America © 2010)

as well as with SD-PS-OCT during dynamically performed tensile tests as shown in Fig. 83.8: PS-OCT cross-sections of an irregularly shaped elastomer sample which were evaluated with the help of advanced 2D-image processing and phase unwrapping algorithms yielded spatially and temporally resolved stress maps [173].

Further applications of PS-OCT comprise enhanced defect detection in GFRPs as used for the aerospace industry: composite materials for helicopter rotor blades were evaluated with UHR in this way to resolve individual fibers together with the surrounding strain and thus obtain microscopic information on the early stages of damage formation [127]. An evaluation in terms of the ***degree of polarization uniformity*** of dynamically acquired PS-OCT cross-sections taken from GFRPs during fracture tests led also to the early detection of micro-damage sites, even before large-scale delaminations appeared in the reflectivity images or increased stress-induced birefringence could be observed [173], proving in this way the added value which an additional source of contrast can provide.

83.4 Conclusions and Outlook

Within this chapter, a broad range of applications for OCT in NDT has been recalled, ranging from examples of industrial quality control over classification and authentication tasks to the evaluation of materials in research and development. However, this large variety should not cover the fact that outside the biomedical field, OCT still holds the position of an exotic measurement technique, which is not yet routinely applied to material testing and evaluation. Only in the field of surface, thin film, and multilayer metrology, OCT-like sensors and devices based on LCI already found broad acceptance, which is not surprising since some of these techniques were dedicatedly developed for these purposes, some even before the invention of OCT. For the application of OCT according to its original motivation, i.e., the imaging of structures within scattering media, the situation presents itself in a more ambiguous way. The large variety of materials and sample geometries makes it difficult to employ a standard design of the measurement device or to apply a routine protocol even when considering similar applications. As an example, by changing only one component in a sample structure, the whole evaluation technique might be put into question, e.g., when during further product development an additional layer with stronger scattering characteristics has to be inserted in a multilayer structure. Nevertheless, for all these structures made from a variety of technical and natural materials, valuable ground could already be gained with promising examples highlighted in the above sections.

The future of OCT in material testing will further brighten up, especially when considering the new methodological developments driven by the large (mostly biomedical) scientific OCT community. At the same time, additional impetus is expected when the technique is further refined and supplemented with respect to the specific demands in NDT. Concerning industrial production, this would call, e.g., for automated and instantaneous image acquisition and evaluation/processing/quantification as required for giving direct feedback signals in on-line control of the production. Further advancement will come from modular OCT(-like) sensor systems which can flexibly be tailored to the needs, fully integrated into production lines (hardware and software) and also be used in combination with complementary characterization methods (multimodal analysis).

Similar considerations hold true for evaluation tasks in material development and research. Here, besides investing resources in tailored systems, the use and further development of additional contrasting are especially of interest, giving access to complementary information. In this context, OCT vibrography [174] for the analysis of periodic movements or true (full) color imaging [175] in combination with the evaluation of spectroscopic information [176] (e.g., for substance identification) shall be mentioned. Molecular contrast arising from optical (nonlinear) phenomena leads to second harmonic generation (SHG) OCT, coherent anti-Stokes Raman scattering (CARS) OCT, or pump-probe (PP) OCT [177, 178], representing techniques which might equally prove useful, as exemplified in Fig. 83.9 for combined OCT and SHG-OCT imaging to distinguish zinc corrosion products by using a compact 1,550 nm broadband femtosecond fiber laser as light source.

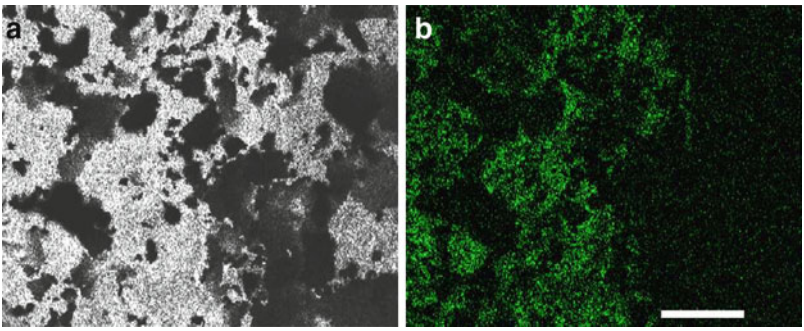

Fig. 83.9 Scanning OCM en face image (**a**) and corresponding SHG-OCM (**b**) image of zinc oxide (*left region*, SHG-active) and hydrozincite-covered surface (*right region*, SHG-inactive, scale bar: 1 mm) (Images by A. Prylepa and D. Stifter, Christian Doppler Laboratory for Microscopic and Spectroscopic Material Characterization, Johannes Kepler University Linz, Austria)

A promising trend for future applications of OCT in NDT is to exploit the extension to other than the usually used wavelength ranges. Ultrathin technical layers could in this way be rendered accessible, as suggested for the soft X-ray and XUV range [179]. Similarly, thick and strongly scattering media would take profit from longer wavelengths, with techniques as principally demonstrated for interferometric THz imaging [180] or for surface metrology in the IR range [181].

Finally, all these recent developments as well as the know-how generated by the applications presented within this chapter will lead – in conjunction with novel photonic components and devices, together with an integration of complementary technologies and a careful reevaluation of formerly presented measurement concepts – to an even stronger sign of life of OCT in the field of NDT.

Acknowledgements The financial support by the Federal Ministry of Economy, Family, and Youth and the National Foundation for Research, Technology, and Development is gratefully acknowledged.

References

1. D. Huang, E.A. Swanson, C.P. Lin, J.S. Schuman, W.G. Stinson, W. Chnag, M.R. Hee, T. Flotte, K. Gregory, C.A. Puliafito, J.G. Fujimoto, Optical coherence tomography. Science **254**, 1178 (1991)
2. D. Stifter, Beyond biomedicine: a review of alternative applications and developments for optical coherence tomography. Appl. Phys. B **88**, 337 (2007)
3. E.A. Swanson, M.R. Hee, G.J. Tearney, J.G. Fujimoto, Application of optical coherence tomography in nondestructive evaluation of material microstructure, in S*ummaries of Papers of the CLEO'96 Conference*, vol. 9, (1996), p. 326. Anaheim, USA
4. M. Bashkansky, P.R. Battle, M.D. Duncan, M. Kahn, J. Reintjes, Subsurface defect detection in ceramics using an optical gated scatter reflectometer. J. Am. Ceram. Soc. **79**, 1397 (1996)

5. M. Bashkansky, M.D. Duncan, M. Kahn, D. Lewis III, J. Reintjes, Subsurface defect detection in ceramics by high-speed high-resolution optical coherent tomography. Opt. Lett. **22**, 61 (1997)
6. S. Ishida, N. Nishizawa, Quantitative comparison of contrast and imaging depth of ultrahigh-resolution optical coherence tomography images in 800–1700 nm wavelength region. Biomed. Opt. Express **3**, 3582 (2012)
7. G. Eder, H. Janeschitz-Kriegl, Polymer crystallization, in *Processing of Polymers*, ed. by H.E.H. Meijer (Wiley-VCH, Weinheim, 1997), p. 270
8. P. Targowski, M. Iwanicka, Optical coherence tomography: its role in the non-invasive structural examination and conservation of cultural heritage objects – a review. Appl. Phys. A **106**, 265 (2011)
9. G. Beheim, Remote displacement measurement using a passive interferometer with a fiber-optic link. Appl. Opt. **24**, 2335 (1985)
10. M. Davidson, K. Kaufman, I. Mazor, F. Cohen, An application of interference microscopy to integrated circuit inspection and metrology. Proc. SPIE **775**, 223 (1987)
11. A. Dubois, K. Grieve, G. Moneron, R. Lecaque, L. Vabre, C. Boccara, Ultrahigh-resolution full-field optical coherence tomography. Appl. Opt. **43**, 2874 (2004)
12. M. Davidson, K. Kaufman, I. Mazor, First results of a product utilizing coherence probe imaging for wafer inspection. Proc. SPIE **921**, 100 (1988)
13. B.S. Lee, T.C. Strand, Profilometry with a coherence scanning microscope. Appl. Opt. **29**, 3784 (1990)
14. G.S. Kino, S.S.C. Chim, Mirau correlation microscope. Appl. Opt. **29**, 3775 (1990)
15. C.J.R. Sheppard, M. Roy, M.D. Sharma, Image formation in low-coherence and confocal interference microscopes. Appl. Opt. **43**, 1493 (2004)
16. L. Deck, P.D. Groot, High-speed noncontact profiler based on scanning white-light interferometry. Appl. Opt. **33**, 7334 (1994)
17. P.J. Caber, Interferometric profiler for rough surfaces. Appl. Opt. **32**, 3438 (1993)
18. T. Dresel, G. Haeusler, H. Venzke, Three-dimensional sensing of rough surfaces by. Appl. Opt. **31**, 919 (1992)
19. R.C. Youngquist, S. Carr, D.E.N. Davies, Optical coherence-domain reflectometry: a new optical evaluation technique. Opt. Lett. **12**, 158 (1987)
20. H.H. Gilgen, R.P. Novak, R.P. Salathe, W. Hodel, P. Beaud, Submillimeter optical reflectometry. J. Lightwave Technol. **7**, 1225 (1989)
21. K. Takada, K. Chida, J. Nod, Trench Depth Measurement System for VLSI DRAM's Capacitor Cells Using Optical Fiber and Michelson Interferometer. J. Lightwave Technol. **LT-5**, 881 (1987)
22. S. Ortiz, D. Siedlecki, L. Remon, S. Marcos, Optical coherence tomography for quantitative surface topography. Appl. Opt. **48**, 6708 (2009)
23. M.M. Amaral, M.P. Raele, J.P. Caly, R.E. Samad, J. Vieira, A.Z. Freitas, Roughness measurement methodology according to DIN 4768 using optical coherence tomography (OCT). Proc. SPIE **7390**, 73900Z (2009)
24. I.B. Couceiro, T. Ferreira da Silva, L.V.G. Tarelho, C.L.S. Azeredo, I. Malinovski, H.P.H. Grieneisein, W.S. Barros, G.V. Faria, J.P. von der Weid, M.M. Amaral, M.P. Raele, A.Z. de Freitas, Development of traceability methodology for optical coherence tomography (OCT) using step height standard as calibration reference. Proc. SPIE **8082**, 80822P (2011)
25. T. Wilson (ed.), *Confocal Microscopy* (Academic, London, 1990)
26. S. Kuwamura, I. Yamaguchi, Wavelength scanning profilometry for real-time surface shape measurement. Appl. Opt. **36**, 4473 (1997)
27. U. Schnars, W. Jüptner, *Digital Holography* (Springer, Berlin, 2005)
28. W. Lyda, M. Gronle, D. Fleischle, F. Mauch, W. Osten, Advantages of chromatic-confocal spectral interferometry in comparison to chromatic confocal microscopy. Meas. Sci. Technol. **23**, 054009 (2012)

29. M. Wurm, C. Hofer, H. Traxler, A. Zabernig, B. Harrer, Vermessung der Laserbohrungen in faserverstärktem Graphit mittels Optischer Kohärenztomographie, in *Proceeding of the Industrial Computed Tomography – CTC* (Wels Austria, 2010), p. 133
30. T. Hellmuth, R. Börret, K. Khrennikov, 3-dimensional scanning of grinded optical surfaces based on optical coherence tomography. Proc. SPIE **6671**, 66710X (2007)
31. M. Sergeeva, K. Khrenikov, T. Hellmuth, R. Boerret, Sub surface damage measurements based on short coherent interferometry. J. Europ. Opt. Soc. Rapid Publ. **5**, 10003 (2010)
32. K.-E. Peiponen, E. Alarousu, M. Juuti, R. Silvennoinen, A. Oksman, R. Myllylä, T. Prykäri, Diffractive-optical-element-based glossmeter and low coherence interferometer in assessment of local surface quality of paper. Opt. Eng. **45**, 043601 (2006)
33. M. Juuti, H. Tuononen, T. Prykäri, V. Kontturi, M. Kuosmanen, E. Alarousu, J. Ketolainen, R. Myllylä, K.-E. Peiponen, Optical and terahertz measurement techniques for flat-faced pharmaceutical tablets: a case study of gloss, surface roughness and bulk properties of starch acetate tablets. Meas. Sci. Technol. **20**, 015301 (2009)
34. P. Targowski, M. Góra, M. Wojtkowski, Optical coherence tomography for artwork diagnostics. *Laser Chem.* **2006**, Article ID 35373 (2006)
35. E. Jonathan, Non-contact and non-destructive testing of silicon V-grooves: a non-medical application of optical coherence tomography (OCT). Opt. Las. Eng. **44**, 1117 (2006)
36. W.J. Walecki, V. Souchkov, K. Lai, T. Wong, T. Azfar, Y.T. Tan, P. Van, S.H. Lau, A. Koo, Low-coherence interferometric absolute distance gauge for study MEMs structures. Proc. SPIE **5716**, 182 (2005)
37. W.J. Walecki, A. Pravdivtsev, K. Lai, M. Santos II, G. Mikhaylov, M. Mihaylov, A. Koo, Fiber-optics low-coherence integrated metrology for in-situ non-contact characterization of Wafer curvature for Wafers having non-uniform substrate and thin film thickness. Mater. Res. Soc. Symp. Proc. **875**, 249 (2005)
38. A. Dubois, A.C. Boccara, Real-time reflectivity and topography imagery of depth-resolved microscopic surfaces. Opt. Lett. **24**, 309 (1999)
39. T. Anna, C. Shakher, D.S. Mehta, Simultaneous tomography and topography of silicon integrated circuits using full-field swept-source optical coherence tomography. J. Opt. A Pure Appl. Opt. **11**, 045501 (2009)
40. S. Beer, P. Seitz, A smart pixel array with massively parallel signal processing for real-time optical coherence tomography performing close to the physical limits. IEEE Conf. Proc. Res. Microelectron. Electron. **2**, 135 (2005)
41. P. Lambelet, Parallel optical coherence tomography (pOCT) for industrial 3D inspection. Proc. SPIE **8082**, 80820X (2011)
42. B. Heise, D. Stifter, Quantitative phase reconstruction for orthogonal-scanning differential phase-contrast optical coherence tomography. Opt. Lett. **34**, 1306 (2009)
43. P.J.L. Webster, J.X.Z. Yu, B.Y.C. Leung, M.D. Anderson, V.X.D. Yang, J.M. Fraser, In situ 24 kHz coherent imaging of morphology change in laser percussion drilling. Opt. Lett. **35**, 646 (2010)
44. M. Wiesner, J. Ihlemann, H.H. Müller, E. Lankenau, G. Hüttmann, Optical coherence tomography for process control of laser micromachining. Rev. Sci. Instrum. **81**, 033705 (2010)
45. Y. Kim, E. Seo Choi, W. Kwak, Y. Shin, W. Jung, Y.-C. Ahn, Z. Chen, Three-dimensional non-destructive optical evaluation of laser-processing performance using optical coherence tomography. Opt. Laser Technol. **40**, 625 (2008)
46. R. Schmitt, G. Mallmann, P. Peterka, Development of a FD-OCT for the inline process metrology in laser structuring systems. Proc. SPIE **8082**, 808228 (2011)
47. P.J.L. Webster, L.G. Wright, K.D. Mortimer, B.Y. Leung, J.X.Z. Yu, J.M. Fraser, Automatic real-time guidance of laser machining with inline coherent imaging. J. Laser Appl. **23**, 022001 (2011)
48. M. Gora, P. Targowski, A. Kowalczyk, J. Marczak, A. Rycyk, Fast spectral optical coherence tomography for monitoring of varnish ablation process, in *Lasers in the*

Conservation of Artworks, LACONA VII Proc, ed. by M. Castilleo (Taylor & Francis, London, 2008), p. 23
49. E.A. Kwiatkowska, J. Marczak, R. Ostrowski, W. Skrzeczanowski, M. Sylwestrzak, M. Iwanicka, P. Targowski, Absolute LIBS stratigraphy with optical coherence tomography. Proc. SPIE **7391**, 73910F (2009)
50. M.L. Dufour, G. Lamouche, V. Detalle, B. Gauthier, P. Sammut, Low-coherence interferometry, an advanced technique for optical metrology in industry. Insight **47**, 216 (2005)
51. L. Giniunas, R. Karkockas, R. Danielius, Accurate remote distance sensing by use of low-coherence interferometry: an industrial application. Appl. Opt. **37**, 6729 (1998)
52. V.V. Ivanov, M.A. Noviko, A.D. Tertyshnik, V.A. Markelov, V.A. Goryunov, Remote gauging with fiber optic low-coherence tandem interferometry: new industrial applications. Proc. SPIE **4900**, 548 (2002)
53. W.J. Choi, S.P. Jung, J.G. Shin, D. Yang, B.H. Lee, Characterization of wet pad surface in chemical mechanical polishing (CMP) process with full-field optical coherence tomography (FF-OCT). Opt. Express **19**, 13343 (2011)
54. S. Lawman, H. Liang, High precision dynamic multi-interface profilometry with optical coherence tomography. Appl. Opt. **50**, 6039 (2011)
55. D.C. Adler, J. Stenger, I. Gorczynska, H. Lie, T. Hensick, R. Spronk, S. Wolohojian, N. Khandekar, J.Y. Jiang, S. Barry, A.E. Cable, R. Huber, J.G. Fujimoto, Comparison of three-dimensional optical coherence tomography and high resolution photography for art conservation studies. Opt. Express **15**, 15972 (2007)
56. J. Czajkowski, T. Prykäri, E. Alarousu, J. Palosaari, R. Myllylä, Optical coherence tomography as a method of quality inspection for printed electronics products. Opt. Rev. **17**, 257 (2010)
57. R. Azzam, N. Bashara, *Ellipsometry and Polarized Light* (North-Holland, Amsterdam, 1987)
58. R.A. Patten, Michelson interferometer as a remote gauge. Appl. Opt. **10**, 2717 (1971)
59. S. Kim, G. Kim, Thickness-profile measurement of transparent thin-film layers by white-light scanning interferometry. Appl. Opt. **38**, 5968 (1999)
60. D. Grigg, E. Felkel, J. Roth, X.C.D. Lega, L. Deck, P.D. Groot, Z. Corporation, Static and dynamic characterization of MEMS and MOEMS devices using optical interference microscopy. Proc. SPIE **5455**, 5455 (2004)
61. S.K. Debnath, S.-W. Kim, M.P. Kothiyal, P. Hariharan, Spectrally resolved phase-shifting interference microscopy: technique based on optical coherence tomography for profiling a transparent film on a patterned substrate. Appl. Opt. **49**, 6624 (2010)
62. J. Schwider, L. Zhou, Dispersive interferometric profilometer. Opt. Lett. **19**, 995 (1994)
63. T. Endo, Y. Yasuno, S. Makita, M. Itoh, T. Yatagai, Profilometry with line-field Fourier-domain interferometry. Opt. Express **13**, 695 (2005)
64. I. Abdulhalim, R. Dadon, Multiple interference and spatial frequencies' effect on the application of frequency-domain optical coherence tomography to thin films' metrology. Meas. Sci. Technol. **20**, 015108 (2009)
65. W.J. Walecki, K. Lai, V. Souchkov, P. Van, S. Lau, A. Koo, Novel noncontact thickness metrology for backend manufacturing of wide bandgap light emitting devices. Phys. Status Solidi C **2**, 984 (2005)
66. K.A. Serrels, M.K. Renner, D.T. Reid, Optical coherence tomography for non-destructive investigation of silicon integrated-circuits. Microelectron. Eng. **87**, 1785 (2010)
67. K. Wiesauer, M. Pircher, E. Götzinger, S. Bauer, R. Engelke, G. Ahrens, G. Grützner, C. Hitzenberger, D. Stifter, En-face scanning optical coherence tomography with ultra-high resolution for material investigation. Opt. Express **13**, 1015 (2005)
68. D. Stifter, A.D.S. Dufau, E. Breuer, K. Wiesauer, P. Burgholzer, O. Höglinger, E. Götzinger, M. Pircher, C.K. Hitzenberger, Polarisation-sensitive optical coherence tomography for material characterisation and testing. Insight **47**, 209 (2005)
69. G.J. Tearney, M.E. Brezinski, J.F. Southern, B.E. Bouma, M.R. Hee, J.G. Fujimoto, Determination of the refractive index of highly scattering human tissue by optical coherence tomography. Opt. Lett. **20**, 2258 (1995)

70. T. Fukano, I. Yamaguchi, Simultaneous measurement of thicknesses and refractive indices of multiple layers by a low-coherence confocal interference microscope. Opt. Lett. **21**, 1942 (1996)
71. M. Haruna, M. Ohmi, T. Mitsuyama, H. Tajiri, H. Maruyama, M. Hashimoto, Simultaneous measurement of the phase and group indices and the thickness of transparent plates by low-coherence interferometry. Opt. Lett. **23**, 966 (1998)
72. H. Maruyama, T. Mitsuyama, Y. Kiyomura, M. Haruna, Evaluation of hardening of UV-light cured epoxy by simultaneous measurement of refractive index and thickness using the low coherence interferometry. IEICE Trans. Electron. **J85-C**, 103 (2002)
73. H. Lv, A. Liu, J. Tong, X. Yi, Q. Li, X. Wang, Y. Ding, Nondestructive measurement of refractive index profile of gradient refractive index rod lens. Rev. Sci. Instrum. **81**, 103104 (2010)
74. A. Nemeth, R. Gahleitner, G. Hannesschläger, G. Pfandler, M. Leitner, Ambiguity-free spectral-domain optical coherence tomography for determining the layer thicknesses in fluttering foils in real time. Opt. Lasers Eng. **50**, 1372 (2012)
75. T. Prykäri, J. Czajkowski, E. Alarousu, R. Myllylä, Optical coherence tomography as an accurate inspection and quality evaluation technique in paper industry. Opt. Rev. **17**, 218 (2010)
76. E. Alarousu, L. Krehut, T. Prykäri, R. Myllylä, Study on the use of optical coherence tomography in measurements of paper properties. Meas. Sci. Technol. **16**, 1131 (2005)
77. T. Arecchi, M. Bellini, C. Corsi, R. Fontana, M. Materazzi, L. Pezzati, A. Tortora, Optical coherence tomography for painting diagnostics. Proc. SPIE **5857**, 58570Z (2005)
78. H. Liang, M.G. Cid, R.G. Cucu, G.M. Dobre, A.G. Podoleanu, J. Pedro, D. Saunders, En-face optical coherence tomography – a novel application of non-invasive imaging to art conservation. Opt. Express **13**, 69 (2005)
79. P. Targowski, B. Rouba, M. Góra, L. Tymińska-Widmer, J. Marczak, A. Kowalczyk, Optical coherence tomography in art diagnostics and restoration. Appl. Phys. A **92**, 1 (2008)
80. M. Elias, C. Magnain, J.M. Frigerio, Contribution of surface state characterization to studies of works of art. Appl. Opt. **49**, 2151 (2010)
81. A. Szkulmowska, M. Góra, M. Targowska, D. Stifter, E. Breuer, P. Targowski, Applicability of optical coherence tomography at 1.55 55 μm mu;m to the examination of oil paintings, in *Lasers in the Conservation of Artworks*, ed. by J. Nimmrichter, W. Krautek, M. Schreiner (Springer, Berlin/Heidelberg/New York, 2005), p. 487
82. A. Rodriguez, J.U. Kang, Y. Huang, Real-time 4D non-invasive subsurface corrosion inspection using ultrahigh-speed, Fourier-domain optical coherence tomography. Proc. SPIE **8155**, 81550W (2011)
83. F. Xu, H.E. Pudavar, P.N. Prasad, Confocal enhanced optical coherence tomography for nondestructive evaluation of paints and coatings. Opt. Lett. **24**, 1808 (1999)
84. M. Hughes, M. Spring, A. Podoleanu, Speckle noise reduction in optical coherence tomography of paint layers. Appl. Opt. **49**, 99 (2009)
85. J. Czajkowski, T. Fabritius, J. Ulański, T. Marszałek, M. Gazicki-Lipman, A. Nosal, R. Śliż, E. Alarousu, T. Prykäri, R. Myllylä, G. Jabbour, Ultra-high resolution optical coherence tomography for encapsulation quality inspection. Appl. Phys. B **105**, 649 (2011)
86. L. Thrane, T.M. Jørgensen, M. Jørgensen, F.C. Krebs, Application of optical coherence tomography (OCT) as a 3-dimensional imaging technique for roll-to-roll coated polymer solar cells. Sol. Energy Mater. Sol. Cells **97**, 181 (2012)
87. M.-T. Tsai, F.-Y. Chang, Y.-J. Lee, J.-D. Lee, H.-C. Wang, C.-K. Lee, Defect detection and property evaluation of indium tin oxide conducting glass using optical coherence tomography. Opt. Express **19**, 7559 (2011)
88. M.-T. Tsai, Y.-J. Lee, Y.-C. Yao, C.-Y. Kung, F.-Y. Chang, J.-D. Lee, Quantitative phase imaging with swept-source optical coherence tomography for optical measurement of nanostructures. IEEE Photon. Technol. Lett. **24**, 640 (2012)
89. S.-H. Kim, J.-H. Kim, S.-W. Kang, Nondestructive defect inspection for LCDs using optical coherence tomography. Displays **32**, 325 (2011)

90. C.-C. Tsai, Y.-S. Lin, S.-C. Pei, C.-K. Chang, T.-H. Chen, N.-C. Cheng, M.-K. Tsai, C.-C. Lai, W.-Y. Li, C.-K. Wei, S.-L. Huang, Microstructural and microspectral characterization of a vertically aligned liquid crystal display panel. Opt. Lett. **36**, 567 (2011)
91. R. Wilhelm, A. Courtevill, F. Garcia, F. de Vecchi, On-axis, non-contact measurement of glass thicknesses and airgaps in optical systems with submicron accuracy. Proc. SPIE **6616**, 66163P (2007)
92. B.R. Davidson, J.K. Barton, Application of optical coherence tomography to automated contact lens metrology. J. Biomed. Opt. **15**, 016009 (2012)
93. J. Jasapara, S. Wielandy, Characterization of coated optical fibers by Fourier-domain optical coherence tomography. Opt. Lett. **30**, 1018 (2005)
94. J.M.A. Mauritz, R.S. Morrisby, R.S. Hutton, C.H. Legge, C.F. Kaminski, Imaging pharmaceutical tablets with optical coherence tomography. J. Pharm. Sci. **99**, 385 (2010)
95. S. Zhong, Y.-C. Shen, L. Ho, R.K. May, J.A. Zeitler, M. Evans, P.F. Taday, M. Pepper, T. Rades, K.C. Gordon, R. Müller, P. Kleinebudde, Non-destructive quantification of pharmaceutical tablet coatings using terahertz pulsed imaging and optical coherence tomography. Opt. Lasers Eng. **49**, 361 (2011)
96. D.M. Koller, G. Hannesschläger, M. Leitner, J.G. Khinast, Non-destructive analysis of tablet coatings with optical coherence tomography. Eur. J. Pharm. Sci. **44**, 142 (2011)
97. N. Zeng, Y. He, H. Ma, Pearl detection with optical coherence tomography. Chin. J. Lasers **34**, 1140 (2007)
98. N. Zeng, Y. He, H. Ma, Application of optical coherence tomography in nacre identification and characterization. Microw. Opt. Technol. Lett. **50**, 442 (2008)
99. C. Xue, Y. Sun, D. Wang, P. Li, Automated thickness measurement of nacreous layer of seawater pearls based on optical coherence tomography. Proc. Ninth Int. Conf. Hybrid Intell. Syst. **3**, *vol* 1. 332 (2009)
100. D. Stifter, K. Wiesauer, M. Wurm, E. Schlotthauer, J. Kastner, M. Pircher, E. Götzinger, C.K.K. Hitzenberger, Investigation of polymer and polymer/fibre composite materials with optical coherence tomography. Meas. Sci. Technol. **19**, 074011 (2008)
101. N.H. Cho, U. Jung, S. Kim, J. Kim, Non-destructive inspection methods for LEDs using real-time displaying optical coherence tomography. Sensors **12**, 10395 (2012)
102. M.J. Ju, S.J. Lee, E.J. Min, Y. Kim, H.Y. Kim, B.H. Lee, Evaluating and identifying pearls and their nuclei by using optical coherence tomography. Opt. Express **18**, 13468 (2010)
103. M.J. Ju, S.J. Lee, Y. Kim, J.G. Shin, H.Y. Kim, Y. Lim, Y. Yasuno, B.H. Lee, Multimodal analysis of pearls and pearl treatments by using optical coherence tomography and fluorescence spectroscopy. Opt. Express **19**, 6420 (2011)
104. M.-L. Yang, C.-W. Lu, I.-J. Hsu, C.C. Yang, The use of optical coherence tomography for monitoring the subsurface morphologies of archaic jades. Archaeometry **46**, 171 (2004)
105. S. Chang, Y. Mao, G. Chang, C. Flueraru, Jade detection and analysis based on optical coherence tomography images. Opt. Eng. **49**, 063602 (2010)
106. M. Yang, A.M. Winkler, J. Klein, A. Wall, J.K. Barton, Using optical coherence tomography to characterize the crack morphology of ceramic glaze and jade, in *Selected Topics in Optical Coherence Tomography*, ed. by G. Liu (InTech, Rijeka, 2012)
107. H. Liang, M. Sax, D. Saunders, M. Tite, Optical coherence tomography for the non-invasive investigation of the microstructure of ancient Egyptian faience. J. Arch. Sci. **39**, 3683 (2012)
108. M.-L. Yang, A.M. Winkler, J.K. Barton, P.B. Vandiver, Using optical coherene tomography to examine the subsurface morphology of Chinese glazes. Archaeometry **51**, 818 (2009)
109. J. Kunicki-Goldfinger, P. Targowski, M. Góra, P. Karaszkiewicz, P. Dzierzanowski, Characterization of glass surface morphology by optical coherence tomography. Stud. Conserv. **54**, 117 (2009)
110. S.G. Demos, M. Staggs, K. Minoshima, J. Fujimoto, Characterization of laser induced damage sites in optical components. Opt. Express **10**, 1444 (2002)

111. G.M. Guss, I.L. Bass, R.P. Hackel, C. Mailhiot, S.G. Demos, In situ monitoring of surface postprocessing in large-aperture fused silica optics with optical coherence tomography. Appl. Opt. **47**, 4569 (2008)
112. J. Choi, K.-S. Lee, J.P. Rolland, T. Anderson, M.C. Richardson, Nondestructive 3-D imaging of femtosecond laser written volumetric structures using optical coherence microscopy. Appl. Phys. A **104**, 289 (2011)
113. K. Minoshima, A.M. Kowalevicz, I. Hartl, E.P. Ippen, J.G. Fujimoto, Photonic device fabrication in glass by use of nonlinear materials processing with a femtosecond laser oscillator. Opt. Lett. **26**, 1516 (2001)
114. J. Reyes-Esqueda, L. Vabre, R. Lecaque, F. Ramaz, B.C. Forget, A. Dubois, B. Briat, C. Boccara, G. Roger, M. Canva, Y. Levy, F. Chaput, J.-P. Boilot, Optical 3D-storage in sol – gel materials with a reading by optical coherence tomography-technique. Opt. Commun. **220**, 59 (2003)
115. S.R. Chinn, E.A. Swanson, Multilayer optical storage by low-coherence reflectometry. Opt. Lett. **21**, 899 (1996)
116. M.D. Duncan, M. Bashkansky, J. Reintjes, Subsurface defect detection in materials using optical coherence tomography. Opt. Express **2**, 540 (1998)
117. M. Bashkansky, D. Lewis III, V. Pujari, J. Reintjes, H.Y. Yu, Subsurface detection and characterization of Hertzian cracks in Si3N4 balls using optical coherence tomography. NDT&E **34**, 547 (2001)
118. J.G. Sun, Z.P. Liu, Z.J. Pei, N.S.L. Phillips, J.A. Jensen, Optical methods for nondestructive evaluation of subsurface flaws in silicon nitride ceramics, in *Corrosion, Wear, Fatigue, and Reliability of Ceramics, vol. 29, no. 3*, ed. by J. Salem, E.R. Fuller, T. Ohji, A. Wereszczak (Hoboken, Wiley, 2008), p. 181
119. J. Veilleux, C. Moreau, D. Lévesque, M. Dufour, M. Boulos, Optical coherence tomography for the inspection of plasma-sprayed ceramic coatings. J. Therm. Spray Technol. **16**, 435 (2007)
120. W.A. Ellingson, R.J. Visher, R.S. Lipanovich, C.M. Deemer, Optical NDE methods for ceramic thermal barrier coatings for nondestructive evaluation. Mater. Eval. **64**, 45 (2006)
121. R. Su, L. Mattsson, Depth profiling in alumina ceramic by optical coherence tomography, In *Proceeding of 7th In nternational Conference Multi-Material Micro Manufacture*, (2011), Bourg en Bresse and Oyonnax, France. p. 316
122. R. Su, M. Kirillin, P. Ekberg, A. Roos, E. Sergeeva, L. Mattson, Optical coherence tomography for quality assessment of embedded microchannels in alumina ceramic. Opt. Express **20**, 4603 (2012)
123. S.-C. Pei, T.-S. Ho, C.-C. Tsai, T.-H. Chen, Y. Ho, P.-L. Huang, A.H. Kung, S.-L. Huang, Non-invasive characterization of the domain boundary and structure properties of periodically poled ferroelectrics. Opt. Express **19**, 7153 (2011)
124. M.Y. Kirillin, A.V. Priezzhev, R. Myllyla, Effect of paper porosity on OCT images: Monte Carlo study. Proc. SPIE **7022**, 702214 (2008)
125. I.S. Chronakis, N.D. Mekras, K. Wiesauer, E. Breuer, D. Stifter, G.F. Fuentes, Y. Qin, MASMICRO micro-/nano-materials processing, analysis, inspection and materials knowledge management. Int. J. Adv. Manuf. Technol. **47**, 963 (2009)
126. D. Stifter, P. Burgholzer, O. Höglinger, E. Götzinger, C.K. Hitzenberger, Polarisation-sensitive optical coherence tomography for material characterisation and strain-field mapping. Appl. Phys. A **76**, 947 (2003)
127. K. Wiesauer, M. Pircher, E. Götzinger, C.K. Hitzenberger, R. Oster, D. Stifter, Investigation of glass–fibre reinforced polymers by polarisation-sensitive, ultra-high resolution optical coherence tomography: internal structures, defects and stress. Compos. Sci. Technol. **67**, 3051 (2007)
128. J. Williams, W. Broughton, T. Koukoulas, S. S. Rahatekar, Plasma treatment as a method for functionalising and improving dispersion of carbon nanotubes in epoxy resins. *J. Mater. Sci.* published online (2012)

129. J.P. Dunkers, F.R. Phelan, D.P. Sanders, M.J. Everett, W.H. Green, D.L. Hunston, R.S. Parnas, The application of optical coherence tomography to problems in polymer matrix composites. Opt. Lasers Eng. **35**, 135 (2001)
130. J.P. Dunkers, D.P. Sanders, D.L. Hunston, M.J. Everett, W.H. Green, Comparison of optical coherence tomography, X-ray computed tomography, and confocal microscopy results from an impact damaged epoxy/E-glass composite. J. Adhes. **78**, 129 (2002)
131. J.P. Dunkers, F.R. Phelan, C.G. Zimba, K.M. Flynn, D.P. Sanders, R.C. Peterson, R.S. Parnas, X. Li, J.G. Fujimoto, The prediction of permeability for an epoxy/ E-glass composite using optical coherence tomographic images. Polym. Compos. **22**, 803 (2001)
132. J.P. Dunkers, R.S. Parnas, C.G. Zimba, R.C. Peterson, K.M. Flynn, J.G. Fujimoto, B.E. Bouma, Optical coherence tomography of glass reinforced polymer composites. Compos. Part A **30**, 139 (1999)
133. B. Heise, S.E. Schausberger, S. Häuser, B. Plank, D. Salaberger, E. Leiss-Holzinger, D. Stifter, Full-field optical coherence microscopy with a sub-nanosecond supercontinuum light source for material research. Opt. Fiber Technol. **18**, 403 (2012)
134. F. Awaja, B. Arhatari, K. Wiesauer, E. Leiss, D. Stifter, An investigation of the accelerated thermal degradation of different epoxy resin composites using X-ray microcomputed tomography and optical coherence tomography. Polym. Degrad. Stab. **94**, 1814 (2009)
135. G. Latour, J.-P. Echard, B. Soulier, I. Emond, S. Vaiedelich, M. Elias, Structural and optical properties of wood and wood finishes studied using optical coherence tomography: application to an 18th century Italian violin. Appl. Opt. **48**, 6485 (2009)
136. C. Lee, S.-Y. Lee, J.-Y. Kim, H.-Y. Jung, J. Kim, Optical sensing method for screening disease in melon seeds by using optical coherence tomography. Sensors **11**, 9467 (2011)
137. C. Fan, G. Yao, 3D imaging of tomato seeds using frequency domain optical coherence tomography. Proc. SPIE **8369**, 83690F (2012)
138. J.C. Clements, A.V. Zvyagin, K.M.M.D. Silva, T. Wanner, D.D. Sampson, Optical coherence tomography as a novel tool for non-destructive measurement of the hull thickness of lupin seeds. Plant Breed. **123**, 266 (2004)
139. I.V. Meglinski, C. Buranachai, L.A. Terry, Plant photonics: application of optical coherence tomography to monitor defects and rots in onion. Laser Phys. Lett. **7**, 307 (2010)
140. M. Leitner, G. Hannesschläger, A. Saghy, A. Nemeth, S. Chassagne-Berces, Optical coherence tomography for quality control and microstructure analysis in food. Proc. 11th Int. Congr. Eng. Food – ICEF11 **II**, 1175 (2011)
141. N. Nishizawa, S. Ishida, M. Hirose, S. Sugiyama, T. Inoue, Y. Mori, K. Itoh, H. Matsumura, Three-dimensional, non-invasive, cross-sectional imaging of protein crystals using ultrahigh resolution optical coherence tomography. Biomed. Opt. Express **3**, 735 (2012)
142. W.-J. Choi, G.-H. Min, B.-H. Lee, J.-H. Eom, J.-W. Kim, Counterfeit detection using characterization of safety feature on banknote with full-field optical coherence tomography. J. Opt. Soc. Korea **14**, 316 (2010)
143. K. Fujiwara, O. Matoba, Detection and evaluation of security features embedded in paper using spectral-domain optical coherence tomography. Opt. Rev. **18**, 171 (2011)
144. K. Fujiwara, O. Matoba, High-speed cross-sectional imaging of valuable documents using common-path swept-source optical coherence tomography. Appl. Opt. **50**, H165 (2011)
145. M. Otaka, H. Yamamoto, Y. Hayasaki, Manually operated low-coherence interferometer for optical information hiding. Opt. Express **14**, 9421 (2006)
146. W.Y. Oh, S.H. Yun, B.J. Vakoc, G.J. Tearney, B.E. Bouma, Ultrahigh-speed optical frequency domain imaging and application to laser ablation monitoring. Appl. Phys. Lett. **88**, 103902 (2006)
147. S. Meissner, J. Herold, L. Kirsten, C. Schneider, E. Koch, 3D optical coherence tomography as new tool for microscopic investigations of nucleate boiling on heated surfaces. Int. J. Heat Mass Transfer **55**, 5565 (2012)

148. P. Hierzenberger, G. Eder, E. Leiss-Holzinger, D. Stifter, In-situ monitoring of polymer crystallization by optical coherence tomography, in *Proceeding of 27th World Congress of the Polymer Society (Marrakech*, 2011), p. 5
149. V. Srinivasan, V. Pamula, K.D. Rao, M. Pollack, J.A. Izatt, R. Fair, V. Srinivasan, V. Pamula, K.D. Rao, M. Pollack, J.A. Izatt, R. Fair, V. Srinivasan, V. Pamula, K.D. Rao, M. Pollack, J.A. Izatt, R. Fair, 3-D imaging of moving droplets for microfluidics using optical coherence tomography, in *Technical Digest of the 7th International Conference on Micro Total Analysis Systems – microTAS-2003*, ed. by M.A. Northrup, K.F. Jensen, D.J. Harrison (TRF, San Diego, 2003), p. 1303
150. C. Xi, D.L. Marks, D.S. Parikh, L. Raskin, S.A. Boppart, Structural and functional imaging of 3D microfluidic mixers using optical coherence tomography. PNAS **101**, 7516 (2004)
151. M. Villiger, C. Pache, T. Lasser, Dark-field optical coherence microscopy. Opt. Lett. **35**, 3489 (2010)
152. L. Vabre, V. Loriette, A. Dubois, J. Moreau, A.C. Boccara, Imagery of local defects in multilayer components by short coherence length interferometry. Opt. Lett. **27**, 1899 (2002)
153. S.E. Schausberger, B. Heise, C. Maurer, S. Bernet, M. Ritsch-Marte, D. Stifter, Flexible contrast for low-coherence interference microscopy by Fourier-plane filtering with a spatial light modulator. Opt. Lett. **35**, 4154 (2010)
154. J.M. Schmitt, OCT elastography: imaging microscopic deformation and strain of tissue. Opt. Express **3**, 199 (1998)
155. D. Stifter, E. Leiss-Holzinger, B. Heise, J.-L. Bouchot, Z. Major, M. Pircher, E. Götzinger, B. Baumann, C.K. Hitzenberger, Spectral domain polarization sensitive optical coherence tomography at 1.55 μm: novel developments and applications for dynamic studies in materials science. Proc. SPIE **7889**, 78890Z (2011)
156. E. Leiss-Holzinger, D.U. Cakmak, B. Heise, J.-L. Bouchot, E.P. Klement, M. Leitner, D. Stifter, Z. Major, Evaluation of structural change and local strain distribution in polymers comparatively imaged by FFSA and OCT techniques. Express Polym. Lett. **6**, 249 (2012)
157. K. Gastinger, S. Winther, K.D. Hinsch, Low-coherence speckle interferometer (LCSI) for characterization of adhesion in adhesive-bonded joints. Proc. SPIE **4933**, 59 (2003)
158. K.D. Hinsch, G. Gülker, H. Helmers, Checkup for aging artwork – Optical tools to monitor mechanical behaviour. Opt. Lasers Eng. **45**, 578 (2007)
159. P.D. Ruiz, J.M. Huntley, R.D. Wildman, Depth-resolved whole-field displacement measurement by wavelength-scanning electronic speckle pattern interferometry. Appl. Opt. **44**, 3945 (2005)
160. S. Chakraborty, P.D. Ruiz, Measurement of all orthogonal components of displacement in the volume of scattering materials using wavelength scanning interferometry. J. Opt. Soc. Am. A **29**, 1776 (2012)
161. M.H. De la Torre Ibarra, P.D. Ruiz, J.M. Huntley, Simultaneous measurement of in-plane and out-of-plane displacement fields in scattering media using phase-contrast spectral optical coherence tomography. Opt. Lett. **34**, 806 (2009)
162. S.J. Kirkpatrick, R.K. Wang, D.D. Duncan, OCT-based elastography for large and small deformations. Opt. Express **14**(24), 373 (2006)
163. Y.-C. Ahn, W. Jung, Z. Chen, Turbid two-phase slug flow in a microtube: simultaneous visualization of structure and velocity field. Appl. Phys. Lett. **89**, 064109 (2006)
164. L. Wang, W. Xu, M. Bachman, G.P. Li, Z. Chen, Phase-resolved optical Doppler tomography for imaging flow dynamics in microfluidic channels. Appl. Phys. Lett. **85**, 1855 (2004)
165. Y.-C. Ahn, W. Jung, J. Zhang, Z. Chen, Investigation of laminar dispersion with optical coherence tomography and optical Doppler tomography. Opt. Express **13**, 8164 (2005)
166. S. Jaradat, M. Harvey, T.A. Waigh, Shear-banding in polyacrylamide solutions revealed via optical coherence tomography velocimetry. *Soft Matter* advance publication, (2012). doi:10.1039/c2sm26395e

167. M. Gora, M. Pircher, E. Götzinger, T. Bajraszewski, M. Strlic, J. Kolar, C.K. Hitzenberger, P. Targowski, Optical coherence tomography for examination of parchment degradation, *Laser Chem.* Article ID 68679 (2006)
168. R. Engelke, G. Ahrens, N. Arndt-Staufenbiehl, S. Kopetz, K. Wiesauer, B. Löchel, H. Schröder, J. Kastner, A. Neyer, D. Stifter, G. Grützner, Investigations on possibilities of inline inspection of high aspect ratio microstructures. Microsyst. Technol. **13**, 319 (2006)
169. K. Wiesauer, M. Pircher, E. Götzinger, C.K. Hitzenberger, R. Engelke, G. Ahrens, G. Grützner, D. Stifter, Transversal ultrahigh-resolution polarization sensitive optical coherence tomography for strain mapping in materials. Opt. Express **14**, 5945 (2006)
170. B. Heise, K. Wiesauer, E. Götzinger, M. Pircher, C.K. Hitzenberger, R. Engelke, G. Ahrens, G. Grützner, D. Stifter, Spatially resolved stress measurements in materials with polarisation-sensitive optical coherence tomography: image acquisition and processing aspects. Strain **46**, 61 (2010)
171. K. Wiesauer, A.D.S. Dufau, E. Götzinger, M. Pircher, C.K. Hitzenberger, D. Stifter, Non-destructive quantification of internal stress in polymer materials by polarisation sensitive optical coherence tomography. Acta Mater. **2785**, 3 (2005)
172. O. Jung-Taek, K. Seung-Woo, J. Oh, S. Kim, Polarization-sensitive optical coherence tomography for photoelasticity testing of glass/epoxy composites. Opt. Express **11**, 1669 (2003)
173. D. Stifter, E. Leiss-Holzinger, Z. Major, B. Baumann, M. Pircher, E. Götzinger, C.K. Hitzenberger, B. Heise, Dynamic optical studies in materials testing with spectral-domain polarization-sensitive optical coherence tomography. Opt. Express **18**, 25712 (2010)
174. E.W. Chang, J.B. Kobler, S.H. Yun, Subnanometer optical coherence tomographic vibrography. Opt. Lett. **37**, 3678 (2012)
175. L. Yu, M.K. Kim, Full-color three-dimensional microscopy by wide-field optical coherence tomography. Opt. Express **12**, 6632 (2004)
176. F.E. Robles, C. Wilson, G. Grant, A. Wax, Molecular imaging true-colour spectroscopic optical coherence tomography. Nat. Photonics **5**, 744 (2011)
177. B.E. Applegate, C. Yang, J.A. Izatt, Theoretical comparison of the sensitivity of molecular contrast optical coherence tomography techniques. Opt. Express **13**, 8146 (2005)
178. C. Vinegoni, J.S. Bredfeldt, D.L. Marks, S.A. Boppart, Nonlinear optical contrast enhancement for optical coherence tomography. Opt. Express **12**, 331 (2004)
179. S. Fuchs, A. Blinne, C. Rödel, U. Zastrau, V. Hilbert, M. Wünsche, J. Bierbach, E. Frumker, E. Förster, G.G. Paulus, Optical coherence tomography using broad-bandwidth XUV and soft X-ray radiation. Appl. Phys. B **106**, 789 (2012)
180. J.L. Johnson, T.D. Dorney, D.M. Mittleman, Enhanced depth resolution in terahertz imaging using phase-shift interferometry. Appl. Phys. Lett. **78**, 835 (2001)
181. P.D. Groot, J. Biegen, J. Clark, X.C.D. Lega, D. Grigg, Optical interferometry for measurement of the geometric dimensions of industrial parts. Appl. Opt. **41**, 3853 (2002)

OCT Technology Transfer and the OCT Market

84

Eric A. Swanson

Keywords
Commercialization of optical coherence tomography • Entrepreneurship • Optical coherence tomography • Optical coherence tomography market • Technology transfer • Translational medicine

84.1 Introduction

The field of optical coherence tomography (OCT) has blossomed dramatically since the first studies by various researchers around the world began in the late 1980s and early 1990s. Since then cumulatively, there have been dozens of companies created, over a hundred research groups working on or with OCT, over a thousand OCT patents issued, over 10,000 research articles published, tens of millions of patients scanned with OCT, hundreds of millions of venture capital and corporate R&D dollars invested, hundreds of millions of dollars in company acquisitions, and over a billion of dollars of OCT system revenue. Ophthalmic OCT reimbursements for clinical OCT procedures surpassed $1B in 2010 alone! The discovery and development of OCT has had, and will continue to have, a major economic, scientific, and medical impact. For example, OCT has had a tremendous impact on treatments for blinding eye diseases, and there is a patient somewhere in the world undergoing an ophthalmic OCT examination every several seconds. With OCT applications in cardiovascular, gastrointestinal, and other applications advancing, the impact will likely increase.

Eric Swanson is a founder of Advanced Ophthalmic Devices (acquired by Carl Zeiss Meditec), Lightlab Imaging (acquired by St. Jude Medical), and has numerous patents that are licensed to various OCT companies. Mr. Swanson also served on the board of NinePoint Medical Imaging and several other high-tech companies.

E.A. Swanson
Gloucester, MA, USA
e-mail: eric@curata.com

© Springer International Publishing Switzerland 2015

W. Drexler, J.G. Fujimoto (eds.), *Optical Coherence Tomography*,
DOI 10.1007/978-3-319-06419-2_86

The success of OCT is due to an array of factors starting with the underlying interferometric optical principles that enable high sensitivity (quantum limited due to heterodyne local oscillator gain), high-dynamic range (due to electric field detection), high lateral and depth resolution (in a way that partially decouples the two), and relatively low-cost compact systems that can achieve high speed, in situ optical imaging at depths which are clinically relevant to many major diseases and industrial applications. Beyond the physical principles, the success of OCT involves a complex ecosphere involving academics and industry engaging in research and development, publishing papers, filing patents, starting new product lines at existing companies or completely new startup companies, clinical studies, government funding, venture capital, and more. There is a clear pattern of federal dollars, technology/applications development, publications, and patents leading to transfer to for-profit startups or established companies.

Researchers from academics are supported by government funding, tuition, industry, and other means. Part of the satisfaction and responsibility of researchers using government funding is to make an impact in the world. This can be done through a variety of ways, one of which is the commercialization or technology transfer of their research to industry. There are many ways to approach commercialization and technology transfer, several of which will be outlined later in this chapter. Commercialization of new technology into products that are useful and that people will buy is very challenging, especially in the medical diagnostic device market. It's hard to get product development funds; it is hard to recruit top staff; it is hard to develop robust, safe, and manufacturable products; it is hard to get products approved by the various regulatory and reimbursement bodies; it is hard to prove clinical value; it is hard to beat the competition; and it is hard to make a profit that is necessary to keep this flywheel going and workers employed to maintain the current product(s) and start building the next product. All these things and more are required for a successful commercial product. Researchers sometimes believe that demonstrating feasibility in the lab is the biggest step, and the job is 90 % complete. In truth, from a commercialization perspective, it is usually only the first 10 % of the job and 90 % of the work remains to be done. Laboratory demonstrations are the first step in a long road toward commercialization.

This chapter will describe some of the history and factors involved in OCT technology transfer and give a snapshot of the current OCT market. It describes the ecosystem that has surrounded OCT commercial development including the role of government funding, publications, patents, and the role startup and established companies have played in bringing complex new products to clinical practices. It also briefly describes some of the impact of the technology and its future potential.

84.2 Academic Publications

One of the most successful and obvious ways to accelerate the transfer of OCT technology is to publish peer-reviewed journal articles and present research results at conferences. Figure 84.1 shows an example of the dramatic growth

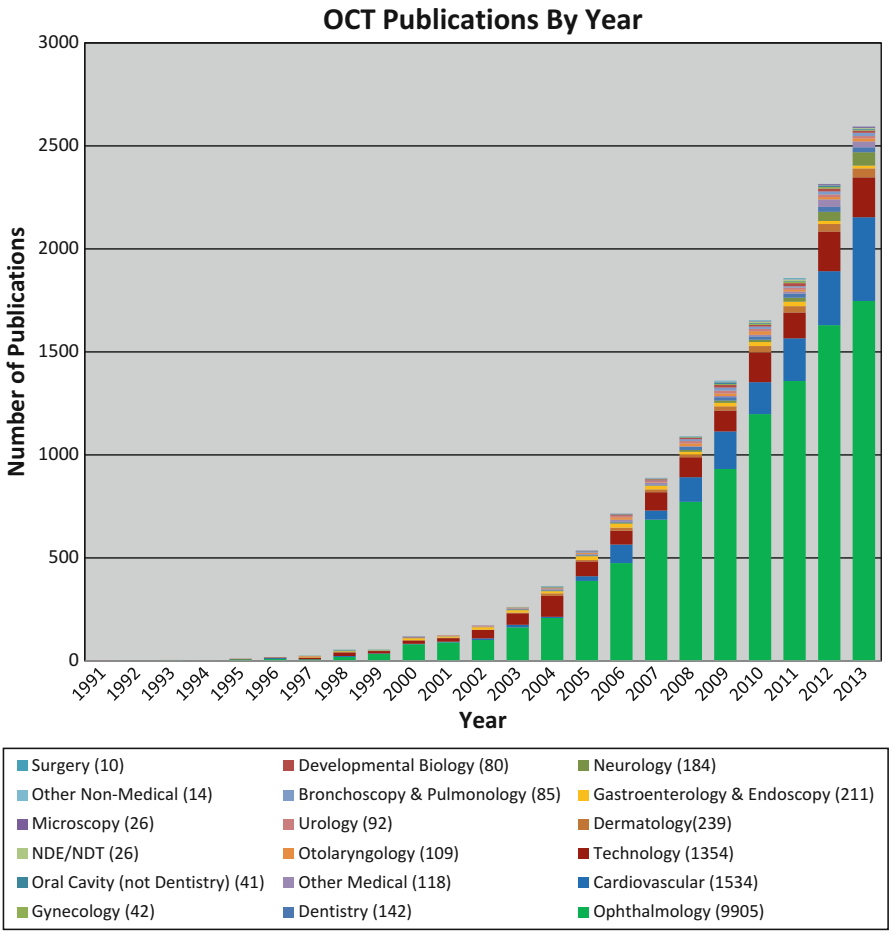

Fig. 84.1 Yearly OCT publications in PubMed categorized by application

in OCT papers since the first "OCT" paper by Huang et al. in 1991. A few things are very obvious, including the dramatic rate of growth of OCT publications (~200 papers/year) and that the publications are dominated by ophthalmology, followed by cardiology, and general technology. The legend below the figure shows the number of cumulative publications by subject area from 1991 to 2013.[1]

[1]In this analysis, only title and abstract were considered. The result is that this data probably underestimates the number of OCT publications but is a good bound. Another limitation is it can be difficult to categorize a publication into a particular subject area, and often publications are in multiple subject areas, and it is often a blurry call if the paper is about fundamental technology or about an application of the technology. Note this data is based on the PubMed database has many good attributes, but there are also limitations in that it doesn't cover every journal, and the number of journals it covers has increased over time.

It is interesting to consider what is driving these publications and the relative breakdown into each subject area. The answer is a combination of fertile and promising research frontiers, availability of government funding, clinical needs and trials, and very importantly, the availability of commercial, regulatory approved OCT products. Certainly, ophthalmic publications would not have grown so dramatically if (1) OCT was not a promising and effective technology for ophthalmology, (2) the NIH National Eye Institute and other government agencies around the word did not provide significant funding, and (3) a commercial company did not produce a reliable and field-able product early on to provide a catalyst for the entire process. These ophthalmic publications are dominated by researchers using commercial instruments, and Zeiss released its first ophthalmic OCT product around 1996 and was the only company making such a product for a good part of a decade – the formative years of this market's development. A similar point is also true for cardiovascular OCT. Cardiovascular/intravascular publications are currently the second largest publication category in OCT. Lightlab (acquired by St. Jude Medical in 2010) obtained its first regulatory approval in 2004. Like Zeiss, Lightlab was almost a decade ahead of other entries into this new market. Examining Fig. 84.1 around the dates of 1996 (2004) shows the start of a big increase in ophthalmic (cardiovascular) publications, in large part, as result of introduction of these new medical products into their respective markets and use by clinicians in clinical settings. These are two clear examples of the power of successful translation of technology from the research environment to the commercial environment. Not only has this resulted in many more publications because clinicians can use fully engineered and approved instruments in their studies and trials, it also dramatically accelerated bringing the technology to patient care (which improved the diagnosis and treatment of blinding ophthalmic diseases and promises similar advances for deadly cardiovascular disease), and it brought financial rewards and market share to the companies that took the business risks and were first to market.

It is interesting to speculate to what extent is publication history a bellwether for future commercial opportunities and are those commercial opportunities subject to the popular trends within funding agencies or are they matched with the best areas for potential impact. Upon examining the data, it seems that funding agencies and subsequent researcher publications do sometimes go off onto dead-end roads, but that those roads usually don't last very long. In addition, as we will see later in this chapter, the number of startup companies and new products from existing companies seem roughly to follow the number of publications. For example, there are several companies in the process of commercializing OCT for new applications such as in the dermatology and gastroenterology markets, the next two highest ranking publication areas in the Fig. 84.1.

84.3 Patents

Patents are obviously another important component of OCT technology transfer and the OCT marketplace in general. Patents play many roles, and the motives to

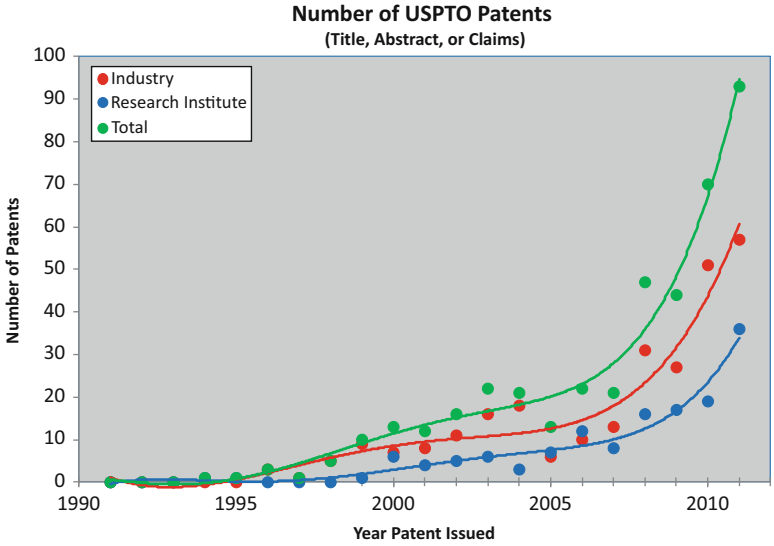

Fig 84.2 Yearly OCT USPTO issued patents

file them are varied. The motive for academics can be either to help enable a startup company the professor or student is involved in or to seek a share in the royalty fees by licensing to a company they are not involved in.[2] Many academics that start companies have licensed patents they authored from their institution, usually under exclusive terms. Exclusive fundamental patents can be a key factor in solidifying equity financing from investors. If a technology is relatively new, patents are especially important because they protect the substantial investment that is necessary to develop and validate the technology. In addition, patents can serve as a historical record of invention, much the way peer-reviewed journal articles do. For example, MIT documented swept source OCT (SS-OCT) systems in most of its earliest OCT patents dating back to 1991, even though the first MIT SS-OCT journal publication was not submitted for publication until 1996. The motives for filing patents in industry are also diverse. Patents can be filed in an effort to provide protection from a competitor entering a market, to ensure that the company has a right to continue to produce, to generate revenue, or for other motives.

Figure 84.2 shows the number of US Patent and Trademark Office (USPTO) patents issued by year that have OCT in the title, abstract, or claims. This Figure shows three curves: the total number of patents, the number of academic patents, and the number of industry patents. It is interesting that even in the early years, industrial patents outpaced university patents. This is, in part, due to the fact that many research institutions do not have the financial resources to file large

[2]In the United States, the Bayh-Dole Act states that universities need to share royalties with the inventor.

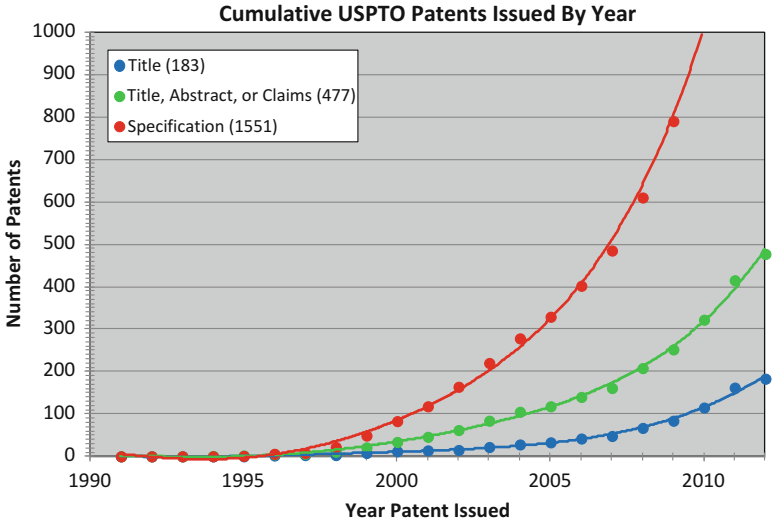

Fig 84.3 Cumulative OCT USPTO issued patents. Cumulative total since 1990 to September 2012 is shown in legend

numbers of patents, and, until recently, publications, research support, and recognition at conferences were key criteria for academic career success. Now, with more emphasis on translation of technology, these criteria may change and result in more academic patents.

Figure 84.3 shows the cumulative number of USPTO patents that have OCT in the title; title, abstract, or claims; and the entire specification. It is clear that the number of issued patents rose initially around 1995, followed by a significant increase around 2007, and there are now over 1,000 issued patents that contain OCT in the specification for the United States and many more patents in Europe and elsewhere. As with publications, it is difficult to determine what an OCT patent is, and there are clearly other patents that do not mention the term OCT, but would impact OCT systems. For example, a patent on a rotary single-mode fiber joint could impact OCT cardiovascular and endoscopic systems, even though it may not mention the word OCT.

Patents are sometimes classified as fundamental or incremental. It is very difficult to get a fundamental patent to issue now that OCT is over 20 years old. In fact, many of the fundamental patents from early years on time-domain OCT, swept source OCT, and full-field OCT systems, scanning techniques, probes, and disposables have expired or are about to expire. Thus, the many of recent patents may represent incremental patents. The role of an individual patent versus a portfolio of patents can be different in an academic setting versus an industrial setting. In an academic setting, patent filings are often focused on more fundamental ideas because it is very costly and risky for a university to develop a large portfolio of patents. Thus, university technology licensing offices will usually not file on incremental ideas. This is also, in part, due to university licensing offices

expecting the licensee companies to file the incremental patents. In industry, a large patent portfolio which may contain many incremental patents can be very important to thwart potential litigation even though it can be hard to place a value on a patent portfolio that is never challenged in court.

Patents can be licensed exclusively or nonexclusively. Licenses to startup companies often are exclusive, whereas licenses to larger companies tend to have a significant fraction of nonexclusive terms [1–3]. In the United States, most university licenses to startups tend to have a combination of fees, equity (1–5 %), and royalties (1–5 %) stakes in startup companies as well as revenue and market due diligence milestones that allow the university to change the licensing terms if the company is not progressing as agreed to in the commercialization process. Often, startup companies and their investors don't want to see precious early company cash going to university licensing offices so they often trade equity for upfront fees. Universities are becoming more stringent about restricting the fields of use to a license grantee in order to avoid situations where a license is given in a field that is never commercially developed. Startup companies and their investors often want exclusivity in the broadest fields of uses, even though this is contrary to the near-term goals of startups which must often focus on a particular market for many years in order to become successful.

It is mainly universities and "patent trolls" that license to industry.[3] Licensing to industry is difficult, and the patent has to be very powerful, as industry has a strong disincentive to give up precious margin (revenue) in the face of market pressures for profitability. Furthermore, while universities typically develop multiple patents in different areas, the vast majority of the licensing revenue is in a very small percentage of their licenses and patents. It is estimated that about one in 200 university patent licenses generate in excess of $1M in any 1 year [3]. At one leading US University between ~85 % of the total royalty and fee income came from the top ~12 patent families. Thus the vast majority of the licensing revenue comes from a small number of big hits. It is probable that a significant fraction of university patents are never licensed at all [1–3]. Patenting law is complex and varies from country to country and over time. For example, US patent law has recently shifted from "first to invent" to "first to file."

Recent trends suggest that patents are playing a more prominent role in the industry. There have been recent major news stories about the increasing value of industrial patent portfolios, particularly in big industries such as wireless where giants such as Apple, Motorola, Google, Microsoft, Samsung, and others are battling for market share [4]. For example, Google bought Motorola Mobility partly for its patent profile for ~$12B in 2011. As another example Apple and Samsung have been embroiled in many patent related lawsuits around the globe, with billions of dollars in damages claimed between them. It seems unlikely in the near term that

[3]Patent troll is a derogatory term for a company that creates or acquires patents and often use what some feel are unsavory tactics against alleged infringers in a manner that is aggressive and often they have no intention to produce any products of their own.

OCT patents will be this litigious, and part of the reason is Apple sells ~$1B in iPhones per week – a long way from OCT sales volumes. In fact, there have only been a very small number of OCT patent battles. But as the revenue stakes increase, so does the likelihood of patent litigation and some of the ugliness of patent trolls and big company tactics being used against small companies [4]. For example, a small startup company is often in no financial position to litigate against an established large competitor, nor are they in a position to fight a competitor litigating against them – even if the apparent legal metrics of the cited patent infringement seem on the side of the small company. Legal battles involving patents can easily exceed $1M and that can be a big chunk of the available cash for small companies.

In summary: patents are important in the OCT technology transfer process and the OCT market in general; patents play a particularly prominent role in startup companies; it is difficult to have a fundamental patent issue after ~25 years of technology development; a significant percentage of university patents are never licensed, the majority of value in university patents comes from a small fraction of the issued patents, and the motives for universities and industry filing patents can be quite different. It is clear that the number of research and industrial sponsored OCT patents is increasing, and this is due to many factors, including the fact that the underlying commercial market is growing, as well as the general high-tech industry-wide increase in the importance of patents.

84.4 Government Funding in OCT

The US government and other governments around the world have been large supporters of funding for research and development in OCT and its applications. This includes funding for basic science and technology as well as applications of the technology including clinical studies and trials. As with journal publications and patents, it is difficult to determine what is OCT funding and even more difficult to track down all the potential sources of OCT government funding around the world. A snapshot of some examples of government funding is shown in Fig. 84.4. This plot contains cumulative funding in OCT for US National Science Foundation (NSF), US National Institutes of Health (NIH), Canada, and the United Kingdom.[4] This data assumes if "Optical Coherence Tomography" is mentioned in the title, abstract, or summary of the grant mentioned, then it was counted as an OCT grant. This data is drawn from a more comprehensive analysis contained in reference [5].

Figure 84.4 illustrates several things, foremost of which is that there has been a steady increase in funding, and in aggregate, this cumulative funding approached $0.5B in the last decade. The actual total could be far in excess of this, approaching

[4]The Canadian data is from the combined Canadian funding from Natural Sciences and Engineering Research Council (NSERC), Canadian Institutes of Health Research (CIHR), and National Cancer Institute of Canada (NCIC). The UK data is combined UK funding from Engineering and Physical Sciences Research Council (EPSRC), Biotechnology and Biological Science Research Council (BBSRC), and Medical Research Council (MRC).

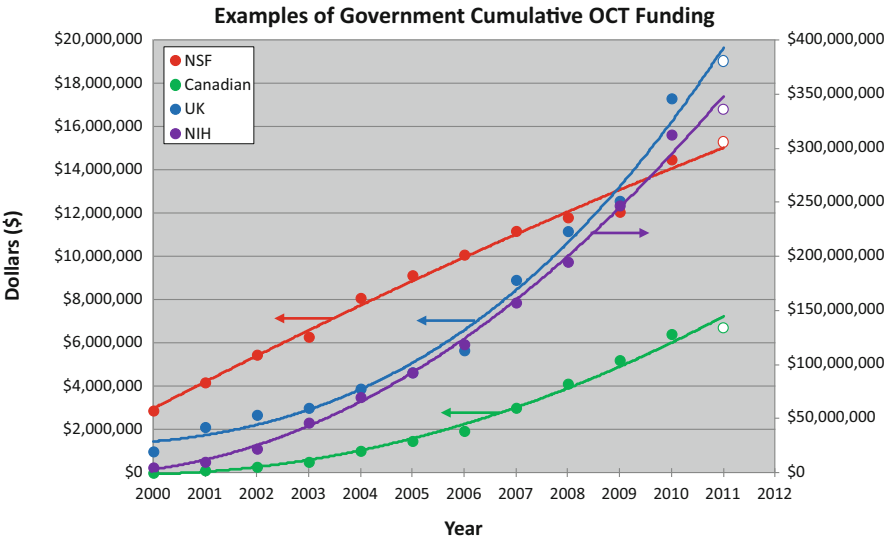

Fig. 84.4 Examples in growth of government funding in OCT. The NSF, Canadian, and UK funding are on the left vertical axis, and the NIH funding vertical axis is on the right. 2011 is a partial year's result

well over $1B since this analysis does not count numerous major sources of OCT funding in the United States, Europe, Japan, Russia, China, and other countries. The majority of funds shown here have come from the NIH, and within the NIH, the National Eye Institute (NEI) has accounted for much of the funding to date [5]. The NEI money has supported ophthalmic clinical studies and clinical trials, which can be expensive. One potential noteworthy trend is that NSF funding appears to be growing at a smaller rate than other sources. This does not bode well for US researchers and industry because NSF funds are better matched to fundamental technology development which is key to future innovation and commercialization.

A question arises as to whether or not this $500M to $1B of worldwide government funding has been effective. Most would say the result is an unqualified success from many metrics. OCT in ophthalmology alone has had over ~100 M procedures, been a major sight saver, created a paradigm shift in ophthalmic practices around the world, generated over $1B in capital equipment sales, generated over $1B in reimbursement in 2010 alone, and created many jobs in the process [5]. With OCT commercialization in other clinical specialties such as cardiovascular, gastroenterology, and oncology, the return on investment and clinical impact on healthcare could continue to be impressive.

It is interesting to speculate about where OCT R&D dollars will come from in the future. In the past, the majority of funding for R&D has come from the government. But with the OCT market approaching ~$0.5B/year it is clear that R&D from industry will begin to play a significant role just as it has in other mature industries such as microprocessors and telecommunications. In the financial

statements of public and private companies, the percentage of revenue spent in R&D can vary from 15 % to 50 % or more. For mature OCT companies with established product lines, the R&D expense number is lower (~15 %), whereas for small startup companies the number can be much higher. Assuming 20 % of a $0.4B market yields an industrial R&D expenditure of ~$80 M/year in 2012. This is about the same level as the yearly US government-sponsored R&D spending in 2012 as seen in Fig. 84.4. Thus, the current government and industry R&D expenditures are roughly of the same magnitude.

This trend does not diminish the importance and necessity of future university research and the government funds that support it. OCT is still an emerging field, and there are large gaps between what industry will fund and the government can fund. Government funding supports new technology development, clinical research, and clinical validation studies. This support continues to be critical and highly leveraged, since industrial funds alone may not support OCT innovation in some of the most new and promising areas for the future.

In summary, the amount of cumulative government spending around the world has exceeded $0.5B, government funding has had a profound effect on the development and commercialization of OCT products, the financial return on this government spending has been outstanding, and continued government support is needed to continue to speed new applications of OCT to market to benefit patient care and commerce. Successful entry of commercial OCT products can accelerate this funding and its positive impact on commerce and clinical care, as is clearly the case in ophthalmology and cardiology.

84.5 Some Examples of Technology Transfer to the Market

Success with technology transfer and the launch of any new product line within a startup company or within an established company is extremely hard. It's difficult and risky to hit all the milestones necessary in the marketplace: to raise funds; recruit and build a team; develop new technology, qualify it, and get regulatory clearances set up manufacturing lines, product support, and quality systems; prove value in clinical studies and clinical trials; get reimbursement; make a profit with the necessary profit margin to reinvest money into supporting existing products and R&D for new products to keep and grow market share; and return profit to the shareholders and keep workers employed. For these reasons, as mentioned previously, academic research is usually only the first 10 % of the job of commercialization, and technology translation often takes much longer and is much harder than expected.

Figure 84.5 (which is similar to that shown in references [6, 7]) shows one qualitative timeline for evolution and phases of a new medical product such as OCT. This suggests that it takes on the order of 3–5 years to design, develop, and qualify a product to enter a new market. Startups have the additional burden during this phase of developing the other aspects of their business (regulatory, sales, marketing, manufacturing, etc.). It then takes another 3–5 years for that product to gain market relevance by, for example, proving efficacy and cost savings though

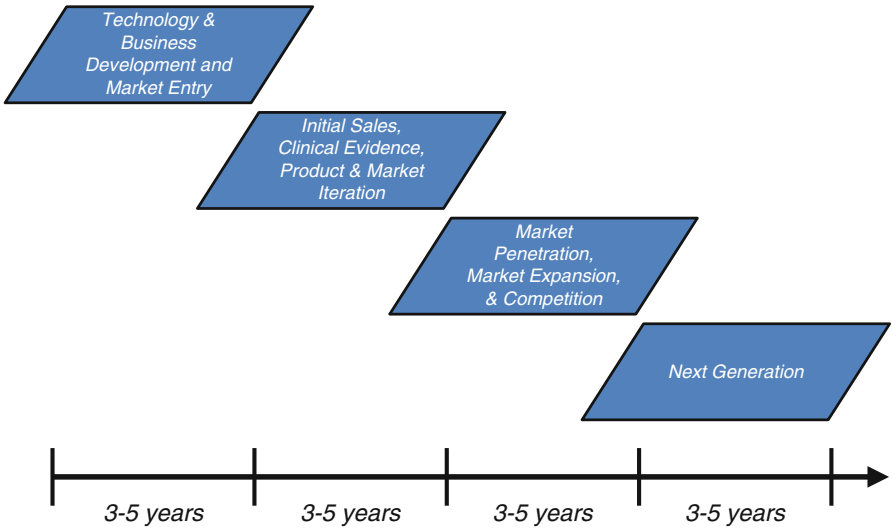

Fig. 84.5 Phases of product evolution ("five-year rule")

clinical studies and clinical trials. Beyond that, it can take another 3–5 years to ramp into significant market penetration, explore and expand into closely related markets, and face competitive pressures. To reach the end of this phase can take 10–15 years. The timeline for additional companies developing a competitive product in a market where a prior product has already received regulatory clearance and some level of market penetration can be, and usually is, much faster than that shown above. The first company often paves the way in regulatory bodies and the market at large. Thus, the second company to enter a new market gets an easier road, but has a disadvantage in the ensuing fight for market share.

Of course not every product falls into this simple phased model, but it is interesting that Advanced Ophthalmic Devices (AOD) and Lightlab Imaging which were among the first OCT companies followed this general pattern. AOD was an OCT startup founded in 1992 out of MIT and acquired by Zeiss in 1994. Lightlab Imaging was also an MIT OCT startup founded in 1998. Lightlab was acquired by Goodman Corporation in 2002 and then acquired by St. Jude Medical in 2010. It is interesting to note that both Zeiss/AOD and St. Jude/Lightlab Imaging led the next significant competitor entry into their respective markets by almost a decade. For both companies, this translated to high risk followed by high reward in obtaining a large market share. Zeiss had shipped ~$100M's in ophthalmic OCT products before a significant scale competitor emerged. St. Jude is currently at ~$100 M/year run rate. Perhaps more important than the profits and market share, the successful transition of the technology had a massive impact in bringing critical diagnostic and research tools to impact clinical care for blinding ophthalmic diseases and deadly cardiovascular disease, accelerating progress by almost a decade.

Figure 84.6 illustrates how OCT in ophthalmology followed the general trend of Fig. 84.5 and further shows the high degree of correlation that makes up this

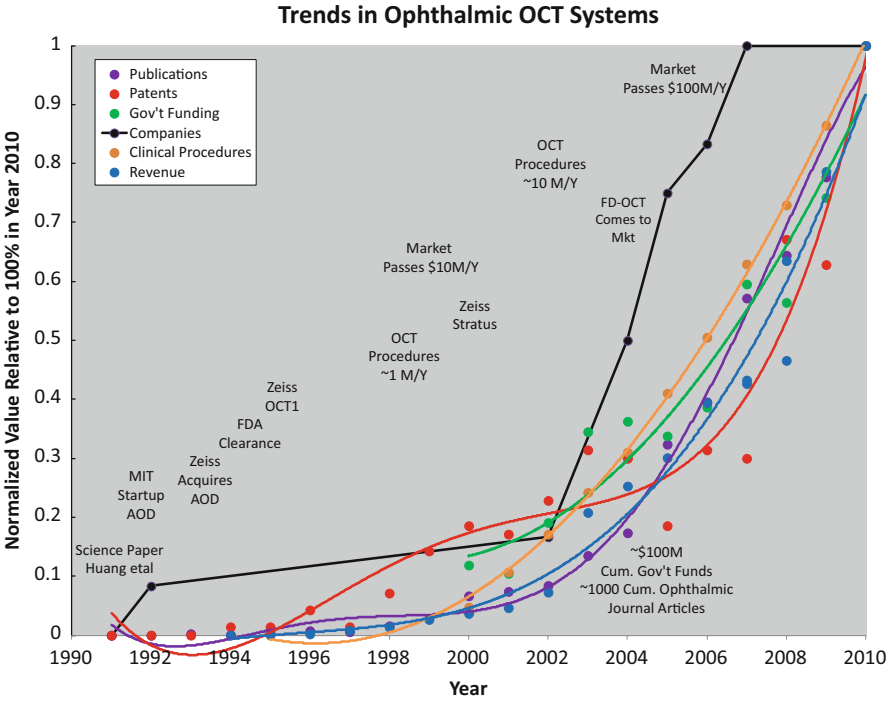

Fig. 84.6 Trends in the ophthalmic OCT system market. (The government funding shown is total NIH funding, but that funding is dominated in this time period by ophthalmology. Similarly, the patents are all OCT patents not just ophthalmology. The clinical procedures are based on Medicare data and were extracted from reference [8].) All the data are normalized to 2010

ecosphere of publications, patents, government funding, companies starting OCT ophthalmic products, clinical ophthalmic procedures (based on CPT code 92135), and revenue for the ophthalmic OCT market. AOD started in 1992, and Zeiss acquired it in 1994 and released its first product in 1996 – 4 years later and within the time period shown in phase 1 of Fig. 84.5. Zeiss shipped ~400 units of its first-generation product (OCT1/2) and gained critical clinical evidence and validation on utility, releasing its second-generation OCT product Stratus in 2002 – 6 years later and within that period shown in phase 2 of Fig. 84.5. There was significant market penetration of Stratus and then around 2007 when Zeiss and several other companies released spectral domain SD-OCT technology – 5 years later and within the time frame shown in phase 3 of Fig. 84.5. It is interesting to note that while commercialization of Fourier domain OCT technology (both SD-OCT and SS-OCT) was a major boost to OCT system utility and capability, the market penetration and clinical utility of TD-OCT had reached a significant level prior to introduction of Fourier domain OCT to the ophthalmic marketplace. While there are now many ophthalmic OCT companies, Zeiss still maintained the largest market share as of 2013.

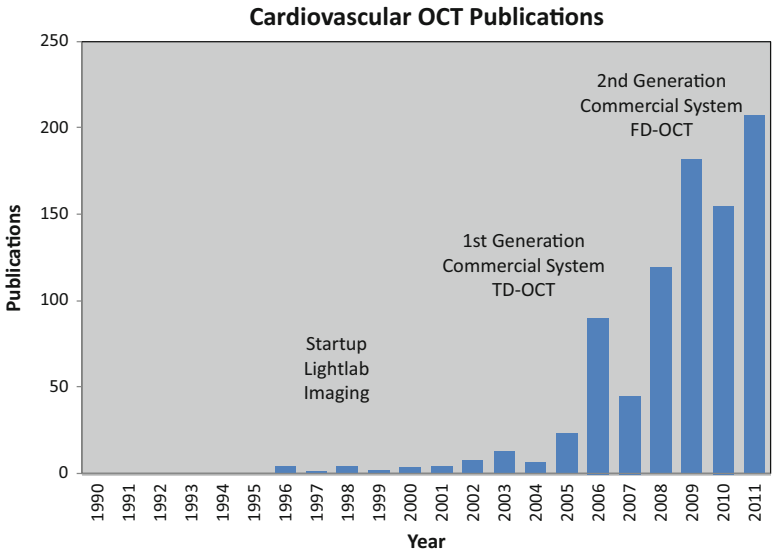

Fig. 84.7 Estimated number of cardiovascular/intravascular OCT publications

Cardiology followed a very similar trajectory as shown in Figs. 84.7 and 84.8. Lightlab Imaging (originally incorporated as Coherent Diagnostic Technology) was founded in 1998 and initially focused on the microscopy and GI markets (for Barrett's esophagus). About a year later, the company changed direction and focused on cardiology. In 2004, Lightlab commercially released its first-generation TD-OCT cardiovascular system in Europe – 6 years later and within the phase 1 shown in Fig. 84.5. By 2005/2006, there were over 1,000 in-man clinical procedures. By 2008, there were approximately 10,000 clinical procedures. Between 2004 and 2009, intravascular OCT gained market relevance – a 5-year period commensurate with phase 2 shown in Fig. 84.5. In 2009, Lightlab released its second-generation swept source/Fourier domain (SS-OCT) cardiovascular product, and in 2013, revenue is estimated to be ~$100M/year, and the number of cumulative clinical procedures has exceeded 100,000. This cardiovascular OCT path was very similar to that experienced in ophthalmology in that it began with a MIT startup company that was eventually acquired by a larger company, a first-generation system paved the way for understanding clinical utility and the market in general, followed by a second-generation system that increased market growth. Also, there was nearly a decade year gap before a scale competitor introduced a product into the marketplace.

Another successful example of OCT technology transfer is Optopol. Optopol was initially distributing ophthalmic equipment and producing devices such as ophthalmic projectors, refraction units, Placido ring corneal topographers, and automated perimeters. Ophthalmic OCT was an attractive market opportunity and for them. Optopol had a leading ophthalmic OCT research group close by, the Nicolaus Copernicus University (NCU). NCU researchers had received significant

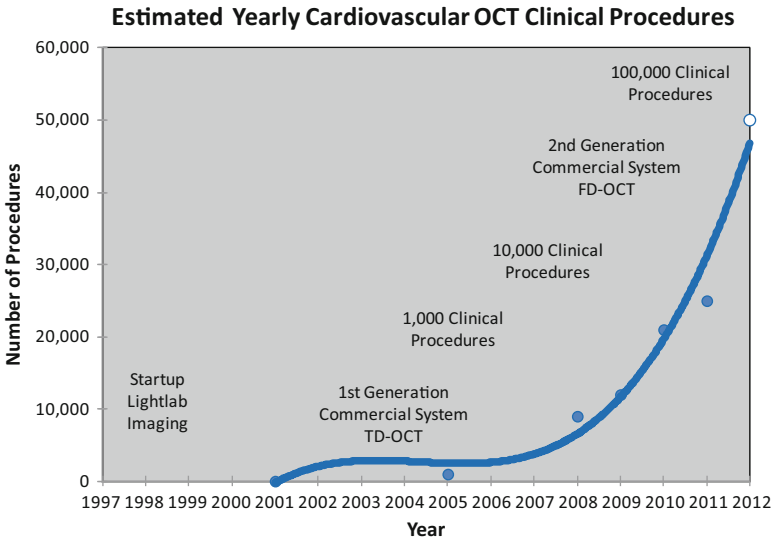

Fig. 84.8 Estimated number of cardiovascular/intravascular OCT clinical procedures. Also shown on chart are cumulative clinical procedures

government funding and had a working SD-OCT clinical prototype. In 2005, an agreement between Optopol and NCU was signed. In addition to transferring technology from NCU to Optopol, the agreement also created an R&D office at NCU. The idea was to create opportunities for jobs in industry for NCU graduate students. In 2009, Canon Inc. acquired Optopol for $94M.

Bioptigen is a different example of an OCT startup. Bioptigen was founded in 2004 and is a supplier of OCT to the preclinical (small animal) and clinical ophthalmology research market, including a handheld SD-OCT product for pediatric ophthalmologists. Bioptigen has strong ties to academic work at Duke University, and Bioptigen is exclusive licensee to patent portfolios from Case Western Reserve University and Duke University. Bioptigen introduced the first commercial ultrahigh resolution UHR SD-OCT system in 2006 and received FDA clearance for the first handheld SD-OCT instrument for ophthalmology in 2012. Government sources played a strong role in funding the company. Initial funding included SBIR grants. Early on, Bioptigen had won in excess of $7M in SBIR awards directly or indirectly in partnership with others, while total equity financing is only $3.8M, none of which came from traditional venture capital. This shows the government can play a big role in both funding research and industrial activities.

There are also examples of highly successful startup companies starting with minimal academic connections and government support. A good example is Optovue. Optovue was founded in ~2004 and was the first to get FDA approval for an ophthalmic SD-OCT system and by 2010 had revenues of ~$50M/year. Optovue was a classic startup company and currently remains privately held. While Optovue interacts closely with academic researchers, the technology transfer

relationship into Optovue was quite different in that it relied heavily on the passion and technical and business expertise of the founder, Jay Wei. He was the lead OCT engineer on the development and release of the early Zeiss OCT products.

There are many other examples of successful technology transfer from universities to startups and established companies (as shown in the Table 84.1). There are also clear examples of companies that have started organically or through association with universities that have not yet been successful from a business perspective. The poor execution is sometimes a combination of bad timing, inexperienced management and/or engineers, insufficient funding, bad choice of markets that didn't develop or are taking a long time to develop, missed milestones, bad luck, or a combination of these and other factors. Even location can be an important factor in the success of a startup. There are several specific regions around the world that have a long track record of fostering startups; these areas have an ingrained startup culture with more risk tolerance and a local economy with access to a talent pool and industrial infrastructure and equity financing (e.g., venture capital) that can be highly beneficial to the success of young companies. These advantages are simply not available in many regions of the world. In startup companies, delays in product development or missed milestones can be deadly, as investors quickly grow impatient and compeition moves on. In large established companies, there is often a bigger financial base and other resources to buffer negative effects. Note that there is a wide range in the amount and types of funding raised by the companies listed in Table 84.1. It ranges from a few million dollars to well over $100M. To bring a successful complex medical device product to market can be quite expensive and is most often well over $10M to hit profitability. The more complex the technology, market, regulatory hurdles, and reimbursement hurdles the higher the number.

84.6 Commercial OCT System Companies

There are ~40 OCT system companies in the market as of mid 2012 in varying stages of maturity.[5] There were even more startups and established companies in stealth mode that have started or are looking to start new OCT related products. There are also several OCT companies that have stated over the past decade and gone out of business or stopped OCT development some of which are listed. Figure 84.9 shows a graph of some of these companies and the approximate time that significant resources were invested in new OCT product development efforts (as of mid 2012). Table 84.1 shows some additional data on these companies including whether their technology initiated as a startup company and/or if there was a strong connection with an academic institution. Some of the data was supplied directly from the companies, and some of the data was estimated where no input was supplied from the company.

[5]There are other OCT companies that currently exist or started in this time period but are not listed here due to their small scale and/or company status or desire to remain confidential.

Table 84.1 Companies with OCT system products in the market or in development

OCT system companies	Academic	Startup	OCT market focus	Comments
AGFA Healthcare			Dermatology systems	Product developments start in 2010. CE Mark 9/5/2011. FDA in process. Technology developed internally
Alcon (LenSx)		Y	Laser technology for cataract surgery that used OCT guidance	LenSx was founded in 2006, was acquired by Alcon for $744 M in 2010. Much of LenSx technology is not focused on OCT. However, OCT being used for laser surgical guidance
Avinger		Y	OCT-guided catheters for chronic total occlusion and atherectomy	Founded 2008. OCT effort started ~2008. OCT product pending FDA clearance (expected Nov 2013)
Bioptigen	Y	Y	Ophthalmic and research OCT systems	Cofounded in 2004 by Dr. Joseph Izatt at Duke University. FDA approval in 2006
Canon (Optopol)	Y	Y	Ophthalmic OCT systems	Optopol founded in 1992, and its OCT effort started in 2005. Canon Medical acquired Optopol for $94 M in 2009. Optopol had strong connections to leading researchers at Nicolaus Copernicus University, and OCT work started at Optopol in 2005 when an agreement with NCU was signed
Carl Zeiss Meditec (AOD)	Y	Y	Ophthalmic OCT systems	Advanced Ophthalmic Devices (AOD) was founded in 1992 by Eric Swanson, Dr. James Fujimoto, and Dr. Carmen Pulifiato at MIT and Harvard Medical School in 1992. Zeiss acquired AOD in 1994. Zeiss developed and released several generation of products: TD-OCT, OCT1/1996, OCT2/2000, Stratus/ 2002, Visante/2005, FD-OCT Cirrus 2007
Colibri Technologies	Y	Y	Cardiovascular OCT	Colibri was founded in 2007 and originated from research conducted at Sunnybrook Health Sciences Centre in Toronto, Canada. Sunnybrook is affiliated with the University of Toronto
Compact Imaging		Y	OEMing compact OCT systems	Founded ~2011. Product in development
Diagnostic Photonics	Y	Y	Surgical-guided OCT systems	Cofounded in 2008 by Dr. Stephen Boppart and Dr. Scott Carney at the University of Illinois at Urbana Champaign

Heidelberg Engineering			Ophthalmic OCT systems	OCT effort started ~2005 when Heidelberg acquired 4optics AG (Lubeck Germany) in 2005. First OCT FDA clearance 2006. 2007 released FD-OCT
Heliotis AG	Y	Y	Microscopy OCT Markets	Heliotis was founded in 2005 and was a spin-off of Swiss Center for Electronics and Microtechnology, a government-sponsored research institution in Switzerland. Shipments ~2007
Imalux	Y	Y	OCT for ENT, gynecology, and urology	Imalux was founded in 2000 by Drs. Felix Feldchtein, Alexander Sergeev, Valentin Gelikonov, and Grigory Gelikonov from the Institute of Applied Physics at the Russian Academy of Sciences. OCT efforts started around 2002. FDA clearance in 2004. Shipments 2005
ISIS Sentronics		Y	Inspection systems: semiconductors, automotive, films, coatings, and medical	ISIS Sentronics GmbH was founded by CEO Dr. Alexander Knüttel in 2006. ISIS Optronics was founded in 1999 and first sales of SkinDex300 in 2000
LLTech	Y	Y	FF-OCT microscopy systems for research and pathology for ex vivo tissue/biopsies assessment	LLTech was cofounded in 2007 by Dr. Claude Boccara and Bertrand Le Conte de Poly at ESPCI Paris Tech University in France and licensed CNRS (National Center for Scientific Research) technology. First OCT funding in 2009. Research market approval 2011 (CE and United States)
MedLumics		Y	OCT systems using integrated optics for cardiology and oral surgery	Founded in 2009. A-round investment in 2011. Company focused on integrated optical photonic circuits to lower size and costs
Michelson Diagnostics		Y	Dermatology market for diagnosis, staging, and monitoring of nonmelanoma skin cancer	Michelson Diagnostics OCT effort started in 2007. Michelson was spun out of an established medium-sized optical engineering company. FDA approval 2010. Shipments 2012
Nidek			Ophthalmic OCT systems	OCT effort started ~2007. 2009 RS-3000 Product Announced
NinePoint Medical	Y	Y	Endoscopic OCT systems for gastroenterology	Founded in 2010 and licensed patents and other IP and receives assistance from the Harvard/MGH. FDA approval 2011. Shipments 2013
Novacam Technologies	Y	Y	3D metrology for industrial and medical markets	Founded in 1997 and OCT systems began in 2004/2006. Novacam works closely with and licensed technology from National Research Council Canada. Shipments ~1999

(*continued*)

Table 84.1 (continued)

OCT system companies	Academic	Startup	OCT market focus	Comments
PhotoniCare	Y	Y	Handheld OCT for otolaryngology and primary care applications	Co-founded in 2013 by Dr. Stephen Boppart and Dr. Ryan Shelton at the University of Illinois at Urbana-Champaign. Product in development
Abbot Medical Optics		Y	Laser cataract surgery systems that used OCT guidance	Abbot Medical Optics acquired Optimedica for $400M in 2013. Optimedica was founded in 2004 and much of the technology was not focused on OCT but on laser surgery. But OCT was integrated to help guide the surgical procedure
OptoMedical Technologies GmbH			Universal OCT camera add-ons for medical imaging	Founded in 2010
Optos (Opko/ Ophthalmic Technologies Inc.)		Y	Ophthalmic OCT systems	Ophthalmic Technologies Incorporated (OTI) founded in ~2002. Acquired by OPKO in 2007 for ~ $15 M. Optos acquire OTI from OPKO in 2011 for ~ $38M. OTI got FDA clearance in 2005, sold in Japan in 2003 via Nidek
Optovue		Y	Ophthalmic OCT systems	Founded in 2004 and was the first to FDA approval for SD-OCT. FDA approval 2006/RTVue, 2010/iVue
Santec			Medical, and nonmedical OCT systems and OEM market	Santec OCT technology R&D started ~2004. Shipments ~2005
Schwind eye-tech-solutions			Refractive and therapeutic corneal surgery	Uses OCT to guide laser surgical ophthalmic procedures. Product release ~2009. Product start ~2007 (estimate). Acquired by Bausch + Lomb in 2012
Shenzhen Moptim Imaging	Y	Y	Ophthalmic and inspection OCT systems	Moptim was founded in 2004 and started in collaboration with Shenzhen Tsinghua University in China. They are currently focused in China market. Chinese regulatory approval ~2009
St. Jude (Lightlab Imaging)	Y	Y	Cardiovascular OCT systems	Founded in 1998 by Eric Swanson, Dr. James Fujimoto, and Dr. Mark Brezinski at MIT as a Joint Venture with Zeiss. Goodman Ltd acquired Lightlab in 2002. St. Jude Medical then acquired Lightlab for $90 M in 2010. TD-OCT 2004/EU, 2006/China, 2007/Japan, FD-OCT 2009/EU, 2010/USA

Technolas Perfect Vision			Refractive and cataract surgical products	Uses OCT to guide laser surgical ophthalmic procedures. Product release ~2011. Product start ~2009 (estimate). Acquired by Bausch + Lomb in 2012
Terumo	Y		Cardiovascular OCT systems	Terumo entered a joint development agreement and licensed numerous patents and other IP and receives assistance from the MGH research in 2004. 2012 European Approval
Thorlabs			Research and OEM market	Thorlabs collaborates with numerous universities; the majority of Thorlabs OCT technology was developed organically around 2004. Shipments ~2005
Tomey		Y	Ophthalmic OCT systems	Tomey is a 40-year old company, and its OCT technology started ~2007. Announced SS-OCT system in 2008
Tomophase		Y	Pulmonary OCT systems	Founded in 2003 (seed) and got A-round in 2005. Founders all came from telecom backgrounds. In April 2014, Tomophase Corp. was acquired by a Chinese company called Winstar, and is now named Tomophase Inc
Topcon Medical Systems	Y		Ophthalmic OCT systems	Topcon Medical Systems OCT effort started 2004. FDA clearance in 2007. Licensing of technology from Tsukuba University, then collaborated during the development
Tornado Spectral Systems		Y	On-chip spectrometers for OCT systems	Founded in 2010 and started OCT in 2011. Developing on-chip spectrometers for OCT applications using photonic integrated circuit technology
Volcano Corporation	Y		Cardiovascular OCT systems. OEMing OCT subsystems through Axsun	Cardiospectra was founded in 2005 by Marc Feldman and Thomas Milner from University of Texas at Austin. Volcano acquired Cardiospectra in 2007 for $63 M for its start in OCT. Volcano also acquired Axsun for its OCT laser technology in 2008 for $21.5 M. In 2013 Volcano announced it was canceling its OCT development and in 2014 Volcano announced it was divesting Axsun Technologies

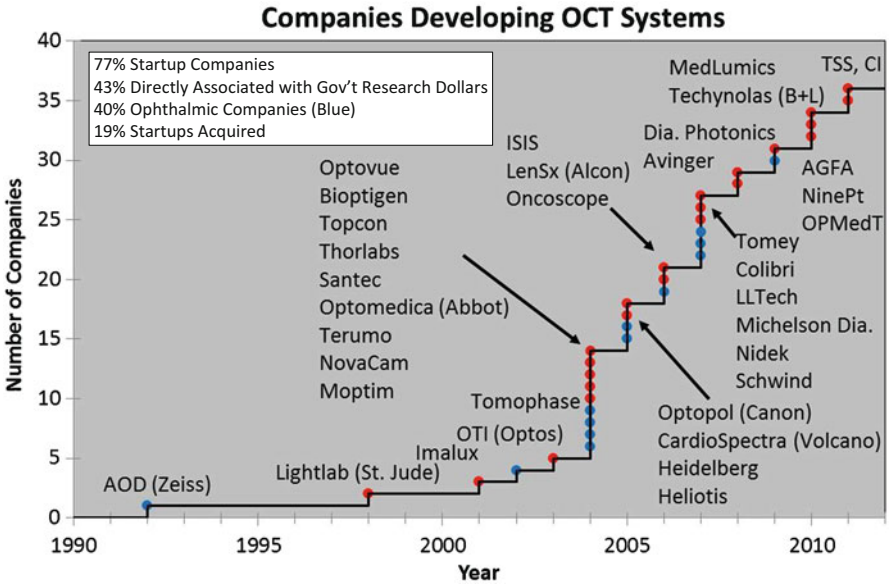

Fig. 84.9 Startups or established companies OCT product development start as of mid 2012

As shown in Fig. 84.9, there was a slow start to OCT system companies. Advanced Ophthalmic Devices, Lightlab Imaging, Imalux, Ophthalmic Technologies Incorporated, and Tomophase were among the first five OCT companies and were all startup companies – a clear testament to the entrepreneurial spirit and power of startups. It is interesting to note that ~75 % of these companies were at one point, startup companies. Additionally, almost one half of these companies owe their start to strong ties with academic institutions that had significant sources of government funding. Of the companies listed, 14 are related to ophthalmology. In the 2005 time frame, there was a lot of activity in new OCT product starts.

Approximately 19 % of the startup companies have been acquired by larger established companies for a total purchase price of ~$300M (not including LenSx, Optimedica, and Technolas which were acquired for large sums but mainly for there non-OCT technology. As of mid 2013, no startup company has gone to the public market for financing.

The end of this chapter shows pictures of some examples of OCT system products in the marketplace.

84.7 OCT Market Size Estimates

It is difficult to get precise data on the worldwide OCT system market. There are many manufacturers, some with direct sales channels and some with sales supported with distributors that have markups; there are a wide variety of models with differing

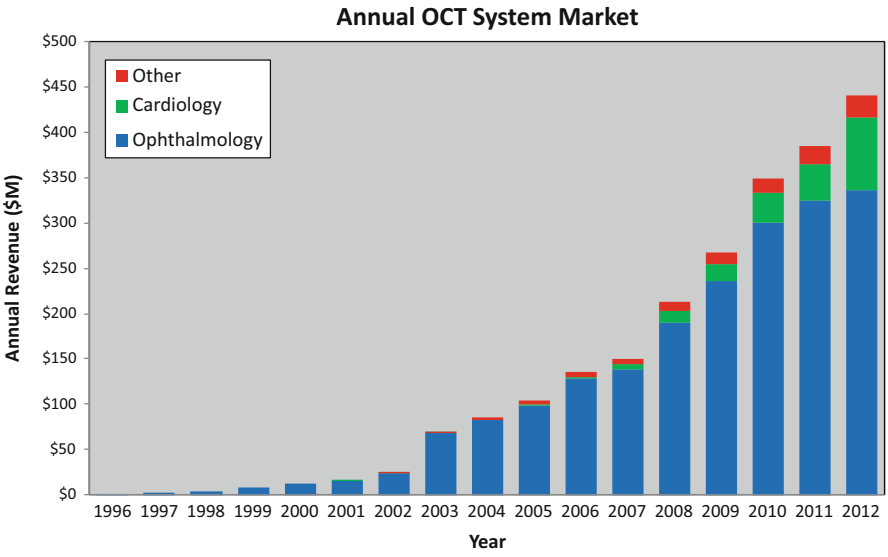

Fig. 84.10 Estimated OCT system annual market size

capabilities and a wide variety of price points. A coarse estimate of the historical OCT system world market is shown in Fig. 84.10. This data was arrived at by a combination of means and represents equipment manufacturers, not end user sales which can often pay higher prices due to distributor costs. While the exact values are subject to some error, one thing is certain: the market has grown dramatically over the past decade and likely exceeded $400M/year in 2012.

It is clear the market has grown dramatically over the past decade and will most likely pass $0.5B in 2013 or shortly thereafter. The majority of the revenue today is clearly from ophthalmology; this is due to the fact that ophthalmology was the first market to be entered, and OCT has proven to be a very powerful tool in ophthalmology, becoming a standard of care. However, cardiovascular OCT is growing rapidly, and many of the startup companies in dermatology, gastroenterology, urology, gynecology, and other markets are just beginning to reach maturity. This should continue to grow the market.

84.7.1 Ophthalmology

As of mid 2012, there are about ten companies in the diagnostic ophthalmology OCT market, plus four more that are using OCT to guide laser surgical procedures in ophthalmic applications. Figure 84.11 shows the estimated growth in total US OCT procedures, the allowed OCT-related Medicare service (based on CPT codes 92132, 92133, 92134, and 92135 used to bill for OCT), and the estimated yearly OCT billing charges [8, 9]. It is impressive that the worldwide OCT billing in 2010

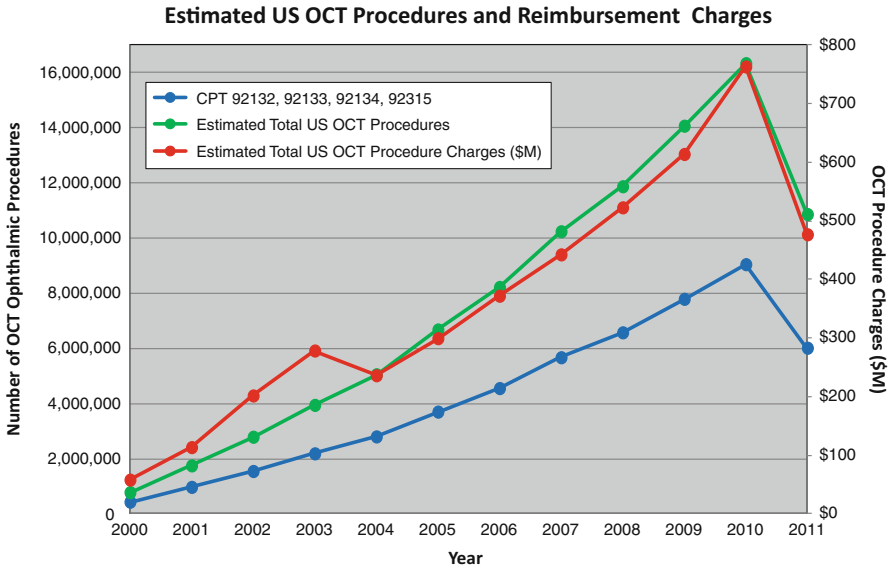

Fig. 84.11 Yearly OCT-related CPT Medicare services, estimated US OCT procedures, and OCT procedure charges

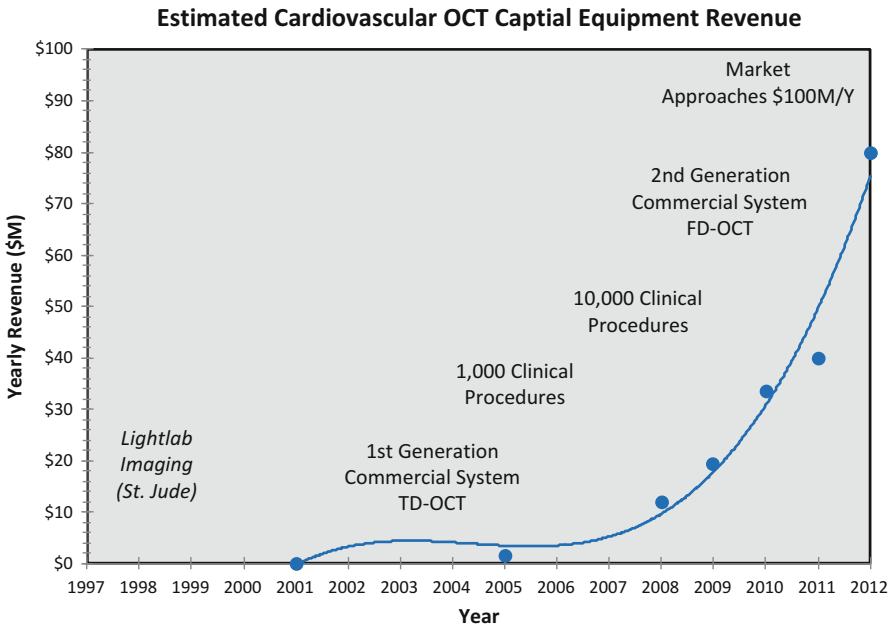

Fig. 84.12 Estimated OCT cardiovascular market

most likely exceeded $1B and was ~$750 M in the United States alone in 2010. This large spending has caught the eye of regulators, who dramatically reduced the Medicare reimbursement allowance in 2011 [8, 9]. This reduction is clearly seen in Fig. 84.11. In 2011 US Medicare policy eliminated CPT code 92135 and split into three new codes: 92132 anterior segment, 92133 optic nerve, and 92134 posterior segment [9]. More relevant in that year, the code was changed from allowing for separate billing of each eye to only allow billing once whether one or two eyes were scanned. Over $100M in reimbursement payments in the United States vanished as a result of this reimbursement change.

This could create a dampening effect on ophthalmic revenue growth. However, there is still a strong opportunity in the optometry market, and much of the developing world still does not have access to any ophthalmic OCT technology. Furthermore, since there is strong clinical evidence that OCT improves clinical outcome, OCT procedures will likely continue to increase and be performed as a standard of care, even though reimbursements have decreased nearly a factor of two. For example, ophthalmologists may perform and bill for fundus photography which has a higher reimbursement, but still do OCT unbilled. Furthermore, even though the OCT Medicare reimbursement rate has dramatically reduced the ROI, it is still attractive for many practices. For example, assuming an ophthalmic OCT instrument costs ~$60k, the blended weighted reimbursement is ~$44, a procedure takes 30 min is used 8 h/day at 100 % utilization yields revenue of ~$200 k/year. Even allowing for costs including technicians taking the exam, doctor reviews, infrastructure, cost of capital, and less than 100 % utilization still yields a very attractive ROI.

It is interesting to estimate the total worldwide ophthalmic OCT procedures. However, there is no readily available data showing the number of worldwide procedures or a reliable breakdown of the US versus international sales of ophthalmic OCT instruments. A coarse assumption is simply to assume the number of world procedures in 2011 was ~2X that of the US procedures. This approach yields a total of worldwide patient procedures in excess of 20M per year and close to one patient per second every day worldwide, a rather amazing achievement for a fairly new technology.

84.7.2 Cardiology

The cardiovascular market segment has been growing rapidly since Lightlab Imaging/St. Jude Medical started shipping its cardiovascular SS-OCT system. The OCT cardiovascular market is expected to continue to grow relative to the intravascular ultrasound (IVUS) market, which is currently around $500M/year. An estimate of the cardiovascular OCT market is shown in Fig. 84.12. It seems likely the market will be ~$100 M/year in 2014, and the market leader is currently St Jude Medical which started shipping commercially in the U.S. in 2010 following the earlier shipments of products by LightLab Imaging in Japan and Europe in 2004.

In 2012, Terumo started shipping its cardiovascular SS-OCT Product in Europe and Japan, and Avinger has introduced an atherectomy catheter that incorporates OCT imaging.

Cardiovascular OCT has been used in clinical research to study mechanisms of coronary artery disease in vivo and to assess percutaneous coronary intervention. But it is uncertain yet to what extent cardiovascular OCT will be adopted into routine clinical practice. Will its usage cap near the IVUS market levels or grow beyond IVUS? The cardiovascular OCT market is already ~25 % of the ophthalmic OCT market. Yet the number of cardiovascular OCT procedures (~50 k) is a small fraction of the number of ophthalmic procedures (~30M). The potential for intravascular OCT to impact patient care and grow market size depends upon whether research demonstrates clear clinical benefits that will lead to indications for intravascular OCT imaging. If such indications are identified, intravascular OCT growth could be dramatic because the number of percutaneous coronary interventional procedures and other intravascular procedures exceeds 1M per year. However, current outcomes in these procedures are relatively good without the use of OCT imaging, and it is unclear as of yet how improved visualization of intravascular structure will improve everyday procedural outcomes. It is also unknown what other functions a future intravascular OCT device, or multimodal device, might provide to further improve outcomes.

There are major research efforts currently underway, such as the Massachusetts General Hospital OCT Registry, to address these important questions and help guide the development and application of the technology in cardiovascular medicine. Important areas for further investigation include the use of OCT to guide percutaneous coronary intervention, including stent selection and deployment, and also the identification of high-risk, vulnerable plaque lesions. The detailed information about coronary plaque morphology provided by OCT may also allow cardiologists to better understand patient risk for future events and therefore modify therapy accordingly.

84.7.3 Other Markets

There are numerous other medical and nonmedical markets for OCT. There are companies developing or already selling OCT and related technology for gastroenterology, dermatology, ENT, urology, gynecology, microscopy, digital pathology, pulmonology, and dentistry, not to mention numerous nonmedical applications such as general purpose research OCT equipment microscopes and NDE/NDT applications. These markets offer growth for the future, but have not yet reached the levels of ophthalmology or cardiology. As of 2012, most of them have not achieved a significant yearly revenue rate in excess of ~$10M/year. In some ways, ophthalmology had an advantage in that it started first as was less invasive and risky and costly to start clinical studies and trials than say cardiology. But commercial efforts are underway in these developing OCT markets, and many of them are very large markets (~$B) where OCT could eventually play an important role.

84.8 Potential Future Trends in OCT

There are many ways OCT could evolve in the future. While details are impossible to predict, it seems a safe bet that both the fundamental technology and its applications will continue to improve and further penetrate existing markets and enter new markets. One exciting technology area where there has been and will continue to be a lot of focus and progress is in software. There are many aspects to this software frontier including the need for efficient algorithms for dealing with collection and real-time processing of extremely large data sets, software for manipulating and visualizing large 3D images, eliminating motion artifacts, and segmentation and feature extraction, as well as development of Doppler, birefringence, and other functional OCT software. Already much of the differentiation in the crowded ophthalmic OCT marketspace is in the software and database front. Its seems clear that for busy clinicians to efficiently deal with what are becoming very large OCT data sets that automated disease detection software will be important software technology area.

Technology for high-performance broadband and tunable light sources will also likely change significantly over the next few years. As of 2012, there are only a few swept source lasers that are commercially available, and this will undoubtedly change in the near future. The design of miniature low-cost scanning probe technology is an area that still seems in its infancy. There are very promising techniques to utilize MEMs, electro-optics, and other approaches to make tiny and low cost scanning medical needle, endoscope, catheter, and guidewire OCT probes. Another very promising area of technology research is integrated photonic circuits (PICs) for lowering the cost and size of OCT imaging engines. While there are a few commercial efforts mainly focused on SD-OCT systems, it seems likely SS-OCT photonic integrated circuits will also play a role in the future, particularly silicon- and InP-based systems where great strides have been made in the telecommunication industry. Such miniaturization and cost reduction offered by multifunction photonic integrated circuits might allow OCT to further penetrate existing markets and to penetrate new cost-sensitive markets such as the optometry market and primary care practice perhaps even low cost and simple enough for home use someday in the distant future. The area of post-optical detection signal/image processing is another exciting research area and includes topics such as synthetic aperture, digital holography, holoscopy, and computational adaptive optics. Such approaches offer many possible advantages such as eliminating need for deformable mirrors in adaptive optics systems and breaking the conventional trade-off between lateral resolution and Rayleigh range.

A factor that comes into play when thinking about future commercial opportunities for OCT component technology such as a new swept source laser, PIC, or similar items is that the current OCT value chain can make it difficult to get a return on an investment for some business plans. For example, the current total yearly market for OCT systems is ~10,000 units. If a startup wants to develop and sell a new laser, it might take between $5M and $50M dollars. If the laser sells in the

marketplace for $1,000, that's a total market size ~$10M and not a very attractive payback opportunity for investors, and no single laser company would own 100 % of the market anyway. If the laser sells for more (e.g., $10k), then there will be pushback from the system vendors selling products into the various medical markets who are facing price competition from competitors and cost pressure from insurers. This can make it difficult for a stand-alone technology company to make good financial progress in supplying the OCT systems market. A partial solution is to find other non-OCT markets for the technology or grow vertically by adding more functionality around the laser to increase the market value of the product. Business climates cycle in and out of time periods where vertical integration is rewarded and when it is not. The other solution is that much of this technology will come out of established multifunction technology companies that sell many components into many markets – and this is the current situation in the OCT marketplace. It is different calculus if a component supplier is shipping into the OCT disposable market due to the large opportunity for reoccurring revenue.

Another exciting future trend for OCT may be in integrating OCT with therapeutic technology. The future of integrating OCT with therapeutic technology seems particularly promising, and companies such as OptiMedica, LenSx, Schwind, Technolas Perfect Vision, Zeiss, Avinger, and others are already working on commercializing. The promise of low cost easy to used OCT screening devices or using OCT to guide therapeutic procedures on a microscopic scale and treating "what you see when you see it" is very appealing. For example, for the large gastroenterology and pulmonary disease management expenditures today, it seems quite possible that in the long term, integrated diagnostic/therapeutic devices could have major market opportunities in these and other areas.

Somewhat similar to integrating OCT with therapeutic technology is multimodality imaging. The future of multimodality diagnostic imaging (e.g., combining OCT and other imaging technology) also seems promising but perhaps faces a few more barriers. On the positive side, the vision of simultaneously getting the best information out of two or more simultaneous diagnostic imaging technologies seems quite attractive. For example, OCT could be used to get 3D morphological microstructural information and fluorescence or Raman or IR technology to get addition molecular or spectroscopic information. Similar comments apply for photoacoustic techniques. On the negative side, the cost of the capital equipment and any associated disposable devices may increase to a point where they are not justified. Other factors such as reimbursement could come into play where, for example, an existing ophthalmic instrument (e.g., fundus camera) and an OCT system could be integrated and prove to be cost-effective for the clinician practice.

Predicting the next medical markets in which OCT will be very successful is more difficult than predicting technology evolution. Figure 84.1 may provide good insight. After ophthalmology and cardiology, the next most published segments include gastroenterology, dermatology, dentistry, neurology, otolaryngology, urology, and pulmonology. Combining this quantitative data with the current availability of commercial approved devices might yield better insight into the next medical

successes. Some of the companies in these spaces are indicated in Table 84.1. They all have significant challenges relative to ophthalmology where from the start there was a clear dearth of technological capability and clear clinical need and a noninvasive procedure and in cardiology where there was an established IVUS technology that could be outperformed in speed and resolution by OCT. There remain large screening, diagnostic, and surgical guidance markets (~$B) where there is a need for improved patient outcomes but the barrier from entrenched products and clinical processes and the technology and economic challenges of the new approaches are significant.

Imaging tools for cancer remains a pressing need in society and a daunting technology challenge. It's made all the more harder because cancer is not one disease. It remains unclear to what extent OCT will provide a key tool to meet this challenge, but there is very promising research work going on in this area including using OCT for cancer margin assessment and to replace or augment current digital pathology tools. It seems highly likely new and novel optical imaging technologies, including OCT, will play a role in future commercial products for fighting cancer. Several existing OCT companies are already focusing on this challenge.

A major factor influencing the future of what medical markets OCT will be successful in will be the current and future health-care cost environment. There are major economic challenges around the world, particularly in the United States, in providing good healthcare while containing health-care cost from escalating to unsustainable levels. In the distant past, a new medical product could more easily be introduced based on improved patient care. Today, it is far more beneficial if a new product significantly lowers costs and improves patient care and to the extent the lowering of costs are clear and beneficial, the better. Further to the extent the cost savings is at the procedure level vs the process level, or at both the better. Reimbursement plays a major factor in the success of medical device companies and their products. It's one thing to get regulatory approval to sell a product, it's yet another to get reimbursement from insurers. In the United States, CPT codes are numbers assigned to every medical task and service provided to a patient. These codes are used by insurers to determine the amount of reimbursement the doctor, nurse, or hospital will receive by the insurer. Even if a generic CPT code can be used for billing or a specific tailored CPT code exists for a procedure, there is still the big step to convince all the major insurers to approve it under the various medical plans and further to convince hospitals to purchase the equipment, and for that, it is highly beneficial that the hospital be able to make a profit, or at a minimum break even, on the cost of purchase and the cost per procedure. Finally as the accumulated reimbursement levels on CPT codes get very large, the regulators may clamp down on the payments as they did in ophthalmology.

Another factor that may influence the future of what medical markets OCT will be successful in could be the changing demographics of society. For example, in some countries, there is the aging of population base, a increase in obesity, and/or dramatic changes in eating habits, the effects of which have not fully played out over time. Such effects could impact what diagnostic tools are needed in the future.

84.9 Summary

The historical growth of commercial OCT has been impressive from the viewpoint of market size, economic impact, and more importantly, for its impact on clinical medicine and patient care. The majority of the commercial efforts have initiated from startup companies – an impressive record and statement to the power of entrepreneurism. Almost half of the current OCT system companies had, or continue to have, strong ties to academic research. Over the past decade, cumulative government funding around the world totaled ~$1B and powered much of this academic and clinical research, which in turn created and powered an ecosystem that enabled startups and new OCT product launches.

While ophthalmology and cardiology are established markets, there remain some wide-open markets for OCT. Research publications (e.g., Table 84.1) may be a good predictor of what markets will be the most successful in the near term. The companies that are first to market face a long challenging process of plowing the field that can take ~10 years. However, they not only can obtain and hold market share for many years but more importantly, can accelerate the translation of research into the clinic by many years, potentially reducing morbidity and mortality.

Now that OCT is nearly 25 years old, the future of technology transfer will undoubtedly begin to change, and industry will play a more prominent role in advancing technology. The nature of how OCT technology is transferred into industry will change, and it is possible startup companies will play a smaller role in the established OCT markets but continue to play a role in new developing markets. It is likely that industrial spending and investment are already reaching levels commensurate with government spending in R&D. This trend happens in many maturing industries. However, this does not obviate the need for continued government funding as it is very clear that the majority of medical markets that could benefit from OCT have not yet been commercialized and remain too risky for significant industrial and venture capital investment. Industry is clearly hesitant to make the large investments needed to develop nonestablished OCT applications, even with the relatively mature technology that may exist today. In order to succeed, a medical diagnostic or interventional device or procedure requires evidence-based data showing improved care and lower costs. This requires multiple clinical studies and trials which is another place where government investment is critical. The return on investment of taxpayers support remains as attractive as it ever was in terms of improved healthcare and quality of life, economic impact, and improved understanding of diseases which will improve diagnosis and treatment even more in the future.

It is exciting to wonder what will be the next big commercial successes for OCT. If its successful expansion continues, OCT will have impacted the world not only in economic and job creation terms and in helping diagnose and treat blinding ophthalmic disease on a routine global basis but also by improving understanding, diagnosis, and treatment of deadly cardiovascular disease and cancer, the #1 and #2 leading causes of death in the industrialized world.

Acknowledgements I would like to thank the following people for helpful discussion and contributions to this chapter. James Fujimoto, Joseph Schmitt, Jay Wei, Chris Petersen, David Huang, Jack Turner, Maciej Wojtkowski, Wolfgang Drexler, Peter Norris, Bertrand Le Conte de Poly, Lori Pressman, Eric Buckland, Rainer Nebosis, Brian Courtney, Masataka Tei, Ralph Johnston, Chris Ritter, Charles Carignan, Ewa Mentel, Gaku Takeuchi, Adam Wax, Arjun Desai, Sabrrina Klinkert, Jim Fulton, Michael Kempe, Jon Holmes, Frederic Sweeny, Eduardo Margallo, and Aaron Aguirre.

Appendix: Examples of Existing OCT Commercial Products

Below are some representative examples of existing OCT commercial products. There are more OCT system products on the market than those listed here, and several of the companies listed have multiple products.

Cirrus-HD OCT 5000 from Zeiss

Optovue Inc. RTVue and Handheld iVue OCT systems for ophthalmology

Topcon 3DOCT-2000 for ophthalmology

Nidek RS-3000 Advance for Ophthalmology

Heidelberg Engineering Spectralis OCT for ophthalmology

Canon OCT-HS100

Tomey Casia SS-1000 System for ophthalmology

Bioptigen Envisu C2300 SDOCT

Optos SLO/OCT System for Ophthalmology

St. Jude ILUMIEN™ OPTIS™ PCI Optimization System

Avinger Inc. Lightbox for guiding chronic total occlusions crossings and atherectomy

Terumo Lunawave Intravascular Imaging Console

Imalux Inc. Product for ENT, gynecology, and urology

Michelson Diagnostics VivoSight Hand-Held Dermatological Scanner

Santec IVS-300 Compact OCT System for research, industrial, biology, and medical applications

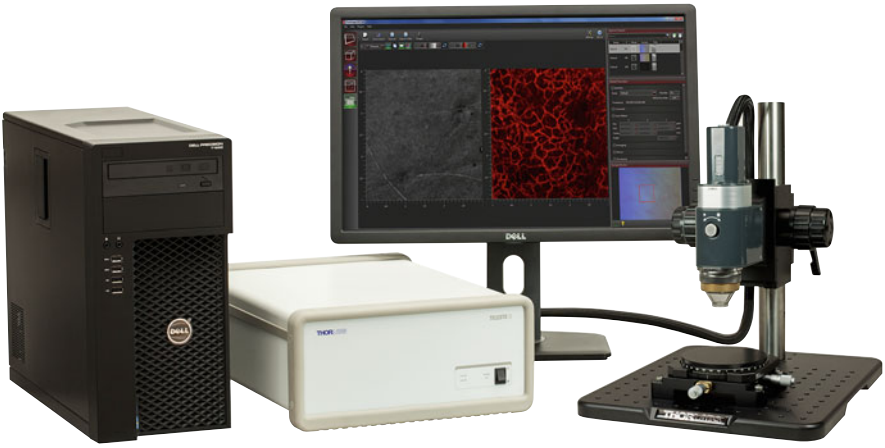

Thorlabs Telesto series Spectral Domain OCT System

Agfa HealthCare SKINTELL System for dermatology

LLTech high-resolution 1μm in 3D FF-OCT scanner

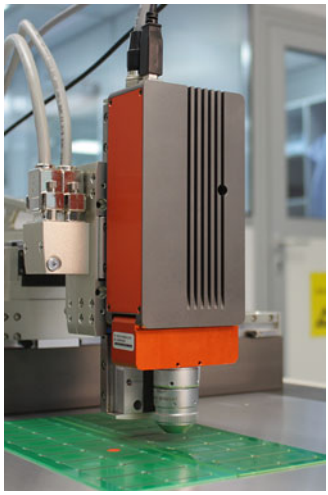

Heliotis AG: Ultra-Fast OCT sensor for automated inspection machines

NinePoint Medical Inc. NvisionVLE(tm) Imaging System for endoscopic applications; initial focus on gastroenterology

Abbot Medical Optics OCT Enabled Catalys System for Laser Cataract Surgery. Image courtesy of Abbott Medical Optics, Inc

Tomophase OCTIS Gen2 Console

VICTUS® Femtosecond Laser Platform with 2S-OCT technology

Schwind AMARIS 750S Excimer Laser for laser eye surgery with optional available integrated online pachymetry

References

1. L. Pressman et al., The licensing of DNA patents by US academic Institutions: an empirical survey. Nat. Biotechnol. **24**(1), 31–39 (2006)
2. F.M. Scherer, D. Harhoff, Technology policy for a world of skew-distributed outcomes. Res. Policy **29**, 559–566 (2000)
3. Association of University Technology Managers Survey: FY 2000, AUTM 10th Anniversary Edition, http://www.provendis.info/fileadmin/info/pdfs/1248.pdf
4. C. Duhigg, S. Lohr, The Patent, Used as a Sword, *The New York Times*, 8 Oct 2012
5. E. Swanson, Optical Coherence Tomography Used $500M Federally Funded Research Over The Past Decade: *How was it Used, What was Accomplished, and What's to Come*?, www.octnews.org, 16 Jul 2011 and BioOptics World, 1 Sept 2011
6. M. Kempe, From research to routine medical diagnostics. Biomed. Eng. (2012). doi:10.1515/bmt-2012-4531
7. M. Kaschke, S. Meyer, M. Everett, C. Grahl, Optical coherence tomography: a case study in Medical Imaging Adoption. Biophotonics Optik. Photonik. **4**(4), 24–28 (2009)
8. E. Swanson, D. Huang, Ophthalmic OCT Reaches $1 Billion Per Year: But Reimbursement Clampdown Clouds Future Innovation, www.octnews.org, 9 Jul 2011 and Retinal Physician, 1 May 2011
9. E. Swanson, Estimates of Ophthalmic OCT Market Size and the Dramatic Reduction in Reimbursement Payments, www.octnews.org, 1 Dec 2012